JOURNAL OF THE ELECTROCHEMICAL SOCIETY

ELECTROCHEMICAL SCIENCE

JANUARY 1970

ES

Solid Ionics—Solid Electrolyte Cells

Takehiko Takahashi* and Osamu Yamamoto

Department of Applied Chemistry, Faculty of Engineering, Nagoya University, Furo-Cho, Chikusa-Ku, Nagoya, Japan

ABSTRACT

The characteristics of the solid electrolyte cells $Ag/RbAg_4I_5/Te$ and $Ag/RbAg_4I_5/Se$ have been studied. The open-circuit voltages of these solid electrolyte cells were 0.217V and 0.265V, respectively, at 20°C. These cells could discharge in the temperature range of −75° to 150°C. Only a small polarization was observed at relatively high current density discharge. Diffusion coefficients of Ag in these systems were also evaluated from the time-dependent behavior of the cell voltage as a function of current density.

Although the various types of solid electrolyte cells have been investigated by many authors (1-3), most of them were able to discharge only in the microampere range at room temperature, the reason being the poor conductivity of the electrolyte used. Recently, as higher ionic conductivity solid electrolytes have been found (4-8), a high performance solid electrolyte cell operating in a milliampere range at ambient temperature has been developed.

Previous investigations on solid electrolyte have dealt almost exclusively with the simple compounds like silver halides, the highest conductivity of which was between 10^{-6} and 10^{-5} ohm^{-1} cm^{-1} at room temperature. In recent years, in order to find high ionic conductivity solids, the solid state reaction products of binary and ternary systems have been studied by Takahashi, Bradley and Owens, and Ag_3SI (4), $Ag_2Hg_{0.25}S_{0.5}I_{1.5}$ (5), $Ag_4HgSe_2I_2$ (6), and $RbAg_4I_5$ (7, 8) have been found to have high ionic conductivities at room temperature (Table I).

Accordingly by using these high ionic conductivity solids as electrolytes, it is possible to make an excellent solid electrolyte cell by combining it with a suitable electrode. As silver ions are charge carriers in these compounds, silver is always used for the anode. The cathode material of solid electrolyte cells should have the properties of: (*i*) showing as positive a potential as possible, (*ii*) ease of forming thin film, (*iii*) a low discharge polarization, and (*iv*) discharge product functioning as a silver ion conductor. Requirements *i* and *ii* are necessary for attaining compactness and high voltage of the cell, while requirements *iii* and *iv* are for obtaining a high current density. Takahashi *et al.* (9) reported a solid electrolyte cell, $Ag/Ag_3SI/I_2$, and Argue *et al.* (10) the cell $Ag/RbAg_4I_5/RbI_3$, with cell voltages of 0.67 and 0.66V, respectively, and these cells can discharge at relatively high current density. The ionic conductivity of solids such as Ag_3SI and $RbAg_4I_5$ is relatively unstable in iodine atmosphere, especially at high temperature, and iodine vapor is so highly corrosive for metals, that the cell must be gastight. In this paper a solid electrolyte cell is described in which the vapor pressure of the cathode material is very low over a wide temperature range and the high voltage is maintained during discharge even at a high current density. Results of our search for substances which satisfy the above stated requirements have indicated tellurium and selenium to be excellent. Tellurium is a solid having a very low vapor pressure and high electrical conductivity (2.6 ohm^{-1} cm^{-1} at 20°C) at room temperature and a melting point of 450°C. Furthermore, tellurium is capable of forming a thin film easily by vacuum evaporation. The melting point of selenium is 217°C and the vapor pressure at room temperature is low enough. The electrical conductivity of selenium, 10^{-5} ohm^{-1} cm^{-1} at room temperature, is substantially less than that of tellurium. Selenium can also form a thin film readily by vacuum evaporation. In this paper, the performances of the cell $Ag/RbAg_4I_5/Te$ or Se are described.

Experimental

Preparation of the solid electrolyte, $RbAg_4I_5$.—The solid electrolyte, $RbAg_4I_5$, was prepared according to the method described by Owens and Argue (8). Weighing of 0.8 mole fraction of silver iodide and 0.2 mole fraction of rubidium iodide was followed by mixing and grinding. The mixture was sealed in a glass tube under vacuum, and it was heated at 500°C for 2 hr. Then after being cooled abruptly, it was maintained at 160°C for 15 hr thereby to synthesize $RbAg_4I_5$. The x-ray diffraction pattern of the resulting $RbAg_4I_5$ showed a cubic structure, lattice parameter being 11.0Å at 25°C, the value of which was identical with those in the literature (11, 12). The electrical conductivity measured at 1000 Hz was 1.7×10^{-1} ohm^{-1} cm^{-1} at 25°C. $RbAg_4I_5$ melted incongruently at 235°C.

Table I. Conductivity of ionic conductors at 25°C

Substance	Conductivity at 25°C, ohm^{-1} cm^{-1}
Ag_3SI	1×10^{-2}
$Ag_4HgSe_2I_2$	2×10^{-2}
$Ag_2Hg_{0.25}S_{0.5}I_{1.5}$	7×10^{-2}
$RbAg_4I_5$	2.4×10^{-1}

* Electrochemical Society Active Member.

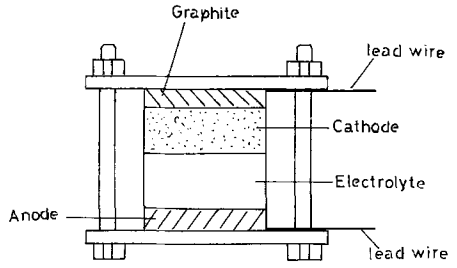

Fig. 1. Schematic diagram of the solid electrolyte cell

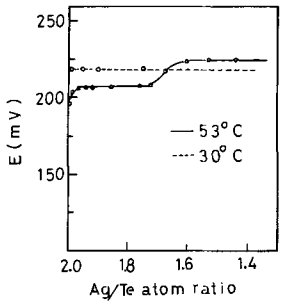

Fig. 2. EMF of the cell $Ag/RbAg_4I_5/Ag\text{-}Te$ vs. ratio of Ag/Te at 30° and 53°C.

Cell structure.—In this experiment, the electrolyte, $RbAg_4I_5$, was placed between the anode which consisted of a tablet of a mixture of silver powder and $RbAg_4I_5$ and the cathode. The cell assembly is shown in Fig. 1. A mixture of 0.6g $RbAg_4I_5$ and 0.3g 200 mesh passed silver powder and 1.2g $RbAg_4I_5$ were stacked in laminar arrangement and pressed into a tablet of 1.2 cm diameter to form anode and electrolyte, respectively. As the cathode material, the mixtures of Te and Ag_2Te (2g:1g), Se and Ag_2Se (1g:2g), Te, Ag_2Te, graphite and $RbAg_4I_5$ (0.3g: 0.1g:0.1g:0.7g) or Se, Ag_2Se, graphite, and $RbAg_4I_5$ (0.3g:0.1g:0.1g:0.7g) were used in the form of tablets pressed at 5 tons/cm^2. The cell was sealed in a vessel together with a silica gel.

Results and Discussion

Open circuit voltage.—The measured open-circuit voltages of the cells

$$Ag/RbAg_4I_5/Te - Ag_2Te \quad (I)$$

$$Ag/RbAg_4I_5/Se - Ag_2Se \quad (II)$$

at different temperatures are shown in Table II. In the silver-tellurium system, in addition to the compound Ag_2Te, an intermediate phase $Ag_{1.66-x}$ Te ($x = 0.03 \sim 0.045$) has been suggested to exist at room temperature by Kracek *et al.* (13).

The cell reaction of cell (I), therefore, may be considered to be either the formation of Ag_2Te or $Ag_{1.66-x}Te$ as represented by the following chemical equation

$$2Ag + Te = Ag_2Te \quad [1]$$

or

$$(1.66 - x)Ag + Te = Ag_{1.66-x}Te \quad [2]$$

In order to clarify the above consideration, the emf of the cell

$$Ag/RbAg_4I_5/Ag\text{-}Te \quad (III)$$

has been determined as a function of the Ag/Te ratio at 30° and 53°C, and the results are shown in Fig. 2 to indicate that, at room temperature, although Ag_2Te is the only compound that exists in the Ag_2Te-Te system, at 53°C, in addition to Ag_2Te, an intermediate phase $Ag_{1.66-x}Te$ is recognized where x is about $0.03 \sim 0.05$, the cell emf of which is 0.207V.

Kiukkola and Wagner (14) calculated the standard molar free energy of formation of α-Ag_2Te, (a high-temperature modification of Ag_2Te) from the measured emf of the cell, $Ag/AgI/Ag_2Te$-Te to be -11.4 kcal/mole at 250°C. This value corresponds to a cell voltage of 248 mV. Further, the emf of the cell, $Ag/AgNO_3$/Ag-Te has been determined at room temperature by Puschin (15) to be about 200 mV. However, no accurate

Table II. Open-circuit voltage of the cell $Ag|RbAg_4I_5|Te$ and $Ag|RbAg_4I_5|Se$

Temp, °C	$Ag\|RbAg_4I_5\|Te$ Cell OCV (V)	$Ag\|RbAg_4I_5\|Se$ Cell OCV (V)
20	0.217	0.265
60	0.219	0.268
100	0.223	0.271

standard molar free energy of formation of β-Ag_2Te (a lower temperature modification of Ag_2Te) has been reported. From the temperature dependence of the standard free energy of formation of β-Ag_2Te calculated by the emf of the cell (I), it follows that

$$2Ag(s) + Te(s) = Ag_2Te(s)$$
$$\Delta F° = -8.47 - 0.0048\,T \text{ kcal}$$
$$\Delta H° = -8.47 \text{ kcal}, \quad \Delta S° = 4.8 \text{ eu} \quad [3]$$

The standard molar entropy of Ag_2Te at 298°K is obtained as

$$S°_{Ag_2Te} = \Delta S° + 2S°_{Ag} + S°_{Te}$$
$$= 4.8 + 2 \times 10.206 + 11.88 = 36.09 \text{ eu} \quad [4]$$

The reaction of cell (II) may be considered to be the formation of Ag_2Se represented by Eq. [5]

$$2Ag + Se = Ag_2Se \quad [5]$$

Kiukkola and Wagner (14) measured the emf of the cell $Ag/AgI/Se\text{-}Ag_2Se$ at high temperature. Using thermodynamic data of α-Ag_2Se and the enthalpy and entropy changes of Ag,Se and Ag_2Se between 298° and 500°K, they calculated that $\Delta F° = -11.94$ kcal, $\Delta H° = -11.38$ kcal, and $\Delta S° = 5.24$ eu at 298°K. Thermodynamic data calculated from our experimental results are as follows

$$2Ag(s) + Se(s) = Ag_2Se(s)$$
$$\Delta F° = -11.18 - 0.00345\,T \text{ kcal}$$
$$\Delta H° = -11.18 \text{ kcal}$$
$$\Delta S° = 3.45 \text{ eu}$$

and the standard molar entropy of Ag_2Se at 298°K is obtained as

$$S°_{Ag_2Se} = \Delta S° + 2S°_{Ag} + S°_{Se}$$
$$= 3.45 + 2 \times 10.206 + 10.0 = 33.86 \text{ eu} \quad [6]$$

Anodic polarization of $Ag/RbAg_4I_5/Ag$.—The solid electrolyte $RbAg_4I_5$ has an ionic conductivity high enough to produce only a very small ohmic potential drop at current densities of the order of milliampere per square centimeter. However, large polarization at the boundary between the electrode and the electrolyte would make the solid electrolyte cell so constructed not usable.

The anodic polarization of the cell, $Ag/RbAg_4I_5/Ag$, was measured using a silver plate reference electrode put in the electrolyte at the cathode side of the cell. It is shown in Fig. 3. As the measurements were carried out with a current interrupter, the measured overvoltage is free from resistance polarization. A plot of logarithm of current density *vs.* overvoltage gives a straight line with slope of about 22 mV at lower current densities. However, above 10 mA/cm^2 at 25°C and 1 mA/cm^2 at 0°C, the overvoltage rapidly increases with current density and tends to increase gradually with time.

Cathode polarization of the cells, $Ag/RbAg_4I_5/Te\text{-}Ag_2Te$ *and* $Ag/RbAg_4I_5/Se\text{-}Ag_2Se$.—The discharge reactions of the above cells are Eq. [1] for the tellurium cathode and Eq. [5] for the selenium cathode, respec-

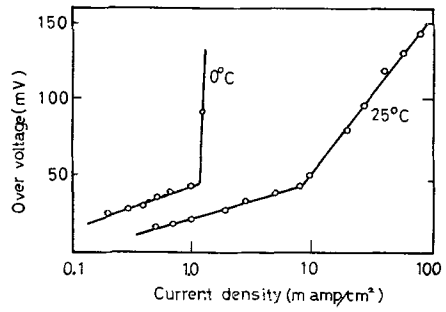

Fig. 3. Anodic polarization of the cell Ag/RbAg$_4$I$_5$/Ag

tively. Accordingly, the reaction product Ag_2Te or Ag_2Se is deposited on the boundary between the electrolyte and the cathode. Therefore, in order to maintain the continuous discharge, silver must move through the reaction product layer, and the transport of silver in Ag_2Te and Ag_2Se may be the rate-determining step of the discharge reaction at higher current drain.

The time dependence of the voltages of the cells, Ag/RbAg$_4$I$_5$/Te-Ag_2Te and Ag/RbAg$_4$I$_5$/Se-Ag_2Se, was measured; results at 25°C are shown in Fig. 4 at various current densities. These curves indicate that the cell voltage decreases linearly with discharge time and the slope increases with current density. Polarization voltages at various temperatures are shown in Fig. 5. These relations also give the straight lines at each temperature and the slope is found to decrease with increasing temperature.

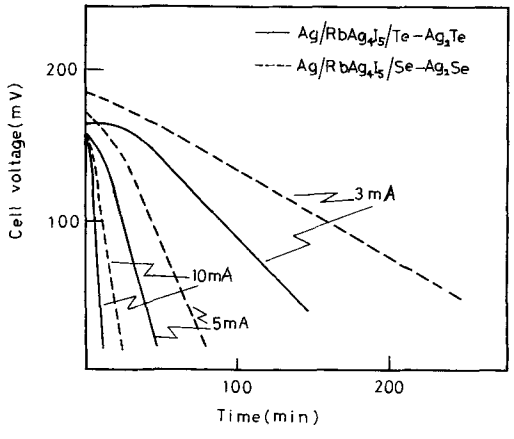

Fig. 4. Voltage *vs.* time of the cells Ag/RbAg$_4$I$_5$/Te-Ag_2Te and Ag/RbAg$_4$I$_5$/Se-Ag_2Se at 25°C.

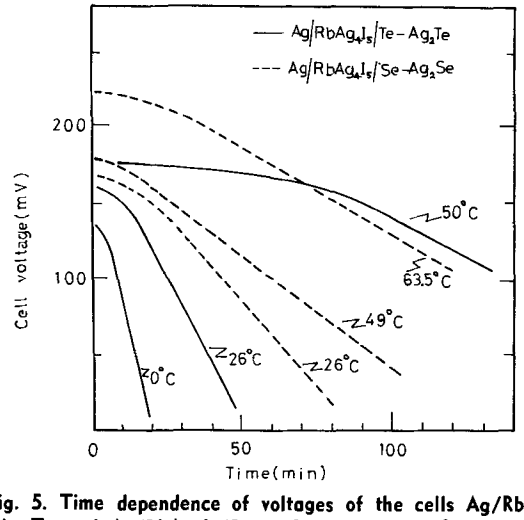

Fig. 5. Time dependence of voltages of the cells Ag/RbAg$_4$I$_5$/Te-Ag_2Te and Ag/RbAg$_4$I$_5$/Se-Ag_2Se at 5 mA/cm^2 constant current discharge.

These curves can be divided into three parts. The initial part corresponds to the rapid decrease of the cell voltage within 1 sec, the second part to the non-linear decrease of it for several minutes, and the third part to the linear decrease of the cell voltage. The analysis of the linear part of the curve has been carried out as follows, considering that the transport of silver in reaction product is the rate-determining step of the discharge reaction.

In order to maintain continuous discharge, silver must move through the reaction product layer. The current density I is given by

$$I = -\frac{eN\mathbf{F}^2}{RT} D_{Ag} \frac{\delta \mu_{Ag}}{\delta x} \qquad [7]$$

where D_{Ag} is the diffusion coefficient of silver in Ag_2Te or Ag_2Se, μ_{Ag} the chemical potential of silver, N the amount of silver/cm^2 in Ag_2Te or Ag_2Se, and x the distance from the electrolyte side of Ag_2Te or Ag_2Se. Integrating Eq. [7] with respect to x, we obtain

$$lI = -\frac{eN\mathbf{F}^2}{RT} D_{Ag} [\mu_{Ag}(x = l) - \mu_{Ag}(x = 0)] = \frac{eN\mathbf{F}}{RT} D_{Ag} \Delta E \qquad [8]$$

where l is the thickness of Ag_2Te or Ag_2Se layer, and ΔE the potential difference in Ag_2Te or Ag_2Se. In the discharge process, if the cell reaction product grows uniformly on the cathode surface obeying Faraday's law

$$l = \frac{mIt}{2\rho \mathbf{F}} \qquad [9]$$

where ρ is the specific gravity of Ag_2Te or Ag_2Se (8.32 for Ag_2Te and 8.0 for Ag_2Se, respectively), m the molecular weight of Ag_2Te or Ag_2Se, and t the discharge time. Inserting Eq. [9] into Eq. [8] and rearranging, one obtains

$$\Delta E = \frac{m}{2\rho \mathbf{F}} \times I^2 t \Big/ \frac{eN\mathbf{F}}{RT} D_{Ag} \qquad [10]$$

and

$$\frac{d\Delta E}{dt} = \frac{m}{2\rho \mathbf{F}} \times I^2 \Big/ \frac{eN\mathbf{F}}{RT} D_{Ag}$$

Thus a plot of $d\Delta E/dt$ *vs.* I^2 should give a straight line with a slope of 3.93 x 10^{-12} (T/D_{Ag}) (V·cm^4/sec·A^2) for the tellurium cathode and 3.13 x 10^{-12} (T/D_{Ag}) (V·cm^4/sec·A^2) for the selenium cathode, respectively. This has been confirmed for tellurium at room temperature as shown in Fig. 6. The results substantiate the above concept (Fig. 6). The diffusion coefficients of silver in Ag_2Te and Ag_2Se calculated from the experimental $d\Delta E/dt$ values using Eq. [10] with appropriate value of the slope of Fig. 6 at various temperatures (−15° ~ 120°C) are plotted in Fig. 7 *vs.* the reciprocal of the absolute temperature. The current density in the range of 2-10 mA/cm^2 was used to determine the diffusion coefficient. For

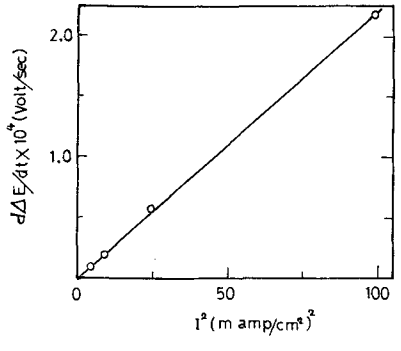

Fig. 6. $d\Delta E/dt$ *vs.* I^2 of the cell Ag/RbAg$_4$I$_5$/Te-Ag_2Te at 26°C

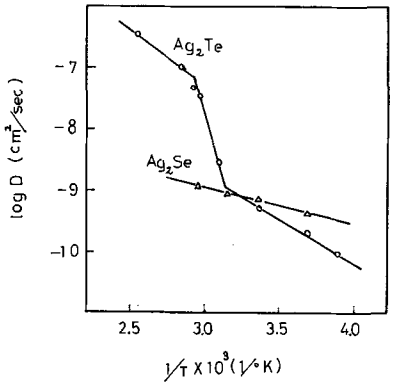

Fig. 7. Temperature dependence of diffusion coefficient of Ag in Ag_2Te and Ag_2Se.

β-Ag_2Se a good straight line is shown, but for β-Ag_2Te, a jump of the diffusion coefficient is indicated at near 50°C. This jump can be attributed to the intermediate compound $Ag_{1.66-x}Te$, described earlier in the paper. It exists above 50°C in the Ag-Te system. Silver will have a higher diffusion coefficient in $Ag_{1.66-x}Te$ than in Ag_2Te.

Characteristics of the cells $Ag/RbAg_4I_5/RbAg_4I_5$-Te *and* $Ag/RbAg_4I_5/RbAg_4I_5$-Se.—According to the measurement of the cathodic polarization, it was found that the potential drop in the cell reaction product Ag_2Te or Ag_2Se became a dominant factor for the cell voltage in long time current drain. For practical use, the mixture of tellurium and the electrolyte $RbAg_4I_5$, and selenium and the electrolyte $RbAg_4I_5$ should be used as the cathode in order to enlarge the surface area on which the charge transfer reactions would take place.

A mixture of 0.7g $RbAg_4I_5$, 0.5g tellurium, 0.1g Ag_2Te, and 0.1g graphite was pressed into a tablet 1.2 cm in diameter to form the cathode. The cell so constructed had an internal resistance of 1 ohm at room temperature. Typical discharge curves are shown in Fig. 8 together with the case of the selenium base cathode.

The cell with the tellurium-base cathode was somewhat rechargeable. In Fig. 9, typical charge and discharge curves are shown. The cell voltage increases rapidly to about 600 mV at overcharge. With charge-discharge cycling, the cell performance deteriorated, for example, in ten cycles, the cell capacity was reduced to about two-thirds of the initial value.

One advantage of this type of solid electrolyte cell is to have the wide range of operating temperature, theoretically, up to 235°C, the melting point of the electrolyte $RbAg_4I_5$. If AgI is used in place of the

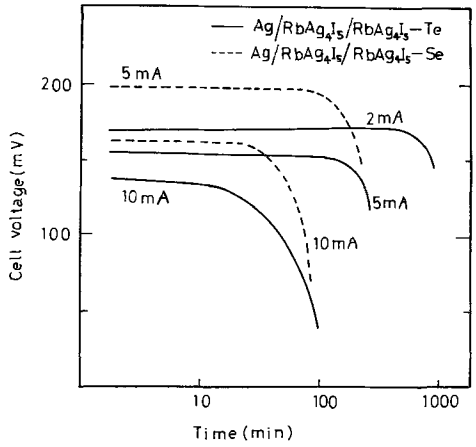

Fig. 8. Time dependence of voltage of the cells $Ag/RbAg_4I_5/RbAg_4I_5$-Te and $Ag/RbAg_4I_5/RbAg_4I_5$-Se.

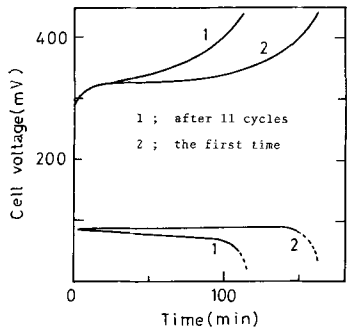

Fig. 9. Charge and discharge curves of the cell $Ag/RbAg_4I_5/RbAg_4I_5$-Te at a current density of 10 mA/cm² at 25°C.

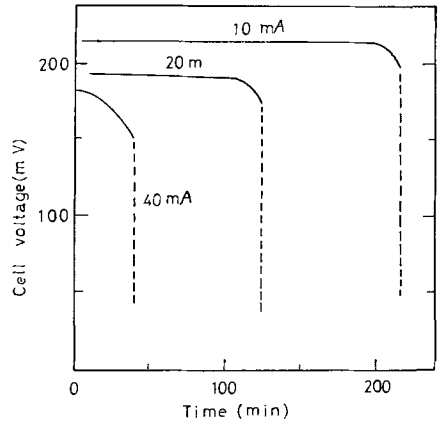

Fig. 10. Time dependence of voltage of the cell $Ag/RbAg_4I_5/RbAg_4I_5$-Te at 150°C.

electrolyte $RbAg_4I_5$, the cell can be operated up to 350°C at which the eutectic mixture of tellurium and Ag_2Te melts. However, this type of cell cannot be discharged at high current density below 147°C, because at this temperature silver iodide transforms from high ionic conductivity α-modification to low ionic conductivity β-modification. For example, the discharge curves at 150°C are shown in Fig. 10. At high temperature, there is no appreciable polarization even at a current density of 10 mA/cm². On the other hand, at −75°C, when it is discharged with a current density of 0.1 mA/cm², the cell voltage becomes 90 mV.

Conclusion

Although the solid electrolyte cells, $Ag/RbAg_4I_5/Te$, and $Ag/RbAg_4I_5/Se$ exhibit a lower open-circuit voltage than a cell in which halogen is used as the cathode material, the cell of this type is capable of discharging with a current density of several milliamperes per square centimeter even at room temperature. Tellurium and selenium can be used as cathode materials up to 350° and 217°C (their respective melting points) and fully gastight cells can be readily fabricated.

When tellurium is used as cathode, the thin film cathode can be formed in a simple manner by vacuum evaporation, so that the entire cell can be made extremely thin.

Sulfur or oxygen cannot be used conveniently as the cathode material instead of tellurium or selenium, since Ag diffusion through the cell reaction product, Ag_2S or Ag_2O, is very low at room temperature. As a result, characteristics of the cell are greatly inferior to that of tellurium or selenium at room temperature.

Manuscript submitted March 28, 1969; revised manuscript received Aug. 20, 1969.

Any discussion of this paper will appear in a Discussion Section to be published in the December 1970 JOURNAL.

REFERENCES
1. K. Lehovec and J. Broder, *This Journal*, **102**, 208 (1954).
2. J. L. Weininger, *ibid.*, **106**, 475 (1959).
3. W. J. van der Grinten, U.S. Pat. 2,793,244 (1957).
4. T. Takahashi and O. Yamamoto, *Denki-Kagaku*, **32**, 610 (1964).
5. O. Yamamoto and T. Takahashi, *ibid.*, **35**, 264 (1967).
6. T. Takahashi, K. Kuwabara, and O. Yamamoto, *ibid.*, **36**, 350 (1968).
7. J. N. Bradley and P. D. Greene, *Trans. Faraday Soc.*, **63**, 424 (1967).
8. B. B. Owens and G. R. Argue, *Science*, **157**, 308 (1967).
9. T. Takahashi and O. Yamamoto, *Electrochim. Acta*, **11**, 779 (1966).
10. G. R. Argue, I. J. Groce, and B. B. Owens, 6th International Power Source Symposium. Brighton (1968), p. 241.
11. S. Geller, *Science*, **157**, 310 (1967).
12. J. N. Bradley and P. D. Greene, *Trans. Faraday Soc.*, **65**, 2516 (1967).
13. F. C. Kracek, C. J. Ksanda, and L. J. Cabri, *Am. Mineralogist*, **51**, 14 (1966).
14. K. Kiukkola and C. Wagner, *This Journal*, **104**, 379 (1957).
15. N. Puschin, *Z. anorg. u. allgem. Chem.*, **56**, 1 (1908).

The Products of the Anodic Oxidation of an Iron Electrode in Alkaline Solution

H. Graham Silver and Elfriede Lekas

Bayside Research Center of General Telephone & Electronics Laboratories, Inc., Bayside, New York

ABSTRACT

X-ray diffraction patterns have been recorded of the surface of an activated iron electrode during anodic oxidation in 30% KOH. At the end of the first plateau (−0.8V relative to a Hg/HgO reference electrode), only α-Fe and $Fe(OH)_2$ are detected. At the end of the second plateau (0.0V), α-Fe and δ-FeO(OH) are detected on the first discharge. On subsequent discharges, a gradual conversion to α-Fe and Fe_3O_4 is observed. In 30% KOH saturated with LiOH, α-Fe and Fe_3O_4 are detected at the end of the second plateau on the first and subsequent cycles.

The anodic discharge of a fully charged iron electrode in alkaline solutions (*e.g.*, 5*N* KOH) occurs at two discrete voltage levels. The first at −0.85V *vs.* Hg/HgO corresponds to the conversion of metallic iron to $Fe(OH)_2$ (1, 2). However, the nature of the products formed during the second anodic process at −0.65V is contradictory, various workers regarding this process as the conversion of metallic iron to $Fe(OH)_3$ (3) or the oxidation of $Fe(OH)_2$ to Fe_2O_3 (2) or $Fe(OH)_3$ (4, 5).

In more recent studies of the products of the anodic oxidation of an iron electrode in alkaline solution, x-ray diffraction patterns of the iron electrode surface have been recorded during discharge by *in situ* techniques (6, 7). Well-defined diffraction peaks for $Fe(OH)_2$ during anodic discharge at −0.8V *vs.* Hg/HgO along the first plateau are reported. However, once again, the nature of the products of the second anodic process is still unclear. One group of workers reports that the major oxidized phase generated at the end of the second plateau (about −0.3V) is Fe_3O_4 (6). Another group presents strong evidence for the formation of δ-FeO(OH), and not Fe_3O_4, on the lower plateau (7).

As a result of these contradictory observations, a careful re-examination of the chemical compounds generated on the surface of an iron electrode during anodic oxidation in alkaline solution, has been undertaken using x-ray diffraction techniques.

Experimental

A carbonyl iron electrode 2 x 2 x 0.025 in. and weight ~5g was cut from a carbonyl iron plaque obtained from Sylvania Electronic Components, Emporium, Pennsylvania. After the four corners of the electrode had been trimmed in order to enable it to fit into a Teflon ring of diameter 2.25 in., it was activated[1] and charged at 0.5A for 3 hr in 30% KOH electrolyte using a nickel counter electrode. The iron electrode was then slipped into the Teflon ring, which was attached in the vertical position to the rotatable wheel of a modification of a specially designed sample holder (8, 9). The lower half of the electrode was immersed in 30% KOH, and, as the wheel rotated at ¼ rev sec^{-1}, a thin film of electrolyte at room temperature was constantly maintained over the upper surface of the electrode, which was exposed to air.

An x-ray beam produced by a Siemens Kristalloflex 4 constant potential generator, utilizing Cu radiation at 35 kV and 18 mA, was directed at this exposed upper surface and the intensity of the reflected radiation measured, after it had passed through a LiF monochromator, into a Geiger counter detector. Excellent peak to background diffraction patterns were thus obtained. A 4° prescatter slit and 1° receiving slit were used in the monochromator and an angular range of 10°-75° (2θ) was recorded using goniometer scan speeds of ¼° and 1° min^{-1}. The resulting x-ray diffraction pattern was then compared with the x-ray patterns listed in the ASTM powder diffraction data file (10).

The electrode was removed from the Teflon ring, again charged at 0.5A for 3 hr in 30% KOH and then discharged to the end of (*a*) the first plateau (−0.8V *vs.* Hg/HgO reference) and (*b*) the second plateau (0V *vs.* Hg/HgO reference) at a discharge current of 0.2A, at which points x-ray diffraction patterns were again recorded, as described previously. The iron electrode was then repeatedly charged and discharged to the end of the second plateau, x-ray diffraction patterns being recorded after each cycle for the completely discharged state. The whole procedure was repeated using, as the cycling electrolyte, 30% KOH saturated with LiOH and the results of the two series of runs compared.

For the rotating iron electrode technique here described, there is the possibility that atmospheric oxy-

[1] Ten minutes in 1*N* H_2SO_4, rinse > 3 min in cold, running, distilled water, then 1 hr in 100 ml of a solution of 32g S dissolved in 1 liter 30% KOH with occasional agitation.

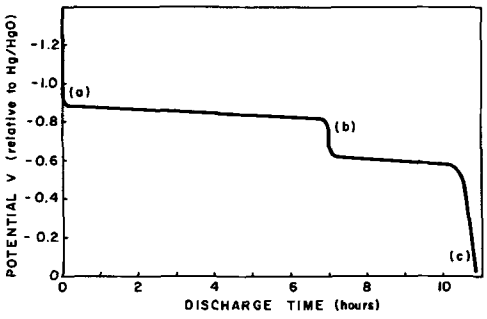

Fig. 1. Discharge curve for an iron electrode vs. a Hg/HgO reference electrode in 30% KOH.

gen could react with that section of the wetted iron surface exposed to the air, to form a surface oxide. However, previous observations (7) indicated that this does not occur, as was fully borne out in the present work. For example, no changes were observed in the products of the anodic oxidation of an iron electrode discharged to the end of the first plateau (−0.8V *vs.* Hg/HgO reference) even after leaving the electrode rotating, but constantly covered with the thin film of electrolyte, for over 24 hr. However, care was taken not to remove an iron electrode unnecessarily, at any point during its charge/discharge cycle, from the alkaline electrolyte and leave it exposed to the atmosphere, except for the few seconds when transfer from the cycling apparatus to the x-ray sample holder was affected.

Moreover, although fresh electrolyte was used each day for all the experimental procedures described, it was found that the use of 30% KOH, which had been left exposed to the atmosphere for over a week and had absorbed considerable CO_2, did not produce results at variance with those to be reported. The presence of dissolved carbonate in the alkaline electrolyte apparently did not affect the products of the anodic oxidation of the iron electrode.

Results and Discussion

A typical discharge curve of the potential of the iron electrode discharged at 0.2A (measured against a Hg/HgO reference electrode) in 30% KOH, is shown in Fig. 1. X-ray diffraction patterns were recorded at points a, b, and c, as well as of the uncharged electrode. The lines are broad in some cases possibly due to small crystallite size. From an analysis of these x-ray diffraction patterns, a definitive identification of the compounds generated on the electrode at these points, was made and is shown in Table I. The experimental results are shown in Table II together with the ASTM standard lines for α-Fe, $Fe(OH)_2$, δ-FeO(OH), and Fe_3O_4 for comparison.

The uncharged electrode, whether activated or unactivated, gave an x-ray diffraction pattern which corresponded to that of α-Fe as listed in the ASTM file. Moreover, no reflections due to a sulfide of iron were detected on the surface of the uncycled freshly activated iron electrode, even though the latter had turned black.

The freshly charged iron electrode (point a) always produced an x-ray diffraction pattern characteristic of α-Fe. Occasionally, after cycling the electrode back and forth over the first plateau, very weak lines were observed in the charged state, which were attributed

Table I. Identification of compounds

State-of-charge	Uncharged	Charged (point a)	End 1st plateau (point b)	End 2nd plateau (point c)
Phase	α-Fe	α-Fe	α-Fe $Fe(OH)_2$	α-Fe δ-FeO(OH) or Fe_3O_4

Table II. Experimental results

Experimental data Discharge to (*vs.* Hg/HgO)			ASTM Standards							
			α-Fe		$Fe(OH)_2$		δ-FeO(OH)		Fe_3O_4	
−0.8V d, Å	0.0V d, Å	0.0V d, Å	d, Å	I/I₁	d, Å	I/I₁	d, Å	I/I₁	d, Å	I/I₁
		4.87							4.85	40
4.61					4.60	100	4.61	20		
		2.97							2.97	70
2.83					2.82	80				
	2.56	2.53					2.55	100	2.53	100
2.41		2.43			2.40	100			2.42	10
	2.24						2.26	100		
		2.10							2.10	70
2.03	2.03	2.02	2.03	100						
1.78					1.78	80				
	1.70	1.71					1.69	100	1.71	60
1.63		1.61			1.63	80			1.61	85
1.54					1.54	60				
	1.47	1.48					1.47	100	1.48	85
1.43	1.43	1.43	1.43	19						
1.35					1.35	60				

to traces of $Fe(OH)_2$. At the end of the first plateau (point b), only the diffraction patterns due to $Fe(OH)_2$ and α-Fe were observed, as shown in Fig. 2.

Ample evidence was accumulated with this and other electrodes prepared, activated and cycled in the same manner, that, on the first discharge of the iron electrode to the end of the second plateau (point c), δ-FeO(OH) was always formed (7). However, on subsequent cycles, a gradual conversion to Fe_3O_4 was observed to occur, the x-ray diffraction patterns of both compounds being detected simultaneously. Finally, after 9 or 10 cycles, only the diffraction pattern of Fe_3O_4 was observed (6). The series of changes is shown in Fig. 3.

Moreover, if an electrode, which had been discharged once to the end of the second plateau (point c), was then stored in a covered container of 30% KOH for several days, there was an aging process, which apparently converted the δ-FeO(OH) to Fe_3O_4. The aging process, which is a chemical reaction taking between 5 and 6 days for completion, involves a partial reduction of the ferric ion to ferrous ion and may be expressed as follows

$$Fe^\circ + 8FeO(OH) = 3Fe_3O_4 + 4H_2O$$

On electrochemically reducing the δ-FeO(OH) during the charging process, Fe_3O_4 is stated to be the first reduction product formed on the way through $Fe(OH)_2$

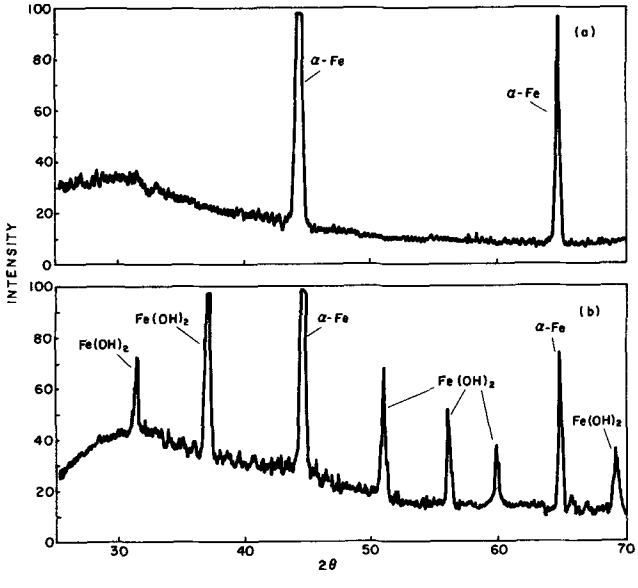

Fig. 2. X-ray diffraction patterns of activated iron electrode: (a) fully charged electrode (point a on discharge curve in Fig. 1); (b) electrode discharged to end of first plateau (point b on discharge curve in Fig. 1).

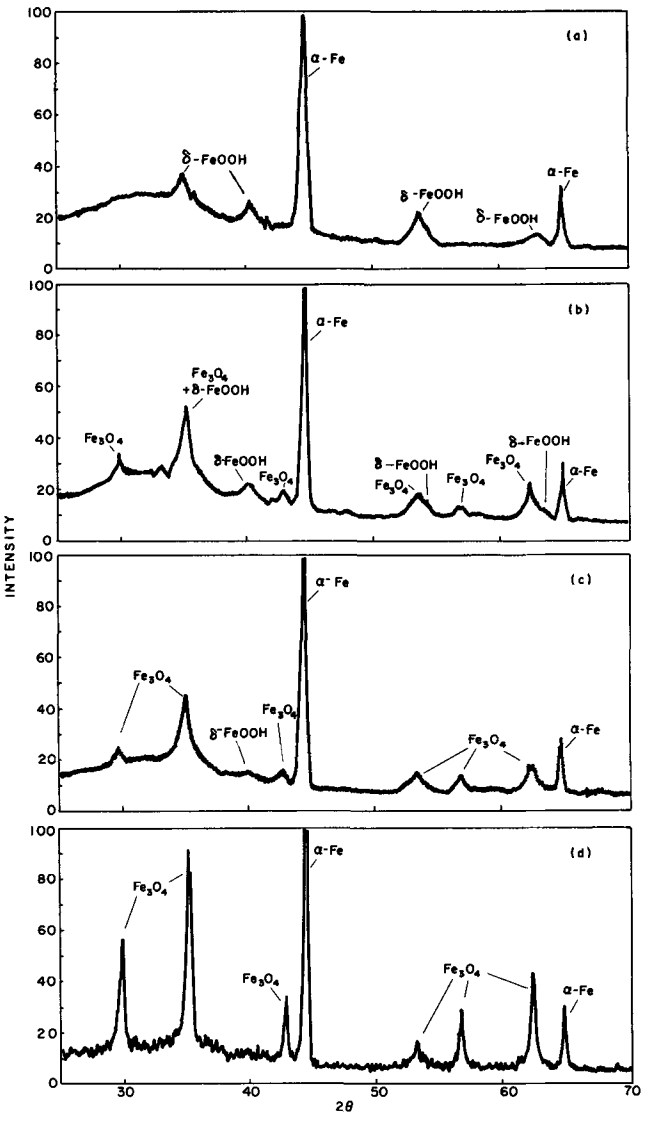

Fig. 3. X-ray diffraction patterns of activated iron electrode: (a) electrode discharged to end of second plateau (point c on discharge curve in Fig. 1), once; (b) electrode discharged to end of second plateau, four times; (c) electrode discharged to end of second plateau, five times; (d) electrode discharged to end of second plateau, ten times.

to metallic α-Fe (11). If all the Fe_3O_4 is not completely reduced during the charging process, then, on subsequent discharge, there is a possibility that, owing to the increasing presence of crystallites of Fe_3O_4, the $Fe(OH)_2$ will gradually cease to oxidize completely to the +3 state, *i.e.*, to δ-FeO(OH). The oxidation process will halt when two out of three Fe^{2+} ions have been converted to the Fe^{3+} ion, *i.e.*, to Fe_3O_4.

On discharging an electrode at 0.5A from the end of the 1st plateau to the end of the 2nd plateau, *i.e.*, a higher rate discharge, an incomplete oxidation of the carbonyl iron occurred, since mainly α-Fe and $Fe(OH)_2$, but only a trace of Fe_3O_4 or δ-FeO(OH), were detected. Discharges at rates greater than 0.25A always gave incomplete oxidation of the carbonyl iron particles and were never used if a definitive identification of the compounds generated on the 2nd plateau was important. However, in this case, the incompletely oxidized electrode was stored in a covered container of 30% KOH for about a month and periodically re-examined by x-ray diffraction to observe whether changes in the line intensities or in the chemical composition of the surface had occurred. No significant changes were noted, although there was a slight decrease in the α-Fe line intensity and a corresponding increase in the $Fe(OH)_2$ line intensity. This observation is not unexpected since the reaction of Fe with water or OH^- ion in solution to form $Fe(OH)_2$ is thermodynamically possible (12). Thus, it would appear that $Fe(OH)_2$ is quite stable in alkaline solution and does not oxidize readily, since no special precautions were taken to exclude oxygen from the solution and container. This is in complete contrast to laboratory-prepared $Fe(OH)_2$ which, after both washing free of alkali and drying in a nitrogen atmosphere, oxidizes immediately on contact with air, to form a brown product, presumably $Fe_2O_3 \cdot nH_2O$ (13). Moreover, although the domain of stability of $Fe(OH)_2$ is completely included in that of Fe_3O_4 and, in the massive state, it is stated that $Fe(OH)_2$ decomposes spontaneously to a mixture of magnetite and iron (14):

$$4Fe(OH)_2 = Fe_3O_4 + Fe + 4H_2O$$

this does not appear to have occurred in this case.

An iron electrode which had been discharged once to the end of the second plateau (α-Fe and δ-FeO(OH)) and stored in a covered container of 30% KOH for a month, was re-examined by x-ray diffraction and found to have converted, as expected, to α-Fe and Fe_3O_4. The electrode was charged at 0.5A for 9 hr and then discharged at 0.2A to the end of the second plateau. Although the normal discharge time for such an electrode is usually between 12 and 14 hr, the potential of this electrode fell to zero after only 2¼ hr. After two further chargings of 3 hr at 0.5A, the discharge time fell to (a) 1½ hr and (b) ½ hr, and presumably would have fallen to zero after further cycles. An x-ray diffraction pattern of the completely discharged electrode surface was then taken, and only α-Fe was detected with possible traces of Fe_3O_4. Presumably, this inability to build up oxide/hydroxide compounds of iron is the reason for the low capacity and may be caused by a very thin, but electrically, poorly conductive, layer of γ-Fe_2O_3 having formed on the iron particles composing the electrode surface (15-17). The oxides Fe_3O_4 and γ-Fe_2O_3 are known to be structurally closely related (18-20).

From an analysis of the x-ray diffraction patterns obtained with the activated iron electrode cycled in 30% KOH saturated with LiOH, the compounds generated on the electrode at several points along the discharge half-cycle, were identified and are shown in Table III.

Contrary to what was observed for the iron electrode cycled in 30% KOH, Fe_3O_4 was formed on this electrode on the first and subsequent discharges to the end of the second plateau. Even after a 4½ hr overdischarge given to the electrode on reaching 0V *vs.* the Hg/HgO reference electrode, α-Fe and Fe_3O_4 were the only compounds detected. No changes were observed in the x-ray diffraction patterns of the fully discharged electrode surface, after storing the electrode in a covered container of the KOH/LiOH mixed electrolyte for about 20 days. Moreover, no lithium compounds were detected on any of the iron electrodes cycled in the KOH/LiOH electrolyte (21, 22).

Conclusion

An x-ray diffraction study of the surface of an activated iron electrode discharged in 30% KOH to different points along the discharge half-cycle has identified the following phases: charged electrode, α-Fe; end of 1st plateau, α-Fe and $Fe(OH)_2$; end of 2nd plateau (discharged), α-Fe, δ-FeO(OH), or Fe_3O_4. On the first

Table III. Compounds generated on the electrode

State-of-charge	Charged (point a)	End 1st plateau (point b)	End 2nd plateau (point c)
Phase	α-Fe	α-Fe $Fe(OH)_2$	α-Fe Fe_3O_4

discharge of the iron electrode to the end of the second plateau, δ-FeO(OH) was always formed. However, on subsequent cycles, a gradual conversion to Fe_3O_4 was observed. The same conversion was observed on aging a once-discharged electrode in the alkaline electrolyte for several days. For an electrode cycled in 30% KOH saturated with LiOH, the following phases were identified: charged electrode, α-Fe; end of 1st plateau, α-Fe and $Fe(OH)_2$; end of 2nd plateau (discharged), α-Fe, Fe_3O_4 (always).

Acknowledgment

The authors would like to thank Paul Lublin for the interest that he has shown in this work.

Manuscript submitted June 4, 1969; revised manuscript received Sept. 22, 1969.

Any discussion of this paper will appear in a Discussion Section to be published in the December 1970 JOURNAL.

REFERENCES

1. F. Förster, *Z. Elektrochem.*, **14**, 285 (1908).
2. F. Förster and P. Herold, *ibid.*, **16**, 461 (1910).
3. O. Faust, *ibid.*, **13**, 161 (1907).
4. P. Krassa, *ibid.*, **15**, 490 (1909).
5. F. F. Faizullin, E. D. Kochman, and A. I. Turashev, *Trudy Kazan. Univ.*, **116**, 77 (1956).
6. A. J. Salkind, C. J. Venuto, and S. U. Falk, *This Journal*, **111**, 493 (1964).
7. T. K. Teplinskaya, N. N. Fedorova, and S. A. Rozentsveig, *Zh. Fiz. Khim.*, **38**, 2176 (1964).
8. J. Burbank and C. P. Wales, Naval Research Lab. Report 6050, March 1964.
9. J. Burbank and C. P. Wales, *This Journal*, **111**, 1002 (1964).
10. ASTM "X-ray Powder Data File," Philadelphia, Pa. (1968).
11. L. I. Lyamina and K. M. Gorbunova, *Elektrokhimiya*, **1**, 546 (1965).
12. W. M. Latimer, "The Oxidation States of the Elements and Their Potentials in Aqueous Solutions," 2nd ed., Prentice-Hall, Inc. (1952).
13. F. A. Cotton and G. Wilkinson, "Advanced Inorganic Chemistry," 2nd ed., Interscience Publishers (1966).
14. J. M. West, "Electrodeposition and Corrosion Processes," Chap. 4, Van Nostrand Co., London (1965).
15. M. Cohen, *Can. J. Chem.*, **37**, 286 (1959).
16. M. C. Bloom and L. Goldenberg, *Corrosion Sci.*, **5**, 623 (1965).
17. C. L. Foley, J. Kruger, and C. J. Bechtoldt, *This Journal*, **114**, 994 (1967).
18. J. D. Bernal, D. R. Dasgupta, and A. L. Mackay, *Clay Min. Bull.*, **4**, 15 (1959).
19. E. J. Fasiska, *Corrosion Sci.*, **7**, 833 (1967).
20. K. J. Gallagher, W. Feitknecht, and U. Mannweiler, *Nature*, **217**, 1118 (1968).
21. M. C. Bloom, M. Krulfeld, and W. A. Fraser, *Corrosion*, **19**, 327t (1963).
22. J. B. Moore, Jr., and R. L. Jones, *This Journal*, **115**, 576 (1968).

Formation of New Phases during Anodic Dissolution of Zn-Rich Cu-Zn Alloys

Howard W. Pickering

Edgar C. Bain Laboratory for Fundamental Research, United States Steel Corporation, Research Center, Monroeville, Pennsylvania

ABSTRACT

Preferential anodic dissolution of Zn from brass is examined from the point of view of the volume diffusion mechanism. Results from x-ray investigations of partially dissolved γ-brass (Cu 65 a/o (atomic per cent) Zn) and ε-brass [Cu 86 a/o Zn] specimens show the appearance of new, more Cu-rich, intermediate and terminal phases. Gradients in chemical composition also result within individual phases and are always in the direction of copper enrichment. These results indicate that preferential anodic dissolution of Zn from Cu-Zn alloy occurs to a significant extent via interdiffusion of the constituent metals in the alloy. Volume diffusion at 23°C may be operative via excess mono- and divacancies, with divacancy diffusion prevailing at high total vacancy concentrations. A few data are presented on the preferential vaporization of Zn from Cu-Zn alloy.

In previous papers (1, 2) it was concluded from x-ray and electron diffraction investigations that preferential dissolution of Cu from Cu-Au alloy occurs via solid state diffusion of Cu and Au in the alloy. Detection of volume diffusion by diffraction methods generally requires optimum sensitivity, and this may explain why other investigators (3-5) using electron diffraction and photographic film methods have not observed similar effects. This is particularly true in transmission electron diffraction experiments (5) since one necessarily examines a very early stage of dissolution when volume diffusion cannot be very pronounced. At such a stage surface diffusion may play a significant role although this can hardly continue during a longer span of attack.

The present paper, as a continuation of the earlier work, investigates the role of volume diffusion in the preferential dissolution of Zn from Cu-Zn alloy by x-ray diffraction. The analogous process of the preferential vaporization of Zn from the same alloys is also investigated. Preliminary results indicate that the formation of new phases does occur during preferential dissolution of Zn from Cu-Zn alloys (6), as does also the much earlier x-ray data (1934) of Stillwell and Turnipseed (7). Other data of Forty and Humble (8) are in agreement with the occurrence of volume diffusion during dezincification of α-brass.

X-ray investigations are easy to make on partially dissolved Cu-Zn specimens, and the interpretation, although requiring much effort due to the many lines of the Cu-Zn phases, is straightforward. Two features of interest may occur in the diffraction patterns of partially dissolved specimens. Both are indicative of a gradient in the chemical composition of the alloy and as such both are evidence that solid state diffusion

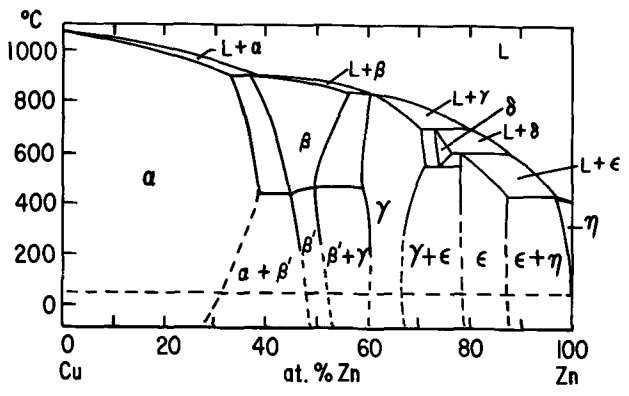

Fig. 1. Phase diagram of the Cu-Zn alloy system

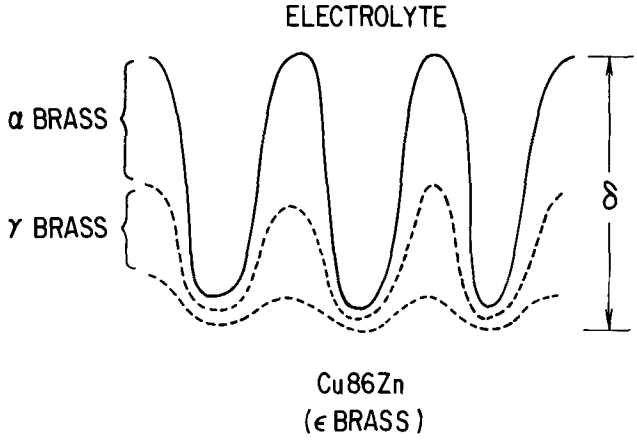

Fig. 2. Diffusion layers after early primary pore formation. With increasing time of dissolution the thickness, δ, over which compositional differences exist becomes increasingly larger than the average diffusion distance ($\lesssim$ one-half the pore wall thickness).

occurs during anodic dissolution of the alloy (see Discussion section).

The first and most clearly recognizable feature is the appearance in the diffraction pattern of new peaks due to the formation of new phases. New phases may form at certain compositions within the gradient if they have a lower free energy than the starting phase. The probable phases at room temperature of the Cu-Zn alloy system are alpha (α), ordered beta (β'), gamma (γ), epsilon (ϵ), and eta (η) phases as shown in Fig. 1.[1] Thus, the preferential dissolution of Zn from ϵ-brass ($\sim$ 76 to 86 a/o Zn) may lead to the formation of γ-, β'-, and α-phases within regions of Zn-depleted alloy. New peaks corresponding to γ-, β'-, and α-phase may then appear in the diffraction pattern. Similarly, preferential dissolution of Zn from γ-brass may result in formation of α- and β'-phases. New peaks due to α and β' would then be observed in the diffraction patterns.

The second feature is a change of the average position of the peaks of a particular phase in the direction of Cu enrichment. This may happen if the lattice parameter within a single phase region varies with composition. This is the method of analysis which was used successfully in the aforementioned x-ray investigations of anodically dissolved Cu-Au alloys.

Since the depth of x-ray penetration is very much greater than the actual solid state diffusion distance, extensive surface roughening is required before sufficient diffracted intensity is obtained from regions of interdiffusion (1); the thickness of the resulting porous layer, δ, approximates the depth of the region of interdiffusion. Very extensive surface roughening has been demonstrated for preferential dissolution of Cu from Cu-Au alloy by polarization capacity measurements (10, 11), and the formation of porous layers have often been reported, especially for Cu-Zn and Cu-Au alloys (12). Surface roughening and the formation of new phases during dissolution of ϵ-brass may occur as illustrated in Fig. 2 if α and γ are the stable, more Cu-rich phases at room temperature.

Analogous to the situation at elevated temperatures (13-17) there may develop in the interdiffusion regions large internal stresses due to local variations in lattice parameter; plastic deformation and recrystallization may then occur in the presence of high excess concentrations of vacancies. Also, porosity at a fine scale may develop giving effectively a fine particle size. Although these developments will affect the diffraction of x-rays, they will not be easily recognizable while there occurs simultaneously the formation of new phases and large changes in composition (lattice parameter) which produce gross changes in the diffracted intensity. Conversely, their presence will not seriously interfere with the identification of new phases or of large changes in lattice parameter of an existing phase.

[1] The β' phase may be unstable at room temperature, in accord with the results of Shinoda and Amado (9) who indicate a eutectoid decomposition into α and γ at about 255°C.

Experimental Procedure

In order to test for the occurrence of Cu and Zn interdiffusion during preferential dissolution of Zn from Cu-Zn alloys, x-ray investigations were carried out on samples of ϵ- and γ-brass anodically dissolved at 23°C. Single-phase alloys of γ- and ϵ-brass were prepared. The alloys were induction melted under helium in a zirconia crucible from starting metals of 99.999% Cu and 99.999% Zn. The compositions of the alloys were determined by chemical analysis to be Cu 65 a/o Zn (Cu 65 Zn) and Cu 86 a/o Zn (Cu 86 Zn). The Cu 65 Zn and Cu 86 Zn ingots were homogenized in small evacuated silica capsules for 2 weeks at 700°C and for 5 weeks at 380°C, respectively. These homogenization treatments produced fully single-phase ϵ- and γ-brass with an average grain diameter of 1-2 mm, as determined by metallographic examination of mechanically polished and etched samples. Visual examination of the silica capsules after the homogenization treatment indicated negligible loss of Zn.

Disk-shaped specimens about 0.1 cm thick were cut from the 1.25 cm (diameter) ingots using a cut-off wheel on the ϵ-brass ingot and a spark cutter on the more brittle γ-brass ingot. Some of the ϵ-brass specimens were annealed in a small evacuated silica capsule at 380°C for 2 hr, and given a light polish with 4/0 emery, but for others only coarser mechanical polishing was done in order to remove cold-worked or Zn-depleted material at the surface. Both procedures gave essentially the same results in the x-ray investigations. The γ-brass specimens were mechanically polished, 320 emery followed with 4/0 emery, to remove Zn-depleted material at the surface resulting from the spark cutting operation.

Nickel-filtered Cu or vanadium-filtered Cr radiation was used to examine the partially dissolved specimens (2). To reduce atmospheric absorption of the soft Cr radiation, the Cr target, specimen and scintillation counter were enclosed in a helium-filled bag. Calibration of the diffractometer stage was made against a gold standard. The arrangement permitted an accuracy of about $\pm 0.01°$ which was better than required. Since the x-rays "reflect" from rather than pass through the specimen, information is obtained on changes in composition which occur in a volume of alloy next to the surface; some variation in the volume of material sampled may occur if the depth of penetration of the x-rays is appreciably influenced by the degree of porosity.

A closed Pyrex cell containing a Pt wire counter-electrode was used to dissolve the specimen at a controlled current density in the range, 1-5 mA/cm^2. Prepurified helium was passed through the cell in order to remove oxygen. A mercury-mercurous sulfate elec-

trode connected to the cell via a Luggin capillary was used to measure the potential of the specimen during dissolution. The potentials are all reported relative to the standard hydrogen electrode (SHE). Electrical contact to the specimen was made with a Teflon-coated Cu rod which has one end slotted and fitted with a tightening screw. The small contact area between the sample and rod was sealed from the environment with lacquer. Contact between the specimen and the electrolyte completed the circuit, so that current flowed during the entire time the specimen was in contact with the electrolyte. At the end of each dissolution period the specimen was withdrawn from the electrolyte, rinsed in water and methanol, and dried prior to x-ray examination. Periodic metallographic examination was performed to observe the formation of porous layers.

Data were obtained with several electrolytes: 1*N* H_2SO_4 and the buffered solutions (pH ~ 5): 1*N* Na_2SO_4-0.05*N* $NaC_2H_3O_2$-0.05*N* $HC_2H_3O_2$, 1*N* $ZnSO_4$-0.05*N* $NaC_2H_3O_2$-0.05*N* $HC_2H_3O_2$, 1*N* $ZnCl_2$-0.05*N* $NaC_2H_3O_2$-0.05*N* $HC_2H_3O_2$ and 0.1*N* $HC_2H_3O_2$-0.1*N* $NaC_2H_3C_2$.

Anodic Dissolution Investigations

X-ray results for ϵ-brass.—The x-ray patterns obtained from specimens of ϵ-brass prior to dissolution show only peaks due to ϵ-brass. After anodic dissolution in all of the electrolytes, new peaks belonging to γ-phase appear in the diffraction patterns. Identification of γ-phase is positive in view of the many peaks of γ which appear in the region $35 < 2\theta < 150°$, and the fact that no superposition due to other Cu-Zn phases occurs in the case of several of these peaks. Table I lists the intensities observed for the various diffracting planes of γ-phase using the patterns obtained after dissolution of ϵ-brass. These data are compiled from x-ray patterns where diffraction due to other phases of Cu-Zn and especially oxides and hydroxides were weak.

Figure 3 shows a segment of three patterns out of 40 obtained at intermittent stages of dissolution at 5 mA/cm² of a single-phase ϵ-brass specimen in the buffered 1*N* Na_2SO_4 electrolyte. The single electrode potential, *E*, of the ϵ-brass specimen was −0.5V. The top pattern, taken prior to dissolution, shows only peaks due to the starting ϵ-phase. After about 20 to 30

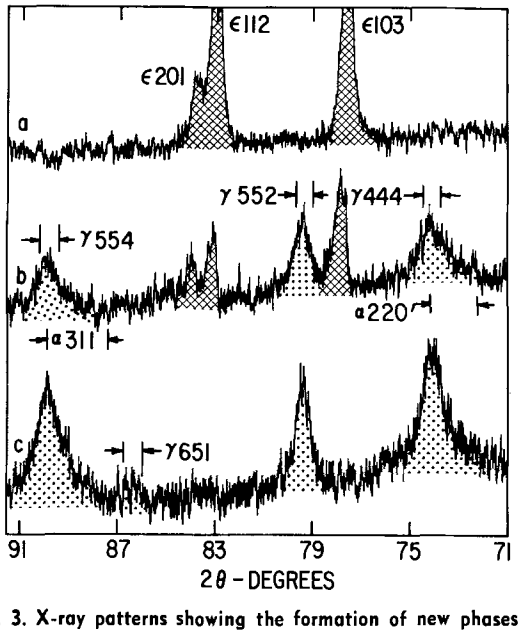

Fig. 3. X-ray patterns showing the formation of new phases during dissolution of ϵ-brass at 5 mA/cm² in buffered 1*N* Na_2SO_4 of pH ~ 5. Cu radiation. The dotted and cross-hatched peaks belong to the newly forming γ- and disappearing ϵ-phases, respectively: (a) prior to dissolution; (b) after dissolution for 67 min (20 C/cm²); and (c) after dissolution for 370 min (110 C/cm²).

Table I. Observed intensities of γ-phase peaks after anodic dissolution of ϵ-brass (5 mA/cm² in 1*N* Na_2SO_4-0.05*N* $HC_2H_3O_2$-0.05*N* $NaC_2H_3O_2$), after vaporization of ϵ-brass (420°C and 5 x 10^{-5} mm Hg) and of a powder sample from Westgren and Phragmen (18). Superscripts indicate γ lines for which other phases may contribute to the total intensity. W, weak; VW, very weak; M, medium; S, strong; VS, very strong; abs, absent.

γ-Brass hkl	$h^2+k^2+l^2$	Anodic dissolution	Vaporization	Powder sample of γ brass (18)
222	12	W	M	W
321	14	W	M	W
400	16	abs	abs	abs
330, 411*‡	18	VS	VS	S
420	20	abs	W	VW
332	22	W	M	M
422*	24	M	W	W
431, 510	26	abs	W	W
521×	30	VW	VW	abs
440	32	abs	VW	abs
433, 530	34	abs	VW	abs
442, 600‡×	36	S	S	S
532, 611	38	abs	VW	W
620×	40	abs	abs	abs
541	42	abs	VW	abs
622	44	W	M	abs
631*	46	W	M	W
444*	48	S	W	M
543, 550, 710	50	VW	W	W
640×	52	abs	W	abs
552, 633, 721‡	54	S	S	S
642	56	abs	VW	VW
730	58	VW	abs	abs
651, 732	62	VW	W	W
800*×	64	abs	abs	abs
554, 741, 811*	66	S	MS	S
644, 820	68	VW	W	W
653*	70	VW	VW	VW
660, 822*‡×	72	M	MS	S
743, 750, 831	74	VW	VW	W
662×	76	W	W	W
752	78	VW	VW	VW
840	80	abs	VW	
833, 910×	82	VW	VW	
842	84	abs	abs	
655, 761, 921	86	abs	VW	
664	88	abs	VW	
754, 851, 930‡	90	VW	W	
763, 932	94	abs	abs	
844*×	96	abs	abs	
770, 853, 941	98	VW	M	
860, 10,0,0	100	abs	abs	
772, 10,1,1	102	VW	W	
862, 10,2,0	104	abs	VW	
943, 950	106	abs	abs	
666, 10,2,2‡	108	abs	VW	
765, 952, 10,3,1,*	110	abs	abs	
774, 855, 871*	114	M	W	
864, 10,4,0*	116	abs	abs	
961 10,3,3*	118	VW	VW	
10,4,2*	120	M	W	
954	122		VW	

* α-brass has a line within the 2θ range of this γ-brass line.
‡ β′-brass has a line within the 2θ range of this γ-brass line.
× ZnO has a line within the 2θ range of this γ-brass line.

min at 5 mA/cm² (6 to 9 C/cm²), new peaks due to γ-phase are first detected. The new peaks grow and those due to the starting ϵ-phase diminish in intensity as dissolution continues. The middle pattern taken at an intermediate stage of dissolution shows three of the new γ-peaks (filled with dots), γ554, γ552, and γ444. At a much later time of dissolution shown in the bottom pattern, γ is still the predominant phase, although some α-phase also is indicated as is discussed next.

In the middle pattern the γ554 and γ444 peaks are asymmetrical with increased diffracted intensity on the right side. Both of these regions of increased intensity correspond to 2θ positions of α-phase, *viz.*, α311 and α220. The left and right boundaries of the α311 and α220 2θ regions shown in Fig. 3 correspond to pure Cu and Cu 30 a/o Zn, respectively. It can be seen that symmetric peaks are normal for γ-phase by examining the γ552 peak for which diffraction from neighboring γ640 ($77.3 < 2\theta < 78.0°$) and γ642 ($80.8 < 2\theta < 81.5°$) is negligible and for which no superposition by other phases occurs.

An alternative explanation of the asymmetry is that part or all of the increased intensity of the γ554 and γ444 peaks is due to weakly diffracting γ800 and γ631 at $2\theta \cong 88.5°$ and $2\theta \cong 72.5°$, respectively. This is not supported though by the results at later times of dis-

solution where the diffracted intensity causing the asymmetry is decreased whereas γ-peaks generally are stronger, as seen for example in the bottom pattern of Fig. 3. On the other hand these data are in accord with a shift of the average compositions of α-phase and γ-phase material with time of dissolution toward their Cu-rich boundaries, where both phases have nearly identical 2θ positions, 74.3° for γ444 and α220 and 90.1° for γ554 and α311.

A single-phase ϵ-brass specimen also was dissolved potentiostatically at −455 mV (SHE) and intermittently examined with x-rays. The x-ray results were the same as already described for the amperostatic case (Fig. 3).

Detailed examination of the x-ray patterns shows also that the average position of the peaks of the starting ϵ-phase shifts in the direction of Cu-enrichment of the alloy. This result is observed at relatively early periods of dissolution before the peaks of new phases show. A typical result is shown in Fig. 4 for the {110} line of ϵ-phase. For the largest amount of dissolution used in this series (pattern c of Fig. 4) the average position of the ϵ-peak is at $2\theta \cong 112.1°$ and diffracted intensity extends to $2\theta \cong 113.0°$, compared to the starting average position, $2\theta \cong 111.8°$ (pattern a). A shift to higher 2θ values corresponds to Cu-enrichment of the affected material. An emerging gamma peak, γ541, is just recognizable in pattern c at $2\theta \cong 113.2°$.

All peaks which appeared in the diffraction patterns between $16 < 2\theta < 150°$ were attributable to ϵ-, γ-, or α-brass, except after prolonged dissolution (> 7 hr at 5 mA/cm² or 120 C/cm²) in the buffered electrolytes of pH ≅ 5 when extra, weak peaks due to ZnO appeared.

The presence or absence of ordered β'-brass could not be resolved due to superposition of other Cu-Zn peaks (mainly γ-phase) and the limited amount of data. A detailed comparison of γ-peak intensities as a function of dissolution time would be helpful in this regard, as would also data at longer times when the diffracted intensity from γ-phase has decreased.

X-ray results for γ-brass.—X-ray results for γ-brass show features similar to those in Fig. 3 and 4 for ϵ-brass. After anodic dissolution broad diffracted intensity occurs at the 2θ regions of α-phase accompanied by a decrease in intensity of the γ-peaks. The average position of the new α peaks shifts with increasing amounts of dissolution from a 2θ value corresponding to α brass of high Zn content to a value corresponding to essentially pure Cu. Also shifts in composition within the starting γ-phase are observed at the early stages of dissolution and are in the direction of Cu-enrichment (as in Fig. 4 for the ϵ-brass sample).

X-ray results for two-phase ($\epsilon + \eta$) brass.—X-ray results were also obtained for a two-phase alloy consisting of a small amount of the terminal Zn-rich η-brass in a matrix of ϵ-brass. This is the "as-melted" rather than the homogenized condition of the Cu 86 a/o Zn alloy. X-ray patterns taken after early stages of dissolution in the buffered chloride solution show the η-peaks to fall off rapidly compared to the ϵ-peaks with increasing amounts of dissolution. Then new peaks due to γ-phase are detected (> 6 C/cm² passed), and the x-ray patterns thereafter are similar to those obtained from completely single-phase ϵ-brass specimens as already discussed (Fig. 3 and 4).

Auxiliary investigations.—Cross-sectional metallographic examination of partially dissolved ϵ- and γ-brass specimens (Fig. 5) shows that a poorly reflecting layer forms not unlike the porous layers (1, 2) found in partially dissolved Cu-Au alloys. The layers formed in Cu-Zn specimens apparently also are porous. This was indicated by metallographic examination, by the tendency of the layers to flake and crumble, and by seepage of liquid out of the layer.

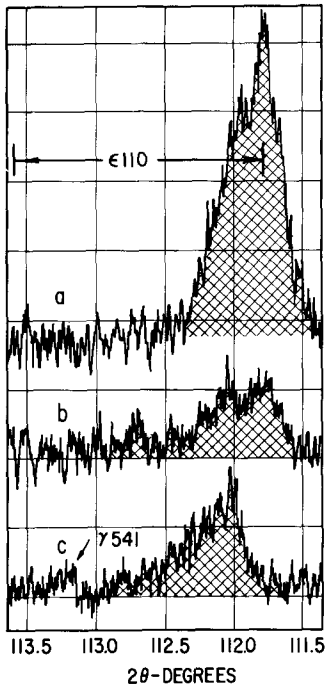

Fig. 4. X-ray diffraction patterns of dissolved ϵ-brass illustrating increased diffracted intensity at the more Cu-rich compositions within the single-phase region of ϵ. Cr. radiation. (a) After 6.7 min at 5 mA/cm² (2 C/cm²) in the buffered Na_2SO_4 solution of pH 5; (b) after 16.7 min (5 C/cm²); (c) after 50.0 min (15 C/cm²).

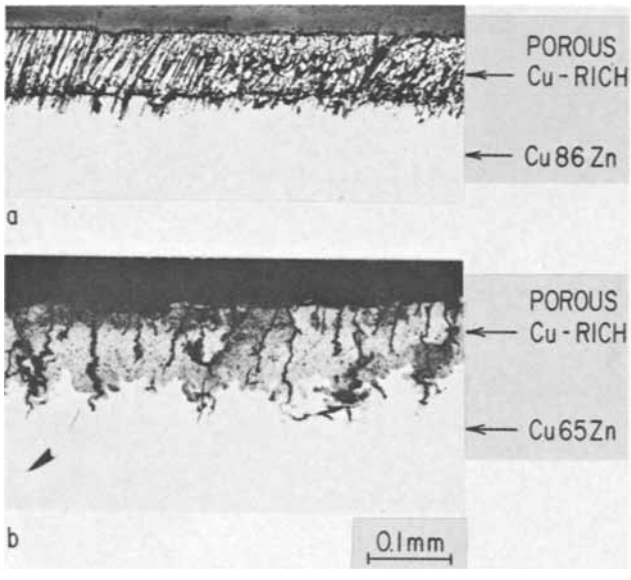

Fig. 5. Cross sections of anodically dissolved ϵ-brass and γ-brass specimens illustrating the porous, Cu-rich layer which forms during preferential dissolution of Zn. Unetched. (a) ϵ-brass after 103 C/cm² passed and (b) γ-brass after 140 C/cm² passed.

The number of moles of Zn dissolved per unit area is $it/2\mathbf{F}$ where i is the current density based on the geometrical surface area, t is the time, and $\mathbf{F}$ is the Faraday constant. The Zn content of a porous layer of depth δ per unit area is $\delta N^{o}_{Zn}/V_m$, where N^{o}_{Zn} is the mole fraction of Zn in the bulk alloy and V_m is the molar volume. If it is assumed that all of the Zn is removed to a depth of δ one has

$$\delta = \frac{it}{2\mathbf{F}} \frac{V_m}{N^{o}_{Zn}}$$

For $V_m \cong 8$ cm³/mole[19] and $it = 103$ and 140 C/cm² for the ϵ- and γ-samples in Fig. 5, one obtains calcu-

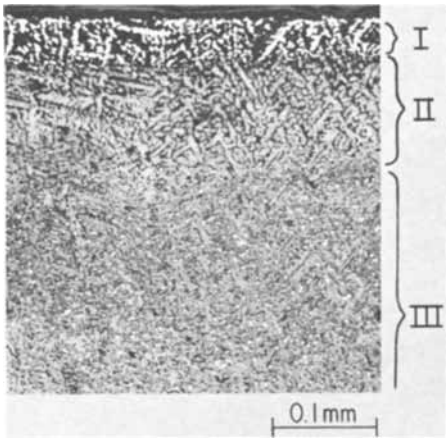

Fig. 6. Cross section of a two-phase sample consisting of $\epsilon + \gamma$-phases after dissolution at 1 mA/cm^2 in 0.1*N* $HC_2H_3O_2$-0.1*N* $NaH_2C_3O_2$ for 15 hr (54 C/cm^2). Layer I, both phases dissolved to an appreciable extent; layer II, only η-phase dissolved; layer III, undissolved two-phase alloy.

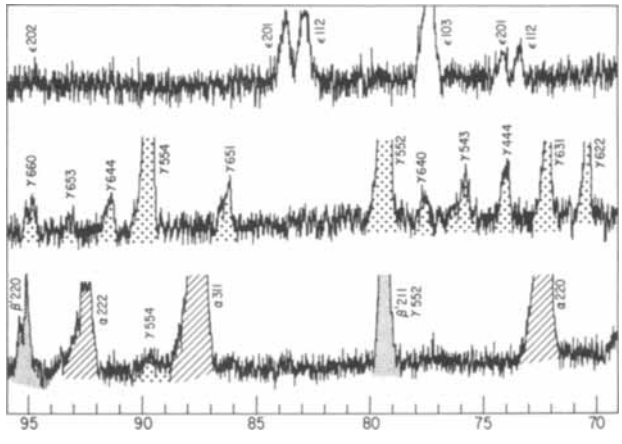

Fig. 7. X-ray diffraction patterns of ϵ-brass after vaporization at 420°C and 5 x 10^{-5} mm Hg. Cu radiation. The peaks with dots, more dense random dots, and cross-hatching belong to the newly forming γ-, β'-, and α-phases, respectively. (a) Prior to vaporization; (b) after ½ hr vaporization; (c) after 10 hr vaporization.

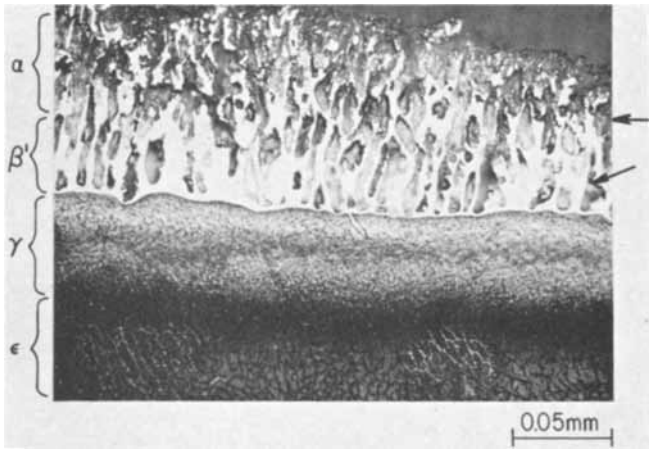

Fig. 8. Cross section of the ϵ-brass specimen used to obtain the diffraction data in Fig. 10. Arrows point to pores. Etched with 5% Nitol followed with saturated picral acid.

lated values of $\delta = 0.05$ and 0.09 mm, respectively. These values are, respectively, about one-half and about equal to the depth measured on the micrographs, and indicate that for ϵ-brass only about one-half and that for γ-brass nearly all of the original Zn within the depth δ has been dissolved. This is in agreement with the x-ray data after large amounts of dissolution which show the porous region of ϵ-brass to consist of γ (and possibly β') and α-brass, and of γ-brass to consist of Cu-rich α-phase.

Metallographic examination of the as-melted two-phase ($\epsilon + \eta$) specimens after dissolution shows that the dispersed η-phase dissolves faster than the matrix ϵ-phase, and to such an extent that η-phase situated beneath the surface also is attacked, probably via interconnection with η-phase originally at the surface. This is seen in the cross section of Fig. 6 which was taken at an advanced stage of dissolution of one of the specimens, and shows a layer (I) of porous alloy at the surface, another layer (II) consisting of undissolved ϵ-phase and holes where η had existed, and furthest in from the surface the as yet completely undissolved two-phase alloy.

Chemical analysis of the electrolyte (*a*) after dissolution of ϵ-brass showed no trace of Cu for current densities in the range of 1 to 5 mA/cm^2, and (*b*) after dissolution of γ-brass showed only a small amount of Cu for even the highest current densities of 5 mA/cm^2. Hence strong preferential dissolution of Zn occurs for both alloys during dissolution at the aforementioned current densities in accord with the x-ray and metallographic data and with the polarization curves for the individual components presented elsewhere (20).

Elevated Temperature Vaporization of Cu-Zn

Similar experiments involving preferential vaporization of Zn from single-phase Cu 86 Zn (ϵ-brass) and Cu 65 Zn (γ-brass) were carried out at 420°C and 5 x 10^{-5} mm Hg. The x-ray results of these experiments are in basic agreement with the voluminous literature on the vaporization of Zn from Cu-Zn alloys. The α-, β'-, and γ-phases are stable at 420°C, as Elam (21) and others have shown. This is illustrated in a sequence of patterns obtained at different stages of vaporization of ϵ-brass in Fig. 7.

Figure 8 shows in cross section that there are four roughly parallel layers next to the surface. These are the α-, β'-, γ-, and ϵ-phases,[2] proceeding inward from the surface according to metallographic and electron microprobe examinations. The α- and β'-layers, although not distinguishable in this micrograph, were distinguishable in the microscope by their color difference. The α- and β'-layers are filled with pores, whereas pore formation is not observed within the γ- and ϵ-layers. The porosity appears in large part to be due to surface roughening.

Figure 9 shows in cross section an originally single phase γ-brass specimen after vaporization at 420°C and 5 x 10^{-5} mm Hg. The γ-β' interface is shown, and the β'-α interface could readily be seen under the microscope. In the α-layer immediately adjacent to the surface, severe porosity has resulted, and in the β'-layer relatively few, very large voids have formed, many of which do not appear connected to the surface. Under the microscope it was seen that α-phase had formed at the surface of all of the porous structure which appeared to be connected to the external surface, in accord with vaporization of Zn from these surfaces; on the other hand α-phase was not observed to have formed at the surface of the large voids within the β'-layer.

Discussion

Volume diffusion during anodic dissolution.—Anodic dissolution which occurs via the interdiffusion of the components in the alloy is consistent with and appears to be the only satisfactory explanation of, the formation of new alloy phases during preferential dissolution of Zn from brass. Neither the often-mentioned ionization-redeposition nor the surface diffusion mechanism appears capable of producing new alloy

[2] This micrograph does not give the proper ratio of the phase widths due to edge effects. γ is relatively thicker than shown.

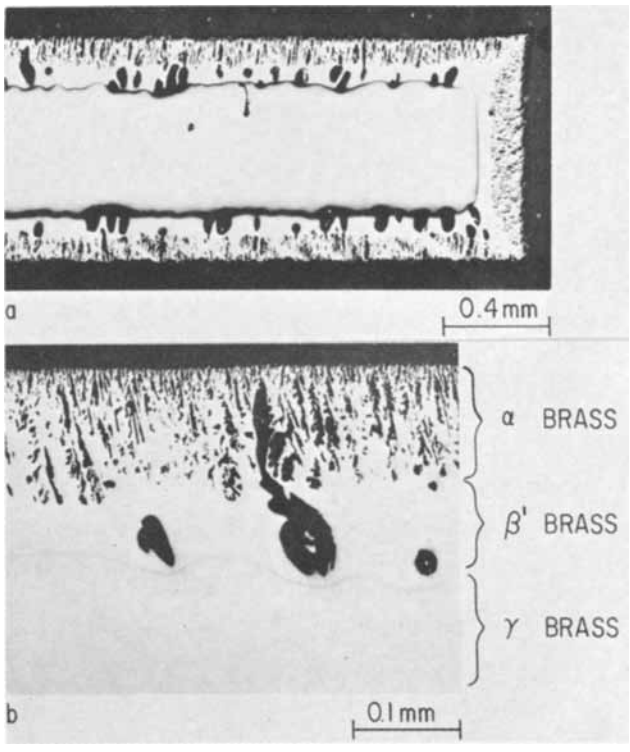

Fig. 9. Cross section of a γ-brass specimen after vaporization at 420°C and 5 x 10^{-5} mm Hg. Etched electrolytically in dilute sulfuric acid.

containing appreciable amounts of the less noble metal. Wagner (22) has calculated the gradients of the potential and of the various ionic species within a pit for anodic dissolution of Cu-Au alloy at the bottom of the pit. From these results he was able to establish that redeposition of Au is thermodynamically impossible on the side walls of the pit, in the absence of "coupling" of the anodic reactions. Rather, he found that there is the tendency for Au to dissolve at the side walls when Au dissolution occurs at the bottom of the pit. There is also the tendency for Cu to dissolve at the side walls irrespective of the presence or absence of the coupling process. Hence, thermodynamic considerations appear to rule out the formation of Cu-Au alloy on the side walls of porous structure by a cathodic deposition process, while anodic dissolution of the alloy occurs at the advancing front of the porous structure. Even without calculations this may be understood when one considers that the potential in the electrolyte for anodic polarization increases with increasing distance into the pit. The same holds for anodically dissolving Cu-Zn alloys.

The accumulation of alloy deposits by migration of adatoms over the surface requires a significant concentration of adatoms of the less noble metal. On polarizing a pure metal anodically, one has to expect a decrease in the number of adatoms in comparison to the state of equilibrium. This is the reverse of the situation for cathodic polarization, which is discussed especially by Bockris and Damjanovic (23). The concentration of adatoms of the less noble metal of a binary alloy, therefore, may be expected to be low at the advancing front of the porous structure where most of the anodic dissolution occurs, and furthermore to be even lower along the side walls in accord with the sign of the potential gradient in the electrolyte. Hence it seems highly unlikely in this case, too, that deposits may form which contain appreciable amounts of the less noble metal by a process involving surface migration of adatoms of the less noble metal.

Volume diffusion at room temperature requires the presence of excess divacancies which may be created

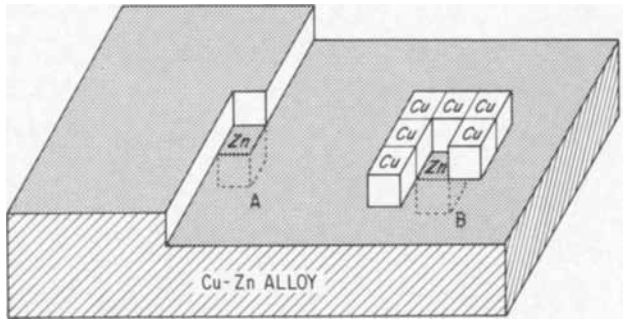

Fig. 10. Variations on the model of vacancy formation offered by Pickering and Wagner (1).

at the surface by a high driving force for dissolution (1). A model for divacancy formation at the surface has been presented which involves ionization from terrace sites of atoms of the less noble metal. It has been questioned whether the operating overvoltages are sufficient to dissolve atoms directly from terrace sites (24). Direct ionization from a terrace site, however, may not be necessary. Sketch A of Fig. 10 shows a Zn atom in a position directly beneath a kink. Dissolution of this Zn atom may occur in the normal kink-ledge-terrace sequence by moving into the neighboring kink position. Schwoebel (25) has considered vacancy formation by a similar rearrangement at a kink. Variation B involves adatoms of the more noble metal (Cu) which may be only momentarily in the positions shown.[3] The designated Zn atom in the layer beneath the adatoms may move up into the "pocket" of the adatoms, thereby creating a vacancy in the underlying atom layer. Divacancies may form similarly, or by the joining of monovacancies which may have a higher mobility in the surface layer(s) than in the bulk alloy.

Using activation energies reported by Ramstetter *et al.* (26) for movement of mono- and divacancies in Cu, it was shown in an earlier work (1) that diffusion of divacancies in Cu is reasonably rapid at room temperature. Monovacancies on the other hand were calculated to be virtually immobile. There is some disagreement in the literature on the activation energy for migration of monovacancies, but even using the lowest value, $E_{\square}^{m} = 0.9$ eV of Simmons and Balluffi (27) one finds that monovacancies are not particularly mobile in copper at 25°C. With $E_{\square}^{m} = 0.9$ eV the diffusivity of monovacancies, $D_{\square}$, in pure copper at 25°C equals 0.9 x 10^{-16} cm²/sec, and for $t = 1000$ s the root-mean-square displacement is only ~40°A. It is a more significant point, however, that at high total concentrations of vacancies the concentration of divacancies exceeds that of monovacancies. Hence, even if monovacancies were highly mobile, interdiffusion still may occur predominantly via the divacancies.

Although data on the mobility of vacancies in Cu-Zn alloys are not available, the greater intrinsic diffusivity of Zn in α brass (the Kirkendall effect) indicates that vacancy migration is faster in α brass than in pure Cu. Also the elevated temperature interdiffusion of Cu and Zn is known to increase with increasing addition of Zn to Cu throughout the α and γ composition range, e.g., as in ref. (13) and (28-30). Hence it seems reasonable to conclude that excess divacancies as well as possibly monovacancies greatly enhance the interdiffusion of Cu and Zn during preferential dissolution of Zn from Cu-Zn alloys at room temperature.

The x-ray results for the two-phase (ε + η) alloy show that the more Zn-rich phase, η, dissolves faster.

[3] The concentration of adatoms of the more noble metal may be quite high if the more noble metal does not dissolve at the potential which prevails during dissolution of the less noble metal

This is in agreement with other data which show that the higher the zinc content of the alloy the lower is the required potential to sustain a given rate of Zn dissolution, (20, 31-33) and with the often-made observation that in two-phase $\alpha + \beta'$ alloys, the more Zn-rich β' phase dissolves faster (34).

The results of investigations on the (preferential) vaporization of Zn from ϵ- and γ-brass were qualitatively the same as for anodic dissolution at room temperature with the exception that for the latter peaks due to β' were not resolved. Also metallographic examination shows severe porosity (Fig. 8, 9) which appears to be the result of both surface roughening and internal void formation. The conclusion that certain voids have formed internally is substantiated by the observation that α-phase does not form at the surfaces of these voids; *i.e.*, if the voids, instead, were connected to the external surface, vaporization accompanied by formation of α-phase would occur from their surfaces as at all external surfaces.

Internal void formation has often been observed as, for example, in the work of Balluffi and co-workers (14, 15) and others (35, 36) during vaporization of Zn from α-brass and during other processes involving interdiffusion of Cu and Zn at higher temperatures ($\gtrsim$700°C). Internal void formation has generally been understood (37-39) as due to the accumulation of excess vacancies, with local supersaturation of vacancies being the result of unequal diffusivities of the component metals (Kirkendall effect).

The occurrence of surface roughening during preferential dissolution or vaporization is in agreement with theoretical considerations by Wagner (40) and by Harrison and Wagner (41). They found that if diffusion (within the alloy) of the reacting species to the surface is rate controlling, there is the tendency for surface roughening to occur, and they and others have shown experimentally the occurrence of surface roughening when this condition is met.

Equilibrium phases.—During the formation of the new phases at room temperature the concentration of vacancies must greatly exceed the equilibrium value in view of the need for a very large vacancy population if appreciable diffusion is to occur in the first place (1). Hence there is the question as to what extent the new phase formed during anodic dissolution are characteristic of the corresponding, equilibrium, room-temperature phases. In the elevated-temperature vaporization of Zn the new phases which form are for all practical purposes identical, or very soon become so, to the equilibrium phases. This can readily be checked since the equilibrium structure can be obtained in annealing experiments. Contrary to the situation at elevated temperatures, an independent determination of the equilibrium phases at room temperature by chemical diffusion is not, practically speaking, possible. Indeed it is for this reason that phase diagrams at room temperature are not available for most alloys.

A change in γ-phase in the 250°-320°C range is indicated in the data of Köster (42) and others (43, 44), although the nature of the change is not clear. More recently Melikhov *et al.* (45) have reported that a change in lattice parameter and crystal structure of γ-phase occurs ~275°C. The data in the present paper do not confirm this.

Concluding Remarks

The most definitive and important result of this investigation is the demonstration of the occurrence of new phases during preferential dissolution of Zn from Zn-rich Cu-Zn alloys. This in turn means that interdiffusion of Cu and Zn in the alloy occurs as an integral part of the mechanism of preferential dissolution of Zn from brass.

Evolving out of these investigations is the interesting possibility that preferential dissolution in conjunction with x-ray diffraction analysis may be used as a tool for determining and roughly mapping out the stable phases of alloy systems at room temperature.

Acknowledgment

The author is especially grateful to Dr. Carl Wagner of the Max Planck Institute für Physikalische Chemie, and Drs. J. C. M. Li, R. A. Oriani, L. S. Darken, and S. S. Brenner and Mr. L. Zwell for valuable discussions and helpful comments. He also wants to acknowledge the skillful assistance of Mr. P. J. Byrne in the anodic dissolution, vaporization, and x-ray phases of the investigation, and of Mr. R. M. Lytle in the metallographic work. All except Professor Wagner are staff members of the E. C. Bain Laboratory for Fundamental Research of the United States Steel Corporation.

Manuscript submitted April 4, 1969; revised manuscript received Aug. 29, 1969.

Any discussion of this paper will appear in a Discussion Section to be published in the December 1970 JOURNAL.

REFERENCES

1. H. W. Pickering and C. Wagner, *This Journal*, **114**, 698 (1967).
2. H. W. Pickering, *ibid.*, **115**, 143 (1968).
3. K. Hashimoto, S. Ogawa, and S. Shimodaira, *Trans. Jap. Inst. Metals*, **4**, 42 (1963).
4. K. Hashimoto, T. Goto, W. Suëtaka, and S. Shimodaira, *ibid.*, **6**, 107 (1965).
5. P. R. Swann, *Corrosion*, **25**, 149 (1969).
6. H. W. Pickering, Conference on the Fundamental Aspects of Stress Corrosion Cracking, Columbus, Ohio (1967), NACE, p. 175, R. W. Staehle, Editor, (1969).
7. C. W. Stillwell and E. S. Turnipseed, *Ind. and Eng. Chem.*, **26**, 740 (1934).
8. A. J. Forty and P. H. Humble, Proceedings of the 2nd International Conference on Metallic Corrosion, NACE (1963), p. 80; Conference on the Fundamental Aspects of Stress Corrosion Cracking, Columbus, Ohio (1967), NACE p. 64, R. W. Staehle, Editor (1969).
9. G. Shinoda and Y. Amano, *Trans. Jap. Inst. Metals*, **1**, 54 (1960).
10. H. W. Pickering, *This Journal*, **115**, 690 (1968).
11. C. Wagner, *ibid.*, **116**, 343 (1969).
12. A. list of references is found in ref. (1).
13. F. Rhines and R. F. Mehl, *Trans. AIME*, **128**, 185 (1938).
14. R. W. Balluffi and L. L. Seigle, *Acta Met.*, **3**, 170 (1955); *ibid.*, **5**, 449 (1957).
15. V. Y. Doo and R. W. Balluffi, *ibid.*, **6**, 428 (1958).
16. J. A. Brinkman, *ibid.*, **3**, 140 (1955).
17. H. Yamaguchi, *Oyo Butsuri*, **32**, 911 (1963); **33**, 171 (1964).
18. A. Westgren and G. Phragmen, *Phil. Mag.*, **1**, 311 (1925).
19. E. A. Owen and L. Pickup, *Proc. Roy. Soc.*, **A140**, 179 (1933).
20. H. W. Pickering and P. J. Byrne, *This Journal*, **116**, 1492 (1969).
21. C. F. Elam, *J. Inst. Metals*, **43**, 217 (1930).
22. C. Wagner, Unpublished memorandum, June 12, 1965.
23. J. O'M. Bockris and A. Damjanovic in "Modern Aspects of Electrochemistry," J. O'M. Bockris and B. E. Conway, Editors, Vol. 3, p. 224, Butterworths (1964).
24. D. Vermilyea, Discussion to ref. (6), p. 176.
25. R. L. Schwoebel, *J. Appl. Phys.*, **38**, 3154 (1967).
26. R. Ramstetter, G. Lampert, A. Seeger, and W. Schüle, *Phys. Status Solidi*, **8**, 863 (1965). W. Schüle, A. Seeger, D. Schumacher, and K. King, *ibid.*, **2**, 1199 (1962).
27. R. O. Simmons and R. W. Balluffi, *Phys. Rev.*, **129**, 1533 (1963).
28. U.S. Landergren, C. E. Birchenall, and R. F. Mehl, *Trans. AIME*, **206**, 73 (1956).
29. A. Kuper, D. Lazarus, J. R. Manning, and C. T. Tomizuka, *Phys. Rev.*, **104**, 1536 (1956).
30. R. F. Mehl and C. F. Lutz, *Trans. AIME*, **221**, 561 (1961).

31. H. G. Feller, Habilitationsschrift, Technische Universität Berlin (1965); *Corr. Sci.*, **7**, 259 (1968).
32. H. Sugawara and H. Ebiko, *Corr. Sci.*, **7**, 513 (1967).
33. I. K. Marshakov and V. P. Bogdanov, *Russian J. Phys. Chem.*, **38**, 1041, 1043 (1964).
34. G. Joseph and M. T. Arce, *Corr. Sci.*, **7**, 597 (1967).
35. J. Brett and L. Seigle, *Acta Met.*, **11**, 467 (1963).
36. F. N. Rhines and B. J. Nelson, *Trans. AIME*, **156**, 195 (1944).
37. L. C. Correa da Silva and R. F. Mehl, *ibid.*, **191**, 155 (1951).
38. R. S. Barnes, *Proc. Phys. Soc.*, **65B**, 512 (1952).
39. F. Seitz, *Acta Met.*, **1**, 355 (1953).
40. C. Wagner, *This Journal*, **103**, 571 (1956).
41. J. D. Harrison and C. Wagner, *Acta Met.*, **7**, 722 (1959).
42. W. Köster, *Z. Metallkunde*, **32**, 151 (1940).
43. T. Matsuda, *Science Reports*, Tohoku Univ., **11**, 251 (1922).
44. H. Imai, *ibid.*, **11**, 313 (1922).
45. V. D. Melikhov, K. K. Kasymbekova, T. P. Polyakova, and A. A. Presnyakov, *Phys. Metals Metallog.*, **16**, 54 (1963).

Characterization of Corrosion Layers on Aluminum by Shifts in the Aluminum and Oxygen X-Ray Emission Bands

P. D. Gigl, G. A. Savanick, and E. W. White

Materials Research Laboratory, The Pennsylvania State University, University Park, Pennsylvania

ABSTRACT

An x-ray emission technique is outlined for the characterization of thin layers of aluminum oxides, aluminum oxyhydroxides, and aluminum hydroxides on aluminum. Shifts in the Al Kβ and O Kα x-ray emission lines of standard compounds are presented and are then used to characterize thin corrosion layers on aluminum.

Characterization of aluminum oxides, aluminum oxyhydroxides, and aluminum hydroxides can present serious problems when they are poorly crystallized and especially when they occur as thin layers on metal substrates. This study was undertaken to establish the feasibility of using shifts in the aluminum K-emission band (Al Kβ) and the oxygen K-emission band (O Kα) to determine the chemistry and short-range structure of various corrosion products on aluminum and its alloys. It has been well established that K-emission bands of the second and third period elements undergo significant changes among various compounds, but consistent rules governing such changes have not been established (1, 2). A major purpose of this investigation is to develop methods for identifying thin Al-O-OH layers on aluminum.

In the case of anhydrous aluminum oxides and alumino silicates it has been shown that Al Kβ shifts depend on the number of oxygens coordinating the Al^{3+} and also on the mean Al-O distance in a given structure (3). More recently a study was undertaken on some of the compounds in the Al-O-OH system using the Al Kβ line but the results were not very definitive (4). The principal result of that study was to establish for the first time the characteristic difference in the Al Kβ from α-Al_2O_3 *vs.* γ-Al_2O_3.

The oxygen K-emission band has been studied in considerable detail by at least three investigators, but their results have not led to a quantitative interpretation of the shifts (5-7). The most recent of these studies indicated that bond character may be the most common factor contributing to changes in the O Kα (7).

Experimental

A set of reference standards for the common Al-O-OH compounds was commercially obtained or synthesized and carefully characterized to confirm their structure and composition. These compounds included: α- and γ-Al_2O_3, boehmite [AlO(OH)], diaspore [AlO(OH)], gibbsite [$Al(OH)_3$], and bayerite [$Al(OH)_3$]. These standards were studied in the form of thin (2-5μ thick layers) deposited from dilute suspension in carbon tetrachloride onto polished surfaces of ¼ in. diameter spectrographic grade carbon rods.

An ARL model EMX electron microprobe operated at 20 keV and 1.5-3.7 x 10^{-8}A specimen current was used to excite and analyze the x-ray spectra. An electron beam diameter of about 100 μm was used in order to minimize specimen damage. A 4-in. radius curved crystal spectrometer, which displays wavelength directly for an ammonium dihydrogen phosphate (ADP) crystal, was used with a thin formvar window flow proportional counter.

An ADP crystal (2d = 10.64Å) was scanned at 0.01 Å/min to diffract the first order Al Kβ line. A clinochlore crystal (2d = 28.39Å) was scanned at 0.0267 Å/min to diffract the oxygen Kα line. The resolution of the ADP is approximately 1000 ($\lambda/\Delta\lambda$) at 8Å and the clinochlore crystal (8) has a resolution of about 500 at 25Å. The Al Kβ peak count rates were in the range of 10-50 counts/sec while the O Kα peak count rates varied from 20 to 50 counts/sec. The peak positions were measured at two-thirds height and could be reproduced within ±0.0026Å for Al Kβ and ±0.0027Å for O Kα. This relatively poor precision in individual measurements of peak positions results from a random error in bringing the specimen to the proper position on the spectrometer circle. By taking the average of eight to ten separate scans, confidence in the mean value approaches ±0.0008Å in each case.

It is imperative to work at quite low specimen currents and large elecrton beam diameters, otherwise the action of the electron beam can induce decomposition of the hydrated films in the time required to record the spectrum. Fortunately, in the microprobe one can monitor the specimen current as an indication of specimen decomposition. A slight decrease in specimen current is a sensitive indication of dehydration. A range of ±0.1 x 10^{-8}A was taken as a safe specimen current variation for a single peak scan.

Results

Typical spectra recorded in this study are reproduced in Fig. 1 and 2. Data on changes in peak position and line widths are shown in Table I. The values are recorded as changes in peak position as measured at 2/3 height and referenced to the peak of α-Al_2O_3.

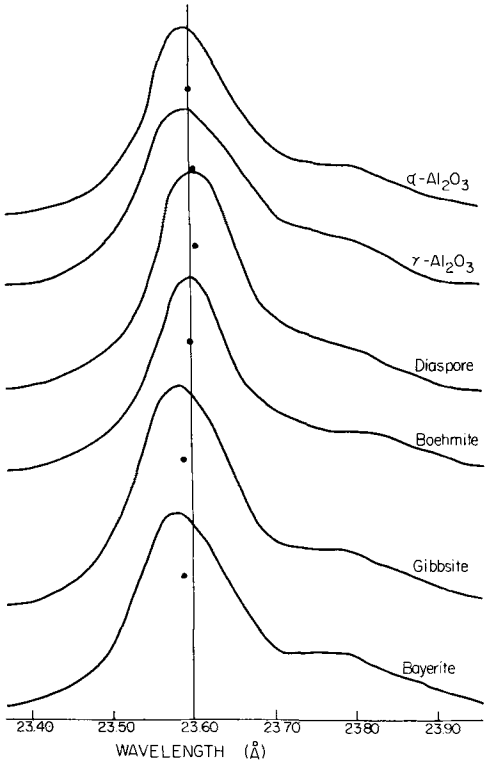

Fig. 1. O Kα emission spectra of the aluminum hydroxides, oxyhydroxides, and oxides given in Table I. Note the wide band widths of γ-Al_2O_3, gibbsite, and bayerite. The 2/3 height peak positions are indicated by the dots in the diagram.

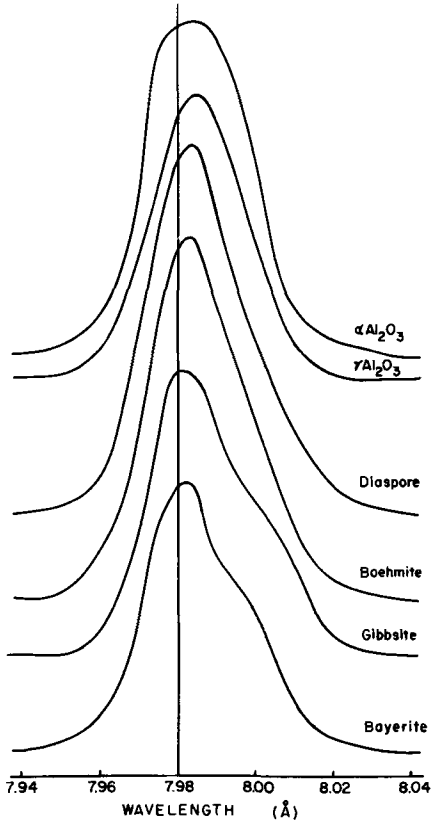

Fig. 2. Al Kβ emission spectra of the same materials shown in Fig. 1. Note the long wavelength shoulder of gibbsite and bayerite.

Figure 1 is a compilation of the O Kα emission bands from the standards. Each band consists of a well-defined main peak with a tail on the longer wavelength side. The γ-alumina and diaspore, corundum and boehmite, gibbsite and bayerite form comparable pairs at similar wavelengths. With corundum as the reference, the O Kα peaks from γ-alumina and diaspore occur at longer wavelengths while gibbsite and bayerite are at shorter wavelengths. The association of greater widths of the O Kα peaks from the $Al(OH)_3$ compounds together with their occurrence at shorter wavelengths is a distinctive feature. γ-alumina also exhibits a broad band, but it falls at significantly longer wavelength than the peaks from $Al(OH)_3$ compounds.

Table I. O Kα and Al Kβ wavelength shifts of the hydroxides, oxyhydroxides, and oxides of aluminum. The wavelength of the band from corundum was used as the reference position.

Standard	Formula	ΔOK (Å × 10⁴)	OKα width 2/3 ht (Å × 10⁴)	ΔAlKβ (Å × 10⁴)	AlKβ width 2/3 ht (Å × 10⁴)
Corundum	α-Al_2O_3	0	91	0	27
γ-Alumina	γ-Al_2O_3	45	107	1	23
Diaspore	AlO(OH)	67	86	−11	21
Boehmite	AlO(OH)	−16	86	−7	25
Gibbsite	$Al(OH)_3$	−99	104	−14	20
Bayerite	$Al(OH)_3$	−120	104	−23	20

Figure 2 is a compilation of the Al Kβ emission bands from the powder standards. The separation of 2/3 peak position is not very pronounced. Another difficulty is the low intensity of the Al Kβ emission. Consequently, a clear-cut distinction cannot be made by position alone. The shape of the curves can be used to distinguish the $Al(OH)_3$ compounds from the lower hydrates by means of the peak shoulder on the long wavelength side of the emission band.

Application to corrosion problems.—Wafers cut from an aluminum ingot were oxidized in hydrothermal cold seal pressure vessels under the conditions shown in Table II. The O Kα and the Al Kβ emission bands were recorded without disturbing or removing the oxide layer. The results are given in Table II and indicate that a complex oxide layer is formed.

In the case of the O Kα peaks there is a definite change of wavelength toward that obtained from the aluminum trihydroxides as the oxidation time is increased. The presence of bayerite [$Al(OH)_3$] was confirmed on sample C by x-ray diffraction, but no crystalline products could be detected on the other samples with thinner oxide layers.

The use of the Al Kβ peak shift is somewhat complicated by the presence of the aluminum substrate. The electron beam voltage must be drastically reduced for the thin oxide coatings in order to limit the Al Kβ emission to just the oxide film. Using this limitation, one can estimate the oxide layer thickness by assuming an electron beam range relation of $R(mg/cm^2) = 0.572\ E^{1.67}$ with E in MeV (9) and a linear loss of maximum electron beam energy (E) with depth in the oxidation layer that is assumed to have a density of 2.5. The maximum electron beam energy is taken as the largest beam potential which does not produce aluminum x-radiation from the aluminum substrate. Sample A, the thinnest oxide layer, was calculated to be about 0.5 μm. Because of the substrate interference and the lower intensity of x-ray emission, the Al Kβ band is not as useful as the O Kα band.

Summary

Shifts in the x-ray emission band positions and shapes from aluminum and especially oxygen for the hydroxides, oxyhydroxides, and oxides of aluminum have been shown to be large enough to be used to differentiate among the six compounds dealt with in this study. Unknown reaction products can be identified through the application of the data contained in Table I and Fig. 1 and 2, provided that the unknown is a single phase of one of the compounds.

In the case of complex corrosion layers consisting of more than one compound, there is a problem of

Table II. Results from the corrosion study of oxidation layers on aluminum. Bayerite was detected by x-ray diffraction on sample C.

Sample	Temp, (°C)	Pressure, (psi)	Time	$\Delta OK\alpha$ (Å × 10^4)	$OK\alpha$ width 2/3 ht (Å × 10^4)	$AlK\beta$ (Å × 10^4)	$AlK\beta$ width 2/3 ht (Å × 10^4)	Electron beam voltage of $AlK\beta$ series (kV)
Unoxidized	—	—	—	—	—	−176	27	20
A	125	2900	5 min	−16	99	−8	25	8
B	125	2900	4 hr	−67	88	−14	22	15
C	100	2800	20 hr	−96	91	−10	23	15

superposition of emission bands from the various compounds; consequently the layers cannot be positively identified by this method. On the other hand, chemical changes in oxidation layer as thickness increases can be observed quite easily, and trends in the dominating chemistry and short-range structures are indicated by the band positions and shapes. This method can also be extended to study changes in chemistry with depth in stratified oxidation layers. By incrementing the electron beam voltage over a range from about 3 to 40 keV, the maximum depth of x-ray emission will be incremented over a range of about 0.1 to 15 μm. Thus the x-ray emission bands recorded at various keV settings will contain the sum of x-ray emission from all layer components to that depth.

The oxygen band is not as well resolved as reported recently by Chun and Handel (7). However, it is advantageous to use the electron microprobe to study peak shifts because they can be recorded quickly (15 min per scan) on a linear intensity scale. Only a very small sample is required and the method is nondestructive. The ability to study very small areas (5-100 μm in diameter) on a sample surface makes this aspect of microprobe analysis particularly useful in the study of layers of nonuniform thickness. It will also be of considerable value in studies of how layers vary from grain to grain on chemically and structurally complex alloy systems.

The main advantages of this technique is that one can study types of surface layers *in situ* under conditions of relatively high spatial resolution with respect to area and depth. This work stresses the use of the oxygen K-emission band which is essentially free of interference from the metallic substrates. By using the newly introduced clinochlore analyzing crystal one can detect oxide layers as thin as about 25Å (10). In comparison, Auger electron spectroscopy will undoubtedly emerge as a complementary tool, but it is not yet clear as to what its relative importance will be eventually. Certainly the problem of sample decomposition is common to both techniques. Resolution in most Auger spectrometers is such that one could not measure the chemical shift as sensitively as reported here. Finally, by using x-ray instrumentation with a broad electron beam (up to ½ in. diameter), the thickness sensitivity could be improved to detect oxide layers as thin as about 2Å (one atomic layer) which is comparable to that in Auger spectrometry.

As we increase our knowledge of how a material's chemistry and structure influence the wavelength and shape of the x-ray emission bands this method should became more useful as a general method for characterization of surface layers on materials.

Acknowledgment

This work was done with the support of the Office of Naval Research, contract number (NR-032-502).

Manuscript submitted May 8, 1969; revised manuscript received Sept. 29, 1969.

Any discussion of this paper will appear in a Discussion Section to be published in the December 1970 JOURNAL.

REFERENCES

1. L. G. Parratt, *Rev. Mod. Phys.*, **31**, 616 (1959).
2. D. H. Tomboulian, *Handbuch der Physik*, **30**, 246 (1957).
3. E. W. White and G. V. Gibbs, *Am. Mineralogist*, **54**, 931 (1969).
4. E. W. White and R. Roy, *Mat. Res. Bull.*, **2**, 395 (1967).
5. H. M. O'Bryan and H. W. B. Skinner, *Proc. Roy. Soc. (London)*, **A176**, 229 (1940).
6. D. W. Fischer, *J. Chem. Phys.*, **42**, 3814 (1965).
7. H. V. Chun and D. Hendel, *Z. Naturforsch.*, **22a**, 1401 (1967).
8. W. L. Baun and E. W. White, *Anal. Chem.*, **41**, 831 (1969).
9. R. D. Birkhoff, *Handbuch der Physik*, **34**, 135 [Table 22] (1968).
10. W. H. Knausenberger, K. Vedam, E. W. White, and W. Zeigler, *Appl. Phys. Letters*, **14**, 43 (1969).

Effect of Nickel in Cr-Ni Stainless Steels on the Critical Potential for Stress Corrosion Cracking

H. H. Lee† and H. H. Uhlig*

Department of Metallurgy and Materials Science, Massachusetts Institute of Technology, Cambridge, Massachusetts

ABSTRACT

Increasing amounts of alloyed Ni in 20% Cr stainless steels improve resistance to stress corrosion cracking in part by shifting to more noble values the critical potentials below which failures are not observed. When the critical potential for any alloy becomes more noble than the corresponding corrosion potential (>26% Ni) the alloys are resistant to $MgCl_2$ at 130°C for >200 hr. Nevertheless, rapid failure of such alloys up to 35% Ni, and probably including 45% as well, can be induced by anodic polarization to a potential which is noble to the corresponding critical value.

Gradual drift of corrosion potentials to more noble values, eventually exceeding the critical potentials, is the likely cause of stress corrosion cracking in practice of <45% Ni stainless steels. Above 45% Ni, structural factors at the surface of plastically deforming alloys become dominant, and failures do not occur regardless of the prevailing potential. Pure nickel is anodic to the 20% Cr-Ni stainless steels and can be used as sacrificial anode to protect them cathodically against stress corrosion cracking. The over-all data support the mechanism of failure based on stress sorption cracking.

The critical potential for stress corrosion cracking (scc) of 18-8 stainless steel in boiling $MgCl_2$ above which failure occurs, but not below, has been reported by Hines and Hoar (1), Barnartt and van Rooyen (2), Smialowski and Rychik (3), and by Uhlig and Cook (4); and similarly in boiling $CaCl_2$ by Brennert (5). Most of the reported values are consistent with the value -0.15 ± 0.01V (SHE) despite variations of chloride concentration, temperature, and applied stress, plus the use of several commercial sources of 18-8 stainless steels in the tests. Uhlig and Cook (4) showed in addition that the critical potential [-0.145V (SHE)] for Type 304 cold-rolled 18-8 stainless steel in $MgCl_2$ boiling at 130°C is shifted by tens of millivolts in the noble direction by salt additions which act as inhibitors of scc, *e.g.*, sodium acetate or sodium nitrate. When the concentration of added salt was sufficient to shift the critical potential to a value more noble than the corrosion potential, cracking did not take place within the maximum test period (200 hr), whereas in the absence of added salts the cracking time was 1 hr or less. Minimum inhibiting concentrations approximated 1% sodium acetate or 2.5% sodium nitrate based on the weight of the $MgCl_2$ solution.

The effect of alloyed Ni to increase resistance of austenitic stainless steels to scc, and to confer essential immunity in amounts greater than 45 w/o (weight per cent) is well known both through laboratory tests and practical service exposures (6, 7). The beneficial effect of nickel has been attributed to higher stacking fault energy (8) leading to tangled rather than coplanar arrays of dislocations when the alloy is plastically deformed, thereby making crack propagation more difficult (9). However, coplanar arrays of dislocations, although seemingly necessary, are not a sufficient condition for scc, as was shown by examination of many different kinds of alloys. Other unknown factors apparently enter the mechanism in addition to dislocation arrangement (9-11).

The results on inhibiting salts cited above suggested that the effect of alloyed Ni may be to shift the critical potential for cracking to more noble values rather than to alter the metallurgical structure of the alloy, or that perhaps both factors are relevant. The present work was undertaken to explore this possibility.

† Electrochemical Society Student Member.
* Electrochemical Society Active Member.

Experimental

A series of stainless steels containing variable Ni was prepared in the laboratory from deoxidized-decarburized electrolytic iron, carbonyl nickel (courtesy International Nickel Company), and high-purity chromium obtained from the Electrometallurgical Company. Two exceptions were the high- and low-nitrogen 20% Ni alloys which were supplied by courtesy of the Naval Research Laboratory and prepared from electrolytic Fe and Cr, and carbonyl Ni. The former alloys were melted in vacuum, the furnace then filled with 1 atm purified N_2 and the melting continued for about 5 to 10 min. The latter step was essential because it had been shown earlier that austenitic pure stainless steels are relatively resistant to scc unless they contain a minimum amount of interstitial nitrogen (12-14). Casting was accomplished by drawing the melt from the N_2 atmosphere into 7 mm diameter Vycor tubing and quenching in water. The ingots were homogenized for 24 hr at 1050°C in argon and then water quenched. They were cold rolled to 0.04 in. (0.016 cm) equivalent to about 80% reduction in thickness. Chemical analyses are given in Table I. The lower N content of the 18.9% Cr, 20.0% Ni alloy was intentional. The lower N content of the 49.4 and 57.8% Ni alloys, on the other hand, compared to other alloys of the series

Table I. Composition of stainless steels (w/o)

Cr	Ni	C	N
18.6	9.4	0.002	0.14
18.6*	19.5	0.001	0.13
18.9*	20.0	0.001	0.036
20.4	25.7	0.003	0.18
19.9	30.8	0.001	0.19
20.8	34.8	0.002	0.15
19.7	49.4	0.006	0.07
18.7	57.8	0.006	0.06
17.8**	82.2	—	—

* Prepared by Naval Research Laboratory.
** Cr-Ni binary alloy cast in He. Used only for corrosion potential measurements.

was probably a result of diminished solubility of N in stainless steels of increasing Ni content (15). The solubility of N in pure Ni at 1600°C for example is about 0.001%.

Specimens were sheared to 1-3/4 x 3/16 x 0.04 in. (4.5 x 0.5 x 0.1 cm) and tested in the cold-rolled state with the rolling direction parallel to the long dimension. Cold-rolled specimens were chosen because of their shorter cracking times compared to times required for annealed specimens (13). Specimens were abraded to No. 0 emery paper, degreased in benzene, and pickled in 25 v/o (volume per cent) H_2SO_4, 25 v/o HCl at 90°C for 5 min followed by a pickle in 15 v/o HNO_3, 5 v/o HF at the same temperature and time. Specimens were immediately bent beyond the elastic limit to a span of 1-5/8 in. (4.1 cm), transferred by means of a metal gauge to insulated holders of the test apparatus, adjusted to a final span of 1-7/16 in. (3.7 cm) and held in this position by a compressed spring. The spring insured that tests in $MgCl_2$ boiling at 130°C were carried out under conditions of essentially constant flow stress. Failure time was recorded by an electric clock. Other details of the test have been described previously (13).

Controlled potential tests made use of the Heathkit or Wenking potentiostats. The 250 ml test cell (Fig. 1) was equipped with two opposing side arms separated by glass frits, each containing auxiliary electrodes of platinized titanium, and a center arm also separated by a glass frit in which a Luggin capillary was connected to a saturated calomel electrode at room temperature. Solutions in the side arm were of $MgCl_2$ of slightly lower concentration than the boiling solution inside the cell. Preliminary tests established that the geometry of the cell and the high conductivity of the electrolyte made any corrections for IR drop unnecessary. A Ni wire 0.025 in. (0.065 cm) diameter was spot welded to one end of the stressed specimen and completely encased in small diameter Teflon tubing in order to reduce any current reaching the wire. Because of accumulating electrolysis products, controlled potential runs were not carried out beyond 100 hr in comparison with simple immersion tests which were run to a maximum of 200 hr.

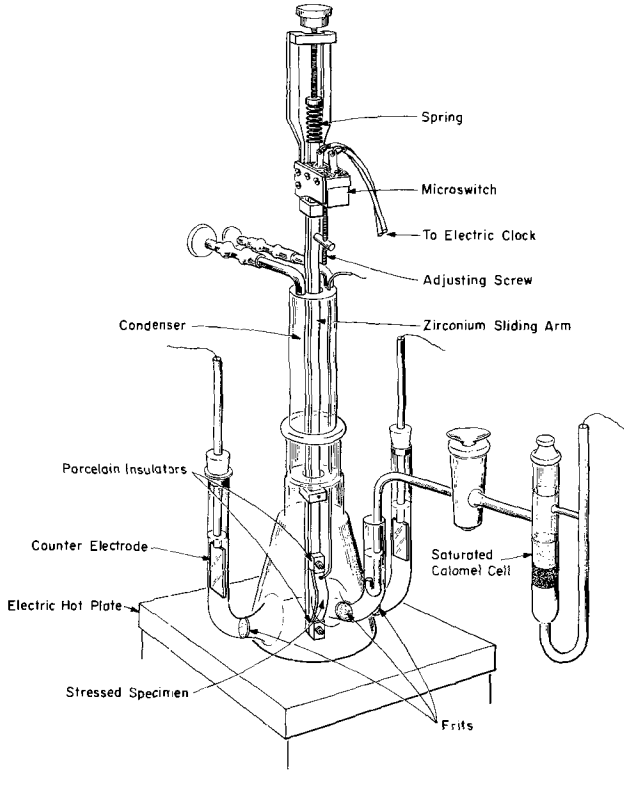

Fig. 1. Test cell for measuring critical potentials of stainless steels in boiling $MgCl_2$ solution.

Corrosion potentials were measured for the unstressed alloys partly immersed for at least 20 hr in the boiling $MgCl_2$ solution at 130°C avoiding immersion of the spot-welded junction to the connecting Ni wire. Barnartt and van Rooyen (2) showed previously that stress does not appreciably affect the potential behavior of stainless steels in $MgCl_2$ solution. All potentials are reported on the standard hydrogen scale, omitting corrections for liquid junction and thermal gradients.

Results

Figure 2 shows that failure time of the alloys in $MgCl_2$ at 130°C increases with Ni content. At and above 30.8% Ni, the alloys were not susceptible to scc within the maximum time of test (200 hr). The 19.5% Ni alloy shown in Fig. 2 is that containing 0.13% N. The similar alloy containing only 0.036% N did not fail within 200 hr, confirming previous results on the detrimental effect of interstitial nitrogen (12-14).

Anodic polarization of the otherwise resistant 30.8% and 34.8% Ni alloys induced total failure by cracking within a few hours. Pitting accompanied cracking at the most noble applied potentials. However, alloys containing 49.4% Ni or more (or the 20% Ni low-N alloy) could not similarly be made to fail when anodically polarized 10 or 20 mV more noble than the corrosion potentials. Prolonged anodic polarization or polarization to still more noble potentials served only to induce random pitting without cracking.

The relation of time to failure at various constant applied potentials for all susceptible alloys is shown in Fig. 3 and 4 together with corrosion potentials at the

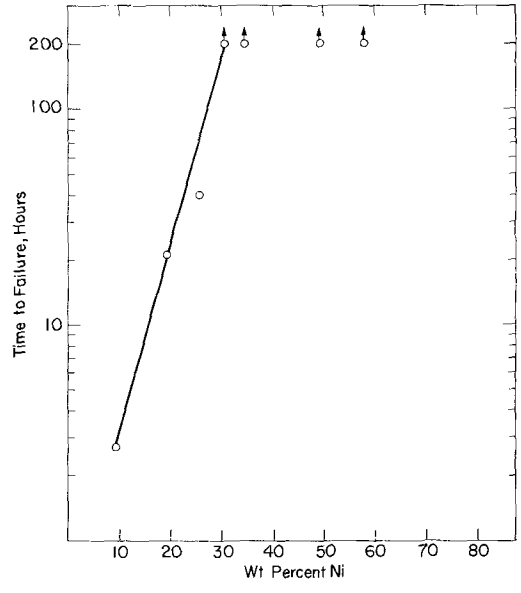

Fig. 2. Stress corrosion cracking of 20% Cr stainless steels in $MgCl_2$ at 130°C as a function of Ni content.

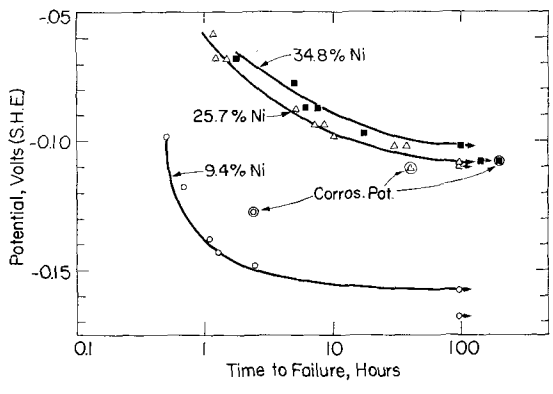

Fig. 3. Effect of applied potential on stress corrosion cracking of 20% Cr stainless steels in $MgCl_2$ at 130°C.

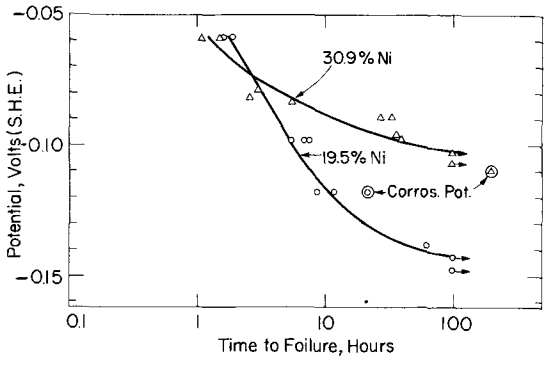

Fig. 4. Effect of applied potential on stress corrosion cracking of 20% Cr stainless steels in $MgCl_2$ at 130°C.

end of 24 hr. A critical potential below which the alloy did not fail within the maximum time of test (100 hr) is clearly defined for the 9.4% Ni alloy at −0.15 to −0.16V which is in reasonable agreement with corresponding potentials reported previously for commercial 18-8. For higher Ni alloys, the critical potentials lie at less negative (more noble) values. The precise value for each alloy at 100 hr is defined to within better than ±5 mV, and it is likely that such values also apply to longer times. The one apparent exception is the 19.5% Ni alloy for which the slope of potential *vs.* failure time is still appreciable at 100 hr. The critical potential for this alloy, corresponding to long failure times, may lie therefore somewhat below −0.14V.

A plot of critical and corrosion potentials (Fig. 5) shows that a crossover occurs at about 26% Ni. Although critical potentials for scc were not observed for alloys above 34.8% Ni, the corrosion potentials of high Ni alloys tend toward increasingly noble values. Surprisingly, the value for pure Ni drops to −0.18V which is consistently more active than the corrosion or critical potentials of any of the alloys. Barnartt and van Rooyen (2) previously observed that Ni, although initially active, may become noble to 18-8 after long exposure times, but their observations apply to $MgCl_2$ boiling at 146°C. At 130°C, a reversal of potential was never observed. The active value for Ni accounts for the observation of Cook (16) that even a small length of exposed Ni wire coupled to 18-8 specimens immersed in the $MgCl_2$ test solution serves to cathodically protect 18-8 against scc. In other words, Ni acts as a sacrificial anode. The coupled Ni wire, however, did not affect time to failure under conditions of controlled potential. The 49.4% Ni or 57.8% Ni alloys, for example, did not crack when anodically polarized using either Ni wire or a wire of the sample composition

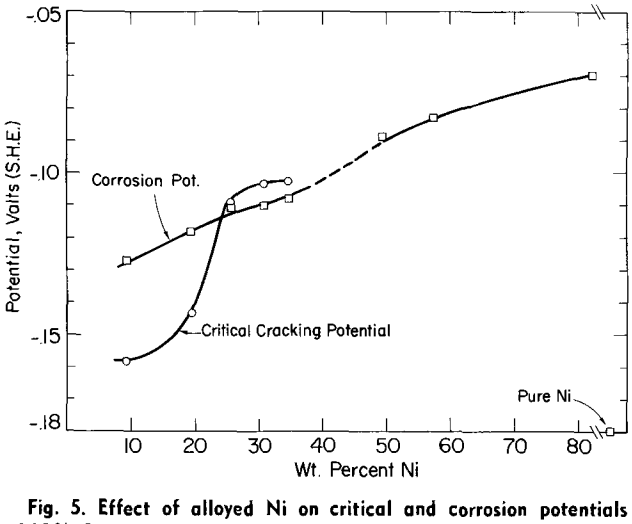

Fig. 5. Effect of alloyed Ni on critical and corrosion potentials of 20% Cr stainless steels in $MgCl_2$ at 130°C.

as the test specimen. Furthermore the measured critical potential for commercial 18-8 was the same using either Ni or 18-8 wires (16). Neumann and Griess (17) reported earlier that Ni-plated austenitic stainless steels, even when the coating was discontinuous, prevented scc in a solution containing dissolved oxygen and 50 ppm chloride at 300°C. Nickel in this instance presumably also polarized the stainless steel below its critical potential.

Discussion

The present results lend further support to the view that susceptibility to scc can occur only if the corrosion potential is noble to the critical potential. Alloyed Ni shifts the critical potential in the noble direction; when the corrosion potential is exceeded, cracking no longer occurs. This is the same relation reported for 18-8 by Uhlig and Cook (4) when inhibiting concentrations of sodium acetate or nitrate are added to $MgCl_2$ solution, the critical potential being shifted by the added salts to values which are noble to the corrosion potential. In other words, alloyed Ni up to 34.8% (and perhaps up to at least 45%) increases resistance of stainless steels to scc in part by a mechanism which parallels that of inhibiting salt solutions.

At least two factors may account for the crossover composition (Fig. 5) coming at about 26% rather than at 45% Ni corresponding to observed immunity in less pure or in commercial alloys. The first is that the present pure alloys contain only nitrogen as a sensitizing impurity. Commercial alloys, by way of comparison, contain many additional impurities which can accelerate cracking, a number of which were listed by Lang (18). The second factor is the relatively short exposure times used of necessity in the present tests. Copson (7) for example, ran tests up to 30 days. Furthermore, our results, as well as those of others (1, 2, 19), show that the corrosion potential tends in time to drift toward more noble values; hence it is probable that the corrosion potentials for alloys containing 30.8% and 34.8% Ni eventually become noble to their critical potentials, at which time but not before, failure takes place. Absence of an observed critical potential for alloys containing 49.4% or more Ni (probably >45% Ni) suggests that such alloys are immune to scc for structural reasons related for example to unfavorable dislocation arrays, low N solubility and similar factors.

Drift of Corrosion Potential and Pitting

Why does the corrosion potential drift toward more noble values? It is not considered likely that the passive film normally associated with stainless steels is accountable despite recurring mention of this possibility in the literature. There are several reasons for reaching this conclusion: (*i*) Potentiostatic polarization curves in $MgCl_2$ solutions at the test temperatures show no evidence of a passive region (2-4). Furthermore, (*ii*) addition of HCl to the $MgCl_2$ test solution which should break down or dissolve passive films shifts the corrosion potential in the noble direction opposite to the direction accompanying any supposed loss of passivity (2). In accord with the noble shift, scc of 18-8 stainless steel occurs in shorter times compared to the nonacidified $MgCl_2$ solution (20). (*iii*) Pre-exposure of unstressed 18-8 to $MgCl_2$ test solution at 154°C is found to affect subsequent scc behavior of the stressed alloy. This occurs not because a surface film is disrupted, as Hoar and Hines suggested (19), but instead because of a metallurgical change in the alloy induced at 154°C (21). The same subsequent shorter failure times are observed whether the specimens are heated at 154°C in the boiling $MgCl_2$ solution or in air. (*iv*) Finally, the corrosion potential of 18-8 in $MgCl_2$ at 130°C is active to the hydrogen electrode potential in the same solution indicating that the alloy is in the active state (4).

The trend of potential, therefore, may be caused by (*i*) changing composition of $MgCl_2$ solution, *e.g.*, changing *p*H, or accumulation of metal ions; (*ii*) changing

composition of the alloy surface, *e.g.*, preferential dissolution of specific alloy components or redeposition of cations like Ni^{++}; (*iii*) formation of a hydrated oxide film acting as a diffusion barrier [similar to a film of $Fe(OH)_2$ on iron exposed to water, or $PbSO_4$ on Pb exposed to H_2SO_4]. The first possibility was eliminated by changing the $MgCl_2$ solution after 24 hr and noting that the potentials of several alloys were unchanged in the new solution after a few minutes exposure. The second possibility is more difficult to assess, especially since relevant composition changes may concern only monolayer quantities. Certainly preferential dissolution of stainless steel components in an acid pickling solution is not observed. Furthermore, if Ni^{++} were to redeposit, the potential would drift in the active, not in the noble direction, since the corrosion potential of Ni in $MgCl_2$ at 130°C is decidedly active to that of any of the present stainless steels. A surface alloy change is possible, therefore, but not probable. Finally, the third possibility appears to be the most plausible because a surface film showing weak interference colors becomes visible after several hundred hours' exposure to $MgCl_2$ at 130°C (at 154°C the film is black). Chemical analysis of the resultant $MgCl_2$ solution for heavy metals compared to weight loss of the immersed stainless steel specimens suggests that the film after 190 hr exposure grows to a thickness of about 4500Å. The analysis indicates furthermore that the film probably consists mostly of $Fe(OH)_3$, perhaps partially hydrated, which might be expected on the basis that $Ni(OH)_2$ is more soluble than $Fe(OH)_3$ or $Cr(OH)_3$. Detailed data are given in Table II.

Although a more complete quantitative analysis of the film and its structure require further detailed investigation, there is no doubt that the film exists, that it is relatively thick, and that as it forms it appreciably reduces the uniform corrosion rate of stainless steels in $MgCl_2$ solution (20). It is the reduction in corrosion rate that likely accounts for the shift of corrosion potential in the noble direction. The responsible film is obviously not the usual passive film on stainless steels both because the film is very much thicker than the passive film, and because there is no evidence of a Flade potential.

The presence of a surface reaction product film explains why anodic polarization may induce corrosion pitting, particularly at noble potentials. The alloy dissolution rate is expected to be higher at local sites of the metal surface where the reaction product film is thinner or absent, hence corrosion tends to be localized. Pitting usually begins only after a certain induction period presumably because of the time necessary to establish an adequate surface film.

For the highest Ni alloys, it was observed that a linear succession of pits often tended to localize in the areas of maximum tensile stress and that failure therefore could be interpreted as occurring perhaps by pitting rather than by cracking. It is probable, however, because nucleation of pits is usually random, that in such instances cracks form first, and that the resultant crevices become favored sites for accelerated localized attack because of exposed film-free metal. A linear succession of pits, therefore, was interpreted as evidence of prior failure by scc.

Mechanism of scc

Several mechanisms of scc have been proposed, the many details of which lie outside the scope of the present paper. Discussion will be limited to the electrochemical theory dependent on anodic dissolution of metal atoms at the tip of a crack, and to the theory of stress sorption cracking dependent on dissociation of strained metal atom bonds at the crack tip weakened by adsorption of damaging ions (22). On the basis of the electrochemical mechanism, it is not certain why alloyed Ni should shift the critical potential for scc in the noble direction. It can be assumed, for example, as in typical instances of cathodic protection, that the critical potential is related to the open-circuit anode potential. Hines and Hoar made this assumption (1). Then the anode potential can be assumed to move in the more noble direction the higher the Ni composition for reasons similar to those applying to observed shift of the corrosion potential. But the fact that the corrosion potentials for 30.8% and 34.8% Ni stainless steels are *active* to their respective critical potentials casts doubt on this possibility, as well as on any model of scc based on a galvanic cell the anode of which is situated at the tip of a growing crack. The corrosion potential of a galvanic cell must always be noble to the open-circuit anode potential; the inverse can never occur. Assuming that only partial cathodic polarization toward the open-circuit anode potential suffices to prevent scc is not of any help to the electrochemical model because such polarization always shifts the potential in a direction active, not noble, to the corrosion potential.

Bearing on this matter are observations that anodic polarization curves for 18-8 in $MgCl_2$ at 130°C show no evidence of increased polarization (corresponding to decreased corrosion) in the presence of sodium acetate which inhibits scc (4). Furthermore, anodic polarization curves in $MgCl_2$ at 130°C as obtained presently for the 20% Ni low-N alloy which resists scc are identical to the corresponding curves for the 19.5% Ni high-N alloy which is susceptible to scc.

On the basis that the mechanism of stress sorption cracking applies instead, Ni shifts the critical potential in the noble direction because Ni has less affinity for Cl^- than does either Cr or Fe. For example, the standard free energies of formation of $NiCl_2$, $FeCl_2$, and $CrCl_2$ at 25°C are −65.1, −72.2, and −85.2 kcal, respectively (23). Hence, if these values are used as a qualitative measure of Cl^- affinities, a more positive applied potential is required the higher the Ni content, as is observed, to affect adequate adsorption of Cl^- on defect sites of plastically deforming alloy accompanying reduction of the cohesive strength of surface metal bonds. On this view, electrochemical factors may affect the corrosion potential which in turn determines whether adsorption of Cl^- is favorable or unfavorable for crack initiation and growth, but the mechanism is not one of dissolution of metal atoms at the tip of the crack. It is one of physical parting of metal atoms instead for which adsorbed components of the environment play a major role, analogous to the role of specific metal atoms as cause of liquid metal embrittlement, *e.g.*, cracking of stressed brass by liquid Hg. The critical potential is interpreted accordingly as that value above which Cl^- ions adsorb on appropriate defect sites of plastically deforming stainless steel, and below which Cl^- ions desorb.

In addition to factors of the environment leading to adsorption, it is also obviously necessary for scc that the surface defect structure of the metal must be favorable for adsorption. For example, the 20% Ni low-N alloy is found not to crack despite anodic polarization to relatively noble values, contrary to the 19.5% Ni high-N alloy which fails whether polarized or not. Further evidence comes from the lack of failure of alloys containing 49.4% or more Ni despite anodic polarization.

The above considerations therefore lead to the conclusion that necessary and sufficient conditions for scc are (*i*) a potential favorable to adsorption of damaging components of the environment on appropriate defect sites of the metal surface, (*ii*) both a metallurgical

Table II. Chemical analyses of $MgCl_2$ solution after immersion of stainless steel specimens for 190 hr at 130°C

	Cr	Ni	Fe
Composition of alloy	19.0%	21.3%	(59.7%)
Heavy metal ions in solution	20.4%	33.2%	(46.4%)
Wt. loss of 190 cm^2 stainless steel spec.	= 11.9 mg		
Total Cr, Ni, Fe found in $MgCl_2$ solution	= 26.5 mg		
Difference (assumed equal to O or OH)	= 14.6 mg		
	or	0.077 mg/cm^2	

0.077 mg OH/cm^2 = 0.161 mg $Fe(OH)_3/cm^2$
Thickness of metal hydroxide (d = 3.6) = 4470Å

structure and tensile stress which produce surface defect sites on which adsorption succeeds.

Acknowledgment

This research was supported by the United States Army Research Office-Durham to whom the authors express their appreciation.

Manuscript submitted June 20, 1969; revised manuscript received ca. Sept. 15, 1969. This was Paper 82 presented at the Detroit Meeting, Oct. 5-9, 1969.

Any discussion of this paper will appear in a Discussion Section to be published in the December 1970 JOURNAL.

REFERENCES

1. J. Hines and T. Hoar, *J. Appl. Chem. (London)*, **8**, 764 (1958).
2. S. Barnartt and D. van Rooyen, *This Journal*, **108**, 222 (1961).
3. M. Smialowski and M. Rychik, *Corrosion*, **23**, 218 (1967).
4. H. H. Uhlig and E. W. Cook, Jr., *This Journal*, **116**, 173 (1969).
5. S. Brennert, *Jernkont. Ann.*, **144**, 560 (1960).
6. M. Scheil, *J. Iron and Steel Inst.*, **174**, 218 (1953).
7. H. Copson in "Physical Metallurgy of Stress Corrosion Fracture," T. Rhodin, Editor, p. 247, Interscience Publishers, New York (1959).
8. W. Robertson and A. Tetelman in "Strengthening Mechanisms in Solids," p. 217, Am. Soc. Metals, Metals Park, Ohio (1962).
9. P. Swann, *Corrosion*, **19**, 102t (1963).
10. D. Douglass, G. Thomas, and W. Roser, *ibid.*, **20**, 15t (1964).
11. T. Evans and D. Burr, *Brit. Corros. J.*, **1**, 192 (1966).
12. H. Uhlig, R. White, and J. Lincoln, Jr., *Acta Met.*, **5**, 473 (1957).
13. H. Uhlig and R. White, *Trans. Am. Soc. Metals*, **52**, 830 (1960).
14. H. Uhlig, "Corrosion and Corrosion Control," p. 280, John Wiley & Sons, Inc., New York (1963).
15. J. Humbert and J. Elliott, *Trans. AIME*, **218**, 1076 (1960).
16. E. Cook and H. Uhlig, Unpublished data.
17. P. Neumann and J. Griess, *Corrosion*, **19**, 345t (1963).
18. F. Lang, *ibid.*, **18**, 378t (1962).
19. T. Hoar and J. Hines, *J. Iron Steel Inst.*, **182**, 124 (1956).
20. H. Uhlig and J. Lincoln, Jr., *This Journal*, **105**, 325 (1958).
21. H. Uhlig and J. Sava, *Corros. Sci.*, **5**, 291 (1965).
22. H. H. Uhlig in "Proceedings, Fundamental Aspects of Stress Corrosion Cracking, Ohio State University," R. Staehle, Editor, p. 86, National Association of Corrosion Engineers, Houston, Texas (1969).
23. W. Latimer, "Oxidation Potentials," Prentice-Hall, New York (1952).

Magnetic Properties of Electrodeposited Nickel-Iron-Phosphorus Thin Films

Koichi Mukasa, Masayoshi Sato, and Masao Maeda

Department of Electronics, Faculty of Engineering, Hokkaido University, Sapporo, Japan

ABSTRACT

The effect of hypophosphite ions in the plating bath on the uniaxial magnetic anisotropy in nickel-iron thin films electrodeposited on uniaxially scratched substrates was investigated. It was observed that the presence of hypophosphite ion in the plating bath results in a decrease of the uniaxial magnetic anisotropy. This decrease of the uniaxial magnetic anisotropy was found to be due to the decrease of the saturation magnetization of the films electrodeposited from the plating bath containing hypophosphite ions. Three possibilities for the effect of the phosphorus on the saturation magnetization are considered.

Nickel-iron thin films which were electrodeposited in an applied magnetic field may prove useful as computer memory and logic elements. Recently, the electrodeposited thin films have been investigated by many authors because of the simplicity of their preparation. It is known that the nature of the substrate surface affects the magnetic properties of thin films. For example, the magnetic properties of electrodeposited films are known to be a very sensitive function of the scratches of the substrate surface (1).

Many workers have shown that one can achieve uniaxial magnetic anisotropy in deposited permalloys by depositing on a surface scratched predominantly in one direction (2-5). And, in a previous paper (6), it was reported that this uniaxial anisotropy constant K_u is described as

$$K_u = \frac{1}{2} \cdot (N_t - N_p) \cdot I_s^2 + \frac{3}{2} \cdot 2\sigma \sin^2\theta \qquad [1]$$

where N_t and N_p are the demagnetizing factor of the film in the direction perpendicular and parallel to the scratches, respectively, σ is the tensile stress in the film, and λ is the saturation magnetostrictive constant.

It is known that the presence of hypophosphite ions in the plating bath results in phosphorus in the deposits (7, 8). This is true also in the case of electroless deposition (9). Mechanical properties (8, 9), metallurgical structure (10-12), and magnetic properties (13-15) of Ni-P and Ni-Fe-P films have been investigated in detail. And it was observed for films electrodeposited on a smooth surface that the coercive force and anisotropy field of Ni-Fe-P films are small compared with that of Ni-Fe films (7). In this work the effects of sodium hypophosphite ($NaH_2PO_2 \cdot H_2O$) in the plating bath on the uniaxial magnetic anisotropy in nickel-iron thin films electrodeposited on uniaxially scratched substrates were investigated. That is, the uniaxial magnetic anisotropy studied in this work is not the anisotropy induced in the film by depositing in the presence of magnetic field, but the anisotropy achieved in the film by depositing on a surface scratched predominantly in one direction.

Experimental Procedures

Films used in this work were electrodeposited at room temperature. The chemical compositions of the electrolyte were $NiSO_4 \cdot 6H_2O$ (140 g/liter), $FeSO_4 \cdot$

$7H_2O$ (20 g/liter), H_3BO_3 (15 g/liter), NH_4Cl (16 g/liter), and $NaH_2PO_2 \cdot H_2O$ (0 ~ 5 g/liter). A rolled nickel plate was used as the anode. The current density of deposition was 25 mA/cm². Films used for the measurement of magnetic torque curves and of saturation magnetization were electrodeposited on scratched copper substrate. The diameter and the thickness of films used for the measurement of the torque curves were 1 cm and 500Å. The diameter of films used for the measurement of the saturation magnetization was 0.5 cm and the five films of 5000Å in thickness were measured in a group. The saturation magnetization of both films electrodeposited from the bath containing 0 and 5 g/liter hypophosphite concentration did not vary much with thickness for thickness less than 5000Å. And, especially for films electrodeposited from the bath with hypophosphite, it was observed that the variation of the saturation magnetization was small. Thus the films of 5000Å in thickness were used for the measurement of the saturation magnetization because of the convenience of the facilities in the Sucksmith's balance measurement. Films used for the measurement of the film thickness and for the observation of the electron micrography were electrodeposited on the substrate which was made from ordinary microscope cover glass which had been coated with vacuum evaporated layers of chromium and copper.

The torque curves were measured by means of a torque magnetometer in a uniform magnetic field of 13 kOe at room temperature. The saturation magnetization was measured by Sucksmith's ring balance in a nonuniform magnetic field of about 10 kOe. The film thickness was measured by multibeam interferometry. For the observation of electron diffraction and transmission electron micrography, the copper layer attached to the deposits having thickness of 250Å was dissolved in a solution of sodium cyanide (20 g/liter). The electron beam which was accelerated by 130 kV was perpendicular to the surface of the films. The content of phosphorus in the films was measured by the use of the x-ray microanalyzer and colorimetric method.

Results and Discussion

Thickness of films.—In order to examine the effects of phosphorus on the film thickness, the thicknesses of the films electrodeposited from the bath with and without the hypophosphite were measured as a function of the plating time, and the results are shown in Fig. 1. It is seen in Fig. 1 that the measured thicknesses of the films increase with increasing plating time for the plating time less than 30 sec when the films are electrodeposited from the plating bath without hypophosphite, but the measured thickness of the films is thicker than the thickness which is calculated from the weight of the film and the density data (16) by about 25%. Thus it is considered that the thin films electrodeposited from the plating bath without hypophosphite include voids, as was discussed in a previous report (6).

In the case of the films electrodeposited from the plating bath with hypophosphite, it was known that the films contain phosphorus (5). The measured thickness of the films with phosphorus is equal to the thickness of the films without phosphorus as seen in Fig. 1, so that the sodium hypophosphite content in the bath (0 ~ 5 g/liter) seems to have no influence on the thickness of the films. If it is assumed that the density of Ni-Fe-P alloys is equal to the density of Ni-Fe alloys, the thicknesses of films both with and without phosphorus were the same when it was calculated from the weight of the films. Accordingly, it is also considered that the films containing phosphorus will include voids, as well as in the case of the deposits without phosphorus.

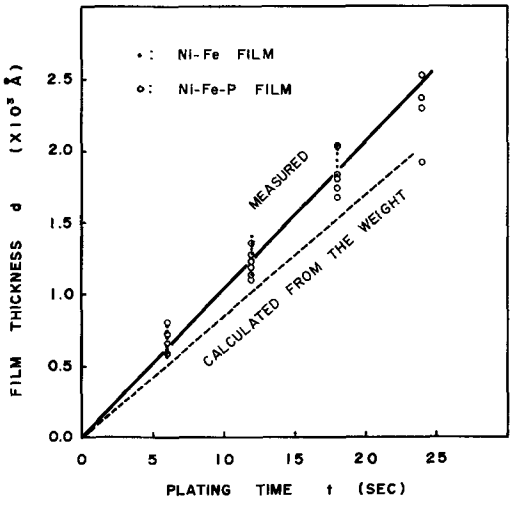

Fig. 1. Thickness of films, *d*, plotted as a function of plating time, *t*, for Ni-Fe and Ni-Fe-P thin films {$NaH_2PO_2 \cdot H_2O$ (5 g/liter) in plating bath}.

Figure 2 shows the two interference patterns by multibeam interferometry for the films electrodeposited from the plating bath containing hypophosphite; one is for the film electrodeposited with stirring the plating bath during the deposition and the other is for the film electrodeposited without stirring. It is seen in Fig. 2(a) that, for the film electrodeposited

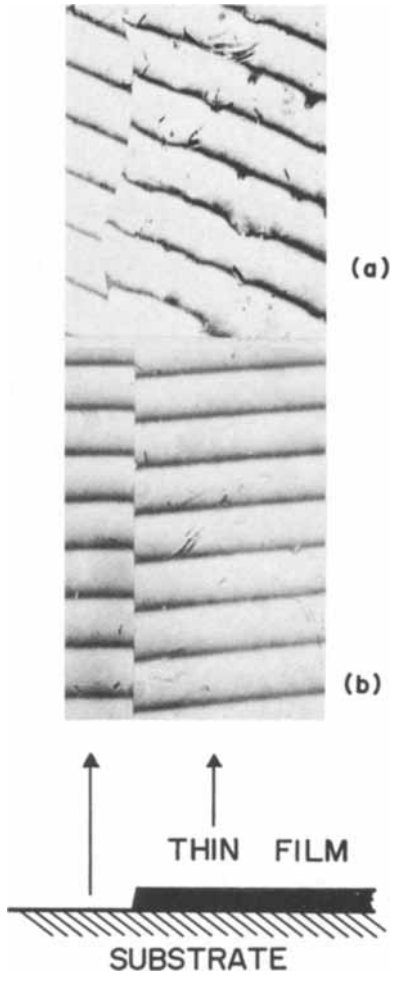

Fig. 2. Interference patterns by multibeam interferometry for the films electrodeposited from the plating bath containing hypophosphite: (a) for films electrodeposited without stirring the plating bath, (b) with stirring. The thickness of the films is about 1500Å.

without stirring during the deposition, the fringes of the interference pattern are spaced irregularly; that is, the surface roughness of the films is observed, but the roughness vanishes when the plating bath is stirred during the electrodeposition as seen in Fig. 2(b). Accordingly, it may be said that the surface roughness of the films containing phosphorus is due to hydrogen bubble formation.

Uniaxial magnetic anisotropy of Ni-Fe-P films.—Figure 3 shows the measured effective uniaxial magnetic anisotropy constant, K_u^* (17), as a function of the concentration of the hypophosphite in the plating bath from 0 to 5 g/liter. The measured K_u^* was calculated from the torque maximum divided by an apparent volume of the films. The measured K_u^* in Fig. 3 decreases with increasing hypophosphite concentration. For example, the values of the measured K_u^* are about 1.3×10^5 erg/cc and 4.0×10^4 erg/cc for the film without hypophosphite and for the film more than 2 g/liter hypophosphite concentration, respectively.

Since the composition of films used in this work is about 75Ni-25Fe, it is considered that the measured K_u^* is due to shape contribution alone as magnetostriction contribution will be small for this composition (6). The effective uniaxial magnetic anisotropy constant, K_u^*, which is a function of the volume of the nonmagnetic inclusions, of thin films electrodeposited on a surface scratched predominantly in one direction is described as

$$K_u^* = \frac{v}{v^*} \cdot K_u = \frac{v}{v^*} \frac{1}{2} (N_t - N_p) I_s^2 = \frac{1}{2} (N_t - N_p) \cdot \frac{v^*}{v} \cdot I_s^{*2} \quad [2]$$

where v^* and v are the volume of magnetic films with and without the nonmagnetic inclusions, respectively. As was stated in a previous section, the value of v^*/v was constant for both Ni-Fe and Ni-Fe-P films. In an attempt to explain the behavior of the measured K_u^* in Fig. 3, the effective saturation magnetization, I_s^*, was measured as a function of hypophosphite concentration and is shown in Fig. 4. It is seen in Fig. 4 that the effective saturation magnetization, I_s^*, decreases with increasingly hypophosphite concentration and becomes constant for films with more than 2 g/liter hypophosphite. It may be understood qualitatively from the decrease of I_s^* in Fig. 4 and Eq. [2] that the value of K_u^* decreases with increasing hypophosphite.

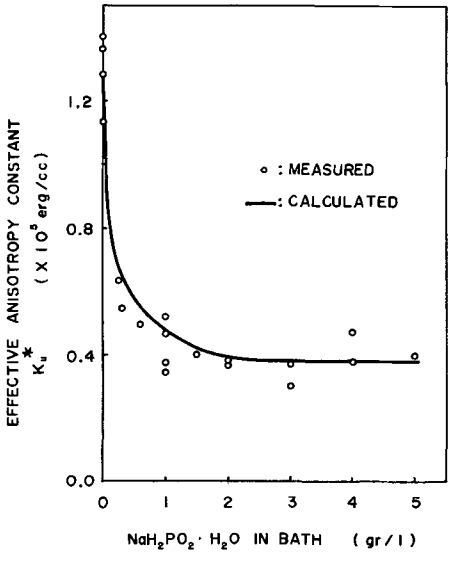

Fig. 3. Effective uniaxial magnetic anisotropy constant, K_u^*, plotted as a function of the concentration of the hypophosphite in the plating bath, together with the solid curve calculated from Eq. [2].

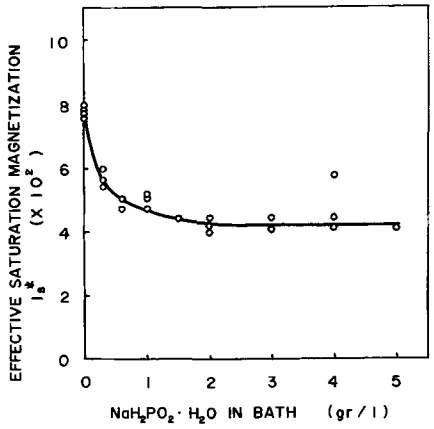

Fig. 4. Effective saturation magnetization, I_s^*, plotted as a function of the concentration of the hypophosphite in the plating bath.

Next, we shall calculate the value of K_u^* as a function of hypophosphite concentration from Eq. [2] using the measured values of I_s^* in Fig. 4. The values of $(N_t - N_p)$ are determined from the measured values of K_u^* and I_s^* for films without phosphorus. Assuming the constant value of $(N_t - N_p)$ calculated above remains unchanged in the cases of the deposits containing phosphorus, the calculated K_u^* is shown in Fig. 3 by the solid curve. It is seen in Fig. 3 that the measured K_u^* is in good agreement with the calculated K_u^*. Accordingly, it is concluded that the decrease of the effective uniaxial magnetic anisotropy constant in Ni-Fe-P films is due to the decrease of the effective saturation magnetization of the films with phosphorus. Thus, the variation of the measured K_u^* in Fig. 3 is well interpreted in terms of the variation of the effective saturation magnetization, I_s^*, in Fig. 4. And the assumption that the value of $(N_t - N_p)$ is constant may be valid since the surface roughness, which affects the value of $(N_t - N_p)$, of films electrodeposited on scratched substrate surfaces probably does not vary with the concentration of the hypophosphite ions in the plating bath.

Effects of the phosphorus on the saturation magnetization.—As was seen in Fig. 4, the effective saturation magnetization, I_s^*, decreases with increasing hypophosphite concentration in the bath. On the other hand, no change in thickness and in weight with hypophosphite concentration was observed as was stated in the first section. Thus it becomes evident that the saturation magnetization, I_s, varies with hypophosphite concentration. It has been observed that the composition of films electrodeposited without hypophosphite in the bath was about 75Ni-25Fe, that iron concentration in the film increases with increasing hypophosphite concentration, and that the Fe-Ni ratio and the phosphorus concentration are constant for films electrodeposited with more than 2 g/liter hypophosphite concentration. Thus it will be considered that the decrease of the saturation magnetization does not depend on the increase of the Fe-Ni ratio but on the increase of phosphorus content in the film. And it is considered that the saturation magnetization becomes constant as shown in Fig. 4 because of the phosphorus content becoming constant for films electrodeposited with more than 2 g/liter hypophosphite concentration. Thus the result that the uniaxial magnetic anisotropy becomes constant as shown in Fig. 3 may be due to the result that the saturation magnetization becomes constant as shown in Fig. 4.

We discuss why the saturation magnetization, I_s, decreases with increasing hypophosphite concentration. The electron transmission micrographs and electron

transmission diffraction patterns of the film are shown in Fig. 5(a) and (b); (a) is for the films without phosphorus and (b) is for the films with phosphorus. It is seen in Fig. 5 that the diffraction pattern for the films without phosphorus can be indexed as a face-centered-cubic structure. It is also seen in Fig. 5 that, with increasing hypophosphite concentration, the diffraction line of the films becomes broader. Therefore, as effects of the phosphorus on I_s* of the electrodeposited Ni-Fe films, three possibilities can be considered.

1. In Fig. 5(b), it is observed that the diffraction rings for the films with phosphorus become broader. Goldenstein *et al.* (10) obtained a similar result concerning the diffraction pattern of chemically deposited Ni-P films, and concluded that Ni-P deposits are amorphous liquidlike structures. It may then be assumed from the diffraction pattern shown in Fig. 5(b) that the electrodeposited Ni-Fe-P films used in this work are partially amorphous or that the lattice of the films is distorted. Then the decrease of saturation magnetization may be explained.

2. In Fig. 5(b), it is observed that the diffraction rings become broader, but a few reflections in the diffraction patterns are distinguishable. Graham *et al.* (9) obtained a similar result concerning the diffraction pattern of chemically deposited Ni-P films and concluded that Ni-P deposits were polycrystalline and that phosphorus dissolves in crystalline nickel-iron. Therefore, on the basis of his viewpoint, it may be said that according to the band theory proposed by Stoner the magnetic moment decreases.

3. In Fig. 5(b), it is observed that the diffraction rings become broader, and it is seen from the micrographs that the grain, if what is seen in the micrographs is grain, becomes smaller. Graham *et al.* (9) obtained a similar result concerning the electron diffraction and the micrography of chemically deposited Ni-P films, and concluded that this result was due to the effect of fine grain size. Therefore, following his conclusion, it may be said that the decrease of saturation magnetization is due to superparamagnetism, which was discussed for isolated small single-domain particles and closely packed ferromagnetic films with different strengths of interaction (18).

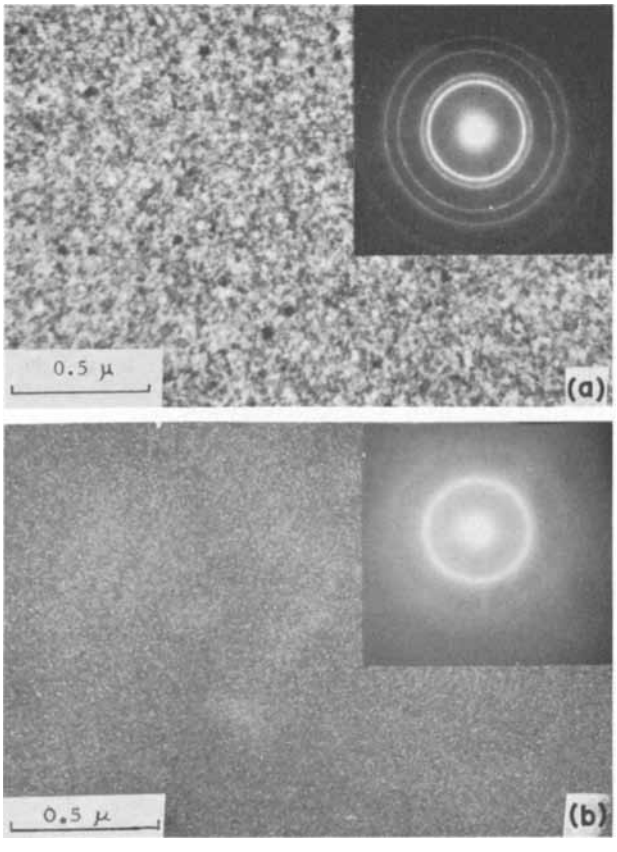

Fig. 5. Electron transmission micrographs and electron transmission diffraction patterns of the films without phosphorus (a) and with phosphorus (b).

Summary

1. It was observed that the presence of hypophosphite ions in the plating bath results in a decrease of the effective uniaxial magnetic anisotropy in nickel-iron thin films electrodeposited on unidirectionally scratched substrates.

2. It was also observed that the presence of hypophosphite ions results in a decrease of saturation magnetization of films.

3. The decrease of the effective uniaxial magnetic anisotropy was found to be due to the decrease of the saturation magnetization of films electrodeposited from the plating bath containing hypophosphite ions.

4. As effects of the phosphorus on the saturation magnetization of nickel-iron thin films, three possibilities are considered.

Acknowledgments

The authors would like to thank Professor T. Takeyama for his advice, Mr. G. Tomita for his cooperation in taking the electron micrographs, Professor M. Nagayama and Dr. S. Kawamura for their advice on the colorimetric method and for supplying the microbalance, and Dr. H. Fujiwara for his advice on multibeam interferometry.

Manuscript submitted July 10, 1969; revised manuscript received Sept. 24, 1969.

Any discussion of this paper will appear in a Discussion Section to be published in the December 1970 JOURNAL.

REFERENCES

1. R. F. Soohoo, "Magnetic Thin Films," p. 19, Harper & Row (1965).
2. J. C. Lloyd and R. S. Smith, *J. Appl. Phys.*, **30,** 274s (1959).
3. M. Maeda and K. Mukasa, *Japan. J. Appl. Phys.*, **4,** 557 (1965).
4. S. Morioka *et al.*, *J. Japan, Inst. Metals*, **28,** 722 (1964).
5. W. D. Doyle, *Phys. Stat. Sol.*, **17,** k67 (1966).
6. M. Satō, K. Mukasa, and M. Maeda, *Japan. J. Appl. Phys.*, **8,** 468 (1969).
7. W. O. Freitag, J. S. Mathias, and G. DiGuilio, *This Journal*, **111,** 35 (1964).
8. M. Maeda and K. Mukasa, *Japan. J. Appl. Phys.*, **6,** 895 (1967).
9. A. H. Graham, R. W. Lindsay, and H. J Read, *This Journal*, **112,** 401 (1965).
10. A. W. Goldenstein, W. Rostoker, F. Schossberger, and G. Gutzeit, *ibid.*, **104,** 104 (1957).
11. M. Schlesinger and J. P. Marton, *J. Phys. Chem. Solids*, **29,** 188 (1968).
12. J. P. Marton and M. Schlesinger, *This Journal*, **115,** 16 (1968).
13. P. A. Albert, Z. Kovac, H. R. Lilienthal, T. R. McGuire, and Y. Nakamura, *J. Appl. Phys.*, **38,** 1258 (1967).
14. A. F. Schmeckenbecher, *This Journal*, **113,** 778 (1966).
15. H. H. Zappe, *J. Appl. Phys.*, **38,** 4536 (1967).
16. R. M. Bozorth, "Ferromagnetism," p. 105, D. Van Nostrand Co. (1951).
17. H. Fujiwara, *J. Phys. Soc. Japan*, **20,** 2092 (1965).
18. W. Hellenthal, *IEEE Trans. Magnetics*, **MAG-4,** No. 1, 11 (1968).

Polarographic Studies of Bivalent Germanium in Perchloric and Hydrochloric Acids

Kuan Pan and Y. Chang Fu

Department of Chemistry and Chemistry Research Center, National Taiwan University, Taipei, Taiwan, China

ABSTRACT

Polarographic behavior of the Ge(II) ion was studied in mixtures of $HClO_4$ and HCl at various H_3O^+ ion concentrations and ionic strengths at 5° intervals from 20° to 35°C. The cathode reduction of Ge(II) at a dropping mercury electrode was found to be $Ge^{++} + 2e = Ge^0$ for $[H^+] > 2M$ in mixed solutions of $HClO_4$ and $NaClO_4$. In the presence of Cl^- ion at 25°C, the reduction of Ge(II) was found to be a two-electron reversible reaction. The formation of $GeCl_3^-$ and $GeOCl_2^=$ was presumed from the polarographic data. The cathode reduction is expressed by $GeCl_3^- + 2e = Ge^0 + 3Cl^-$ ($[H^+] > 5.0M$) and $GeOCl_2^= + 2H^+ + 2e = Ge^0 + 2Cl^- + H_2O$ ($[H^+] < 1.0M$).

The existence of complex anion GeX_3^- in halogen acid solutions was reported by Tchakirian (1) and Karantassis *et al.* (2) and confirmed by the observation of Raman spectra by Tchakirian and his collaborators (3, 4). By reducing Ge(IV) to the Ge(II) state with hypophosphite in hydrochloric acid solution, a cathode wave due to the reduction, Ge(II) + 2e = Ge, was found by Alimarin and Ivanov-Emin (5), while an anodic wave due to the oxidation, Ge(II) = Ge(IV) + 2e, was observed by Cozzi and Vivarelli (6). The polarographic behavior of Ge(II) in hypophosphorous acid and hydrochloric acid was subsequently reinvestigated by Everest (7). In any of the aforementioned investigations, however, no evidence has been given for the existence of the single Ge^{++} ion in aqueous solution.

In order to observe the polarographic behavior of Ge(II) ion in acid solutions, therefore, the present investigators (8) have prepared Ge(II)-perchlorate which, though unstable, may be expected to give a reduction wave of Ge^{++} or $Ge(H_2O)_6^{++}$ ion in perchloric acid solution at a dropping mercury electrode. The purpose of the present investigation is, therefore: first, to make a polarographic study of Ge(II) ion in perchloric acid and in a mixture of hydrochloric and perchloric acids without the presence of hypophosphite; and, second, to find the ligand number of chloride of the Ge(II)-chloride complex ion and its reduction mechanism at a dropping mercury electrode.

Experimental

All chemicals used, except germanium dioxide (Alfa Inorganic Inc. Chemicals, 99.999% purity), were of Baker Analyzed Reagent grade. A mixture of Ge(II)-chloride and hypophosphite was prepared by reducing Ge(IV) to Ge(II) with sodium hypophosphite in hydrochloric acid, according to Everest (7).

Germanium(II)-hydroxide (9, 10) was prepared by neutralizing the mixture of Ge(II)-chloride and hypophosphite with dilute ammonia solution. The brownish yellow precipitate was washed repeatedly with deaerated water in a current of deoxygenated nitrogen until the ammonium, chloride, and hypophosphite ions were free from the wash liquid as determined by the qualitative tests.

Solutions of Ge(II)-perchlorate in perchloric acid and Ge(II)-chloride in hydrochloric acid were prepared by dissolving Ge(II)-hydroxide in the corresponding acid. Another solution of Ge(II)-chloride was prepared by dissolving the solid germanium dichloride, obtained from the reaction of germanium tetrachloride with germanium (11) in hydrochloric acid for comparison. The content of bivalent germanium was determined, after addition of the Ge(II) solution to a greater amount of ceric sulfate solution, by potentiometric titration with a standard solution of ferrous sulfate.

Polarograms were taken with a Yanagimoto Type PB-105 pen-recording polarograph using a H-type cell and a saturated calomel electrode. In order to prevent the electrolyte solution from evaporating during passage of nitrogen gas, a gas-washing bottle containing the corresponding acid or the mixed acids of the same concentration was inserted between washing bottles for gas purification and the polarographic cell in the thermostat at 25° ± 0.1°C. A 0.001% gelatin solution was used as the maximum suppressor.

Results and Discussion

Polarographic behavior of Ge(II)-perchlorate.—A well-defined cathode wave was observed in polarograms of Ge(II) in the mixtures of perchloric acid and sodium perchlorate at various hydronium ion concentrations and ionic strengths at 25°C (Table I), and in those at constant hydronium ion concentration and various ionic strengths at 5° intervals from 20° to 35°C (Table II). Above $[H_3O^+] = 2.0M$, the value of $E_{1/2}$ of the cathode wave is practically independent of hydronium ion concentration at constant ionic strength, which shifts to a more positive value with increasing ionic strength, as shown in Table I. At

Table I. Dependence of half-wave potential of germanium (II) on hydronium ion concentration and ionic strength* of the mixture of $HClO_4$ and $NaClO_4$ at 25°C

$[H^+]$ \ I	1.0	2.0	3.0	4.0	5.0
5.0					−0.360
4.0				−0.370	−0.360
3.0			−0.395	−0.375	−0.360
2.0		−0.425	−0.396	−0.380	−0.360
1.0	−0.425	−0.385	−0.370	−0.340	−0.315

* Both ion concentrations and ionic strength are given in gram ions per liter and $E_{1/2}$ in volts *vs.* SCE.

Table II. The half-wave potential of germanium (II) in $HClO_4$ and $NaClO_4$ at various ionic strengths and temperatures at $[H^+] = 1.0M$

$\sqrt{I}$ \ t°C	20°	25°	30°	35°
2.225	−0.330	−0.315	−0.310	−0.300
2.000	−0.350	−0.340	−0.335	−0.330
1.733	−0.380	−0.370	−0.355	−0.360
1.414	−0.410	−0.385	−0.390	−0.380
1.000	−0.420	−0.425	−0.415	−0.410

Table III. The values of $-E_{1/2}$ for Ge (II) in the mixtures of $HClO_4$, $NaClO_4$, and NaCl at 25°C ($[H^+] = 1.0M$)

$\sqrt{I}$ \ [Cl⁻]	0.25	0.50	0.75	1.00	1.25	1.75
2.225	0.335	0.350	0.355	—	0.375	0.390
2.000	0.345	0.355	0.370	—	0.390	0.395
1.733	0.350	0.370	0.375	—	0.395	0.400
1.414	0.360	0.375	0.390	—	0.400	0.405
1.000	0.370	0.385	0.400	0.405	—	—

constant hydronium ion concentration, $[H_3O^+] = 1.0M$; however, the value of $E_{1/2}$ shifts to a more negative value with decreasing ionic strength, as shown in Table II.

Though plots of $\log i/(i_d - i)$ *vs.* $E_{d.e.}$ give a slope of 0.03, we could not make sure that the reaction $Ge^{++} + 2e = Ge$ in $HClO_4$ is reversible since the value of $(E_{3/4} - E_{1/4})$ changes from 0.04 to 0.08, and the Ge(II) ion is so unstable in $HClO_4$ that the diffusion current decreases as time progresses. The positive shift in $E_{1/2}$ with increasing ionic strength at constant hydronium ion concentration may be attributable to the decrease in activity, while the positive shift in $E_{1/2}$ with decreasing hydronium ion concentration at constant ionic strength may be attributable to the possible change in aquo struction of the electroactive species, say from $Ge(H_2O)_6^{++}$ to $Ge(OH)_n(H_2O)_{6-n}^{2-n}$.

Polarographic behavior of Ge(II) in the mixtures of chloride and perchlorate ions.—The bivalent germanium has been found to be more stable toward hydrolysis and oxidation in hydrochloric acid than in perchloric acid. The values of $E_{1/2}$ obtained from the cathode wave of Ge(II) in the mixtures of HCl, NaCl, and $NaClO_4$ at various chloride ion concentrations and ionic strengths at constant hydronium ion concentration, $[H^+] = 1.0M$, are indicated in Table III. By plotting $E_{1/2}$ *vs.* $\sqrt{I}$ at various chloride ion concentrations at 25°C, a series of straight lines was obtained as shown in Fig. 1. The slope of these linear plots changes from 0.027 to 0.036 as the chloride ion concentration changes from 0.25 to 1.75M; *viz.*, $0.0591/n = 0.027$, 0.029, 0.032, 0.033, and 0.036 with $[Cl^-] = 0.25$, 0.50, 0.75, 1.25, and 1.75M, respectively. The fact that plots of $\log i/(i_d - i)$ *vs.* $E_{d.e.}$ for Ge(II) in the mixtures of HCl and $NaClO_4$ at various chloride ion concentrations and ionic strengths give $n = 2$, and the value of $(E_{3/4} - E_{1/4})$ changes in the range of $0.03 \sim 0.04$, indicates the cathode reduction to be a reversible two-electron process.

In the mixtures of hydrochloric acid and sodium chloride at constant ionic strength and chloride ion concentrations, $I = [Cl^-] = 5.0$, 4.0, and 3.0M, the half-wave potential is independent of hydronium ion concentration when $[H^+]$ is higher than 1.5M, as shown in Table IV. In the mixtures of hydrochloric acid and ammonium chloride, as well as ammonium hydroxide and ammonium chloride at constant ionic strength, $I = 0.48$; however, the half-wave potential in volts *vs.* SCE varies with pH of the solution at 25°C. The values of $E_{1/2}$ are given as functions of pH as follows

$$E_{1/2} = -0.362\text{-}0.059\,pH \quad (pH\ 1 \sim 2)$$

and

$$E_{1/2} = -0.165\text{-}0.055\,pH \quad (pH\ 7.6 \sim 9)$$

Table IV. Dependence of half-wave potential on hydronium ion concentration at 25°C

		$I = 5.0$, $[Cl^-] = 5.0M$			
$[H^+]$	0.53	1.07	1.60	2.13	2.67
$-E_{1/2}$	0.425	0.445	0.455	0.455	0.455
		$I = 4.0$, $[Cl^-] = 4.0M$			
$[H^+]$	0.53	1.06	1.58	2.11	2.64
$-E_{1/2}$	0.420	0.445	0.450	0.450	0.450
		$I = 3.0$, $[Cl^-] = 3.0M$			
$[H^+]$	0.50	1.00	1.50	2.00	2.50
$-E_{1/2}$	0.420	0.440	0.450	0.450	0.450

Dependence of $E_{1/2}$ on Cl^- ion concentration in mixtures of HCl, NaCl, and $NaClO_4$ at constant H_3O^+ ion concentration and various ionic strengths is shown in Fig. 2. The data are summarized in Table III. Dependence of $E_{1/2}$ on Cl^- ion concentration at constant ionic strength, $I = 5.0$, and various H_3O^+ ion concentrations is shown in Fig. 3. The slope of these linear plots changes from 0.09 to 0.06 as H_3O^+ ion concentration decreases from 5.0 to 1.0M. Dependence of $E_{1/2}$ on

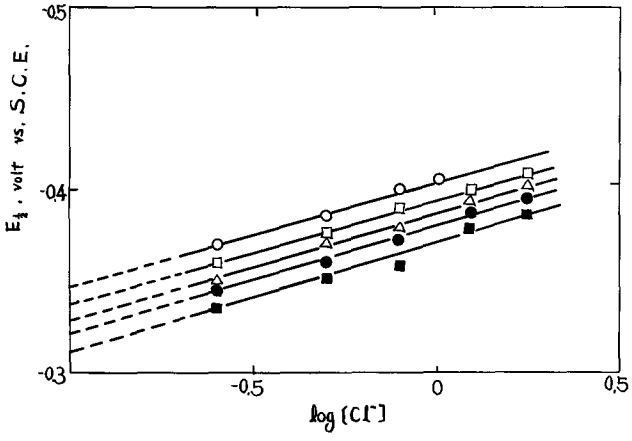

Fig. 2. Dependence of $E_{1/2}$ on Cl^- ion concentration in mixtures of HCl, NaCl, and $NaClO_4$ at $[H^+] = 1.0M$ (25°C): $I = 1.0$, ○; 2.0, □; 3.0, △; 4.0, ●; 5.0, ■.

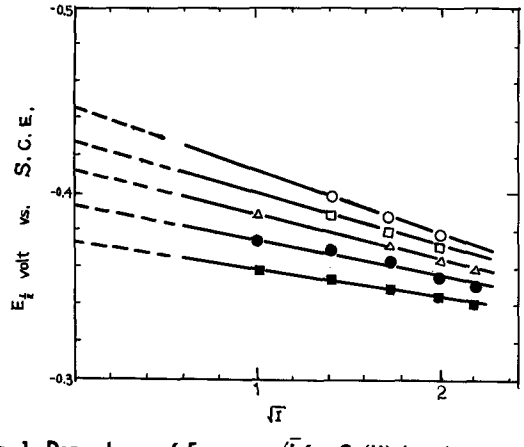

Fig. 1. Dependence of $E_{1/2}$ on $\sqrt{I}$ for Ge(II) in mixtures of Cl^- and ClO_4^- ions at $[H^+] = 1.0M$ at 25°C: $[Cl^-] = 0.25$, ■; 0.50, ●; 0.75, △; 1.25, □; and 1.75M, ○.

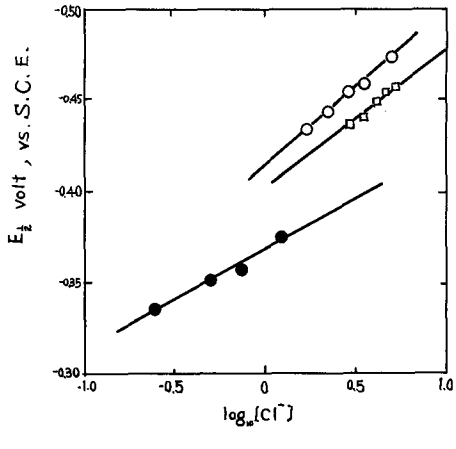

Fig. 3. Dependence of $E_{1/2}$ on Cl^- ion concentration in mixtures of HCl, NaCl, and $NaClO_4$ at $I = 5.0$ (25°C): $[H^+] = 1.0$, ●; 3.0, □; 5.0, ○.

H_3O^+ ion concentration at constant Cl^- ion concentration and ionic strength is shown in Table IV.

Assuming Ge(II) to be cationic in property in acid solution, it can be expected to form complex $Ge(H_2O)_xCl_p^{2-p}$ or be abbreviated as $GeCl_p^{2-p}$. Since the cathode reduction of Ge(II) has been assigned to be a two-electron reversible reaction at a dropping mercury electrode, the half-wave potential may be expressed in the following form

$$E_{1/2} = e + \frac{0.0591}{n} \log \frac{K_c f_c k_a}{f_a k_c f^p_{Cl^-}} - p \frac{0.0591}{n} \log [Cl^-] \quad [1]$$

Taking the second term of the right-hand side of Eq. [1] as a constant at constant H_3O^+ ion concentration and ionic strength, the slope of the linear plots of $E_{1/2}$ *vs.* log $[Cl^-]$ is given by

$$\Delta E_{1/2}/\Delta \log [Cl^-] = -p(0.0591/n) \quad [2]$$

From the experimental results obtained above, therefore, the ligand number of chloride is given by $p = 3$ for $[H^+] > 5.0M$ and $p = 2$ for $[H^+] < 1.0M$.

In the mixtures of hydrochloric acid and perchlorate at $[H^+] = 1.0M$, the values of i_d/C are 4.71, 4.60, and 5.89 and those of the diffusion constant, $i_d/C\ m^{2/3}\ t^{1/6}$, are 3.49, 3.39, and 4.41 at ionic strengths, $I = 5.0$, 3.0, and 1.0, respectively. Though the diffusion current and half-wave potential of Ge(II) have been shown to change with the concentrations of Ge(II) and H_3O^+ ion as well as the ionic strength, at constant hydronium ion concentration the value of i_d/C decreases with increase in ionic strength. At constant hydronium ion concentration and ionic strength, however, the diffusion current is proportional to the concentration of Ge(II). The fact that the chloride ligand number is 3 for $[H^+] > 5.0M$, and 2 for $[H^+] < 1.0M$, and that the half-wave potential is independent of H_3O^+ ion concentration for $[H^+] > 1.5M$ and the linear plot of $E_{1/2}$ *vs.* pH gives a slope of 0.059 for pH < 1.0 at 25°C, appears to support the mechanism of the cathode reduction at the dropping mercury electrode

$$GeCl_3^- + 2e = Ge^o + 3Cl^- \quad ([H^+] > 5.0M)$$

and

$$GeOCl_2^{--} + 2H^+ + 2e = Ge^o + 2Cl^- + H_2O \quad ([H^+] < 1.0M)$$

Acknowledgment

This work was carried out as part of the research projects of the Chemistry Research Center, National Taiwan University, CRC-5602 and CRC-5702, which were supported by the National Council on Science Development, Republic of China.

Manuscript submitted May 15, 1969; revised manuscript received Aug. 12, 1969.

Any discussion of this paper will appear in a Discussion Section to be published in the December 1970 JOURNAL.

REFERENCES

1. A. Tchakirian, *Compt. Rend.*, **192**, 233 (1931).
2. T. Karantassis and L. Capatos, *ibid.*, **199** 64 (1934); **201**, 74 (1935).
3. H. Volkringer, A. Tchakirian, and M. Freymann, *ibid.*, **199**, 292 (1934).
4. A. Tchakirian and H. Volkringer, *ibid.*, **200**, 1758 (1935).
5. I. P. Alimarin and B. N. Ivanov-Emin, *J. Appl. Chem. (U.S.S.R.)*, **17**, 204 (1944).
6. D. Cozzi and S. Vivarelle, *Mikrochemic ver. Mikrochim. Acta*, **36/37**, 594 (1951).
7. D. A. Everest, *J. Chem. Soc.*, **1953**, 660.
8. Kuan Pan and Y. C. Fu, *J. Chin. Chem. Soc., II*, **11**, 176 (1964).
9. L. M. Dennis and R. E. Hulse, *J. Am. Chem. Soc.*, **52**, 3553 (1930).
10. David A. Everest and H. Terrey, *J. Chem. Soc.*, **1950**, 2082.
11. L. M. Dennis and H. L. Hunter, *J. Am. Chem. Soc.*, **51**, 1190 (1929).

Electrical Conductivities of Molten Aluminum Chloride-Potassium Chloride Mixtures

C. R. Boston,[1] L. F. Grantham, and S. J. Yosim

Atomics International Division of North American Rockwell Corporation, Canoga Park, California

ABSTRACT

The electrical conductivities of aluminum chloride-potassium chloride mixtures were measured over the composition range 15-80 m/o (mole per cent) $AlCl_3$ and at temperatures of 180°-1080°C. A minimum at 33 m/o $AlCl_3$ and a maximum at 50 m/o were observed in the equivalent conductivity as a function of composition. The system was considered as consisting of the two binary systems, KCl-$KAlCl_4$ and $KAlCl_4$-Al_2Cl_6, since the compound $KAlCl_4$ is extremely stable in the liquid. The compound $KAlCl_4$ had a maximum specific conductance with temperature near 1000°C. The negative deviations of conductivity isotherms for the KCl-$KAlCl_4$ system are apparently due to large differences in anion polarizabilities, whereas the positive deviations for the $KAlCl_4$-Al_2Cl_6 system are attributed to basic changes in melt structure.

Aluminum halide-alkali halide mixtures are of interest as solvents because of their low melting points and their great range of acidic properties as the composition is varied. Previous conductivity measurements (1-8) on these systems have been limited for the most part to compositions between 50 and 80 m/o AlX_3, since below 50 m/o the liquidus curve rises very rapidly, and above 80 m/o a two-liquid phase region usually occurs. Also, most measurements have been made below 300°C because of the high vapor pressures characteristic of these mixtures. This work extends the composition range to 15 m/o $AlCl_3$ and the temperature range to over 1000°C. No attempt was made to determine conductivities above 80 m/o since independent, visual measurements showed that this system does not exhibit normal consolute behavior.

Experimental

Aluminum chloride was prepared from high-purity aluminum metal and HCl (9). Anhydrous KCl was

[1] Present address: Metals and Ceramics Division, Oak Ridge National Laboratory, Oak Ridge, Tennessee 37830.

prepared from reagent-grade material by a method similar to that used by Boston and Smith (10) for the purification of LiCl-KCl eutectic. The $AlCl_3$-KCl mixtures were prepared by weighing the components into conductivity cells in a dry box purged with high-purity argon.

The type of conductivity cell used was a modification (11) of that described by Grantham and Yosim (12). This cell was designed to permit accurate conductivity measurements of molten salt systems at high temperatures and pressures and was especially well suited to the study of aluminum chloride-containing systems over a wide temperature and composition range. The tungsten electrode material used in these cells was found to be inert to $AlCl_3$-KCl mixtures even at temperatures of 1000°C.

The procedure for measuring electrical conductivities has been described (12) previously. Conductivities were found to be frequency insensitive in the range 1-5 kHz. To prevent cell rupture an external pressure was applied to the conductivity cell for only one composition—70 m/o $AlCl_3$. The technique (13) for applying external pressure to the cell consisted of enclosing it in a pressurized Hastelloy N container and applying pressures slightly greater than the internal vapor pressure of the salt.

Results

The specific conductivities, K, are plotted against temperature in Fig. 1. Equivalent conductivities, Λ, were calculated using the density data of Morrey and Carter (14) for the mixtures. The conductivity and density data of Van Artsdalen and Yaffe (15) were used for pure KCl. Specific conductivity was plotted against composition at various temperatures in Fig. 2, and a similar plot of equivalent conductance is shown in Fig. 3. For convenience, compositions were calculated on the basis of KCl and monomeric $AlCl_3$, even though liquid aluminum chloride exists as Al_2Cl_6

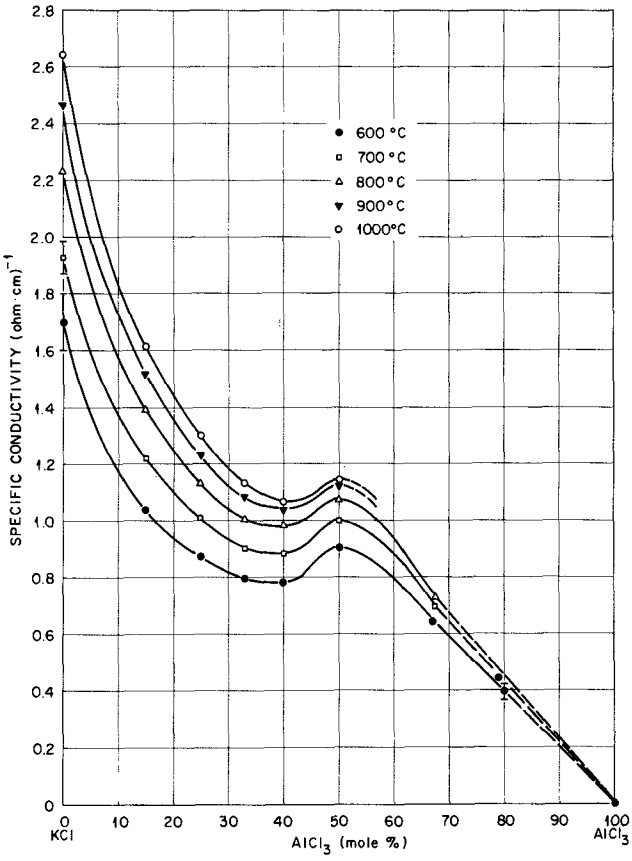

Fig. 2. Specific conductivity vs. composition for various temperatures.

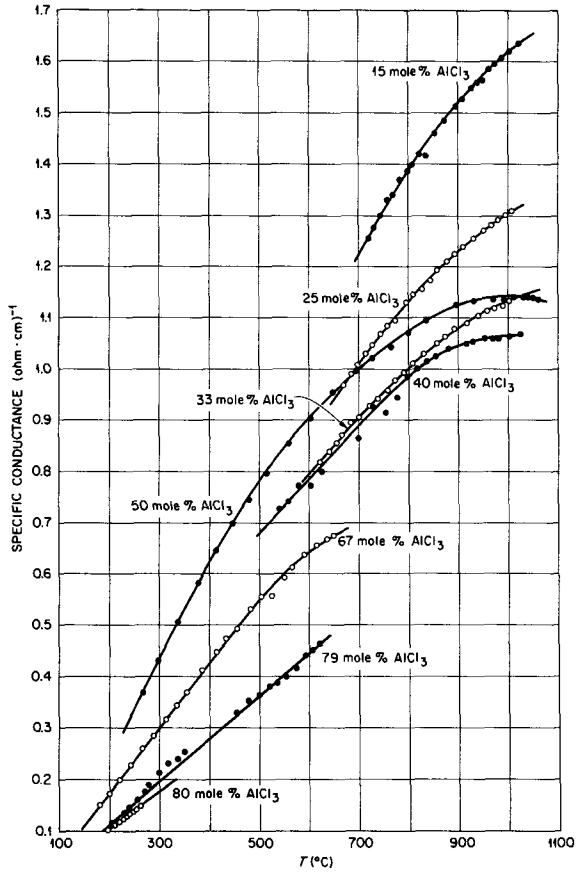

Fig. 1. Specific conductance vs. temperature for various compositions.

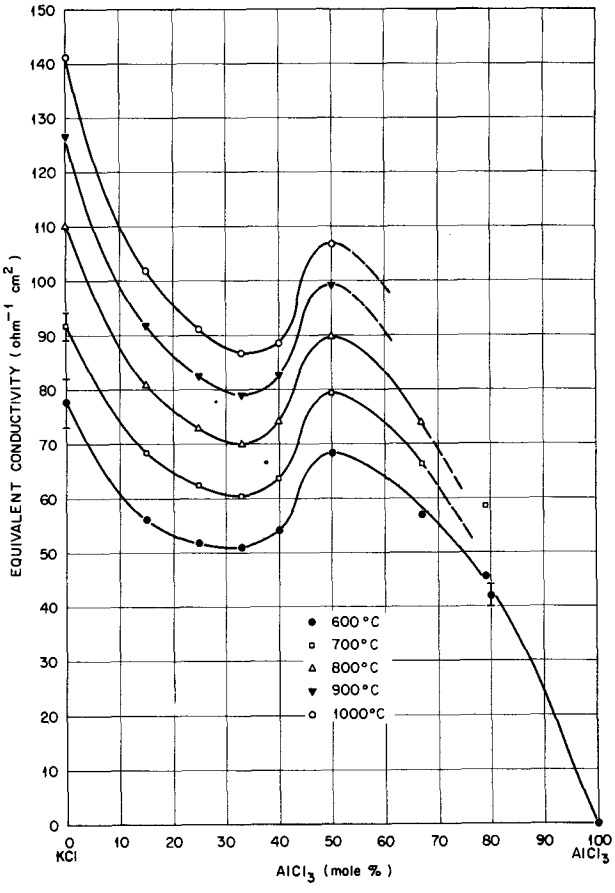

Fig. 3. Equivalent conductivity vs. composition for various temperatures.

dimers (16). For the complete system, the general shapes of the conductivity isotherms are essentially unchanged by use of the dimeric formula. However, in later discussions when the aluminum chloride-rich region is considered as a separate system, the dimeric nature of aluminum chloride is emphasized by use of the formula Al_2Cl_6.

From these plots one can see that the deviations from additivity were quite large. The deviations were negative on the KCl-rich side and positive on the $AlCl_3$-rich side and were relatively insensitive to temperature. The larger deviations (60-80%) occurred at compositions near 50-70 m/o $AlCl_3$.

Values of K from smoothed curves of K *vs.* T were used in constructing Fig. 2 and 3. It is interesting to note that, if the low-temperature linear portions of the K *vs.* T plots were extrapolated to obtain conductivities at higher temperatures, this raised the conductivity isotherms near 50 m/o $AlCl_3$ thus making the deviations from additivity even larger in this region.

The conductivity *vs.* temperature curves in Fig. 1 have the same general shape as those often observed (11) for pure compounds. The conductivities at first increase linearly with temperature but gradually the slopes decrease, resulting in a conductivity maximum. For the $AlCl_3$-KCl mixtures, the temperature of maximum conductivity, T_{max}, was usually above the temperature-pressure limits of the apparatus, an exception being the 50 m/o mixture, corresponding to the compound $KAlCl_4$, where T_{max} was about 1000°C.

Discussion

Many studies have been made of conductivity changes with composition in binary molten-salt mixtures. Deviations from additivity have usually been interpreted as evidence for changes in the degree of ionic association in the melt or of actual compound formation. Delimars'kii (17) suggests that in a qualitative way deviations from additivity can be correlated with phase diagrams in that such deviations tend to increase in both number (positive and negative) and magnitude as the phase diagram becomes more complex, *i.e.* with progression from solid solutions to eutectics and finally to congruently melting compounds. The more stable the compounds in the liquid phase, the greater the deviations from additivity.

The phase diagram (18, 19) for $AlCl_3$-KCl shows eutectics at 49.0 m/o $AlCl_3$, 250°C, and at 67 m/o $AlCl_3$, 128°C. A two-liquid region extends from 82 to 99 m/o $AlCl_3$. A congruently melting compound, $KAlCl_4$, melts at 256°C and is quite stable in the liquid phase. Grothe (20) reports a vapor pressure at this composition of 22 mm Hg at 700°C, and extrapolation of his data indicates that the vapor pressure is still less than 1 atm at 1000°C. Several Raman studies (21-23) of the liquid indicate the presence of tetrahedral tetrachloroaluminate ions even though there is some disagreement about details in the spectra. Dewing (24) has shown that the corresponding sodium compound, $NaAlCl_4$, even exists in the vapor phase. Thus, the phase diagram for $AlCl_3$-KCl is fairly complex with at least one very stable compound so that one might expect large deviations from additivity for conductivity isotherms.

Potassium chloride-rich mixtures.—Since the 1:1 compound is so stable, it may be more reasonable to consider the KCl-$AlCl_3$ system as consisting of the two separate systems, KCl-$KAlCl_4$ and $KAlCl_4$-Al_2Cl_6. When this is done, the equivalent conductivities for the KCl-$KAlCl_4$ system show negative deviations from simple additivity over the entire composition range. The maximum deviation at 600°C was 28% and occurred near 50 m/o $KAlCl_4$. The equivalent conductance of $KAlCl_4$ at 600°C was 136 ohm^{-1} cm^2.

Negative deviations of this magnitude have been observed even for relatively simple systems such as LiCl-KCl which shows a 26% deviation (15) from additivity at 800°C. The explanation offered by Van Artsdalen and Yaffe (15) for such negative deviations was in terms of a contracted or expanded chloride semilattice as one substitutes Li^+ or K^+, respectively. The over-all conductivity being determined largely by cation mobility might be expected to decrease as the chloride semilattice contracts and increase as it expands. However, this explanation would predict positive deviations at high LiCl compositions where the chloride semilattice is expanded by K^+ additions, but they actually found negative deviations. Furthermore, this interpretation would predict positive deviations instead of the negative deviations observed in this study at low $AlCl_4^-$ composition where the chloride semilattice is again expanded by addition of the large $AlCl_4^-$ ions. These authors also measured equivalent conductivities for the KCl-KI system, which bears some resemblance to the KCl-$KAlCl_4$ system (common cation and different anions). Again, negative deviations were observed over the entire composition range. Markov and Shumina (25) have shown that negative deviations are actually to be expected for noninteracting mixtures and have derived the equation, $\lambda_{mix} = x_1^2\lambda_1 + x_2^2\lambda_2 + 2x_1x_2\lambda_1$, to predict the equivalent conductivity of such mixtures. The x's are mole fractions, and λ's are equivalent conductivities. The derivation assumes random mixing and an over-all rate of transposition of ions in the melt which is determined by the lesser conducting constituent. However, the deviations observed for KCl-$KAlCl_4$ were approximately twice those predicted. The maximum deviation from both simple additivity (−28%) and the theoretical (Markov-Shumina) curve (−17%) occurred near 50 m/o $KAlCl_4$.

The negative deviations observed by Van Artsdalen and Yaffe for the KCl-KI system, mentioned above, were also greater (−4%) than those predicted by the Markov-Shumina equation, and it has been suggested (17) that this is due to the difference in polarizabilities of the chloride and iodide ions. Following this line of reasoning, the much larger deviations observed here for the KCl-$KAlCl_4$ system would indicate an even greater difference in polarizabilities of the Cl^- and $AlCl_4^-$ ions. Thus, polarizabilities would appear to fall in the order, $I^- > Cl^- >> AlCl_4^-$.

The only previous conductivity measurements on KCl-rich mixtures of KCl and aluminum chloride are those of Grothe (6). The compositions measured were 43, 35, and 7 m/o KCl-$KAlCl_4$. This was sufficient to show that strong negative deviations and, in fact, a minimum in conductance occurred with change in composition. However, the composition range was insufficient to locate either the minimum or the point of maximum deviation. Although our conductivities are in fairly good agreement with those of Grothe, we disagree with his interpretation. He suggests that the replacement of poorly conducting, dimeric K_2Cl_2 by the more highly conducting $KAlCl_4$ would explain the increase in conductivity between 43 and 7 m/o KCl. Since independent evidence for K_2Cl_2 is lacking, we feel that the suggestion of such specific entities to explain these results is unnecessary. Certainly, one might argue for varying degrees of association in the melt as implied when discussing relative anion polarizabilities, but the suggestion of dimer formation does not appear justified.

We feel that the large negative deviations observed in the KCl-$KAlCl_4$ system are best explained in general terms in the following way. Pure molten-salt conductivities appear to be largely a function of cation mobility with the size of the anion being much less important than its polarizability. In this system it appears that cation mobility is considerably greater in the pure $AlCl_4^-$ semilattice than in the pure Cl^- semilattice—the equivalent conductivity of $KAlCl_4$ being almost twice that of KCl. This is not too surprising, since one would expect the $AlCl_4^-$ ion to be

less polarizable than the chloride ion, thus giving less resistance to cation migration. In the mixed anion semilattice the cations have a lower mobility as reflected by the Markov-Shumina equation (*i.e.*, negative deviations), and may be even lower than in either pure anion semilattice alone (*i.e.*, minima, as observed here) when anion polarizabilities differ greatly. Thus, the large negative deviations observed for KCl-$KAlCl_4$ represent an extreme case of conductivity behavior observed previously in such systems as KCl-KI.

Aluminum chloride-rich mixtures.—Equivalent conductivity (and, to a lesser degree, specific conductivity) isotherms show positive deviations on the aluminum chloride-rich side of the KCl-$AlCl_3$ composition diagram shown in Fig. 3. When a similar plot is made for $KAlCl_4$-Al_2Cl_6, the deviations are even more apparent with a maximum positive deviation from additivity of about 50% occurring near the 50 m/o composition. This is apparently due to the drastic change in the nature of molecular Al_2Cl_6 when it reacts with $AlCl_4^-$ to form such species as $Al_2Cl_7^-$. In this way aluminum chloride changes from a nonconducting (26) entity to an ionic species contributing to the over-all conduction of the mixtures. Evidence for $Al_2X_7^-$ ions in these melts is indirect and consists of phase diagrams (19, 27) and vapor pressure measurements (24, 28).

The aluminum chloride-potassium chloride system bears some resemblance to both the $MgCl_2$-KCl (29) and the $ZnCl_2$-KCl (30) systems. All three cases involve the breakdown of associated structures as KCl is added. Neutral Al_2Cl_6 dimers in the liquid are broken to form ionic species as described above, while the network structure of liquid $ZnCl_2$ also breaks down to form smaller ionic units. The structure of liquid $MgCl_2$ is less certain, but one would expect the relative degrees of association to be in the order $AlCl_3$ (dimers) >>> $ZnCl_2$ (network) >> $MgCl_2$ > KCl. As might be expected, similarities in conductivity isotherms are observed for these three systems. Negative deviations are found in the KCl-rich region, while positive deviations appear on the other (acidic) side of the composition diagram. The deviations are less pronounced for the $MgCl_2$-KCl and $ZnCl_2$-KCl mixtures than for aluminum chloride-potassium chloride mixtures in keeping with the above order of degrees of association.

In summary then, the KCl-rich mixtures (*i.e.*, KCl-$KAlCl_4$ system) appear to be of the simple "noninteracting" type with the large negative deviations being mainly due to the large difference in anion polarizabilities. The aluminum chloride-rich mixtures (*i.e.*, $KAlCl_4$-Al_2Cl_6 system), on the other hand, show large positive deviations presumably due to a basic change in melt structure on mixing. Thus, the aluminum chloride-potassium chloride system may be thought of as an extreme example of behavior which has been observed to a lesser extent for systems such as KCl-KI and KCl-$ZnCl_2$.

Acknowledgments

This work was supported by the U.S. Atomic Energy Commission and performed while one of the authors (CRB) was on leave from the Oak Ridge National Laboratory. The authors wish to thank Mr. E. Harrelson for technical assistance and J. Brynestad of the Oak Ridge National Laboratory for providing the high-purity aluminum chloride.

Manuscript submitted May 8, 1969; revised manuscript received Sept. 16, 1969.

Any discussion of this paper will appear in a Discussion Section to be published in the December 1970 JOURNAL.

REFERENCES

1. E. Ya. Gorenbein, *Zh. Obshch. Khim.*, **18**, 1427 (1948).
2. E. Ya. Gorenbein and E. E. Kriss, *ibid.*, **19**, 1978 (1949).
3. Y. Yamaguti and S. Sisido, *J. Chem. Soc. Japan*, **62**, 304 (1941).
4. R. Modorikawa, *J. Electrochem. Soc. Japan*, **24**, 23 (1956).
5. A. I. Kryagova, *J. Gen. Chem. USSR*, **9**, 2061 (1939).
6. H. Grothe, *Z. Elektrochem.*, **53**, 362 (1949).
7. R. H. Moss, Thesis, University Microfilms No. 12730.
8. R. Midorikawa, *J. Electrochem. Soc. Japan*, **24**, 83 (1956).
9. N. J. Bjerrum, C. R. Boston, and G. P. Smith, *Inorg. Chem.*, **6**, 1162 (1967).
10. C. R. Boston and G. P. Smith, *J. Phys. Chem.*, **62**, 409 (1958).
11. L. F. Grantham and S. J. Yosim, *J. Chem. Phys.*, **45**, 1192 (1966).
12. L. F. Grantham and S. J. Yosim, *ibid.*, **38**, 1671, (1963).
13. L. F. Grantham, E. B. Harrelson, P. H. Shaw, and C. M. Larsen, *Rev. Sci. Instr.*, **39**, 699 (1968).
14. J. R. Morrey and D. G. Carter, *J. Chem. Eng. Data*, **13**, 94 (1968).
15. E. R. Van Artsdalen and I. S. Yaffe, *J. Phys. Chem.*, **59**, 118 (1955).
16. R. L. Harris, R. E. Wood, and H. L. Ritter, *J. Am. Chem. Soc.*, **73**, 3151 (1951)
17. Yu. K. Delimars'kii and B. F. Markov, "Electrochemistry of Fused Salts," The Sigma Press, Publishers, Washington, D.C. (1961).
18. J. Kendall, E. D. Crittenden, and H. K. Miller, *J. Am. Chem. Soc.*, **45**, 963 (1923).
19. W. Fischer and A. L. Simon, *Z. Anorg. Allgem. Chem.*, **306**, 1 (1960).
20. H. Grothe, *Z. Elektrochem.*, **54**, 216 (1950).
21. H. Gerding and H. Houtgraaf, *Rec. Trav. Chim.*, **72**, 21 (1953).
22. K. Balasubrahmanyam and L. Nanis, *J. Chem. Phys.*, **42**, 676 (1965).
23. D. E. H. Jones and J. L. Wood, *Spectrochim. Acta*, **23A**, 2695 (1967).
24. E. W. Dewing, *J. Am. Chem. Soc.*, **77**, 2639 (1955).
25. B. F. Markov and L. A. Shumina, *Dokl. Akad. Nauk SSSR*, **110**, 411 (1956).
26. C. R. Boston, S. J. Yosim, and L. F. Grantham, "The Electrical Conductivity of Aluminum Chloride Liquid and Supercritical Vapor," *J. Chem. Phys.*, **51**, 1669 (1969).
27. V. I. Mikheeva, S. M. Arkhipov, and T. V. Revzina, *Zh. Neorgan. Khim.*, **13**, 1946 (1968).
28. T. Narita, T. Ishikawa, and R. Midorikawa, *Denki Kagaku*, **36**, 300 (1968).
29. H. Grothe, *Aluminum*, **38**, 320 (1962).
30. F. R. Duke and R. A. Fleming, *This Journal*, **104**, 251 (1957).

The Mechanism of Hydrogen Evolution at a Stainless Steel Electrode in Basic Solution

R. N. O'Brien and P. Seto[1]

Department of Chemistry, University of Victoria, Victoria, British Columbia, Canada

ABSTRACT

The mechanism of the hydrogen evolution reaction at the stainless steel Type 304 (18.20% Cr, 18.20% Ni, austenitic) was investigated in the presence of plain NaOH solutions and with various ions added. It is concluded that the mechanism is

$$H_2O + M + e \underset{}{\overset{\text{(slow)}}{\rightleftharpoons}} M\text{-}H; \quad 2M\text{-}H \overset{\text{(fast)}}{\rightarrow} H_2$$

Tafel parameters are given.

While the hydrogen evolution reaction has been most frequently studied at the platinum (1), the dropping mercury (2), the iron (3-5), the silver (6, 7), and the nickel (8-11) electrodes, it has yet to be studied at the commercial austenitic stainless steel (s.s.) Type 304 metal in strong sodium hydroxide solution. The electrolytic evolution of hydrogen at the s.s. 304 alloy in the alkaline media was undertaken because of the possibility of industrial application. The elemental composition of commercial austenitic s.s. 304 is listed as 18-20% Cr, 18-20% Ni, 2% Mn, 1% Si, 0.08% max C, 0.045% P, 0.03% S, and the rest Fe (12). The structure of the metal alloy is therefore very complex and, hence, its surface. Furthermore, a passivating film of unknown structure and nature exists on the surface on exposure to air or oxidizing media (13). The thickness of the ultrathin film ranged from 30 to 60Å (14). It is this thin film that gives a shiny luster characteristic to the alloy surface. It is speculated that the passive film disappears either under hydrogen evolution conditions (13, 15), or pickled with HCl (13), or pickled with Br_2|MeOH mixture (14).

Theory

In neutral or alkaline solutions, four mechanisms for the electrolytic hydrogen evolution at the solid metal electrodes are regarded as possible. The mechanisms can be represented by:

$$(A)\quad H_2O + M + e \underset{\underline{1}}{\overset{\text{(slow)}}{\rightleftharpoons}} M\text{-}H; \quad 2M\text{-}H \overset{\text{(fast)}}{\underset{\underline{2}}{\rightarrow}} H_2 \qquad b = 120\ \text{mV}$$

$$(B)\quad H_2O + M + e \overset{\text{(fast)}}{\rightleftharpoons} M\text{-}H; \quad 2M\text{-}H \overset{\text{(slow)}}{\rightarrow} H_2 \qquad b = 30\ \text{mV}$$

$$(C)\quad H_2O + M + e \overset{\text{(slow)}}{\rightleftharpoons} M\text{-}H;$$
$$H_2O + M\text{-}H + e \overset{\text{(fast)}}{\underset{\underline{3}}{\rightarrow}} H_2 + OH^- \qquad b = 120\ \text{mV}$$

$$(D)\quad H_2O + M + e \overset{\text{(fast)}}{\rightleftharpoons} M\text{-}H;$$
$$H_2O + M\text{-}H + e \overset{\text{(slow)}}{\rightarrow} H_2 + OH^- \qquad b = 40\ \text{mV}$$

where M represents a metal site on which a water molecule can be discharged to form an adsorbed intermediate M-H and each step is rated fast or slow relative to the other in the mechanism. Several criteria, such as the Tafel slopes, the stoichiometric number, and the concentration of M-H, are available for distinguishing the above mechanisms (1, 10, 16, 19, 22). An experimental criterion such as the maximum current density as the mechanism changes from one mechanism to another, sometimes called the limiting current density, is also available (1).

[1] Present address: Chemistry Department, University of Western Ontario, London, Ontario, Canada.

Experimental

Electrodes and procedures.—Commercial austenitic stainless steel Type 304 rods supplied by Atlas Steel Company were employed as test electrodes. Electrodes of surface areas of 0.23 and 0.44 cm^2 were prepared as described previously (17). Similar electrolytic cells and experimental procedures were also employed.

Polarizing circuit.—An electronic current interrupter technique similar to that described by Hoey and Cohen (18) was used to isolate the ohmic and activation overpotentials. As shown in Fig. 1(a), the test electrode was polarized *via* the counterelectrode by a constant current source. As usual this constant current source was composed of a high-capacity 90V dry cell battery and a variable high-resistance box. A pulse generator and a vacuum diode were inserted between the current source and the electrolytic cell to interrupt the polarizing current. Negative current pulses ($T_r < 22$ nsec) were drawn from the General Radio Pulse Generator Type No. 1217-B which was powered by its analogous GR Power Supply Type No. 1201-B. The pulse repetition frequency (PRF) and the pulse duration employed were 100 Hz and 100 μsec, respectively. Current interruption was obtained by adjusting the amplitude of the negative pulses to a slightly larger value than the current supplied by the battery source. The 6AL5 vacuum diode did not conduct during the time of each negative pulse. As a result, for each 10-msec period, the current flowed in the circuit for 9.9 msec and the electrolysis current was interrupted for 0.1 msec (100 μsec). The polarizing current was measured with a Simpson's microammeter while any noise in the circuit was filtered by the 10-μf electrolytic capacitor.

The switching on and off of the polarizing current resulted in a build up and decay of the electrode potential which was monitored by a Tektronix Type

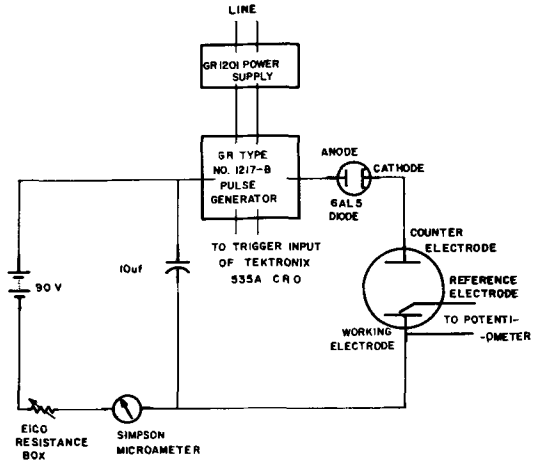

Fig. 1(a). Stainless steel electrode polarizing circuit.

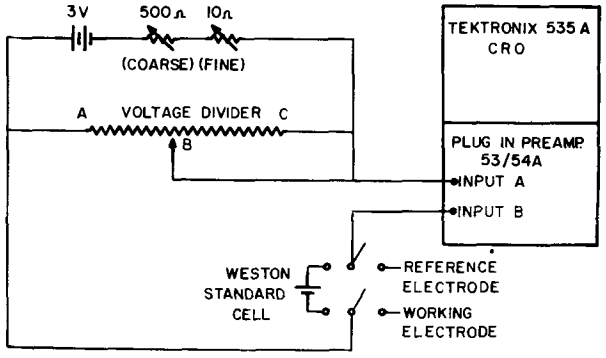

Fig. 1(b). Switching and monitoring circuit.

535 A C.R.O. as shown in Fig. 1(b). By synchronizing the interruption rate with the time base of the C.R.O., a stationary trace was obtained on the C.R.O. screen. The inputs were amplified with a Tektronix Type D preamplifier. It should be noted that the C.R.O. acted as the galvanometer in the usual potentiometer circuit; hence, the electrode potentials were monitored simultaneously.

Results and Discussion

A typical Tafellian plot of decreasing-increasing-decreasing current density runs is shown in Fig. 2. The combination of the lower Tafel slope and of the lower overpotential indicated that the initial electrode surface was less contaminated by absorbed impurities during the first decreasing run. Generally, the electrode potential went up after prolonged electrolysis. For this reason, the average initial down runs are reported.

The cathodic electrode potential-log apparent current density relationships for 0.10, 1.0, 3.0, 5.0, and 10M NaOH solutions are shown in Fig. 3. With the exception of the 5M NaOH solution, a general trend of decreasing overpotential with decreasing NaOH concentration can be observed. The Tafel plots converged at current densities higher than 10 mA/cm^2. Below 10 mA/cm^2 the lines diverged to their respective reversible potential given by the Nernst equation. Tafel parameters calculated from the Tafel equation

$$\eta = \epsilon - \epsilon_r = a - b \log i_c \qquad [1]$$

are summarized in Table I.

It can be seen that the b values decreased with increasing NaOH concentration which may be caused by the same trend in the transfer coefficient. Symmetrical potential energy surfaces were obtained for the 3.0M NaOH ($\alpha = 0.50$). The Tafel slopes 134-105 mV are compatible with mechanisms *A*, *C*, and *D* (1, 10, 20, 23). Mechanism *D* can be ruled out because the electrode surface must be highly covered with atomic hydrogen for the mechanism to be operative. It is unlikely that the stainless steel surface would be covered with a monolayer of H atoms because of the low exchange current density (Table I). In fact the activity of s.s. 304 metal is intermediate between Fe (3) and Ni (9) as compared in Table II. From current-time transient measurements, it was found that a monolayer of adsorbed atomic hydrogen was not reached in the present range of current densities studied.

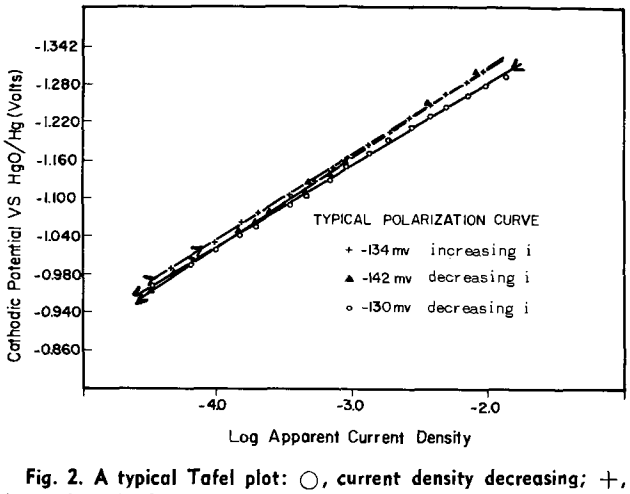

Fig. 2. A typical Tafel plot: ○, current density decreasing; +, increasing; ▲, decreasing.

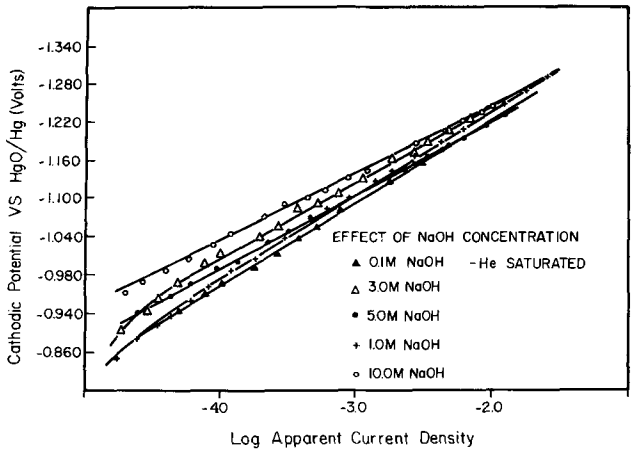

Fig. 3. Effect of electrolyte concentration

Addition of NaF, NaCl, NaI, $BaCl_2$, and $LaCl_3$ did not significantly affect the rate of hydrogen evolution. The anions F^-, Cl^-, and I^- were probably repelled from the highly negatively charged metal surface. The multivalent cations should remain beyond the reaction plane since their hydration numbers should be quite high.

As shown in Fig. 4, iodate ion was very electroactive at the stainless steel surface in alkaline media. The IO_3^- ion was probably reduced according to the equation

$$IO_3^- + 3\,H_2O + 6e = I^- + 6OH^- \qquad [2]$$

It is obvious that the iodate ions were competing with H_2O molecules to be reduced since, at higher IO_3^- concentrations, the discharge of water molecules was shifted to higher electrode potentials.

Uhlig (13) and Popat and Hackerman (15) speculated that the shiny passive film, which is characteristic of Cr-Fe, Cr-Ni, and Cr-Ni-Fe alloys, would dissolve under cathodic hydrogen evolution conditions. This concept should be true in acid solutions. The Pourbaix diagram of a chromium-water system (21)

Table I. Tafel parameters

[NaOH], mole/liter	$-a$ (volt)	b (volt)	$-\log i_o$	α
0.10	0.720	0.134	5.37	0.45
1.0	0.677	0.133	5.09	0.45
3.0	0.622	0.121	5.14	0.50
5.0	0.657	0.115	5.71	0.53
10.0	0.560	0.105	5.38	0.58

$\alpha = \eta$ at $i_c = 1$ A/cm^2, b = Tafel slope, i_o = exchange current density, α = transfer coefficient.

Table II. Tafel parameters in 0.1M NaOH solutions

Metal	b (volt)	$-a$ (volt)	i_o (amp/cm^2)	η, at 10^{-3} amp/cm^2
Ni (9)	0.092	0.487	1.2×10^{-5}	−0.176
Fe (3)	0.120	0.726	8.7×10^{-7}	
s.s. 304	0.134	0.720	4.2×10^{-6}	−0.325

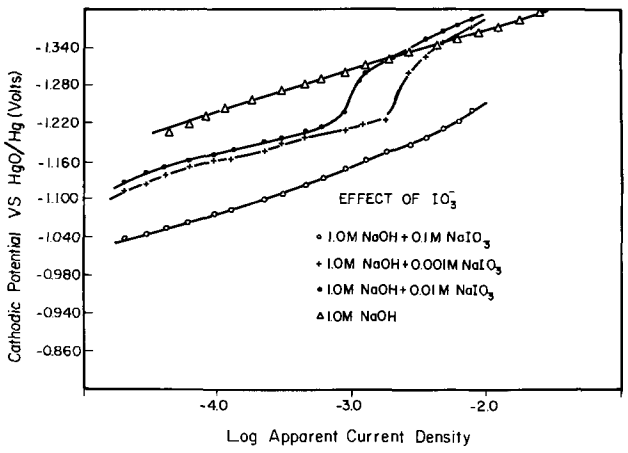

Fig. 4. Effect of iodate ion concentration

showed that $Cr(OH)_2$ or CrO_2^- could exist at the potential and at the *p*H ranges covered in this work. Similar potential-*p*H diagrams do not show the existence of any nickel or iron hydroxides/oxides under the same conditions. After the three runs as shown in Fig. 2 (over a period of 3 hr) visual examination of the stainless steel metal surface showed that the characteristic shiny luster remained. Addition of ammonia decreased the hydrogen overvoltage significantly as shown in Fig. 5. The reagent ammonia may have dissolved some chromium hydroxides and/or oxides (20), resulting in a modification of the *M-H* interaction energy. Since the alloy comprised about 70% Fe, it would be expected that the color of the oxide-free and carbon-impregnated (0.08% max) alloy would be black. After prolonged electrolysis at 12.5 mA/cm² for a 44-hr period or at 4 A/cm² for 2½ hr, the electrode surface became black, the characteristic color of carbon steel. The black material could be scraped off gently and a new shiny surface appeared. When the black material was not scraped off, a shiny surface reappeared on dipping into nitric or chromic acid. This suggested that an oxide is present throughout on the s.s. alloy lattice. The electrolytic evolution of hydrogen at an oxide surface has been studied by Makrides (11) and has been discussed by Frumkin (23) and Makrides (9, 11).

A maximum current density for one mechanism of about 4.5 A/cm² was obtained in 1.0M NaOH solution as shown in Fig. 6. It is unlikely that the observed curvature is due to solution concentration polarization as the stirring rate was increased considerably and no effect noted. An electrode of surface area of 0.02 cm² was used to obtain the curve so that solution heating effect was avoided. The phenomenon of the

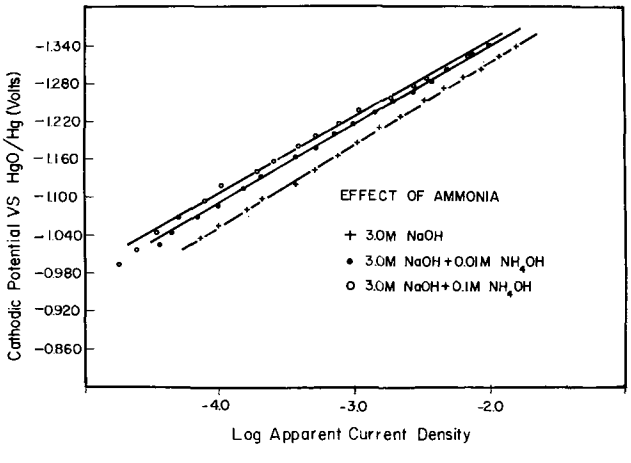

Fig. 5. Effect of ammonia concentration

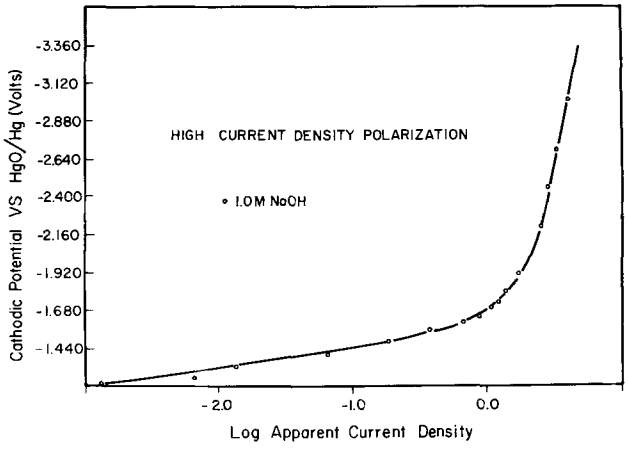

Fig. 6. Limiting current density in 1.0M NaOH

infinite Tafel slope has been interpreted as the maximum rate at which atomic hydrogen combination can occur (1, 10). At this stage the electrode surface is believed to be saturated with atomic hydrogen (monolayer) and mechanism *D* provided an alternative or parallel path to mechanism *A*.

Acknowledgment

This work was partially supported by the National Research Council and Defence Research Board of Canada to whom our thanks are due.

Manuscript submitted Aug, 28, 1968; revised manuscript received Sept. 23, 1969.

Any discussion of this paper will appear in a Discussion Section to be published in the December 1970 JOURNAL.

REFERENCES

1. J. O'M. Bockris and A. M. Azzam, *Trans. Faraday Soc.*, **48**, 145 (1952).
2. J. O'M. Bockris and R. G. H. Watson, *J. Chim. Phys.*, **49**, C70 (1952).
3. N. Pentland, J. O'M. Bockris, and E. Sheldon, *This Journal*, **104**, 182 (1957).
4. E. Kelly, *ibid.*, **112**, 124 (1965).
5. M. A. V. Devanathan, F. Starchurski, and W. Beck, *ibid.*, **110**, 886 (1964).
6. H. Gerischer and W. Mehl, *Z. Elektrochem.*, **59**, 1049 (1955).
7. M. A. V. Devanathan, J. O'M. Bockris, and W. Mehl, *J. Electroanal. Chem.*, **1**, 143 (1959-1960).
8. M. A. V. Devanathan and M. Selvaratnam, *Trans. Faraday Soc.*, **56**, 1820 (1960).
9. A. C. Makrides, *This Journal*, **109**, 977 (1962).
10. J. O'M. Bockris and E. C. Potter, *J. Chem. Phys.*, **20**, 614 (1952).
11. A. C. Makrides, *This Journal*, **113**, 1158 (1966).
12. "Metals Handbook," Vol. 1, 8th Ed., American Society for Metals (1961).
13. H. H. Uhlig, "Corrosion and Corrosion Control," John Wiley & Sons, New York (1963).
14. T. N. Rhodin, *Corrosion*, **12**, 123t (1956).
15. P. V. Popat and N. Hackerman, *J. Phys. Chem.*, **65**, 1201 (1961).
16. B. E. Conway, "Theory and Principles of Electrode Processes," Ronald Press, New York (1964).
17. R. N. O'Brien and K. V. N. Rao, *This Journal*, **112**, 1245 (1965).
18. S. Schuldiner and A. S. White, *ibid.*, **97**, 433 (1950).
19. J. O'M. Bockris, "Modern Aspects of Electrochemistry," Vol. 1, Edited by Bockris and Conway, Butterworths, New York (1954).
20. "Handbook of Physics and Chemistry," 45th Ed., The Chemical Rubber Co., Cleveland, (1964-1965).
21. M. Pourbaix, "Atlas of Electrochemical Equilibria in Aqueous Solutions," Pergamon, New York (1966).
22. E. Gileadi and B. E. Conway, "Modern Aspects of Electrochemistry," Vol. 3, Edited by Bockris and Conway, Butterworths, Washington, D.C. (1964).
23. A. N. Frumkin, *Disc. Faraday Soc.*, **1**, 57 (1947).

Mechanisms and Kinetics of H_2 Dissociation and Open-Circuit Accumulation of H Atoms during the Formation of the Equilibrium H_2/H^+ Electrode on Platinum

Murray Rosen[*,1] **and Sigmund Schuldiner**[*]

Electrochemistry Branch, Naval Research Laboratory, Washington, D. C.

ABSTRACT

The rate at which dissolved H_2 dissociates and accumulates on a clean, H- and O-free Pt electrode as the reversible H_2/H^+ electrode is formed has been studied under dissociation, diffusion, and mixed control. The kinetics of the open-circuit hydrogen accumulation reaction (h.a.r.) in H_2-saturated (1 atm) 1M H_2SO_4 were determined by a galvanostatic double-pulse method in which the first pulse strips the surface, and the second pulse measures the amount of H accumulated in a given time. Under dissociation control, the accumulation of the first 70% of the equilibrium concentration of H obeys a second-order kinetic relation in which the maximum rate at zero time is 4.46 mA/cm^2. As the h.a.r. proceeds, the initial reaching of zero volt cannot be equated with equilibrium of the H_2/H^+ reaction. A slower rearrangement of adsorbed and dermasorbed H atoms occurs before thermodynamic equilibrium is reached. The hydrogen oxidation limiting current density of 2 mA/cm^2 (0.05-0.7V, vigorous H_2 stirring) is shown to be the geometric average of $i_{diss,max}$ (4.46 mA/cm^2) and $i_{diff,max}$ (geom) (7.25 mA/cm^2). This mixed control indicates that diffusion causes the effective H_2 partial pressure at the electrode surface to be reduced from 1 to 0.45 atm. Only a small fraction of the total number of Pt atoms which are associated with H atoms at equilibrium are active dissociation sites. Non-faradaic charging corrections were found to be complex and involved adsorption/desorption processes as well as double-layer charging.

The object of this study is to determine the kinetics of H_2 dissociation and the instantaneous rate of accumulation of H atoms which associate with a clean Pt electrode; or, in terms of Pt atoms, the instantaneous rate of disappearance of available Pt atoms which can associate with H atoms. A known, Pt electrode/solution interface is electrochemically prepared by applying a galvanostatic pulse of predetermined amplitude and length. The amount of accumulated H atoms or the corresponding loss of available Pt atoms is obtained from the amount of H atoms oxidized on a second pulse that is applied a known time after the first pulse. The solution is either vigorously stirred with H_2 or is a quiescent H_2-saturated solution, both at $P_{H_2} = 1$ atm.

The experimental procedure for applying two identical galvanostatic pulses separated in time by a preset counter has been previously described (1, 2). In the present study, pulses of two different coulombic contents (current density x time) are used so that for the initial pulse either one of two final polarization potentials are reached. In one case, the amplitude and length of the first pulse of a set are fixed so that the electrode is polarized to 1.76V thereby oxidizing all the H associated with the electrode and forming just one monolayer of Pt-O_{ad} on the surface (1, 2). In the second case, the amplitude and length of the first pulse of a set is fixed so that the electrode is polarized to 0.8V thereby oxidizing essentially all the Pt-associated H but not forming any Pt-O_{ad}. Consequently, the loss of available Pt atoms or gain of H atoms is studied: (*a*) when the process occurs on a clean, H- and O-free Pt electrode immediately after the electrode is stripped of a monolayer of Pt-O_{ad} and (*b*) when the process occurs on a clean, H- and O-free Pt electrode immediately after the electrode is stripped of atomic H. In the first case, the Pt-O_{ad} + H_2 reaction occurs first, depleting the interface region of H_2 both by reaction and dilution.

Hence, for the first case, the dissociation of H_2 that follows the removal of Pt-O_{ad} begins under conditions in which the concentration of H_2 at the interface is different from the concentration in the bulk of the solution. On the other hand, in the second case, the dissociation of H_2 takes place at a solution interface free of an H_2 diffusion layer. Consequently, a method for determining the rate at which the H_2/H^+ equilibrium is established at clean, H- and O-free Pt under H_2 diffusion-controlled and H_2 dissociation-controlled conditions is provided.

The pulse length for case (*b*) was not set to polarize the Pt electrode to 0.88V, the potential at which Pt-O_{ad} has been observed to first form (3), because the end of the H oxidation and the beginning of the Pt-O_{ad} region is not sharply defined. The limit of 0.8V was chosen so that Pt-O_{ad} formation would be insignificant. It also is evident that at 0.8V the residue of H atoms is negligibly small.

To facilitate reporting and discussing the results for the H atom accumulation reaction (h.a.r.), four experimental cases based on the initial pulse polarization limits [cases (*a*) and (*b*)] and the stirring conditions are defined in terms of the symbols used in the graphical representation of the data. Cases ▲ and △ represent initial pulse polarization to 1.76V in rapidly stirred and quiescent solutions, respectively. Cases ● and ○ represent initial pulse polarization to 0.8V in rapidly stirred and quiescent solutions, respectively.

Experimental

The closed system of glass pipe construction, the helium and hydrogen purification, and the Pt electrode and miniature glass reference electrodes have been previously described (3, 4). The general procedures

* Electrochemical Society Active Member.
[1] National Academy of Sciences-National Research Council Postdoctoral Research Associate at NRL.

for solution preparation, electrochemical cell, and solution cleaning and pre-electrolysis techniques have been reported in the same references. Ultrapure sulfuric acid (E. Merck A. G., Darmstadt) was used. The Pt bead working electrodes were 0.668 and 0.332 true cm^2 in the two systems used. These true areas were determined from the linear oxygen atom adsorption region of anodic charging curves taken in clean, H_2-saturated 1M H_2SO_4 solution (3). All current densities in this paper are in true areas, so defined, unless otherwise noted. For cleanliness criteria *see* Ref. (2, 5). All results were obtained at 25° ± 1°C. All potentials are reported with reference to the normal hydrogen electrode (NHE).

Galvanostatic anodic pulses (1-2 A/cm^2) were provided by an Electro Pulse Model 3450C or Model 3450D pulse generator. A Tektronix Type 547 oscilloscope with Type 1A1 or 1A5 plug-in was used to display the data which was then recorded on film. The solution *IR* drop was largely removed from the display when using the 1A1 unit by subtracting the appropriately attenuated rectangular pulse at the generator output from the signal across the cell. The 1A5 unit is equipped with a Comparison Voltage Circuit which by use of a panel dial can be equated to the solution *IR* drop. A Hewlett-Packard 5214L Electronic Preset Counter provided accurately spaced triggering pulses to the pulse generators. The time intervals (10^{-3} to 100 sec) between the two pulses were known to within 10^{-3} sec. For time intervals greater than 100 sec, the second pulse was triggered manually with the time interval being known to about 0.1 sec.

For cases ● and ○, the preset time (time between initiation of the first and second pulses) can be considered to be "real" time, *t*, because the open-circuit decay immediately following the first pulse is extremely rapid, allowing H atoms to be observed on the second pulse well within 5 msec. In addition, the time correction due to the length of the first pulse is insignificant compared to the open-circuit time for h.a.r.

Since in cases ▲ and △, the Pt-O_{ad} + H_2 reaction has to occur before H_2 begins dissociating and accumulating on the surface at a detectable rate, the time, τ_o, for the Pt-O_{ad} reaction to be completed has to be determined and then subtracted from the preset time read on the counter to obtain "real" time, *t*, for h.a.r.

Experimentally, two different systems consisting of cleaning trains, gas-tight cells, and Pt electrode beads were used in case ▲, and τ_o's are 0.46 sec (0.668 cm^2) and 0.25 sec (0.332 cm^2). The 0.668 cm^2 electrode was used for case △ (τ_o = 0.545 sec) and cases ● and ○. When the solution was stirred, the H_2 flow rate into the cell was from 500 to 700 ml/min. The time interval waited between each set of double pulses was at least 7 min.

Results

H.A.R.—The amount of hydrogen dissociated and accumulated following a time, *t*, is considered equal to the amount of H oxidized by the second pulse. Any H atom contribution by H^+ reduction would be negligible because of anodic double-layer discharge and positive potential during open-circuit decay. The term q_H ($\mu C/cm^2$) represents the total H associated with the electrode. Two examples (Fig. 1) of first (traces 1, 2) and second (traces 1′, 2′) pulses of case ● are typical illustrations of a set for any polarization and stirring condition. As the time allowed for open-circuit decay is increased from 0.045 sec (traces 1, 1′) to 0.047 sec (traces 2, 2′), the amount of q_H observed on the second pulses (traces 2′ *vs.* 1′) has increased while at the same time the potential reached as the second pulse is applied is less noble (0.15 *vs.* 0.16V). From such oscilloscope traces, q_H can be plotted as a function of time. Figure 2 shows a q_H *vs.* log *t* plot to permit display of the total time.

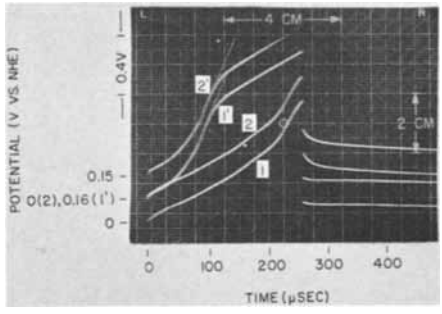

Fig. 1. Two typical sets of anodic charging curves for the double-pulse method. Case ● (see Symbols). Time interval between first (1) and second pulse (1′) is 0.045 sec. Time interval between first (2) and second pulse (2′) is 0.047 sec. Open-circuit potential on first pulses (1, 2) is 0.000V. Open-circuit potential on second pulses (1′, 2′) is 0.16 and 0.15V, respectively.

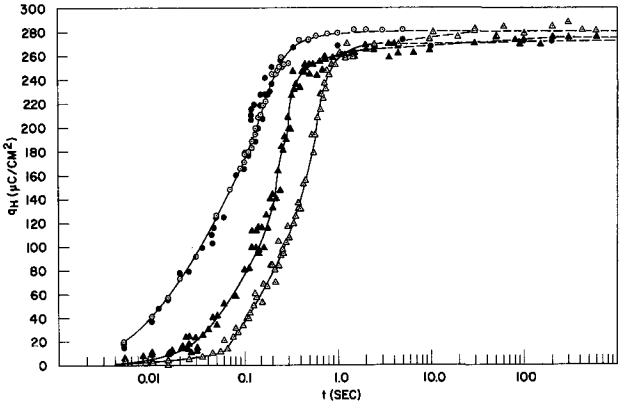

Fig. 2. Dependence of q_H on *t* for various cases. See Symbols

Double-layer correction.—In order to be able to calculate q_H from the raw data (Fig. 3), which includes double-layer discharging, the value of the charge required to polarize the double layer, q_{dl}, over the same potential limits must be determined. The value of q_{dl} can be determined by integrating the area under a C_{dl} *vs.* *E* curve, where C_{dl} represents the double-layer capacitance at a potential, *E*. The limits for the integration are set by the instantaneous potential, *E*, that the system decays to after the first pulse (Fig. 4) and by the end of the hydrogen region of the second pulse (0.8 or 0.88V). The value of C_{dl} can be calculated from the slope of an *E* *vs.* *t* oscilloscope trace taken by

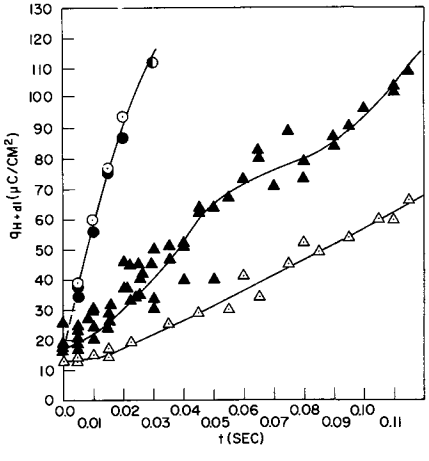

Fig. 3. Total amount of charge, q_{H+dl}, required to oxidize H atoms accumulated after first pulse and to charge double-layer capacitance after times, *t*, for various cases. See Symbols.

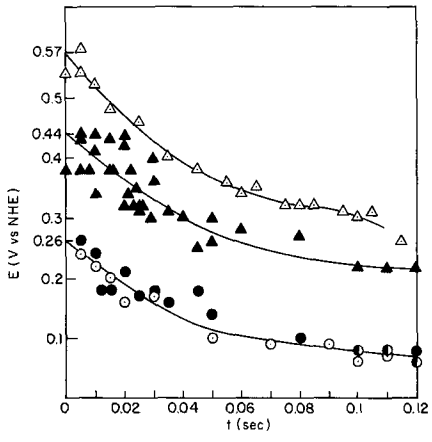

Fig. 4. *E vs. t* during h.a.r. for various cases. See Symbols

either a long constant current charging pulse (5 μsec) or a short pulse ($\sim$ 100 nsec).

The C_{dl} as a function of E has been determined using 5 μsec pulses by Schuldiner and Roe (3), and an average value of 40 μF/cm^2 between 0.2 and 0.8V was determined. However, recent measurements at the same laboratory (6) using $\sim$ 100 nsec pulses gave a significantly different C_{dl} *vs.* potential relation with an average value of 19 μF/cm^2. Quite obviously, the earlier higher value for capacitance reflects significant contributions from faradaic and other processes, *e.g.* hydrogen oxidation at lower potentials and probably adsorption-desorption processes especially at the higher potentials. However, to use the shorter pulse corrections for the entire potential range would include such adsorption-desorption contributions in q_H at higher values of E. The correction used becomes increasingly more important as the initial potential at the start of the second pulse becomes less noble.

The transitional potential above which corrections are based on the longer pulses is taken to be 0.34V because this is the beginning potential for charging curves taken in He-saturated solutions (3). Below this potential of 0.34V, corrections are based on measurements taken with the 100 nsec pulses so that the total charge due to H oxidation can be more accurately measured. Above 0.34V, corrections based on the longer pulses are used so that the unknown probable adsorption-desorption processes can be subtracted out.

The reliability of this complex correction procedure can be demonstrated by comparing the q_{dl} determined by the above procedure to the value of q_{dl} determined by extrapolating the q_{H+dl} *vs. t* plot (Fig. 3) to zero time. The values determined from Fig. 3 for q_{dl} at $t = 0$ are 17, 17, and 12 μC/cm^2 for overlapping cases ● and ○, and for cases ▲ and △, respectively. The values determined by the double-layer correction procedure used are 18.5, 16, and 11 μC/cm^2, respectively. The potential at zero time for each experiment can be found by extrapolating to zero time the *E vs. t* plot (Fig. 4).

Equilibrium establishment.—The dissociation of H_2 and accumulation of H atoms continues until the system reaches equilibrium. During this time, the potential first decays rapidly and then levels off as the system reaches equilibrium. The relative rates for potential decay for all four cases are compared in Fig. 5. An example of the time required for a system to reach equilibrium is shown in Fig. 6 for case ●. Here three sets of double pulses were taken at pulse-interval time, t, equal to 0.2, 2.0, and 200 sec. In order to be sure that the system was initially at the H_2/H^+ equilibrium, each set of double-pulse measurements was spaced at least 7 min apart.

Discussion

H.A.R.—Figure 2 shows that the net rate of H atom accumulation is the greatest when first pulse polarization is limited to 0.8V (cases ● and ○) so that Pt-O_{ad} does not form. The h.a.r. for these cases is largely independent of stirring conditions (a small stirring effect is indicated in Fig. 5—compare traces 1 and 2—which show a significant stirring effect below 0.1V) indicating that a major diffusion component to the reaction control for case ● does not exist. Also, H_2 dissociation and accumulation of H atoms proceeds rapidly after the first pulse is terminated.

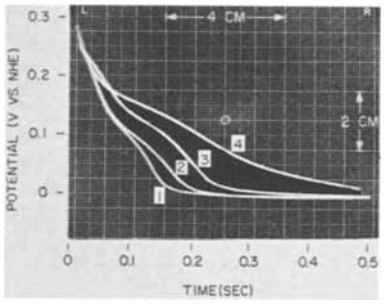

Fig. 5. Oscilloscope traces for potential *vs.* time relation of h.a.r. for Case ●, trace 1; Case ○, trace 2; Case ▲, trace 3; Case △, trace 4. See Symbols.

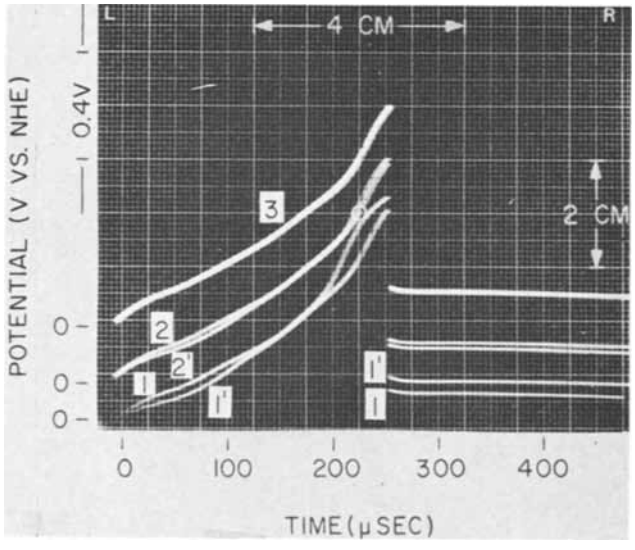

Fig. 6. Effect of *t* on the amount of accumulated H and polarization behavior. Case ●. Pulse interval time between 1 and 1′ is 0.2 sec; between 2 and 2′ is 2.0 sec; between 3 and 3′ (3 and 3′ overlap) is 200 sec.

On the other hand, cases ▲ and △ show a diffusion dependency and a period where the initial build-up of H atoms increases relatively slowly. The diffusion dependency arises from the preceding Pt-O_{ad} + H_2 reaction which depletes the solution at the electrode interface of molecular hydrogen, simultaneously generates water, and establishes a diffusion gradient that is only partially decreased by stirring (case ▲). As to be expected, the diffusion dependency is greater for the quiescent solution (case △) than it is for case ▲. The scatter of points for each case is random. The results of cases ▲ and △ indicate that diffusion gradients continue to exist until the equilibrium H_2/H^+ exchange is established. The initially slow h.a.r. is attributed to removal of the last traces of Pt-O_{ad} and to an initial lag in diffusion of H_2 to the surface.

The rounding off to the limiting q_H plateau in Fig. 2 represents the approach of system equilibrium as the concentration of accumulated H atoms reaches its limiting value, q_{H_∞}. As illustrated in Fig. 2, equilibrium is not reached in the same manner for all cases. In case ○, the plateau is formed soon after the round-

ing off occurs, whereas in case △ there is an additional rise following the rounding off before equilibrium values of q_H are observed. As will be shown later, the reproducibility of the measured equilibrium concentration of hydrogen, q_{H_x}, is poor. This variation is attributed to the presence of gaseous H_2 which contacts the electrode surface and can contribute to the measured q_H.

As can be seen in Fig. 2, the plateau value of q_{H_x} for quiescent solutions is slightly higher than those values for the stirred solutions. This difference also is attributed to effects of gaseous H_2. Stirring may reduce the actual electrode coverage with H_2 gas.

Equilibrium establishment.—The criteria used to determine when a system reached equilibrium are based on the matching of the first and second charging and decay curves (Fig. 6). Since the first charging curve is from the equilibrium H_2/H^+ reaction, a match by the second pulse gives the time required to reach equilibrium at open circuit. The matching of the potential decay, shown in Fig. 6 as parallel lines on the right side of the picture, is a very sensitive indication of the maximum polarization of the first and second pulses. An interesting point is seen at the $t = 0.2$ and 2.0 sec curves of Fig. 6 (curves 1, 1′, 2, 2′). In all these cases, E is zero, but the overlapping of the charging curves does not begin until about 0.3V. Moreover, prior to the overlapping there is a potential region for which the charging curves of the second pulse dip below those charging curves of the first pulses indicating that less polarization is required to oxidize the same number of H atoms in this potential range. This difference is attributed to the transient distribution of weakly and strongly adsorbed and dermasorbed H atoms which are not in the equilibrium distribution for curves 1′ and 2′. Thus, even though the active, weakly bonded H atoms which establish the equilibrium potential are present at virtually their equilibrium concentration, the equilibrium distribution of all the H atoms associated with Pt is not established in these cases. The relative rates at which equilibrium is established for the four cases are seen in the curves of Fig. 2. However, it must be kept in mind that both an E of zero volt and a q_{H_x} accumulation of H atoms are required for true equilibrium since distributions of $q_H < q_{H_x}$ can give zero volt.

Diffusion gradient.—The effect of a substantial gradient produced by the preceding Pt-O_{ad} removal reaction has already been mentioned as the primary reason for the dissimilar results of cases ▲ and △ as compared with the results of cases ● and ○. By plotting q_H *vs.* t for case ▲ and △ (Fig. 7), it can be determined whether or not a constant diffusion gradient is established. The required linear relationship is found only for the curve of case △ above 0.2 sec. This relationship requires that the concentration of H_2 at the surface remains very small and constant. Hence, the h.a.r. is under nearly complete diffusion control and occurs at a constant rate of 3.1 x 10^{-4} A/cm² as given by the slope between 0.2 and 0.7 sec (80 and 240 μC/cm²). When the solution is stirred, case ▲, a definite linear region is not observed, indicating that the h.a.r. is most likely under mixed diffusion and dissociation control.

The initial plateau for case △ (0-0.06 sec) most likely represents the interaction of H_2 with the last traces of atomic O which reduces the net value of q_H. From 0.06 to about 0.16 sec a transition to the linear diffusion-controlled h.a.r. occurs.

E vs. q_H.—In order to compare the transient concentration of accumulated H atoms to those obtained under steady-state conditions, a plot of E *vs.* q_H was prepared (Fig. 8). The data in this curve are the average values for five different methods of determinations of E *vs.* q_H. These are: (*a*), (*b*) the transient ●, ○ cases; (*c*) previously reported (3) steady-state data for which the potential was controlled by the partial pressure of stirred H_2 and $H_2 + O_2$ mixtures, and (*d*), (*e*) unreported steady-state potentiostatic relations between q_H and E in both H_2 and helium-stirred solutions determined at this laboratory. All q_H values have been corrected for double-layer capacitance by the method indicated under the heading *Double-layer correction* in the Results section of this paper. Since the values obtained by these five different methods are the same within the experimental precision, they are all lumped together in Fig. 8 (average values are ○ points), where the spread of all the data is shown by the hatched lines. The E *vs.* q_H relationships for cases ▲ and △ do not fit the Fig. 8 data and are plotted separately in Fig. 9 (the dotted line represents the curve in Fig. 8).

As can be seen in Fig. 8, E *vs.* q_H follows an almost linear relation after the initial rapid decay. Most important is the fact that the transient (cases ● and ○) data are essentially the same as the steady-state, open-circuit, and potentiostatic data indicating that either parameter q_H or E can be used to define the system.

On the other hand, comparing Fig. 8 and 9, the curves indicate that for the same quantity of H atoms, q_H, less potential decay has been achieved in cases ▲ and △. These differences may be explained by considering the effect of H_2 diffusion. Since the diffusion gradient created by the Pt-O_{ad} removal reaction is limiting the supply of H_2 to the surface, the partial pressure of H_2 at the surface ($P_{H_2,S}$) is less than it is in the bulk. Hence, since q_H and $P_{H_2,S}$ determine the measured potential, it is more positive for the cases ▲ and △.

Diffusional effects also account for the E *vs.* q_H relation for case △ from 140 μC/cm² and above (Fig. 9). The diffusion dependency causes a time lag during which H associated with the electrode may migrate to other lattice sites on the surface or is dermasorbed.

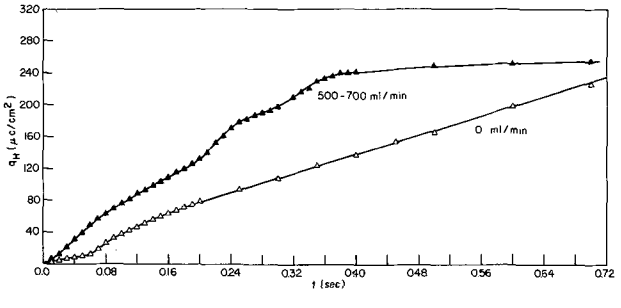

Fig. 7. q_H *vs.* t for cases ▲ and △. H_2-stirring rate for ▲ was 500-700 ml/min, and for △ was 0 ml/min.

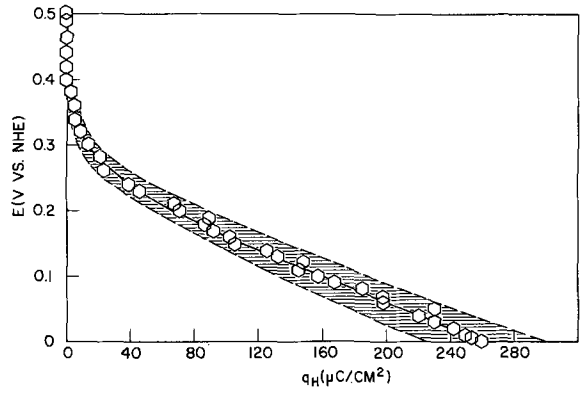

Fig. 8. E *vs.* q_H. Summary of all cases primarily not under diffusion control. See Symbols for definition of ○. Hatched lines show spread of data.

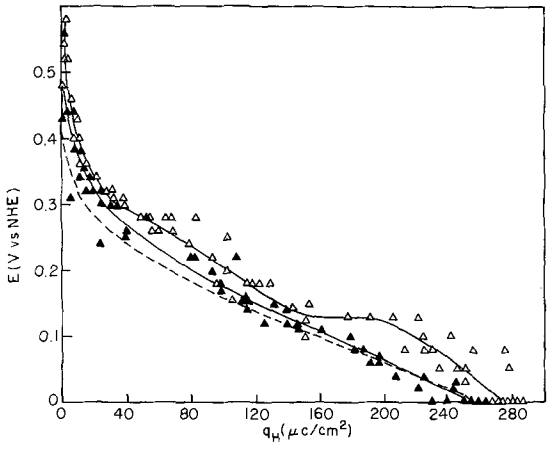

Fig. 9. E vs. q_H for cases ▲ and △ which are primarily under diffusion control. Broken line is data for ○ (Fig. 7). See Symbols.

Such behavior suggests that, in terms of time and/or potential, not all H atom-Pt associations are equivalent and that given sufficient time rearrangements can occur. In the other cases, where diffusion dependency is less or does not exist, rearrangements have less effect on the E *vs.* q_H relations.

If rearrangement of H atoms does occur, then sometime before equilibrium is reached the rearrangement effects should cause the dE/dq_H to decrease at a faster rate. Note that this does occur between 200 and 280 $\mu C/cm^2$ (△, Fig. 9). Any possibility that enough time was not allowed for equilibrium to be reached is rejected in light of Fig. 2 which shows cases ○ and △ coming to equilibrium at the same q_H.

Hydrogen regions.—Previous (3) charging curve data taken from the H_2/H^+ equilibrium potential of zero volt have shown that H ionization can be considered to occur in six potential regions. In the present study, these regions are investigated using many more samples to obtain much greater detail and, consequently, the limiting potential of each region is more precisely determined.

For each charging curve at time t for cases ● and △, q_H for each region is plotted as a function of log t (Fig. 10) to show the rate at which the various H regions (HR) accumulate H atoms both in the presence and absence of an H_2 diffusion layer. The assumption made in constructing these curves is that regions, *i.e.* HR_1, HR_2, *etc.*, exist and are being filled. The potential decay to a particular potential (E) is related to these regions. This assumption, however, should not be taken so that only higher potential regions are being first filled since extremely small amounts of H atoms may exist in the lower potential regions simultaneously. In short, a few atoms may accumulate in HR_1 and HR_2, but not enough to significantly affect E. This requirement is necessitated by the opinion that HR represents different forms and degrees of association between H atoms and Pt. It should be emphasized that the value of an HR accumulation plot lies in demonstrating, on a relative basis only, that different regions acquire H atoms at different times and at different rates.

Examining the results of case ● (Fig. 10), the following points can be established. When the h.a.r. begins, H atoms simultaneously fill the $HR_{6,5,4}$ regions (but note that none of them are filled to their equilibrium levels or fill at the same rate). When the lower potential regions ($HR_{1,2}$) begin filling, the processes are rapid and reach a definite maximum and finally level off at a lower q_H.

In case △, when the h.a.r. begins, only the HR_6 and HR_5 regions accumulate H atoms, and other than the fact that longer times are required, the patterns of filling $HR_{6,5,4}$ are about the same as for case ●. However, in case △, $HR_{3,2,1}$ do show differences from case ●. To be noted are the higher peaks for $HR_{1,2}$ and the rapid filling of HR_3 after an initial lag. These differences in association with observations in the potential decay curves (Fig. 5) may explain the E *vs.* q_H behavior of case △ in terms of the rearrangement of H atoms in the several regions.

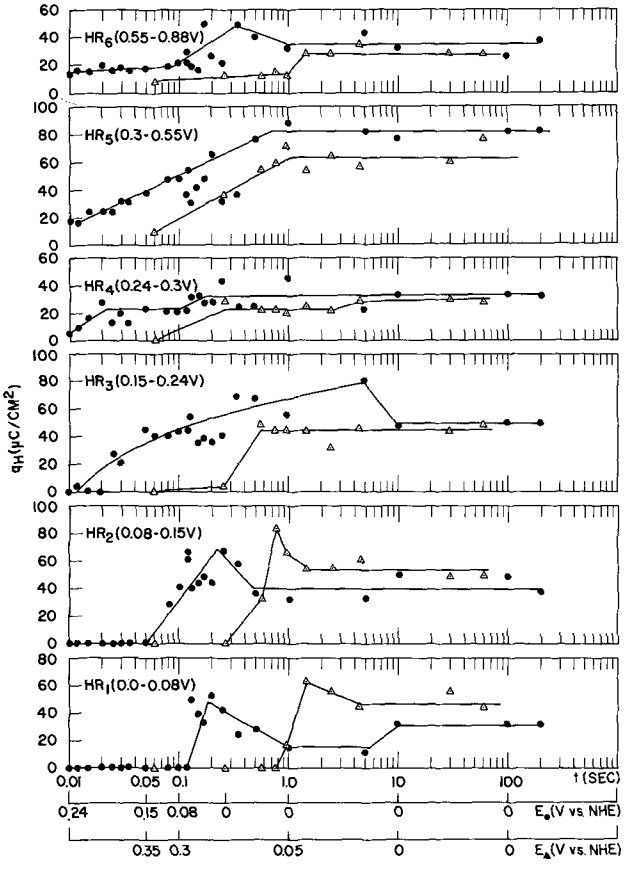

Fig. 10. Relationships between q_H vs. t (and E) for each of the six hydrogen oxidation regions, HR_{1-6} for cases ● and △. See Symbols.

Upon examining Fig. 5, one notes that the last break in the E *vs.* t curve as the equilibrium potential is approached corresponds for case ● (curve 1, 0.15 sec) to the maximum of HR_1 (0.15 sec, Fig. 10), whereas for case △ (curve 4, Fig. 5, 0.3 sec) the last break corresponds to the beginning of HR_2 (0.3 sec, Fig. 10). Timewise, for case △, it can be seen that at 0.3 sec HR_3 also begins to fill. The HR_3 of case ●, however, does not reach its maximum value until about 5 sec or its equilibrium value until 10 sec, either of which is after HR_1 has peaked. The opposite behavior is true in case △. The significance of this extended period of time in case ● has been brought out already by case ● reaching equilibrium (Fig. 6, t = 2 sec) where, even though HR_4 is filled and HR_3 is not, the potential decays to zero volt. Consequently, it is concluded that, because of the time lag produced by the diffusion layer, a rearrangement process occurs which allows HR_3 to be filled. The equilibrium values for each region must be the same for cases ● and △, and the differences seen in Fig. 10 must be due to the effects of adsorbed H_2 gas and experimental error.

The question as to which regions determine the open-circuit potential at time t is difficult to answer. One may conclude that all regions could influence the potential in a partitioning manner, *i.e.* at any E; all regions will contain some H atoms that influence the potential to some, but not equal, degrees. However, the reason why the E *vs.* q_H relation should be virtually linear is not apparent.

Mechanisms and Kinetics

H.A.R. kinetics.—The rate at which the H_2/H^+ equilibrium is established on Pt can be measured in terms of the disappearance of available Pt sites or in terms of the accumulation of H atoms. The net h.a.r. may be written as

$$H_2 + 2Pt \underset{k_2}{\overset{k_1}{\rightleftharpoons}} 2Pt\text{-}H \qquad [1]$$

The following kinetic relationship can be written for the rate of the h.a.r., $d[Pt\text{-}H]/dt$

$$\frac{d[Pt\text{-}H]}{dt} = 2k_1 [H_2] [Pt]^2 - 2k_2 [Pt\text{-}H]^2 \qquad [2]$$

$$\tfrac{1}{2}\frac{d[Pt]}{dt} = \frac{d[H_2]}{dt} = -\tfrac{1}{2}\frac{d[Pt\text{-}H]}{dt} \qquad [3]$$

Assuming that the reverse reaction is negligible and that $2k_1 [H_2]$ is a constant, rate Eq. [2] converted to electrical units becomes

$$\frac{d(Pt\text{-}H)}{dt} = k'_1 (Pt)^2 \qquad [4]$$

where $d(Pt\text{-}H)/dt$ is in $\mu A/cm^2$, (Pt-H) and (Pt) are in $\mu C/cm^2$, and k'_1 is in $cm^2/\mu C$ sec.

Since (Pt-H) + (Pt) = q_{H_∞}, Eq. [4] can be written in terms of (Pt-H), *i.e.*

$$\frac{d(Pt\text{-}H)}{dt} = k'_1 [q_{H_\infty} - (Pt\text{-}H)]^2 \qquad [5]$$

Integrating Eq. [5], and since at $t = 0$ the integration constant is $1/q_{H_\infty}$, the h.a.r. rate equation can be written as

$$\frac{1}{q_{H_\infty} - (Pt\text{-}H)} = k'_1 t + 1/q_{H_\infty} \qquad [6]$$

where (Pt-H) is q_H at time t. Equation [6] was tested for cases ▲ and △ (Fig. 11) and cases ● and ○ (Fig. 12). For cases ▲ and △ where a diffusion gradient is present, the kinetic plots (Fig. 11) are curved during the accumulation of the first 180 and 140 $\mu C/cm^2$, respectively.

For case ● (Fig. 12), a straight line whose slope of 0.059 $cm^2/\mu C$ sec, equal to k_1', is observed from the extrapolated zero time to 0.11 sec. Case ○ follows the same straight line up to 0.07 sec, but then deviates. This is due to the stirring effect noted in Fig. 5 at potentials below 0.1V. At longer times, the ● points do not fall on the straight line indicating that the assumed kinetic model for the h.a.r. may break down. Due to the scatter, the reproducibility of measurement of q_H is poor. Nevertheless, during the linear portion about 64% (180/280) of q_{H_∞} has been accumulated. It

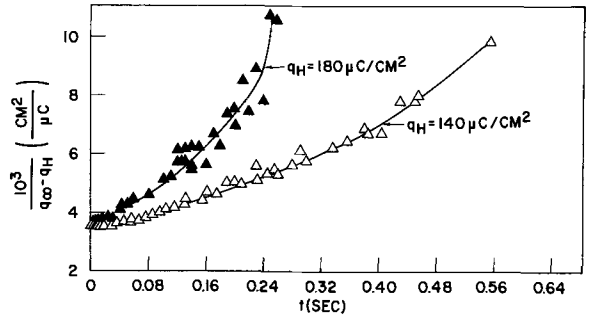

Fig. 11. Plot showing that cases ▲ and △ do not fit kinetic model (Eq. [6]). See Symbols.

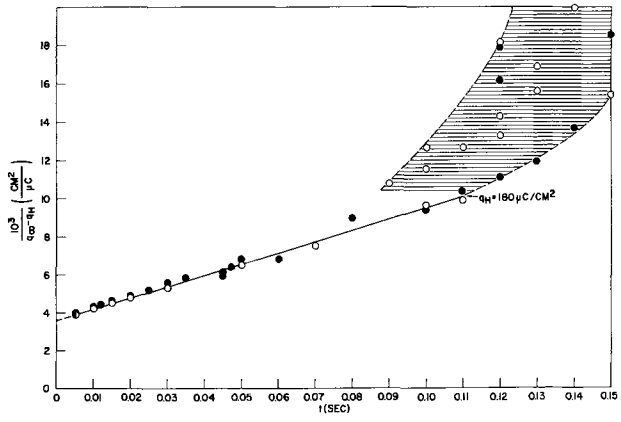

Fig. 12. Fit of data for cases ● and ○ to kinetic model (Eq. [6]). See Symbols.

is interesting to note that 0.11 sec corresponds to the time when HR_1 begins to accumulate H atoms.

To further test the validity of the kinetic model, the instantaneous rates of case ● calculated from Eq. [4] were plotted and gave the curve shown in Fig. 13. The instantaneous rate from the "chain rule" calculation of Breiter (7)

$$\frac{d(Pt\text{-}H)}{dt} = \frac{d(Pt\text{-}H)}{dE} \times \frac{dE}{dt} \qquad [7]$$

were determined also and are shown as "■" points in Fig. 13. Equation [7] does not depend on a specific kinetic model. The value of $d(Pt\text{-}H)/dE$ was obtained from Fig. 8, and the value of dE/dt was obtained from a potential decay curve (Fig. 5). The curve in Fig. 13 was determined by differencing q_H changes in each msec of time during decay and then obtaining an average △(Pt-H) value over each 10 msec interval.

The agreement between the "■" points and the curve in Fig. 13 is reasonably good down to a potential of 0.10V. The disagreement between "■" points at small values of t reflects the difficulty in reading small changes on a potential decay curve under conditions where rates of decay are very fast. The scatter of "■" points below 0.10V most likely reflect the error in determining q_H as equilibrium is reached (*see* Fig.

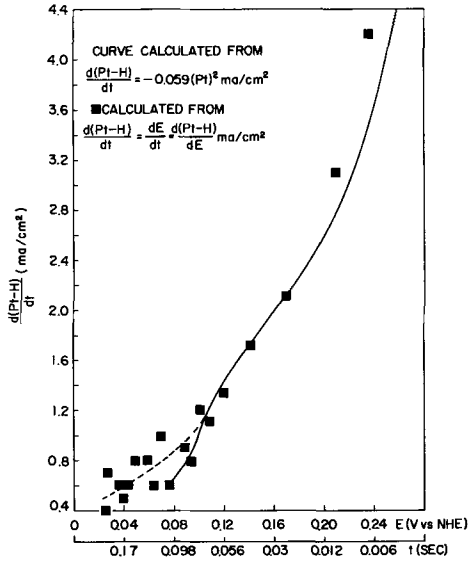

Fig. 13. Comparison of dependence of rates of h.a.r. on E and t for cases ● and ○ calculated from kinetic model and from instantaneous rate by "chain rule" calculation. Broken line is average of ■ points on graph. See Symbols.

12). The fact that the solid line curve deviates significantly from the average of the "■" points, as indicated by the broken line in Fig. 13, implies that the h.a.r. kinetic model does break down above 0.11 sec (*see* Fig. 12).

Hydrogen regions.—The h.a.r. kinetic model fits down to 0.10V for cases ● and ○. The maximum rate at which the h.a.r. can proceed on an H- and O-free Pt electrode in the absence of a diffusion gradient for H_2 occurs at $t = 0$. Calculating this rate using Eq. [4] at the estimated $t = 0$ value gives 4.46 mA/cm². As t increases, the number of available Pt atoms for H atom association decreases, and the net rate at which additional H atoms are accumulated rapidly decreases and would, of course, be zero at equilibrium. In other words, the rate at which the H_2/H^+ equilibrium is reached on an initially H- and O-free Pt electrode can be described by Eq. [4] and is primarily dependent on the rate at which H atoms accumulate in $HR_{6,5,4,3}$. Once H atoms begin to accumulate in $HR_{2,1}$, the kinetic model expressed by Eq. [4] no longer holds.

The departure from the kinetic model of Eq. [4] cannot be explained by the reverse reaction in Eq. [1] becoming significant. Correcting the kinetic model for an H atom combination reaction only would lower the calculated net rate, whereas the correct kinetic model must increase the rate (Fig. 13).

Maximum H_2 diffusion current.—Schuldiner (8) found that from about 0.05 to 0.7V a limiting current density, i_L, of 2 mA/cm² (true area) is obtained for H_2 oxidation in vigorously stirred (>1000 ml H_2/min) solution of 1M H_2SO_4, $P_{H_2} = 1$ atm. The often argued question as to whether i_L is diffusion or dissociation controlled can be examined in view of the present results.

Our results have shown that, in the absence of a diffusion layer, the maximum rate at which H_2 dissociates and H atoms accumulate on a clean, H- and O-free Pt electrode (0.26V, $t = 0$) is 4.46 mA/cm² (Fig. 13). Since the exchange current density for H atom oxidation/reduction is about 0.4 A/cm² (6), the rate of H atom oxidation at potentials in excess of 0.05V would be greater and would increase with increasingly positive potentials. Therefore, the maximum rate at which H_2 could be oxidized on an H- and O-free Pt electrode in the absence of a diffusion layer would be 4.46 mA/cm² and would be dissociation controlled. Hence, a comparison of the i_L value of 2 mA/cm² under steady-state polarization with the H_2 dissociation rate of 4.46 mA/cm² leads to the conclusion that i_L must be under partial diffusion control.

The contribution of the diffusion current density (geom. area) to i_L can be calculated. The oxidation of H under steady-state potentiostatic conditions can be limited by either $H_2 \xrightarrow{I} H_{2,s} \xrightarrow{II} 2H$ or a combination of diffusion (I) and dissociation (II). The terms H_2, $H_{2,s}$, and H refer to hydrogen in the bulk solution, surface, and associated with the electrode as H atoms, respectively. Under steady-state conditions, the rate of H_2 oxidation is not dependent on the h.a.r. since at any potential the steady-state concentration of (Pt-H) has been reached and, if the potential is positive enough (>0.3V), (Pt-H) is effectively zero. It is diffusion and/or dissociation of H_2 which then becomes rate determining.

The basis of calculating the contribution of the diffusion current density to i_L is writing separate equations for the dissociation current density, i_{diss}, and for the diffusion current density, i_{diff} (true area for the present argument). Since under steady-state, potentiostatic conditions at the limiting current density, dissociation and diffusion must occur at the same rate, so that

$$i_L = i_{diss,\,L} = i_{diff,\,L}$$

From these equations a relationship for i_L in terms of $i_{diff,\,max}$ (geom. area) and $i_{diss,\,max}$ can be derived. The latter terms represent the maximum rate at which H_2 would be oxidized by either total diffusion or total dissociation control.

The diffusion current density (true area), i_{diff}, is given here as being ½ the Nernst diffusion equation (9) because we have found that our Pt bead electrodes have roughness factors of about 2; thus, i_{diff} (geom.) $\approx 2\, i_{diff}$

$$i_{diff} = \frac{DF(C_b - C_s)}{2 \times 10^3\,\delta} = \frac{(1 - C_s/C_b)}{2}\left(\frac{DFC_b}{\delta \times 10^3}\right) \quad [8]$$

[$i_{diff,\,max}$ (geom.) is given by the last parenthesized term on the right.] Here D is the diffusion coefficient, F is the faraday, C_b is the concentration of H_2 in the bulk of the solution in equiv./L, C_s is the concentration at the surface, and δ is the "effective thickness" of the diffusion layer.

Converting to H_2 partial pressures, C_b and C_s are equal to $1.33 \times 10^{-3}\, P_{H_2,b}$ and $1.33 \times 10^{-3}\, P_{H_2,s}$, respectively (Eq. [5], Ref. 9). Since $P_{H_2,b} = 1$ atm

$$i_{diff} = \frac{i_{diff,\,max}\ (\text{geom.})}{2}(1 - P_{H_2,s}) \quad [9]$$

Equations for the dissociation/combination step, assuming a Langmuir isotherm are

$$i_{diss} = k_{diss}\,(1 - \theta)^2 P_{H_2,s}$$

and

$$i_{comb} = k_{comb}\,\theta^2$$

At equilibrium

$$i_{diss} = i_{comb} = i_o = k_{diss}\,(1 - \theta_o)^2$$

where θ is the fraction of available Pt dissociation sites covered with H atoms, θ_o is the value of this fraction at equilibrium, and i_o is the exchange current density for the dissociation reaction. The net i_{diss} when the back reaction is negligible is

$$i_{diss} = i_o\left(\frac{1 - \theta}{1 - \theta_o}\right)^2 P_{H_2,s} \quad [10]$$

The maximum current under dissociation control is when $P_{H_2,s} = 1$ atm and $\theta = 0$.
Hence

$$i_{diss} = i_{diss,\,max}\,(1 - \theta)^2 P_{H_2,s} \quad [11]$$

For the limiting current density, $i_{diss} \to i_L \leftarrow i_{diff}$, and $\theta = 0$; hence, Eq. [9]

$$i_{diff,\,L} = i_L = \frac{i_{diff,\,max}\ (\text{geom.})}{2}(1 - P_{H_2,s,L}) \quad [9a]$$

and Eq. [11] becomes

$$i_{diss,\,L} = i_L = i_{diss,\,max}\,P_{H_2,s,L} \quad [11a][2]$$

Solving Eq. [9a] or [11a] for $P_{H_2,s,L}$ and then substituting for $P_{H_2,s,L}$ in the other equation, the geometric averaging of $i_{diff,\,max}$ and $i_{diss,\,max}$ for i_L is obtained, *i.e.*

$$i_L = \frac{(i_{diss,\,max}) \times (i_{diff,\,max}(\text{geom.}))}{(2\, i_{diss,\,max}) + (i_{diff,\,max}(\text{geom.}))} \quad [12]$$

or

$$\frac{1}{i_L} = \frac{2}{i_{diff,\,max}\ (\text{geom})} + \frac{1}{i_{diss,\,max}} \quad [13]$$

Therefore, since i_L is known (2×10^{-3} A/cm²) and since $i_{diss,\,max}$ is $i_{h.a.r.,\,max}$ (4.46×10^{-3} A/cm²), $i_{diff,\,max}$ (geom.) is found to be 7.25×10^{-3} A/cm². Equation [13] is similar to the one derived by Castellan (10).

Schuldiner (8) has shown that for 0.05 to 0.7V, i_L is independent of potential. This behavior necessitates

[2] Thus, $P_{H_2,s,L} = \dfrac{2\ \text{mA/cm}^2}{4.46\ \text{mA/cm}^2} = 0.45$ atm, which is the effective partial pressure of H_2 at the electrode surface at i_L.

the conclusion that the majority of the H atoms associated with the electrode above 0.05V are not adsorbed on Pt atoms that are required for H_2 dissociation. The total number of Pt atoms which are associated with H atoms at equilibrium is considered to be equivalent to 260 ± 40 μC/cm^2 (not one monolayer = 210 μC/cm^2). However, only a small portion of that total number of Pt atoms are actually involved in H_2 dissociation, and it is this small number of Pt atoms that are "covered" when $\theta = 1$. Otherwise, on the basis of the total number of Pt atom association with H atoms, 260 μC/cm^2, the fraction of Pt atoms associated with H atoms would go from 0.81 at 0.05V to 0.62 and 0.42 at 0.10 and 0.15V, respectively (*see* Fig. 8), while at the same time i_L remains constant. However, by defining θ as the fraction of available Pt dissociation sites covered with H atoms, θ must be approximately zero above 0.05V under conditions of the i_L described by Schuldiner (8). In the definition used for θ, the relationship between Pt sites available for H_2 dissociation and actual number of Pt atoms is not necessarily on a basis of one atom to one site; *e.g.*, a site may involve junction of two atoms.

It is not definite whether the effective coverage of available Pt dissociation sites with H atoms, the potential near and at equilibrium, and the relation with HR_1 and possibly HR_2 are all related, but our results indicate that they probably are related. As is shown in Fig. 10, above 0.05V (*e.g.*, 0.15 sec) the number of H atoms in HR_1 is about zero, and the number of H atoms in HR_2 is only about 50 μC/cm^2. If θ is to be equated with $HR_{1,2}$, then it must follow that, under steady-state conditions above 0.05V, H_2 molecules are dissociated and are oxidized at Pt sites which are equivalent to $HR_{1,2}$, but whose H content is virtually zero.

Diffusion-layer thickness.—The "effective thickness" of the diffusion layer, δ, can be calculated for case △ (quiescent solution) and for the potentiostatic steady-state oxidation of hydrogen (stirring rate > 1000 ml/min). In the latter case, δ is 8.6 x 10^{-4} cm as calculated from Eq. [8]

$$i_{diff,\,max}(geom.) = 7.25 \times 10^{-3}\ A/cm^2 = \frac{DFC_b}{\delta \times 10^3}$$

where D is 4.87 x 10^{-5} cm^2/sec (11). For case △, δ can also be calculated from the right-hand side of Eq. [8] since the latter is equal to the slope of q_H *vs.* t (Fig. 7, 0.2-0.7 sec). Since C_s would be small, δ is 1 x 10^{-2} cm, and $i_{diff,\,max}$(geom.) is 0.62 mA/cm^2 under these conditions.

A comparative calculation of δ for case △ can be made by first calculating the depth, d, of hydrogen depletion caused by reducing a monolayer of Pt-O_{ad} (420 μC/cm^2 of Pt-O_{ad}). The depth is given by

$$d\ cm = \frac{\text{mole } H_2/cm^2\ (geom.)}{\text{mole } H_2/cc\ solution} \qquad [14]$$

where the numerator is

$$\frac{420 \times 10^{-6} C}{cm^2} \times \frac{equiv.}{9.65 \times 10^4 C} \times \frac{mole}{2\ equiv.} \times 2 = \frac{4.35 \times 10^{-9}\ \text{mole } H_2}{cm^2\ (geom.)} \qquad [14a]$$

and the denominator is

$$\frac{\text{mole } H_2}{22{,}400\ cc\ H_2} \times \frac{0.0149\ cc\ H_2}{cc\ solution} = \frac{6.65 \times 10^{-7}\ \text{mole } H_2}{cc\ solution} \qquad [14b]$$

Equation [14a] is multiplied by 2 because d must be calculated on a geometric area basis, and 1 cm^2 true area is about 0.5 cm^2 geometric area. The H_2 solubility in 1M H_2SO_4 term in Eq. [14b] is taken from Ref. (12). Hence, d is 6.5 x 10^{-3} cm. To complete the comparative calculation, it is necessary to make $\delta = 2d$ because diffusion Eq. [8] assumes a linear H_2 diffusion gradient which means that the diffusion layer will be only one half depleted of H_2 in 6.5 x 10^{-3} cm. Thus, δ calculated this way is 1.3 x 10^{-2} cm and is comparable to the δ value (1.0 x 10^{-2}) determined from Fig. 7.

Conclusions

1. The open-circuit hydrogen accumulation reaction (h.a.r.) under dissociation control obeys the following second-order kinetic relation

$$i_{h.a.r.} = i_{diss} = dq_H/dt = 0.059(275\text{-}q_H)^2 \qquad 0 \leq q_H < 180\ \mu C/cm^2$$

The $i_{diss,\,max} = 4.46 \times 10^{-3}$ A/cm^2 $\qquad q_H \sim 0\ \mu C/cm^2$

2. The open-circuit h.a.r. under diffusion control was measured in a quiescent solution where i_{diff} (geom.) ≡ 6.2 x 10^{-4} A/cm^2. The "effective thickness" of the diffusion layer in quiescent solution is 1.0 x 10^{-2} cm.

3. Only a small number of the total number of Pt atoms which are associated with H atoms at equilibrium (260 ± 40 μC/cm^2) are involved in the available Pt dissociation sites.

4. Under potentiostatic steady-state hydrogen oxidation (0.05-0.7V, vigorous H_2 stirring), the limiting current density (2 x 10^{-3} A/cm^2) was shown to be under mixed dissociation and diffusion control. The $i_{diss,\,max}$ = 4.46 x 10^{-3} A/cm^2 and the $i_{diff,\,max}$ (geom.) = 7.25 x 10^{-3} A/cm^2 show that, even though the H_2 oxidation is primarily dissociation controlled, diffusion does cause the effective hydrogen partial pressure at the electrode surface to be reduced from an applied pressure of 1 to 0.45 atm. The "effective thickness" of this diffusion layer is 8.6 x 10^{-4} cm.

5. The h.a.r. under dissociation control reaches zero volt in about 0.3 sec, but at least 100 sec are required to reach the equilibrium Pt-associated H atom concentration.

6. The h.a.r. under diffusion control reaches zero volt in about 10 sec, but also requires at least 100 sec to reach the equilibrium Pt-associated H atom concentration.

7. Items 4 and 5 show that a slow rearrangement of adsorbed and dermasorbed H atoms are required before the Pt-H_2/H^+ electrode reaches thermodynamic equilibrium.

8. Nonfaradaic charging corrections were found to be complex and involved adsorption/desorption processes as well as double-layer charging.

SYMBOLS

case ●	h.a.r. in H_2-stirred solution, first pulse polarization to 0.8V
case ○	h.a.r. in quiescent solution, first pulse polarization to 0.8V
case ▲	h.a.r. in H_2-stirred solution, first pulse polarization to 1.76V
case △	h.a.r. in quiescent solution, first pulse polarization to 1.76V
C_b	Concentration of H_2 in the bulk of the solution, equiv./L
C_s	Concentration of H_2 at the surface, equiv./L
C_{dl}	Double-layer capacitance, μF/cm^2
d	Depth from the electrode which the Pt-O_{ad} + H_2 reaction depletes H_2 from the solution, cm
D	Diffusion coefficient for H_2, 4.87 x 10^{-5} cm^2/sec (11)
E	Potential, V
h.a.r.	Hydrogen accumulation reaction of dissociated H_2 adsorbed on and/or dermasorbed with the Pt electrode
H	Hydrogen atoms, associated with the Pt electrode either by adsorption or dermasorption
H_2	Dissolved molecular hydrogen

$H_{2,s}$	H_2 at the electrode surface
HR_i	H region-H oxidation potential region observed during an anodic charging pulse
i	Current density or reaction rate on true area basis, A/cm²
i_{comb}	Rate of H atom combination
i_{diff}	Rate of H_2 diffusion in solution
$i_{diff,L}$	i_{diff} under limiting conditions
$i_{diff,max}$	Maximum i_{diff} under conditions of pure diffusion control
$i_{diff,max}(geom.)$	Maximum i_{diff} on a geometric area basis
i_{diss}	Rate of H_2 dissociation to 2H
$i_{diss,L}$	i_{diss} under limiting conditions
$i_{diss,max}$	Maximum i_{diss} under conditions of pure dissociation control
i_L	Limiting current density
i_o	Exchange current density for i_{diss}
$i_{h.a.r.}$	Reaction rate of h.a.r.
k_{diss}	Rate constant for the dissociation reaction, A/cm²
k_{comb}	Rate constant for the combination reaction, A/cm²
k_1	Rate constant for h.a.r., cm⁵/mole² sec
k'_1	$2k_1(H_2)$ converted to electrical units, cm²/μC sec
$P_{H2,b}$	Bulk partial pressure of H_2, atm
$P_{H2,s}$	Surface partial pressure of H_2, atm
$P_{H2,s,L}$	Partial pressure of $H_{2,s}$ at i_L, atm
q_H	Amount of H associated with Pt electrode via h.a.r. at time t as measured by the second pulse, μC/cm²
q_{H_∞} or q_r	Equilibrium concentration of H associated with Pt electrode at equilibrium, μC/cm²
q_{H+dl}	Net q_H + amount of double-layer capacitance charging, μC/cm²
t	Elapsed "real" time for h.a.r.
δ	"Effective thickness" of the H_2 diffusion layer, cm
θ	Fraction of available Pt dissociation sites covered with H
θ_o	Value of θ at equilibrium
τ_o	Time required for potential decay due to Pt-O_{ad} + H_2 reaction, sec
■	$i_{h.a.r.}$ calculated from the chain rule $(d(Pt\text{-}H)/dE)\ (dE/dt)$
○	Average q_H *vs.* t value for cases ● and ○ and steady-state measurements where potential control was either potentiostatic in He- or H_2-saturated solution or by mixtures of H_2, He, and O_2

Acknowledgments

The authors are indebted to Dr. D. R. Flinn of the Naval Research Laboratory and to Professor P. H. Emmett of Johns Hopkins University for stimulating discussions and suggestions concerning this work.

Manuscript submitted April 7, 1969; revised manuscript received *ca.* July 31, 1969.

Any discussion of this paper will appear in a Discussion Section to be published in the December 1970 JOURNAL.

REFERENCES

1. T. B. Warner and S. Schuldiner, *This Journal*, **115**, 28 (1968).
2. S. Schuldiner and B. J. Piersma, *J. Catalysis*, **13**, 413 (1969).
3. S. Schuldiner and R. M. Roe, *This Journal*, **110**, 332 (1963).
4. S. Schuldiner and R. M. Roe, *ibid.*, **110**, 1142 (1963).
5. S. Schuldiner and T. B. Warner, *J Phys. Chem.*, **68**, 1223 (1964).
6. M. Rosen, D. R. Flinn, and S. Schuldiner, *This Journal*, **116**, 1112 (1969).
7. M. W. Breiter, *Ann. N. Y. Acad. Sci.*, **101**, 709 (1963).
8. S. Schuldiner, *This Journal*, **115**, 362 (1968).
9. S. Schuldiner, T. B. Warner, and B. J. Piersma, *ibid.*, **114**, 343 (1967).
10. G. W. Castellan, *ibid.*, **108**, 277 (1961).
11. B. E. Conway, "Electrochemical Data," p. 174, Elsevier Publishing Co., Amsterdam (1952).
12. "International Critical Tables," Vol. 3, p. 271 (1928).

Current Distributions on Plane, Parallel Electrodes in Channel Flow

W. R. Parrish and John Newman

Inorganic Materials Research Division, Lawrence Radiation Laboratory, and Department of Chemical Engineering, University of California, Berkeley, California

ABSTRACT

Current distributions on two plane, parallel electrodes embedded in the walls of a flow channel have been calculated for separation distance between electrodes to electrode length ratios of 0.5, 1, and 10. Secondary current distributions were calculated using the linear and Tafel polarization laws. Using the Tafel polarization law, current distributions were calculated at various fractions of the limiting current. In all cases considered, the electrodes are nearly independent of one another if the height to length ratio is ten or more.

Many industrial electrochemical processes use channel flow between two plane, parallel electrodes as shown in Fig. 1. The limiting current distribution for this flow geometry is well known (1). A procedure for determining current distribution below the limiting current has been outlined previously (1). The method uses the concept of having concentration variations restricted to a thin diffusion layer very near each electrode surface (2), allowing the bulk region and the diffusion layers to be treated separately. The same concept has been applied previously to the rotating disk electrode (3, 4) and to the single plane electrode (5).

In the treatment of the problem, the following assumptions are made:

1. The electrodes are embedded in infinite, parallel, plane, insulating walls.

2. Fully developed, laminar flow exists, and the velocity profile can be considered linear inside the diffusion layer. Thus, the diffusion layer thickness should be small compared with the distance between

Key words: electrochemical mass transfer, electrode kinetics, current distribution.

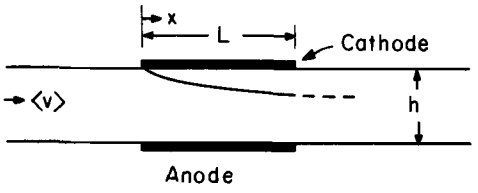

Fig. 1. Plane electrodes in the walls of a flow channel

the walls. In such diffusion layers it is appropriate to neglect diffusion in the direction parallel to the electrode.

3. Dilute solution theory with constant physical properties is applicable.

4. The transport equations used here apply to either single salt deposition or ions reacting in an excess of supporting electrolyte. The effect of ionic migration for intermediate cases is not considered.

Mathematical Formulation of Problem

The general approach to the problem is outlined in ref. (1) through (5). The potential in the bulk region satisfies Laplace's equation

$$\frac{\partial^2\Phi}{\partial x^2} + \frac{\partial^2\Phi}{\partial y^2} = 0 \qquad [1]$$

where Φ is the potential measured by a reference electrode of the same type as the working electrode. The appropriate boundary conditions are

$$\partial\Phi/\partial y = 0 \text{ at } y = 0 \text{ and } y = h \text{ for } x < 0 \text{ and } x > L \qquad [2]$$

$$\partial\Phi/\partial y = -\,i/\kappa_\infty \text{ at } y = 0 \text{ and } y = h \text{ for } 0 < x < L \qquad [3]$$

Equation [2] applies to the insulating surfaces bounding the electrodes, and Eq. [3] relates the normal potential gradient to the electrode current density i, where κ_∞ is the solution conductivity in the bulk region. The current is taken to be positive on the anode and negative on the cathode.

The solution (1) to Eq. [1] with the boundary conditions is

$$\Phi(x,y) = \Phi^* - \frac{1}{2\pi\kappa_\infty} \times \left\{ \int_0^L i_{\text{cath}}(x') \ln[\sinh^2(\pi(x-x')/2h) + \sin^2(\pi(y-h)/2h)]\,dx' + \int_0^L i_{\text{anode}}(x') \ln[\sinh^2(\pi(x-x')/2h) + \sin^2(\pi y/2h)]\,dx' \right\} \qquad [4]$$

where the anode is at $y = 0$ and the cathode is at $y = h$. The potential very near the cathode surface is then

$$\Phi^o{}_{\text{cath}}(x) = \Phi^* - \frac{1}{2\pi\kappa_\infty} \times \left\{ \int_0^L [i_{\text{cath}}(x') \ln \sinh^2(\pi(x-x')/2h) + i_{\text{anode}}(x') \ln \cosh^2(\pi(x-x')/2h)]\,dx' \right\} \qquad [5]$$

The expression for the anodic potential is the same as above except that the subscripts are reversed. These potentials represent the potentials of the bulk region extrapolated to the electrode surface as if the actual current prevails but there is no concentration variation near the electrodes. The integration constant, Φ^*, is determined by the requirement that the total currents for the two electrodes must be equal in magnitude, *i.e.*

$$\int_0^L [i_{\text{cath}}(x') + i_{\text{anode}}(x')]\,dx' = 0 \qquad [6]$$

To obtain a relationship between the current and concentration on each electrode, an equation has been derived from the limiting current expression

$$i_{\text{lim}}(x) = -\frac{n\mathbf{F}D}{(1-t)} \frac{c_\infty}{\Gamma(4/3)} \left(\frac{2<v>}{3hDx}\right)^{1/3} \qquad [7]$$

Application of Duhamel's theorem (6) yields an equation which is applicable to either electrode (1)

$$i(x) = \frac{n\mathbf{F}D}{(1-t)\Gamma(4/3)} \left(\frac{2<v>}{3hD}\right)^{1/3} \times \int_0^x \frac{dc_o(x')}{dx'} \frac{dx'}{(x-x')^{1/3}} \qquad [8]$$

For many electrode reactions, the current density and surface overpotential, η_s, can be related by

$$i(x) = i_o(c_o/c_\infty)^\gamma \times \{\exp[\alpha Z\mathbf{F}\eta_s/RT] - \exp[-\beta Z\mathbf{F}\eta_s/RT]\} \qquad [9]$$

where α and β are characteristic parameters of the electrode reaction, and i_o is the exchange current density at the bulk concentration. The exchange current density is assumed to be proportional to the surface concentration, c_o, raised to the power γ. The surface overpotential on each electrode is related to the electrode potential, V, by

$$\eta_s = V - \Phi^o - \eta_c \qquad [10]$$

The concentration overpotential, η_c, is taken to be (2)

$$\eta_c = -(RT/Z\mathbf{F})[\ln(c_\infty/c_o) - t(1 - c_o/c_\infty)] \qquad [11]$$

where

$$Z = -z_+z_-/(z_+ - z_-) \text{ for a single salt} \qquad [12]$$

$$Z = -n \text{ with supporting electrolyte} \qquad [13]$$

The transference number, t, is zero if there is an excess of supporting electrolyte. The number Z was inserted into Eq. [9] in order to make more simple the dimensionless parameters which describe the system. For a solution of a single salt, the effect of the variation of conductivity across the diffusion layer is included in Eq. [11], and in this case the derivation was restricted to a metal deposition reaction. The kinetic parameters are αZ and βZ, not α and β alone.

Numerical Calculations

To calculate current and concentration distributions on the two electrodes, two sets of five equations must be solved simultaneously; these are Eq. [5], [8], [9], [10], and

$$i_{\text{avg}} = \frac{1}{L} \left| \int_0^L i(x)\,dx \right| \qquad [14]$$

i_{avg} is a specified average current density applying to both electrodes (Eq. [14] replaces Eq. [6]). For a given distribution of total overpotential, $\eta_c + \eta_s$, Eq. [8] was solved in conjunction with Eq. [9] and [10] using the method of Acrivos and Chambré (7). Simpson's method was used to evaluate Eq. [14]. Gaussian quadrature integration, using 96 points (8), was used to calculate the total overpotential in Eq. [5]. To get intermediate values of the integrand required for the Gaussian integration, Lagrange's interpolation formula was used. Simpson's method had been used for evaluating Eq. [5], but was found to be less accurate and efficient than the Gaussian method. The singularity at $x' = x$ in Eq. [5] was eliminated by adding and subtracting $i(x)$ as suggested by Kantorovich and Krylov (9).

The answers were considered satisfactory if they did not change by more than 1% when the number of evenly spaced intervals was increased by 20. The required number of intervals varied between 100 and 180, depending on the uniformity of the current and concentration distributions.

The following doubly reiterative procedure was used:

1. As a first guess, the total overpotential was assumed constant over the entire electrode. The overpotentials were calculated from Eq. [9] using $i(x) = i_{avg}$ and $c_o = c_\infty$.
2. For a given overpotential distribution, the current and concentration distributions were calculated from Eq. [8], [9], [10], and [11].
3. The average current was then calculated and compared with i_{avg}. If the two values differed by more than 0.001%, the overpotential distribution was changed uniformly by adding a constant to each value. The new overpotentials were then put back into step 2. The constant was found by assuming that the overpotential at $x = 0$ was proportional to the calculated average current density or its logarithm for the cathode or the anode, respectively.
4. Using the current distributions that satisfy Eq. [14], new values of the overpotentials were calculated from Eq. [5] and [10]. If the old and new values differed by more than 0.1%, the two values were averaged (usually with unequal weights because of stability problems) and put back into step 2.

This numerical procedure works well for the range of current distributions considered in this paper. Three to eight iterations were required to obtain convergence in the inner loop, and the convergence rate depended on how near the overpotential distributions were to the "correct" values. Up to 70 iterations were required in the outer loop. The required number of outer iterations increased with increasing nonuniformity of the current and concentration distributions.

Results

Eight parameters are required to define completely each problem, h/L, the transference number, t, α, β, and γ which are characteristic of the electrode reaction (although it is not necessary, the same kinetic parameters are assumed to apply to both electrodes), and three dimensionless quantities which are analogous to those defined for the flat plate (5) and the rotating disk (3) electrodes

$$J = ZFLi_o/RT\kappa_\infty \qquad [15]$$

$$N = \frac{nZF^2Dc_\infty}{(1-t)RT\kappa_\infty}\left(\frac{6<v>L^2}{hD}\right)^{1/3} \qquad [16]$$

$$\delta = |i_{avg}|\, ZFL/RT\kappa_\infty \qquad [17]$$

where J, N, and δ represent the dimensionless exchange, average limiting, and average current densities. The average limiting current corresponds to $\delta = 0.807N$, obtained by substituting Eq. [7] and [14] into [17].

The two extreme cases are the primary and limiting current distributions which are shown in Fig. 2 for several values of h/L. The primary current distribution occurs when the electrode is reversible and there are no concentration effects ($N = \infty$, $J = \infty$). The primary current distribution (1) is

$$i/i_{avg} = \frac{\epsilon \cosh \epsilon/K(\tanh^2 \epsilon)}{\sqrt{\sinh^2 \epsilon - \sinh^2 (2x-L)\epsilon/L}} \qquad [18]$$

where $\epsilon = \pi L/2h$ and $K(m)$ is the complete elliptic integral of the first kind.

The limiting current occurs when the current distribution is limited by the mass transfer rate through the diffusion layer and is given by

$$i/i_{avg} = (2/3)(x/L)^{-1/3} \qquad [19]$$

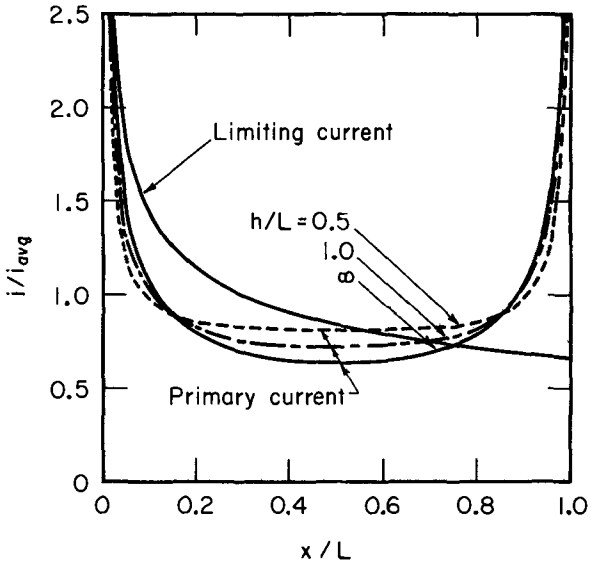

Fig. 2. Primary and limiting current distributions on channel electrodes.

Secondary current distributions occur when there is a surface overpotential but no mass transfer effects ($N = \infty$). If the current density is small ($\delta << J$), the polarization law [9] can be linearized to give

$$i = (\alpha + \beta)(ZF/RT)i_o\eta_s \qquad [20]$$

Using the coefficient in Eq. [20] [which, after multiplication by L/κ_∞, becomes $(\alpha + \beta)J$] as a parameter, Wagner (10) calculated secondary current distributions for the two cases of $h/L = \infty$ and $h/L << 1$. Linear secondary current distributions are shown in Fig. 3 for $(\alpha + \beta)J$ equal to 8π (this corresponds to Wagner's parameter $a/k_c = 4\pi$) and several values of h/L. To give an indication of current uniformity, the ratio of the maximum to minimum current density has been plotted in Fig. 4 as a function of $(\alpha + \beta)J$ and h/L.

If the average current is much greater than the exchange current ($\delta >> J$), Tafel polarization will ap-

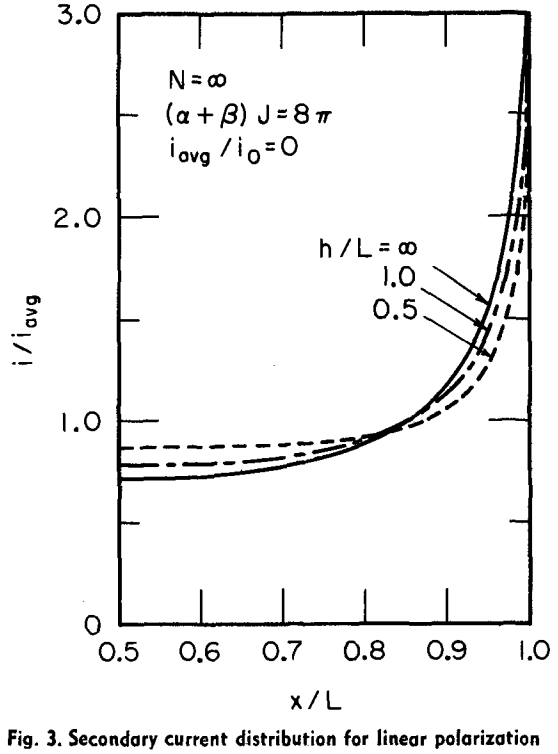

Fig. 3. Secondary current distribution for linear polarization

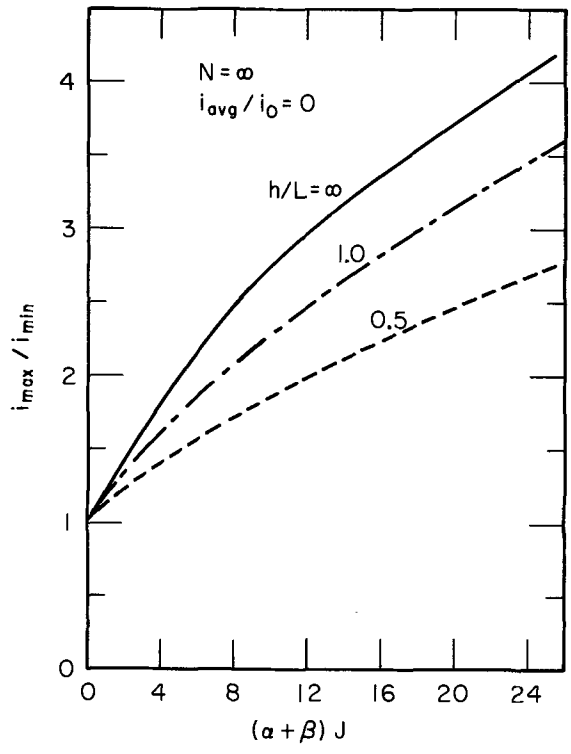

Fig. 4. Ratio of maximum to minimum current for linear polarization as a function of the parameter $(\alpha + \beta)J$.

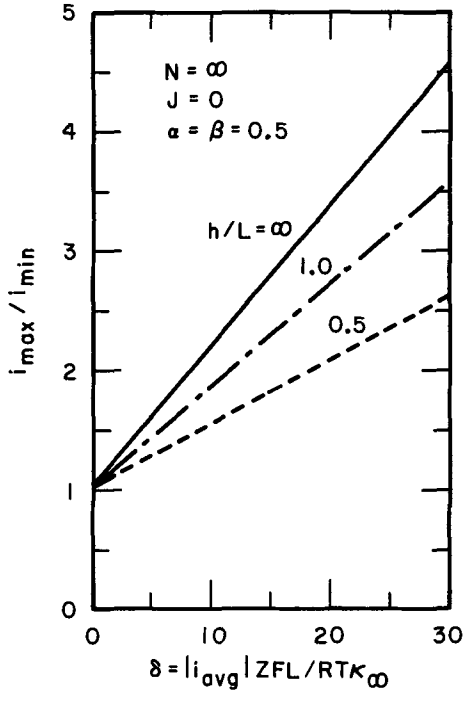

Fig. 6. Ratio of maximum to minimum current for Tafel polarization with no mass transfer effects as a function of the dimensionless average current.

ply. Equation [9] can then be written as

$$\eta_s = -(RT/ZF\beta)[\ln|i| - \ln i_o] \qquad [21]$$

for the cathode. (For the anode, α replaces β and the minus sign is omitted.) Poddubnyi, Rudenko, and Formin (11) have calculated secondary current distributions for Tafel polarization and $h/L = \infty$. Figures 5 and 6 show current distributions and current uniformity curves for Tafel kinetics.

As can be seen in Fig. 3 through 6, the current distributions become increasingly more sensitive to h/L as the ratio decreases. For all the cases considered, the current distributions for $h/L = 10$ were very close to the distributions for $h/L = \infty$.

Because mass transfer effects are important at higher current densities, we used Tafel polarization in calculating current distributions involving concentration effects. Figure 7 shows the current distribution on the cathode at various fractions of the limiting current and for three values of h/L. The current distribution on the anode is shown in Fig. 8 for a current which is 95% of the limiting current. Near the front of each electrode, the current drops rapidly, behaving like a secondary current distribution. However, on the cathode, mass transfer effects become more important with

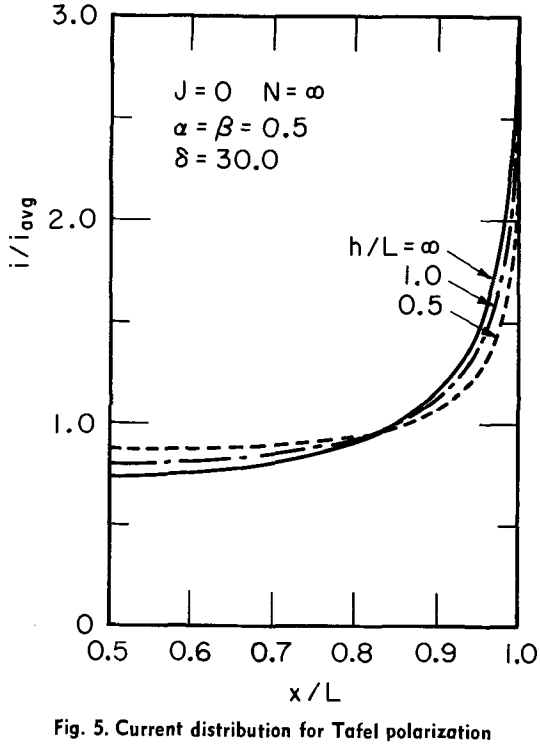

Fig. 5. Current distribution for Tafel polarization

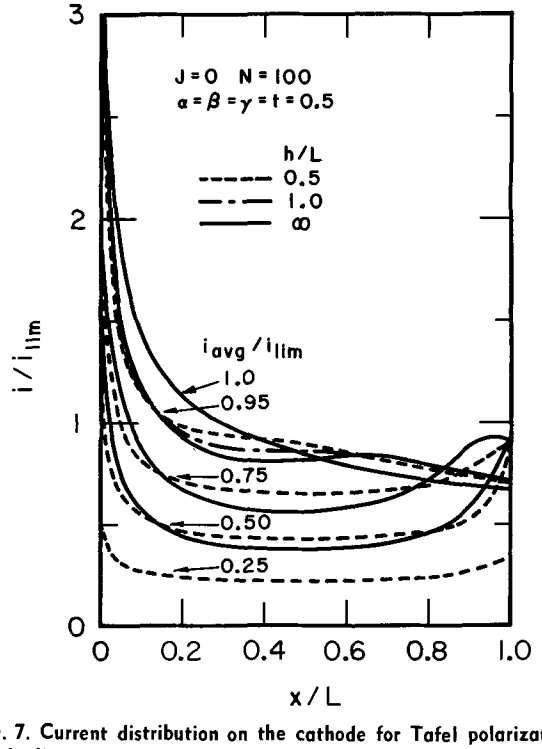

Fig. 7. Current distribution on the cathode for Tafel polarization near the limiting current.

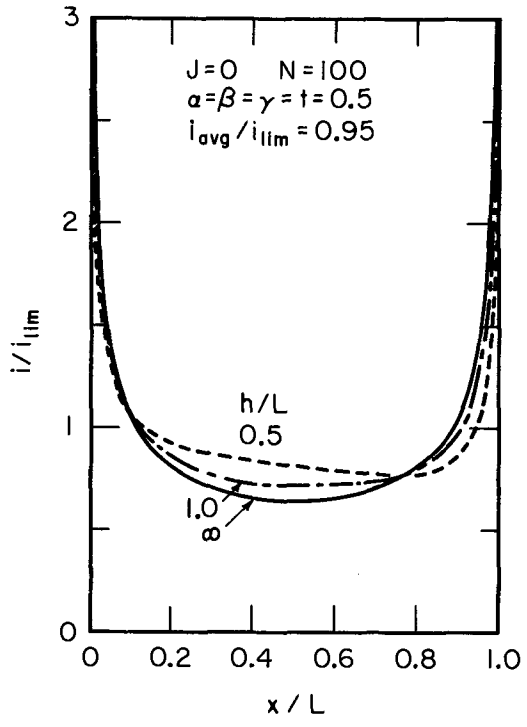

Fig. 8. Current distribution on the anode for Tafel polarization with the current at 95% of the cathodic limiting current.

increasing x/L. As the concentration profiles for the cathode show in Fig. 9, the cathodic current cannot continue to behave like a secondary current because the reactant concentration has been lowered inside the diffusion layer. But concentration effects are relatively unimportant on the anode, and the anodic current continues to resemble a secondary current distribution. The interaction between the two electrodes through Laplace's equation is very apparent for the case of $h/L = 0.5$.

The above considerations explain the maxima in the cathodic current densities. These arise from a compromise between the secondary and limiting distributions of current. The depletion of the diffusion layer eventually begins to be felt, although the local value of the limiting current density can be exceeded [compare with the disk (3)].

For the cathode, at higher current densities, the concentration drops rapidly at the front of the electrode and, as x/L increases, the concentration increases slightly before decreasing again for h/L equal to 1.0 or more. This behavior is caused by the rapid depletion of reactant at the beginning when the current density is very high. However, after the current has dropped, the concentration has a chance to increase by diffusion into the diffusion layer. Then, when the current increases, the concentration starts decreasing again. A similar but opposite behavior occurs on the anode as is shown in Fig. 10.

Although not shown, current and concentration distributions were calculated for N equal to 5 and 20, for comparable fractions of the limiting current and h/L as discussed above. At the lower values of N, the differences between the current distributions at h/L of 0.5 and infinity were less than 5 and 12% on cathode and anode at $x/L = 0.5$. Thus, for these lower values of N, some idea of the cathodic current distribution can be obtained from ref. (5). This result is in harmony with the observation that large values of the conductivity and hence small values of N and δ mean that the electrodes behave independently since they were coupled only through the ohmic potential drop. For an infinite value of the conductivity, the problem is similar to one of mass transfer and nonelectrochemical catalysis (1, 12).

Conclusions

A general approach, applied previously to flat plate and rotating disk electrodes, has been used to calculate current distributions on two plane, parallel electrodes embedded in the walls of a flow channel. The method of solution takes into account mass transfer effects as well as electrode kinetics and ohmic drop in the bulk region. The same approach should be applicable to other flow geometries if the velocity gradient is known at the electrode surface and if the potential distribution in the bulk region can be obtained from Laplace's equation.

Based on the above results, the two electrodes can be treated separately if h/L is ten or more. This is also a fairly good approximation for h/L down to 0.5 if the current density (or $(\alpha + \beta)J$ in the case of linear polarization) is relatively small. This assumption greatly reduces the numerical work required to calculate current and concentration distributions on electrodes in flow channels.

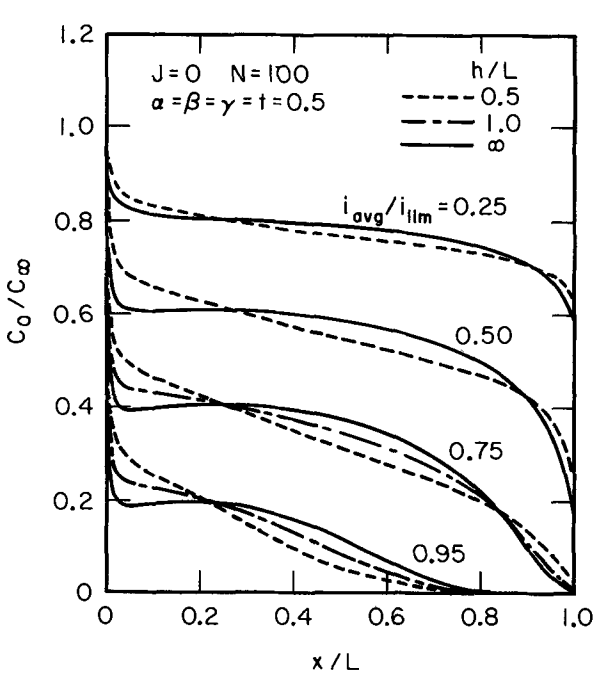

Fig. 9. Surface concentration distribution on the cathode for Tafel polarization near the limiting current.

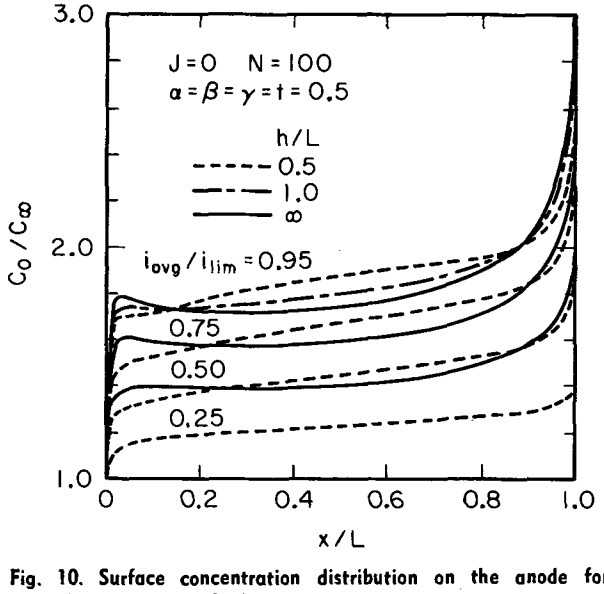

Fig. 10. Surface concentration distribution on the anode for Tafel polarization near the limiting current.

Acknowledgment

This work was supported by the United States Atomic Energy Commission.

NOMENCLATURE

c_o, concentration at electrode surface, mole/cm^3
c_x, bulk concentration of reactant, mole/cm^3
D, diffusion coefficient of reactant or of binary electrolyte, cm^2/sec
$\mathbf{F}$, Faraday's constant, 96,487 coul/equiv
h, height of flow channel, cm
i, normal current density at electrode surface, A/cm^2
i_{avg}, magnitude of average current density, A/cm^2
i_{lim}, average limiting current density, A/cm^2
i_o, exchange current density, A/cm^2
J, dimensionless exchange current density (see Eq. [15])
K, complete elliptic integral of the first kind
L, length of electrode, cm
n, number of electrons produced when one reactant ion or molecule reacts
N, dimensionless limiting current (see Eq. [16])
R, universal gas constant, joule/mole-deg
t, transference number of reactant
T, absolute temperature, °K
$<v>$, average velocity, cm/sec
V, potential of electrode, V
x, distance along electrode, cm
y, normal distance from electrode, cm
z_i, charge number of species i
Z, see Eq. [12] and [13]
α,β,γ, parameters of kinetic expression (see Eq. [9])
$\Gamma(4/3) = 0.89298$, the gamma function of 4/3
δ, dimensionless average current density (see Eq. [17])
$\epsilon = \pi L/2h$
η_c, concentration overpotential, V
η_s, surface overpotential, V
κ_x, conductivity of bulk solution, ohm^{-1}-cm^{-1}
Φ, potential in bulk solution, V
Φ^o, potential in bulk solution extrapolated to electrode surface, V
Φ^*, integration constant (see Eq. [4])

Manuscript submitted April 7, 1969; revised manuscript received Aug. 29, 1969.

Any discussion of this paper will appear in a Discussion Section to be published in the December 1970 JOURNAL.

REFERENCES

1. John Newman, *Ind. Eng. Chem.*, **60** [4], 12 (1968).
2. John Newman, *Intern. J. Heat Mass Transfer*, **10**, 983 (1967).
3. John Newman, *This Journal*, **113**, 1235 (1966).
4. John Newman, *ibid.*, **114**, 239 (1967).
5. W. R. Parrish and John Newman, *ibid.*, **116**, 169 (1969).
6. H. S. Carslaw and J. C. Jaeger, "Conduction of Heat in Solids," 2nd Ed., p. 30, Clarendon Press, Oxford (1959).
7. Andreas Acrivos and P. L. Chambré, *Ind. Eng. Chem.*, **49**, 1025 (1957).
8. Milton Abramowitz and I. A. Stegun, Editors, "Handbook of Mathematical Functions.," p. 919, National Bureau of Standards. Washington, D.C. (1964).
9. L. V. Kantorovich and V. J. Krylov, "Approximate Methods of Higher Analysis," translated by C. D. Benster, p. 101, Interscience Publishers, Inc., New York (1959).
10. Carl Wagner, *This Journal*, **98**, 116 (1951).
11. N. P. Gnusin, N. P. Poddubnyĭ, E. N. Rudenko, and A. G. Formin, *Elektrokhim.*, **1**, 452 (1965).
12. D. E. Rosner, *This Journal*, **113**, 624 (1966).

Emf of Isothermal and Nonisothermal Formation Cells of Molten Silver Halides

C. R. Metz*,[1] and R. L. Seifert*

Department of Chemistry, Indiana University, Bloomington, Indiana

ABSTRACT

Studies of isothermal formation cells by the electronic commutator method gave the following equations for $E°$ of formation of silver halides.

AgCl (478°-731°C): $E° = 0.9081 - 0.280 \times 10^{-3} (t - 455) + 0.110 \times 10^{-6} (t - 455)^2$

AgBr (447°-743°C): $E° = 0.7997 - 0.288 \times 10^{-3} (t - 432) + 0.097 \times 10^{-6} (t - 432)^2$

AgI (558°-730°C): $E° = 0.5720 - 0.227 \times 10^{-3} (t - 558) + 0.220 \times 10^{-6} (t - 558)^2$

The $E°$'s and derived formation constants $\Delta G°$, $\Delta H°$, $\Delta S°$, and $\Delta C°_p$ are compared with values obtained by others from calorimetric data and by use of reversible formation cells. Nonisothermal data reveal that large errors in reversible cell measurements will result from small temperature changes produced at the cathode by adding halogen from outside the cell. Combination of the iso- and nonisothermal data gives the following values, in mV/deg, for the thermoelectric power of molten silver halide thermocells.

AgCl (500°-700°C): $\theta_{Ag} = -0.378 \quad \theta_{Cl_2} = -0.725 + 2.4 \times 10^{-4} (t - 500)$

AgBr (500°-700°C): $\theta_{Ag} = -0.417 \quad \theta_{Br_2} = -0.776 + 3.5 \times 10^{-4} (t - 500)$

AgI (600°-700°C): $\theta_{Ag} = -0.432 \quad \theta_{I_2} = -0.859$

These values agree with direct determinations within the present rather large error limits. However, consistencies in the observed variations suggest that in formation cells the concentration gradients of solutes resulting from solution of silver and halogen at the electrodes may produce a significantly greater potential drop in the thermal gradient of a nonisothermal formation cell than in the corresponding thermocell, having a smaller gradient of only one solute.

The important thermodynamic quantities, $\Delta G°$, $\Delta H°$, $\Delta S°$, and $\Delta C°_p$ for the formation of a binary molten electrolyte, can be evaluated most readily from measurements over a range of temperature of $E°$ for its formation cell, *i.e.* a reversible voltaic cell in which the cell reaction is the formation of the electrolyte from its constituent elements. Such measurements have been made for a number of molten chlorides, bromides, and iodides with the cell $C|M|MX_n(liq)|X_2,C$, where X_2 is the halogen Cl_2, Br_2, or I_2, and M is the metal of the halide MX_n. However, when cells have been used in which the halogen has been introduced at the carbon cathode from an external source, different investigators have in many cases obtained widely varying results with the same halide. Apparently this is due primarily to thermal gradients within the cells and/or to depolarization when the halogen is introduced too slowly or does not contact the entire surface of the electrode or, as in some cases, when its flow has been interrupted during emf measurements. The pulsed electrolysis, or electronic commutator, technique for determining the reversible $E°$ of such cells has been shown to be reliable in studies with silver chloride (1) and lead chloride (2). In each case, however, a temperature existed above which it was not possible to produce cells free of depolarization, 910°C for AgCl and 640°C for $PbCl_2$ (extended to 865°C with chlorine atmosphere above the melt). Below these temperatures the cells met the requirements of reproducible emf, absence of hysteresis effects, and adherence to the Nernst equation with changing pressure. The reproducibility of emf values indicated a precision of measurement greater than that achieved in most earlier studies by the conventional reversible cell method.

In the commutator method, square-wave current pulses are passed between inert graphite electrodes in the molten halide to form the constituents of a reversible cell. Pulsing cycles have ranged from 0.04 to 1.0 sec, with current pulse lengths of 0.008-0.25 sec. Cell emf is determined as a function of time between pulses. If satisfactorily functioning electrodes are formed, there is rapid decay of overpotential, followed by a slow, essentially linear emf decay resulting from diffusion of one or both reactants from the electrode(s). The linear, diffusion-controlled portion of the emf decay curve is extrapolated to current-off time to obtain the reversible cell emf for the reactant activities at that time. Pulse current and/or pulse time are increased until a constant value is obtained for this extrapolated emf of the cell at 760 Torr. This is $E°$ for the cell if mutual solubilities of cell constituents are very low. If mutual solubilities of the elements and the salt are significant, proper corrections must be made by use of the Nernst equation. Observation of the shape of the emf decay curve and its change, if any, with time and with increasing pulsing current reveals whether the electrodes are functioning satisfactorily, whether maximum activities at 1 atm have been obtained, and whether convection currents that produce fluctuating electrode temperature are present in the cell. The cell signal, therefore, gives more information about the state and functioning of the cell than is available to one employing the conventional reversible cell method. Because no gas bubbles through the melt from an external source, it is easier to maintain a uniform cell temperature. A more detailed discussion of the technique has been given by Warner (3).

In this investigation isothermal measurements were made with silver bromide and silver iodide to deter-

Key words: formation cell, nonisothermal cell, fused salt, silver halides.

* Electrochemical Society Active Member.

[1] Present address: Department of Chemistry, Indiana University-Purdue University at Indianapolis, Indianapolis, Indiana.

mine whether suitable bromine and iodine electrodes can also be achieved by this technique. Measurements with silver chloride were repeated because the improved equipment and techniques permit greater precision and accuracy than could be achieved in the earlier investigation (1). The emf of these three halide formation cells was also measured under nonisothermal conditions to determine the magnitude of error arising from relatively small temperature differences between the cell electrodes and, by combination with the isothermal data, to derive emf values of silver and halogen thermocells for the three silver halides.

Experimental

Reagents.—Reagent grade silver chloride (Fisher Scientific Company) was used. The silver bromide (Goldsmith Brothers) had stated purity of 99.9% and the AgI was certified by the supplier (Fisher Scientific Company) to have silver content of 45.95%. No additional purification was attempted. After overnight evacuation of each cell, the halide was melted under vacuum. Dry, oxygen-free nitrogen was then introduced and permitted to flow slowly through the upper part of the cell container. A bubbler, with adjustable head of Halo-carbon polychlorotrifluoroethylene oil, was used to maintain a nitrogen pressure of 760 Torr in the cell.

Electrodes.—Each electrode consisted of a short length of spectroscopic graphite rod (Ultra Carbon Corporation, lot 1001-5, 3/32 in. diam) the pointed end of which had been thermally pretreated as described by Warner (2, 3). The graphite was sealed in a 4-mm ID fused quartz tube by evacuating the tube and, by heating, collapsing the quartz onto the graphite from 1 cm above the pointed end of the electrode for a length of 1-2 cm, which covered the junction of a platinum wire lead with the graphite. The quartz tube below the seal provided a hood about the electrode.

This construction of the electrodes resulted in the following cell after silver, Ag, and halogen, X_2, were liberated at the graphite electrodes by electrolysis pulses

$$(-)\ \mathrm{Cu|Pt|C|Ag|AgX(liq)|X_2,C|Pt|Cu}\ (+) \quad [A]$$

The cell diagram [A] is written to include all interfaces up to the measuring circuit. The copper-platinum junctions were at room temperature and the platinum-graphite junctions were at the electrode temperatures.

Temperature measurement.—Cell temperatures were determined with Pt-$Pt_{90}Rh_{10}$ thermocouples, calibrated against a Leeds and Northrup Reference Thermocouple (certified maximum error of ±0.75°C below 1100°C). Each thermocouple was protected from electrolysis products by a close-fitting fused-quartz sheath containing a small amount of the molten salt as heat transfer medium. A differential thermocouple, with junctions 2.5 cm apart in a fused-quartz sheath, was used to detect thermal gradients in the melt.

Electronic commutator and associated circuitry.—The circuit used was similar to that employed by Warner (3), but was modified to provide total on- and off-time cycles as large as 1.1 sec and to reduce instability and noise in the observed signal. Circuit details are given elsewhere (4). During the period of diffusion-controlled emf decay, the cell emf was balanced against a L&N type K-3 potentiometer and the difference signal, amplified by a Philbrick Type P2 d-c amplifier, was displayed on a Tektronix Type 585A CRO with Type D plug-in unit and was readily compared with a trace for grounded input. The horizontal sweep was internally triggered at any desired time following the current-off pulse from the commutator. Cell emf at any desired time during a single trace could be determined with a precision of about ±0.03 mV. However, due to small convection currents within the cell or other transient effects, successive traces wandered randomly from an average, or midpoint, value by ±0.1 mV under the best conditions at the lower temperatures to as much as ±1.0 mV at the highest temperatures. A midpoint trace was used to determine the cell emf.

Isothermal cell.—The melt was held in a 50-cc Triangle RR Morganite alumina crucible, contained in a 5.7-cm OD x 61-cm closed-end Coors alumina tube. This outer tube fitted into a 6.3-cm ID x 24-cm well in a 12.5-cm OD x 28-cm Hastelloy X heat ballast inside a 12.8-cm ID x 31-cm crucible furnace. The alumina tube was closed at the top by an aluminum plate making a gastight O-ring seal with a water-cooled aluminum ring sealed to the tube by quartz cement. A 4.5-cm diam x 1.8-cm graphite cover was placed on the 50-cc crucible to function as a heat shield, to reduce convection currents immediately above the cell, and to reduce loss of salt by evaporation. Its effectiveness was limited by the four holes passing through it to admit the electrodes, thermocouple, and differential thermocouple. Further details are given elsewhere (4).

Electrodes and thermocouples were inserted after the halide had been melted under vacuum and positive pressure of purified nitrogen had been established. The electrodes and the thermocouple for measurement of cell temperature were placed at the same level in the melt. Pressure inside the cell was adjusted to 760 Torr and current was pulsed through the cell until a steady value was obtained for the cell emf extrapolated to current-off time. About 15 min were usually required. Pulsing current or the ratio of on- to off-time was increased until the extrapolated emf became constant with further increase in current. The vapor pressures of the silver halides (5, 6) and the solubility of silver in silver chloride and silver bromide (7, 8) are negligible in the temperature ranges of these measurements. In the absence of quantitative data concerning the solubility of silver in silver iodide and of each halogen in the corresponding silver halide, it has been assumed that these solubilities are negligible, and that the observed maximum extrapolated emf values at 1 atm are $E°$ values. For this assumption to introduce an error of 0.1 mV in the reported values of $E°$, a solubility would have to exceed 0.2 m/o (mole per cent); for an error of 0.5 mV, 0.8 m/o. After a prolonged period of measurements, depolarization of cell emf occasionally became apparent. This resulted from growth of a silver dendrite to a point near the halogen electrode and was eliminated by rotation of the silver electrode or insertion of new electrodes.

The electrolyte temperature at the level of the electrodes was maintained constant within ±0.1°C during measurements near 450°C and ±0.5°C near 750°C. The maximum vertical temperature gradient was 1.9°C/cm, observed during a measurement at 650°C. For each set of data, $E°$ determinations were made both while ascending and descending the temperature range. Maximum temperature for measurement was determined by the point at which it was impossible to attain constant extrapolated emf by increase in pulsing current. Reproducibility was determined by making successive runs for each halide with different samples of the halide and by using more than one electrode pair in six of the eight runs. The electrodes differed in the size and location of the opening in the hood and in the area of exposed graphite surface.

Nonisothermal cell.—The nonisothermal data were obtained with a U-shaped fused-quartz cell having 15-mm ID x 36-cm vertical arms and a horizontal tube, 4 mm ID x 13.5 cm. A graphite electrode and thermocouple were inserted in each cell arm so that the thermocouple junction was at the same height and approximately at the same distance from the cell wall

as the electrode. The cell was heated in an H furnace, permitting independent temperature control of the two electrode compartments. Each vertical arm of the cell was enclosed for a height of 19 cm inside the furnace by a heavy-wall Inconel tube to aid in maintaining a uniform temperature. The temperature of one electrode was held at a constant reference value while that of the other electrode was set at various values within ±50°C of the reference temperature. Cell emf was determined as described for the isothermal cells, except that the cell was open to the atmosphere. Emf corrections to 760 Torr were calculated. Corrections were also made for the thermoelectric emf introduced by the platinum-graphite junctions at the electrodes and for small changes in the reference electrode temperature during a series of measurements.

Results

Isothermal cells.—Typical data are given in Table I for the cell C|Ag|AgCl(liq)|Cl_2,C. A total of 56 determinations of $E°$ were made for silver chloride in the temperature range 478.4°-731.3°C, 54 for silver bromide (447.0°-742.9°C), and 44 for silver iodide (558.1°-730.4°C). For each halide the regression coefficients were evaluated for the best representation of the data by linear through fifth-order polynomials in temperature, using the method given by Bennett and Franklin (9). Computations by a CDC 3600 computer gave the regression coefficients with error estimate, the standard deviation of the experimental data for each order equation, and an analysis of variance to determine the proper order of equation to employ. Although higher order equations were valid for some individual runs, for the combined data for each halide analysis of variance indicated that quadratic equations should be used to express $E°$ as a function of temperature. Constants a, b, and c for the resulting quadratic equations, with their estimated errors based on a 99% probability limit, are given in Table II, and are to be used in the equation

$$E°\,(\text{volt}) = a - bW + cW^2 \qquad [1]$$

W is 0.001 $(t - t_{m.p.})$ where t is the cell temperature in °C, and $t_{m.p.}$ is the arbitrarily accepted melting point of the halide (Table II). The standard deviations of the experimental points from these equations for AgCl, AgBr, and AgI were ±0.7, ±0.8, and ±0.8 mV, respectively. Values of $E°$ calculated by these equations within the experimental temperature ranges have possible errors, based on a 99% probability limit, of ±0.42, ±0.54, and ±0.57 mV, respectively. The experimental points are shown on the difference plots given in Fig. 1, 2, and 3. In each figure the dark curve corresponds to Eq. [1] and Table II. The light curves represent results of electrochemical measure-

Table I. Typical data for the cell C|Ag|AgCl(liq)|Cl_2,C

Temperature	515.9°C
Pressure	760 Torr
Cell resistance	6.2 ohms
Pulsing current	32 mA
Current on time	0.18 sec
Current off time	0.87 sec
Trigger delay time	0.44 sec
EMF at end of off time	0.8904V
Slope	−0.35 mV/sec
$E°$ (extrapolated)	0.8907V
Signal reproducibility	±0.3 mV

Table II. Coefficients for use in Eq. [1], [2], [3], [4], and [5] to calculate $E°$, $\Delta G°$, $\Delta S°$, $\Delta H°$, and $\Delta C°_p$ of formation for liquid silver halides

	AgCl	AgBr	AgI
W:	10^{-3} $(t - 455)$	10^{-3} $(t - 432)$	10^{-3} $(t - 558)$
a:	0.9081 ± 0.00074	0.7997 ± 0.00075	0.5720 ± 0.00057
b:	0.280 ± 0.015	0.288 ± 0.015	0.227 ± 0.026
c:	0.110 ± 0.049	0.097 ± 0.044	0.220 ± 0.149
d:	20.942 ± 0.017	18.442 ± 0.017	13.191 ± 0.013
e:	6.46 ± 0.35	6.64 ± 0.35	5.23 ± 0.60
f:	2.54 ± 1.13	2.24 ± 1.01	5.07 ± 3.44
g:	5.07 ± 2.26	4.47 ± 2.03	10.15 ± 6.87
h:	25.64 ± 0.27	23.13 ± 0.26	17.54 ± 0.51
i:	3.69 ± 1.65	3.16 ± 1.43	8.43 ± 5.71
Exptl. range:	478°-731°C	447°-743°C	558°-730°C

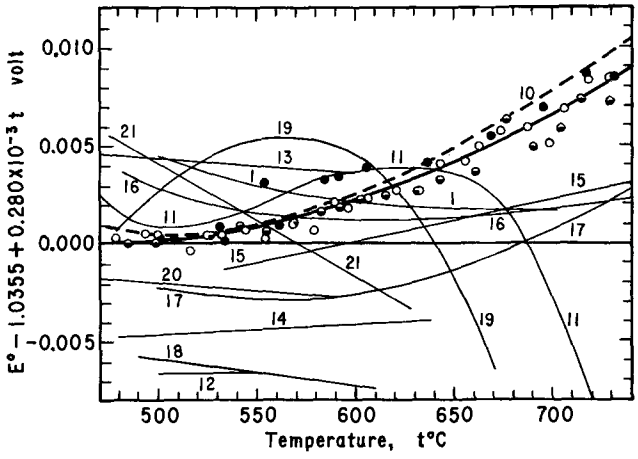

Fig. 1. $E° - (a - bW)$ for the cell C|Ag|AgCl(liq)|Cl_2,C for three independent runs, indicated by ○, ◒, ●. Dark curve is based on constants in Table II used in Eq. [1]. Dashed curve is based on thermochemical data (10). Light curves represent electrochemical measurements by investigators who are identified by the curve numbers, which correspond to entries under References.

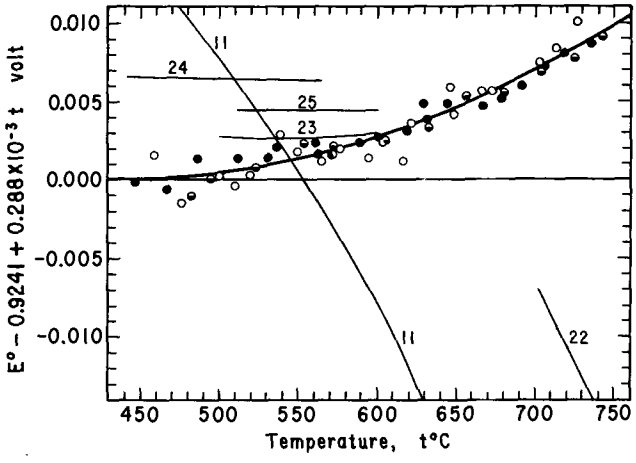

Fig. 2. $E° - (a - bW)$ for the cell C|Ag|AgBr(liq)|Br_2,C for three independent runs, indicated by ○, ◒, and ●. Dark curve is based on constants in Table II used in Eq. [1]. Numbered curves represent measurements by other investigators, (11, 22-25).

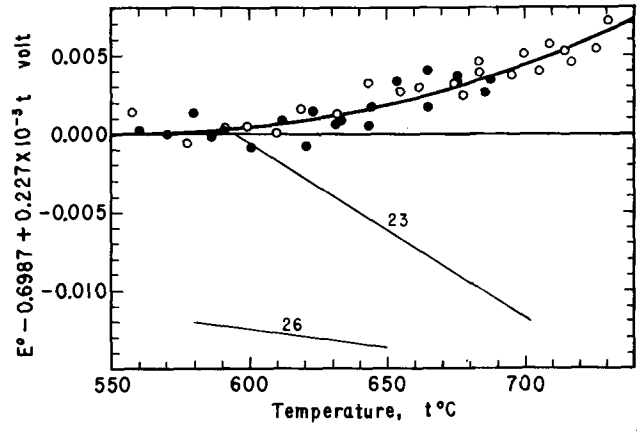

Fig. 3. $E° - (a - bW)$ for the cell C|Ag|AgI(liq)|I_2,C for two independent runs, indicated by ○ and ●. Dark curve is based on constants in Table II used in Eq. [1]. Numbered lines represent measurements by other investigators, (23) and (26).

ments by other investigators who are identified by the numbers of the curves, which correspond to entries under References. Some of these investigators present their results only as a linear equation. This linearity is preserved in these figures by plotting all results relative to the line defined by the first two terms in Eq. [1], *i.e.* by plotting differences of $E°$ from $a - bW$ where a, b, and W are given in Table II for each halide.

In Fig. 1 the dashed curve corresponds to $E°$'s calculated by Hamer, Malmberg, and Rubin (10) from thermochemical data. A five-term equation of the form they used in their calculations was used to interpolate between the values they give for $E°$ at 500°, 600°, 800°, 1000°, and 1500°C. The dashed curve lies within the 99% probability limit for the dark curve from 491° to 626°C. The data for curve 1 were obtained by the electronic commutator polarization method during its early development. Temperature measurement and control were not as accurate as for the present measurements. Data for curves 11 and 12 were obtained by the polarization method in which the halide was electrolyzed for a considerable time and the emf of the resulting cell was measured as rapidly as possible thereafter. The remaining curves are based on data obtained by the conventional reversible cell method. The data for curves 1, 11, and 13-18 were free from or had been corrected for the thermoelectric emf resulting from the temperature gradient in dissimilar leads to the cell electrodes. The authors of (12), (19), (20), and (21) do not state whether this correction was made for the silver and graphite leads in their cells. If it was not made, the corresponding curves in Fig. 1 may be low by as much as 1.0 mV at 450°C to 2.1 mV at 750°C, depending on the temperature at the connection of the electrode materials with the measuring circuit. Curves 11 and 19 show clearly the effect of depolarization at high temperatures resulting from rapid diffusion of chlorine from the cathode. Similar drop in emf was observed in this investigation at temperatures above the ranges for which data are reported. Some or all of the variation between curves in Fig. 1, 2, and 3 not resulting from depolarization may result from temperature gradients within the cells. Halogen introduced from outside the conventional reversible cell must be preheated to exactly the cell temperature. As shown by the measurements with nonisothermal cells in this investigation, cooling of the chlorine electrode by only 7°C produces the same vertical displacement (5 mV) of a point at 600°C in Fig. 1 as an error of 20°C in measurement of the temperature of an isothermal cell.

In Fig. 2 and 3, curves 11, 22, and 23 were obtained by the polarization method. [Czepinski's results (11) for AgI are not shown in Fig. 3 because they lie below −0.030V on the scale plotted, and Weber's (22) results for AgCl are not shown in Fig. 1 because they lie above 0.027V.] Graphite electrodes were used for curves 11 and 22. Silver and graphite electrodes were used for curves 23 but it was not stated whether correction was made for the thermoelectric emf present. Curves 24-26 are based on properly corrected reversible formation cell data. The values of $E°$ calculated from thermochemical data by Hamer, Malmberg, and Rubin (27) differ from the dark curves, calculated by Eq. [1] and Table II, by 0.45, 0.44, −0.07, −0.05, and −0.85 mV for AgBr at 450°, 500°, 550°, 600°, and 800°C, respectively, and by 0.15 and −1.95 mV for AgI at 600° and 800°C. Except for the values at 800°C, which is above our experimental temperature range (Table II), these differences are all within the 99% probability error limits of the equations given by Eq. [1] and Table II. However, disagreement is greater with other compilations based on thermochemical measurements.

Equations for $\Delta G°$, $\Delta S°$, $\Delta H°$, and $\Delta C°_p$ of formation of each liquid silver halide from silver and the corresponding halogen can be derived from Eq. [1]. Values of constants d, e, f, g, h, and i are given in Table II for use in the following equations (gibbs = cal/deg).

$$\Delta G° \text{ (kcal/mole)} = -d + eW - fW^2 \quad [2]$$

$$\Delta S° \text{ (gibbs/mole)} = -e + gW \quad [3]$$

$$\Delta H° \text{ (kcal/mole)} = -h + iW + fW^2 \quad [4]$$

$$\Delta C°_p \text{ (gibbs/mole)} = i + gW \quad [5]$$

Values calculated by these equations are given in Table III for each halide at its reference temperature (for which $W = 0$) and at multiples of 100° up to 1000°K. To one significant figure, the 99% probability error limits computed from the error terms in Table II are the same for the AgCl and AgBr results, being ±0.02 kcal/mole for $\Delta G°_f$, ±0.3 gibbs/mole for $\Delta S°_f$, and ±0.3 kcal/mole for $\Delta H°_f$. For AgI the corresponding terms are ±0.01 kcal/mole, ±0.6 gibbs/mole, and ±0.6 kcal/mole, respectively. For $(\Delta C°_p)_f$ the 99% probability error limits are best stated as percentages of the values given for $(\Delta C°_p)_f$ in Table III, being ±44.5% for AgCl, ±45.1% for AgBr, and ±67.9% for AgI (which are also the percentage errors of f in Table II).

Table III also includes the corresponding thermodynamic formation constants calculated by the equations of Wicks and Block (28) for AgCl and AgBr and values estimated by them for AgI at 1000°K. Their equations are based on a survey of thermodynamic literature published through 1959. For AgCl the values of $\Delta S°_f$, $\Delta H°_f$, and $(\Delta C°_p)_f$ agree well within the 99% probability error limits of Eq. [3-5]. However, the differences for $\Delta G°_f$ are three times the calculated 99% probability error limit. Except for the $(\Delta C°_p)_f$ values, where the error limits are large for the electrochemically determined values, agreement is poor for AgBr, as is the agreement between the values calculated by Eq.[2-4] for AgI at 1000°K and those estimated by Wicks and Block (28). For AgBr their values of $\Delta G°_f$ and $\Delta H°_f$ are less negative by as much as 4.44 and 3.46 kcal/mole, respectively; and for AgI at 1000°K their estimated values of $\Delta G°_f$ and $\Delta H°_f$ are more negative by 6.50 and 8.57 kcal/mole, respectively. These

Table III. Comparison of thermodynamic formation constants calculated by Eq. [2-5] and Table II with values calculated by equations derived by Wicks and Block (28)

(Values in parentheses are for temperatures beyond the range given for the equations. Values in brackets are estimates by Wicks and Block.)

Halide	Temp, °K	$\Delta G°_f$ (kcal/mole)		$\Delta S°_f$ (gibbs/mole)		$\Delta H°_f$ (kcal/mole)		$(\Delta C°_p)_f$ (gibbs/mole)	
		Eq. [2]	W & B	Eq. [3]	W & B	Eq. [4]	W & B	Eq. [5]	W & B
AgCl	728	−20.94	−20.90	−6.47	−6.66	−25.65	−25.75	3.7	4.99
	800	−20.49	−20.44	−6.09	−6.20	−25.36	−25.40	4.1	4.84
	900	−19.91	−19.85	−5.60	−5.64	−24.94	−24.92	4.6	4.63
	1000	−19.37	(−19.31)	−5.09	(−5.16)	−24.46	(−24.47)	5.1	(4.43)
AgBr	705	−18.44	−14.30	−6.65	−7.66	−23.13	−19.70	3.2	3.82
	800	−17.83	−13.60	−6.22	−7.19	−22.81	−19.35	3.6	3.63
	900	−17.23	−12.90	−5.77	−6.77	−22.43	−19.00	4.1	3.43
	1000	−16.68	(−12.24)	−5.32	(−6.42)	−22.00	(−18.66)	4.5	(3.23)
AgI	831	−13.19		−5.24		−17.55		8.4	
	900	−12.87		−4.52		−16.94		9.1	
	1000	−12.45	[−18.95]	−3.53	[−5.60]	−15.98	[−24.55]	10.1	

differences for $\Delta G°_f$ are considerably greater percentage-wise than those between the $E°$ data for AgBr and AgI and the $E°$ values calculated from thermochemical data by Hamer, Malmberg, and Rubin (27). Since both sets of authors utilized essentially the same compilations of thermochemical data, their results differ because of differences in the selection of the data they considered most reliable and in the techniques used to interpolate and extrapolate from the available data.

Wicks and Block (28) utilize as $\Delta H°_{298}$ for AgCl, AgBr, and AgI the values −30.36, −20.06, and −22.3 kcal/mole, respectively, attributing them to their Ref. (112) [Rossini *et al.*, "Selected Values of Chemical Thermodynamic Properties," NBS Circ. 500, (1952)]. The corresponding values actually given in NBS Circ. 500 are −30.362, −23.78, and −14.91 kcal/mole. The value −22.3 kcal/mole used for AgI by Wicks and Block is given in their Ref. (11). The source of their value −20.06 kcal/mole for AgBr is not apparent. Values given in the references referred to in the compilations utilized by Wicks and Block range from −22.7 to −23.81 kcal/mole. If the NBS Circ. 500 value of −23.78 kcal/mole had been used by Wicks and Block for $\Delta H°_{298}$ of AgBr, their values for $\Delta G°_f$ at 705°, 800°, 900°, and 1000°K would be −18.02, −17.32, −16.62, and −15.96 kcal/mole, which are less negative than our values by 0.42, 0.51, 0.61, and 0.72 kcal/mole; and their values for $\Delta H°_f$ at 705°, 800°, 900°, and 1000°K would be −23.42, −23.07, −22.72, and −22.38 kcal/mole, which are more negative than our values by 0.29, 0.26, 0.29, and 0.38 kcal/mole. When the equation for $\Delta G°_f$ of AgBr given by Wicks and Block (28) is used to calculate $E°$ values in the temperature range of Fig. 2, the corresponding difference values, calculated as for Fig. 2, vary from −0.180V at 450°C to −0.184V at 750°C, lying far below all the electrochemical data shown in Fig. 2. The value estimated by Wicks and Block (28) for $\Delta G°_f$ of AgI at 727°C corresponds to an $E°$ value that would lie at 0.188V on the ordinate scale of Fig. 3. Since these values lie so far from the electrochemical determinations, it follows that, at least for AgBr and AgI, the selection and utilization of thermochemical data by Hamer, Malmberg, and Rubin (27) provide more reliable values of $E°$ and the thermodynamic formation constants than that by Wicks and Block (28).

Nonisothermal formation cells.—The complete diagram for the nonisothermal silver halide formation cells, including all interfaces up to the measuring circuit, is as follows

$$(-)\ \underbrace{\mathrm{Cu}\mid\mathrm{Pt}\mid\mathrm{C}}_{t_{room}}\mid\underbrace{\mathrm{Ag}\mid\mathrm{AgX}}_{t_{Ag}}\mid\underbrace{(\mathrm{liq})\mid\mathrm{X_2,C}}_{t_{X_2}}\mid\underbrace{\mathrm{Pt}\mid\mathrm{Cu}}_{t_{room}}\ (+) \qquad [B]$$

where t_{room} is room temperature and t_{Ag} and t_{X_2} represent the temperatures of the silver and halogen electrode chambers, respectively. To correct for the Pt-graphite thermoelectric emf present in the circuit, a determination was made of the thermoelectric power, $\theta_{Pt\text{-}C}$, of a Pt-C-Pt thermocouple constructed with a graphite rod of the type used to make the cell electrodes. Based on emf measurements with one junction held at 0°C and the other at temperatures in the range t =25°-1100°C and the convention that the emf of the thermocouple is the potential of the platinum lead from the hot junction relative to that from the cold junction, the thermoelectric power was found to be

$$\theta_{Pt\text{-}C}(\mathrm{mV/deg}) = -3.3 \times 10^{-3} - 19.2 \times 10^{-6}\, t \qquad [6]$$

The correction $\theta_{Pt\text{-}C}(t_{X_2} - t_{Ag})$, where $\theta_{Pt\text{-}C}$ is taken at $t = (t_{Ag} + t_{X_2})/2$, was subtracted from the observed emfs of the nonisothermal cell [B] to obtain E', the emf that would have been observed if the temperature change from electrode temperatures to room temperature had occurred in graphite leads, as in schematic cell [C]

$$(-)\ \underbrace{\mathrm{Cu}\mid\mathrm{C}}_{t_{room}}\mid\underbrace{\mathrm{Ag}\mid\mathrm{AgX}}_{t_{Ag}}\mid\underbrace{(\mathrm{liq})\mid\mathrm{X_2,C}}_{t_{X_2}}\mid\underbrace{\mathrm{C}\mid\mathrm{Cu}}_{t_{room}}\ (+) \qquad [C]$$

The resulting values of E' for cell [C] are plotted in Fig. 4. Each series of measurements, in which one electrode was held at constant temperature, t_{ref}, and the other at variable t, may be represented by the linear equation

$$E'(\mathrm{volt}) = \alpha + \beta \times 10^{-4}\,(t - t_{ref}) \qquad [7]$$

Table IV gives the values of α and β for each series of measurements, as calculated by the method of least squares, and also gives the standard deviations of the data from the corresponding lines in Fig. 4. With each value of t_{ref} in Table IV is given its standard deviation during the series of measurements. The error

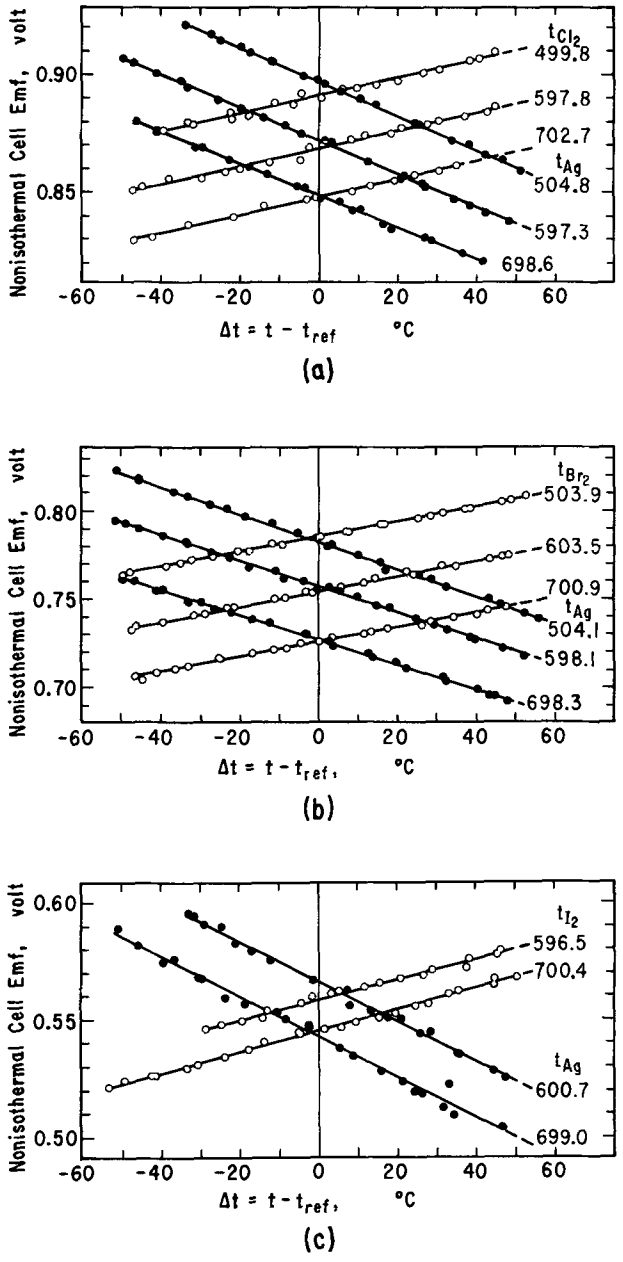

Fig. 4. Emf, E', of the nonisothermal formation cells [C] as a function of the temperature difference between the electrodes. ○ for constant $t_{X_2} = t_{ref}$ and variable $t_{Ag} = t$. ● for constant $t_{Ag} = t_{ref}$ and variable $t_{X_2} = t$. For each line t_{ref} is given at the right. (a) Silver chloride cell, X = Cl. (b) Silver bromide cell, X = Br. (c) Silver iodide cell, X = I.

Table IV. Constants for Eq. [7] to represent the nonisothermal cell data and their standard deviations

Halide	Reference electrode	t_{ref} (°C)	$E°_{ref}$ (volt)	α	β	Standard deviation (mV)
AgCl	Ag	504.8 ± 0.4	0.8944	0.8972	−7.21 ± 0.12	±0.5
		597.3 ± 0.8	0.8705	0.8720	−7.07 ± 0.14	±0.7
		698.6 ± 1.0	0.8464	0.8488	−6.75 ± 0.20	±0.8
	Cl_2	499.8 ± 0.6	0.8958	0.8911	3.86 ± 0.32	±1.2
		597.8 ± 1.0	0.8704	0.8687	3.83 ± 0.32	±1.4
		702.7 ± 1.6	0.8455	0.8480	3.85 ± 0.24	±0.8
AgBr	Ag	504.1 ± 0.6	0.7794	0.7827	−7.78 ± 0.13	±0.7
		598.1 ± 0.9	0.7545	0.7568	−7.36 ± 0.19	±1.1
		698.3 ± 0.7	0.7299	0.7266	−7.10 ± 0.16	±0.9
	Br_2	503.9 ± 0.3	0.7795	0.7851	4.24 ± 0.10	±0.5
		603.5 ± 0.7	0.7532	0.7543	4.34 ± 0.13	±0.7
		700.9 ± 0.8	0.7293	0.7253	4.13 ± 0.19	±0.9
AgI	Ag	600.7 ± 0.6	0.5627	0.5662	−8.59 ± 0.44	±1.7
		699.0 ± 0.9	0.5444	0.5426	−8.59 ± 0.58	±2.7
	I_2	596.5 ± 0.4	0.5636	0.5586	4.28 ± 0.34	±1.2
		700.4 ± 0.9	0.5441	0.5452	4.51 ± 0.18	±1.0

term for β is the estimate of confidence based on a 99% probability limit.

Values of $E°_{ref}$ in Table IV were calculated by Eq. [1] and Table II for the isothermal cell [A] at t_{ref}. The random variation (up to 5.6 mV) between $E°_{ref}$ and α no doubt results primarily from failure to eliminate temperature gradients within the electrode chambers of the nonisothermal cells. Small temperature differences must have existed between electrode and thermocouple in one or both chambers. Since the electrode and thermocouple placements were not changed during the series of measurements for each reference temperature, any error from this source was fairly constant for the reference electrode and, although somewhat variable in magnitude, always in the same direction for the other electrode. This would shift each average line in Fig. 4 to left or right, with little influence on the slope, which is the characteristic utilized in the following discussion.

The data in Table IV, for the nonisothermal formation cells, can be combined with data in Table II, for the isothermal formation cells, to obtain emf's for the silver halide thermocells. This provides a means of checking the self-consistency of all the electrochemical data involved, and in this case provides information regarding the iodine-silver iodide thermocell which has apparently not yet been studied.

As seen from the following cell diagrams, the sum of the interphase potential differences in a silver halide thermocell with halogen electrodes at temperatures t_{ref} and t (suppose, for the time being, that t is the temperature of the hotter electrode)

$$\underbrace{\mathrm{C,X_2|AgX}}_{t_{ref}}\underbrace{\mathrm{|X_2,C}}_{t} \quad (E_{th,X_2}) \qquad [D]$$

equals the sum of the interphase potential differences in the series combination

$$\underbrace{\mathrm{C,X_2|AgX|Ag|C}}_{t_{ref}} - \underbrace{\mathrm{C|Ag|AgX}}_{t_{ref}}\underbrace{\mathrm{|X_2,C}}_{t}$$

$$(E = -E°_{ref} + E'_{Ag}) \qquad [E]$$

where $E°_{ref}$ is the emf of the isothermal formation cell [A] at t_{ref}, and E'_{Ag} is the emf of nonisothermal formation cell [C] with the silver electrode held at the constant reference temperature. Similarly, the sum of interphase potential differences in

$$\underbrace{\mathrm{C|Ag|AgX|X_2,C}}_{t_{ref}} - \underbrace{\mathrm{C,X_2|Ag}}_{t_{ref}}\underbrace{\mathrm{X|Ag|C}}_{t}$$

$$(E = E°_{ref} - E'_{X_2}) \qquad [F]$$

where E'_{X_2} is the emf of cell [C] with the halogen electrode held at the constant reference temperature, equals the sum for the thermocell

$$\underbrace{\mathrm{C|Ag|Ag}}_{t_{ref}}\underbrace{\mathrm{X|Ag|C}}_{t} \quad (E_{th,C|Ag}) \qquad [G]$$

If the liquid AgX phases were pure, the potential drop induced by the temperature gradient between electrodes in the thermocells would equal that in the corresponding nonisothermal formation cells. However, the molten silver halide in the formation cells contains a concentration gradient of dissolved halogen (presumably present primarily as X_3^-) and of dissolved silver (probably present primarily as Ag_2^+ or $Ag_n^{(n-1)+}$). The halide in the thermocell with halogen electrodes then contains a small concentration gradient of X_3^-, resulting from the small difference in solubility of X_2 at t and t_{ref}; whereas, in the corresponding portions of halide melt in the two formation cells, the concentration gradients of X_3^- are much greater and there is also an opposing gradient of Ag_2^+ at very low concentrations. For each solute the concentration gradient in one formation cell opposes that in the other cell. Therefore any accompanying potential gradients are opposed, but their net contribution to potential drop will equal that resulting from the smaller concentration gradient in the thermocell only if the potential drop accompanying concentration change is dependent only on the concentrations of the solute at the electrodes and if the contribution to potential drop resulting from temperature gradient is independent of solute concentration. The corresponding situation, with X_3^- and Ag_2^+ interchanged, exists in the thermocell with Ag electrodes and the corresponding combination of formation cells. If the net effect of the potential gradients resulting from the concentration gradients is negligible in every case, or if it is essentially the same for a combination of formation cells as for the corresponding thermocell, then the observed emf of each thermocell, [D] or [G], should equal that of the corresponding combination of formation cells, [E] or [F].

To deal with the contingency where $t < t_{ref}$, *i.e.*, where the variable temperature electrode in the thermocell is cooler than the constant reference temperature electrode and Δt (Fig. 4) is negative, the following algebraic conventions must be introduced.

By convention, the emf of a thermocell, E_{th}, like that of a thermocouple, is the potential of the lead from the hotter electrode relative to that of the lead from the cooler electrode. The emf of the silver halide formation cells [A], [B], and [C] is the potential of the lead from the halogen electrode relative to that of the lead from the silver electrode. It is then necessary to use $\pm$ in Eq. [8], [9], and [10], according as $\Delta t = \pm$, so that

$$E_{th,X_2} = \pm E\,[D] = \pm (E'_{Ag} - E°_{ref}), \text{ for } \Delta t = \pm \qquad [8]$$

$$E_{th,C|Ag} = \pm E\,[G] = \pm (E°_{ref} - E'_{X_2}), \text{ for } \Delta t = \pm \qquad [9]$$

In past studies of thermocells with silver electrodes, silver leads have connected the electrodes with the measuring circuit or correction has been made for the thermoelectric emf introduced by use of different leads. Since the values of E' plotted in Fig. 4 and calculated by Eq. [7] are for graphite leads, cell [C], it is necessary to correct Eq. [9] for the graphite-silver thermoelectric emf, E_{C-Ag}, to obtain values comparable with reported emf's for thermocells with silver electrodes and leads

$$\underbrace{\mathrm{Ag|AgX}}_{t_{ref}}\underbrace{\mathrm{|Ag}}_{t} \quad (E_{th,Ag}) \qquad [H]$$

This gives

$$E_{th,Ag} = \pm (E°_{ref} - E'_{X_2}) - E_{C-Ag}, \text{ for } \Delta t = \pm \qquad [10]$$

where E_{C-Ag} is the potential of the carbon lead from the hot junction of a C-Ag-C thermocouple relative

to that of the carbon from the cold junction. E_{C-Ag} and $E_{th,Ag}$ are both negative quantities.

Combination of published Ag-Pt thermoelectric data (29) with Pt-C data for the graphite used in this investigation, Eq. [6], gave

$$E_{C-Ag}(mV) = -(2.31 \times 10^{-3} + 3.99 \times 10^{-6}\,\Delta t + 7.98 \times 10^{-6} t_{ref})\Delta t \quad [11]$$

The maximum value of $-E_{C-Ag}$ was only 0.407 mV.

Thermocell data are expressed as thermoelectric power, $\theta = (\partial E_{th}/\partial t)_{t_{ref}}$. Therefore, from Eq. [7], [8], [10], and [11]

$$\theta_{X_2}(mV/deg) = (\partial E_{th,X_2}/\partial t)_{t_{ref}} = 0.1\,\beta_{Ag} \quad [12]$$

where β_{Ag} is the value of β in Table IV for Ag reference electrode, and

$$\theta_{Ag}(mV/deg) = (\partial E_{th,Ag}/\partial t)_{t_{ref}} = -0.1\,\beta_{X_2} + 2.31 \times 10^{-3} + 7.98 \times 10^{-6} t_{ref} \quad [13]$$

where β_{X_2} is β in Table IV for halogen reference electrode. Values thus obtained from the formation cell data are compared in Table V with thermocell data. The average of β for different reference temperatures in Table IV has been used to calculate θ_{X_2} and θ_{Ag} except where variation with temperature is consistent and exceeds the probable experimental error.

For θ_{Ag} the seven literature values with AgCl thermocells cover a range of 0.205 mV/deg or 43% of the midrange value; the three with AgBr thermocells, a range of 0.064 mV/deg or 13%; and the three with AgI, 0.12 mV/deg or 26%. If the early thermocell values by Reinhold (20) are disregarded, the ranges become 0.045, 0.010, and 0.015 mV/deg, respectively. The four literature values of θ_{Cl_2} cover a range of 0.040 mV/deg or 6%. There is only one literature value for θ_{Br_2}, by Reinhold (20), and none for θ_{I_2}.

Values of θ_{Ag} calculated by Eq. [13] from formation cell data (Table IV) are less in absolute value than the averages of the experimental thermocell values by 0.047, 0.054, and 0.030 mV/deg or 11, 11, and 6% for the AgCl, AgBr, and AgI cells, respectively. If the values by Reinhold (20) are disregarded the differences are, respectively, 0.021, 0.034, and 0.066 mV/deg or 5, 8, and 13% less in absolute value. The corresponding 99% probability error limits given by Eq. [12] and Table IV for the calculated θ_{Ag} values are ±.03, ±0.02, and ±0.03 mV/deg for AgCl, AgBr, and AgI, respectively. The value of θ_{Cl_2} for 600°C from Eq. [12] and Table IV is 0.031 mV/deg or 5% greater in absolute value than the average of the thermocell values and that of θ_{Br_2} at the melting point of AgBr is 0.185 mV/deg or 30% greater in absolute value than the single value by Reinhold (20). The 99% probability error limits for the calculated values are ±0.02 mV/deg for θ_{Cl_2} and θ_{Br_2} and ±0.06 mV/deg for θ_{I_2}. Possible errors in the thermocell data may in some cases be of comparable magnitude, although most of the values are reported to three figures.

Table V. Thermoelectric power of silver halide thermocells

Thermocell	θ (mV/deg)	Temperature range (°C)	Reference
Ag|AgCl|Ag	−0.378	500-700	Eq. [13]
	−0.400	470-570	(18)
	−0.58	465-550	(20)
	−0.395	455-650	(30)
	−0.420	490-590	(31)
	−0.375	500-900	(32)
	$-0.404 + 6.47 \times 10^{-5}(t - 500)$	500-630	(33)
	$-0.402 + 1.6 \times 10^{-5}(t - 500)$	640-825	(34)
Cl_2|AgCl|Cl_2	$-0.725 + 2.4 \times 10^{-4}(t - 500)$	500-700	Eq. [12]
	−0.695	500-645	(18)
	−0.664	500-900	(32)
	−0.655	500-900	(35)
	−0.667	480-680	(36)
Ag|AgBr|Ag	−0.417	500-700	Eq. [13]
	−0.51	425-500	(20)
	−0.456	450-550	(31)
	$-0.446 + 5.5 \times 10^{-5}(t - 500)$	450-600	(37)
Br_2|AgBr|Br_2	$-0.776 + 3.5 \times 10^{-4}(t - 500)$	500-700	Eq. [12]
	−0.61	425-465	(20)
Ag|AgI|Ag	−0.432	600-700	Eq. [13]
	−0.39	560-600	(20)
	−0.505	540-625	(31)
	−0.490	560-650	(38)
I_2|AgI|I_2	−0.859	600-700	Eq. [12]

The differences between the experimental thermoelectric power values of the silver halide thermocells and the corresponding values calculated by Eq. [12] and [13] are therefore of the same order of magnitude as the sum of the possible errors. There is some consistency among the differences in that, for all three halides, the calculated value of each θ_{Ag} is less negative than the corresponding average thermocell value and, for each of the two halides for which thermocell values are available, the calculated value of θ_{X_2} is more negative than the thermocell value. However, this may be fortuitous or result from an undetected systematic error. Therefore, within present experimental errors Eq. [12] and [13] and the assumptions involved may be considered to be valid, at least for cells in which the solubilities of the reactants at the electrodes are low. To detect effects of concentration and thermal gradients in such cells will require greatly improved accuracy of measurement.

To obtain quantitative data related to the influence of simultaneous thermal and concentration gradients on the potential drop in a molten salt, it may be more profitable to use only formation cells, isothermal and nonisothermal, because the concentration gradients are greater in such cells than in thermocells. The sum of interphase potential differences in the combination

$$\underbrace{C|Ag|AgX}_{(a),\,t}\,\underbrace{|X_2,C - C,X_2|AgX|Ag|C - C|Ag|}_{(b),\,t_{ref}}\,\underbrace{AgX|X_2,C}_{(c),\,t}$$

equals that in an isothermal formation cell (d), C|Ag|AgX|X_2,C, at temperature t. The effect on potential drop in AgX resulting from thermal gradient in cell (a) cancels that in cell (c) unless each is influenced by the concentration gradients of Ag_2^+ and X_3^-, each of which is opposed to the thermal gradient in one cell but not in the other, so that they will not have compensating effects unless the effect of concentration gradient of Ag_2^+ equals that of X_3^- in each cell. From left to right, the concentration increase of X_3^- in cell (a) is essentially the same as its decrease in (b); the increase of Ag_2^+ in (b) is essentially the same as its decrease in (c). The remaining concentration changes of Ag_2^+ in (a) and X_3^- in (c) are essentially the same as in cell (d). Therefore the net influence of concentration gradient on potential drop in the AgX of cell (d) should equal that in the cell combination (a) + (b) + (c) unless the latter is influenced by the thermal gradients in (a) and (c). If there is no such influence, then

$$E^\circ_t = E'_{X_2} - E^\circ_{t_{ref}} + E'_{Ag} \quad [14]$$

From Eq. [7], where the constant α equals E° at t_{ref}

$$dE^\circ/dt\ (mV/deg) = 0.1(\beta_{Ag} + \beta_{X_2}) \quad [15]$$

By Eq. [1] and [15] and Tables II and IV, with β values averaged as for Table V, dE°/dt is always less negative than $0.1(\beta_{Ag} + \beta_{X_2})$. For AgCl cells at 500°, 600°, and 700°C the differences are 0.070 ± 0.05, 0.068 ± 0.05, and 0.066 ± 0.05 mV/deg, respectively; for AgBr at the same temperatures, 0.077 ± 0.04, 0.061 ± 0.04, and 0.046 ± 0.04 mV/deg; and for AgI at 600° and 700°C, 0.210 ± 0.09 and 0.254 ± 0.09 mV/deg. These calculated differences range from two to four times those obtained when comparing thermocells with isothermal plus nonisothermal formation cells and the 99% probability error limits are a smaller fraction of the differences. As might be expected, the differences for AgBr are closer to those for AgCl than to those for AgI.

In every case the calculated difference is in the direction such that, if there is an interaction between

thermal gradient and concentration gradients in non-isothermal formation cells, its net effect is to increase the potential of the high-temperature electrode relative to that of the cooler electrode if the gradients of temperature and Ag_2^+ concentration are in the same direction and to decrease its relative potential if the gradients of temperature and X_3^- concentration are in the same direction. Although the possible existence of systematic errors, unrecognized and therefore uncorrected, precludes firm quantitative conclusions, the results suggest that the net effect in silver halide cells may be of the order of hundredths of a millivolt per degree and therefore capable of evaluation with increased accuracy of measurement of cell potentials and electrode temperatures.

Acknowledgments

This work was supported by the U.S. Atomic Energy Commission. One of us (C. R. M.) is grateful for the award of a terminal year fellowship by the National Institute of General Medical Science and for the use of computing facilities at Purdue University during manuscript preparation.

Manuscript submitted April 22, 1969; revised manuscript received Sept. 24, 1969.

Any discussion of this paper will appear in a Discussion Section to be published in the December 1970 JOURNAL.

REFERENCES

1. A. F. Wilde and R. L. Seifert, *This Journal*, **108**, 1059 (1961).
2. T. B. Warner and R. L. Seifert, *J. Phys. Chem.*, **69**, 1034 (1965).
3. T. B. Warner, "Determination of E° of Formation of Molten Lead Chloride Using an Electronic Commutator," Ph.D. Thesis, Indiana University (1963); available from University Microfilms, Ann Arbor, Mich.
4. C. R. Metz, "Electronic Commutator Emf Measurements of Cells Containing Molten Silver and Lithium Halides," Ph.D. Thesis, Indiana University (1966); available from University Microfilms, Ann Arbor, Mich.
5. D. R. Stull, *Ind. Eng. Chem.*, **39**, 544 (1947).
6. H. Bloom, J. O'M. Bockris, N. E. Richards, and R. G. Taylor, *J. Am. Chem. Soc.*, **80**, 2044 (1958).
7. J. D. Corbett and S. Winbush, *ibid.*, **77**, 3964 (1955).
8. J. D. Van Norman, *This Journal*, **112**, 1126 (1965).
9. C. A. Bennett and N. L. Franklin, "Statistical Analysis in Chemistry and the Chemical Industry," pp. 224-225, 245-255, 423-426, J. Wiley & Sons, Inc., New York (1954).
10. W. J. Hamer, M. S. Malmberg, and B. Rubin, *This Journal*, **103**, 8 (1956).
11. V. Czepinski, *Z. Anorg. Allgem. Chem.*, **19**, 208 (1899).
12. S. Sternberg and D. I. Marchidan, *Z. Physik. Chem.*, **218**, 250 (1961).
13. E. J. Salstrom, *J. Am. Chem. Soc.*, **55**, 2426 (1933).
14. I. G. Murgulescu and S. Sternberg, *Rev. Chim. Acad. Rep. Populaire Roumaine*, **2**, 251 (1957).
15. S. Senderoff and G. W. Mellors, *Rev. Sci. Instr.*, **29**, 151 (1958).
16. M. B. Panish, F. F. Blankenship, W. R. Grimes, and R. F. Newton, *J. Phys. Chem.*, **62**, 1325 (1958).
17. J. Leonardi and J. Brenet, *Compt. Rend.*, **261**, 113 (1965).
18. B. F. Markov and E. B. Kuzyakin, *Ukr. Khim. Zh.*, **32**, 1180 (1966).
19. R. Suchy, *Z. Anorg. Allgem. Chem.*, **27**, 152 (1901).
20. H. Reinhold, *ibid.*, **171**, 181 (1928).
21. K. H. Stern, *J. Phys. Chem.*, **60**, 679 (1956).
22. O. H. Weber, *Z. Anorg. Allgem. Chem.*, **21**, 305 (1899).
23. I. G. Murgulescu, S. Sternberg, L. Medintev, and C. Mustetea, *Electrochim. Acta*, **8**, 65 (1963).
24. E. J. Salstrom and J. H. Hildebrand, *J. Am. Chem. Soc.*, **52**, 4650 (1930).
25. I. G. Murgulescu and D. I. Marchidan, *Rev. Chim. Acad. Rep. Populaire Roumaine*, **3**, 47 (1958).
26. S. Sternberg, I. Adorian, and I. Galasiu, *J. Chim. Phys.*, **62**, 63 (1965).
27. W. J. Hamer, M. S. Malmberg, and B. Rubin, *This Journal*, **112**, 750 (1965).
28. C. E. Wicks and F. E. Block, *U. S. Bur. Mines Bull.*, 605 (1963).
29. H. F. Stimson, J. F. Swindells, and R. E. Wilson, "American Institute of Physics Handbook," 2nd Ed., D. E. Gray, Editor, pp. 4-8, McGraw-Hill Book Co., Inc., New York (1963).
30. H. Holtan, Jr., *Koninkl. Ned. Akad. Wetenschap., Proc.*, **56B**, 498 (1953).
31. B. F. Markov, *Doklad. Akad. Nauk S.S.S.R.*, **108**, 115 (1956).
32. S. Senderoff and R. I. Bretz, *This Journal*, **109**, 56 (1962).
33. J. Dupuy and J. Ruch, *Compt. Rend., Ser. C.*, **262**, 1512 (1966).
34. C. Sinistri and E. Pezzati, *Z. Naturforsch.*, **22a**, 590 (1967).
35. H. P. Meissner, D. C. White, and G. D. Uhlrich, *Advan. Energy Conversion*, **5**, 205 (1965).
36. W. Fischer, *Z. Naturforsch.*, **21a**, 281 (1966).
37. J. Ruch and J. Dupuy, *Compt. Rend., Ser. C.*, **261**, 957 (1965).
38. A. Kvist, A. Randsalu, and I. Svensson, *Z. Naturforsch.*, **21a**, 184 (1966).

Electrode Studies in Nonaqueous Electrolytes

I. The Lithium Electrode in $LiClO_4$-Propylene Carbonate Solutions

Stuart G. Meibuhr

Electrochemistry Department, Research Laboratories, General Motors Corporation, Warren, Michigan

ABSTRACT

The electrochemical properties of the smooth lithium electrode in $LiClO_4$-propylene carbonate solutions were studied at temperatures up to 70°C by galvanostatic methods. For the range of current densities, temperatures, and $LiClO_4$ concentrations studied, the anodic and cathodic polarization data were symmetrical through zero current density. Values for the exchange current density, i_o, were calculated at each experimental condition; at 28°C and 1M $LiClO_4$, i_o was 0.95 ± 0.05 mA/cm². The ΔH^*_o value was 8.5 ± 0.3 kcal/mole, and α had a temperature independent value of about 0.67. The electrochemical reaction order was 1 for concentrations up to 1M in Li^+ ion.

The extensive interest in organic electrolyte batteries (1-3) has produced a recent increase in the number of investigations of electrochemical phenomena in solutions of organic solvents. However, only a limited amount of work has been devoted to the study of the electrode kinetics at solid electrodes.

Rao has examined the electrode reactions at the cathodes of copper (4) and lead (5) in a 1M $LiAlCl_4$-propylene carbonate (PC) solution, whereas Burrows and Jasinski (6) studied the lithium anode in 1M $LiClO_4$-PC at 28°C. From the slope of their current-polarization data, a value for the exchange

current density (i_o) is calculated to be 0.0275 mA/cm^2. Scarr (7), however, reported a value for i_o of about 0.6 mA/cm^2 at 23°C in a $LiClO_4$-PC solution. Zotov and Khlystova (8) found that the process of lithium deposition from LiCl-dimethylformamide solutions was crystallization limited.

The purpose of this work was to study the electrochemical properties of the smooth lithium electrode in $LiClO_4$-PC solutions at temperatures up to 70°C. Two series of experiments were performed. The lithium reference electrode in $LiClO_4$-PC solutions was evaluated by investigating the open-circuit potential of a Li/Li^+ concentration cell at ambient temperature; and the Li/Li^+ electrode kinetics were studied by analyzing the data obtained by anodically and cathodically polarizing Li electrodes in $LiClO_4$-PC solutions.

Experimental

Materials.—The propylene carbonate solvent, obtained from Jefferson Chemical Company, was vacuum distilled at 3-4 mm of mercury using a 90-cm long column packed with glass rings. The first 30% of the pot charge that distilled was discarded. The next 60% was collected and used in these experiments. The distilled PC had a water content of <35 ppm; the analysis was performed by the Karl Fischer method in an apparatus exposed to the air; consequently, the actual amount of water was probably considerably below the 35-ppm level. Gas chromatographic analysis of distilled PC showed only one impurity peak. A typical chromatogram (using the thermal conductivity detector) is given in Fig. 1. The post-PC peak was identified as ethylene carbonate, and its concentration was calculated at about 0.5% (9). Only one other impurity could be detected; about 20 ppm of 1, 2 propanediol was present in the distillate.

The $LiClO_4$ was of the highest purity available; it was (*a*) dried at 150° in a vacuum oven for at least 16 hr, (*b*) cooled in vacuum, and (*c*) transferred promptly to a dry box.

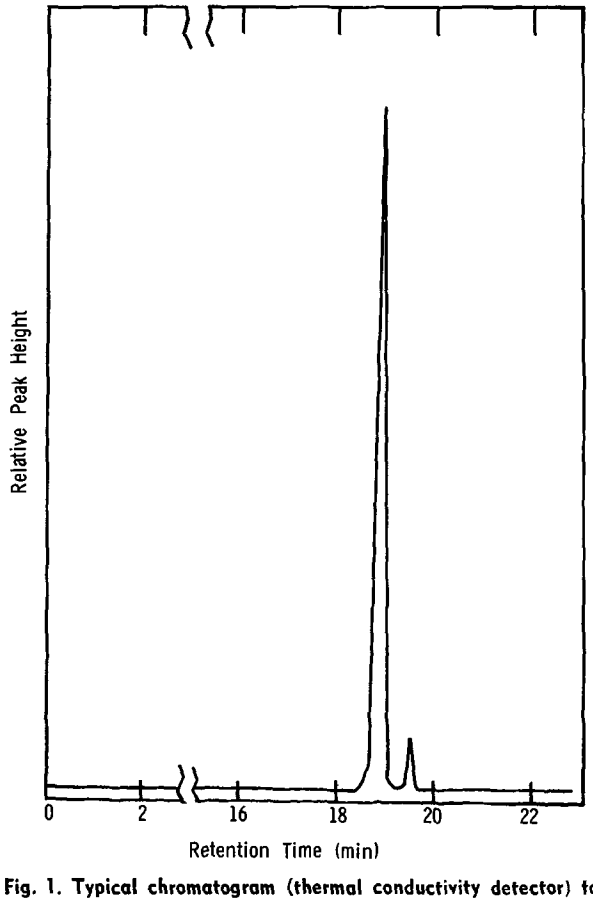

Fig. 1. Typical chromatogram (thermal conductivity detector) for distilled PC.

Solutions of concentrations ≧ 1M were made by weighing in a dry box sufficient solute to add to 100 ml of PC. The less concentrated solutions were prepared by diluting the concentrated solutions with PC. All solutions were stored over solid lithium which could act as a getter for water (6). These solutions also showed a water content <35 ppm. The solutions were stored in ungreased, ground glass stoppered bottles in the water, O_2, and N_2 free atmosphere of the dry box [manufactured by Vacuum Atmospheres Corporation, (VAC)].

Lithium electrodes (0.08 cm^2 in area) were prepared in the VAC dry box by sealing a bright lithium wire (metal impurities = 0.01% obtained from Alfa Inorganics Company), approximately 40 mm long, in epoxy resin. A small alligator clip, which was attached to one end of the wire for making electrical contacts, was partially sealed in the epoxy also. When hard, one end of the potted wire was ground to expose the bright lithium surface with an area equal to the cross-sectional area of the wire. Three such electrodes served as the test, counter, and reference electrodes.

Equipment.—The potential measurements of the Li/Li^+ concentration cells were performed in a glass U-tube with the arms (ID = 8 mm) separated with a fritted glass disk.

The galvanostatic measurements were performed in a glass cell mounted over a hot plate shown schematically in Fig. 2. The three epoxy-sealed lithium electrodes and a thermometer were inserted in inlet ports in the glass cell cover, and the solution was stirred with argon bubbling through a glass frit in the cell. The solution temperature could be maintained within ± 0.5°C. The argon gas that was bubbled through the solution contained 6% H_2 because the presence of H_2 was necessary to regenerate the copper turnings in the O_2-removal furnace. It was found that the presence of H_2 did not affect the measurements.

Because of the relatively low specific conductivity [approximately 10^{-2} ohm^{-1} cm^{-1} for 1M $LiClO_4$ at 25°C (10, 11)] of these solutions, it was necessary to measure the resistance between the working and reference electrodes (12) before each experiment. This solution resistance was determined from the oscilloscope trace of a single current pulse. The electrical circuit mounted outside the dry box was similar to one described previously (13) except that a variable resistor was in series with the single cell lead-acid battery; with this resistor, the current flowing through the circuit could be varied. With the oscilloscope operating at 20 μsec/cm, the *iR* loss was determined at 6-8 different currents. The largest current that was pulsed was always larger than the maximum current used during a polarization run. For a given set of conditions, repeat determinations of R gave values within

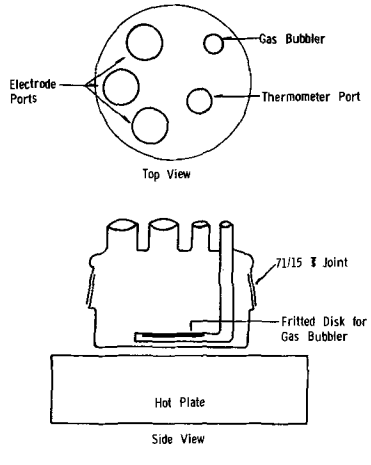

Fig. 2. Polarization cell

10% of one another. These values of R were used to obtain iR-free polarization curves. The current was determined from the iR drop across a 1000-ohm precision resistor.

Experimental method.—All electrochemical measurements and associated materials handling were performed in the VAC dry box.

The potential of the concentration cell

$$\underset{c_1}{\text{Li/LiClO}_4\text{-PC//LiClO}_4\text{-PC/Li}}\ \ \underset{c_2}{}$$

was measured for values of $c_1 = 0.5$ or 1.0M and $c_2 = 0.1$ to 1.0M. Included in the measured emf was an unknown junction potential which was estimated using the Henderson equation (14)

$$E_j = RT/F \frac{\lambda^o_+ - \lambda^o_-}{\lambda^o_+ + \lambda^o_-} \ln \frac{c_1}{c_2} \qquad [1]$$

where λ^o_+ and λ^o_- are the limiting ionic mobilities of Li^+ and ClO_4^-, respectively. The values of λ^o_+ for Li^+ have been determined in dimethylsulfoxide as 11.4 (15), in dimethyl formamide as 25 (16), and in formamide as 8.5 (16). Applying Walden's rule, the value for λ^o_+ in PC becomes 8.7. The value for λ^o_- can be calculated from

$$\Lambda_o = \lambda^o_+ + \lambda^o_-$$

The value for Λ_o has been determined to be 30.4 (11); hence, λ^o_- is 21.7.

The polarization studies were made in the following manner. Sixty milliliters of solution were added to the cell, and the electrodes were placed in position. The solution was bubbled with argon presaturated with PC. The potential between the working and reference electrodes was monitored with a Keithley electrometer. When this potential came to a steady value <0.5 mV, the voltage leads were connected to the oscilloscope and Polaroid prints were made of the traces obtained by applying a single pulse to the working electrode at 6-8 different values. The iR correction could then be calculated for each current for which the polarization was measured. When equilibrium was again regained (as indicated above), the anodic polarization run was made for increasing values of the current. In some experiments a cathodic run was made when the system returned to equilibrium. Before a duplicate anodic run was made, the test electrode was removed from solution, dried, and repolished to expose a fresh lithium surface. It was necessary to redetermine the resistance between the working and reference electrodes after each repolishing step.

The exchange current densities were calculated from the equation

$$i_o = iRT/\eta_{iR-free}F \qquad [2]$$

where $\eta_{iR-free} = E_{exptl} - E_{oc} - iR$.

Results and Discussion

Concentration cell studies.—Table I shows the measured emf values for the cell together with the calculated E_j values and the corrected emf values. The data show a 68 ± 1 mV change/decade of Li^+ ion concentration. Considering the assumptions that were made in calculating the E_j values, the potential responded to the varying Li^+ ion concentration in reasonable accordance with the Nernst equation. Thus, a solid lithium electrode immersed in solutions of Li^+ ion from 0.1 to 1M behaved satisfactorily for a reference electrode, in agreement with results (6) obtained by measuring (*a*) the stability of potential with time and (*b*) the recovery of the electrode after micropolarization.

Table I. Concentration cell studies

c_1 (M)	c_2 (M)	Cell potential (V)	E_j (V)	Corrected emf (V)
0.5	1.0	−0.0335	+0.0077	−0.0258
0.5	0.25	+0.0245	−0.0077	+0.0168
0.5	0.1	+0.060	−0.0178	+0.0422
0.5	0.5	0.000	—	0.000
1.0	1.0	0.000	—	0.000
1.0	0.1	+0.095	−0.0255	+0.0695

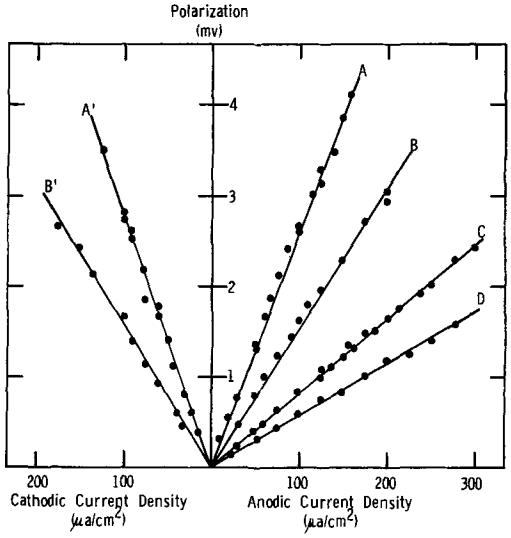

Fig. 3. Current density-iR free polarization data for a 1M $LiClO_4$ solution. Curves A, A', 29°C; B, B', 43°C; C, 58°C; D, 67.5°C.

Polarization studies.—Figure 3 shows typical anodic and cathodic iR-free polarization data; these were taken at 28° in a solution of 1M $LiClO_4$. Under all experimental conditions, the current density-polarization plots were linear; the slope of the cathodic portion agreed with the slope of the anodic branch within 4%. Duplicate anodic polarization runs produced slopes which were within 10% of one another. The i_o variations with temperature and Li^+ ion concentration are summarized in Table II.

The anodic and cathodic i_o values for a 1M $LiClO_4$ solution at 28° were 0.95 ± 0.05 mA/cm² determined in five separate experiments over a period of months. This value is about 35 times greater than the value calculated from data of Burrows and Jasinski (6). An extrapolation of the log i_o − $1/T$ data to lower temperatures (Fig. 4, curve C) for the 1M solution yielded an i_o value at 23° of 0.7 mA/cm². This value agreed with the 0.65 value reported by Scarr also at 23° (7). One explanation for the large discrepancy between the i_o value calculated from Burrows and Jasinski (6) on the one hand and the values given by Scarr (7) and the present work on the other hand is that in the former case the polarization values may have included the solution iR loss. If this occurred, the calculated i_o values would be too low, the magnitude depending on the exact value for the included iR drop. If a resistance value of about 235 ohms is

Table II. The i_o values for different experimental conditions

$LiClO_4$ concentration (M)	Temperature, °C	i_o mA/cm²
2	28.5	0.56
	41	1.25
	53	1.85
	61.5	2.35
1	28	0.95
	43	1.8
	58	3.4
	67.5	5.25
0.5	29	0.4
	49	0.75
	61	1.05
	69	1.25
0.1	28	0.114
	40	0.24
	49	0.3
	57	0.42

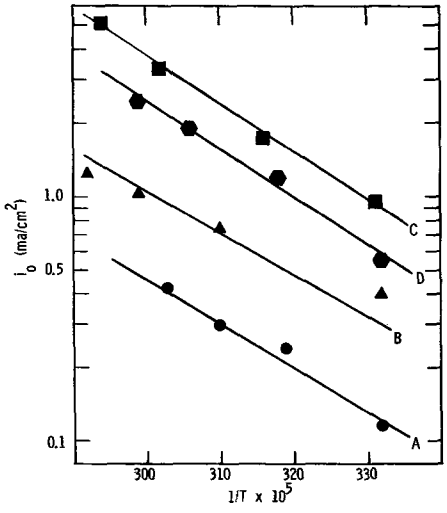

Fig. 4. Plot of the i_o values against $1/T$. Curve A, 0.1M; B, 0.5M; C, 1.0M; D, 2.0M $LiClO_4$.

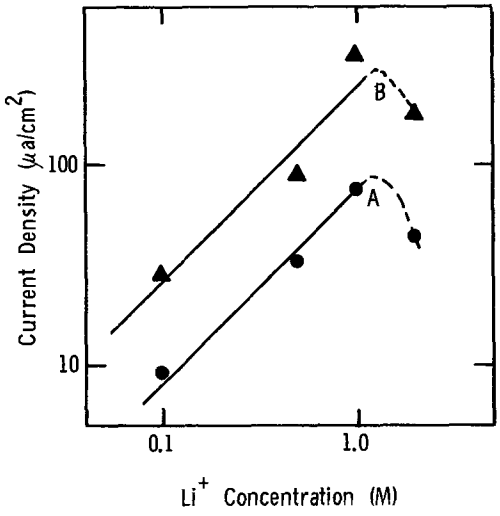

Fig. 6. Determination of the reaction order for solutions containing only $LiClO_4$. Curve A, 28°C; B, 70°C.

assumed (and this value is reasonable for a 1M $LiClO_4$ solution having the electrodes spaced approximately 1 cm apart), the calculated value for i_o then agrees with the value determined in this work.

From the results of the temperature effect on the polarization, the enthalpy of activation at zero polarization (ΔH_o^*) was calculated using the equation

$$\frac{\partial \ln i_o}{\partial (1/T)} = \frac{\Delta H^*_o}{R} \qquad [3]$$

The values of i_o were calculated from the slopes of the polarization plots using Eq. [2]. Plots of the log i_o against $1/T$ are given in Fig. 4. The lines were drawn parallel to give the best fit for all the points in that figure. The value obtained for ΔH^*_o was 8.5 ± 0.3 kcal/mole. This value is of the order of magnitude expected for metal dissolution and deposition.

The transfer coefficient, α, was calculated indirectly from the slope of the plot $\partial \log i_o / \partial \log C_{Li^+}$ (17). The data in Fig. 5 (curve A) yield a value for α of about 2/3; this value remained constant with increasing temperature.

The electrochemical reaction order can be obtained by plotting the log i, at constant overvoltage, against the log of the apparent concentration of a given species (18). In Fig. 6 is shown the current density dependence on the Li^+ ion concentration in solution. Curve A represents data at 28°C whereas curve B denotes data at 70°C. Several important items of note include: the linear plots are parallel; their slope equals 1; and at concentrations above 1M there is a marked change in the reaction order. The change may be associated with the causes for the decrease in conductivity (10, 11) at $LiClO_4$ concentrations greater than 1M. Also, in these concentrated solutions ion association may occur. The current density value associated with the 2M solution (see Fig. 6) corresponds to a Li^+ ion concentration of about 0.6M in the linear region. This concentration is about 1/3 the amount of Li^+ ion added to the solution. More polarization data at Li^+ ion concentrations greater than 1M and the Li^+ ion activity coefficients are needed before an unambiguous explanation for the apparent change in reaction order can be presented.

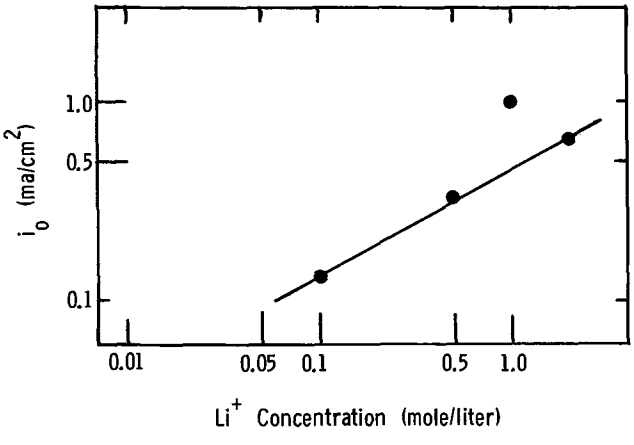

Fig. 5. Determination of the $(1-\alpha)$ value. Temperature, 28°

It may be concluded from these studies that the data for the dissolution and deposition of lithium from solutions containing only $LiClO_4$ are consistent with the charge transfer rate-determining step

$$Li \rightleftharpoons Li^+ + e$$

Acknowledgments

The author is grateful to the following members of the Research Laboratories of the General Motors Corporation: to Roger Gatrell[1] and Bernard E. Nagel of the Chemistry Department for the chromatographic analysis; to Charles R. Wiese of the Electrochemistry Department for his assistance with this work; and to Dr. James P. Hoare for his valuable suggestions during the preparation of the manuscript.

Manuscript received May 15, 1969. This paper was Paper 204 presented at the New York meeting, May 4-9 1969.

Any discussion of this paper will appear in a Discussion Section to be published in the December 1970 JOURNAL.

[1] No longer with General Motors Corporation.

REFERENCES

1. R. Jasinski, *Electrochem. Technol.*, **6**, 28 (1968); *Electroanal. Chem. and Interfacial Electrochem.*, **15**, 89 (1967).
2. H. N. Seiger and A. E. Lyall, Paper No. 680454 presented to the Society of Automotive Engineers at the Detroit Meeting, May 20-24, 1968.
3. K. H. M. Braeuer, *Proc. 20th Ann. Power Sources Conf.*, **20**, 57 (1966).
4. M. L. B. Rao, *This Journal*, **114**, 13 (1967).
5. M. L. B. Rao, *ibid.*, **114**, 665 (1967).
6. B. Burrows and R. Jasinski, *ibid.*, **115**, 365 (1968).
7. R. Scarr, Paper No. 161 presented at the New York Meeting of the Society May 4-9, 1969.
8. N. A. Zotov and K. B. Khlystova, *Elektrokhimiya*, **2**, 1444 (1966).
9. S. G. Meibuhr, B. E. Nagel, and R. Gatrell, Submitted for publication.

10. D. P. Boden, *Proc. 20th Ann. Power Sources Conf.*, **20**, 63 (1966).
11. S. G. Meibuhr, Unpublished data.
12. J. N. Butler, Paper No. 127 presented at the Dallas Meeting of the Society, May 7-12, 1967.
13. J. P. Hoare, *Electrochim. Acta*, **9**, 599 (1964).
14. P. Henderson, *Z. Phys. Chem.*, **59**, 118 (1907); S. Glasstone, "Introduction to Electrochemistry," p. 213, D. Van Nostrand, Inc., Princeton, N. J. (1956).
15. J. S. Dunnett and R. P. H. Gasser, *Trans. Faraday Soc.*, **61**, 922 (1965).
16. D. S. Reid and C. A. Vincent, *Electroanal. Chem. and Interfacial Electrochem.*, **18**, 427 (1968).
17. P. Delahay, "Double Layer and Electrode Kinetics," p. 165, Interscience Publishers, Inc., New York (1965).
18. K. J. Vetter in "Transactions of the Symposium on Electrode Processes," p. 47, E. B. Yeager, Editor, John Wiley & Sons, Inc., New York (1961).

Electrode Oxidation of Hydrazine and Related Compounds in Liquid Ammonia Electrolytes

M. H. Miles*, [1] **and P. M. Kellett**

Naval Weapons Center, Corona Laboratories, Corona, California

ABSTRACT

Potential sweep investigations of the electrochemical oxidation of hydrazine on platinum in liquid ammonia electrolytes yield current-potential curves which depend markedly on the nature of the electrolyte anion present. These anion effects are interpreted in terms of the principle of soft and hard acids and bases and specific adsorption at the electrode. In general, the "harder" the electrolyte anion, the better is the performance of the hydrazine anode. Low-temperature studies show that hydrazine can be electrochemically oxidized in liquid ammonia at −60°C, demonstrating the high reactivity of this fuel. The oxidation of hydrazine on platinum appears to be a diffusion-controlled, highly irreversible reaction. Hydrazine is also electrochemically oxidizable in liquid ammonia on Ir, Rh, Re, Pd, V, Mo, Au, and on nitrocarbides and nitrides of transition metals. Of various substituted hydrazine compounds tested, only hydroxylamine compared with hydrazine in reactivity.

Fuel cells using hydrazine are emerging from the laboratory (1, 2); this development is a result of fundamental research on the electrochemical oxidation of this reactive fuel (3-6). Except for a few results in several organic electrolytes and hydrogen fluoride electrolytes (7), this research has been limited to aqueous solutions. Contrary to earlier work by Hammer (8), we have established that hydrazine can be electrochemically oxidized in liquid ammonia electrolytes (9). The high electrochemical activity of hydrazine and its infinite solubility in liquid ammonia make hydrazine attractive for use as a soluble fuel in low-temperature fuel cells with liquid ammonia electrolytes. Furthermore, the use of hydrazine as a fuel appears to be thermodynamically more favorable in liquid ammonia than in aqueous electrolytes, because of the abnormal stability in liquid ammonia of the hydrogen ions produced in the electrochemical oxidation of hydrazine (10).

Experimental

The chemicals used include Baker reagent hydrazine sulfate and Matheson hydrazine hydrate (99-100%). Hydrazine sulfate is convenient to handle and undergoes ammonolysis (11)

$$N_2H_4 \cdot H_2SO_4 + 2NH_3 \rightarrow N_2H_4 + (NH_4)_2SO_4$$

to produce anhydrous hydrazine and insoluble ammonium sulfate. The electrolyte solutions were prepared from anhydrous ammonia (Matheson Company, 99.99%) and vacuum-dried, reagent-grade salts.

Inorganic salt solutions of liquid ammonia were prepared in a special flask which permits vacuum drying of the salt and formation of the solution without exposure to air. Various salts, such as NH_4SCN, NH_4I, $LiNO_3$, $LiClO_4$, NaSCN, and NaI form ammonia solutions where the vapor pressure of NH_3 at ambient temperature is below 1 atm (9, 12). Unless stated otherwise, these solutions having a salt concentration of about 5-10M were used. These liquid ammonia solutions were taken into a drybox and poured into a vacuum-tight, controlled-atmosphere electrochemical cell fitted with screw cap thermometer adapters with O-rings (Scientific Glass Apparatus) which seal the electrodes. A smaller, three-compartment cell equipped with the screw cap thermometer adapters was used for the low-temperature studies; anhydrous ammonia was condensed directly into the cell thermostatted at −60°C. A special pressurized cell (13) was used for investigations where the vapor pressure of ammonia exceeds 1 atm. The reference electrode used for all measurements was $Pb/Pb(NO_3)_2$ (saturated) with a single glass microcrack separating the reference electrode and solution. Further details of the electrochemical measurements are given elsewhere (9).

For low-temperature investigations, slush baths of dry ice in organic solvents conveniently cover the liquid range of ammonia and provide temperature control of ±1°C (14). A dry ice slush bath of a mixture of o-xylene and m-xylene was used for studies at −60°C while 3-heptanone was used for the −35°C bath.

Results and Discussion

Electrocatalysts for hydrazine oxidation.—Various nitrocarbides, nitrides, carbides, and borides of transition metals and alloys prepared by the Bureau of Mines, Pittsburgh Coal Research Center under NASA contract No. 12,300, were tested as catalysts for the electrochemical oxidation of hydrazine in acid liquid ammonia solutions. In general, the nitrogen-containing compounds, such as the nitrocarbides and nitrides, showed more promise as catalysts than the other

* Electrochemical Society Active Member.
[1] Present address: Department of Chemistry and Physics, Middle Tennessee State University, Murfreesboro, Tennessee.
Key words: adsorption, ammonia, anions, electrocatalysts, fuel, hydrazine, hydroxylamine, oxidation, platinum, temperature.

compounds. However, it appears that none of these compounds show catalytic activity comparable to that for platinum.

Various transition metals were also tested as catalysts for the electrochemical oxidation of hydrazine in liquid ammonia electrolytes. The metals iridium, rhodium, rhenium, and palladium showed catalytic activity comparable to that for platinum. Hydrazine oxidation was also observed on vanadium, molybdenum, and gold. Tantalum, titanium, aluminum, wolfram, zirconium, chromium, and gallium were all found to be inactive for hydrazine oxidation. Hydrazine was also tested on cobalt, copper, iron, indium, lead, mercury, and tin, but oxidation of the metal itself obscured the results.

Tests of other related compounds on platinum.—Several substituted hydrazine compounds were tested for electrochemical oxidation on Pt in liquid ammonia electrolytes including phenylhydrazine, 1,2-diphenylhydrazine, 1,2-dimethylhydrazine dihydrochloride, 2,4-dinitrophenylhydrazine, carbohydrazide, and hydroxylamine hydrochloride. All showed evidence for oxidation on Pt; however, only hydroxylamine showed reactivity comparable to that for hydrazine.

Constant current and potential scan methods were used in testing these various compounds. Figure 1 gives the results for constant current oxidation of $N_2H_4 \cdot H_2SO_4$ and $NH_2OH \cdot HCl$ on Pt in stirred NH_3-$LiNO_3$ solutions. Similar results were obtained in NH_4NO_3 and NH_4SCN ammonia electrolytes; *i.e.*, almost 4 electrons/molecule for hydrazine oxidation and about 2 electrons/molecule for the oxidation of hydroxylamine. This suggests that the net oxidation reactions for these compounds in ammonia electrolytes are

$$N_2H_4 \rightarrow N_2 + 4H^+ + 4e^-$$
$$NH_2OH \rightarrow \tfrac{1}{2}N_2O + \tfrac{1}{2}H_2O + 2H^+ + 2e^-$$

Nitrous oxide is also believed to be a major product in the electrochemical oxidation of hydroxylamine in dimethylsulfoxide (15).

The constant current oxidation of the other compounds did not give the sharp inflections observed for hydrazine and hydroxylamine (Fig. 1); hence, the electron yield per molecule was indeterminate for the oxidations of these other compounds.

Anion effects.—Potential scan investigations of hydrazine oxidation on platinum in various concentrated salt-ammonia solutions show that the results depend markedly on the nature of the electrolyte anion. Figures 2, 3, and 4 give the results in NH_3-NH_4SCN, NH_3-NH_4I, and NH_3-NH_4NO_3, respectively. Oxidation of the iodide ion (Fig. 3) tends to obscure part of the hydrazine oxidation peak. Figure 4 shows the interesting build-up when time is allowed between potential sweeps of a second hydrazine oxidation peak at about +0.2V in the nitrate solutions, as well as a peak build-up at about −0.2V due to hydrogen oxidation. This build-up with time of a second hydrazine oxidation peak was also observed in NH_3-NH_4ClO_4 solution at 0°C, but in NH_3-NH_4SCN and NH_3-NH_4I no such effect was observed. The rest potential (V_R) was −0.15V in the nitrate solution and +0.15V in the thiocyanate solution; however, V_R in NH_3-NH_4SCN gradually shifted over a period of several days to the −0.15V value. Results in neutral ammonia solutions (NH_3-NaSCN, NH_3-NaI, and NH_3-$LiNO_3$) were very similar to those in the acid solution containing the same anion.

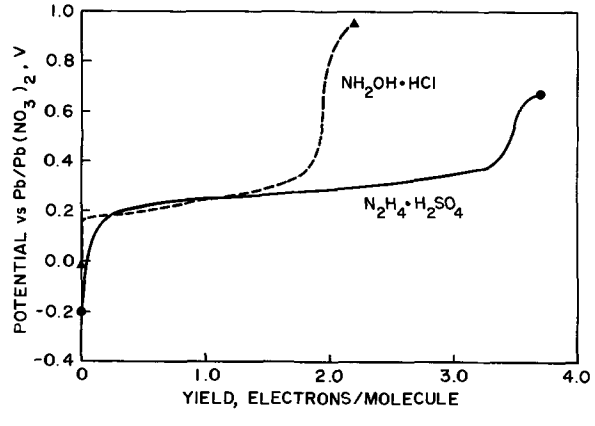

Fig. 1. Constant current oxidation of $N_2H_4 \cdot H_2SO_4$ and $NH_2OH \cdot HCl$ in stirred NH_3-$LiNO_3$ solutions using platinum electrode of about 50 cm² geometrical area. I = 1.00 mA; T = 20°C.

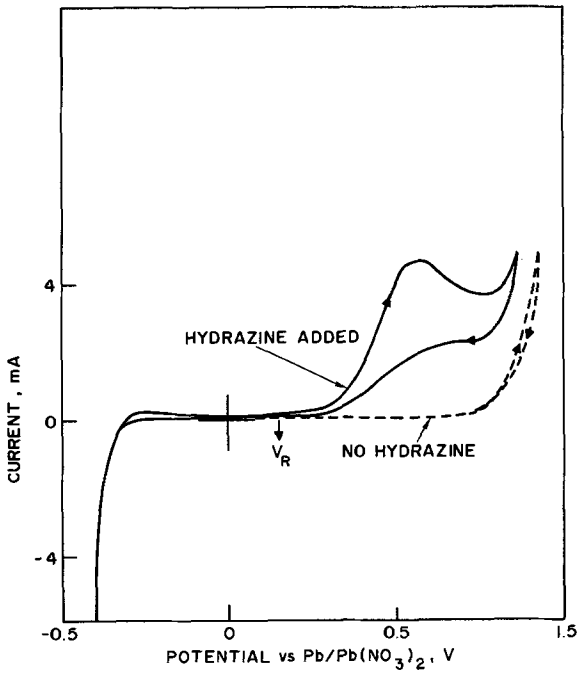

Fig. 2. Cyclic voltammogram for 0.02M $N_2H_4 \cdot H_2SO_4$ in NH_3-NH_4SCN at 20°C using platinum wire electrode with geometrical area = 0.3 cm². v = 250 mV/sec.

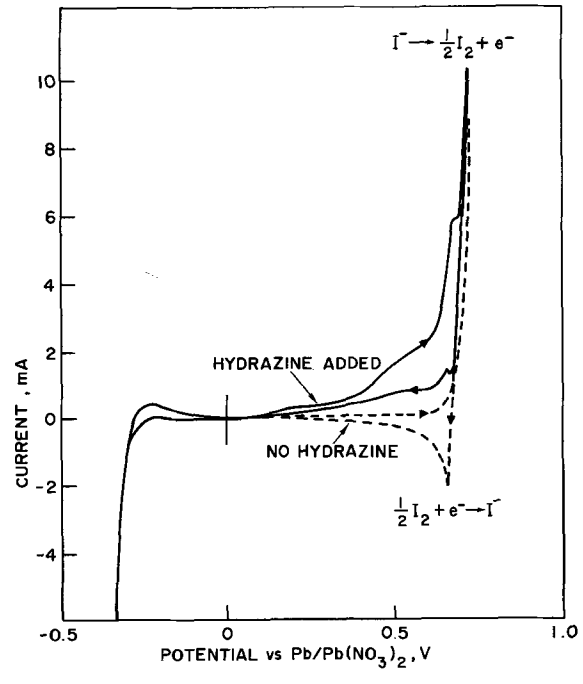

Fig. 3. Cyclic voltammogram for 0.02M $N_2H_4 \cdot H_2SO_4$ in NH_3-NH_4I at 20°C using platinum wire electrode with geometrical area = 0.3 cm². v = 250 mV/sec.

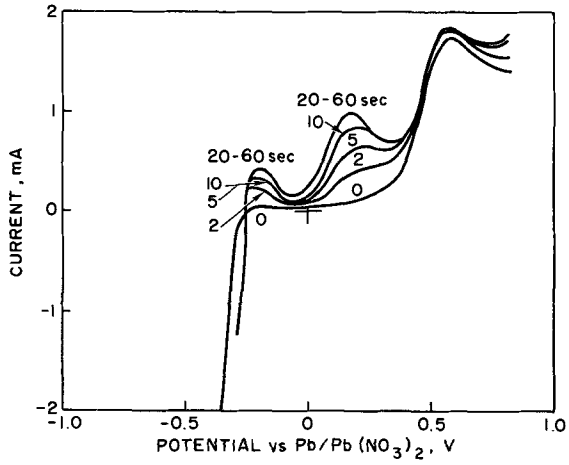

Fig. 4. Effect of allowing time between potential sweeps on current potential curves for 0.02M $N_2H_4 \cdot H_2SO_4$ in NH_3-NH_4NO_3 at 20°C using platinum disk electrode with geometrical area = 0.2 cm^2. Electrode potentiostatted at −0.35V between sweeps. v = 250 mV/sec.

Investigations were also conducted at about 25°C in 1M salt-ammonia solutions in the pressurized electrochemical cell fixture. The results were practically identical to those obtained at atmospheric pressure in the concentrated salt-ammonia solutions containing the same anion. For example, Fig. 5 shows cyclic voltammograms for hydrazine oxidation in 1M $LiNO_3$-ammonia solution at about 25°C in the pressurized cell giving the usual two oxidation peaks observed in nitrate solutions. No reduction of the oxidized species was ever observed (*see* Fig. 2, 3, and 5), indicating that the hydrazine oxidation is highly irreversible.

Low-temperature studies of hydrazine oxidation at −60°C and −35°C were made in 1M NH_4Cl, 1M NH_4Br, and 1M NH_4I ammonia solutions in order to evaluate the relative effect of these halogen anions on the reaction. Results are given in Fig. 6 and 7. Note that, in the NH_4Cl solution, hydrazine oxidation at −60°C is observed near the potential of the Pb reference. The oxidation current obtained is dependent on the anion present, increasing in the order $I^- < Br^- < Cl^-$. At −35°C, the oxidation current in the bromide solution approaches that for the chloride solution as the potential increases. Similar hydrazine

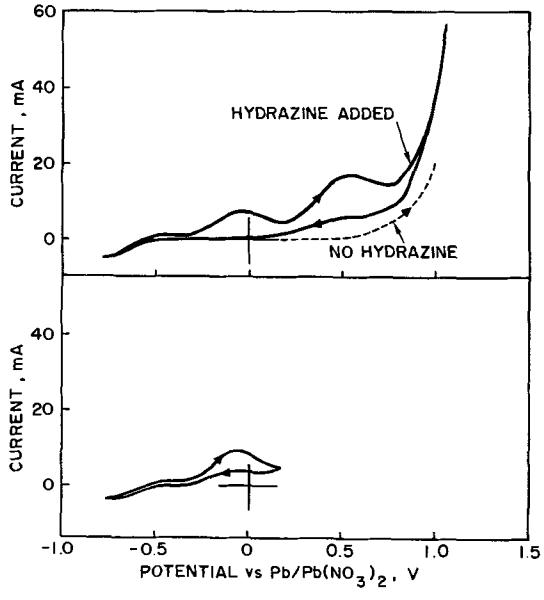

Fig. 5. Cyclic voltammograms for 0.02M $N_2H_4 \cdot H_2SO_4$ in NH_3-1M $LiNO_3$ in pressurized cell at about 25°C using platinum disk electrode with geometrical area = 1 cm^2. v = 250 mV/sec. In the bottom voltammogram the anodic sweep range is reduced.

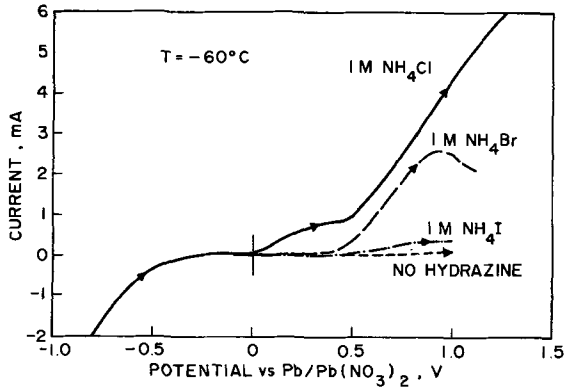

Fig. 6. Current potential curves for 0.2M $N_2H_4 \cdot H_2O$ in 1M NH_4Cl, 1M NH_4Br, 1M NH_4I ammonia solutions at −60°C using platinum wire electrode with geometrical area = 0.2 cm^2. v = 250 mV/sec.

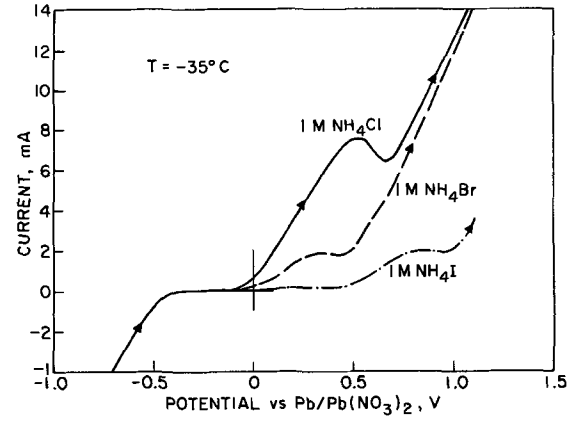

Fig. 7. Current potential curves for 0.2M $N_2H_4 \cdot H_2O$ in 1M NH_4Cl, 1M NH_4Br, and 1M NH_4I ammonia solutions at −35°C using platinum wire electrode with geometrical area = 0.2 cm^2. v = 250 mV/sec.

investigations in 1M NH_4NO_3 solution at −60°C yield an oxidation current intermediate between that in the chloride and iodide solutions; however, the build-up when time is allowed between potential sweeps of a second hydrazine oxidation peak does not occur readily at these low temperatures.

Discussion of anion effects.—The observed anion effects can be interpreted in terms of the principle of soft and hard acids and bases (SHAB) and specific adsorption at the platinum electrode. The SHAB principle states that hard acids prefer to bond to hard bases and soft acids prefer to bond to soft bases (16). Bulk metals, such as platinum, have the properties of soft acids (16, 17); hence, soft bases will tend to bond to platinum, blocking the active sites on the metal. Barclay (18) has shown that the classification of anions in terms of softness can be related to the potential at the point of zero charge (E_{pzc}) which shifts cathodically with increasing specific anion adsorption. Table I shows the relationship between E_{pzc} for mercury and Pearson's classification of the anion in terms of the SHAB principle.

The SHAB principle predicts that the order of anion specific adsorption will not vary greatly with the solvent, which is the case experimentally as anions appear to be specifically adsorbed in the same general order in most solvents (19, 20). Since both NH_3 and H_2O are classified as hard bases (21), the order and extent of anion specific adsorption should be similar in these two solvents.

The SHAB principle also predicts that the order of anion specific adsorption will not vary with the electrode metal used. Experimentally it is found that, as

Table I. Relationship between potential of zero charge (E_{pzc}) for mercury in aqueous solutions and softness of anions

Anion	E_{pzc} (*v vs.* NHE)	Pearson's classification of anion
$S^=$	−0.638	Soft
I^-	−0.451	Soft
SCN^-	−0.347	Soft
Br^-	−0.293	Borderline
NO_3^-	−0.236	Hard
ClO_4^-	−0.228	Hard
Cl^-	−0.219	Hard
$SO_4^=$	−0.196	Hard
OH^-	−0.196	Hard
F^-	−0.195	Hard

Salt concentrations were 0.1M except for $S^=$ (0.5M) [*see* Ref. (18)].

for mercury, halide adsorption decreases in the order $I^- > Br^- > Cl^-$ on platinum (22), gallium (23), and cadmium (24). However, the potential regions where anion adsorption is significant will depend on the electrode metal used, since the point of zero charge depends markedly on the nature of the metal (25-30). Barclay (18) considers the electrode at the point of zero charge to be soft. Anodically increasing the potential from the point of zero charge results in increased anion adsorption; however, the electrode becomes increasingly harder (as an acid) as the potential increases, and it is feasible that soft anions could be desorbed and hard anions or bases adsorbed at extreme positive polarization.

Hydrazine and ammonia are clasisfied as hard bases (21), while I^- and SCN^- are soft bases (Table I), which should interact strongly with platinum (soft acid) and block the active surface. In the SCN^- and I^- solutions, only in the extreme anodic potential region are these soft anions desorbed sufficiently to allow hydrazine access to the surface (Fig. 2 and 3), while, in the NO_3^- (hard base) solution, hydrazine competes for access to the surface at lower potentials (Fig. 4 and 5). Because of the much higher concentration of NO_3^- than N_2H_4, time is required for hydrazine to reach a steady-state concentration on the electrode surface (Fig. 4). Results at −60° and −35°C show that hydrazine can be electrochemically oxidized at lower potentials and give higher currents in Cl^- solution than in I^- solution, while Br^- solutions are intermediate (Fig. 6 and 7), indicating that, in accord with the SHAB principle, the softer anions more effectively block the platinum surface. The passivity produced with the soft anions is probably caused by the saturation of the free valencies of the electrode surface by the chemisorbed anions (31).

Peak current and peak potential analysis.—The effect of the potential sweep rate (v) and reactant concentration (C) on the peak current (I_p) and peak potential (E_p) is useful in extracting information from potential scan experiments. For a diffusion-controlled process with linear diffusion, we have the following three general cases (32):

1. *Reversible, soluble reactants and products*
   $I_p \propto v^{1/2}C$, $E_p \neq f(v,C)$
2. *Reversible, insoluble product*
   $I_p \propto v^{1/2}C$, $E_p \neq f(v)$, $E_p = f(C)$
3. *Highly irreversible*
   $I_p \propto v^{1/2}C$, $E_p = f(v)$, $E_p \neq f(C)$

For an adsorption or desorption controlled process, we have the following two general cases (33):

1. *Reversible (quasi-equilibrium)*
   $I_p \propto v$, $I_p \neq f(C)$, $E_p \neq f(v,C)$
2. *Highly irreversible*
   $I_p \propto v$, $I_p \neq f(C)$, $E_p = f(v)$, $E_p \neq f(C)$

The current-potential curves for hydrazine oxidation in NH_3-NH_4SCN as a function of v are given in Fig. 8, and Fig. 9 shows the results in NH_3-NH_4NO_3 solution. Potentiostating the electrode at −0.35V for

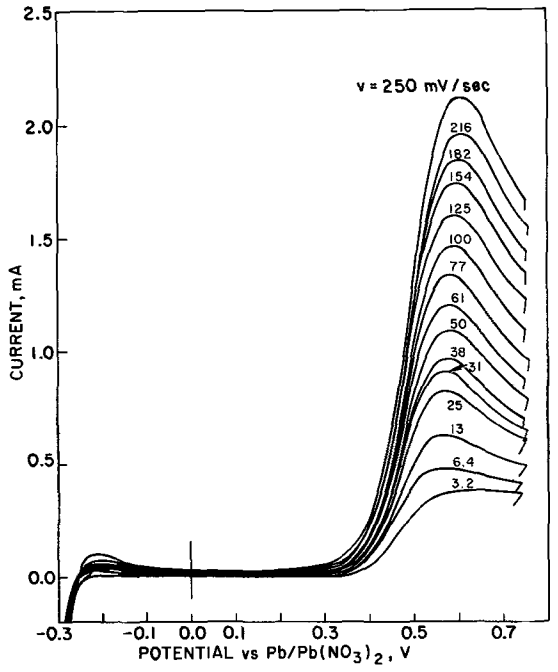

Fig. 8. Effect of sweep rate on current potential curves for 0.02M $N_2H_4 \cdot H_2SO_4$ in NH_3-NH_4SCN at 20°C using platinum disk electrode with geometrical area = 0.2 cm². Electrode potentiostatted for 30 sec at −0.35V between sweeps.

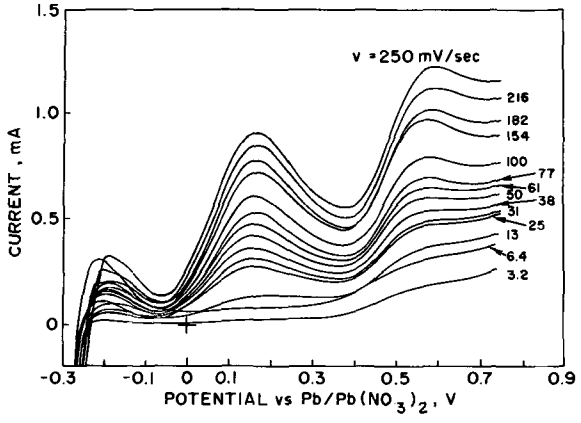

Fig. 9. Effect of sweep rate on current potential curves for 0.015M $N_2H_4 \cdot H_2SO_4$ in NH_3-NH_4NO_3 at 20°C using platinum disk electrode with geometrical area = 0.2 cm². Electrode potentiostatted for 30 sec at −0.35V between sweeps.

30 sec prior to the potential sweep establishes a steady-state condition for the hydrazine oxidation (*see* Fig. 4). Note that the nitrate solution gives a much higher hydrogen oxidation peak near −0.2V than the thiocyanate solution, again illustrating the anion effect described above.

Experimentally, I_p is found to be proportional to $v^{1/2}$ and C for hydrazine oxidation in the NH_4SCN and NH_4NO_3 ammonia solutions (Fig. 10, 11, and 12). This indicates that, where active sites on the metal are available, diffusion of hydrazine to those sites is the rate-determining step rather than adsorption, desorption, or kinetic steps.

The peak potential, E_p, becomes more anodic with increasing v for hydrazine oxidation in liquid ammonia electrolytes, but the shift is rather small; E_p also becomes more anodic with increasing hydrazine concentration. (The rest potential also shifts from −0.18V with 0.001M hydrazine to −0.13V with 0.01M hydrazine.) The behavior of E_p does not clearly fit any of the general cases mentioned above; however, the evolution of nitrogen in the hydrazine oxi-

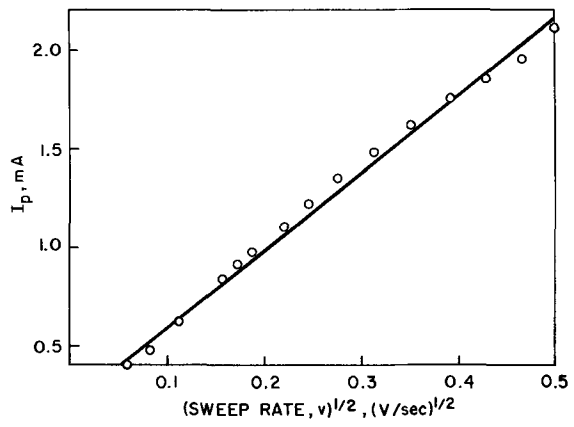

Fig. 10. Relationship of peak current to sweep rate for the results of Fig. 8.

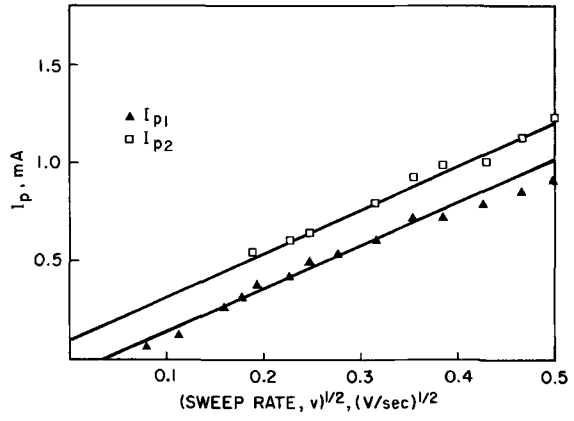

Fig. 11. Relationships of peak currents to sweep rate for the results of Fig. 9.

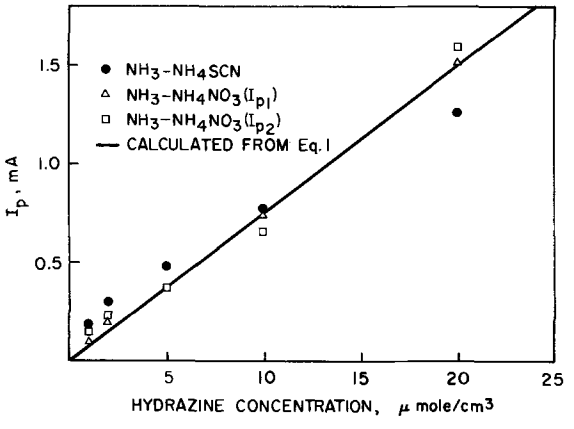

Fig. 12. Relationship of peak current to hydrazine sulfate concentration in NH_3-NH_4 SCN and NH_3-NH_4NO_3 at 20°C using platinum disk electrode with geometrical area = 0.2 cm^2. v = 125 mV/sec.

dation is a highly irreversible process. Experimental evidence for the irreversibility of hydrazine oxidation is shown by the absence of any corresponding reduction peaks.

For a diffusion-controlled, highly irreversible process (32)

$$I_p = 3.04 \times 10^5 n (\alpha n_a)^{1/2} A D^{1/2} C v^{1/2} \quad [1]$$

at 20°C. Comparing the shape of the current-potential curves for hydrazine oxidation in liquid ammonia electrolytes (Fig. 8, and 9) with standard curves given by Delahay (32), we can determine graphically that $\alpha n_a = 0.5 \pm 0.1$ for all observed peaks. Using $n = 4$ for hydrazine oxidation (Fig. 1), the diffusion coefficient for hydrazine can be calculated from Eq. [1], yielding $D_{N_2H_4} = 1 \times 10^{-6}$ cm^2 sec^{-1} in both the NH_3-NH_4SCN electrolyte and the NH_3-NH_4NO_3 electrolyte at 20°C. Viscosity determinations gave 3.2 centipoise for the NH_3-NH_4SCN solution and 4.4 centipoise for the NH_3-NH_4NO_3 solution, both measured at 20.0°C. The expected variation in diffusion coefficients due to this difference in viscosity is small compared with experimental errors. Using $n = 4$, $\alpha n_a = 0.5$, and $D_{N_2H_4} = 1.5 \times 10^{-6}$ cm^2 sec^{-1} in Eq. [1] gives reasonable agreement with experiment for the effect of hydrazine concentration on I_p up to 0.02M hydrazine concentrations (Fig. 12, solid line is calculated from Eq. [1]). Higher concentrations tend to give peak currents smaller than calculated.

Summary

The main results of this study are:

1. Hydrazine can be electrochemically oxidized in liquid ammonia elecrolytes on Pt, Ir, Rh, Re, Pd, V, Mo, and Au. Nitrocarbides and nitrides of transition metals also show activity for hydrazine oxidation.

2. Substituted hydrazine compounds can also be electrochemically oxidized in liquid ammonia electrolytes on Pt, but hydroxylamine was the only compound tested which compared with hydrazine in reactivity. Oxidation of hydroxylamine in liquid ammonia electrolytes yields about 2 electrons/molecule.

3. Current-potential curves obtained for the electrochemical oxidation of hydrazine on Pt in liquid ammonia electrolytes depend markedly on the nature of the electrolyte anion present. These anion effects can be interpreted in terms of the principle of soft and hard acids and bases and specific adsorption at the platinum electrode. The "harder" the electrolyte anion, the better will be the performance of the hydrazine anode.

4. Low-temperature studies show that hydrazine can be electrochemically oxidized at −60°C. The limitation of the reaction at this low temperature by anion adsorption rather than by slow kinetics demonstrates the high reactivity of hydrazine.

5. The electrochemical oxidation of hydrazine on Pt in liquid ammonia electrolytes appears to be a diffusion-controlled, highly irreversible reaction.

Acknowledgments

The authors wish to thank Dr. S. J. Szpak and Dr. W. S. Harris for helpful discussions, and Dr. R. E. Panzer for the use of his pressurized electrochemical cell.

SYMBOLS

A	Electrode area, cm^2
C	Concentration, mole cm^{-3}
D	Diffusion coefficient, cm^2 sec^{-1}
E_p	Peak potential, volt
I_p	Peak current, amperes
n	Number of electrons involved in net electrode reaction
n_a	Number of electrons involved in rate-determining step
V_R	Rest potential, volt
v	Potential sweep rate, volt sec^{-1}
α	Anodic transfer coefficient

Manuscript submitted May 16, 1969; revised manuscript received *ca.* Sept. 29, 1969. This was Paper 49 presented at the Detroit Meeting, Oct. 5-10, 1969.

Any discussion of this paper will appear in a Discussion Section to be published in the December 1970 JOURNAL.

REFERENCES

1. G. E. Evans and K. V. Kordesch, *Science*, **158**, 1148 (1967).
2. H. A. Liebhafsky and E. J. Cairns, "Fuel Cells and Fuel Batteries," pp. 414-419, John Wiley & Sons, Inc., New York (1968).
3. R. Glicksman, *This Journal*, **108**, 922 (1961).
4. S. Karp and L. Meites, *J. Am. Chem. Soc.*, **84**, 906 (1962).

5. A. J. Bard, *Anal. Chem.*, **35**, 1602 (1963).
6. S. Szpak, P. Stonehart, and T. Katan, *Electrochim. Acta*, **10**, 563 (1965).
7. L. G. Austin, "Fuel Cells—A Review of Government Sponsored Research, 1950-1964," p. 270, NASA Report SP-120, Washington, D. C. (1967).
8. R. N. Hammer, "Some Electrochemical Studies of Chloramine and Hydrazine," Ph.D. Thesis, University of Illinois, pp. 31-34 (1954).
9. M. H. Miles and P. M. Kellett, *This Journal*, **115**, 1225 (1968).
10. W. L. Jolly, *J. Phys. Chem.*, **58**, 250 (1954).
11. L. F. Audrieth and B. A. Ogg, "The Chemistry of Hydrazine," pp. 170-173, John Wiley & Sons, Inc., New York (1951).
12. G. Jander, H. Spandau, and C. C. Addison, "Chemistry in Nonaqueous Ionizing Solvents, Vol. I, Chemistry in Anhydrous Liquid Ammonia, Part I, Anorganische und Allgemeine Chemie in Flüssigem Ammoniak," Interscience Publishers, John Wiley & Sons, Inc., New York (1966).
13. R. E. Panzer, To be published.
14. A. M. Phipps and D. N. Hume, *J. Chem. Educ.*, **45**, 664 (1968).
15. A. D. Goolsby and D. T. Sawyer, *J. Electroanal. Chem.*, **19**, 405 (1968).
16. R. G. Pearson, *J. Am. Chem. Soc.*, **85**, 3533 (1963).
17. M. J. Frazer, *New Scientist*, **33**, 662 (1967).
18. D. J. Barclay, *J. Electroanal. Chem.*, **19**, 318 (1968).
19. R. Payne, *J. Am. Chem. Soc.*, **89**, 489 (1967).
20. R. Payne, *1968 C.I.T.C.E. Meeting, Extended Abstracts*, **47** (1968).
21. R. G. Pearson, *J. Chem. Educ.*, **45**, 581 (1968).
22. M. W. Breiter, *Electrochim. Acta*, **8**, 925 (1963).
23. D. C. Grahame, *Anal. Chem.*, **30**, 1736 (1958).
24. J. M. Kolotyrkin, *This Journal*, **108**, 209 (1961).
25. P. Delahay, "Double Layer and Electrode Kinetics," pp. 126-128, John Wiley & Sons, Inc., New York (1965).
26. R. S. Perkins, R. C. Livingston, T. N. Anderson, and H. Eyring, *J. Phys. Chem.*, **69**, 3329 (1965).
27. D. D. Bodé, Jr., T. N. Anderson, and H. Eyring, *J. Phys. Chem.*, **71**, 792 (1967).
28. D. D. Bodé, Jr., T. N. Anderson, and H. Eyring, *This Journal*, **114**, 72 (1967).
29. I. Morcos, *J. Electroanal. Chem.*, **20**, 479 (1969).
30. T. R. Beck, *J. Phys. Chem.*, **73**, 466 (1969).
31. A. N. Frumkin, *This Journal*, **107**, 461 (1960).
32. P. Delahay, "New Instrumental Methods in Electrochemistry," pp. 115-129, Interscience Publishers, New York (1954).
33. S. Srinivasan and E. Gileadi, *Electrochim. Acta*, **11**, 321 (1966).

The Electrocrystallization of Zinc Dendrites in High-Purity, and Inhibitor Doped, Alkaline Zincate Solutions

John W. Diggle*,[1] and A. Damjanovic

The Electrochemistry Laboratory, University of Pennsylvania, Philadelphia, Pennsylvania

ABSTRACT

The influence of electrolyte purity on the initiation times and propagation rates of zinc dendrites grown in alkaline zincate solution is examined. No significant difference was found to exist between the results obtained in the present high-purity systems and those reported previously for the unpurified system. It is proposed that this is due to the fact that the zinc deposition potential is so far removed from the pzc of zinc that the electrode coverage with impurities present in unpurified solutions is far below that known to affect both morphology and kinetics. Evidence supporting this view was obtained in the case of benzene-doped zincate solutions, where 10^{-4} mole liter^{-1} benzene did not affect the growth of dendrites. Lead and organic cation-doped zincate solutions were found to be effective in retarding dendrite initiation, the degree of retardation depending on their concentration.

In a previous paper (1) a mechanism for the dendritic electrocrystallization of zinc was proposed in which the role of impurities was not considered. The crystallization was performed under conditions where rigorous purification of solutions was not made, and the purpose of the present paper is to ascertain whether, and to what extent, the presence of impurities may have influenced previous results and thus have affected subsequent theoretical analysis.

It is known that the presence of impurities influences greatly both the type of morphology obtained in metal electrodeposition and also the kinetic parameters (2-5). For example, the presence of 10^{-8} mole liter^{-1} of n-decylamine was found (3) to be effective in preventing a full development of pyramids on the (100) face of copper single crystals; and 10^{-7} mole liter^{-1} completely prevented their formation. These observations are particularly pertinent to the present investigation, since the initiation of zinc dendrites was proposed (1) to be due to a pyramidal type of growth under linear diffusion control. The adsorption of certain impurity molecules at specific sites would then be expected to prevent the initiation of dendrites. The extent of electrode coverage required to inhibit completely the formation of dendrites can be estimated by considering that there are, for instance, 10^8 screw dislocations/cm^2 from which a pyramidal growth and hence a dendrite may arise (1); therefore at least 10^8 molecules/cm^2 are required to prevent development of pyramids. This is equivalent to a coverage of about 10^{-6} (assuming one molecule of impurity per atom in the metal surface). However, in the case of n-decylamine adsorption on Cu, it was found (3) that an estimated coverage $>10^{-4}$ was required to promote truncation of pyramids. Under conditions where $\theta < 10^{-4}$, *i.e.*, at very low decylamine concentrations ($< 10^{-8}$ mole liter^{-1}) and at potentials far from pzc of Cu, no effect on morphology was noted.

The presence of impurities has been proposed by Price, Vermilyea, and Webb (6) to be important in the growth of metal whiskers, in which a critical current density, required to sustain growth, is dependent on the third root of the impurity concentration in the

* Electrochemical Society Active Member.
[1] Present address: Corporate Research Laboratories, Allied Chemical Corporation, Morristown, New Jersey.
Key words: zinc, dendrites, electrocrystallization, electrodeposition, inhibition.

solution. However, a discrepancy in the derivation of the exact critical current density-impurity concentration negates this third root dependence; nevertheless, some dependence of the growth rate on impurity concentration can be expected if the impurity molecule is adsorbed and buried by the advancing metal-electrolyte interface.

In conclusion, a survey of the literature on the influence of impurities in metal deposition suggests that some dependence on both the initiation and propagation of dendrites is to be expected, provided that the impurity molecule is adsorbed.

Experimental

Solution preparation.—The system chosen for the investigation of the effect of solution purity was 10% potassium hydroxide-0.1M zincate solution, $\eta = -100$ mV, and room temperature (~27°C).

Rigorous purification of potassium hydroxide solution was carried out as follows: Approximately 100 ml of saturated potassium hydroxide solution in conductivity water was treated with 5 ml 1% H_2O_2 in order to oxidize any oxidizable impurities present, the excess hydrogen peroxide being decomposed by heating the solution for 1 hr at 70°-80°C.[2] This treated solution was then transferred to an all-glass pre-electrolysis cell, and sufficient redistilled conductivity water was added to it to reduce the KOH concentration to 10%. All operations, from the moment of adding the concentrated KOH to the pre-electrolysis cell, are carried out in a closed, all-glass system.

The solution was then pre-electrolyzed in a three-electrode system composed of two gold gauze electrodes (area 50 cm^2 each) and a palladium subsidiary electrode in a compartment isolated from the main pre-electrolysis system by a fine frit (Fig. 1). One gold electrode was held manually at the zero charge potential (+1.1V HE, as measured against the palladium electrode) in order to adsorb any neutral organic molecules. The second gold electrode was held at +1.6V HE. The palladium electrode was chosen as the counter-electrode so that hydrogen atoms, instead of evolving as H_2, would be absorbed and therefore minimize the contamination of the purified potassium hydroxide. The pre-electrolysis was performed in a N_2 atmosphere [the N_2 being purified according to Mattson and Bockris (7)]. In order to purge the system of any evolved O_2 and to destroy any H_2O_2 which could be produced[3] at the gold electrode held at +1.1V HE, N_2 was continually bubbled through the electrolyte maintained at 70°-80°C.

Following 24 hr pre-electrolysis, a portion of the purified KOH solution was transferred to a usual three-compartment cell (9) and, after saturation with O_2, the O_2 evolution reaction on platinum was carried out. The current density at which the electrode begins to depolarize is taken as a measure of the purity of the solution (9, 10). The O_2 evolution test was repeated for different times of pre-electrolysis, as well as upon the "impure" KOH solution prepared as outlined in previous work (1).

The preparation of zincate solution was carried out by adding a suitable quantity of the purified KOH solution to a half saturated zinc amalgam (~1% Zn/Hg), and dissolving the required amount of zinc. The preparation of the zinc amalgam, the subsequent transfer of KOH, and the zinc dissolution process were all carried out in a closed all-glass system.

The final zincate concentration was then determined by EDTA titration in buffered pH 10 media (11); the zincate concentration was adjusted to 0.10M by additional short periods of zinc dissolution. This solution was then transferred, through a closed system, to the test cell (1).

[2] The influence of dissolved silicates has been found to be negligible in the present work (see section on possible influence of dissolved silicates introduced during purification).

[3] H_2O_2 formation at the +1.1V gold electrode is possible due to the partial reduction of oxygen produced at the +1.6V gold electrode (8).

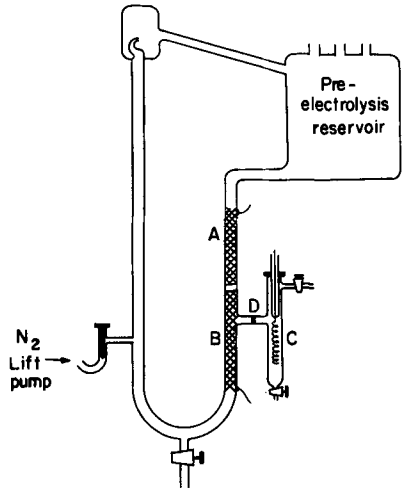

Fig. 1. Circulatory pre-electrolysis system comprising of a gold electrode controlled at the pzc (A), a gold electrode controlled at a high anode potential (B), and a subsidiary palladium electrode (C) separated from the main system by a fine frit (D).

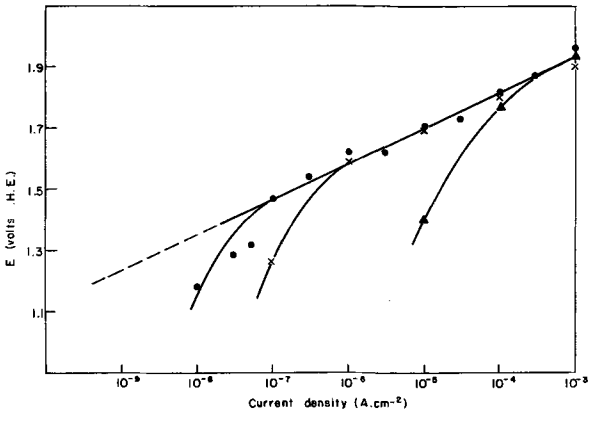

Fig. 2. Electrode potential E (volts HE) *vs.* current density for the evolution of oxygen on platinum as a function of 10% potassium hydroxide solution purity. ▲, No pre-electrolysis; ×, 24 hr pre-electrolysis; and ●, 72 hr pre-electrolysis.

Electrode preparation and procedure.—Electrode preparation and all procedures involved in total current-time and dendrite length-time measurements were identical to those outlined previously (1).

Results

Criteria for potassium hydroxide solution purity.—Figure 2 shows the plots of log i *vs.* E (HE) for the oxygen evolution on Pt for three states of purity. The Tafel slope is 0.118V, in agreement[4] with previous work in 1N KOH. Extrapolation of the linear E-log i plots to the reversible oxygen potential produces $i_o = 10^{-9}$ A-cm^{-2}, as compared (9) to 10^{-8} A-cm^{-2} obtained from the high current density region in 1*N* KOH.

Total current-time phenomenon.—The total current density for zinc deposition (based on geometric area) *vs.* time of deposition is shown in Fig. 3 for various degrees of solution purification. No significant effect of purification was observed. The initiation time for rapid current increase due to dendrite appearance, τ_i, is seen to be the same regardless of purification.

The influence of benzene, lead (added as Pb_3O_4), and tetraethyl ammonium bromide doped zincate solution (10^{-4} mole liter^{-1} dopant) are shown in Fig. 4. Benzene is seen to have no effect, tetraethyl ammonium bromide has some effect on the initiation time,[5] and

[4] It was noted that no break was found in the Tafel slope at low overpotentials, as was previously reported (9).

[5] The initiation time elongation has been shown not to occur in 10^{-4}M KBr doped zincate solutions. Thus the effect is due to $(C_2H_5)_4N^+$.

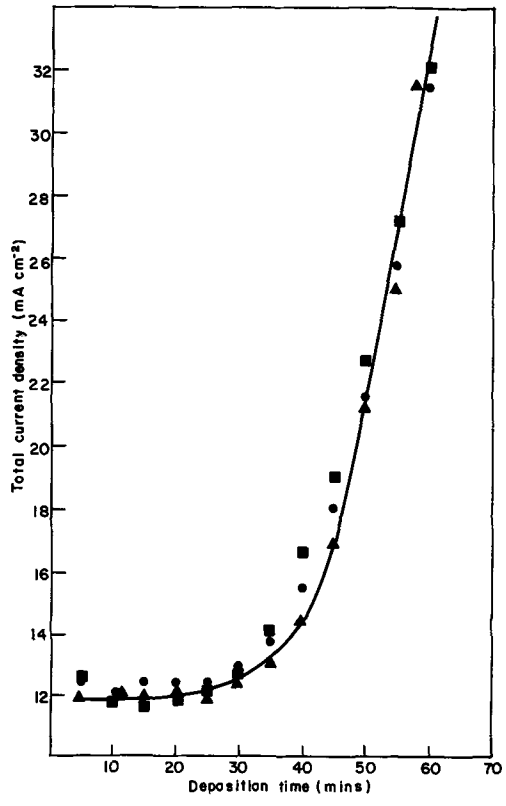

Fig. 3. Total current density vs. deposition time as a function of zincate solution purity for the conditions: 10% KOH + 0.1M zincate, $\eta = -100$ mV, and $T = 27°C$. ●, Impure system; ▲, 10^{-6} purity (24 hr pre-electrolysis); and ■, $<10^{-7}$ purity (72 hr pre-electrolysis).

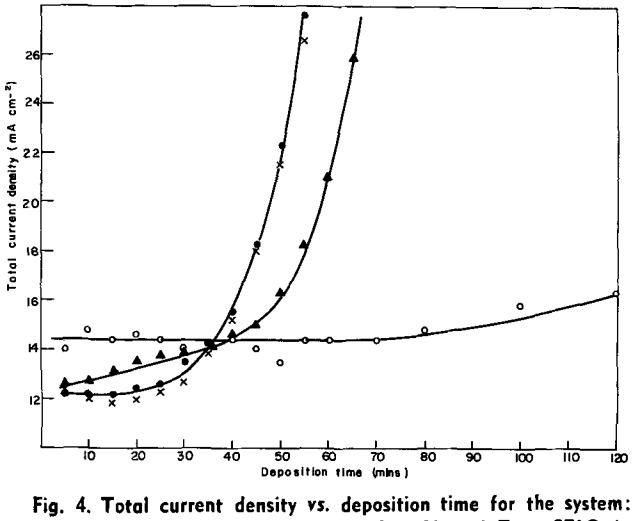

Fig. 4. Total current density vs. deposition time for the system: 10% KOH + 0.1M zincate, $\eta = -100$ mV, and $T = 27°C$, in the presence of 10^{-4}M benzene (×), lead (○), and tetraethyl ammonium bromide (▲). The blank impure system is represented by (●).

lead completely suppresses dendrites. The influence of lead on zinc morphology has also been shown earlier by Kudryavtsev (12).

Dendrite length-time behavior.—The dendrite length, y, *vs.* time of deposition as a function of solution purity, is shown in Fig. 5. Table I summarizes these results in terms of the dendrite tip current density, i_{tip}. The influence of purification is again seen to be negligible, both in terms of growth rate and initiation time, τ_d.[6]

[6] The notation used here is that of a previous paper (1). τ_i is the initiation time as determined by the time of rapid current increase (Fig. 3), whereas τ_d is that initiation time obtained by extrapolating the dendrite length-time of deposition line to zero dendrite length (Fig. 5).

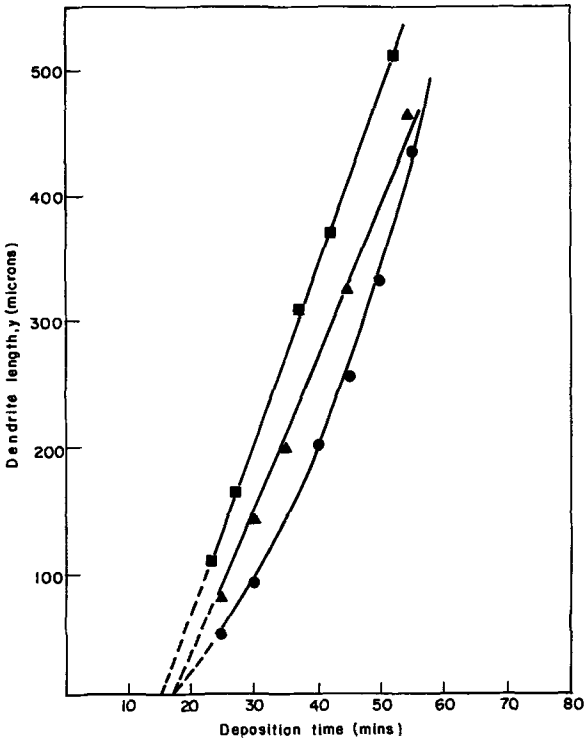

Fig. 5. Dendrite length, y, vs. deposition time as a function of zincate solution purity. Conditions and symbols identical to those in Fig. 3. Extrapolation of growth line to y = 0 produces initiation time, τ_d.

Possible influence of dissolved silicates introduced during purification.—The addition of 10^{-2}M silicate to an unpurified 0.1M zincate solution was found to be ineffective in terms of both the initiation time and the propagation rate, *i.e.*, a propagation rate of 14 μmin^{-1} was observed for the silicate doped zincate system for $\eta = -100$ mV and $T = 25°C$, compared to 15 μmin^{-1} reported previously (1) for the identical unpurified zincate system.

Discussion

Those impurities which were present within the "impure" system investigated earlier (1) clearly do not influence the results obtained, either in terms of the initiation time or the growth rate. This, then, leads to the question, "What type of impurity is present in the impure system, and why does it not influence the results?"

Since some impurities were clearly present in the impure system (Fig. 2), comparison with any impurity theory (6) (Table I) will be invalid if it can be shown that the impurities are not adsorbed and therefore are ineffective in reducing the dendrite growth rate. However, if the impurities are adsorbed, then a comparison of the present results with the Price, Vermilyea, and Webb theory (6) would indicate that the impurity theory is invalid in the present experiments.

Figure 4 shows that the influence of 10^{-4}M benzene, lead, and tetraethyl ammonium bromide on the total

Table I. Comparison of experimental dendrite tip current densities, i_{tip}, as a function of impurity level with that calculated from Price, Vermilyea, and Webb (6) theory on whisker growth

Impurity level, c_i (moles/liter)	i_{tip} experimental (A-cm²)	i_{tip} calculated*
10^{-4}	0.37 ± 0.02	4.6×10^{-2} K
10^{-6}	0.38 ± 0.02	10^{-2} K
2×10^{-7}	0.42 ± 0.02	5.9×10^{-3} K

* $i_{tip} = \left(\frac{K_2}{K_1}\right)^{2/3}\left(\frac{1}{\tau_{tip}}\right)^{1/3} c_i^{1/3} = K c_i^{1/3}$.

current density-time phenomenon. Benzene has no influence, $(C_2H_5)_4NBr$ increases the initiation period, τ_i, but does not prevent dendrites, whereas 10^{-4}M Pb completely suppresses dendritic growth. Further experiments have shown that 10^{-6}M Pb is ineffective in suppressing dendrites when $\eta = -100$ mV.

It may be concluded, therefore, that the impurity present in previous work was either:

(*A*) A neutral organic molecule whose adsorption is completely inhibited because the experimental zinc deposition potential (−1.5V NHE) is nearly IV negative to the zero charge potential (−0.65V NHE) (13) for zinc. From the work of Heiland, Gileadi, and Bockris (14), and the theoretical analysis of Bockris, Gileadi, and Müller (15) on the adsorption of benzene on Pt in pH = 11 solutions, the surface coverage drops sharply to near zero when the potential is 0.4V away from the zero charge potential. Furthermore, from the work of Damjanovic, Paunovic, and Bockris (3, 4) the coverage of n-decylamine was estimated as 10^{-5} at a potential 0.25V from the zero charge potential of Cu. Thus, it is easily seen that the coverage of zinc by benzene, at −0.85V from zero charge potential, can be $<10^{-6}$, and probably a great deal lower; or

(*B*) Metallic cations whose concentration was less than or equal to 10^{-6}M.

The ineffectiveness of positively charged organic cations in preventing dendrites (at least up to 10^{-4}M) may be related to the fact that, although they are positively charged, as the potential in the electric double layer goes increasingly negative, it is observed (16, 17) that such large cations can be desorbed. It is also reported (16) that this negative potential, required for desorption, becomes increasingly negative as the concentration of the organic cation increases.

Conclusions

1. Impurities present in previously reported work (1) have been shown to be ineffective in producing changes in dendrite initiation and propagation. The presence of organic molecules has been suggested which, due to the fact that the zinc deposition potential is far from zero charge potential, are not adsorbed to an extent sufficient to influence either morphology or kinetics. This was demonstrated in the case of benzene-doped electrolytes. Thus, in the absence of adsorbed impurities, any comparison with the Price, Vermilyea, and Webb theory (6) will be invalid.

2. The presence of lead has been shown to be effective in retarding dendritic growth; 10^{-4}M renders complete inhibition, whereas 10^{-6}M is ineffective (both with reference to $\eta = -100$ mV).

3. The presence of tetraethyl ammonium bromide (10^{-4}M) was shown to be effective in increasing the initiation time, but ineffective, at least at this concentration, in preventing dendrites.

4. The results in the section on dissolved silicates and the negligible difference found between unpurified and highly purified systems, indicates that silicates are ineffective as inhibitors for dendrites under the present conditions.

Acknowledgments

The many discussions and the encouragement of Professor J. O'M. Bockris are gratefully acknowledged. We also acknowledge the helpful discussions held with Mr. Ernst Cohn, Professor B. Lovrecek, and Mr. Z. Nagy. Financial support from the National Aeronautics and Space Administration (Contract NsG-325) is gratefully acknowledged.

Manuscript submitted May 20, 1969; revised manuscript received Sept. 11, 1969.

Any discussion of this paper will appear in a Discussion Section to be published in the December 1970 JOURNAL.

REFERENCES

1. J. W. Diggle, A. R. Despic, and J. O'M. Bockris, *This Journal*, **116**, 1503 (1969).
2. H. Fischer, *Electrochim. Acta*, **2**, 50 (1960).
3. A. Damjanovic, M. Paunovic, and J. O'M. Bockris, *J. Electroanal. Chem.*, **9**, 93 (1965).
4. A. Damjanovic, M. Paunovic, and J. O'M. Bockris, *Electrochim. Acta*, **10**, 111 (1965).
5. H. Fischer, *J. Electrochem. Soc. Japan*, **35**, 169 (1968).
6. P. B. Price, D. Vermilyea, and M. B. Webb, *Acta Met.*, **6**, 524 (1958).
7. E. Mattson and J. O'M. Bockris, *Trans. Faraday Soc.*, **55**, 1586 (1959).
8. A. Damjanovic, M. A. Genshaw, and J. O'M. Bockris, *J. Electroanal. Chem.*, **15**, 173 (1967).
9. A. Damjanovic, A. Dey, and J. O'M. Bockris, *Electrochim. Acta*, **11**, 791 (1966).
10. J. O'M. Bockris and A. K. M. S. Huq, *Proc. Roy. Soc. (London)*, **A237**, 271 (1956).
11. F. J. Welcher, "The Analytical Uses of EDTA," p. 149, Van Nostrand (1958).
12. N. T. Kudryavtsev, *Tr. Konf. Korr. Metal.*, **2**, 175 (1943).
13. Chuang-Hshin Cha and Z. A. Iofa, *Dokl. Akad. Nauk*, **131**, 137 (1960).
14. W. Heiland, E. Gileadi, and J. O'M. Bockris, *J. Phys. Chem.*, **70**, 1207 (1966).
15. J. O'M. Bockris, E. Gileadi, and K. Müller, *Electrochim. Acta*, **12**, 1301 (1967).
16. A. N. Frumkin, in "Advances in Electrochemistry, Electrochemical Engineering," Vol. 1., P. Delahay and C. W. Tobias, Editors, Interscience Publishers, New York (1961).
17. B. Lovrecek and D. Cipris, *J. Electroanal. Chem.*, **11**, 44 (1966).

Electrical Polarization Experiments on Silver Chloride

Y. J. van der Meulen[1] and F. A. Kröger

Department of Materials Science, University of Southern California, Los Angeles, California

ABSTRACT

The electronic conductivity in AgCl equilibrated with either chlorine or silver was measured at temperatures between 100° and 425°C. The measurements were carried out for crystals containing various amounts of divalent cationic impurities. A clear distinction could be made between a native Frenkel disorder controlled region and an impurity controlled conductivity region. The emf of the cell $Cl_2|AgCl|Ag$ was found to agree with the value calculated from tabulated thermodynamic data. Combination of our results with published data for the band gap and the chlorine induced absorption in AgCl shows that the latter stems from self-trapped rather than from free holes.

In silver chloride as in a number of other halides in a neutral atmosphere ionic conductivity strongly prevails at temperatures ranging from room temperature up to the melting point (455°C) (1, 2). The electronic component of the current is small and normally goes unnoticed. Previous investigators arrived at values for the electronic (hole) conductivity from the tarnishing rate of silver by chlorine (T = 300°-400°C) (1) and from the increase of the current through the crystal on changing from a nitrogen to a chlorine ambient (T = 50°-200°C) (3). Both methods are feasible over a limited temperature range only; moreover no distinction can be made between conduction by electrons and by holes.

As was first suggested by Hebb (4) and Wagner (5) the ionic part of the current can be blocked by the use of a material, that does not contain the constituents of the crystal, for one of the electrodes. The other one may contain the constituents and is preferably chosen to do so in order to fix the electrochemical potentials of the crystal at that side of the cell. Thus, for silver chloride, one can use a carbon anode and a silver cathode, or a carbon cathode and a carbon/chlorine anode. Comparable experiments have been published in detail for silver bromide (6, 7). For silver chloride only a few results were reported previously (6). These did not conform to existing theory and were highly irreproducible.

It was the purpose of the present investigation to determine the electronic conductivity of silver chloride as a function of temperature using both silver and chlorine as the chemically active electrode. Both undoped and Cd-doped crystals were used.

Theory

The equations governing the one-dimensional, electronic current flow through an ionic crystal with one reversible and one inert electronically conducting electrode have been derived before (5, 8, 9). Thus for the cell

$$+ \text{C}, \text{Cl}_2\ (1\ \text{atm})\ |\text{AgCl}|\text{C}, \text{N}_2 - \qquad \text{(I)}$$

we have

$$i_{tot} = i_h + i_e = \frac{RT}{LF}\left\{ \sigma_h(\text{I})\ (1 - e^{-EF/RT}) + \sigma_e(\text{I})\ (e^{EF/RT} - 1) \right\} \qquad [1]$$

And for the cell

$$- \text{Ag}|\text{AgCl}|\text{C}, \text{N}_2 + \qquad \text{(II)}$$

we find

$$i_{tot} = i_e + i_h = \frac{RT}{LF}\left\{ \sigma_e(\text{II})\ (1 - e^{-EF/RT}) + \sigma_h(\text{II})\ (e^{EF/RT} - 1) \right\} \qquad [2]$$

[1] On leave of absence from Utrecht State University, Utrecht, The Netherlands.

Here L is the cell constant, defined as the ratio of the thickness of the crystal and the effective electrode contact area (dimension: cm^{-1}); E is the applied voltage; $\sigma_e(\text{I})$ and $\sigma_h(\text{I})$ are the specific electron and hole conductivities in AgCl equilibrated with Cl_2 (1 atm.), $\sigma_e(\text{II})$ and $\sigma_h(\text{II})$ are the corresponding conductivities for the equilibrium with Ag ($a_{Ag} = 1.0$). These conductivities depend on the composition of the crystal and are different for pure and doped crystals. The other symbols have their usual meaning.

Equations [1] and [2] are valid under the condition that the ionic current is completely suppressed. However, a residual ionic contribution to the current may arise from chlorine evolution at the blocking electrode and is to be expected for conditions under which the steady-state chlorine pressure at this electrode is relatively high.

The chlorine evolved may be absorbed by the carbon and diffuses away or is flushed away. For cell I this condition exists at lower applied voltages where the equilibrium chlorine pressure at the blocking electrode is described by $p_{Cl_2} = e^{-2EF/RT}$. For cell II, the equilibrium chlorine pressure at the inert electrode is described by $p_{Cl_2} = e^{-2(E_d - E)\,F/RT}$. Here E_d is the decomposition voltage, *i.e.*, the voltage for which $p_{Cl_2} = 1$ atm. Thus, in this case the chlorine evolution becomes important at higher applied voltages. The theoretical hole and electron currents together with the deviations to be expected from the unavoidable chlorine evolution are schematically depicted in Fig. 1a and b for T = 246°C. Although a total current has been indicated as well, it should be stressed that the relative size of the components is unknown in advance and will vary from one case to another.

From the figures it can be seen that i_e can best be determined from measurements on cell II at low applied voltage. Thus we find σ_e (II). The determination

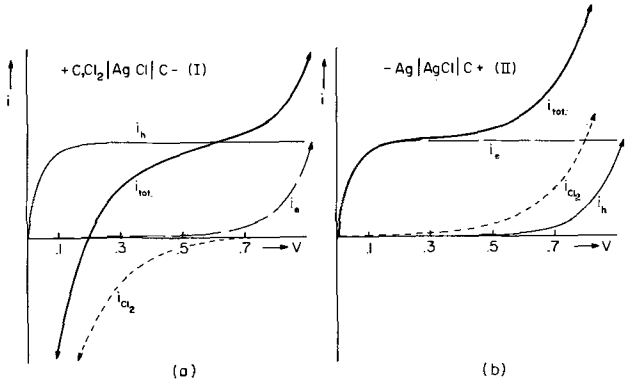

Fig. 1. Partial and total currents (schematic) at T = 246°C for cell I (a) and cell II (b). The relative size of the three current components is arbitrary.

of the σ_h (I) can best be done in cell I at higher applied voltage, as we expect only a small electron contribution in this configuration.

σ_h (I) and σ_h (II) are related through the free energy of formation of AgCl, as can be seen by considering the relevant defect equilibria

$$Ag_{Ag}^x + V_i^x \rightleftarrows V'_{Ag} + Ag^{\cdot}_i ; H'_F \quad [3]$$

$$V^x_{Ag} \rightleftarrows V'_{Ag} + h^{\cdot} ; H_A \quad [4]$$

$$\tfrac{1}{2}(Cl_2)_g \rightleftarrows Cl_{Cl}^x + V_{Ag}^x ; H_{Cl2V} \quad [5]$$

In pure and weakly doped crystals the defects formed by Frenkel disorder [3] are the dominant species. Thus, indicating concentrations by square brackets

$$[V'_{Ag}] \approx [Ag^{\cdot}_i] \quad [6]$$

and

$$[V'_{Ag}] \approx K'_F{}^{1/2} \quad [7]$$

From [4]

$$K_A = \frac{[V'_{Ag}]\,[h^{\cdot}]}{[V^x_{Ag}]} = \frac{K'_F{}^{1/2}\,[h^{\cdot}]}{[V^x_{Ag}]} \quad [8]$$

From [5]

$$K_{Cl2V} = \frac{[V^x_{Ag}]\,[Cl^x_{Cl}]}{p_{Cl_2}{}^{1/2}} = \frac{[V^x_{Ag}]}{p_{Cl_2}{}^{1/2}} \quad [9]$$

Thus [8] + [9] gives

$$[h^{\cdot}] = \frac{K_A K_{Cl2V}}{K'_F{}^{1/2}}\, p_{Cl_2}{}^{1/2} = \frac{K_{Cl2Vh}}{K'_F{}^{1/2}}\, p_{Cl_2}{}^{1/2} \quad [10]$$

We may write $\sigma_h(I) = [h\cdot(I)]qv_h$, $\sigma_h(II) = [h\cdot(II)]qv_h$, in which q is the electronic unit charge, v_h is the hole mobility and $[h\cdot(I)]$ and $[h\cdot(II)]$ are the hole concentrations in AgCl in equilibrium with Cl_2 and Ag, respectively. Then

$$\sigma_h(I)/\sigma_h(II) = p_{Cl_2}{}^{1/2}(I)/p_{Cl_2}{}^{1/2}(II) = 1/p_{Cl_2}{}^{1/2}(II) \quad [11]$$

Now in cell II

$$a_{Ag}(II) \cdot p_{Cl_2}{}^{1/2}(II) = p_{Cl_2}{}^{1/2}(II) = K_T = e^{-\Delta G/RT} \quad [12]$$

ΔG being the standard free enthalpy of formation in AgCl.

Thus finally

$$\sigma_h(I) = \sigma_h(II)\, e^{\Delta G/RT} \quad [13a]$$

For the electrons we find correspondingly

$$\sigma_e(I) = \sigma_e(II)\, e^{-\Delta G/RT} \quad [13b]$$

The last formulas enable us to correlate data found in measurements on one cell with data found for the other cell arrangement.

In doped samples, or in samples containing residual contamination, the impurities dominate the defect equilibria at lower temperatures and Eq. [6] and [10] do not apply anymore. For Cd we have

$$[Cd^{\cdot}_{Ag}] \approx [V'_{Ag}] \quad [14]$$

and using [8] and [9] we find in this extrinsic region

$$[h^{\cdot}] = \frac{K_A K_{Cl2V}}{[Cd^{\cdot}_{Ag}]}\, p_{Cl_2}{}^{1/2} = \frac{K_{Cl2Vh}}{[Cd^{\cdot}_{Ag}]}\, p_{Cl_2}{}^{1/2} \quad [15]$$

Thus it can be seen that Eq. [11] through [13b] remain valid in this region.

The various equilibria for the intrinsic Frenkel disorder controlled region are summarized in Table IV. The numerical data for the thermodynamic parameters result from our experiments as will be discussed in a later section.

Experimental

General set-up and procedures.—Measurements were carried out both on a nominally undoped and on Cd-doped AgCl crystals. The doped crystals were grown from a melt containing 1 x 10^{18} and 1.8 x 10^{20} atoms Cd/cm^3, respectively. At room temperature second phase segregation occurred in the heavily doped crystal. Complete redissolution took place, however, on reheating to the lowest measuring temperature.

Disk-shaped samples were cut from the boules with a jeweler's saw. The surfaces were polished on various grades of polishing paper and successively etched in HNO_3 and NH_4OH. Samples were rinsed with deionized water and with acetone, and dried on filter paper. The thickness of the samples thus obtained varied from 0.5 to 2.5 mm.

Subsequently the samples were mounted in a Pyrex polarization cell (Fig. 2). This cell was designed to allow both sides of the crystal to be kept in a different ambient. The crystal was sandwiched between two tubes, c, that pressed against the outer edge. Tension was provided by a stretched rubber collar, g. Current contacts to the crystal were made by hollow carbon electrodes, b. For some of the experiments one of these electrodes was covered with evaporated silver or silver foil. The electrodes were centrally mounted on Pyrex glass tubes, m, that could be adjusted separately. In order to avoid complications resulting from the attack of chlorine on platinum, the sections of the main outgoing leads subjected to elevated temperature were made of carbon yarn. The danger of attack by chlorine also prevented the use of a Pt blocking electrode, which otherwise might have been preferable.

Both the preparation and the mounting of the sample were done under red light. The cell was shielded from light during the measurements. Nitrogen and chlorine were used as ambients. The nitrogen was passed over a catalyst (ICI 29-1) to remove traces of oxygen. Both gases were dried with Union Carbide molecular sieves. To insure gas purity glass tubing was used throughout.

The measuring cell was contained in a furnace, the temperature control and stability of which were better than 0.5°C. After assembling, the cell was thoroughly flushed with nitrogen. It as then heated to 390°C and

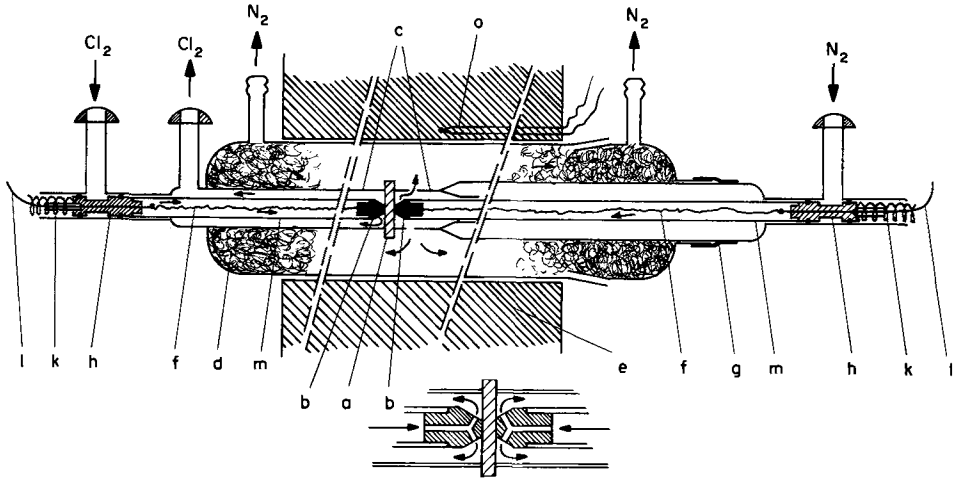

Fig. 2. Polarization cell (detail; electrode configuration): a, crystal; b, carbon electrodes; c, glass tubes; d, glass wool insulation; e, furnace; f, carbon electrode leads; g, rubber collar; h, Teflon end pieces; k, coiled springs; l, outgoing platinum leads; m, electrode mounting tubes; o, thermocouple. The direction of the gas flow is indicated by arrows.

the tubes, c, were pressed on the crystal. Due to the plasticity of AgCl at that temperature this resulted in a gastight seal. The cell was then cooled to 200°C and the carbon electrodes were pushed against the crystal. The nitrogen at the left-hand side was replaced by chlorine, and a polarizing voltage of 400 mV was applied to the crystal (Cl_2-side positive). Following Raleigh the electrode contact was optimized by heating the cell until surface melting set in. This was indicated by an abrupt rise in the cell current. The cell was then cooled down again, and the electrode springs were released. The i-V characteristics were measured for a number of temperatures for the configurations I and II.

The latter arrangement was effected by first replacing the chlorine by nitrogen and then increasing the cell voltage for a short time above the decomposition limit. For some slices of crystal, measurements were only carried out in the second configuration, and the silver electrode consisted of evaporated silver or silver foil. During all experiments a gas stream of 5-20 cm^3/min was maintained through both electrode compartments. The d-c electrical circuit is schematically shown in Fig. 3a.

The sample and electrode geometry were of rather ill-defined dimensions. To determine the cell constant of each sample, the a-c resistivity (at 5-50 kc) was measured as a function of temperature. These measurements when combined with literature data for the specific resistivity as a function of doping concentration and temperature (10), not only yielded the cell constant but also the concentration of electrically active foreign constituents (Cd). The a-c bridge circuit is schematically shown in Fig. 3b. The measurements were usually carried out after the polarization experiments had been finished. Results with and without silver plating the electrodes were somewhat different. At the highest temperatures, the relatively high resistivity of the carbon yarn had to be taken into account.

Inspection of the sample and the contacts after completion of the measurements showed that as a rule the electrodes adhered firmly to the crystal. Samples had not darkened visibly even after runs of a month's length, the surface was very smooth, probably as a result of local melting.

Current fluctuations and their prevention.—Measurements on the cell I configuration went off smoothly, and only minor problems were encountered. Measurements on the cell II configuration, however, presented a different picture. The current in this case was very unstable showing sharp positive peaks. Moreover the time required to establish a new equilibrium value of the current after a charge of the applied voltage was much longer than for cell I. Various attempts were made to correct these problems. They included the use of silver foil as a cathode instead of electrolytically deposited silver, and the use of a mixed carbon-silver electrode, consisting of a carbon electrode that had only partially been covered with evaporated silver in a dotted pattern. These modifications were not successful; moreover they made it impossible to carry out successively measurements on the same sample for both configurations. The

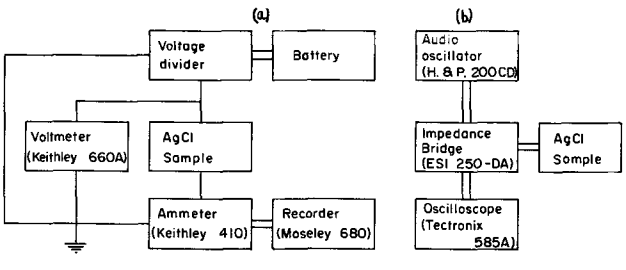

Fig. 3. (a) Electrical circuit for d-c polarization measurements; (b) bridge circuit (a-c) for measuring the cell constant L.

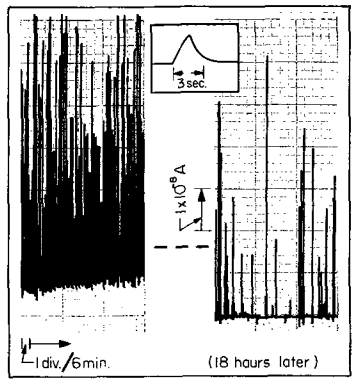

Fig. 4. Current fluctuations registered for a cell Ag|AgCl|C before and after an 18-hr long annealing period. In all cases the annealing finally eliminated virtually all excursions. Cell voltage = 500 mV, T = 300°C. Inset: The form of a single current fluctuation registered at a higher magnification of the time base.

best results were obtained at temperatures above 350°C, after annealing the crystals at the highest operating temperature and voltage for an extended period. This treatment directly followed the electrodeposition of silver on one of the electrodes and eliminated the sharp current fluctuations almost completely (Fig. 4).

We are inclined to believe that the breaks are bursts of ionic conduction released when a trapped dislocation breaks loose from a pinning point. Annealing may be assumed to result in the removal of the most loosely trapped dislocations from the space charge region near the blocking electrode, "loosely" being defined with respect to the applied field. An alternative explanation could be that the contact between crystal and electrode is not perfect. Thus there exist unpolarized regions at the surface of the crystal. On establishing contact with one of these spots a burst of ionic current could arise from the polarization of that region.

Experimental Results

Cells of type I.—I-V characteristics were measured on AgCl samples mounted between a chlorine (1 atm) anode and a carbon cathode at temperatures ranging from 98° to 426°C. Care was taken not to exceed the decomposition voltage at a given temperature. The curves all show a well-defined saturation of the hole current (Fig. 5a and b). At lower applied voltages the effect of chlorine evolution at the blocking electrode can be seen clearly. Use of platinum foil as an electrode material could have sealed off the crystal better, but was precluded by the formation of platinum chlorides at the temperatures and chlorine pressures involved.

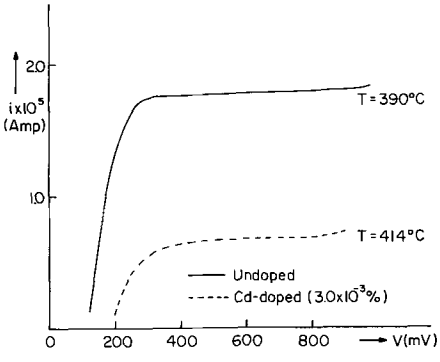

Fig. 5a. I-V characteristics for undoped and lightly Cd-doped AgCl crystals in cell configuration I. A second rise in the current at the highest applied voltages is barely perceptible. The difference in the saturation current is mainly due to a difference in cell constant.

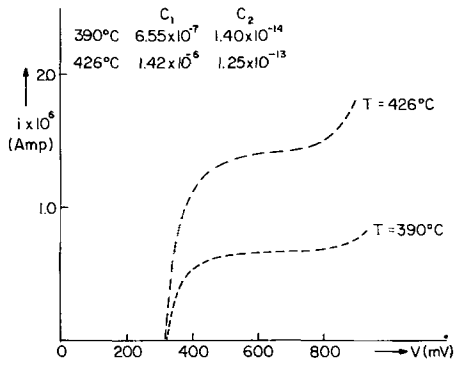

Fig. 5b. I-V characteristics for the heavily doped AgCl crystal. The exponential contribution at higher applied voltage is much more pronounced than in the previous case (Fig. 5a). The hole conduction has become smaller. The values obtained for C_1 and C_2 (Eq. [16]) have also been indicated.

In the case of the undoped and lightly doped material only at $T > 390°C$ some evidence was found of a contribution by electrons to the current at the highest applied voltages ($E > 850$ mV). Nowhere did this contribution exceed 4% of the total current.

In the case of the heavily doped crystal the saturation of the hole current is evident again, but now a rise in the current at higher applied voltage indicates a contribution by electrons as well. The high-voltage part of the curves found in the last case can be represented by

$$i_{tot.} = i_h + i_e = C_1(1 - e^{-EF/RT}) + C_2(e^{EF/RT} - 1) \quad [16]$$

The best values for C_1 and C_2 have been indicated in Fig. 5. By entering now the measured values of $i_{sat}(T)$ and the cell constant L in Eq. [1], $\sigma_h(I)$ is found as a function of temperature. The result for undoped material is plotted in Fig. 6. The change is slope at 210°C is related to the transition from the extrinsic, Cd-dominated range at lower temperature to the Frenkel disorder controlled, intrinsic region at higher temperature. It can be seen that the transition for the lightly doped crystal takes place at a higher temperature (255°C). The heavily doped crystal remains extrinsic up to the highest temperature (426°C).

The discrepancy in the intrinsic, high-temperature region between the curves as found for the undoped and the lightly doped crystals gives some idea of the accuracy with which L can be determined: The two curves should almost coincide. Also entered in the same figure are the results found by Wagner from the rate constant of bromination (1) and by Luckey from the excess conductivity (3).

The a-c conductivity of the crystals examined relative to the conductivity of very pure AgCl (10, 11) is shown in Fig. 7. The curves of the undoped and lightly doped crystals have been adjusted to fit the $\sigma/\sigma_0 = 1$ level at higher temperature, *i.e.*, in the intrinsic region. Comparison of these curves with literature data concerning doped crystals indicates a divalent impurity mole fraction of $5 \times 10^{-6} - 10^{-5}$ in the undoped material and a Cd^{++} mole fraction of 3.0×10^{-5} ($=7 \times 10^{17}$ at. Cd/cm³) in the lightly doped material. For the heavily doped crystal spectrochemical analysis indicated a Cd^{++} hole fraction of 1.82×10^{-2} ($=4.2 \times 10^{20}$ at. Cd/cm³). Both values are close to the Cd concentration of respectively 1×10^{18} and 1.8×10^{20} cm^{-3} in the melt.

Cells of type II.—The best reproducible measurements on cells of type II were obtained while working with the lightly doped crystal. Doping is unimportant in this case because all measurements were carried out at relatively high temperature well outside the extrinsic region. Up to an applied voltage $E = 600$ mV the graphs are well described by Eq. [2].

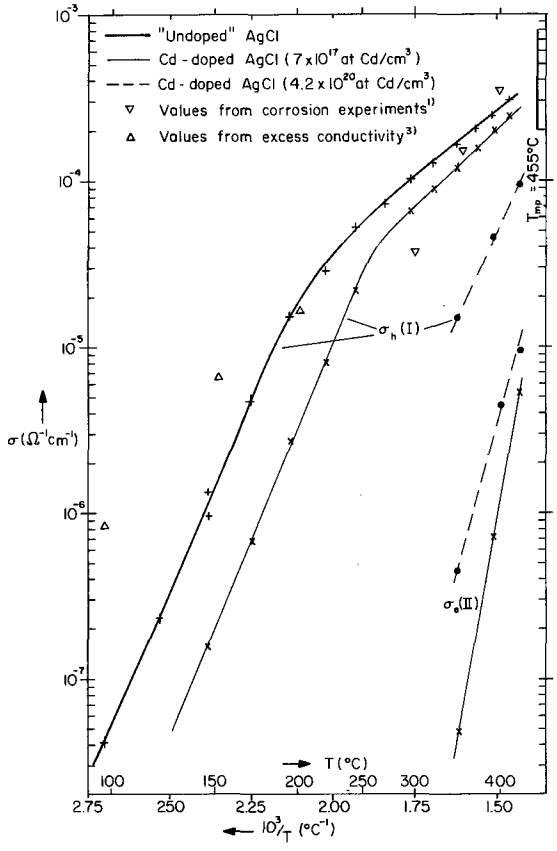

Fig. 6. Conductivity vs. temperature for AgCl containing various amounts of divalent cationic impurities. Both the hole conductivity $\sigma_h(I)$ and the electron conductivity $\sigma_e(II)$ are shown. The influence of the impurity concentration on the transition temperature is obvious. Values for the electronic conductivity by Wagner and Luckey have also been entered in the graph.

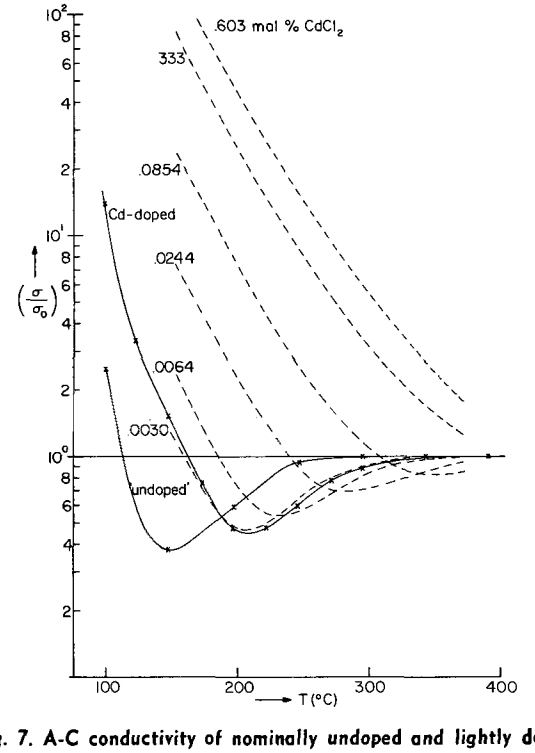

Fig. 7. A-C conductivity of nominally undoped and lightly doped AgCl relative to the conductivity of pure AgCl as a function of temperature. Dashed curves were taken from ref. (10).

The resulting values for $\sigma_e(II)$ and $\sigma_h(II)$ are given in the first columns of Table I. The third column gives values of $\sigma_h(I)$ determined from cells I. The fifth

Table I. Electron and hole conductivities in AgCl + Cd (7×10^{17} at./cm^3)

T, °C	σ_e(II), ohm^{-1} cm^{-1}	σ_h(II), ohm^{-1} cm^{-1}	σ_h(I), ohm^{-1} cm^{-1}	$e^{\Delta G/RT}$	σ_h(II)$_{exp}$, ohm^{-1} cm^{-1}	σ_e(II)σ_h(II)$_{exp}$, ohm^{-2} cm^{-2}
343	4.8×10^{-8}	1.44×10^{-11}	1.20×10^{-4}	$10^{7.80}$	1.92×10^{-12}	9.2×10^{-20}
390	7.1×10^{-7}	1.64×10^{-10}	1.93×10^{-4}	$10^{7.10}$	1.54×10^{-11}	1.10×10^{-17}
426	5.3×10^{-6}	7.9×10^{-10}	2.70×10^{-4}	$10^{6.60}$	6.8×10^{-11}	3.6×10^{-16}

Table II. Electron and hole conductivities in AgCl + Cd (4.2×10^{20} at./cm^3)

T, °C	σ_e(II), ohm^{-1} cm^{-1}	σ_h(II), ohm^{-1} cm^{-1}	σ_h(I), ohm^{-1} cm^{-1}	$e^{\Delta G/RT}$	σ_h(II)$_{exp}$, ohm^{-1} cm^{-1}	σ_e(II)σ_h(II)$_{exp}$, ohm^{-2} cm^{-2}
343	4.44×10^{-7}	6.77×10^{-11}	1.49×10^{-5}	$10^{7.80}$	2.4×10^{-13}	1.07×10^{-19}
390	4.48×10^{-6}	1.04×10^{-9}	4.60×10^{-5}	$10^{7.10}$	3.7×10^{-12}	1.66×10^{-17}
426	9.3×10^{-6}	3.71×10^{-9}	9.4×10^{-5}	$10^{6.60}$	2.4×10^{-11}	2.23×10^{-16}

column contains values for $\sigma_h(II)_{expected}$ calculated from $\sigma_h(I)$ using Eq. [13a]. It is seen that $\sigma_h(II) \approx 10 \times \sigma_h(II)_{exp}$. This indicates that either $\sigma_h(II)$, $\sigma_h(I)$, or ΔG must be in error.

Electromotive force measurements between 295° and 426°C on a cell Ag|AgCl|C,Cl_2 gave values that are within 1% of the ones calculated from $E = -\Delta G/F$ using tabulated values (12, 13) in the calculation of ΔG. On the other hand $\sigma_h(I)$ seems to be beyond doubt. Thus $\sigma_h(II)_{exp}$ must be correct. This leaves only $\sigma_h(II)$ as possibly erroneous. It seems most likely that this is due to the fact that most of the extra current interpreted as $\sigma_h(II)$ is actually an ionic current due to decompositon of the crystal as a result of chlorine evolution at the anode (cf. Fig. 1b). The fact that it is possible to describe this contribution to the total current by an exponential function may be accidental.

The last column of Table I shows the product $\sigma_e(II)\sigma_h(II)_{exp}$. This product equals $K_i q^2 \mu_e \mu_h$ and should not depend on whether the sample under consideration is pure or doped, or is in the extrinsic or intrinsic conductivity range.

Measurements on the heavily doped crystal could not be fitted satisfactorily by Eq. [2]. Thus in this case we used

$$i_{tot} = C_1(1 - e^{-EF/RT}) + C_2(e^{EF/RT} - 1) + C_3E \quad [17]$$

The third term is equivalent to an ohmic contribution to the total current. This could be caused by leakage along the surface of the crystal. The numerical value of the constant C_3 varied from 10^{-8} at 343°C to 1.5×10^{-7} at 426°C. Omission of the third term did not result in a pronounced change in C_1 or C_2, but simply made the curve fitting far worse. Values found for $\sigma_e(II)$ and $\sigma_h(II)$ for this crystal have been entered in Table II. Here again the expected value of $\sigma_h(II)$ has been calculated and tabulated. The discrepancy between the observed and expected values of $\sigma_h(II)$ is in this case even higher than in the previous case where electronic conduction in the intrinsic ionic range was examined. Instead of showing a decrease as expected for $\sigma_h(II)$ in the presence of high [Cd], the value of $\sigma_h(II)$ has actually increased. The product $\sigma_e(II)\sigma_e(I)_{exp}$ has again been entered in the last column of Table II. Both sets of electron conductivity data have been plotted in Fig. 6. Figure 8 shows the values of $\sigma_e(II)\,\sigma_h(II)_{exp}$ from Tables I and II. These values were determined on crystals that are intrinsic and extrinsic in ionic defects. It is seen that the two sets of data agree satisfactorily and can be described by the equation

$$\sigma_e\sigma_h = 2.70 \times 10^{10} \times 10^{-1.81 \times 10^4 \times T^{-1}} \text{ (ohm cm)}^{-2} \quad [18]$$

This agreement can be considered as an over-all check on the reliability of the results.

Discussion

The conductivity data found from our experiments may be combined with published data of the free hole concentration to yield the hole mobility as a function of temperature. Moser (14) and Ulrici, Koswig, and Stasiw (15) measured the chlorine induced absorption in AgCl. They found a maximum absorption around 800 mμ and a half width of approximately 1.60 eV. At a given temperature the absorption is proportional to the square root of the chlorine pressure and inversely proportional to the concentration of divalent cations in the crystal. These findings prove that the absorption is due to a positive species, almost certainly holes; it cannot be caused by holes trapped at silver vacancies as suggested earlier (16), for this species is effectively neutral (V^x_{Ag}). An estimate of the number of absorbing centers N′ per cm^3 may be obtained using the Smakula equation. It seems best in our case to use a modified expression derived without considering the Lorentz local field (17).

$$N' f_{ab} = 1.43 \times 10^{16} \times n_o \times K(E)_{max} \Delta E \text{ cm}^{-3} \quad [19]$$

Here n_o is the index of refraction, K_{max} the maximum absorption constant in cm^{-1}, and ΔE the half width in eV; f_{ab}, the oscillator strength, can be considered as an adjustable parameter. The reported measurements (14, 15) give an identical result (Table III) for N'_h as a function of T

$$N'_h f_{ab} = 8.0 \times 10 \times T^{5.34} \text{ cm}^{-3} \quad [20]$$

If the absorption is attributed to free holes, μ'_h may be obtained from

$$\mu'_h\,(T) = \frac{\sigma_h(I)}{N'_h(T)\,q} \text{ cm}^2 \text{ V}^{-1} \text{ sec}^{-1} \quad [21]$$

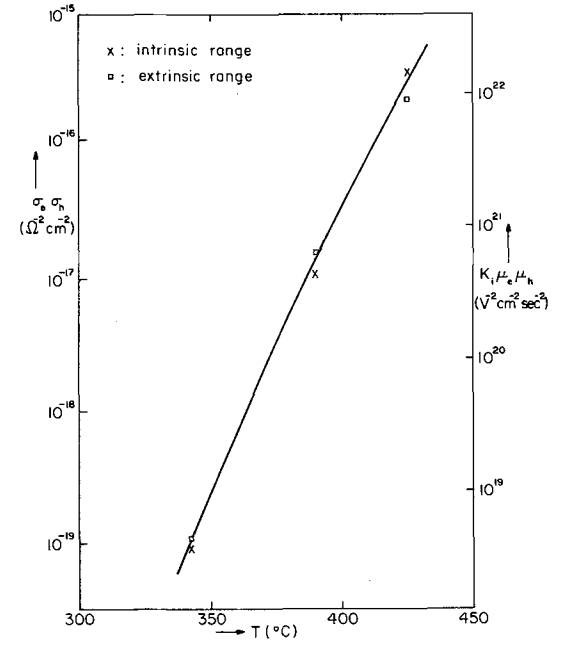

Fig. 8. The product $\sigma_e(II)\,\sigma_h(II)_{exp}$ (left-hand scale) and $K_i\mu_e\mu_h$ (right-hand scale) as a function of temperature for lightly doped (intrinsic conductivity range) and heavily doped (extrinsic conductivity range) silver chloride.

Table III. Values of $\mu'/f_{ab} = f(T)$, using $N'_h f_{ab}$ calculated from literature (14, 15) with the modified Smakula equation, and σ_h from our experiments. Also shown are $K_i \exp(E_{ex}/kT)$ calculated from optical data (19) using Eq. [25] and [26], and $K_i \mu_e \mu_h$ calculated from the experimental results using Eq. [28]

T, °C	$\frac{10^3}{T}$, °K^{-1}	$N'_h f_{ab}$, cm^{-3}	σ_h, ohm^{-1} cm^{-1}	μ'_h/f_{ab}, cm^2 V^{-1} sec^{-1}	$K_i e^{E_{ex}/kT}$, cm^{-6}	$K_i \mu_e \mu_h$, cm^{-2} V^{-2} sec^{-2}
441	1.40	—	—	—	2.7×10^{21}	—
393	1.50	9.5×10^{16}	2.60×10^{-4}	1.69×10^{-2}	4.2×10^{19}	7.4×10^{20}
352	1.60	6.9	1.80	1.60	7.3×10^{17}	1.15×10^{19}
315	1.70	5.1	1.25	1.52	1.15×10^{16}	—
282	1.80	3.7	8.6×10^{-5}	1.45	1.74×10^{14}	—
253	1.90	2.7	6.0	1.38	3.0×10^{12}	—

Values of σ_h (I) in the intrinsic region (Fig. 6) can be expressed as

$$\sigma_h\ (I) = 6.37 \times 10^{-2} \times e^{-3.67 \times 10^3 \times T^{-1}}\ \text{ohm}^{-1}\,\text{cm}^{-1} \quad [22]$$

or, expanding the exponential as a power of T

$$\sigma_h\ (I) = 9.16 \times 10^{-22} \times T^{6.18}\ \text{ohm}^{-1}\,\text{cm}^{-1} \quad [23]$$

Combination of [21] and [23] gives

$$\mu'(T)/f_{ab} = 7.16 \times 10^{-3} \times T^{0.84}\ \text{cm}^2\,\text{V}^{-1}\,\text{sec}^{-1} \quad [24]$$

Values at various temperatures are given in Table III. Since f_{ab} should be a number close to unity it is seen that μ'_h is rather low and nearly temperature independent.

Another line of approach can be taken by calculating K_i from

$$K_i = N_e N_h = g_c g_v\, 4 \left(\frac{2\pi kT}{h^2}\right)^3 \left(\frac{m_e^*\, m_h^*}{m_e^2}\right)^{3/2} e^{-E_g/kT}\ \text{cm}^{-6} \quad [25]$$

Here E_g is the width of the forbidden gap; g_c and g_v are the statistical weights of the conduction and valence band: $g_c = 1$, $g_v = 12$ (18). We use $m_e^* = 0.3\ m_e$ and, tentatively, $m_h^* = m_e$. Brown's optical data (19) for $T > 300$°K can be represented by

$$E_g - E_{ex} = 3.39 - (1.02 \times 10^{-3})\,T\ \text{eV} \quad [26]$$

E_{ex}, the exciton dissociation energy, is unknown but will be retained in the expression for K_i obtained from [25] and [26]

$$K_i e^{E_{ex}/kT} \approx 3.00 \times 10^{46} \times 10^{-1.79 \times 10^4 \times T^{-1}}\ \text{cm}^{-6} \quad [27]$$

Values calculated from (27) are also given in Table III. Combining [18] with

$$\sigma_e(I)\ \sigma_h(I) = N_e\, N_h\, q^2\, \mu_e\, \mu_h = K_i\, q^2\, \mu_e\, \mu_h \quad [28]$$

we get

$$K_i\, \mu_e\, \mu_h = \frac{\sigma_e \sigma_h}{q^2} = 1.05 \times 10^{48} \times 10^{-1.81 \times 10^4 \times T^{-1}}\ (\text{cm V sec})^{-2} \quad [29]$$

Values for $\sigma_e \sigma_h$ were taken from Fig. 8. The result is given in Table III. By dividing $K_i\, \mu_e \mu_h$, which results completely from our experiments, by $K_i e^{-E_{ex}/kT}$, which was calculated from optical data, we arrive at

$$\mu_e \mu_h\, e^{-E_{ex}/kT} = 35 \times 10^{-2 \times 10^2 \times T^{-1}}\ \text{cm}^4\,\text{V}^{-2}\,\text{sec}^{-2} \quad [30]$$

or

$$\mu_e \mu_h \approx 35 \times e^{(E_{ex} - 0.04)/kT}\ \text{cm}^4\,\text{V}^{-2}\,\text{sec}^{-2} \quad [31]$$

The Hall mobility of electrons in AgCl has been measured by several authors up to 400°K (20-22). The high-temperature results can be expressed as

$$\mu_e = 2.54 \times 10^5 \times T^{-3/2} \approx 3.45 \times \exp\,(0.083/kT)\ \text{cm}^2\,\text{V}^{-1}\,\text{sec}^{-1} \quad [32]$$

The latter part of the equation is an approximation holding in the range 600°-700°K. Combination of [31] and [32] gives

$$\mu_h = 10 \times \exp\,(E_{ex} - 0.123)/kT\ \text{cm}^2\,\text{V}^{-1}\,\text{sec}^{-1} \quad [33]$$

Comparison with the value of μ'_h/f_{ab} derived from [21], reveals a considerable discrepancy. The ratio between μ_h and μ'_h can be written

$$\mu_h/\mu'_h \approx 2.65 \times 10^2 \times f_{ab}^{-1} \times \exp\,(E_{ex} - 0.076)/kT \quad [34]$$

This ratio varies from 61.5 to 74.5 between 600° and 700°K for $E_{ex} = 0$ and $f_{ab} = 1$ and it becomes larger with increasing E_{ex} and decreasing f_{ab}.

A possible explanation for the deviation of μ_h/μ'_h from unity may be that the optical absorption as found by Moser and Ulrici, *et al.* does not originate from free hole absorption but has to be assigned to self-trapped holes at an energy level E_T slightly above the valence band. Indications of the occurrence of self trapping have been found previously in electron spin resonance experiments at low temperature (23). The use of N'_h stemming from the optical absorption to calculate the hole mobility is then not justified: $N'_h = (N_h)_{\text{self trapped}}$.

The expected ratio between free and self-trapped holes is

$$\frac{(N_h)_{s.t.}}{N_h} = \frac{N_T e^{\Delta E/kT}}{N_V} = \frac{2 \times 2.3 \times 10^{22} \times e^{\Delta E/kT}}{g_v \times 2\left(\frac{2\pi mkT}{h^2}\right)^{3/2}} = 10.7 \times \exp\,(\Delta E + 0.083)/kT \quad [35]$$

N_T = trap density = 2 x number of atoms per cm^3 on one sublattice, N_V = density of states in the valence band, $\Delta E = E_T - E_V$, E_V being the energy of the edge of the valence band. This ratio must equal the ratio between the two mobilities (34):

$$\frac{(N_h)_{s.t.}}{N_h} = \frac{N'_h}{N_h} = \frac{\mu_h}{\mu'_h} \quad [36]$$

From [34], [35] and [36] we finally find

$$\Delta E = E_{ex} + (3.21 - \ln f_{ab})\ kT - 0.16\ \text{eV} \quad [37]$$

The calculation restricts the validity of [37] primarily to the 600°-700°K range. If, instead of using the modified equation, we had used the original version of Smakula's equation, which includes the Lorentz field, the result would have been, again for $T = 600$°-700°K,

$$\Delta E = E_{ex} + (1.75 - \ln f_{ab})\ kT - 0.16\ \text{eV} \quad [38]$$

With reasonable values of E_{ex} (0.10 eV $< E_{ex} <$ 0.20 eV), Eq. [37] and [38] lead to values for ΔE between 0.04 and 0.22 eV at $T = 650$°K and $f_{ab} = 1$. A lower oscillator strength tends to shift these values slightly upwards: for $f_{ab} \approx 1/2$ we find ΔE between 0.08 and 0.26 eV, values that are quite acceptable.

Thus it seems that the discrepancy between the mobility values can be explained by the fact that the chlorine-induced extra absorption in AgCl originates from self-trapped rather than free holes. This situation contrasts with the one found in AgBr, where the analysis did not point to self-trapped holes (24).

In the alkali and ammonium halides the valence band is mainly due to Cl^- ions and a self-trapped hole can be considered to be a Cl_2^- molecule ion, as

Table IV. Reactions involving structure elements of AgCl and AgBr and the parameters of their reaction constant $K = K_0 \exp(-H/kT)$, with $K^0 = \exp(\Delta s/k)$

Reaction	K	AgCl		AgBr	
		H, eV	ΔS, cal. °K^{-1}·mole^{-1}	H, eV	ΔS, cal. °K^{-1}·mole^{-1}
$\frac{1}{2}X_2(g) \rightleftarrows X_X^x + V'_{Ag} + h^\cdot$	K_{X_2Vh}	0.91	−22.2	0.84	−8.9
$Ag(s) + V_i^x \rightleftarrows Ag_i^\cdot + e'$	K_{Ag}	2.64	26.0	2.28	25.9
$Ag_i^\cdot + V'_{Ag} \rightleftarrows Ag_{Ag}^x + V_i^x$	K'^{-1}_F	−1.14	−8.32	−1.06	−13.5
$AgX(s) \rightleftarrows Ag(s) + \frac{1}{2}X_2(g)$	K_{AgX}^{-1}	1.29	12.38	1.13	+12.2
$0 \rightleftarrows e' + h^\cdot$	K_I			3.19	15.7
	K_i (opt.)	3.70	7.9	2.97 + E_{ex}	17.9

has been confirmed by various means (25, 26). In AgCl the valence band is mainly due to Ag^+ ions and a self-trapped hole center should consist of Ag^{2+} + 6 neighboring Cl^- atoms. Further evidence, that the optical absorption in chlorinated crystals may well originate from self-trapped holes, stems from observations on AgCl: Cu^{2+} (27). After selective illumination of the crystals at liquid helium temperature an absorption band speculatively assigned to a $(CuCl_6)^{4-}$ complex was found which was very similar to the one produced by chemically injected holes (14).

The trapping energy according to [37] and [38] is in our case somewhat temperature dependent. It must be remembered that approximations included in [36] and [37] restrict these expressions to the range 600°-700°K. Furthermore, a linear temperature dependence of the band gap may not be quite correct, and a possible temperature dependence of the exciton energy has been neglected. Thus it is the absolute value of ΔE rather than its temperature dependence that seems most important.

As mentioned earlier, the various equilibria for the intrinsic region have been summarized in Table IV together with the results for both AgCl and AgBr. For AgCl we put $f_{ab} = 1.0$, $E_{ex} = 0.15$ eV, $p_{Cl_2} = 1$ atm and the number of molecules $N = 2.33 \times 10^{22}$ cm^{-3}.

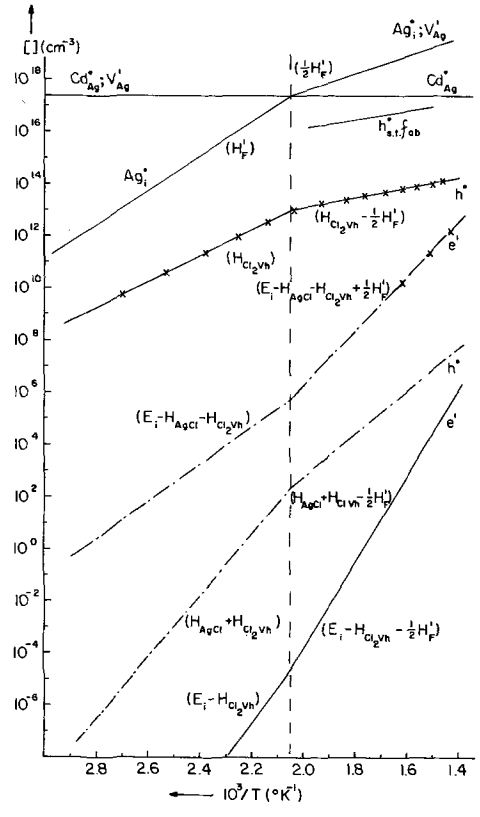

Fig. 9. Concentrations of the imperfections in AgCl + 10 ppm Cd as a function of temperature. Solid lines, AgCl in equilibrium with Cl_2 (1 atm); broken lines, Ag-Cl in equilibrium with Ag ($a_{Ag} = 1.0$). The slopes of the various lines are given in brackets.

The data taken on the undoped sample have been used. The value of K_{AgCl} was calculated at $T = 500$°K. The value found for K'_F agrees well with the low-temperature value reported by Müller (2). For AgBr we modified the results from an earlier publication (16). K'_F was taken from ref. (24), the value of K_{AgBr} was also calculated for $T = 500$°K, and the hole mobility was taken to be $\mu_h = 8 \times 10^6 \times T^{-2.69}$ cm^2 V^{-1} sec^{-1} (29) rather than $\mu_h = 1.5 \times 10^{14} \times T^{-5.5}$ cm^2 V^{-1} sec^{-1} (7). It can be seen that for AgBr the result for K_i agrees very well with the result of optical measurements and that the differences between AgCl and AgBr are quite acceptable.

Figure 9, finally, shows the concentrations of ionic and electronic defects in AgCl + 10 ppm Cd equilibrated with, respectively, 1 atm Cl_2 and Ag(s). Note the bends in the concentration of holes and electrons at the temperature where the ionic defects change from being impurity controlled to Frenkel disorder controlled. In the plotting of the data the same values of the various parameters have been used as before.

Acknowledgment

Thanks are due to Dr. F. Moser, Eastman Kodak Research Laboratories, Rochester, New York for putting at the authors' disposal the undoped and lightly doped AgCl crystals. This work was supported by the Directorate of Chemical Sciences, Air Force Office of Scientific Research under Contract AF-AFOSR-68-1405.

Manuscript received Aug. 13, 1969.

Any discussion of this paper will appear in a Discussion Section to be published in the December 1970 JOURNAL.

REFERENCES

1. C. Wagner, *Z. physik. Chem.*, **B32**, 447 (1936).
2. P. Müller, *Physica Stat. Sol.*, **12**, 775 (1965).
3. G. W. Luckey, *Discussions Faraday Soc.*, **28**, 113 (1958).
4. M. H. Hebb, *J. Chem. Phys.*, **20**, 185 (1952).
5. C. Wagner, *Z Elektrochem.*, **60**, 4 (1956).
6. B. Ilschner, *J. Chem. Phys.*, **28**, 1109 (1958).
7. D. O. Raleigh, *J. Phys. Chem. Solids*, **26**, 329 (1965).
8. F. A. Kröger, "The Chemistry of Imperfect Crystals," North-Holland Publishing Co., Amsterdam (1963).
9. D. O. Raleigh, "Progress in Solid State Chemistry," H. Reiss, Editor, Pergamon Press, **3**, 104 (1967).
10. H. C. Abbink and D. S. Martin, *J. Phys. Chem. Solids*, **27**, 205 (1966).
11. P. Müller, *Physica Stat. Sol.*, **21**, 693 (1967).
12. D. R. Stull and G. C. Sinke, "Thermodynamic Properties of the Elements," American Chemical Society, Washington, D. C. (1956).
13. O. Kubaschewski and E. L. Evans, "Metallurgical Thermochemistry," Pergamon Press, London (1955).
14. F. Moser, *J. Appl. Phys.*, **33S**, 343 (1962).
15. W. Ulrici, H. D. Koswig, and O. Stasiw, *Physica Stat. Sol.*, **12**, 545 (1965).
16. F. A. Kröger, *J. Phys. Chem. Solids*, **26**, 901 (1965).
17. D. L. Dexter, *Phys. Rev.*, **101**, 48 (1956).
18. P. Scop, *ibid.*, **139**, 934 (1965).
19. F. C. Brown, *J. Phys. Chem.*, **66**, 2386 (1962).
20. J. R. Haynes and W. Shockley, *Phys. Rev.*, **82**, 935 (1951).

21. B. A. Snavely, *Physica Stat. Sol.*, **9**, 709 (1965).
22. T. Masumi, R. K. Ahrenkiel, and F. C. Brown, *ibid.*, **11**, 163 (1965).
23. M. Höhne and M. Stasiw, *ibid.*, **2**, 247 (1968).
24. P. B. P. Phipps and F. A. Kröger, *J. Phys. Chem. Solids*, **30**, 1435 (1969).
25. F. W. Patten, *Phys. Letters*, **21**, 277 (1966).
26. T. J. Neubert and J. A. Reffner, *ibid.*, **23**, 2780 (1962).
27. Moser, F., Private communication.

Technical Notes

Influence of Porosity of Thin Gold Layers Used as the Substrate for Electrodeposited Permalloy

F. E. Luborsky

General Electric Research and Development Center, Schenectady, New York

The substrate requirements for the vacuum deposition of NiFe films suitable for static memory operation are well documented (1, 2) and reasonably well understood. Of particular interest is the recent study (3) of various metallic underlayers; the observed effects on the Permalloy properties were attributed to the microstructure and morphology of the underlayers. Similar requirements and effects are expected in the case of the substrate used for electrodeposition of NiFe. In many cases, these substrates use a thin gold film over a copper base (4, 5). The gold film has two characteristics needed to produce Permalloy films with the required magnetic characteristics: a very fine grain size and an electrode potential (4) close to that of Permalloy in the electrolyte in use.

In this note, we will show some interesting fluctuations in the magnetic properties and composition of the Permalloy as the thickness of the gold underlayer is increased. The minimum thickness of gold required to achieve good magnetic properties will be shown to correspond to the completion of a change in the character of the cathode potential *vs.* time for the deposition of NiFe at constant current. The change in these cathode potentials, as the gold thickness increases, is most likely due to the "covering" of the copper by the gold.

Samples were prepared, as previously described (5, 6), on 0.010 in. thick copper substrates plated with about 5-10μ of copper, varying thicknesses of gold, and finally 600Å of Permalloy. All samples were annealed in an easy axis field of 1000 Oe before the magnetic measurements (5, 6). The gold films were deposited from a proprietary (7) electrolyte, Orosene 999, at room temperature, at a pH of 4.5, and at a current density of 12 mA/cm^2. The grain size of the gold films were all in the range of 90-130Å, as determined from x-ray line broadening for films from 500 to 5000Å thick. Line widths were not corrected for any stress contribution, and thus these grain sizes may be somewhat larger. There was no evidence for any crystal orientation in any of the films. The average surface roughness (center line average) of the substrates after depositing the copper was 250Å as averaged over 0.025 cm intervals. This roughness did not change on depositing gold up to thicknesses of 10,000Å.

The electrolytes used for the Permalloy deposition contained nickel and iron sulfates, boric acid, and thiourea as previously described (5). They were operated under conditions to obtain the zero magnetostrictive composition, 81.5% Ni, when deposited on gold (4-6, 8). The magnetic properties resulting from depositing a 600Å thick Permalloy film, using the above conditions, onto copper substrates with increasing thicknesses of a gold film are shown in Fig. 1. For thicknesses of gold on the substrate of more than about 300Å, the properties are independent of gold thickness; namely the coercive force along the easy axis, H_c, the coercive force along the hard axis $H_{c,\perp}$, the anisotropy field H_k, and the anisotropy dispersion α_q. Below about 300Å of gold H_c, $H_{c,\perp}$, H_k', and α_q increase sharply. These changes in properties may be due to a combination of many factors that are changing as the gold film becomes very thin, *e.g.*, the Permalloy composition may change, its crystallite size may change, the strain between the substrate and the Permalloy film may change, and the roughness may change.

The change in composition with gold thickness was determined by three independent measurements: x-ray fluorescence, saturation magnetization M_s, and magnetostriction. The results obtained from each of these, shown in Fig. 2, all agree with one another. Compositions were obtained from x-ray fluorescence through the use of alloy film standards normalized

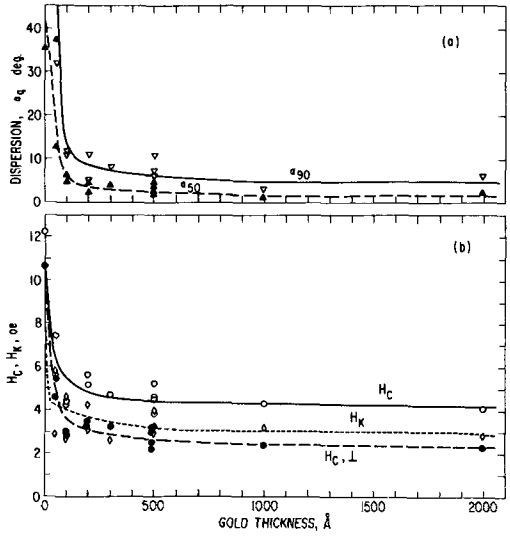

Fig. 1. Magnetic properties of Permalloy films 600Å thick, all deposited under the same conditions, but onto substrates with increasing thicknesses of gold deposited over 5μ of electrodeposited copper. NiFe deposited at 28°C, pH = 2.5, 4.3 mA/cm^2, 160 mg/l of thiourea, 19% Fe^{++} to Fe^{++} + Ni^{++}. Measurements made after an easy axis magnetic anneal of 4 hr at 150°C.

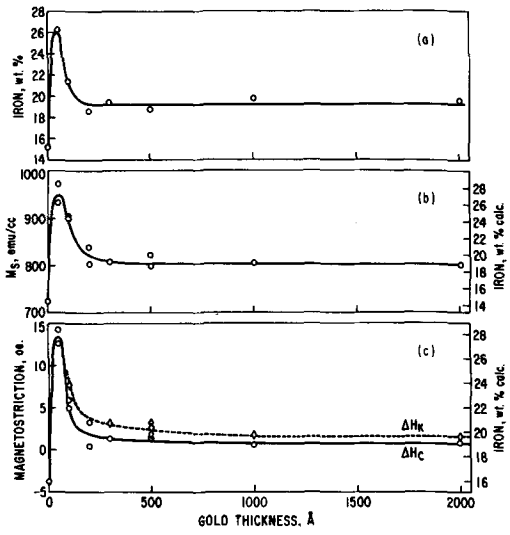

Fig. 2. Average film composition from (a) x-ray fluorescence, (b) saturation magnetization and (c) magnetostriction for films reported in Fig. 1.

to 81.5% Ni for a zero magnetostrictive film. The x-ray fluorescence also showed that all the films were the same thickness to within ± 1%. Compositions were obtained from the M_s measurement using a value of 17.5 (emu/cm³)/w/o Ni for M_s *vs.* composition through the 81.5% Ni point, as obtained from published (9) data. Compositions were calculated from the magnetostriction measurements using the value (6) of 1.46 Oe change in H_k/w/o Ni for the 0.06% strain used in this work. The change in the average Permalloy composition for substrates with very thin Au layers must be due to the change in substrate potential with increasing gold thickness. It appears from these measurements that about 200-300Å of gold are required to remove the influence of the copper.

The cathode potential measured during the deposition of the Permalloy on substrates with different Au thicknesses are shown in Fig. 3. Although the time response of the recorder was only ~ 0.2 sec (equivalent to the deposition of about 10-15Å of NiFe) the initial potentials, plotted in Fig. 4, still vary in a consistent manner with the thickness of the gold film. The open circuit or equilibrium potentials of a copper electrode, shown in Fig. 4, show the same trend with increasing thicknesses of gold. The results of Fig. 3 and 4 also indicate that about 300Å of gold are required to completely remove the influence of the copper substrate.

In a previous paper (5) it was shown that the deposited copper substrates had a grain size of 350-500Å and that NiFe deposited on this copper, from the same electrolyte as used in this work, had the same 350-500Å grain size, while deposition on gold films with a

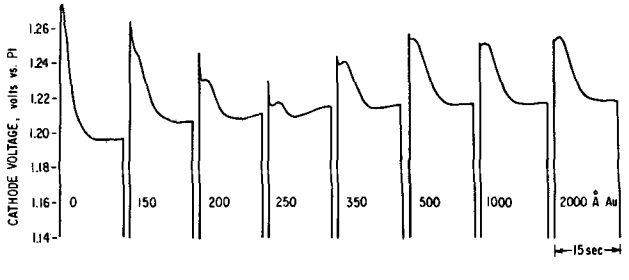

Fig. 3. Potential *vs.* time for deposition of 600Å of NiFe onto substrates with increasing thicknesses of gold. NiFe deposited at 38°C, pH = 2.50, 13.1 mA/cm², 320 mg/l thiourea, 17.75% Fe^{++} to Fe^{++} + Ni^{++}.

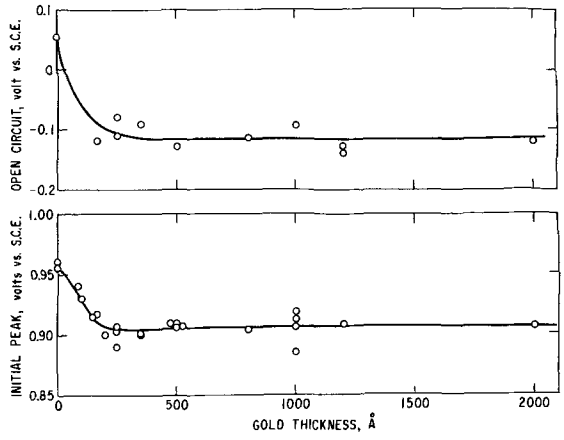

Fig. 4. Initial cathode potential and the open circuit cathode potential as a function of gold thickness for samples prepared as in Fig. 3.

100Å grain size produced NiFe with a 100Å grain size. Thus, it appears that the NiFe deposits epitaxially on both the copper and the gold. In the range of gold film thicknesses where the gold film is discontinuous or has large regions of copper exposed, it is expected that the NiFe film will have regions both with the fine grain size and the coarser grain size. The dispersion α_q will then decrease as the fraction of the film with the larger grain size decreases since α_q is proportional to grain size (1). Since these films are magnetostrictive, the dispersion will also be affected by the difference in strain between the NiFe and Au and between NiFe and Cu.

We conclude that the poor magnetic properties of Permalloy deposited on films of gold less than about 250Å thick results from the influence of the copper substrate. This influence appears as a change in the electrode potential which affects the Permalloy composition; a change in the local grain size of the substrate which affects the local grain size of the Permalloy; and a change probably in the local stress in the Permalloy film. Each of these changes is known to increase H_c, H_k, and α_q. Gold films thicker than about 250Å appear to eliminate the effect of the copper and can be used as substrates to prepare nonmagnetostrictive films with H_c = 4 Oe, H_k = 3 Oe, and $\alpha_{50} < 1°$ for films 600Å thick.

Acknowledgment

The contributions of B. J. Drummond in carrying out the experimental work is greatly appreciated. Helpful discussions with R. Girard of CNRS, Grenoble, are acknowledged.

Manuscript submitted July 23, 1969; revised manuscript received Sept. 26, 1969.

Any discussion of this paper will appear in a Discussion Section to be published in the December 1970 JOURNAL.

REFERENCES

1. M. Prutton, "Thin Ferromagnetic Thin Films," Butterworth Co. Ltd., London (1964).
2. R. F. Soohoo, "Magnetic Thin Films," Harper and Row, New York (1965).
3. K. Y. Ahn and J. R. Freedman, *IEEE Trans. Mag.*, **MAG-3,** 157 (1967).
4. R. Girard, *J. Appl. Phys.*, **38,** 1423 (1967).
5. F. E. Luborsky, *IEEE Trans. Mag.*, **MAG-5,** 106 (1969).
6. F. E. Luborsky, *J. Appl. Phys.*, **38,** 1445 (1967).
7. Technic, Inc. P. O. Box 965, Providence, Rhode Island.
8. F. E. Luborsky and W. D. Barber, *J. Appl. Phys.*, **39,** 746 (1968).
9. E. Kneller, "Ferromagnetismus," p. 148-150, Springer-Verlag, Berlin (1962).

Properties of a Leached K^+-Selective Glass Electrode

I. Altug and M. L. Hair

Research & Development Laboratories, Corning Glass Works, Corning, New York

The origin of the electrochemical potential which arises when a glass membrane is inserted between solutions of different concentrations has been investigated for many years. This potential is the basis of the glass electrode, giving a standard technique for measuring *p*H. Interest recently has centered on the selectivity of various glasses toward monovalent and divalent cations. Eisenman (1) obtained a correlation between the electrochemical selectivity and ratio of alkali metal to alumina in the glass. Thus, glasses with a high Na/Al ratio are preferentially sensitive to K^+ over Na^+, whereas if Na/Al is less than 3, the glasses are preferentially sensitive to Na^+ over K^+.

Recently we showed that porous glass (with a controlled pore diameter, dry, of approximately 40Å) behaves as an ionic membrane and its properties are adequately accounted for by the Theorell-Meyer-Sievers theory (2). This theory applies to monovalent cations and assumes no selectivity between the various ions. The porous glass membrane, however, has a considerable selectivity. Thus, in its normal, porous state, K_{CaK}^{pot} is approximately 15, whereas K_{NaK}^{pot} is about 1.8. However, when the porous glass was sintered, the membrane potential increased, the calcium selectivity decreased and, just prior to complete sintering, the selectivity of K^+ over Na^+ increased (3). A maximum value of $K_{NaK}^{pot} = 10$ was eventually obtained. This value corresponds to the highest selectivity observed with normal K^+-selective glass electrodes, yet the glass composition (96% SiO_2, 3% B_2O_3, 1% Na_2O) bears no relationship to the compositional ratios projected by Eisenman.

As it is known what happens when a porous glass is gradually sintered so as to become essentially nonporous, it seemed of interest to leach a conventional potassium-selective glass electrode and measure the change in its electrochemical properties. An NAS_{27-4} glass membrane (59% SiO_2, 27% Na_2O, 4% Al_2O_3), which had originally been tested as a potassium electrode, was kept in aqueous solution for 17 months prior to the determination of its ion selectivity. The membrane potentials were measured using the techniques described previously, (3) and the selectivities of K^+ and Na^+ relative to Ca^{2+} were measured.

Freshly prepared K^+-selective glasses do not exhibit appreciable ion selectivity unless they have been stored in aqueous solution for a considerable time to produce a hydrated layer on the surface of the glass. This membrane was no exception, and a six-week immersion in $NaHCO_3$ solution was required to produce the maximum K_{NaK}^{pot} value of 10. At this point, there was negligible response to Ca^{2+}. However, after aging for 17 months, it was found that the divalent response had increased, while the selectivity of K^+ relative to Na^+ had decreased from 10 to 5.6. On further leaching, the glass rapidly became completely porous and eventually fell apart.

On immersing any glass in aqueous solution, at least two processes occur. One is an ion exchange in which the alkali metal ions in the glass are replaced by protons. The second is a dissolution of either one phase or the whole of the glass network. It is probably the first process that gives rise to the hydrated layer necessary for K^+ selectivity. If the leaching process that occurs with the NAS_{27-4} glass can be considered to be the reverse of the sintering of a porous glass (both affecting the hydration state of the medium), then it is possible that these apparently different types of glass would have similar electrochemical properties. The selectivity constants obtained for the leached NAS_{27-4} membrane

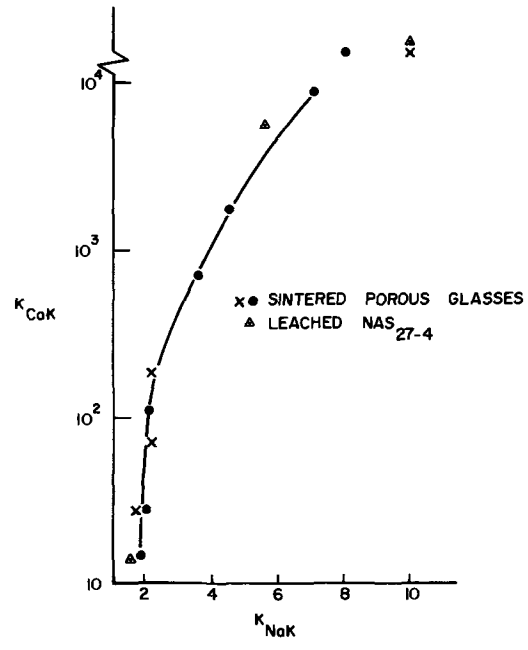

Fig. 1. Selective behavior of sintered porous glasses compared with NAS_{27-4}.

are plotted in Fig. 1 with the data previously reported for sintered porous glasses. The properties of the partially leached aluminosilicate glass are almost identical with those obtained for a partially sintered porous glass. Complete leaching of the NAS_{27-4} membrane formed a completely porous, fragile membrane whose electrochemical properties were similar to those of a porous glass.

The ion selectivity of the sintered porous glasses was explained on the basis of very small "pores" of the order of 2-3Å in the resultant membrane. The leaching of a sodium aluminosilicate glass, particularly if it shows very fine phase separation or clustering of the alkali metal ions, can also give rise to small "pores" within the glass. The leached layer then approximates a molecular sieve, rather than a silica gel. This analogy has been previously suggested by Garfinkel (4) on the basis of diffusion measurements on both "wet" and "dry" samples of NAS_{27-4}. Furthermore, the leaching of both alkali silicate and alkali aluminosilicate (5) glasses is known to give rise to materials with molecular sieve properties and pore sizes in the range of 2-7Å. The present results indicate the formation of such a hydrated layer on the surface of K^+-selective glass electrodes.

Manuscript received June 6, 1969.

Any discussion of this paper will appear in a Discussion Section to be published in the December 1970 JOURNAL.

REFERENCES

1. G. Eisenman, *Biophys. J.*, **2**, 2, 259 (1962).
2. I. Altug and M. L. Hair, *J. Phys. Chem.*, **72**, 599 (1968).
3. I. Altug and M. L. Hair, *ibid.*, **72**, 2976 (1968).
4. H. Garfinkel and H. E. Rauscher, *J. Appl. Phys.*, **37**, 2169 (1966).
5. L. S. Yastrebova, A. A. Bessonov, S. S. Khvaschev, *Mater. Vses. Soveshch. Tseolitam, 2nd, Leningrad 1964*, pp. 229-234 (1965). See *C.A.* **64**, 19149c (1966).

A High-Speed Switch for Isolation of the Reference Electrode Circuit to Hold-Off IR Changes during Current Interruption or Pulsing

David R. Flinn,[1]* Murray Rosen,[1]* and Sigmund Schuldiner*

Electrochemistry Branch, Chemistry Division

and James D. Fahey

Electronics Division, Naval Research Laboratory, Washington, D. C.

Determination of electrochemical parameters by current interruption or by pulse polarization is difficult in dilute solution because of high solution resistance. The sensitivity of the oscilloscope or other recording device is limited due to overdriving and the resultant saturation of the electronic amplifiers by the solution IR component which is much larger than the electrode polarization component. Besides the loss in sensitivity many microseconds or even milliseconds may be required before the correct potential may be recorded.

By the use of a field-effect transistor (FET), it is possible to construct a simple device through which the potential response of a reference electrode may be recorded over any desired time interval. The potential response measured between the reference and working electrodes may be "held-off" until the applied current is completely shut off.

The field-effect transistor acts as a simple toggle switch or relay contact. In the open or off state, it has an impedance in the order of 10^{12} ohm. In the conduction or on state, it has an impedance of approximately 15 or 20 ohm. The minimum time from off to on or on to off states can be as fast as 1.5 to 2 nsec (1, 2). The actual transition time depends on the rise and fall time of the gating pulse used.

By using the FET in conjunction with a high input impedance operational amplifier, the reference electrode sees no apparent change in impedance from the off to the on state of the FET and, therefore, there is no differential change in loading of the reference electrode. Thus a much higher input impedance is provided than normally available from an oscilloscope probe. Also, with the use of a wide bandwidth operational amplifier, there should be no significant loss in oscilloscope bandwidth capabilities. This FET switch should prove capable of replacing mercury relays in many applications, without the difficulties inherent in such mechanical devices (3).

For current interruption measurements an applicable switching circuit is shown in Fig. 1a. The FET (2N4859) is biased to the nonconducting state by the −15V from the power supply. Any signal which will raise the gate control signal input to a potential of approximately −1V will render the source (S)-to-drain (D) of the FET fully conducting, with a negligible resistance as compared to the high input impedance operational amplifier. The gate must not be driven positive, however, as this potential will be transferred to the drain point. Input signals as large as 50V may be "held-off" by this FET in its nonconducting state.

In most applications, a potential step from some point in the cell polarization or measurement circuitry (*e.g.*, pulse generator) will be available for the FET gating control. In many cases the gate potential of the recording oscilloscope may be used as the gate control signal.

In our application (Fig. 1) the FET drain was fed into a Model 1011 Philbrick/Nexus operational amplifier. The high impedance (10^{11} ohm) and low input capacitance (4 pF) of this amplifier prevents loading of the FET. Although an amplifier gain of 2 is shown here, any reasonable value may be used.

The 1N914 diode between the amplifier (plus) input and ground serves to provide a current path for the small amplifier bias current (<30 pA). For the circuit of Fig. 1a, the direction of this diode is unimportant for small signal applications. Where signals greater than the breakdown value of the diode are to be examined, the direction of the diode may be reversed. With the diode in the circuit the effective input impedance is approximately 5 x 10^9 ohm.

For pulse polarization applications, the FET switch may be used in the reverse sense to that shown in Fig. 1a. In Fig. 1b the gate connections are made so that the FET is normally conducting. The FET may be rendered nonconducting for any desired time period by a gate control potential of −4V or greater.

The effective switching time for the circuit of Fig. 1a is illustrated in Fig. 2-4. In Fig. 2, a small d-c potential applied to the FET source is gated through the FET after about 1μsec. The true switching time is much faster than the 0.7 μsec shown here, but is masked by ringing. The upper curve of Fig. 3 illustrates a typical galvanostatic high current density anodic pulse polarization of a platinum electrode in H_2-saturated, 1M H_2SO_4 solution. For the lower curve of Fig. 3, the FET has been gated into the conducting mode after about 3 msec, thereby holding-off the potential response to the reference electrode for that period of time.

In Fig. 4, curve (a) shows the potential-time response to a 2 μsec constant current pulse applied to the same electrode used for Fig. 3, with the FET switch conducting throughout the entire response shown. Curve (b) of Fig. 4 was made at ten times greater sensitivity, with the FET gated on only after pulse

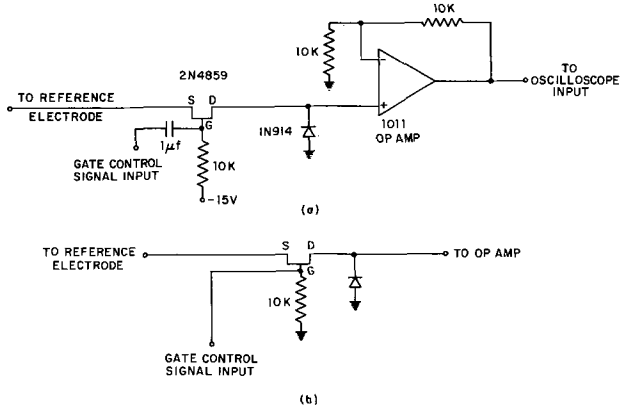

Fig. 1(a). Switching circuit with FET in normally nonconducting mode. A signal of 12-14V through the gate control signal input will render the FET conducting; Fig. 1(b) FET in normally conducting mode. A gate control input signal more negative than −4V will render the FET nonconducting.

* Electrochemical Society Active Member.
[1] National Academy of Sciences-National Research Council Postdoctoral Research Associate at NRL.

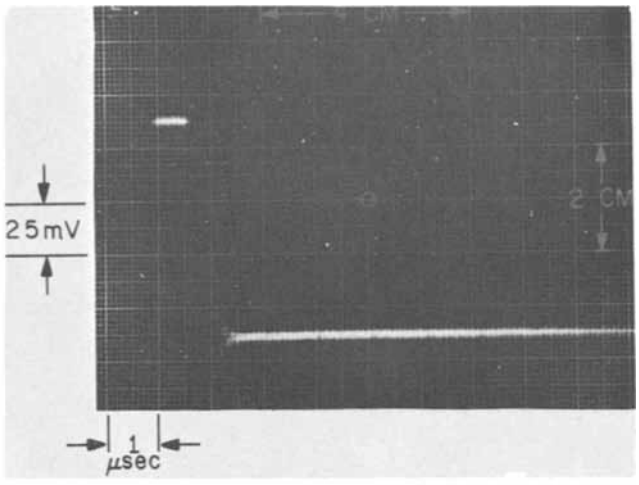

Fig. 2. Small d-c potential gated through the FET circuit of Fig. 1(a) after about 1 μsec. Line at upper left is ground potential.

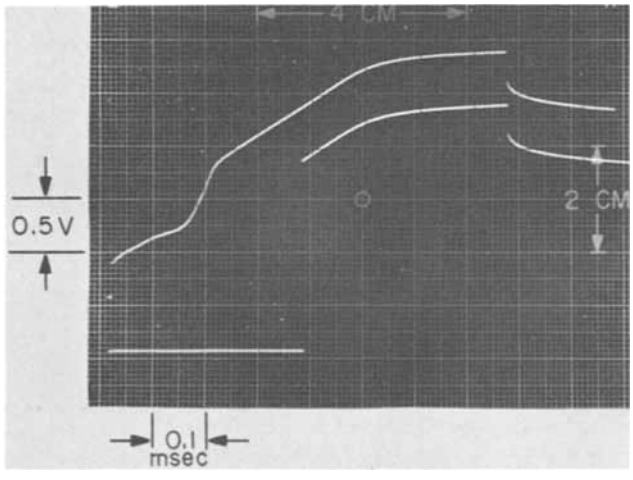

Fig. 3. Upper curve: galvanostatic high current density anodic pulse polarization of a platinum electrode in H_2-saturated, 1M H_2SO_4 solution; lower curve: same as upper curve except that FET switch is rendered conducting after about 3 msec. Lower curve has been displaced downward to separate traces.

cut-off. This illustrates that the solution IR component can be virtually eliminated and the electrode polarization response can be measured at high precision.

No photograph is shown for the response of the circuit of Fig. 1b to a 2 μsec constant current pulse applied under the same conditions to the same electrode used in Fig. 3 and 4 because the result is essentially identical with that observed in Fig. 4. The line visible at the lower left in Fig. 4 represents the ground potential which in this case is the potential of the working and reference electrodes. Under other experimental conditions or with some other reference electrodes the

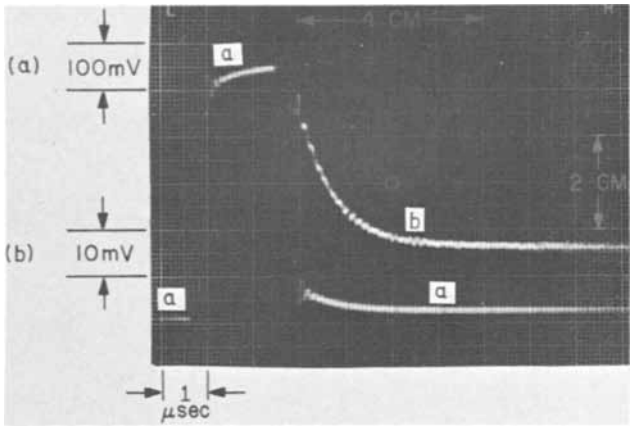

Fig. 4. Potential response to 2 μsec galvanostatic anodic pulse for same electrode used in Fig. 3. (a) FET conducting throughout; vertical sensitivity of 0.1 V/div; (b) FET conducting only after pulse cut-off; vertical sensitivity of 10 mV/div.

potential of the reference electrode will be different from that of the grounded working electrode.

The advantage of the circuit of Fig. 1b over the one of Fig. 1a is that the cell potential is recorded both prior to and after a pulse polarization perturbation. The potential at the + input of the operational amplifier, while the FET is biased off during the pulse period, depends to some extent on the risetime of the signal used to render the FET nonconducting. A transient voltage spike may appear which is caused by the very small amount of charge required to bias the FET, which in turn can charge the small capacitance (4 pF) of the amplifier. With proper adjustment of the FET gating signal risetime, this transient may be entirely eliminated. The circuit of Fig. 1a also may be used for pulse polarization studies, but an independent measurement of the initial cell potential must be made, either by shorting across the FET or by gating the FET on without polarizing the cell.

The 2N4859 used here is an n-channel FET. For holding off large negative going signals a p-channel FET would offer an advantage in that a lower gating potential could be used than for an n-channel FET. Also, the positive gate bias which is required may be more convenient in some applications.

Manuscript submitted Sept. 16, 1969.

Any discussion of this paper will appear in a Discussion Section to be published in the December 1970 JOURNAL.

REFERENCES

1. R. McIntyre, "FET Applications Handbook," J. Eimbinder, Editor, Chap. 17, Tab Books, Blue Ridge Summit, Pa. (1967).
2. L. J. Sevin, "Field-Effect Transistors," McGraw-Hill Book Co., New York (1965).
3. P. Delahay and D. J. Kelsh, *J. Electroanal. Chem.*, **16**, 116 (1968).

Brief Communications

Auger Electron Analysis of Electropolished High-Purity Aluminum

C. G. Dunn* and L. A. Harris

Research and Development Center, General Electric Company, Schenectady, New York

The topography of electropolished aluminum has been studied extensively (1-12), but the composition of the surface reaction film has received little attention. It is generally believed to be an amorphous oxide of aluminum formed either in the electrolyte or subsequently on exposure to water or air. Holló (8) obtained a porous oxide film on aluminum electropolished in phosphoric acid/n-butyl alcohol. Halfawy (12) concluded from electron diffraction data that the surface of aluminum electropolished in perchloric acid/acetic anhydride was initially free of oxide. Morize and Lacombe (13) reached the same conclusion from solution potential measurements. On the other hand Beck *et al.* (14) stated that electropolishing in typical baths produced an aluminum surface containing perchlorate ions which prevented the subsequent formation of high resistivity anodic oxide films. Similarly, using aluminum specimens initially electropolished in a perchloric acid electrolyte, one of the authors (CGD) observed surface reactions (to be described elsewhere) that indicated impurity contamination by the electropolish. These observations in fact led to the present study by Auger electron emission (15) of atom species present on electropolished aluminum.

* Electrochemical Society Active Member.

The Auger analyses were made on electropolished aluminum sheet of 99.999% purity and on similar specimens chemically treated to remove residual films or reaction products. Electropolishing involved raising the voltage beyond the first current maximum to a point within the polishing region (16, 6) (about 15V) and holding the voltage constant for 3 min or more in a 1:4 (by volume) solution of perchloric acid (71%) in absolute ethanol maintained between 5° and 10°C. After thorough rinses in alcohol and in distilled water, samples were dried in a stream of clean nitrogen.

Auger analyses of electropolished samples revealed the presence of O, C, S, Cl, and N (top curve of Fig. 1). Treatments after electropolishing such as 10 min in 30% NaOH at room temperature, or 5 to 10 min in 10% HNO_3 at 90°C, had the following effects on surface concentrations: a slight reduction in oxygen and carbon, a significant decrease in sulfur, a decrease in chlorine to nondetectable levels, and no significant change in nitrogen (middle and bottom curves of Fig. 1). Treatments in an oxide stripping bath (35 ml of 85% phosphoric acid and 20g of chromic acid per liter) (17) at 90°C appeared to remove most of the chlorine in 1 min and perhaps all of it in 10 min. Reactions in this oxide stripping bath, as Fig. 2 shows, resulted in surface films containing appreciable

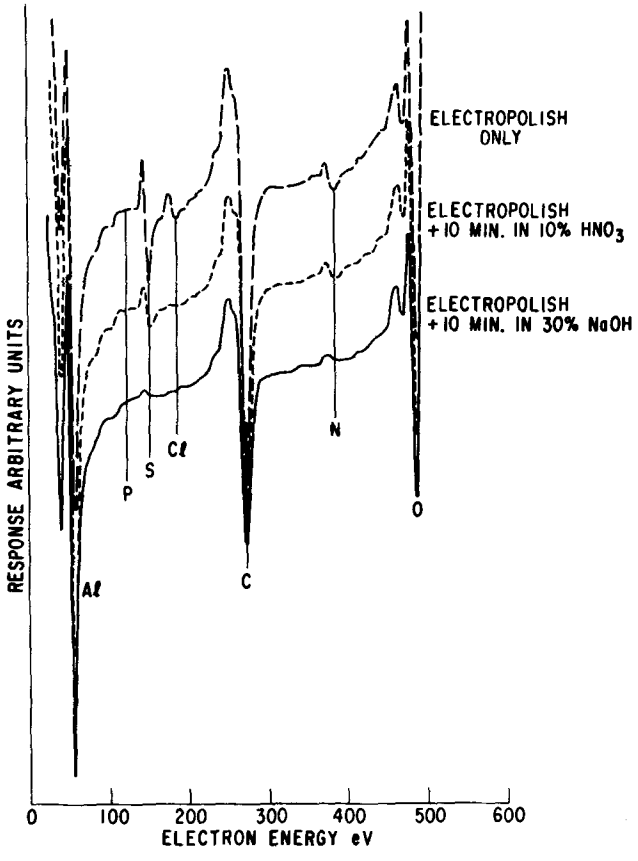

Fig. 1. Auger spectra of electropolished aluminum before and after chemical treatments.

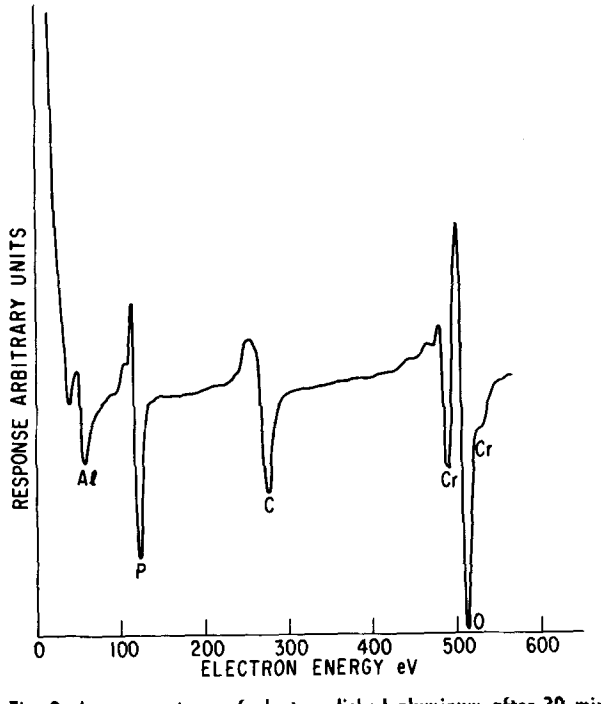

Fig. 2. Auger spectrum of electropolished aluminum after 30 min in a phosphoric acid/chromic acid bath at 90°C and a thorough wash in water.

amounts of phosphorus and chromium. The latter result confirms other published work, particularly the tracer studies of Lewis and Plumb (18) on radioactive phosphorus and chromium initially added as phosphates and chromates in their phosphoric acid/chromic acid bath.

Since the composition of the electropolishing bath consisted mainly of C, H, O, and Cl, and since the Auger analysis revealed the presence of C, O, and Cl on electropolished aluminum samples, we conclude that elements in the polishing bath, particularly chlorine and carbon can enter in a surface reaction product and contaminate the aluminum. The oxygen contamination could originate from the water in the washing treatment, from exposure to air (12, 13), or from the electrolyte. The source of the nitrogen and sulfur contamination was not determined.

Acknowledgment

The authors are grateful to A. N. DeTommasi for assistance in experimental work.

Manuscript received Aug. 14, 1969.

Any discussion of this paper will appear in a Discussion Section to be published in the December 1970 JOURNAL.

REFERENCES

1. G. L. Buchnell and G. A. Geach, *Nature*, **164**, 231 (1949).
2. A. F. Brown, *ibid.*, **163**, 961 (1949); "Metallurgical Applications of the Electron Microscope," p. 103, Institute of Metals (1950).
3. G. L. Buchnell, G. A. Geach, and N. C. Welsh, *Research*, **5**, 289 (1952).
4. P. Bussy, *Rev. Met.*, **50**, 629 (1953); **52**, 116 (1955).
5. N. C. Welsh, *J. Inst. Metals*, **85**, 129 (1956).
6. A. W. Agar and R. S. M. Revell, "Electron Microscopy," p. 324, Proceedings of Stockholm Conference (1956).
7. M. Gy. Holló, *Acta. Met.*, **8**, 265 (1960); *Rev. Met.*, **57**, 23 (1960).
8. Y. Didier and M. Froment, *Compt. rend.*, **256**, 1766 (1963).
9. P. E. Doherty and R. S. Davis, *J. Appl. Phys.*, **34**, 619 (1963).
10. J. J. Randall, Jr., and W. J. Bernard, *ibid.*, **35**, 1317 (1964).
11. H. A. Francis, *ibid.*, **38**, 715 (1967).
12. M. Halfawy, *Rev. Met.*, **48**, 787 (1951).
13. P. Morize and P. Lacombe, *Compt. rend.*, **222**, 658 (1946).
14. A. F. Beck, M. A. Heine, E. J. Caule, and M. J. Pryor, *Corrosion Sci.*, **7**, 1 (1967).
15. L. A. Harris, *J. Appl. Phys.*, **39**, 1419 (1968).
16. A. L. De Sy and H. Haemers, *Stahl u. Eisen*, **61**, 185 (1941).
17. R. B. Mason and C. J. Slunder, *Ind. Eng. Chem.*, **39**, 1602 (1947).
18. J. E. Lewis and R. C. Plumb, *Int. J. Appl. Radiation and Isotopes*, **1**, 33 (1956).

Theoretical Electromotive Forces of Metal-Halogen Cells

Some Recalculations Based on Recent Data

Reuben E. Wood* and Walter J. Hamer*

National Bureau of Standards, Washington, D. C.

Since the publication of the calculations of Hamer, Malmberg, and Rubin on the theoretical electromotive forces of cells containing a single solid or molten chloride (1), fluoride (2), bromide (2), or iodide (2), new data have become available, and tabulations of thermodynamic properties, particularly those of Stull *et al.* (3), have been published. We have used these newer data to recalculate emfs for the cases covered by the JANAF tabulations (3). We shall not here attempt to evaluate the reliability of data leading to the differing results, but shall only indicate the cases in which substantial discrepancies exist between the older and newer values.

Both the tabulations of Hamer, Malmberg, and Rubin (H) and those in the JANAF publications (J) give values (emfs in the H tables, ΔG°'s in the J tables) at 25°C (298.15°K). At higher temperatures the H tables give values at rounded Celsius temperatures, the J tables at rounded Kelvin temperatures. As a representative high temperature, 1100°K was chosen. This required only a short extrapolation of the H values from 800°C.

Table I compares, for cases in which a difference of 100 millivolts or more in the standard emfs of formation (2.3 kcal [1] per equivalent difference in ΔG°), the emfs given by H and those we have calculated from the ΔG's given by J. It can be pointed out that for those cases in which the higher temperature comparison can be made, most of the discrepancies are of the same order of magnitude and in the same direction at both temperatures. This suggests strongly that the usual

* Electrochemical Society Active Member.
[1] One thermocalorie (defined) = 4.1840 joules.

Table I. Formation potentials having reported values differing from each other by more than 100 mV (2.3 kcal/equiv) at either 298° or 1100°K

	298°K		1100°K	
Salt	J	H	J	H
AlF_3	4.94	4.25	4.19	3.61
AlI_3	1.05	1.18		
$BeCl_2$	2.32	2.43		
CsF	5.45	5.22	4.53	4.33
CsCl	4.30	4.19	3.44	3.32
FeF_3	3.36	3.17	2.75	2.62
FeI_2	0.58	0.76	0.31_4	0.30_6
HgF_2	1.94	1.80		
Hg_2I_2	0.58	0.68		
LiBr	3.51	3.57	2.89	3.03
LiI	2.79	2.91		
MgF_2	5.55	5.44	4.83	4.72
PbI_2	0.90	1.01		
$TiBr_4$	2.10	2.43		
$TiCl_3$	2.26	2.15		
$TiCl_4$	1.91	1.75		
TiF_3	4.64	4.33	4.03	3.81
TiF_4	4.04	3.79		
TiI_3	1.40	1.41	0.98	0.88
WBr_5	0.71	0.32		
WBr_6	0.57	0.28		
WCl_2	1.14	0.63		
WCl_4	1.10	0.56		
WCl_5	1.00	0.54		
WCl_6	0.79	0.51		
$ZrBr_2$	1.94	2.53	1.51	1.97
$ZrBr_3$	2.10	2.43	1.51	1.99
$ZrBr_4$	1.88	2.01		
$ZrCl_2$	2.64	2.90		
ZrF_3	4.94	4.81		
ZrF_4	4.69	4.59		
ZrI_2	1.37	2.04	1.00	1.47
ZrI_3	1.37	1.92		
ZrI_4	1.25	1.50		

cause of the discrepancies lies chiefly in the evaluation of the ΔG's at 25°C and not in different choices of heat capacity data required to evaluate the ΔG's or emfs at other temperatures.

Manuscript received Sept. 4, 1969.

Any discussion of this paper will appear in a Discussion Section to be published in the December 1970 JOURNAL.

REFERENCES

1. W. J. Hamer, M. S. Malmberg, and B. Rubin, *This Journal*, **103**, 8 (1956).
2. W. J. Hamer, M. S. Malmberg, and B. Rubin, *ibid.*, **112**, 750 (1969).
3. D. R. Stull, Project Director, JANAF THERMOCHEMICAL TABLES, distributed by CLEARINGHOUSE for Scientific and Technical Information. Original tabulation PB 168 370, 1965; addenda PB 168 370-1, 1966; PB 168 370-2, 1967; PB 168 370-3, 1968.

JOURNAL OF THE ELECTROCHEMICAL SOCIETY

SOLID STATE SCIENCE

JANUARY 1970

Kinetics of the Phosphidation of Copper

Shiro Ueda, Yoshinori Sasaki, Mikio Matsuura, and Shuichi Nishimura

Department of Synthetic Chemistry, Faculty of Engineering, Chiba University, Yayoicho, Chiba, Japan

ABSTRACT

A study on the kinetics of the phosphidation of copper sheets exposed to phosphorus vapor was undertaken at temperatures of 400°-650°C and at phosphorus partial pressures between 0.8 and 110 Torr. The phosphidation rate increased with rising temperature and with increasing partial pressure of the phosphorus vapor. When the phosphide layer reached a certain thickness, a transition from a linear rate to a parabolic or a cubic one took place. The relation between the phosphorus vapor pressure, P, (0.8-110 Torr) and the linear rate constant, K_l, (3.3-200 x 10^{-5} g/cm^2-min) found in the initial stage gave $K_l \propto P^{0.83}$ at 500°C. In general, the phosphides obtained have been composed of Cu_3P or the mixture of Cu_3P and CuP_2. The CuP_2-formation at temperatures above 600°C seldom has been observed from the x-ray patterns of the phosphides.

Preparations and structures of copper phosphides have been extensively investigated by many authors (1). However, no investigation involving the rate of phosphidation of copper has been made except by Edwards and Murphy (2).

The present study was undertaken to provide further information concerning the kinetics of the attack of phosphorus vapor on copper sheets at elevated temperatures.

Experimental

Materials.—Copper sheet.—Commercial copper sheets of high purity (more than 99.95%), about 15 mm wide, 30 mm long, and 0.3 mm thick, were employed in this work. They were polished through 3-0 emery paper. After degreasing with trichloroethylene or toluene in a soxhlet-type apparatus, they were treated with a mixture of 50 parts of nitric acid and 1 part of hydrofluoric acid to remove surface oxides, after which they were washed with alcohol and acetone. They were transferred in a desiccator filled with argon dried over phosphorus pentoxide.

Red phosphorus.—Commercial red phosphorus (amorphous) was treated with a boiling 8% solution of sodium hydroxide for about 3 hr to remove any yellow phosphorus, then with dilute hydrochloric acid and with a dilute solution of potassium cyanite to remove trace amounts of metals or their compounds contained in the red phosphorus. After washing with distilled water, the refined red phosphorus was preserved in a desiccator which was filled with argon dried over phosphorus pentoxide.

Apparatus and Procedure

It is necessary to carry out phosphidation of metals in the absence of air to avoid formation of metal oxides, metal nitrides, or various oxides of phosphorus. In this study, an apparatus depicted in Fig. 1 was used to evade these problems.

A copper sheet was suspended from a quartz helix (sensitivity 0.1 mm/mg) hanging from a glass hook inside the top of a quartz reactor. The extension of the quartz helix caused by the weight increase of the specimen was measured using a cathetometer with a precision of 0.01 mm.

A quartz cell filled with the refined red phosphorus was placed at the bottom of the reactor. The temperatures of the specimen and of the red phosphorus were controlled independently with two automatic regulators. The rate of sublimation of red phosphorus was controlled by adjustment of the temperature of the lower electrofurnace. Since the gaseous P_4 molecule scarcely dissociates into P_2 molecule at temperatures below 800°C, the phosphorus vapor can be regarded as consisting of P_4 molecules over the temperature range from 400° to 650°C employed in this work.

An argon carrier gas was dried by passing through phosphorus pentoxide and deoxygenated by passing through heated active copper, and then introduced into the bottom of the reactor from the heated side tube at a flow rate of 100 ml/min and at 1 atm. The extension of the quartz helix was in practice unaffected by the flow of the carrier gas. Partial pressures of phosphorus vapor were calculated from the rate of sublimation to P_4 vapor and the flow rate of this carrier gas.

Results and Discussion

Plots of the weight gain per unit area against the elapsed time are shown in Fig. 2(a) and (b), which

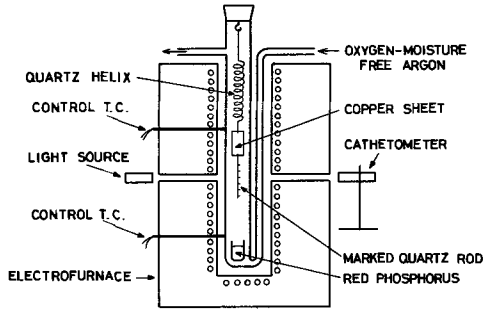

Fig. 1. Schematic diagram of the reaction apparatus

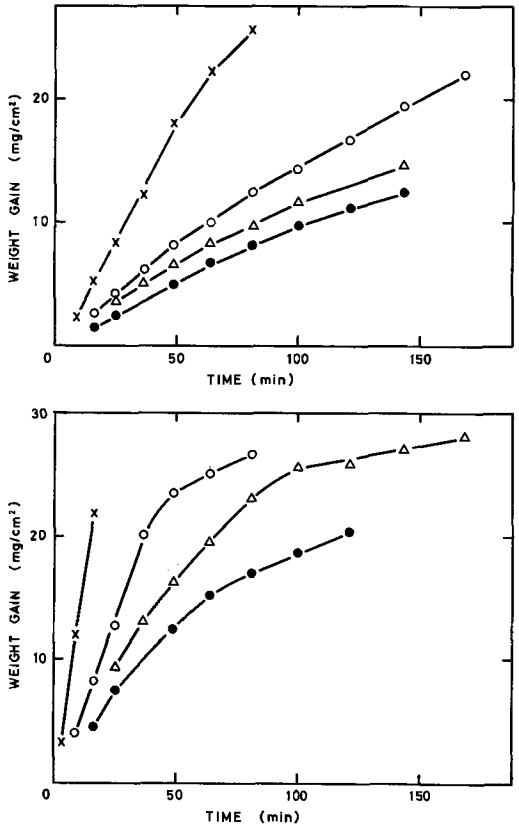

Fig. 2. Phosphidation of copper between 400° and 650°C at phosphorus partial pressures of (a) (top) 3.7 and (b) (bottom) 13.2 Torr: × 650°; ○ 600°; △ 500°; ● 400°C.

represent the results of the phosphidation of copper sheets at phosphorus partial pressures of 3.7 and 13.2 Torr, respectively. It is obvious from Fig. 2 that the weight of the copper sheet increased with rising temperature, and that phosphidation appears to follow approximately a linear rate law in the early stage.

Figure 3 represents the results of the influence of partial pressures of phosphorus vapor between 0.8 and 110 Torr at 500°C. By varying the partial pressure of phosphorus vapor the phosphidation rate of copper can be altered considerably. It will be seen that at the pressures below 6.7 Torr the phosphidation proceeded nearly according to a linear rate law while at pressures above 13.2 Torr, up to 110 Torr, it approximately followed a parabolic or a cubic rate law in the advanced stage. The log-log plots of the data for the

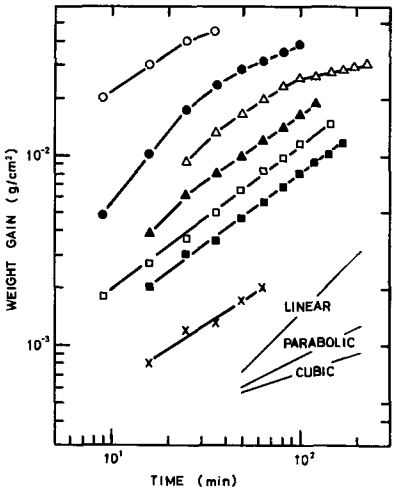

Fig. 3. Influence of the phosphorus partial pressure at 500°C: ○ 110; ● 19.2; △ 13.2; ▲ 6.7; □ 3.7; ■ 2.5; × 0.8 Torr.

Table I. Linear rate constants for the phosphidation of copper

Temp, °C	Pressure, Torr	n*	$K_1 \times 10^3$ g/cm²-min
400	3.7	1.0	0.1
	13.2	0.9	0.28
500	0.8	0.6	0.033
	2.5	0.7	0.09
	3.7	0.7	0.12
	6.7	0.7	0.18
	13.2	0.7	0.34
	19.2	1.0	0.76
	110.0	—	2.0
600	3.7	0.9	0.15
	13.2	1.2	0.54
650	3.7	1.0	0.35
	13.2	1.4	1.5

* $w = kt^n$; w, weight gain per unit area; t, time; k, rate constant.

pressure of 3.7 Torr at 650°C and for the pressure of 13.2 Torr at 600°C show transition from linear to parabolic or cubic behavior after a certain thickness is reached. The linear kinetics in the early stages may indicate phase boundary control.

The rate constant, K, can be obtained by extrapolating log t to zero. However, only approximate values of the slope were evaluated from Fig. 3, inasmuch as the extrapolation cannot be applied for any curve. Since all the phosphidations approximately followed a linear rate law in the early stage, the linear rate constants, K_1, were obtained from each slope in Fig. 2 and from the slopes on the weight gains *vs.* time plots of the data given in Fig. 3. These values are summarized in Table I.

Needlelike crystals of phosphide formed at 650° and 600°C under pressures of 3.7 and 13.2 Torr, at 500°C under pressures ranging from 2.5 to 110 Torr, and at 400°C under a pressure of 13.2 Torr, but not at 500°C under a pressure of 0.8 Torr and at 400°C under a pressure of 3.7 Torr. As most of the phosphidations proceeded with the formation of numerous mounds and needles, the reaction appears not necessarily to follow the parabolic rate law which is based on the assumption of a plane parallel scaling film. As illustrated in Fig. 3, the phosphidation behaved according to mixtures of linear, parabolic, and cubic rate laws.

X-ray powder diffraction patterns of the typical phosphides obtained in this work are illustrated in Fig. 4, in which those of Cu_3P and CuP_2 were quoted from the ASTM card (4) and from the result given by Oloffson (3), respectively. The phosphide layer appears to consist almost entirely of Cu_3P at the lower partial pressures of phosphorus vapor, while at 500°C and the partial pressures between 6.7 and 110 Torr the formation of CuP_2 was also observed.

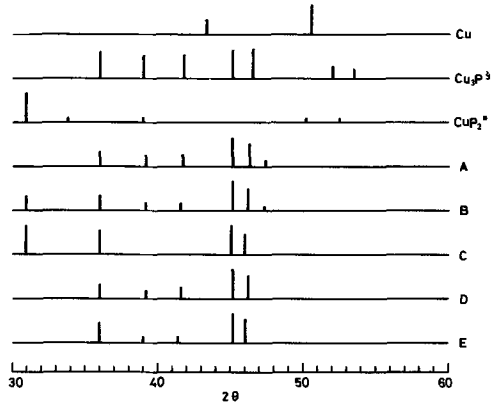

Fig. 4. Sketched line diagrams from the x-ray patterns of the obtained phosphides, (θ, diffraction angle). A, 13.2 Torr, 600°; B, 13.2 Torr, 500°; C, 13.2 Torr, 400°; D, 3.7 Torr, 500°; E, 3.7 Torr, 400°C.

§ ASTM card (4), * Oloffson (3).

It is interesting that no product other than Cu_3P was formed at 600° and 650°C. It is known that CuP_2 decomposes to form Cu_3P in the temperature range from 600° to 800°C with an evolution of P_4 vapor. The partial pressure, P_{Torr}, of phosphorus vapor composed of P_4 molecules is given for this decomposition as a function of the absolute temperature, T, as follows

$$\log P_{Torr} = -11{,}370/T + 13.827$$

According to this equation, the partial phosphorus pressures of a mixture of CuP_2 and Cu_3P, for example, at 600° and 500°C, are $10^{1.3}$ and $10^{-0.9}$ Torr, respectively. The reason why the formation of CuP_2 at 600° and 650°C has been seldom observed is revealed from this readily decomposable property of CuP_2.

The phase diagram of the copper-phosphorus system has been determined up to 15% copper. According to this diagram, the solubility of phosphorus in metallic copper is about 1.6% at 650°C and about 1.5% at 600°C. A semilogarithmic plot of K_1 for 3.7 and 13.2 Torr against the reciprocal of the temperature is shown in Fig. 5. The appearance of a quite high increase in value of K_1 at 650°C is presumed to be attributable to a predominance of phosphorus dissolution process in metallic copper.

A graph showing the dependence of the linear rate constant on the partial pressure of phosphorus vapor at 500°C is given in Fig. 6. The dependence interestingly gives a straight line, whose slope corresponds to 0.83, in spite of the approximate value of K_1. It may be interpreted in terms of a phosphorus chemisorption equilibrium followed by a rate-determining step governed by nucleation and growth of the phosphide nuclei.

It seems reasonable to conclude that in the initial stage the chemisorption of phosphorus at the phosphide-phosphorus interface is responsible for the phosphidation rate. It may be suggested that the appearance of a parabolic rate in the advanced stage is a result of the rate-determining diffusion of phosphorus or copper ion through the phosphide layer.

The present difficulties in the explanation of the phosphidation mechanism result from the complicated structure of the copper phosphide scaling layer and lack of information concerning the phosphorus chemisorption and the diffusion of phosphorus and copper ion.

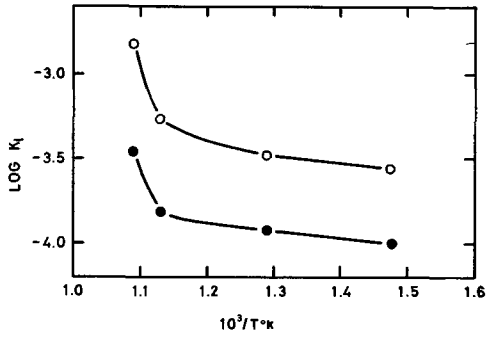

Fig. 5. Temperature dependence of the linear rate constant between 400° and 650°C: ○ 13.2; ● 3.7 Torr.

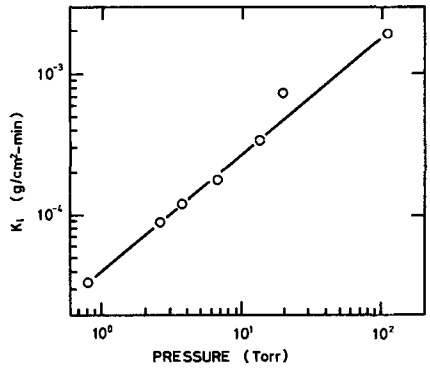

Fig. 6. Phosphorus vapor pressure dependence for linear rate of the phosphidation of copper at 500°C.

Summary and Conclusions

A study on the kinetics of the elevated temperature phosphidation of copper sheets was undertaken. The weight increase of the copper sheets exposed to phosphorus vapor (P_4 molecule) in an argon carrier gas was determined by measuring the extension of the quartz helix suspending the sample copper sheet.

The phosphidation rate increased with increasing temperature from 400° to 650°C and also with increasing phosphorus partial pressures from 3.7 to 13.2 Torr.

The relation between the phosphorus vapor pressure, P, (0.8-110 Torr) and the linear rate constant, K_1, (3.3-200 x 10^{-5} g/cm²-min) found in the initial stage gave $K_1 \propto P^{0.83}$ at 500°C.

In general the phosphidation proceeded nearly according to a linear rate law in the early stage, while it approximately followed a parabolic or a cubic rate law in the advanced stage. The transitions appeared to take place when the phosphide layer reached a certain thickness.

The phosphides obtained have been composed of Cu_3P or the mixture of Cu_3P and CuP_2. The formation of CuP_2 at temperatures above 600°C seldom has been observed from the x-ray patterns.

From the experimental results the rate-determining step seems to change from an adsorption to a diffusion step with the increasing thickness of the phosphide layer. The growth of numerous phosphide mounds and needles complicates the phosphidation mechanism.

Manuscript submitted May 5, 1969; revised manuscript received Sept. 16, 1969.

Any discussion of this paper will appear in a Discussion Section to be published in the December 1970 JOURNAL.

REFERENCES

1. J. W. Mellor, "A Comprehensive Treatise on Inorganic and Theoretical Chemistry," vol. VIII, p. 833, Longmans, Green and Co. Ltd., London (1962). L. Gmelin, "Gmelins Handbuch der Anorganischen Chemie," 60, Cu(B), p. 904, Verlag-Chemie, Weinheim, Germany (1961). J. R. Van Wazer, "Phosphorus and its Compounds," Vol. 1, p. 123, Interscience Publishers, Inc., New York (1958).
2. C. A. Edwards and A. J. Murphy, *J. Inst. Met.*, **27**, 183 (1922).
3. O. Oloffson, *Acta Chem. Scand.*, **19**, 229 (1965).
4. X-Ray Powder Data File, American Society for Testing Materials, 1916.

Fluorescence Properties of Alkaline Earth Oxyanions Activated by Divalent Ytterbium

Frank C. Palilla,* Brian E. O'Reilly, and Victor J. Abbruscato

The Bayside Research Center of General Telephone and Electronics Laboratories Inc., Bayside, New York

ABSTRACT

The luminescence of Yb^{2+} in alkaline earth phosphates and vanadates is reported. Particular attention has been given to those compositions possessing apatite and spodiosite structures. Emissions from Yb^{2+} are broad and sensitive to host composition. Single and double emission bands are observed which exhibit a variety of temperature dependent relationships. The decay of the Yb^{2+} fluorescence, under cathode-ray excitation, is short.

Spectroscopic studies of rare earth ions have concentrated largely on the interpretation of the inner shell 4f-4f transitions of the rare earth ions. There are generally a large number of 4f-4f emissions in the fluorescence spectrum of a rare earth ion, and they are relatively sharp and easily resolved at liquid nitrogen or helium temperatures. Consequently changes in the emission features brought about by the environment of the rare earth ions are useful in arriving at a quantitative description of the crystal field. However, this is not true for the 4f-5d emission spectra of rare earth ions. Due to the strong interaction of the 5d orbitals with the crystal field, there are a few very broad 4f-5d emission bands. As a result, the 4f-5d fluorescence spectra are not easily interpreted and do not readily lend themselves to basic investigations of the quantum process. Nonetheless, there have been some attempts to do so. For example, Blasse and Bril (1) have described the absorption bands of Ce^{3+}-activated phosphors in terms of the crystal field splitting of the 5d(^{2}D) state. Wood and Kaiser (2) have described the absorptions of Sm^{2+} in the alkaline earth fluorides. The latter investigations used a strong-field formulism to describe the 5d levels and a weak field formulation to describe the 4f levels of Sm^{2+}. An approximate energy level diagram was constructed by combining the 5d and 4f levels. Blasse *et al.* (3) have used the same approach to describe the energy level scheme of Eu^{2+}-activated silicates.

The rare earth ions which most commonly exhibit 4f-5d fluorescence spectra are Ce^{3+}, Eu^{2+}, and Yb^{2+}. There have been relatively few investigations of the spectroscopic properties of Yb^{2+}, even though this ion can have only 4f-5d transitions, since its ground state is $4f^{14}$. Butement (4) has investigated the absorption and emission properties of Yb^{2+} in $SrCl_2$, $BaCl_2$, and of $YbCl_2$ in aqueous media. Kaplyanskii and Feofilov (5) and Feofilov (6) have reported on the emission and absorption spectrum of Yb^{2+} in CaF_2. Bryant (7) has observed and interpreted the free ion emission spectrum of Yb^{2+}. Probably the most complete analysis of a Yb^{2+} absorption spectrum was given by Piper, Brown, and McClure (8), who carried out a complete quantum calculation of Yb^{2+} in $SrCl_2$, taking into consideration the electrostatic interaction, spin orbit coupling, and crystal field.

This paper reports the results of investigations of the emission and excitation spectra of Yb^{2+} in the Ba, Sr, and Ca chlorophosphates with apatite structure, $M_5(PO_4)_3Cl$, the Ca chlorophosphate and chlorovanadate with spodiosite structure, M_2PO_4Cl, and Sr orthophosphate. Some of these matrices have previously been reported as effective hosts for Eu^{2+}, and the Eu^{2+} emission was reported to be sensitive to host composition (9). The Yb^{2+} emission features in these hosts were also found to vary and the results are described herein.

* Electrochemical Society Active Member.

Experimental

The alkaline earth halophosphates and halovanadates were formed in the following manner. The halophosphates were formed by firing appropriate mixtures of Yb_2O_3, $MHPO_4$ (M = Ca, Sr, Ba) and the corresponding halide MCl_2 in hydrogen (9). Similarly, the calcium halovanadate was prepared by firing the appropriate mixture of Yb_2O_3, V_2O_5, $CaCO_3$, and $CaCl_2$ in air, as described by Banks *et al.* (10). The halide is added in excess for fluxing purposes. Reaction temperatures used for synthesis ranged from 800° to 1300°C. The temperature ranges for formation of the spodiosite and apatite structures were 800°-1050°C and 1100°-1300°C, respectively. After the reaction was complete (> 1 hr), the melt was air quenched to room temperature and the excess MCl_2 leached out with hot H_2O washings.

The alkaline earth orthophosphates, unlike the halophosphates, did not require preparation under hydrogen atmosphere for efficient luminescence response under CR excitation. Appropriate mixtures of Yb_2O_3, $MHPO_4$, and MCO_3 can be reacted in either air, nitrogen, or hydrogen. An alternative mixture consisting of only $MHPO_4$ + Yb_2O_3 does, however, require a hydrogen atmosphere to yield an efficient phosphor. Either procedure requires that the starting materials be fired at temperatures above 1200°C for periods of at least 2 hr; the samples are then air quenched to room temperature.

Activator concentration used in either the halo- or orthophosphates can be between 0.0025 and 0.10 gram-atom per gram-atom of host cation.

The excitation and emission spectra were recorded with a Hitachi MPF-2A fluorescence spectrophotometer and corrected for instrumental response by a computer program. The correction curve for the emission spectra was obtained with the use of a NBS standard lamp. The correction curve for the excitation spectra was generated with the use of sodium salicilate and rhodamine B as standards. The relative excitation spectra are expressed in quanta as a function of wavelength.

The temperature measurements were taken under x-ray excitation using a Mo tube. The phosphor was deposited on a copper plate which was then fitted into the slot of a metal block dewar. The temperature was measured with the use of a copper-constantan thermocouple which was in contact with the copper plate while the spectra were recorded. A ¼ meter Jarrell-Ash monochromator and photomultiplier tube with a S-10 response were used to record the spectra. Since the centers of the emission bands shift with temperature, the spectra were corrected for photomultiplier and monochromator discrimination. The areas under the curves recorded at the various temperatures were then compared. The temperature dependencies under uv excitation were found to correspond to those observed under x-ray excitation. The three emission

Table I. Peak wavelengths of emission and excitation bands at room and liquid-nitrogen temperatures

Host	Yb^{2+} emission, nm	Excitation, nm	Reflection, nm	Decay, μsec	Emission color
$Ba_5(PO_4)_3Cl$	624 (RT) 648 (LNT)	290, 335, 387, 404 280, 322, 382	275, 316, 343, 380	16	Orange Red
$Sr_5(PO_4)_3Cl$	560 (RT) 445 610 (LNT) 450 (LNT)	268, 315, 350, 375 289, 306, 332, 369 290, 315, 348, 395	270, 304, 325, 370	21	Yellow Yellow
$Ca_5(PO_4)_3Cl$	622 (LNT) 525 (LNT) 435 (LNT)	300, 328, 372 284, 313, 349 292, 345, 378			Yellowish-green
Ca_2PO_4Cl	505 (RT) 510 (LNT) 455 (LNT)	291, 328, 400 271, 292, 322, 395 282, 311, 330, 400	280, 317, 387	58	Green Greenish-blue
Ca_2VO_4Cl	436 (RT) 462 (LNT)	330 band edge 320 band edge			Blue Blue
$Sr_3(PO_4)_2$	432 (RT) 440 (LNT)	280, 318, 345, 377 287, 322, 347, 370	265, 305, 346		Blue Blue

bands in Ca apatite are exceptionally temperature dependent and decay rapidly on heating above liquid nitrogen temperature. Because of the difficulty in recording the change in intensity over the narrow temperature range at which emission occurs, only visual observations were made and therefore not included in Fig. 9.

The decay times were measured by pulsing the grid of a demountable CR tube. The emitted radiation was detected by a 1P21 photomultiplier tube which drove a Tektronix 535 oscilloscope. The trace on the oscilloscope was photographed, and the time to decay to 10% of initial brightness was measured from the photographs.

Results

The emission bands of the Yb^{2+}-activated phosphors were found to vary considerably with host. Their room and liquid nitrogen temperature emission and excitation spectra, along with the room-temperature reflectance spectra, are shown in Fig. 1-8. Table I gives peak wavelengths of the emission and excitation bands at room and liquid-nitrogen temperature, emission color, and the peak of the reflectance bands at room temperature.

Except for the calcium phosphate apatite, all the Yb^{2+}-activated phosphors have moderate response under CR excitation. The exponential decay times to 10% of the initial brightness of the phosphors under CR excitation are also listed in Table I.

The temperature dependence of the emission intensities of the Yb^{2+}-activated phosphors varied considerably from host to host (Fig. 9). For example, the Ca phosphate apatite shows no emission at room temperature while the emission from the Sr orthophosphate phosphor is still evident at 300°C. Even in those hosts where two or three emission bands are present, these bands exhibit a marked difference in their temperature dependence. Thus, at liquid nitrogen temperature the Sr apatite shows a bluish-white emission due to two bands centered at 450 and 620 nm, while at room temperature this phosphor exhibits a yellow emission which results from the quenching of the 450 nm emission.

It was also noted that under high energy photon excitation, *i.e.* x-ray radiation from a Mo target, the emissions correspond to those observed under uv excitation in all cases except that for the calcium apatite phosphor. In this case, the emission observed under uv excitation at 435 nm is not observed under x-ray excitation.

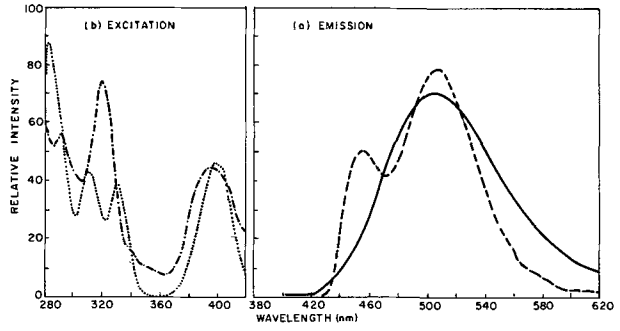

Fig. 1a. Emission spectra of $Ca_2PO_4Cl:Yb^{2+}$ at room (solid line) and liquid nitrogen (broken line) temperatures under 375 nm excitation; Fig. 1b. Liquid nitrogen excitation spectra for the 455 nm (·····) and 510 (·–·–·–·) emission bands of Yb^{2+} in Ca_2PO_4Cl.

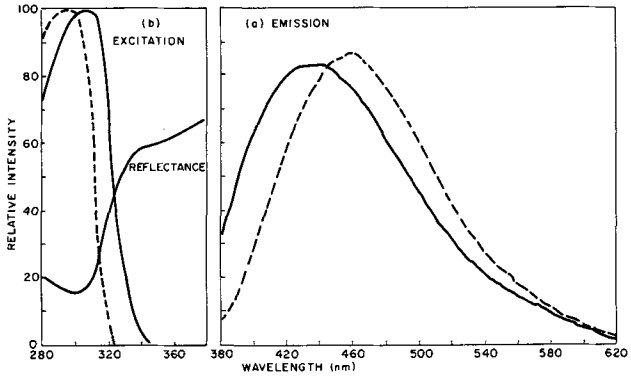

Fig. 2a. Emission spectra of $Ca_2VO_4Cl:Yb^{2+}$ at room (solid line) and liquid nitrogen (broken line) temperatures under 315 nm excitation; Fig. 2b. Excitation spectra at room (solid line) and liquid nitrogen (broken line) temperatures for the emission band of $Ca_2VO_4Cl:Yb^{2+}$. The diffuse reflectance spectrum for this phosphor is also shown.

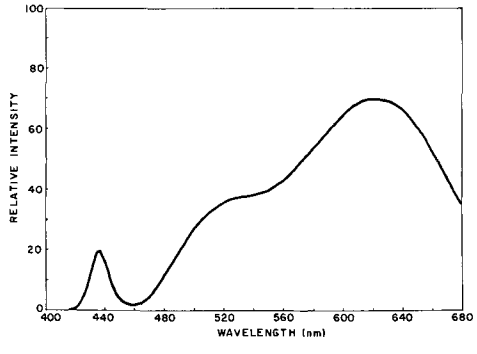

Fig. 3. Emission spectrum of $Ca_5(PO_4)_3Cl:Yb^{2+}$ at liquid nitrogen temperature under 370 nm excitation.

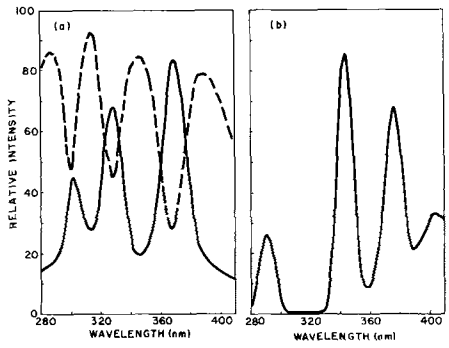

Fig. 4. Excitation spectrum at liquid nitrogen temperature for the emission bands of Yb^{2+} in $Ca_5(PO_4)_3Cl$: (a) 620 nm (solid line) and 525 nm (broken line) emissions; (b) 435 nm emission.

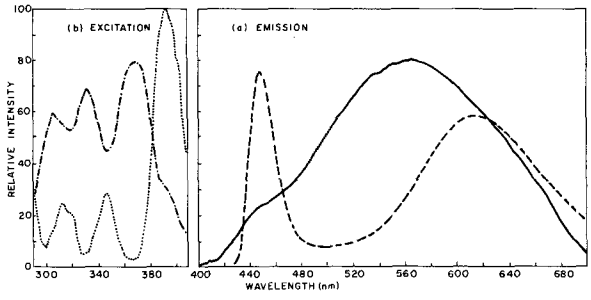

Fig. 5a. Emission spectra of $Sr_5(PO_4)_3Cl:Yb^{2+}$ at room temperature (solid line) under 380 nm excitation and at liquid nitrogen temperature (dashed line) under 350 nm excitation; Fig. 5b. Liquid nitrogen excitation spectra for the 450 nm (·····) and 610 nm (·–·–·–·) emissions of $Sr_5(PO_4)_3Cl:Yb^{2+}$.

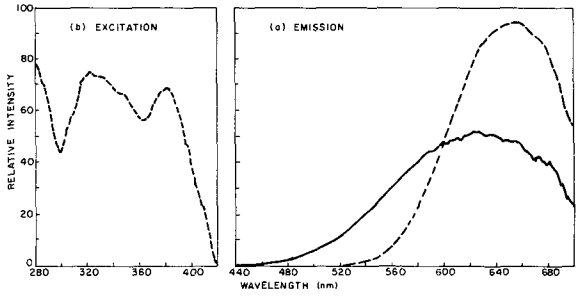

Fig. 6a. Emission spectra of $Ba_5(PO_4)_3Cl:Yb^{2+}$ at room (solid line) and liquid nitrogen temperatures (dashed line) under 366 nm excitation; Fig. 6b. Liquid nitrogen excitation spectrum for the 650 nm emission of Yb^{2+} in $Ba_5(PO_4)_3Cl:Yb^{2+}$.

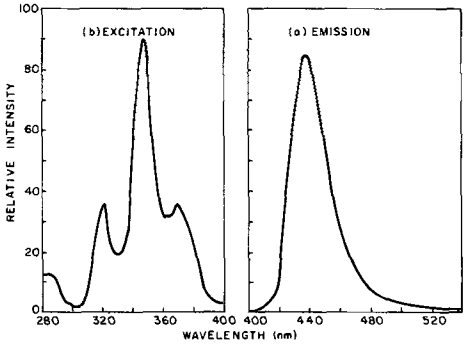

Fig. 7a. Emission spectrum of $Sr_3(PO_4)_2:Yb^{2+}$ at liquid nitrogen temperature under 366 nm excitation; Fig. 7b. Liquid nitrogen excitation spectrum for the 440 nm emission band of Yb^{2+} in $Sr_3(PO_4)_2$.

Discussion

In the free ion calculation of the energy levels of Yb^{2+}, Bryant (7) has shown that for the first excited state levels ($4f^{13}5d^1$) the Jj coupling scheme is the most appropriate, since Yb^{2+} has strong spin-orbit coupling constants (J_f = 2950.2 cm^{-1}, J_d = 1211 cm^{-1}). In this scheme the $4f^{13}$ core is coupled as in Yb^{3+} to form $^2F_{7/2}$ and $^2F_{5/2}$ states (J_1). The spin and orbital angular momentum of the 5d electron is coupled to form $d_{3/2}$, $d_{1/2}$ orbitals (j). The angular momenta J_1 and j are coupled to form states with a total angular momentum J. However, the electrostatic interactions between the $4f^{13}$ and $5d^1$ electrons cannot be neglected, as shown by the relatively large (≈8000 cm^{-1}) (7) splitting of the $[^2F_{7/2}]d_{3/2}$, $[^2F_{7/2}]d_{5/2}$, $[^2F_{5/2}]d_{3/2}$, and $[^2F_{5/2}]d_{5/2}$ levels (Fig. 10). Figure 10 shows the $4f^{13}5d^1$ free ion energy level scheme. All the electric dipole transitions from the $^1S_0$ ground state to these levels, except those where $J = 1$, are not allowed due to the $\Delta J = 0, \pm 1$ (not $0 \leftrightarrow 0$) selection rule. Of these, the $J = 1$ level of the $[^2F_{5/2}]d_{5/2}$ state is predominantly ^1P in character, and therefore the transition to the ground state is spin allowed; the $J = 1$ levels of the $[^2F_{7/2}]d_{5/2}$ and $[^2F_{5/2}]d_{3/2}$ states are predominantly ^3D and ^3P in character (7), and therefore the transition to the ground state is not allowed because of the $\Delta S = 0$ selection rule. Piper *et al.* (8) have investigated the effect of a cubic crystal field on the free ion levels of Yb^{2+}. They obtained good agreement with the absorption spectrum of Yb^{2+} in $SrCl_2$ by calculating the mixing of the un-allowed states with the ^1P state in cubic symmetry and taking a Dq value of 800 cm^{-1} for the crystal field strength. Only those levels which had T_{1u} symmetry in a cubic

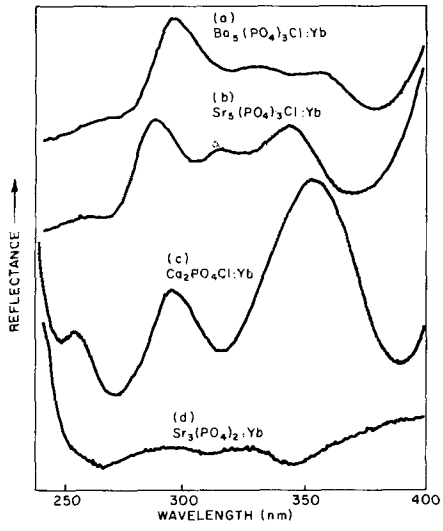

Fig. 8. Diffuse reflectance spectra of the phosphors: (a) $Ba_5(PO_4)_3Cl:Yb^{2+}$; (b) $Sr_5(PO_4)_3Cl:Yb^{2+}$; (c) $Ca_2PO_4Cl:Yb^{2+}$; and (d) $Sr_3(PO_4)_2:Yb^{2+}$.

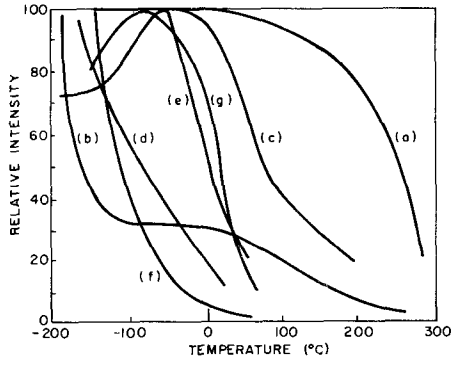

Fig. 9. Temperature dependence of fluorescence intensity of the phosphors: (a) $Sr_3(PO_4)_2:Yb^{2+}$; (b) $Ca_2VO_4Cl:Yb^{2+}$; (c) $Ca_2PO_4Cl:Yb^{2+}$ (510 nm emission); (d) $Ca_2PO_4Cl:Yb^{2+}$ (455 nm emission); (e) $Ba_5(PO_4)_3Cl:Yb^{2+}$; (f) $Sr_5(PO_4)_3Cl:Yb^{2+}$ (450 nm emission); and (g) $Sr_5(PO_4)_3Cl$ (610 nm emission) under x-ray excitation.

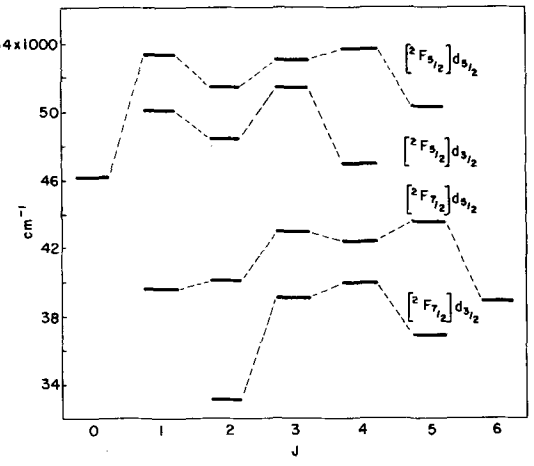

Fig. 10. Experimental free ion $4f^{13}5d$ levels of Yb^{2+} as determined by Bryant (7).

field were considered, since this is the symmetry of the ^1P state in a cubic field. In this treatment, no reasonable approximations were possible, since the electrostatic interactions, the spin-orbit coupling, and the crystal field for Yb^{2+} were of the same magnitude.

The electrostatic and spin-orbit coupling interactions tend to make the transitions from the lower levels of the $4f^{13}5d^1$ to the ground state not allowable. The effect of the crystal field is to make the transitions partially allowable. Therefore the decay times for the Yb^{2+} transitions should be longer than is observed for Ce^{3+} ($\approx 10^{-7}$ sec) and Eu^{2+} ($\approx 10^{-6}$ sec), where the crystal field effects are dominant (3). However, they should be shorter than the decay times of the 4f-4f transitions in the rare earth ions ($\approx 10^{-3}$ sec), where the effects of the crystal field are minimal. Indeed, decay times of the Yb^{2+} emissions in the hosts described in this paper under CR excitation are of the order of 10-60 x 10^{-6} sec to 10% I_0 (Table I).

The Ca, Sr, Ba apatites and the Ca spodiosite lattices have two low symmetry metal ion sites, C_3, C_s and C_2, C_s point symmetries, respectively. Contrary to the case in $SrCl_2$, where the high symmetry of the crystal field allows only a select few number of states to mix with the ^1P state, in the spodiosite and apatite metal ion sites all the $[^2F_{7/2}]d_{3/2}$ and $[^2F_{7/2}]d_{5/2}$ states can mix with the ^1P state. Furthermore, the crystal field can totally remove the degeneracy of the J states, so that there can be a total of 80 individual levels. The $[^2F_{5/2}]d_{3/2}$ and $[^2F_{5/2}]d_{5/2}$ states are not considered because they are too far above the ground state to be observed. Since the Yb^{2+} ion in these hosts exhibits only four main absorption and excitation bands in the 400-280 nm region, we are probably not observing the splitting of the individual J states within the $[^2F_{7/2}]d_{3/2}$ and lower lying $[^2F_{7/2}]d_{5/2}$ states, at least not at liquid nitrogen temperatures. The effect of the crystal field is probably to broaden the J states.

The excitation spectra for the Yb^{2+} emissions show relatively sharp and well-defined bands, *e.g.*, Fig. 1B, 4. This is in contrast to the excitation spectra of other activators whose emissions also involve $4f^n5d^1 \rightarrow 4f^{n+1}$ transitions, *e.g.*, Ce^{3+} and Eu^{2+}, but whose excitation spectra are relatively broad and without fine structure (3, 9). In the absence of appropriate theoretical calculations, these differences can be explained qualitatively in the following way: In the case of Ce^{3+}, whose lowest excited configuration is $4f^05d^1$, the energy level scheme can be explained on the basis of the splitting of the pure 5d orbital by the crystal field (1). The excited state levels are therefore expected to interact strongly with the crystal field leading to broad excitation bands. On the other hand, the Yb^{2+} and Eu^{2+} excited states are $4f^{13}5d^1$ and $4f^65d^1$, respectively, and therefore contain a large degree of f orbital character. As a result the crystal field does not broaden these levels to the same extent that the pure d-character excited states of Ce^{3+} are broadened. However, in the case of Eu^{2+}, the observed broadening can be attributed instead to the greater complexity of its electronic structure in comparison to that of Yb^{2+}. The $4f^6$ core in Eu^{2+} has a ^7F Russell-Saunders state, which will couple with the d electron to produce the lowest lying $4f^65d^1$ levels. The total multiplet splitting of the ^7F state is observed to be approximately 5000 cm^{-1} in Eu^{3+}. Indeed, Freiser *et al.* (11) have observed the structure of the lowest lying uv absorption band of EuF_2 at 20°K and have attributed the seven observable bands to the individual J components of the ^7F state. At room temperature thermal broadening will result in the observation of one broad band. Finally, Yb^{2+} is unique in the sense that the $4f^{13}$ core produces only a $^2F_{7/2}$ and a $^2F_{5/2}$ level, which are well separated by a strong spin-orbit coupling parameter. Consequently, this leads to a relatively well-defined excitation spectrum.

Ca *chlorophosphate and vanadate spodiosite systems.*—The emission spectra of Yb^{2+}-activated Ca chlorophosphates and vanadates with spodiosite structure at liquid nitrogen and room temperature are shown in Fig. 1A, 2A. The fluorescence spectrum of the phosphate spodiosite at liquid nitrogen temperature exhibits two bands centered at 455 nm and 505 nm. As evident in Fig. 1B, the excitation spectrum at liquid nitrogen temperature for each band is distinct and relatively sharp ($\lambda_{1/2} \approx 20$ nm).

The Ca chlorovanadate of spodiosite structure exhibits only one broad band emission at liquid nitrogen temperature (Fig 2a), which is centered at 460 nm. The broad band excitation spectrum is similar to the reflectance spectrum of the unactivated vanadate (Fig. 2b) and is undoubtedly due to absorption into the vanadate host which is followed by transfer to the Yb^{2+} ion. If we assume that the Yb^{2+} is distributed between the two available lattice sites, then the single emission band may be either a composite of the fluorescence of ions on both sites or representative of luminescence from one site only. The complex nature of the fluorescence intensity *vs.* temperature curve of the vanadate compound (Fig. 9b) supports the argument that there are two overlapping emissions present. The temperature relationship appears to approximate a composite of that observed for the two emissions in the Ca phosphate spodiosite (Fig. 9c, d).

Ba, Sr, *and* Ca *chlorophosphates with apatite structure.*—At liquid nitrogen temperatures the emission spectra of Yb^{2+} in the Ba, Sr, and Ca apatites consist of one, two, and three bands as shown in Fig. 3, 5, and 6. The presence of three fluorescence bands in the Ca apatite, which has two available sites for the activator, implies that at least two of the bands are a result of transitions of the Yb^{2+} in the same site. The blue emissions centered at 455 and 435 nm in the Sr and Ca apatites show relatively small Stokes shifts of approximately 3700 and 1700 cm^{-1}. The lowest lying excited states for these emissions are at 390 and 405 nm. This small Stokes shift is probably also responsible for the relative sharpness of these emissions ($\lambda_{1/2} \approx$ 500-600 cm^{-1}). In contrast the emission centered at 620 nm in Ca apatite has a Stokes shift of approximately 11,000 cm^{-1} and an emission halfwidth of approximately 3000 cm^{-1}.

Among the apatites, the Yb^{2+} emission intensity in the Ca compound is the one most influenced by temperature, while the Yb^{2+} emission intensity in the Ba compound is the least affected (Fig. 9). This trend among isostructural hosts is also found to be true for the Eu^{2+} emission intensities in the silicates (3). The smaller size of the sites in the Ca compound allows for a stronger vibronic interaction of the activator excited state and the host and a higher probability of a nonradiative transition.

In the phosphors where there is more than one emission band, the emissions with the smaller Stokes

shifts have a lower quenching temperature. For example, as can be seen in Fig. 9f and g, in Sr apatite the 450 nm emission is thermally quenched at a much lower temperature than the 610 nm emission. This is unusual, since Blasse *et al.* (3) have shown that in Eu^{2+}-activated silicates the emissions that have the larger Stokes shifts usually have a much lower quenching temperature, due to a higher probability of crossover between the ground state and excited state of the activator ion.

Sr *orthophosphate system.*—The $Sr_3(PO_4)_2$ lattice also provides two divalent metal ion sites which have slightly higher symmetries (D_{3d},C_{3v}) than those in the apatite and spodiosite structures. The emission of Yb^{2+} in $Sr_3(PO_4)_2$ shows only one main absorption band at room and liquid nitrogen temperatures. In this compound the emission intensity *vs.* temperature curve (Fig. 9a) is not complex, and therefore there probably is emission from predominantly only one site.

Acknowledgments

The authors are grateful to J. Ragusin for his assistance in the experimental work. Helpful discussions with C. S. Wiggins, S. Natansohn, and R. Amster are acknowledged. The use of a computer program to apply the correction functions to the recorded spectra was supplied by O. J. Sovers. The C.R. decay measurements were recorded by V. D. Meyer.

Manuscript submitted April 22, 1969; revised manuscript received Oct. 6, 1969. This was Paper 62 presented at the New York Meeting, May 4-9, 1969.

Any discussion of this paper will appear in a Discussion Section to be published in the December 1970 JOURNAL.

REFERENCES

1. G. Blasse and A. Bril, *J. Chem. Phys.*, **47**, 5139 (1967).
2. D. L. Wood and W. Kaiser, *Phys. Rev.*, **126**, 2079 (1962).
3. G. Blasse, W. L. Wanmaker, J. W. ter Vrugt, and A. Bril, *Philips Res. Repts.*, **23**, 189 (1968).
4. F. Butement, *Trans. Faraday Soc.*, **44**, 617 (1948).
5. A. Kaplyanskii and P. Feofilov, *Opt. and Spect.*, **13**, 129 (1962).
6. P. Feofilov, *ibid.*, **1**, 992 (1956).
7. B. W. Bryant, *J. Opt. Soc. Am.*, **55**, 771 (1965).
8. T. S. Piper, J. P. Brown, and D. S. McClure, *J. Chem. Phys.*, **46**, 1353 (1967).
9. F. C. Palilla and B. E. O'Reilly, *This Journal*, **115**, 1076 (1968).
10. E. Banks, M. Greenblatt, and R. W. Schwartz, *Inorg. Chem.*, **7**, 1230 (1968).
11. M. J. Freiser, S. Methfessel, and F. Holtzberg, *J. Appl. Phys.*, **39**, 900 (1968).

The Deposition and Physical Properties of Aluminosilicate Films

S. K. Tung[1] and R. E. Caffrey

Bell Telephone Laboratories, Incorporated, Allentown, Pennsylvania

ABSTRACT

A CO_2-H_2-$AlCl_3$-$SiCl_4$ process used to deposit various compositions of aluminosilicate films on a silicon substrate held at various temperatures is described. The film deposition rate with a total vapor (0.42 Al_2Cl_6 + 0.58 $SiCl_4$) concentration of 0.12 v/o (volume per cent) in the gas phase is 2500 Å/min at 1100°C and 150 Å/min at 880°C with an activation energy of 42.5 kcal/mol. in this temperature range. The deposition rate is increased as the Al_2Cl_6 concentration is increased. The chemical composition of the films was determined by x-ray fluorescence. The films were smooth to the eye but grainy at 12,000 times. A compositional relationship between indices of refraction of Al_2O_3 (1.76) and SiO_2 (1.46) was found. The dielectric strength of the films (6×10^6 — 1.7×10^7 V/cm) was found to be similar to SiO_2 (5-6 $\times 10^6$ V/cm) or higher.

Sodium diffusion data for aluminosilicate films and silica films are presented. For a given film depth sodium concentration in an aluminosilicate film is less than the concentration in a silica film. CV measurement of an MIS capacitor gave a typical surface charge (Q_{ss}) of 1-2 $\times 10^{11}$/cm^2. Films of less than 50% Al_2O_3 were etchable in concentrated hydrofluoric acid or in buffered hydrofluoric acid. Films of greater than 50% Al_2O_3 were somewhat resistant to hydrofluoric acid but were etched in hot (180°C) phosphoric acid with a rate about 100 Å/min.

The beam-lead-sealed-junction (BLSJ) technology has been developed in order to eliminate the need for vacuum sealed packages in high reliability semiconductor devices and circuits. For application to bipolar devices BLSJ structures utilize the Lepselter metallurgy and silicon nitride (1). To apply this same technology to insulated gate field effect transistors the dielectric film used must have a stable and a low surface charge density in order to achieve and maintain a low threshold voltage. In addition the film must provide resistance to sodium penetration in order to achieve long-term stability. Although silicon nitride (Si_3N_4) films have been shown to be good barriers to alkali ions (2) they normally exhibit a comparatively high surface charge density which yields a higher than desired threshold voltage (> 2V). Several techniques, *i.e.*, *in situ* cleaning and *in situ* oxide deposition, were used in an effort to improve the properties of the Si_3N_4 films (3). However, the characteristic surface charge density of such films was too high for the required devices. Thus another insulator film was sought. This search has led to alumina, an insulator which, when placed over a thin film of SiO_2 satisfies the requirements.

The deposition of metal (Si, Al, Ti) oxide on silicon by the reaction of the respective metal halide compound

[1] Present address: IBM Components Division, Essex Junction, Vermont.

with a hydrogen-carbon dioxide mixture had been studied previously by Tung and Caffrey (4). A film composed of a mixture of aluminum oxide and silicon dioxide had also been cursorily studied. This paper discusses more recent work on deposited aluminosilicate film using the H_2-$SiCl_4$-$AlCl_3$ system and discusses process parameters, physical properties, and the composition of the films.

Experimental

The system employed for deposition was a vertical, single wafer system developed for deposition of epitaxial silicon and silicon dioxide (4). To deposit an aluminosilicate film, sources of both aluminum and silicon were required, and $AlCl_3$ and $SiCl_4$ were used. Because $AlCl_3$ is a solid, and has a low-vapor pressure at room temperature, it was necessary to vaporize $AlCl_3$ at an appropriate elevated temperature in the region of 95°-115°C. Aluminum chloride exists as a dimer (Al_2Cl_6) in the gaseous state (5). The dimer was kept in the gaseous state, diluted with hydrogen (H_2), and delivered to the reaction zone close to the silicon substrates unreacted and still in the gaseous state. This was accomplished by placing the aluminum chloride source in a specially designed saturator within an oven and wrapping the gas line downstream of the oven with heating tape to heat the gas line 30°-50°C hotter than the oven temperature. Al_2Cl_6 and $SiCl_4$ vapors in H_2 were carefully monitored by means of flowmeters and were admitted to the reaction chamber simultaneously. The compositions of the Al_2Cl_6 and $SiCl_4$ vapor mixtures were calculated from the respective source temperatures and the corresponding flow rates. Figure 1 shows a schematic drawing of the system used for aluminosilicate film deposition.

The aluminosilicate films were usually deposited on 50 ohm-cm, p-type silicon slices. Occasionally 10 ohm-cm, n-type silicon slices or slices of other resistivities were used for deposition studies. In general the oxide deposition was independent of the silicon substrate resistivity.

A typical aluminosilicate deposition was performed in the following manner. The silicon substrate was etched with a 2% (by volume) hydrogen chloride (HCl) gas in H_2 at 1275°C for 10 min. This operation removed approximately 12μ of silicon and gave a clean, strain-free surface. After gas etching the oxide deposition was done either (*a*) by lowering the slice temperature from 1275°C to the deposition temperature ($\leq$ 950°C) and admitting the reactant gases or (*b*) by lowering the temperature from 1275°C to approximately 800°C, admitting the reactant gases and raising the slice temperature to the deposition temperature ($\geq$ 950°C). The latter procedure was designed to deposit a film without any etching occurring at the oxide-free silicon interface. Such a phenomenon has been occasionally observed at the SiO_2-Si interface when SiO_2 was deposited at high temperatures ($\geq$ 1200°C). The deposition procedure chosen depended on the deposition temperature used because etching of the interface was not observed in aluminosilicate deposition at $\leq$ 1000°C.

The rate of deposition of an aluminosilicate film deposited from a gaseous mixture of 42% Al_2Cl_6 and 58% $SiCl_4$ was studied as a function of temperature. The deposition procedure was that outlined in method (*a*) above. The gas mixture had a total vapor ($SiCl_4$ + Al_2Cl_6) concentration of 0.12 v/o. The carbon dioxide (CO_2) concentration was about 1%.

Results and Discussion

Factors affecting the rate of oxide deposition.—A plot of logarithm of the deposition rate *vs.* $1/T$ where T is absolute temperature resulted in a straight line and is shown in Fig. 2. The activation energy derived from the slope is 42.5 kcal/mol. As a comparison the activation energy for SiO_2 deposition from the CO_2-H_2-$SiCl_4$ process was 51.6 kcal/mol (4) and the activation energy for Al_2O_3 deposition from the CO_2-H_2-$AlCl_3$ process was 30.3 kcal/mol.

Figure 3 is a plot of the deposition rate at 1100°C *vs.* the percentage of Al_2Cl_6 vapor concentration in an Al_2Cl_6-$SiCl_4$ vapor mixture, which constituted 0.1% of the total gas input to the reactor. The deposition procedure was that outlined previously in method (*a*). This figure indicates a tendency for the deposition rate to increase as the percentage of Al_2Cl_6 vapor concentration is increased; however, the deposition rates of the SiO_2-rich aluminosilicate compositions were higher

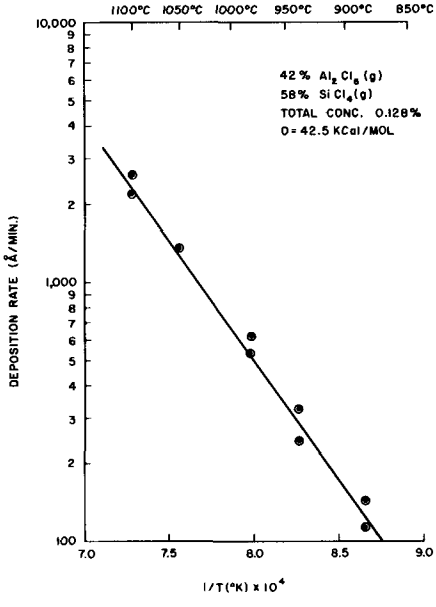

Fig. 2. Deposition rate vs. 1/substrate temperature

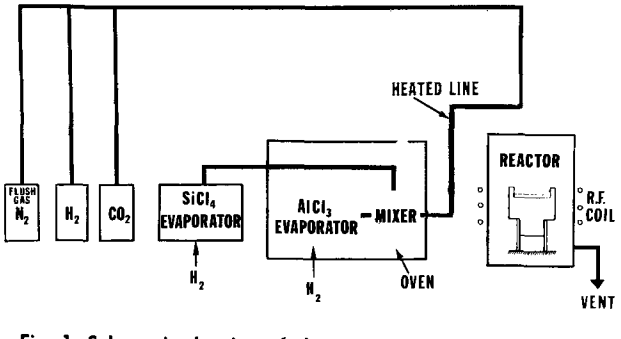

Fig. 1. Schematic drawing of the system used for aluminosilicate film deposition.

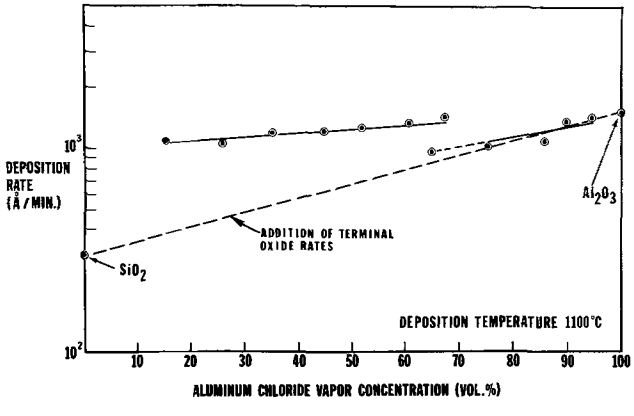

Fig. 3. Deposition rate at 1100°C vs. aluminum-chloride vapor concentration in (Al_2Cl_6-$SiCl_4$) vapor mixture.

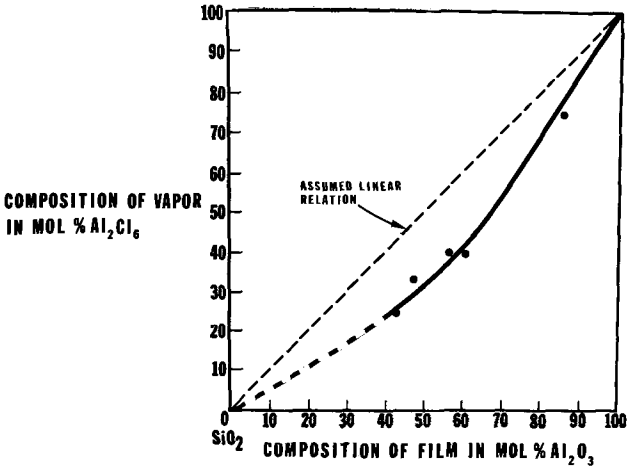

Fig. 4. Calculated composition of Al_2Cl_6 in vapor vs. composition of Al_2O_3 in film determined by x-ray fluorescence.

than the expected values. If a simple hydrolysis reaction were the deposition mechanism, one would have expected a simple addition of the percentages of the individual oxide rates (Fig. 3, broken line) for the aluminosilicate deposition rates; thus, a simple hydrolysis reaction is not sufficient to account for the deposition rate of aluminosilicate films. The break in the two regions is not explained except to note that the electron diffraction patterns of the films changed near the break. That is, the film structure was polycrystalline with an associated amorphous background on the low side of the Al_2Cl_6 concentration and was polycrystalline with preferred orientation on the high side of the Al_2Cl_6 concentration. These results will be discussed more extensively in a later paper.

The deposition rate was averaged in several trial runs at various gas compositions by depositing slices for various times and measuring the thickness with an uv-visible spectrophotometer (6). The measured thickness was corrected by a factor deduced from the composite index of refraction according to the vapor composition. The measured film thickness should be corrected by a factor derived from the actual film composition. However, the correction factor is not a very sensitive function of the refractive index, and thus the thickness is not in great error. The error in the real thickness is estimated to be no greater than 4 per cent. The spectrophotometric method used to make the thickness measurements was discussed in reference (6) and was calibrated by multiple-beam interferometry.

Chemical composition of aluminosilicate films.—An x-ray fluorescent technique was used to determine the compositions of aluminosilicate films deposited on tantalum substrates. Tantalum was employed because of its limited fluorescence contribution to the measurement of the film; hence all the counting can be attributed to the film only. Figure 4 shows the resultant data showing the composition of Al_2Cl_6 in the vapor *vs.* measured Al_2O_3 in the film.

If similar over-all reaction rates for the hydrolysis of Al_2Cl_6 and $SiCl_4$ are assumed, the solid aluminosilicate film should have the same composition as the respective vapor constituents. This relationship is shown as a broken line in Fig. 4. Experimentally the actual alumina (Al_2O_3) composition in the film was slightly higher than that of Al_2Cl_6 in the vapor state. This deviation is thought due to a rate difference between the hydrolysis reaction of aluminum chloride (Al_2Cl_6) and that of silicon tetrachloride ($SiCl_4$), *i.e.*, Al_2O_3 deposited faster than SiO_2 (see Fig. 3).

Film structure and composition.—The film structure was determined by electron diffraction. When the aluminum chloride concentration (Al_2Cl_6) was 15% or less the films were found to be amorphous. As the Al_2Cl_6 concentration is increased, the film becomes more crystalline. However, the crystalline film structure is complex and is composed of andalusite, sillimanite, κ- and α-alumina depending on the vapor concentration and the deposition temperature. These structures will be discussed in detail in another paper.

Some properties of aluminosilicate films.—Surface characteristics.—The aluminosilicate films usually were transparent and smooth to the eye; however, the film surface (at 12,000 × magnification) was somewhat grainy when compared with a deposited SiO_2 film surface. Figures 5a and 5b show electron micrographs of surface replicas of aluminosilicate and SiO_2 films, respectively.

Index of refraction.—The indices of refraction of the films were measured with an ellipsometer. Figure 6 shows a plot of index of refraction versus oxide composition. The oxide composition was the vapor composition corrected according to Fig. 4. The deviation of the points from a straight line relationship in Fig. 6 probably represents a small error resulting from the use of empirical corrections of the calculated gas compositions.

Dielectric strength.—The dielectric strengths of the films measured with a ROYCO anodicator are given in Table I. It can be noted that the value for pure alumina was found to be about the same as that for SiO_2 (4). For a mixed oxide film of approximately 50% Al_2O_3 the values were somewhat higher.

Sodium diffusion and surface charge density.—Aluminosilicate films deposited at 900°C with a composition of approximately 50% Al_2O_3 and 50% SiO_2 were investigated for their response in sodium diffusion and also for evaluation of surface charge density. The sodium diffusion experiment was done by a radioactive tracer technique (7). $Na^{22}Cl$ and $Na^{23}Cl$ were evaporated onto the film and heated at 600°C in forming gas for 22 hr. The film was then etched, and the Na^{22} activity was counted. Figure 7 shows a plot of total sodium concentration *vs.* film depth. The result indicates that when 750Å of the film was removed the sodium concentration in the film dropped from 7×10^{19} at./cm^3 to 1.2×10^{17} at./cm^3. As a comparison, sodium diffusion data on a steam grown silica film under similar heat-treatment conditions is also shown in Fig. 7. It can be noted that the concentration of Na^{22} in the SiO_2 film for a given film depth was an order of magnitude or more higher than the concentration in an aluminosilicate film.

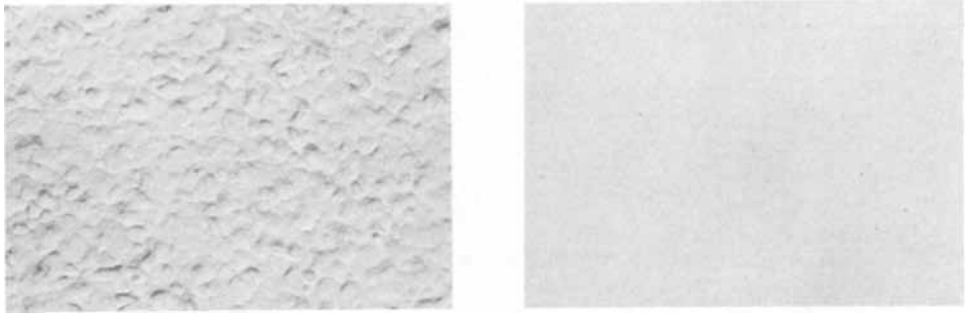

Fig. 5. Electron micrographs of oxide film surfaces (carbon platinum replica). Fig. 5a. (left), aluminum oxide and silicon dioxide mixture; Fig. 5b (right), silicon dioxide film. (Magnification 7200X)

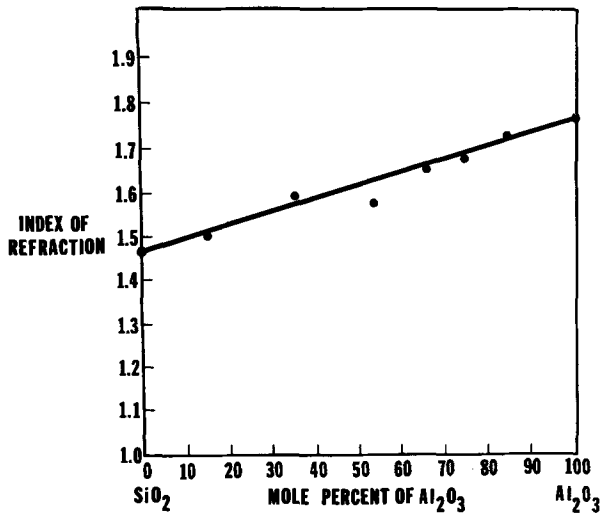

Fig. 6. Index of refraction vs. aluminosilicate film composition

The total surface charge density was evaluated by means of a C-V measurement of a metal-insulator-semiconductor (MIS) capacitor. Typically 1-2x10^{11}/cm^2 was observed.

Etching.—Aluminosilicate films deposited at 1100°C with a composition of 50% Al_2O_3 or higher showed resistance to hydrofluoric acid (48%). Films with less than 50% of Al_2O_3 could be etched in concentrated HF or in ammonium fluoride buffered HF acid. However, etch figures such as those shown in Fig. 8 were developed after etching in buffered HF. These effects were thought due to the precipitation of etching products during the etching. No etch figures were observed when films were etched in concentrated HF. Tillotson (8) observed similar etching figures and attributed them to etching solutions. He stated: "The form of the etch figures is independent of the chemical composition of the glass, and is determined by the composition of the etching solution; *i.e.*, buffered HF." Hot phosphoric acid was found capable of etching the films not etched in HF. A typical rate for hot (180°C) H_3PO_4 of films with greater than 50% Al_2O_3 was about 100 Å/min.

Summary

A CO_2-H_2-$AlCl_3$-$SiCl_4$ process has been described for depositing aluminosilicate films of various compositions on silicon substrates held at various temperatures. The activation energy for the deposition process was found to be 42.5 kcal/mol from about 850° to 1100°C. The deposition rate increased as the aluminum chloride vapor concentration increased.

The chemical composition of the films as measured by an x-ray fluorescence technique gave higher values than the respective vapor constituents. The error of this measurement is estimated to be less than 5%.

Table I. Film dielectric strength as measured with an anodicator*

Film composition calculated from vapor composition		Dielectric strength
Al_2O_3 (%)	SiO_2 (%)	(V/cm)
100	—	5.95 × 10^6
100	—	6.95 × 10^6
81.9	18.1	7.20 × 10^6
75.5	24.5	6.04 × 10^6
60.6	39.4	1.27 × 10^7
50.7	49.3	1.91 × 10^7
43.5	56.5	1.11 × 10^7
35.0	65.0	6.36 × 10^6
14.6	85.4	6.90 × 10^6
—	100	5-6 × 10^6

* ROYCO Co.

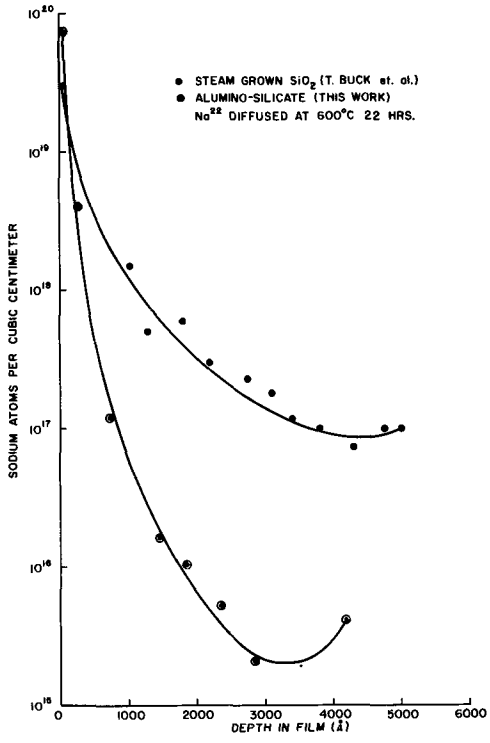

Fig. 7. Sodium profile in aluminosilicate film

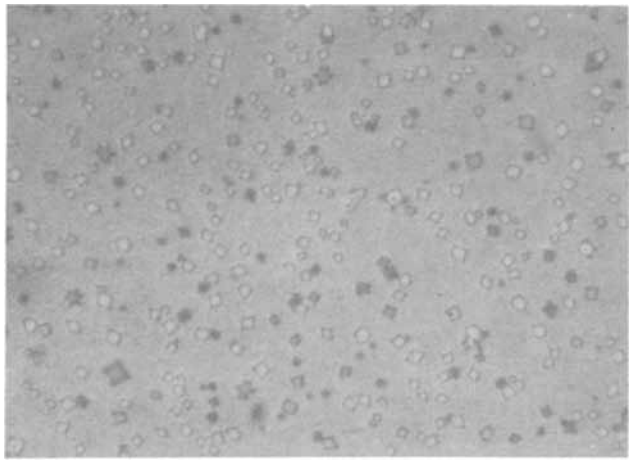

Fig. 8. Etch figure of aluminosilicate film in buffered hydrofluoric acid. Magnification 450X.

Aluminosilicate film surfaces appeared smooth to the eye, but were grainy at a magnification of 12,000×. The index of refraction of the films seemed to bear a simple relationship to indices of Al_2O_3 and SiO_2. The dielectric strengths of the films were the same or somewhat higher than that of SiO_2. Sodium diffusion data of aluminosilicate film and data of silica film were compared. For a given film depth the sodium concentration in aluminosilicate films was significantly lower than the concentration in similarly treated silica films. Measurement of a typical MIS capacitor gave a surface charge density of 1-2x10^{11}/cm^2. Films of less than 50% Al_2O_3 can be etched in concentrated hydrofluoric acid or in buffered hydrofluoric acid. Films of greater than 50% Al_2O_3 showed resistance to HF, but can be etched in hot (180°C) phosphoric acid with a rate about 100 Å/min.

Acknowledgment

The sodium diffusion experiment by Mr. J. Dalton and Metal-Insulator-Semiconductor measurements and discussion of the measurements by Dr. H. Nigh are gratefully acknowledged.

Manuscript submitted Dec. 6, 1968; revised manuscript received ca. Sept. 11, 1969.

Any discussion of this paper will appear in a Discussion Section to be published in the December 1970 JOURNAL.

REFERENCES

1. G. H. Schneer, W. Van Gelder, V. E. Hauser, and P. F. Schmidt, *IEEE Trans. on Electron Devices*, May, 1968.
2. V. Y. Doo, *IEEE Trans. on Electron Devices*, ED-13, 561 (1966).
3. V. E. Hauser, Private communication.
4. S. K. Tung and R. E. Caffrey, *Trans. Met. Soc. AIME*, **233**, 572 (1965).
5. N. V. Sidgwick, "Chemical Elements and Their Compounds," Oxford University Press (1952).
6. F. Reizman, *J. Appl. Phys.*, **36**, 3804 (1965).
7. T. M. Buck, F. G. Allen, J. V. Dalton, and J. D. Struthers, *This Journal*, **114**, 862 (1967).
8. E. W. Tillotson, Jr., *J. Ind. Eng. Chem.*, **9**, 937 (1917).

Growth and Properties of Thin Germanium Films

D. J. Dumin

RCA Laboratories, Princeton, New Jersey

ABSTRACT

Germanium films have been grown via the pyrolysis of GeH_4-H_2 mixtures on thin films of silicon grown on spinel and sapphire. The thin layer of silicon (≈1000Å) was used to produce improved crystal structure in the germanium layer. In addition, the silicon undercoating provided improved adhesion of the germanium to the substrate, particularly at germanium growth temperatures above 700°C. The electrical properties of the films are described in terms of substrate orientation, silicon and germanium growth temperatures, and doping density. Both p- and n-type films 2 μm thick have been grown reproducibly with mobilities in excess of 1200 cm^2/V sec at carrier concentrations in the $10^{16}/cm^3$-$10^{17}/cm^3$ range. These films were sufficiently perfect to allow observation of the indirect-direct transition in the conduction band at 0.8 ev in the optical absorption data.

Epitaxial growth of semiconducting films on insulating substrates has been reported for such material combinations as silicon-on-sapphire (1), silicon-on-spinel (2), germanium-on-sapphire (3), germanium-on-spinel (4), germanium-on-calcium floride (5), and gallium arsenide-on-sapphire (6). Various techniques for transporting the semiconductor have been reported with vacuum deposition, chemical vapor transport, hydride decomposition, and reduction from the halide being used. With respect to germanium films on insulating substrates, relatively high carrier mobilities have been reported in films thicker than 10 μm. In particular, 20-40 μm thick films deposited by chemical vapor transport on sapphire have had mobilities of 1500 and 560 cm^2/V sec at carrier concentrations of $3 \cdot 10^{16}/cm^3$ and $9 \cdot 10^{18}/cm^3$ in p- and n-type films, respectively (3). Polycrystalline germanium films vacuum deposited on sapphire (7) and glass (8) have had mobilities as high as 1455 and 270 cm^2/V sec, respectively, for film thicknesses of the order of 8-17 μm.

The mobility of germanium-on-insulator films is known to drop as the film thickness is reduced; however, mobilities as high as 800 cm^2/V sec have been reported on 2 μm thick p-type films vacuum deposited on calcium fluoride (5). We have been studying the electrical characteristics of germanium films less than 10 μm thick grown on sapphire and spinel substrates via the decomposition of germane-hydrogen mixtures. The mobilities reported for germanium films grown on spinel in the hydride system have been relatively low, and the electrical characteristics of these films appear to be dominated by crystalline imperfections (4).

It has been shown that defects in both heteroepitaxial silicon (9) and germanium (10) are partially self-annihilating as the films grow thicker. Recently, evidence has been presented indicating that the defects can behave electrically as relatively deep donors and acceptors in silicon-on-sapphire films (11) and as shallow acceptors in germanium-on-sapphire or spinel films (12). Thus, any improvement in the crystal structure of the initial germanium layer grown near the germanium-substrate interface would be expected to lead to an improvement in the properties of the films as reflected in both a higher mobility and a lower defect and shallow acceptor concentration. In the case of germanium-on-spinel films grown via decomposition of GeH_4, it was observed that, as the growth temperature increased, the mobility rose and the acceptor concentration dropped (4). However, at growth temperatures in excess of 700°C, the films tended to agglomerate, and, while good single crystals of germanium could be grown on the spinel at growth temperatures in excess of 700°C, the films were often either discontinuous or highly nonuniform in thickness. It proved impossible to grow 1-2 μm thick germanium films on sapphire or spinel at growth temperatures above 700°C because of the tendency of the germanium to agglomerate. Also, films grown on the spinel in the hydride system often were so poorly bonded to the substrate that they could be removed easily from the substrate by scratching.

In order to attempt to grow thin germanium films at higher growth temperatures and to provide a good nucleating layer, it was decided to try using a very thin (≈ 1000Å) layer of silicon grown on the sapphire or spinel at a high temperature prior to growth of the germanium layers. This paper describes the results of experiments conducted using a thin layer of silicon as the undercoat for the germanium. The improvement in the quality of the germanium layer will be shown to be reflected electrically in both lower acceptor concentration and higher Hall mobilities than have previously been obtained using the hydride system. The improvement in the film quality was also reflected optically in a sharp indirect-direct transition in the absorption data. A somewhat analogous scheme has recently been successfully used for the growth of GaAs on Ge-on-sapphire (13).

Experimental Techniques

The experimental techniques used to grow the films are similar to those previously described for growing heteroepitaxial silicon (14) and germanium (4), and only the salient features will be discussed here. The films were grown via decomposition of GeH_4 or SiH_4 in

hydrogen in a vertical reaction chamber utilizing RF heating of a silicon susceptor and water cooling of the reactor walls. The doping of the films was controlled by adding dilute mixtures of B_2H_6, or AsH_3 in H_2 to the gas stream during growth. The film thickness was monitored during growth and controlled to the nearest 0.05 μm by using infrared interference techniques (15).

The substrates were $(1\bar{1}02)$ oriented sapphire wafers or (111) and (100) oriented spinel wafers approximately 300 μm thick. Both materials were mechanically polished to a scratch free surface and were subjected to a 1200°-1400°C heating in H_2 prior to growth to restore a single crystal surface to the wafer. The silicon undercoat was grown at various temperatures between 1000° and 1200°C at an average growth rate of 5 μm/min, and unless stated otherwise, was about 1000Å thick. The temperature was then lowered to the germanium growth temperature, and the germanium was grown at temperatures between 500° and 900°C at a growth rate of 2 μm/min. In order to maintain the germanium growth rate of 2 μm/min, it was necessary to increase the GeH_4 flow rates as the substrate temperature was lowered below 700°C. When no dopant was added to the GeH_4 supply, the GeH_4-H_2 mixture used to grow the films produced 2-3 ohm-cm p-type germanium when grown on 40 ohm-cm n-type Ge or 25 ohm-cm p-type germanium, which indicates that this GeH_4 supply was contaminated with acceptors to levels of the order of low-10^{15}/cm^3. The undesired doping due to impurities in the gas supplies was small when compared to the doping levels considered in the experiments performed on the germanium films.

The Hall mobility and resistivity of these films were measured using six terminal etched Hall bars and the carrier concentration derived from the Hall data under the assumption that the ratio of drift to Hall mobility was unity. The deformation of several of the films was measured on a cross section microscope using a previously described technique (16). The films were isotropically deformed and under a compressive stress of about 10^9 dynes/cm^2 which is slightly less than the stress measured in silicon-on-sapphire films (16). The optical absorption coefficient in the energy range from 0.5 to 1.2 ev was determined by measuring the optical density of several films on a Cary Model 14 CMR spectrophotometer.

The Hall mobility and resistivity of several 0.1 μm thick layers of silicon-on-sapphire and spinel were measured to determine what effects the silicon undercoating would have on the measured electrical properties of the germanium films. In general, the Hall mobilities of the silicon undercoatings were 60-120 cm^2/V sec and the carrier concentrations were of the order of 10^{15}-10^{16}/cm^3. Thus the shunting effects of the thin silicon layer could be neglected when interpreting the measurements made on the thicker, higher mobility germanium films.

A schematic sketch of the structure of a typical film grown on sapphire is shown in Fig. 1. The thickness of the interdiffused silicon-germanium region was estimated at less than 500Å by using a diffusion constant of Si in Ge of 10^{-14} cm^2/sec at 850°C (17). The possible effects of this interdiffused alloy region and of the aluminum autodoping on the electrical characteristics of the films will be considered below in some detail.

Experimental Results

Germanium growth temperature.—The temperature at which the germanium was grown strongly influenced the electrical characteristics of the films. At very low growth temperatures and very high growth temperatures, the Hall mobilities were low, and, as in the case of silicon-on-sapphire (14) or spinel (18), there was a growth temperature at which the highest mobility was obtained.

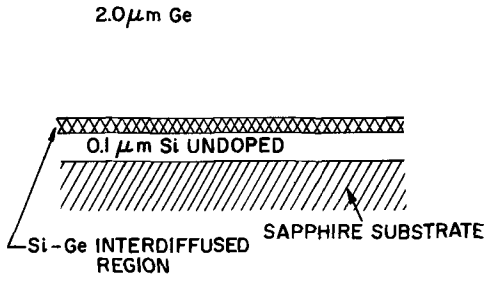

Fig. 1. Schematic sketch of a germanium film grown on a thin layer of silicon-on-sapphire.

Measured values of Hall mobility and carrier concentration are shown in Fig. 2 and Fig. 3, respectively, for 2 μm thick p-type Ge films grown on 0.1 μm of silicon on $(1\bar{1}02)$ sapphire. The silicon undercoat was grown at 1125°C. No intentional doping was added to the gas stream during growth of these films. The films were single crystal (100) oriented as determined from spot patterns on Laue back reflection photographs. These films are compared with some previously reported 2 μm thick germanium films grown directly on sapphire and spinel. Since it proved to be impossible to grow continuous 2 μm thick germanium films on the insulator at growth temperatures above 700°C without the benefit of the thin silicon undercoating, the comparison with films grown directly on the insulators has only been made for growth temperatures below 700°C.

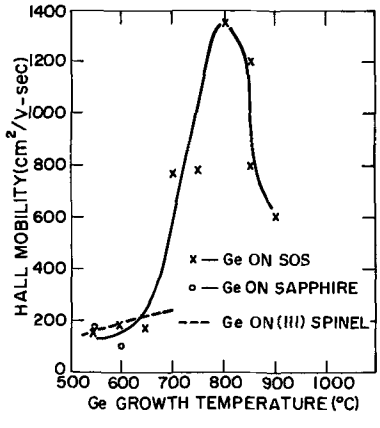

Fig. 2. Measured values of Hall mobility of 2 μm undoped germanium films as a function of germanium growth temperature. Films were p-type.

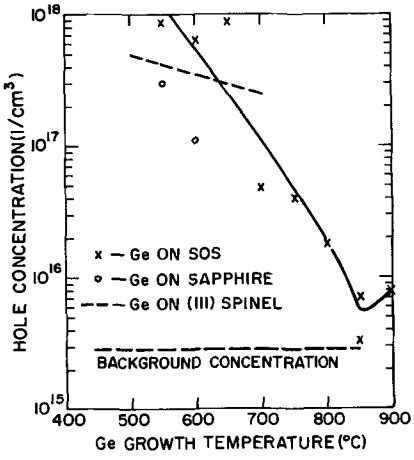

Fig. 3. Carrier concentration vs. germanium growth temperature for p-type films grown with no intentional added dopant.

As seen in Fig. 2, the highest mobility films were obtained at growth temperatures in the vicinity of 800°-850°C where Hall mobilities in excess of 1000 cm^2/V sec were obtained. The mobility fell off at both higher and lower growth temperatures. The resistivity of all of the films rose as the growth temperature increased and films of the order of 1-2 ohm-cm were obtained at growth temperatures of 850°-900°C. The lowest carrier concentrations were obtained at growth temperatures of 850°-900°C. The data of Fig. 2 and Fig. 3 show that the optimum germanium growth temperature was around 800°-900°C where both high mobilities and low acceptor concentrations were obtained when the thin silicon undercoating was present.

No doping was purposely added to these films and yet the hole concentration measured in Fig. 3 was, in general, dropping as the growth temperature increased. Similar effects of lowered carrier concentrations as a function of increasing growth temperatures have been reported in Ge-on-spinel (4) and Ge-on CaF_2 (5) and has been attributed to the action of defects acting as acceptors (5). The possibility that impurities could be doping the films should be considered, however. The fact that the carrier concentration dropped as the growth temperature increased would argue against an autodoping process based on either aluminum originating from the back of the wafer or from the silicon undercoating.

The thickness of the silicon undercoating had relatively little effect on the measured electrical characteristics of the films, provided, of course, that the thickness of the silicon was small compared to the germanium thickness. The silicon undercoating was varied in thickness from 0.04 to 0.3 μm and the mobility and carrier concentration of 2 μm thick germanium films grown on these undercoatings did not appear to significantly vary. Several of the undoped p-type germanium films were annealed at 850°C in H_2 for 1 hr to 4 hr immediately after growth, and no significant changes in the electrical characteristics of these films were found when compared with unannealed films.

Silicon growth temperature and substrate orientation.—The temperature at which the silicon undercoat was grown and the substrate orientation played an interrelated role in determining the electrical properties of the germanium layers. In order to demonstrate the relationship between silicon growth temperature and substrate orientation on the properties of the germanium films, a series of germanium films were grown on silicon undercoatings grown at different temperatures on three orientations of substrates. The substrate orientations and growth temperatures chosen for this experiment are shown in Fig. 4, where published curves of Hall mobility *vs.* growth temperature for 2 μm thick silicon-on-sapphire and silicon-on-spinel films are plotted (19). Silicon films 0.1 μm thick were grown at the six orientation-temperature points shown in Fig. 4. On top of these thin undercoatings, 2 μm thick films of undoped germanium were grown. The electrical characteristics of these films are described in Table I. All of the films were p-type, and

Table I. Properties of germanium films grown on 0.1 μm layers of silicon grown at different temperatures and on different substrate orientations. Germanium films were grown with no impurities intentionally added during growth and all of the films were p-type.

Substrate	Silicon growth temp, °C	Hall mobility, cm^2/V sec	Resistivity, ohm-cm	Carrier concentration, l/cm^3
$(1\bar{1}02)$ Sapphire	1050	1040	1.2	$5.5 \cdot 10^{15}$
$(1\bar{1}02)$ Sapphire	1125	1200	1.5	$3.5 \cdot 10^{15}$
$(1\bar{1}02)$ Sapphire	1200	360	0.3	$6 \cdot 10^{16}$
(100) Spinel	1200	730	0.7	$1.3 \cdot 10^{16}$
(111) Spinel	1125	250	0.16	$1.4 \cdot 10^{17}$
(111) Spinel	1200	870	0.8	$9 \cdot 10^{15}$

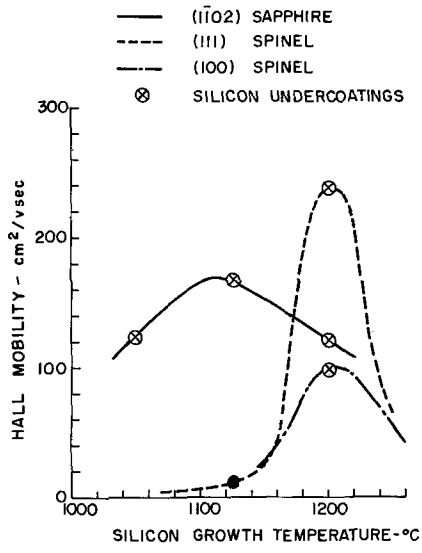

Fig. 4. Hall mobility of 2 μm thick silicon-on-sapphire and silicon-on-spinel films as a function of orientation and growth temperature. Points marked were chosen for growth of the silicon undercoatings. Curves taken from ref. (14) and (18).

the carrier concentration and Hall mobility were reasonably well correlated with the mobility of the thicker silicon films grown on the insulators.

For example, of the three films grown on silicon-on-$(1\bar{1}02)$ sapphire, the highest Hall mobility and the lowest carrier concentration were measured on the film grown on silicon grown at 1125°C. This temperature is relatively close to the maximum in the mobility *vs.* growth temperature curve for thicker silicon-on-$(1\bar{1}02)$ sapphire. The film grown on the silicon grown at 1050°C had a higher carrier concentration than the film grown on the silicon grown at 1125°C, which would argue against a doping mechanism based on autodoping of the films by aluminum. These same general comments apply to the three films grown on silicon-on-spinel where the highest mobility and lowest carrier concentration were measured in the film grown on the silicon grown on (111) spinel at 1200°C.

Variation in mobility with doping density.—The variation in the Hall mobility of boron and arsenic doped films was measured as a function of carrier concentration in the range between $10^{15}/cm^3$ to $10^{19}/cm^3$. The dopant was added to the gas stream as B_2H_6 or AsH_3 during growth. The Hall mobilities of the p-type films are compared with mobilities reported for bulk germanium (20) in Fig. 5. The films were grown on silicon grown on $(1\bar{1}02)$ sapphire at temperatures between 1050° and 1100°C. At higher carrier concentrations the mobility of both the films and bulk germanium dropped due to ionized impurity scattering. At the lower concentrations, the mobility rose and was

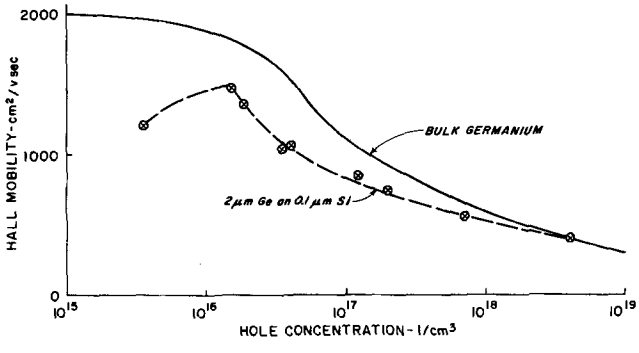

Fig. 5. Hall mobility of p-type germanium films as a function of carrier concentration.

about 60% of bulk values for films with carrier concentrations of the order of 10^{16}-10^{17}/cm^3. The dominant scattering mechanism in these films, as determined from Hall data taken as a function of temperature, was phonon scattering and is described in detail in another paper (12). The film doped $3.5 \cdot 10^{15}$/cm^3 was an undoped germanium layer and would be typical of the undoped films in which defects, acting as acceptors, dominated the electrical properties. In films grown such that the defect density was higher and defect scattering more important, the measured values of Hall mobility were considerably lower than those in Fig. 6. For example, the undoped film grown with carrier concentration of $6 \cdot 10^{16}$/cm^3 described in Table I had a mobility of 360 cm^2/V sec, while the boron doped films grown with similar carrier concentrations, but presumably lower defect densities, had mobilities of the order of 1000 cm^2/V sec.

An attempt was made to grow boron doped films, with a constant boron concentration, on silicon-on-sapphire undercoatings grown at various growth temperatures. The measured values of Hall mobilities of 2 μm thick germanium films on silicon-on-(1$\bar{1}$02) sapphire, doped 10^{16}/cm^3 $\pm$ 30% as a function of growth temperature of the silicon undercoating are shown in Fig. 6. The range in the doping density of the films represents the degree of reproducibility of the present growth system at what is presently considered low doping levels. Although the Hall mobility of these films varied with the silicon growth temperature, the relatively low values often obtained with undoped films were not obtained. In fact, the highest p-type mobilities have consistently been obtained on films containing a small amount of boron doping.

When describing the measurements made on the n-type films as a function of doping density, two effects must be kept in mind. One is that the measured values of electron density represented the difference between the donor (As) density and the defect-caused acceptor density. The n-type films were thus compensated to varying degrees, and, at doping levels comparable to the defect density, low values of mobility may be measured. The second effect concerns the variation of defect density with film thickness. The defects acted as acceptors, and the defect density increased as the film thickness decreased (5, 12). Thus, the portion of the germanium near the silicon interface contained both a higher defect density and a higher acceptor density. This effect, of course, was present in the p-type films. In the n-type films this compensation-thickness variation implied that the films were highly nonuniform in electrical properties as a function of thickness, and the measured values of

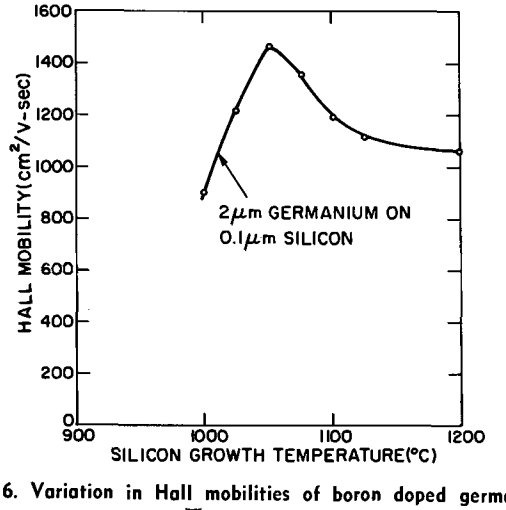

Fig. 6. Variation in Hall mobilities of boron doped germanium films grown on silicon-on-(1$\bar{1}$02) sapphire. Mobilities were measured on films grown on silicon grown at different temperatures.

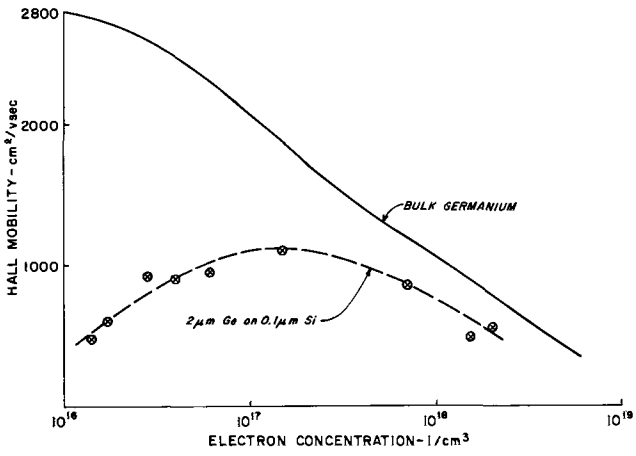

Fig. 7. Hall mobility of n-type germanium films as a function of carrier concentration.

Hall mobility *vs.* carrier concentration shown in Fig. 7 should be taken as indicating an average over the film thickness. The mobility of the outermost layer was higher than the material near the silicon-germanium interface, and on the most lightly doped wafers the germanium near the silicon-germanium interface was over-compensated with defect-acceptors and was p-type (12).

From the variation in Hall mobility with electron concentration as plotted in Fig. 7, it is seen that at high electron concentrations, the mobility paralleled the bulk values (21) where mobilities of 60% bulk mobility have been observed. As the carrier concentration was reduced to the low 10^{17}/cm^3 range, the defect-acceptor compensation became important and dominated the Hall data to concentrations of the order of 10^{16}/cm^3. No 2 μm n-type films have been grown with carrier concentrations lower than 10^{16}/cm^3, which represents the present limits due to the defect-acceptor density.

Absorption coefficient measurements.—The absorption coefficient of several 2 μm thick germanium films was measured in the energy range from 0.5 to 1.2 ev. Two films grown on thin silicon layers with mobilities in excess of 1000 cm^2/V sec and one film grown directly on sapphire with a mobility of 200 cm^2/V sec were used. All three films had smooth surfaces with no large surface structure visible. The absorption coefficient *vs.* energy is plotted in Fig. 8 for these three films. The two films grown on silicon had both lower

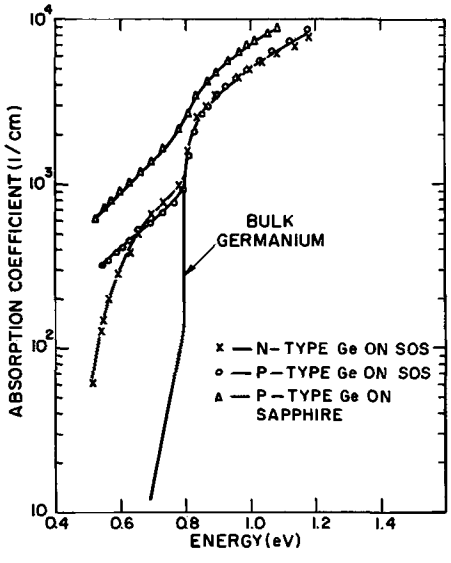

Fig. 8. Absorption coefficient of germanium films with and without the silicon undercoating.

values of absorption coefficient and showed a sharp increase in absorption coefficient at 0.8 ev. The film grown directly on the sapphire had higher values of absorption and only a small increase in absorption coefficient at 0.8 ev. In bulk Ge the increase in absorption coefficient at 0.8 ev has been attributed to excitation of the direct transition to a minimum in the conduction band at $\kappa = [000]$ (22). The absorption coefficients measured on the germanium films grown on silicon-on-sapphire were considerably lower than values reported for germanium directly deposited on sapphire (23). It should be noted that both the thinness of the silicon undercoating and the larger band gap of silicon effectively eliminated the silicon from interfering with these optical measurements.

Discussion and Conclusions

The usefulness of using a thin silicon undercoating to bond germanium films to an insulator has been demonstrated by comparing the electrical and optical properties of these films with films grown directly on the insulator. The silicon undercoating appears to act as a bonding agent to firmly attach the germanium to the sapphire. Even though the silicon undercoating was far from crystallographically perfect, it was sufficiently well structured to allow the high mobility germanium films to be grown using the hydride system.

The effects of the growth parameters on the electrical characteristics of the film were summarized by measuring the film properties grown on various orientations of sapphire and spinel and by varying both the germanium and silicon growth temperatures. The electrical properties of the germanium films depended heavily on the silicon film quality, and it appears as if the highest mobility germanium films were grown on the silicon grown near the optimum growth temperature for that particular substrate and substrate orientation. This makes both (111) spinel and $(1\bar{1}02)$ sapphire attractive for use as a substrate provided the differences in the silicon mobility-growth temperature curves for these two materials are known.

The maximum in the Hall mobility-germanium growth temperature curve shown in Fig. 2 did not occur at the same growth temperature as the minimum in the hole concentration-growth temperature curve shown in Fig. 3. The highest mobility p-type films grown with either no added impurities or with boron added to the films occurred at carrier concentrations of about $1\text{-}2 \cdot 10^{16}/cm^3$. If the defect-acceptor had an activation energy of about 0.15 ev, the Fermi level would lie below this energy in the films doped $2 \cdot 10^{16}/cm^3$, and the acceptor would be neutral, while in the films doped $3 \cdot 10^{15}/cm^3$, the Fermi level would lie above the acceptor energy, and the defect-acceptor would be ionized (24). The larger scattering center associated with the charged center would be expected to result in lower mobilities. While this agreement is highly speculative it would explain the apparent discrepancy in the data shown in Fig. 2 and 3. The assignment of an activation energy for the defect acceptor of 0.15 ev is in reasonable agreement with the multiple shallow levels found in bulk germanium (25).

The effects of the silicon undercoat on the measurement of the electrical properties of the germanium has been neglected even though these silicon layers were doped in the 10^{15}-$10^{16}/cm^3$ range and had mobilities as high as 60-100 cm^2/V sec. Over the range of doping densities and mobilities being considered here, the effects of this silicon underlayer on the measured electrical characteristics of the germanium were certainly negligible. The thin silicon layer was shunted by a thicker layer of germanium which had a higher mobility than the silicon. There was some interdiffusion of the silicon and germanium but this interdiffused region was only of the order of 0.06 μm. The doping density of several silicon undercoatings was measured after the germanium films had been removed and no significant changes in thickness or doping density could be observed when these layers were compared with some test films of thin silicon. Thus, it would also appear that the aluminum present in the thin silicon undercoating was not appreciably doping the germanium film, which would agree with calculations based on the known diffusion constant of Al in Si[26] and Ge[27] at 800°-900°C.

The Hall mobility-carrier concentration data presented in Fig. 7 show the effect of the defect-acceptor on compensating the lightly doped n-type germanium films. The compensation became more significant as the carrier concentration dropped and it was impossible to grow 2 μm thick n-type films with carrier concentrations below $10^{16}/cm^3$. If the defect-acceptor concentration can be used as a measure of the film quality, then the p-type, undoped films reported here have both lower acceptor concentration and higher mobility than have been reported on other similar thickness germanium films. The mobilities and carrier concentrations measured on the n-type films also attest to the relatively high quality of these films grown on the thin silicon undercoating.

The compatibility of the silane-germane system has been used to grow silicon-germanium alloys with composition that could be varied from 30 to 100% Si. These alloys were 1-2 μm thick films, were single crystal, and had measured values of Hall mobilities of the order of 100-150 cm^2/V sec.

In passing, it should be noted that oxygen in the reactor, either in form of a leak or in the form of an oxide on the silicon underlayer, led to agglomeration of the germanium films. The problems associated with growing germanium in the presence of minute traces of oxygen have been discussed recently (28).

Acknowledgments

The author is extremely indebted to C. W. Mueller for many enlightening discussions and to R. O. Wance and J. Corboy for assistance in performance of the electrical measurements.

Manuscript submitted March 21, 1969; revised manuscript received Aug. 29, 1969. This was Paper 129 presented at the New York Meeting, May 4-9, 1969.

Any discussion of this paper will appear in a Discussion Section to be published in the December 1970 JOURNAL.

REFERENCES

1. B. W. Bicknell, J. M. Charig, B. A. Joyce, and D. J. Stirland, *Phil. Mag.*, **9**, 965 (1964); H. M. Manasevit and W. I. Simpson, *J. Appl. Phys.*, **35**, 1349 (1964); C. W. Mueller and P. H. Robinson, *Proc. IEEE*, **52**, 1487 (1964).
2. V. H. Seiter and Ch. Zaminer, *Z. Agnew, Physik.*, **20**, 158 (1965); H. M. Manasevit and D. H. Forbes, *J. Appl. Phys.*, **37**, 734 (1966); H. Schlotterer and Ch. Zaminer, *Phys. Stat. Sol.*, **15**, 399 (1966); P. H. Robinson and D. J. Dumin, *This Journal*, **115**, 75 (1968).
3. R. F. Tramposch, *Appl. Phys. Letters*, **9**, 83 (1966).
4. D. J. Dumin, *This Journal*, **114**, 749 (1967).
5. B. W. Sloope and C. O. Tiller, *J. Appl. Phys.*, **38**, 140 (1967).
6. H. M. Manasevit, *Appl. Phys. Letters*, **12**, 156 (1968).
7. M. C. McKinnon and B. A. MacIver, *J. Appl. Phys.*, **38**, 4924 (1967).
8. J. E. Davey, *Appl. Phys. Letters*, **8**, 164 (1966).
9. H. Schlotterer and Ch. Zaminer, *Phys. Status Solids*, **15**, 399 (1966).
10. B. W. Sloope and C. O. Tiller, *J. Appl. Phys.*, **37**, 887 (1966).
11. D. J. Dumin, *Bull. Am. Phys. Soc.*, **14**, 394 (1969). To be published in *Solid-State Electron.*
12. D. J. Dumin, 1969 International Conference on Thin Films, Boston, April 28-May 2, 1969, to be published in J. Vacuum Science and Technology.
13. R. L. Zanowick, *This Journal*, **114**, 146C, (1967).
14. D. J. Dumin, *J. Appl. Phys.*, **38**, 1909, (1967); D. J. Dumin, *ibid.*, **36**, 2700 (1965).
15. D. J. Dumin, *Rev. Sci. Instru.*, **38**, 1107 (1967).
16. D. J. Dumin, *J. Appl. Phys.*, **36**, 2700 (1965).

17. B. Ya. Pines and I. P. Grebennik, *Soviet Physics-Crystallography*, **8**, 11 (1963).
18. P. H. Robinson and D. J. Dumin, *This Journal*, **115**, 75 (1968).
19. Data shown in Fig. 5 was taken from ref. (14) and (18).
20. F. A. Trombore and A. A. Tartaglia, *J. Appl. Phys.*, **29**, 1511 (1958); O. A. Goligova, B. Ya. Moizhes, and L. S. Stil'bans, *Soviet Phys.-Solid State*, **3**, 2259 (1962).
21. P. P. Debye and E. M. Conwell, *Phys. Rev.*, **93**, 693 (1954); R. G. Zhurkin, U. S. Zemskov, and K. V. Yurkina, *Soviet Phys.-Solid State*, **3**, 2545 (1962).
22. R. Braunstein, A. R. Moore, and F. Herman, *Phys. Rev.*, **109**, 695 (1958).
23. J. Wales, G. J. Lovitt, and R. A. Hill, *Thin Solid Films*, **1**, 137 (1967).
24. E. Spenke, "Electronic Semiconductors," pp. 310-312, McGraw-Hill Book Co., New York (1958).
25. L. F. Konorova, *Soviet Phys.-Solid State*, **10**, 2233 (1969).
26. R. C. Miller and A. Savage, *J. Appl. Phys.*, **27**, 1430 (1956).
27. B. I. Boltaks, V. P. Gragchak, and T. D. Dzhafarov, *Soviet Phys.-Solid State*, **6**, 2542 (1965).
28. R. F. Adamsky, K. H. Behrndt, and W. T. Brogan, Paper presented at 1969 International Conference on Thin Films, Boston, April 28-May 2, 1969.

Some Recent Developments in Fused Glass Films on Semiconductor Devices

M. Dumesnil* and R. Hewitt

Fairchild Semiconductor Research and Development Laboratory, Palo Alto, California

ABSTRACT

An investigation of methods developed to fabricate and deposit glass films in the near-colloidal state and with a sodium content of less than 10 ppm is described. A brief review of the characteristics and charge effects in high lead glass films is given. Several examples of lead glasses and their application as films on aluminum metallized silicon devices for scratch protection, corrosion resistance, and in mesa isolated structures are presented.

The deposition of dielectric films on metallized silicon devices and microcircuits is primarily directed at the formation of a secondary dielectric layer for crossover or two-layer metal interconnection, mechanical protection of the metal conductor lines, and device stability in nonhermetic packaging. Since aluminum is commonly used as the conductor metal, this puts an upper limit on the secondary dielectric application temperature (577°C Al-Si eutectic). Three low-temperature dielectric deposition techniques are available: glass sedimentation, rf sputtering, and vapor deposition. In contrast to the last two methods, which can produce the equivalent of high-temperature softening point glasses on relatively low-temperature substrates, glass sedimentation requires glass materials of low-temperature softening point. Sedimentation has the advantage of rapid film formation, greater thickness (1.5-6μ or more), simple deposition equipment, and the capability of bonding face-to-face diffused, metallized silicon wafers in the construction of mesa isolated devices.

The recent development of a convenient method of sodium analysis at low levels by flame spectrophotometry has simplified the analysis and control of sodium in materials associated with the processing of semiconductor devices. It has also made possible the evolution of techniques for the processing of substantially low sodium glass. Very good agreement is obtained between sodium content and the drift indicated by MOS C-V analysis.

After a brief review of the physical characteristics and charge effects of lead glasses applicable by sedimentation and low temperature fusion, this paper describes an investigation of methods to fabricate glass in the colloidal state at a sodium level less than 10 ppm. Several examples of lead glass films and their application for silicon device metal scratch protection, corrosion resistance, and in mesa isolated structures are presented.

* Electrochemical Society Active Member.

General Properties of Lead Glass Films

Physical properties.—Sedimented glass is the earliest type of secondary insulating films applied on transistors and diodes. The application of sedimented glass films on silicon devices was first reported by Perri *et al.* (1961) (1), Langdon *et al.* (2), Davis *et al.* (3), and Kerr (4). Pliskin and Conrad (5) showed the importance of the solvent system used in the deposition technique. The first major commercial application of this method is on the silicon diodes and transistors incorporated in IBM's system 360.

In comparison with alternative dielectric deposition methods which utilize either vacuum or a gas phase, sedimentation involves a finely subdivided solid (a glass) set in position by its ability to flow under application of heat. After lowering its viscosity to a point where the solid powder is converted into a continuous transparent film, the layer returns on cooling from its soft state to the brittle, hard characteristic of glass. Glass films of excellent clarity and uniformity can be obtained by sedimentation. The technique involves placing a wafer at the bottom of a centrifuge cup and filling the cup with a measured amount of glass suspension. Centrifugation for a few minutes at about 2000g deposits the glass on the wafer as a fairly adherent layer. A drying and firing step transforms the layer to a glossy, clear film. The two decisive factors resulting in smooth, defect-free films are the glass particle size and the properties of the organic solvents. The smaller the glass particle size, the better. A combination of solvents with widely different dielectric constants but similar viscosity and drying rate is necessary to obtain consistently uniform glass layers (5). The technique is incorporated in the process outline shown in Fig. 1. Glass-coated planar devices are masked and etched to expose the metal contacts. Devices scheduled to be mounted face down are then covered with a metal mask through which a 1-2 mil thick aluminum layer is deposited to form the required metal pads for inverted bonding.

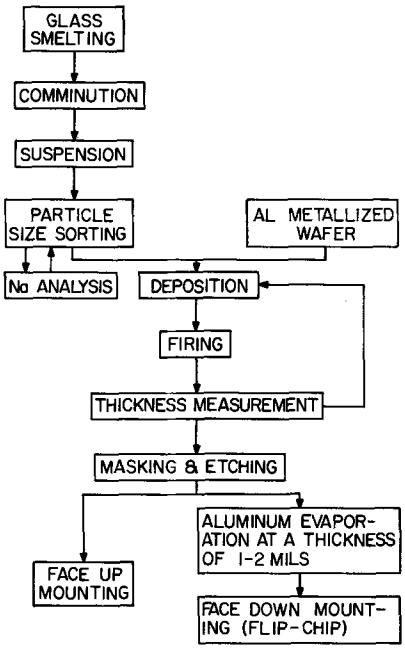

Fig. 1. Fused glass film process outline

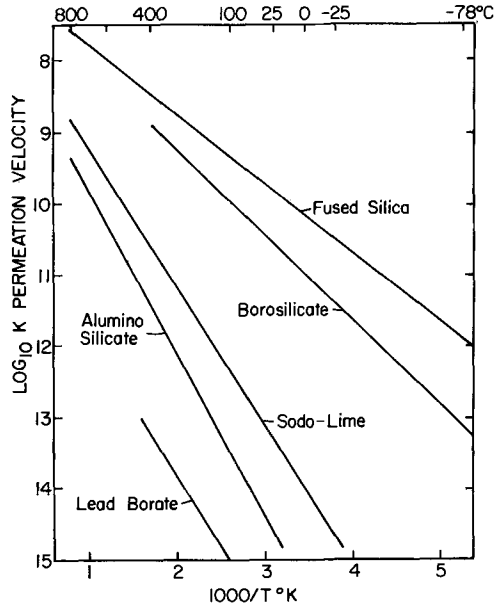

Fig. 2. Helium permeation rates as a function of glass composition [F. J. Norton, *J. Appl. Phys, 28,* 34 (1957)].

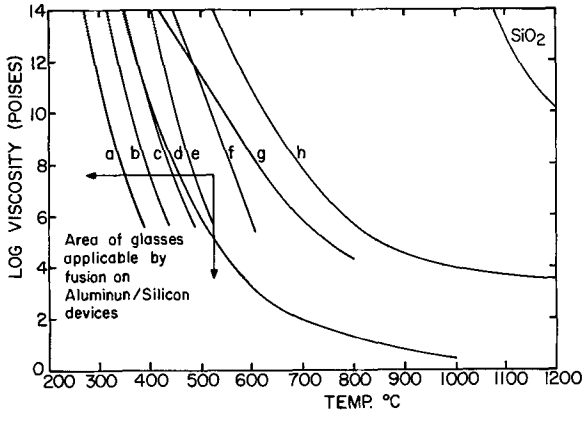

Fig. 3. Relationship between temperature and viscosity of lead glasses, ref. (7) and (8).

The application of a glass film on an oxidized silicon wafer without undesirable cracks in the glass which would impair the effectiveness of the glass film as a hermetic seal requires the selection of a glass with a thermal expansion closely matching silicon to minimize strain. The presence of a layer of SiO_2 between the glass and silicon improves the situation since a graded seal is formed at the silica-glass interface by the solution of the glass into silica to a depth averaging 400-800Å, depending on the time and temperature of fusion. Therefore, the thinner the glass film, the greater the permissible mismatch in thermal expansion. It is possible to apply glass films with a thermal expansion as high as 100 x 10^{-7} 1/°C if the thickness of the glass remains no higher than 1.5μ. Tests with low expansion but high melting glasses demonstrate that mechanically stable 5-15μ thick films can be applied on silicon with glasses having an expansion α no greater than 45 x 10^{-7} 1/°C.

Interest in lead glasses stems from the well-known low gas permeability (Fig. 2) and low alkali diffusivity through high lead glasses which are attributable not only to the large size of the lead cation, but also to the ability of lead to polarize the surrounding oxygen ions and become part of the network. Although lead is not a glass former, PbO and SiO_2 become compatible at high temperature. Both Si^{4+} and Pb^{2+} ions can form stable symmetrical polyhedra due to the polarizability of the Pb^{2+} and O^{2-} ions with silicon to form the normal regular SiO_4 tetrahedron, each oxygen ion being linked to three Pb^{2+} ions and one Si^{4+} ion. This structural picture shows good agreement with the electron diffraction patterns of high lead silicate glasses. The lack of visible absorption of lead glasses suggests that the PbO_6 groups become fairly regular octahedra on cooling the melt. Glasses in the lead corner of the lead borosilicate system possess a uniquely combined balance of low softening temperature, high electrical resistivity, low power factor, and fair moisture resistance. Figure 3 compares the temperature dependence of the viscosity η, and Table I compares the corresponding α, of some typical high lead glasses with two commercial glasses and with fused silica. The significant difference in high lead glasses is the very steep slope of $\Delta\eta/\Delta T$, advantageous in reaching rapidly the working range necessary to obtain a smooth film from the compacted glass powder. It is worthwhile to note that for application on aluminum metallized devices, the glass viscosity curve must intersect the enclosed area in the lower left-hand corner of Fig. 3.

The parent ternary phase diagram, shown in Fig. 4, is useful in determining the liquid temperature which corresponds to the minimum glass smelting temperature as a function of composition. This diagram, however, representing by definition a system in thermodynamic equilibrium, does not tell us whether a glass will be formed by cooling a binary or ternary melt and what properties the glass will assume. If a glass is formed, its softening point will roughly follow the trend of the liquidus-solidus points shown in the diagram. The information the phase diagram will predict exactly is the constitution of the crystalline phases

Table I. Composition in weight per cent and thermal expansion of glasses in Fig. 3

	PbO	B_2O_3	Al_2O_3	SiO_2	$\alpha \times 10^7$ 1/°C (25°-300°C)
a	88	12			120
b	85	7.5		7.5	117
c	85			15	108
d	75	11	11	3	84
e	76	24			93
f	72			28	74
g	Corning glass #0120				94
h	Corning glass #0800				84
i	Fused SiO_2			100	5

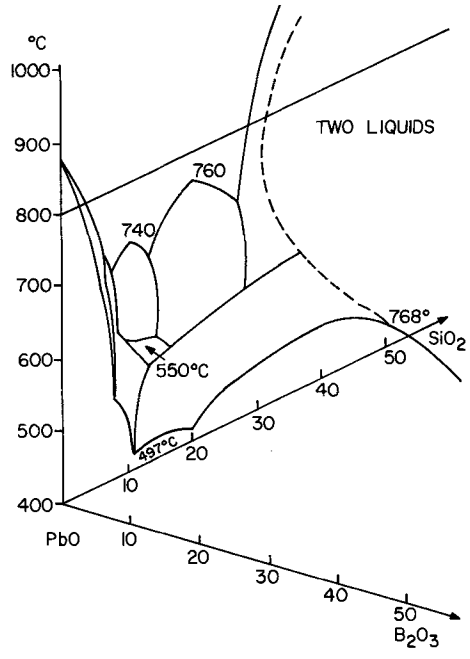

Fig. 4. High lead corner of the ternary phase diagram $PbO-B_2O_3-SiO_2$, ref. (6).

appearing in the glass on partial or complete devitrification, *i.e.*, recrystallization.

The $PbO-B_2O_3-SiO_2$ ternary contains a most extensive glass forming region. A plot of the softening points as a function of composition produces the envelope shown in Fig. 5. Glasses with a softening point lower than 560°C are limited to the high lead and high boron corners. The excessive water solubility of the high boron oxide glasses rules them out of consideration. The thermal expansion coefficient α of the glasses in the lead borosilicate system is plotted in Fig. 6 and 7. Starting from the binary lead oxide-silica tie line, both α and η decrease initially on addition of boron oxide, but beyond a certain amount of boron α increases (6,7). The lowest points in the valley represent the region of maximum proportion of boron with four oxygen instead of three as nearest neighbors. The presence of up to 10% by weight alumina in lead glasses decreases

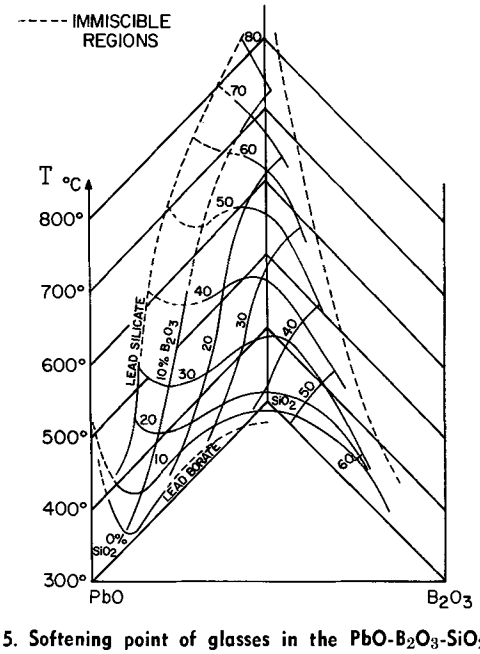

Fig. 5. Softening point of glasses in the $PbO-B_2O_3-SiO_2$ system [R. F. Geller, E. N. Bunting, A. S. Creamer, *J. Research NBS, 20,* 57 (1938) R.P. 1064].

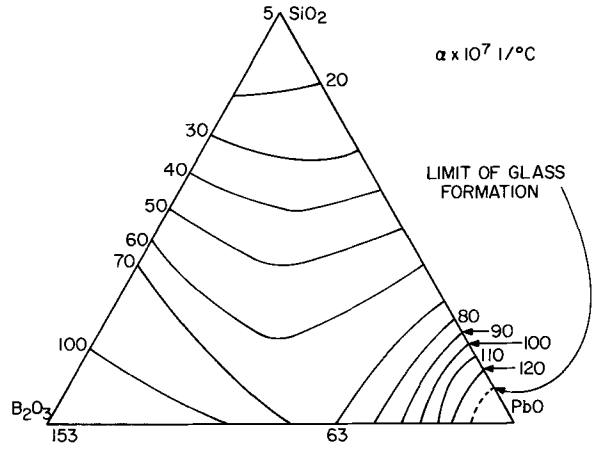

Fig. 6. Linear thermal expansion of glasses in the $PbO-B_2O_3-SiO_2$ system [R. F. Geller, E. N. Bunting, A. S. Creamer, *J. Research NBS, 20,* 57 (1938) R.P. 1064].

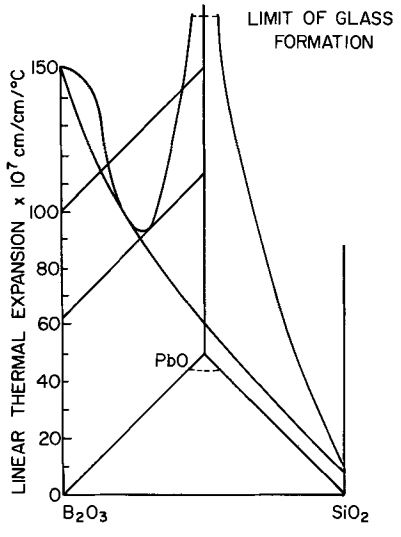

Fig. 7. Three-dimensional plot of the linear thermal expansion of glasses in Fig. 6.

α without unduly increasing the softening point or decreasing the viscosity/temperature slope (8,9). Further lowering of α is achievable by the partial replacement of lead oxide by zinc oxide. The properties of four typical lead glasses of increasing compositional complexity are listed in Table II.

The average strain produced in silicon by lead glass films with different linear thermal expansions was derived from the measured radius of curvature of silicon strips parallel to [112] covered with a layer of thermal oxide and a fused glass layer on one side only. As expected, a compressive stress in silicon was found as evidenced by the negative radius in the six samples in Table III. These compressive stresses in silicon can be compared with the 2950 kg/cm² tensile stress caused by the thermal oxide layer on silicon. Although the maximum thickness of glass which can be formed on oxidized silicon without cracks is inversely proportional to the glass thermal expansion, the induced stress in silicon is not. This seeming contradiction may be resolved by considering the relative amount of thermal oxide dissolved by each glass (Fig. 8) (10).

Space-charge polarization in lead glass films.—The capacitance-voltage analysis of metal-insulator-semiconductor (MIS) capacitors is a sensitive detection method to study charge transport and polarization effects in insulators. Three types of effects are distinguishable: drift of mobile cations within the dielectric, dipole-type polarization, and charge transfer between the dielectric and the silicon electrode. The in-

Table II. Physical properties of selected low melting lead glasses

	A	B	C	D
Refractive index	1.91	1.85	1.78	1.76
Dielectric constant	16	15.5	15	14
Soft. point ($10^{7.6}$ poises)	440°	490°	530°	530°
Resistivity @ 25°C in Ωcm	10^{14}	10^{14}	10^{14}	10^{15}
Specific gravity	5.3	5.2	4.4	4.1
Thermal expansion (20°-400°C) × 10^7 1/°C	79	68.3	58	47.5
Composition	Lead borosilicate	Lead aluminoborosilicate		Lead zinc aluminoborosilicate
Maximum applicable thickness on oxidized Si wafer without craze line on etching	1.5μ	2.2μ	3.3μ	4.2μ
Etchability		Dilute HNO_3		

Table III. Average strain produced in oxidized silicon by lead glasses

Glass No.	α*	Glass thickness, μ	Initial oxide thickness, μ	Final oxide thickness, μ	−R, cm	Fusion temp, °C	Average, kg/cm²
B	68.3	1.7	0.5	0.4	21,000	550	21.5
		2.0	0.5	0.4	8,400	550	51.2
C	58.0	2.17	0.5	0.47	1,525	550	282
		3.0	0.5	0.47	900	550	478
D	47.5	2.3	0.5	0.47	1,665	550	259
		4.1	0.5	0.47	398	550	1080
SiO_2 (thermal)	5	1.0	—	—	—	—	−2950

* (20°-400°C) × 10^7 1/°C.

sulator layer may be either a single or multilayer dielectric.

Kerr (11) first reported the use of the MIS method to study polarization in several glasses in the lead-aluminoborosilicate and zinc-aluminoborosilicate systems deposited on bare silicon by sedimentation and fusion. The initial surface charge levels were quite low ($N_{FB} < 2.7 \times 10^{11}/cm^2$), indicating that this technique of applying glass causes a very low density of surface states or charge density in the insulator. For each glass ΔV_{FB} was approximately symmetric under positive and negative bias with no tendency for ΔV_{FB} to saturate. All the glasses had 10^{19} sodium at./cm³ or more; that is, greater than 100 ppm Na. Snow and Dumesnil (12) provided a quantitative theoretical model for the case of a double-layer dielectric and an experimental application to a sedimented glass layer containing 75% PbO, 12% SiO_2, 10% B_2O_3, and 3% TiO_2 by weight (glass A) on thermally oxidized silicon. Ion migration in deposited glass films can be studied more easily and more quantitatively by this method. As expected, it was found that the C-V characteristic shifted in the positive direction after application of a negative gate bias and vice versa. The amount of the shift ΔV increased with the length of time the bias was applied, but eventually approached a saturation value ΔV_{sat}. The rate at which ΔV approached its saturation value was used to obtain the ionic mobility or the diffusion coefficient. The results obtained for the 75% lead glass were compared with direct diffusion data for lead ions in a glass of similar composition (75% PbO-25% SiO_2). The excellent agreement indicated that lead is the mobile ion.

The time dependence of the long-term drift under positive bias which is shown in Fig. 9 does correlate with sodium content, and the following mechanism was proposed. After applying a positive bias, the lead ions in the glass migrate rapidly toward the glass-SiO_2 interface until the field in the glass is reduced to zero. The lead ions appear to be immobile in the SiO_2 and hence, if there were no alkali ions present, the drift would saturate as in the negative bias case. The situation we actually have, however, is a uniform concentration of Na^+ ions in the field-free glass layer and zero concentration of Na^+ ions in the high-field SiO_2 layer. Ions in the glass near the oxide interface will tend to diffuse in the concentration gradient. On reaching the glass-oxide interface, they will enter the high-field region and will be swept across the oxide by the field to

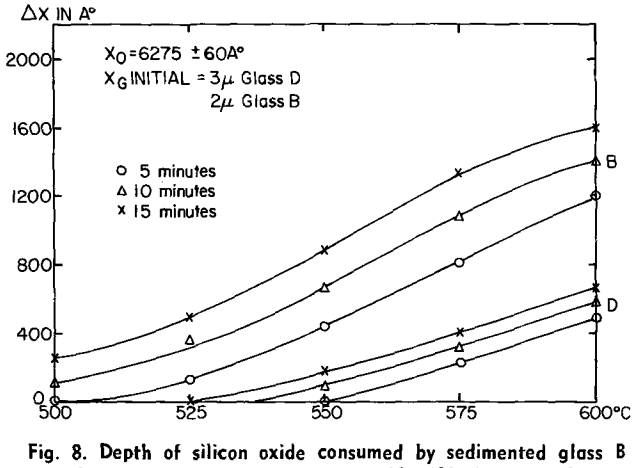

Fig. 8. Depth of silicon oxide consumed by sedimented glass B and D films in the temperature range 500°-600°C for 5, 10, and 15 min.

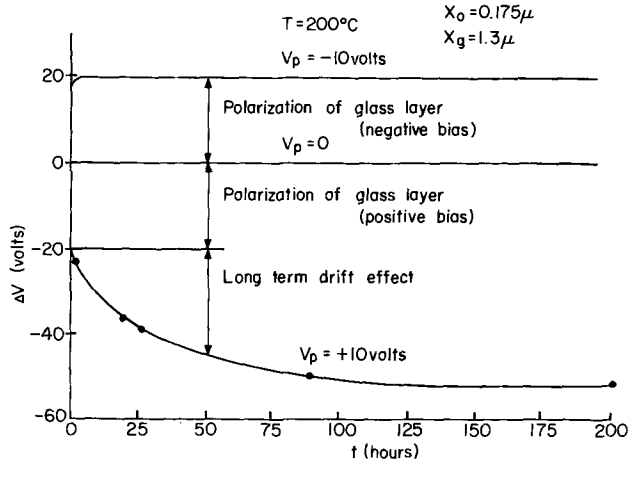

Fig. 9. Shift of the C-V characteristic with time under positive, negative, and zero bias at 200°C. Note that there is a rapid initial polarization which is symmetrical under positive and negative bias, but only under positive bias is there an additional long-term drift effect.

appear at the oxide-silicon interface. The situation is identical to the boundary-layer model developed in (13), and the solution for the excess charge induced in the silicon by the ions accumulated at the oxide-silicon interface is

$$Q_s'(t) = 2qN_0(Dt/\pi)^{1/2}$$

for $t << 4x_g^2/\pi^2D$. The data in Fig. 9 show approximately this square root of time dependence. The data can be replotted as Q_s' *vs.* $t^{1/2}$ and the slope of such a plot used to calculate D from the above equation. N_0 is the initial sodium concentration in the glass and was 3×10^{18} cm^{-3} for this sample. In this manner one obtains for the diffusion coefficient of sodium in the glass at 200°C a value of about 10^{-19} cm^2/sec at this temperature. Aside from this remarkably low diffusion coefficient, all aspects of the above model are in agreement with the experiments described earlier, including the fact that after a unit has been drifted under positive bias for many hours, it can be recovered and drifted again in only a few minutes. This shows that the slow step in the original drift was gettting the ions out of the glass, and that field transport in the SiO_2 layer is very fast, in agreement with previous work (13).

Sodium analysis and control.—Space-charge polarization studies add considerably to our understanding of the instability problems associated with early sedimented glass films. The diffusion coefficient of sodium being very low in high lead glass, this type of insulator should be an efficient barrier to external sodium. The internal sodium level in the glass layer must be, however, drastically reduced if long-term stability in silicon devices is to be achieved. A refined flame spectrophotometric method has been used to analyze and control the sodium content in glass at each processing step. The method has been described elsewhere (14). It utilizes a modified Beckman Model DU spectrophotometer, the instrument being carefully tuned to the sodium emission line with a sodium standard. The method is relatively inexpensive and simple to use, with a detection limit in water of 0.05 ppb sodium. Table IV lists the typical sodium content of commercial metal oxides used in glass preparation. The wide variations in alkali content of commercial chemicals require a careful choice of sources and an analysis of each new lot. Sodium analyses of a series of the same glass smelted in platinum indicated no increase in sodium at a level averaging 12-15 ppm. A comparison of these analyses with the expected calculated sodium content is shown in Table V. Glass comminution was investigated next. A substantial sodium level increase occurs during mechanical size reduction of glass by ball milling. Sodium contamination increases linearly with milling time, so an alternative comminution method was adapted for the production of high-purity glass powder. The resulting dry powder is ultrasonically mixed with an organic solvent and centrifuged at 1000g to precipitate all particles larger than 1μ. The supernatant liquid is calibrated in terms of height of suspension per micron of glass thickness. Analysis of this glass powder shows no measurable increase in sodium above the initial content of the metal oxides acting as glass components. To obtain some measure of possible alkali impurity contributed by this technique, two borate glasses were prepared and ground into a 1μ powder. Table VI demonstrates the effectiveness of the process at the 4 and 6 ppm sodium level.

Table IV. Sodium content of commercial metal oxides

Materials	Sodium content, ppm
Lead oxide PbO	None detected
Zinc oxide ZnO	<1
Aluminum oxide Al_2O_3	23
Anhydrous boron oxide B_2O_3	280
Boric acid H_3BO_4	20
Silicon dioxide SiO_2	18
Titanium dioxide TiO_2	300
Bismuth oxide Bi_2O_3	34
Niobium pentoxide Nb_2O_5	15
Antimony oxide Sb_2O_3	21
Vanadium pentoxide V_2O_5	48
Zinc fluoride ZnF_2	4

Table V. Sodium content of lead glass A

	Calculated Na content, ppm
75% by weight PbO	0
12% by weight SiO_2	18 ppm × 0.12 = 2.2
10% by weight B_2O_3	20 ppm × 0.10 = 2.0
3% by weight TiO_2	300 ppm × 0.03 = 9.0
	Total 13.2

Applications in Semiconductor Device Technology

Effects on device characteristics.—The space-charge polarization effect present in high lead content glass films limits their application to device areas not affected by this polarization or where the glass is above the metallization layer. To date over two million device hours, including operating life, high-temperature reverse bias, and 300°C storage, have been accumulated with type A, B, and D glassed small-geometry npn and pnp bipolar transistors in hermetic metal cans. The sodium content in these glasses was maintained at a value of less than 45 ppm. These lifetest studies extending to 4000 hr detected no surface parameter drift nor any unusual failure mode. The leakage current remained below 20 na at 50V base-collector reverse biased junction. However, an appreciable decrease in h_{FE} during the initial glassing operation is observable with sensitive low current h_{FE} devices. This h_{FE} drop was prevented by the addition of a thin silicon nitride layer at the oxide-glass interface. All glass-coated bipolar devices in which the sodium content of the glass layer was greater than 100 ppm invariably experienced a one to three order of magnitude increase in leakage current within a few hours of thermal stress.

Device scratch protection.—A 2μ layer of glasses type B, C, and D over the surface of a microcircuit is effective in eliminating practically all scratches and shorts in a dense aluminum intraconnection arising from the normal handling of a processed wafer during electrical sorting, scribing, dicing, optical inspection, and final packaging steps.

To measure the mechanical strength provided by sedimented glass films over etched aluminum films, localized mobile pressure was applied by means of a wedge-shaped diamond stylus moving at the rate of 1 in./min. The tip area being equal to 0.15 mm^2, a 10g stylus pressure is equal to a force of 7 kg/cm^2. The stylus pressure was increased by increments of 5g from 5 to 20g. Densely metallized silicon wafers were utilized, the aluminum thickness on the devices being equal to 1.4μ. The effect of the stylus was observed in two areas: between the metal lines to measure the indentation depth produced by the diamond point in the dielectric surface, and over the metal pattern. It was noted that an increasing pressure will eventually induce cracks localized at the aluminum edges followed, with further pressure, by collapse of the dielectric and entrainment of the metal over some distance.

The failure point was taken as the pressure required to smear aluminum metal from one line to the next in a dense pattern without concern for dielectric crack

Table VI. Analysis of two low sodium processed glasses

Sample	Sodium content, ppm
Lead zinc borate glass	6
Lead zinc borate glass powder	6
Lead borate glass	4
Lead borate glass powder	4

Table VII. Mechanical strength of dielectric films over an aluminum pattern on oxidized silicon

	Thickness in microns	Mechanical strength in grams over 1.4μ Al
Vapor deposited oxide	1	<5
RF sputtered silicon nitride	1	<5
RF sputtered SiO_2	1	<5
Multicomponent vapor deposited oxide	1.5	15
Sedimented glass B	1.5	15
Sedimented glass C	2	15-20
Sedimented glass D	3.5	>20

Note: 10g stylus pressure = 7 kg/cm².

formation. The mechanical strength required in a dielectric film to provide a notable yield improvement in manufacturing is of the order of 15g. A comparison between sedimented glass films and other dielectric films deposited at a temperature lower than 550°C is shown in Table VII. This table indicates that sufficient scratch resistance of a 1.4μ aluminum pattern is in general provided by dielectric films which can be formed 1.5μ thick or more.

Corrosion protection.—For effective surface protection of semiconductor devices, the glass film should have long-term stability to ambient attack, particularly moisture. The water stability and the effect of moisture on various glass films can in general be compared by physical examination, weight loss, thickness difference, and infrared spectroscopy. Weight loss and film thickness measurements are generally inadequate, except for highly stable glasses, since glass dissolution can be offset by water absorption. The relative compositional changes of some of the glass components can be determined with infrared spectroscopy by the sharpness and shifts of band positions. The presence of water and silanol groups can be detected by this method (15).

Surface attack of a lead glass film is easily detected visually by the appearance of pitting or colored fringes, accompanied by loss of gloss. A lead glass can be affected by a decrease in film thickness or by preferential leaching of the glass components to form a porous structure. Of the two modes of attack, preferential leaching is the most undesirable. In thicker films, it often increases the tensile stress in the glass to the point of initiating fracture lines. Boron is the element most susceptible to be selectively removed in a high lead glass. To prevent this effect the boron concentration in the glass formulation can be reduced or the network tightened by the addition of titania. TiO_2 even in small concentrations is quite effective in increasing the water and acid resistance of lead glasses, its specificity being related to its small size (0.64Å) and high coordination number (12).

Prolonged moisture exposure at elevated temperature was simulated by accelerated high-pressure steam treatment in a gold-plated pressure vessel. Exposure to 16 psi steam is equivalent to eight times the exposure at 95°/95% relative humidity. Practically all the high lead glasses are severely pitted when exposed to steam. The addition of a few per cent titania to the lead glasses maintains a bright, shiny surface on the glass even after exposure to 16 psi steam for 400 hr.

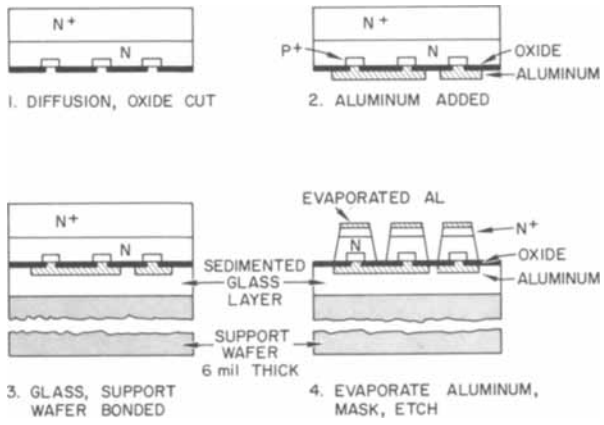

Fig. 10. Step-by-step processing of mesa isolated diode array

A second series of high-pressure steam treatments included the addition of cured epoxy resin powder to simulate the condition encountered by epoxy encapsulated devices exposed to moisture. Increased stress occurs when cured epoxy is added to the samples in a high pressure vessel. The comparative stability of various low-temperature dielectric films to high pressure steam is seen in Table VIII. Although titania-containing sedimented glass films withstand a long-term exposure to high pressure steam, only glass D resisted the presence of epoxy. Glass-coated devices packaged in epoxy resin survive a 72-hr high-pressure steam treatment, whereas non-surface-protected devices will fail within a few hours under similar conditions.

Sedimented glass in mesa isolated structures.—Mesa isolated integrated planar devices are fabricated commercially by sealing face down a diffused, metallized wafer with glass type D on a backing silicon wafer. The back of the active wafer is thinned to approximately 20μ and an isolation pattern etched in the silicon. On exposure of the bottom side of the original top thermal oxide the individual devices are in fact isolated, being connected only by the first metal pattern on the other side of the thermal oxide and now buried in the glass layer. At this point the metal pads are exposed by photoetching. Since the glass sealing step is performed at a temperature lower than 560°C standard, optimized pnp or npn devices are utilized. Similarly, the technique is applicable to the construction of diode arrays (Fig. 10), described elsewhere (16), and the combination of pnp's and npn's in one single structure (17). In the latter case, the metal pads of the substrate devices are exposed by photoetching together with the bottom side of the top pads (Fig. 11 and 12). A major advantage of mesa isolation when compared with p-n junction and most dielectric isolation processes is simplicity of design fabrication, fewer steps, and better electrical performance.

Conclusions

By suitable refinements glass comminution can be used to reproducibly fabricate glass in the near-colloidal state with a sodium content of less than 10 ppm. The lower sodium contamination limit provided by this method has not been determined but appears to be appreciably less than 1 ppm. The major source of contamination now arises from the commercially pur-

Table VIII. Corrosion resistance of dielectric films

		Steam treatment		Steam & Cured Epoxy	
	μ	16 hr/16 psi	16 hr/55 psi	16 hr/16 psi	16 hr/55 psi
Vapor deposited oxide	1	Interference fringes		Interference fringes	Some pinholes visible
RF sputtered silicon nitride	1	No attack	—	No surface attack but numerous cracks	
RF sputtered SiO_2	1	No attack	—	—	Excellent film
Sedimented glass B	2	No attack		Breakdown	Severe breakdown
Sedimented glass D	3.5	No attack		No attack	Good film, no attack

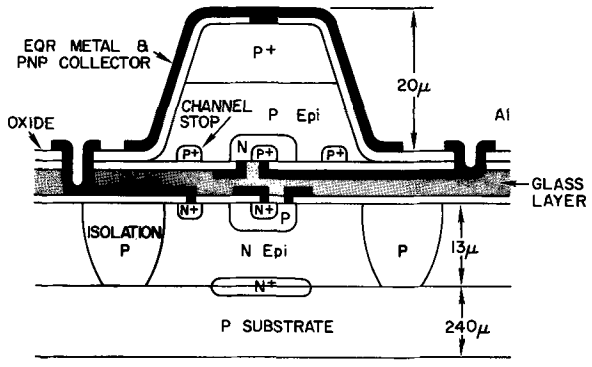

Fig. 11. Cross section of mesa isolated pnp on npn device

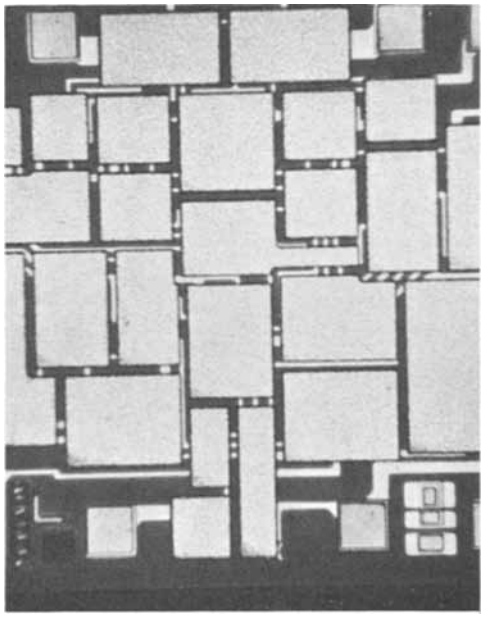

Fig. 12. Mesa isolated linear integrated circuit. The rectangular grey surfaces are the back side of the top devices.

chased metal oxides utilized in the synthesis of the lead glasses.

It was found that silicon planar bipolar devices remain electrically stable when covered with a fused lead glass film containing no more than 50 ppm sodium. The application of this type of film must be limited because of polarization and drift effects to device areas not affected by strong electrical fields.

Lead glass films are applicable for corrosion resistance and aluminum scratch protection and as a bonding layer in mesa isolated structures.

Acknowledgment

The authors wish to acknowledge the preliminary development on mesa isolation carried out by J. Schroeder and R. Rusert. B. Yurash and R. Ceynowa conducted the flame analyses reported in this paper and R. Erkson prepared most of the samples. The authors also wish to thank H. Sello, G. Moore, B. Deal, and E. Snow for their helpful advice and encouragement during the course of this work.

Manuscript submitted July 14, 1969; revised manuscript received Sept. 9, 1969. This was Paper 41 presented at the New York Meeting of the Society, May 4-9, 1969.

Any discussion of this paper will appear in a Discussion Section to be published in the December 1970 JOURNAL.

REFERENCES

1. J. A. Perri, H. S. Lehman, W. A. Pliskin, and J. Riseman, Recent News Paper presented at the Detroit Meeting of the Society, Oct. 1-5, 1961.
2. J. L. Langdon, W. E. Mutter, R. P. Pecoraro, and K. K. Schaegraf, Paper presented at the Electron Devices Meeting, Washington, D. C., Oct. 27, 1961.
3. E. M. Davis, W. E. Harding, and R. S. Schwartz, Paper presented at WESCON, San Francisco, Aug. 22, 1963.
4. D. R. Kerr, *Proc. IEEE*, **51**, 1142 (1963).
5. W. A. Pliskin and E. E. Conrad, *Electrochem. Technology*, **2**, 196 (1964).
6. R. F. Geller and E. N. Bunting, *J. Res. Natl. Bur. Std.*, **23**, 275 (1939).
7. J. Gallup and A. Dingwall, *Am. Cer. Soc. Bull.*, **36**, 47 (1957).
8. R. H. Dalton, *J. Amer. Ceram. Soc.*, **39**, 109 (1956).
9. H. M. Hoogendoorn *et al.*, U. S. Pat. No. 3,309,399, Feb. 7, 1967.
10. W. A. Pliskin, *This Journal*, **114**, 620 (1967).
11. D. R. Kerr, *IBM J. Res. Develop.*, **8**, 385 (1964).
12. E. H. Snow and M. E. Dumesnil, *J. Appl. Phys.*, **37**, 2123 (1966).
13. E. H. Snow, A. S. Grove, B. E. Deal, and C. T. Sah, *ibid.*, **36**, 1664 (1965).
14. B. Yurash and B. E. Deal, *This Journal*, **115**, 1191 (1968).
15. W. A. Pliskin, Paper presented at the American Ceramic Society Meeting, Washington, D. C., May 1966.
16. H. Claussen and R. Rusert, *Electronics*, **41**, 75 (1968).
17. D. Oberlin, Paper presented at the Electron Devices Meeting, Washington, D. C., Oct. 1968.

Flux Growth of Cubic CuCl Crystal Using a Small Thermal Gradient

Sidney G. Parker* and Jack E. Pinnell

Texas Instruments Incorporated, Dallas, Texas

ABSTRACT

Cubic CuCl crystals can be used to modulate light by application of an electric field. Because it is difficult to grow large, strain-free crystals from the melt, crystals have been grown by vapor transport and from molten salt or flux solutions. We have grown single crystals up to 25 x 15 x 7 mm from flux solutions with a small thermal gradient between the crystal growth region and the charge. Crystals were grown from KCl, $SrCl_2$, and $PbCl_2$ fluxes. Use of a KCl flux leads to cellular growth and bubble inclusions caused by constitutional supercooling and decomposition of CuCl. Similar inclusions and growth behavior were not noted for the other fluxes. The electro-optical properties of the CuCl crystals differed as a function of the growth media. The CuCl crystals also differ in their properties from those grown from the same fluxes using the Bridgeman technique with a larger thermal gradient. Good crystal growth is more likely to be obtained with a small thermal gradient, but poor mixing caused by lack of strong convection currents may influence growth.

Cubic CuCl is a material whose refractive index can be changed by application of an electric field. Therefore, CuCl has been used for modulation of light in the 0.5-10 μm range (1). Because the percentage of modulation depends on crystal length transversed by the light, large crystals are desired.

It is difficult to grow large, strain-free, cubic CuCl crystals from the melt because the material freezes with a hexagonal structure at 420°C and transforms to a cubic structure at 407°C. Vapor transport (2), flux growth (3, 4), and aqueous solution in gel (5) have been used to grow crystals below the transition temperature. CuCl forms eutectics (6) with numerous halides which can be used for flux growth. The Bridgeman technique has been applied to flux growth of CuCl, but we chose to use a small thermal gradient technique we had used successfully for the flux growth of cubic ZnS crystals (7).

Experimental

Figure 1 is a diagram of the crystal growth apparatus. Because the loaded growth tubes were pushed into the furnace at the desired operating temperature, these tubes were made of quartz to reduce thermal shock.

Reagent grade CuCl was further purified for these experiments by dissolving it in concentrated HCl solution and precipitating by dilution with H_2O. This was followed by a sublimation step that gave CuCl of the purity listed in Table I. The flux halides, KCl, RbCl, $SrCl_2$, $PbCl_2$, and $BaCl_2$, were reagent grade and were not further purified.

Phase diagrams were constructed from differential thermal analysis data for some of the systems which were not discussed in the literature. These diagrams, shown in Fig. 2, were necessary to establish the operating conditions for possible crystal growth. For crystal growth, 2-8 m/o (mole per cent) of flux was dissolved in the CuCl by heating to about 400°C, then the mixture was quickly quenched and placed in the growth tube to serve as the charge at the cooler end containing the heat sink. Additional CuCl was placed at the higher temperature end of the growth tube to serve as the main source of CuCl for crystal growth. The system was outgassed at 150°C and 10^{-3} Torr for 1 hr, then cooled to 25°C before it was sealed off at 10^{-5} Torr. The tubes were then pushed into furnaces which were at the desired operating temperature and had the proper thermal gradient between the crystal growth and charge regions. Growth continued for 2-4 weeks, after which the furnace was shut off and the tubes were cooled to 25°C over a 3-hr period.

* Electrochemical Society Active Member.

Table I. Impurities in CuCl used for crystal growth

Source of CuCl	Impurities, ppm (wt)* Mn	Pb	Mg	Si	Ni	Fe	Al	Ag
Reagent grade	3.0	6.7	52.8	39.9	66.7	50.4	6.0	60.1
Re-ppt. and sublimed	ND	ND	6.4	ND	ND	ND	ND	78.9

* Determined by emission spectrographic analysis.

Results and Discussion

Most work was done with KCl or $SrCl_2$ fluxes because they have wide temperature and compositional ranges from which CuCl crystals can be obtained. Because of a peritectic with about 4 m/o $BaCl_2$, the system $BaCl_2$-CuCl was not studied for CuCl crystal growth. RbCl and $PbCl_2$ were also investigated as fluxes.

A few unsuccessful attempts were made to grow on a CuCl seed crystal, but the seeds dissolved before growth conditions were established. Thus, crystal growth was limited to self-nucleation, which began in the coolest regions at the heat sink. The conditions for crystal growth are listed in Table II. A wide range of conditions was used for each flux, but the ones listed in Table II appeared to give the largest crystals. Generally, concentrations of flux greater than those listed have led to inclusions of flux in the CuCl crystals. Temperature gradients of up to 30°C were used, but caused the growth of many small crystals.

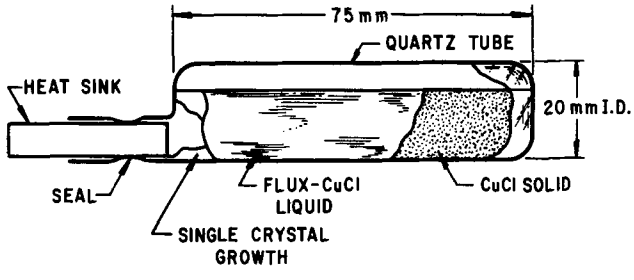

Fig. 1. Apparatus for flux growth of cubic CuCl

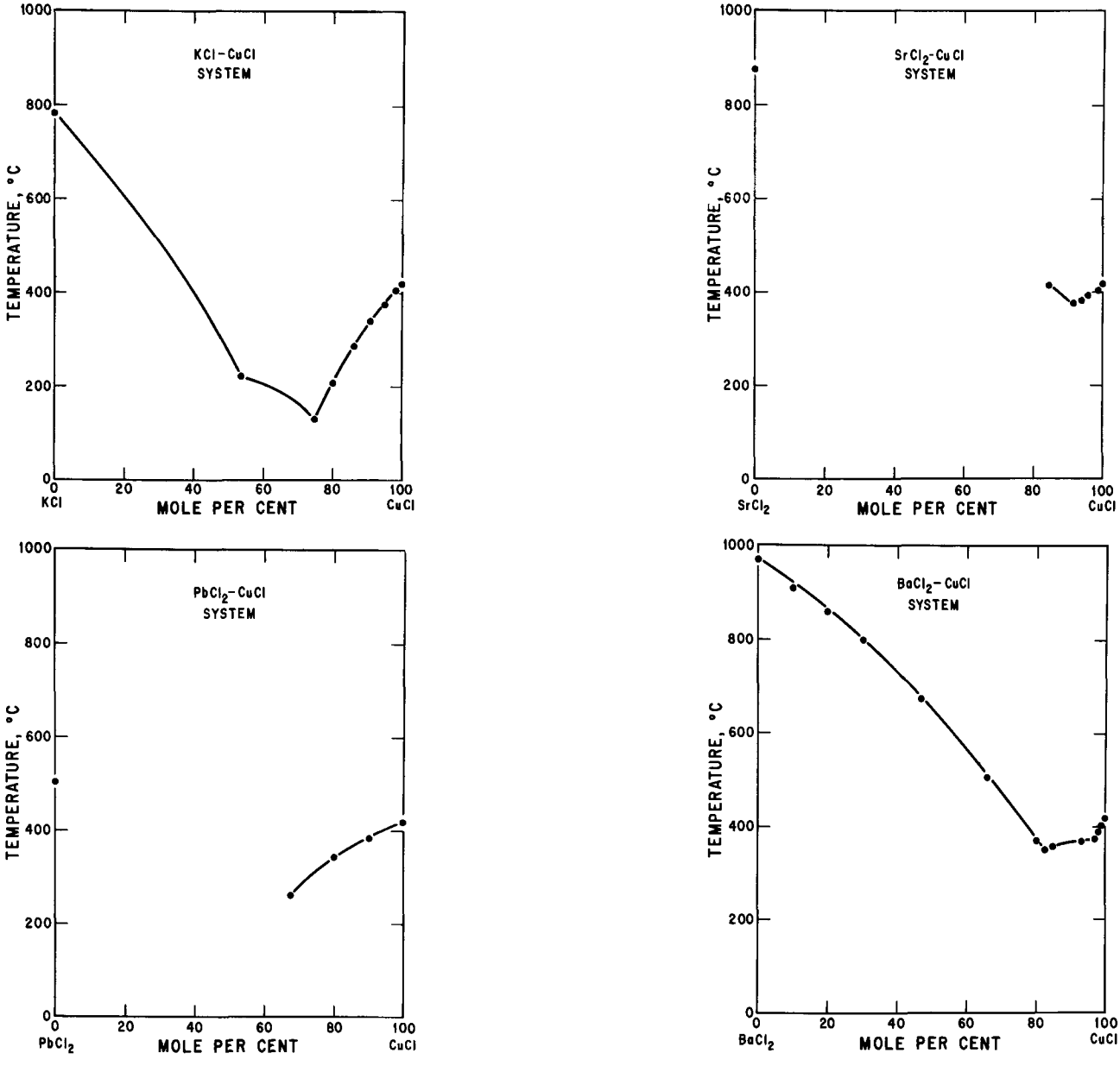

Fig. 2. Phase diagrams for (a) (top left) KCl-CuCl; (b) (top right) $SrCl_2$-CuCl; (c) (bottom left) $PbCl_2$-CuCl; (d) (bottom right) $BaCl_2$-CuCl.

CuCl crystals up to 25 x 15 x 7 mm in size were grown from all the fluxes except RbCl, which gave smaller crystals. The concentration of impurities in typical crystals grown from different fluxes is given in Table III. Crystals grown from KCl are rather pure, while those grown from $PbCl_2$ and $SrCl_2$ contain much flux. There seems to be little correlation between the amount of flux in the crystals and the resistivity. The amount of flux occluded in the crystals increased with decreasing operating temperatures.

As shown in Table IV, crystals grown from KCl usually had much greater optical transmission than those from the other fluxes. The inclusion of flux during growth from $SrCl_2$ or $PbCl_2$ probably contributed

Table II. Conditions* for growth of CuCl crystals from flux melts

Flux solvent	Flux, m/o	Temperature at growth end, °C	Temperature at feed end, °C	Source of CuCl	Growth period, days	Comments
KCl 9747-77	6	345	352	Reagent grade	20	Clear crystals, 2½ cm in length
KCl 9747-42	7.4	387	394	Reagent grade	27	Opaque crystals, 12 mm in length
KCl 9747-132	6	346	351	Sublimed	33	Clear crystals, 2½ cm in length
KCl 10210-35	6	366	376	Reppt. & sublimed	18	Semi-transparent crystals, 2½ cm in length
$SrCl_2$ 9747-104	2.7	383	391	Reppt. & sublimed	14	Smoky crystals, 13 mm in length
$PbCl_2$	2.7	387	393	Reppt. & sublimed	17	Slightly opaque crystals, 13 mm or more in length
RbCl 10210-4	6	348	352	Reppt. & sublimed	32	Clear crystals, 13 mm in length

* Typical conditions for growth.

Table III. Concentration of impurities in flux grown CuCl crystals

Flux* solvent	Impurities, ppm K	Sr	Pb	Rb	Mg	Si	Fe	Ag	Resistivity, ohm-cm
N9747-148[a] $PbCl_2$	N.D.	N.D.	500	N.D.	1	1	6.4	N.D.	1.5×10^8
N9747-77, 132[a] KCl	N.D.	N.D.	N.D.	N.D.	0.5	0.3	N.D.	N.D.	1.5×10^6
N9747-76[a] $SrCl_2$	N.D.	10	N.D.	N.D.	1	1	N.D.	N.D.	3.5×10^7
N10210-43 RbCl	N.D.	N.D.	50	>0.1%	0.1	N.D.	0.5	100	—
Reppt. & sublimed[b]	N.D.	N.D.	N.D.	N.D.	0.6	0.8	N.D.	N.D.	—

[a] All crystals grown from reppt. and sublimed CuCl.
[b] Presented as reference for impurity pick-up from flux.
* Impurities in flux 10-50 ppm.

Table IV. Properties of CuCl crystals grown from flux

Run No.	Source of CuCl	Flux	% Transmission* per mm	Resistivity, ohm-cm	Rotation*‡/mm of length, degrees	Electric breakdown, V/cm
9747-77	Reagent grade	KCl	79	1.5×10^6	4.1	400
9747-132	Sublimed	KCl	57	1.8×10^6	3.5	375
10210-53	Reppt. and sublimed	KCl	28	1.7×10^7	4.6	500
10210-52	Reppt. and sublimed with $CuCl_2$ added	KCl	64	5.3×10^6	7.0	700
10210-45	Reppt. and sublimed	$SrCl_2$	38	3.5×10^7	4.3	800
10210-4	Reppt. and sublimed	RbCl	40	1.5×10^7	8.0	300
9747-125	Reagent grade	$PbCl_2$	52	1.5×10^8	7.0	1000

* Transmission and modulation at 5500A.
‡ Electric field of 300 V/cm applied to (111) planes with optical beam perpendicular to the field.

to the reduced transmission, but there was no direct correlation between transmission and impurity level. That the transmission of crystals from $SrCl_2$ and $PbCl_2$ is less than that of crystals grown from KCl is in disagreement with the results reported by Soga *et al.* (3) for crystals grown from these same fluxes by a Bridgeman technique. The differences in the occlusions or defects which give the crystals their opaque character may be caused by the different thermal gradients used in the two methods. In our experiments thermal gradients of 2°-7°C/in. were used, while crystals have been grown by the Bridgeman technique with a gradient of 20°-50°C/in. Small gradients should aid in obtaining a better crystal growth (7, 8), but this may be negated by constitutional supercooling and poor mixing which are likely to occur with small thermal gradients. Constitutional supercooling (9) would lead to cellular growth and entrainment of solvent at the grain boundaries. Large thermal gradients would cause greater mixing and tend to minimize supercooling effects. Use of a large thermal gradient of 15°-30°C/in. in our system led to polycrystalline growth probably because of simultaneous formation of many nucleation centers. Evidence of cellular growth in some growth runs is illustrated in Fig. 3 which shows a cross section of a CuCl crystal grown from flux with a small gradient. X-ray back reflection confirmed that the material was polycrystalline.

The purity of the CuCl affected not only the resistivity but also the optical transmission of CuCl crystals, particularly those grown from KCl. CuCl which was purified by sublimation contained traces of $CuCl_2$ but material produced by reprecipitation from HCl solution and then sublimed was relatively free of $CuCl_2$ and other impurities. Yet crystals grown from the purer CuCl were more opaque, as noted in Table IV. Figure 4 shows that CuCl crystals grown in KCl flux from the purer CuCl contained bubbles, which in many cases were arranged in a periodic manner. Because as-received CuCl did not give crystals containing voids, it was thought that these voids were somehow related to the equilibrium between CuCl and $CuCl_2$. When 1-5 m/o $CuCl_2$ was added to the reprecipitated and sublimed CuCl, the number of voids

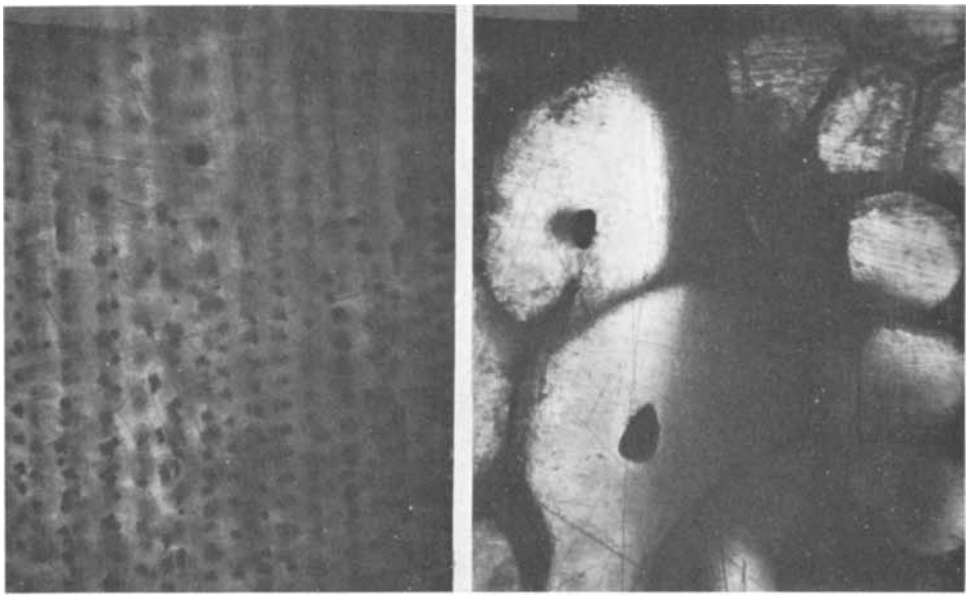

Fig. 3. CuCl crystals grown from KCl flux and showing evidence of cellular growth: (a) (left) parallel to growth direction; magnification 160X approximately; (b) (right) normal to growth direction; magnification 32X approximately.

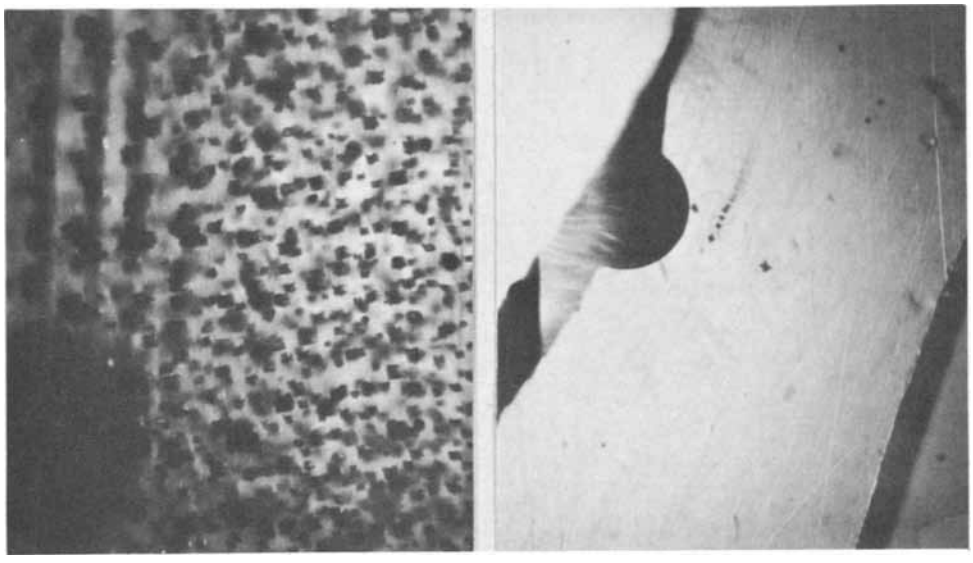

Fig. 4. CuCl crystals grown from KCl flux: (a) (left) high-purity CuCl; (b) (right) high-purity CuCl with $CuCl_2$ added. Magnification 160X approximately.

was greatly reduced. A comparison of CuCl crystals grown from high purity CuCl and crystals from a CuCl-$CuCl_2$ mixture is given in Fig. 3.

Only a few randomly distributed voids were formed with the other fluxes. Some CuCl crystals were grown from a flux composed of 2 m/o each of KCl and $SrCl_2$. These crystals were semitransparent and did not contain voids, but did have 10-50 ppm of Sr.

In the limited number of experiments made with RbCl, bubble formation was much less than in the experiments with KCl. The reduced bubble formation is reflected in the increased optical transmission for crystals grown from RbCl, although the amount of RbCl in the crystals is large. The resistivities for crystals from KCl and RbCl were about the same. Transmission of crystals from RbCl was about the same as or greater than that of crystals from $SrCl_2$ or $PbCl_2$; this is contrary to results obtained with the Bridgeman technique.

Optical rotation was measured by first crossing the direction of the polarizers, then determining the number of degrees of rotation necessary to return to the original light intensity while applying an electric field. The electrodes were on the (111) planes; the light was at right angles to the electrodes, thus giving a transverse mode. The electric breakdown of the CuCl crystals was usually much lower than that of crystals grown by other techniques (3). Thus, the number of impurities as well as their state of incorporation in the CuCl crystals seem to greatly influence the electro-optical properties.

Summary

Rather large cubic CuCl crystals were grown from several alkali or alkaline halides by using a small thermal gradient of 5°-12°C between the feed region and the crystal growth region.

The properties of the crystals grown by this technique are different from those of crystals grown by a Bridgeman technique, in which a large thermal gradient exists between the growing crystal and the melt. Some evidence of constitutional supercooling was found with the small thermal gradient.

Crystals grown in KCl flux from high-purity CuCl contained bubbles which were related to the breakdown of CuCl to give $CuCl_2$.

Manuscript received July 30, 1969.

Any discussion of this paper will appear in a Discussion Section to be published in the December 1970 JOURNAL.

REFERENCES

1. C. D. West, *J. Opt. Soc. Am.*, **43**, 335 (1953).
2. A. Neuhous and K. Recker, in "Crystal Growth," by H. S. Peiser, pp. 235-240, Pergamon Press, Oxford (1967).
3. M. Soga, R. Imaizumi, Y. Kondo, and F. Okabe, *This Journal*, **115**, 388 (1967).
4. J. Rivera, L. A. Murray, and P. A. Hoss, *J. Cryst. Growth*, **1**, 171 (1967).
5. A. F. Armington and J. J. O'Conner, *ibid.*, **3,4**, 367 (1969).
6. M. K. Reser, "Phase Diagrams for Ceramists," pp. 585-586, American Ceramic Society (1964).
7. S. G. Parker and J. E. Pinnell, *J. Cryst. Growth*, **3, 4**, 490 (1969).
8. E. Kaldis, *J. Phys. Chem. Solids*, **26**, 1701 (1967).
9. R. A. Laudise, in "Crystal Growth," by H. S. Peiser, p. 8, Pergamon Press, Oxford (1967).

Oxidation and Decarburization Kinetics of Iron-Carbon Alloys

G. J. Billings,[1] W. W. Smeltzer,* and J. S. Kirkaldy

Department of Metallurgy and Materials Science, McMaster University, Hamilton, Ontario, Canada

ABSTRACT

The early stages of the oxidation-decarburization kinetics have been investigated for austenitic iron alloys of carbon contents 0.23-1.07 w/o exposed to carbon dioxide-carbon monoxide atmospheres at the temperature of 950°C. Complex reaction behavior was observed for these alloys in the range 10-100 v/o carbon dioxide. The initial selective oxidation of carbon from sheet specimens exhibited linear kinetics. During late stage scale growth of wustite crystals, decarburization occurred by gaseous transport of carbon oxides through pores in the oxide. An oxidation-decarburization model based on surface controlled reaction steps accounted most adequately for decarburization and wustite formation before onset of control by diffusion processes.

Oxidation of a metal-carbon alloy is an unusual process since the metal oxides are generally solids and the carbon oxides are gaseous (1-7). The character of the reaction is therefore strongly circumscribed by the location of the carbon-oxygen reaction. Webb *et al.* (1) have recognized two possible reaction sequences: (*a*) rapid decarburization occurs by gas penetration through cracks in the scale, and (*b*) decarburization occurs without scale rupture due to carbon diffusion in both the metal and scale leading to the occurrence of the oxygen reaction at the oxide/gas interface. Engell and Peters (2) and Engell and Bohnenkamp (3, 4) have examined these propositions for alloys containing 0.1-0.8 w/o carbon on exposure in various atmospheres over the temperature range 750°-1050°C. They noted that decarburization occurred without scale rupture. While the alloys oxidized parabolically in air, this dependence could not be attributed to sequence (*b*) since carbon solubility in wustite was found to be so low that its diffusion through the scale had to be discounted as a significant reaction step. Furthermore, when specimens were exposed to carbon dioxide atmospheres, the wustite scale grew by the linear kinetics usually associated with a phase boundary reaction. Since decarburization involved both carbon diffusion in the metal and carbon transport through the scale, these authors concluded that formation of pores in the scale permitted effusion of gaseous carbon oxides. Although Langer and Trenkler (5) have suggested that both carbon and iron may diffuse sufficiently rapidly through the scale to react with the gaseous reactants at the oxide/gas surface, the results recently obtained by Manenc *et al.* (6) and Boggs and Kachik (7) for carbon gradients in the alloy have demonstrated that a compact scale essentially acts as a barrier to carbon diffusion.

It would therefore appear that decarburization of an iron-carbon alloy during oxidation involves depletion of carbon by its diffusion in the metal and by effusion through pores in the oxide scale as gaseous carbon oxides. This investigation was undertaken using metallographic and gravimetric techniques to clarify the reaction mechanism in the early stages of oxidation for alloys containing 0.23-1.07 w/o carbon exposed to carbon dioxide-carbon monoxide atmospheres at a temperature sufficient for stabilization of austenite and wustite.

Experimental

Specimens were prepared from disks 0.25 in. thick cut from 1 in. diameter homogenized alloy bars of carbon contents in the range 0.23-1.07 w/o. Analyses are recorded in Table I. In the case of the 0.23 w/o carbon alloy, disks were directly cold rolled to sheets 0.07 cm thick. Sheets of the higher carbon alloys, however, could be obtained only after soaking at 1000°C in argon and hot rolling. Rectangular plate specimens, 1 x 1.5 cm, were cut from the sheets and polished, finishing with 1μ diamond abrasive.

Flowing carbon dioxide-carbon monoxide atmospheres at 1 atm pressure were utilized for oxidation tests. Carbon dioxide, 99.95 v/o pure, was dried by passage through columns containing magnesium perchlorate, reduced copper oxide, and activated alumina. The carbon monoxide, minimum purity of 99.6 v/o, was further purified by passage through columns containing magnesium perchlorate and ascarite. The gases were metered with capillary flowmeters, mixed in a Pyrex bulb packed with glass wool, and directed through Pyrex tubes to an inlet at the bottom of the oxidation tube. To prevent thermal segregation of the gases, the flow rate was maintained at 0.6 cm/sec.

The vertically mounted mullite reaction tube contained a calibrated 5 mil Nispan-C wire spring which was raised or lowered by a winch to position the specimen in the furnace. Weight changes of an oxidizing specimen were recorded by following the spring extension with a cathetometer. In a typical experiment, the apparatus was evacuated to 10^{-4} Torr and the furnace adjusted within $\pm$ 2°C of the test temperature. The oxidation cell was then returned to atmospheric pressure by the introduction of nitrogen followed by the reaction gas in desired proportion, and the reaction tube was purged for 1 hr. A specimen carrying the normal room temperature oxide film was then lowered into the furnace and the weight changes were recorded. On completion of the test, the specimen was raised to the portion of the tube at room temperature and cooled in the flowing gas. A specimen was mounted in epoxy resin for metallographic examination.

Results

All results were obtained from specimens exposed at the temperature of 950°C. Typical weight-change curves for exposures up to 500 min are illustrated in Fig. 1 and

Table I. Chemical analyses of alloys

w/o Carbon	w/o Impurity element
0.231	Ni—0.033
0.623	Mn—0.020
1.065	Mo—0.015
	Si—0.010
	Cb, P, S—0.005
	Al, Cr, Cu, Ti, V—0.002
	B—0.001

[1] Present address: Central Secondary School, Hamilton, Ontario, Canada.

* Electrochemical Society Active Member.

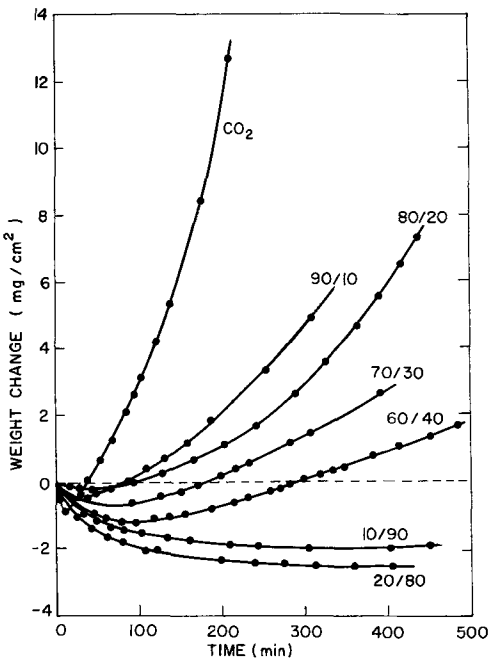

Fig. 1. Oxidation-decarburization kinetics of the Fe-1.07 w/o C alloy in CO_2-CO atmospheres at 1 atm pressure (atmospheres are designated by the ratio P_{CO_2}/P_{CO}).

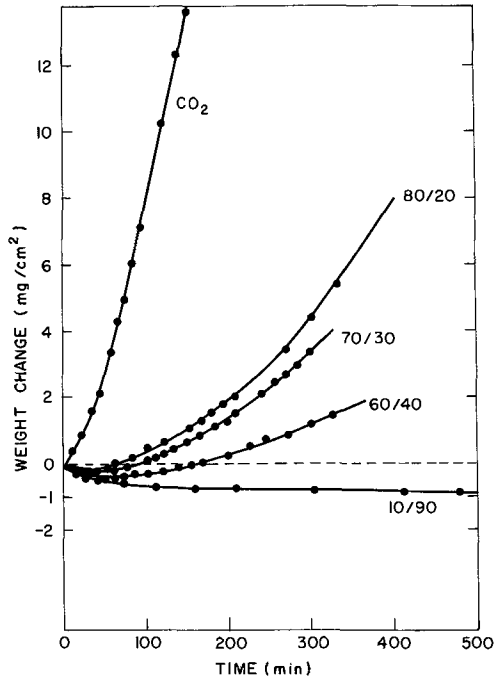

Fig. 2. Oxidation-decarburization kinetics of the Fe-0.62 w/o C alloy in CO_2-CO atmospheres at 1 atm pressure (atmospheres are designated by the ratio P_{CO_2}/P_{CO}).

2. Under reducing atmospheric conditions with respect to wustite (< 30 v/o CO_2), the negative slopes of the decarburization curves become smaller with increasing exposure time. For atmospheres containing greater than 30 v/o carbon dioxide, the slopes of the curves initially exhibited negative values due to weight losses, but ultimately became positive due to wustite formation.

Since the reaction curves were approximately linear during the initial and final stages of exposure, the initial and final linear reaction rate constants were extracted and recorded for the three alloys in Table II. Results for the 1.07 w/o carbon alloy are notable in that the initial rate revealed the most extreme negative

Table II. Initial and final linear reaction rate constants for iron-carbon alloys containing 1.07, 0.62, and 0.23 w/o carbon at 950°C in carbon dioxide-carbon monoxide atmospheres (the negative values refer to weight losses of specimens)

Alloy w/o C	Atmosphere P_{CO_2}, atm	Initial slope mg O/cm², min	Final slope mg O/cm², min
1.065	1.0	−0.113; 0.108	0.086
	0.9	−0.054	0.048
	0.8	−0.018; −0.015	0.026; 0.020
	0.7	−0.023; −0.022	0.009; 0.011
	0.6	−0.027; −0.024	0.009
	0.5	−0.034; −0.028	0.003
	0.3	−0.041; −0.032	0.00015; 0.00033
	0.2	−0.055; −0.048	
	0.1	−0.025; −0.032	
0.623	1.0	0.036; 0.039	0.080; 0.081
	0.8	−0.013	0.025
	0.7	−0.013	0.014
	0.6	−0.020	0.009
	0.1	−0.028; −0.021	
0.231	1.0	0.037; 0.028	0.096; 0.092
	0.8	−0.006	0.020
	0.6	−0.016	0.010
	0.2	−0.019	

value in pure carbon dioxide, a smaller extreme near 30 v/o carbon dioxide, and the least extreme value near 80 v/o carbon dioxide.

To ascertain the carbon loss during simultaneous oxidation of iron and carbon, several specimens were quenched after different intervals and analyzed for residual carbon. The equilibrium carbon concentration in the iron is essentially zero for atmospheres containing greater than 60 v/o carbon dioxide, and it is 0.05 w/o carbon for the atmosphere of 30 v/o carbon dioxide. Results from the above experiments for the 1.07 w/o carbon alloy are shown in Fig. 3 in comparison to the over-all reaction kinetics. Decarburization was essentially complete for the specimen exposed 2 hr in a 30 v/o carbon dioxide atmosphere when lateral growth of wustite was insufficient to interfere with surface decarburization. In the pure carbon dioxide atmosphere, lateral growth of wustite and onset of linear scale growth tends to stifle decarburization, and the carbon content of the alloy approached its equilibrium value more slowly.

The surfaces of specimens exhibited thermal etching at grain boundaries when decarburized under reducing conditions for wustite formation. Metallographic examination of the metal after oxidation under conditions for wustite formation gave results in accord with the observations of Engell and Bohnenkamp (3, 4). As illustrated in Fig. 4, the structure shows typical carbon diffusion profiles, the amount of pearlite being proportional to the carbon content.

In the metal oxidation regions, wustite grows laterally from nuclei distributed randomly over the metal

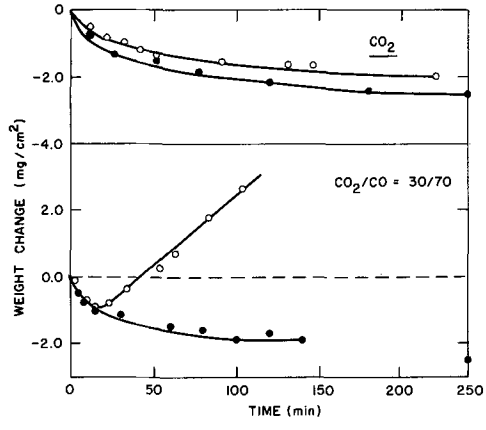

Fig. 3. Curves for oxidation-decarburization kinetics (○) and carbon loss (●) for an Fe-1.07 w/o C alloy in CO_2-CO atmospheres. (The weight loss for carbon for complete decarburization by each atmosphere is shown on the right-hand ordinate).

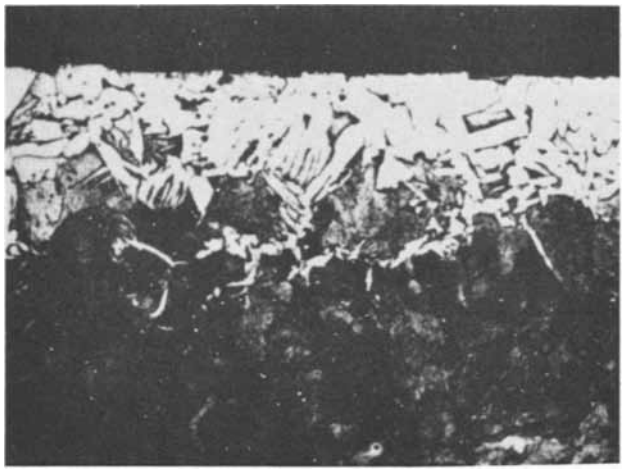

Fig. 4. Structure of the Fe-1.07 w/o C alloy after exposure for 25 min in 60/40 CO_2-CO atmosphere (250X). (Ferrite is white and pearlite is dark in color.)

surface. These nuclei, which expand vertically more than laterally, coalesce until only a scale consisting of oxide crystals is visible. The scale exhibits good adherence to the metal, and the oxide crystals are characterized by very rugged surfaces consisting of macroscopic ledges. Impingement of these surfaces presumably leads to formation of pores in the scale.

These considerations may be discussed by referring to tests on the 1.07 w/o carbon alloy since wustite growth was similar for the three alloys studied. As illustrated in the micrographs of Fig. 5 obtained from specimens exposed in a 60 v/o carbon dioxide atmosphere, the wustite nuclei have grown after 5 min to considerable thickness over a large fraction of the metal surface. Oxide coverage was only slightly more extensive after 10 min. Coalesced areas then appear, and developing porosity may be associated with the crystal boundaries. There is microscopic evidence for porosity in the scales on specimens exposed up to about 30 min, Fig. 6. Metallographic cross sections illustrated that both surfaces of a scale were irregular and that the impingement of crystals is associated with small regions of iron protruding into the oxide. The observations showed that the wustite weight increased with increasing pressure of carbon dioxide. For example, coverage of the surfaces in pure carbon dioxide was essentially complete after 30 min.

Discussion

Several possibilities involving diffusion and surface control processes must be examined in order to elucidate the decarburization kinetics for the cases of nonscaling and scaling of the base-metal iron. It is therefore essential to consider carbon diffusion in the metal substrate and the nature of the scale with regard to transfer of carbon oxides.

The decarburization range.—The simplest possibility is that decarburization is controlled by the rate of carbon diffusion in the metal when the oxidizing potential is insufficient for wustite formation. This is obtained simply from the desorption conditions for a plane sheet (8, 9). The result of a sample calculation is shown in Fig. 7 corresponding to a 1.07 w/o carbon alloy exposed to a 10 v/o CO_2 atmosphere. The calculation is based on published results for carbon concentrations and diffusion coefficients (10, 11) and involves the assumption that the surface carbon concentration is the equilibrium value for the atmosphere used. Since the observed decarburization rate in the early stages of the reaction is much smaller than the calculated value,

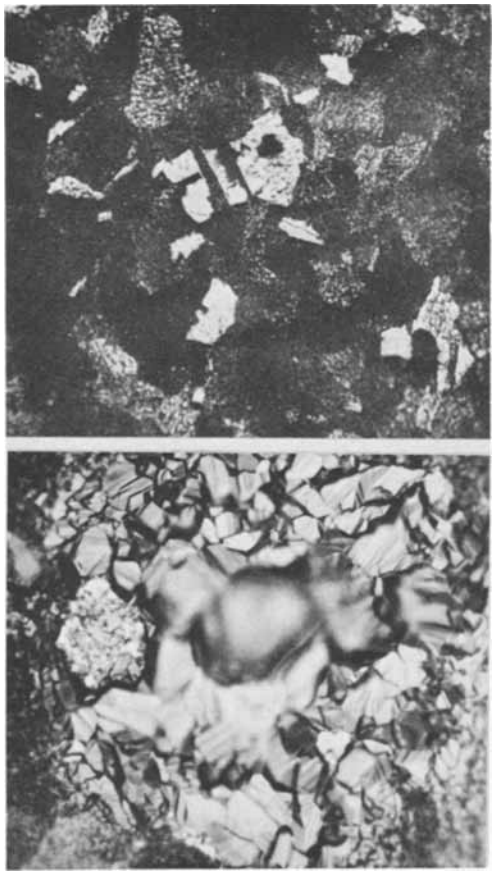

Fig. 5. Topographies of the Fe-1.07 w/o C alloy specimens after exposure to a 60/40 CO_2-CO atmosphere. Upper micrograph: 5 min exposure (magnification 195X); lower micrograph: 25 min exposure (magnification 422X).

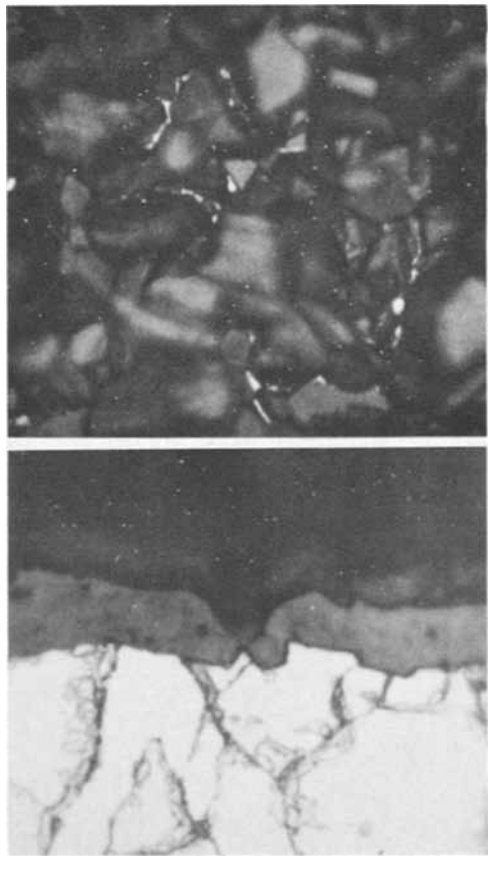

Fig. 6. Porous wustite scale on the Fe-1.07 w/o C alloy specimens after exposure to a 60/40 CO_2-CO atmosphere. Upper surface micrograph: 70 min exposure (magnification 252X); lower cross-section micrograph: 10 min exposure (magnification 1020X.)

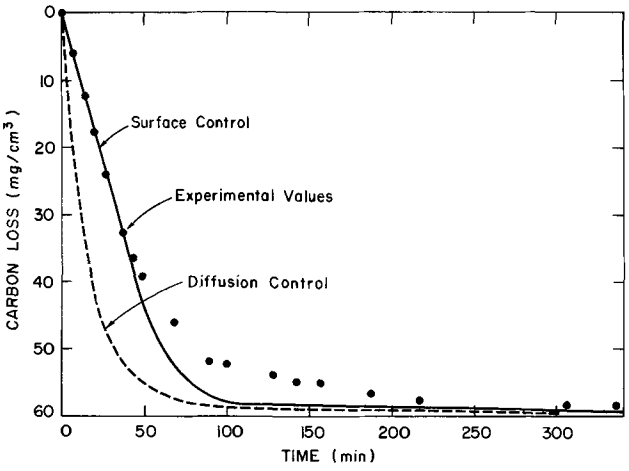

Fig. 7. Comparison of curves calculated for surface and diffusion controlled decarburization to experimental results for an Fe-1.07 w/o C alloy exposed in a 10/90 CO_2-CO atmosphere. The diffusion control curve was that calculated from equations for a finite plate [8], [9]; the surface control curve was calculated from Eq. [3] in integrated form and the experimental value of k_1.

decarburization must be inhibited initially by chemical reaction at the metal surface.

We therefore consider the transfer of oxygen from a carbon dioxide atmosphere to react with carbon at the surface of iron. Two parallel reaction chains have been considered by Doehlemann (12). In the first chain

$$CO_2 = O^*_{ads} + CO \qquad \text{(slow)} \qquad [1]$$

$$O^*_{ads} + C = CO \qquad \text{(fast)} \qquad [2]$$

O^*_{ads} refers to oxygen absorbed on sites where it reacts with carbon. That is, the reaction rate is not dependent on the surface diffusion of oxygen to an active site to react with carbon. Doehlemann applied the theory of chemical kinetics to this sequence of reactions with the assumption that the dissociation of carbon dioxide is the rate-determining step to obtain the following expression for the reaction rate

$$R_1 = k_1 \, p_{CO_2} \left(1 - \frac{C_e}{C}\right) \qquad [3]$$

where k_1 is the rate constant for dissociation of CO_2, and where C and C_e are the carbon concentrations after a given exposure period and the equilibrium value, respectively, for a specified carbon dioxide-carbon monoxide atmosphere.

In atmospheres of higher oxidizing potential, the decarburization kinetics may assume a parallel dependence upon the dissociation step for carbon dioxide and a surface diffusion step of adsorbed oxygen to an active site for reaction with carbon. Doehlemann (12) has also considered this chain of reactions

$$CO_2 = O_{ads} + CO \qquad \text{(fast)} \qquad [4]$$

$$O_{ads} = O^*_{ads} \qquad \text{(slow)} \qquad [5]$$

$$O^*_{ads} + C = CO \qquad \text{(fast)} \qquad [6]$$

where O_{ads} refers to inactive adsorbed oxygen. It was assumed that the adsorbed oxygen is in local equilibrium with the atmosphere and the occupied random surface sites, the controlling reaction [5] being a short surface diffusion step in which O_{ads} migrates to active sites to form O^*_{ads}. The reaction rate may then be written as

$$R_2 = k_5 \frac{p_{CO_2}}{p_{CO}} \left(1 - \frac{C_e}{C}\right) \qquad [7]$$

where k_5 is the rate constant for surface diffusion. Consequently, the net initial decarburization rate may be expressed as

$$R_{dec} = R_1 + R_2 = (k_1 p_{CO_2} + k_5 \, p_{CO_2}/p_{CO})(1 - C_e/C) \qquad [8]$$

It is conceivable that k_5 has a value relative to k_1 such that the second term in Eq. [8] is insignificant in the pure decarburization range at $p_{CO_2} < 0.3$ atm but becomes significant at higher pressures approaching 1 atm. Doehlemann (12) found for the decarburization of alloys fabricated from electrolytic iron that the ratio $k_1/k_5 \simeq 20$ at 920°C whereas Grabke (13) recently demonstrated that the decarburization rate of alloy foil containing high-purity iron was dependent only on $k_1 p_{CO_2}$ at temperatures in the range 800°-1000°C in atmospheres up to those sufficiently oxidizing for wustite formation. As shown by the plots in Fig. 8, it would appear that the initial decarburization rate for the alloys of this work, which is directly dependent upon the partial pressure of carbon dioxide, is correctly described by Eq. [3]. It will be shown, however, that this consideration is only valid for pure decarburization at low pressures of carbon dioxide; the term $k_5 p_{CO_2}/p_{CO}$ becoming significant in the oxidation-decarburization range.

The oxidation-decarburization range.—It is essential to consider both concurrent decarburization and wustite formation in the atmospheres of sufficient oxidizing potential for stability of wustite. Since randomly distributed oxide nuclei would be present on the surface after partial reduction of the air formed room temperature film at the reaction temperature, adsorbed oxygen would react with iron at these nuclei boundaries. Lateral growth of oxide would then be determined by complicated processes for oxygen adsorption and surface diffusion. By analogy with the rate processes for decarburization, two limiting oxidation cases may be considered. In the first reaction chain, carbon dioxide dissociating at active sites adjacent to the oxide nuclei would determine the reaction rate. The second reaction chain would involve a rate-determining surface diffusion step for adsorbed oxygen from the randomly distributed sites to these active oxidation sites.

The first oxidation chain may be represented by

$$CO_2 = O^{**}_{ads} + CO \qquad \text{(slow)} \qquad [9]$$

$$O^{**}_{ads} + Fe = FeO \qquad \text{(fast)} \qquad [10]$$

where the dissociation of carbon dioxide at the active

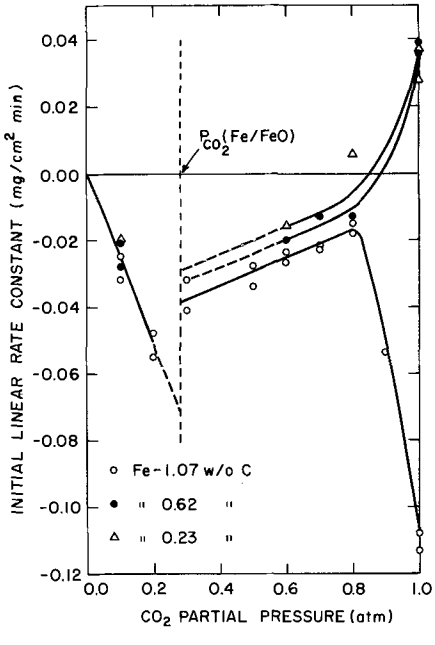

Fig. 8. Initial oxidation-decarburization linear rate constants as a function of CO_2 partial pressures. Symbols (○), (●), and (△) are for the 1.07, 0.62, and 0.23 w/o carbon alloys respectively.

sites is the rate-determining step. The surface coverage of adsorbed oxygen then corresponds to the value for equilibration of iron with wustite. A detailed balance of the reactions with this restriction gives for the initial oxidation rate

$$R_3 = k_9 P_{CO_2} (1 - K P_{CO}/P_{CO_2}) \quad [11]$$

where the constant K represents the gas pressure ratio for equilibration of wustite with iron and k_9 is the rate constant for dissociation of carbon dioxide at the active oxidation sites.

The reaction chain for oxygen surface diffusion as the rate determining step is

$$CO_2 = O_{ads} + CO \quad \text{(fast)} \quad [4]$$

$$O_{ads} = O^{**}_{ads} \quad \text{(slow)} \quad [12]$$

$$O^{**}_{ads} + Fe = FeO \quad \text{(fast)} \quad [10]$$

If the species given in [4] and [10] are regarded as being at equilibrium concentrations for the atmospheric oxidizing potential and the iron-wustite reaction, the resulting expression for the oxidation rate is of the form

$$R_4 = k_{12}k_4 P_{CO_2}/P_{CO} \left(1 - \frac{k'_{12}}{k_{12}K_4K_{10}} P_{CO}/P_{CO_2}\right) \quad [13]$$

where K_4 and K_{10} are the equilibrium constants for reactions [4] and [10], and k_{12} and k'_{12} are the forward and backward rate constants for the surface diffusion steps. Accordingly, a concentration gradient of adsorbed oxygen would then exist from the iron surface to the Fe/FeO boundary for surface diffusion of oxygen.

Thus, the initial rate for lateral growth of wustite on the surface may be expressed as

$$R_{oxid} = R_3 + R_4 = k_9 P_{CO_2} (1 - K\ P_{CO}/P_{CO_2}) + k_{12}K_4 P_{CO_2}/P_{CO} \left(1 - \frac{k'_{12}P_{CO}}{k_{12}K_4K_{10}P_{CO_2}}\right) \quad [14]$$

The net initial reaction rate in the oxidation-decarburization range is therefore the summation, $R_{dec} + R_{oxid}$, given by Eq. [8] and [14]. They are comprised of two leading terms, one being directly proportional to the partial pressure and dissociation rate of carbon dioxide and the other to the P_{CO_2}/P_{CO} ratio and the rate constants describing the oxygen surface diffusion to the active decarburization and oxidation sites.

These considerations may be demonstrated by examining the plots of the net initial reaction rates *vs.* gas consumption for the three alloys investigated, Fig. 8. A sharp break in the reaction rate curve at the partial pressure of carbon dioxide for wustite formation is due to retention of partial coverage of oxide resulting from partial reduction of the air-formed film. This oxide would act as nuclei for subsequent growth of wustite. In the intermediate pressure range, $0.3 < P_{CO_2} < 0.8$, reactions [1] and [9], as described by Eq. [3] and [11], involving dissociation of carbon dioxide must be rate limiting since the net reaction rate involving both decarburization and oxidation are directly dependent on carbon dioxide pressure. It is to be noted that the effective contribution of the decarburization reaction was larger for an alloy of higher carbon concentration which would be associated with the larger number of active carbon surface sites for dissociation of the reactant gas. Contributions to reaction control associated with the P_{CO_2}/P_{CO} ratio, Eq. [7] and [13], appear to become effective at carbon dioxide pressures exceeding 0.8 atm. Apparently the surface coverage of adsorbed oxygen became sufficient in atmospheres of high oxidation potential for reactions [5] and [12] to enter into competition for oxygen by diffusion to one of the other of the active decarburization and oxidation sites. The oxidation rate was dominant for the alloys containing 0.23 and 0.62 w/o carbon. On the other hand, decarburization wins out over oxidation in the case of the 1.07 w/o carbon alloy where oxygen diffused preferentially by shorter diffusion paths to the decarburization sites.

Model for the oxidation-decarburization reaction kinetics.—A model based on the growth of a wustite scale from oxide nuclei randomly distributed on the alloy surface may be advanced to generate the shape of the reaction curves. The nuclei, as illustrated in Fig. 9, are regarded for simplicity as spherical caps which grow laterally and vertically, their lateral growth reducing decarburization in proportion to the areal coverage of the alloy surface. The rate constants k_o and k_d may then be defined to describe the vertical growth of wustite and the decarburization process, respectively. A large number of nuclei covering a fraction of the surface corresponding to A_o is assumed to be present at the commencement of the reaction due to partial reduction of the air formed oxide film on exposure of the specimen at the reaction temperature. This coverage at time, t, is defined by the relationship

$$A(t) = 1 - (1 - A_o) \exp(-at) \quad [15]$$

where a is the rate constant for lateral growth of wustite in order that the oxide coverage of the surface will vary from $A(0) = A_o$ at $t = 0$ to $A(\infty) = 1$ for complete coverage at very long times.

Since the weight change of a specimen may be expressed as

$$\Delta W = \Delta W_o + \Delta W_d \quad [16]$$

where ΔW_o is the oxidation weight gain and ΔW_d is the decarburization weight loss, the instantaneous rates given by means of Eq. [15] and [16] are

$$\frac{d\ \Delta W_o}{dt} = k_o A = k_o [1 - (1 - A_o) \exp(-at)] \quad [17]$$

$$\frac{d\ \Delta W_d}{dt} = -k_d (1 - A) = -k_d (1 - A_o) \exp(-at) \quad [18]$$

Upon integration of Eq. [17] and [18] followed by substitution into [16]

$$\Delta W = k_o \left[t - \frac{1 - A_o}{a} (1 - \exp - at) \right] - k_d \left[\frac{1 - A_o}{a} (1 - \exp - at) \right] \quad [19]$$

It may be shown that Eq. [19] describes the shape of the reaction curves by examining several limiting approximations. The initial weight change of a specimen found to occur by a linear rate relationship would be given by

$$\Delta W(0) = [-k_d + (k_d + k_o) A_o] t \quad [20]$$

When the alloy surface is covered completely by a wustite scale at long exposure intervals, the linear relationship would be

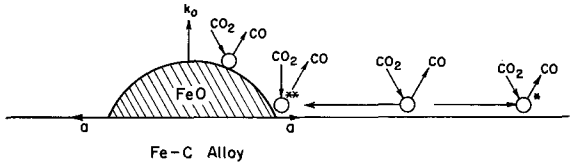

Fig. 9. Oxidation-decarburization model for a large number of oxide nuclei distributed randomly on the alloy surface. The nuclei are spherical caps covering a fractional area A_o at the commencement of the reaction. The rate constant, a, defines the lateral growth rate of wustite, k_o is the rate constant for vertical wustite growth, O* and O** represent oxygen adsorbed at active decarburization and oxidation sites.

$$\Delta W(\infty) = k_o t \qquad [21]$$

neglecting any decarburization due to effusion of gaseous carbon oxides at wustite crystallite boundaries. Equation [19] may also be solved for the time corresponding to the minimum observed in the reaction curves where oxidation and decarburization occur at equal rates. This relationship is

$$t_m = \frac{1}{a} \ln k_o/(k_o + k_d)(1 - A_o) \qquad [22]$$

We see therefore that the reaction curves illustrated in Fig. 1 and 2 have a shape described by Eq. [19]. One further qualitative point of agreement of the model with the reaction kinetics may be noted by examining the terms in Eq. [22]. Since the rate constant, a, for lateral growth of wustite is the leading term and corresponds to R_{oxid}, Eq. [14], it would be expected to show a dependence on both the partial pressure of carbon dioxide and the pressure ratio P_{CO_2}/P_{CO}. Moreover, this constant determines the location of the minimum of the curve, the larger is its value, the shorter is t_m, and they should be inversely proportional. We have plotted $1/t_m$ *vs.* P_{CO_2} in Fig. 10 obtained from the reaction curves for the 1.07 w/o C alloy, and the predicted tendency is clearly shown. At low partial pressures of carbon dioxide, 0.3 to 0.8 atm, the magnitude of the rate constant is proportional to pressure since the dissociation step of carbon dioxide at active oxidation sites is most important. Its magnitude then becomes dependent on the P_{CO_2}/P_{CO} ratio for atmospheres at high partial pressures of carbon dioxide since the active oxidation sites at wustite nuclei boundaries enter into competition with active decarburization sites for adsorbed oxygen supplied by surface diffusion.

It is clear that this simple model reproduces the qualitative character of all features of the reaction. However, it does not take account of long time decarburization by gaseous transport at oxide crystallite boundaries in the scale and the known change of the oxidation to parabolic kinetics at very long times. The linear behavior implies that the surface control reaction is much slower than the diffusion of iron through the scale to the reaction front at its external surface. According to earlier work on the linear kinetics for wustite formation on pure iron (14, 15), the oxidation rate constant k_o, Eq. [21], would be expected to show a proportional dependence on the partial pressure of carbon dioxide greater than that for equilibration of wustite with iron. Values of the linear reaction rate constants obtained for the three alloys at long exposures are plotted in Fig. 11, and it is to be seen that

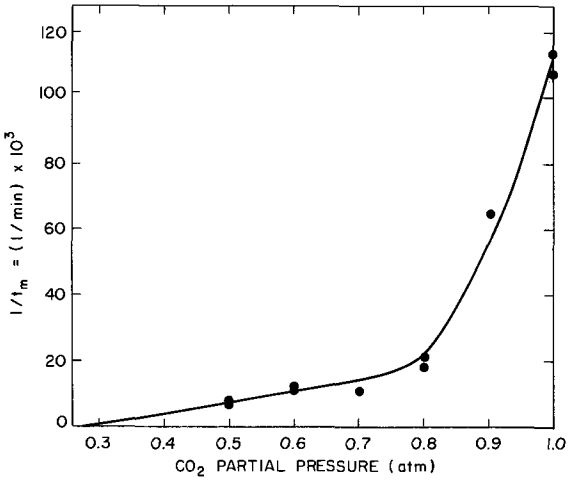

Fig. 10. Variation of time for kinetic minima with partial pressure of carbon dioxide for concurrent oxidation of iron and carbon for 1.07 w/o C alloy.

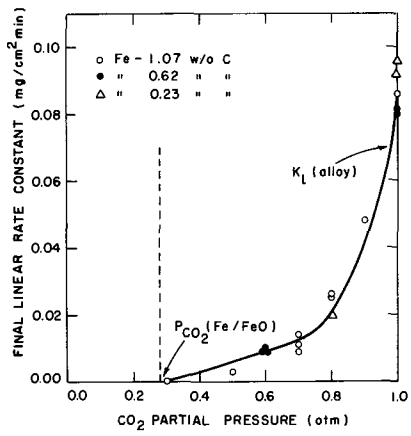

Fig. 11. Final oxidation-decarburization linear rate constants as a function of CO_2 partial pressure.

they do show this proportional dependence up to a carbon dioxide partial pressure of 0.8 atm and a larger dependence at higher pressures. Apparently wustite formation is enhanced and decarburization decreased at these latter pressures. Since the scales on the alloys are porous, a larger area for wustite formation at external and internal surfaces would lead to less effective porosity and decreased decarburization. These properties would lead to the higher observed rates for wustite formation but the complex processes involved, however, are not amenable to simple analysis.

Summary

An investigation has been carried out on the oxidation-decarburization kinetics and the morphological development of the wustite scale on iron alloys containing 0.23-1.07 w/o carbon exposed to carbon dioxide-carbon monoxide atmospheres at a temperature sufficiently high for stabilization of the metal as austenite. Under reducing atmospheric conditions with respect to wustite formation, the decarburization rate increased with increasing pressure of carbon dioxide, but decreased with increasing exposure time due to onset of carbon diffusion in the metal substrate. Growth of wustite stifled decarburization in proportion to the areal coverage by oxide. In the late stage of the reaction decarburization occurred only by gaseous effusion of carbon oxides through pores in the scale. The magnitudes of the initial linear oxidation-decarburization rate constants were examined as a function of carbon dioxide partial pressure. These constants showed a direct dependence at low pressure while at high pressure they were dependent on both the partial pressure of carbon dioxide and the P_{CO_2}/P_{CO} ratio. An explanation was advanced for this behavior by considering both oxidation and decarburization to be controlled by a chain of surface reactions where either dissociation of carbon dioxide at active oxidation and decarburization sites or surface diffusion of adsorbed oxygen to these active sites acted as rate determining steps. Finally, an oxidation-decarburization model based on stifling of the decarburization reaction by lateral growth of wustite was advanced to generate the general features of the reaction curves.

Acknowledgments

This research was supported by a grant from the American Iron and Steel Institute to W. W. Smeltzer. G. J. Billings wishes to express his appreciation of the award of an Ontario Graduate Fellowship. This paper is based on his thesis submitted to McMaster University in partial fulfillment of the requirements for the M.Sc. degree.

Manuscript submitted June 2, 1969; revised manuscript received Aug. 28, 1969. This was Paper 412 presented at the Montreal Meeting of the Society, Oct. 6-11, 1968.

Any discussion of this paper will appear in a Discussion Section to be published in the December 1970 JOURNAL.

REFERENCES

1. W. W. Webb, J. T. Norton, and C. Wagner, *This Journal*, **103**, 112 (1956).
2. H. J. Engell and F. K. Peters, *Arch Eisenhuttenw.*, **28**, 567 (1957).
3. K. Bohnenkamp and H. J. Engell, *ibid.*, **33**, 359 (1962).
4. K. Bohnenkamp and H. J. Engell, Proc. 1st Inst. Congress Metallic Corrosion, p. 215, Butterworths Publishers (1962).
5. K. Langer and H. Trenkler, *Berg-und Huttenmann Monatshefte*, **110**, 291 (1965).
6. J. Manenc, M. Bojic, and J. Benard, C. *R. Acad. Sci. Paris*, **264**, 1573 (1967).
7. W. E. Boggs and R. H. Kachik, *This Journal*, **116**, 424 (1969).
8. J. Crank, "The Mathematics of Diffusion," p. 45, University Press, Oxford (1956).
9. A. T. McKay, *Proc. Phys. Soc.*, **42**, 547 (1930).
10. C. Wells and R. F. Mehl, *Trans. AIME*, **140**, 279 (1940).
11. R. P. Smith, *J. Am. Chem. Soc.*, **68**, 1163 (1946).
12. E. Doehlemann, *Z. Elektrochem.*, **42**, 561 (1936).
13. H. J. Grabke, Proc. 3rd Int. Congress Catalysis, p. 928, North-Holland Publishing Co. (1964).
14. W. W. Smeltzer, *Trans. AIME*, **218**, 674 (1960); *Acta Met.*, **8**, 377 (1960).
15. F. S. Pettit, R. Yinger, and J. B. Wagner, Jr., *ibid.*, **8**, 617 (1960).

Decarburization of an Iron 0.8 w/o Carbon Alloy in the Presence of a Wustite Scale

A. S. Reeves[1] and W. W. Smeltzer*

Department of Metallurgy and Materials Science, McMaster University, Hamilton, Ontario, Canada

ABSTRACT

The decarburization kinetics have been investigated for an austenitic Fe-0.81 w/o C alloy in the presence of a wustite scale exposed to a carbon dioxide atmosphere or vacuum at 950°C. During the stage of linear reaction kinetics in carbon dioxide, iron oxidation was approximately tenfold more rapid than carbon oxidation. The latter reaction occurred predominately with carbon dioxide rather than by reduction of wustite. The primary rate-controlling steps in decarburization were reaction steps at the alloy surface with a small resistance possibly occurring to the passage of carbon oxides by pores in the scale. The maximum area affected by porosity in a scale was 2-3%. Under vacuum decarburization conditions, the effectiveness of the pores in the wustite scale as a means of transport for carbon oxides was dependent on its thickness and the concentration of carbon at the metal/oxide interface.

An oxidation-decarburization model based on surface controlled reaction steps has been shown previously by Billings *et al.* (1) to account most adequately for the initial rates of decarburization and wustite formation on austenitic iron-carbon alloys on their exposure in carbon dioxide-carbon monoxide atmospheres. The initial selective oxidation of carbon from sheet specimens exhibited linear kinetics, and decarburization occurred by gaseous transport of carbon oxides through pores in the oxide during the late stage growth of wustite crystals. The purpose of this investigation was to obtain additional information for interpretation of the decarburization reaction at relatively long exposure intervals. The reaction kinetics consisting of simultaneous oxidation of iron and carbon were allowed to occur until a layer of wustite formed on the metal surface. Decarburization was then allowed to proceed without wustite formation.

Experimental

The methods for preparing the Fe-0.81 w/o C alloy and the method for carrying out the reaction tests at 950°C in flowing carbon dioxide at 1 atm pressure were identical to those methods previously reported (1). Rectangular plate specimens of the alloy, 0.7 x 0.5 x 0.3 cm, were polished finishing with 1μ diamond paste. During oxidation-decarburization of a specimen, the flow rate of the carbon dioxide gas was maintained at 0.6 cm/sec. Vacuum decarburization of a specimen *in situ* was carried out at a residual pressure of 10^{-5} Torr.

Specimens were mounted in epoxy resin for metallographic examination. Both cross sections and tapered sections through the oxide layer at angles less than 5° from the surface plane were used. Where etching of the metal surface was employed, the etchant was 2% nital.

Carbon analyses of oxidized specimens were carried out by the Orsat method. An entire specimen was combusted after removal of the wustite layer by pickling in dilute hydrochloric acid at room temperature until visual examination showed complete removal of oxide. It was established that the loss of metal by this pickling procedure was negligible.

Results

When a specimen is exposed to carbon dioxide at 950°C, the observed change in weight is the result of both wustite growth and carbon loss. The reaction curves and the carbon analyses of specimens reacted under various conditions will be shown, as well as photomicrographs illustrating structural features of the metal and oxide scale.

Reaction kinetics.—Typical reaction curves for the Fe-0.81 w/o C alloy in carbon dioxide are shown in Fig. 1. The initial slope of a curve was positive giving way to a region of constant slope and finally a region of decreasing slope as the reaction tended to become partially governed by diffusion processes. In the previous research (1), the initial slope in the reaction curve was found to be positive for Fe-0.6 w/o C and negative for Fe-1.07 w/o C. The value from the present work is intermediate between these values. The linear reaction rate constant calculated from the data in Fig. 1 is 0.093 ± 0.012 mg/cm^2 min.

An abrupt change from weight increase to weight decrease was usually observed immediately after

[1] Present address: Defence Research Establishment Atlantic, Dartmouth, Nova Scotia.

* Electrochemical Society Active Member.

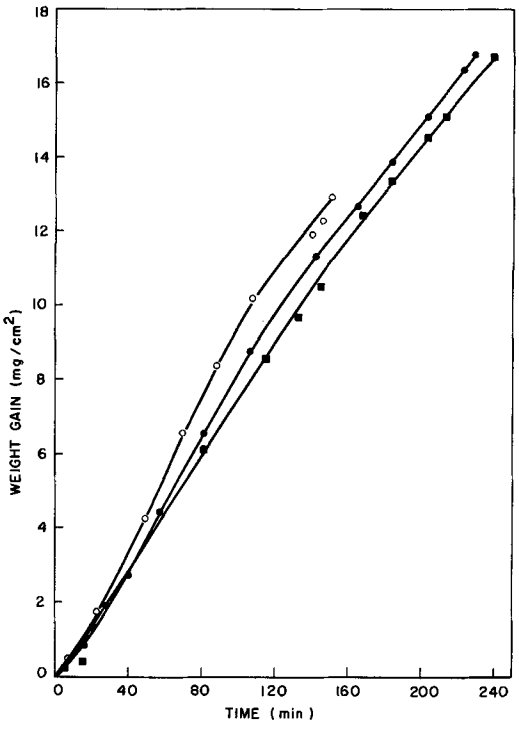

Fig. 1. Reaction kinetics of Fe-0.81 w/o C alloy in carbon dioxide at 1 atm. pressure at 950°C.

shutting off the carbon dioxide supply and allowing a scaled specimen to react under vacuum. The results are shown in Fig. 2. The loss of carbon from a specimen became continuously slower with increasing exposure time. Moreover, the rate of carbon loss decreased as the oxide thickness increased. With very thick oxide scales, approximately 100μ thick, decarburization was not observed during the time of the experiments.

Carbon analyses.—Specimens were oxidized in carbon dioxide for different intervals and then analyzed for residual carbon. The upper graph in Fig. 3 shows the carbon loss during the oxidation-decarburization period. Carbon loss occurred after an initial period of more rapid rate over an extended period by a constant rate equal to 6.0 x 10^{-3} mg/cm^2 min. Microscopic examination of the wustite scales illustrated that the onset of the linear rate behavior corresponded approximately to coverage of the metal surface with wustite.

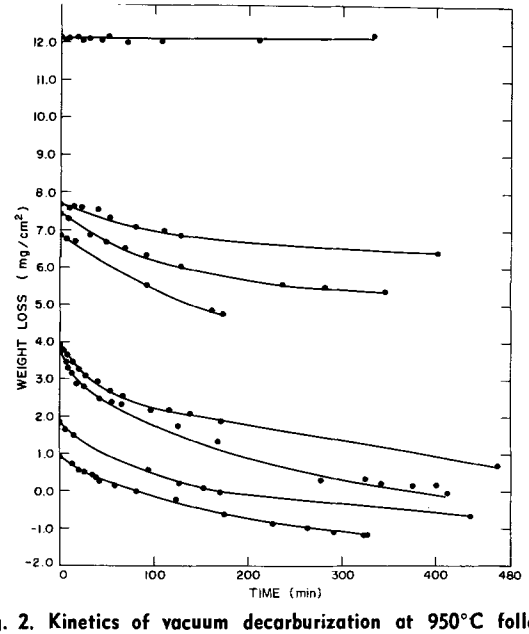

Fig. 2. Kinetics of vacuum decarburization at 950°C following immediately after oxidation in carbon dioxide.

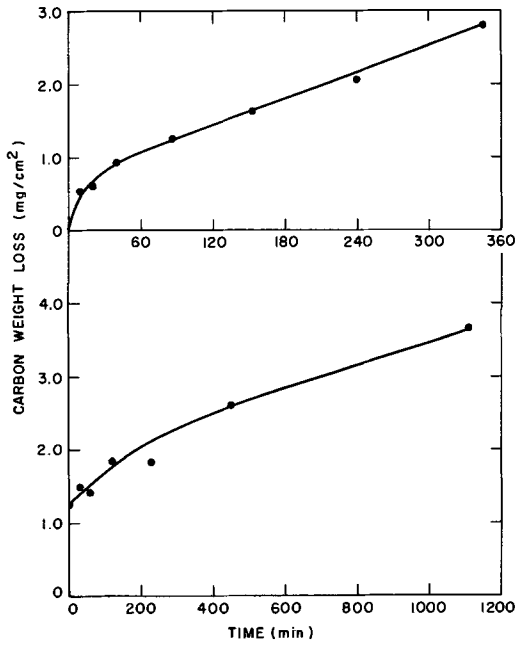

Fig. 3. Carbon loss from a specimen during oxidation in carbon dioxide (upper graph) and during vacuum decarburization after exposure to carbon dioxide for 90 min (lower graph).

In another series of experiments, the reaction time in carbon dioxide was kept constant at 90 min. Specimens were then decarburized under vacuum and analyzed for residual carbon. These results are given in the lower graph of Fig. 3. Carbon loss by oxide reduction at approximately 1.7 x 10^{-3} mg/cm^2 min occurred more slowly than during reaction of a specimen in carbon dioxide.

Metallography.—When a specimen was exposed to carbon dioxide, the surface became covered with wustite crystallites within a period of 30-40 min. The growth of the crystallites was very irregular, the general trend being toward larger size crystallites as the oxide layer thickened. The oxide was generally very adherent to the metal as shown in Fig. 4. Sometimes, however, reaction of carbon with wustite occurred at the metal interface with the result that voids were formed, and iron precipitated at the interface, as shown in Fig. 5. It appeared that blistering of the scale occurred at these regions. Figure 6 taken from a tapered section of a specimen suggests this possibility. The micrograph of the metal shows

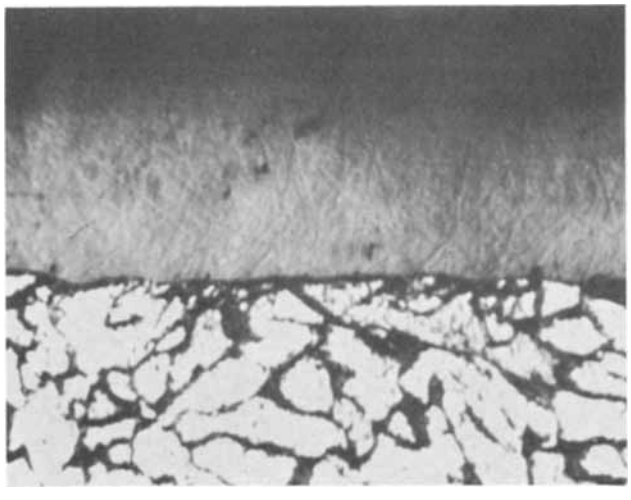

Fig. 4. Metal/oxide interface after oxidation of the specimen in carbon dioxide (Magnification 200X).

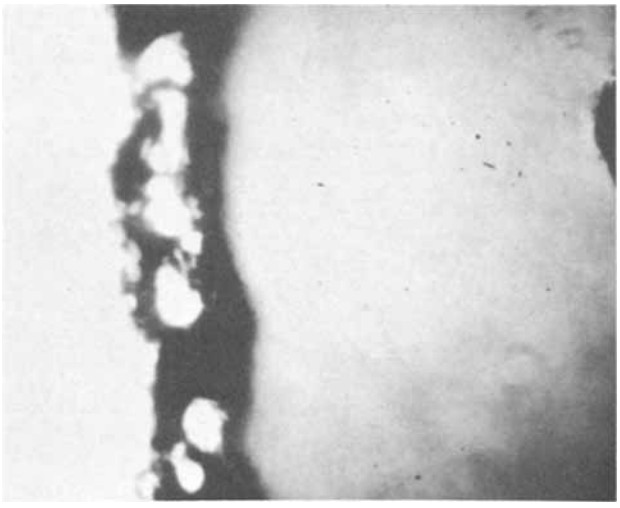

Fig. 5. Void formation and iron precipitation at metal/oxide interface after oxidation in carbon dioxide (Magnification 380X).

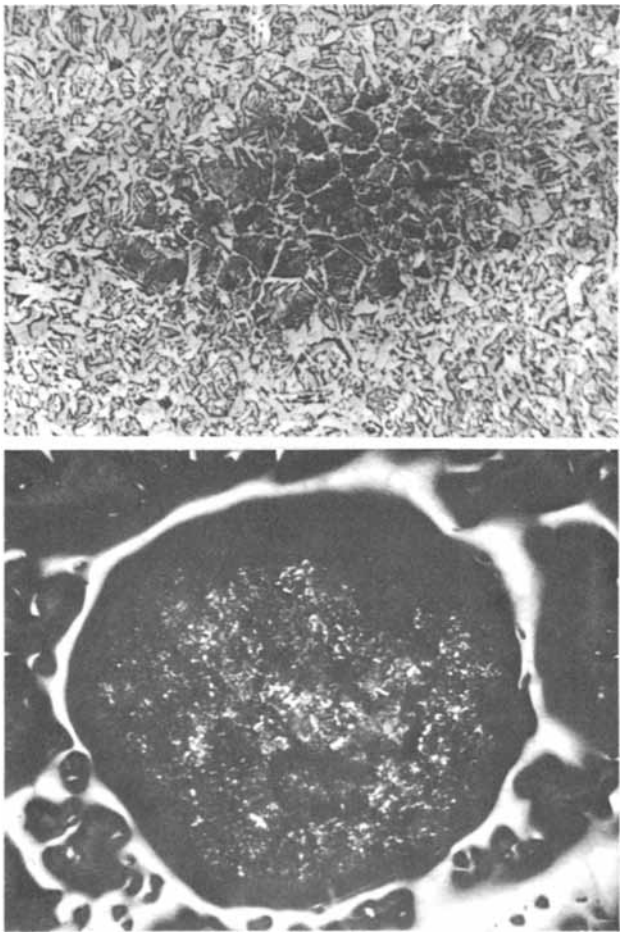

Fig. 6. Taper sections of a specimen after oxidation in carbon dioxide. Upper micrograph, metal surface showing nonuniform carbon content, dark area is of larger pearlite content due to higher carbon content (magnification 100X); lower micrograph, blistering of oxide, the central area of the blister is the underlying metal.

an area of high carbon content surrounded by an area of extensive decarburization. In the other micrograph showing the presence of wustite, the scale appears to be ruptured and the dark etching of the underlying metal suggests that this may be a high-carbon area.

Void formation and iron precipitation at the metal/oxide interface became a general feature when an oxidized specimen was allowed to decarburize under vacuum. As shown in Fig. 7, this interface became

Fig. 7. Void formation and iron precipitation at metal/oxide interface after vacuum decarburization of oxidized specimen for 3 hr at 950°C (magnification 400X).

extremely uneven as wustite was reduced, and voids were formed at the interface. In this photomicrograph, the void volume (39%) is of the same order of magnitude as the difference in the volume of the metal and oxide (43%). This appeared to be a common feature of the decarburization reaction by wustite reduction. An additional effect apparently caused by the presence of pores in the scale through which carbon monoxide escaped could be seen by taper-section metallography. As shown in Fig. 8, spires of metal, which extended into the wustite scale, developed at the surfaces of pores during reduction of wustite by carbon monoxide. In the case of a thin scale, wustite could be completely reduced in some places exposing areas of reduced metal. Cross sections of these regions, as illustrated in Fig. 9, also showed the presence of the iron spires formed by the reduction of wustite at the walls of pores.

Discussion

The observations are consistent with the proposition that decarburization is controlled largely by the reaction steps at the alloy surface with pores in the wustite scale possibly offering a small resistance to the transfer of gaseous carbon oxides. These pores

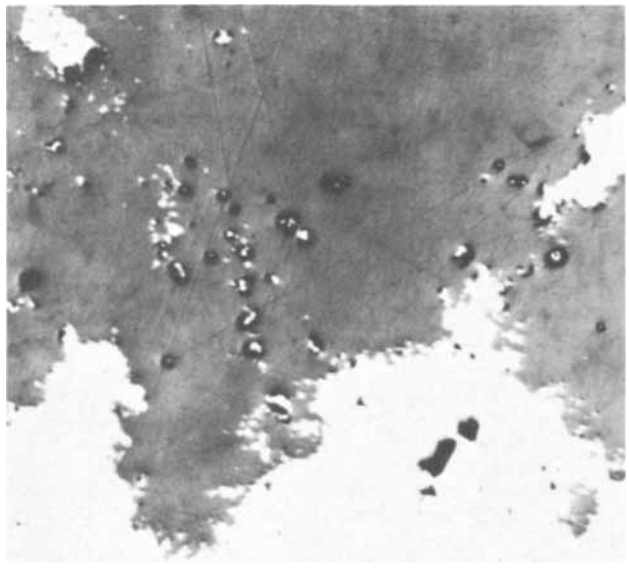

Fig. 8. Taper section of metal and oxide scale after vacuum decarburization of specimen (magnification 170X). Iron precipitation extends into wustite scale at pores.

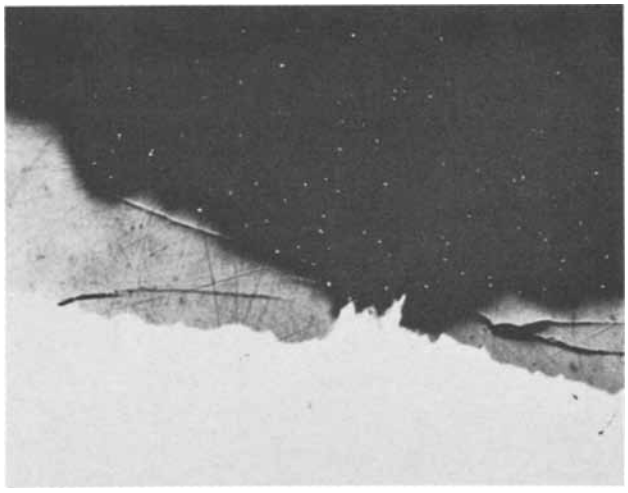

Fig. 9. Cross section of oxidized specimen after vacuum decarburization showing iron spires associated with oxide porosity (magnification 170X).

remain effective for gas transport under conditions which would appear to be a complex function of the original carbon content in the alloy, the exposure atmosphere, and the amount of wustite formation.

Decarburization was relatively rapid and wustite formation relatively slow during the initial stages of the reaction. Nevertheless, the reaction kinetics for both processes became approximately constant after 30 min. The linear weight gain corresponding to both oxidation and decarburization was 0.093 mg/cm^2 min (Fig. 1) while the decarburization rate was 0.006 mg/cm^2 min (Fig. 3). This latter rate is equal to an oxygen consumption of 0.008 mg/cm^2 min assuming that the reaction product is carbon monoxide. Thus, iron oxidation occurred approximately tenfold more rapidly than carbon oxidation in the steady-state condition for the Fe-0.81 w/o C alloy exposed in a carbon dioxide atmosphere.

It was found in the previous investigation that iron and carbon both enter into competition for adsorbed oxygen resulting from the dissociation of carbon dioxide during the early stages of the reaction (1). Since lateral growth of wustite blocks active decarburization sites and stifles this reaction, the area of metal exposed to the atmosphere approaches a small value, the atmosphere finally contacting the alloy through pores where wustite crystallites impinge on one another. An estimate may be made of this area affected by porosity during the steady-state oxidation-decarburization condition. In the absence of wustite formation, a carbon loss of 0.21 mg/cm^2 min would be expected using data from Fig. 8 and Eq. [3] of ref. (1). The actual loss, 0.006 mg/cm^2 min, is much lower. Assuming that this decrease is caused by the areal coverage of wustite stifling decarburization, the above rate shows that 2-3% of the surface area is affected by porosity. This is a maximum estimate since any influence of the P_{CO_2}/p_{CO} ratio in the expression for the decarburization rate, Eq. [8] of ref. (1), was neglected. Also, account could not be given to any possible resistance arising from geometry of pores to gas access to the metal surface.

The rate-controlling steps in decarburization would appear to be associated with the reaction at the alloy surface and transport of gaseous carbon oxides through the scale. If the surface reaction was completely rate controlling, the pores in the scale need only be large enough to permit free passage of carbon oxides to and from the metal surface. On the other hand, a constant resistance to gas flow would be required if transport of the carbon oxides through a thickening scale became rate determining. To account for this behavior in the case of the decarburization reaction of these alloys exposed in air, Sachs (2) has suggested that a resistance to gas flow cannot be due to friction along the walls which would increase with scale thickness. He suggests therefore that the resistance is caused by a single narrow restriction in each pore which remains open as long as sufficient carbon monoxide is evolved. It would appear, however, that the decarburization rate observed under the exposure condition employed in this investigation is largely controlled by the surface reaction steps. Even when the surface was covered with a thick scale, the relatively rapid passage of carbon dioxide through the pores was sufficient to maintain the surface decarburization reaction involving adsorbed oxygen at least threefold more rapid than under the condition of oxygen supply from wustite during its reduction (Fig. 3). Also, the decarburization rate was not independent of wustite scale thickness and decreased with time when this reaction proceeded by direct reduction of wustite in vacuum (Fig. 2). These characteristics suggest that the rates of the surface reactions coupled with the supply of carbon to the reaction sites are the most significant factors for determining the kinetics under scaling and nonscaling conditions.

The pores in the scale remained effective for the transfer of carbon oxides up to the longest exposure interval in the carbon dioxide atmosphere. Under vacuum decarburization conditions, however, the rate of carbon loss was a function of the amount of wustite formed and the residual carbon in the alloy. To obtain additional information on this relationship, the instantaneous rates for vacuum decarburization were obtained by taking limiting tangents to the plots in Fig. 2. These rates are plotted *vs.* the scale thickness in Fig. 10. Decarburization became negligible when the scale thickness exceeded 100μ and the residual carbon content of the alloy was less than 0.5 w/o. It would appear therefore that the reaction of carbon with wustite may reach a state of equilibrium in the absence of a reactive atmosphere. Engell (3) calculated an equilibrium pressure of 16 atm for the carbon monoxide gas arising from the reaction of carbon in a 0.5 w/o C alloy with wustite at 950°C. This value, which is accurate probably to a factor of not greater than five by present limitations of thermodynamic data (4, 5), would represent the maximum pressure to be found in a closed pore of the wustite scale at the metal interface since the carbon concentration is the average concentration of an oxidized specimen. Peters and Engell (5, 6) also measured the adherence of wustite to iron and iron-carbon alloys by determining the force required to separate the scale from the metal and obtained values ranging from 100 atm for pure iron to 30 atm for Fe-0.6 w/o C. This latter value lies in the range of the calculated equilibrium

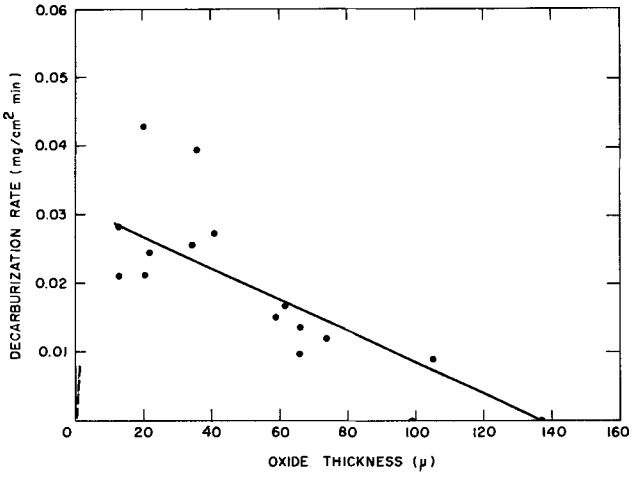

Fig. 10. Dependence of the initial vacuum decarburization rates on wustite scale thickness of the Fe-0.81 w/o C alloy immediately after oxidation in carbon dioxide at 950°C.

pressure of carbon monoxide, which suggests, as was found, that the wustite may become protective to decarburization at carbon contents below a critical value in the absence of a reactive atmosphere.

This investigation dealing with the reaction kinetics and observations on the structural features of the alloy and scales has substantiated the consideration that the reaction of carbon dioxide and wustite with carbon from an iron alloy occurs predominantly at the metal/oxide interface (1, 5-7). Carbon monoxide only reduced wustite at walls of pores to form a metal decoration as spires extending into the scale (Fig. 8). During vacuum decarburization, the small voids which appear at the metal/oxide interface could be accounted for by the difference in volume between wustite reduced and iron formed. These phenomena associated with the surface decarburization reaction and passage of carbon oxides through a porous wustite scale were most common. One other feature, blistering of the scale from the alloy did occur. Apparently growth and coalescence of wustite crystallites occasionally annihilated porosity in a scale at small localized areas, carbon build-up subsequently occurred and sufficient pressure of carbon monoxide was generated from the reaction of carbon with wustite for blistering of scale (Fig. 6). This type of reaction, nevertheless, was only of minor significance.

Summary

An investigation has been carried out on the oxidation and decarburization kinetics of a Fe-0.71 w/o C alloy at 950°C. Iron oxidation occurred approximately tenfold more rapidly than carbon oxidation under the steady-state reaction condition in the carbon dioxide atmosphere. The rate-controlling steps for decarburization were associated with the reaction at the alloy surface and possibly with a small constant resistance to passage of gaseous carbon oxides by pores in the wustite scale. A comparison of decarburization rates in the absence and presence of wustite indicated that the area of the surface affected by porosity was a maximum of 2-3%. Also, it was possible to show that these pores in the scale remained effective for gas transport at scale thicknesses less than 100μ and residual carbon contents in the alloy greater than 0.5 w/o under the conditions of vacuum decarburization. A small degree of scale blistering from the alloy surface was found to occur by the generation of a high pressure of carbon monoxide from the reaction of carbon with wustite at areas where growth and coalescence of the oxide crystallites annihilated scale porosity.

Acknowledgments

This research was supported by a grant from the American Iron and Steel Institute to W. W. Smeltzer. E. S. Reeves expresses his appreciation to the Defence Research Board of Canada for provision of a leave of absence from employment, and for financial assistance in the form of a Defence Research Board Scholarship. This paper is based on his thesis submitted to McMaster University in partial fulfilment of the requirements for the M.Sc. degree.

Manuscript submitted June 2, 1969; revised manuscript received Aug. 28, 1969.

Any discussion of this paper will appear in a Discussion Section to be published in the December 1970 JOURNAL.

REFERENCES

1. G. J. Billings, W. W. Smeltzer, and J. S. Kirkaldy, *This Journal*, **117**, 111 (1970).
2. K. Sachs, Proc. 1st Int. Congress Metallic Corrosion, p. 219, Butterworths Publishers (1962).
3. H. J. Engell, *Z. Elektrochem.*, **63**, 842 (1959).
4. F. D. Richardson, *J. Iron Steel Inst.*, **175**, 33 (1953).
5. F. K. Peters and H. J. Engell, *Arch. Eisenhuttenw.*, **28**, 567 (1967).
6. F. K. Peters and H. J. Engell, *ibid*, **30**, 275 (1959).
7. K. Bohnenkamp and H. J. Engell, Proc. 1st. Int. Congress Metallic Corrosion, p. 215, Butterworths Publishers (1962).

The Sublimation Pressure and Sublimation Coefficient of (100) Oriented Lead Telluride Single Crystals

Edward E. Hansen and Zuhair A. Munir

Department of Materials Science, School of Engineering, San Jose State College, San Jose, California

ABSTRACT

The sublimation pressure of (100) oriented single crystals of lead telluride was measured by the torsion-Langmuir method over the temperature range of 871°-993°K. The resulting expression for the free-surface sublimation pressure is $\log P(\text{atm}) = -(1.085 \pm 0.049)\ 10^4/T + (6.716 \pm 0.536)$ where T is the absolute temperature and the quoted errors are the standard deviations. Equilibrium sublimation pressures, as determined by the torsion-effusion technique in the temperature range of 919°-1042°K, were found to obey the expression: $\log P(\text{atm}) = -(1.109 \pm 0.026)\ 10^4/T + (7.119 \pm 0.261)$. Calculations of the third-law enthalpies for free-surface and equilibrium sublimations gave the values 54.95 ± 0.37 and 54.34 ± 0.13 kcal/mole, respectively.

Because of their properties as semiconductors, the chalcogenides of lead have been the object of considerable interest in recent years (1-3). A common method of preparation of thin films of these compounds employs a vapor deposition technique. In order to interpret the properties of the deposited films and to select suitable conditions for deposition, it is necessary to know the vapor pressure and the sublimation mechanism of these semiconductors.

Pashinkin and Novoselova (4) determined the sublimation rates from porous samples of lead telluride employing the Knudsen and Langmuir-like methods. Combining the results of these methods they concluded that the sublimation coefficient of lead telluride was essentially one. More recently, Brebrick and Strauss (5), employing an optical absorption method, determined the partial optical densities of vapors in equilibrium with solid lead telluride. They then used

the results of ref. (4) to calculate partial pressures of $Te_2(g)$ and PbTe(g) over PbTe(s).

Since vapor pressure values measured over free porous surfaces represent only upper limits, a total understanding of the sublimation mechanism of lead telluride is not complete without knowledge of the sublimation rates from single crystal samples. Furthermore, it would seem highly desirable to determine the equilibrium vapor pressure of this compound using the weight-loss-independent torsion method.

Experimental

The torsion-effusion and torsion-Langmuir methods have been adequately described in recent publications (6, 7). Detailed description of the apparatus used in this investigation has been given elsewhere (8).

Cylindrical cells made from National Carbon ZT101 Grade graphite were used in the torsion-effusion study. Previous experience with identical cells proved the absence of leakage around the friction-fitted lids (8). Graphite blocks with diagonally situated sample wells were used in the torsion-Langmuir portion of this study. Geometric descriptions of all cells used in this work as well as the appropriate Freeman-Searcy force correction factors (9) appear in Table I.

Temperatures were measured by means of a calibrated Pt-Pt/10% Rh thermocouple inserted inside a dummy cell which is situated about 1 cm below the torsion cell in the center portion of a tungsten heating element. Calibration of this thermocouple was accomplished by measuring the freezing points of aluminum, silver, and copper samples placed inside the dummy cell. As an additional check on the validity of results obtained in this apparatus the vapor pressures of tin, zinc, and silver were redetermined in the range from 10^{-6} to 10^{-3} atm. These measurements gave third-law $\Delta H°_{298}$ values of 72.4 ± 0.1, 31.6 ± 0.2, and 68.49 ± 0.05 kcal/mole, respectively. Hultgren *et al.* (10) list $\Delta H°_{298}$ values of 72.2, 31.2, and 68.10 for the above-mentioned elements, respectively.

Lead telluride samples were obtained as cylindrically shaped ingots with approximate diameters of 1.5 cm. These ingots, which had been prepared from "99.9999% pure" elements by the Bridgeman technique, were examined by x-ray methods. The resulting Laue patterns showed them to be single crystals with the easy cleavage (100) planes perpendicular to the cylinder major axis (lead telluride has the NaCl structure). Furthermore, Debye-Scherrer powder patterns indicated the presence of the lead telluride phase only.

Wafer samples (about 1 mm thick) to be used in the torsion-Langmuir experiments were obtained by means of a spark cutter. Laue photographs showed that the orientation of the faces of the wafers was within 2° of the (100) planes of the crystal. Powder samples used in the torsion-effusion experiments were filed from the ingots using a tungsten carbide file.

The congruency of sublimation of powder and single crystal samples of lead telluride was established from x-ray evidence. Samples which had been heated in vacuum, at temperatures and for time periods corresponding to about 30% weight loss, showed no discernible change in the x-ray patterns. The only observable change was a darkening of color of the heated powders at or near their surface. Crystallographic examinations of heated wafers showed no change in their orientation even after they had suffered up to about 80% weight loss by vacuum heating.

Table I. Torsion cell characteristics

Cell	Sublimation area,* cm² a_1	a_2	Moment arm, cm q_1	q_2	Orifice depth/radius $(l/r)_1$	$(l/r)_2$	Freeman-Searcy factor
			Torsion-effusion				
A	0.0446	0.0446	1.292	1.277	2.60	2.60	0.506
B	0.0312	0.0312	1.243	1.303	3.16	3.16	0.459
C	0.0060	0.0060	1.274	1.289	7.28	7.28	0.274
			Torsion-Langmuir				
L	0.0789	0.0778	0.8720	0.8720	—	—	—
M	0.3164	0.3164	0.8720	0.8720	—	—	—

* This quantity is the orifice area in torsion-effusion cells and is the surface area of the sample in the torsion-Langmuir runs.

Results

Figure 1 shows the results of the vapor pressure measurements of both the torsion-effusion and torsion-Langmuir studies of lead telluride.

Using three cells, torsion-effusion sublimation pressures were measured between 919° and 1079°K. Calculations of the mean free path to orifice diameter ratios, λ/d, showed a systematic increase in the pressure results as this ratio fell significantly below one. Thus only vapor pressure values whose λ/d ratios were greater than one were included in all subsequent calculations. Based on the following reaction

$$PbTe(s) = PbTe(g) \qquad [1]$$

the least-square fit of the torsion-effusion data in the temperature range of 919°-1042°K was found to be

$$\log P(\text{atm}) = -(1.109 \pm 0.026)\ 10^4/T + (7.119 \pm 0.261) \qquad [2]$$

where P is the pressure, T is the absolute temperature, and the quoted errors are the standard deviations. Based on Eq. [1] and [2] second-law heat and entropy changes at 980°K were calculated to be 50.7 kcal/mole and 32.6 eu, respectively. Using reported Cp values (11, 12) the corresponding thermodynamic quantities at 298°K, $\Delta H°_{298}$ and $\Delta S°_{298}$, were found to be 54.9 ± 1.2 kcal/mole and 39.1 ± 1.2 eu. In order to determine third-law $\Delta H°_{298}$, free-energy functions were calculated from reported heat capacity data for PbTe(g) (11) and PbTe(s) (12). These calculations whose results appear in Table II gave an average value of $\Delta H°_{298}$ of 54.34 ± 0.13 kcal/mole.

Figure 1 also shows the results of the torsion-Langmuir studies of the sublimation from (100) oriented crystals of lead telluride. Employing a least-square fit for these data the expression for the sublimation pressure over the temperature range of 871° to 993°K was found to be

$$\log P(\text{atm}) = -(1.085 \pm 0.049)\ 10^4/T + (6.716 \pm 0.536) \qquad [3]$$

where T is in degrees Kelvin and the stated errors are the standard deviations. Second-law calculations of the heat and entropy of sublimation gave $\Delta H°_{932}$ =

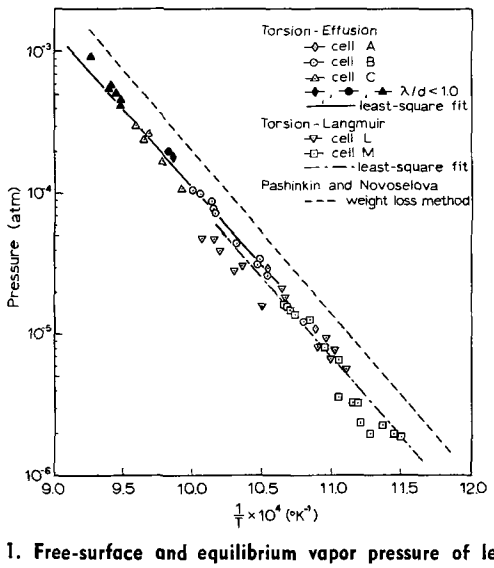

Fig. 1. Free-surface and equilibrium vapor pressure of lead telluride.

Table II. Third-law heats of sublimation of lead telluride: torsion-effusion

T, °K	P, atm	Δfef, cal/deg mole	λ/d	$\Delta H°_{298}$, kcal/mole
		Cell A		
919	1.10×10^{-5}	36.55	9.39	54.44
949	2.87×10^{-5}	36.42	3.71	54.28
986	8.93×10^{-5}	36.24	1.24	54.00
1014	1.89×10^{-4}	36.10	0.61	53.88*
		Cell B		
925	1.22×10^{-5}	36.53	10.16	54.58
949	2.60×10^{-5}	36.42	4.89	54.47
954	3.33×10^{-5}	36.37	3.86	54.24
955	3.13×10^{-5}	36.39	4.09	54.35
969	4.64×10^{-5}	36.32	2.80	54.41
985	7.20×10^{-5}	36.24	1.83	54.37
986	7.75×10^{-5}	36.24	1.71	54.28
987	8.80×10^{-5}	36.21	1.50	54.10
996	1.06×10^{-4}	36.19	1.26	54.16
996	9.74×10^{-5}	36.19	1.37	54.33
1017	2.00×10^{-4}	36.09	0.68	53.96*
		Cell C		
1008	1.08×10^{-4}	36.12	2.86	54.71
1022	1.65×10^{-4}	36.06	1.89	54.54
1033	2.53×10^{-4}	36.01	1.24	54.20
1035	2.48×10^{-4}	36.00	1.27	54.34
1042	2.94×10^{-4}	35.97	1.08	54.32
1054	4.29×10^{-4}	35.92	0.75	54.10*
1055	4.64×10^{-4}	35.92	0.69	53.99*
1057	5.05×10^{-4}	35.91	0.64	53.90*
1062	5.87×10^{-4}	35.88	0.55	53.81*
1063	5.77×10^{-4}	35.87	0.56	53.88*
1079	9.19×10^{-4}	35.80	0.36	53.63*

* Data not included in calculating $\Delta H°_{298}$ average.

49.6 kcal/mole and $\Delta S°_{932} = 30.7$ eu, respectively. Using the cited heat capacity data the corresponding values at 298°K were calculated to be 53.4 ± 2.3 kcal/mole and 36.9 ± 2.4 eu. Free-energy functions, calculated from Cp data referred to above, were used to calculate third-law heat of free-surface sublimation. Results of these calculations are shown in Table III. From this table an average value of $\Delta H°_{298}$ was found to be 54.95 ± 0.37 kcal/mole.

Discussion

The congruency of sublimation of lead telluride established in this work by x-ray methods is in agreement with observations made by others (4, 13). Porter (13), using mass spectrometric techniques, studied the composition of vapors effusing from graphite Knudsen cells containing solid lead telluride. His observations showed PbTe(g) to be the most significant gaseous species over PbTe(s). From optical absorption measurements, Brebrick and Strauss (5) concluded that PbTe(g) constitute about 98% of the sublimate from lead telluride.

Table III. Third-law heats of sublimation of lead telluride: torsion-Langmuir

T, °K	P, atm	Δfef, cal/deg mole	$\Delta H°_{298}$, kcal/mole
	Cell M		
871	1.86×10^{-6}	36.74	54.84
874	1.98×10^{-6}	36.73	54.90
880	2.26×10^{-6}	36.71	55.04
887	1.97×10^{-6}	36.68	55.69
893	2.36×10^{-6}	36.65	55.72
895	3.20×10^{-6}	36.65	55.30
898	3.21×10^{-6}	36.64	55.48
906	3.53×10^{-6}	36.62	55.78
906	6.57×10^{-6}	36.62	54.65
911	7.49×10^{-6}	36.58	54.70
913	8.02×10^{-6}	36.57	54.68
913	7.92×10^{-6}	36.57	54.70
927	1.24×10^{-5}	36.52	54.67
932	1.39×10^{-5}	36.49	54.72
934	1.48×10^{-5}	36.48	54.71
936	1.53×10^{-5}	36.47	54.77
938	1.61×10^{-5}	36.46	54.77
	Cell L		
901	5.60×10^{-6}	36.63	54.65
908	7.67×10^{-6}	36.60	54.49
910	6.49×10^{-6}	36.59	53.99
911	7.27×10^{-6}	36.59	54.75
913	9.19×10^{-6}	36.58	54.44
915	7.81×10^{-6}	36.57	54.85
917	8.11×10^{-6}	36.57	54.90
937	1.80×10^{-5}	36.47	54.51
941	2.08×10^{-5}	36.45	54.46
953	1.52×10^{-5}	36.39	55.68
965	3.01×10^{-5}	36.34	55.03
971	2.83×10^{-5}	36.30	55.46
980	3.91×10^{-5}	36.27	55.31
985	4.61×10^{-5}	36.25	55.25
993	4.68×10^{-5}	36.20	55.62

The existence of equilibrium conditions inside the torsion-effusion cells was demonstrated by the observation that measured pressures showed no dependency on orifice size (14). The only deviation from equilibrium conditions came from data points for which the λ/d ratio was less than one. These points which correspond to nonmolecular flow conditions (15) were not included in the thermodynamic calculations.

Effects of volume diffusion through the walls of the torsion cell, and of surface diffusion around the orifice were examined. The former effect contributes no net torque to the cell and hence is of little significance in any study employing the torsion method. In accordance with theoretical considerations (16) a check was made on the magnitude of the surface diffusion effect. Results of such analyses proved the insignificance of any loss of material by means of surface diffusion around the orifice.

Because of the relatively small thickness (~1 mm) of the lead telluride samples used in the torsion-Langmuir experiments, and in view of the manner in which they were positioned and held on the graphite cells (approximately three fourths of their surface was in contact with graphite), it is unlikely that the phenomenon of evaporation-cooling (17) can create a significant temperature gradient across the samples and thus lead to erroneously low free-surface sublimation pressures. The negative deviation of the reported pressures at the high temperature end of the torsion-Langmuir studies may be suspected of being caused by evaporation-cooling. However, on examination of the remainder of the data, it becomes difficult not to attribute this deviation to the experimental scatter in the reported pressure results.

Torsion-Langmuir studies on (100) oriented crystals gave sublimation pressures somewhat lower than the equilibrium values in the corresponding temperature range. Based on this pressure difference, calculations of the sublimation coefficient, α, at 1000°K gave a value of about 0.7. In spite of the uncertainties in the data used in the calculation of this coefficient, justification for the reported value of α is based on the theoretical treatment given by Hirth and Pound (18). According to this treatment sublimation coefficients of low-index crystalline planes are expected to have a theoretical value of considerably less than one, even for such nondissociative sublimation processes as that of Eq. [1]. Measured sublimation rates from oriented single crystals of silver have in effect demonstrated this (19).

Acknowledgments

The authors gratefully acknowledge the technical assistance of Walter Mounts and Arthur Cooper. The assistance of Mrs. Phyllis Ashe and Mrs. Sylvia Peaker in the preparation of this manuscript is also acknowledged.

Manuscript submitted March 17, 1969; revised manuscript received Aug. 15, 1969.

Any discussion of this paper will appear in a Discussion Section to be published in the December 1970 JOURNAL.

REFERENCES

1. C. Agabaev, B. Gol'tsman, E. Nensberg, and A. Petrov, *Izv. Akad. Nauk. SSR, Neorg, Mat.*, **4**, 621 (1968).
2. L. S. Palatnik and V. K. Sorokin, *ibid.*, **4**, 337 (1968).
3. R. A. Smith, *Adv. Phys.*, **2**, 321 (1953).

4. A. S. Pashinkin and A. V. Novoselova, *Russ. J. Inorg. Chem.* (English translation, Chem. Soc., London), **4**, 1229 (1959).
5. R. F. Brebrick and A. J. Strauss, *J. Chem. Phys.*, **40**, 3230 (1964).
6. Z. A. Munir and A. W. Searcy, *This Journal*, **111**, 1170 (1964).
7. R. C. Blair and Z. A. Munir, *J. Phys. Chem.*, **72**, 2434 (1968).
8. W. T. Lee and Z. A. Munir, *This Journal*, **114**, 1236 (1967).
9. D. A. Schulz and A. W. Searcy, *J. Chem. Phys.*, **36**, 3099 (1962).
10. R. Hultgren, R. L. Orr, P. D. Anderson, and K. K. Kelley, "Selected Values of Thermodynamic Properties of Metals and Alloys," John Wiley & Sons, Inc., New York (1963).
11. K. K. Kelley, U.S. Bur. Mines Bull. 584 (1960).
12. C. Hirayama, *J. Chem. Eng. Data*, **9**, 65 (1964).
13. R. F. Porter, *J. Chem. Phys.*, **34**, 583 (1961).
14. K. Motzfeld, *J. Phys. Chem.*, **59**, 139 (1955).
15. K. D. Carlson, P. W. Gilles, and R. J. Thorn, *J. Chem. Phys.*, **38**, 2064 (1963).
16. N. A. Gokcen, *J. Phys. Chem.*, **69**, 3538 (1965).
17. R. S. Bradley and P. Volans, *Proc. Roy. Soc. (London)*, **217A**, 508 (1953).
18. J. P. Hirth and G. M. Pound, *Prog. in Mater. Sci.*, **11**, 1 (1963).
19. J. P. Hirth and G. M. Pound, *Trans. AIME*, **215**, 932 (1959).

Technical Notes

Multiple Activation of YVO_4

S. Faria* and D. T. Palumbo

Sylvania Electric Products Inc., Chemical and Metallurgical Division, Towanda, Pennsylvania

The YVO_4 matrix serves as an efficient host for many rare earth (1) and nonrare earth (2) activators. Most works treat the singly activated systems or the combination of a rare earth and non-rare-earth activator (3, 4) or at most two rare earths in combination (5), except in the case of Brixner and Abramson (6) where emissions due to low concentrations of rare earth impurity were observed. In this note we discuss the spectra of YVO_4 multiply activated with combinations of Dy, Er, Sm, Eu, Bi, or In. Our aim was to prepare a single component phosphor having the same chromaticity as Illuminant A.

Experimental

The phosphors were prepared using conventional procedures as described in previous papers (2a, 5). The uncorrected emission spectra were recorded with a Perkin-Elmer Hitachi MPF-2A spectrophotometer. The phosphors were tested in 40W low-pressure fluorescent lamps for light output and color rendering index (7).

* Electrochemical Society Active Member.

Experimental Results

YVO_4:Dy,Er,Sm,Eu.—Because of its strong emission at low concentrations, Dy was selected as the primary activator. Various concentrations of the other rare earth elements (Er,Sm,Eu) were then added to YVO_4:Dy(0.003). The amounts required to approximate the Illuminant A energy distribution were usually less than the optimum concentration needed for the singly activated YVO_4. For example, the optimum Eu content was between 3 and 5 m/o (mole per cent) in YVO_4, while in YVO_4:Dy(0.003), 0.3-0.5 m/o Eu was sufficient to initiate quenching of the Dy emission. The emission spectrum of YVO_4:Dy(0.003) is shown in Fig. 1. Other rare earths are known to emit their major characteristic emission lines in the spectral area not occupied by the Dy multiplets. Rare

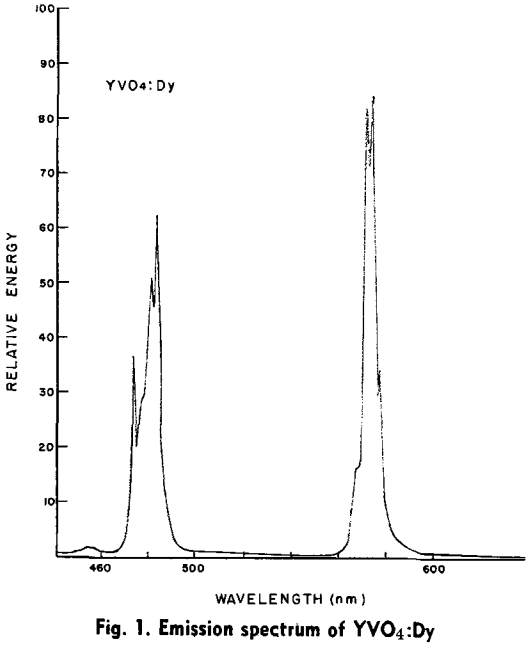

Fig. 1. Emission spectrum of YVO_4:Dy

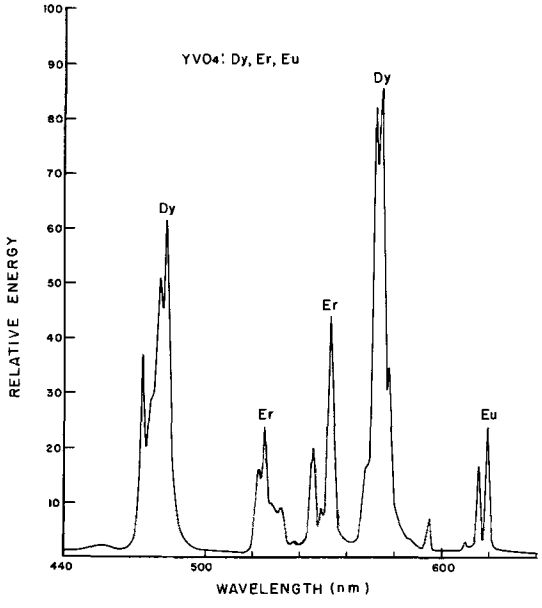

Fig. 2. Emission spectrum of YVO_4:Dy, Er, Eu

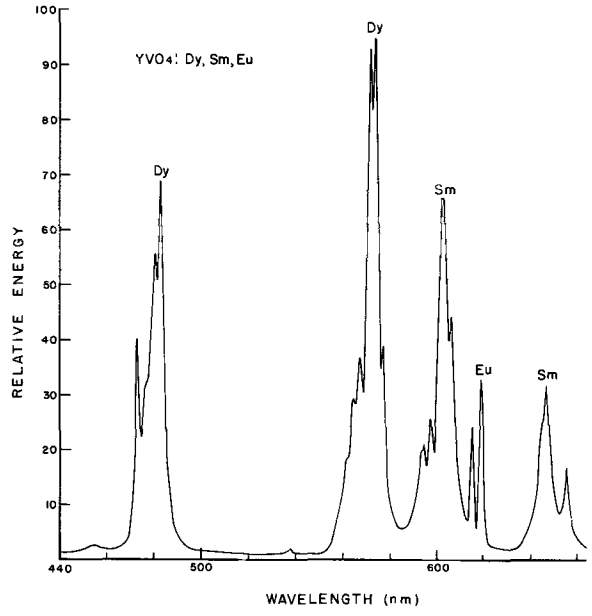

Fig. 3. Emission spectrum of YVO_4:Dy, Sm, Eu

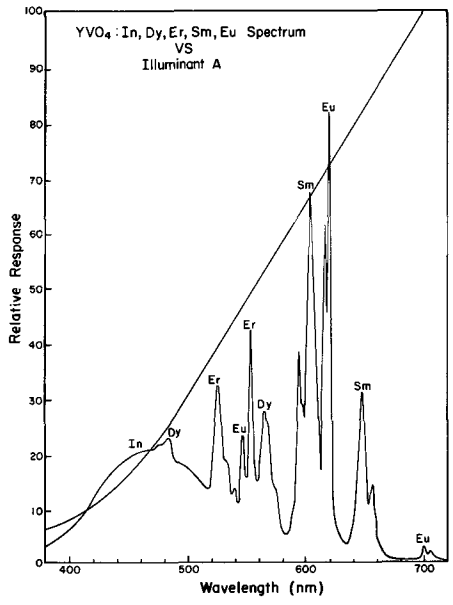

Fig. 5. Emission spectrum of YVO_4:In, Dy, Er, Sm, Eu

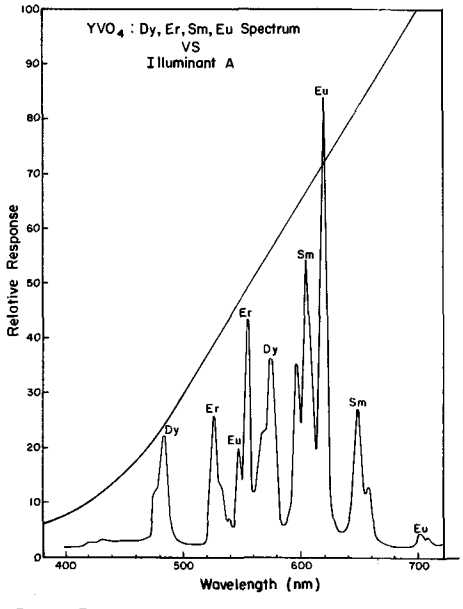

Fig. 4. Emission spectrum of YVO_4:Dy, Er, Sm, Eu

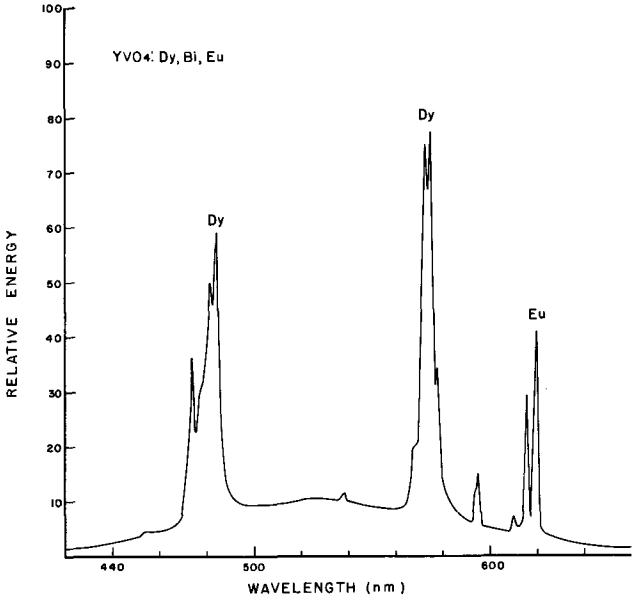

Fig. 6. Emission spectrum of YVO_4: Dy, Bi, Eu

earth elements known to emit between the two Dy multiplets are Tb at 543nm, Er at about 550nm, and Ho at about 545nm. Of these three, Er was the only one to show strong intensities in the presence of Dy and small traces of Eu. Figure 2 shows the emission spectrum of YVO_4:Dy(0.003), Er(0.007), and Eu (0.0003). Erbium lines are shown to be very strong at 525, 545, and about 555 nm. In the long-wavelength spectral region, *i.e.*, beyond the 575 nm Dy lines, Sm and Eu are the most intense rare earth emitters.

Samarium was incorporated together with Dy and Eu. Figure 3 shows Sm lines appearing at about 600 and around 645 nm. In this spectrum the concentration of Sm was 0.008 while Dy was kept at 0.003 and Eu at 0.0003. The addition of Er to YVO_4:Dy,Eu,Sm fills the gap in the emission spectrum between the Dy multiplets. Figure 4 shows the emission spectrum of all these rare earths, Dy, Er, Sm, and Eu. Figure 4 gives the spectrum of YVO_4:Dy,Er,Sm,Eu compared to Illuminant A (tungsten lamp at 2848°K) which is shown as the superimposed line. The composition of the phosphor represented in Fig. 4 is YVO_4:Dy(0.0007), Er(0.008), Sm(0.005) and Eu(0.0025). Note that the Dy lines are still very strong even in the presence of more than ten times as much Er, seven times as much Sm, and three times as much Eu. This phosphor composition, however, lacks some blue and red emission compared to the Illuminant A distribution.

YVO_4:In,Dy,Er,Sm,Eu.—The blue emission of YVO_4:Dy,Er,Sm,Eu was enhanced by incorporating In, a non-rare-earth element. By adjusting the proportions of each rare earth and by using about 2 m/o In, a chromaticity closer to Illuminant A was obtained. The color coordinates of the YVO_4:In(0.02), Dy (0.0007), Er(0.008), Sm(0.005), Eu(0.0025) phosphor shown in Fig. 5 were $x = 0.429$ and $y = 0.393$ with 254 nm excitation, compared to $x = 0.448$ and $y = 0.408$ for Illuminant A.

YVO_4:Dy,Bi,Eu.—The addition of Bi to YVO_4:Dy,Eu introduced the typical broad emission band of YVO_4:Bi (3, 4) with a peak at about 550 nm. Dy, Eu, and Bi were incorporated in YVO_4 yielding a phosphor with the following composition, YVO_4:Dy(0.003), Bi(0.002), Eu(0.002). The emission spectrum is shown in Fig. 6. By slightly increasing the Dy content to 0.004 in this phosphor, we obtain color characteristics close to

Illuminant A. The x color coordinate was 0.438 and the y was 0.403, measured in 40W fluorescent lamps with an output of about 2500 lumens and a color rendering index of 50.

Summary

YVO_4 can simultaneously accommodate a multiplicity of rare earth and non-rare-earth activators, each emitting its characteristic spectral lines or bands. Although the color of Illuminant A can be obtained with reasonable light output, the gaps in the spectral energy distribution, as a consequence of the use of line emitters, give poor color rendition.

Manuscript received June 9, 1969; revised manuscript received Aug. 8, 1969. This was a Recent News Paper presented at the New York Meeting of the Society, May 4-9, 1969.

Any discussion of this paper will appear in a Discussion Section to be published in the December 1970 JOURNAL.

REFERENCES

1a. F. C. Palilla, A. K. Levine, and M. Rinkevics, *This Journal*, **112**, 776 (1965); 1b. R. C. Ropp, *ibid.*, **115**, 940 (1968).
2a. S. Faria and C. W. Fritsch, Jr., *ibid.*, **116**, 155 (1969); 2b. G. Blasse, *Philips Res. Rept.*, **23**, 344 (1968).
3. S. Z. Toma, F. F. Mikus, and J. E. Mathers, *ibid.*, *Journal*, **114**, 953 (1967).
4. R. K. Datta, *ibid.*, **114**, 1057 (1967).
5. S. Faria and D. T. Palumbo, *ibid.*, **116**, 157 (1969).
6. L. H. Brixner and E. Abramson, *ibid.*, **112**, 70 (1965).
7. Publication C.I.E. No. 13, (E-1.3.2) 1965.

Epitaxially Grown Graded Heterojunctions of (Zn, Cd)S

W. J. Biter and R. B. Lauer[1]

University of Delaware, Newark, Delaware

In this communication we wish to report the epitaxial growth of CdS crystals on ZnS single crystal substrates. Due to the elevated temperatures at which these heterojunctions are grown there exists a transition region between the pure ZnS and the pure CdS. The transition region which has its origin in interdiffusion is a region of spatially dependent energy gap (1). The heterojunctions at 80°K show blue photoluminescence on the ZnS side and green photoluminescence on the CdS side. The majority of the work done on epitaxy in the II-VI compounds has been limited to the deposition of thin films of one II-VI onto another II-VI, either by chemical transport, vacuum evaporation, or flow method (2).

The technique used to grow the heterojunctions was basically the self-sealing method of Piper and Polich (3), except that an orientated ZnS single crystal was placed in the tip of the growth tube as shown in Fig. 1. [The ZnS crystal was grown in this laboratory and had impurities on the order of 10 ppm (4). The CdS powder was Semi-Elements and 99.999% pure.] The ZnS single crystal was orientated so that its c-axis was parallel to the axis of the growth tube. The ZnS single crystal was chemically etched in HCl prior to use. The optimum conditions for the successful epitaxial growth of CdS onto the ZnS were: (*a*) charge temperature of 1120°C; (*b*) an initial temperature difference of 20°C between the charge and the face of the ZnS; (*c*) a drive rate of 1.3 cm/day; and (*d*) a temperature gradient of 20°C/cm in the growth zone. The ambient used was 100 mm of Hg of HCl and 660 mm of Hg of H_2S. These crystal growth parameters represent optimum values. The HCl is added for doping; however, it probably increases the transport process as well. The duration of the growth run was 24 hr giving CdS regions of about 1 cm thick. The CdS crystal was composed of a number of large single crystals.

Back reflection Laue photographs showed that the c-axis of the epitaxially deposited CdS crystal was parallel to the c-axis of the ZnS substrates. Preliminary microscopic observations indicated that the transition region was between 50 and 100 μm thick. By means of electron microprobe analysis the exact spatial extent as well as the ratio of Zn to Cd in the transition region could be determined. Electron microprobe data for a typical heterojunction are shown in Fig. 2. Since a concentration gradient exists in the

[1] Present address: Itek Corporation, Lexington, Massachusetts.

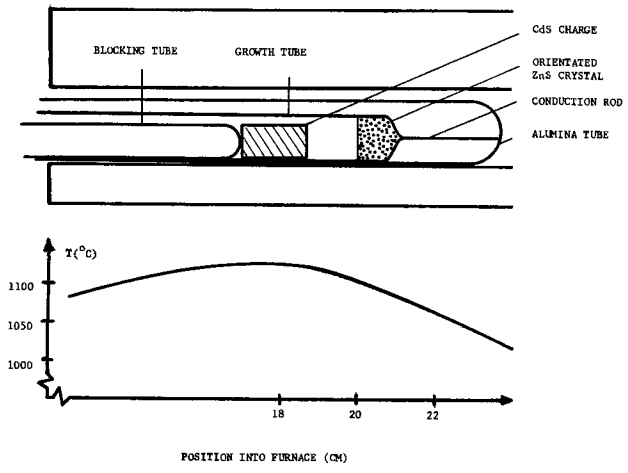

Fig. 1. Furnace and temperature profile for the growth of epitaxial heterojunctions of (Zn, Cd)S.

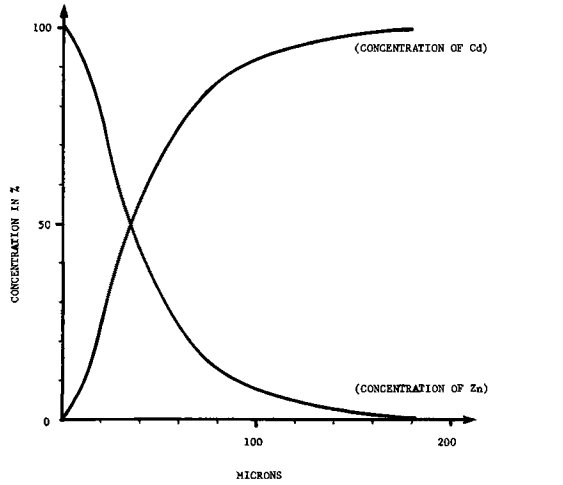

Fig. 2. Concentration of Zn and Cd as a function of position in (Zn, Cd)S graded heterojunctions.

system, it is necessary to consider the transition region as a region of spatially dependent energy gap (5).

Owing to the complex nature of the interdiffusion process it is impossible to relate the diffusion to a specific type of diffusion, or to calculate an exact diffusion constant. This technique of epitaxial crystal growth does serve as a method for obtaining graded heterojunctions of II-VI compound systems, and should be readily applicable to such systems as CdS on ZnTe or CdSe on ZnS. Although it is impossible to generalize on the nature of the interdiffusion process, an order of magnitude diffusion constant characterizing the diffusion process can be obtained from the electron microprobe data by taking the two end points and assuming that the diffusion follows the relation $C(x,t) = C'$ erfc $(x^2/4Dt)^{1/2}$. The value of D obtained for 1100°C is 10^{-11}cm^2/sec. This value most likely represents a weighted average value for the combined diffusion of Zn into CdS and Cd into ZnS.

Acknowledgment

The authors would like to thank Professor Ferd Williams for his constant encouragement. This work was partially supported by the United States Army Research Office—Durham, Contract No. DA-31-124-ARO (D)-173.

Manuscript submitted July 3, 1969; revised manuscript received Oct. 13, 1969.

Any discussion of this paper will appear in a Discussion Section to be published in the December 1970 JOURNAL.

REFERENCES

1. Y. Marfaing, G. Cohen-Solal, and F. Bailly, *J. Phys. Chem. Solids*, Suppl. 549 (1966).
2. R. J. Caveney, *J. Cryst. Growth*, **2**, 85 (1968).
3. W. W. Piper and S. J. Polich, *J. Appl. Phys.*, **32**, 1278 (1961).
4. Indradev, Materials Res. Bull., **1**, 173 (1966).
5. Thaddeus Gora and Ferd Williams, *Phys. Rev.*, **177**, 1179 (1969).

SEM Observation of Self-Healing Breakdown in Thermally Grown SiO_2 Films

P. Wang* and N. Van Buren

General Telephone and Electronics Laboratories, Inc., Woburn, Massachusetts

and P. Edraos

Rome Air Development Center, Griffiss AFB, New York

During a study of switching in thin dielectric films, we observed, through a low-power microscope in a darkened room, faint bluish light emission generally along the periphery of the top electrode when a gradually increasing negative potential was applied. A typical test vehicle was a thin silicon dioxide film (between 0.06 and 0.1 μm thick) grown by thermal oxidation at 1050°-1100°C in a clean environment on a p-type silicon substrate of 0.002-0.008 ohm-cm resistivity. An evaporated gold film was used to provide backside contact, and the top electrodes were formed by electron beam evaporation of thin aluminum (of approximately 0.1 μm thickness) to form dots through a metal mask. The light emission was generally concurrent with an increase in leakage current observable on a Tektronix 575 curve tracer, beginning at well below bulk breakdown field strength. At a potential near, or slightly exceeding, bulk breakdown the device switched from a high resistance state, typically greater than 10^7 ohms, to a high conductance state of typical resistance of less than 100 ohms for a 0.020 in. diameter Al dot. By means of an appropriate current pulse, the device could be switched back to the high resistance state. The transition time for the switching effect is submicrosecond. The switching cycle might be repeated for tens or even hundreds of times with little visually detectable change in the appearance of the device structure until it failed. Its failure was usually accompanied by a white flash and a partially damaged top electrode. This was true for either devices on a slice or devices mounted on a transistor base with aluminum wire bonded contacts.

It is known (1, 2) that in an actual dielectric thin film structure there are weak spots in the dielectric material which must be cleared out by self-healing breakdowns before the true bulk electrical breakdown can be seen. For thin dielectric films and thin aluminum top electrodes, as in our case, the breakdown may be dominated by either structural defects or field distortion, which may be due to surface roughness or to the irregular edge of the electrode which is shaped by evaporation with a mask. Electrical breakdown in dielectric material may be due to an electronic avalanche caused by the stripping and acceleration of electrons by the applied field. In our devices, breakdown usually occurred at voltages between 60 and 100V. Sometimes, we observed a series of bluish light spots before the device was turned on. Since scanning electron microscopy has been of value in the study of semiconductor device failure, we decided to examine our devices in a JEOLCO model JSM scanning electron microscope by both secondary electron mode and beam-induced-current mode. Phase-contrast microscopy was also used to examine the test devices (before and after SEM study) for minute structural changes.

Selected open devices were examined on the JEOL scanning electron microscope with step increase in the applied bias to the aluminum top electrode. Each voltage step was held for several minutes, and Polaroid photographs were taken of the CRT displays. For instance, in device DS-0035-1B-6, the following figures show the beam-induced-current mode image of devices under varying bias. Figures 1a and 1b are at bias voltages less than 45V. The luminous effect at the periphery is explained as due to the enhanced conduction near the electrode edge at which a fringing electric field can accelerate injected beam-electrons toward the positive return. However, when a continuous bias of −50V was applied, we began to see microplasmas in the device areas, as shown in Fig. 1c to 1e. These three pictures show a sequence of self-healing breakdowns and a growing number of locations where beam-induced current gradually ceased to flow. We propose that these breakdowns in the area of the mask-evaporated aluminum electrode occurred at thinly covered spots on the dielectric film, and that those at the edge occurred where the deposited aluminum film was thinner, feathering out to the edge. In

* Electrochemical Society Active Member.

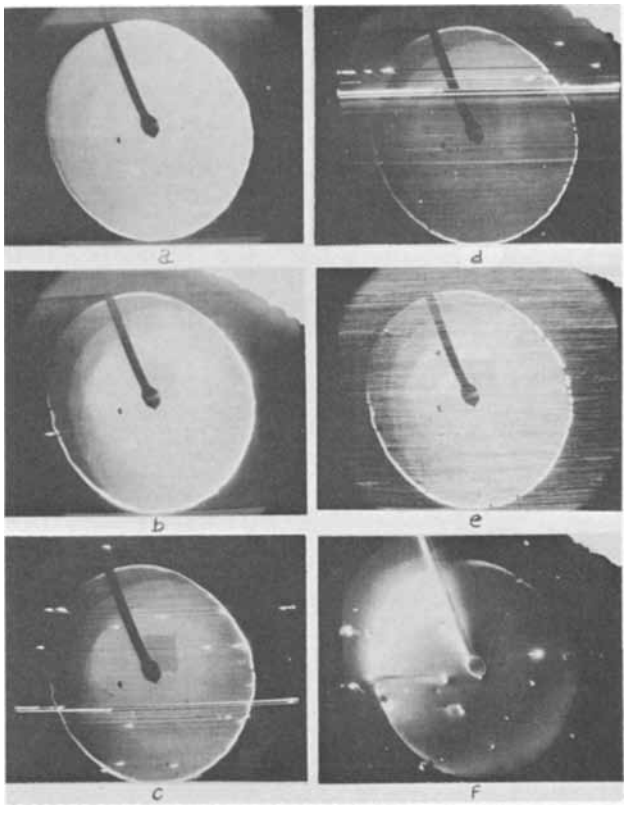

Fig. 1 SEM photographs of Al/SiO_2/p^+ Si thin film device: a, BIC Mode —20V; b, BIC Mode —45V; c, BIC Mode —50V, frame No. 1; d, BIC Mode —50V, frame No. 2; e, BIC Mode —50V, frame No. 3; f, SE Mode (voltage contrast) —50V. Magnification 90X.

such locations, the electrons of the scanning beam could most readily penetrate the negatively biased electrode, thus entering a strong accelerating field toward the positive electrode. Such electron current, at high field, then avalanched causing discharge of the device capacitance through the small breakdown region, generating enough heat to evaporate and/or fuse the thin film, resulting in disconnection from the bias. Thereafter, only thicker aluminum nearby remained biased, and being relatively impenetrable, the scanning beam had much less opportunity to be injected into the field. As seen in Fig. 1e, only the edge was bright at the fringing field, and the weak spots inside the dielectric film were essentially eliminated by the single-hole-propagated self-healing breakdown mechanism. Physical damage to the electrode may be seen in the voltage contrast, secondary electron mode photograph shown in Fig. 1f. A picture (inverted) taken later by means of a Reichert metallograph with phase-contrast attachment (Fig. 2) further illustrates the physical damage introduced during SEM examination. There is a one-to-one correspondence between the light spots and the burned areas.

Additional support to the proposed model was obtained by capacitance measurement of test devices on a General Radio conductance-capacitance bridge. Device capacitance was measured initially and after each of several pulsed switching cycles. Each cycle resulted in a small decrease in capacitance, due to localized

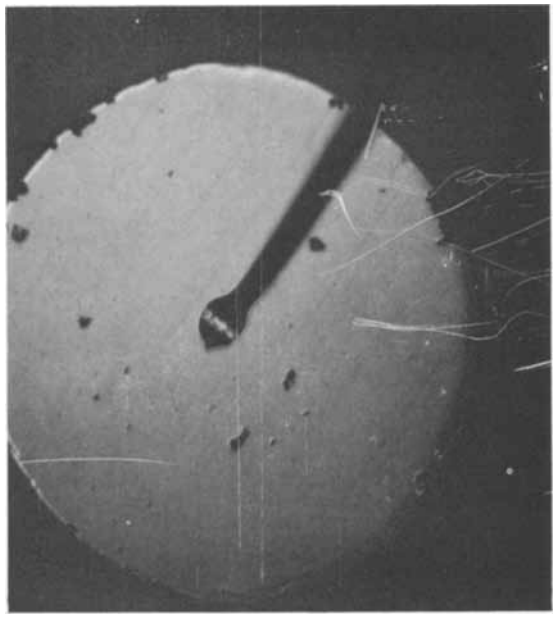

Fig. 2. Phase-contrast micrograph of same device after SEM examination, Magnification 125X.

erosion of aluminum near a conduction path, amounting to a few per cent or tenths per cent. Ultimately, the device under test would remain in a conductive state, or its capacitance would decrease substantially (say, to 10%) due to gross upper electrode destruction.

This phenomenon was observed in aluminum oxide, silicon nitride and silicon nitride-on-silicon dioxide films, and in silicon oxide films with sputtered molybdenum top electrodes. In these film devices, switching appears to occur at fields slightly above bulk breakdown and to proceed by a destructive mechanism. Although these devices may function for a large number of cycles, we cannot predict their life expectancy. We have attempted to modify the structure of the dielectric films by means of x-ray (40 kV) and high energy neutron (3 and 14 MeV) irradiation and by introduction of impurities during device fabrication with the hope that different modes of switching in these films would result. However, no significant difference in their switching behavior was observed.

Acknowledgment

The authors wish to acknowledge the valuable discussion on the subject of dielectric breakdown in silicon oxide thin films with Professor N. Klein of the Faculty of Electrical Engineering, Israel Institute of Technology. The scanning electron micrographs were taken by Mr. Joshua Varon of GT and E Laboratories, Bayside Research Center.

This work was supported by U. S. Air Force Contract No. F30-602-68-C-0159.

Manuscript received Aug. 20, 1969.

Any discussion of this paper will appear in a Discussion Section to be published in the December 1970 JOURNAL.

REFERENCES

1. N. Klein, *Trans. IEEE*, **ED-13**, 788 (1966).
2. N. Klein, Paper 456 presented at the Montreal Meeting of the Society, Oct. 6-11, 1968.

Brief Communication

Residual Impurities in High-Purity Epitaxial GaAs

C. M. Wolfe,* G. E. Stillman, and E. B. Owens

Lincoln Laboratory, Massachusetts Institute of Technology, Lexington, Massachusetts

Vapor and liquid epitaxial growth techniques have been notably successful in obtaining low concentrations of electrically active impurities in GaAs, and the total ionized impurity densities in the higher purity samples have been analyzed in some detail (1). By using a vapor growth method we have obtained epitaxial layers with total ionized impurity densities as low as 6.9 x 10^{13} cm^{-3} ($\mu_{77°K}$ = 210,000 cm^2/V-sec) (2). However, little is known about the residual total impurity content of these high-purity epitaxial layers, and the residual electrically active impurities have not been identified. Here we report the results of mass spectrographic analyses with detection limits down to 1 x $10^{15}cm^{-3}$ for samples of epitaxial GaAs with total ionized impurity concentrations as low as 7.6 x 10^{13} cm^{-3} ($\mu_{77°K}$ = 200,000 cm^2/V-sec).

The epitaxial samples analyzed here were grown on Cr-doped semi-insulating substrates with the $AsCl_3$-Ga-H_2 vapor flow system. Electrical measurements and mass spectrographic analyses were performed on either the same sample or samples grown during the same run. The Cr-doped substrates and the Sn ohmic contacts for the electrical measurements together with the regrown region below the contacts were removed before the mass spectrographic analyses.

The electrical measurements were performed in the van der Pauw configuration on symmetrically-shaped samples at a magnetic field of 5 kG. The shallow donor concentration (N_D) and the total acceptor concentration (N_A) were determined to within an estimated 10% by analyzing the temperature dependence of the Hall constant with the usual single donor statistics and/or by using the Brooks-Herring equation for ionized impurity scattering to analyze the Hall mobility at a temperature where other scattering mechanisms are minimal (3). When both analyses could be performed on the same sample, the results were in excellent agreement.

The results of these analyses for five epitaxial samples with total ionized impurity concentrations ($N_D + N_A$) from 2.6 x 10^{15} to 7.6 x $10^{13}cm^{-3}$ together with the measured mobilities at 300° and 77°K are shown in Table I. The properties of an undoped horizontal Bridgman grown crystal (sample No. 1) are shown for comparison. It is clear from these data that the epitaxial samples have a considerably lower electrically active impurity content than the melt grown sample. The sample thicknesses (last column in Table I) were generally large enough to obtain detection limits in the low $10^{15}cm^{-3}$ range for the mass spectrographic analyses.

The mass spectrographic analyses were performed with a double focusing mass spectrograph of the Mattauch-Herzog geometry (4) using a rf spark discharge as the ion source and a photographic plate as the detector. Pieces of the sample were used as self electrodes in the spark system. Only the singly charged ion lines were used in the quantitative evaluation. The lines were measured with a densitometer-analog computer system that corrected for the photoplate response and integrated the corrected intensity values as each line was scanned. Background corrections were made by subtracting the values obtained by integrating the spectral background immediately adjacent to each line for the same time interval required to scan that line. The photoplate was calibrated by the Churchill two-line method (5).

Table I. Results of electrical analyses

Sample No.	$\mu_{300°K}$, cm^2/V-sec	$\mu_{77°K}$, cm^2/V-sec	N_D, cm^{-3}	N_A, cm^{-3}	Thickness, μm
1	4400	6700	4.3 x 10^{16}	2.7 x 10^{16}	355
2	7700	53,000	1.8 x 10^{15}	8.0 x 10^{14}	135
3	8100	120,000	2.5 x 10^{14}	1.6 x 10^{14}	400
4	7500	155,000	1.0 x 10^{14}	9.0 x 10^{13}	295
5	8000	185,000	6.6 x 10^{13}	4.8 x 10^{13}	175
6	8200	200,000	4.6 x 10^{13}	3.0 x 10^{13}	150

It was assumed that the system was equally sensitive for all elements except that correction was made for the known mass effect on photoplate sensitivity (6). This assumption is necessitated by the lack of appropriate standards and can lead to errors as large as a factor of three in the absolute value of the concentrations reported. However, since it seems probable that the behavior of any one impurity would be the same in the ionization of all GaAs samples, it is estimated that the relative values for any one element in the several samples would be correct to within some 25%.

The results of these analyses for elements which have been reported to be donors in GaAs (O, Si, Sn, Te, Pb) and for elements reported to be acceptors (C, Fe, Cu, Zn, Cd) (7), together with the results of the electrical measurements for N_D and N_A from Table I, are shown in Table II. The nominal detection limit (NDL) for each sample is given in the last column. Other impurities which were detected in some samples at levels generally below $10^{16}cm^{-3}$ were N, Al, K, Ca, V, Sr, and Ta. It is interesting to note that no large difference in total impurity content is observed between the melt grown sample (sample No. 1) and the epitaxial samples or between the epitaxial samples with the highest and lowest electrically active impurity concentrations. This is in contrast to the three orders of magnitude difference in electrically active impurity content in these samples. The dominant impurities in all the samples are oxygen (2 x 10^{17} —1 x $10^{18}cm^{-3}$) and carbon (4 x 10^{17} —3 x $10^{18}cm^{-3}$). The total concentrations of possible donors and acceptors are greatly in excess of the electrically active donors and acceptors.

Obviously, with these high total impurity levels it is difficult to assign responsibility for the observed electrical activity to any particular impurity. Oxygen is generally believed to be a deep donor so that it would probably not be observed in the temperature range (4.2°-300°K) of the electrical measurements. The hydrogenic nature of the residual electrically active donors (8) strongly suggests a simple substitutional impurity and any of the remaining possible donors could be electrically active in a simple substitutional site. Silicon is observed in the melt grown

* Electrochemical Society Active Member.

Table II. Results of mass spectrographic analyses

Sample No.	N_D	O	Si	Sn, cm^{-3}	Te	Pb	NDL
1	4.3×10^{16}	1×10^{18}	4×10^{15}	—	—	—	1×10^{15}
2	1.8×10^{15}	4×10^{17}	—	4×10^{16}	1×10^{17}	2×10^{16}	7×10^{15}
3	2.5×10^{14}	4×10^{17}	—	—	—	—	2×10^{15}
4	1.0×10^{14}	3×10^{17}	1×10^{16}	—	1×10^{16}	—	1×10^{15}
5	6.6×10^{13}	2×10^{17}	—	—	2×10^{16}	—	2×10^{15}
6	4.6×10^{13}	2×10^{17}	—	—	9×10^{15}	—	2×10^{15}

Sample No.	N_A	C	Fe	Cu, cm^{-3}	Zn	Cd	NDL
1	2.7×10^{16}	4×10^{17}	—	—	—	4×10^{16}	1×10^{15}
2	8.0×10^{14}	3×10^{18}	4×10^{15}	7×10^{15}	4×10^{16}	2×10^{16}	7×10^{15}
3	1.6×10^{14}	8×10^{17}	—	—	—	—	2×10^{15}
4	9.0×10^{13}	8×10^{17}	—	—	—	—	1×10^{15}
5	4.8×10^{13}	1×10^{18}	—	—	—	—	2×10^{15}
6	3.0×10^{13}	5×10^{17}	—	—	—	—	2×10^{15}

sample and in the epitaxial sample with the lowest detection limit in the analysis, while large amounts of Te are detected in most of the epitaxial samples.

The electrical analyses should detect all electrically active acceptors. Carbon is observed in all the samples, and all the other possible acceptors are found in large quantities in the lowest purity epitaxial sample. Although these acceptors were not found in the other epitaxial samples, it should be noted that the nominal detection limits are much higher than the concentrations of electrically active acceptors.

The high total impurity contents found in high-purity epitaxial GaAs are similar to those observed in high-purity silicon ($N_D + N_A \sim 10^{13}cm^{-3}$) where large quantities of oxygen ($10^{15} - 10^{18}cm^{-3}$), carbon ($10^{15} - 10^{20}cm^{-3}$), and aluminum ($10^{15} - 10^{17}cm^{-3}$) have been detected by various analytical techniques (9). The large Al content in silicon is believed to be rendered electrically inactive by the formation of compounds with oxygen. Considering the high levels of possible donors and acceptors and the high levels of oxygen observed in epitaxial GaAs, it is conceivable that similar effects also occur in GaAs.

We conclude that the high density of apparently electrically inactive impurities in high-purity epitaxial GaAs suggests the possibility of complicated impurity interactions in the solid and makes the identification of the residual electrically active impurities a formidable problem.

Acknowledgment

This work was sponsored by the Department of the Air Force.

Manuscript received Sept. 19, 1969.

Any discussion of this paper will appear in a Discussion Section to be published in the December 1970 JOURNAL.

REFERENCES

1. J. Whitaker and D. E. Bolger, *Solid State Commun.*, **4**, 181 (1966); D. V. Eddolls, *Phys. Stat. Sol.*, **17**, 67 (1966); D. E. Bolger, J. Franks, J. Gordon, and J. Whitaker, "Proc. Intern. Symp. GaAs, Reading, 1966," p. 16, Institute of Physics and The Physical Society (1967); M. Maruyama, S. Kikuchi, and O. Mizuno, *This Journal*, **116**, 413 (1969).
2. C. M. Wolfe, G. E. Stillman, W. T. Lindley, L. Krohn, Jr., and J. O. Dimmock, Solid State Research Report, p. 8, Lincoln Lab., M.I.T. (1969:1).
3. C. M. Wolfe, G. E. Stillman, and J. O. Dimmock, To be published.
4. J. Mattauch and R. Herzog, *Z. Physik*, **89**, 786 (1934).
5. J. R. Churchill, *Ind. Eng. Chem., Anal. Ed.*, **16**, 653 (1944).
6. E. B. Owens, *Appl. Spectry.*, **16**, 148 (1962).
7. O. Madelung, "Physics of III-V Compounds," pp. 223-231, John Wiley & Sons, Inc., New York (1964).
8. G. E. Stillman, C. M. Wolfe, and J. O. Dimmock, *Solid State Commun.*, **7**, 921 (1969).
9. E. Spenke, Paper No. 265; W. Bonsels and J. L. Lambert, Paper No. 312; W. C. J. Gebauer, Paper No. 313; C. Gross, G. Gaetano, T. N. Tucker, and J. A. Baker, Recent News Paper No. 333. All presented at the New York Meeting of the Society, May 4-9, 1969.

JOURNAL OF THE ELECTROCHEMICAL SOCIETY

ELECTROCHEMICAL TECHNOLOGY

JANUARY 1970

A New Fast-Charging Power Source

P. Bro* and N. Marincic*

P. R. Mallory & Company, Incorporated, Laboratory for Physical Science, Burlington, Massachusetts

ABSTRACT

A new rechargeable system has been developed comprising the cell: $Cd/ZnCl_2$, $CdCl_2$, $NaClO_4/AgCl/Ag$. Practical cells have been made which can be charged at rates between 30° and 90°C *via* a dual charging process involving the primary deposition of zinc and its subsequent replacement by cadmium from solution. The open-circuit voltage of the cells is 0.75V, and they can be discharged at either high or low rates with low overvoltages. No gas evolution occurs at the high rates of charge, and sealed cells have been operated through ten cycles with discharge efficiencies above 95%. The high rate capability is associated with a low specific capacity and a low energy density.

A new type of rechargeable cell has been developed which is capable of being charged with impunity at rates as high as 90°C. The cells give low charge recoveries when charged at low rates, and they are restricted in use to fast-charging regimes only, where they operate with high coulombic efficiencies. No such restrictions apply to the discharge of the cells; they may be discharged at either high or low rates. The purpose of this report is to describe the work which led to the development of the cells and to describe their mode of operation and their essential operating characteristics.

The search for a fast-charging, aqueous, electrochemical system led us to examine the intrinsic charging rate capability of a large number of anodes and cathodes in a variety of electrolytes. Our objective was to find a set of matching electrodes that could be charged to useful specific capacities at the 100°C rate without any gas being produced at the electrodes during the high rate of charge. It became apparent that anodes formed by deposition from concentrated solutions of an anode salt had much higher specific rate capabilities than anodes formed *via* solid-solid transformation processes such as the charging of cadmium anodes from cadmium oxide or hydroxide in an alkaline electrolyte. The same general principle applied to the cathodes, except that in this case the dissolved species would be the anion of the cathode active material. In addition, other limitations had to be considered, such as the solubility of the active material and the possible occurrence of passivation.

The only cathode found to be satisfactory was the Ag/AgCl electrode, and its high rate charging characteristics have been reported already (1). The most promising fast-charging anode was the Zn/Zn^{+2} electrode, and its mass transfer limiting rate characteristics have been reported (2). The experimental data available in the literature (3) on the $Zn/ZnCl_2/AgCl/Ag$ cell indicated that it had a high self-discharge rate. We found that the self-discharge rate could be reduced to a tolerable value by decreasing the zinc chloride concentration of the electrolyte, and we proceeded to develop practical $Zn/ZnCl_2/AgCl/Ag$ cells. However, gas accumulated in the cells on long-term active stand due to the corrosion of the zinc in the acidic electrolyte, and the gas bubbles caused current inhomogeneities which led to the formation of dendrites and cell shorts during subsequent high rate charges. Because of the gassing, the $Zn/ZnCl_2/AgCl/Ag$ cells could not be considered for any practical applications.

Attention was then focused on the $Cd/CdCl_2/AgCl/Ag$ system as the second choice for the development of a fast-charging cell. The low half-cell voltage of the cadmium electrode, its relatively high hydrogen overvoltage (4), and its charging rate characteristics (5) suggested that practical cells would be feasible. $Cd/CdCl_2/AgCl/Ag$ cells were constructed and operated at charging rates between 10° and 100°C with apparently satisfactory results. However, the discharge efficiency of the cells varied between about 60 and 90%. Extensive studies indicated that cadmium chloride induced a structural transformation of the glassy film of silver chloride on the cathode which changed to a powdery form and lost contact with the substrate. The rate of the silver chloride transformation process could be reduced to a tolerable level by decreasing the cadmium chloride concentration to 0.1M $CdCl_2$ or less, but such an electrolyte could not support the high charging rates sought for the rechargeable system. We were thus confronted with the dilemma that the high-rate $Zn/ZnCl_2/AgCl/Ag$ system could not be used because of gassing on long-term stand and the high-rate $Cd/CdCl_2/AgCl/Ag$ system could not be used in the high-rate charging mode.

The dilemma was resolved by developing a dual charging process consisting of the following sequence:

1. *Electrical charging*:

$$ZnCl_2 + 2e^- \rightarrow Zn + 2Cl^-$$
$$2Ag + 2Cl^- \rightarrow 2AgCl + 2e^-$$

2. *Electrochemical exchange*:

$$Zn + CdCl_2 \rightarrow Cd + ZnCl_2$$

This scheme depended on the selection of an electrolyte with a sufficiently high zinc chloride concentration to give the required electrical charging rate and an

* Electrochemical Society Active Member.

amount of cadmium chloride in solution such that the cadmium chloride concentration would be less than 0.1M $CdCl_2$ at the end of the exchange reaction. It was found to be successful in eliminating both the long-term gassing associated with the zinc anode and the deterioration of the silver chloride cathode caused by high concentrations of cadmium chloride. Although the exchange reaction proceeded more slowly than did the electrical charging process, it did not prevent the immediate use of the cell. In fact, on immediate use the zinc anode participated in the discharge and a greater cell voltage was realized than with pure cadmium alone.

Cell Design and Experimental Procedures

The characteristics of the Ag/AgCl electrode (1) indicated that charge densities of about 2 mAh/cm^2 could be obtained on flat cathodes at current densities up to 300 ma/cm^2, and the characteristics of the Zn/Zn^{+2} electrode (2) showed that charge densities of 2 mAh/cm^2 could be obtained on flat anodes at current densities below 360 mA/cm^2 in a 2.0M $ZnCl_2$ electrolyte. Therefore, it should be possible to operate parallel-plate type cell structures with anodes and cathodes of equal areas. Flat circular cells were constructed with an interelectrode spacing of 0.4 cm, and they were operated under a variety of conditions. All the cells failed after a few cycles, and the dominant cause of failure was the shorting of the cells due to zinc dendrites. Attempts were made to eliminate the shorting problem by using flat cells with anode areas twice those of the cathodes and by using peripheral current baffles tapering from a large diameter on the anode side to a small diameter on the cathode side. It was found that the shortness of the current path was inadequate to spread the current over the entire anode, and the cells failed after a few cycles again due to dendrite formation.

The cell structures were changed, therefore, to a concentric arrangement with a central silver rod as a cathode substrate and a peripheral cadmium cylinder as an anode substrate. The design is shown schematically in Fig. 1 and a photograph of the cell and its components is shown in Fig. 2. The cylindrical cell worked satisfactorily. Two features of the design appeared to be of some importance: the shape of the end baffles and the absorber structure. The former was shaped to reduce the deleterious edge effects observed during the charging of the anode, and the absorber decreased the intensity of the convective flows of the electrolyte during charging which otherwise caused a nonuniform current density on the electrodes and a subsequent premature failure. The cells were filled in a vacuum chamber using a degassed electrolyte to avoid the entrapment of air bubbles in the cells.

The electrolyte contained 2.0 moles/liter of zinc chloride (AR), 1.5 moles/liter of sodium perchlorate

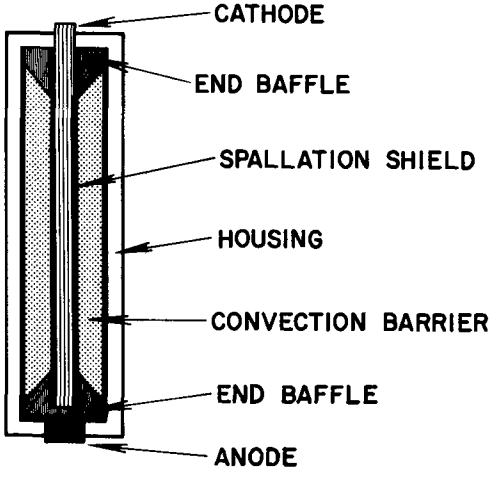

Fig. 1. Schematic diagram of cell

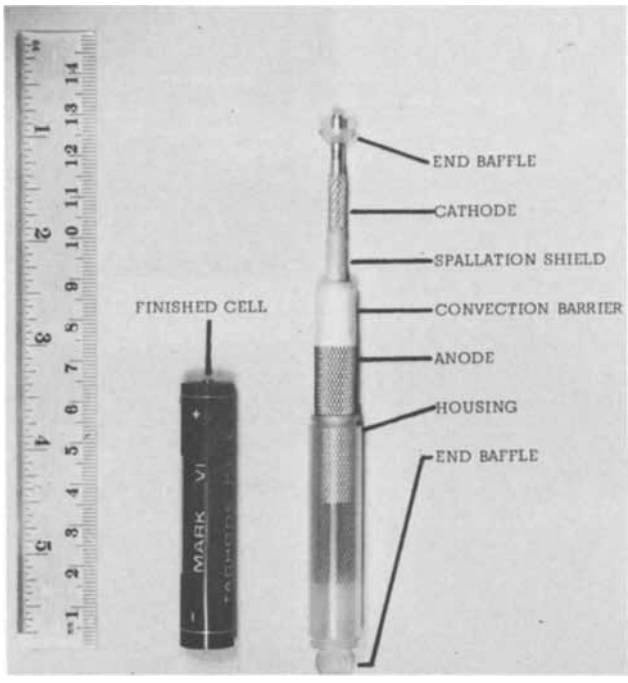

Fig. 2. Assembled cell and component parts

(AR), and an amount of cadmium chloride (AR) sufficient to give a concentration below 0.1 mole/liter on the completion of the charging process. It was necessary to employ the sodium perchlorate as a supporting electrolyte to increase the conductivity of the solution.

The cells were charged and discharged under constant current conditions using a Harrison power supply, Model 6286A, and a Greibach ammeter, Model 700, to measure the cell current with an accuracy of ± 0.5%. The charge-discharge curves were recorded with a Sargent recorder, Model DSRG, and the cell voltage was fed to the recorder *via* a Hewlett Packard d-c null voltmeter, Model 413A.

Experimental Results

The electrochemical evaluation of the cells was performed under ambient conditions at 25° ± 2°C. A typical charging curve is shown in Fig. 3A for a cell charged at the 40°C rate to a capacity of 50 mAh. The voltage remained constant at 2V during the first minute of charge. Then, it increased rapidly and reached 5V at the end of the charge after 1.5 min. The increase in the voltage toward the end of charge was probably due to the increasing resistance of both the silver chloride film and the diffusion layer at the electrode which becomes depleted in charge carriers. The open-circuit voltage of the cell immediately after charge was that of the Zn/AgCl couple, 1.05V, but it decreased to 0.75V on standing as the zinc was replaced by cadmium, Fig. 3B. The Zn/AgCl potential persisted for about half an hour, and the Zn/Cd exchange required slightly less than an hour to reach completion. The discharge curve of a cell discharged at the 2°C rate is shown in Fig. 3C. The load voltage remained constant at 0.6V until the end of discharge approached when it fell to zero at the exhaustion of the cell capacity.

The overvoltage of the cell on discharge is shown in Fig. 4. It increased linearly with the current density which indicated a purely ohmic impedance of 1.5 ohms for the 50 mAh unit.

The cyclability of the cell is represented by the data in Table I for charging rates between 30° and 90°C for cells with capacities of 33 and 50 mAh. The charge recoveries were generally greater than 90% with an average value of 96% throughout ten cycles.

The self-discharge rates of the cells were determined by charging the cells and leaving them on open-circuit

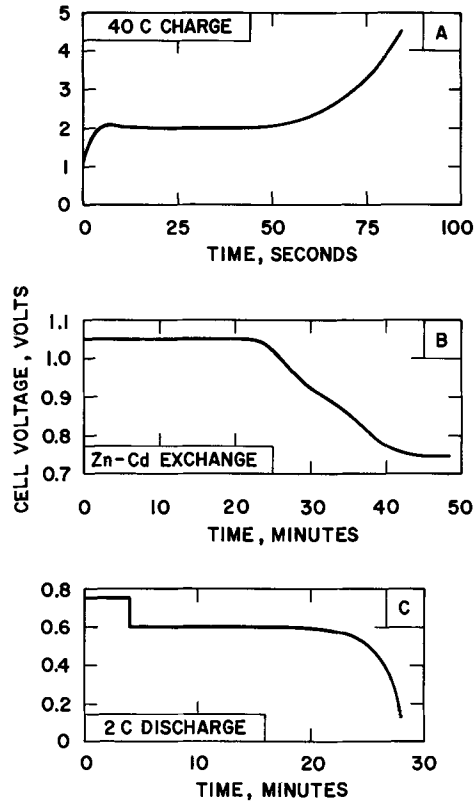

Fig. 3. Voltage characteristics of 50-mAh cell

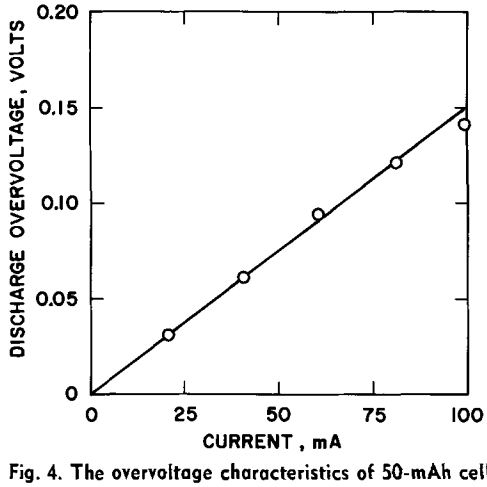

Fig. 4. The overvoltage characteristics of 50-mAh cell

stand for various periods of time before discharge. The results are shown in Fig. 5 for a 50-mAh cell. The data indicated a spontaneous initial rate of loss of capacity of about 0.5 mAh/day. However, the self-discharge rate decreased noticeably after about a month and more than 60% of the capacity remained after 3 months.

Table I. Cycling behavior of Cd(Zn)/AgCl cell*

Charging rate capacity, mAh	30°C 33	60°C 33	90°C 33	40°C 50	80°C 50
Cycle					
1	96.5	99.5	96.2	92.5	91.7
2	97.5	98.0	98.9	96.8	96.0
3	97.5	98.0	99.5	99.0	89.5
4	98.2	98.1	95.3	97.5	95.1
5	97.2	101.0	95.0	98.2	96.2
6	97.2	105.0	100.0	99.1	97.0
7	97.5	99.5	96.3	92.0	95.0
8	97.2	98.0	96.3	97.7	97.5
9	93.0	97.5	92.0	99.0	98.5
10	92.2	96.6	85.5	98.0	81.6

* 2°C Discharge rate. Per cent charge recovery tabulated.

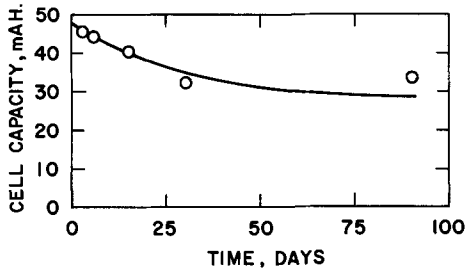

Fig. 5. The self-discharge rate at 25° ± 2°C.

Discussion of the Results

The composition of the electrolyte used for the cell was based on a compromise between the various effects discussed on a previous page. A concentration of about 2 moles/liter of zinc chloride appeared to give a sufficient concentration of zinc ions to satisfy the charging rate requirements of the anode, and the associated chloride ion concentration was adequate for the high rate charging of the cathode without causing an unduly high rate of dissolution of the cathode by complexation. The concentration of the supporting electrolyte, 1.5 moles/liter of sodium perchlorate, was close to the maximum permissible concentration for the system which did not cause the precipitation of any solution component. The concentration of cadmium chloride was determined by the requirement that its concentration should not exceed 0.1 mole/liter upon completion of the Zn/Cd exchange and the additional requirements of the total charge of the cell and the volume of electrolyte needed to fill the cell. For the 50-mAh cell, this amounted to 0.365 mole/liter of cadmium chloride.

The dual charging mode was developed to overcome the difficulties associated with the evolution of hydrogen on the zinc electrode on stand. Since the zinc electrode has an active life of about an hour in the cell per cycle, it was of interest to consider the extent of a possible gas accumulation in the cells during extended cycling. The rate of hydrogen evolution calculated from experimental data would, for a 50-mAh deposit of zinc in 2M zinc chloride, amount to less than one tenth of a microliter per hour which suggested that a deleterious gas accumulation would probably not occur except for extended cycling regimes. Furthermore, since the zinc is oxidizing while present on the anode, it is likely that a smaller gassing rate will prevail in the cells.

It was thought that the self-discharge of the cells might be caused by the dissolution of silver chloride due to complexation with chloride ions and its subsequent reduction on the anode. Separate experiments established that this mode of loss of silver chloride amounted to about 0.4 $\mu A/cm^2$ in a 2M zinc chloride solution which agreed well with the low rate of self-discharge reached after a month. However, the observed initial rate of loss was ten times this value, and it is probable, therefore, that another process dominates the initial self-discharge of the cells. It is thought that the slow structural transformation of silver chloride caused by the residual cadmium chloride may contribute significantly to the observed self-discharge rate. A quantitative assessment of the rate of this process is not available.

An attractive feature of the cells is their very long projected shelf life in the uncharged state which can be further enhanced by the use of a silver substrate for the anode.

It is characteristic of the cells we have discussed so far that they can be charged to only low capacities, principally because of their nonporous electrode structures. The energy density of the 50-mAh units is 0.9 whr/lb. Although we have no data on conventional rechargeable cells charged at comparable °C rates, it is probable that energy densities of 1 whr/lb can be

realized with, *e.g.*, nickel-cadmium cells if they are charged at their rated currents for the short periods of time required to give comparable °C rates. However, it is also probable that they will produce gas which the $Cd/ZnCl_2$, $CdCl_2$, $NaClO_4/AgCl/Ag$ cells do not do. The voltage transition associated with the Zn/Cd exchange process may limit the usefulness of the system for some applications.

Conclusions

The rechargeable Cd(Zn)/AgCl cells operated satisfactorily at constant current charging rates between 30° and 90°C *via* the dual charging process involving the primary deposition of zinc and its spontaneous replacement by cadmium from solution.

The fast-charging cells had an open-circuit voltage of 0.75V and an ohmic impedance of 1.5 ohms on discharge. The available data suggest that the half life of charge retention was more than 3 months. The cell capacity was limited to about 50 mAh because flat, nonporous electrodes were used in the configuration discussed in this paper.

It appears that the specific charging rate capability of the Cd(Zn)/AgCl system exceeds that of any other available aqueous system by a considerable margin. However, the realizable energy density of the cell is only 0.9 whr/lb. No parasitic reactions occurred at the high charging rates, and the cells were completely sealed without the need for any venting structures. The average charge recovery through 10 cycles exceeded 95%.

Manuscript submitted May 19, 1969; revised manuscript received *ca.* Sept. 7, 1969.

Any discussion of this paper will appear in a Discussion Section to be published in the December 1970 JOURNAL.

REFERENCES

1. P. Bro and N. Marincic, *This Journal*, **116**, 1338 (1969).
2. P. Bro and N. Marincic, *ibid.*, **116**, 448 (1969).
3. D. P. Boyd and R. H. Comyn, "A Fast-Charge Power Supply," Tech. Report 1354, July 1967, Harry Diamond Laboratories.
4. K. J. Vetter, "Electrochemische Kinetik," p. 432, Springer Verlag, Berlin (1961).
5. P. Bro and N. Marincic, *This Journal*, **116**, 1176 (1969).

Zinc Sulfide D-C Electroluminescent Displays

A. Vecht, N. J. Werring, R. Ellis, and P. J. F. Smith

Division of Materials and Molecular Science, Woolwich Polytechnic, London, England

ABSTRACT

A study of the materials preparation of zinc sulfide powders activated by manganese and copper has yielded direct-current electroluminescent cells with considerably improved performance. Investigation of the forming process has led to new cell configurations which are described. Some low-voltage characteristics are illustrated, 0.5 ft-L being obtained at 20V. The main problem of deterioration is discussed.

Although the emphasis of research work on the electroluminescence of II—VI compounds has shifted almost entirely from the Destriau type cell (1) to single-crystal junction devices (2), the potential of large-area electroluminescent displays made from powders should not be neglected. The requirement is still for displays and arrays of the order of 100-1000 cm^2. At present, the use of single-crystal devices for these applications must be ruled out. Apart from the prohibitive cost of large arrays of such devices, single-crystal slices greater than 5-10 cm^2 are not available. Furthermore, the current requirements of a junction device working at 1V would be in the region of 50A for a 500 cm^2 display, assuming 1% power efficiency at 500 ft-L. (This represents 500A/500 cm^2 area at a more realistic efficiency of 0.1%.)

The present position of d-c EL phosphors was reviewed recently (3) and it was shown that, with good materials control, both bright and efficient large areas can be produced (4) using powder phosphor layers. It was demonstrated that two different types of powder could be made. The first type is prepared by a slurrying technique, in which the activators are added to prefired ZnS powder (post-activation), and the second type involves the addition of the activator during the precipitation of ZnS (simultaneous-activation). Both types are then fired and may be subsequently copper coated to give high brightness panels which exhibit an electrochemical forming process. The simultaneously activated phosphors were found to be more suitable for low-voltage operation and the present investigation is confined to this type.

Preparative

The phosphors were prepared by the methods previously described in detail (4). Essentially, the powders were doped with manganese and copper during precipitation and were given a copper coating treatment. The activator concentrations were 0.25% manganese and 0.1% copper by weight.

Having prepared the phosphor, the construction of the d-c EL cell is extremely simple. The phosphor is mixed with a fixed weight of organic binder, shaken in an ultrasonic bath, and spread onto a moving plate of tin oxide conducting glass placed on a chromatographic spreader. The thickness of the electroluminescent panel is controlled by the height of the spreader gate over the conducting glass substrate, and usually ranges from 20 to 80 μm. Using this technique, areas up to 6 in. square can be prepared.

Cell Configurations

D-C electroluminescent powder cells have been constructed in two principal configurations: the conventional "through" cell and the gap cell (4). These are illustrated in Fig. 1 and 2. For the "through" electroluminescence cell, a back electrode of evaporated aluminum or a painted layer of colloidal graphite is applied. For experimental purposes, the area of this electrode (normally the cathode) is 0.5 cm^2. The gap electroluminescence cell is prepared by depositing the phosphor layer on an insulating surface between two planar electrodes. The region of light emission (Fig. 2) is dependent on the forming process.

When a d-c voltage is initially applied to a copper-coated phosphor in either a "through" or gap cell structure, the onset of light emission is accompanied by an irreversible fall in current. Similar effects have been observed on thin films (5-7). Upon the completion of the forming process, a line of relatively insulating particles across which most of the voltage drop occurs will have been produced. The "unformed" portions of

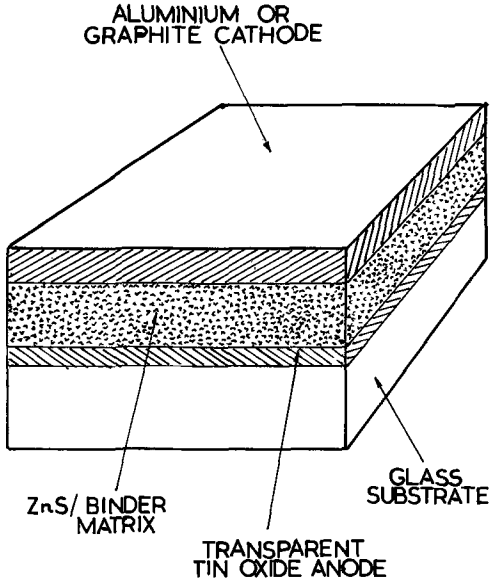

Fig. 1. Conventional powder "through" electroluminescence cell

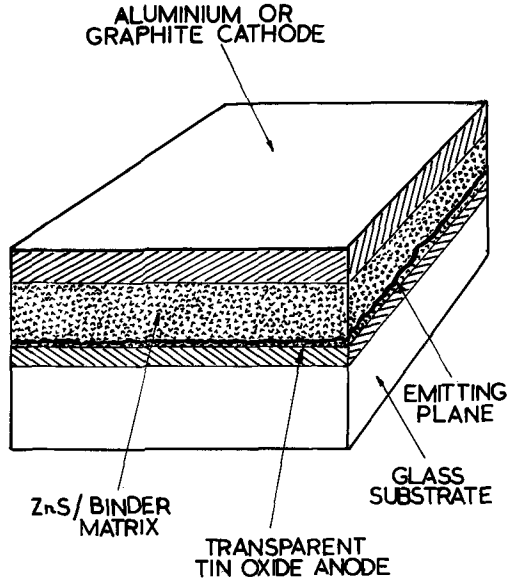

Fig. 3. "Through" cell showing plane of light emission. Thickness of powder-binder layer 50 μm.

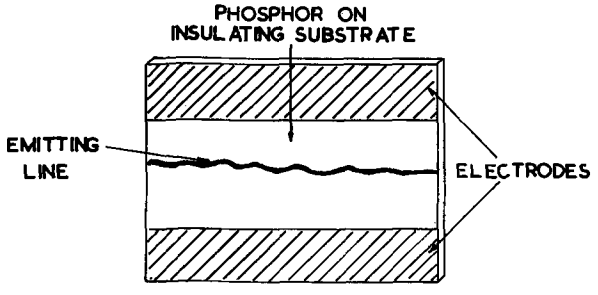

Fig. 2. A simple gap electroluminescence cell on a glass substrate. Graphite electrodes.

the phosphor layer will remain conducting and act as an extension of the electrodes. In the gap cell a similar line of insulating particles will emit light.

The forming process is believed to occur as the result of copper diffusion due to heating in the presence of an applied field. Thus, the power dissipation profile which is dependent on the local variation of defects, thickness and copper concentrations, will determine the path and shape of the emitting area. Similarly, in the "through" cell, a continuous plane or planar area will form that will emit light. Fortunately, this plane is produced adjacent to the conducting glass when this is made the anode (*see* Fig. 3).

Forming also takes place with reversed polarity but, in this case, the plane of emission is near to the back electrode. The efficiency is much lower due to light absorption in the bulk of the phosphor layer. Consequently, to minimize the effects of absorption, cells in the "through" mode must be operated with the conducting glass as the anode.

If a constriction is introduced between the electrodes of an unformed gap cell so that increased voltage stress will occur in a particular region, light emission will subsequently occur at that region. This can be achieved in many ways. For example, if a stylus is run along the surface of a gap cell, the line of light will follow the indentation produced.

A new type (8) of gap cell can be produced simply by making a narrow break in a conducting substrate and painting a layer of phosphor over it. If a voltage is applied, the current will tend to flow through the bulk of the layer as shown in Fig. 4A. Once over the break, the electrons will take the shortest path back to the conducting coating. At a sufficiently high power dissipation, the forming process takes place in the phosphor region adjacent to the conducting substrate and on the positive side of the break (Fig. 4B), and light

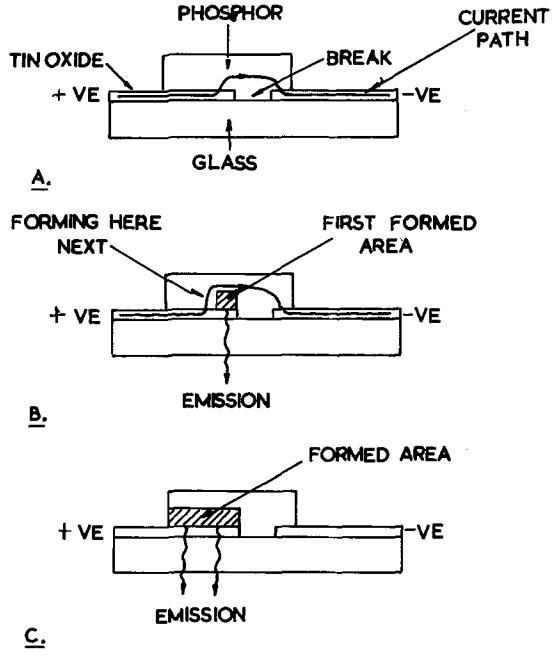

Fig. 4. Stages in the forming process of a modified gap cell

emission occurs. This region now becomes more resistive and the lowest resistance path for current flow moves toward the positive electrode and the forming process is repeated in the adjacent region. Eventually, the band of light emission will extend from the break in the conducting coating to the edge of the phosphor layer (Fig. 4C). Using this technique, simple numerical displays have been constructed (Fig. 5). It can be seen from Fig. 4C that the gap cell is in fact equivalent to a "through" cell, in which the top layer of unformed conducting phosphor acts as the back electrode.

Low-Voltage Operation

In order to be compatible with transistor circuitry, it is preferable that the operating voltage be relatively low (30V). By increasing the surface copper concentration and making thinner panels, the operation voltage has been reduced. As shown in Fig. 6, we have achieved 0.5 ft-L at 20V, increasing to 14 ft-L at 30V. For cross-matrix arrays, the discrimination ratio [defined as the ratio of the brightness at a particular voltage to the brightness at half that voltage (9)] is an

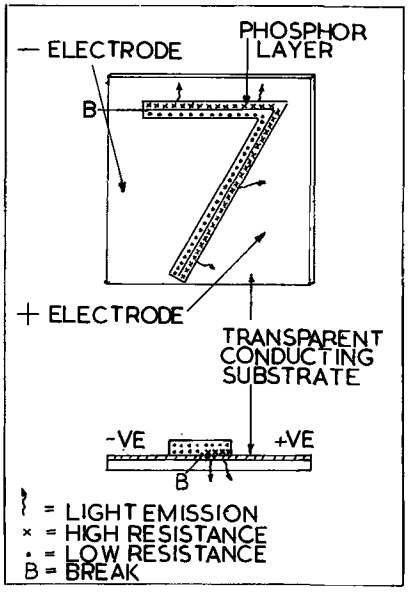

Fig. 5. Simple numeric gap cell type display

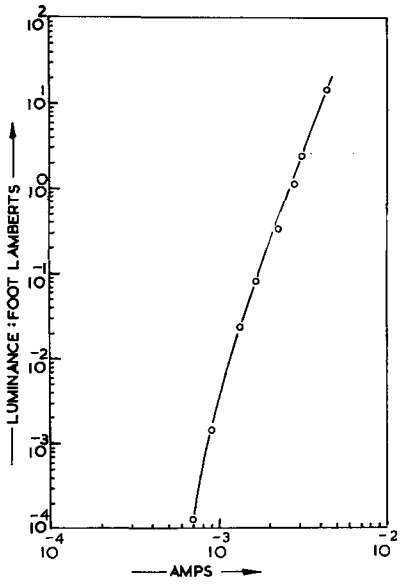

Fig. 7. Luminance-current characteristic of copper-coated phosphor. Area 0.5 cm^2. "Through" cell.

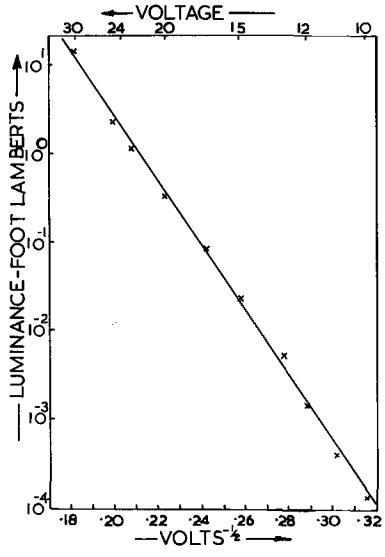

Fig. 6. Luminance-voltage characteristic of copper-coated phosphor. Area 0.5 cm^2. "Through" cell.

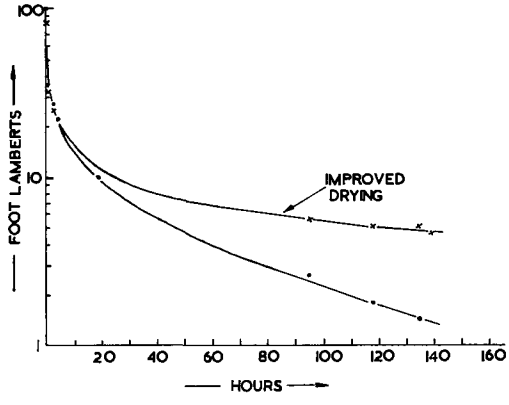

Fig. 8. Life curve, showing the effect of dry nitrogen atmosphere. "Through" luminescence cell at 100V.

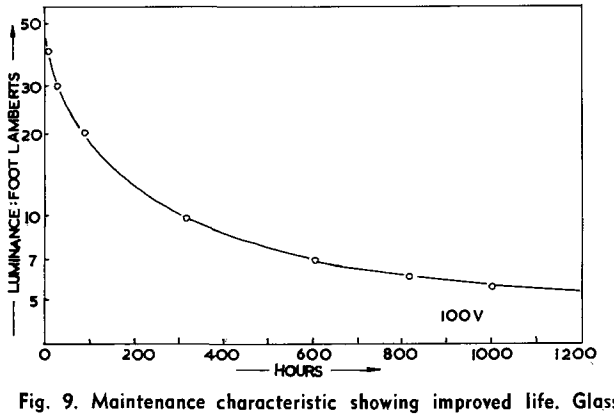

Fig. 9. Maintenance characteristic showing improved life. Glass encapsulated "through" cell with dry nitrogen atmosphere.

important parameter. Figure 6 indicates a discrimination ratio of 600 at 30V. The dependence of light output on current for the same device is illustrated in Fig. 7. It can be seen that the luminance increases by five orders of magnitude for less than an order increase in current.

Maintenance

The major problem still to be overcome is the short life under continuous operation of these devices. Although the life requirements of at least 5000 hr continuous operation have not yet been realized, improved characteristics are being obtained. At an early stage of the investigation, the devices were sealed in dry air to exclude moisture. These gave relatively poor results. The sealing of the devices in a glass vessel containing dry nitrogen with a powerful drying agent (such as magnesium perchlorate) yielded improved results as illustrated in Fig. 8.

The mechanism of the deterioration process is not yet fully understood. So far, relatively short half lives have been obtained with panels operating at low voltage or high brightness. However, an intermediate range of panels gave promising results. As illustrated in Fig. 9, a half life of 900 hr from 10 ft-L has been obtained.

As with conventional a-c phosphor layers, the impedance increases with operating time. This is not accompanied by a fall in efficiency; therefore the life of the panels can be considerably improved by stepwise voltage application (6). For example, one of our panels which initially emitted 100 ft-L at 60V again yielded this figure at 80V after having reached its half life. Another method of achieving a more useful life is the introduction of an appropriate series resistance. As the resistance of the phosphor layer increases the fraction of the voltage dropped across the layer will rise (10).

Conclusions

The potential of large-area displays made from powdered ZnS phosphors used under d-c excitation has been largely neglected and now affords exciting promise. The main problem to be resolved is that of life. Further improvement in the lifetime can be expected when the factors influencing the diffusion of impurities and defects under an applied field are more fully understood.

Acknowledgments

The authors wish to acknowledge their thanks to the Ministry of Technology and the Governing Body of Woolwich Polytechnic for continued sponsorship of the d-c electroluminescent project. They are particularly indebted to Mr. J. H. Williamson for some device preparation.

Manuscript submitted April 29, 1969; revised manuscript received Sept. 12, 1969. This was Paper 92 presented at the New York Meeting, May 4-9, 1969.

Any discussion of this paper will appear in a Discussion Section to be published in the December 1970 JOURNAL.

REFERENCES

1. G. Destriau, *J. Chim. Phys.*, **33**, 587 (1936).
2. M. Aven and D. A. Cusano, *J. Appl. Phys.*, **35**, 606 (1964).
3. A. Vecht and N. J. Werring, *Brit. J. Appl. Phys.*, Jan. 1970.
4. A. Vecht, N. J. Werring, R. Ellis, and P. J. F. Smith, *Brit. J. Appl. Phys., Ser. 2*, **2**, 953 (1969).
5. P. Goldberg and J. W. Nickerson, *J. Appl. Phys.*, **34** (6), 1601 (1963).
6. R. C. King, Dallas Meeting, Electrochem. Soc. Meeting, Dallas, May 7-12, 1967.
7. W. Uchida, *Jap. J. Appl. Phys.*, **7** (4), 378 (1968).
8. Patent applied for.
9. W. A. Thornton, *J. Appl. Phys.*, **33** (10), 3045 (1962).
10. H. F. Ivey, *Illum. Engr.*, **55**, 13 (1960).

Stabilization of Small, Pyrophoric Iron Particles by Surface Polymerization

M. Robbins, J. H. Swisher, H. M. Gladstone, and R. C. Sherwood

Bell Telephone Laboratories, Incorporated, Murray Hill, New Jersey

ABSTRACT

Pyrophoric iron powders, produced by the reduction of α- and γ-Fe_2O_3 in H_2, have been stabilized with respect to air oxidation by a method of surface polymerization which results in the formation of a plastic film around the particles. The polymer-coated iron was subjected to various heat treatments in air and O_2 saturated with H_2O to test its resistance to oxidation. The iron was highly resistant to oxidation as long as the decomposition temperature of the polymer was not exceeded (between 140° and 180°C). Therefore, this method of stabilization holds promise in overcoming a major problem in the use of fine particles of magnetic metals and alloys for permanent magnets and magnetic recording applications.

Submicron particles of magnetic metals and alloys have been of continuing industrial interest, especially for their use as permanent magnets and magnetic tape materials. The main problem in the use of these materials is their tendency to oxidize in air. Iron prepared by the reduction of fine particles of Fe_2O_3 at low temperatures burns upon exposure to air, while fine particles of Fe prepared by other methods, such as reduction from solution (1) or electrolytic reduction (2), oxidize more slowly. Stabilization of Fe particles for a limited period of time can be attained by immersion in organic solvents such as acetone, benzene, *etc.* A different method of stabilizing small metal particles is reported here. This method involves polymerization of a monomer on the surface of the particles which results in their encapsulation in a plastic film.

Experimental

Iron for the initial experiments was prepared from freeze-dried (3) $FeSO_4$ powder which was calcined at 700°C for 5 hr to form α-Fe_2O_3. The average particle diameter of the resulting Fe_2O_3 was about 0.1μ (1000Å), as determined by electron microscopy. Acicular Fe was also employed in the experiments; it was prepared by reducing acicular [Fig. 1(a)] γ-Fe_2O_3 obtained from Charles Pfizer and Company, Inc. (Type MO-4526). The average particle dimensions were 0.1 by 0.5μ.

Both the α- and γ-Fe_2O_3 materials were reduced to Fe in hydrogen at 350°C for a minimum time of 3 hr. The resulting iron powder, after cooling to room temperature in H_2, was highly pyrophoric and oxidized immediately upon exposure to air.

For the polymer coating experiments, the iron powder was allowed to cool to room temperature in the H_2 atmosphere. The sample was then lowered into a beaker of the monomer, tetraethylene glycol dimethacrylate,[1] which was contained in the cold end of the reaction tube. This particular monomer has the advantage that there are two polymerizable groups which cause a 3-dimensional structure to form during polymerization.

Dilute monomer solutions were also used to decrease the thickness of the monomer coating and hence the thickness of the polymer. Dilutions of 1:1, 1:6, and 1:15 (monomer to benzene) were used.

Following removal from the furnace, the monomer-coated samples were held for several hours at 60°C in a vacuum oven to remove the benzene. The powder was then placed in a beaker of mineral oil, which was stirred vigorously to avoid clumping of the particles. The mineral oil-coated particle slurries were heated to 110°C and held for 4 hr to effect polymerization of the monomer.

[1] Tetraethylene glycol dimethacrylate

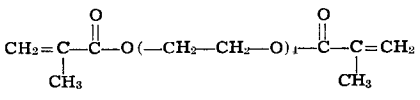

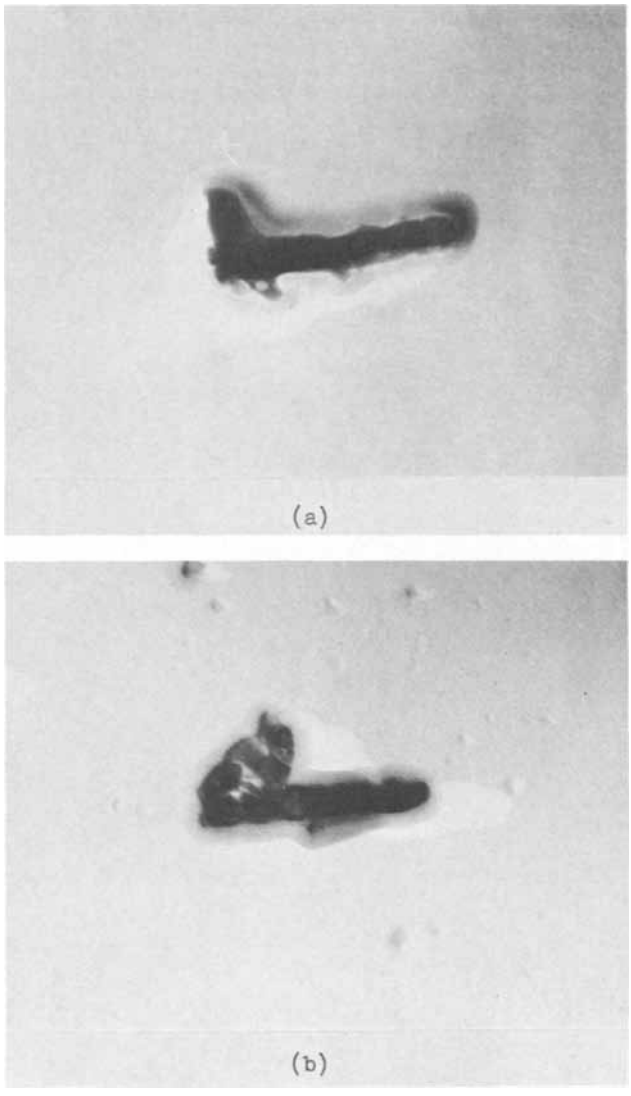

Fig. 1. Electron photomicrographs (27,000X) of (a) γ-Fe_2O_3 starting material and (b) reduced Fe using the γ-Fe_2O_3 as starting material. Polymer coating [gray coating around particle in (b)] was made using 1:15 monomer to benzene dilution.

The slurries were then allowed to cool and the Fe powder removed by filtration. Excess mineral oil was removed by washing the sample with hexane. X-ray diffraction using Cr-Kα radiation indicated the presence of iron with no observable second phase. The electron photomicrographs in Fig. 1(a) and 1(b) show that the shape of the acicular α-Fe_2O_3 was maintained during reduction to iron and that no apparent change in particle size occurred. Some pores in the powders developed, however, because of the difference in density between Fe and Fe_2O_3.

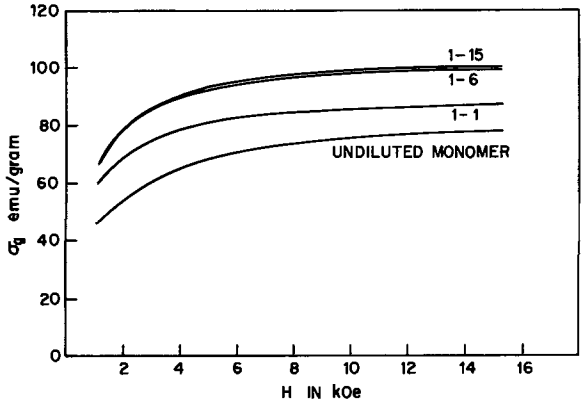

Fig. 2. Magnetic moment (σ in emu/g) vs. applied field for polymer-coated Fe samples using undiluted and diluted monomer solutions.

Results

Results obtained from room-temperature magnetic measurements on iron samples treated in various monomer dilutions are shown in Fig. 2. The observed magnetic moments per gram of material are significantly smaller than for uncoated Fe (σ = 218 emu/g), which indicates that the weight fractions of polymer in the materials are appreciable. With increasing dilution of the monomer with benzene, the polymer film becomes thinner and the magnetic moment increases. Coercivity measurements made on pressed bars of polymer-coated iron yielded coercive forces of $\sim$ 250 oe. Intrinsic coercivities ($I^{H}c$) of $\sim$ 1000 oe have been measured. The bars, which were magnetized after pressing, exhibited a remanent moment, indicating that some alignment of the acicular particles had occurred during pressing.

The results of tests designed to measure oxidation resistance in various media are given in Table I. In these tests, comparisons were made between polymer-coated iron and iron which had been stabilized by flowing a mixture of N_2 saturated with acetone over the sample at room temperature.

After each heat treatment, the samples were examined for oxidation under a microscope. Magnetic moment measurements were also made on many of the samples, which provided a more sensitive means of detecting oxidation. While the sample prepared with a 1:6 monomer dilution showed a 10% change in moment after 40 hr in air at 140°C, the sample prepared with 1:15 dilution was the only one that showed measurable changes in moment at both 140° and 97°C.

Discussion and Conclusions

We have shown that pyrophoric metal particles can be stabilized with respect to air oxidation. Aging tests which were made (Table I) show that this method affords better protection than stabilization with organic solvents. Although magnetic measurements made over time periods longer than those shown in

Table I. Results of oxidation resistance tests on iron powders stabilized with acetone and stabilized by polymer coating

		Test conditions				
Starting material	Passivation treatment	97°C, 67 hr in air	140°C, 40 hr in air	180°C, 18 hr in air	140°C, 24 hr in wet O_2	Immersion in 2*N* HCl
α-Fe_2O_3, γ-Fe_2O_3	None	← Pyrophoric →				
α-Fe_2O_3	Stabilized with acetone	Stable	Oxidized	Oxidized	Partially oxidized	Rapidly oxidized
α-Fe_2O_3, γ-Fe_2O_3	Undiluted monomer	Stable	Stable	Oxidized	Stable	Very slowly oxidized
γ-Fe_2O_3	1:1 Monomer to benzene	Stable	Stable	—	—	Very slowly oxidized
γ-Fe_2O_3	1:6 Monomer to benzene	Stable ($\Delta\sigma$ = 0)	Moderate oxidation ($\Delta\sigma$ = 10%)	—	—	Very slowly oxidized
γ-Fe_2O_3	1:15 Monomer to benzene	Slight oxidation ($\Delta\sigma$ = 3%)	Moderate oxidation ($\Delta\sigma$ = 15%)	—	—	Very slowly oxidized

Table I should be made, the results of oxidation tests at elevated temperatures indicate that room-temperature oxidation should not be a problem.

The room-temperature moment of the sample prepared with a 1:6 monomer dilution (σ = 100 emu/g) is significantly higher than that of γ-Fe_2O_3 ($\sigma \approx 80$ emu/g), which is presently used in magnetic tapes. The coercive force can be increased if desired by substituting Fe-Co alloys for Fe.

An advantage of the monomer used in this experiment is that polymerization can also be brought about by electron beam irradiation (4), which may be of use in some applications. Although we used tetraethylene glycol dimethacrylate exclusively in our study, there are many other monomers which may be used for polymer coatings.

Acknowledgments

The authors would like to thank Mr. E. A. Nesbitt and Mr. E. O. Fuchs for their help in making coercivity measurements. We also thank Miss S. E. Koonce for providing the electron micrographs.

Manuscript received Aug. 22, 1969.

Any discussion of this paper will appear in a Discussion Section to be published in the December 1970 JOURNAL.

REFERENCES

1. A. L. Oppegard, F. J. Darnell, and H. C. Miller, *J. Appl. Phys.*, **32**, 1845 (1961).
2. F. E. Luborsky, *ibid.*, **32**, 171 S (1961).
3. F. J. Schnettler, F. R. Monforte, and W. W. Rhodes, "Science and Ceramics," Vol. 4, pp. 79-90, British Ceramics Society, Manchester, England (1968).
4. J. V. Schmitz and E. J. Lawton, *Science*, **113**, 718 (1951).

The Optimum Number of Cells in an Amalgam Process Chlorine Plant

Fumio Hine*[1]

Kyoto University at UJI, Japan

ABSTRACT

The optimum number of cells in a chlorine plant has been calculated as a function of a coefficient, α, of the formula: Plant cost = Constant (Plant size)$^{\alpha}$, and the ratio of the a-c power cost, c, to the annual fixed charge, $\overline{Fc}$. The labor cost for plant operation is also discussed, but it is a small factor in deciding the optimum number of cells.

Deciding the plant capacity, the number of cells to be installed, and the optimum conditions of operation in a chlorine plant depends on the market situation, the power cost, the labor rate, the cell type, and other factors. The plant size should meet the market, but too small a plant is not economical. In general, the manufacturing cost decreases with increasing plant size if the plant is operated at nearly full capacity.

The optimum current density of the amalgam-type chlorine cell as a function of the investment and the power cost has been discussed in a previous paper (1).

The number of cells, N, or conversely the cell current load, I, in kiloamperes, is a major factor in optimizing a chlorine plant having the capacity of P metric tons per day by Faraday's law as follows:

$$P = 31.8 \times 10^{-5}\ nIN \text{ (metric tons } Cl_2\text{/day)} \quad [1]$$

where n is the current efficiency of the cell in per cent.

The number of cells to be installed is discussed from the economic point of view in this paper.

Investment

The total investment of a chlorine plant includes the costs of the cell room, the rectifier, the brine purification system, the handling of crude salt, chlorine and caustic, and other auxiliaries. Of these, the investment for the cell room and the rectifier room varies with the number of cells, but other costs are almost independent and are only a function of the plant capacity.

The cell-room cost depends on the plant size, the number of cells, or the amperage of the circuit, and the operating current density of the cells. It increases slightly with the number of cells, because the cost of a small cell is rather high.

The rectifier cost per kilowatt was shown in the previous report to be

$$\text{Rectifier cost per kw} = \text{Constant (Voltage)}^{-\delta}\ (\$/\text{kw}) \quad [2]$$

where δ = 0.15-0.16. Therefore, the rectifier cost is as follows:

$$\begin{aligned}\text{Rectifier cost} &= \text{Constant (kA of cell, } I\text{)} \\ &\quad \times \text{(Number of cells, } N\text{)} \\ &\quad \times \text{(voltage per cell, } v\text{)} \\ &\quad \times (Nv)^{-\delta} \\ &= \text{Constant } (P/n)\ (v)^{1-\delta}\ (N)^{-\delta} \text{ (dollars)}\end{aligned} \quad [3]$$

where v is the voltage of a cell including intercell bus bars in volts.

According to the previous report, the investment, J, consisting of the costs for the rectifier, the cells including graphite anode and mercury, and the cell room including connecting bus and piping, is shown by the next equation:

$$J = J_0 \left(\frac{P}{100}\right)^{\alpha} \left(\frac{i}{100}\right)^{\gamma} \quad \text{(dollars)} \quad [4]$$

where J_0 is the plant cost, in dollars, of a 100-tons/day plant operated at 100 A/dm^2, and i the current density in A/dm^2, and α = 0.926 and γ = −0.740. However, α becomes large for the modern chlorine plant: say 0.96-0.98.

Assume (2) that Eq. [4] is feasible for the cost estimation per unit cell, J_1, in dollars, that is,

$$J_1 = J_0 \left(\frac{P/N}{100}\right)^{\alpha} \left(\frac{i}{100}\right)^{\gamma} \quad (\$/\text{cell}) \quad [5]$$

* Electrochemical Society Active Member.
[1] Present address: Nagoya Institute of Technology, Gokiso-cho, Nagoya 466, Japan.

Since the chlorine plant of P tons/day in capacity has N cells, the plant cost, J, also in dollars, is N times J_1 as follows:

$$J = J_0 N \left(\frac{P/N}{100}\right)^{\alpha} \left(\frac{i}{100}\right)^{\gamma}$$

$$= J_0 (N)^{1-\alpha} \left(\frac{P}{100}\right)^{\alpha} \left(\frac{i}{100}\right)^{\gamma} \quad \text{(dollars)} \quad [6]$$

The total fixed charge, Fc(total), per unit production in \$/ton-Cl_2, which consists of depreciation, tax, maintenance, and supplies, is as follows:

$$Fc(\text{total}) = \frac{J}{365P}\frac{\beta}{100} + Fc' \quad (\$/\text{ton-Cl}_2) \quad [7]$$

where β is a coefficient depending on the location and situation, and is about 15-40%, and Fc' is the fixed charge based on the sum of the investment for brine purification, handling of chlorine and caustic, and other plant facilities not dependent on cell size.

Cost of Electric Power

The cost of electric power per unit of production, Ec, in \$/ton-Cl_2, was also shown in the previous report:

$$Ec = 0.756 \times 10^5 \left(\frac{c'}{n}\right) v$$

$$= 0.756 \times 10^5 \left(\frac{cv}{n}\right)\left(\frac{100}{m'}\right) \quad (\$/\text{ton-Cl}_2) \quad [8]$$

where c' and c are the prices of d-c and a-c power in \$/kwhr, respectively, and m' is the conversion efficiency of the rectifier in %, which is a function of the terminal voltage, V, in volts. It also depends on the type of rectifier. An example of the m' *vs.* V curve of a silicon rectifier is shown in Fig. 1 (3). Therefore, the following equation can be obtained:

$$\frac{100}{m'} = \frac{1}{1 - \frac{m}{V}} \cong 1 + \frac{m}{V} \quad [9]$$

where m is a characteristic value of the rectifier and is 1.45 in this case. Substituting this into Eq. [8],

$$Ec = 0.756 \times 10^5 \left(\frac{cv}{n}\right)\left(1 + \frac{m}{V}\right)$$

$$= 0.756 \times 10^5 \left(\frac{c}{n}\right)\left(v + \frac{m}{N}\right) \quad (\$/\text{ton-Cl}_2) \quad [10]$$

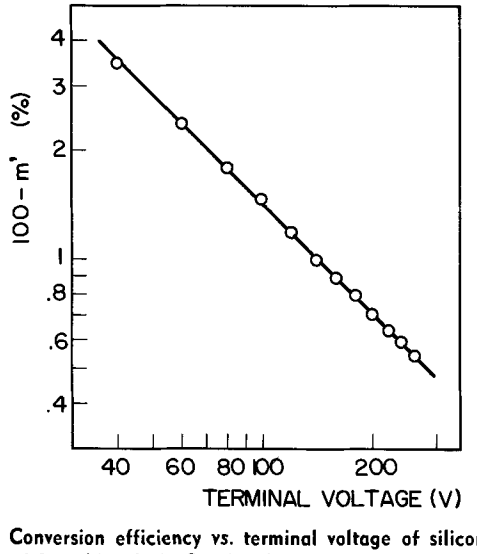

Fig. 1. Conversion efficiency vs. terminal voltage of silicon rectifier (quoted from Mitsubishi Catalog, L30901B, p. 13).

Labor Cost

The labor cost per unit production is greatly affected by several factors such as the size, layout, location and situation of the plant, the type and number of cells, the degree of automation and the labor rate, and the labor quality. Estimation of the labor cost, Lc, is therefore complicated.

A de Nora cell plant is operated by only three men per shift, and the operating man-hours for various sizes of plant up to 36 cells is almost constant according to Monsanto (4). The labor per shift in the de Nora cell plant is surprisingly small, and the layout of the plant is said to be a major factor in reduction of the labor cost.

Gardiner (5) points out that the man-hours per unit of production in an Olin cell plant decrease considerably with increasing the plant capacity, but he also indicates that the labor cost varies with the location and situation even though the plant capacity and the cell size are much the same.

Grosselfinger and Schuecker (6) obtained a relationship between the electric power cost and the labor requirements for anode adjustment in the Uhde cell.

Burt of Olin Mathieson emphasized in private conversation with the author that the labor cost in a chlorine plant is much affected by labor quality; that is, the well-trained workers are able to reduce considerably the direct and indirect costs of operation. A Japanese engineer, Sugino (7), expressed almost the same opinion.

Introduction of automatic process control in a chlorine plant is also effective in cost reduction, but there is an optimum point because the equipment costs are high.

In the past, labor requirements for cell operation were greatly affected by the number of cells, but this is a small factor in a modern plant. A typical 100-tons/day chlorine plant having thirty 100 kA cells requires five men per shift for operating brine purification, cell room, and rectifiers; but, in a 200-tons/day plant, additional labor is only one man per shift.

Since anode adjustment consumes most of the labor for cell operation, the labor cost may increase with the size and number of cells. In practical experience, however, the man-hours for cell operation are almost independent of the size, because a modern large cell is provided with automatic interelectrode control devices and other improved equipment. The effect of the number of cells on labor cost is relatively small for this reason.

The Japanese Ministry of Labor surveyed the trend in man-hours in chlor-caustic plants for the years 1955-1966. Using these data (7), the average man-hours per unit of production have been evaluated as a function of the plant capacity. As shown in Fig. 2, the logarithm of man-hours *vs.* the logarithm of plant capacity is a straight line with a slope of about -1.5, which is a significant result.

Suppose two plants of different sizes: the one having a capacity of 50 tons/day and the other 200 tons/day. The man-hours per unit of production of these plants are 4.5 and 0.4, respectively, according to Fig. 2. Therefore, the total man-hours per day in the small plant should be 4.5 x 50; that is, this plant may require 9-10 men per shift for operation, in contrast with 0.4 x 200 man-hours per day or only 3-4 men per shift in the large plant. It is not unreasonable, because large plants, such as 150-200 tons/day, are new, but several small plants in Japan have operated over 20 years and modernization of these old plants is limited. Some Japanese engineers claim that the slope of the logarithm of man-hours *vs.* logarithm of plant size is about unity according to their experience.

In conclusion, the labor cost, Lc, is roughly shown by the next equation:

$$Lc = \overline{Lc}\left(\frac{P}{100}\right)^{-1} \quad (\$/\text{ton-Cl}_2) \quad [11]$$

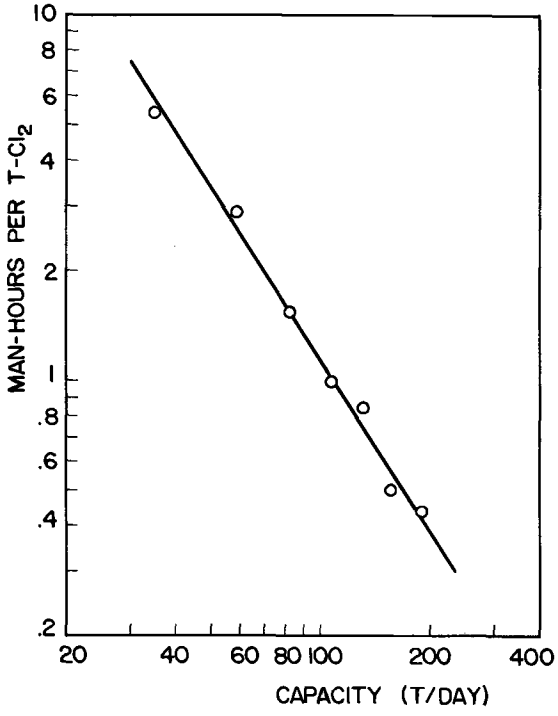

Fig. 2. Man-hours vs. plant capacity in the amalgam-type chlorine plant.

where $\overline{Lc}$ is Lc, also in \$/ton-Cl_2, for a 100-tons/day chlorine plant. The total man-hours for a 100-tons/day plant are about 1.15 per ton chlorine. The labor for the cell room is about 35-40% of the total man-hours. Assuming that the labor rate is \$3.50/hr, the labor cost for the cell room in a 100-tons/day plant is about \$1.50/ton-Cl_2.

Optimum Number of Cells

Assume that the manufacturing cost, Mc, is the sum of the total fixed charge, Fc(total), and the total operating cost, Oc(total), as follows:

$$Mc = Fc(\text{total}) + Oc(\text{total}) \qquad [12]$$

Of these, Oc(total) consists of the power cost, the labor cost, and other expenses, Oc(other), which is almost independent of the number of cells installed, that is,

$$Oc(\text{total}) = Ec + Lc + Oc(\text{other}) \qquad [13]$$

Substituting Eq. [7] and [13] into Eq. [12], we have the optimum number of cells, N(opt), by the differentiation of Mc with respect to N, that is,

$$\frac{dMc}{dN} = \frac{dFc(\text{total})}{dN} + \frac{dOc(\text{total})}{dN}$$

$$= \frac{1}{365P}\frac{\beta}{100}\frac{dJ}{dN} + \frac{dEc}{dN} = 0 \qquad [14]$$

$$N(\text{opt}) = \left[\frac{1-\alpha}{276\times10^5}\frac{J_0}{P}\frac{\beta}{100}\left(\frac{P}{100}\right)^{\alpha}\left(\frac{i}{100}\right)^{\gamma}\left(\frac{n}{cm}\right)\right]^{1/(\alpha-2)}$$

$$= \left[\frac{276\times10^5}{1-\alpha}\frac{cm}{n\overline{Fc}}\right]^{1/(2-\alpha)} \qquad [15]$$

where $\overline{Fc}$ is the annual fixed charge corresponding to J. Thus, the larger the annual fixed charge, the smaller is the optimum number of cells to be installed.

On the other hand, if the cost of d-c electric power is high, the number of cells should be increased. The slope of the investment *vs.* plant capacity curve, α, is also a large factor to N(opt). When α is small, N(opt) becomes small. Since α is close to 1, a small variation of α or $(1-\alpha)$ affects N(opt) very much.

Assuming that $\overline{Fc}$ = \$2000, c = 5 mills/kwhr, n = 95%, and m = 1.5, the optimum number of cells from Eq. [15] is 14 and 51 for α = 0.93 and 0.98, respectively.

Generally speaking, variations of both n and m are small, but c varies from 2 to 10 mills/kwhr. Both $\overline{Fc}$ and α are functions of the cell type, the plant location, the plant layout, and other conditions, and $(1-\alpha)\overline{Fc}$ varies from \$50 to \$400 at present. From Eq. [15], the optimum number of cells is a function of α and the ratio of the a-c power cost to the annual fixed charge. Figure 3 shows N(opt) as a function of $cm/n\overline{Fc}$ or $c/\overline{Fc}$ at constant values of m and n (assuming m = 1.5 and n = 95% in this case) for a reasonable range of α.

It is clear that the value of α for the plant under consideration is most important for discussion of the subject, while it is complicated in practice. Experience in plant design and construction must be depended on for an answer.

The average cost of a-c power in Japan is about 8 mills/kwhr, and the annual fixed charge is \$2000-\$2500; hence, $c/\overline{Fc} \times 10^6$ is 3.2 = 4.0. The coefficient α is not small today as described above. If α = 0.960 and $c/\overline{Fc} \times 10^6$ = 4.0, the optimum number of cells is 36 from Eq. [15] or Fig. 3. Therefore, the 92-kA cells are preferable for the 100-tons/day chlorine plant, assuming 95% current efficiency. The optimum number of cells described by Eq. [15] is independent of the plant size. Then a large chlorine plant, such as 500 tons/day, requires a very large cell. However, a cell up to 300 kA is the largest now available. Consequently, the exact number of cells installed is limited by the cell size also. Larger cells should be developed continuously with increase in production capacity in a plant. The requirement of surprisingly large cells such as 500 kA might not be far away, and reduction of α is an important subject for the design engineer.

Acknowledgments

The author wishes to express his thanks to Dr. W. C. Gardiner, Olin Mathieson Chemical Corporation, and to Dr. Toshiyuki Sugino, Ajino-moto Company, for their helpful advice and supplying useful data for this work.

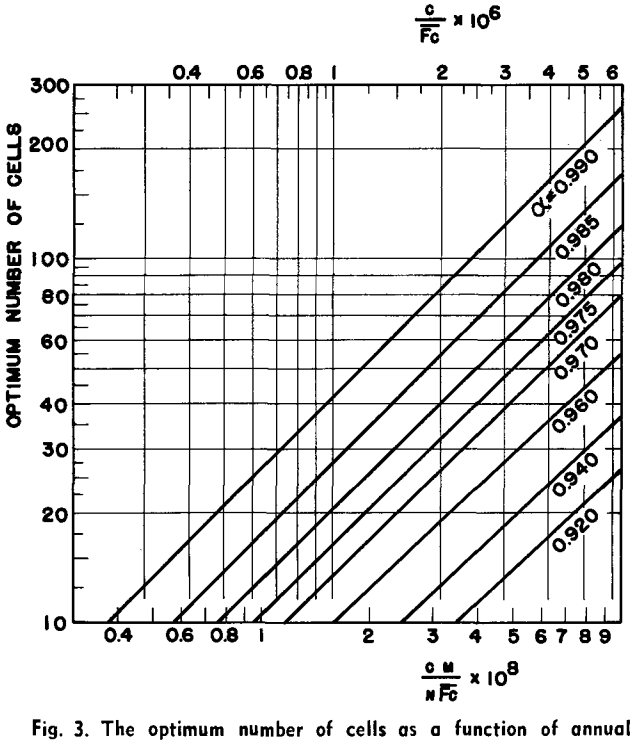

Fig. 3. The optimum number of cells as a function of annual fixed charge and the a-c power cost.

Manuscript submitted Feb. 26, 1969; revised manuscript received ca. Sept. 26, 1969.

Any discussion of this paper will appear in a Discussion Section to be published in the December 1970 JOURNAL.

REFERENCES

1. F. Hine, *Electrochem. Technol.*, **6**, 69 (1968).
2. H. A. Quigley, *Chem. Eng.*, Aug. 29, 1966, p. 97.
3. Catalog of Mitsubishi Electric Co., L30901B, p. 13.
4. M. M. Silver, Paper 103 presented at Electrochem. Soc. Meeting, Cleveland, May 1-6, 1966.
5. W. C. Gardiner, Private communication.
6. F. B. Grosselfinger and J. Schuecker, *Chem. Age India*, **12**, 540 (1961).
7. Private communication from T. Sugino.

SYMBOLS AND UNITS

c	A-C power cost	mills/kwhr
Ec	Power cost per unit production	\$/ton-Cl_2
Fc(total)	Total fixed charge	\$/ton-Cl_2
Fc'	Fixed charge independent of the cell size	\$/ton-Cl_2
$\overline{Fc}$	Annual fixed charge based on J	dollars
I	Amperage	kiloamperes
i	Current density	A/dm^2
J	Investment depending on the cell size	dollars
J_o	J of a 100-t/day plant operated at 100 A/dm^2	dollars
J_1	Investment for a cell ($=J/N$)	\$/cell
Lc	Labor cost	\$/ton-Cl_2
$\overline{Lc}$	Lc in a 100-t/day chlorine plant	\$/ton-Cl_2
Mc	Manufacturing cost	\$/ton-Cl_2
m'	Conversion efficiency of rectifier	%
m	Coefficient depending on m'	
N	Number of cells installed	
N(opt)	Optimum number of cells	
n	Current efficiency of cell	%
Oc(total)	Total operating cost	\$/ton-Cl_2
Oc(other)	Indirect operating cost	\$/ton-Cl_2
P	Production capacity of a plant	tons-Cl_2/day
V	Terminal voltage of rectifier ($= Nv$)	volts
v	Cell-to-cell voltage	volts
α, β, γ, and δ	Coefficients	

Oxide Film Studies on Iron in Electrochemical Machining Electrolytes

James P. Hoare*

Electrochemistry Department, Research Laboratories, General Motors Corporation, Warren, Michigan

ABSTRACT

Electrodes made from soft iron were polarized potentiostatically in solutions of NaCl, $NaNO_3$, $Na_2Cr_2O_7$, and $NaClO_3$, and the films formed were stripped from the iron surface with constant current stripping pulses. The amount of charge associated with the oxide layer was determined as a function of the potential. In general, the oxide film formed in the passive region is dissolved by the anion in the transpassive region. The Cl^- ion is so efficient in dissolving oxide films on iron that no protective film is formed, and wild cutting is obtained. Such poor oxide-dissolving anions as the chromates protect the surface too well, and machining takes place at high potentials with sparking. Only ClO_3^- ion behaves in such an intermediate way that excellent finishes are obtained with good dimensional control at high metal removal rates.

In the electrochemical machining (ECM) process, the electrolyte is one of the most important considerations for successfully obtaining good dimensional control with an excellent surface finish. LaBoda and coworkers (1, 2) have found that $NaClO_3$ electrolytes produced the best results.

It was questioned why $NaClO_3$ produced good dimensional control and fine finishes, whereas NaCl gave poor dimensional control (wild cuts) and $Na_2Cr_2O_7$ cut at high potentials with poor finishes. From steady-state polarization studies (3, 4) on iron electrodes, an explanation for the ECM behavior of these electrolytes for cutting steel was presented in terms of the build-up and breakdown of an oxide film. According to the literature, the corrosion of iron in solutions of chromates (5, 6), carbonates (7), and phosphates (8) is inhibited by the formation of a passive film of γ-Fe_2O_3. The oxide film present on machined samples of steel in $NaClO_3$ electrolytes was identified as γ-Fe_2O_3 by electron diffraction techniques (4). The differences in behavior of these electrolytes were related to the properties of the passivating film of γ-Fe_2O_3 formed on the steel surface. These conclusions (3, 4) have been criticized by Boden and Evans (9).

In the work reported here, the build-up and the breakdown of the protective film of γ-Fe_2O_3 on iron samples in NaCl, $Na_2Cr_2O_7$, $NaNO_3$, and $NaClO_3$ electrolytes were investigated as a function of potential by means of constant current stripping pulses.

Experimental

The test electrodes were small beads (~0.065 in. in diameter and 0.044 cm^2 in area) melted at the end of soft iron wires (35 mils) and held in the reducing part of a burning H_2 jet to reduce any oxides. These beads were then embedded in polyethylene so that only a hemisphere was exposed to the electrolyte. Teflon spaghetti was used to cover the wire leads. Such electrodes were mounted in triplicate in a Teflon cell (10) along with an α-Pd reference electrode (11). The cell was filled with the proper electrolyte and was preelectrolyzed for 24 hr against removable Pt electrodes. Finally, oxygen was bubbled through the cell at a rate of about 300 cc/min, and the iron electrode was held at a given potential with a 61R Wenking potentiostat until a steady current was reached. At this point, the potentiostat was disconnected by a mechanical switch, and a constant current stripping pulse was applied to the electrode from a pulsing circuit

* Electrochemical Society Active Member.

employing a mercury-wetted relay (12). The trace of the stripping curve was displayed on an oscilloscope and photographed. From the trace, the quantity of charge associated with the oxide-reduction plateaus of the traces was determined.

The following electrolytes, corresponding to those studied under actual conditions, were investigated: NaCl (275 g/liter), $NaNO_3$ (350 g/liter), $Na_2Cr_2O_7$ (100 g/liter), and $NaClO_3$ (350 g/liter). All potentials were recorded with a General Radio Electrometer, Model 1230-A, and reported against the normal hydrogen electrode (NHE). To do this, the potential of the saturated calomel electrode (SCE) against a Pt/H_2 electrode was determined for each solution. The α-Pd electrode is 50 mV more noble than a Pt/H_2 electrode in the same solution, and a value of 245 mV was used as the potential of the SCE *vs.* NHE.

Only the apparent area obtained from the geometric dimensions of the exposed beads was used in this work. Any consideration of a true area was hopeless because each time the bead was held at a given anodic potential the oxide layer formed was reduced by the following cathodic stripping pulse. In this way the true area was continually changed so that only an apparent area can be used as a working device. The transition times were determined from the traces of the stripping pulses by the intersection of the tangents drawn at the points of inflection as described elsewhere (13).

Results

A plot of the steady value of the current for given values of the controlled potential recorded just before the potentiostat was disconnected is presented in Fig. 1. These curves are in good agreement with those previously reported (3, 4). Alongside the curves in Fig. 1 are letters which refer to the traces of the corresponding stripping pulses shown in Fig. 2. Only selected traces are recorded in Fig. 2, but the quantity of charge, Q_{ox}, corresponding to the amount of oxide reduced during the arrests appearing in the traces for all points, was calculated from $Q_{ox} = I\tau A$ and is given in Fig. 3. Here, I is the value of the constant current applied during the stripping pulse, A is the apparent electrode area, and τ is the transition time of the oxide reduction arrest in the stripping pulse.

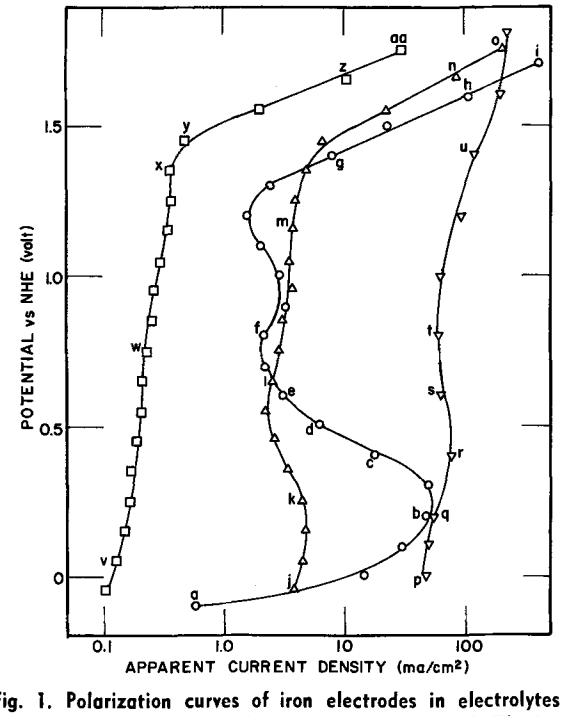

Fig. 1. Polarization curves of iron electrodes in electrolytes of $NaClO_3$, ○; $NaNO_3$, △; NaCl, ▽; and $Na_2Cr_2O_7$, □. The letters correspond to the traces of the stripping pulses shown in Fig. 2.

Discussion

For good dimensional control in the ECM process, it is desirable that the region of the workpiece opposite to and a gap distance away from the cutting face of the tool be corroded while those regions of the workpiece further away, such as the sides, be protected. The protecting agent is a film of cubic oxide which is either Fe_3O_4 or γ-Fe_2O_3 or both, or a mixture of the two (14, 15). In general, most of the traces in Fig. 2 exhibit only one arrest although two may be detected in such traces as Fig. 2d, 2e, 2g, 2z, and 2aa. Nagayama and Cohen (16) found a layer of Fe_3O_4 under the layer of γ-Fe_2O_3 on iron passivated in borate buffer solutions. For the sake of simplicity, we will refer to the protective layer as one of γ-Fe_2O_3 in further discussions.

At the high currents (500-1200 A/in.^{2}) used in ECM, the *IR* drop appearing across the electrolyte gap between the tool and workpiece may assume large values so that the potential drop across the double layer (which controls the rate of the electrochemical corrosion process) at points remote from the cutting face of the tool (such as the sides of a plunge-cut hole) may be much lower than at points directly opposite the cutting face of the tool (such as the bottom of the hole). It is assumed that acceptable cutting rates are achieved when the potential has reached a value corresponding to the transpassive region of the polarization curve (such as points i and o in Fig. 1). This condition exists at the bottom of the plunge-cut hole. If the *IR* drop is large enough, the effective potential at points remote from the tool cutting face will be decreased to a point corresponding to the passive region of the polarization curve (such as point m in Fig. 1). Consequently, how well a given electrolyte provides dimensional control will depend on how sharp the transition from the passive to the transpassive state is with respect to potential. As this transition becomes less sharp, it requires a larger solution path (*IR* drop) to bring the potential into the passive region. As a result, cutting along the sides of the workpiece (wild cutting) results.

In the series of traces, Fig. 2a to 2i, it is seen that the oxide film in $NaClO_3$ begins to form in the region of the critical current at point b in Fig. 1. There is a linear increase in the film thickness with potential (*see* Fig. 3) until point f is reached, followed by a slow thinning of the film up to point g in the beginning of the transpassive region. With increasing potential in the transpassive region, the film is rapidly removed so that at point i the protective film has practically disappeared, and rapid ECM can take place.

In the case of $NaNO_3$ (Fig. 2j to 2o), the oxide film forms at much lower potentials than in $NaClO_3$ but increases more slowly with potential. Also, the oxide is removed in the transpassive region more slowly. Since the polarization curve for $NaNO_3$ lies above that for $NaClO_3$ in the transpassive region, the current at a given potential is smaller in $NaNO_3$ than in $NaClO_3$. This fact is in agreement with the observation that steel is machined more slowly in $NaNO_3$ than in $NaClO_3$. Because the film is removed more slowly in $NaNO_3$, the transition from the passive to the transpassive state is less abrupt, predicting that the dimensional control is not as good as in $NaClO_3$. This conclusion has been verified in actual ECM operation on steel.

A protective film is not formed on iron in NaCl solutions as evidenced by the large currents drawn even at very low anodic potentials in Fig. 1. Although a porous, nonprotecting film is formed at low anodic potentials (*see* Fig. 2p to 2u), it is completely removed at the higher potentials as seen in Fig. 3. Consequently, metal removal can take place at points well remote from the cutting face of the tool. This behavior produces wild cutting with the resultant poor dimensional control.

At the other extreme, iron in chromate solutions is covered by a strongly passivating film (Fig. 2v to 2aa)

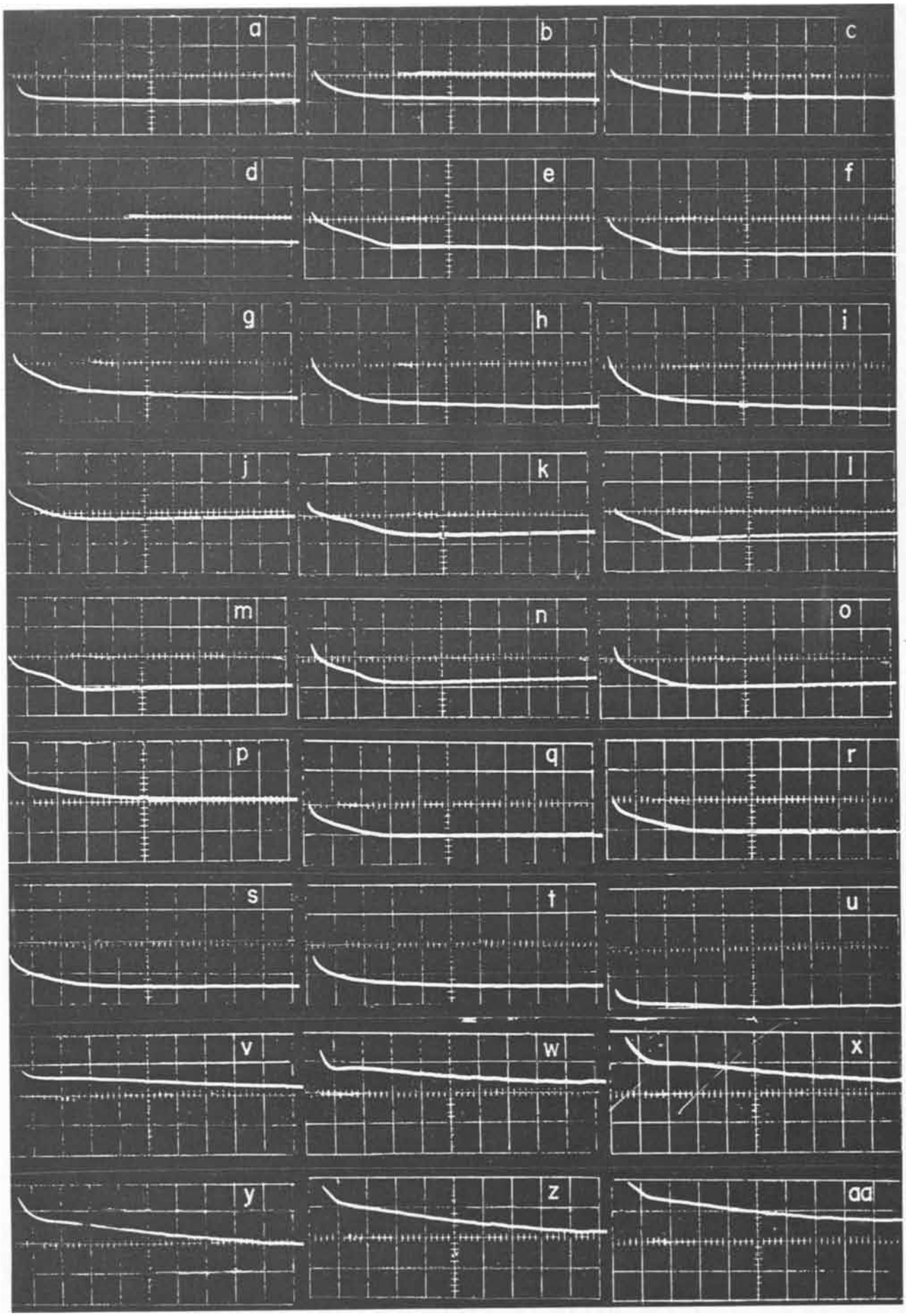

Fig. 2. Trace of the constant current stripping pulses applied to iron electrodes in solutions of $NaClO_3$ (a-i), $NaNO_3$ (j-o), NaCl (p-u), and $Na_2Cr_2O_7$ (v-aa). X-axis = 20 msec/cm; Y-axis = 500 mV/cm; current = 4.2 mA.

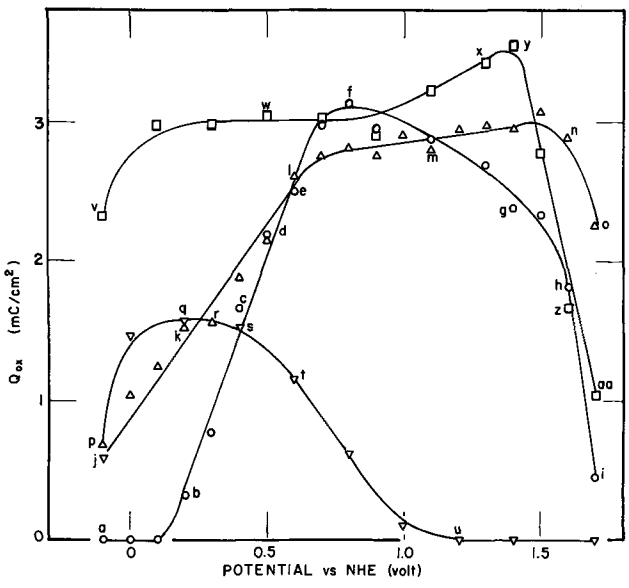

Fig. 3. A plot of the amount of charge, Q_{ox}, formed on the iron surface as a function of the potential in solutions of $NaClO_3$, ○; $NaNO_3$, △; NaCl, ▽, and $Na_2Cr_2O_7$, □. The charge was calculated using apparent area values since true areas could not be estimated. It is the relative shape of the curves that is important.

in most of the potential region studied in Fig. 1 and 3. Although an abrupt removal of the film takes place in the transpassive region (Fig. 3), this effect takes place at much higher potentials than for $NaClO_3$ (Fig. 1). Under such conditions, sparking may take place during the actual ECM operation on steel, and poor finishes are obtained. This conclusion has also been verified in the actual ECM of steel.

For successful ECM operation, it is seen that an electrolyte must be chosen which forms a protecting film on the metal surface but not so protecting that very high anodic potentials are required to remove it as in the case of $Na_2Cr_2O_7$. In addition, the sharper the transition from the passive to the transpassive state takes place, the better is the dimensional control.

As pointed out by Hoar (17), the ability of the anion to penetrate and dissolve a film formed on the metal surface may be the fundamental point in these considerations. The Cl^- ion is a very efficient agent for penetrating and dissolving films of iron oxides so that the iron surface in solutions of Cl^- ion is not passivated by a protective oxide film. In fact, Cl^- ion is so efficient that it has not been possible to achieve acceptably machined steel parts with chloride electrolytes modified by the additions of other anions such as $SO_4^=$ or $CrO_4^=$ ions contrary to that predicted in the literature (9). Anions such as the chromates, phosphates, and carbonates are such poor dissolving agents of iron oxides that, either machining cannot be obtained with such electrolytes, or ECM occurs at such high potentials that poor finishes result from the sparking that takes place.

Intermediate in behavior between chlorides and chromates are electrolytes such as nitrates and chlorates. Of these, the $NaClO_3$ electrolyte is far superior to the other for ECM applications from the standpoint of quality of the surface finish, rate of machining, degree of dimensional control, and economy. The ClO_3^- anion has the fortunate properties of producing a good protective film of γ-Fe_2O_3 on iron surfaces and of producing a sharp transition from the passive to the transpassive state at relatively low anodic potentials.

Manuscript submitted July 23, 1969; revised manuscript received Oct. 13, 1969.

Any discussion of this paper will appear in a Discussion Section to be published in the Deember 1970 JOURNAL.

REFERENCES

1. M. A. LaBoda and M. L. McMillan, *Electrochem. Technol.*, **5**, 340 (1967).
2. M. L. McMillan and M. A. LaBoda, *ibid.*, **5**, 346 (1967).
3. J. P. Hoare, *Nature*, **219**, 1034 (1968).
4. J. P. Hoare, M. A. LaBoda, M. L. McMillan, and A. J. Wallace, *This Journal*, **116**, 199 (1969).
5. T. P. Hoar and U. R. Evans, *J. Chem. Soc.*, **134**, 2476 (1932).
6. M. Cohen and A. F. Beck, *Z. Elektrochem.*, **62**, 696 (1958).
7. M. J. Pryor and M. Cohen, *This Journal*, **100**, 203 (1953).
8. H. H. Uhlig, D. N. Triadis, and M. Stern, *ibid.*, **102**, 59 (1955).
9. P. J. Boden and J. M. Evans, *Nature*, **222**, 377 (1969).
10. J. P. Hoare, *This Journal*, **109**, 858 (1962).
11. D. J. G. Ives and G. J. Janz, "Reference Electrodes," p. 112, Academic Press, New York (1961); J. P. Hoare, *G. M. Eng. J.*, **9**, No. 1, 14 (1962).
12. J. P. Hoare, *Electrochim. Acta*, **9**, 599 (1964).
13. S. Trasatti, *Electrochim. Metall.*, **2**, 12 (1967).
14. U. R. Evans, "The Corrosion and Oxidation of Metals," p. 136, St. Martin's Press, New York (1960).
15. J. P. Hoare, "The Electrochemistry of Oxygen," p. 375, Interscience Publishers, New York (1968).
16. M. Nagayama and M. Cohen, *This Journal*, **109**, 781 (1962); **110**, 670 (1963).
17. T. P. Hoar, *Corrosion Sci.*, **7**, 341 (1967).

Technical Note

Diffusion of Zinc through Films of Refractory Metals on GaAs

John C. Marinace*

International Business Machines Corporation, Research Division, Yorktown Heights, New York

To make ohmic contacts of minimal resistance in GaAs injection lasers, one practice has been to alloy plated metals to the GaAs wafer surfaces (1). The alloying must be thorough, otherwise the resistance will be high. When the laser junction is shallow (say, < 3 or 4μ), the alloyed contacts can penetrate the junction, either during the liquid formation of the alloying step or during subsequent laser operation under high current-density conditions.

* Electrochemical Society Active Member.

Another drawback of the alloying method is that the surface tension of the liquid tends to cause it to "ball up," and then freeze into an uneven layer. This hinders subsequent processing of the wafer and mounting of the lasers. The purpose of this paper is to describe a method of overcoming these difficulties, at least on the p-side of a laser wafer.

This method, incidentally, was discovered serendipitously during an investigation of useful maskants against Zn diffusion into GaAs. Instead of being useful maskants, it was found that films of W, Mo, or Cr barely impeded, if at all, the diffusion of Zn into GaAs, GaP, or GaAlAs. Moreover, no liquefaction of the films occurred during the diffusion process.

Other workers at about the same time found that W or Mo could be used effectively as diffusion masks in silicon technology (2, 3).

Experimental

As a result of these findings, the following process was devised for laser fabrication: A chemically polished {100} GaAs wafer (Sn doped, $\sim 2 \times 10^{18}/cm^3$) is coated with 2000-3000Å of W on its polished surface. This filming of W can be done by vacuum evaporation, using an electron gun as a heat source. Alternatively, the W film can be deposited by the hydrogen reduction of WF_6, at about 500°C.

The W-coated wafer is then put through its regular diffusion process. In the case shown in Fig. 1, the coated wafer and 5 mg of $ZnAs_2$ were sealed in a silica ampoule of 11 mm ID and 75 mm length. The ampoule was kept at 750°C for 4 hr and then at 850°C for 0.75 hr. The wafer is lapped on the surface opposite the W film until the wafer is $\sim 100\mu$ thick. Thin layers of Au, Sn, and In are plated on the lapped surface, and in a forming gas atmosphere the wafer is heated rapidly to 450°C and then cooled quickly. Indium is then electroplated on both the alloyed surface and the W film. The wafer is cleaved into bars, which bars are then sawed into lasers. The W does not interfere with the cleaving.

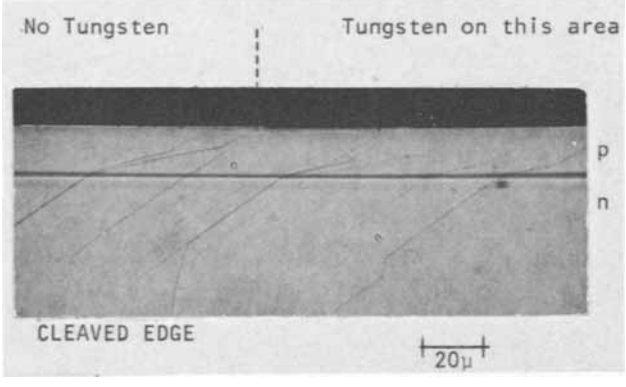

Fig. 1. Cleaved and stained edge of diffused wafer. ~2000Å of W is on wafer surface to the right of the dotted line. Diffusant source was ZnAs; diffusion time was 4 hr at 750°C plus 0.75 hr at 850°C. This wafer was then used in second controlled experiment described in text.

Because the junction profile is substantially unchanged by the presence of the W film, it is very likely that the Zn concentration at the GaAs-W interface is the same as the C_0 of Zn on an uncoated wafer after Zn diffusion. The value of C_0 under conditions of the diffusion procedure set forth above is $\sim 2 \times 10^{20}$; this probably accounts for the observed low electrical resistance at the GaAs-W interface. Nonohmic contacts are observed when W is filmed on n- or p-type GaAs doped in the 10^{18} range or less. When the W is evaporated on an already diffused wafer, the contact is ohmic but of higher resistance than when the Zn is diffused through the W.

Two controlled experiments were carried out to compare the series resistances of lasers using the new W film contacting method. The dimensions of the lasers were nominally of 50μ width, 250μ length, and 100μ thickness and were mounted under compression between In-coated Cu plates.

In one experiment the junction depth was quite shallow (2μ) and the average series resistance was about the same for the two groups: $\sim$ 120 mohm as measured on a Tektronix Model 575 curve tracer at 1A current.

In another experiment in which the junction depth was 17μ (*see* Fig. 1), the average series resistances were as follows:

(*a*) Conventional plating-alloying both sides (1)	100 mohm
(*b*) New W method	70
(c) Indium only on p-side; plating-alloying on n-side	120

The contacts of group (c) above tend to degrade under high current density conditions; that is, the resistance increases slowly. This degradation has not been observed in either the new W-film method contacts or the conventional alloying-plating contacts.

W films have been used successfully on GaP and GaAlAs; Zn was diffused through the films, and a low contact resistance resulted.

Mo and Cr films have not been studied as extensively as have the W films, but their behavior seems similar.

Acknowledgments

The writer gratefully acknowledges the cooperation of J. J. Cuomo, E. L. Wilkie, Anne R. Benoric, R. C. McGibbon, and others.

Manuscript received June 20, 1969.

Any discussion of this paper will appear in a Discussion Section to be published in the December 1970 JOURNAL.

REFERENCES

1. J. C. Marinace, *IBM J. Res. Develop.*, **8**, 543 (1964).
2. D. M. Brown, W. E. Engeler, M. Garfinkel, and P. V. Gray, *This Journal*, **115**, 874 (1968).
3. D. M. Brown, W. E. Engeler, M. Garfinkel, and P. V. Gray, *Solid-State Electron.*, **11**, 1105 (1968).

JOURNAL OF THE ELECTROCHEMICAL SOCIETY

ELECTROCHEMICAL SCIENCE

FEBRUARY 1970

A Kinetic Study of the Electrochemical Reduction of Manganese Dioxide in a Homogeneous Phase

J. P. Gabano, J. Seguret, and J. F. Laurent

Fundamental Research Laboratory, Société des Accumulateurs Fixes et de Traction, "La Pile Leclanché" Department, Poitiers, France

ABSTRACT

The electrochemical behavior of MnO_2 electrodes during cathodic reduction in buffered medium (1M KOH) was studied on the basis of diffusion of protons into the solid phase according to Coleman's theory. The kinetics of the process was followed by means of a diffusion equation which predicts the general form of the discharge satisfactorily during potentiostatic and galvanostatic reductions. A method for determining the product of the active surface area of the electrode by the square root of the diffusion coefficient of protons in the crystal lattice is given and results are compared for various samples of MnO_2.

Numerous studies have been undertaken by various authors for the purpose of studying the electrochemical reduction processes of manganese dioxides. In most cases, such studies have resulted in defining some factors which can influence the performance of galvanic cells using manganese dioxide; unfortunately due to the extreme complexity of the so-called depolarization reaction involved in reduction processes, it is often difficult to find correlations among the properties under study.

However in recent years, new data have appeared, one of the most interesting aspects of which is concerned with the electrochemical reduction of manganese dioxide in a homogeneous phase. The reduction process involves a special mechanism of diffusion in the solid state (1-6). In our previous studies (7), some properties relating to the physicochemical structure of manganese dioxide have been examined by various methods (chemical analysis, thermogravimetric analysis, x-ray diffraction, etc). In the present work the research has been extended to studies of the kinetics of the electrochemical reduction of γ and ρ manganese dioxides from various sources in ordinary use in dry cells of the Leclanché type.

In the course of the present study, the fundamental mechanisms involved in the reduction processes were first reviewed. The basic equations for describing the processes were established, and their possible application was considered in the simple case of reductions carried out under potentiostatic or galvanostatic conditions. The validity of such a treatment has been checked by experimental study of some synthetic and natural manganese dioxides. The electrochemical reductions were carried out in a buffered medium of well-defined composition (1M KOH) by means of the cell described by Appelt (8). Intrinsic constants have been deduced for characterizing the relative electrochemical reactivity of the dioxides under study.

Basic Equations

The electrochemical or chemical reduction of manganese dioxides of the γ and ρ type has already been shown (9) to take place in a topochemical reaction in a homogeneous phase and to progress up to the formation of groutite, MnOOH, according to the simplified reaction mechanism

$$MnO_2 + e + H^+ \rightarrow MnOOH$$

The protons supplied by the electrolytic medium pass into the crystal, whereas, the electrons coming either from the outer circuit (in the case of an electrochemical reaction) or from the oxidation of the reducing agent (in the case of a chemical reaction) allows the valence of an equivalent number of Mn^{4+} ions to change into Mn^{3+} ions so that the electrical neutrality of the lattice is maintained. If it is assumed that the electrons can freely move in the solid phase, only the accumulation of protons in the surface layers of the crystal produces a diffusion toward the deeper layers, thus controlling the reduction kinetics. The two oxides, MnO_2 and MnOOH, cause the formation of only one phase. This reaction proceeds as if the lower oxide forming on the surface of the manganese dioxide particles diffuses to the inside of these particles, thus giving a compound having an intermediate oxidation state when the equilibrium in the phase is reached. Thus for a given degree of reduction, the equilibrium resulting from such a mechanism could be represented by the following equations (10-13)

$$2\left(x-\frac{3}{2}\right)MnO_2,\ 2(2-x)\ MnOOH + 2dxH^+ + 2dxe$$

$$\rightleftarrows 2\left(x-dx-\frac{3}{2}\right)MnO_2,\ 2(2-x+dx)\ MnOOH$$

or

$$MnO_{2(x-1)}(OH)_{2(2-x)} + 2dxH^+ + 2dxe^- \rightleftarrows MnO_{2(x-dx-1)}(OH)_{2(2-x+dx)}$$

x being the oxidation state of the intermediate defined by the ratio O/Mn.

In the kinetic processes of the electrochemical reduction at a dioxide electrode in a buffered elec-

trolyte, the variations in the electrode potential are due to variations in the oxidation state in the surface layers of the crystal. The value of the surface oxidation state x_s can be deduced as a function of time t and reduction current i according to the relation (14-18)

$$x_s = x_o - \frac{V}{FS\sqrt{D}\sqrt{\pi}} i\sqrt{t} \qquad [1]$$

In this expression, x_o is the initial oxidation state of the dioxide, V the average volume occupied by one molecule of the species $MnO_{2(x-1)}(OH)_{2(2-x)}$, F Faraday's constant, S the electrochemically active surface of the electrode, and D the diffusion coefficient of protons in the crystal.

According to the electrical conditions imposed on the electrode, the validity of the above theory may be verified.

Potentiostatic Conditions

The electrode potential being fixed, the surface oxidation state, x_s, remains constant, and in this case relation [1] may be written in the following way

$$x_o - x_s = \frac{V}{FS\sqrt{D}\sqrt{\pi}} i\sqrt{t}$$

that is

$$\log i = \frac{-1}{2}\log t + \log k \qquad [2]$$

with

$$k = \frac{FS\sqrt{D}\sqrt{\pi}}{V}(x_o - x_s) \qquad [3]$$

By determining k at a known x_s corresponding to the imposed potential $E(x_s)$, it is possible to determine the product $S\sqrt{D}$ which is characteristic of the dioxide electrode under study. The value of x_s can be approximately determined in the case of a buffered electrolytic medium, from the following relation

$$E(x_s) = E^{o\prime} - 2.3\frac{RT}{F}\log\left(\frac{2 - x_s}{x_s - \frac{3}{2}}\right) \qquad [4]$$

$E^{o\prime}$ is a constant. $E(x_o)$ is related to x_o by the same relation, that is

$$E(x_o) = E^{o\prime} - 2.3\frac{RT}{F}\log\left(\frac{2 - x_o}{x_o - \frac{3}{2}}\right) \qquad [5]$$

By calculating the difference $\Delta E = E(x_s) - E(x_o)$ representing the polarization imposed on the electrode, x_s can be determined taking the value of x_o into account. However, the application of these various relations implies that the electrode kinetics are controlled only by the diffusion process in the solid phase, and other processes which might cause other electrode polarizations are excluded.

Galvanostatic Conditions

In the case of galvanostatic conditions imposed on the electrode, the previously established relation [1] remains valid. Moreover, if the following relation is assumed

$$K = \frac{V}{FS\sqrt{D}\sqrt{\pi}} \qquad [6]$$

the electrode potential $E(x_s)$ may be written in the following way

$$E(x_s) = E^{o\prime} - 2.3\frac{RT}{F}\log\left(\frac{2 - x_o + Ki\sqrt{t}}{x_o - \frac{3}{2} - Ki\sqrt{t}}\right) \qquad [7]$$

which leads to a linear representation of the coordinate system

$$E(x_s), \log\left(\frac{2 - x_o + Ki\sqrt{t}}{x_o - \frac{3}{2} - Ki\sqrt{t}}\right)$$

Experimental

Manganese dioxides tested.—Three types of manganese dioxide were tested: a common electrolytic manganese dioxide, γ; a ρ manganese dioxide obtained by disproportionation of a sesquioxide in sulfuric acid medium; and a natural manganese dioxide, consisting of mainly ramsdellite.

Electrolytes.—All measurements were carried out in a buffered medium of 1M potassium hydroxide. Some determinations were also made in a 1M solution of deuterated potassium hydroxide (KOD) in heavy water (D_2O). In all cases, the electrolytes were carefully deaerated by previously bubbling purified nitrogen through them.

Reduction cell.—The experimental device described by APPELT and PUROL (8) was used with a constant electrolyte rate of 5 ml/min through the cell. The rate was controlled by a peristaltic pump. With such a mode of operation, concentration polarization was avoided in the electrolyte in the vicinity of the electrode during the reduction. The depolarizing mass distributed on a surface area of 3.2 cm^2 was a mixture of manganese dioxide and acetylene black (6%): its weight varied in the range of 0.05-0.2g. The counterelectrode was a perforated zinc anode through which the electrolyte could flow. The separator was a nylon fabric. The reference electrode employed the Hg/HgO/1M KOH system. In all cases, determinations were carried out at 25°C.

Types of reduction studied.—Potentiostatic reduction.—The equilibrium potential of each kind of manganese dioxide was determined in a separate experiment by recording potential time curves to confirm a steady state.

In a second experiment the sample was first subjected to its equilibrium potential. A TACUSSEL potentiostat of the PRT 20-2Z type with three electrodes was used for this purpose. The current was simultaneously measured by a recorder (TACUSSEL EPL1). The current dropped almost immediately to practically zero, thereby indicating that the electrode was in equilibrium with test solution. A potential more negative than the equilibrium potential was then imposed on the electrode, so that the manganese dioxide was potentiostatically reduced. The current-time curve was recorded.

Galvanostatic reduction.—A suitable potentiostatic polarization was imposed on the dioxide electrode to bring it quickly to the equilibrium potential in the test electrolyte. Then the electrode was subjected to galvanostatic conditions (reduction at a constant current), and the corresponding potential in relation to the reference electrode was recorded as a function of time.

Results and Discussion

Potentiostatic reduction.—Influence of the type of dioxide.—Figure 1 shows various current-time relations obtained from the potentiostatic reductions carried out in 1M KOH medium on the tested manganese dioxides. The weight of depolarizing mix was equal to 0.2g. The reduction time in minutes has been plotted as abscissa, and the corresponding current in milliamperes delivered by the electrode is shown as ordinate. The imposed cathodic polarization is −25 mV.

Examination of this figure leads to the following conclusions. For any type of manganese dioxide, the relationship thus obtained results in lines having a slope of −½ in agreement with the previously established relation [2]

$$\log i = -\tfrac{1}{2}\log t + \log k$$

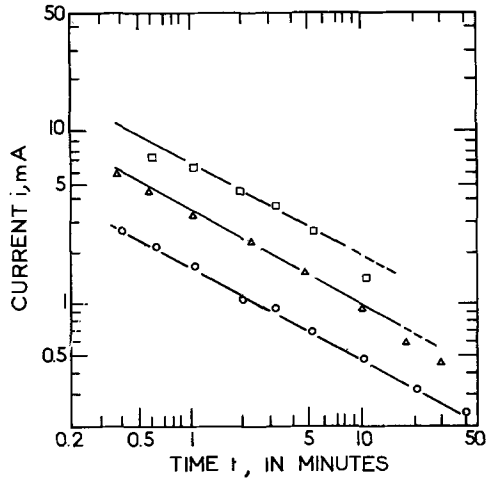

Fig. 1. Potentiostatic reductions carried out on various kinds of manganese dioxide in 1M KOH medium and for a value of the cathodic polarization $\Delta E = -25$ mV. The weight of depolarizing mix is 0.2g. □ Electrolytic MnO_2; △ chemical MnO_2; ○ natural MnO_2 (ramsdellite).

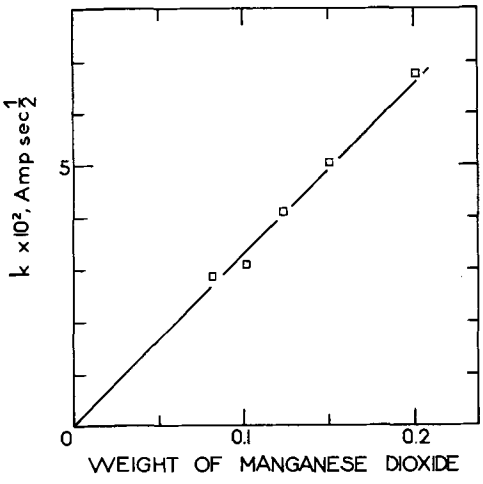

Fig. 2. Variation of k as a function of weight of manganese dioxide used for an electrolytic manganese dioxide and for a cathodic polarization value $\Delta E = -25$ mV.

which shows, that under such conditions, the cathodic reduction phenomenon is limited only by the diffusion process of protons in the crystal of the depolarizer.

The theoretical relationship is even more closely followed as the manganese dioxide becomes well crystallized. With ramsdellite which represents the most highly organized structure, the relation is followed during reduction periods of about 40 min; there is not such good agreement for the more amorphous forms, ρ-MnO_2 and γ-MnO_2. Thus, with electrolytic γ manganese dioxide, deviation from the theoretical relationship appears after a reduction period of 10 min. Such deviations are caused by the fact that the solid wherein the diffusion process takes place can be considered as a semi-infinite medium only as a first approximation, that is only on the scale of the crystallite the dimensions of which limit its continuity. On the other hand, the application of such a theory implies that diffusion takes place in a preferential direction which could, for instance, be one of the better defined crystal orientations of the lattice. This may explain why the best results have been obtained with the most highly crystallized form of MnO_2 (ramsdellite).

The determination of parameter

$$k = \frac{FS\sqrt{D}\sqrt{\pi}}{V}(x_0 - x_s)$$

may be made from the lines obtained for each kind of manganese dioxide tested. Parameter k represents the value of the reduction current intensity at time $t = 1$ sec. In the diffusion equation k has a unit of amp $sec^{1/2}$. It depends partially on the cathodic polarization and partially on the active surface area of the electrode which is directly proportional to the amount of manganese dioxide.

In all cases, the perfect proportionality existing between the value of parameter k and the amount of manganese dioxide present in each test has been verified by varying the weight of the depolarizing mix for a constant polarization of the electrode.

Figure 2 shows the line obtained for electrolytic, γ manganese dioxide by plotting as abscissa the amount of manganese dioxide used in each test, and as ordinate the corresponding value of k for a constant cathodic polarization of -25 mV. By determining the slope of this line, the value of k can be extrapolated to 1g of manganese dioxide which is the selected unit of weight.

Influence of imposed polarization.—The influence of cathodic polarization, ΔE, on the potentiostatic current-time curves has been studied for each type of manganese dioxide tested, at constant depolarizing mix weight. For natural dioxide (ramsdellite), the result was in agreement with the theory for values of ΔE in the -25 to -80 mV range. Figure 3 shows, on a logarithmic scale, the reduction time (in minutes) as abscissa and the corresponding current (in milliamperes) as ordinate for the natural dioxide. The potentiostatic reductions for various values of cathodic polarization have been carried out in 1M KOH medium for a weight of depolarizing mix of 0.2g. Examination of this figure leads to the following conclusions.

At any polarization imposed on the electrode, a series of linear relations of $-\frac{1}{2}$ slope are obtained.

The deviation from the theoretical relationship appears earlier with higher cathodic polarization imposed on the electrode. This may be explained by the fact that the diffusion in the solid phase does not take place in a semi-infinite medium as assumed in the mathematical derivation.

For each value of the cathodic polarization, the parameter k (value of the current at time $t = 1$ sec) has been measured from the preceding experimental determinations. The variation $\Delta x = x_0 - x_s$ corresponding to the imposed variation $\Delta E = E(x_s) - E(x_0)$

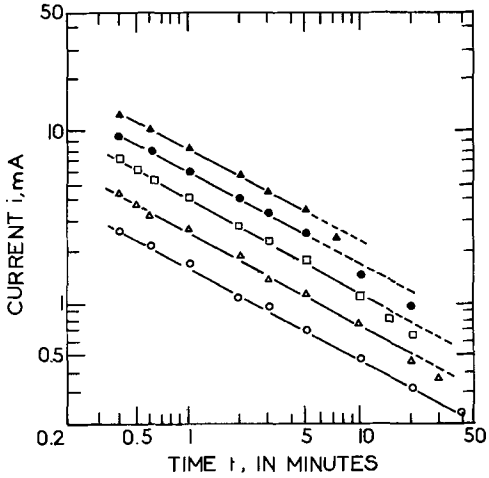

Fig. 3. Potentiostatic reductions carried out on a natural manganese dioxide (ramsdellite) in 1M KOH medium for various values of the cathodic polarization ΔE expressed in mV. The depolarizing mix weight is 0.2g. ▲—80 mV, ●—70 mV, □—50 mV, △—38 mV, ○—25 mV.

has been deduced, taking into account relations [4]-[5] and the value of x_0.

Figure 4 shows Δx as abscissa and parameter k as ordinate. The line thus obtained (white squares) agrees with Eq. [3]

$$k = \frac{\mathbf{F}S\sqrt{\pi}\sqrt{D}}{V}\Delta x$$

The slope of this line

$$\frac{\partial k}{\partial \Delta x} = \frac{\mathbf{F}\sqrt{\pi}}{V} S\sqrt{D}$$

is a means of obtaining parameter $S\sqrt{D}$ which is characteristic of the manganese dioxide electrode tested. This parameter obviously depends on the amount of dioxide involved in the reduction process.

Influence of the electrolyte.—In order to define the influence of the nature of the electrolyte some determinations have been made in a medium consisting of 1M deuterated potassium hydroxide (KOD) in heavy water (D_2O). The potentiostatic reductions were effected on 0.2g of depolarizing mix for cathodic polarization values identical to those described above. However, the natural dioxide used in this test was previously treated for several weeks with heavy water. The solution was renewed several times during the operation, and then the dioxide was dried at 110°C.

Figure 4 also shows (black squares) the relation between k and Δx for this particular case. The line thus obtained shows a lower slope than in the preceding case (reductions carried out in 1M KOH).

The ratio of the slopes $\partial k/\partial \Delta x$ for reductions carried out in 1M KOH in H_2O and 1M KOD in D_2O, respectively, has been found to be 1.4. It is interesting to note that the ratio is very near the theoretical value (1.414) (19).

Practical results obtained with various manganese dioxides.—It has been shown that for each manganese dioxide the electrochemical reduction of which is limited by a diffusion process in the solid phase, a product $S\sqrt{D}$ representing its electrochemical activity can be determined (Eq. [4]).

Several values of the main parameters characterizing these dioxides are shown in Table I, together with the products $S\sqrt{D}$ obtained from potentiostatic reductions carried out in 1M KOH medium.

Values of $S\sqrt{D}$ have been calculated for 1g of dioxide, taking into account the MnO_2 content of the tested samples. The determination of the average molar volume V required for the evaluation of product $S\sqrt{D}$ has been effected from previously obtained (7) results.

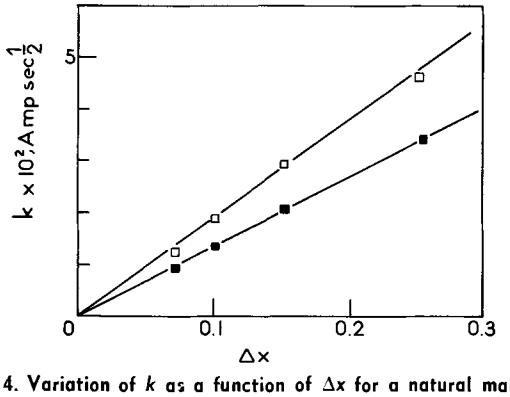

Fig. 4. Variation of k as a function of Δx for a natural manganese dioxide (ramsdellite) and for a depolarizing mix weight of 0.2g. □ Determinations made from potentiostatic reductions in 1M KOH in H_2O; ■ determinations made from potentiostatic reductions in 1M KOD in D_2O.

Table I. Values of the main parameters

Kind of dioxide	% MnO_2	x_0	$E(x_0)$/Hg/HgO/KOH 1M, mV	$S\sqrt{D}$, cm³ sec$^{-1/2}$ g^{-1}
Electrolytic γ MnO_2	90	1.97	+120	5.07×10^{-4}
Chemical ρ MnO_2	81	1.95	+110	2.45×10^{-4}
Natural MnO_2 (ramsdellite)	75	1.96	+95	1.43×10^{-4}

Table II. Diffusion coefficient of protons in the crystal

Kind of dioxide	S BET, m² g^{-1}	$S\sqrt{D}$, cm³ sec$^{-1/2}$ g^{-1}	D, cm² sec^{-1}
Electrolytic γ MnO_2	55	5.07×10^{-4}	8×10^{-19}
Chemical ρ MnO_2	30	2.45×10^{-4}	6.7×10^{-19}
Natural MnO_2 (ramsdellite)	18	1.43×10^{-4}	7×10^{-19}

In Table I, the value of product $S\sqrt{D}$ may be seen to vary from 1 to 5 x 10^{-4} cm³ sec$^{-1/2}$ g^{-1} according to the depolarizing activity of the manganese dioxide tested.

Knowing the BET surface area, it is possible to deduce in first approximation the diffusion coefficient of protons in the crystal, as is shown in Table II.

Galvanostatic reductions.—In order to complete the results obtained by the potentiostatic reductions, some reductions were effected at constant current on the three kinds of manganese dioxide tested.

Figure 5 shows, as abscissa, in a logarithmic scale the ratio

$$\frac{2 - x_0 + Ki\sqrt{t}}{x_0 - \frac{3}{2} - Ki\sqrt{t}}$$

for various values of reduction time, t, as ordinate, the corresponding potential reached by the dioxide electrode in relation to the reference system, after correcting for the ohmic polarization measured by the interrupted current method (20). In order to calculate K, the values of $S\sqrt{D}$ (in cm³ s$^{-1/2}$ g^{-1}) previously determined by the potentiostatic method were used. The i values were calculated for one gram of dioxide.

Examination of Fig. 5 leads to the following remarks.

With any kind of dioxide, the relation gives a line the slope of which is equal to 0.060V, which is in

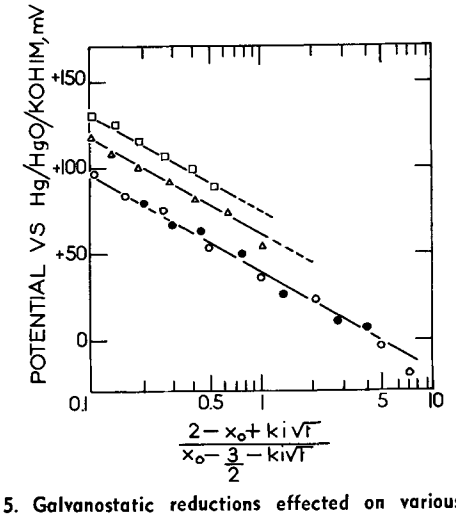

Fig. 5. Galvanostatic reductions effected on various kinds of manganese dioxide in 1M KOH medium for various reduction rates, i, imposed on a depolarizing mix weight of 0.2g. □ electrolytic MnO_2, i = 1 mA; △ chemical MnO_2, i = 1 mA; ○ natural MnO_2 (ramsdellite) i = 1 mA; ● natural MnO_2 (ramsdellite) i = 2 mA.

agreement with theory (2.3 $RT/\mathbf{F}$). The potential is expressed as follows

$$E(x_s) = E^{\circ\prime} - 2.3\frac{RT}{\mathbf{F}}\log\left[\frac{2 - x_o + Ki\sqrt{t}}{x_o - \frac{3}{2} - Ki\sqrt{t}}\right]$$

The theoretical relationship is more closely followed as the manganese dioxide becomes more highly crystallized. This agrees with the hypotheses previously stated from the potentiostatic determinations. The galvanostatic reduction method therefore corroborates the results obtained by the potentiostatic method.

Conclusions

This work has resulted in some general views of the protonic reduction process in the solid phase, which has been mentioned frequently by various authors to explain the mechanisms involved in the electrochemical reduction of γ and ρ manganese dioxides.

The following points have particularly been stressed in this work, which started from theoretical consideration based both on thermodynamics and on the physicochemistry of the solid state.

The behavior of manganese dioxide during its electrochemical reduction may be analyzed to a first approximation by means of an equation representing a diffusion process in the solid state; such equation may be expressed in a particularly simple form if the crystal of the dioxide is assumed to be a semi-infinite medium.

Under the experimental conditions imposed on the system (either potentiostatic or galvanostatic) the validity of this equation can be demonstrated with the restrictions associated with the semi-infinite nature of the crystal of dioxides at the beginning of the electrochemical reduction. The equation is followed more closely as the kind of dioxide tested becomes more highly crystallized.

A characteristic parameter, $S\sqrt{D}$, the product of the active surface area of the dioxide electrode multiplied by the square root of the diffusion coefficient of protons in the crystal, has been determined for 1g samples of dioxides. With such a parameter it has been possible to compare the depolarizing activity of several dioxides of the γ and ρ types. Some determinations were also made in a deuterated electrolyte.

The knowledge of the reduction mechanism gained in this study should be helpful in directing the physicochemical treatments of manganese dioxides in order to obtain a high electrochemical activity for use in galvanic cells.

Acknowledgment

The authors wish to express their thanks to Dr. R. C. Osthoff, Manager of the Electrochemical Systems Branch of General Electric, Research and Development Center, for his assistance in the presentation of this paper.

Manuscript submitted June 10, 1969; revised manuscript received *ca.* Oct. 7, 1969.

Any discussion of this paper will appear in a Discussion Section to be published in the December 1970 JOURNAL.

REFERENCES

1. J. J. Coleman, *Trans. Electrochem. Soc.*, **90,** 545 (1946).
2. J. P. Brenet, *C. R. Acad. Sci., Paris,* **231,** 543 (1950).
3. J. P. Brenet, *Proc. CITCE 1956 Madrid,* **8,** 394 (1958).
4. W. Feitknecht, H. R. Oswald, and V. Feitknecht-Steinmann, *Helv. Chem. Acta,* **43,** 1947 (1960).
5. H. Bode, A. Schmier, and D. Berndt, *Z. Elektrochem.*, **66,** 586 (1962).
6. K. J. Vetter and N. Jaeger, *Electrochim. Acta,* **11,** 401 (1966).
7. J. P. Gabano, B. Morignat, E. Fialdes, B. Emery, and J. F. Laurent, *Z. Physik. Chem.*, **46,** 359 (1965).
8. K. Appelt and H. Purol, *Electrochim. Acta,* **1,** 326 (1959).
9. J. P. Gabano, B. Morignat, and J. F. Laurent, *Electrochem. Technol.*, **5,** 532 (1967).
10. K. J. Vetter, *Z. Elektrochem.*, **66,** 577 (1962).
11. K. J. Vetter, *This Journal,* **110,** 596 (1963).
12. A. Kozawa and R. A. Powers, *This Journal,* **113,** 871 (1966).
13. J. P. Gabano, *C. R. Acad. Sci. Paris,* **264,** 262 (1967).
14. A. B. Scott, *This Journal,* **107,** 941 (1960).
15. F. Kornfeil, *ibid.*, **109,** 349 (1962).
16. A. Era, Z. Takehara, and S. Yoshizawa, *Electrochim. Acta,* **12,** 1199 (1967).
17. P. Brouillet, A. Grund, F. Jolas, and R. Mellet, *C. R. Acad. Sci.*, **257,** 3390 (1963).
18. P. Brouillet, A. Grund, F. Jolas, and R. Mellet, 4th International Battery Symposium Brighton (1964).
19. A. Kozawa and R. A. Powers, *This Journal,* **115,** 122 (1968).
20. G. Geard, G. Gerbier, and J. P. Gabano, 4th International Battery Symposium Brighton (1964).

Discharge Mechanism of the V_2O_5 Electrode

Kenneth R. Newby[1] and Allen B. Scott*

Department of Chemistry, Oregon State University, Corvallis, Oregon

ABSTRACT

The behavior of V_2O_5 single crystals, grown from the melt, during cathodic polarization and recovery, has been investigated. The dependence of potential on *p*H showed that the only plausible reduction product was a solid oxide or oxyhydroxide, polarization being due to the formation of a solid solution. In the *p*H range 2.0-5.5, the curve of electrode potential *vs.* time during both polarization and recovery was accurately predicted by an equation, already applied to MnO_2, derived from the assumption that the product is removed from the surface by diffusion into the electrode. Using tritium as a tracer, it was shown that hydrogen is incorporated in the electrode during discharge at *p*H 4.7. The activation energy for diffusion was found to be 6.7 kcal/mole, which is consistent with bipolar diffusion of protons and electrons.

Vanadium pentoxide as a cathode in electrochemical cells has previously been studied to a limited extent. Watson and Scott (1) studied polycrystalline V_2O_5 electrodes in an acid electrolyte saturated with dissolved V_2O_5. They found that, for low constant-current discharges, polarization curves for this electrode were qualitatively similar to those for MnO_2 in an alkaline medium. These authors were partially successful in applying a theory developed (2) for MnO_2 to these discharge curves. This theory is based on the assumption that polarization is caused by an accumulation of reduced product in solid solution on the electrode surface and that recovery is a result of the subsequent diffusion of the product into the electrode. Its application to MnO_2 has been demonstrated quantitatively (3).

Shukler and Kuz'min (4) studied the cathodic behavior of pressed pellet electrodes made of 80% V_2O_5 and 20% graphite. These authors used H_2SO_4 as an electrolyte and worked at higher apparent current densities than Watson and Scott. They concluded that the V_2O_5 electrode is reduced directly to a second solid phase on the electrode surface. This phase was identified as one containing V(IV).

Here we attempt to determine the discharge mechanism for single crystalline V_2O_5 in NH_4Cl buffered solutions and to show under what experimental conditions the theory applicable to MnO_2 can be expected to predict the discharge and recovery curves.

Experimental

Electrode preparation.—Single crystals of V_2O_5 were grown using a modification of a method originally due to Arsen'eva and Kurchatov (5) and supplied to this laboratory by Boros in a private communication.

The crystals were grown in a platinum crucible in an air atmosphere. Baker analyzed (99.5%) V_2O_5 was melted at 690°C and a small seed of crystalline V_2O_5 was placed on the melt surface. The temperature was then slowly raised until only a single crystallite remained. At this point the melt was cooled at a rate of approximately 1°C/3 min for a total of 10°-20°C. The single crystal grew as a thin, flat sheet on the surface of the melt with the *ac* crystallographic plane parallel to the surface of the melt. The crystal was removed before it reached the edge of the crucible by lifting it from the surface of the melt with a stainless steel spatula.

Crystals could be grown to a diameter of 5 cm (the diameter of the platinum crucible) and a thickness in excess of 3 mm by the above method. However, for convenience a crystal was usually removed from the melt with dimensions of approximately 20 x 10 x 2 mm. The underside of the crystal was covered with polycrystalline material frozen during the process of removal. For the purposes of this study, in which only the top surface of the crystal was presented to the electrolyte, the presence of this material on the back of the crystal was no disadvantage. The top surface was plane, lustrous, and over a large part of its area was, on microscopic examination in reflected light, free of appearances of polycrystallinity. Regions which appeared to be polycrystalline at or near the surface were discarded.

Two methods of attaching leads to the V_2O_5 crystals were used. In one, a hot Pt wire was driven into one end of the oxide crystal which melted and resolidified around the wire. In the other method a copper wire was soldered to a gold leaf which had been deposited on the back of the crystal. After the electrical contact was made, a heavy coat of paraffin was applied to all parts of the crystal except the surface which was to be presented to the electrolyte.

Electrolyte *p*H was measured by means of a Beckman Zeromatic *p*H meter. A Systems Research Corporation Model 5501 differential voltmeter was used to measure the electrode potential with reference to the saturated calomel electrode as a function of electrolyte *p*H. The cell was held in a thermostat at 25° ± 0.2°C.

For counting solutions containing tritium, a 1 ml sample of the solution was pipetted into 10 ml of Bray's solution (6) and counted three times, for periods of 5 min, on a Packard Tri-carb Liquid Scintillation Counting System Model 314 EX. In the original solutions in which electrodes were treated the tritium concentration was such that 28.0 counts/min corresponded to one μ-equivalent of hydrogen. Corrections were made for background and color quenching due to dissolved V_2O_5.

The cell for determining the polarization and recovery curves contained the V_2O_5 cathode, a spectroscopic grade carbon anode, a saturated calomel reference electrode with a Luggin tip having an internal radius less than 0.5 mm placed 2 mm from the cathode, a stirrer, and a gas dispersion tube for either O_2 or N_2. The cell was maintained within 0.2° of any chosen temperature between 0° and 45°C by means of a thermostat. The discharge current was held constant by means of a circuit (7) using a Heathkit Model EUW-194 operational amplifier, and was measured by means of a calibrated microammeter. The potential of the V_2O_5 electrode with respect to the saturated calomel electrode was recorded using a Hewlett-Packard Model 7100 BM recording potentiometer.

Results and Discussion

Effect of pH on electrode potential.—During cathodic discharge in acid medium the reaction may be written

* Electrochemical Society Active Member.
[1] Present address: Bell Telephone Laboratories, Inc., Murray Hill, New Jersey.
Key words: vanadium pentoxide, cathodic polarization, discharge.

$$V_2O_5 + ne^- + n'H^+ + mH_2O = \text{product} + pH_2O \quad [1]$$

where "product" represents the reduced form of the vanadium pentoxide and n, n', m, and p may individually have any value including zero.

At 25°C the Nernst equation for this reaction is

$$E = E_o - \frac{0.059}{n} \log \frac{[\text{product}]\,[H_2O]^p}{[V_2O_5]\,[H^+]^{n'}\,[H_2O]^m} \quad [2]$$

where [ ] represents the activity of the enclosed species.

If the activity of the water is taken as the activity of pure water, and if the activity ratio of the V_2O_5 and the product remains constant when the pH is varied, then Eq. [2] reduces to

$$E = E_o' - 0.059\frac{n'}{n}\text{pH}$$

where E_o' includes E_o and other constants. Thus under these assumptions the slope of the curve of electrode potential *vs.* pH is $-0.059(n'/n)$.

The variation of the V_2O_5 electrode potential with pH, in NH_4Cl solution whose pH was adjusted by addition of NH_3 or HCl, is shown in Fig. 1, for pH between approximately 2.0 and 5.5. When the pH was outside this range, the potential was unsteady. The experiment was conducted both on a freshly prepared electrode which had never been discharged and on electrodes which had been discharged to varying degrees and then allowed to recover for two days.

The slopes of the curves in Fig. 1, determined by least-squares analysis were, for A through D, −0.064, −0.054, −0.058, and −0.060, respectively, with an average value of -0.059 ± 0.005 V/pH unit. This is good evidence that the activities of both V_2O_5 and the product are independent of pH and that $n = n'$.

The data on single crystals confirm the previous result of Watson and Scott (1) on polycrystalline vanadium pentoxide electrodes and also that reported by Shukler and Kuz'min (3) on pressed pellet electrodes.

It has been previously shown (1) that, for the cathodic discharge of V_2O_5 at pH < 5.3, if the number of electrons equals the number of protons the product must be a solid. The reduction may involve loss of oxygen to the electrolyte, exemplified by the reaction

$$V_2O_5 + 2e^- + 2H^+ = V_2O_4 + H_2O$$

or by incorporation of hydrogen and water in the solid electrode exemplified by the reaction

$$V_2O_5 + 2e^- + 2H^+ + H_2O = 2VO(OH)_2 \quad [3]$$

The observation that steady potentials were unattainable outside pH 2.0-5.5 is probably due to the following factors, among others: at pH <2 the product dissolves to an appreciable extent; at pH >5.5 the product is oxidized by oxygen dissolved in the electrolyte.

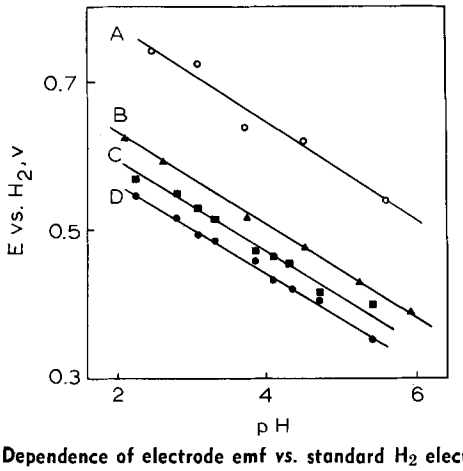

Fig. 1. Dependence of electrode emf *vs.* standard H_2 electrode on pH at 25°C. Curve A is for unreduced V_2O_5; B, C, and D are for partially reduced V_2O_5.

Discharge in tritiated solutions.—In order to demonstrate whether or not hydrogen is incorporated in the V_2O_5 electrode during cathodic discharge, electrodes were discharged in tritium-containing solutions. After a recovery period, the electrodes were anodically charged in a nontritiated electrolyte to recover tritium incorporated during the discharge, and this electrolyte was then counted. Because a considerable amount of tritium was adsorbed or otherwise adhered to the electrode after immersion in tritiated solution even if no discharge current was passed, a standard procedure for rinsing and soaking electrodes was developed to provide suitable "blank" comparisons.

Each electrode initially was allowed to stand for a minimum of 1 hr in 1*N* NH_4Cl solution which contained 25 μc/ml of tritium. The electrode was then rinsed for 1 min with manual agitation successively in each of three 10-ml distilled water baths followed by one 3-hr rinse in a fourth 10-ml distilled water bath. The fourth rinse served as a predischarge blank for the adsorbed tritium on a given electrode. Following the predischarge blank the electrode was returned to the tritiated electrolyte and discharged at a measured current for 3 hr. After discharge the electrode was allowed to recover in the tritiated solution for a minimum of 1.5 hr. At the completion of the recovery period the electrode was rinsed as described above for the blank except that in the fourth distilled water bath the electrode was made an anode and oxidized for 3 hr at a current equal to or slightly less than the discharge current. This charging procedure was undertaken to reverse the discharge reaction and, thereby, aid in the release to the bath of tritium incorporated in the electrode. After the discharge and charge operations, a postdischarge blank was made. The procedure for this was identical to that of the predischarge blank.

Table I shows clearly that tritium was incorporated during discharge, the discharge-charge treatment yielding on the average significantly higher activity than either of the blanks. Some tritium may have been retained in the electrode in most cases even after the charging process, as the postdischarge blank was generally higher than the predischarge blank. An additional cause for higher postdischarge blanks may be an increase in surface roughness caused by charging and discharging which would result in increased adsorption of tritiated solution. From the number of Faradays passed during discharge, and the difference in counting rate between the entries in the discharge-charge column and the predischarge blanks, a rough value for the current efficiency for incorporation of hydrogen during discharge was calculated. It approached 60% in some samples, but was generally lower and highly variable. In part, the low current efficiency may be due to failure to recover all of the tritium during charging; in part it may arise from isotope effects during electrolysis; further in the case of samples 4 and 7 hydrogen gas evolution was ob-

Table I. Comparison of electrode treatments in tritiated solution

Sample	Counting rate, per minute			Current efficiency, %
	Predischarge blank	Discharge-charge	Postdischarge blank	
1	216	526	97	23
2	101	750	268	47
3	64	715	258	37
4	70	374	487	17
5	48	720	98	55
6	26	1397	493	58
7	26	242	210	27
8	26	708	429	52
9	32	640	255	55

served to occur, which would account for the low current efficiency observed.

We conclude from this experiment that the cathodic discharge of V_2O_5 involves largely if not entirely the incorporation of hydrogen in the solid electrode. If the product is in solid solution with V_2O_5, it is meaningless to specify its formula. For some purposes, it may be convenient to represent the reduced material as a solid solution of $VO(OH)_2$ in V_2O_5; however, this representation has the disadvantage that $VO(OH)_2$ cannot diffuse as such in solid solution with V_2O_5 unless oxygen diffuses as well as hydrogen, an unlikely occurrence at the temperatures of interest. The most satisfactory representation is simply a solid solution of hydrogen in V_2O_5.

Polarization and recovery mechanism.—On the basis of the results of the foregoing experiments, we propose that single crystalline V_2O_5 is polarized during discharge by an increasing concentration of hydrogen (probably as an oxyhydroxide) in solid solution; on discontinuing the current, recovery occurs by diffusion of protons, accompanied by electrons, into the interior of the electrode.

Representing the reduction product, as a solid solution of hydrogen in V_2O_5, by the formula $V_2O_5 \cdot H$, the cathode reaction is

$$V_2O_5 + e^- + H^+ = V_2O_5 \cdot H$$

and the Nernst equation for constant pH is

$$E = E_o'' - (RT/F) \ln \frac{[V_2O_5 \cdot H]}{[V_2O_5]}$$

where E_o'' includes E_o and a term involving the pH.

Formulated in this way, the cathode reaction is the formal analogue (8) of the cathode reaction for MnO_2 at moderate current density and pH in the middle range. It must be noted that a different choice of electrode reaction, *e.g.*, Eq. [3], leads to apparent differences in the Nernst equation. These differences disappear if the reference functions for activity are properly chosen on the basis of site-occupancy, as they should, since the representation of solids by molecular formulas is arbitrary.

The dependence of electrode potential upon time should then follow the equation (2, 3)

$$E = E_o'' + 2.303(RT/F) \log \left[\frac{A}{t^{1/2} - (t - \tau)^{1/2}} - 1 \right] \quad [4]$$

where t is the time and τ is the time at which the discharging current is broken. This relation is derived from the solution of Fick's equation for one-dimensional diffusion in a semi-infinite body, with constant flux onto the surface. Provided the proposal above is correct, [4] should apply more accurately to a large single crystal than to the polycrystalline electrodes previously studied.

In obtaining [4], if the activities of V_2O_5 and $V_2O_5 \cdot H$ are replaced by the respective mole fractions, A is given by

$$A = C_o (\pi D)^{1/2}/2\phi \quad [5]$$

with D the diffusion coefficient for the product, C_o the concentration of pure solid V_2O_5 in equivalents/volume, and ϕ the flux of hydrogen through the surface in equivalents/area x time.

Single crystals were discharged and allowed to recover in an NH_4Cl electrolyte, using a range of current densities, temperatures, and pH's. The pH was adjusted by addition of NH_3 or HCl. In previous work with polycrystalline electrodes (1) it was necessary to saturate the electrolyte with V_2O_5 to prevent dissolution of the electrodes; with single-crystal electrodes the rate of dissolution was so small that experiments of several hours duration could be carried out in V_2O_5-free electrolytes with no detectable dissolution provided the pH was within the range 2.0-5.5. This avoided the complication of the possibility of simultaneous reduction of dissolved as well as solid V_2O_5.

Figure 2 shows the polarization during discharge, and the recovery, of a V_2O_5 electrode at pH = 4.7 and current density 48 μA/cm^2. The current was broken at 20 sec.

An apparently instantaneous drop in potential at the start of the discharge, with an approximately equal instantaneous rise on breaking the current, resulted from ohmic polarization, with possibly some contribution due to activation polarization. The original recorder tracings (Fig. 2a) were corrected by removing the segments which appeared to be vertical. The origin of the ohmic polarization was chiefly in the high resistivity (around 100 ohm cm) of the electrode itself, since so-called pseudo-ohmic polarization was made small by use of the Luggin tip. The magnitude of the ohmic polarization was affected by a change in the method of connecting leads (see "Experimental") but there was no other effect of lead location on the shape of the polarization and recovery curves. Due to the extreme initial steepness of the recovery curve, and the finite response time of the recorder, the correction for ohmic polarization at the start of recovery could not be made with accuracy by inspection of the original tracing. However, since the only effect of the correction is to move the recovery curve up or down with respect to the discharge curve, the magnitude of the correction was determined to be that which allowed the same value of E_o'' to be used for both the discharge portion and the recovery portion in fitting the observed data to Eq. [4]. The remaining polarization, shown in Fig. 2b, 3, 5, and 6, is ascribed to solid concentration polarization.

In Fig. 2b, experimental points taken at several values of t from the original tracing, corrected as described, are shown. The constants E_o'' and A of Eq. [4] may be found from the values of E and t at any pair of points on the discharge portion of the curve. The best fit of the experimental points to the equation, during discharge, was given by the constants E_o'' = 0.421V and A = 7.7 sec$^{1/2}$. The recovery curve, *i.e.*, E at $t > 20$ sec, was then calculated with these constants. The full curve of Fig. 2b shows the variation of E with t for both discharge and recovery calculated according to Eq. [4]. The agreement with observation is good.

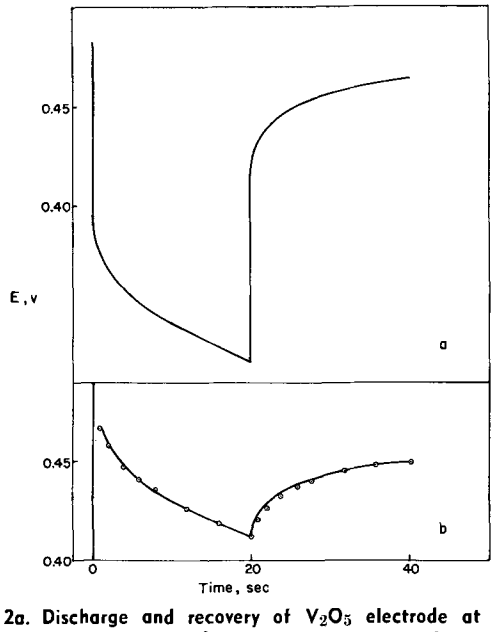

Fig. 2a. Discharge and recovery of V_2O_5 electrode at pH 4.7 and current density 4 μA/cm^2; b after correcting for IR drop on discharge and IR rise on recovery. Points, experimental observations from corrected recorder tracing; full curve, calculated from Eq. [4].

The adherence to Eq. [4] shown in this example is typical of 50 polarization experiments, in which 12 different electrodes were used, provided the *p*H was in the range 2.0-5.5, and the current density and τ were such that τ was somewhat less than $4A^2/9$. At $t \rightarrow 0$, the Nernst equation yields $E \rightarrow \infty$. Except at t near zero, or slightly greater than τ, at which times also the error due to finite recorder response time is apparent, Eq. [4] with constants obtained as above fit the experimental discharge and recovery curves, on the average, within ± 1 mV. The same electrode could be discharged, allowed to recover until E had returned within a few mV of the initial value, and then discharged again; Eq. [4] was followed equally well on the second (and subsequent) discharges as upon the first. We conclude that, under the conditions given, both the polarization during discharge and the recovery are satisfactorily accounted for by the mechanism proposed.

The theory was further tested by examining the dependence of A on the current density. Since A varies as the reciprocal of the flux of the diffusing species onto the surface, it should be linear with i^{-1}, where i is the current density. Figure 3 displays corrected discharge and recovery curves for the same electrode at three different currents. Since the electrode area was maintained constant, the current and current density were proportional. Figure 4 shows the relation between A, found as described above, and the reciprocal of the current, for curves of Fig. 3 and others obtained using additional values of the current. The linearity, and passage through the origin, is satisfactory.

The effects of variation in *p*H, oxygen-content of the electrolyte, stirring, and temperature were next examined.

According to [5], A should be independent of *p*H; however, this was not found to be true. In Fig. 5 are shown the results of discharge at constant current density but varying *p*H. Polarization was made less severe, and recovery more rapid, by lowering the *p*H; this corresponds to an apparent increase in A with decrease in *p*H. There are two probable causes: at *p*H < 2.0 the rate of dissolution of tetravalent vanadium is significant, so that polarization by the mechanism above is minimized by the simultaneous removal of product by dissolution and diffusion into the solid, while the recovery rate is correspondingly enhanced. At all *p*H's the rate of the competing reaction to form H_2 is favored by a decrease in *p*H, so that the actual flux of diffusant may be decreased as a higher proportion of the transferred charge is consumed in H_2 generation.

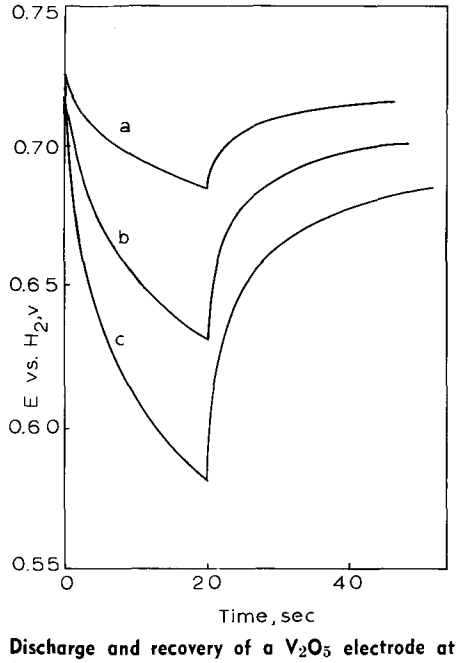

Fig. 3. Discharge and recovery of a V_2O_5 electrode at *p*H 3.1. Current, μA: a, 36; b, 80; c, 123.

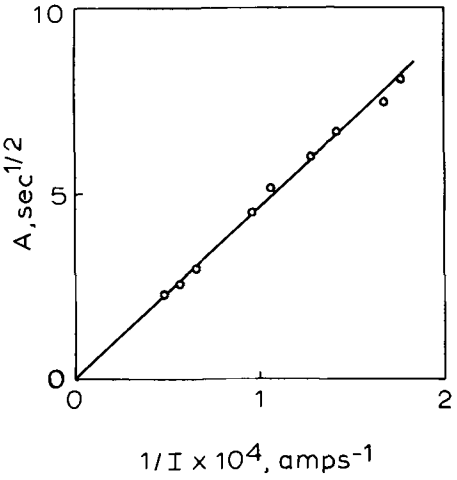

Fig. 4. Dependence of A on current for discharge of the vanadium pentoxide electrode.

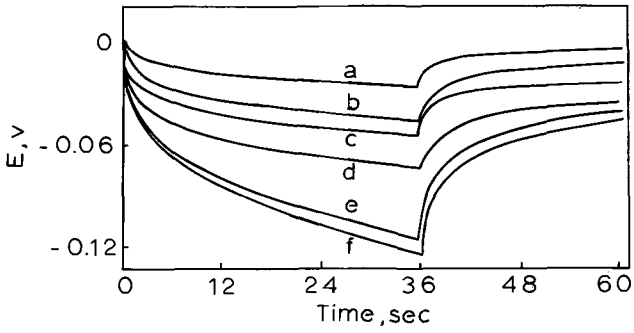

Fig. 5. Effect of *p*H and stirring on the polarization of a V_2O_5 electrode at 61 μA. *p*H: a, 0.7; b, 1.7; c, 3.0; d, 4.5; e, 7.0 stirred; f, 7.0 not stirred. Curves a-d represent both stirred and unstirred discharges. Ordinate of each curve has been shifted so that $E = 0$ at $t = 0$.

At high *p*H's, tetravalent vanadium is oxidized by dissolved oxygen. As shown in Fig. 5, rapid stirring decreased the degree of polarization in an aerated electrolyte of *p*H $= 7$, but had no significant effect at lower *p*H's. It appears that recovery in such a solution is assisted by oxidation of the reduced product and that the rate of oxidation is at least in part governed by the rate of diffusion of dissolved oxygen to the electrode. Several experiments were performed in solutions which had been either freed of oxygen by bubbling N_2 through the solution, or saturated with O_2. In all cases where *p*H ≥ 7 the presence of O_2 in solution clearly reduced the degree of polarization.

The variation of A with *p*H, and the likelihood that evolution of H_2 may compete with the assumed electrode reaction makes the calculation of D from A and ϕ unreliable, since ϕ cannot be related unambiguously to the current density. If it is assumed that ϕ is actually given by $i/\mathbf{F}$, and that the measured surface area is the true surface area, the diffusion coefficient for protons, accompanied by electrons, in V_2O_5 may be calculated for the example shown in Fig. 2, to be $D = 6 \times 10^{-15}$ cm^2/sec. The coefficient for protons alone is one-half this value (11). There are few reported values for other oxides with which to compare this result. The data of Thomas and Lander (12), extrapolated to room temperature, lead to $D \sim 10^{-16}$ cm^2/sec for the bipolar diffusion coefficient for hydrogen in ZnO. The rough value reported above for hydrogen in V_2O_5 appears on this basis to be of a reasonable order of magnitude.

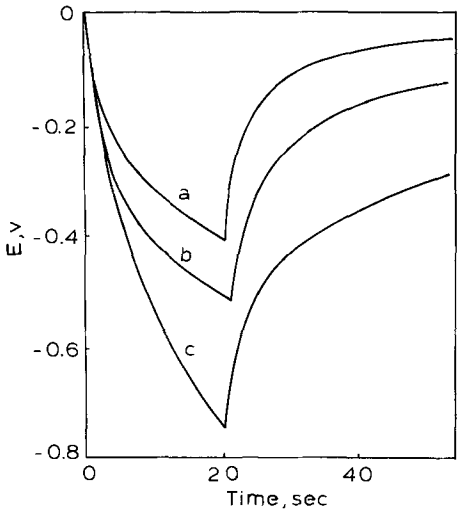

Fig. 6. Effect of temperature on the discharge of a V_2O_5 electrode. Temperature: a, 33°C; b, 16°C; d, 4.5°C; current: 120 μA. Ordinate of each curve has been shifted so that $E = 0$ at $t = 0$.

The effect of temperature upon polarization and recovery is shown in Fig. 6. Letting

$$D = D_0 \exp(-\Delta E/RT)$$

where ΔE is an activation energy for diffusion, it is clear that, provided the current density is constant and the current efficiency for production of the diffusing species is not strongly influenced by temperature, a curve of 2 log A *vs.* T^{-1} should be linear. Figure 7 shows such a relation for the curves of Fig. 6, along with similar data for additional temperatures. From the slope, the value of ΔE was found to be 6.7 kcal/mole.

The magnitude of ΔE is comparable to activation energies reported in some other instances of what is thought to be proton diffusion in oxides, *e.g.*, 3.2 kcal/mole in MnO_2 (9), 13 kcal/mole in α-$Al_2O_3 \cdot H_2O$ (10), and 4.5 kcal/mole in ice (10). For metal ions in oxides, ΔE has been found to be roughly an order of magnitude higher, and it is generally higher still for oxide ions, so that this value of ΔE is consistent with

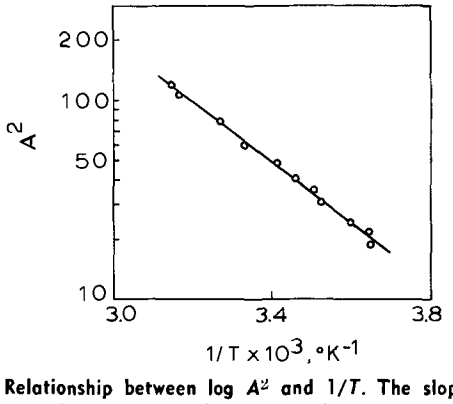

Fig. 7. Relationship between log A^2 and $1/T$. The slope corresponds to an activation energy of 6.7 kcal/mole.

the proposed mechanism involving the diffusion of protons.

A limitation of the simple diffusion theory, already pointed out (2), became apparent when the discharge was carried out for extended periods. Equation [4] predicts that an inflection should occur in the curve of E *vs.* t, during discharge, at $t = 4A^2/9$; further the slope should become infinitely negative at $t = A^2$, that is when the surface is completely reduced. It is evident that A^2 is the analogue of the "transition time" in the chronopotentiometric equation of Sand (13). In fact, both the inflection downward and the later abrupt decrease in potential, where they were observed at all, always occurred at times longer than those predicted. We ascribe this result to the fact that the surface, instead of being a geometrical plane as assumed in the theory, is actually the layer, perhaps a unit-cell edge or more deep, whose composition determines the electrode potential. We are unaware of any satisfactory way to improve the theory by a consideration of the detailed structure of the surface; consequently, in testing the theory we limited ourselves to discharges for times considerably less than $4A^2/9$.

The results reported here differ greatly from those of Shukler and Kuz'min (4). In view of the differences in the electrolyte and apparent current density, and the circumstance that they used polycrystalline material mixed with graphite, this is to be expected. Under the conditions used here, our results all support the conclusion that the reduction product includes hydrogen and forms a solid solution in V_2O_5.

Acknowledgment

The authors wish to acknowledge the assistance of C. Bryden in the preparation of single crystals and D. J. Reed for his aid in the experiments involving tritium. This work was supported in part by the Office of Naval Research. The assistance provided by a NDEA Fellowship is gratefully acknowledged by K. R. Newby.

Manuscript received Oct. 9, 1969.

Any discussion of this paper will appear in a Discussion Section to be published in the December 1970 JOURNAL.

REFERENCES

1. N. V. Watson and A. B. Scott, *This Journal*, **112**, 883 (1965).
2. A. B. Scott, *ibid.*, **107**, 941 (1960).
3. F. Kornfeil, *ibid.*, **109**, 349 (1962).
4. Y. S. Shukler and L. L. Kuz'min, *J. Appl. Chem. USSR*, **39**, 1240 (1966).
5. A. N. Arsen'eva and B. V. Kurchatov, *J. Exp. Theoret. Phys. USSR*, **4**, 576 (1934).
6. G. H. Bray, *Anal. Biochem.*, **1**, 279 (1960).
7. H. V. Malmstadt, C. G. Enke, and E. C. Toren, Jr., "Electronics for Scientists," p. 368, Benjamin, New York (1963).
8. W. C. Vosburgh, *This Journal*, **106**, 839 (1959).
9. A. Era, Z. Takehara, and S. Yoshizawa, *Electrochim. Acta*, **12**, 1199 (1967).
10. Y. Wei and R. B. Bernstein, *J. Phys. Chem.*, **63**, 738 (1959).
11. J. Bardeen, W. Brattain, and W. Schockley, *J. Chem. Phys.*, **14**, 714 (1946).
12. D. G. Thomas and J. J. Lander, *ibid.*, **25**, 1136 (1956).
13. "Electroanalytical Chemistry," A. J. Bard, Editor, Vol. I, p. 159, Dekker, New York (1966).

The Anodic Oxidation of Silicon Nitride Films on Silicon

Terrance B. Tripp

Research and Development Laboratories, Sprague Electric Company, North Adams, Massachusetts

ABSTRACT

The anodic oxidation of silicon nitride films prepared by chemical-vapor-deposition on silicon was studied at six current densities between 4.0 and 13.0 mA/cm^2. It was found that the rate of conversion of silicon nitride to silicon dioxide is independent of time and that the conversion efficiency increases with increasing current density. The onset of film growth from the substrate does not occur until a significant time after the whole film has been rendered easily soluble in HF. It is postulated that the initial product of conversion is an easily soluble, mixed oxide-nitride which must subsequently be converted to oxide before film growth from the substrate can begin. This idea is supported by the behavior of the field strength in the film during the conversion process.

Recently Schmidt and Wonsidler (1) have reported that chemical-vapor-deposited films of silicon nitride on silicon can be converted to silicon dioxide by electrochemical oxidation. The present investigation was undertaken to obtain quantitative data on this anodization process. This information can be used to compare the nature of the conversion of silicon nitride with the formation of anodic oxide films on metals such as silicon and tantalum.

Experimental

The silicon nitride films were grown on 10 ohm cm <111> p-type silicon wafers using the silane-hydrogen-ammonia reaction of chemical-vapor deposition (2). A 1:1000:10 ratio by volume of silane-hydrogen-ammonia was used with a substrate temperature of approximately 900°C. Prior to depositing the nitride, a 12,000Å layer of thermal silicon dioxide was grown on the substrate and a round, 2.5 cm^2 window was opened in this film near the center of the wafer by photolithographic methods (3). This layer of thermal oxide served as an electrically insulating barrier which assured that the anodization was confined to the well-defined area of the window.

The initial thickness of the nitride film was measured by ellipsometry. Samples were selected and matched to give sets with a film thickness variation of less than ± 20Å. Such a set was used for each current density studied. The samples were pressed against a 2 cm ID Viton O-ring mounted in the side of the anodization cell in such a way that the window of silicon nitride was exposed to the electrolyte. In order to reduce heating effects, the plate used to hold the wafer against the O-ring was a block of brass into which cooling fins were machined. During anodization, air was blown over the fins to enhance heat transfer. No temperature rise was detectable with a thermocouple imbedded in the plate very near the surface in contact with the sample. The anodizations were carried out at room temperature using a constantly stirred electrolyte of ethylene glycol + 2% water, 0.4M in KNO_3. Constant current, supplied with an Electronic Measurements Model C633B power supply, was measured with a Keithley 610A electrometer. To measure the voltage drop across the film and substrate a platinum wire, imbedded in glass up to its tip, was placed very near the surface of the sample. The voltage drop between this electrode and the sample substrate during anodization was measured with a Keithley 610A electrometer and recorded with an Esterline Angus Model AW recorder. The contribution to the total voltage by the substrate and contact resistance was about 25V.

The thickness of the converted film and remaining silicon nitride film after anodization was measured interferometrically by taking advantage of the great difference in solubility of the films in HF. First, the surface of each sample was masked with wax to leave two narrow channels of the film exposed, and the film was etched for 2 sec in 48% HF. Next, half the length of each channel was masked with wax, and the film was etched again for several minutes (the etching time varied somewhat with the thickness of the silicon nitride) in 48% HF. After removing the wax, the depth of the channels was measured by interferometry with a Cryolab Model TD-550 thin film thickness determinator. The depth of the channels in the area etched for 2 sec was taken as the thickness of the layer of film produced by the conversion of the silicon nitride. The depth of the channels in the area etched for a longer time was taken as the total thickness of the film.

Results and Discussion

The conversion behavior of 1000Å silicon nitride films at a current density of 7.5 mA/cm^2 (calculated from total current and window area with no roughness factor) is summarized in Fig. 1. The rate of conversion and the total film growth rate were found to be constant also at five other current densities between 4.0 and 13.0 mA/cm^2. Results are summarized in terms of the conversion rate and total film growth rate in Table I. Results obtained from the conversion of a number of samples for the same length of time indicated that the thickness of converted film produced agreed from sample to sample to within about ±20A. Total film thickness was reproducible to within ±50Å.

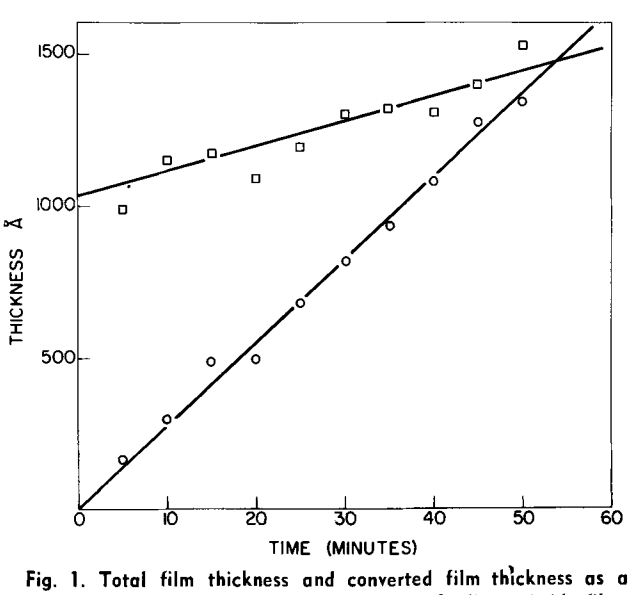

Fig. 1. Total film thickness and converted film thickness as a function of time during the anodic oxidation of silicon nitride films on silicon at a current density of 7.5 mA/cm^2. □ Total film thickness; ○ converted film thickness.

Table I. Conversion rate, total film growth rate, and normalized conversion rate for the anodization of silicon nitride films on silicon at various current densities

Current densities, mA/cm²	Total film growth rate, Å/min	Conversion rate, Å converted film formed/min	Normalized conversion rate ($1/i\ dD/dt$), $\left(\frac{\text{Å converted film}}{\text{formed} \times \text{cm}^2}\right)$ / min × mA
4.0	3.93	13.1	3.28
5.5	5.50	18.9	3.44
7.5	8.20	27.4	3.65
9.0	10.5	35.0	3.89
11.0	12.0	46.4	4.22
13.0	8.0	56.3	4.33

The results from converting 500Å films indicated that the conversion rate is essentially independent of initial film thickness.

Schmidt and Wonsidler (1) report that at a current density of 7 mA/cm² a 1000Å film of silicon nitride is completely converted (presumably as indicated by etch rate) in about 10 min. They used a 7.5 v/o (volume per cent) solution of pyrophosphoric acid in tetrahydrofurfuryl alcohol as electrolyte. In contrast, the present results indicate that it takes about 55 min to convert the same thickness film when the current density is 7.5 mA/cm². The difference in results is most likely due to a difference in the silicon nitride films used or possibly a difference in anodization efficiency of the different electrolytes. In any case, the present results were found to be reproducible for the films studied.

A current efficiency of 1.0% was calculated assuming that the conversion reaction is (1)

$$6\,O^{=} + Si_3N_4 \rightarrow 3SiO_2 + 2N_2 + 12e^{-}$$

The density of the silicon nitride film was taken as 3.1 g/cm³ (see below), and the initial material was considered to be stoichiometric silicon nitride. A similarly low current efficiency has been observed for the anodization of silicon in this electrolyte system (4).

A constant conversion rate is the behavior one would expect for constant current anodization, provided the current efficiency is independent of time and the composition and density of the film are uniform. As the normalized conversion rates ($1/i\ dD/dt$, where i is the current density and D is the converted film thickness) listed in Table I show, the efficiency of conversion increases with increasing current density. In fact, an increase in efficiency with current density has been reported for the anodization of silicon (5). Figure 2 shows the variation with current density of D/D_o, where D is the thickness of the completely converted film and D_o is the initial thickness of the nitride film. This ratio decreases at higher current densities indicating that the increase in conversion efficiency may not be due to a variation in the ratio of ionic to electronic current but to a change in the nature of the conversion, *i.e.*, possibly the initial product of anodization is a mixed oxide-nitride which is easily soluble in concentrated HF and contains a greater percentage of residual nitrogen at higher current densities. Schmidt and Wonsidler (1) have proposed that the conversion reaction involves the evolution of nitrogen gas and, consequently, with increasing current density the increased gas evolution rate produces more porous films. Thus, a given thickness of silicon nitride would produce a thicker converted film with increasing current density, a trend which they reported was observed. Such results are not in agreement with the present study.

In an attempt to detect residual nitrogen in converted films, IR absorption spectra were measured with a Beckman IR 10 spectrometer for films which had been completely converted. No silicon nitride absorption band could be detected. However, the intensity of this absorption band in such films could be below the sensitivity of the instrument or even be absent in a mixed film. The oxide band at 1020-1040 cm^{-1} (6) was present with high intensity.

Figure 3 summarizes the progress of anodization of 500Å films over a time period well beyond the point where the whole film becomes easily soluble in HF. Of interest is the increase in the film growth rate about 5 min after the entire film becomes easily soluble in HF. Some indication of the significance of this change in slope can be deduced from Fig. 4 which shows the voltage build-up during the anodization of both a 500Å silicon nitride film and 10 ohm cm silicon. A change in voltage build-up rate occurs during the anodization of the silicon nitride at a time which corresponds to the break in film growth rate. Furthermore, the build-up rate after the slope change is almost identical to that for the anodization of silicon. Thus, it would appear that the slope change signals the point at which the growth of oxide from the substrate begins. If during anodization, a mixed oxide-nitride film is initially produced as postulated, then what might occur between the time when the film becomes easily soluble in HF and the time when film growth from the substrate begins is the further electrochemical elimination of nitrogen from the film.

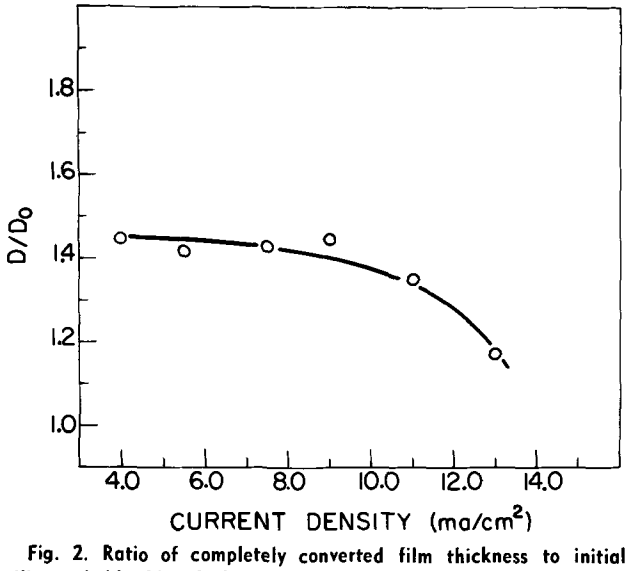

Fig. 2. Ratio of completely converted film thickness to initial silicon nitride film thickness as a function of current density.

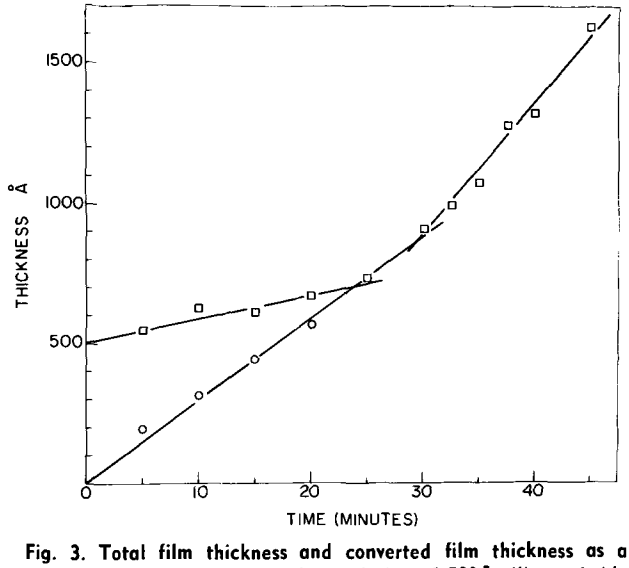

Fig. 3. Total film thickness and converted film thickness as a function of time during the anodic oxidation of 500Å silicon nitride films on silicon at a current density of 7.5 mA/cm². □ Total film thickness; ○ converted film thickness.

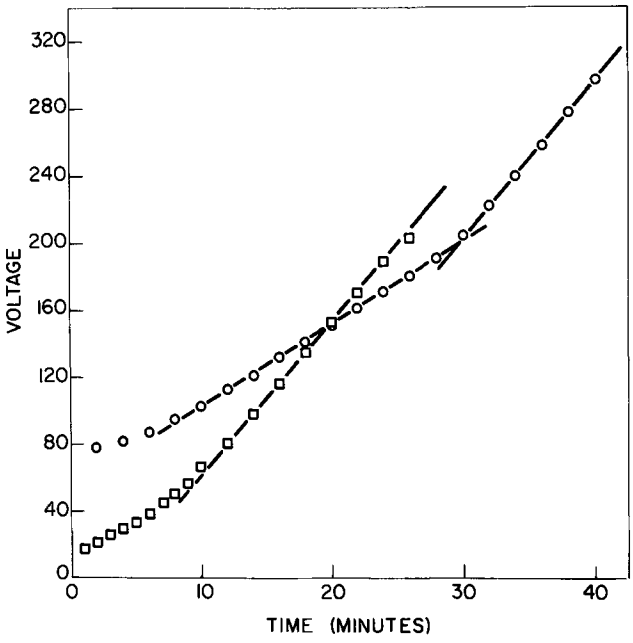

Fig. 4. Voltage as a function of time during the anodic oxidation of silicon and a 500Å silicon nitride film at a current density of 7.5 mA/cm². □ Ten ohm cm silicon; ○ silicon nitride on silicon.

This conclusion is supported by a calculation, based on the densities of silicon nitride and silicon dioxide, of the expected thickness of the converted film to be produced by a given thickness of silicon nitride. Choosing as representative of the limited published data (6-8) on the density of silicon nitride and silicon dioxide films the values 3.1 and 2.2 g/cm³, respectively, one calculates that the complete conversion of a 500Å silicon nitride film should produce a 900Å silicon dioxide film. The change in film growth rate occurs at a thickness of 875Å while the whole film becomes easily soluble in HF at a thickness of 710Å.

It is not possible to calculate from the experimental data the field strength in the converted portion of the film during anodization without making unjustifiable assumptions. Nevertheless, the field in the film being grown directly from the substrate can be calculated if it is assumed that the field in the completely converted silicon nitride film remains constant and is given by the ratio of voltage to film thickness at the point where the change in film growth rate occurs. With these assumptions, the voltage drop across the substrate grown film is simply the difference between the observed voltage and its value at the point where the film growth rate changes. A similar rule applies for the film thickness. The results of such a calculation are summarized in Table II and indicate that the field strength in the new film growing from the substrate is constant at 1.93×10^7 V/cm. Schmidt and Michel (5) observed that the field in the oxide film during the anodization of silicon is constant. Furthermore, this calculated field is in good agreement with the value $1.9 \pm 0.03 \times 10^7$ V/cm² for the field in the oxide film during the anodization of 10 ohm cm p-type silicon. This field was evaluated from voltage build-up and film thickness data obtained in this laboratory by room temperature anodization of silicon at a current density of 7.5 mA/cm² using the electrolyte ethylene glycol + 2% water, 0.04M in KNO_3.

Table II. Calculated field across the substrate-formed-film during anodization of silicon nitride films on silicon at a current density of 7.5 mA/cm²

Anodization time, min	Field × 10^{-7} V/cm
32.0	1.95
34.0	1.93
36.0	1.96
38.0	1.94
40.0	1.93
42.0	1.93
44.0	1.93

A detailed understanding of the progress of the anodization cannot be deduced from the present results alone. Based on unpublished data for the anodization of thermally grown silicon dioxide, Schmidt (9) has suggested that a conversion gradient might be established in the film during anodization by the penetration of hydroxyl ions into the film. Conceivably even the only slightly converted material near the leading edge of this gradient would be easily soluble in concentrated HF. If this is the case, then the whole film would become easily soluble in concentrated HF when the leading edge of the gradient arrives at the silicon surface. A change in film growth kinetics would not occur, however, until complete conversion of the nitride film.

Summary

The rate of conversion of silicon nitride films on silicon was found to be constant in the current density range 4.0-13.0 mA/cm². The initial product of conversion appears to be a mixed oxide-nitride in which the residual nitrogen content increases with increasing current density. This mixed film continues to be converted to oxide for a time after the whole film has been rendered easily soluble in HF. A change in film growth rate and voltage build-up rate then occurs which signals the onset of film growth from the substrate.

Acknowledgments

The author is indebted to Dr. D. M. Smyth and Dr. R. J. Dreiner for many helpful discussions and to Dr. P. F. Schmidt for comments and suggestions. The silicon nitride films were prepared by R. Holmstrom.

Manuscript submitted June 2, 1969; revised manuscript received ca. Sept. 30, 1969. This was Paper 29 presented at the New York Meeting, May 4-9, 1969.

Any discussion of this paper will appear in a Discussion Section to be published in the December 1970 JOURNAL.

REFERENCES

1. P. F. Schmidt and D. R. Wonsidler, *This Journal*, **114**, 603 (1967).
2. V. Y. Doo, D. R. Nichols, and G. A. Silvey, *ibid.*, **113**, 1279 (1966).
3. J. M. Doyle, "Thin-Film and Semiconductor Integrated Circuitry," Chap. 2, McGraw-Hill Book Co., New York (1966).
4. E. F. Duffek, E. A. Benjamini, and C. Mylroie, *Electrochem. Technol.*, **3**, 75 (1965).
5. P. F. Schmidt and W. Michel, *This Journal*, **104**, 230 (1957).
6. W. A. Pliskin and H. S. Lehman, *ibid.*, **112**, 1013 (1965).
7. T. L. Chu, G. H. Lee, and G. A. Gruber, *ibid.*, **114**, 717 (1967).
8. P. Popper and S. N. Ruddlesden, *Trans. Brit. Ceram. Soc.*, **60**, 603 (1961).
9. P. F. Schmidt, Private communication.

A Calorimetric Study of the Electroless Deposition of Nickel

J.-P. Randin[1] and H. E. Hintermann*

Laboratoire Suisse de Recherches Horlogères, Neuchâtel, Switzerland

ABSTRACT

A calorimetric study of electroless nickel deposition was made, with the aim of establishing the energy balance for the system. The heat of reaction of chemically reduced nickel by hypophosphite, as well as the heats of oxidation of hypophosphite and nickel, and the heat of ionization of water, was measured at 94°C.

A calorimetric study of electroless nickel deposition was performed, with the aim of establishing the energy balance for the system. It was shown in a previous publication (1) that the as-plated alloy is composed of a nickel phase and a nickel phosphide, Ni_2P, phase. Hence, the heat of formation of the Ni_2P must be contained in the heat of reaction of the deposition. The DTA of the deposit showed, indeed, that the energy evolved during heating corresponds almost exactly to the heat of formation of Ni_3P from Ni_2P (2, 1).

A study of the literature shows that four principal reaction mechanisms have been proposed to explain the chemical plating of nickel by reduction with hypophosphite:

1. The atomic hydrogen mechanism proposed by Brenner and Riddell (3, 4), then successively supported by several authors, among them Gorbunova and Nikiforova (5), Panchenko and Krokhina (6), Gutzeit (7, 8), Fléchon (9), and Levy (10),
2. The hydride transfer mechanism suggested by Hersch (11), by analogy with the reduction of nickel salts by borohydride ions, and later modified by Lukes (12),
3. The electrochemical mechanism proposed by Brenner and Riddell (4). Machu (13), Müller (14), and Ishibashi (15) adopted this theory with some modifications, while Hickling and Johnson (16) proposed an electrochemical alternative to the atomic hydrogen mechanism,
4. The mechanism involving hydrolyzed nickel with hydroxyl ions proposed by Cavallotti and Salvago (17).

Among these four, only the hydride transfer mechanism and that involving hydrolyzed nickel account for the observed values of the molar ratio Ni^{2+} deposited/$H_2PO_2^-$ consumed, which is always lower than 0.50, as well as the variations of this ratio with pH (18). Further, the results of Sutyagina, Gorbunova, and Glazunov (19), concerning the origin of the hydrogen evolved in the course of the reaction, can be explained also by any of these two mechanisms. The lamellar structure of the deposit, as well as the behavior of baths containing iron, cobalt, and nickel (17), suggests that the most probable mechanism may be that involving hydrolyzed nickel.

In the present work, the heat of formation of the chemically reduced nickel deposit was measured at 94°C, a temperature at which the deposition rate is high. For this temperature, however, heats of reaction cannot be calculated accurately on the basis of the tabulated values at 25°C, since the heat capacities of ions in aqueous media are not known. Therefore, it is necessary to measure the heats of reaction of the oxidation of hypophosphite to orthophosphite and of nickel to Ni^{2+} besides that of the over-all reaction of the chemical deposition of nickel.

In the three principal reactions investigated, hydrogen appears as a reaction product. Therefore measurements were carried out at constant volume and under practically adiabatic conditions to determine the energy content ΔE.

Experimental Procedure

Materials.—The purest sodium hypophosphite[2] was used. Its purity was determined by iodometry (20) and cerometry (21). The average of the two measurements showed that the reagent used was 100 ± 0.5% pure. The accuracy of the titrations was not sufficient to justify a correction, and therefore the hypophosphite was used without further purification, considering it as a 100% pure reagent.

The nickel used was carbonyl-nickel powder,[3] containing: C, 0.05-0.10%; O_2, 0.10%; S, <0.001%; Fe, <0.01%; Ni, balance. This reagent was used without further purification. In the calculations, the impurity proportion was neglected.

Deionized water was used to prepare the sodium hydroxide solutions and to measure the heats of dilution. Prior to use, it was purged for 1 hr at its boiling point with argon to remove traces of CO_2.

In those reactions where hydrogen evolution occurs, the solution was saturated with this gas before being introduced into the Dewar. By this method, the heat of solution of hydrogen did not have to be taken into account.

Other chemicals used were generally "pro analysi" grade.[4]

Apparatus and calorimetric measurements.—The temperature of the thermostat was maintained at 94°C with a relative variation of ±0.005°C. The thermostat was large enough to contain two calorimeters, so that it was possible to work either in a direct, or in a differential mode.

The principal element of the calorimeter shown in Fig. 1 is a Dewar vessel of 1 liter capacity, closed by means of a Teflon stopper, 60 mm thick. The seals were made gas-tight with Viton "O" rings.[6] Stirring was achieved with a glass paddle, turned magnetically at 250 rpm. The magnet was sealed in glass. The thermistors used had a resistance of about 6 kohms at 94°C (100 kohms at 20°C) and were matched to ±1%.[6] The 50-ohm heater was constructed out of Karma alloy[7] wire of 0.10 mm diameter and was insulated from the reaction medium by a glass tube in the form of a coil. Each end of the resistance wire was connected through a short piece of platinum wire, sealed in glass, to the copper leads. Thus, thermal leakage along the copper wires was minimized. The glass bulb containing the reagent was attached to the glass rod by a nylon or platinum wire. The

* Electrochemical Society Active Member.
[1] Present address: Department of Chemistry, Case Western Reserve University, Cleveland, Ohio 44106.

[2] Siegfried AG, 4800 Zofingen.
[3] Type 122, The International Nickel Company (Mond) Ltd., sold by Fluka AG, 9470 Buchs.
[4] E. Merck AG, Darmstadt, Germany.
[5] Angus-Viton-O-Ringe VA 75, Angst & Pfister AG, 8052 Zürich.
[6] Type F 15 MP, ITT Standard AG, 8036 Zürich.
[7] British Driver-Harris.

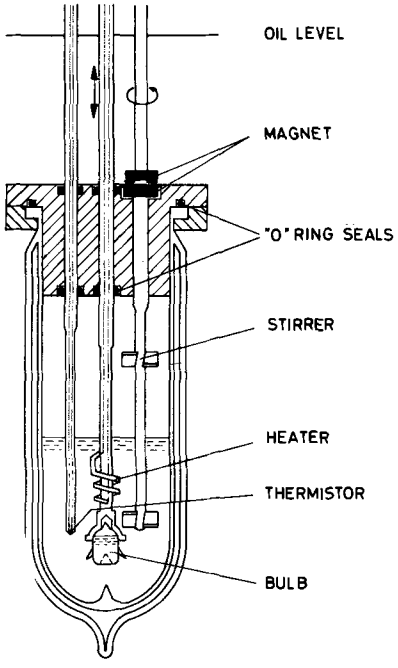

Fig. 1. Calorimeter

platinum wire was used in hydrochloric acid, the nylon wire in electrolytes for the deposition of electroless nickel and for oxidation of hypophosphite, since these reactions are catalyzed by metals.

The calorimeter was allowed to reach equilibrium in the thermostat overnight. The temperature inside the calorimeter was previously brought to the desired initial temperature by the internal heater. The initial temperature of each run was 94.00° ± 0.05°C. The glass bulb was broken by lowering the supporting rod to a glass protrusion welded to the bottom of the Dewar vessel. After the calorimeter had returned to its equilibrium temperature, one or two subsequent calibrations were performed by electrical heating over the same temperature interval. For the determination of the heat of reaction of the nickel deposition the working order was reversed. The calibration preceded the breaking of the bulb to minimize the time during which nickel and orthophosphite could be oxidized.

The temperature change during each experiment was measured by means of unit similar to that described by Nancollas and Hardy (22), consisting of an oscillator, bridge, amplifier, and synchronous detector. The two arms of the bridge included either a thermistor and a reference resistor if the temperature of one Dewar was measured against an external reference, or two thermistors, if the measurement was differential. An a-c bridge was used, and the signal amplified in the usual way, a sensitivity of 16 mV/0.001°C for 1V of the bridge voltage being obtained.

An electronic timer controlled the heating circuit, which was composed of a standard resistance[8] connected in series with the calorimeter heater. The circuit was supplied by a stabilized voltage. The electrical energy dissipated in the heater was determined by measuring the potential drop across the standard resistor and the calorimeter heater, using a digital voltmeter Solartron LM 1420.2.

The volume of liquid used was generally 500 cm³. For measurements of heats of dilution, the accurate volume was calculated on the basis of the weight of the reagent in the bulb to attain the desired dilution. Wherever possible, the proportion of reagents was chosen so as to have an increase of temperature of 0.2-0.3°C. In the measurements of the heat of dilution, the size of the calorimeter did not allow this condition to be realized; therefore, the accuracy of these determinations was less precise.

The calibration of the calorimeter is difficult, because, to our knowledge, no well-authenticated heats of reaction have been measured at 94°C. However, the heat of ionization of water at 25°C is well known (23), and the heat capacity of aqueous solutions of hydrochloric acid, sodium hydroxide, and sodium chloride, between 10° and 120°C, have been studied by Ackermann (24). From the values reported by these authors, the heat of neutralization at 367°K can be calculated to: $\Delta H°_{N(367°K)} = -10.15$ kcal/mole. The error in this value is certainly higher than 1%, because Ackermann extrapolated the heat capacities to infinite dilution from three measurements made at concentrations of 0.5, 1.0, and 2.0M. As is shown below (Table V and VIII), a value of $\Delta H_{(367°K)} = -10.08 \pm 0.05$ kcal/mole, was found within work, for a dilution of $n = 4000$ (n = mole ratio of water to solute), a value which is in good agreement with that calculated at infinite dilution from the data of the literature.

Results and Discussion

Oxidation of hypophosphite.—The oxidation of hypophosphite to orthophosphite and to phosphate is catalyzed by different metals. The data of the literature are limited to the reactions occurring at ambient temperature (25); therefore, the activities of several metals were studied at 94°C to choose the best catalyst for the oxidation of hypophosphite to orthophosphite which, at the same time, would not be too efficient for the oxidation to phosphate. The catalytic activity of Pd, Co, Ni, and Cu was studied in acid, neutral, and alkaline medium. In Table I, the amount of phosphate formed, expressed in per cent of the initial amount of hypophosphite, is reported for each catalyst at different *p*H values. The experiments were performed at constant pressure, with 100 mM hypophosphite in 2 liters of reaction medium. At time O, the catalyst is added, then, at regular time intervals, samples are removed to determine hypophosphite, orthophosphite, and phosphate concentrations. With the amount of catalyst used, all the hypophosphite was oxidized to orthophosphite after about 10 min. In Table I, only the amounts of phosphate formed as a function of the time of reaction are reported.

At *p*H lower than 6, the catalyst dissolves in the reaction medium. Calorimetric conditions were slightly different from those used in the preliminary experiments. The catalyst was added to the reaction medium,

Table I. Oxidation of hypophosphite to orthophosphate and phosphate at constant pressure

Solution volume, 2000 cm³; initial $H_2PO_2^-$ content, 100 mM; temperature, 94°C.

Catalyst	Weight of catalyst, g	Medium	*p*H	Phosphates formed after ($mMPO_4^{-3}/mMH_2PO_2^-$, %) 1 hr	2 hr	4 hr	8 hr
		H_2O	≃6	59.4	95.4	100	100
Pd/Al_2O_3[a] (10% Pd)	5.0	$NaHCO_3$	9.6	9.96	13.3	19.0	29.6
		NaOH	12.5	1.96	3.32	7.32	13.6
Raney nickel[b]	≃2	H_2O	≃6	7.72	14.8	20.6	40.3
		$NaHCO_3$	9.6	0.74	1.64	3.14	5.30
		NaOH	12.5	0.12	0.40	1.42	4.80
Raney cobalt[b]	≃2	H_2O	≃6	5.44	9.36	11.0	11.7
		$NaHCO_3$	9.6	1.22	2.44	4.62	8.00
		NaOH	12.5	0.50	1.34	3.62	9.26
Raney copper[b]	≃10	H_2O	≃6	0.76	1.76	4.42	7.34
		$NaHCO_3$	9.6	0.28	0.50	0.70	1.72
		NaOH	12.5	0.00	0.00	0.00	0.12

[a] Engelhard Industrien AG, 8039 Zürich.
[b] Fluka AG, 9470 Buchs.

[8] General Radio Company.

then, after stabilization of the temperature overnight, the bulb containing the hypophosphite was broken. The temperature-time curve was plotted; after the calorimeter had returned to its equilibrium temperature, electrical calibration was carried out. The operation required between 5 and 7 hr, during which no sampling could be made. Results obtained are given in Table II. The approximate duration of the reaction indicates the time interval between the breaking of the bulb and the point at which the temperature, being at its maximum, begins to fall. For copper in alkaline medium, the very slow kinetics observed can be explained by the fact that the catalyst is oxidized and therefore loses its activity. This metal does not offer the best conditions for calorimetric measurements. The same is true of palladium, which catalyzes strongly the oxidation of orthophosphite to phosphate. Raney nickel in alkaline medium is the best catalyst for the oxidation to orthophosphite and the least for the oxidation of this compound to phosphate.

In this work electroless nickel plating in acid media is of interest. For the following reasons the reactions were carried out in alkaline solutions and from the results thus obtained values corresponding to acid media were calculated: (*a*) the amount of phosphate formed by oxidation of orthophosphite is much lower in alkaline than in neutral or acid medium; in fact this amount is low enough to be neglected; (*b*) the catalyst is not oxidized itself to any appreciable amount in alkaline medium, whereas it is in neutral or acid solution; (c) the reaction kinetics is more rapid in alkaline than in neutral or acid medium.

The amount of Raney nickel used was about 25 cm^3 of an aqueous suspension containing about 300 g/l of catalyst. This quantity allows the reaction to proceed to completion in about 10 min. The heat of adsorption of hydrogen on the Raney nickel catalyst was not taken into account. This is justified by the fact that at 94°C the amount of adsorbed hydrogen extrapolated from data measured at ambient temperature, 50° and 80°C (26), is negligible.

Calorimetric measurements were performed with initial concentrations of sodium hydroxide between 0.037 and 0.280*N*, corresponding to a *p*H $\geq$ 12 at the end of the reaction. At lower concentrations of hydroxide ions, the oxidation of orthophosphite to phosphate can no longer be neglected. For example, at a *p*H of about 10, the amount of phosphate formed after 5-7 hr at 94°C corresponds to about 17% of the initial amount of hypophosphite. On the other hand, at *p*H $\geq$ 12 only 0.6% of phosphate was formed during the same time. From this value one can deduce that for the time of the calorimetric measurements of the principal chemical reaction, which was about 30 min, only about 0.05% of hypophosphite was oxidized to phosphate. The initial concentrations of sodium hydroxide used corresponded to $NaOH \cdot 200H_2O$, $NaOH \cdot 750H_2O$, and $NaOH \cdot 1500H_2O$. Table III gives the results of these measurements. Heat values are expressed in defined thermochemical calories, 4.1840 absolute joules. The

Table II. Oxidation of hypophosphite to orthophosphate and phosphate at constant volume

Solution volume, 500 cm^3; initial $H_2PO_2^-$ content, 6 mM; temperature, 94°C

Catalyst	Weight of catalyst	Medium	*p*H	Phosphate formed after 6 hr $mMPO_4^{-3}$/$mMH_2PO_2^-$, %	Approximate duration of reaction, min
Pd/Al_2O_3 (10% Pd)	0.8	H_2O	$\simeq$6	44.4	90
		NaOH	12.5	12.1	60
Raney nickel	$\simeq$5	H_2O	$\simeq$6	6.1	70
		NaOH	12.5	0.6	10
Raney copper	$\simeq$17	H_2O	$\simeq$6	2.8	60
		NaOH	12.5	1.3	180

Table III. Heats of reaction for the oxidation of hypophosphite in alkaline media

Run	NaOH, *N*	$H_2PO_2^-$, mM	$q_{obs.}$, cal	$-\Delta E_{367°K}$, kcal/mole
1	0.0370	5.797	167.40	28.88
2		6.501	189.56	29.16
3		5.994	172.75	28.82
4		5.277	153.59	29.11
5		5.529	160.13	28.96
6		5.522	159.00	28.79
			Average	28.95 ± 0.13
1	0.0745	7.528	219.33	29.14
2		5.944	171.78	28.90
3		5.852	170.69	29.17
4		5.543	161.48	29.13
5		6.451	187.55	29.07
6		5.457	157.94	28.94
			Average	29.06 ± 0.09
1	0.280	5.506	160.30	29.11
2		5.544	162.66	29.34
3		6.118	177.34	28.99
4		5.911	172.39	29.16
5		6.583	188.96	28.17
			Average	29.06 ± 0.21

errors cited in this table, as anywhere else in this study, are twice the standard deviations of the mean.

Measurements of the heat of reaction at dilutions of sodium hydroxide corresponding to $n = 200$, 750, and 1500 show that the variation of ΔE as a function of n is negligible. The mean of the three sets of measurements can be considered to a good approximation as practically identical with that corresponding to the reaction

$$NaH_2PO_2 \cdot 26H_2O + NaOH \cdot 4000H_2O = Na_2HPO_3 + H_2 + 4026H_2O$$

$$\Delta E_{367°K} = -29.02 \pm 0.11 \text{ kcal/mole} \quad [1]$$

The heat of dilution of sodium hypophosphite corresponds to the reaction

$$NaH_2PO_2 \cdot 26H_2O + 3974H_2O = NaH_2PO_2 \cdot 4000H_2O$$

$$\Delta H_{367°K} = -1.162 \pm 0.015 \text{ kcal/mole} \quad [2]$$

Results are reported in Table IV. By subtracting the heat of dilution of hypophosphite, reaction [2], from the heat of the reaction [1], we obtain

$$NaH_2PO_2 \cdot 4000H_2O + NaOH \cdot 4000H_2O = Na_2HPO_3 + H_2 + 8000H_2O$$

$$\Delta E_{367°K} = -27.86 \pm 0.13 \text{ kcal/mole} \quad [3]$$

and, by addition of ΔnRT, $\Delta H_{367°K} = -27.13 \pm 0.13$ kcal/mole, the heat content of the reaction at constant pressure.

Heat of neutralization of NaOH *by* HCl.—In order to calculate the heat of reaction of the oxidation of hypophosphite to orthophosphite in acid medium from its corresponding value in alkaline medium, the heat of neutralization of hydroxide ions by protons had to be determined. Moreover, this heat of neutralization serves to calibrate the calorimeter, since its heat of reaction is the only one known at 367°K.

Dilutions as above were used, that is $n = 4000$. The reaction corresponds to the equation

Table IV. Heat of dilution of hypophosphite

Run	$H_2PO_2^-$, mM	$q_{obs.}$, cal	$-\Delta H_{367°K}$, kcal/mole
1	6.909	7.869	1.139
2	7.133	8.254	1.157
3	7.046	8.359	1.186
4	6.847	7.990	1.167
5	6.818	7.926	1.162
		Average	1.162 ± 0.015

Table V. Heat of neutralization of NaOH by HCl

Run	HCl 0.996N, mM	$q_{obs.}$, cal	$-\Delta H_{367°K}$, kcal/mole
1	3.389	36.47	10.76
2	3.631	38.82	10.69
3	3.497	37.42	10.70
4	3.492	37.63	10.78
5	3.514	37.60	10.70
6	3.499	37.71	10.70
		Average	10.74 ± 0.04

$$HCl \cdot 55H_2O + 2(NaOH \cdot 4000H_2O) = NaCl + NaOH + 8056H_2O$$
$$\Delta H_{367°K} = -10.74 \pm 0.04 \text{ kcal/mole} \quad [4]$$

Experimental results are reported in Table V. The heat of dilution of 0.996N hydrochloric acid was also measured (Table VIII); it corresponds to the reaction

$$HCl \cdot 55H_2O + 3945H_2O = HCl \cdot 4000H_2O$$
$$\Delta H_{367°K} = -0.663 \pm 0.004 \text{ kcal/mole} \quad [5]$$

Therefore, by subtracting reaction [5] from reaction [4]

$$HCl \cdot 4000H_2O + 2(NaOH \cdot 4000H_2O) = NaCl + NaOH + 12001H_2O$$
$$\Delta H_{367°K} = -10.08 \pm 0.05 \text{ kcal/mole} \quad [6]$$

Finally, the oxidation of hypophosphite to orthophosphite in acid medium follows by subtracting reaction [6] from reaction [3]. This may be expressed in ionic form as

$$H_2PO_2^- \cdot 4000H_2O + H_2O = HPO_3^{2-} + H_2 + H^+ + 4000H_2O$$
$$\Delta H_{367°K} = -17.05 \pm 0.18 \text{ kcal/mole} \quad [7]$$

Oxidation of nickel.—The oxidation of carbonyl-nickel powder was carried out in hydrochloric acid because hydrogen is evolved from it quantitatively (27). The reaction was performed without an accelerator (chloroplatinous acid) which would cause a side reaction (28), whose energy is not known at 94°C. Heats of solution of nickel as a function of the concentration of hydrochloric acid are reported in Table VI. For an acid concentration lower than 1N, the reaction is too slow (1 hr at 0.5N) to allow an accurate calorimetric measurement. The heat of wetting of nickel plus the heat of vaporization of water into the internal bulb volume is positive and equal to 0.43 ± 0.05 cal. The measurement was made with 14 mM nickel in 500 cm³ water. The heats observed, q_{obs}, reported in Table VI are corrected by this value.

The heats of reaction of the oxidation of nickel are of interest at pH values between 4 and 6, since chemical nickel plating occurs within these limits. Although the dilution of protons is then very large, a dilution of $n = 4000$ is adopted as before. In order to refer the values measured at acid concentrations of 1-8N ($n = 55$ to 6), to a value of $n = 4000$, it is necessary to consider the following set of reactions, as Richards *et al.* (28-30) showed.

The heat of the reaction corresponding to the equation

$$a\,Ni + b\,(HCl \cdot cH_2O) = a\,H_2 + [a\,NiCl_2 + (b - 2a)HCl + bc\,H_2O] + q' \text{ cal} \quad [8]$$

Table VI. Heats of reaction for the oxidation of nickel in hydrochloric acid

Run	HCl, N	Ni, mM	$q_{obs.}$, cal	$-\Delta E_{367°K}$, kcal/mole
1		12.42	145.27	11.70
2		14.19	160.05	11.28
3	1.005	14.73	167.98	11.41
4		13.90	161.53	11.62
5		14.81	174.50	11.78
			Average	11.56 ± 0.19
1		11.76	143.45	12.20
2		13.65	165.43	12.12
3	2.030	13.92	169.09	12.15
4		13.88	171.05	12.32
5		14.08	170.10	12.08
			Average	12.17 ± 0.08
1		12.80	144.50	11.29
2		13.68	154.71	11.31
3	4.027	14.00	157.59	11.25
4		12.58	143.79	11.43
5		13.20	150.64	11.42
			Average	11.34 ± 0.07
1		12.51	132.39	10.59
2		12.09	129.78	10.73
3	7.350	12.27	130.60	10.64
4		12.66	133.59	10.56
5		14.59	157.86	10.82
			Average	10.67 ± 0.10

was measured. On dividing by a in order to find the amount of heat evolved by the solution of 1 mole of nickel

$$Ni + b/a\,(HCl \cdot cH_2O) = H_2 + \left[NiCl_2 + \left(\frac{b}{2a} \Big/ a\right) HCl + bc/a\,H_2O \right] + q \text{ cal} \quad [9]$$

The following additional reactions are necessary in order to reduce the result to the reaction required

$$b/a\,(HCl \cdot cH_2O) + (4000b/a - bc/a)H_2O = b/a\,(HCl \cdot 4000H_2O) + x \text{ cal} \quad [10]$$

$$[NiCl_2 + ((b - 2a)/a)HCl + bc/a\,H_2O] + (4000b/a - bc/a)\,H_2O = \left[NiCl_2 + \left(\frac{b}{2a} \Big/ a\right) HCl + (4000b/a)H_2O \right] + y \text{ cal} \quad [11]$$

$$NiCl_2 \cdot 8000H_2O + \left[\left(\frac{b}{2a} \Big/ a\right)(HCl \cdot 4000H_2O)\right] = \left[NiCl_2 + \left(\frac{b}{2a} \Big/ a\right) HCl + (4000b/a)H_2O \right] + z \text{ cal} \quad [12]$$

From these reactions, by elimination or cancellation, the desired result is

$$Ni + 2(HCl \cdot 4000H_2O) = H_2 + NiCl_2 \cdot 8000H_2O + [q + (y - x) - z] = Q \text{ cal} \quad [13]$$

Table VII gives values of coefficients and energies corresponding to the various dilutions for several hydrochloric acid concentrations. Values of q and y are taken from Table VI and IX. The value x is extrapolated at the concentrations of acid used, from the heats

Table VII. Calorimetric data used to calculate the heat of reaction for the oxidation of nickel

HCl, N	a, M	b, M	c, M	$-q$	$-x$	$-y$	$-Q$
				(kcal/mole)			
1.005	0.01409	0.5025	54.4	11.56 ± 0.19	23.78 ± 0.14	29.60 ± 0.39	17.38 ± 0.72
2.030	0.01335	1.015	26.7	12.17 ± 0.08	88.65 ± 1.67	94.43 ± 0.37	17.95 ± 2.12
4.027	0.01322	2.014	12.7	11.34 ± 0.07	—	—	—
7.350	0.01264	3.675	6.4	10.67 ± 0.10	—	—	—
				Average	$\Delta E_{367°K} = -17.67 \pm 1.58$		

Table VIII. Heats of dilution of hydrochloric acid

Run	HCl, N	HCl, mM	$q_{obs.}$, cal	$-\Delta H_{367°K}$, kcal/mole
1		6.794	4.558	0.671
2		6.910	4.546	0.658
3	0.996	6.888	4.563	0.663
4		7.004	4.633	0.662
5		6.919	4.576	0.662
			Average	0.663 ± 0.004
1		7.029	8.189	1.165
2		6.992	8.259	1.181
3		7.034	7.843	1.115
4	2.000	7.093	8.020	1.131
5		7.019	7.988	1.138
6		6.936	8.140	1.174
			Average	1.151 ± 0.022

of dilution reported in Table VIII, and multiplied by the ratio b/a.

The fact that the quantity $(y - x)$ is a difference of similar quantities obtained in precisely the same way increases the ease of determining it accurately. Any systematic errors in x would also appear in y and hence, would be eliminated from the result $(y - x)$. This is also the case in the other principal measurements of this work, since the heat of dilution of the reagent is subtracted from the heats of reaction of the oxidation of hypophosphite and of the neutralization of NaOH by HCl.

The value a being practically the same for all the acid concentrations, the term b/a increases strongly with concentration. Hence, as the apparatus limited the volume to 500 cm^3 and the same dilution had to be maintained, the measurements of the heat of dilution for HCl 4.027 and 7.350N are less precise than those obtained at lower concentrations. At high acid concentrations, the error of the measurement reaches approximately the same value as the difference $(y - x)$; it is for that reason that only the heats of dilution of HCl 1.005 and 2.030N were measured. The experimental results are reported in Table VIII regarding the heats of dilution of hydrochloric acid (reaction [10]), and in Table IX concerning the heat of dilution of the residual solutions (reaction [11]).

The heat of reaction [12] was measured by Richards *et al.* (29) at a dilution of 200, that is to say for the mixture $(1/n\ MCl_n) \cdot 200H_2O$ in an excess of $HCl \cdot 200H_2O$, at 20°C. For the chlorides of Zn, Al, Mg, Cd, and Fe, this heat of mixing is zero. Therefore it can be expected that this energy is also zero or negligible for nickel chloride at a dilution of 4000 and at 94°C. Several measurements of the heat of mixing of $NiCl_2 \cdot 8000H_2O$ in an excess of $HCl \cdot 4000H_2O$ showed that this energy can be considered as being negligibly small.

Finally, for reaction [13], the mean value of the heats of reaction obtained at acid concentrations of 1 and 2N (Table VII), is

$$\Delta E_{367°K} = -17.67 \pm 1.58 \text{ kcal/mole},$$
$$\text{whence } \Delta H_{367°K} = -16.94 \pm 1.58 \text{ kcal/mole}$$

Table IX. Heats of dilution of final solutions Ni^{2+}-HCl

Run	Solution composition, mM Ni^{2+}/g sol.	Ni^{2+}, mM	$q_{obs.}$, cal	$-\Delta H_{367°K}$, kcal/mole
1		0.1977	5.734	29.00
2		0.1971	5.795	29.40
3	0.027725	0.1985	5.989	30.17
4	(HCl 0.977N)	0.1998	5.939	29.72
5		0.1971	5.856	29.71
			Average	29.60 ± 0.39
1		0.09305	8.760	94.14
2		0.09252	8.703	94.07
3	0.025843	0.09289	8.831	95.06
4	(HCl 2.003N)	0.09313	8.776	94.23
5		0.09311	8.812	94.64
			Average	94.43 ± 0.37

Chemical deposition of nickel.—An acid bath of the following composition was used: $NiCl_2 \cdot 6H_2O$, 30 g/l; $CH_2(OH)COOH$, 30 g/l; $COOH(CH_2)_2COOH$, 10 g/l; NaF, 3 g/l; NaOH to adjust to the desired *p*H. The reducing agent was sodium hypophosphite. Deionized water used for the bath preparation was purged at its boiling point with argon to remove traces of CO_2.

The deposition was performed on seeds of nickel, previously plated chemically to palladium. For each *p*H value of the bath studied, seeds were prepared in an identical solution as follows: 35 cm^3 $PdCl_2$ M/1000 were introduced for each liter of this solution, which was 0.1M in sodium hypophosphite, at 94°C. After about 10 min, the solution was filtered and the seeds of palladium, coated with nickel, were washed and dried at about 100°C. For use in the actual deposition study, these seeds were introduced into the bulb of the calorimeter, which was subsequently broken when the calorimeter temperature reached equilibrium. This method was preferred to the use of a suspension of nickel seeds placed directly in the bath or in the bulb since it avoided partial dissolution of nickel before the run commenced.

The weight of seeds needed for each run to proceed to completion in about 30 min at constant volume was about 1g. This amount was small enough relative to the deposited nickel and phosphorus to determine these quantities with accuracy. At constant pressure, 0.2g were sufficient for the reaction to occur in less than 15 min. The influence of pressure on the electroless deposition process can explain the difference of about one order of magnitude between the amount of catalyst needed to take the reaction to completion in a given time at constant pressure or volume. Sallo, Swenson, and Carr (31) studied this effect and showed that the rate of nickel deposition, from a bath containing little buffer and no complexing agent, decreases with increasing pressure. The reverse is true for the same bath when subjected to ultrasonic vibrations. For a highly buffered bath containing a complexant, the rate of nickel deposition increases with the pressure. Sallo *et al.* concluded that the deposition rate from the former bath is controlled by a diffusion process whereas for the latter the area of hydrogen-free catalytic surface is rate controlling. The effect of pressure is attributed to the influence of the size of hydrogen bubbles formed at the active areas. According to the findings of Sallo *et al.*, it is very likely that the bath used in this study could be controlled by a transport process since the rate of nickel deposition decreases with increasing pressure. On the other hand, one may anticipate the behavior of the bath from Le Chatelier's principle, regarding the reactions which occur during the electroless process (Table XI).

In the experiments described here, the solid area being very large with regard to the plating bath volume, the oxidation of nickel and orthophosphite can occur to a considerable extent. In order to minimize these side reactions, the time during which they could occur must be kept as short as possible. Therefore the usual order of the calorimetric manipulations was inverted; the electrical calibration preceded the measurement of the heat of reaction. After breaking the bulb, the reaction was allowed to continue until the temperature, being at its maximum, began to fall. This generally required between 20 and 40 min. The reaction was then stopped as quickly as possible by quenching, after removal of the calorimeter. The deposit was filtered, washed with water, and dried at about 100°C. The amount of electroless nickel deposited was found from the difference between the initial weight of the seeds and the weight after plating. The phosphorus content of the deposit was deduced analytically in the same way.

The determination of residual hypophosphite in the filtrate of the bath after reaction showed that, in the experimental conditions of this study, 95-97% of the reducing agent was consumed in the experiment. The

Table X. Heat of reaction of electroless nickel deposition in acid media

Run	Initial pH	Final pH	w/o P of deposit	$H_2PO_2^-$ utilized, mM	Ni deposited, mM	P deposited, mM	$q_{obs.}$, cal	$-\Delta E_{obs.}$	$-\Delta H_{obs.}$	$-\Delta H_{calc.}$	$[\Delta H_{calc.} - \Delta H_{obs.}]$	$-\Delta H$ Ni_2P
								kcal/mole $H_2PO_2^-$ at 367°K				
1	5.97	5.56	1.11	14.50	5.56	0.12	158.7	10.9	10.5	10.7 ± 0.8	−0.2	0.4
2	5.93	5.52	0.96	14.19	5.95	0.11	148.8	10.5	10.1	10.1 ± 0.9	0.0	0.3
3	5.87	5.49	1.05	14.08	5.52	0.11	154.1	10.9	10.5	10.5 ± 0.8	0.0	0.3
4	5.87	5.49	0.68	14.46	5.52	0.07	162.9	11.3	10.8	10.7 ± 0.8	+0.1	0.2
5	5.78	5.46	2.06	14.56	5.61	0.22	165.6	11.4	10.9	10.7 ± 0.8	+0.2	0.7
6	5.08	5.02	2.45	14.47	4.87	0.23	172.2	11.9	11.4	11.5 ± 0.8	−0.1	0.7
7	5.08	5.02	2.23	14.24	4.71	0.20	169.5	11.9	11.4	11.6 ± 0.8	−0.2	0.6
8	5.08	5.02	2.23	14.51	4.93	0.21	171.9	11.8	11.4	11.5 ± 0.8	−0.1	0.6
9	5.01	4.98	2.65	13.06	4.07	0.21	159.8	12.2	11.8	12.0 ± 0.7	−0.2	0.7
10	5.01	4.98	2.50	12.86	4.05	0.20	159.8	12.4	12.0	11.9 ± 0.7	+0.1	0.7
11	5.12*	5.09	5.91	14.29	4.52	0.54	177.1	12.4	11.9	12.2 ± 0.8	−0.3	1.7
12	5.05*	5.05	5.95	14.36	4.05	0.49	192.0	13.4	12.9	12.7 ± 0.8	+0.2	1.5
13	5.05*	5.04	5.72	14.45	4.36	0.50	181.0	12.5	12.1	12.4 ± 0.8	−0.3	1.5
14	5.05*	5.03	6.33	14.24	4.53	0.58	185.7	13.0	12.6	12.2 ± 0.8	+0.4	1.8
15	5.04*	5.02	6.15	14.37	4.64	0.58	180.0	12.5	12.1	12.1 ± 0.8	0.0	1.8
16	4.60*	4.57	7.96	14.29	3.54	0.58	194.0	13.6	13.1	13.4 ± 0.7	−0.3	1.8
17	4.60*	4.59	8.07	14.10	3.62	0.60	196.8	14.0	13.5	13.2 ± 0.7	+0.3	1.9
18	4.60*	4.56	9.15	14.31	3.15	0.60	198.5	13.9	13.4	13.9 ± 0.7	−0.5	1.9
19	4.48*	4.47	10.13	14.42	2.85	0.61	209.5	14.5	14.0	14.2 ± 0.6	−0.2	1.9
20	4.42*	4.37	10.04	14.33	2.80	0.59	207.1	14.5	13.9	14.3 ± 0.6	−0.4	1.8
21	4.20*	4.20	8.43	13.26	3.05	0.53	178.3	13.5	13.0	13.7 ± 0.7	−0.7	1.8
22	4.17*	4.14	11.55	13.90	2.02	0.50	221.1	15.9	15.3	15.1 ± 0.5	+0.2	1.6
23	4.01*	3.96	9.30	12.88	2.66	0.51	183.9	14.3	13.8	14.1 ± 0.7	−0.3	1.7
24	4.00*	3.99	9.27	12.71	2.39	0.46	181.1	14.3	13.7	14.3 ± 0.6	−0.6	1.6

* Filtrate from seed preparation used as plating bath.

amount of phosphate in the filtrate being lower than 1% of that of the hypophosphite consumed at $pH \geq 5$ and lower than 2% at $pH \leq 4.5$, this amount has not been taken into account in the energy balance. The orthophosphite concentration of the filtrate was also determined in order to check the material balance concerning phosphorus compounds. In all runs, the hypophosphite consumed corresponded, within experimental error, to the sum: orthophosphite + phosphorus + phosphate.

The calorimetric results of the heat of reaction of electroless nickel deposition are summarized in Table X, which also includes corresponding analytical data. The heats of reaction are referred to the amount of hypophosphite consumed.

For the reaction mechanisms proposed, the total heats of reaction were calculated from the partial heats of reaction stated in Table XI. This table also summarizes the proposed stoichiometries. The experimental results obtained in this work for the heat of oxidation of hypophosphite and nickel, as well as for the heat of ionization of water, were used, through Hess' law, to calculate the heat of deposition of electroless nickel. In Table XI, the electrochemical mechanism is not reported. The stoichiometry of this mechanism is, indeed, the same as that of the atomic hydrogen mechanism given in this table; therefore, values calculated for the second mechanism also are valid for the first one.

Heats of reaction for the deposition of phosphorus indicated in Table XI are estimated on the basis of the most recent data of the literature, which are collected in Table XII. When the heat capacities are known, one can calculate the term $\int_{298°K}^{367°K} C_P dT$, and hence the enthalpy at 367°K. When the heat capacities are not known, one can assume that, to a first approximation, the sum of $\Delta C_P dT$ is zero in the temperature interval considered, that is to say that, for the calculation of the heats of deposition of phosphorus at 367°K, the enthalpies of these substances at 298°K have been used. The error resulting from this approximation is negligible. It might be said, in this context, that some values of enthalpy vary considerably from one author to the other. For example, for orthophosphoric acid H_3PO_3 (aq), the most recent value from NBS tables (32) is $H°_f = -230.6$ kcal/mole, whereas Skinner (33) proposes -226.5 ± 0.8 kcal/mole. In this work, NBS values were adopted, where available.

In the total heat of reaction of the electroless nickel deposition, previous experimental result has been taken into account (1), *i.e.*, that the phosphorus is included in the as-plated deposit as nickel phosphide, Ni_2P, and not as elementary phosphorus. Then, the heat of formation of phosphorus is added to that corresponding to the formation of Ni_2P. For this latter energy, the tabulated value was used (34). Results from DTA (2), for samples containing less than 10% phosphorus, confirm that value, while for samples with more than 10% phosphorus, the adopted value for the heat of formation of Ni_2P would be a little too low. If the experimental heat of reaction corresponds to the calculated one, by taking into account the heat of formation of Ni_2P, this will give supplementary evidence of the existence of a Ni_2P phase in as-plated alloy.

Results of Table X need some comment. The plating bath was studied at several *p*H values, as was the case for the analytical study (18). For values of $pH \leq 4.5$, the behavior of the bath does not correspond to that observed in the previous study, *i.e.*, the phosphorus content is irregular, often higher than that expected, which could mean that, in the present experimental conditions, nickel is dissolved at a relatively high rate. This consideration led to the use of a bath, which was the filtrate of the bath used for the preparation of seeds after readjustment of its *p*H and its Ni^{2+} concentrations. At *p*H 5.0, depositions were carried out in the fresh bath and in that already used. Results show that, at this *p*H, the behavior of these two baths is the same.

The error for the calculated heats of reaction, given in Table X, is the proportion of the errors corresponding to the partial reactions indicated in Table XI. One has to add to it about ±0.1 kcal/mole, to take into account the errors in the analytical determinations of nickel, phosphorus, and hypophosphite. The experimental error is not reported in Table X; it is estimated, on the basis of other measurements of the heats of reaction, to be ±0.2 kcal/mole. The heat of wetting of seeds, as well as the heat of vaporization of water in the bulb volume, is negligible. Heats of oxidation of nickel and hypophosphite are given for a dilution of $n = 4000$. In order to refer the heats of reaction of electroless nickel deposition to this dilution, the heats of dilution of the bath before and after the reaction were measured. The difference between these two determinations is of the order of the limit of error of

Table XI. Calorimetric data used to calculate total heat of reaction of electroless nickel deposition, from partial reactions, for the mechanisms proposed, ΔH at 367°K in kcal/mole

Hydride transfer mechanism		Atomic hydrogen mechanism		Mechanism involving hydrolyzed nickel	
Partial ionic reactions:					
$H_2PO_2^- + H_2O = HPO_3^{2-} + 2H^+ + H^-$		$H_2PO_2^- + H_2O = HPO_3^{2-} + H^+ + 2H$			
$Ni^{2+} + 2H^- = Ni + H_2$		$Ni^{2+} + 2H = Ni + 2H^+$			
$H_2PO_2^- + H^- = P + 2OH^- + 1/2H_2$		$H_2PO_2^- + H = P + H_2O + OH^-$			
$H^+ + H^- = H_2$		$2H = H_2$			
Deposition of nickel:					
$2[H_2PO_2^- + H_2O = HPO_3^{2-} + H^+ + H_2]$	$\Delta H = -34.10 \pm 0.36$	$H_2PO_2^- + H_2O = HPO_3^{2-} + H^+ + H_2$	$\Delta H = -17.05 \pm 0.18$	$Ni^{2+} + 2OH^- = \begin{matrix} OH \\ Ni_{(s)} \\ OH \end{matrix}$	$\Delta H \cong 0$
$Ni^{2+} + H_2 = Ni + 2H^+$	$\Delta H = 16.94 \pm 1.58$	$Ni^{2+} + H_2 = Ni + 2H^+$	$\Delta H = 16.94 \pm 1.58$	$\begin{matrix} OH \\ Ni_{(s)} \\ OH \end{matrix} + 2H^+ = 2H_2O$	$\Delta H = 20.16 \pm 0.10$
				$2H_2O \equiv 2H^+ + 2OH^-$	$\Delta H = -34.10 \pm 0.36$
				$2[H_2PO_2^- + H_2O \equiv HPO_3^{2-} + H^+ + H_2]$	$\Delta H = 16.94 \pm 1.58$
$2H_2PO_2^- + Ni^{2+} + 2H_2O = Ni + 2HPO_3^{2-} + 4H^+ + H_2$	$\Delta H = -17.16 \pm 1.94$	$H_2PO_2^- + Ni^{2+} + H_2O = Ni + 3H^+ + HPO_3^{2-}$	$\Delta H = -0.11 \pm 1.76$	$Ni^{2+} + 2OH^- = \begin{matrix} OH \\ Ni_{(s)} \\ OH \end{matrix}$	$\Delta H \cong 0$
				$2OH^- + 2H^+ = 2H_2O$	$\Delta H = -20.16 \pm 0.10$
Deposition of phosphorus:				$2H_2PO_2^- + Ni^{2+} + 2H_2O = Ni + 2HPO_3^{2-} + 4H^+ + H_2$	$\Delta H = -17.16 \pm 1.94$
$2H_2PO_2^- = P + HPO_3^{2-} + H_2O + 1/2H_2$	ΔH estimated -3 ± 1	$3/2H_2PO_2^- + 1/2H^+ = P + 3/2H_2O + 1/2HPO_3^{2-}$	ΔH estimated 6 ± 1	$2H_2PO_2^- + H^+ = P_{Ni} + H_2PO_3^- + H_2O + 1/2H_2$	ΔH estimated -3 ± 1
$P + 2Ni = Ni_2P$	$\Delta H = -44.0 \pm 0.3$	$P + 2Ni = Ni_2P$	$\Delta H = -44.0 \pm 3.0$	$P + 2Ni = Ni_2P$	$\Delta H = -44.0 \pm 3.0$
	ΔH estimated -47 ± 4		ΔH estimated -38 ± 4		ΔH estimated -47 ± 4
Oxidation of hypophosphite:					
		$H_2PO_2^- + H_2O = HPO_3^{2-} + H^+ + H_2$	$\Delta H = -17.05 \pm 0.18$		

the measurement, that is to say about ±0.1 kcal/mole. This contribution to the heat of reaction of the electroless nickel deposition will be neglected.

All experimental results obtained for the heat of reaction of electroless nickel deposition, from pH values of 5.8 to 4.0, correspond, within the limits of error reported in Table X, to the heats of reaction calculated on the basis of the reaction mechanisms proposed. The difference between the observed heat and that calculated, as well as the contribution of the heat of formation of Ni_2P to the total heat of reaction, is reported in Table X. One can see that, for the experiments carried out at high pH values, the contribution of the heat of formation of Ni_2P to the total heat of reaction is of the order of the experimental error. By contrast, for runs 11-24, the contribution of the heat of formation of Ni_2P is clearly greater than this error. If the energy had not been included in the calculation of the total heat of reaction, the experimental heat of reaction would be about 2 kcal/mole $H_2PO_2^-$ more exothermic than the calculated value for runs 11-24. This represents about 15% of the evolved energy for runs 11-15. Therefore, this study is a further confirmation of the existence of Ni_2P in as-plated deposit.

Finally, one can remark that, in practice, when the reaction is performed at constant pressure, the positive heat of vaporization induced by the hydrogen evolution largely counter balances the exothermic heat of reaction of the electroless nickel deposition. Thus, the total phenomenon is endothermic.

Conclusions

Heats of oxidation of hypophosphite to orthophosphite and of nickel to Ni^{2+} were measured at 94°C. They are, respectively, $\Delta H_{367°K} = -17.1 \pm 0.2$ and -16.9 ± 1.6 kcal/mole, at a dilution of $n = 4000$. From the literature data at 25°C given in Table XII, values of $\Delta H°_{298°K} = -16.6$ kcal/mole for the oxidation of hypophosphite and $\Delta H°_{298°K} = -15.3$ kcal/mole for the oxidation of nickel were obtained. The heat of neutralization of NaOH by HCl measured at a dilution of $n = 4000$ is $\Delta H_{367°K} = -10.08 \pm 0.05$ kcal/mole, while the value calculated from (23) and (24) is $\Delta H_{N(367°K)} = -10.15$ kcal/mole.

The energy balance of the over-all system can be established only when the heat of formation of Ni_2P is included in the calculation of the total heat of reaction. This being so, all experimental results obtained for the heat of reaction of electroless nickel deposition, from pH values of 5.8-4.0, correspond to the calculated heats of reaction. From the results of this study, the energy balance of the over-all system can be established. The study of the deposit showed (1, 2) that it contains a nickel phase and a nickel phosphide, Ni_2P, phase. The DTA of as-plated deposits revealed that the energy evolved during heating corresponds approximately to the heat of formation of Ni_3P from Ni_2P. Therefore, the heat of formation of Ni_2P must be contained in the heat of reaction of the electroless nickel deposition in aqueous media. This is precisely the result of this study, since the calculated value of the heat of reaction of electroless nickel deposition, which includes the heat of formation of Ni_2P corresponds within the limits of error to that experimentally obtained. This result constitutes additional evidence for the presence of a nickel phosphide phase in as-plated deposits.

Several authors (39, 40, 41), studying other alloys than NiP, suggested that the principal condition for the formation of "cryptocrystalline" structure is the occurrence of a chemical reaction in the crystallization zone. Solid products of such surface reactions interfere with the normal growth of the crystallite and, therefore, induce the formation of a liquid-like structure. In the electroless nickel deposition, the origin of the liquid-like state of the deposit therefore can be explained in the same way, since the codeposited

Table XII. Tabulated enthalpies at 298°K and calculated enthalpies at 367°K

Substance	$\Delta H°_{f,298°K}$, kcal/mole	Ref.	$\int_{298°K}^{367°K} C_p dT$ (kcal/mole)	Ref. for C_p	$\Delta H_{f,367°K}$, kcal/mole
$H_2PO_2^-$ (aq)	−146.7	(32)	—	—	—
$H_2PO_3^-$ (aq)	−231.7	(32)	—	—	—
HPO_3^{2-} (aq)	−231.6	(32)	—	—	—
P white (s)	0	def.	2.20 1.87	(36) (37)	2.20 1.87
Ni^{2+} (aq)	−15.3	(35)	—	—	—
Ni (s)	0	def.	0.44	(36), (37)	0.44
H_2O (l)	−68.315	(32)	1.24	(36), (37)	−67.08
H^+ (aq)	0	def.	0	def.	0
OH^- (aq)	−54.970	(32)	−2.2	(38)	−57.17
H_2 (g))	0	def.	0.475	(36), (37)	0.475
Ni_2P (s)	−44.0±3.0	(34)	—	—	—

phosphorus immediately reacts with nickel to produce the nickel phosphide Ni_2P.

Acknowledgment

The authors wish to thank Professor P. Dinichert, Director of the L.S.R.H., for his advice and interest in this work, and for permission to publish this paper. They also thank Professor K. Bernauer for his criticisms and suggestions during the redaction of the manuscript. They are grateful to Mr. W. Bettex for the design and construction of the electronic units, to the staff of the workshop for manufacturing the thermostat and accessories, and to Mr. E. Widmer for constructing the glass-ware. The authors acknowledge the valuable assistance of Dr. R. D. Cowling in the translation of the manuscript.

Manuscript submitted July 7, 1969; revised manuscript received *ca.* October 7, 1969. This was Paper 141 presented at the Detroit Meeting of the Society, Oct. 5-9 1969. This paper is based in part on a dissertation by one of the authors (J.-P. R.) in partial fulfillment of the requirements for a Ph.D. degree.

Any discussion of this paper will appear in a Discussion Section to be published in the December 1970 JOURNAL.

REFERENCES

1. J.-P. Randin and H. E. Hintermann, *This Journal*, **115**, 480 (1968).
2. J.-P. Randin, P. A. Maire, E. Saurer, and H. E. Hintermann, *ibid.*, **114**, 442 (1967).
3. A. Brenner and G. E. Riddell, *J. Res. Nat. Bur. Std.*, **37**, 1 (1946); *Proc. Amer. Electroplaters' Soc.*, **33**, 16 (1946).
4. A. Brenner and G. E. Riddell, *J. Res. Nat. Bur. Std.*, **39**, 385 (1947); *Proc. Amer. Electroplaters' Soc.*, **34**, 156 (1947).
5. K. M. Gorbunova and A. A. Nikiforova, *Zhur. Fiz. Kim.*, **28**, 883 (1954); *C. A.*, **49**, 6060h (1955).
6. S. M. Panchenko and M. A. Krokhina, *Vestnik. Machinostroeniya*, **34**, [12], 68 (1954); *C. A.*, **49**, 6070g (1955).
7. G. Gutzeit, *Plating*, **46**, 1158, 1275, 1377 (1959); **47**, 63 (1960).
8. G. Gutzeit, "Symposium on Electroless Nickel Plating," ASTM Special Technical Publication No. 265, p. 3, ASTM, Philadelphia (1959).
9. J. Fléchon, Thesis, Nancy (1960).
10. D. J. Levy, *Proc. Amer. Electroplaters' Soc.*, **50**, 29 (1963).
11. P. Hersch, *Trans. Inst. Metal Finishing*, **33**, 417 (1955-1956).
12. R. M. Lukes, *Plating*, **51**, 969 (1964).
13. W. Machu and S. El-Gendi, *Metalloberfläche*, **13**, 97 (1959).
14. K. Müller, *ibid.*, **14**, 65 (1960).
15. S. Ishibashi, *Heimeji Hogyo Daigaku Kenkyu Hokden*, **13**, 68 (1961); *C. A.*, **56**, 1283g (1961).
16. A. Hickling and D. Johnson, *J. Electroanal. Chem.*, **13**, 100 (1967).
17. P. Cavalloti and G. Salvago, *Electrochim. Metal.*, **3**, 239 (1968).
18. J.-P. Randin and H. E. Hintermann, *Plating*, **54**, 523 (1967).
19. A. A. Sutyagina, K. M. Gorbunova, and M. P. Glazunov, *Doklady Akad. Nauk. SSSR*, **147** 1133 (1962); *C. A.*, **58**, 6517a (1963).
20. J. P. McCloskey, *Plating*, **51**, 689 (1964).
21. D. N. Bernhart, *Anal. Chem.*, **26**, 1798 (1954).
22. G. H. Nancollas and J. A. Hardy, *J. Sci. Instrum.*, **45**, 290 (1967).
23. V. B. Parker, "Thermal Properties of Aqueous Uni-univalent Electrolytes," National Standard Reference Data Series, p. 62, National Bureau of Standards, Washington, D. C. (1965).
24. T. Ackermann, *Z. Elektrochem.*, **62**, 411 (1958).
25. Gmelins Handbuch der anorganische Chemie, Phosphor Teil C, 16C, p. 107, 8th ed., Verlag Chemie, Weinheim (1965).
26. *ibid.*, Nickel Teil A 1, p. 618, 8th ed., Verlag Chemie, Weinheim (1967).
27. O. Kubaschewski, E. Ll. Evans, and C. B. Alcock, "Metallurgical Thermochemistry," 4th ed., p. 100, Pergamon Press, Oxford (1967).
28. T. W. Richards and L. L. Burgess, *J. Am. Chem. Soc.*, **32**, 431 (1910).
29. T. W. Richards, A. W. Rowe, and L. L. Burgess, *ibid.*, **32**, 1176 (1910).
30. T. W. Richards and T. Thorvaldson, *ibid.*, **44**, 1051 (1922).
31. J. S. Sallo, J. I. Swenson, and J. M. Carr, *This Journal*, **109**, 389 (1962).
32. D. D. Wagman *et al.*, National Bureau of Standards Technical Note 270-3, U. S. Government Printing Office, Washington, D. C. (1968).
33. H. A. Skinner, *Pure Appl. Chem.*, **8**, 113 (1964).
34. *Ibid.*, Ref. (27), p. 340.
35. F. D. Rossini *et al.*, National Bureau of Standards Circular 500, U. S. Government Printing Office, Washington, D. C. (1952).
36. *Ibid.*, Ref. (27), pp. 398-403.
37. Handbook of Chemistry and Physics, 45th, ed., p. D-33, Chemical Rubber Publishing Co., Cleveland (1964).
38. G. N. Lewis and M. Randall, revised by K. S. Pitzer and L. Brewer, "Thermodynamics," 2nd ed., p. 400, McGraw-Hill Book Co., New York (1965).
39. K. M. Gorbunova and A. A. Sutyagina, *Electrochim. Acta*, **10**, 367 (1965).
40. K. M. Gorbunova, *ibid.*, **1**, 217 (1959).
41. V. Kohlschütter, *Trans. Faraday Soc.*, **31**, 1181 (1935); *Helv. Chim. Acta*, **22**, 277 (1939).

Anion Effects in Copper Deposition

David W. Hardesty*

Electrochemistry Department, Research Laboratories, General Motors Corporation, Warren, Michigan

ABSTRACT

Preliminary investigation has demonstrated that surface morphology of epitaxial copper electrodeposits is influenced by the anion of the electrolyte. Effects due to the use of sulfate, sulfamate, dimethylsulfamate, methane-sulfonate, benzene-sulfonate, perchlorate, fluoborate, nitrate, chloride, and acetate anions were studied. Observed changes in surface structural details are consistent with adsorption of the anion on the cathode as an important influencing factor, but other factors can and do produce similar results.

It has been observed that iron and chromium can be deposited epitaxially only from singular electrolytes using particular deposition conditions. Iron is so deposited from ferrous chloride electrolyte (1) and chromium from a fluoride "catalyzed" chromic acid solution (2) at temperatures above 80°C. From other electrolytes, deposits of both metals become coarse grained with well-developed preferred orientation. In addition, internal stress decreases as bath temperature is increased. Surface morphology of the plane-facetted epitaxed deposits of iron and chromium is similar in so many respects to that of copper deposits, which have been studied intensively (3-10), that deposition under control of a "bunching mechanism" was concluded to have occurred. It has been shown previously that with similarly specific operating conditions, nickel, cobalt, lead, and zinc (11, 12) are deposited epitaxially with morphologies characteristic of growth by bunching.

The cited work has largely been concerned with deposits from sulfate electrolytes. Limited comparisons with copper deposited from perchlorate and nitrate electrolytes (13, 14) indicated that the habit, or characteristic morphology, developed was correlated with overvoltage during deposition. Very similar habit development was observed in deposits from copper sulfamate solutions, but significant detail differences are observable in illustrative photomicrographs (15).

In the course of an investigation (16) of mechanisms and kinetics of copper deposition from several electrolytes, results obtained were interpreted as indicative of blocking of deposition sites by specific adsorption of anions as one of several factors which influence growth of electrodeposits. In view of the role of adsorbable additives in practical plating processes (17), it is reasonable to expect that such specific adsorption, the effect of which varies with anion size, can result in modifications of the external form and internal structure of electrodeposits.

Since the structure and morphology of iron and chromium are so specifically dependent on the anion used in the electrolyte, the effects of anions of different sizes on the characteristic habit of epitaxial copper deposits were examined. Deposits from acidic copper electrolytes were prepared and their surface forms compared to those obtained from the well-studied sulfate electrolytes.

Experimental

Solutions.—With three exceptions, all solutions contained 0.5M cupric salt and 0.5M excess or free acid. In all cases, the solution was prepared by dissolution of the constituent compounds in distilled water, followed by agitation with 2 g/l activated carbon and filtration after settling overnight. When not in use, the solutions were stored in glass bottles and were filtered before use after storage.

Sulfate, nitrate, chloride, and acetate solutions were prepared from reagent grade salts and acids. Due to limited solubility of cupric acetate, copper concentration was only 0.05M and total cation concentration was adjusted to 0.5M by addition of sodium acetate. Dilute sulfate solutions containing 0.05M $CuSO_4$, 0.45M Na_2SO_4 or $MgSO_4$, and 0.5M H_2SO_4 were also prepared.

Sulfamate (amidosulfonate), citrate, perchlorate, methane-sulfonate, and benzene-sulfonate electrolytes were prepared by slowly adding dissolved acid to a vigorously stirred slurry of reagent grade (assay 55.5% Cu) copper carbonate until effervescence ceased, at which time the remainder of the acid was added. No difficulty was encountered except that solubility limited the benzene-sulfonate solution to 0.35M in the copper salt and free acid.

Dimethyl-sulfamate solution was made with acid prepared by hydrolysis of N,N-dimethylsulfamoyl chloride (18). The twice-recrystallized acid melted at 165°-170°C after washing with ether. Since this acid contained traces of chloride, it was dissolved in water, stirred with a small quantity of AgO, allowed to settle overnight, and filtered. Excess silver was removed by cementation on a spiral of clean copper wire. Chloride ion was not detected by the Bunsen test after this treatment. The copper dimethyl-sulfamate electrolyte was then prepared.

In all cases, deposition at room temperature (25° ± 1°C) was carried out in 500 ml volumes of electrolyte in 600 ml Pyrex beakers. Mild agitation, by a Teflon-coated stirring magnet was held nearly constant by adjusting the stirrer speed to just below that where a visible vortex formed.

Under these conditions of stirring, the apparent limiting current density in the copper sulfate electrolyte was above 100 mA/cm². Without mechanical agitation, the apparent limiting current density was about 10 mA/cm². Above these values, the deposits rapidly became polycrystalline and tended to be powdery or dendritic.

The same anode (2.5 x 8.0 x 0.6 cm) of high-conductivity copper was used throughout. Before placing the anode in any electrolyte, it was cleaned by immersion in 25% (by volume) nitric acid and thoroughly rinsed in distilled water.

Some polarization measurements were made using a copper reference electrode in a Luggin-Haber capillary, positioned at the edge of the cathode. Cathode-to-reference electrode potentials were measured with a high impedance electrometer[1] and recorded, together with the current used, on a two-channel recorder.[2] The potential measurement and recording apparatus were standardized using a laboratory potentiometer.[3]

Electrodes.—After etching in nitric acid, the reference electrodes were prepared by plating (on 20-gauge copper wire) from the studied electrolyte for 2 min at low current density (anode-wire voltage of 10-15 mV).

* Electrochemical Society Active Member.

[1] Model 610B, Keithley Instruments, Inc., Cleveland, Ohio.
[2] Mosely Autograf, Hewlett-Packard Company, Pasadena, California.
[3] Type K-3, Leeds & Northrup Company, Philadelphia, Pennsylvania.

Current (maintained constant manually to within 0.5 mA) was obtained from a 100-ohm voltage divider across the terminals of a 1.5V dry cell. Current density was usually between 5 and 10 mA/cm^2, and deposit thickness was constant at 15 μm on the copper substrates, areas of 1.0-2.0 cm^2, cut from large-grained, oxygen-free, cast copper anodes and mounted in 3.2-cm diameter epoxy resin[4] castings. These were prepared initially by metallographic grinding and polishing. The disturbed surface layer was removed using a procedure described by Epelboin (19) which consists of a two-step chemical polish followed by electropolishing. Complete removal of the abrasively distorted surface layer is revealed by disappearance of "lines" from the bright copper surface in the second step of the chemical polishing stage. Later, it was found that a flatter surface could be obtained by manual polishing of the cathodes on nonwoven polypropylene cloth[5] (stretched over a plate glass surface) moistened with the second-step chemical polishing solution, then electropolished for 5 min at 1.4-1.8V in 60% phosphoric acid. After examination, deposits were removed by grinding, and the cathodes were repolished before plating again. The columnar structure of the 1-cm thick samples permitted repeated grinding and polishing without requiring redetermination of orientations of individual grains since these are readily recognizable and relocated without undue difficulty. The grains of interest are those with surfaces close (within 10°) to {100} orientations as determined from back reflection Laué photographs. On these grains, the platelet habit found by Pick *et al.* (3) of deposits plated at 10 mA/cm^2 from the sulfate electrolyte provided a convenient, readily reproducible criterion for selection of suitable grains for study.

Microscopy.—Examination of the surfaces of deposits was done on a bench metallograph equipped with a camera.[6] Facet angles were measured, as appropriate, with a microgoniometer.[7] On facets nearly parallel to the surface, interference microscopy could provide limited information on facet contours.

Results

Deposits from the acetate and chloride electrolytes were unsatisfactory, although interesting. In both baths, the initial deposit appeared to be normal, but in a few seconds became rough and powdery in appearance. The acetate electrolyte changed from its original copper blue color to a brilliant, deep blue (comparable to a cobalt blue) and the deposit, under the microscope, was found to consist of extremely small particles, apparently agglomerated into balls. The chloride electrolyte changed from blue to a grass-green and, on standing, became milky with a suspension of finely divided solids. The deposit from this electrolyte was found to consist of octahedral particles, some of which were elongated into blunt needle-like shapes.

The deposits from sulfate, dilute sulfate, perchlorate, and fluoborate electrolytes, at the same current densities, were indistinguishable from each other and compared quite well in appearance with those of Pick *et al.* (3). The deposit from the sulfate electrolyte, in Fig. 1, is typical. The dark material at some of the steps is the first polycrystalline deposit appearing after plating for an hour at 10 mA/cm^2. The apparently planar surfaces actually have slight, irregular curvature which can be seen only by use of the interference microscope. At current densities below 10 mA/cm^2, the pyramidal habit to be seen in Fig. 2a (plated at 5 mA/cm^2 for 2 hr) predominates. This form appears at first glance to be octahedral but is, in fact, non-

[4] Resin 502, Hardener 951, Ciba Products Company, Summit, New Jersey.
[5] Fiber Products Division, Kendall Company, Walpole, Massachusetts.
[6] "Dynazoom," Bausch and Lomb, Inc., Rochester, New York.
[7] Model GM-3, Unitron Instrument Company, Newton Highlands, Massachusetts.

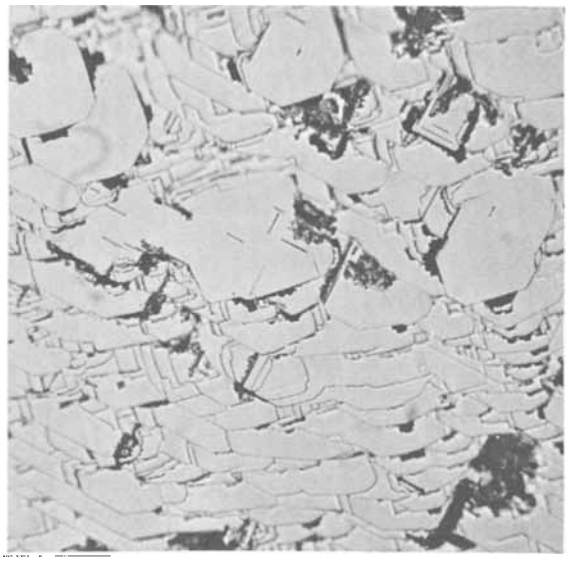

Fig. 1. Copper (0.6 μm thick) plated from 0.5M $CuSO_4$-0.5M H_2SO_4 at 10 mA/cm^2 on copper substrate. Magnification, 200X.

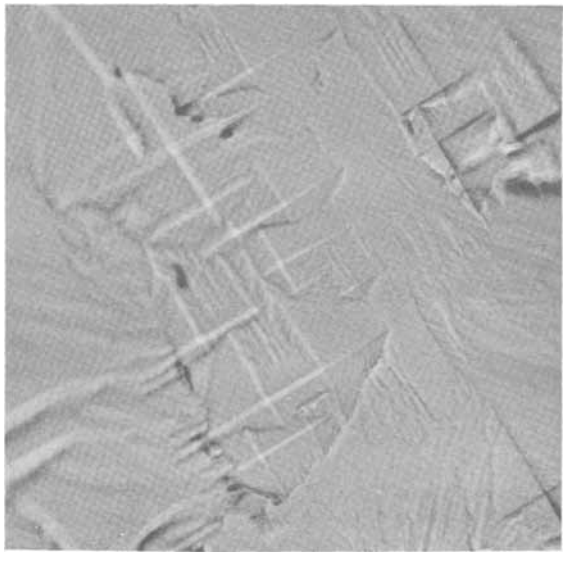

Fig. 2a. Copper plated from 0.5M $CuSO_4$-0.5M H_2SO_4 at 5 mA/cm^2 showing pyramidal and "roof-top" forms. The "comb" of the ridge is the <110> direction. Magnification, 400X.

planar. Figure 2b shows a corresponding deposit from the fluoborate bath.

Deposits from sulfamate, dimethyl-sulfamate, methane-sulfonate, and benzene-sulfonate baths have forms which, though similar in over-all shapes to deposits from the sulfate electrolyte, appear to be more complex. This is particularly noticeable in the pyramidal forms produced at 5 mA/cm^2, illustrated in Fig. 2c and d. These pyramidal forms and the less prominent, ridged forms show distinct and regular steps. These steps are edges of {100} surfaces and are parallel to <100> directions. In deposits from methane-sulfonate and benzene-sulfonate electrolytes, these forms are much more irregular and, although recognizable, have very different characteristics. In these deposits, pyramids tend to be rounded and steps are very fine and irregular in shape, as illustrated in Fig. 2e.

In deposition from the sulfamate electrolyte over extended periods, it was found that octahedral tipped, branchless "dendrites" grew from the edges of the cathodes, as observed by Kikuchi (20). Also, an acicular precipitate appeared in this electrolyte. When filtered out of the solution, no more of this precipitate appeared until deposition was attempted. The precipi-

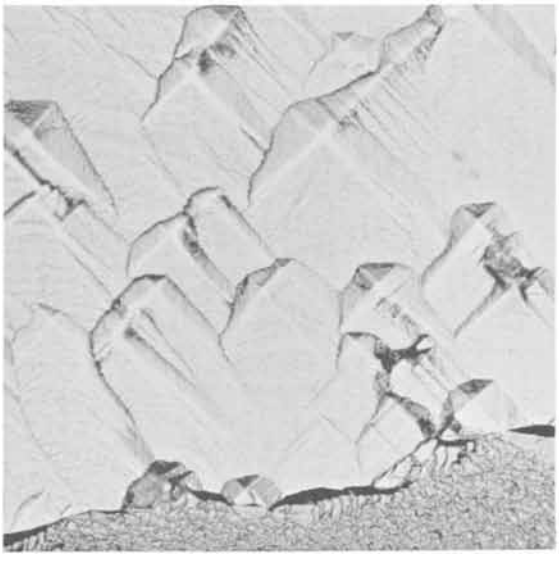

Fig. 2b. Deposit from 0.5M $Cu(BF_4)_2$-0.5M HBF_4 at 5 mA/cm^2. Magnification, 300X.

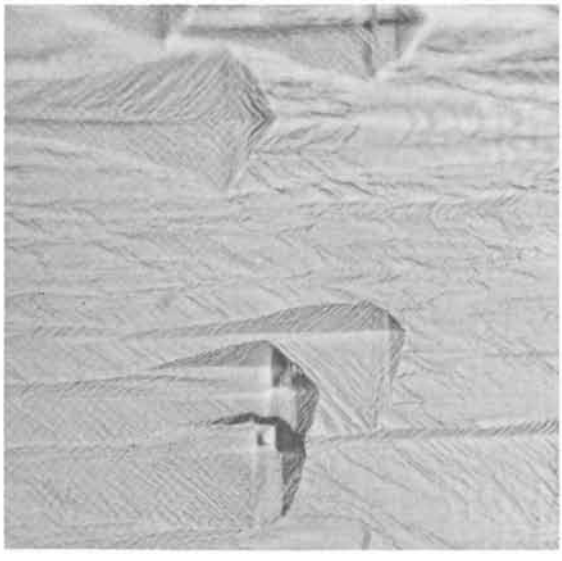

Fig. 2d. Deposit from 0.5M $Cu[(CH_3)_2SO_3]_2$-0.5M $H[(CH_3)_2SO_3]$ bath. Magnification, 400X.

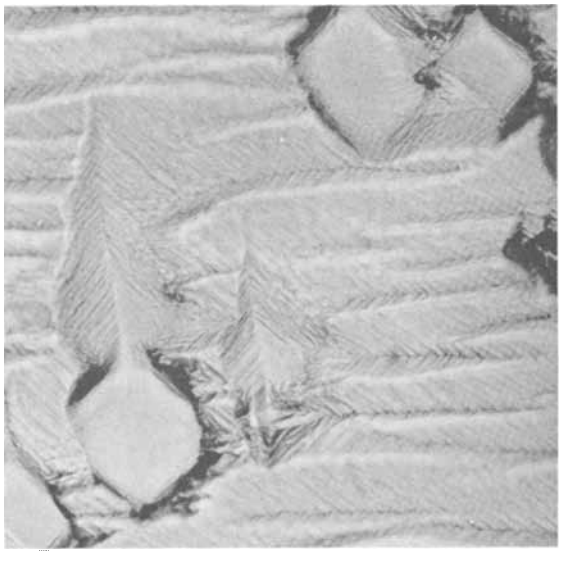

Fig. 2c. Deposit from 0.5M $Cu(NH_2SO_3)_2$-0.5M HNH_2SO_3 bath at 5 mA/cm^2 showing regular steps in ridges and pyramids. Magnification, 400X.

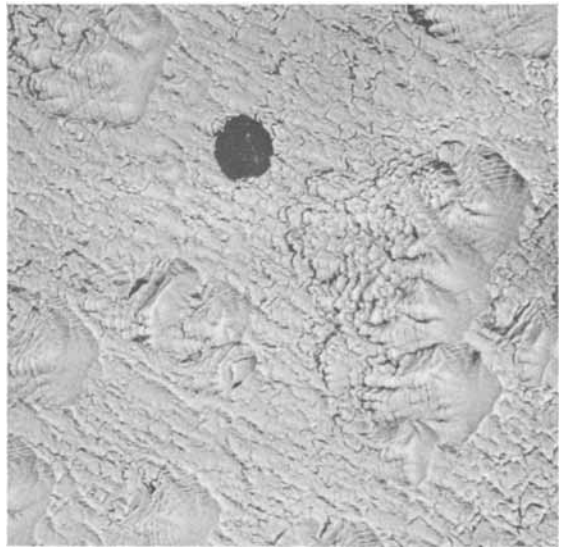

Fig. 2e. Deposit from 0.5M $Cu(CH_3SO_3)_2$-0.5M HCH_3SO_3 bath. Magnification, 400X.

tate dissolved readily in dilute (10%) nitric acid to give an initially pale green solution which turned blue in a short time. A comparable precipitate, formed in the methane-sulfonate electrolyte, behaved similarly when dissolved in nitric acid.

Since, in strongly acid solutions (pH <3), sulfamate ion hydrolyzes rapidly to ammonium bisulfate, a sulfate electrolyte containing 0.25M NH_4HSO_4 was prepared. The deposit obtained (Fig. 3) was quite similar in appearance to that from the sulfamate solution. When periodic reverse current (45 sec direct, 15 sec reverse) was used to prepare a deposit from sulfate electrolyte, the appearance was also very similar to a sulfamate deposit as illustrated in Fig. 4a. The effect of periodic reverse current is not very reproducible since another trial yielded the deposit shown in Fig. 4b.

In Fig. 5, the deposit from a citrate electrolyte is seen to consist of isolated or clustered nodules on grain surfaces with grain boundaries shown by lines of larger globular nodules. The current density was initially 5 mA/cm^2 but rapidly decreased to less than 1 mA/cm^2 and could not be restored to the original value by raising the applied voltage.

Overvoltages measured during deposition from sulfate, sulfamate, methane-sulfonate, and benzene-sulfonate solutions were not appreciably different. In all these electrolytes, the final overvoltage was 80-90 mV at 5 mA/cm^2, but in the sulfamate and methane-sulfonate baths, the initial overvoltage was about 50 mV and rose steadily over 20-30 min to the final value.

Discussion

The most important result of this work is that, for solutions of nominally comparable compositions, the surface morphology, or habit, of copper deposits is rather radically affected by the anion present. Bockris and Enyo (16) had found anion effects in their work, but since their investigation was oriented toward study of kinetics and mechanism of deposition, it was not feasible to examine the deposits. It was suggested that the results obtained were consistent with specific adsorption of anions on the copper cathode and that the potential of zero charge for copper is such that this adsorption will occur. It was further suggested that the differences in observed double layer capacities in sulfate or perchlorate and sulfamate electrolytes were

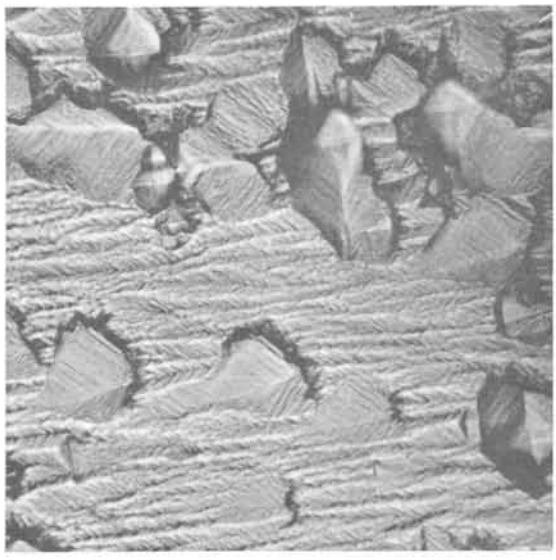

Fig. 3. Deposit from 0.5M $CuSO_4$-0.5M H_2SO_4 containing 0.25M NH_4HSO_4. Magnification, 400X.

Fig. 4b. Copper deposited from the same electrolyte using the same periodic reverse current cycle as in Fig. 4a. Magnification, 400X.

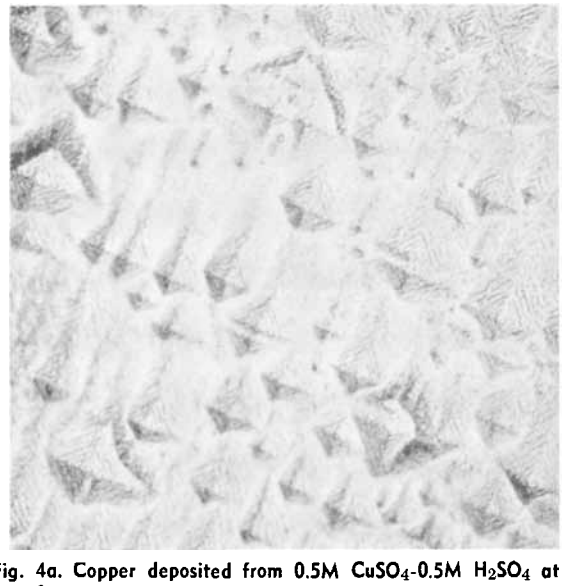

Fig. 4a. Copper deposited from 0.5M $CuSO_4$-0.5M H_2SO_4 at 20 mA/cm^2 using periodic reverse current cycle of 45 sec direct and 15 sec reverse. Magnification, 400X.

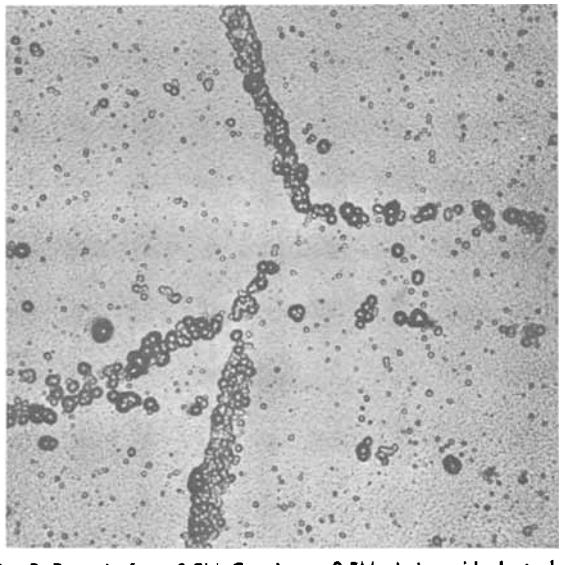

Fig. 5. Deposit from 0.5M Cu citrate-0.5M citric acid electrolyte. Magnification, 200X.

attributable to differences in polarizability, due to differences in the sizes of these ions.

In the work reported here, the results show that deposits from sulfate, perchlorate, and fluoborate have so many surface characteristics in common as to indicate the anions also must have important characteristics in common. The most probable factor is their "shape." All of these ions are regular tetrahedra, with the oxygen atoms in sulfate and perchlorate, and fluorine in fluoborate, equidistant from the central sulfur, chlorine, or boron atom, respectively. These ions are very nearly the same size and have many other similarities (idiomorphic salts, solubilities of salts, dissociation, etc.) (21). Thus, it can be concluded logically that, if specifically adsorbed on copper cathodes, these ions should have similar effects on surface structures.

It appears that changing from sulfate to the sulfamate electrolyte resulted in modifications of the bunching of layers. While the over-all or gross habit remains similar to that of sulfate deposits, details of surface topographies of deposits from the sulfamate and dimethyl-sulfamate electrolytes indicate that uniform steps are formed during growth. It seems reasonable to postulate that the replacement of an oxygen atom in sulfate ion by the amido group (NH_2^-) thus significantly altered the shape or structure of the anion. If, by this substitution, the adsorptive characteristics are enhanced, which is indicated by the double layer capacity of copper in sulfamate solution (16), it is conceivable that step heights could be modified accordingly. The structure of the sulfamate ion is a distorted tetrahedron in which the S-O distances and N-S-O bond angles are smaller than corresponding values in the sulfate ion, presumably due to the electron-deficient NH_2 group (21). Thus, there is reason to believe that this ion has different polarizability and adsorptive behavior than the regular, symmetrical sulfate ion. Replacement of the hydrogen atoms on the amido group by methyl groups to form the dimethyl-sulfamate ion enlarges this ion, and symmetry is even less regular. Distribution of electrons in this ion is a matter of speculation, but its size is such that it could serve, if adsorbed, to block several sites for deposition of copper atoms and thereby account for larger and more uniform step heights. However, addition of ammonium bisulfate to a copper sul-

fate solution produces the same morphological effects observed in sulfamate deposits. In strongly acid solutions (pH <3), sulfamic acid hydrolyzes rapidly to form ammonium and sulfate ions (23, 24). The formation of uniform steps may be due to the presence of the ammonium ion in the sulfamate electrolyte. Presumably, dimethyl-sulfamate ion is subject to similar hydrolytic decomposition [to $(CH_3)_2NH_2^+$?], and the steps observed in these deposits result.

Presence of extraneous or specially structured ions in the electrolyte is not necessary to develop uniformly stepped pyramids or ridges, however, since periodic reverse current (see Fig. 4a) can also produce this result, but not consistently as evidenced by the deposit illustrated in Fig. 4b.

The rather diffuse layering seen in Fig. 2e in deposits from methane-sulfonate solutions, and the even more irregular topography of deposits from benzene-sulfonate electrolyte, do indicate that changes in structure and symmetry of the sulfate ion do affect the surface structure of epitaxial copper deposits. Since overvoltages are not very different from those during depositon from sulfate solution, the effects can be attributed reasonably to differences in adsorption at the cathode.

Another influence which may be operative is the possible effect of ion pairing between the divalent cupric ion and the monovalent sulfamates and sulfonates. In these solutions, the excess acid present may favor the formation of ion pairs such as $[Cu^{++} \cdot CH_3SO_3^-]^+$. Yet another factor which should be considered is the "hydration sheath" of loosely held water molecules which surround ions in solution. The binding forces in these sheaths may also be important in determining the detailed morphological structuring of deposits.

The identical surface morphologies of deposits from the dilute sulfate electrolyte and from the more concentrated solution are of interest. This indicates that it may be feasible to plate copper from these more dilute solutions without impairment of the quality of the deposit. Further, it also shows that the deposition process is essentially independent of cupric ion concentrations, possibly because activity (effective ion concentration) in the more concentrated solutions is not very different from that in the dilute solution.

The behavior of the citrate electrolyte is puzzling. Copper forms complexes with citrate only at relatively high alkalinity. The shape of the small amount of nodules suggests that an inhibiting film formed as the copper was deposited from a complex which may have developed in the high pH cathode film.

The changes which occurred in the acetate and chloride electrolytes may also be due to complexation with the copper species in the electrolyte. Involved could be effects of pH changes in the electrolyte at the electrodes, formation and stability of cupric and cuprous ion complexes, and even more complicated reactions. Proposals of explanations would require investigation of reaction and electrode kinetics, an interesting and difficult exercise obviously outside the scope of this work.

The results obtained in this work are of value, primarily, because several fundamentally interesting problems appear to be involved. Exploration of these may be expected to contribute to improved understanding of electrodeposition processes, provided suitable experimental techniques can be devised. For example, Reddy (25) has analyzed the relationships between electrode kinetics and morphology and pointed out that they are interdependent, thereby furnishing another avenue of attack on the problem.

Manuscript submitted July 23, 1969; revised manuscript received Oct. 2, 1969.

Any discussion of this paper will appear in a Discussion Section to be published in the December 1970 JOURNAL.

REFERENCES

1. J. D. Thomas, O. J. Klingenmaier, and D. W. Hardesty, Paper presented at Annual Technical Conference, Institute of Metal Finishing, Scarborough, England, April 29-May 3, 1969.
2. D. W. Hardesty, In press.
3. H. J. Pick, G. G. Storey, and T. B. Vaughan, *Electrochim. Acta*, **2**, 165 (1960).
4. T. B. Vaughan and H. J. Pick, *ibid.*, 179.
5. S. C. Barnes, G. G. Storey, and H. J. Pick, *ibid.*, 195.
6. G. G. Storey and S. C. Barnes, *Trans. Inst. Metal Finishing*, **37**, 11 (1960).
7. N. A. Economou, H. Fischer, and D. Trivich, *Electrochim. Acta*, **2**, 207 (1960).
8. N. A. Economou and D. Trivich, *ibid.*, 292.
9. N. A. Economou and D. Trivich, *ibid.*, **3**, 298 (1961).
10. A. Damjanovic, M. Paunovic, and J. O'M. Bockris, *J. Electroanal. Chem.*, **9**, 93 (1965).
11. J. M. Keen and J. P. G. Farr, *This Journal*, **109**, 668 (1962).
12. D. R. Cliffe and J. P. G. Farr, *ibid.*, **111**, 299 (1964).
13. S. C. Barnes, *Electrochim. Acta*, **5**, 79 (1961).
14. L. Peraldo Bicelli and G. Poli, *ibid.*, **11**, 289 (1966).
15. L. Peraldo Bicelli and C. Romagnani in "Symposium on Sulfamic Acid and Its Electrometallurgical Applications," p. 155, Italian Association of Metallurgy, Milan (1966).
16. J. O'M. Bockris and M. Enyo, *Trans. Faraday Soc.*, **58**, 1187 (1962).
17. E. H. Lyons, Jr., "Fundamental Principles" in "Modern Electroplating," 2nd ed., F. A. Lowenheim, Editor, p. 25, John Wiley & Sons, Inc., New York (1963).
18. R. Behrend, *J. Liebigs Ann. Chem.*, **222**, 129 (1884).
19. I. Epelboin, *Electrochim. Acta*, **2**, 205 (1960).
20. M. Kikuchi, *Tokyo Kogyo Shikensha Hokoku*, **55**, 35 (1960); *CA*, **60**, 11612c (1964).
21. N. V. Sidgwick, "The Chemical Elements and Their Compounds," pp. 410, 914, Oxford University Press, London (1950).
22. C. J. Brown and E. G. Cox, *J. Chem. Soc. (London)*, **142**, 1 (1940).
23. L. Peraldo Bicelli in "Symposium on Sulfamic Acid and Its Electrometallurgical Applications," p. 23, Italian Association of Metallurgy, Milan (1966).
24. R. Piontelli, B. Mazza, and P. Pedeferri, *ibid.*, p. 81.
25. A. K. N. Reddy, *Electrochim. Acta*, **11**, 277 (1966).

Electrolytic Reductive Coupling

XVIII.[1] Hydrodimerization of Activated Olefin A *vs.* Cross-Coupling with Activated Olefin B as a Function of Cathode Voltage

Manuel M. Baizer,* John P. Petrovich, and Donald A. Tyssee

Central Research Department, Monsanto Company, St. Louis, Missouri

ABSTRACT

It is shown that in mixed reductive coupling of activated olefins A and B, in which A is reduced at the more anodic voltage, the ratio of cross-coupled product HABH to self-coupled product HAAH rises substantially as the controlled potential is made more negative. Diethyl maleate (DEM) was chosen as an example of A and ethyl acrylate (EA) and acrylonitrile (AN) as examples of B. Previously reported fluctuations of voltage along the cathode surface are confirmed and may lead to unexpected formation of HBBH. The results of cyclic voltammetry of DEM in the presence of EA or AN and of a kinetic study of the addition of a carbanion to these same acceptors in bulk are interpreted to indicate that the reductive coupling of DEM with the acceptors occurs largely but not exclusively at the electrode surface.

Among the synthetic advantages amply illustrated for electrolytic reductions at extrinsically controlled potentials are: (*a*) selective reduction of only one of two potentially electroreducible groups in one molecule, as in 9-(*o*-iodophenyl) acridine (2); (*b*) reduction of a molecule to one of two possible major end-products, *e.g.*, a ketone to an alcohol or to a pinacol (3); (c) mixed reductive coupling (4) between activated olefins A and B, in which A is reduced more anodically than B, to yield 1 and 2 without 3 [1]

$$A + B \xrightarrow[H_2O]{F} \underset{1}{HA\text{-}AH} + \underset{2}{HA\text{-}B\text{-}H} + \underset{3}{HB\text{-}B\text{-}H} \quad [1]$$

The present paper reports an apparently new phenomenon associated with electrode potential control. In [1] when diethyl maleate (DEM) is an example of A and ethyl acrylate (EA) and acrylonitrile (AN) are examples of B, the ratio of cross-coupled products (**5** or **6**) to hydrodimer (**4**) can be

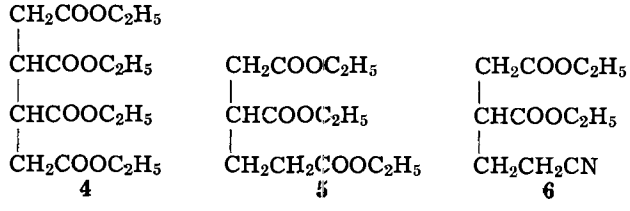

made to vary considerably depending upon the cathode voltage used; **5** or **6**/**1** increases as the cathode voltage increases (negatively) toward the value needed for reduction of B. By judicious choice of voltage one may, therefore, maximize the yield of **2** or, alternatively, reduce A to **1** even in the presence of B (which might be an impurity) without forming significant quantities of **2**.

It has been reported previously (1) that, when A is *trans*-ethyl-3-cyanoacrylate and B is acrylonitrile, electrolysis of a mixture of A and B leads overwhelmingly to **7** (with a small amount of the isomeric hydrodimer **8**) and to only a trace of the cross-coupled product **9**.

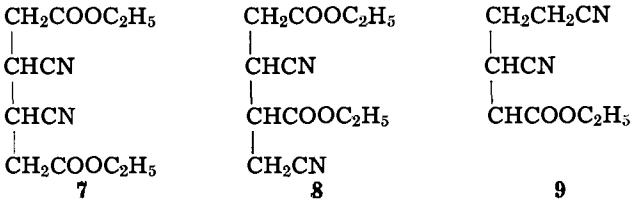

It is shown now that even here the ratio **9**/**7** + **8** increases dramatically as the cathode voltage is made more negative.

Experimental

Reagents.—The diethyl maleate (Matheson, Coleman, and Bell) contained 6% diethyl fumarate according to vpc analysis. Ethyl acrylate and acrylonitrile were high-quality products redistilled and stored over a trace of *p*-nitrosodimethylaniline stabilizer. The dimethylformamide (DMF) and tetraethylammonium *p*-toluenesulfonate were purified as described previously (1). The *trans*-ethyl 3-cyanoacrylate was of the same batch as described previously (1). The preparation of **4** and **6** needed as vpc standards has been reported (1). Compound **5** was obtained by electrolytic reductive coupling of diethyl fumarate and ethyl acrylate. It had the correct elemental analysis, bp 113°-115° (0.15 mm), n^{24}D 1.4380 [reported (5) n^{20}D 1.4390]. Compounds **7** and **9** were available from previous work (1).

Equipment.—The electrolysis cell and associated equipment (6) employed a mercury cathode, area 55 cm^2. The SCE controlling the potentiostat (1.6 ampere Model, Chemical Electronics Company, Newcastle, England) had a salt bridge which was placed at the circumference of the mercury pool. It terminated in a medium porosity sintered disk which was positioned about 1 mm above the surface of the mercury when the stirrer was on. For measurements of the variation of cathode voltage along the mercury surface, the magnetic bar stirrer was replaced by a small glass stirrer in the catholyte. A second calomel cell containing a salt bridge, bent so that it could be positioned under the alundum cup and swivelled to permit readings in an arc from the center of the cell to the circumference, was used along with the "controlling" SCE (Fig. 1).

Analytical methods.—For the experiments with diethyl maleate a vpc analysis was developed, using di-

* Electrochemical Society Active Member.
[1] For Part XVII see (1).

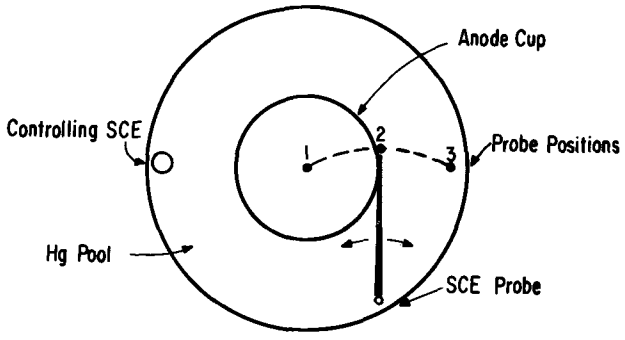

Fig. 1. Arrangement for measuring variation in cathode voltage along surface of mercury.

methyl terephthalate as an internal standard, for the quantitative determination in the mixture of products isolated from the electrolyses of (in order of elution): solvents, diethyl succinate, diethyl adipate, standard, **5**, adiponitrile, **6**, bis-cyanoethyl ether, and **4**. Either of two columns was used: (*a*) a 6-ft, ⅛ in. diameter stainless steel column packed with 80-100 mesh Chromosorb W (N.A.W.) coated with 6% by weight of diethyleneglycol succinate. The instrument was programmed from 180° to 225°C at a rate of 10°/min and held at 225° until all peaks had eluted; (*b*) a similar column packed with 80-100 mesh Chromosorb W (N.A.W.) coated with 10% by weight of Carbowax 20M. The instrument was programmed from 125° to 225° at 50°/min and held at 225° until all peaks had eluted.

In the vpc analysis of the products from ethyl 3-cyanoacrylate a 6-ft, ⅛ in. diameter stainless steel column packed with 10% Apiezon "L" on Chromosorb W (N.A.W.) was used isothermally at 190°. No internal standard was used, and, for comparison purposes, area per cents were taken equal to weight per cents.

Procedures.—The cathode chamber was charged with 50.0g tetraethylammonium p-toluenesulfonate, 5-8 ml of water, a total of 0.75 mole the acceptor olefin(s) (ethyl acrylate, acrylonitrile, or an equimolar mixture of the two) and enough DMF to bring the total volume to *ca.* 150 ml. The anolyte was a saturated aqueous solution of the same salt. The catholyte was stirred and deaerated with nitrogen for 15 min. The cathode voltage was then preset by potentiostat (*vs.* SCE)[2] and from a buret a mixture of 12.9g (0.075 mole) of diethyl maleate and 2.5 ml of acetic acid was added dropwise at a rate sufficient to sustain a current of 0.3-0.5A. Acetic acid was available for dropwise addition from a second buret to maintain the pH in the bulk of the catholyte slightly higher than 7 as measured externally by moist Hydrion paper. After addition was complete, the electrolysis was allowed to proceed at the same cathode voltage until the current fell to 40-60 mA. The catholyte was then diluted with an equal volume of ice water and extracted with five 75-ml portions of methylene chloride. The extracts were washed three times with water and dried over magnesium sulfate. The filtered solution was heated on a water bath at *ca.* 100 mm until no further volatile materials were removed. The residual liquid was analyzed by vpc. Data are summarized in Table I.

The experiment with ethyl 3-cyanoacrylate was conducted similarly except that the catholyte contained 75 ml of AN, 25 ml of DMF, and 6 ml of H_2O; 8.63g (0.069 mole) of ester-nitrile was used in the dropwise addition. After half had been added at −1.450V, a 25-ml sample of catholyte was removed for analysis, the volume replaced by an equal volume of starting catholyte mix, and the remaining half of the ester-nitrile was added at −1.500V. The final catholyte was analyzed in the same manner as the first sample. Suitable arithmetical adjustments permitted the calculation of the quantities of products made in each period. Data are summarized in Table II.

In the experiment in which the variation of the voltage along the mercury surface was measured the catholyte was the same as in runs 4-6 (Table I); small amounts of diethyl maleate were added incrementally in order to achieve the currents at which measurements were desired (Table III). The "monitoring" voltage was read on a DANA Model 5500 digital voltameter fitted with accessory module number 130.

Kinetics (electrochemical).—The method used for obtaining the rate constants is the same as described

[2] In a preliminary experiment the catholyte was charged as in run 1, the cathode voltage preset at −0.51V and increased negatively by small increments while "instantaneous" current readings were made. It was found that between −1.05 and −1.62V a current of only 63-75 mA was sustained (due to reduction of the stabilizer); at more negative voltages reduction of EA began. As discussed later, the conclusion that mixed coupling could safely be carried out at −1.50V without formation of diethyl adipate was, however, incorrect.

Table I. Electrolysis of 0.075 mole diethyl maleate added dropwise to catholyte containing 0.75 mole acceptor mono-olefins; 15°-20°

Run	Apparent cathode voltage (SCE) (−)	Catholyte: Acceptor	Catholyte: ml H_2O	Catholyte: ml DMF	Products, mM: DES[a]	CCP[b]	TEBT[c]	DEA[d]	ADN[e]	mM CPP / mM TEBT	A-hr end of addn. to end of expt.
1	1.314	EA	8	59	26.0	1.18	3.64	0	—	0.324	0.70
2	1.425	EA	8	59	35.1	5.95	8.50	0	—	0.700	0.17
3	1.500	EA	8	59	27.2	12.1	6.00	8.66	—	2.03	0.28
4	1.314[f]	AN	8	72	34.6	0	1.00	—	0	0	0.43
5	1.425	AN	8	72	43.1	4.71	3.88	—	0	1.21	0.38
6	1.500	AN	8	72	55.0	13.1	1.34	—	8.90	9.75	0.61
7	1.425	EA + AN	8	55	52.2	0.764[g] + 4.97[h]	3.68	Trace	0	0.207[g] + 1.35[h]	0.13
8	1.425	EA + AN	5	58	34.0	0.72[g] + 4.94[h]	2.47	Trace	0	0.291[g] + 1.98[h]	—

[a] Diethyl succinate. [b] Cross-coupled product, *i.e.*, compound 5 when EA was used, compound 6 when AN was used. [c] Tetraethyl butanetetracarboxylate, **4**. [d] Diethyl adipate. [e] Adiponitrile. [f] Experiment not run to completion; 24.2 millimoles of DEM recovered. [g] From EA. [h] From AN.

Table II. Electrolysis of 0.069 moles ethyl 3-cyanoacrylate added dropwise to catholyte containing 1.12 moles AN; 6°-10°

Run	Apparent cathode voltage (SCE) (−)	ml H_2O	ml DMF	ECP[c]	CCP[d]	DDA[e]	ADN[f]	mM CCP[d] / mM DDA[e]
1A[a]	1.450	6	25	1.45	0.668	16.2	0	0.0412
1B[b]	1.500	6	25	1.06	1.83	16.5	Trace	0.111

[a] Twenty-five ml removed after half the ethyl 3-cyanovalerate had been added and completely reduced. Quantities of products calculated on basis of 135/25 of sample. [b] Corrected for materials left in catholyte after removal of first sample. [c] Ethyl 3-cyanopropionate. [d] Cross-coupled product, *i.e.*, compound **9**. [e] Diethyl 2,3-dicyanoadipate, *i.e.*, compound **7**. [f] Adiponitrile.

Table III. Variation of cathode voltage with current (density) and position of salt bridge; 16°-16.5°

"Apparent" voltage vs. SCE (−)	Voltage vs. SCE (−) at positions 1	2	3	Current, mA
1.200	1.205	1.200	1.200	1.56
1.314	1.319	1.316	1.316	1.56
1.314	1.340	1.309	1.317	44.0
1.314	1.339	1.314	1.316	50.0
1.314	1.335	1.312	1.315	60.0
1.314	1.35-1.37[a]	1.29-1.31	1.31-1.32	156
1.314	1.35-1.38	1.31-1.33	1.31-1.32	208
1.425	1.464	1.434	1.434	116
1.425	1.470	1.440	1.441	138
1.425	1.47-1.49	1.41-1.45	1.43-1.46	130
1.425	1.47-1.49	1.43-1.47	1.45-1.47	172
1.425	1.49-1.53	1.45-1.48	1.47-1.49	260
1.425	1.48-1.50	1.41-1.45	1.40-1.41	286
1.425	1.52-1.57	1.46-1.51	1.46-1.50	338
1.500	1.539	1.514	1.514	185
1.500	1.55-1.58	1.52-1.55	1.53-1.55	234
1.500	1.51-1.55	—	—	286
1.500	1.53-1.57	1.50-1.53	1.51-1.54	340
1.500	1.59-1.63	1.49-1.56	1.53-1.57	468
1.500	1.57-1.63	1.49-1.54	1.49-1.53	470
1.500	1.57-1.61	1.47-1.53	1.51-1.54	500
1.500	1.60	1.50	1.53	520

[a] At currents greater than *ca.* 100 mA fluctuations of registered cathode voltage were too rapid to permit determination of an average, so that the range is indicated.

previously (7). The concentration of diethyl fumarate was 2 x $10^{-3}M$, EA and AN were 1.0*M* in each run. The solvent was dimethylformamide containing 0.1*M* tetraethylammonium perchlorate.

Kinetics (solution).—The solutions contained 1*M* diethyl ethylmalonate, 0.1*M* EA or AN and 1 x $10^{-4}M$ tetraethylammonium hydroxide in ethanol as solvent. At appropriate times 1 ml of the solution was removed and added to 1 ml of a solution of 0.1*M* diethyl adipate and sufficient acetic acid to stop the reaction in ethanol as solvent. The analysis was done by vpc using diethyl adipate as an internal standard and a 6-ft, 10% Carbowax 20M on Chromosorb W, programmed from 100° to 220° at 15°/min. A plot of ln [product] *vs.* time curved due to the disappearance of base. A smooth curve was drawn through the points and the tangent to the curve at low conversion was used to calculate *k*. The runs were done in pairs, EA and AN, side-by-side at room temperature. The average value for the relative rate constants AN/EA for several runs was 9.2. The maximum value obtained was 11.0 and the minimum was 7.6. All attempts to use dimethylformamide failed due to the extremely rapid disappearance of the catalyst in this solvent. The disappearance of base is due to the facile saponification of diethyl ethylmalonate.

Reductive cyclization of **6** *to* **10**.—Diethyl α-(2-cyanoethyl) succinate (**6**, 47.0g, 2.1 x 10^{-1} moles), Raney cobalt (6.0g), absolute ethanol (120 ml), and ammonia (17.0g, 1 mole) were placed in a 300-ml bomb and heated at 100° under an initial hydrogen pressure of 1500 psi until hydrogen uptake was no longer observed (*ca.* 4 hr) (8). The reaction mixture was filtered, the solvent removed under vacuum, and the residue crystallized from 350 ml of cyclohexene to give 27.2g (1.5 x 10^{-1} moles) of **10**, ethyl 2-oxo-3-piperidineacetate (72%), mp 77°-79°. The infrared spectrum (nujol) has peaks characteristic of ester and amide functions at 1735 and 1650 cm^{-1}, respectively; nmr spectrum (τ, $CDCl_3$): 2.8 (broad singlet, 1H, NH), 5.6 (quartet, J = 7 cps, 2H, OCH_2), 6.4 (unresolved multiplet, 2H, NCH_2), 7.03 (unresolved multiplet, 3H, H α to carbonyl), 8.0 (unresolved multiplet, 4H, ring H), 8.5 (triplet, J = 7 cps, 3H, CH_3).

Anal.—Calcd. for $C_9H_{15}NO_3$: C, 58.38; H, 8.22; N, 7.57. Found: C, 57.88; H, 8.26; N, 7.49.

3-Piperidinethanol.—Ethyl 2-oxo-3-piperidineacetate (9.2g, 5 x 10^{-2} moles) was added in portions to 7.2g (1.9 x 10^{-1} moles) of $LiAlH_4$ in 150 ml of diethyl ether at room temperature over a 2-hr period. After refluxing for 6 hr and cooling, water was slowly added to destroy excess $LiAlH_4$. The mixture was filtered and the solid washed several times with ethanol. The amino-alcohol (3.1g, 2.4 x 10^{-2} moles) was isolated by vacuum distillation: bp 94°-96° (0.28 mm) [lit. (9-11) bp 120°-123° (4-6 mm)]; $n^{24}D$ 1.4897 [lit. (9-11) $n^{21}D$ 1.4880, $n^{25}D$ 1.4920, 1.4888]; nmr spectrum (τ, $CDCl_3$): 6.3 (broad singlet, NH and OH), 6.45 (triplet, 2H, OCH_2), 6.9-8.5 (unresolved multiplet, 11H).

Discussion of Results

In working with the reaction systems described here it is necessary to adopt a series of compromises. One must take cognizance of (*a*) the ready saponification of diethyl maleate (6) (pH and temperature-dependent); (*b*) the electroreducibility of ethyl hydrogen maleate (12); (c) the cyanoethylation of water (pH dependent); (*d*) the anionic oligomerizability/polymerizability of ethyl acrylate and acrylonitrile (proton donor concentration dependent); (*e*) the facile formation of diethyl succinate (proton donor concentration dependent); and (*f*) the facile formation of tetraethyl butanetetracarboxylate (diethyl maleate/water concentration dependent). Conditions were chosen so as to eliminate complicating side reactions [*e.g.*, formation of bis(2-cyanoethyl ether)], minimize the probability of favoring only hydrodimerization (therefore, dropwise addition of DEM), and to accept perhaps higher than necessary yields of DES in order to avoid polymerization. The penalty paid for the last compromise was to increase the possibility of "bulk" rather than electrode reactions (1). Attempts were not made to maximize yields of cross-coupled products at the expense of all other products; the focus of attention was on the ratio of cross-to-self-coupled products. Any DEM anion radical (or derived anion) which ended as DES or any DEM which was saponified was equally unavailable for formation of either coupled product.

Even though the quantity of water added to the catholyte is carefully measured, the concentration of water during a run and from run to run varies due to uncontrollable changes in the porosity of the diaphragm (1). Therefore, as mentioned above, it is not the absolute yield of DES (water dependent) which is significant but the ratio CCP/TEBT.

It is evident from the data in Table I that whether ethyl acrylate or acrylonitrile is the acceptor olefin the yield of reduced cross-coupled product with diethyl maleate compared to the yield of hydrodimer rises sharply as the voltage is made more negative. These results are consistent with our previous suggestion (1) concerning "induced" reactivity of acceptor olefins in electric fields. It is interesting that under certain circumstances (runs 1, 4) very little if any mixed coupling can be made to occur. This may explain reported (13) deviations in the success of obtaining cross-coupled products.

There is another factor affecting the ratio of coupled products: it cannot be ignored but cannot be evaluated clearly. Despite attempts to keep the rates of addition of DEM to the catholyte fairly constant from run to run (6-8 hr) and the effort to maintain comparable current densities (0.3-0.5 A/55 cm^2), the bulk concentrations, although small, of unreduced DEM in the runs at the more positive cathode voltages must have been higher than that at the more negative voltages. The higher concentration *per se* would have favored TEBT formation in the more anodic electrolysis (in accordance with results) but so would the greater reactivity of DEM in the more cathodic electrolyses (not in accordance with results).[3]

The reason for the formation of hydrodimers of the acceptor olefins (runs 3 and 6) as an "apparent" cath-

[3] The coulombs passed in the period between the end of DEM addition and the end of the experiment is a measure of the terminal concentration of DEM in the catholyte. While in run 1 (0.70 A hr) it was higher than in run 2 (0.17 A hr), in run 2 it was lower than in run 3 (0.28 A hr). Likewise, in run 6 (0.61 A hr) it was higher than in run 5 (0.38 A hr).

ode voltage at which they "should" not be reduced is clear from a consideration of the variation of cathode voltage with position of the salt bridge (14) and with current densities (Fig. 1 and Table III). At the currents used in these preparative runs the cathode voltages at certain areas of the mercury cathode may be as much as 0.13V more negative than "apparent" at the more negative voltages and may, therefore, overlap the beginning of the reduction waves of the acceptors. This phenomenon has been reported before (14). This type of preparative cell, otherwise very convenient, must be used cautiously for controlled potential electrolyses in which the desired reduction is < *ca.* 0.2V removed from an undesired reduction. Even at a "fixed" potential, the fluctuations may in some cases be significant (30-40 mV). Since, however, the same geometry was maintained throughout the runs reported in Table I, the conclusions concerning the reductive couplings involving DEM are the same whether one refers to the "apparent" cathode voltage or to the "true" cathode voltage (position 1, Table III).

It will be noted that in similar separate experiments (run 5 *vs.* run 2, run 6 *vs.* run 3) and even more in competitive experiments (runs 7 and 8) considerably more cross-coupled product was formed from AN as acceptor (→ **6**) than from EA (→ **5**). It was of interest to diagnose these results by the most feasible experiments which would differentiate between the reactions of DEM anion radical/diethyl succinate anion with acceptors at the electrode/in the "bulk" of solution.

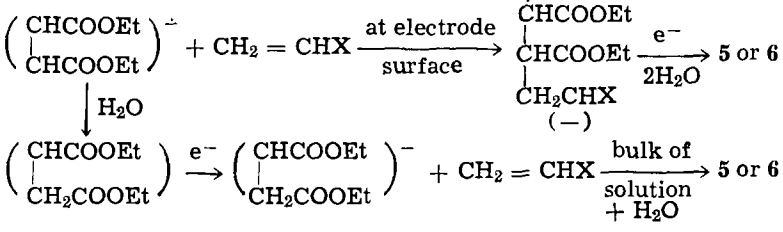

Cyclic voltammetry provided the answer for the first of these coupled questions. For the second, diethyl succinate anion could, unfortunately, not be used successfully in the Michael reaction; therefore, diethyl ethylmalonate anion, which reacts with acceptors to give only 1:1 products, was chosen for the comparison of AN and EA as acceptors in a "bulk" reaction.[4]

Rate constants for the reaction of EA and AN separately with the anion radical electrochemically generated from diethyl fumarate (DEF)[5] were measured by cyclic voltammetry by the procedure described previously (7). Using 2 x $10^{-3}M$ DEF, the rate constant for the disappearance of the anion radical in the absence of EA and AN is 0.30 sec^{-1} with DMF as solvent and 0.1*M* tetraethylammonium perchlorate as the supporting electrolyte. The rate constant measured in the presence of 1*M* EA was 0.46 sec^{-1}, and in the presence of 1*M* AN was 0.43 sec^{-1}. The ratio of the rate constants for the attack of the anion radical of DEF on AN and EA separately is 0.81. In macroscale cross-coupling electrolysis, if all of the products could be formed at the electrode surface, the cross-coupled product **5** would be formed at 1.2 times the rate of the cross-coupled product **6**. In fact, however, using the TEBT formed as a common denominator, and comparing Runs 2 and 5, **6** predominates by a factor of 1.7.

These results are in apparent contradiction to what would be predicted from cyclic voltammetric data only. However, it must be recognized that in bulk electrolyses the distribution of products obtained must depend not only on the rates of the reactions at the electrode but also on the rates of reaction in the "bulk" of solution outside the influence of the electric field. Cyclic voltammetry yields information exclusively about the first category; a normal Michael reaction "in bulk" yields information exclusively about the second category. The actual product distribution determined experimentally must reflect contributions from both electrode and bulk reactions.

Rate constants for a typical Michael reaction of EA and AN were measured using the diethyl ethylmalonate anion as the donor. The reactions were conducted in ethanol as solvent using tetraethylammonium hydroxide as the catalyst. The ratio of the rate constants for the reaction of AN and EA toward the same donor was 9.2. The fact that the observed rate ratio AN/EA of 1.7 from comparative macroelectrolysis lies between the values of 0.81 for the electrode reaction and 9.2 for the solution reaction again indicates that both of these reactions are occurring in macroelectrolysis.

The demonstrated increased reactivity of each acceptor alone (EA or AN) toward the maleate anion radical donor as the cathode voltage is made more negative must not be interpreted to indicate that their relative separate reactivities will hold when both are present together. Now questions of specific adsorption and cation effects may intervene (17). Examination of the data of runs 7 and 8, Table I, indicates a rate ratio of 6.5 for AN/EA in contrast to the value of 1.7 obtained for runs 2 and 5. The yield of CCP from AN is nearly constant in runs 5, 7, and 8, while the yield of the CCP from EA decreases sharply in runs 7 and 8 from that in run 2. The preferential adsorption of an AN-tetraethylammonium ion complex (17) on the electrode surface, thereby largely excluding EA from the reactive environment, may be the cause of the significant change in relative reactivities observed. The effect may not be unique for AN (17) and may explain the high reactivity of the β-substituted acrylonitriles reported previously (7).

Finally, it should be mentioned that compound **6**, prepared much more conveniently by a one-step electrochemical synthesis than by a multistep chemical route (18), is in itself an interesting intermediate. Catalytic reduction of **6** in ethanol with excess ammonia over Raney cobalt at 100° and 1500 lb gave an almost quantitative yield of ethyl 2-oxo-3-piperidine acetate **10**, mp 77°-79°, (with correct elemental analysis and consistent nmr spectrum) and none of the isomeric 7-membered lactam **11**. Reduction of the

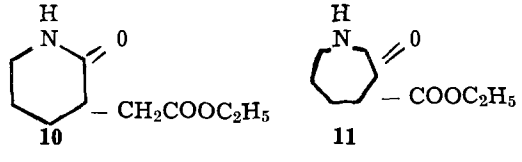

carbethoxymethyl group of **10** with lithium aluminum hydride yielded the corresponding known (9) amino-alcohol whose *p*-bromobenzenesulfonamide melts at 97°-98.5° (correct analysis).

Acknowledgment

We are grateful to John L. Chruma for excellent technical assistance.

Manuscript received Aug. 12, 1969.

[4] It is assumed that steric effects will not influence the relative reactivities of AN and EA toward this model anion. Cf (15).

[5] It has been shown that the same anion radical is formed from either DEF or DEM (16).

Any discussion of this paper will appear in a Discussion Section to be published in the December 1970 JOURNAL.

REFERENCES

1. J. P. Petrovich and M. M. Baizer, *This Journal*, **116,** 749 (1969).
2. J. J. Lingane, C. G. Swain, and M. Fields, *J. Am. Chem. Soc.*, **65,** 1348 (1943).
3. M. J. Allen and A. H. Corwin, *ibid.*, **72,** 114, 117 (1950).
4. M. M. Baizer, *J. Org. Chem.*, **29,** 1670 (1964); K. Sugino, K. Shirai, and T. Nonaka, *Bull. Chem. Soc. Japan*, **37,** 1895 (1964).
5. L. Ruzicka, A. B. de Almeida, and A. Brack, *Helv. Chim. Acta*, **17,** 183 (1934); S. J. Birch, W. J. Oldham, and E. A. Johnson, *J. Chem. Soc.*, **1947,** 818.
6. M. M. Baizer, *This Journal*, **111,** 215 (1964).
7. J. P. Petrovich, M. M. Baizer, and M. R. Ort, *ibid.*, **116,** 743 (1969).
8. J. W. Lynn, *J. Org. Chem.*, **21,** 578 (1956).
9. H. Najer, R. Giudicelli, J. Loiseau, and J. Menin, *Bull. Soc. Chim. France*, 2831 (1963).
10. R. L. Malan and P. M. Dean, *J. Am. Chem. Soc.*, **69,** 1797 (1947).
11. R. Merchant and C. S. Marvel, *ibid.*, **50,** 1197 (1928).
12. M. M. Baizer and J. P. Petrovich, *This Journal*, **114,** 1023 (1967).
13. J. Wiemann and M. L. Bouguerra, *Compt. rend.*, **265,** 751 (1967).
14. J. E. Harrar and I. Shain, *Anal. Chem.*, **38,** 1148 (1966); L. Meites, *Pure Appl. Chem.*, **18,** 3 (1969); G. L. Booman and W. B. Holbrook, *Anal. Chem.*, **35,** 1793 (1963).
15. D. E. Floyd and S. E. Miller, *J. Org. Chem.*, **16,** 882 (1951).
16. S. F. Nelsen, *Tetrahedron Letters*, **1967,** 3795.
17. A. P. Tomilov, E. V. Kryukova, V. A. Klimov, and I. N. Brago, *Soviet Electrochemistry*, **3,** 1352 (1967).
18. P. C. Mitter and A. C. Roy, *J. Indian Chem. Soc.*, **5,** 47 (1928).

Densities and Molar Volumes of Molten Alkali Carbonate Binary Mixtures

P. L. Spedding

Department of Chemical and Materials Engineering, The University of Auckland, Auckland, New Zealand

ABSTRACT

Density and molar volumes were determined for the molten lithium, sodium, and potassium carbonate binary mixtures over the complete composition range. Molar volumes of the sodium-potassium carbonate binary exhibit ideal behavior but the lithium binaries show positive deviations in the 0.25 to 0.67% mole lithium carbonate region. An attempt is made to handle the results using thermodynamic reasoning. It is possible to give a detailed explanation of the observed behavior by postulating that inbalances in repulsive cation interactions, caused by the relatively small size of the lithium ion, forces changes in anion-cation bonding in the melt microstructures.

Valuable insight into the nature of liquid structure can be gained from precise thermodynamic data of molten salts. Such information would be particularly relevant at the present time because of the absence of an adequate general theory of liquids. In particular, variations of density and molar volume with both temperature and melt compositions provide information on corresponding changes taking place in melt structure. Furthermore, accurate density data are an essential prerequisite to an adequate interpretation of certain other experimental data, *e.g.*, in the calculation of transport phenomena such as equivalent conductance.

The alkali metal carbonates have been studied extensively in recent years both from an interest in the fundamental structural and transport properties of pure salts and mixtures and also for their importance as electrolytes in the high-temperature fuel cell (1-5). This present study was undertaken as part of an integrated fuel cell research program aimed at obtaining a better understanding of the actual processes involved in the molten carbonate-type cell.

Experimental

The Archimedian single bob densitometer was used because of its simplicity, accuracy, and precision at higher temperatures. The method depends on the availability of suitable surface tension and expansion data (6, 7). If these data were lacking, the two-bob densitometer would have to be used (8). The pycnometer was not used because it was found that a suitable reference liquid for high-temperature work was difficult to obtain. Even when this aspect was avoided by using thermal expansion corrections, the surface tension difficulties encountered made the method unreliable for high-temperature work (9).

The apparatus (Fig. 1) was similar to that used for other molten carbonate studies (5). The densitometer section of the apparatus consisted of a salt bath (K) contained in an 80% Au 20% Pd alloy crucible which was supported on a 25/20 stainless steel frame (O). The crucible was provided with two small lifting holes (J) near its rim to facilitate handling in and out of the furnace. A precision laboratory jack (V), external to the furnace, enabled the crucible and support frames to be moved vertically. A thick pyrophyllite plug (R), fitted with a silicone rubber seal (T) and cooled by external water coils (S), provided a gas seal at the furnace base while still allowing vertical movement. Reproducible depth of bob immersion was ensured by a probe, height-sensing device (M). Ideally the carbonate melts should have been maintained under dry carbon dioxide at a pressure well in excess of their dissociation pressure in order to ensure the melt compositions (5). In practice it was not possible, with this relatively inexpensive type of apparatus, to maintain gas pressure during weight measurements because the bob suspension required free movement during a determination. Conditions were compromised in that a suitable carbon dioxide pressure was maintained during the 5-hr temperature equilibration by sealing the suspension hole at the top of the furnace. During the short time an actual weighing was conducted, carbon dioxide

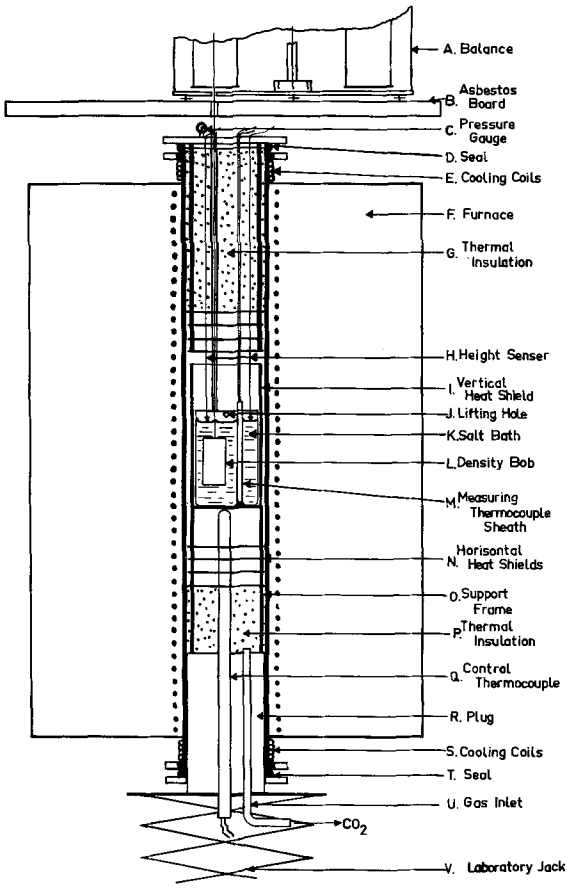

Fig. 1. Archimedian densitometer

was allowed to flow slowly down past the bob suspension wire through a special anticondensation sleeve. The absence of condensation was checked by weighing of the suspension wire after it had been exposed to operating conditions. It has been reported that the gas flow does not adversely affect the results obtained and that any decomposition which may take place during the short measurement period would be on the surface of the salt and so have an insignificant effect on the results (6, 7).

Analytical reagent grade lithium, sodium, and potassium carbonates were used in the preparation of the salt baths. The carbonates were dried initially at 120°C to constant weight and kept in a desiccator prior to weighing of the salt bath material. The salt bath was premelted in a furnace under a carbon dioxide atmosphere, care being taken to ensure that no bubbles were formed in the melt. The bath was solidified slowly and stored in a desiccator until it was used in the densitometer. Density readings were taken at increasing and then at decreasing temperatures. The weights used were calibrated against a substandard set of weights to ensure accuracy. The volume of the density bob was determined by weighing in air of a known density and then in water to a known depth of immersion. The water used was distilled, deionized, and deaerated. The calibration was carried out in a constant temperature room. The following equation applied. Difference between the two weights of masses in air $+ 2\pi r\gamma \cos\theta/g$ = Bob volume $\times$ Difference in density of water and air. Seven separate series of determinations taken at intervals over the molten salt density determinations gave the average volume of the density bob as 2.87675 $\pm$ 0.00027 cc. A further check of the bob volume was made by determining the density of benzene and carbon tetrachloride, and agreement with published data was within $\pm$ 0.01%. Corrections for surface tension (γ) and expansion (10) of the density bob in the melt were applied. In the former case the data of Janz and Lorenz (1) for the pure melts were used and the binary mixture values calculated assuming ideal melt behavior which is of sufficient accuracy for these circumstances (11). One of the most serious sources of error of the density bob method is bubble formation on the bob surface during an actual determination. Bubble formation has been attributed to minute traces of water in the melt, and in the present work this was completely eliminated by use of the premelting technique.

Results

The density data measured for the binary lithium, sodium and potassium carbonate mixtures are detailed in Fig. 2 to 4. The constants for the temperature-density equations were calculated using the method of least squares (12) and are listed in Tables I to III. The calculated accuracy of the determinations was in the region of $\pm$ 0.015%.

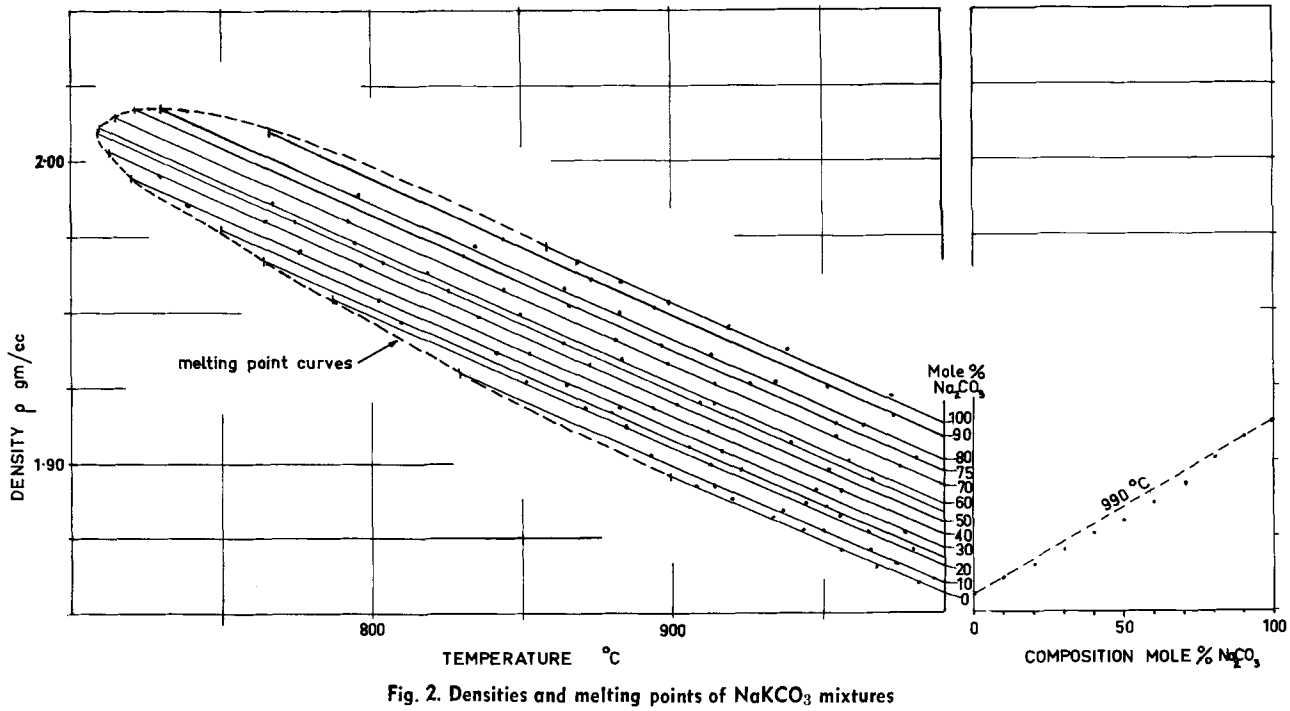

Fig. 2. Densities and melting points of $NaKCO_3$ mixtures

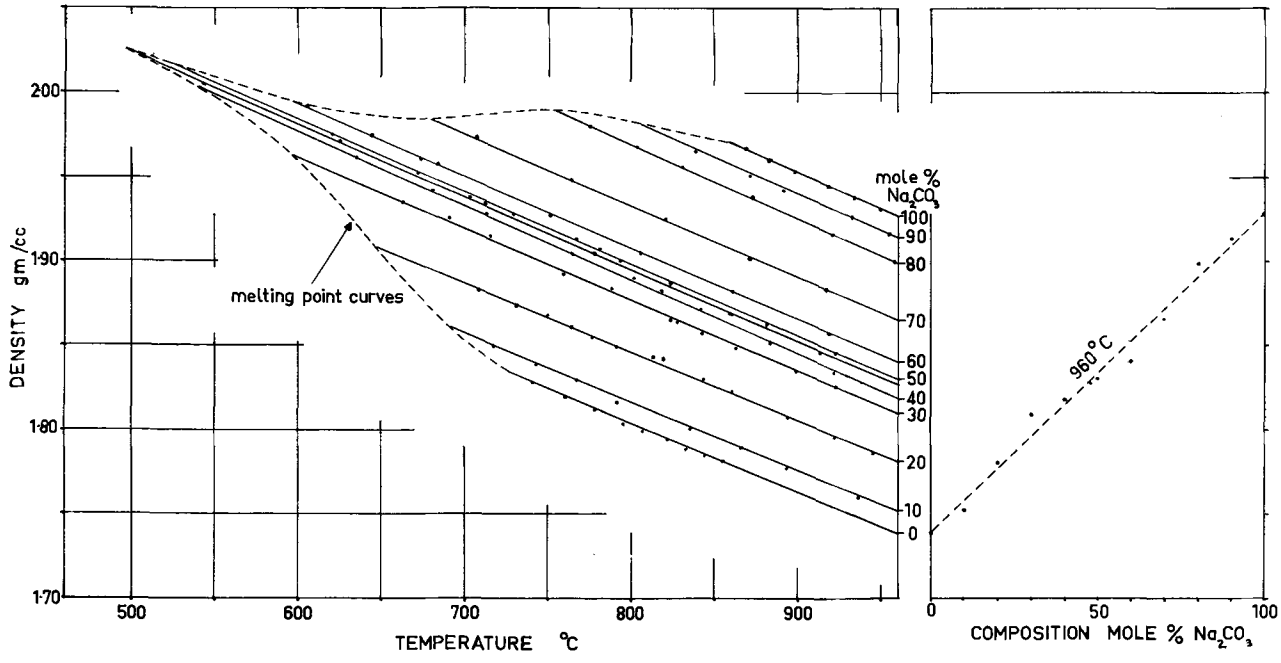

Fig. 3. Densities and melting points of $LiNaCO_3$ mixtures

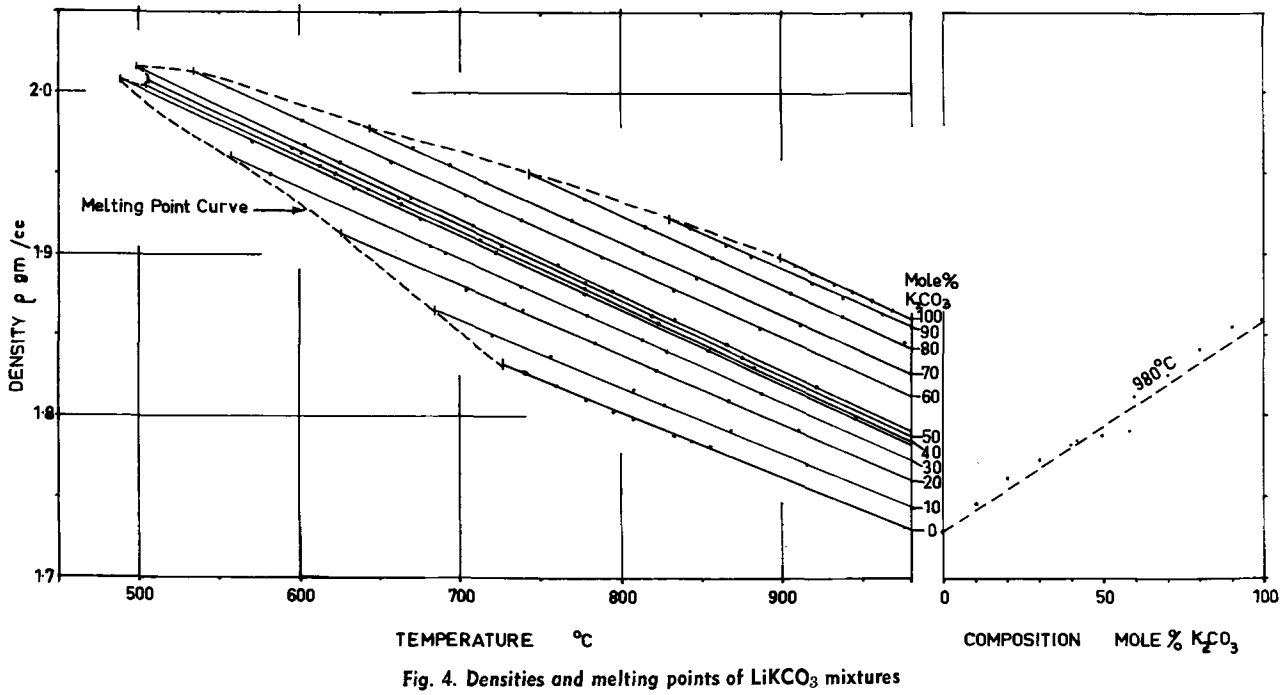

Fig. 4. Densities and melting points of $LiKCO_3$ mixtures

Discussion

Comparison with reported data.—Most of the reported data on the densities of molten alkali metal carbonates are incomplete or possess inconsistencies (1, 4, 13-17), Vorobev *et al.* (17) and Janz and Lorenz (1, 4) have suggested this is due to the lack of reasonable precautions being taken in certain instances to prevent thermal decomposition of the melt. The wide scatter and abnormal behavior of much of the data makes it highly probable that this criticism is well justified. When comparisons are drawn between the remaining data it is found that certain inconsistencies exist which are difficult to reconcile. The present work resolve these by showing agreement with the data of Vorobev *et al.* (17) and Janz and Lorenz (1) in the region of the eutectic compositions and the pure components, respectively, but poor agreement elsewhere.

Temperature-density data.—The most notable aspect of the results is the linear relationship which exists between density and temperature even at points quite close to the melting point. The temperature coefficient, *b*, exhibits a reasonably smooth change from one pure component composition to the other. This is in contrast with most other reported carbonate data but seems to be the more reasonable behavior to expect.

Composition-density data.—The sodium-potassium carbonate mixture exhibits a slight negative deviation from lineality. This is the usual behavior to be expected from a mixture of two similar salts. The lithium binary mixtures, on the other hand, show a change in the sign of the deviation from linear behavior at the eutectic compositions. This abnormal behavior of the lithium binary mixtures arises from a clustering of the composition-density data around the eutectic and is in accord with other thermodynamic data reported for these systems (5).

Composition—molar volume data.—Calculated molar volume data are detailed in Fig. 5. The sodium-potas-

Table I. Densities of lithium-sodium carbonate binary mixtures

$\rho = a - b\,T$ g/cc*

Media, m/o Li_2CO_3	a	$b \times 10^3$	t°C range
100	2.2365 ± 0.0076	0.4041 ± 0.0071	741-856
90	2.2435 ± 0.0043	0.3991 ± 0.0040	717-930
80	2.2885 ± 0.0036	0.4120 ± 0.0033	708-945
70	2.3474 ± 0.0091	0.4378 ± 0.0084	663-923
60	2.3557 ± 0.0047	0.4337 ± 0.0044	636-920
53.3	2.3581 ± 0.0013	0.4325 ± 0.0004	542-915
50	2.3532 ± 0.0029	0.4249 ± 0.0028	620-923
40	2.3653 ± 0.0033	0.4262 ± 0.0033	607-919
30	2.3890 ± 0.0118	0.4230 ± 0.0112	674-918
20	2.4461 ± 0.0038	0.4437 ± 0.0034	775-958
10	2.4443 ± 0.0047	0.4301 ± 0.0042	839-955
Na_2CO_3	2.4532 ± 0.0064	0.4267 ± 0.0052	868-973

* T = ° Kelvin.

Table II. Densities of lithium-potassium carbonate binary mixtures

$\rho = a - b\,T$ g/cc*

Media, m/o Li_2CO_3	a	$b \times 10^3$	t°C range
100	2.2365 ± 0.0076	0.4041 ± 0.0071	741-856
90	2.2687 ± 0 0031	0.4180 ± 0.0029	720-915
80	2.2966 ± 0.0036	0.4264 ± 0.0034	704-911
70	2.3251 ± 0.0017	0.4390 ± 0.0016	682-888
62	2.3526 ± 0.0007	0.4532 ± 0.0007	570-945
60	2.3593 ± 0.0024	0.4569 ± 0.0024	611-883
50	2.3599 ± 0.0023	0.4548 ± 0.0023	595-875
42.7	2.3711 ± 0.0008	0.4623 ± 0.0008	602-921
40	2.3795 ± 0.0011	0.4527 ± 0.0009	601-886
30	2.4184 ± 0.0139	0.4761 ± 0.0135	671-911
20	2.3942 ± 0.0032	0.4385 ± 0.0029	776-976
10	2.4094 ± 0.0062	0.4422 ± 0.0052	842-981
K_2CO_3	2.4295 ± 0.0085	0.4543 ± 0.0694	907-981

sium carbonate mixture exhibits ideal behavior while the lithium binary mixtures show a positive deviation from ideality only in the vicinity of the 50% molar compositions. The deviation is observed to increase as the cation size difference in the melt increases. This nonideal behavior for the lithium mixtures is in line with other reported data for these systems such as the tracer diffusion coefficients (5). In order to explain the diffusion data it was postulated, among other things, that the interionic bonds of the melt were

Table III. Densities of sodium-potassium carbonate binary mixtures

$\rho = a - b\,T$ g/cc*

Media, m/o Na_2CO_3	a	$b \times 10^3$	t°C range
100	2.4532 ± 0.0064	0.4267 ± 0.0054	868-973
90	2.4862 ± 0.0013	0.4581 ± 0.0011	844-973
80	2.4723 ± 0.0018	0.4520 ± 0.0016	796-963
75	2.4614 ± 0.0026	0.4465 ± 0.0022	811-980
70	2.4509 ± 0.0019	0.4419 ± 0.0016	792-976
60	2.4506 ± 0.0015	0.4467 ± 0.0007	767-959
58	2.4413 ± 0.0006	0.4406 ± 0.0005	773-966
50	2.4359 ± 0.0015	0.4393 ± 0.0014	730-952
40	2.4278 ± 0.0019	0.4366 ± 0.0017	739-956
30	2.4240 ± 0.0019	0.4375 ± 0.0016	802-977
25	2.4243 ± 0.0013	0.4405 ± 0.0012	810-951
20	2.4130 ± 0.0019	0.4329 ± 0.0016	851-980
10	2.4179 ± 0.0037	0.4419 ± 0.0030	893-987
K_2CO_3	2.4295 ± 0.0085	0.4543 ± 0.0694	907-981

loosened in the vicinity of the 50% mole compositions as some type of short ranged structure of a covalent nature was formed in the melt. The present density data, in line with density studies of other systems (18, 19), lend further weight to this explanation. In this case the effect is attributable to the widely differing sizes of the constituent cations as there is an increasing deviation from ideality when the cation size difference is increased. The asymmetry is provided either by reason of the large difference in cation polarizing power or from purely geometrical considerations. Phase diagrams for the binary and ternary carbonate systems reveal that compounds are formed from the lithium melts. There is no doubt that the congruently melting compound $LiKCO_3$ is formed in the lithium-potassium system (2) but there is controversy over the formation of a $LiNaCO_3$ compound because, it is argued that the lithium-sodium system shows simple eutectic behavior (2). The present work supports the suggestion of a $LiNaCO_3$ compound being formed in line with evidence from thermal and x-ray analysis data (20, 21). Formation of such compounds would result in a reduction in electrical conduction in the composition region. This is in line with the reported electrical conductance studies of these systems (4, 5).

Partial molar volumes.—The partial molar volumes for the nonideal lithium carbonate binaries were cal-

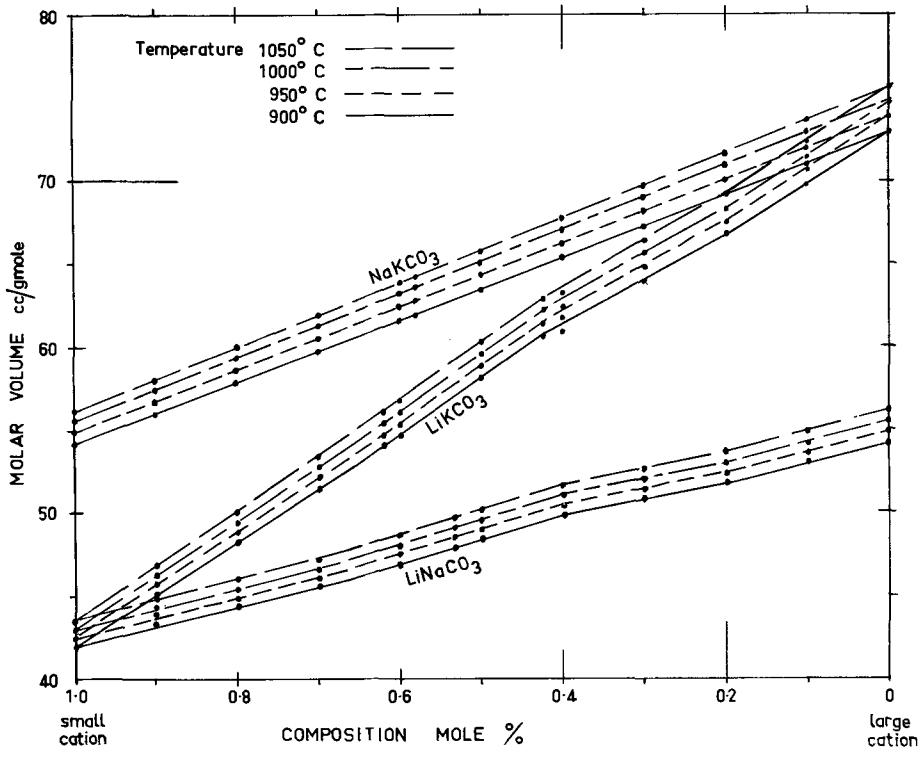

Fig. 5. Molar volumes of the alkali metal carbonate binary mixtures.

Table IV. Partial molar volumes ($\overline{V}$) of the lithium carbonate binary mixtures, cc/gmole

	Mole fraction Li_2CO_3					
	1.0-0.67	0.67-0.5	0.4	0.3	0.25	0.25-0.0
	900°C					
Li_2CO_3	41.9	41.9	42.9	43.3	43.7	41.9
Na_2CO_3	54.3	55.7	54.5	54.5	54.3	54.3
Li_2CO_3	41.9	42.3	43.8	43.8	43.8	41.9
K_2CO_3	73.6	74.3	72.9	72.9	72.9	72.9
	950°C					
Li_2CO_3	42.4	42.4	43.5	43.7	44.0	42.4
Na_2CO_3	54.9	56.3	55.0	55.0	54.9	54.9
Li_2CO_3	42.2	42.8	44.6	44.6	44.6	42.4
K_2CO_3	74.5	75.4	73.8	73.8	73.8	73.8
	1000°C					
Li_2CO_3	42.9	42.9	44.0	44.2	44.5	42.9
Na_2CO_3	55.5	57.0	55.6	55.6	55.5	55.5
Li_2CO_3	42.9	43.7	45.3	45.3	45.3	42.9
K_2CO_3	75.4	76.4	74.7	74.7	74.7	74.7
	1050°C					
Li_2CO_3	43.4	43.4	44.6	45.0	45.2	43.4
Na_2CO_3	56.1	57.8	56.3	56.2	56.1	56.1
Li_2CO_3	43.4	43.8	46.0	46.0	46.0	43.4
K_2CO_3	76.5	77.4	75.6	75.6	75.6	75.6

culated, at convenient temperatures and compositions, by the method of intercepts from the data of Fig. 5. As the nonideality was confined to the 50 m/o (mole per cent) region, the actual intercept determination was applied there only and the values were then extrapolated assuming ideal behavior. The tangents to the curves were constructed using the general method of Hoelscher and Springer (23) and checked by the "squint test" (24). It should be realized that the error of the molar volumes was magnified in the calculation of the partial molar values because of the long extrapolations involved. Values for the partial molor volumes are detailed in Table IV. It can be seen from these data that the solution behaves normally up to the 25 m/o and beyond the 66.7 m/o lithium carbonate compositions. In the intervening region there is initially an increase in partial molar volume of the minor component. The partial molar volume exhibits the usual behavior with respect to temperature.

It is instructive to discuss all changes in molar volume of the melts relative to a chosen reference state (25). For convenience the reference state is taken as the melting point of the higher molecular weight component of the mixture. The implication behind the assumption is that there is a basic microscopic reference lattice structure of the liquid which predominates over the entire region of temperature and composition involved. The molar volume (V) can then be considered to be a function of only two variables, the temperature (T) and the mole fraction of the lower molecular weight component in the mixture (n_2)

$$V = f(T, n_2) \qquad [1]$$

$$dV = (\partial V/\partial T)_{n_2}\, dT + (\partial V/\partial n_2)_T dn_2 \qquad [2]$$

where $(\partial V/\partial T)_{n_2}$ is the rate of change of molar volume with temperature at a fixed composition, *i.e.*, the thermal expansivity. From the density data when n_2 is constant

$$\rho = f(T)$$

i.e.,

$$V = M/f(T) \qquad [3]$$

In the present case

$$(\partial V/\partial T)_{n_2} = bM/(a - bT)^2 \qquad [3a]$$

The second term in Eq. [2], $(\partial V/\partial n_2)_T$, is the isothermal rate of change of molar volume with composition. From molar volume data

$$V = f(n_2) \qquad [4]$$

In the present case

$$(\partial V/\partial n_2)_T = \overline{V}_1 - \overline{V}_2 \quad \text{at} \quad 1 \geq n_2 \geq 0 \qquad [4a]$$

that is, the isothermal rate of change of molar volume with composition is equal to the difference between the partial molar volumes ($\overline{V}$) of the two components in the melt, when the mixture behaves ideally. In the case of the lithium binaries the nonideal section n_2 = 0.25-0.67 can be accommodated by including two new linear functions. Finally, from [2], the change in molar volume above the melting point of the higher molecular weight component can be found

$$\Delta V = \int_{To}^{T} (\partial V/\partial T)_{n_2}\, dT + \int_{n_2=0}^{n_2=n_2} (\partial V/\partial n_2)_T\, dn_2 \qquad [5]$$

and more simply, for convenience

$$\Delta V = \int_{To}^{T} \Delta V_T\, dT + \int_{n_2=0}^{n_2=n_2} \Delta V_{n_2}\, dn_2 \qquad [5a]$$

where ΔV_T and ΔV_{n_2} are the rate change of molar volume with temperature and composition, respectively, used in Fig. 6.

Using this analysis on the data it is possible to separate the respective effect of these two integral terms of [5a] on the molar volume change beyond the standard state. Resulting data are shown in Fig. 6 from which it can be seen clearly that both the change due to temperature and composition are not entirely independent of the other variable; the effect of temperature exhibiting a decrease in volume change with increasing composition of the higher molecular weight component particularly in the vicinity of the pure components, and the effect of composition showing a slight increase in volume change with temperature. The magnitude of these deviations is small, being between 0.5 to 2.0%. In Fig. 6 the effect is shown only for the sodium-potassium carbonate mixtures in order to avoid confusion but the other binaries show a similar effect. It would be expected that the thermal expansivity would alter with composition because it is a property which depends on the nature of the components in the mixtures. However, what is more notable is that the expansion is not regular over the composition range even with ideal melts such as the sodium-potassium carbonate binary. Such variations are in line with studies on binary solids and are presumably connected with interactions in the melt. The same is true of the thermal effects exhibited by the change of molar volume with composition.

It is possible to explain the sudden nonideal volume increase shown in Fig. 5 by reference to the microscopic structural arrangement of the melts along lines suggested by Ward and Janz (4). If the anions are considered as rigid units built up of three interpenetrating oxygen atoms (Fig. 7), then a cation can occupy various contact positions around such a unit (26). These positions, designated as A, B, and C, correspond to symmetrical positions of the cation in contact with, respectively, 2 and 1 oxygen atoms of the anion. The cation can assume intermediate positions depending on the packing of the molecule. The most flexible of these sites is obviously the B and C positions where the cation can move over a relatively large portion of the exposed oxygen atom surface with which it has contact. This type of siting is designated as D cation position. A change in volume of an alkali metal carbonate

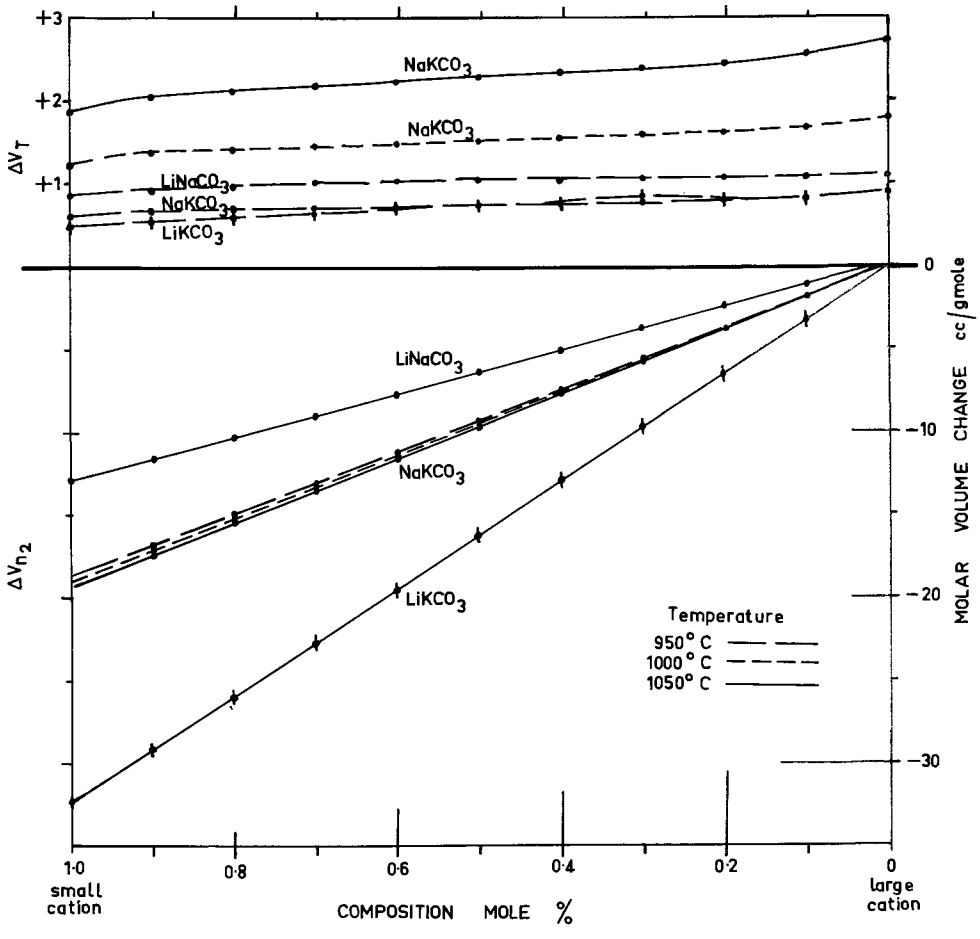

Fig. 6. Molar volume change of the alkali metal carbonate binary mixtures. The temperature effect is shown only for the $NaKCO_3$ mixture.

molecule is possible if a cation is moved from one site to another. With the alkali metal carbonates the anions pack together forming a distorted tetrahedron of four oxygen atoms around an alkali metal ion (27). The cation atoms would then be in a C-3D siting between the anions while every fourth cation in a crystal unit forms an A — A bond. A close examination of the increase in partial molar volume of the lithium binaries reveals that movement of the cations between various sites can provide a feasible explanation for the observed increase in volume of the minor component. For example, with the lithium-sodium carbonates mixtures, the partial molar volume of sodium carbonate increases suddenly by 2.6% at the 66.7 m/o lithium composition and remains constant until about the 50 m/o composition. This corresponds to a shift from A — A bonding of two anions by a sodium atom to an A — D type bonding. Similarly, the lithium carbonate shows a partial molar volume increase of 3.8% at the 25 m/o lithium composition. Again this corresponds to a shift of anion bonding by the lithium cation from A — A to A — D type. In the case of the lithium-potassium binary, corresponding increases in the partial molar volume of the potassium and lithium carbonate of 2.2% and 5.1%, respectively, again aline with A — A to A — D type shift of cation siting. Such a change of bonding of the minor additive in the lithium carbonate binaries implies a drop of coordination number in the particular composition region involved. Determination of such data would provide a positive test of the proposed site change mechanism.

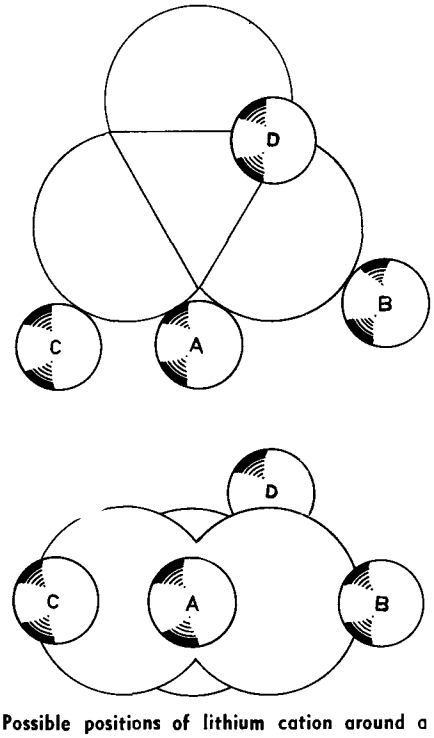

Fig. 7. Possible positions of lithium cation around a carbonate anion.

The flexibility of the D-type bond will depend to a great extent on the size of the cations in both A and D sites. As the size of the cation is increased for the D site and decreased for the A site the flexibility of movement of the cation in the D site will be reduced, *i.e.*, the siting tends toward the B or C positions. Comparison of the lithium-sodium and lithium-potassium binaries shows that the D site tends more toward B or C positions when the size of the diluting cation is increased. This is in agreement with the general predictions regarding cation siting already presented. Another detail of the results which supports the cation siting premise is the almost linear increase in partial

molar volume which is observed for the nonideal region.

Nonideal behavior of these lithium binaries occurs between the small/large cation ratios of 2/1 to 1/3, that is, at definite molar ratios. In the first place the basic reason for the proposed shift in cation siting could well be due to the relatively small sized lithium ion being able to fit between two anions held together by a larger cation in an A — A type bond. This would permit the lithium ion with its greater charge density to influence the larger A — A sited cation. When the small/large cation ratio is above 2/1, the larger cation is, on the average, influenced evenly by lithium ions. As the ratio falls below this point, there is an inbalance of influence because, on an average, large cations are now not influenced by lithium ions alone and an inbalance in repulsive influence forces the larger cation from the A — A site bond. This inbalance continues as the small/large cation ratio falls until it passes below 1/3 ratio. In such circumstances the greater charge density of the lithium ions conceivable would enable them to take the A — A siting thus bringing back ideal behavior to the melt.

Acknowledgment

Grateful acknowledgment is made to the Reserve Bank of Australia for a grant for fuel cell research, part of which has been used to finance the above study. Thanks are due to Dr. R. Mills of the Australian National University for helpful discussions.

Manuscript submitted April 10, 1969; revised manuscript received Oct. 16, 1969.

Any discussion of this paper will appear in a Discussion Section to be published in the December 1970 JOURNAL.

REFERENCES

1. G. J. Janz and M. R. Lorenz, *This Journal*, **108**, 1052 (1961).
2. G. J. Janz and M. R. Lorenz, *J. Chem. Eng. Data*, **6**, 321 (1961).
3. G. J. Janz and F. Saegusa, *This Journal*, **110**, 452 (1963).
4. A. T. Ward and G. J. Janz, *Electrochim. Acta*, **10**, 849 (1965).
5. P. L. Spedding and R. Mills, *This Journal*, **112**, 594 (1965); **113**, 599 (1966); *J. Phys. Chem.*, **70**, 4077 (1966).
6. J. O'M. Bockris, J. L. White, and J. D. MacKenzie, "Physico-Chemical Measurements at High Temperatures," p. 198, Butterworth, London (1959).
7. J. S. Peake and M. R. Bothwell, *J. Am. Chem. Soc.*, **76**, 2653 (1954).
8. J. O'M. Bockris, J. W. Thomlinson *et al.*, *Trans. Faraday Soc.*, **52**, 299 (1956); **54**, 1822 (1958).
9. M. Bloom *et al.*, *Aust. J. Chem.*, **19**, 1591 (1966).
10. P. L. Spedding, *J. Less Common Metals*, **7**, 395 (1964).
11. N. K. Broadman, A. R. Palmer, and E. Heyman, *Trans. Faraday Soc.*, **51**, 277 (1955).
12. H. Margenau and G. H. Murphy, "The Mathematics of Physics and Chemistry," 2nd ed., p. 519, D. Van Nostrand & Co., New York (1957).
13. E. Brunner, *Z. anorg. Chem.*, **38**, 350 (1904).
14. K. Arndt, *Z. Elektrochem.*, **13**, 509 (1907).
15. E. Ryschkewitsh, *Z. Elektrochem.*, **39**, 531 (1933).
16. V. D. Polyakov and S. I. Berul, *Izv. Ionkh. Akad. Nauk. SSSR Sekt. Fiz. Khim. An.*, **22**, 170 (1953).
17. G. V. Vorobev *et al.*, *Izv. Anal. Inst. Obs. Neorg. Khim. Akad. Nauk. SSSR Sekt. Fiz. Khim.*, **26**, 164 (1955).
18. N. K. Broadman, F. H. Dorman, and E. Heyman *J. Phys. Chem.*, **53**, 375 (1949).
19. H. Bloom *et al.*, *Trans. Faraday Soc.*, **49**, 1458 (1953).
20. W. Eitel and W. Skaliks, *Z. anorg. Chem.*, **183**, 263 (1929).
21. S. Tamaru and M. Kamada, *Z. Elektrochem.*, **41**, 93 (1953).
22. L. F. Volkova, *Izv. Sib. Otdel Akad. Nauk SSSR*, **7**, 33 (1958).
23. R. P. Hoelscher and C. M. Springer, "Engineering Drawing and Geometry," 2nd ed., pp. 4-17, John Wiley & Sons, Inc., New York (1961).
24. A. G. Worthing and J. Geffner, "Treatment of Experimental Data," p. 88, John Wiley & Sons, Inc., New York (1943).
25. D. Papousek and J. Kucirek, *Russ. J. Phys. Chem.*, **34**, 76 (1960).
26. J. Zarzycki, *Discussions Faraday Soc.*, **32**, 38 (1961).
27. J. Zemann, *Acta. Cryst.*, **10**, 664 (1957).

Electrode Potentials of Several Redox Couples in Molten Fluorides

H. W. Jenkins,[1] G. Mamantov,* and D. L. Manning

Department of Chemistry, University of Tennessee, Knoxville, Tennessee, and Analytical Chemistry Division, Oak Ridge National Laboratory, Oak Ridge, Tennessee

ABSTRACT

The standard electrode potentials ($E°$) of the following redox couples were determined in molten LiF-BeF_2-ZrF_4 (65.6-29.4-5.0 m/o (mole per cent) and LiF-NaF-KF (46.5-11.5-42.0 m/o) at 500°C from emf measurements on galvanic cells using Ni(II)/Ni reference electrode, contained in a boron nitride compartment. The $E°$ of the Ni(II)/Ni couple was set at 0.000V. In LiF-BeF_2-ZrF_4: Be(II)/Be −2.120V, Zr(IV)/Zr −1.792V (not $E°$), Cr(II)/Cr −0.701V, Cr(III)/Cr(II) −0.514V, Fe(II)/Fe −0.410V, and Fe(III)/Fe(II) 0.166V. In LiF-NaF-KF: Fe(II)/Fe −0.390V and Fe(III)/Fe(II) −0.200V. The more anodic value of $E°$ of the Fe(III)/Fe(II) couple (as compared to the Fe(II)/Fe couple) in LiF-BeF_2-ZrF_4 in comparison to LiF-NaF-KF reflects the higher acidity (modified Lux-Flood concept) of the LiF-BeF_2-ZrF_4 melt.

Electrode potentials give a direct measure of thermodynamic stability of electroactive species relative to one another in a given solvent and provide information useful in electroanalytical chemistry. Interest in electrode potentials in molten fluorides at the Oak Ridge National Laboratory stems from their importance in nuclear reactor technology. A number of electrode potentials have been determined in molten chloride solvents from emf measurements on electrochemical cells (1-3). Few electrode potentials

* Electrochemical Society Active Member.
[1] Oak Ridge Associated Universities Fellow, University of Tennessee.

have been measured in molten fluorides. Grjotheim (4) has measured the potentials of several metal ion/metal electrodes in NaF-KF (40-60 m/o) at 850°C. Baes (5) has calculated electrode potentials in LiF-BeF_2 (66-34 m/o) from ionic equilibria data. Hitch and Baes (6) have measured the potential of a Be(II)/Be electrode *vs.* a HF/H_2 electrode in LiF-BeF_2 (66-34 m/o); the reversibility of the HF/H_2 electrode was studied previously by Dirian, Romberger, and Baes (7). Mellors and Senderoff (8) have estimated several electrode potentials from chronopotentiometric measurements in LiF-NaF-KF (46.5-11.5-42.0 m/o).

Results of other measurements have been summarized elsewhere (9-11).

Experimental

Materials.—Two fluoride salt mixtures were used as solvents in this investigation:

1. LiF-NaF-KF (46.5-11.5-42.0 m/o, liquidus temperature 454°C).
2. LiF-BeF_2-ZrF_4 (65.6-29.4-5.0 m/o, liquidus temperature 434°C).

These two salt mixtures and the following anhydrous fluoride salts were obtained from the Reactor Chemistry Division of the Oak Ridge National Laboratory (12): NiF_2, FeF_2, FeF_3, CrF_2, CrF_3, and LiF-BeF_2 (66-34 m/o). None of these salts received any further pretreatment; however, all were stored in an inert atmosphere until their use. Boron nitride used in the construction of the reference electrode was grade A or HP (Carborundum Company). The boron nitride was kept in a desiccator except for the time required for machining.

Equipment.—The melt (~400g) is contained in a graphite cell which is enclosed in the drybox-furnace system. This system and the Ni(II)/Ni reference electrode contained in a boron nitride compartment that were employed in this investigation have been described previously (13). All emf measurements were made with a Moseley X-Y recorder Model 2D-2A (input impedance 1 megohm). In some cases, in order to expand the recorder scales, the emf was first amplified using a Keithley 600A electrometer.

High-purity nickel and iron wires, coiled several times on the end to increase the surface area, were employed as indicator electrodes for the Ni(II)/Ni and Fe(II)/Fe couples, respectively. Beryllium, zirconium, and chromium indicator electrodes were constructed by attaching a threaded 1 to 1.5 in. long piece of the desired metal to a long, ⅛ in. diameter nickel rod. The beryllium and zirconium electrodes were cleaned with emory paper and rinsed in acetone. The other electrodes were rinsed with acetone and distilled water and then dried.

Procedure.—Voltammetric current-potential curves recorded in each melt were used to identify impurities and approximate their concentrations. Removal of common metal ion impurities, Ni(II), Fe(II), and Cr(II), in the LiF-BeF_2-ZrF_4 melt was accomplished by reduction with zirconium metal. Removal of these impurities in the LiF-NaF-KF melt was accomplished by pre-electrolysis employing either a graphite or platinum cathode.

The emf measurements were made as a function of concentration (except for Be(II)/Be and Zr(IV)/Zr couples); the concentration of the solute species was varied by addition of the anhydrous salt. It was established from the stability of emf measurements and from variations of the voltammetric peak current that homogeneity of solutions was attained by waiting about 1 hr between additions and measurements; the melt was stirred periodically (either manually or mechanically) during that time. EMF measurements were recorded over a 15-30 min period to insure stability of the values.

Solute concentration was determined either by spectrophotometric analysis of a sample taken at the time of the corresponding emf measurement or from a voltammetric current-potential curve recorded at the time of the corresponding emf measurement.

Since a significant junction potential across the boron nitride membrane has been observed (13) (this potential, although stable, was of the order of 100 mV in some experiments), it was necessary to relate the potential of each reference electrode to a common point; in this study, the standard potential of the Ni(II)/Ni couple. This was accomplished by measuring the potential of the reference electrode with respect to a Ni(II)/Ni electrode in the bulk of the melt and extrapolating the measured value by means of the Nernst equation to a value with respect to a unit mole fraction solution of Ni(II).

Results and Discussion

Three concentration scales are commonly employed in molten salts: molality (m), molarity (M), and mole fraction (X). Concentrations are expressed in mole fraction for this study; however, for dilute solutions molality and molarity can be readily related to mole fraction. At 500°C the relationships for LiF-BeF_2-ZrF_4 are given by (14)

$$m = 25.5\,X$$

$$M = 62.2\,X$$

For LiF-NaF-KF the relationships are given by

$$m = 24.2\,X$$

$$M = 52.6\,X$$

The potential of the hypothetical unit mole fraction Ni(II)/Ni electrode was set arbitrarily at 0.000V in these measurements.

Since beryllium metal readily reduces Zr(IV), it was not possible to measure the potential of the Be(II)/Be couple in LiF-BeF_2-ZrF_4. However, the potential of this couple was measured in LiF-BeF_2 (66-34 m/o) by isolating the couple in a boron nitride compartment and measuring the cell emf *vs.* a Ni(II)/Ni electrode in the bulk of a LiF-BeF_2-ZrF_4 melt as the function of the Ni(II) concentration. In these measurements, the emf may have included a junction potential between the two melts plus the previously observed potential drop across the boron nitride wall. Since there was no way to ascertain the magnitude of the junction potential, it was included in the standard electrode potential of the Be(II)/Be couple. The standard state of the Be(II) was taken as the solvent composition, LiF-BeF_2 (66-34 m/o).

The potential of the Zr(IV)/Zr couple was determined by measuring the potential of a zirconium rod immersed in the LiF-BeF_2-ZrF_4 melt. The potential of this rod was stable to ±0.01V over a five day period. The standard electrode potentials of the Fe(II)/Fe, Fe(III)/Fe(II), and Ni(II)/Ni couples were determined in both solvents while the standard electrode potentials of the Cr(II)/Cr and Cr(III)/Cr(II) couples were determined only in the LiF-BeF_2-ZrF_4 melt.

Standard electrode potentials for the various couples were determined from plots of emf *vs.* the logarithm of concentration of the solute species (approximately 5×10^{-5} to 10^{-3} mole fraction) in the bulk of the melt. For each electrode couple, a line having the slope predicted by the Nernst equation was drawn through the data points. These lines were extrapolated to either a unit mole fraction or a Ox/Red ratio of unity to determine the standard electrode potential. Nernstian reversibility was confirmed from a fit of the data points to such lines which was good in all cases except the Cr(II)/Cr couple. For the Cr(II)/Cr couple, the data tended toward a lower slope than predicted by the Nernst equation.

Table I. Standard electrode potentials in molten fluorides*

Electrode couple	Measured,[a] V		Calculated,[b] V
	LiF-BeF_2-ZrF_4	LiF-NaF-KF	LiF-BeF_2
Be(II)/Be	−2.120		−2.211[c]
Zr(IV)/Zr	−1.792[d]		−1.772
U(IV)/U(III)[e]	−1.480		−1.517
Cr(II)/Cr	−0.701		−0.789
Cr(III)/Cr	−0.639		
Cr(III)/Cr(II)	−0.514		
Fe(II)/Fe	−0.410	−0.390	−0.413
Fe(III)/Fe	−0.218	−0.327	
Ni(II)/Ni	0.000	0.000	0.000
Fe(III)/Fe(II)	+0.166	−0.200	

* Temperature 500°C.
[a] Standard state for all solutes except beryllium(II) and zirconium(IV) (see footnote [d]) is the hypothetical unit mole fraction solution. The beryllium(II) standard state is the solvent composition, LiF-BeF_2 (66-34 m/o). The estimated accuracy is ±0.01V.
[b] Values calculated by Baes (5) converted to 500°C.
[c] Experimentally determined value (6).
[d] This potential was not extrapolated to the hypothetical unit mole fraction solution since the activity coefficient of ZrF_4 changes by more than tenfold from 5 m/o to infinite dilution (5).
[e] See ref (15).

The standard electrode potentials determined in this study at 500°C are listed in Table I. Values determined for the Fe(III)/Fe and Cr(III)/Cr couples were calculated from the standard electrode potentials of the Fe(III)/Fe(II), Fe(II)/Fe, Cr(III)/Cr(II), and Cr(II)/Cr couples using a standard approach (16). For the sake of comparison, the standard electrode potentials calculated by Baes(5) in LiF-BeF_2 (66-34 m/o) at 500°C are included in Table I where available. The trend in the values determined in LiF-BeF_2-ZrF_4 agrees well with that calculated in LiF-BeF_2; however, in all instances, the values determined in this study are lower than those calculated by Baes. The 91 mV difference between the two values for the Be(II)/Be couple could be due partially or totally to the inclusion of a junction potential in the value determined in this study. The other differences observed between the two sets of values range from 3 mV for the Fe(II)/Fe couple to 88 mV for the Cr(II)/Cr couple.

These differences may be due to the greater stability of the higher oxidation state relative to the lower oxidation state in LiF-BeF_2 than in LiF-BeF_2-ZrF_4. Such an effect may be caused by the formation of a very stable ZrF_x^{4-x} complex which would make LiF-BeF_2-ZrF_4 a more acidic (using the modified Lux-Flood concept) solvent than LiF-BeF_2 by the reduction of the activity of the basic species, free F^-. The same effect, in a more pronounced example, is observed when comparing the relative stability of Fe(III) to Fe(II) in LiF-NaF-KF and LiF-BeF_2-ZrF_4. In LiF-NaF-KF where all of the F^- is present as free F^-, the standard potential of the Fe(III)/Fe(II) couple is 0.190V anodic to the Fe(II)/Fe standard potential. However, in LiF-BeF_2-ZrF_4 where the free F^- activity is reduced by the formation of BeF_4^{-2} and ZrF_x^{4-x} complexes, the standard potential of the Fe(III)/Fe(II) couple is 0.576V anodic to the Fe(II)/Fe couple. Thus, Fe(III) is 0.386V or 8.8 kcal more stable relative to Fe(II) in LiF-NaF-KF than in LiF-BeF_2-ZrF_4.

Acknowledgment

This research was sponsored by the United States Atomic Energy Commission under contract with the Union Carbide Corporation and Contract AT-(40-1)-3518.

Manuscript submitted June 9, 1969; revised manuscript received Sept. 20, 1969.

Any discussion of this paper will appear in a Discussion Section to be published in the December 1970 JOURNAL.

REFERENCES

1. S. N. Flengas and T. R. Ingraham, *Can. J. Chem.*, **35**, 1139, 1254 (1957); **36**, 780, 1103, 1662 (1958).
2. H. A. Laitinen and C. H. Liu, *J. Am. Chem. Soc.*, **80**, 1015 (1958).
3. H. C. Gaur and W. K. Behl in "Proceedings of the First Australian Conference on Electrochemistry," p. 543, J. A. Friend and F. Gutmann, Editors, Pergamon, Oxford (1965).
4. K. Grjotheim, *Z. Physik. Chem., N. F.*, **11**, 150 (1957).
5. C. F. Baes, Jr. in SM-66/60, "Thermodynamics," Vol. I, IAEA, Vienna (1966).
6. B. F. Hitch and C. F. Baes, Jr., *Inorg. Chem.*, **8**, 201 (1969).
7. G. Dirian, K. A. Romberger, and C. F. Baes, Jr., U.S.A.E.C. Report ORNL-3789, 76 (1965).
8. G. W. Mellors and S. Senderoff in "Applications of Fundamental Thermodynamics to Metallurgical Processes," pp. 81-103, G. R. Fitterer, Editor, Gordon and Breach, New York (1967).
9. A. F. Alabyshev, M. F. Lantratov, and A. G. Morachevskii, "Reference Electrodes for Fused Salts," Sigma Press, Washington, D. C. (1965).
10. G. J. Janz, "Molten Salts Handbook," Academic Press, New York (1967).
11. G. Mamantov in "Molten Salts: Characterization and Analysis," G. Mamantov, Editor, M. Dekker, New York (1969).
12. W. R. Grimes, D. R. Cuneo, F. F. Blankenship, G. W. Keilhotz, H. F. Poppendiek, and M. T. Robinson in "Fluid Fuel Reactors," p. 584, J. A. Lane, H. G. MacPherson, and F. Moslan, Editors, Addison-Wesley, Reading, Mass. (1958).
13. H. W. Jenkins, G. Mamantov, and D. L. Manning, *J. Electroanal. Chem.*, **19**, 385 (1968).
14. H. W. Jenkins, Ph.D. Dissertation, University of Tennessee, 1969.
15. H. W. Jenkins, G. Mamantov, D. L. Manning, and J. P. Young, *This Journal*, **116**, 1712 (1969).
16. B. E. Douglas and D. H. McDaniel, "Concepts and Models of Inorganic Chemistry," p. 143, Blaisdell, New York (1965).

Proton Effects in the Electrochemistry of the Quinone Hydroquinone System in Aprotic Solvents

B. R. Eggins and J. Q. Chambers†

Department of Chemistry, University of Colorado, Boulder, Colorado

ABSTRACT

Electrochemical and spectroscopic techniques have been used to study the benzo-, duro-, tetrachloro-, and *p*-xyloquinone-hydroquinone couples in nonaqueous solvents. The proton transfer reactions which are coupled to the electron transfer steps are elucidated. Oxidation of the hydroquinone leads to the protonated quinone species, while reduction of the quinones in the presence of a proton source gives mixtures of the corresponding hydroquinone, its conjugate base, and the free semiquinone, depending on the amount and strength of the proton donor used. Oxidation of the hydroquinones is postulated to proceed *via* a dimer of the one-electron intermediate. Preliminary results are reported on the electrochemical behavior of solutions containing the quinhydrone charge-transfer complex.

The vast majority of organic electrode processes involve proton transfers coupled with electron transfers. Proton transfers are generally very rapid reactions and cannot be studied using conventional polarographic techniques. We have studied the quinone-hydroquinone (Q-QH_2) system which has been considered the classical organic reversible redox reaction (1, 2)

$$Q + 2H^+ + 2e^- = QH_2 \qquad [1]$$

Such systems are often used to test new electrode materials, new electrochemical techniques, and new solvent systems. They are also involved in biological electron transport (3).

Studies by Vetter (4) on the quinhydrone system at platinum electrodes in aqueous solutions using Tafel plots led to the following suggested mechanism

$$\begin{aligned} pH < 5 \quad Q + H^+ &= QH^+ \\ QH^+ + e^- &= QH \\ QH\cdot + H^+ &= QH_2\cdot^+ \\ QH_2\cdot^+ + e^- &= QH_2 \end{aligned} \qquad [2]$$

which can be expressed as a HeHe mechanism. At $pH > 6$ Vetter suggests that the mechanism is eHeH.

There is some conflict between these mechanisms and the work of Hale and Parsons (5) in which polarographic waves at pH 4 were analyzed by the Koutecky method and potential energies of the various species were estimated to elucidate a pathway following the species of lowest energy. These workers suggest that the mechanism is either HeeH or eHeH, and favor the former.

Several researchers including Peover (6), Wawzonek (7), Elving (8), Kolthoff (9), and Osteryoung (10) have studied proton effects on the reduction of quinones in aprotic solvents, but not in great detail. We have studied proton effects in the nonaqueous electrochemistry of the Q/QH_2 system (11) and have characterized the oxidation of QH_2 in acetonitrile (12) using electrochemical techniques over a wide time scale. The products and an intermediate have been detected by cyclic voltammetry (13).

Experimental Section

Most of the experimental procedures were standard and have been described in part elsewhere (14, 15).

Reagent grade chemicals were used. Duroquinone was obtained from Aldrich Chemical Company; *p*-benzoquinone, *p*-xyloquinone, tetrachloroquinone, and *p*-benzohydroquinone were obtained from Eastman Chemical Company. The *p*-benzoquinone was resublimed before use. The hydroquinones were prepared from the corresponding quinones following the method given by Vogel (16). Practical grade pyrrolidine and Analytical Grade pyridine obtained from Matheson, Coleman, and Bell were used without further purification. For most of the studies, acetonitrile of high purity was employed as the solvent.

Two platinum electrodes were used in this study. For measurement at long times a commercial Beckman platinum inlay electrode was used, geometric area: 0.212 cm^2. The other electrode had a geometric area of 0.0134 cm^2 and was used for measurements at short times. The experimental area of this electrode was determined using the known diffusion coefficient of potassium ferrocyanide (17) and found to be 0.0135 cm^2 after correcting for edge effects by the method of Soos and Lingane (18). This electrode was usually polished to a mirror finish using 0.3μ lapping compound before recording individual current-potential (i-E) curves. The mechanical pretreatment gave reproducible results in the nonaqueous systems under study.

The potentiostat was based on the design of Brown *et al.* (19) and provided for compensation of the resistance between the tip of the reference electrode and the working electrode input. At all but the fastest sweep rates employed (*ca.* 2 x 10^3 V/sec), close to 100% iR compensation could be achieved. At the fastest sweep rates the peak potential and current function data contain small contributions from iR terms although qualitative features of the i-E curves are still significant. All peak potential data in this paper are given *vs.* an aqueous SCE.

Controlled potential electrolyses were carried out on 10 mM solutions of hydroquinones by conventional techniques. The product was isolated, after neutralization of the solution (where necessary) with sodium carbonate, by removal of the acetonitrile under vacuum and extraction of the residue with ether or cyclohexane. The quinone products were identified by cyclic voltammetry and melting points. Visible and u.v. spectra were obtained using a Cary Model 14 spectrometer. *In situ* electrolyses were performed in the cavity of a Varian Model V4502 spectrometer following standard procedures.

Results and Discussion

Oxidation of hydroquinone.—The oxidation of benzohydroquinone (QH_2) at platinum electrodes in acetonitrile is irreversible, producing quinone (Q) in a two-electron step.

$$QH_2 \rightarrow Q + 2H^+ + 2e^- \qquad [3]$$

$$Q + H^+ \rightleftharpoons QH^+ \qquad [4]$$

Cyclic voltammograms of QH_2 (Fig. 1) at slow sweep

† Address correspondence to this author at Dept. of Chemistry, University of Tennessee, Knoxville, Tenn. 37916.

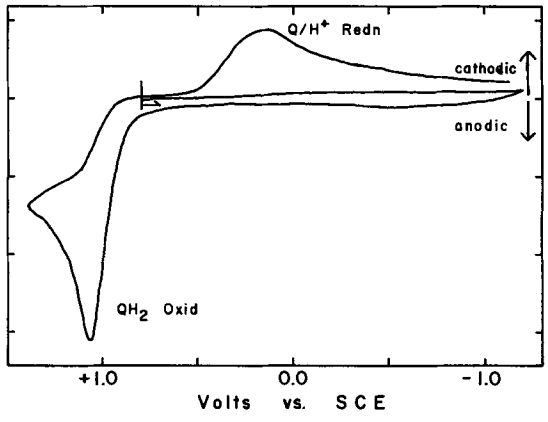

Fig. 1. Cyclic voltammogram of *p*-benzohydroquinone oxidation: 1.82 x 10^{-3}M QH_2, 0.1M TEAP, CH_3CN, 0.12 V/sec, 0.1 mA/division.

rates show one irreversible two-electron oxidation wave (I) followed by one irreversible two-electron reduction wave (II) on the cathodic sweep. The number of electrons involved in each wave was determined by double potential step chronoamperometry (20). The diffusion coefficient of QH_2 is 3.16 ± 0.15 x 10^{-5} cm^2 sec^{-1}. The peak width for wave I at a sweep rate of 0.12 V/sec is 95 mV indicating irreversibility and a transfer coefficient of 0.5. Controlled potential electrolysis of QH_2 and of durohydroquinone gave good yields of the respective quinones.

Wave II involves the reduction of Q/H^+ mixtures to the hydroquinone monoanion, QH^-, which is rapidly protonated in the presence of excess protons.

$$Q + H^+ + e^- \longrightarrow QH\cdot \xrightarrow{e^-} QH^- \xrightarrow{H^+} QH_2 \quad [5]$$

This scheme was established by observation of the effect of proton donors on the cyclic voltammograms of the various quinones. Reduction of a 2:1 mixture of perchloric acid to quinone gives a cyclic voltammogram essentially identical to Fig. 1 in that only the QH_2 oxidation wave is observed on the anodic cycle. With a ratio of 1:1 perchloric acid to quinone, reduction waves can be seen in the cyclic voltammograms corresponding to Eq. [5] and [6]

$$Q + e^- \leftrightharpoons Q\cdot^- \quad [6]$$

followed by oxidation waves on the reverse scan arising from the oxidation of semiquinone ($Q\cdot^-$), QH^-, and QH_2 (see Fig. 2). The peak potential of wave II

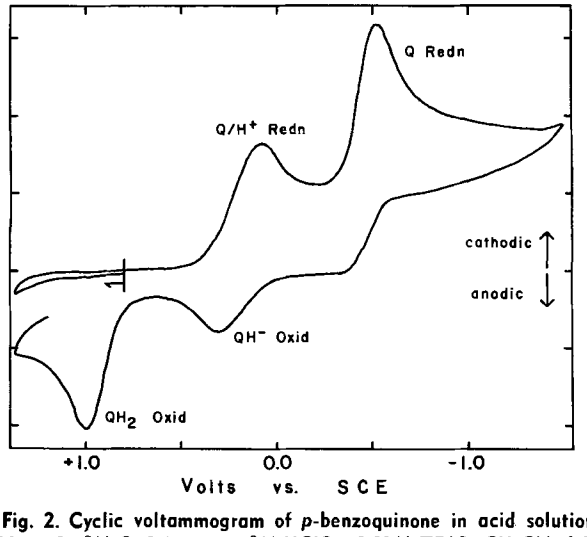

Fig. 2. Cyclic voltammogram of *p*-benzoquinone in acid solution: 1.52 x 10^{-3}M Q, 1.91 x 10^{-3}M $HClO_4$, 0.01M TEAP, CH_3CN, 0.12 V/sec, 0.05 mA/division.

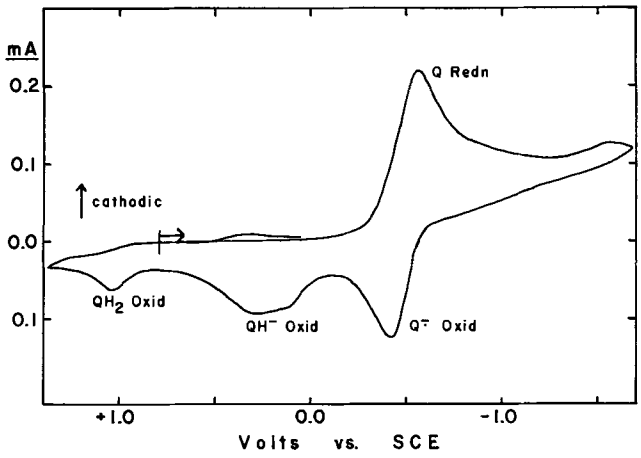

Fig. 3. Cyclic voltammogram of *p*-benzoquinone in the presence of a weak proton donor: 1.87 x 10^{-3}M Q, 2.3 x 10^{-3}M benzoic acid, 0.1M TEAP, CH_3CN, 0.12 V/sec.

(Eq. [5]) varies between 0.0 and 0.2V, depending on the hydrogen ion activity. When *p*-toluenesulfonic or picric acid is used as the proton donor, waves I and II shift to more positive potentials as the acid concentration is increased. The shift is roughly 30 mV in $E_{p/2}$ per tenfold increase in the hydrogen ion activity. A quantitative explanation of this dependence is difficult since the peak widths are also a function of the acidity. The peak width for wave II is *ca.* 0.2V and dependent on sweep rate, suggesting kinetic complications as well as irreversibility.

The diffusion coefficient of the quinone species is 2.9 x 10^{-5} cm^2 sec^{-1}. This was determined by chronoamperometric measurements on wave II in $Q/HClO_4$ mixtures using the Cottrell equation. The apparent *D* value for wave II varies as the quinone ring is substituted by methyl groups. The diffusion coefficient of the solvated proton (H_3O^+?) in acetonitrile/$HClO_4$ mixtures is 2.1 x 10^{-5} cm^2 sec^{-1}.

Evidence for the formation of QH^- in the reduction of Q/H^+ mixtures is as follows. Cyclic voltammograms of quinone in the presence of weak proton donors, *e.g.*, 1:1 benzoic acid to Q, exhibit an oxidation wave at *ca.* +0.3V on the reverse or anodic-going sweep (Fig. 3). This wave is attributed to the oxidation of QH^-. Direct evidence for the oxidation of QH^- was difficult to obtain as addition of excess tetra-*n*-butylammonium hydroxide to QH_2 results in the formation of Q^{2-} and $Q\cdot^-$ (detected by cyclic voltammetry), but not QH^-. With a 1:1 ratio of QH_2:Bu_4NOH a precipitate forms and all electrochemical waves disappear. This precipitate is ascribed to $Bu_4N^+QH^-$ by Badoz-Lambling and Demange-Guerin (21, 22). However, addition of the nonhydroxylic base, pyrrolidine [pK_a in water: 11.27 (23); compared to pK_a's for QH_2 of 9.85 and 11.40 (24)] to QH_2 in acetonitrile results in a decrease in the height of the QH_2 wave and the appearance of an oxidation wave at +0.28V to +0.45V depending on the amount of base added. Assignment of this wave to the oxidation of QH^- is consistent with the acid-base chemistry of QH_2.[1] No Q^{2-} oxidation wave is observed, presumably because pyrrolidine is a weaker base than the dianion. Pyrrolidine itself is oxidized at +1.08V and a product is reduced at −0.88V.

These results can be explained either by a scheme involving "preprotonation" of the quinone to form QH^+ near the electrode surface followed by uptake of an electron or by one-electron reduction of H^+ followed by hydrogen atom transfer to Q. The latter process is feasible since H^+ is reversibly reduced in acetonitrile at a well polished platinum electrode in the region of 0.0V. The pK of QH^+ has been reported

[1] Since this paper was submitted for publication, Parker (42) has reported a similar observation using 2,6-lutidine as the base.

to be −1.0 in aqueous solutions (25). However, there is some dispute over this value since quinone species which are stable in concentrated acid solutions give pK values considerably lower on a Hammett acidity function scale (26, 27). Badoz-Lambling and Demange-Guerin (21) report that benzoquinone is not protonated in N,N-dimethylformamide on the basis of spectrophotometric studies. We find that the absorption spectrum of Q in acetonitrile changes considerably on addition of perchloric acid up to a concentration of 1*M*, showing a new maximum at 353 mμ. These changes are caused by chemical reactions of Q with $HClO_4$, including possible QH^+ formation.

If the basicity of Q is as high as suggested by Biedermann (25), the QH^+ scheme is an attractive explanation for wave II. This scheme is in accord with the kinetic character of the wave and the appearance of the wave at roughly the same potential on both mercury and platinum electrodes. Hale and Parsons (5) have suggested the QH^+ species to explain the reduction of Q in aqueous solutions. Furthermore, the wave seems to be independent of the state of the electrode surface in contrast to the proton wave which varies by several hundred millivolts depending on the platinum electrode pretreatment.

For these reasons, we favor QH^+ as the intermediate in the reduction of $Q/HClO_4$ mixtures. However, in the rest of this paper, this wave (Eq. [5]) will be referred to as the "Q/H^+ wave" which is meant to indicate that the order of proton and electron transfer is open to question.

The process has characteristics similar to catalytic hydrogen waves (28), except that clearly the quinone nucleus is reduced, evidenced by the reduction products detected on the reverse cycle of the cyclic voltammograms. This is similar to the reduction of protonated species in other nonaqueous solvents. For example, Spritzer *et. al.* (29) found that reduction of pyridinium ion in pyridine leads to reduction of the pyridine ring and a coupling product, in contrast to the behavior in aqueous solutions (28).

Chemical complications.—As the sweep rate is increased, wave II disappears completely, and the current function for the QH_2 oxidation wave decreases considerably. This behavior is shown in Fig. 4. However, the corresponding current function for the reduction of Q plus acid (Eq. [5]) remains almost constant with increasing sweep rate on both mercury and platinum electrodes. This result was not expected. We had tentatively ascribed the decrease of the current function of wave II to a slow protonation of Q prior to electron transfer (11).[2] However the observation of a constant current function for the Q/H^+ wave in the $Q/HClO_4$ mixtures implies that protonation of Q, the forward step in Eq. [4], is fast on the time scale of the electrochemical experiment and suggests that the decrease in the current function for wave II shown in Fig. 4 is due to some other kinetic complication.

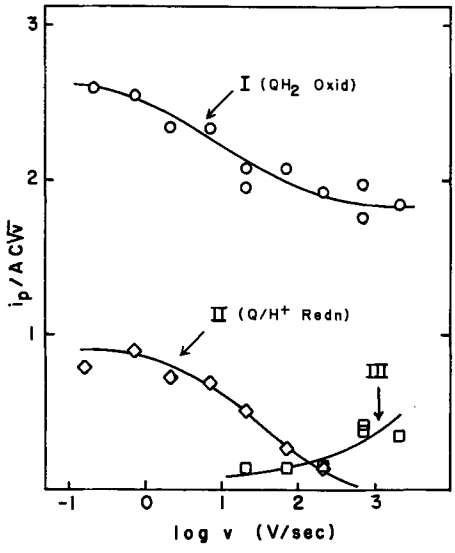

Fig. 4. Variation with sweep rate of current functions for waves I, II, and III of QH_2 cyclic voltammograms. Units: i_p in amperes, A in cm^2, C in moles/liter, and V in volts/sec.

To eliminate the possibility that the difference in the behavior of the current functions for wave II in Fig. 4 and the Q/H^+ wave obtained in a $Q/HClO_4$ mixture was due to the water added with the $HClO_4$, the following experiment was carried out. A 2×10^{-3} *M* QH_2 solution in acetonitrile was exhaustively electrolyzed at a large platinum electrode to produce a "dry" solution, $2 \times 10^{-3}M$ in Q and 4×10^{-3} in $HClO_4$. At slow sweep rates the *i-E* curve obtained on this solution was essentially identical to the reverse cycle of the QH_2 oxidation: one irreversible two-electron Q/H^+ reduction wave was present. However this wave did not disappear at fast sweep rates, but exhibited behavior identical to the $Q/HClO_4$ mixture. In addition several experiments were carried out in which freshly dried molecular sieves were added to the working electrode compartment. Current function data were obtained in agreement with Fig. 4, which indicates that trace amounts of water present in acetonitrile were not producing spurious results.

At a sweep rate of about 10 V/sec a new reduction wave (III) appears on the reverse cycle of the QH_2 oxidation cyclic voltammogram at about −0.3 to −0.4V. This wave becomes more prominent as wave II disappears as is shown in Fig. 4 and the figure in ref. (12). This wave does not correspond to the small Q reduction wave in the cyclic voltammograms of $Q/HClO_4$ mixtures which appears at potentials more negative than −0.5V. Waves II and III were the only reduction processes evident in the cyclic voltammograms at potentials more positive than −2.0V.

The most striking feature of these results is the complete disappearance of the Q/H^+ reduction wave at fast sweep rates. This must mean that the QH· intermediate which is formed in the oxidation of QH_2

$$QH_2 \rightarrow QH\cdot + H^+ + e^- \qquad [7]$$

is not oxidized further by a simple one-electron step at this time scale. Direct evidence for the fate of the protonated semiquinone, QH·, is lacking, but a likely possibility is that it disproportionates to Q and QH_2 *via* a hemiketal intermediate, Eq. [8].

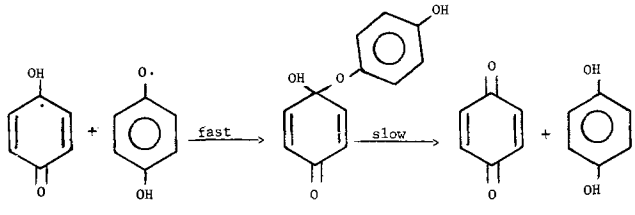

[8]

The hemiketal intermediate, $(QH)_2$, is a dimer of the one-electron intermediate oxidation state, and its formation would account for the decrease of the current function for the main oxidation wave. If the initial concentration of QH_2 is reduced from 2.11 to 0.96 *mM*, the current function for wave I decreases much more rapidly with sweep rate indicating that the chemical step following the initial oxidation process (Eq. [7]) is bimolecular. This is in accord with a dimerization step such as Eq. [8].

Formation of $(QH)_2$ has precedent in the literature. Oxidation of durohydroquinone monomethyl ether by alkaline ferricyanide in benzene mixtures leads to the corresponding dimethoxy derivative which can be isolated as a stable product (30). Also oxidation of substituted phenols leads to products with analogous

[2] This mechanism has been recently suggested by Parker (42).

structures (31,32). The observed half-life of this species, estimated from the decrease of the current function of the Q/H$^+$ wave, is *ca.* 0.1 sec. Under the acidic conditions of the QH_2 electrolysis solutions, the proposed intermediate would be expected to be unstable. Ketals and acetals are known to decompose in an acid catalyzed reaction *via* an intermediate of the type (33):

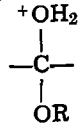

The half-life of $(QH)_2$ shows qualitatively the expected decrease with increasing hydrogen ion concentration.

In addition to QH_2, the electrochemical oxidation of durohydroquinone (DQH_2), p-xylohydroquinone (XQH_2), and tetrachlorohydroquinone was examined in an effort to extend the generality of the conclusions. The behavior of these hydroquinones is analogous to that of QH_2. The current functions for wave I decrease in each case and waves II and III appear on the reverse cycle for DQH_2 and XQH_2. Cyclic voltammograms of DQH_2 and the corresponding current functions for waves I, II, and III are shown in Fig. 5 and 6. Wave III is observed at lower sweep rates for DQH_2

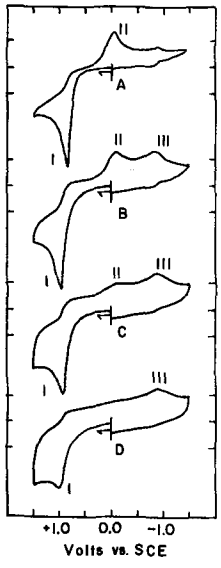

Fig. 5. Cyclic voltammograms of durohydroquinone oxidation: 2.12 x 10^{-3}M DQH_2, 0.1M TEAP, CH_3CN. (A) 1.80 V/sec, 0.02 mA/division; (B) 18.0 V/sec, 0.05 mA/division; (C) 180 V/sec, 0.2 mA/division; (D) 600 V/sec, 0.5 mA/division.

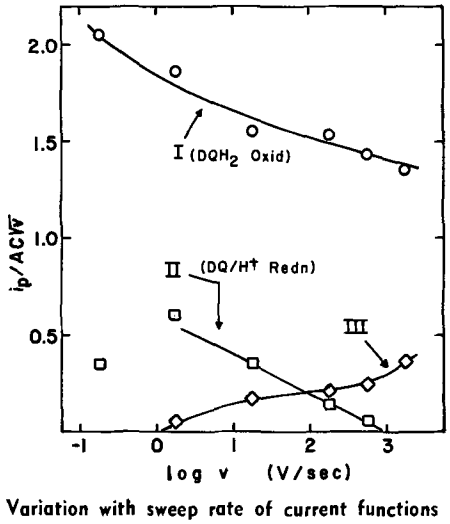

Fig. 6. Variation with sweep rate of current functions for waves I, II, and III of DQH_2 cyclic voltammograms. Units: same as Fig. 3.

and XQH_2 and at potentials fairly close to the reversible one-electron reduction of the corresponding quinone. Wave III occurs at −0.83V for DQH_2 and −0.59V for XQH_2, while the quinones are reduced at −0.83 and −0.54V, respectively, under the same conditions. The intermediates formed from DQH_2 and XQH_2 are more stable than the intermediate formed from QH_2. This conclusion is based on the assumption that wave II disappears when the time scale of the experiment competes with the half-life of the dimer.

The behavior of DQ in the presence of perchloric acid is interesting. First, a considerable excess of acid (6:1) is required to completely eliminate the one-electron DQ reduction wave at −0.83V at a sweep rate of 6 V/sec. With increasing sweep rate the peak potential of the DQ/H$^+$ wave shifts from 0.18V at 0.6V/sec to −0.52V at 600 V/sec and the current function decreases by one half. This suggests that the rate of protonation of DQ is slow.

Nature of wave III.—Identification of the reduction process responsible for wave III is not straightforward. This wave first appears at moderately fast sweep rates and spectroscopic or product identification techniques cannot be applied. However some pertinent observations can be made. First of all, wave III is due to the reduction of some quinone species and not free protons. While protons are reduced in the potential region where wave III appears for QH_2, a proton wave would be expected to occur at roughly the same potential regardless of the hydroquinone oxidized. On the contrary, wave III is dependent on the nature of the hydroquinone in both its peak potential and ease of formation. In an effort to trap the protons released, millimolar concentrations of pyridine were added to the solution. This resulted in the appearance of wave III at slower sweep rates, but the peak potentials still varied considerably with the hydroquinone oxidized. In the absence of pyridine, wave III appears at −0.3V for QH_2 and −0.83V for DQH_2, while $HClO_4$ is reduced in the region of 0.0V. These differences are difficult to rationalize in terms of assignment of wave III to a proton reduction. Furthermore, wave III is observed at a similar potential on a nonaqueous carbon paste electrode (34), in contrast to the proton wave which appears at higher overvoltages on carbon paste than on platinum.

Another possible process for wave III is reduction of the quinone assisted by protons supplied by QH_2 in the diffusion layer. This could proceed by protonation of $Q\cdot^-$ by QH_2

$$Q \overset{e^-}{\rightleftharpoons} Q\cdot^- \xrightarrow{QH_2} QH\cdot \xrightarrow{e^-} QH^- \xrightarrow{H^+} QH_2 \qquad [9]$$

or by the reduction of a Q-QH_2 hydrogen bonded complex to give a preprotonation wave

$$Q\ldots HQH \xrightarrow{e^-} QH\cdot + QH^- \xrightarrow{H^+} 2QH_2. \qquad [10]$$
$$\qquad\qquad\qquad\quad \Big| \xrightarrow{e^-} QH^-$$

Peover (6) has invoked both schemes in the reduction of different carbonyl compounds in the presence of weak proton donors. However, both schemes are somewhat unsatisfactory descriptions of wave III since protons available in the diffusion layer from Eq. [7] would be more effective proton donors than QH_2. In other words, assignment of wave III to either of these processes is not consistent with the mobile equilibrium for the protonation of Q (or the formation of QH·) which is observed experimentally at these time scales. Because this equilibrium is fast, the absence of a Q/H$^+$ wave implies that the concentration of free Q is close to zero in the vicinity of the electrode surface. Quinone solutions containing a large excess of QH_2 do exhibit a wave in the potential region where wave

III is observed. This process is thought to occur according to Eq. [10] and is discussed below.

Reduction of the hemiketal species, $(QH)_2$, formed in Eq. [8] is an interesting possibility for wave III.

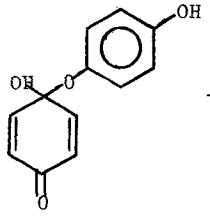

$$+ 2H^+ + 2e^- \rightarrow 2QH_2 \qquad [11]$$

Reduction of duroquinone dimethyl ketal in aqueous solutions occurs at more positive potentials than reduction of duroquinone at the same *p*H (35). Hemiketals would be expected to behave similarly and so the assignment of wave III, which is more positive than the quinone wave, to the hemiketal is reasonable.

The appearance of wave III at slower sweep rates in the presence of pyridine is consistent with an intermediate such as the hemiketal whose stability is dependent on the hydrogen ion activity. Invoking this species to explain wave III is also consistent with the behavior of different hydroquinones and the disappearance of the Q/H^+ wave in each case. Moreover its formation by dimerization of $QH\cdot$ is chemically straightforward, and the position (E_p) of the wave relative to the quinone wave is acceptable.

We have proposed that wave III might be due to reduction of quinhydrone on the grounds that in solutions containing 0.02*M* Q and an excess of QH_2, resulting in appreciable equilibrium concentration of quinhydrone, a wave is observed in the region of wave III (12). This suggestion also represents a "one-electron" intermediate state in the oxidation process and explains the decrease of the current function of wave I and the disappearance of the Q/H^+ wave. However, the bonding of quinhydrone in solution is primarily charge transfer in nature (36) and reduction of charge transfer complexes usually occurs at potentials more negative than the reduction potential of the acceptor molecule (37). On this basis alone, assignment of wave III to reduction of quinhydrone species is questionable. *In situ* spectrophotometric observation of the intermediates might permit a distinction to be made between these possibilities since the hemiketal should have a characteristic absorption in the 210 to 230 mμ region (35, 38).

Mechanism.—On the basis of the above discussion we propose the following mechanism for the oxidation of hydroquinones in acetonitrile at a platinum electrode (wave I)

$$QH_2 \rightleftharpoons QH_2^{+}\cdot + e^- \qquad [12a]$$

$$QH_2^{+}\cdot \longrightarrow QH\cdot + H^+ \qquad [12b]$$

$$2QH\cdot \xrightarrow{\text{fast}} (QH)_2 \qquad [12c]$$

$$(QH)_2 \xrightarrow{\text{slow}} Q + QH_2 \qquad [12d]$$

$$Q + H^+ \rightleftharpoons QH^+ \qquad [12e]$$

This mechanism explains the decrease of the current functions for wave I toward values of unity and the disappearance of the Q/H^+ wave. At short times the oxidation proceeds to the one-electron intermediate state, postulated to be $(QH)_2$.

Electrode surface effects.—Experiments were carried out in high concentrations of perchloric acid using both acetonitrile and nitromethane as a solvent in an unsuccessful attempt to detect the $QH_2^{+}\cdot$ or $DQH_2^{+}\cdot$ species by cyclic voltammetry. Occasionally a prominent cathodic wave was observed at +0.6 to +0.7V which could be ascribed to the reduction of a platinum oxide or a solution impurity.

In some experiments QH_2 and DQH_2 were oxidized on a "platinized platinum" surface, prepared by taking the electrode through an oxidation and reduction cycle for 10 min at 100 c/sec. Qualitatively the cyclic voltammograms are similar to those on "smooth" platinum, except that wave III is observed at slower sweep rates and the current function for wave II does not decrease until faster sweep rates. Similar behavior is observed on oxidized electrodes. Gentle polishing with 0.3μ lapping compound restores the electrode to its original activity.

The increase of wave II on a "platinized platinum" surface is difficult to explain in terms of Eq. [12] or any scheme ascribing wave III to an intermediate chemical species. Some chronocoulometric experiments were performed in an effort to detect adsorbed intermediates in the electrode process, but the data did not permit significant conclusions to be drawn. However, these results can be tentatively interpreted by suggesting that the reactions of $QH\cdot$ and $DQH\cdot$ (Eq. [12c]) are partly heterogeneous in nature. A more meaningful explanation awaits further experimental data and a better description of the oxidized electrode surface.

Other solvents.—Cyclic voltammograms of QH_2 were also obtained in dimethylsulfoxide and nitromethane. They are qualitatively similar to those in acetonitrile except that the peak potentials varied as shown in Table I. A detailed study at different sweep rates was made in nitromethane in which current function behavior similar to that in acetonitrile was observed.

Reduction of "quinhydrone solutions".—In low concentrations of quinhydrone the appearance of the cyclic voltammograms is that of a mixture of QH_2 and Q. The QH_2 acts to protonate $Q\cdot^-$ and to suppress the $Q\cdot^-/Q^{2-}$ couple to some extent. Esr indicates that $Q\cdot^-$ radical anions are present in the electrolysis solutions.

However, if the concentration of quinhydrone is sufficiently high, a wave is observed at *ca.* −0.3V. At slow sweep rates no Q reduction wave is observed between −0.5 and −0.6V. On the anodic cycle a broad wave is evident between +0.13 to +0.37V which can be assigned to oxidation of QH^-. No wave corresponding to $Q\cdot^-$ oxidation is seen. This behavior is shown in Fig. 7.

The solution chemistry is complicated in this case since the QH_2 molecule can function both as a donor molecule in a charge transfer complex and as a proton donor. The formation constant for the charge transfer complex between Q and QH_2 in acetonitrile is 0.083 ± 0.004 1 mole^{-1}. This was measured by following the charge transfer band at *ca.* 440 mμ and is in agreement with literature values for other nonaqueous solvents (39). Thus in concentrated quinhydrone solutions or in the presence of a large excess of QH_2 (0.5*M*) there exist an appreciable equilibrium concentration of the charge transfer complex. Assignment of the prewave at −0.3V to reduction of this quinhydrone species could explain the above observations. However, this is unlikely in view of the properties of quinhydrone in solution. The bonding in this species is primarily charge transfer in nature (36). In complexes of this type the acceptor molecule, Q, formally

Table I. Peak potentials of QH_2 in different solvents

Solvents	E_p[a] of waves for QH_2		
	I	II	III
MeCN	1.12[b]	0.13[b]	−0.34[c]
DMSO	0.98[d]	−0.31[d]	—
$MeNO_2$	0.86[e]	−0.23[e]	−0.61[f]

[a] V *vs.* SCE.
[b] 2 V/sec.
[c] 20 V/sec.
[d] 4 V/sec.
[e] 1.5 V/sec.
[f] 15 V/sec.

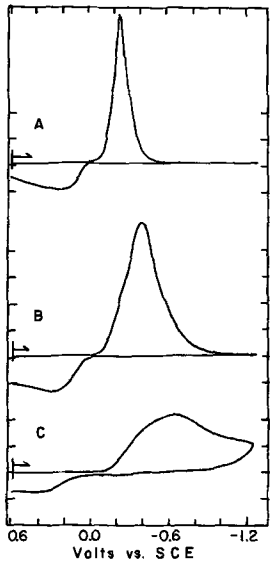

Fig. 7. Cyclic voltammograms of "quinhydrone" solutions: 0.5M QH_2, 0.02M, Q, 0.1M TEAP, CH_3CN. (A) 0.191 V/sec, 0.05 mA/division; (B) 1.12 V/sec, 0.1 mA/division; (C) 11.2 V/sec, 0.5 mA/division.

accepts electronic charge from the donor molecule which will act to decrease the electron affinity of the acceptor and hence its reduction potential. This is the behavior Peover has observed with a series of strong acceptor molecules such as chloranil with hydrocarbon donor molecules (37). Thus the presence of a prewave in the concentrated quinhydrone solutions is more likely to be a result of the proton donor than the charge transfer properties of QH_2. This suggests that a protonation scheme such as Eq. [9] or [10] might be the basis for the prewave at −0.3V.

However there are several features of this reduction process which cannot be explained on the basis of simple schemes such as Eq. [9] and [10]. First, the shift of the prewave from the $Q/Q\cdot^-$ wave is *ca.* 0.25-0.3V which is greater than shifts observed in systems in which Eq. [9] is operative (40). Second, as the sweep rate increases the wave broadens considerably and the peak potential shifts to more negative potentials at *ca.* 0.1V per decade increase in the sweep rate. Even with 10:1 phenol to Q the shift of the prewave is *ca.* 0.18V and a similar shift of 0.1V per decade increase in sweep rate occurs. Little is known about the quantitative aspects of preprotonation behavior such as described by Eq. [10] apart from the brief mention by Peover (6). The properties of this wave are qualitatively similar to those of the previously mentioned duroquinone reduction wave in excess perchloric acid.

In addition the wave at −0.3V does not have the usual shape for a peak voltammogram as can be seen in Fig. 7. At slow sweep rates the *i-E* curve is almost a symmetrical bell curve on both mercury and platinum. Potentiostatic current-time curves also exhibit unusual behavior as the currents fall sharply to zero at long times. The peak current is not proportional to the concentration of Q in solution. A plot of peak current *vs.* concentration exhibits marked positive deviations from linearity at low concentrations. This behavior is to be contrasted with the Q-phenol mixtures which show diffusion controlled waves at all sweep rates. All these phenomena indicate that kinetic as well as adsorption effects are taking place to complicate the electrode process for the reduction of Q− QH_2 mixtures.

Conclusions

The principle mechanistic conclusions of this work are as follows.

1. In the presence of strong proton donors, Q is reduced in a two-electron process, probably *via* the protonated quinone, QH^+. The protonation equilibrium is fast on the time scale of the electrochemical experiment. The duroquinone system behaves in a similar manner, but the protonation of DQ appears to be slower than the protonation of Q.

2. Weak proton donors act to protonate the semiquinone, $Q\cdot^-$, which gives rise to the usual electrochemical protonation scheme first reported by Hoijtink (41). Hydroquinone, QH_2, appears to fall in this category, but the reduction mechanism in the presence of excess QH_2 is complicated and not completely understood.

3. The oxidation of hydroquinones in acetonitrile shows two-electron character at long times but one-electron character at short times when it is postulated to proceed *via* a dimer of $QH\cdot$ which may be a quinone hemiketal.

Acknowledgment

This work was supported by a grant from the Public Health Service 5-RO1-GM14815.

Manuscript submitted May 27, 1969; revised manuscript received Oct. 3, 1969.

Any discussion of this paper will appear in a Discussion Section to be published in the December 1970 JOURNAL.

REFERENCES

1. G. W. Milner, "Principles and Applications of Polarography," p. 515, Longmans, London (1962).
2. W. Mansfield Clark, "Oxidation-reduction Potentials of Organic Systems," Baillière, Tindall, and Cox, London (1960).
3. F. L. Crane in "Biological Oxidations," T. P. Singer, Editor, p. 533, Interscience Publishers, New York (1968).
4. K. J. Vetter, "Electrochemical Kinetics," p. 483, Academic Press, New York (1967).
5. J. H. Hale and R. Parsons, *Trans. Faraday Soc.*, **59**, 1429 (1963).
6. (a) P. H. Given and M. E. Peover, *J. Chem. Soc.*, **1960**, 385; (b) M. E. Peover, *ibid.*, **1962**, 4540.
7. S. Wawzonek, R. Berkey, E. W. Blaha, and M. E. Runner, *This Journal*, **103**, 456 (1956).
8. W. R. Turner and P. J. Elving, *ibid.*, **112**, 1215 (1965).
9. I. M. Kolthoff and T. B. Reddy, *ibid.*, **108**, 980 (1961).
10. R. A. Osteryoung, R. L. McKisson, P. H. Dutch, G. Lauer, and E. B. Luchsinger, "Development of a Light-weight Battery System," Final Report, Contract DA-36-039 SC-88925 (1962), AD290 326; J. N. Butler, *J. Electroanal. Chem.*, **14**, 89 (1967).
11. B. R. Eggins and J. Q. Chambers, Abstracts of the Midwest ACS Meeting, Manhattan, Kansas, Oct. 1968, p. 23.
12. B. R. Eggins and J. Q. Chambers, *Chem. Comm.*, **1969**, 232.
13. Z. Galus, H-Y. Lee, and R. N. Adams, *J. Electroanal. Chem.*, **5**, 17 (1963).
14. S. H. Cadle, P. R. Tice, and J. Q. Chambers, *J. Phys. Chem.*, **71**, 3517 (1967).
15. J. Q. Chambers, A. D. Norman, M. R. Bickell, and S. H. Cadle, *J. Amer. Chem. Soc.*, **90**, 6056 (1968).
16. A. I. Vogel, "A Text-book of Practical Organic Chemistry," p. 749, John Wiley & Sons, New York (1962).
17. M. Von Stackelberg, M. Pilgram, and V. Toome, *Z. Elektrochem.*, **57**, 342 (1953).
18. Z. G. Soos and P. J. Lingane, *J. Phys. Chem.*, **68**, 3821 (1964).
19. E. R. Brown, T. G. McCord, D. E Smith, and D. D. DeFord, *Anal. Chem.*, **38**, 1119 (1966).
20. T. Kambara, *Bull. Chem. Soc. Japan*, **27**, 523 (1954); W. M. Schwartz and I. Shain, *J. Phys. Chem.*, **69**, 30 (1965).
21. J. Badoz-Lambling and G. Demange-Guerin, *Anal. Letters*, **2**, 123 (1969).
22. G. Demange-Guerin, *C. R. Acad. Sci., Paris*, **266**, 784 (1968).
23. A. Albert and E. P. Serjeant, "Ionisation Constants of Acids and Bases," Methuen, London (1962).
24. J. H. Baxendale and H. R. Hardy, *Trans. Faraday Soc.*, **49**, 1140 (1953).

25. G. Biedermann, *Acta Chem. Scand.*, **10**, 1340 (1956).
26. T. Handa, *Bull. Chem. Soc. Japan*, **28**, 483 (1955).
27. A. Beauchamp and R. L. Benoit, *Can. J. Chem.*, **44**, 1607 (1966).
28. J. Heyrovsky and J. Kuta, "Principles of Polarography," p. 413, Academic Press, New York (1966).
29. M. S. Spritzer, J. M. Costa, and P. J. Elving, *Anal. Chem.*, **37**, 211 (1965).
30. C. Martius and E. Eilingsfeld, *Ann.*, **607**, 159 (1957).
31. H.-D. Becker, *J. Org. Chem.*, **30**, 982, 989 (1965).
32. M. A. DaRooge and L. R. Mahoney, *ibid.*, **32**, 1 (1967).
33. D. J. Cram and G. S. Hammond, "Organic Chemistry," p. 272, McGraw-Hill Book Co., New York, (1959).
34. L. S. Marcoux, K. B. Prater, B. G. Prater, and R. N. Adams, *Anal. Chem.*, **37**, 1446 (1965).
35. B. R. Eggins, Ph.D. Thesis, University of Warwick, 1968.
36. H. Tsubmura, *Bull. Chem. Soc. Japan*, **26**, 304 (1953).
37. M. E. Peover, *Trans. Faraday Soc.*, **60**, 417 (1964).
38. W. Dürckheimer and L. A. Cohen, *Biochem.*, **3**, 1948 (1964).
39. R. E. Moser and H. G. Cassidy, *J. Amer. Chem. Soc.*, **87**, 3463 (1965).
40. J. Janata and H. B. Mark, Jr., *J. Phys. Chem.*, **72**, 3616 (1968).
41. G. I. Hoijtink, J. von Schooten, E. de Boer, and W. I. J. Aalbersberg, *Rec. Trav. Chem., Pays Bas*, **73**, 355 (1954).
42. V. D. Parker, *Chem. Comm.*, **1969**, 716.

The Anodic Behavior of Zinc Electrodes in Potassium Hydroxide Electrolytes

M. N. Hull,* J. E. Ellison, and J. E. Toni*

Power Sources Division, Electronic Components Laboratory, U. S. Army Electronics Command, Fort Monmouth, New Jersey

ABSTRACT

The electrochemical oxidation of zinc anodes in potassium hydroxide solutions of 0.5-5.0M has been studied under stationary and hydrodynamic conditions. Linear sweep voltammetry and rotating ring-disk electrode techniques were employed to elucidate the different processes involved in the electrode reaction. Two different surface films are formed on zinc anodes. The first of these causes a small retardation in the rate of dissolution of the electrode in the active region while the second causes passivation. Measurements with rotating ring-disk arrangements indicate that the "dissolution-precipitation" model for the formation of these films may not be correct. The majority of the current passed in those regions where the surface is covered by a film is utilized in direct electrochemical oxidation of the zinc to soluble products and not in processes associated with thickening of the surface layer.

Many previous studies of the anodic behavior of zinc electrodes in alkaline electrolytes have reported the existence of both passivating and nonpassivating films on the electrode surface during electrolysis (1-11). These films have been reported as having a range of colors varying from extremely black (4, 5) in some cases to very white in others (6). It appears, however, that apart from the work of Breiter and Powers (1) and Powers (2), no firm correlation between the effect of these films on the current-voltage (i-v) curves for zinc dissolution, their color, and the nature and convective conditions of the electrolyte has yet been reported. Indeed relatively few studies have been reported of the i-v behavior of zinc anodes recorded under potentiostatic conditions and in these no systematic study of the dissolution process at different scan rates was conducted. In addition, there appears to be no general agreement between different workers as to the exact form of these i-v curves, primarily due to the differing and in some cases, ill-defined convective conditions employed in each case. Thus, Vozdvizhenskii and Kochman (3) reported two peaks in the i-v curves recorded in 2 and 5M KOH solutions before passivation whose relative heights depended on the scan rate (not given) which was employed. These peaks were believed to reflect the formation of two oxides which differed in their degree of hydration, solubility and rate of formation. Again, Breiter and Powers (1) observed distinctly different i-v curves recorded at scan rates of approximately 1.0 mV.sec^{-1} depending on the convective conditions of the 7M KOH solution which they used. Under quiescent conditions the current rose to a peak at -1.27V (Hg-HgO) with increasing anodic voltage and then passed through a small "hump" before the onset of passivity at ~ -1.0V. In stirred solution the current initially rose fairly rapidly to the same potential at which the peak was observed in the unstirred case and from there continued to rise until passivation occurred but with a greatly reduced slope. Elder (12), who also studied the dissolution of zinc in unstirred 7M KOH solution, found that at a scan rate of 2.8 mV.sec^{-1} the current passed through a small peak at -1.12V and then commenced to rise again just before the onset of passivation. The peak potential and current were found to obey the relationship

$$E_p = -0.701 + 0.5246 \log i_p$$

for scan rates within the range 0.56-139.0 mV.sec^{-1}. In contrast, Ashton and Hepworth (10) observed no peaks in the i-v curves recorded in 0.5N NaOH although it is not clear from their work exactly what stirring conditions, if any, were employed. In this case the current rose to a limiting value which was maintained with increasing anodic potential until passivation.

It is therefore evident from the above examples that the i-v behavior of zinc anodes in alkaline electrolytes is very unclear and therefore merits reinvestigation under more clearly defined conditions with regard to both the stirring of the electrolyte and the concentration. In the following work the i-v behavior of zinc wire electrodes in various concentrations of KOH solu-

* Electrochemical Society Active Member.

tions has been studied by the technique of linear sweep voltammetry as a function of both the stirring conditions in the electrolyte and the scan rate. In addition visual observations concerning the nature and color of the various films formed on the surface were made and correlated with the form of the i-v curves recorded at the slower scan rates.

With a knowledge of the general patterns of behavior of the i-v curves and their dependence on both the stirring conditions and the presence or absence of surface films, the dissolution process was further studied using the rotating ring-disk technique which has given added insight into the over-all dissolution process under even more rigorously defined mass transfer conditions. Although this technique would appear to be admirably suited for this type of study only the Russian school appears to have attempted any measurements along these lines. For example, Popova *et al.* (7, 13, 14) have studied the anodic dissolution of passivated zinc anodes by the rotating disk technique but have shed little light on the behavior of zinc anodes during the "active" region of the dissolution process. However, from the i-v curves which they have published one can see that the current rise prior to the onset of passivation did exhibit two distinct regions of differing slope in qualitative agreement with the work of Breiter mentioned above. With regard to the use of a rotating ring-disk arrangement to study the anodic dissolution of zinc, the work of Oshe *et al.* (15) appears to be the only investigation reported to date. No conclusions were drawn from this work concerning the mechanism of the dissolution of zinc, but the results did suggest that in the passive region the nonstationary flow of current caused by a step change in the electrode potential arises from an additional electrochemical dissolution of the zinc and not from processes involved with thickening of the oxide layer.

Preliminary observations are therefore also presented here of sweep measurements obtained with a zinc disk electrode surrounded by either a graphite or a zinc ring, the potential of which was held at a sufficiently cathodic potential that all of the oxidized species transported to the ring were immediately reduced. Some postulations concerning the factors which influence the over-all dissolution process are presented from these two types of study.

Experimental Procedure

The electrical arrangement which was used to obtain the i-v curves with wire electrodes is shown in Fig. 1a. In this the triangular voltage signal was supplied from a Tacussel GSTP-2 function generator to the input of a Tacussel PRT potentiostat and was used to drive the Y-axis of a 564 Tektronix memory oscilloscope which was operated in the X-Y mode. The current flowing through the cell was measured differentially across a resistor in the counterelectrode circuit and was recorded on the X-axis of the oscilloscope.

For measurements with the ring-disk arrangement the circuitry shown in Fig. 1b was used. Since it is not possible to operate two independent electrodes connected to the same ground, *i.e.*, the ring and the disk, at different potentials with respect to a reference electrode, the potentiostats were operated in the reverse mode to that shown in Fig. 1a. In this a large platinum gauze electrode was used as a common counterelectrode for both the ring and the disk and this was connected to "ground." This electrode was polarized cathodically from a second platinum gauze electrode (not shown) to the point of hydrogen evolution and under these conditions maintained a relatively stable potential (±5 mV) as current was passed through it to the ring and the disk. The stability of this electrode was constantly monitored with respect to a Hg-HgO reference electrode. The ring and the disk were connected to the control terminals of separate potentiostats operated in the follower mode and could be held at different fixed potentials or scanned independently with respect to the platinum gauze electrode held at ground potential. A complete discussion of this electrical circuit will be published elsewhere (16). In the experiments described here the ring was held at a fixed potential while the disk was anodically polarized at a scan rate of 10 mV.sec^{-1}. Two memory oscilloscopes, operated in the X-Y mode, were used to record independently the ring and the disk current each as a function of the disk electrode potential. Simultaneously during the potential sweep the collection efficiency N was obtained from a trace of the ring current as a function of the disk current recorded on a Honeywell 550 X-Y plotter.

In the experiments with wire electrodes zinc wire of 99.9999% purity and of 0.076 cm diameter was used. The electrode was sheathed in heat shrinkable Teflon tubing to leave an area of 0.05 cm^2 exposed to the electrolyte. Before a sweep was performed the electrode was pretreated by stepping to a potential of 1.0V positive to the open-circuit rest potential for a period of 1.0 msec. This procedure produced an oxide film on the electrode surface which was then dissolved off when the potential was stepped back to the open-circuit value. The sweep was initiated after the current had decayed to zero (approximately 5 msec.).

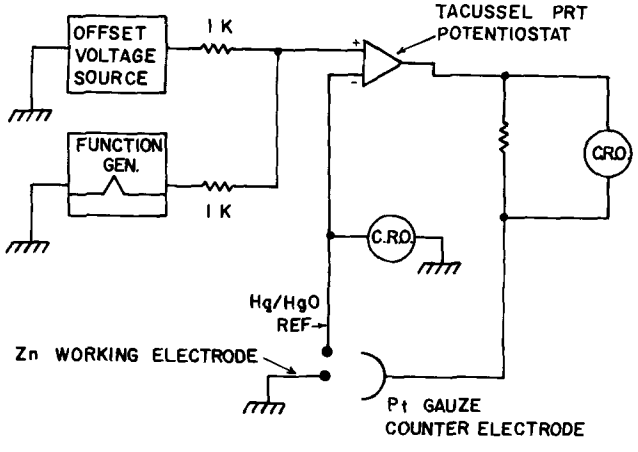

Fig. 1a. Electrical circuitry used for experiments with wire electrodes.

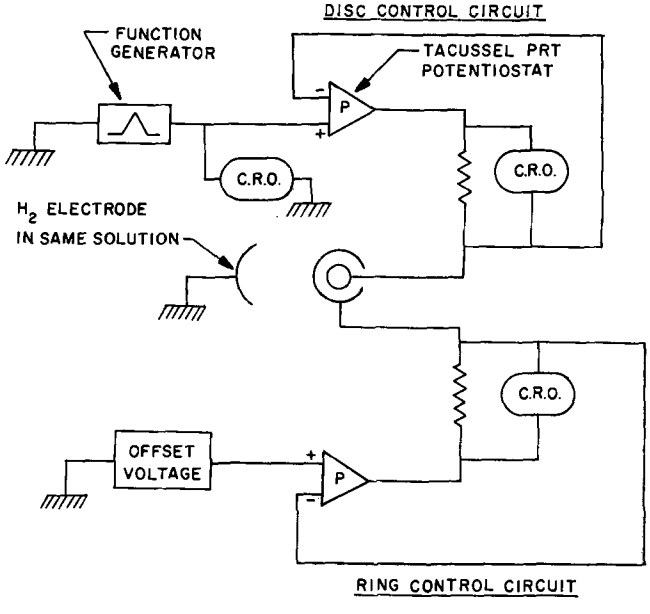

Fig. 1b. Electrical circuitry used for rotating ring-disk experiments.

In the ring-disk experiments two all-Teflon electrode configurations were used. In the first of these a zinc disk (99.99%) was surrounded by a pyrolytic graphite ring and had the dimensions $r_1 = 1.05$, $r_2 = 1.40$, $r_3 = 3.20$ mm ($N = 0.653$). In the second a zinc disk-zinc ring arrangement was used of dimensions $r_1 = 2.55$, $r_2 = 3.30$, and $r_3 = 3.78$ mm ($N = 0.248$). The electrodes were rotated at rates between 50-5000 rpm by means of a servoregulated motor supplied by Electro Devices Inc., and the rotation speed was accurately measured with a General Radio 1153-AP digital frequency meter.

The electrolyte was prepared by dissolving the required weight of Merck reagent KOH pellets in nitrogen-saturated doubly distilled water and was contained in an all-Teflon cell which had provision for the bubbling of nitrogen gas either through or over the electrolyte. Observation of the zinc wire electrodes was performed by means of a Western Electric Laboratory microscope having a maximum magnification of 100 times.

Results

Figure 2 shows the i-v behavior of a zinc electrode in unstirred 5*N* KOH recorded at scan rates of 12.5 and 130.0 V.sec^{-1}. At these sweep rates the form of the curves are independent of the convective conditions in the electrolyte and only one peak is observed on the forward sweep before the onset of passivation. Generally the potential of passivation shifts to more anodic values as the scan rate is increased until eventually at scan rates of the order of several hundred volts per second the point of passivation merges with the current rise associated with the onset of oxygen evolution. Concurrently with the increase in scan rate the total charge passed during the region of active dissolution falls to a minimum value of approximately 20.0 millicoulombs/cm^2 (geometrical area) for scan rates in excess of 500 V.sec^{-1}. Assuming that all of the zinc which is oxidized is utilized as ZnO in passivation of the electrode, then this charge would correspond to an oxide thickness of the order of 70 atomic layers.

At decreasing scan rates the i-v curves begin to show much more detail, and the influence of the stirring conditions in the electrolyte on the form of the curves becomes more pronounced. In Fig. 3 the i-v curves recorded at a scan rate of 82.0 mV.sec^{-1} in both stirred and unstirred 5*N* KOH are shown. The general behavior is that the dissolution current rises steadily with increasing anodic potential to a peak value whose magnitude is strongly dependent on both the electrolyte concentration and the stirring conditions in the electrolyte. After passing through this

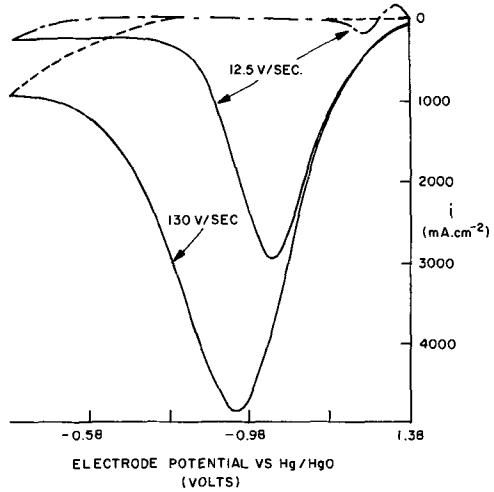

Fig. 2. Current-voltage curves of a zinc wire electrode in unstirred 5*N* KOH at scan rates of 12.5 and 130.0 V.sec^{-1}.

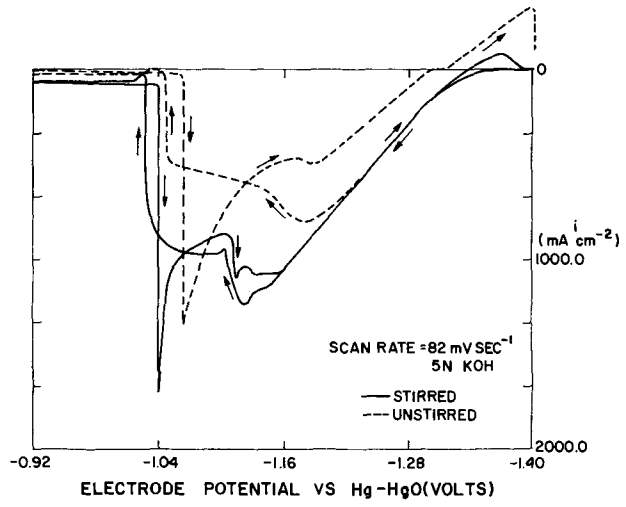

Fig. 3. Current-voltage curves of a zinc wire electrode in both stirred and unstirred 5*N* KOH recorded at a scan rate of 82.0 mV.sec^{-1}.

peak the current is fairly constant in the stirred electrolyte but falls off slowly in unstirred electrolyte until complete passivation occurs at approximately −1.04V.

The reverse sweeps show that the increased rate of chemical dissolution of the passivating film in the stirred electrolyte causes reactivation of the electrode to occur at a more anodic potential than for the unstirred case. Apart from this the general form of the reverse curves are quite similar in that the current falls from the relatively high values attained immediately after reactivation to pass once more through a well-defined peak in the same potential region as that observed during the forward sweep. Near the end of the reverse sweep a broad region is observed where dissolution products remaining close to the electrode surface are reduced.

Interesting changes in the form of these curves take place as both the electrolyte concentration and the sweep rate are decreased. For example, in Fig. 4 the i-v curves recorded at the same scan rate but in 1*N* KOH are shown. One can see as before that in both cases the current rises to a well-defined peak. However, in the stirred electrolyte the current undergoes a further increase in the potential region between that of the peak and the onset of passivity while the slow fall observed in this potential region for the unstirred 5*N* KOH case is less pronounced. In addition the reverse sweeps show that with the decrease in the electrolyte concentration from that shown in the previous figure the rate of dissolution of the passivating film has also decreased and the potential of reactivation

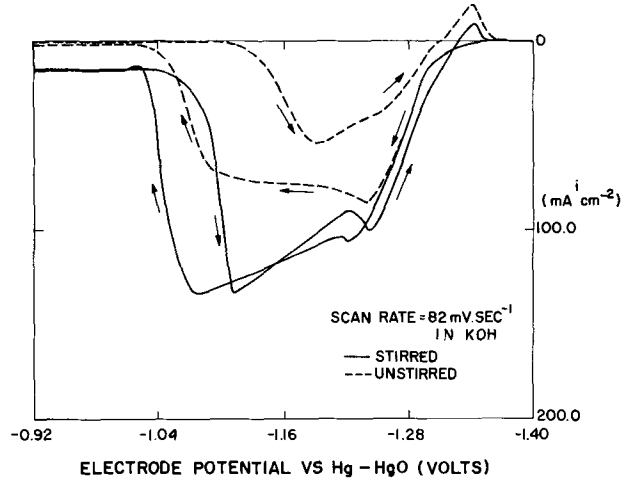

Fig. 4. Current-voltage curves of a zinc wire electrode in both stirred and unstirred 1*N* KOH (scan rate as in Fig. 3).

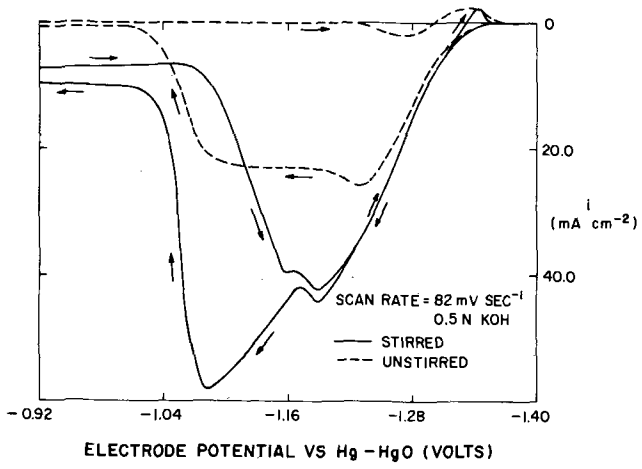

Fig. 5. Current-voltage curves of a zinc wire electrode in both stirred and unstirred 0.5*N* KOH (scan rate as in Fig. 3 and 4).

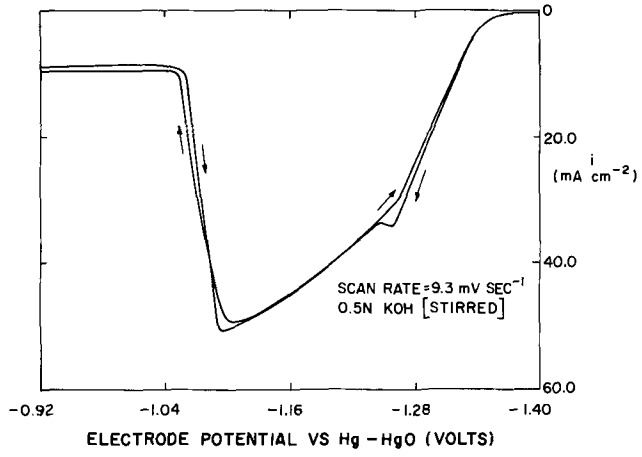

Fig. 8. Current-voltage curve of a zinc wire electrode in stirred 0.5*N* KOH (scan rate as in Fig. 6 and 7).

has therefore moved to more cathodic values particularly in the case of the unstirred electrolyte. These trends are illustrated to a more marked degree in the i-v curves for 0.5*N* KOH shown in Fig. 5. Here the current rise after the peak is now very pronounced in the stirred case and little or no reactivation of the electrode is observed in the time required for completion of the reverse sweep.

Figures 6 to 8 which show the anodic behavior of zinc in these same three concentrations of KOH electrolyte but at the slower scan rate of 9.3 mV.sec^{-1} reveal several additional details. In the 5*N* KOH case shown in Fig. 6 current oscillations are observed to be

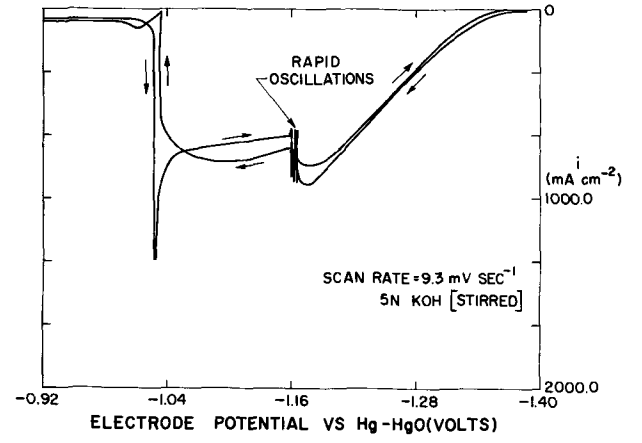

Fig. 6. Current-voltage curve of a zinc wire electrode in stirred 5*N* KOH recorded at a scan rate of 9.3 mV/sec^{-1}.

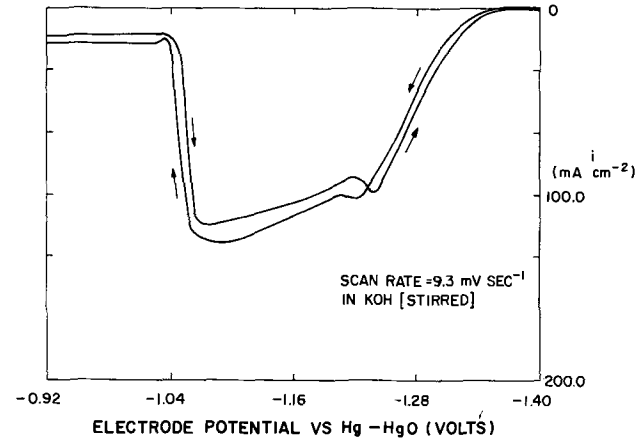

Fig. 7. Current-voltage curve of a zinc wire electrode in stirred 1*N* KOH (scan rate as in Fig. 6).

associated with the peak in both the forward and reverse sweeps in stirred electrolyte while after passivation has occurred the current passes through another small peak before levelling off at a slowly rising value of the dissolution current. In the 1*N* and 0.5*N* KOH electrolytes at this scan rate (Fig. 7 and 8) it is evident that this peak behavior after passivation is less pronounced in the weaker electrolyte.

Figure 9 shows an i-v curve recorded at a scan rate of 1.1 mV.sec^{-1} in unstirred 5*N* KOH and summarizes our observations concerning film formation during the over-all dissolution process. At potentials less anodic than that of the peak (point B) the surface of the electrode remains bright and the development of etch patterns are clearly visible. At B a milky white film forms which in the absence of stirring slowly flakes from the electrode surface in the region C-D. At point D, as the current begins to fall, the surface beneath this film can be observed to be growing dark in color until, after passing through a region of intense current oscillation, the passivated surface at F is very black. This black film however undergoes a rapid lightening of color in the region of the small current peak (FGH) to leave the surface covered by a white crystalline passivating layer. Moreover, this latter color change appears to be somewhat of a reversible process since on the reverse sweep in the region J-K, just prior to complete reactivation of the electrode, the light colored coating begins to darken again and at *K*, where the surface is a mixture of light and dark areas, the current oscillates once more between the active and passive states. Eventually, when a stable current state is attained at *L*, the electrode is wholly covered

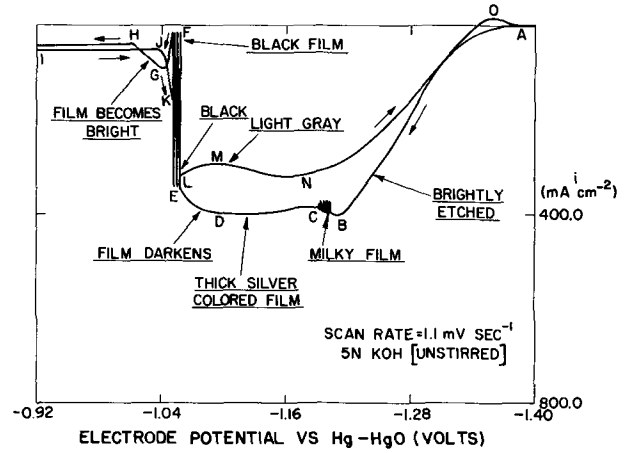

Fig. 9. Current-voltage curve of a zinc wire electrode in unstirred 5*N* KOH recorded at a scan rate of 1.1 mV.sec^{-1}.

by a very black film which now permits active dissolution of the electrode to proceed. This film in the region L-M undergoes another gradual lightening in color to leave the electrode surface with a similar appearance to that observed in the same potential region on the forward sweep.

Using a rotating ring-disk electrode (C-Zn) the i-v curves shown in Fig. 10a were recorded at three different rotation speeds for a scan rate of 10.0 mV.sec^{-1}. The corresponding curves shown in Fig. 10b refer to the reduction current observed at the ring as a function of the disk potential while the ring was maintained at a fixed potential of −1.45V (Hg-HgO), *i.e.*, at a sufficiently cathodic potential to immediately reduce those oxidized zinc species which are swept over from the disk. In general the form of the i-v curves observed at both the ring and the disk are extremely similar if care is taken to maintain reproducible conditions on the surface of the ring by mechanically cleaning off the deposited layer after each sweep. In addition the peak potential is independent of the rotation rate and occurs at a value of −1.2V for a scan rate of 10 mV.sec^{-1}.

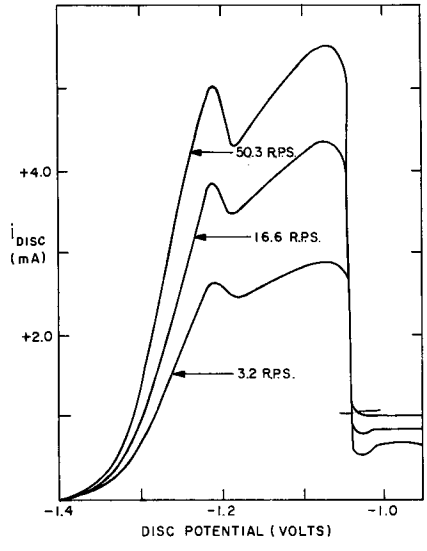

Fig. 10a. Current-voltage curves recorded on the disk of a C-Zn ring-disk electrode at different rotation rates. Scan rate = 10 mV.sec^{-1}; 1*N* KOH; electrode area = 0.035 cm^2.

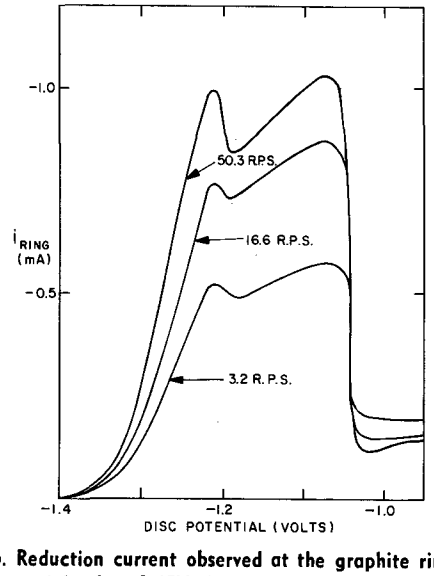

Fig. 10b. Reduction current observed at the graphite ring held at a fixed potential of −1.45V (Hg-HgO) for the current-voltage curves shown in Fig. 10a.

As the rotation rate is increased one can see from the figure that the slope of the i-v curve between the peak and the onset of passivation becomes greater and that the small current peak after passivation disappears. The observed collection efficiency *N* for the two ring-disk systems employed is constant for all regions of the i-v curves, *i.e.*, there is no change in this parameter when measured before the peak, between the peak and the onset of passivity or in that region where the electrode is in a passivated state.

In order to test whether the dissolution process was diffusion controlled for any particular set of experimental conditions, plots of the peak current and also the maximum current observed just prior to the passivation were drawn as a function of the square root of the rotation speed for a fixed scan rate. No significant regions of linearity were observed as is illustrated in Fig. 11 where a plot of the peak current as a function of $\omega^{1/2}$ is drawn. At rotation rates below approximately 600 rpm a straight line is observed which could be indicative of mass transfer control although the linear portion has a positive intercept on the current axis instead of passing through zero as required by the Levich (17) equation. Deviations such as this from the Levich equation have been observed before for other diffusion-controlled reactions at a rotating disk and have been fully discussed by Riddiford (18). It seems clear however that with increasing rotation speed diffusion control of the over-all reaction becomes increasingly less important.

Discussion

The preceding results show clearly that the i-v curves of zinc electrodes in KOH solutions are strongly dependent on the convective conditions in the electrolyte. It is quite evident however that there is only one main peak in both the forward and reverse curves although an additional small broad peak may be identified on the forward sweep immediately following the onset of passivation, particularly in the more concentrated and unstirred solutions. Prior to the peak potential in the active region there does not appear to be any visible films on the electrode surface, and thus unhindered dissolution of the zinc anode occurs. At the peak, however, the dissolution process becomes retarded by the formation of a film on the surface which acts as a barrier layer to either the passage of zinc species from the electrode to the solution or conversely the approach of additional hydroxyl ion species to the unoxidized surface. This barrier layer, which according to Nikitina (8) has the chemical composition of ϵ-$Zn(OH)_2$, is probably formed by the adsorption of the electrolyte anions at the peak potential (19) rather than by a precipitation process from zincate saturated layers adjacent to the electrode surface

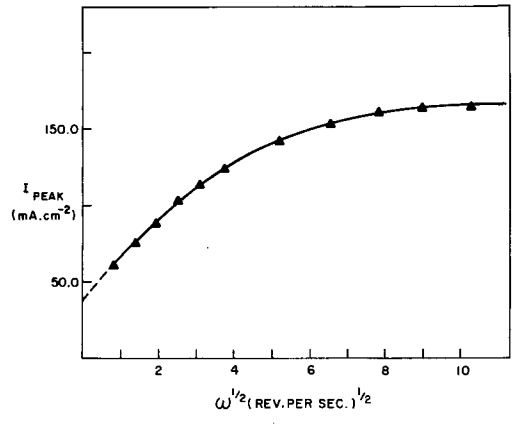

Fig. 11. Plot of the peak current observed at a rotating zinc disk electrode in 1*N* KOH as a function of the square root of the rotation rate.

as suggested before (1). If indeed the previously suggested "dissolution-precipitation model" were valid for the film formation at this point then one would be obliged to explain the further increase in the dissolution current at potentials more positive than that of the peak in terms of thickening of the surface film accompanied by its chemical dissolution at a rate limited by the diffusion of zincate ions away from the electrode surface. In addition one would not expect the current on the ring to undergo any further increase after the peak potential was reached on the disk if the limiting rate of diffusion of zincate ions into the solution had been reached at that point. The evidence is, therefore, that the film of zinc hydroxide is directly formed on the zinc surface once a certain critical potential is exceeded and further dissolution of the electrode is then determined by the thickness and hence by the rate at which transport processes can occur within this layer. One might expect that the layer thickness would be determined by the stirring conditions in the electrode vicinity and in the case of, for example, the rotating disk experiments that the thickness would decrease with increase in the rate of rotation. These conclusions are in agreement with the experimental observations since the slope of the i-v curve in the region between the peak and the onset of passivation increases with increase in the rotation rate reflecting a decrease in the resistance and hence a decrease in the thickness of the film. Further support for these views is found in the lack of linearity of the plots of the peak current *vs.* $\omega^{1/2}$ at rotation rates in excess of 600 rpm. At rotation rates below this value it could be advanced that the thickness of the diffusion layer is such that transport of the zincate species away from the electrode surface is the controlling process. However it is quite evident from the approach of the peak current to a limiting value at higher rotation speeds that the rate-controlling step under these conditions is occurring prior to the diffusive transport of the zincate product into the bulk of the electrolyte. This rate-controlling step is most probably associated with the transport of ions across the surface film under the action of the local electrical field existing across the film between the metal surface and the electrolyte.

At the onset of passivation a definite change on the electrode surface occurs. The sudden drop in the oxidation current with the observed visible changes in the color of the surface film within a narrow and well-defined range of electrode potential is indicative of a sharp change in the nature and conductivity of this layer. This change reflects a change in the composition of the film from that of the hydroxide to that of the oxide. Since, prior to the onset of passivation, it is quite probable that the zinc surface is covered by an adsorbed layer of hydroxide ions, one could postulate that formation of the initial monomolecular layer of oxide on the surface proceeds by a deprotonation reaction accompanied by the formation of water according to

$$Zn(OH^-)_{ads} \rightleftarrows ZnO + H^+ + 2e^-$$
$$H^+ + OH^- \rightarrow H_2O$$

The above reaction sequence can explain the presence of the intense oscillations of the current in this region of the i-v curve at slow scan rates since as the passivation reaction tends to proceed the resulting decrease in the pH of the solution layers adjacent to the electrode surface tends to drive the thermodynamic potential at which the passivating oxide is stable toward more positive values. Attainment of a stable passive state therefore is not reached until a sufficiently anodic potential is achieved that the local pH change in the electrode vicinity does not reverse the passivation step. It is also quite likely that during this region of current oscillation the electrode surface becomes disrupted with the result that a high concentration of interstitial zinc particles become incorporated into the passivating layer and impart to it the characteristic black coloration. That this black surface film does indeed contain an excess of zinc above that of stoichiometrically balanced zinc oxide is borne out by the subsequent electrode behavior after passivation where the current passes through a small oxidation peak (region FGH of Fig. 9) and the film then becomes bright. It is not evident however how the oxide film on the return sweep can again become rich in zinc prior to reactivation of the electrode assuming that the black film formed in this region is indeed one which is rich in zinc. In addition it is also not clear why this black film should permit the metal to dissolve actively after reactivation unless its mode of formation is such that a more porous layer is produced on the surface compared to that formed during the passivation step.

Finally, the constancy of the collection efficiency N over the whole of the i-v curve indicates that the fraction of the current which is utilized in formation of the surface films at either the peak potential or during the onset of passivity is so small that there is no detectable fall in the amount of the reducible species arriving at the ring. Further, one would have expected that, as the applied field across each of the surface films was increased by the increasing anodic voltage, the films would undergo a corresponding gradual increase in thickness. Again the constancy of N between those potential regions where the surface is free of films and those where films are present shows that if, indeed such thickening of the surface layers does occur, it cannot be detected from measurements of this type. Thus the majority of the current produced at the disk for all regions of the i-v curves is utilized in direct electrochemical oxidation of the zinc to soluble products.

During the review stage of the manuscript one of the reviewers questioned the low value of 0.2 for the collection efficiency when the graphite-zinc arrangement was used ($N_{theor} = 0.653$). Since the time we did the experiments reported here we have been able to achieve values very close to the theoretical collection efficiency using much narrower gaps and rings than those reported above. We found that with graphite rings all of the zinc was deposited on the inner circumference of the ring if the gap was very wide and low values of N were obtained. We are now using very thin gaps and rings and the observed values of N come out close to the expected value. We shall be reporting this in more detail in a later publication. The main point is, however, not that N has a low value but that it is constant throughout the whole of the active region of dissolution. Out latest experiments with the redesigned electrode configuration confirm this constancy of N for unamalgamated zinc disk electrodes surrounded by either a graphite or an amalgamated (and nonamalgamated) zinc ring.

Manuscript submitted July 8, 1969; revised manuscript received Sept. 23, 1969. This was Paper 239 presented in part at the New York Meeting of the Society, May 4-9, 1969.

Any discussion of this paper will appear in a Discussion Section to be published in the December 1970 JOURNAL.

REFERENCES

1. M. W. Breiter and R. W. Powers, *This Journal*, **116**, 719 (1969).
2. R. W. Powers, Paper 369 presented at the Montreal Meeting of the Society, Oct. 6-11, 1968.
3. G. S. Vozdvizhenskii and E. D. Kochman, *Russ. J. Phys. Chem.*, **39**, 347 (1965).
4. K. Huber, *This Journal*, **100**, 376 (1953).
5. K. Huber, *Z. Elektrochem.*, **62**, 675 (1958).
6. H. Fry and M. Whitaker, *This Journal*, **106**, 606 (1959).
7. T. I. Popova, N. A. Simonova, and B. N. Kabanov, *Soviet Electrochemistry*, **3**, 1273 (1967).

8. Z. Ya. Nikitina, *J. Appl. Chem.*, (*USSR*), **31**, 209 (1958).
9. N. A. Hampson and M. J. Tarbox, *This Journal*, **110**, 95 (1963).
10. R. F. Ashton and M. T. Hepworth, *Corrosion*, **24**, 50 (1968).
11. N. A. Hampson, M. J. Tarbox, J. T. Lilley, and J. P. G. Farr, *Electrochem. Technol.*, 2, 309 (1964).
12. J. P. Elder, *This Journal*, **116**, 757 (1969).
13. T. I. Popova, N. A. Simonova, and B. N. Kabanov, *Soviet Electrochemistry*, **2**, 1347 (1966).
14. T. I. Popova, G. L. Vidovitch, N. A. Simonova, and B. N. Kabanov, *ibid.*, **3**, 860 (1967).
15. A. I. Oshe, Ya. Ya. Kulyavik, T. I. Popova, and B. N. Kabanov, *ibid.*, **2**, 1356 (1966).
16. J. E. Toni and A. A. Pilla, To be submitted for publication.
17. V. G. Levich, "Physicochemical Hydrodynamics," p. 69, Prentice-Hall Inc., New York (1962).
18. A. C. Riddiford, "Advances in Electrochemistry and Electrochemical Engineering," Vol. 4, p. 47, P. Delahay, Editor, Interscience Publishers, New York (1966).
19. J. P. G. Farr and N. A. Hampson, *J. Electroanal. Chem.*, **13**, 433 (1967).

Frequency Dispersion in Capacity Measurements at a Disk Electrode

John Newman

Inorganic Materials Research Division, Lawrence Radiation Laboratory, and Department of Chemical Engineering, University of California, Berkeley, California

ABSTRACT

The geometry of an electrode system affects the frequency dispersion of impedance measurements if the primary current distribution on the electrode is nonuniform. This effect is treated for a disk electrode embedded in an insulating plane with the counterelectrode at infinity. The apparent capacity is found to approach zero at large frequencies. The frequency dependence of the apparent capacity will be much smaller for a spherical electrode tangent to an insulating plane. The latter system is also treated briefly.

We investigate here the alternating-current impedance of a disk electrode embedded in an infinite, insulating plane, with the counterelectrode at infinity. The distribution of current over the surface of such a disk electrode is, in general, nonuniform. Figure 1 depicts equipotential surfaces in the medium near a disk, where the solution adjacent to the disk electrode is at a uniform potential; this is the so-called "primary potential distribution," for which the distribution of current on the surface of the disk is given by (1)

$$i = 0.5\, i_{avg}/[1 - (r/r_0)^2]^{1/2} \qquad [1]$$

With an alternating current, the current can pass from the electrode to the solution either by means of a faradaic electrode reaction or by charging the double-layer capacity. Attention here is primarily focused on the double-layer capacity. The impedance can then be represented by an equivalent circuit consisting of a series combination of a resistor and a capacitor (Fig. 2). However, the values of the effective resistance and double-layer capacity of the equivalent circuit are not independent of frequency. Several factors may contribute to this "frequency dispersion."

If the electrode surface is rough, the peaks and valleys will be accessible to a different degree at different frequencies (2). Second, if the frequency becomes large relative to the kinetics of ion sorption in the double layer, then the apparent double-layer capacity will depend on frequency (3). The occurrence of faradaic reactions will also cause a frequency dependence of the values in the equivalent circuit in Fig. 2. Finally, the current distribution will be different at different frequencies, and this will lead to a frequency dispersion, as suggested by Bauer, Spritzer, and Elving (4).

The last factor is investigated theoretically here in order that an experimentally observed frequency dispersion due to this factor will not be erroneously attributed to one of the first factors mentioned. Consequently, the electrode surface is taken here to be smooth, and the true double-layer capacity (per unit area) C is taken to be independent of frequency. Except for large organic ions, the kinetics of ion sorption should not affect the double-layer capacity until frequencies of 1 Mc are reached. The possibility of faradaic reactions will also be included, without, however, consideration of the Warburg impedance due to concentration changes near the electrode.

At low frequencies, the reactive impedance of the double layer predominates over the resistive impedance of the electrolytic solution. Consequently, the current distribution is uniform over the surface of the

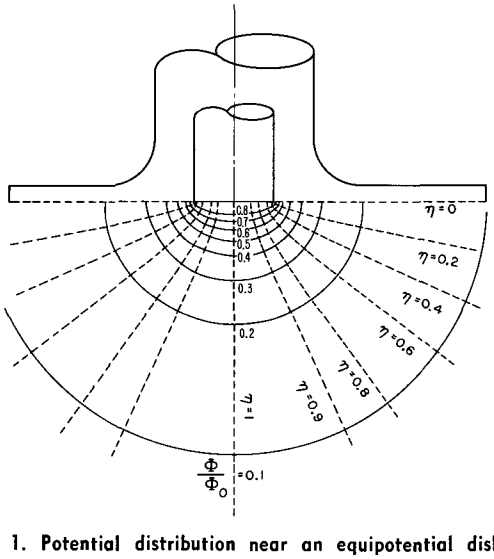

Fig. 1. Potential distribution near an equipotential disk in an insulating plane.

Key words: frequency dispersion, double-layer capacity, current distribution, disk electrode, dropping mercury electrode, polarography.

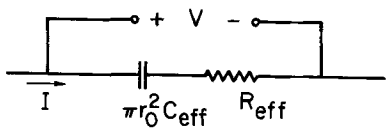

Fig. 2. Equivalent circuit of disk system. Here, C_{eff} and R_{eff} can be regarded as the apparent double layer capacity and the apparent resistance of the electrolytic solution, if faradaic reactions are of negligible importance.

disk, and C_{eff} corresponds to the true double-layer capacity. At high frequencies, the reactive impedance becomes small, and the primary current distribution is a good approximation. Hence, the effective resistance approaches the value for the primary distribution (1)

$$R_{eff} \to 1/4\, r_o\, \kappa \text{ as } \omega \to \infty \qquad [2]$$

As we shall see, C_{eff} approaches zero at high frequencies, in marked contrast to the situation at a hanging mercury drop or dropping mercury electrode.

If, however, faradaic reactions can occur, the low-frequency limit will no longer yield the true double-layer capacity, since the reactive impedance is large compared to the faradaic impedance with which it is in parallel. Information about the true double-layer capacity can then be obtained only at intermediate frequencies with due allowance for the nonuniform current distribution.

For rough electrodes, the low-frequency limit will yield the true electrode area if the true double-layer capacity is known (in the absence of faradaic reactions). However, the determination of the true double-layer capacity from impedance measurements at higher frequencies will not be straightforward.

This investigation is also relevant to the frequency dependence of classical conductivity cells [see, for example, Robbins (5)].

Mathematical Model

The potential in the solution satisfies Laplace's equation

$$\nabla^2 \Phi = 0 \qquad [3]$$

The potential at infinity will be taken to be zero

$$\Phi \to 0 \text{ as } r^2 + z^2 \to \infty \qquad [4]$$

and, since the current density is zero on the insulating plane around the disk electrode, the normal component of the potential gradient will also be zero there

$$\partial\Phi/\partial z = 0 \text{ at } z = 0, r > r_o \qquad [5]$$

At the disk, the normal component of the current density, which contributes to the total current passing to the electrode, is given by

$$i = C\frac{\partial(V - \Phi_o)}{\partial t} + (\alpha + \beta)\frac{i_o ZF}{RT}(V - \Phi_o) = -\kappa\frac{\partial\Phi}{\partial z} \quad \text{at } z = 0, r \leq r_o \qquad [6]$$

where V is the potential of the electrode, Φ_o is the potential in the solution adjacent to the electrode, κ is the conductivity of the solution, C is the true double-layer capacity, and $(\alpha + \beta) i_o ZF/RT$ relates to the kinetics of the faradaic reaction, here taken to be linear. Thus double-layer charging and a faradaic reaction can both contribute to the passage of current from the electrode to the solution. The last equality relates the current density to the normal component of the potential gradient in the solution.

For an alternating current, the electrode potential can be expressed as[1]

$$V = V_o e^{j\omega t} \qquad [7]$$

where V_o is the amplitude of the applied potential. Correspondingly, the potential in the solution can be expressed in terms of a complex potential U which is independent of time

$$\Phi = V_o e^{j\omega t} U(r,z) \qquad [8]$$

The results of the analysis can be expressed in terms of two dimensionless quantities

$$\Omega = \frac{\omega C r_o}{\kappa} \quad \text{and} \quad J = (\alpha + \beta)\frac{i_o ZF r_o}{RT\kappa} \qquad [9]$$

Ω can be regarded as a dimensionless frequency and J as a dimensionless exchange current density. $\Omega = 1$ when, for example, $C = 30\ \mu f/cm^2$, $r_o = 0.25$ cm, $\kappa = 0.05$ (ohm-cm)$^{-1}$, and $\omega = 0.67 \times 10^4$ sec^{-1} (or 10,500 Hz). $J = 0.0194$ when, in addition, $i_o = 0.1$ mA/cm^2 and $(\alpha + \beta)Z = 1$. The results are expressed in terms of C/C_{eff}, the ratio of the true double-layer capacity to the apparent capacity, and $4r_o\kappa R_{eff}$, the ratio of the effective resistance to the resistance for the primary distribution (see Eq. [2]). At low frequencies, $C/C_{eff} \to 0$ unless $J = 0$, and, for small values of J, $4r_o\kappa R_{eff} \to (4/\pi)(1 + 1/J)$.

The secondary current distribution, when $\Omega = 0$, has been discussed before (6).

Analysis

Since Φ satisfies Laplace's equation, U also satisfies Laplace's equation. In rotational elliptic coördinates η and ξ, the solution satisfying the condition at infinity and the condition on the insulating part of the disk can be expressed as (6)

$$U = \sum_{n=0}^{\infty} B_n P_{2n}(\eta) M_{2n}(\xi) \qquad [10]$$

where $P_{2n}(\eta)$ is the Legendre polynomial of order $2n$ and $M_{2n}(\xi)$ is a Legendre function with known properties (6). Since a similar development has recently been used to treat the current distribution on a rotating disk electrode below the limiting current (6), these mathematical details will not be repeated here. In the present case, the coefficients B_n will be complex.

This solution allows the potential and the potential derivative near the electrode to be expressed as

$$U_o = \sum_{n=0}^{\infty} B_n P_{2n}(\eta) \qquad [11]$$

and

$$\left.\frac{\partial U}{\partial z}\right|_{z=0} = \frac{1}{r_o\eta}\left.\frac{\partial U}{\partial \xi}\right|_{\xi=0} = \frac{1}{r_o\eta}\sum_{n=0}^{\infty} B_n P_{2n}(\eta) M'_{2n}(0) \qquad [12]$$

Substitution into the boundary condition [6] on the disk electrode gives

$$(j\Omega + J)\left[1 - \sum_{n=0}^{\infty} B_n P_{2n}(\eta)\right] = -\frac{1}{\eta}\sum_{n=0}^{\infty} B_n P_{2n}(\eta) M'_{2n}(0) \qquad [13]$$

where the dimensionless parameters Ω and J are given by Eq. [9].

This approach derives its economy from the fact that Eq. [10] is an appropriate solution of Laplace's equation. Hence, the problem of solving a partial differential equation is reduced to the determination of the coefficients B_n from Eq. [13]. Multiplication of this equation by $\eta P_{2m}(\eta)$ and integration with respect to η gives an infinite set of equations for this purpose

[1] Strictly speaking, one takes the real part of such complex expressions: $V = Re\{V_o e^{j\omega t}\} = V_o \cos(\omega t)$.

$$B_m = -\frac{4m+1}{M'_{2m}(0)}(j\Omega + J)\int_0^1 \eta P_{2m}(\eta)\left[1 - \sum_{n=0}^{\infty} B_n P_{2n}(\eta)\right] d\eta \quad [14]$$

One can truncate this set of equations by carrying only a finite number of terms in the sum in the integrand. Higher accuracy can, of course, be obtained by carrying more terms.

After the coefficients B_n have been obtained, one needs to calculate the impedance of the system. The total current is given by

$$I = \int_0^{r_0} i2\pi r dr = -2\pi r_0^2 \kappa \int_0^1 \eta \frac{\partial \Phi}{\partial z}\bigg|_{z=0} d\eta = -2\pi r_0 \kappa V_0 e^{j\omega t} B_0 M_0'(0) \quad [15]$$

where the change of variable from r to η is effected by means of the relation

$$r/r_0 = \sqrt{1-\eta^2} \text{ on the disk} \quad [16]$$

Since, furthermore, $M_0'(0) = -2/\pi$, the impedance is

$$Z = V/I = 1/4r_0\kappa B_0 \quad [17]$$

We wish to compare this with the impedance of the series resistor-capacitor combination given in Fig. 2 and supposed to represent the resistance of the solution and the capacity of the double layer. Thus

$$Z = R_{eff} + 1/j\omega C_{eff}\pi r_0^2 \quad [18]$$

Comparison with Eq. [17] allows us to determine R_{eff} and C_{eff} from calculated values of B_0

$$4r_0\,\kappa R_{eff} = B_{or}/(B^2_{or} + B^2_{oi}) \quad [19]$$

and

$$C/C_{eff} = (\pi/4)\Omega B_{oi}/(B^2_{or} + B^2_{oi}) \quad [20]$$

where B_{or} and B_{oi} represent the real and imaginary parts of B_0, respectively.

Results

Table I represents the effective resistance and capacity as a function of the dimensionless frequency Ω and for several values of J, the parameter describing the faradaic reactions. One sees that in the absence of faradaic reactions ($J = 0$) the effective resistance varies by only 8% from the high-frequency limit to the low-frequency limit. The effective capacity gives no high-frequency limit. The presence of faradaic reactions can change considerably the character of the impedance when interpreted in terms of the equivalent circuit of Fig. 2.

Low-Frequency Limit

In the absence of faradaic reactions one obtains at low frequencies a uniform, imaginary current density of small magnitude. As a first approximation

Table I. Effective resistance and capacitance as a function of frequency

$\omega Cr_0/\kappa$	$4r_0\,\kappa R_{eff}$	C/C_{eff}	$4r_0\,\kappa R_{eff}$	C/C_{eff}	$4r_0\,\kappa R_{eff}$	C/C_{eff}
	$J = 0$		$J = 0.1$		$J = 1$	
0	1.08076	1.0	13.81194	0	2.34368	0
0.1	1.08073	1.00010	7.44572	0.50009	2.33106	0.00997
0.2	1.08066	1.00039	3.62593	0.80037	2.29465	0.03873
0.5	1.08013	1.00241	1.56867	0.96385	2.08868	0.20168
1	1.07835	1.00931	1.20335	0.99906	1.70571	0.50658
2	1.07234	1.03307	1.10336	1.02950	1.32015	0.82435
5	1.05205	1.12341	1.05705	1.12084	1.09978	1.06500
10	1.03344	1.23630	1.03478	1.23430	1.04657	1.20762
20	1.01945	1.37207	1.01982	1.37078	1.02312	1.35674
50	1.00875	1.57278	1.00882	1.57215	1.00943	1.56606
100	1.00461	1.73438	1.00462	1.73404	1.00480	1.73084
200	1.00238	1.90092	1.00238	1.90074	1.00243	1.89909
500	1.00098	2.12577	1.00098	2.12570	1.00099	2.12502
∞	1.0	—	1.0	—	1.0	—

$$B_{ni} \to -\frac{\pi}{4}\frac{\Omega P^3_{2n}(0)}{(2n-1)(n+1)}(4n+1) \text{ as } \Omega \to 0 \quad [21]$$

In particular, $B_{oi} \to \pi\Omega/4$. The real components are of order Ω^2. In particular

$$B_{or} \to \frac{\pi^2}{4^2}\Omega^2 \sum_{n=0}^{\infty} \frac{(4n+1)P^4_{2n}(0)}{(2n-1)^2(n+1)^2} \quad [22]$$

Substitution of these results into Eq. [19] and [20] gives low-frequency limits for the effective resistance and capacity which agree with the appropriate entries in Table I.

High-Frequency Limit

At high frequencies, the surface potential U_0 becomes uniform and real. $B_{or} \to 1$, and $B_{nr} \to 0$ for $n \neq 0$. The imaginary components of the B coefficients are also small. However, the primary current distribution is infinite at the edge of the disk. This is not possible at finite frequencies on account of the impedance of the interface. Hence, a singular-perturbation problem is encountered. The situation is so severe that the value of B_{oi} cannot be determined in a straightforward manner.

Let us examine the singular nature of the problem. The primary potential distribution will be a valid approximation everywhere except in a small region near the edge of the disk. We use rotational elliptic coordinates (6) to investigate this region

$$r = r_0\sqrt{(1-\eta^2)(1+\xi^2)} \text{ and } z = r_0\eta\xi \quad [23]$$

Both ξ and η are small near the edge of the disk, and we can write

$$(r - r_0)/r_0 = \frac{1}{2}(\xi^2 - \eta^2) \text{ and } z/r_0 = \eta\xi \quad [24]$$

These coordinates thus reduce to parabolic coordinates in the region under consideration. (Because this region is small, results obtained for the potential distribution will also be valid near the edge of any electrode at high frequencies if the electrode is flush with an insulating surface at its edge.)

Near the edge of the disk the potential U therefore satisfies the equation

$$\frac{\partial^2 U}{\partial \eta^2} + \frac{\partial^2 U}{\partial \xi^2} = 0 \quad [25]$$

The boundary condition on the surface of the disk, $\xi = 0$, is

$$j\Omega(1 - U_0) = -\frac{1}{\eta}\frac{\partial U}{\partial \xi}\bigg|_{\xi=0} \quad [26]$$

Far from the disk, the potential approaches the primary distribution (1) as approximated for small ξ

$$U \to 1 - \frac{2}{\pi}\tan^{-1}\xi \approx 1 - \frac{2}{\pi}\xi \text{ as } \xi \to \infty \quad [27]$$

Furthermore, on the surface of the insulator

$$\partial U/\partial \eta = 0 \text{ at } \eta = 0 \quad [28]$$

By defining stretched variables as follows

$$\bar{U} = (1 - U)\frac{\pi}{2}\sqrt{\Omega}, \quad \bar{\eta} = \eta\sqrt{\Omega}, \quad \bar{\xi} = \xi\sqrt{\Omega} \quad [29]$$

the problem in the edge region can be made independent of the parameter Ω. The problem then becomes

$$\frac{\partial^2 \bar{U}}{\partial \bar{\eta}^2} + \frac{\partial^2 \bar{U}}{\partial \bar{\xi}^2} = 0 \quad [30]$$

$$j\bar{U}_0\bar{\eta} = \partial\bar{U}/\partial\bar{\xi} \text{ at } \bar{\xi} = 0 \quad [31]$$

$$\partial\bar{U}/\partial\bar{\eta} = 0 \text{ at } \bar{\eta} = 0 \quad [32]$$

$$\bar{U} \to \bar{\xi} \text{ as } \bar{\xi} \to \infty \quad [33]$$

From these results one can conclude that in the original coordinate system the size of this region is of order r_o/Ω, while $1 - U_o$ is of order $\Omega^{-1/2}$ and the (dimensionless) current density $j\Omega(1 - U_o)$ is of order $\Omega^{1/2}$.

The problem posed by Eq. [30] through [33] was solved by finite-difference methods by successive overrelaxation. The results for the surface potential $\bar{U}_o$, which is proportional to the current density, are given in Fig. 3. The current density approaches the primary distribution far from the edge of the disk, but it is more uniform in the edge region where the impedance of the interface prevents the current density from becoming infinite. However, the high currents predicted by the primary distribution are not prevented totally from reaching the disk; the current is just spread out over a larger region. The disturbance of the real component of the current density generates a comparable disturbance in the imaginary component.

The singular-perturbation treatment of the edge region at high frequencies permits these phenomena to be clarified in a definitive manner and permits an economy in the calculations by defining a problem in which no parameters appear. An accurate treatment of the edge region would otherwise require a very fine mesh if Laplace's equation were to be solved by finite-difference methods over the whole disk simultaneously.

As we have seen, the impedance of the system is tied up in the B_o coefficient. This coefficient can be expressed as

$$1 - B_o = \int_0^1 (1 - U_o)\, d\eta \quad [34]$$

and we know that $B_{or} \to 1$ as $\Omega \to \infty$. The primary distribution (see Eq. [1]), which applies over the central region of the disk, can be expressed as

$$1 - U_o = -2j/\pi\Omega\eta \quad [35]$$

We can obtain useful results by proceeding in the following manner. The imaginary part of Eq. [34] is

$$B_{oi} = -\int_0^1 (1 - U_o)_i d\eta = -\frac{2}{\pi\Omega}\int_0^{\sqrt{\Omega}} \bar{U}_{oi} d\bar{\eta} \quad [36]$$

where, in the last expression, we have used the variables appropriate to the edge region. We now break this up into several parts

$$B_{oi} = \frac{-2}{\pi\Omega}\left[\int_0^b \bar{U}_{oi} d\bar{\eta} + \int_b^{\sqrt{\Omega}} \left(\bar{U}_{oi} + \frac{1}{\eta}\right) d\bar{\eta} - \int_b^{\sqrt{\Omega}} \frac{1}{\bar{\eta}} d\bar{\eta}\right] \quad [37]$$

The last integral can be evaluated analytically. The next to the last integral has an upper limit which approaches infinity as $\Omega \to \infty$. Since $\bar{U}_{oi} \to -1/\bar{\eta}$ as $\bar{\eta} \to \infty$, it is permissible to set this limit equal to infinity.

Thus we obtain the following high-frequency limit for B_{oi}

$$B_{oi} = \frac{4A}{\pi\Omega} + \frac{\ln\Omega}{\pi\Omega} \quad [38]$$

where

$$A = -\frac{1}{2}\left[\int_0^b \bar{U}_{oi} d\bar{\eta} + \int_b^{\infty} \left(\bar{U}_{oi} + \frac{1}{\bar{\eta}}\right) d\bar{\eta} + \ln b\right] \quad [39]$$

The value of A should be independent of the value of b. However, it is broken up in this way since the first integral is unbounded as $b \to \infty$ and the second integral is unbounded as $b \to 0$. Evaluation from the information plotted in Fig. 3 gives $A = 0.563$. The high-frequency limit for B_{or} is

$$1 - B_{or} = \frac{2}{\pi\Omega}\int_0^{\infty} \bar{U}_{or} d\bar{\eta} \quad [40]$$

Substitution of Eq. [38] and [40] into Eq. [19] and [20] gives the high-frequency limits

$$4r_o\kappa R_{eff} \to 1 \text{ and } C/C_{eff} \to A + \frac{1}{4}\ln\Omega \text{ as } \Omega \to \infty \quad [41]$$

This asymptotic form for C/C_{eff} and values from Table 1 for $J = 0$ are plotted in Fig. 4. Satisfactory agreement is reached for large values of Ω.

Discussion and Conclusions

The most important result of this work is the fact that there is no high-frequency limit for C/C_{eff}. Consequently, the apparent capacity of a disk electrode embedded in an insulating plane should be expected to vary considerably with frequency. This conclusion is related to the fact that the primary current density becomes infinite at the edge of the disk. Since this effect is related critically to the edge region, the high-frequency behavior will be affected significantly by the detailed geometry at the edge. If the disk is slightly inset in the plane, a finite limit would be obtained.

Since this effect is related to the edge region, a similar conclusion would apply to a flat electrode of any shape embedded in an insulating plane. In contrast, for a mercury drop on an insulating plane, the primary current density does not become infinite, and the frequency-dependence of C/C_{eff} is considerably less (see Appendix).

A similar singular-perturbation problem in the edge region would arise at finite frequencies for large values of J. Since the behavior of the secondary current distribution in the edge region is not of critical interest, there is no compelling reason to pursue this problem. However, the correct determination of the behavior of C/C_{eff} at high frequencies required a consideration of the edge region.

Bauer, Spritzer, and Elving (4) report impedance measurements at a pyrolytic graphite disk electrode.

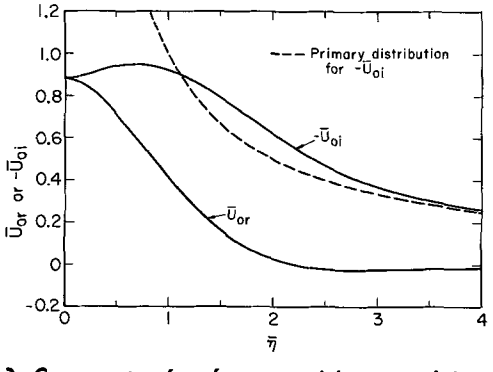

Fig. 3. Components of surface potential expressed in stretched variables for the region near the edge of the disk at high frequencies.

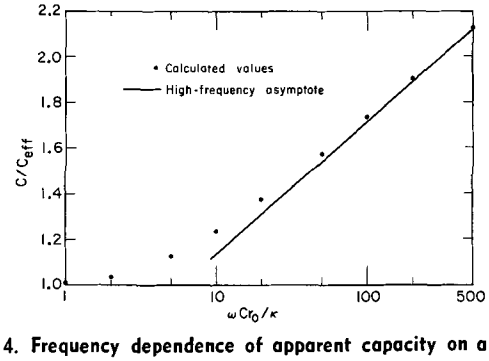

Fig. 4. Frequency dependence of apparent capacity on a smooth disk in the absence of faradaic reactions.

Their results show that the apparent capacity varies by about a factor of 2 while the apparent resistance varies by about a factor of 10. The latter result, interpreted in terms of the present analysis, suggests that faradaic reactions are not of negligible importance.

APPENDIX

A Drop Electrode on a Plane

A mercury drop at the end of a capillary tube is sometimes treated as a spherical electrode tangent to an insulating plane. The frequency dependence of the apparent capacity due to shielding by the capillary tip is inherently much less than that for a disk because the primary current distribution does not become infinite anywhere. The capillary tip can, of course, be designed to minimize the shielding and thus reduce the frequency dispersion further.

Here we use tangent-sphere coordinates (7) ν and μ

$$r = \frac{2r_o\mu}{\mu^2 + \nu^2}, \quad z = \frac{2r_o\nu}{\mu^2 + \nu^2} \qquad [42]$$

where r and z are cylindrical coordinates, with their origin at the *base* of the drop. The surface of the spherical drop is then given by $\nu = 1$. The current density relation on the surface of the drop, analogous to Eq. [6], [13], or [26] becomes

$$(j\Omega + J)(1 - U_o) = \frac{1 + \mu^2}{2}\frac{\partial U}{\partial \nu} \quad \text{at} \quad \nu = 1 \qquad [43]$$

The solution to Laplace's equation satisfying the conditions at infinity and on the insulating plane is expressed as

$$U = (\mu^2 + \nu^2)^{1/2}\int_0^\infty G(p)\frac{\cosh p\nu}{\cosh p} J_o(p\mu)\,dp \qquad [44]$$

The function $G(p)$ is analogous to the B_n coefficients used for the disk, but for the drop no discrete eigenvalues are found. By substitution of this expression into the boundary condition on the drop surface, it is possible to derive a differential equation for $G(p)$

$$2(j\Omega + J)(G - e^{-p}) = p\tanh p\frac{d^2G}{dp^2} + \left(\tanh p + \frac{2p}{\cosh^2 p}\right)\frac{dG}{dp} - \tanh p\left[\tanh p + p + \frac{2p}{\cosh^2 p}\right]G \qquad [45]$$

and $G = 1$ at $p = 0$ and $G = 0$ at $p = \infty$. The impedance Z of the system will then be given by

$$\frac{1}{4\pi\kappa r_o Z} = \int_0^\infty \frac{G(p)\,dp}{\cosh p} \qquad [46]$$

The primary potential distribution, applicable for large values of Ω or J and corresponding to $U_o = 1$, is given by $G(p) = e^{-p}$. The primary distribution has been treated by Maxwell (8) and by Matyáš (9) and has been plotted by de Levie (2). The primary current distribution on the drop is

$$\frac{i}{i_{avg}} = \frac{(1 + \mu^2)^{3/2}}{2\ln 2}\int_0^\infty \frac{J_o(p\mu)p\,dp}{\cosh p} \qquad [47]$$

and is plotted by de Levie. The value of i/i_{avg} at $\mu = 0$ (the bottom of the drop) is here calculated to be 1.3215, in good agreement with de Levie's graph.

For high frequencies we can obtain a second approximation directly from the differential equation

$$G(p) = e^{-p} + j(\tanh p + 2p/\cosh^2 p)/2\Omega\cosh p \qquad [48]$$

Substitution into the integral for the impedance gives the high-frequency limits for the resistance and capacitance of the equivalent circuit.

$$4\pi r_o\kappa R_{eff} = 1/\ln 2 = 1.4427 \text{ and } C/C_{eff} = 1.1352 \qquad [49]$$

The value for the resistance limit can also be inferred from the results of Maxwell. The capacitance in the equivalent circuit of Fig. 2 should now be represented by $4\pi r_o^2 C_{eff}$. Thus, C/C_{eff} is the ratio of the true double-layer capacity to the apparent double-layer capacity and has the same meaning as for the disk. However, the resistance ratio $4\pi r_o\kappa R_{eff}$ is the ratio of the resistance to that for a free sphere not attached to a blunt capillary tube.

Table II. Effective resistance and capacitance for a drop on a plane, in the absence of faradaic reactions (J=0)

$\omega C r_o/\kappa$	$4\pi r_o\kappa R_{eff}$	C/C_{eff}
0	?	1.0
0.1	1.5755	1.0016
1	1.5056	1.0632
10	1.4443	1.1330
∞	1.4427	1.1352

At low frequencies, the current distribution becomes uniform and $C/C_{eff} \to 1$. However, it is difficult to force the current to the surface of the drop near the point of contact, and the effective resistance might be expected to increase considerably more than was found for the disk. The solution for G at low frequencies becomes a singular-perturbation problem. Since little interest in this limit has been expressed, the problem was not pursued.

The drop problem is quite different from the disk problem. Here the high-frequency limit is relatively easy to obtain, but the low-frequency limit is difficult. For the disk the apparent capacity varies considerably with frequency; for the drop the apparent resistance varies considerably. These differences are directly related to the fact that the primary current distribution becomes infinite at the edge of the disk and becomes zero near the point of contact of the drop. Some results for intermediate frequencies are given in Table II. These values are in satisfactory agreement with the experimental results of Tessari, Delahay, and Holub (10). In particular, the factor 1/ln 2 gives a good account of the shielding effect of the capillary on the effective resistance.

Acknowledgment

Henry H. Bauer drew the author's attention to the disk problem. Robert de Levie suggested the drop problem and supplied a copy of Matyáš's paper. The author is indebted to Simon Goren for fruitful suggestions on how to treat the drop problem. In his class he treats the primary distribution by the method used here. This work was supported by the United States Atomic Energy Commission.

Manuscript submitted May 12, 1969; revised manuscript received Oct. 9, 1969.

Any discussion of this paper will appear in a Discussion Section to be published in the December 1970 JOURNAL.

NOMENCLATURE

B_n	coefficients in series expansion of the potential
C	double-layer capacity (f/cm²)
C_{eff}	apparent double-layer capacity in the equivalent circuit
G	distribution function for drop
i	current density (A/cm²)
I	total current (A)
j	$\sqrt{-1}$
J	dimensionless parameter for linear electrode kinetics
J_o	Bessel function of order zero
M_{2n}	Legendre function discussed in ref. (6)
p	separation parameter for drop

P_{2n}	Legendre polynomial or order $2n$
r	radial position from axis of disk (cm)
r_0	radius of disk or drop (cm)
R_{eff}	apparent resistance in the equivalent circuit (ohm)
t	time (sec)
U	complex potential in the solution (V)
U_0	value of U at the disk surface
V	electrode potential relative to infinity (V)
V_0	amplitude of applied potential
z	distance from plane of disk (cm)
Z	impedance of the system (ohm)
η	rotational elliptic coordinate
κ	conductivity of the solution ($ohm^{-1} - cm^{-1}$)
μ	tangent-sphere coordinate
ν	tangent-sphere coordinate
ξ	rotational elliptic coordinate
Φ	potential in the solution (V)
Φ_0	value of Φ at the electrode surface
ω	frequency of applied potential (radian/sec)
Ω	dimensionless frequency

REFERENCES

1. John Newman, *This Journal*, **113**, 501 (1966).
2. Robert de Levie, "Electrochemical Response of Porous and Rough Electrodes," in "Advances in Electrochemistry and Electrochemical Engineering," **6**, 329-397 (1967).
3. Paul Delahay, "Double Layer and Electrode Kinetics," Interscience Publishers, New York (1965).
4. H. H. Bauer, M. S. Spritzer, and P. J. Elving, *J. Electroanal. Chem. Interfacial Electrochem.*, **17**, 299 (1968).
5. G. D. Robbins, *This Journal*, **116**, 813 (1969).
6. John Newman, *ibid.*, **113**, 1235 (1966).
7. Parry Moon and D. E. Spencer, "Field Theory Handbook," Springer-Verlag, Berlin (1961).
8. J. C. Maxwell, "A Treatise on Electricity and Magnetism," Vol. 1, p. 273, Dover Publications, Inc., New York (1954). (An unaltered republication of the third edition of 1891.)
9. Zdeněk Matyáš, *Ceska Spolecnost Nauk, Prague Trida Mathematicko Prirodovedecka Vestnik*, **30**, 1 (1944).
10. G. Tessari, P. Delahay, and K. Holub, *J. Electroanal. Chem. Interfacial Electrochem.*, **17**, 69 (1968).

The Electrochemical Reduction of m-Dinitrobenzene in Liquid Ammonia Solutions

William H. Tiedemann and Douglas N. Bennion***

School of Engineering and Applied Science, University of California, Los Angeles, California

ABSTRACT

The reduction of meta-dinitrobenzene has been studied in a NH_4NO_3-NH_3 solution at 0.0°C. Two separate electrochemical techniques, the rotating disk and the potential step, were employed to determine the over-all number of electrons transferred in the first and second waves of the reduction. The first and second waves occurred at −0.08 and −0.25V *vs.* Pb reference electrode, respectively. To within experimental accuracy, four electrons were transferred in each wave. The diffusion coefficient of meta-dinitrobenzene in a NH_4NO_3-NH_3 solution was measured using a modified Stoke's diaphragm cell and found to be a 1.83 x 10^{-6} cm^2/sec.

It has been shown by Spindler and Pritchard (1) that meta-dinitrobenzene (m-DNB) is an effective cathodic depolarizer in several battery systems. The electrochemical reduction of m-DNB has been studied in aqueous media by Jackson and Dereska (2) and by Ehlers and Sease (3). In addition, the possible use of m-DNB in liquid ammonia batteries has prompted studies of m-DNB reduction in liquid ammonia systems by Harris and Matson (4), Schaer (5), and Kuwana and Darlington (6).

In these investigations the following objectives appeared to be of interest: (*i*) the number of electrons transferred in the over-all electrochemical reduction of m-DNB; (*ii*) the number of waves occurring in the reduction; (*iii*) the number of electrons transferred in each wave; (*iv*) the products of each wave; (*v*) the effect of *p*H and solvent on the waves and the products; and (*vi*) a detailed description of intermediate steps in the reaction.

Ehlers and Sease (3) used a combination of potentiostatic and polarographic reduction techniques to study the cathodic reduction of m-DNB among other polynitro aromatic compounds in aqueous media. They were able to show that there are two waves in the total reduction and that eight electrons were transferred in the over-all reaction. However, they were unable to determine the number of electrons transferred in each wave. Of all the polynitro aromatic compounds which they studied, m-DNB is the only compound in which they could not say that four electrons were transferred in each wave.

Harris and Matson (4) studied the constant current reduction of m-DNB in a NH_4SCN-NH_3 solution using a voltage trace technique. From inflections in the voltage trace, the number of equivalents transferred per mole of material reduced can be inferred provided multiple reaction paths do not occur. They reported that m-DNB undergoes two successive four electron reductions. Schaer (5) also studied the reduction of m-DNB in NH_4SCN-NH_3 solutions. He employed constant potential coulometry and reported that eight electrons were obtained in the over-all reduction.

Jackson and Dereska (2) used polarographic and potentiostatic techniques to study the mechanism of the cathodic reduction of m-DNB in aqueous solution at various *p*H values. They obtained two waves with four electrons in each wave. They were able to isolate the product of the first wave as 3-nitrophenylhydroxylamine (3NPHA). However, they were not able to isolate the product of the second wave. The inability of previous researchers (3-5) to isolate the product of the first wave was apparently due to the techniques employed. Jackson and Dereska (2) found that below 100% reduction the product of the first wave is all

** Electrochemical Society Student Associate.
* Electrochemical Society Active Member.

3NPHA. However, near 100% reduction no identifiable product was obtained (the residue turned brown). They proposed that the mixed product observed when 100% reduction is approached for the first wave indicates that reduction of the first nitro group does not occur completely before reduction of the second group begins.

The present study was undertaken in order to clarify some of the previous results obtained in NH_4SCN-NH_3 solutions. Since it has been observed (6) that the SCN^- ion reacts slowly with m-DNB to produce a radical anion, a solution of NH_4NO_3-NH_3 (which does not react with m-DNB) was employed in this study. The m-DNB molecule is protonated in the solution since the solution behaves like a strong acid as shown by Given and Peover (7) and Schaer (5).

To demonstrate consistency and accuracy of results, two separate and independent electrochemical techniques were employed, the rotating disk electrode (8) and the potential step (9). Only the over-all reactions associated with the first and second waves will be considered.

Experimental

Reagents.—Ammonia (NH_3) was obtained from Matheson Company and was further purified by two successive single stage distillations. Conductance was used as a measure of purity of the NH_3 obtained in the final distillation. The conductance was determined as 1×10^{-8} mho/cm. NH_4NO_3 obtained from Sargent Company was vacuum dried at 100°C for 24 hr. A solution of NH_4NO_3-NH_3 (0.37 mole fraction of NH_4NO_3) was prepared by condensing NH_3 from a container which has been previously weighed into a glass vessel containing a known weight of NH_4NO_3. After the desired amount of NH_3 had been condensed, the container of NH_3 was weighed to determine the quantity of NH_3 transferred to the glass vessel. The solution was then stored at 0.0°C. The m-DNB used was Eastman's highest purity and was recrystallized once from chloroform and vacuum dried at 50°C for 24 hr. All solutions of varying concentrations of m-DNB in NH_4NO_3-NH_3 were prepared at the same time by adding a known volume of NH_4NO_3-NH_3 into a flask containing a known weight of m-DNB. The volume of each solution so prepared was about 300 ml. The resulting solutions were light yellow in color.

Apparatus.—A detailed description of the equipment used in the rotating disk and potential step experiments has been given (10). The essential features shall be discussed briefly. A Dumore lathe quill was employed to hold the rotating electrode in a vertical position. A pulley-belt system was used to transmit the desired angular velocity to the rotating electrode via the Dumore quill. The eccentricity at the face of the electrode was determined to be less than 0.001 of an inch. The surface of the electrode consisted of a platinum disk surrounded by Teflon (see Fig. 1). A glass tube was used to connect the cell to a Viton rubber seal. The system was air tight. No NH_3 leak could be detected.

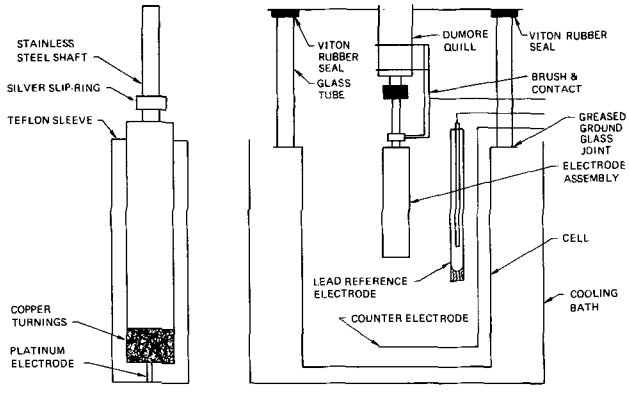

Fig. 1. Rotating disk electrode and electrochemical cell

The spherical platinum electrode used in the potential step experiments was prepared by West Glass Corporation. The average geometrical area of the sphere was determined using an optical comparator. The counterelectrode consisted of a platinum wire mesh cylinder. The cell was sealed with standard, ground glass joints. The cell was air tight, and no NH_3 odor could be detected outside the cell. The rotating disk, after being polished, and the spherical electrode were electrochemically cleaned in chromic acid, washed in redistilled water, and vacuum dried at 150°C for 24 hr.

A cracked-glass lead reference electrode described by Panzer (11) was used in both experiments. The reference electrode consisted of a cracked glass tube filled with NH_3 solution saturated with $LiNO_3$ and $Pb(NO_3)_2$ and contained a strip of lead wire. The ohmic resistance across the cracked glass was about 5×10^5 ohms. Due to this large resistance, a 610B Keithley electrometer which had an internal resistance of 10^{14} ohm was used.

An Anotrol 4700 M potentiostat was used in the potential step experiments as well as in the potentiostatic work with the rotating disk.

A Stokes-type diaphragm cell (12) was used to measure the diffusion coefficient of m-DNB in NH_4NO_3-NH_3 solutions at 0°C. The only modification of significance to Stokes' cell was the replacement of the stoppered ends by Teflon stopcocks.

Procedure.—Approximately 120 ml of a m-DNB-NH_4NO_3-NH_3 solution were used in each experiment. Experiments were conducted on blank solutions of NH_4NO_3-NH_3 to determine the contribution of extraneous reactions to the measured currents. The resulting current was found to be less than 0.5% of the current obtained from the smallest concentrations of m-DNB used. This indicates that the impurity level was low enough not to interfere with the measurements made in these experiments.

Rotating disk electrode.—The electrochemical cell, shown in Fig. 1, which had been cooled to 0.0°C in an ice bath, was flushed several times with NH_3 gas before about 120 ml of solution were added. Several cathodic pulses, lasting about 5 sec, were applied to the electrode before the experiment was begun in order to reduce impurities remaining on the surface. The rotation speed was set by adjusting the control unit which was connected to a d-c motor. The rotation speed was measured with a General Radio Strobotac (Type 1531-A) and recorded. Both galvanostatic and potentiostatic cathodic reductions were performed (which produced the same η *vs.* i curve). When a steady-state condition was reached, the values for the current and potential (*vs.* a lead reference electrode) were recorded and a new setting of the current or potential was made. This procedure was continued until the run was terminated, *i.e.*, a limiting current was reached. Then the rotating speed and/or the concentration of m-DNB was changed and the above procedure repeated.

Potential step.—The same procedure for filling the cell and cleaning the electrode as described above was used in the potential step experiments. The potential (*vs.* a lead reference electrode) sufficient to produce a limiting current at the surface of the electrode was set on the potentiostat. A potential pulse was then applied to the cell. The response was displayed on an oscilloscope and a permanent record was obtained on polaroid film. The potential was changed to determine if a true limiting current had been reached. The oscilloscope was fitted with a projected graticule to eliminate parallax and increase the accuracy of the readings. The concentration was changed and the above procedure repeated.

Diaphragm cell.—The cell was flushed with NH_3 gas. This was done to eliminate entrapment of air in the pores of the diaphragm. A syringe was used to fill the cell. The side containing the dilute solution was filled first. The cell was inverted, and the concentrated solution added to the second compartment. A vacuum pump was connected to the cell so that trapped gas in the pores was removed. A period of several hours was allowed for prediffusion in the diaphragm. The two compartments of the cell were refilled and the experiment begun. The cell was thermostated in a glycol bath at 0.0° ± 0.2°C. The experiment was terminated after 192 hr. The concentration in the bottom compartment changed from 0.0202 to 0.0191M, and the concentration in the top compartment changed from 0.0010 to 0.0023M.

The final concentrations in the two compartments of the cell were analyzed by removing a known volume of solution from each compartment and allowing the NH_3 to evaporate at room temperature. The m-DNB was extracted from the residue by adding spectrograde ether to the residue. The ether was then transferred to a flask, and the ether was allowed to evaporate. The remaining m-DNB was weighed.

The cell was calibrated by Dunning (13). Stokes (12) claimed 0.2% accuracy for this method. Our calibration runs had a mean deviation of 9.2%. This variation is due to small amounts of gas trapped in the diaphragm. Better degassing procedures are needed to improve this accuracy.

Results

Rotating disk.—The equation governing the use of the rotating disk electrode was developed by Levich (8). Riddiford (14), and Newman (15) have since made a Schmidt number correction. Applying their suggested correction to this system, the equation is

$$i_{lim} = \frac{nFD^{2/3}\ C^{\circ}\ \omega^{1/2}}{1.63\ \nu^{1/6}} \qquad [1]$$

where 1.61 in Levich's original derivation is now changed to 1.63 using the Schmidt number correction.

The cathodic reduction of m-DNB in NH_4NO_3-NH_3 solution at 0.0°C on the rotating disk occurred in two waves. The first wave appears at about −0.08V *vs.* a lead reference electrode and the second wave occurred at −0.25V. A typical plot of η *vs.* i as a function of rotation speed is shown in Fig. 2. A plot of i_{lim} *vs.* $\omega^{1/2}$ for the first and second waves resulted in a straight line which passed through the origin as predicted by

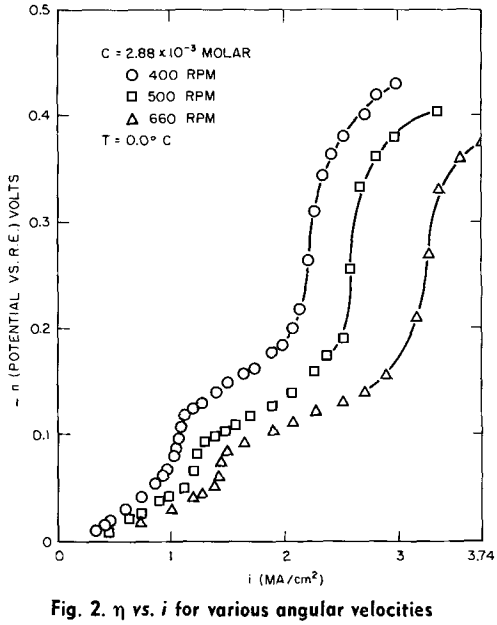

Fig. 2. η *vs.* i for various angular velocities

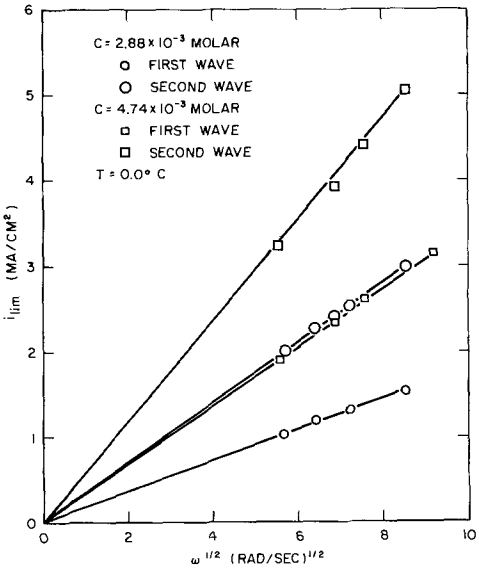

Fig. 3. Effect of varying the disk velocity on the limiting diffusion current for m-DNB reduction.

Eq. [1] (see Fig. 3). A plot of

$$\frac{1.63\ \nu^{1/6}\ i_{lim}}{F\ \omega^{1/2}}\ vs.\ C^{\circ}$$

also resulted in straight lines passing through the origin as predicted by Eq. [1] (see Fig. 4). The slope of the plot in Fig. 4 yields $nD^{2/3}$; n is the over-all number of electrons transferred and D is the diffusion coefficient of the bulk species diffusing to the surface of the electrode. The diffusion coefficient of m-DNB in NH_4NO_3-NH_3 at 0.0°C as measured by the diaphragm cell method was found to be 1.83 x 10^{-6} cm²/sec. The type of species present in the NH_4NO_3-NH_3 solution is the protonated m-DNB molecule (5, 7). Using the value of the diffusion coefficient determined in this work, the values of the number of electrons for the first and second waves were found to be 4.14 and 3.91, respectively.

Potential step.—The equation developed for the limiting current at the surface of a spherical electrode has been presented by Delahay (9) and is shown in Eq. [2]

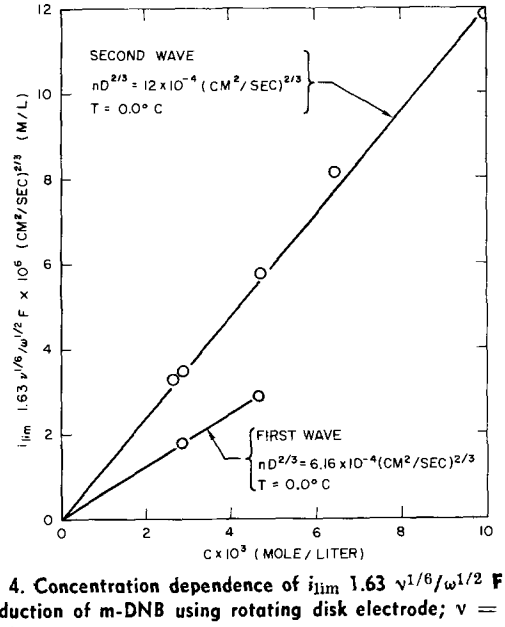

Fig. 4. Concentration dependence of i_{lim} 1.63 $\nu^{1/6}/\omega^{1/2}$ F vs. C° for reduction of m-DNB using rotating disk electrode; ν = 0.0408 stokes (10).

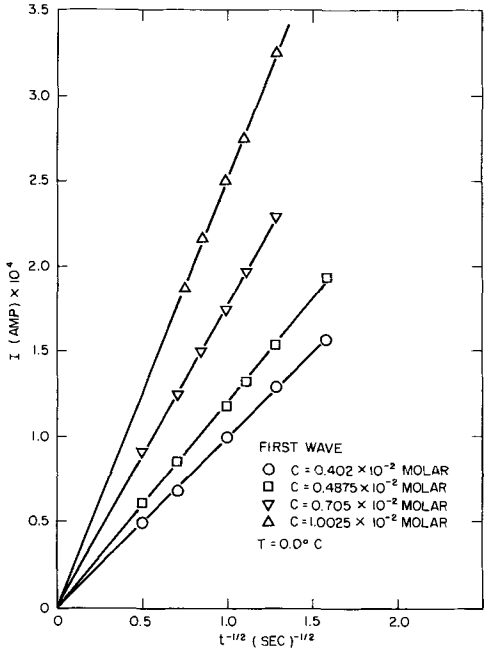

Fig. 5. Variation of the limiting diffusion current with time for the reduction of m-DNB using the potential step for the first wave.

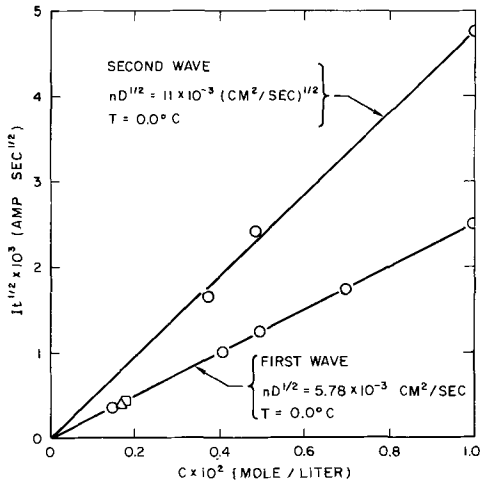

Fig. 6. Concentration dependence of $I\ t^{1/2}$ for the reduction of m-DNB using the potential step.

$$I_{\text{lim}} = \frac{n\mathbf{F}AD^{1/2}\ C^\circ}{\pi^{1/2}\ t^{1/2}} + \frac{n\mathbf{F}AD\ C^\circ}{r^\circ} \qquad [2]$$

For short response times (a few seconds), $(n\mathbf{F}ADC^\circ)/r^\circ$ is negligible compared to

$$\frac{n\mathbf{F}AD^{1/2}\ C^\circ}{\pi^{1/2}\ t^{1/2}}$$

Therefore, for $t < 4$ sec Eq. [2] reduces to the following

$$I_{\text{lim}} = \frac{n\mathbf{F}AD^{1/2}\ C^\circ}{\pi^{1/2}\ t^{1/2}} \qquad [3]$$

The current was plotted *vs.* $t^{-1/2}$ for several concentrations (Fig. 5). The plot produced straight lines which intersected the origin as predicted by Eq. [3]. Figure 6 contains the plots for the first and second wave of

$$I_{\text{lim}}\ t^{1/2}\ vs.\ C^\circ$$

Again it is observed that a straight line results which passes through the origin. The over-all numbers of electrons transferred in the first and second waves are determined from the slopes of the plots in Fig. 6 and the previously determined diffusion coefficient. They were found to be 4.24 and 3.92, respectively.

Discussion

Table I summarizes values of the number of electrons transferred in each wave as determined in this work as well as in the literature cited. As can be seen, the agreement between the results obtained in this paper and that obtained by previous researchers is good.

Based on the similarities between the system of Jackson and Dereska (2) (m-DNB in H_2O with H^+ ions) and that of the system described in this paper (m-DNB in NH_3 with NH_4^+ ions), and the consistency of results, it appears that the over-all reaction mechanism proposed by Jackson and Dereska (2) is the same for ammonia, the system being considered here. Therefore, by replacing H^+ with NH_4^+, we obtain the following

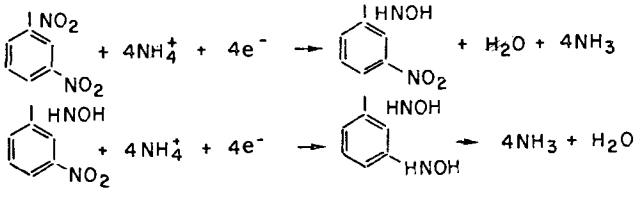

A detailed description of the intermediate steps in the cathodic reduction of m-DNB was not attainable in this study since the NH_4^+ ion concentration could not be varied sufficiently. If one were to use $LiNO_3$ as the supporting electrolyte, the effects of variations in NH_4^+ ion concentration could be examined and details of the reaction mechanism studied.

Acknowledgment

This work was supported by the Electrochemistry Branch of the Naval Weapons Center, Corona, California, on Contract Number N123-(62738)57439A.

Manuscript submitted Aug. 11, 1969; revised manuscript received *ca.* Oct. 20, 1969.

Any discussion of this paper will appear in a Discussion Section to be published in the December 1970 JOURNAL.

LIST OF SYMBOLS

η	potential between the working electrode and reference electrode, V
i	average current density, mA/cm²
i_{lim}	limiting current density, mA/cm²
n	number of electrons produced in one wave from one molecule or ion
I_{lim}	limiting current, mA
$\mathbf{F}$	Faraday's constant, coulomb/equiv.
D	diffusion coefficient of species reacting at surface of electrode, cm²/sec

Table I. Summary of results for reduction of m-DNB

	System	1st Wave	2nd Wave	Total
Ehlers and Sease	H_2O	—	—	8
Jackson and Dereska	H_2O	4	4	8
Harris and Matson	NH_3-NH_4SCN	4	4	8
Schaer	NH_3-NH_4SCN	—		8 ± 10%
This work, P.S.	NH_3-NH_4NO_3	4.24 ± 0.14	3.92 ± 0.1	8.16 ± 0.24
This work, R.D.	NH_3-NH_4NO_3	4.14 ± 0.24	3.91 ± 0.21	8.05 ± 0.40

C° concentration of reacting species in the bulk of solution, moles/liter
ω angular velocity, radians/sec
ν kinematic viscosity, cm^2/sec
π 3.1416
t time, sec
A geometric area of sphere, cm^2
r° radius of sphere, cm

REFERENCES

1. W. C. Spindler and R. J. Pritchard, *"Advances in Battery Technology Symposium," So. Calif-Nevada Section of the Electrochem. Soc.*, **1**, 21 (1965).
2. G. W. Jackson and J. S. Dereska, *This Journal*, **112**, 1218 (1965).
3. V. E. Ehlers and J. W. Sease, *Anal. Chem.*, **31**, 16 (1959).
4. W. S. Harris and G. N. Matson, Naval Ordnance Center, Corona Lab., Report 7241, 1962.
5. M. J. Schaer, Naval Ordnance Center, Corona Lab. Report 737, 1967.
6. T. Kuwana and R. K. Darlington, Naval Ordnance Center, Corona Lab., Report 697, 1967.
7. P. H. Given and M. E. Peover, *J. Chem. Society*, **1960**, 385.
8. V. G. Levich, "Physiochemical Hydrodynamics," Prentice-Hall, Cliffside, N.J. (1962).
9. P. Delahay, "New Methods in Electrochemistry," Interscience Publishers, New York (1954).
10. W. H. Tiedemann, "Conductance and Electrochemical Behavior of m-Dinitrobenzene in Liquid Ammonia Solutions," M.S. Thesis, University of California, Los Angeles, June 1968.
11. R. E. Panzer and G. E. McWilliams, Naval Ordnance Center, Corona Lab., Report 689, 1966.
12. R. H. Stokes, *J. Am. Chem. Soc.*, **72**, 763 (1950).
13. J. S. Dunning, "The Electrochemical Reduction of meta-Dinitrobenzene in Dimethylsulfoxide," M.S. Thesis, University of California, Los Angeles, June, 1968.
14. A. C. Riddiford, *Advan. Electrochem. Electrochem. Eng.*, **4** (1966).
15. J. Newman, *J. Phys. Chem.*, **70**, 1327 (1966).

Rotating Ring-Disk Electrodes

I. Fundamentals of the Digital Simulation Approach. Disk and Ring Transients and Collection Efficiencies

Keith B. Prater[1] and Allen J. Bard*

Department of Chemistry, The University of Texas at Austin, Austin, Texas

ABSTRACT

A digital simulation technique has been used to treat electrode reactions occurring at the rotating ring-disk electrode (RRDE). The method of treating normal diffusion, normal and radial convection, and homogeneous kinetics at the RRDE is discussed and results for the transient and steady-state currents at the disk and ring electrodes in the absence of kinetic complications are given. Where comparisons are possible, the simulated results were found to be in excellent agreement with previous theoretical treatments.

The rotating ring-disk electrode (RRDE) was introduced in 1959 by Frumkin and Nekrasov (1). The addition of a ring electrode to the rotating disk electrode permitted the detection of products formed by electrode reactions and provided a steady-state method for investigating coupled chemical reactions. However, the mass transfer conditions existing at the RRDE are rather complex, and the mathematical treatment of the RRDE, especially in the presence of kinetic complications, is difficult. A general mathematical treatment was not given until 1966 when a series of papers by Albery and Bruckenstein (2-9) appeared. In these papers, Albery and Bruckenstein presented an exact treatment of the steady-state collection efficiency as a function of electrode geometry in the absence of kinetic complications (3). They also presented approximate treatments of first- and second-order follow up reactions. Unfortunately, as pointed out by Albery (10), the treatment of the first-order case is not applicable to any practical electrode without further approximations. Their second-order treatment is limited to certain regions of rotation rate and rate constant. Furthermore, expansion of these treatments to more complex mechanisms, such as ECE reactions and electrogenerated chemiluminescence (11), seems unlikely.

In this series of papers, we present the results of the application of a digital simulation technique to this problem. This technique is capable of generating a theoretical working curve for any particular electrode under any imaginable kinetic situation. The simulation technique used is a modification of that introduced to electrochemical problems by Feldberg (12) and most fully described in a recent chapter (13). This paper also discusses the mathematical background of the method and gives a detailed description of other applications of this technique.

The principal problem encountered in simulating the RRDE is that, due to the normal and radial convective flow, the concentrations of all species are functions of two spatial variables, X, the normal distance from the electrode surface, and R, the radial distance from the axis of rotation. It is here that this paper differs from those previously presented.

Digital Simulation Method

Digital model.—In a digital simulation of an electrochemical system, one first divides the solution into a number of small volume elements. These volume elements will henceforth be called "boxes" regardless of shape. The shapes of these boxes are chosen in such a way that one can reasonably assume that the solution within each box is homogeneous. For an RRDE, the symmetry of the system suggests the following model. The solution is first divided into thin parallel layers which are Δx cm thick. The electrode is placed in the center of the first layer, parallel to the planes dividing the layers. Then each layer is divided into a cylindrical box of radius $\frac{1}{2}\ \Delta r$ cm which is centered about the axis of rotation, and a series of concentric annular boxes Δr cm wide (Fig. 1). The parameter, Δr, is chosen in such a way that the pertinent radii of

* Electrochemical Society Active Member.
[1] Present address: University of Texas at El Paso, El Paso, Texas.

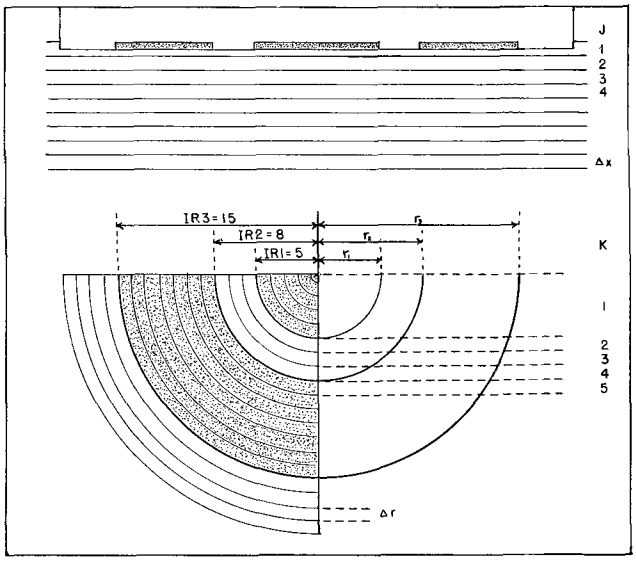

Fig. 1. Digital simulation model of the rotating ring disk electrode.

the electrode, r_1 (the radius of the disk electrode), r_2 (the radius to the inner edge of the ring electrode), and r_3 (the radius to the outer edge of the ring electrode), can be satisfactorily approximated by

$$r_1 = (IR1\text{-}0.5)(\Delta r)$$
$$r_2 = (IR2\text{-}0.5)(\Delta r)$$
$$r_3 = (IR3\text{-}0.5)(\Delta r) \quad [1]$$

where $IR1$, $IR2$, and $IR3$ are integers and correspond to the number of boxes necessary to represent the particular radial distances. Obviously, the smaller Δr is (*i.e.*, the greater the number of annular boxes), the better the approximation is likely to be. Unfortunately, the number of boxes must be weighed against the length of computation time and some compromise reached.

In the interest of minimizing computation time, one can very reasonably assume that the disk electrode is a uniformly accessible surface. This condition holds under usual experimental conditions where an excess of supporting electrolyte is present (14). This means that in each layer, the solution in the cylindrical volume of radius $(IR1\text{-}0.5)(\Delta r)$ centered about the axis of rotation is homogeneous and can be represented by one large cylindrical box.

For the sake of simplicity the following convention is used. Each box is referred to by its layer number, J, and its radial number, K. The layer containing the electrode is the $J = 1$ layer, and all other layers are numbered consecutively outward from the electrode. Within any layer, the large central cylindrical box is called the $K = 1$ box, and all the annular boxes are numbered consecutively outward from this box. The large cylindrical box in the first layer ($J = 1$, $K = 1$) corresponds to the disk electrode. Similarly, the appropriate first layer ($J = 1$) annular boxes correspond to the gap region, the ring electrode region, or the outer insulation region.

A concentration for each of the active species in solution is then assigned to each box. This concentration is associated with the center of each box. Thus, in the particular case of the boxes in the first layer, the concentrations in those boxes correspond to the concentrations at the electrode surface. Before electrolysis begins, all boxes are assigned concentrations which correspond to the bulk concentration of the solution. At the beginning of electrolysis, $t = 0$, the concentrations in those first layer boxes corresponding to the disk and ring electrodes are changed to reflect appropriate boundary conditions. These changes result in a concentration gradient between some of the corresponding boxes in the first and second layers. Using a finite difference representation of Fick's second law, the extent to which the concentrations in these boxes are changed by diffusion across the boundary between them in a time interval, Δt, is calculated. These changes in the original array of concentrations produce a new array reflecting the effects of diffusion during this first time interval. In all calculations we assume, following the arguments of Albery and Bruckenstein (3), that radial diffusion is negligible when compared with radial convection.

In the case of a rotating electrode, convection is also taking place during the same time interval, Δt. From the treatment by Levich (15) of convection to a rotating disk electrode one can calculate the normal and radial components of fluid velocity at any point near the electrode. Thus, one can calculate the distance a given fluid volume will travel in the normal and radial directions in a time, Δt. If, for example, this calculation reveals that the volume element in the Kth ring of the Jth layer at the end of Δt seconds has traveled a distance ΔJ in the normal direction and a distance ΔK in the radial direction, then by replacing the concentration in the J, Kth box in the existing array with the concentration at $J + \Delta J$, $K - \Delta K$, a new array is generated which reflects the effects of both diffusion and convection for a time Δt.

If, in addition, one or more species undergo homogeneous reactions, this can be simulated by calculating, for each box containing the appropriate species, the amount by which each species will be depleted or increased according to the appropriate rate law in a time Δt. This generates an array which represents the expected concentration profile of the simulated system at a time Δt after the initiation of electrolysis. From this profile, the current observed at this point in an experiment can be calculated by assuming that the current is proportional to the difference between the concentrations in the corresponding boxes in the first and second layers, *i.e.*, the flux at the electrode surface. After making the adjustments to the concentrations in the appropriate boxes due to the passage of current, the above process is repeated to give a new concentration profile and current at $t = 2\Delta t$ and so on until the steady state has been attained. In the limit, as $\Delta x \to 0$, $\Delta t \to 0$, and $\Delta r \to 0$, the calculated current-time behavior and the steady-state currents should approach those observed experimentally.

Initial and boundary conditions.—Let us now consider the simulation in greater detail by discussing the following situation. The solution initially contains only species A at bulk concentration C^o_A. At time $t = 0$, the potential of the disk electrode is stepped to a potential on the limiting current plateau for the reaction

$$A \pm ne \to B \quad [2]$$

We consider the case where species B undergoes a first order homogeneous reaction to give some electroinactive species, X, by the reaction

$$B \xrightarrow{k_1} X \quad [3]$$

The potential of the ring electrode is such that all B reaching the ring electrode is instantaneously converted back to A by

$$B \mp ne \to A \quad [4]$$

In digital simulations, to make each computation as general as possible, all calculations are done in terms of dimensionless parameters. Hence, all concentrations are normalized with respect to the initial concentration of bulk species A. Thus, the initial fractional concentration of species A in any box is

$$F_A(J,K) = C^o_A/C^o_A = 1.0 \quad [5]$$

and the fractional concentrations of species B and X are

$$F_B(J,K) = 0.0$$
$$F_X(J,K) = 0.0 \quad [6]$$

At the initiation of electrolysis, $t = 0$, the boundary conditions for the disk box in the case of a potential step to the limiting current region are

$$F_A(1,1) = 0.0$$
$$F_B(1,1) = 1.0$$
$$F_X(1,1) = 0.0 \quad [7]$$

For those first layer boxes which correspond to the ring electrode, the initial boundary conditions are

$$F_A(1,K_R) = 1.0$$
$$F_B(1,K_R) = 0.0$$
$$F_X(1,K_R) = 0.0 \quad [8]$$

where K_R represents all values of K corresponding to the ring electrode region.

Diffusion effects.—These conditions set up a concentration gradient between the first and second layer disk boxes ($J = 1$, $K = 1$) and ($J = 2$, $K = 1$), which gives rise to diffusion across the boundary between these boxes. The amount of material crossing the boundary in Δt seconds can be calculated using the finite difference representation of Fick's second law

$$\Delta F_A(J,K) = DM_A[F_A(J+1) - F_A(J,K)] - DM_A[F_A(J,K) - F_A(J-1,K)] \quad [9]$$

or

$$\Delta F_A(J,K) = DM_A[F_A(J+1,K) - 2F_A(J,K) + F_A(J-1,K)] \quad [10]$$

This states that for any time interval, Δt, the change in the fractional concentration of species A in the J,Kth box is the difference between the amount of A entering from the adjacent box of higher concentration and the amount of A going into the adjacent box of lower concentration. The amount entering or leaving the box is proportional to the concentration gradient across the boundary. The proportionality factor, DM_A is given by

$$DM_A = D_A \Delta t/(\Delta X)^2 \quad [11]$$

where D_A is the diffusion coefficient of species A and ΔX is the width of one layer. The parameter, Δt, is defined below. By applying Eq. [10] to all boxes and then replacing $F_A(J,K)$ by $F_A(J,K) + \Delta F_A(J,K)$, a new array of concentrations is generated which represents the effects of diffusion for a time interval Δt. The concentrations of species B and X are similarly treated. For this technique to converge, DM_A must have a value less than 0.5 (13). In most of these calculations, DM_A was taken to be 0.45.

Convection effects.—The parameter, Δt, is the real time length of one iteration. Thus

$$\Delta t = t_k/L \quad [12]$$

where t_k is some experimentally known time or time dimensioned variable, and L is the number of iterations used to simulate that time. To evaluate the appropriate form of t_k, consider the equation for the velocity of convective fluid flow in the direction normal to the electrode. In the region near the electrode, this is given by (15)

$$v_X = -0.51\,\omega^{3/2}\,\nu^{-1/2}\,X^2 \quad [13]$$

where ω is the rotation rate in radians/second, ν is the kinematic viscosity in square centimeters per second, and X is the distance from the electrode surface. The velocity in the X direction may be represented by the derivative, dX/dt. Thus

$$dX/dt = -0.51\,\omega^{3/2}\,\nu^{-1/2}\,X^2 \quad [14]$$

Solving the above, for X and evaluating between t_2 and t_1, one obtains

$$\frac{1}{X_2} - \frac{1}{X_1} = -0.51\,\omega^{3/2}\,\nu^{-1/2}\,(t_2 - t_1) \quad [15]$$

If we let $t_2 - t_1 = \Delta t$, then X_1 and X_2 represent the distance of a particular solution volume from the electrode surface at the beginning and end of the time interval, Δt. In terms of the layer number, J, the distance from the electrode surface to the center of any box is given by $(J - 1)(\Delta X)$. Let

$$XJ = J - 1 \quad [16]$$

and

$$X_1 = XJ(\Delta X) \quad [17]$$

then X_2 is the position in the old array of the solution volume which will be in the center of the Jth box at the end of the time interval, Δt. It is convenient to let

$$X_2 = (XJJ)\Delta X \quad [18]$$

where XJJ is a nonintegral distance from the electrode expressed in terms of numbers of boxes.

We can now rewrite Eq. [15] as

$$\frac{1}{XJJ} - \frac{1}{XJ} = -0.51\,\omega^{3/2}\,\nu^{-1/2}\,\Delta X\,\Delta t \quad [19]$$

or

$$XJJ = XJ/[1 - (XJ)(0.51\,\omega^{3/2}\,\nu^{-1/2}\,\Delta X \Delta t)] \quad [20]$$

The product $(0.51\,\omega^{3/2}\,\nu^{-1/2}\,\Delta X \Delta t)$ is dimensionless and is designated V_{NAUT}, that is

$$V_{NAUT} = 0.51\,\omega^{3/2}\,\nu^{-1/2}\,\Delta X \Delta t \quad [21]$$

From Eq. [11]

$$\Delta X = (D_A \Delta t/DM_A)^{1/2} \quad [22]$$

Thus

$$V_{NAUT} = 0.51\,\omega^{3/2}\,D_A^{1/2}\,\nu^{-1/2} DM_A^{-1/2} \Delta t^{3/2} \quad [23]$$

Using Eq. [12]

$$V_{NAUT} = 0.51\,\omega^{3/2}\,D_A^{1/2}\,\nu^{-1/2}\,DM_A^{-1/2}\,t_k^{3/2}\,L^{-3/2} \quad [24]$$

Letting

$$t_k = \omega^{-1}\,\nu^{1/3}\,D_A^{-1/3}\,(0.51)^{-2/3} \quad [25]$$

$$V_{NAUT} = DM_A^{-1/2}\,L^{-3/2} \quad [26]$$

then

$$XJJ = XJ/[1 - (XJ)(V_{NAUT})] \quad [27]$$

Note that the above substitutions render the calculation of the effects of convection not only dimensionless, but also strictly in terms of simulation variables. By replacing the concentrations now at the center of each box with the concentrations at the distance calculated from Eq. [27], a new array representing the effects of diffusion and convection normal to the electrode for a time, Δt, is generated.

In a similar manner, the effects of convection in the radial direction can be calculated. Beginning with the equation for fluid velocity in the radial direction near the electrode (15)

$$v_R = -0.51\,\omega^{3/2}\,\nu^{-1/2}\,XR \quad [28]$$

where R is the distance from the axis of rotation, one obtains

$$dR/dt = -0.51\,\omega^{3/2}\,\nu^{-1/3}\,XR \quad [29]$$

Solving Eq. [29] one obtains

$$\ln(R_2) - \ln(R_1) = -0.51\,\omega^{3/2}\,\nu^{-1/2}\,X\,(t_2 - t_1) \quad [30]$$

As before, R_2 and R_1 are the positions of a solution volume at times t_2 and t_1. Rearranging and substituting for X and $(t_2 - t_1)$

$$\ln(R_1/R_2) = 0.51\,\omega^{3/2}\,\nu^{-1/2}\,XJ\,\Delta X\,\Delta t \quad [31]$$

If we let

$$R_1 = RK(\Delta r) \quad [32]$$

and

$$R_2 = RKK(\Delta r) \quad [33]$$

and combine terms, we get

$$\ln(RK/RKK) = (V_{NAUT})(XJ) \quad [34]$$

and finally

$$RKK = RK \exp\left[-(V_{NAUT})(XJ)\right] \quad [35]$$

where

$$RK = K + IR1 - 2 \quad [36]$$

and is the radial distance of the solution volume in the center of the Kth box from the axis of rotation. RKK is the present position of the solution volume which will be at RK at the end of the Δt interval. Equation [35] allows the generation of an array of concentrations which represents the effects of diffusion and both normal and radial convection for a time, Δt.

Kinetic effects.—For a first order disappearance of species B from the J, Kth box, one can write the rate law in the form

$$\Delta C_B(J,K)/\Delta t = -kC_B(J,K) \quad [37]$$

Normalizing the concentrations by dividing both sides of the equation by C^o_A, and remembering that $F_B(J,K) = C_B(J,K)/C^o_A$, we have

$$\Delta F_B(J,K) = -k\Delta t\, F_B(J,K) \quad [38]$$

or substituting for Δt

$$\Delta F_B(J,K) = -[k\omega^{-1}\nu^{-1/3} D_A^{-1/3}(0.51)^{-2/3}]F_B(J,K)/L \quad [39]$$

The dimensionless collection of terms in brackets in Eq. [39] is called XKT, so that

$$XKT = k\omega^{-1}\nu^{1/3} D_A^{-1/3}(0.51)^{-2/3} \quad [40]$$

This is the dimensionless rate parameter which is used in the calculations. Rewriting Eq. [39], we get

$$\Delta F_B(J,K) = -XKT[F_B(J,K)]/L \quad [41]$$

Similarly, the expression for the appearance of species X is

$$\Delta F_X(J,K) = XKT[F_B(J,K)]/L = -\Delta F_B(J,K) \quad [42]$$

By replacing $F_B(J,K)$ with $F_B(J,K) + \Delta F_B(J,K)$ and $F_X(J,K)$ with $F_X(J,K) + \Delta F_X(J,K)$, an array of concentrations which represents the concentration profile one would expect to observe under these conditions after Δt seconds is generated.

Calculation of current.—The fractional flux of a species, Z, moving from a $J = 2$ box into a $J = 1$ box is given by

$$FF_Z(K) = DM_Z[F_Z(2,K) - F_Z(1,K)] \quad [43]$$

The contribution to the current from a given box, K, can be expressed as

$$i(K) = [FF_Z(K)](C^o_A)[A(K)\Delta X](n\mathbf{F})/\Delta t \quad [44]$$

where $A(K)$ is the area of the Kth box (thus $A(K)\Delta X$ is the volume of that box). Rearranging and substituting for ΔX and Δt we get

$$i(K)/n\mathbf{F}C^o_A = FF_Z(K)\, A(K)\, D_Z^{1/2} DM_Z^{-1/2} L^{1/2} t_k^{-1/2} \quad [45]$$

Substituting for t_k and rearranging we have

$$i(K)/(0.51)^{1/3} n\mathbf{F}C^o_A D_Z^{2/3}\omega^{1/2}\nu^{-1/6} = FF_Z(K)\, A(K)\, L^{1/2} DM_Z^{-1/2} \quad [46]$$

If we divide both sides of Eq. [46] by the area of the disk electrode, A_D, we have

$$i(K)/(0.51)^{1/3} n\mathbf{F}A_D C^o_A D_Z^{2/3}\omega^{1/2}\nu^{-1/6} = FF_Z(K) L^{1/2} DMZ^{-1/2} A(K)/A_D \quad [47]$$

Both sides of Eq. [47] are now dimensionless and the simulation variables are all on one side of the equation.

Equation [47] can be used to calculate the current at the disk electrode. That is

$$i_d/(0.51)^{1/3} n\mathbf{F}A_D C^o_A D_A^{2/3}\omega^{1/2}\nu^{-1/6} = FF_A(1)\, L^{1/2} DM_A^{-1/2} \quad [48]$$

In the case of a potential step to the limiting current plateau, since $F_A(1,1) = 0.0$, the fractional flux becomes

$$FF_A(1) = DM_A F_A(2,1) \quad [49]$$

The dimensionless parameters on each side of Eq. [48] are called ZD. Thus, in terms of experimental variables

$$ZD = i_d/(0.51)^{1/3} n\mathbf{F}A_D C^o_A D_A^{2/3}\omega^{1/2}\nu^{-1/6} \quad [50]$$

while in terms of the simulation

$$ZD = DM_A^{1/2} F_A(2,1)\, L^{1/2} \quad [51]$$

Similarly, the current at the ring electrode can be calculated. Using Eq. [47]

$$i_r/(0.51)^{1/3} n\mathbf{F}A_D C^o_A D_B^{2/3}\omega^{1/2}\nu^{-1/6} = L^{1/2} DM_B^{-1/2} \sum_{K_R} FF_B(K)A(K)/A_D \quad [52]$$

where the summation is over all radial boxes, K, corresponding to the ring electrode.

The dimensionless parameter on each side of Eq. [52] are called ZR. Thus, in terms of experimental variables

$$ZR = i_r/(0.51)^{1/3} n\mathbf{F}A_D C^o_A D_B^{2/3}\omega^{1/2}\nu^{-1/6} \quad [53]$$

while in terms of simulation variables

$$ZR = L^{1/2} DM_B^{-1/2} \sum_{K_R} FF_B(K)\, A(K)/A_D \quad [54]$$

If the potential at the ring is such that all B reaching the ring is instantly converted into A, then $F_B(1,K_R) = 0.0$ and Eq. [43] becomes

$$FF_B(K_R) = DM_B F_B(2,K_R) \quad [55]$$

Therefore, Eq. [54] becomes

$$ZR = L^{1/2} DM_B^{1/2} \sum_{K_R} F_B(2,K)\, A(K)/A_D \quad [56]$$

Note that

$$ZR/ZD = (i_r/i_d)(D_A/D_B)^{1/2} \quad [57]$$

The quotient i_r/i_d is the collection efficiency, N. Thus

$$ZR/ZD = N(D_A/D_B)^{1/2} \quad [58]$$

Though it is not necessary to do so, we will assume that $D_A = D_B$, and thus

$$ZR/ZD = N \quad [59]$$

Redefinition of boundary conditions.—At this point, the first iteration in the calculation is completed. It is now necessary to modify the boundary conditions at the disk and ring electrodes as follows.

At the disk

$$F_A'(1,1) = 0.0 \quad [60]$$

$$F_B'(1,1) = F_B(1,1) + DM_A[F_A(2,1)] - DM_B[F_B(1,1) - F_B(2,1)] \quad [61]$$

$$F_X'(1,1) = F_X(1,1) - DM_X[F_X(1,1) - F_X(2,1)] \quad [62]$$

Equation [61] states that the new fractional concentration of B at the disk, $F_B'(1,1)$, is the old fractional concentration of B at the disk, $F_B(1,1)$, plus the amount of A which diffused into the disk and is transformed (with passage of current) into B, less the B which diffuses out.

Equation [62] states that the new concentration of X at the disk, $F_X'(1,1)$, is given by the old concentration less the X which diffuses out.

The new boundary conditions at the ring electrode are

$$F_A'(1,K_R) = F_A(1,K_R) + DM_B[F_B(2,K_R)] - DM_A[F_A(1,K_R) - F_A(2,K_R)] \quad [63]$$

$$F_B'(1,K_R) = 0.0 \quad [64]$$

$$F_X'(1,K_R) = F_X(1,K_R) - DM_X[F_X(1,K_R) - F_X(2,K_R)] \quad [65]$$

At this point the calculation of the effects of diffusion, convection and kinetics are repeated, then currents are calculated at $t = 2\Delta t$, and the process is continued until steady state is reached.

Boundary conditions for constant current.—It is also of interest to simulate the application of a constant current step to the disk electrode. This is done simply by modifying the disk electrode boundary condition in the above simulation. The boundary conditions for constant current at the disk are given by

$$F_A'(1,1) = F_A(1,1) - \text{FLUX} - DM_A[F_A(1,1) - F_A(2,1)] \quad [66]$$

$$F_B'(1,1) = F_B(1,1) + \text{FLUX} - DM_B[F_B(1,1) - F_B(2,1)] \quad [67]$$

$$F_X'(1,1) = F_X(1,1) - DM_X[F_X(1,1) - F_X(2,1)] \quad [68]$$

where F_A', F_B', and F_C' are the new fractional concentrations of species A, B, and C; F_A, F_B, and F_C are the old fractional concentrations. FLUX is the amount of A transformed into B by electrolysis during each Δt interval and is given by

$$\text{FLUX} = (i_{cc}/i_L)\ (0.776)\ (DM_A/L)^{1/2} \quad [69]$$

where i_{cc} is the applied constant current and i_L is the limiting current for species A.

Results

A Fortran program based on the methods of the previous section was written; a listing and discussion of this program is available (16). Calculations for a number of different electrode geometries were carried out on a Control Data Corporation Model 6600 computer and processing times quoted refer to compilation and execution times on this.

Effect of number of iterations.—From Eq. [12] and [22] it is clear that the number of iterations, L, determines the magnitude of Δx and Δt; the larger L, the closer the simulation will approximate the physical system. A simple test of the simulation is to compare the computed steady state current at the disk with that predicted by the Levich equation (15)

$$i_{S.S.} = 0.62\, n\mathbf{F}AC^{o}D^{2/3}\omega^{1/2}\nu^{-1/6} \quad [70]$$

When $L = 50$, the simulated steady-state current at the disk electrode is only 96.5% of the Levich equation limiting current. When $L = 1000$, however, the simulated disk current is 99.5% of the theoretical current. Similar results are obtained for the simulated collection efficiency. A simulation with $L = 50$ yields a collection efficiency 9% higher than that predicted by Albery and Bruckenstein (3) for an electrode with $IR1 = 83$, $IR2 = 94$, and $IR3 = 159$. When $L = 1000$, the simulated collection efficiency agrees to within 0.5% with the theoretical value.

Unfortunately, the computation time required to attain the steady state when $L = 1000$ is prohibitively long, requiring about 25 min of computer time. It was found, however, that identical results could be obtained from a simulation with $L = 50$, which requires only 25 sec of computer time, if a slight modification is made in the calculation of the effects of convection.

If Eq. [27] and [35] are modified as follows

$$XJJ = XJ/[1.0 - (1.11 \cdot XJ \cdot V_{NAUT})] \quad [71]$$

$$RKK = RK \exp[-1.03\,(XJ)\,(V_{NAUT})] \quad [72]$$

the results obtained with $L = 50$ are in close agreement with those using $L = 1000$ and the unmodified convection equations. The introduction of adjustable parameters into digital simulations involving convection has been successful in other cases (13). Note that the factors in Eq. [71] and [72] are valid only for $L = 50$ and $DM_A = 0.45$. There will be slightly different factors for different values of these parameters.

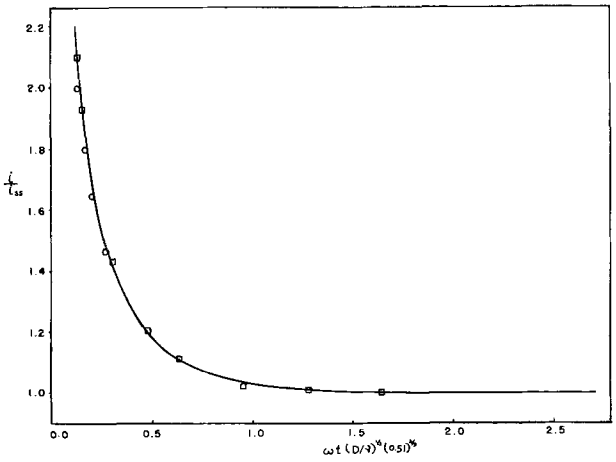

Fig. 2. Simulated disk current transient for potential step at disk: ⊙ theoretical work of Bruckenstein and Prager (17); ⊡ theoretical work of Siver (18).

Figure 2 shows the simulated disk current transient. The solid line is actually two curves, one generated using $L = 1000$ and the other using $L = 50$ and the correction factors. For all practical purposes, they are identical. The simulated curve is also compared with the theoretical and experimental work of Prager and Bruckenstein (17) and the approximate treatment of Siver (18). Both are in good agreement with the simulation.

Figure 3 shows the concentration profile of species A at steady state as a function of distance from the electrode surface in the normal direction. Curves b and c are the results of simulations using $L = 1000$, and $L = 50$ and the correction factors, respectively. On this scale, they are indistinguishable. Curve a is the theoretical concentration profile given by Riddiford (19). The agreement is quite satisfactory and indicates that the correction factors do not adversely affect the concentration profile.

Collection efficiencies.—Table I presents the simulated collection efficiencies in the absence of kinetics for a number of different electrode geometries. In these calculations $L = 50$ and the correction factors given in Eq. [71] and [72] were used. In all cases the simulated collection efficiencies are in excellent agreement with the theoretical collection efficiencies of Albery and Bruckenstein (3). Identical steady-state collection efficiencies are also predicted when the boundary conditions at the disk electrode correspond to a constant current step rather than a potential step. This is as would be expected. Furthermore, the steady-state collection efficiencies are unaffected by the mag-

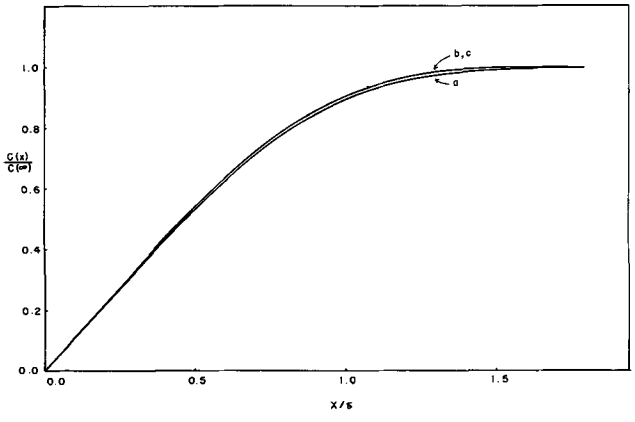

Fig. 3. Concentration profile of species at the disk: a, theoretical curve by Riddiford (19); b, simulated curve, $L = 1000$; c, simulated curve, $L = 50$, correction factors used. $\delta = 1.805\, D^{1/3}\nu^{1/6}\omega^{-1/2}$.

Table I. Simulated collection efficiencies for different electrode geometries

r_2/r_1	r_3/r_1	Collection efficiencies	
		Simulated[a]	Calculated[b]
1.05	1.261	0.339	0.340
1.05	1.361	0.408	0.409
1.05	1.472	0.463	0.464
1.07	1.161	0.209	0.210
1.07	1.271	0.321	0.323
1.07	1.371	0.391	0.391
1.07	1.483	0.449	0.449
1.09	1.201	0.226	0.226
1.09	1.301	0.320	0.321
1.09	1.521	0.449	0.447

[a] L = 50, correction factors used. Computation time about 20 sec per calculation.
[b] Calculated from tables in (3).

nitude of the current step, provided the current is smaller than the limiting current.

Ring transients.—From an approximate treatment of ring current transients (RCT), Albery (9) suggested that these could be employed to study fast homogeneous reactions of species generated at the disk electrode. Bruckenstein and Feldman (20) introduced the concept of the transit time from disk to ring electrode and suggested its application to the determination of rate constants of homogeneous reactions. Bruckenstein and Napp (21) have also shown that the RCT can be used to determine the amount of adsorption of electrogenerated products.

Figure 4 shows the RCT obtained when either a potential step or a current step is applied to the disk electrode and the ring electrode is held at a potential where all product reaching it is electrolyzed. The computed results for the RCT are identical for L = 1000 or for L = 50 and the modified convection equations.

Note that the current at the ring rises more rapidly when a potential step is applied. This is caused by the large instantaneous current which results at the disk when the potential is stepped (Fig. 2). The RCT, normalized by the steady-state ring current, due to a current step is independent at the magnitude of the current step.

We can compare the simulated RCT's with transit times predicted by Bruckenstein and Feldman (20). The appropriate equation given by them for the transit time (the time interval between the potential step at the disk and the appearance of current at the ring) in the absence of complications is

$$\omega t' D^{1/3} \nu^{-1/3} (0.51)^{2/3} = B[\log (r_2/r_1)]^{2/3} \qquad [73]$$

where ω is in radians/sec, t' is the transit time, and r_1 and r_2 are the radii of the disk and inner edge of the ring, respectively. Bruckenstein and Feldman (20) take B = 2.87, while a slightly different method of carrying out the integration in the derivation yields B = 2.28. Figure 5 shows the simulated RCT's for a potential step at the disk for electrodes of different geometries. Also shown are the transit times calculated from Eq. [73] for B-values of 2.28 and 2.87. A useful definition of the transit time, corresponding to Eq. [73] with B = 2.28, is that time at which the current is approximately 2% of the steady-state ring current. Taking the transit time at a given fraction of the steady-state current seems preferable for many electrodes to methods involving extrapolations of the rising current region of the RCT.

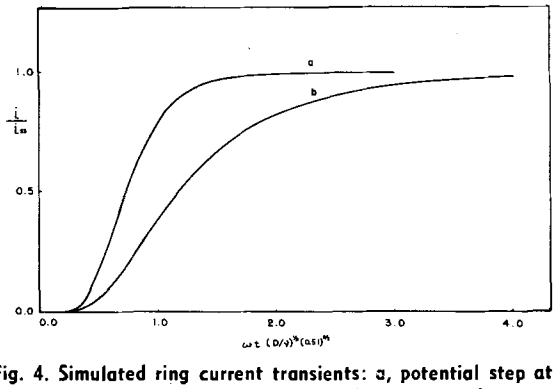

Fig. 4. Simulated ring current transients: a, potential step at the disk; b, current step at the disk; L = 50, correction factors used.

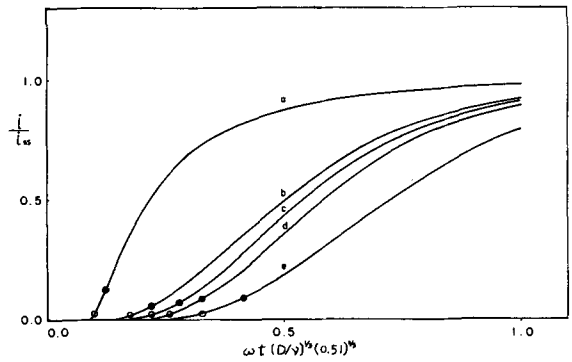

Fig. 5. Simulated transit times: a, $IR1$ = 2000, $IR2$ = 2040, $IR3$ = 2080; b, $IR1$ = 100, $IR2$ = 105, $IR3$ = 147; c, $IR1$ = 100, $IR2$ = 107, $IR3$ = 148; d, $IR1$ = 100, $IR2$ = 109, $IR3$ = 152; e, $IR1$ = 83, $IR2$ = 94, $IR3$ = 159; L = 50, correction factors used. The points correspond to transit times calculated using Eq. [73] with B = 2.28 (open points) and 2.87 (solid points).

We can also compare our results with those of Albery (9) who treated the RCT for the current step condition. For a thin-ring thin-gap electrode, he obtained two approximate equations, one which is valid at long times and the other which is more valid at short times. Figure 6 shows the simulated RCT for the current step condition at a fairly thin-ring thin-gap electrode ($IR1$ = 2000, $IR2$ = 2040, $IR3$ = 2080). Also plotted are points obtained from Albery's equations. The agreement is acceptable and points out the limits within which the approximate equations are valid. Unfortunately, these equations cannot be employed for most practical electrodes which are not of the required thin-ring thin-gap configuration.

Conclusion

The digital simulation technique has been shown to give theoretical results for transient and steady state behavior which are in good agreement with previous theoretical treatments and experiments. The digital simulation approach has the advantage of being directly applicable to situations involving more complex boundary conditions and coupled first and second order homogeneous chemical reactions. Results of dig-

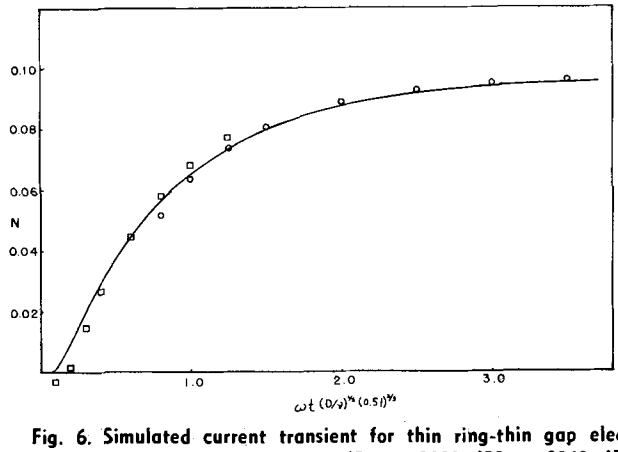

Fig. 6. Simulated current transient for thin ring-thin gap electrode with current step at the disk: $IR1$ = 2000, $IR2$ = 2040, $IR3$ = 2080; L = 50, correction factors used from Albery's Eq. [3.4] (9) using pre-exponential factors. ○ 0.94; □ 0.81.

ital simulations under these conditions and for electrogenerated chemiluminescence at the RRDE, and applications of these treatments, will be given in future papers.

Acknowledgment

The support of The Electrochemical Society, Mobil Oil Corporation and the Eastman Kodak Company for fellowships to one of us (K.B.P.) and the Robert A. Welch Foundation and the National Science Foundation (AP-6688X) are gratefully acknowledged. The authors are indebted to J. T. Maloy for helpful discussions during the course of this work.

Manuscript received April 18, 1969.

Any discussion of this paper will appear in a Discussion Section to be published in the December 1970 JOURNAL.

REFERENCES

1. A. N. Frumkin and L. N. Nekrasov, *Doklady Akad. Nauk. SSSR*, **126**, 115 (1959).
2. W. J. Albery, *Trans. Faraday Soc.*, **62**, 1915 (1966).
3. W. J. Albery and S. Bruckenstein, *ibid.*, **62**, p. 1920.
4. W. J. Albery, S. Bruckenstein, and D. T. Napp, *ibid.*, p. 1932.
5. W. J. Albery, S. Bruckenstein, and D. C. Johnson, *ibid.*, p. 1938.
6. W. J. Albery and S. Bruckenstein, *ibid.*, p. 1946.
7. W. J. Albery and S. Bruckenstein, *ibid.*, p. 2584.
8. W. J. Albery and S. Bruckenstein, *ibid.*, p. 2596.
9. W. J. Albery, *ibid.*, **63**, 1771 (1967).
10. W. J. Albery, M. L. Hitchman, and J. Ulstrup, *ibid.*, **64**, 2831 (1968).
11. J. T. Maloy, K. B. Prater, and A. J. Bard, *J. Phys. Chem.*, **72**, 4348 (1968).
12. S. W. Feldberg and C. Auerbach, *Anal. Chem.*, **36**, 505 (1964).
13. S. W. Feldberg, "Electroanalytical Chemistry," Vol. 3, A. J. Bard, Editor, Marcel Dekker, Inc., New York (1969).
14. W. J. Albery and J. Ulstrup, *Electrochim. Acta*, **13**, 281 (1968).
15. V. G. Levich, "Physiochemical Hydrodynamics," Prentice-Hall, Englewood Cliffs, N.J. (1962).
16. K. B. Prater, Ph.D. Dissertation, University of Texas at Austin, 1969.
17. S. Bruckenstein and S. Prager, *Anal. Chem.*, **39**, 1161 (1967).
18. Yu G. Siver, *Russ. J. Phys. Chem.*, **33**, 533 (1959).
19. A. C. Riddiford, "Advances in Electrochemistry and Electrochemical Engineering," P. Delahay and C. W. Tobias, Editors, Interscience, New York (1966).
20. S. Bruckenstein and G. Feldman, *J. Electroanal. Chem.*, **9**, 395 (1965).
21. S. Bruckenstein and D. T. Napp, *J. Am. Chem. Soc.*, **90**, 6303 (1968).

The Equivalent Conductance of Electrolytes in Mixed Solvents

XII. Magnesium Sulfate in Water-Ethanol Solvents

Edward S. Amis and J. F. Casteel

Department of Chemistry, University of Arkansas, Fayetteville, Arkansas

ABSTRACT

The equivalent conductance of magnesium sulfate was measured at 25.00°, 35.00°, and 45.00°C in pure water and in 20.1, 40.7, 60.2, and 80.1 w/o (weight per cent) ethanol. Viscosity, temperature, and dielectric effects are calculated for the conductance process. Also the observed data were compared to the theoretical requirements of the Onsager equation.

Several studies have been made (1-10) in these laboratories of the equivalent conductance of different valence types of electrolytes in various solvent compositions over a range of temperatures. Even the simple salt, potassium chloride (1), has been shown to deviate, depending on the solvent and temperature, from the requirements of the Onsager equation. In other cases interesting suggestions as to the nature of the ions in solution (8) and as to solvent structure and solvation effects (7) have resulted from the conductance data. Since magnesium chloride (10) in ethanol-water solvents gave highly curved phoreograms with corresponding wide deviation from the theoretical Onsager plots, it seemed of special interest to study the conductivity of magnesium sulfate, the anion of which is also bivalent, in order to observe the expected marked curvature of the phoreograms of this salt in the water-ethanol solvent system and to investigate the deviations, also expected to be large, from the Onsager theory. Magnesium sulfate seemed to be of special interest since extensive conductivity work on bi-bivalent electrolytes in water-ethanol mixtures at various temperatures had not been reported.

The conductivity of magnesium sulfate has been studied at various temperatures in water (11) and at 25°C in ethanol-water mixtures ranging from 5 to 50 w/o ethanol (12). This present study includes conductivity measurements at 25.00°, 35.00°, and 45.00°C in various weight per cents of ethanol up to and including 80 w/o, which is the limiting weight per cent of ethanol for measurable concentrations of magnesium sulfate using our conductivity apparatus.

Experimental

All weights were previously standardized against NBS weights. The temperature of the thermostated oil baths were held to ±0.01°C at 25.00°, 35.00°, and 45.00°C. Densities of the mixed solvents were determined with a calibrated arm-pycnometer. In this manner the solvent composition was found within ±0.1%. The viscosities of the solvent mixtures were obtained from the literature (13). Dielectric constants of the mixtures were interpolated from the data of Akerlof (14).

Resistances were measured with a Jones and Joseph 60,000 ohm bridge at a frequency of 1000 Hz. Resistances were accurate to ±1.0 ohm. The L&N conductivity cells had cell constants of 5.3886 and 1.0430.

Conductivity water was prepared in the manner described by Foster and Amis (1). Pure ethanol was prepared by the method of Smith (15). The specific

conductance of pure water (1-3 x 10^{-7} mhos) and ethanol (4-7 x 10^{-8} mhos) agreed favorably with those found by Goldenberg and Amis (6). Solutions were prepared by adding a known amount of magnesium sulfate stock solution to the preweighed solvent. Necessary amounts of pure ethanol were added to restore the solvent composition. Magnesium sulfate (reagent grade Baker's Analyzed) was recrystallized from conductivity water three times, then vacuum dried to the heptahydrate.

Calculation Procedure

Onsager's equation for a completely dissociated bivalent electrolyte is given by

$$\Lambda = \Lambda_o - \left[\frac{4.6085 \times 10^6 \Lambda_o}{(DT)^{3/2}} + \frac{231.52}{(DT)^{1/2}\eta} \right] \sqrt{C} \quad [1]$$

where: Λ = equivalent conductance, Λ_o = equivalent conductance at infinite dilution, η = viscosity of the solvent, D = dielectric constant of the solvent, and T = absolute temperature. The term in the square bracket is called the Onsager slope, γ. Λ_o for all the runs were obtained by the Fuoss-Shedlovsky (16) theory. By application of this theory we determined the equilibrium constant, K, for the dissociation and the correct Λ_o.

The Fouss and Shedlovsky method uses the equation

$$\frac{F(Z)}{\Lambda} = \frac{1}{\Lambda_o} + \frac{C\Lambda f^2}{K\Lambda_o^2 F(Z)} \quad [2]$$

where: K = ionization equilibrium constant

$$Z = \gamma \Lambda_o^{-3/2} \sqrt{C\Lambda} \quad [3]$$

where: γ = Onsager slope and C = concentration in equivalents per liter

$$F(Z) = 1 - Z\,[1 - Z\,(1 - Z\,\{1 - -\}^{-1/2})^{-1/2}]^{-1/2} \quad [4]$$

Redefining C in terms of moles per liter c, the activity coefficient can be expressed as follows

$$-\ln f_\pm = \frac{\dfrac{\epsilon^3}{(DkT)^{3/2}} \left[\dfrac{\pi N_o}{1000}\right]^{1/2} (\nu_+ + \nu_-)^{1/2} (z_+ z_-)^{3/2} (c\alpha)^{1/2}}{1 + \dfrac{G\epsilon^3}{(DkT)^{3/2}} \left[\dfrac{\pi N_o}{1000}\right]^{1/2} (\nu_+ + \nu_-)^{1/2} (z_+ z_-)^{3/2} (c\alpha)^{1/2}} \quad [5]$$

Where $\mathring{a}$ was approximated by $\dfrac{G|z_+ z_-|\epsilon^2}{2DkT}$ and G was a converging factor.

$$\alpha = \frac{\Lambda}{\Lambda_o F(Z)} \text{ (the degree of dissociation)} \quad [6]$$

where: N = Avogadro's number, π = 3.14159, k = Boltzmann gas constant, D = dielectric constant, z_+ = charge of the positive ion, z_- = charge of the negative ion, ν_+ = number of positive ions per molecule, and ν_- = number of negative ions per molecule.

Preliminary values of Λ_o used in the Fuoss-Shedlovsky calculation were obtained with a least squares analysis using an IBM 7040 computer of the log Λ *vs.* $C^{1/2}$, which gave the values in the form

$$Y = a_o + a_1 X + a_2 X^2 + \ldots + a_\eta X^\eta \quad [7]$$

where Y represents log Λ and X the square root of the concentration in equivalents per liter. Initial values of log Λ_o from Eq. [7] were used to calculate the extrapolated values of Λ_o, *i.e.*, Λ_o(extrap). The Λ_o (extrap) values were used as the preliminary values of Λ_o for the Fuoss-Shedlovsky method, Eq. [2] and the most acceptable values of K and Λ_o (F-S) for the electrolyte in each solvent composition were found.

A brief outline of the Fuoss-Shedlovsky method is presented to help clarify the calculation procedure. The left hand side of Eq. [2] is plotted against $C\Lambda f^2_\pm / F(Z)$. The best straight line is obtained by a linear least squares analysis and is extrapolated to abscissa zero, thus obtaining $1/\Lambda_o$. The slope of the straight line is calculated and gives $1/K\Lambda_o^2$. Since Λ_o is known from the intercept, the value of K can be obtained from the slope. Actually, the value of K is calculated only after a reiterative calculation of the best value of Λ_o. The reiterative procedure consists of inserting in Eq. [2] the initial values of Λ_o obtained by use of Eq. [7]. This preliminary value of Λ_o permits a calculation of Z, $F(Z)$, α, and $f_\pm$. The reiteration proceeds from each extrapolated better value of Λ_o to yield better values of Z, $F(Z)$, α, and $f_\pm$. This reiterative procedure continues until Λ_o becomes constant within any desired limits. In the case of our data, the limit of the self-consistent values of Λ_o was chosen to be 0.0001% of the preceding value.

It can be easily seen from Eq. [2] and specifically from Eq. [5] that the numbers of ions per formula of electrolyte and the valence of the ions must be defined in order to calculate $f_\pm$, γ, Z, $F(Z)$, and eventually Λ_o and K. In order to determine the numbers and the valence of the ions produced by an electrolyte in solution, an ionization scheme must be postulated. Whatever ionization scheme is selected, it must result in values of ν_+, ν_-, z_+, and z_- which, when inserted in the equations given above, will permit a computer evaluation of Λ_o and K. Since the Fuoss-Shedlovsky calculation (Eq. [2]) is very discriminatory (8) with respect to the ν and z values used, only a limited number of ionization schemes are available to an investigator. The theory as formulated permits only one choice of type of ionization scheme for any particular set of data. A wrong choice of an ionization scheme for a particular set of data results in one of three objectional features in the calculation:

(*A*) The reiterative calculation will not converge.

(*B*) Impossible values of Λ_o and K will be obtained.

(*C*) $A\sqrt{-1}$ factor will result which generally appears in the $F(Z)$ function, thus making the calculation impossible.

With these limitations in view, the following ionization schemes were finally selected for the different solvent compositions in order to evaluate Λ_o(F-S) and K:

Solvent	Ionization scheme
H_2O	$MgSO_4 \rightarrow Mg^{2+} + SO_4^{2-}$
20.1%	$MgSO_4 \rightarrow Mg^{2+} + SO_4^{2-}$
40.7%	$2MgSO_4 \rightarrow Mg^{2+} + Mg(SO_4)_2^{2-}$
60.2%	$2MgSO_4 \rightarrow Mg^{2+} + Mg(SO_4)_2^{2-}$
80.1%	$MgSO_4 + H_2O \rightarrow MgOH^{1+} + HSO_4^{1-}$

After the values of Λ_o(F-S) and K were calculated, they were substituted into Eq. [1] and a value of Λ, *i.e.*, Λ(calc), was obtained for each concentration. Then these calculated values of Λ were used to recalculate Λ_o(F-S) and K to check for self-consistency in the program and to give an indication of the accuracy of the method of calculation.

Values of Λ_o(F-S) and Λ_o(extrap) were used to calculate the energy of activation of the conductance process by the following procedure. The energy of activation of viscous flow, $\Delta E\eta$, is given by (17)

$$\eta = e^{\Delta E\eta / RT} \quad [8]$$

then

$$\Delta E_\eta = \frac{d(\ln\eta)R}{d\left(\frac{1}{T}\right)} \qquad [9]$$

Pederson and Amis (9) used the following equations for the calculation of $\Delta E_{\Lambda_o exp}$ and $\Delta E_{\Lambda_o cal'd}$

$$\Delta E_{\Lambda_o exp} = -\frac{d(\ln\Lambda_o)R}{d\left(\frac{1}{T}\right)} \qquad [10]$$

$$\Delta E_{\Lambda_o cal'd} = \left[2\frac{d(\ln D)}{d\left(\frac{1}{T}\right)} + \frac{d(\ln\eta)}{d\left(\frac{1}{T}\right)} + 2\frac{d(\ln T)}{d\left(\frac{1}{T}\right)}\right] R \qquad [11]$$

The slopes were calculated by use of Eq. [7] at the temperature of 35°C. $\left[\frac{d(Y)}{d(X)}\right]_x = a_1 + a_2 X$ where $Y = \ln D, \ln\eta, \ln\Lambda_o, \ln T$; where $X = 1/T$, and where $T = 308.15$°K.

Numerical values given by these calculations are presented in the Discussion of Data section.

Discussion of Data

The observed and calculated equivalent conductance data are recorded in Table I. Plots of observed and calculated values of Λ *vs.* $C^{1/2}$, the square root of the concentration in equivalents per liter, are shown in Fig. 1-3. From the figures it can be seen that the agreement between observed and calculated values of Λ is good. In Fig. 1 are included the data from the International Critical Tables (11) for magnesium sulfate in water at 25.00°C. It is obvious from the graph that these data agree well with the present data. The data

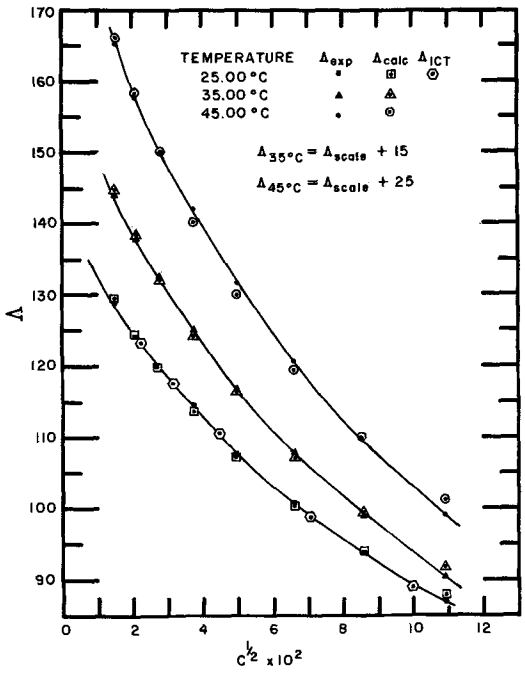

Fig. 1. Observed and calculated equivalent conductance of $MgSO_4$ in water.

Table I. Observed and calculated equivalent conductance of magnesium sulfate in water

Solution	Temperature 25.00° ± 0.01°C $C \times 10^4$	Λ obs	Λ calc	Temperature 35.00° ± 0.01°C $C \times 10^4$	Λ obs	Λ calc	Temperature 45.00° ± 0.01°C $C \times 10^4$	Λ obs	Λ calc
a	119.83	86.804	87.843	119.41	105.41	106.97	119.10	124.08	126.38
b	74.005	93.721	93.915	73.731	114.03	114.32	73.521	134.69	135.04
c	44.146	100.78	100.20	43.988	122.97	122.08	43.862	145.54	144.33
d	24.840	107.80	107.09	24.756	131.86	130.74	24.682	156.62	154.84
e	14.214	114.49	113.50	14.161	140.15	138.94	14.119	166.95	164.96
f	7.835	119.9	119.7	7.806	147.7	147.0	7.784	175.0	175.0
g	4.403	124.2	124.8	4.387	152.8	153.7	4.375	182.7	183.5
h	2.237	128.9	129.4	2.228	158.8	159.9	2.222	190.2	191.4
a	69.443	39.399	39.459	69.079	51.033	51.116	68.680	62.936	63.563
b	54.398	41.663	41.750	54.120	54.060	54.170	53.806	66.794	67.130
c	49.138	42.687	42.697	48.884	55.409	55.437	48.604	68.532	68.635
d	32.625	46.483	46.443	32.458	60.510	60.468	32.273	75.086	74.717
e	26.160	48.437	48.414	26.027	63.196	63.129	25.878	78.574	78.026
f	21.068	50.582	50.310	20.961	65.968	65.698	20.842	82.046	81.284
g	13.573	54.059	53.996	13.504	70.877	70.726	13.427	88.656	87.872
h	9.252	57.05	57.00	9.206	75.02	74.86	9.154	94.19	93.51
i	6.317	59.80	59.76	6.285	78.80	78.67	6.250	99.23	98.90
j	3.846	62.87	62.92	3.826	83.00	83.08	3.805	105.0	105.4
k	3.021	64.20	64.27	3.006	84.85	84.98	2.989	107.5	108.3
l	1.946	66.13	66.41	1.937	87.48	88.00	1.926	111.2	113.0
a	110.93	13.774	13.826	110.04	17.652	17.634	109.11	21.366	21.436
b	81.544	15.213	15.250	80.867	19.130	19.430	80.184	23.641	23.712
c	45.030	18.202	18.299	44.664	23.466	23.475	44.270	28.568	28.692
d	40.054	19.076	18.976	39.724	24.545	24.365	39.376	29.904	29.806
e	20.832	23.165	22.964	20.661	30.044	29.698	20.477	36.844	36.537
f	17.828	24.059	23.981	17.682	31.295	31.074	17.523	38.491	38.291
g	10.674	27.812	27.564	10.586	36.372	35.969	10.476	45.028	44.580
h	9.760	28.37	28.20	9.860	37.13	36.86	9.593	45.98	45.70
i	5.583	32.49	32.36	5.537	42.82	42.66	5.480	53.48	53.28
j	5.196	33.02	32.90	5.153	43.57	43.43	5.107	54.49	54.27
k	2.323	38.41	38.85	2.304	51.28	52.02	2.280	64.92	65.75
l	1.187	42.10	43.29	1.177	56.40	58.68	1.165	72.56	74.90
a	159.29	3.7258	3.6652	157.80	4.4238	4.3467	156.25	4.9845	4.9215
b	128.98	4.0344	4.0099	127.78	4.7849	4.7533	126.52	5.3918	5.3646
c	127.82	4.0504	4.0253	126.63	4.8024	4.7715	125.38	5.4119	5.3846
d	92.310	4.5842	4.6072	91.453	5.4296	5.4609	90.549	6.1132	6.1408
e	81.753	4.8023	4.8412	80.996	5.6894	5.7390	80.196	6.4048	6.4478
f	56.716	5.5293	5.6066	56.191	6.5489	6.6517	55.634	7.3753	7.4620
g	43.492	6.1112	6.2239	43.091	7.2532	7.3923	42.665	8.1723	8.2912
h	35.220	6.6641	6.7600	34.894	7.8965	8.0354	34.548	8.9174	9.0182
i	21.739	8.0740	8.1354	21.510	9.6086	9.7048	21.296	10.855	10.917
j	19.890	8.2423	8.4033	19.506	9.9354	10.072	19.310	11.216	11.337
k	12.795	9.8976	9.9129	12.660	11.855	11.877	12.534	13.448	13.428
l	8.969	11.26	11.27	8.796	13.60	13.60	8.708	15.52	15.45
m	6.814	12.85	12.45	6.742	15.52	15.01	6.675	17.34	17.10
n	3.712	15.64	15.28	3.640	19.10	18.62	3.604	21.87	21.49
o	1.694	20.70	19.50	1.677	25.48	23.98	1.660	29.63	28.26
a	8.681	1.309	1.310	8.590	1.312	1.313	8.496	1.318	1.319
b	5.846	1.570	1.602	5.784	1.590	1.623	5.721	1.605	1.642
c	3.552	2.094	2.027	3.514	2.126	2.058	3.476	2.163	2.088
d	1.722	2.897	2.831	1.704	2.953	2.891	1.685	3.017	2.950
e	1.069	3.374	3.510	1.058	3.466	3.601	1.046	3.547	3.693

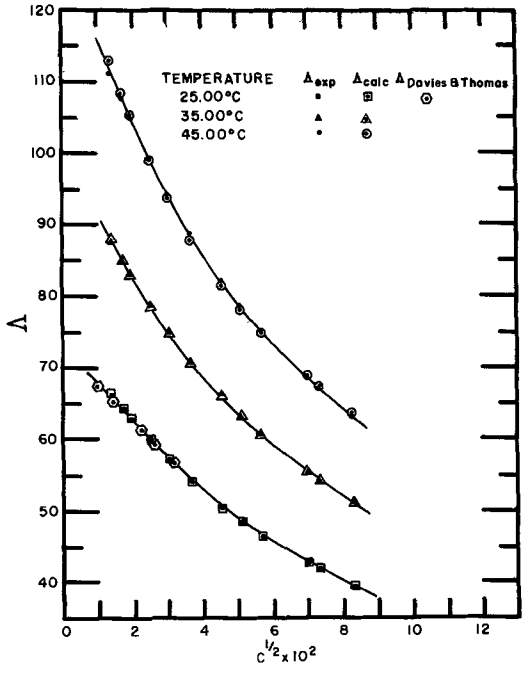

Fig. 2. Observed and calculated equivalent conductance of $MgSO_4$ in 20.1 w/o ethanol.

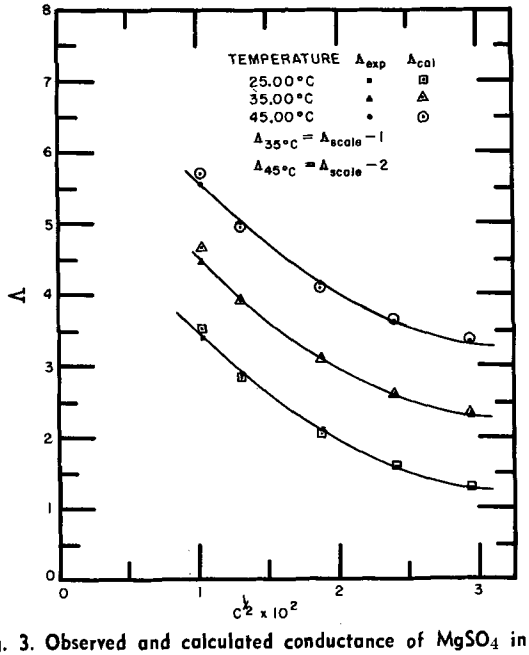

Fig. 3. Observed and calculated conductance of $MgSO_4$ in 80.1 w/o ethanol.

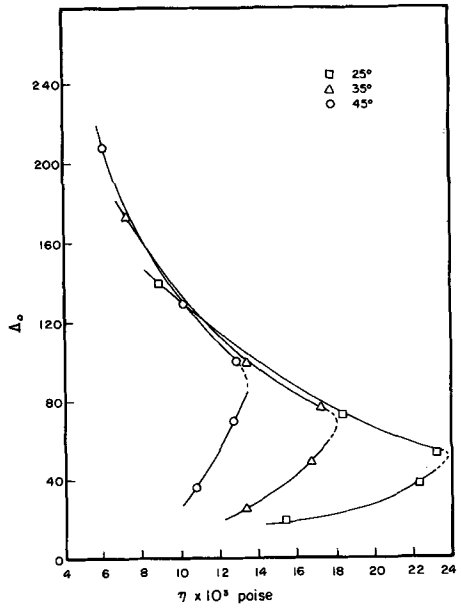

Fig. 4. Dependence of equivalent conductance (Λ_0) on viscosity of E + OH — H_2O solvents.

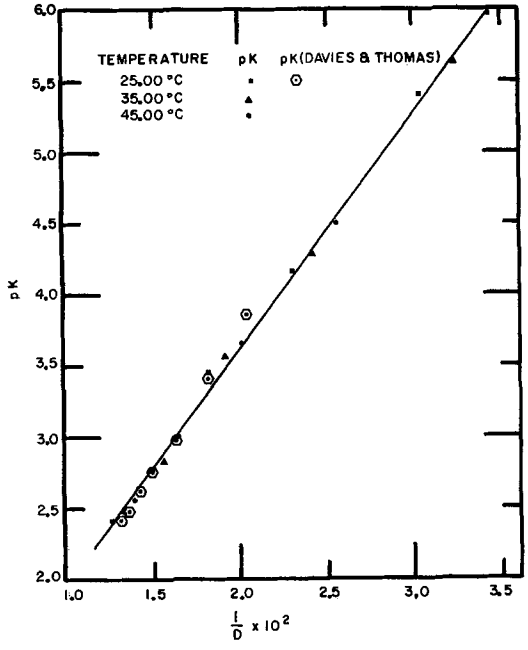

Fig. 5. Plot of pK vs. $1/D$ at 25°, 35°, and 45°C

of Davies and Thomas (12) for both 20 and 40 w/o ethanol also agree well with our data for both 20.1 and 40.7 w/o ethanol. The agreement between the sets of data can be seen in Fig. 2 for 20.1 w/o ethanol at 25.00°C.

There is good agreement between the values of Λ_0(extrap) and $\Lambda_0(F\text{-}S)$, shown in Table II, in water, 20.1 and 40.7 w/o ethanol, and poor agreement in 60.2 and 80.1 w/o ethanol. The discrepancies between $\Lambda_0(F\text{-}S)$ and Λ_0(extrap) in 60.2 and 80.1 w/o ethanol were not due to imprecision or error in the data but resulted from a failure of the theory in the ethanol rich solvents which is probably due to the formation of more than one complex by association of the ions of the electrolyte. This multiplicity of complexes was not accounted for by one simple ionization scheme; however, the ionizations presented previously, or others comparable to them in the numbers of ions and their charges produced per formula of electrolyte, must have been the predominate ionizations or else the calculations would have run into the problems listed in the calculation section.

In Table II are presented the values of $\Lambda_0(F\text{-}S)$ and $\Lambda_0(F\text{-}S$ calc) and of K and K(calc). The agreement between the two sets of Λ_0 and the two sets of K is good. From the care used in purifying chemicals, making measurements, and performing calculations, the differences between the values of $\Lambda_0(F\text{-}S)$ and K obtained from measured values of Λ and from values of Λ calculated by inserting the values of $\Lambda_0(F\text{-}S)$ and K back into the Fuoss-Shedlovsky equations is certainly indicative of the self-consistency of the data and of the calculations. These differences, which are slight, are perhaps the best indication of the accuracy of the $\Lambda_0(F\text{-}S)$ and K obtained by use of the Fuoss-Shedlovsky method since there are no absolute values of these quantities available for comparison.

The ratio of the observed slope to the Onsager slope is shown for water and 20.1 w/o ethanol. The ratio

Table II. Properties of the solvent and derived conductivity data

w/o Ethanol	Dielectric constant	Viscosity $\eta \times 10^2$	$\Lambda_o(F\text{-}S)$	$\Lambda_o(F\text{-}S)$ calc	Λ_o(extrap)	Observed slope / Onsager slope		$K \times 10^5$ $K(F\text{-}S)$	$K(F\text{-}S$-calc)
				25.00					
00.0	78.54	0.8949	139.18	139.19	138.52	1.788	1.246	388.9	389.0
20.1	66.71	1.830	73.70	73.70	75.93	2.499	1.349	169.8	169.8
40.7	54.76	2.334	54.01	54.07	55.21		1.260	34.51	34.40
60.2	43.45	2.225	38.15	38.00	36.36		0.849	6.830	6.887
80.1	32.85	1.745	19.64	19.70	5.987		0.343	0.404	0.401
				35.00					
00.0	75.00	0.7208	172.84	172.85	172.51	2.044	1.246	333.6	333.6
20.1	63.46	1.341	98.41	98.42	100.52	2.756	1.320	150.2	150.2
40.7	52.06	1.721	75.84	75.99	74.19		1.305	27.10	26.97
60.2	41.25	1.665	50.71	50.54	38.91		0.844	5.328	5.386
80.1	30.90	1.335	25.32	25.40	6.194		0.338	0.243	0.241
				45.00					
0.00	71.59	0.5970	208.10	208.13	207.89	2.206	1.242	290.8	290.6
20.1	60.45	1.010	130.03	130.10	130.31	2.756	1.313	100.9	100.7
40.7	49.40	1.289	99.82	99.98	98.32		1.287	22.41	22.32
60.2	39.05	1.270	70.84	70.40	44.70		0.900	3.267	3.309
80.1	29.05	1.080	36.05	36.23	6.404		0.389	0.119	0.118

becomes so great at weight per cents above 20.1 that they are not considered to be significant. This extreme deviation from the Onsager theory for sulfates in higher weight per cents of ethanol was also noted by Davies and Thomas (12). Also shown in Table II is the product $\Lambda_o\eta$, which is relatively constant for 0.00, 20.1, and 40.7 w/o ethanol. Values of $\Lambda_o\eta$ in 60.2 and 80.1 w/o ethanol show marked decreases compared to the values in the first three solvents. This corresponds to the observation by Than and Amis (10) on the magnesium chloride in the water-ethanol system.

The reasonable consistency of $\Lambda_o\eta$ in the water-rich solvents and its decrease in the ethanol solvents is in harmony with the reasonable ratio of the observed slope to the Onsager slope in the water-rich solvents and the unreasonable values to the ethanol-rich solvents. The plots of $\Lambda_o(F\text{-}S)$ *vs.* viscosity (Fig. 4) show the dependence of equivalent conductance at infinite dilution of magnesium sulfate on viscosity. This dependence has the broad finger shape which has been shown to exist in alkali metals in water-ethanol mixtures (1, 9, 10).

Plots of $-\log K$ *vs.* $1/D$ (Fig. 5) for the three temperatures show a linear relationship from 0.00 to 80.1 w/o ethanol. The plots indicate that the relationship between $pK(-\log K)$ and $1/D$ is independent of temperature. The data of Davies and Thomas (12) are inserted for comparison. The agreement between their measured values of K and our calculated values is good. The values of K show that the presented ionization schemes are reasonable since they decrease very rapidly with decreasing dielectric constant.

If $\log \Lambda_o(F\text{-}S)$ is plotted *vs.* $1/T$ (Fig. 6), straight lines result for water for 20.1 and 40.7 and slightly curved lines for 60.2 and 80.1 w/o ethanol; therefore, the energy of activation must be calculated at a particular temperature for the two latter curves. The Fuoss-Shedlovsky method seems to weigh higher temperatures more heavily; thus, the increase in the value of Λ_o is greater for a given increase in temperature at higher temperature as shown in Table II. Therefore the slope $d(\ln\Lambda_o)/d(1/T)$ is much more negative than one would find by the use of Λ_o's obtained by a simple extrapolation.

The dotted line (Fig. 7) shows the values of $\Delta E_{\Lambda_o\text{exp}}$ (extrap), *i.e.*, calculated from Λ_o(extrap). This is what one would expect considering the values of K. Also, this curve is in agreement with the shape of the $\Delta E_{\Lambda_o\text{exp}}$ curve found by Than and Amis (10). The results of these calculations are recorded in Table III.

Manuscript submitted May 12, 1969; revised manuscript received *ca.* Sept. 12, 1969.

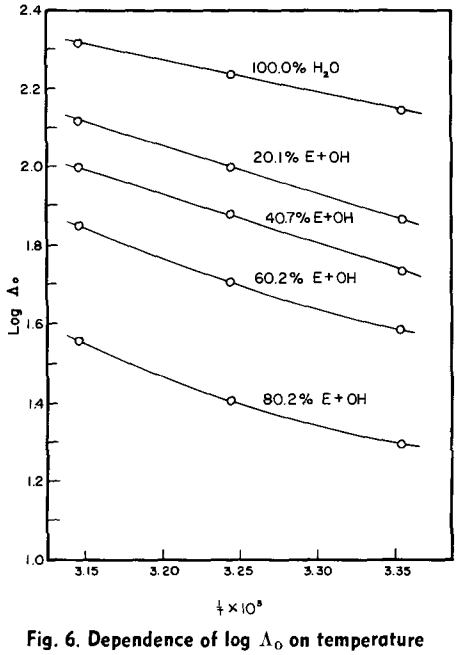

Fig. 6. Dependence of log Λ_o on temperature

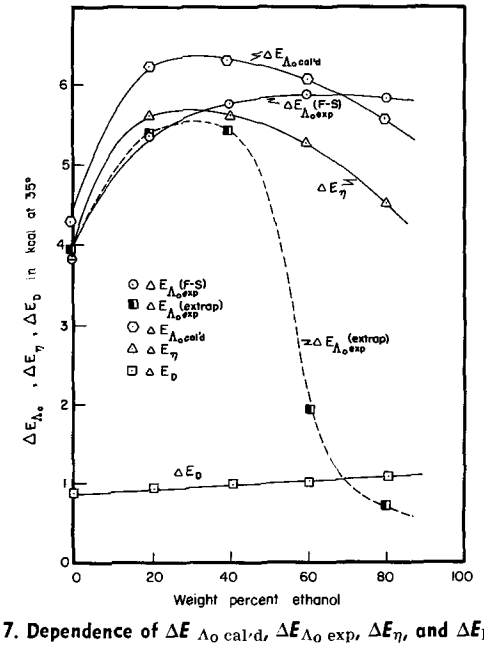

Fig. 7. Dependence of $\Delta E_{\Lambda_o \text{ cal'd}}$, $\Delta E_{\Lambda_o \text{ exp}}$, ΔE_η, and ΔE_D on solvent composition.

Table III. Energies of activation for the conductance process in calories

Solvent	$\Delta E_{\Lambda_0 exp}$ (F-S)	$\Delta E_{\Lambda_0 exp}$ (extrap)	$\Delta E_{\Lambda_0 cal'd.}$
Water	3779	3826	4297
20.1%	5350	5402	6235
40.7%	5761	5439	6318
60.2%	5874	1947	6080
80.1%	5858	635	5594

Any discussion of this paper will appear in a Discussion Section to be published to the December 1970 JOURNAL.

REFERENCES

1. N. G. Foster and E. S. Amis, Z. *physik. Chem. NF*, **3**, 365 (1955).
2. N. G. Foster and E. S. Amis, *ibid.*, **7**, 360 (1956).
3. R. Whorton and E. S. Amis, *ibid.*, **7**, 9 (1956).
4. R. Whorton and E. S. Amis, *ibid.*, **17**, 300 (1958).
5. N. Goldenberg and E. S. Amis, *ibid.*, **22**, 63 (1959).
6. N. Goldenberg and E. S. Amis, *ibid.*, **30**, 65 (1961).
7. N. Goldenberg and E. S. Amis, *ibid.*, **31**, 10 (1962).
8. D. Roach and E. S. Amis, *ibid.*, **35**, 274 (1962).
9. L. G. Pedersen and E. S. Amis, *ibid.*, **36**, 199 (1963).
10. A. Than and E. S. Amis, *ibid.*, **58**, 196 (1968).
11. International Critical Tables, 6, Table 2, p. 236.
12. C. W. Davies and G. O. Thomas, *J. Chem. Soc.*, **3**, 3660 (1958).
13. Bingham and Jackson, Bull. Bureau Standards, **14**, 59 (1918-1919).
14. G. C. Akerlof, *J. Am. Chem. Soc.*, **54**, 4125 (1932).
15. E. L. Smith, *J. Chem. Soc. (London)*, **1927**, 1288.
16. R. M. Fuoss and T. Shedlovsky, *J. Am. Chem. Soc.*, **70**, 1496 (1949).
17. W. J. Moore, "Physical Chemistry," 2nd Ed., p. 431, Prentice Hall, Englewood Cliffs, N.J. (1958).

Technical Notes

Thermal Stability of a Propylene Carbonate Electrolyte

Raymond Jasinski and Susan Carroll

Tyco Laboratories, Inc., Bear Hill, Waltham, Massachusetts

Lithium-organic electrolyte batteries are, in principle, superior in a number of aspects to many aqueous electrolyte battery systems. One of the aspects may be prolonged performance at elevated temperatures, *e.g.*, 160°-200°F (71°-94°C). This temperature range is not accessible, for example, to aqueous zinc batteries because of the increased corrosion of this electrode.

Obviously then, one requirement for lithium batteries intended to operate at these temperatures is compatibility of the negative electrode with the electrolyte. In this note are described preliminary studies on the thermal stability of lithium, and other selected battery components with IN$LiClO_4$-propylene carbonate electrolyte, a system employed by a number of groups in developing prototype batteries [see ref. (5) and (2)].

Experimental

The propylene carbonate was distilled and analyzed according to the method described in ref. (1). Sufficient $LiClO_4$ (G. F. Smith, anhydrous grade) was added to make a 1*N* solution which was then further dried by passage down a column of crushed and dried Molecular Sieves. This procedure has been shown to reduce the water content to less than 10 ppm (4). The absence of gassing on insertion of the lithium was consistent with a dry solution.

The first tests were qualitative in nature. Approximately 10 ml of the electrolyte was placed in a 50-ml beaker containing the component of interest. The open beaker was set on a hot plate; a thermocouple, inserted into the bottom of the beaker, was used to monitor temperature. Results are shown in Table I.

In the first run ($LiClO_4$ + PC) the solution was taken to dryness, with no obvious reaction. A second solution was held at 180° for 5 hr with similar results. Heating the electrolyte with lithium metal also provided no obvious reaction. However, the inclusion of acetylene black and sulfur resulted in a violent reaction when the temperature reached the values shown. Only a small amount of electrolyte was lost by evaporation.

Table I. Stability of 1*N* $LiClO_4$-PC solutions

Material	Temperature, °C	Result
$LiClO_4$ in PC	To dryness	Stable
$LiClO_4$ in PC	180 (5 hr)	Stable
$LiClO_4$ in PC + Ni_3S_2	To dryness	Stable
$LiClO_4$ in PC + acetylene black	215	Exploded
$LiClO_4$ in PC + sulfur (flowers)	260	Burned
$LiClO_4$ in PC + lithium (sheet)	240	Stable

To confirm these processes in working cells, a C-size battery was built in a Leclanché-type configuration. The positive was a paste of nickel oxide, sulfur, and acetylene black (10%) with $LiClO_4$-PC). A high current pulse (2A for 30 sec) was applied resulting in immediate explosion.

A more quantitative evaluation of the compatibility of metallic lithium with the electrolyte was made as follows. Three lithium rods, scraped clean of visible nitride and oxide films within an argon atmosphere dry box (Vacuum Atmospheres Corporation) were placed in a three-compartment glass cell. The counter and test electrodes were separated by a glass frit; the reference electrode was separated from the anode by a Luggin capillary. The anode was a cylinder, ⅜ in. diameter.

The test cell was then sealed, removed from the glove box, and placed in an oven thermostatted at + 160°F. A constant current of 1.27 mA was maintained. The effective current density at the anode was 1 mA/cm^2; this is based on using only the area facing the counterelectrode. That this was reasonable was indicated by the fact that pronounced electrochemical dissolution of lithium occurred only on the side facing the center electrode, as would be expected.

The reference electrode-anode voltage was followed continuously with time; these data are shown in Fig. 1. Visual observations were periodically made of the electrode surfaces and the appearance of the electrolyte. The electrolyte remained clear and colorless; no gassing was noted; the anode surface maintained its metallic luster; a slight tarnish was visible on the reference electrode after 800 hr, resembling the form of lithium deposited on the cathode. The appearance of the cathode change markedly. Lithium electrodeposits as an amorphous powder which is only very loosely adherent and not metallic in appearance. It is not possible to judge, from the electrode appearance, whether the electrolyte is stable under such conditions; however the electrolyte in the vicinity of the cathode did remain clear and colorless.

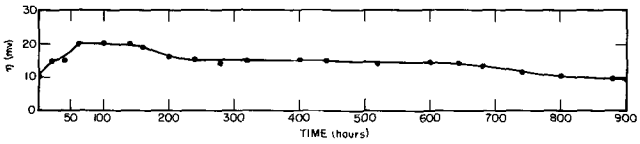

Fig. 1. Time dependence of the reference electrode, anode potential shown for lithium electrodes immersed in 1N $LiClO_4$-PC at +160°F.

Discussion

Consider first the compatibility experiments described by Table I. No gross decomposition was noted in heating the electrolyte alone or in the presence of lithium sheet. More sensitive gas chromatographic evidence indicates some electrolyte decomposition at and above 150°C (1). The electrolyte was not compatible at high temperatures with acetylene black and sulfur. The first material has often been used as a conductive binder in positive plates; sulfur has been suggested as a positive plate material (2, 3). Particular caution should be used in handling positives formed from carbon, sulfur, and lithium perchlorate: This combination resembles closely the classical composition of gun powder.

The electrochemical method is felt to be a particularly severe test of system compatibility, since fresh lithium surface is continuously exposed to the electrolyte at the anode and cathode. Thus, thin but protective films become much less effective in retarding gross decomposition of the electrolyte. As shown in Fig. 1, the polarization of the lithium anode remains relatively constant; there is no indication of any major deterioration in performance with time. The reason for the minor improvement after 600 hr has not been established. Two explanations are possible. First, small amounts of film on the anode are slowly lost by electrochemical dissolution of the electrode and hence it improves with time. Second, small amounts of film deposit on the reference electrode and it slowly deteriorates with time. In either event, the effect is small, a few millivolts over a 900-hr test.

The conclusion to be drawn from these experiments is that there is not a gross decomposition of the electrolyte by anodically discharging lithium metal at 160°F which would prohibit its use in a working battery. This is a necessary although not a sufficient condition for the development of high temperature lithium batteries. Oxidizable materials such as sulfur and acetylene black are not compatible with $LiClO_4$-PC at elevated temperature.

Acknowledgments

This work was carried out under Contract No. N00019-68-C0402 for the Naval Air Systems Command and Contract No. F19628-68-C-0052 for the Air Force Cambridge Research Laboratories.

Manuscript submitted July 31, 1969; revised manuscript received Oct. 29, 1969.

Any discussion of this paper will appear in a Discussion Section to be published in the December 1970 JOURNAL.

REFERENCES

1. R. Jasinski and S. Kirkland, *Anal. Chem.*, **39**, 1663 (1967).
2. M. Rao, U.S. Pat. 3,413,154, Nov. 26, 1968.
3. J. Coleman and M. Bates, Proceed. Sixth Int. Power Symposium, Brighton, England, p. 289, Pergamon Press, Sept. 1968.
4. R. Jasinski and S. Carroll, *Anal. Chem.*, **40**, 1908 (1968).
5. R. Jasinski, "High Energy Batteries," Plenum Press, New York (1967).

A Laboratory Cell for Testing Anode Materials

A. Tasch, L. E. Vaaler,* and J. M. Finn, Jr.*

Carbon Products Division, Union Carbide Corporation, Cleveland, Ohio

Scaled down diaphragm and mercury cells have been used for many years for the laboratory evaluation of anode materials for chlorine cells. The preparation, operation, and maintenance of these laboratory cells required considerable effort, and, as a result, the present investigation was initiated for the purpose of developing a new laboratory cell that would permit a more precise procedure for the study of the fundamentals of corrosion and the development of improved product. A simple system for depolarizing the cathode was conceived and resulted in a test cell which does not require a diaphragm or brine source. In the new cell the chlorine ion is oxidized to chlorine at the test anode, and the bath is replenished by reduction of chlorine gas bubbled through a porous graphite cathode. Conditions in this cell can be controlled more easily than in the laboratory cell used previously (1).

Apparatus

Figure 1 is a simplified sketch of the cell and the functioning electrodes. The corrosive environment is contained in a battery jar and consists of 30 liters of sodium chloride solution at a concentration of 220 g/l and saturated with chlorine.

Anode and anode support.—Figure 2 is a photograph of the anode parts and assembly.

The anode sample, 1.129 ± 0.002 in. in diameter, provided a corroding surface of 1 in.^{2}. The sample thickness was chosen as a result of corrosion depth measurements (2) which showed that anode graphites may be attacked to a depth of as much as 8 mm below the surface. The thickness of ½ in. (12.7 mm) used in the laboratory cell was, therefore, more than adequate to show the full corrosive attack. The sample edge was drilled and tapped (5-40 tap) to a depth of ½ in. to provide means for attaching an electrical conductor.

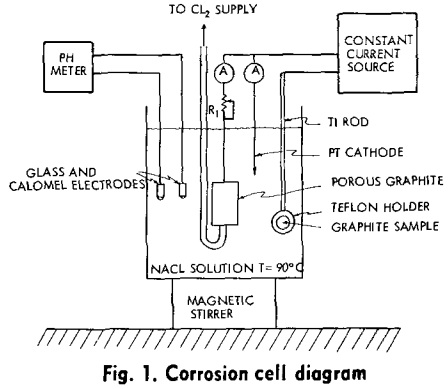

Fig. 1. Corrosion cell diagram

* Electrochemical Society Active Member.

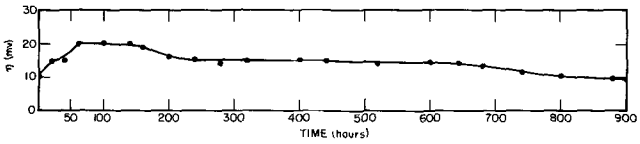

Fig. 1. Time dependence of the reference electrode, anode potential shown for lithium electrodes immersed in 1N $LiClO_4$-PC at +160°F.

Discussion

Consider first the compatibility experiments described by Table I. No gross decomposition was noted in heating the electrolyte alone or in the presence of lithium sheet. More sensitive gas chromatographic evidence indicates some electrolyte decomposition at and above 150°C (1). The electrolyte was not compatible at high temperatures with acetylene black and sulfur. The first material has often been used as a conductive binder in positive plates; sulfur has been suggested as a positive plate material (2, 3). Particular caution should be used in handling positives formed from carbon, sulfur, and lithium perchlorate: This combination resembles closely the classical composition of gun powder.

The electrochemical method is felt to be a particularly severe test of system compatibility, since fresh lithium surface is continuously exposed to the electrolyte at the anode and cathode. Thus, thin but protective films become much less effective in retarding gross decomposition of the electrolyte. As shown in Fig. 1, the polarization of the lithium anode remains relatively constant; there is no indication of any major deterioration in performance with time. The reason for the minor improvement after 600 hr has not been established. Two explanations are possible. First, small amounts of film on the anode are slowly lost by electrochemical dissolution of the electrode and hence it improves with time. Second, small amounts of film deposit on the reference electrode and it slowly deteriorates with time. In either event, the effect is small, a few millivolts over a 900-hr test.

The conclusion to be drawn from these experiments is that there is not a gross decomposition of the electrolyte by anodically discharging lithium metal at 160°F which would prohibit its use in a working battery. This is a necessary although not a sufficient condition for the development of high temperature lithium batteries. Oxidizable materials such as sulfur and acetylene black are not compatible with $LiClO_4$-PC at elevated temperature.

Acknowledgments

This work was carried out under Contract No. N00019-68-C0402 for the Naval Air Systems Command and Contract No. F19628-68-C-0052 for the Air Force Cambridge Research Laboratories.

Manuscript submitted July 31, 1969; revised manuscript received Oct. 29, 1969.

Any discussion of this paper will appear in a Discussion Section to be published in the December 1970 JOURNAL.

REFERENCES

1. R. Jasinski and S. Kirkland, *Anal. Chem.*, **39**, 1663 (1967).
2. M. Rao, U.S. Pat. 3,413,154, Nov. 26, 1968.
3. J. Coleman and M. Bates, Proceed. Sixth Int. Power Symposium, Brighton, England, p. 289, Pergamon Press, Sept. 1968.
4. R. Jasinski and S. Carroll, *Anal. Chem.*, **40**, 1908 (1968).
5. R. Jasinski, "High Energy Batteries," Plenum Press, New York (1967).

A Laboratory Cell for Testing Anode Materials

A. Tasch, L. E. Vaaler,* and J. M. Finn, Jr.*

Carbon Products Division, Union Carbide Corporation, Cleveland, Ohio

Scaled down diaphragm and mercury cells have been used for many years for the laboratory evaluation of anode materials for chlorine cells. The preparation, operation, and maintenance of these laboratory cells required considerable effort, and, as a result, the present investigation was initiated for the purpose of developing a new laboratory cell that would permit a more precise procedure for the study of the fundamentals of corrosion and the development of improved product. A simple system for depolarizing the cathode was conceived and resulted in a test cell which does not require a diaphragm or brine source. In the new cell the chlorine ion is oxidized to chlorine at the test anode, and the bath is replenished by reduction of chlorine gas bubbled through a porous graphite cathode. Conditions in this cell can be controlled more easily than in the laboratory cell used previously (1).

Apparatus

Figure 1 is a simplified sketch of the cell and the functioning electrodes. The corrosive environment is contained in a battery jar and consists of 30 liters of sodium chloride solution at a concentration of 220 g/l and saturated with chlorine.

Anode and anode support.—Figure 2 is a photograph of the anode parts and assembly.

The anode sample, 1.129 ± 0.002 in. in diameter, provided a corroding surface of 1 in.^{2}. The sample thickness was chosen as a result of corrosion depth measurements (2) which showed that anode graphites may be attacked to a depth of as much as 8 mm below the surface. The thickness of ½ in. (12.7 mm) used in the laboratory cell was, therefore, more than adequate to show the full corrosive attack. The sample edge was drilled and tapped (5-40 tap) to a depth of ½ in. to provide means for attaching an electrical conductor.

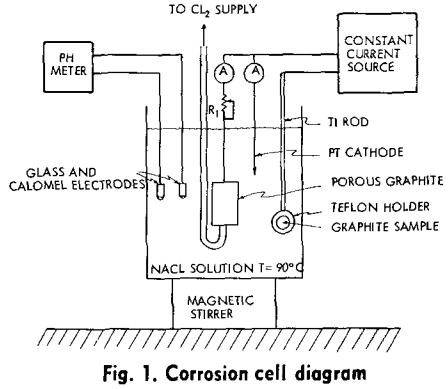

Fig. 1. Corrosion cell diagram

* Electrochemical Society Active Member.

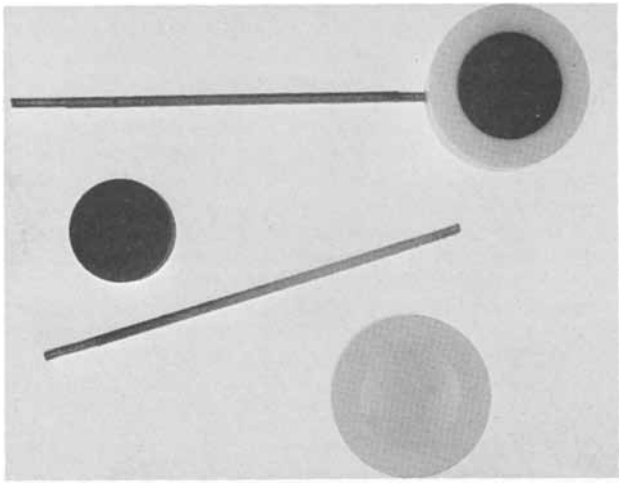

Fig. 2. Anode components and assembly

The test anode was pressed into a cylindrical Teflon holder that protected all but one face of the graphite from attack. The inside diameter of the Teflon can be as much as 0.005 in. larger than the outside diameter of the graphite and still maintain adequate protection. Current was carried to the anode through a ⅛ in. diameter titanium rod which had a 6-40 threaded end to provide an interference fit with the graphite.

Cathode.—The most critical assembly of the laboratory test cell is the chlorine depolarized cathode. This electrode supplies chloride ions to the bath through the reduction of chlorine gas. The cathode consists of a porous graphite block threaded to a ½ in. diameter graphite rod which acts as a physical support as well as an electrical conductor. A glass tube attached to the bottom of the block conducts the chlorine gas to the bath. Porous graphite (PG-25) having the greatest gas permeability was used for the block so that a minimum of gas pressure would provide an adequate supply of chlorine. It was usually found necessary to bubble chlorine through the block for a period of 3-4 days at a pH of 2.0 before normal operation of the cell was initiated. After four to six months of operation, the porous block began to disintegrate rapidly and was replaced. The graphite support rod corroded in the area between the bath level and the cover and also needed periodic replacement.

In addition to the chlorine depolarized cathode, a small platinum wire cathode, connected in parallel, produced hydrogen gas and hydroxyl ions. The platinum cathode simulates, in a controlled manner, leakage of caustic into the anolyte in a diaphragm cell or hydrogen evolution (with OH^- ion formation) on a mercury cathode.

Covers and supports.—The top of the jar was covered with a 1-in. thick Lucite plate which supported the samples, heater, pH electrodes, and cathode and prevented the evaporation of the liquid. The Lucite does not appear to react with the gas or bath and, after one year of operation, there were few signs of deterioration. The cover was drilled with four holes 3½ in. in diameter. Each of four Lucite stoppers made to fit these holes supported four anode assemblies so that 16 samples could be tested simultaneously. Figure 3 shows the cover in place and the location of the various electrodes.

pH Measurement.—The pH of the solution was measured through the use of glass and calomel electrodes by normal techniques and instrumentation. The pH calibration, however, was obtained by using a buffer in a salt solution at 90°C. The two electrodes were located in the center of the cell directly above the cathode block. This position, determined by experimentation, is electrically "neutral" so that the pH

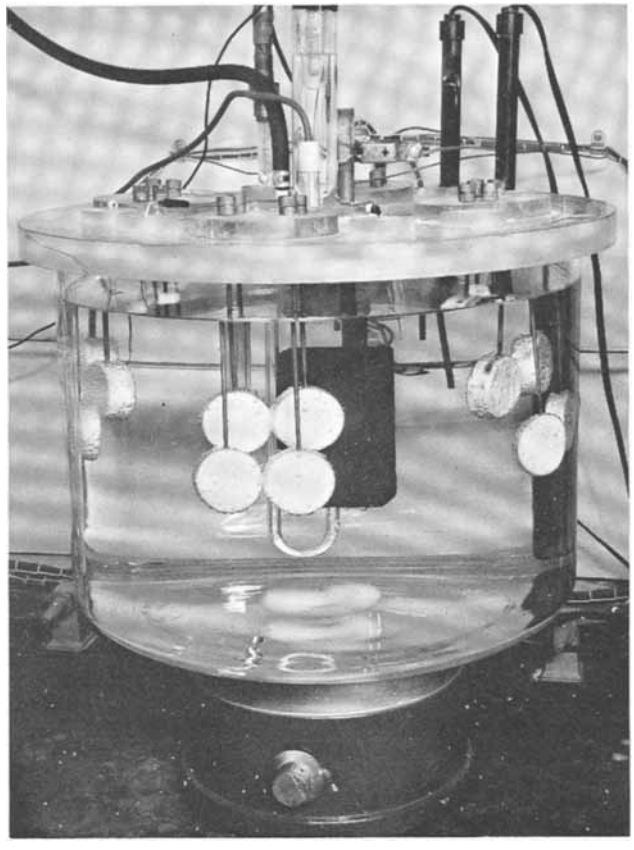

Fig. 3. Photograph of corrosion cell showing location of electrodes.

measurement is affected very little by the electric field associated with the current flow to the anode samples. This arrangement makes it possible to record the correct pH automatically with a recording potentiometer.

Heating and stirring.—The cell bath was maintained at 90°C by means of glass-covered immersion heaters in conjunction with an on-off type control unit. Two 500W units were found to be sufficient even with no thermal insulation of the battery jar.

The uniformity of conditions throughout the bath was insured through the use of a magnetic stirrer under the glass container. Determinations of pH, showed that the variation of this parameter, throughout the bath, is within the error of the measuring instrument (0.1 unit).

Power supply and constant current source.—The electrical current for cell operation was obtained from a rectifier with a variable 30V, 50A, unfiltered output. Filter networks and transistorized constant current circuits were used to produce ripple-free direct current to the anodes. Figure 4 is a schematic of the filter network and the simple one-transistor circuit which maintained the current at a level determined by the setting of R_3. The constant current was obtained by operating the transistor on the flat portion of its col-

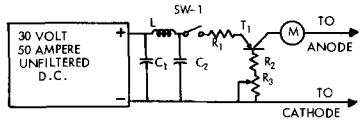

L = 0.025 H, 4 AMP.
C_1 & C_2 = 4000 MF 50 WVDC
R_1 = 2 Ω 20 WATT
R_2 = 100 Ω 2 WATT
R_3 = 10K Ω 2 WATT POTENTIOMETER
T_1 = 2N441 TRANSISTOR
SW-1 = SPST
M = 0-3 AMPERES, D.C.

Fig. 4. Schematic diagram of anode power source

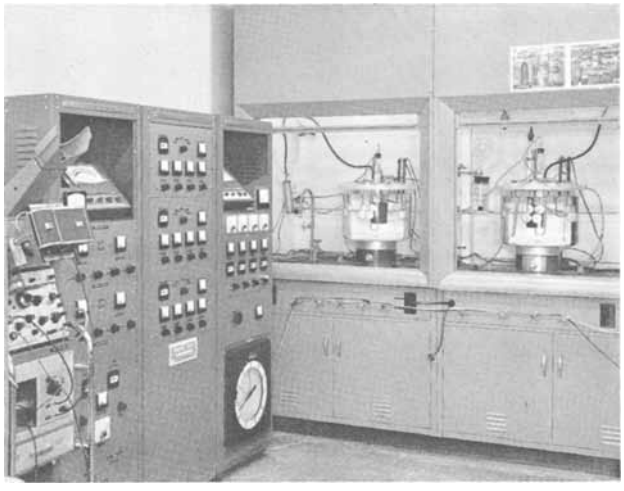

Fig. 5. Two test cells and control equipment

lector characteristic. A current density of 0.8 A/in.^{2} was used since this value is typical of commercial diaphragm cell operation. The constant current circuit maintained this level with a tolerance of ±3% when steady-state operating conditions were achieved. Figure 5 shows two test cells in operation, the power source, and control equipment.

Chlorine supply.—The flow of chlorine to the cathode must be great enough to replenish the chloride removed at the anodes and to keep the electrolyte saturated with the gas. To achieve these conditions, chlorine gas was supplied from a stainless steel manifold which was connected to a pressure cylinder containing 150 lb of liquid chlorine. The gas, taken from the manifold, was metered through a Monel valve, passed through a drier of calcium sulfate, and then through a glass bubbler which permitted the flow rate to be adjusted visually. From the bubbler, the Cl_2 passed through a neoprene hose to the glass tube of the cathode assembly. The neoprene hose and graphite cathode block deteriorate in service and must be replaced periodically. Maintenance of the cell, therefore, has been reduced to this simple replacement procedure.

Operation and Experimental Procedure

The best results[1] were obtained by corroding the test samples in the brine solution for five days, washing in hot water for one day, and drying at 110°C for one day. The first five days of corrosion were considered "break-in" time, during which the corrosion rate was highly variable. Conditions were sufficiently stable thereafter to obtain reproducible results during successive five day corrosion periods so that the determination of corrosion rates required a total elapsed time of two weeks.

The test anodes were weighed before installation and following washing and drying after the corrosion period. The weight loss per 1000 A hr of operation is defined as the "corrosion rate" that characterizes the anode material.

The operating parameters of the laboratory cell were selected on the basis of laboratory investigations and commercial operating conditions. The conditions used to obtain the corrosion data presented in this paper were the following: temperature = 90° ± 1°C; current density = 0.8 ± 0.02 A/in.^{2}; brine concentration = 220 ± 10 g/l; I_{pt} = 15% of total cathode current.

The value of I_{pt} (the platinum cathode current) was adjusted by means of R_1 in Fig. 1. By setting this current to various percentages of the total current the pH of the solution could be changed as shown in Fig. 6. In an alternate mode of operation, the platinum cathode was used as an element to control pH at a selected value. For the data presented in this paper the platinum cathode current was adjusted to 15% of the total current because this value produced a pH in the range from 3.0 to 4.0 for the types of graphites examined. This pH is in the range existing in production diaphragm cells.

[1] In an alternate procedure, it was found possible to follow the external corrosion of the anode via changes in its archimedean volume (contained brine and all). The anode was periodically removed and weighed, without washing, above and under a salt solution (220 g/l) of exactly known density. From these data the volume was precisely determined.

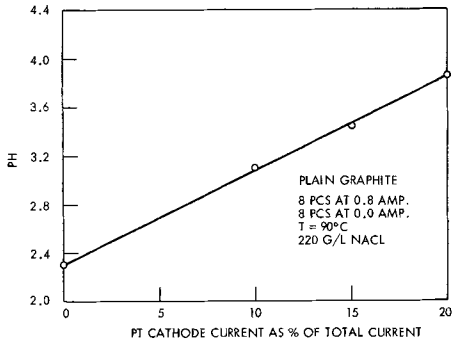

Fig. 6. Effect of Pt cathode current on electrolyte pH

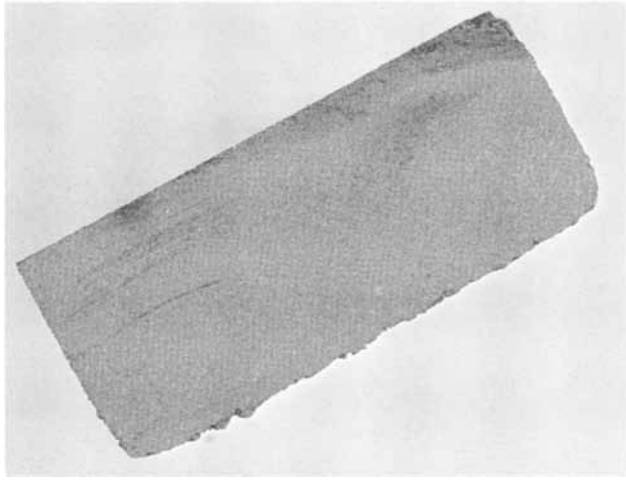

Fig. 7. Cross section of corroded sample

Experimental Results

Figure 7 is a photograph of a cross section through the diameter of a corroded sample indicating that corrosion is reasonably uniform except for some rounding near the circumference. This result indicates that the current density is uniform over most of the surface and somewhat higher at the edges. More elaborate means of assuring a uniform current density could have been provided but would have interfered with free convection and gas escape at the electrode surface.

The corrosion rates of four samples taken from an experimental oil-treated graphite anode are presented in Table I. The average value for the first week was obtained during the "break-in" period and, therefore, should not be compared with the data of subsequent

Table I. Oil-treated anode corrosion rate

Anode No.	Corrosion rate, g/KAH		
	1st Week	2nd Week	3rd Week
1	3.78	4.31	4.00
2	3.85	4.37	4.32
3	3.64	4.31	4.28
4	3.86	4.35	4.26
Avg	3.78	4.34	4.22
	σ = 0.10	σ = 0.03	σ = 0.14

σ = Standard deviation.

Table II. Corrosion rates of anode graphite (g/KAH)

Sample No.	Plain graphite	Sample No.	Oil-treated graphite
1	3.34	1	2.97
2	3.41	2	2.20
3	3.61	3	2.94
4	3.64	4	3.29
5	3.61	5	3.18
6	3.56	6	2.84
7	3.68	7	2.83
8	3.57	8	2.85
	Avg = 3.55		Avg = 3.55
	σ = 0.12		σ = 0.32

σ = Standard deviation.

corrosion periods. The excellent agreement between the average values for the second and third weeks demonstrates the reproducibility of the measurements.

The effect on service life of impregnating graphite with linseed oil is shown in Table II. The samples for the two sets of data involved the same base stock and processing except for the linseed oil treatment. A 20% reduction in corrosion rate was obtained through the use of linseed oil as the impregnating material.

The relatively large standard deviation for the oil-treated graphite was due primarily to the exceptionally low value of corrosion rate of oil-treated sample 2. There was nothing unusual about the appearance of this sample and it is suspected that there was an error in weighing. If sample 2 is omitted, the results show that the cell functions very well in the evaluation of plain and oil-treated graphite and can distinguish between oil-treated graphites as demonstrated by a comparison of the data of Tables I and II.

Samples of oil-treated graphite, through which no current was passed, were immersed in the cell in which the eight oil-treated samples which carried current were being tested. This technique was used to compare the extent of chemical corrosion (no current) with chemical plus electrochemical (current) corrosion. The average weight loss due to chemical corrosion was 28% of the total weight loss of the samples carrying current. This loss is appreciable and does not involve the mechanical erosion that occurs at a conducting electrode at which gas is produced. Conceivably mechanical corrosion could accelerate the corrosion rate on the nonconducting samples.

With the accuracy of control of the meaningful parameters and the simplicity of operation, the apparatus described has become a useful laboratory tool for studying the corrosion of anodes for use in chlorine cells.

Acknowledgment

The authors wish to express their appreciation to N. J. Johnson and M. Janes for the helpful suggestions regarding chlorine chemistry and the discussions of the chlor-alkali industry in general. The assistance of M. G. Swartz in the operation and maintenance of the test cells has been invaluable.

Manuscript submitted July 28, 1968; revised manuscript received *ca.* Oct. 20, 1969. This was Paper 267 presented at the Boston Meeting of the Society, May 5-9, 1968.

Any discussion of this paper will appear in a Discussion Section to be published in the December 1970 JOURNAL.

REFERENCES

1. N. J. Johnson, *Trans. Electrochem. Soc.*, **86**, 127, 1944.
2. R. Geise, L. E. Vaaler, A. J. Kallfelz, *This Journal*, **111**, 73C, Abstract 170 (1964).

The Electrochemical Decomposition of Propylene Carbonate on Graphite

A. N. Dey* and B. P. Sullivan*

Laboratory for Physical Science, P. R. Mallory & Company, Inc., Burlington, Massachusetts

Propylene carbonate (PC) became one of the most commonly used solvents for organic electrolyte batteries after the successful electrodeposition of lithium (1) from a PC solution of its salt. The solvent was also considered to be relatively stable with lithium. Considerable (2, 3) attention was given to the purification of the solvent to remove the supposedly electroactive impurities, *e.g.*, water. There was no information available regarding the electroactivity of PC itself. We wish to present evidence in this report to show that PC is electrochemically decomposed on the graphite cathode to propylene gas and carbonate ion with almost 100% coulombic efficiency.

Experimental

Propylene carbonate (Eastman Kodak) was vacuum distilled at 120°C, 1.2 mm Hg.

Anhydrous $LiClO_4$ was used as received from G. Fredrick Smith Company.

The graphite rods (⅛ in. diameter), used as working electrodes, were of special spectroscopic type (National AGKSP) supplied by Fisher Scientific Company.

Lithium ribbons (Foote Mineral Company) pressed on stainless steel exmet were used as reference and counterelectrodes.

* Electrochemical Society Active Member.

Perkin Elmer Model 801 gas chromatograph (GC) was used for analysis of the gas and the electrolyte. The column used was Porapak Q with a He flow rate of 20 cc/min, hot wire detector temperature of 200°C, and detector current of 200 mA. The column temperature of 60°C was used for gas analysis.

The water content of our electrolyte was found to be 0.09% (volume).

The cell.—The schematic diagram of the cell is shown in Fig. 1. The working electrode was a graphite rod (A) connected with the platinum wire which was sealed in a glass tube. The electrical connection was made using a copper wire dipped in the mercury pool in the glass tube. The reference (C) and the counterelectrodes (B) were spot welded with the Pt wires from two other glass tubes. The glass container (D) connected with the cell was filled with the PC and the level of the PC in the side arm was adjusted up to the tip of the side arm (as shown in Fig. 1) using dry argon stream, prior to the electrolysis. On electrolysis the evolved gas displaced an equivalent volume of PC from the container (D) and was collected in the container (E) and weighed. The volume of the gas evolved was determined from the weight of the displaced PC. The method was found to be sensitive enough to measure gas volumes of 0.005 cc or more. Also, the PC in

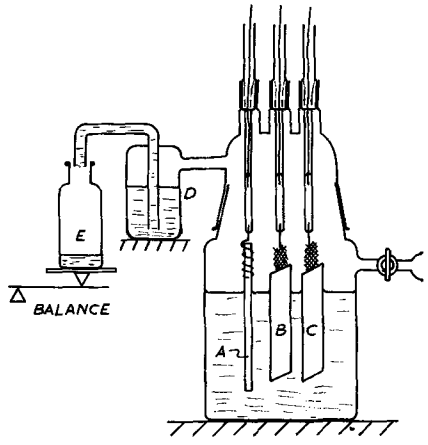

Fig. 1. Cell for the measurement of rate of gas evolution: (A) graphite cathode, (B) and (C) lithium counter and reference electrode, (D) PC container, and (E) container for the weighing of the displaced PC.

container (D) prevented transport of moisture and other impurities from the atmosphere to the cell electrolyte. The cell was assembled in the dry box in an argon atmosphere, and the subsequent gassing experiment was carried out in the open atmosphere. The weight changes due to the evaporation of PC were found to be negligible.

The chemical evolution of gas (H_2) with the lithium electrodes in the electrolyte, was found to be exceedingly low ($< 1\%$ of the gas) during the duration of the gassing experiment. The entire amount of the evolved gas was found to be generated electrochemically at the graphite cathode only.

Experimental Procedure.—Galvanostatic experiments were carried out using Regatron Constant Current Power Supply, Model C-612, (Electronic Measurements Inc.). The electrolyte used was 1(M) $LiClO_4$ in PC. The potential of the graphite working electrode, *vs.* Li reference, and the volume of gas evolved was recorded as a function of time, on passage of a constant current. During electrolysis the graphite rod electrode was found to disintegrate slowly. However, the gassing rate and the potential-time curves were found to be reasonably reproducible when a new graphite rod was used for each run.

At the end of the run the samples of gas and the electrolyte were removed and analyzed by GC. The graphite electrode and the disintegrated materials were collected from the cell on a filter paper (in the dry box) and washed thoroughly with tetrahydrofuran to remove all PC. The electrode along with the disintegrated materials were then acidified with phosphoric acid and the evolved gas was removed by bubbling prepurified argon and was passed first through a cold trap and then through a standard solution of $Ba(OH)_2$. The CO_2 in the gas was quantitatively determined by titrating $Ba(OH)_2$ solutions.

Results and Discussion

A typical chronopotentiogram (corrected for IR) on a graphite electrode in 1(M) $LiClO_4$-PC electrolyte is shown in Fig. 2. The open-circuit voltage of +2.75V *vs.* Li reference dropped sharply on the passage of cathodic current (2 mA/cm^2) and a relatively steady plateau voltage of approximately +0.6V *vs.* Li was observed. During this galvanostatic electrolysis a substantial evolution of gas was observed on the graphite cathode. The rate of gas evolution at an apparent current density of 2 mA/cm^2 is plotted in Fig. 3 for two electrodes of different size. On doubling the total current (same current density) the increase in the rate of gassing was found to be more than double. The

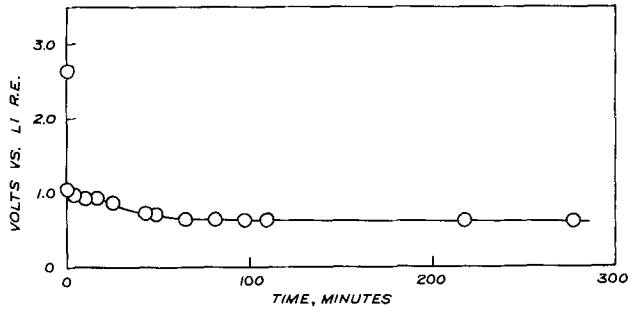

Fig. 2. Chronopotentiogram on graphite electrode in 1M $LiClO_4$-PC electrolyte. Apparent current density = 2 mA/cm^2.

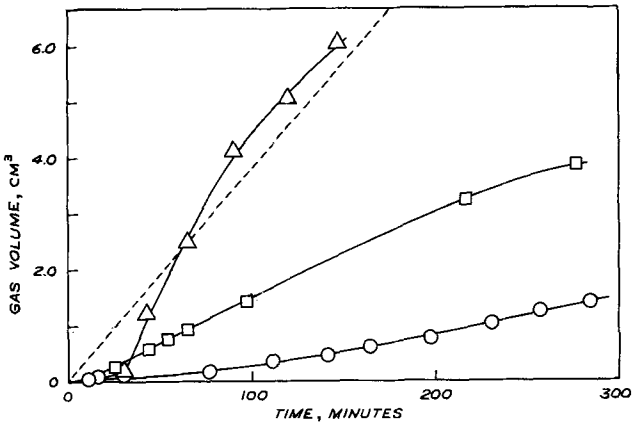

Fig. 3. Rate of gas evolution plots: □ rate of gas evolution at 2 mA/cm^2, total current = 10 mA; in 1M $LiClO_4$-PC; ○ rate of gas evolution at 2 mA/cm^2, total current = 5 mA; in 1M $LiClO_4$-PC; △ rate of gas evolution at 2 mA/cm^2, total current = 5 mA; in 1M $LiClO_4$-PC saturated with propylene; - - - theoretical rate of gas evolution at 5 mA current.

gassing rate was also found to be increased substantially on increasing the current density.

The gas chromatographic analysis of the evolved gas showed that the major ($> 95\%$) component consisted of propylene. The presence of CO_2, H_2, and ethylene in trace quantities ($< 1\%$) was also detected. The G.C. analysis of the electrolyte, after electrolysis, also showed the presence of propylene, as a major new component, and traces of water. No other new component was detected in the electrolyte.

We propose the following electrochemical reaction to explain the formation of propylene.

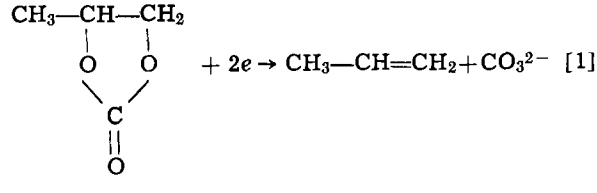

Based on the above reaction it was possible to determine the coulombic efficiency of gas evolution. The dotted line in Fig. 3 represents the theoretical rate of gas evolution at 5 mA current according to reaction [1]. Apparently, the observed rates are considerably lower. However, we found that propylene was highly soluble in PC. Therefore, the gassing experiment was then carried out in a propylene saturated 1M $LiClO_4$-PC electrolyte. Results in Fig. 3 show that the experimental rate in propylene saturated solution is quite close to the theoretically expected rate.

Reaction [1] also predicts the stoichiometric formation of Li_2CO_3 (insoluble) as a result of the electrochemical decomposition of PC. This was analyzed by determining the amounts of CO_2 evolved on acidifying

Table I. Determination of Li_2CO_3 in the graphite electrode after electrolysis

Apparent current density, mA/cm²	Coulombs passed	Moles of CO_2 observed	Theoretical moles of CO_2 based on reaction [1]	Coulombic efficiency, %
1	185	1.14×10^{-3}	0.96×10^{-3}	118
2	418	2.20×10^{-3}	2.16×10^{-3}	102
2	306	1.63×10^{-3}	1.59×10^{-3}	102
2	393	1.98×10^{-3}	2.04×10^{-3}	97

The coulombic efficiency was again found to be approximately 100%.

the electrode after the electrolysis. Results are shown in Table I.

Formation of trace amounts of H_2 and CO_2 could be due to the chemical and/or electrochemical decomposition of H_2O present in the electrolyte. However, the decrease in the water content did not show any measurable effect on the formation of the main products, *viz.*, propylene and CO_3^{2-}. Thus, the effect of H_2O (0.09% vol) in the above reaction was of minor importance, if any.

It was thus established that PC could be electrochemically decomposed quite efficiently on graphite substrates at potentials substantially positive to that of lithium. However, we found that at higher current densities the potential of the graphite electrode slowly decreased to less than 0V *vs.* Li reference and lithium deposition ensued. Under these circumstances, both the decomposition of PC and the lithium deposition occurred on graphite. This could explain the previously observed (2) inefficient lithium deposition on graphite. On metals like Pt, Ni, Cu, etc., the cathodic chronopotentiogram in 1(M) $LiClO_4$-PC usually consisted of three short voltage plateaus prior to lithium deposition as observed (4) in our laboratory earlier. One of those could be due to the decomposition of PC. On metals like Pt, Ni, Cu, etc., the overvoltage for the lithium deposition could be relatively lower than on graphite and thus lithium deposition became the predominant cathodic reaction, whereas on graphite the decomposition of PC was the predominant reaction at low current densities.

Graphite was one of the most common conductive mixes used for practical battery cathodes. The above finding thus raises a serious question regarding the validity of many cathodic efficiency measurements and also regarding the feasibility of using PC for practical organic electrolyte batteries. Measurements of the kinetics of lithium electrode in PC may also be in error because of the solvent decomposition reaction discussed above.

Similar electrochemical decompositions were observed in other solvents and will be discussed in a future publication.

Acknowledgment

The authors wish to thank Dr. Per Bro and Dr. Robert Selim for helpful discussions.

Manuscript submitted Sept. 3, 1969; revised manuscript received Oct. 19, 1969.

Any discussion of this paper will appear in a Discussion Section to be published in the December 1970 JOURNAL.

REFERENCES

1. W. S. Harris, "Electrochemical Studies in Cyclic Esters," Thesis, University of California, 1958.
2. R. G. Selim, K. R. Hill, and M. L. B. Rao, "Research and Development of a High Capacity Nonaqueous Secondary Battery," Final Report, NASA CR-54969, P. R. Mallory & Co. Inc., December 1965.
3. R. Jasinski, B. Burrows and P. Malachesky, "High Energy Batteries," Final Report AD 823304, Tyco Laboratories, Oct. 1967.
4. A. N. Dey, *This Journal*, **114**, 823 (1967).

JOURNAL OF THE ELECTROCHEMICAL SOCIETY

SOLID STATE SCIENCE

FEBRUARY 1970

The Mechanical Behavior of Anodic Coatings on Deformed Aluminum

N. J. Cochrane[1] and R. J. Block

Department of Chemical Engineering and Materials Science, The University of Oklahoma, Norman, Oklahoma

ABSTRACT

Aluminum monocrystals and polycrystalline wire having coatings were deformed in boric acid. The behavior of the coatings was studied using a potential technique to determine the progress of film rupture and by optical metallography. The results suggest that the coating-substrate interface is capable of sustaining significant shear strain.

The rupturing of oxide coatings on metals is believed to play a part in stress corrosion cracking (1) and in the corrosion of cold worked metals (2). As a result, the behavior of barrier-type passive coatings has become a subject of some interest (3-6). In the present paper we describe experiments in which the initiation of fracture in the coating was accurately determined relative to the yield strain of the substrate. The behavior of the coating was studied metallographically to determine its response to the deformation processes. Both aluminum crystals and polycrystalline wire were used as substrate material.

Experimental

The experimental technique, after Logan (1), involved extension of the specimen in a 0.4M boric acid electrolyte while simultaneously measuring its potential relative to a saturated calomel electrode. The specimens, mounted in glass or Lucite balls, were electropolished, stripped of residual films, and either placed open circuited in the boric acid or anodized at 90V prior to extension. The treatments produced barrier coatings 100 and 1300Å in thickness. Coating thicknesses were estimated using the technique of Hunter and Fowle (7), and the usual 14 Å/V relationship.

Results

Figure 1 is a tracing of the load-extension, potential-extension chart records of one of the single crystals tested. The magnitude of the potential difference between specimen and electrode is plotted as a positive value. The crystal was of square cross section ⅛ in. of a side by 1.0 in. gauge length. The orientation of this crystal is given in Fig. 2.

Examination of the 100Å coating after increments 1 and 5 showed only slip plane traces which were apparent on both faces of the crystal. After sufficient extension, the 1300Å coating was found to crack. Cracking always initiated on the crystal surface most nearly perpendicular to the Burgers' vector of the primary slip system. Often a pattern of cracks had developed on the $(\bar{2}\bar{1}0)$ face of the crystal before any cracks had appeared on the $(1\bar{2}2)$ surface. Using round monocrystals, it was verified that displacements causing slip steps rather than surface shears were responsible for crack initiation in the coating. Slip displacements in the absence of corresponding cracks were clearly evident beneath the coating and may be seen in Fig. 3 and 4. Once formed, the cracks always propagated along directions normal to the tensile axis, encircling the crystal.

Conversion of the load-extension data to resolved shear stress-strain curves showed that the crystal ended stage I midway through the second strain increment and deformed in stage II thereafter. Figure 1 shows a small but reproducible delay of about 0.03% extension between yielding of the crystal and onset of film rupture in the 100Å coating. This value is about an order of magnitude less than the maximum extension reported by Bradhurst and Leach (8) for a 20Å film on an aluminum alloy. The difference may be the result of fracture of the coating across fewer but larger slip steps on the monocrystals used here. The delay appears in increments 1 and 5 as well as

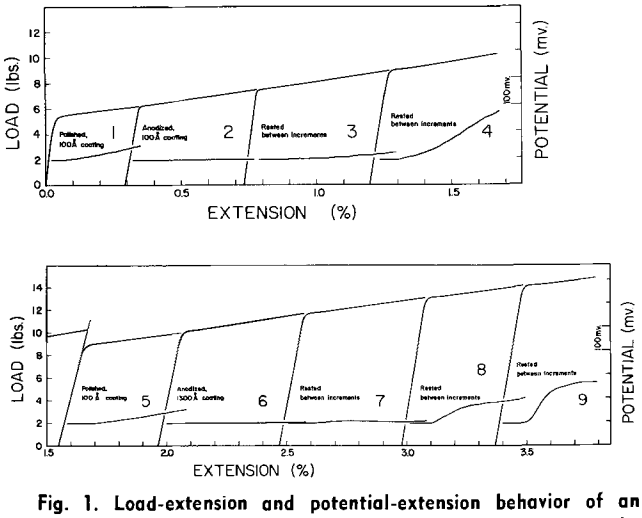

Fig. 1. Load-extension and potential-extension behavior of an aluminum single crystal. Treatment of the specimen prior to the strain increment is indicated.

[1] Now with the U. S. Air Force, Elgin AFB, Florida.

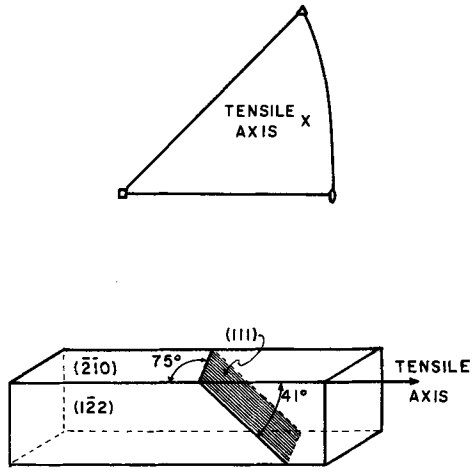

Fig. 2. Stereographic and geometric representation of the crystal used in the sequence of Fig. 1.

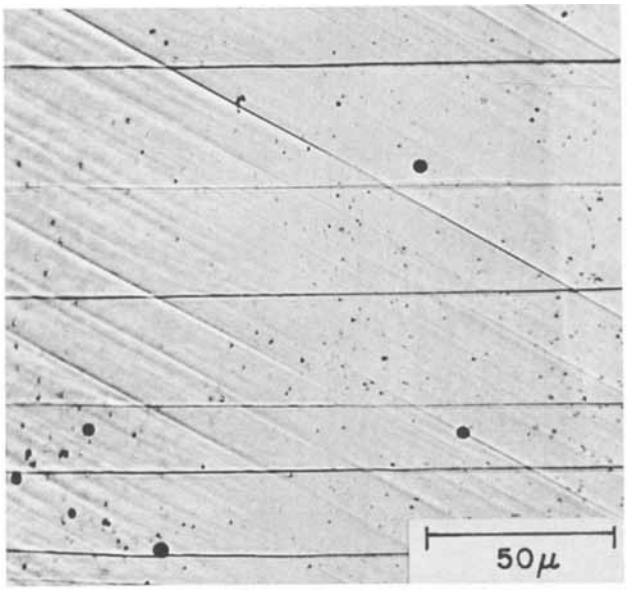

Fig. 3. Photomicrograph of the (2̄10) surface of a crystal having the same orientation as in Fig. 2. The specimen was anodized at 90V and extended 2%. The tensile axis is vertical. Horizontal cracks and diagonal slip plane traces are shown.

increments 4, 8, and 9. In these latter cases flow in the substrate initially caused film rupture where old cracks in the anodized coating had been repaired with the 100Å coating during the rest period between strain increments. Later in these increments new cracks formed in the 1300Å coating.

The surfaces of anodized specimens for which extension had been interrupted before a sharp potential change had occurred (as after increments 2, 3, 6, and 7) showed only slip plane traces equivalent to the diagonal markings visible in Fig. 3. It was verified that a change in specimen potential occurred only with the appearance of circumferential cracks in the coating. Here one is forced to conclude that the coating can remain intact over the shear displacements and slip steps present at the coating substrate interface. The diagonal markings must then be slip plane traces viewed through the transparent coating.

The anodized coating sustained about 1% extension of the substrate before fracture initiated (increments 2-3 and 6-7). Once again one might expect larger extensions with more isotropic substrates. In experiments with annealed aluminum wires having a grain size of 0.002 in., the difference between yielding and the onset of film rupture was about 1.4% extension.

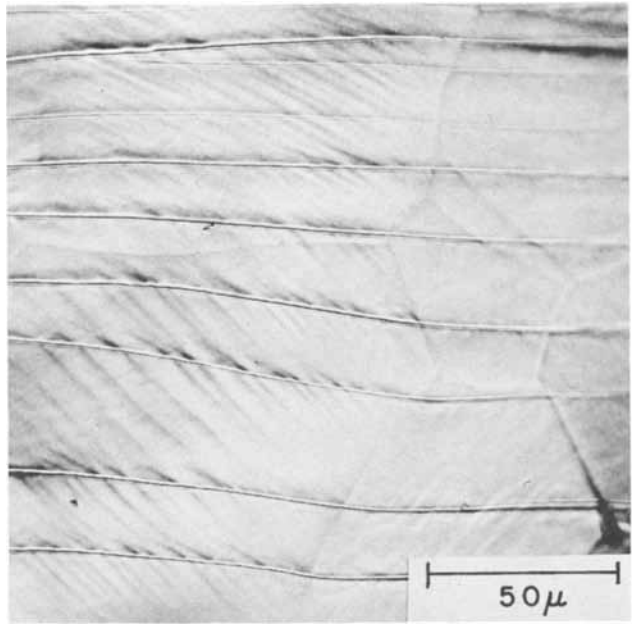

Fig. 4. Photomicrograph of a polycrystalline aluminum wire, anodized at 90V and extended 3.7%. The tensile axis is vertical.

This value is about the same as has been reported elsewhere (8, 9).

Discussion

The results of these studies raise several questions about how thick anodic coatings accommodate deformation of the substrate. Crack propagation appears to be a macroscopic phenomenon in which the film and substrate seem to behave as though they were concentric cylinders under axial load. Cracks which open independent of slip plane traces are most easily pictured as occurring with localized detachment of the coating just ahead of the growing crack. However, the mechanism for crack propagation may also describe how the film accommodates shear of the underlying surface without cracking. The high shearing stresses induced in the coating at slip plane traces could be relieved by interfacial slip, shear of the film or detachment over an area adjacent to the slip plane trace. The first of these mechanisms was invoked by Edeleanu and Law (9) to explain the relaxation of stress between cracks in anodic coatings. Shear of the coating appears to be unlikely in view of the very brittle behavior of isolated coatings observed by Bradhurst and Leach (8) and the present experiments which showed that substrate exposure (potential changes) did not generally accompany the formation of slip lines in the substrate. Shear of the coating may also be eliminated on the basis of observations described below.

Detachment may also be ruled out because of somewhat more indirect evidence. After sufficient extension of the substrate, the thick anodized coatings were observed to buckle, as shown in Fig. 5. Buckling is the result of a decrease in the cross sectional perimeter of the specimen as it elongates. The coating detaches and becomes raised from the surface as indicated by the interference fringes in the micrograph. Buckles in coatings always ran parallel to the tensile axis, and when fully developed, from crack to crack. Figure 5 shows several buckles passing over regions of well defined slip lines where the surface displacements should be fairly large, yet the buckles are not deflected by the slip plane traces. It is also apparent that the coating where raised is unbroken by the slip plane. Therefore, one might conclude that the coating can remain unbroken and adherent to the substrate across slip plane traces even after considerable deformation.

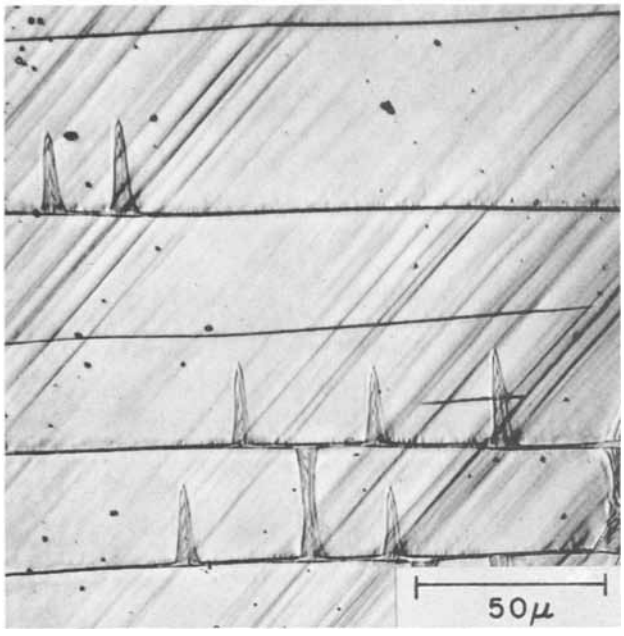

Fig. 5. Photomicrograph of an aluminum single crystal, anodized at 90V and extended 14%. The vertical structures are buckles in the coating.

It appears that the only model which survives is the equivalent of a rather viscous glue which can deform in shear while still firmly bonding the coating to the substrate. The strength of thick coatings was sufficient to require shear of the glue while apparently the opposite situation was obtained with the thinner coating which cracked along the slip plane traces. It seems reasonable to suggest that the characteristics required of the interfacial glue may reside in the misfit dislocations (10) which accommodate film and substrate.

Acknowledgments

The authors wish to express their appreciation to Mr. Parviz Mehdizadeh for his helpfulness throughout the study. This work was supported by the U.S. Atomic Energy Commission (Contract AT-(40-1)-3401) whose support is gratefully acknowledged, and is based on a thesis for the degree of Master of Science.

Manuscript submitted Aug. 15, 1969; revised manuscript received Nov. 3, 1969.

Any discussion of this paper will appear in a Discussion Section to be published in the December 1970 JOURNAL.

REFERENCES

1. H. L. Logan, *J. Res. Nat. Bur. Stand.*, **48**, 99 (1952).
2. U. R. Evans, "Corrosion and Oxidation of Metals," p. 386, St. Martin's Press, New York (1960).
3. D. H. Bradhurst and J. S. Ll. Leach, *This Journal*, **113**, 1245 (1966).
4. S. F. Bubar and D. A. Vermilyea, *ibid.*, **113**, 892 (1966).
5. S. F. Bubar and D. A. Vermilyea, *ibid.*, **114**, 882 (1967).
6. J. C. Grosskreutz and M. B. McNeil, *J. Appl. Phys.*, **40**, 355, (1969).
7. M. S. Hunter and P. Fowle, *This Journal*, **101**, 481 (1954).
8. D. H. Bradhurst and J. S. Ll. Leach, *Trans. Brit. Ceram. Soc.*, **62**, 793 (1963).
9. C. Edeleanu and T. J. Law, *Phil. Mag.*, **7**, 513 (1962).
10. H. A. Francis, *J. Appl. Phys.*, **38**, 715 (1967).

Fluorescence and Energy Transfer in $SrZnP_2O_7:UO_2^{+2}$

M. V. Hoffman*

General Electric Company, Lighting Research Laboratory, Nela Park, Cleveland, Ohio

ABSTRACT

An efficient green phosphor has been found in $SrZnP_2O_7:UO_2^{+2}$. Optimum formulation of host matrix, cation substitutions, and activator concentrations have been made and tested in fluorescent lamps. The structure has not been determined, but it is suggested that it may be a UO_2^{+2}-stabilized structure differing from the apparent host matrix of $SrZnP_2O_7$. Efficient energy transfer by radiationless transfer has been found to Eu^{+3} and Nd^{+3}.

The fluorescence of uranium in solids and in liquids is well known and has been thoroughly described in the literature (1, 2). A recent paper by Blasse (3) on the emission characteristics of many uranium-activated compounds with related cubic structures also includes a review of the literature on uranium-activated phosphors. Both green and red emission have been reported for uranium activation, and from these papers, it is apparent that the emission spectra depend on the lattice environment and on the particular uranium-oxygen group. Blasse attributes the green emission in certain phosphors to U^{+6} in octahedral positions, occupying a normal crystallographic site. The spectra of this type of phosphor consist of overlapping bands, varying in peak position and relative intensity, dependent on the structure and influenced by all the surrounding O^{-2} ions.

Another source of green emission is the uranyl group $(O—U—O)^{+2}$, a linear molecular species. These spectra are primarily influenced by the linear or axial U—O bonds, while the equatorial field from the other four U—O bonds exerts only a small influence and does not greatly modify the spectra (4). The emission consists of at least six relatively strong lines, and the absorption contains about 14 lines in the ultraviolet and blue region and a continuum in the ultraviolet. These emission and absorption characteristics are consistent with respect to relative band position, band spacing, and intensity in all matrices in which they are found. By this optical data, the presence of U^{+6} in the uranyl group can be distinguished from U^{+6} in a UO_6^{+6} or UO_4^{+2} group.

* Electrochemical Society Active Member.

Key words: luminescence, $SrZnP_2O_7:UO_2^{+2}$, energy transfer, UO_2^{+2} to Eu^{+3}, uranyl emission, strontium Zn phosphate luminescence.

Rabinowitch and Belford (5) have described the literature on the spectra of UO_2^{+2} in solids such as nitrates, chlorides, sulfates, phosphates, and acetates, and have included much of the earlier work of Dieke and Duncan (6). While it is possible to describe and identify the UO_2^{+2} spectra, little correlation has been possible with the structure in which the ion can be found. In general, the solid materials on which most spectra measurements have been made are hydrates, or formed by decomposition of hydrates, and contain UO_2^{+2} as a major matrix constituent.

The phosphor described here is activated by UO_2^{+2} as determined by its spectra, in a crystalline matrix based on $SrZnP_2O_7$. The structural incorporation of the UO_2^{+2} in this phosphor has not yet been determined.

Procedure.—The starting materials used to prepare the phosphor were standard grades normally used in commercial luminescent materials. These were $SrHPO_4$ and $ZnNH_4PO_4$, prepared for phosphor production, ZnO, $(NH_4)_2HPO_4$, and $UO_2(C_2H_3O_2)_2 \cdot 2H_2O$, purchased as reagent grade material. Uranyl acetate has a flaky consistency which makes uniform mixing difficult. The most satisfactory method was to incorporate the activator by coprecipitation. This was achieved by the addition of NH_4OH to an acid solution containing Zn^{+2}, UO_2^{+2}, and a slight excess of PO_4^{-3} ions. When the precipitate was fired to determine loss on ignition, the product did not retain the uranyl ion, but was arbitrarily calculated as "$(Zn_{1-x}U_x)_2P_2O_7$." Compensation with x or $x + 0.01$ moles ZnO gave the required stoichiometry, showing that the precipitated material had close to the assumed ratio of $Zn/U/PO_4$ even though the oxygen compensation for the uranium was not known. Even though mixing procedures were simplified and were made more efficient by the use of this precipitate, wet mixing in acetone was still found to be necessary to obtain complete diffusion of the UO_2^{+2} during firing.

Firing was in air, in quartz or platinum crucibles, at 800°C for 1 hr followed by 900°C for 2 hr or more. The brightness of the fired material is highly dependent on the preparative technique and formulation, which must include a precise stoichiometry, thorough dispersion of the activator, and a final firing at about 900° ± 10°C.

Formulation and phase relations.—All formulations and activator contents are given as moles per mole of $SrZnP_2O_7$. The identification of the activator as UO_2^{+2} is shown by its absorption and emission in a later section. These characteristic measurements, combined with microscopic examination and x-ray diffraction were used to determine the compositional limitations in the phosphor and the compatibility phase relations of the systems. The phosphor is a matrix of $SrZnP_2O_7$ with the activator, UO_2^{+2}, calculated as additive to the pyrophosphate. The activator can be accepted in amounts up to about 0.10 mole UO_2^{+2} per $SrZnP_2O_7$. Beyond this limit, microscopic examination shows the presence of a second compound. The addition of a full mole of UO_2^{+2} to $SrZnP_2O_7$ results in the formation of this second phase, which is a dark green compound, highly refractory, well crystallized, and easily identifiable by microscopic examination. An orthophosphate formula of $SrZnUO(PO_4)_2$, with U as +4, can be written for this material. Diffuse reflectance measurements showed good agreement with line absorption found for U^{+4} in CaF_2 (7) and no absorption or emission characteristic of UO_2^{+2}.

From optical data, the phosphor can be limited to a material of composition which is variable between $SrZnP_2O_7$ to $SrZnP_2O_7$:0.10 UO_2^{+2}. Above the UO_2^{+2} solid solution limit, the system contains two phases, each containing uranium, but in different oxidation states.

A further requirement of the phosphor is that the SrO=ZnO=P_2O_5=1 ratio must be maintained. Any deviation from this ratio, such as would result from substituting UO_2^{+2} for Sr, for Zn or for P_2O_5, results in the loss of the characteristic UO_2^{+2} absorption and emission. Further, every attempt to provide charge compensation for UO_2^{+2} had the same result. Therefore, the phosphor composition lies only along the join between $SrZnP_2O_7$ and $SrZnUO(PO_4)_2$.

X-ray diffraction patterns of $SrZnP_2O_7$ and of the phosphor show the addition and intensification of new lines with increasing additions of UO_2^{+2}, and a decrease in intensity of some of the host matrix lines. Close to the solid solution limit, a slight shift in a few lines was found. This introduction of new lines with UO_2^{+2} additions could indicate interstitial incorporation of the activator. The x-ray diffraction pattern of the orthophosphate compound closely resembles the additive lines found in the phosphor. For this reason, x-ray diffraction is a poor tool to define compositional and solid solution limits. The XRD patterns of the three materials are compared in Table I. These were obtained on a General Electric XRD 5 using CuKα radiation.

Optical Characteristics

Procedures.—The spectral energy distributions were measured on a direct reading spectroradiometer with a grating monochromator, corrected for photocell response, similar to that described by Brown (8). The spectral slit width is 10Å. The diffuse reflectance spectra were obtained on a Cary 14 recording spectrophotometer and are relative to CaF_2 as a standard. It is modified by the insertion of a 7-54 filter between the sample and detector when measuring between 250 and 360 nm to avoid interference from emission from the sample.

The excitation spectra were obtained by illuminating the sample at 45° normal incidence with a beam of 10-15Å spectral band width obtained from a Cary spectrophotometer, Model No. 14, and focusing the luminescence onto the entrance slit of a ¼ meter JACO monochromator which was set to give the maximum luminescence signal. The light which was chopped immediately before entering the monochromator, was detected by an EMI 9558 QB photomultiplier and the signal was synchronously amplified by a P.A.R. HR-8

Table I. X-ray diffraction patterns

$SrZnP_2O_7$:0.06UO_2^{+2}*			$SrZnP_2O_7$*			$SrZnUO_x(PO_4)_2$†		
2θ	d	I	2θ	d	I	2θ	d	I
12.7	6.95	22	12.9	6.86	29			
13.84	6.39	18	13.96	6.34	15			
14.1	6.28	16				14.1	6.27	45
16.7	5.30	21				16.8	5.27	45
18.1	4.89	7				18.2	4.87	20
19.8	4.48	16	19.96	4.09	8	19.7	4.51	25
21.5	4.13	42				21.6	4.11	100
22.4	3.96	25				22.5	3.95	72
23.6	3.77	10				23.6	3.77	16
24.14	3.68	10	24.4	3.64	6	24.0	3.70	40
25.7	3.46	6	25.8	3.44	7			
26.7	3.33	100	26.9	3.32	100			
27.4	3.25	78	27.5	3.24	60	27.6	3.23	62
28.4	3.14	39	28.4	3.14	28	28.0	3.18	10
29.0	3.07	66	29.1	3.07	60	28.5	3.13	45
29.5	3.03	37				29.6	3.02	85
30.1	2.96	37	30.2	2.95	38			
30.8	2.90	37	30.9	2.89	38			
32.5	2.75	10	33.5	2.67	49	32.7	2.74	30
33.4	2.68	45	33.7	2.65	43			
34.5	2.59	36	34.7	2.58	34	34.1	2.63	40
35.3	2.54	13				35.2	2.55	20
35.5	2.53	19	35.6	2.52	17			
36.2	2.48	10				36.5	2.46	20
36.9	2.44	13	36.9	2.43	13			
39.2	2.29	17	39.2	2.29	18			
39.6	2.27	15	39.6	2.27	17			
41.0	2.20	17	40.4	2.22	7			
41.6	2.17	12	41.1	2.19	20			
43.3	2.09	9	41.7	2.16	10			
44.0	2.06	48	44.1	2.05	47			
45.9	1.98	37	44.6	2.03	11			
47.5	1.91	17	45.9	1.97	47			

* Data taken from slow scan x-ray diffraction pattern.
† Data taken from a fast scan x-ray diffraction pattern.

lock-in amplifier whose output was recorded on a strip chart recorder. The excitation signal was normalized by dividing by the energy present in the exciting beam which was determined below 330 nm using sodium salicylate phosphor. Between 330 and 600 nm, Rhodamine B was used as the standard. Both have essentially constant quantum efficiencies in the regions specified.

The decay rates of the phosphors were measured by exciting with a brief (2 μsec duration) light pulse (General Radio Strobotac filtered by a 2537Å interference filter). The luminescence was collected by lenses and passed through a JACO ¼ meter monochromator (200Å spectral band width) onto the cathode of a photomultiplier (Amperex 150 AVP). The voltage across the load resistor was displayed *vs.* time on an oscilloscope (Tektronix Type 535A) and photographed with a Polaroid camera. The pictures were measured and the decay data plotted on semilog paper to obtain the decay times.

Measurements.—The spectral distribution of the phosphor at room temperature is shown in Fig. 1, measured against a standard commercial lamp phosphor, Zn_2SiO_4:Mn. The diffuse reflectance is shown in Fig. 2. Comparison of these spectra with the data presented by Bell and Biggers (9) confirm that the absorbing and emitting species is UO_2^{+2} (Table II). The Bell and Biggers data was resolved in the region 3325-5000Å, from spectra of UO_2^{+2} in perchlorate media. At 77°K, the emission spectra of the phosphor retained the relative intensities of the lines, except that the line at 482 nm was quenched, and the side bands on the low energy side were resolved, as the line emission narrowed. The diffuse reflectance spectra did not change in line width or intensity at 77°K.

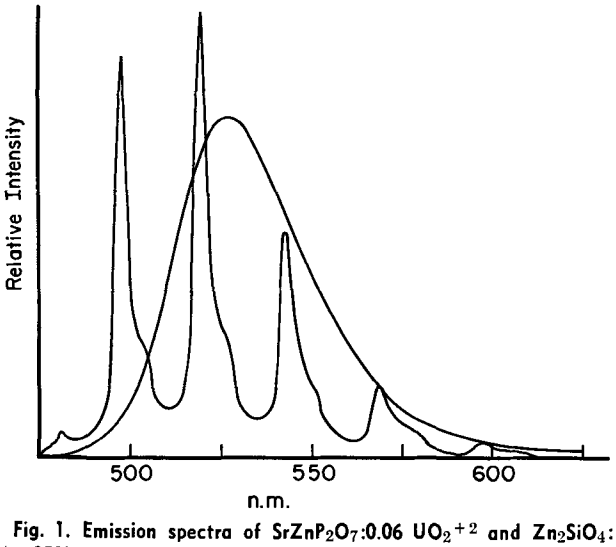

Fig. 1. Emission spectra of $SrZnP_2O_7$:0.06 UO_2^{+2} and Zn_2SiO_4:Mn. 2537 excitation; relative intensities comparable.

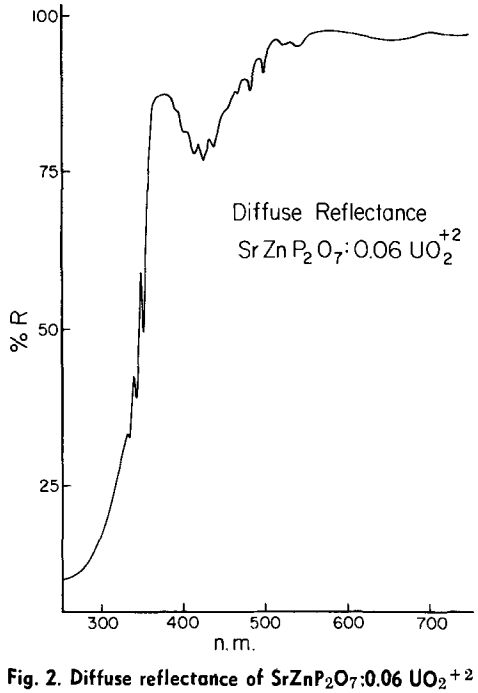

Fig. 2. Diffuse reflectance of $SrZnP_2O_7$:0.06 UO_2^{+2}

Table II.

Line No.	$SrZnP_2O_7$:0.06 UO_2^{+2} λ nm	Wave No.	UO_2^{+2}, ref. (9)
	UO_2^{+2} absorption		
1	496	20,100	20,582
2	481	20,800	21,331
3	465	21,500	22,062
4	451	22,200	22,740
5	435.5	22,900	23,414
6	423.5	23,600	24,118
7	411	24,350	24,829
8	400	25,000	25,539
9	388	25,800	26,253
10	375	26,700	27,021
11	363	27,600	27,738
12	350	28,600	28,557
13	341	29,350	29,173
14	332	30,100	30,147
	UO_2^{+2} emission		
1	482	20,800	21,270
2	498	20,200	20,502
3	519	19,250	19,636
4	543	18,300	18,774
5	568	17,600	17,917
6	593	16,870	17,081

The excitation was measured by monitoring the 519 nm emission line (Fig. 3 and 4). The excitation follows the absorption with the same band spacing and intensity. The excitation data also show additional small peaks which could indicate the position of vibronic levels. These peaks were not resolved in the diffuse reflectance.

Phosphor evaluation.—The relative intensities of the UO_2^{+2} emission bands do not change with compositional or processing variables, but several factors influence the absolute intensity. Substitutions in the host matrix can be made. When a larger ion is substituted, such as Ba for Sr or Cd for Zn, the brightness is increased. The substitution of smaller ions, Mg for Zn and Ca for Sr, decreases the brightness. This change may reflect the need for a slightly larger crystal lattice to accommodate the UO_2^{+2} ion better. These changes are shown in Fig. 5. The change in brightness with activator concentration is shown in Fig. 6 and is further confirmation of the extent of the solid solution range. A 0.20 substitution Ba for Sr and 0.06 UO_2^{+2} was used in the phosphor formulation for optimum brightness in lamp tests.

The brightness was also found to be dependent on particle size, regardless of whether the size was obtained by milling, classification, or as a result of the

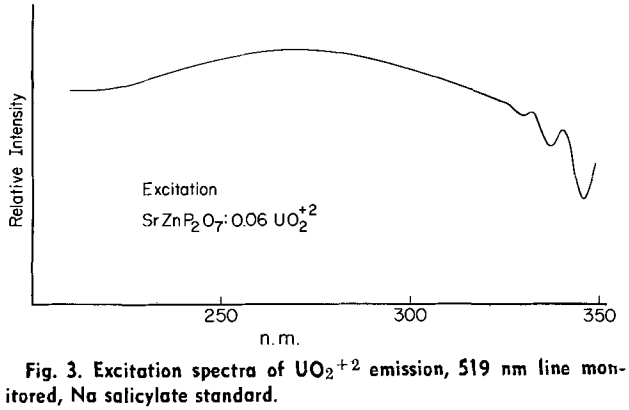

Fig. 3. Excitation spectra of UO_2^{+2} emission, 519 nm line monitored, Na salicylate standard.

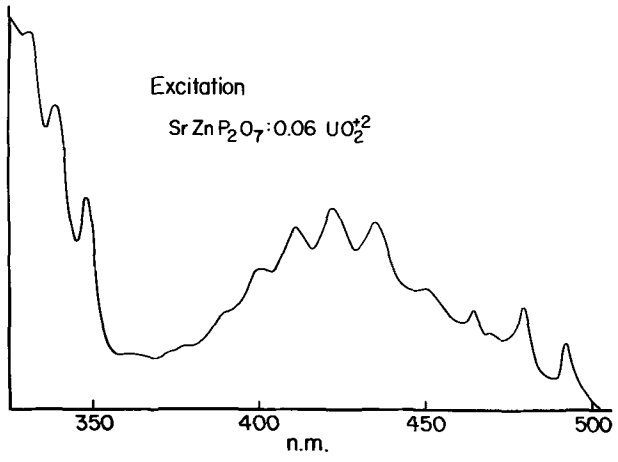

Fig. 4. Excitation spectra of UO_2^{+2} emission, 519 nm line monitored, Rhodamine B standard.

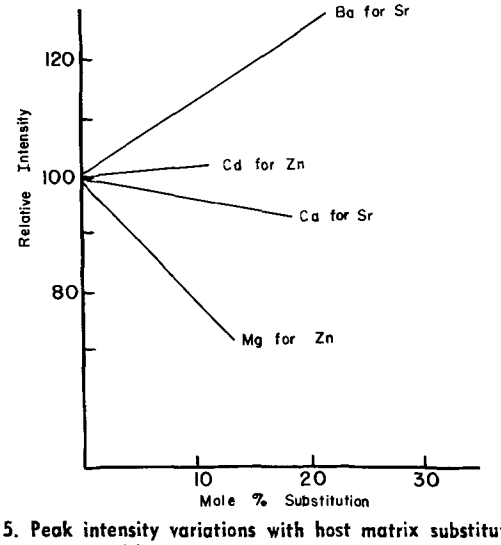

Fig. 5. Peak intensity variations with host matrix substitution in $SrZnP_2O_7$:0.06 UO_2^{+2}, 2537 excitation.

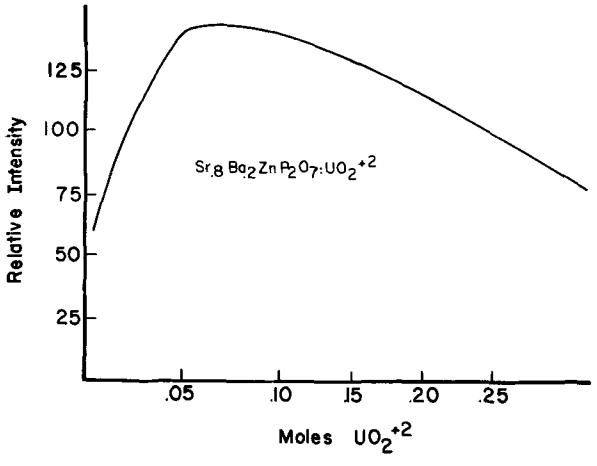

Fig. 6. Peak intensity variations with UO_2^{+2} content, 2537 excitation.

firing procedures used. The best phosphors had an average particle diameter (Fisher SSS) of 12 to 15μ. Firing temperature was the greatest single factor in determining brightness, by its effect on particle size growth. Reduction of the size by milling lowered the brightness by creating very small particles, but classification by separation or refiring did not change the size-brightness correlation. This proved to be a detriment in application in fluorescent lamps, since the particles were too large to make a satisfactory lamp coating without a milling step. The milling necessary to give adequate coating appearance resulted in a loss of brightness of 20-30%.

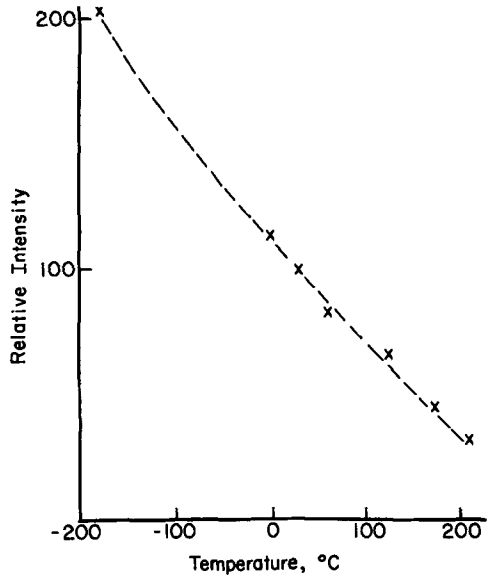

Fig. 7. Peak intensity variation with temperature, 2537 excitation

An additional detriment to lamp application is the decrease in peak intensity with temperature, as shown in Fig. 7. The decrease is large enough to reduce the intensity 8-10% at the operating temperature of a standard fluorescent lamp.

Lamp data were obtained in F 40 T 12 fluorescent lamps, and typical data are shown in Table III. While the lumen level is low for a green phosphor, and below that calculated from relative spectral distributions such as Fig. 1, the lumen maintenance is uniformly good. These results show that the UO_2^{+2} ion can be stable in a fluorescent lamp, if incorporated in a suitable matrix.

Energy transfer.—The transfer of energy from UO_2^{+2} to rare earth ions has been reported in solids, in glass, and in solutions (10-14). The rare earths involved in these systems have included Nd, Eu, Pr, Ho, Er, and Tm. Decay measurements were made by Gandy *et al.* (10) for the $UO_2^{+2} \rightarrow Nd^{+3}$ transfer in barium crown glass and by Zhabotinskii *et al.* (11) in $Cs_2[UO_2Cl_4]$ with transfer to several rare earths. These showed a decrease in the lifetime of the uranyl ion, and the transfer was attributed to radiationless transitions from the resonance level of UO_2^{+2} to the rare earth.

In measuring the $UO_2^{+2} \rightarrow Eu^{+3}$ energy transfer in solutions, Kropp (14) found quenching of the UO_2^{+2} emission with Eu^{+3} enhancement, but the lifetime of the UO_2^{+2} emission was too short to measure. He attributed the transfer to absorption by the $^5D_1$ or $^5D_2$ level of Eu^{+3} of the UO_2^{+2} emission. A similar mechanism was proposed by DeShazer and Cabezas (12) for Eu^{+3} in a glass host.

In this phosphor, efficient energy transfer has been found from UO_2^{+2} to Eu^{+3} and to Nd^{+3}. To a lesser extent, transfer was also found to Sm^{+3}. With Eu^{+3} in $SrZnP_2O_7$ substituting on a Sr site, the emission

Table III. Lamp data, F40T12 lamps

Hours burned	Lumens	LPW
0	1470	37.1
100	1469	37.1
500	1394	35.4

is very weak under all excitations. The spectra, shown in Fig. 8, show evidence of extensive crystal field splitting of the Eu^{+3}. Excitation of the Eu^{+3} emission in $SrZnP_2O_7$ is close to linear between 220 and 280 nm and then decreases to essentially no response at 350 nm. With the incorporation of UO_2^{+2}, the emission, the intensity, and the excitation of Eu^{+3} change. The emission of an optimized sample is shown in Fig. 9, in which the dominant Eu^{+3} emission is the $^5D_0$-$^7F_2$ transition. Changes in relative intensities within the multiplets indicate some change in the Eu^{+3} symmetry resulting from the presence of UO_2^{+2}. The intensity is increased by 60-fold over the Eu^{+3} spectra shown in Fig. 8. The excitation of the Eu^{+3} is now identical to that of the UO_2^{+2} activator, showing the same structure.

This change in Eu^{+3} spectra will occur with as little as 0.002 moles UO_2^{+2} incorporated in the phosphor matrix. Additional UO_2^{+2} does not change the Eu^{+3} transitions, and the spectra of both emitting ions remain the same for all Eu^{+3} and UO_2^{+2} concentrations. Changes in the relative intensities of the two spectra occur as the UO_2^{+2} emission is quenched by the transfer to Eu^{+3}. A typical change is shown in Fig. 10. Optimum Eu^{+3} emission is found between 0.003 and 0.005 Eu, with about 0.06 UO_2^{+2}.

Similar transfer and enhancement was found for Nd^{+3}, in which the emissions at 875 and 1060 nm were measured. The Nd^{+3} spectra did not change with the addition of UO_2^{+2}. A 50-fold enhancement was measured with 0.004 Nd^{+3} in a sample with 0.06 UO_2^{+2}

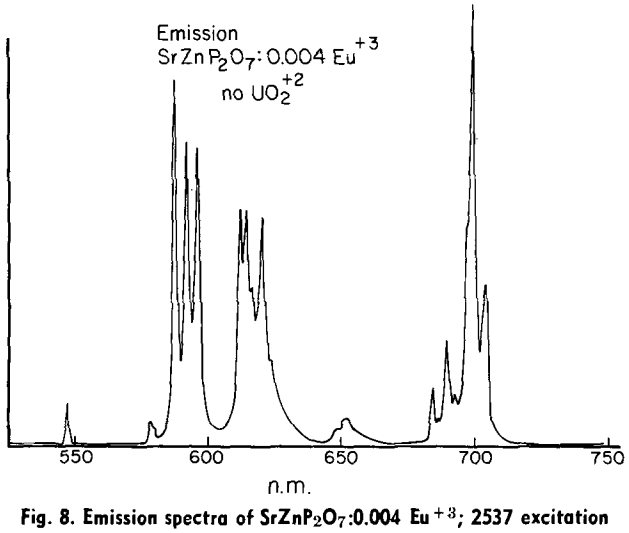

Fig. 8. Emission spectra of $SrZnP_2O_7$:0.004 Eu^{+3}; 2537 excitation

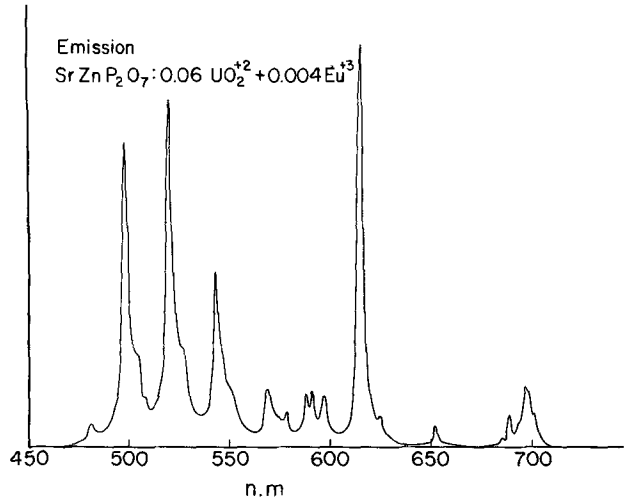

Fig. 9. Emission spectra of $SrZnP_2O_7$:0.06 UO_2^{+2}:0.004 Eu^{+3}; 2537 excitation.

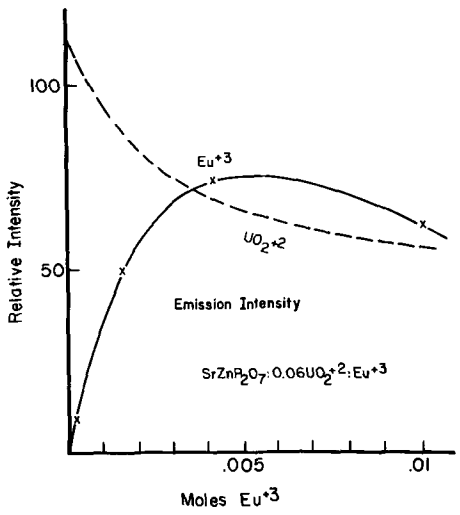

Fig. 10. Relative peak intensity of Eu^{+3} and UO_2^{+2} with Eu^{+2} concentration, 2537 excitation.

added. The excitation of the enhanced Nd^{+3} emission also follows the UO_2^{+2} excitation spectra.

Decay measurements were made on the UO_2^{+2} emission for variations in activator concentration and also with rare earths incorporated. Results are shown in Table IV. This shows energy transfer by a radiationless process from UO_2^{+2} to Eu^{+3} and to Nd^{+3} and Sm^{+3}. No transfer is apparent for Ho^{+3} or Er^{+3} and is questionable for Pr^{+3} from both the decay and the emission measurements.

Discussion

The interesting and perhaps unique aspect of this phosphor is in the incorporation of the UO_2^{+2} ion as an activator in variable amounts, resulting in an efficient phosphor, in a crystalline matrix which does not have a logical site for substitution. The UO_2^{+2} ion has been shown to be linear, with the U—O bond length between about 1.7-1.9Å, depending on the structure in which it is found (4, 15). The full O—U—O^{+2} ion would require 3-4Å distance to be accommodated in the structure, as well as charge compensation. This is a very large ion to be substituted in a matrix containing Sr (1.12Å) and Zn (0.74Å). Several facts indicate that the phosphor is not a substitutional solid solution of UO_2^{+2} in $SrZnP_2O_7$. The stoichiometric requirement of SrO=ZnO=P_2O_5=1, with UO_2^{+2} as an additive must be met. Deviations from this ratio would result in the presence of strontium or zinc phosphates, either metaphosphates or one of several orthophosphates, as a second phase. These compounds when prepared with UO_2^{+2} do not fluoresce efficiently, or absorb unusually. If present in amounts of several per cent, none of these would be expected to greatly reduce the total emission intensity. With this phosphor, this is not the case. Even deviations of a few mole per cent from the exact stoichiometry result in the loss of much of the UO_2^{+2} incorporation in the phosphor. It would appear that the phosphor consists of a structure stabilized by the presence of the O—U—O^{+2} ion, present in a range of up to about 0.10 mole per $SrZnP_2O_7$. Further, this

Table IV. Decay times, μsec

$SrZnP_2O_7$:0.06 UO_2^{+2}, x Eu^{+3}		$SrZnP_2O_7$:0.03 UO_2^{+2}:0.001 R^{+3}	
x	μsec	R	μsec
0	174	—	173
0.0002	139	Eu	131
0.0015	134	Nd	80
0.0040	97	Sm	84
0.0100	76	Pr	120
		Ho	145
		Er	152

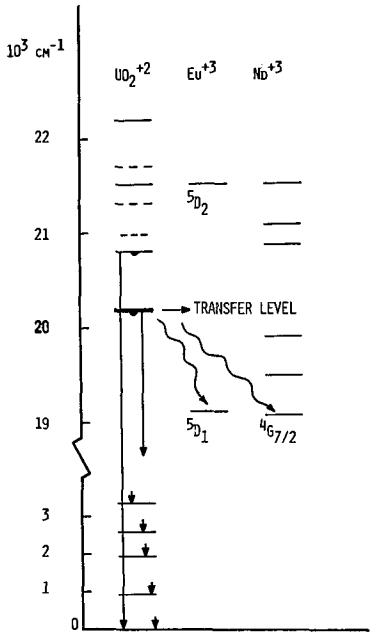

Fig. 11. Partial energy level diagram. UO_2^{+2} levels determined by absorption (—) or excitation (- -).

structure is limited to a narrow composition line along the join between $SrZnP_2O_7$ and $SrZnUO(PO_4)_2$.

Preliminary work on the structures indicates that the unactivated $SrZnP_2O_7$ is possibly orthorhombic and that the phosphor is a monoclinic distortion.

An additional indication that a structural modification of $SrZnP_2O_7$ may be caused by UO_2^{+2} incorporation comes from the differences between the Eu^{+3} spectra in each structure. In the phosphor $SrZnP_2O_7$:UO_2^{+2}:Eu^{+3}, the dominant Eu^{+3} transition is the $^5D_0$-$^7F_2$, while in $SrZnP_2O_7$:Eu^{+3}, the spectra is more complex (Fig. 9 and 8). If the $SrZnP_2O_7$ stoichiometry is not maintained, but with UO_2^{+2} and Eu^{+3} present, the emission is a mixture of the two spectra, with greatly reduced $SrZnP_2O_7$:UO_2^{+2} emission. By analogy to the phase relations, the deviations in stoichiometry could place the composition in a two phase region, identifiable by the emission spectra as $SrZnP_2O_7$:Eu^{+3} and $SrZnP_2O_7$:UO_2^{+2}:Eu^{+3}.

The UO_2^{+2} emission is essentially from a level centered at 20,200 cm^{-1} to the ground state and vibronic levels above the ground state. At 77°K, the emission at 482 nm (20,800 cm^{-1}) is quenched, and side bands of the major emissions are resolved. These are about 250 cm^{-1} lower in energy than the major emission and 5-10% as intense. The existence of this second set of emission lines with a band spacing of about 850 cm^{-1} suggests the possibility of two sites for the UO_2^{+2} ion.

The mechanism of energy transfer as shown by decay measurements agrees with the mechanism proposed by Gandy *et al.* (10) and by Zhabotinskii *et al.* (11). Excitation spectra of Eu^{+3} and Nd^{+3} emission also show that the energy transfer is from the 20,200 cm^{-1} level, however, there is no exact agreement with the rare earth levels. An energy level diagram of this part of system is shown in Fig. 11, and includes the positions of the additional weak UO_2^{+2} levels found in the excitation spectra. The closest levels of Eu^{+3} are about 1000-1300 cm^{-1} from the transferring UO_2^{+2} level. The Nd^{+3} ion has a somewhat better match. The R.E.$^{+3}$ ions listed in Table IV all show a decrease in decay times and, therefore, possible energy transfer, although emission was not found for most of these ions. The three ions showing emission have energy levels at about 19,000 cm^{-1}, showing that this is probably the recipient level. This is the $^5D_1$ level of Eu^{+3} and the $^4G_{7/2}$ level of Nd^{+3}.

No definite evidence of emission from either the $^5D_2$ or $^5D_1$ levels of Eu^{+3} were found in the phosphor. The more probable emissions from these levels would be masked by the UO_2^{+2} emission. No evidence of Eu^{+3} absorption was found in either diffuse reflectance or excitation curves.

Acknowledgments

The author would like to express her appreciation to Dr. R. A. Hewes and Miss E. J. Wilson for the optical and decay measurements, to Miss J. R. Cooper for the x-ray work and for the technical assistance of Diane Karla, Robert Kattler, and Lana Funaro in sample preparation and evaluation.

Manuscript submitted Aug. 18, 1969; revised manuscript received *ca.* Oct. 24, 1969. This was Paper 73 presented at the New York Meeting of the Society, May 4-9, 1969.

Any discussion of this paper will appear in a Discussion Section to be published in the December 1970 JOURNAL.

REFERENCES

1. F. A. Kroger, "Some Aspects of the Luminescence of Solids," Chap. IV, Elsevier Publishing Co., New York (1948).
2. W. A. Weyl, "Coloured Glasses," Dawson's of Pall Mall, London (1959).
3. G. Blasse, *This Journal*, **115**, 738 (1968).
4. S. P. McGlynn and J. K. Smith, *J. Mol. Spectr.*, **6**, 164-187 (1961).
5. E. Rabinowitch and R. L. Belford, "Spectroscopy and Photochemistry of Uranyl Compounds," MacMillan Co. (1964).
6. G. H. Dieke and A. B. F. Duncan, "Spectroscopic Properties of Uranium Compounds," McGraw-Hill Publishing Co., New York (1949).
7. J. G. Conway, *J. Chem. Phys.*, **31**, 1002 (1959).
8. R. L. Brown, *Illum. Engr.*, **61**, 230 (1966).
9. J. T. Bell and R. E. Biggers, *J. Mol. Spectr.*, **18**, 247-275 (1965).
10. H. W. Gandy, R. J. Ginther, and J. F. Weller, *Appl. Phys. Letters*, **4**, 188 (1964).
11. M. E. Zhabotinskii *et al.*, *Zh. Eksperim. i Teor. Fiz.*, **49**, 1689 (1965), *CA*-64-12058h.
12. L. G. DeShazer and A. Y. Cabezas, *Proc. IEEE*, **52**, 1355 (1964); and U. S. Patent 3,417,345.
13. A. Kitamura, *J. Phys. Soc. Japan*, **20**, 1283 (1965).
14. J. L. Kropp, *J. Chem. Phys.*, **46**, 843 (1967).
15. S. K. K. Jatkar, A. V. Khedekar, and A. J. Mukhedkar, *J. Univ. Poona*, Sci. Tech., No. 34, pp. 59-66 and pp. 67-72 (1968).

The Preparation and Crystallography of Cadium Zinc Sulfide Solid Solutions

Paul Cherin, Edward L. Lind, and Edward A. Davis[1]

Xerox Corporation, Rochester, New York

ABSTRACT

Single crystals and powders of $Cd_{(1-x)}Zn_xS$ were grown using chemical transport with iodine. These components form a continuous series of solutions over the entire range of x, 0 to 1. The wurtzite structure was produced over the entire range. The lattice parameters and the composition of the solid solutions were determined to approximately 1% using x-ray diffractometry techniques. The results provide a definitive calibration of lattice constants for the wurtzite structure of solid solutions of CdS and ZnS and allow the analysis of $Cd_{(1-x)}Zn_xS$ samples. The variation of lattice parameters with composition was found to obey Vegard's law. The variation of the c/a ratio with composition was also linear. The ideal ratio, assuming close packing of hard spheres, occurred at 70% ZnS. The volume relationship with composition showed a slightly negative deviation from linearity. A least squares method for refining lattice parameters is described.

Cadmium sulfide and zinc sulfide are of considerable importance as phosphors and photoconductors. Because the size and electronic structure of the cations are so similar, these materials readily form a continuous series of solid solutions. Thus, this is a system in which systematic variation of photoelectronic properties is possible simply by adjusting the composition of the solid solutions.

In this paper we describe a method of preparing single crystals of $Cd_{(1-x)}Zn_xS$ which have uniform composition, show no tendency to order, and are relatively free from strain. Precise measurement of the variation of the lattice parameters with composition was done because of the considerable disagreement existing in the literature (1-5). Future investigators will be able to use the results presented here to determine accurately the composition of their $Cd_{(1-x)}Zn_xS$ single crystals and powders. It will be shown that the solutions are not ideal at room temperature even though the variation of a and c with composition obeys Vegard's law. The c/a axial ratio is computed and plotted as a function of composition. A variety of optical and electrical measurements on these crystals has been published elsewhere (6-9).

Structure

Cadmium sulfide and zinc sulfide can crystallize in two polymorphic modifications, either in a cubic sphalerite structure or as a hexagonal wurtzite structure. Throughout most of the composition range of $Cd_{(1-x)}Zn_xS$, the wurtzite structure is the stable one. Only when the concentration of zinc sulfide nears 100% does the sphalerite form predominate. In this paper, we are concerned only with the wurtzite modification.

The wurtzite phase can be considered as two interpenetrating hexagonal structures, one composed of cations and the other of anions. All the atoms lie in the center of tetrahedra containing unlike atoms at the corners. Regular tetrahedra can pack as efficiently as spheres. For rigid, close packed tetrahedra the ideal c/a ratio is 1.633. Many wurtzite structures deviate from this ideal value. It has been suggested (10, 11) that this deviation occurs because of the partial ionic character of the bonds. Distortion in the c/a ratio can lead to an increase in lattice energy, if the bonds have some ionic character. Within a group of the periodic table, the pairs forming bonds having the most ionic character tend to deviate most from the ideal ratio (10, 11). This empirical rule holds in the case of ZnS and CdS where the c/a ratios are 1.6376 and 1.6238, respectively.

Key words: crystallography, sulfide, solid solutions, cadmium, zinc.

[1] Present address: Cavendish Laboratory, University of Cambridge, Cambridge, England.

Method of Preparation

In the range of temperatures at which these crystals may be grown, the vapor pressure of CdS is so much greater than ZnS at a given temperature, that it is impossible to grow mixed crystals of $Cd_xZn_{(1-x)}S$ (12) from a mixture of the vapors of CdS and ZnS by themselves. However, in the presence of iodine, the equilibrium constants for the reaction of ZnS and CdS with iodine are close enough to result in cotransport. Chemical transport with iodine vapor is, therefore, a convenient means for growth of homogeneous single crystals of $Cd_{(1-x)}Zn_xS$. The crystal sizes achieved by this method were found to be suitable for electrical and optical studies (6-9).

Preparation

Weighed quantities of G. E. luminescent grade ZnS and CdS powders were tumbled in a container overnight and fired in an open boat at 800°C under flowing nitrogen to remove water vapor and volatile salts. A small, but insignificant, amount of the more volatile CdS was lost during this process. The powder was transferred to an 8-in. quartz ampoule and evacuated to 10^{-6} Torr. Sufficient iodine, which had been previously triple sublimed in vacuum to remove permanent gases, was distilled into the ampoule to provide 5 mg iodine per cc of vapor space in the final ampoule (13). The ampoule was sealed off under vacuum and placed in a two-zone furnace. Inadvertent nucleation centers of ZnS or CdS in the growth end of the ampoule were removed by leaving the ampoule overnight with its charge end at a temperature range of 775°-800°C and growth end at a range of 875°-900°C. Subsequently the ampoule was positioned in the furnace so that a suitable growth gradient was obtained. For low proportions of ZnS, the charge end was held at temperatures of 875°-925°C with the growth end at the range 825°-850°C. As the ZnS fraction was increased, the temperatures of both charge and growth ends was increased so that for 95% ZnS crystals the temperature ranges were at 925°-975° and 850°-875°C, respectively. Growth was allowed to proceed from 72 to 80 hr.

Polycrystalline solid solutions were prepared by firing mixtures of the above mentioned ZnS and CdS powders in an open boat at 850°C (controlled to ± 5°C) for 5.5 to 6.5 hr while under a continuous

flow of nitrogen. Samples were slowly cooled in the furnace while the flow of nitrogen was continued.

Determination of Composition

The method of determining the composition of the solid solutions is described in detail elsewhere (15). This technique employed a set of physical mixtures of CdS and ZnS of known composition. The ratio of the intensity of the x-ray emission lines of zinc and cadmium was plotted against the molecular ratio of ZnS to CdS. If care is taken to minimize matrix effects, this plot is virtually linear.

This plot was used to determine the composition of a series of $Cd_{(1-x)}Zn_xS$ solid solutions by x-ray spectroscopy methods, which acted as secondary standards. Debye-Scherrer photographs were taken of the secondary standards, and the distances between the diffraction lines (S) were measured at high values of the Bragg scattering angle. A plot of $(\cos S/4)^{-1}$ *vs.* the composition results in a smooth curve which is nearly linear and which subsequently was used for composition determinations of the crystals and powders.

The purpose of this procedure is twofold. First, when the amount of material available is small, it is not possible to obtain sufficiently high x-ray emission intensities. Then statistical variation in the counts causes considerable error in the composition determined. Second, a higher relative accuracy is obtained by the Debye-Scherrer method. By the techniques described, the composition could be determined absolutely to ± 0.5% and relatively to ± 0.2 m/o (mole per cent) using only 0.1 mg of sample.

It was found that the actual composition and the nominal composition as determined by the known weights of CdS and ZnS in the initial mixture were identical within the limits of error previously stated.

Determination of Lattice Parameters

A North American Philips diffractometer was used to record the lines diffracted from the finely ground solid solution. The solid particles chosen were uniform (between 250-500 mesh). The radiation was CuKα (monochromatic); the scanning speed was (⅛)°/min; a 1° divergence slit was used in conjunction with a 4° preslit and a 1° scatter slit. Diffraction lines were generally recorded out to the limit of the diffractometer, *i.e.* to 145° in 2θ. A NaCl standard was added to the samples to correct for possible minor misalignment.

The diffraction lines were indexed using approximate values of the a and c parameters. These parameters were then refined by fitting the calculated values of $1/d^2$, where d is the lattice spacing, to the observed values using a least squares technique (see Appendix).

Results

The lattice parameters a and c were determined and plotted as a function of composition. These are shown in Fig. 1 and 2, respectively. The variation obeys Vegard's law within the error limits. All the points fall within three times the standard deviation. The relationship between the parameters and the concentration may be expressed as

$$a = 4.1370 - 0.3165x$$
$$c = 6.7168 - 0.4597x$$

where x is the mole fraction of ZnS.

The errors tended to increase toward the high ZnS concentration. This is the region in which the free energy of the wurtzite structure approaches that of the sphalerite structure. Thus, some strain and defects are to be anticipated. The sample containing 95% ZnS did contain some of the cubic sphalerite. The concentration ratio of wurtzite to sphalerite was approximately 9/1. It was assumed that the ZnS concentration was the same in both phases. This assumption was supported by the agreement of the wurtzite a and c parameters with Vegard's law at 95% of ZnS. Additionally, the lattice parameter of the cubic cell containing 95% ZnS agreed with the parameter found assuming a linear relationship with composition.

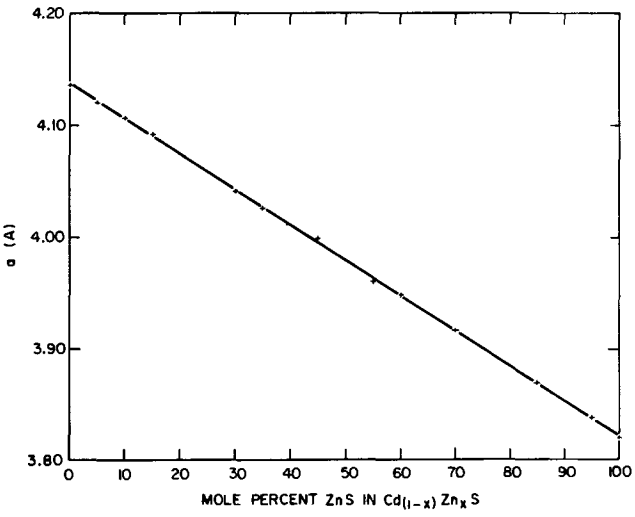

Fig. 1. Lattice parameter a as a function of composition

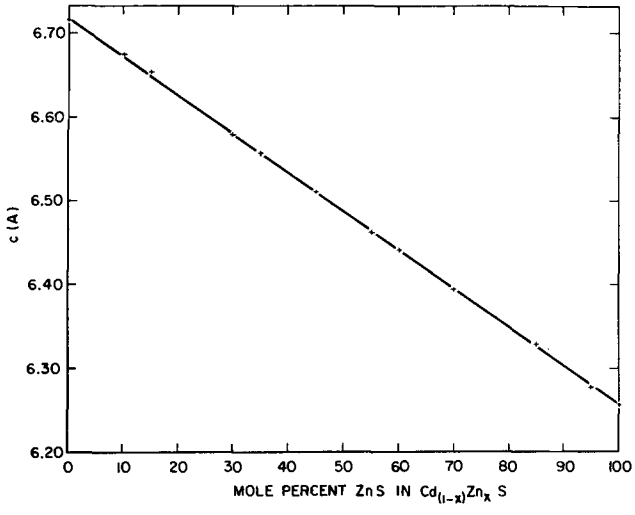

Fig. 2. Lattice parameter c as a function of composition

The c/a ratios were calculated as a function of the composition and are shown in Fig. 3. This variation is linear and may be expressed as $c/a = 1.6238 + 0.01376x$. This relationship is interesting because at $x = 0.70$, $c/a = 1.633$. It was mentioned earlier that distortion in the c/a ratio is related to long range coulombic forces (10, 11). Although the ionic character of the solid solutions does decrease from 0% ZnS to 100% ZnS, there is probably nothing unique in the bonding at 70% ZnS, where $c/a = 1.633$, the ideal ratio. In CdS the tetrahedra tend to be compressed, while in ZnS

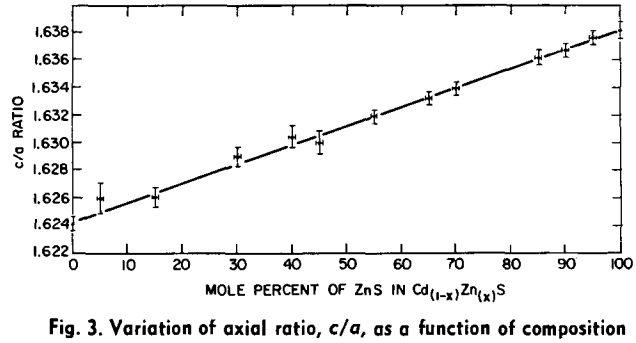

Fig. 3. Variation of axial ratio, c/a, as a function of composition

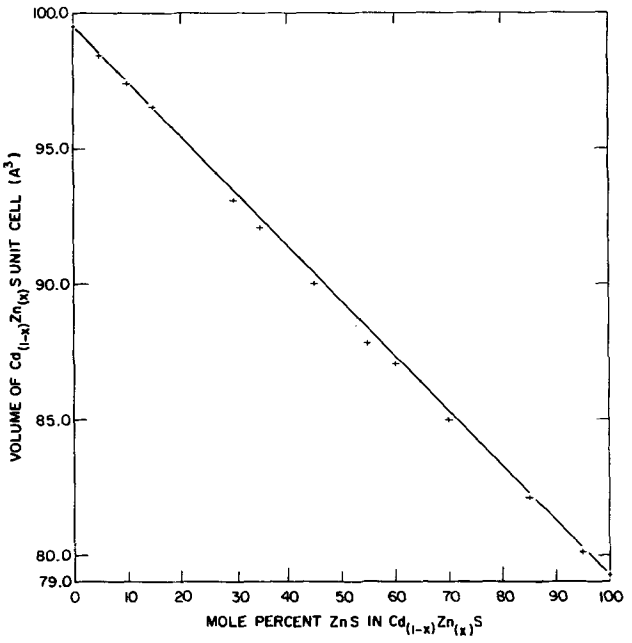

Fig. 4. Unit-cell as a function of composition

the c-axes of the tetrahedra are elongated. At 70% ZnS the average tetrahedron happens to have an axial ratio of 1.633.

The variation of unit-cell volume with concentration has been plotted in Fig. 4. A slightly negative deviation from linearity can be observed. Thus, the solutions are not ideal at room temperature although they might well have been at the temperature of preparation. If the solutions had been ideal, the partial molar volumes would have been additive and the volume variations linear.

The variations of a, c, c/a, and unit cell volume with composition are given in Table I.

Discussion

The variation of the lattice parameters with composition as found by previous investigators (summarized below) is, for the most part, somewhat different than that reported here. Much effort has been expended to make our results as accurate as possible.

The quality of our crystals has been ascertained by other measurements, which would have most probably revealed any imperfections, such as severe strain, inhomogeneity, large concentrations of defects, etc. These measurements include electron microscopy, electron microprobe studies, fluorescence, x-ray precession, Laue measurements, and studies in a polarizing microscope. Spectroscopic analysis for heavy metals shows less than 3 ppm copper and less than 1 ppm of silicon. Fluorescence analysis did not detect the presence of iodine, suggesting that its concentration was no more than 100 ppm. This is in agreement with Beun, Nitsche, and Bölsterli (14). The sharpness of the powder diffraction lines contributed additional evidence.

Table I. Variation of lattice parameters with composition

Mole per cent of ZnS	a (A)	c (A)	c/a	V (A^3)
0	4.1360 ± 0.0006	6.7162 ± 0.0014	1.6238	99.495
5	4.1206 ± 0.0005	6.6937 ± 0.0010	1.6244	98.425
10	4.1068 ± 0.0005	6.6747 ± 0.0008	1.6253	97.489
15	4.0925 ± 0.0005	6.6537 ± 0.0008	1.6258	96.507
30	4.0413 ± 0.0005	6.5793 ± 0.0008	1.6280	93.055
35	4.0265 ± 0.0004	6.5580 ± 0.0007	1.6287	93.076
45	3.9945 ± 0.0006	6.5111 ± 0.0009	1.6300	89.970
55	3.9604 ± 0.0008	6.4631 ± 0.0015	1.6319	87.788
60	3.9489 ± 0.0006	6.4424 ± 0.0013	1.6315	87.000
70	3.9167 ± 0.0006	6.3956 ± 0.0015	1.6329	84.965
85	3.8693 ± 0.0007	6.3297 ± 0.0012	1.6359	82.067
95	3.8380 ± 0.0006	6.2786 ± 0.0023	1.6359	80.092
100	3.8195 ± 0.0007	6.2552 ± 0.0008	1.6377	79.026

The standard deviations obtained from the least square computations indicate a rather precise determination of lattice parameters (Table I). The limiting factor is, however, the composition determination. This is the most difficult step, because of the similarity in properties of zinc and cadmium. For this reason, physical methods were utilized instead of chemical techniques. As had been mentioned earlier, much effort was made to determine the composition of the solid solutions (15). The method used is rather sensitive to small changes in composition. Repeated measurements were made and the results were reproducible within 0.5%.

Early measurements of the lattice parameters of the $Cd_{(1-x)}Zn_xS$ system were made by Vitrikhovskii and Mizetskaya (1) using Debye-Scherrer methods. Their results show large positive deviation of a and c from Vegard's law by as much as 0.01A. Their data have considerable scatter, especially for the c parameter. It is not clear what method was used to determine compositions.

Chan's measurements (2) of the variation of the a-axis with composition also reflected more scatter than our data, although a linear relationship was shown. Single crystal techniques were used by this worker. In addition, the voltametry and stripping analysis used to determine composition presented problems, because of interference of one cation with the measurement of the other.

Ballentyne and Ray's (3) measurements indicated very large negative deviations from Vegard's law. They used Debye-Scherrer methods and determined compositions using chemical methods which might explain their different results.

Ortman and Treplow (4) reported that the a and c parameters followed Vegard's law. They plotted their results on a rather compressed scale so that deviations up to 0.01A did not show. Several of their points did not fall on the lines.

In a rather recent effort, Kane, Spratt, Hershinger, and Kahn (5) measured the lattice parameters of evaporated films. Using Debye-Scherrer methods, they found that a and c deviated negatively from Vegard's law. They determined compositions indirectly by monitoring the amount of CdS and ZnS that evaporated from separate boats. Their parameter determinations at high concentrations of ZnS, however, assumed an ideal c/a ratio.

Summary

A continuous series of substitutional solid solutions of $Cd_{(1-x)}Zn_xS$ were prepared. Both the powders and the single crystals appeared to be homogeneous and relatively strain free. The wurtzite structure was the most stable throughout the series at the temperature of preparation. However, some sphalerite phase formed at the 95% ZnS composition. The composition determinations were done using physical methods which avoided problems due to the similarities in properties of zinc and cadmium. The lattice parameter variation with composition was linear. The c/a ratio also showed a linear variation. The ratio reached the ideal value of 1.633, assuming close packing of hard spheres, at 70% ZnS. This was probably due to an averaging effect rather than to any profound change in long range bonding forces. The variation of volume with composition showed a negative deviation from linearity. Thus, the solid solutions are not ideal at room temperature, since the partial molar volumes are not additive.

The pertinent results are given in Table I to enable future workers to easily determine the composition of their solid solutions.

Acknowledgments

The authors would like to thank Fred Knier for his help in preparing the solid solutions, Chester Bielan for his aid in determining the compositions, and George

Fekete and Phyllis Unger for their aid in collecting and analyzing the diffraction data.

Manuscript submitted Aug. 11, 1969; revised manuscript received Oct. 29, 1969.

Any discussion of this paper will appear in a Discussion Section to be published in the December 1970 JOURNAL.

APPENDIX

Least squares fit of $(1/d_c)^2$ *to* $(1/d_o)^2$

In reciprocal lattice parameters, $1/d^2$ is linear, *i.e.*,

$$1/d^2 = S_{11}h^2 + S_{22}k^2 + S_{33}l^2 + S_{12}hk + S_{23}kl + S_{31}lh,$$

where

$$S_{11} = b^2c^2\sin^2\alpha/V^2$$
$$S_{12} = 2abc^2(\cos\alpha\cos\beta - \cos\gamma)/V^2$$
$$S_{22} = c^2a^2\sin^2\beta/V^2$$
$$S_{23} = 2a^2bc(\cos\beta\cos\gamma - \cos\alpha)/V^2$$
$$S_{33} = a^2b^2\sin^2\gamma/V^2$$
$$S_{31} = 2ab^2c(\cos\gamma\cos\alpha - \cos\beta)/V^2$$

a, b, c are the unit cell lengths, α, β, γ are the angles, and V is the volume of the cell.

The sum of the squares minimized is

$$\sum_{i}^{N} W_i[1/d_i^2 - (S_{11}h_i^2 + S_{22}k_i^2 + \text{--------} + S_{31}l_ih_i)]^2$$

where N is the number of diffraction peaks observed. The weights, W_i, were taken as

$$W_i = 1/\sigma_i^2$$

$$\sigma_i = \left[\frac{d(1/d^2)}{d(2\theta)}\right]\Delta(2\theta_i), = \frac{8\sin 2\theta_i\,\Delta(2\theta_i)}{\lambda}$$

and $\Delta(2\theta_i)$ was taken to be the uncertainty in reading the peak position due to broadness or noise.

REFERENCES

1. N. I. Vitrikhovskii and I. B. Mizetskaya, *Soviet Physics-Solid State*, **2**, 2301 (1961).
2. F. L. Chan, "Advances in X-Ray Analysis," Vol. 5, p. 142, W. M. Mueller, Editor, Plenum Press, New York (1961).
3. D. W. G. Ballentyne and B. Ray, *Physica*, **27**, 337 (1961).
4. H. Ortman and H. Treplow, *Z. Naturforschung*, **16A**, 910 (1961).
5. W. Kane, J. P. Spratt, L. W. Hershinger, and I. H. Khan, *This Journal*, **113**, 136 (1966).
6. E. A. Davis and E. L. Lind, *J. Phys. Chem. Solids*, **29**, 79 (1968).
7. E. A. Davis, R. E. Drews, and E. L. Lind, *Solid State Comm.*, **5**, 573 (1967).
8. R. E. Drews, E. A. Davis, and A. G. Leiga, *Phys. Rev. Letters*, **18**, 1194 (1967).
9. G. Lucovsky, E. L. Lind, and E. A. Davis, p. 1150 "II-VI Semiconducting Compounds." Proceedings of the Int. Conf. of II-VI Compounds at Brown University, D. J. Thomas, Editor, W. A. Benjamin Inc. (1967).
10. G. A. Jeffries, G. S. Parry, and R. L. Mozzi, *J. Chem. Phys.*, **25**, 1024 (1956).
11. F. Keffro and A. M. Portis, *ibid.*, **27**, 675 (1957).
12. P. Goldfinger and J. Drouart, Final Technical Report under ARDC Contract. AF61 (J14)-868, October, 1957.
13. R. Nitscke, H. V. Bolsterli, and M. Lichtensteiger, *J. Phys. Chem. Solids*, **21**, 199 (1961).
14. J. A. Beun, R. Nitsche, and H. U. Bölsterli, *Physica*, **28**, 184 (1962).
15. P. Cherin, E. Davis, and C. Bielan, *Anal. Chem.*, **40**, 611 (1968).

Broad Emission and Excitation Bands in Y_2O_3 and YVO_4

S. Z. Toma and D. T. Palumbo

Sylvania Electric Products Inc., Chemical and Metallurgical Division, Towanda, Pennsylvania

ABSTRACT

Pure yttrium oxide has three x-ray-excited emission bands in the blue-u.v. region of the spectrum. Addition of thallium gives a broad emission peaking at about 580 nm with a decay time of less than 20 nanosec and Eu^{3+} emission in this matrix can be sensitized with thallium and bismuth absorption bands. On lowering the temperature from room to liquid N_2 both Y_2O_3:Bi and YVO_4:Bi show new emissions as well as complex differences in the excitation spectra. The results in Y_2O_3:Bi are discussed on the basis of bismuth occupying two centers in this matrix.

Numerous studies on the optical properties of rare earth-activated Y_2O_3 and YVO_4 have appeared (1-7). Considerably less work, however, has been reported on activators with broad absorption and emission bands in these matrices, the emphasis being primarily on bismuth activation at room temperature (8-12), and more recently on indium in YVO_4 (13). In both YVO_4:Bi (8, 9, 11) and Y_2O_3:Bi (10-12) only some of the bands arising from bismuth addition are experimentally established and their corresponding electronic transitions are not clearly understood. As will become evident below, two factors contribute to this: (*a*) in Y_2O_3:Bi, the large number and strong overlap of the observed emission and excitation bands makes difficult the isolation and study of the individual bands, with a similar problem existing in YVO_4:Bi where the matrix absorption overlaps that obtained on Bi^{3+} addition; and (*b*) the differentiation of Bi-matrix from predominantly free ion transitions ($6s \rightarrow 6p$) is difficult since host luminescence exists in the absence of any activators. The problem is analogous to the case of $CaWO_4$ and $CaWO_4$:Pb where the luminescence on addition of Pb^{2+} is usually considered to arise from Pb-perturbed tungstate groups (14, 15).

The present work concerns a study of Y_2O_3:Bi and YVO_4:Bi at liquid nitrogen temperature with a comparison to the results obtained at room temperature. The optical properties of Y_2O_3, Y_2O_3:Tl, Y_2O_3:Eu,Tl, and Y_2O_3:Eu,Bi were also investigated.

Experimental

Phosphors were prepared from intimate mixtures of high-purity raw materials by solid state reactions. For activated and pure YVO_4, proper amounts of Y_2O_3 and Bi_2O_3 were blended with recrystallized NH_4VO_3 and fired for 2 hr at 950°C.

Phosphors with Y_2O_3 as a matrix were synthesized by acetone blending appropriate amounts of thallium (ic) oxide, bismuth oxalate, and yttrium oxalate. The mix was first-step fired at 700°C and refired for 2-3 hr at 1200°C. In europium-containing phosphors, Y^{3+} and Eu^{3+} were coprecipitated as oxalates before addition of bismuth or thallium. This coprecipitation and the high firing temperatures were necessary to obtain high efficiency phosphors. All samples were prepared in air atmosphere unless specified otherwise. The data discussed below were obtained with the following concentrations of various activators: $Y_{0.95}Bi_{0.05}VO_4$, $(Y_{0.995}Bi_{0.005})_2O_3$, $(Y_{0.98}Tl_{0.02})_2O_3$, $(Y_{0.99}Eu_{0.01})_2O_3$, $(Y_{0.983}Eu_{0.01}Bi_{0.007})_2O_3$, $(Y_{0.95}Eu_{0.05})_2O_3$, and $(Y_{0.93}Eu_{0.05}Tl_{0.02})_2O_3$, where the concentrations are for the formulated compositions. In Y_2O_3:Tl a substantial amount of activator is lost on firing and the various thallium-containing phosphors showed more than 90% loss as measured by atomic absorption analysis.

Excitation and emission spectra were obtained with a Perkin-Elmer Model 195 and Hitachi-Perkin-Elmer MPF-2A spectrophotofluorimeters. The Perkin-Elmer Model 195, a prism instrument (16), provided energy-corrected emission and excitation spectra (Fig. 4 and 5) and was used to obtain quantum efficiency data by comparing the phosphors to NBS $MgWO_4$ (17). The Hitachi instrument, though uncorrected (see Fig. 10 and 14 for energy correction factors), provided better separation of the overlapping excitation and emission bands due to its grating optics (Fig. 1 and 7-14). Reflectance spectra were obtained with a Bausch and Lomb Spectronic 505 instrument. A TRW Model 31A instrument was used for decay time measurements.

X-ray-excited emission spectra were recorded using radiation from a tube with a molybdenum target operating at 50 kV and 30 mA. One gram samples were pressed into pellets 1 cm in diameter and the emission measured from the excitation side of the sample. An EMI 9558B photomultiplier and a 1-meter Jarrell-Ash monochromator were used to record the spectra.

Results

YVO_4, YVO_4:Bi.—Pure YVO_4 shows a blue emission peaking at about 440 nm at both room and liquid N_2 temperature. YVO_4:Bi at room temperature gives a broad, yellowish emission peaking at 560 nm under both short and long wavelength ultraviolet excitations. The emission color at liquid N_2 temperature, however, is determined by the energy of exciting radiation. A blue emission peaking at 440 nm dominates under short wavelength excitations (< 300 nm), whereas only the yellowish emission of bismuth appears at longer (340 nm) wavelengths. Figure 1 shows the excitation spectra for both these emissions. As the emission wavelength, at which the excitation spectrum is measured, is gradually increased above 440 nm, an increase in peak height of the excitation band at about 340 nm occurs relative to that of the higher energy band. Figure 1 also shows the excitation spectrum for the peak emission of pure YVO_4 at 440 nm and liquid N_2 temperature.

Y_2O_3.—Three x-ray-excited emission bands are observed with maxima at approximately 340, 365, and 400 nm. The spectrum appears in Fig. 2. Possible contribution of chemical impurities to this matrix emission is difficult to rule out. However, several samples of Y_2O_3, considered to be of high purity by the suppliers and by our own analysis, gave similar spectra. On converting the same materials to YVO_4, a high intensity emission, characteristic of the vanadate matrix, was always observed.

Y_2O_3:Tl *and* Y_2O_3:Eu, Tl.—The reflectance, emission and excitation spectra of Y_2O_3:Tl prepared in air are shown in Fig. 3, 4, and 5. Varying thallium concentrations formulated up to 10 a/o (atom per cent) gave an optimum brightness at about 2% added thallium, with a quantum efficiency of 25% under 254 nm excitation.

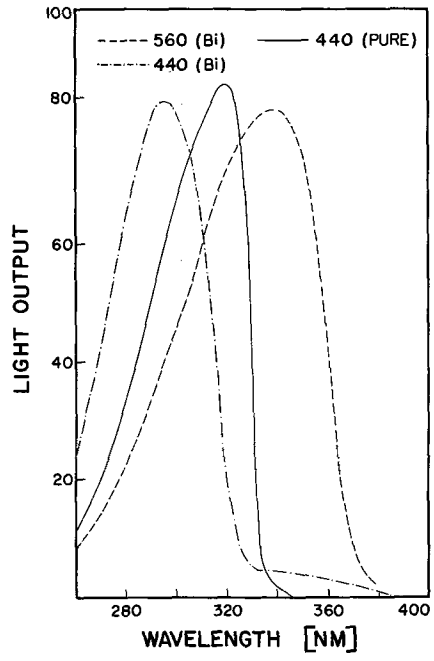

Fig. 1. Excitation spectra at liquid N_2 temperature of pure YVO_4 and $Y_{0.95}Bi_{0.05}VO_4$. The numbers are emission wavelengths in nanometers at which the excitation spectra were measured.

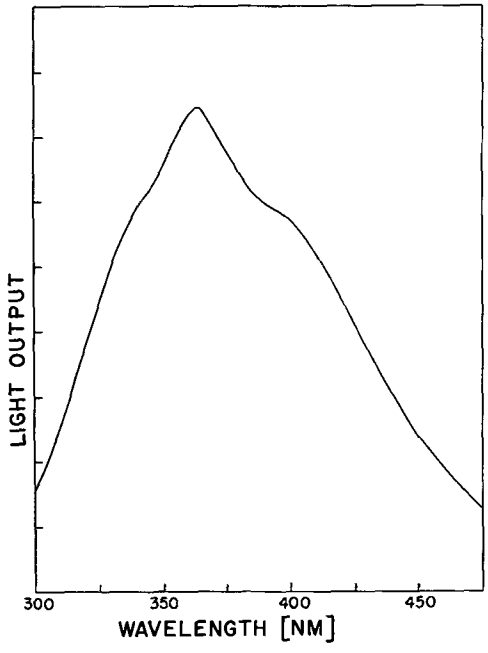

Fig. 2. Matrix luminescence of Y_2O_3 excited by x-rays

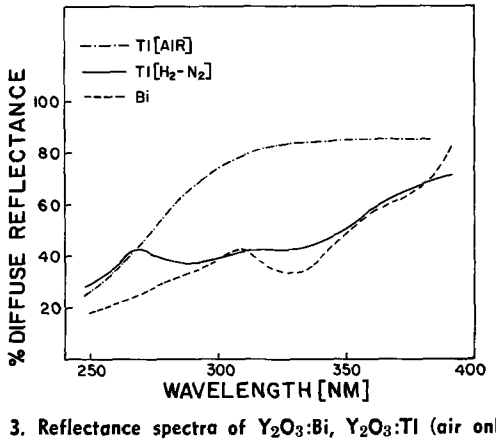

Fig. 3. Reflectance spectra of Y_2O_3:Bi, Y_2O_3:Tl (air only), and Y_2O_3:Tl refired in reducing atmosphere.

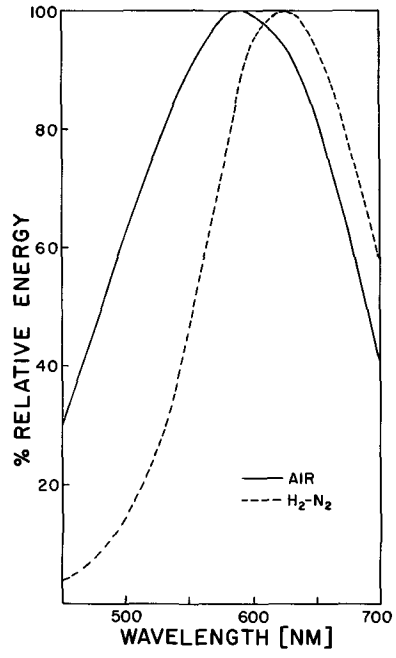

Fig. 4. Y_2O_3:Tl emission spectra: solid line (air) with 254 nm excitation; dashed line (H_2-N_2) with 365 nm excitation.

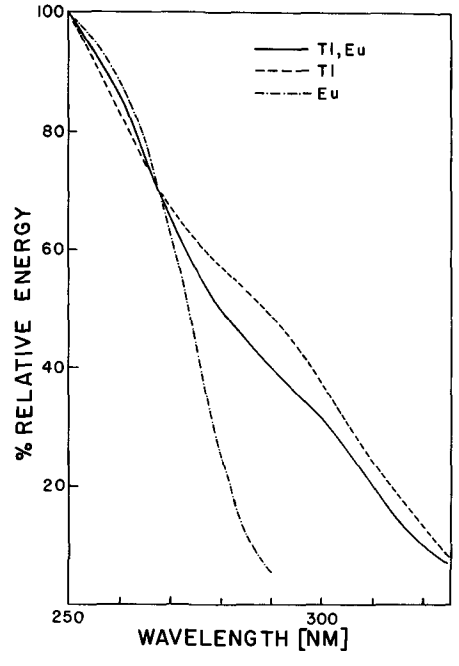

Fig. 5. $(Y_{0.95}Eu_{0.05})_2O_3$, $(Y_{0.95}Eu_{0.05})_2O_3$:Tl, and Y_2O_3:Tl excitation spectra: dashed line for 580 nm emission, solid and dot-dashed lines for the europium emission at 611 nm. The latter's weak (f-f) excitation lines are not shown.

A fluorescence decay time of less than 20 nanosec was observed. Refiring for 1 hr at 1000°C in N_2-H_2 (10%) atmosphere gives a material with distinctly different optical properties, the absorption and emission bands extending to longer wavelengths (Fig. 3, 4) and the emission intensity decreasing.

Addition of thallium to Y_2O_3:Eu alters the excitation spectrum of Eu^{3+} emission at 611 nm (Fig. 5). The broad excitation band for this emission (5, 12) is extended to longer wavelengths. A decrease in emission intensity is observed under 254 nm excitation whereas enhancement is seen at longer (*e.g.*, 290 nm) excitation wavelengths. The effect is gradual, increasing with increasing amounts of added thallium. Figure 5 shows the spectrum of the phosphor formulated with 2 a/o Tl. A comparison of the relative brightness of Y_2O_3:Eu and Y_2O_3:Eu,Tl at various excitation wavelengths can be made by comparing the corresponding excitation curves after a 20% scaledown of the Y_2O_3:Eu,Tl curve.

Energy transfer from Tl to Eu is demonstrated in Fig. 5, where the excitation spectrum for the 611 nm Eu^{3+} emission in Y_2O_3:Eu,Tl is in the same energy region and similar to that observed for Tl emission in Y_2O_3:Tl. Further indication of the transfer is provided by the observed decrease in intensity of the broad-band thallium emission on addition of increasing amounts of europium (0.1-1.0 a/o) at constant, 2 a/o thallium concentration.

Y_2O_3:Bi *and* Y_2O_3:Eu,Bi.—At room temperature Y_2O_3:Bi has two emission bands in the visible at about 405 and 500 nm. Their respective excitation band maxima, three for each emission (12), are shown schematically in Fig. 6 and labeled as g bands for the green emission at 500 nm and b bands for the blue emission at 405 nm.

Exact positions of some of these band maxima are difficult to ascertain due to strong overlap with adjacent bands. Furthermore, from the measurement standpoint, it is difficult to establish the "pure" bands associated with each emission, also due to this overlap. The problem is common to most measurements on this phosphor and some of the excitation and emission spectra shown below are for wavelengths slightly displaced from the proper maxima in efforts to isolate the bands of interest.

The reflectance spectrum of Y_2O_3:Bi appears in Fig. 3. A quantum efficiency of about 40% was obtained at room temperature using 340 nm exciting radiation. The 500 nm emission, which was the only band we were able to isolate using Corning filter CS3-74, has a decay time of 5×10^{-7} sec at room temperature.

Figure 7 shows a comparison of Y_2O_3:Bi emission at room and liquid N_2 temperature under 371 nm excitation. A similar comparison appears in Fig. 8 with 350 nm excitation. The effect on the excitation bands of lowering the temperature appears in Fig. 9 for the 500 nm emission. Note the decrease in intensity of 330 (2 g) relative to the 344 nm (1 g) band with decreasing temperature. Simultaneously, excitation in the energy region of the 2 g band (325 nm) gives a new emission in the visible at about 430 nm (Fig. 10). The excitation spectrum of the 430 nm band (Fig. 11) is dominated by the 330 nm band but with some contribution from the 371 (1 b) and 338 nm (2 b) bands of the 405 nm emission. This contribution decreases when excitation spectra are measured for emissions at longer wavelengths than 430 nm (further away from the 405 nm emission to minimize overlap) and at 500 nm (Fig. 9) very little of the 1 b and 2 b bands remain.

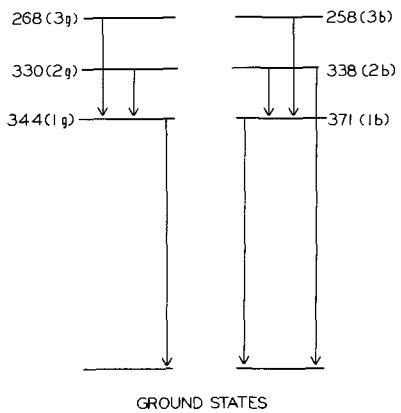

Fig. 6. Schematic representation of the excitation band maxima in nanometers for the 500 nm (g bands) and 405 nm (b bands) emissions in Y_2O_3:Bi. Arrows indicate electronic transitions at room temperature discussed in the text. The g and b designations also represent the electronic states responsible for the corresponding excitation bands.

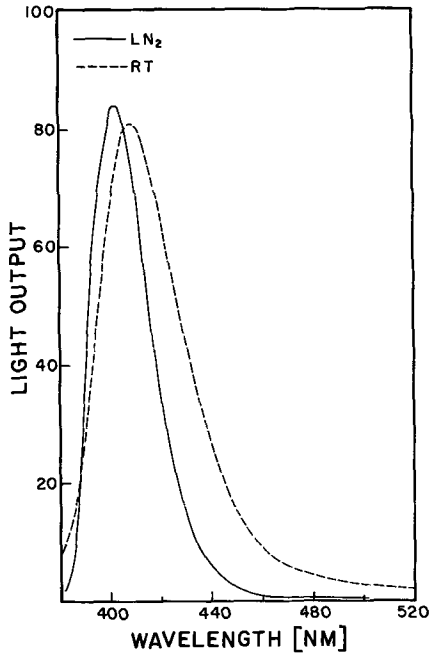

Fig. 7. Emission spectra of Y_2O_3:Bi excited at 371 nm

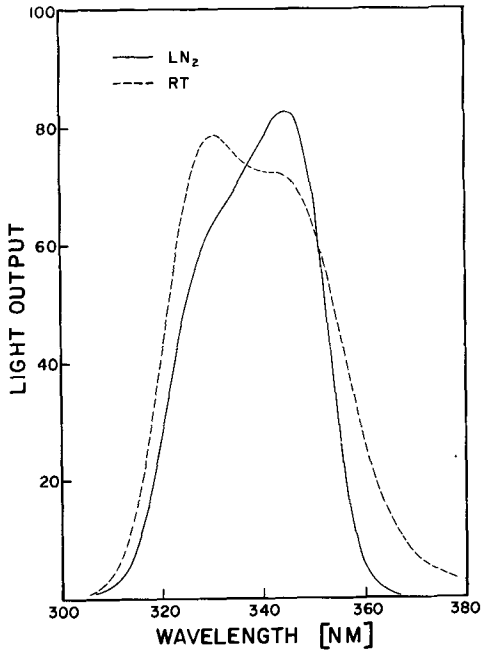

Fig. 9. Excitation spectra of Y_2O_3:Bi for the 500 nm emission

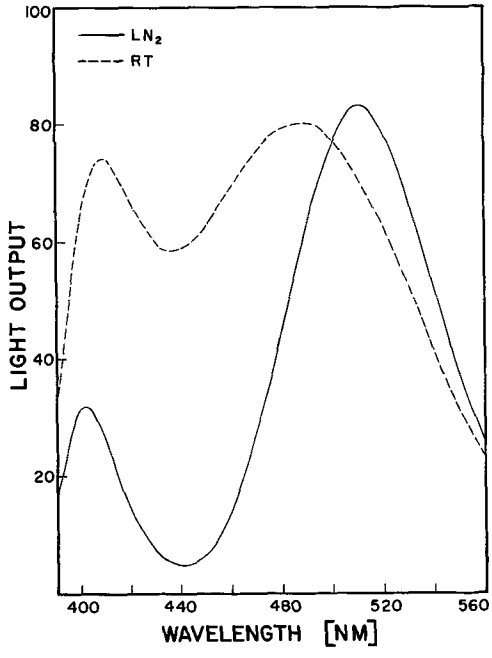

Fig. 8. Emission spectra of Y_2O_3:Bi excited by 350 nm radiation

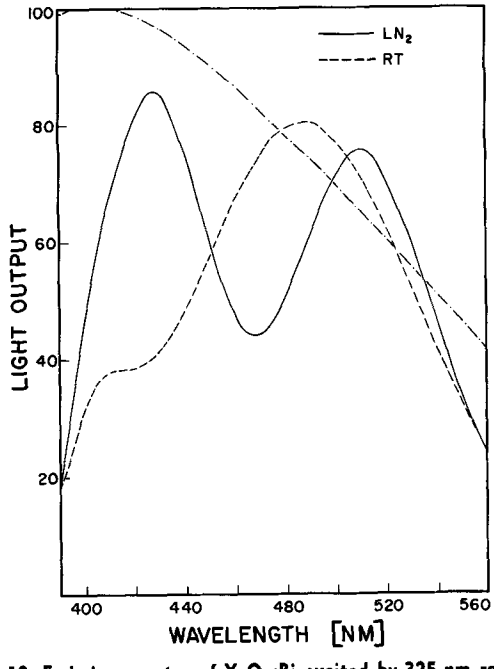

Fig. 10. Emission spectra of Y_2O_3:Bi excited by 325 nm radiation. The dot-dashed curve shows the relative sensitivity of the grating-photomultiplier combination used.

Qualitatively similar effects are observed on comparing the excitation spectra for the 405 nm emission at room and liquid N_2 temperatures (Fig. 12 and 13). Note that the excitation band at 338 nm (2 b) in Fig. 12 decreases in intensity relative to that at 371 nm (1 b) on cooling to liquid N_2 temperature. At the same time (Fig. 13) the emission band at about 355 nm, under 338 nm excitation, now dominates the emission spectrum. This u.v. emission can also be ascertained at room temperature but with considerably weaker intensity than the 405 nm band and less resolved from it.

Energy transfer from Bi to Eu has been reported, considering only the 500 nm emission (10). Figure 14 gives the excitation spectra of Y_2O_3:Eu,Bi measured at 611 nm for the Eu^{3+} emission and at 450 nm, where both the 405 and 500 nm emissions of Bi contribute. Both the b and g excitation bands of bismuth are shown to sensitize the Eu^{3+} emission, this being a further similarity between the two sets of bands.

Discussion

The room temperature excitation spectrum of YVO_4:Bi extends to longer wavelength than that for the pure matrix. However, no structure can be ascertained at these long wavelengths. At liquid N_2 temperature (Fig. 1), bismuth addition introduces a discrete band peaking at about 340 nm. It is interesting to note that this is the energy region of the 1 g (344 nm), 2 g (330), and 2 b (338) excitation bands in Y_2O_3:Bi. The appearance of higher energy emission peaking at 440 nm in YVO_4:Bi may be compared to similar results obtained on rare earths additions to this matrix. Palilla *et al.* (2) observed that although additions of 0.5 m/o (mole per cent) of Dy^{3+}, Tm^{3+}, Sm^{3+}, or Eu^{3+} almost completely quench the luminescence of YVO_4 at room temperature, it reappears with high intensity on cooling these phosphors to liquid

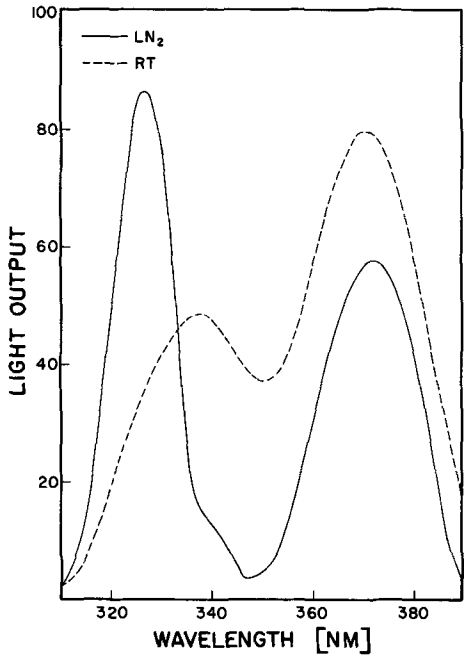

Fig. 11. Excitation spectra of Y_2O_3:Bi for the 430 nm emission

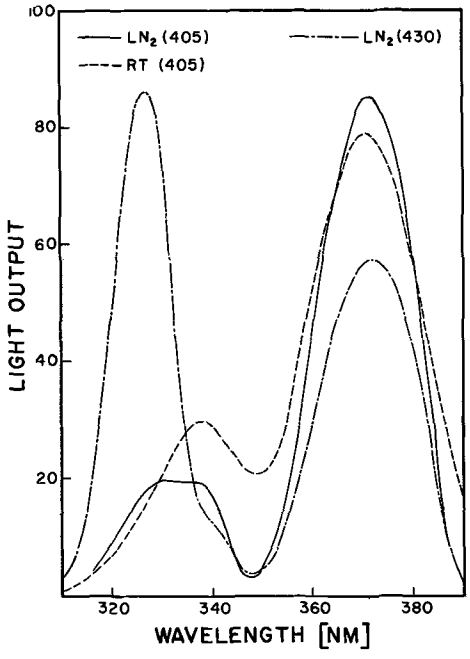

Fig. 12. Excitation spectra of Y_2O_3:Bi for the 405 nm and 430 nm emissions.

N_2 temperature. This suggests that the 440 nm emission observed in YVO_4:Bi at liquid N_2 temperature may be due to host luminescence since the maximum of the emission band of pure YVO_4 is also at 440 nm. However, the difference in the energies of the maxima of the excitation bands for the 440 nm emission in YVO_4 and YVO_4:Bi (Fig. 1) is not understood if in both phosphors the luminescence arises from the common host.

The absorption of pure Y_2O_3 has been reported at wavelengths lower than 225 nm (3,18). In this and the similar oxides of scandium and lanthanum the bands are generally ascribed to electron transfer transitions from oxygen to the trivalent cations (18-20). Further study of the three emission bands observed with x-ray excitation in Y_2O_3 was difficult since attempts to observe any u.v.-excited luminescence, within our instrumental capabilities, were not successful.

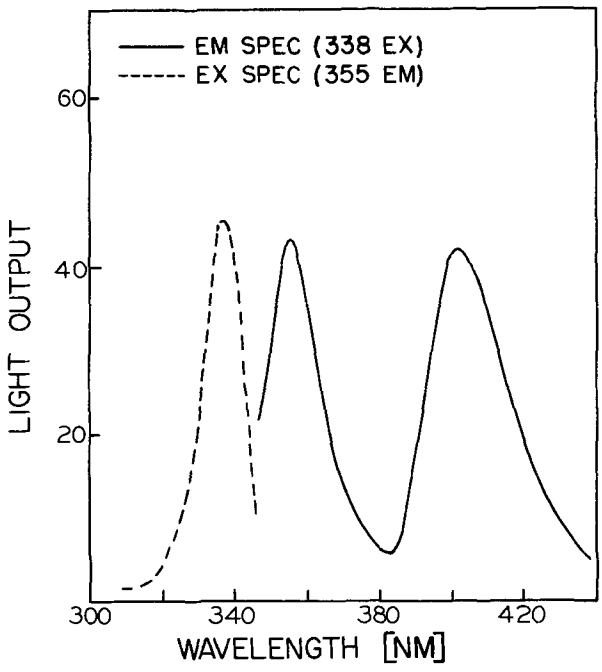

Fig. 13. U.V. emission in Y_2O_3:Bi at liquid N_2 temperature with its corresponding excitation band.

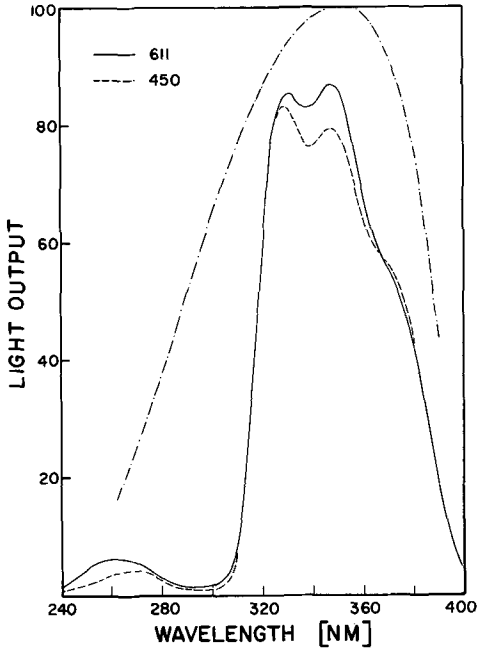

Fig. 14. Excitation spectra for the 611 and 450 nm emissions in Y_2O_3:Eu,Bi at room temperature. The dot-dashed curve shows the relative intensity of the grating-xenon lamp combination used.

Although monovalent thallium is well known as an activator, its trivalent state with $5d^{10}$ configuration is not commonly considered as such. The question of the particular oxidation state of thallium in the matrix with a trivalent cation is, then, of some relevance. Comparing the size and charge of Tl^+ (1.49Å) and Tl^{3+} (1.05) to Y^{3+} (1.06) and considering that Tl_2O_3 is isomorphous with Y_2O_3, the trivalent state of thallium can be favored in nonreduced Y_2O_3:Tl. Further evidence for this is the change in optical properties observed on refiring in H_2-N_2 atmosphere, which presumably can be due to a reduction in the oxidation state of Tl^{3+}. It is also interesting to note that the reduced material absorbs in the same energy region as trivalent bismuth (Fig. 3), the latter being isoelectronic with Tl^+.

Absorption of a trivalent thallium ion in Y_2O_3 can arise either from transitions in the thallium-oxygen bond or the free ion $d^{10} \rightarrow d^9s$. The latter have been considered in alkali halides containing Cu^+ and Ag^+ (21). Their absorption coefficients are smaller by one or two orders of magnitude than those of Pb^{2+} and Ti^+. If the spectra arise from $d^{10} \rightarrow d^9s$ (forbidden) transitions, then their energy in alkali halides is larger than the corresponding transitions in the gaseous state (21). The spectra of nonreduced Y_2O_3:Tl are difficult to understand as arising from such $d^{10} \rightarrow d^9s$ transitions, since their lowest energy in gaseous Tl^{3+} is at 75052 cm^{-1} (22), whereas the absorption of Y_2O_3:Tl occurs at appreciably longer wavelengths. This absorption, however, may be compared to that observed for the hexachlorocomplexes of Pb^{4+} (23), the latter being isoelectronic with Tl^{3+}. Two broad and intense absorption bands are observed at 307 and 208 nm with the high molar extinction coefficient of 9700 and 24000, respectively. These have been interpreted as possibly due to an electron transfer from a predominantly ligand orbital to the empty s orbital of Pb^{4+} which is filled in Pb^{2+} complexes (23). Similar allowed transitions may occur in the thallium-oxygen center in nonreduced Y_2O_3:Tl and the observed short decay time is compatible with such transitions.

The spectra of Y_2O_3:Bi at room temperature show that the green emission at 500 nm can be excited with three bands (1-3 g). Thus, the electronic states responsible for the 3 g and 2 g excitation bands are not the emitting states, since the same emission is observed with the lower energy 1 g band. Radiationless transitions, then, from the 2 g and 3 g to the 1 g state must occur and these are indicated schematically in Fig. 6. The probability for such transitions at temperature T may be considered as proportional to an exponential factor containing T and other parameters pertaining to the configuration coordinate curves of the respective electronic states (24). On lowering the temperature to that of liquid N_2, the probability for transitions, as for example from 2 g to 1 g, can decrease and allow at least some emission from 2 g state, *i.e.*, direct radiative transition from 2 g to the ground state. The new emission at 430 nm (Fig. 10) can be understood as arising from such a transition and is consistent with related excitation spectra given earlier. A similar interpretation applies to the origin of 355 nm emission band, *i.e.*, a radiative transition from 2 b to the ground, electronic state.

In prior work (12), the 405 and 500 nm emissions of bismuth were assumed to arise from different centers in Y_2O_3, for example the C_2 and S_6 sites. The additional emission bands at 355 and 430 nm as well as their corresponding excitation spectra are quite compatible with such an assignment; one center for the 500 and 430 nm emissions and a differing one for the 405 and 355 nm emissions.

Manuscript submitted June 18, 1969; revised manuscript received Nov. 3, 1969. This was Paper 75 presented at the New York Meeting of the Society, May 4-9, 1969.

Any discussion of this paper will appear in a Discussion Section to be published in the December 1970 JOURNAL.

REFERENCES

1. L. G. Van Uitert, R. C. Linares, R. R. Soden, and A. A. Ballman, *J. Chem. Phys.*, **36**, 702 (1962).
2. F. C. Palilla, A. K. Levine, and M. Rinkevics, *This Journal*, **112**, 776 (1965).
3. N. C. Chang, *J. Appl. Phys.*, **34**, 3500 (1963).
4. T. Kano and Y. Otomo, *This Journal*, **116**, 64 (1969).
5. H. Forest and G. Ban, *This Journal*, **116**, 474 (1969).
6. S. Faria and D. T. Palumbo, *ibid.*, **116**, 157 (1969).
7. R. W. Mooney and S. Z. Toma, *J. Chem. Phys.*, **46**, 4544 (1967).
8. S. Z. Toma, F. F. Mikus, and J. E. Mathers, *This Journal*, **114**, 953 (1967).
9. R. K. Datta, *ibid.*, **114**, 1057 (1967).
10. R. K. Datta, *ibid.*, **114**, 1137 (1967).
11. G. Blasse and A. Bril, *J. Chem. Phys.*, **48**, 217 (1968).
12. S. Z. Toma and D. T. Palumbo, *This Journal*, **116**, 274 (1969).
13. G. Blasse, *Philips Res. Rept.*, **23**, 344 (1968); S. Faria and C. W. Fritsch, *This Journal*, **116**, 155 (1969).
14. F. A. Kroger, "Some Aspects of the Luminescence of Solids," Elsevier Publishing Co., Inc., New York (1948).
15. D. Curie, "Luminescence in Crystals," chap. III, Methuen and Company Ltd., London (1963).
16. W. Slavin, R. W. Mooney, and D. T. Palumbo, *J. Opt. Soc. Am.*, **51** (1961).
17. A. Bril and W. Hoekstra, *Philips Res. Rept.*, **16**, 356 (1961).
18. H. J. Borchardt, *J. Chem. Phys.*, **39**, 504 (1963).
19. H. H. Tippins, *J. Phys. Chem. Solids*, **27**, 1069 (1966).
20. C. K. Jorgensen, "Absorption Spectra and Chemical Bonding in Complexes," p. 168, Pergamon Press, Inc., New York (1962).
21. D. S. McClure, "Electronic Spectra of Molecules and Ions in Crystals," Part II, Academic Press Inc., New York (1959).
22. C. E. Moore, "Atomic Energy Levels," NBS Circular 467, **3**, 207 (1958).
23. Ref. 20, p. 164. See also Eq. 54, p. 61.
24. C. C. Klick and J. E. Schulman, *Solid State Phys.*, **5**, 99-104 (1957).

Diffusion of Manganese in Single Crystalline Manganous Oxide

J. B. Price[1] and J. Bruce Wagner, Jr.*

Materials Research Center, Northwestern University, Evanston, Illinois

ABSTRACT

The self diffusion of $^{54}_{25}Mn$ in monocrystalline manganous oxide has been studied in order to investigate the predominant lattice defect in MnO_{1+x} in the low oxygen pressure region of the phase field. In the low oxygen pressure region of the MnO_{1+x} phase field the material exhibits apparent n-type behavior. A graph of log D^{T}_{Mn} *vs.* log P_{O_2} for a temperature of 1032°C exhibits a constant slope of $+1/5.4$ for $10^{-18} \leq P_{O_2} \leq 10^{-8}$ atm. This pressure dependence is consistent with the model for doubly ionized cation vacancies over the range of composition studied.

The oxide, MnO_{1+x}, is nonstoichiometric with a maximum deviation from stoichiometry of approximately 15% (1-4). The high temperature region of the MnO_{1+x} phase field is shown in Fig. 1. In regions B and C the oxide is oxygen excess (1, 4) according to the following quasi-chemical reaction

$$\tfrac{1}{2}\, O_2(g) \rightleftarrows O_{xs} + V_{Mn}^{m'} + m\oplus \qquad [1]$$

where O_2 is an oxygen molecule, O_{xs} is an excess oxygen atom on a regular oxygen site, $V_{Mn}^{m'}$ is a negatively charged manganese vacancy, $\oplus$ is an electron hole (4), and m is the degree of ionization of the vacancy. Classically m takes on a value of 0, 1, or 2. In region B, m equals 2 (1, 4), and m equals 1 in region C (1, 4). In regions B and C the electrical conductivity (1, 4) is proportional to the concentration of electron holes, $[\oplus]$ or p. In the region of the MnO_{1+x} phase field shown in Fig. 1, $0.05 < \sigma < 8.0$ (ohm-cm)$^{-1}$. For dilute solutions the ideal mass action law predicts that

$$p = [\oplus] = (m)^{1/(1+m)}\, P_{O_2}{}^{+1/2(m+1)} \exp\{-\Delta G°_f/(1+m)RT\} \qquad [2]$$

where the brackets, [], denote concentration, P_{O_2} is the oxygen partial pressure, $\Delta G°_f$ is the Gibbs free energy for reaction [1], R is the gas law constant, and T is the absolute temperature, In regions B and C the electrical conductivity is

$$\sigma = e\mu_{\oplus}\, p \qquad [3]$$

where the conductivity, σ, is in reciprocal ohm-cm, e is the electronic charge in coulombs, the electron hole mobility, $\mu_{\oplus}$, is in cm^2/v-sec, and p is the number of holes/cm^3, given by Eq. [2]. In regions B and C the differential form of the oxygen pressure dependence of the conductivity is

$$\left[\frac{\partial \log \sigma}{\partial \log P_{O_2}}\right]_T = \frac{1}{2(1+m)} \qquad [4]$$

where it is assumed that $\mu_{\oplus}$, $\Delta G°_f$, and m are not functions of concentration (4). Data from the thesis Eror (1) and from Hed and Tannhauser (4) are shown in Table I. Both Eror and Hed found satisfactory agreement between the value of $1/2(m+1)$ determined from conductivity studies and the value of $1/2(m+1)$ determined from thermogravimetric studies in regions B and C. The concentration of cation vacancies and the deviation from stoichiometry may be computed from thermogravimetric data (1, 4). The oxygen pressure dependence of the deviation from stoichiometry is

$$\left[\frac{\partial \log x}{\partial \log P_{O_2}}\right]_T = \frac{1}{2(1+m)} \qquad [5]$$

where x, $0 < x < 1/3$, is the deviation from stoichiometry in MnO_{1+x}. The oxidation studies of Fueki and Wagner (9) further substantiate the predominance of the cation vacancies in region B.

The apparent p-n boundary (1-4) occurs at approximately $P_{CO_2}/P_{CO} = 1$ in the temperature range 800°-1500°C. For ratios less than $P_{CO_2}/P_{CO} = 1$, the value of $1/2(m+1)$ derived from conductivity studies is negative. Eror (1) and Hed (4) were unable to correlate their conductivity and thermogravimetric data in region A because neither was able to detect weight changes in region A. Hed and Tannhauser (4) showed that the weight change between the p-n boundary and the Mn-MnO boundary would be less than 25 μg/g if cation vacancies predominated in region A. The limit of resolution for the systems used

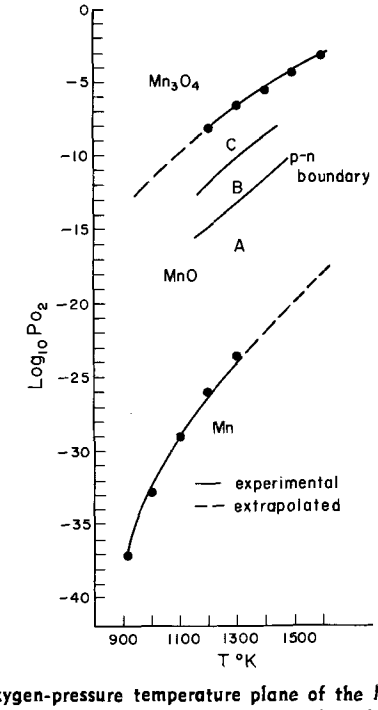

Fig. 1. Oxygen-pressure temperature plane of the MnO_{1+x} phase field; the Mn-MnO_{1+x} and MnO_{1+x}-Mn_3O_4 boundaries are taken from ref. (4, 5, 6, 7, and 8), the P-N boundary is taken from ref. (3), and the sub-regions are defined in ref. (4).

* Electrochemical Society Active Member.

[1] Present address: Central Research Laboratories, Motorola, Inc., Phoenix, Arizona 85008.

Key words: diffusion Mn into MnO; defect equil. MnO.

Table I. Oxygen pressure dependence of the electricol conductivity

Temperature, °C	Eror (1, 16) $\left(\frac{1}{2(m+1)}\right)$ Region A	Eror (1, 16) $\left(\frac{1}{2(m+1)}\right)$ Region B	Hed and Tannhauser (4) $\left(\frac{1}{2(m+1)}\right)$ Region A	Hed and Tannhauser (4) $\left(\frac{1}{2(m+1)}\right)$ Region B	Hed and Tannhauser (4) $\left(\frac{1}{2(m+1)}\right)$ Region C
900	$-\frac{1}{5.4}$	$\frac{1}{5.9}$	—	—	—
1000	$-\frac{1}{5.9}$	$\frac{1}{5.7}$	—	—	—
1100	$-\frac{1}{6.4}$	$\frac{1}{5.2}$	—	—	—
1210	—	—	$-\frac{1}{6.6}$	$\frac{1}{6.6}$	—
1280	—	—	$-\frac{1}{7.1}$	$\frac{1}{5.7}$	$\frac{1}{3.9}$
1375	—	—	—	$\frac{1}{6.0}$	$\frac{1}{4.0}$
1500	—	—	—	$\frac{1}{5.8}$	$\frac{1}{3.7}$

by Hed and Eror is 25 μg/g, or 25 x 10^{-4}%. Hed and Tannhauser (4) demonstrated that MnO_{1+x} in region A could be n-type, electronically, if $\mu_{\ominus} > 10\ \mu_{\oplus}$. Using the analysis of Becker and Frederikse (10), Hed computed the oxygen pressure dependence of p from his own conductivity data for the oxygen pressure range $-2.5 \leq \log P_{CO_2}/P_{CO} \leq +2$ at 1100° and 1300°C. He found no inflection point or minimum in log (const. p^2) *vs.* log P_{O_2} at or near the apparent p-n boundary. He concluded that at the p-n boundary $n\mu_{\ominus} = p\mu_{\oplus}$ and that $p > n$. As p decreases, the electron contribution to the conductivity eventually dominates because $\mu_{\ominus} > \mu_{\oplus}$ even though $p \geq n$. Gvishi, Tallan, and Tannhauser (11) confirmed that $\mu_{\ominus} > \mu_{\oplus}$ by Hall measurements on single crystals of MnO.

Self diffusion studies with the $^{54}_{25}$Mn isotope would be more sensitive to small changes in the deviation from stoichiometry than thermogravimetric analysis and would therefore compliment the conductivity studies made in region A. Accordingly the present study was carried out.

Boundary Value Problem

An infinitesimally thin layer of $^{54}_{25}$Mn placed on the surface of a thin slab of MnO_{1+x} will have the following distribution after t seconds (12)

$$N(\xi,t) = \frac{Q}{\sqrt{\pi Dt}} \exp\ (-\xi^2/4Dt) \qquad [6]$$

where Q is the number of $^{54}_{25}$Mn atoms initially on the surface per square centimeter of surface, D is the diffusion coefficient, $N(\xi,t)$ is the number per cubic centimeter ξ centimeter below the surface after a diffusion anneal of t seconds. It is assumed that all the $^{54}_{25}$Mn diffuses into the sample, that it does not change the composition of the sample, that it diffuses through the bulk only, that $I(\xi,t) = \text{const. } N(\xi,t)$, and that $I_o = \text{const. } Q$. Then

$$I(\xi,t) = \frac{I_o}{\sqrt{\pi Dt}} \exp\ (-\xi^2/4Dt) \qquad [7]$$

where $I(\xi,t)$ is the number of counts per second per cubic centimeter at a depth of ξ cm, and I_o is the number of counts per second per square centimeter initially at the surface. The tracer diffusivity, $D_{Mn}{}^{T}$ (hereafter simply, D), may be calculated from the tracer distribution, $I(\xi,t)$; it may be calculated also from the integrated distribution

$$I_k = I_o \operatorname{erfc} \frac{k}{\sqrt{4Dt}} \qquad [8]$$

where k is the thickness of material removed prior to counting. Equation [8] may be rearranged (13) so that it is amenable to graphical solution

$$50\left(2 - \frac{I_k}{I_o}\right) = 50\left(1 + \operatorname{erf}\frac{k}{\sqrt{4Dt}}\right) \qquad [9]$$

A graph of 50 $(2 - I_k/I_o)$ *vs.* $k/\sqrt{t}$ yields a straight line with intercept at 50 $(2 - I_k/I_o)$ equal to fifty on probability paper. Analysis via Eq. [7] is the sectioning method (12), and analysis via Eq. [8] is the Gruzin method (12). It was experimentally verified that absorption corrections to Eq. 8 were unnecessary because the 0.84 m.e.v. radiation emitted by $^{54}_{25}$Mn is relatively unattenuated in MnO_{1+x}.

Table II. Analyses of MnO crystals

As-received boule
Analytical Laboratory "A"
Ca, Co, Fe, Si, V, Al, Cr, Cu, Mo, Ni, Ag, and Pb all <1 ppm wt (Ti = 0.001 wt %)

Diffusion samples		
Analytical Laboratory "A"	Analytical Laboratory "B"	
Ca, Co, Fe, Si, V, Al, Cr, Cu, Mo, Ni, Ag Pb <1 ppm wt Ti = 0.001 wt %	Ca	0.01 to 0.1 wt %
	Co	0.001 to 0.01
	Fe	0.001 to 0.01
	Si	0.001 to 0.01
	V	0.001 to 0.01
	Al	0.0005 to 0.006
	Cr	0.0005 to 0.005
	Cu	0.0005 to 0.005
	Mo	0.0005 to 0.005
	Ni	0.0005 to 0.005
	Ti	0.0005 to 0.005
	Ag	0.0001 to 0.001
	Pb	0.0001 to 0.001

Experimental Procedure

Rectangular slabs approximately 200 x 100 x 30 mils were cleaved from single crystal boules of MnO_{1+x}. Two typical analyses are presented in Table II. The samples were equilibrated at a given oxygen pressure and temperature in a vertical tube furnace. The oxygen pressure was fixed with a flowing mixture of CO_2 and CO. The time required to equilibrate a sample at a given oxygen pressure and temperature was computed from the appropriate value of the chemical diffusivity. Using an electrical conductivity technique (14) the composition dependence of the chemical diffusivity of MnO_{1+x} was determined before the radiotracer studies were initiated. It was assumed that the as-received MnO_{1+x} boules were highly nonstoichiometric; to test the assumption, several as-received samples were equilibrated to a composition near the MnO_{1+x} — Mn_3O_4 boundary, P_1 in Fig. 2. The equilibration was monitored with d-c conductivity readings.

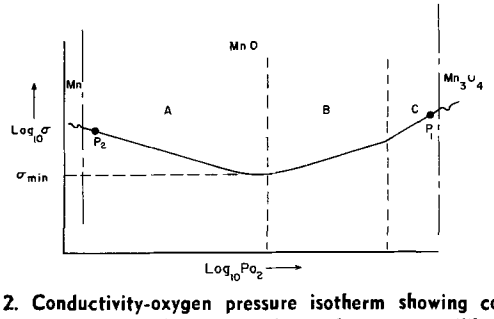

Fig. 2. Conductivity-oxygen pressure isotherm showing composition, P_1 to which several as-received samples were equilibrated to determine the approximate composition of as-grown samples.

The characteristic curve of Fig. 2 shows the conductivity variation with oxygen pressure at constant temperature. If the as-grown sample composition were in region A, *e.g.*, P_2 in Fig. 2, the conductivity would initially decrease, reach a minimum, and then increase to the equilibrium value corresponding to P_{O_2} final, *e.g.*, P_1 in Fig. 2. If the initial composition were in region B, the conductivity would increase monotonically to the final value. If the initial composition were in region C to the right of, or at a higher deviation from stoichiometry than the final equilibrium composition of this experiment, the conductivity of the sample would monotonically decrease with time until it reached the equilibrium value (P_1 in Fig. 2). The latter behavior was found with all as-grown samples tested. Therefore, the as-received samples were oxygen-rich, the composition being close to the MnO_{1+x}-Mn_3O_4 boundary, corresponding to a composition near P_1 in Fig. 2.

Radiotracer diffusion samples were equilibrated and diffused in pairs in platinum baskets. The oxygen pressure and temperature combinations at which samples were equilibrated are given in Table III. The equilibrated samples were polished on one face with 500A silicon carbide paper. On the polished face was placed a drop of neutral, aqueous $^{54}_{25}MnCl$ solution containing about 2 μcuries of $^{54}_{25}Mn$. The drop of $^{54}_{25}MnCl$ was dried under a lamp in approximately 30 min. The pair of samples was then placed, active faces together, in a platinum basket in the cold zone of the diffusion anneal furnace. The same CO_2/CO mixture which was used for the prediffusion anneal was used for the diffusion anneal. The samples were lowered into the hot zone via a magnetic coupling between a magnetic drive wheel inside the gas system and a concentric magnetic ring outside the gas system. The minimum diffusion anneal was 100 min, and the maximum diffusion anneal was 1300 min. The diffusion anneal was terminated by raising the sample from the hot zone to the cold zone of the furnace in about 5 sec. Prior to mounting, at least one diffusion length of material was lapped from each edge and from the back face of each sample to minimize errors from surface diffusion. The diffused samples were mounted in a room temperature setting plastic inside a magnetic stainless steel ring.

A microscope was focused on the top surface of the sample, and an attached dial gauge was zeroed. After each successive layer was lapped from a sample the amount removed was read on the dial gauge after the microscope was refocused. The initial count rate was I_o. Succeeding activity measurements were made of the total remaining sample, I_k, and of the grindings, $I(\zeta,t)$.

Results

In Fig. 3 are the results of twenty-two radiotracer experiments. The oxygen pressure dependence of the cation diffusivity, $[(\partial \log D_{Mn}{}^T)/(\partial \log P_{O_2})]_T$, is given in Table IV. Lacombe *et al.* (2) have presented direct experimental data from which the activation energy

$$Q^* = \left[\partial \log D_{Mn}{}^T / \partial \log \frac{1}{T} \right]_{P_{O_2}} \quad [10]$$

may be calculated. From their manganese oxidation experiments Fueki and Wagner (9) have calculated $D_{Mn}{}^T$ *vs.* $\log P_{CO_2}/P_{CO}$; from these data and the equilibrium constant for the dissociation of CO_2, Q^* may be calculated. By assuming parallel isotherms the

Table III. Experimental conditions for radiotracer experiments

Temp, °C	P_{O_2} atm
1141	10^{-7}
1032	10^{-8}, 10^{-10}, 10^{-12}, 4×10^{-14}, 10^{-15}, 10^{-16}, 10^{-17}, 10^{-18}
935	10^{-11}
852	4×10^{-18}

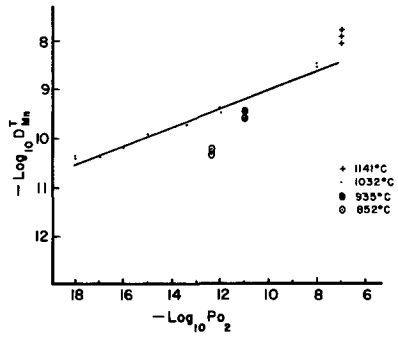

Fig. 3. Experimental data for $D_{Mn}{}^T$ of this study

1141°, 935°, and 852°C data of the present study were extrapolated so that an approximate value of Q^* could be calculated for comparison with the data of Fueki (9) and of Lacombe (2). The results are given in Table V.

Approximately half of the diffusion profiles did not extrapolate to the point 50 $(2 - I_k/I_o)$ equal to fifty, see Fig. 4. Where the data did not extrapolate to fifty the profile was translated so that it would intercept 50 $(2 - I_k/I_o)$ equal to fifty, the dotted line in Fig. 4. The differences between the corrected profile and the experimental profile are due to the experimental errors in the location of the plane k equal to zero and in the measurement of I_o as discussed below. Referring to Eq. [9]

$$50\left(2 - \frac{I_k}{I_o \pm \delta}\right) = 50\left(1 + \text{erf}\frac{k \pm \Delta}{\sqrt{4Dt}}\right) \quad [11]$$

the data in Fig. 5 may be interpreted on the basis that δ and Δ of Eq. [11] are not equal to zero. There is a constant error in the measurement of I_o and k. The error in the location of k equal to zero was due to the occasional presence of a very thin layer of the plastic mount on the top surface of the crystal. The plastic mount had to be removed before the measuring microscope could be focused on the top surface of the crystal. One or two microns of the crystal were inadvertently removed with the excess cold mount so that the point k equal to zero was one or two per cent uncertain. Because of evaporation losses during the diffusion anneal the measured value of I_o was approximately 10% uncertain. For experimental data containing nonzero values of Δ and δ the profile extrapolates to some value of $I_k/I_o \neq 1$ at k equal to zero. The appropriate way to adjust the profile for the nonzero values of Δ and δ is to translate the curve as shown in Fig. 4, curve B. The appropriate value of D was calculated from the translated curve. See the dashed curve in Fig. 4. For the data in Fig. 4 the value of D

Table IV. Comparison of experimental determination of the oxygen pressure dependence of $D_{Mn}{}^T$ in MnO_{1+x}

$\left[\frac{\partial \log D_{Mn}{}^T}{\partial \log P_{O_2}}\right]_T$	Temperature, °C	Oxygen pressure range (atm)	Investigators
$\frac{1}{5.4}$	1032	10^{-8} to 10^{-18}	This study
$\frac{1}{6.7}$	1000	10^{-10} to 10^{-16}	Lacombe *et al.* (2) (interpolated)
Variable	1000	10^{-15} to 10^{-20}	
$\frac{1}{6}$	1000	10^{-20} to 20^{-23}	
$\frac{1}{7}$	1000	10^{-10} to 10^{-14}	Fueki and Wagner (9)

Table V. Approximate value of the activation energy, Q^*, compared with the data of Lacombe and of Fueki

Q^* kcal/mole	19	22	36	20	20	30	31	26	26
P_{O_2} (atm)	10^{-10}	10^{-10}	10^{-11}	10^{-13}	10^{-14}	10^{-16}	10^{-17}	10^{-20}	10^{-22}
Investigator	Lacombe (2)	Fueki (9)	This study				Lacombe (2)		

Table VI. Results of a least squares analysis of the $\log_{10} D_{Mn}{}^T$ vs. $\log_{10} P_{O_2}$ data at 1032°C

$\log_{10} D_{Mn}{}^T$	−8.59	−8.96	−9.34	−9.60	−9.89	−10.1	−10.3	−10.5
$\log_{10} P_{O_2}$	−8.0	−10	−12.0	−13.4	−15	−16	−17	−18

calculated from the translated curve differs from the value of D calculated from the experimental curve by 20%. All the samples were sectioned to a depth of at least twice $\sqrt{Dt}$, and it was found that in most samples the γ intensity did not go to zero; it dropped to a constant value of approximately 10% of I_0. This residual activity, or tail (15), was subtracted point by point from the profile. If the ratio of the residual activity to I_0 was two tenths or less there was no measurable difference between D computed from data including the tail and D computed from data with the tail subtracted out. If the ratio of the residual activity to I_0 exceeded two tenths the experiment was repeated on another sample.

Only one experiment was conducted so that both Eq. [7] and [8] could be used to analyze the data for D on the same sample. The sample was lapped and counted using the Gruzin method, but at 30μ intervals, layers approximately 4μ thick were removed on circular grinding paper and counted. The counting errors in the sectioning data were appreciable because the net count rate from the grindings was always less than the background count rate. However, the difference between D computed from the sectioning data and D computed from the residual activity data, 23%, was close to the average experimental error of 18%.

The linear absorption coefficient for the $^{54}{}_{25}Mn$ γ radiation was also measured. Slabs of monocrystalline MnO_{1+x} were placed over an active diffusion sample, and the decrease in count rate per each slab added was measured. The area of the absorber slabs was at least twice the area of the source. The experimental value of the linear absorption coefficient, μ, was comparable to the value computed from reference data (17)

$$\mu \text{ (calc)} = 0.3 \text{ cm}^{-1}$$

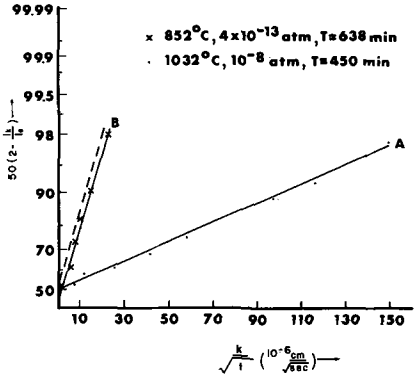

Fig. 4. Two radiotracer profiles of 50 $(2 - I_k/I_0)$ vs. $k/\sqrt{t}$ from which $D_{Mn}{}^T$ was determined to be: (A) 3 x 10^{-9} cm²/sec for 1032°C, 10^{-8} atm P_{O_2}, t = 450 min, and (B) 5 x 10^{-11} cm²/sec for 852°C, 4 x 10^{-13} atm $P_{O}{}^2$, t = 638 min. Curve A intercepted the ordinate at 50 $[2 - I_k/I_0]$ = 50 as required by theory, see text. Curve B did not. It was translated as shown by the dashed line to intercept the ordinate at 50. This offset indicates an experimental error. See text.

$$\mu \text{ (exp.)} = 0.1 \text{ cm}^{-1}$$

Therefore the absorption correction to Eq. [8] was not necessary as was noted previously.

The average percentage deviation of the experimental data about the $\log_{10} D - \log_{10} P_{O_2}$ regression line at 1032°C was 16%. The data computed from a least squares analysis of $\log_{10} D$ vs. $\log_{10} P_{O_2}$ at 1032°C are given in Table VI. Each datum point studied corresponded to some fixed value of temperature and oxygen pressure. At many of the data points several repeat experiments were conducted, each on a different sample. At all data points at least two samples were analyzed. Each experimental value of D was compared to the average value at that datum point to compute a per cent deviation in the sense of Eq. [12]

$$\% \text{ deviation} = \frac{\Delta D}{D(\text{avg})} \times 10^2 \qquad [12]$$

where

$$\Delta D = D(\text{avg}) - D(\text{exp.}) \qquad [13]$$

and

$$D(\text{avg}) = \sum_{i=1}^{j} D_i/j \qquad [14]$$

The average per cent deviation was 18%. The standard deviation in the log $D_{Mn}{}^T$ vs. log P_{O_2} data at 1032°C is 0.1.

Discussion

The oxygen pressure dependence of the electronic conductivity of MnO_{1+x} in region A could yield a model involving a manganese interstitial

$$MnO(s) \rightleftarrows \frac{1}{2} O_2(g) + Mn_i{}^{m\cdot} + m\ominus \qquad [15]$$

where $Mn_i{}^{m\cdot}$ is an ionized interstitial, $\ominus$ is an electron, and m is an integer, either one or two. With this model the differential form of the oxygen pressure dependence of the electrical conductivity is

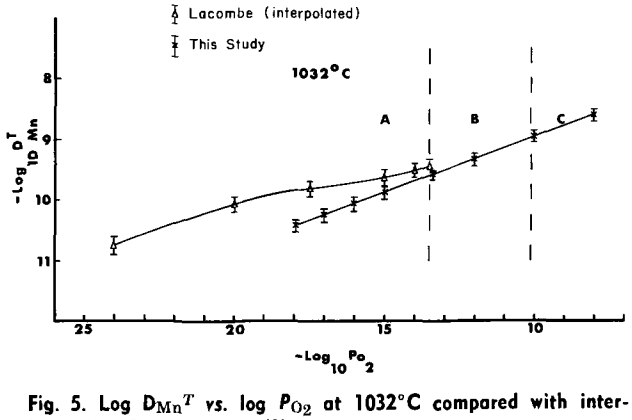

Fig. 5. Log $D_{Mn}{}^T$ vs. log P_{O_2} at 1032°C compared with interpolated data from Lacombe (2).

$$\left[\frac{\partial \log \sigma}{\partial \log P_{O_2}}\right]_T = -\frac{1}{2(m+1)} \quad [16]$$

An oxygen vacancy would yield the same oxygen pressure dependence for the conductivity

$$MnO(s) \rightleftarrows \frac{1}{2} O_2(g) + V_O^{m\cdot} + m\ominus \quad [17]$$

where $V_O^{m\cdot}$ is an oxygen vacancy with m positive charges.

As suggested by Hed and Tannhauser (4) a doubly ionized cation vacancy would yield a similar oxygen pressure dependence for the electrical conductivity if

$$\mu_- n >> \mu_+ p \quad [18]$$

and

$$np = n_i^2 = n_{io}^2 \exp(-E_g/RT) \quad [19]$$

where n_i is the intrinsic concentration of carriers, n_{io} is a constant, and E_g is the band gap expressed here in cal/mole. The conductivity is given by

$$\sigma = e(\mu_- n + \mu_+ p) \quad [20]$$

and

$$p \propto P_{O_2}^{1/2(m+1)} \quad [21]$$

so that combining [18], [19], [20], and [21] yields

$$\sigma \propto P_{O_2}^{-1/2(m+1)} \quad [22]$$

for n-type MnO. With their conductivity data and the analysis of Becker and Frederikse (10), Hed and Tannhauser substantiated this latter model.

The self diffusivity of manganese is proportional to the concentration of defects responsible for the mobility of the manganese, presumably either cation vacancies or cation interstitials. In regions B and C of the T-P_{O_2} diagram (Fig. 1), the predominant defect is the cation vacancy (1-4), the concentration of which is proportional to $P_{O_2}^{1/2(m+1)}$. In region B the data of this study, of the study of Lacombe *et al.* (2), and the study of Fueki and Wagner (9) verify that D is proportional to $P_{O_2}^{1/2(m+1)}$, where m equals approximately two. For region A Eq. [15] predicts that D should be proportional to $P_{O_2}^{-1/2(m+1)}$, the oxygen pressure dependence of the concentration of manganese interstitials if manganese interstitials were the predominant defect. There would necessarily result a minimum value of D near the composition corresponding to the boundary between regions A and B. Both the data of Lacombe and the data of the present study show no minimum value for D. If Eq. [17], the oxygen vacancy model, were valid for region A, the mobile cation defect in region A would be the low concentration vacancy. There would be an intrinsic region near the region A-region B boundary because the material would be transforming from oxygen excess in region B to oxygen deficit in region A. The cation diffusivity, D, would decrease monotonically across the phase field with an inflection point in the intrinsic region. The oxyyen pressure dependence of D would be $P_{O_2}^{-1/2(m+1)}$. Although Lacombe has rejected the oxygen vacancy model, his data seem to support it. Reasoning that if the oxygen vacancy were the predominant point defect in region A there would be appreciable oxygen transport in an electric field, Lacombe *et al.* (2) eliminated the oxygen vacancy model by showing that the ionic conductivity was dominated by the cation contribution. By assuming parallel isotherms we have interpolated Lacombe's radiotracer diffusion data for comparison with the data of the present study, see Fig. 5. The error bars on the interpolated data points of Lacombe were taken from equivalent data points at 1000° and 1100°C. The experimental data points of the present study are given with the computed regression line. The agreement between the two sets of data is very satisfactory. The diffusion activation energy, Q^*, is also consistent with the cation vacancy model. The differences in the data, Fueki's at 10^{-10} atm ($Q^* = 22$ kcal/mole), Lacombe's (interpolated) at 10^{-10} atm ($Q^* \cong 19.3$ kcal/mole), and our extrapolated value at 10^{-11} atm ($Q^* \cong 36$ kcal/mole), are attributed to experimental error and extrapolation.‡ The data of Lacombe, Q^* *vs.* P_{O_2} from 10^{-10} to 10^{-22} atm, will be discussed further because they require the least interpretation and extrapolation. For a vacancy diffusion model it is known that $Q^* = [\Delta H^\circ_f/(m+1) + \Delta H_m]$ where ΔH°_f is the enthalpy for reaction 1, the enthalpy of formation of an ionized vacancy and m electron holes and ΔH_m denotes the enthalpy of movement of the manganese ions. This is the notation of Eror, and it is consistent with the notation of Hed and Tannhauser if one notes that $\Delta H^\circ_f = \Delta h^\circ_f + E_1 + E_2$ where Δh°_f is the enthalpy of formation of a neutral cation vacancy, and E_1 and E_2 are the first and second ionization energies of the cation vacancy. The enthalpy of motion for diffusion will show a discontinuity when plotted *vs.* composition or P_{O_2}, wherever there is a change in diffusion mechanism. If $\Delta H^\circ_f/(m+1)$ may be determined for each value of P_{O_2} at which Q^* has been calculated, it would be possible to calculate ΔH_m at each value of P_{O_2}.

In the p-region of the phase field

$$\sigma = \mu_{\oplus} p\, e = \text{const}\, P_{O_2}^{\frac{1}{2(m+1)}} \exp\left\{-\frac{\Delta H^\circ_f + (m+1)\,\Delta H^\ddagger_{\oplus}}{(m+1)RT}\right\}$$

and

$$\left[\frac{\partial \ln \sigma}{\partial\, 1/RT}\right]_{P_{O_2}} = -\left(\frac{\Delta H^\circ_f}{m+1} + \Delta H^\ddagger_{\oplus}\right) \quad [23]$$

These data are available from Eror (1, 16) and are reproduced in Table VII. At 7×10^{-10} atm $[\Delta H^\circ_f/(m+1)]$ is -6 kcal/mole, and from Lacombe's data at 10^{-10} atm Q^* is 19 kcal/mole. Therefore, at 7×10^{-10} atm, ΔH_m is 25 kcal/mole. In the n-region of the phase field

$$\sigma = ne\mu_{\ominus} = [n^2_{io}/p]\, e\mu_{\ominus} \exp(-E_g/RT)$$
$$= \text{const}\, P_{O_2}^{-1/2(m+1)} \exp\left\{\left[\Delta H^\circ_f - (m+1)\left(E_g + \Delta H^\ddagger_{\ominus}\right)\right]\Big/(m+1)RT\right\} \quad [24]$$

where ΔH°_f is the enthalpy of formation of a doubly ionized cation vacancy, E_g is the intrinsic energy gap

Table VII. Sum of the activation energies for defect formation and electrical conduction for MnO_{1+x} in the 800°-1200°C temperature range (1)

$\frac{\Delta H^\circ_f}{m+1} - E_g - \Delta H^\ddagger_{\ominus}$ (kcal/mole)	P_{O_2} atm	$\frac{\Delta H^\circ_f}{m+1} + \Delta H^\ddagger_{\oplus}$ (kcal/mole)	P_{O_2} atm	$\frac{\Delta H^\circ_f}{m+1}$ (kcal/mole)	$\Delta H^\ddagger_{\oplus}$ (kcal/mole)
-53.7 ± 1.1*	10^{-17}	7.0 ± 0.3**	10^{-9}		
-52.4 ± 1.3	10^{-18}	7.0 ± 0.3	7×10^{-10}	-5.9 ± 0.6	12.9 ± 0.9
-51.7 ± 0.8	10^{-19}	8.0 ± 0.4	10^{-11}		
		8.0 ± 0.7	2.5×10^{-13}		

* 95% confidence level.
** Probable error.
‡ Because only one datum point of Q^* at a given P_{O_2} was available, it was not possible to assign confidence limits to these energy values.

(4), and $\Delta H^{\ddagger}_{\ominus}$ is the enthalpy of motion of an electron. Then

$$\left[\frac{\partial \ln \sigma}{\partial\, 1/RT}\right]_{P_{O_2}} = + \left(\Delta H^{\circ}_f/(m+1) - E_g - \Delta H^{\ddagger}_{\ominus}\right) \quad [25]$$

and from Hed and Tannhauser (4), $E_g + \Delta H^{\ddagger}_{\ominus} = 2.49$ eV or 57.4 kcal/mole. From the data of Eror we have at 10^{-19} atm O_2, $\left(\Delta H^{\circ}_f/(m+1) - E_g - \Delta H^{\ddagger}_{\ominus}\right) = -51.7 \pm 0.8$ kcal/mole. Combining the data one calculates $\Delta H^{\circ}_f/(m+1) = 5$ kcal/mole. At 10^{-20} atm O_2 $Q^* = 26$ kcal/mole and ΔH_m is then calculated to be 21 kcal/mole at approximately 10^{-20} atm O_2. Within experimental error ΔH_m is 22.2 kcal/mole and is shown to be a representation of the same diffusion process in both regions A and B. Also it is evident that the temperature dependence of the conductivity is dominated by the term E_g in the n-regions of regions A. In regions B and C, σ is almost independent of temperature. The above calculations probably yield only approximate agreement owing to the large errors in each energy term. Nevertheless, the magnitude of the energy terms is reasonable. A similar calculation assuming diffusion via interstitial jumps in the n-region yields clearly unreasonable values for the energy terms as can be seen in what follows. If the predominant lattice defects are interstitials at low oxygen pressures, then a plot of log conductivity *vs.* reciprocal temperature at constant oxygen pressure yields a slope whose value gives $\left[\Delta H^{\circ}_f/(m+1) + \Delta H^{\ddagger}_{\ominus}\right] = +51.7 \pm 0.8$ kcal/mole at 10^{-19} atm where $\Delta H^{\ddagger}_{\ominus}$ denotes the migration enthalpy of electrons and ΔH°_f denotes the enthalpy for the ex-solution of oxygen (formation of interstitials) according to Eq. [15]. Under this assumption, combining the value, $Q^* = [\Delta H^{\circ}_f/(m+1) + \Delta H_m] = 26$ kcal/mole, and $\left[\Delta H^{\circ}_f/(m+1) + \Delta H^{\ddagger}_{\ominus}\right] = 51.7$ kcal/mole yields $\left[\Delta H_m - \Delta H^{\ddagger}_{\ominus}\right] = -26$ kcal/mole or $\Delta H_m = -26 + \Delta H^{\ddagger}_{\ominus}$ where ΔH_m denotes the migration enthalpy of interstitial cations for the purposes of this calculation. A reasonable value of ΔH_m is ≈ 35 kcal as it should be larger than the similar energy term for the enthalpy of motion via vacancies. If so, the enthalpy of migration for electrons would amount to ≈ 61 kcal/mole which is clearly unreasonable. Again the evidence points to cation vacancies as the predominant lattice defect in MnO.

The temperature dependence of the electrical conductivity at constant P_{O_2} does not provide data for a straightforward calculation of $\Delta H^{\circ}_f/(m+1)$ in the intrinsic region. Thermogravimetric data would provide values of $\Delta H^{\circ}_f/(m+1)$ in the intrinsic region, but these data are not available. Other data are not available then for a consistency check of the temperature dependence of Lacombe's diffusion data in the intrinsic region. However, the inflection points in the diffusivity isotherms are not consistent with a cation vacancy model.

If the majority lattice defect in region A were a cation vacancy, via Eq. [1] the oxygen pressure dependence of the cation diffusivity would be $P_{O_2}{}^{+1/2(m+1)}$. There would be no minimum or inflection point in the log D_{Mn^T} — log P_{O_2} data. The diffusion data of the present study are thus consistent with the model wherein cation vacancies are the predominant lattice defect in MnO.

Summary

The data, log D_{Mm^T} *vs.* log P_{O_2} at 1032°C, of this study are consistent with the cation vacancy model proposed by Hed and Tannhauser (4).

In region C there is agreement between conductivity and thermogravimetric analysis. In region B all studies of conductivity, thermogravimetry, oxidation, and radiotracer diffusion yield an oxygen pressure dependence of approximately +1/6. The predominant defect in region C is a singly ionized cation vacancy, and in region B the predominant defect is a doubly ionized cation vacancy. In region A the oxygen pressure dependence of the conductivity is −1/6, there is no measurable weight change, and the oxygen pressure dependence of the cation diffusivity is +1/6. The computed oxygen pressure dependence of the electron hole concentration is +1/4 in region C and +1/6 in regions A and B, with no inflection point at the region A-region B boundary. Further, the oxygen pressure dependence of the cation diffusivity is +1/5.4 throughout regions A and B, and the activation energy for motion, ΔH_m, is the same in both regions. Therefore, we conclude that throughout the high temperature region of the MnO_{1+x} phase field, MnO_{1+x} is oxygen excess with cation vacancies, including region A. Further arguments supporting this conclusion are presented by F. A. Kröger (18) who showed that the thermodynamically stable forms of MnO, FeO, CoO, and NiO are all oxygen excess.

Acknowledgment

This work was supported by the Advanced Research Projects Agency through a grant from the Materials Research Center of Northwestern University. It is part of the Ph.D. thesis of J. B. Price, Northwestern University, 1968.

Manuscript submitted April 2, 1969; revised manuscript received Oct. 10, 1969. This was paper 530 presented at the Montreal Meeting of the Society, Oct. 6-11, 1968.

Any discussion of this paper will appear in a Discussion Section to be published in the December 1970 JOURNAL.

REFERENCES

1. N. G. Eror, Ph.D. Thesis, Northwestern University, 1965.
2. J. P. Bocquet, M. Kawahara, and P. Lacombe, *Compt. Rend.*, **265**, 1318 (1967).
3. A. Duquesnoy and F. Marion, *ibid.*, **256**, 2862 (1963).
4. A. Z. Hed and D. S. Tannhauser, *J. Chem. Phys.*, **47**, 2090 (1967).
5. C. B. Alcock and S. Zador, *Electrochim. Acta*, **12**, 673 (1967).
6. D. Q. Kim, Y. Wilbert, and F. Marion, *Compt. Rend.*, **262C**, 756 (1966).
7. A. Muan and W. C. Hahn, Jr., *J. Phys. Chem.*, **63**, 1826 (1959).
8. K. Schwerdtfeger and A. Muan, *Trans. Am. Inst. Mining, Met. Petrol. Engrs.*, **239**, 1114 (1967).
9. K. Fueki and J. B. Wagner, Jr., *This Journal*, **112**, 384 (1965).
10. J. H. Becker and H. P. R. Frederikse, *J. Appl. Phys.*, Suppl. 33, 447 (1962).
11. M. Gvishi, N. M. Tallan, and D. S. Tannhauser, *Solid State Commun.*, **6**, 135 (1968).
12. C. Leymonie, "Radioactive Tracers in Physical Metallurgy," John Wiley & Sons, New York (1963).
13. M. S. Seltzer, Private communication.
14. J. B. Price and J. B. Wagner, Jr., *Z. Physik. Chem. N. F.*, **49**, 257 (1966).
15. K. Zanio, Ph.D. Thesis, Northwestern University (1966).
16. N. Eror and J. B. Wagner, Jr., Elec. Div. Electrochem. Soc. Extended Abs. No. 28-137, Spring Meeting, 1965.
17. "Handbook of Chemistry and Physics," 47th Edition, The Chemical Rubber Publishing Co., Cleveland.
18. F. A. Kröger, *J. Phys. Chem. Solids*, **29**, 1889 (1968).

The Equilibrium and Free Surface Sublimation Pressures of Oriented Single Crystals of Bismuth Telluride

Iraj Y. Kashkooli and Zuhair A. Munir

Department of Materials Science, School of Engineering, San Jose State College, San Jose, California

ABSTRACT

The equilibrium and free surface sublimation pressures of bismuth telluride were determined by the torsion-effusion and torsion-Langmuir techniques, respectively. Based on a least-square fit, the expression for the equilibrium pressure in the temperature range of 722°-828°K was found to be: $\log P$ (atm) $= (7.579 \pm 0.373) - (1.020 \pm 0.029)\ 10^4/T$, where T is the absolute temperature and the given uncertainties are the standard deviations. A similar treatment of the results of free surface pressure over basal plane oriented single crystals gave the following expression for the apparent total pressure in the temperature range of 741°-793°K: $\log P$ (atm) $= (10.312 \pm 0.693) - (1.280 \pm 0.053)\ 10^4/T$. Assuming the sublimation reaction Bi_2Te_3 (S) = 2 BiTe (g) + ½ Te_2 (g), average third-law enthalpies and activation enthalpies of sublimation at 298°K were found to be 127.4 ± 1.2 and 133.1 ± 1.8 kcal/mole, respectively. Calculated values of the sublimation coefficient varied from 0.14 at 722°K to 0.39 at 828°K.

Probably because of its thermoelectric properties, the telluride of bismuth, Bi_2Te_3, has been the object of considerably more thermodynamic investigations than the corresponding compounds of other group V elements (1-3). However, until the recent studies of Gorbov and Krestovnikov (4), and Boncheva-Mladenova *et al.* (5) no vapor pressure measurements had been reported on this compound.

Based on the assumption that the sublimation of bismuth telluride is according to

$$Bi_2Te_3(S) = Bi(g) + BiTe(g) + Te_2(g) \qquad [1]$$

Gorbov and Krestovnikov (4) calculated the sublimation pressures from weight loss determinations. In an added note, however, these authors suggested that better agreement between calculated and measured thermodynamic functions can be achieved if the sublimation reaction of bismuth telluride is written as follows

$$Bi_2Te_3(S) = 2\,BiTe(g) + 1/2\,Te_2(g) \qquad [2]$$

Assuming an identical reaction, Boncheva-Mladenova *et al.* (5) reported sublimation pressures of polycrystalline bismuth telluride employing the Knudsen and Langmuir techniques.

Mass spectrometric studies by Porter and Spencer (6) showed the presence of the gaseous species BiTe, Bi, and Te_2 over liquid bismuth telluride. However, lack of similar mass spectrometric information regarding solid bismuth telluride renders sublimation pressure values calculated from weight loss data subject to considerable doubt. In this paper we report results of sublimation studies on bismuth telluride using the weight-loss-independent torsion-effusion and torsion-Langmuir methods for the experimental conditions of equilibrium and free surface sublimations, respectively.

Experimental

The torsion-effusion and torsion-Langmuir methods have been discussed in several publications (7-9), and the apparatus used in this study has been described in a recent paper (10).

The torsion cells used in this investigation, which were made of National Carbon ZT101 grade graphite, have similar geometric configurations to those described earlier (8, 9).

Single crystalline bismuth telluride used in this study had been previously prepared from 6-nine pure tellurium and bismuth by the Bridgman technique. X-ray examinations of an ingot prepared by this technique showed it to be a single crystal with an easy cleavage basal plane parallel to its major axis. To be used in the torsion-Langmuir experiments, wafers of bismuth telluride, about 1.5 mm thick, were cleaved off the ingot following a liquid-nitrogen quench. When x-rayed these wafers were found to be single crystalline with facial orientations corresponding to the basal plane [Bi_2Te_3 has the tetradymite type hexagonal lattice (11)].

In agreement with others (5) the sublimation of bismuth telluride was found to be congruent. X-ray examinations of samples which had previously been heated in vacuum at temperatures and for periods of time corresponding to no less than 30% weight loss gave patterns identical to those obtained from unheated samples. Furthermore, metallographic examinations of the heated samples proved the absence of any second phase which may have not been detected by the x-ray analyses, *e.g.*, amorphous tellurium.

Temperatures were measured by means of a calibrated Pt-Pt/10% Rh thermocouple imbedded inside a dummy cell situated about 2 cm below the torsion cell. Determination of the temperature profile of the heating element indicated that the torsion and dummy cells are well within the constant temperature portion of the profile. Calibration of the thermocouple was accomplished by redetermining the freezing point of pure samples of aluminum, silver, and copper which were placed inside the dummy cell.

Ambient pressures, as measured in the vicinity of the heating element, were maintained at 2×10^{-5} Torr or less throughout this study.

As a check on the reliability of pressure results obtained using the present apparatus, the vapor pressure of silver was redetermined in the range of 10^{-3} to 10^{-6} atm. From over 30 vapor pressure determinations the third-law heat of vaporization of silver was calculated to be 68.3 ± 0.4 kcal/mole which is in good agreement with the value reported by Hultgren *et al.* (12) of 68.1 ± 0.3 kcal/mole.

Results

Equilibrium sublimation.—Figure 1 shows the results of equilibrium pressure determinations, calculated from torsion deflections in the temperature range of 722°-828°K, and plotted as $\log P$ vs. $1/T$, where P is the total sublimation pressure of bismuth telluride

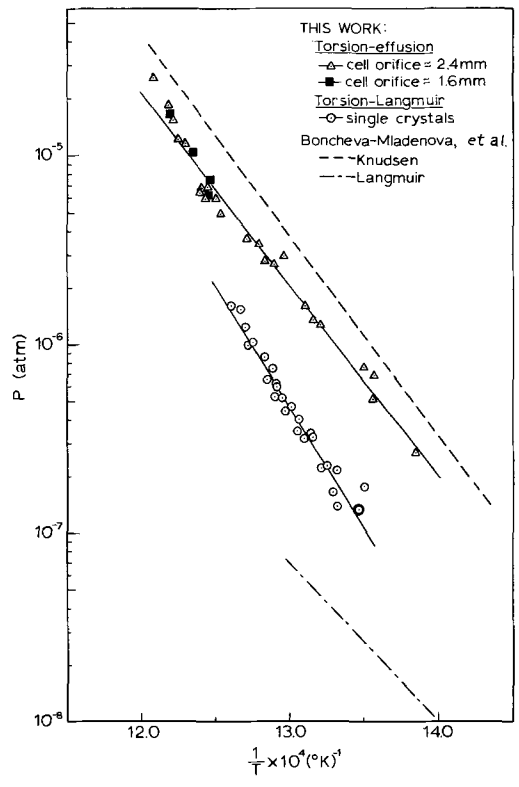

Fig. 1. Sublimation pressure of bismuth telluride

and T is the absolute temperature. Employing a least-square method of analysis these results can be expressed as

$$\log P\ (\text{atm}) = (7.579 \pm 0.373) - (1.020 \pm 0.029)\ 10^4/T \qquad [3]$$

where the quoted uncertainties are the standard deviations. If the reaction given by Eq. [2] is assumed to be the one describing the sublimation process of bismuth telluride, then the expression for the equilibrium constant becomes

$$K = (P_{BiTe})^2 \cdot (P_{Te_2})^{1/2} \qquad [4]$$

where P_{BiTe} and P_{Te_2} are the partial pressures of the gaseous species BiTe and Te_2, respectively. From kinetic theory considerations the relationship between these partial pressures is

$$\frac{P_{BiTe}}{P_{Te_2}} \frac{2}{1/2} \left[\frac{(\text{m.w.})Te_2}{(\text{m.w.})BiTe}\right]^{1/2} \qquad [5]$$

where (m.w.)Te_2 and (m.w.)BiTe refer to the molecular weights of the two species. Finally, since the total pressure is the sum of these partial pressures, *i.e.*,

$$P_T = P_{BiTe} + P_{Te_2} \qquad [6]$$

an expression (similar to that of Eq. [2]) relating the equilibrium constant, K, with temperature can be derived. From such an expression second-law heat and entropy of sublimation were calculated and corrected to 298°K using reported thermodynamic functions (13). These calculations gave values of $\Delta H°_{298}$ and $\Delta S°_{298}$ of 121.6 ± 5.0 kcal/mole and 93.5 ± 6.3 eu, respectively.

Third-law calculations, based on Eq. [2] and using reported free energy functions for Te_2(g) (14), BiTe(g) and Bi_2Te_3(S) (4, 13), are shown in Table I. Table I also shows the results of mean-free-path to orifice diameter calculations, which were based on a molecular diameter of BiTe(g) of 3.48Å, and the assumption of ideal gas law. The average value of the third-law $\Delta H°_{298}$ of sublimation was found to be 127.4 ± 1.2 kcal/mole.

Table I. Equilibrium pressures and heats of sublimation of bismuth telluride

T, °K	P, atm	λ/d	$\Delta H°_{298}$, kcal/mole	T, °K	P, atm	λ/d	$\Delta H°_{298}$, kcal/mole
722	2.70×10^{-7}	417	127.4	802	7.53×10^{-6}	11.1	127.4
737	6.87×10^{-7}	167	126.5	803	6.97×10^{-6}	18.0	128.5
737	5.18×10^{-7}	222	127.5	804	6.05×10^{-6}	20.8	128.5
741	7.65×10^{-7}	151	126.7	804	6.36×10^{-6}	13.3	128.3
757	1.29×10^{-6}	91.2	127.3	805	6.70×10^{-6}	18.8	128.3
759	1.36×10^{-6}	86.9	127.4	806	6.53×10^{-6}	19.3	128.5
763	1.61×10^{-6}	73.9	127.4	810	1.04×10^{-5}	8.2	127.2
771	2.98×10^{-6}	40.3	126.3	813	1.16×10^{-5}	10.9	127.2
775	2.70×10^{-6}	44.8	127.3	816	1.22×10^{-5}	10.4	127.5
779	2.81×10^{-6}	43.2	127.8	818	1.55×10^{-5}	8.2	126.8
781	3.46×10^{-6}	35.1	127.3	820	1.66×10^{-5}	5.2	126.8
786	3.65×10^{-6}	33.6	127.8	821	1.85×10^{-5}	6.9	126.5
798	4.98×10^{-6}	25.0	128.4	828	2.58×10^{-5}	5.0	126.1
799	6.03×10^{-6}	20.7	127.8				

Free-surface sublimation.—The free surface sublimation pressures of oriented single crystals of bismuth telluride, which were obtained from torsion-Langmuir deflection measurements, are shown in Fig. 1. Least-square analysis of these results obtained in the temperature range of 741°-793°K gave the following expression for the apparent total pressure over basal-plane oriented bismuth telluride crystals

$$\log P\ (\text{atm}) = (10.312 \pm 0.693) - (1.280 \pm 0.053)\ 10^4/T \qquad [7]$$

where T is the absolute temperature and the given uncertainties are the standard deviations. Again using the procedure outlined by Eq. [4] through [6], second-law activation heat and entropy values were calculated with the resulting values for $\Delta H^{\pm}_{298}$ and $\Delta S^{\pm}_{298}$ of 151.3 ± 6.4 kcal/mole and 124.6 ± 7.5 eu, respectively.

Calculations of the third-law heat of sublimation, which were based on reported free-energy functions (13, 14), are shown in Table II. An average $\Delta H^{\pm}_{298}$ of 133.1 ± 1.8 kcal/mole was obtained from these calculations. From results obtained in this study the sublimation coefficient, defined as the ratio of the free-surface-to-equilibrium pressures, was found to vary from 0.14 to 0.39 over the corresponding temperature limits of 722°-828°K.

Discussion of Results

The assumption of equilibrium conditions inside the torsion-effusion cells was based on examinations of theoretical factors governing effusion cells (15, 16). Use of two cells with orifice areas differing by a factor of about two showed no dependence of measured pressures on the orifice size. Moreover, the calculated third-law heats of sublimation showed no deviation with a decrease in the λ/d ratio reported in Table I. Thus in accordance with the cited theoretical considerations, the reported torsion-effusion pressures are the equilibrium sublimation pressures of bismuth telluride.

The reasonably good agreement (within 5%) between the calculated third-law and second-law equi-

Table II. Free surface pressures and activation heats of sublimation of bismuth telluride single crystals

T, °K	P, atm	$\Delta H^{\pm}_{298}$, kcal/mole	T, °K	P, atm	$\Delta H^{\pm}_{298}$, kcal/mole
741	1.77×10^{-7}	132.1	770	4.49×10^{-7}	133.4
745	1.34×10^{-7}	133.8	772	5.24×10^{-7}	133.1
745	1.33×10^{-7}	133.8	774	5.98×10^{-7}	132.9
750	1.39×10^{-7}	134.5	774	6.18×10^{-7}	132.8
750	2.17×10^{-7}	132.9	775	5.31×10^{-7}	133.6
753	1.64×10^{-7}	134.4	776	7.50×10^{-7}	132.4
755	2.30×10^{-7}	133.5	778	6.60×10^{-7}	133.2
757	2.23×10^{-7}	133.9	779	8.60×10^{-7}	132.3
760	3.25×10^{-7}	133.0	784	1.03×10^{-6}	132.4
761	3.37×10^{-7}	133.0	786	1.00×10^{-6}	132.9
764	3.20×10^{-7}	133.7	788	1.25×10^{-6}	132.3
765	4.09×10^{-7}	132.9	789	1.53×10^{-6}	131.7
766	3.51×10^{-7}	133.7	793	1.61×10^{-6}	132.1
768	4.73×10^{-7}	132.9			

librium heats of sublimation suggests that the sublimation mechanism of Bi_2Te_3 is in accordance with Eq. [2]. Agreement between published pressure results (4, 5), which were calculated from weight loss data assuming the reaction of Eq. [2], and those measured directly in this work can be taken as additional support for the plausibility of the assumed mechanism. Reported $\Delta H°_{298}$ values (4, 5) are within 2% of the value calculated in this paper.

On the other hand, the relatively large discrepancy ($\sim$ 14%) between second-law and third-law activation enthalpies may be interpreted as suggesting a mode of sublimation under free-surface conditions which is somewhat different from that under equilibrium. That it is possible to have differences in the mode of sublimation under free surface and equilibrium conditions, has been shown in at least one investigation (17). The existence of a layer structure in Bi_2Te_3 (18) (Te — Te — Bi — Te — Bi — Te — Te — Bi .....) may possibly contribute to a dual nature in the sublimation modes of this compound.

In addition to the ease with which cleavage takes place along basal planes of Bi_2Te_3, choice of this orientation in the free surface sublimation study was based on previous experience on other hexagonal systems in which the sublimation rates of basal planes were found to be lower than those of prismatic planes (19) and thus offer a greater degree of departure from equilibrium. Rates of sublimation from these basally oriented crystalline faces, which were constant at any given temperature, thus represent a state of "apparent" or pseudo-equilibrium. Such low rates of sublimation may result from the formation or desorption energetics of the two gaseous species leaving the surface.

Acknowledgments

The authors are grateful for the technical assistance of Walter Mounts, Arthur Cooper, and Lou Schallberger, and for the assistance of Mrs. Sylvia Peaker, Mrs. Phyllis Ashe, and Mr. Peter Enright in the preparation of the manuscript.

Manuscript submitted Aug. 11, 1969; revised manuscript received *ca.* Oct. 7, 1969.

Any discussion of this paper will appear in a Discussion Section to be published in the December 1970 JOURNAL.

REFERENCES

1. A. F. Ioffe, "Semiconductor Thermoelements" [in Russian], Izd. AN SSR, Moscow (1960).
2. H. J. Goldsmid, "Applications of Thermoelectricity," Methuen, London (1960).
3. J. H. Westbrook, Editor, "Intermetallic Compounds," John Wiley & Sons, Inc., New York (1967).
4. S. I. Gorbov and A. N. Krestovnikov, *Zh. Neorg. Mater.*, **2**, 1702 (1966).
5. (a) Z. Boncheva-Mladenova, A. S. Pashinkin, and A. V. Novoselova, *ibid.*, **2**, 1542 (1966); (b) Z. Boncheva-Mladenova, A. S. Pashinkin, and A. V. Novoselova, *ibid.*, **4**, 291 (1968).
6. R. F. Porter and C. W. Spencer, *J. Chem. Phys.*, **32**, 943 (1960).
7. R. D. Freeman in "The Characterization of High Temperature Vapors," J. L. Margrave, Editor, Ch. 7, John Wiley & Sons, Inc., New York (1967).
8. W. T. Lee and Z. A. Munir, *This Journal*, **114**, 1236 (1967).
9. R. C. Blair and Z. A. Munir, *J. Phys. Chem.*, **72**, 2434 (1968).
10. Z. A. Munir and M. J. Mitchell, *J. High Temp. Sci.*, in press (1969).
11. P. W. Lange, *Naturwiss.*, **27**, 133 (1939).
12. R. Hultgren, R. L. Orr, P. D. Anderson, and K. K. Kelley, "Selected Values of Thermodynamic Properties of Metals and Alloys," John Wiley & Sons, Inc., New York (1963).
13. S. I. Gorbov and A. N. Krestovnikov, *Russ. J. Phys. Chem.*, **40**, 505 (1966).
14. R. D. Stull and G. Sinke, "Thermodynamic Properties of the Elements," Am. Chem. Soc., Washington (1956).
15. K. Motzfeld, *J. Phys. Chem.*, **59**, 139 (1955).
16. K. D. Carlson, P. W. Gilles, and R. J. Thorn, *J. Chem. Phys.*, **38**, 2064 (1963).
17. J. Berkowitz and W. A. Chupka, *ibid.*, **45**, 4289 (1966).
18. Ch. 20 in ref. (3).
19. Z. A. Munir, *J. High Temp. Sci.*, in press (1969).

Selected Area Electron Diffraction Study of α-Fe_2O_3 Platelet Growths Twinned on Twist Grain Boundaries

R. L. Tallman* and E. A. Gulbransen*

Westinghouse Research Laboratories, Pittsburgh, Pennsylvania

ABSTRACT

Broad, rounded draperylike platelet growths result from the oxidation of unannealed iron in dry oxygen at 400°C. Their skewed sandwich structure is a new type of twinning in which the composition plane is a twist grain boundary. This twin interface and the platelet faces are on the basal plane. A 13.174° twist angle is common; 21.787°, 26.66°, and 35.22° were also found. Such a rounded platelet would be expected to result from the proposed internal diffusion mechanism.

Three distinct families of α-Fe_2O_3 growths have been observed in the gaseous oxidation of relatively pure irons (1, 2). These are whiskers, bladelike platelets, and broad, rounded platelets. Whiskers have been found to show the axial twist characteristic of an axial screw dislocation (3, 4). The bladelike platelets are contact twins with the composition plane parallel to the blade face and to the mirror plane relating the two orientations (4, 5). The blade face is on the rhombohedral plane, (010) of the primitive structural rhombohedron.

This paper presents the structure, or structures, of the broad, rounded platelets together with all the selected area electron diffraction patterns important to the determination of these structures. Comments on some features of the probable growth mechanism and their broader significance are also provided.

* Electrochemical Society Active Member.

Experimental

The broad, rounded platelets examined in this work were chosen from many produced in oxidation experiments which were part of some earlier studies (1, 2). The iron wire, 0.007 in. thick, obtained from the National Bureau of Standards, contained <200 ppm metallic impurities and about 140 ppm carbon. The unannealed wire was washed, degreased, and rinsed with ethyl alcohol. Then the wire was oxidized 48 hr at 400°C in an atmosphere of oxygen which had been dried by a trap cooled by solid carbon dioxide in acetone. Broad, rounded platelets have also been observed in oxidations in dry oxygen at up to 500°C of Battelle iron wires of higher purity.

Conditions determining growth of whiskers, bladelike platelets, and broad, rounded platelets.—The broad, rounded platelet growths predominated among the growths on the unannealed wires. Areas of platelets and areas of whiskers developed on annealed wires; whisker growth seems likely to be the growth to be expected for annealed wires under the least complex conditions. The broad, rounded platelet growth seems to be associated with some plastic deformation of the iron, but this may involve an undetermined impurity effect. The 10 μm breadths of the platelets may be permitted by the preferred orientation (texture) of the grains always found in the surface of fine iron wires.

The whisker and broad, rounded platelet growths are replaced by bladelike platelet growths (1, 2, 5) when the atmosphere is water vapor (with at least some oxygen). The absence of bladelike platelets among the whiskers and broad, rounded platelets indicates that the water vapor concentration is less than some unknown limit. Experiment (2) has shown this limit to be smaller, itself, than 3%.

Selected Area Electron Diffraction Study of Broad, Rounded Platelet Structures

Earlier work (1, 2) has established that the broad, rounded platelets are α-Fe_2O_3. This was accomplished with a simple electron diffraction camera. Patterns from a standard were taken alternatively with patterns from 0.007 in. iron wires densely covered with broad, rounded platelets of α-Fe_2O_3. The d-spacings measured were all α-Fe_2O_3 d-spacings, and the intensities compared satisfactorily with x-ray powder diffraction intensities. The patterns also compare satisfactorily with electron diffraction patterns of fine α-Fe_2O_3 powder. The spot shapes and intensity distributions of such platelet patterns are consistent with the shape and preferred orientation of the platelets. The large, thin total cross section of these growths results in an extreme predominance of their diffraction in such patterns.

The platelets themselves having been adequately proved to be α-Fe_2O_3, selected area diffraction patterns of large numbers of platelets were measured to determine the instrument constant for selected area diffraction. The satisfactory indexing of such patterns further confirms that the broad, rounded platelets are α-Fe_2O_3.

In this paper a set of three indices will refer to the face-centered rhombohedral (morphological) unit cell; a set of four, to the structural (triple) hexagonal unit cell. Information concerning these unit cells and the d-spacings and transformations of indices can be found in the associated previous publications (3-5).

General description of the platelets.—Figure 1 shows a broad, rounded platelet with a typical S-curve. Stereoscopic images have also shown platelet S-curvature. A dark field image showing three approximately parallel bend contour lines has been obtained from another platelet. Since only one diffracted beam passed the objective aperture, there were at least two points of inflection in the cross section normal to the bend

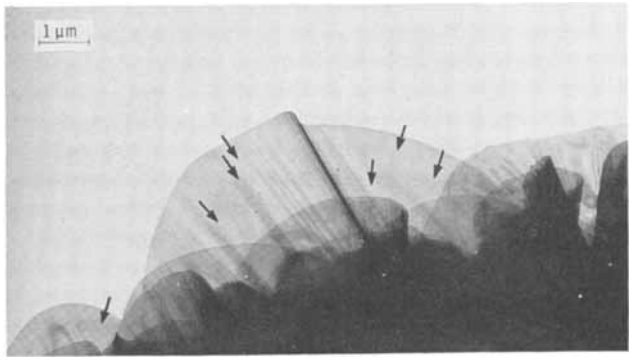

Fig. 1. Broad, rounded platelets of α-Fe_2O_3 on a 175 μm diameter iron wire after 48 hr in dry O_2 at 400°C. Each arrow indicates a step in thickness tracing the edge at a stage in the platelet growth.

contours. This draperylike curvature is common, but some broad, rounded platelets are nearly flat.

Figure 2 is an artist's attempt to show the curved surfaces and twinned structure of the broad, rounded platelets. The arrows indicating the [$\bar{1}$10] directions of the two crystals show the relative twist about [111] which relates the two crystal orientations. The approximate [$\bar{1}$10] growth direction and bend axis is common.

Heights of the broad, rounded platelets range to 4 μm and breadths to 10 μm. Both in thickness and in thickness uniformity, the broad, rounded platelets appear to be similar to the bladelike platelets (1, 2, 4, 5). Thicknesses are estimated to be commonly in the range 150-300Å.

The four structures determined suggest that all broad, rounded platelets are contact twins with one twin interface. The twin interface, or composition plane, is a twist grain boundary on the basal plane, parallel to the platelet faces. This could be called a skewed sandwich structure.

The four structures found are different in that their twist angles are different. Other differences between the platelets, such as differences in shape, thickness, bend contours, etc., might be expected to accompany the difference in structure. However, these differences have not been correlated with the twist angle

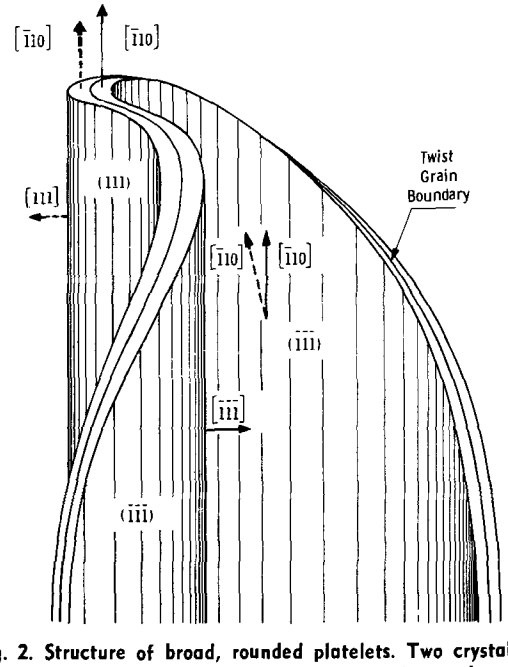

Fig. 2. Structure of broad, rounded platelets. Two crystal orientations indicated by rhombohedral indices; thickness shown exaggerated by a factor of five or more.

variation, primarily because such features have not been studied sufficiently.

Special twist angles.—Two of the twist angles have special significance in that they rotate lattice point rows in the basal plane into coincidence. This results in a repeating pattern in the boundary structure with a small two-dimensional hexagonal unit cell. If the twist angle were small, one could imagine the boundary to consist of a hexagonal array of islands of coherency separated by axial screw dislocations. This is the common picture of small angle twist grain boundaries (6, 7). Then the special twist angles would introduce long-range translational symmetry into such an array. The fact that the special twist angles are found suggests that this concept has some validity unexpected for such large twist angles. That is, the interface structure has some special stability (reduced energy).

Common twist angle.—Figures 3 and 4 indicate the indexing of the diffraction patterns obtained from two platelets which show the most common twist angle. That angle is calculated to be 13.174° = 2 arc csc$\sqrt{76}$. The calculation is based on the coincidence of the double diffraction patterns about the $2\bar{2}0$ spots and the incident beam. The planes $(32\bar{5}0)$ and $(23\bar{5}0)$ of the two crystals, as well as the directions $[32\bar{5}0]$ and $[23\bar{5}0]$, are rotated into coincidence by this twist angle.

Each drawing in Fig. 3 and 4 shows the diffraction from one face crystal. In each figure the two hexagonal patterns of circles are related by the twist angle, 13.174°.

The rotation indicated in the diffraction pattern of each face crystal results from the curved nature of the broad, rounded platelets. Both showed bend contours roughly perpendicular to the iron wire surface, and, therefore, along what might be considered the growth directions. This is the most common bending. The bend contours lie parallel to the projection of the axis of the rotation of the bending. For these two platelets the bending seems to be nearly exactly about $[\bar{1}10]$ for the platelet faces whose pattern drawings do not show the indices. (That is why these patterns are more symmetrical than those showing the indices.) That this $[\bar{1}10]$ direction, toward eight o'clock in the drawings, lies parallel to the bend contours is confirmed by the relative rotation of image and diffraction (determined with asbestos fibers).

The growth directions of the broad, rounded platelets are in the region of the $[\bar{1}10]$ directions of the two faces. This $[\bar{1}10]$ direction (face-centered rhombohedral, morphological indices) is also the growth direction of the whiskers and bladelike platelets (3-5).

In both Fig. 3 and 4 the beam is nearly parallel to the threefold axis near one extreme of the bending. This orientation is indicated by the hexagonal patterns of open circles. The patterns differ in that the bending brings (001) parallel to the beam in Fig. 3 and (110) parallel in Fig. 4.

Of nineteen platelets for which the selected area diffraction patterns were available and suitable, thirteen gave patterns indicating the 13.174° twist angle. Other twist angles have been determined for three of the remaining six.

Uncommon twist angle.—Figure 5 indicates the indexing for the one platelet with the special twist angle 21.787° = 2 arc csc$\sqrt{28}$. The angle is that required to rotate $3\bar{3}1$ of the drawing at the right of Fig. 5 into

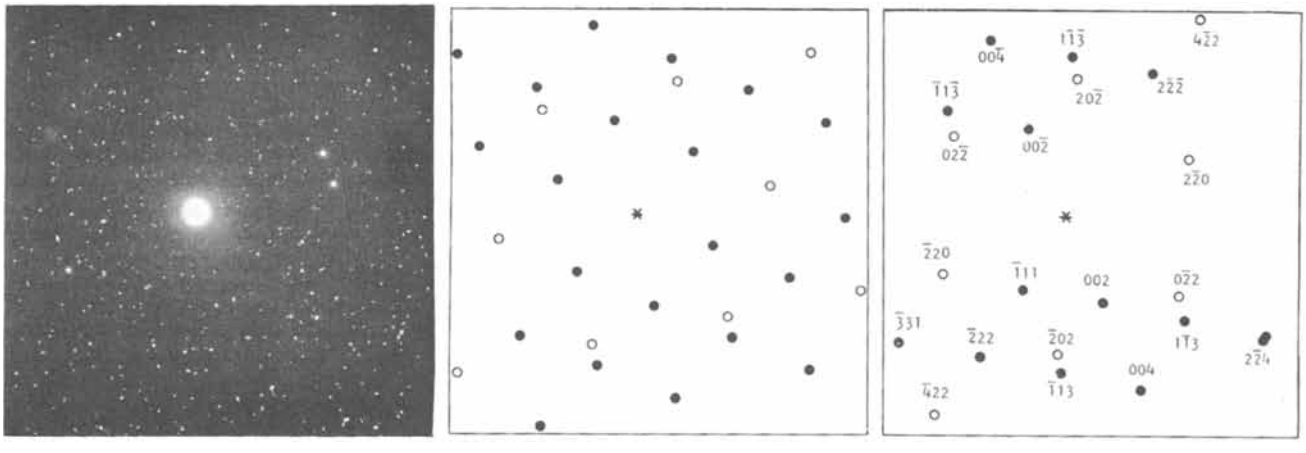

Fig. 3. Broad, rounded platelet, α-Fe_2O_3, twist angle 13.174° = 2 arc csc$\sqrt{76}$. The pattern is the sum of the drawings

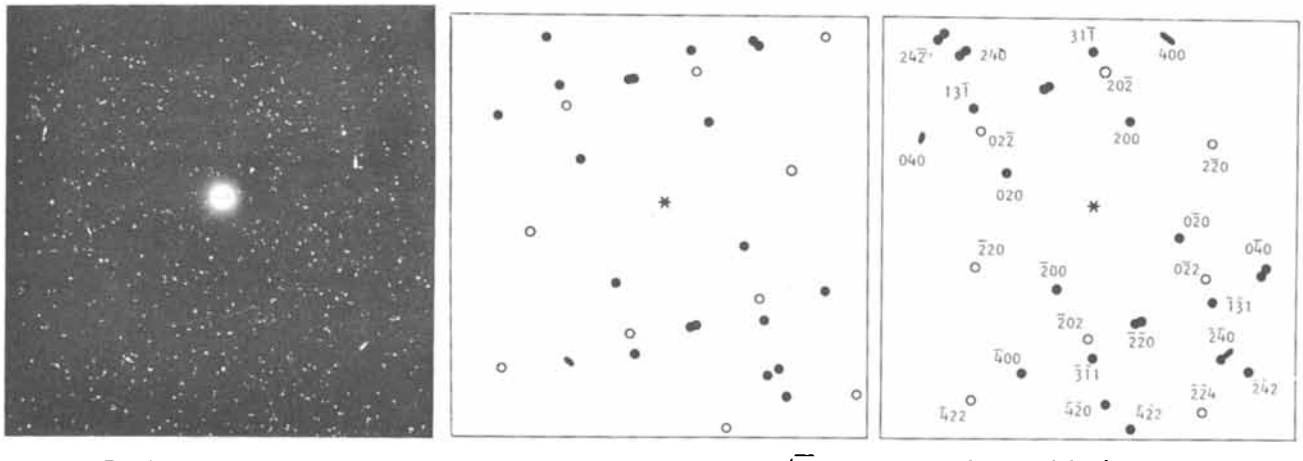

Fig. 4. Broad, rounded platelet, α-Fe_2O_3, twist angle 13.174° = 2 arc csc$\sqrt{76}$. The pattern is the sum of the drawings

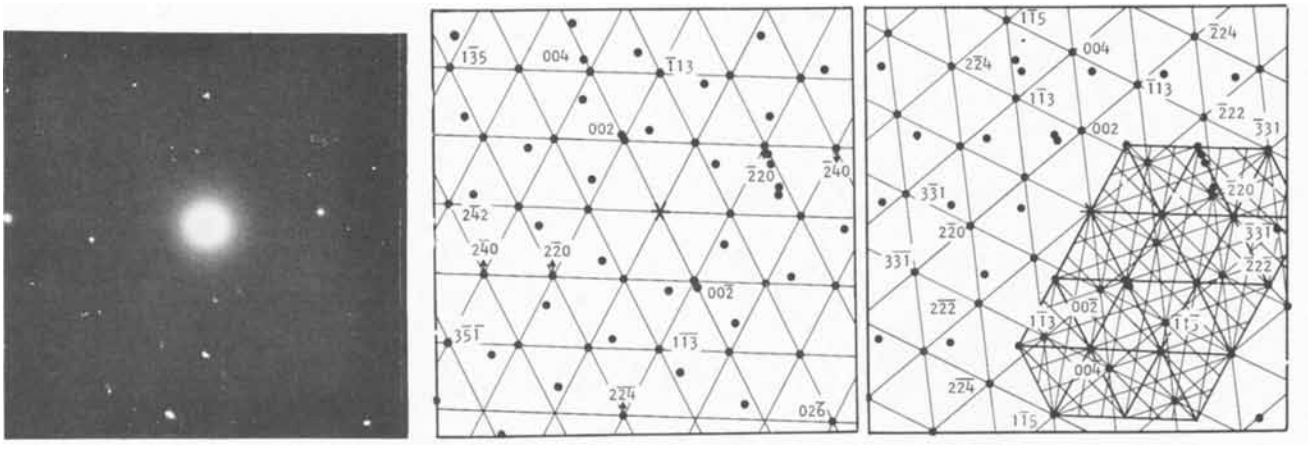

Fig. 5. Broad, rounded platelet, α-Fe_2O_3, twist angle 21.787° = 2 arc csc$\sqrt{28}$

its position in the row of reciprocal lattice points including 2$\bar{4}$0, of the drawing at the left. This rotation brings the direction [21$\bar{3}$0] into coincidence with the direction [12$\bar{3}$0] [and the planes, (21$\bar{3}$0) and (12$\bar{3}$0), into coincidence as well].

A portion of the array of the left drawing is drawn in heavier lines at the lower right of the drawing at the right. In this area the regular array of intersections of the additional finer lines indicates the positions of the spots of the double diffraction pattern, which is too weak to reproduce satisfactorily. As in the case of the 13.174° twist, the pattern of the double diffraction spots is continuous and includes the incident beam spot and the indexed spots for both orientations. The special twist angle results in coincidences among the reflections from the two platelet faces. These are the intersections common to the two arrays.

Not so special twist angles.—Figure 6 represents the indexing of the one diffraction pattern indicating a measured twist angle of 35.22 ± 0.2°. This pattern is the second of three in a series. The specimen was rotated approximately 8° for the second pattern, and approximately 4° more for the third. The rotation was about an axis normal to the beam and to the arrows on the drawing. Arrows pointing to positions at smaller Bragg angles indicate the positions of spots most intense in the first pattern. Arrows pointing to larger Bragg angles indicate spots most intense in the third. The rotation is out of 5 o'clock, into 11 o'clock on the patterns. With this information, the orientation of the platelet is apparent from the effect of the rotation on the spot positions and intensities.

The unindexed weak spots and the changes in spot position with platelet orientation in the beam indicate diffraction that can be described by continuous reciprocal lattice rods normal to the platelet face. The diffraction from bladelike platelets was also characterized by continuous relrods (4, 5).

Figure 7 indicates the indexing of the pattern for the only platelet having a measured 26.66 ± 0.2° twist angle. Some of the double diffraction pattern is shown in the drawings. In these drawings, as in Fig. 5, the same spots are shown in two drawings, each of which shows the indexing for one face of the platelet.

The bending of this platelet has produced streaked reflections. The long streaks indicated by the fine lines of the drawing are observed on the original plates. Such streaks are also describable by continuous relrods.

The arrows from the 131 and 13$\bar{1}$ spots of the left-hand drawing indicate the positions, on the lines of the drawing, of the intersections of the axial rows of reciprocal lattice points containing the 13$\bar{1}$ and $\bar{1}$31 points. The other arrows of the two drawings indicate directions to the positions at the correct Bragg angles for the diffraction indexed at the arrows. The bending of the crystal was such that this diffraction was "bypassed"; furthermore, as a result of this bending, angles in the reciprocal lattice are not faithfully presented by the pattern.

The angles 26.66° and 35.22° do not approximate angles required to rotate to coincidence rows of lattice points sufficiently closely spaced (*i.e.*, along directions with sufficiently small indices) that some special significance is indicated. However, it may be of some significance that 13.174° + 13.174° = 26.348°, and 13.174° + 21.787° = 34.961°. The possibility of two interfaces in these platelets, with twist angles that sum to give the measured twist angles, has not been substantiated

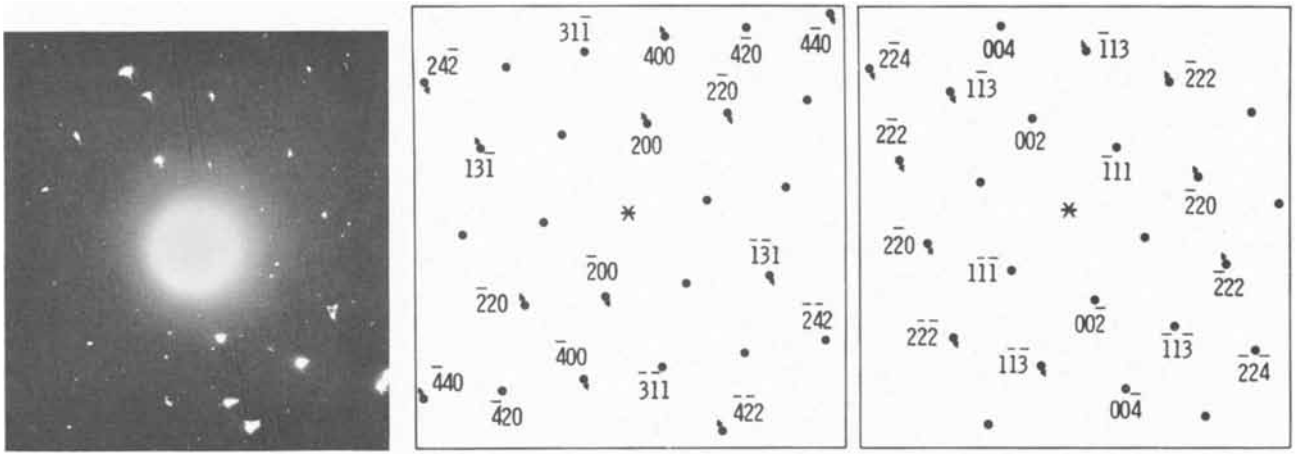

Fig. 6. Broad, rounded platelet, α-Fe_2O_3, twist angle 35.22 ± 0.2°

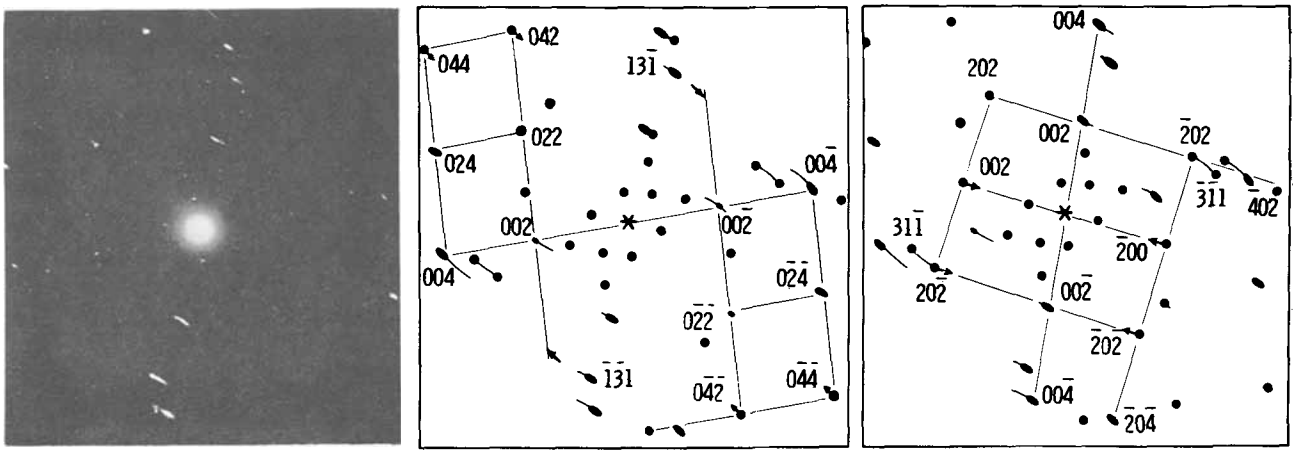

Fig. 7. Broad, rounded platelet, α-Fe_2O_3, twist angle 26.66 ± 0.2°

by the observation of diffraction from a third, intermediate orientation. Furthermore, two twist boundaries, even if relatively stable, one would expect to have more energy than one nondescript twist boundary on a parallel plane.

Curvature and stresses in the platelets.—A dark field image for the four reflections $0\bar{2}2$ and $\bar{1}3\bar{1}$ of Fig. 4, measures 6.7 μm between the bend contours $0\bar{2}2$ and $\bar{1}3\bar{1}$ for the crystal rotated about [2$\bar{2}$0] by the bending. The approximate radius of curvature, 12 μm, is given by 6.7 μm/2sin(ϕ/2), where ϕ = 32.35°, the rotation between the positions for the $0\bar{2}2$ and $\bar{1}3\bar{1}$ reflections. For a 300Å thickness, maximum tensile strain (at the surface) of 1.25 x 10^{-3} results from this curvature. The strain is multiplied by the appropriate stiffness constant (8), c_{11} = 2.42 x 10^{12} dyne cm^{-2}, to calculate the maximum tensile stress, 3.0 x 10^9 dyne cm^{-2}, or 44,000 psi.

Maximum shear stresses of the order of 10^6 dyne cm^{-2} can be estimated to result where such curvatures are involved in draperylike folds. The appropriate shear modulus (8) is c_{44} = 0.85 x 10^{12} dyne cm^{-2}. For some crystalline materials (9, 10), critical shear stresses have been measured to be smaller than the shear modulus by a factor of 10^5. The shear stresses resulting from the bending of the platelets should be sufficient to produce slip on the composition plane, for which the critical shear stress is likely to be less than the estimated 10^7 dyne cm^{-2}. Edge dislocations at the twist boundary should result from this slip. The many images of dislocations in the platelets have not been studied in this work, however, nor have the apparent dislocation loops.

The bend contours of many platelets show the platelet edges less curved, or partially straightened, relative to the base of the platelet. The unrelieved stresses associated with the bent crystals should cause their edges to straighten. The configuration of the growth sites must be curved when the growths are examined after oxidation. Presumably, growth sites are curved initially. However, they may change in curvature during oxidation or cooling. The cracks and discontinuities observed in some platelets may have resulted from stresses occurring after their growth, possibly on cooling. A further consideration is that the curvature of a platelet would vary with a variation in twist angle. The twist angle might change (in time, or with further growth) so as to increase the interface area having a special, low-energy twist angle.

Special defects, Moire fringes, and further contrast effects, possibly resulting from magnetic structure, have not been studied.

General Discussion of the Platelet Structures

Some further general comments can be made about these platelets. The twist angles have all been given as positive, but a distinction could be made as to which face is rotated in the positive sense relative to the other. The two possibilities, which could be indicated by negative and positive values of the same twist angle, are enantiomorphs, or mirror images of one another.

The composition plane very likely has islands of coherency for the 13.174° twist such that the structure is repeated through each island, from one twin through into the other (with the twist distributed over several layers on the basal plane). This most simple structure can be thought of as the result of a rotation on the interface plane of half a single crystal relative to the other half.

However, evidence is not available to prove, for any of the twist angles, that the structure is so simple. Two further possible operations may be necessary. The rotation, most likely on a plane of octahedral positions, may be accompanied by a translation over the interface by some fractional distance. Furthermore, a layer of oxygen ions and a layer of iron ions may be missing at the interface.

That absence of two such layers and only two such layers need be considered can be shown as follows: Number the oxygen layers in the unit cell 1, 3, 5, 7, 9, and 11. Lattice points are at center ($\bar{3}$) on levels 0, 4, and 8 (twelfths of the hexagonal c dimension), in the even-numbered (iron) layers. The lattice translation relates layers 1, 5, and 9. But these are in mirror orientation to 7, 11, and 3 by the operation of the c-glide planes on {11$\bar{2}$0}. Removing layers 2 and 3 (or 3 and 4) puts 1 in contact with 5, and no rotation with translation will bring the ordered structure back. Removing 2, 3, 4, and 5 (or 3, 4, 5, and 6) puts 1 in contact with 7; but 7 is related to 3 by translation, and so the structure obtained can be ordered by a translation in the basal plane. Similar arguments handle the question of iron positions and other possible numbers of missing planes of atoms. The removal of layer 3 is enantiomorphic to the removal of layer 9, however. Consequently, if layers are missing, each twist angle represents four possible enantiomorphic structures.

Moiré patterns and screw dislocation arrays.—The broad, rounded platelets can be expected to give rotational Moiré patterns (6, 7). However, micrographs at sufficiently high resolution have not yet been obtained for the broad, rounded platelets. Such observations of Moiré fringes on twist grain boundaries may be confused with the images of the screw dislocations to be expected where the twist angle α is not too great (11).

The distance H between parallel screw dislocations (the diameter of the hexagon of screw dislocations about an island of coherency) is given by $H = b/2\sin(\alpha/2)$ where b is the magnitude of the Burgers vector of the screw dislocations. Hexagons 21.9 and 13.3Å

across are calculated for the 13.174° and 21.787° twist boundaries, respectively. That some order can exist between such screw dislocations so close together is evidenced by the relative stability of these structures indicated by their existence.

Twist grain boundaries with translational symmetry on planes of threefold symmetry.—Rotations about the threefold axis by angles $\alpha = 2 \text{ arc sin } (h - k)/2\sqrt{h^2 + hk + k^2}$ bring lattice point rows into coincidence. The angles 21.787° and 13.174° bring the point rows $k\bar{h}O$, $2k2\bar{h}O$, $3k3\bar{h}O$, . . . into coincidence for hk values 21 and 32, respectively, for which $h - k = 1$.

Discussion of growth mechanisms.—Tip and edge growth.—Observations by Takagi (12) indicate that whiskers and bladelike platelets grow from the tip. He observed their further growth from the "stumps" of broken growths and also some effects of temperature changes. The further growth of broken broad, rounded platelets has not been observed.

However, some broad, rounded platelets are marked by thickness variations at what appear to be outlines of the platelet outer edge as it was at various times during growth by addition at the outer edge. Figure 1 shows such markings in two platelets. The outlines are such as would result if the growth rate normal to the platelet edge had been approximately uniform over the length of the platelet edge. That is, any one outline is everywhere approximately at the same distance from the platelet edge. The only alternative, growth by addition at the base edge, would not be expected to produce such markings, which indicate smooth, rounded outlines of areas decreasing in breadth as the growth progresses. Except for thickening growth, the shape (outline) of thin crystal growths in general must result from edge growth. In the case of these rounded platelets, growth must be at the outer edge.

A precedent for the consideration of growth from the base as a possible alternative mechanism lies in the observation by Markali (13) of evidence suggesting that Nb_2O_5 whiskers grow from the base by a mechanism involving plastic deformation of the oxide layer.

Iron transport.—We apply here the arguments for internal iron diffusion mechanisms, some of which have been presented previously (3-5). Iron must be transported from the base to the tip or edge to produce the growth of the α-Fe_2O_3 whiskers and platelets. Internal diffusion mechanisms involving linear and planar defects are proposed primarily on the basis of the arguments against other transport mechanisms:

Lattice diffusion coefficients (14) are nearly isotropic at higher temperatures and are far too small to account for significant growth in the range 400°-500°C.

Caplan and Cohen (15) have failed to detect a weight loss in measurements on Fe_2O_3 in flowing atmospheres at 1200°C. Vapor transport of iron oxides or hydroxides at lower temperature is severely limited by these experiments and by common experience with turbines, steam generators, etc.

Coble (16) determined that the α-Fe_2O_3 compaction on sintering at 750°C proceeds at a rate determined by the iron lattice diffusion coefficient. His results provide an upper limit on the surface diffusion coefficient because surface diffusion is a competing process which produces no compaction. This upper limit is too small, by a factor of at least 10^4, to supply the iron incorporated in the whisker and bladelike platelet growths at rates of 1 to 100Å sec^{-1}. Growth rates of the broad, rounded platelets are likely to be comparable; they are known to exceed 0.1Å sec^{-1} from heights found after 48 hr oxidations. It seems excessive to propose both surface transport by an unknown mobile iron-oxygen species (somehow absent in the sintering experiments) and the poisoning of competing surface growth sites.

The shapes of the three growth types observed (whiskers, bladelike platelets, and broad, rounded platelets) can be qualitatively understood to result from the internal diffusion of iron because the shapes match the symmetry of the internal defects. This is a point in favor of the internal diffusion mechanism.

Large twist angles.—One may question why only platelets with large twist angles have been observed. The calculated density of dislocations increases with twist angle, indicating increasing disorder. It may be that the larger twist angles we have found on observing only the tall growths result in larger diffusion coefficients for iron at the twist grain boundary.

Base structures.—The symmetry and perfection of the platelet growths suggest the presence of unknown special structures at their bases. The ability of these special structures to supply the iron diffusing in the platelets is a feature of the internal diffusion hypothesis. Future studies of iron oxidation and of mechanisms for the transformation of Fe_3O_4 to α-Fe_2O_3 might well include a search for the structures and mechanisms associated with the growths of α-Fe_2O_3.

Conclusion

The structures of the broad, rounded platelets have been successfully deduced from electron diffraction patterns. These platelets and their growth have been described to the extent permitted by the available information. The diffusion of iron in the internal twist boundaries of these platelets is the only transport mechanism against which we find no strong arguments.

It seems self-evident that crystal growth resulting from diffusion along internal defects will predominate in general when lattice diffusion is small and the external paths of vapor transport and surface diffusion are precluded. Grain boundary and lattice defect diffusion should be especially important to oxide growth in metal oxidation at ordinary temperatures.

Acknowledgments

The oxidation experiments which provided the specimens for this work were performed by T. P. Copan, who also obtained the electron micrograph of Fig. 1.

This work was supported in part by the Office of Naval Research under Contract No. Nonr-4949(00).

Manuscript submitted June 12, 1968; revised manuscript received July 30, 1969. This was Paper 421 presented at the Montreal Meeting of the Society, Oct. 6-11, 1968.

Any discussion of this paper will appear in a Discussion Section to be published in the December 1970 JOURNAL.

REFERENCES

1. E. A. Gulbransen and T. P. Copan, *Discussions Faraday Soc.*, **28**, 229 (1959).
2. E. A. Gulbransen, *Mem. Sci. Rev. Met.*, **62**, 253 (1965).
3. R. L. Tallman and E. A. Gulbransen, *This Journal*, **114**, 1227 (1967).
4. E. A. Gulbransen and R. L. Tallman, "Chemical Physics of Surface Reactions of Metals," AD-653 723, Clearinghouse, Springfield, Va.
5. R. L. Tallman and E. A. Gulbransen, *This Journal*, **115**, 770 (1968).
6. P. B. Hirsch, A. Howie, R. B. Nicholson, D. W. Pashley, and M. J. Whelan, "Electron Microscopy of Thin Crystals," p. 169, pp. 357 ff, Butterworths, Washington (1965).
7. S. Amelinckx, "The Direct Observation of Dislocations," pp. 67 ff, pp. 309 ff, Academic Press, New York (1964).
8. H. B. Huntington, in "Solid State Physics," **7**, F. Seitz and D. Turnbull, Editors, Academic Press, Inc., Publishers, New York (1958).
9. J. Weertman and J. R. Weertman, "Elementary Dislocation Theory," p. 3, The Macmillan Co., New York (1964).

10. C. Kittel, "Introduction to Solid State Physics," p. 325, John Wiley & Sons, Inc., New York (1953).
11. Hirsch *et al.*, *op. cit.*, p. 365.
12. R. Takagi, *J. Phys. Soc. Japan*, **12**, 1212 (1957).
13. J. Markali, in "Mechanical Properties of Engineering Ceramics," pp. 93-102, Proc., Conf., Raleigh, N. C., Interscience Publishers, New York (1961).
14. W. C. Hagel, *Trans. Met. Soc. AIME*, **233**, 1949 (1965).
15. D. Caplan and M. Cohen, *This Journal*, **108**, 438 (1961).
16. R. L. Coble, *J. Am. Ceram. Soc.*, **41**, 55 (1958).

Technical Notes

The Effect of Emitter Perimeter-to-Area Ratio on Current Gain after Temperature Treatment

C. C. Mai and T. S. Whitehouse

Semiconductor Division, Sylvania Electric Products Inc., Woburn, Massachusetts

It is well known (1-3) that the d-c current gain of a transistor increases after treatment in hydrogen at temperatures above 300°C. From this experiment it was found that this change of d-c current gain is directly related to the perimeter-to-area ratio of the emitter. This indicates that the mechanism causing this change is the variation of generation-recombination current at the intersection of the junction and the silicon-silicon dioxide interface.

Experiments and Results

Four different sets of transistors with emitter perimeter-to-area ratios in the range of 2.7-6.7 mil^{-1} were employed. They were typical npn planar transistors with boron and phosphorus diffusions. The surface oxides, about 0.6μ thick, were grown by steam oxidation at 1050°C.

Ten transistors from each set were annealed for 1 hr at 450°C in a nitrogen ambient. Ten other transistors from each set were annealed for 1 hr at 450°C in a forming gas ambient (95% nitrogen, 5% hydrogen). The d-c current gains were measured at collector currents ranging from 10 μA to 10 mA. The data are plotted in Fig. 1, 2, 3, and 4. It is evident that the current gain, h_{FE}, is greater for transistors treated with forming gas and that the degree of difference is directly related to the perimeter-to-area ratio of the emitter. Also, the difference in h_{FE} is dependent on collector current, as expected.

In Fig. 5 the ratios of h_{FE} of forming-gas-treated units to h_{FE} of nitrogen-treated units are plotted against the perimeter-to-area ratios of the emitter at a collector current of 10 μA and at the peak current gain. The curves show that there is a relatively greater effect of forming-gas treatment at low current levels, but the effect also appears at peak gain.

In a second experiment one set of ten transistors was treated in the sequence listed in Table I. h_{FE} was measured after each treatment. The data indicate that the high value of h_{FE} due to a previous forming-gas treatment can be reduced by baking in nitrogen. h_{FE} does not decrease further with additional baking. When the transistors were treated in forming gas again, h_{FE} rose to the same high value obtained before. Further forming-gas treatment did not effect h_{FE} further.

Discussion

The reciprocal of d-c current gain ($1/h_{FE}$) is a function of three factors: emitter efficiency, base transport, and recombination on the surface. At a fixed current level the surface term is proportional to (4)

$$\frac{S\,As}{A}$$

where S = surface recombination velocity
A = area of the emitter and
As = surface area where recombination takes place. The term As is proportional to the emitter perimeter and hence the surface term is proportional to the perimeter-to-area ratio of the emitter.

Since S is multiplied by As/A, any change in S becomes magnified as the perimeter-to-area ratio becomes greater. Thus, the fact that h_{FE} increases with this ratio with forming-gas treatment shows that the surface recombination velocity was decreased. Also, the surface contribution to h_{FE} has its greatest effect

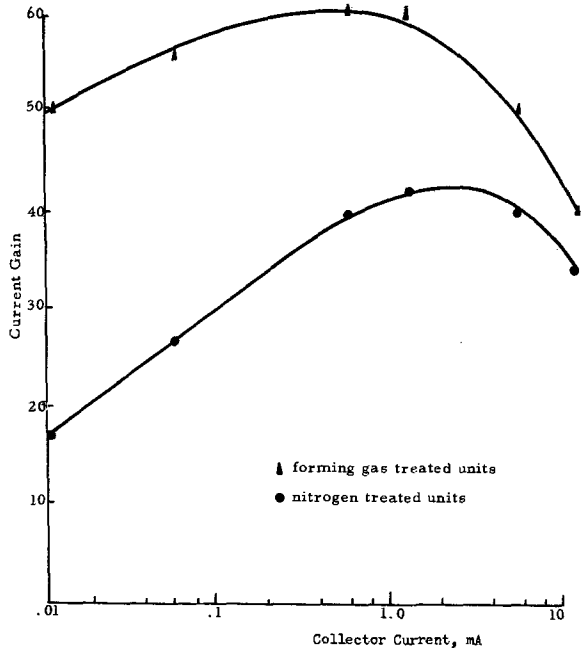

Fig. 1. Current gain vs. collector current for emitter perimeter-to-area ratio of 6.7, mil^{-1}.

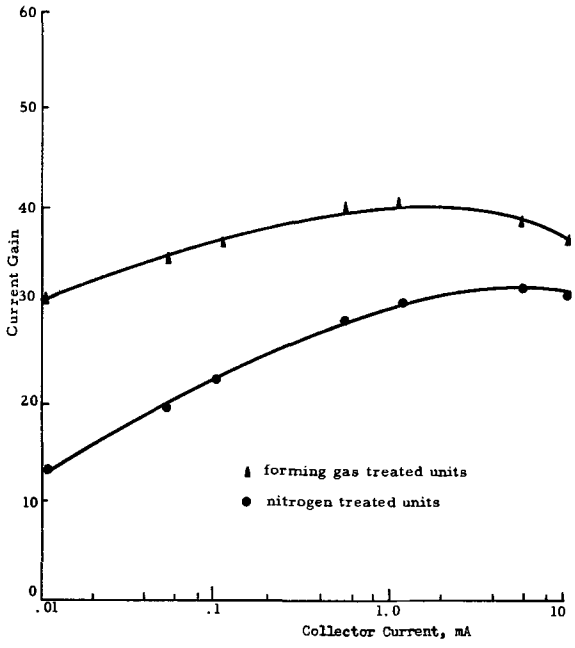

Fig. 2. Current gain vs. collector current for emitter perimeter-to-area ratio of 4.5, mil^{-1}.

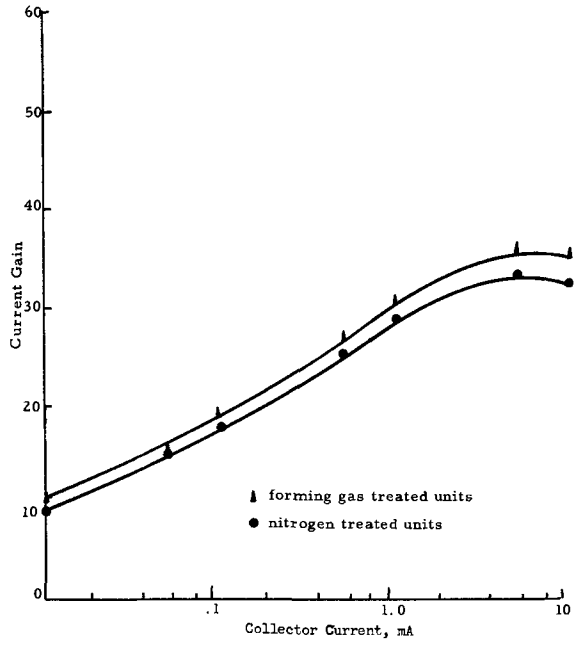

Fig. 4. Current gain vs. collector current for emitter perimeter-to-area ratio of 2.7, mil^{-1}.

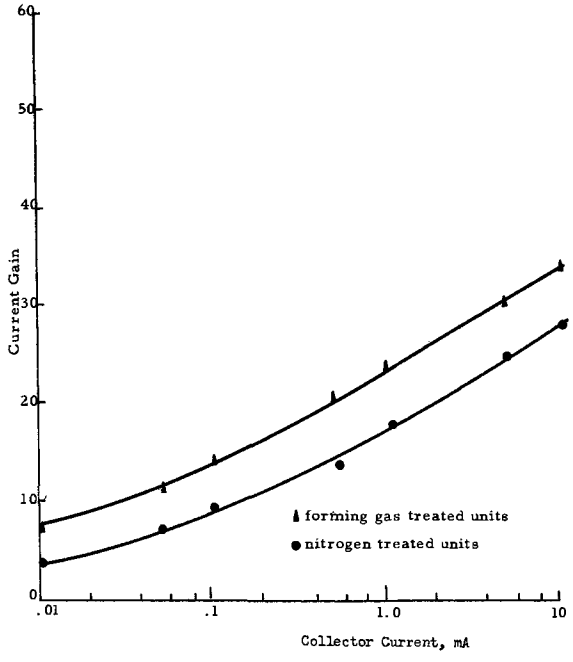

Fig. 3. Current gain vs. collector current for emitter perimeter-to-area ratio of 3.7, mil^{-1}.

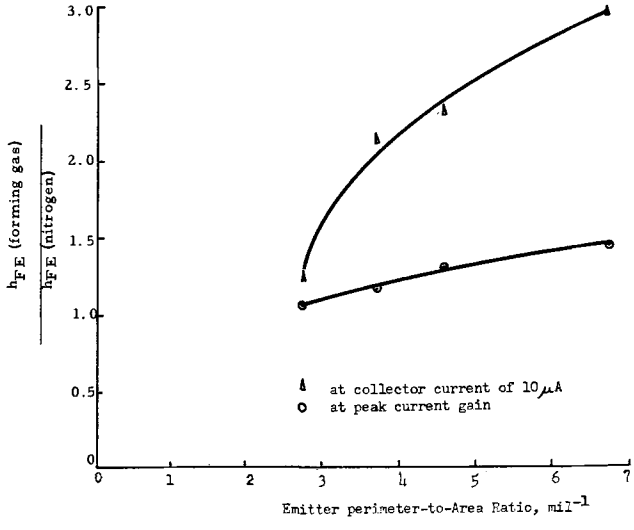

Fig. 5. Ratios of current gain of forming-gas-treated units to that of nitrogen-treated units vs. the emitter perimeter-to-area ratio.

on h_{FE} at low currents (4). Figure 5 shows that the forming-gas effect is greatest at low currents, giving added evidence that surface recombination velocity is being decreased by the forming-gas treatment.

The experimental result that the increase is h_{FE} in forming-gas-treated transistors is directly dependent on the perimeter-to-area ratio suggests that the hydrogen in the emitter base junction at the silicon-silicon dioxide interface decreases the surface recombination velocity. One possible explanation for the effect of forming gas is that the hydrogen in the gas combines with the unsaturated bonds at the interface, lowering the surface recombination velocity and hence increasing h_{FE}.

This paper has also shown that the h_{FE} changes due to baking in forming gas in nitrogen are reversible, which demonstrates that the hydrogen can be removed from the junction by out-diffusion.

Table I. Sequential treatment

Temp, °C	Time, hr	Ambient	h_{FE}
450	1	Forming gas	58.0
200	1	Air	57.5
450	1	N_2	50.5
450	1	N_2	50.5
450	0.25	Forming gas	58.0
450	2	Forming gas	58.0

Conclusion

When transistors are heat-treated in forming gas at temperatures above 300°C, the surface recombination velocity decreases and the current gain increases. The current gain increase is greater as the perimeter-to-area ratio of the emitter increases and the collector current decreases. The effect can be reversed by baking the transistor in nitrogen.

Manuscript received July 14, 1969; revised manuscript received Oct. 28, 1969.

Any discussion of this paper will appear in a Discussion Section to be published in the December 1970 JOURNAL.

REFERENCES

1. A. A. Bergh and C. Y. Bartholomew, *This Journal*, **115**, 1282 (1968).
2. J. Blum *et al.*, Paper 55 presented at the Toronto Meeting of the Society, May 3-7, 1964.
3. K. Busen and J. Lindmayer, *Trans. Met. Soc. AIME*, **233**, 536 (1965).
4. W. M. Webster, *Proc. IRE*, **42**, 914 (1954).

Further Verification of a Model for Diffusion from Doped Oxides

M. L. Barry* and J. Manoliu

Fairchild Semiconductor, Research and Development Laboratory, Palo Alto, California

In a recent article (1) we presented and verified a model describing the diffusion from a deposited doped oxide into a semiconductor substrate. Subsequently, in related work dealing with diffusion into polycrystalline silicon, we found additional experimental evidence verifying this model. In short, we find that junctions after diffusion from a deposited oxide are deeper in polycrystalline silicon than in single-crystal silicon because the diffusivity of the dopant is higher in the polycrystalline material. However, the sheet conductivities are the same for both types of silicon since the diffusion process is limited by diffusion within the oxide source.

Figure 1 shows a general one-dimensional case for diffusion of a dopant from a uniformly doped oxide into a semiconductor substrate. In the work to be described, the layer of undoped barrier oxide has been reduced to a minimum and may be disregarded. We have shown previously that for the case where the deposited oxide is thick compared to the diffusion length in the oxide, the concentration of dopant in the semiconductor after diffusion is given by

$$C_2(x,t) = C_s \operatorname{erfc}\,(x/2\sqrt{D_2 t}) \qquad [1]$$

and

$$C_s = \frac{C_o\sqrt{D_1/D_2}}{1 + (1/m)\sqrt{D_1/D_2}} \qquad [2]$$

where C_o is the initial concentration of dopant in the oxide, D_1 and D_2 are the diffusivities of the dopant in the oxide and in the semiconductor, respectively, and m, the segregation coefficient, is the ratio of the surface concentration of the dopant in the semiconductor to the surface concentration in the oxide. If the substrate is silicon with a reasonably high resistivity (about 2 ohm-cm for most cases) of opposite type from the diffusing dopant, Eq. [1] and [2] can be manipulated to yield

$$x_j = 2\sqrt{D_2 t}\ \text{argerfc}\ (C_B/C_s) \qquad [3]$$

and

$$I/V = 8.15 \times 10^{-23}\,\bar{\mu}\,C_s\sqrt{D_2 t} = 8.15 \times 10^{-23}\,\bar{\mu}\,\frac{C_o}{1 + (1/m)\sqrt{D_1/D_2}}\sqrt{D_1 t} \qquad [4]$$

where x_j is the junction depth resulting from the diffusion, I/V is the sheet conductivity as measured with a standard 4-point probe, C_B is the bulk concentration of carriers in the substrate, $\bar{\mu}$ is the effective mean mobility of the carriers, and the constant, 8.15×10^{-23}, contains the electronic charge and the spreading-current factor for the 4-point probe.

Since argerfc (C_B/C_s) is only a weak function of C_s, the junction depth for a given diffusion time depends primarily on the diffusivity of the dopant in the semiconductor; on the other hand, if $(1/m)\sqrt{D_1/D_2}$ is small compared to 1 (and this appears to be the case for both boron and phosphorus in silicon), the I/V will depend primarily on the diffusivity of the dopant in the oxide. The same analysis applied to Eq. [2] indicates the surface concentrations will vary inversely with the diffusivities in the silicon. Equations [2], [3], and [4] then predict that if diffusions are made from the same deposited oxide into silicon substrates in which the diffusivities of the dopant vary widely, the resulting junction depths and surface concentrations will reflect this variation while the sheet conductivities will remain nearly the same. Another way of describing this is to say that for the ratios of D_1 and D_2 which occur in silicon oxide and silicon, the process is limited by the total quantity of dopant which can diffuse out of the oxide, and this total quantity is nearly independent of the sink into which it is diffusing.

Experimental verification of the above conclusions has been found for the case of diffusion from a doped oxide into intrinsic polycrystalline silicon with a typical crystallite size of 0.3μ. The silicon was deposited by the thermal decomposition of silane, and the phosphorus-doped oxide was deposited at 400°C by the oxidation of silane and phosphine. In all cases, the polycrystalline silicon was much thicker than the junction depth after diffusion, so there was no problem of saturating the polycrystalline layer. As Table I

* Electrochemical Society Active Member.

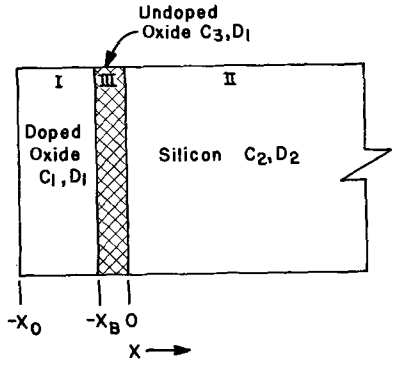

Fig. 1. Diffusion from a deposited doped oxide through a barrier oxide into a semiconductor substrate.

Table I. Diffusion from phosphorus-doped silicon oxide into polycrystalline and single-crystal silicon

Temp, °C	I/V polycrystalline / I/V single-crystal	x_j polycrystalline / x_j single-crystal
1000	0.8	2.8
1100	0.9	2.6
1200	0.9	3.0

shows, there is a very large enhancement of the junction depth in the polycrystalline silicon compared to single-crystal silicon, but very little difference between the sheet conductivities, or I/V's, for the two substrates. That this is not just due to decreased carrier mobilities in the polycrystalline silicon is shown by the enhancement of both x_j and I/V in polycrystalline material after a normal gaseous-source predeposition where the diffusion is not oxide limited.

This type of diffusion appears to offer an improved technique for measuring the diffusivity of dopants in the oxide, since as shown in Eq. [4] the sheet conductivity is relatively insensitive to D_2, the diffusivity of dopant in the polycrystalline silicon. However, before quantitative results can be reported, the effective mobilities of carriers in polycrystalline silicon must be determined. This information, as well as the mechanism of the diffusion of dopants in polycrystalline silicon in relation to the structure of the silicon will be described in a subsequent paper.

Manuscript submitted July 31, 1969; revised manuscript received Nov. 3, 1969.

Any discussion of this paper will appear in a Discussion Section to be published in the December 1970 JOURNAL.

REFERENCE

1. M. L. Barry and P. Olofsen, *This Journal*, **116**, 854 (1969).

Recombination-Generation Centers Caused by 60°-Dislocations in Silicon

M. C. Collet

Philips Research Laboratories, N. V. Philips' Gloeilampenfabrieken, Eindhoven-Netherlands

The importance to device fabrication of the dislocation density in semiconducting material has been recognized more and more in recent years.

Many experiments have been carried out on the influence of dislocations in silicon on device parameters such as leakage current, breakdown voltage, and noise. This field has been reviewed recently by Queisser (1). In the methods used in these experiments to introduce the dislocations the samples had to be at 800°C or higher for at least half an hour. This treatment is quite sufficient to enable impurities to diffuse through the crystal and to interact with the dislocations. Because of this it is impossible to know whether the measured effects are caused only by dislocations or by impurities interacting with these dislocations.

An exception can be made for the experiments of Glaenzer and Jordan (2) on the influence of dislocations on lifetime in silicon, where the interaction between the dislocations and slow diffusants like O, C, B, and P was avoided. However these lifetime measurements were carried out on bulk silicon. Here the dislocations are surrounded by space charge cylinders. According to the authors this makes it very difficult for majority carriers to reach the dislocations, so that the recombination rate is strongly decreased and astonishingly high lifetimes of about 200 μsec at room temperature are found for silicon with a dislocation density of 10^7 cm^{-2}. Nevertheless they were able to measure the energy levels associated with edge dislocations.

In the experiments we are reporting here the generation rate of minority carriers was measured in depletion layers. Dislocations occurring in these regions will not be shielded by space charge cylinders, and their influence on recombination-generation rates can be assumed to be much more pronounced. This is a typical situation for most devices containing p-n junctions, because their characteristics are strongly influenced by recombination-generation centers present in the depleted region of the junction.

The depletion layer was obtained by biasing the gate of a MOS capacitor made on our samples. This bias induces an inversion layer at the silicon surface with a depletion layer underneath. A sudden increase in bias causes an instantaneous increase of the depletion layer thickness followed by a slow relaxation to the equilibrium value. The relaxation time is governed by the rate at which minority carriers are generated in the depletion layer and it can be measured by monitoring the high-frequency capacitance of the MOS during the relaxation of the depletion layer. Because one starts the measurement with an inversion layer at the surface the influence of surface states on generation is negligible. A more complete description of this method can be found in the literature (3-5).

Introduction of the Dislocations

Dislocation-free, Czochralski grown, (111) oriented, 10 ohm cm phosphorus doped silicon slices, with a 1.5 in. diameter were lapped and polished to a final thickness of 300μ. The slices were etched 40μ on each side and cleaned by repetitive boiling in HNO_3 alternated with rinsing in deionized water and dipping in HF. This treatment was directly followed by oxidation at 1200°C in dry oxygen in a double walled quartz tube. The oxide thickness was 0.25μ. The oxide layer was stripped from the back face of the wafer, and a phosphorus diffusion at 1100°C was carried out. Such a diffusion is known to getter metallic impurities from silicon.

Next the slices were scribed and broken into four quarters. By means of two pressure contacts a voltage was applied to such a sample. The current flowing through the sample heated it. When a part of the sample became intrinsic, because of thermal generation, that part showed a negative temperature coefficient of resistivity, and it attracted most of the current. This part reached a temperature of about 900°C while the rest of the sample remained at a relatively low temperature. The stresses caused by the temperature gradient were sufficient to cause plastic deformation.

Figure 1a shows a sample during deformation and Fig. 1b shows an x-ray topograph of a sample after the treatment. The deformation has caused slip along (111) planes. Points at the edge of the crystal acted as dislocation sources. The dislocations ran from the edge into the crystal up to the point where the crystal was too cold to permit further glide. This caused the (111) slip planes to be densely packed with dislocations. The slip bands are visible as white stripes in the topograph.

The dislocations in those slip planes were lying along <110> directions in a herring bone pattern. The Burgers vector, which is the same for all dislocations in one such slip plane, could be determined by the contrast criterion for x-ray diffraction. Dislocations crossing the depletion layers of the MOS capacitors with which we measured the generation rate were found to be of the 60° type.

Using this method mean dislocation densities of 10^7 cm^{-2} were created in less than 5 sec, including

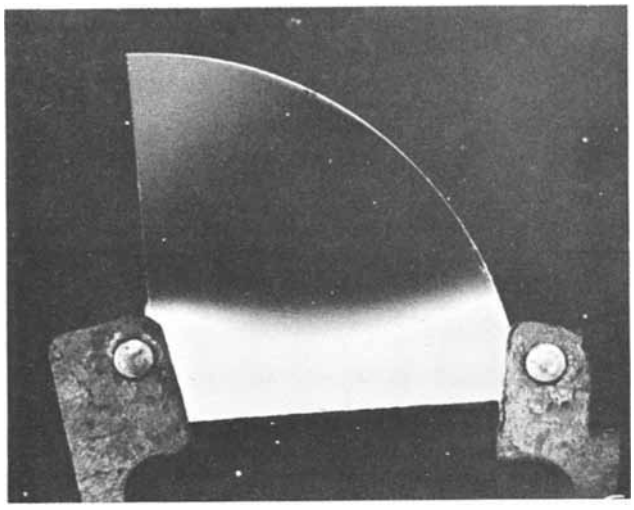

Fig. 1a. Photograph of a sample during deformation. Hot zone between the pressure contacts is at about 900°C.

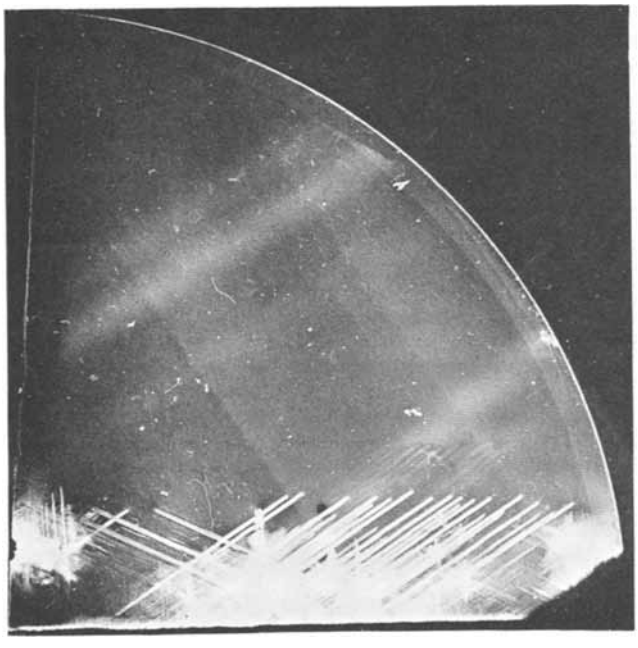

Fig. 1b. X-ray topograph of a deformed sample

heating and cooling times. The short duration of the heat-treatment prevents impurities such as O, C, B, and P from diffusing toward the dislocations. Fast diffusants like Cu, Au, and Fe could diffuse to the dislocations from within a radius of 100μ. As mentioned above, we tried to keep their concentration as low as possible by means of gettering by phosphorus diffusion.

After the introduction of the dislocations the MOS capacitors needed for the generation rate measurements were completed by the evaporation of 0.5 mm diameter aluminum dots on top of the oxide layer.

Results of Generation Rate Measurements

Figure 2 shows an x-ray topograph of a sample with dislocations. Spots where the generation rate of minority carriers has been measured are indicated by numbers. At 4, 5, and 6 the crystal is still dislocation free, although at 5 the temperature reached 900°C during deformation and at 6 an elastic strain field is present, caused by one of the pressure contacts used for heating the sample. Notwithstanding these differences the same low generation rate was found at these three places. But whenever the generation rate was measured on parts of the crystal containing high dislocation densities significant increases in generation rate were found. Spots 1 and 2, for example, showed a 300-

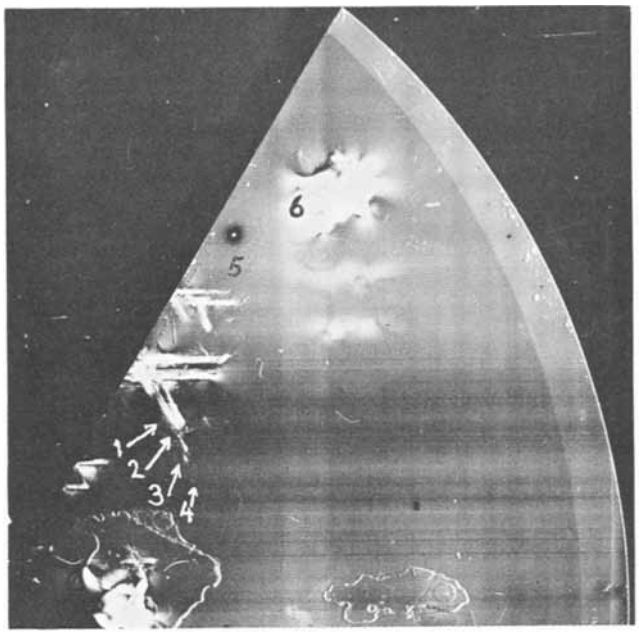

Fig. 2. X-ray topograph of one of the samples on which generation rate measurements were performed.

fold increase and spot 3 a 30-fold increase in generation rate.

The correlation between increased generation rate and the presence of dislocations proves that plastic deformation introduces generation-recombination centers. It does not prove that the dislocations are responsible for these centers, because plastic deformation introduces not only dislocations, but also vacancies, divacancies, vacancy impurity complexes, and possibly interstitials. Such point defects may also cause an increase in generation rate.

The energy levels associated with these point defects are known, mostly from measurements on electron-irradiated samples (6). If we can determine the energy levels of the centers which cause the increase in generation rate in the samples, the possible contribution of those point defects can also be identified.

For this purpose the temperature dependence of the generation rate was measured. To interpret these measurements the Shockley-Read theory for recombination-generation was applied (7).

In Fig. 3 the ratio of generation rate and intrinsic charge carrier concentration is plotted logarithmically against the inverse of absolute temperature. Curves A, B, and C have been measured on spots on three different samples where 60°-dislocations were present. Curve D was measured on the same sample as curve A but on a dislocation free spot.

Each of the drawn curves in Fig. 3 has been constructed by the summation of two straight lines, whose slopes are indicated.

According to the Shockley-Read theory the generation rate in a depleted layer is equal to

$$U = n_i \left[\tau_{n_0} \exp \frac{q}{kT} (E_t - E_i) + \tau_{p_0} \exp \frac{q}{kT} (E_i - E_t) \right]^{-1}$$

$E_t - E_i$ = distance in eV between the center of the energy gap and the recombination-generation center's level. For $E_t - E_i > 0$ the recombination-generation center's level is in the lower half of the energy gap and *vice versa*. The other symbols have their usual meaning.

For the material containing 60°-dislocations energy levels are found at $|E_t - E_i| = 0.20$ eV and at $|E_t - E_i| = 0.06$ eV.

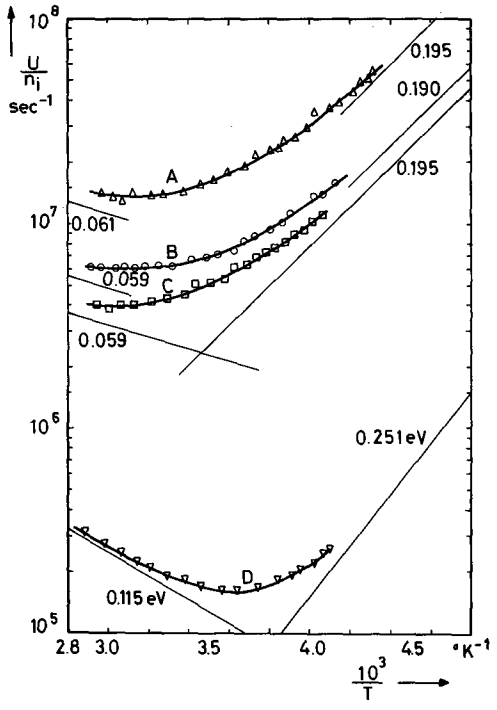

Fig. 3. Ratio of generation rate and intrinsic carrier concentration plotted logarithmically against the inverse of absolute temperature.

The line associated with the 0.20 eV level has a positive slope. If $|E_t - E_i| > 0$ it follows from the above equation that $\tau_{p_0}/\tau_{n_0} >> 1$ and the center is a donor. If $|E_t - E_i| < 0$, $\tau_{n_0}/\tau_{p_0} >> 1$, in this case the center is an acceptor. These data fit the second acceptor level of the divacancy, and they also fit the acceptor level of the vacancy-phosphorus complex. Because the energy levels associated with 60° dislocations have not been reported, the 0.20 eV level found here can be explained as being due to divacancies, vacancy-phosphorus complexes, or dislocations. The experimental evidence allows no choice between these possibilities.

For the 0.06 eV level the combinations $E_t - E_i > 0$ and $\tau_{n_0}/\tau_{p_0} > \frac{1}{4}$ or $E_t - E_i < 0$ and $\tau_{p_0}/\tau_{n_0} > \frac{1}{4}$ are found. The monovacancy and iron cause centers which fit these data. But the monovacancy is known to be mobile at very low temperatures (6) and thus should have been annealed out. If iron causes the high generation rates in the deformed part of our samples, we should have found it in the dislocation-free part of the same sample as well.

Curve D, however, shows that iron is not present in this part of the crystal. Thus the 60°-dislocations remain as the most probable explanation of the 0.06 eV level.

Conclusion

Dislocations of the 60°-type are able to cause an increase of several orders of magnitude in generation rate. In n-type silicon this behavior can be described by one Shockley-Read type recombination-generation center with an energy level at a distance of 0.06 eV from the center of the energy gap. If this level is situated in the upper half of the energy gap, it probably acts as a donor, if in the lower half, it probably acts as an acceptor.

Also present after plastic deformation was a center with a level at 0.20 eV from the middle of the energy gap. This level may be due to divacancies, vacancy-phosphorus complexes or dislocations.

Acknowledgments

It is a pleasure to thank M. V. Whelan for the adaptation of the generation measurements to our purpose and for many stimulating discussions and L.M.C. Goossens for his valuable assistance during these experiments.

Manuscript received Sept. 2, 1969.

Any discussion of this paper will appear in a Discussion Section to be published in the December 1970 JOURNAL.

REFERENCES

1. H. J. Queisser in "Semiconductor Silicon," R. R. Haberecht and E. L. Kern, Editors, p. 585, Electrochemical Society (Spring Meeting), New York (1969).
2. R. H. Glaenzer and A. G. Jordan, *Solid-State Electron.*, **12**, 247 (1969).
3. M. Zerbst, *Z. Angew. Phys.*, **22**, 30 (1966).
4. F. P. Heiman, *IEEE Trans.*, **ED-14**, 781 (1967).
5. S. R. Hofstein, *ibid.*, **ED-14**, 785 (1967).
6. J. W. Corbett in "Electron Radiation Damage in Semiconductors and Metals," Suppl. 7, to "Solid State Physics," F. Seitz and D. Turnbull, Editors, p. 70, Academic Press Inc., New York (1966).
7. W. Shockley and W. T. Read Jr., *Phys. Rev.*, **87**, 835 (1952).

A New Striation Etch for Silicon

Manfred Kämper

Siemens AG., Wernerwerk für Bauelemente, Werk Halbleiter Laboratorium, Pretzfeld, Germany

A new method has been worked out to reveal a striation etch in silicon crystals in a fast and definite way. The method is fast, furnishes a shining surface, and works on silicon of a very wide range of resistance. Previous etchants are slower (1-4), give a more or less rough surface (1, 3), and work mainly on highly doped material (1-4).

The silicon wafer is lapped on one side with 800 SiC or Al_2O_3 grit with the assistance of 3% NaOH in the slurry on a cast iron plate. The lapped wafer is then chemically polished by a mixture of 2 parts hydrofluoric acid 38%, 5 parts acetic acid 96%, and 3 parts nitric acid 100%. It would be preferable to let the wafer roll in a polypropylene beaker during the etch. The temperature of the etchant initially should be 20°C and should be allowed to warm up during the etch. Under these conditions the etching time would be 10-15 min, and the resulting surface is shining.

After these lapping and polishing processes a special treatment precedes the actual striation etch. The wafer is treated with a mixture of 1 part acetic acid 96% and 1 part nitric acid 100% for 1 min at about 50°C, rinsed with deionized water, and warmed up with 50% KOH solution until hydrogen is evolved over the whole surface. This should take from 15 to 30 sec. The wafer is then rinsed at once with deionized water and finally with acetic acid 96%, under which the wafer should be kept up to the actual striation etch. The time between the last treatment and the following striation etch should not be too long.

The etchant for the striation consists of, e.g., 20 ml hydrofluoric acid 48% and 10 ml acetic anhydride, to

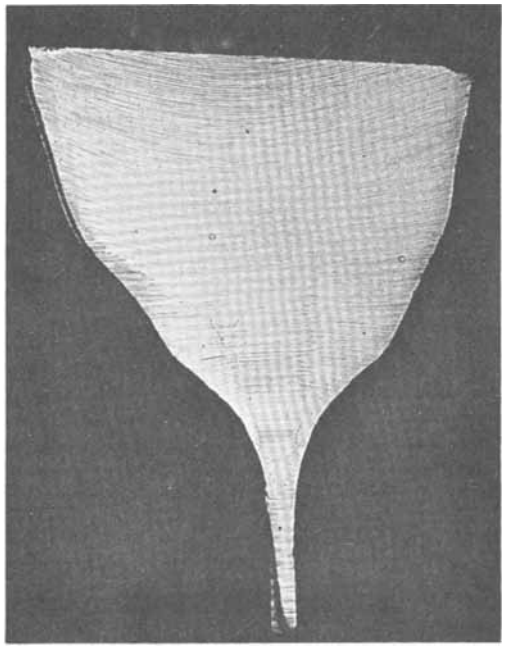

Fig. 1. Longitudinal section out of the cone of a dislocation free single crystal silicon rod with the seed. The center facet above the seed vanishes when the rotation is switched from concentric to excentric.

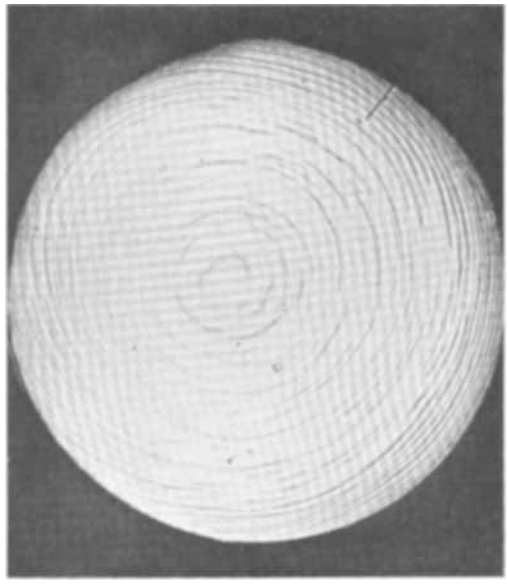

Fig. 2. Transverse section out of a dislocation free single crystal silicon rod. Some swirls can be seen parallel to the striation spiral.

which 10 drops of a 0.5M $NiSO_4 \cdot 7H_2O$ solution in HF 48% and 4 drops of a 10M HNO_3 solution in HF 48% are added. The 4 drops of 10M HNO_3 solution can be substituted by 20 drops of 1M V_2O_5 solution in HF 48%. The latter gives a somewhat more shining surface than the former, but the sensitivity is not as large.

The striation etch is carried out under strong illumination, the exact intensity of which is not critical. The etching time is 10-20 min. During the etch one can follow the development of the striation which becomes visible after 2 min.

During the etch the surface will stain, revealing continuous color changes. The formation of that colored film indicates the start of the etch. Should no film form on the surface, one can start the formation by adding 1 more drop of the oxidant (HNO_3 or V_2O_5 in Hf) to the solution while stirring, causing the local concentration of the oxidants to be increased at the surface for a short time. After the etch, the wafer is rinsed with water, methanol, 50% KOH solution, water, and finally methanol in the given order. The KOH solution takes off the colored film.

The essentials of this method seem to be the special treatment of the surface before the actual striation etch and the composition of the striation etchant. Treatment of the surface includes the passivation with $CH_3COOH:HNO_3$ 1:1 and the activation with 50% KOH. Passivation leads to a more even evolution of hydrogen on the surface in the second step. Use of acetic acid to wet the surface after the KOH treatment is better than the proposed (2) use of methanol, because methanol reacts with the striation etchant and furnishes a cloudy surface at times. Concerning the reaction mechanism the addition of acetic anhydride to the striation etchant seems to lower the surface tension. The concentration of HF is not lowered much by the addition of acetic anhydride as it would be in the case of use of acetic acid. The efficiency of other species (like acetylfluoride) in the solution cannot be excluded for the practical effect, that nearly no bubbles form on the surface during the etch. Bubble formation has been a major problem with previous etchants.

The addition of Ni^{2+} ions in most instances furnishes a more shining and reflecting surface. In special cases as with p-materials, which sometimes are not etched as readily as n-materials, the quantity of $NiSO_4$ can be increased. The method works for crystals with resistivities ranging from 10^{-3} ohm cm up to 2 to $3 \times 10^{+3}$ ohm cm. For higher resistivities, the etching time may be somewhat longer.

Usually a longitudinal test piece out of a silicon rod is etched better than a transverse test piece. This is because the gradient of the resistivity generally is steeper in the former than in the latter.

A more detailed discussion of the mechanism will be given elsewhere.

Acknowledgment

For taking the photographs the author is indebted to Mr. Nagorsen.

Manuscript received Sept. 29, 1969.

Any discussion of this paper will appear in a Discussion Section to be published in the December 1970 JOURNAL.

REFERENCES

1. W. D. Edwards, *Can. J. Phys.*, **38**, 439 (1960).
2. A. Mühlbauer, Z. *Naturforsch.*, **20a**, 1089 (1965).
3. T. F. Ciszek in "Semiconductor Silicon," R. R. Haberecht and E. L. Kern, Editors, pp. 156, 166, Electrochemical Society (1969).
4. F. Vieweg-Gutberlet, *Solid-State Electron.*, **12**, 731 (1969).

JOURNAL OF THE ELECTROCHEMICAL SOCIETY

ELECTROCHEMICAL TECHNOLOGY

FEBRUARY 1970

Technology of Solid Electrolyte Coulometers

John H. Kennedy, Fred Chen,* and John Willis

Department of Chemistry, University of California, Santa Barbara, California

ABSTRACT

A pulse discharge technique for reading solid electrolyte coulometers was studied and found to be superior to constant current readout. The technique can be applied to any solid electrolyte system which holds an open-circuit voltage for several seconds. A double-cell configuration for information storage with cyclic use was investigated. An initial charge setting could be retained for a number of cycles, but conditions are extremely critical. Any slight coulometric error will continue to add to or subtract from the initial charge so that after several cycles errors become quite large. Coulometers containing Ag_3SBr show excellent characteristics at temperatures as low as −70°C, but are poor at temperatures above ambient. Palladium and graphite do not offer any electrochemical advantages over gold as an indicator electrode other than the extremely sharp voltage rise on graphite.

In previous publications, it was demonstrated that solid electrolyte cells could function as moderately accurate coulometers (1, 2). However, this work concentrated on material and cell preparation, cell resistance, electronic conductivity contribution, and coulometric accuracy at constant current. It was shown that highest accuracy was obtained when the cells were "read" (*i.e.*, determining the amount of silver plated on an inert gold electrode by anodic stripping) under the same conditions that they were plated. In order to achieve accurate integration of a varying current, other methods besides constant current readout have been examined.

In this paper, considerations that are necessary for practical solid state electrolytic integrators are explored. These include integration readout with pulse discharge, use of double-cell configuration for information storage, operating temperature range, and possible substitutes for the gold indicator electrode.

Experimental

Materials.—Silver iodide.—Commercial silver iodide (B and A) was used as received.

Silver sulfide bromide.—Ag_3SBr was prepared according to the procedure described in a previous publication and designated as method II (2).

Silver sulfide iodide.—Ag_3SI was prepared according to a procedure analogous to that developed for Ag_3SBr using potassium iodide in place of potassium bromide.

Rubidium silver iodide.—$RbAg_4I_5$ was prepared according to the method described by Owens and Argue (3). It should be noted that our material had the same chemical composition as that reported by Owens and Argue, but our material was not handled in a dry box. The material was stored in a desiccator, and pellets were coated with Microshield plastic to minimize hydrolysis. However, the material is quite sensitive to moisture, and the poor results presented below may be partially due to decomposition taking place while the cell was under test.

Silver metal.—Engelhard Type G-3 fine silver powder.

Gold metal.—Wilkinson 99.99%, 5-15μ gold powder.

Procedures.—Cell preparation.—Cells in the form of pellets were prepared by powder compression described previously (1, 2). Double cells for cycling were prepared with a layer of silver followed by a layer of electrolyte, a layer of gold, a second layer of electrolyte, and finally a second layer of silver. These cells were 0.5 in. in diameter and weighed about 2.0g.

Graphite electrodes.—Hexamethylenetetramine, Durite D-5143, and powdered graphite were mixed together in ethanol in the ratio 2:10:88. The ethanol was then evaporated under vacuum and the graphite dried at 235°C overnight. The mixture was reground and pressed in the same manner as the powdered metal electrodes. Hexamethylenetetramine, which catalyzes the curing of the Durite binder, could have some effect on the graphite electrode. However, in its absence the graphite did not press properly yielding cells with little mechanical strength. The normal amount was 2% of the total weight, and changes in this ratio did not appear to affect the electrochemical properties of the graphite cells.

Pulse discharge readout.—A Bissett-Berman Corporation EDR-300 E-Cell Digital Readout was used for pulse discharge readout of cells. Either 5000 or 10,000 ohms resistance was used in series to decrease peak currents. A schematic diagram is shown in Fig. 1.

Temperature control.—An Associated Testing Laboratory SW-5101 environmental chamber was used for temperatures other than ambient.

Constant current readout.—A Bissett-Berman Corporation E-Cell Digital Coulometer was used for constant current charging of cells and for those experiments designated as constant current readout. This unit has a built-in trigger which cuts off the constant current supply when cell voltage reaches a predetermined value.

* Electrochemical Society Student Member.

Key words: coulometer; coulometry; electrolyte, solid; silver sulfide bromide; silver sulfide iodide; rubidium silver iodide; silver iodide; integrator, electrolytic; pulse discharge.

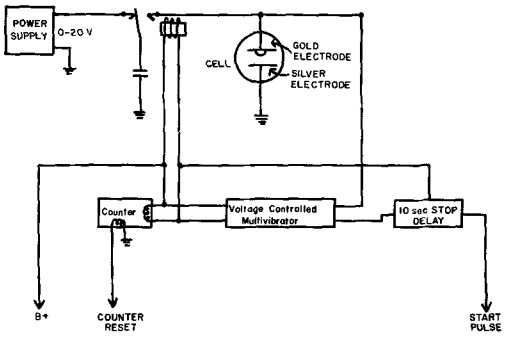

Fig. 1. Capacitative discharge current/time monitor. Courtesy of Bissett-Berman Corporation.

Charge setting for double cells.—A Harrison 6112A d-c power supply was used to clean by anodic stripping the gold surface *vs.* each of the silver electrodes with the use of a needle probe. The probe consisted of a copper wire, sharpened at the end and held or clamped on the center gold layer while the cell was clamped in place. After anodic stripping, a predetermined amount of silver was plated on the gold by applying a constant current between one silver electrode and the needle probe to the gold electrode. A Bissett-Berman E-Cell Digital Coulometer was used for this procedure.

Cycling.—A constant current was applied between the two silver electrodes until the voltage across the cell reached a preset cut-off value. After noting the time, the current was then reversed either manually or automatically and run until the voltage again reached the cut-off value. As an example, odd-numbered cycles were cut off at +0.5V while even-numbered cycles were cut off at −0.5V. For automatic reversal, after the cell reached the preset voltage and the current was disconnected, the cell polarity was rotated by a stepping relay and current reapplied to initiate a new cycle. The cycle times were recorded by following the cell voltage on a Moseley Model 7100B dual channel recorder.

Controlled potential electrolysis.—Samples of potassium iodide in 0.5F H_2SO_4 were electrolyzed at +0.70V *vs.* SCE for 30 min using a Beckman Electroscan 30. The 0.5F H_2SO_4 supporting electrolyte was pre-electrolyzed for 5 min and showed less than 1 mcoulomb of charge on the coulometers.

Results and Discussion

Pulse discharge method for reading solid electrolyte coulometers.—It was shown previously that, when constant current readout was used for solid electrolyte cells, the charge recovered was a function of the current level. As the current was increased, the error became more negative. The main reason for inaccurate readout for these devices is that the actual experimental function normally observed, applied voltage at the operating current, is not the function indicating the complete stripping of silver from the gold electrode, which is a gold electrode potential *vs.* a reference. Although three-electrode systems have been used for basic studies, current must be interrupted for each measurement to eliminate polarization. Applied voltage includes silver electrode potential, silver electrode/electrolyte polarization, electrolyte *IR* drop, and gold electrode/electrolyte polarization in addition to the desired gold electrode potential. The polarization voltages and *IR* drop vary with current and, thus, it is easy to see why readout accuracy varies with current level. It was also shown that accuracy improved with succeeding cycles under the same operating conditions as the cell appeared to become "conditioned" to these conditions (2). If the operating conditions such as current or temperature changed, new conditioning cycles were required to regain high readout accuracy.

The pulse discharge method circumvents these problems by measuring, at least approximately, the gold electrode potential, and triggers a cutoff when a potential develops indicative of complete silver stripping. In principle, a capacitor is discharged through the cell equivalent to 0.100 mcoulomb of charge. The voltage across the cell is monitored as is done in the conventional constant current mode. However, after the pulse, the voltage drops rapidly as the *IR* drop and polarization voltages decay, and when the cell voltage falls below 0.25V another pulse of charge is delivered. While silver remains on the gold electrode, the potential is essentially zero since it is being measured against the counter silver electrode. When all the silver has been stripped by the pulses of charge, a gold electrode potential develops which does not decay rapidly with time. Actually, since the measurement is still a two-electrode case as opposed to a cell containing a reference third electrode, the auxiliary silver electrode will not be strictly a reference potential. However, polarization which develops during the pulse will have 10 sec to decay which is sufficient time to consider the auxiliary silver electrode as a reference potential. As soon as the cell potential remains above 0.25V for 10 sec, the circuit is inactivated, and the number of pulses which were delivered can be read on a counter. The values of 0.25V and 10-sec time period for voltage decay were established for liquid electrolyte timers, but turn out to be convenient for the solid electrolyte coulometers reported here. The only modification necessary was the addition of 5000-10,000 ohms resistance in series with the cell to slow down the capacitor discharge. The equipment is designed to deliver peak currents of 10 mA which led to shorting for some of our solid electrolyte cells. The resistors cut the pulse peak currents to about 1 mA or less, although the slower pulses do require a somewhat longer running time. The actual time for readout is not inversely proportional to pulse current since a major fraction of time is associated with the final few pulses when the voltage is decaying slowly, but still reaching 0.25V in less than 10 sec. The 10-sec delay is arbitrary, but for most of our experiments the difference between 5, 10, or 20 sec was 1-2% and often just a pulse or two.

Accuracy of the pulse discharge readout method was checked by charging the cells at constant current and using the pulse discharge for stripping. The pulse discharge equipment was calibrated to ±0.5% by the manufacturer and was reproducible to ±0.2%. Since the output is digital, there is an absolute uncertainty of ±0.1 mcoulomb. This need not be an inherent limitation since the instrument could be designed to give pulses of 0.01 or 0.001 mcoulomb. The constant current source used for checking the pulse discharge method was calibrated to ±0.1%. The results in Table I show that this method is as accurate and reproducible as the constant current method results given in Table III of Ref. (2). In addition, it was noted that very little "conditioning" was required (Table II) contrary to the results when constant current readout was em-

Table I. Pulse discharge results for constant current charge

Charge conditions			Pulse discharge,* mcoulomb	Avg error, %	Avg dev., mcoulomb
Current, μA	Time, sec.	Charge, mcoulomb			
360	50	18.0	18.0	0.0	0.1
	100	36.0	35.9	−0.3	0.1
	200	72.0	71.5	−0.7	0.1
	500	180.0	180.4	+0.2	0.3
	1000	360.0	350**	−2.8	—
100	100	10.0	10.1	+1.0	0.1
	150	15.0	15.0	0.0	0.1
	200	20.0	19.5	−2.5	0.2
	500	50.0	49.8	−0.4	0.1
36	200	7.2	7.5	+4.2	0.1
	500	18.0	18.0	0.0	0.1
	1000	36.0	35.7	−0.8	0.1
10	1000	10.0	10.0	0.0	0.1

* Average of 8 trials.
** Pellet broke after 4 trials, average of 4.

Table II. Successive cycle results using pulse discharge

Charge: 100 sec at 360 μA = 36 mcoulombs

Cycle No.	Readout, mcoulombs
1	35.7
2	35.9
3	35.9
4	35.9
5	35.9
6	35.9
7	36.1
8	36.0
9	35.9

ployed in which the first few cycles were usually 3-8% away from succeeding charge-discharge cycles [*see* Fig. 9, Ref. (2) for typical results]. This behavior for pulse discharge supports the concept that this method of readout is less dependent on previous history and charging conditions than the constant current method. To emphasize this difference, a cell was cleared at 100 μA, charged at 100 μA, and read out at various constant currents. At currents above 100 μA, the cell was cleared at 100 μA before the next charge was applied. The results in Table III show how a cell conditioned at 100 μA will give low results at higher currents and high results at lower currents. As the current level is increased, polarization and *IR* drop increase, causing the 0.5V cutoff voltage to be reached sooner. A cell conditioned at 100 μA will be most accurate when subsequent stripping is performed at 100 μA. At currents lower than 100 μA less polarization and *IR* drop will allow the cell to run longer, while at currents above 100 μA the cell will run short.

A small effect was even noted when various charging currents were employed with a constant readout current. This was unexpected from the concept that polarization and *IR* depend only on the stripping current level. However, silver deposition conditions do play a part in the polarization observed during stripping and would account for this observation.

To illustrate the use of solid electrolyte cells as coulometers, a program of various amounts of charge applied at various current levels was used followed by pulse discharge readout. Table IV shows results of a series of integrations on one cell. To date, over 20 cells have been operated as coulometers with similar results. Again the readouts were accurate to 1-2%, although occasionally a higher error was observed suggesting that some silver had become separated from the gold electrode. Contrary to constant current readout, the pulse discharge showed no tendency for values to reach some limiting value when several integrations under the same conditions in a row were performed (*see* Table IV which lists a set of runs in the order performed). Also, there was no evidence for different results because of different previous runs. An example is seen in Table IV in which integration No. 13 was the same as No. 8 with essentially the same result even though the preceding integrations were different. Thus, integration of a variable current input can be accomplished with the solid electrolyte systems using the pulse discharge technique. However, the cells still show changes in charge setting when a hold period between charge and discharge is present, similar to the constant current results. Also, high-temperature results (> 50°C) were poor even for immediate readout. In fact, at elevated temperatures, the open-circuit voltage fell so rapidly that pulse discharge could not be employed. Even when fully stripped, the gold electrode would not retain an open-circuit potential > 0.25V for 10 sec, which is necessary for cutoff. At constant current, large positive errors were observed. The inability of the cell to hold a charge during an idle period and the inability of the gold electrode to hold an open-circuit potential is related to the residual current of the cell which is also a measure of electronic conductivity in the electrolyte (2). As temperature is increased, the electronic contribution increases rapidly explaining the open-circuit decay as well as the extra time required to bring the cell to 0.5V. This obvious shortcoming could limit the device to ambient or lower temperatures with only short idle periods. However, as preparation techniques for Ag_3SBr improved, the residual current was decreased an order of magnitude and further improvement may still be possible.

To illustrate the use of a solid electrolyte coulometer for controlled potential electrolysis, iodide solutions were oxidized at +0.70V *vs.* SCE. The solid electrolyte cell was in series with the electrolysis and, after the current decayed to background level, the coulometer was read using pulse discharge. The results are shown in Table V.

Low-temperature studies.—Conductivity of Ag_3SBr as a function of temperature is given in Ref. (2). The cells exhibit reasonable resistances of < 100 ohms as low as −70°C. Timing accuracy at constant current for cells at low temperature is shown in Table VI. Negative errors which were observed in general prob-

Table III. Effect of varying stripping current for fixed charging current

Clear: strip at 100 μA
Charge: 100 sec at 100 μA

Stripping current	Error, %
10	+35
36	+21
100	+4
360	−6
1000	−21

Table IV. Integration results

Charging time, sec				Total charge mcoulombs	Pulse-discharge readout mcoulombs	% Error
10 μA	36 μA	100 μA	360 μA			
500	140	50	—	15.04	14.5	−3.3
500	140	50	—	15.04	14.6	−2.7
500	140	50	—	15.04	13.6	−10.5
500	140	50	—	15.04	14.8	−2.0
—	150	50	—	10.4	10.4	0.0
—	150	50	—	10.4	10.5	+1.0
—	150	50	—	10.4	10.3	−1.0
—	100	100	100	49.6	48.9	−1.4
500	—	—	50	23.0	23.2	+0.9
200	200	200	—	29.2	28.6	−2.1
500	200	100	50	40.2	40.3	+0.2
—	200	100	50	35.2	35.2	0.0
—	100	100	100	49.6	48.7	−1.8
—	150	50	—	10.4	10.1	−2.9*
—	150	50	—	10.4	10.1	−2.9*

* Operated at −70°C.

Table V. Controlled potential electrolysis results

Iodide taken, mcoulombs	Iodide found, mcoulombs	% Error
161.0	161.1	+0.1
161.0	161.2	+0.1
322.0	326.2	+1.3

Table VI. Low-temperature timing accuracy

(Constant current charge and discharge)
Charge time: 200 sec

Current, μA	Temp, °C	Strip time,* sec	Avg dev., %	% Error
36	0	200.4	0.1	+0.2
100	0	198.9	0.1	−0.6
36	−25	199.2	0.1	−0.4
100	−25	194.4	0.2	−2.8
36	−50	192.7	0.4	−3.7
100	−50	191.5	0.2	−4.2
10	−70	192.9	1.0	−3.6
36	−70	192.1	0.9	−4.0
100	−70	195.0	0.5	−2.5

* Average of 8 cycles after 2 conditioning cycles.

ably result from the higher polarization voltages and *IR* drop leading to premature cutoff. Precision was excellent although the results at −70°C definitely showed less precision than the higher temperatures. Charge hold showed a slight negative drift at −70°C reaching −7.5% at 25 hr. In general, charge hold characteristics were better at low temperature.

With pulse discharge, positive or negative errors were observed at −70°C, depending on plating current, and again showed poor precision. However, an experiment at −70°C gave excellent results which are given in Table IV. Results at −25°C were similar to constant current readouts with an average of −1.9% when a charge of 400 sec at 36 μA was applied to the cell.

It should be noted that behavior at low temperature was markedly better than at elevated temperature with extremely sharp cutoff both at constant current and pulse discharge. Constant current cutoff depends on sulfide oxidation effects which are less at low temperatures. Sharper pulse discharge cutoff coincides with the slower decay of open-circuit potential at low temperature after silver has been stripped from the gold electrode. Solid electrolyte coulometers operated well at room temperature or below, including better charge storage and sharper cutoff characteristics as the temperature was decreased. Accuracy and precision became somewhat poorer below −25°C, but cutoff characteristics and general performance remained good to −70°C, the lowest temperature studied. Cells could be operated at 35°-50°C using constant current readout, but pulse discharge could be employed only below 35°C.

Double-cell configuration for information storage.— The normal mode of operation of these coulometers (*i.e.*, plating a certain amount of silver on a gold electrode and subsequent stripping) destroys the information which was stored on the gold indicator electrode. In developing a device which stored the original information, a double-cell configuration has been used and tested. The cell consists of a silver, solid electrolyte, gold, solid electrolyte, silver five-layer pellet in which the center gold indicator electrode is given an initial charge setting *vs.* one of the silver electrodes. Current is then passed through the entire pellet which strips silver from one side of the gold while plating an equivalent amount on the other side. When the cell reaches a preset cutoff voltage (normally 0.5V), the current is reversed. Some of the pellets have undergone several thousands of such cycles. A recorder trace showing voltage *vs.* time is shown in Fig. 2,

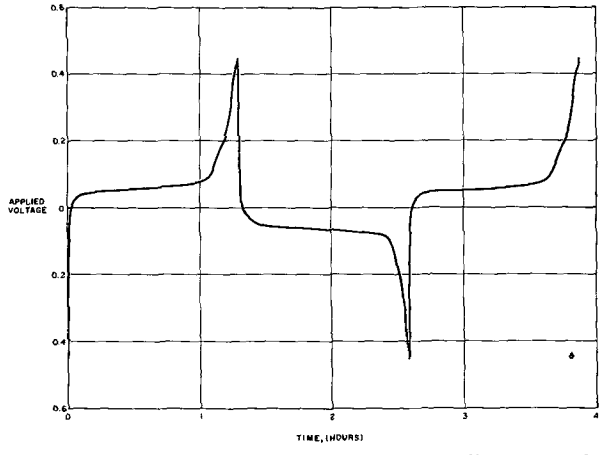

Fig. 2. Cell voltage *vs.* cycle time. Ag_3SBr pellet operated at 36 μA, 25°C with 0.5V automatic cutoff and current reversal. Cycle time approximately 4000 sec. (Note: The voltage across the cell was measured from the output of a VTVM because the recorder impedance was only 1 megohm. The voltage rise across the cell from 0.45 to 0.5V was more rapid than the VTVM response which appears on the recorder trace as a cutoff of 0.45V.)

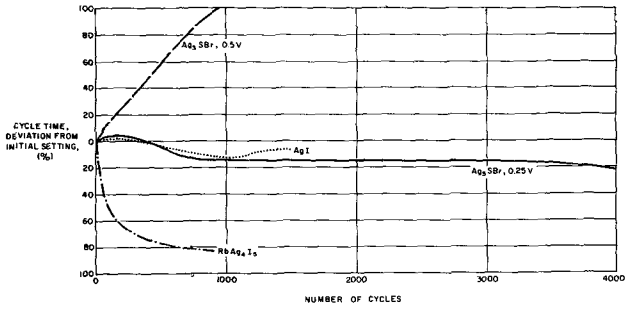

Fig. 3. Cycle time changes with number of cycles.

Ag_3SBr	0.5V	100 μA	216 sec initial
Ag_3SBr	0.25V	100 μA	166 sec initial
$RbAg_4I_5$	0.5V	100 μA	340 sec initial
AgI	0.5V	3.6 μA	425 sec initial

while cycle time *vs.* cycle number is shown for some of the pellets in Fig. 3.

The results for Ag_3SBr were interesting in that, with 0.5V cutoff, the cycles ran long (+0.1%/cycle) while, with 0.25V cutoff, the cycles ran short (−0.02%/cycle). This difference can be explained by the sulfide oxidation which occurs at 0.35V (2). In driving the voltage to 0.5V, some oxidation of sulfide occurs on one side of the gold, while an equivalent amount of silver is plated on the other side. When the current is reversed, this silver is stripped on the second side, but will cause an equivalent amount of silver to be plated on the first gold side. Silver is plated in preference to sulfur reduction because the sulfide cycle is irreversible. Thus, every time some sulfide is oxidized, more silver plate enters the system and the cycle time gets progressively longer. The effect would be even more dramatic except for the tendency to run short (seen at 0.25V cutoff and probably the same type of effect with $RbAg_4I_5$) which tends to compensate for the sulfide effect. This balance between low and high results is also affected by temperature; the cycle time increases at higher temperature and decreases at lower temperatures. Another operating problem with Ag_3SBr was encountered using manual cycling. Any time the pellet was left idle for long periods of time, such as 1-3 days, the cycle time would increase significantly. Manual cycle drift averaged +0.80%/cycle at 36 μA but only +0.09% when cycled automatically. However, when changes associated with idle periods were subtracted, the cycle drift averaged +0.11/cycle in good agreement with automatic cycling.

Results for AgI in Fig. 3 show that, under these specified conditions, AgI can be used for over a thousand cycles without large changes in charge setting, indicating the 100% coulombic efficiency. It should be noted that lower currents (3.6 *vs.* 100 μA) had to be used with AgI since its conductivity is nearly 1000 times smaller than Ag_3SBr or $RbAg_4I_5$.

Negative errors are normally encountered with solid electrolyte cells during anodic stripping. Silver may lose contact with the electrolyte or the gold electrode, and thus is not oxidized during stripping. Silver iodide exhibits this same effect with larger amounts of charge, but the very small amounts of charge used in these experiments could be repeatedly cycled with little loss.

Cycle time for $RbAg_4I_5$ pellets decreased rapidly, but these results may only be reflecting the fact that the tests were not carried out in a dry box. It is known that $RbAg_4I_5$ is a satisfactory electrolyte when protected from the atmosphere (4), although experiments of this type have not been reported before.

It appears that with careful choice of operating conditions, such as 0.25V cutoff voltage for Ag_3SBr, the double-cell configuration can be used to store initial information and to use this information for determining cycle time for many cycles. However, the

latitude of these conditions is much more limited than for single shot timing or integration.

Indicator electrodes.—The primary requirement for an indicator electrode is that it be sufficiently more noble than the metal used for tabulating charge so that an observable voltage rise can be observed when the indicator electrode is clear. When silver is used for coulometry, only a few materials exhibit this nobility including gold, platinum group, and carbon (1, 2, 5, 6). When normal trigger circuits are used, the voltage rise should be at least 0.2-0.3V and preferably $>$ 0.5V. Voltage rises for palladium and graphite are given in Fig. 4.

In addition to this primary requirement, the open-circuit voltage must not decay so quickly that a cutoff cannot be achieved when pulse discharge is considered. Open-circuit voltage decays after stripping for palladium and graphite electrodes are also shown in Fig. 4. Only graphite with Ag_3SBr electrolyte gave sufficiently slow voltage decay for pulse discharge.

Timing accuracy at constant current was checked for currents of 10-360 μA and for periods of 36-360 sec for Ag_3SBr and Ag_3SI using palladium and graphite electrodes in place of gold. Although readouts were quite reproducible with standard deviations of about 1-3%, accuracy was poor with average errors ranging from −40% to +131%. Pulse discharge gave similar poor results. The only advantage graphite exhibited over gold was its very sharp cutoff. This was caused by two effects. First, there was no voltage plateau at 0.35V which has been attributed to sulfide oxidation (2). Evidently, the irreversible oxidation of sulfide on gold is even more irreversible on graphite. The second effect appeared to be poor electrode/electrolyte contact which would mean less effective area for the same size pellet. The smaller area would have less capacitance and, thus, a sharper voltage rise. The poor contact, however, also led to low results. At this time, there does not appear to be an indicator electrode more suitable than gold for solid electrolyte silver coulometers.

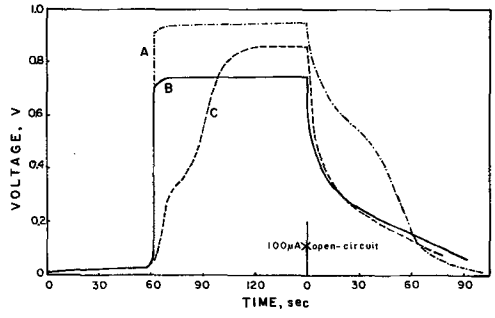

Fig. 4. Voltage rise and open-circuit decay for graphite and palladium electrodes: (A) C/Ag_3SBr/Ag, (B) C/Ag_3SI/Ag, (C) Pd/Ag_3SBr/Ag.

Acknowledgments

The authors wish to thank Bissett-Berman Corporation for specialized test equipment including a pulse discharge EDR-300 unit, and N. Stieb for designing the modifications necessary for automatic cycling. One of the authors (F.C.) is indebted to the Latin American Scholarship Program of American Universities, the University of California, Santa Barbara, and the Instituto para la Formacion y Aprovechamierto de Recursor Humanor for financial support.

Manuscript submitted July 22, 1969; revised manuscript received Nov. 4, 1969.

Any discussion of this paper will appear in a Discussion Section to be published in the December 1970 JOURNAL.

REFERENCES

1. J. Kennedy, F. Chen, and A. Clifton, *This Journal*, **115**, 918 (1968).
2. J. Kennedy and F. Chen, *ibid.*, **116**, 207 (1969).
3. B. B. Owens and G. R. Argue, *Science*, **157**, 308 (1967).
4. G. R. Argue, B. B. Owens, and I. J. Groce, *Proc. Ann. Power Sources Conf.*, **22**, 103 (1968).
5. T. Takahashi, *Denki Kagaku*, **36**, 481 (1968).
6. O. Yamamoto and T. Takahashi, *ibid.*, **36**, 894 (1968).

Accurate Temperature Control for Laboratory Furnaces Using Thermocouple Modulation

John G. Burt

Nuclear Engineering Department, The Ohio State University, Columbus, Ohio

ABSTRACT

A solid state circuit utilizing field effect transistors in a free running multivibrator configuration is discussed as a method for improving temperature regulation of galvanometer movement controllers. The circuit when used in conjunction with on-off controllers will maintain temperature to ±0.2°C at 1000°C.

Frequently it is necessary to maintain the temperature of a muffle or tube furnace at a set point with control accuracy of ±1°C at 1000°C for extended periods of time. This small tolerance is generally far beyond the limit of on-off galvanometer temperature controllers presently available. The proportioning controllers which will satisfy this requirement are generally quite expensive and this high cost very often precludes their use in many experiments conducted in the laboratory. This work deals with a reasonably simple and inexpensive modification to on-off galvanometer controllers which will greatly improve the short- and long-term temperature fluctuation about the set point.

With most laboratory furnaces and their associated galvanometer on-off controllers, there are two effects which contribute to the variation above and below the set point temperature: thermal inertia of the furnace and galvanometer pivot friction. The first factor is the result of furnace winding and thermocouple proximity, while the second comes from the finite friction present in the galvanometer movement (1). The result of these two factors is a dead zone about the set point where the galvanometer movement is not affected by slight changes in the thermocouple signal, and an oscillation in furnace temperature having a period of 5-15 min depending on the location of the thermocouple relative to the heating elements.

Reid has discussed a method for reducing the short- and long-term temperature fluctuation by modulating the thermocouple signal with a low-frequency a-c voltage (2). The superposition of the a-c signal on the d-c thermocouple output results in a voltage that drives the galvanometer above and below the dead zone that surrounds the set point. This effectively turns the controller on and off once during each modulated cycle, the ratio of "on" to "off" time being determined by the average d-c signal. The power delivered to the windings is proportioned in time such that the furnace cannot oscillate with its natural frequency, and the effect of the dead zone is minimized.

The original method used to obtain this "Guoy" modulation was mechanical, using resistance wire and a rocking pool of mercury, and as such is subject to breakdown when used for extended periods of time. This effort has been directed toward replacing the mechanical modulator with a solid state electronic circuit, which is not as susceptible to failure. During the last few years, field effect transistors have been developed to the point where very high input impedances can be obtained at low cost; thus oscillators and multivibrators having extremely low frequencies can be constructed using moderate-sized capacitors. In this particular circuit, two n-channel FET's are used in a free running multivibrator configuration to obtain a square wave having a period of about 10 sec. Ten seconds was chosen since the galvanometer movement is damped and cannot follow any signal having a period of less than 5 sec/cycle.

The circuit shown in Fig. 1 functions as follows. When power is applied, both FET's are in the "on" mode as the gates are at essentially the same potential as the sources. As S_1 is closed, capacitor C_1 is charged through Q_2 to the full supply voltage of the battery. When this switch is released (a push button is used for S_1), the source of Q_1 immediately returns to near ground and C_1 drives the gate of Q_2 about 4V negative with respect to ground. This negative pulse turns Q_2 off as the gate is now negative compared to the source of Q_2. C_1 discharges through R_2 according to the R_2C_1 combination allowing the gate of Q_2 to return to ground. At this point, Q_2 will turn on driving the gate of Q_1 negative *via* coupling capacitor C_2, turning Q_1 off. The RC decay at the gate of Q_1 eventually turns Q_1 on and the sequence is repeated. The square wave obtained from the two FET's is integrated by the 1-meg resistors and the 4-μf capacitor to obtain a double ramp function which is more suitable for driving the galvanometer. Q_3 and Q_4 are pnp silicon transistors used in a common collector mode to drive the low impedance load which will be added to the galvanometer circuit. The 1-ohm resistor added to the galvanometer was chosen for two reasons; the addition of more than 1-2 ohms will alter the dampening of the galvanometer and require recalibration of the temperature scale, while any load of less than 1 ohm is difficult to drive with the output transistors. The two trimpots are incorporated into the circuit in order to adjust the magnitude of the modulating signal for optimum results. This adjustment also makes it possible to use the circuit to drive various types of thermocouples since the output voltage varies from one type to the next. When platinum-rhodium thermocouples are used, the modulating signal need only be about 1/10 mV, while for chromal-alumal it must be about 1 mV in order to sweep through the dead zone at 1000°C.

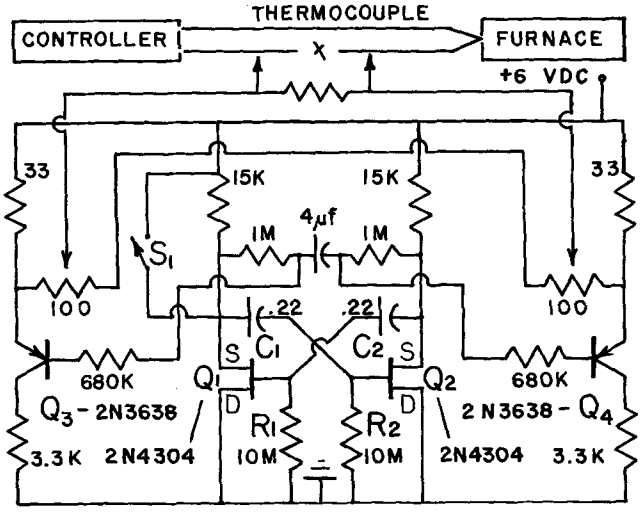

Fig. 1. Solid state circuit utilizing field effect transistors

In summary, it is recommended that mercury relays be used for switching power to the furnace windings as the frequent switching due to the modulation will quickly wear out ordinary metal contactors. Improved performance will also be obtained by switching from a low-to high-power mode at more elevated temperatures rather than complete on-off operation. The best regulation has been observed when the maximum power is applied about 60-70% of each cycle, and the modulating signal set for minimum amplitude which allows switching once during each modulated cycle. Good long-term regulation will require a reference junction which is maintained to ±0.05°C or better, and an ice bath in a vacuum Dewar has been found quite satisfactory. Using these precautions it has been possible to take a controller that maintained 1000° ± 4.0°C prior to this modification, and obtain regulation of ±0.3°C at this operating temperature for 4-6 hr. Short-term fluctuations over a period of 15-20 min are less than 0.2°C. Experimental runs were conducted at 1020°C using a Marshall 10-in. OD tubular furnace in conjunction with a Leeds & Northrup speedomax H-AZAR strip recorder. Span and zero suppression were adjusted for a 20°C span at this operating temperature and fluctuations of 0.10°C were observable. The furnace was operated without modulation to observe temperature variation and oscillation. Modulation was then imposed on the thermocouple and the regulation recorded for extended periods of time.

Manuscript received Sept. 15, 1969.

Any discussion of this paper will appear in a Discussion Section to be published in the December 1970 JOURNAL.

REFERENCES

1. C. H. L. Goodman, *J. Sci. Instr.*, **43**, 395 (1966).
2. W. T. Reid, "Temperature, Its Measurement and Control in Science and Industry," p. 611, Reinhold Publishing Corp., New York.

Electrodeposition of Lead-Antimony Alloys

J. W. Dini and J. R. Helms

Material Science Division, Sandia Laboratories, Livermore, California

ABSTRACT

Two fluoborate solutions capable of producing sound, thick lead-antimony deposits are described. One contains peptone and resorcinol in addition to lead and antimony fluoborates, while the other contains beta-naphthol in place of the peptone and resorcinol. Property data for some deposits are presented as well as influence of operating conditions and bath composition on antimony concentration of deposits.

Sound, thick lead electroforms have been produced by electroplating in fluoborate solution (1). However, as expected, the lead deposits were quite soft (hardness of 8 Knoop with a 5-g load) and highly subject to marring and scratching during handling. In an effort further to improve lead electroforms, a method was sought for increasing their hardness and strength. The method investigated, codepositing antimony with lead in a fluoborate solution, was chosen because antimony and/or tin is frequently used as an alloy to increase the strength of lead castings, and, of the two metals, antimony imparts the most hardness and strength to the lead (2). The fluoborate solution was chosen because past experience indicated that this solution was the best possible choice for electrodeposition of lead-antimony alloys (1, 3, 4-9).

The study revealed that fluoborate solutions are indeed capable of producing sound, thick electroforms of lead-antimony alloys, and that these alloys are harder and have higher tensile strengths than pure lead. In general, the study showed that as the antimony composition of a deposit is increased the deposit becomes harder and stronger.

During the course of the study, it was found that:

To obtain an alloy with a fixed antimony composition required the use of a pure lead anode wrapped tightly in filter paper and bagged with Dacron.

Although fluoborate solutions containing either resorcinol and peptone or beta-naphthol functioned equally well, deposits produced with the resorcinol-peptone bath bubbled when quickly heated to the melting point. There were no supplemental studies of the effects of addition agents.

An increase in the antimony concentration of the plating bath increased the antimony concentration of the deposit.

For a given bath composition, an increase in current density or a decrease in temperature lowered the antimony concentration of the deposit.

Preliminary Experiments

Antimony content of deposit.—Initially, a 1-liter bath was used that contained 460 ml/liter lead fluoborate concentrate, 0.23 g/liter peptone, and 0.23 g/liter resorcinol. Antimony was added in small amounts as antimony fluoborate (*see* Table I for composition of lead and antimony fluoborate concentrates). The anode was chemically pure lead and of the same dimensions as the cathode (2¼ x 4 in.). Panels were plated for 30 min at 30 A/ft², and the antimony content of the deposit was determined by using a copper coulometer during the plating operation and the calculation technique described by DuRose and Hutchison (10). As shown in Table II, the antimony content of the deposit increased as the antimony content of the solution increased.

Immersion deposition.—During testing, it became obvious that antimony was being deposited on the lead anode by displacement when the bath was not electrolyzed. At the end of the first day of plating, the lead anode was left in the bath overnight. The next morning there was a bright displacement coating of antimony on the anode. The antimony content of the alloy produced in the bath after the antimony was removed from the anode was 7.8%, whereas the previous evening it was 18.0%. Since the plating times were short enough that the amount of antimony deposited out of solution was minimal, it was evident that most of the antimony had been removed from the solution by displacement on the lead anode.

Displacement deposition of antimony on anodes in alloy plating baths has been discussed in the literature. Booe noticed the immersion with lead-tin anodes in a solution containing lead, tin, and antimony fluoborate (11). He obviated the phenomenon by wrapping the anodes with paper to limit the amount of solution coming in contact with the anode. Schaefer and Mohler also had the same trouble when plating lead-tin-antimony alloys, but decided the problem was not that serious because the rate at which antimony immersion plated on the anode was only about one fourth of the rate at which the antimony was electrodepositing at the cathode (12).

Because both the data from the test under discussion and past experience indicated that immersion deposition could be a problem, the anodes in all following experiments were wrapped tightly with two layers of Whatman #42 filter paper and bagged with Dacron. This did not completely prevent immersion plating but minimized it by limiting the amount of solution coming in contact with the anode. In addition, when the baths were not being used, the anodes were removed from the solution.

Table I. Composition of lead and antimony fluoborate concentrates

Lead fluoborate (A)	
	g/liter
Lead	503
Free fluoboric acid	161
Free boric acid	45
Antimony fluoborate (B)	
	g/liter
Antimony	191
Free fluoboric acid	36
Free hydrofluoric acid	78

(A) Harshaw Chemical Co., Cleveland, Ohio
(B) Allied Chemical Co., General Chemical Div., New York, N. Y.

Table II. Effect of antimony concentration on alloy composition[1]

Antimony concentration in plating solution (g/liter)	Antimony concentration of deposit (w/o)
2	0.8
4	1.5
6	4.1
8	8.0
10	13.2
11.5	18.0

[1] The solution contained 460 ml/liter lead fluoborate concentrate, 0.25 g/liter peptone, and 0.25 g/liter resorcinol, and was operated at 27°C. Plating time was 30 min at 30 A/ft².

Table III. Effect of a pure antimony anode on alloy composition[A]

Antimony added to bath as antimony fluoborate (g/liter)	Total antimony added as antimony fluoborate (g/liter)	Antimony content of deposit (w/o)	Total A-hr electrolysis per liter
0	0	0.5	1.2
2	2	6.1	2.4
2	4	9.6	3.5
0	4	16.5	4.6
0	4	22.7	5.8
0	4	26.6	10.0

[A]Solution contained 460 ml/liter Harshaw Lead Fluoborate concentrate, 0.25 g/liter peptone, and 0.25 g/liter resorcinol. Volume was 1 liter, plating current density 35 A/ft², and temperature 27°C.

Antimony vs. lead anode.—In a second experiment similar to the one described earlier, an antimony anode was used instead of the lead one. A small amount of antimony was added to the plating solution and then a series of panels were plated. As time progressed, the antimony content of the deposits increased even though no more antimony was added to the bath as antimony fluoborate. This increase occurred because antimony went into solution at the anode faster than it plated out at the cathode, thereby gradually increasing the antimony content of the bath (*see* Table III). With a 93% lead-7% antimony anode, preferential electrolytic dissolution of antimony was noted, thus gradually increasing the antimony content of the bath.

The work with the various anode systems showed that the best approach for obtaining an alloy with a fixed antimony composition was to use a pure lead anode and additions of antimony fluoborate as the solution was depleted of antimony. Use of anodes containing antimony precluded keeping the antimony content of the deposit at fixed levels.

Physical Properties

Experimental procedures.—To determine the effect of the antimony content on the physical properties of the electrodeposited alloy, electroforms approximately 30 mils thick were produced by plating for 8 hr at 25 A/ft² in a 40-liter solution (*see* Table II for composition). (Thicker deposits were not produced because the process would have required more than the 8 hr of a typical working day.) The mandrels were 3- by 6-in. aluminum panels, and a Mohler-Schaefer box was used to assure uniform deposition during plating (13). Prior to plating, the mandrels were zincated and given a cyanide copper strike. The antimony content of the deposits was increased by adding antimony fluoborate to the plating bath. The solution was continuously filtered through a unit containing a Dacron filter tube, and an electric stirrer with a plastic stirring rod provided the agitation. The anodes were of chemically pure lead, wrapped with filter paper and bagged with Dacron. The anode-to-cathode ratio was about 2 to 1. During plating, the alloy composition was determined with a copper coulometer (10). Tensile specimens were prepared by using a Tensilkut template, as described by Dini and Helms (1).

Results

The electroforms produced appeared to be quite sound. Those low in antimony content had the dull, gray appearance typical of lead. As the antimony content of the alloy increased, the deposits became brighter and their tensile strength and hardness increased in a relatively linear fashion (*see* Fig. 1 and 2). The tensile data shown agree fairly well with published data for cast lead-antimony alloys (2). Elongation of the electroformed alloys was essentially *nil* in all cases, and the structure of the alloys, examples of which are shown in Fig. 3, was fine grained.

Peptone-Resorcinol vs. Beta-Naphthol Bath

When the alloy deposits were quickly heated to their melting point, vigorous outgassing and bubbling occurred, and an odor similar to that of burnt peptone was evident. In addition, a carbonaceous film would occasionally appear on the surface of a heated part. This phenomenon was attributed to decomposition of organics which had been occluded in the deposits during plating. A few experiments revealed that, of the two organic additives used in the solution, peptone was the major culprit in the heating problem. Attempts at producing deposits without either one or both of the organic additives resulted in rough, noduled deposits that were completely unacceptable.

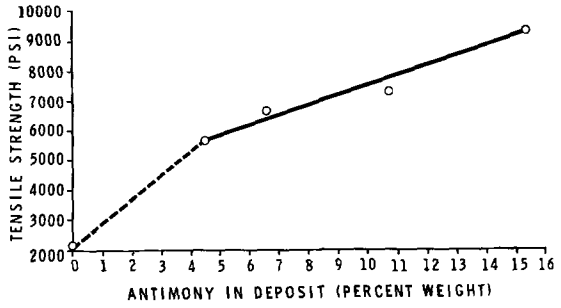

Fig. 1. Effect of antimony content in the deposit on tensile strength.

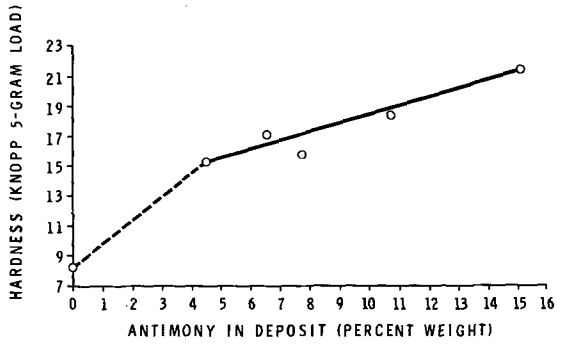

Fig. 2. Effect of antimony content in the deposit on hardness

At this point, it should be mentioned that this bubbling phenomenon was also obtained with tin-lead electrodeposits produced in a standard fluoborate bath containing peptone and resorcinol as additives (14). This finding led to the conclusion that this type of reaction is probably prevalent for most deposits produced in fluoborate solution containing organic additives. For thin deposits, the problem is probably not of consequence; however, when deposits are thick and joining or soldering operations have to be performed, difficulties could be experienced.

A few other organic additives, including catechol, hydroquinone, and beta-naphthol, were evaluated in the lead-antimony solution. It was found that smooth, thick deposits could be produced in a solution containing beta-naphthol, and when these deposits were heated the bubbling was not nearly as extensive as with the peptone-resorcinol system. Figure 4 compares a deposit produced in the peptone-resorcinol bath with one produced in the beta-naphthol bath. Both were quickly heated to their melting points shortly after plating. Because the beta-naphthol bath produced good deposits that did not bubble when heated, the physical properties of the deposits obtained with this bath were further investigated.

Beta-naphthol bath.—To evaluate the effect of current density and temperature on the antimony concentration of deposits produced in the beta-naphthol bath, a series of experiments was run with a 40-liter solution containing beta-naphthol as the organic additive (*see* Table IV). The antimony concentration of the plating solution was checked after each plating test by Langford's permanganate technique (15) and then readjusted with additions of antimony fluoborate. Cur-

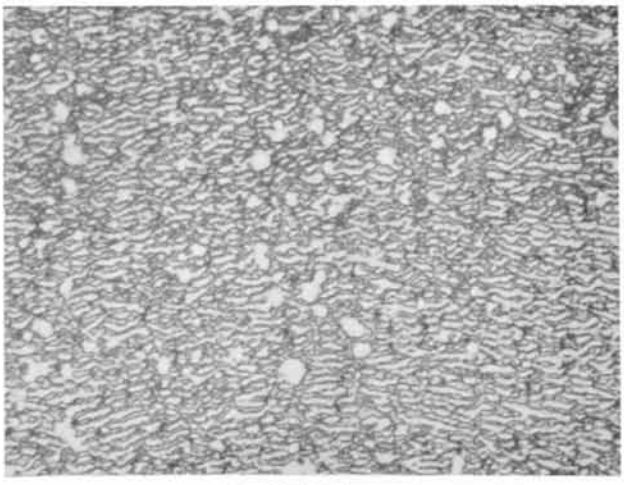

Fig. 3. Cross sections of deposits produced in solution containing lead fluoborate, antimony fluoborate, peptone, and resorcinol. Etchant was a solution containing acetic acid, nitric acid, and glycerol. Magnification was 1000X. Current density was 25 A/ft².

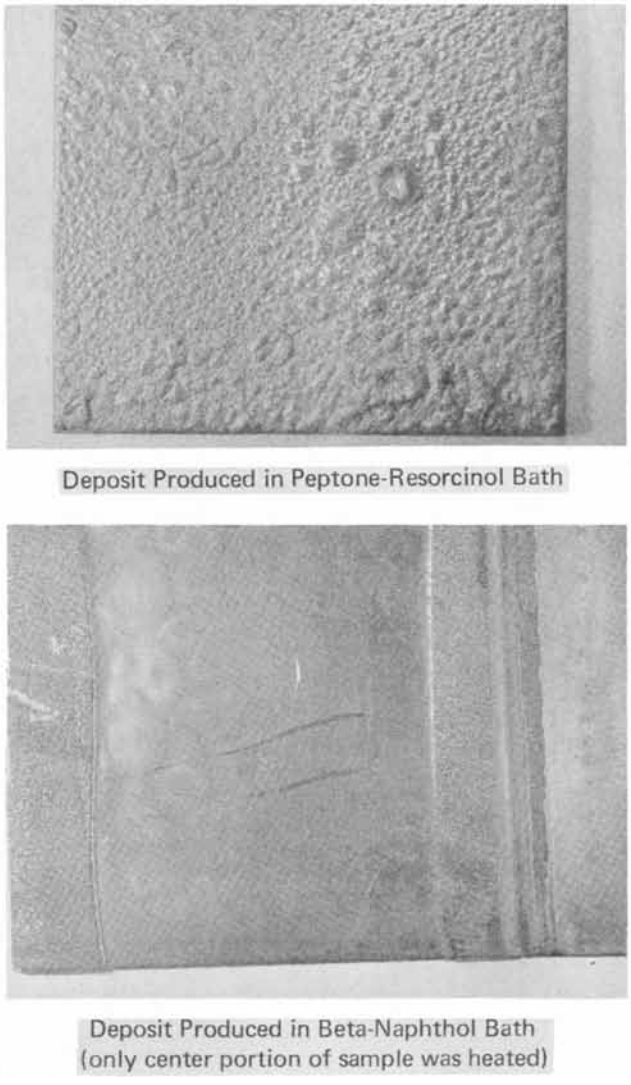

Fig. 4. Comparison of deposits produced in peptone-resorcinol and beta-naphthol baths. Note the bubbling effect on the deposit produced in the peptone-resorcinol bath.

rent density effects were checked at two antimony concentration levels, 0.43 and 0.98 g/liter.

The results, included in Table IV, show that for both series evaluated the antimony concentration increased as the current density decreased. As expected, the bath containing the higher amount of antimony in solution produced deposits higher in antimony content. The temperature data (*see* Table V), which were obtained only on the bath containing 0.43 g/liter antimony, showed that as the temperature increased the antimony content of the deposit increased.

These trends for lead and antimony are typical for less noble and more noble metals in a normal alloy plating system.

Table IV. Effect of current density on antimony concentration of alloy

Current density[1] (A/ft²)	Antimony content (w/o)	Antimony content of bath[2] Before plating (g/liter)[3]	After plating (g/liter)[3]
10	5.3	0.43	0.30
20	4.0	0.43	0.35
30	2.1	0.43	0.32
40	2.0	0.43	0.36
10	11.8	0.98	0.74
20	6.7	0.98	0.78
30	5.8	0.98	0.80
30	4.5	0.98	0.85

[1] Five A-hr of plating time were used on all experiments. Deposit thickness was approximately 6 mils.
[2] In addition to the antimony listed above, the bath also contained 460 ml/liter lead fluoborate concentrate and 2.5 g/liter beta-naphthol. Temperature was 52°C. Volume was 40 liters.
[3] Determined by analytical technique described by Langford (15).

Table V. Effect of temperature on antimony concentration of alloy[1]

Temperature (°C)	Antimony content of deposit (w/o)	Antimony content of bath[2] Before plating (g/liter)[3]	After plating (g/liter)[3]
42	3.2	0.43	0.38
52	4.0	0.43	0.35
65	5.7	0.43	0.38

[1] Five A-hr of plating time were used on all experiments. Current density was 20 A/ft². Deposit thickness was approximately 6 mils.
[2] In addition to the antimony listed above, the bath also contained 460 ml/liter lead fluoborate concentrate and 2.5 g/liter beta-naphthol. Volume was 40 liters.
[3] Determined by analytical technique described by Langford (15).

Acknowledgments

The author would like to acknowledge the help of C. W. Karfs, 8312, Materials Application, who did the metallographic work; S. Grisby, 8125, Environmental Test, who performed the tensile tests; H. C. Feemster, 8311, Materials Science, who provided chemistry sup-

port; and T. E. Dadian, 8312, Materials Application, who helped perform the fusion studies.

Manuscript submitted May 23, 1969; revised manuscript received Oct. 23, 1969.

Any discussion of this paper will appear in a Discussion Section to be published in the December 1970 JOURNAL.

REFERENCES

1. J. W. Dini and J. R. Helms, *Metal Finishing*, **67**, 53 (1969).
2. "Metals Handbook," 8th Ed., Vol. 1, American Society for Metals, Metals Park, Ohio, (1961).
3. A. Brenner, "Electrodeposition of Alloys," Vol. II, Academic Press, New York (1963).
4. W. G. Knox, *Metal Ind.*, **18**, 264 (1920).
5. P. P. Beliaev and O. B. Khalatova, *Korroziya i Borba s Nei*, **6**, 48 (1940).
6. A. L. Hitchens, U.S. Pat. 2,634,235 (1953).
7. C. L. Faust, U.S. Pat. 2,718,494 (1955).
8. R. T. Putnam and E. J. Roser, *Plating*, **42**, 1133 (1955); *Proc. Am. Electroplaters' Soc.*, **42**, 38 (1955).
9. D. L. Cox, *Plating*, **51**, 976 (1964).
10. A. H. DuRose and D. M. Hutchison, *ibid.*, **40**, 470-477, 497, 630-633 (1953).
11. J. M. Booe, U.S. Pat. 2,458,827 (1949).
12. R. A. Schaefer and J. B. Mohler, U.S. Pat. 2,461,350 (1949).
13. J. B. Mohler and R. A. Schaefer, *Monthly Review of the American Electroplaters' Society*, **34**, 1361 (1947).
14. "Metal Finishing Guidebook," 37th Ed., Metals and Plastics Publications, Inc., Westwood, N. J. (1969).
15. K. E. Langford, "Analysis of Electroplating and Related Solutions," 3rd Ed., Robert Draper Ltd., Teddington, Middlesex, England (1962).

The Effect of a Silicon-Boron Phase on Thermally Grown Silicon Oxide Films

William A. FitzGibbons,[1] Thomas Kloffenstein,*[2] and Karl M. Busen*[3]

Research and Development Laboratories, Sprague Electric Company, North Adams, Massachusetts

ABSTRACT

It is shown in the present paper that silicon oxides etch more slowly when they are thermally grown on samples with a silicon-boron phase, whereas oxides grown on samples without a phase exhibit the normal etching rate of SiO_2. One also can observe that the maximum variation in etching rates is different for samples with and without a phase. A removal of the phase prior to oxidation reduces variation of the etching rate considerably (by a factor of five in some cases).

In the processing of silicon planar devices or integrated circuits, dopants are being used which convert predetermined regions of a silicon wafer from one conductivity type to another. The dopants enter the wafer *via* openings in a protective silicon oxide mask. To form the openings, photoresist processes are utilized where silicon oxide is coated with a layer of light-sensitive photoresist material and where in subsequent steps this material is exposed, developed, and selectively removed in places which conform to a device pattern. At these places, the silicon oxide can be etched off so that the openings for the dopants are formed.

The etching must be controlled carefully to avoid residues in the openings and/or undercuttings. This phenomenon commonly arises when part of the silicon oxide has been adulterated by a glass-forming substance as phosphorus oxide. Pliskin and Gnall (1) have reported that in this case one finds a faster etching rate for glass than for the oxide itself. Such a difference in etching rate can lead to undercutting.

The appearance of residues in openings is another phenomenon which can be related to a difference in etching rates between a glass and SiO_2. For formation of the openings, timed etching is normally applied and the duration is often adjusted to etching rates of pure silicon oxide. If boron glass occupies the openings, timed etching may not be sufficient to remove all of it, because, as is demonstrated later, boron glass has a lower rate than SiO_2. This residue can be related directly to contact resistance problems.

The present article deals specifically with conditions under which a boron glass is formed and with the etching behavior of the glass and its influence on device fabrication. Generally the glass forms in an oxidizing atmosphere on top of samples which are composed of a silicon substrate and a boron-rich surface layer. Such a layer can be observed after execution of a deposition step, during which a boron source is generated for subsequent drive-in diffusion. In this step, a silicon slice is exposed to high concentrations of diborane (B_2H_6). The layer consists most likely of a silicon-boron phase. Its formation and its nature have been described recently (2, 3). For convenience, some details concerning the phase are repeated here. The phase was observed to form on silicon substrates which were exposed for 5 min and more to an ambient of $N_2 + O_2 + B_2H_6$ (300-1000 ppm) with a total flow of 2 liters/min. The temperature ranged from 930° to 1100°C and the oxygen concentration was 1% at all times. Glass etches such as buffered HF or diluted HF did not attack the phase; however, a mixture of $HF:HNO_3:CH_3COOH = 1:2:6$ or a low-temperature oxidation with subsequent etching in diluted HF removed it. The oxidation was carried out at 600°C in a flow of wet oxygen.

The phase acts as a source for the diffusion of boron into silicon. This diffusion, which takes place together with the formation of the phase, is called prediffusion. For the processing of semiconductor devices, normally an additional heating cycle, the drive-in diffusion is applied in order to obtain a deeper penetration of the prediffused boron into the substrate. During the drive-in diffusion, the sample is exposed to an oxidizing atmosphere and it is this processing step which produces the boron glass we are discussing.

Experimental

For the experiments, several lots were prepared with each lot having three samples. To make condi-

* Electrochemical Society Active Member.
[1] Present address: IBM Corporation, Box A, Essex Junction, Vermont.
[2] Present address: Fairchild Semiconductor, Mountain View, California.
[3] Present address: Zenith Corporation, Chicago, Illinois.

Table I. Deposition cycles

Deposition	B_2H_6 concentration
I	Very low (~100 ppm)
II	Low (~200 ppm)
III	Medium (~300 ppm)

tions for the investigations "realistic," the samples were structured as if they were going to be used for circuit processing, which means that p-type silicon substrates were n-type diffused (with high surface concentration), overgrown with an n-type epitaxial layer, oxidized, covered with photoresist, exposed, developed, stripped of photoresist, subjected to a glass etch, and exposed to different boron depositions as described in Table I.

All samples were then treated by a glass etch. After that, the samples in each deposition cycle were divided into two groups with one group going through ellipsometric measurement #1, phase removal, ellipsometric measurement #2, drive-in, and the other group going through ellipsometric measurement #1 and drive-in. The procedures are summarized in Fig. 1(a).

Data for the deposition cycle have been given in the introduction. The etch, applied after deposition, consisted of $HF:H_2O = 1:10$. The first ellipsometric measurement was done for identification of the boron-silicon phase. For an identification, the relative phase change Δ was determined from the polarizer setting of the ellipsometer. The instrument used was a Gaertner Model L119. A phase layer was considered to be present when the Δ values, as read by the ellipsometer, were different from Archer's value for a cleanest etched silicon surface ($\Delta = 175°$) (4). Under the conditions in this experiment, a Δ of 160° represents a thin-phase layer while a Δ of 130° can be considered a thick phase. The phase removal was achieved by either the low-temperature oxidation with subsequent HF etching [Ref. (3)] or by a special process. To see how effective the removal was, a second ellipsometric measurement was taken. For drive-in, the samples were heated at 1130°C in an oxidizing atmosphere until about 5000Å-thick oxide layers were obtained. No evidence of any silicon-boron or other unetchable phase was apparent after any drive-in cycle used.

The oxides which formed during drive-in were investigated for their etching rate [Fig. 1(b)] by measuring their thicknesses ellipsometrically before and after 3-min etching in a slow glass etch (700 ml of 40% NH_4F solution + 100 ml of 49% HF at 23°C). A special computer program was set up (5) to determine the oxide thickness from ψ and Δ values (change in amplitude ratio and relative phase change) measured at 5461Å under an angle of incidence of 70° and assuming that the index of refraction was $n_1 = 1.456$ for the oxide and $n_2 = 4.05 - 0.028\,i$ for the silicon substrate; n_1 was obtained by comparison of measurements at two different angles of incidence (50° and 70°).

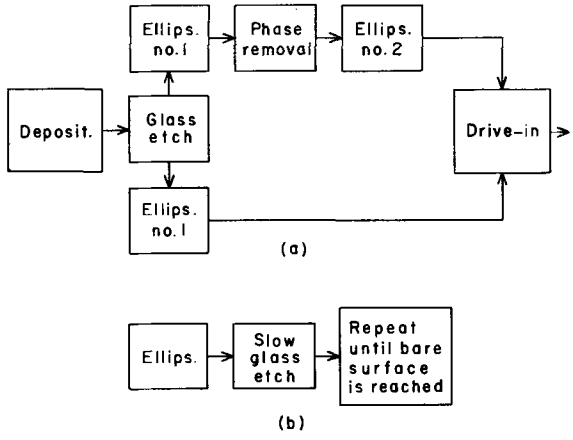

Fig. 1. Procedures for sample evaluation: (a) preparation of samples for drive-in; (b) determination of the etching rate.

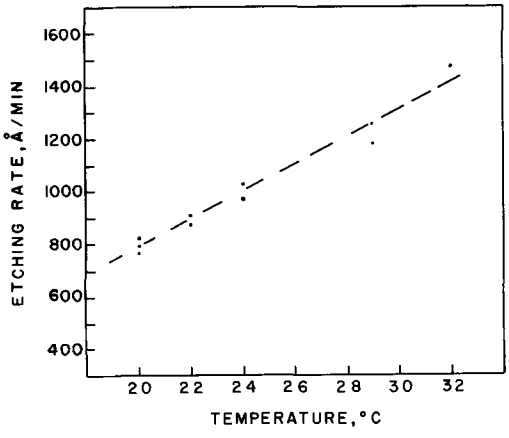

Fig. 2. Etching rate of thermally grown pure silicon oxide vs. temperature.

The results of the measurements are summarized in Table II. The Δ values show that the phase grows with an increase in B_2H_6 concentration. Oxides on samples, where a phase layer existed had on the average about 10% lower etching rates (lots C and D) than oxides which were grown on samples where the phase layer was either very thin or had been removed. One can further observe that the samples with a thicker-phase layer (lot D) acquire thicker oxides after drive-in. For comparison, etching rates as a function of temperature were determined for thermally grown SiO_2. Figure 2 shows that the etching rate of SiO_2 at 23°C is 950 Å/min which is about the same as that for the oxides in lot A and lot B in Table II. This indicates strongly that, for samples with nearly nonexistent phases or for samples without a

Table II. Determination of etching rates for oxides on samples with and without a phase

Lot	Sample No.	Dep. cycle	Δ After dep. and glass etch (°)	Phase removal	Oxide thickness after drive-in (Å)	Etching rate (Å/min)	Maximum variation in etching rate (Å/min)
A	69	I	176	None	4940	986	17
	70	I	172	None	4920	969	
	71	I	176	None	4917	974	
B	75	II	166	Yes	4952	965	28
	76	II	168	Yes	4906	993	
	77	II	172	Yes	4941	965	
C	63	II	172	None	4933	915	41
	64	II	167	None	4934	874	
	65	II	164	None	4936	907	
D	72	III	148	None	5044	843	57
	73	III	150	None	5065	900	
	74	III	150	None	5070	893	

phase, the grown oxide is SiO_2. We find also that for boron glasses there is a larger variation among the etching rates than for SiO_2. The maximum variation for etching rates within a given lot has been entered into the last column of Table II. The extremely large variation of etching rate has been verified by special investigations which have shown that depending on the flow conditions and on the position of the samples the phase can vary from slice to slice in a particular lot or can even vary over a single slice.

After this trend had been established, 36 more samples were prepared with varying phase thicknesses. Of the samples in each group, six samples were subjected to low-temperature oxidation and etching, six samples to the special process for phase removal, and six samples were left untreated. Half of the samples in each subgroup of six were then subjected to a drive-in cycle with wet/dry oxidation, the other half to a cycle with dry/wet/dry oxidation. Again etching rates and their variations were evaluated for oxides grown during drive-in. In Table III are found the results for this part of the investigation. For reasons of economy, individual samples and drive-in cycles (it was found that the cycles had no influence on the etching rate) are not listed in Table III, but only lots of samples which underwent the specified processes. For each lot, the maximum variations in etching rate are found in the last three columns. The trend shown in Table II is now substantially confirmed; namely, that a silicon boron phase leads to an oxide, which etches about 10% slower than pure silicon oxide does and that oxides grown on a phase have a higher maximum variation in etching rate than SiO_2 has. The structure of this oxide has not been investigated but it is tentatively assumed that the substance which forms the oxide is a boron glass.

In a final experiment to provide additional information on the nature of the investigated oxides, oxides of various thicknesses were thermally grown on silicon slices. The oxide-covered slices were then exposed to a B_2H_6 concentration of 1000 ppm for 5 min and were post-annealed in the same furnace for 15 min in an N_2 + 2% O_2 flow. Table IV shows the oxide thickness before and after the B_2H_6 exposure. The thicknesses which were measured with the ellipsometer increased from 500 to 700Å during the B_2H_6 treatment. The etching rate of the oxide was found to change with depth. The upper 2000Å had a rate of 2/5 of that of the remaining oxide. The latter had the same rate which clean, thermally grown SiO_2 has. The effect of the changing etching rate can be seen by etching a step in the oxide and taking interference pictures. They show undercutting. The smaller etching rates, common to oxides grown on phase layers and to oxides prepared by deposition of boron oxide on SiO_2, are indicative of the boron glass nature of the oxides grown on phase layers.

Table III. Etching rates for deposition cycle

Deposition cycle	Phase not removed (Å/min)	Phase removed by oxidation (Å/min)	Phase removed by special process (Å/min)
II	777-957	916-948	895-986
III	633-910	936-986	924-956

Table IV. Oxide grown by exposure to B_2H_6

Sample No.	Growth condition	Thickness after growth (Å)	Thickness after exposure to B_2H_6
1	Dry O_2	1415	2070
2	Dry O_2	2350	2800
3	Dry O_2	3297	4050
4	Wet O_2	4075	4725
5	Wet O_2	5675	6420

Summary and Discussion

In the preceding section, it was shown that oxides grown on a silicon-boron phase have a lower and more erratic etching rate than pure SiO_2. When and if a silicon-boron phase does exist, the lower temperature oxidation prior to drive-in will remove all traces of it. This procedure reduces the etching rate variations by a factor of 3 to 5. High variations in etching rates for samples of the same lot can be related to variations of the phase. It was, furthermore, shown that exposing pure silicon oxide to diborane results in a glass which etches at about twice the rate as does SiO_2.

The last observation explains the undercutting during photoresist processes when one assumes that there are two discrete oxide layers under the photoresist layers. When an opening in such a layer is exposed to a glass etch, the difference in lateral etching rates between SiO_2 and the boron glass causes uneven erosion.

The formation of a boron glass on top of a phase layer during drive-in oxidation can lead to another disturbing effect. When such a glass forms in openings for contacts of a planar device, times etching which is normally adjusted to pure silicon oxide may not be sufficient to remove all of the glass from the openings. In this case, contact resistance problems can result. It was actually observed that upon removal of the phase such problems ceased to exist. Because the appearance of the phase is erratic under certain conditions, one can expect that without phase removal procedures there can be an erratic appearance of contact problems, too, even for the same lot or slice. Thus, phase removal offers a good tool for control of yield. It should be pointed out that according to the investigations the contact resistance problem is not directly associated with an unetchable silicon-boron phase but follows from the formation of the boron glass during drive-in.

Acknowledgment

The authors appreciate measurements and helpful discussions given by Dr. M. Ghezzo of these laboratories.

Manuscript submitted July 2, 1969; revised manuscript received Oct. 13, 1969. This was Recent News Paper 358 presented at the New York Meeting, May 4-9, 1969.

Any discussion of this paper will appear in a Discussion Section to be published in the December 1970 JOURNAL.

REFERENCES

1. W. A. Pliskin and R. P. Gnall, *This Journal*, **111**, 872 (1964).
2. K. M. Busen, W. A. FitzGibbons, and W. K. Tsang, *ibid.*, **115**, 291 (1968).
3. K. M. Busen, W. A. FitzGibbons, and T. Kloffenstein, *Electrochem. Technol.*, **6**, 256 (1968).
4. R. J. Archer, *J. Opt. Soc. Am.*, **52**, 970 (1962).
5. M. Ghezzo, Unpublished work.

Cell Voltage during the Electrolytic Production of Manganese Dioxide

F. R. A. Jorgensen

Division of Mineral Chemistry, C.S.I.R.O., Port Melbourne, Victoria, Australia

ABSTRACT

The components of the cell voltage (*viz.*, anodic potential, *IR* drop through the deposit, *IR* drop through the electrolyte, and cathodic potential) are discussed for a range of operating conditions and the discussion illustrated with a record of pilot cell data obtained over a period of 32 days of operation. Growth of the deposit was found to occur from the deposit/electrolyte interface and electrical transport through the deposit was by semiconduction.

Gamma manganese dioxide for use as a depolarizer in high-capacity dry cells can be prepared by the electrolysis of a hot aqueous manganese sulfate solution (1). During this operation, manganese dioxide forms as a massive deposit at the anode and hydrogen is liberated at the cathode. A typical voltage drop across an operating cell has not been discussed in detail in the literature and, apart from a few isolated measurements by Kissin (2) and Steinhoff (3), little is known about the individual electrode processes in these electrolytes. The mechanism of deposition is also not completely understood. Marx (4) concluded that the deposit formed at the actual electrode surface, while both Marx and Schrier and Hoffman (5) concluded that the deposit was nonconducting and electrical transport was *via* pores through the deposit. Van Arsdale and Maier (6), however, treated the electrode processes as occurring at the deposit/electrolyte interface and stated that the deposit was conducting. In view of this lack of information and doubt as to the actual mechanism of formation of the massive deposits, advantage was taken during the operation of a small pilot plant electrolytic cell to conduct a series of experiments to further our understanding of this electrolytic process.

Experimental

In the pilot cell, high-density oil-impregnated graphite was used as the electrode material for both anodes and cathodes, the relative arrangement of which is shown in plain view in Fig. 1. The electrodes were housed in a polypropylene-lined steel tank through which the heated cell liquor was circulated at the rate of 2 gpm by a peristaltic pump. Fresh feed was metered to the cell, displacing spent electrolyte through an overflow pipe to maintain a constant level. The cell was operated under the following conditions: T, 95°C; H_2SO_4, 50-55 g/liter; Mn^{2+}, 55-60 g/liter; anode C.D., 10.0 A/ft² (10.8 mA/cm²); cathode C.D., 6.8 A/ft² (7.3 mA/cm²). Figure 1 also shows the position of a polypropylene strip which was suspended in the electrolyte some distance in front of one of the anodes. This strip served the same purpose as a marker in high-temperature oxidation experiments and was used to detect whether the deposit grew from the graphite or the electrolyte interface.

The cell was operated for 32 days during which time the deposit attained a thickness of 1 in. The deposit was remarkably uniform in thickness, thus indicating a uniform distribution of current to all parts of the anodes. After a 2-hr start-up period, measurements were made of the potential at the surface of the growing deposit relative to a Hg-$HgSO_4$ reference electrode. The latter was sited external to the cell and was connected to one of the anodes *via* a probe which was filled with 1N H_2SO_4. After each measurement, the probe was rotated away from the electrode to prevent incorporation in the deposit. A current interrupter, employing high-current switching transistors, was used when required to remove the current for approximately 10^{-4} sec. The *IR*-free potential measurements were made at the moment of interruption using a cathode ray oscilloscope as null indicator. The equipment is shown in schematic form in Fig. 2.

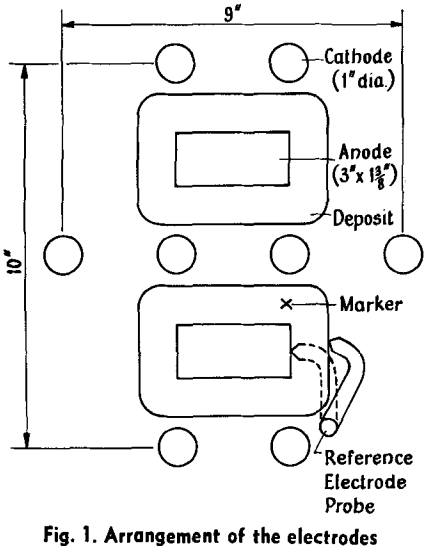

Fig. 1. Arrangement of the electrodes

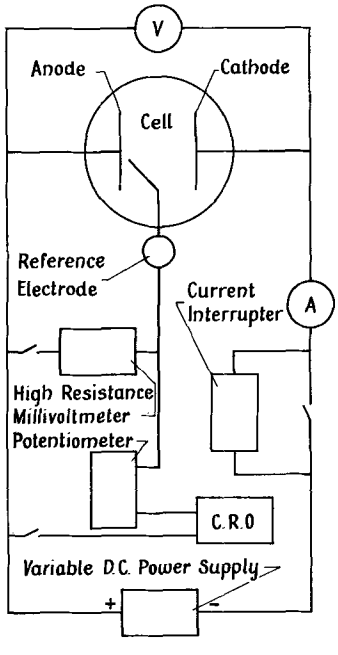

Fig. 2. Cell instrumentation

On completion of the run the anodes were quickly removed from the cell and washed, the deposit was stripped from the anodes, and samples retained for chemical and x-ray diffraction analysis. Samples of the material were subsequently sectioned on a diamond saw and the individual sections analyzed for total manganese (7) and available oxygen (8). These figures were used to establish the value of "n" in the formula MnO_n.

Results and Discussion

Figure 3 shows point values of the cell voltage as a function of time. The results were characterized by the initial rapid rise to a level of 2.75V and thereafter by a slow decrease to 2.60V at the end of the run. Fluctuations occurred due to cracking of the deposit and to a lesser extent to minor variations in the electrolyte composition during the course of the run. In the following discussion, the over-all cell voltage has been broken down into the following components: anodic potential, *IR* drop through the deposit, *IR* drop through the electrolyte, and cathodic potential.

Anodic reaction.—At the end of the run, inspection of the anodes revealed that the polypropylene marker had become incorporated in the deposit and had not been pushed ahead of it. This shows conclusively that deposit formed at the electrolyte and not at the graphite interface. The deposit on one of the anodes was also noted to be touching a cathode. No short-circuiting of the cell had occurred, however, so that if the deposit was conducting it must be concluded, in agreement with Nichols (9), that the presence of a very high contact resistance prevented the leakage of a significant amount of current. Further inspection revealed the presence of some pores in the deposit. They were few in number, however, and appeared to have resulted from the healing of cracks. In many cases, the pores were blind and did not lead to either face of the deposit. These observations discount the suggestions made by Schrier and Hoffman (5) that the formation of the deposit took place by a mechanism involving pores through the deposit and support the view that a reaction of the type proposed by Vetter (10) occurs at the deposit/electrolyte interface. This electrochemical reaction may be represented by the following equation

$$Mn^{2+} + (n + m)H_2O \rightarrow MnO_n \cdot mH_2O + 2nH^+ + 2(n - 1)e \quad \ldots (A)$$

Figure 4 shows anode potential, corrected for *IR*, as a function of the electrolysis time. It can be seen that in the first 50 hr there was a rapid polarization to potentials in excess of 1400 mV *vs.* NHE, after which the potential decreased and thereafter remained practically constant at 1330 mV *vs.* NHE. Unfortunately, the point values shown in Fig. 4 do not allow the full magnitude of the polarization to be determined as this occurred over a week end when the cell was unattended. Separate tests indicated, however, that during this phase of the electrolysis polarizations of as high as 1800 mV *vs.* NHE were attained. In a limited number of tests, graphite anodes were found to exhibit the initial polarization on every occasion that they were tested; for platinum anodes, however, the effect was not always observed but appeared to be dependent on surface preparation. A possible explanation of the above behavior is that the initial oxide film formed on the surface of the anodes was incapable of maintaining the reaction at the rate of the impressed current and the electrodes polarized to potentials where alternate reactions were possible. At these high potentials, the initial oxide film either underwent a dissolution or was recrystallized, the net effect being that nuclei of the desired form were created on the surface after which the potential settled to a level characteristic of electrolysis conditions.

Additional information concerning the final steady state anodic reaction was obtained from a series of laboratory scale tests carried out at constant anode potentials. The form of the potential *vs.* steady state current density relation is shown in Fig. 5 from which it is evident that for the electrolyte (*i.e.*, one containing 50 g/liter H_2SO_4 and 50 g/liter Mn^{2+} as $MnSO_4$), and degree of agitation used in these tests, a limiting diffu-

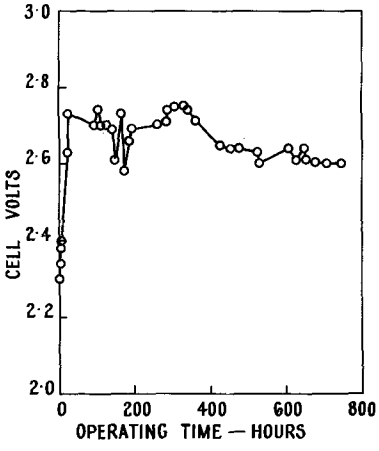

Fig. 3. Cell volts as a function of operating time

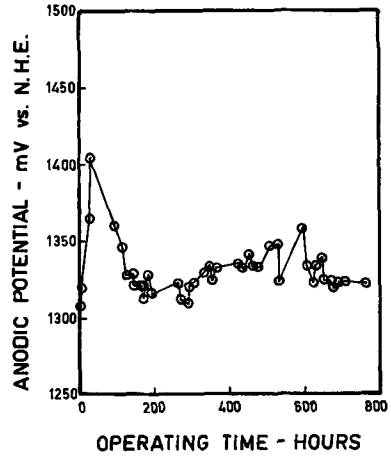

Fig. 4. Anodic potential, corrected for *IR* drop, as a function of operating time.

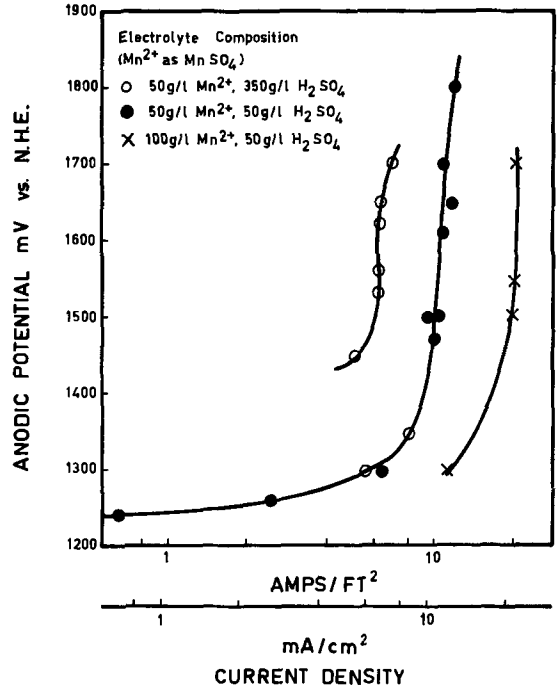

Fig. 5. Anodic current density, at the surface of the deposit, as a function of the potential of formation.

sion condition was approached at values of the current density exceeding 10 A/ft² (10.8 mA/cm²). Increasing the manganese concentration of the electrolyte to 100 g/liter Mn^{2+} approximately doubled the limiting diffusion current, while an increase of the acid content to 350 g/liter was found to halve the limiting current density. For the electrolytes containing 50 and 100 g/liter of Mn^{2+}, anodic current efficiencies of close to 100% were attained until the potential exceeded 1400 mV *vs.* NHE after which the efficiency declined. For the electrolytes containing 350 g/liter of acid, however, the anodic current efficiencies were only of the order of 50%.

X-ray diffraction analysis of ground samples of the deposit confirmed the γ structure and chemical analysis of thin sections revealed the presence of a composition gradient through the deposit which reflected the effect of variations in the anode potential on the composition of the deposited material. The composition gradient is shown in Fig. 6. Chemical analysis also showed the presence of a very thin layer of degraded material, having an *n* value of 1.83, at the electrode surface. This material was in contact with ⅛ in. of partially oxidized graphite. Additional pilot plant tests which involved the removal of anodes after 50 and 400 hr of operation showed that most of the attack on the graphite occurred during the first 50 hr of operation when the electrodes were polarized to high potentials. Extension of the operating time to 780 hr did not produce any measurable increase in the deterioration of the anodes.

Conductivity of the deposit.—The voltage drop associated with the passage of the current through the deposit is shown in Fig. 7. During the first 50 hr of operation, the *IR* drop over the deposit rapidly increased to approximately 300 mV, after which there was a steady increase as the deposit thickened. Fluctuations evident in the record were probably caused by the formation and subsequent healing of cracks in the deposit. The initial rise in the graph is associated with the first 50 hr of operation when the electrodes were polarized to high potentials and represents a high resistance contact at the electrode surface due to the presence of a layer of partially oxidized electrode material and degraded MnO_2. Deposits produced on platinum electrodes which experienced the initial polarization to high potentials did not show the sudden rise in *IR* component. These observations support the above view.

There is a lack of information concerning the semiconducting properties of γMnO_2. Pons and Brenet (11) have, however, reported a value of 13 ohm-cm for the

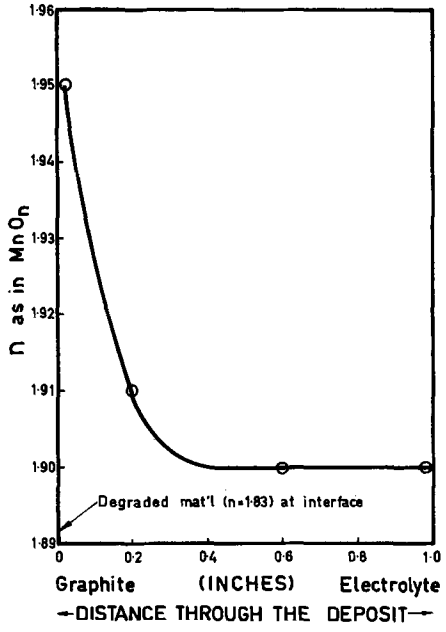

Fig. 6. Composition gradient through the deposit

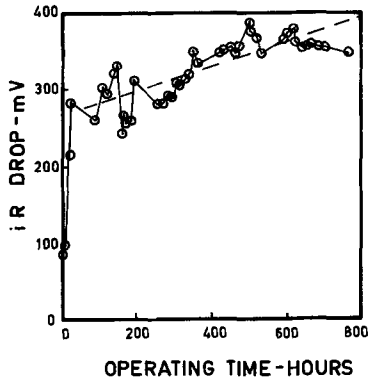

Fig. 7. *IR* drop across the deposit as a function of operating time.

resistivity measured at room temperature and Gabano and his associates (12) have determined semiconduction activation energies for a wide range of composition. Calculations utilizing these data show that under the present conditions (*T*, 95°C; average *n* value of the deposit 1.91) the conductivity of γMnO_2 should be 0.4 ohm^{-1} cm^{-1}. This agrees fairly well with the value of 0.25 ohm^{-1} cm^{-1} obtained from the steadily increasing *IR* values. The latter, which correspond to the increase in *IR* due to the growth of the deposit, are indicated on Fig. 7 by the dashed line.

The above discussion was based on measurements carried out with the reference probe at a fixed distance of 8 in. above the bottom of an anode. Two hours before the completion of the run, however, the probe was traversed over the whole of the 19½ in. of the anode that was submerged in the electrolyte. The *IR*-free potential was independent of position and constant at 1330 mV *vs.* NHE, while the potential drop across the deposit was found to vary from 344 mV at the bottom to 333 mV at the top of the electrode. Calculations taking the current and conductivity of the graphite (8.5 x 10^3 ohm^{-1} cm^{-1}) into account showed the voltage drop, associated with the flow of current through the graphite, to be approximately 10 mV. When allowance was made for this factor, the voltage drop across the deposit was also found to be independent of position.

Conductivity of the electrolyte.—The conductivity values of various manganese sulfate/sulfuric acid solutions were determined in a heated conductivity cell and the results are shown in Fig. 8. It can be seen that, over the range of concentration used in the present work, conductivity of the electrolyte was independent of manganese concentration but increased linearly with increasing acid concentration. It is also apparent that the conductivity of the electrolyte was less than that of the deposit (0.16 *cf.* 0.25 ohm^{-1} cm^{-1}). Hence,

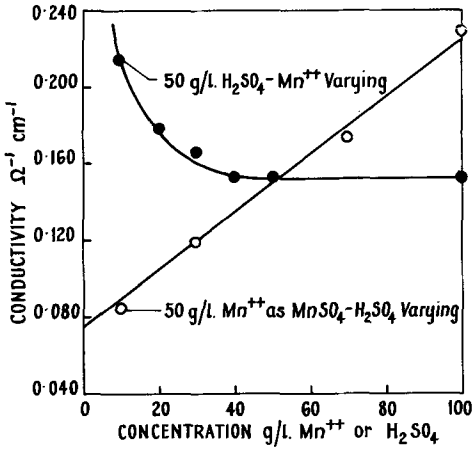

Fig. 8. Conductivity of manganese sulfate electrolytes at 95°C

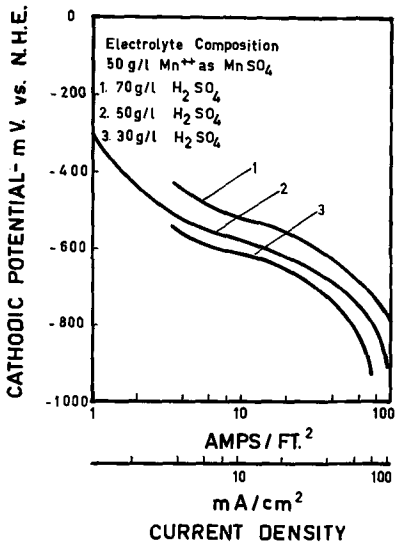

Fig. 9. Cathodic current density as a function of potential

as the deposit increased in thickness it reduced the length of the solution path and there was a net reduction in the over-all cell resistance.

Some of the decrease in cell volts, evident from Fig. 3, could also have been due to the reduction in current density at the surface of the growing deposit. It was shown however that, after the initial polarization had passed, the *IR*-corrected anode potential remained practically constant at 1330 mV *vs.* NHE. This is consistent with electrolysis conditions in the pilot cell corresponding to the flat portion of Fig. 5 where the anode potential is relatively unaffected by variations in current density. Hence under the present conditions the decrease in cell volts was due solely to the reduced length of the solution path.

Cathodic reaction.—Electrolytes containing from 30 to 70 g/liter of H_2SO_4 and Mn^{2+} as the sulfate were used in a well-stirred laboratory cell to determine the effect of electrolyte composition on the overvoltage associated with the hydrogen evolution reaction at the cathodes. As would be expected, manganese concentration had little effect but varying the acid concentration made appreciable differences to the potential of the reaction. From Fig. 9 it can be seen that under the conditions used in this work the cathodes would have been operating at a potential of −560 mV *vs.* NHE.

Conclusions

1. Evidence has been presented to show that massive electrodeposits of manganese dioxide function as semiconductor electrodes; that is, the anodic reaction occurred at the interface between the deposit and the electrolyte, while electrical transport through the deposit was by semiconduction.
2. Results obtained from the operation of a small pilot plant cell showed that for most of the run the cell operated at a voltage of from 2.75 to 2.60V. Analysis of the results showed that the combined anodic and cathodic electrochemical reactions accounted for 1.90V, and that the remaining 0.85-0.70V was associated with the passage of the current through the deposit and the electrolyte. The conductivity of the electrolyte was less than that of the deposit, and as the deposit thickened there was a resultant slight decrease in the over-all cell voltage.

Acknowledgments

The author wishes to thank Dr. W. T. Denholm and Mr. R. Dorin, members of the Division of Mineral Chemistry, C.S.I.R.O., the former for devising the system of *IR* measurement and the latter for assistance with the experimental program. The financial support of the Electrolytic Zinc Company of Australasia Limited is also gratefully acknowledged.

Manuscript submitted April 21, 1969; revised manuscript received Oct. 24, 1969.

Any discussion of this paper will appear in a Discussion Section to be published in the December 1970 JOURNAL.

REFERENCES

1. C. A. Hampel, "The Encyclopedia of Electrochemistry," p. 790, Reinhold Publishing Corp., New York (1964).
2. G. H. Kissin, Final Report Project No. 107-7, Georgia Institute of Technology, State Engineering Experiment Station, July 30, 1949.
3. O. W. Storey, E. Steinhoff, and E. R. Hoff, *This Journal*, **86**, 344 (1944).
4. P. Marx, U. S. Bur. Mines Inform. Circ. No. 7464 (1948).
5. E. Schrier and R. Hoffman, *Chem. Eng.*, **62**, 152 (1954).
6. G. D. Van Arsdale and C. G. Maier, *Trans. Electrochem. Soc.*, **33**, 109 (1918).
7. J. J. Lingane and R. Karplus, *Ind. Eng. Chem.*, **18**, 191 (1946).
8. I. M. Kolthoff and E. B. Sandell, "Textbook of Quantitative Inorganic Analysis," 3rd Ed., p. 575, MacMillan Co., New York (1952).
9. G. W. Nichols, *Trans. Electrochem. Soc.*, **62**, 393 (1932).
10. K. J. Vetter, *This Journal*, **110**, 591 (1963).
11. L. Pons and J. Brenet, *Compt. Rend.*, **260**, 2483 (1965).
12. J. P. Gabano, B. Morignat, and J. F. Laurent, *Electrochem. Technol.*, **5**, 531 (1967).

Conductivity of Sodium Chlorate-Sodium Chloride-Water System at High Temperature

R. A. Crawford,* W. B. Darlington,[1] and L. B. Kliever[2]

Research Department, Industrial Chemicals Division, PPG Industries, Barberton, Ohio

ABSTRACT

The conductivity of the $NaClO_3$-NaCl-$H_2O_{(l)}$ system for temperatures above 80°C was investigated. The $NaClO_3$ concentration ranged from 412 to 1354 g/1000g H_2O and the NaCl concentration varied from 74 to 177 g/1000g H_2O. Temperature and $NaClO_3$ concentration were both significant variables in affecting the conductance of the salt solution. Regression analysis was used to determine the coefficients for a series of empirical conductance equations. These model equations used various concentration terms, as square root, linear, square, and logarithmic, and are compared to experimental results. Only two equations are reported and these equations predict the experimental data within ±0.005 mho cm^{-1} for the concentration ranges and temperatures studied.

A common method for the industrial preparation of sodium chlorate uses a solution containing around 600 g/liter $NaClO_3$ and 120 g/liter NaCl at a temperature of 45°C. With the development of newer electrode systems and improved cell design, $NaClO_3$ may be produced using solutions having higher $NaClO_3$ concentrations and cells operating at higher temperatures. The objective of this work was to obtain contour maps at various temperatures so optimum salts concentrations could be used. Since the over-all production system may determine the concentration of one of the salts, a range of values, or a contour surface, was required. The range of salts concentrations reported here varies from 328g $NaClO_3$/liter (412 g/1000g H_2O) to 842g $NaClO_3$/liter (1354 g/1000g H_2O) and from 57g NaCl/liter (74 g/1000g H_2O) to 120g NaCl/liter (177 g/1000g H_2O).

Shedlovsky (1), using the theoretical equations developed by Onsager, found an empirical equation for the determination of $\Lambda°$. Lorenz (2) replaced the original square root concentration term with an empirical parameter that was characteristic for each group of electrolytes. The Lorenz equation is shown in Eq. [1].

$$\Lambda = \Lambda° - AC^n \qquad [1]$$

Knibbs and Palfreeman (3) studied the $NaClO_3$-NaCl-H_2O system for temperatures up to 80°C, $NaClO_3$ concentrations up to 600 g/liter, and NaCl concentrations up to 250 g/liter. They did not attempt to correlate their data to empirical equations. As with the study of Knibbs and Palfreeman, the system in this paper is not a simple or a dilute system. There are two anions and one cation present and the total ionic strength is much greater than allowed by any of the empirical equations developed. Because of this, we are attempting to find empirical equations that best fit our data.

Experimental

After determining the area of interest with preliminary studies, two series of runs were made using the following procedure. A conductance cell was constructed by sealing a commercial pipette-type conductivity cell with platinized electrodes in a 1-liter Erlenmeyer flask. The connection was made near the bottom of the flask so a sample of the electrolyte solution could be drawn up between the electrodes for a conductance measurement. A Teflon stopcock at the top of the pipette cell allowed it to be sealed from the atmosphere. The Erlenmeyer flask was fitted with an "O" ring joint in which a circle of hydrophobic membrane material[3] was held in place by Viton "O" rings. This membrane permitted air to escape from the cell (because the cell contents expand after placing in the constant temperature bath) but was impermeable to water vapor. A 24/40 joint was modified so it could be fitted with a rubber septum and this was inserted in the top of the Erlenmeyer. Additional solution was added to the cell from a hypodermic syringe equipped with a 6-in. long 20-gauge needle that was inserted through the rubber septum. This allowed us to introduce the sample near the bottom of the cell. Stirring in the cell was done with a Teflon covered magnetic stirring bar that was actuated by an air driven magnetic motor immersed in the constant temperature bath. The conductivity cell was calibrated with 1.0 demal KCl at 25°C using the data of Jones and Bradshaw (4). The cell constant was 98.98 cm^{-1}. The cell was connected, using a grounded, shielded cable, to a Beckman Model RC-18 conductance bridge with an accuracy of 0.1%.

The solutions to be measured were prepared gravimetrically by weighing the correct amount of salts and water into the Erlenmeyer flask described earlier. All weights were corrected to vacuo. The flask was placed in the constant temperature bath and after the desired temperature had been attained, the conductance cell was filled with sample. The conductance was monitored for a period of time until the conductance did not vary by more than ±5 μmhos on successive measurements.

If a dilution was to be made for another conductance measurement at a different concentration, the following procedure was used. The solution to be added was drawn into the syringe, the syringe weighed, the contents added to the cell as previously described, and the empty syringe reweighed to give a tare weight. The solution was thoroughly stirred and the conductance obtained as described above.

The constant temperature bath used for these studies was an oil-filled recirculating bath. The temperature was regulated to ±0.02°C by a mercury-in-glass thermoregulator and its associated relay. The regulator activated a 250-w infrared heat lamp mounted above the bath, thereby avoiding thermal lags obtained with immersion heaters.

The temperature was measured with a Beckman thermometer calibrated in increments of 0.01°C. This

* Electrochemical Society Active Member.

[1] Present address: Research Department, PPG Industries, Corpus Christi, Texas 78408.

[2] Present address: Phillips Petroleum Company, Akron, Ohio 44308.

Key words: conductivity, specific conductance, NaCl-$NaClO_3$ conductivity in H_2O, empirical specific conductance models, specific conductance above 80°C, specific conductance at high salt concentration.

[3] Acopor WC-800, Gelman Instrument Company, Ann Arbor, Michigan.

thermometer was calibrated using a laboratory platinum resistance thermometer which in turn had been calibrated against a National Bureau of Standards reference.

Chemicals.—The KCl was recrystallized J. T. Baker reagent grade assaying 99.7% KCl before recrystallization.

The $NaClO_3$ was J. T. Baker reagent grade assaying 100.0% $NaClO_3$.

The NaCl was Fisher ACS reagent grade.

All materials were dried at 110°-120°C under a pressure of 1-2 Torr for at least 24 hr prior to use. The chemicals were stored over P_4O_{10}. The conductivity water used for preparing all solutions was obtained by redistilling water in a quartz still.

Results

These runs were performed at 90.00° ± 0.02°C and 97.50° ± 0.02°C at several NaCl and $NaClO_3$ concentrations. Some effort to statistically balance these data points was tried, but complete balance was not possible because of solubility limits. The data points are given in Table I. There was randomization within a series to help remove bias. In the 90.0°C series, runs No. 5, 9, and 10 were replicated and gave an average conductance value of 0.44341 ± 0.00451 mho cm^{-1}. In the 97.5°C series, runs No. 14 and 15 were replicated and gave an average value of 0.48088 ± 0.00030 mho cm^{-1}.

Since our objective was to obtain the best empirical equation from our data and to obtain contour maps from these equations, many different models were tried. Acceptable models were subject to the following restrictions:

(*a*) A significant regression mean square[4]
(*b*) The two series of data had to be compatible indicating no temperature interaction[5]
(*c*) The R Square term should be close to 1 indicating that most of the data were included in the regression sum of squares[6]
(*d*) The standard error term should be small

The data were analyzed using regression analysis. In this technique, the parameters associated with a model equation containing one dependent and one or more independent variables per equation are estimated using a least-squares technique. Using these results, one estimates the random error associated with the response (standard error) and places confidence limits on the parameters.

Many models, from very simple models utilizing only linear concentration terms to complicated models using a combination of half power, linear, quadratic, logarithmic, and interaction terms, were tried. All calculations were performed on an IBM 360 or a time-sharing computer. All calculations have the concentrations in molal units and temperature in °C, either as original or coded data.

The simple models did not fulfill all of the above criteria and the complicated models did not improve the R^2 or reduce the standard error sufficiently to warrant their use. Therefore, only two models are described in this paper.

The first model equation was a full polynomial in the variables. In order to separate the quadratic effects from the linear effects, that is decrease the confounding, and at the same time improve the determinant of the correlation matrix, the data were coded. This involved transforming the coordinates of the system so the centroid of the data points approximately correspond to the origin of the transformed variables. The transformed model equation is given in Eq. [2].

$$K = 4.6028 \times 10^{-1} + 8.5861 \times 10^{-5} \cdot C_1 + 1.296 \times 10^{-6} \cdot C_1^2 - 8.7904 \times 10^{-5} \cdot C_2 - 5.5571 \times 10^{-8} \cdot C_2^2 - 6.7264 \times 10^{-7} \cdot C_1 \cdot C_2 + 4.1267 \times 10^{-3} \cdot T \quad [2]$$

where:

K = Specific conductance in mho cm^{-1}
T = [°C − 93.75°C]
C_1 = [NaCl concentration − 130 g/1000g H_2O]
C_2 = [$NaClO_3$ concentration − 870 g/1000g H_2O]

This model gave a statistically significant regression equation and the equation had a standard error of 4.66 x 10^{-3} mho cm^{-1}. The plot back is shown in Table II. It is observed that the maximum error is only slightly greater than 1%, with most of the errors less than 1%.

Contour maps of these data were obtained and the one for 97.5°C is shown in Fig. 1. The contour map for the 90.0°C is not shown; however, it has the same form except that the specific conductance values were smaller. Equation [2], when reduced to its canonical form, is the equation for a hyperbola with the center of the plateau at a coded NaCl concentration of −98 g/1000g H_2O and a coded $NaClO_3$ concentration of −200 g/1000g H_2O. The specific conductance at this point is calculated to be 0.44526. The experimental

[4] The preliminary data indicated that at least $NaClO_3$ concentration was significant in affecting specific conductance.
[5] The preliminary data indicated that specific conductance was linearly related to temperature.
[6] The R Square = Regression SS/Total SS.

Table I. Data points for investigation of specific conductance as a function of $NaClO_3$ and NaCl concentration

Run No.	Temp, °C	$NaClO_3$ conc, g/1000g H_2O	NaCl conc, g/1000g H_2O	Sp cond, mhos cm^{-1}
1	90.00	853.2	87.77	0.44393
2	90.00	1175	109.7	0.41336
3	90.00	593.6	91.97	0.45832
4	90.00	1354	150.1	0.38681
5	90.00	872.3	131.2	0.44472
6	90.00	504.5	116.7	0.46479
7	90.00	612.2	149.7	0.47448
8	90.00	901.3	177.7	0.44469
9	90.00	874.6	129.1	0.44387
10	90.00	875.9	131.4	0.44165
11	97.50	412.2	113.1	0.49334
12	97.50	525.5	73.80	0.48714
13	97.50	796.0	128.2	0.47378
14	97.50	875.9	131.4	0.48110
15	97.50	876.0	131.6	0.48067
16	97.50	901.3	177.7	0.48227
17	97.50	1175	109.7	0.44500
18	97.50	1151	176.1	0.43897
19	97.50	1354	150.1	0.41879

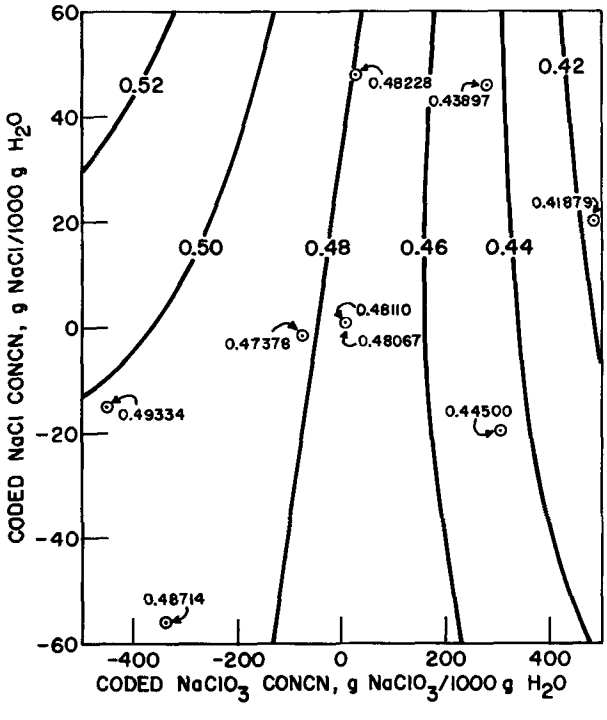

Fig. 1. Contour surface, using Eq. [2], for specific conductance as a function of NaCl and $NaClO_3$ concentration and a coded temperature of +3.75°C (97.5°C).

points are included in Fig. 1 and it is observed that the fit, in most cases, is quite good.

This model equation, unfortunately, has some inherent errors. The first is that it predicts continually increasing conductance values at: (*a*) high NaCl concentration and low $NaClO_3$ concentration, and (*b*) low NaCl and high $NaClO_3$ concentrations. We know this is incorrect because association at high concentrations should decrease the conductance. This equation also predicts continually decreasing values of conductance at high NaCl and $NaClO_3$ concentrations and at low NaCl and $NaClO_3$ concentrations, which would be expected. Solubility effects are ignored in this and subsequent analyses. Another difficulty with this equation is that the specific conductance should approach zero as the actual NaCl and $NaClO_3$ concentrations approach zero. This equation predicts a specific conductance of 0.281 mho cm^{-1} at zero salts concentrations.

Since the constant term and coded data in Eq. [2] prevented the specific conductance from approaching zero, the constant term in the second model was deleted. This change would force the equation to go through zero if the data were not coded.

A model that fits the theoretical equation a little better is given in Eq. [3] and [4]. Equation [3] gives the 90.0°C model

$$K = 4.0292 \times 10^{-2} \cdot C_1^{1/2} + 1.6577 \times 10^{-2} \cdot C_2^{1/2} - 1.3221 \times 10^{-3} \cdot C_1 - 3.2127 \times 10^{-4} \cdot C_2 - 4.2414 \times 10^{-7} \cdot C_1 \cdot C_2 \quad [3]$$

and Eq. [4] gives the 97.5°C model

$$K = 4.227 \times 10^{-2} \cdot C_1^{1/2} + 2.2105 \times 10^{-2} \cdot C_2^{1/2} - 1.8805 \times 10^{-3} \cdot C_1 - 4.7733 \times 10^{-4} \cdot C_2 + 7.1351 \times 10^{-8} \cdot C_1 \cdot C_2 \quad [4]$$

where

C_1 = NaCl concentration in g/1000g H_2O
C_2 = $NaClO_3$ concentration in g/1000g H_2O

The model represented by these equations gives a standard error of 5.55 x 10^{-3} mho cm^{-1} and a statistically significant regression equation. The plot back data are shown in Table II and it is observed that the fit is about as good as the fit obtained with Eq. [2]. This is very satisfying because we have forced this model to give a zero specific conductance at zero NaCl and $NaClO_3$ concentration.

A contour map of 97.5°C data is shown in Fig. 2. The contour map for the 90.0°C data is not shown, but will have the same general shape as Fig. 2. Equation [4] predicts a maximum specific conductance of 0.498 mho cm^{-1} at a NaCl concentration of 135 g/1000g H_2O and a $NaClO_3$ concentration of 565 g/1000g H_2O.

Equations [3] and [4] obviously predict that the specific conductance goes to zero as the salts concentrations go to zero. Also, as the salts concentrations get extremely large, the specific conductance goes to zero, and of course, goes negative beyond this point. This zero specific conductance value is well beyond solubility limits, however. These equations also predict that when one of the salts is constant at zero concentration and the other is steadily increased, the specific conductance passes through a maximum. This behavior would be expected experimentally.

Table II. Tabulation of difference between empirical model equations and experimental data

Run No.	Difference values (Expt value-calc. value) in mho cm^{-1} Eq. [2]	Eq. [3] or [4]	% Deviation from expt point Eq. [2]	Eq. [3] or [4]
1	-2.446×10^{-4}	4.101×10^{-3}	−0.06	0.92
2	-2.349×10^{-3}	2.632×10^{-4}	−0.57	0.06
3	2.163×10^{-3}	3.442×10^{-3}	0.47	0.75
4	1.933×10^{-3}	2.772×10^{-3}	0.46	0.72
5	1.776×10^{-5}	-4.195×10^{-3}	0.00	−0.94
6	-5.050×10^{-4}	-1.505×10^{-3}	−0.11	−0.32
7	5.164×10^{-3}	4.768×10^{-3}	1.09	1.00
8	-2.978×10^{-3}	2.274×10^{-3}	−0.67	0.51
9	-4.529×10^{-4}	-4.670×10^{-3}	−0.10	−1.05
10	-2.748×10^{-3}	-6.931×10^{-3}	−0.62	−1.57
11	-4.675×10^{-3}	1.583×10^{-3}	−0.95	0.32
12	1.981×10^{-3}	4.498×10^{-3}	0.41	0.92
13	-7.932×10^{-3}	-1.424×10^{-2}	−1.67	−3.00
14	5.752×10^{-3}	-1.824×10^{-4}	1.20	−0.04
15	5.314×10^{-3}	-6.076×10^{-4}	1.10	−0.13
16	3.662×10^{-3}	9.567×10^{-3}	0.76	1.98
17	-1.725×10^{-3}	2.954×10^{-3}	0.39	0.66
18	-5.339×10^{-3}	-5.239×10^{-3}	−1.22	−1.19
19	2.962×10^{-3}	2.115×10^{-3}	0.71	0.50
	Std dev.		±0.67	±1.32

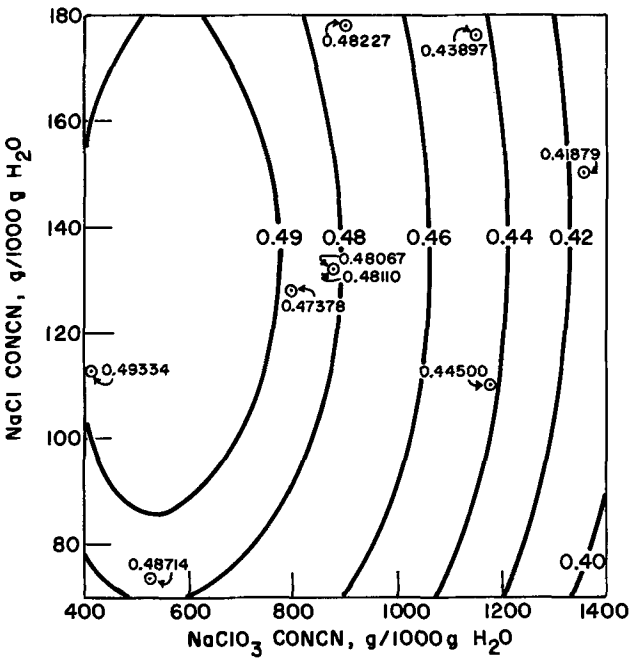

Fig. 2. Contour surface, using Eq. [4], for specific conductance as a function of NaCl and $NaClO_3$ concentration and a temperature of 97.50°C.

There is no justification for using our equations to predict specific conductance of solutions far removed from the range of our experimental data. The only reason for doing this was that we felt the best equation would be one that, at least approximately, predicted specific conductances throughout the entire soluble region, in addition to predicting accurately specific conductance within the range of experimental data. Then, if at some later date we or some other investigators extended the range of experimental data points, only minor changes in the parameters of Eq. [3] or [4] would be required to make it an acceptable equation.

Discussion

From a practical point of view, our equations allow one to calculate specific conductance for a wide range of temperatures and concentrations. Of all the empirical models tried, those given in Eq. [2], [3], or [4] predict the specific conductance best for the concentrations encompassed by the experimental data. Equation [3] or [4] appears to predict the specific conductance best for any NaCl or $NaClO_3$ concentration within the range of solubilities. Since we lack data for extended ranges of concentrations, the above is our best estimate of the contour surface. A major discrepancy between Eq. [2] and [4] is in the area of low $NaClO_3$-high NaCl concentration. In this area, Eq. [2] predicts a continuously increasing specific conductance, a condition we know cannot exist. On the other hand, Eq. [4] predicts an absolute maximum and its value is less than 0.50 mho cm^{-1}, a phenomenon we would, *a priori*, expect. Within the experimental concentration range, Eq. [2] yields a smaller standard deviation when experimental data points are compared to calculated data points; whereas, Eq. [4] appears to predict the expanded concentration range better. Our

data do not determine which equation describes the surface more accurately.

One major problem with all of these models is that the standard deviations of the regression coefficients are, in some cases, large when compared to the regression coefficient. In these cases, some of the terms in our various models may have been zero, or at least we could not have proven it to be non-zero statistically. As mentioned earlier, this could only be resolved by additional experimental work, specifically more replicated experiments.

In conclusion, we have used statistical methods to determine acceptable empirical equations for predicting specific conductance values for concentrated $NaClO_3$ and NaCl solutions at elevated temperatures. We have shown two equations; one gives accurate specific conductance values for a limited range of NaCl-$NaClO_3$ concentrations and the other gives less accurate specific conductance values over a more extended range of concentrations. It is hoped that additional experimental data can be generated so more correct and accurate equations may be found to describe this system.

Acknowledgments

The authors wish to express their gratitude to Mr. David Kirbawy who wrote the computer programs and obtained the statistical analysis of these data.

Manuscript submitted April 29, 1969; revised manuscript received Sept. 19, 1969. This was Paper 268 presented at the Chlorates and Perchlorates Symposium at the Boston Meeting, May 5-9, 1968.

Any discussion of this paper will appear in a Discussion Section to be published in the December 1970 JOURNAL.

REFERENCES

1. T. Shedlovsky, *J. Am. Chem. Soc.*, **54**, 1405 (1932).
2. R. Lorenz, *Z. Anorg. Chem.*, **108**, 191 (1919); **114**, 209 (1920).
3. N. V. S. Knibbs and H. Palfreeman, *Trans. Faraday Soc.*, **16**, 402 (1920).
4. G. Jones and B. C. Bradshaw, *J. Am. Chem. Soc.*, **55**, 1780 (1933).

The Calculation of Cathode Current Efficiency and Metal Loss in a Small Alumina Reduction Cell

V. Anthony Cammarota, Jr.,* and David Schlain*

College Park Metallurgy Research Center, Bureau of Mines, United States Department of the Interior, College Park, Maryland

ABSTRACT

Experimental data from a small Hall cell were used to show the relationship between the cathode current efficiency and the carbon monoxide-carbon dioxide content of the anodic gas. The equation, $CE = 0.45\ (\%\ CO_2) + 47.6$, was developed and shown to give reliable estimates of aluminum production. In this equation, the volume per cent of carbon dioxide is corrected for the Boudouard reaction which varies in amount with anode type and operating conditions. A second and equally effective equation is, $CE =$ Anode $CE - EL$, where Anode CE is based on the oxygen in the anodic gases and EL is metal efficiency loss resulting from solubility and vaporization. The minimum value of EL is the solubility of metal in the electrolyte, which in the small cell was estimated to be 0.12%. Calculations made with experimental and literature data show that under industrial conditions the Pearson and Waddington equation gives good estimates of cathode current efficiency, because the lower efficiency indicated by the excess carbon monoxide from the Boudouard reaction compensates for the EL factor.

The Pearson and Waddington equation, developed as a means of relating the cathode current efficiency in commercial aluminum cells to the anodic gas composition (1), is

$$CE = 0.5\ (\%\ CO_2) + 50 \qquad [1]$$

Equation [1] is based on the following reasoning: (*a*) At the cathode, aluminum-bearing ions are reduced to metal with 100% current efficiency; an equivalent quantity of oxygen is liberated at the anode, and all of the oxygen combines with carbon to form CO_2. The over-all reaction is expressed by

$$2Al_2O_3 + 3C \rightarrow 4Al + 3CO_2 \qquad [2]$$

(*b*) All of the CO which appears in the anodic gas results from the reaction between various reduced species and CO_2. In terms of equivalent aluminum, this is

$$2Al + 3CO_2 \rightarrow Al_2O_3 + 3CO \qquad [3]$$

If there is no reoxidation of aluminum as expressed by reaction [3], then the anodic gas is 100% CO_2 and the cathode current efficiency, as calculated by means of Eq. [1], is 100%. If all the CO_2 reacts with reduced species, then the anodic gas is 100% CO and the current efficiency is 50%. In commercial practice, the gas contains 60-80% CO_2 which is equivalent to a current efficiency of 80-90%.

Work by other investigators led to the conclusion that the relationship between gas composition and cathode efficiency as expressed in Eq. [1] was valid but inaccurate because it did not account for certain other reactions which also occur. Beck (2), with an experimental alumina reduction cell, correlated gas analysis data with current efficiency. The results showed that more CO was generated than can be accounted for by reaction [3], and that this excess CO is the product of the reaction between carbon dioxide and carbon, commonly referred to as the Boudouard reaction

$$CO_2 + C \rightleftarrows 2CO \qquad [4]$$

The equilibrium is strongly displaced to the right at 950°-1000°C. Accordingly, Beck introduced the g term, the ratio of carbon in the gas to carbon theoretically

* Electrochemical Society Active Member.

Key words: Hall cell, anodic gas, alumina, reduction, current efficiency, metal loss, solubility, vaporization, specific carbon consumption.

oxidized to CO_2. Another correction term, Z, was added that accounts for the oxidation or loss of cathode products by reactions other than that with CO_2 and also for electronic conduction. The equation, as modified by Beck, becomes

$$CE = g[50 + 0.5\ (\%\ CO_2)] - Z \qquad [5]$$

This was later amended to include electronic conduction as a separate entity (3)

$$CE = \{g[50 + 0.5\ (\%\ CO_2)] - Z\}\left\{1 - \frac{Z'}{100}\right\} \qquad [6]$$

where Z' is the percentage of electronic loss.

Kostukov (4) derived the formula

$$CE = [50 + 0.5\ (N_{CO_2} + n_{CO_2})]n_c \qquad [7]$$

where N_{CO_2} is the volume per cent of CO_2 in the anodic gas, n_{CO_2} is the portion of CO_2 that reacts with hydrogen gas from the cracking of hydrocarbons in the baking zone of Soderberg anodes, and n_c is the Boudouard correction term.

An equation which corrects for air leakage was derived by Hamlin and Richards (5).

Saakyan (6) did not apply correction terms, and a plot of his cathode current efficiency *vs.* CO_2 content yielded the equation

$$CE = 0.22\ (\%\ CO_2) + 73 \qquad [8]$$

An excellent discussion on methods of determining current efficiency by the use of equations such as those given above and on variables affecting current efficiency was given by Thonstad (7).

One of the objectives of the work at the Bureau of Mines was to design a cell which would operate at high cathode current efficiencies for evaluating anode materials. During the course of this work, it was found that the data obtained in the small experimental cell would fit the Beck modification of the Pearson and Waddington equation if values for g and Z were first determined for that temperature and current density. With the use of g and Z, two general equations have been derived which give accurate predictions of cathode current efficiency. A third equation, similar to Saakyan's, was also derived, but it is less acceptable.

Experimental

The alumina reduction cell (Fig. 1) differed in construction and operation from a commercial cell—it was externally heated, electrolysis was conducted under an argon atmosphere so that there was no possibility for reaction of carbon with air, and there was no crust over the electrolyte and no layer of solid electrolyte next to the cell wall. There were no periodic additions of alumina during the operation of the cell.

The cell was located on a graphite support in a gas-tight 6-in. diameter vertical Inconel[1] tube through which the purified argon flowed. The argon entered the cell through orifice, H, or through the anode bus bar slip-hole and carried the gaseous reaction products out through the gas exit tube, B, to the gas collection bottles. The cell liner, L, cover, F, splash baffle, G, and anode sleeve, I, were machined from dense, premium-grade boron nitride, which is inert to the molten electrolyte. The splash baffle collected anode dust and prevented splashing into the gas exit tube. The anode sleeve ensured a specific exposed anode surface area. The anode, K, had an area of 3.80 in.^{2} and was placed 1.5 in. from the cathode and about 1 in. below the electrolyte surface. The cell, M, was machined from dense, fine grained graphite and was continuous with the 2-in. diameter cathode, N, which fitted snugly into the liner bottom. The cell voltage was measured between the anode potential rod, C, and the inside control thermocouple, O. The anode and cathode bus bars, D and P, extended to points near the electrode surfaces, and contained within them Chromel-Alumel thermocouples, E and Q.

[1] Reference to specific brands is made to facilitate understanding and does not imply endorsement of such items by the Bureau of Mines.

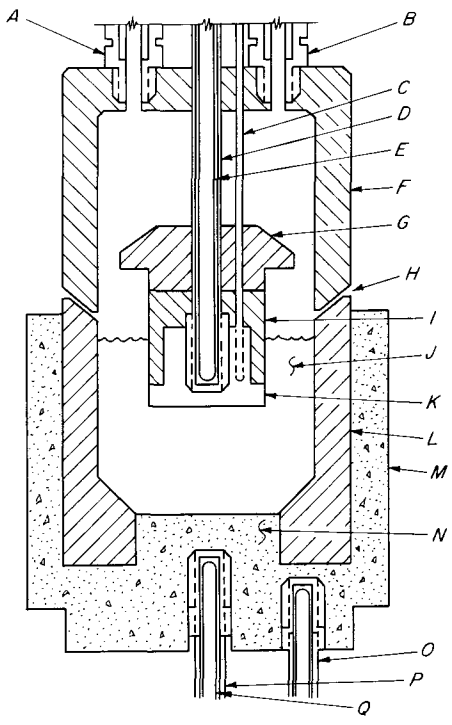

Fig. 1. Reduction cell assembly: A—manometer tube, B—gas exit tube, C—anode potential rod, D—anode bus bar, E—anode thermocouple, F—boron nitride cover, G—splash baffle, H—orifice, I—sleeve, J—electrolyte, K—anode, L—boron nitride crucible liner, M—graphite crucible, N—cathode, O—control thermocouple, P—cathode bus bar, Q—cathode thermocouple.

The anodes were either machined from large industrial anode blocks or were prepared from raw materials in the laboratory. The raw materials were either commercial coke and pitch or experimental coke and pitch binder made from lignite.

The furnace was heated by six silicon carbide resistance rods equally spaced around the tube. Temperatures were measured with Chromel-Alumel thermocouples and the anode and cathode temperatures were recorded to within 1°C on an adjustable zero-adjustable range recorder. The cell temperature was controlled through a proportional reset controller by the inside control-thermocouple and the furnace-thermocouple connected in parallel. The furnace was equipped with a fan to cool the furnace tube and cell quickly after a run. The electrolyte was normally frozen within 3-4 min, and the aluminum within 15-17 min after the run was completed. A copper coulometer with stainless steel cathodes was used to measure the quantity of electricity passing through the cell.

The electrolyte was composed of 85.6% natural Greenland cryolite, 7.4% reagent-grade CaF_2, and 7% anhydrous reagent-grade aluminum oxide. The cell, completely assembled in the furnace tube with 440-600g of charge, was dried overnight at 500°C under flowing argon. After the electrolyte had been brought to operating temperature, the anode was lowered to within 1.5 in. of the cathode. The anode and cathode temperatures were adjusted to within 1°C of electrolysis temperature before the beginning of each reduction.

Reductions were performed at anode current densities of 2.5, 5, and 10 A/in.^{2} (asi) and at 980° and 1000°C. The total current for each run was 38 A-hr. For the purpose of anodic gas collection and analysis, the electrolysis time was divided into six equal portions; gas composition was essentially constant in periods two through six. The cell gases first passed through scrubbers to remove water, dust, halides, and cyanides; then through CO_2 absorption bottles; and finally through copper(II) oxide at 600°C to oxidize the CO

to CO_2 and the H_2 to water. Immediately after the electrolysis ended, the cell was quickly fan-cooled. In this way, the quantities of CO_2, CO, and H_2 evolved during each electrolysis were determined.

After each run, the electrolyte, including the material machined from the cathode surface and from the liner, was analyzed for aluminum by the standard hydrogen evolution method. The anode and all carbonaceous material on the cell interior and electrolyte surface were analyzed for carbon to give a material balance check and anode consumption values.

Results

Initially, experiments were conducted in the alumina reduction cell with anodes cut from large industrial anodes in order to determine the effect of cell variables and the reproducibility of results. For a series of standard runs at 980°C and 5 asi anode current density, the cathode current efficiency based on aluminum produced was 81-83%. Anode current efficiency, based on the oxygen evolved as CO_2 and CO was 91-92%. The volume ratio of CO to CO_2 in the anodic gas was 0.389-0.419. Specific carbon consumption calculated from carbon in the anodic gas is a measure of the excess carbon oxidized over the theoretical amount, assuming 100% CO_2 formation at the anode. Specific carbon consumptions ranged from 1.06 to 1.08. These results showed that the cell could be operated at a high current efficiency with a variation of 1-2 percentage units.

The Pearson and Waddington equation is based on the assumption that the anode and cathode current efficiencies are equal. Therefore, a plot of anode current efficiency *vs.* % CO_2 in the anodic gas should give a straight line according to Eq. [1]. However, Fig. 2 shows that data obtained in the experimental cell do not form the straight line relationship unless the gas volume and the composition are corrected for the amount of CO_2 reacting with carbon to form CO as shown in reaction [4]. The correction factor for the Boudouard reaction is the g term in Beck's Eq. [5]. We therefore have the relationship

$$\text{Anode } CE = g[50 + 0.5\ (\%\ CO_2)] \qquad [9]$$

The g term is equal to the specific carbon consumption as defined above. Data obtained in the experimental cell at College Park show that the value of the specific carbon consumption is dependent on variables such as anode current density, temperature, the raw materials, and anode manufacturing processes. Some typical values associated with electrolysis conditions or anode type are shown in Table I.

In order to obtain data for a cathode current efficiency equation, electrolyses were conducted under standard conditions at 980° and 1000°C and at 5 and 10 asi. The cathode current efficiencies from these runs were plotted (Fig. 3) against the volume per cent of CO_2 after correcting it for the Boudouard reaction.

Table I. Effect of anode material and electrolysis conditions on specific carbon consumption

Anode type	Electrolysis °C	Electrolysis asi	Specific carbon consumption (g)
Cut from industrial anode blocks	980	5	1.06
Laboratory, commercial coke and binder	980	2.5	1.13
	980	5	1.11
	980	10	1.06
	1000	2.5	1.20
	1000	5	1.11
	1000	10	1.11
Laboratory, commercial coke and lignite binder	1000	5	1.19
	1000	10	1.13

Table II. Average *EL* values

	Anode current density, asi		
	2.5	5	10
980°C	12.8 (a)	7.1	6.7 (a)
1000°C	13.4	6.5	5.4

(a) Based on one electrolysis.

The points fall along a line which is almost parallel to the Pearson and Waddington line as obtained from Eq. [1], but 6-7 current efficiency units below it. This difference in cathode current efficiency is equal to the metal loss by mechanisms other than reaction with CO_2, and it will be called *EL*. An attempt will be made to break *EL* into component losses. The Beck equation, written with *EL* substituted for *Z*, is

$$\text{Cathode } CE = g[50 + 0.5\ (\%\ CO_2)] - EL \qquad [10]$$

Substituting Anode *CE* according to Eq. [9]

$$\text{Cathode } CE = \text{Anode } CE - EL \qquad [11]$$

Data obtained earlier in electrolyses done at several temperatures and current densities and with an average cell pressure differential of 15 cm water or less were used to evaluate the *EL* term. Since a total of 38 A-hr was used in each experiment, electrolysis times were shorter at the higher current densities. The average values of *EL* are given in Table II. The term *EL* decreases with increasing current density because there is less vaporization during the shorter electrolysis times. The *EL* values at electrolyte temperatures of 980° and 1000°C are substantially the same. It was assumed that in this cell there is no electronic conduction and hence no correction is necessary.

With these predetermined *EL* values for the electrolysis conditions used, it is possible to use Eq. [11]

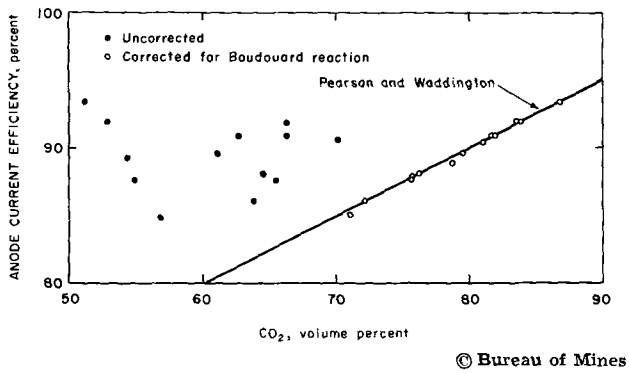

Fig. 2. Anode current efficiency as a function of carbon dioxide content of anodic gas.

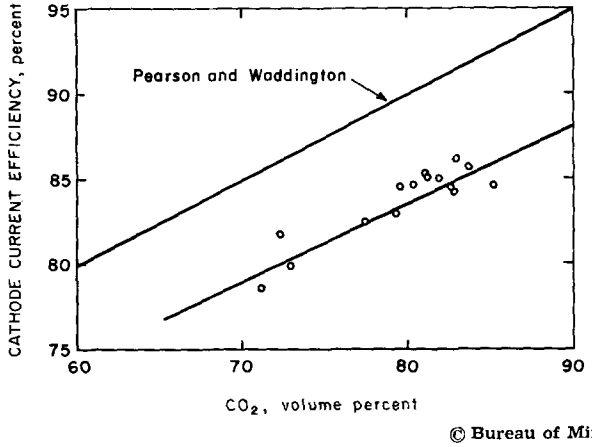

Fig. 3. Cathode current efficiency as a function of corrected volume per cent carbon dioxide.

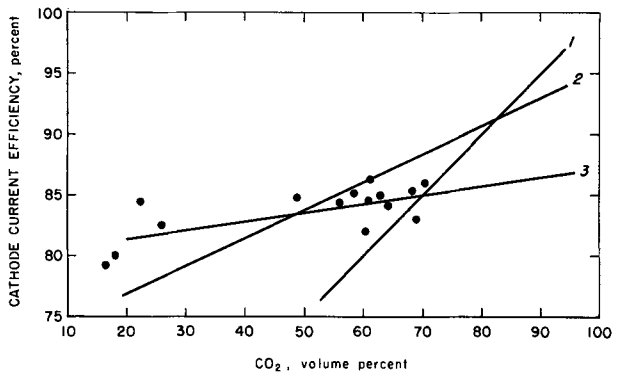

Fig. 4. Cathode current efficiency as a function of uncorrected volume per cent of carbon dioxide: 1—Pearson and Waddington, 2—Saakyan, 3—Bureau of Mines Eq. [13].

to calculate cathode current efficiencies and to compare them with those based on the aluminum actually produced. This was done with a set of experiments performed in the small cell. The data given in Table III show very good agreement between experimental and calculated cathode current efficiencies, the average difference being only 1.0 unit.

A least-squares fit of the cathode current efficiencies and corrected volume per cents of CO_2 given in Fig. 3 results in the general equation

$$CE = 0.45\ (\%\ CO_2) + 47.6 \qquad [12]$$

The data used in Fig. 3 were replotted in Fig. 4 (line 3) except that the values for per cent CO_2 were not corrected for the Boudouard reaction. In this case, the points fall along a line for which the equation is

$$CE = 0.076\ (\%\ CO_2) + 79.9 \qquad [13]$$

The line for Eq. [13] varies greatly from the Pearson and Waddington line because in the experiments on which Eq. [13] is based the specific carbon consumption was 1.07-1.50, whereas the Pearson and Waddington equation is based on the assumption that the specific carbon consumption is 1.00. Equation [13] is more similar to Saakyan's Eq. [8] which is also based on experimental data but, obviously, with different specific carbon consumptions. It is apparent that Eq. [13] is insensitive to small changes in the CO_2 content of the gas.

The cathode current efficiencies were calculated for the experiments in Table III by using Eq. [12] and [13], and compared in Table IV with the experimental values and with those obtained by Eq. [11]. Efficiencies calculated by Eq. [11] agree well with those calculated from Eq. [12]. Equation [13] often results in large deviations in current efficiency because it is relatively insensitive to changes in the CO_2 concentration in the gases, and the gas composition is not indicative of cathode current efficiency if the specific carbon consumption is high.

Table III. Calculated and experimental cathode efficiencies

Temp, °C	C.D., asi	*EL*	Current efficiency, % Experimental Anode	Experimental Cathode	Calculated Cathode (a)	Difference
980	5	7.1	91.4	84.0	84.3	0.3
1000	5	6.5	89.8	84.6	83.3	1.3
1000	5	6.5	92.2	85.2	85.7	0.5
1000	5	6.5	86.3	79.6	79.8	0.2
1000	5	6.5	84.2	80.0	77.7	2.3
1000	5	6.5	84.4	76.6	77.9	1.3
1000	5	6.5	85.6	81.0	79.1	1.9
1000	10	5.4	90.6	85.2	85.2	0.0

(a) Eq. [11].

Table IV. Comparison of experimental and calculated cathode current efficiencies

Experimental	*CE* = Anode *CE-EL* [11]	*CE* = 0.45 (% CO_2) + 47.6 [12]	*CE* = 0.076 (% CO_2) + 79.9 [13]
84.0	84.3	84.8	84.8
84.6	83.3	83.4	84.5
85.2	85.7	85.4	81.6
79.6	79.8	80.2	82.3
80.0	77.7	78.3	82.1
76.6	77.9	78.5	82.4
81.0	79.1	79.6	84.7
85.2	85.2	84.1	84.3

Figure 5 compares the manner in which Eq. [12] and [13] reflect the change in current efficiency with time during a single experiment. The data are for a 3-hr experiment at 980°C and 5 asi using an anode cut from a large industrial anode. The insensitivity of Eq. [13] to changes in anodic gas composition is well illustrated by its linearity almost from the beginning. On the other hand, Eq. [12] shows a gradual increase in efficiency for about the first hour, after which a steady state is reached at 85-87% efficiency. During this time, the specific carbon consumption is increasing from 1.02 to 1.10, where it remains for the duration of the run. Current efficiency based on oxygen recovered increases from 72 to 92%. This means that the initially high CO content of the gas is produced from reoxidation of aluminum and not from the Boudouard reaction.

A possible explanation for this high initial rate of oxidation is that, at the beginning of an experiment in the small cell, there is no pool of aluminum on the graphite cathode. Initially, the aluminum product is in the form of many tiny globules, or a mist, and has not yet coagulated into larger globules with less surface area. Because of bath convection caused by the anode heating about 10°C more than the cathode, there is an excessive amount of aluminum being carried into the vicinity of the anode where reoxidation occurs. In almost every electrolysis conducted, this pattern is evident.

An attempt was made to improve the estimation of efficiency by splitting *EL* into a solubility component and a vaporization component. The solubility of aluminum has been reported at 0.1% (11). Taking the nominal value of 0.1%, the amount of aluminum dissolved was calculated for each of a series of runs, at 1000°C and 5 asi, in which the cell pressure differential varied between 6 and 35 cm water. The calculated soluble aluminum in each electrolyte was divided by the theoretical aluminum produced and expressed in current efficiency units. This solubility component was subtracted from *EL* in each of these runs to give the vaporization component, which was plotted *vs.* average cell pressure differential in Fig. 6. In the range of 8-12 cm water, where most of the electrolyses for the data in Table IV were conducted, the vaporization varies between 1 and 4, but most of the time is in the 2-3

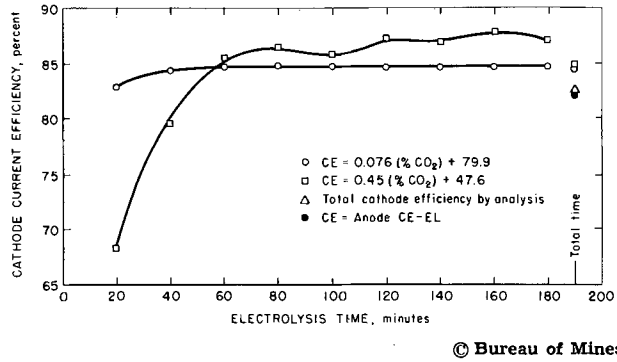

Fig. 5. Change in calculated cathode current efficiency with time for an extended electrolysis at 980°C, 5 asi.

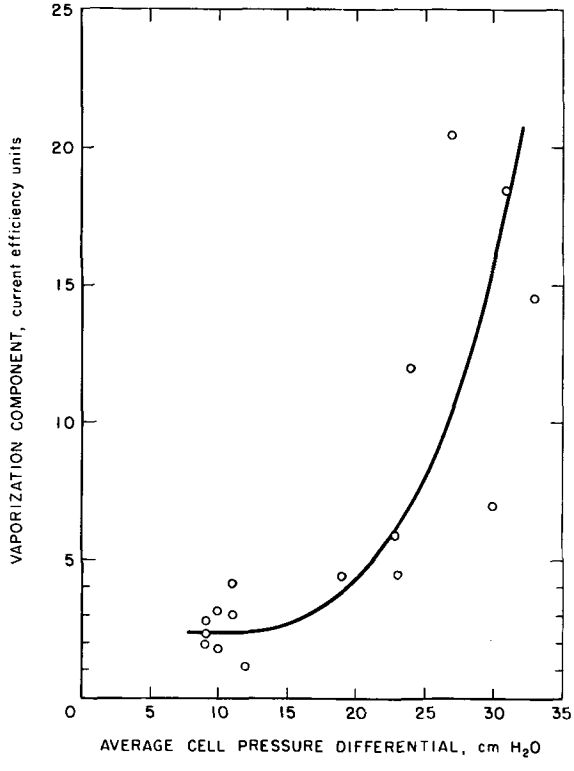

Fig. 6. Vaporization component as a function of cell pressure differential at 1000°C, 5 asi.

range. In subsequent electrolyses, the value for the vaporization component was taken as 2.5 at 1000°C and 5 asi for pressure differentials up to 15 cm water. The solubility component, estimated as described above, varied from 3.9 to 4.6 current efficiency units. The individual values for *EL*, calculated by adding vaporization and solubility components, varied from 6.4 to 7.1. The *EL* value for experiments at 1000°C and 5 asi is 6.5 current efficiency units (Table III). Hence, the use of *EL* values obtained from estimates of solubility and vaporization would not significantly improve the calculation of current efficiency. These components are not known accurately enough and, in addition, pressure fluctuations affect vaporization enough so that it overshadows any small changes in solubility.

Discussion

Although the Pearson and Waddington equation does not contain any of the correction terms used in the more recent equations, it has been found to give reliable current efficiency values under normal commercial operating conditions; Bureau of Mines' work with the small experimental cell has verified this. The corrections for vaporization and solubility on one hand and for the Boudouard reaction on the other are opposite in sign and have approximately the same value in the small cell under the usual operating conditions.

The manner in which the corrections *g* and *EL* in Eq. [10] may offset each other to make the Pearson and Waddington equation a reasonably good approximation is illustrated with a set of data obtained in the small cell. Considering that, in the Boudouard reaction the volume of CO produced is twice that of the CO_2 that reacts, the CO_2 content of the anodic gas can be corrected for the Boudouard reaction in the following way

$$\% CO_{2c} = \frac{CO_{2a} + CO_{2b}}{CO_{2a} + CO_a - CO_{2b}} \times 100 \qquad [14]$$

where CO_{2c} is the corrected volume, CO_{2a} and CO_a are experimentally determined, and CO_{2b} is involved in the Boudouard reaction. The results of these calculations are shown in Table V. The last column is the

Table V. Relative magnitude of corrections

Experimental cathode current efficiency, %	*g*	% CO_{2a}	% CO_{2c}	Corrections in Eq. [10], per cent cathode CE: *EL*	½(% CO_{2c}-% CO_{2a})
82.3	1.13	57.7	78.4	6.9	10.4
85.0	1.12	63.0	81.9	6.0	9.5
84.6	1.11	61.1	79.6	5.3	9.3
78.7	1.10	58.5	74.1	8.4	7.8
85.4	1.08	68.1	81.1	5.2	6.5
85.9	1.08	70.3	83.7	5.9	6.7
81.9	1.07	60.4	72.3	4.3	6.0
83.0	1.06	69.0	79.3	6.7	5.2

apparent decrease in cathode current efficiency resulting from the Boudouard reaction, on the basis of one-half unit change in aluminum current efficiency per one unit change in volume per cent of CO_2 according to Pearson and Waddington.

The relationship between apparent decrease in cathode current efficiency, as indicated by the change in gas composition, and specific carbon consumption is shown in Fig. 7. Also plotted, as the right-hand ordinate, is the *EL* term for each of these electrolyses. The value of *EL* is usually 4-7 units. The intersection of this range with the apparent decrease in cathode current efficiency from the Boudouard reaction gives a value for *g* of 1.04-1.08. This means that, in electrolyses is which *g* ranges from 1.04 to 1.08, the Pearson and Waddington equation should give reliable results because the Boudouard reaction and *EL* corrections will offset each other.

In Fig. 8, the experimental cathode current efficiency is plotted *vs.* the experimental CO_2 content. For values

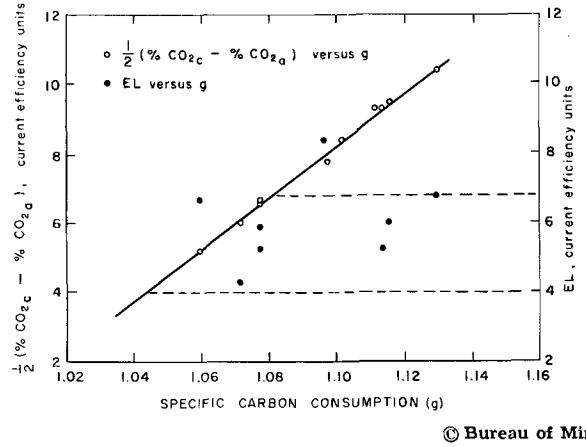

Fig. 7. Relationship between errors in Pearson and Waddington equation introduced by Boudouard reaction and by losses of metal.

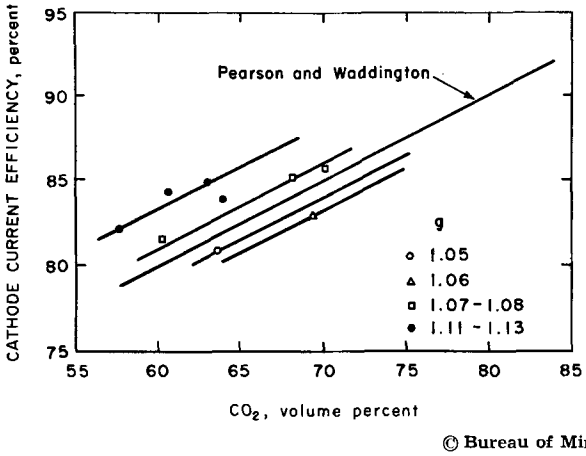

Fig. 8. Experimental data showing ranges of specific carbon consumption in which the Pearson and Waddington equation gives good results. (The volume per cent of CO_2 is uncorrected.)

of g between 1.05-1.08, the actual current efficiency is within 1.5-2 percentage units of the value calculated by the Pearson and Waddington equation. As g increased to 1.11-1.13, the deviation became greater. The EL value for all of these experiments was about 6-7.

An examination of the literature also supports these findings. Beck (2) found that for g equal to 1.04-1.07 there was good agreement between the experimental current efficiencies and those calculated from the Pearson and Waddington equation. As g became less than 1.04, the experimental value was significantly below the calculated one. This agrees with the conclusions derived from Fig. 7. When g is less than 1.04, the amount of Boudouard reaction corresponds to an EL value of less than 4, so that aluminum loss is not sufficiently accounted for, and the calculated efficiency is greater than the actual one.

An analysis was also made of the data presented by Saakyan (6). These data show specific carbon consumption values of 1.05-1.08 that correspond to his correction factor, K, of 4-6. Subtraction of a nominal value of 5.0 from Saakyan's current efficiency yields the plot shown in Fig. 9. Very good agreement occurs when the specific carbon consumption is 1.05-1.08. The deviations from Pearson and Waddington with changes in specific carbon consumption are well illustrated. Again it is shown that the Boudouard reaction fortuitously accounts for metal loss in the cell. It is interesting to note that our value for metal loss varies between 6 and 7, which is slightly above that indicated in Saakyan's work and the value of 5 taken by Beck.

The value of the specific carbon consumption is significant in that it serves as an indicator of anode reactivity. For example, the data in Table I show that the coke which results from lignite pitch is more reactive than that which comes from coal-tar pitch. It seems specific carbon consumption or g can be used as an index number to signify relative anode quality.

An attempt was made to correlate the experimental values of EL with those that could be calculated from physical data available in the literature. The reactions that may take place are given below

$$Na_3AlF_6 \rightleftarrows 2NaF + NaAlF_4 \quad [15]$$

$$5\,NaAlF_4 \rightarrow Na_5Al_3F_{14} + 2AlF_3 \quad [16]$$

$$6NaF + Al \rightarrow 3Na + Na_3AlF_6 \quad [17]$$

$$3Na + 2AlF_3 \rightarrow Al + Na_3AlF_6 \quad [18]$$

Reaction [15] represents the dissociation of cryolite at 1000°C (8). The volatile sodium tetrafluoroaluminate, upon slow cooling in the gas exit tube, forms chiolite and aluminum (III) fluoride as in reaction [16] (9). As aluminum is formed in the electrolyte, it can react according to Eq. [17] with sodium fluoride to form sodium vapor (9). This sodium vapor reacts [18] at about 600°C with aluminum (III) fluoride in the gas exit tube to form aluminum and cryolite (9).

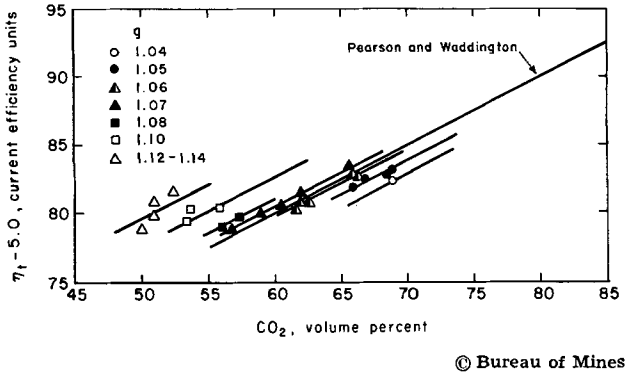

Fig. 9. Data taken from Saakyan (6) to show values of g for which Pearson and Waddington equation gives good results. (Volume per cent of carbon dioxide is uncorrected.)

Thus, aluminum is lost from the cell. This may also explain why sodium is not detected when the system is opened.

The experimental values for EL in Table III were compared to calculated values based on the solubility of aluminum in the melt and on vaporization losses resulting from reactions summarized in reactions [15] through [18]. First, an estimate was made of aluminum lost in the small cell by using electrolyses conducted for 1 hr. In 1-hr, vaporization loss would be at a minimum. The total metal loss was the difference between aluminum theoretically produced and the sum of aluminum actually produced and aluminum lost by reoxidation. The metal lost in six experiments at 1000° or 980°C and at 10 asi was an average of 0.15% of the weight of the electrolyte. Second, an estimate was made of vaporization losses. The data for vapor pressure of sodium over cryolite-aluminum melts is given by Stokes (10). Taking the partial pressure to be about 20 Torr at 1000°C, the number of moles of sodium (n_{Na}) is

$$n_{Na} = \frac{P_{Na}}{760} = 2.63 \times 10^{-2}\ \text{moles/molar volume} \quad [19]$$

This corresponds to a sodium loss of 0.33 g/hr of electrolysis, which is equivalent to about 0.13g aluminum. Expressed as current efficiency units, this is 1 unit lost per hour of electrolysis. Subtraction of 0.13g aluminum equivalent from the total of 0.15% loss (0.68g) gave an estimated solubility of 0.12%. This value is in good agreement with solubilities reported in the literature (11, 12).

Average EL values were calculated on the basis of a vaporization loss of one current efficiency unit per hour and a solubility of 0.12%. These values are compared with experimental values for EL in Table VI.

The agreement between calculated and experimental EL values is excellent for 2-hr electrolyses, but poor for the 4-hr run. In the latter case, volatilization may be greater than expected because of longer time at slowly changing electrolyte composition. For the 1-hr electrolysis, only one run was available at low pressure differential.

Conclusions

Data obtained in a small batch-type, externally heated Hall cell show that cathode current efficiency equations based on CO_2 content of the anodic gas are valid, provided corrections are made for the reaction of CO_2 and carbon to form CO, and for metal losses. Two equations provide accurate estimates of aluminum production

$$\text{Cathode } CE = \text{Anode } CE - EL$$

where Anode $CE = g\,[50 + 0.5\ (\%\ CO_2)]$, and

$$\text{Cathode } CE = 0.45\ (\%\ CO_2) + 47.6$$

where % CO_2 is corrected for the Boudouard reaction. The value of EL and the constants in the second equation vary somewhat with current density and temperature. EL is primarily a correction for losses resulting from solubility of aluminum in the electrolyte and for vaporization of metal values.

The specific carbon consumption (g) is a measure of anode reactivity.

Table VI. Comparison of experimental and calculated values of EL

Temp, °C	Time, hr	EL	
		Calculated	Experimental
980	1	5.6	6.7[a]
980	2	6.8	7.1
1000	2	6.6	6.5
1000	4	8.5	13.4

[a] One electrolysis.

The Pearson and Waddington equation gives good estimates of cathode current efficiency in commercial cells because under normal operating conditions the metal losses resulting from solubility and vaporization, which amount to 4-7 cathode current efficiency units, are fortuitously balanced by the results of the Boudouard reaction.

The estimate of volatilized and soluble aluminum derived for the small cell are in good agreement with physical data in the literature. These estimates together with the estimate for aluminum loss by reaction with CO_2 seem to account for all losses in the small cell.

Manuscript received July 7, 1969. This was Paper 285 presented at the Boston Meeting, May 5-9, 1968.

Any discussion of this paper will appear in a Discussion Section to be published in the December 1970 JOURNAL.

REFERENCES

1. T. G. Pearson and J. Waddington, *Disc. Faraday Soc.*, **1**, 307 (1947).
2. T. R. Beck, *This Journal*, **106**, 710 (1959).
3. T. R. Beck, *ibid.*, **107**, 577 (1960).
4. A. A. Kostukov, *Non-Ferrous Metals USSR (English Transl.)*, **36**, No. 3, 38 (1963).
5. J. D. Hamlin and N. E. Richards, "Extractive Metallurgy of Aluminum," Vol. 2, Edited by G. Gerard, p. 51, Interscience Publishers, New York (1963).
6. P. S. Saakyan, *Non-Ferrous Metals USSR (English Translation)*, **36**, No. 12, 41 (1963).
7. J. Thonstad, *Tidsskr. Kjemi, Bergvesen Met. (English Transl.)*, **26**, No. 4 (1966).
8. W. B. Frank and L. M. Foster, *J. Phys. Chem.*, **64**, 95 (1960).
9. E. H. Howard, *J. Am. Chem. Soc.*, **76**, 2041 (1954).
10. J. J. Stokes, Jr., and W. B. Frank, "Extractive Metallurgy of Aluminum," Vol. 2, Edited by G. Gerard, pp. 3-14, Interscience Publishers, New York (1963).
11. J. Thonstad, *Can. J. Chem.*, **43**, 3429 (1965).
12. W. E. Haupin, *This Journal*, **107**, 232 (1960).

JOURNAL OF THE ELECTROCHEMICAL SOCIETY

ELECTROCHEMICAL SCIENCE

MARCH 1970

On the Oxidation-Reduction Mechanism of the Cadmium Metal-Cadmium Hydroxide Electrode

Yutaka Okinaka*

Bell Telephone Laboratories, Incorporated, Murray Hill, New Jersey

ABSTRACT

Electrochemical oxidation-reduction processes of the $Cd/Cd(OH)_2$ electrode in concentrated alkaline solutions were investigated by using a rotating ring-disk electrode as well as a stationary electrode. Results support the mechanism that the anodic oxidation of Cd to $Cd(OH)_2$ in the active potential range proceeds entirely through the dissolution-precipitation sequence, while the cathodic reduction of $Cd(OH)_2$ takes place both through the solution phase and by a direct solid-state mechanism.

The mechanism of anodic oxidation of cadmium metal and cathodic reduction of the oxidation product in strongly alkaline solutions is of interest in understanding the behavior of the cadmium electrode in nickel-cadmium batteries. In spite of much effort in recent years by a number of investigators, the reaction mechanism is still incompletely understood. For example, two radically different mechanisms have been proposed in the literature for the anodic reaction: the dissolution-precipitation mechanism (1-6) and the solid-state oxidation mechanism involving ionic transport through the $Cd(OH)_2$ film (7-9). The formation of CdO has been the subject of discussion of many investigators. Croft (7), Falk (10), and Armstrong *et al.* (11) found no evidence of CdO formation, whereas Huber (2), Huber and Stucki (2a), Breiter and Weininger (12), and Breiter and Vedder (13) reported experimental results indicating the formation of CdO. It has been suggested that CdO is formed as the primary product before its conversion to $Cd(OH)_2$ (3, 3a, 5) or as a result of a secondary reaction that occurs after $Cd(OH)_2$ is formed (12, 14). Most recently, Devanathan and Lakshmanan (6) proposed a mechanism in which the CdO formation occurs in parallel with the formation of $Cd(OH)_2$. Rozentsveig *et al.* (1), Huber (2), Lake and Casey (3, 3a), Breiter and Weininger (12), and Devanathan and Lakshmanan (6) suggested that it is the CdO layer, and not $Cd(OH)_2$, that causes the passivation which limits the extent of anodic oxidation of cadmium metal. Milner and Thomas (15) state that even if CdO does form, it will not play any significant role under the normal operating conditions of nickel-cadmium batteries, because they are not ordinarily negative-limited and passivation ought not to occur. It is recognized, however, that under certain conditions the cell does become negative-limited on discharge, even when significant excess of charged cadmium is present. Thus, understanding the cause of the passivation of cadmium metal is of great practical interest. The mechanism of the cathodic reduction of $Cd(OH)_2$ has been studied to a much lesser degree than its anodic counterpart (7, 12, 13, 16) in spite of its importance in relation to the charging process of the battery cadmium electrode. Croft (7) and Rubin (16) believe that the cathodic process occurs by a solid-state mechanism without involving the solution phase.

The present investigation using a rotating ring-disk electrode was undertaken in order to obtain information on the role of soluble cadmium species during the anodic as well as the cathodic process. The technique is now well known as a powerful method for detecting and determining the concentration of soluble intermediate species formed at an electrode surface (17).

Experimental

Both the disk and ring were made of 99.99% pure cadmium metal. Epoxy resin was used as the insulating material. The electrode had the following dimensions: r_1 (disk radius) = 4.7 mm, r_2 (r_1 plus the thickness of insulating ring) = 5.1 mm, r_3 (r_2 plus the thickness of cadmium ring) = 5.7 mm, and r_4 (radius to the outer edge) = 6.4 mm. Before each experiment, the surface of the electrode was polished mechanically with 4/0 emery paper wetted with methanol, cleaned with methanol and water, and cathodized in 6.9M KOH at 0.5 mA for at least 1 hr to obtain an oxide-free surface. The electrode was kept immersed in deaerated water when not in use. The speed of rotation was 2100 rpm unless otherwise stated.

A half-charged cadmium electrode of sintered-plate-type served as the reference electrode to control and measure the potential of the disk electrode. It was placed in a compartment which was connected to the main part of the cell through a salt bridge with a capillary tip. A platinum coil served as the counterelectrode. A second, half-charged cadmium electrode placed in a compartment separated by a fine sintered glass disk served as the reference-counterelectrode for the ring electrode circuit. A constant voltage of -0.2V was applied to the ring electrode against the reference-counterelectrode from a battery-voltage divider arrangement. Because the ring current was always small (< 0.3 mA) as compared to the charge

* Electrochemical Society Active Member.

Key words: cadmium, cadmium hydroxide, anodic oxidation, cathodic reduction, anodic film, rotating ring-disk electrode.

capacity of the reference-counterelectrode (200 mA·hr), the polarization of the latter was negligible. By taking current-potential curves in 6.9M KOH saturated with $Cd(OH)_2$, it was confirmed that the potential of −0.2V lies well within the mass transfer limiting current region for the reduction of dissolved cadmium species.

The stationary cadmium electrode used in the experiments for the calculation of ionic conductivity of the anodic film was constructed by press-fitting a pure cadmium rod in Teflon. The electrode surface was polished first mechanically with 4/0 emery paper and then chemically in concentrated nitric acid and in a 1:1 mixture of concentrated phosphoric acid and 30% hydrogen peroxide. The apparent surface area of the electrode was 0.317 cm^2.

A Wenking 64TR potentiostat with an MP64 motor potentiometer was used in both galvanostatic and controlled-potential experiments. Potassium hydroxide was of analytical reagent grade (Baker, low chloride and low iron) and used without further purification. The solution was deaerated by bubbling purified nitrogen. All experiments were conducted at room temperature.

Results and Discussion

Potential scan experiment.—Anodic process.—The disk potential was scanned at a speed of 100 mV/min first in the anodic direction to various potentials and then in the cathodic direction, while currents at both the disk and the ring electrode were being recorded. In the anodic scan (Fig. 1, solid line) the disk current (i_{disk}) — disk potential (E_{disk}) curve exhibited a sharp peak due to the active oxidation of the disk followed by a passivation process. The corresponding ring current (i_{ring}) — E_{disk} curve also showed a sharp maximum at the disk potential where i_{disk} became maximum. The magnitude of i_{ring} at the peak was equal to 230 μA in this experiment. The concentration of dissolved cadmium at the disk surface, c^o, can be calculated from this value with the aid of the following equation (17)

$$c^o = \frac{i_{ring}\,\delta}{nFAND} \qquad [1]$$

where

$$\delta = 1.61\left(\frac{D}{\nu}\right)^{1/3}\sqrt{\frac{\nu}{\omega}} \qquad [2]$$

and A is the area of the disk electrode in cm^2, N the collection efficiency (17, 18), D the diffusion coefficient of the dissolved cadmium species in $cm^2 \cdot sec^{-1}$, δ the diffusion layer thickness in cm, ν the kinematic viscosity of the solution in $cm^2 \cdot sec^{-1}$, and ω the angular velocity of rotation of the electrode. By using the numerical values $n = 2$, $\mathbf{F} = 96500$ coulombs, $A = 0.677$ cm^2, $N = 0.311$ [calculated from electrode geometry with the aid of the Albery-Bruckenstein Eq. (6.1) in ref. (18)], $D = 0.51 \times 10^{-5}$ $cm^2 \cdot sec^{-1}$ for $Cd(OH)_3^-$ in 6.9M KOH (19), $\nu = 1.67 \times 10^{-2}$ $cm^2 \cdot sec^{-1}$ [calculated from density 1.2854 and viscosity 2.147 centipoise (15)], and $\omega = 219.8$ sec^{-1} (2100 rpm), the value of c^o at the peak potential was calculated to be equal to 1.06×10^{-3}M. The equilibrium solubility of cadmium hydroxide in 6.9M KOH at 25°C determined by various investigators (19-23) ranges from 1.2 to 1.6×10^{-4}M. Thus, the concentration of dissolved cadmium species at the disk surface at the peak potential was about 7 to 9 times larger than the equilibrium solubility of cadmium hydroxide. Such a large degree of supersaturation can be understood only in terms of the dissolution-precipitation mechanism, in which cadmium metal first dissolves anodically and the dissolved species subsequently form a precipitate of $Cd(OH)_2$ on the metal surface. Supersaturation is required to form nuclei in the initial stages of precipitation.

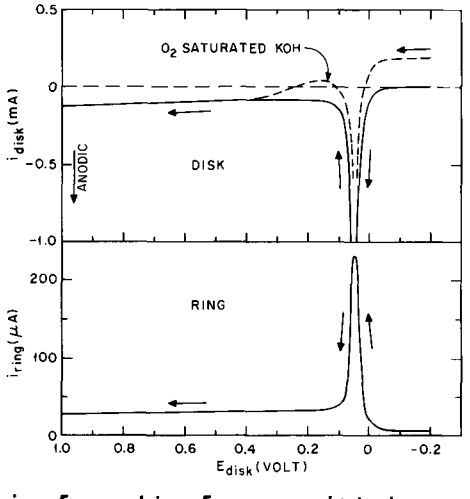

Fig. 1. i_{disk}-E_{disk} and i_{ring}-E_{disk} curves obtained on anodic scan of E_{disk} at 100 mV/min in 6.9M KOH. Speed of rotation, 2100 rpm. Broken line, same electrolyte saturated with oxygen.

The cause of passivation was the subject of discussion of the papers by Rozentsveig *et al.* (1), Lake and Casey (3, 3a), Breiter and Weininger (12), and Devanathan and Lakshmanan (6). These authors postulated that passivation is due to formation of a thin continuous film of CdO, although the different groups of authors suggested different mechanisms for the film formation. The ring-disk electrode experiment does not provide any conclusive information on the mechanism of passivation. However, there are evidences which show that passivation is not simply due to complete coverage of the cadmium surface with $Cd(OH)_2$ crystals. First, a simple microscopic observation of the passivated surface shows the coverage with crystalline products to be incomplete. Second, the reduction of oxygen continues after passivation up to about +0.4V as shown by the dotted line in Fig. 1. This curve was obtained in 6.9M KOH saturated with oxygen at atmospheric pressure. The rate of potential scan had no effect on the oxygen current between 100 and 1 mV/min. If the cadmium metal surface were completely covered with an insulating layer of $Cd(OH)_2$ on passivation, no oxygen reduction would continue to such a positive potential. The result supports the view that the passivation is due to the formation of a thin film of CdO, which appears to have a relatively high electronic conductivity under the present conditions of film formation. [Conductivity values ranging from 100 to 500 $ohm^{-1} \cdot cm^{-1}$ have been reported for bulk CdO (24).] In agreement with Breiter and Weininger (12), the structure of the entire film may be pictured in such a way that a number of $Cd(OH)_2$ crystals are imbedded in an extremely thin passivating layer of CdO. As will be discussed later, this passivating layer appears to be insoluble or only very slowly soluble in alkali, whereas $Cd(OH)_2$ in the film is soluble in the electrolyte to a significant extent.

Figure 1 also shows that the disk current after passivation increases slightly as the potential becomes more positive than about +0.4V and approaches +1.0V, while the ring current in the corresponding potential range decreased slightly. It is considered that the disk current in the passive potential range consists of two components: the current necessary for replenishment of the dissolved part of the $Cd(OH)_2$ crystals by further oxidation of the metal, and that for the growth of CdO. The former component is expected to be determined by either the equilibrium solubility or the rate of chemical dissolution of the $Cd(OH)_2$ crystals and hence independent of potential, while the latter component may be potential-dependent. The results of infrared spectroscopic investigation recently reported by Breiter and Vedder (13) indicate that an increasing amount of CdO is formed at more anodic potentials. On the other hand, the magnitude of i_{ring} after passivation of the disk (about 30 μA at +0.2V) corresponds to a concentration of the dissolved cad-

mium species at the disk surface equal to 1.4 x 10^{-4}M, as calculated from Eq. [1]. This concentration agrees with the equilibrium solubility of $Cd(OH)_2$ under the conditions of the present experiment. The observed decrease in i_{ring} with E_{disk} apparently indicates a slight decrease in the rate of chemical dissolution of the film during the potential scan.

Cathodic process—The $i_{disk} - E_{disk}$ curves 1 and 2 in Fig. 2 were obtained by reversing the direction of potential sweep immediately after terminating the anodic sweep (Fig. 1) at +1.0 and at +0.2V, respectively. In curve 1 a prewave is noted prior to the large cathodic peak. This prewave was first reported by Breiter and Weininger (12) in more dilute KOH solutions (0.2 and 1M). In 6.9M KOH we observed that the prewave appeared only after the sweep reversal was made at a potential more positive than about +0.4V. In curve 2, which was obtained by reversing the potential sweep at +0.2V, the prewave was totally absent, while a very small prewave was visible when the potential scan was reversed at +0.5V (not shown in Fig. 2). Breiter and Weininger attributed the prewave to the reduction of CdO on the basis that the reduction of $Cd(OH)_2$ is not thermodynamically possible at about +0.04V where the prewave begins to appear. It is of interest to note in Fig. 2 that the ring current exhibited no marked change in the potential range of the prewave, while it decreased rapidly as the disk current increased further toward the peak. This result clearly shows that the reduction of the substance yielding the prewave, presumably CdO, does not proceed through the formation of soluble intermediates. In view of the relatively high electronic conductivity, it is not surprising that CdO is reduced directly without an intermediate dissolution step. It is considered that the reduction of an electronic conductor can take place on its surface, and, when the molar volume of the reduction product is smaller than that of the oxidized material, it can continue to completion with all ionic motions in the solution phase. Thus, the reduction of CdO to Cd does not require ionic conductivity of CdO. The fact that a larger prewave appears on reversal of potential sweep at a more positive potential is consistent with Breiter and Vedder's finding (13) that a greater amount of CdO is formed at a higher anodic potential.

That the reduction of $Cd(OH)_2$ takes place, at least partially, through the formation of a soluble intermediate is indicated by the rapid decrease in i_{ring} starting at about 0 volt and the increase in i_{ring} observed when the disk circuit was opened after the termination of potential sweep at −0.2V (see Fig. 2). This subject will be discussed further in subsequent sections.

Galvanostatic experiment.—Anodic process.—When the disk was made an anode at a constant current, the ring current rapidly increased to a maximum and then decreased gradually until the disk passivated. As an example, the result obtained at i_{disk} = 0.5 mA is shown in Fig. 3. The disk was at open circuit before application of the current. The magnitude of i_{ring} during the active oxidation of the disk (up to 8 min, and $E_{disk} < 60$ mV) was always greater than 40 μA, which corresponds to a concentration of soluble cadmium species at the disk surface greater than 1.8 x 10^{-4}M. Comparison of this value with the equilibrium solubility 1.2 to 1.6 x 10^{-4}M shows that supersaturation persisted during the entire period of active anodic oxidation of the disk. The result clearly demonstrates that the dissolution-precipitation mechanism was operative during the galvanostatic anodic oxidation. The decrease in i_{ring} with time shows that the concentration of dissolved cadmium at the disk surface decreases as the latter becomes covered with $Cd(OH)_2$. This may be anticipated for two reasons. First, the ring current is proportional to the "average" concentration of the dissolved species over the disk surface. Hence, even if the dissolution reaction and the precipitation reaction continue at a constant rate, the uncovered area of the disk surface at which the dissolution reaction takes place should decrease with time, resulting in a decrease in the "average" concentration. Second, as the disk surface becomes covered to an increasing extent, more sites for precipitation become available; thus, the rate of precipitation of $Cd(OH)_2$ on the disk surface is expected to increase with time. This also should result in a decrease in the surface concentration of the dissolved species.

Cathodic process.—After the anodic polarization at 0.5 mA, the disk was open-circuited and then cathodically polarized at the same current. During the cathodic polarization, the disk current was interrupted a few times to see the effect of opening the circuit on the ring current. Results are shown in Fig. 4. During the initial reduction of the anodic film, the disk electrode was only slightly polarized, while the ring current continued to decrease. It is significant to note that when the disk current was interrupted, the ring current rapidly increased. This increase in ring current clearly shows that the reduction of the $Cd(OH)_2$ film takes place at least partially through the dissolved cadmium species. After the disk current was turned on again and the potential reached the hydrogen evolution region, the disk current was interrupted for the second time. This again caused a sharp rise in ring current, indicating that $Cd(OH)_2$ was still present on the disk surface in spite of the fact that hydrogen evolution was taking place. The existence of $Cd(OH)_2$ during the hydrogen evolution is also seen from the result that cathodic polarization at 0.05 mA after the 0.5 mA experiment permitted further reduction of $Cd(OH)_2$ without hydrogen evolution (Fig. 4, right half). It is noteworthy that the final current inter-

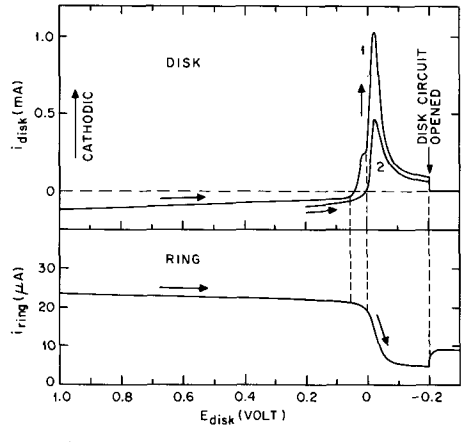

Fig. 2. i_{disk}-E_{disk} and i_{ring}-E_{disk} curves obtained on cathodic scan of E_{disk} after anodic scan. 2100 rpm. (The behavior for 60 sec after opening the disk circuit is shown to the right of −0.2V.)

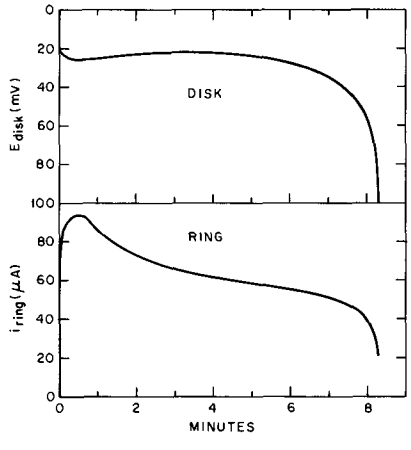

Fig. 3. Galvanostatic anodization of disk in 6.9M KOH at 2100 rpm, i_{disk} = 0.5 mA.

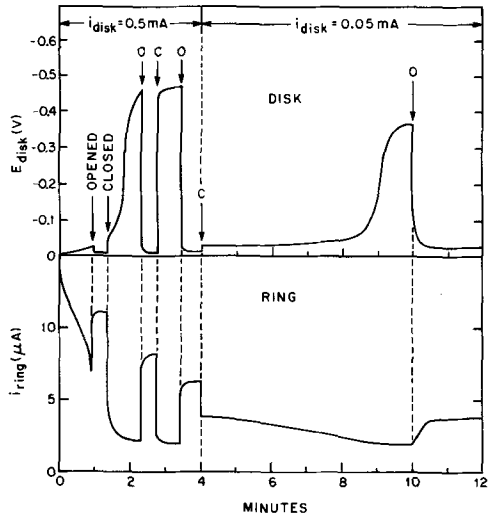

Fig. 4. Galvanostatic cathodic reduction after anodic oxidation at 0.5 mA, 2100 rpm.

ruption after 10 min still caused an increase in ring current. Evidently, the rate of solution of the $Cd(OH)_2$ film is quite slow.

Potentiostatic experiment.—Anodic process. Current-time curves obtained on applying various anodic potentials to the disk electrode are reproduced in Fig. 5. Again, from the magnitude of i_{ring} it is clear that the anodic reaction proceeds through the dissolution-precipitation sequence.

An attempt was made to calculate the rate constant for the precipitation process from these current-time curves. In order to carry out the calculation, it is necessary to formulate the reaction scheme. The form of dissolved cadmium species present in equilibrium in concentrated alkaline solutions has been studied by several investigators (19-22). Visco and Sonner (19) recently reinvestigated the subject and established that the dissolved cadmium species exists in the form of $Cd(OH)_3^-$ in solutions of KOH from 2 to 15*M*. Thus, in agreement with Milner and Thomas (15) we shall write

$$Cd + 3\,OH^- \rightleftarrows Cd(OH)_3^- + 2e^- \qquad [3]$$

$$Cd(OH)_3^- \xrightarrow{k} Cd(OH)_2 + OH^- \qquad [4]$$

where k is defined as the heterogeneous rate constant for the precipitation reaction. The current consumed in the formation of CdO, if any, at the small anodic potentials (<40 mV) is negligible. Suppose that the electron transfer reaction [3] is sufficiently fast that the disk current, except during the short initial transient period, is controlled by the rate of the precipitation reaction [4] and/or the rate of mass transfer of $Cd(OH)_3^-$. The former is given by kc^o while the latter by $(D/\delta)\ c^o$; thus the total rate of disappearance of $Cd(OH)_3^-$ is given by $(k + D/\delta)\ c^o$. Assuming that the disk current flows only through the uncovered area, we can write

$$i_{disk} = 2FA(1 - \theta)\left(k + \frac{D}{\delta}\right) c^o \qquad [5]$$

where θ is the fraction of the disk surface covered by $Cd(OH)_2$. Combination of this expression with Eq. [1] yields

$$i_{disk} = \frac{\delta}{ND}(1 - \theta)\left(k + \frac{D}{\delta}\right) i_{ring} \qquad [6]$$

The values of i_{disk} and i_{ring} being known at various times from the experimental current-time curves, it should be possible to calculate k provided that θ is known. Since θ cannot be determined readily, we calculated k at various times with θ set equal to zero and plotted it against time to find the value of k at $t = 0$ by extrapolation. The result is shown in Fig. 6. The two curves obtained at 35 mV at 1000 and 3950 rpm show that k is practically unaffected by the speed of rotation, which constitutes a partial check of Eq. [6]. The observed increase of k with time is partly due to the fact that the surface coverage was ignored in the calculation, but it is attributable mainly to an increase in the number of nuclei for the precipitation with increasing coverage and hence with time. The precision and reproducibility of this experiment was not very good; it was especially sensitive to the surface preparation. Therefore, no quantitative significance should be attached to the observed effect of potential on $k_{t=0}$. The results simply show that the method can be used, in principle, to calculate the rate constant of the precipitation reaction, and that $k_{t=0}$ was approximately 1 to 3 x 10^{-3} cm · sec^{-1} under the particular conditions used in this experiment.

Cathodic process.—The disk electrode was first anodized at +40 mV for 10 min at 6.9M KOH at 2100 rpm. The potential was then suddenly switched to −40 mV while both i_{disk} and i_{ring} were being recorded. Results are shown by curves 1 and 2 in Fig. 7. When the rotation was stopped during the reduction, both i_{disk} and i_{ring} decreased, and they increased again when rotation was resumed. The ring current more than doubled when the disk circuit was opened after 90 sec. These results clearly show that the anodic film does dissolve in the electrolyte, and the reduction of the dissolution product takes place at the disk electrode. This is also clear from comparison of the ring current-time curve during the reduction of the film (curve 2) with that

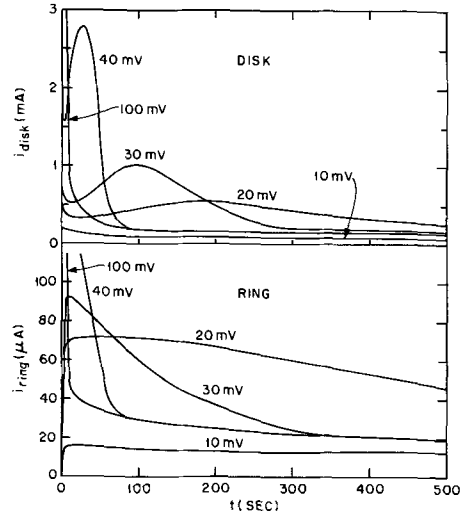

Fig. 5. Potentiostatic anodization of disk in 6.9M KOH at various potentials, 2100 rpm.

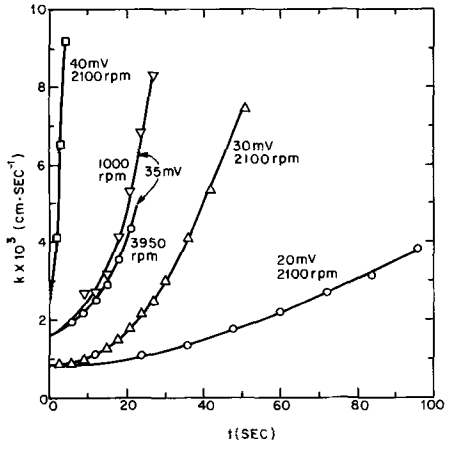

Fig. 6. Heterogeneous precipitation rate constant calculated from i_{disk}-t and i_{ring}-t curves.

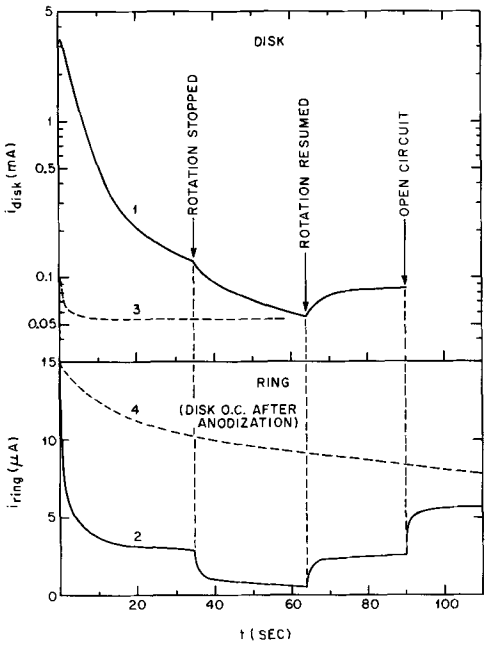

Fig. 7. i_{disk}-t (curve 1) and i_{ring}-t (curve 2) curves during potentiostatic reduction at −40 mV of the film formed at +40 mV on the disk in 6.9M KOH. Also included are (curve 3) i_{disk}-t curve for reduction of $Cd(OH)_3^-$ at −40 mV in 6.9M KOH saturated with $Cd(OH)_2$, and (curve 4) i_{ring}-t curve during free dissolution in 6.9 KOH at open circuit of the film formed on the disk at +40 mV. 2100 rpm for all curves.

during free dissolution of the film at open circuit (curve 4). The latter was obtained by first preanodizing the disk electrode under the same conditions as for curve 1 and then opening the disk circuit. While these experimental results show that the reduction of the anodic film takes place at least partly through the solution phase, this mechanism alone does not seem to be sufficient to account for the very large disk current observed during the initial period of reduction in curve 1. The steady-state reduction current measured in 6.9M KOH saturated with $Cd(OH)_2$ was only 53 μA at −40 mV (curve 3 in Fig. 7). Clearly, if the reduction proceeded solely through the dissolved intermediate, the dissolution of the anodic film would have to be extremely fast to account for the large initial disk current. Actually, however, the dissolution rate of the film was found to be rather slow. For example, the ring current due to the free dissolution of the film (curve 4) continued to decrease slowly for about 1.5 hr until the current finally reached zero. We also found that during the initial period of about 10 sec, the disk current was unaffected by stopping and resuming the rotation.

These experimental results suggest that in the initial stages the cathodic reduction of the film proceeds to a significant degree by the direct mechanism without going through the solution phase, while in the later stages the contribution of the solution-reduction mechanism becomes more significant. It may be speculated that when the cadmium metal is mostly covered with the film, the reduction takes place largely by the direct mechanism involving no soluble intermediate. As the reduction progresses, an increasing portion of the cadmium metal surface becomes exposed to the electrolyte, which increases the contribution of the reduction through the solution phase. It would be desirable to have more quantitative information as to the extent of contribution of each of the two mechanisms to the over-all reduction process. However, the experimental technique employed here could not yield such information.

On the basis of their current-interruption experiment during the galvanostatic anodic oxidation of cadmium metal in KOH, Farr and Hampson (9) reported that the solubility of the anodic film in the electrolyte is negligible. They observed that the total passivation time was independent of the duration of current interruption up to 80 hr. It would appear that the result of our ring-disk electrode experiment is at variance with that of Farr and Hampson's current interruption experiment. This apparent contradiction can be understood if it is assumed that the passivation occurs because of the formation of a thin insoluble film, which may consist of CdO as postulated by Breiter and Weininger (12), while the major oxidation product, $Cd(OH)_2$, dissolves in the electrolyte to give rise to the reduction current at the ring electrode. Thus, the result of current interruption experiments reported by Farr and Hampson does not necessarily mean that the entire film is insoluble.

Electrical conductivity of the film.—The solid-state growth mechanism originally postulated by Croft (7) and supported by Farr and Hampson (9) requires the rate of transport of ions such as Cd^{++}, OH^-, or H^+ in the film to be large. These ions may migrate or diffuse through the interior of the crystalline lattice, through defects in the film, or through grain boundaries or pores in the film. In order to obtain some information on the magnitude of the ionic conductivity of the film, potentiostatic anodic current-time curves obtained at a stationary planar cadmium electrode were analyzed according to the method described by Franck (25) and also by Fleischmann and Thirsk (26). The analysis should be regarded as only very approximate because the actual film is not uniform in composition as well as in thickness.

Suppose that a metal electrode given is already covered entirely with an anodic film of a uniform thickness. If an anodic current i flowing for time dt results in an increase in film thickness by $d\delta_f$ by a solid-state ionic transport mechanism, the following equation should hold

$$\frac{d\delta_f}{dt} = \frac{m}{n\mathbf{F}A\rho} i \qquad [7]$$

where m is the molecular weight of the substance composing the film, A is the area of the electrode, and ρ the density of the film. If the film dissolves during its growth, the total current i must be corrected for the current corresponding to the rate of dissolution of the film. This correction is unnecessary if the solution is presaturated with the material of the film, because no further dissolution of the film will take place during the solid-state growth in such a solution. The total potential drop between the metal and the solution can be written as

$$\Delta V = i\left(R_{m/f} + \frac{\delta_f}{\sigma A} + R_{f/s}\right) \qquad [8]$$

where $R_{m/f}$ and $R_{f/s}$ are the resistances of metal-film and film-solution interfaces, respectively, and σ is the specific conductivity of the film. It is assumed here that all three components of the total potential drop vary linearly with current. Under potentiostatic conditions (ΔV = const.), the following relation can be derived readily from [7] and [8]

$$\frac{1}{i^2} = \frac{1}{i_o^2} + \frac{2m}{n\mathbf{F}A^2\sigma\rho(\Delta V)} t \qquad [9]$$

where i_o is the current at $t = 0$. It is expected from this equation that plotting i^{-2} against t should yield a straight line, and its slope should permit calculation of σ.

An experiment was carried out with a stationary cadmium electrode with $A = 0.317$ cm² in 6.9M KOH saturated with $Cd(OH)_2$. The electrode was first anodized at +0.100V for 90 min, at which time the electrode surface was assumed to be completely covered

with a film. The potential was then stepped up to +0.300V. The i^{-2} — t plot at the two potentials is shown in Fig. 8. At +0.100V the relation was not linear as may be expected, whereas a good straight line was obtained at +0.300V except for the first several minutes. Since the amount of CdO formed in this potential range is believed to be negligibly small as indicated by the absence of cathodic prewave in the potential scan experiment (see Fig. 2), it may be assumed that the current observed at +0.300V was consumed entirely for the growth of $Cd(OH)_2$ by a solid-state ionic transport mechanism. In calculating the ionic conductivity σ from the slope of the straight line, the actual surface area of $Cd(OH)_2$ crystals which is in contact with the electrolyte should be used for A. However, since this is an unknown quantity, we are compelled to use the apparent electrode area for A to find the order of magnitude of σ. With $n = 2$, $A = 0.317$ cm^2, $m = 146.43$, $\rho = 4.79$ g · cm^{-3}, and $\Delta V = 0.2$V, we obtain $\sigma = 1.7 \times 10^{-10}$ ohm^{-1} · cm^{-1}. The experiment was repeated by forming the initial film at +0.0952V and stepping up the potential to +0.196V. The i^{-2} — t plot at the latter potential yielded a straight line with $\sigma = 2.0 \times 10^{-10}$ ohm^{-1} · cm^{-1} in good agreement with the value found from Fig. 8. The conductivity value is comparable to that found for anodic films of $PbSO_4$, 3.5×10^{-10} (26) or 1×10^{-9} ohm^{-1} · cm^{-1} (27).

The increase in "average" film thickness due to the solid-state growth at +0.300V in the experiment of Fig. 8 was calculated from the integration of the current-time curve over the 70-min period. It amounted to 0.044μ. On the other hand, the average film thickness prior to application of the potential step was estimated to be approximately 0.14μ. This value was calculated by integration of the current-potential curve which was obtained in a separate experiment by scanning the potential from +0.1 to −0.3V at a speed of 0.1 V/min after potentiostatic film formation at +0.1V. Thus, the increase in film thickness due to the solid-state growth at +0.3V corresponds to about 30% of the thickness of the film formed at +0.1V.

The results described above show that in the potential range after passivation, the film does grow by the solid-state ionic transport mechanism. In the potential range of active oxidation (<0.05V), however, the contribution of ionic transport process to the film formation is negligible. It can be estimated that the solid-state film growth is limited to only about 0.01μ for $\Delta V = 0.05$V.

Summary and Conclusion

1. The formation of a dissolved intermediate species during the anodic and cathodic processes of cadmium metal in concentrated alkaline solutions was demonstrated by using the ring-disk electrode technique.

2. The dissolution-precipitation mechanism prevails in the active range of potential. The contribution of solid-state growth mechanism is negligible in this potential range, and practically all current flows through exposed areas of the cadmium metal.

3. The result of this investigation supports the view expressed by previous investigators (1-3a, 6, 12) that passivation is not the result of complete blocking of the cadmium metal surface by $Cd(OH)_2$ crystals but rather is due to the formation of a thin, continuous film of CdO next to metallic cadmium. This passive film appears to be insoluble or only very slowly soluble in alkali.

4. In the passive range of potential the $Cd(OH)_2$ crystals grow on top of the passive layer by a solid-state ionic transport mechanism. The ionic conductivity of the $Cd(OH)_2$ film is of the order of 10^{-10} ohm^{-1} · cm^{-1}.

5. The quantity of CdO formed increases with increasing anodic potential, and in 6.9M KOH it becomes detectable by cathodic reduction if the anodization potential is brought to a value more positive than +0.4V *vs.* the equilibrium potential of $Cd/Cd(OH)_2$.

6. The cathodic reduction of CdO occurs at a potential about 40 mV less cathodic than that of $Cd(OH)_2$ without forming a soluble intermediate.

7. The reduction of $Cd(OH)_2$ occurs both by a direct mechanism and through the solution phase. The contribution of the latter mechanism increases as the reduction progresses and as the area of exposed cadmium metal increases.

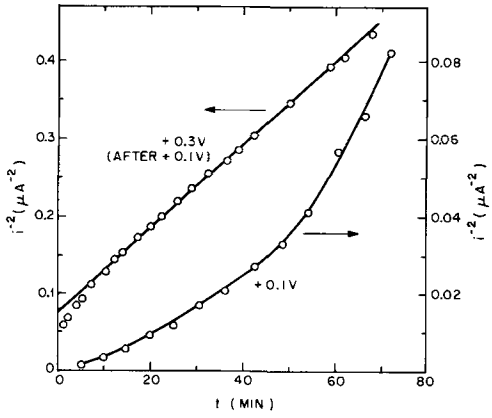

Fig. 8. i^{-2}-t plot for calculation of ionic conductivity [stationary electrode in 6.9M KOH saturated with $Cd(OH)_2$].

Acknowledgment

The author is grateful to D. R. Turner, P. C. Milner, and R. E. Visco for helpful suggestions and discussions.

Manuscript submitted July 23, 1969; revised manuscript received *ca.* Nov. 5, 1969. This was Paper 48 presented in part at the Philadelphia Meeting of the Society, Oct. 9-14, 1966.

Any discussion of this paper will appear in a Discussion Section to be published in the December 1970 JOURNAL.

REFERENCES

1. S. A. Rozentsveig, B. V. Ershler, E. L. Strum, and M. M. Ostania, *Trudy Soveshehaniya Elektrokhim. Akad. Nauk, SSSR, Otdel. Khim, Nauk,* **1950,** 571 (1953).
2. K. Huber, *This Journal,* **100,** 376 (1953).
2a. K. Huber and S. Stucki, *Helv. Chim. Acta,* **51,** 1343 (1968).
3. P. E. Lake and E. J. Casey, *This Journal,* **105,** 52 (1958).
3a. P. E. Lake and E. J. Casey, *ibid.,* **106,** 913 (1959)
4. I. Sanghi, S. Visvanathan, and S. Ananthanarayanan, *Electrochim. Acta,* **3,** 65 (1960).
5. S. Yoshizawa and Z. Takehara, *ibid.,* **5,** 240 (1961).
6. M. A. V. Devanathan and S. Lakshmanan, *ibid.,* **13,** 667 (1968).
7. G. T. Croft, *This Journal,* **106,** 278 (1959).
8. G. T. Croft and D. Tuomi, *ibid.,* **108,** 915 (1961).
9. J. P. G. Farr and N. A. Hampson, *Electrochem. Technol.,* **6,** 10 (1969).
10. S. U. Falk, *This Journal,* **107,** 661 (1960).
11. R. D. Armstrong, E. H. Boult, D. F. Porter, and H. R. Thirsk, *Electrochim. Acta,* **12,** 1245 (1967).
12. M. W. Breiter and J. L. Weininger, *This Journal,* **113,** 651 (1966).
13. M. W. Breiter and W. Vedder, *Trans. Faraday Soc.,* **63,** 1042 (1967).
14. R. W. Ohse, *Z. Elektrochem.,* **64,** 1171 (1960).
15. P. C. Milner and U. B. Thomas, in "Advances in Electrochemistry and Electrochemical Engineering," C. W. Tobias, Editor, Vol. 5, Interscience Publishers, New York (1967).
16. E. J. Rubin, Abstract No. 51, Extended Abstracts of Papers Presented at the Chicago Meeting of the Society (1967).
17. V. G. Levich, "Physicochemical Hydrodynamics," translated by Scripta Technica, Inc., Prentice-Hall, Inc., Englewood Cliffs, N. J. (1962).
18. W. J. Albery and S. Bruckenstein, *Trans. Faraday Soc.,* **62,** 1920 (1966).
19. R. E. Visco and R. H. Sonner, Abstract No. 7, Extended Abstracts of Papers Presented at the Detroit Meeting of the Society (1969).

20. P. E. Lake and J. M. Goodings, *Can. J. Chem.*, **36**, 1089 (1958).
21. D. E. Ryan, J. R. Dean, and R. M. Cassidy, *ibid.*, **43**, 999 (1965).
22. E. M. Jost, Extended Abstract of Battery Division of the Society, **11**, 130 (1966).
23. J. P. Harivel, B. Morignat, J. Migeon, and J. P. Laurent, Advances in Battery Symposium of the Electrochemical Society, Southern California-Nevada Section, Dec. 4, 1965.
24. A. R. Hutson, in "Semiconductors," N. B. Hannay, Editor, Chap. 13, Reinhold Publishing Corp., New York (1959).
25. U. F. Franck, in "Verband deutchen Physikalischer Geselschaften, Halbleiterprobleme," W. Schottky, Editor, Vol. II, p. 214, Friedr. Vieweg u. Sohn, Braunschweig (1955).
26. M. Fleischmann and H. R. Thirsk, *Trans. Faraday Soc.*, **51**, 71 (1955).
27. P. Ruetschi and B. D. Cahn, *This Journal*, **104**, 406 (1957).

Kinetics of the Solid Lithium Electrode in Propylene Carbonate

Robert F. Scarr*

Union Carbide Corporation, Consumer Products Division, Research Laboratory, Cleveland, Ohio

ABSTRACT

Kinetic parameters for solid lithium electrodes have been evaluated at 23° ± 1°C for $LiClO_4$ in propylene carbonate at several concentrations between 0.1 and 1.0M. Polarization data obtained by the interrupted current method agree with that obtained by a pulse technique. Depending on its treatment, the electrode exhibits one of two levels of activity. This phenomenon is believed to be due to the presence of a film formed by reaction between lithium metal and the solvent or impurities. The film is broken down at higher current densities, effecting an increase in electrode area. The area increase has been corroborated by double-layer capacitance measurements. Standard exchange current of a film-free electrode in $LiClO_4$ is 1.78 ± 0.33 mA/cm².

Lithium metal is a promising material for use as an anode in nonaqueous battery systems. Besides being one of the more active metals and possessing a very low equivalent weight, lithium has been shown, at least in the case of its amalgam, to be a highly reversible electrode. Cogley and Butler (1) have evaluated the so-called "true" exchange current for lithium amalgam in LiCl-dimethyl sulfoxide electrolyte at approximately 3 mA/cm².

The present investigation is a study of the kinetics of the solid lithium electrode in another solvent of current interest, propylene carbonate. The electrolyte was $LiClO_4$, a soluble lithium salt commonly used in nonaqueous battery studies. Due to the nature of experimental conditions and the existence of interfering processes, the results obtained should be considered preliminary. At this early stage of our understanding of this system, rigorous measures, such as correction for double-layer effects of activity coefficients, were not used in analysis and interpretation of experimental results.

Experimental

Most of the current-voltage data for the lithium electrode reaction were obtained by the interrupted current technique. This type of measurement represents steady-state conditions for the test electrode, and permits the polarization to be corrected for ohmic drop. A pulse method was also used.

Cell current was controlled by a Tacussel Model PIT 20-2X potentiostat in a galvanostatic mode. The control signal was supplied from a variable-gain inverting adder which summed a constant d-c potential and a single 100-μsec pulse from a Tektronix Model 160 Pulse Generator.

The pulse amplitude was initially adjusted to counterbalance exactly the d-c potential. The result was a signal wherein the d-c level corresponded to closed-circuit operation and the pulse period to the open-circuit condition. For the pulse experiments, the d-c level was nulled. Variation in the closed-circuit current was achieved by changing the gain of the adder. Steady-state cell voltages were measured on a Dana Model 5400 digital voltmeter. Transient cell potential and cell current were observed on a Tektronix Model 564 Storage Oscilloscope with a Model 3A3 dual channel differential amplifier using the a.c.-coupled input. The settling time for the current interruption, defined as 97% of the full step, was less than 2 μsec, as shown in Fig. 1.

The cell for this work was a 50-ml Pyrex beaker with a tight-fitting Teflon top which held the three electrodes with vertically oriented surfaces. All electrodes, test, counter, and reference, were pieces of

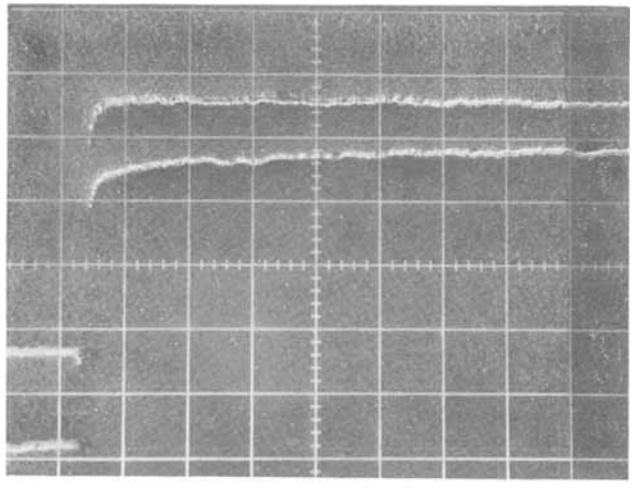

Fig. 1. Typical oscilloscope trace showing current interruption for lithium metal electrode in 0.1M $LiClO_4$. Upper trace: current, 500 μA/cm. Lower trace: potential 50 mV/cm. Sweep rate: 5 μsec/cm.

* Electrochemical Society Active Member.
Key words: lithium electrode kinetics, film formation on lithium, lithium in propylene carbonate.

99.96% lithium foil obtained from Foote Mineral Company. This foil was known to contain 100 ppm potassium, 200 ppm sodium, and 150 ppm calcium. The test electrode was a flat plate, 0.5 x 1.0 cm, exposed to electrolyte on both sides, and surrounded by the counterelectrode which was suspended around the perimeter of the cell. Though nearly cylindrical, this geometry may have led to nonuniform distribution of the current at the electrode surface. According to Wagner (2), the current density at the edges of the electrode could, for the conditions employed in this particular experiment, be as much as twice that of the average based on a parallel-plate model for the cell. The effects of nonuniform current distribution should, however, largely cancel in the determination of the kinetic parameters from the average current, and, in view of the preliminary nature of the work, this effect shall be disregarded.

The reference electrode was situated adjacent to and in the same plane as the test electrode. Lithium metal is known to be a stable reference electrode, and in the present work was found not to vary more than 1 mV from an auxiliary twin reference electrode, even after prolonged use. The area of the test electrode was controlled and known. Prior to their use, the surfaces of the electrodes were cleaned by brushing with Carborundum cloth.

During the earliest work, those parts of the test electrode not intended to contact the electrolyte were coated with Microtex masking lacquer. Later, this substance was shown by gas chromatography (g.c.), to introduce trace quantities of unknown organic contaminants into the electrolyte. Consequently, the use of the masking lacquer was discontinued, and the electrode area was controlled instead by cutting away all unwanted metal. The electrode of the desired size was suspended just below the surface of the electrolyte by a thin thread of lithium metal remaining from the original piece. The results obtained using this type electrode were, however, no different than those where the lacquer was used.

The entire cell and associated work area were incorporated in a glove box containing a purified, continuously renewed argon atmosphere. Oxygen was removed from the argon by passing it over hot copper turnings and water vapor was removed with Linde 13X Molecular Sieve. During quiescent periods, the argon flow rate was 0.8-1.3 std ft^3/hr, which corresponds to an hourly rate of 15-23% of the box capacity. The flow rate was considerably higher at times when the transfer chamber was opened. The humidity in the box was monitored by a Panametrics Hygrometer, Model 1000, and throughout the course of the work was progressively reduced to about 5 ppm water vapor. The nitrogen content of the atmosphere was below limits detectable by g.c. Under these conditions, lithium metal remained visually bright and clean indefinitely. Ambient temperature within the box was 23° ± 1°C.

Propylene carbonate was purified by vacuum distillation from a Podbielniak column at 8 mm Hg and 100°-105°C column head temperature. The resulting product still contained some low level contamination, probably 1,2-propanediol. It is known (3) that the glycols are virtually impossible to remove completely. Ultrapure lithium perchlorate made by vacuum fusion was obtained from Anderson Physical Laboratories, and was used without further purification. After preparation, electrolytes were stored over Linde 4A Molecular Sieves and occasionally also stored in the presence of lithium wool.

The normal procedure was first to obtain data at increasing levels of anodic polarization, followed by decreasing the current back to open circuit, each point requiring 3-8 min to establish. This pattern was then repeated in the cathodic direction. Nonohmic steady-state polarization was evaluated by extrapolating the initial region of the potential-time curves back to the initiation of the pulse, then subtracting the obtained ohmic drop from the steady-state cell voltage. The electrode potential could be determined with an error of ±2% of the IR drop or 1 mV, whichever was the greater.

Current-voltage data were then plotted according to the Allen-Hickling method (4). In this technique, polarization data are corrected for the back reaction by plotting the logarithm of the function $I/1 - \exp(\eta/\beta)$ *vs.* the overvoltage, η, where I is the current density and $\beta = RT/F$. A one-electron process is assumed. This permits data points very close to equilibrium to be taken into account. In addition, cathodic and anodic branches are colinear, thereby reinforcing one another.

Results and Discussion

The current-voltage behavior of the electrode seemed to depend in part on the humidity of the glove-box atmosphere. During the initial phases of this work, the water vapor content of the glove box was approximately 30 ppm. A current-voltage plot typical of these conditions is given in Fig. 2, where the circles represent data taken under increasingly positive polarization and the triangles the opposite direction. The cathodic branches of these plots were seldom colinear with the anodic branches, and usually fell away (to higher polarization) as the current density increased. The lithium deposits corresponding to this region were loose, granular, and poor in quality.

The average exchange current density, I_0, for 1M $LiCO_4$ at this stage of the work was found to be about 0.64 ± 0.04 mA/cm^2, and the cathodic transfer coefficient, α, about 0.63 ± 0.02. The corresponding kinetic parameters for 0.2M $LiClO_4$ were 0.32 ± 0.01 mA/cm^2 and 0.69 ± 0.01, respectively. The cathodic transfer coefficient calculated from the dependency of exchange current on lithium-ion concentration was in good agreement with the slope of the Allen-Hickling plots.

At this point, glove-box conditions were improved to the extent that water vapor was reduced to about 15 ppm. All measurements were then repeated using new batches of materials. A pronounced change in polarization behavior was found to occur. Although the water vapor was thereafter reduced even further to 5 ppm, no additional change in results occurred.

Current-voltage curves characteristic of those obtained are illustrated in Fig. 3. Data points taken under the initial increasing anodic polarization indicated very clearly the usual linear region with an exchange current approximately equal to the previous measurements. At a point midway in the series, however,

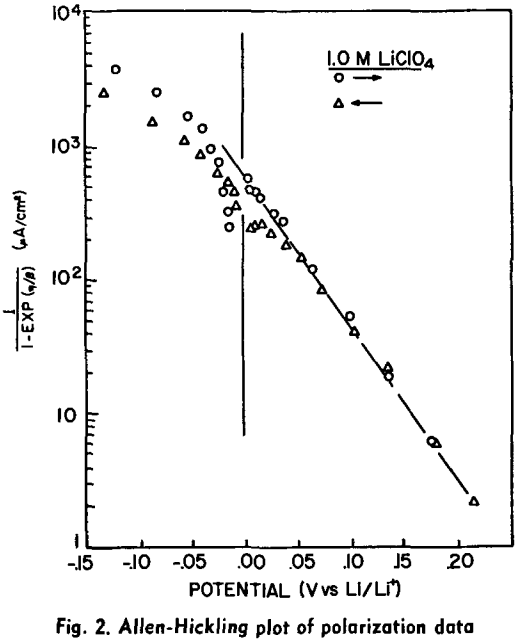

Fig. 2. Allen-Hickling plot of polarization data

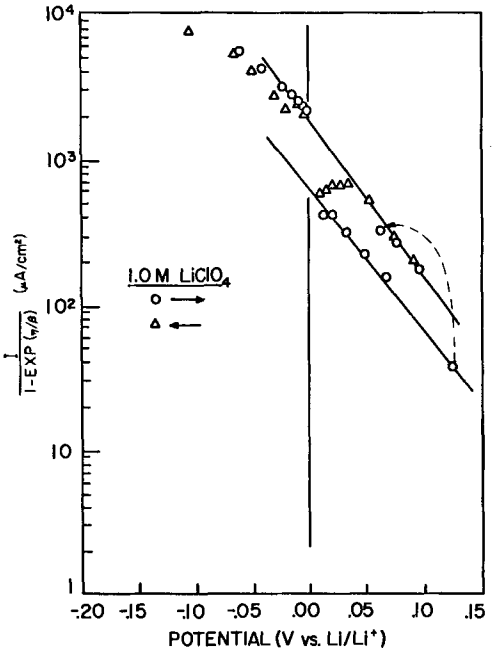

Fig. 3. Allen-Hickling plot of polarization data; later results

usually in the range of 2-5 mA/cm², the overpotential suddenly diminished, as shown by the dashed line. These latter data points, as well as those taken under subsequent decreasing current, define a second linear region with a higher exchange current. The extension of the upper line was often colinear with the cathodic branch, as illustrated in Fig. 3. After an electrode had once achieved the active condition, subsequent anodic treatments resulted in retracing the upper curve, as shown in Fig. 4 for 0.2M $LiClO_4$.

The linearity of the anodic branch of the current-voltage plot indicates that electron transfer is the rate-determining phenomenon in this region. Steady-state conditions are superseded at current densities above 15 mA/cm² where diffusion polarization is presumed to take effect.

The dual Tafel behavior is believed to be due to the existence of an insulating film on the electrode surface which initially covers many of the active sites available for reaction. Such a film is not the normal product of anodization of lithium metal but is probably the result of a side reaction with the solvent or an impurity. This interpretation is supported by the observation by Cogley and Butler (5) of a waxy film deposited on lithium amalgam in propylene carbonate electrolyte.

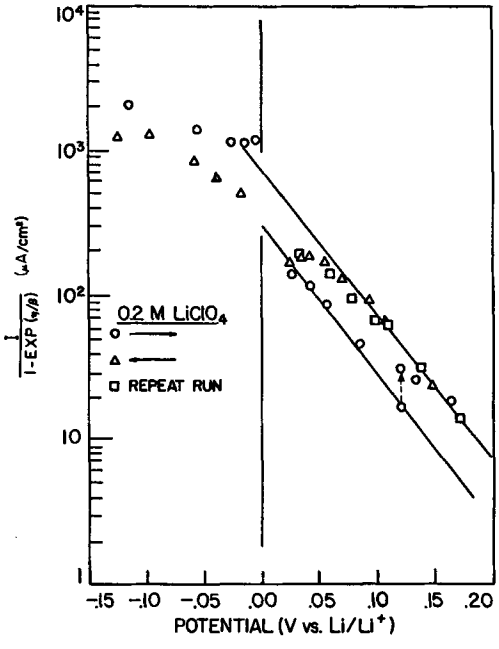

Fig. 4. Allen-Hickling plot of polarization data showing retracing of upper curve.

As the current is increased under interrupter conditions, the effect of the film can be overcome, causing the effective area of the electrode to be abruptly increased. This point occurs when the rate of creating new sites through either dissolution or deposition exceeds that of film formation. Film formation is probably limited by the rate of diffusion of reactant through solution.

Film formation may be catalyzed by the presence of water, hence the dependence on the humidity of the glove box. Of the two levels of activity, the upper is probably more representative of the intrinsic properties of the electrode because of the absence of the film. The electrode remains in this enhanced mode as long as the current appreciably exceeds the rate of film formation. Below this point, the film is reformed, causing the downward decay of the Allen-Hickling plots.

Independent evidence has been obtained that a reactive substance which might lead to film formation is present in the electrolyte system. Linear sweep voltammetry of propylene carbonate solutions of various electrolytes has revealed the presence of two cathodic peaks between 0.0 and 1.0V with respect to Li/Li^+. These peaks might be attributed to formation of lithium intermetallic compounds with the substrate. The peaks have been observed in this laboratory, however, even in the complete absence of lithium ion, or where lithium compounds are not expected to form, such as for nickel electrodes shown in Fig. 5. Furthermore, it may be shown from thermodynamic data that propylene carbonate may be expected to decompose in this potential region.

The film formation theory was further confirmed by applying current pulses rather than current interruptions to the electrode. In the case of pulses, the amount of material removed from the electrode is negligible, hence the film would be expected to maintain its integrity. Figure 6 shows the results of an electrode which was subjected to both pulse and current interruption techniques. The circles, open and solid, represent the first pulse experiment for ascending and descending current, respectively. The usual shift in polarization was not observed, indicating that the film remained intact.

The current interruption run, denoted by the triangular data points, was made the next day. The first few points are therefore considerably lower than the pulse series due to further film formation which occurred overnight. Nevertheless, midway through the run, the electrode switched to the enhanced state and remained

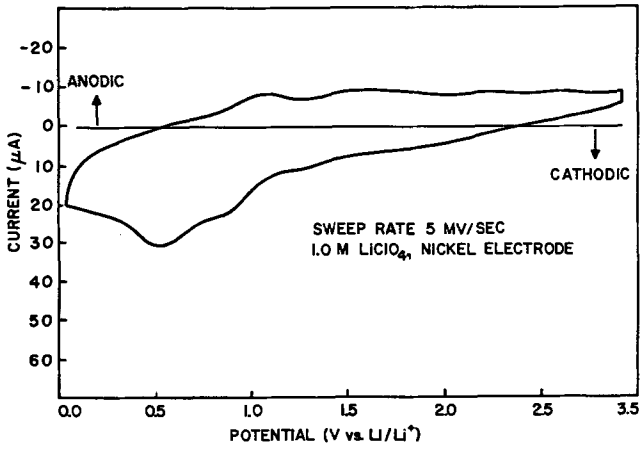

Fig. 5. Voltammetric sweep of nickel electrode in $LiClO_4$ electrolyte.

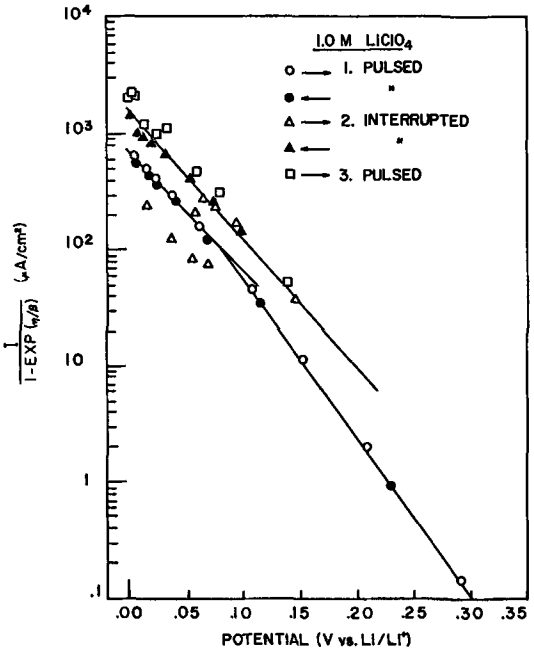

Fig. 6. Allen-Hickling plot for combined current interrupter/pulse procedure.

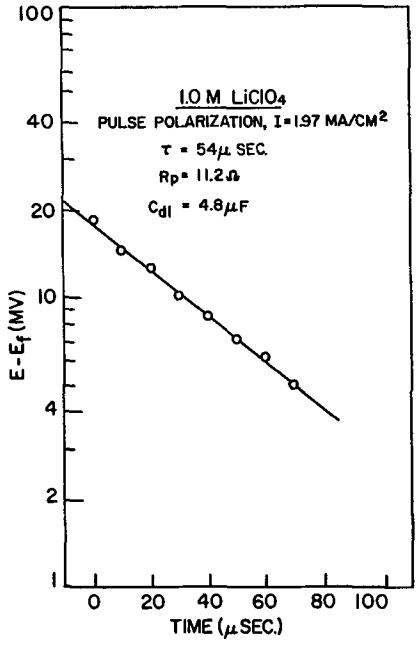

Fig. 7. Log plot of potential response after pulse

in that condition for the balance of the experiment. The square points are for another pulse series immediately following the interrupter run. It is seen that the activity of the electrode remained high during this period. The agreement between the pulsed and interrupted results indicates further that there was no temperature increase during the interrupter series due to resistive heating of the electrolyte.

Table I. Double-layer capacity and polarization resistance for pulsed runs, 1M $LiClO_4$

	C_{dl} $\mu F/cm^2$	R_p ohm
Lower curve	2.4	20.4
Upper curve	5.2	9.3

As further characterization of the insulating effect of the film, an indication of the area change was obtained by evaluating the double-layer capacity (C_{dl}) from pulse data, both before and after the interrupter run. Using a parallel resistor-capacitor equivalent circuit as a model for the double layer, C_{dl} was evaluated from the slope of log potential *vs.* time plots, as in Fig. 7. Because of the experimental difficulties in making such measurements under film-forming conditions and because of the marginal fitness of the model in this range of overpotential, C_{dl} values should be considered valid only for purposes of comparison. As shown in Table I for 1M $LiClO_4$, the double-layer capacity, hence electrode area, does increase roughly in proportion to the increase in exchange current while the polarization resistance (R_p) is seen to decrease. The exchange current calculated from R_p, 2.7 mA/cm^2, is in good agreement with that obtained from the interrupted current measurements, *vide infra.*

Due to the irreproducibility and nonlinearity of the Allen-Hickling plots for the cathodic data, kinetic parameters were determined largely from anodic measurements. Only where the cathodic data tended to substantiate anodic results were they utilized. The character of the results from the cathodic region may probably be attributed to a mixed-electrode process involving both metal deposition and solvent decomposition. Convection is ruled out as an explanation for the nonlinearity because of the agreement between interrupter and pulse data.

The combined pulse-interrupter measurements were carried out at several concentrations of electrolyte. The exchange currents evaluated by this means, as well as those obtained by the conventional interrupter procedure, were combined to give the results listed in Table II. As one means of determining the transfer coefficient, α, these data are plotted *vs.* log concentration in Fig. 8. The straight lines represent the data according to a least-squares analysis; the numerical parameters for the least-squares lines are given as the last entry in Table II. The data obtained by the pulse technique are solid points, while those obtained by interruption are shown as open points. The relationship of the upper and lower curves is seen very clearly. The data from the earliest experiments obtained before the dual effect was encountered are represented by the crosses and the dashed line, and are in good agreement with the lower curve.

The transfer coefficient has been determined both from the polarization slope and from the concentration

Table II. Li/$LiClO_4$ electrode kinetic parameters at 23°C

C_{Li^+} (mole/liter)	Upper curve			Lower curve		
	I_0 mA/cm^2	b_c mV/dec	α	I_0 mA/cm^2	b_c mV/dec	α
1.0	1.76 ± 0.10	92 ± 2	0.64 ± 0.01	0.69 ± 0.16	96 ± 5	0.61 ± 0.03
0.5	1.22 ± 0.03	100 ± 14	0.59 ± 0.08	0.53 ± 0.05	98 ± 2	0.60 ± 0.02
0.2	0.76 ± 0.07	94 ± 2	0.62 ± 0.01	0.33 ± 0.08	92 ± 4	0.64 ± 0.03
0.1	0.49 ± 0.09	92 ± 5	0.64 ± 0.03	0.30 ± 0.02	92 ± 9	0.64 ± 0.06
$\frac{\Delta \log I_0}{\Delta \log C}$	1.78 ± 0.33	130 ± 5	0.45 ± 0.02	0.67 ± 0.25	96 ± 13	0.61 ± 0.08

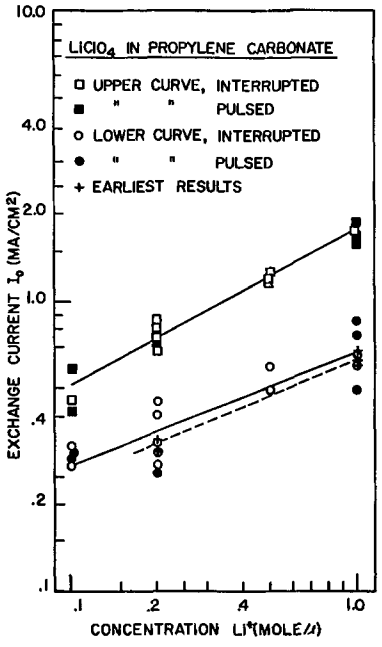

Fig. 8. Exchange current-concentration plot for $LiClO_4$

dependence of exchange current. The first method, while normally preferred, suffers from the influence of surface films and interfering corrosion processes at low currents. The second method may produce erroneous results because no correction has been made for double-layer effects or for activity coefficients. For the majority of cases, an average value for the transfer coefficient of 0.62 is obtained, but for the reasons stated the reliability of this figure is somewhat in question. The standard exchange current obtained by both methods is *ca.* 1.8 mA/cm². Standard deviations for these values are given in Table II. The principal factor in the scatter of the kinetic parameters from run to run is probably the irreproducibility of the film. This is supported by the qualitative observation that the data scatter for the lower state of electrode activity is somewhat greater than for the more active state where the film is supposedly absent. The above kinetic parameters may be compared with those of Cogley and Butler (5) who obtained values of 0.75 and 8.6 mA/cm², respectively, for Li(Hg)-LiCl in DMSO.

It is concluded that the solid lithium electrode is indeed active enough to compare favorably with other electrodes presently utilized in primary battery applications. While the formation of a film with some component of the electrolyte may reduce the apparent activity of the metal, the electrode discharge performance should improve under continuous drain conditions which tend to remove the film. In the final analysis, such a film may actually prove beneficial as a protective layer during idle periods.

Acknowledgments

The author is pleased to acknowledge the assistance of Mr. Peter Briedis in obtaining the experimental data, and the helpful discussions of Professor Ernest B. Yeager, Case Western Reserve University.

Manuscript submitted Aug. 6, 1969; revised manuscript received Nov. 17, 1969. This was Paper 161 presented at the New York Meeting, May 4-9, 1969.

Any discussion of this paper will appear in a Discussion Section to be published in the December 1970 JOURNAL.

REFERENCES

1. David R. Cogley and James N. Butler, *J. Phys. Chem.*, **72**, 4568 (1968).
2. C. Wagner, *This Journal*, **98**, 116 (1951).
3. R. Jasinski, B. Burrows, and P. Malachesky, Final Report, Contract NOw 66-0621-C, Tyco Labs., Inc. (Oct. 1967).
4. P. L. Allen and A. Hickling, *Trans. Faraday Soc.*, **53**, 1626 (1957).
5. David R. Cogley and James N. Butler, Final Report, Contract AF 19 (628) 5525, Tyco Labs., Inc. (Dec. 1968).

PbO_2 in the Lead-Acid Cell

II. Cycling and Overcharge on Pure and Antimonial Lead Grids

Everett J. Ritchie*

Eagle-Picher Industries, Incorporated, Joplin, Missouri

and Jeanne Burbank*

Naval Research Laboratory, Washington, D. C.

ABSTRACT

Three representative lead oxides were used in fabricating lead-acid cells with pure and antimonial lead grids. The cells were cycled and overcharged. Positive plates were removed at intervals and the active material was examined by x-ray diffraction, electron microscopy, and by spectroscopy. Bulk densities of the active materials were also determined. The cells with pure lead grids usually had somewhat lower capacities than the corresponding antimonial cells, and lost approximately 80% of their initial capacity between 5 and 10 cycles. None of the antimonial cells suffered major capacity loss during the 21 cycles comprising the test. The rate of loss in bulk density of the PbO_2 was higher in the pure lead cells. This and the loss in capacity have been attributed to the grain growth and anhedralization that take place more rapidly when antimony is absent. Antimony appears to act as a nucleating catalyst for the PbO_2 and inhibits crystal growth.

The fully charged positive electrode of the lead-acid cell is a porous polycrystalline aggregate of PbO_2. The individual crystallites are usually of submicroscopic dimensions (1), and the aggregate must retain its mechanical strength and electrical continuity under stringent requirements: percolation of H_2SO_4 throughout the mass, cyclic volume changes between PbO_2 and $PbSO_4$ during electrode operation, and vigorous O_2 gas evolution during overcharging. The ability of

* Electrochemical Society Active Member.

the working electrode to withstand such use is the combined result of several factors. Voss and Huster (2) have shown that, in antimonial cells, the durability of the PbO_2 mass is related to the depth of discharge during cycling, with deep or complete discharges most destructive. The composition of the supporting grid alloy has an effect on the cycle life of the active material. Under usual conditions, plates made with antimonial alloy grids have significantly longer cycle life than those with nonantimonial lead grids (3, 4).

In general, the strength of polycrystalline aggregates has been shown to be related to their microstructures (5, 6), and it has been suggested that the durability of a PbO_2 aggregate is related to the morphology of the particles as seen in the electron microscope (3, 7).

In the first phase of this study, electrodes fabricated from three representative lead oxides were oxidized while supported on pure and antimonial lead grids (8). The resultant PbO_2 was examined by x-ray diffraction and electron microscopy, and it was concluded that the freshly anodized mass comprised compound spikes of crystals of approximately 0.5μ average diameter, which were overgrown with smaller sessile crystallites, 0.1μ or less in diameter. The descriptive terminology was selected because botanical analogy is frequently employed to describe crystal formations. Such a geometrical morphology readily explains the difference in surface area of the polycrystalline mass when measured by gas absorption methods, about 7 m^2/g, and the value of 14 to 24 m^2/g, calculated on the basis of x-ray line broadening (4, 9). The very small sessile crystallites lie within the range that gives rise to a limited degree of x-ray line broadening (10). Since the smaller crystallites cover the larger crystals, and because the specific x-ray absorption of lead is high, the entire mass appears to consist of the smaller crystallites. In such a specimen, the underlying larger crystals contribute little to the x-ray diffraction pattern, although the larger crystals may make up the major fraction of the total weight of the sample. Kordes (4) determined from neutron diffraction that the interior portions of the crystals or agglomerates of PbO_2 electrodes appeared to have better "crystallinity" than the outer layers or grain boundary material. This was borne out by the direct examination of PbO_2 by electron microscopy (8). In further agreement with the conclusions of Kordes (4), it was observed that the initial oxidation, or formation of PbO_2, was not significantly different when antimonial or pure lead supporting grids were employed.

It was also found that there was no significant difference in the initial morphology of the active material among the three representative oxides employed, although the oxide that originally contained Pb_3O_4 gave rise to the largest individual crystals (8).

Table I. Cell characterization*

Oxide	Description	9-Plate cells** D†	F	G	3-Plate cells*** D	F	G
A	A milled nonleady litharge	64	1.050	1.250	65	1.0585	1.2247
C	A ball-mill leady litharge containing 25% free lead	64	1.100	1.250	65	1.0585	1.2247
H	A furnaced litharge containing 25% Pb_3O_4	64	1.100	1.250	66	1.0585	1.2247

* Pastes of each oxide were applied to pure and 7% antimonial lead grids, and positive and negative plates were pasted with the same materials at the same time.
** Materials used in fabrication of these cells are characterized in Ref. (11).
*** Materials used in fabrication of these cells are characterized in Ref. (8).
† Symbols signify: *D*—wet paste density in g/in.^{3}; *F*—sp gr H_2SO_4 used in formation; *G*—sp gr H_2SO_4 used in the cycling and overcharging routines, Table II.

The present phase of the study was undertaken to determine: whether electrochemical cycling and overcharge in H_2SO_4 has an effect on the crystal morphology of PbO_2, whether differences in active material morphology attributable to the presence of antimony in the grid metal could be observed, as indicated by earlier studies (3, 4), and whether differences could be ascribed to the original oxides from which the electrodes were fabricated.

Materials and Methods

Three representative lead oxides, designated *A*, *C*, and *H*, were used in this study. The metals and individual oxide production batches were characterized in detail in earlier reports (8, 11). Conventional battery plates were hand pasted and cured following standard practice for each of the oxides using pure and antimonial lead grids, nominally 7% Sb by weight. No additives were used in plate fabrication, and positive and negative plates were pasted with identical materials. From these plates, 12 full-sized 9-plate cells were assembled for electrochemical cycling and overcharge tests (12). Six small 3-plate cells (2 negatives and 1 positive) were manually cycled a few times. These experiments are summarized in Tables I and II.

Two each of the positive and negative plates were removed from six of the 9-plate cells after 11 cycles. These were replaced by heavy plastic sheets to retain approximately the normal element-electrolyte balance

Table II. Capacity cycling and overcharge procedures

9-Plate cells						3-Plate cells*		
Cycle No.	Discharge rate (A)	Cut-off voltage	Cycle No.	Discharge rate (A)	Cut-off voltage	Cycle No.	Discharge rate (A)	Grids
1, 3, 5, 8, 10, 18	3**	1.75	13, 20	100	1.00	1, 3 2, 4	1.0 0.5	Pure lead
2, 9, 12***	150	1.00	14, 21	50	1.70			
4, 7, 19	150	1.00	15	25	1.70	1, 4-8	1.0	Antimony alloy
6, 11†	20	1.70	16 17	12 6	1.70 1.75	2, 3	0.5	

* The 3-plate cells were cycled at ambient room temperature which varied between 20°-30°C. A positive plate potential *vs.* Hg/Hg_2SO_4 of 0.75-0.8V was used as the cut-off voltage.
** The 20-hr rate at 26.67°C (80°F).
*** Cycles 2, 9, and 12 were run at −17.78°C (0°F). All others were run at 26.67°C (80°F).
† Following 11 cycles, 6 cells (one of each type oxide and grid) were removed from the cycle test. After removal of two each of the positive and negative plates, these cells were placed on the following overcharge regime: overcharge, 120 hr at 2.5A; stand, 48 hr less the time required for; high rate discharge, 75A at 37.78°C (100°F) to a cut-off voltage of 1.00V. Failure was reached when the cell capacity fell below 40% of the initial capacity at the 75-A discharge rate.
Note: The charging schedule for the 9-plate cells was to restore 135% of the capacity discharged on the previous discharge. The schedule for the 3-plate cells was to restore 125% of the capacity discharged on the previous discharge at constant current. If the on-charge voltages or the specific gravity of the electrolyte were not stable, charging was continued until the readings indicated a fully charged condition or a defective cell.

and cell packing, prior to continuing with the overcharge phase of the study. After reassembly as 5-plate cells, the pure lead cells were placed on the overcharge test for 2 weeks, and the antimonial cells for 5 weeks. The remaining six 9-plate cells were continued on the cycle test for a total of 21 cycles.

The small 3-plate cells were assembled in polyethylene bags which were shimmed externally to approach a normal element-electrolyte balance. A Hg/Hg_2SO_4 reference electrode was placed in each 3-plate cell, and current, positive plate, and cell voltages were recorded continuously. After formation, these pure lead cells were given 4 cycles, and the antimonial cells 8 cycles.

Fully charged positive plates were removed from the cells at selected intervals and, after blotting off excess electrolyte, the plates were dried in air at room temperature or at 60°-71.1°C (140°-160°F). The plates were weighed before and after removal of the active material. The PbO_2 was examined by x-ray diffraction and electron microscopy by the same techniques described earlier (8). Positive active materials from the 9-plate cells were analyzed spectrographically for antimony, and their bulk densities were measured by the method of Dittman and Sams (13).

Results and Discussion

During operation of a PbO_2 electrode in H_2SO_4, changes in capacity (2, 14), electrical continuity (15-17), bulk density (13), and particle size (4) take place in the electrode mass. Ultimately it fails to deliver adequate electrical capacity, and must be replaced. Some of these changes have been examined in this study to determine the nature of the difference in behavior of PbO_2 when supported on pure and antimonial lead grids, and to compare the behavior of three representative lead oxides.

Capacity.—Discharge capacities of the cells used in this study are given in Table III, and Fig. 1 shows the change in actual cell capacity at the 20-hr rate with cycling at 26.67°C (80°F). The cells with pure lead grids usually had somewhat lower capacities than the corresponding antimonial cells, and lost approximately 80% of their initial capacity between 5 and 10 cycles. High rate discharges showed less difference between antimonial and pure lead cells, and this may be attributed to the relatively small amount of active material required to take part in such cycles (14, 18). It has also been suggested (12) that in the pure lead cells a barrier layer may form between the grid and active material and may offer less resistance at high than at low discharge rates. None of the antimonial

Table III. Discharge capacities of the 9-plate cells (A-hr/kg of dry unformed active material)

Cycle No.	Pure lead grids Oxide A	Pure lead grids Oxide C	Pure lead grids Oxide H	Antimonial grids Oxide A	Antimonial grids Oxide C	Antimonial grids Oxide H
1	103.4	120.3	128.4	130.0	139.0	137.3
2	30.7	31.0	30.7	31.6	24.8	29.4
3	97.5	94.0	134.6	139.7	144.1	149.3
4	47.1	50.0	45.1	49.4	50.0	50.6
5	97.5	95.9	123.4	140.7	139.1	144.7
6	87.8	90.6	102.3	111.4	116.0	112.2
7	40.4	28.4	46.9	53.8	54.3	56.9
8	93.5	35.1	75.0	149.8	147.2	151.4
9	25.7	22.0	20.7	31.0	27.7	27.4
10	24.0	31.5	25.2	142.2	141.7	146.1
11	45.8	59.3	64.9	119.9	116.9	118.0
12	19.7	18.1	17.5	27.2	26.4	26.4
13	41.7	52.1	47.2	61.5	61.5	59.3
14	43.0	58.0	52.0	71.0	69.0	71.0
15	40.0	69.0	62.0	100.0	99.0	99.0
16	49.0	43.0	62.0	124.0	121.0	123.0
17	21.0	21.0	20.0	137.1	133.4	136.6
18	14.3	24.3	12.3	147.4	146.6	147.2
19	14.5	20.8	18.0	38.8	37.3	37.5
20	3.6	22.8	23.5	65.6	66.0	65.5
21	17.0	46.0	18.0	78.7	77.2	70.0

* Values for cycles 1-11 are the average of two cells; those for cycles 12-21 are for single cells.

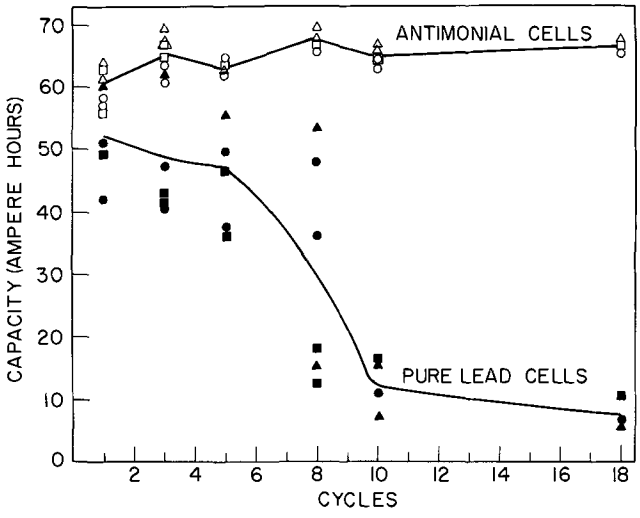

Fig. 1. Actual cell capacities at the 20-hr rate discharged at 26.67°C (80°F). Three of the pure lead cells had failed by the 8th cycle and all had failed by the 10th. None of the antimonial cells had failed at the conclusion of the test at 21 cycles. ●, Oxide *A*; ■, oxide *C*; and ▲, oxide *H* on pure lead grids. ○, Oxide *A*; □, oxide *C*; and △, oxide *H* on 7% Sb-Pb grids.

cells suffered major capacity loss in the cycle tests of this investigation. Visual examination of the positive plates at the conclusion of the cycle tests indicated that the pure lead cells failed by degradation of the active material, while the antimonial cells would have failed because of grid corrosion although none reached failure during these cycles (12).

Overcharge.—During the first week of the overcharge test, Table II, there were indications that the soft lead cells were beginning to short out. These cells were opened and the lead whiskers and bridges removed, and the cells returned to the line. During the second week the shorting problem became general, and the soft lead cells were removed from test at the end of the second week. The antimonial cells did not begin to show shorting troubles until the end of the fourth week, and their test was discontinued after 5 weeks.

The combination of 11 deep capacity cycles and overcharge is evidently a very severe regime for the lead-acid cell. Visual examination of the positive plates indicated that in the pure lead cells the active material failed, while in the antimonial cells the grids limited cell life. In addition, it appears that antimonial grids grow to a greater extent than pure lead grids in the overcharge test, whereas the pure lead grids grow to a greater degree than the antimonial ones during cycling.,

Utilization of PbO_2.—During cycle operation of the positive plate of the lead-acid cell, only a fraction of the active material is actually used. Nominally every kilogram of PbO_2 is capable of giving 224 A-hr capacity. The coefficient of use varies with the rate and ambient conditions of discharge, usually lying in the range of 10-50% of theory (14). The coefficient of use also appears to depend on the grid metal, with the same active material paste yielding less capacity with pure lead grids than when supported on antimonial grids. Representative values of the coefficient of use for the cells in this study are given in Table IV. The values of 18-63% utilization obtained with the plates and conditions of this study lie within the accepted operating range. Differences among the three oxides were less on antimonial than on pure lead grids.

Bulk density.—The bulk or apparent density of the positive active material decreases with cycling (13). Figure 2 shows the change in bulk density of plates fabricated with the three oxides on pure and antimonial lead grids. On pure lead, the rate of density loss

Table IV. Average utilization coefficients of PbO_2* (U. C. in A-hr/kg)

Discharge rate (A)	Pure lead grids Oxide A U.C.	A %**	C U.C.	C %	H U.C.	H %	Antimonial lead grids Oxide A U.C.	A %	C U.C.	C %	H U.C.	H %
3	97.6	43.6	100.2	44.7	123.9	55.3	137.5	61.4	138.0	61.6	141.2	63.1
20	85.2	38.0	87.6	39.1	96.6	43.1	112.1	50.0	112.8	50.3	112.2	50.1
150	42.3	18.9	48.4	21.6	44.8	20.0	51.3	22.9	51.1	22.8	52.9	23.6

* Representative values for cells in good condition operating at 26.67°C (80°F).
** Percentage utilization calculated on the basis of a maximum capacity of 224 A-hr/kg of PbO_2.

was greater than for the same active material supported on antimonial lead grids. The rate of change in the bulk density is more significant than the actual magnitude since it is the change that is of interest. Changes occurred with all oxides on both pure and antimonial lead grids; however, the rate of density loss was greater on the pure lead grids.

The bulk density of a porous granular aggregate depends on the degree of close packing of the individual solid particles. Within the mass, pores may be opened by actual removal of material throughout the structure. This mechanism does not alter the over-all volume of the mass. Decrease in the apparent density may also result from an over-all volume expansion of the aggregate with a corresponding increase in the internal pore volume. In such an expanded mass, the individual particles are less closely packed. This is the characteristic of granular masses that gives rise to the phenomenon known as dilatancy (19-21). Dilatancy was first described and named by Reynolds in 1885 (19) who noted the most familiar example: the drying out of an area of wet beach sand around each step as a person walked along the shoreline, followed by a resurfacing of the water after the weight was removed. Reynolds demonstrated that application of force to a granular mass, not rigidly contained, caused an expansion or dilation of the mass, and an increase in internal porosity. The disruption of an unconfined granular mass resulting from a localized stress is not limited to nearest-neighbor particles, but is propagated through the structure for considerable distances (19-21).

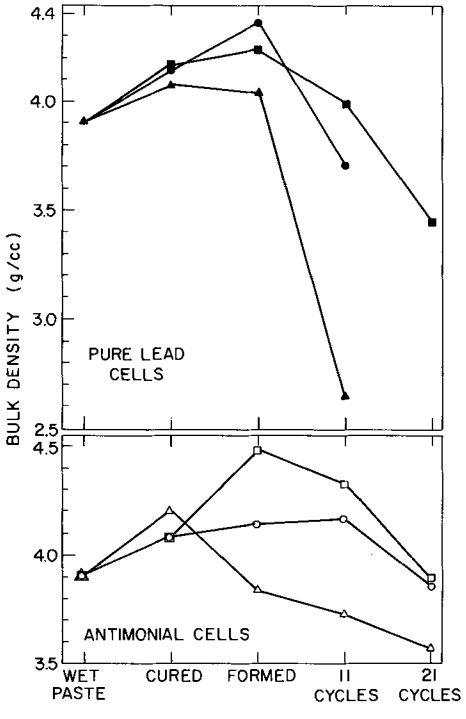

Fig. 2. Bulk density of the positive active material at various stages of the study. The rate of density loss is markedly greater for the pure lead cells. The plates containing oxide *H* were considerably less dense than the other two oxides and this may be attributed to the growth of the largest crystals of PbO_2 in these plates, and dilatant behavior of the active material. ○ and ●, oxide *A*; □ and ■, oxide *C*; △ and ▲, oxide *H*.

The volume contraction of a granular mass upon pulverization is also a very familiar effect, but the reverse action, the expansion of a close-packed granular array upon growth of the individual particles, is less commonly appreciated.

The decrease in bulk density of the cycled PbO_2 electrode probably results from both the opening up of internal voids by conversion of relatively low density materials to the high density PbO_2 during formation, and by an over-all volume increase owing to an increase in individual particle size. It may well be that the growth of the individual particles exerts sufficient force to cause the granules to shift from their initially more close-packed configuration. This suggests that it is grain growth that causes the expansion of the apparent volume of the PbO_2 electrode during cell operation. The relation of this expansion process to positive plate life, warping, and grid fracture has been pointed out by Dittman and Sams (13).

X-ray diffraction examination.—The major solid phase of the fully charged electrodes was identified by x-ray diffraction to be rutile type β-PbO_2 in all positive plates. Some plates showed one broad extra diffraction peak of low intensity in the vicinity of the position of the strongest line in the diffraction pattern of α-PbO_2. It is not possible to make an identification on the basis of a single diffraction line; therefore, the plates used in this study may or may not have contained a small amount of α-PbO_2. Tetragonal PbO, Sb, Sb_2O_3, and several other lead oxides also have strong diffraction peaks in this position. During cycling of the plates, this extra line disappeared from the diffraction patterns.

It has been reported earlier (4, 8, 22) that there is some evidence of a small degree of preferred orientation in freshly formed PbO_2 electrodes. This is suggested by the deviation in relative intensities of the diffraction lines from those of the standard pattern. This effect was not eliminated by hand grinding of the specimens in a mortar and pestle and sieving through 125-μ mesh screens; however, electrochemical cycling of the electrodes gradually eliminated this deviation. It may be that the deviation from standard intensities is caused by crystal anisotropy of a degree insufficient to give the usual mixture of broad and slender peaks in the diffraction patterns. The intensity of the diffraction patterns also increased with cycling, and this can be attributed to an increase in crystal size to give more efficient diffraction of x-rays. The degree of crystallinity did not, however, become sufficient to give good resolution of the K_α doublet. The small sessile crystallites of the freshly formed PbO_2 appeared to be about 10^{-5} cm in average diameter (8). Line broadening is present but slight in the range 10^{-5} to 10^{-6} cm, and line broadening resulting from

anisotropy of the small crystallites would not necessarily be distinguishable in such a specimen (10). Distortion of the lattice may also give rise to similar effects in the diffraction patterns of the freshly formed PbO_2 electrodes. It is not feasible in these specimens to distinguish between these possible causes of the peculiarities in the diffraction patterns, and all factors may be present in the electrochemically formed PbO_2 mass.

Geometrical morphology and the effect of antimony.—The particle morphology of the PbO_2 undergoes marked change during cycling in H_2SO_4. In addition, the presence of antimony in the grid metals appears to have a most significant effect during cycle operation of the cells. All three oxides included in this study underwent similar changes with cycling, and for this reason only selected electron micrographs of changes in oxide *A* on both pure and antimonial lead grids are presented here as representative of the three oxides. Oxide *H*, that initially gave rise to the largest crystals upon formation (8), again produced the largest PbO_2 crystals in this study. This greater grain growth is reflected in the greater loss of bulk density of oxide *H* compared to oxides *A* and *C*, Fig. 2.

Figure 3 shows an electron micrograph of freshly formed PbO_2 electrode material made from oxide *A*. The agglomerates are believed to be true spherulites made up of very small crystals that have grown on the surfaces of somewhat larger skeletal crystals (8). This structure changes with cycling, and Fig. 4 (*a*) shows the morphology after four cycles on pure lead supporting grids. The increase in particle size is clearly apparent. The smallest crystallites are no longer present, and the spherulitic character has largely disappeared. The spiney growth on the surface of a larger grain in the center of the photograph appears to be a stage in the alteration of a spherulitic formation. The same oxide supported on antimonial lead, Fig. 4 (*b*), shows a marked loss of spherulitic morphology after 8 cycles; however, the particle size is smaller than when pure lead grids were used as in Fig. 4 (*a*). The accumulation of antimony in the electrode mass is progressive, Table V, and the change shown by comparing Fig. 3, 4 (*b*), 5, and 6 (*b*) is believed to be the result of the gradual increase in the antimony content of the positive active material. This is further borne out by comparing the appearance of the active materials after 11 capacity cycles plus overcharge, Fig. 6 (*a*) and (*b*). Here the effect of antimony on the

Fig. 3. Electron micrograph of a carbon replica of PbO_2 from oxide *A* after formation on 7% antimonial lead grids. These agglomerates appear to be true spherulites of small sessile crystals overgrown on spikes of larger crystals. Marker equals approximately 1μ.

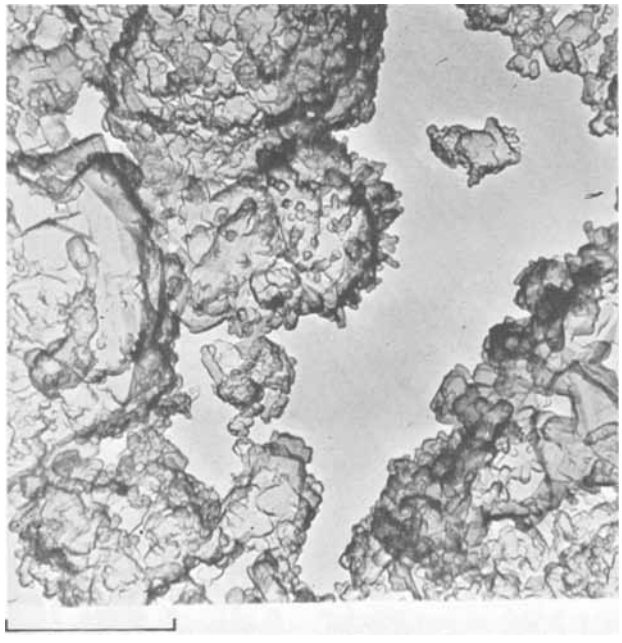

Fig. 4(*a*). Electron micrograph of a carbon replica of PbO_2 from oxide *A* after 4 cycles on pure lead grids. The smallest sessile crystallites have disappeared and the particle size is larger than the freshly formed material, Fig. 3. The spiked formation at the center of the photograph suggests that the smallest crystals are consumed in discharge, and the recharge process involves deposition on the residual crystals of PbO_2 so that they become larger with each cycle.

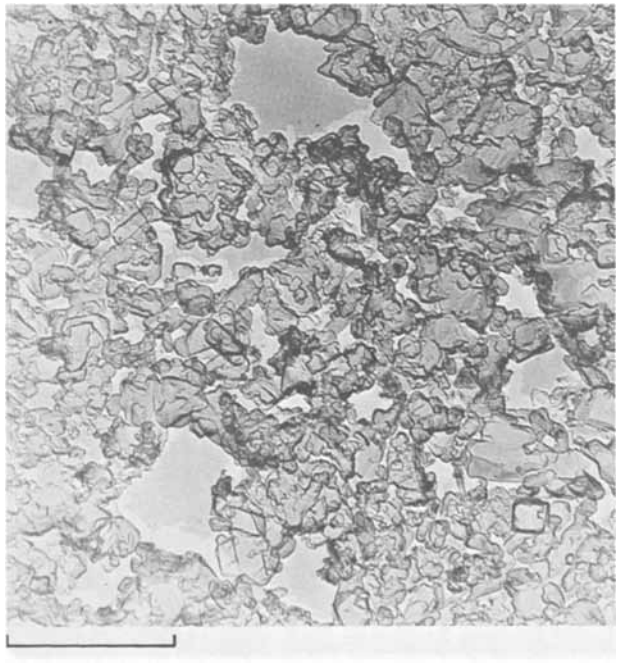

Fig. 4(*b*). Electron micrograph of a carbon replica of PbO_2 from oxide *A* after 8 cycles on 7% Sb-Pb alloy grids. Cycling has produced considerable grain growth and the small crystallites originally present after formation have been consumed; however, the 11 cycles have not resulted in grains of the size seen in Fig. 4(*a*) after 4 cycles on pure lead. Many of these crystals appear to have surface and edge defects that may serve as active sites for the discharge reaction. Markers equal approximately 1μ.

active material is especially apparent. In the pure lead cell, there has been marked grain growth and anhedralization of the PbO_2 particles. The small crystallites present after formation have disappeared, and the particles have the smooth surfaces and rounded outlines associated with so-called normal crystal growth (23, 24). The active material from the antimonial cell, on the other hand, has regained its spherulitic form, the individual crystallites are larger than those in the freshly formed material, Fig. 3, but smaller than those in the pure lead cell, Fig. 6 (*a*). They have irregular convoluted surfaces and edges. The

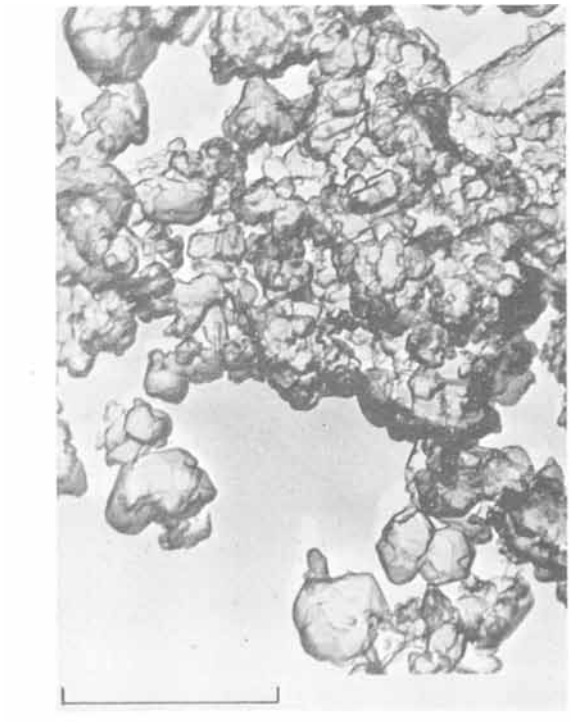

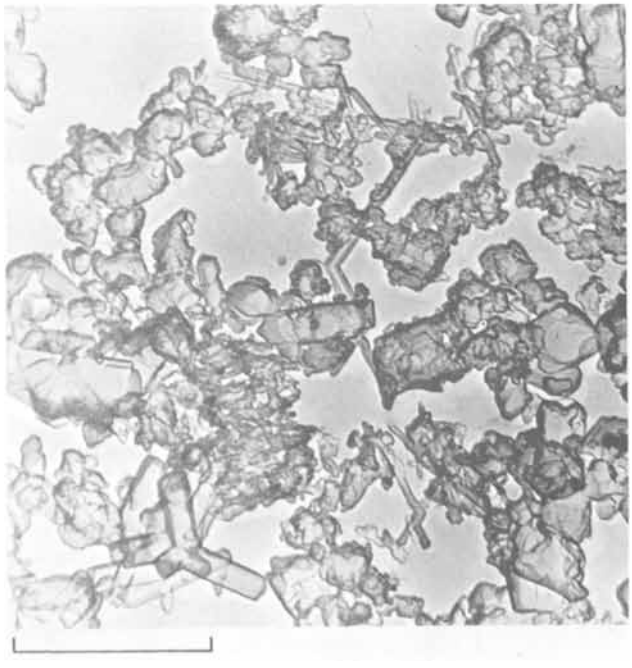

Fig. 5. Electron micrographs of carbon replicas of PbO_2 from oxide *A* after 21 cycles on 7% Sb-Pb alloy grids. *(a) Top:* The accumulation of Sb in the active material, Table V, has apparently acted as a growth inhibitor for the PbO_2 so that the individual crystals do not grow significantly in size after 8 cycles. *(b) Bottom:* A considerable fraction of this active material is made up of very slender prismatic crystals that have in some instances been overgrown with small sessile crystals. Markers equal approximately 1μ.

Table V. Spectrographic analysis for Sb in positive active material

Oxide	Grid	After formation	After 11 cycles	After 21 cycles	After 11 cycles plus overcharge
A	Pb	BL*	BL	BL	0.004**
	7% Sb	0.094	0.100	0.24	0.31
C	Pb	BL	0.0017	0.001	0.002
	7% Sb	0.094	0.140	0.27	0.29
H	Pb	BL	BL	0.001	0.001
	7% Sb	0.075	0.120	0.28	0.35

* BL—below the limit of the method used, or less than 0.001% Sb.

** Accumulation of the relatively small amounts of antimony in the pure lead cells may be the result of contamination inadvertently introduced during testing.

PbO_2 taken from the antimonial cells was a lighter brown than that from the pure lead cells which was very dark brown, almost jet black.

These direct observations are in agreement with conclusions of earlier studies (3, 4) comparing antimonial and nonantimonial cells. The increase in particle size and change from spherulitic to regular crystal growth appear to be the cause of the early disintegration of the positive active material in nonantimonial cells. It appears that during cycling the larger crystals grow at the expense of the smaller ones. The initial electrical capacity of the electrodes has been attributed to the large surface area of the small crystallites (4). As grain growth occurs, the surface area and electrical capacity would decrease. In addition, the structural strength of the granular mass would be expected to decrease owing to dilatant behavior as mentioned previously.

The PbO_2 particles in the pure lead cells grow more rapidly and to a larger size than those in the antimonial cells, resulting in more rapid paste disintegration and failure. Antimony retards the crystal growth rate so that these effects are less rapid. However, even in antimonial cells, the bulk density of the mass gradually decreases, Fig. 2, and the autoradiographic studies of Bode *et al.* (15-17) indicate that, at the end of life of antimonial cells, pockets of PbO_2 become electrically isolated so that they may not be discharged. This is readily explained by the long-range effects of stresses in granular masses.

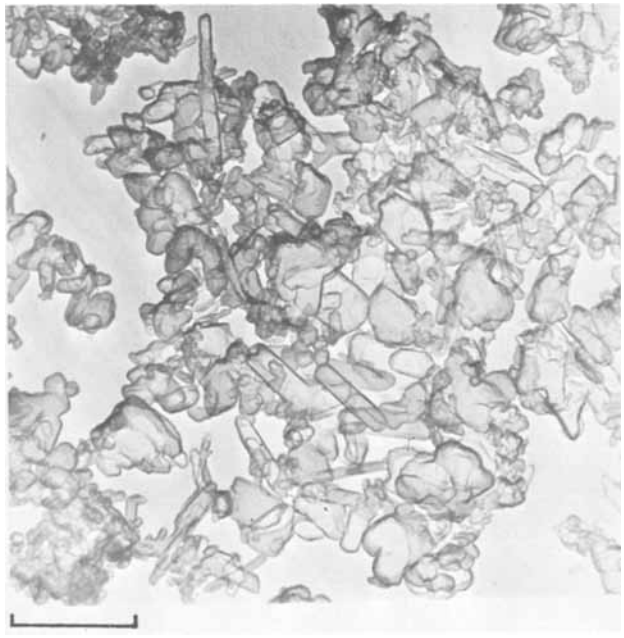

Fig. 6(*a*). Electron micrograph of a carbon replica of PbO_2 from oxide *A* after 11 cycles plus 2 weeks' overcharge on pure lead grids. Marked grain growth and anhedralization are visible in this example. The crystals have smooth surfaces and edges.

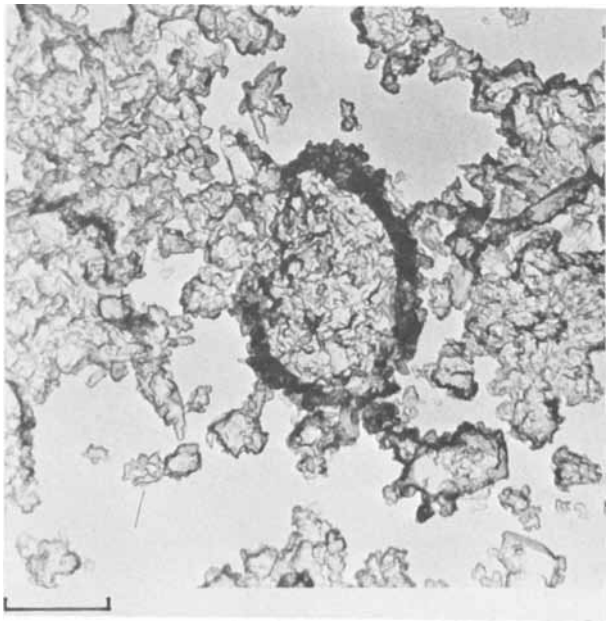

Fig. 6(*b*). Electron micrograph of a carbon replica of PbO_2 from oxide *A* after 11 cycles plus 5 weeks' overcharge on 7% Sb-Pb alloy grids. The Sb present in this active material appears to have promoted the nucleation of many small crystals and to have inhibited the growth of larger crystals. The surfaces and edges of the individual crystals contain many flaws that may indicate a high degree of electrochemical activity. This cell had failed on the overcharge test by grid corrosion. Markers equal approximately 1 μ.

The mechanism by which antimony has the above effect on the morphology of PbO_2 is not defined. It may be concluded that essentially it acts as a nucleating agent for PbO_2, simultaneously inhibiting crystal growth. It may accomplish this by entering the PbO_2 lattice by substitutional solid solution. This could give rise to an increased number of nucleating centers on the surfaces of the PbO_2 crystals. Incorporation into the lattice has been suggested as the cause of a similar effect of Sb_2O_3 on crystallization of rutile type CrO_2 (25). Up to 2% by weight of the antimony oxide can enter the CrO_2 lattice with no detectable change in lattice parameters. In this case, the antimony has been said to act as a nucleating catalyst producing small highly acicular crystals. Electrochemically, pentavalent antimony is the stable species at the potentials of the PbO_2 electrode in acid solutions (26). In crystalline oxides, the oxygen coordination is the same for Pb^4 and Sb^5 (27), and the spectrographic results, Table V, and radioactive tracer analyses (28, 29) indicate that antimony remains associated with the PbO_2 electrode mass. Thus it seems likely that antimony can enter the PbO_2 lattice, occupying Pb^4 positions in the oxygen octahedra. Quite another mechanism is also possible. The antimony may be adsorbed at the growth sites on the PbO_2 crystal surfaces, probably preferentially on the fastest growing faces, and act as a growth inhibitor. Under these circumstances, nucleation would be a secondary effect. The complexities of full mechanism definition and coordination of electrochemical and crystallization processes have been emphasized by Bockris and Razumney (24). It is apparent that further effort is required to define the mechanism by which antimony promotes nucleation of PbO_2 and inhibits crystal growth. When this is understood, it may be possible to select another material that will serve the same functions and at the same time be free of the detrimental side effects of antimony in the lead-acid cell (14).

Acknowledgment

The work of one of us (EJR) was performed under a research contract with the International Lead Zinc Research Organization.

Manuscript received Sept. 24, 1969.

Any discussion of this paper will appear in a Discussion Section to be published in the December 1970 JOURNAL.

REFERENCES

1. J. Burbank, *This Journal*, **111**, 765 (1964).
2. E. Voss and G. Huster, "The Effect of Depth of Discharge on the Cycle Life of Positive Lead-Acid Plates," in "Performance Forecast of Selected Static Energy Conversion Devices," 29th Meeting of AGARD Propulsion and Energetics Panel, Liege, Belgium, June 12-16, 1967. G. W. Sherman and L. Devol, Editors, p. 57.
3. J. Burbank, *This Journal*, **111**, 1112 (1964).
4. D. Kordes, *Chem. Ing. Tech.*, **38**, 638 (1966).
5. C. S. Smith, *AIME Trans.*, **175**, 15 (1948).
6. L. H. Van Vlack, "Microstructure of Ceramic Materials," Proc. of a Symposium, p. 1, Nat. Bur. Standards Misc. Pub. 257, April 6, 1964.
7. J. Burbank, in "Batteries," D. H. Collins, Editor, p. 43, Pergamon Press, New York (1963).
8. J. Burbank and E. J. Ritchie, *This Journal*, **116**, 125 (1969).
9. E. Voss and J. Freundlich in "Batteries," D. H. Collins, Editor, p. 73, Pergamon Press, New York (1963).
10. H. P. Klug and L. E. Alexander, "X-Ray Diffraction Procedures," John Wiley & Sons, Inc., New York (1954).
11. E. J. Ritchie, "Assistance to Naval Research Laboratory on Lead-Acid Battery Research," 1st Semi-Annual Rpt., Project LE-84, International Lead Zinc Research Organization, Jan.-June 1964.
12. E. J. Ritchie, *ibid.*, 2nd Semi-Annual Rpt., July-Dec. 1964.
13. J. F. Dittmann and J. F. Sams, *This Journal*, **105**, 553 (1958).
    Note: There is a misprint in this article; on p. 553, line 26, col. 1, the word "water" should read "wax." A detailed description of this method of plate density measurement also appears in Ref. (12), Appendix p. 62.
14. G. W. Vinal, "Storage Batteries," 4th Ed., John Wiley & Sons, New York (1955).
15. H. Bode and J. Euler, *Electrochim. Acta*, **11**, 1211 (1966).
16. H. Bode and J. Euler, *ibid.*, **11**, 1221 (1966).
17. H. Bode, J. Euler, E. Rieder, and H. Schmitt, *ibid.*, **11**, 1231 (1966).
18. H. Bode, H. Panesar, and E. Voss, *Naturwissenschaften*, **55**, 541 (1968).
19. O. Reynolds, *Phil. Mag.*, **20**, 469 (1885).
20. C. F. Jenkin, *Proc. Roy. Soc. (London)*, **131**, 53 (1931).
21. E. N. DaC. Andrade and J. W. Fox, *Phys. Soc. London Proc.*, **62B**, 483 (1949).
22. N. E. Bagshaw, R. L. Clarke, and B. Halliwell, *J. Appl. Chem.*, **16**, 180 (1966).
23. A. Van Hook, "Crystallization Theory and Practice," ACS Monograph 152, Reinhold Publishing Corp., New York (1961).
24. J. O'M. Bockris and G. A. Razumney, "Fundamental Aspects of Electrocrystallization," Plenum Press, New York (1967).
25. T. J. Swoboda, P. Arthur, Jr., N. L. Cox, J. N. Ingraham, A. L. Appegard, and M. S. Sadler, *J. Appl. Phys.*, **32**, Suppl. 3, 374 (1961).
26. A. L. Pitman, M. Pourbaix, and N. de Zoubov, *This Journal*, **104**, 594 (1957).
27. R. W. G. Wykoff, "Crystal Structures," 2nd Ed., Vol. 1, Interscience Publishers, New York (1963).
28. W. Herrmann and G. Pröpstl, *Z. Elektrochem.*, **61**, 1154 (1957).
29. W. Herrmann, W. Ilge, and G. H. Proepstl in "U.N. Peaceful Uses of Atomic Energy," Proc. 2nd Intern. Conf. Geneva, Sept. 1958, p. 272, Pergamon Press, New York (1959).

The Adsorption of Vanadium(III) on Mercury from Thiocyanate Solutions and Its Electrochemical Consequences

Fred C. Anson* and Josip Caja[1]

Gates and Crellin Laboratories of Chemistry, California Institute of Technology, Pasadena, California

ABSTRACT

The adsorption of V(III) on mercury electrodes in thiocyanate electrolytes has been measured chronocoulometrically. The adsorption is not strongly dependent on potential except in the vicinity of the V(III)/V(II) half-wave potential. The adsorbing species is a V(III)-thiocyanate complex containing one or more thiocyanates. The adsorption of V(II) also occurs, but is much weaker than that of V(III). A minimum value for the exchange current for the V(III)/V(II) couple in the adsorbed state has been estimated coulostatically. Although this exchange current is quite large, 0.5 A/cm^2, its magnitude can be largely accounted for by the enhancement of the reactants' surface concentrations produced by their adsorption.

The spontaneous adsorption of electrochemical reactants on the surface of electrodes often produces complications in the study of the kinetics of their electrode reactions. An electrode process that can proceed by more than one pathway, *e.g.*, via both the adsorbed and unadsorbed reactants, corresponds to a complex equivalent circuit which contains elements that cannot be evaluated in separate experiments in the absence of the reactants. As a result, a larger number of kinetic parameters must be extracted from the rate data, and confidence in the accuracy and uniqueness of the resulting kinetic parameters is weakened. Under these circumstances, it is advantageous to have independent quantitative information on the extent of adsorption of the reactants because the kinetic data can then be analyzed with one less adjustable parameter.

The technique of chronocoulometry (1) is well suited to provide the desired quantitative adsorption data. It has been applied in the present study to evaluate the adsorption of V(III) and V(II) on mercury electrodes in thiocyanate solutions. The V(III)/V(II) system was chosen for several reasons. It offered an opportunity to compare the adsorption of a transition metal redox couple with the extensively studied anion-induced adsorption of white metal cations (2-6) [Cd(II), Zn(II), Pb(II), In(III)]. Second, the equilibrium adsorption of V(III) and V(II) could be measured in poised solutions containing both halves of the redox couple, thus allowing the potential dependence of the adsorption in the vicinity of the half-wave potential to be determined. Analogous data for the white metal cations are less straightforward to obtain because of the difficulties associated with the preparation and storage of metal amalgam electrodes. Finally, the V(III)/V(II) system was attractive because the electrode kinetics of the couple have been extensively studied (7-14) in electrolytes where no reactant adsorption occurs. It was hoped that a comparison of these rates with those measured with adsorbed reactants would contribute to an understanding of the effect of adsorption on the rate of electrochemical charge transfer for a simple redox reaction.

Experimental

Techniques.—The adsorptions of V(III) and V(II) (which shows very little adsorption) were evaluated at potentials removed from the half-wave potential by double potential-step chronocoulometry (1). The theory and practice of this technique have been described (15, 2). To measure V(III) adsorption the electrode potential was stepped from various initial values, E_i, to −900 mV, where the rate of reduction of V(III) is diffusion limited, and then back to E_i. To search for V(II) adsorption the potential was stepped from various initial values, well cathodic of $E_{1/2}$, to −300 mV where the oxidation of V(II) is diffusion limited in thiocyanate solutions.

Data acquisition and analysis were performed by means of the computer-based apparatus previously described (16). In most cases, data points (*i.e.*, the value of the charge passed up to each time) were recorded (automatically) every 400 μsec. Typically, 100 such points were obtained during the first potential step and another 100 following the return of the potential to its initial value. The amount of adsorbed V(III) was evaluated, as before, (3, 16) from regression analysis of the two sets of data points according to the theoretical equations of double potential-step chronocoulometry (15).

The double potential-step technique was not useful at values of E_i near $E_{1/2}$, where both V(III) and V(II) are present, because the coupling between the mass transfer process and the Nernstian limit on the electrode reaction rate greatly complicates the theoretical analysis. A modified single potential-step chronocoulometric method was employed to evaluate the adsorption in these cases. Details are described in the section on Results and Discussion.

To evaluate q^m, the charge density on the mercury electrode, in solutions where the electrode was ideally polarizable, *i.e.*, when only V(III) or V(II) was present, the charge flowing into a potentiostated dropping mercury electrode (dme) was measured and analyzed as previously described (2, 17, 18). The same experimental procedure was also employed with poised solutions containing both V(III) and V(II) in which the dme behaved as a nonpolarizable electrode. As is explained later, these experiments yielded values of q^m plus a fraction of the amounts of adsorbed V(III) and V(II) rather than q^m alone. Measurements of q^m with the dme were also performed by means of the computer-based data acquisition and analysis system (16).

Coulostatic experiments designed to measure large electrode reaction rates were performed with conventional circuitry (19). The potential-time transients were obtained photographically with a Tektronix Type C-12 camera and a Type 531 CRO with a Type W preamplifier. This combination recovered from being driven off scale within 1.0 μsec or less, but experimental data free from ohmic perturbations were usually not available at times shorter than 1.5 μsec.

Reagents.—All solutions were prepared from reagent grade salts and triply distilled water. Recrystallization of the salts produced no changes in the experimental results. Evidence for the quality of the reagents was

* Electrochemical Society Active Member.
[1] Permanent address: Institute Rudjer Bosković, Zagreb, Yugoslavia.

the good agreement between values of the electrode charge measured in these experiments and those previously obtained (by others) for the same electrolytes from double layer capacitance measurements. Solutions of V(II) were prepared by controlled potential reduction of V(V) at a stirred mercury pool at −1100 mV in the same cell employed for the subsequent electrochemical measurements. Solutions of V(III) were prepared by oxidation of V(II) at the mercury pool at −300 mV. With supporting electrolytes containing more than 0.01M thiocyanate the spontaneous reaction between V(V) and SCN^- was not negligible. Therefore, with these solutions V(V) was reduced to V(IV) by reduction at the mercury pool at −100 mV before any thiocyanate was added.

The concentrations of V(III) and V(II) were determined polarographically. The source of V(V) was V_2O_5 dissolved (after prolonged stirring) in 0.5M perchloric acid. All test solutions were 0.01-0.02M in $HClO_4$. Higher acidities were avoided to minimize the slow acid catalyzed decomposition of thiocyanate. Calculations show that the hydrolytic dimer of V(III) (20) constituted less than 1% of the total V(III) present in all solutions studied.

Solutions were deoxygenated with prepurified nitrogen that had been passed successively through copper turnings at 350°C and a trap maintained at −77°C. The ionic strength of all solutions was adjusted to 1.0M with $NaClO_4$. Measurements were carried out at 25° ± 2°C. All potentials are referred to the saturated calomel electrode.

Apparatus.—The hanging mercury drop electrode was a commercially available unit (Brinkman Instruments, Inc.) modified to improve the electrical contact (21). The mercury pool electrode used for the controlled potential generation of V(III) and V(II) served as the auxiliary electrode in the chronocoulometric and coulostatic experiments.

The electronic control device used to impose potential perturbations on the indicator electrode and to measure the current and coulomb responses consisted of appropriately connected operational amplifiers (Philbrick Type SP 656), mercury wetted relays, bias potentiometers, and switches. Its design and operation were essentially identical to previously described units (16, 22).

Results and Discussion

Two major aspects of the electrochemistry of the V(III)/V(II) couple have been studied: the adsorption of V(III) on mercury and the kinetics of the V(III)/V(II) couple in the adsorbed state. In order sensibly to address the second aspect the results of the adsorption studies are required so these will be discussed first.

V(III) *adsorption in the absence of* V(II).—The adsorption of V(III) was searched for in perchlorate, bromide, iodide, and thiocyanate electrolytes by double potential step chronocoulometry (1, 2). Only in thiocyanate solutions was significant adsorption detected. The standard double-step chronocoulometric technique depends on the assumption that the product of the electrode reaction is not adsorbed on the electrode. Two lines of evidence indicated that the adsorption of V(II) in thiocyanate solutions is very small: (*i*) single potential-step chronocoulometry with pure V(II) solutions gave intercepts of charge *vs.* $(\text{time})^{1/2}$ plots which matched (within ±0.5 $\mu C/cm^2$) the charge change obtained between the same two potentials in the absence of V(II); (*ii*) when reactant but not product is adsorbed, the slopes of the chronocoulometric plots for the forward and reverse potential steps are unequal, the reverse slope being larger. The ratio of the slopes can be calculated from a knowledge of the amount of adsorbed reactant (15). Thus, if products were adsorbed, the calculated and observed slope ratios would disagree. As the data in Table I show,

Table I. Calculated and observed slope ratios for double potential step chronocoulometric measurements with 1 mM V(III) in thiocyanate[a]

$-E_i$, mV	$F\Gamma_{V(III)}$, $\mu C/cm^2$	Reverse slope/forward slope	
		calculated[b]	observed
250	14.1	1.27	1.26
300	14.2	1.27	1.27
350	13.6	1.26	1.27
400	13.0	1.25	1.24

[a] Supporting electrolyte was 0.1M NaSCN-0.9M $NaClO_4$-0.01M $HClO_4$. The potential was stepped from E_i to −900 mV and back. [b] Slope ratios were calculated from $S_r/S_f = 1 + a_1 F\Gamma_{V(III)}/S_f\tau^{1/2}$, where S_r and S_f are the reverse and forward slopes, respectively, τ is the duration of the first potential step, and a_1 is defined in (15); for the experimental conditions employed $a_1 = 0.966$.

the calculated and observed slope ratios are in good agreement indicating little or no adsorption of V(II).

Table II summarizes the data obtained on V(III) adsorption at various potentials and thiocyanate concentrations. The rather slight dependence of the adsorption on the electrode potential is evident. The values of q^m in Table II were obtained in two ways: (*i*) the charge flowing into a dme potentiostated in the V(III)-SCN solution of interest was determined (17, 18); (*ii*) the value of q^m at −900 mV, the potential to which the electrode was stepped, was measured as in (*i*). Then the difference in charge between the initial potential and −900 mV was obtained, in the usual way (15), from the intercept of the chronocoulometric plot for the reverse step. Subtraction of the value of q^m at −900 gave the value of q^m at the initial potential in the presence of the adsorbed V(III). Both procedures gave the same values for q^m, but the chronocoulometric method was preferable because of difficulties in eliminating traces of reducible or oxidizable impurities which contributed undesirably large faradic components to the total charge consumed in the dme experiments with the V(III) solutions.

Figure 1 shows that the adsorption of V(III) is only weakly affected by changes in the amount of adsorbed thiocyanate ions. Values of Γ_{SCN^-} used in Fig. 1 were evaluated from the data of Wroblowa *et al.* (23) obtained in pure thiocyanate solutions by assuming that the adsorption of thiocyanate in pure and mixed electrolytes would be the same at corresponding salt activities (24).

The data in Table II and Fig. 1 contrast with similar data for the thiocyanate-induced adsorption of Cd(II) (2) and Zn(II) (25, 26) in that the adsorption of V(III) is less affected by changes in potential, electrode charge, and adsorbed thiocyanate than are the white metal cations. We believe these smaller dependences reflect a difference in the mode of adsorption of V(III). The white metals are believed to be adsorbed as uncharged, cation-anion complexes by bond

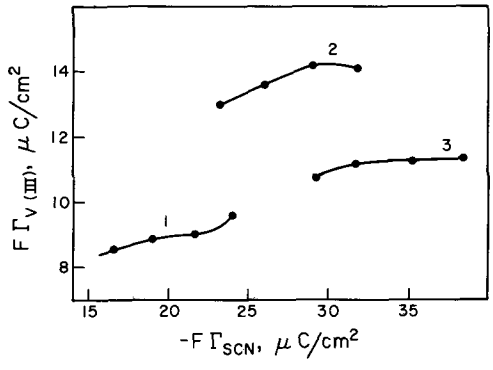

Fig. 1. Adsorbed V(III) *vs.* adsorbed SCN^-. Supporting electrolyte: 1, 0.01M NaNCS-0.98M $NaClO_4$-0.01M $HClO_4$; 2, 0.1M NaNCS-0.89M $NaClO_4$-0.01M $HClO_4$; 3, 0.99M NaNCS-0.01M $HClO_4$.

Table II. Values of $\Gamma_{V(III)}$ and q^m in thiocyanate electrolytes[a]

[SCN⁻], M:	0.01		0.03		0.10		0.30		1.0	
$-E_i$, mV	q^m, μC/cm²	$F\Gamma_{V(III)}$, μC/cm²	q^m, μC/cm²	$F\Gamma_{V(III)}$, μC/cm²	q^m, μC/cm²	$F\Gamma_{V(III)}$, μC/cm²	q^m, μC/cm²	$F\Gamma_{V(III)}$, μC/cm²	q^m, μC/cm²	$F\Gamma_{V(III)}$, μC/cm²
	[V(III)] = 1.0 mM									
250	8.5	9.6	10.1	12.7	14.6	14.1	15.8	14.1	17.4	11.4
300	6.3	9.0	7.6	11.8	12.0	14.2	13.0	13.4	14.9	11.3
350	3.6	8.9	5.4	11.3	9.7	13.6	10.9	13.3	12.5	11.2
400	0.8	8.6	3.7	10.8	7.8	13.0	9.1	12.8	10.4	10.8
	[V(III)] = 0.5 mM				[V(III)] = 0.5 mM					
250	8.9	6.4			14.1	12.8				
300	6.8	5.8			11.7	12.7				
350	4.6	5.3			9.8	12.2				
400	2.3	4.9			7.7	11.2				
	[V(III)] = 0.3 mM				[V(III)] = 0.1 mM					
250	9.9	6.6			13.7	8.0				
300	7.7	5.7			11.8	7.4				
350	5.8	4.9			9.6	7.0				
400	3.7	4.3			7.6	5.9				
					[V(III)] = 2.0 mM					
250					13.7	15.8				
300					11.8	15.2				
350					9.6	14.8				
400					7.6	14.0				
	[V(III)] = 0									
250	9.6		10.6		14.2		16.4		18.7	
300	7.9		8.6		12.3		13.7		15.5	
350	6.9		—		10.1		11.6		13.0	
400	4.2		4.8		8.3		9.3		10.7	

[a] All solutions contained 0.01M $HClO_4$ and were adjusted to an ionic strength of 1.0 with $NaClO_4$.

formation with additional anions which are specifically adsorbed on the electrode (2, 5, 6). Vanadium(III), on the other hand, is more likely to be adsorbed by means of the same thiocyanate anions with which it is complexed in the bulk of the solution. This assertion is based primarily on related experiments with Cr(III) thiocyanate complexes (27) which, because of their substitution inertness, can be studied in the absence of any free thiocyanate anions. The adsorption of these Cr(III) complexes is decreased monotonically by the addition of thiocyanate anions as the latter compete for the available electrode surface. Thus, the adsorption of the Cr(III)-thiocyanate complex results exclusively from the interaction between the coordinated thiocyanate and the mercury surface.[2]

An analogy has been drawn (27) between the adsorption of Cr(III)-SCN complexes on mercury electrodes and the homogeneous reaction

$$CrNCS^{2+} + Hg^{2+} = CrNCSHg^{4+} \quad [1]$$

which proceeds extensively from left to right (28, 29). The V(III) analog of reaction [1] cannot be observed because of the substitution lability of V(III), but the adsorption of the V(III)-thiocyanate complex on mercury can be observed, and it shares too many of the behavioral aspects of the Cr(III)-thiocyanate adsorptions to ignore the likely connection.

The adsorption of the Cr(III) complex is thought to arise from increases in the ligand field strength of the nitrogen atom in the coordinated thiocyanate molecule when a mercury-sulfur bond is formed at the sulfur atom in the same molecule (27, 30). The driving force for adsorption according to this scheme would be less for the doubly charged V(II) than for triply charged V(III) because of the smaller ligand field splitting, Δ, and similarly less for the d^2 V(III) ion than for the d^3 Cr(III) ion; the observed relative adsorptions of these three ions are in this order.

[2] Adsorption of metallic ions on mercury via coordinated ligands was proposed by O'Dom and Murray (4) in the case of indium adsorption from iodide electrolytes. We have argued against this mechanism for adsorption in the case of white metal cations (3), but we favor it in the case of transition metal cation adsorption induced by thiocyanate (27).

Identity of the adsorbed-V(III) *species.*—Attempts to determine the composition of the adsorbed V(III) complex were largely unsuccessful. The adsorption reaches a maximum at a concentration of thiocyanate near 0.1M (see Table II), but it does not seem justified to identify this adsorption maximum with the maximum concentration of a particular V(III)-thiocyanate complex because increasing the thiocyanate concentrations also increases the adsorption of free thiocyanate anions which compete for the available electrode surface with all V(III)-thiocyanate complexes. Furthermore, the available data on the formation constants for complexation of V(III) with thiocyanate are not adequate to allow the relative concentrations of the various possible V(III)-thiocyanate complexes to be calculated. Furman and Garner (31) showed that $VNCS^{2+}$ is the predominate complex formed in solutions 5 mM in V(III) and SCN^-, but evidence for higher complexes was clear at higher thiocyanate concentrations, such as prevailed in the present experiments.

Experiments with the Cr(III)-thiocyanate complexes, where the identities of the adsorbing species were certain (27), showed that the adsorption increased considerably as the number of coordinated thiocyanate ions increased from one to three. Similar behavior in the substitution-labile V(III)-thiocyanate system could lead to the preferential adsorption of a complex containing more than one thiocyanate, even if the higher complex were a relatively minor constituent in the solution.

In several previous studies (3, 6, 20), information on the charge of the adsorbing species was obtained from measurements of the changes in the rates of irreversible electrode reactions produced by the adsorption. This approach failed in the present instance for the lack of suitable electrode reaction whose rate could be measured in the narrow potential "window" between the reduction of V(III) and the oxidation of mercury in the thiocyanate supporting electrolytes.

V(III) *adsorption in the presence of* V(II).—In solutions containing mixtures of V(III) and V(II) the standard double potential-step chronocoulometric

techniques is not applicable because the separation of double layer charging from faradaic reduction of adsorbed V(III) is no longer possible by means of the intercepts of the two plots of charge *vs.* appropriate functions of time. This inseparability of double layer and faradaic charge has been subjected to extensive analysis and discussion by Delahay and co-workers (32-34) and Sluyters and co-workers (35, 36). Review articles with treatments of this topic have also appeared (37-39). The ramifications of charge inseparability for the present experiments become clear if a single potential-step chronocoulometric experiment is contemplated: suppose the potential of a mercury electrode is stepped from its equilibrium value in a V(III)-V(II) mixture to −900 mV where the reduction of V(III) is diffusion limited. Plots of the total charge passed at time, t, *vs.* $t^{1/2}$ are linear and have intercepts on the charge axis equal to the sum of the amount of V(III) adsorbed at the equilibrium potential and the difference in the charge on the electrode between the initial potential and −900 mV. If the usual chronocoulometric analysis were applied, the charge on the electrode at the initial and final potentials would be measured in independent experiments and the resulting difference in charge subtracted from the observed intercept to obtain the amount of adsorbed V(III). The value of the charge on the electrode, q^m, at −900 mV can be obtained, as described in the Experimental section, from measurements of the charge flowing into a dme potentiostated at −900 mV in a solution containing V(II) but no V(III). However, if the same procedure is followed at the equilibrium potential with the mixture of V(III) and V(II), the value of q^m at the initial potential is not obtained. Instead, the sum of q^m plus a fraction of the amounts of V(III) and V(II) adsorbed at the equilibrium potential is obtained. This result has been anticipated in previous work by others (40, 41), but it has, so far as we are aware, never been explicitly tested by experiment. For this reason, it seems useful to give a, largely unoriginal, thermodynamic analysis of the expected results along with those obtained experimentally.

We shall consider a mercury electrode at equilibrium in a solution containing the salts NaNCS, $V(NCS)_2$, and $V(NCS)_3$. The electrocapillary equation for this system is (42)

$$-d\gamma = q^m\,dE^- + \Gamma_{Na+}d\mu_{NaNCS} + \Gamma_{V(III)}(d\mu_{V(NCS)_2} + \mathbf{F}\,dE^-) + \Gamma_{V(II)}d\mu_{V(NCS)_2} \quad [2]$$

where it has been assumed that the V(II)-V(III) couple functions as a reversible redox couple; *i.e.*

$$d\mu_{V(NCS)_3} = d\mu_{V(NCS)_2} + \mathbf{F}\,dE^- \quad [3]$$

And where γ is the interfacial tension, q^m is the charge density on the mercury, E^- is the potential of the mercury electrode with respect to an electrode reversible to thiocyanate ion, the μ's and Γ's are the chemical potentials and surface excesses of the subscripted species, respectively, and $\mathbf{F}$ is the Faraday. Suppose a series of measurements of the interfacial tension are made in solutions containing varying ratios of V(III) to V(II) but with a constant total concentration of vanadium, C^*.

$$C_{V(III)} + C_{V(II)} = C^* = \text{const.} \quad [4]$$

Under these conditions Eq. [3] and [4] can be combined to yield

$$d\mu_{V(NCS)_2} = -\mathbf{F}\left(\frac{C^* - C_{V(II)}}{C^*}\right)dE^- \quad [5]$$

Substituting [5] into [2] and rearranging gives (2)

$$-d\gamma = \Gamma_{Na+}d\mu_{NaNCS} + \left[q^m + \mathbf{F}\Gamma_{V(III)} - \mathbf{F}(\Gamma_{V(III)} + \Gamma_{V(II)})\left(\frac{C^* - C_{V(II)}}{C^*}\right)\right]dE^- \quad [6]$$

which leads to

$$-\left(\frac{d\gamma}{\partial E^-}\right)_{\mu_{NaNCS}} = q^m + \frac{\mathbf{F}}{C^*}(\Gamma_{V(III)}C_{V(II)} - \Gamma_{V(II)}C_{V(III)}) \quad [7]$$

Thus, a measurement of the slope of the electrocapillary curve at potentials where both V(II) and V(III) are present does not give q^m, but a more complex quantity dependent on the concentrations and surface excesses of V(III) and V(II).

The measurement of the charge flowing into a potentiostated dme in a V(II)-V(III)-thiocyanate mixture, according to the procedure described in the Experimental section (2, 17, 28), amounts to an experimental evaluation of the slope of the electrocapillary curve. This assertion seems quite reasonable because the time scale of the experiment is several seconds and the heterogeneous rate constant for the V(II)/V(III) couple in thiocyanate media is greater than 10^{-2} cm/sec so that there is no reason to doubt that thermodynamic equilibrium prevails throughout the data collection. Note also that so long as the thiocyanate concentration is large compared with the total vanadium concentration, as the ratio of V(III) to V(II) is changed, the derivative with the respect to E^- is essentially the same as the derivative with respect to E_{ref}, the potential measured *vs.* a fixed-potential reference electrode.

An experimental test of this analysis is given in Fig. 2 which gives "charge"-potential curves for two supporting electrolytes in the absence and presence of V(III) and V(II). With the sodium perchlorate electrolyte the values of charge obtained from the dme experiment are the same, within experimental error (±0.4 μC/cm²), whether or not the V(III)/V(II) couple is present. This accords with the chronocoulometric result that no adsorption of V(III) or V(II) could be detected in pure perchlorate electrolytes; the second term in Eq. [7] is thus zero at all potentials and the true charge on the electrode, q^m, is obtained in the presence, as well as in the absence of the V(III)/V(II) couple. [This conclusion ignores any nonspecific adsorption of V(III) and V(II) in the diffuse layer, but this is negligibly small at the ionic strength (μ = 1.0) and vanadium concentrations (C^* = 1 mM) employed.]

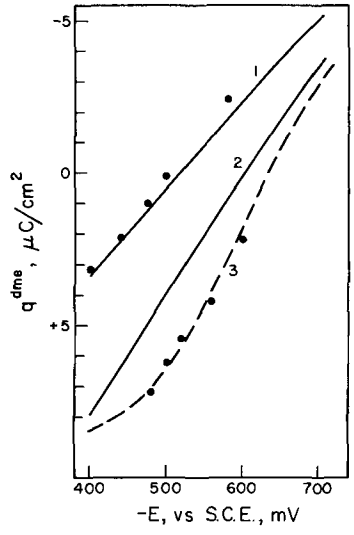

Fig. 2. Potential dependence of the values of q^{dme} obtained with a dropping mercury electrode. Solution compositions: 1, 1M $NaClO_4$; 2, 3, 0.1M NaNCS-0.9M $NaClO_4$. Solid lines are for the pure supporting electrolytes; plotted points represent values obtained in the same electrolyte in the presence of vanadium: [V(III)] + [V(II)] = 1.0 mM. All solutions also contained 0.02M $HClO_4$.

A different result is obtained with the mixed perchlorate-thiocyanate electrolyte (Fig. 2). With this supporting electrolyte the charge-potential curves do not coincide in the absence and presence of V(III) and V(II). Again, this behavior accords with the chronocoulometric result that substantial V(III) adsorption occurs from 0.1M NaNCS solutions. Equation [7] predicts that in a solution where $C_{V(III)} = C_{V(II)} = \frac{C^*}{2}$, the value of "charge" resulting from the dme experiment should be given by $\left[q^m + \frac{\mathbf{F}}{2} (\Gamma_{V(III)} - \Gamma_{V(II)} \right]$. Values of $\mathbf{F}\,\Gamma_{V(III)}$ and $\mathbf{F}\,\Gamma_{V(II)}$ obtained chronocoulometrically for a solution containing 0.5 mM V(III) and 0.5 mM V(II) are 7 ± 1 μC/cm^2 and 0 ± 1 μC/cm^2, respectively. Thus, if q^m were unaffected by the adsorption of V(III), the expected value of charge resulting from the experiment with a dme poised at the equilibrium potential would be 3.5 μC/cm^2 greater in the presence of 0.5 mM V(III) and V(II) than in their absence. The observed difference (Fig. 2, $E = -520$ mV) is 3 μC/cm^2. Comparable agreement was obtained at other potentials in the vicinity of the half-wave potential which supports the analysis given above. The inseparability of faradaic from nonfaradaic charge with poised electrodes in Nernstian systems where substantial reactant adsorption occurs is also clearly demonstrated.

One may inquire why more total charge is supplied by the potentiostat to the dme in the presence of V(III) and V(II) even if the (not directly measurable) value of q^m is not changed by the adsorption of V(III). The explanation is that as the drop grows some of the V(III) at its surface is "consumed" by being adsorbed on the electrode. The Nernstian balance of V(III) and V(II) at the electrode is thereby disturbed, and the potentiostat supplies the additional charge necessary to oxidize enough V(II) to restore the ratio V(III)/V(II) to its initial value. This faradaic charge will be supplied at just the same rate as is the nonfaradaic charge needed to maintain the charge density, q^m, because both charge-consuming processes are proportional to the rate of change of the electrode's area. It is just this indistinguishability in time that renders the two kinds of charge experimentally inseparable.

The comparison made above of the separation near $E_{1/2}$ of the two charge-potential curves for the thiocyanate electrolyte in Fig. 2 with the separation calculated on the basis of Eq. [7] depended on a knowledge of $\Gamma_{V(III)}$ and $\Gamma_{V(II)}$ at potentials near $E_{1/2}$. However, the inseparability of the faradaic and nonfaradaic charges just described prevents the direct measurement of the double layer charging corrections which must be subtracted from the observed intercepts of chronocoulometric charge-(time)$^{1/2}$ plots to obtain values for $\Gamma_{V(III)}$. This leaves the question of how the values of $\Gamma_{V(III)}$ and $\Gamma_{V(II)}$ quoted above as prevailing at potentials near $E_{1/2}$ were obtained. In two ways: the simplest was to assume, on the basis of the behavior observed at potentials removed from $E_{1/2}$, where separation of faradaic and nonfaradaic charges is no problem, that a negligible change in q^m at potentials near $E_{1/2}$ is produced by the adsorption of V(III). Then the charge change measured in the absence of vanadium for a potential step from initial potentials near $E_{1/2}$ to -900 mV could be subtracted from the chronocoulometric intercept obtained in the presence of vanadium to obtain $\Gamma_{V(III)}$. The reasonableness of the assumption on which this method is based was checked by evaluating $\Gamma_{V(III)}$ by a second method and comparing the results.

The second route to values for $\Gamma_{V(III)}$ took advantage of the fact that measurements of q^m at -900 mV by the dme procedure gave the same result, -9.5 μC/cm^2, in the presence and absence of V(II). The intercepts, I, of chronocoulometric (charge *vs.* $t^{1/2}$) plots for potential steps to -900 mV from initial equilibrium potentials in solutions containing both V(III) and V(II) are therefore given by Eq. [8]

$$I = \mathbf{F}\,\Gamma_{V(III)} + q^m{}_{-900} - q^m{}_{E_i} = \mathbf{F}\,\Gamma_{V(III)} - q^m{}_{E_i} - 9.5 \quad [8]$$

An independent relation between the same quantities results from the dme charge measurements with the poised solution at E_i. From Eq. [7]

$$-\left(\frac{\partial \gamma}{\partial E}\right) = q^{dme}{}_{E_i} = q^m{}_{E_i} + \beta\,\mathbf{F}\,\Gamma_{V(III)} \quad [9]$$

where $q^{dme}{}_{E_i}$ is the charge supplied to the growing drop at a rate proportional to its change in area and $\beta = C_{V(II)}/C^*$. Equations [8] and [9] can be solved simultaneously to yield values for $\mathbf{F}\Gamma_{V(III)}$ (as well as $q^m{}_{E_i}$).

Both of the methods were applied to obtain values of $\Gamma_{V(III)}$ at potentials near $E_{1/2}$, and the resulting data are summarized in Table III. The agreement between the values of $\Gamma_{V(III)}$ obtained by the two methods is only fair presumably because the assumption that q^m is unaffected by the adsorption of V(III) is not strictly valid and also because of the relatively large uncertainties associated with the values of $q^{dme}{}_{E_i}$ obtained from the dme experiments in poised solutions. However, the data do demonstrate unambiguously that a substantial amount of V(III) is adsorbed in the vicinity of the half-wave potential for the couple.

The strong potential dependence of $\Gamma_{V(III)}$ near $E_{1/2}$ reflects the fact that the concentration of V(III) is very potential dependent near $E_{1/2}$ (Nernst equation). A similar dependence on the concentration of V(III) is also observed at potentials well anodic of $E_{1/2}$ (Table II).

With reference to the ideas of Delahay *et al.* (32-34), it may be worth noting that in the present instance, the evaluation of $\Gamma_{V(III)}$ by the combination of the chronocoulometric intercept with the dme charge measurement (Eq. [8] and [9]) accomplishes a separation of the total charge into faradaic ($\mathbf{F}\Gamma$) and nonfaradaic ($q^m{}_{E_i}$) components. However, this separation is not *a priori* because it resorts to the non-thermodynamic chronocoulometric measurements. Nevertheless, this tactic can be helpful in evaluating the "true double-layer capacitance"; *i.e.*, $\left(\frac{\partial q^m}{\partial E}\right)$, in the presence of reactant adsorption. Just such use is made of this possibility in the experiments on the kinetics of the V(III)-V(II) couple in thiocyanate solutions to be described next.

Effects of V(III) *adsorption on the kinetics of the* V(III)-V(II) *couple.*—The problem of measuring the rate of a rapid electrode reaction when the reactant is adsorbed on the electrode has long plagued electro-

Table III. Comparison of the values for $\Gamma_{V(III)}$ obtained by two different methods

Supporting electrolyte: 0.9M $NaClO_4$-0.1M NaNCS-0.01M $HClO_4$
[V(II)] + [V(III)] = 1.0 mM

$-E$, mV *vs.* SCE	$\mathbf{F}\Gamma_{V(III)}$,[a] μC/cm^2, from intercept	$\mathbf{F}\Gamma_{V(III)}$,[b] μC/cm^2 from intercept and dme measurements
480	9.7 ± 0.4	7.2 ± 1.5
500	8.9	7.3
520	7.2	7.6
550	3.9	2.4

[a] These values were obtained by subtracting from the intercepts of chronocoulometric charge-(time)$^{1/2}$ plots the charge consumed in stepping the electrode from the same initial equilibrium potential to -900 mV in the supporting electrolyte alone. The reproducibility of each value was *ca.* ±0.4 μC/cm^2.

[b] These values were calculated by combining Eq. [8] and [9] to give $(1 - \beta)\mathbf{F}\Gamma_{V(III)} = I - q^{dme} - 9.5$. The reproducibility of each calculated value was *ca.* ±1.5 μC/cm^2.

chemical kineticists. A large number of theoretical analyses and experimental attacks on the problem have been made [ref. (43-50) are a representative but not comprehensive set of examples]. They all boil down to extrapolations to infinite frequencies or vanishingly small times where, it is assumed, only adsorbed reactant can be reacting because of the finite times required to transport unadsorbed reactant from the solution to the electrode surface. This philosophy was applied to the V(III)-V(II) couple in thiocyanate solutions in the present experiments by means of the coulostatic technique (19): small charges were injected into a hanging mercury drop electrode initially at its equilibrium potental in a solution containing approximately equal concentrations of V(III) and V(II). The resulting, open-circuit, potential-time transients were observed on an oscilloscope, recorded photographically, and analyzed to obtain information about the kinetics of the electrode reaction. To carry out the analyses of the transients, values of the differential double-layer capacitance are required (51, 52) and the appropriate value of the capacitance is that for solutions containing the reactant couple. When no reactant adsorption occurs the double-layer capacitance measured at the same potential in reactant-free supporting electrolyte is usually an excellent approximation of the capacitance in the presence of reactant. When reactant adsorption is known to occur, as with V(III) in thiocyanate solutions, the approximation that there is no change in double-layer capacitance is much poorer. Furthermore, the *a priori* inseparability of faradaic current and double-layer charging current referred to earlier complicates attempts to evaluate the true double-layer capacitance in the presence of reactant adsorption (47-50).

The approach adopted in the present experiments was as follows: values of $q^m{}_{E_i}$ at various values of E_i were obtained by simultaneous solution of Eq. [8] and [9] as described earlier. A plot of these values of $q^m{}_{E_i}$ *vs.* potential in the vicinity of $E_{1/2}$ was made. The slope of the resulting line gives the appropriate differential double-layer capacitance for use in analyzing the coulostatic potential-time transients. The experimental errors involved in obtaining the values of $q^m{}_{E_i}$ leave some uncertainty in the value of the double-layer capacitance in the presence of vanadium as is indicated in Fig. 3. It seems likely that the capacitance is actually about the same, 46 μF/cm^2, in the presence of vanadium as in the pure supporting electrolyte. However, the slope of the dashed rather than the solid line in Fig. 3 was used to evaluate the

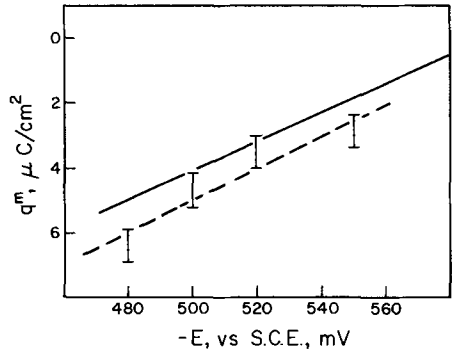

Fig. 3. Charge-potential curves. The solid line is the result of measurements of q^m with the dme procedure in pure supporting electrolyte

0.1M NaSCN-0.9M $NaClO_4$-0.02M $HClO_4$

Its slope corresponds to a double-layer capacitance of 46 μF/cm^2. The four points marked with bars were obtained from the corresponding points in Fig. 2 by subtracting the appropriate fraction of $\Gamma_{V(III)}$ as calculated from Eq. [7]. The length of the bars indicates the range of the values obtained in replicate experiments. The dashed line through the four points corresponds to a double-layer capacitance of 50 μF/cm^2.

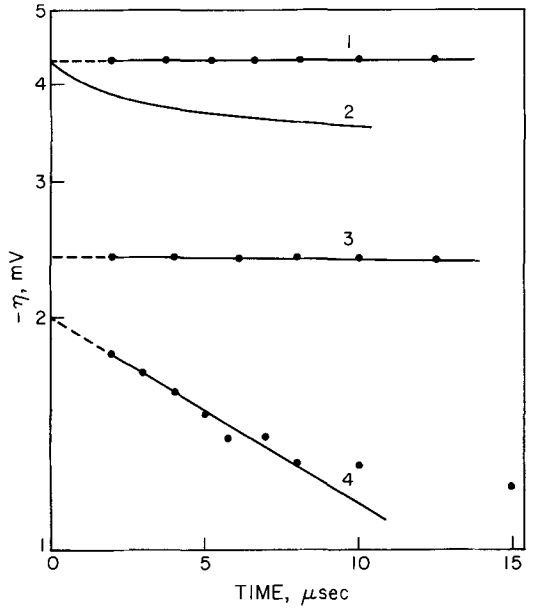

Fig. 4. Cathodic coulostatic relaxation transients for V(III)/V(II) in thiocyanate. 1, Supporting electrolyte alone: 0.1M NaSCN-0.9M $NaClO_4$-0.02M $HClO_4$; 2, calculated diffusion limited relaxation transient in the same electrolyte as 1 for [V(III)] = [V(II)] = 0.5 mM; 3, experimental transient in the same electrolyte as 1 with [V(III)] = [V(II)] = 0.5 mM; 4, as in 3 except [V(III)] = [V(II)] = 5 mM. The overvoltage, η, is plotted on a logarithmic scale. In each case, the initial potential was −520 mV and the charge injected was −0.176 μC/cm^2.

capacitance as 50 μF/cm^2 in the presence of V(III) and V(II). The true value of the capacitance should be bracketed by these two values.

Curve 3 in Fig. 4 shows a typical cathodic potential-time relaxation transient obtained with 0.5 mM V(III) and 0.5 mM V(II) in a 0.1M NaNCS-0.9M $NaClO_4$ supporting electrolyte. It is unusual in that even at the shortest times at which measurements could be made, the observed potential is well below the value that is obtained in the same electrolyte without vanadium, curve 1. Curve 2 is the calculated transient that would be observed for a diffusion limited electrode reaction with the same bulk concentrations of V(III) and V(II) and the double-layer capacitance of the supporting electrolyte. It is clear from curve 2 that very little of the difference between curves 1 and 3 can be attributed to the reaction of the bulk reactants, especially at the shortest observable times. The potential difference between curves 1 and 3 could arise either from a large difference in the double-layer capacitance for the two solutions or from the very rapid faradaic reaction of adsorbed V(III). However, the double-layer capacitance has been shown to increase by no more than 4 μF/cm^2 (from 46 to 50 μF cm^2) in the presence of V(III) and V(II) (Fig. 3), while a change of 30 μF/cm^2 would be required to account for the difference between curves 1 and 3 in Fig. 4. Thus, the faradaic reaction of adsorbed V(III) seems clearly to be the source of this difference.

As a check on these conclusions, a set of coulostatic experiments was also carried out in a bromide supporting electrolyte where substantial anion adsorption occurs, but no evidence of V(III) adsorption was obtained in chronocoulometric measurements. Figure 5 shows the results: essentially no difference at the shortest times between the curves obtained in the presence and absence of V(III) and V(II). These results with the bromide electrolyte confirm that V(III) adsorption in the thiocyanate electrolyte is the reason for the differences between curves 1 and 3 in Fig. 4. It seems reasonable, therefore, to use the difference between these two curves to calculate a value for the exchange current for the adsorbed V(III)/V(II) couple. Unfortunately, only a lower limit on the rate

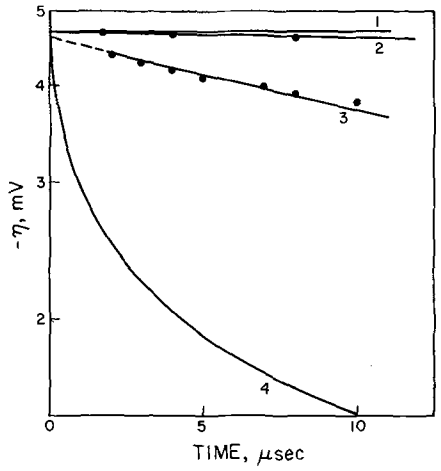

Fig. 5. Cathodic coulostatic relaxation transients for V(III)/V(II) in bromide. Supporting electrolyte: 1M NaBr-0.02M $HClO_4$. 1, Supporting electrolyte alone; 2, experimental transient with [V(III)] = [V(II)] = 0.5 mM; 3, experimental transient with [V(III)] = [V(II)] = 5 mM; 4, calculated diffusion limited transient for [V(III)] = [V(II)] = 5 mM. The overvoltage, η, is plotted on a logarithmic scale. In each case, the initial potential was −470 mV and the charge injected was −0.239 $\mu C/cm^2$.

can be obtained because the essentially constant level of the potential-time transient at the shortest accessible times (curve 3, Fig. 4) indicates that the reduction of the adsorbed V(III) is completed by the time the ohmic potential drop decays to negligible values, *ca.* 1.5 μsec. At $t = 1.5$ μsec, the difference between curves 1 and 3 amounts to 1.8 mV which corresponds (on the basis of the double-layer capacitance in the presence of adsorbed V(III) obtained from Fig. 3) to 0.090 $\mu C/cm^2$ of charge. This charge difference can be attributed to the reduction of the same amount of adsorbed V(III). Thus, 0.090 $\mu C/cm^2$ of V(III) were reduced within 1.5 μsec. The minimum average faradaic current flowing during this period was thus 60 mA/cm^2 and the average overvoltage during this period was 3.4 mV. If the same linearized current-potential relation commonly used to analyze the kinetics of unadsorbed reactants (53) is applied to the present case, a value of the minimum exchange current can be calculated

$$I = I_o \frac{\mathbf{F}}{RT} \eta \qquad [10]$$

where I is the faradaic current, I_o is the exchange current, η is the overvoltage, and $\mathbf{F}/RT = 0.0392$ mV^{-1} at 25°C. Equation [10] leads to $I_o = 0.50$ A/cm^2 as the minimum value of the exchange current for the adsorbed reactants.

If positive instead of negative charge is injected in the coulostatic experiment, the resulting anodic transient duplicates the cathodic transient. This indicates that sufficient V(II) is adsorbed to provide a symmetrical relaxation pathway via the adsorbed reactants. The chronocoulometric value for V(II) adsorption at $E_{1/2}$ was 0 ± 1 $\mu C/cm^2$, but the coulostatic measurements are more sensitive for detection of small quantities of adsorbed reactant. Hence, 0.5 $\mu C/cm^2$ was taken as a reasonable value for the amount of adsorbed V(II).

The rather large minimum exchange current obtained for the V(III)/V(II) couple in the adsorbed state contrasts with the smaller exchange currents previously measured for this couple in electrolytes where no reactant adsorption was involved (7-14). This large difference might be regarded as an instance of true catalysis by the electrode surface, *i.e.*, electrocatalysis. Before reaching this conclusion however, it is necessary to compare the exchange currents for the homogeneous (no reactant adsorption) and heterogeneous (both reactants adsorbed) cases with equivalent concentrations of reactants. "Equivalent concentrations" for these two cases implies homogeneous concentrations that expose the electrode surface to the same amounts of reactants per square centimeter as are adsorbed in the heterogeneous case. The molar reactant concentration that is required to match the cross-sectional concentration in the bulk of a homogeneous solution with a surface concentration of adsorbed reactant, Γ_i, can be calculated from Eq. [11]

$$C_i = \frac{C_{H_2O}}{\Gamma_{H_2O}} \Gamma_i \qquad [11]$$

where C_i is the required molar reactant concentration, $C_{H_2O} = 55.5$M, and Γ_{H_2O} is the number of moles of water per square centimeter in the bulk of the solution; for pure water $\Gamma_{H_2O} = 2.7 \times 10^{-9}$ moles/cm^2 (54).

For the V(III)-V(II) system under consideration the surface concentrations of the two oxidation states at −520 mV estimated from chronocoulometric measurements of their adsorptions are $\Gamma_{V(III)} = 7.5 \times 10^{-11}$ moles/cm^2 and $\Gamma_{V(II)} = 5.2 \times 10^{-12}$ moles/cm^2. The matching homogeneous bulk concentrations calculated from Eq. [9] are $C_{V(III)} = 1.5$M and $C_{V(II)} = 0.10$M. It is the exchange current that would be measured in an (hypothetical) experiment with a solution containing these calculated concentrations of V(III) and V(II) that must be compared with the exchange currents observed with adsorbed reactants in order to assess whether the adsorption has had an effect on the electrochemical reactivity of the V(III)/V(II) couple.

To make this comparison a value for the homogeneous exchange current for the V(III)/V(II) couple in the same electrolyte is needed. Coulostatic relaxation transients for solutions 0.5 mM in V(III) and V(II), such as curve 3 in Fig. 4, are not suitable for this purpose at any accessible times because the corrections for mass-transfer contributions to the relaxation are sizeable and complex with reactant concentrations this low (51). For this reason, the coulostatic experiment was repeated with a solution ten times more concentrated in vanadium ([V(III)] = [V(II)] = 5 mM). The resulting transient is shown as curve 4 in Fig. 4. The slope of the straight line drawn through the points at the shortest times (before mass transfer begins to slow down the relaxation) with the double layer capacitance obtained from the data in Fig. 3 lead (51) to an exchange current of 69 mA/cm^2.

To check on the reasonableness of this value the experiment was repeated in a 1M NaBr electrolyte where there are no complications from adsorbed reactants. Curve 3 in Fig. 5 shows the relaxation transient that resulted. Its slope corresponds to an exchange current of 29 mA/cm^2 which makes the exchange current obtained in the thiocyanate electrolyte seem reasonable.

Taking the value of 69 mA/cm^2 for a solution 5 mM in V(III) and V(II) and assuming that the transfer coefficient, α, is 0.5, one calculates that the exchange current that would correspond to a solution containing 1.5M V(III) and 0.1M V(II) is 5.4 A/cm^2. This value is ten times greater than the estimated minimum exchange current with adsorbed reactants in the 0.1M NaNCS-0.9M $NaClO_4$ electrolyte. It is, therefore, not possible to observe any electrocatalytic effects if they are present. The increase in rate arising merely from the increased concentrations of reactants is so large that it effectively masks any enhancement (or depression) in the electrochemical reactivity of the complexes resulting from their adsorption.

The much higher reaction rates (exchange currents) observed with adsorbed reactants are to be expected because of the large increase in their surface concentrations which are produced by even rather weak adsorption (10^{-12} moles/cm^2 or less). This fact may often permit the reaction rate for both the adsorbed and nonadsorbed reactants to be evaluated because the

characteristic relaxation times for the two kinetic pathways may be sufficiently different for two distinct relaxations to be observed. The present case is such an example: the adsorbed V(III) is reduced so much more rapidly than the dissolved V(III) that the latter's rate of reduction can be measured without serious contributions from the reaction of the adsorbed species (curve 4, Fig. 4). Some complications might be anticipated from contributions of the adsorbed reactant to the slower relaxation of the dissolved reactant because the overvoltage which controls the rate of both processes continues to change. It is likely that curve 4 in Fig. 4 departs from linearity at longer times (lower overvoltages) for this reason. Nevertheless, the initial slope of this curve should provide a reasonable estimate of the exchange current for the homogeneous reaction.

Nürnberg (55) has suggested recently that weak adsorption of V(III) and V(II) may occur in perchlorate electrolytes. We could find no evidence for this chronocoulometrically nor even in the much more sensitive coulostatic experiments. Relaxation transients obtained in 1M $NaClO_4$ extrapolated to the same initial overvoltage as was obtained in blank experiments, *i.e.*, they resembled curve 3 in Fig. 5 rather than curve 4 in Fig. 4, and the calculated exchange currents [I_o = 250 $\mu A/cm^2$ with 0.5 mM V(III) and V(II)] agreed with previous measurements (7-9).

Sluyters and co-workers have reported on the kinetics of a number of metal/metal amalgam electrode reactions in which weak reactant adsorption occurs (35, 36, 56-58). In every case, the exchange currents were too large to be measured (with the a-c bridges employed) when reactant adsorption was evident. Similar behavior has also been observed by others (46, 59) and this apparent generality lead Sluyters and co-workers to speculate recently (60) as to whether there might not be "a causal connection between (electrochemical) reversibility and specific adsorption" of reactants. One conclusion arising from the present investigation is that concentration enhancement rather than true catalysis may often be the source of the much larger electrode reaction rates observed with adsorbed reactants. Essentially the same point has been made by Mairanovskii in discussing the polarography of adsorbed organic reactants (61, 62).

It seems likely that electrode reactions which are inherently slower than those so far investigated may permit a clearer distinction to be made between rate enhancements due to true catalytic adsorption and those arising only from concentration enhancement by adsorption. Kinetic studies of a number of transition metal thiocyanates are presently under way in this laboratory to explore this possibility.

Acknowledgments

The coulostatic circuit employed was constructed by Chaim Yarnitzky who also served as a reliable and extremely helpful source of electronic expertise. Roger Abel contributed freely and expertly to the programming and maintenance of the digital computerized data acquisition system. Thoughtful and critical comments and suggestions were supplied by Donald Barclay. This work was supported by the National Science Foundation. This paper is Contribution No. 3913, Gates Crellin Laboratories of Chemistry, California Institute of Technology.

Manuscript submitted Aug. 1, 1969; revised manuscript received Sept. 23, 1969.

Any discussion of this paper will appear in a Discussion Section to be published in the December 1970 JOURNAL.

REFERENCES

1. F. C. Anson, *Anal. Chem.*, **38**, 54 (1966).
2. F. C. Anson, J. H. Christie, and R. A. Osteryoung, *J. Electroanal. Chem.*, **13**, 343 (1967).
3. F. C. Anson and D. J. Barclay, *Anal. Chem.*, **40**, 1791 (1968).
4. G. W. O'Dom and R. W. Murray, *J. Electroanal. Chem.*, **16**, 327 (1968).
5. D. J. Barclay and F. C. Anson, *This Journal*, **116**, 438 (1969).
6. Z. Kowalski and F. C. Anson, *ibid.*, **116**, 1208 (1969).
7. J. E. B. Randles and K. W. Somerton, *Trans. Faraday Soc.*, **48**, 937 (1952).
8. J. E. B. Randles, *Can. J. Chem.*, **37**, 238 (1959).
9. K. M. Joshi, W. Mehl, and R. Parsons, *Trans. Symp. Electrode Processes, Philadelphia, Pa., 1959*, 249 (1961).
10. S. Sathyanarayana, *J. Electroanal. Chem.*, **7**, 403 (1964).
11. Y. Israel and L. Meites, *ibid.*, **8**, 99 (1964).
12. V. S. Srinivasan, G. Torsi, and P. Delahay, *ibid.*, **10**, 165 (1965).
13. J. E. B. Randles and D. R. Whitehouse, *Trans. Faraday Soc.*, **64**, 1376 (1968).
14. K. K. Niki and N. Hackerman, *J. Phys. Chem.*, **73**, 1023 (1969).
15. J. H. Christie, R. A. Osteryoung, and F. C. Anson, *J. Electroanal. Chem.*, **13**, 236 (1967).
16. G. Lauer, R. Abel, and F. C. Anson, *Anal. Chem.*, **39**, 765 (1967).
17. J. N. Butler and M. L. Meehan, *J. Phys. Chem.*, **69**, 4051 (1965); *ibid.*, **70**, 3581 (1966).
18. G. Lauer and R. A. Osteryoung, *Anal. Chem.*, **39**, 1866 (1967).
19. P. Delahay and A. Aramata, *J. Phys. Chem.*, **66**, 2208 (1962).
20. T. W. Newton and F. B. Baker, *Inorg. Chem.*, **3**, 569 (1964).
21. R. H. Wopschall and I. Shain, *Anal. Chem.*, **39**, 1527 (1967).
22. F. C. Anson and D. A. Payne, *J. Electroanal. Chem.*, **13**, 35 (1967).
23. H. Wroblowa, Z. Kovac, and J. O'M. Bockris, *Trans. Faraday Soc.*, **61**, 1523 (1965).
24. E. Dutkiewicz and R. Parsons, *J. Electroanal. Chem.*, **11**, 100 (1966).
25. R. A. Osteryoung and J. H. Christie, *J. Phys. Chem.*, **71**, 1348 (1967).
26. G. Lauer and R. A. Osteryoung, *Anal. Chem.*, **41**, 1882 (1969).
27. D. J. Barclay, E. Passeron, and F. C. Anson, In press.
28. J. N. Armor and A. Haim, Abstracts, XX ACS Meeting, Atlantic City, N. J., 1968.
29. M. Orhanovic and N. Sutin, *J. Am. Chem. Soc.*, **90**, 4286 (1968).
30. F. A. Cotton, D. M. L. Goodgame, M. Goodgame, and A. Sacco, "Advances in the Chemistry of Coordination Compounds," p. 123, McMillan, New York (1961).
31. S. C. Furman and C. S. Garner, *J. Am. Chem. Soc.*, **73**, 4528 (1951).
32. P. Delahay, *This Journal*, **113**, 967 (1966).
33. P. Delahay, *J. Phys. Chem.*, **70**, 2086 (1966); *ibid.*, p. 2373; *ibid.*, **71**, 3360 (1967).
34. P. Delahay and G. G. Susbielles, *ibid.*, **70**, 3150 (1966).
35. M. Sluyters-Rehbach, B. Timmer, and J. H. Sluyters, *J. Electroanal. Chem.*, **15**, 151 (1967).
36. B. Timmer, M. Sluyters-Rehbach, and J. H. Sluyters, *ibid.*, **15**, 343 (1967).
37. W. H. Reinmuth, *Anal. Chem.*, **40**, 185R (1968).
38. F. C. Anson. *Ann. Rev. Phys. Chem.*, **19**, 83 (1968).
39. R. Parsons in "Advances in Electrochemistry and Electrochemical Engineering," P. Delahay, Editor, In press.
40. D. C. Grahame and R. B. Whitney, *J. Am. Chem. Soc.*, **65**, 1548 (1942).
41. D. M. Mohilner, *J. Phys. Chem.*, **66**, 724 (1962).
42. D. M. Mohilner in "Electroanalytical Chemistry," Vol. 1, A. J. Bard, Editor, M. Dekker, Inc., New York (1966).
43. H. A. Laitinen and J. E. B. Randles, *Trans. Faraday Soc.*, **51**, 54 (1955).
44. M. Senda and P. Delahay, *J. Phys. Chem.*, **65**, 1580 (1961).
45. D. M. Mohilner and P. Delahay, *ibid.*, **67**, 588 (1963).
46. A. M. Baticle and F. Perdu, *J. Electroanal. Chem.*, **12**, 15 (1966); *ibid.*, **13**, 364 (1967).
47. P. Delahay, *ibid.*, **19**, 61 (1968).
48. B. Timmer, M. Sluyters-Rehbach, and J. H. Sluyters, *ibid.*, **19**, 73 (1968).
49. M. Sluyters-Rehbach, B. Timmer, and J. H. Sluyters, *ibid.*, **19**, 305 (1968).

50. D. J. Kooijman, *ibid.*, **19**, 365 (1968).
51. P. Delahay, *J. Phys. Chem.*, **66**, 2204 (1962).
52. W. H. Reinmuth, *Anal. Chem.*, **34**, 1272 (1962).
53. P. Delahay, "Double Layer and Electrode Kinetics," Chap. 7, Interscience Publishers, New York (1965).
54. R. Parsons and M. A. V. Devanathan, *Trans. Faraday Soc.*, **49**, 673 (1953).
55. H. W. Nürnberg, *Electrochim. Acta*, **13**, 1004 (1968) (Discussion).
56. M. Sluyters-Rehbach, B. Timmer, and J. H. Sluyters, *Rec. Trav. Chim.*, **82**, 553 (1963).
57. M. Sluyters-Rehbach and J. H. Sluyters, *ibid.*, **83**, 217, 967 (1964).
58. B. Timmer, M. Sluyters-Rehbach, and J. H. Sluyters, *J. Electroanal. Chem.*, **18**, 93 (1968).
59. J. R. Galli and R. Parsons *ibid.*, **10**, 245 (1965).
60. M. Sluyters-Rehbach, B. Timmer, and J. H. Sluyters, *ibid.*, **19**, 305 (1968).
61. S. G. Mairanovskii, *ibid.*, **3**, 166 (1962).
62. S. G. Mairanovskii, "Catalytic and Kinetic Waves in Polarography," p. 128, Plenum Press, New York (1968).

Thermogalvanic Cells: Equations for Special States and Ionic Mobilities

Philip B. Lorenz

Bartlesville Petroleum Research Center, Bureau of Mines, U. S. Department of the Interior, Bartlesville, Oklahoma

ABSTRACT

Linear phenomenological equations for processes in thermogalvanic cells are set up in two forms. One form is used for examining the nature of six special states: the thermal and shorted initial states, and the isothermal, thermal, shorted, and adiabatic steady states. With aqueous electrolytes the following are predicted: a large variation in the Soret effect and a moderate variation in the Peltier heat with changes in electrical state; a difference between electrical and thermal transference numbers; and a small temperature gradient set up by the flow of current under adiabatic conditions. The other form of the equations is used for examining the mobility of ions in a thermal field and a comparison with the mobility in an electrical field or a concentration gradient. Introduction of electrostatic potential as a variable suggests a way of measuring thermodynamic properties of individual ions.

The thermogalvanic cell serves as a prototype for processes involving electric potentials of chemical and thermal origin. The spontaneous electric potentials in the earth are of considerable importance in logging of oil wells and other geophysical analytical methods. With ordinary geothermal gradients, the thermal component of a measured potential can amount to many millivolts. This part of the potential has received less than its share of attention, although electrochemical and electrokinetic potentials have been considered extensively.

For all kinds of potentials, a systematic formulation by means of linear phenomenological equations provides a sound basis for further understanding of the processes. A variety of formulations has been presented (1-5), but some are more convenient for making predictions than others. It is illuminating to compare the work that has been done with the isothermal concentration cell.

For the latter system, one formulation in particular has been used for describing the behavior of the cell under a variety of experimental conditions (6). The variables in this formulation are current, potential, diffusion rate, and gradient of chemical potential, which are closely related to experimental quantities. A special state is the steady state when electrical current maintains a constant concentration gradient. This state is relatively unfamiliar, but has been used as a basis for a separation procedure (7).

The more abstract formulation in terms of electrochemical potentials (8) leads to a relation between electrical and diffusion mobility that amounts to an extension of the Nernst-Einstein equation to finite concentrations.

The purpose of the present work is to extend the same treatment to the thermogalvanic cell. From the formulation in terms of experimental quantities, we find that there are six special states. The characteristics of two of these states have long been considered, *viz.*, the steady state of "Soret equilibrium" and the "initial" state of uniform concentration when the temperature gradient is first established. However, when the various possible electrical and thermal constraints are permuted, there are three other steady states and one other initial state.

From the formulation in terms of electrochemical potentials, we gain more information about the individual properties of the migrating ions. This information is of theoretical interest and, moreover, is needed for a knowledge of the behavior of mixed electrolytes.

Key words: initial state, ionic activity coefficient, ionic entropy, ionic mobility, Peltier heat, Soret coefficient, steady state, thermal emf, thermogalvanic cell.

The Cell

The salient features of the analysis can be seen in the simple case of a cell with a single electrolyte in a single solvent, with all the gradients in one dimension. The electrodes are reversible to one of the ions according to the reaction

$$(1/z_r)\,[M] \rightarrow (1/z_r)\,r^z + e^- \qquad [1]$$

where [M] is a substance, or a group of substances, *e.g.*

$$[M] = [\tfrac{1}{2}H_2],\ [AgCl - Ag],\ [\tfrac{1}{2}PbO + \tfrac{1}{2}H_2O - \tfrac{1}{2}Pb]$$

$$r = H^+, \qquad Cl^-, \qquad OH^-$$

For definiteness, the cell will be oriented so that reaction [1] takes place as written at the left, and in reverse at the right. All fluxes and forces will be taken as positive from left to right (Fig. 1). Thus, the cell emf

$$E = \tilde{\Delta\mu_r}/z_rF \qquad [2]$$

is positive when the right-hand electrode has the sign of the r ion. E is a difference function that is formally converted to a gradient in the subsequent treatment.

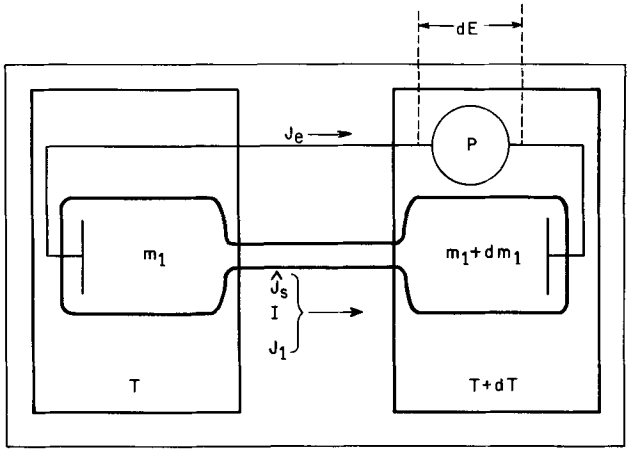

Fig. 1. Schematic diagram of thermogalvanic cell

Phenomenological Equations and Experimental Coefficients

The flux of solvent is eliminated by assuming the Hittorf convention. The electrolyte flux is then a straightforward experimental quantity in a cell such as that shown schematically in Fig. 1. The thermal flux will be represented by the flux of entropy. The reason for this choice is that the coefficients of the equations can be more conveniently interpreted than when heat flux is used directly.

The total entropy flux includes a convective term for bulk transport that results from the frame of reference anchored to the solvent. However, it is the nonconvective portion of the flux, $\overline{J}_s$, that is conjugate with the temperature gradient (5), and moreover the quantity

$$\hat{J}_s = \overline{J}_s - \Sigma_i \overline{S}_i J_i$$

is the conjugate flux when ordinary chemical or electrochemical potentials are used in place of the total chemical potentials that include the temperature variation.[1] For the processes under consideration, $\hat{J}_s$ is unaffected by the frame of reference; it is the "reduced heat flow" divided by the temperature (5). The reduced heat flow is measured calorimetrically as the heat accumulation on one side of the cell and depletion on the other. (The two quantities are not equal, but the difference is a second order effect.)

By the use of [2] and transformations that have been discussed previously (6), the phenomenological equations for the thermogalvanic cell can be put into the form

$$\begin{aligned} \hat{J}_s &= L_{11}\nabla T + L_{12}\nabla E + L_{13}\nabla\mu_1 \\ I &= L_{12}\nabla T + L_{22}\nabla E + L_{23}\nabla\mu_1 \\ J_1 &= L_{13}\nabla T + L_{23}\nabla E + L_{33}\nabla\mu_1 \end{aligned} \qquad [3]$$

The Onsager reciprocal relations have been incorporated into Eq. [3]. A modificaton of these equations is less symmetrical but more closely related to familiar experimental quantities

$$\begin{aligned} \hat{J}_s &= C_{11}\nabla T + C_{12}\nabla \ln m_1 + C_{13} I \\ J_1 &= C_{21}\nabla T + C_{22}\nabla \ln m_1 + C_{23} I \\ E &= C_{31}\nabla T + C_{32}\nabla \ln m_1 + C_{33} I \end{aligned} \qquad [4]$$

where m_1 is the molal concentration of the electrolyte. In this case $C_{21} = C_{12}/A$, $C_{32} = -C_{23}A$, and $C_{31} = -C_{13}$, where $A = \nu RT(1 + d \ln \gamma_\pm/d \ln m_1)$. Expressions for the coefficients of [3] and [4] in terms of conventional experimental quantities are given in Table I.[2] Extra terms appear in the L-coefficients because diffusion and thermal conductivity are measured with no electric current rather than with no electric potential. Table II gives examples of numerical values.

[1] For the system under consideration, $\hat{J}_s$ can be expanded to $\overline{J}_s - \overline{S}_M J_M - \overline{S}_1 J_1$, where J_M is a fictitious flux of electrode material; or $\hat{J}_s$ can be transformed to $J_{sk} + \hat{S}_r J_r + \hat{S}_g J_g + \hat{S}_e J_e + [\overline{S}_e + \overline{S}_r/z_r - \overline{S}_M/z_r]J_e$, where the term in brackets is the calorimetric entropy of the electrode reaction.

Table I. Coefficients of [3] and [4]

Subscript	$-L$	$-C$
11	$(K + \pi_{sm}^2\kappa/F^2T)/T$	K/T
12	$-\pi_{sm}\kappa/TF$	$\hat{S}_1 m_1 D$
13	$(\hat{S}_1 m_1 D/A) + (\pi_{sm} t_g \kappa/n_g F^2 T)$	π_{sm}/TF or ϵ
22	κ	$m_1 D$
23	$t_g\kappa/n_g F$	$-t_g/n_g F$
33	$(m_1 D/A) + (t_g/n_g F)^2\kappa$	$1/\kappa$

Table II. Values of coefficients for common inorganic aqueous electrolytes at 25°C (MKS units)

0.01N KCl Ag/AgCl electrode	Effect of species and electrode at 0.01N	Variation with concentration	References
C_{11} -2.03×10^{-3}	Small	Small	(9, 10)
C_{22} -1.92×10^{-8}	Li_2SO_4: -0.9×10^{-8} HCl: -3.2×10^{-8}	Proportional	(11)
C_{33} -7.07	HCl: -2.4 $LaCl_3$: -21	Inversely proportional	(12)
C_{12} -1.30×10^{-7}	LiI: $+0.9 \times 10^{-7}$ H_2SO_4: -26×10^{-7}	$(A - B\sqrt{m})m$ (roughly $\times$ 5 per decade of conc.)	(1, 3, 11)
C_{13} $+6.39 \times 10^{-4}$	HCl: -3.5×10^{-4} KI with Ag/AgI: $+2 \times 10^{-4}$	$A - B\sqrt{m}$ (roughly $\times$ 0.7 per decade of conc.)	(3, 13)
C_{23} -5.08×10^{-6}	LiCl: -3×10^{-6} HCl: -8×10^{-6}	Small	(12)
A 4.73×10^3	Proportional to ν	Small	(11)

Special States

There are three "initial" states: the isothermal initial state (IIS); the thermal initial state (TIS), in which a temperature gradient is established in the absence of electric current and before material fluxes have produced a significant concentration gradient; and the shorted initial state (SIS), which is the TIS with electrodes short-circuited. There are four steady states, two induced by the flow of current and two by a temperature gradient. In the former category belong the isothermal steady state (ISS) and the adiabatic steady state (ASS), the later produced by an adiabatic flow of current until the fluxes of solute and entropy both cease. The steady states produced by a thermal gradient are the thermal steady state (TSS) or Soret equilibrium in the absence of current, and the shorted steady state (SSS), which is the TSS with electrodes short-circuited.

Expressions equal to the various ratios under these special conditions are listed in Table III. Expressions is braces are included only for completeness. To get expressions compact enough for tabulation, it was necessary to develop the shorthand portrayed in Table IIIa. Examination of Tables II, III, and IIIa leads to the following conclusions:

1. The effect of electrical state (SIS and SSS) on thermal conductivity of aqueous electrolytes is very small, 1 part in 10^5 for 0.01N KCl and not over 1% in extreme cases. In fused salts or semiconductors this effect could be quite substantial, as much as 30%.

2. The Peltier heat of 0.01N KCl is increased about 6% by the establishment of ISS. This varies in sign and magnitude with electrolyte species. It depends on a large Soret coefficient and reasonable gegenion transference number. The increase is larger at low concentration; however, both the steady state and the low

[2] The thermal and electrical conductivities of the external circuit contribute to the over-all process, and the coefficients of Table I are, to a slight extent, approximations.

Table III. Expressions equal to various ratios

	0 =	IIS $\nabla T, \nabla m_1$	TIS $\nabla m_1, I$	SIS $\nabla E, \nabla m_1$	ISS $J_1, \nabla T$	TSS J_1, I	SSS $J_1, \nabla E$	ASS J_s, J_1
Thermal conductivity × $1/T$	$\hat{J}_s/\nabla T$		C_{11}	$C_{11}W_{13}$		$C_{11}W_{12}$	$L_{11}(1 - L^2_{13}/L_{11}L_{33})$	0
Peltier coefficient × $1/T$	$\hat{J}_s/I$	C_{13}		$\left\{\frac{C_{13}W_{13}}{W_{13}-1}\right\}$	$C_{13}U_{13}$		$\left\{\frac{C_{13}W_{13}}{W_{13}-1}X\right\}$	
Thermal emf	$\nabla E/\nabla T$		$-C_{13}$			$-C_{13}U_{13}$		$\{-C_{13}Z\}$
Electrical resistivity	$\nabla E/I$	C_{33}			$C_{33}W_{32}$			$C_{33}W_{23} + Y$
Soret coefficient	$\frac{\nabla \ln m_1}{\nabla T}$					$-C_{21}/C_{22}$	$-\frac{C_{21}}{C_{23}}\frac{U_{12}}{W_{23}}$	$\left\{-\frac{C_{21}U_{32}}{C_{22}U_{13}(U_{23}-1)}\right\}$
Transference	J_1/I	C_{23}		$\frac{C_{23}U_{12}}{U_{12}-1}$	0	0	0	0
Steady-state concentration	$\nabla \ln m_1/I$				$-C_{23}/C_{22}$		$\left\{-\frac{C_{23}U_{12}}{C_{22}U_{13}(U_{12}-1)}\right\}$	$-\frac{C_{23}}{C_{22}}\frac{U_{23}}{W_{12}}$

concentration increase the power required to transfer heat.

3. The foregoing effect in 3 is numerically equal to the difference in thermal emf between initial state (TIS) and Soret equilibrium (TSS).

4. The electrical resistance as usually measured with alternating current depends only on the distributed resistivity due to distributed concentration. Values in Table III refer to an increase in current flow and the simultaneous adjustment of the system to a new steady state. In this case $\nabla E/I$ is almost double the normal resistivity.

5. The Soret effect is defined for TSS, but, if the concept is extended to other steady states, the coefficient for 0.01*N* KCl is reversed in sign and increased eightfold in magnitude by short circuiting (SSS). This change is large for any system with a large Peltier coefficient and a reasonable gegenion transference number. It varies greatly with the electrolyte species; the sign is not always reversed.

6. The transference of electrolyte by current in 0.01*N* KCl is about 6% smaller when the current is generated by a thermal gradient than when it is generated by an applied emf. This means that a larger portion of the current is carried by the reversible ion when the current is thermally generated.

7. The concentration gradient in the current-induced steady state is virtually the same under isothermal (ISS) and adiabatic (ASS) conditions. In the adiabatic case, the temperature gradient is $-C_{13}U_{13}/C_{11}W_{12}$, which for 0.01*N* KCl is an increase in the direction of current flow of 0.33 deg m^{-1} A^{-1} (0.0033 deg cm^{-1} A^{-1}). This value depends primarily on the Peltier coefficient, but it also increases significantly with an increase in the Soret coefficient.

Phenomenological Equations and Mobilities

The other form of the equations to be considered is

$$\hat{J}_s = \Omega_{ss}\nabla T + \Omega_{sr}\nabla\tilde{\mu}_r + \Omega_{sg}\nabla\tilde{\mu}_g$$

$$J_r = \Omega_{sr}\nabla T + \Omega_{rr}\nabla\tilde{\mu}_r + \Omega_{rg}\nabla\tilde{\mu}_g$$

$$J_g = \Omega_{sg}\nabla T + \Omega_{rg}\nabla\tilde{\mu}_r + \Omega_{gg}\nabla\tilde{\mu}_g \quad [5]$$

Table IIIa. Shorthand for Table III and values (dimensionless) for 0.01*N* KCl

$1 - W_{12} = C_{12}C_{21}/C_{11}C_{32}$	$+0.96 \times 10^{-7}$
$1 - W_{23} = C_{23}C_{32}/C_{22}C_{33}$	-0.94
$1 - W_{13} = C_{13}C_{31}/C_{11}C_{33}$	-2.82×10^{-6}
$1 - U_{12} = C_{13}C_{32}/C_{12}C_{23}$	$+16.6$
$1 - U_{23} = C_{21}C_{13}/C_{23}C_{11}$	-1.7×10^{-6}
$1 - U_{13} = C_{12}C_{23}/C_{13}C_{22}$	-5.7×10^{-2}
$L_{13}^2/L_{11}L_{33}$	$+1.20 \times 10^{-5}$

$X = (1 - L_{13}^2/L_{11}L_{33})/(1 - L_{13}L_{32}/L_{12}L_{33})$
$Y = (1 - U_{23}/W_{12})(1 - W_{23}) + (W_{13} - 1)U_{13}/W_{12}$
$Z = 1 + (W_{23} - 1)U_{23}/(W_{13} - 1)U_{13} + (W_{13} - 1)U_{13}/W_{12}$

These equations emphasize the contributions of the separate ions to the cell process. Here the coefficients are thermal and electrochemical mobilities.[3] Their relation to the coefficients of Eq. [4] are

$$\Omega_{ss} = C_{11} + C_{13}^2/C_{33} = -(K + \pi^2_{sm}\kappa/T\mathbf{F}^2)/T$$

$$\Omega_{sr} = \nu_r[(C_{12}/A) + C_{13}(C_{23} + 1/n_r\mathbf{F})/C_{33}] = t_{r\kappa}\pi_{sm}/Tz_r\mathbf{F}^2 - \nu_r\hat{S}_1 m_1 D/A$$

$$\Omega_{sg} = \nu_g[(C_{12}/A) + C_{13}C_{23}/C_{33}] = t_{g\kappa}\pi_{sm}/Tz_g\mathbf{F}^2 - \nu_g\hat{S}_1 m_1 D/A$$

$$\Omega_{rr} = \nu_r^2[(C_{22}/A) + (C_{23} + 1/n_r\mathbf{F})^2/C_{33}] = -t_r^2\kappa/z_r^2\mathbf{F}^2 - \nu_r^2 m_1 D/A$$

$$\Omega_{gg} = \nu_g^2[(C_{22}/A) + C_{23}^2/C_{33}] = -t_g^2\kappa/z_g^2\mathbf{F}^2 - \nu_g^2 m_1 D/A$$

$$\Omega_{rg} = \nu_r\nu_g[(C_{22}/A) + C_{23}(C_{23} + 1/n_r\mathbf{F})/C_{33}] = -t_r t_g\kappa/z_r z_g\mathbf{F}^2 - \nu_r\nu_g m_1 D/A \quad [6]$$

To develop a relation among mobilities, a special symbol is defined for the entropy of transfer when the electric current is carried by one ion alone

$$\hat{S}_{Ir} = (\hat{J}_s/J_r)_{J_g=\nabla T=0} \quad [7]$$

$$\hat{S}_{Ig} = (\hat{J}_s/J_g)_{J_r=\nabla T=0} \quad [8]$$

By use of the relations

$$J_g = \nu_g J_1 \quad [9]$$

$$J_r = \nu_r J_1 + I/z_r\mathbf{F} \quad [10]$$

it is found that

$$\hat{S}_{Ir} = z_r\mathbf{F}[C_{13} - C_{12}C_{23}/C_{22}] = t_g\hat{S}_1/\nu_r - z_r\pi_{sm}/T \quad [11]$$

$$\hat{S}_{Ig} = z_g\mathbf{F}[C_{13} - C_{12}(C_{23} + 1/n_r\mathbf{F})/C_{22}] = t_r\hat{S}_1/\nu_g - z_g\pi_{sm}/T \quad [12]$$

From Eq. [6], [11], and [12], it follows that

$$\Omega_{sr} = \Omega_{rr}\hat{S}_{Ir} + \Omega_{rg}\hat{S}_{Ig} \quad [13]$$

$$\Omega_{sg} = \Omega_{gg}\hat{S}_{Ig} + \Omega_{rg}\hat{S}_{Ir} \quad [14]$$

The left-hand side of each equation represents the mobility of the ion under the sole influence of a thermal gradient. From a thermodynamic point of view, $-\hat{S}_{Ir}\nabla T$ is the "thermal force" for the migration of

[3] $\Omega_{rr} = (c/z_r\mathbf{F})u_r$ where c is equivalent concentration and u_r = (migration speed)/(voltage gradient).

r-ions accompanied by the electrode reaction. Thus, $\hat{S}_{Ir}$ serves to convert the electrochemical mobility, Ω_{rr}, into a part of the thermal mobility. This first term is the principal term. The second term involves Ω_{rg}, which is sometimes called a drag coefficient, and represents a kinetic interaction between the two ions. This interaction introduces a correction term into the thermal mobilitites, so that they are not identical with the electrochemical mobilities.

A similar situation exists in the relation between electrical and diffusion mobility. For the electrolyte, it is seen from Eq. [6] that

$$m_1 D/A = (t_r t_g \kappa/n_r^2 \mathbf{F}^2) - \Omega_{rg}/\nu_r \nu_g \quad [15]$$

and for the self-diffusion of a single ion, it can be shown that, approximately

$$m_r D_r/\nu_r RT = (t_r \kappa/z_r n_r \mathbf{F}) - \Omega_{rg}/\nu_g \quad [16]$$

In both cases, the second term on the right is a correction to the ideal Nernst equation. It has been shown (8) that Ω_{rg} is proportional to $\sqrt{m}$ at high dilution, so in the limit, thermal, electrical, and diffusion mobilities of the i-ion are all equal to Ω_{ii}. The nonequality of mobilities at higher concentration is introduced by the differing conditions of measurement.

Properties Associated with Individual Ions

The quantities $\hat{S}_{Ir}$ and $\hat{S}_{Ig}$ represent a composite of processes in the solution, in the external circuit, and at the electrodes. When $\hat{S}_{Ir}$ is expanded to show the entropy contribution of each process

$$\hat{S}_{Ir} = (\bar{\bar{S}}_r + z_r \bar{\bar{S}}_e - \bar{S}_M) \quad [17]$$

where $\bar{\bar{S}}_r$ is the entropy transported by the r-ion in solution, $\bar{\bar{S}}_e$ is the entropy transported by the electron in the wire, and $\bar{S}_M$ is the aggregate of molar entropies in the group [M]. The right-hand side of [17] is the same as the expression (3) for the thermoelectric power of the cell in Soret equilibrium, since by reciprocity

$$(\hat{J}_s/J_r)_{J_g=\nabla T=0} = -z_r \mathbf{F} (dE/dT)_{J_1=I=0} \quad [18]$$

Equations [17] and [18] are of value in developing expressions that suggest a measurement of thermodynamic properties of individual ions.

For illustration of the reasoning, consider first the electron in the wire. The differential of its total potential in the thermal gradient at zero electric current is (3)

$$d\bar{\mu}_e = -\bar{\bar{S}}_e dT \quad [19]$$

But if the temperature of a charged, isolated conductor M is raised, the increase in the total potential of the electrons is $d\bar{\mu}_e = -S_e dT$. If the conductor is connected with a sample of the same material at the original temperature, there will be a slight shift of charge because of the decreased escaping tendency at higher temperature. The electrons migrate from the cold end to the hot end until the thermal and electrical fields balance. The total potential is determined by the change in electrostatic (Volta) potential, ψ, as well as the temperature

$$d\bar{\mu}_e = -\bar{S}_e dT - \mathbf{F} d\psi \quad [20]$$

Equating [20] and [19]

$$d\psi = (\hat{S}_e/\mathbf{F}) dT \quad [21]$$

The electrostatic potential is measurable in principle, although a comparison of values at different temperatures would be less simple than measurements of isothermal changes. Table IV gives calculations from Eq. [21] for copper and platinum. The thermally induced electrostatic potential is a few microvolts per degree. This effect would probably be masked by the variations in local electrostatic potential due to inhomogeneous surfaces.

Table IV. Electrostatic potentials (μV/deg) on metals calculated from electronic entropies (joule/deg)

	Pt	Cu
$\bar{\bar{S}}_e$[a]	0.10	−0.045
$\bar{S}_e$[b]	0.05	+0.033
$\hat{S}_e$	0.05	−0.078
$d\Psi/dT$	2.0	−3.3

[a] Temkin and Khoroshin (14).
[b] Statistical value based on 1.0 free electron per atom for Cu and 0.6 for Pt (15).

Now the differential of the total potential for the r-ion can be easily derived by setting up the condition for equilibrium, *i.e.*, reversibility, at the electrodes. The expression is (3)

$$d\bar{\mu}_r = z_r \mathbf{F} dE + [z_r \bar{\bar{S}}_e - \bar{S}_M] dT = d\tilde{\mu}_r + [z_r \bar{\bar{S}}_e - \bar{S}_M] dT \quad [22]$$

Then, by use of

$$d\bar{\mu}_1 = \nu_r d\bar{\mu}_r + \nu_g d\bar{\mu}_g = \nu_r d\tilde{\mu}_r + \nu_g d\tilde{\mu}_g - \bar{S}_1 dT \quad [23]$$

it follows that

$$d\bar{\mu}_g = d\tilde{\mu}_g + [z_g \bar{\bar{S}}_e - (z_g/z_r) \bar{S}_M - \bar{S}_1/\nu_g] dT \quad [24]$$

When the thermogalvanic cell is in an initial state (IIS), $dE/dT = \pi_{sm}/T\mathbf{F}$, and this can be combined with [11], [17], and [22] to give

$$d\bar{\mu}_r = (-\bar{\bar{S}}_r + t_g \hat{S}_1/\nu_r) dT = -\bar{S}_r dT + z_r \mathbf{F} d\psi \quad [25]$$

Here ψ is to be taken as the electrostatic potential at the surface of the solution. Thence

$$(d\psi/dT)_{in} = (-\hat{S}_r + t_g \hat{S}_1/\nu_r)/z_r \mathbf{F} \quad [26]$$

Example calculations from Eq. [26] are given in Table V. Separate calculations (a) and (b) are made from different estimates of $\hat{S}_r$. The chief difference lies in the choice of a value for $\bar{S}_r$ for the hydrogen ion, which was −4.5 eu in (a) and −5.5 eu in (b). This makes an appreciable change in the predicted surface potential difference. In principle, since $\bar{S}_H$ is the basis for all conventional ionic entropies, measurements of surface potentials could be used to get actual ionic entropies (16).

When a cell is in Soret equilibrium, according to [17] $dE/dT = -\hat{S}_{Ir}/z_r \mathbf{F}$, and [25] is replaced by

$$d\bar{\mu}_r = -\bar{\bar{S}}_r dT = -\bar{S}_r dT + RT\, d \ln \gamma_r m_r + z_r \mathbf{F} \psi \quad [27]$$

Table V. Electrostatic potentials (μV/deg) on 0.01*N* electrolytes calculated from entropies of transport (joule/deg)

		KCl	HCl	KOH
Reversible ion		Cl	H	K
t_g		0.490	0.175	0.735
$\hat{S}_1$[a]		7.1	43.9	63.5
$\hat{S}_r$	(a)[a]	7.5	40.6	0.0
	(b)[b]	2.1	43.2	7.1
$(d\Psi/dT)_{in}$	(a)	−41	−341	484
	(b)	+14	−368	409
$(d\Psi/dT)_{st}$	(a)	−40	−193	329
	Δ	3.5	22.0	32.0

[a] According to de Bethune (1).
[b] According to Agar (3).

where the second term on the right is the variation of Lange's "real potential" with concentration, and γ_r is some function of concentration that amounts to an activity coefficient for the reversible ion. Under the same conditions

$$d \ln m_1/dT = -\hat{S}_1/A \quad [28]$$

Now since $m_r = \nu_r m_1$

$$(d\psi/dT)_{st} = -\hat{S}_r + (S_1/\nu)[(1 + d \ln \gamma_r/d \ln m_1)/(1 + d \ln \gamma_\pm/d \ln m_1)] \quad [29]$$

Values given in Table V are based on the assumption that the quantity in square brackets is unity, *i.e.*, that the ionic activity coefficient is directly proportional to the mean activity coefficient of the electrolyte. The last line of the table shows differences that would result from a 10% change in the square brackets. This suggests a possible way of getting a numerical comparison of the activity coefficient of an electrolyte with an activity coefficient for its ions.

Manuscript submitted July 31, 1969; revised manuscript received Nov. 7, 1969.

Any discussion of this paper will appear in a Discussion Section to be published in the December 1970 JOURNAL.

LIST OF SYMBOLS

A	activity correction, defined under Eq. [4]
c	concentration; equivalent · m^{-3}
C	coefficients of Eq. [4]
D	Fick diffusion coefficient; formula-wt $m^{-2} \cdot sec^{-1}$
e	electron (species)
E	Cell emf; V (sign of right-hand electrode)
g	gegenion (species to which electrodes are not reversible)
I	current density; A · m^{-2}
J_1, J_r, J_g	flux density of electrolyte, r-ion, g-ion; formula-wt · m^{-2} · sec^{-1}
$\bar{\bar{J}}_s, \hat{J}_s, J_{sk}$	entropy flux density: total nonconvective, "calorimetric," heat conduction (see footnote 1); joule · deg^{-1} · m^{-2} · sec^{-1}
K	Fourier thermal conductivity; joule · m^{-1} · sec^{-1} · deg^{-1}
L	coefficients of Eq. [3]
m	molal concentration; formula-wt · (kg of solvent)$^{-1}$
M	species in electrode reaction, Eq. [1]
$n_g = \nu_g z_g = -\nu_r z_r = -n_r$	
r	reversible ion (species)
R	gas constant; joule · deg^{-1} · $mole^{-1}$
$\hat{S}_1, \hat{S}_r, \hat{S}_g, \hat{S}_e$	Eastman entropy of electrolyte, r-ion, g-ion, electron; joule · deg^{-1} · (formula-wt)$^{-1}$
$\bar{S}$	(various subscripts) partial molal entropy; joule · deg^{-1} · (formula-wt)$^{-1}$
$\bar{\bar{S}}$	(various subscripts) transported entropy; $= \hat{S} + \bar{S}$
$\hat{S}_I$	entropy of current transfer, Eq. [7] and [8]
t	Hittorf transference number
T	temperature; deg Kelvin
u	ionic mobility; $m^2 \cdot sec^{-1} \cdot V^{-1}$
z	algebraic valence of ion
ϵ	"thermoelectric power" in the initial state; V · deg^{-1}
$\gamma_\pm$	molal activity coefficient
κ	specific electric conductivity; $ohm^{-1} \cdot m^{-1}$
μ_1	chemical potential of electrolyte; joule · (formula-wt)$^{-1}$
$\tilde{\underline{\mu}}$	electrochemical potential of ion
$\underline{\mu}$	total chemical potential (including temperature term)
$\nu_+, \nu_-, \nu_r, \nu_g$	number of cations, anions, r-ions, g-ions, into which electrolyte dissociates
$\nu = \nu_+ + \nu_-$	
π_{sm}	Peltier coefficient: heat absorbed from outside when current passes from solution to metal; joule · equivalent^{-1}
ψ	electrostatic (Volta) potential; V
Ω	coefficients of Eq. [5]

REFERENCES

1. A. J. de Bethune, *This Journal*, **107**, 829 (1960).
2. S. R. De Groot and P. Mazur, "Non-Equilibrium Thermodynamics," Chap. 13, Interscience Publishers, Inc., New York (1962).
3. J. N. Agar, in "Advances in Electrochemistry and Electrochemical Engineering," Vol. 3, Paul Delahay, Editor, Chap. 2, Interscience Publishers, New York (1963).
4. E. A. Guggenheim, "Thermodynamics," 5th ed., Chap. 13, North Holland Publishing Co., Amsterdam (1967).
5. R. Haase, "Thermodynamics of Irreversible Processes," Chap. 4, Addison-Wesley Publishing Co., Reading, Mass. (1969).
6. G. W. Murphy and R. C. Taber, International Symposium on Saline Water Conversion, National Acad. Sciences—National Research Council Publication *568*, p. 196, Washington, D. C. (1958).
7. J. Piguet, W. Kuhn, and H. Kuhn, *Helv. Chim. Acta*, **34**, 1183 (1951); G. W. Murphy, *Ind. Eng. Chem.*, **50**, 1181 (1958).
8. P. B. Lorenz, *J. Phys. Chem.*, **65**, 704 (1961).
9. Handbook of Chemistry and Physics, 45th ed., p. E-2. Chemical Rubber Publishing Co., Cleveland (1964).
10. International Critical Tables, Vol. 5, p. 229, McGraw-Hill Book Co., New York (1929).
11. R. A. Robinson and R. H. Stokes, "Electrolyte Solutions," pp. 461, 479, and 494. Butterworths Scientific Publications, London (1955).
12. H. S. Harned and B. B. Owen, "The Physical Chemistry of Electrolytic Solutions," 3d ed., pp. 697 and 699. Reinhold Publishing Corp., New York (1958).
13. R. Haase and H. Schönert, *Z. physik. Chem. (Frankfurt)*, **25**, 193 (1960).
14. M. I. Temkin and A. V. Khoroshin, *Zhur. Fiz. Khim.*, **26**, 500 (1952).
15. N. F. Mott and H. Jones, "The Theory of the Properties of Metal and Alloys," p. 316, Dover Publications, Inc. New York (1958).
16. P. B. Lorenz and A. S. Coolidge, *This Journal*, **112**, 1041 (1965).

Thermodynamic Properties of Molten Mixtures of Cobalt Chloride with Some Alkali Halides

Drannan C. Hamby[1] and Allen B. Scott*

Department of Chemistry, Oregon State University, Corvallis, Oregon

ABSTRACT

Thermodynamic properties including the activity coefficient, and the partial molar free energy, enthalpy, and entropy of mixing have been determined for the solute $CoCl_2$ in the solvents KCl, NaCl, LiCl, and 1:1 NaCl-KCl. Values of the properties were established by measuring the reversible emf of cells of the type

$$Co|CoCl_2, MCl|Cl_2,C$$

where M represents an alkali metal cation. Cell emf's were determined over a range of concentration from approximately 10^{-4} to as high as 8.3×10^{-1} mole fraction of solute and temperatures ranging from the melting points of the solvents to 900°C. Experimentally determined values of the quantity $\Delta G°$, the standard change in Gibbs function for the reaction

$$Co(c) + Cl_2(g) \rightarrow CoCl_2(l)$$

have been found to agree to within 1 kcal with values calculated on the basis of Brewer's (19) tabulation: the agreement with values calculated from other data in the literature is not as close, but is still within the stated limits of uncertainty of the data. Reference electrodes of the type

$$Ag|AgCl, MCl||$$

which utilized solid porcelain as a bridge, were immersed in the same melts and allowed continuous monitoring of chlorine electrode potentials as solute concentrations varied.

This report concerns electrochemical cells which may be designated

$$Co|CoCl_2(N), MCl\ (1 - N)|Cl_2, C$$

where

$$N = \frac{\text{moles solute}}{\text{moles solvent} + \text{moles solute}}$$

and MCl is KCl, NaCl, 1:1M NaCl-KCl or LiCl. Reference electrodes of the type

$$Ag|AgCl\ (N), MCl\ (1 - N)||$$

similar to those described by Lamb and Labrie (1) and Littlewood (2) were also placed in the melts of the cells described above. The solvent, MCl, was always the same on both sides of the membrane. This arrangement allowed continuous measurement of the quantity

$$\Delta E' = E'_{Ag} - E_{Ag}$$

where E'_{Ag} and E_{Ag} are emf's for the cell

$$Ag|AgCl\ (N_{AgCl}), MCl||MCl, CoCl_2(N_{CoCl_2})|Cl_2, C$$

in the respective cases $N_{CoCl_2} \neq 0$ and $N_{CoCl_2} = 0$. The magnitude of $\Delta E'$ is useful in determining the limits of $CoCl_2$ concentration over which one may convert potentials measured with the Ag reference electrode to potentials based on the chlorine reference electrode without correcting for junction effects.

Cell emf's were determined over the ranges of solute concentration and temperature shown in Table I.

Experimental data have been extrapolated to unit mole fraction of $CoCl_2$ to establish a basis for the calculation of solute activities and partial molar free energies, enthalpies, and entropies of mixing of $CoCl_2$ in the various solvents.

Experimental

Several experimental details have been described in a previous paper and will not be repeated here (3). These include cell envelope and chlorine electrode design; cleaning procedures; gas metering method; furnace, temperature control, and temperature measurement; emf measurements and instrumentation; measurement of thermoelectric emf's developed by electrode pairs; details concerning preparation of the Ag|AgCl reference electrodes; and source and treatment of metal electrodes.

The chlorine, argon, and HCl gases were Matheson Company "high purity." The HCl and chlorine gases were passed over $Mg(ClO_4)_2$ and hot (500°C) powdered graphite (Ultra Carbon UF-4-S) before entering the cell. The argon was passed over $Mg(ClO_4)_2$ or P_2O_5 and then over hot Cu at 500°C; the Cu was in the form of pellets formed by reduction of CuO with H_2. The gas delivery system was glass except for a few inches of rubber tubing near the cell top.

The salts used in this work were:

NaCl *and* KCl.—Reagent grade materials were further purified by passage through ion exchange columns (4, 5). The salts were then vacuum desiccated and oven dried at 120°C in air for 48 hr. After two moles of salt were weighed into the cell crucible, the salts were subjected to two days vacuum-oven treatment at temperatures up to 200°C and pressures of approximately 10^{-2} mm Hg. The crucible was then transferred to the cell, in air, and the salt was again held at a pressure of approximately 10^{-2} mm Hg while being slowly brought to near its melting point over a two day period. Fusion was carried out under dry HCl and the salt was then chlorinated in the presence of carbon (6).

Table I. Concentration and temperature ranges

Cell	Solvent	T, °C	Solute range, N_{CoCl_2}
I	KCl	800-900	9.7×10^{-4}-4.8×10^{-1}
II	NaCl	800-900	1.4×10^{-4}-5.3×10^{-1}
III	1:1 NaCl-KCl	700-900	5.0×10^{-4}-5.4×10^{-1}
IV	LiCl	700-800	1.1×10^{-3}-8.3×10^{-1}

[1] Present address: Linfield College, McMinnville, Oregon.
* Electrochemical Society Active Member.

LiCl.—Reagent grade was used. Drying procedure was the same as for NaCl and KCl.

$CoCl_2$.—Reagent grade $CoCl_2 \cdot 6H_2O$ was initially vacuum oven dried at approximately 10^{-2} mm Hg at 200°C. The salt was subsequently dried for at least 4 hr under flowing dry HCl at 400°C. It was then transferred to weighing bottles in a glove bag under nitrogen, capped, and stored in a desiccator over P_2O_5 until used.

A schematic diagram of the cell envelope and electrodes is shown in Fig. 1. Each cell contained one Ag|AgCl reference electrode housed in a ½ in. diameter McDanel PT 38 MV30 porcelain tube, a Vycor sheathed chromel-alumel thermocouple, two chlorine electrodes, and one 6 mm Vycor tube, constricted to a capillary at the lower end, which protected the Co electrode from direct attack by dissolved chlorine (7). The Co electrode was immersed in the melt several minutes before its use in an emf determination. At other times it was positioned above the melt inside the protection tube where it was protected by a dry argon atmosphere. Equalization of melt concentration inside and outside the metal electrode compartment was achieved by purging with dry argon and allowing the compartment to refill.

After solvent preparation was complete and the electrodes were immersed, continuous monitoring of the chlorine electrode potential with respect to the Ag|AgCl reference electrode was begun. Subsequently, solute was added, either by electrolysis at low concentrations ($N < 10^{-3}$) or as the bulk anhydrous $CoCl_2$ powder at higher concentrations; transfer to the cell involved brief exposure to the atmosphere. Cell emf's were measured as a function of temperature, the usual sequence being high, low, and intermediate temperatures.

At any nominal bath concentration three samples of the melt were taken through the vacuum port by means of an acid-washed, flamed, 6 mm Vycor tube. Cobalt in the samples was determined spectrophotometrically at 520 nm in aqueous solution as the soluble red complex anion formed by Co^{++} and nitroso-R salt (sodium 1-nitroso-2-hydroxynaphthalene-3,6-disulfonate) (8). Aqueous solutions of known concentration of $CoCl_2$ were used to establish a curve of absorbance per cm *vs.* concentration. The limit of error (99% confidence level) of bath concentration, based on deviations of the original 10 standardizing absorbances from the least squares line, and also on the deviations of 10 other absorbance values for samples made up from the original standard solution, is taken to be +3% of bath concentration. This estimate is based on dilutions to yield absorbance values in the range 0.2 to 0.7 cm^{-1}.

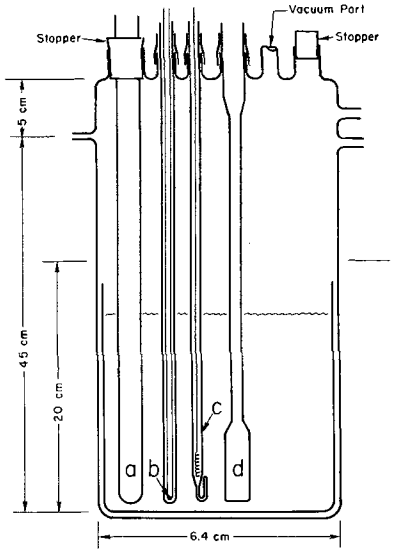

Fig. 1. Schematic diagram of cell envelope and electrodes: a, Ag reference electrode; b, thermocouple; c, Vycor protection tube; d, chlorine electrode.

Results

Reversibility of Co and chlorine electrodes was verified as reported previously (3). The treatment of the primary cell data is illustrated in Fig. 2 for cell III, solvent 1:1 NaCl-KCl. All emf's have been corrected for thermoelectric effects. In all cases the relationship of cell emf to temperature was assumed to be linear. The uncertainty in the determination of the slopes was estimated to be 5 x 10^{-5} V/degree. From Fig. 2 and similar plots cell emf's were read at constant temperature to prepare the curves shown in Fig. 3. Straight lines, giving the best fit by least

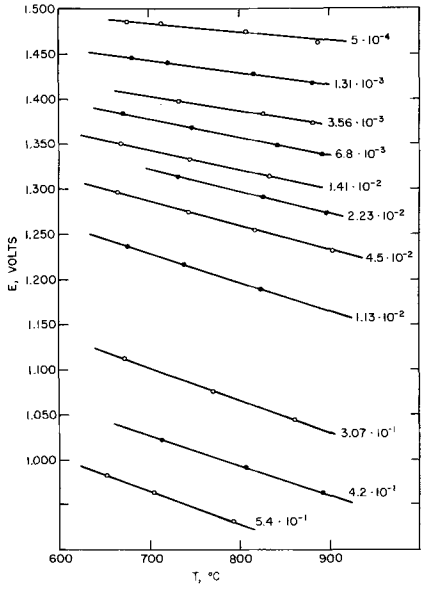

Fig. 2. Primary data for cell III, 1:1 NaCl-KCl solvent. Solute concentrations are indicated.

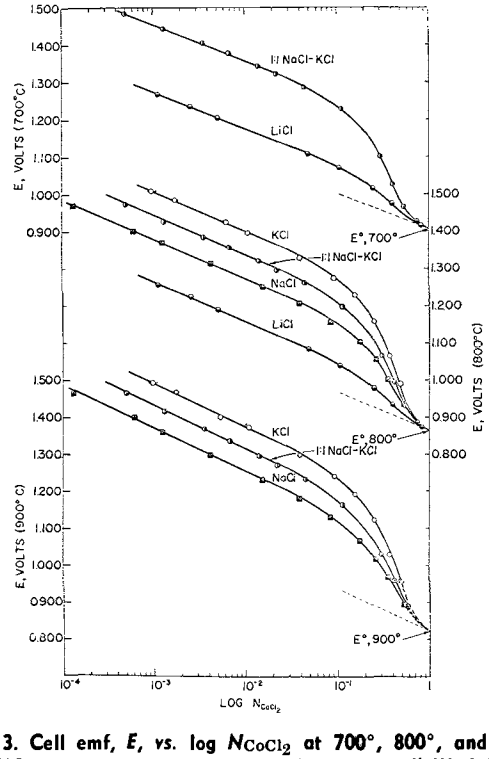

Fig. 3. Cell emf, *E*, *vs.* log N_{CoCl_2} at 700°, 800°, and 900°C. Cell I KCl solvent, ○; cell II, NaCl solvent, ■; cell III, 1:1 NaCl-KCl solvent, ◑; cell IV, LiCl solvent, ◒. Uncertainty in concentration is indicated by extended bars where the magnitude of the uncertainty exceeds the size of the symbol representing the data point. Dashed lines; Raoult's law slope.

Table II. Least squares treatment of the low concentration data
$Co|CoCl_2(N), MCl(1-N)|Cl_2,C$

Solvent, MCl	T, °C	Observed slope, $dE/d \log_{10} N$, V	Intercept, V	Nernst slope, V	σ, V*	n†
KCl	800	−0.106	1.192	−0.106	0.002	4
KCl	900	−0.116	1.146	−0.116	0.002	4
NaCl	800	−0.108	1.055	−0.106	0.003	6
NaCl	900	−0.116	1.020	−0.116	0.004	6
1:1 NaCl-KCl	700	−0.0969	1.164	−0.0965	0.002	6
1:1 NaCl-KCl	800	−0.105	1.127	−0.106	0.002	6
1:1 NaCl-KCl	900	−0.116	1.083	−0.116	0.002	6
LiCl	700	−0.0981	0.980	−0.0965	0.001	4
LiCl	800	−0.107	0.943	−0.106	0.002	4

* σ = standard deviation.
† n = number of data points.

squares analysis, for the low concentration data are shown, and the slopes of these lines are compared with the Nernst equation value, 2.303 $RT/2\mathbf{F}$, in Table II.

The data of Fig. 3 have been extrapolated to unit mole fraction, using Raoult's law to predict a limiting slope as $N \rightarrow 1$, in order to establish the values of E° at 700° and 800°C. The thermodynamic functions for the assumed cell reaction

$$Co(c) + Cl_2(g) \rightarrow CoCl_2 \text{ (in liq. soln. at conc. } N) \quad [1]$$

have been calculated on the basis of the definitions

$$\lim_{N \rightarrow 1} \frac{a}{N} = 1$$

$$a = N\gamma$$

where a, N, and γ refer to the solute, $CoCl_2$. Thus, the standard and reference states of the solute are chosen as the pure liquid with the properties of the pure liquid at the temperature of the experiment and one atmosphere total pressure. The standard state for Cl_2 was taken as the pure gas at one atmosphere pressure. Corrections for variation in barometric pressure and depth of immersion of the Cl_2 electrode were estimated to be definitely less than 1 mV and were neglected. The reference function for the metallic reactants is mole fraction and the reference and standard states for the metals are taken as the pure elements in their stable modification at one atmosphere total pressure, at 1 atm pressure, and the temperature of the experiment. Thus, for Co the stable phase and standard state is the β phase, stable from 718°K to 1400°K at 1 atm pressure (11). The partial molar Gibbs function of mixing and the partial molar enthalpy and entropy of mixing are given by

$$\overline{G} \equiv \Delta G - \Delta G^\circ = -2\mathbf{F}E - \Delta G^\circ$$
$$\overline{H} \equiv \Delta H - \Delta H^\circ$$
$$\overline{S} \equiv \Delta S - \Delta S^\circ = 2\mathbf{F}\left(\frac{\partial E}{\partial T}\right)_p - \Delta S^\circ$$

where ΔG°, ΔH°, and ΔS° are the standard changes for reaction [1]. The excess free energy of mixing is given by

$$\overline{G}^E \equiv \overline{G} - RT \ln N = RT \ln \gamma$$

The values of $\Delta G^\circ = -2\mathbf{F}E^\circ$ determined in this study are given in Table III along with values calculated from data in the literature (9, 10, 11).

The quantity $\Delta S^\circ = 18.5$ eu was determined by extrapolating a curve of ΔS *vs.* log N to $N = 1$; the scatter of the data indicate an uncertainty of at least ±2 eu in this quantity.

Emf values were read at selected concentrations from the curves of Fig. 3 and used to calculate the values of the functions given in Tables IV through VII. Values of $\overline{S}$ given in the table are smoothed values based on graphs of ΔS *vs.* log N_{CoCl_2} and the value of ΔS° mentioned above.

The Ag|AgCl reference electrodes incorporated in cells I through IV are described in Table VIII. E'_{Ag} was found to be independent of N_{CoCl_2} up to $N_{CoCl_2} = 10^{-2}$. The values of E'_{Ag} given in the tables are average values, corrected for thermoelectric emf's, taken over the duration of the experiments with $CoCl_2$ concentrations up to $N = 10^{-2}$. The maximum deviation from the average is given. Nonzero values of $\Delta E' = E'_{Ag} - E_{Ag}$ were observed at higher concentrations; these values are plotted in Fig. 4 along with similar data for nickel electrodes and the solute $NiCl_2$ taken from an earlier paper (3).

Discussion

The cobalt electrode has been studied in fused salts by Flengas and Ingrahm (12), Laitinen and Liu (13), Stromatt (14), and Trzebiatowski and Kisza (15). Flengas and Ingrahm used the reference electrode

$$Ag|AgCl\ (N), 1{:}1\ NaCl\text{-}KCl||$$

where the double line represents an asbestos fiber, to measure the potential of the Co electrode as a function of $CoCl_2$ concentration up to $N = 6.12 \times 10^{-2}$ at 710°C in 1:1 NaCl-KCl. In an independent experiment the potential of the reference was established with respect to the chlorine electrode in the same solvent. Thus, the cell emf's for the $CoCl_2$ formation cell may be calculated from Flengas and Ingrahm's data. Corrections for thermoelectric effects of 4-5 mV were included in a later paper; however, as discussed previously (3) for the case of Ni, the polarity of the correction is in doubt. Flengas and Ingrahm's earlier data points without thermoelectric correction for the Ag-Co couple all lie within ±6 mV of the least squares line given in Table II. The majority of the points lie above the least squares line, and it is believed that proper inclusion of the thermoelectric correction would leave the two sets of data in good agreement.

Stromatt has carried out a rather extensive but unpublished study of solvent effects on nickel and cobalt electrodes at fixed solute concentration. Measurements of cobalt electrode potentials with respect to a chlorine electrode were taken at or near 0.1M and normalized to 0.1M at 670°C. Solvent composition was varied over wide ranges for the mixtures NaCl-KCl, LiCl-KCl, and LiCl-NaCl; however, measurements were not

Table III. Standard free energy of formation, $CoCl_2(l)$

Temp, °C	−ΔG°, kcal a	b	c	d	e
700		45.9	46.7	41.9	41.8
800	45.1	43.6	44.8	39.3	40.0
900		41.3	43.0	37.0	38.0
1000	41.5	39.1	41.2		

Column a, Hamer *et al.* (9); b, Kubaschewski *et al.* (10); c, Wicks and Block (11); the β phase of Co was assumed present at temperatures above 718°K and the heat capacity of liquid $CoCl_2$ was estimated to be 24.2 cal/mole deg, the mean of the values given for liquid $NiCl_2$ and $FeCl_2$ (10); d, calculated from data of ref. (19), using linear interpolation of the free energy function; e, this study.

Table IV. KCl solvent, cell I

N_{CoCl_2}	E (volts)		$\bar{G}$ (kcal)		$\bar{G}^E$ (kcal)		γ		$\bar{S}$ (eu)	$\bar{H}$ (kcal)
	800°C	900°C	800°C	900°C	800°C	900°C	800°C	900°C	800°C	800°C
0.00100	1.507	1.491	−29.7	−30.9	−15.0	−14.8	9.01×10^{-4}	1.78×10^{-3}	11	18
0.00300	1.457	1.435	−27.4	−28.3	−15.0	−14.7	8.92×10^{-4}	1.80×10^{-3}	9	18
0.00700	1.418	1.393	−25.6	−26.3	−15.0	−14.8	8.92×10^{-4}	1.78×10^{-3}	7	18
0.0200	1.370	1.339	−23.3	−23.9	−15.0	−14.7	8.78×10^{-4}	1.81×10^{-3}	5	18
0.0500	1.323	1.288	−21.2	−21.5	−14.8	−14.5	9.72×10^{-4}	1.98×10^{-3}	3	18
0.0700	1.299	1.263	−20.1	−20.3	−14.4	−14.1	1.16×10^{-3}	2.33×10^{-3}	2	18
0.100	1.272	1.235	−18.8	−19.0	−13.9	−13.7	1.46×10^{-3}	2.83×10^{-3}	2	17
0.150	1.234	1.196	−17.1	−17.3	−13.0	−12.8	2.23×10^{-3}	4.08×10^{-3}	1	16
0.200	1.197	1.160	−15.4	−15.6	−11.9	−11.8	3.72×10^{-3}	6.26×10^{-3}	1	14
0.250	1.160	1.125	−13.7	−14.0	−10.7	−10.8	6.62×10^{-3}	1.00×10^{-2}	1	13
0.300	1.120	1.090	−11.8	−12.4	−9.3	−9.6	1.31×10^{-2}	1.66×10^{-2}	1	11
0.350	1.081	1.056	−9.0	−10.8	−6.8	−8.3	4.18×10^{-2}	2.80×10^{-2}	1	9
0.400	1.044	1.023	−8.3	−9.3	−6.4	−7.1	5.10×10^{-2}	4.71×10^{-2}	0	9
0.500	0.973	0.947	−5.0	−5.8	−3.5	−4.1	1.94×10^{-1}	1.84×10^{-1}	0	5
0.700	0.891	0.862	−1.2	−1.8	−0.4	−1.0	8.17×10^{-1}	6.65×10^{-1}	0	1
0.900	0.868	0.831	−0.2	−0.4	0	−0.1	1	9.6×10^{-1}	0	0
1.00	0.864	0.822	0	0	0	0	1	1	0	0

Table V. NaCl solvent, cell II

N_{CoCl_2}	E (volts)		$\bar{G}$ (kcal)		$\bar{G}^E$ (kcal)		γ		$\bar{S}$ (eu)	$\bar{H}$ (kcal)
	800°C	900°C	800°C	900°C	800°C	900°C	800°C	900°C	800°C	900°C
0.00100	1.379	1.372	−23.8	−25.4	−9.0	−9.3	1.44×10^{-2}	1.88×10^{-2}	14	9
0.00300	1.329	1.316	−21.5	−22.8	−9.1	−9.3	1.42×10^{-2}	1.89×10^{-2}	12	8
0.00700	1.290	1.273	−19.7	−20.8	−9.1	−9.2	1.42×10^{-2}	1.91×10^{-2}	10	9
0.0200	1.242	1.221	−17.4	−18.4	−9.1	−9.3	1.40×10^{-2}	1.97×10^{-2}	8	9
0.0500	1.198	1.169	−15.4	−16.0	−9.0	−9.0	1.46×10^{-2}	2.08×10^{-2}	6	9
0.0700	1.178	1.147	−14.5	−15.0	−8.8	−8.8	1.59×10^{-2}	2.31×10^{-2}	5	9
0.100	1.153	1.120	−13.3	−13.8	−8.4	−8.4	1.92×10^{-2}	2.74×10^{-2}	5	8
0.150	1.120	1.083	−11.8	−12.0	−7.8	−7.6	2.62×10^{-2}	3.81×10^{-2}	4	8
0.200	1.091	1.052	−10.5	−10.6	−7.0	−6.9	3.69×10^{-2}	5.28×10^{-2}	3	7
0.250	1.063	1.023	−9.2	−9.3	−6.2	−6.0	5.38×10^{-2}	7.51×10^{-2}	3	6
0.300	1.032	0.977	−7.7	−8.1	−5.2	−5.3	8.81×10^{-2}	1.05×10^{-1}	2	6
0.350	1.002	0.972	−6.4	−6.9	−4.1	−4.5	1.45×10^{-1}	1.47×10^{-1}	2	4
0.400	0.977	0.950	−5.2	−5.9	−3.3	−3.8	2.17×10^{-1}	1.99×10^{-1}	2	3
0.500	0.940	0.909	−3.5	−4.0	−2.0	−2.3	3.97×10^{-1}	3.66×10^{-1}	1	3
0.700	0.890	0.852	−1.2	−1.4	−0.4	−0.5	8.50×10^{-1}	8.11×10^{-1}	1	0
0.900	0.868	0.830	−0.2	−0.4	0	−0.1	1.00	9.71×10^{-1}	0	0
1.00	0.864	0.822	0	0	0	0	1.00	1.00	0	0

Table VI. 1:1 NaCl-KCl solvent, cell III

N_{CoCl_2}	E (volts)			$\bar{G}$ (kcal)			$\bar{G}^E$ (kcal)			γ			$\bar{S}$ (eu)	$\bar{H}$ (kcal)
	700°C	800°C	900°C	700°C	800°C	900°C	700°C	800°C	900°C	700°C	800°C	900°C	800°C	800°C
0.00100	1.454	1.446	1.433	25.2	26.8	28.2	11.9	12.1	12.1	2.16×10^{-3}	3.39×10^{-3}	5.62×10^{-3}	12	14
0.00300	1.407	1.394	1.377	23.1	24.4	25.6	11.8	12.1	12.1	2.21×10^{-3}	3.48×10^{-3}	5.67×10^{-3}	10	14
0.00700	1.373	1.355	1.335	21.5	22.6	23.7	11.9	12.1	12.1	2.19×10^{-3}	3.48×10^{-3}	5.60×10^{-3}	9	13
0.0200	1.328	1.307	1.282	19.4	20.4	21.2	11.9	12.1	12.1	2.23×10^{-3}	3.44×10^{-3}	5.58×10^{-3}	6	14
0.0500	1.283	1.258	1.227	17.3	18.2	18.7	11.9	11.8	11.7	2.55×10^{-3}	3.97×10^{-3}	6.63×10^{-3}	4	14
0.0700	1.262	1.235	1.202	16.4	17.1	17.5	11.2	11.5	11.3	3.01×10^{-3}	4.66×10^{-3}	7.78×10^{-3}	4	13
0.100	1.238	1.208	1.172	15.3	15.9	16.1	10.8	11.0	10.7	3.73×10^{-3}	5.87×10^{-3}	9.87×10^{-3}	3	13
0.150	1.202	1.172	1.132	13.6	14.2	14.3	9.9	10.2	9.9	5.87×10^{-3}	8.55×10^{-3}	1.45×10^{-2}	2	12
0.200	1.169	1.138	1.097	12.1	12.6	12.7	9.0	9.2	9.1	9.70×10^{-3}	1.34×10^{-2}	2.01×10^{-2}	2	11
0.250	1.137	1.105	1.065	10.6	11.1	11.2	7.9	8.2	8.0	1.66×10^{-2}	2.18×10^{-2}	3.26×10^{-2}	1	10
0.300	1.102	1.070	1.033	9.0	9.5	9.7	6.7	6.9	6.9	3.21×10^{-2}	3.86×10^{-2}	5.14×10^{-2}	1	9
0.350	1.068	1.037	1.044	7.4	8.0	8.4	5.4	5.7	5.9	6.13×10^{-2}	6.78×10^{-2}	7.83×10^{-2}	1	7
0.400	1.031	1.007	0.977	5.7	6.6	7.2	4.0	4.6	5.0	1.30×10^{-1}	1.14×10^{-1}	1.14×10^{-1}	1	6
0.500	0.979	0.948	0.922	3.3	3.9	4.6	1.9	2.3	2.9	3.68×10^{-1}	3.34×10^{-1}	2.84×10^{-1}	1	3
0.700	0.930	0.890	0.857	1.1	1.2	1.6	0.3	0.4	0.7	8.45×10^{-1}	8.34×10^{-1}	7.36×10^{-1}	0	1
0.900	0.911	0.868	0.830	0.2	0.2	0.4	0.0	0.0	0.1	1	1	9.71×10^{-1}	0	0
1.00	0.907	0.864	0.822	0.0	0.0	0.0	0.0	0.0	0.0	1	1	1	0	0

Table VII. LiCl solvent, cell IV

N_{CoCl_2}	E (volts)		$\bar{G}$ (kcal)		$\bar{G}^E$ (kcal)		γ		$\bar{S}$ (eu)	$\bar{H}$ (kcal)
	700°C	800°C	700°C	800°C	700°C	800°C	700°C	800°C	800°C	800°C
0.00100	1.274	1.265	−16.9	−18.5	3.6	3.8	0.158	0.170	13	5
0.00300	1.227	1.213	−14.8	−16.1	3.5	3.7	0.162	0.175	11	4
0.00700	1.192	1.173	−13.2	−14.3	3.6	3.7	0.160	0.178	9	5
0.0200	1.148	1.125	−11.1	−12.0	3.6	3.7	0.160	0.175	7	5
0.0500	1.109	1.083	−9.3	−10.1	3.5	3.7	0.161	0.175	5	5
0.0700	1.093	1.065	−8.6	−9.3	3.4	3.6	0.169	0.184	5	4
0.100	1.075	1.044	−7.8	−8.3	3.3	3.4	0.182	0.203	4	4
0.150	1.052	1.017	−6.7	−7.1	3.0	3.0	0.210	0.244	3	4
0.200	1.032	0.997	−5.8	−6.1	2.7	2.3	0.253	0.334	2	4
0.250	1.015	0.978	−5.0	−5.3	2.3	2.0	0.305	0.386	2	3
0.300	0.999	0.962	−4.2	−4.5	1.9	1.7	0.374	0.455	2	3
0.350	0.986	0.947	−3.6	−3.8	1.6	1.4	0.435	0.519	1	3
0.400	0.974	0.933	−3.1	−3.2	1.3	1.1	0.507	0.586	1	2
0.500	0.952	0.912	−2.1	−2.2	0.7	0.6	0.698	0.772	1	1
0.700	0.926	0.886	−0.9	−1.0	0.2	0.1	0.927	0.970	0	1
0.900	0.911	0.868	−0.2	0.2	0	0	1	1	0	0
1.00	0.907	0.864	0	0	0	0	1	1	0	0

Table VIII. Ag|AgCl, MCl reference electrodes

Cell	N_{AgCl}	Solvent	E'_{Ag} (volts) 700°	800°
I	5.5×10^{-3}	KCl		1.131 ± 4 mV
II	6.0×10^{-2}	NaCl		1.030 ± 2 mV
III	6.6×10^{-3}	1:1 NaCl-KCl	1.074 ± 2 mV	1.074 ± 2 mV
IV	7.3×10^{-2}	LiCl	0.975 ± 2 mV	0.969 ± 2 mV

carried out utilizing the pure alkali metal chlorides as solvents. Comparison of Stromatt's data with the present data require, in the case of 1:1 NaCl-KCl, both a temperature and a thermoelectric adjustment of data. Temperature coefficients of emf from the present study and Handbook (17) thermoelectric values were used to make the necessary corrections. The value 1.378V at $N_{CoCl_2} = 6.63 \times 10^{-3}$ calculated from Stromatt's data is in good agreement with that found in the present study, 1.375V.

Trzebiatowski and Kisza (15) have studied the cells

$$Co|CoCl_2(N), MCl\ (1 - N)\,|Cl_2,C$$

where MCl is KCl, NaCl, or LiCl. Five concentrations were studied in the case of KCl, three for NaCl, and only two for LiCl. Both the cell emf's and temperature coefficients may be compared with the present work. The emf values reported by Trzebiatowski and Kisza are higher in all cases than those reported here; the magnitude of the disagreement ranges from 7 to over 30 mV. Trzebiatowski and Kisza (31) made no corrections for thermoelectric effects, the magnitude of which would depend on experimental arrangement and can, in this case, be as high as 20 to 30 mV. Correction for thermoelectric effects might improve the agreement between the two sets of data; however, it must also be noted that their slopes, $dE/d \log N$, for KCl deviate rather strongly from the Nernst values, indicating the possibility of mixed electrode reactions. Values of dE/dT determined by Trezebiatowski and Kisza are uniformly lower than those determined in this study, the two sets of data differing by a factor of about 1.5.

The apparent lack of agreement between certain values of $\Delta G°$ reported in Table III requires comment. Values in columns a, b, and c are calculated from thermochemical data and are all based on $\Delta H°_{298} = -77.8$ kcal, given by Rossini (18). The uncertainty in this quantity is given by Kubaschewski (10) as ±4 kcal. Brewer *et al.* (19) obtained $\Delta H°_{298} = -74 \pm 1$ kcal, using the heat of solution given by Bichowsky and Rossini (20) and the data of Jellinek and Uloth (21) for the heat of reaction of $CoCl_2$ with H_2. Our directly determined values of $\Delta G°$, which are generally about 4 kcal less negative than those in columns a, b, and c, support the values of $\Delta H°_{298}$ given by Brewer *et al.* At the same time the agreement of our values with the others listed is, in general, not outside the uncertainty quoted for Rossini's $\Delta H°_{298}$.

Quite clearly, additional differences appear among the values of $\Delta G°$, arising from the considerable spread in the values chosen for the heat capacity and heat of fusion of $CoCl_2$.

Egan (22), from measurements on the cell

$$Co|CoCl_2(c)|BaCl_2(c), AgCl\ (N = 0.2)\,|Ag$$

found $\Delta G°$ at 400° and 450° to be, respectively, 2.7 and 2.5 kcal less negative than that calculated by Wicks and Block, which again suggests that $\Delta H°_{298}$ should be less negative than the value given by Rossini.

A small error may arise in the present work from the dilution of Cl_2 by vapors of the melt. At 800°C the vapor pressures of NaCl, KCl, and $CoCl_2$ are 4.5×10^{-4}, 9.1×10^{-4}, and 4.0×10^{-2} atm, respectively; at 900°C the pressures are, respectively, 2.7×10^{-3}, 5.0×10^{-3}, and 1.7×10^{-1} atm (23, 24, 25). No data are available for mixtures. The error from this source would increase with solute concentration and temperature. Two cases are considered: $N = 0.83$ at 800°C and $N = 0.5$ at 900°C. Assuming Raoult's law to apply (which seems unlikely as $CoCl_2$ is known to form complexes with the alkali halides which should markedly reduce its vapor pressure), and taking $a_{Cl_2} = P_{Cl_2}$, the errors arising from dilution of Cl_2 by $CoCl_2$ vapor would be 1.6 and 4.5 mV, respectively. The latter amount is an upper limit for the error from this source, and it has been assumed that at lower temperatures and concentrations the error could be disregarded. No attempt was made to correct the data, since vapor pressures over the mixtures are not known.

The negative deviations of the solute from Raoult's law observed in this work follow a well established pattern with respect to solvent cation, *i.e.*, the magnitude of $\overline{G}^E$ becomes greater in the order LiCl < NaCl < 1:1 NaCl-KCl < KCl. In the case of the solute $CoCl_2$ it is reasonable to attribute the observed deviations, at least at low concentrations, to the formation of the tetrahedral complex anion, $CoCl_4^=$. The existence of this ion has been demonstrated spectroscopically at low concentration in a number of fused chlorides (26-28). There is also evidence (27) which would indicate tetrahedral coordination for this particular solute even at high concentrations.

A comparison of the degree of departure from ideality of the solutes $NiCl_2$, $CoCl_2$, and $MgCl_2$, as measured by $\overline{G}^E$, is of interest. Values of $\overline{G}^E$ for these solutes in KCl at 800° are given in Fig. 5. At concentrations below $N = 0.1$ there are significant differences in the degree of departure of the solutes from ideality. $CoCl_2$ exhibits the greatest departure followed by $NiCl_2$ and $MgCl_2$. The same order is exhibited by these solutes in the solvent 1:1 NaCl-KCl at 800°C (13, 16). It is interesting to note that the order, $CoCl_2 > NiCl_2 > MgCl_2$, is reflected by the hexacoordinate crystal radii of Co (II), Ni (II), and Mg (II). These radii are 0.72, 0.69, and 0.66Å, respectively (32). However, it is not suggested that the observed ordering should be attributed simply or even primarily to differences in ionic radii.

In Fig. 6 the variation of the partial molar entropy of mixing of $CoCl_2$, $\overline{S}$, is shown as a function of log N_{CoCl_2}. The solid curve corresponds to the equation

$$\overline{S} = -R \ln N$$

that is, the value predicted by ideal mixing (Raoult's

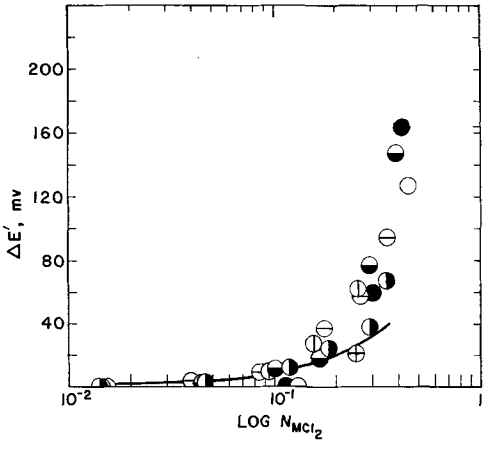

Fig. 4. Values of $\Delta E'_{Ag} = E'_{Ag} - E_{Ag}$ vs. log N_{RCl_2}, 800°C

Solute, RCl_2	Solvent MCl	Symbol
$NiCl_2$	1:1 NaCl-KCl	○
$NiCl_2$	LiCl	◑
$NiCl_2$	KCl	◒
$CoCl_2$	KCl	⊖
$CoCl_2$	NaCl	⊖
$CoCl_2$	1:1 NaCl-KCl	●
$CoCl_2$	LiCl	⊕

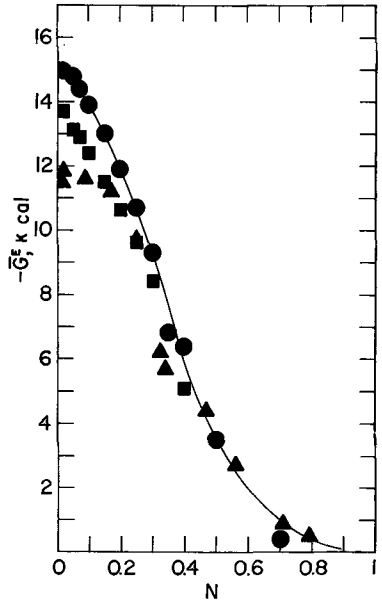

Fig. 5. Excess partial molar free energy, $\bar{G}^E$, vs. mole fraction for the solutes $MgCl_2$ ▲, $NiCl_2$, ■, and $CoCl_2$, ●, in KCl at 800°C. The $MgCl_2$ data are those of Niel and Clark (16).

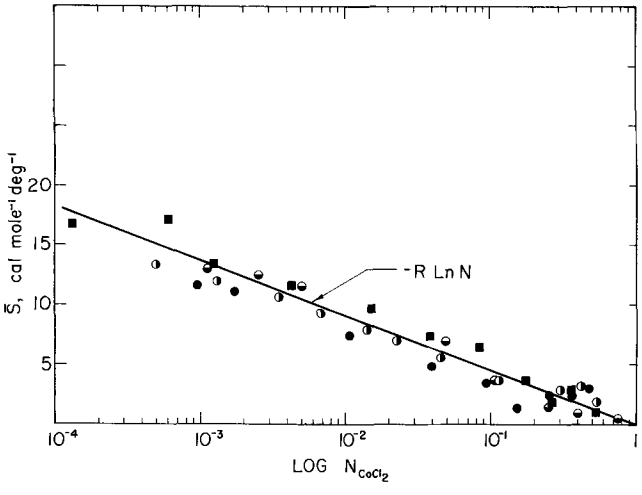

Fig. 6. Partial molar entropy of mixing for $CoCl_2$, $\bar{S}$, as a function of log N_{CoCl_2}. Solid line is $\bar{S} = -R \ln N$. Symbols are related to cells and solvents as in Fig. 3.

law) or the Temkin model (30).[2] Within the uncertainty in $\bar{S}$, the solutions follow this relation. The entropy of mixing for a number of models have been discussed previously for $NiCl_2$ solutions (3) and the conclusion was reached that, while some models (such as the vacancy model) may be ruled out on the basis of the observed entropy of mixing, the data are insufficiently accurate to allow one to select unambiguously the most representative model.

The calculation of the potential of a particular metal electrode, R, with respect to the chlorine electrode from data available on the cells

$$R|RCl_2(N), MCl(1-N)||AgCl(N'), MCl(1-N')|Ag$$
$$Ag|AgCl(N'), MCl(1-N')||MCl|Cl_2,C$$

is frequently of interest. Detailed consideration of cell reactions (29) indicates that an error $\Delta E'$, defined above, is involved in the calculated potential.

Provided the two surfaces of the membrane each act as an electrode reversible to the M^+ ion (which would be expected, for example if transport through the membrane were solely by means of the M^+ ion), it may be shown that

$$\Delta E' = -(RT/F) \ln a_{MCl}$$

where a_{MCl} is the activity of MCl in the RCl_2 (N), MCl ($1 - N$) solution. The solid curve in Fig. 4 gives the value of $\Delta E'$ calculated from this relation assuming that $a_{MCl} = N_{MCl}$. Experimental results for the solutes $CoCl_2$ and $NiCl_2$ are in good agreement at $N_{RCl_2} < 5 \times 10^{-2}$ and in fair agreement in most of the solvents up to $N_{RCl_2} = 0.1$.

If this result, valid for both $NiCl_2$ and $CoCl_2$, is taken also to be valid for $FeCl_2$, the Ag|AgCl,MCl|| reference electrode may be used reliably in place of the chlorine electrode to study low-concentration solutions of $FeCl_2$, which otherwise would undergo oxidation by chlorine. In this case E_{Ag} may be determined (*i.e.*, with $N_{FeCl_2} = 0$) by comparison with the chlorine electrode; E'_{Ag} may then be taken as

$$E'_{Ag} = E_{Ag} - (RT/F) \ln N_{MCl}$$

for $N_{FeCl_2} \lesssim 0.1$.

Acknowledgments

The initial encouragement by W. J. Kroll to undertake this research, and his continued interest is acknowledged with thanks. The authors are also indebted to D. A. Nissen, K. Stern, R. D. Walker, and Robert Stromatt for useful discussions and information, to Linda Schuerman for help in salt preparation, and to the Tektronix Foundation and Linfield Research Institute for valued support.

Manuscript submitted July 22, 1969; revised manuscript received Nov. 10, 1969. This was Paper 189 presented at the New York Meeting of the Society, May 4-9, 1969.

Any discussion of this paper will appear in a Discussion Section to be published in the December 1970 JOURNAL.

REFERENCES

1. R. J. Labrie and V. A. Lamb, *This Journal*, **106**, 896 (1959).
2. R. Littlewood, *Electrochim. Acta*, **3**, 270 (1961).
3. D. C. Hamby and A. B. Scott, *This Journal*, **115**, 704 (1968).
4. W. J. Fredericks, F. E. Rosztoczy, and J. Hatchett, Final Report, SRI Project No. PAU-3523, Menlo Park (1963).
5. W. J. Fredericks, L. W. Schuerman, and L. C. Lewis, Final Report, AF-AFOSR-217-63, Project Task: 9762-02, Oregon State University, (1966).
6. D. A. Nissen, Ph.D. Thesis, Oregon State University (1964).
7. J. Greenberg and B. R. Sundheim, *J. Chem. Phys.*, **29**, 1029 (1958).
8. F. Snell and C. Snell, "Colorimetric Methods of Analysis," Vol. II, A. D. Van Nostrand, New York (1958).
9. W. J. Hamer, M. S. Malmberg, and B. Rubin, *This Journal*, **103**, 8 (1956).
10. O. Kubaschewski, E. Evans, and C. B. Alcock, "Metallurgical Thermochemistry," Pergamon Press, New York (1967).
11. C. Wicks and F. Block, *U.S. Bur. Mines Bull. 605*, 85 (1963).
12. S. N. Flengas and T. R. Ingrahm, *Can. J. Chem.*, **35**, 1139 (1957).
13. H. A. Laitinen and C. Liu, *J. Am. Chem. Soc.*, **80**, 1015 (1958).
14. R. Stromatt, Battelle Northwest, Personal Communication (1966).
15. W. Trzebiatowski and A. Kisza, *Bul. De L'Acad. Polonaise des Sci., Series des Sci. Chem.*, **9**, 605 (1961).
16. D. E. Neil and H. M. Clark, *J. Chem. Eng. Data*, **10**, 21 (1965).
17. American Institute of Physics Handbook, pp. 4-8, McGraw-Hill Book Co., New York (1957).
18. F. D. Rossini *et al.*, *Natl. Bur. Std. U.S. Circ. 500.*
19. L. Brewer *et al.*, "The Thermodynamic Properties of the Halides," in "Chemistry and Metallurgy of Miscellaneous Materials: Thermodynamics, Vol.

[2] The same relationship, modified by an added constant, may be shown to hold if the solute obeys Henry's law over a range of temperatures.

IV-19B," L. L. Quill, Editor, p. 135, McGraw Hill Book Co., New York (1950).
20. F. R. Bichowsky and F. D. Rossini, "The Thermochemistry of the Chemical Substances," Reinhold, Publishing Co., New York (1936).
21. K. Jellinek and R. Uloth, *Z. Physik. Chem.*, **119**, 161 (1926).
22. J. J. Egan, U. S. A. E. C. BNL-9343.
23. J. L. Barton and H. Bloom, *J. Phys. Chem.*, **60**, 1413 (1956).
24. H. Bloom *et al.*, *J. Am. Chem. Soc.*, **80**, 2044 (1958).
25. H. Schafer, *Z. Anorg. u. Allgem. Chem.*, **278**, 300 (1955).
26. D. M. Gruen and R. L. McBeth, *Pure Appl. Chem.*, **6**, 23 (1963).
27. C. A. Angell and D. M. Gruen, *J. Inorg. Nucl. Chem.*, **29**, 2243 (1967).
28. H. A. Øye and D. M. Gruen, *Inorg. Chem.*, **4**, 1173 (1965).
29. D. C. Hamby, Ph.D. Thesis, Oregon State University (1968).
30. T. Førland, *Discussions Faraday Soc.*, **32**, 122 (1961).
31. W. Trzebiatowski, Polska Akademia Nauk, Instytut Niskich Temperatur, Wrocław, Poland, Personal communication (1969).
32. L. H. Ahrens, *Geochim. Cosmochim. Acta*, **2**, 155 (1952).

Thermodynamics of Lithium Iodide in Anhydrous Dimethyl Sulfoxide

Mark Salomon

National Aeronautics & Space Administration, Electronics Research Center, Cambridge, Massachusetts

ABSTRACT

The thermodynamic properties of LiI in dimethyl sulfoxide have been determined by the emf method. Results are consistent with the concept that anions are less solvated in the aprotic solvent, but that the order of increasing solvation is $Cl^- < Br^- < I^-$. The significance of individual ionic solvation energies is (qualitatively) discussed.

Previous thermodynamic studies in dimethyl sulfoxide (DMSO) have involved either the LiCl (1-3) or LiBr (4) salt-solvent systems. The present work extends the measurements to the LiI-DMSO system. The work was carried out by emf measurements on the cell

$$\text{Li}|\text{LiI-DMSO}|\text{TlI, Tl(Hg)} \qquad [1]$$

These emf measurements were transferred to emf's for the solid thalium cell

$$\text{Li}|\text{LiI-DMSO}|\text{TlI, Tl} \qquad [2]$$

by reference to the cell

$$\text{Tl}|\text{Tl}^+|\text{Tl(Hg)} \qquad [3]$$

The relation between the emf's of cells [1]-[3] is

$$\mathcal{E}_2 = \mathcal{E}_1 - \mathcal{E}_3$$

and the values for $\mathcal{E}_3$ as a function of temperature were obtained from the data of Richards and Daniels (5).

The standard potential of cell [2], $\mathcal{E}_2^\circ$, was obtained from

$$\mathcal{E}_2 = \mathcal{E}_2^\circ - \frac{2RT}{\mathbf{F}} \ln (m_\pm \gamma_\pm) \qquad [4]$$

where $\gamma_\pm$ was evaluated from (6)

$$\ln \gamma_\pm = -\frac{A\, m^{1/2}}{1 + m^{1/2}} + 2\beta m \qquad [5]$$

In Eq. [4] and [5], $m_\pm$ and $\gamma_\pm$ are the mean molalities and activity coefficients, respectively; A is the Debye-Hückel constant; β is a constant and all other terms have their usual significance [*e.g.*, see ref. (4)].

Finally by reference to the cell

$$\text{Li}|\text{Li}^+|\text{Tl}^+|\text{Tl} \qquad [6]$$

the solubility product for TlI can be calculated from

$$\ln K\,\text{sp (TlI)} = (\mathcal{E}_2^\circ - \mathcal{E}_6^\circ)\mathbf{F}/RT \qquad [7]$$

In DMSO at 25°C, $\mathcal{E}_6^\circ = 2.641$V (4).

Experimental

All cells, solutions, and equipment used were identical to those reported earlier (4, 7). Reagent grade $LiI \cdot 3H_2O$ was dried at 240°C under vacuum for 24 hr [cf. ref. (11), (12)]. One batch of 2.73% Tl (by weight) amalgam was used for all the runs. The potentials of cell [1] were recorded over a period of 3 to 4 days and a constant potential (to within 0.1 mV) was usually attained on the second day. Below solution concentrations of 0.1*M*, the emf's of cell [1] exhibited continual drift, decreasing slowly over the entire time the cells were studied. Stable potentials were not reached, and no data are reported for these small concentrations.

Results

The cells were studied at 25°, 35°, and 45°C. To evaluate $\mathcal{E}_2^\circ$, the Guggenheim approximation was used (6). This approximation was found to fit other very similar systems quite well (1-4, 7, 8). In this method a plot of $\mathcal{E}'$ *vs.* m is extrapolated to infinite dilution. Here $\mathcal{E}'$ is defined as

$$\mathcal{E}' = \mathcal{E}_2 + \frac{2RT}{\mathbf{F}}\left\{\ln m_\pm - \frac{A\, m^{1/2}}{1 + m^{1/2}}\right\}$$

A typical plot is shown in Fig. 1 for the data at 25°C. Results for all three temperatures are shown in Table I. Energies and enthalpies in Table I were obtained as follows: calculated $\mathcal{E}_2^\circ$ values were fitted to a second order polynomial, *i.e.*

$$\Delta G_2^\circ\ (\text{DMSO}) = -39.313 - 0.11172 \cdot T + 2.1637 \cdot 10^{-4} \cdot T^2\ \text{kcal/mole}$$

and ΔH_2° and ΔS_2° are obtained by differentiating this relation with respect to temperature. A similar treatment for cell [2] in aqueous solutions (9) gives the following relation

$$\Delta G_2^\circ\ (H_2O) = -44.771 - 0.04387 \cdot T + 5.7264 \cdot 10^{-5} \cdot T^2\ \text{kcal/mole}$$

Activity coefficients of LiI for the three temperatures are given in Table II. These $\gamma_\pm$ values were calculated

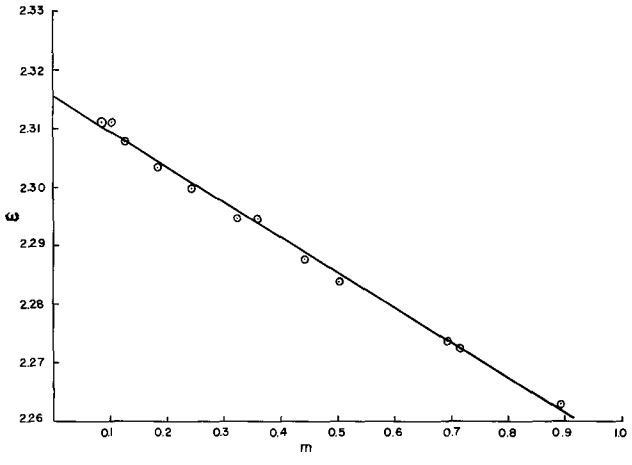

Fig. 1. Plot of E' vs. molality at 25°C

from Eq. [4] using the $\mathcal{E}_2°$ values listed in Table I. Finally a value for the TlI solubility product was calculated from Eq. [7]. It is found that K_{sp} (TlI) $= 3.1 \cdot 10^{-6}$, and this value can be compared to K_{sp} (TlBr) $= 6.0 \cdot 10^{-7}$ (4) and K_{sp} (TlCl) $= 5.9 \cdot 10^{-7}$ (3).

Discussion

The solvation of ions in dipolar aprotic solvents differ significantly from aqueous systems (10, 4, 7, 8). Evidence for specific ion properties comes mainly from solubilities (10) and free-energy and enthalpy data (4, 7, 8, 11, 12). Significant insight into the nature of solvation processes in DMSO can be achieved by comparing free energies, enthalpies, and entropies of transfer, $\Delta G_t°$, $\Delta H_t°$, and $\Delta S_t°$, respectively, from water to DMSO. Comparisons of these quantities involving many solvents has been made elsewhere (4, 7, 8). Tables III and IV list those quantities for the transfer of the Li-halide salts from water to DMSO.

Inspection of Tables III and IV reveal information supporting previous interpretations (4, 7, 8, 10) that the degree of solvation of the anion increases in the order $Cl^- < Br^- < I^-$. This is dramatically demonstrated by plotting ln $\gamma_\pm$ *vs.* $m^{1/2}$; such a plot is shown in Fig. 2. The shape of these plots are very similar to the aqueous data [*e.g.*, see (13)] with the exception that (*i*) the aqueous data is shifted upward by about 0.2 — 0.4 lnγ units and, (*ii*) the lnγ plot for LiCl in H_2O shows a minimum at about $m = 0.4$ whereas no such minimum is observed for LiCl in DMSO. Since this minimum is associated with solvation effects (13),

Table I. Thermodynamic quantities for cell [2]*

°C	$\Delta G_{2,m}°$	β	$\Delta H_{2,m}°$	$\Delta S_{2,m}°$	$\mathcal{E}_{2,m}°$
25	−53.39	0.581	−58.55	−17.30	2.3152
35	−53.19	0.578	−59.86	−21.63	2.3065
45	−52.96	0.558	−61.21	−25.96	2.2964

* All data in this table are based on molal scale. $\mathcal{E}°$ is in volts; $\Delta G°$ and $\Delta H°$ are in kcal mole^{-1}, $\Delta S°$ is in eu, and β is in kg/mole.

Table II. Mean molal activity coefficients of LiI in DMSO

m	$\gamma_\pm$ 25°C	35°C	45°C
0.10270	0.5644	0.5853	0.5900
0.12677	0.5696	0.5451	0.5628
0.18630	0.5559	0.5883	0.5932
0.24380	0.5535	0.5710	0.5767
0.32250	0.5646	0.5851	0.5885
0.36076	0.5432	0.5635	0.5685
0.44181	0.5832	0.6026	0.6053
0.50181	0.6045	0.6235	0.6251
0.69333	0.6619	0.6814	0.6826
0.71890	0.6698	0.6915	0.6942
0.89290	0.7485	0.7708	0.7718

Table III. Free energies of transfer of Li-Salts from H_2O to DMSO*

Salt	$\Delta G_{t,m}°$ 25°C	35°C	45°C
LiCl	4.865	5.121	5.353
LiBr	2.515	2.792	3.064
LiI	−0.626	−0.340	−0.022

* $\Delta G_t°$ values in kcal/mole (molal scale).

Table IV. Energetics of transfer of Li-halides from H_2O to DMSO at 25°C*

Salt	$\Delta G_t°$	$\Delta H_t°$	$\Delta S_t°$	$\partial\Delta H_t°$	Ref.
LiCl	4.865	−3.12	−26.78	2.55	(1)
		−2.05		3.38	(11)
LiBr	2.515	−5.67	−27.46	0.0	(4)
		−5.43			(11)
LiI	−0.626	−8.69	−27.03	−3.02	This work
		−9.07		−3.64	(11)

* $\Delta G_t°$ and $\Delta H_t°$ are in kcal/mole and $\Delta S_t°$ is in eu. All are based on the molal scale.

it is apparent that the solvation of LiCl in DMSO is smaller than it is in H_2O as proposed earlier (4, 7, 10). This can now be demonstrated (qualitatively) as follows. It is well known that the "true" molality, m', of a given solution differs from the conventional molality, m, by (13)

$$m' = m/(1 - 0.001\ hm) \qquad [8]$$

In Eq. [8], h is the solvation number and arises from the fact that in a solution containing m moles of solute in 1000g of solvent, there are 1000/mw — hm moles of free solvent (mw is the molecular weight). The corresponding relation between the "true" and conventional activity coefficients is therefore

$$\ln \gamma = \ln \gamma' - \frac{h}{\nu} \ln a_1 - \ln (1 - 0.001\ hm \cdot \mathrm{mw}) \qquad [9]$$

where ν is the total number of ions into which the solute molecule dissociates and a_1 is the solvent activity. We assume [cf. Robinson and Stokes, ref. (13)] that lnγ' is given by the Debye-Hückel relation

$$\ln\gamma' = -A\sqrt{m'}/(1 + Ba_i\sqrt{m'}) \qquad [10]$$

where m' is obtained from Eq. [8]. The solvent activity coefficient can be calculated from the observed activity coefficients (ln$\gamma_\pm$) by use of the Gibbs-Duhem equation

$$\ln a_1 = -\int_0^{X_2} \frac{X_2}{1 - X_2}\, d \ln a_2$$

In this equation a_1 and a_2 are, respectively, the solvent

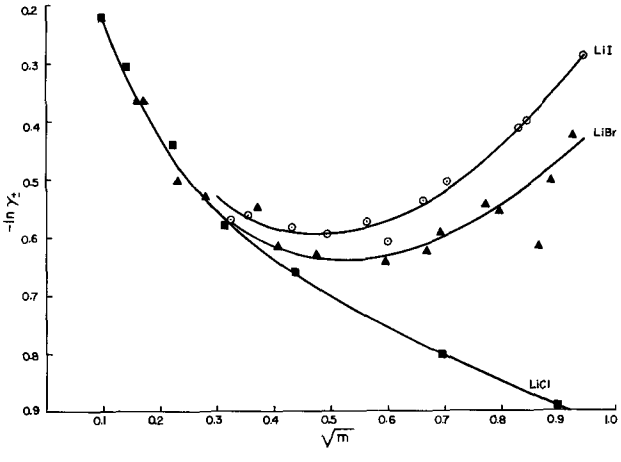

Fig. 2. Plot of *ln* $\gamma_\pm$ *vs.* $m^{1/2}$ for lithium halides in DMSO: ○, present data for LiI, ▲, LiBr (4), ■, LiCl (1, 2).

and solute activities, and X_1 and X_2 are the corresponding mole fractions. To obtain an exact integral, the $\ln a_2$ term was fit to the polynomial

$$\ln a_2 = \alpha + \beta X_2 + \gamma X_2^2$$

so that

$$\ln a_1 = \beta (X_2 + \ln X_1) + \gamma (X_1^2 - 4X_1 + 2\ln X_1 + 3.0)$$

Finally in order to evaluate the solvated radii term (a_i in Eq. [10]) we use the approximate relation [cf. ref. (13)]

$$a_i = [3V (h - \Delta)/4\pi]^{1/3} + r_+ + r_- \qquad [11]$$

where V is the volume occupied by 1 solvent molecule ($1.185 \cdot 10^{-22}$ cc for DMSO), r_+ and r_- are the crystal radii of the cation and anion, respectively, and Δ is an adjustable parameter called the "penetration distance." In the present calculations, values of 0.1 and 1.0 were taken for Δ in the aqueous and nonaqueous systems. It should be pointed out that several serious limitations exist in this calculation (see below) and the results, while qualitative, do in fact reflect the differences in solvation between the solvents H_2O and DMSO. Equation [9] was easily solved by an iteration procedure on an IBM 7094 computer by slowly increasing h from 0 in steps of 0.05. The iteration was carried out until the calculated $\ln\gamma_\pm$ (Eq. [9]) equaled the observed value to within ± 0.001 units. The results of these calculations are shown in Table V. The effect of changing Δ from 0.1 to 1.0 is small as indicated in this table. While the calculations are not, by any means, quantitative, they are significant in the sense that they do demonstrate that the various Li-salts are less solvated in the organic solvent than they are in water. The fact that h in Table V increases from Cl^- to I^- in both solvents is fortuitous and results from the simplified treatment for a_i (Eq. [11]) used in these calculations (13). A more exact treatment (14) equates the experimental activity coefficient, γ, to three contributions, *i.e.*

$$\log \gamma = \log f_c + \log f_h + \log f_{so}$$

where the f's are rational activity coefficients and the subscripts c, h, and so refer, respectively, to coulombic, hydration, and mutual salting-out interactions. The first two terms can be calculated simply as discussed by Conway (14), but the salting-out term requires specific knowledge of partial molal volumes. The lack of such data prevents the accurate determination of solvation numbers.

Single ion contributions to ΔG_t°, ΔH_t°, and ΔS_t° are of interest since they are important in comparing solvent kinetic effects (10, 11, 15) as well as distinguishing between specific solvation effects between anions and cations. In Table IV, it is seen that both the enthalpy and energy of transfer of the anion become more negative in going from Cl^- to I^-. This is demonstrated for the enthalpy of transfer in the last column of Table IV where $\partial\Delta H_t^\circ$ is the relative (to Br^-) enthalpy of transfer of the anion from H_2O to DMSO, *i.e.*

$$\partial\Delta H_t^\circ = \Delta H_t^\circ(X^-) - \Delta H_t^\circ(Br^-)$$

The fact that ΔS_t° is almost independent of the nature of the anion indicates that the increase in solvent structure in transferring the salt to DMSO is largely a cation effect. Using the approach described by Feakins (16), where individual energy contributions are given by

$$\Delta G_t^\circ(MX) = \Delta G_t^\circ(M^+) + k/r_- \qquad [12]$$

or

$$\Delta G_t^\circ(MX) = \Delta G_t^\circ(X^-) - m/r_+ \qquad [13]$$

it was found that Eq. [13] gave satisfactory results for the alkali-chloride-N-methyl formamide system (7). In these equations, k and m are constants and the intercept of a plot of $\Delta G_t^\circ(MX)$ *vs.* $1/r$ gives the single ion value for the free energy of transfer. However in the course of the present work, use of Eq. [12] has led to values for $\Delta G_t^\circ(Li^+)$ of the order of -30 kcal/mole, $\Delta G_t^\circ(Cl^-)$ values of $+35$ kcal/mole, and $\Delta H_t^\circ(X^-)$ values which were in complete disagreement with those more reasonable values found by Arnett and McKelvey (23). This demonstrates the complete breakdown of Eq. [12] for the present data but does not indicate that the use of Eq. [13] is invalid. Indeed the use of Eq. [13] over [12] is to be preferred (16) especially when one is transferring salts to solvents more basic than water. It has been suggested (17) that the use of equations such as [12] and [13] should be corrected for mutual polarization arising from dispersion forces, *i.e.*

$$\Delta G_t^\circ = \Delta G_t^\circ(\text{el}) + \Delta G_t^\circ(\text{neut})$$

where ΔG_t°(el) is given by Eq. [12] or [13] and ΔG_t°(neut) is proportional to r^2 and can be estimated from solubility data of rare gases in the two solvents (17). ΔG_t°(neut) contributions can be evaluated by use of Henry's law

$$p/c = \exp\{(\mu_s^\circ - \mu_g^\circ)/RT\}$$

Here μ_s° and μ_g° are the chemical potentials of the solute (unit concentration) in solution and gas phase, respectively, p is the partial pressure, and c is the concentration in solution. Using this equation together with the data for rare gas solubilities in DMSO (18) and H_2O (19), it is found from a plot of ΔG_t°(neut) *vs.* r^2 that ΔG_t°(neut) for Li^+, Cl^-, Br^-, and I^- is 244, -285, -390, and -551 cal/mole, respectively (values are based on molal units). The resulting plot of $\Delta G_t^\circ(MX) - \Delta G_t^\circ$(neut) *vs.* $1/r_-$ still gave $\Delta G_t^\circ(Li^+)$ values close to -30 kcal mole^{-1} and $\Delta H_t^\circ(Li^+)$ values close to 20 kcal/mole thereby indicating that ΔG_t°(el) in Eq. [14] cannot be evaluated simply by a $1/r$ (Born)-type law. In fact in highly polarizable solvents such as DMSO (10), the possibility of ion-quadrupole and ion-induced quadrupole probably become significant. For example in H_2O, which has a lower polarizability than does DMSO, the interaction energy between an ion and the H_2O quadrupole is, for a linear alignment

$$E_\theta = e\theta/d^3$$

where θ is the quadrupole moment ($\sim 2.10^{-26}$ esu); e is the electronic charge and d is the diameter of the water molecule ($\sim 3.10^{-8}$ cm). E_θ is therefore of the order of 5 kcal/mole and is by no means insignificant [cf. ref. (20)]. In the aprotic solvents such as DMSO and propylene carbonate, dipole moments are high (10) and are attributed to the highly charged oxygen center and a very diffuse negative charge spread out over the remainder of the molecule. The success of applying Eq. [13] to evaluate $\Delta G^\circ(X^-)$ from a series of salts such as LiCl, NaCl, KCl would appear to arise from the fact that the cations are very much less polarizable and that the major interaction energy is an ion-dipole one whereas anions, which must interact with the polarizable end of the solvent molecule, do not behave so simply. Further demonstration of this cation *vs.* anion effect can be seen from work on other solvent systems where individual ionic contributions to ΔG_t° are always made on the basis of some extrathermodynamic assumption involving the cation (21, 22). This effect is also significant for transfers between hydrogen-bonded (protic) solvents as individual ΔG_t° values between H_2O and methanol were always significantly

Table V. Solvation numbers in H_2O and DMSO at 25°C

Salt	H_2O^1	H_2O^2	$DMSO^1$	$DMSO^2$
LiCl	4.2	4.5	0.2	1.0
LiBr	4.5	5.0	0.2	1.0
LiI	7.5	7.7	1.5	1.8

[1] $\Delta = 0.10$.
[2] $\Delta = 1.00$.

higher for the anion plot (Eq. [12]) than for the cation plot (Eq. [13]) as discussed by Feakins (16).

Acknowledgment

The author is grateful to Dr. J. N. Butler for many helpful discussions and for making available experimental data prior to publication [cf. ref. (8)].

Manuscript submitted Sept. 2, 1969; revised manuscript received Nov. 10, 1969.

Any discussion of this paper will appear in a Discussion Section to be published in the December 1970 JOURNAL.

REFERENCES

1. W. H. Smyrl and C. W. Tobias, *This Journal*, **115**, 33 (1968).
2. G. Holleck, D. R. Cogley, and J. N. Butler, *ibid.*, **116**, 952 (1969).
3. D. R. Cogley and J. N. Butler, *ibid.*, **113**, 1074 (1966).
4. M. Salomon, *ibid.*, **116**, 1392 (1969).
5. T. W. Richards and F. Daniels, *J. Am. Chem. Soc.*, **41**, 1732 (1919).
6. E. A. Guggenheim, *Phil. Mag.*, **19**, 588 (1935).
7. M. Salomon, *J. Phys. Chem.*, **73**, 3299 (1969).
8. J. N. Butler and J. C. Synnott, "Thermodynamics of LiCl in Dimethyl Formamide," in course of publication.
9. A. J. deBethune, T. S. Licht, and N. Swendeman, *This Journal*, **106**, 617 (1959).
10. A. J. Parker, *Chem. Rev.*, **69**, 1 (1969); this major review gives many references to ion-solvation in dipolar aprotic solvents.
11. R. F. Rodewald, K. Mahendran, J. L. Bear, and R. Fuchs, *J. Am. Chem. Soc.*, **90**, 6698 (1968).
12. Y. Wu and H. L. Friedman, *J. Phys. Chem.*, **20**, 501 (1966).
13. R. A. Robinson and R. H. Stokes, "Electrolyte Solutions," Butterworths, London (1959).
14. J. E. Desnoyers and B. E. Conway, *J. Phys. Chem.*, **68**, 2305 (1964).
15. M. Salomon, *ibid.*, **70**, 3853 (1966).
16. D. Feakins and P. Watson, *J. Chem. Soc.*, **1963** 4734; see also D. Feakins, "Physico-Chemical Processes in Mixed Aqueous Solvents," F. Franks, Editor, Elsevier Publishing Co., New York (1967).
17. C. L. DeLigny and M. Alfenaar, *Recueil*, **84**, 81 (1965).
18. J. H. Dymond, *J. Phys. Chem.*, **71**, 1829 (1967).
19. W. F. Linke, "Solubilities," American Chemical Society, Washington, D. C. (1965).
20. A. D. Buckingham, *Discussions Faraday Soc.*, **24**, 151 (1957).
21. H. Strehlow, "The Chemistry of Non-Aqueous Solvents," J. J. Lagowski, Editor, Chap. 4, Academic Press, New York (1966).
22. J. F. Coetzee and J. J. Campion, *J. Am. Chem. Soc.*, **89**, 2513, 2517 (1967).
23. E. M. Arnett and D. R. McKelvey, *ibid.*, **88**, 2598 (1966).

Oxygen Reduction on Oxide-Free Platinum in 85% Orthophosphoric Acid: Temperature and Impurity Dependence

A. J. Appleby*

Institute of Gas Technology, Chicago, Illinois

ABSTRACT

Oxygen electrode kinetics in 85% orthophosphoric acid have been studied as a function of temperature and impurity level in the electrolyte. It is shown that the mechanism of reaction is the same as that in N perchloric acid, and that rate constants and Tafel slopes are dependent on impurity adsorption. Hydrogen peroxide is not a significant reaction product, at least at high temperatures. The activation energy of the reaction at the reversible potential was determined to be 22.9 ± 0.9 kcal.

Work carried out in recent years on the oxygen electrode on platinum in acid solution has stressed the importance of the surface oxides on the metal whose half-wave reduction potential is close to that for oxygen reduction at all pH values (1). Some workers have noted inhibition of the oxygen reduction process by oxides of platinum (2-6); in other cases the reaction was accelerated (1).

The majority of workers consider that a two-stage reduction takes place, with hydrogen peroxide as an intermediate (4-7). This product was either reduced or spontaneously decomposed (8) on the platinum surface at the same potentials as those of its formation. However, in other cases no hydrogen peroxide was detected as a reaction product (3, 9).

Recent work has shown that oxide-free platinum (10, 11) under high-purity conditions is more active than oxidized platinum (12) for oxygen reduction in dilute acid and is kinetically quite different (11, 12). It has also been shown that under these conditions impurity adsorption is associated with the formation of hydrogen peroxide (13) which is produced in a process parallel to the main reaction of oxygen reduction direct to water (14).

As it is evident from the literature that a wide variation of results has been obtained in the past under different conditions in acid electrolytes, an examination of oxygen reduction on oxide-free platinum under different conditions of impurity level and temperature in 85% orthophosphoric acid has been carried out to determine the effect of these variables on kinetics.

Experimental

To reduce the possibility of attack by the electrolyte (85% orthophosphoric acid), especially at the highest temperatures of study, all parts of the electrochemical cell in contact with the acid were constructed from fused silica. The reference electrode was a dual bubbling hydrogen electrode in the same electrolyte as that used in the cell. All potentials quoted in this paper are referred to this electrode (HRE potentials). The counterelectrode was a large-area platinum grid. Working electrodes were 1 cm^2 platinum foils of zone-refined (nominal 99.999%) grade hung on platinum wires. They could be moved up or down as required

* Electrochemical Society Active Member.

by means of sliding seals. All gaskets and seals in the equipment were of Teflon or Viton A. A general description of the layout of the cell and ancillary equipment together with the cleaning procedure used has been published (15).

Hydrogen for the reference electrodes and oxygen or oxygen-nitrogen mixtures for the working compartment of the cell were passed through presaturators containing 85% orthophosphoric acid before being led into the cell. The cell and presaturators were maintained at the required temperatures in the range 25.1-136.1°C in a thermostatic oil bath. The hydrogen and oxygen used were of Matheson ultrahigh-purity-grade, and the nitrogen was of 99.997% purity. All gases contained less than 0.1 ppm oxidizable organics, but as a further precaution the hydrogen and oxygen or oxygen-nitrogen mixture were passed over a bed of platinized asbestos at 300°C before going to the cell. Reproducible oxygen-nitrogen mixtures of known oxygen partial pressure were made using capillary flowmeters and a mixing chamber. During experiments, oxygen or oxygen-nitrogen mixtures were normally bubbled through the cell at the rate of approximately 10 ml/min.

The platinum foil or disk electrodes were degreased, and washed with HCl, conductivity water, and the electrolyte itself before use. The electrolyte was normally prepared by a succession of hydrogen peroxide treatments to remove oxidizable matter, although in some experiments untreated analytical reagent-grade 85% (14.6M) orthophosphoric acid was used.

The majority of measurements were carried out galvanostatically using a conventional battery-operated, high-resistance circuit, although with the rotating ring-disk electrode a potentiostat was used. The ring-disk electrode was used to investigate the role of hydrogen peroxide in the oxygen reduction reaction. Its construction will be discussed elsewhere.

Results

Electrode activation.—The work of Damjanovic and Brusic (11) has emphasized the difference in kinetic character for the oxygen reduction reaction between "bare" or "reduced" platinum surfaces, and platinum which has been subjected to anodizing or other intensive oxidation (12). The importance of obtaining a reproducible surface has been often stressed in the literature. Accordingly, it was decided in these experiments to use a standard electrochemical method of surface preparation for all the working electrode specimens.

After preparation of the electrodes by the method described above, the platinum specimens were hung until required above the electrolyte level in a pure oxygen atmosphere in the cell. After specimens were lowered into the cell, they were subjected to an anodic galvanostatic pulse, followed by a series of about three anodic and cathodic pulses between 1.0V and 50 mV at a current density of 10^{-3} A/cm^2. The final pulse was in every case cathodic, after which the electrodes were allowed to reach their rest potentials. In the initial anodic pulse the electrodes were allowed to reach a maximum potential of 1.2-1.3V. A series of preliminary experiments established that the maximum potential of this activation procedure, provided it was above about 1.1V and below approximately 1.4V, was unimportant. Pulsing above 1.4V led to electrodes of slightly increased activity. This may be attributed to an increase in surface energy (increase in the number of surface defects) on reduction of the phase oxide monolayer formed at these potentials (16, 17).

The major purpose of this activation procedure was to desorb impurities on the electrode surface (18). Any phase oxide or adsorbed oxygen radicals formed at high potentials are reduced in the cathodic portion of the pulse. It was established that potentiostating the electrodes at 0.25V for long periods, a procedure which should slowly remove any "dermasorbed" oxygen initially present in the platinum (19), made no difference to the final behavior of the electrode. This activation method is essentially similar to the electrochemical treatment used by Damjanovic and Brusic (11). However, their procedure involved exposing the electrode to a potential of 1.7V for a period of several seconds, which produced an electrode with similar kinetic character but higher activity (by a factor of 2) than chemically treated or thermally reduced electrodes.

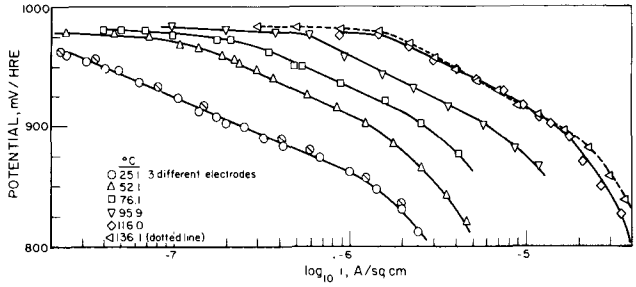

Fig. 1. Cathodic Tafel plots on oxide-free platinum, pure electrolyte.

Rest potentials.—In clean (hydrogen peroxide treated) electrolyte saturated with oxygen at 1 atm pressure, the platinum electrodes after pulsing attained rest potentials in the range 985-1000 mV. A slow rise was noted over a period of several hours, when a maximum potential of about 1010-1015 mV was reached. A slow decay followed; a final potential of about 990-1000 mV was noted after 24 hr, which would remain constant[1] thereafter. The rest potentials were not significantly temperature-dependent, but at the highest temperatures studied they tended to be a few millivolts lower. Values of rest potentials, generally close to those noted in other aqueous media, are considered to be due to a mixed potential mechanism to explain the low value of the rest potential compared with the thermodynamic value for the oxygen electrode (about 1.2V at 25°C). In this mechanism, the cathodic process is oxygen reduction, and the anodic process is considered to be either platinum oxidation (20) or the oxidation of impurities (21).

Tafel plots.—Galvanostatic Tafel plots were made immediately after electrode activation at six different temperatures in the range 25.1°-136.1°C. They are illustrated in Fig. 1. Equilibrium was quickly attained at each point within 1-2 min, after which the potential remained steady for 15-20 min. This period was followed by a very slow decay of potential at constant current, which was more rapid at lower potentials. This may be attributed to the slow deactivation of the electrode by impurities diffusing in from the solution. It was noted that deactivation was most rapid at high oxygen bubbling rates, which would indicate a diffusion-controlled process. A similar effect has been noted, though at lower potentials, in 0.1*N* sulfuric acid using a rotating disk electrode when the electrolyte had been similarly purified (13). The original potential could then be restored by pulsing to either 1.0V or 50 mV, which desorbed the impurities responsible.

Results thus obtained were very reproducible; the data for three different electrodes cut from the same sample of platinum foil are shown together on the plot for 25.1°C (Fig. 1). Results at higher temperatures for different electrodes were within 10 mV. It may be seen in each case that a high-potential region exists in which there is little change of potential with current density, followed by a Tafel region, followed by a region of higher slope leading to the limiting-current region. Results are generally simlar to those reported by Damjanovic and Brusic (11) in 0.1*N* perchloric acid at room temperature. It should be noted that the Tafel lines at 116.0° and 136.1°C are prac-

[1] Over a period of weeks.

tically coincident because of the rapid increase in water vapor pressure over phosphoric acid, and hence the fall in oxygen partial pressure in this temperature range. Table I lists the Tafel slopes and extrapolated exchange current values, together with values of $1/\alpha$, where α is the transfer coefficient. In each case, the exchange current values have been obtained by extrapolating back to the value of the reversible potential at the temperature of experiment, calculated for gaseous water from the data of Lewis and Randell (22), and corrected for the water vapor pressure over 85% orthophosphoric acid (23). The figures quoted in Table I refer to the theoretical emf of the cell

$$H_{2(1-p)\ atm} \quad 85\%\ \text{orthophosphoric acid} \quad O_{2(1\ atm)}$$

where p is the water vapor pressure over the electrolyte. The exchange current values have been corrected for the oxygen partial pressure and are expressed for a standard pressure of 1 atm. The correction has been made on the basis of first-order oxygen reduction kinetics at constant potential (see below). It is apparent from Table I that the Tafel slopes, at least above 900 mV, are very close to RT/F.

Kinetic data in analytical-grade acid.—A number of experiments were carried out in analytical-grade acid to determine the effect of traces of oxidizable impurities on the system. Such impurities have been detected in orthophosphoric acid and have been identified as traces of phosphorous and hypophosphorous acids (24). On immersion, chemically cleaned electrodes generally took up rest potentials of about 750 mV (at 25°C) to 920 mV (at 136°C) in analytical-grade electrolyte.

After cathodic polarization, higher values were noted: 886 mV at 25.1°C, 916 mV at 76.1°C, and 941 mV at 116.0°C. Within 24 hr, these values had fallen considerably, to about 600 mV at 25°C and 800 mV at 136°C.

Galvanostatic Tafel plots.—A steady-state galvanostatic Tafel plot was made at each temperature on electrodes that had been allowed to stay on open circuit in the solution for 1 hr so that equilibrium could be reached between the electrode surface and the residual impurities in the solution. A high current density in the appropriate range was applied to the electrode, and an ascending steady-state Tafel plot was made. The electrode was left at each point for sufficient time for less than 1 mV change in 5 min to occur. Normally, steady state was achieved within 10 min.

Downward Tafel plots were similar, but had somewhat lower slopes, registering lower potentials in the low current density part of the plot. Downward plots taken on electrodes which had been in the solution 24 hr were normally steep (slope $\sim 2RT/F$), and showed more evidence of electrode deactivation (higher polarizations at low current densities).

To show the effect of impurity desorption by pulsing to 50 mV, a second plot was made at each temperature. These are illustrated in Fig. 2 for 25°-95°C. For these Tafel plots the electrode was activated by pulsing before each point since it was noted that slow deactivation over a period of some minutes took place. The potential eventually returned to values close to the initial curve for each current density studied. A much more effective method of electrode activation

Table I. Kinetic data in purified 85% orthophosphoric acid

Temp, °C	E_{rev} at 1 atm O_2, mV HRE	Slope, mV/decade	$1/\alpha$	i_o, A/cm²
25.1	1260	62	1.04	3.8×10^{-13}
52.1	1236	67	1.04	1.4×10^{-11}
76.1	1219	70	1.03	8.6×10^{-11}
95.9	1203	72	0.98	4.4×10^{-10}
116.0	1182	80	1.04	5.0×10^{-9}
136.1	1161	82	1.01	1.2×10^{-8}

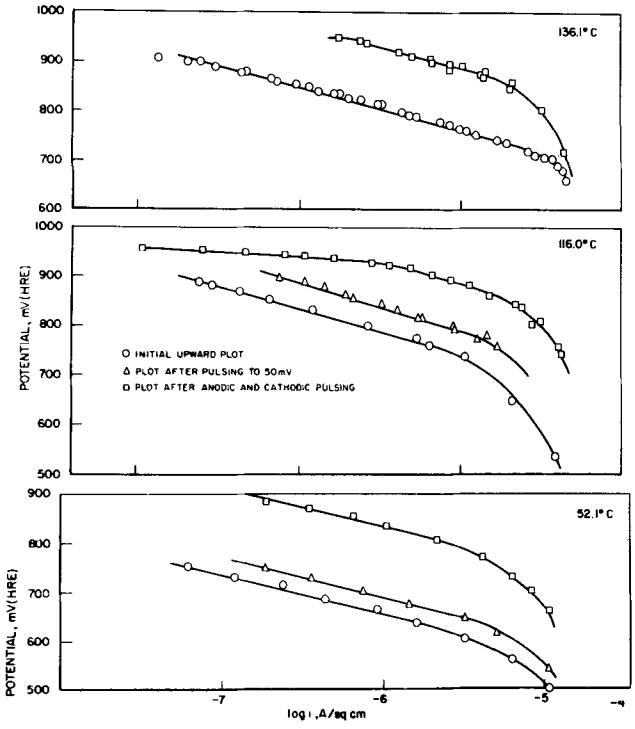

Fig. 2. Cathodic Tafel plots on oxide-free platinum, analytical-grade electrolyte.

was shown to be a method of pulsing between 50 mV and 1.2V before each galvanostatic point. Results of this method are also shown in Fig. 2. Deactivation was in this case exceptionally rapid compared with a purified solution, and was dependent upon the rate of stirring of the solution. A typical potential-time curve for such an activated electrode (after pulsing to 50 mV) is shown in Fig. 3. The electrode surfaces obtained by this technique are probably essentially free from adsorbed impurities after pulsing, as the plots of maximum potential reached after pulsing against log current density (Fig. 2) are close to the steady-state plots obtained in purified electrolyte (Fig. 1).

Tafel slopes, $1/\alpha$ values, and extrapolated apparent exchange current values for the steady-state plots in analytical-grade acid are given in Table II.

Order of reaction for oxygen.—The effect of oxygen partial pressure in the Tafel region at 52.1°C in purified electrolyte has been published (25). For this experiment oxygen was diluted with nitrogen to give the partial pressure required before being led into the cell. The results obtained indicate that the reaction is essentially first order for oxygen at constant potential.

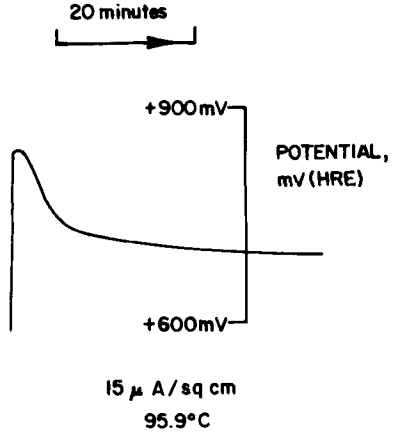

Fig. 3. Decay curve of electrode activity in analytical-grade electrolyte.

Table II. Kinetic data in analytical-grade acid

Temp, °C	Initial plot Tafel slope, mV/decade	$1/\alpha$	i_o Corrected for oxygen partial pressure, A/cm² Initial plot	After anodic and cathodic pulsing
25.1	89	1.51	5.0×10^{-14}	2.5×10^{-12}
52.1	82	1.29	4.6×10^{-13}	3.6×10^{-11}
76.1	87	1.28	3.8×10^{-12}	4.3×10^{-10}
95.9	81	1.11	3.5×10^{-11}	1.7×10^{-9}
116.0	91	1.18	1.4×10^{-10}	6.1×10^{-9}
136.1	90	1.11	7.4×10^{-10}	1.6×10^{-8}

Hydrogen peroxide formation.—An examination of the contribution of oxygen reduction to hydrogen peroxide to the over-all process was carried out using a rotating ring-disk electrode at 3140 rpm in the purified electrolyte at 76.1° and 116.0°C. The electrode disk had an area of 0.212 cm² and was treated before use in the same way as the platinum for electrodes. During the experiments, the lightly platinized electrode ring was maintained at a potential of 1.3V, at which oxidation of any hydrogen peroxide produced in the oxygen reduction reaction at the disk will be diffusion-controlled.

The shapes of the oxygen reduction waves obtained at 76.1° and 116.0°C are shown in Fig. 4. At 76.1°C, the reduction wave has the appearance of a double wave as noted for instance on mercury in dilute acid solutions (26). In the latter case, the first wave corresponds to oxygen reduction to hydrogen peroxide, and the second wave corresponds to oxygen reduction direct to water.

The data obtained on hydrogen peroxide oxidation at the ring as a function of disk potential are also shown on Fig. 5. As the collection factor of the ring electrode in the apparatus used is 0.35, hydrogen peroxide production only accounts for a maximum of approximately 16% of the total oxygen consumed, the figure being considerably less (under 5%) at 116.0°C. It is clear that the double-wave effect cannot therefore be attributed to oxygen reduction to hydrogen peroxide.

It was noted that pulsing of the disk between 1.2V and 50 mV would restore the disk current to about 60 μA in the potential range 0.75-0.3V, corresponding to the value of limiting current for the 4-electron process of oxygen reduction. The limiting current value then gradually fell, over a period of some minutes, down to the values in Fig. 2, the rate of fall being most rapid in the potential range 400-500 mV. In the

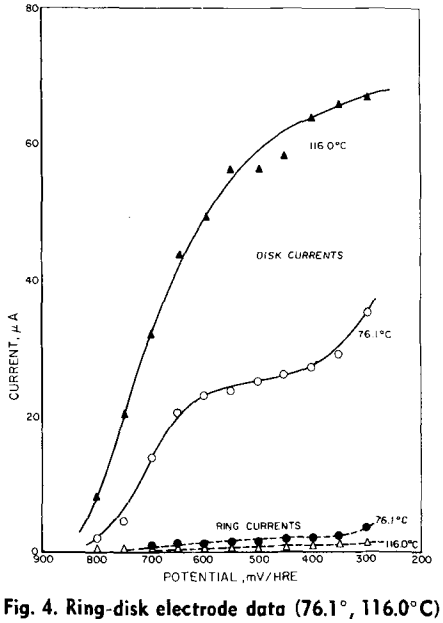

Fig. 4. Ring-disk electrode data (76.1°, 116.0°C)

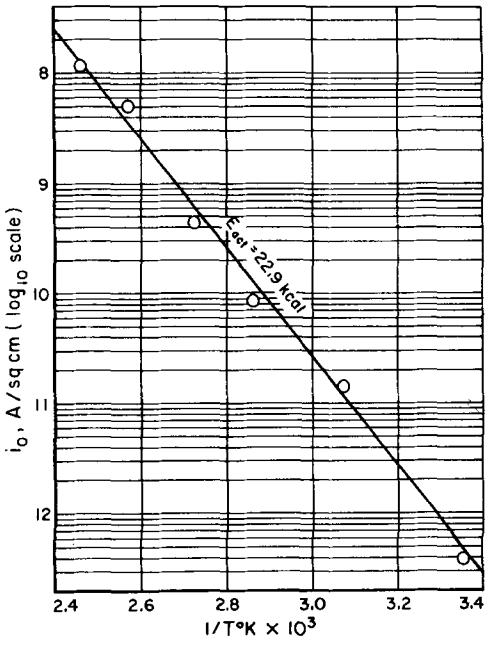

Fig. 5. Arrhenius plot for exchange current values on oxide-free platinum.

Tafel region the rate of deactivation of the electrode was very small. These results are similar to those noted by Müller and Nekrasov (27) in dilute sulfuric acid, which these authors attributed to anion adsorption in the double-layer region (below about 800 mV), so that oxygen reduction sites on the electrode surface are blocked. Damjanovic, Genshaw, and Bockris (13) have recently shown that in dilute sulfuric acid this deactivation effect only occurs in the presence of nonoxidizable impurities which are not removed by extended pre-electrolysis or by hydrogen peroxide treatment. They conclude that anion adsorption is not directly responsible as deactivation is apparently controlled by the slow diffusion of some species to the electrode surface. This species can only be removed from the electrolyte by the use of a large-area platinum adsorber electrode potentiostated for extended periods at the potential of maximum deactivation (about 300-400 mV in dilute sulfuric acid), which is removed from the solution taking with it the impurities at the end of the operation. The nature of these capillary-active impurities is open to question; they may be traces of organic greases or adsorbable foreign ions.

Müller and Nekrasov (27) have shown the deactivating effect of chloride ions in acid solutions, and Müller and Sobol (28), the corresponding effect of divalent cations on oxygen reduction in alkaline solutions. It is certainly possible that polyphosphates are responsible in this present case.

Damjanovic *et al.* (13) have shown that hydrogen peroxide production in acid solution is associated with the presence of these capillary-active materials, and they attribute this to the blocking of high-energy sites on the electrode surface, where O-O bond dissociation (and direct reduction of O_2 to water) takes place. When impurities are eliminated, little H_2O_2 results.

In the present case, very little peroxide was detected as a reaction product, but it is certainly possible that catalytic decomposition of hydrogen peroxide takes place during the time occupied in diffusion from the disk to the ring, so that the collection factor of the electrode is effectively reduced. The precursor of hydrogen peroxide produced in the reaction is, according to Nekrasov (29), the O_2H^- ion adsorbed on the electrode. This material may be expected to become progressively more unstable (and liable to dissociate) with rise in temperature, so that

the yield of hydrogen peroxide will fall, even in the presence of adsorbed impurities.

At 116.0°C the oxygen reduction wave shows much less the influence of any impurities in the solution. It is therefore apparent that their heat of adsorption on platinum is comparatively low.

We may conclude from these data that hydrogen peroxide is only a minor product of oxygen reduction on oxide-free platinum in concentrated phosphoric acid at temperatures of interest in the operation of fuel cell cathodes.

Activation energy for oxygen reduction.—The activation energy for oxygen reduction on oxide-free platinum at the reversible potential has been obtained from the Arrhenius plot (Fig. 5) of the extrapolated exchange current values (corrected to atmosphere oxygen pressure) in purified electrolyte. The value obtained is 22.9 ± 0.9 kcal. This is considerably higher than the value on oxidized platinum (13.1 kcal) (15) and is close to the value reported for the oxygen electrode reaction in alkaline solution (12, 30). No activation energy correction has been made in the present case for changes in oxygen solubility or water activity of the electrolyte, but such corrections are small.

As has been already noted, the nonoxidizable capillary-active material has no effect on Tafel slopes and exchange currents (13), so further purification is not expected to significantly influence these quantities or the activation energy.

Discussion of Mechanism

In pure solutions, oxygen reduction on oxide-free platinum is first-order, and the Tafel slope is $RT/\mathbf{F}$. Under the conditions of the experiment it is not possible to obtain any other relevant kinetic parameters which might further clarify the mechanism. It is not possible to obtain the order of reaction for (H^+) at constant ionic strength in concentrated phosphoric acid; as oxygen evolution takes place on an oxidized surface, no direct determinations of the stoichiometric number are possible as the near-equilibrium and anodic regions are not accessible.

Under Langmuir adsorption conditions, we may use the following relation for α, the measured transfer coefficient (12, 31-33)

$$\alpha = \beta n + \frac{n_a}{\nu}$$

where β is the symmetry factor of the rate-determining step, ν is the stoichiometric number of the rate-determining step, n is the number of electrons transferred in the rate-determining step, and n_a is the total number of electrons transferred before the rate-determining step. Assuming that the rate-determining step is a charge transfer with $\beta = \frac{1}{2}$ and that only one electron is transferred in the rate-determining step,[2] with the experimental value of α equal to 1

$$n_a/\nu = \tfrac{1}{2}$$

The only solution is $n_a = 1$, $\nu = 2$. $n_a = 2$, $\nu = 4$ is not possible as only 4 electrons are involved in the over-all reaction.

However, if $\nu = 2$, *i.e.*, two identical charge-transfer reactions occur for one unit of the over-all process, then the chemical order of reaction for O_2 must be ½, not 1 as is experimentally observed. Hence, under Langmuir conditions the rate-determining step cannot be a charge-transfer unless β has the nonphysical value of unity.

If the rate-determining step is a chemical process

$$n = 0, \text{ and } n_a/\nu = 1$$

Again, for unit oxygen reaction order, ν must be 1, hence $n_a = 1$; that is, the data are consistent with a chemical step following a 1-electron transfer.

The above analysis applies only to 1:1 coupled mechanisms (31). For more complex paths in which chemical steps control without preliminary charge-transfer other possibilities exist. Gnanamuthu and Petrocelli (34) have provided a useful list of possible oxygen reaction mechanisms, which includes 1:1 and more complex paths, with kinetic parameters evaluated assuming Langmuir adsorption.

Tafel slopes of $RT/\mathbf{F}$ appear in certain complex paths, which also satisfy the experimental oxygen reaction order requirement. Again neglecting paths involving 2-electron charge transfers, the only reactions which satisfy the above conditions are as follows, "S" in each case being an undefined surface site. The calculated Tafel slope follows each reaction

A. $O_2 + S + S - H_2O \rightarrow SOH + SO_2H$	∞
(rds) $SO_2H + SH_2O \rightarrow SOH + SH_2O_2$	$RT/\mathbf{F}$
[the "hydrogen peroxide path" (35)]	
B. $O_2 + S + SH_2O \rightarrow SOH + SO_2H$	∞
(rds) $SO_2H + S \rightarrow SO + SOH$	$RT/\mathbf{F}$
["metal peroxide" (35) or Conway and Bourgault (36) paths]	
C. $S + O_2 + e^- \rightarrow SO_2^-$	$2RT/\mathbf{F}$
(rds) $SO_2^- + H^+ \rightarrow SO_2H$	$RT/\mathbf{F}$[3]
[Ives (37) or Hoare's (38) paths].	

Damjanovic and Brusic (11) have pointed out that their H^+ reaction order data (rate $\propto [H^+]^{3/2}$) for dilute perchloric acid are inconsistent with mechanism C, which is first order in H^+. Similarly, the complex (nonconsecutive) mechanisms A and B, which are zero-order in H^+, are not in agreement with their experimental data.

Consequently, it appears that the present results, and the results of Damjanovic and Brusic (11), are not explicable assuming Langmuir adsorption. These authors have, however, noted that in the potential range in which results are obtained, platinum is covered by less than monolayer quantities of water oxidation fragments [—OH and —O, with the latter predominating (21)].

Experimentally, a linear relationship between steady-state coverage and potential holds in N perchloric and sulfuric acids (11, 21). This coverage-potential relationship implies that the heat of adsorption of the oxygen radicals on the platinum surface falls off linearly with increasing potential and increasing coverage (21). If one assumes that the intermediates in the oxygen electrode process follow a similar isotherm to that of the adsorbed water fragments (11), then it is possible to show the experimental data are consistent with the mechanism

$$S + O_2 \rightarrow SO_2$$

$$\text{(rds)} \qquad S - O_2 + H^+ + e^- \rightarrow SO_2H$$

followed by

$$SO_2H + 3H^+ + 3e^- \rightarrow 2H_2O$$

which proceeds by unknown (though rapid) steps.

The isotherm which describes the adsorption of intermediates in the reaction is thus the Temkin isotherm, in which the heat of adsorption of a particular species is dependent on the total coverage of all species on the electrode (39). As Böld and Breiter (40) have shown, it is necessary to assume that Temkin adsorption of oxygen and —OH radicals takes place on platinum in order to explain the experimental cyclic voltammetric scans in dilute perchloric and sulfuric acid. Similar plots are obtained in concentrated phosphoric acid (41), and hence it is reasonable to assume that the same isotherm applies in this case. A complete analysis of this mechanism is given as the Appendix.

[2] It is assumed that a two electron transfer would require too high an activation energy.

[3] Gnanamuthu and Petrocelli (34) point out that the slope may be greater than $RT/\mathbf{F}$ if the plane of closest approach for the adsorbate and the Helmholtz plane are not identical.

One may only speculate on steps following the rate-determining step. As shown by Damjanovic, Genshaw, and Bockris (13), hydrogen peroxide production in dilute sulfuric acid is accompanied by impurity adsorption, which results also in lower reaction rates. The same has been shown here to take place in concentrated phosphoric acid. The next steps of the reaction therefore probably are

$$(a) \qquad SO_2H \rightarrow SO + SOH \xrightarrow{3H^+} 2H_2O + 2S$$

or

$$(b) \qquad SO_2H + H^+ + e^- \xrightarrow{3e^-} SH_2O_2 \rightarrow S + H_2O_2$$

[or perhaps $2SO_2H \rightarrow 2S + H_2O_2 + O_2$ ref (1)]

The first reaction will take place only preferentially if the heats of adsorption of the product are sufficiently high. In the presence of adsorbed electron-donating impurities the net heat of adsorption of negative species (for instance —O_2H) on the electrode surface should be lowered. From the previous discussion, this will reduce the over-all reaction rate and make reaction (*b*) above the preferred step.[4]

It should be noted that in absence of impurities the reaction

$$S - O_2 + H^+ + e^- \rightarrow S - O_2H$$

will take place under Langmuir conditions of adsorption, with low total coverage of adsorbate, in the double-layer region (below about 750 mV HRE). In the presence of impurities, again Langmuir conditions will occur, now involving high coverages of capillary-active adsorbate. In this case, however, much lower rate constants would be expected, as the adsorbed material will depress the heat of adsorption of the reaction product —O_2H.

We have noted that in the presence of gross amounts of oxidizable impurity (untreated electrolyte) the rest potential is depressed. This is to be expected if the rest potential is a mixed potential, with anodic process diffusion-controlled impurity oxidation and the cathodic process oxygen reduction. The effect of pulsing the electrode desorbs impurities from its surface (18) and leaves more sites available for reaction. If the heat of adsorption of impurities is potential-dependent, the final Tafel plot will appear to be the locus of a family of normal (Langmuirian) Tafel plots of $2RT/\mathbf{F}$ slope, but with changing rate constant, according to impurity coverage. If coverage falls with increase in overpotential, a slope of less than $2RT/\mathbf{F}$ will occur. If a rise in coverage with increasing potential occurs, a net slope greater than $2RT/\mathbf{F}$ results.

Slopes between $RT/\mathbf{F}$ and $2RT/\mathbf{F}$ are frequently observed on oxygen reduction electrodes, and have been observed in impure solutions during the course of this work, on the electrodes which have been in contact with the solution for 1 hr. After 24 hr in the solution, high coverages of strongly bound impurities may be considered to be present. These materials probably do not appreciably desorb during the Tafel plot so that slopes close to theoretical for a 1-electron charge transfer, with no previous charge transfer, under Langmuirian conditions ($2RT/\mathbf{F}$) occur, although at high overpotential.

It is interesting to note when large amounts of strongly adsorbable anion are present (*e.g.*, in HCl solution) slopes appreciably greater than $2RT/\mathbf{F}$ occur (8), probably indicating progressively increasing adsorption of anion with overpotential. In addition, the adsorbed anion effectively prevents SO_2H breakdown on the electrode surface, as H_2O_2 appears to be the primary reaction product (8, 44).

[4] This is perhaps equivalent to saying high energy sites for direct reduction of O_2 to H_2O are blocked.

On this basis, it is possible to rationalize past data for oxygen reduction on bare platinum in acid solutions. When electrodes are given a preparative treatment consisting of anodic and cathodic pulsing (or hydrogen pretreatment at high temperature), slopes close to $RT/\mathbf{F}$ are obtained. In other cases, slopes are obtained which depend more on potential-dependent impurity adsorption than on oxygen electrode kinetics as such.

Similarly, due to the higher slopes of Tafel plots obtained under impure conditions, apparent exchange current values might be higher (Tables I and II) than under pure conditions. This does not imply higher rate constants, but indicates that the observed slope is too high due to potential-dependent electrode deactivation.

Finally, the rate-determining step for oxygen reduction on phase-oxide-free platinum

$$S - O_2 + H^+ + e^- \rightarrow SO_2H$$

appears to be common to all aqueous acid electrolytes which are stable at oxygen-electrode potentials, regardless of temperature or concentration. In acids with anions which are not strongly adsorbed, this reaction will take place under Temkin conditions at potentials above 750 mV, with an approximate slope of $RT/\mathbf{F}$.

APPENDIX

Oxygen Reduction under Temkin Adsorption Conditions

The arguments for the derivation of a Temkin-type rate-controlling equation are as follows. Consider the above reaction taking place at a potential V, under charge-transfer control, at a potential sufficiently far from equilibrium to make the backward reaction negligible.

The rate equation would be

$$i_{\text{forward}} = \mathbf{F}\frac{kT}{h}(\theta^*)[H^+]\left(\exp -\frac{[\Delta G^{\neq} + (1-\beta)(\Delta G_p - \Delta G_r)]}{RT}\right)\cdot \exp\left(\frac{-\beta\mathbf{F}V}{RT}\right) \quad [1]$$

where k, h, and $\mathbf{F}$ have their usual meanings, θ^* is the oxygen coverage on the electrode, $\Delta G^{\neq}$ is the free energy of activation in absence of adsorption, ΔG_r is the free energy of adsorption of reactants (O_2 only, as we assume H^+ is not specifically adsorbed), ΔG_p is the free energy of adsorption of products (—O_2H), and β is the symmetry factor.

Assuming $\beta = \frac{1}{2}$

$$i_{\text{forward}} = \mathbf{F}\cdot\frac{kT}{h}\theta^*[H^+]\left(\exp -\frac{[\Delta G^{\neq} + \frac{1}{2}(\Delta G_p - \Delta G_r)]}{RT}\right)\exp\left(\frac{-\mathbf{F}V}{2RT}\right) \quad [2]$$

If we write $\Delta G = \Delta H - T\Delta S$ in each case

$$i_{\text{forward}} = \text{const.}\ \theta^*[H^+]\left(\exp -\frac{[\Delta H^{\neq} - T\Delta S^{\neq} + \frac{1}{2}(\Delta H_p - \Delta H_r) - \frac{1}{2}T(\Delta S_p - \Delta S_r)]}{RT}\right)\exp\left(\frac{-\mathbf{F}V}{2RT}\right) \quad [3]$$

We make the assumption that a potential-dependent adsorption of reactants and products occurs, which may be reasonably described by a Temkin isotherm in the range of $0.2 > \theta_T > 0.8$, where θ_T is the total coverage on the electrode of strongly bonded adsorbed species (39). These constitute primarily O radicals at high potential (21). We then obtain

$$i_{\text{forward}} = \text{const.}\ \theta^*[H^+]\left(\exp -\frac{[\Delta H^{\neq} - T\Delta S^{\neq} + \frac{1}{2}(\Delta H_p + q_p\theta_T - \Delta H_r + q_r\theta_T) - \frac{1}{2}T(\Delta S_p - \Delta S_r)]}{RT}\right)\exp\left(\frac{-\mathbf{F}V}{2RT}\right) \quad [4]$$

where ΔH_r and ΔH_p are the heats of adsorption at low coverage, and q_r and q_p are enthalpy-coverage factors for reactants and products. It is understood that q is positive for a reduction in heat of adsorption; $\Delta H^{\neq}$ and $\Delta S^{\neq}$ are the enthalpy and entropy of activation in absence of adsorption.

$$i_{forward} = \text{const. } \theta^* \cdot [H^+] \left(\exp - \frac{[\tfrac{1}{2}(q_p - q_r)\theta_T - \tfrac{1}{2}T(\Delta S_p - \Delta S_r)]}{RT} \right) \exp\left(\frac{-FV}{2RT}\right) \quad [5]$$

We must now substitute a relation for θ^* in terms of P_{O_2}. It is reasonable to assume that θ^* is very low, and that oxygen adsorption follows a Langmuir isotherm, so that

$$P_{O_2} = A \frac{\theta^*}{1 - \theta_T} \exp(\Delta G/RT) \quad [6]$$

where ΔG is the free energy of adsorption of oxygen.[5] However, according to our previous postulate, that heat of adsorption of the reactants depends on θ_T, we may write

$$P_{O_2} = A \left(\frac{\theta^*}{1 - \theta_T}\right) \exp \frac{(\Delta H_r - T\Delta S_r + q_r\theta_T)}{RT} \quad [7]$$

Assuming changes in entropy of adsorption with coverage are negligible (42) we may write

$$P_{O_2} = A \left[\frac{\theta^*}{1 - \theta_T}\right] \exp\left[\frac{\Delta H_r - T\Delta S_r}{RT}\right] \exp\left[\frac{q_r\theta_T}{RT}\right] \quad [8]$$

which is basically a modified Frumkin isotherm.

We have seen from Eq. [5] that

$$i \propto \theta^*$$

and we have found experimentally that

$$i \propto P_{O_2}$$

Now, from Eq. [8]

$$P_{O_2} \propto \theta^*$$

for small values of θ^* provided that the expression

$$\exp[(\Delta H_r - T\Delta S_r + q_r\theta_T)/RT] \quad [9]$$

from Eq. [8] does not substantially change with θ_T.

Assuming that ΔS_r does not depend on total coverage (42) and, as we noted experimental first-order dependence between $\theta_T = 0.1$ (at low potentials) and $\theta_T \sim 0.2$ (at about 1000 mV) to within 10%, then

$$\exp(\Delta H_r/RT) > 0.9 \exp[(\Delta H_r + q_r\theta_T)/RT] \quad [10]$$

This inequality gives the upper limit of q_r, the lower limit being 0. Thus,

$$\exp - 0.1\, q_r/RT > 0.9$$

giving

$$0.1\, q_r/RT < 0.1$$

Hence

$$q_r < 0.6 \text{ kcal/mole}^6$$

We may conclude, therefore, that q_r is small; it has been shown that q_p is about 23 kcal/mole in N perchloric and sulfuric acids (11, 21).

Assuming θ^* is small

$$\frac{\partial}{\partial P_{O_2}}\left(\frac{\theta^*}{1 - \theta_T}\right) \sim \partial\theta^*/\partial P_{O_2}$$

and, substituting Eq. [8] in Eq. [5] we have

$$i = \text{const. } P_{O_2}[H^+] \left[\exp - \frac{[\tfrac{1}{2}(q_p - q_r)\theta_T - \tfrac{1}{2}T(\Delta S_p - \Delta S_r)]}{RT}\right] \exp - \left(\frac{[\Delta H_r - T\Delta S_r + q_r\theta_T]}{RT}\right) \exp\left(\frac{-FV}{2RT}\right) \quad [11]$$

which gives, as ΔH_r is constant

$$\text{const. } P_{O_2}[H^+] \exp - \left[\frac{\tfrac{1}{2}(q_p + q_r)\theta_T - \tfrac{1}{2}T(\Delta S_p + \Delta S_r)}{RT}\right] \exp\left(\frac{-FV}{2RT}\right) \quad [12]$$

Again, assuming that changes in θ do not influence ΔS_p or ΔS_r, we obtain

$$i \propto P_{O_2}[H^+] \exp - \left(\frac{\tfrac{1}{2}(q_p + q_r)\theta_T}{RT}\right) \exp\left(\frac{-FV}{2RT}\right) \quad [13]$$

It should be noted that this is basically the same equation as that derived by Damjanovic and Brusic (11) except that their equation predicts that weaker adsorption of reactants would cause an increase in the reaction rate; that is, they have $-q_r$, not $+q_r$ in their equation.

Damjanovic and Brusic (11) have shown that for platinum an approximately linear variation of coverage exists in the intermediate coverage region ($0.2 < \theta < 0.8$) and that the potential for unit coverage changes by 60 mV per unit of pH.

Hence, where K is constant, we obtain

$$\theta(V, pH) = K \cdot V + K(RT/F) \cdot pH + \text{const.} \quad [14]$$

Substituting in Eq. [13] we obtain

$$i \propto P_{O_2}[H^+] \left(\exp - \frac{[\tfrac{1}{2}(q_p + q_r) \cdot (KV + K(RT/F)pH)]}{RT}\right) \exp\left(\frac{-FV}{2RT}\right) \quad [15]$$

From published data (11, 21) we find that $q_p \approx 23$ kcal/mole. Hence we may write, as $q_r << q_p$

$$i \propto P_{O_2}[H^+] \left(\exp - \frac{\tfrac{1}{2}q_p[KV + K(RT/F)pH]}{RT}\right) \exp\left(\frac{-FV}{2RT}\right) \quad [16]$$

Under equilibrium conditions, neglecting pre-exponential terms in the forward and backward Temkin rate expressions (21) and as "q" is large (43)

$$q\,\delta\,\theta = F\,\delta\,V$$

That is, the change in heat of adsorption in the interval ΔV is equal to the change in electrochemical potential.[7]

Hence

$$q = F\left(\frac{\partial V}{\partial \theta}\right)_{pH} \quad [17]$$

and, from Eq. [14]

$$(\partial V/\partial\theta)_{pH} = \frac{1}{K} \quad [18]$$

where q refers to any strongly bound species.

Substituting Eq. [17] and [18] in Eq. [16], we obtain

$$i \propto P_{O_2}[H^+] \left(\exp - \frac{[\tfrac{1}{2}FV + \tfrac{1}{2}RT(pH)]}{RT}\right) \exp\left(\frac{-FV}{2RT}\right) \quad [19]$$

or

[5] The constant A has been introduced in Eq. [6] to allow ΔG to represent the free energy of adsorption of oxygen at low coverage.

[6] This implies also that ΔH_r is small, which is reasonable as oxygen is adsorbed as molecules.

[7] It should be noted that it may perhaps be more accurate to write

$$F\delta V = \Delta\Delta G$$

where $\Delta\Delta G$ is the equilibrium change in free energy of adsorption of the intermediate in the interval δV. If we substitute this quantity in Eq. [2], it is not then necessary to suppose that the entropy of adsorption is coverage-independent (42).

$$i \propto P_{O_2}[H^+]^{3/2} \exp\left(-\frac{FV}{RT}\right) \quad [20]$$

This equation has a Tafel slope of RT/F, and has the correct oxygen partial pressure and pH-dependence (11).

Acknowledgment

The author wishes to thank Pratt & Whitney Aircraft Division of United Aircraft Corporation, and the sponsors of this work under the TARGET fuel cell program, for permission to publish this paper. The help of the various members of IGT who assisted in preparation is also greatly appreciated.

Manuscript submitted Aug. 1, 1969; revised manuscript received *ca.* Nov. 12, 1969.

Any discussion of this paper will appear in a Discussion Section to be published in the December 1970 JOURNAL.

REFERENCES

1. D. T. Sawyer and L. V. Interrante, *J. Electroanal. Chem.*, **2**, 310 (1961).
2. M. W. Breiter, *Electrochim. Acta*, **9**, 441 (1964).
3. C. C. Liang and A. L. Juliard, *J. Electroanal. Chem.*, **9**, 390 (1965).
4. E. I. Khrushcheva, N. A. Shumilova, and M. R. Tarasevich, *Elektrokhim.*, **1**, 730 (1965).
5. L. Müller and L. N. Nekrasov, *Dokl. Akad. Nauk. S.S.S.R.*, **157**, 416 (1964).
6. L. Müller and L. N. Nekrasov, *J. Electroanal. Chem.*, **9**, 282 (1965).
7. J. P. Hoare, *This Journal*, **112**, 602 (1965).
8. G. Bianchi and T. Mussini, *Electrochim. Acta*, **10**, 445 (1965).
9. J. J. Lingane, *J. Electroanal. Chem.*, **2**, 296 (1961).
10. A. Damjanovic and J. O'M. Bockris, *Electrochim. Acta*, **11**, 376 (1966).
11. A. Damjanovic and V. Brusic, *ibid.*, **12**, 615 (1967).
12. A. Damjanovic, A. Dey, and J. O'M. Bockris, *ibid.*, **11**, 791 (1966).
13. A. Damjanovic, M. A. Genshaw, and J. O'M. Bockris, *This Journal*, **114**, 466 (1967).
14. A. Damjanovic, M. A. Genshaw, and J. O'M. Bockris, *J. Chem. Phys.*, **45**, 4057 (1966).
15. A. J. Appleby, *J. Electroanal. Chem.*, **24**, 97 (1970).
16. H. A. Laitenen and C. G. Enke, *This Journal*, **107**, 773 (1960).
17. A. K. N. Reddy, M. Genshaw, and J. O'M. Bockris, *J. Electroanal. Chem.*, **8**, 406 (1964).
18. S. D. James, *This Journal*, **114**, 1113 (1967).
19. S. Schuldiner and T. B. Warner, *ibid.*, **112**, 212 (1966).
20. J. P. Hoare, *ibid.*, **109**, 858 (1962).
21. H. Wroblowa, M. L. B. Rao, A. Damjanovic, and J. O'M. Bockris, *J. Electroanal. Chem.*, **15**, 139 (1967).
22. G. Lewis and M. Randell, "Thermodynamics and Free Energy of Chemical Substances," McGraw-Hill Book Co., New York (1923).
23. Monsanto Corporation, Technical Bulletin *1-239*.
24. J. Bravacos, M. Bonnemay, E. Levart, and A. A. Pilla, *Compt. Rend. Acad. Sci. Paris*, **265**, 337 (1967).
25. A. J. Appleby and A. Borucka, *This Journal*, **116**, 1212 (1969).
26. V. S. Bagotskii and I. E. Yablokova, *Z. Fiz. Khim.*, **27**, 1663 (1953).
27. L. Müller and L. N. Nekrasov, *Dokl. Akad. Nauk. SSSR*, **154**, 437 (1964).
28. L. Müller and V. V. Sobol, *Elektrokhim.*, **1**, 111 (1965).
29. L. N. Nekrasov, *ibid.*, **2**, 438 (1966).
30. H. P. Stout, *Discussions Faraday Soc.*, **1**, 246 (1947).
31. A. C. Riddiford, *Electrochim. Acta*, **4**, 170 (1961).
32. T. P. Hoar, *Proc. 8th Meeting CITCE, Madrid 1956*, p. 439, Butterworths, London (1958).
33. H. Mauser, *Z. Elektrochem.*, **62**, 419 (1958).
34. D. S. Gnanamuthu and J. V. Petrocelli, *This Journal*, **114**, 1036 (1967).
35. J. O'M. Bockris, *J. Chem. Phys.*, **24**, 817 (1956).
36. B. E. Conway and P. L. Bourgault, *Can. J. Chem.*, **40**, 1690 (1962).
37. D. J. Ives and G. J. Janz, "Reference Electrodes—Theory and Practice," p. 365, Academic Press, New York (1961).
38. J. P. Hoare, *This Journal*, **112**, 849 (1965).
39. B. E. Conway and E. Gileadi, *Trans. Faraday Soc.*, **58**, 2493 (1962).
40. W. Böld and M. Breiter, *Electrochim. Acta*, **5**, 145 (1961).
41. O. A. Petrii, R. V. Marvet, and Zh. N. Malysheva, *Elektrokhim.*, **3**, 962 (1967).
42. R. Parsons, *Trans. Faraday Soc.*, **54**, 1053 (1958).
43. T. Biegler and R. Woods, *J. Electroanal. Chem.*, **20**, 347 (1969).
44. A. Damjanovic, Private communication (1969).

Rotating Ring-Disk Electrodes

II. Digital Simulation of First and Second-Order Following Chemical Reactions

Keith B. Prater[1] and Allen J. Bard*

Department of Chemistry, The University of Texas at Austin, Austin, Texas

ABSTRACT

A digital simulation technique has been employed to treat the steady-state and transient ring current behavior at the rotating ring-disk electrode (RRDE) for cases where the intermediate generated at the disk electrode undergoes a first- or second-order homogeneous chemical reaction leading to a nonelectroactive species. Where comparisons were possible, the results were found to be in good agreement with previous approximate theoretical treatments. Working curves are provided which allow determination of rate constants of the homogeneous reactions from ring-current-rotation rate data.

The rotating ring-disk electrode (RRDE) was introduced by Frumkin and Nekrasov (1) as a means of detecting intermediates of electrode reactions. An intermediate, B, is generated at the disk electrode by the reaction

$$A \pm ne \rightarrow B \quad [1]$$

and B is detected at the ring electrode by applying a sufficient potential such that all B reaching the ring is transformed back to A by the reaction

$$B \pm ne \rightarrow A \quad [2]$$

If B is a stable species, then the ratio of the current at the ring electrode to the current at the disk electrode is a function only of the geometry of the electrode (2). This ratio is called the collection efficiency, N, and is given by the expression

[1] Present address: University of Texas at El Paso, El Paso, Texas.
* Electrochemical Society Active Member.

$$N = -i_r/i_d \quad [3]$$

If species B undergoes a chemical reaction which depletes its concentration as it passes from the disk to the ring, then the observed collection efficiency under these conditions, N_k, (the kinetic collection efficiency) will be smaller than that found in the absence of these reactions. In this case, the collection efficiency is a function, not only of electrode geometry, but also of the rate constant of the reaction, the rotation rate, ω, and other solution parameters.

Albery and Bruckenstein (3) have given an approximate treatment of steady-state kinetic collection efficiencies for the first-order EC mechanism (where EC denotes an electron transfer followed by a chemical reaction)

$$B \xrightarrow{k_1} X \quad [4]$$

in which B reacts to give an electro-inactive species X. This treatment is valid only for extremely thin-ring thin-gap electrodes and then only for certain values of k_1/ω. In a later paper, Albery, Hitchman, and Ulstrup (4) modified the previous treatment to make it applicable to a wider range of electrode geometries. Albery (5) has also treated the ring current transients for this mechanism in the case of a constant current at the disk electrode.

Albery and Bruckenstein (6) have also given an approximate treatment of the second-order EC mechanism

$$B + C \xrightarrow{k_2} Y + Z \quad [5]$$

where C, Y, and Z are electro-inactive species. Unfortunately, the treatment of this mechanism is valid only for very small values of the parameter $k_2C^\circ_A/\omega$ where C°_A is the bulk concentration of species A.

Albery, Hitchman, and Ulstrup (4) have presented experimental work to support the modified treatment of the first-order case, and Johnson and Bruckenstein (7) have investigated the second-order case. In both of these studies, however, the systems chosen did not strictly conform to the above mechanisms in that in all cases one product of the homogeneous following reaction was the starting species, A. Thus, the experimental studies were more related to the catalytic reaction mechanism; a theoretical treatment of that case will be given in a later paper.

In this paper, we present the results of the application of a digital simulation technique (8) to the first- and second-order EC mechanisms. In addition to steady-state kinetic collection efficiencies, ring current transient behavior is presented. This simulation technique can be applied to any electrode and the results are valid for any value of the rate parameters, k_1/ω and $k_2C^\circ_A/\omega$.

Digital Simulation Method

The basic method for the digital simulation of the RRDE including the simulation of the first-order EC mechanism has been presented in a previous paper (8). Only two modifications of the simulation technique previously presented are necessary in order to simulate the second-order EC mechanism. First, the collection efficiency for such a process will be determined not only by the value of the rate constant, k_2, the rotation rate, ω, and the bulk concentration of species C, C°_C. For the second-order case, then, an additional parameter, m, given by

$$m = C^\circ_C/C^\circ_A \quad [6]$$

must be specified. Thus in setting up the initial conditions, the fractional concentration of species A in any box will be

$$F_A(J,K) = 1.0 \quad [7]$$

and the initial fractional concentration of species C in any box will be

$$F_C(J,K) = m \quad [8]$$

A second difference between the treatment of the first- and second-order cases concerns the form of the dimensionless rate parameter. The pertinent rate law for the second-order mechanism is

$$-dC_C/dt = -dC_B/dt = k_2C_BC_C \quad [9]$$

In terms of the simulation this becomes

$$-\Delta C_C = -\Delta C_B = k_2C_BC_C\Delta t \quad [10]$$

Dividing through by C°_A and letting

$$C_C/C^\circ_A = F_C \quad [11]$$

and

$$C_B/C^\circ_A = F_B \quad [12]$$

then Eq. [10] becomes

$$-\Delta F_C = -\Delta F_B = k_2F_BC_C\Delta t \quad [13]$$

Replacing C_C by $F_CC^\circ_A$ and using the equation (Eq. [12] and [25], ref. (8))

$$\Delta t = t_k/L = \nu^{1/3}D_A^{-1/3}\omega^{-1}L^{-1}(0.51)^{-2/3} \quad [14]$$

one obtains

$$-\Delta F_C = -\Delta F_B = k_2t_kC^\circ_AF_BF_C/L \quad [15]$$

The product $k_2t_kC^\circ_A$ is the dimensionless rate parameter applicable to this mechanism and is called XKTC. Thus

$$XKTC = k_2t_kC^\circ_A = k_2C^\circ_A\omega^{-1}\nu^{1/3}D_A^{-1/3}(0.51)^{-2/3} \quad [16]$$

where as before ν is the kinematic viscosity and D_A is the diffusion coefficient of species A.

The effects of kinetics on the concentration in any box may be taken into account by replacing the existing concentrations of B and C, F_B and F_C by

$$F'_B(J,K) = F_B(J,K) - \Delta F_B(J,K) \quad [17]$$

$$F'_C(J,K) = F_C(J,K) - \Delta F_C(J,K) \quad [18]$$

Other than these two modifications, the simulation is identical to that previously presented.

A digital computer program based on the digital simulation model with the appropriate modifications was used to obtain the results which will be presented. These results were obtained by first selecting a value for the appropriate dimensionless rate parameter

$$XKT = (0.51)^{-2/3}k_1\omega^{-1}\nu^{-1/3}D_A^{-1/3} \quad [19]$$

for the first-order case or XKTC for the second-order case. In the second-order case, a value for the parameter m was also specified. The computation was then carried out until a steady state was attained. This computation yields both steady-state kinetic collection efficiencies, N_k, and the ring current transients as functions of the dimensionless rate parameters and m. In all cases unless otherwise stated, L = 50 and D_m = 0.45 and the appropriate correction factors were used.

First-Order Results

Steady-state behavior.—The simulated collection efficiency *vs.* XKT curve for an electrode approximating the thin-ring thin-gap electrode treated by Albery and Bruckenstein is shown in Fig. 1 and 2. In Fig. 1, the simulation is compared with Albery and Bruckenstein's Eq. [6.4] (3) in the region of small XKT. The entire simulated curve is shown in Fig. 2 as is the comparison with their Eq. [5.8] (3). These graphs show clearly the regions in which the approximate treatments of Albery and Bruckenstein apply for an electrode of this geometry. These regions of applicability are quite close to those suggested by Albery and Bruckenstein.

In a later paper (4), Albery pointed out that the thin-ring thin-gap treatment is not valid for most

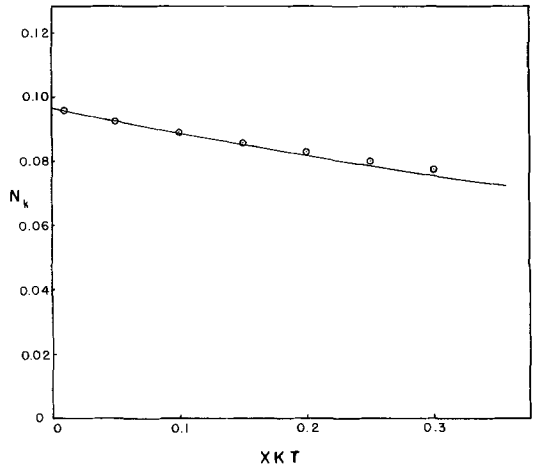

Fig. 1. Collection efficiency vs. XKT for a first-order following reaction at a thin-ring thin-gap electrode (IR1 = 2000, IR2 = 2040, IR3 = 2080). ⊙ Comparison with Albery's Eq. [6.4] (2). XKT = $k_1\omega^{-1}D^{-1/3}\upsilon^{1/3}(0.51)^{-2/3}$.

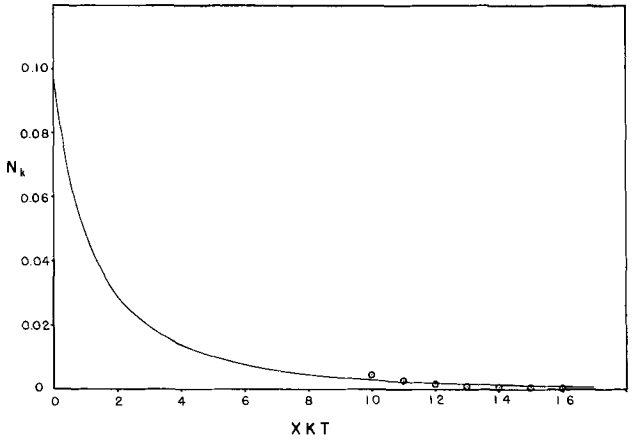

Fig. 2. Collection efficiency vs. XKT for a first-order following reaction at thin-ring thin-gap electrode (IR1 = 2000, IR2 = 2040, IR3 = 2080). ⊙ Comparison with Albery's Eq. [5.8] (2). XKT = $k_1\omega^{-1}D^{-1/3}\nu^{1/3}(0.51)^{-2/3}$.

practical electrodes, and he presented a modified theory which should be applicable to a wider range of electrode geometries. The results of the simulation of the two electrodes for which Albery presented his calculations are shown in Fig. 3 as well as Albery's calculated values for the collection efficiency as a function of $(XKT)^{1/2}$. The agreement over this range of XKT values is excellent.

It is interesting to consider the effect of electrode geometry on the range of applicability of different electrodes to studies of first-order following reactions. The results of the simulation of three different electrodes are given in Fig. 4. Electrode A is the electrode previously presented which approximates the thin-ring thin-gap electrode. Electrode B is one of Albery's electrodes. It has a fairly thin gap and a moderately thin ring. Electrode C which has been used in these laboratories has a comparatively wide gap and ring. The simulated working curves show, as expected, that the thin-ring thin-gap electrode (A) is the most applicable of the three for studying extremely fast reactions, while electrode C, with a wider gap is more useful for slow reactions. The point to be made here is that while electrodes similar to electrode A should be used for studying fast reactions, they are not useful for slow reactions ($k \leq 0.1$) because even at the lowest usable rotation rates such a reaction does not proceed to any detectable extent in the time required for species B to reach the ring electrode. In these cases, electrodes with gaps as wide as that in electrode C or even wider should be used

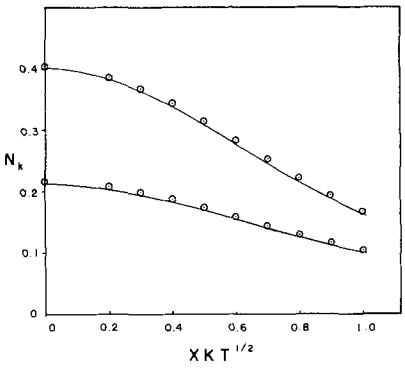

Fig. 3. Collection efficiency vs. $(XKT)^{1/2}$ for a first-order following reaction for two electrodes of different geometries

a. $r_1 = 0.3635$	$r_2 = 0.3777$	$r_3 = 0.4835$
IR1 = 200	IR2 = 208	IR3 = 266
b. $r_1 = 0.4770$	$r_2 = 0.4869$	$r_3 = 0.5222$
IR1 = 820	IR2 = 837	IR3 = 898

⊙ Comparison with Albery's Fig. 2 (4). XKT = $k_1\omega^{-1}D^{-1/3}\upsilon^{1/3}(0.51)^{-2/3}$.

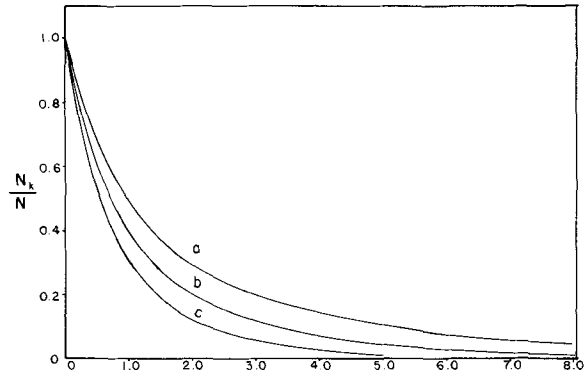

Fig. 4. Collection efficiency vs. XKT for a first-order following reaction for three electrodes of different geometries. XKT = $k_1\omega^{-1}D^{-1/3}\upsilon^{1/3}(0.51)^{-2/3}$. a, $r_2/r_1 = 1.02$, $r_3/r_2 = 1.02$; b, $r_2/r_1 = 1.04$, $r_3/r_2 = 1.28$; c, $r_2/r_1 = 1.14$, $r_3/r_2 = 1.70$.

For this first-order case, identical steady-state collection efficiencies are predicted when the boundary condition at the disk electrode corresponds to a constant current step instead of a potential step. The constant current boundary condition at the disk affects only the transient and not the steady-state behavior of the collection efficiency.

Transient behavior.—The simulated ring current transients (RCT) for this mechanism due to a potential step at the disk are shown in Fig. 5. Each curve represents the RCT for the specified value of the dimensionless rate parameter, XKT. As must be the case, the steady-state currents are seen to decrease with increasing values of XKT. An interesting feature of these curves is that, unlike the RCT in the absence of a following reaction, the ring current passes through a maximum before attaining steady state. This is because under the potential step condition, a very large instantaneous flux of species B is generated at the initiation of electrolysis [see Fig. 2, ref. (8)]. The short time interval between the generation of this large flux of B and the detection of B at the ring does not permit the homogeneous reaction to reduce the concentration of B to its eventual, lower steady-state value. Hence a maximum in the ring current is observed. Identical simulation results are obtained if the simulation is carried out with L = 1000 and no correction factors. This effect is more clearly shown in

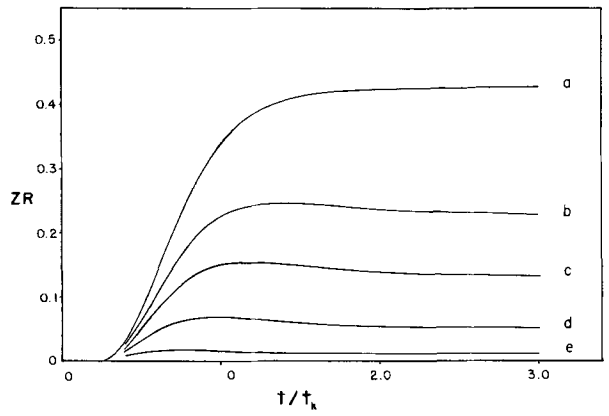

Fig. 5. Ring current transients for a first-order following reaction for different values of XKT. a, 0.0; b, 0.5; c, 1.0; d, 2.0; e, 4.0. Zr $= i_r/(0.51)^{1/3}nFA_DC^\circ {}_AD_B^{2/3}\omega^{1/2}\upsilon^{-1/6}$. XKT $= k_1\omega^{-1}D^{-1/3}\upsilon^{1/3}(0.51)^{-2/3}$. Simulated with IR1 = 83, IR2 = 94, IR3 = 159.

Fig. 6 in which the RCT's have each been normalized by the eventual steady-state current for each value of XKT. This plot also points out that the value of $\omega t\ D^{1/3}\nu^{-1/3}(0.51)^{2/3}$ at which the ring current is one-half (or any other fraction) of the steady-state value is a function of XKT and could in principle be used to determine the rate constant, as has been suggested by Albery (5).

These results can be compared with those obtained using a constant current boundary condition at the disk. The results of two simulations which differed only in the boundary condition at the disk are shown in Fig. 7. Note that no maximum is observed when a constant current is applied to the disk. The effect of the rate parameter on the normalized RCT's with a constant current step at the disk is shown in Fig. 8. As before, the value of the time parameter, $\omega t\ D^{1/3}\nu^{-1/3}(0.51)^{2/3}$, at a specified fraction of the steady-state current is a function of the rate parameter, XKT. It should also be pointed out that these normalized curves are independent of the value of the applied constant current.

Second-Order Results

Steady-state behavior.—A series of curves of N_k *vs.* (XKTC) (m) for different values of m, for a following second-order reaction and for the disk electrode held at a potential where the limiting current for the conversion of A to B occurs, is shown in Fig. 9. Also shown in Fig. 9 is the simulated collection efficiency

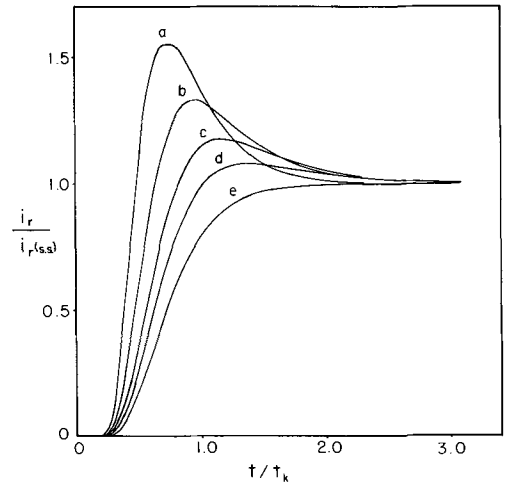

Fig. 6. Ring current transients for a first-order following reaction for different values of XKT. a, 4.0; b, 2.0; c, 1.0; d, 0.5; e, 0.0. Curves are normalized by the steady-state current at each value of XKT. Simulated for IR1 = 83, IR2 = 94, IR3 = 159. XKT $= k_1\omega^{-1}D^{-1/3}\upsilon^{1/3}(0.51)^{-2/3}$.

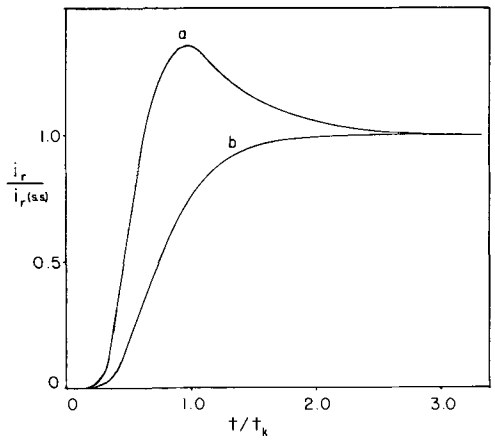

Fig. 7. Ring current transients for a first-order following reaction for XKT = 2.0, IR1 = 83, IR2 = 94, IR3 = 159. $t_k = \omega^{-1}D^{-1/3}\upsilon^{1/3}(0.51)^{-2/3}$. a, Potential step at the disk electrode; b, constant current at the disk electrode.

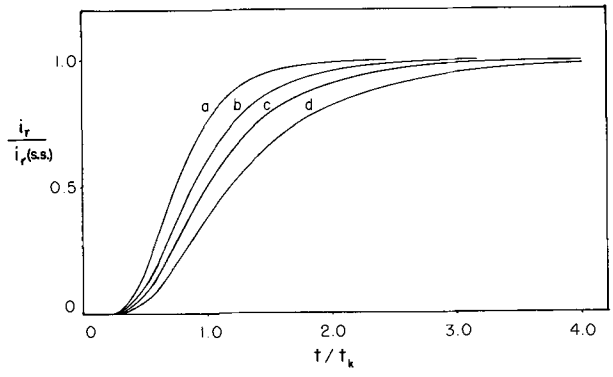

Fig. 8. Ring current transients for a first-order following reaction with constant current at the disk for different values of XKT. $t_k = \omega^{-1}D^{-1/3}\upsilon^{1/3}(0.51)^{-2/3}$. a, 2.0; b, 1.0; c, 0.5; d, 0.0. IR1 = 83, IR2 = 94, IR3 = 159.

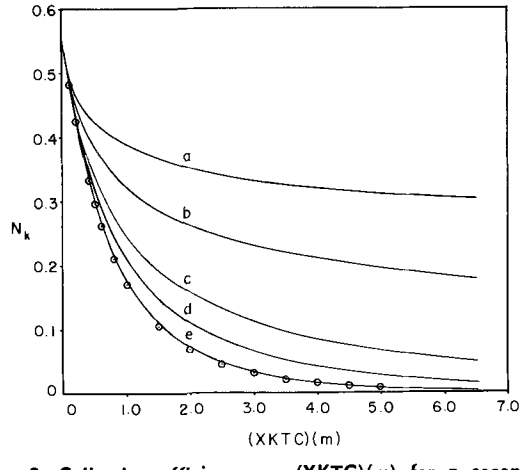

Fig. 9. Collection efficiency *vs.* (XKTC)(m) for a second-order following reaction for different values of m $= C^\circ_C/C^\circ_A$. a, 0.10; b, 0.20; c, 0.50; d, 1.0; e, 10.0. ⊙ Simulated first-order curve. IR1 = 83, IR2 = 94, IR3 = 159. XKTC $= k_2\omega^{-1}C^\circ {}_AD^{-1/3}\upsilon^{1/3}(0.51)^{-2/3}$.

curve for a first-order following reaction. Note that when C is in tenfold excess, the second-order curve is almost indistinguishable from the first-order curve; thus when m = 10.0, the second-order process can be treated as a pseudo-first-order one.

In the case of this second-order mechanism, unlike that of a following first-order reaction, the simulated collection efficiencies presented here are valid only for the case $i_d = i_{lim}$. If a constant current less than the limiting current were applied to the disk, differ-

ent collection efficiencies would be observed as pointed out by Albery and Bruckenstein (6). The simulation of the effects of a constant current less than the limiting current can easily be done, but there seems to be little reason to do so.

In the treatment of this case by Albery and Bruckenstein (6), the current at the disk electrode is adjusted to a value where the concentrations of B and C are equal at the inner edge of the ring electrode. Under these conditions, the current at the ring due to species B will be dependent on the rate of the reaction between B and C and is given by the following equation

$$i_r = BnF\pi r_2^2 D_A \omega^{3/2} \nu^{-1/2} k_2^{-1} \quad [20]$$

The constant, B, was originally calculated to be 590 (6) but more recently has been given as 210 (7). The disk current necessary to produce the appropriate conditions is given by

$$i_d = 620nF\pi r_1^2 D_A^{2/3} \omega^{1/2} \nu^{-1/6} C^\circ_C (1 - F(\alpha))^{-1} \quad [21]$$

where $F(\alpha)$ is a geometrical parameter of the electrode which has been tabulated by Albery and Bruckenstein (2). Note that for the particular value of m, given by

$$m = C^\circ_C / C^\circ_A = 1 - F(\alpha) \quad [22]$$

Eq. [21] becomes

$$i_d = 620nF\pi r_1^2 D_A^{2/3} \omega^{1/2} \nu^{-1/6} C^\circ_A \quad [23]$$

This is precisely the limiting current due to species A as predicted by the Levich equation. Thus from Eq. [20] and [23], N_k in this case is given by

$$N_k = (B/620)(r_2/r_1)^2 \omega k_2^{-1} C^\circ_A{}^{-1} D^{1/3} \nu^{-1/3} \quad [24]$$

or

$$N_k = (B/620)(r_2/r_1)^2 (0.51)^{2/3} (XKTC)^{-1} \quad [25]$$

Note that Eq. [24] must at best be valid only as $\omega/k_2 C^\circ_A$ approaches zero where it accurately predicts that, under these conditions, N_k approaches zero. At the other limit, as $\omega/k_2 C^\circ_A$ approaches infinity, Eq. [24] predicts that N_k should increase without bound, while in reality the actual upper limit is N, the collection efficiency in the absence of kinetic complications.

To compare the digital simulation results with those of Albery and Bruckenstein (6), an electrode of a given geometry was chosen, and m was adjusted according to Eq. [22]. Values of N_k at various values of XKTC with i_d at its limiting value can then be used to investigate the useful range of Eq. [24].

Simulated collection efficiencies *vs.* 1/XKTC are shown in Fig. 10 for one of Albery's electrodes under these conditions. Also shown is the line predicted by Eq. [25] using B = 210. The simulation yields curves which approach the proper limits (zero or N) for the extreme values of $\omega/k_2 C^\circ_A$. In the region of small $\omega/k_2 C^\circ_A$, the simulated curve is approximately linear, but the agreement with Eq. [25] depends on the particular geometry. The slope of the simulated curve as $\omega/k_2 C^\circ_A$ approaches zero yields a value of B of about 260, but it seems that the use of the entire simulated working curve would be preferable to an approximate linearization near $\omega/k_2 C^\circ_A = 0$.

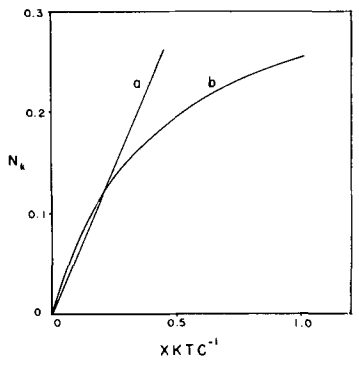

Fig. 10. Collection efficiency *vs.* $(XKTC)^{-1}$ for a second-order following reaction. m = 0.60. IR1 = 200, IR2 = 208, IR3 = 266. $XKTC = k_2\omega^{-1}C^\circ_A D^{-1/3}\upsilon^{1/3}(0.51)^{-2/3}$. Curve a is a plot of Eq. [25]; curve b is the simulated curve.

Albery and Bruckenstein's recommended experimental procedure involves variation of i_d at values below the limiting current and at constant ω to obtain the i_r values used in fitting Eq. [24]. It appears that a more straight forward procedure when working curves such as those in Fig. 9 are available, would involve maintaining i_d at its limiting value and studying the variation of N_k with ω and m. The value of k_2 is then obtained by fitting the experimental results to these working curves.

Transient behavior.—A description of RCT's for second-order following reactions has not been given previously. The simulation shows that the RCT's for the second-order mechanism are similar to those for the first-order case. As shown in Fig. 11, the extent to which a maximum is predicted in the potential step case is a function of the ratio of the bulk concentrations of species A and C. If A is in excess, then the maximum is small because very little B disappears on its way to the ring and the RCT approaches the RCT in the absence of a following reaction. If C is in excess, then the maxima are similar to those obtained for the first-order case.

Conclusion

The digital simulation technique is capable of describing both the steady-state and transient behavior at the RRDE for systems involving homogeneous reactions following the electrode reaction for a wide range of electrode geometries, ω and R. Although the simulation technique permits the calculation of the transient behavior of the ring current, there are many experimental problems involved in measuring these transients. The most important problem is that adsorption of the intermediate, B, on the disk electrode will delay and smear out the RCT while desorption of B produced from adsorbed A will produce a maximum similar in form to the one predicted for this kinetic case, even in the absence of kinetic effects. Bruckenstein (9) has considered cases like this and their effects on transients. Since adsorption of either product or reactant is so frequently found, the observation of the maxima predicted by the simulation will be difficult. For the same reason, the use of RRDE transient measurements to investigate the kinetics of homogeneous reactions is probably less profitable and more difficult, than the corresponding steady-state measure-

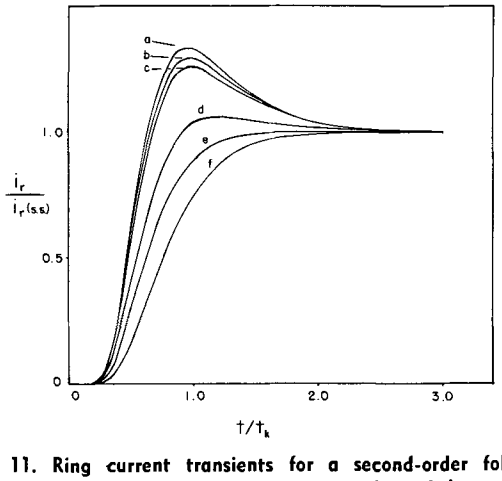

Fig. 11. Ring current transients for a second-order following reaction with a potential step at the disk. $t_k = \omega^{-1}D^{-1/3}\upsilon^{1/3}(0.51)^{-2/3}$. IR1 = 83. IR2 = 94, IR3 = 159. The curves are all generated for $(XKTC)(m)$ = 2.0 at different values of m; also shown is the first-order curve. a, First-order; b, 10.0; c, 5.0; d, 1.0; e, 0.5; f, 0.1.

ments. We might point out that adsorption interferes in a similar way in other types of electrochemical transient measurements (*e.g.*, cyclic voltammetry and chronopotentiometry).

The method of obtaining rate constants proposed here involves setting the disk current at its limiting value, observing the ring current as a function of ω, and fitting the results to working curves for the particular RRDE employed. This technique should prove just as useful, and operationally somewhat easier, than the technique suggested by Albery and Bruckenstein (6). The relatively small value of m which yields essentially pseudo-first-order behavior ($m > 10$) suggests that a good fit to the first-order working curves does not necessarily indicate that a second-order reaction is not involved.

Acknowledgment

The support of the Mobil Oil Corporation and the Eastman Kodak Company for fellowships to one of us (K.B.P.) and the Robert A. Welch Foundation and National Science Foundation (GP 6688X) are gratefully acknowledged. The authors are indebted to J. T. Maloy for helpful discussions during the course of this work.

Manuscript submitted May 29, 1969; revised manuscript received *ca.* Nov. 17, 1969.

Any discussion of this paper will appear in a Discussion Section to be published in the December 1970 JOURNAL.

REFERENCES

1. A. N. Frumkin and L. N. Nekrasov, *Doklady Akad. Nauk. SSSR*, **126**, 115 (1959).
2. W. J. Albery and S. Bruckenstein, *Trans. Faraday Soc.*, **62**, 1920 (1966).
3. W. J. Albery and S. Bruckenstein, *ibid.*, 1946 (1966).
4. W. J. Albery, M. L. Hitchman, and J. Ulstrup, *ibid.*, **64**, 2831 (1968).
5. W. J. Albery, *ibid.*, **63**, 1771 (1967).
6. W. J. Albery and S. Bruckenstein, *ibid.*, **62**, 2584 (1966).
7. D. C. Johnson and S. Bruckenstein, *J. Am. Chem. Soc.*, **90**, 6592 (1968).
8. K. B. Prater and A. J. Bard, *This Journal*, **117**, 207 (1970).
9. S. Bruckenstein and D. T. Napp, *J. Am. Chem. Soc.*, **90**, 6303 (1968).

Technical Notes

Ultrafine Porous Polymer Membranes as Battery Separators

Joseph L. Weininger* and Fred F. Holub

General Electric Research and Development Center, Schenectady, New York

In nonaqueous galvanic systems, based on organic solvents, it is important to keep soluble ions of the cathodic reactant from the anode. Conventional ion exchange membranes have been used (1, 2) for this purpose, but have not been able to support appreciable current densities. In solvent exchange only an insufficient amount of organic solvent, *e.g.* propylene carbonate or dimethyl sulfoxide, replaces water in the ion exchange resin. To obviate this problem and obtain a separator for organic electrolyte cells, an alternate method of ion exclusion is reported in this note.

It is possible to restrict migration of solvated ions by reducing the pore size of microporous membranes below a certain limit. Different methods are known of producing microporous polymers by the introduction of additives into a thermoplastic resin and following this by the removal of the additive to leave a porous structure. For example, Sargent and Safford (3) introduced anionic surfactants into polyethylene and processed the mixture. After the additive is leached out, there remains a microporous structure. Similarly, in the present method ultrafine porous polymer membranes are prepared. These membranes are flexible, about 50% porous, and, most importantly, have extremely fine pore size. The average pore size is between 40 and 120Å.

Membranes were prepared by adding sodium benzoate or other salts of benzoic acid to the melted polymer in a weight ratio of 70-85 parts of benzoate to 30-15 parts of polymer. The salt does not dissolve in the polymer, but forms a dispersion or colloidal suspension. In processing, the polymer was milled on differential rolls with the benzoate salt at 140°-160°C for polyethylene or 170°-180°C for polypropylene. The mixtures were then cooled close to the softening point of the polymer and sheeted into 0.005-in. thick films. The final leaching of the sheets occurred in water at 20°-55°C. The salt was generally extracted in 1-16 hr. However, leaching is almost complete within 5-10 min.

In some cases the polymers were also irradiated with high energy electrons of 20 Mr at a dose rate of 10 Mr/min before or after extraction of the salt. This irradiation step was employed to improve the thermal and mechanical properties of the porous polymer for possible later use at greater than ambient pressures and temperatures. Irradiation after leaching was more effective in strengthening mechanical and thermal properties, but by this treatment the smallest pores were closed by cross-linking.

Membranes were tested routinely for porosity, gas permeability, and electrolytic conductivity. The porosity was determined by density measurements, the gas permeability from nitrogen flow as a function of applied pressure, and the electrolytic conductivity was measured at 1 kHz with a conductance bridge after filling the membrane with 1M KCl.

The known porosity of 40-50% corresponds to the initial weight ratio of polymer and additive. The conductivity is of the same order of magnitude as that of the solution filling the membrane. This shows an open continuous pore structure. Finally, small gas permeability is a measure of small pore diameters.

From the magnitude of the conductivity, a tortuosity factor can be calculated. It is the ratio of the actual electrolytic conductance to that expected at the given porosity and thickness for a structure with straight pores, normal to the surfaces.

The properties of three membranes are listed in Table I. They are given as examples of the magnitudes

* Electrochemical Society Active Member.

Table I. Geometry, gas permeability, and electrolytic conductivity of membranes

Composition before leaching (parts by weight)			
Polyethylene*	1	1	
Polypropylene			1
Sodium benzoate	3.5	4	4
Porosity (per cent)	52	55	51
Thickness (in.)	0.0033	0.0064	0.005
Nitrogen flow (ml/min/cm²)			
at 5.3 psi	12.0	5.9	2.6
at 65.3 psi	33.4	27.5	13.5
Resistance of membrane filled with 1M KCl (ohm)	0.48	0.31	0.95
Conductivity (mho/cm)	2.9×10^{-3}	6.7×10^{-3}	2.2×10^{-3}
Tortuosity factor	3.1	1.2	4.0

* Density—0.948 g/cm³, melt index 0.2.

involved and are representative of the very large number of membranes which were prepared from high-density polyethylene and highly crystalline polypropylene together with salts of benzoic acid as the additives.

The median pore size of these membranes is about 40-120Å. Materials of different pore size are illustrated in Fig. 1, 2, and 3. Figure 1 is an electron micrograph of a porous polyethylene sheet prepared by dissolving an anionic surfactant in polyethylene and subsequently removing the additive (3). Figures 2 and 3 show porous polyethylene and polypropylene prepared by the present method. In Fig. 1 the pores have a dimension of about 1μ (10,000Å), whereas in the other membranes most of the visible pores are about 100Å large. The majority of pores are smaller than 100Å median upper limit.

To obtain a quantitative estimate of the pore distribution, the following widely divergent physical methods were used to determine the pore sizes:

1. Electron microscopy.
2. Capillary flow—mercury intrusion porosimetry.
3. Capillary flow—liquid permeability.
4. Gas diffusion—Knudsen flow.
5. Small angle x-ray scattering.

Each of these methods has its specific limitation so that the quantitative values obtained indicate the limits of pore sizes rather than their distribution. However, a distribution curve can be constructed, combining the results of the above physical methods. Figure 4 shows the qualitative distribution of pore diameters on a logarithmic scale. The distribution ordinate, $\Delta N/N$, is

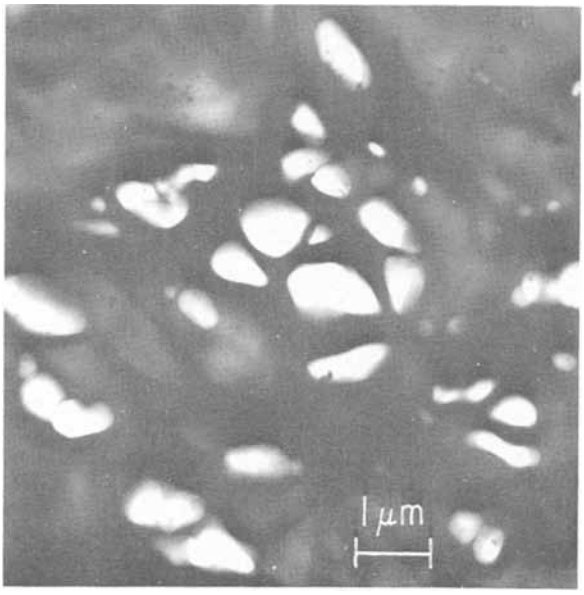

Fig. 1. Electron micrograph of porous polyethylene membrane, prepared with anionic surfactant as additive. 10,000X.

Fig. 2. Electron micrograph of ultrafine porous polyethylene membrane. 100,000X.

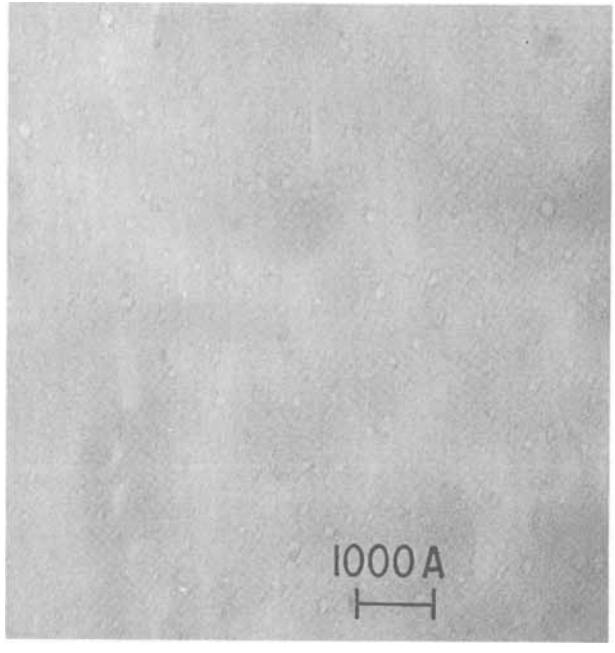

Fig. 3. Electron micrograph of ultrafine porous polypropylene membrane. 100,000X.

a qualitative estimate of the abundance of pores with different diameters. The numbered bars and the single point above the curve correspond to the different methods and the range of pore diameters obtained with them.

These membranes are now being used as separators in rechargeable organic electrolyte systems, containing a negative lithium electrode and a positive bromine electrode: $\ominus$ Li(on Ni)/0.2M LiBr + 0.8M $LiClO_4$ in propylene carbonate(PC)/porous polyethylene membrane/1.5M Br_2 + 1.6M LiBr in PC/porous C $\oplus$. With excess bromine solution, the cell is limited in current efficiency by lithium utilization, which, therefore, becomes a measure of self-discharge caused by bromine diffusion to the negative electrode. Table II shows the utilization of lithium as a function of cycle life. These results were obtained by charging and discharging the cell in 45-min half cycles, charging the cell at 4.2V and 1 mA/cm², discharging it at approxi-

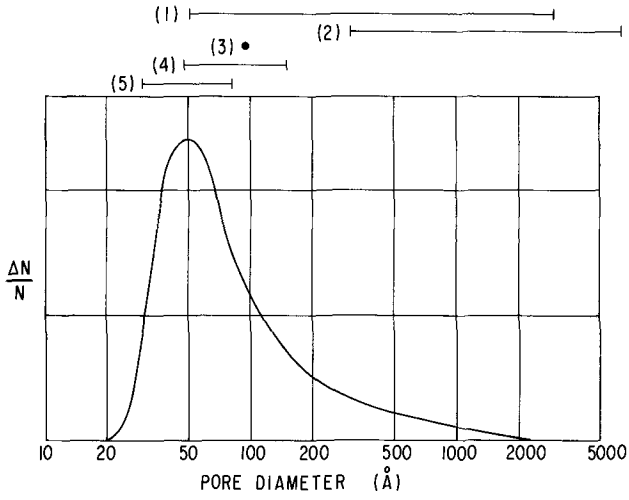

Fig. 4. Distribution of pore diameters in ultrafine porous membrane.

mately 3.2V and at a current density to match complete discharge in each cycle; for example, 0.9 mA/cm^2 for 90% utilization in the first 100 cycles.

Such use of the galvanic system as a secondary cell is made possible by the presence of the porous membrane as separator. Electro-osmotic measurements indicate that each tribromide ion and bromine molecule is associated with 4-6 molecules of the solvent. The solvated entity is less than 20Å in size, but this size in combination with its polar character, and the larger transport number of the positive ion, prevents bromine from reaching the lithium electrode compartment, except through the largest pores of the separator. Additional evidence for this is adduced from comparable experiments with porous Vycor glass which has a uniform pore diameter of 60Å. In this latter case, no bromine diffusion or migration occurs.

Table II. Utilization of lithium in lithium-bromine cell on continuous cycling

Cycle No.	0-100	100-300	300-1785
Approx % utilization	90	70	30

The alternative of using ion exchange membranes as separators in the nonaqueous system fails, because it has not been possible to exchange the solvent water in the ion exchange membrane with a sufficient amount of organic electrolyte to render it conducting. For example, a conventional cation exchange membrane was equilibrated with lithium ions, vacuum dried, and equilibrated with organic solvent (PC), or water was replaced stepwise by PC. In both cases, the conductivity of the cation exchange membrane in its organic form was about 2 x 10^{-9} mho/cm as compared with 0.46 x 10^{-3} mho/cm for the ultrafine porous separator in operation of the lithium-bromine cell, and 1.5 x 10^{-3} and 0.94 x 10^{-3} mho/cm, respectively, for the initial solutions in the positive and negative electrode compartments of the above cell.

Acknowledgments

The authors are grateful to E. F. Koch, W. J. Ward, D. G. LeGrand, and F. W. Secor who supplied electron micrographs, x-ray, and other measurements of the membrane material.

Manuscript submitted Sept. 2, 1969; revised manuscript received Nov. 17, 1969.

Any discussion of this paper will appear in a Discussion Section to be published in the December 1970 JOURNAL.

REFERENCES

1. A. N. Dey, *This Journal*, **115**, 160 (1968).
2. A. N. Dey and M. L. B. Rao, Preprint, 6th Intern. Power Sources Symp. Brighton, Sept. 1968.
3. D. E. Sargent and M. M. Safford, U.S. Pat. 3,378,506, April 1968.

Electroreduction of β-Diketones on Mercury

E. Kariv, J. Hermolin, and E. Gileadi

Institute of Chemistry, Tel-Aviv University, Ramat-Aviv, Israel

The electroreduction of ketones has been widely reported in the literature (1-6). Dimers formed by reductive coupling are often found, in particular in the presence of mercury or amalgams (1). β-Diketones are of special interest since they can follow several reduction pathways when reduced electrochemically (7). The polarography of some β-diketones has been studied (7-11) and different products were obtained by varying the conditions of electrolysis (7). Cyclopropandiols formed by intramolecular reactions have been proposed as intermediates in chemical reduction (12-14) and recently such compounds formed during electroreduction have been isolated (15).

The reduction of dimedone (I) on a mercury cathode was studied. Butanol, methanol, isopropanol, or DMF were used as solvents. Tetraethyl-ammonium-p-toluene sulfonate which was used as the electrolyte increased the solubility of the reactant and reduced the rate of simultaneous hydrogen evolution.

The product of the reaction has been separated and identified as the dimer (III), formed by a single electron transfer per molecule of dimedone (I). The same product was proposed before (8) on the basis of a polarographic determination of the number of electrons transferred in the reaction. However, no attempt was made to separate and identify the product in this previous study. The dimer (III) is a β-hydroxy-ketone which loses two molecules of water easily to yield the dimer (IV) with a conjugated double-bond system.

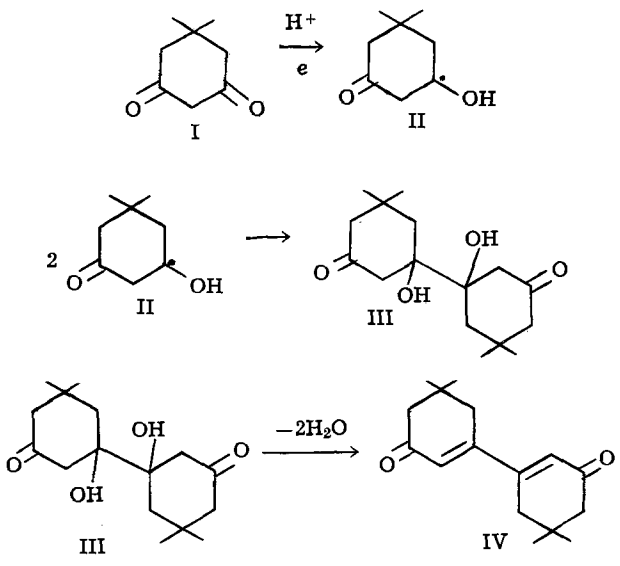

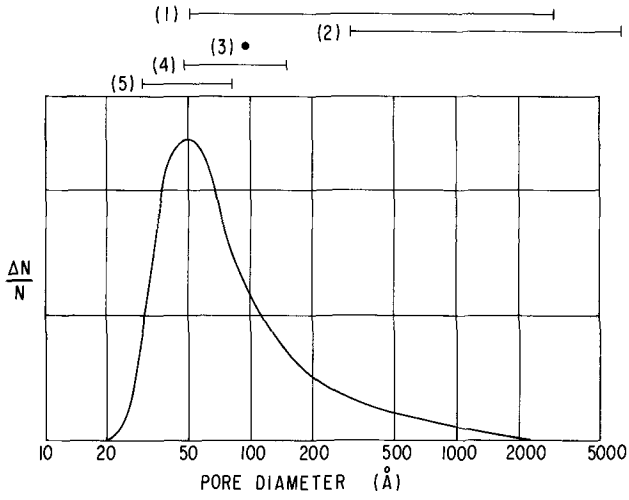

Fig. 4. Distribution of pore diameters in ultrafine porous membrane.

mately 3.2V and at a current density to match complete discharge in each cycle; for example, 0.9 mA/cm^2 for 90% utilization in the first 100 cycles.

Such use of the galvanic system as a secondary cell is made possible by the presence of the porous membrane as separator. Electro-osmotic measurements indicate that each tribromide ion and bromine molecule is associated with 4-6 molecules of the solvent. The solvated entity is less than 20Å in size, but this size in combination with its polar character, and the larger transport number of the positive ion, prevents bromine from reaching the lithium electrode compartment, except through the largest pores of the separator. Additional evidence for this is adduced from comparable experiments with porous Vycor glass which has a uniform pore diameter of 60Å. In this latter case, no bromine diffusion or migration occurs.

Table II. Utilization of lithium in lithium-bromine cell on continuous cycling

Cycle No.	0-100	100-300	300-1785
Approx % utilization	90	70	30

The alternative of using ion exchange membranes as separators in the nonaqueous system fails, because it has not been possible to exchange the solvent water in the ion exchange membrane with a sufficient amount of organic electrolyte to render it conducting. For example, a conventional cation exchange membrane was equilibrated with lithium ions, vacuum dried, and equilibrated with organic solvent (PC), or water was replaced stepwise by PC. In both cases, the conductivity of the cation exchange membrane in its organic form was about 2 x 10^{-9} mho/cm as compared with 0.46 x 10^{-3} mho/cm for the ultrafine porous separator in operation of the lithium-bromine cell, and 1.5 x 10^{-3} and 0.94 x 10^{-3} mho/cm, respectively, for the initial solutions in the positive and negative electrode compartments of the above cell.

Acknowledgments

The authors are grateful to E. F. Koch, W. J. Ward, D. G. LeGrand, and F. W. Secor who supplied electron micrographs, x-ray, and other measurements of the membrane material.

Manuscript submitted Sept. 2, 1969; revised manuscript received Nov. 17, 1969.

Any discussion of this paper will appear in a Discussion Section to be published in the December 1970 JOURNAL.

REFERENCES

1. A. N. Dey, *This Journal*, **115**, 160 (1968).
2. A. N. Dey and M. L. B. Rao, Preprint, 6th Intern. Power Sources Symp. Brighton, Sept. 1968.
3. D. E. Sargent and M. M. Safford, U.S. Pat. 3,378,506, April 1968.

Electroreduction of β-Diketones on Mercury

E. Kariv, J. Hermolin, and E. Gileadi

Institute of Chemistry, Tel-Aviv University, Ramat-Aviv, Israel

The electroreduction of ketones has been widely reported in the literature (1-6). Dimers formed by reductive coupling are often found, in particular in the presence of mercury or amalgams (1). β-Diketones are of special interest since they can follow several reduction pathways when reduced electrochemically (7). The polarography of some β-diketones has been studied (7-11) and different products were obtained by varying the conditions of electrolysis (7). Cyclopropandiols formed by intramolecular reactions have been proposed as intermediates in chemical reduction (12-14) and recently such compounds formed during electroreduction have been isolated (15).

The reduction of dimedone (I) on a mercury cathode was studied. Butanol, methanol, isopropanol, or DMF were used as solvents. Tetraethyl-ammonium-p-toluene sulfonate which was used as the electrolyte increased the solubility of the reactant and reduced the rate of simultaneous hydrogen evolution.

The product of the reaction has been separated and identified as the dimer (III), formed by a single electron transfer per molecule of dimedone (I). The same product was proposed before (8) on the basis of a polarographic determination of the number of electrons transferred in the reaction. However, no attempt was made to separate and identify the product in this previous study. The dimer (III) is a β-hydroxy-ketone which loses two molecules of water easily to yield the dimer (IV) with a conjugated double-bond system.

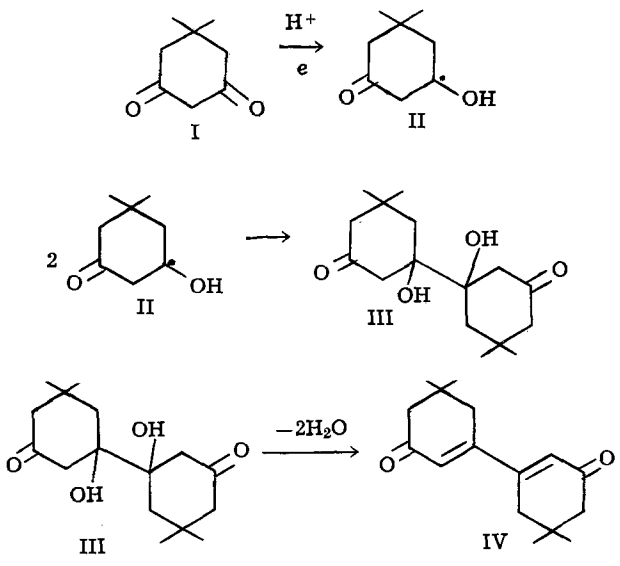

Product identification.—The dimer (III) has been isolated as sparingly soluble white crystals (methanol), mp 226°C (corr.). It had no absorption in the u.v. region. *IR* (KBr) 3440 (OH) and 1690 cm^{-1} (C = 0); mass spectrum m/e 282, 264, 246; molecular weight (by bp elevation) 280.

The dimer (IV) has been isolated as yellow platelets, mp 180°C (corr.). U.V. max (95% C_2H_5OH) 286 mμ (ε21900); *IR* (KBr) no absorption in the OH region, 1655 cm^{-1} (C = 0); nmr ($CDCl_3$) δ 1.08 (singlet 12H), 2.31 (singlet 4H), 2.4 (doublet 4H) and 6.28 ppm (multiplet 2H); mass spectrum m/e 246; molecular weight 247. Upon very mild dehydration on florisil at room temperature, pure dimer (III) yielded exclusively the dimer (IV).

The combined Faradaic yield for the dimers (III) and (IV) was 30-70% depending on both potential and the concentration of reactant in solution.

Kinetic studies.—Current-potential measurements were taken on a dropping mercury electrode equipped with a tapper which knocks off equal sized drops at equal intervals of time (*ca.* 0.2 sec). The maximum current (observed just before the drop is knocked off) was measured, and the current density was calculated from the average drop weight, assuming that the drops were hemispherical.

A wave due to reduction of dimedone is observed at −1.5 to −1.8V *vs.* SCE, depending on the concentration of reactant in solution, as shown in Fig. 1. The shape of the curves and the reduction potentials are not essentially affected by changing the solvent. The reaction is first order at lower concentrations and potential, but tends to zero order as the concentration and/or potential are increased. A limiting current is observed at higher potentials, as shown in Fig. 2, where the values of the current, corrected for background current, are plotted *vs.* potential. This behavior implies a rate-determining surface reaction, with reaction limited currents, as found also by Conway *et al.*

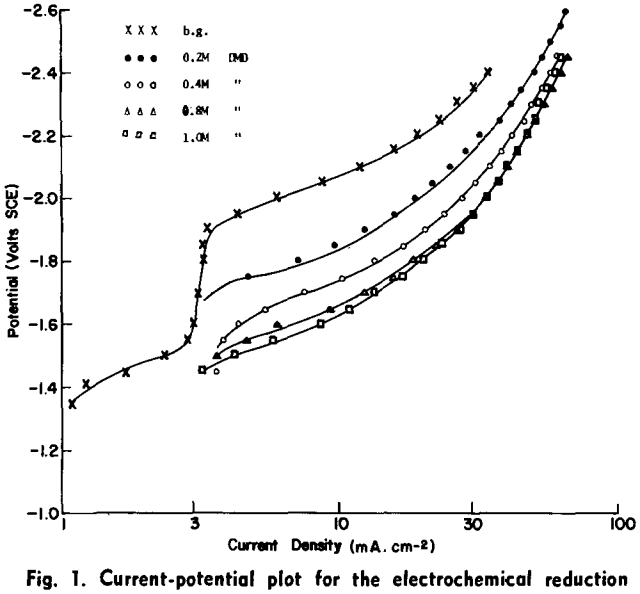

Fig. 1. Current-potential plot for the electrochemical reduction of dimedone on mercury. 1M tetraethyl p-toluene-sulfonate in n-butanol.

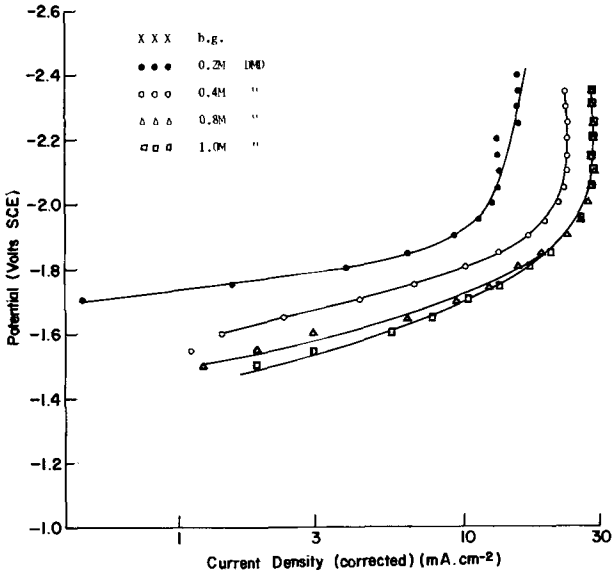

Fig. 2. Data of Fig. 1 corrected for background current

(5) for the reduction of acetophenone on mercury. It is also consistent with the product (III) formed by combination of two radicals (II) which are unstable in the homogeneous phase and can only have a substantial steady-state concentration on the electrode surface.

Acknowledgment

This work was supported in part by the Fund for the Encouragement of Research of the "Histadrut."

Manuscript submitted Sept. 11, 1969; revised manuscript received *ca.* Nov. 17, 1969.

Any discussion of this paper will appear in a Discussion Section to be published in the December 1970 JOURNAL.

REFERENCES

1. F. D. Popp and H. P. Schultz, *Chem. Rev.*, **62**, 19 (1962).
2. P. Zuman, *Collection Czech. Chem. Commun.*, **33**, 2549 (1968).
3. P. Zuman and B. Turcsanyi, *ibid.*, **33**, 3090 (1968).
4. P. Zuman, B. Turcsanyi, and A. K. Mills, *ibid.*, **33**, 3205 (1968).
5. B. E. Conway, E. J. Rudd, and L. G. M. Gordon, *Disc. Faraday Soc.*, **45**, 87 (1968).
6. P. Zuman, D. Barnes, and A. Ryvolova-Kejharova, *ibid.*, **45**, 202 (1968); (*see* this paper for further references).
7. D. H. Evans and E. C. Woodbury, *J. Org. Chem.*, **32**, 2158 (1967).
8. J. C. Pariaud, J. Modiano, R. Sorel, and R. Stefani, *Compt. Rend.*, **239**, 1217 (1954).
9. R. H. Philp, R. L. Flurry, and R. A. Day, *This Journal*, **111**, 328 (1964).
10. R. Pasternak, *Helv. Chim. Acta*, **31**, 753 (1948).
11. H. Adkins and F. W. Cox, *J. Am. Chem. Soc.*, **60**, 1151 (1938).
12. E. Wenkert and E. Kariv, *Chem. Comm.*, **1965**, 570.
13. K. M. Baker and B. R. Davis, *Chem. Ind. (London)*, **1966**, 768.
14. N. J. Cusack and B. R. Davis, *J. Org. Chem.*, **30**, 2062 (1965).
15. T. J. Curphey, C. W. Amelotti, T. P. Layloff, R. L. McCartney, and J. H. Williams, *J. Am. Chem. Soc.*, **91**, 2817 (1969).

JOURNAL OF THE ELECTROCHEMICAL SOCIETY

SOLID STATE SCIENCE

MARCH 1970

Preparation of Single Crystals of Cuprous Oxide in an Arc-Image Furnace

Dan Trivich* and **Gordon P. Pollack**[1]

Department of Chemistry, Wayne State University, Detroit, Michigan

ABSTRACT

A crucible-free technique for pulling single-crystal cuprous oxide from the melt has been developed, involving the use of an arc-image furnace to form a melt on the top of a cylindrical ingot of cuprous oxide. Single crystals approximately 1 cm in diameter and 3.5 cm long were grown along [111], [110], and [111] directions by the use of oriented seeds. The crystals were found to cleave preferentially along (111) planes. A count of chemical etch pits on (111) faces indicates a dislocation density of 10^4 to 10^5 cm^{-2}.

Cuprous oxide has been the subject of a number of investigations mainly because of its interesting electrical properties which depend on a departure from stoichiometry. It has been only recently that single crystals have become available for these investigations. These single crystals of cuprous oxide have been prepared by grain growth from polycrystalline cuprous oxide (1-4), by careful oxidation of single-crystal copper (5), and by hydrothermal methods (6). However, while these single crystals are useful for many studies, the methods have the disadvantage of giving usually thin samples with a limited control of orientation.

Attempts to grow cuprous oxide from the melt in our laboratory and elsewhere have been hampered by the reactivity of molten cuprous oxide with the standard crucible materials. Zucker (7), who used the Czochralski method to grow single crystals of Cu_2O from the melt, investigated a number of crucible materials of which sintered magnesia was found to be least reactive.

Because of this reactivity problem, it would be preferable to dispense with the use of crucibles. We have developed a crucible-free method of growing cuprous oxide single crystals from the melt by use of an arc-image furnace. We report here some details of this procedure and of the quality of the crystals obtained.

Crystal Growth Procedure

Essentially, the method consists of the use of focused radiation from a carbon arc to form a melt on top of a cylindrical ingot of cuprous oxide. The surface tension of the molten cuprous oxide is sufficient to hold the melt in place. Single crystals are then pulled from this melt by the Czochralski technique which consists of partial immersion and withdrawal of a seed crystal. Since the present method dispenses with the use of crucibles, the crucible contamination problems associated with past methods have been eliminated.

The basic design of the arc-image furnace used in these experiments has been described by Poplawsky and Thomas (8). The source of the radiant energy is a high-intensity carbon arc powered by an a.c.-d.c. motor generator supplying 150A d.c. at 78V. Imaging is accomplished by a double-paraboloid system (9) using two 150-cm parabolic mirrors set on a vertical axis with the carbon arc at the focus of the lower mirror and the partially molten ingot at the focus of the upper mirror. The crystal pulling mechanism provides for both rotation and vertical translation of the seed and the bulk material. Final temperature control is obtained by varying the position of the melt in relation to the focused image of the arc. The rotation and translation functions are motorized but final control of the position and rotation is attained by manual adjustment of the motor controls according to the judgment of the operator who views the work stage through a telescope.

The starting material for the preparation of the bulk material in the experiments reported here was high-purity copper metal (99.999+% pure, supplied by the American Smelting and Refining Company) usually in the form of 9-mm rods or sometimes 0.3- x 0.3- x 15-cm^3 strips. These were oxidized completely to Cu_2O by heating in air in a separate furnace at 1030°C for 3 days. The rods of Cu_2O were then transferred to the arc-image furnace where they were fed from above into the focus of the upper mirror and thus melted and deposited onto a high-purity copper base. By gradual feeding in of the source rods and downward withdrawal of the work stage from the melt zone, an ingot of bulk material 3.5 cm in diameter and 3 cm high could be built up. The work stage could also be surrounded by a Pyrex envelope to provide for control of the atmosphere. Usually the ingot build-up procedure was carried out under reduced pressure (2 Torr) in order to aid in the removal of gas bubbles trapped in the melt.

For the crystal growth process, the above procedure was essentially reversed so that material was transferred upward from the ingot to a Cu_2O seed crystal, but with more stringent control requirements. The crystal growth was begun by properly adjusting the power to the arc and the position of the ingot of bulk material in relation to the focal point so that a melt of the correct size and temperature was produced. A seed crystal, cut from a plate of cuprous oxide grown by the grain growth method (1), was then

* Electrochemical Society Active Member.
[1] Present address: Texas Instruments, Inc., P.O. Box 5936, M.S. 147, Dallas, Texas 57222.

merged with the melt. Material was transferred to the seed by upward vertical translation of both the seed and the bulk material at the correct relative rates. The crystal growth was usually carried out in air at 1 atm with a seed withdrawal rate of 1.5-2.0 cm/hr and rotation rates of 32 and 12 rpm in the same direction for the seed and bulk material, respectively.

Results and Evaluation of Crystals

The crystals obtained by this method were typically about 8-10 mm in diameter and 3-5 cm long. Difficulties with obtaining larger stable molten zones have thus far limited the maximum obtainable diameter to about 10 mm. Also, the length of the samples obtained is presently limited by the burning time of the carbon arc. No preference for direction of growth was observed since equal success was obtained for growth along the [100], [110], and [111] directions. The crystals were found to cleave preferentially along the (111) planes. Some typical samples are shown in Fig. 1.

The single-crystal character of the samples was evaluated by examining ground faces for grain boundaries and by back-reflection Laue x-ray diffraction. Grain boundaries when present were revealed by grinding a flat surface on the sample and then etching the surface with 0.5*N* NaCN solution. Under adequately controlled conditions the first portion of the sample pulled from the melt was invariably single crystal in character, but there was frequently a tendency for the growth to become coarsely polycrystalline toward the end of the sample. On the average, grain boundaries were found to appear approximately ¾ of the way down the sample. This deterioration of the structure toward the bottom end of the sample was further confirmed by x-ray analysis in that secondary diffraction spots became apparent. However, it was possible with care to grow samples which were single crystal in character over the entire length.

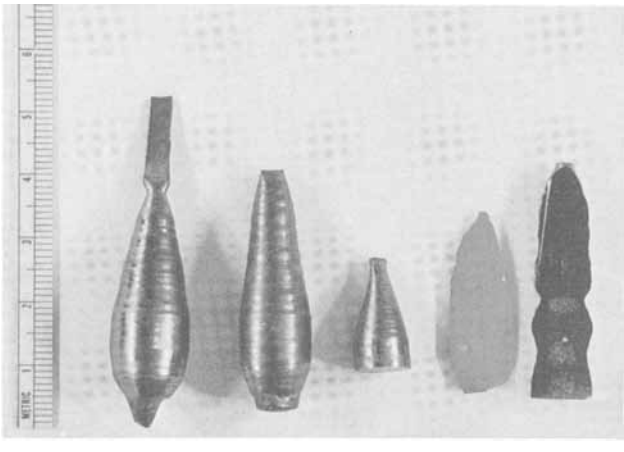

Fig. 1. Samples of Cu_2O as grown by the arc-image furnace method. The two samples at the left are single crystals as grown; the first has the seed still attached. The third sample was cut to reveal a cross section for examination. The fourth sample shows the ground surface of a lengthwise slice, showing the absence of grain boundaries. The fifth sample shows polycrystalline regions in a ground and etched slice.

Examination of cross sections of the samples revealed a number of pinhole-size voids which apparently originated from gas bubbles trapped in the viscous melt and subsequently transferred to the crystal. Subjecting the melt to a moderate vacuum before a run diminished but did not eliminate the voids. It is possible that these bubbles provided nucleation sites for the secondary crystallization that occurred. Another factor that probably contributed to the poor structure at the bottom of the samples is the basic instability of the carbon arc as a heat source.

In order to obtain a measure of the dislocation density in these samples, the density of chemical etch pits on the (111) planes was determined. Samples were prepared by first grinding a flat surface on the sample and then chemically polishing in a solution containing 17% HNO_3, 41.5% H_3PO_4, and 41.5% HAc (5) to remove the surface damage. The etch pits were developed by immersion of the sample for 30 sec in a solution containing 12% copper nitrate and 10% nitric acid (10). The etch pit density was found to vary across a plane perpendicular to the growth axis, typical values being 10^4 to 10^5 cm^{-2} near the center. The density of etch pits was also found to increase down the length of the sample.

The increase in etch pit density toward the center of the sample was probably due in part to the temperature distribution in the melt zone during the crystal growth. As shown for the double-paraboloid type of arc-image furnace (8), the melt-zone has a large radial temperature gradient which leads to a highly concave liquid-solid interface. Samples formed by solidification through such an interface could contain large stresses which would lead to the production of the dislocations.

Manuscript submitted July 24, 1969; revised manuscript received Oct. 17, 1969.

Any discussion of this paper will appear in a Discussion Section to be published in the December 1970 JOURNAL.

REFERENCES

1. R. S. Toth, R. Kilkson, and D. Trivich, *J. Appl. Phys.*, **31**, 117 (1960).
2. G. Blankenburg and K. Kassel, *Ann. Physik.*, **10**, 201 (1952).
3. Y. I. Gritsenko, *Izvest. Akad. Nauk, Ser. Fiz.*, **21**, 153 (1957).
4. M. Grosmann, *J. Chim. Phys.*, **10**, 1129 (1965).
5. Y. Ebisuzaki, *J. Appl. Phys.*, **32**, 2027 (1961).
6. A. Kinoshita and T. Nakano, *Japan. J. Appl. Phys.*, **6**, 656 (1967).
7. R. S. Zucker, *This Journal*, **112**, 417 (1965).
8. R. P. Poplawsky and J. E. Thomas, *Rev. Sci. Instr.*, **31**, 1303 (1960).
9. T. S. Laszlo, "Image Furnace Techniques," Vol. V of "Techniques of Inorganic Chemistry," John Wiley & Sons, New York (1965).
10. A. I. Andrievskii and G. F. Mocharnyuk, *Kristallografiya*, **8**, 120 (1963).

Fast-Decay Phosphors

A. Bril, G. Blasse, and J. A. de Poorter

Philips Research Laboratories, N.V. Philips' Gloeilampenfabrieken, Eindhoven, The Netherlands

ABSTRACT

Decay times, efficiencies, and spectral energy distributions of a number of Ce^{3+}-activated phosphors have been determined. Decay times as short as 25-30 nsec are found for YPO_4-Ce, YOCl-Ce, and $YAl_3B_4O_{12}$-Ce; the two first-named phosphors show a weak, the last a strong, afterglow. The techniques of measurement have been described.

Ce^{3+}-activated phosphors are known as phosphors with very short decay times. The emission is ascribed to a 5d → 4f transition in the Ce^{3+} ion. The decay time is found to be shorter than 100 nsec due to the fact that an allowed transition is involved. Recently Ropp (1) summarized the results previously obtained and gave new data on Ce^{3+}-activated rare earth phosphates. The decay times of the latter phosphors are about 30 nsec, *i.e.* shorter than reported previously for Ce^{3+} phosphors. Awazu and Muto (2) described sensitization of YPO_4-Ce by the incorporation of thorium ions, leading to a higher photoluminescent efficiency.

The emission band of Ce^{3+}-activated phosphors has a doublet character due to the splitting ($\approx$2000 cm^{-1}) of the ground state ($^2F_{7/2}$,$^2F_{5/2}$). The emission is nearly always located in the blue or ultraviolet region of the spectrum. An exception is the yellow emission of the phosphor $Y_3Al_5O_{12}$-Ce which has been recently described (3).

In this paper, decay times, efficiencies, and spectral energy distribution of the emissions are given for several Ce^{3+}-activated phosphors, especially yttrium, scandium, and lanthanum phosphates and borates and yttrium oxychloride.

The cerium-activated phosphors find application in: (*a*) Flying-spot cathode-ray tubes for the TV transmission of films and slides. For color TV, an emission is required covering the whole visible spectrum. (*b*) A special type of color-TV receiving tube, the so-called index tube where an ultraviolet emitting phosphor is required in order to obtain the index signal (4).

Experimental

The preparation of the phosphors has been described by us earlier (5). The cerium concentration is 1-2%.

The decay times are measured both with ultraviolet and cathode-ray excitation. With cathode-ray excitation, a square pulse of voltage is displayed to the grid of the electron gun of a demountable cathode-ray tube, so that the phosphor can be irradiated during a variable time and with a variable repetition frequency. The method is analogous to that described previously by Bril and Klasens (4), but now much shorter times can be measured due to the use of a square-wave oscillator giving short pulses with a very short rise time (Tektronix Type 109, rise time 0.25 nsec, repetition frequency 550-720 pulses/sec) in combination with an oscilloscope with a wide frequency band (Philips No. 3330, bandwidth 70 MHz). The oscilloscope pictures were photographed with the aid of a Polaroid camera. To find all decay components, it is necessary to irradiate the phosphor with a wide range of excitation times in succession. Suppose a short and a long decay time component of equal efficiency are present, of *e.g.* 50 nsec and 1 msec. When the phosphor is then irradiated with a pulse of about 50 nsec duration, the maximum height of the rise and decay curve of the 1 msec component is negligible with respect to that of the 50 nsec component (the areas under the curves being equal). As a consequence, the long decay time component may be overlooked. This difficulty is avoided by exciting the phosphor for longer times also.

With ultraviolet excitation, use was made of two methods. (*a*) The TRW Nanosource instrument shown schematically in Fig. 1. The radiation source is a hydrogen discharge lamp for short-wavelength u.v. or a nitrogen discharge lamp for long-wavelength u.v.; the duration of the exciting pulses is 4 nsec or 9 nsec, the rise time less than 1.6 or 4 nsec, respectively, while the repetition frequency can be varied from zero to 5 KHz. The exciting radiation is filtered in such a way that the desired u.v. region is transmitted and imaged on the phosphor. The emitted radiation passes a filter transmitting only the fluorescence and is then collected by a photomultiplier with fast response time. With this instrument, the excitation time cannot be prolonged beyond a few nanoseconds which is a disadvantage as mentioned above. (*b*) Therefore, an additional method is used: longer decay times with u.v. radiation can be measured with the aid of a set-up described previously (6), using a cathode-ray tube with a fast, u.v.-emitting phosphor. In this case, u.v. pulses of shorter and longer duration can be obtained by modulation of the electron beam with a square-wave oscillator.

The spectral energy distributions were measured with the aid of a Jarrell-Ash 0.50m grating monochromator (15000 g/in., blazed at 750 nm). In the blue and ultraviolet region, the measurements were carried out in second order of the grating. As a detector, a photomultiplier with S20 photocathode was used (EMI 9558 Q), the current of which is amplified with the aid of a phase-sensitive a-c amplifier. To obtain the emitted power as a function of wavelength from the measured photocurrent, a correction for the varying instrumental response G as a function of λ has to be made (G consists of the variation of the response of the photomultiplier and of the transmission of the monochromator). This correction has been applied automatically, using a circuit whose diagram is given

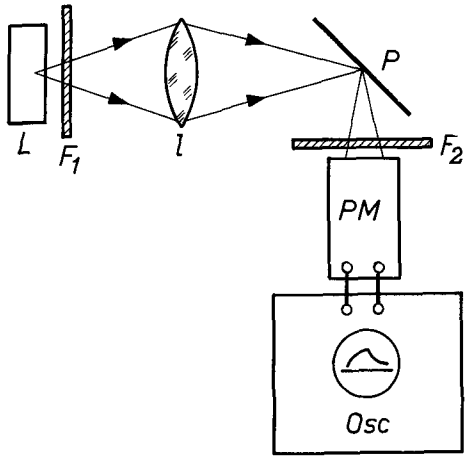

Fig. 1. Schematic diagram of the Nanosource instrument for decay time measurement: L = lamp, F_1 = ultraviolet transmitting filter, l = lens, F_2 = ultraviolet absorbing filter, PM = photomultiplier, Osc = oscilloscope, P = phosphor.

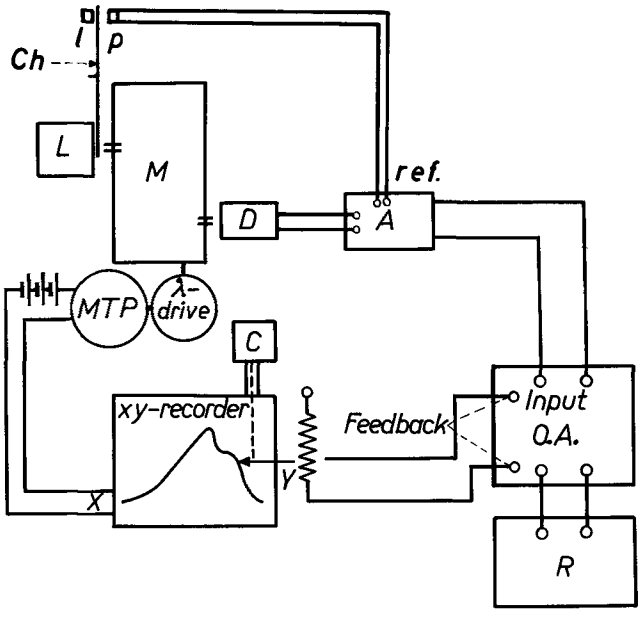

Fig. 2. Schematic diagram of automatic correction for instrumental response in spectral energy distribution measurements: *L* = light source, *M* = monochromator, *D* = detector, *Ch* = chopper (770 Hz), *l* = lamp, *p* = photodiode, *ref.* = reference signal, *A* = phase sensitive amplifier, *O.A.* = operational amplifier, *R* = recorder, *MTP* = multiturn potentiometer, *C* = curve follower.

in Fig. 2. On the axis of the wavelength drive, a multiturn potentiometer is fixed, to which a voltage of a few volts are applied. The variable voltage of the multiturn potentiometer is fed to the X-circuit of a flat-bed XY recorder. On this recorder, a piece of paper is placed on which the instrumental response $1/G = f(\lambda)$ is drawn. This curve is read with the aid of a curve follower. In this way a variable resistance, proportional to the value of $1/G(\lambda)$, taken from the built-in Y-potentiometer, is displayed to the feedback channel of an operational amplifier (Hewlett-Packard-Dymec). The normal signal $i(\lambda)$ of the photomultiplier is fed to an input channel of this amplifier. The output of the operational amplifier then gives the product of the two signals $I(\lambda) = i(\lambda) \cdot 1/G(\lambda)$, representing the emitted radiant power per constant wavelength interval (in arbitrary units). In the u.v. region, the correction factor $G(\lambda)$ proved to be nearly constant. Apparently, the instrumental response did not change much in this wavelength region.

Results and Discussion

In Table I, the decay times, the efficiencies and the maxima of the emission bands are given, both for cathode-ray and ultraviolet excitation. Some of the data, together with excitation and reflection spectra,

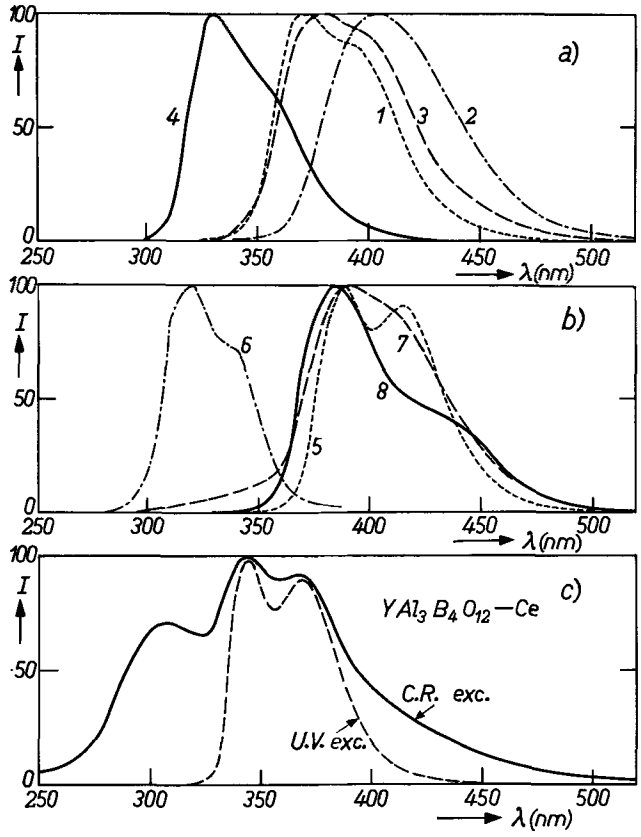

Fig. 3. Spectral energy distribution of the fluorescence. Along the ordinate, the radiant power per constant wavelength interval (*I*) in arbitrary units is given: (*a*) (cathode-ray excitation) 1. $Ca_2MgSi_2O_7$-Ce, 2. $Ca_2Al_2SiO_7$-Ce, 3. YOCl-Ce, 4. YPO_4-Ce. (*b*) (cathode-ray excitation) 5. YBO_3-Ce, 6. $LaPO_4$-Ce, 7. $Sc_2Si_2O_7$-Ce, 8. $ScBO_3$-Ce. (c) $YAl_3B_4O_{12}$-Ce, ——— cathode-ray excitation, - - - - u.v. excitation.

have already been published but are given here for completeness (7). In Fig. 3, the spectral energy distribution curves with cathode-ray excitation for some phosphors are given.

Generally, the doublet character of the emission (see introductory paragraphs) can be observed. However, sometimes a third, very short wavelength u.v. band is present, which has been ascribed to fluorescence from higher 5d-levels (6). For $Y_3Al_5O_{12}$-Ce, $ScBO_3$-Ce, and $Sc_2Si_2O_7$-Ce, this very short wavelength emission is present with u.v. excitation, but is absent or only weakly present with cathode-ray excitation. On the contrary for $YAl_3B_4O_{12}$-Ce such a third band is found with cathode-ray excitation but is absent with u.v. excitation. For $LaBO_3$-Ce, this very short wavelength

Table I. Some properties of Ce^{3+}-phosphors

Phosphor **	τ C.R. nsec	τ U.V. nsec	δ C.R. % of max int.	η C.R. (20 kV) %	q_{max} U.V. %	λ_{max} of emission band (room temp) C.R. excit. (20 kV) nm	λ_{max} of emission band (room temp) U.V. excit. (253.7 nm) nm
$Y_3Al_5O_{12}$-Ce	70*	55	6	3.5	~70	550	340,360,550
$YAl_3B_4O_{12}$-Ce	30	25	18	2	40	305,345,365	345,365
YOCl-Ce	25	25	1.5	3.5	60	380,400	380
YPO_4-Ce	25	25	1.5	2.5	30	330,355	335,355
$LaPO_4$-Ce	35		1.5	2	40	320,340	320,335
$ScBO_3$-Ce	40	35		2	70	385,420	330,385,420
YBO_3-Ce	60*	30		2	50	385,415	390,415
$LaBO_3$-Ce	25*			0.2	35	310,355,380	315,355,380
$Sc_2Si_2O_7$-Ce	35	30		1.5	65	390,410	335,390,420
$Ca_2Al_2SiO_7$-Ce	50	50	9	4.5		405	
$Ca_2MgSi_2O_7$-Ce	80*	45	3	4		370,395	

τ : Decay time, where the 1/*e* value of the initial intensity is reached (excitation pulse < 10 nsec).
δ : Percentage of the initial intensity 80 μsec after the end of the pulse of 20 μsec duration.
η : Radiant efficiency (energy conversion efficiency), C.R. excitation (20 kV).
q : Quantum efficiency, U.V. excitation.
* : Nonexponential decay.
** : The Ce concentration is 1-2%.

band is present for both types of excitation. The reason for the difference in behavior of the two types of excitation is not understood.

For u.v. excitation, the decay time τ is given, defined as the time at which the $1/e$-value of the initial intensity at the end of the pulse is reached. These values for τ are obtained for short-duration pulse excitation (less than 10 nsec), leading generally to exponential decay curves.

In some Ce-activated phosphors, more decay components are present. For $Ca_2Al_2SiO_7$-Ce, for example, it is well known that in the freshly prepared phosphor at least two decay components are present, from which the slower component disappears during life (8). Moreover, this phosphor and many other Ce^{3+}-activated phosphors show a strong deviation from the exponential law at much longer times (see Fig. 4). A long afterglow occurs, milliseconds even. This may be due to release of excitation energy stored in traps as a consequence, *e.g.* of impurities or imperfections in the host lattice. This long afterglow is troublesome in some applications such as the index-color-TV receiving tube. Therefore, for cathode-ray excitation we give not only the decay time τ ($1/e$-value), but in the 4th column of Table I also a value δ, defined as the percentage of the initial intensity 80 μsec after the end of an excitation pulse of 20 μsec duration. From the table it can be seen that δ varies considerably for the phosphors measured: it is 18% for $YAl_3B_4O_{12}$-Ce, while only 1.5% is found for YOCl-Ce, YPO_4-Ce, and $LaPO_4$-Ce. These latter phosphors are therefore suitable in cases where not only a short decay time but also a low-intensity afterglow is required (9).

For $LaPO_4$-Ce, Ropp (1) gives a value of 32 nsec close to our value of 35 nsec. For calcium magnesium silicate, Ropp gives 114 nsec for cathode-ray excitation ($1/e$-value), while we find a value of 80 nsec for our $Ca_2MgSi_2O_7$-Ce. This difference may be due to another composition of the substance, so that the long decay time components are different (moreover, these depend also on the duration of the excitation pulse). In this respect, it is remarkable that for our $Ca_2MgSi_2O_7$-Ce we measure a decay time of 50 nsec with an exponential decay curve for u.v. excitation when a very short excitation pulse of less than 10 nsec is used. With cathode-ray excitation, however, the curve is found to be nonexponential when extended over long enough times, *e.g.* 500 nsec (see Fig. 4; excitation pulse also less than 10 nsec). For the $1/e$ value, we find $\tau = 80$ μsec.

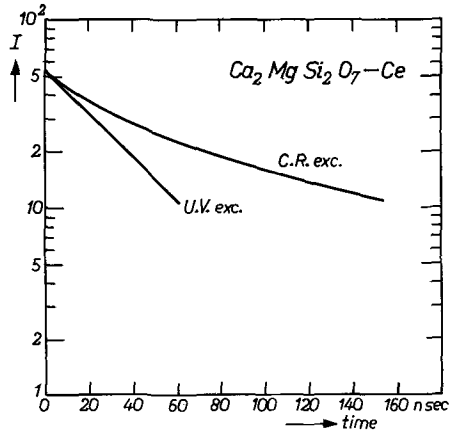

Fig. 4. Decay curves of $Ca_2MgSi_2O_7$-Ce for cathode-ray and u.v. excitation.

Acknowledgments

The authors are indebted to Mr. J. de Vries, Mr. C. J. Loyen, and Mr. M. M. A. Janssen for their valuable technical assistance.

Manuscript submitted April 7, 1969; revised manuscript received *ca.* Dec. 3, 1969. This was Paper 81 presented at the New York Meeting, May 4-9, 1969.

Any discussion of this paper will appear in a Discussion Section to be published in the December 1970 JOURNAL.

REFERENCES

1. R. C. Ropp, *This Journal*, **115**, 531 (1968).
2. K. Awazu and K. Muto, *ibid.*, **116**, 282 (1969).
3. G. Blasse and A. Bril, *Appl. Phys. Letters*, **11**, 53 (1967).
4. J. Davidse, *Philips Res. Repts.*, **19**, 112-280 (1964).
5. A. Bril and H. A. Klasens, *Philips Res. Repts.*, **7**, 421 (1952).
6. A. Bril, H. A. Klasens, and P. Zalm, *ibid.*, **8**, 393 (1953).
7. G. Blasse and A. Bril, *J. Chem. Phys.*, **47**, 5139 (1967).
8. A. Bril, J. de Gier, and H. A. Klasens, *Philips Tech. Rev.*, **15**, 233 (1954).
9. A. H. Gomes de Mesquita and A. Bril, *This Journal*, **116**, 171 (1969) and *Mat. Res. Bull.*, **4**, 643 (1969).

The Efficiency of Cathode-Ray Phosphors

I. Measurement

G. W. Ludwig* and J. D. Kingsley

General Electric Research and Development Center, Schenectady, New York

ABSTRACT

The cathode-ray efficiency of a variety of phosphors has been studied, including (ZnCd)S:Ag, Zn_2SiO_4:Mn, ZnO:Zn, and oxide hosts activated with Eu^{3+}, Tb^{3+}, and other rare earths. In addition to the basic measurement of efficiency at 10 kV, the voltage dependence was measured over the range 0.2-20 kV and analyzed following Gergely.

One of the most important parameters of a cathode-ray phosphor is its power efficiency: the watts of radiant output per unit power in the incident electron beam. The measurement of absolute efficiency has been discussed by Bril (1). He determined the incident power by measuring the accelerating voltage and the sample current. A thermopile having a flat spectral response was used to detect the emitted radiation. To calibrate the thermopile and obtain an absolute efficiency measurement, Bril replaced the phosphor plaque with MgO of known reflectivity, irradiated it with a standard lamp, and measured the detector output. (If, instead, the radiated power is detected with a photomultiplier, one must calibrate its spectral response and measure the spectral energy distribution

* Electrochemical Society Active Member.

from the phosphor.) Bril found efficiencies ranging from 0.2 to 21% for a set of standard phosphors obtained from the National Bureau of Standards.

Many workers have contented themselves with measurement of relative efficiency. For example, Buchanan *et al.* (2) used a set of commercial phosphors as standards (accepting published efficiency figures for them) to calibrate the response of their detection system. The booklet "RCA Phosphors" (3) quotes relative radiant energy (*i.e.*, efficiency) of phosphors taking the output from RCA Phosphor No. 33-W-2A (Zn_2SiO_4:Mn) to be 100.

Only scattered values for the efficiencies of many of the newer phosphor materials are available in the literature. Moreover, the efficiency of a particular phosphor may be substantially influenced by preparatory and/or handling techniques. Therefore, it was deemed worthwhile to investigate the efficiency of a sizable number of phosphors, both new and old. The measurements on the older ones form a basis of comparison for the newer ones. We have measured commercial phosphors, the standard phosphors from the NBS studied by Bril, YVO_4 doped with rare earths, Eu-doped oxide phosphors such as Gd_2O_3 and Y_2O_2S, etc.

In addition to the basic measurement of efficiency at 10 kV, the relative efficiency has been studied over the range 0.2-20 kV. The resulting curves have been analyzed in terms of a formula suggested by Gergely (4) for de-excitation associated with the surface of the phosphor particles. From the analysis one obtains three parameters characterizing a phosphor, including a characteristic (or "dead") voltage. Of course, such measurements are of considerable interest for evaluating phosphors for low voltage applications, and have not been available for most phosphors hitherto.

For some hosts, such as YVO_4, there is reason to expect that the ratio of the cathode ray to u.v. efficiency will be a constant independent of the activating impurity or its concentration. To allow a check on this expectation, the absolute efficiency of many of the phosphors has been measured under excitation at 2537Å.

We have been interested in correlating the cathode-ray efficiency with other phosphor parameters. In a companion paper (5) we discuss the processes involved in cathode-ray excitation, and the use of photons of energy up to ~25 eV to simulate fast electron excitation. Comparison is made there between cathode-ray efficiency and efficiencies observed under u.v. excitation. Experimental techniques and results are presented and discussed in this paper.

Experimental Techniques

Preparation of phosphor plaques.—Phosphor powders for investigation under cathode-ray excitation were obtained from several sources including the General Electric Company Chemical Products Business Section, Cleveland; The National Bureau of Standards; and commercial sources. Shortly before use, the powders were sieved through a 400 mesh screen, or a coarser screen for relatively coarse powders.

Phosphor plaques were prepared having a phosphor weight in the range 8-14 mg/cm². Such a weight was adequate to produce plaques having no areas covered so lightly that the electron beam could penetrate completely through the phosphor layer.

The phosphor plaques were prepared by settling the powdered phosphor in a 3 in. diameter cylinder onto 1 x 2 in. pure silver (or aluminum) plates. Silver was chosen because it is an excellent electrical and thermal conductor, minimizing electrical charging and temperature rise, and is an excellent reflector for visible light from the settled phosphors. Some plaques were prepared by settling in water without binder, while for others a LiOH binder was used. In the latter case 380 cc of barium acetate solution (0.060 g/liter) was first poured into a cylinder containing a silver plate.

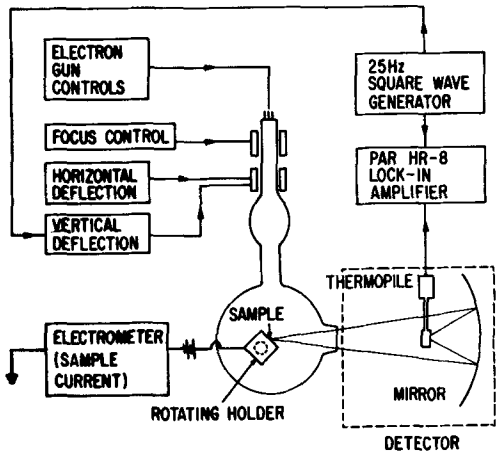

Fig. 1. Apparatus used to measure cathode-ray efficiency of phosphors.

A suspension of the phosphor in 240 cc of lithium hydroxide solution (0.4 g LiOH/liter) was then added. The phosphor was allowed to settle, the liquid slowly drained through an outlet, and the plaque allowed to air-dry at room temperature.

Cathode-ray excitation.—The plaques were excited using the apparatus shown in Fig. 1. The demountable cathode-ray tube will accept four plaques. The sample holder is a copper block which is thermally isolated by a length of stainless steel tubing, so that measurements may be made in the temperature region 77°-420°K. An electron beam from a commercially available oxide cathode gun (10FP4) was magnetically focused onto a plaque and magnetically deflected to produce a raster of the desired size. The plaque was oriented at 45° to the incident beam, while the emitted light passed through a quartz port at 90° to the beam. The beam voltage was adjusted in the range 0.2-10 kV by applying the potential to the electron gun. Post-acceleration of the beam was used to obtain voltages up to 20 kV. The sample holder, which was near ground potential, was biased positive relative to nearby parts of the tube so that secondary electrons were collected and the measured sample current was equal to the total incident electron beam current, the measurement error being a few per cent.

Absolute efficiency measurements were made at 10 kV or occasionally 20 kV beam voltage. For such measurements a thermopile[1] was used as the detector element. To high accuracy such detectors produce a response which is proportional to the total incident radiant energy independent of its wavelength. The electron beam was swept vertically at a frequency of 25 Hz, and a spherical mirror was used to focus the light on the active surface of the thermopile. Since the image of the phosphor was twice as long as the active surface of the detector, the thermopile signal was square wave modulated at the vertical scan frequency. This signal was synchronously detected using a Princeton Applied Research Model HR-8 lock-in amplifier. A 25 Hz square wave was used both to synchronize the vertical scan and as an input to the lock-in amplifier operated in the selective external mode. When a measurement was completed, the sample holder was rotated to position a new sample in the electron beam, and micrometer drives were employed to so reposition the thermopile as to maximize the signal from it.

The thermopile is sensitive to radiant energy from the phosphor in the infrared and ultraviolet as well as in the visible portion of the spectrum. In cases where information concerning the spectral distribution of the radiation was of interest, energy ranges were isolated by interposing appropriate filters in the light path to the thermopile.

[1] The thermopile was a Model RSL-6S obtained from Charles M. Reeder and Co., Detroit, Mich.

The relative efficiency of phosphors was measured as a function of beam voltage over the range 0.2-20 kV. In these measurements, use of the thermopile detector was abandoned in favor of the greater sensitivity of a photomultiplier such as a 1P21. In order to maintain a raster of standard size, it was necessary to adjust the focus coil voltage and the horizontal and vertical deflection coil voltages at each value of beam voltage. The photomultiplier tube used as the detector was positioned directly in front of the quartz window with no collecting optics for the light.

Phosphor emission spectra were also taken with cathode ray excitation. A lens in front of the quartz window served to focus the emitted light on the entrance slit of a ½ meter Jarrell-Ash spectrometer.

Ultraviolet efficiency at 2537Å.—The absolute radiant efficiency of a phosphor under u.v. excitation customarily is defined as the emitted radiant power divided by the power absorbed from the incident beam. We have measured this efficiency by a technique similar to that of Bril and Hoekstra (6). A block diagram of our apparatus is shown in Fig. 2. Radiation from a 4w germicidal lamp, consisting largely of the mercury line at 2537Å, was mechanically chopped at 13 Hz. A narrow band interference filter passed a band centered near 2537Å and suppressed other components. The radiation was reflected from an MgO plaque onto a thermopile and synchronously detected using a Perkin-Elmer Model 107 amplifier. The MgO plaque then was replaced by a geometrically similar phosphor plaque. Readings of the thermopile signal were taken both with and without interposing a filter (which removes 2537Å radiation) between the plaque and thermopile. The absolute efficiency, η_{2537}, and reflection coefficient, r_{2537}, of the phosphor were then calculated from the formulas (6)

$$r_{2537} = \rho(V_P - V_{PF}\tau^{-1})/V_{MgO} \quad [1]$$

$$\eta_{2537} = \frac{\rho}{\tau(1-r)}\frac{V_{PF}}{V_{MgO}} \quad [2]$$

In [1] and [2] V_{MgO}, V_P, and V_{PF} are the thermopile signals from the MgO plaque, the phosphor with no filter interposed, and the phosphor with attenuating filter for 2537Å interposed, respectively. The parameters ρ and τ are the reflectivity of the MgO and the transmission of the filter for the fluorescent radiation. The formulas assume equal transmission of the quartz window of the thermopile for 2537Å and the fluorescent radiation.

Results

The relative light output of phosphors under cathode-ray excitation was studied from 0.2 to 20 kV. Typical results for the light output per unit current are shown in Fig. 3. At high voltage the output approaches a straight line through the origin, while at low voltage it falls substantially below the line. As the voltage is lowered the incident electrons penetrate

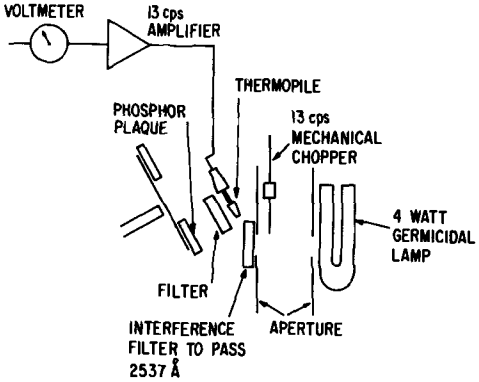

Fig. 2. Apparatus used to measure absolute efficiency of phosphors under 2537Å excitation.

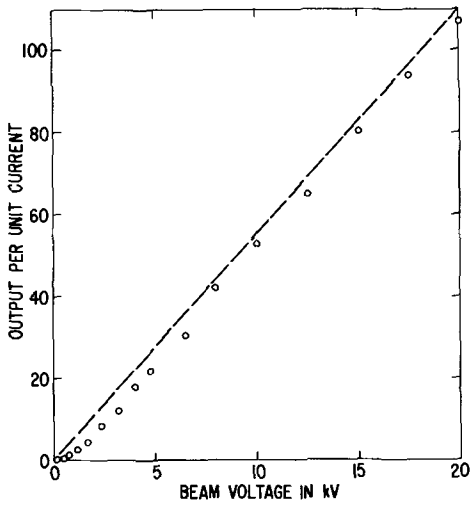

Fig. 3. Relative light output of a Gd_2O_3:Eu phosphor as the beam voltage is varied.

the phosphor grains less and less. It is generally accepted that the decrease in power efficiency at low beam voltage is associated with surface loss.

Gergely (4) has analyzed the voltage dependence of cathodoluminescence under a set of simplifying assumptions. He assumes a range for the incident electrons of the form

$$R = KV^b \quad [3]$$

where K and b are material constants. He approximates the excitation density as uniform throughout the range. He assumes that free carriers are produced which diffuse through the phosphor and recombine at the surface, characterized by a surface recombination velocity. The result of his analysis is that the efficiency, normalized to 1 at high voltage, is given by [*cf.* his Eq. (8)]

$$\eta_N = 1 - Q\left[\frac{1-\exp(-\beta R)}{\beta R}\right] \quad [4]$$

where β is the inverse of the diffusion length and Q is a surface recombination loss parameter. However, we can use the range relation of Eq. [3] to express η_N in terms of the beam voltage V and a characteristic voltage V_0

$$\beta R \equiv (V/V_0)^b \quad [5]$$

$$\eta_N = 1 - Q\frac{1-\exp[-(V/V_0)^b]}{(V/V_0)^b} \quad [6]$$

Plots of η_N for $b = 1.5$ and different values of Q are shown in Fig. 4. For $Q = 0$ (no surface loss) η_N is in-

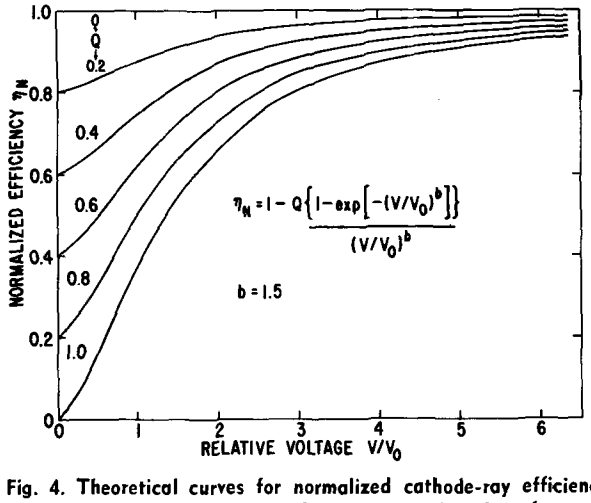

Fig. 4. Theoretical curves for normalized cathode-ray efficiency as a function of voltage for different strengths of surface recombination.

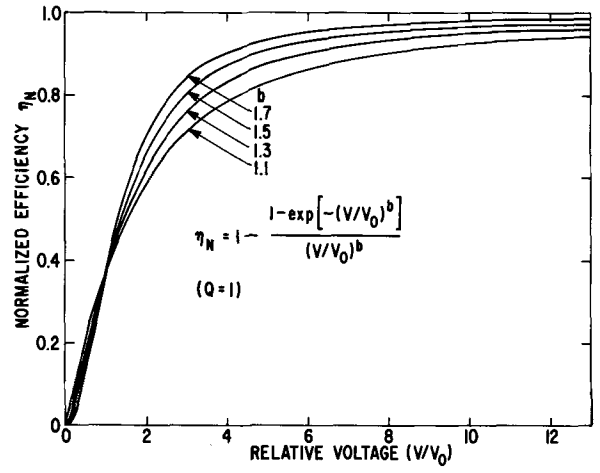

Fig. 5. Theoretical curves for normalized cathode-ray efficiency for different range-voltage relations.

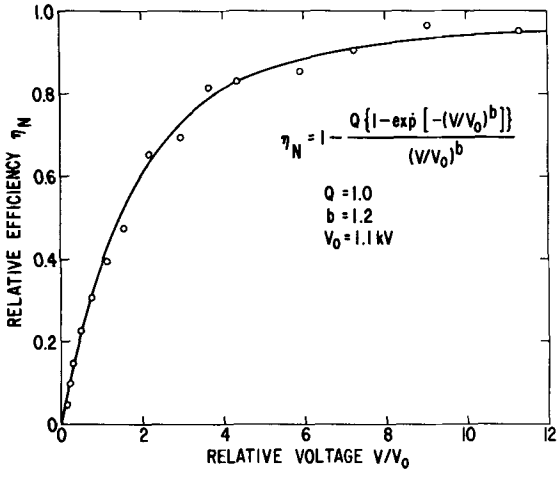

Fig. 6. Normalized efficiency of a Gd_2O_3:Eu phosphor compared with Eq. [6] of the text.

dependent of voltage. As Q increases toward 1, the limiting efficiency at low voltage approaches zero. In all cases, the η_N approaches unity at high voltage.

In Fig. 5 η_N is plotted for $Q = 1$ and different values for b. Large b implies that the range rises rapidly with voltage. Correspondingly, for b large the efficiency rapidlly approaches unity as the voltage increases.

Gergely's assumption that energy transport in the phosphor grain is by diffusion of free carriers may not apply to many of the phosphors of present interest. However, it does seem possible to fit the experimental data rather well by a curve of the form Eq. [6] with judicious choice of the parameters V_0, b, and Q. Data were matched to that equation in the following way: We normalized the efficiency to 1 at high voltage and extrapolated the efficiency to zero voltage to find $Q = 1 - \eta_N(0)$. V_0 can be found by realizing that at V_0, $\eta_N = 1 - Q(1 - e^{-1})$, while the parameter b is found by matching curves such as those of Fig. 5.

The experimental data of Fig. 3, normalized at high voltage, were replotted as normalized efficiency *vs.* normalized voltage in Fig. 6. There is reasonable agreement between the experimental points and the calculated curve for η_N.

The efficiency of the phosphors at 10 kV was measured using the thermocouple detector.[2]

[2] No correction was applied for absorption of the emitted light internal to the phosphor or on reflection by the metal backing plate. It can be shown that the correction factor needed to convert measured to intrinsic efficiencies is approximately $2/(1 + R)$ where R is the reflectivity of the phosphor-backing plate combination [*c.f.* ref. (7)]. For sulfide phosphors, settled on aluminum, we find $R \sim 0.8$, while for most other phosphors, settled on silver, $R > 0.9$.

The absolute efficiency and reflection coefficient under excitation at 2537Å were calculated using Eq. [1] and [2], assuming at value $\rho = 0.91$ for the reflectivity of MgO (1) and using a measured value $\tau = 0.92$ for the visible transmission of the Pyrex filter used to attenuate 2537Å radiation.

Values for the cathode-ray efficiency at 10 kV, η_{cr}, the parameters V_0, b and Q describing the voltage dependence of the efficiency, and the parameters η_{2537} and r_{2537} describing the efficiency and reflection coefficients under 2537Å radiation are given for various phosphors in Tables I-V. Unless otherwise indicated, samples were obtained from J. Rabatin.

Comments and discussion.—Cathode-ray efficiencies of commercial and NBS standard phosphors (Tables IA and II).—Bril (1) has published efficiency values for a number of standard phosphors obtained from the National Bureau of Standards. The booklet, "RCA Phosphors" (3) lists the efficiency of a series of RCA commercial phosphors relative to a Zn_2SiO_4:Mn phosphor. We have used Bril's (1) and Hardy's (8) published efficiency for Zn_2SiO_4:Mn to set the absolute efficiency scale for the RCA phosphors: a relative efficiency of 100 apparently corresponds to an absolute efficiency of 6%.

Figure 7 shows our detector reading for a number of phosphors along with the efficiency as published by Bril or as derived above for RCA phosphors. The efficiency scale for our detector readings can be set by drawing a straight line on the basis of the experimental points. The substantial deviations from the line are attributed partly to random errors, partly to differences in measurement conditions (beam voltage and current, plaque preparation, etc.), and partly to real differences in efficiency between different phosphor lots. Our measurements on the same phosphor lot are repeatable to ±5% or so; that is for two successive measurements η_1 and η_2 it generally is true that

$$0.95\,\eta_1 - 0.5 < \eta_2 < 1.05\,\eta_1 + 0.5$$

where η_1 and η_2 are expressed in per cent.

We have also made an independent determination of the efficiency scale for our detector readings. The thermopile was irradiated with light from a standard lamp, the energy output of which previously had been calibrated by the National Bureau of Standards. The light

Table IA. Cathode-ray excitation of NBS phosphors

Phosphor	NBS Number	η_{cr} (%)	V_0 (kV)	b	Q	η_{Bril}* (%)
Zn_2SiO_4:Mn	1021	4.7	1.3	1.2	0.89	8
ZnS:Cu	1022	12.4	2.2	1.4	0.99	11
(Zn,Cd)S:Ag	1023	18.7	2.4	1.4	0.97	19
(Zn,Cd)S:Cu	1024	9.7	3.1	1.4	1.00	12
$Zn_3(PO_4)_2$:Mn	1025	3.1	1.4	1.2	0.91	6
$CaWO_4$:Pb	1026	3.4	1.5	1.3	0.92	3
$MgWO_4$	1027	2.9	2.5	~1.9	1.00	2.5
Zn_2SiO_4:Mn	1028	6.8	1.6	1.4	0.89	6

* See Ref. (1).

Table IB. 2537Å excitation of NBS phosphors

Phosphor	NBS Number	Present measurements η_{2537} (%)	Present measurements r_{2537} (%)	Bril & η_{2537} (%)	Hoekstra† r_{2537} (%)
Zn_2SiO_4:Mn	1021	22	25	35	30
$CaWO_4$:Pb	1026	45	4	41	5
$MgWO_4$	1027	49.5	4	43	6
Zn_2SiO_4:Mn	1028	33	3	33	6
$CaSiO_3$:Pb,Mn	1029	10	10	29*	11
$(MgO)_x(As_2O_5)_y$:Mn	1030	34	4	30	4
$3Ca_3(PO_4)_2 \cdot Ca(F,Cl)_2$:Sb,Mn	1031	32	10	34*	14
$BaSi_2O_5$:Pb	1032	66	10	55*	14

† See Ref. (7).
* Measured with excitation over the 2500-2750Å band.

Table II. Cathode-ray excitation of some commercial phosphors

Phosphor	Designation	Source	η_{cr} (%)	V_0 (kV)	b	Q	η_{PB}* (%)
ZnS:Cu	33-Z-245A (P31)	RCA	17.5	1.5	~1.3	0.95	22
ZnS:Ag	33-Z-646A (P11)	RCA	19.6	1.8	~1.3	1.00	21
(Zn,Cd)S:Ag	118-322PL47 (TV green)	GE	21	2.8	1.6	1.00	
(Zn,Cd)S:Ag	33-Z-658A (TV green)	RCA	21	2.1	1.5	1.00	14.9
(Zn,Cd)S:Cu	33-Z-601B (P2)	RCA	7.9	2.1	1.6	1.00	7.1
Y_2O_2S:Eu	33-Y-256 R05-31	RCA	13	1.2	1.4	1.00	
ZnO:Zn	33-Z-613A	RCA	11.8	~6.5		0.3	2.6
ZnO:Zn	CE8036-5	N. J. Zinc	5.1	5.5		0.6-0.8	
Zn_2SiO_4:Mn	33-W-2A	RCA	4.8				6.0

*The booklet "RCA Phosphors" (2) lists the total relative radiant energy from phosphors under cathode-ray excitation. η_{PB} is the cathode-ray efficiency calculated assuming that a total relative radiant energy of 100 corresponds to an efficiency of 6% [see A.E. Hardy, ref. (10)].

was mechanically chopped at 26 Hz and the detector output read with the lock-in amplifier. In this way we obtained a value for the detector sensitivity for 25 Hz square wave modulation. The absolute efficiency scale could then be set by estimating the fraction of the total emitted light from the phosphor gathered by the mirror and focused onto the thermopile. The efficiency scale estimated in that way agreed within about 10% with the scale as estimated in the preceding paragraph from measurements on standard phosphors.

Ultraviolet efficiency of NBS phosphors (Table IB).—A comparison between our measurements of u.v. efficiency and those of Bril and Hoekstra (6) on the NBS standard phosphors is given in Table IB. Our measurements tend to be slightly higher. The average could be made to agree more closely if a lower value for the parameter ρ, the reflectivity of our MgO plaque for 2537Å radiation, were assumed.

YVO_4:RE *phosphors (Table III).*—The cathode-ray efficiency of all the YVO_4:RE samples fell in the range 1-7%, with YVO_4:Eu being the most efficient. All of the phosphors showed high surface loss ($Q \cong 1$), and the parameter b in the range-voltage relation ($R \sim V^b$) was measured to be 1.4 ± 0.2. The characteristic voltage V_0 is a measure of the voltage (and hence depth within the phosphor grain) at which surface de-excitation is still important. We find that V_0 varies somewhat with the activator and is largest in the unactivated sample where one might expect energy transport over relatively large distances, since there are no purposely added activators to trap the excitation.

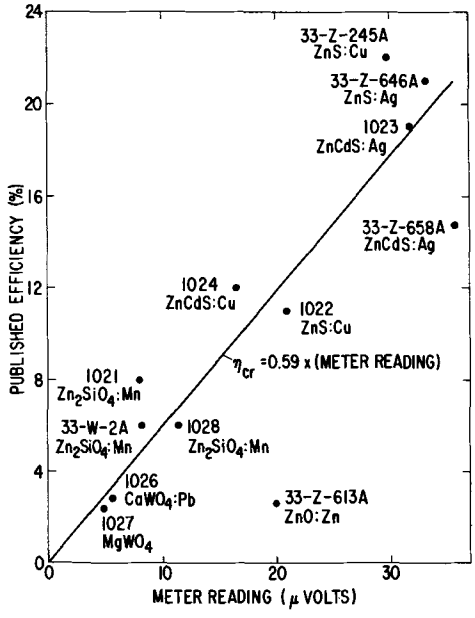

Fig. 7. Calibration of the cathode-ray efficiency scale using standard and commercial phosphors.

It is generally accepted that YVO_4 phosphors are host-sensitized in both cathode-ray and u.v. excitation; the excitation energy is absorbed by the lattice and transported to activators via the VO_4^{-3} groups. Thus, both the cathode-ray efficiency and the u.v. efficiency at 2537Å are expressible as the product of two efficiencies, one describing the excitation of VO_4^{3-} groups by fast electrons (or 2537Å photons), and the other the production of luminescence from VO_4^{3-} excitation. The latter efficiency will depend on the activator and other impurities present in the sample, but should be the same for cathode-ray and 2537Å excitation. The former efficiency differs for cathode-ray and 2537Å excitation, but may not be sensitive to the impurities and defects in the sample unless they produce traps which intercept the excitation energy before the VO_4^{3-} groups are excited. In the absence of such traps we expect the ratio η_{cr}/η_{2537} to be the same for all samples and activators. Indeed, we find $\eta_{cr}/\eta_{2537} = 0.16 \pm 0.03$. On the other hand, Kano and Otomo report on impurities, such as Mo, W, and Ta which apparently produce traps such that the cathode-ray efficiency is reduced while the photoefficiency at 2537Å is largely unaffected (9).

Eu^{3+} *activated oxide, oxysulfide, and oxyhalide phosphors (Table IV).*—Except for the oxyhalides, all of the Eu^{3+} activated phosphors which we investigated are at least as efficient as YVO_4:Eu, the most efficient being Gd_2O_3:Eu and Y_2O_2S:Eu. All show strong surface losses ($Q \simeq 1$) and are reasonably efficient under 2537Å excitation.

Tb^{3+} *activated oxyhalide and oxysulfide phosphors (Table V).*—Except for YOCl, the phosphors in Table V are at least moderately efficient under both cathode ray and 2537Å radiation.

Acknowledgments

The authors are indebted to D. T. F. Marple for valuable discussions and to S. J. Lubowski for assistance with the measurements. We also wish to thank

Table III. C.-R. and u.v. excitation of YVO_4:RE phosphors

Activation	η_{cr} (%)	V_0 (kV)	b	Q	η_{2537} (%)	τ_{2537} (%)	η_{cr}/η_{2537}
None	2.4	2.0	1.3	0.98			
0.6% Eu	4.1-4.9	1.4	1.3	0.98	30	2	0.14-0.16
2.5% Eu	6.0-6.7	1.2	1.3	1.00	37	2	0.16-0.18
10% Eu	5.9	1.2	1.4	1.00	33	2	0.18
20% Eu	3.4	1.7	1.5	0.99	22	3	0.15
0.8% Sm	3.0	0.9		1.00	23	4	0.13
0.8% Dy	3.6	1.1	1.6	0.98	24	4	0.15
0.8% Ho	1.3	1.2	1.6	0.97	8	3	0.16
0.8% Er	2.3	1.3	1.6	1.00	16	3	0.16
0.8% Tm	4.4	0.9	1.1	1.00			

Table IV. C.-R. and u.v. excitation of Eu^{3+}-activated oxide, oxysulfide, and oxyhalide phosphors

Phosphor	Eu^{3+} conc (%)	Designation	η_{cr} (%)	V_o (kV)	b	Q	η_{2537} (%)	τ_{2537} (%)
Y_2O_3	4.5		6.5	0.7	1.3	0.97	35	24
Gd_2O_3	5	N-125-1	9.6	1.1	1.1	1.00	41	9
Gd_2O_3		GOR-53*	11.7	0.9	1.1	0.99	44	21
Gd_2O_3		1327-121 PL-4	11.7	1.0	1.1	1.00	42	10
$Na_2OGd_2O_3$	1	N124-1	8.7	3.7	1.5	1.00	32	18
	5	N124-2	8.8	2.6	1.5	1.00	38	5
Y_2O_2S		GG10	13.1	1.2	1.1	1.00	26	6
La_2O_2S		N329-B	10.8	1.3	1.1	1.00	21	6
Gd_2O_2S		N322-C	10.2	1.9	1.1	1.00	22	5
YOF	4.5		~0.5	1.0	1.1	0.90	16	18
YOCl	5		2.9	2.8	~1.5	1.00	20	17

*A Sylvania phosphor.

Table V. C.-R. and u.v. efficiency of Tb^{3+}-activated oxyhalide and oxysulfide phosphors

Phosphor	Tb^{3+} conc (%)	Designation	η_{cr} (%)	V_o (kV)	b	Q	η_{2537} (%)	τ_{2537} (%)
YOF	5	1479*	3.8	1.3	1.1	0.97	27	38
YOCl	5	Y124-1	0.1	1.6	1.2	0.80	9	28
La_2O_2S	1	N54-A	11.8	0.6	1.1	1.00	23	4

* Obtained from J. Sarver, General Electric Company Lighting Research Laboratory.

J. Rabatin for preparing many of the phosphor samples.

Manuscript received Aug. 11, 1969. This was Paper 60 presented at the New York Meeting of the Society, May 4-9, 1969.

Any discussion of this paper will appear in a Discussion Section to be published in the December 1970 JOURNAL.

REFERENCES

1. A. Bril in "Luminescence of Organic and Inorganic Materials," p. 479, Kallman and Spruck, Editors, John Wiley & Sons, New York (1967).
2. R. A. Buchanan, K. W. Wickersheim, J. L. Weaver, and E. E. Anderson, *J. Appl. Phys.*, **39**, 4342 (1968).
3. "RCA Phosphors" TPM-1508B 1-66, obtained from RCA, Parts and Devices, 415 South St., Harrison, N. J.
4. G. Gergely, *J. Phys, Chem. Solids*, **17**, 112 (1960).
5. J. D. Kingsley and G. W. Ludwig, *This Journal*, **117**, 353 (1970).
6. A. Bril and W. Hoekstra, *Philips Research Repts.*, **16**, 346 (1961).
7. A. Bril and H. A. Klasens, *ibid.*, **7**, 401 (1952).
8. A. E. Hardy, *RCA Engineer*, **2**, 12 (1965); A. E. Hardy, *Trans. Electrochem. Soc.*, April 1947.
9. T. Kano and Y. Otomo, *This Journal*, **116**, 64 (1969).

The Efficiency of Cathode-Ray Phosphors

II. Correlation with Other Properties

J. D. Kingsley and G. W. Ludwig*

General Electric Research and Development Center, Schenectady, New York

ABSTRACT

In cathode-ray excitation of a phosphor the energy of the fast electrons appears, in an intermediate stage, as excitation of the valence shell electrons. We have used photons of energy up to 25 eV to simulate cathode-ray excitation. Attempts to account for cathode-ray efficiencies on the basis of the photoexcitation efficiencies give agreement in some cases and substantial lack of agreement in others. A correlation between high plasma resonance energy and low cathode-ray efficiency is pointed out.

In the preceding paper (1) we have presented measurements of the cathode-ray efficiency of a variety of phosphor materials. In this paper we discuss the processes involved in cathode-ray excitation (2). We then seek to correlate the cathode-ray efficiency with results of other experiments, notably with the photoefficiency observed under u.v. excitation.

When a fast electron enters a phosphor it loses energy predominantly by ionizing electrons from the inner shells of atoms. The penetration of fast electrons and the processes whereby the excitation energy is transferred to valence-shell electrons and from them to the activator atoms are discussed. Photons of energy up to ~25 eV have been used to simulate the excitation of phosphors by fast electrons. Comparison is made between observed cathode-ray efficiencies and expectations based on the photoexcitation measurements. In addition, a correlation between low cathode-ray efficiency and high plasma resonance energy is pointed out. While our crude models meet with some measure of success in accounting for observed cathode-ray efficiencies, there is substantial lack of agreement in other cases. Thus, the understanding of cathode-ray efficiency still is in a primitive state and much remains to be done.

* Electrochemical Society Active Member.

The penetration of fast electrons into phosphor materials is summarized, and the host excitation thereby produced is discussed. We present and discuss methods for estimating cathode-ray efficiency on the basis of photoexcitation efficiency in the u.v. and make some concluding comments.

Penetration of Fast Electrons (3)

As a fast electron passes through a medium it interacts with nearby atoms via Coulomb forces. An electron with a kinetic energy in the 20 kV range is not sufficiently energetic to displace nuclei from their lattice sites. Rather, it is scattered elastically by the nuclear potential as screened by the electrons of the medium. However, in passing near an atom a fast electron can impart a sufficient electromagnetic pulse to a bound electron to cause it to ionize. The energy loss of a fast electron is predominantly by ionization of electrons from inner shells of atoms, and is given approximately by Bethe's formula (4)

$$-\frac{dE}{dX} = \frac{2\pi Ne^4}{E} \ln\left[\frac{E}{E_i}\sqrt{2.717/2}\right] \qquad [1]$$

Here E is the electron energy, X is the path length, N

is the density of bound electrons, e is the electronic charge, 2.717 is the base of natural logarithms, and E_i is an average ionization energy for the bound electrons. Since the logarithmic term is slowly varying, dE/dX is approximately inversely proportional to the electron energy, and the maximum excitation density occurs near the end of the electron's path. Equation [1] is only valid as long as the energy lost in an ionization event is small compared with the electron's energy ($E_i << E_j$). With the reservation that the initial energy must be large compared with E_i, Eq. [1] can be integrated to give the relation between electron energy and integrated path length.

In estimating the spatial distribution of the energy dissipated by incident fast electrons, account must be taken of the deflections suffered by the electrons in elastic scattering events. The problem is a difficult one because the electrons suffer multiple collisions and undergo both small and large angle deflections. Thus, the initial trajectory of an electron is completely lost before it dissipates its energy.

Spencer (5) has made numerical calculations of the energy dissipation in a series of different elements for the experimentally important case of a plane perpendicular source of fast electrons of a given energy. His numerical results include values for the electron range and for the excitation intensity as a function of depth. The excitation intensity shows a peak which moves deeper into the material as the initial electron energy is increased.

Ehrenberg and King (6) have made an interesting experimental study of the penetration of electrons into a phosphor crystal. They focused a narrow electron beam onto a flat crystal face. The luminous glow through an adjacent face at right angles to the first was enlarged with a microscope and photographed using a series of different exposures. Contours of equal brightness could be traced out, giving a direct measure of the distribution of excitation within the crystal. At high incident electron energy the excited volume resembled a sphere joined to the surface by a narrow neck. As the electron energy was decreased, the neck shortened until at low energy the excited volume was roughly hemispherical. From measurements at different energy Ehrenberg and King were able to deduce to range-energy relation. For a range of different phosphors they found a practical range $P \propto E^{1.7\pm0.1}$.

The penetration of fast electrons in nonluminous materials has also received much experimental attention (7).

There is a close correspondence between the experimental and the theoretical determinations of the spatial distribution of energy loss. For example, the determinations of the voltage-range relation are consistent. Thus, a reasonable understanding of the basic features of the penetration of electrons into matter has been achieved.

Lattice Excitation Produced by the Fast Electrons

From Eq. [1] we see that to first approximation a sufficiently fast electron loses energy to each bound electron of an atom at the same rate. Since there are more inner shell electrons than valence shell electrons, the former account for the major part of the energy loss. Thus, the major primary excitations produced by a fast electron are fast secondaries and excited ions.

In the second stage of the excitation process, excited ions lose energy by Auger transitions in which one outer shell electron is ejected from the ion, while a second such electron falls into the hole in the inner shell. Energetic secondary electrons can also cause ionization. Thus, a shower of energetic secondaries and ionized atoms is formed. As more and more ionization of the medium is produced by repetition of the above processes, the average energy of each excitation of course decreases. A fraction of the incident primary electrons and their secondaries leave the solid, resulting in a back-scattering loss which typically

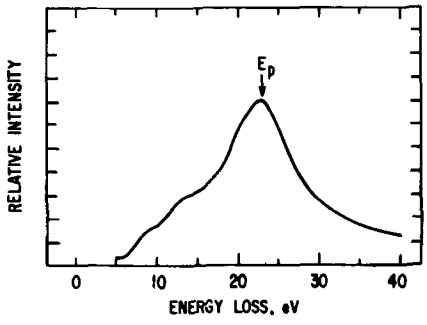

Fig. 1. Energy loss spectrum for fast electrons incident on an Al_2O_3 film [after Swanson (12)].

amounts to about 10% of the energy of the primaries. In addition, a very small fraction (~1%) of the excitation is lost by x-ray emission.

As the average energy of the secondary electrons falls below the binding energy of deep inner shell electrons, energy loss to valance shell electrons becomes relatively more important. Loss to these electrons has been described in terms of the longitudinal dielectric function, $\epsilon^L(k,\omega)$, which is dependent on both the energy lost, $\hbar\omega$, and the momentum transferred, $\hbar k$. The complex longitudinal dielectric function

$$\epsilon^L(k,\omega) = \epsilon_1{}^L(k,\omega) + i\epsilon_2{}^L(k,\omega)$$

and the energy loss to the valence-shell electrons are related by

$$-Im\frac{1}{\epsilon^L(k,\omega)} = \frac{\epsilon_2{}^L}{(\epsilon_1{}^L)^2 + (\epsilon_2{}^L)^2} \qquad [2]$$

Energy loss of relatively energetic electrons (~20 keV) to valence-shell electrons can be determined directly by the characteristic energy loss measurement (8, 9).[1] A thin foil of the solid under investigation is prepared. The foil is irradiated with monoenergetic electrons, and the electrons passing through it are analyzed in energy. In addition to the electrons which pass through without loss, one observes electrons which have lost energies characteristic of the solid. For some metals, the loss occurs mainly at one reasonably well-defined energy and multiples thereof; for Al such a loss occurs at about 15 eV. No optical absorption band occurs at this energy, and it thus does not represent an interband transition. The loss peak rather occurs at the resonant energy for longitudinally polarized, collective oscillations in the density of the Al valence electrons. These oscillations are the so-called plasma oscillations.

Plasma resonance phenomena[1] have been discussed by Bohm and Pines (10) and Nozieres and Pines (11). They arise from the Coulomb interaction between electrons. One can show that plasma resonance occurs near an energy given by

$$E_p \equiv \hbar\left(\frac{4\pi N_v e^2}{m}\right)^{1/2} \qquad [3]$$

Here N_v is the valence electron density and m is the mass of a free electron.

Swanson's measurement (12) of the energy loss spectrum of an oxygen-dominated lattice, Al_2O_3, is shown in Fig. 1. The loss peak occurs near the plasma resonance energy as calculated from Eq. [2]. However, the great width of the peak indicates that any collective oscillation is very short lived, soon decaying to other forms of host excitation. The bumps on the broad loss peak presumably represent interband transitions and/or exciton transitions.

Characteristic energy loss measurements have been made for CdS (13), but not for most other phosphor lattices.

[1] References (8) and (9) are review articles discussing plasma resonance phenomena and the characteristic energy losses of electrons in solids.

The energy loss of fast electrons to valence-shell electrons can also be estimated from the optical properties of the material (14, 15). The optical properties are described by the transverse complex dielectric function $\epsilon^T(k,\omega)$. For $k \simeq 0$ excitations $\epsilon^T \simeq \epsilon^L$, and ϵ^T can be used in place of ϵ^L in the loss function [2].

Figure 2 shows Swanson's comparison (12) between $\epsilon_2^L[(\epsilon_1^L)^2 + (\epsilon_2^L)^2]^{-1}$ as deduced from energy loss of fast electrons in Al_2O_3 and $\epsilon_2^T[(\epsilon_1^T)^2 + (\epsilon_2^T)^2]^{-1}$ determined from the optical constants of the material.

We have measured the optical constants of single crystals of the phosphor host YVO_4 as a function of photon energy in the region 3-25 eV (16). The real and imaginary components of the transverse dielectric function were determined by a Kramer's-Kronig analysis of the reflectivity data. They are shown in Fig. 3 along with the energy loss function as estimated from ϵ^T.

The loss function has a broad maximum near the plasma resonance energy as given by Eq. [3]. The structure on the curve is attributed to interband and/or exciton transitions.

Of major concern in cathodoluminescence are the excitations produced by relatively low energy secondary electrons. Since the momentum loss varies as $E^{-1/2}$, there will be comparatively large momentum transfer associated with energy loss of slow electrons.

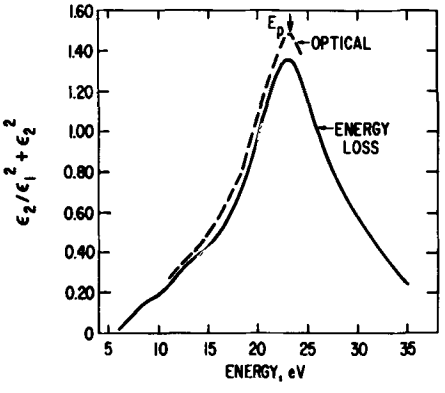

Fig. 2. Energy loss function $\epsilon_2/(\epsilon_1^2 + \epsilon_2^2)$ of Al_2O_3 as determined from optical and from energy loss measurements [after Swanson (12)].

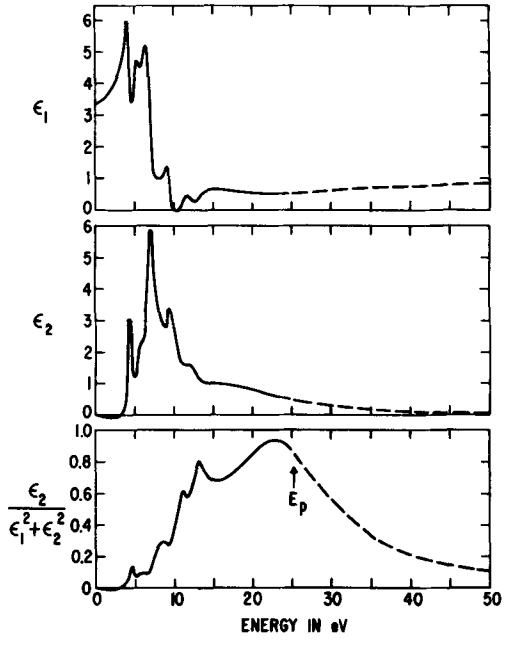

Fig. 3. Real and imaginary parts of the dielectric constant, ϵ_1 and ϵ_2, respectively, and the energy loss function $\epsilon_2/(\epsilon_1^2 + \epsilon_2^2)$, as deduced from a Kramer's-Kronig analysis of reflectivity data for a YVO_4 single crystal.

Unfortunately, there is no direct information on $\epsilon^L(k,\omega)$ for k appreciably different from zero. As k increases, plasmon creation tends to be suppressed in favor of interband transitions. No estimates are available on how severely the loss function is affected. It is likely, however, that in most phosphors the energy of fast electrons ultimately goes to exciting valence-shell electrons in a fundamental loss band similar to that shown in Fig. 3.

Estimation of Cathode-Ray Efficiencies

The excitation of luminescence by energetic electrons can be described by the following sequence of steps:

1. The primary electrons lose energy predominantly by exciting electrons from inner shells of ions, thereby leaving a trail of fast secondaries and excited ions. They also excite valence-shell electrons.

2. The excited ions decay, principally by Auger transitions, producing additional secondary electrons and excited ions. A small fraction (about 1%) of the excitation is lost through x-ray emission.

3. The processes of 1 and 2 continue, each successive step reducing the average energy of the secondaries and excited ions, and increasing the excitation of the valence shell electrons.

4. Except for the roughly 10% lost by back-scattering and x-ray emission, all of the energy of the primary electrons ultimately appears as excitations of the valence-shell electrons in the "fundamental energy loss region" from a few electron volts to several 10's of eV. The excitations initially formed may consist of a mixture of free electrons and holes, plasmons, and excitons. We will neglect the excitons, since probably few are formed initially. Moreover, the plasmons decay, principally into interband excitations, almost immediately. It is as though energetic-hole pairs were excited directly by the energetic primary and secondary electrons.

5. The total excitation energy of a typical electron-hole pair is 20-30 eV. This energy consists of the band gap energy plus the energy of the energetic electron relative to the conduction band minimum and that of the energetic hole relative to the valence band maximum. An energetic electron (or hole) can excite an additional electron-hole pair if its energy exceeds a threshold energy E_t. It can also excite phonons. Theoretical calculations (17) by Kane and Mahan show that a very energetic charge carrier loses much more energy to pair creation than it does to phonon excitation. However, as its energy decreases, the cross-section for pair creation decreases, while the phonon cross-section remains essentially constant. Obviously, a carrier with a kinetic energy less than E_t can excite phonons but not pairs. It may also excite defects or impurities, including activators. (However, we assume that the excitation of activators at this stage is negligible.) Carriers having insufficient energy to excite additional electron-hole pairs eventually thermalize by phonon emission.

6. Activators are excited by thermalized pairs. One possible mechanism is through successive capture of an electron and a hole. This mechanism is very likely operative in II-VI compounds and other semiconductors. A second mechanism involves the initial formation of an exciton, which then migrates to an activator and excites it. This mechanism is thought to be important in YVO_4, $CaWO_4$, and similar materials. The activator relaxes to the emitting state and fluoresces, usually with the emission of part of the energy as phonons.

The loss of potential excitation energy occurs principally in steps 5 and 6. The energy available from one thermalized electron hole-pair is E_g, the band gap energy. In all cases for which information is available, one pair produces at most one emitted photon, with energy $h\nu_e$, so that the energy efficiency of step 6 is

no greater than $h\nu_e/E_g$. Let us make the assumption that the number of emitted photons per thermalized pair produced under cathode-ray excitation is equal to the quantum efficiency η_q, which is observed for photoexcitation just above the absorption threshold. Then the radiant efficiency of step 6 will be that which is observed for excitation with u.v. radiation; $\eta_{u.v.} = \eta_q \frac{h\nu_e}{h\nu}$, with $h\nu \simeq E_g$. If the mean energy required to make a pair is E_x, the efficiency of step 5 is E_g/E_x, and the over-all cathode-ray energy efficiency is given by (18)

$$\eta_{c\text{-}r} = (1 - \eta_{back}) \frac{E_g}{E_x} \frac{h\nu_e}{E_g} = (1 - \eta_{back}) \frac{E_g}{E_x} \eta_{u.v.}(E_g) \quad [4]$$

where η_{back} is the fraction of the energy lost by backscattering.

Equation [4] is useful only if we have an independent means for determining E_x. In principle, E_x could be calculated if the dielectric function $\epsilon^L(\omega,k)$ were known out to large values of k, corresponding to appreciable momentum transfer. However, as mentioned previously, at best $\epsilon^L(k,\omega)$ is known for small k, where it can be deduced from optical measurements. Mahan (17) has calculated E_x for YVO_4 by neglecting any dependence of the loss function on momentum and assuming that the energies of the hole and electron produced in each pair creation event are equal. Under these assumptions, he estimates E_x to be about two times the threshold energy for optical absorption.

A simple model which allows us to estimate E_x describes the host as having parabolic valence and conduction bands. It assumes that the probability of an energetic electron (or hole) creating a pair is much larger than the probability of its losing energy to phonons if and only if its energy exceeds some threshold energy, E_{te} (or E_{th}). Then, as is shown in the appendix, it is generally true that the maximum energy an electron-hole pair can have without being able to excite additional pairs is $E_g + E_{te} + E_{th} = 4E_g$. This value, $4E_g$, is an upper limit for E_x which would be realized only if both charge carriers were produced with energies just under their respective thresholds in each excitation event. The minimum value E_x can have is E_g. This occurs if the energy of the high energy electrons is channelled entirely into creation of electron-hole pairs in which both carriers have zero kinetic energy. We thus find $E_g < E_x < 4E_g$.

Various estimates of E_x have appeared in the literature (19, 20).[2] Such data as are available are consistent with E_x values between $2E_g$ and $4E_g$.[3]

Information on the efficiency of a phosphor under photoexcitation in the photon energy range up to ~40 eV is of interest relative to an understanding of its cathode-ray efficiency for several reasons:

(*a*) Measurement of the radiant efficiency at the band gap energy, $\eta_{u.v.}(E_g)$, may be combined with estimates of E_x/E_g and $(1 - \eta_{back})$ to yield a prediction of the cathode-ray efficiency from Eq. [4].

(*b*) The region up to ~40 eV is the energy range in which the excitation energy of fast electrons eventually shows up as excitations of the valence shell electrons. If excitations of a given energy are sufficiently similar, whether produced optically or by fast electrons, then one expects the cathode-ray efficiency to be a weighted average of the photoexcitation efficiency over this energy range. The weighting function to be used is the relative amount of excitation produced by fast electrons at each energy; the energy loss function as determined optically might be a suitable approximation.

We have studied the photoexcitation efficiency of a number of phosphors in the range of photon energies $3 < h\nu < 25$ eV by exciting them with u.v. from a vacuum monochromator. (Experimental limitations have thus far prevented us from extending the measurements to higher energy.) The luminescent output was compared with that from a sodium salicylate plaque assumed to have a quantum efficiency which is independent of photon energy over the range of interest. Measurement of the absolute radiant efficiency at 2537Å and a value of the average emission energy $h\nu_e$ could then be used to compute the absolute quantum efficiency and absolute radiant efficiency as a function of photon energy. Several representative quantum efficiency curves are shown in Fig. 4.

The energy dependence of the quantum efficiency is most readily interpreted for Zn_2SiO_4:Mn samples. Between 4 and 5.5 eV the photoexcitation appears to be associated with absorption by the Mn activator, since the strength depends on the Mn concentration. Host absorption apparently sets in at about 5.5 eV. From 6 to 14 eV the quantum efficiency remains roughly constant between 70 and 90%. We interpret this to mean that each absorbed photon yields either one or no emitted photons. At 14 eV the quantum efficiency begins to rise, indicating that some of the absorbed photons yield more than one emitted photon. A 14 eV photon produces an electron and a hole at least one of which has sufficient energy to excite a second electron-hole pair. Thus, for one or both carriers $5.5 < E_t < 14 - 5.5$ or $5.5 < E_t < 8.5$.

The quantum efficiency curves for YVO_4:Eu, Gd_2O_3:Eu, and $CaWO_4$:Pb shown in Fig. 4 are not as readily interpreted. For energies slightly greater than the absorption threshold, the efficiency reaches values of 80-100%. At intermediate energies (~8 eV) the quantum efficiency falls. We believe that this decrease in efficiency occurs partly because of surface de-excitation and partly because the intrinsic or bulk efficiency of the excitation produced in this energy range is less. The absorption coefficient $\alpha(h\nu)$ for far u.v. photons is high for the phosphors in question. For example, for YVO_4 $\alpha \sim 10^6$ cm^{-1} for $h\nu > 7$ eV, and the bulk of the u.v. radiation is absorbed within 100Å of the surface. The depth over which surface deactivation

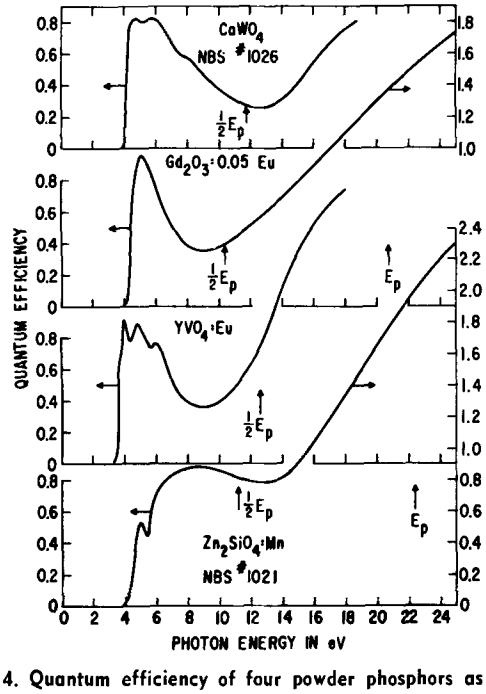

Fig. 4. Quantum efficiency of four powder phosphors as a function of the energy of the incident u.v. photons.

[2] Shockley (19) and Klein (20) have given estimates of E_x. However, their estimates are based on a model wherein the incident fast electrons (of perhaps 20 keV energy) continually lose energy by phonon emission as well as by electron-hole production. According to Mahan (17), such a model is unrealistic.

[3] Data on pair production summarized by Klein (20) is consistent with values $2.7 \leq E_x/E_g \leq 4.0$ for the semiconductors Ge, Si, GaAs, SiC, PbO, and CdS.

is important, for electron excitation, is given approximately by the electron range $R(V_0)$, where V_0 is the characteristic voltage as determined from the voltage dependence of the cathode-ray efficiency. As estimated from the voltage-range relation,[4] 40Å < $R(V_0)$ < 1000Å for most phosphors, and $R(V_0) \sim$ 130Å for YVO_4:Eu. Consequently, a substantial part of the dip in the quantum efficiency curve may be due to surface de-excitation, assuming that u.v. produces the same kind of excitation as fast electrons.

The decrease in quantum efficiency near 8 eV may also be due to a change in the excitation mechanism. Near the excitation edge it is likely that excitons are formed directly by the absorption of the u.v. photons. As the photon energy is increased, one expects to encounter a threshold for the formation of free electrons and holes. The quantum efficiency for fluorescent emission may be lower for free carriers, because they are susceptible to nonradiative trapping processes which do not effect neutral excitons. The increase in efficiency at 10-12 eV is believed due to internal multiplication.

Parameters describing the photoexcitation and cathode-ray excitation of several phosphors are summarized in Table I.[5]

Let us compare the measured cathode-ray efficiency of several phosphors of Table I with an estimate based on Eq. [4]. Taking $1 - \eta_{back} = 0.9$ and $1 < E_x/E_g < 4$, we estimate that $0.22 < \eta_{c\text{-}r}/\eta_{u.v.}(E_g) < 0.9$. For a typical value $E_x/E_g = 3$, $\eta_{c\text{-}r} = 0.3\ \eta_{u.v.}(E_g)$. Unfortunately, E_g is not known for most phosphors, and perhaps the best we can do is to assume that $\eta_{u.v.}(E_g) \simeq \eta_{u.v.}^{max}$, where $\eta_{u.v.}^{max}$ is the maximum radiant efficiency in the near ultraviolet. Figure 5 shows experimental values of $\eta_{c\text{-}r}$ plotted *vs.* 0.3 $\eta_{u.v.}$. There is rough agreement for Gd_2O_3:Eu and $Na_2OGd_2O_3$:Eu, while the remaining materials have $\eta_{c\text{-}r} << 0.3\ \eta_{u.v.}^{max}$. One source of the discrepancy may be the assumption that $\eta_{u.v.}(E_g) = \eta_{u.v.}^{max}$; the maximum in $\eta_{u.v.}$ may correspond to the excitation of excitons rather than free carriers. It is also possible that our assumption of a sharp threshold E_t for pair creation is at fault. If the probability of pair creation increases slowly above threshold, the effect would be to raise E_x and decrease the expected $\eta_{c\text{-}r}$.

Let us now make the assumption that excitations in the fundamental loss region produced optically yield the same luminescent efficiency as the excitations of the same energy produced by fast electrons. Since we do not know the spectrum of excitations produced by fast electrons in the phosphors in question, we simply compare $\eta_{c\text{-}r}$ with 0.9 $\eta_{u.v.}$, where $\eta_{u.v.}$ denotes the range of photoexcitation efficiencies observed between 9 and 25 eV, and the factor 0.9 takes into account the back-scattering loss in fast electron excitation. (No correction for surface de-excitation has been applied.) The comparison is made in Fig. 6. There is rough agreement for several phosphors including Gd_2O_3:Eu and Y_2O_3:Eu. For $MgWO_4$, $CaWO_4$:Pb, and Zn_2SiO_4:Mn $\eta_{u.v.}$ is high compared with $\eta_{c\text{-}r}$, and application of a surface correction would only worsen the agreement.

[4] The voltage-range relation was calculated by assuming that the range $R = 0.4I$, where I is the integrated path length. In turn, I was calculated using the formula given on p. 753 of ref. (6).

[5] See Ref. (1) for additional information concerning these parameters and their measurement.

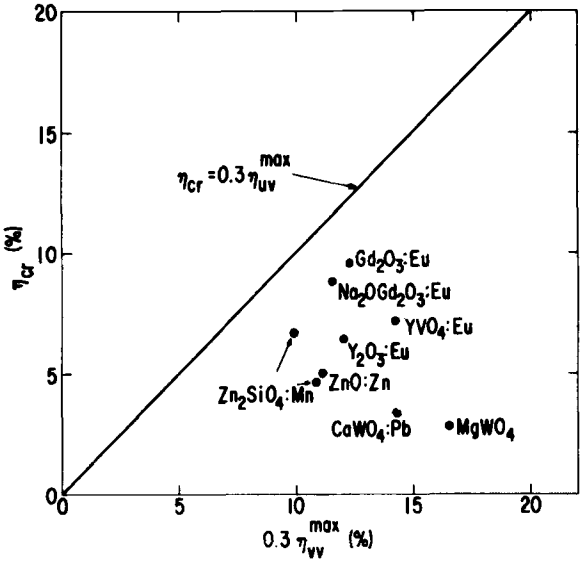

Fig. 5. Comparison between maximum photoexcitation efficiency in the near u.v. and cathode-ray efficiency.

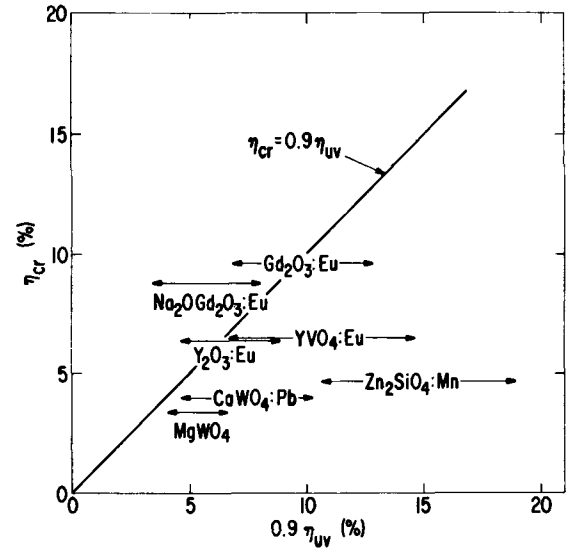

Fig. 6. Comparison between the photoexcitation efficiency in the range $\frac{1}{2}E_p < h\upsilon_{incident} < E_p$ and the cathode-ray efficiency.

The above attempt to relate $\eta_{c\text{-}r}$ to the vacuum ultraviolet photoexcitation efficiency has thus met with very limited success. But the excitations made by photons and electrons may have different momenta and a different division of energy among electrons and holes. Thus, there may be a fundamental difficulty in relating the two kinds of measurement. The cathode-ray efficiency seems to be more variable and sensitive to phosphor preparation than the near u.v. photoefficiency. For example, by incorporation of certain impurities, Kano and Otomo (21) were able to substantially reduce the cathode-ray efficiency of YVO_4:Eu while leaving the near u.v. efficiency largely un-

Table I. Parameters describing the luminescence of selected phosphors

Phosphor	Designation	V_0 (kV)	$R(V_0)$ (eV)	$h\nu_e$ (eV)	$h\nu$ (eV)	η_a (%)	$0.3\eta_{u.v.}^{max}$ (%)	$\eta_{c\text{-}r}$ (%)	E_p (eV)
ZnO:Zn	CE8036-5	5.5	1200		3.4		11.1	5.1	20.9
Zn_2SiO_4:Mn	1021	1.3	140	2.45	6.0	88	10.8	4.7	22.3
$CaWO_4$:Pb	1026	1.5	150	2.5	4.6	88	14.4	3.4	23.6
$MgWO_4$	1027	2.5	380	2.5	4.4	97	16.5	2.9	24
Zn_2SiO_4:Mn	1028	1.6	200	2.34	4.9	70	9.9	6.8	22.3
YVO_4:Eu		1.2	130	2.0	4.0	90	14.2	6.5	25
Y_2O_3:Eu		0.7	64	2.0	5.2	100	~12	6.5	21.8
Gd_2O_3:Eu	N-125-1	1.0		2.0	5.0	100	12.2	9.6	19.2
$Na_2OGd_2O_3$:Eu	N-124-2	~3	640	2.0	5.0	94	11.5	8.8	~19
ZnS:Ag	33-2-646A			2.82	3.7			19.6	16.3

affected. Pairs having appreciable energy and momentum may undergo trapping and nonradiative decay processes which pairs having low energy and momentum avoid (perhaps because the latter pairs quickly form excitons). Further progress in understanding cathode-ray efficiency is made difficult by a lack of knowledge of how important undesired trapping processes may be, and thus how high the efficiency might be in their absence. Additional knowledge about the excitations produced by fast electrons and about exciton formation, surface de-excitation, band gap energies, etc., would be useful.

We have noticed a correlation between high plasma resonance energy of a phosphor host and low cathode-ray efficiency (see Fig. 7). We know of no phosphor having $E_p > 21$ eV and $\eta_{c\text{-}r} > 8\%$. The very efficient phosphor hosts (Zn,Cd)S:Ag and Gd_2O_3:Eu have $E_p \approx 15.4$ and 20.8 eV, respectively. One simple model for phosphor excitation is that the energy of the fast electrons is used exclusively to produce plasmons and that each plasmon decays to form one electron-hole pair, with no further multiplication ($E_x = E_p$). Assuming $\eta_q = 1$, we find $\eta_{c\text{-}r} = (1 - \eta_{back})h\nu_e/E_p$ from Eq. [4]. This relation is obeyed to within ±30% for about one third of the samples for which we have made the comparison. However, other phosphors (such as ZnS:Ag) show a higher $\eta_{c\text{-}r}$ than the above model predicts, indicating that $E_x < E_p$.

Concluding Comments

We have presented several models of the excitation mechanisms involved in cathodoluminescence. Each of these models is capable of "explaining" the efficiencies of only a fraction of the materials we have investigated. We thus do not have, as yet, a generally applicable picture of cathodoluminescence. The reasons for the failure of our models in many instances are understandable, but the means for improving them are not obvious.

A thorough understanding of cathodoluminescence appears to require a more detailed knowledge of the band structure, excitation processes, and decay processes in the energy range from the band gap to the plasmon energy. This knowledge is not easily acquired either experimentally or theoretically. Determination of the optical constants of more phosphor materials and a more detailed understanding of the vacuum u.v. excitation spectra and surface de-excitation may be useful.

There are some comparatively certain conclusions which one can draw, however. Specifically, the more efficient phosphors are expected to be, and in practice turn out to be, those with small band gaps and low

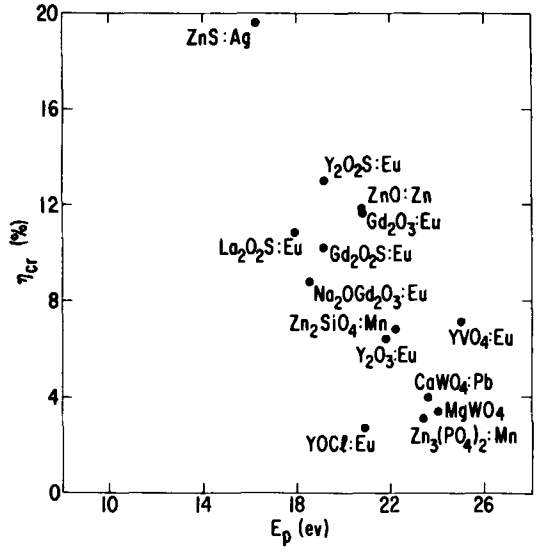

Fig. 7. Cathode-ray efficiency and calculated plasma resonance energy $E_p \equiv \eta(4\pi Ne^2/m)^{1/2}$ of a series of phosphors.

Table II. Some compounds having low plasma resonance energy (see Eq. [3])

Compound	E_p (eV)
Cs_2O	9.9
CsI	10.5
Hg_2I_2	12.2
BaS	12.6
BaI_2	12.6
Gd_2S_3	13.3
NaI	13.6
LaI_3	13.6
HgSe	14.2
CdS	14.5
ThC_2	14.5
HgS	14.8
La_2S_3	16
ZnS	16.3
ThOS	17.1
$LaCl_3$	17.4
$GdCl_3$	18.0

plasma resonance energies. Thus, an empirical search for new phosphor hosts may be more fruitful if the materials investigated are those which tend to have small E_g and $\eta\omega_p$. Obviously, the band gap cannot be arbitrarily small if a material is to emit visible emission efficiently at room temperature. As a guide, we have listed a number of materials with low E_p in Table II.

Acknowledgments

The authors are indebted to G. D. Mahan and D. T. F. Marple for many valuable discussions and to S. J. Lubowski for assistance with the measurements.

Manuscript received Aug. 11, 1969. This was Paper 60 presented at the New York Meeting, May 4-9, 1969.

Any discussion of this paper will appear in a Discussion Section to be published in the December 1970 JOURNAL.

APPENDIX

Threshold Energies for Pair Creation by an Energetic Carrier

We assume that the host has parabolic conduction and valence bands, and use the subscripts e and h to denote electron and hole, respectively. The smallest possible energy for pair creation corresponds to the case where the momenta of all the particles are parallel or antiparallel. We assume that momentum is conserved without the aid of phonons or impurities and equate the momentum loss of the energetic carrier to the total momentum of the pair

$$\Delta p = p_e + p_h \qquad [A\text{-}1]$$

Furthermore, we equate the energy loss of the energetic carrier to the total energy of the created pair

$$[p_0^2 - (p_0 - \Delta p)^2]/2m = E_g + p_e^2/2m_e + p_h^2/2m_h \qquad [A\text{-}2]$$

Solving for p_0 and eliminating p_h we find

$$p_0 = \frac{m}{\Delta p}\left[E_g + \frac{\Delta p^2}{2m} + \frac{p_e^2}{2m_e} + \frac{(\Delta p - p_e)^2}{2m_h}\right] \qquad [A\text{-}3]$$

The minimum value of p_0 can be found by differentiating Eq. [A-3] with respect to Δp, and with respect to p_e, and equating each to zero and solving the pair of simultaneous equations. The minimum occurs for $\Delta p = 2m(m_e + m_h)E_g/(m + m_e + m_h)$ and $p_e = 2m(m_e)^2E_g/[(m + m_e + m_h)(m_e + m_h)]$. The threshold energy for pair creation is then given by

$$E_t = [1 + m/(m_e + m_h)]E_g \qquad [A\text{-}4]$$

For $m = m_e = m_h$, $E_t = 3/2\ E_g$. For $m_e << m_h$, $E_{te} = E_g$, $E_{th} = 2E_g$. We find that $E_{te} + E_{th} + E_g = 4E_g$, independent of the effective masses.

REFERENCES

1. G. W. Ludwig and J. D. Kingsley, *This Journal*, **117**, 348 (1970).
2. See G. F. J. Garlick in "Luminescence of Inorganic Solids," p. 685, P. Goldberg, Editor, Academic

Press, New York (1966), for a review of the physics of cathodoluminescence.
3. For a review of electron penetration of matter see R. D. Birkoff, "Handbook of Physics" Vol. 34, p. 53, Springer Verlag, Berlin (1958).
4. H. A. Bethe, "Handbook of Physics," Vol. 24, pp. 1, 519, Springer Verlag, Berlin (1933).
5. L. V. Spencer, *Phys. Rev.*, **98**, 1597 (1955); L. V. Spencer, NBS Monograph 1 (1959) (Washington: National Bureau of Standards).
6. W. Ehrenberg and D. E. N. King, *Proc. Phys. Soc.*, **81**, 751 (1963).
7. See, for example, V. E. Coslett and R. N. Thomas, *Brit. J. Appl. Phys.*, **15**, 883, 1283 (1964).
8. O. Klemperer and J. P. G. Shepherd, *Adv. Phys.*, **12**, 355 (1963).
9. H. Raether, *Ergeb. Exakt. Naturw.*, **38**, 84 (1965).
10. D. Bohm and D. Pines, *Phys. Rev.*, **82**, 625 (1951); *ibid.*, **85**, 338 (1952); *ibid.*, **92**, 609 (1953).
11. P. Nozieres and D. Pines, *ibid.*, **113**, 1254 (1959) and reference therein.
12. N. Swanson, *ibid.*, **165**, 1067 (1968).
13. F. Pradal and C. Gout, *Compt. Rend.*, **252**, 2687 (1961).
14. See, for example, refs. (11), 13), and (16).
15. F. Stern, *Solid State Phys.*, **15**, 299 (1963).
16. J. D. Kingsley and G. W. Ludwig, *J. Appl. Phys.*, To be published.
17. E. O. Kane, *J. Phys. Soc. Jap.*, **21**, Suppl. 37 (1966); G. D. Mahan, Unpublished.
18. Compare p. 699 of Ref. (2).
19 W. Shockley, *Solid State Electronics*, **2**, 35 (1961).
20. C. A. Klein, Proc. Int. Conf. Semiconductor Phys., Kyoto, 1966, *J. Phys. Soc. Japan*, **21**, Suppl. 307 (1966).
21. T. Kano and Y. Otomo, *This Journal*, **116**, 64 (1969).

Anomalous Thermal Behavior of Boron-Doped Low-Temperature Ge Epitaxial Layers

M. Berkenblit,* T. B. Light, and A. Reisman*

IBM Watson Research Center, Yorktown Heights, New York

ABSTRACT

Recently, conditions have been defined for the growth of mirror-smooth layers of Ge on either Ge or semi-insulating GaAs by the GeI_2 disproportionation reaction. In attempting to dope such layers with p-type impurities under the defined surface-rate-limited growth conditions, it was observed that order-of-magnitude decreases in resistivity occurred on heating the grown layers to temperatures higher than the original growth temperature. This indicated that impurities were initially incorporated in an electrically inactive state. Results are presented which show this behavior to be increasingly pronounced for fast growth rates and low substrate temperatures. and growth conditions to minimize the effect are defined.

Recently, conditions were defined for the growth of mirror-smooth layers of Ge on Ge or semi-insulating GaAs (110) substrates by the GeI_2 disproportionation reaction (1). In attempting to fabricate devices in layers that were boron doped and grown under defined surface-rate-limited growth conditions, a marked thermal instability was detected. It was observed that material grown at 350° exhibited an order of magnitude decrease in resistivity as a consequence of a process step which required temperatures higher than the original growth temperatures (*e.g.*, 700°C As diffusion for diode fabrication). As a consequence, it was difficult to achieve control of resistivities of 0.1 ohm-cm or greater. Initial attempts at preparing As-diffused diodes in B-doped Ge layers grown at 350°C under the surface limiting conditions described in reference (1) resulted in devices with soft reverse characteristics.

Investigation of the anomalous behavior demonstrated that the thermal instability is a function of the temperature at which the layer is grown, the growth rate and to some degree the concentration of the added impurity. The results presented in this paper are mainly concerned with B-doped Ge. Ga-doped samples, prepared using a solid source of $GaCl_3$, were shown to exhibit a similar resistivity change following heat treatment. Within the limits of the experiment, As-doped layers did not behave in this manner. In the following, conditions are defined for layer growth and annealing which permit stabilization of the electrical behavior and the maintenance of the desired surface smoothness.

Experimental Procedure

Germanium epitaxy.—The Ge layers were grown in a horizontal reactor under the required high-velocity and high-GeI_2-concentration conditions described previously by the authors (1). Substrate temperature was varied from 350° to 410°C, and the velocity and concentration of the carrier and reactant gases were adjusted upwards with increasing temperature in order to maintain surface-reaction-rate limiting conditions. The Ge source bed was held at 600°-620°C. A 15% H_2-85% He mixture was used as a carrier gas at an input flow rate of 900-1500 cc/min [room-temperature average linear-gas-stream velocity (l.g.s.v.) at the substrate equal to 190-320 cm/min]. The I_2 source temperature for the HI generator was varied from 65° to 85°C (±0.2°C at a given temperature), which is equivalent to a range of HI pressures of 11.0-39.2 Torr.

Purification of the carrier gas, preparation of the substrates, and the use of a vacuum chuck substrate holder to protect the surface during Ge deposition have been described in detail previously, as have a number of general considerations regarding the low-temperature disproportionation reaction (1-4).

Doping.—The prime source for p-type doping was BI_3. The use of BBr_3 and $GaCl_3$, as well as elemental Ga with which HI was reacted, were tested and found to be unsuitable as a means of introducing a controlled impurity concentration into the reactive gas stream. During the course of the investigation, a method was developed for the *in situ* synthesis of BI_3 which made available a reproducible source of boron and eliminated the problems of handling a highly reactive material (5). Arsenic as an n-type impurity was obtained from the *in situ* decomposition of AsH_3 carried into the reactor as a dilute mixture in 15% H_2-85% He.

Annealing.—Germanium layers, grown by the iodide process as well as by other deposition techniques, and bulk Ge wafers were annealed at 500°C for 16 hr in a

* Electrochemical Society Active Member.

Table I. Resistivity of bulk Ge and epitaxial Ge layers on Ge or GaAs substrates annealed at 500°C for 16 hr

Deposition process	Deposition temperature, °C	"As grown" resistivity of Ge layer	Resistivity after 16 hr at 500°C
GeI_2 (BI_3)	350	0.1 to >12 ohm-cm, p-type and n-type (low BI_3)	p-type ~0.02 ohm-cm
Bulk Ge wafers (n-or p-type)	—	—	No change
$GeCl_4$ (B_2H_6)	800	~0.1 ohm-cm, p-type	No change
GeH_4 (B_2H_6)	650	~0.1 ohm-cm, p-type	No change
GeI_2 (no BI_3)	350	n-type	Slight change

quartz tube furnace in a 15% H_2-85% He ambient. A comparison was made between the iodide process and the other deposition methods, and with bulk material, to obviate the possibility of an impurity present in the annealing furnace causing the resistivity shift, and to determine whether the method of deposition influenced the results.

Measurement of electrical characteristics.—A 3-point-probe spreading-resistance technique was used to determine the resistivities of the "as grown" layers and to follow the changes resulting from the various anneal cycles. Van der Pauw samples were prepared from a number of samples for Hall-mobility and active-impurity-concentration determinations. Planar diodes were fabricated by As diffusion at 700°C for 30-60 min through openings in vapor-deposited SiO_2 layers. The diode area was about 1.8×10^{-5} cm^2. The reverse characteristics of the diodes were measured from 0.2V to breakdown.

Results and Discussion

Table I shows the variation of resistivity with annealing for samples of Ge from various sources. It may be observed that B-doped Ge layers (approximately 0.1 ohm-cm), grown at 350°C at a rate of 5 μm/hr, exhibit a very pronounced decrease in resistivity to <0.02 ohm-cm as a result of a heat treatment at 500°C. Such behavior was found to be characteristic of the p-type Ge grown by the iodide process and was not observed in Ge deposited at higher temperatures by other methods (pyrolysis of GeH_4 at 650°C and the reduction of $GeCl_4$ at 800°C). Ge wafers cut from bulk grown material, both p- and n-type, showed no change following heat treatment. In layers grown by the iodide process without BI_3 or any other intentionally added impurity present in the vapor stream, only a slight shift in resistivity could be detected after heat treatment.[1] Similar slight changes were observed some years earlier by Marinace *et al.* (6, 7), and were attributed by them to incorporated iodides. From the above results it is clear that iodide contamination in the grown layers does not contribute significantly to the anomalous resistivity effect. Finally, the instability of the deposited-Ge layer was similar whether the substrate used was Ge or GaAs.

The major conclusion from the information in Table I is that boron appears to be incorporated to a large degree in an electrically inactive state at 350°C under the nonequilibrium growth conditions employed, and is subsequently activated by an annealing process. Significantly, in previous work, B-doped Ge layers, grown at 350°C under flux conditions approaching equilibrium, did not exhibit a resistivity shift. All of the above indicate that the resistivity changes observed are a consequence of the growth parameters, primarily, and the attendant mechanism of impurity incorporation during the specific growth procedure used.

The extent to which growth rate affects the observed stability of B-doped Ge was studied in a series of depositions at 350°C. It was found that the resistivity change following annealing at 500°C was large (approximately an order of magnitude) for layers grown at rates of 2-10 μm/hr. For layers grown at 1.2 μm/hr the effect was somewhat diminished, and at an 0.8 μm/hr growth rate there was less than a 10% change in resistivity. It should be noted that, as the growth rate was reduced, the epitaxial-layer surface quality deteriorated and the layers were less suitable for fine-line device fabrication. Consequently, as equilibrium growth conditions were approached, electrical stability was gained at the expense of surface quality.

The resistivity change, after annealing the deposited Ge layers, was reduced markedly also as a result of a relatively small increase in substrate temperature. In order to retain surface-rate-limiting growth conditions and attendant surface smoothness, it was necessary to increase the vapor phase concentration and velocity as the substrate temperature was increased. This, of course, resulted in an enhanced growth rate with increasing temperature; for example, at 385°C it was necessary to employ a growth rate of approximately 20 μm/hr in order to obtain surfaces comparable to those obtained at 350°C at a rate of 5 μm/hr. At 400°C deposition temperatures, the growth rates were of the order of 25-30 μm/hr. In this range, however, some degradation of surface quality resulted, since the maximum practical concentration and velocity obtainable in the system employed was only marginally adequate.

A summary of the deposition parameters is shown in Table II. The flux requirements in terms of HI vapor pressure, carrier gas input, and average linear-gas-stream velocity at the substrate site are listed together with the resulting growth rates. The BI_3 concentration is an approximate value required to provide an "as grown" resistivity of 0.1 ohm-cm.

A numerical comparison of the relative stabilities of layers deposited at various substrate temperatures was estimated by calculating a ratio of inactive boron in the "as grown" layer to the total boron in the layer. Spreading resistance values for resistivity were converted to carrier concentration using the curves of Sze and Irvin (8). The total boron concentration, C_T, was obtained from the resistivity of the annealed sample (neglecting corrections for charge carrier compensation and mobility). The concentration of inactive boron, C_T-C_I, was taken as the difference between the annealed value, C_T, and the value derived from the "as grown" resistivity, C_I. $(C_T\text{-}C_I)/C_T$ represents the fraction of the boron that is incorporated into the "as grown" Ge layer in an electrically inactive state. Figure 1 is a plot of this ratio as a function of substrate temperature. The inactive boron fraction is seen to decrease from 0.83 to 0.12 in the substrate temperature interval 350°-400°C, respectively. This is consistent with the observed decrease in the BI_3 concentration required in the gas phase (Table II).

A further evaluation of the effect of substrate temperature during growth and annealing was made from Hall mobility data. Van der Pauw samples were prepared from Ge layers grown on semi-insulating GaAs substrates at 350° and 385°C. The insulating substrates were used to provide isolation of the epitaxial film. Half of each Ge/GaAs structure was given an extended anneal (48 hr at 500°C) to insure complete equilibration of the Ge layer. The results are shown in Fig. 2a

Table II. Deposition parameters used to obtain smooth surfaces as a function of temperature

Substrate temperature, °C	HI vapor pressure, Torr	Flow rate, cc/min	L.G.S.V. cm/min	Growth rate, μm/hr	BI_3 concentration, ppm	$\frac{C_T - C_I}{C_T}$
350	11.0	900	190	5	90	0.83
385	27.6	1200	250	20	70	0.58
400	27.6	1500	320	25	50	0.12

[1] "As grown," undoped layers were high resistivity n-type (of the order of 2 ohm-cm), and they remained high resistivity after annealing (some samples converted to p-type high resistivity and others remained n-type, but with a higher resistivity).

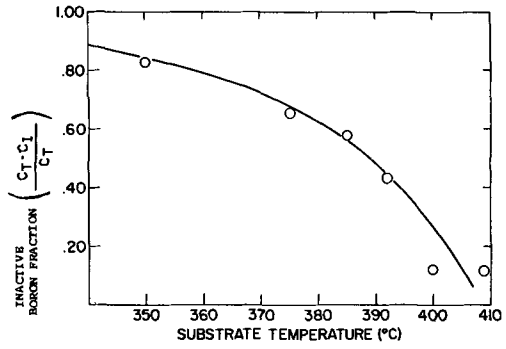

Fig. 1. Variation of the fraction of inactive boron with substrate temperature.

and 2b as plots of mobility *vs.* carrier concentration. The solid lines represent published data for bulk mobility (9). The shape of the curves at the high carrier concentration end (dashed portions) was obtained from values determined by Woods (of these laboratories) on bulk material. Samples grown at 385°C exhibit a Hall mobility close to that of bulk mobility at room temperature. Following annealing at 500°C, the resistivity of these samples decreases slightly and is accompanied, as expected, by a similarly small decrease in Hall mobility. Samples grown at 350°C exhibit a Hall mobility considerably smaller than the bulk value. Following annealing there is a considerable resistivity change accompanied by a somewhat smaller Hall mobility change. The Hall mobility of such samples at room temperature following annealing is still, however, considerably smaller than the bulk value.

For these same samples measured at 77°K, the following is observed: the mobility of the sample grown at 385°C and annealed at 500°C is essentially the bulk value, whereas that of the sample grown at 350°C and annealed at 500°C shows a significant increase from the "as grown" value, but is still less than the bulk value. Unaccountably, when measured at 77°K, the layer grown at 385°C exhibited essentially bulk mobility following annealing, but the carrier concentration decreased after annealing. In view of the results for both the annealed and unannealed layers deposited at 385°C, this last result is unexpected and as yet unexplained. What does appear to be clear, however, is that with a slight increase in growth temperature of the layers, one obtains Hall mobilities more nearly approximating bulk values. As we shall show below, diodes fabricated from layers grown at different temperatures show leakage characteristics that correlate with Hall data in the sense that, as Hall mobilities approach bulk values, diode characteristics improve.

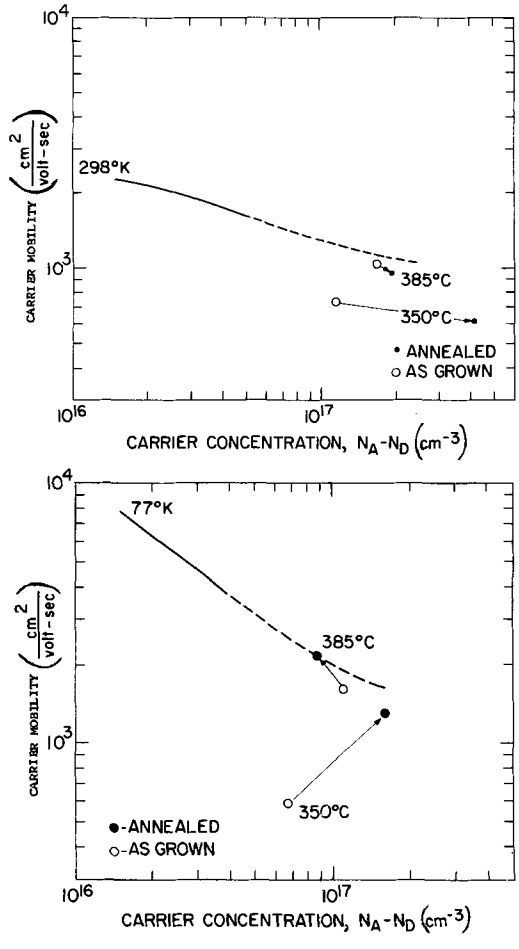

Fig. 2. Hall mobility *vs.* carrier concentration, as-grown and after annealing at 500°C. a, Room temperature; b, liquid nitrogen temperature.

The characteristics of diffused diodes made in Ge layers grown under various conditions of growth rate, substrate temperature, and annealing time were compared. All of the Ge layers were given at least a standard annealing treatment of 500°C for 16 hr before diode fabrication.

Typical reverse characteristics are shown in Fig. 3 for diodes in bulk Ge, and in high- and low-temperature epitaxial layers of Ge deposited on Ge and GaAs substrates. Diodes formed in bulk Ge and in Ge epitaxial layers, deposited by the reduction of $GeCl_4$, were indistinguishable from one another. The Ge layers deposited on GaAs substrates by the pyrolytic dissociation of GeH_4 were more heavily doped, with the result that they had a lower breakdown voltage; below breakdown, the characteristics are equivalent to those for bulk Ge.

As seen from Fig. 3, the B-doped layers formed by the disproportionation of GeI_2 at 350°C yielded soft reverse *I-V* characteristics, whether deposited on Ge or on GaAs substrates. As the reverse voltage increases, it eventually reaches a saturation value at about the expected breakdown voltage.

The major difference between diodes fabricated in layers grown at higher and lower temperatures is seen in the slope, n, of the log I *vs.* log V characteristic in the pre-breakdown region. Thus, $n = \Delta \log I/\Delta \log V$. If $n \rightarrow 0$, then this is indicative of what is normally termed a hard diode characteristic. If $n \rightarrow 1$, a resistance-like or soft characteristic is indicated.

Figure 4 gives a summary of the values of n for typical diodes in epitaxial layers formed by different high- and low-temperature epitaxial processes. The B-doped layers produced by the high-temperature processes ($GeCl_4$ and GeH_4) yield acceptable diodes, even when deposited on GaAs substrates (via the GeH_4 process). It should be noted that Ge layers deposited on GaAs using the GeH_4 process are plastically deformed (10). Consequently, the question of crystal perfection influencing these results was tested. An As-doped layer on Ge, produced by the low temperature process (GeI_2

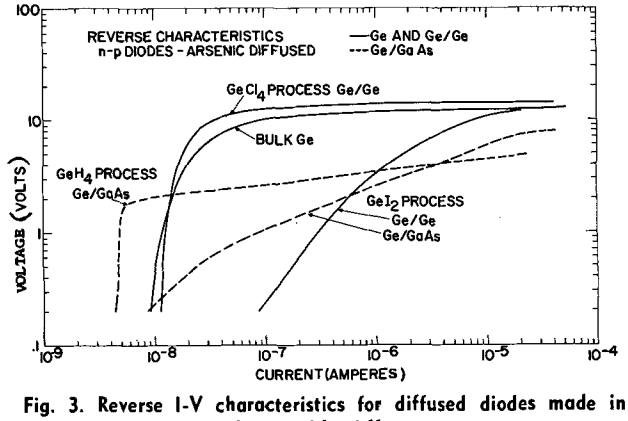

Fig. 3. Reverse I-V characteristics for diffused diodes made in bulk Ge and in Ge layers deposited by different processes.

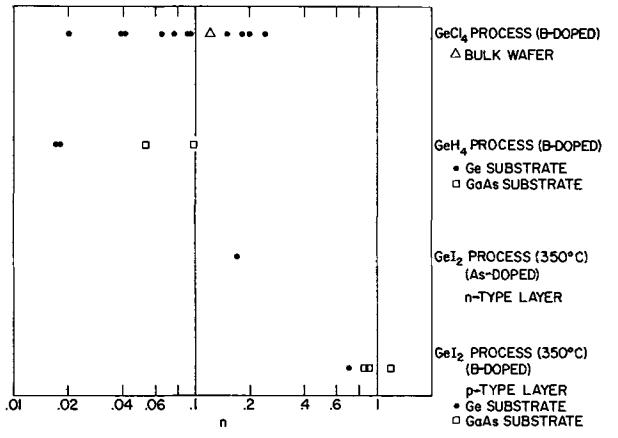

Fig. 4. Measured values of the pre-breakdown slope (n = Δlog I/Δlog V) of I-V characteristics for diodes made in bulk Ge and Ge layers deposited by different processes.

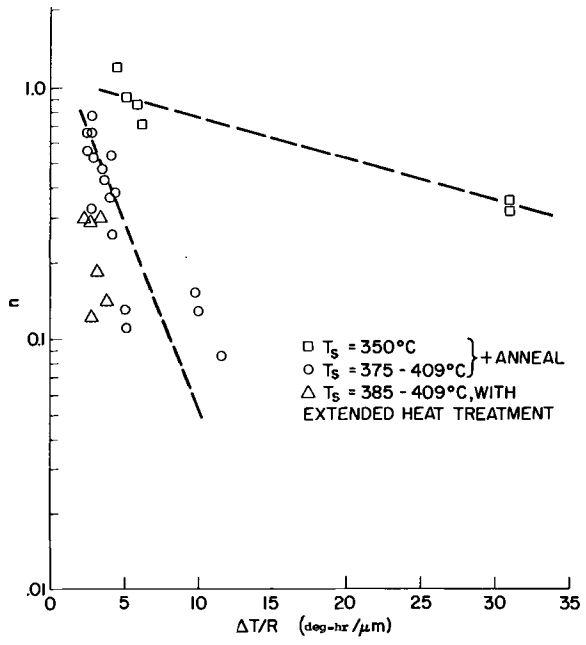

Fig. 5. Measured values of the pre-breakdown slope (n = Δlog I/Δlog V) of V-I characteristics for diodes made in Ge layers deposited under different conditions of substrate temperature, T_S, and deposition rate, R.

at 350°C substrate temperature), also yielded acceptable diodes. We can see from the data of Fig. 4 that neither substrate type nor plastic deformation are important factors leading to high values of n, but that low deposition temperatures combined with the use of B doping does result in high values of n.

The effects of substrate temperature and growth rate on n are shown in Fig. 5. Log n is plotted against the ratio $\Delta T/R$, where ΔT is defined arbitrarily as the substrate temperature, T_S, minus 325°C, and R is the growth rate in μm/hr. The ratio $\Delta T/R$ is used, since it is expected that the incorporation of active B would be enhanced by larger ΔT or smaller R. Most of these data are for layers grown on Ge substrates.

As mentioned previously, all of the Ge layers from which these data were obtained were annealed at 500°C for 16 hr prior to diode fabrication. Some of the samples were given extended heat treatments at 500°C for 32-48 hr or at 800°C for 45 min. The n-values for these samples were about a factor or two lower than would be expected from the substrate temperature, growth rate, and standard anneal.

It can be seen, then, that the growth conditions which lead to minimal changes in resistivity also lead to improved diode reverse characteristics. The resistivity data indicate that the B dopant present in the 350°C layers is not all incorporated into electrically active sites in the Ge lattice. The mobility data indicate that there is an extra scattering mechanism taking place in these layers. The inactive B may be associated with imperfections which adversely affect the mobility.

Summary

1. The resistivities of Ge layers deposited at the lower substrate temperature (350°C), using high GeI_2 concentrations and high carrier gas velocities, were thermally unstable (exhibiting resistivity decreases of a factor of 10) and the mobilities were low.

2. The resistivities of Ge layers deposited at the higher substrate temperatures (>375°C) showed much less thermal instability (10% decrease in resistivity at 400°C) and yielded satisfactory diodes after annealing.

3. The thermal instability is attributed to incomplete incorporation of electrically active B in the Ge lattice.

Acknowledgments

The authors wish to thank M. Sampogna for assistance in growing the Ge layers, M. E. Cowher for the Hall measurements, S. A. Sharpe for making diode measurements, and R. A. Laff for many helpful discussions.

Manuscript received Sept. 9, 1969.

Any discussion of this paper will appear in a Discussion Section to be published in the December 1970 JOURNAL.

REFERENCES

1. M. Berkenblit, A. Reisman, and T. B. Light, *This Journal*, **115**, 966 (1968).
2. A. Reisman and M. Berkenblit, *ibid.*, **112**, 315 (1965).
3. A. Reisman, M. Berkenblit, and A. Alyanakyan, *ibid.*, **112**, 241 (1965).
4. A. Reisman and A. Alyanakyan, *ibid.*, **111**, 1154 (1964).
5. M. Berkenblit and A. Reisman, To be submitted as a Technical Note.
6. J. C. Marinace, *IBM J. Res. and Dev.*, **4**, 248 (1960).
7. W. E. Baker and D. M. J. Compton, *ibid.*, **4**, 269 (1960).
8. S. M. Sze and J. C. Irvin, *Solid State Electronics*, **11**, 599 (1968).
9. H. Fritzche, *Phys. Rev.*, **99**, 406 (1955).
10. T. B. Light, M. Berkenblit, and A. Reisman, *This Journal*, **115**, 969 (1968).

High-Dose Implantations of P, As, and Sb in Silicon: A Comparison of Room-Temperature Implantations Followed by a 550°C Anneal and Implantations Conducted at 600°C

Billy L. Crowder

IBM Thomas J. Watson Research Center, Yorktown Heights, New York

and John M. Fairfield[*,1]

IBM Components Division, East Fishkill Laboratory, Hopewell Junction, New York

ABSTRACT

A study has been made of room-temperature implantations of large doses of P, As, and Sb into Si substrates, followed by annealing in the temperature range 550°-600°C and of implantations of these species into Si substrates maintained at 600°C. Neutron activation combined with anodic oxidation and HF stripping techniques was used to determine the profiles of the implanted ions. Electrical evaluation of the implanted layers by Hall effect and sheet resistivity measurements in conjunction with anodic oxidation and HF stripping techniques yielded profiles of the net electrically active species. The profiles obtained for 600°C implantations are markedly orientation dependent since the crystalline nature of the Si lattice is maintained during the implantation. Most of the P, As, or Sb ions implanted at room temperature are electrically active after annealing at 550°-600°C, and the carrier mobility observed in the implanted layer approaches that observed in comparably doped bulk Si. Only a small fraction of the ions implanted at 600°C are electrically active and uncompensated, and the carrier mobility in these layers reflects the increased scattering due to charged compensating defects.

In the process of ion implantation doping of silicon at room temperature, the overlapping of disordered regions produced by the energetic heavy ions eventually results in the formation of a completely amorphous region extending to the surface of the silicon substrate, provided the implanted dose is sufficiently large (1). The recrystallization of such amorphous regions occurs in the temperature range 500°-600°C and results in epitaxial regrowth onto the underlying undamaged Si substrate (1,2). If the substrate is maintained at a high enough temperature (*e.g.*, greater than 400°C for dose rates normally employed in ion implantation) during the implantation process, enough radiation damage is annealed during the course of the implantation to preclude the formation of a completely amorphous region (3). In a previous publication, the presence of a completely amorphous region was demonstrated to be advantageous in achieving a large fraction of the implanted species electrically active and uncompensated (P, As, and Sb in Si) at a low annealing temperature (*e.g.*, 600°C) (4). The purpose of the present paper is to expand these initial investigations. The profiles (total and net electrically active) for P, As, and Sb implanted into Si have been investigated for (*a*) room-temperature implantations followed by a 550°-600°C post implantation anneal and (*b*) implantations into Si substrates maintained at 600°C. The total doses employed were sufficiently large to produce a visible amorphous region for the room-temperature implantations.

Experimental

The group V ions were implanted into Si samples using a Cockcroft-Walton accelerator capable of operation to 300 kV. The ions P and As were obtained from gaseous species (PF_5, AsH_3) in an oscillating electron source of our design (5). An Ar plasma was used to heat solid Sb in a quartz crucible suspended inside the same source, thereby obtaining a sufficient vapor pressure of Sb. The ion beam was focussed, mass analyzed magnetically, and scanned uniformly over the sample (4 cm^2). In the case of Sb, Sb^{123} was employed since this isotope, upon neutron activation, yields Sb^{124} which has a 60.9-day half life. The Si substrates were <100> wafers cut from Czochralski-grown crystals, which were boron doped and 1 ohm-cm resistivity. The substrates were lapped and chemically polished. It was possible to heat the samples as high as 700°C during implantations. The total dose was obtained by integrating the current from the samples (room-temperature implantations) or from a beam profile monitor (high-temperature implantations). The currents were measured with a Faraday cup. Dose rates were typically 1-5 $\mu A\ cm^{-2}$. For this study, accurate target alignment (*i.e.*, within 0.1°) was not available since the beam sweep was over approximately ±1°.

After implantation, the wafers to be used for obtaining the total profile of the implanted species were subjected to a thermal neutron flux $10^{13}\ cm^{-2}\ sec^{-1}$ for a few days to produce P^{32}, As^{76}, or Sb^{124} depending on the implanted species. After sufficient time for the Si^{31} (half life 2.5 hr) to decay, the wafers were sectioned by anodizing and dissolving the anodic oxide in dilute HF. A radiochemical assay by liquid scintillation counting was performed on the resultant solutions to determine the specific activity of each section; precautions were taken to insure against the loss of any radioactive material and to avoid cross contamination. The system was calibrated by including a standard wafer of known impurity concentration with each group of activated wafers. Half-life determinations and γ-ray spectral analyses were used for positive identification of the isotopes.

The electrical evaluation of ion-implanted layers utilizing Hall effect and sheet resistivity measurements on van der Pauw configurations in conjunction with anodic oxidation and HF stripping techniques has been described fully by Mayer, Marsh, Shifrin, and Baron

* Electrochemical Society Active Member.
[1] Present address: SEMI, 1910 W. Cheryl Drive, Phoenix, Arizona.

(6). In the following experiments, the electrical profiling operation was performed in one sample holder (Fig. 1). This design allows etching, anodic oxide formation, and electrical measurements to be performed *in situ*, with electrical contacts being applied only once. To facilitate good electrical contact to the implanted regions, diffused contact pads (As doped) were utilized. Clover-leaf van der Pauw configurations (Fig. 2) were obtained by etching techniques employing a 3:2:1 mixture of nitric acid, acetic acid, and hydrofluoric acid. Contact to the diffused contact pads was achieved by evaporated Al. A fifth large-area Al contact was evaporated onto the rear of the wafer (for use in evaluating the effectiveness of the electrical isolation provided by the p-n junction formed by the implanted species in the B-doped Si substrates). The contacts were sintered at 450°C for 5 min. Electrical contact was made by fastening Pt wires to the Al pads by means of conducting Ag paste.

The anodic oxide growth (and consequent Si removal) was accomplished *in situ* by the insertion of a Pt cathode into the sample holder (Fig. 1) and the use of the Hall contacts and the rear contact to complete the circuit. The electrolyte used was a 0.001*N* solution of potassium nitrate in N-methylacetamide to which was added 3% water. The film growth was terminated automatically by presetting the limiting voltage on a constant current power supply. Typical oxide film thicknesses ranged from 430 to 1000Å (corresponding to 200-460Å of Si removed).

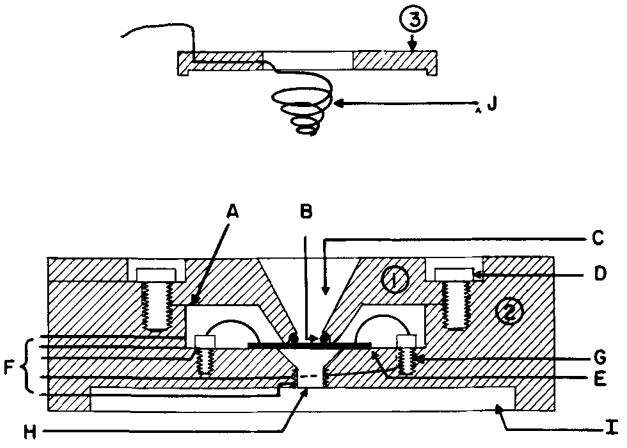

Fig. 1. The sample holder used for stripping and measurements consists of three parts. The holder consists of two Teflon parts, 1 and 2, which fit together well enough to provide a seal at A to protect the contact areas from anodizing and etching solutions. An "o" ring provides a seal at B between the Si wafer, E, and the upper section, 1, thus defining a reservoir, C, for containing anodizing and etching solutions. The upper and lower sections, 1 and 2, are held together by nylon screws, D. Electrical contacts terminate in a Jones plug, F, which has five connections, four to the van der Pauw sample and one to the back of the Si substrate. Contact to the van der Pauw sample is provided by Pt wires attached to the Al pads (Fig. 2) and soldered to the posts, G. Contact to the back of the sample is provided by Ag paste between Al on the wafer and the contact, H. A groove, I, in the lower section fits over one pole face of the magnet, allowing reproducible alignment of the sample. The section 3 constructed from Teflon and with a Pt cathode, J, provides a reproducible cell geometry for the anodic oxidation.

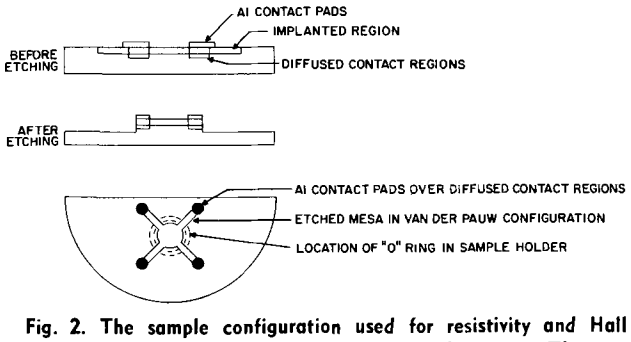

Fig. 2. The sample configuration used for resistivity and Hall measurements is a modified van der Pauw configuration. The test sample is produced by etching a mesa, relying on the junction to provide electrical isolation from the substrate. The portion of the sample which is stripped is inside the area delineated by the "o" ring.

Electrical measurements were made by conventional d-c potentiometric techniques. The van der Pauw configuration is ideally suited to stripping techniques in that a viton "o" ring seal may be inserted between the contact pads and the central region (Fig. 2). The contacts are unaffected by the etching and oxide growth to be performed on the central region and therefore need be applied only once. The magnetic field used for the Hall measurements was 7.5 kilogauss. At the beginning of a stripping run, typical currents, provided by a constant current power supply, were 10^{-4} A and were reduced as the sample resistance increased to minimize the voltage drop across the sample contacts but yet maintain sufficient sensitivity in the Hall measurement.

At the conclusion of a stripping experiment, one has a set of sheet Hall coefficients and sheet resistivities corresponding to a number of successive removals of a known quantity of Si. These data can be reduced to a profile of the concentration and mobility of carriers as a function of the depth from the surface. The details of this data reduction are fully explained in Ref. (6).

The samples which were used for electrical evaluation were implanted under identical conditions to those used to obtain the total profile of implanted atoms with neutron activation analysis and stripping techniques. The use of two separate samples was dictated by the fact that, during the process of neutron activation, massive damage to the sample is incurred which would also influence the annealing characteristics of electrical properties of the implanted ions.

Experimental Results and Discussion

Profiles of implanted species.—Typical profiles obtained by neutron activation and stripping techniques are presented for P (Fig. 3), As (Fig. 4), and Sb (Fig. 5) implanted into <100> silicon wafers. For the P implantations (Fig. 3), the energy of the ions was 280 keV and the dose was 9 x 10^{15} cm^{-2} (room-temperature implantation) and 3 x 10^{15} cm^{-2} (600°C implantation). The room-temperature implantation exhibits a somewhat smaller most probable range, R_p, than the 600°C implantation (0.38 and 0.42μ, respectively). The significant difference in the profile obtained at 600°C relative to the profile obtained at room temperature is the markedly more asymmetric and broader distribution of ions which penetrate more deeply into the Si substrate than the most probable range. For As implantations (Fig. 4), similar results were obtained [R_p = 0.19μ (room temperature) and 0.24μ (600°C)]. The implantation parameters for these As implantations were: 280 keV, total dose = 4 x 10^{15} cm^{-2} (room temperature) and 3 x 10^{15} cm^{-2} (600°C). The solid curve in Fig. 4 was obtained for a <100> silicon substrate misoriented by 7° during the 600°C implantation of 3 x 10^{15} As cm^{-2} (the data points are omitted for clarity).

During the room-temperature implantations, most of the implanted ions impinge on amorphous Si, since the total dose in all cases was more than sufficient to produce a completely amorphous region extending to the substrate surface. Crystalline effects such as channeling were thus not important for most of the ions implanted at room temperature, since channeling is markedly reduced when sufficient lattice disorder is present (7, 8). During 600°C implantations, much of the damage is continuously annealed (3), and crystalline effects, such as channeling, were important

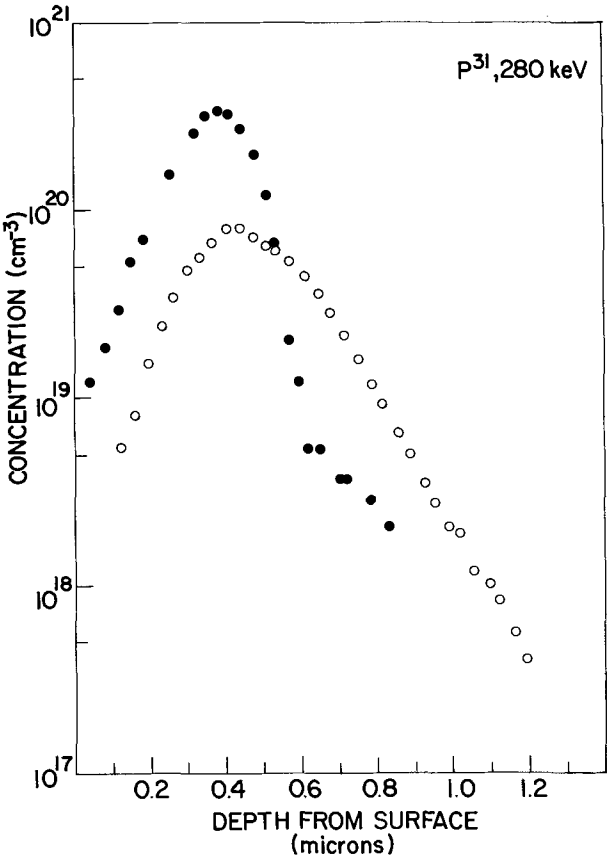

Fig. 3. Implantation profiles of P^+, 280 keV, into <100> Si. Open circles, ○, represent 500°C implant (3 x 10^{15} cm^{-2}), and closed circles, ●, represent room-temperature implant (9 x 10^{15} cm^{-2}).

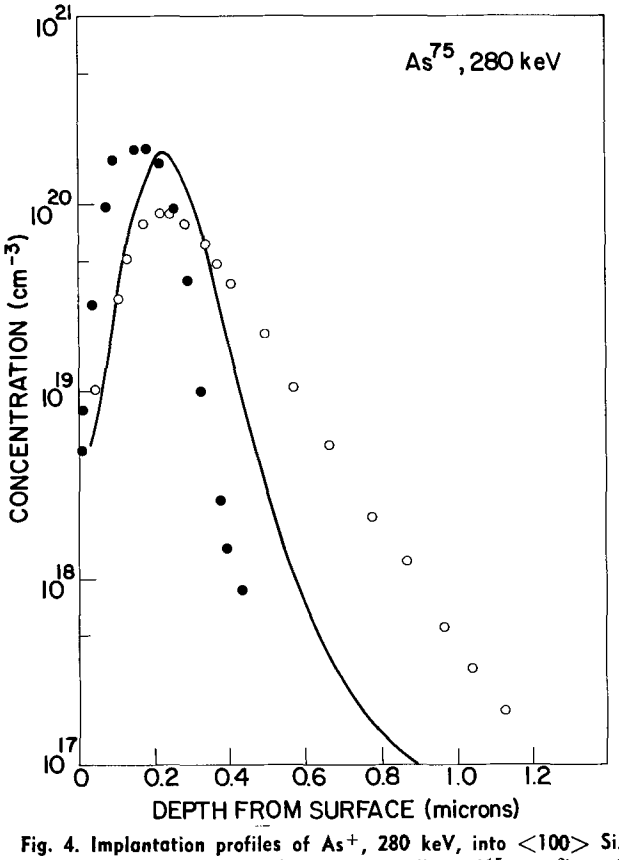

Fig. 4. Implantation profiles of As^+, 280 keV, into <100> Si. Open circles, ○, represent 600°C implant (3 x 10^{15} cm^{-2}), and closed circles, ●, represent room-temperature implant (4 x 10^{15} cm^{-2}), and the solid line represents 600°C implant (3 x 10^{15} cm^{-2}) in which the <100> wafer was misoriented by 7 deg.

during the entire implantation. The asymmetry in the 600°C implantations is thus due to crystalline effects (channeling) and the orientation of the substrate is important, as evidenced in the marked difference in profiles obtained at 600°C for the <100> silicon substrate and the <100> silicon substrate misoriented by 7°. Although not shown in Fig. 4, a nearly identical profile to that obtained for the <100> silicon substrate was observed for 280 keV As (3 x 10^{15} cm^{-2}) implanted into a <111> silicon wafer at 600°C (no misorientation).

Figure 5 depicts the profile obtained from a room-temperature Sb^{123} implantation (120 keV, 1 x 10^{15} cm^{-2}) into <100> Si. The deeply penetrating tail is undoubtedly due to channeling effects present during the initial stages of the implantation when the amount of lattice disorder is not sufficient to prevent such effects, as has been experimentally verified for As implantations at room temperature (7).

Profile of net electrically active species.—A comparison of the profile of total P atoms (280 keV, 8 x 10^{15} cm^{-2}) with the net electrically active carriers is presented in Fig. 6. The implantations were conducted at room temperature into <100> Si substrates. The electrically active profile was obtained after a series of 30 min isochronal anneals from 500° to 800°C. After the 550°C isochronal anneal, the sheet resistivity of this implantation was 14 ohms/sq with a corresponding carrier concentration of 6.4 x 10^{15} cm^{-2}. After the 800°C annealing step, the sheet resistivity was 12 ohms/sq with a corresponding 6.1 x 10^{15} carriers cm^{-2}. Most of the implantation is thus electrically active after only a 550°C, 30 min anneal.[2] From Fig. 6, it is apparent that essentially all of the P atoms implanted are electrically active after an 800°C anneal, except perhaps in the tail region beyond 0.6μ. The carrier mobility of this sample as a function of carrier concentration is presented in Fig. 7, which indicates that the mobility in the implanted layer is comparable to what would be observed for bulk Si of comparable doping levels [after Irvin (9)].

Quite a different situation is observed for P implantations conducted at 600°C (Fig. 8). The implantation parameters were 300 keV, 1.5 x 10^{16} P cm^{-2}, 600°C, Si substrate <100> orientation. The carrier concentration is markedly lower than the concentration of implanted P atoms. In addition, the mobility of the carriers in this sample is markedly lower than that predicted for bulk Si of comparable carrier concentrations, perhaps indicating increased scattering by charged compensating defects responsible for the lack of complete electrical activity of the implanted P atoms (Fig. 7).

Analogous results were also obtained for As and Sb implantations; namely, room-temperature implantations followed by a 600°C anneal produced material in which most of the implanted species are electrically active with a mobility characteristic of bulk Si of comparable doping levels, while 600°C implantations yielded layers in which most of the implanted atoms are not electrically active and uncompensated and the mobility observed is markedly lower than expected for uncompensated bulk Si of comparable carrier concentrations, indicative of appreciable scattering by defect centers.

The profiles resulting from annealing room-temperature implantations of As (280 keV, 4 x 10^{15} cm^{-2},

[2] The carrier concentration referred to here is an effective carrier concentration cm^{-2} determined from the sheet Hall coefficient of the entire implanted layer by the simple relationship $[n^*_s = 1/(R_H e)]$, where n^*_s is the effective number of carriers cm^{-2}, R_H is the measured sheet Hall coefficient, and e is the electronic charge. The number of carriers cm^{-2} determined from this measurement is always lower than the true number cm^{-2} obtained by integrating over the observed carrier distribution. This occurs because the sheet Hall coefficient is a weighted average which favors carriers of higher mobility [see Ref. (6) for a good discussion of this point]. The decrease in resistivity and the decrease in effective carriers cm^{-2} upon annealing to 800°C is due primarily to the fact that the tail of the distribution becomes electrically active only at the higher annealing temperature. This point is discussed more fully in connection with Fig. 9 of the text.

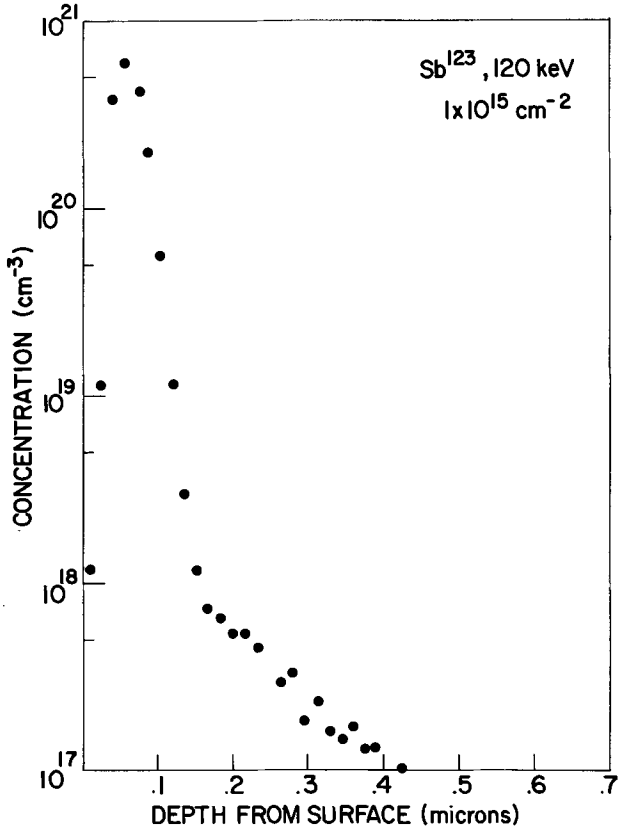

Fig. 5. Implantation profile of Sb^+, 120 keV, into <100> Si. The total implanted dose was 1 x 10^{15} cm^{-2}.

<100> Si) for 30 min at either 550° or 800°C are shown in Fig. 9. The observed carrier concentration beyond 0.36μ in the sample annealed at 500°C exhibits a marked fall-off relative to that in the sample annealed at 800°C. This phenomenon is due to only a small fraction of the implanted As atoms being electrically active and uncompensated in this tail region in the sample annealed at 550°C rather than to a diffusion of As atoms occurring in the sample annealed at 800°C. In a previous study, it was determined that no noticeable diffusion of implanted As atoms occurred at temperatures below 850°C (7). An attractive explanation of this phenomenon is that the amorphous Si layer did not extend as deep as 0.36μ and thus a temperature much higher than 550°C would be required to achieve a large fraction of the implanted ions in the tail as electrically active and uncompensated. This is consistent with the previously published annealing characteristics of P and As implantations at doses below the critical dose required to produce an amorphous Si layer (4).

Summary

As in our previous study (7), for sufficiently high doses of P, As, or Sb ions, the profiles obtained by room-temperature implantations are relatively insensitive to crystalline orientation. "Tailing," due to channeling in the initial stages of the implantation (7), is more pronounced for P than for As or Sb (*i.e.*, for equal doses, a larger fraction of the implanted ions is partially channeled for P than for As or Sb) as expected, since more damage per ion produced by the heavier As or Sb would curtail channeling at an earlier stage. In this paper, we have demonstrated that, for 600°C implantations, crystalline effects remain important during the entire implantation and that the orientation of the substrate is important in determining the final profile.

Implantations conducted into Si substrates maintained at 600°C result in only a fraction of the implanted ions electrically active and uncompensated. The carrier mobility in such implanted layers reflects

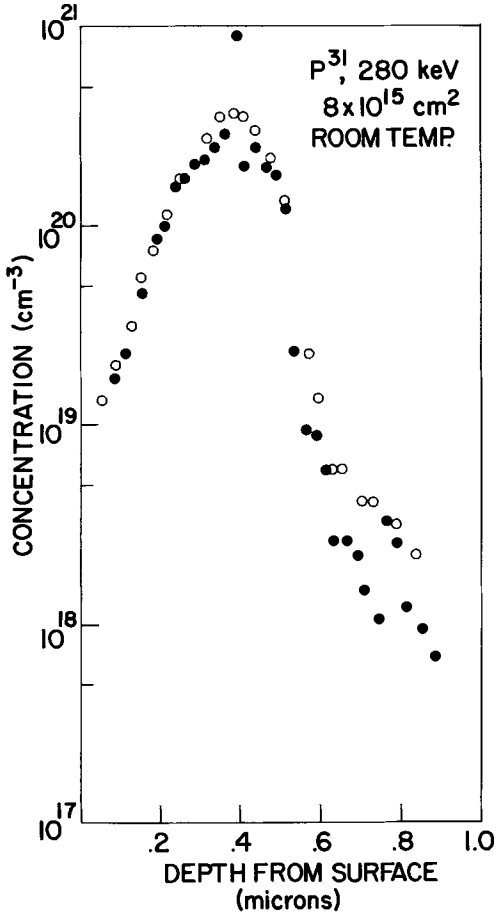

Fig. 6. Room-temperature implantation profile of P^+, 280 keV, 8 x 10^{15} cm^{-2}, into <100> Si. Open circles, ○, represent the total P as determined by neutron activation, and closed circles, ●, represent the carrier concentration, as determined by Hall and sheet resistivity measurements, after annealing at 800°C for 30 min.

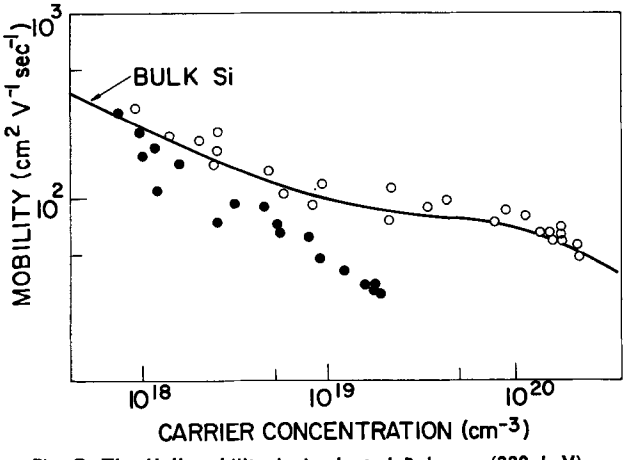

Fig. 7. The Hall mobility in implanted P layers (280 keV) as a function of the observed carrier concentration. Open circles, ○, represent the Hall mobility for a room-temperature implantation followed by a 800°C anneal (see Fig. 6 for profile). Closed circles, ●, represent the Hall mobility observed in an implant conducted at 600°C (see Fig. 8 for profile). The solid line represents the mobility in bulk Si after Irvin [Ref. (9)].

increased scattering from charged defects yielding mobilities markedly lower than that expected from uncompensated bulk Si of comparable carrier concentrations. In contrast to this behavior, high-dose implantations of P, As, or Sb into Si substrates at room temperature followed by a 550°-600°C anneal yield the majority of the implanted carriers electrically active

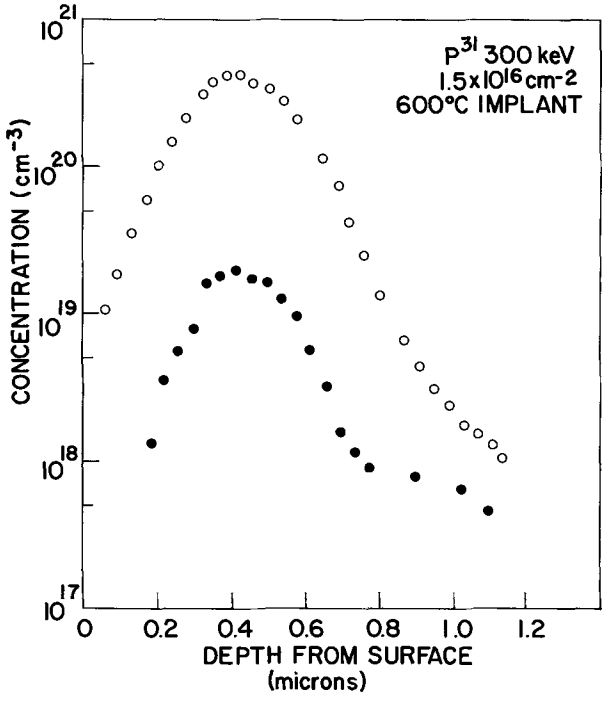

Fig. 8. 600°C implantation profile of P^+, 280 keV, 1.5 x 10^{16} cm^{-2}, into <100> Si. Open circles, ○, represent the total P as determined by neutron activation, and closed circles, ●, represent the carrier concentration, as determined by Hall and sheet resistivity measurements.

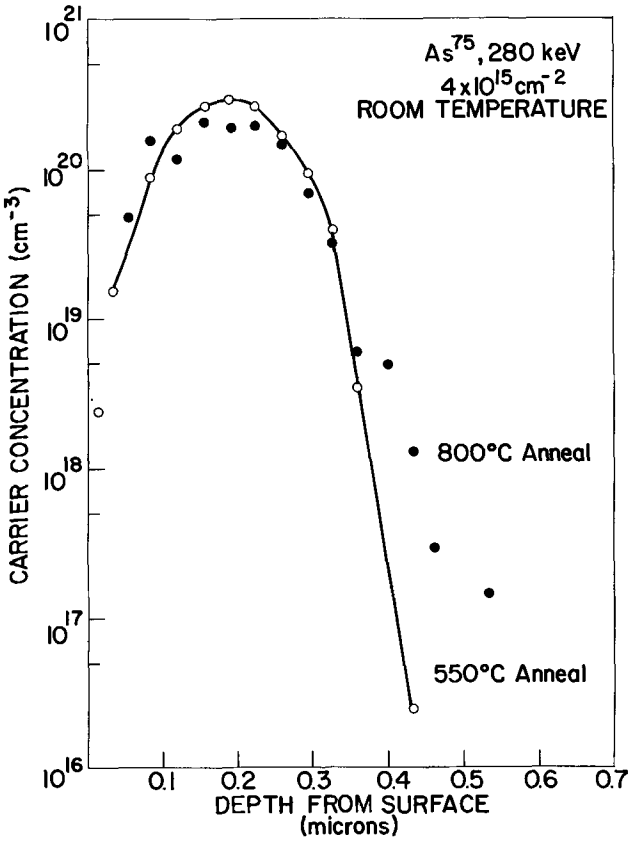

Fig. 9. Carrier concentration profiles of As^+, 280 keV, 4 x 10^{15} cm^{-2}, implanted into room-temperature <100> Si. Open circles, ○, represent the carrier concentration observed after a 550°C, 30 min anneal. Closed circles, ●, represent the observed carrier concentration after a 800°C, 30 min anneal.

and uncompensated with carrier mobilities approaching that expected for bulk Si of comparable doping levels. Temperatures markedly higher than 550°C are required to render the atoms in the tail of the distribution of room temperature implantations of P, As, or Sb electrically active and uncompensated, presumably due to the fact that these atoms lie outside the amorphous Si surface layer.[3]

Acknowledgments

The authors acknowledge Dr. F. F. Morehead for useful consultation, Dr. B. J. Masters for consultation and use of the tracer laboratory, W. N. Hammer for the design of the sample holder used in these experiments and for technical assistance, and G. Jung and N. A. Penebre for valuable technical assistance.

Manuscript submitted Aug. 1, 1969; revised manuscript received Nov. 28, 1969.

[3] Note added in proof: This comment applies only to that portion of the tail of the distribution which lies outside the amorphous Si layer but within a layer which, although crystalline, is heavily damaged. Ions still deeper within the crystal (e.g., channeled ions) in a region of lower damage density may require lower annealing temperatures.

Any discussion of this paper will appear in a Discussion Section to be published in the December 1970 JOURNAL.

REFERENCES

1. R. S. Nelson and D. J. Mazey, *Int. Conf. on Applications of Ion Beams to Semiconductor Technology, 1967, Grenoble, France*, p. 337.
2. J. W. Mayer, L. Erkisson, S. T. Picraux, and J. A. Davies, *Can. J. Phys.*, **46**, 663 (1968).
3. J. A. Davies, J. Denhartog, L. Eriksson, and J. W. Mayer, *ibid.*, **45**, 4053 (1967).
4. B. L. Crowder and F. F. Morehead, *Appl. Phys. Letters*, **14**, 313 (1969).
5. B. L. Crowder and N. A. Penebre, *Rev. Sci. Instr.*, **40**, 170 (1969).
6. J. W. Mayer, O. J. Marsh, G. A. Shifrin, and R. Baron, *Can. J. Phys.*, **45**, 4073 (1967).
7. J. M. Fairfield and B. L. Crowder, *Trans. Met. Soc. AIME*, **245**, 469 (1969).
8. K. E. Manchester, *This Journal*, **115**, 656 (1968).
9. I. Irvin, *Bell System Tech. J.*, **41**, 387 (1962).

Contact Resistance in Diffused Resistors

I. F. Chang

IBM Burlington, Components Division, Essex Junction, Vermont

ABSTRACT

The metal-silicon interface resistance is an important factor in the total resistance value of a diffused resistor. A contact correction term has to be considered for the design of resistors on an integrated circuit chip. This correction term is explored both experimentally and theoretically. Experimental results of contact correction are obtained for aluminum, sputtered molybdenum, and pyrolytic molybdenum to silicon contacts of various dimensions. Theoretically, a modified transmission line (MTL) model is introduced to describe the contacts of the diffused resistors. This model is based on the considerations of the geometry and the fabrication processes of the diffused resistor and its contacts. Model calculations compare very well with experimental findings. Thus, the equations derived from the MTL model can be used as design formulas to estimate a realistic value of the contact correction term for any given contact size and fabrication process, provided the process parameters are determined experimentally. In addition, the lower limit of the contact correction term is also obtained based on geometrical considerations only.

The design of monolithic integrated circuits requires a set of simple and correct device formulas as a design guide. For a diffused resistor, one usually uses the simple formula (1) for the resistance, R

$$R = \rho_s \frac{L}{W} \quad [1]$$

where L and W are the resistor length and width. The sheet resistance, ρ_s, is defined (2) as

$$\rho_s = \frac{\rho}{X_j} = \frac{1}{q\mu N X_j} \text{ (for uniform doping profile)} \quad [2]$$

or

$$\rho_s = \frac{1}{q\bar{\mu}\int_0^{X_j} N(x)\,dX} \text{ (for graded doping profile)} \quad [3]$$

where ρ is the resistivity and X_j is the junction depth of the diffusion. $N(x)$ is the doping profile and q and $\bar{\mu}$ are, respectively, the charge and average mobility of the majority carriers. When formula [1] is used in practice, it is often found to be yielding incorrect resistance values for actual diffused resistors. This discrepancy exists because the contacts to the resistor are contributing some resistance to the over-all resistor value. This extra resistance is particularly important in the design of low value resistors and resistors with tracking requirements. Therefore, one must add a contact correction term to Eq. [1] as

$$R = \rho_s \frac{L}{W} + 2R_{cc} \quad [4]$$

in order to achieve a correct design. R_{cc} is defined as the contact correction term per single contact. It is the intention of this work to analytically determine the added term, R_{cc}, such that Eq. [4] can be used as a design formula.

In general, the contact correction term may consist of several parts which may be caused by various different or combined mechanisms. For instance, the current crowding phenomenon due to the geometry of the resistor contacts can contribute to the R_{cc} term. This effect has been studied by Kennedy and Murley (3) using a two-dimensional model. The electric field distribution in the resistor is numerically determined. The current crowding in the vicinity of the ohmic contacts is clearly shown in their graphical presentation. Their model assumes a perfect metal-semiconductor interface which is never the case. In reality, one may have a metal semiconductor alloy at the contact region which may or may not be ohmic. The nonohmic type contacts fall outside the range of our concern here. The ohmic type, depending on the metallurgical processes, of course, contributes some resistance to R_{cc}.

A few measurements (4-6) of metal-silicon contacts have been performed in the past. However, these studies were made on large contacts and did not consider the chemical and metallurgical processes involved in the integrated circuit technology necessary for fabricating the diffused resistors. In particular, there is evidence (7) indicating that sometimes conductive or nonconductive films may exist at the metal-semiconductor interface. These films could be either by-products of some chemical masking processes or left-overs of imperfect cleaning and etching processes. They may also contribute to the contact correction term.

The above-mentioned possible contributions to R_{cc} can occur simultaneously and cannot be separately determined by experimental measurements. However, the contact correction term as a whole may be analytically obtained. This work intends to show that an analytic formula can be used to calculate the contact correction term as a whole for all sizes of contacts provided two process parameters are experimentally determined. This is necessary since R_{cc} is definitely a function of fabrication processes.

The measurements and the results of various metallurgical contacts of various sizes are described. Experimental data of contacts from aluminum, sputtered molybdenum, and pyrolytic molybdenum to silicon have been statistically compiled. An analytic model simulating a metal contact of a diffused resistor is introduced. Model calculations are compared with experimental results. A formula for the contact correction term is obtained. Furthermore, based on geometrical considerations only, a formula for contact correction can be derived to serve in the lower limit cases of R_{cc} for any given size of contacts. Conclusions are made.

Measurements

In order to study the contact correction term with respect to geometry and dimensions, resistors with various contact sizes and shapes were designed on a chip. Figure 1 shows a typical resistor pattern. All dimensions, W, a, d are nominal wafer dimensions. The side diffusion effect and contact over etch effect has been accounted for in the design. Two metal pads were connected to each contact so that one could be used as a voltage terminal and one as a current terminal. Thus, any contact resistance introduced by mea-

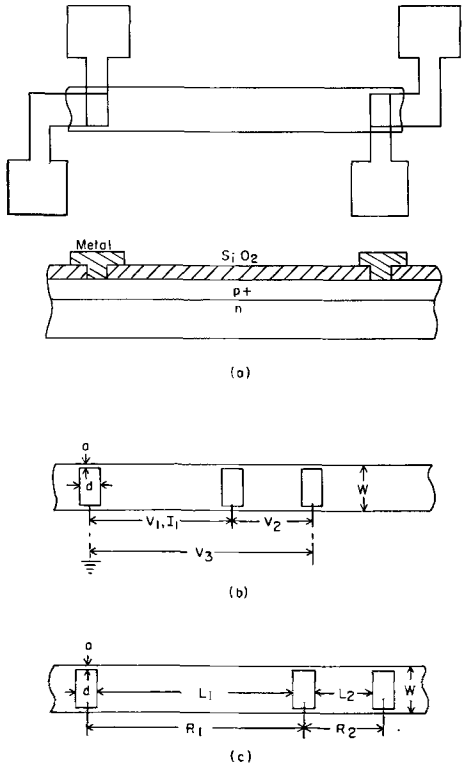

Fig. 1. Resistor test pattern for measurement of contact correction.

suring probes are excluded from the measurements. All the measurements were performed on the COSMIC programmed tester using an IBM 1130 computer. By program instruction, two probes can be chosen to be current terminals which supply constant current at 1 or 10 mA levels. The remaining probes sequentially measure the potentials on different contacts with respect to the grounded current terminal. The program is repeated when the test probes step on to the next chip. The series of measurements, according to the information they provide, can be classified as follows:

1. The measurement of resistor value with respect to the current direction into the contact: The current is applied to two contacts through any pair of pads as shown in Fig. 1(a). The potential between two pads is recorded accordingly. Resistor values derived from these measurements, however, do not show significant differences.

2. The measurement of R_c (defined below): The current is applied between two adjacent contacts on a long diffused resistor. Voltages on one contact and its neighboring contact [shown in Fig. 1(b)] are recorded. Thus R_c is defined as

$$R_c = \frac{V_2}{I_1} = \frac{V_1 - V_3}{I_1} \qquad [5]$$

3. The measurement of the contact correction term and sheet resistance of the diffused resistor: Fig. 1(c) shows the scheme for measuring two resistors with identical contacts. From measured resistor value R_1 and R_2 we obtain the sheet resistance and the contact correction term of the diffused resistor

$$\rho_s = \frac{W(R_1 - R_2)}{L_1 - L_2} \qquad [6]$$

$$R_{cc} = \frac{R_2L_1 - R_1L_2}{2(L_1 - L_2)} \qquad [7]$$

The above measurements were performed on a large number of chips. Different wafers were made with aluminum, sputtered molybdenum, and pyrolytic molybdenum contacts. In all cases, the metal deposition is made immediately after a conventional light hydrofluoric acid etch. In the case of molybdenum contacts, a thin layer of platinum silicide is formed at the interface in order to make good ohmic contact with molybdenum. The results of ρ_s, R_{cc}, and R_c obtained from the chips on these wafers have a fairly tight distribution. The mean values, peak values, and ranges of these measured results are shown in Table I. The sheet resistances obtained are essentially within a few per cent deviation from the mean values. Thus, only the mean values are shown in the table. The experimentally determined contact correction term is plotted as a function of contact width and length in the next section when comparison is made with the MTL model calculations. It can be seen from the table that the molybdenum contacts, in general, have higher contact correction values than the aluminum contacts.

Modified Transmission Line (MTL) Model

As mentioned before, the contact correction term not only depends on the geometry of the contact but also depends on the chemical and metallurgical processes involved in making the diffused resistor and its contacts. Therefore, one can only take an analytic approach to arrive at a useful formula. The formula should be such that an integrated circuit designer could use it to calculate contact corrections for various

Table I. Mean and peak values and ranges of measured results

	x_j (μ)	ρ_s ohm/sq	Wafer →| d |← □ W-2a: W (mils)	d (mils)	W-2a (mils)	Distribution of R_{cc} (ohm): Mean	Peak	Range	Distribution of R_c (ohm): Mean	Peak	Range	Eq. [18] R_{cc} (ohm)
					2.0	7	7	4-9	3.5	3	1-5	0.98
				0.5	1.0	14	15	10-18	7	5	4-9	1.96
					0.5	24.5	26	18-32	15.4	13	9-21	
Al	1.2	94	2.3									3.92
					2.0	9	8	6-14	7	6	1-8	0.98
				0.3	1.0	18.5	19	13-24	14	15	6-19	1.96
					0.5	34	32	24-42	26.5	26	18-39	3.92
					2.0	7.7	7	5-10	3.7	3	1-6	1.29
				0.5	1.0	15.3	16	13-19	7.5	6	5-9	2.575
					0.5	25	26	20-30	16.5	15	12-18	5.16
Sputtered Mo	1	148	3.3									
				0.5					28	27	23-31	
				1.0	0.3				14	13	12-16	8.59
				2.0					4	5	1-6	
					2.0	8.2	9	6-10	4.4	6	3-7	1.38
				0.5	1.0	17.5	17	11-21	10	10	9-14	2.76
					0.5	31	30	26-35	21	21	18-24	5.52
Pyrolytic Mo	1	159	3.3									
				0.5					34	35	30-38	
				1.0	0.3				16	15	14-20	9.21
				2.0					7	7	2-8	

sizes of contacts and resistors. Any process parameter involved in the formula should be experimentally measured for any given fabrication process.

Recently Berger (8) has proposed a transmission line (TL) model to describe the contact problem. However, when it is applied to the cases discussed here, one finds that the TL model calculations do not agree with the experimental results presented in the section on Measurements. Nevertheless, if certain modifications are made, a correct and useful formula for contact correction can be derived. The modifications are based on fabrication process considerations. We introduce these modifications along with a brief description of the TL model below.

The TL model assumes a parameter, σ_c, conductivity per unit area, to describe the contact sheet resistance. The series resistance beneath the contacts is described by the same sheet resistance, ρ_s, of the diffused resistor. This is not always a valid assumption, since in most cases the contact region is a metal-semiconductor alloy which will definitely have different resistivity. Furthermore, the contact width is assumed to be the same as the diffused resistor in the TL treatment. This approximation will lead to errors when the contact width is much smaller than the resistor width. However, considering the two assumptions above, an equivalent circuit can be drawn for the contact. Figure 2(a) shows the equivalent circuit in which R' and G' are defined as follows

$$R' = \frac{\rho_s}{W} \qquad [8]$$

$$G' = \sigma_c W \qquad [9]$$

The transmission line equation for this equivalent circuit can be written in terms of the load voltage and the load current. For open end termination, one obtains

$$V = E_R \cosh(\gamma y) \qquad [10]$$

$$I = \frac{E_R}{Z_o} \sinh(\gamma y) \qquad [11]$$

where

$$Z_o = \left(\frac{R'}{G'}\right)^{1/2} = \frac{1}{W}\left(\frac{\rho_s}{\sigma_c}\right)^{1/2}$$

$$\gamma = (R'G')^{1/2} = (\rho_s \sigma_c)^{1/2}$$

and E_R and I_R are the voltage and the current, respectively, at the load end. From Eq. [10] and [11] one can derive the following

$$R_{cc} = \left.\frac{V}{I}\right|_{y=d} = \frac{Z_o}{\tanh(\gamma d)} = \frac{1}{W}\frac{(\rho_s)^{1/2}(\sigma_c)^{-1/2}}{\tanh[(\rho_s\sigma_c)^{1/2}d]} \qquad [12]$$

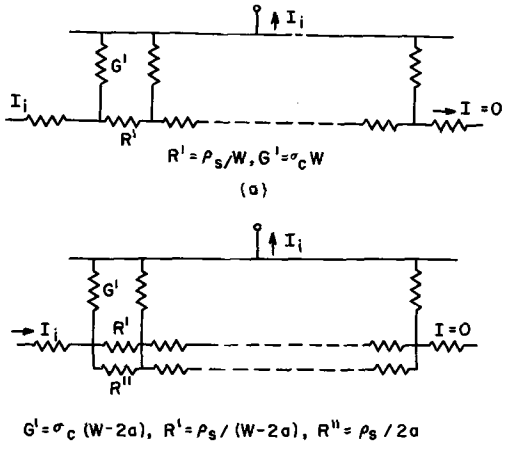

Fig. 2(a). Equivalent circuit for TL model. (b). Equivalent circuit for MTL model.

$$R_c = \left.\frac{E_R}{I}\right|_{y=d} = \frac{Z_o}{\sinh(\gamma d)} = \frac{1}{W}\frac{(\rho_s)^{1/2}(\sigma_c)^{-1/2}}{\sinh[(\rho_s\sigma_c)^{1/2}d]} \qquad [13]$$

Equation [12] gives the input impedance which is equivalent to the contact correction term R_{cc}, and Eq. [13] is the transfer impedance identified as R_c. From Eq. [12] and [13] one obtains the parameter

$$\sigma_c = \frac{1}{\rho_s}\left[\frac{1}{d}\cosh^{-1}\frac{R_{cc}}{R_c}\right]^2 \qquad [14]$$

which can be determined by the experimental measurement.

If the TL model were correctly predicting the contact correction term, then σ_c determined from Eq. [14] should be a constant regardless of contact size. However, this is not the case. The reason is that R_{cc}/R_c varies with the contact width W. This can be illustrated in another fashion. For example, we measured

$$\rho_s = 161 \text{ ohms/sq}$$
$$R_{cc} = 17 \text{ ohms}, R_c = 10 \text{ ohms}$$
$$W = 1 \text{ mil}, d = 0.5 \text{ mil}$$

for a typical sample of pyrolytic molybdenum contacts. The calculated σ_c of Eq. [14] is 0.0317 ohm/mil^2. However, when substituting this value into Eq. [12] and [13], one obtains values of R_{cc} and R_c, 87.9 and 51.43, which are far above the values we measured.

In view of the fabrication processes used for making the contacts, the above result is expected. When certain fabrication processes are used, they are likely to produce metal-semiconductor alloy at the contacts. This alloy may consist of the semiconductor material and the same metal used for the contact, or a different kind of metal. For example, in the case of our molybdenum test wafers platinum is used to form platinum silicide between the molybdenum and silicon at the contacts. Therefore, the assumption made in the TL model should be modified.

A new parameter

$$\rho_s' = \frac{\rho'}{X_j} \neq \rho_s$$

is introduced here to represent the series resistance at the contacts. A further modification should be made, that is to take into account the fact that the contact width is usually designed to be smaller than the resistor width. An exact treatment of this case would be too complicated. However, one could approximate this case by employing a parallel resistor scheme shown in the modified equivalent circuit, Fig. 2(b). Therefore, the contact correction term is

$$R_{cc} = \frac{\left[\left(\frac{\rho_s'}{W-2a} /\!/ \frac{\rho_s}{2a}\right)/\sigma_c(W-2a)\right]^{1/2}}{\tanh\left\{\left[\left(\frac{\rho_s'}{W-2a} /\!/ \frac{\rho_s}{2a}\right)\sigma_c(W-2a)\right]^{1/2} d\right\}} \qquad [15]$$

and

$$R_c = \frac{\left[\left(\frac{\rho_s'}{W-2a} /\!/ \frac{\rho_s}{2a}\right)/\sigma_c(W-2a)\right]^{1/2}}{\sinh\left\{\left[\left(\frac{\rho_s'}{W-2a} /\!/ \frac{\rho_s}{2a}\right)\sigma_c(W-2a)\right]^{1/2} d\right\}}$$

$$R_{cc}/R_c = \cosh\left\{\left[\left(\frac{\rho_s'}{W-2a} /\!/ \frac{\rho_s}{2a}\right)\sigma_c(W-2a)\right]^{1/2} d\right\} \qquad [16]$$

where $A /\!/ B = \dfrac{AB}{A+B}$.

At this point, we can directly compare the experimental data with the results of the MTL model, specifically, Eq. [15] and [16]. From Table I, R_c and R_{cc} of

Table II. Calculated ρ_s' and σ_c of metallurgical contact

Wafer	Al	Sputtered Mo	Pyrolytic Mo	
ρ_s	94	148	159	ohm/sq
ρ_s'	33.75	44	39.8	ohm/sq
σ_c	0.2178	0.202	0.1784	ohm/mil

the widest contacts are used to determine ρ_s' and σ_c by Eq. [15] and [16]. Table II shows the calculated ρ_s' and σ_c of all three different metallurgical contacts. The sheet resistance, ρ_s, of different wafers is also included in the table. Since the model predicts the contact correction term for all contact sizes once the process parameters ρ_s' and σ_c are determined, we could calculate R_c and R_{cc} as functions of contact width, which is equal to $W - 2a$, and the contact length, d. The results of aluminum, sputtered molybdenum, and pyrolytic molybdenum coated wafers are plotted in Fig. 3, 4, and 5, respectively. The contact correction, R_{cc}, and R_c are plotted as functions of the contact width with the contact length as a parameter. The experimental data are included in these figures for comparison. The agreement is very good. One notes that all three figures show the effect of the contact width on the contact correction, that is, the smaller the width the higher the contact correction. Furthermore, the measured and calculated results of aluminum contacts with $d = 0.3$ mil and $d = 0.5$ mil are given in Fig. 3 which indicates that R_{cc} is higher for smaller d. In the case of molybdenum contacts, three

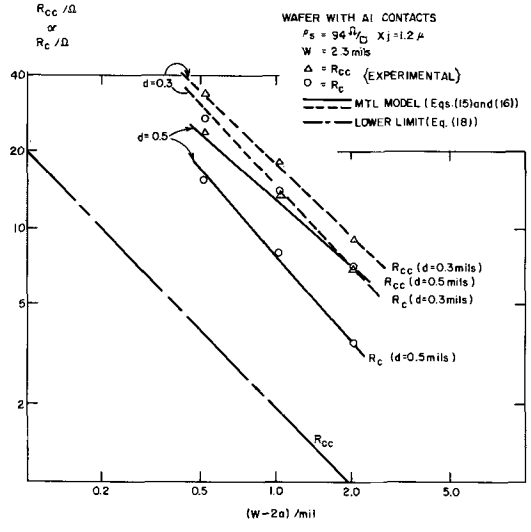

Fig. 3. Contact correction for aluminum contacts

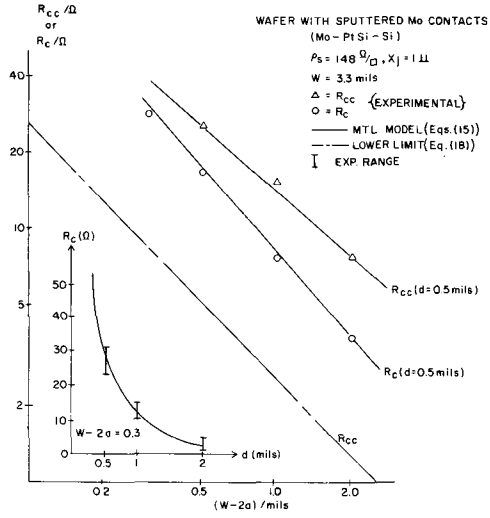

Fig. 4. Contact correction for sputtered molybdenum contacts

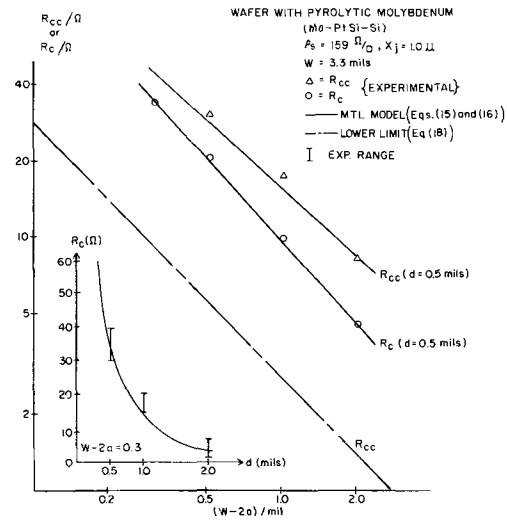

Fig. 5. Contact correction for pyrolytic molybdenum contacts

contacts with identical widths but different lengths were measured. Calculations made as a function of contact length, d, are compared with the data. This is shown in the left hand corners of Fig. 4 and 5. The data fall on the curves of the formulated hyperbolic functions.

Since the calculations agree very well with the measured results, we conclude that these curves shown in Fig. 3, 4, and 5 for different metal contacts can be used to estimate the contact correction term for any given size of contact. In other words, Eq. [15] and [16] can be used as design formulas for the contact correction of diffused resistors. For example, if the sputtered molybdenum contacts of size $W = 0.8$ mil and $d = 0.5$ mil were to be used, one would obtain the contact correction term to be 17 ohms by Fig. 4.

It is interesting to know whether one can obtain a lower limit for the contact correction by considering only the geometry of the contact and the resistor. If this limit could be obtained in an analytical form, it will be a useful formula in addition to Eq. [15] and [16]. Let us consider a simple case which assumes that the contact holes have the same width as the resistor. A perfect, intimate metal-semiconductor contact is also assumed. With these considerations, we see only the geometrical effect on contact correction, R_{cc}. We can now represent this resistor by a two dimensional mathematical model originally due to Hall (9, 10) and recently evaluated in detail for thin film resistors by Ting (11). The model assumes that the metal surfaces are at constant potential and so does the center cross section of the diffused resistors since $L >> X_j$. Then the resistance, R_{AC}, can be calculated by making use of the Schwartz-Christoffel transformations (12, 4). One obtains

$$R_{AB} = 2R_{AC} = 2\left[\rho_s \frac{L}{2W} + \frac{2}{\pi}\frac{\rho_s X_j}{W} \ln\left(\frac{2}{1 - e^{-\pi d/x_j}}\right)\right] \quad [17]$$

where ρ_s and X_j are defined as in Eq. [2]. In normal practice, the contact length, d, is at least one order of magnitude higher than X_j. Therefore, the exponential term in Eq. [17] can be neglected. Comparing Eq. [4] and [17] we obtain

$$R_{cc} = 0.441 \frac{\rho_s X_j}{W} \quad [18]$$

This result is arrived at entirely from geometrical considerations. It is applicable only when the metal-semiconductor contact resistance is negligible. Therefore, Eq. [18] serves as a lower limit formulation of R_{cc}. Together with Eq. [15] and [16] they serve as design formulas. In Table I, Fig. 3, 4, and 5, the lower limit data derived from Eq. [18], are also shown for comparison.

Conclusions

A useful formula for the contact correction term is derived from the MTL model. Model calculations compare very well with experimental data of various metal-silicon contacts. Equations [15] and [16] of this analytic model are recommended to be design formulas for diffused resistors. Furthermore, a lower limit for the contact correction term can be established by considering the geometry of the diffused resistor only. This lower limit together with the MTL results can sufficiently serve as guide lines in the design work of diffused resistors on an integrated circuit chip.

Acknowledgment

The author has benefited from discussions with J. J. Chang, M. Klein, and S. K. Tung. The technical assistance from L. Bilodean, J. Coullahan, J. G. Kessler, and G. Slayton is greatly appreciated.

Manuscript submitted Aug. 11, 1969; revised manuscript received ca. Dec. 2, 1969.

Any discussion of this paper will appear in a Discussion Section to be published in the December 1970 JOURNAL.

REFERENCES

1. H. Dicken, *Electronic Industries*, Oct. (1962).
2. A. S. Grove, "Physics and Technology of Semiconductor Devices," John Wiley & Sons, New York (1967).
3. D. P. Kennedy and P. C. Murley, *IBM J. of Research and Dev.*, **12**, 242 (1968).
4. M. V. Sullivan and J. H. Eigler, *This Journal*, **104**, 226 (1957).
5. Q. J. Mengali and M. R. Seiler, *Adv. Energy Conv.*, **2**, 59 (1962).
6. R. C. Hooper, J. A. Cunningham, and J. G. Harper, *Solid State Elec.*, **8**, 831 (1965).
7. I. F. Chang, S. Dash, and S. K. Tung, Unpublished.
8. H. H. Berger, IEEE Intntl. Solid State Circuits Conference, Philadelphia, Feb. 1969.
9. F. B. Hagedorn and P. M. Hall, *J. Appl. Phys.*, **34**, 128 (1963).
10. P. M. Hall, *Thin Solid Films*, **1**, 277 (1967).
11. C. Y. Ting, Private communication, Preprint.
12. F. W. Carter, *J. Inst. Elec.*, **64**, 115 (1926).

Interface Properties of Si-(SiO_2)-Al_2O_3 Structures

M. T. Duffy* and A. G. Revesz[1]

RCA Laboratories, Princeton, New Jersey

ABSTRACT

Aluminum oxide films have been deposited on silicon substrates at 420°C by thermal decomposition of aluminum-isopropoxide. An electrical evaluation of the interface properties of Si-Al_2O_3 and Si-SiO_2-Al_2O_3 structures has been made. MOS capacitance measurements have shown the important role of a postdeposition heat treatment in O_2 in eliminating room-temperature hysteresis and reducing the scatter in flat-band voltage values of Si-Al_2O_3 structures. This treatment has an overriding effect on the influence of deposition conditions on interface properties. The density of interface states varies from 10^{10} to 10^{11} cm^{-2} $(eV)^{-1}$, and the flat-band voltage (for ~1000Å oxide) is about +2V. The flat-band voltage gradually shifts to more positive values under large negative bias (field ~10^6 V/cm) at 250°C. There is a strong tendency toward localized conduction in these films and there are indications that conduction is controlled by the interface(s) rather than by the bulk material. This problem was alleviated by growing a thin SiO_2 film (~200Å) on Si prior to deposition. The interface properties of Si-SiO_2-Al_2O_3 structures depend on the Si orientation. For (100) orientation, the density of interface states is about 10^{10} cm^{-2} $(eV)^{-1}$ and the flat-band voltage is zero. The radiation resistance of deposited Al_2O_3 is better than that of SiO_2 and comparable to that of Al_2O_3 films prepared by plasma anodization. Irradiation by 1 MeV electrons under +10V bias introduces a density of positive oxide charge of a few times 10^{12} e/cm^2.

Silicon dioxide films are widely used for passivation of silicon device surfaces. The technological importance of these devices led to extended research activity which yielded a reasonably good understanding of the properties of the oxide film and the oxide-silicon interface (1). However, some problems remain unsolved. These include a somewhat high radiation sensitivity and the inability to obtain positive flat-band voltage values relative to silicon. In addition, the relatively low value of the dielectric constant of SiO_2 makes the use of an insulator with higher dielectric constant desirable.

Recently, Al_2O_3 films have drawn the attention of several workers (2-8). A comparison of the bulk properties of Al_2O_3 and SiO_2 (*see* Table I) shows Al_2O_3 superior in some respects, including higher dielectric constant and greater density. Other advantages are the lower radiation sensitivity and greater impermeability to impurity diffusion. The ability to deposit films at temperatures as low as 400°C is also desirable.

The purpose of this work was to explore the potential of Al_2O_3 in MOS devices. Hence, we were mainly concerned with interface properties. MOS measurements have been performed on Si-Al_2O_3 and Si-SiO_2-Al_2O_3 structures and their stability and radiation resistance examined.

Experimental

Thin film deposition.—Thin dielectric films of aluminum oxide have been deposited on silicon substrates by the pyrolysis of Al-isopropoxide in the presence of oxygen (2). The alkoxide vapors were transported to the rf-heated substrates by bubbling helium through the molten alkoxide at 125°C. This gas was subsequently mixed with nitrogen and oxygen. The deposition temperature was usually 420°C, but in some cases depositions have been performed at various tempera-

Table I. Comparison of Al_2O_3 and SiO_2

	Bond strength, kcal/mole	Density	Volume per g atom O, cm^3	Dielectric constant
SiO_2	104	2.20	13.7	3.8
Al_2O_3	138	3.5-4.0	8.5-9.7	~7.5

* Electrochemical Society Active Member.
[1] Present address: COMSAT Laboratories, Clarksburg, Maryland.

tures from 350° to 925°C. The experimental arrangement of the rf system was the same as that reported by Duffy *et al.* (9).

Both p- and n-type silicon substrates of (111) and (100) orientation were used. The resistivity was usually 10 ohm-cm, but some degenerate substrates were also used for dielectric investigations. The wafers were cleaned by standard chemical means prior to deposition and had a residual SiO_2 film of about 30Å. Because of conduction problems associated with Si-Al_2O_3 structures, Al_2O_3 films were also deposited on Si-SiO_2 samples prepared by thermally oxidizing silicon in dry O_2 at 1100°C. The oxide thickness was usually 200Å. The oxidation was followed by 15 min He annealing at 1100°C prior to deposition of Al_2O_3; these processes were performed *in situ*. Postdeposition heat treatments in He, N_2, H_2, and O_2 have also been investigated. For electrical evaluation, MOS contacts were provided by vacuum deposition of aluminum.

Measurements.—Thickness and refractive index values were determined by ellipsometry at the mercury wavelength 5461Å in the case of Al_2O_3 films up to 1400Å. In the case of SiO_2-Al_2O_3 structures, the SiO_2 film thickness was separately determined after etching off the Al_2O_3 film in phosphoric acid. Film structure was determined by reflection electron diffraction and the morphology by optical microscopy. Some films were analyzed by mass spectrometry using an ultrapure gold electrode for sparking.

The frequency dependence of the dielectric constant and loss tangent was determined in the range 10^2 to 10^5 Hz on a capacitance bridge. These measurements were performed on films deposited on degenerate silicon or on Si-Al_2O_3 structures which showed strong accumulation at zero bias.

Interface properties were studied by the MOS capacitance and conductance methods (1). Most capacitance-voltage (C-V) measurements were made at 1 MHz using an automatic recording apparatus (10). Many specimens were also examined by an MOS impedance method in the frequency range 3 x 10^2 to 10^5 Hz using phase-sensitive detection (11). MOS measurements also gave information on the apparent resistivity (as an order of magnitude) of films with appreciable d-c conduction. Computer analysis of the C-V curves gave the surface charge density as a function of energy within the Si forbidden band. From this information the charge density at flat-band condition, Q_{FB} (charges/cm^2), and the interface state density, Q_{SS} (/cm^2 · eV), were determined. The interface state density was also determined from the MOS conductance (G-V) measurements assuming a uniform distribution (energy-wise) of these states in the Si forbidden band (12).

The stability of the charge distribution was measured by applying positive and negative voltages for varying times to the gate electrodes of samples kept in He atmosphere at 250°C. Differences between C-V measurements, made both before and after the bias-temperature (BT) tests, indicated the resulting charge redistribution.

Radiation resistance measurements were made by irradiating MOS units, while under applied gate bias, with 1-MeV electrons. The fluence level corresponding to each bombardment was 10^{14} e/cm^2 and a bombardment was made at each of the gate voltages 0, −2, −5, −10, +2, +5, +8, and +10V successively. MOS capacitance measurements were performed after each bombardment and the density of induced charge determined.

Results

Bulk properties.—Aluminum oxide films ranging in thickness up to 8000Å have been obtained. The deposition rate was usually about 100 Å/min at 420°C but in some cases deposition was performed at a slower rate (17 Å/min). The etch rate was about 90 Å/min in 85% H_3PO_4 at 40°C. The refractive index varied from 1.60 to 1.68. Films deposited at temperatures up to 700°C were noncrystalline, and remained noncrystalline even after O_2 treatment for 30 min at 700°C. By contrast, films deposited at 925°C and also those heated in O_2 at 800°C were polycrystalline. Films were uniform and did not show any discernible structure when examined by optical microscopy. An order of magnitude estimate of the impurity-to-aluminum ratio (atomic) was obtained by mass spectrometry. The ratio for Zn, Cu, and Cr was 10^{-3}; for S, 10^{-2}; and for C, 10^{-2} to 10^{-1}.[2]

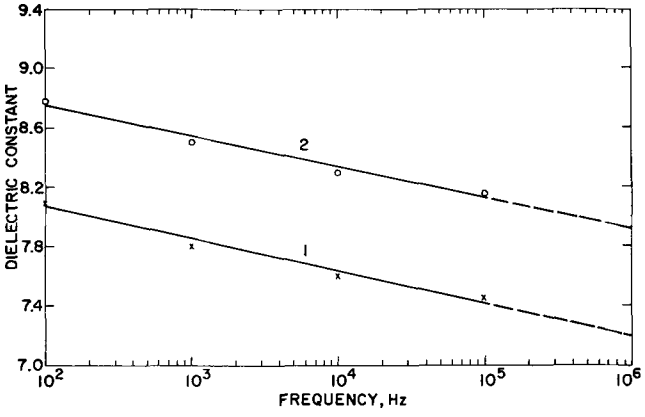

Fig. 1. Frequency dependence of dielectric constant of Al_2O_3. Curve 1, as deposited; curve 2, oxygen treated.

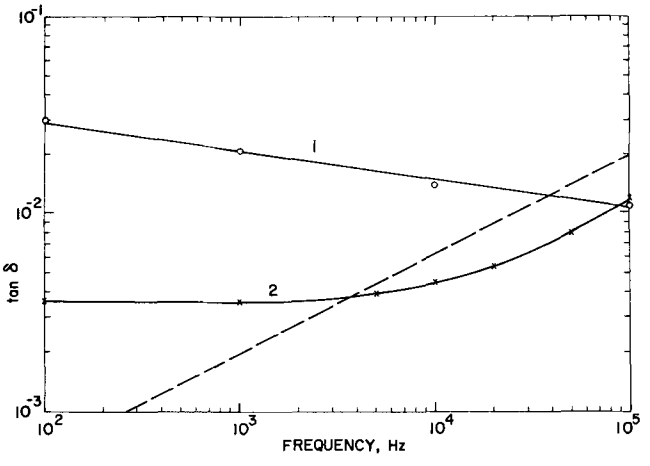

Fig. 2. Loss tangent vs. frequency. Curve 1, as deposited on degenerate silicon; curve 2, deposited on ~ 10 ohm-cm silicon and heat treated in O_2. The upward trend of curve 2 results from the resistance of the substrate; the broken curve approximates the expected effect.

The dielectric constant and loss tangent are frequency dependent; typical curves are presented in Fig. 1 and 2. The curve labeled 1 in both figures represent data obtained on an untreated film which was deposited on degenerate silicon, while the curves labeled 2 represent the data from measurements on a sample which received an *in situ* postdeposition O_2 treatment at 700°C. The substrate in this latter case was ~ 10 ohm-cm silicon; the series resistance of this substrate accounts for the upward trend in curve 2, Fig. 2. The broken curve approximates the expected effect. The results of Fig. 1 and 2 indicate that the O_2 treatment increases the dielectric constant and decreases the apparent value of the loss tangent.

[2] These results were originally obtained as impurity-to-silicon ratios. Since the depth of the crater produced by sparking is much larger (~5μ) than the oxide thickness (~1000Å), large errors may be introduced in conversion to the above form. However, the experimental value of the Al/Si ratio corresponds to 6 × 10^{22} Al atoms/cm^3 in the oxide which approximates the calculated value 4.3 × 10^{22} (taking the density as 3.7 g/cm^3). The O/Al ratio was about unity, in good order of magnitude agreement with the theoretical value 1.5. Also the Al/Si ratio for a blank Si specimen was three orders of magnitude lower than that of the Si-Al_2O_3 specimen. From these considerations, the order of magnitude values of impurity content are probably correct.

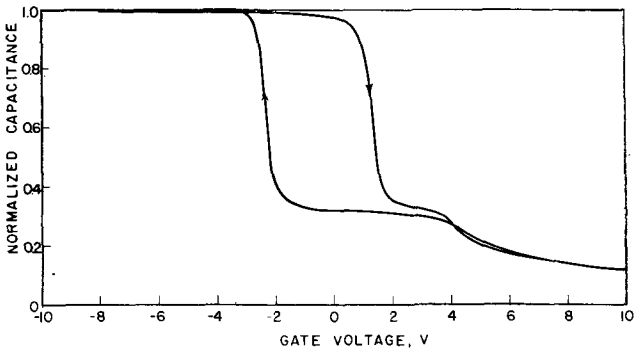

Fig. 3. Typical MOS capacitance curve for 1000Å Al_2O_3 film

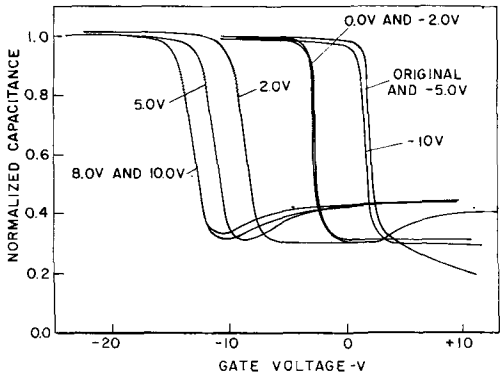

Fig. 4. Effect of electron irradiation on MOS capacitance of 1400Å Al_2O_3 film. The parameter is the gate bias during irradiation.

Interface properties.—The C-V behavior of as-deposited Si-Al_2O_3 structures shows large scatter in flat-band voltage values and large room-temperature hysteresis. A typical example is shown in Fig. 3. The extent of the hysteresis depends on the deposition temperature and rate of deposition. Higher deposition temperatures and slower deposition rates favor reduced hysteresis and less scatter in flat-band voltage values. The nature of the hysteresis is such that negative and positive gate biasing results in a shift of the flat-band voltage toward more positive and negative values, respectively. Postdeposition heat treatments in He, N_2, and H_2 were unsuccessful in modifying the C-V behavior. However, a heat treatment in O_2 at 700°C eliminated the room-temperature hysteresis and reduced the flat-band voltage scatter. This treatment had an overriding effect on the influence of the deposition conditions on interface properties.

After oxygen treatment, the charge density at flat-band condition varied from -5×10^{11} e/cm^2 to -1.5×10^{12} e/cm^2 [3] (corresponding to +1.4 to 3.6V flat-band voltages for 1000Å oxide film) as determined from C-V measurements at 1 MHz. The density of interface states, determined from G-V measurements, varied from 10^{10} to 10^{11} states/$cm^2 \cdot$ eV.

Bias-temperature (BT) tests on O_2-treated specimens revealed that the charge distribution in the Si-Al_2O_3 structures is unstable. The principal effect is a shift in the flat-band voltage to more positive values under negative bias. The extent of this shift is typically about 4.5V for 1000Å oxide after the application of −5V gate bias for 5 min at 250°C. The application of −10V usually led to excessive conduction. Positive biasing did not cause a shift to more negative values, and in some cases actually caused a shift toward more positive voltages.

A typical set of C-V curves obtained after successive irradiation of a 1400Å film (under varying bias) with 1-MeV electrons as previously described is presented in Fig. 4. Bombardment under +10V bias led to a shift (normalized to 1000Å oxide thickness) of −9.8V. This corresponds to an induced charge of 4.6×10^{12} e/cm^2 at flat-band condition. The smallest shift observed for +10V bias was −6.4V, corresponding to an induced charge of 2.7×10^{12} e/cm^2. No significant effect results from irradiation under negative bias. The density of interface states was found to increase slightly during bombardment; a typical value is 2×10^{11} to 7×10^{11} states/$cm^2 \cdot$ eV. In the case of Al_2O_3 samples which were not treated in oxygen, the induced oxide charge was unstable. The negative shift in flat-band voltage resulting from irradiation decreased after the irradiation was stopped.

Conduction.—Most MOS capacitors showed very varied d-c conduction behavior. Conduction was usually observed during C-V measurements as a decrease in the set bias when gate contact was made. This decrease in applied bias is due to d-c current flow through the capacitor. This conduction is localized in the sense that a given sample had conducting and nonconducting capacitors. It has not been possible to correlate this behavior with process parameters including postdeposition oxygen treatment, nor with morphological defects. However, it has been found that conduction developed or became greatly enhanced during BT tests, even when samples were heated in helium at 250°C without bias; *e.g.*, a sample which initially showed no apparent conduction (estimated $\rho > 10^{12}$ ohm-cm), had an apparent resistivity of about 10^8 ohm-cm after heating in He at 250°C for 10 min. The largest change was observed for a polycrystalline specimen which had been deposited at 925°C. No noticeable conduction occurred before the BT test, but after applying −5V at 250°C for 5 min in He the apparent resistivity changed to less than 10^4 ohm-cm. In general, the development of conduction was accompanied by the occurrence of the Schottky depletion layer capacitance (13) as observed in the C-V measurements (*see* Fig. 3) on both O_2-treated and untreated specimens, while nonconducting samples did not exhibit the Schottky depletion layer capacitance. Some samples developed this depletion capacitance during electron bombardment, but this effect and the induced charge were unstable and reverted at a diminishing rate to the original state after irradiation. During the relaxation process, the Schottky capacitance disappeared (*see* Fig. 5).

Si-SiO_2-Al_2O_3 *structures.*—The problem of conduction associated with Al_2O_3 films was alleviated by growing a SiO_2 film (~200Å) before deposition of Al_2O_3 (1000-1300Å). The double insulator structures did not show any hysteresis effects, even when no post-deposition O_2 treatment was applied. In contrast to the case of Si-Al_2O_3 structures, both the flat-band voltage and the density of interface states characteristic of the double insulator structures depend on the Si crystallographic orientation. Typically, for (111) orientation the flat-band voltage is about −2.5V (corresponding to about 7×10^{11} e/cm^2 charge density) for a combination of 1000Å Al_2O_3 and 200Å SiO_2 films, and

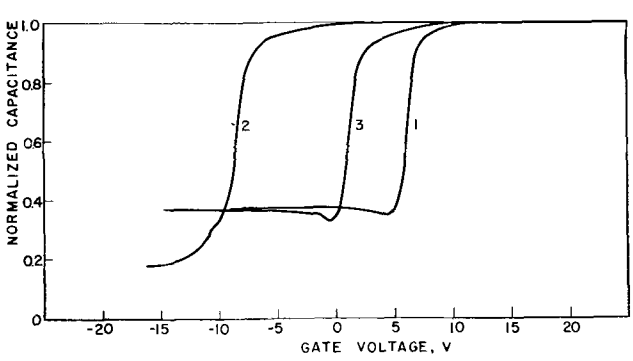

Fig. 5. Unstable charge distribution resulting from electron irradiation. Curve 1, C-V behavior before bombardment; curve 2, after bombardment at −5V gate bias; curve 3, final state after termination of relaxation process at room temperature.

[3] *e* Represents the absolute value of the electronic charge.

the interface state density varies from 4 x 10^{10} to 2 x 10^{11} states/cm^2 · eV. For (100) orientation the flat-band voltage is approximately zero, and the interface state density varies from 1 x 10^{10} to 4 x 10^{10} states/cm^2 · eV. Similar results were obtained on both n- and p-type substrates.

Bias-temperature tests revealed that the charge distribution in the double insulator structure is also unstable. This is demonstrated in Fig. 6 where the flat-band voltage is plotted as a function of time for which the bias was applied. The principal effect is caused by negative biasing. In the range from −5 to −13V, the change in flat-band voltage is approximately proportional to the change in bias. The effect of a given negative bias saturates with time even when the sequence of applying negative bias is interrupted by the application of positive bias (*see* part B of Fig. 6). Unlike Si-Al_2O_3 structures, the composite films consistently showed a shift in the flat-band voltage under positive bias during the BT test. The extent of this shift is time dependent and varies from 1 to 4.5V. The magnitude of the bias apparently has no influence on this shift. The effect of positive bias was independent of whether the BT test started with negative or positive bias.

A different instability behavior was observed for Si-SiO_2-Al_2O_3 structures which were not treated in O_2 after deposition of Al_2O_3 (*see* Fig. 7). Before the BT test, the specimen had an appreciable d-c conduction and the C-V curve showed the development of the Schottky capacitance. After applying +5V for 5 min at 250°C, both the d-c conduction and the Schottky capacitance disappeared, and the flat-band voltage shifted to a more negative value. Application of −5V bias shifted the flat-band voltage to a more positive value; the extent of the shift is comparable to that shown in Fig. 6. It also led to the reappearance of the Schottky capacitance and d-c conduction. The C-V curve is now distorted and reveals a hysteresis which is in the opposite sense to that observed for Si-Al_2O_3 structures.

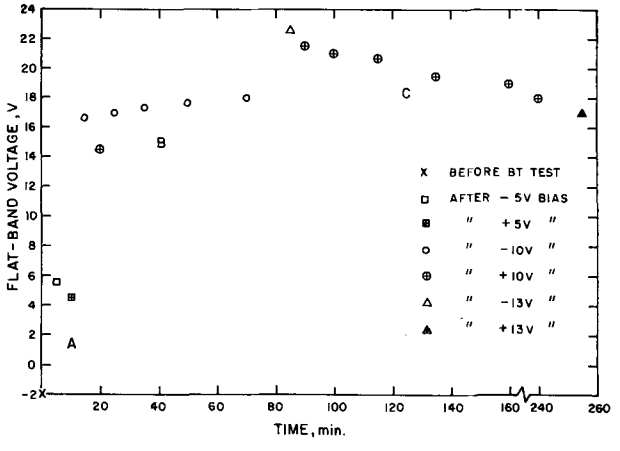

Fig. 6. Flat-band voltage as a function of time for which gate bias was applied during bias-temperature tests on a Si-SiO_2-Al_2O_3 composite structure corresponding to 200Å SiO_2 and 1000Å Al_2O_3.

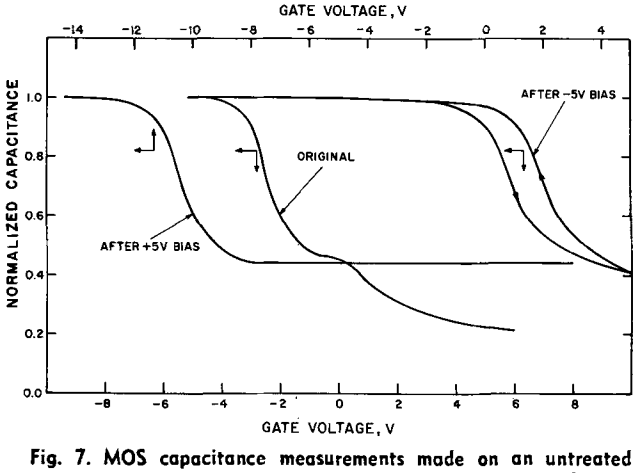

Fig. 7. MOS capacitance measurements made on an untreated Si-SiO_2-Al_2O_3 specimen during bias-temperature tests (200Å SiO_2 and 1100Å Al_2O_3).

Although the conduction problem was largely alleviated by growing a thin SiO_2 film before the deposition of Al_2O_3, the double insulator structures still showed localized conduction to a greater extent than thermally grown SiO_2.

Electron bombardment of the double insulator structures caused negative shifts in the flat-band voltage under positive bias and positive shifts under negative bias. The scatter in the results was quite large. Nevertheless, even the largest shift at +10V bias (about −20V) was less than that observed for dry oxygen-grown SiO_2 of comparable thickness (about −50V). Aluminum oxide films alone show better radiation resistance than the SiO_2-Al_2O_3 structures. The bias dependence of the radiation induced charge did not show the asymptotic behavior characteristic of SiO_2 or Al_2O_3 films alone. Also, the charge distribution was generally unstable even at room temperature. The radiation behavior of the Si-SiO_2-Al_2O_3 interface system requires more study.

Discussion

Bulk properties.—No systematic study of the effect of deposition parameters on bulk properties has been undertaken in this investigation. This has been treated in detail by Aboaf (2). Our measured values of refractive index are higher than those reported in Ref. (2), but are still lower than the refractive index of γ-Al_2O_3 (1.7) or α-Al_2O_3 (1.765). These differences may represent differences in density or mole refraction. The frequency dependence of the dielectric constant is typical of a noncrystalline dielectric (14). Oxygen-treatment at 700°C (Fig. 2) decreases the apparent value of tan δ; this value, 3.5 x 10^{-3} at 10^3 Hz, is comparable to that reported (2) for Al_2O_3 deposited in the absence of O_2 and is lower than the value 7.5 x 10^{-3} given for O_2-deposited films. The tan δ values represented by curve 1, Fig. 2, are larger than expected on the basis of Ref. (14). This may be due to d-c conduction through the film of the untreated sample.

The crystallization behavior of these films upon annealing exhibits a similar trend to that reported by Aboaf (2) but differs significantly from that reported by Nishimatsu *et al.* (7) who report crystallization at 500°C. It appears from Ref. (7) that the deposition of alumina films was performed in the absence of oxygen, while in the present work oxygen has been used. Matsushita and Koga (4) have shown that pyrolytic alumina films deposited in the absence of oxygen and at high deposition rates can have an Al_2O_3 content as low as 80%, the remaining film possibly consisting of polymer impurity, while those films deposited at low deposition rates in the presence of oxygen contain as high as 100% Al_2O_3. They also report significant differences in insulating properties of the two types of films. The above differences in crystallization behavior may be due to differences in impurity content of the respective films, and it is expected that significant differences in interface properties will also occur. That this is so can be seen from a review of the results reported here and in Ref. (7).

Interface properties.—The charge instability effects, including hysteresis, displayed by Si-Al_2O_3 structures show the same trend as reported for Si-SiO_2(grown)-SiO_2(deposited) structures (15) but differ from those of the Si-Si_3N_4 system (16).

The diminished hysteresis obtained at higher deposition temperatures and lower deposition rates suggests that this effect is associated with incomplete oxidation of the Al-alkoxide, possibly the presence of H^+ or

OH^- ions in the oxide. The effectiveness of a post-deposition O_2 treatment in eliminating the hysteresis may result from the deactivation of these species upon further oxidation.

Another possibility is that the O_2 treatment modifies the defect structure of the Si-Al_2O_3 interface. Such a process could be a modification of the defect structure of the residual SiO_2 (~ 30Å) on the silicon surface. A "densification" of this oxide prior to deposition of Si_3N_4 was reported (17) to have a large influence on the charge transfer behavior of the Si-Si_3N_4 interface. However, the hysteresis associated with Si-Al_2O_3 structures is in the opposite sense to that expected for such a transfer mechanism at the Si-Al_2O_3 interface. The observed hysteresis is similar to that resulting from charge transfer at the gate electrode or ionic polarization of the oxide resulting from ions present or produced by field ionization of defects in the Al_2O_3 film. However, the presence of a 200Å thick SiO_2 film between the Si and Al_2O_3 eliminates the hysteresis. It is unlikely that these mechanisms could be greatly influenced by the presence of a 200Å SiO_2 film except insofar as that the field in the latter is about twice as high as in the Al_2O_3 film. Thus, it has not been possible to explain the observed hysteresis in terms of charge transfer at the gate electrode. We cannot, at present, propose a satisfactory model for the hysteresis effects in Si-Al_2O_3 structures.

In agreement with previous reports (4-7), the Al_2O_3 film (including the Si-Al_2O_3 interface) is associated with negatively ionized acceptor states. By contrast, Al_2O_3 films produced by plasma anodization of aluminum have an associated positive charge (3). However, after a hydrogen heat treatment, the charge in the plasma-grown oxide becomes negative. A typical final value is -8×10^{10} e/cm^2. This behavior has been attributed to electron and hole capture during anodization and subsequent emptying of traps by thermal excitation. The fact that the negative charge density is higher for deposited than for plasma-grown oxide suggests that trapped holes in the latter partially compensate the negative charge due to trapped electrons. No appreciable hole injection can occur during chemical deposition because of the absence of a high electric field across the oxide. Consequently, the apparent negative charge density is larger.

Because of the frequent development of excessive conduction during the BT tests, no detailed study of the charge instability was made. The observations indicate, however, that the instability may be due to a redistribution of positive or negative ions which were originally in the vicinity of the Si-oxide or oxide-gate interface, respectively. As in the case of Si-SiO_2 structures (1), such a process could result in a voltage asymmetric instability, but in the opposite sense. Another possibility is that under negative bias electrons are injected from the gate electrode into the oxide, leading to positive space charge in the silicon. This process seems plausible in view of the general tendency toward electron trapping in Al_2O_3. The occasionally observed positive shifts under positive bias are similar, but again in the opposite sense, to the slow trapping instability associated with imperfect Si-SiO_2 interface structures (1). This can be attributed to the injection of electrons from silicon in Al_2O_3 and trapping near the interface.

Si-Al_2O_3 structures are more resistant to high energy electron radiation than MOS devices using SiO_2 as insulator. Bombardment of 1000Å of Al_2O_3 under +10V gate bias produces a flat-band voltage shift of −9.8V (4.6×10^{12} e/cm^2 induced charge) which compares with ~ −50V for SiO_2 (18) (1.3×10^{13} e/cm^2 induced charge). Since the dielectric constant of Al_2O_3 is about twice as large as that of SiO_2, an identical change in the surface charge, as due to irradiation, gives rise to only half the shift in the flat-band voltage.

It can be seen from Fig. 4 that, like SiO_2 and plasma-grown Al_2O_3 (3), the effect of positive bias under irradiation saturates. The behavior under negative bias is, however, different from the other cases. In the case of SiO_2, irradiation under negative bias also results in an increase in the positive oxide charge (though to a lesser extent than under positive bias). Irradiation of plasma-grown Al_2O_3 under negative bias leads to an increase of the negative oxide charge. This has been attributed to electron trapping in the Al_2O_3 film (3). The difference in behavior between chemically deposited and plasma-grown Al_2O_3 can again be explained by the presence of trapped holes in the latter.

The results of irradiation experiments demonstrate that the defect structure of Al_2O_3 is different from that of SiO_2. The predominant feature of the latter is an abundance of hole traps which capture the radiation-produced holes. This results in a net positive charge in the oxide (18). Recent investigations of radiation effects in SiO_2 and Al_2O_3 films, using the thermoluminescence glow curve technique, showed that polycrystalline Al_2O_3 has a large density of traps (probably both hole and electron traps) which hardly increases with irradiation, whereas the pre-irradiation trap density in SiO_2 is low but increases substantially during irradiation (19). Because of the presence of electron traps in Al_2O_3, the net trapped positive charge is much less than in SiO_2. Another contributing effect could be the recombination of radiation-generated electrons and holes before significant trapping takes place. From our observations, it is evident that Al_2O_3 has a greater tendency toward conduction than SiO_2. On the other hand, samples showing no observable d-c conduction were not more sensitive to radiation than those showing some conduction. However, there are indications that conduction is controlled by the interface(s) so that appreciable movement of electrons and/or holes might occur in the oxide without giving rise to d-c conduction. The instability of the induced charge in samples which did not receive an O_2 treatment possibly resulted from such recombination, and demonstrates again the effect of this treatment in changing the defect structure of the oxide.

Conduction.—Most conducting samples exhibit the Schottky depletion capacitance during C-V measurements. This indicates that the minority carriers (electrons for p-type material) cannot accumulate in the silicon space-charge region but are injected into the oxide and drift to the positively biased gate electrode. Similar behavior has also been observed in Si-SiO_2 structures where the SiO_2 film was prepared by anodic oxidation of silicon. This oxide film shows localized conduction to a greater extent than thermally grown SiO_2 (1). This behavior differs from that observed for Si-SiO_2 structures having a large density of interface states (20), since holding the gate under positive bias did not lead to accumulation of minority carriers in the space-charge region and, thus, to the disappearance of the Schottky capacitance. Rather the behavior is similar to that reported for semiconductor-electrolyte systems where injection of electrons from a p-type semiconductor into the electrolyte occurs when the latter is under negative bias (21).

The simultaneous development of conduction and Schottky capacitance in BT-stressed samples suggests that conduction is controlled by the interface(s). Processes (*e.g.*, heat treatment, irradiation) which affect interface properties have a large influence on the observed conduction. The nature of the interface(s) apparently changes from blocking to injecting and in many cases electron and/or hole injection at the Si-Al_2O_3 interface controls the conduction. That Al_2O_3 films have a greater tendency toward conduction than SiO_2 films has also been observed by Matsushita and Koga, especially for pure Al_2O_3 (4). It would be premature to speculate on the exact mechanism of conduction, but it is unlikely that it is a bulk-controlled Frenkel-Poole mechanism as proposed for silicon nitride (16).

Si-SiO_2-Al_2O_3 *structures.*—The fact that, in contrast to Si-Al_2O_3 structures, the surface state density of the Si-SiO_2-Al_2O_3 structures is orientation dependent corroborates the argument that this dependence is related to the mechanism by which the SiO_2 film grows on silicon (1). When the insulator is deposited instead of grown no orientation dependence can be observed.

The charge instability associated with these structures under negative gate bias is probably due to injection of electrons from the gate into the Al_2O_3 and/or to field ionization of defects in Al_2O_3. In the latter mechanism, positive ions and electrons are generated by the field and the electrons repelled to the Al_2O_3-SiO_2 interface which they cannot penetrate. Such a mechanism has been proposed to explain the instability behavior of Si-SiO_2(grown)-SiO_2(deposited) structures (15). The instability under positive bias is probably due to Na^+ ions since no attempt was made to provide a sodium-free environment during the growth of the SiO_2 film. It is unlikely that it is caused by injection or trapping since the instability effect is independent of the magnitude of the positive bias and the extent of flat-band voltage shift during previous negative biasing (*see* Fig. 6).

The stability behavior of Si-SiO_2-Al_2O_3 structures, which did not receive a postdeposition O_2 treatment, requires more study. This behavior (Fig. 7) again demonstrates that d-c conduction is controlled by the interface(s), which, in turn, can be modified by the BT tests.

Summary and Conclusions

1. Thermal decomposition of Al-isopropoxide at ~ 420°C results in noncrystalline Al_2O_3 films whose refractive index varies from 1.60 to 1.68. The dielectric constant at 100 kHz is about 7.5, and the tan δ is about 0.01. The MOS capacitance curves show large scatter and room-temperature hysteresis.

2. Postdeposition heat treatment in oxygen at 700°C reduces this scatter and eliminates the hysteresis. This treatment overrides the effects on interface properties of the deposition conditions. A typical value of the flat-band voltage (for 1000Å thick film) is +2.0V. The density of interface states varies from 10^{10} to 10^{11} states/cm^2 · eV. Localized conduction occurs frequently in these films; there are indications that it is controlled by the interface(s).

3. Bombardment with 1 MeV electrons (fluence = ~ 10^{14} e/cm^2) under positive bias results in a relatively small shift in the flat-band voltage; the smallest value observed was −6.4V under +10V bias (equivalent to 2.7 x 10^{12} e/cm^2 surface charge). Bombardment under negative bias has practically no effect.

4. The conduction observed in Si-Al_2O_3 structures was greatly reduced by growing ~200Å thick SiO_2 film on silicon prior to the Al_2O_3 deposition. Typical flat-band voltages for ~1200Å total insulator thickness are −2.5V and zero volt for (111) and (100) orientations, respectively. The corresponding interface state densities are 4 x 10^{10} − 2 x 10^{11} e/cm^2 · eV and 1 x 10^{10} − 4 x 10^{10} e/cm^2 · eV.

5. Under large negative bias (corresponding to about 10^6 V/cm field) at 250°C, the flat-band voltage shifts to more positive values. At a given bias, a stable situation can be achieved within roughly 20 min. Positive bias shifts the flat band to more negative values but only by about 1V.

6. The results reported here differ significantly from those of Nishimatsu *et al.* (7). This is particularly marked in the crystallization behavior of the respective alumina films and the charge instability phenomena, including hysteresis, associated with Si-Al_2O_3 and Si-SiO_2-Al_2O_3 structures. These differences may be due to differences in impurity content of the films resulting from differing preparation conditions (*e.g.*, presence or absence of oxygen during deposition).

The results reported here have been obtained without using special clean technology. The radiation resistance of the Si-Al_2O_3 structures, the positive values of the flat-band voltage, the lack of significant instability effects of prestressed samples, and the value of dielectric constant make Al_2O_3 attractive from the viewpoint of device fabrication. However, the problem of localized conduction must be brought under control.

Acknowledgments

R. J. Evans and R. A. Soltis collaborated in the experimental work. A. Waxman and K. H. Zaininger cooperated in the MOS measurements and also participated in discussions. D. Richman critically read the manuscript. The authors are indebted to all.

Manuscript submitted June 25, 1969; revised manuscript received Nov. 11, 1969.

Any discussion of this paper will appear in a Discussion Section to be published in the December 1970 JOURNAL.

REFERENCES

1. For a review, *see* A. G. Revesz and K. H. Zaininger, *RCA Rev.*, **29**, 22 (1968).
2. J. A. Aboaf, *This Journal*, **114**, 948 (1967).
3. A. Waxman and K. H. Zaininger, (*a*) *Appl. Phys. Letters*, **12**, 109 (1968); (*b*) *Proc. IEEE*, To be published.
4. M. Matsushita and Y. Koga, Paper 90 presented at Electrochem. Soc. Meeting, Boston, May 5-9, 1968.
5. H. Nigh, Paper 476 presented at the Montreal Meeting of the Society, Oct. 6-11, 1968.
6. S. K. Tung and R. E. Caffrey, "Thin Film Dielectrics," Edited by F. Vratny, Electrochemical Society Softbound Symposium Series (1969).
7. S. Nishimatsu, T. Tokuyama, and M. Matsushita, *ibid.*
8. K. Nagano, S. Iwauchi, and T. Tanaka, *Japan. J. Appl. Phys.*, **8**, 277 (1969).
9. M. T. Duffy, C. C. Wang, A. Waxman, and K. H. Zaininger, *This Journal*, **116**, 234 (1969).
10. K. H. Zaininger, *RCA Rev.*, **27**, 341 (1966).
11. J. Sewchun and A. Waxman, *Rev. Sci. Instr.*, **37**, 1195 (1966).
12. E. H. Nicollian and A. Goetzberger, *Appl. Phys. Letters*, **7**, 216 (1965).
13. K. H. Zaininger, "Field Effect Transistors," p. 41, Edited by J. T. Wallmark and H. Johnson, Prentice-Hall, Inc., Englewood Cliffs, N. J. (1966).
14. M. Gevers and F. K. du Pre, *Trans. Faraday Soc.*, **42**, 47 (1946).
15. Y. Haneta and S. Nakanuma, *Japan. J. Appl. Phys.*, **6**, 1176 (1967).
16. S. M. Hu, D. R. Kerr, and L. V. Gregor, *Appl. Phys. Letters*, **10**, 97 (1967).
17. J. Scott and J. T. Wallmark, *RCA Rev.*, **30**, 335 (1969).
18. K. H. Zaininger and A. G. Holmes-Siedle, *RCA Rev.*, **28**, 208 (1967).
19. J. P. Mitchell, IEEE Transactions on Nuclear Science NS-15, 154 (1968).
20. D. M. Brown and P. V. Gray, *This Journal*, **115**, 760 (1968).
21. R. Memming, *Philips Res. Repts.*, **19**, 323 (1964).

Oxygen Diffusion in Monoclinic Zirconia

D. J. Poulton and W. W. Smeltzer*

Department of Metallurgy and Materials Science, McMaster University, Hamilton, Ontario, Canada

ABSTRACT

Oxygen-18 enriched oxygen and carbon dioxide-carbon monoxide atmospheres have been used in the determination of the oxygen self-diffusion coefficient in monoclinic zirconia at 990°C. Oxygen exchange measurements were made on zirconia spheres in the average size ranges of 90 and 126μ. The diffusion coefficient was found to be independent of both oxygen partial pressure over the range 1-10^{-19} atm and sphere size. The value of the diffusion constant has been used with previously determined electrical conductivity data to verify postulates of a defect model involving oxygen ion vacancies for monoclinic zirconia.

The nature of the defect structure and the transport properties of oxygen in monoclinic zirconia have been the subjects of several recent investigations (1, 2). For example, Vest, Tallan, and Tripp (3) measured the electrical conductivity of zirconia at 990°C as a function of oxygen pressure from 1 to 10^{-23} atm and found an electronic semiconductor, with the transition from n-type to p-type conductivity occurring at approximately 10^{-16} atm. Their results have been further discussed by Kröger (1) who advanced a Schottky-type model involving both isolated oxygen vacancies and zirconium vacancies singly associated with oxygen vacancies, and also by Douglass and Wagner (2) who proposed an anti-Frenkel type model involving oxygen vacancies and interstitials. It is predicted by both of these models that oxygen ionic conductivity may be considered to be predominant at moderately low oxygen pressures, between the extremes of n- and p-type electronic conductivity.

Recently, Madeyski and Smeltzer (4, 5) have applied the gas-solid oxygen-18 exchange technique to determine the oxygen self-diffusion coefficient in monoclinic zirconia prepared as annealed spheres at temperatures in the range 800°-1000°C and at oxygen pressures close to atmospheric. In this paper, these results have been extended at 990°C to oxygen partial pressures as low as 10^{-19} atm, by the use of oxygen-18 enriched CO-CO_2 atmospheres.

Experimental

In Fig. 1, a schematic drawing of the gas preparation train and the reaction apparatus is given. The oxygen exchange apparatus is identical to that previously described (5).

The preparation of microspheres of near-stoichiometric ZrO_2 in the size ranges 75-105μ and 105-147μ by oxidation of 99.92 w/o (weight per cent) zirconium sheet (4), and of oxygen gas containing about 1.3 a/o (atomic per cent) ^{18}O has already been described (5). Carbon dioxide containing about 0.9 a/o ^{18}O was prepared by equilibrating normal carbon dioxide with oxygen-18 enriched water in the five-liter flask shown on the diagram, followed by removal of the water by trap-to-trap distillation between dry ice-acetone and liquid nitrogen traps. Carbon monoxide containing about 0.9 a/o ^{18}O was prepared by exposing either the oxygen or the CO_2 prepared as above to an excess of activated charcoal for approximately 24 hr at 1000°C, followed by transfer through three liquid nitrogen traps to a 5-liter storage flask with the aid of a Toepler pump. The equality of the oxygen-18 enrichment in the carbon monoxide and carbon dioxide was carefully checked by mass spectrometric analysis and adjusted to better than 0.2 relative per cent difference.

Microspheres of stoichiometric zirconia were first annealed for 24 hr in the reaction chamber containing a CO-CO_2 atmosphere of normal isotopic composition and desired oxygen partial pressure. Oxygen partial pressures were calculated from the free energies of formation of carbon monoxide and carbon dioxide as tabulated by Rossini *et al.* (6). In a few experiments, pure oxygen was used at pressures of approximately 0.5 atm. At the conclusion of the anneal, the normal gases were pumped out and an oxygen-18 enriched CO-CO_2 atmosphere of identical oxygen partial pressure was admitted. The progress of the exchange reaction was then followed by taking approximately ten samples of the gas atmosphere over a total time period of generally about 30 hr.

Oxygen self-diffusion coefficients D^* were obtained from the mass spectrometric analyses of the gas samples with the aid of the error function equation developed by Carmen and Haul (7)

$$\frac{Q - Q_1}{Q_2 - Q_1} = \frac{\gamma_1}{\gamma_1 + \gamma_2} \operatorname{eerfc} \frac{3\gamma_1}{\lambda}\sqrt{\tau} + \frac{\gamma_2}{\gamma_1 + \gamma_2} \operatorname{eerfc} \frac{-3\gamma_2}{\lambda}\sqrt{\tau} \quad [1]$$

where

$$\gamma_1 = \frac{1}{2}\left[\sqrt{1 + \frac{4\lambda}{3}} + 1\right], \gamma_2 = \gamma_1 - 1, \quad \tau = D^*t/a^2 \quad [2]$$

In this equation, Q, Q_1, and Q_2 represent the atom fraction of oxygen-18 in the atmosphere at time t, in the oxide at zero time (taken as the natural abundance 0.00204), and in the atmosphere at zero time, respectively; a is the sphere radius and λ is the ratio of the total mass of oxygen in the gas atmosphere to that in the solid oxide. These calculations were performed with the aid of a computer.

Results and Discussion

Plots of the results, $\sqrt{\tau}$ *vs.* $\sqrt{t}$, are illustrated in Fig. 2-4. For clarity, successive plots have been dis-

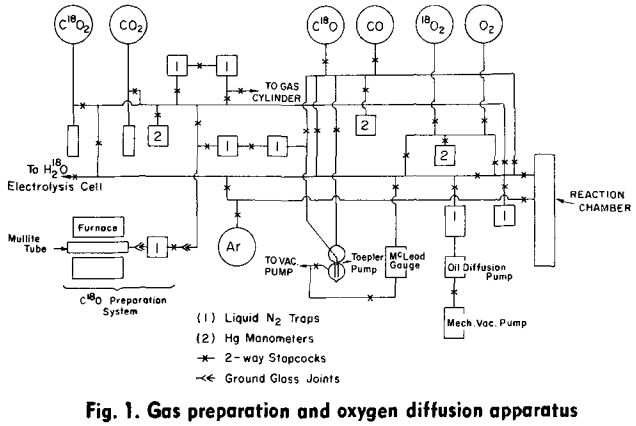

Fig. 1. Gas preparation and oxygen diffusion apparatus

* Electrochemical Society Active Member.

placed by $\sqrt{\tau} = 0.03$ in Fig. 2-3 and $\sqrt{\tau} = 0.04$ in Fig. 4. Since they are linear and extrapolate to the origin, oxygen diffusion in the spheres would appear to determine the exchange kinetics. In Fig. 5, the values of the self-diffusion coefficient D^* have been plotted against the oxygen partial pressure over the range 10^{-19}-1 atm. Least squares analysis of these results demonstrated that the oxygen self-diffusion coefficient was independent of both oxygen partial pressure and sphere size, and to have the value

$$D^* = (1.9 \pm 0.3) \times 10^{-12} \text{ cm}^2 \text{ sec}^{-1} \quad [3]$$

This result agrees favorably with the value $D^* = 1.98 \times 10^{-12}$ cm^2 sec^{-1} calculated for $P_{O_2} \sim 0.5$ atm from the Arrhenius equation presented earlier (5).

The partial electrical conductivity due to oxygen ions may be related to the oxygen self-diffusion coefficient

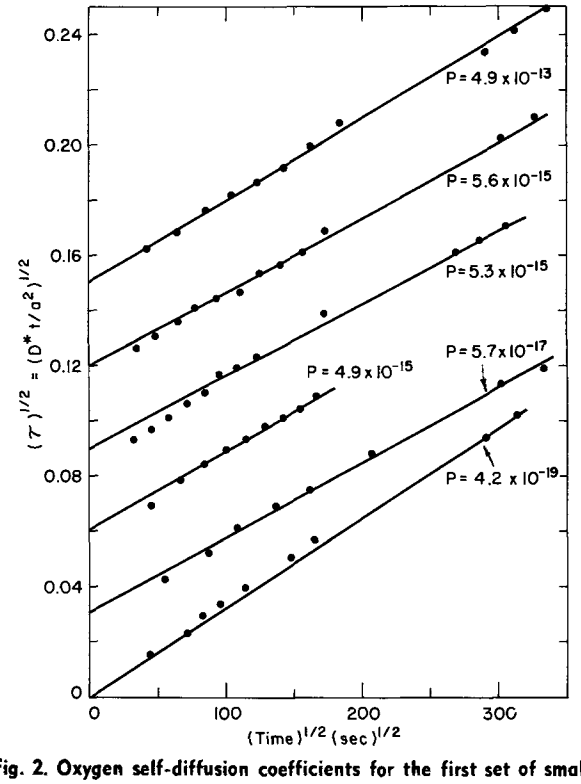

Fig. 2. Oxygen self-diffusion coefficients for the first set of small spheres, 75-105μ in diameter.

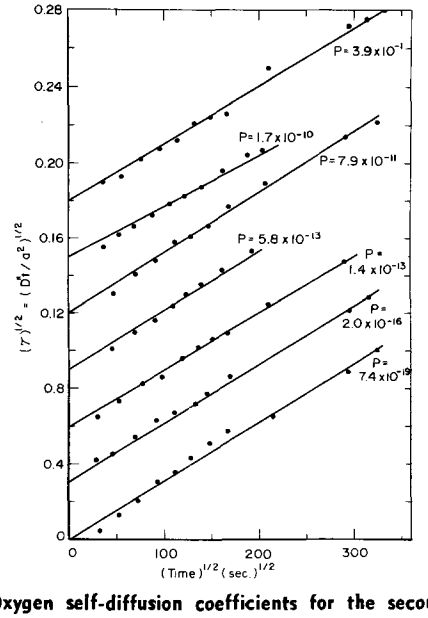

Fig. 3. Oxygen self-diffusion coefficients for the second set of small spheres, 75-105μ in diameter.

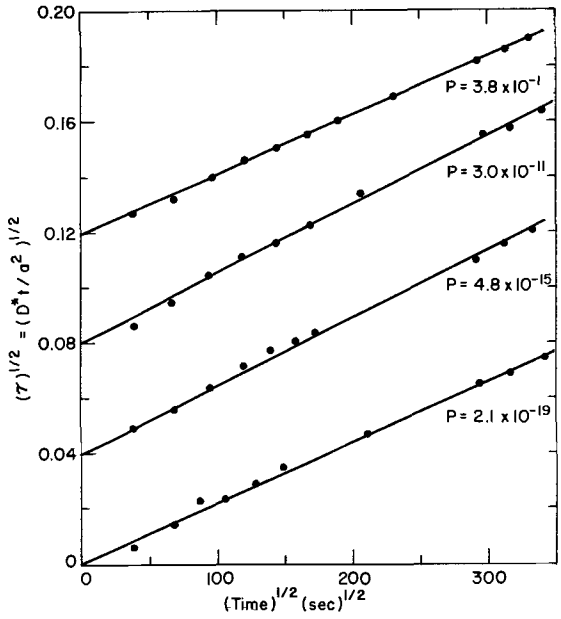

Fig. 4. Oxygen self-diffusion coefficients for large spheres, 105-147μ in diameter.

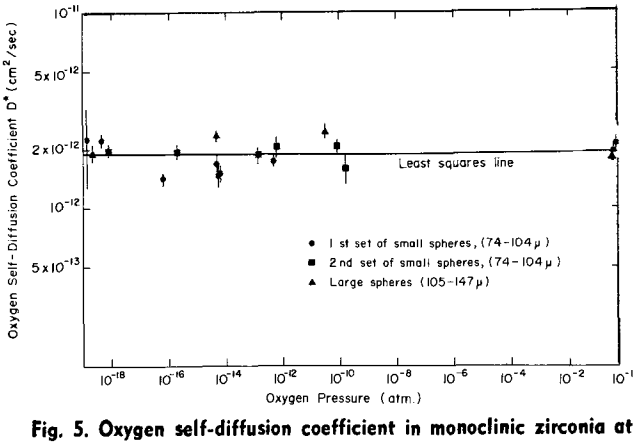

Fig. 5. Oxygen self-diffusion coefficient in monoclinic zirconia at 990°C.

by means of the Nernst-Einstein relationship to a first approximation by the following expression

$$\kappa_{ion} = \frac{4F^2D^*}{V_mRT} = 3.2 \times 10^{-7} \text{ ohm}^{-1} \text{ cm}^{-1} \text{ at } 990°\text{C} \quad [4]$$

where V_m, the molar volume of oxide, is equal to 21.15 cm^3 mole^{-1}. In Fig. 6, the ionic conductivity at 990°C is compared with the total electrical conductivity, as determined by Vest *et al.* (3). As illustrated by the pressure dependency of the conductivity, n-type conductance is predominant at $P_{O_2} \leq 10^{-18}$ atm and p-type conductance is predominant at $P_{O_2} \geq 10^{-10}$ atm. It is also to be seen that the ionic conductance, which is independent of oxygen pressure over the range 10^{-19}-1 atm, lies within the range typical of both the intrinsic and n-type electrical conductivity.

If it is assumed that the minimum value of the total electrical conductivity is associated with oxygen ion migration, the excess electrical conductivity illustrated in Fig. 6 at 10^{-17} atm for the polycrystalline hot-pressed zirconia may be explained as being due to short-circuit anionic conductivity. This behavior associated with structure would appear to be most probable since the total weight per cent of zirconia in the compacts and spheres is of the same order of magnitude, 99.82 *vs.* 99.92 w/o. In previous investigations on the oxygen diffusional properties of the microspheres and polycrystalline oxide (5, 8), it has been shown that

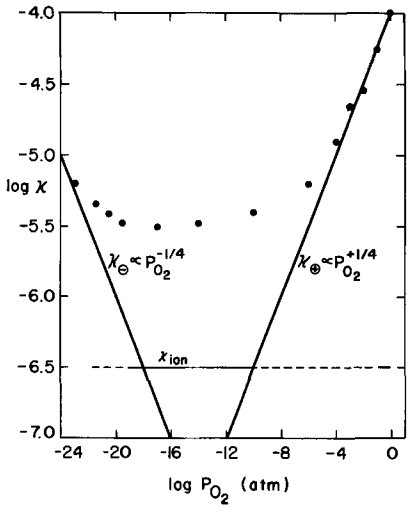

Fig. 6. Ionic and electronic conductivity of monoclinic zirconia at 990°.

the diffusion rate was much larger in the latter structure and of values typical for short-circuit diffusion in the temperature range 750°-950°C. Accordingly, the apparent electrical conductivity κ_{app} is written in terms of the lattice conductivity κ_L and boundary conductivity κ_B as follows

$$\kappa_{app} = \kappa_L (1 - f) + \kappa_B f \quad [5]$$

where f is the fraction of oxygen ion sites at line defects such as dislocations and crystal boundaries. The values of f may be estimated from the ionic conductivity calculated here together with an estimate of κ_B derived from the results of oxygen diffusion measurements in polycrystalline zirconia slabs performed earlier (8). If one estimates that $f = 0.1$ in the polycrystalline slabs, D_B at 990°C is found to be approximately 3×10^{-8} cm²/sec, from which one obtains $\kappa_B = 5 \times 10^{-3}$ ohm^{-1} cm^{-1}. Substituting these values into Eq. [5] and solving for f, one obtains $f = 5 \times 10^{-4}$. This represents somewhat defective material with 0.05% of the oxygen lattice sites located at crystal boundaries or line defects such as dislocations.

Two defect models involving oxygen ion vacancies have been proposed for monoclinic zirconia from which theoretical predictions may be made on the variation of the electronic and ionic conductivities as a function of oxygen pressure. Kröger (1) has proposed a Schottky-type model involving zirconium vacancies singly associated with oxygen vacancies, as follows

$$\text{nil} \rightleftarrows (\square_{Zr}\square_O)'' + \square_O{\cdot\cdot} \quad K_1 = C_A C_{\square} \quad [6]$$

where C_A denotes the concentration of associated vacancies. On the other hand, Douglass and Wagner (2) have proposed anti-Frenkel disorder, similar to that found for calcium fluoride by Ure (9)

$$\text{nil} \rightleftarrows \square_O{\cdot\cdot} + O_i'' \quad K_1' = C_{\square} C_i \quad [7]$$

Equations for the production of electrons and electron holes, and for the incorporation of oxygen from the gas phase, which are common to both models, may be written as follows

$$\text{nil} \rightleftarrows e' + h{\cdot} \quad K_2 = C_\theta C_\oplus \quad [8]$$

$$\frac{1}{2} O_2 + \square_O{\cdot\cdot} + 2e' \rightleftarrows O_L \quad K_3 = \frac{1}{C_{\square} C_\theta^2 P_{O_2}^{1/2}} \quad [9]$$

where O_L represents a lattice oxygen ion. From these equations, together with the appropriate approximation for the electroneutrality condition, equations for the oxygen pressure dependence of the various defects may be written.

Under conditions in which the zirconia exists with nearly ideal stoichiometric composition, the electroneutrality condition may be expressed by

$$C_{\square} = C_i = K_1'^{1/2} \quad \text{or} \quad C_{\square} = C_A = K_1^{1/2} \quad [10]$$

and it follows from Eq. [6] to [9]

$$C_\theta = K_3^{-1/2} K_1^{-1/4} P_{O_2}^{-1/4} \quad [11]$$

and

$$C_\oplus = K_2 K_3^{1/2} K_1^{1/4} P_{O_2}^{1/4} \quad [12]$$

At very low oxygen pressures, where an excess of oxygen vacancies exists in oxygen-deficit zirconia, the electroneutrality condition may be expressed by

$$2C_{\square} = C_\theta \quad [13]$$

and from [9] it follows that

$$2C_{\square} = C_\theta = \left(\frac{2}{K_3}\right)^{1/3} P_{O_2}^{-1/6} \quad [14]$$

At very high oxygen pressures, in oxygen-rich zirconia, the electroneutrality relationship may be expressed in terms of either oxygen interstitials or zirconium vacancies associated with oxygen vacancies, as follows

$$2C_i = C_\oplus \quad \text{or} \quad 2C_A = C_\oplus \quad [15]$$

Using Eq. [6]-[9], it may be seen that

$$2C_i = C_\oplus = (2K_1' K_2^2 K_3)^{1/3} P_{O_2}^{1/6} \quad [16]$$

or

$$2C_A = C_\oplus = (2K_1 K_2^2 K_3)^{1/3} P_{O_2}^{1/6} \quad [17]$$

depending on whichever model is selected. It is therefore seen that the two models are mathematically equivalent, with O_i'' in the anti-Frenkel model corresponding directly to $(\square_{Zr}\square_O)''$ in the Schottky model, provided that, in the Schottky model, further association of a second oxygen vacancy or dissociation of the complex is neglected.

The ionic and electronic conductivity of zirconia may now be explained by reference to these models. Figure 6 shows that the ionic conductivity is independent of oxygen pressure over the range $1\text{-}10^{-19}$ atm. Apparently, the solid behaves as an intrinsic semiconductor in which the total oxygen defect concentration involving oxygen vacancies and interstitials is fixed by the value of the constant, K_1 or K_1', being much greater than the value of the constant K_2. That the value observed for the ionic conductivity refers to both formation and movement of oxygen vacancies has been shown by the fact that the activation energy for oxygen diffusion in spheres at 0.5 atm pressure, 56 kcal (5), is approximately twice that observed for oxygen diffusion in plates of columnar zirconia of identical composition (8). Hence, the electroneutrality relation would not appear to be markedly influenced by impurities present in the oxide specimens and accordingly may be defined by Eq. [10], within the experimentally accessible pressure range. Consequently the concentrations of electrons and holes would be given by Eq. [11] and [12], respectively.

The partial electronic conductivity, κ_e, may be expressed by

$$\kappa_e = \kappa_\theta + \kappa_\oplus = \mathbf{F}(\mu_\theta C_\theta + \mu_\oplus C_\oplus)/V_m \quad [18]$$

where $\mathbf{F}$ is the Faraday constant, V_m the molar volume, and μ_θ and $\mu_\oplus$ the mobilities of electrons and positive holes. Substituting Eq. [11] and [12] into [18], it is found that

$$\kappa_e = \frac{\mathbf{F}}{V_m} [\mu_\theta K_3^{-1/2} K_1^{-1/4}) P_{O_2}^{-1/4} + (\mu_\oplus K_2 K_3^{1/2} K_1^{1/4}) P_{O_2}^{+1/4}] \quad [19]$$

The electronic conductivity has been shown in Fig. 6 where it is seen that a $P_{O_2}^{+1/4}$ relationship is consistent

with Vest *et al.*'s results at $P_{O_2} = 1\text{-}10^{-4}$ atm. The low pressure data does not extend to a sufficiently low pressure to verify the $P_{O_2}^{-1/4}$ relationship.

The partial ionic conductivity, κ_{ion}, in terms of the mobilities for the point defects is given by

$$\kappa_{ion} = 2\mathbf{F}\,(\mu_{\square} C_{\square} + \mu_A C_A)\,/V_m \qquad [20]$$

or

$$\kappa_{ion} = 2\mathbf{F}\,(\mu_{\square} C_{\square} + \mu_i C_i)\,/V_m \qquad [20a]$$

depending on which defect model is selected. If the Schottky disorder type were present, the zirconium vacancies present in the associates would be expected to contribute somewhat to μ_A, resulting in a zirconium self-diffusion coefficient within a few orders of magnitude of the oxygen self-diffusion coefficient. However, if the anti-Frenkel defect model were present, the cationic lattice would be nearly perfect compared to the anionic lattice and the zirconium self-diffusion coefficient would be several orders of magnitude lower than the oxygen self-diffusion coefficient. Unfortunately, data on zirconium self-diffusion in pure zirconia is lacking. Extrapolation of data on zirconium self-diffusion in calcia-stabilized zirconia at 1700°-2200°C (10) to 990°C, would indicate D^*_{Zr}/D^*_O to be approximately 10^{-6}, apparently favoring the anti-Frenkel model as the predominant defect structure for monoclinic zirconia. However, in stabilized zirconia, the concentration of zirconium vacancies or oxygen interstitials (dependent on which model is chosen) is expected to be lower than the value for pure zirconia by an amount dependent on the equilibrium constant for association of oxygen vacancies with calcium ions in stabilized zirconia (1). Thus the value of D^*_{Zr} in pure zirconia can be expected to be higher, and it is therefore concluded that a decision on which defect model is important for either oxide must await the experimental determination of values for D^*_{Zr} in pure zirconia.

Conclusions

The oxygen self-diffusion coefficient in monoclinic zirconia microspheres at 990°C was determined to be $D^* = 1.9 \times 10^{-12}$ cm^2 sec^{-1}. This value is independent of both sphere size in the range 90-126μ and oxygen pressure in the range $1\text{-}10^{-19}$ atm. A comparison of the partial electrical conductivity due to oxygen ions as calculated from the Nernst-Einstein relationship to the total conductivity of hot-pressed compacts indicates monoclinic zirconia to be an n-type electronic conductor at $P_{O_2} \leq 10^{-18}$ atm and a p-type electronic conductor at $P_{O_2} \geq 10^{-10}$ atm, with predominant oxygen ionic transport at intermediate pressures. The excess electrical conductivity exhibited by the polycrystalline compact at intermediate pressures is believed to be due to short-circuit anionic conductivity, with an estimate of approximately 0.05% of the oxygen ions situated at line defects. Although data for zirconium diffusion in stabilized zirconia would appear to support the anti-Frenkel model as the predominant defect model for pure zirconia, it is impossible to draw a conclusion until a value for the zirconium self-diffusion coefficient in pure zirconia has been measured.

Acknowledgments

The authors were indebted to R. Kelly for helpful discussions. D. J. Poulton wishes to acknowledge the award of a post-doctoral research fellowship and funds to support this investigation from the National Research Council of Canada.

Manuscript submitted July 14, 1969; revised manuscript received Oct. 31, 1969. This was Paper 122 presented at the Detroit Meeting, Oct. 5-9, 1969.

Any discussion of this paper will appear in a Discussion Section to be published in the December 1970 JOURNAL.

REFERENCES

1. F. A. Kröger, *J. Am. Ceram. Soc.*, **49**, 215 (1966).
2. D. L. Douglass and C. Wagner, *This Journal*, **113**, 671 (1966).
3. R. W. Vest, N. M. Tallan, and W. C. Tripp, *J. Am. Ceram. Soc.*, **47**, 635 (1964).
4. A. Madeyski and W. W. Smeltzer, *Mat. Res. Bull.*, **2**, 427 (1967).
5. A. Madeyski and W. W. Smeltzer, *ibid.*, **3**, 369 (1968).
6. F. D. Rossini, K. S. Pitzer, R. L. Arnett, R. M. Braun, and G. C. Pimental, "Selected Values of Physical and Thermodynamic Values of Hydrocarbons and Related Compounds," Carnegie Press, Pittsburgh (1953).
7. P. C. Carman and R. A. W. Haul, *Proc. Royal Soc. (London)*, **222A**, 109 (1954).
8. A. Madeyski, D. J. Poulton, and W. W. Smeltzer, *Acta Met.*, **17**, 579 (1969).
9. R. W. Ure, *J. Chem. Phys.*, **26**, 1363 (1957).
10. W. H. Rhodes and R. E. Carter, *J. Am. Ceram. Soc.*, **49**, 244 (1966).

Technical Notes

Luminescent Properties of Eu^{2+} and $Eu^{2+} + Mn^{2+}$ Activated $BaMg_2Si_2O_7$

Thomas L. Barry*

Sylvania Lighting Center, Sylvania Electric Products Incorporated, Danvers, Massachusetts

Recently, a great deal of work has been done on divalent europium activation of silicate phases (1-9), largely devoted to three ternary systems:

1. CaO — MgO — SiO_2
2. SrO — MgO — SiO_2
3. BaO — MgO — SiO_2

and their respective bounding binary systems. In particular, joins and isothermal sections between phases with analogous formulas were considered; examples of this being the 3-1-2 and 2-1-2 (RO-MgO-SiO_2) compounds in the ternary isothermal sections (common in all three systems) and the 2-1 compounds in the bounding alkaline earth oxide-silica binary joins. Such selections are easily understandable due to the wide variety of substitution possible in such compositional regions and the accompanying changes in the excitation and emission spectra which may be studied.

* Electrochemical Society Active Member.

Key words: phosphors alk earth silicates, luminescence alk earth silicates, subsolidus phase relations, europium (2+) activation, emission spectra, excitation spectra, energy transfer Eu(2+) to Mn(2+), sensitizer and activator dependencies.

The subsolidus phase relationships in the BaO-MgO-SiO_2 system were initially studied by Klasens, Hoekstra, and Cox (10) and recently redone by Argyle (11), the latter reporting three new compounds ($3BaO \cdot 5SiO_2$; $5BaO \cdot 8SiO_2$; $BaO \cdot MgO \cdot 3SiO_2$). The features of the two diagrams which are pertinent to this luminescence study, however, are identical.

Figure 1, taken from the work of Argyle (11), gives the subsolidus relationships. Five ternary compounds exist in the system luminescence being studied in the 3-1-2 and 2-1-2 compounds (1, 5, 7). A compound with the 1-2-2 stoichiometry occurs only in this system. It does not form in the other two ternary systems mentioned. This compound melts congruently at 1600°C and provides the matrix on which the luminescence studies of this paper have been conducted.

Other features of Fig. 1 which are referred to later are the observations that (*A*) the 1-2-2 compound lies on a binary join between $BaMgSiO_4$ (1-1-1) and $MgSiO_3$ (1-1), and also between $BaSi_2O_5$ (1-2) and MgO; (*B*) the compounds $BaSiO_3$ (1-1) and Mg_2SiO_4 (2-1), and BaO plus $MgSiO_3$ (1-1) possess such stoichiometries that when mixed in the proper proportions and completely reacted yield the 1-2-2 compound.

Experimental

Of the starting materials, the barium carbonate, silicic acid, and manganese carbonate were luminescent-grade chemicals, the barium chloride hexahydrate and ammonium chloride were commercially available reagent grade chemicals; the basic magnesium carbonate was a Mallinckrodt analytical reagent containing less than 0.005% sulfate as an impurity; and the europium oxide was 99.9% purity. Assays were run on those materials where it was necessary to compensate for sorbed water. Appropriate proportions of the raw materials were dry blended in a Spex Mixer/Mill for 15 min to obtain starting mixtures. The blended mixtures were fired in a wet forming-gas atmosphere (80% nitrogen-20% hydrogen passed through water at temperatures around 50°C) at temperatures between 950° and 1250°C and times of from 1 to 4 hr. The particular combination employed depended on the flux combination and/or concentration. Lower temperatures and longer times were used when a concurrent double flux of NH_4Cl and $BaCl_2$ was used (*e.g.*, 4 hr at 1000°C) and higher temperature and shorter time when just a relatively small amount of NH_4Cl was employed (*e.g.*, 1 hr at 1200°C). After firing, the samples were cooled to near room temperature in the reducing atmosphere. Chemical analysis of phosphors prepared as described showed no chloride retained in the finished phosphor. This established chloride as a flux, influencing the luminescence of the phosphor produced and the course of the reaction yet not being incorporated in the matrix.

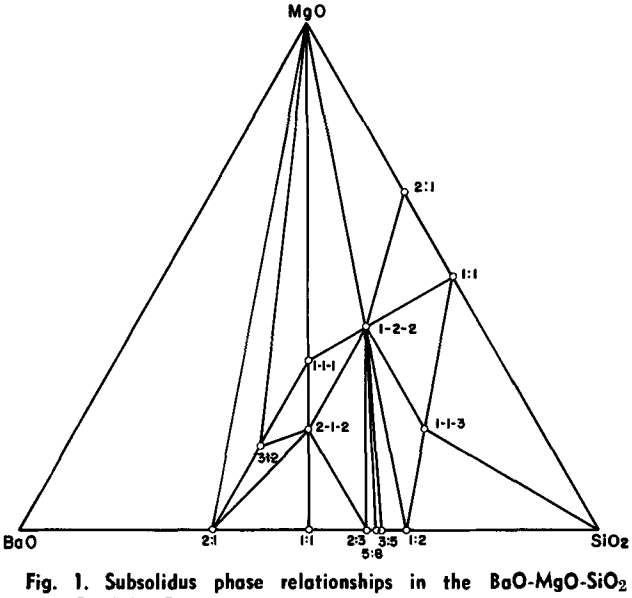

Fig. 1. Subsolidus phase relationships in the BaO-MgO-SiO_2 system. [Ref. (11)].

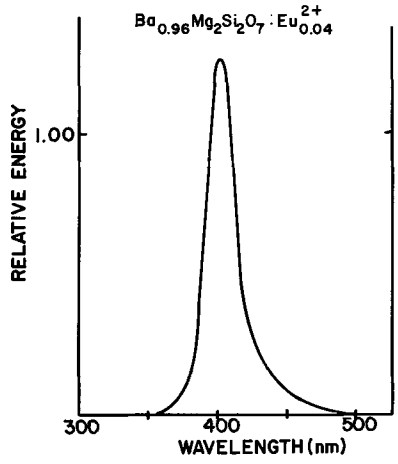

Fig. 2. Spectral energy distribution curve for $Ba_{0.96}Mg_2Si_2O_7:Eu^{2+}_{0.04}$ (2537Å excitation).

A Norelco diffractometer with filtered CuKα-radiation was used in phase identification for virtually every run on every sample. Excitation spectra were obtained with a modified Hitachi Perkin-Elmer fluorescence spectrophotometer, Model MPF-2A, which has been corrected for the output from the source. The emission spectra and peak height measurements were determined using equipment and techniques previously described by Eby (12). The luminescence intensities given in Fig. 2, 3, 4, 6, and 7 were obtained *vs.* $Zn_2SiO_4:Mn^{2+}$ (Relative Energy = 1.00) as a standard and are thus directly comparable.

Results and Discussion

Luminescent properties of $BaMg_2Si_2O_7:Eu^{2+}_{0.04}$.—When the 1-2-2 compound is prepared under equilibrium conditions (flux methods described in experimental section) and activated by divalent europium, a phosphor whose SED curve (254 nm excitation) is given in Fig. 2 is obtained. This phosphor responds to both long- and short-wavelength u.v. as well as to cathode-ray excitation giving an emission band peaking at 400 nm and a width at half height of 25 nm.

The peak wavelength of this phosphor is considerably less (~35 nm) than those obtained from compounds or crystalline solutions with a 3-1-2 stoichiometry (1, 5). These phases had previously yielded the shortest peak wavelengths of the alkaline earth silicates reported to date. Additionally, the luminescence intensity of this compound (1-2-2) at its peak wavelength is greater than the vast majority of the 3-1-2 phases at their particular peak wavelengths.

Luminescent properties of nonequilibrium preparations.—When equilibrium is not attained in synthesizing this phosphor (when no fluxing action is employed), an SED curve such as that given in Fig. 3 may be characteristic of the assemblage obtained. Three peaks are evident in the composite SED curve. Data from x-ray diffraction and u.v. microscope studies previously reported on by Bouchard (13) have been used to explain such a distribution. Employing these methods, the formation and identification of a reaction intermediate have been established. The intermediate phase,[1] $BaMgSiO_4:Eu^{2+}$, in many instances is difficult to detect in spectral energy data due to overlapping peaks, and in x-ray patterns due to the small amount present. This phase is immediately obvious when viewed under the u.v. microscope since its peak (440

[1] A 1-1-1 reaction intermediate was also observed in the synthesis of ternary compounds in the CaO-MgO-SiO_2 system by Drs. A. L. Smith and A. D. Power, of Radio Corporation of America, especially when the larger alkaline earth oxide to silica ratio in the blend was 1:2, as is the ratio in the present work.

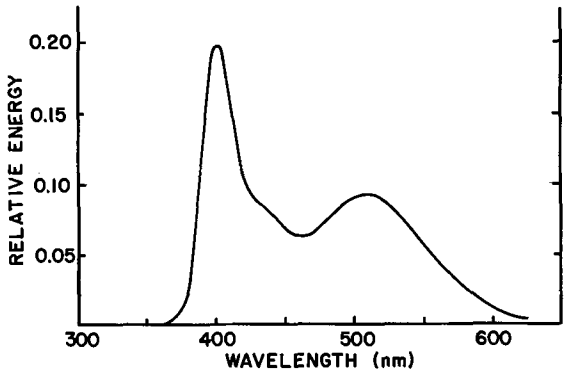

Fig. 3. Spectral energy distribution curve for a nonequilibrium assemblage (no flux employed in synthesis).

nm) is displaced approximately 40 nm from that of the violet peak of the major phase. In addition to the presence of this intermediate which may be detected as a shoulder in the emission peak in the violet region, a second, broader peak appears in the green region of the spectrum.

This is a much grosser effect than the one just described. This green emission was at first thought to be due to an additional secondary phase. Microscopic examination utilizing ultraviolet radiation showed the emission bands to be due to individual crystallites, rather than multiple emission from crystallites composed of intergrown phases. Thus crystallites giving rise to the individual emission bands could be separated. X-ray diffraction data taken on separated fractions showed only the (1-2-2) phase to be present, and the same degree of crystallinity, whether dominated by either green or violet emission. Thus these two emission bands are due to divalent europium in two different positions in the same lattice. The violet emission is attributed to the substitution of Eu^{2+} in Ba^{2+} sites. The green emission, which results from a metastable condition and can be removed by prolonged heating is possibly due to substitution of Eu^{2+} for Mg^{2+}, or more likely the incorporation of Eu^{2+} in structural holes in the lattice (as in feldspars).

An attempt was made to take advantage of the fact that $BaMgSiO_4:Eu^{2+}$ is formed as an intermediate when the constituent oxides are reacted. This compound and enstatite ($MgSiO_3$) were synthesized and reacted to form $BaMg_2Si_2O_7:Eu^{2+}$ according to the following reaction

$$BaMgSiO_4: Eu^{2+} + MgSiO_3 \rightarrow BaMg_2Si_2O_7:Eu^{2+}$$

Note that in Fig. 1 the product (the finished phosphor) lies on a binary join between these reactants.

Although a well-reacted product could be obtained at somewhat lower temperatures (100°-150°C) than required to react the constituent oxides (x-ray evaluation), the luminescence of these samples was considerably less (~50-60%) than that of the samples prepared from the oxide raw materials. An additional reaction, represented by another binary join in Fig. 1, between $BaSi_2O_5$ and MgO was also explored.

$$BaSi_2O_5:Eu^{2+} + 2MgO \rightarrow BaMg_2Si_2O_7:Eu^{2+}$$

Better results were anticipated here as syntheses involving silicate and oxide materials are generally considered to be more reactive than syntheses when the reactants are both silicates. However, the output of the phosphor prepared in this manner was only 25-30% of that prepared from the constituent oxides.

The two other schemes investigated involved reacting two silicates or an oxide and a silicate

$$BaSiO_3:Eu^{2+} + Mg_2SiO_4 \rightarrow BaMg_2Si_2O_7:Eu^{2+}$$
$$BaO:Eu^{2+} + 2MgSiO_3 \rightarrow BaMg_2Si_2O_7:Eu^{2+}$$

with the correct stoichiometries to yield the desired product. These proved to be even less successful.

Incorporation of other alkaline earth ions.—Since no (1-2-2) compound exists in either the CaO or SrO analogs of the $BaO-MgO-SiO_2$ system, varying compositions between compounds with analogous formulas is not a possibility. Attempted Ca^{2+} or Sr^{2+} substitution for Ba^{2+} in this matrix resulted in a decrease in the luminescence intensity in both instances. With Sr^{2+}, the drop is gradual up to the 0.20 atom fraction Sr^{2+} formulation, followed by a quite drastic decrease in the luminescence intensity for formulations containing greater Sr^{2+} concentrations. At the same time, an emission band from a secondary phase emerges at (460-470 nm) attributable to $Sr_2MgSi_2O_7:Eu^{2+}$. The appearance of this compound is easily rationalized, as no 1-2-2 compound forms in the $SrO-MgO-SiO_2$ system. The composition which corresponds to this stoichiometry falls in a three-phase field. The compound $Sr_2MgSi_2O_7$ is the only one efficiently activated by divalent europium. The other two phases are forsterite (Mg_2SiO_4) and enstatite ($MgSiO_3$) which are not efficiently activated by Eu^{2+} for exciting radiation between 180 and 320 nm.

When the incorporation of Ca^{2+} is attempted, the luminescence intensity again drops with increasing Ca^{2+} concentration, in this case in almost a continuous manner. The SED curves of these samples show the appearance of a new emission band at 445 nm due to the diopside ($CaMgSi_2O_6:Eu^{2+}$) secondary phase formed. Beyond 0.30 atom fraction calcium, the intensity of the 445 nm band also drops and a third band at 535 nm due to the formation of akermanite ($Ca_2MgSi_2O_7:Eu^{2+}$) results.

These observations again may be explained due to the nonexistence of a compound with the 1-2-2 stoichiometry in the $CaO-MgO-SiO_2$ system. Again formulating to this stoichiometry leads to a composition falling in a three-phase field where diopside ($CaMgSi_2O_6$), forsterite (Mg_2SiO_4), and akermanite ($Ca_2MgSi_2O_7$) are in equilibrium. The changes in the relative amounts of the phases, which can be efficiently activated by divalent europium, can thus be observed in the SED curves run on these samples. These data are intended only to show in a qualitative manner the detrimental effect on the luminescence intensity of attempted Ca^{2+} or Sr^{2+} substitution for Ba^{2+} in this matrix under the specific conditions of synthesis employed (4 hr at 1200°C).

Double activation with Eu^{2+} *and* Mn^{2+}.—The SED curve of the phosphor which results when both europium and manganese are incorporated as activators is given in Fig. 4. The emission from Eu^{2+} remains at 400 nm, and a new band appears at 690 nm due to emission from Mn^{2+}. The SED curve in Fig. 4 is for

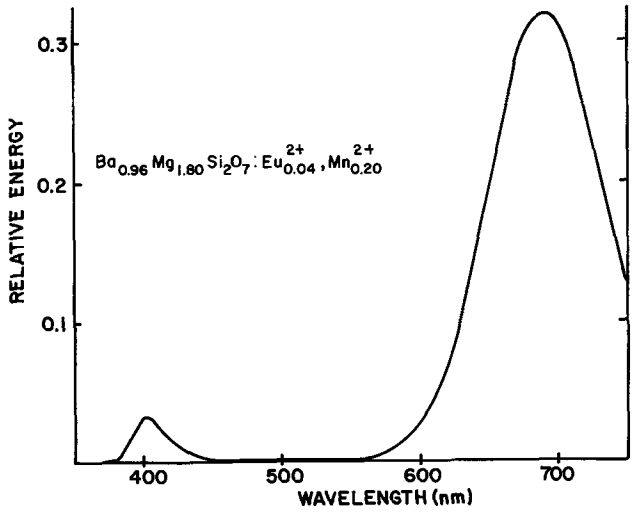

Fig. 4. Spectral energy distribution curve for the europium, manganese doubly activated phosphor, $Ba_{0.96}Mg_{1.80}Si_2O_7:Eu^{2+}{}_{0.04}$, $Mn^{2+}{}_{0.20}$.

the phosphor when the formulation allows for Eu^{2+} substitution for Ba^{2+} and Mn^{2+} substitution for Mg^{2+}. More detail of the effect on luminescence intensity of the substitution schemes which allow for the incorporation of the activator ions is given in a subsequent section of this paper.

Figure 5 presents the excitation spectra for emission peaked at 400 nm, in samples with Eu activator only, or 690 nm in those having Eu + Mn or Mn alone. Identity of the excitation spectra for the first two shows there is $Eu^{+2} \rightarrow Mn^{+2}$ energy transfer, while the third curve shows that direct excitation of Mn (sensitivity was increased 10 to 100 times over that used for the others to obtain this curve) is weak.

Effect of Mn^{2+} and Eu^{2+} concentrations on luminescence intensity.—The effect of varying the manganese concentration, as the Eu^{2+} is held constant, on the two emission bands is shown in Fig. 6. Data are given for two postulated substitution schemes.

(*A*) $Ba_{1-x-y}Mg_2Si_2O_7:Eu_x^{2+}, Mn_y^{2+}$

(*B*) $Ba_{1-x}Mg_{2-y}Si_2O_7:Eu_x^{2+}, Mn_y^{2+}$

In the series run covering both substitution schemes, x was held constant at 0.04, and y was varied from 0.10 to 0.50 in steps of 0.10. In the first scheme (*A*), maximum red emission at 690 nm, due to emission

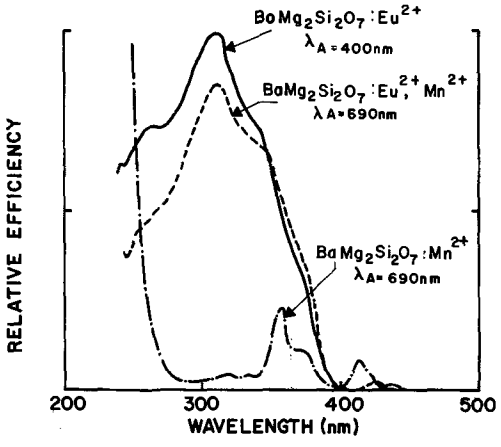

Fig. 5. Excitation spectra of $BaMg_2Si_2O_7:Eu^{2+}$, $BaMg_2Si_2O_7:Mn^{2+}$, and of the doubly activated phosphor $BaMg_2Si_2O_7:Eu^{2+}, Mn^{2+}$.

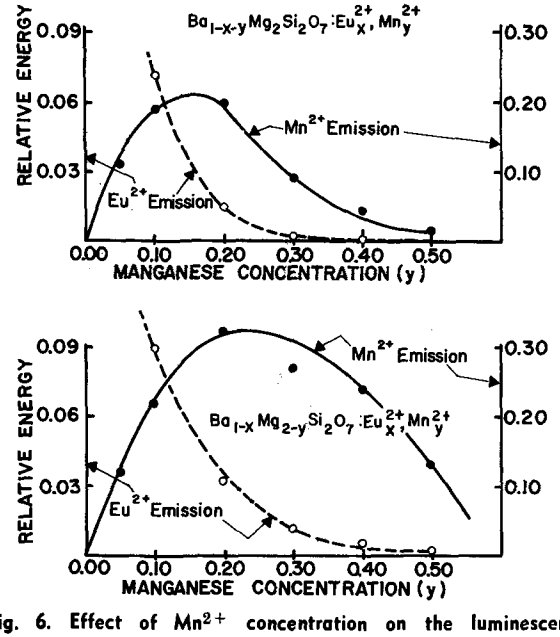

Fig. 6. Effect of Mn^{2+} concentration on the luminescence intensity according to two postulated substitution schemes, $Ba_{0.96-y}Mg_2Si_2O_7:Eu^{2+}{}_{0.04}, Mn^{2+}{}_y$, and $Ba_{0.96}Mg_{2-y}Si_2O_7:Eu^{2+}{}_{0.04}, Mn^{2+}{}_y$.

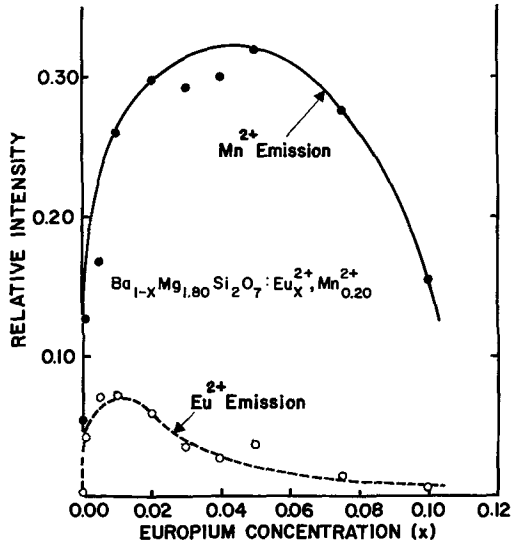

Fig. 7. Effect of Eu^{2+} sensitizer concentration, at optimum Mn^{2+} activator concentration, on the luminescence intensity of the phosphor $Ba_{1-x}Mg_{1.80}Si_2O_7:Eu^{2+}{}_x, Mn^{2+}{}_{0.20}$.

from manganese, occurs at $y = 0.10$-0.20 and falls off drastically at $y = 0.30$, probably due to concentration quenching. When a value of $y = 0.50$ is reached in this scheme, the typical emission bands as in Fig. 4 are extremely weak and some line emission from Eu^{3+} now appears. For the same substitutions made according to scheme (*B*), maximum red emission occurs for $y = 0.20$ and is 50% greater than the maximum achieved in scheme (*A*).

Even at $y = 0.50$ in scheme (*B*), substantial emission due to Mn^{2+} is realized. These results show that maximum red emission from manganese is realized in scheme (*B*) and intimate that manganese substitutes for magnesium rather than barium in this pyrosilicate phase. This scheme is more in line with simple crystal chemical considerations, such as ionic size and phase relations in magnesium silicate–manganese silicate systems.

The effect of varying that Eu^{2+} concentration when the Mn^{2+} is held at the optimum value is shown in Fig. 7. Initially, there is a rise in both europium and manganese emission. The initial rise in europium emission is due to improved u.v. absorption by the phosphor as the europium concentration is increased. The initial rises are followed by a decrease in europium and a further increase in manganese emission as the energy transfer process becomes more efficient. Finally, a decrease in both emissions as europium self-quenching sets in and less energy is available for transfer to manganese.

Acknowledgments

The author gratefully acknowledges the encouragement and valuable discussions during this investigation with Dr. K. H. Butler and Dr. M. J. B. Thomas. Appreciation is likewise extended to Mr. A. Rudis for the synthesis and spectral measurements on the samples and to Miss M. Skeadas for the x-ray diffraction data.

Manuscript submitted Aug. 18, 1969; revised manuscript received *ca.* Nov. 25, 1969. This was Paper 77 presented at the New York Meeting, May 4-9, 1969.

Any discussion of this paper will appear in a Discussion Section to be published in the December 1970 JOURNAL.

REFERENCES

1. G. Blasse, W. L. Wanmaker, J. W. ter Vrugt, and A. Bril, *Philips Res. Repts.*, **23**, 189 (1968).
2. G. Blasse, W. L. Wanmaker, and J. W. ter Vrugt, *This Journal*, **115**, 673 (1968).
3. G. Blasse, W. L. Wanmaker, and J. W. ter Vrugt, *ibid.*, **115**, 65*C* (1968).
4. T. L. Barry, *ibid.*, **115**, 65*C* (1968).

5. T. L. Barry, *ibid.*, **115**, 733 (1968).
6. T. L. Barry, *ibid.*, **115**, 1181 (1968).
7. R. K. Datta, "Proceedings of the 7th Rare Earth Research Conference," Vol. II, 585 (1968).
8. T. L. Barry, *This Journal*, **116**, 123C (1969).
9. W. A. McAllister and W. A. Thornton, *ibid.*, **116**, 123C (1969).
10. H. A. Klassens, A. H. Hoekstra, and A. P. M. Cox, *ibid.*, **104**, 93 (1957).
11. J. F. Argyle, Ph.D. Thesis, The Pennsylvania State University (1963); Univ. Microfilms (Ann Arbor, Michigan), Order No. 64-1378, 201 pp.
12. J. E. Eby, Paper 27 presented at Electrochem. Soc. Meeting, Toronto, May 3-7, 1964.
13. A. C. Bouchard, *This Journal*, **115**, 1279 (1968).

Effect of Water Vapor on the Combustion of Flash-Heated Beryllium Droplets[1]

Jack L. Prentice

Michelson Laboratories, Naval Weapons Center, China Lake, California

Corrosion and corrosion processes are of exceptional importance to both science and technology. In particular, oxide transport in the Be-BeO-H_2O system through corrosion processes is of importance in the fields of ceramics, nuclear reactor technology, and propellant combustion. The reaction

$$BeO_{(solid)} + H_2O_{(gas)} \rightleftharpoons Be(OH)_{2(gas)}; \quad \Delta H°_{298} = +42 \text{ kcal/mole} \quad [1]$$

is reported to be the principal process and is probably the one of importance here although there is as yet no spectroscopic identification of the gaseous species $Be(OH)_2$. The process has both advantages and disadvantages, depending on where it is encountered. In ceramics and nuclear reactor technology, oxide transport through corrosion processes results in damaged or destroyed apparatus (with possible dire consequences). In some industrial applications, the process is either employed to grow large BeO single crystals or to produce high-purity BeO of very fine crystallite size ($\sim 1\mu$). In propellant combustion, the mechanism of combustion of the beryllium metal additive can be changed by the presence of significant amounts of water vapor.

To this author's knowledge, no previous demonstration of oxide transport from burning beryllium droplets has been reported. Such a phenomenon is described in this communication.

When submillimeter diameter Be particles were burned at atmospheric pressure in air, carbon dioxide, or a mixture of 20% oxygen in argon, long, well-formed hexagonal whiskers of BeO were formed on the droplet surface during the intermediate phases of burning (1, 2). Continued oxidation accompanied by rising droplet temperature resulted in total encapsulation of the droplet by molten beryllia. Repetition of such experiments with the gases saturated with water vapor at room temperature results in the prevention of oxide accumulation on the droplet surface, and neither whisker formation nor encapsulation occurs.

In our combustion experiments, each Be particle, nominally 500μ in diameter, was prepared and ignited by exposing a small square of Be foil to the thermal pulse from a high-intensity xenon flash discharge lamp. In this technique, developed by Nelson (3), a metal foil, 1.6 mm on a side and 12.7μ thick, was permitted to fall freely through a glass reaction vessel in which an appropriate oxidizer was provided and whose top was surrounded by a helical quartz flash lamp. As the particle passed through the lamp area, the lamp was fired electrically and the foil ignited, forming a sphere. Individual burning particles were quenched on Pyrex plates at various distances from the flash lamp and withdrawn for study with a scanning electron microscope (SEM). By judicious sampling, a complete picture of the evolution of the burning particle geometry may be reconstructed.

Figure 1 is a composite of SEM photomicrographs sketching the evolution of particle geometry for Be burning in a dry oxygen-argon mixture. The figure shows random growth of ill-formed BeO on a spongy, unmolten Be substrate, growth of hexagonal whiskers of BeO on a molten droplet of Be (mp = 1556°K), and finally encapsulation of the Be droplet by molten BeO

[1] This work was sponsored by the National Aeronautics and Space Administration under NASA Work Order 6032.

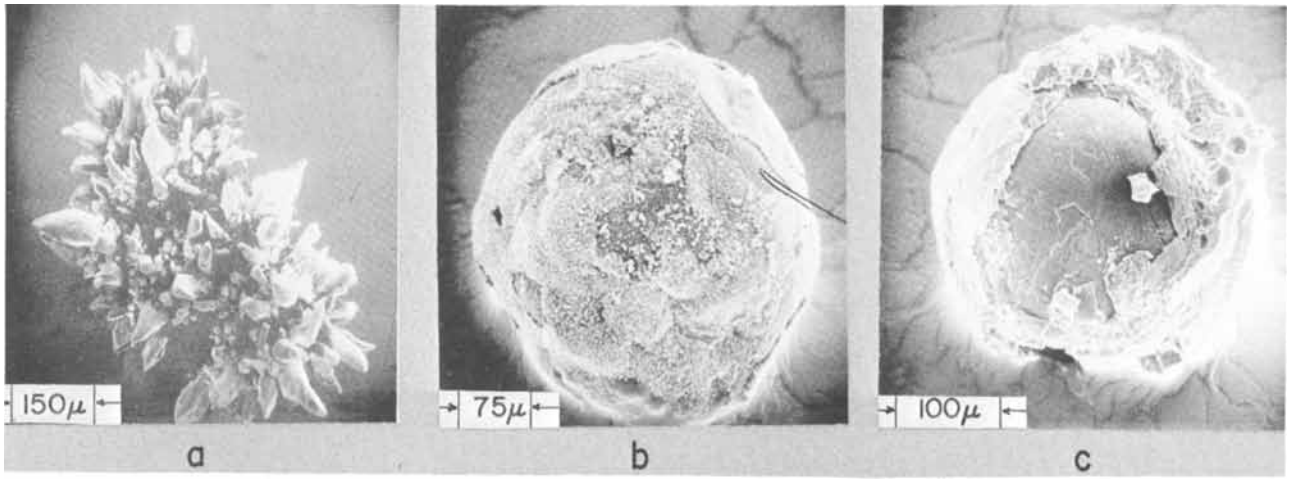

Fig. 1. SEM micrographs sketching the evolution of particle geometry for flash-ignited beryllium foil burning in a mixture of 20% oxygen-argon at 705 ±5 Torr. Particles quenched at (a) 20, (b) 30, and (c) 40 cm from the lamp.

(mp = 2820°K). Shortly after encapsulation, radiative heat loss from the extensive beryllia surface lowers the temperature enough to freeze the oxide, vapor phase combustion is terminated, and particle temperature decays to ambient. These specimens were quenched at 20, 30, and 40 cm from the lamp and represent burning times (*i.e.*, time from ignition to quench) of about 250-500 msec. Figure 1(c) shows a specimen in which the heavy surface oxide has fractured on cooling.

Optimum beryllium combustion proceeds by a vapor phase mechanism. The ambient temperature must therefore be kept high enough to keep the encapsulat-

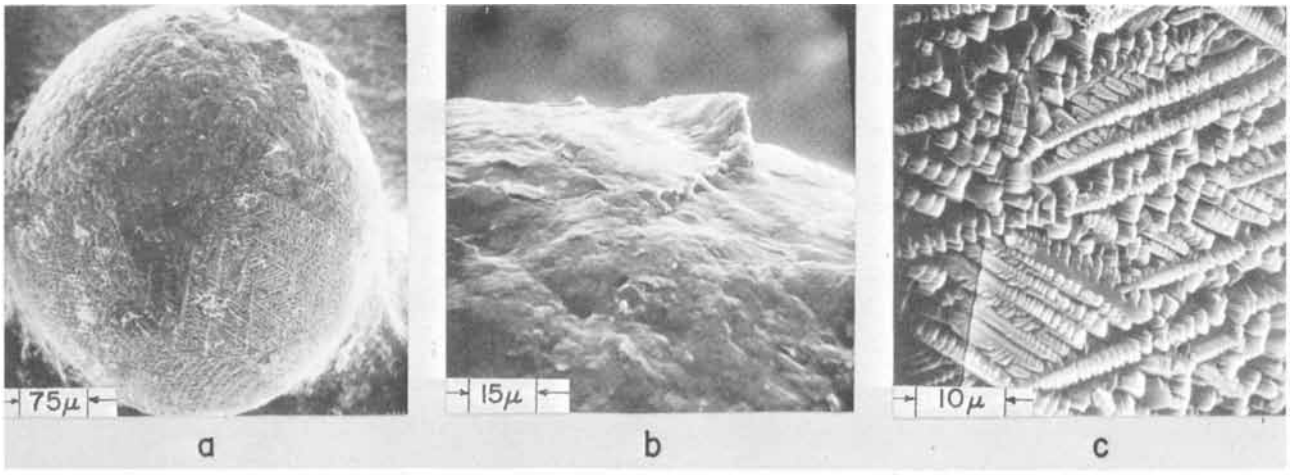

Fig. 2. SEM micrographs of flash-ignited beryllium particle quenched while burning in 1 atm of 20% oxygen-argon saturated with water vapor at 28°C. Note clean surface burning.

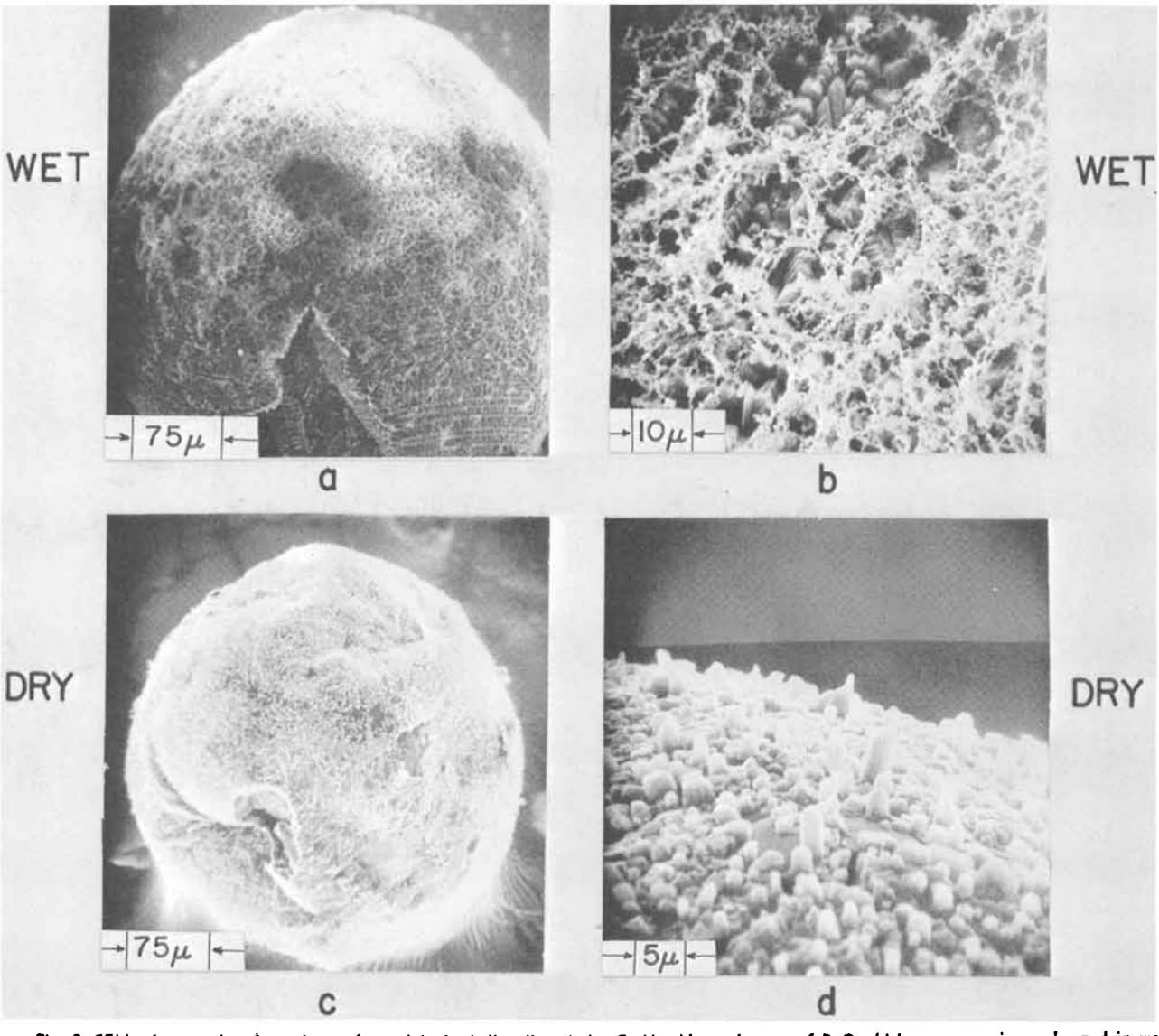

Fig. 3. SEM micrographs of specimens burned in both "wet" and dry O_2/Ar. Note absence of BeO whiskers on specimens burned in wet gas (a, b). Both specimens (a, c) quenched 30 cm from flash lamp.

ing oxide molten or the vapor phase combustion will be stifled and the droplet combustion will be forced to proceed *via* the much slower process of oxidizer diffusion through the oxide crust and subsequent surface reaction. Gulbransen and Andrew (4) have shown that the vapor pressure of beryllium may be reduced by as much as 100-fold by an oxide coating 0.4μ thick at 1200°K. Thus, oxide skins or films on burning beryllium particles similar to that in Fig. 1c, which may be as much as 50μ thick, must surely exert a retarding effect on combustion efficiency.

Figure 2 is a composite of SEM photomicrographs showing the effect of burning a beryllium particle in an oxygen-argon mixture saturated with water vapor. No trace of hexagonal whisker formation exists on specimens burned in the presence of water. When examined by low-power ($\sim$60X) optical microscopy, such specimens appear as shiny, bright metallic-looking spheres as contrasted with the opaque, milky-white oxide encapsulated specimens in Fig. 1. Figure 3 contrasts beryllium droplets quenched while burning in "wet" and dry oxygen-argon.

Douglas (5) has reviewed the high-temperature thermodynamics of the BeO-H_2O system and has postulated that higher gaseous hydrates of beryllium oxide may be important at high temperature. For example, he suggests that the trimer $(BeO)_3 \cdot H_2O$ is prevalent above about 1850°K. The analysis indicates that the JANAF thermodynamic data may be in error and that at temperatures above 2500°K there would be more BeO in the gas phase than indicated by the JANAF tables which assume $BeO \cdot H_2O$ to be the gaseous species. Douglas' analysis indicates that at 2000°K the partial pressure of $(BeO)_3 \cdot H_2O$ would be only about 10% of that of $BeO \cdot H_2O$, but at 3000°K the partial pressure of $(BeO)_3 \cdot H_2O$ would be 100 times that of the monomer $Be(OH)_2$.

The experiments reported here appear to lend support to the conclusions of Douglas. The specimen in Fig. 2 shows that no BeO has accumulated on the droplet surface indicating that BeO is being destroyed or removed at least as fast as it is being formed. The JANAF data indicate that this should occur only at temperatures $\geq$ 4500°K, and yet the physical condition of the quenched particles shown in the figures leads to the conclusion that the droplet temperature was somewhere between 1600° and 2800°K (between melting points of metal and oxide). Lack of oxide accumulation on the droplet as shown in Fig. 2 is difficult to reconcile with the reaction in Eq. [1] where only one BeO molecule is transpired by each water molecule. In view of the observed rate of oxide removal and the probable droplet temperature, it would appear that higher gaseous hydrates than the monomer are involved in the oxide transport processes during combustion of beryllium droplets in wet gases.

In reporting on a study of beryllium particle combustion in a flat-flame burner, Maček and Semple (6) report that addition of $\sim$ 1% water to their flame gases resulted in an increase of burning time of about 30%. The presence of water also resulted in lower droplet temperatures and narrower particle tracks than when burning in dry gases. Maček and Semple suggest that, despite the significant change in burning rate, only a slightly modified vapor phase diffusion model is adequate to describe the combustion. They leave open the cause of the flame zone contraction but suggest that it may be due to reduced vapor pressure of beryllium caused by an exceptionally heavy preignition deposit of oxide in the presence of water which persists during combustion. The quenched beryllium particles shown in Fig. 2 and 3 demonstrate that such is not the case. [For a more extensive discussion of this matter, *see* Ref. (7).]

Narrower particle tracks (relative to dry gases) and lower color temperatures are characteristic of flash-ignited beryllium droplets burning in wet gases. The reaction in Eq. [1] is endothermic by 42 kcal/mole and thus it or a similar reaction of the form

$$nBeO_{(c)} + H_2O_{(g)} \rightleftharpoons (BeO)_n \cdot H_2O_{(g)} \qquad [2]$$

should be a significant energy sink during droplet combustion in the presence of water vapor. Thus the oxide transport process is seen to have an effect on the flame temperature, flame radius, droplet geometry, burning rate, and burning mechanism.

Manuscript submitted Sept. 29, 1969; revised manuscript received *ca.* Dec. 22, 1969.

Any discussion of this paper will appear in a Discussion Section to be published in the December 1970 JOURNAL.

REFERENCES

1. J. L. Prentice, *J. Am. Ceram. Soc.*, **52**, 564 (1969).
2. J. L. Prentice, Preprint #69-2, Spring Meeting, Western States Section/The Combustion Institute, China Lake, Calif., April 28-30, 1969.
3. L. S. Nelson, *Pyrodynamics*, **3**, 121 (1965).
4. E. A. Gulbransen and K. F. Andrew, *This Journal*, **97**, 383 (1950).
5. T. B. Douglas, NBS Report 9389, p. 105, July 1966.
6. A. Macek and J. McK. Semple, "Proceedings, 12th Symposium (International) on Combustion, The Combustion Institute, Pittsburgh, Pennsylvania," p. 71 (1969).
7. J. L. Prentice and K. J. Kraeutle, NWC TP 4658, Naval Weapons Center, China Lake, Calif., Jan. 1969.

Epitaxial Growth of $GaAs_xP_{1-x}$ from the Liquid Phase

K. K. Shih*

IBM Thomas J. Watson Research Center, Yorktown Heights, New York

$GaAs_xP_{1-x}$ is a useful material because it emits visible light efficiently from p-n junctions (1). $GaAs_xP_{1-x}$ has been prepared in various ways such as by vapor transport in both closed-tube (2) and open-tube (3, 4) systems, and by horizontal Bridgman (5) and solution growth (6) methods. For a number of materials, the liquid phase epitaxial method of growth has produced grown-in p-n junctions of superior quality; for example, as evidenced by the improved luminescent properties in the case of GaAs (7), GaP (8), and $Ga_xAl_{1-x}As$ (9). In the present work, the liquid phase epitaxial method has been employed to grow single crystals in p-n junctions of $GaAs_xP_{1-x}$ on GaP single-crystal substrates. The growth parameters and some luminescent properties of the junctions are described.

The vertical growth method described by Rupprecht *et al.* (9) was employed. This method permits the

* Electrochemical Society Active Member.

formation of both sides of a p-n junction in a single cooling cycle. An alumina crucible charged with Ga, GaAs, and GaP was contained in a vertical quartz tube. For n-type growths, the donor dopant, Te, was added; the acceptor, Zn, was added for p-type growths. The epitaxial layers were deposited mostly on B($\bar{1}\bar{1}\bar{1}$) oriented GaP substrates supported on a graphite holder. GaP single-crystal substrates were grown by the solution growth method (10) and zone-bomb method (11). GaAs substrates have been tried but they dissolved in the melt which contains Ga, GaAs, and GaP during the growth process. High-purity forming gas was passed through the system prior to and during the overgrowth cycle. The layers deposited during cooling from 955° to 860°C.

The composition of the deposited layers was adjusted by varying the proportions of GaAs and GaP added to the melt. In order to form built-in p-n junctions, the first layer, an n-type layer about 2 mils thick, was deposited on an n-type substrate with carrier concentration about 10^{17} cm^{-3} by cooling from 955° to 900°C. Then the melt was counterdoped, with sufficient acceptor dopant to overcompensate the previous dopant, and cooling was continued to 860°C to produce a p-layer about 2 mils thick, then the substrate with deposit was lifted from the melt. It was found that the best results were obtained when the melt which contained Ga and different amounts of dissolved GaAs was "saturated" with GaP, depending on the desired composition, with none or a slight excess floating on the melt. It is recognized that this is not a true equilibrium since the melts are not stable in the presence of either of these pure components. This situation is generally encountered in liquid epitaxy experiments and pseudo-equilibrium appears to be achieved when the remaining undissolved solid becomes coated with a layer of the mixed compound, thus preventing further dissolution.

In order to establish the conditions for this pseudo-equilibrium, the take-up of GaP by melts containing various amounts of dissolved GaAs was measured. The experiment was similar to that reported by Hall (12) and the amount dissolved was determined by weight loss. The results at 945° and 955°C are shown in Fig. 1.

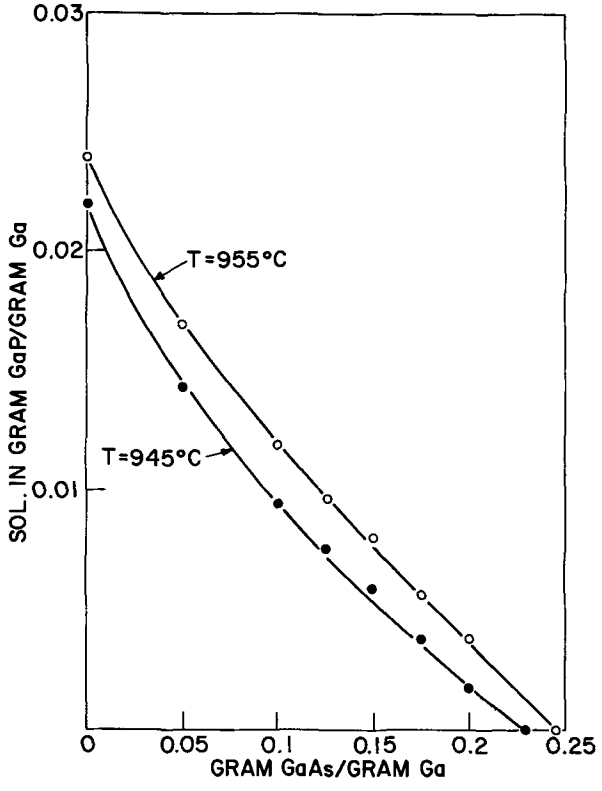

Fig. 1. Solubility of GaP in Ga-GaAs melt at 945° and 955°C

The information in Fig. 1 is helpful for determining the amount of GaAs and GaP which should be used in order to grow good GaAs$_x$P$_{1-x}$ p-n junctions.

The deposits had smooth surfaces when grown on either side of the (111) oriented GaP substrates, but material grown on the B($\bar{1}\bar{1}\bar{1}$) surface looks a little better. A terraced or sometimes coarse granular surface resulted if the substrate was off more than 1° from the (111) orientation. Microscopic examination of delineated p-n junctions revealed them to be quite planar, as shown in Fig. 2. By inspecting the color change of the crystal, it seems that the content of GaAs in the ternary alloy increased gradually along the direction of growth.

For the fabrication of electroluminescent diodes, the substrate side of the wafer was thinned to reduce series resistance, then Au-Sn and In-Zn alloy dots were applied to the n and p sides, respectively, of a small cleaved section in an atmosphere of flowing forming gas. The emission spectra were measured with a Bausch-Lomb monochromator. The quantum efficiency was measured with an integrating sphere type of apparatus, using Si photodiodes as detectors.

The electrical and optical properties of a large number of diodes were studied. No GaP-Ga(As, P) heterojunction was observed. The current-voltage characteristics of all diodes had the same general characteristics. The current varied as a function of voltage according to the equation $I = I_0\ (eV/\beta\ kT)$. In the linear region from $I = 10^{-4}$ mA to 5 mA at 300°K, $\beta = 2$ indicating that recombination is in the space-charge region (13).

The diodes emit light from the visible to the infrared range of the spectrum, with the peak energy depending on the composition of the melt from which the epitaxial layers were grown. For example, when 2g GaAs and 0.21g GaP were added to a 20g Ga melt, the resulting diodes emitted light with a peak at about 6800Å with about 70 meV width at 300°K as shown in Fig. 3.

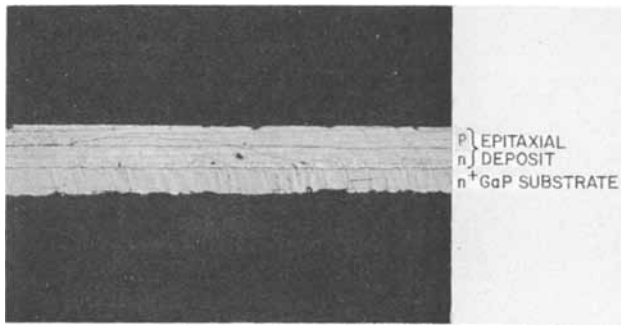

Fig. 2. Typical cross section of a GaAs$_x$P$_{1-x}$ p-n junction structure grown in GaP substrate cleaved and chemically stained to reveal the individual regions.

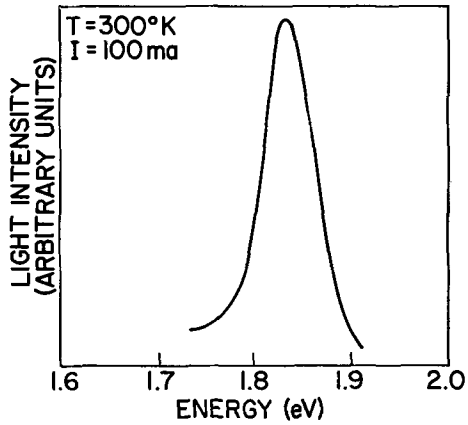

Fig. 3. Spectral distribution of the electroluminescence in GaAs$_x$P$_{1-x}$ diodes.

Because of the narrow width of this emission, it is identified as a band-to-band transition. An external quantum efficiency of about 5 x 10^{-4} at 6800Å at room temperature was measured. This increased by more than a factor of 10 at 77°K. The efficiency may improve by optimizing the doping profile.

Acknowledgments

The author thanks Messrs. R. J. Chicotka, J. Scardefield, and J. M. Woodall, who provided source materials and substrates, and Mr. J. DeGelormo for technical assistance.

Manuscript submitted Sept. 8, 1969; revised manuscript received Dec. 8, 1969. This was Paper 119 presented at the New York Meeting, May 4-9, 1969.

Any discussion of this paper will appear in a Discussion Section to be published in the December 1970 JOURNAL.

REFERENCES

1. *See*, for example, M. R. Lorenz, *Trans. Met. Soc., AIME*, **245**, 539 (1969).
2. N. Holonyak, Jr., D. C. Jillson, and S. F. Bevacqua, "Metallurgy of Elemental and Compound Semiconductors," p. 49, Interscience Publishers, New York (1962).
3. W. F. Finch and E. W. Mehal, *This Journal*, **111**, 814 (1964).
4. J. J. Tietjen and J. A. Amick, *ibid.*, **113**, 724 (1966).
5. N. Ainslie, M. Pilkuhn, and H. Rupprecht, *J. Appl. Phys.*, **35**, 105 (1964).
6. G. A. Wolff, H. E. LaBelle, Jr., and B. N. Das, *Trans. Met. Soc. AIME*, **242**, 436 (1968).
7. H. Nelson, *RCA Rev.*, **24**, 603 (1963).
8. M. R. Lorenz and M. Pilkuhn, *J. Appl. Phys.*, **37**, 4094 (1966).
9. H. Rupprecht, J. M. Woodall, and D. G. Pettit, *Appl. Phys. Letters*, **1**, 81 (1967).
10. L. M. Foster, T. S. Plaskett, and J. E. Scardefield, *IBM J. Res. Develop.*, **10**, 114 (1966).
11. S. E. Blum and R. J. Chicotka, *This Journal*, **115**, 298 (1968).
12. R. N. Hall, *ibid.*, **110**, 385 (1963).
13. C. T. Sah, R. N. Noyce, and W. Shockley, *Proc. IRE*, **45**, 1228 (1957).

Brief Communications

Oxidation Studies on Iron Using the Mössbauer Effect

D. A. Channing and M. J. Graham[1]

Central Electricity Generating Board, Berkeley Nuclear Laboratories, Berkeley, Gloucestershire, United Kingdom

This communication indicates the potential of Mössbauer spectroscopy for quantitative study of high-temperature oxidation processes on iron. In particular, we describe experiments concerning the formation at 500°C of the duplex scale Fe_3O_4 and α-Fe_2O_3.

Johnson-Matthey iron foils of purity 99.9 + % and thickness 9.5 μm were used. Oxidation was performed in one atmosphere of high purity oxygen (B.O.C. grade X). Mössbauer absorption measurements were made on the starting foils and after specified oxidation periods. The spectrometer, a "constant acceleration" instrument, employed a Co^{57}/Pd single-line source and a NaI (Tl) scintillation detector. All spectra were determined with both source and absorber at room temperature using a fixed counting arrangement. Background radiation was essentially unchanged between measurements and $\simeq$ 20% of the recorded counts.

By reference to standard spectra of Fe^{57} in Fe_3O_4 and α-Fe_2O_3, the presence of the two oxides in the scale is immediately established from the measured spectrum. The relative quantities of the oxides, and of unused metal, are obtained from the respective intensities of absorption. Taking n_i as the areal density of Fe^{57} (atoms · mm^{-2}) in the i^{th} component, we may write (1)

$$n_i = kA_i/f_i$$

where A_i is the corresponding total absorption area corrected (upwards) for "saturation effects," f_i is the recoil-free fraction, and k is a constant. The f_i factors are not expected to differ greatly, and our experiments confirm this. Saturation corrections range up to $\simeq$ 15% and may be estimated from tables (2). Thus, roughly, the relative number of resonant atoms in the three components is simply the ratio of observed absorption intensities.

Measurements are presented in Fig. 1-3. Included are the line positions, indexed 1, 2, 3, ..., of the individual components. The spectra for iron and α-Fe_2O_3 are single Zeeman patterns of six lines [ref. (3) and (4, 5), respectively]. For Fe_3O_4, the spectrum comprises two superposed Zeeman patterns which are incompletely resolved (6-8). The first has lines at 1, 3, 5, 7, 9, and 10, the second at 2, 4, 6, 8, 9, and 10.

Figure 1 shows the simultaneous growth of the two phases. The spectra are for a foil oxidized for successive periods up to a total of $\simeq$ 31 hr, by which time most of the metal is consumed. The course of oxidation is best followed by lines α-Fe_2O_3 1, Fe_3O_4 1 and 2, and Fe 1. At all stages, Fe_3O_4 is the major oxide. With continued oxidation, the source of metal is exhausted and the flow of iron to the reaction zone stops. The oxidation of Fe_3O_4 to α-Fe_2O_3 can then be directly investigated and results are displayed in Fig. 2. No metal is detected at $\simeq$ 77 hr, and at $\simeq$ 395 hr the conversion to α-Fe_2O_3 is almost complete. Analogously, if the oxygen supply is cut off once a scale has formed, the reduction by iron of α-Fe_2O_3 to Fe_3O_4 can be directly studied. Thus, in Fig. 3, spectrum (a) was obtained for a foil oxidized 18 hr, and spectrum (b) after a subsequent 1 hr vacuum anneal ($< 10^{-5}$ Torr). Referring to lines α-Fe_2O_3 1 or 6, a marked decrease in α-Fe_2O_3 is clearly evident after the anneal.

Spectral areas are determined as follows. First, we assume that the relative line intensities within each Zeeman pattern remain unaltered throughout the ex-

[1] Present address: Division of Chemistry, National Research Council, Ottawa, Ont., Canada.

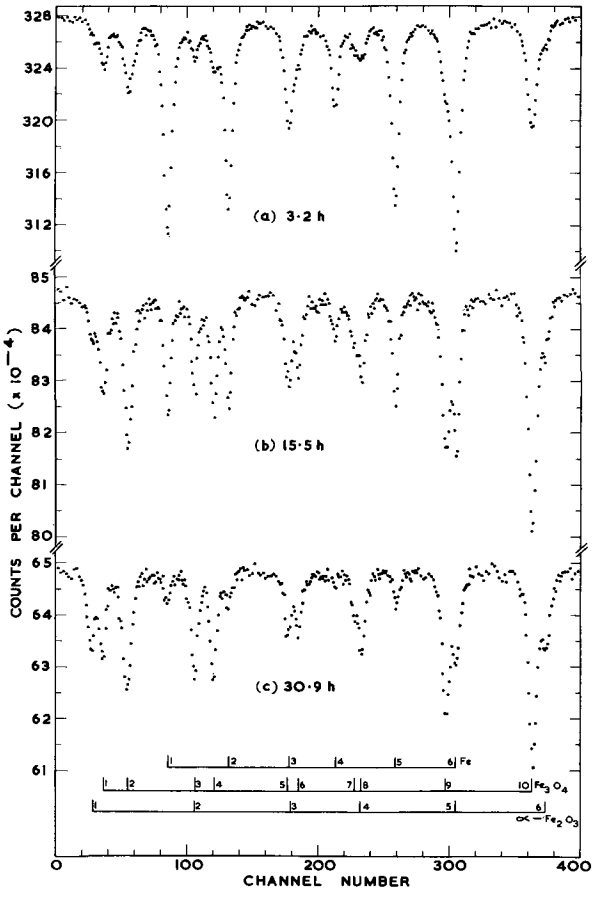

Fig. 1. Mössbauer spectra of a 9.5 μm iron foil heated in 1 atm of oxygen at 500°C for the times specified. Background radiation is not subtracted.

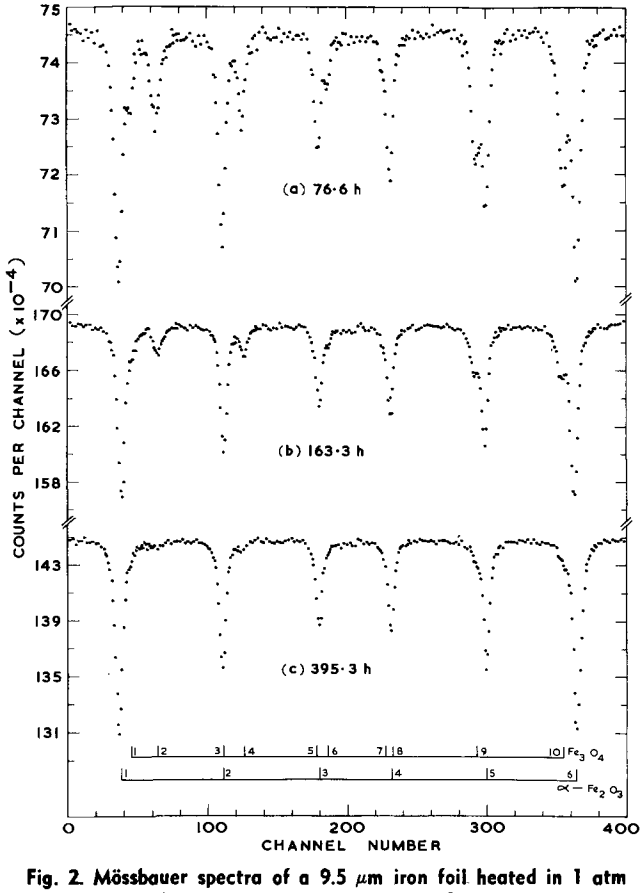

Fig. 2. Mössbauer spectra of a 9.5 μm iron foil heated in 1 atm of oxygen at 500°C for the times specified. (Continued oxidation of the foil used in Fig. 1.) Background radiation is not subtracted.

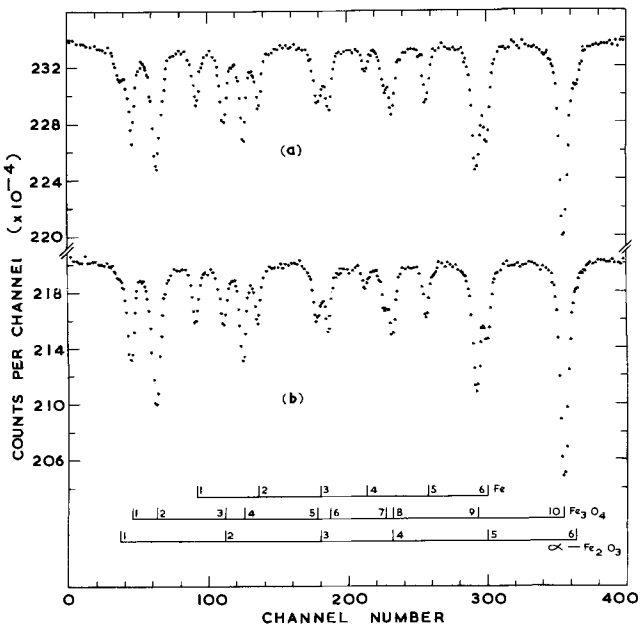

Fig. 3. Mössbauer spectra (a) for a 9.5 μm iron foil heated in 1 atm of oxygen at 500°C for 18 hr, and (b) after a subsequent 1 hr vacuum anneal (also at 500°C). Background radiation is not subtracted.

periments. This appears to be a reasonable assumption. [Significant variations are expected only if major changes in magnetization occur (3). Saturation effects will introduce some variation, but this is small and would not easily be detected.] Having established these ratios, the total absorption areas are then derived by analyzing only the outer most intense lines, specifically Fe 1, Fe_3O_4 10, and α-Fe_2O_3 1 or 6. The ratios adopted (2.7 : 2.2 : 1.0 : 1.0 : 2.2 : 2.7 for iron, 2.7 : 1.5 : 1.0 : 1.0 : 1.5 : 2.7 for both Fe_3O_4 and α-Fe_2O_3) are based upon detailed analysis of the two initial metal spectra, spectrum (c) of Fig. 2 which shows virtually only α-Fe_2O_3, and spectrum (b) of Fig. 3 showing predominantly Fe_3O_4 but also metal. These same four spectra are also used for checking the variation of f_i factors. Thus, noting that the total number of Fe^{57} atoms in a given foil is constant, equations of the type

$$\Sigma_i (A_i/f_i) = A_o/f_{Fe}$$

are solved, where A_o is the corrected starting metal absorption. We find $f_{Fe} : f_{Fe_3O_4} : f_{\alpha\text{-}Fe_2O_3} = 1 : 1.15$ ($\pm$0.15) : 1.20 ($\pm$0.12). Visual curve fitting is employed throughout the analysis, and the absorption of a line is taken as depth times half-width.

More detailed experiments on growing iron oxide films, at temperatures 400°-550°C, are in progress. Our main aim is to provide data for the diffusion of iron ions through Fe_3O_4 and of oxygen ions through α-Fe_2O_3. In preliminary experiments at 700°C, three phase scales of FeO, Fe_3O_4, and α-Fe_2O_3 have been observed and analyzed.

Acknowledgment

This note is published by permission of the Central Electricity Generating Board.

Manuscript submitted July 28, 1969; revised manuscript received Nov. 17, 1969.

Any discussion of this paper will appear in a Discussion Section to be published in the December 1970 JOURNAL.

REFERENCES

1. A. H. Muir, Jr., "Mössbauer Effect Methodology," Vol. 4, p. 75, I. J. Gruverman, Editor Plenum Press, New York (1968).
2. G. Lang, *Nucl. Instr. and Methods*, **24**, 425 (1963).
3. R. S. Preston, S. S. Hanna, and J. Herberle, *Phys. Rev.*, **128**, 2207 (1962).

4. O. C. Kistner and A. W. Sunyar, *Phys. Rev. Letters*, **4**, 412 (1960).
5. F. Van Der Woude, *Phys. Stat, Sol.*, **17**, 417 (1966).
6. R. Bauminger, S. G. Cohen, A. Marinov, S. Ofer, and E. Segal, *Phys. Rev.*, **122**, 1447 (1961).
7. F. Van Der Woude, G. A. Sawatzky, and A. H. Morrish, *ibid.* **167**, 533 (1968).
8. J. M. Daniels and A. Rosencwaig, *J. Phys. Chem. Solids*, **30**, 1561 (1969).

Anodic Oxidation of InSb in Nonaqueous Electrolytes

L. C. Brennan*[1] and N. J. Gri[2]

Avco Laboratories, Cincinnati, Ohio

The anodic oxidation of InSb in aqueous electrolytes has been extensively investigated by Dewald (1). This system was chosen by Dewald because InSb has the zinc blende structure which does not have a center of inversion and thus anodization rates on (111A) and (111B) faces are different. During work carried out at Avco Laboratories, it was found that, at current densities greater than 1 mA/cm^2, anodic oxidation was limited to a film thickness of ~1200Å when the anodization was carried out in an aqueous electrolyte. If anodization was continued to higher voltages, the anodic film began to break down and a black oxidation product was formed. In an attempt to grow thicker films at higher current densities, the anodic oxidation of InSb in nonaqueous or largely nonaqueous electrolytes has been investigated. This report constitutes the initial results of this investigation.

Some of the solutions investigated were: (*a*) n-methylacetamide/KOH, (*b*) tetra-hydro-furfuryl alcohol/KOH, and (*c*) ethylene glycol/sodium tetraborate/H_2O (90% ethylene glycol, 5% $Na_2B_4O_7$. $10H_2O$, 5% H_2O).

The InSb used was supplied by Cominco American Incorporated and was n-type, tellurium doped with a carrier concentration of 1 x 10^{15} at 77°K.

The slices were approximately 1 in. in diameter by 25 mils thick cut parallel to the (111) plane. The B surface was lapped and the A surface was polished to a smooth surface using 3/10μ alumina. Just prior to anodization, the wafers were etched in a 10% solution of HNO_3 in lactic acid for 5 min.

It was found that for all the electrolytes studied, at current densities greater than 1 mA/cm^2, anodization could be carried out to much greater thicknesses than is the case for aqueous electrolytes. For example, at current densities of 1.5 mA/cm^2, it was found that breakdown of the anodized layer occurred at ~1200Å, whereas, for the same current density, breakdown of the anodized layer did not occur up to 5000Å when the films were formed in a solution of sodium pentaborate in ethylene glycol (Soln. C). A possible explanation of the fact that anodization can be carried out to greater thicknesses in nonaqueous electrolytes could be that in nonaqueous electrolytes an outer porous film is formed on an inner compact layer as is the case for the anodization of aluminum. To check this possibility, the nature of the surface was examined using surface replica electron microscopy. The surface replicas were prepared by the colloidal stripping method. Several areas of the sample had a surface structure consisting of a high density of hillocks. However, at the magnifications used (16, 500, X) no evidence of porosity was obtained. No patterns were obtained when this material was examined by electron diffraction indicating that the material is amorphous.

Electrical measurements were taken on the anodized InSb surface using the metal-oxide-semiconductor (MOS) method (2). MOS test units were made by evaporating chromium over the oxide and alloying indium to the back for an ohmic contact. Some of the evaporated surface electrodes were kept less than 100Å thick to allow testing for light-induced surface potential shifts which have been observed (3-5) in thin anodic oxides formed in aqueous electrolytes.

The capacitance-voltage characteristics were obtained at 77°K using a capacitance bridge operating at 1 MHz. A positive interface charge Q_{ss} was observed on all samples. Measured values of Q_{ss}/q were 1-8 x 10^{11} cm^{-2}, showing similarity to those reported by Chang and Howard (6) for thin anodic oxides formed in aqueous electrolytes.

A significant difference has been observed in that light-induced surface potential shifts did not occur in the thick oxides formed in nonaqueous electrolytes. This observation was made in all cases where the MOS samples were strongly illuminated with zero, positive, or negative voltages applied to the surface electrode, in contrast to reported (3-5) surface potential shifts under the same conditions for thin oxides. These results indicate that photon absorption and charge buildup occur within the oxide and not at the semiconductor interface.

Acknowledgments

This work was sponsored in part by the Air Force Material Laboratory, Research and Technology Division, Air Force Systems Command, U.S. Air Force, under Contract Number F3361567C1005.

Manuscript submitted July 14, 1969; revised manuscript received Nov. 17, 1969.

Any discussion of this paper will appear in a Discussion Section to be published in the December 1970 JOURNAL.

* Electrochemical Society Active Member.
[1] Present Address: Fairchild Semiconductor, Mountain View, California.
[2] Present Address: TRW Semiconductor, Lawndale, California.

REFERENCES

1. J. F. Dewald, *This Journal*, **104**, 244 (1957).
2. A. S. Grove, B. E. Deal, E. H. Snow, and C. T. Sah, *Solid State Electronics*, **8**, 145 (1965).
3. R. K. Mueller and R. L. Jacobson, *J. Appl. Phys.*, **35**, 1524 (1964).
4. N. J. Gri, Am. Phys. Soc. Solid State Physics Mtg., Berkeley, March 17-19, 1968.
5. N. J. Gri and L. C. Brennan, Recent News Papers, Boston Meeting of the Society, May 5-9, 1968.
6. L. L. Chang and W. E. Howard, *Appl. Phys. Lett.*, **7**, 210 (1965).

JOURNAL OF THE ELECTROCHEMICAL SOCIETY

ELECTROCHEMICAL TECHNOLOGY

MARCH 1970

Passivation Phenomena and Potentiostatic Corrosion in Molten Alkali Metal Carbonates

H. J. Davis* and D. R. Kinnibrugh

Research Laboratories, Ferranti-Packard Limited, Toronto, Ontario, Canada

ABSTRACT

Potentiostatic corrosion rates of certain metals and alloys in molten carbonates at 680°C have been studied under both partially and fully immersed conditions using a variety of gas atmospheres above the melt. Measurements were made within the range 0.00 to −1.00V *vs.* Au/(O_2 − CO_2) 1:2 reference electrode. Of particular interest was the resistance to corrosion of ferroaluminum-type alloys. These materials have been successfully tested in working molten carbonate fuel cells under conditions where contact between the corrosive electrolyte and a supporting member is unavoidable.

The purpose of this investigation was to determine the suitability of certain metals for structural parts of molten carbonate fuel cell assemblies. In the past, the only materials exhibiting sufficient long-term resistance to the melt have been those based on high-temperature sintered oxides, namely alumina and magnesia. However, these materials are fragile and show poor resistance to thermal shock. From the mechanical point of view, metals would offer many advantages. Up to the present time, most metals have exhibited high corrosion rates when exposed to molten carbonates. Janz and co-workers (1-3) have investigated certain materials for corrosion resistance including the noble metals and some of their alloys and, in addition, nickel, 304 and 347 stainless steels, and silver. The noble metals exhibit a varying amount of resistance to the melt, but are not suitable from the cost point of view. Nickel and, to a lesser extent, 304 and 347 stainless steels are corroded by molten alkali metal carbonates, but some degree of passivation was observed in our measurements. The degree of protection afforded, however, has proved to be insufficient to warrant their use for structural components of molten carbonate fuel cells. Nevertheless, the fact that passivation was observed led us to suspect that other materials were well worth investigating in this respect, especially as certain metal oxides (*e.g.*, alumina) are very resistant to molten carbonates. For this reason, we included some commercial ferroaluminum alloys in our study.

Experimental

The standard technique for obtaining potentiostatic corrosion current densities for metals was adopted. The potentiostat used was a Wenking Model 6622 TRH, and the potential scan was generated by a Wenking motor potentiometer, MP 0.64. The current was recorded by monitoring the voltage drop across a standard resistor by means of either an X-Y recorder (Mosely Model No. 7000 A), or a digital voltmeter. Some details of the electrochemical cell used for these studies are shown in Fig. 1. The reference electrode was of the type described by Borucka (4). The counterelectrode consisted of gold foil spot-welded to gold wire. The crucible containing the melt, the gas pipes, and the various parts of the reference electrode were all of high-purity sintered alumina. The gas atmosphere over the melt could be controlled. The reference electrode was fed continuously with a gas mixture consisting of 67 m/o carbon dioxide and 33 m/o oxygen. The reference electrode assembly was connected to the bulk of the electrolyte by an electrolyte film on the concen-

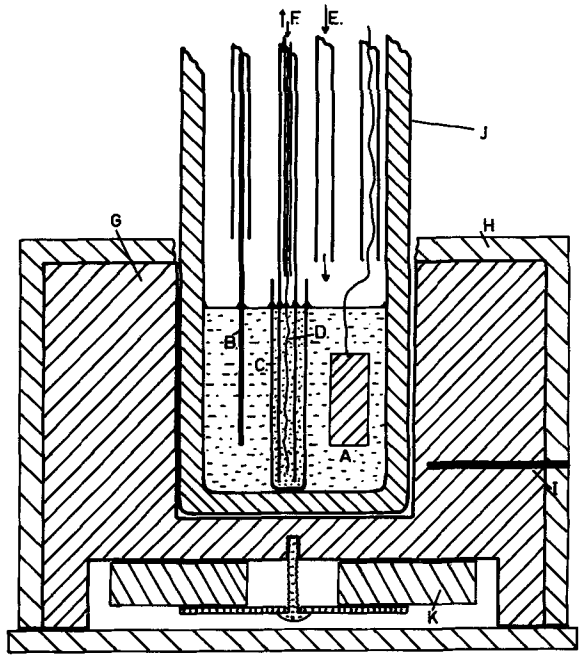

Fig. 1. Apparatus for potentiostatic polarization studies in molten carbonates: A—gold counterelectrode, B—working electrode, C—alumina crucible separator, D—gold reference electrode, E—atmosphere inlet, F—O_2-CO_2 supply for reference electrode, G—stainless steel furnace body, H—thermal insulation, I—thermocouple, J—alumina crucible, K—heater.

* Electrochemical Society Active Member.
Key words: molten carbonate fuel cells, corrosion.

tric alumina separating crucible, C. This was done to avoid the possibility of contamination of the electrolyte in the reference electrode compartment by corrosion products from the test sample. The cell assembly was so arranged that only gold, recrystallized pure alumina, and the test sample were in contact with the melt. This consisted of a binary eutectic mixture of analytical-grade sodium and lithium carbonates. The test sample took various forms which ranged from 0.06 in. diameter wire to strip cut from rolled sheet. The area of immersion of the samples was of the order of 1 cm^2. The samples were cleaned with abrasive paper no finer than 400 grit. No attempt was made to obtain a high degree of finish on the test samples, as the main object was to establish their suitability for structural components of molten carbonate fuel cells.

Table I shows the composition of certain of the metals investigated. These alloys are based on either iron or nickel, with their high-temperature oxidation controlled by formation of chromium or aluminum oxides. The samples were first investigated while completely submerged in the melt. The material under test was spot-welded to 0.01 in. diameter gold wire and the sample was completely immersed such that the meniscus was in contact with the gold wire. In this case, the atmosphere above the melt was continuously swept with a mixture of dry air containing 1% carbon dioxide.

Further measurements were made with corrosion samples only partially submerged in the melt. Under these conditions, the observed currents were strongly dependent on the nature of the gas atmosphere above the melt and reproducible measurements were obtained for oxidizing, neutral, and reducing atmospheres.

Results and Discussion

Measurements with fully submerged samples.—Some of the results obtained under these conditions are seen in Fig. 2. The scan rate was approximately 60 mV/hr. This is a realistic compromise since the traverse should actually be carried out infinitely slowly. The curves were quite reproducible and for the resistant alloys were unaffected by the position on the potential scale from which the scan was started, provided that a short period (typically ¼ hr) was allowed for equilibration. The curves were also unaffected by the direction of scan. The apparent high degree of reversibility at these scan rates can be attributed to the fact that the number of coulombs associated with the formation of a protective oxide film becomes small compared with the product of the background current and time. At high sweep rates (10-150 V/hr), hysteresis was expected and observed. Departure from ideality was considered to be small for sweep rates of 60 mV/hr. The scale of Fig. 2 was chosen to show a direct comparison with the passivation phenomena observed for 347 stainless steel. Nickel is included as a guide to the extent of corrosion which can be observed. It is apparent that certain of the alloys exhibit superior corrosion resistance when compared with either 347 stainless steel or nickel. The exact nature of the surface species restricting corrosion of the samples was not determined, although for the Kanthal and Hoskins alloys it is quite probable that this is an alumina film or reaction products of alumina with the melt, *e.g.*, lithium aluminate.

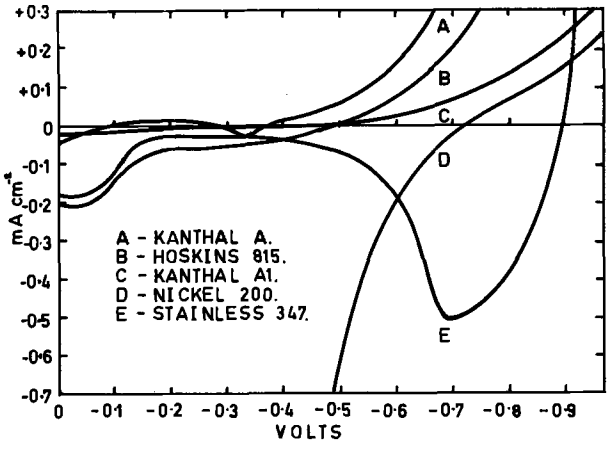

Fig. 2. Potentiostatic polarization curves for fully submerged samples, binary sodium, lithium carbonate eutectic, 680°C.

The open-circuit potential of fully submerged Kanthal A-1 in a binary sodium and lithium carbonate eutectic at 680°C with respect to the gold/oxygen plus carbon dioxide (1:2) reference electrode was also investigated. The voltage between the sample and the reference electrode fell quite rapidly initially and continued to decrease for approximately 6 hr at which time a final potential of approximately —71 mV for the Kanthal A-1 was obtained. This is close to the meniscus potential which might be expected for the gold supporting wire with the particular gas atmosphere present above the melt and suggests complete passivation of the Kanthal. The sample remained mirror-bright after 40 hr of exposure.

In Fig. 3, the alloy Kanthal A is shown. A number of 0.01 in. diameter wires were embedded in a paste mixture of molten carbonate and an inert filler, and heated at 700°C for more than 1000 hr. The wires were not connected to an external circuit, no polarization being applied. This represents a practical utilization of corrosion resistant metals in molten carbonate fuel cells in that the wires were used to reinforce the paste electrolyte and improve its resistance to mechanical and thermal shock prior to melting. It is apparent that the depth of corrosion is hardly significant and, in fact, this wire could not be distinguished from a sample which had not been exposed to the melt.

Based on the assumption that the corrosion rate of totally immersed samples is directly measured by the current density observed, the data in Table II were obtained. The rate of attack was predicted by assuming

Table I. Nominal composition of certain metals investigated

	Fe	Ni	Cr	Co	Al	C	Mn	Si	Ti	Cu	Other
Kanthal A1[1]	Bal.	—	22.0	0.5	5.5	—	—	—	—	—	—
Kanthal A[1]	Bal.	—	22.0	0.5	5.0	—	—	—	—	—	—
Hoskins 875[2]	Bal.	—	22.5	—	5.5	0.1	—	0.5	—	—	—
Hoskins 815[2]	Bal.	—	22.5	—	4.6	0.1	—	0.5	—	—	—
347 S. S.	Bal.	11.0	18.0	—	—	0.1	2.0	1.0	—	—	Cb-Ta 10xC
321 S. S.	Bal.	11.5	18.0	—	—	0.1	2.0	1.0	5xC	—	—
310 S. S.	Bal.	20.5	25.0	—	—	0.3	2.0	1.5	—	—	—
Nikrothal 80[1]	—	Bal.	20.0	—	—	—	—	—	—	—	—
Duranickel 301[3]	0.1	Bal.	—	—	4.5	0.2	0.2	0.5	0.5	—	—
Hastelloy X[4]	18.0	Bal.	22.0	1.5	—	0.1	—	—	—	—	Mo, 9.0, W, 0.6
Hastelloy N[4]	5.0	Bal.	7.0	0.2	0.2	—	0.8	1.0	0.3	0.3	Mo, 17.0, W, 0.5
Nickel 200[3]	0.1	Bal.	—	—	—	0.1	0.2	0.1	0.1	—	—

[1] The Kanthal Corp., Wooster St., Bethel, Conn.
[2] Hoskins Manufacturing Co., 4445 Lawton Ave., Detroit, Mich.
[3] The International Nickel Co. of Canada, Ltd., 55 Yonge St., Toronto 1, Ont., Canada.
[4] Union Carbide Corp., Materials Systems Division, Stellite Works, Kokomo, Ind.

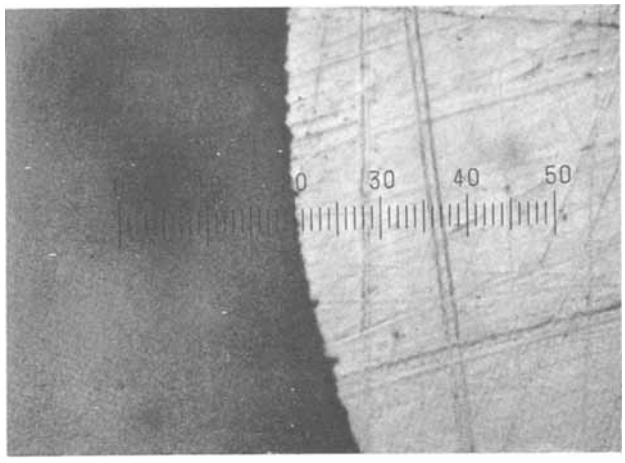

Fig. 3. Cross section of 0.010 in. diameter Kanthal A wire after 1000 hr in 53% lithium aluminate plus ternary sodium, lithium, potassium carbonate eutectic paste at 700°C (1 div = 2×10^{-5} in.).

that the observed current was entirely due to the conversion of iron to the ferrous state. The corrosion rates at two potentials representing approximately the working potentials of the anode and the cathode are given. It is seen that Kanthal A and A1 and some of the other alloys are superior to 347 stainless steel. For samples with low corrosion currents (*e.g.*, Kanthal), the current due to corrosion of the alloy becomes comparable to the current due to the gas reaction.

$$2e + CO_2 + \tfrac{1}{2} O_2 \rightleftharpoons CO_3^{2-}$$

occurring at the meniscus of the 0.01 in. diameter gold supporting wire and actual corrosion rates cannot be estimated with any degree of accuracy. It seems probable, however, that fully submerged Kanthals can have an even lower corrosion rate than those indicated in Table II, since samples which had been exposed under open-circuit conditions at the rest potential remained untarnished for long periods.

Measurements with partially submerged samples.— The highly satisfactory results obtained with certain alloys in the completely submerged condition led to the investigation of their performance in situations more closely akin to those found in some structural components of molten carbonate fuel cells. Under these conditions, they could be in contact both with electrolyte and gaseous phases. The potentiostatic corrosion curves were therefore obtained for samples which were only partially submerged, the unsubmerged portions being exposed to various gas atmospheres. The atmospheres used were either oxidizing (*e.g.*, oxygen/carbon dioxide mixtures), inert (either nitrogen or helium), or reducing (carbon dioxide, nitrogen, hydrogen mixtures), and always contained at least 1% carbon dioxide to limit decomposition of the melt. The total pressure of the gas atmosphere was maintained fractionally greater than the atmospheric pressure.

Table II. Estimated corrosion rates (mm/yr) for fully submerged materials at the electrode working potentials. (Binary sodium, lithium carbonate eutectic, 680°C.)

Metal/alloy	− 850 M. V.	− 100 M. V.
Kanthal A	0	0.02
Kanthal A1	0	0.16
Hoskins 815	0	0.60
347 Stainless	2.2	1.30
Nikrothal 80	0	3.6
310 Stainless	1.5	4.2
321 Stainless	6.9	7.6
Duranickel 301	0	8.0
Nickel 200	0	29.4
Iron	105.0	525.0

The results were plotted in two ways, either by considering the same metal in differing atmospheres or different metals in one atmosphere. The currents for these measurements on partially submerged samples were plotted as a function of the meniscus length on the specimens (*e.g.*, μA cm^{-1}). This was done largely as a consequence of the observation that samples tended to show far greater corrosion currents in the meniscus or electrolyte film regions than in the fully submerged regions. Even this is an approximation, since the submerged part of the electrode will be carrying a small portion of the current.

Figure 4 shows the corrosion currents for alloys in a partially immersed condition, with a 50/50 mole ratio oxygen/carbon dioxide atmosphere. It will be noted that the alloys which previously showed resistance, namely the Kanthal A series and the Hoskins alloys, again show a high degree of resistance to the melt, and exhibit low corrosion currents compared with 347 stainless steel. Hoskins 875 is very similar in composition to Kanthal A1, as is Hoskins 815 to Kanthal A. It is apparent that the oxidizing atmosphere in this case does nothing to destroy any protective film which is likely to be formed on the samples.

In Fig. 5, the oxidizing atmosphere has been replaced by an inert one, namely nitrogen. Helium was investigated and gave results very nearly identical to those for nitrogen. The currents per unit meniscus length are somewhat higher and the positions of zero current have been moved to more negative potentials.

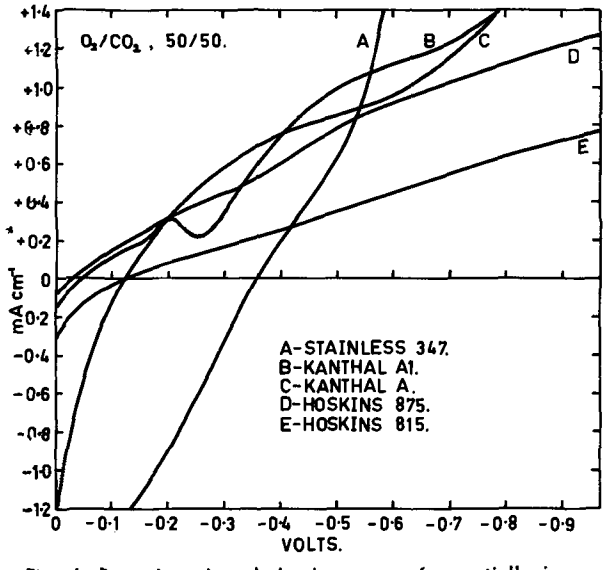

Fig. 4. Potentiostatic polarization curves for partially immersed samples, binary sodium, lithium carbonate eutectic, 680°C.

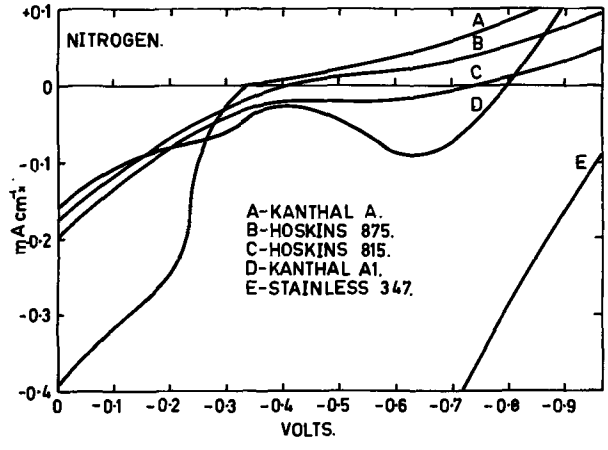

Fig. 5. Potentiostatic polarization curves for partially immersed samples, binary sodium, lithium carbonate eutectic, 680°C.

It is reasonable to assume that the currents at potentials more negative than −0.3V are largely due to formation of oxides and that only a small part of the current is due to the carbon dioxide/oxygen evolution reaction (*see* Fig. 8 and 9). Unfortunately, it is not possible from this experiment to determine the current efficiency of either of these reactions. It will be noted, however, that the position of 347 stainless steel under the same conditions is much inferior. Figure 6 shows the effect of a reducing atmosphere. In this case, all the alloys exhibit net anodic currents for most of the potential range investigated. One of the few conclusions that can be drawn is that appreciable anodic currents can be obtained from all the samples under reducing atmospheric conditions, and any insulating, protective film must therefore be destroyed by the presence of hydrogen at all the potentials of interest. It is not possible to determine what the corrosion rates would be in the potential range −700 to −1000 mV, where the anode is normally operated, since the electrode reaction

$$CO_3^{=} + H_2 \rightarrow CO_2 + H_2O + 2e^-$$

does not necessarily involve corrosion of the metal. However, the formation of steam at 680°C greatly increases the probability of direct chemical corrosion of the metal.

Comparison of the curves obtained for partially immersed samples with a reducing atmosphere, with those obtained for the completely submerged samples attached to 0.01 in. diameter gold wire leads shows that, in both cases, two competing reactions govern the observed corrosion potentials. These are: (*a*) the reactions involving the gas phase, principally in the meniscus region, and (*b*) the normal corrosion reactions occurring where the submerged surface contacts the electrolyte. When the gas phase reaction is limited to that occurring at the meniscus region on 0.01 in. diameter gold supporting wire (*i.e.*, total immersion of the sample), the corrosion reaction might be expected to predominate except in cases where passivation of the sample is almost complete.

For partially submerged samples, however, the gas phase reaction can be enhanced and its current capacity increased by the much greater meniscus length involved. Since in terms of current-carrying capability the electrode process involving the gas phase might now be expected to be much greater than that attributed to the immersed corrosion reactions, the potential moves toward that of the gas reaction

$$CO_3^{=} \rightleftharpoons CO_2 + \tfrac{1}{2}\,O_2 + 2e$$

which is also occurring at the reference electrode. This explains why certain materials, *e.g.*, 347 stainless steel in CO_2/O_2, appear more noble at their rest or corrosion potentials (partially immersed, zero external current) than they do when fully immersed in the melt, despite the fact that in the partially immersed mode they could be corroding by internal currents due to the difference in potential between the meniscus and immersed zones. Under these conditions, therefore, a more "noble" corrosion potential cannot necessarily be interpreted as a decrease in corrosion rate.

In the case of alloys which are protected from high-temperature oxidation by chromic oxide (Fig. 7), behavior, as might be expected (Table I), is somewhat similar to 347 stainless steel, the main difference for Hastelloy N being that the bulk of the material is now nickel. The material appears to corrode in an oxygen/carbon dioxide/nitrogen atmosphere and is comparable to stainless steels in this respect.

Measurements with the nickel-based alloys containing chromium indicated a tendency toward higher corrosion rates with decreasing chromium content. Nickel-based alloys containing aluminum (*e.g.*, Duranickel 301, Inconel 702) did not show the same degree of resistance as the iron-based alloys.

Figure 8 shows the effect of oxidizing and reducing atmospheres on partially submerged gold. The gold in this case appears to be acting as a reversible gas electrode and the potential shift corresponds closely to that which would be expected from the gas composition at the sample compared with the reference electrode. The curve for the atmosphere containing hydrogen is something of a measure of gold's ability to act as a hydrogen electrode, since the high currents for curve B can be attributed to the reaction

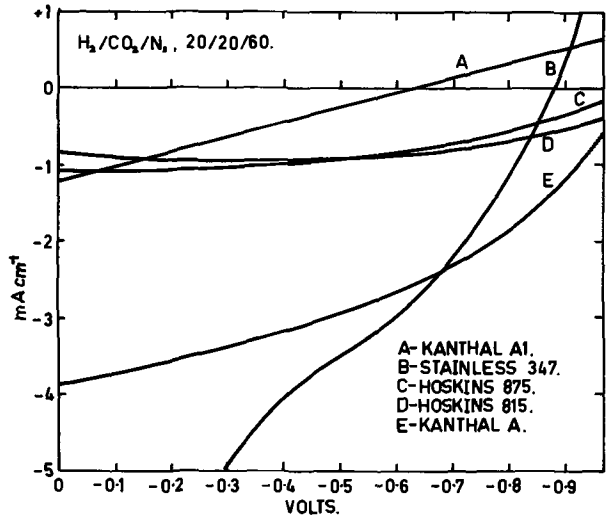

Fig. 6. Potentiostatic polarization curves for partially immersed samples, binary sodium, lithium carbonate eutectic, 680°C.

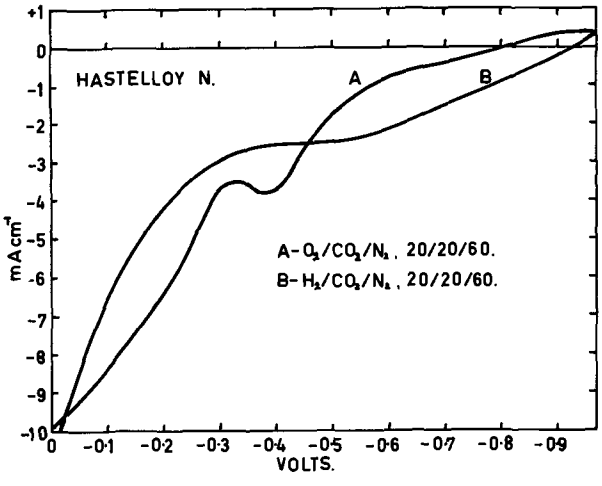

Fig. 7. Effect of gas atmosphere on potentiostatic polarization curves for partially immersed Hastelloy N, binary sodium, lithium carbonate eutectic, 680°C.

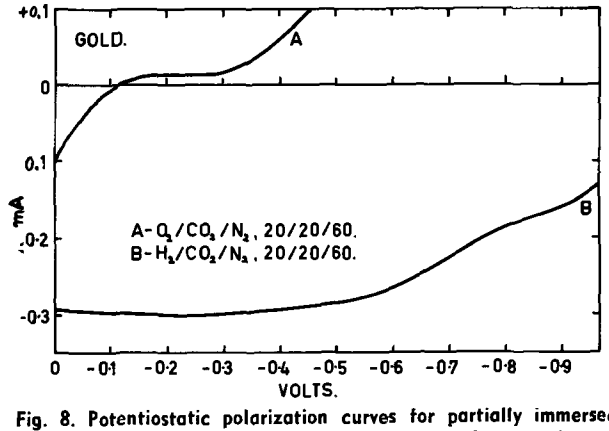

Fig. 8. Potentiostatic polarization curves for partially immersed gold wire (0.76 mm diameter); binary sodium, lithium carbonate eutectic, 680°C.

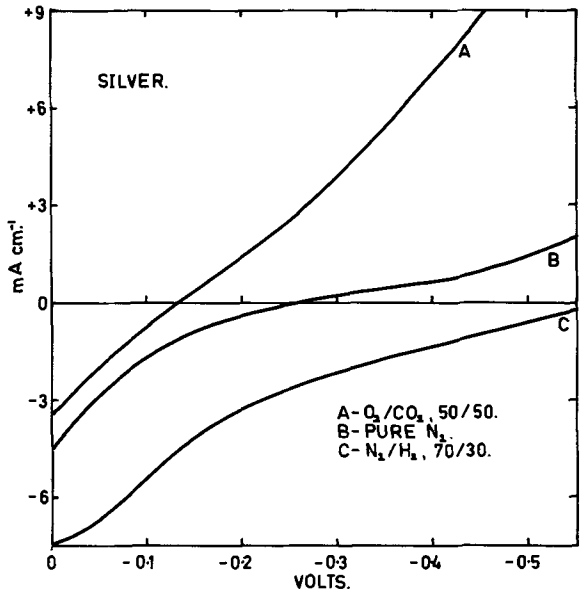

Fig. 9. Potentiostatic polarization curves for partially immersed silver wire (0.04 in. diameter; 0.75 in. immersed), binary sodium, lithium carbonate eutectic, 680°C.

$$H_2 + CO_3^{=} \rightarrow H_2O + CO_2 + 2e$$

The currents for silver (Fig. 9) are higher than might be expected, especially for the nitrogen atmosphere, where anodic currents are in excess of the predicted rate for carbon dioxide-oxygen evolution. The high value was subsequently found to be largely due to the formation of silver dendrites around the melt-atmosphere interface, which enormously increased the surface area of the silver at the three-phase boundary. Similar effects have been observed by Broers (5).

An experiment was carried out to determine the long-term resistance of Kanthal A1 to exposure to air, cathode gases, and other gases in the environment of a working molten carbonate fuel cell. Two disks of the metal were used as anode and cathode supporting members in the cell. The disks were both in contact with the electrolyte and with either anode or cathode and their respective fuel and oxidant gases. Creepage of electrolyte over both the inner and outer surfaces of the disks occurred immediately, but inspection after 1200 hr of operation indicated that the cathode disk was substantially unchanged. Corrosion of the anode disk was appreciable, but nevertheless far superior to any other non-noble metal or alloy so far used under these conditions.

In summary, corrosion of ferroaluminum alloys occurs most rapidly with a molten carbonate film in the presence of a reducing atmosphere, and is very much reduced in the presence of oxygen. The most favorable case appears to be the totally immersed open-circuit condition, where corrosion rates seem likely to be lower than for some noble metals, e.g. platinum.

Manuscript submitted April 24, 1969; revised manuscript received ca. Dec. 11, 1969. This was Paper 352 presented at the Montreal Meeting, Oct. 6-11, 1968.

Any discussion of this paper will appear in a Discussion Section to be published in the December 1970 JOURNAL.

REFERENCES

1. G. J. Janz, E. Neuenschwander, and A. Conté, *Corrosion*, **19**, 292t (1963).
2. G. J. Janz and A. Conté, *Electrochim. Acta*, **9**, 1269 and 1279 (1964).
3. M. D. Ingram and G. J. Janz, *ibid.*, **10**, 783 (1965).
4. A. Borucka, Fuel Cell Symposium, 154th National Meeting of the division of Fuel Chemistry of the American Chemical Society, Chicago, Ill., Sept. 10-15, 1967.
5. G. J. H. Broers, Fifth International Power Sources Symposium, Brighton, Sussex, UK, Sept. 20-22, 1966.

Preparation and Properties of Sputtered Hafnium and Anodic HfO_2 Films

M. T. Thomas[1]

Bell Telephone Laboratories, Incorporated, Murray Hill, New Jersey

ABSTRACT

Hafnium films sputtered at high voltages (4 kV) had a density of 98% of the bulk, specific resistivities as low as 50 μohm-cm and TCR as high as 1580 ppm/°C. Films with a density of 50% of that of the bulk, a specific resistivity of 815 μohm-cm, and TCR of 800 ppm/°C were obtained at the lower sputtering voltages (1.5 kV). High- and low-density films had Hall coefficients of -2×10^{-5} cm³/coulomb and $+12 \times 10^{-5}$ cm³/coulomb, respectively. All the sputtered films had the same hexagonal close-packed structure as the bulk material, although the high- and low-density films had different preferred orientation. The oxide density, anodization constant, and dielectric constant for hafnium oxide were found to be 7.9 g/cm³, 20 Å/V, and 18, respectively. The anodized hafnium oxide had a monoclinic polycrystalline structure with some preferred orientation, $(11\bar{1})$ or (001) plus $(10\bar{2})$. Test capacitors with anodic oxides formed to 100V at 1 mA/cm² had capacitance density values of 0.085 μf/cm², dissipation factors below 0.01 at 1 kHz, and a frequency dependence of capacitance of ±1% in the range of 0.1-100 kHz relative to the 1 kHz value. Temperature coefficient of capacitance values varied from 300 to 600 ppm/°C.

Sputtered and reactively sputtered tantalum films have been investigated in considerable detail with respect to their electrical, structural, and anodization properties. A reliable thin film passive component technology, suitable for integrated circuits, has been developed as an outgrowth of these studies (1). Recent studies on diode sputtered hafnium films showed that capacitors formed from these films by anodic oxidation had interesting properties (2-5).

The purpose of this paper is to present some experimental data on the electrical, structural, and anodization properties of hafnium films. In particular, the

[1] Present address: Washington State University, Department of Physics, Pullman, Washington.

density, resistivity, temperature coefficient of resistance, and the Hall coefficient of these films were studied for different sputtering voltages and sputtering current densities. The structure of these films was determined using reflection x-ray and electron microscope techniques.

The anodization characteristics in various electrolytes using both the constant current and constant voltage methods for anodization were also investigated. Hafnium-anodic hafnium dioxide-gold structures were used to measure the capacitance, temperature coefficient of capacitance, and frequency dependence of capacitance. From all of these measurements, it was possible to determine the hafnium dioxide density, anodization constant, and dielectric constant of anodic hafnium dioxide.

Experimental Procedure

The sputtering experiments were conducted in a CVC 18 in. metal bell jar system which was capable of reaching an ultimate pressure in the low 10^{-6} Torr range. This system consisted of a 15 CFM mechanical fore pump backing a 6 in. diffusion pump (untrapped pumping speed of 1520 liters/sec for air) which was isolated from the experimental chamber by a liquid nitrogen cold trap and a gate valve. The dynamic argon flow d-c sputtering technique was used for all experiments. The substrates could be heated to approximately 400°C and were covered by a shutter so the cathode could be cleaned by presputtering. A thermocouple imbedded in the substrate heater was used to monitor the temperature during all stages of the deposition procedure. Figure 1 shows the geometrical arrangement of the sputtering chamber. The cathode to substrate distance was fixed at 7.62 cm. As can be seen, both sides of the cathode were used to sputter hafnium films simultaneously. Before any films were deposited, the cathode was cleaned of any etching residues by a 3 hr presputter (6).

The cathode consisted of a square hafnium sheet 14.92 cm on a side and 0.145 cm thick, and was supplied by Wah Chang Corporation, Albany, Oregon. The chemical analysis supplied by the manufacturer indicated that the cathode contained 2.15% zirconium with the following other impurities (in ppm): C—90, O-180, Nb—<100, Fe—265, and Ta—<200. All the other impurities were less than 40 ppm. A number of hafnium-coated sapphire slides were analyzed using x-ray fluorescence to detect some of these impurities in the films themselves. No niobium or tantalum peaks were seen above the background signal, but iron and zirconium were detected on all samples tested. By comparing the x-ray fluorescence data obtained from the sputtered material to those taken on a bulk sample, it was found that the concentration of zirconium in the films (for both the 4 and 1 kV sputtered films) was the same as that of the bulk cathode. For zirconium in a hafnium matrix, therefore, there is approximately a one to one transferal of these low-concentration alloying atoms during the sputtering process. The presence of zirconium and iron in the films could be an important factor influencing the behavior of these hafnium films based on the results of metal alloying for thin-film tantalum oxide capacitors (7).

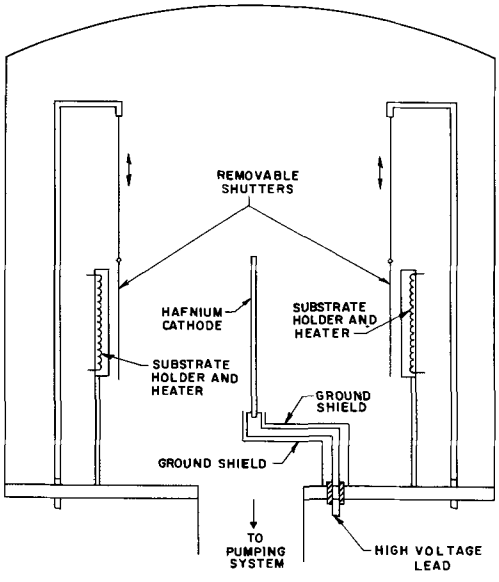

Fig. 1. Schematic of the sputtering chamber

Film Properties as a Function of Sputtering Parameters

The specific resistivity, temperature coefficient of resistance, the Hall coefficient, and the density of the hafnium films were studied as a function of sputtering voltage, sputtering current density, time of presputter, film thickness, and substrate temperature. Most of the films were deposited on 1 x 3 in. Corning alumino-borosilicate glass slides, although the thickness calibrations and the density measurements were performed on films deposited onto 1 in. square sapphire slides. In addition, the structure and topology of the films were examined with x-ray, reflection electron diffraction, electron-transmission, and replica techniques. For the electron transmission studies, very thin hafnium layers were sputtered onto mica, SiO films, and a carbon-coated molybdenum screen.

Hafnium films with electrical properties closest to that of the bulk were obtained with a sputtering voltage of 4000V and a sputtering current density of 0.112 mA/cm^2. These films had a shiny metallic appearance and ranged from 5000 to 6000Å thick (1 hr sputtering time, corresponding to a deposition rate of 80-100 Å/min). The specific resistivity of these films varied from 50 to 68 μohm-cm depending on the substrate temperature and ambient pressure of the system as compared to the bulk value of 35 μohm-cm. The lowest specific resistivities were obtained with the substrate at 400°C and the lowest background gas pressures in the chamber. As might be expected, there was no change in the electrical characteristics of the films resulting from a deposition of a few minutes to a few hours, nor were any changes seen upon varying the presputtering time from 15 min to 2 hr. For most experiments, a presputtering time of 30 min was chosen to insure that the system had reached dynamic equilibrium.

Figure 2 gives the deposition rate for hafnium in μg/(min-cm^2) and the density of the sputtered films in g/cm^3 as a function of sputtering voltage. A constant current density of 0.112 mA/cm^2 and a substrate temperature of 400°C were used for all of these measurements. Because of the large change of film density between the sputtering voltages of 2 and 3 kV, the

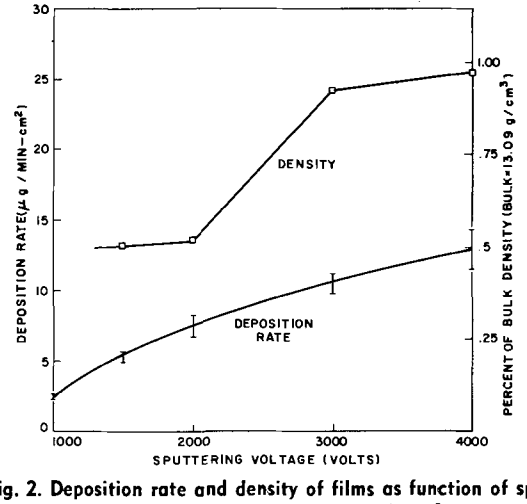

Fig. 2. Deposition rate and density of films as function of sputtering voltage (sputtering current density 0.112 mA/cm^2).

deposition rate is given in terms of the mass per unit area per unit time rather than in angstroms per unit time as is usually done. At 4 kV the density of the films was 12.8 g/cm^3 or about 97.7% of the bulk density, while at 1.5 kV the density dropped to 6.6 g/cm^3 or about one half that of the bulk density. Accompanying this change in density was a change in specific resistivity from about 53 μohm-cm at 4 kV to about 815 μohm-cm at 1.5 kV as shown in Fig. 3. It should be noted that similar changes in the film density and resistivity as a function of sputtering voltage have been reported previously with tantalum (8, 9). However, in contrast to low-density tantalum films, the resistivity of low-density hafnium films did not drift as a function of time after exposure to the atmosphere. This probably means there is not the same large uptake of oxygen by the hafnium films as there is by the tantalum films (8). Figure 3 shows the resistivity at room temperature and the TCR measured between room temperature and liquid nitrogen temperature as a function of the sputtering voltage. Qualitatively, the TCR varies in a manner that would be expected from the resistivity curve; *i.e.*, the TCR decreases when the resistivity increases, although the decrease is not as large as expected on the basis of an impurity scattering mechanism. The 4 kV films had a TCR of about 1580 ppm/°C, while those sputtered at 1 kV had a TCR of about 800 ppm/°C (the bulk TCR value is 4.4 x 10^3 ppm/°C at 20°C).

The low-density hafnium films were quite different in appearance from the high-density films. The former were black, nonmetallic looking, and quite transparent. Light could be seen through even the thickest films (approximately 10,000Å thick, sputtering time: 2 hr). The low-density films have a very porous quality as can be seen in Fig. 4(*a*) which is an electron micrograph taken of a carbon replica of 5000Å film sputtered at 1.5 kV on alumino-borosilicate glass. The films consist of many voids and interconnected islands. It is this very open structure with the many grain boundaries, comparable to low-density tantalum, that contributes to the high specific resistivity observed with these films. For comparison, Fig. 4(*b*) shows a carbon replica of a film sputtered at 4 kV and, as can be seen, these films are much more continuous and uniform. The appearance of the hafnium films is the same when viewed with transmission electron microscopy. For example, Fig. 5(*a*) and 5(*b*) show micrographs of films approximately 400Å thick deposited on SiO films at a voltage of 1.5 and 4 kV, respectively. The appearance of the films was independent of the substrates used for the electron microscope studies. Both the electron diffraction and x-ray diffraction studies show that both the high- and low-density films had the close-packed hexagonal structure which is the normal bulk material structure. The films deposited at 4 kV showed both (10.0) and (00.2) planes

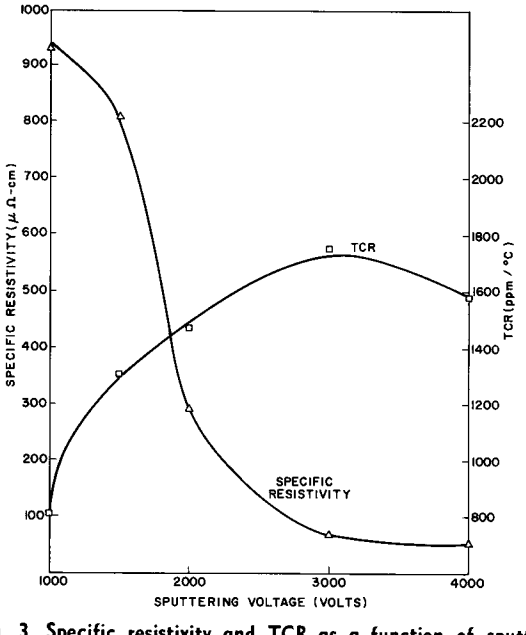

Fig. 3. Specific resistivity and TCR as a function of sputtering voltage (sputtering current density 0.112 mA/cm^2).

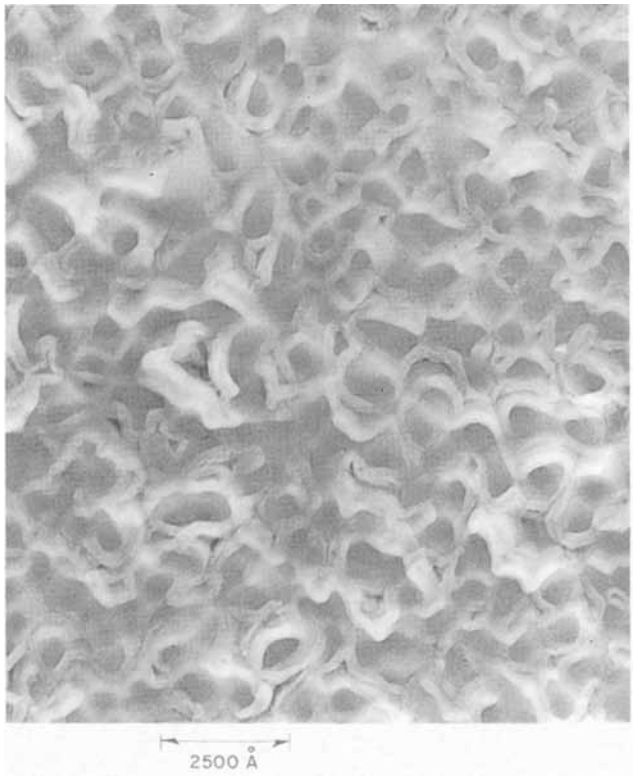

Fig. 4(*a*). Electron micrograph from a carbon replica of a low-density hafnium film, 5000Å thick deposited on a 7059 glass.

Fig. 4(*b*). Electron micrograph taken from a carbon replica of high-density hafnium film, 5000Å thick deposited on 7059 glass.

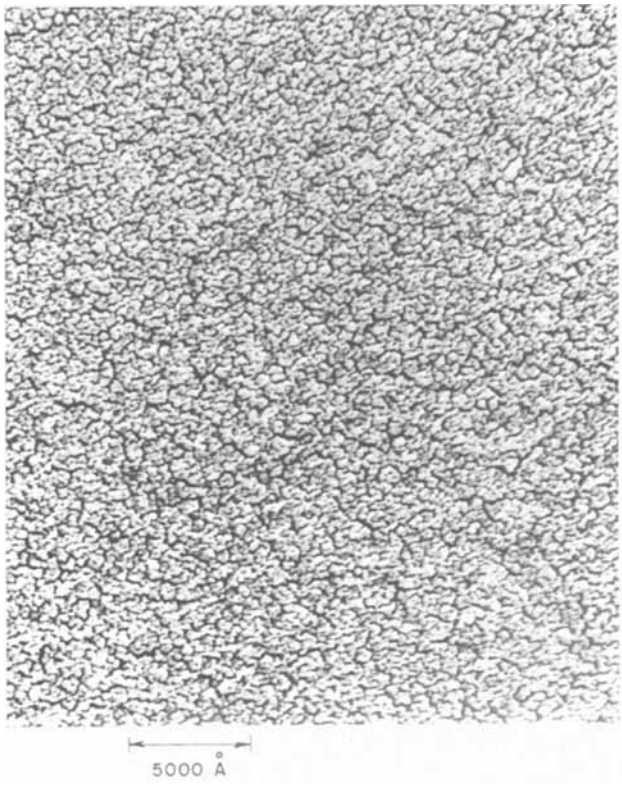

Fig. 5(a). Transmission electron micrograph of low-density hafnium film about 400Å thick deposited on SiO.

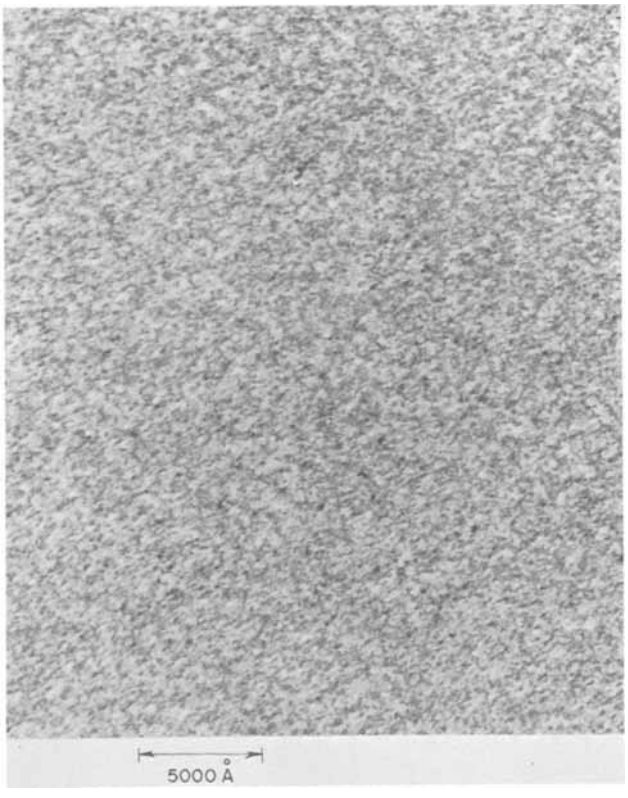

Fig. 5(b). Transmission electron micrograph of a high-density hafnium film about 400Å thick deposited on SiO.

preferentially parallel to the substrate surface, while the films deposited at 1.5 kV had the (10.0) planes about 40° to the substrate surface with no preferred orientation parallel to the substrate surface. At the higher current densities for the films deposited at 4 kV there appeared to be more (00.2) preferred orientation, and at times some (10.1) orientation was observed. Some preferred orientation was seen for films sputtered on cold as well as hot substrates. The crystallite size of both the high- and low-density films was about a few hundred angstroms.

Figures 6 and 7 show the variations of the deposition rate, density, resistivity, and TCR of films sputtered at 4.0 kV, but at various current densities. As would be expected, the deposition rate increases linearly with current density except for the higher currents where backscattering at pressures of the order of 40 x 10^{-3} Torr causes the deposition rate to drop off from the expected rate. There is no appreciable change in the density and only a slight increase in the specific resistivity of the films over the range of current densities investigated—from 0.112 to 0.672 mA/cm^2. The TCR, however, varies more than would be expected from the small change in resistivity, which means that Matthiessen's rule (10) does not apply. White and Woods (11) have reported a departure from Matthiessen's rule for bulk hafnium samples with varying amounts of zirconium. For divalent or multivalent metals which must be described by a two-band model, Matthiessen's rule is not necessarily expected to hold (12). Such materials may have complicated Fermi surfaces which could overlap more than one Brillouin zone and one might have to take into account interband scattering. This situation can vary as a function of crystal orientation for anisotropic materials (hafnium has a hexagonal close-packed structure). The resistivities of these materials are sensitive to changes in the amount and type of impurities present as well as on the orientation in the sample. Generally it is assumed that Matthiessen's rule may be applied to each band separately but not to the total conductivity. As is seen below, one may have to assume two types of carriers for hafnium. Although there was not a large

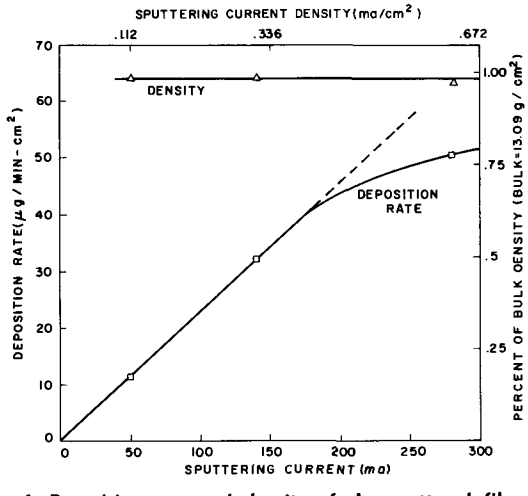

Fig. 6. Deposition rate and density of the sputtered films as a function of sputtering current (sputtering voltage 4000V).

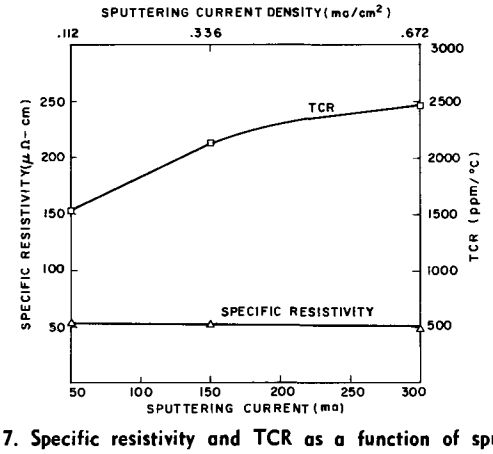

Fig. 7. Specific resistivity and TCR as a function of sputtering current (sputtering voltage 4000V).

change in resistivity with sputtering current, one would expect an additional impurity content in the films sputtered at the lower deposition rates. Also, as mentioned above, there was some effect in the preferred orientation of the film with increasing current density. The films seemed more strongly oriented as the current density increased, which, coupled with a variation in the impurity concentration, might contribute to the changes in TCR seen in Fig. 7.

Figure 8 shows the variation of the Hall coefficient, R, of the hafnium films as the sputtering voltage was varied with a constant sputtering current density of 0.112 mA/cm^2, and Fig. 9 shows the variation in the Hall coefficient for 4 kV sputtering voltage as the current density was varied. As can be seen, the Hall coefficient varied from -2×10^{-5} to $+12 \times 10^{-5}$ cm^3/coulomb as the voltage varied from 4 to 1 kV. Such a change in sign was an unexpected result and indicates that one must assume two types of carriers in hafnium; *i.e.*, both electrons and holes must be present. Vol'Kenshteyn and Galoshina (13) have reported a value of $+4.3 \times 10^{-5}$ cm^3/coulomb at room temperature with hafnium sample of 99.4% purity, the major impurity being 0.5% zirconium. However, they reported a change in sign of the Hall coefficient at 56°K, and at liquid helium temperature R had a value of about -2×10^{-5} cm^3/coulomb. To explain this variation of the Hall coefficient with temperature, Vol'Kenshteyn and Galoshina assumed a two-band model where the effective masses, mobilities, and carrier type differed in each band. In a tabulation of electrical properties of hafnium, Martin and Pizzolato (14) reported a value of the Hall coefficient of -0.16×10^{-5} cm^3/coulomb at room temperature, but unfortunately no information as to the purity of the sample was given. An unambiguous value for the bulk value of the Hall coefficient for hafnium has not been found in the literature.

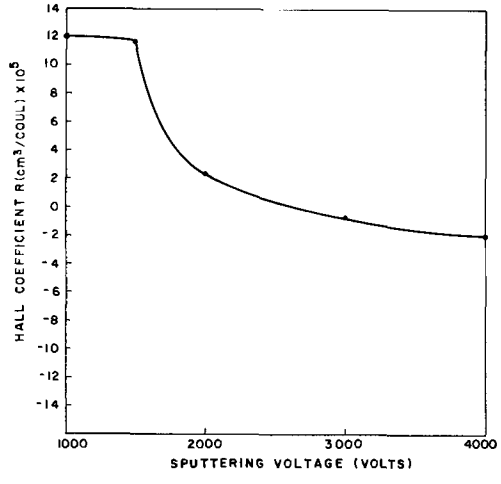

Fig. 8. Hall coefficient of sputtered films as a function of sputtering voltage (sputtering current density 0.112 mA/cm^2).

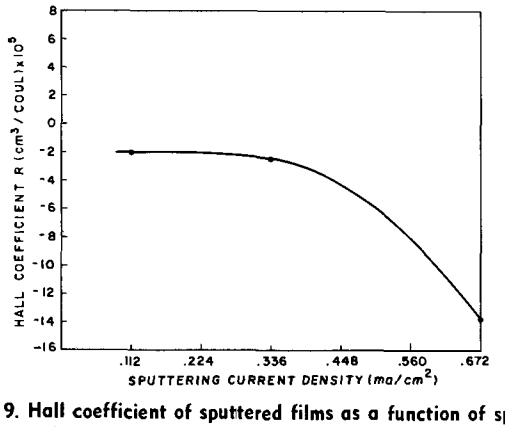

Fig. 9. Hall coefficient of sputtered films as a function of sputtering current density (sputtering voltage 4000V).

The fact that the low-density films have a high resistivity due to their porous and granular structure does not explain the variation in the Hall coefficient. Koppe and Ryan (15) have shown by a theoretical argument that voids and holes in a material do not effect the Hall voltage. Roesch and Willens (16) have reported that the Hall coefficient of titanium has different values and sign depending on the orientation of the sample in the magnetic field. In particular, they reported values of $R_{\parallel} = +4.2 \times 10^{-5}$ cm^3/coulomb and $R_{\perp} = -7.7 \times 10^{-5}$ cm^3/coulomb, where $R_{\parallel}$ and $R_{\perp}$ are the Hall coefficients when the magnetic field is parallel to and perpendicular to the c axis, respectively. For anisotropic media, the Hall coefficient must be considered a tensor quantity rather than a scalar quantity. As was stated above, the low-density films have a preferred orientation different from that of the high-density films which could explain both the change in sign and magnitude of the results measured on the hafnium films. Figure 9 shows the variation of the Hall coefficient with sputtering current density. Again, as was stated above, the greater the current density the more oriented the films became, which could explain the change in the magnitude of the Hall coefficient. Also, there may be more incorporation of impurities at the smaller current densities which might also contribute to the variation seen here. Before any definitive statements can be made concerning the mechanisms responsible for the changes in the Hall coefficient in the sputtered hafnium films, further studies must be performed, including perhaps measurements on pure bulk single crystals.

Anodization Characteristics of Sputtered Hafnium Films

The anodization characteristics of both the 4 kV, 0.112 mA/cm^2 and the 1.5 kV, 0.112 mA/cm^2 sputtered hafnium films were investigated using 0.01% citric acid in water, or equal volumes of aqueous solution of oxalic acid and ethylene glycol, or 1% potassium hydroxide in water as electrolyte. All anodizations were done at room temperature. Of course, the surface temperature of the film may increase slightly during the constant current method of anodization and may rise considerably during the constant voltage method of anodization. High-density hafnium films (4 kV sputtering voltage) anodized in a manner similar to high-density tantalum films, but, in contrast to low-density tantalum films (8), the low-density hafnium films anodized completely at very low forming voltages. Figure 10 shows typical voltage and current *vs.* time plots of anodizations of high-density hafnium films using the constant current technique. Curves A and B correspond to a current density of 1 mA/cm^2, while

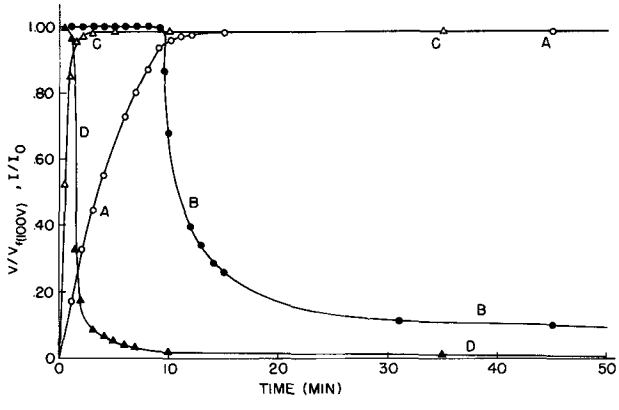

Fig. 10. Anodization characteristics of hafnium sputtered films in saturated aqueous solution of oxalic acid and ethylene glycol (anodized to 100V). Curves A and B, V/V_f and I/I_o, respectively, for 1 mA/cm^2 current density anodization. Curves C and D, V/V_f and I/I_o, respectively, for 5 mA/cm^2 current density anodization.

curves C and D correspond to a current density of 5 mA/cm². In both cases, the forming voltage was 100V. As can be seen, the current dropped to 10% of the starting current I_0 for the 1 mA/cm² anodization, but it dropped to about 1% of the starting current I_0 for the 5 mA/cm² anodizations, implying the oxide may be more dense for the higher current density anodizations. It was observed that there was more gas evolution (oxygen) as the anodizing current density was increased and also at the higher forming voltages. Gas evolution was associated with pinholes that were observed in the oxide. There were only minor differences in the anodization characteristics using the above-mentioned electrolytes. The constant voltage technique of anodization was also tried using the oxalic acid-ethylene glycol solution. The films anodized very rapidly using this method and, at least with the films used, the oxide growth was accompanied by a considerable amount of bubbling on the film surface, *i.e.* gas evolution.

The low-density, 1.5 kV films could not be anodized above 10V which means that all of the metal had been consumed at 10V and therefore no further oxide could be grown at the high voltages. This can be seen in Fig. 11 which shows the voltage *vs.* time curves during anodization of these films at different voltages. Curve A shows an attempt to anodize a film to 130V. Curves B and C show attempts to anodize two different portions of the same slide to 20 and 10V, respectively. In all of these cases, the resulting film was completely transparent. There was, however, a very slight darkish tinge on the film anodized to 10V. Even for the thickest films sputtered at 1.5 kV, approximately 10,000Å, an anodization of 10V produced a clear, transparent film. Such behavior is not too difficult to understand if it is realized that these are highly porous metal films. From the electron micrographs of these films [*see* Fig. 4(*a*) and 5(*a*)], it is seen that these films are composed of many voids and empty spaces. This means that the hafnium metal which forms the boundaries of the voids is of such a size as to be completely anodized at about 10V. Using an anodization constant of 20 Å/V determined below and assuming that twice as much area of the film is exposed to the anodization solution, the film structure should be composed of islands about 400Å in size. This estimate agrees with the size of the crystallites obtained from the structural studies. These anodization characteristics are quite different than those found for low-density tantalum. Low-density tantalum exhibits an induction period during anodization where the voids are filled with oxide followed by the normal anodization characteristics of high-density tantalum films (8). The interpretation of this is that, after the voids in the tantalum film are filled, there is still sufficient metal remaining to produce the typical anodization characteristics.

X-ray investigations show that for both the 4 and 1.5 kV films the oxide formed is monoclinic HfO_2 and that the oxide has a polycrystalline structure rather than being completely amorphous. The crystallite size of the oxide formed on the 4 kV films was approximately the same as those in the film, while for the 1.5 kV films the crystallite size of the oxide was smaller (less than 100Å) than those in the film. There was a slight $(11\bar{1})$ orientation on the oxide from the 4 kV films, and on the oxide from the 1.5 kV films there was a slight (001) and $(10\bar{2})$ orientation. This is not too surprising since the metallic hafnium films had a different preferred orientation. In addition, there appeared an extra diffraction line at the position of the strongest line of the high-temperature HfO_2 tetragonal phase (1965°C).

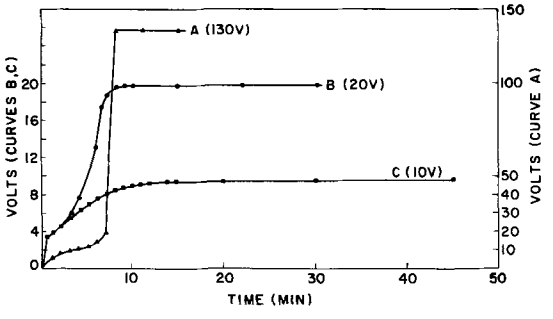

Fig. 11. Anodization characteristics of low-density sputtered hafnium films.

Density, Anodization Constant, Dielectric Constant of HfO_2

Estimates of the density, anodization constant, and dielectric constant for the oxide grown on the sputtered films were obtained from measurements of the mass change during anodization and oxide thickness (17). For these evaluations, the normal stoichiometry of the hafnium oxide was assumed which may not be true, especially at the oxide-hafnium interface. Also, for these calculations the measured value of the 4 kV sputtered film density was used rather than the bulk density of hafnium. The average density of hafnium oxide was found to be 7.9 g/cm³ which is about 19% lower than the bulk value.

Using the calculated value of the oxide film density, the constant current anodization constant was 20 Å/V. For constant voltage anodization, however, the anodization constant was 45 Å/V. In this case, the bulk oxide density was used in the calculation since preliminary data indicate that the oxide formed by constant voltage anodization is higher than that formed by constant current anodization. The scatter in the data includes the bulk value. Qualitatively, the reason for this difference in the anodization constant between two methods of anodization can be explained by noting that for constant voltage anodization the initial stages of oxide growth are accompanied by a large current surge which could develop localized heating on the surface of the film, increasing the temperature and thus enhancing film growth. Huber reported an anodization constant of 65 Å/V for constant voltage anodization (2).

The dielectric constant can be determined from the anodization constant and measured values of capacitance density. The area of each capacitor was 0.105 cm² and both gold and nichrome gold counterelectrodes were used. Table I gives some typical values of the capacitance density and dissipation factors for the three electrolytes used and for various anodization parameters. It should be noted that the capacitance density is a function of the electrolyte, current density during formation, and the technique of formation (constant current or constant voltage).

If the low value of hafnium oxide density is assumed, the dielectric constant is calculated to be 18. However, if the bulk oxide density is assumed, the anodization constant becomes 26.6 Å/V and the dielectric constant has a value of 24 which agrees quite well with the values reported in the literature. For example, Goldstein and Leonhard (18) have reported a value of 24.5 for the dielectric constant of reactively sputtered hafnium dioxide, and Gerstenberg (19) in a recent tabulation of dielectric constants of various thin-film dielectrics formed by anodic oxidation and reactive sputtering listed a value of 25. Huber has reported (2) a dielectric constant of 45 for hafnium oxide formed by constant voltage anodization, and capacitance densities for oxide formed to 130V of about 6.2×10^4 $\mu\mu$f/cm². These capacitance densities agree with those measured during this investigation; *see* Table I. For comparison, the dielectric constant for anodic tantalum oxide formed on sputtered tantalum thin films often reported (18, 19) is 25, and the capacitance density of tantalum oxide formed to 130V is about 10×10^4 $\mu\mu$f/cm². It should be noted that the value of the dielectric con-

Table I. Typical values of capacitance density and dissipation factor at 1 kHz for various anodization conditions

Electrolyte	Anodization condition	Capacitance density, $\mu f/cm^2$	Tan δ
0.01% Citric acid	130V 1 mA/cm²	0.0585	0.010
		0.0583	0.008
		0.0626	0.009
		0.0579	0.021
50-50 Saturated aqueous solution oxalic acid and ethylene glycol	130V 1 mA/cm²	0.0646	0.031
		0.0650	0.031
		0.0651	0.031
		0.0634	0.033
	100V 1 mA/cm²	0.0825	0.016
		0.0809	0.011
		0.0818	0.014
		0.0798	0.036
	100V 5 mA/cm²	0.0747	0.011
		0.0753	0.006
		0.0751	0.006
		0.0714	0.034
	50V 1 mA/cm²	0.1561	0.010
		0.1581	0.007
		0.1624	0.013
		0.1639	0.022
	50V 5 mA/cm²	0.1510	0.008
		0.1505	0.006
		0.1498	0.006
		0.1544	0.006
	100V constant voltage	0.0433	0.052
		0.0441	0.052
		0.0467	0.051
		0.0456	0.050
1% KOH	100V 1 mA/cm²	0.0911	0.005
		0.0923	0.005
		0.0928	0.004
		0.0946	0.004
	100V 5 mA/cm²	0.0889	0.009
		0.0872	0.009
		0.0889	0.009
		0.0852	0.010

stant of Ta_2O_5 formed on bulk tantalum or tantalum foil measured by Young (20) is 27.6.

Frequency and Temperature Dependence of Capacitance

The capacitance and dissipation factor of the test capacitors as a function of frequency in the range from 0.1 to 100 kHz were studied. Only a $\pm 1\%$ variation in $c/c_{1\ kHz}$ was found in this range and there was very little difference in the frequency dependence for the oxides formed in the oxalic acid-ethylene glycol, KOH, and citric acid solutions. This capacitance *vs.* frequency variation agrees very well with that reported by Huber (2). Low values of the dissipation factor, ≤ 0.01 at 1 kHz were measured for all the electrolytes and the normal variation of tan δ with frequency was observed.

The initial attempts to measure TCC indicated that for either gold or nichrome-gold counterelectrodes the capacitance varied in an erratic and nonreproducible fashion as a function of temperature. The gold counterelectrodes seemed to have the wider variations. Only after placing the capacitors in a chamber and evacuating to a few microns did the capacitance as a function of temperature cycle in a reproducible manner and then only after one complete temperature cycle. This behavior was basically the same whether any of the three electrolytes were used or whether constant current or constant voltage anodization was used to form the dielectric. The TCC values varied from about 300 to about 600 ppm/°C, with the lowest values measured with the capacitors formed at constant voltage. It is interesting to note that a change in capacitance of about half that measured by increasing the temperature to 100°C was obtained upon placing the capacitors in a vacuum of a few microns. One possible explanation for this behavior and the erratic capacitance changes is that the capacitors are very sensitive to humidity. This would be expected if the oxide were porous which seems the case for the oxide formed with the anodization conditions used (the anodic oxide density was found to be about 20% lower than that of the bulk oxide). The larger variation observed with the gold counterelectrode could have been caused by adhesion problems. The values of TCC reported here are larger by a factor of 2 to 4 than those reported previously (2, 3), even for those formation conditions that closely approximated those studies.

Conclusions

As is the case with many materials and in particular tantalum, the electrical and structural properties of hafnium are a function of the sputtering parameters. No phase of hafnium equivalent to the β-phase (21) in tantalum was observed but a low-density film was obtained at the low sputtering voltages. In contrast, sputtered niobium (22) exhibits neither a low-density structure nor a β-phase. These low-density films have a large specific resistivity and a large positive Hall coefficient in contrast to the films sputtered at the higher voltages. All of the films sputtered had a hexagonal close-packed structure which was the same as the bulk but with preferred orientations that were dependent on the sputtering conditions. These different preferred orientations may be the cause of the change in sign and magnitude of the Hall coefficient for the different films.

The hafnium films sputtered at 4 kV anodized in a manner similar to tantalum, although the final anodization current did not decrease by the same percentage as that with tantalum. One implication of this might be that there is a larger variation in the stoichiometry of the oxide than with tantalum or the film may have a greater number of defects. This, coupled with the fact that the density of the high-density hafnium films is smaller than the bulk value, could explain the relatively low value of the density of the HfO_2 films. Klerer (17) reported the density of the tantalum oxide formed on the sputtered films smaller than that of the bulk oxide. The anodization constant for hafnium was found to be about 20 Å/V which is somewhat higher than that of tantalum, 16 Å/V. Also, the value of the dielectric constant was determined and found to be 18 using the low value of the oxide density.

One of the problems encountered during anodization, which is not unique with hafnium, was gas evolution during oxide growth and pinholes in the final oxide. Pinholes affect capacitor yields and performance. The capacitance densities, capacitance as a function of frequency, and the leakage current agree reasonably well with those reported previously (2, 3). However, the values of TCC measured were higher by a factor of 2 to 4. In addition, it was found that the capacitors are quite sensitive to the environment, probably humidity, and only after placing the capacitors in an evacuated oven were reproducible capacitance *vs.* temperature data obtained.

One of the interesting facts discovered about the anodic oxide was that it was not amorphous but polycrystalline monoclinic with some preferred orientation. Also, x-ray studies showed a diffraction ring belonging to either the high-temperature tetragonal oxide or the bcc hafnium oxide postulated by Passerini (23).

Acknowledgments

The extensive aid of Mrs. M. H. Read is appreciated for her contributions to the x-ray analysis of these films, as well as helpful discussions with N. Schwartz.

Manuscript submitted March 10, 1969; revised manuscript submitted Dec. 3, 1969.

Any discussion of this paper will appear in a Discussion Section to be published in the December 1970 JOURNAL.

REFERENCES

1. D. A. McLean, N. Schwartz, and E. D. Tidd, *Proc. IEEE*, **52**, 1450 (1964).
2. F. Huber, W. Witt, and W. Y. Pan, *Proc. Third Intern. Vacuum Congress, Stuttgart, June 1965.*
3. F. Huber, W. Witt, W. Y. Pan, and I. H. Pratt, *Proc. IEEE Components Conf., 1966* p. 326.
4. F. Huber, W. Witt, and I. H. Pratt, *Proc. IEEE Components Conf., 1967*, p. 66.
5. F. Huber, *RCA Engineer*, **13**, 57 (1967).

6. Before insertion into the vacuum chamber, the hafnium cathode was etched in a 1% hydrofluoric solution and rinsed in boiling distilled water.
7. N. N. Axelrod, B. H. Vromen, H. D. Guberman, D. J. Harrington, and N. Schwartz, Extended Abs. of Dielectrics and Insulation Div., Electrochem. Soc. Meeting, **3**, 6 (1966); *This Journal*, **113**, 52C (1966).
8. B. H. Vromen, Extended Abs. 7, Electrochem. Soc. Meeting, Cleveland, Ohio, May 1-6, 1966; Extended Abs. 11, Electrochem. Soc. Meeting, Dallas, Texas, May 7-12, 1967.
9. H. J. Scheutze, H. W. Ehlbeck, and G. G. Doerbeck, *10th Nat. Vac. Symp., Boston, Mass.*, p. 434 (Oct. 1963).
10. The resistivity of a metal, which is a function of temperature, can generally be written in the form $\rho(T) = \rho_L(T) + \rho_i$ where $\rho_L(T)$ is the resistivity due to the lattice thermal vibration (phonons) and is a function of temperature, and ρ_i is the resistivity due to impurities and crystal defects. Matthiessen's rule states that if the impurity concentration is small, ρ_i is independent of temperature. *See* C. Kittel, "Introduction to Solid State Physics," 3rd Ed., p. 218, John Wiley & Sons, Inc., New York (1966).
11. G. K. White and S. B. Woods, *Phil. Trans. Roy. Soc. London*, **251**, Series A, 273 (1959).
12. G. T. Meaden, "Electrical Resistance of Metals," p. 82, Plenum Press (1965).
13. N. V. Vol'Kenshteyn and E. V. Galoshina, *Phys. Metals Metallog. (GB)*, **18**, No. 5, 138 (1965).
14. D. R. Martin and P. J. Pizzolato, "Rare Metals Handbook," 2nd Ed., Edited by C. A. Hampel, Chap. 12, p. 205, Reinhold Publishing Corp., (1961).
15. H. Koppe and J. M. Ryan, *Can. J. Phys.*, **29**, 274 (1951).
16. L. Roesch and R. H. Willens, *J. Appl. Phys.*, **34**, 2159 (1963).
17. J. Klerer, *This Journal*, **112**, 896 (1965).
18. R. M. Goldstein and F. W. Leonhard, *Proc. IEEE Components Conf. 1967*, p. 312.
19. D. Gerstenberg, *14th Nat. Vac. Symp. Am. Vac. Soc., 1967*, p. 9.
20. L. Young, *Proc. Roy. Soc.*, **244**, 41 (1958).
21. M. H. Read and C. Altman, *Appl. Phys. Letters*, **7**, 51 (1965).
22. J. Sosniak, To be published, *J. Appl. Phys.*; J. Sosniak and G. W. Hull, Jr., *ibid.*, **38**, 4390 (1967).
23. L. Passerini, *Gazz. Chim. Ital.*, **60**, 762 (1930).

Electrodeposition of Thin Magnetic Permalloy Films

H. V. Venkatasetty*

Honeywell Corporate Research Center, Hopkins, Minnesota

ABSTRACT

A citrate-complexed nickel-iron electrolyte which has a long useful plating life from the point of view concerning the magnetic properties of the plated films and a better plating efficiency compared to the conventional baths has been used to plate thin magnetic films of 80:20 nickel-iron from about 150 to about 8000Å. The magnetic properties, like the coercive force (H_c) and the anisotropy field (H_k), were determined at a known thickness as a function of current density, pH, temperature, and the concentration of citrate ion and the plating conditions optimized. The ferromagnetic domain patterns observed by the Bitter technique as a function of thickness show the same behavior as those observed in evaporated films. Internal stress measurements made as a function of thickness, current density, and temperature show that both the current density and the temperature have significant effect on stress. Photomicrographs of deposits obtained at a wide range of current density show the differences in the structure of the deposits.

Within the last ten years, the study of electrolytic preparation and properties of thin ferromagnetic films of permalloy and permalloy type material useful as memory elements for computers (1-6) has received great attention by research workers. Electrodeposition has the unique advantage in that controlled quantities of elements like P, As, S, *etc.*, can be introduced into the deposit to produce films of varying magnetic properties (2, 5-7). By manipulating the plating parameters, like the current density and the temperature of the bath, the roughness of the surface topography of the substrate material can be varied and, by subsequent plating of ferromagnetic material on such a surface, a wide range of specific desirable magnetic properties can be produced (8). The disadvantage of electroplating lies in the difficulty in controlling the impurity content of the bath, the adsorption of ions on the cathode, and the codeposition of hydrogen. In the conventional permalloy bath where either ferrous sulfate or ferrous formate is used, ferrous ions undergo anodic oxidation to ferric ions during plating. Ferric hydroxide and other hydrolysis products like $Fe(OH)^{++}$ and $Fe(OH)_2^+$ are incorporated into the deposit and affect the magnetic properties of plated permalloy (9).

With a view to preventing the adsorption and inclusion of the ferric compounds in the deposit causing a deleterious effect on the magnetic properties of the permalloy on prolonged plating, citrate ion was added to the solution and the conditions to plate permalloy were optimized. It has been found that permalloy films of good magnetic properties can be obtained from the citrate bath even when used over a long period of time ($\sim$ 25 hr), whereas similar studies with the sulfate bath show that the films exhibit poor magnetic properties after a few hours of use ($\sim$ 10 hr) and a new bath should be used (9). It is also found that the unstirred sulfate bath is very sensitive to small changes in the operating parameters like the current density, pH, and the temperature of the bath, whereas the citrate bath is much less sensitive to the above operating parameters making it easier to reproduce the films with good magnetic properties (9). This paper describes a method for preparing 80:20 nickel-iron films of varying thickness and the effect of plating parameters like the pH, temperature, citrate ion concentration, ferrous sulfate concentration on the magnetic properties of the films. Ferromagnetic domain patterns are observed as a function of film thickness. Stress measurements made with and without saccharin in the bath are also described.

Experimental Procedure

The method of preparation of the bath, though similar to the Ni-Fe-Mo bath prepared by Freitag and Mathias (5), is different from the composition of the

* Electrochemical Society Active Member.
Key words: electrodeposition, permalloy, memory element, thin film, coercive force, anisotropy field.

present bath and the bath is operated at a different pH and current density. The typical plating solution is made with reagent-grade chemicals by dissolving in distilled water about 112g of $NiSO_4 \cdot 6H_2O$, 5g of $FeSO_4 \cdot 7H_2O$, 75g of citric acid and/or sodium citrate, 1.5g of K_2SO_4, 0.0-0.4g of sodium lauryl sulfate, and 1.0g of saccharin, and diluting the solution to 1 liter. The pH is adjusted to 4.8 by sodium hydroxide or citric acid. The plating cell is a liter flask with a flat surface fitted with a Lucite cover that can hold the electrodes rigidly and can be positioned accurately. A platinum sheet was used as anode. Glass slides with chromium and gold evaporated on them were used as substrates and the films were deposited from a nonagitated bath using a sequence of current pulses of varying amplitude (7.5 mA/cm²-18 mA/cm²) with 3 sec on period and 3 sec off period from a constant current source to minimize the concentration gradients across the thickness of the deposit. The bath can be operated from 25° to 45°C, and the films were made at 25°C and 30°C. A coil wound around the bath generates a uniform vertical magnetic field of about 100 Oe.

The coercive force (H_c) and the anisotropy field (H_k) of the films were measured in a 1000 cycle hysteresis loop tracer using the standard procedure (10). The standard spectrophotometric method was used to estimate iron in the deposit (11) at 522 mμ using a Beckman Du spectrophotometer. The iron was precipitated twice and complexed with dipyridyl. The amount of iron in the deposit was calculated with a calibration curve made using 99.8% A.R. grade iron wire. These determinations are accurate to ±2% or better. The thicknesses of the films were estimated from the total weight of the alloy deposited in a given area and these measurements are accurate to ±10%.

The well-known Bitter technique using a Zeiss metallographic microscope was used to observe the domain walls (12, 13). The photomicrographs of the deposits made at different current densities were also obtained using a Zeiss metallographic microscope. The internal stress in the deposits was measured using a Brenner and Senderoff spiral contractometer (14). The copper spiral was coated with gold (~3000Å) and a smooth deposit of copper (~3000Å) using a proprietary copper bath and the procedure recommended by Brenner and Senderoff was used. The measurements are accurate to ±10%.

Results and Discussion

Permalloy films (2000-8000Å) deposited at 7.5 and 10 mA/cm² as a function of pH at 25° and 30°C show that at pH less than 4.5 the deposits are rough looking and give distorted B-H loops (Fig. 1). The deposits plated at pH 4.6-5.2 are shiny and have good magnetic properties and square hysteresis loops in the easy direction (Fig. 1). The deposits plated at pH more than 5.2 are rough looking with high values of H_c and H_k (Fig. 2) with distorted B-H loops. The variation of pH can cause a large variation in nickel content of the alloy deposited from the citrate bath. It has been shown that above pH of 6 the deposit consists mainly of nickel due to the preferential complexing of iron by the citrate ion (15). Apparently, the relative affinity of citrate ion for complexing iron and nickel must vary with pH. The Freitag and Mathias bath seems to be highly sensitive to pH change and it was operated at pH 5.2 (5) which is the limiting end of the pH range applicable to the present bath (Fig. 2). They prepared Ni-Fe-Mo films (600-800Å) which were highly magnetostrictive, whereas the present studies relate to nonmagnetostrictive films covering a wide range of thickness (500-8000Å) since nonmagnetostrictive forms of permalloy comprise the bulk of the magnetic film material used for magnetic storage and switching purpose.

The films of thickness 2000 and 3000Å deposited at different temperatures from 25° to 55°C show that the

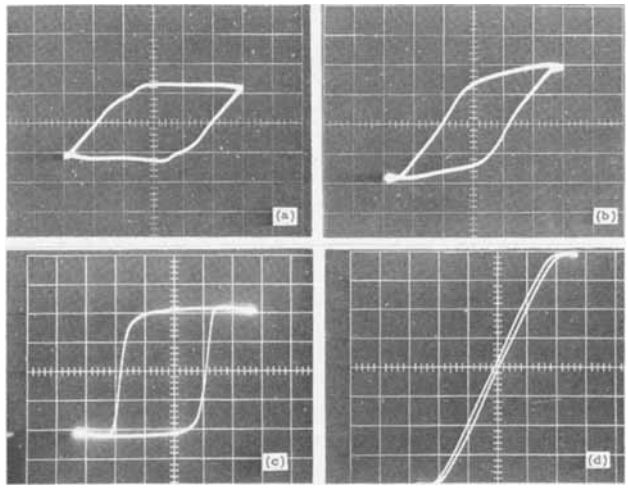

Fig. 1. B-H loops of easy and hard axis of 3000Å Ni-Fe films plated at different pH: (a) easy axis loop at pH 3.7, (b) hard axis loop at pH 3.7, (c) easy axis loop at pH 4.8, (d) hard axis loop at pH 4.8.

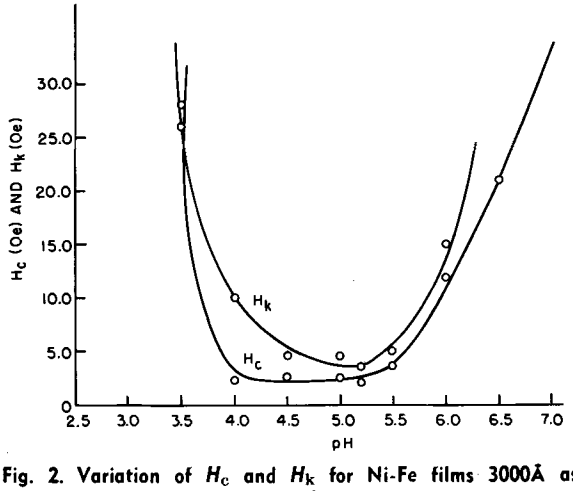

Fig. 2. Variation of H_c and H_k for Ni-Fe films 3000Å as a function of bath pH; C.D. 10 mA/cm² at 30°C.

deposits have good magnetic properties up to 45°C, above which the deposits become rough looking with distorted B-H loops with high values of H_c and H_k (Fig. 3). The magnetic properties of the deposits (~3000Å), H_c and H_k, were studied as a function of the citrate ion concentration. It is found that both H_c and H_k values remain almost constant up to citrate ion concentration of 125 g/liter, above which the H_c and H_k increase (Fig. 4) and the B-H loops are distorted. The effect of citrate ion on the composition of nickel-iron deposit has been described (16). It has been found that the iron content of the alloy increases with increase in the citrate ion concentration in the bath, and the deposits from a bath with very much citrate ion were found to contain organic inclusions (16).

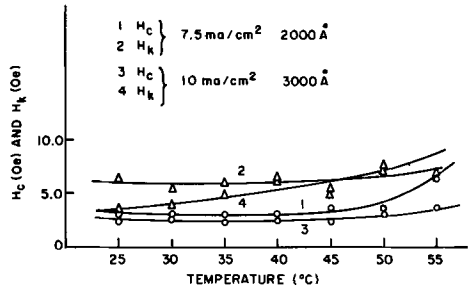

Fig. 3. Variation of H_c and H_k with temperature of the bath

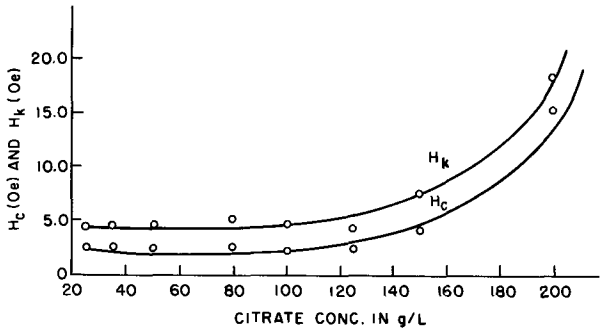

Fig. 4. Variation of H_c and H_k with citrate concentration for Ni-Fe films, 3000Å plated at pH = 4.8.

The chemical analysis of the films with zero magnetostrictive properties showed that the film composition corresponds to 80% nickel and 20% iron by weight. The deposits plated at 25° and 30°C with 7.5 and 10 mA/cm² were very slightly iron-rich below ~ 1000Å, and from 1000Å to 1μ they were all zero magnetostrictive with good magnetic properties (Fig. 5). Experiments done with near zero or zero magnetostrictive films (~ 600-8000Å) to determine the effect of film thickness on H_c and H_k show that, while H_c is very much thickness dependent with a value of 4.2 Oe at ~ 600Å and 1.0 Oe at 8000Å, H_k is less dependent on thickness with a value of 5.2 Oe at ~ 600Å and leveling off at 4.0 Oe from 1000 to 8000Å in good agreement with the results of Wolf for films made from the sulfate-chloride bath (1) (Fig. 6).

Films (~ 3000Å) were deposited from the baths containing varying amounts of ferrous ion concentration at constant nickel ion concentration, and H_c and H_k were measured. At 2.5g of $FeSO_4 \cdot 7H_2O$/liter, the film has high H_c of 15.0 Oe and drops to about 1.2 Oe at 3.75g of $FeSO_4 \cdot 7H_2O$/liter, remains about the same at 5.0g of $FeSO_4 \cdot 7H_2O$/liter, above which it increases steadily to 1.8 Oe at 10.0g of $FeSO_4 \cdot 7H_2O$/liter. At 2.5g of $FeSO_4 \cdot 7H_2O$/liter, the film has H_k of 17.0 Oe, drops to 4.0 Oe at 3.75g $FeSO_4 \cdot 7H_2O$/liter, and remains at 4.0 Oe up to 5.0g of $FeSO_4 \cdot 7H_2O$/liter, above which it increases rapidly with increase of ferrous sulfate in the bath, reaching a value of 9.5 Oe at 10.0g $FeSO_4 \cdot 7H_2O$/liter (Fig. 7). These results are in excellent agreement with those of Wolf (1) and point out the well-known composition dependence of H_k with a minimum value in the zero magnetostrictive range.

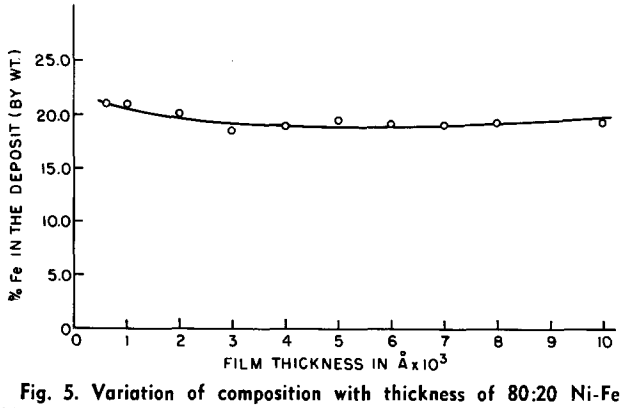

Fig. 5. Variation of composition with thickness of 80:20 Ni-Fe films plated at 25° and 30°C.

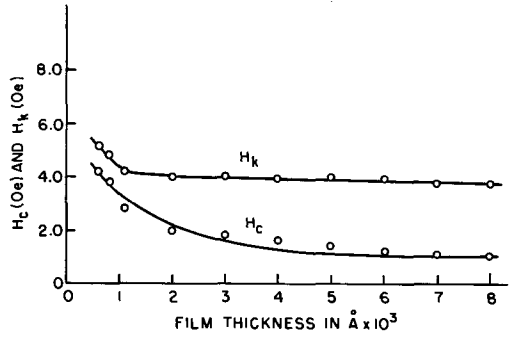

Fig. 6. Variation of H_c and H_k with film thickness for 80:20 Ni-Fe films.

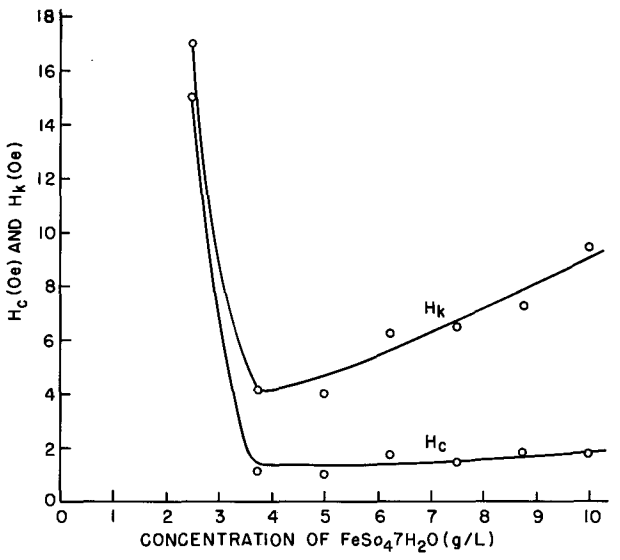

Fig. 7. Variation of H_c and H_k with ferrous sulfate concentration in the bath at constant nickel sulfate concentration for Ni-Fe films, 3000Å.

Experiments run to determine the plating efficiency of the bath at various current densities (7.5-18.0 mA/cm²) at 30°C show that the plating efficiency is about 85% compared to about 60% for conventional sulfate baths. The lower plating efficiency of the sulfate bath can be explained in terms of lower operating pH ~ 2.6 where a significant amount of hydrogen is liberated.

The internal stress developed in an electrodeposited material is possibly caused by the mismatch and disorder in the arrangement of the atoms in the lattice during the growth process. Some of the factors that influence the stress are the substrate roughness, impurities in the bath, temperature, pH, and current density. Stress measurements made as a function of current density and film thickness show that stress is tensile in nature and is very much dependent on plating current density. At each current density, the initial stress is high and levels off with increasing thickness which indicates that the film substrate interface has a great effect on stress. Stress measurements made at 6.5 mA/cm² as a function of temperature show that stress decreases from a value of about 9.7 x 10^9 dynes/cm² at 25°C to about 5.0 x 10^9 dynes/cm² at 47°C. It is found that, on adding weighed quantities of saccharin to the bath, the stress of 6.0 x 10^9 dynes/cm² measured at 5 mA/cm² with no saccharin gradually decreases with increase of saccharin to a constant value of 1.9 x 10^9 dynes/cm² at saccharin concentrations of 1 g/liter and above (Fig. 8). Stress values measured in this work compare favorably with those of Maeda and Mukasa for permalloy (17).

Though it is well known that the domain wall properties are important to the study of ferromagnetic films and their applications, very little work is reported on the domain wall studies of electrodeposited films. Bitter pattern observations were made on demagnetized nickel-iron films as a function of film thickness from ~ 150 to 2800Å. It is apparent from these observations that, as the film thickness increases, the influence of the stray fields on domain wall configuration changes. As predicted from theory, Néel walls are observed at ~ 150 and ~ 250Å films [Fig. 9(*a*), (*b*)], whereas at ~ 600Å cross-tie walls appear [Fig. 9(*c*)], and in thick films ~ 2800Å Bloch walls are observed [Fig.

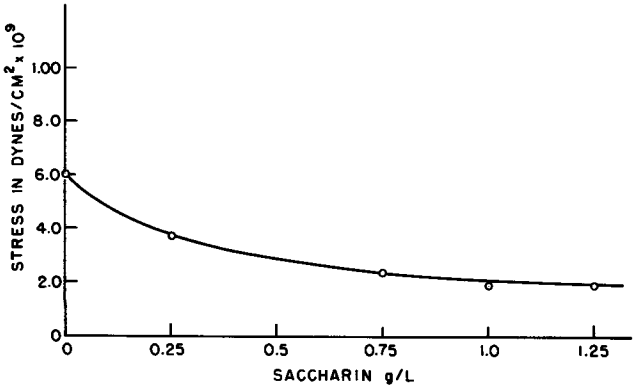

Fig. 8. Effect of saccharin on the residual stress of electrodeposited Ni-Fe films ~ 7000Å.

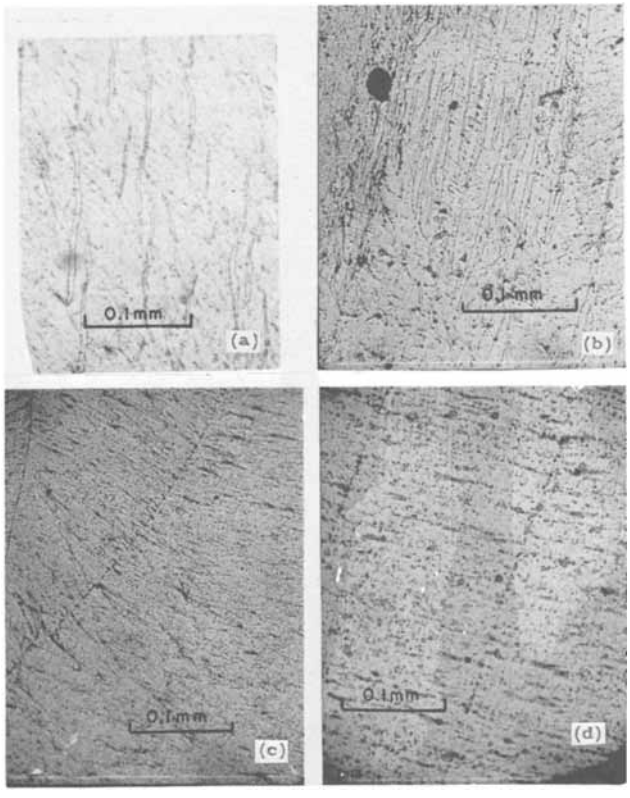

Fig. 9. Bitter patterns of the domain walls in Ni-Fe films as a function of film thickness: (a) Néel walls ~ 150Å Ni-Fe film, easy axis approximately vertical; (b) Néel walls ~ 250Å Ni-Fe film, easy axis approximately vertical; (c) cross-tie walls ~ 600Å Ni-Fe film, easy axis approximately vertical; (d) Bloch walls ~ 2800Å Ni-Fe film, easy axis approximately vertical.

9(*d*)]. The localized field due to the free magnetic pole lying inside the thin ferromagnetic film will be directed parallel to the surface in the case of Néel walls. The colloidal particles of the Bitter solution are used for easy flux closure, thus giving rise to very intense deposits of colloids. In Bloch walls, these localized strong fields lie perpendicular to the surface and hence have a weaker force on the colloidal particles giving rise to poorly defined lines. Cross-tie walls represent a transition from Bloch to Néel walls, wherein the cross-ties serve to decrease the magnetostatic energy (18, 19). Kainuma and Tsuya (20), who studied the domain patterns of electrodeposited Ni-Fe films, could not observe these patterns below 300 magnification, whereas the present observations could be made at magnifications of 60 and above. Maeda and Nukasa (21), who made domain pattern studies of electrodeposited Ni-rich and Fe-rich samples of Ni-Fe films from 400 to

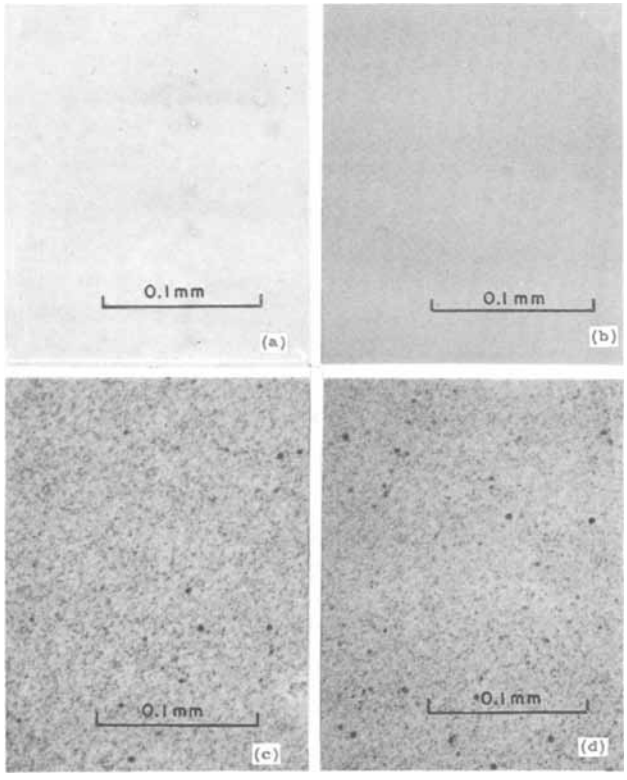

Fig. 10. Photomicrographs of the surface of Ni-Fe films deposited at different current densities: (a) 1 mA/cm², (b) 5 mA/cm² (c) 20 mA/cm², and (*d*) 25 mA/cm².

7000Å, observed cross-tie walls for 450-1300Å and Bloch walls at 7000Å.

The photomicrographs of 80:20 NiFe films plated at different current densities show that the films are smooth and shiny [Fig. 10(*a*), (b)] with low values of H_c, H_k, and easy axis dispersion (α_{90}) and square loop in the easy direction at 1 and 5 mA/cm², whereas at 20 and 25 mA/cm² the deposits become rough [Fig. 10(*c*), (*d*)] with high values of H_c and H_k and easy axis dispersion (22).

Conclusion

It has been shown that, using the citrate bath, 80:20 nickel-iron films of varying thickness with magnetic properties comparable to films made by vacuum deposition can be produced. The bath has a higher plating efficiency and longer useful life and the process has a high degree of reproducibility as compared to the sulfate bath.

Acknowledgments

The author wishes to thank Dr. Jack Sartell for helpful comments, Dr. Olin Lutes for helpful discussions, and Mr. L. L. Egan and Mr. Dave Bergum for technical assistance.

Manuscript submitted Aug. 4, 1969; revised manuscript received *ca.* Dec. 19, 1969.

Any discussion of this paper will appear in a Discussion Section to be published in the December 1970 JOURNAL.

REFERENCES

1. I. W. Wolf, *This Journal*, **108**, 959 (1961).
2. W. O. Freitag, J. S. Mathias, and G. Diljuilio, *ibid.*, **111**, 35 (1964).
3. R. D. Fisher, H. E. Austen, and H. E. Haber, *ibid.*, **111**, 39 (1964).
4. M. W. Sagal, *ibid.*, **112**, 174 (1965).
5. W. O. Freitag and J. S. Mathias, *ibid.*, **112**, 64 (1965).
6. W. O. Freitag, G. Diljuilio, and J. S. Mathias, *ibid.*, **113**, 441 (1966).
7. F. E. Luborsky, *J. Appl. Phys.*, **38**, 1445 (1967).
8. H. D. Richard, J. Humpage, and J. C. Hendy, *IEEE*

Trans. Mag., **MAG-4**, 351 (1968).
9. H. V. Venkatasetty, Unpublished results (1968).
10. H. W. Katz, A. H. Anderson, W. Kayser, U. F. Gianola, H. P. Louis, J. H. Glaser, C. D. Olson, and I. W. Wolf, *IEEE Trans. Mag.*, **MAG-1**, 218 (1965).
11. M. L. Moss and M. G. Mellon, *Ind. Eng. Chem. Anal. Ed.*, **14**, 862 (1942).
12. F. Bitter, *Phys. Rev.*, **38**, 1903 (1931).
13. H. J. Williams and R. C. Sherwood, *J. Appl. Phys.*, **28**, 548 (1957).
14. A. Brenner and S. Senderoff, *J. Res. Nat. Bur. Std.*, **42**, 89 (1949).
15. A. Brenner, "Electrodeposition of Alloys, Vol. I, p. 102, Academic Press, New York (1963).
16. A. Brenner, "Electrodeposition of Alloys," Vol. II, pp. 271, 303, Academic Press, New York (1963).
17. M. Maeda and K. Nukasa, *Japan. J. Appl. Phys.*, **6**, 895 (1967).
18. R. F. Soohoo, "Magnetic Thin Films," p. 46, Harper and Row, New York (1965).
19. S. Methfessel, S. Middelhoek, and H. Thomas, *J. Appl. Phys.*, **31**, 3025 (1960).
20. S. Kainuma and N. Tsuya, *ibid.*, **34**, 795 (1963).
21. M. Maeda and K. Nukasa, *Japan. J. Appl. Phys.*, **4**, 557 (1965).
22. H. V. Venkatasetty and L. L. Egan, Unpublished results (1969).

Vapor Phase Etching of GaAs in the H_2-H_2O Flow System

Chinyueh Lin, Lin Chow, and Kenneth J. Miller*

Department of Chemistry, Northeast Louisiana State College, Monroe, Louisiana

ABSTRACT

The GaAs-H_2O-H_2 etch reaction has been studied as a function of flow rate, temperature, and GaAs surface area. Experimental and calculated equilibrium constants for the reaction have been compared. The formation of Ga_2O_3(s) is considered. The variation of sample surface texture with gas composition is examined.

An understanding of the chemical equilibrium of a reaction is essential for its useful application. In this study, the chemical equilibrium of the GaAs-H_2-H_2O reaction has been studied particularly as this reaction may be applied to the controlled *in situ* etching of samples prior to epitaxial deposition of thin films by chemical transport. Such *in situ* etching may be useful for purity control of substrate surfaces. Since this reaction also takes place at the "source" when H_2O vapor transport is used in epitaxial deposition under a temperature gradient, it is also important to understand its equilibrium to control epitaxial deposition. Various experimental methods have been used in prior studies of this etch reaction (1, 2); in the present study, a horizontal reactor suitable for processing relatively large area samples has been used and the effect of temperature, flow rate, and GaAs surface area on the reaction equilibrium and of gas composition on etched surfaces has been studied.

Experimental

Single-crystal ($\bar{1}\bar{1}\bar{1}$) oriented GaAs sample wafers obtained from the Monsanto Chemical Company were lapped and polished in 1800 grit alumina and with Linde B, and chemically polished in bromine-methanol solution according to the method of Sullivan *et al.* (3). Hydrogen was pre-purified grade obtained from Matheson Company and was further purified by passing through a Pd-Ag diffusion tube purifier. Hydrogen was bubbled through DI water held in a Pyrex saturator immersed in an ice-water bath. For all etching, the H_2O/H_2 mole ratio was $\cong 6 \times 10^{-3}$. Figure 1 shows a schematic drawing of the furnace and furnace temperature profile. A 28 mm ID X 24 in. long quartz reaction tube was used. The furnace temperature profile was constant within $\pm 1°$ over about 5 in. The GaAs sample was placed on a flat quartz sample holder held in the center of the reaction tube by a quartz tube with a test tube end fused to the bottom of the flat sample holder directly below it so that the sample temperature could be measured with a thermocouple. The experimental details of similar flow reactors have been described by Moest (4) and by Lawley (5).

* Electrochemical Society Active Member, to whom correspondence should be addressed.

Results

Figure 2 shows an Arrhenius plot of the data for the etch reaction giving an experimental activation energy of approximately 44 kcal/mole in the 900°-1050°C temperature range for a H_2O-H_2 flow rate of 300 cm^3/min and a H_2O-H_2 gas flow velocity of 50 cm/min. The latter flow rate etched samples at a rate convenient for useful etching, between 0.1-2 μ/min. The sample area used to determine this plot was approximately 3 cm^2, large enough to minimize nonuniform edge etching. It was not possible to distinguish different etch rates between the ($\bar{1}\bar{1}\bar{1}$) and (100) surfaces.

Figure 3 shows a plot of GaAs sample weight loss at 1000°C as a function of H_2O-H_2 flow rate for sample areas > 10 cm^2. A weight loss of approximately 23 X 10^{-4} g/min was obtained at a flow rate of 300 cm^3/min for sample areas > 10 cm^2. However, a weight loss of approximately 5.56 X 10^{-4} g/min was obtained for the 3 cm^2 area normalized to 1 cm^2, as used to obtain Fig. 2. This decrease in weight loss with decrease in surface area at constant flow rate and temperature indicates

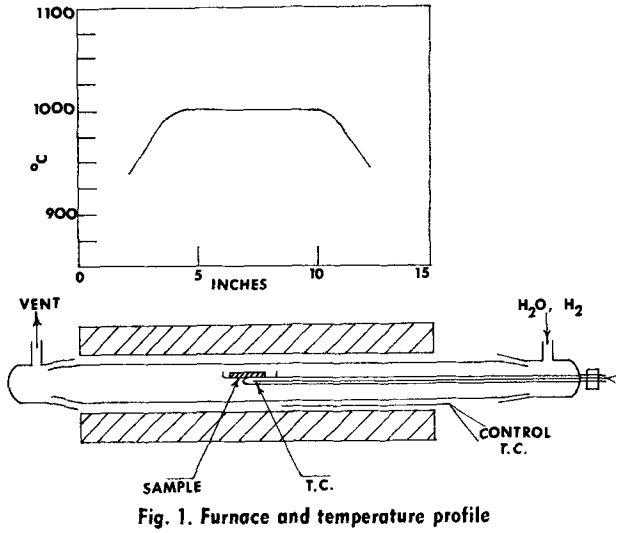

Fig. 1. Furnace and temperature profile

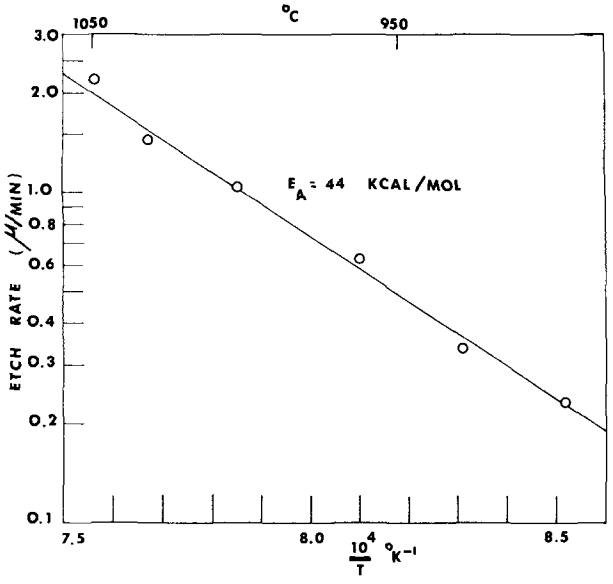

Fig. 2. GaAs etch rate as a function of temperature at H_2O/H_2 mole ratio 6×10^{-3} and H_2O-H_2 flow rate 300 cm³/min.

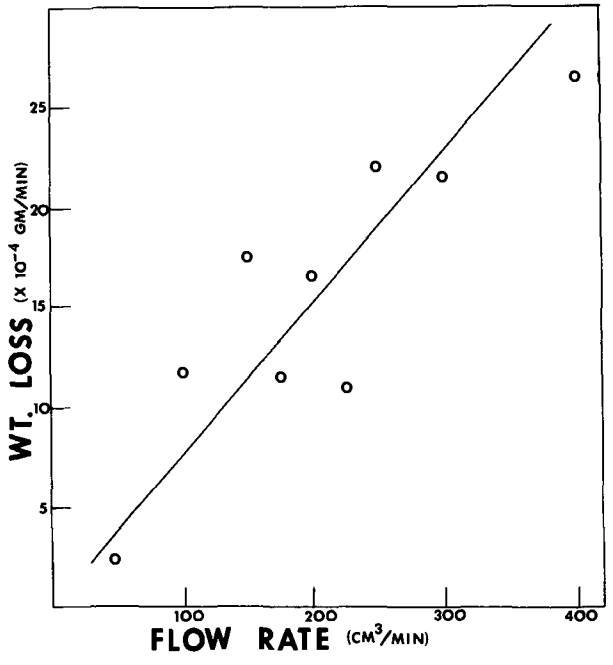

Fig. 3. GaAs weight-loss at 1000°C as a function of H_2O-H_2 flow rate for sample area > 10 cm².

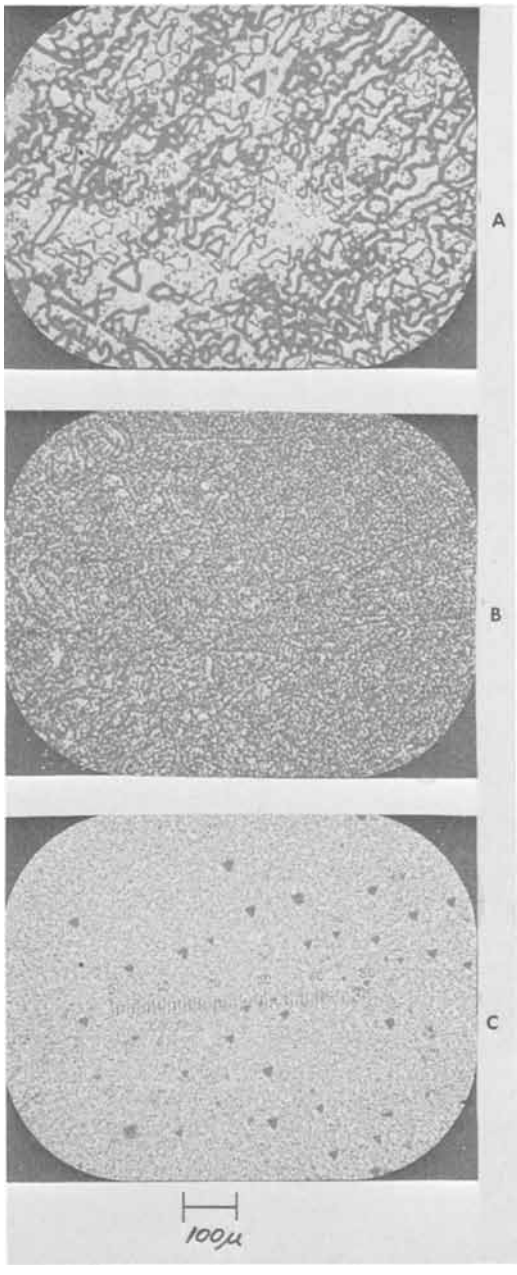

Fig. 4. GaAs ($\bar{1}\bar{1}\bar{1}$) face following etching at 1000°C: A—600 cm³/min, 5 min; B—100 cm³/min plus 300 cm³/min N_2 by-pass, 5 min; C—50 cm³/min plus 400 cm³/min N_2 by-pass, 15 min.

incomplete reactivity of the reactants. The dependence of reaction rate on surface area is not unexpected and is usual for the relatively fast flow rates used when reactions are applied in practice. Figure 3 indicates that the etch rate reaction under the experimental conditions used to obtain the data in Fig. 2 is closer to a steady-state equilibrium than a true thermodynamic equilibrium. If it is assumed that, for sample surface area > 10 cm² the reaction of reactant gases is complete at a flow rate of 300 cm³/min, then sample weight loss under these conditions should be independent of surface area and represent a close to true thermodynamic equilibrium.

Figure 4 shows photomicrographs of the ($\bar{1}\bar{1}\bar{1}$) GaAs face following etching at 1000°C. When the H_2O-H_2 gas composition is diluted with nitrogen, it can be seen that the GaAs surface is smoother and more uniform. The effect of nitrogen on etching is believed to be primarily due to H_2O-H_2 dilution rather than to chemical reaction since etching is taking place at about the decomposition temperature of gallium nitride (6). When (100) surfaces were etched, it was found that they yielded a smoother etched surface as compared to ($\bar{1}\bar{1}\bar{1}$) surfaces etched under the same conditions.

Discussion

The over-all idealized etch reaction, limited by temperature and partial pressures of H_2 and H_2O, can be written

$$GaAs(s) + \tfrac{1}{2}H_2O(g) \rightleftarrows \tfrac{1}{2}Ga_2O(g) + \tfrac{1}{2}H_2(g) + \tfrac{1}{2}As_2(g) \quad [1]$$

where the pressure of As_4 has previously (2) been shown to be less than 10% of the total arsenic pressure above approximately 900°C. An equation showing the variation of the equilibrium constant for [1] with temperature in the 1000°-1400°K range has been obtained using recently evaluated free energy functions for GaAs(s) from Lichter and Sommelet (7), free energy functions for $Ga_2O(g)$ from Cochran and Foster (8) and heats of formation using the data of Arthur (9), and Thurmond and Frosch's (10) value for $\Delta H°_{f298}$ of

$Ga_2O(g)$, as well as data from JANAF Thermochemical Tables (11) and Stull and Sinke (12)

$$\log K_p = \frac{-13.15 \times 10^3}{T} + 8.21 \qquad [1a]$$

At 1000°C, K_p calculated for reaction [1] using [1a] is 7.6×10^{-3} as compared with the value for K_p obtained from the experimental data in Fig. 2 of 2×10^{-3}. The latter experimental value for K_p varies from K_p calculated by about one order of magnitude; however, it should be noted that the thermal data uncertainty of ± 1.5 kcal causes an uncertainty of approximately one order of magnitude in calculated K_p values. The K_p obtained from the experimental data of Fig. 3 where sample area is > 10 cm^2 and flow rate is 300 cm^3/min is 0.9×10^{-2}, comparing more closely with the K_p calculated, than the value obtained at 3 cm^2 sample area, indicating that closer to true thermodynamic equilibrium has been achieved in this case. The method used for the determination of experimental K_p values has previously been described (2). Figure 5 shows smooth semilog plots of K_p for the etch reaction [1] as a function of temperature as calculated from [1a] and as obtained experimentally from the kinetic data of Fig. 2. For comparison, Fig. 5 shows the two experimental values in this temperature range from the work of Michelitsch *et al.* (2). In the latter study, gas velocity was considerably greater than that used in this present study.

The range of partial pressures of H_2O and H_2 in reaction [1] is limited by the formation of $Ga_2O_3(s)$. The reaction for $Ga_2O_3(s)$ formation when p_{H_2O} is relatively high or p_{H_2} relatively low, based on experimental observations, is proposed as

$$\tfrac{1}{2}Ga_2O(g) + H_2O(g) \rightleftarrows \tfrac{1}{2}Ga_2O_3(s) + H_2(g) \qquad [2]$$

An equation showing the variation of K_p for [2] with

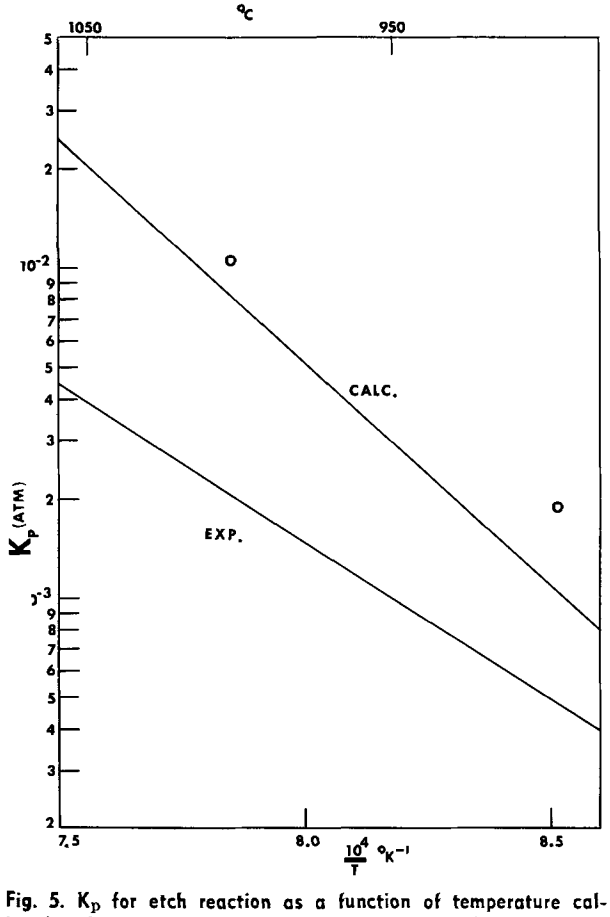

Fig. 5. K_p for etch reaction as a function of temperature calculated and experimentally determined compared with experimental values of Michelitsch et *al.* (o).

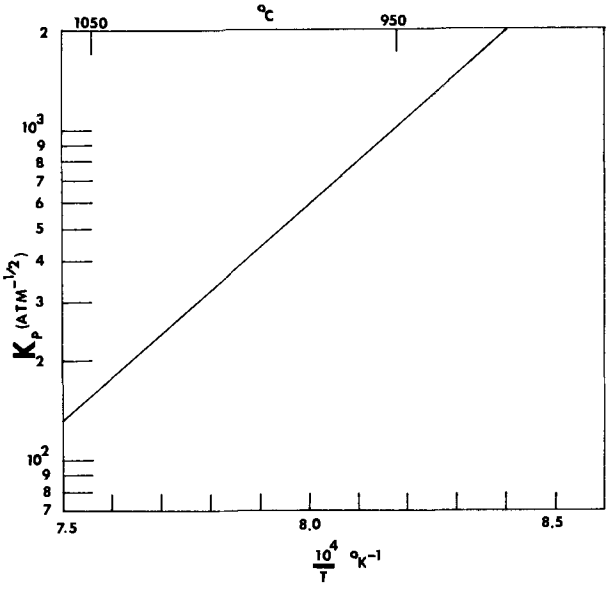

Fig. 6. Calculated K_p for the reaction $\tfrac{1}{2}Ga_2O(g) + H_2O(g) \rightleftarrows \tfrac{1}{2}Ga_2O_3(s) + H_2(g)$.

temperature in the 1000°-1400°K range has been obtained as follows

$$\log K_p = \frac{13.5 \times 10^3}{T} - 8.02 \qquad [2a]$$

Figure 6 shows a smooth semilog plot of K_p calculated from [2a] as a function of temperature, indicating that reaction [2] can affect the etch reaction significantly unless the partial pressure of H_2O is small compared to that of hydrogen. Equation [2a] has been obtained using free energy functions given by Cochran and Foster (8) for $Ga_2O(g)$ and $Ga_2O_3(s)$, $\Delta H°_{f298}$ for $Ga_2O_3(s)$ of −261 kcal/mole (13) and $\Delta H°_{f298}$ for $Ga_2O(g)$ of −21.5 kcal/mole (10).

Acknowledgments

Part of the equipment used was provided by a Western-Electric college equipment gift, and GaAs samples were provided as a gift from the Monsanto Chemical Company.

Manuscript submitted June 20, 1969; revised manuscript received *ca.* Dec. 10, 1969. This was Paper 122 presented at the New York Meeting, May 4-9, 1969.

Any discussion of this paper will appear in a Discussion Section to be published in the December 1970 JOURNAL.

REFERENCES

1. G. E. Gottlieb and J. F. Corboy, Jr., *RCA Review*, **24**, 585 (1963); G. E. Gottlieb, *This Journal*, **112**, 196 (1965).
2. M. Michelitsch, W. Kappallo, and G. Hellbardt, *ibid.*, **111** 1248 (1964).
3. M. V. Sullivan and G. A. Kolb, *ibid.*, **110**, 585 (1963).
4. R. R. Moest, *ibid.*, **113**, 141 (1966).
5. K. L. Lawley, *ibid.*, **113**, 240 (1966).
6. A. Rabenau, "Compound Semiconductors," Vol. 1, p. 174, R. K. Willardson and H. L. Goering, Editors, Reinhold Publishing Corp., New York (1962).
7. B. D. Lichter and P. Sommelet, *Trans. Met. Soc., AIME*, **245**, 1021 (1969), as subsequently revised by authors in Discussion Section of this Journal in reply to R. Blachnik.
8. C. N. Cochran and L. M. Foster, *This Journal*, **109**, 148 (1962).
9. J. R. Arthur, *J. Phys. Chem. Solids*, **28**, 2257 (1967).
10. C. D. Thurmond and C. J. Frosch, *This Journal*, **111**, 184 (1964).
11. JANAF Interim Thermochemical Tables, Thermal Laboratories, Dow Chemical Co. (1960).
12. D. R. Stull and G. C. Sinke, "Thermodynamic Properties of the Elements," American Chemical Society, Washington, D. C. (1956).
13. C. J. Frosch and C. D. Thurmond, *J. Phys. Chem.*, **66**, 877 (1962).

Compatibility of Battery Materials with Fuel Cell Catalysts

C. H. Weeks

CSIRO, Division of Mineral Chemistry, Port Melbourne, Victoria, Australia

Materials for constructing low-temperature fuel cell batteries must be carefully selected not only to resist attack by corrosive electrolytes, but also to avoid poisoning of catalysts. Very few systematic studies of fuel cell catalyst poisoning have been published. Witherspoon and Adams (1) studied a Rh-Pd hydrogen anode catalyst and found that cupric and ferrous ions in solution and a surfactant (Triton x 100) caused some loss of activity, while sulfide ion caused severe poisoning. Terry (2) reports that short life of hydrogen-air cells was attributable to poisoning from sulfur in molded rubber cell frames. Cathro (3) has found that platinum-based formaldehyde anodes fail rapidly in the presence of copper and silver ions in acid solution. Workers at Esso Research and Engineering (4) found that copper poisoned methanol anodes, but that aluminum had no effect.

Active catalysts for the oxidation of both methanol and formaldehyde have been developed in this laboratory (5, 6) and tested successfully for long periods in small-scale fuel cells. Early versions of larger cells and batteries were less successful, showing poor performance and short life, and it was evident that anode catalysts were becoming poisoned by impurities in solution. The experiments described below were undertaken to determine the undesirable impurities and their sources and to investigate possible substitutes.

Experimental

Each test was performed using a covered 2 liter glass pot cell. Five holes in the cover contained leads to the working and counterelectrodes, a probe leading out to a mercury/mercurous sulfate reference electrode, a glass-sheathed immersion heater, and a glass thermistor pocket. Anode catalyst (approx 150 mg of Pt-Re-Sn) was electrodeposited onto a gold-plated expanded tantalum or niobium disk of 13 cm^2 nominal area to form the working electrode. The counterelectrode was platinum gauze, and was surrounded by a glass tube to prevent evolved hydrogen reaching the working electrode. The solution was maintained at 60°C and agitated by the use of a magnetic stirrer unit. The working electrode was supplied with a current of 0.5A (38 mA/cm^2) from an external source. The fuel used was formaldehyde (0.3 ± 0.15M) dissolved in 2M sulfuric acid electrolyte. A few experiments were also performed with methanol (approx 1.0M) as fuel. Results were generally similar to those with formaldehyde.

The procedure for each test was to run the electrode for 50 or more hours to allow it to reach a steady potential, then to introduce a sample of the material to the pot. Where possible, size and physical form of the samples were selected to correspond with the maximum exposure likely in a practical battery. Working electrode potential was recorded daily, and any poisoning effect was detected by the resulting rise in potential. Corrections for *IR* drop were determined by a simple interruption technique.

Results and Discussion

One electrode was tested for several hundred hours in a solution free of impurities, using reagent-grade formaldehyde. The potential remained steady at 0.21 ± 0.02V *vs.* SHE throughout this time. The fuel supply was then changed to commercial 40% formaldehyde which contained some 8 ppm of iron. No evidence of poisoning was observed, and the electrode has now maintained the same potential for over 9000 hr.

The metals aluminum, zinc, and iron were tested as possible poisons. These are often present in liquid fuels stored in steel or aluminum containers and in contact with rubber seals or hoses. Aluminum was introduced to the test pot as chips of commercial metal which slowly dissolved, while the other metals were added as reagent-grade sulfates. In each case, the concentration was approximately 2 g/liter, but no poisoning was detected over periods exceeding 100 hr. This result for iron is in contrast to the poisoning detected by Witherspoon and Adams (1) using alkaline electrolyte and hydrogen anodes.

Further tests were made with 28g of unfilled polypropylene sheet and with 26g of plasticized PVC tube immersed in the solution. Slight poisoning (*see* Fig. 1) was apparent with PVC, perhaps from the plasticizer which was leached out by the acid formaldehyde solution.

Tests with rubbers and components of rubber compounds proved the most informative. As shown in Fig. 2, sulfur cured butyl rubber (used for seals in early battery tests) caused rapid and severe poisoning. Leaching the rubber samples for 4 weeks in a mixture of hot 2M sulfuric acid and ethanol retarded but did not eliminate this poisoning. Three other nonsulfur cured rubbers were tested—a peroxide cured ethylene-

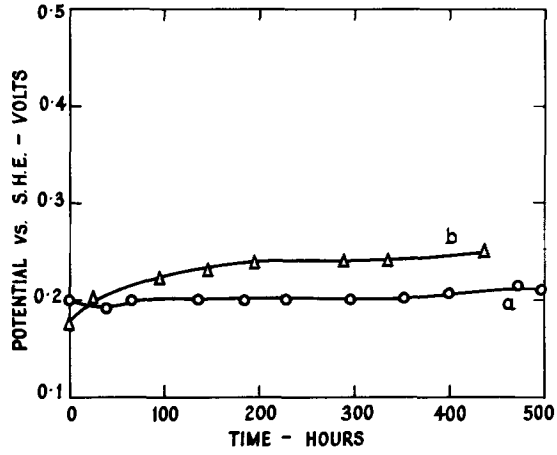

Fig. 1. Effect of plastics on formaldehyde electrodes: (a) 28g polypropylene (Shell KM 61) in cell; (b) 26g plasticized PVC tube (assorted pieces) in cell.

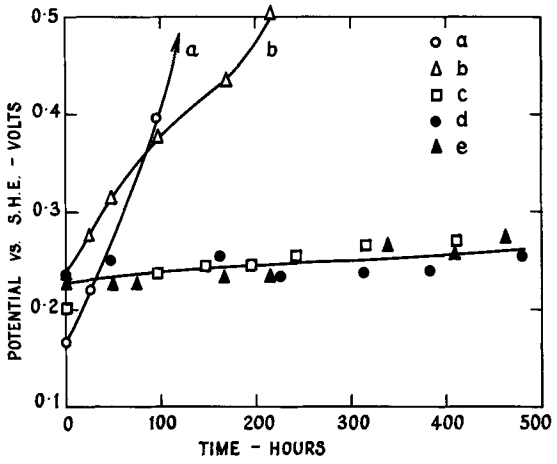

Fig. 2. Effect of rubbers on formaldehyde electrodes: (a) 20g sulfur cured butyl rubber in cell; (b) same as (a), but rubber preleached for 4 weeks in acid-ethanol solution; (c) 14g peroxide cured ethylene-propylene-diene terpolymer in cell; (d) 7g resin cured butyl rubber in cell; (e) 7g Permalux cured chlor-butyl rubber in cell.

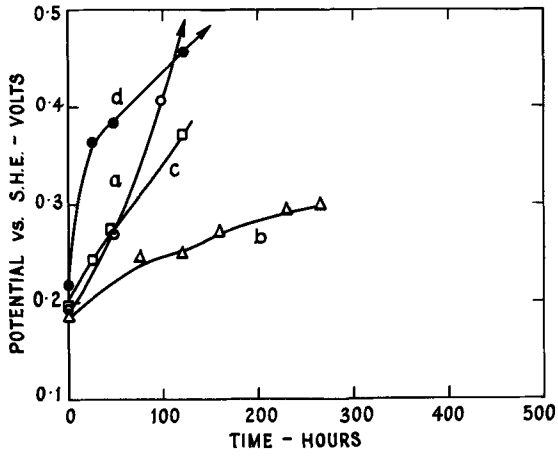

Fig. 3. Effect of rubber formulation components on formaldehyde electrodes: (a) 0.20g commercial sulfur in cell; (b) 0.10g mercaptobenzothiazole in cell; (c) 0.10g tetramethyl thiuram disulfide in cell; (d) 0.10g sodium diethyl dithiocarbamate in cell.

propylene-diene terpolymer, a resin cured butyl rubber, and a Permalux cured chlor-butyl rubber. (Permalux is a diorthotolyl guanidine salt of dicatechol borate.) The resulting potential changes (Fig. 2) were small or negligible. Slow poisoning was observed with some samples of ethylene-propylene-diene rubber, probably a result of contamination with traces of sulfur during manufacture.

Various components of these rubber compounds were then tested individually. Zinc oxide (*see* zinc test above), sample carbon blacks, a process oil, Permalux curing agent, and Santoflex I.P. anti-ozonant (N isopropyl N′ phenyl paraphenylene diamine) were found to cause no significant poisoning. Several sulfur-containing organic compounds, and also a sample of commercial sulfur, caused rapid poisoning (*see* Fig. 3). Evidently the hot acid-formaldehyde solution attacks these compounds, releasing sulfide ion or some other soluble sulfur species equally effective as a catalyst poison. These and similar compounds are widely used in rubber formulations as curing agents, accelerators, and anti-oxidants. Except where the sulfur is present in an oxidized form such as sulfate or polystyrenesulfonic acid, all sulfur-containing organic compounds need to be considered as possible catalyst poisons.

Conclusions

The catalysts used in this study are not affected by substantial concentrations of iron, zinc, and aluminum in solution.

Any sulfur-containing component should be completely eliminated from rubber formulations used for molding fuel cell frames or seals. Sulfur-free formulations are available which show reasonable acid resistance and life and eliminate the risk of catalyst poisoning. Unfilled polypropylene has proved a satisfactory material for construction, unlikely to affect electrode catalysts.

Acknowledgment

The assistance of Dr. K. J. Cathro in preparing the many working electrodes used in this study is gratefully acknowledged.

Manuscript received Nov. 3, 1969.

Any discussion of this paper will appear in a Discussion Section to be published in the December 1970 JOURNAL.

REFERENCES

1. R. R. Witherspoon and R. L. Adams, Extended Abstract No. 344, Electrochem. Soc. Meeting, Montreal, Oct. 6-11, 1968.
2. P. L. Terry, "60 Watt Hydrogen-Air Fuel Cell System," Interim Report, Feb. 1966, U.S. Clearinghouse Fed. Sci. Tech. Information. No. AD 629 220.
3. K. J. Cathro, Unpublished work.
4. Esso Research and Engineering Company, "Hydrocarbon-Air Fuel Cell," Semi-Annual Report, Dec. 1965, U.S. Clearinghouse Fed. Sci. Tech. Information. No. AD 634 078.
5. K. J. Cathro, *Electrochem. Technol.*, **5**, 441 (1967).
6. K. J. Cathro, *This Journal*, **16**, 1608 (1969).

The Electrodeposition of Metals in Porous Glass

Francis P. Fehlner[1]

Research and Development Laboratories, Corning Glass Works, Corning, New York

Porous glass impregnated with a soft superconductor such as lead behaves like a hard superconductor having a high critical magnetic field (1). Schmidt and Charles (2) made such a material by hydrostatically injecting molten metal into the fine capillary labyrinth of porous glass. The metal was dispersed in the glass as filaments or adjoining spheres having a diameter of less than 100Å. In the present work, an electrochemical method has been used to impregnate Corning Code 7930 porous glass with both lead and silver.

[1] Present address: Signetics Corporation, Sunnyvale, California.

Experimental

Glass preparation proved to be the most critical step in the experimental procedure. Samples of 3/16-in. porous glass sheet (pore size: 40-60Å) 1½ in. square were cleaned by boiling in 5% H_2O_2 or baking in air at 500°C. Indium film electrodes, 1 in. square, were evaporated onto one side of the glass and a lead wire was attached to the electrode with indium solder. The edges of the glass and the electroded side were completely covered with paraffin. This was done so that the plating solution could only approach the indium electrode by

passing through the glass. The final step in preparing a sample for electrolysis was humidification of the glass so that it would not crack when it was introduced into the plating solution.

The unsymmetrical a-c electrolysis apparatus is outlined in Fig. 1. A negative d-c bias on the indium electrode is combined with a 60-Hz, half-wave rectified a-c signal to produce an unsymmetrical a-c signal. The waveform produced by this signal is shown in Fig. 2. The positive portion of the voltage waveform applied to the lead or silver electrode brings about plating in the pores of the glass. Conversely, the negative portion causes deplating. The plating/deplating ratio can be adjusted by changing the relative a-c and d-c components of the unsymmetrical a-c signal.

During the lead deposition in porous glass, the unsymmetrical a-c signal was applied for upward of 3 hr. A d-c level of 1V at 30 mA was employed but, because of the d-c blocking resistor located next to the a-c source (Fig. 1), an a-c level of 30 V_{RMS} was required to obtain 7 mA. These numbers are given to show the magnitudes involved, and are to be considered neither exact nor ideal, since some interference occurred between the a-c and d-c portions of the circuit shown in Fig. 1.

The lead-plating solution (3) consisted of the following compounds dissolved in distilled water: $Pb(OH)_2 \cdot 2PbCO_3$, 0.150g ml^{-1}; HF (50%), 0.240g ml^{-1}; and H_3BO_3, 0.105g ml^{-1}. The resulting solution was stirred at room temperature in a Teflon beaker. The counterelectrode was technical-grade sheet lead.

In the case of silver, a solution of 0.133g $AgNO_3$ ml^{-1} of distilled water was used, along with a sheet-silver counterelectrode.

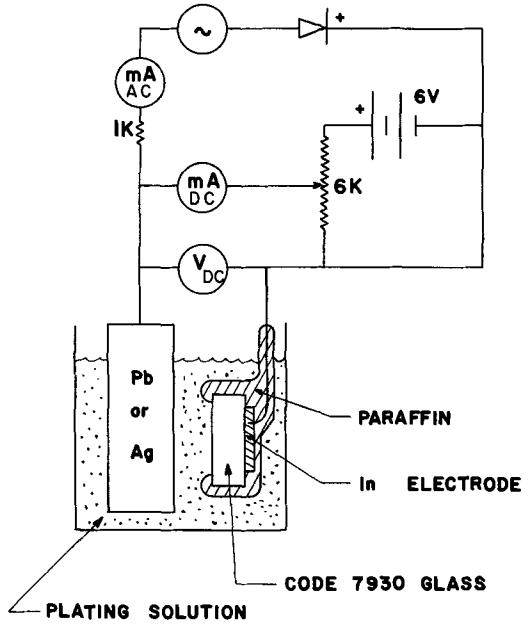

Fig. 1. Diagram of the circuit used for unsymmetrical a-c electrolysis.

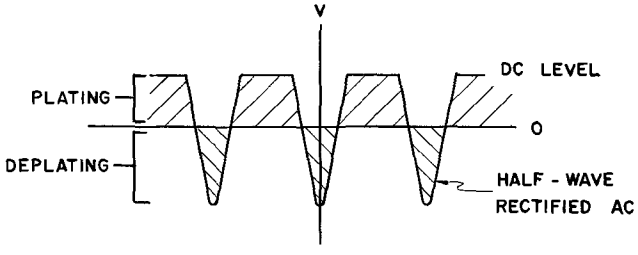

Fig. 2. Waveform of the unsymmetrical a-c voltage across the plating bath. The voltage level refers to the lead or silver electrode. Plating and deplating occur in the pores of the Code 7930 glass.

Results

Deposition of metal in the pores of Code 7930 glass did not begin immediately when a prepared sample was introduced into the plating solution and the unsymmetrical a-c voltage was applied. Instead, there was a lag of approximately 20 min during which the electrolyte diffused from the front of the glass, through the pores, to the indium electrode. After this induction period, a black deposit could be seen to grow over the indium and into the glass. This was the beginning of metal deposition in the pore structure.

Under the influence of a d-c potential alone, portions of the metal deposit grew faster than the rest of the deposit. These "leading dendrites" quickly reached the surface of the glass, preventing further deposition of metal in the pores. The unsymmetrical a-c electrolysis corrected this problem by deplating metal fastest at the points of highest potential gradient, *i.e.* at the "leading dendrites." During the subsequent plating pulse, metal was deposited uniformly over the whole growth front. In this manner, the "leading dendrites" were destroyed and the metal growth front advanced steadily through the sample.

The density of lead electrodeposited in Code 7930 porous glass was not as high as was theoretically possible. After 3 hr, only 10% of the pore volume had been uniformly filled with lead. It should be possible to improve both the rate of deposition and the per cent of pore filling by adjusting the process variables such as temperature and plating/deplating ratio.

Unsymmetrical a-c electrolysis has also been used to deposit filamentary silver in porous glass. Sample preparation and plating conditions similar to those used for lead gave good results. In fact, the silver samples appeared to be of better quality than the lead specimens.

Optical microscopy showed that the metal deposited in porous glass formed a dendritic structure which continuously branched into shorter and shorter limbs.

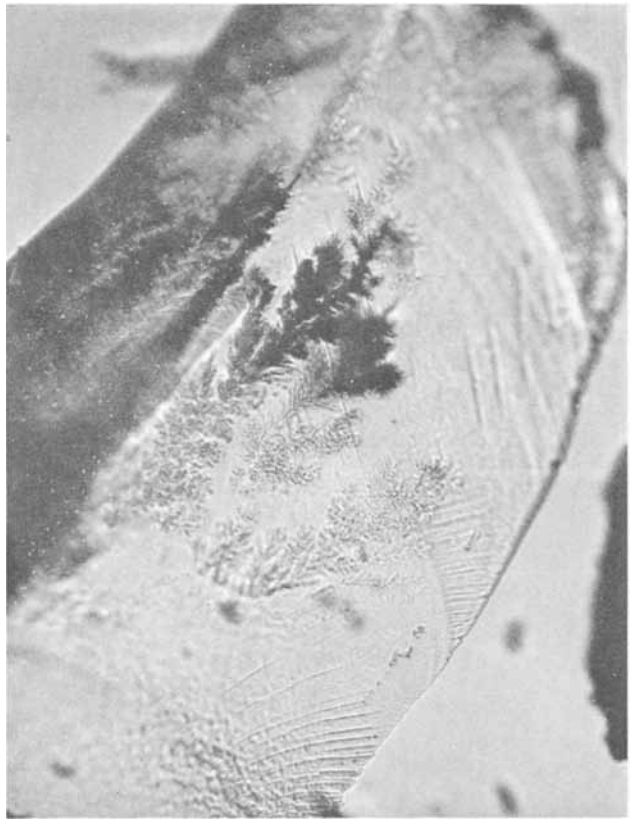

Fig. 3. Photomicrograph of lead electrodeposited in Code 7930 porous glass. Transmitted light; 200X.

An optical micrograph of chips from a lead-impregnated sample is shown in Fig. 3. The diameter of the smallest branches could not be resolved optically, although the dendritic structure, both in the direction of growth and in cross section, was readily visible. Electron microscopy of a silver deposit showed that the diameter of the metal filaments was less than 100Å. This compares well with the pore size of approximately 50Å.

Conclusions

Unsymmetrical a-c electrolysis is a useful method for impregnating the pores of Corning Code 7930 glass with metals. In the case of lead and silver, glass preparation is the most critical step in the procedure. However, it will be necessary to experiment further with the plating parameters, if a denser deposit is desired.

Acknowledgments

The aid of T. H. Elmer, G. Pratt, E. Kennedy, and G. Carrier in carrying out this project is acknowledged.

Manuscript submitted Oct. 2, 1968; revised manuscript received Oct. 9, 1969.

Any discussion of this paper will appear in a Discussion Section to be published in the December 1970 JOURNAL.

REFERENCES

1. C. P. Bean and R. W. Schmitt, *Science*, **140**, 26 (1963).
2. W. G. Schmidt and R. J. Charles, *J. Appl. Phys.*, **35**, 2552 (1964).
3. T. Lyman, Editor, "Metals Handbook," 1948 Ed., p. 719, Am. Soc. for Metals, Cleveland.

A Simple Procedure for Mounting Sodium-Tungsten Bronze Electrodes

R. S. Alwitt* and A. K. Vijh*,[1]

Research and Development Laboratories, Sprague Electric Company, North Adams, Massachusetts

Recently, Mannan (1) has reported a rather elaborate method for mounting sodium-tungsten bronze electrodes in a glass-Teflon assembly. Here, a much simpler procedure, which is a minor variation of our previous suggestion for preparing metallic electrodes (2), is described.

A Na_xWO_3 crystal, C in Fig. 1(*a*), is chiseled with a diamond wheel and/or a diagonal cutter (or a suitable substitute) to give it the form of a crude cone. This chiseled end is deposited in the slightly funneled, flame-polished end of a "Trubore" (or any other) glass tubing, G [Fig. 1(*a*)]. After C is placed in G, this end of the glass tubing, G, is surrounded by a suitable length [Fig. 1(*b*)] of a special, heat-shrinkable, two-layered Teflon tubing available commercially (*e.g.*, "Flotite" manufactured by Pope Scientific Incorporated, Menominee Falls, Wisconsin). The Teflon tubing is then heated by means of a heat gun to $\geqslant$ 330°C *first* at glass-Teflon boundary (shown by 1) and then, after cooling, at the Teflon-glass-bronze boundary (as shown by 2). A compact and satisfactory seal of Teflon thus connects the bronze to the "Trubore" glass tubing. The electrical contact may then be made by means of a copper wire and a mercury drop (or some suitable substitute, *e.g.* Ga-In alloy). The electrode surface may be made smooth by polishing gently on an abrasive wheel with subsequent cleaning by a variety of solvents. A typical electrode thus obtained is shown schematically in Fig. 2.

* Electrochemical Society Active Member.
[1] Present address: Institute of Research, Hydro-Quebec, Varennes, P. Q., Canada.

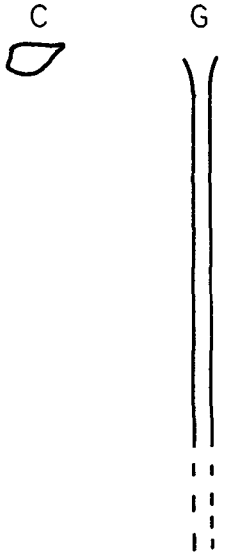

Fig. 1(*a*). A sodium tungsten bronze piece chiseled into a rough cone, C, and a "Trubore" glass tubing, G, with its end slightly funneled and flame polished.

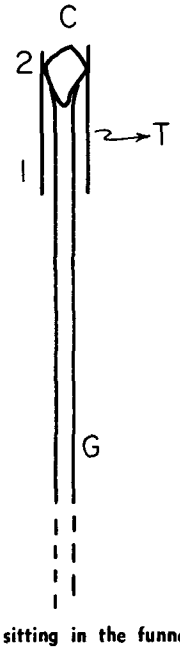

Fig. 1(*b*). Cone, C, sitting in the funneled end of glass tubing, G. The C-G boundary is surrounded by a piece of "Flotite" tubing, T. Heat must be applied first around the region marked 1 and then at 2.

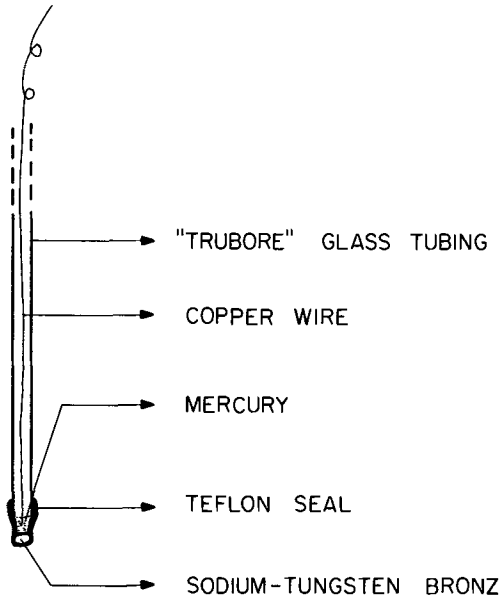

Fig. 2. A schematic representation of a sodium-tungsten bronze electrode mounted in a glass-Teflon assembly.

It may be added that, with slight obvious modifications, the described procedure may be used for mounting *any* metallic (2) or nonmetallic electrode material provided that it can withstand temperatures up to *ca.* 400°C [for substances with somewhat lower melting points, *see* Ref. (2)]. This procedure would thus be expected to be also suitable for preparing electrodes from germanium, silicon, graphite, carbides, borides, and a variety of other materials.

Acknowledgment

Thanks are due to Mr. J. McHardy of the Electrochemistry Laboratory, University of Pennsylvania, for providing sodium-tungsten bronze crystals.

Manuscript received Aug. 1, 1969.

Any discussion of this paper will appear in a Discussion Section to be published in the December 1970 JOURNAL.

REFERENCES

1. R. J. Mannan, Ph.D. Thesis, Univ. of Pennsylvania, Philadelphia, Pa. (1967).
2. A. K. Vijh and R. S. Alwitt, *J. Chem. Ed.*, **46**, 121 (1969).

Erratum

In the paper "Studies on Chlorate Cell Process, V. Theory and Practice of a Modified Technology for Electrolytic Chlorate Production" by M. M. Jaksić, A. R. Despić, I. M. Csonka, and B. Z. Nikolić which was published on pp. 1316-1322 of the September 1969 issue of the JOURNAL, Vol. 116, No. 9, several errors appeared in Appendixes I and II (pp. 1320-1322). The corrected Appendixes follow.

APPENDIX I

One can arrive at Eq. [5] both in the given and an extended form, which takes into account all kinds of losses in the electrolytic production of chlorate for a closed-loop system, by considering the material balance of available chlorine with respect to the cell at quasi steady-state condition, which is defined by [*cf.* (4)]

$$V_c \cdot \left(\frac{dC_{sc}}{d\tau} \right) = 0 \qquad [15]$$

The partial contributions of individual components of production, consumption, and loss of available chlorine during the process would be as follows:

(*a*) Anodic generation of available chlorine, which is converted to chlorate by two possible parallel paths (Eq. [2] and [3])

$$V_c \cdot \left(\frac{dC_{sc}}{d\tau} \right)_{G1} = \frac{t_1 \cdot I}{2\mathbf{F}} \qquad [16]$$

where t_1 is the fraction of current used for generation of chlorine by anodic oxidation of chloride

$$2Cl^- \rightarrow Cl_2 + 2e \qquad [17]$$

with subsequent hydrolysis

$$Cl_2 + 2H_2O \rightleftharpoons HClO + H_3O^+ + Cl^- \qquad [18]$$

and *conversion* (Eq [2]), or further *anodic oxidation* (Eq. [3]) to chlorate.

(*b*) Anodic generation of available chlorine, which is subsequently lost in the electrolytic production process by cathodic reduction

$$ClO^- + H_2O + 2e \rightarrow Cl^- + 2OH^- \qquad [19]$$

is described as

$$V_c \cdot \left(\frac{dC_{sc}}{d\tau} \right)_{G2} = \frac{t_2 \cdot I}{2\mathbf{F}} \qquad [20]$$

where t_2 is the fraction of the current used for generation of that part of available chlorine.

(*c*) Anodic generation of available chlorine, which is subsequently lost by evaporation in the hydrogen stream

$$V_c \cdot \left(\frac{dC_{sc}}{d\tau} \right)_{G3} = \frac{t_3 \cdot I}{2\mathbf{F}} \qquad [21]$$

where t_3 is the fraction of the current used for unhydrolyzed chlorine.

(*d*) Further anodic oxidation of available chlorine to chlorate (Eq. [3]).

$$V_c \cdot \left(\frac{dC_{sc}}{d\tau} \right)_{OX} = -\frac{t_4 \cdot I}{\mathbf{F}} \qquad [22]$$

where t_4 is the fraction of the current for the anodic chlorate formation.

(*e*) Available chlorine consumption by cathodic reduction

$$V_c \cdot \left(\frac{dC_{sc}}{d\tau} \right)_{RED} = -\frac{t_2 \cdot I}{2\mathbf{F}} \qquad [23]$$

which corresponds to Eq. [20].

(*f*) Current losses by chlorine evaporation in the hydrogen stream

$$V_c \cdot \left(\frac{dC_{sc}}{d\tau} \right)_{E} = -\frac{t_3 \cdot I}{2\mathbf{F}} \qquad [24]$$

(*g*) Conversion of available chlorine to chlorate (Eq. [2]) inside the cell (18, 19), which operates as back-mix flow reactor

$$V_c \cdot \left(\frac{dC_{sc}}{d\tau} \right)_{CH} = -3f_c^2 \cdot k_{r,c} \cdot V_c \cdot [HClO]_c^2 \cdot [ClO^-]_c \qquad [25]$$

(*h*) The difference in quantities of available chlorine leaving the cell and entering the cell from the holding volume in the considered time interval (which is equal to the conversion of available chlorine to chlorate inside the holding volume)

$$V_c \cdot \left(\frac{dC_{sc}}{d\tau} \right)_{H} = -q(C_{sc} - C_{sh}) \qquad [26]$$

The material balance (Eq. [15]) thus is given by the following relation

$$\frac{t_1 \cdot I}{2\mathbf{F}} + \frac{t_2 \cdot I}{2\mathbf{F}} + \frac{t_3 \cdot I}{2\mathbf{F}} - \frac{t_4 \cdot I}{\mathbf{F}} - \frac{t_2 \cdot I}{2\mathbf{F}} - \frac{t_3 \cdot I}{2\mathbf{F}} - 3f_c^2 \cdot k_{r,c} \cdot V_c \cdot [\mathrm{HClO}]_c^2 \cdot [\mathrm{ClO}^-]_c - q(C_{sc} - C_{sh}) = 0 \quad [27]$$

Individual fractions of the anodic current are, in that case, connected by the relation

$$t_1 + t_2 + t_3 + t_4 = 1 \quad [28]$$

By combining Eq. [27] and [28], one obtains the explicit expression for the current efficiency on chlorate

$$t_1 = \frac{2}{3} + \frac{2f_c^2 \cdot k_{r,c} \cdot V_c \cdot \mathbf{F}}{I} \cdot [\mathrm{HClO}]_c^2 \cdot [\mathrm{ClO}^-]_c + \frac{2}{3}\mathbf{F}\left(\frac{q}{I}\right) \cdot (C_{sc} - C_{sh}) - \frac{2}{3}(t_2 + t_3) \quad [29]$$

in which further transformations of the second and third terms are possible, as given in the main part of the paper. By dividing all terms of Eq. [27] by three, one can relate the generation and consumption of available chlorine with chlorate production, which means that t_1 also defines the current efficiency in the process of electrolytic chlorate production.

The current losses due to the catalytic decomposition of available chlorine and chlorate, or the anodic oxidation to perchlorate, are practically avoided under normal conditions of production, and thus need not be taken into consideration in the presented analysis.

The fraction of the current loss due to cathodic reduction is given as a ratio of the difference between the theoretical amount of hydrogen (V_o) and that actually produced amount (V_1), to the theoretically given amount (V_o) for a certain duration of electrolysis, namely

$$t_2 = \frac{V_o - V_1}{V_o} \quad [30]$$

The fraction of the current loss due to chlorine evaporation can also be determined by gas analysis as the ratio of percentage fractions of chlorine (Q) and hydrogen (H)

$$t_3 = \frac{Q}{H} \quad [31]$$

under the conditions of negligible cathodic reduction of available chlorine. If it is not negligible, this relation gives the ratio of evaporated chlorine to the theoretical amount of hydrogen developed for the same time interval.

In the presence of dichromate ions, with sufficiently high current densities and in a suitably defined pH region, both kinds of loss tend to zero, and Eq. [29] reduces to Eq. [5].

APPENDIX II

The equation for calculating the current efficiency from the gas analysis, which takes into account all kinds of losses, listed in Appendix I, can be derived using Faradaic stoichiometry, *i.e.* coulometric balance.

Consider the passage of N faradays through the cell during a definite time interval under quasi steady-state conditions of electrolytic chlorate production. This should be distributed as follows:

(*a*) Let x be the fraction of the charge, N, at the anode which is used to oxidize those chloride ions (Eq. [17]), which on discharge give molecular chlorine subsequently lost by evaporation (unhydrolyzed chlorine). Then $x \cdot \mathbf{F}$ produce $x/2$ moles of evaporated chlorine at the anode, and $x/2$ moles of hydrogen at the cathode.

(*b*) Let y be the fraction used to oxidize chloride ions which produce available chlorine to replace that which is consumed by chemical conversion to chlorate (Eq. [2]). Then $y \cdot \mathbf{F}$ produce $y/2$ moles of available chlorine at the anode and $y/2$ moles of hydrogen at the cathode.

(c) Let z be the fraction used to oxidize further the available chlorine into chlorate (Eq. [3]). Then $z/4$ moles of oxygen are produced at the anode and $z/2$ moles of hydrogen at the cathode.

d) Let w be the fraction which produces hypochlorite ions to replace those reduced at the cathode (Eq. [19]). Then $w \cdot \mathbf{F}$ produce $w/2$ moles of available chlorine at the anode and reduce the same amount at the cathode.

All the fractions must sum up to give the total amount of charge as

$$x + y + z + w = N \quad [32]$$

The fraction of oxygen (S) in the gas mixture should then be

$$S = \frac{\mathrm{O_2}}{\mathrm{H_2} + \mathrm{O_2} + \mathrm{Cl_2}} = \frac{\frac{z}{4}}{\left(\frac{x}{2} + \frac{y}{2} + \frac{z}{2} + \frac{z}{4} + \frac{x}{2}\right)} \quad [33]$$

while the content of unhydrolyzed (evaporated) chlorine (Q), obtained by gas analysis, is given by the equation

$$Q = \frac{\mathrm{Cl_2}}{\mathrm{H_2} + \mathrm{O_2} + \mathrm{Cl_2}} = \frac{\frac{x}{2}}{\left(\frac{x}{2} + \frac{y}{2} + \frac{z}{2} + \frac{z}{4} + \frac{x}{2}\right)} \quad [34]$$

The current fraction lost by cathodic hypochlorite reduction ($P = t_2$) is expressed by the following relation

$$P = \frac{\frac{w}{2}}{\left(\frac{x}{2} + \frac{y}{2} + \frac{z}{2} + \frac{w}{2}\right)} \quad [35]$$

The current efficiency of chlorate formation (t_1), which has to be equal to the theoretical amount of electricity required for the yield divided by the actual amount used, is then given, expressed as a fraction of unity, by

$$t_1 = \frac{\frac{y}{2}}{\left(\frac{x}{2} + \frac{y}{2} + \frac{z}{2} + \frac{w}{2}\right)} \quad [36]$$

Equations [33-36] represent a system of four homogenous linear equations, which can be solved for t_1 by eliminating the unknown quantities x, y, z, and w

$$t_1 = \frac{(1 - 2Q - 3S)(1 - P)}{1 - Q - S} \quad [37]$$

The partial fractions of oxygen (S) and chlorine (Q) are determined by the gas analysis, while the determination of the current fraction losses by hypochlorite reduction at the cathode ($P = t_2$) is discussed in Appendix I. Carbon dioxide is added to the oxygen content in the present calculations.

JOURNAL OF THE ELECTROCHEMICAL SOCIETY

ELECTROCHEMICAL SCIENCE

APRIL 1970

Unsteady-State Phenomena on Oxygen Cathodes of Hydrogen-Oxygen Fuel Cells

Joseph O. DeVet,[1] Ronald G. Barile, and Lyle F. Albright

School of Chemical Engineering, Purdue University, Lafayette, Indiana

ABSTRACT

The phenomenon of oxygen transfer to the surface of a platinum cathode has been clarified for a hydrogen-oxygen fuel cell. The cathode which was partially submerged in acid electrolyte was investigated at various steady-state conditions, for various methods of raising and lowering, and at several start-up conditions. Large currents are generated in the cathodic area close to the meniscus because transfer of oxygen is relatively easy there. Larger currents can be obtained by lowering or in some cases by raising a cathode which is partially immersed in the acid electrolyte.

Convincing evidence has been presented recently that the most important reaction zone on the anode of a hydrogen-oxygen fuel cell is the thin portion of the meniscus and the adjacent thin film of electrolyte (1-6). The diffusion path of the hydrogen from the gas phase to the electrode surface is short in this zone, and concentration polarization is reduced (3, 4, 7-9).

Vertical movements of the anode of a hydrogen-oxygen cell partially immersed in acid electrolyte were found by Will (3) to produce significant transient effects. Currents were initially depressed when a platinized anode was raised, but they were increased when it was lowered. Ennis (6) found, however, for a sand-blasted platinum anode that the currents were larger than steady-state with both raising and lowering. Davitt and Albright (5) resolved this apparent anomaly by demonstrating that the character of the surface roughness is important relative to these transient currents. They also reported large initial surges of current with quick anode lowering and increased currents with gradual constant-speed lowering. The average current was found to depend on the rate of anode movements, applied potential, and surface condition.

In the present investigation, unsteady-state current responses during cathode motion were studied. The objectives were to provide detailed data for motion of the oxygen cathode in acid electrolyte similar to those presented by Davitt asd Albright (11) for the anode and to examine further the constant-speed lowering phenomena. Steady-state, stationary-cathode data are compared with the unsteady-state currents. Current changes during lowering are proposed to be similar to the transient currents at cell start-up. Results of cathode raising are explained in terms of changes in the meniscus region.

Experimental

The cell was constructed mainly of borosilicate glass (Pyrex) and consisted of a large cathode chamber separated from the smaller (450 ml) anode chamber by a porous glass disk. The electrolyte was 1*N* sulfuric acid prepared from reagent grade acid and distilled water. A bubbler, which was immersed in the electrolyte 4 in., was shielded by a glass cylinder with an open end immersed 5 in. Oxygen was bubbled through the electrolyte at the rate of about 800 cc/hr and then flowed to the cathode chamber. A glass stirrer was used to agitate the electrolyte and assure its homogeneity. The temperature of the electrolyte was maintained at 30° ± 0.3°C, and the cathode chamber was operated at atmospheric pressure.

The three cathodes used were prepared from platinum foil 0.0125 cm thick and 3 cm wide by 8 cm high. The top of each cathode was spot-welded to a 12 cm length of platinum wire which was connected by copper wire to the external circuit. The first cathode (S) was unaltered foil with a mirror-like surface. It produced low currents which did not achieve steady-state but which decayed over long periods of time. Similar difficulties with smooth platinum has been reported by others (4). Because a reliable steady-state reference could not be developed for this cathode, only limited experimentation was tried with it. The other two cathodes were platinized using 10% chloroplatinic acid and a current density of 10 mA/cm^2. Platinizing for 120 sec produced a "moderately platinized" cathode (henceforth called cathode M) and for 240 sec yielded a "heavily platinized" cathode (cathode H). Roughness factors (BET surface/geometric surface) for the three cathodes were calculated to be 1, 75, and 150 for the smooth, moderately platinized, and heavily platinized cathodes, respectively. These calculations are based on the measured capacitances at the rest potential and the specific capacitance (capacitance/BET surface area) reported earlier (10, 11).

The anode (often partially submerged in the electrolyte) consisted of two rectangular strips of platinum foil totaling 48 cm^2 geometric surface area, which was platinized for 5 min at a current density of 20 mA/cm^2. Hydrogen was continuously supplied to the anode chamber at approximately 800 cc/hr.

Potentials were referred to a Leeds and Northrup saturated calomel electrode (SCE) which has a poten-

[1] Present address: Humble Oil and Refining Company, Baytown, Texas.

tial relative to the normal hydrogen electrode (NHE) of 0.242V at 30.0°C (12). A potentiostat similar to the one described by Schwarz and Shain (13) was used to control the cathode potential. Current measurements were reported continuously on a Sargent Model SR recorder.

A glass tube through which the electrical lead from the cathode was passed was used as a support for the cathode. It was often connected to a motor-driven elevator for adjusting the vertical height of the cathode at various constant rates. Alternatively, the position could be hand adjusted by 2 to 4 cm in less than 1 sec. The currents as reported here for stationary positions of the cathode are the steady-state values obtained after about 20-40 min. For runs at a constant rate of raising, the fully submerged cathode was first allowed to reach a steady-state current before raising was started.

Prior to each run the electrode was cleaned by immersion for 0.5 hr in a solution of 20% reagent grade nitric acid at the boiling point. After a thorough rinse in distilled water the cathode was introduced into the cell, and the cell was allowed to equilibrate 4-12 hr before the start of the run. Experiments with stationary cathodes resulted in currents which were reproducible to within ±3%, while those with moving cathodes were reproducible to within ±5%.

Results

Stationary cathodes.—The current phenomena for the moderately platinized and the heavily platinized cathodes were investigated at cell start-up. In each case, the cathode was immersed in the electrolyte and then allowed to equilibrate in the system for at least 3 hr at open-circuit. The circuit was then closed, and a given potential was applied. Figure 1 indicates resulting current responses reported as mA/cm² for both cathode M (moderately platinized cathode) and cathode H (heavily platinized cathode).

A high initial current was obtained in all cases at start-up, but the current decayed rapidly toward the steady-state value in the first few minutes. Higher initial currents were obtained at 0.158V as compared to 0.558V. The difference in the results for the two cathodes at 0.158V was small. If the cell was shut down (*i.e.*, the circuit was opened) and then restarted within less than 3 hr, the initial current was less than that shown in Fig. 1. Hence equilibration of the cathode with the surroundings is an important consideration.

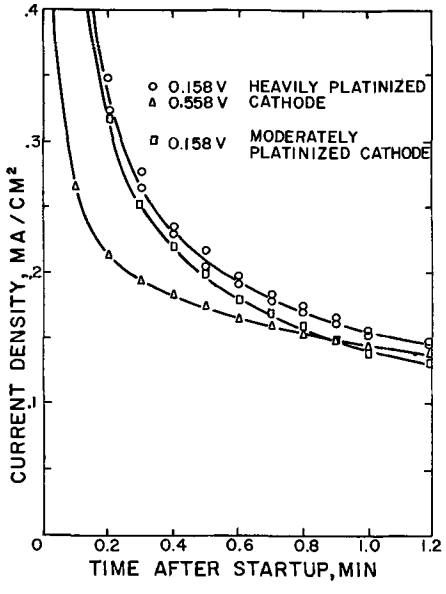

Fig. 1. Current as a function of time after cell start-up for heavily platinized cathode (cathode H) and for moderatively platinized cathode (cathode M).

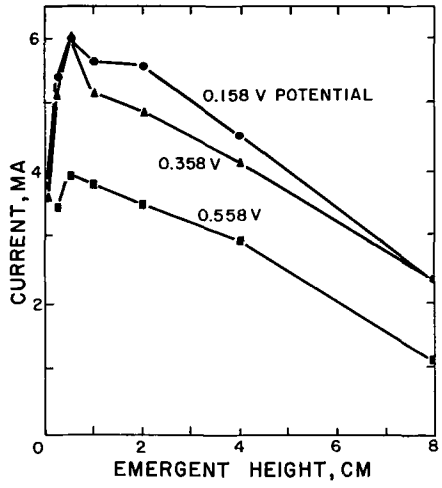

Fig. 2. Current as a function of emergent height for cathode H at three applied potentials.

Steady-state currents were obtained after about 20-40 min, and these currents were investigated as a function of the length of the cathode extending above the surface of the electrolyte, called here the emergent height, h. Figure 2 shows the results for cathode H at heights between fully submerged, $h \leq 0$, and just touching the electrolyte (but with a complete meniscus), $h = 8$ cm. The results for cathode M were essentially identical.

The meniscus contributed the increase in the steady-state current between $h = 0$ and approximately $h = 0.5$ cm (at which height the meniscus was fully developed), or the total current at $h = 8$. In most cases, these two current values were identical within experimental accuracy. The completely submerged cathode of course contributed the current at $h = 0$. The currents at 0.158 and 0.358V were quite similar and significantly higher than those at 0.558V. At about $h = 0.5$ cm, the meniscus produced for cathodes M and H approximately 40% of the total current at 0.158 and 0.358V, and about 30% at 0.558V. The meniscus for the smooth cathode (cathode S) however produced less than 5% of the current for that cathode. At 0.158V, the meniscus for cathodes M and H contributed about 0.38 mA/cm of meniscus length which is in excellent agreement with 0.40 mA/cm found by Maget and Roethlein (4) at 0.156V.

Comparisons of the currents obtained from similarly polarized cathodes and anodes are of interest. Table I gives one such comparison. The results of cathode H at 0.158V and of the anode at 0.55V as used by Davitt and Albright (5) were used to prepare this table. These voltages represent polarizations (deviations from open circuit) for the similarly activated electrodes of about 0.6 and 0.8V, respectively. The current density of the completely submerged cathode was about 60% greater than that of the submerged anode. The meniscus current of the anode was, however, about 4.7 times greater than that of the cathode. Comparisons of the meniscus

Table I. Comparison of currents generated at cathode and anode

	Cathode, (this work)	Anode (5)
Potential SCE	0.158V	0.55V
Polarization	0.6V	0.8V
Dimensions	3 cm × 8 cm	2.5 cm × 8 cm
Geometrical surface area, cm²	48	40
Current when completely submerged, mA	3.8	2.0
Current when completely submerged, mA/cm²	0.08	0.05
Meniscus current, mA	2.2	9.0
Current per linear length of meniscus, mA/cm	0.37	1.8
Estimated current density in meniscus area (0.25 cm meniscus height assumed)	1.5	7.2

currents for an anode (3) and of a cathode (4) at lower polarizations gave a similar result. Current densities in the meniscus region are greater by a factor of about 20 and 150 as compared to the densities in the submerged portions of the cathode and anode, respectively, if it is assumed that the effective height of the meniscus in each case is 0.25 cm.

Rapid height changes of cathodes.—Current-time response was investigated for a rapid change in height (within 1 sec or less) from $h = 2$ to $h = 6$ cm, or vice versa. Lowering cathode H caused the currents at potentials of 0.158 and 0.558V to first surge rapidly above 14 mA and then to decay in a few seconds to within 3 mA of the new steady-state currents at $h = 2$ cm (see Fig. 3). The current-time response when the cathode was quickly lowered from a position completely withdrawn from the electrolyte to a given emergent height h was found to be identical within experimental accuracy to the response for the start-up of the stationary cathode at the same height.

Raising cathode H rapidly caused an initial current depression then a 5-10 mA surge and finally a decay to the steady-state current at $h = 6$ cm, as shown in Fig. 4. The current surges and the time of decay were considerably greater at 0.158V than at 0.558V. The current responses for both rapid raising and lowering were found to be quite similar for cathodes H and M.

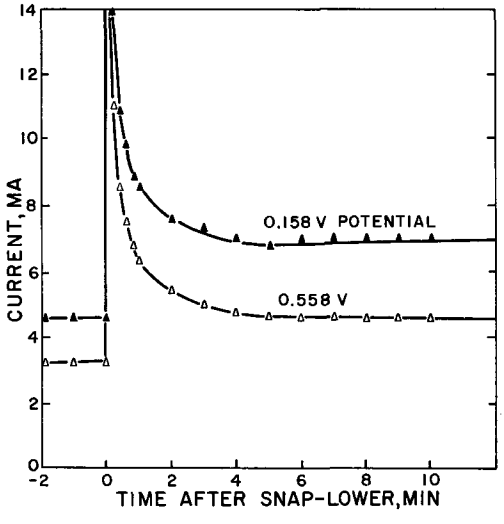

Fig. 3. Current as a function of time after rapid lowering of cathode H.

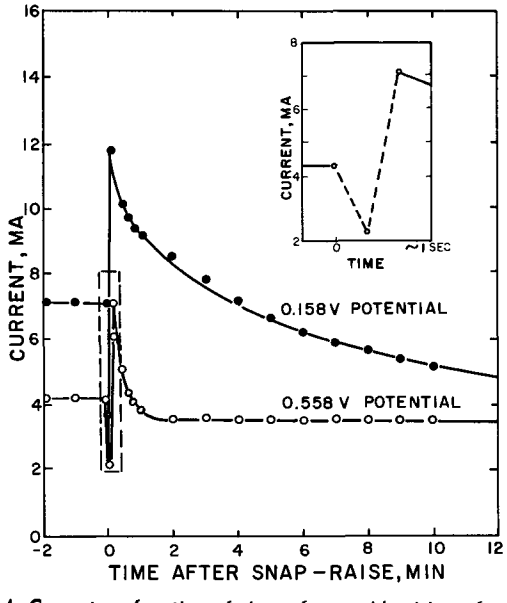

Fig. 4. Current as function of time after rapid raising of cathode H. The insert indicates the current response immediately after raising the cathode at 0.558V.

Constant-speed movement of cathode.—Constant-rate raising or lowering experiments with cathodes M and H were begun with the cathode either completely submerged at steady-state current or completely exposed to an oxygen atmosphere, respectively. Figures 5 and 6 show results for cathode H at 0.558 and 0.158V, respectively. In these figures, the current was plotted *vs.* the emergent height for various rates of lowering and raising. Larger increases of current were obtained especially at 0.158V, as the rate of lowering increased. The currents for the stationary cathode (*i.e.*, zero rate of lowering) are also shown and designated as steady-state currents. About a seven-fold increase was obtained when the rate of lowering was 18.5 cm/min as compared to the currents for the stationary cathodes.

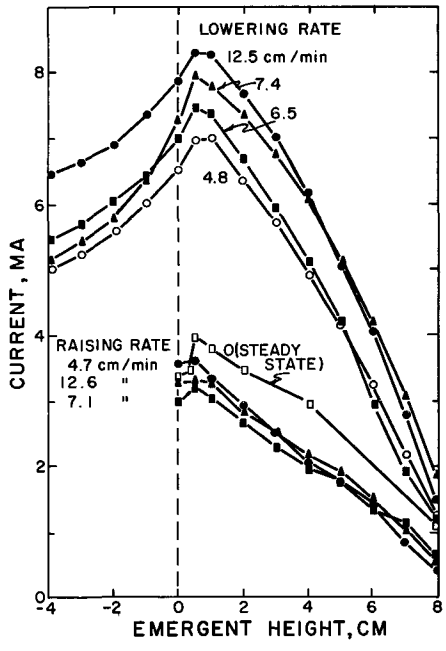

Fig. 5. Current as a function of emergent height during constant-speed motion of cathode H at 0.558V.

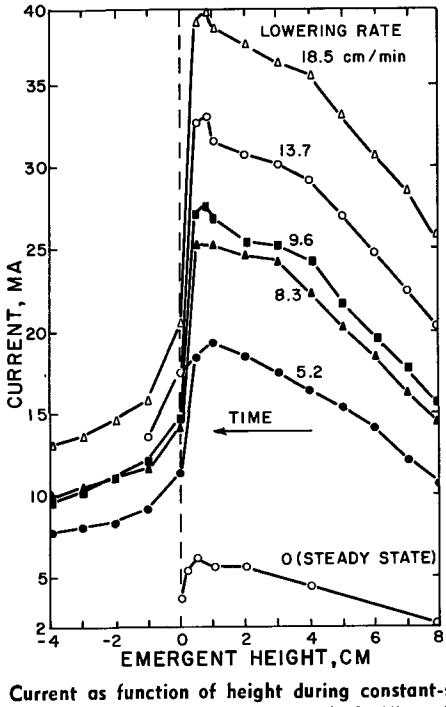

Fig. 6. Current as function of height during constant-speed lowering of the heavily platinized cathode (cathode H) at 0.158V potential.

These higher currents continued even when the cathode was completely submerged in the electrolyte, that is for $h < 0$ cm.

Raising cathode H at rates of 4.7-12.6 cm/min caused the current to decrease slightly as compared to the steady-state values of current when the potential was 0.558V, as also shown in Fig. 5. Larger currents were obtained however at 0.158V when the cathode was raised at constant rates. In general, this trend was proportional to the rate of raising as the rate was increased to about 8 cm/min. About a 2-fold increase of current was obtained at this rate as compared to the currents for the stationary cathode. No significant change in current was noted however between raising rates of 8.0 and 18.4 cm/min.

The average current obtained during either the raising or the lowering of the cathode at constant speed was calculated by averaging the current-emergent height data from 0 to 8 cm. Such an averaging technique is useful in quantitatively comparing how the rate of lowering or raising the cathode affects the current density. Results for raising and lowering at both 0.158 and 0.558V with cathodes H and M are shown in Fig. 7. Cathode H produced slightly higher currents, but the types of electrode surface had relatively less effect as compared to the applied potential and the direction of motion.

Discussion of Results

The general phenomena and current responses noted in the present investigation for various cathodes were quite similar in character to those noted earlier for anodes (5). As had also been found in the anode study, the current generation is controlled to a considerable extent by physical effects rather than by electrochemical ones. Controlling factors for the cathode include transfer of the oxygen to the electrode and the character of both the meniscus and adjoining film.

The results of Fig. 2 indicate that steady-state currents for partially submerged cathodes were diffusion controlled, especially in the range of 0.158-0.358V. In this range, they increased slightly with decreasing potential. Activation control is thought, however, to be limiting at 0.558V and above, at which potentials considerably lower currents are obtained. These conclusions and the general character of the current-height curves are in good agreement with Maget and Roethlein (4).

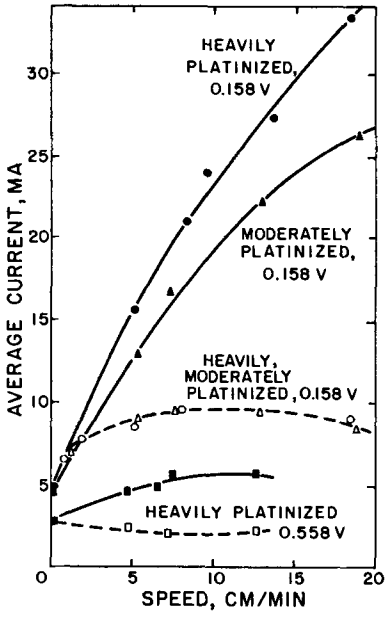

Fig. 7. Average current as a function of speed during constant-speed motion of cathodes (solid lines indicate lowering experiments and dotted lines indicate raising experiments).

Current on fully submerged electrode.—When a gas diffuses through a liquid as is occurring at both the cathode and the anode, the molar flux (N) for such a transfer is expressed by Fick's law (12). For a dilute system, the molar flux through a given thickness of liquid to a flat electrode is proportional to the product of the diffusivity coefficient (D) of the gas and the concentration gradient (ΔC)/L of the gas dissolved in the liquid

$$N_{gas} = D_{gas\text{-}liquid}\, \Delta C/L$$

ΔC is equal to the concentration in the main body of the electrolyte minus the concentration at the electrode surface and L is the diffusion layer thickness. For diffusion-limited conditions such as frequently occur in the case of the submerged cathode or anode (5), the reactant concentration at the surface is essentially zero. The dissolved concentration in the bulk of the electrolyte in this work is almost equal to the saturated concentration since efforts were made to keep the electrolyte saturated.

Using available values for the diffusivity coefficients and for the equilibrium concentrations of the two gases in water (14), the diffusion layers for the cathode and anode were calculated to be in the range 1000-2000 μ thick. For the conditions compared in Table I, the diffusion layer for the cathode was the thicker of the two. These calculations indicate that the ratio of the current densities generated on the submerged portions of a cathode and anode are at least in relatively good agreement with theory if diffusion is the rate-limiting step.

Meniscus current.—Currents generated in the region of the menisci of both the cathode and anode are diffusion controlled (rather than limited) at high polarizations, *e.g.*, 0.158V for the cathode or 0.56V for the anode. The controlling step is slow diffusion but current is nevertheless dependent on potential because the molar driving force, $C_{bulk} - C_{adsorbed}$, varies as $C_{adsorbed}$ varies with potential (3,15). Although the driving force is larger in the fully submerged region where $C_{adsorbed} = 0$, the diffusion length is smaller in the upper portions of the meniscus where the liquid thickness is 50μ or less. Significantly increased current densities are generated in these portions of the meniscus (4).

Raising cathodes.—Rapid raising of cathodes acted to disrupt and extend the stationary meniscus and film which were relatively oxygen-rich as compared to the diffusion layer surrounding the submerged portion of the cathode. The following events likely occur after the cathode is moved:

(*i*) The original meniscus is stretched and thinned. The newly formed meniscus has a lower concentration of oxygen than the original.
(*ii*) Motion of the electrode causes disturbance of the diffusion layer surrounding the cathode, forced convection currents are induced in the electrolyte, and the oxygen transfer rate increases.
(*iii*) Electrolyte clinging to the withdrawn portion of the cathode absorbs oxygen as it drains into the meniscus increasing available oxygen for reaction.
(*iv*) Eventually a stable meniscus is reformed and steady-state concentrations develop resulting in a steady-state current.

These meniscus effects, which likely occur more or less in a chronological order, suggest a rationale for the observed current phenomena after a quick raise of the cathode. Step (*i*) is the reason for the initial drop of current. Sudden meniscus stretching causes a condition similar to a thin film above a stationary meniscus where it has been shown that concentration and ohmic polarization both limit current (4). Steps (*ii*) and (*iii*) are responsible for the higher currents

noted, as shown in Fig. 4, before steady-state conditions are established.

Whether the currents obtained during constant-speed raising are greater or less than the steady-state current depends on the applied potential. Since the slopes of constant-speed raising curves are about equal to the steady-state slopes (see Fig. 5), meniscus changes are presumably responsible for the major deviations from steady-state currents. All the meniscus effects postulated for quick raising should apply to constant-speed raising, but they would occur simultaneously. Meniscus stretching and lower meniscus oxygen concentration would reduce current, whereas forced convection to the submerged electrode and electrolyte draining would counteract this tendency. The over-all effect is a slight decrease in current during steady raising at 0.558V and a moderate increase at 0.15V (not shown) compared to steady state. Note that a slow activation step at 0.558V more than cancels convection and draining during steady raising, but for quick raising the larger molar convection flux apparently increases oxygen concentration at the submerged electrode surface to an extent that the slow reaction is accelerated.

Lowering cathodes.—The large current surges with rapid lowering of the cathode are thought to be caused by at least one of the following two factors:

1. The lower end of the cathode moves into fresh electrolyte in which the concentration of the oxygen is high.

2. The portion of the electrode initially above the electrolyte surface carries some absorbed oxygen (and oxygen dissolved in the electrolyte film) into the electrolyte where it quickly reacts. The exact condition of the oxygen is not known. Some of it may be present as a chemisorbed state and some as a platinum oxide (16). This latter phenomenon is designated as the start-up effect.

It is of interest to note that the relationship between current and time is essentially identical for both quick lowering of the cathode into the electrolyte and for start-up of the cathode after open circuit. The same effects which cause the current surges with quick lowering of the cathode are apparently responsible for the current behavior with constant-speed lowering. A differential area on the cathode surface experiences a surge in current density when it first contacts the electrolyte. The current generated at this area then decays (as at cell start-up, see Fig. 1) as the cathode moves into the electrolyte. The bottom edge of the cathode however continuously encounters fresh electrolyte and its current density will therefore be maintained at a relatively high level.

A simplified model is proposed for a cathode which is lowered at a constant rate into electrolyte. The start-up effect for this model is arbitrarily assumed to apply only to the upper half of the submerged portion of the cathode. The fresh electrolyte effect is assumed to apply to only the lower half of the cathode. Calculations were performed for cathode H at 0.158V. Current densities on the upper half of the submerged portion of cathode H were calculated using the start-up data for this cathode. An arbitrary function for the fresh electrolyte effect was devised so that the predicted value at $h = 4$ cm and 8.3 cm/min fit the actual current data. The function was actually the measured start-up current for time ≥ 0.2 min with the initial current surge replaced by a smoothed curve extrapolated to 0.86 mA/cm^2 at time $= 0$. This same function was used in subsequent calculations for other rates of lowering. Calculated curves for 5.2, 8.3, and 18.5 cm/min are presented in Fig. 8.

The model rather accurately predicts the results for low-speed lowering, but it is less accurate at higher rates. It is inaccurate up to about 20% for 13.7 cm/min and up to 25% for 18.5 cm/min. When the model was modified, however, to include the start-up effect over

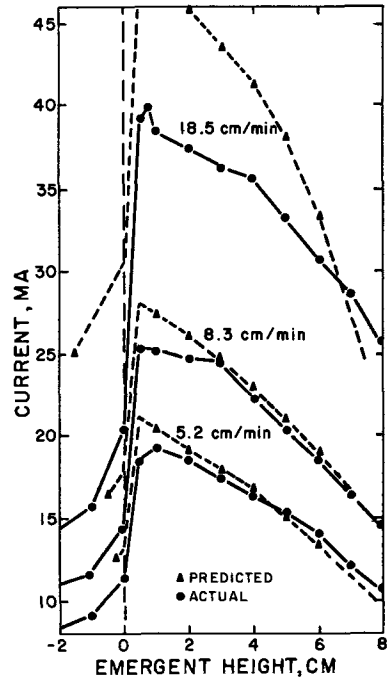

Fig. 8. Predicted model for average current as function of emergent height during constant-speed lowering of cathode H at 0.158V (dotted lines indicate predicted values and solid lines indicate experimental values).

the entire cathode, the model accurately represented the results at 18.5 cm/min. It seems logical that the start-up effect would be more important and the fresh electrolyte effect less important for higher rates of lowering of the cathode. In such cases, the oxygen at or near the cathode would be less depleted between $h = 8$ and $h = 1$ cm, and the relative contribution of oxygen convection from the bulk electrolyte would be reduced.

Figure 9 illustrates qualitatively the proposed manner in which the current density varies with the submerged distance during cathode lowering. These curves are based in part on the model just described. Since the model is accurate at low speeds, the proposed low-speed current density profile is similar to the profiles assumed for the model, *i.e.*, there is a significant fresh electrolyte effect at the lower end of the cathode. The predictions of the model were too high at higher

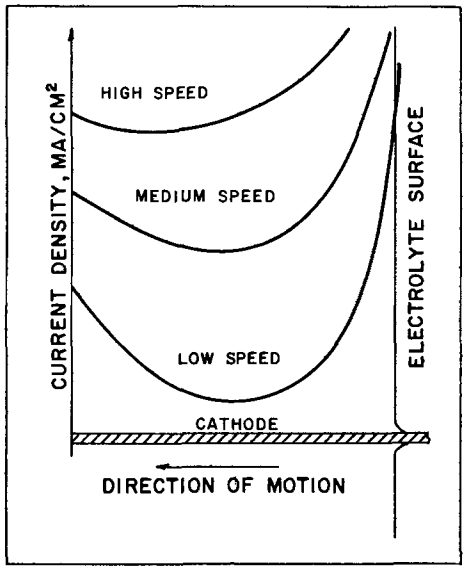

Fig. 9. Proposed family of current density profiles for a cathode being lowered.

speeds, and the error was probably caused by overestimating the importance of the fresh electrolyte effect. The proposed current density profile for high-speed lowering includes less allowance for this effect than does the model.

Conclusions

Transfer of oxygen is controlling in the reactions which occur on the surface of a highly polarized cathode that is partially immersed in a dilute acid electrolyte. Large currents are generated in the cathodic area close to the meniscus because transfer of oxygen is relatively easy there. Larger currents can be obtained by lowering or in some cases by raising a cathode which is partially immersed in the acid electrolyte.

Acknowledgment

The authors wish to thank the Indiana Gas Association for supporting this project.

Manuscript submitted Nov. 14, 1968; revised manuscript received Nov. 24, 1969.

Any discussion of this paper will appear in a Discussion Section to be published in the December 1970 JOURNAL.

REFERENCES

1. R. P. Iczkowski, *This Journal*, **111**, 1078 (1964).
2. T. Katan, S. Szpak, and E. A. Grens, *ibid.*, **112**, 1166 (1965).
3. F. G. Will, *ibid.*, **110**, 145 (1963).
4. H. J. R. Maget and R. Roethlein, *ibid.*, **112**, 1034 (1965).
5. H. J. Davitt and L. F. Albright, *ibid.*, **114**, 531 (1967).
6. R. Ennis, M. S. Thesis, Purdue University, 1965.
7. J. A. Rockette and R. Brown, *This Journal*, **113**, 207 (1966).
8. S. Srinivasan and H. D. Hurwitz, *Electrochem. Acta*, **12**, 495 (1967).
9. S. Srinivasan, H. D. Hurwitz, and J. O'M. Bockris, *J. Chem. Phys.*, **46**, 3108 (1967).
10. H. A. Laitenen and C. G. Enke, *This Journal*, **107**, 773 (1960).
11. R. P. Bowden and E. K. Rideal, *Proc. Royal Soc. London*, **120A**, 80 (1928).
12. J. H. Perry, "Chemical Engineers Handbook," 3rd Edition, p. 1794 (1950).
13. W. M. Schwarz and I. Shain, *Anal. Chem.*, **35**, 1770 (1963).
14. "International Critical Tables," McGraw-Hill Publishing Co., New York (1929).
15. H. A. Liebhafsky and E. J. Cairns, "Fuel Cells and Fuel Batteries," John Wiley & Sons, Inc., New York (1968).
16. *Ibid.*, pp. 371-373.

The Hydrated Nickel Hydroxide Electrode Potential Sweep Experiments

D. M. Mac Arthur*

Bell Telephone Laboratories, Incorporated, Murray Hill, New Jersey

ABSTRACT

The mechanism of the hydrated nickel hydroxide electrode, used in the nickel cadmium battery, is a matter of considerable controversy. Potential sweep experiments were performed on film nickel hydroxide electrodes in an effort to determine the oxidation-reduction mechanism. The existence of more than one reduced structure was confirmed and the structure known as α-nickel hydroxide was studied in detail. A model based on a reversible charge transfer step with a rate-controlling diffusion process was used to analyze the data. The results were in good agreement with the model. The over-all reaction for α-nickel hydroxide was found to be

$$2[3Ni(OH)_2 \cdot 2H_2O] + 6\,OH^- + 3/2KOH \rightleftarrows 2[3NiOOH \cdot 7/2H_2O \cdot 3/4KOH] + 3H_2O + 6e^-$$

The rate-controlling process, which was assumed to be proton diffusion, was found to have a diffusion coefficient of approximately 2×10^{-9} cm^2 sec^{-1}. Evidence for the formation of a poorly conducting layer during discharge of the electrode was found and capacity loss was attributed to this.

The commercial success of the nickel cadmium battery has aroused considerable interest in the nickel electrode used in this battery. Many studies (1-4) have been reported in which the structure and the electrochemical mechanism have been the subject of investigation. No real progress was made in understanding this electrode until recently when several (5-7) investigations achieved some success in understanding the structural modifications of the electrode. Although the structure is now partly understood, the electrochemical mechanism of this electrode is still not clear.

It is well established that the reduced form is $Ni(OH)_2$[1] and the oxidized form is generally believed to be NiO(OH). Both these structures have been shown (6) to exist in two modifications called α and β for the reduced structure and correspondingly γ and β for the oxidized structure. The reduced α form has further been shown to have the formula $3Ni(OH)_2 \cdot 2H_2O$. These structures and their modifications are probably hydrated to a greater or lesser extent. It was also shown that α nickel hydroxide is formed by electrochemical precipitation from $Ni(NO_3)_2$ solutions as used in preparing the electrodes for this study. It was further found that α nickel hydroxide is unstable on standing on open circuit or cycling. Lukovtsev (8) has presented a theoretical argument for a redox mechanism in which proton diffusion through the lattice is one of the reaction steps. Lukovtsev and Slaiden (9) have reported experimental results intended to measure the rate of diffusion of protons in the electrode but their

* Electrochemical Society Active Member.

Key words: batteries, oxide electrodes, nickel hydroxide electrode.

[1] $Ni(OH)_2$ is used here as an abbreviated symbol for the nickel hydroxide electrode which exists in a variety of hydrated forms.

results were only qualitative. Sagoyan (10) used isotopic tracers to show that during the redox reaction, protons are exchanged with the solution while there is very little oxygen exchange.

Feitknecht (11) and coauthors measured the diffusion coefficient of protons in the nickel hydroxide lattice by measuring the rate of exchange of radioactive hydrogen with water vapor. They found that at temperatures above 100°C the enthalpy of diffusion was about 23 kcal deg^{-1} $mole^{-1}$ and D_0 in the expression $D = D_0 \exp(-\Delta H/RT)$ was about 2×10^{-7} cm^2 sec^{-1}, although the latter value could be wrong by several orders of magnitude since the data showed considerable scatter.

Experimental

Electrolysis cell.—A sketch of the cell is shown in Fig. 1. A four-necked flask constructed of alkali resistant Corning No. 7280 glass was used to hold the solution. The working electrode was a disk of high purity Inco 270 Ni which was machined to give a surface area of 1 cm^2. The sides and back of the disk as well as the supporting wire were insulated with heat shrinkable polyethylene tubing. The sides of the disk itself were coated with a thin film of alkali resistant resin glue before the shrinkable tubing was applied since this resulted in a very close fit of the tubing onto the disk. Nonetheless, it was found that in the more concentrated KOH solutions, electrolyte was beginning to work its way between the tubing and the disk after about one week in the solution, and a new electrode would have to be prepared.

The reference electrode was a Hg/HgO electrode in a solution of the same concentration as that in the electrolysis cell. It was connected to a Luggin capillary through a Pyrex glass tube. The counterelectrode was a coiled Pt wire. N_2 was continuously bubbled through the solution from a glass fritted disk.

The screen electrode shown in the diagram was a nickel hydroxide sintered electrode about 1 $in.^2$. It was used for experiments not included in this report but had the additional feature of exposing a large surface area to adsorbable impurities and thus probably helping to keep the working electrode cleaner than would otherwise occur.

Solutions.—Baker analyzed reagent grade KOH was used to prepare solutions in distilled water. Ordinary precautions were taken to minimize carbonate formation. The solution used for precipitating $Ni(OH)_2$ films was 0.5M reagent $Ni(NO_3)_2$ and fresh solution was used in the preparation of each electrode.

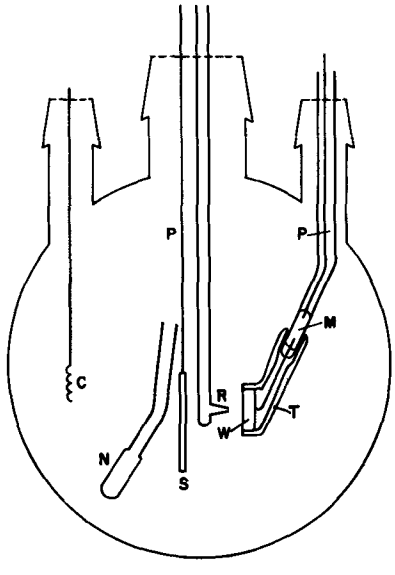

Fig. 1. Electrolysis cell. M, mercury contact; N, nitrogen diffuser; P, platinum wire; R, Luggin capillary; S, screen electrode; T, shrinkable polyethylene tubing; W, working electrode; C, counterelectrode.

Equipment.—A Wenking Model 61RS potentiostat and motor potentiometer were used in the potential control circuit. An X-Y recorder was used to measure current as a function of potential. The X axis was calibrated with a precision voltage calibrator and the Y axis with a precision milliammeter. The X-Y recorder was fitted with microswitches which reversed the direction of the potential scan at any preset voltage. This made it possible to automatically run many scans on an electrode.

Preparation of electrode.—The surface of the disk was polished with several grades of emery paper, the last being 4/0, before washing with 10% HCl and distilled water. It was then immersed in 0.5M $Ni(NO_3)_2$ solution and made cathodic. The counterelectrode was a sheet of Inco 270 nickel. The current distribution was essentially uniform over the cathode surface. After deposition the electrode was washed in running tap water and running distilled water and then immersed in the KOH solution. Scanning was started about 1 min later. All experiments were done at room temperature (25°C).

Currents and deposition times used in the preparation of the electrodes are given in Table I.

Results and Discussion

Aging characteristics.—In preliminary work it appeared that the potential at which the oxidation peak occurred varied with the history of the electrode. The shift in potential was about 50 mV moving to higher potentials as the electrode was cycled or was allowed to stand in KOH. Because the magnitude of the potential shift was similar to that found by Bode (6) and because it occurred while the electrode was immersed in KOH, we assume that this shift in potential corresponds to the conversion of α nickel hydroxide to β nickel hydroxide as described by Bode. It was found that the rate of this conversion was accelerated in more concentrated KOH and while potentiostated in the reduced state. The conversion is illustrated in a series of consecutive scans of an electrode in Fig. 2. The rate of conversion shown here was unusually rapid and was a result of the electrode being potentiostated at reducing potentials for a longer time than that used for the scans in the later work.

According to Bode (6) α-nickel hydroxide is oxidized to the γ structure. The work of Bode and coworkers has not established that γ may be reduced to α. From the results presented here, evidently it is possible to cycle between the α and γ structures, although only for a limited time.

Potential scans at various KOH *concentrations.*—From the preceding work it was found that it was possible to work with the α structure for a reasonable period of time. It was not possible, however, to do the same with the β structure because there always was evidence of at least some α present. As a result, potential scans in KOH of various concentrations were taken only of the α structure in an attempt to obtain the dependence of the reversible potential on the KOH concentration.

Table I. Currents and deposition times for electrode preparation

Current density (mA/cm^2)	Time (min)
1	1
1	2
2	2
2	4
4	4
4	8
4	12

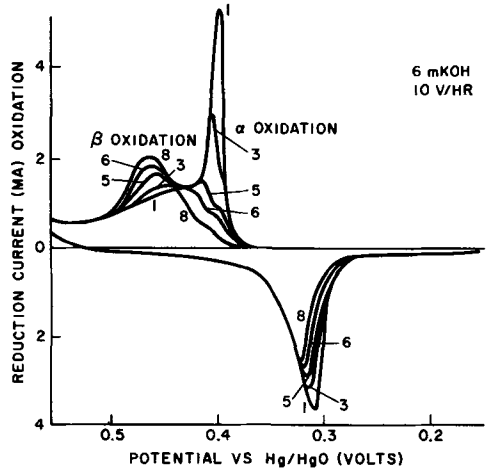

Fig. 2. Consecutive scans of a film electrode. Numbers refer to order of potential scans.

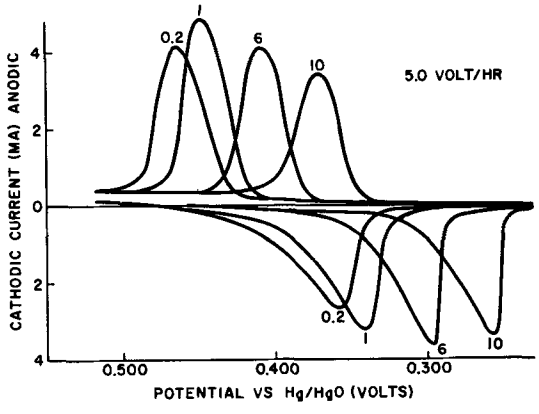

Fig. 3. Potential scans in various KOH solutions. Numbers are molalities.

The well-known hysteresis of the charge-discharge curves for the nickel electrode has suggested that the reaction is irreversible. Examination of the potential scans, however, reveals a potential range where both oxidation and reduction may occur. It was therefore decided to take the reversible potential as that potential at which the oxidation and reduction currents are equal.[2] This reversible potential was found to be influenced to a small extent by the scanning speed but for slow and moderate speeds was essentially independent of the scan rate (see Fig. 4).

Several electrodes were used at each KOH concentration and the reversible potentials of the different electrodes were averaged. Potential scans at the various concentrations are shown in Fig. 3. Since the Hg/HgO reference electrode has the same dependence on hydroxyl ion activity as the nickel electrode, the changes in potential were associated with dependence on KOH and water activities. The reversible potentials found in the different solutions are given in Table II. These potentials are for the reaction

$$HgO + 2[Red] + mKOH \rightarrow Hg + 2[Ox] + nH_2O$$

where [Red] and [Ox] are the reduced and oxidized forms of the $Ni(OH)_2$ electrode and m and n are constants for the reaction. The potential of the reaction may be written as

$$E_r = E_o - 0.0591 \log \frac{[a_{KOH}]^m}{[a_{H_2O}]^n}$$

at 25°C. Substituting the values for E_r and using

[2] The justification for this choice rests on the observation that the reverse current during a scan in either direction was negligible. This phenomenon probably is related to the structural changes taking place in the lattice.

Table II. Reversible potentials in different solutions

KOH (molality)	E_r vs. Hg/HgO (volts)
0.200	0.435
1.00	0.414
6.00	0.382
8.00	0.367
10.0	0.360
12.0	0.348

values given by Akerlof and Bender (12) for a_{KOH} ($= \gamma^{\pm 2} m^2$) and a_{H_2O}, a least squares fit gives

$$E_o = 0.411 \pm 0.003V$$

$$m = 0.494$$

$$n = 0.0012$$

The above chemical reaction may be separated into two half reactions

$$HgO + H_2O + 2e^- \rightarrow Hg + 2OH^-$$

$$2[Red] + mKOH + 2OH^- \rightarrow 2[Ox] + (n+1)H_2O + 2e^-$$

Taking the probable value for n as zero we find the $Ni(OH)_2$ half reaction to be

$$2[3Ni(OH)_2 \cdot 2H_2O]^{3} + 6OH^- + 3/2KOH \rightleftarrows 2[3NiOOH \cdot 7/2H_2O \cdot 3/4KOH] + 3H_2O + 6e$$

Bode (6) has given the formula $[NiO(OH)]_8O_3(OH)K_2$ for the oxidized γ structure. In the present work the same mole ratio of potassium to nickel has been found (1:4) but there is some difference in the water content. This agreement between two different techniques (Bode's formula was based on x-ray analysis) is encouraging. Equations derived by other workers for what was probably $\beta Ni(OH)_2$ are

$$2Ni(OH)_2 \cdot 1.28H_2O + 0.14KOH + 2OH^- \rightleftarrows 2NiOOH \cdot 0.14KOH + 4.56H_2O + 2e^-$$

[Bourgault and Conway (13)]

$$2Ni(OH)_2 \cdot 2H_2O + 2OH^- \rightleftarrows 2NiOOH \cdot H_2O + 4H_2O + 2e^-$$

[Zedner (2)]

$$2Ni(OH)_2 + 2OH^- \rightleftarrows 2NiOOH \cdot 0.2H_2O + 1.8H_2O + 2e^-$$

[Forster (14)]

$$2Ni(OH)_2 + 2OH^- + 0.067KOH \rightleftarrows 2NiOOH \cdot 0.067KOH \cdot 1.16H_2O + 0.84H_2O + 2e^-$$

[Kornfeil (15)]

It may be seen that our dependence on H_2O and KOH is greater than any of these. This is not surprising since our results were obtained for α nickel hydroxide which has a more open structure.

Potential scans at different rates.—Several attempts (9-11) have been made to measure the rate of diffusion of protons in the nickel hydroxide lattice. Only one was successful in obtaining quantitative data and this (11) for temperatures greater than 100°C. There appears to be little data available for proton diffusion coefficients in hydrated lattices at room temperature. A very wide range extending from 10^{-5} cm^2 sec^{-1} for solutions to about 10^{-18} cm^2 sec^{-1} for self-diffusion in solids would appear to encompass reasonable values for the proton diffusion coefficient. With such

[3] We use Bode's formula for $\alpha Ni(OH)_2$.

a wide range of possible values to choose from it appeared that some relatively unsophisticated experiments should be done in order to obtain an estimate of the diffusion coefficient in the hydrated nickel hydroxide lattice.

The model that we use to describe the nickel electrode reaction is a simplified one. It ignores some features that other authors have used, particularly that of phase changes in the solid. Electron transfer through the nickel hydroxide lattice is believed to occur rapidly in comparison to proton transfer (thus the redox reaction $Ni^{II} \leftrightarrows Ni^{III}$ may be regarded as reversible). Protons are released adjacent to the nickel ion sites when Ni^{II} is oxidized to Ni^{III} and a proton vacancy is created when Ni^{III} is reduced to Ni^{II}. During oxidation the proton diffuses to the electrolyte interface where it reacts with OH^- to form a water molecule in the electrolyte. During reduction protons diffuse from the interface into the lattice to fill up the proton vacancy. The rate of the reaction is believed to be controlled by the rate of proton transfer. This reaction meets the following conditions: (*i*) the electrode process is rapid compared with the rate of diffusion, and (*ii*) the reaction product is soluble either in the solution or in the material of the electrode. Randles (16) has solved the semi-infinite diffusion problem for these conditions and obtained the current-voltage relationship for a potential scan. Delahay (17) has shown that the solution may be written in the form

$$i_p = 2.7 \times 10^5 n^{3/2} A D^{1/2} C^\circ V^{1/2}$$

where i_p (A cm^{-2}) is the peak current during a potential scan at 25°C as a function of scan rate V in V sec^{-1}. Accordingly a plot of the peak current against (scan rate)$^{1/2}$ will be a straight line with slope proportional to the area of the electrode (A, cm^2), the square root of the diffusion coefficient (D, cm^2 sec^{-1}) and the initial concentration (C°) which here is taken as the number of nickel sites per unit volume expressed as moles/cm^3. This is simply the density of the nickel hydroxide film divided by the molecular weight. For this calculation the molecular weight used was that of $\alpha Ni(OH)_2 \cdot 2/3H_2O$ and the density was taken as 2.5 g/cm^3, the value found by x-ray measurements (6). Potential scans for a single electrode in 1M KOH at various rates are shown in Fig. 4, and a plot of i_p *vs.* (scan rate)$^{1/2}$ for electrodes of various thickness is given in Fig. 5. The plot shows a linear relationship indicating a diffusion-limited reaction; however, the change in slope as the thickness of the film varied was unexpected. The explanation of this result was sought in the relationship between the thickness of the film, the duration of the experiment, and the diffusion coefficient for the reaction. (It may be noted that it was not possible to increase the thickness of the film beyond that used here since thicker films generally were less adherent.)

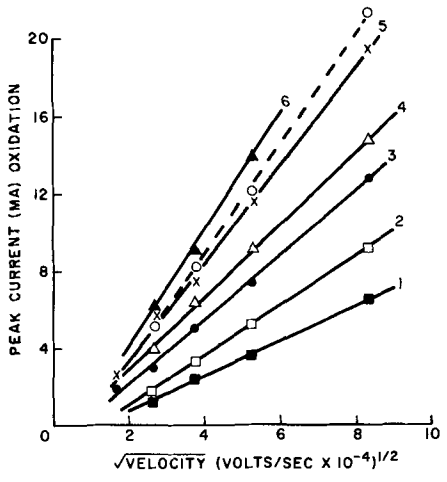

Fig. 5. Oxidation peak height vs. (sweep rate)$^{1/2}$. Numbers refer to films of increasing thickness (0.17, 0.31, 0.51, 0.93, 1.3, 1.8μ). The dashed line was obtained after correction for thicknesss.

An estimate may be made of the maximum diffusion coefficient which would still allow use of the semi-infinite diffusion equation. The depth of the diffusion layer may be estimated as $\sqrt{2Dt}$ where D is the diffusion coefficient and t is the time from the start of the diffusion process. This depth must be less than the film thickness if the semi-infinite diffusion equation is to be applicable or, expressed mathematically

$$d \geq \sqrt{2Dt}$$

where d is the film thickness in centimeters. The time required for the potential to scan through the oxidation peak was about 360 sec. The maximum D allowed, therefore, is about 0.5×10^{-10} cm^2 sec^{-1} for the thickest films (1.8×10^{-4} cm, estimated from the electrode capacity). As will be shown below, D apparently exceeds this value, therefore, it is not surprising that the slope of the lines in Fig. 5 varied with the thickness of the film. In an effort to obtain an approximate value for the diffusion coefficient, an attempt was made to extrapolate from the data to an infinitely thick film.

A plot of the peak current at various scan rates as a function of the electrode capacity (proportional to film thickness) is shown in Fig. 6. These curves were fitted with an empirical equation of the form $i_p = i_{p_\infty}(1 - \exp - 7Q)$ where Q is the capacity of the film and i_{p_∞} is the peak height for an infinitely thick film. The form of this equation was chosen because it approaches a limiting value as the thickness of the film increases. The coefficient of 7 was found to give

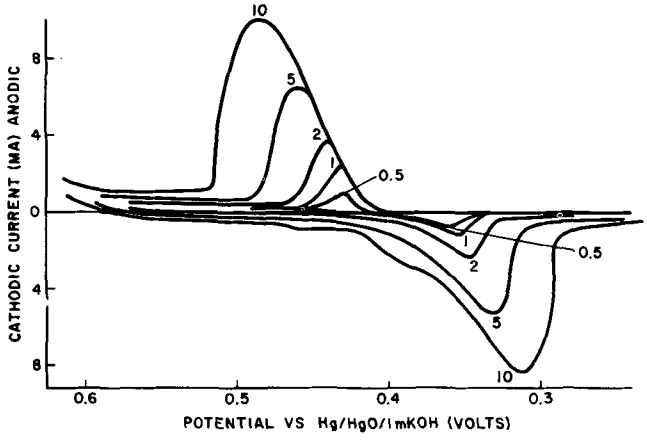

Fig. 4. Potential scan at various sweep rates. Numbers are volts/hour.

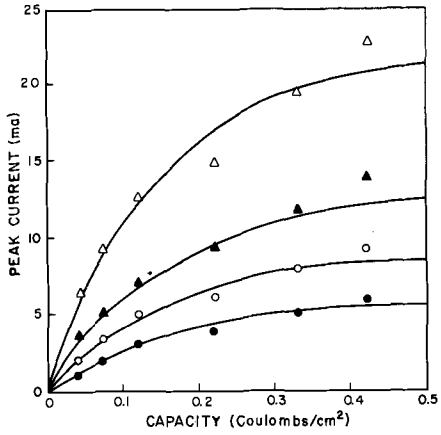

Fig. 6. Oxidation peak current as a function of calculated film thickness. Symbols refer to various scan rates.

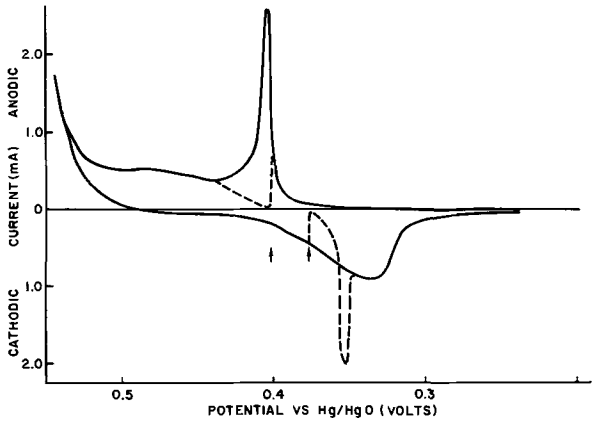

Fig. 7. Interrupted scans. Dashed lines show curves following a pause (arrow) in the scan in 6.0M KOH.

the best fit for the various rates of scan. As may be seen these curves pass below the experimental points for the thickest films. We attribute this to a complicating reaction that occurs with these thicker films. As the film thickness increases, the potential at which the peak current appears is shifted to more anodic potentials where the proposed competing reaction (8)

$$OH^- + NiO_2 \rightarrow NiO(OH) + O_{ads} + e^- \quad [4]$$

begins to take on greater importance. Thus the current is abnormally high for the thicker films.

The values for i_{p_∞} were obtained for each scan rate. These values of i_{p_∞} for which diffusion is presumed to be the only mechanism for introducing protons into the surface layer, are shown in Fig. 5. A dashed line has been drawn through them. From the slope of this line, the diffusion coefficient was found to be 1.9×10^{-9} cm^2 sec^{-1}. It was found that the slope of the line was independent of the electrolyte concentration as indeed it should be for the proposed mechanism. Because of the uncertainties contained in the curve fitting procedure, this value may be considered only an order of magnitude estimate. It is, however, the first quantitative estimate of the diffusion coefficient. This value is about four orders of magnitude smaller than the corresponding value for ions in solution. It suggests that the diffusion occurs in a solid.

Intermittent scans.—The model that has been used for these calculations is that of a reversible charge transfer step with a diffusion limiting process. Although the species involved have not been unambiguously established, we believe the charge transfer step occurs at the nickel ion sites in the lattice. During charging a proton is released at the site and diffuses to the surface. During discharge the proton moves from the surface to the nickel site. The slow step in this reaction is believed to be the proton diffusion process. However, the assumption of a reversible charge step requires further investigation in view of the fact that the open-circuit potential varies depending on whether the electrode has been undergoing oxidation or reduction (18).

This apparent irreversibility was investigated by the use of an intermittent scan technique (Fig. 7). In this procedure the potential scan was stopped at various potentials in the oxidation and reduction regions during successive scans (arrows on Fig. 7). The potential was held constant until the current had fallen to zero. The scan was then continued. In the oxidation region it was noted that the electrode had become almost fully charged during the pause and when the scan was continued there was no unusual increase in current. In the reduction region, however, the electrode did not become completely discharged during the pause and on continuing the scan there was a sharp current peak that occurred at a potential roughly 20 mV more cathodic. This behavior was observed throughout the potential range where reduction occurs.

These results suggest that a poorly conducting film forms during reduction. The film resistance apparently increases when the electrode is held at constant potential and prevents further reduction of the electrode. In order to achieve film breakdown, a potential several tens of millivolts more cathodic is required, at which time a surge of current is noted. There are several compounds which could form this layer; NiO at the substrate interface, Ni_3O_4 or unhydrated $Ni(OH)_2$ at the electrolyte interface. The most likely compound is Ni_3O_4 on the basis of the potentials involved. The standard potential for the nickel hydroxide electrode was found to be 0.411V vs. Hg/HgO. On the hydrogen scale in basic solution this potential is 0.499V. Reduction of $Ni_2O_3 \cdot H_2O$ (which may also be written as $NiO(OH)$) to Ni_3O_4 occurs at a potential of 0.477V as given by Pourbaix (19). Thus the Ni_3O_4 electrode might be expected to have a potential about 20 mV more negative and the apparent irreversibility of the nickel hydroxide electrode reaction possibly is caused by the formation of Ni_3O_4 during reduction.

[4] The surface may be oxidized to the Ni^{IV} state, if not the reaction might be $OH^- + NiO(OH) \rightarrow Ni(OH)_2 + O_{ads} + e^-$.

Acknowledgments

The author is indebted to P. C. Milner, Y. Okinaka, and D. R. Turner for many helpful suggestions.

Manuscript submitted Oct. 2, 1969; revised manuscript received Dec. 12, 1969. Part of this work was Paper 49 presented at the Chicago Meeting, Oct. 15-19, 1967.

Any discussion of this paper will appear in a Discussion Section to be published in the December 1970 JOURNAL.

REFERENCES

1. M. Haissinsky and M. Quesney, *Compt. Rend.*, **224**, 831 (1947).
2. J. Zedner, *Z. Elektrochem.*, **46**, 809 (1905).
3. A. L. Pitman and G. W. Work, NRL Report 4844 (1956).
4. E. Jost and F. Rufenacht, *This Journal*, **113**, 97 (1966).
5. M. A. Aia and F. P. Kober, 153rd National Meeting of the American Chemical Society, Division of Fuel Chemistry, Preprints of papers, 1967.
6. H. Bode, K. Dehmelt, and J. Witte, *Electrochim. Acta*, **11**, 1079 (1966).
7. D. Tuomi, *This Journal*, **112**, 1 (1965).
8. P. D. Lukovtsev, "Soviet Electrochemistry" (Proc. 4th Conf. in Electrochem.), Vol. 3, p. 156, Consultants Bureau, New York (1961).
9. P. D. Lukovtsev and C. J. Slaidin, *Electrochim. Acta*, **6**, 17 (1962).
10. L. N. Sagoyan, *Izv. Akad. Nauk Arm. SSR Khim. Nauki*, **17** (1), 3 (1964).
11. W. Feitknecht, A. Wyttenback, and W. Buser, *Proc. 4th Inter. Symp. Reactivity Solids, Amsterdam* (1960) p. 234.
12. G. C. Akerlof and P. Bender, *J. Am. Chem. Soc.*, **70**, 2366 (1948).
13. P. L. Bourgault and B. E. Conway, *Can. J. Chem.*, **38**, 1557 (1960).
14. F. Forster, *Z. Elektrochem.*, **13**, 414 (1907).
15. F. Kornfeil, *Proc. Ann. Battery Res. Develop. Conf.*, 12th Conf., U.S. Army Signal Corps, 1958.
16. J. E. B. Randles, *Trans. Faraday Soc.*, **44**, 327 (1948).
17. P. Delahay, "New Instrumental Methods in Electrochemistry," p. 119, Interscience Publishers, Inc., New York (1954).
18. D. M. Mac Arthur, Unpublished results.
19. M. Pourbaix, "Atlas of Electrochemical Equilibria in Aqueous Solution," Pergamon Press (1966).

Effect of Electron Donor and Acceptor Elements on Passivity of Copper-Nickel Alloys

F. Mansfeld*,[1] and H. H. Uhlig*

Department of Metallurgy and Materials Science, Massachusetts Institute of Technology, Cambridge, Massachusetts

ABSTRACT

The electron configuration theory of passivity is further evaluated through data obtained for two additional nontransition elements, *i.e.*, Ge and Ga (electron donors) added to Cu-Ni alloys. These studies follow previous investigations on effects of alloyed Zn and Al. Data are also presented for Cu-Ni alloys containing transition metal components, *i.e.*, Fe and Co, which act as electron acceptors. Potentiostatic polarization curves and potential decay-time data in 1*N* H_2SO_4 are employed as an index of passivity, or of its absence. The results show that a critical alloy composition exists for each alloy series at which and for higher electron donor percentages, passivity is no longer observed. The critical composition is interpreted as that at which surface *d* electron vacancies of Ni are just filled by valence electrons from donor elements. Hence, Cu, Ge, Al, and Zn are found to donate 1, 4, 3, and 2 electrons per atom, respectively. Ga donates more nearly 2 electrons per atom, perhaps in accord with the tendency of Ga to form lower valent as well as trivalent compounds. Fe and Co act in accord with their expected behavior as electron acceptors, favoring passivity rather than eliminating it as in the case of electron donors. The present quantitative data lend additional support to the theory and to the concept of a passive film on Cu-Ni alloys made up largely of chemisorbed oxygen, the formation of which is favored by surface *d* electron vacancies. When such vacancies are filled by valence electrons of alloyed component atoms, passive properties are no longer observed presumably because oxygen is no longer chemisorbed.

A previous investigation (1) on passivity of Cu-Ni alloys showed that a critical Ni composition exists above which potentiostatic polarization curves exhibit a typical passive current density qualitatively similar to that shown by nickel, and below which the passive current density disappears and the alloys behave like copper. The critical composition, interpreted in accord with the electron configuration theory of passivity (2), is that at which one electron per Cu atom just fills the available surface *d* electron vacancies of Ni (1.6/atom).[2] When, for example, Zn is alloyed with Cu-Ni (3), the critical composition shifts to a lower Cu/Ni ratio consistent quantitatively with donation of two electrons per Zn atom; similarly when Al is alloyed (4) the contribution is three electrons per Al atom. These facts persuaded us to survey other possible alloy additions, *e.g.*, Ga and Ge which are predicted to contribute 3 and 4 electrons per atom respectively. In addition, the question arose: What would be the effect on the critical composition of Cu-Ni alloys of an added transition element which supplies electron vacancies? According to theory it should shift the critical composition in the opposite direction, that is toward a higher Cu/Ni ratio. Hence, alloys containing Fe and Co, the *d* electron vacancies of which per atom are known from magnetic saturation moment data, were included in the present program.

Experimental

The choice of possible alloying components was limited to those having reasonable solid solubility in Cu-Ni alloys. The passivity of many single phase alloys can be satisfactorily interpreted based on electron sharing, but that of multiphase alloys is more complex. Single phase alloys were presently assured by adding only small concentrations of the components previously named. The maximum amount in each case was estimated from the binary phase diagrams and was later checked by metallographic examination of the swaged and annealed ingots.

Alloys were prepared by induction melting in vacuum using dense pure alumina crucibles. After the alloys were melted, the furnace was filled with purified argon to 1 atm, and the melt was drawn into 7 or 9 mm Vycor tubes, then water quenched. Subsequent additions to the melt were made as required, followed by periodic casting. The ingots were then homogenized in argon in a quartz tube at 850°-950°C for 24 hr, swaged to a smaller diameter, annealed in argon at 850°-950°C for 1 hr, and air cooled while remaining in argon within the quartz tube. They were swaged to the final diameter rod (0.35-0.45 cm) and then annealed and cooled as before.

Alloys were prepared from high-purity Cu (99.999%) and from carbonyl nickel, the latter being supplied by courtesy of the International Nickel Company. Germanium was of semiconductor grade. Gallium of 99.99% purity was weighed in glass bulbs, cooled by solid CO_2, and added to the melt as frozen pellets. Iron was electrolytic grade further decarburized, and cobalt (99.9%) was obtained through courtesy of the Cobalt Information Center at Battelle Memorial Institute. Chemical analyses of the final alloys are listed in Table I.

Electrodes were machined in the form of cylinders approximating 1.5 cm long and 0.3 cm diameter. They were mounted in a special glass holder using a Teflon gasket as described previously (3). After mounting, the electrodes were degreased in hot benzene and then briefly pickled in dilute HCl and H_2SO_4 at 90°C. Subsequent anodic polarization in 1*N* H_2SO_4 before each run assured removal of the cold-worked surface.

Potentiostatic anodic polarization curves were obtained in 1*N* H_2SO_4 deaerated with nitrogen. Either a

* Electrochemical Society Active Member.

[1] Present address: Science Center, North American Rockwell Corporation, Thousand Oaks, California.

[2] It is also possible to show that *d* vacancies of Ni may be filled by donor electrons from Cu independent of surface effects. In this case the assumption is made that mutual coupling of *d* electrons of metal atoms, having a maximum number of vacancies in the gaseous state, is linearly related to concentration of such atoms in the alloy, resulting in the observation that the solid metal contains fewer uncoupled *d* electrons or *d* vacancies the higher its concentration in the alloy. For example, there are 2 *d* vacancies per atom for gaseous Ni but only 0.6 *d* vacancy per atom for solid Ni. On this basis, it is calculated that the *d* band of Ni is filled by electrons from Cu at and below 41 a/o (atom per cent) Ni in conformity with measurements of magnetic susceptibility. H. H. Uhlig, to be published.

Table I Composition of Cu-Ni alloys
Atom per cent

% Cu	% Ni	% Ga	Atomic ratio[a]
Gallium series			
58.2	41.8	—	1.39
57.0	(42.1)[b]	0.9	1.42
56.1	(42.3)	1.6	1.44
55.1	(42.3)	2.6	1.49
54.1	(42.3)	3.6	1.53
52.2	(42.9)	4.9	1.56
52.0	(42.9)	5.1	1.57
50.8	(42.9)	6.3	1.63
51.3	(42.5)	6.2	1.65
48.6	(43.0)	8.4	1.72
49.7	(42.4)	7.9	1.73
47.2	43.2	9.6	1.76
47.0	(43.1)	9.9	1.78
44.4*	(43.2)	12.4	1.89
43.3	(42.7)	14.0	2.00
43.9	42.2	13.9	2.03
Germanium series			
% Cu	% Ni	% Ge	Atomic ratio[a]
58.0	42.0	—	1.38
57.45	(42.15)	0.4	1.40
56.9	(42.2)	0.86	1.43
56.2	(42.1)	1.66	1.49
55.5	(42.3)	2.22	1.52
54.8	(42.2)	3.03	1.59
53.7	(42.2)	4.02	1.65
52.8	(42.6)	4.58	1.67
52.0*	(42.8)	5.26	1.71
51.2	42.4	6.34	1.81
Aluminum series**			
% Cu	% Ni	% Al	Atomic ratio[a]
45.3*	(44.8)	9.9	1.68
Zinc series***			
% Cu	% Ni	% Zn	Atomic ratio[a]
43.0*	(43.1)	13.9	1.65
Iron series			
% Cu	% Ni	% Fe	Atomic ratio[a]
52.9	42.8	4.3	1.12
54.0	(42.9)	3.1	1.17
55.0	(42.4)	2.6	1.22
56.9	(40.7)	2.4	1.32
59.0	(38.5)	2.5	1.44
61.9	(35.5)	2.6	1.62
63.2	(34.3)	2.5	1.72
65.5	(32.2)	2.3	1.90
67.8	29.8	2.4	2.10
(68.5)*†	(29.1)	(2.4)	2.2
Cobalt series			
% Cu	% Ni	% Co	Atomic ratio[a]
52.6	44.1	3.3	1.11
54.4	43.4	(2.2)	1.19
58.1	39.7	(2.2)	1.39
60.3	37.5	(2.2)	1.52
63.1	34.7	(2.2)	1.71
65.7	32.2	(2.1)	1.92
68.2*	29.5	(2.3)	2.14
70.5	27.0	2.5	2.39
Copper-Nickel††			
65.8*	34.2		1.92
68.3*	31.7		2.16

[a] Atomic ratio = (% Cu + n % Y)/% Ni where n is the normal valence of added nontransition element Y. For transition metals (Fe, Co) the atomic ratio = % Cu/(% Ni + % Z) where Z represents the alloyed transition metal.
[b] Values in parentheses obtained by difference.
* Critical composition.
** Complete analyses given in ref. (4).
*** Complete analyses given in ref. (3).
† Extrapolated composition.
†† Complete analyses given in ref. (5).

continuous sweep rate of ±20 mV/min was employed, or a stepwise procedure was used instead for which the potential was kept at a fixed value until the current was relatively constant for at least 2 min. Potential steps were 20 mV in the active and passive regions and 40 mV in the transpassive region. In general, the alloy composition at which the passive current density, i(pass.) converged with the critical current density i(crit.) (polarization in noble-to-active direction), corresponded to disappearance of passivity as presently defined. It occurred at the same composition whichever polarization procedure was followed. Two or more runs were made for each alloy composition.

Measurements were extended into the region of secondary passivity, noble to the region of primary passivity, where either the current density decreased again, or oscillations of current (unstable secondary passivity) and O_2 evolution occurred. The current density was noted just before it decreased or before oscillations occurred, and again at the minimum value beyond which oscillations, if they were observed, diminished and finally ceased. It was assumed that observed oscillations of current accompanied the formation and breakdown of passivity within the secondary region, the minimum current, therefore, corresponding to the passive state. In accord with this assumption, oscillations were not observed for any of the alloys which proved to be nonpassive in the primary region.

Potential decay curves were obtained in 1N H_2SO_4, supplementing polarization data as a measure of passive properties. The alloy was first polarized into the region of secondary passivity (2V) remaining there for 5 min. The polarizing current was then shut off and the potentials recorded corresponding to points of inflection in the potential-time curve using a Keithley No. 602 electrometer as amplifier. The latter insured minimum polarization of the alloy electrode during decay, serving both to improve detection of small discontinuities of slope corresponding to Flade potentials, and the accurate determination of such potentials. Typical potential-time curves are given in ref. (4) and (5).

All measurements were carried out in a constant temperature room maintained at 25° ± 0.5°C.

Results

It was felt advisable to first establish in further detail the potentiostatic polarization characteristics of the binary Cu-Ni alloys in the region of critical composition. Curves for i(crit.) and i(pass.) based on 10 alloys are shown in Fig. 1. Good agreement was found with similar data reported previously by Osterwald and Uhlig (1). Characteristics of secondary passivity and decay potentials for the same alloys were reported earlier (5). Although values of i(crit.) and i(pass.) were readily established for the alloys exhibiting passivity, values of current density analogous to i(crit.) for the nonpassive alloys at which a rapid

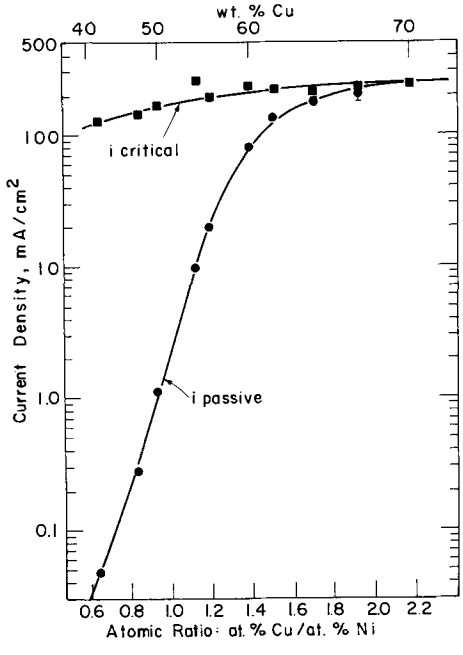

Fig. 1. Critical and passive current densities for copper-nickel alloys obtained from potentiostatic polarization curves (noble → active) in 1N H_2SO_4, 20 mV/min, 25°C.

change of slope occurred beyond the linear Tafel region, were less easily estimated [see, for example, the polarization curve for Cu in Fig. 2, ref. (4)]. The procedure used for the nonpassive alloys and for similar alloys to be described later was to take the value of current density corresponding to the intersection of two straight lines representing polarization data on either side of the region of maximum curvature. The same procedure was used for estimating values of potential corresponding to discontinuities in slope of potential decay curves. The potentials obtained in this manner were less arbitrary than those chosen at some point of maximum change of slope, especially in cases where the change of slope was not marked.

Because of the asymptotic approach of i(pass.) to i(crit.), the critical composition for the Cu-Ni alloy series cannot be determined precisely. It may be taken at the composition corresponding to an atomic ratio of 1.92 or at the higher atomic ratio of 2.16 (Fig. 1). For data obtained in the active-to-noble direction (not shown), typical overshoot in the polarization curves makes it necessary to take the critical composition as that value beyond which a constant difference between i(crit.) and i(pass.) is observed. The same atomic ratio approximating 1.9-2.2 is obtained either way.

Polarization curves corresponding to the region of secondary passivity (5) locate the critical composition at an approximate atomic ratio of 1.7-1.9. Because of the nature of the measurements in this region, these values are considered less reliable than those obtained in the region of primary passivity.

Data for potential decay (5) show that Flade potentials become more noble as the critical alloy composition is approached. The values reported previously for binary Cu-Ni alloys and presently for Cu-Ni alloys with addition elements are more noble than the values reported previously for the 45% Ni-Cu-Al alloys (4). This difference occurs partly because the method of intersecting lines presently used to estimate the potentials leads to somewhat more noble values; the trend, however, is not altered. The particular method employed for estimation does not affect absolute values corresponding to secondary passivity because the change of slope is relatively abrupt. But for Flade potentials of Cu-Ni alloys for which the change of slope is gradual, the method used for estimation becomes more important. The change of slope is so small for Ni compared to that for iron, for example, that Flade (6) originally reported nickel to show no "umschlagspunkt" (Flade potential) at all.

Gallium series.—Curves for i(pass.) and i(crit.) are shown in Fig. 2 with convergence at an atomic ratio of 1.89. Shapes of the curves, in particular a minimum in i(pass.), are similar to those reported earlier for Al additions (4). Convergence occurred at the same ratio whether the data were obtained proceeding from the noble-to-active or active-to-noble directions. Analogous curves for secondary passivity are shown in Fig. 3 showing parallel convergence at an atomic ratio of 1.89 and a similar minimum in the lower current density at an atomic ratio of 1.7.

Decay potentials related to both secondary passivity and to primary passivity (Flade potentials) are shown in Fig. 4. No discontinuities of slope were observed for alloys of atomic ratio greater than that of the critical composition in either the primary or secondary regions, at 0° or 25°C. Instead the potentials decayed smoothly to active values approximating the corrosion potential. This behavior is consistent with the previous conclusion that such alloys are not passive, that is they show no evidence of a decreasing current density or i(pass.) on shift to more noble potentials in typical potentiostatic polarization curves.

Decay potentials for secondary passivity of the Cu-Ni-Ga alloys were not observed at 25°C for alloys of atomic ratio less than 1.53 even though polarization curves indicate passive behavior. The probable reason

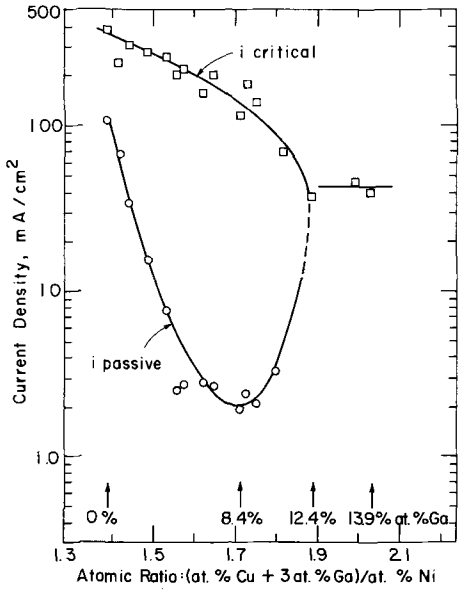

Fig. 2. Critical and passive current densities for copper-nickel-gallium alloys obtained from potentiostatic polarization curves (noble → active) in 1*N* H_2SO_4, stepwise scanning, 25°C.

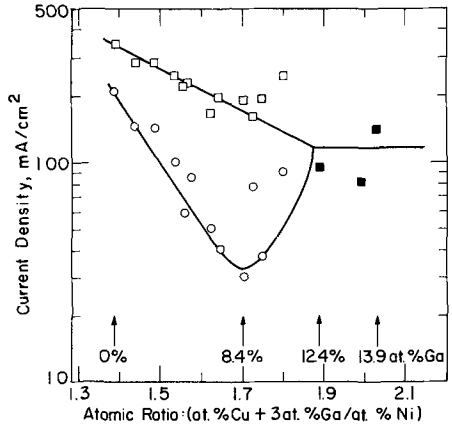

Fig. 3. Upper and lower current densities for secondary passivity of copper-nickel-gallium alloys obtained from potentiostatic polarzation curves (active → noble) in 1*N* H_2SO_4, stepwise scanning, 25°C.

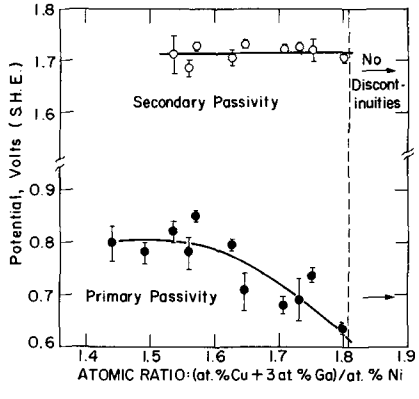

Fig. 4. Potentials corresponding to discontinuities in slope of potential decay-time curves for copper-nickel-gallium alloys in 1*N* H_2SO_4, 25°C. (Each point is average of 4 runs.)

is that the relevant current densities become so high that soluble corrosion products accumulating at the alloy surface rapidly destroy the passive film after the polarizing current is shut off. For the same reason, Flade potentials were not observed below a ratio of 1.44. Decay potentials of Fig. 4 corresponding to secondary passivity are independent of atomic ratio or

gallium content, but the Flade potentials tend toward more active values at higher atomic ratios.

Germanium series.—Curves for i(pass.) and i(crit.) are given in Fig. 5. These show that stepwise polarization measurements lead to higher values of i(crit.) than are observed with continuous polarization measurements, but values for i(pass.) are the same, and the convergence of the two current densities occurs at the same atomic ratio of 1.7. Small additions of Ge decrease values of i(pass.), but only slightly, and larger additions have the opposite effect. A minimum occurs at about 2 a/o (atomic per cent) Ge corresponding to an atomic ratio of 1.5. Values of i(crit.) decrease as the critical alloy composition is approached similar to the behavior of other alloy series of relatively constant Ni content. The trend is opposite in Cu-Ni alloys for which Ni content decreases as the critical composition is approached.

Secondary passivity was observed in the potential region >1.6V for alloys of atomic ratio less than 1.7, but the differences in current density characteristic of secondary passivity were smaller than for the Cu-Ni alloys and less reproducible. For this reason they were not plotted.

Decay potentials corresponding to both the secondary and primary regions of passivity are shown in Fig. 6. Measurements were taken at 1°C because passivity is more stable at low than at room temperature making it possible to discern small discontinuities in potential-time curves similar to those depicted in curves of Fig. 6, ref. (4). The potentials corresponding to secondary passivity lie between 1.7 and 1.8V showing a slight trend toward more active values as the critical composition is approached. The Flade potentials show an even steeper negative slope. Consistent with polarization data, no discontinuities in either the secondary or primary regions were observed at or above an atomic ratio of 1.7 which corresponds to the critical composition shown in Fig. 5, and above which a passive current density is not observed.

Iron and cobalt series.—These series of alloys were made up with variable Cu and Ni contents but approximately constant in Fe (2.5 a/o) or cobalt (2.3 a/o). The shapes of curves for i(pass.) and i(crit.) are similar to those for Cu-Ni (Fig. 7 and 8). Fe and Co, as well as Ni, are transition metals, hence the atomic ratio: a/o Cu/[a/o Ni + a/o (Co or Fe)] groups these addition elements with Ni rather than with Cu with which the nontransition elements are grouped. The critical compositions for convergence of i(pass.) and i(crit.) lie at higher atomic ratios compared to Ga or Ge additions, confirming that alloyed Fe and Co act like Ni.

Convergence of current densities for the Fe series, according to Fig. 7, occurs at an atomic ratio greater than 2.1. The extrapolated ratio is about 2.2, and the corresponding calculated critical composition is given in Table I. Secondary passivity data (Fig. 9) confirm that the critical composition for the Fe series lies above the atomic ratio 2.1. For the Co series the critical composition occurs at or above a ratio 2.14 with some possible justification for choosing 2.39 instead. Secondary passivity data (Fig. 10) lend weight to a critical composition at an atomic ratio 2.1.

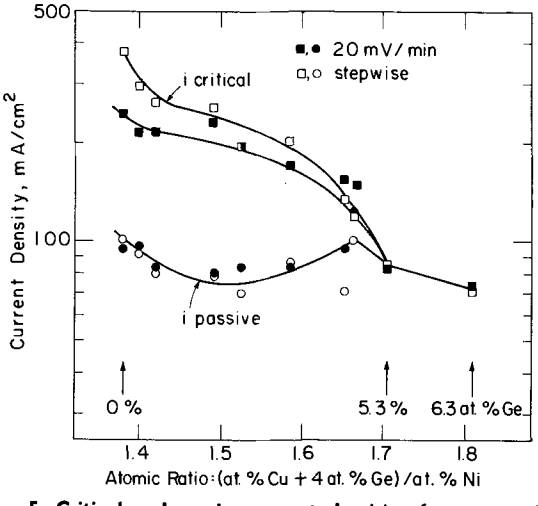

Fig. 5. Critical and passive current densities for copper-nickel-germanium alloys (noble → active) in 1N H_2SO_4, 25°C.

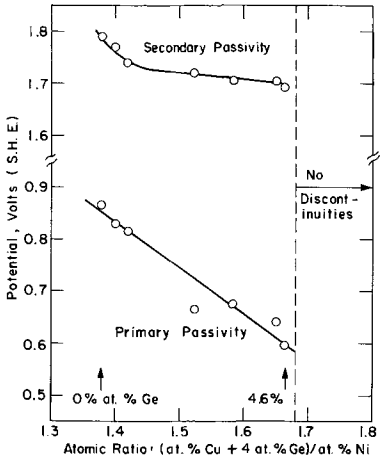

Fig. 6. Potentials corresponding to discontinuities in slope of potential decay-time curves for copper-nickel-germanium alloys in 1N H_2SO_4, 1°C. (Each point is average of 4 runs.)

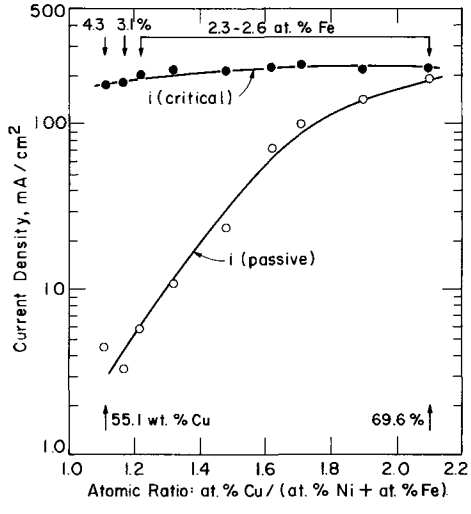

Fig. 7. Critical and passive current densities for copper-nickel-iron alloys (noble → active) in 1N H_2SO_4, 20 mV/min, 25°C

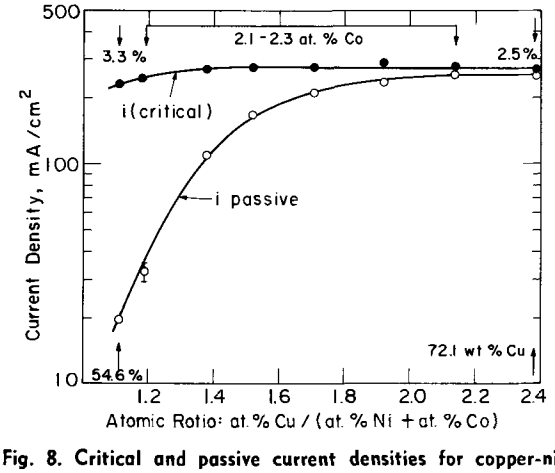

Fig. 8. Critical and passive current densities for copper-nickel-cobalt alloys (noble → active) in 1N H_2SO_4, 20 mV/min, 25°C.

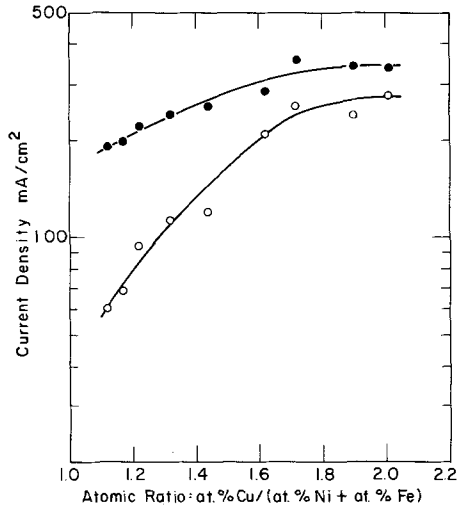

Fig. 9. Upper and lower current densities for secondary passivity of copper-nickel-iron alloys (active → noble) in 1N H_2SO_4, 20 mV/min, 25°C.

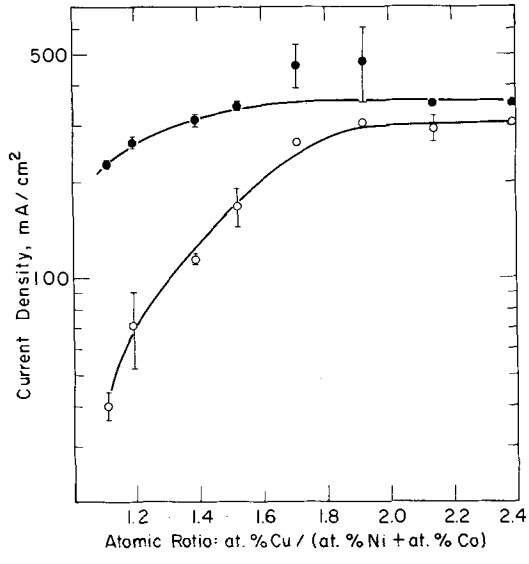

Fig. 10. Upper and lower current densities for secondary passivity of copper-nickel-cobalt alloys (active → noble) in 1N H_2SO_4, 20 mV/min, 25°C.

Although a systematic study was not carried out at this time, preliminary potential decay-time curves for the two series at 25°C showed two discontinuities for the alloys of lowest atomic ratio, but either one or no discontinuity for alloys approaching the critical composition. As mentioned before, it is probable that high current densities characteristic of the critical composition served to destroy passive films before potential decay measurements could be carried out. As with the other alloy series, discontinuities were more pronounced at lower temperatures where passivity decayed less rapidly.

Discussion

It is apparent that as the critical composition is approached, decreasing i(crit.) is usually accompanied by decreasing Flade potential ϕ_F (Al, Ga, Ge series). On the other hand, when i(crit.) increases, ϕ_F also increases (Ni-Cu series), or when the change of i(crit.) is small, change in ϕ_F is small (Zn series). This interdependence can be explained by the relation presented previously (7): $\phi_F - \phi_{corros.}$ = activation polarization + concentration polarization. Since the corrosion potential $\phi_{corros.}$ is observed to be about the same for all the alloys (0.2V), $\phi_F - \phi_{corros.}$ increases as ϕ_F becomes more noble. Furthermore, since the Tafel slope for anodic dissolution of all the alloys in the active region was observed to be about 30 mV, the current density i(crit.) required to polarize to ϕ_F is obviously greater the more noble the value of ϕ_F. Similarly, if ϕ_F becomes more active with alloy composition, corresponding values of i(crit.) show a decreasing trend.

Since the intersection of i(pass.) with i(crit.) at the critical composition occurs at a current density of about 100 mA/cm² or higher, this value corresponds to the removal of about 170 atom layers per second. Limited diffusion in the metal lattice at room temperature accompanied by continuous rapid removal of surface atoms make it likely that surface composition does not differ essentially from the over-all alloy composition.

It will be noted that the absolute values of i(pass.) lead to a less satisfactory correlation with alloy composition than does the present correlation based on both convergence of i(pass.) with i(crit.) and on potential-decay curves. The probable reason is that values of i(pass.), which are proportional to prevailing corrosion rates in the passive state, are subject both to variables of alloy composition additional to those entering formation of the passive film, as well as on prevailing potentials of the metal exposed to the electrolyte. On the other hand, the criteria of passivity used in the present paper merely indicate whether or not a passive film is present without relation to absolute reaction rates. Similarly, current oscillations as presently employed to indicate the presence of a secondary passive film may vary widely depending on the alloy, its environment and the relevant applied potential.

In accord with the discussion presented in earlier papers, the critical composition is interpreted as the specific atom ratio below which surface d electron vacancies exist and above which such vacancies are filled. Nickel on which oxygen of the passive film is adsorbed was assumed to supply 1.6 vacancies per atom (0.6 per Ni atom plus 1 vacancy resulting from electron transfer to adsorbed O). Copper, on the other hand, was assumed to donate 1 electron per atom accounting for a predicted filled d band at 62 a/o Cu or at an atomic ratio Cu/Ni of 1.6. The observed convergence of i(pass.) and i(crit.) according to data of Fig. 1 comes very close to this atomic ratio but is more precisely located at a higher ratio of 1.9 or 2.2.

By similar reasoning, it was shown in accord with prediction that alloyed Zn supplies 2 electrons per atom, the atomic ratio

$$(\text{a/o Cu} + 2\ \text{a/o Zn})/\text{a/o Ni}$$

for convergence of i(pass.) with i(crit.) occurring at 1.65 compared to the theoretical 1.60. Similarly, for alloyed Al, supplying 3 electrons per atom, the corresponding atomic ratio (a/o Cu + 3 a/o Al)/a/o Ni was observed at 1.68. Following the same principles, the critical atomic ratios, all of which are expected at 1.6 for nontransition components, are presently observed at values of 1.9 for Ga and 1.7 for Ge. For the alloyed transition metal Fe, the critical atomic ratio a/o Cu/(a/o Ni + a/o Fe) should also be observed at 1.6 provided that Fe behaves as does Ni, or at some higher value if the number of d electron vacancies per Fe atom is greater than for Ni. The same situation applies to alloyed Co. Data of Table I show that the critical atomic ratios are 2.2 and 2.14, respectively, hence Fe and Co probably contribute more d vacancies per atom than does Ni. Magnetic saturation moment data confirm that d electron vacancies per Fe atom are 2.2 and for Co they are 1.7 (8). At the surface, because of adsorbed oxygen, they are assumed to increase by 1 (2), and hence they become 3.2 and 2.7, respectively. Data of Fig. 1, 7, and 8 show that the differences between i(pass.) and i(crit.) at an atomic ratio of 1.6 are 70 mA/cm² for Cu-Ni, 90 mA/cm² for Cu-Ni-Co, and 180 mA/cm² for Cu-Ni-Fe alloys. Hence at the same atomic ratio, Fe is more effective than Co which

in turn is more effective than Ni, in imparting passivity to Cu-Ni alloys.

At the critical composition the number of vacancies equals the number of donor electrons, therefore the following general relation is expected to hold

$$\text{a/o Cu} + n(\text{a/o Y}) = 1.6(\text{a/o Ni})$$

where n is the number of electrons donated per atom of alloyed element Y. Similarly: a/o Cu = 1.6(a/o Ni) + v(a/o Z) where v is the number of vacancies per transition metal atom Z. It is possible therefore to plot a/o Cu − 1.6(a/o Ni) against n(a/o Y) having negative unit slope for alloyed nontransition elements or electron donors, and similarly against v(a/o Z) with positive unit slope for alloyed transition metals or electron acceptors. Doing so for the critical compositions given in Table I produces a straight line passing above the origin with a slope of 1.35 as shown in Fig. 11. For Ge, n = 4; for Al, n = 3; for Ga, n = 3 (or 2); and for Zn, n = 2. For Fe and Co, v = 3.2 and 2.7, respectively. The Ga point is relatively accurately placed by polarization data both in the primary and the secondary regions. If Ga were to contribute 2 instead of 3 electrons per atom, the point then lies close to the line representing other elements. Consideration, therefore, should be given to this possibility, especially since the chemical properties of Ga have established that it tends to form lower valent compounds much more readily, for example, than does Al (9).

The slope of the line is obviously high; it can be reduced to unity and at the same time pass through the origin in accord with predictions of the equations given heretofore by assuming that Cu donates less than one electron per atom (*e.g.*, 0.7-0.8) and that Ni has fewer vacancies per atom (*e.g.* 1.4-1.5). Justification for modifying the number of donor electrons or *d* vacancies per atom, and also the conditions under which such modifications may be expected to apply, lie outside the scope of the present discussion and are more properly the subject of a future communication. The fact that the points of Fig. 11 lie close to a straight line on either side of the Cu value without additional assumptions, is in itself significant.

Conclusions

The first conclusion derived from the accumulated data, therefore is that several nontransition elements added to the Ni-Cu alloy system apparently donate all or the major part of their valence electrons to the *d* electron vacancies of Ni, and that when such vacancies are filled, passivity is no longer observed. Transition metal additions, to the contrary, favor conditions for passivity by acting as electron acceptors, supplementing the number of *d* vacancies of Ni. These relations support the electron configuration theory of passivity beyond any of the evidence previously available.

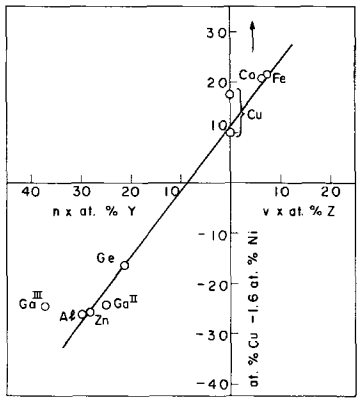

Fig. 11. Plot of excess electrons donated by Cu over surface *d* electron vacancies of Ni at the critical composition of Ni-Cu alloys, vs. electrons per atom donated by nontransition element Y or vacancies per atom supplied by transition metal Z. Assumption: 1.6 vacancy/Ni atom; 1 electron donated/Cu atom.

The second conclusion is that the presently reported relations between *d* band vacancies and observed passivity provide strong support for an adsorbed structure of the passive film having monolayer to multilayer dimensions in accord with the adsorption theory of passivity (10-13). Metals containing *d* band vacancies (transition metals) are well-known to favor chemisorption of oxygen, for example, more so than metals with filled *d* bands (nontransition metals). Passivity in Ni-Cu alloys accordingly is observed only when surface *d* electron vacancies are present; when such vacancies become filled by electrons from alloyed components, the required chemisorption of oxygen making up the passive film does not occur.

The simple band theory, therefore, successfully describes conditions leading to passivity or activity in the present alloys. Similar success has been achieved in explaining magnetic susceptibility (14). Some doubt has been expressed that such a model can adequately explain properties of Ni-Cu alloys such as electrical resistance, electronic specific heat, or thermo-electric properties (15, 16) indicating that refinements of theory are needed. These refinements can be expected as further data become available and as theoretical concepts of alloy structure mature. It is obvious in any event that the property of passivity, which is important not only to Ni-Cu alloys but also to several transition metal alloys, *e.g.*, Cr-Fe (stainless steels), must be included in any extension of present theories of the metallic state to more general explanations of alloy properties.

Acknowledgment

The authors are pleased to acknowledge support of this research by the Shell Companies Foundation.

Manuscript received Dec. 16, 1968. This was Paper 243 presented at the New York Meeting, May 4-9, 1969.

Any discussion of this paper will appear in a Discussion Section to be published in the December 1970 JOURNAL.

REFERENCES

1. J. Osterwald and H. H. Uhlig, *This Journal*, **108**, 515 (1961).
2. H. Uhlig, *Z. Elektrochem.*, **62**, 700 (1958).
3. N. D. Stolica and H. H. Uhlig, *This Journal*, **110**, 1215 (1963).
4. F. Mansfeld and H. H. Uhlig, *ibid.*, **115**, 900 (1968).
5. F. Mansfeld and H. Uhlig, *Corrosion Sci.*, **9**, 377 (1969).
6. F. Flade, *Z. physik. Chem.*, **76**, 513 (1911).
7. H. Uhlig, *This Journal*, **108**, 327 (1961).
8. "American Institute of Physics Handbook," 5-208, McGraw-Hill Book Co., New York (1957).
9. H. Remy, "Lehrbuch der Anorganische Chemie," Vol. I, pp. 374, 440-444, Akadem. Verlag, Leipzig (1960). Carlston *et al.* consider Ga (II) to be a mixture of Ga (I) and Ga (III). *J. Am. Chem. Soc.*, **80**, 1532 (1958).
10. H. H. Uhlig, *Z. Elektrochem.*, **62**, 626 (1958); *Annals N. Y. Acad. Sci.*, **58**, 843 (1954).
11. B. Kabanov, R. Burstein, and A. Frumkin, *Discussions Faraday Soc.*, No. 1 (1947).
12. Ya. Kolotyrkin, *Z. Elektrochem.*, **62**, 664 (1958); *This Journal*, **108**, 209 (1961). Additional Russian references are listed in "Passivity and Protection of Metals Against Corrosion" by N. D. Tomashov and G. Chernova, p. 12, Plenum Press, New York (1967).
13. K. Schwabe and G. Dietz, *Z. Elektrochem.*, **62**, 751 (1958); K. Schwabe, *Electrochim. Acta*, **3**, 186 (1960); *Werkstoffe u. Korrosion*, **18**, 961 (1967).
14. C. Kittel, "Introduction to Solid State Physics," pp. 463, 581, John Wiley & Sons, Inc., New York (1966).
15. B. Coles, *Proc. Phys. Soc.*, **65B**, 221 (1952).
16. D. Pollack, *Acta Met.*, **16**, 1453 (1968).

Oxide Growth on Copper and Alpha-Brasses in Aqueous Ammonia

J. A. S. Green* and H. D. Mengelberg[1]

Research Institute for Advanced Studies, Martin Marietta Corporation, Baltimore, Maryland

and H. T. Yolken*

Institute for Materials Research, National Bureau of Standards, Washington, D. C.

ABSTRACT

An ellipsometric study of the kinetics of oxide growth for pure copper and a series of alpha-brasses immersed in tarnishing ammoniacal environments has established that the growth of the oxide, shown to be cuprous oxide, obeys a linear law in each case, and that the rate of growth increases significantly with (*a*) increasing zinc content of the solid, (*b*) increasing temperature, and (c) the application of anodic potentials. On the basis of these results it is suggested that the oxide is porous and that oxide growth involves the dissolution of metal ions at the base of the pore (anodic reaction) and their deposition at the oxide surface (cathodic reaction), electrons flowing through the oxide film. The influence of zinc content on the oxide-growth rate is attributed to its effect on the dissolution kinetics.

The intergranular stress-corrosion cracking (SCC) of alpha-brass in aqueous ammonia, commonly referred to as season cracking, occurs in those ammoniacal environments which cause tarnishing (1, 2), and it has been suggested that the tarnish plays an important role in the cracking process (3, 4). Electron diffraction (3), x-ray (5), and electron microprobe (6) studies have shown that the tarnish formed on Cu-30 Zn consists mainly of an epitaxed layer of cuprous oxide, Cu_2O, which is severely depleted in zinc with respect to the alloy. The mechanism of tarnishing, however, has not been established. In this respect several investigators (4, 7) have suggested that the tarnish is fully dense and protective, and that the growth process involves the solid-state diffusion of cuprous ions across the film. Conversely, other workers (3, 6, 8) have suggested that it is porous. Tromans and Nutting (8) based their suggestion on the observation of pores at both grain and twin boundaries in replicas of tarnish formed on Cu-30 Zn by exposure to moist ammonia vapor. Forty and Humble (6) supported their conclusion by the fact that when glass tubes containing tarnishing solutions were sealed with thin brass foils, leaks eventually developed even though the foils apparently remained coherent. Electron microscope studies by the latter workers also showed the tarnish to consist of an aggregate of small platelets of crystallites, about 500Å in diameter and about 100Å thick.

The present ellipsometric studies were undertaken to provide quantitative data on the kinetics of the growth process and thereby to clarify the mechanism of tarnish growth. In addition to the kinetic measurements of oxide growth, electron-diffraction studies were carried out to determine the composition of the tarnish for a wide range of alpha-brasses.

Experimental

The studies were carried out on 99.999% pure copper; on brasses, prepared from base metals of similar purity, containing, 5, 10, and 20 w/o (weight per cent) zinc; and on 30 w/o zinc alloy of 99.97% purity. Disks of each material, 1.9 cm in diameter and 0.05 cm in thickness, were cut from annealed sheet and silver-soldered onto a copper base plate. The base plate was firmly attached to a glass specimen holder by a polytetrafluoroethylene seal. The surface of the specimen was prepared by mechanical polishing using ¼ μm diamond abrasive on a napped cloth, followed by electropolishing in a 60/40 orthophosphoric acid/water solution. Finally, before use, the surface was rinsed in distilled water, methanol, and spectro-grade acetone, and then dried in a blast of oxygen. This procedure produced surfaces which gave rise to reproducible results.

The tarnishing ammoniacal solution was prepared by dissolving 8g of electrolytic copper dust in 1 liter of oxygen-saturated 15*N* aqueous ammonia. This solution was the same as that used for previous stress-corrosion studies (2, 9). The refractive index of this solution was 1.3535 at 25°C; small changes of the refractive index of this aqueous solution as a function of temperature were neglected (10).

Electron-diffraction studies were carried out to establish the composition of the tarnish formed on pure copper and all the α-brasses. Metal foils were prepared by electropolishing in orthophosphoric acid/water solution. Diffraction patterns were then obtained both before and after immersing the foil in the tarnishing environment.

The ellipsometric technique and its application to the measurement of the thickness of films formed during corrosion and oxidation has been described in detail elsewhere (11-16). Essentially the technique depends on the fact that the state of polarization of elliptically polarized light incident on a surface is changed on reflection. The change in ellipticity is measured in terms of two parameters, tan ψ and Δ, where tan ψ represents the relative amplitude ratio and Δ, the relative phase retardation of an equivalent set of electric field vectors parallel and normal to the plane of incidence. In addition to the film thickness d, the change in ellipticity on reflection is dependent on several factors such as the optical properties of the media involved, the angle of incidence ϕ, the wavelength of light λ. In terms of these factors, the change in ellipticity may be expressed as

$$(\tan \psi)\, e^{i\Delta} = f(\hat{n}_1, \hat{n}_2, \hat{n}_3, \phi, d, \lambda) \qquad [1]$$

where $\hat{n}$ is the refractive index. For an absorbing medium the latter is a complex quantity which may be expressed as

$$\hat{n} = n(1 - ik) \qquad [2]$$

where n is the real part of the refractive index, k the extinction coefficient (both for a given wavelength),

* Electrochemical Society Active Member.

[1] Research Associate from Martin Marietta Corporation in the Corrosion Section, Institute for Materials Research, National Bureau of Standards, from September 1967 to September 1968.

and i is $\sqrt{-1}$. The suffixes 1, 2 and 3 refer to the environment, the film, and the substrate respectively. Accordingly, for a metal/environment system in which $\hat{n}_1$, $\hat{n}_3$, ϕ and λ are known it is possible to compute values of tan ψ and Δ for films of various thicknesses and optical constants, *i.e.*, n_2 and k_2 values. In this study the computations were carried out using a program developed by McCrackin (17). The thickness of the film then may be determined by selecting the optical constants which provide the closest agreement between the computed data and the experimental results.

In general, the ellipsometer arrangement used in this study was similar to that described by Kruger (13), although some minor modifications were introduced. For instance, due to light absorption, the blue ammoniacal solution required the use of blue light. Thus a monochromater was employed to isolate a blue line ($\lambda = 4358$Å) of the mercury arc. Also to permit rapid filling of the cell (volume $\approx$ 100 cm^3) by a gravity-feed system a large diameter (1.25 cm) inlet tube was connected to the cell. Two platinum electrodes were located in the cell so that when the specimen was completely immersed, the environment completed the circuit between the electrodes and indicated the start of the test on a recorder. The ellipsometer cell was constructed so that the optical axis of the cell windows intersected the plane of the specimen surface giving an angle of 70° with the normal to the surface. Each window of the cell consisted of two optical flats, separated by an evacuated space, in order to avoid condensation of moisture on the outer window at lower test temperatures. To obtain the lower temperatures, the cell was wrapped with cooling coils and insulated with polystyrene foam so that the temperature could be maintained, within ±3°C of the required value, in the range −35° to +25°C. Methanol, precooled in a methanol/dry ice mixture, was used as coolant.

In the ellipsometric technique it is generally necessary to measure the optical parameters of the bare metal surface and usually in solution environments this is accomplished by cathodically protecting the specimen. In this instance, however, this procedure was not possible since cathodic deposition of copper occurred. Thus an alternative procedure was adopted in which the polished specimen was inserted into the cell and the ellipsometric values of the electropolished surface were measured in air. The optical parameters of the "bare" metal surface were then calculated from this data. The "bare" surface was probably covered with an oxide film as a result of washing with water (18) and might also be coated with a thin phosphate film from the electropolishing process (19). However, the ellipsometric parameters as measured *in situ* were found to be virtually unchanged when the electropolished specimen was cathodically polarized in a solution of phosphoric acid (in which there was no dissolved copper) indicating that the electropolished surface was covered by a film which was much thinner than the film thickness to be determined in the ammonia solution.

After the parameters of the initial surface condition had been established, the ammoniacal solution was introduced to the cell and subsequent changes in ellipsometer values were monitored by manual operation of the instrument. For the Cu-30 Zn alloy oxide growth was too rapid to be followed in this manner. In this case the ellipsometer was preset to certain values of Δ and ψ, corresponding to a particular film thickness. It should be noted that in most film-covered systems the Δ values are cyclic and any particular Δ value is repeated at certain intervals which are a function of film thickness (11). The time intervals required for the oxide to attain these preset values are then measured. To do this the photodetector output is recorded, a minimum of light intensity being observed each time the actual parameters of the film approximated the preset values. The interval between successive minima corresponds to an increment of thickness which may be computed. To provide a useful estimate of the increment of thickness the actual ψ value need not be exactly equivalent to the preset values (in most of the experiments in this study ψ is cyclic but the exact values are not repeated, see Fig. 2). It should be emphasized that this method gives only a rough estimate of the rate of film growth, but it was used because no other technique was available to measure the very rapid oxide growth of the Cu-30 Zn alloy.

The rate of oxide growth was measured for pure copper and the α-brasses as a function of temperature, and for the Cu-30 Zn alloy also as a function of applied anodic potential.

Results

The ellipsometric results are presented in polar-coordinate diagrams in which Δ and ψ are the angular coordinate and radial coordinates, respectively. The changes in ellipsometer values, measured as a function of time for pure copper at two temperatures, are shown in Fig. 1. Similar measurements for the series of brasses investigated are illustrated in Fig. 2. Figure 1 shows that, at ambient temperature, the ellipsometer values move in an anticlockwise direction and almost describe a closed loop, while at 10°C the sense of rotation changes to a clockwise direction after one loop.

The fact that the ellipsometer values describe a loop is significant in terms of the thickness of the surface film. For a nonabsorbing film on an absorbing substrate, the film thickness corresponding to a change of 360° in Δ is that thickness which shifts the phase of the incident radiation by an amount equal to its period (11) as shown in Fig. 3a. This thickness, d, is given by

$$d = \frac{\lambda}{2 \cdot n_2 \cdot \sin \phi} \qquad [3]$$

For absorbing films ($k_2 \neq 0$) approximately the same situation exists. It may be seen from the computed

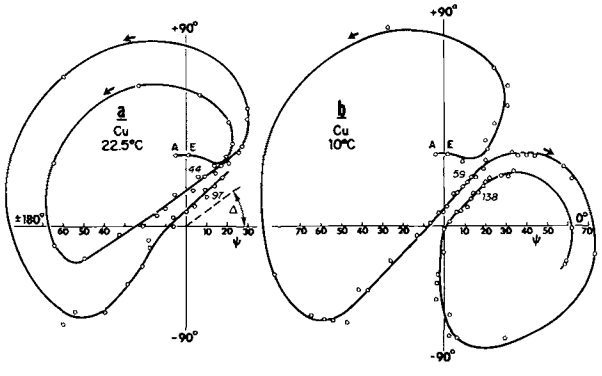

Fig. 1. Experimentally determined ellipsometric curves of Δ and ψ plotted on polar coordinates for the growth of cuprous oxide on copper at (a) 22.5°C and (b) 10°C. In each diagram point A indicates the parameters of the "film-free" surface in air and point E represents the initial surface in the ammoniacal environment. The numbers beside each curve indicate the elapsed time, in minutes, from the moment of immersion.

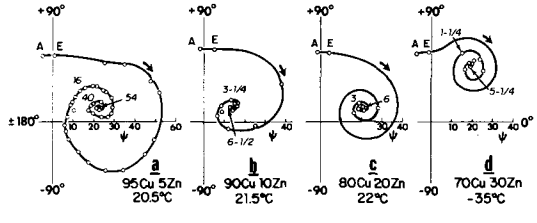

Fig. 2. Experimentally determined ellipsometric curves of Δ and ψ plotted on polar coordinates for the growth of cuprous oxide on a range of brasses. Points A and E and the numbers beside each curve have the same significance as in Fig. 1.

curves shown in Fig. 3 that each 360° rotation about the center of the spiral corresponds to the same increment in film thickness. The electron-diffraction studies showed that for pure copper and all the α-brasses the tarnish film was composed of cuprous oxide Cu_2O. Thus, in this particular case ($\lambda = 4358$Å) if the refractive index, n_2, of Cu_2O is taken as 2.75 (14), then the value of d is approximately 900Å. However changes in the optical constants, *i.e.*, n_2 and k_2 values of the film may alter this estimate of thickness, although in this respect only changes in n_2 will be significant. The observed changes in the direction of rotation of the curves in Fig. 1 and 2 suggest that the optical constants are not the same in every case. Thus it is necessary to determine whether and to what extent these constants change as a function of the experimental variables before making any estimate of film thickness.

To examine whether the changes in the shape of the curves shown in Fig. 1 and 2 are due to changes in n_2 and/or k_2, a series of curves were computed assuming various n_2 and k_2 values for the film. The computations were made using the parameters for the electropolished surface,[2] *i.e.* point A in Fig. 1 and 2, and n_2 and k_2 of the film were assumed to vary between 2.3-3.2 and 0.0-1.0, respectively. Figures 3 and 4 represent a selection of these computed curves. Figure 3 illustrates curves computed assuming constant n_2 (2.75) and varying k_2 (0.0-0.2), while Fig. 4 illustrates curves for constant k_2 (0.2) and varying n_2 (2.5-2.9). These figures show that the changes of shape in the experimental curves of Fig. 1 and 2 are not due to changes in n_2 (Fig. 4) but may be accounted for solely on the basis of small changes in k_2 (Fig. 3) which would not appreciably affect the estimate of film thickness. Figures 3 and 4 also show that the completion of one ellipsometer loop[3] is equivalent to an oxide thickness of 900Å. In fact, the figures show that even if the refractive index, n_2, varied within the range 2.5-2.9, a considerably greater variation than that reported for Cu_2O films grown under different conditions (14), the computed thickness would be in error by only 10%. Using the time to complete one ellipsometer loop as an increment of given thickness it was possible to examine the influence of zinc content, temperature, and applied potential on the kinetics of oxide growth by simply measuring the time required to complete successive loops under the various conditions. These results are presented below.

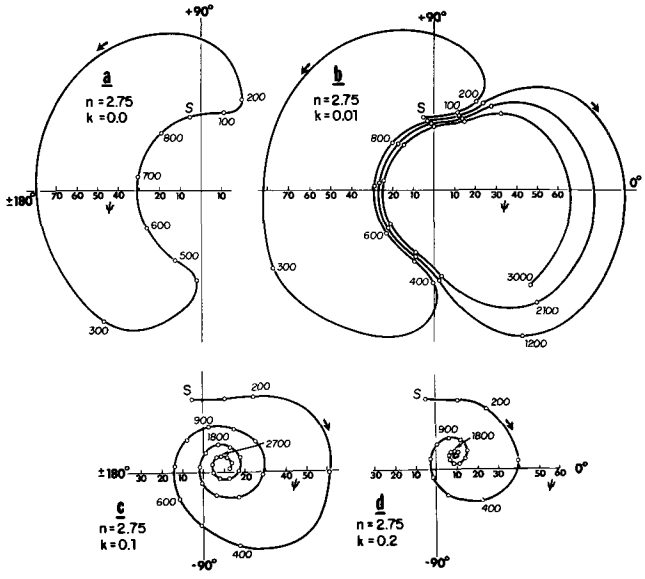

Fig. 3. Computed ellipsometric curves of Δ and ψ plotted on polar coordinates for the growth of cuprous oxide on copper assuming for the oxide constant n (2.75) and varying k (0.0-0.2). In each diagram point S indicates zero film thickness and the numbers beside each curve indicate values of film thickness in angstroms.

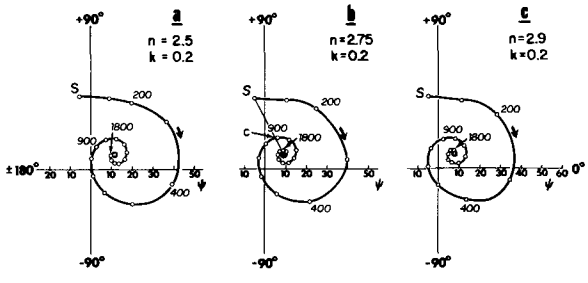

Fig. 4. Computed ellipsometric curves of Δ and ψ plotted on polar coordinates for the growth of cuprous oxide on copper assuming for the oxide varying n (2.5-2.9) and constant k (0.2). Point S indicates zero film thickness and the numbers beside each curve indicate values of film thickness in angstroms.

Influence of zinc content.—Figure 2 and Table I indicate the influence of zinc content on the oxide growth kinetics. Figure 2 shows that curvature of the ellipsometric spiral increases for increasing zinc content of the substrate, and a comparison of this figure with the computed curves of Fig. 3 suggests that the extinction coefficient, k_2, of the oxide increases for increasing zinc content of the brass. Table I shows that the time required to grow an oxide of given thickness decreases with increasing zinc content of the substrate, *i.e.*, the oxidation rate is more rapid the higher the zinc content of the brass. In fact, in the case of Cu-30 Zn the process was found to be so rapid that it could only be followed manually at −35°C. However, by using the technique described earlier in which the ellipsometer was preset to certain values, it was estimated that an oxide of ~ 900Å thickness was formed in ~ 1-2 sec at room temperature.

A further result apparent from Table I is that, for the range of oxide thicknesses studied (0-2700Å), the oxidation process follows a linear law, *i.e.*, the time required for the oxide to grow the second 900Å increment is almost the same as for the first increment. This result, which appears to be valid both over the temperature range investigated (−25°-+25°C) and under conditions of applied potential, is well illustrated in the case of Cu-5 Zn at −20°C, see Table II. In this instance if it is assumed that a 900Å oxide is formed in 37.5 min, then the time required to form

[2] The complex refractive index of the copper substrate was calculated to be 1.5 (1-2.39i). This value is in the range of values reported in Winterbottom's survey (11). It should be pointed out that this value was not substantially changed for the alloys and was therefore also used in all calculations. Changes of the refractive index of the substrate over the temperature range investigated were calculated to be small and were therefore neglected (20).

[3] For a spiral-shaped curve a loop is said to be complete when a line drawn from the beginning to the center of the spiral cuts the spiral itself, *i.e.*, at point C in Fig. 4b.

Table I. Effect of zinc content and temperature on the kinetics of tarnish growth

Metal Substrate	Cu				Cu-5 Zn			Cu-10 Zn			Cu-20 Zn			Cu-30 Zn		
Temperature, °C	−15	−5	10	22.5	−20	0	20.5	−20	0	21.5	−15	0	22	−35	0	22
Time, min, to 900Å	83.5	61	59	44	37.5	17	16	28	6.5	3.7	12	3	1	1	—	*
to 1800Å	200	147	138	97	82	38	40	58	13	6.5	25.5	6.3	3	2.7	—	—
to 2700Å	—	—	—	—	121	—	49.5	75	—	—	38	9.5	5.5	—	—	—

* Process too rapid to measure manually, estimated by rapid recording technique to be ~ 1-2 sec at 22°C.

Table II. Oxidation of Cu-5 Zn at −20°C

Time, min, to	Calculated a) Linear law	Assuming b) Parabolic law	Experimental results
900Å	37.5	37.5	37.5
1800Å	75	150	82
2700Å	112.5	337.5	121

Table III. Effect of applied anodic potential on the oxidation of Cu-5 Zn at 22°C

Time, min, to	Applied potential, mV, SCE −390 (E_{corr})	−330	−300
900Å	37.5	9.7	5
1800Å	82	23.5	10.5
2700Å	121	—	16.5

successive increments of oxide may be calculated assuming both linear and parabolic growth laws. Table II shows that the experimental observations approximate to the values computed assuming the linear law.

Effect of temperature.—For pure copper and the alloys the rate of oxide growth was found to increase with temperature, Table I. The variation in the time required to form an oxide of given thickness as a function of temperature was used to estimate the activation energy of the process. For pure copper a plot of the time to form a 900Å film *vs.* the reciprocal temperature gave an activation energy of 84.44 kjoules/mole (20.2 kcals/mole) for the reaction. For the alloys, however, no estimate of the activation energy was possible as the dependence was not linear over the limited range of temperatures examined.

Effect of anodic potential.—The application of a potentiostatically controlled anodic potential was found to increase the oxidation rate of Cu-5 Zn at 22°C. In fact, the results in Table III suggest that the logarithm of the time to grow a 900Å film follows a linear relationship as a function of applied potential. If it is assumed that the oxide thickness is equivalent to the quantity of material dissolved,[4] then this suggests that a Tafel relationship is operative, *i.e.*, that the logarithm of the current is proportional to the applied potential. Generally a Tafel relationship is obeyed when anodic dissolution under activation control occurs. During these measurements it was also noted that the applied current required to sustain a given potential was virtually constant during film growth, indicating that the oxide formed is not protective.

Discussion

The present results provide considerable insight into the mechanism of oxide growth. The observation of linear kinetics over the thickness range 0-2700Å indicates that diffusion across the film is not rate-controlling. Thus, these results would appear to eliminate an earlier suggestion that the process is controlled by the solid-state diffusion of cuprous ions across the film (4, 7). Furthermore, such a model cannot be reconciled with the rates of film growth observed in the present studies, *viz.*, from $\sim 10^{-8}$ cm/sec for Cu to $\sim 10^{-5}$ cm/sec for Cu-30 Zn. Taking the diffusion coefficient of cuprous ions in cuprous oxide at ambient temperature to be $\sim 10^{-26}$ cm^2/sec (21) and assuming a concentration gradient across a 1 μm film to be $\sim 10^{-3}$ mole/cm^3, then it may be shown that solid-state diffusion of copper ions would give rise to a rate of oxide growth of only $\sim 2.4 \times 10^{-24}$ cm/sec.

The linear growth process and the observation during anodic polarization that the oxide is not protective both support the suggestion (6, 8, 22) that the oxide is porous and that the environment has access to the metal via pores. Thus it is suggested that oxide growth involves dissolution of metal ions at the base of the pore (anodic reaction) and their deposition at the oxide surface (cathodic reaction) electrons flowing through the oxide film. Such a process is also consistent with the earlier observations that the oxide is severely depleted with respect to zinc (6). Moreover, this model can account for the observed growth kinetics. Thus, taking the diffusion coefficient of copper ions in solution at ambient temperatures to be $\sim 10^{-5}$ cm^2/sec (23) and again assuming the concentration gradient of copper ions across a film of 1 μm thickness to be 10^{-3} mole/cm^3, then it may be shown that diffusion in solution would give rise to oxide-growth rates of $\sim 2.4 \times 10^{-3}$ cm/sec.

While in the present work oxide growth is linear over the thickness range 0-2700Å, previous workers (24) have reported that a limiting thickness is eventually reached. It was shown for Cu-30 Zn immersed in Mattsson's solution (1) of pH $\sim$ 7.2, that a limiting thickness of 5 μm was attained, at which point it was suggested that the rate of growth was equal to the rate of dissolution of the oxide. In terms of the present observations it is possible that, for film thicknesses considerably in excess of 2700Å, diffusion through pores would be rate-controlling. Alternatively, oxide growth could be limited either by an increase in the copper ion concentration at the base of the pore which would in itself restrict the dissolution kinetics (25) or by electron transport through the film.

The magnitude of the activation energy of the oxide-growth process for copper, ~20 kcal/mole, and the fact that the process appears to obey a Tafel relationship suggests that the rate-controlling step is anodic dissolution at the base of the pore. Accepting this, then the strong influence of zinc content on the oxide-growth rate of the metal can be attributed to the influence of zinc on the kinetics of anodic dissolution which, in turn, may be attributed to the high thermodynamic activity for dissolution of zinc. It is reasonable to suggest that the dissolution of a copper atom from the surface occurs via some type of active site, such as a kink site or ledge, and that the rate of dissolution of copper atoms is related to the number of such active sites. If zinc atoms, because of their high thermodynamic activity for dissolution, may be dissolved directly from the plane surface producing monotomic pits, then this would lead to the creation of a large number of additional active sites from which dissolution of copper atoms would be facilitated.

While the present results provide a general outline of the mechanism of oxide growth, several details remain to be established. In particular, the specific role (24) of the cupric complex, $Cu(NH_3)_4^{2+}$, in the tarnishing process is not understood. It has been suggested (5) that the reduction of these complexes provides an efficient cathodic reaction but the precise role of this reaction is not clear. Also, it is not understood why the base of the pore remains free of oxide. It is well established that oxide formation is critically dependent on the chemical composition of the environment, particularly on pH (1, 2). However, the way in which the reactions at the base of the pore maintain oxide-free conditions requires further attention. Finally, it would appear that season-cracking might be curtailed by controlling the anodic dissolution reaction at the base of the pores; for example, by the addition of minor alloying elements which might poison the active sites at which dissolution occurs.

Acknowledgments

The authors wish to thank Drs. E. N. Pugh and A. J. Sedriks of the Research Institute for Advanced Studies, Martin Marietta Corp., Dr. J. Kruger of the Institute for Materials Research, National Bureau of Standards, and Dr. D. A. Vermilyea of the Research and Development Center, General Electric Company, for helpful and stimulating discussions during the course of this study. The authors are indebted to the

[4] This assumption is not exact as the zinc, which comprises 5% of the alloy, remains in solution on dissolution.

Corrosion Section of the National Bureau of Standards in whose laboratories this work was carried out and to the Anaconda American Brass Company for providing the alloys used. The financial support of the Office of Saline Water is gratefully acknowledged.

Manuscript submitted April 30, 1969; revised manuscript received Nov. 17, 1969.

Any discussion of this paper will appear in a Discussion Section to be published in the December 1970 JOURNAL.

REFERENCES

1. E. Mattsson, *Electrochim. Acta*, **3**, 279 (1961).
2. E. N. Pugh and A. R. C. Westwood, *Phil. Mag.*, **13**, 167 (1966).
3. A. J. Forty and P. Humble, *ibid.*, **8**, 247 (1963).
4. A. J. McEvily and A. P. Bond, *This Journal*, **112**, 131 (1965).
5. T. P. Hoar and C. J. L. Booker, *Corrosion Sci.*, **5**, 821 (1965).
6. A. J. Forty and P. Humble, in "Environment-Sensitive Mechanical Behavior," p. 421, A. R. C. Westwood and N. S. Stoloff, Editors, Gordon and Breach, New York (1966).
7. E. N. Pugh and A. R. C. Westwood, "Stress Corrosion Testing," p. 228, A.S.T.M.S.T.P. No. 425 (1967).
8. D. Tromans and J. Nutting, *Corrosion*, **21**, 143 (1965).
9. E. N. Pugh, J. V. Craig, and W. G. Montague, *Trans. ASM*, **61**, 468 (1968).
10. Handbook of Chemistry and Physics, 37th Edition, p. 2677, Chemical Rubber Publishing Co., Cleveland (1956).
11. A. B. Winterbottom, "Optical Studies of Metal Surfaces," Vol. 1, Kgl. Norske Findenskab. Selskabs Shrifter (1955), F. Bruns Bokhandel, Trondheim (1955).
12. F. L. McCrackin, E. Passaglia, R. R. Stromberg, and H. L. Steinberg, *J. Res.* Natl. Bur. Std., **67A**, 363 (1966).
13. J. Kruger, *Corrosion*, **22**, 88 (1966).
14. P. C. S. Hayfield, First International Congress on Metallic Corrosion, London, April 1961, Butterworths, London (1962); (a) p. 663, (b) p. 671.
15. V. V. Andreeva, Second International Congress on Metallic Corrosion, New York, March 1963, p. 535, NACE, Houston, Texas (1966).
16. H. T. Yolken and J. Kruger, *This Journal*, **114**, 796 (1967).
17. F. L. McCrackin, Natl. Bur. Std. Tech. Note 479 (1969).
18. J. Kruger, *This Journal*, **108**, 503 (1961).
19. J. N. Allen, *Trans. Faraday Soc.*, **48**, 273 (1952).
20. R. G. Lye, RIAS, Private communication.
21. P. Kofstad, "High-Temperature Oxidation of Metals," p. 99, John Wiley and Sons, New York (1966).
22. D. A. Vermilyea, Proceedings of the International Conference on Fundamental Aspects of Stress-Corrosion Cracking, p. 152, R. W. Staehle, Editor, NACE (1969).
23. See ref. (10), p. 2026.
24. E. N. Pugh, J. V. Craig, and A. J. Sedriks, Proceedings of the International Conference on Fundamental Aspects of Stress-Corrosion Cracking, p. 118, R. W. Staehle, Editor, NACE (1969).
25. J. I. Lauritzen, Natl. Bur. of Std., Private communication.

A Simple Crevice Corrosion Theory

D. A. Vermilyea* and C. S. Tedmon, Jr.*

Research and Development Center, General Electric Company, Schenectady, New York

ABSTRACT

A simple theory for the concentration and potential variation in a crevice is compared with experimental results from a model crevice. A consequence of the theory, confirmed by experiments, is that a small potential difference in a crevice can cause a large concentration change and a corresponding large increase in corrosion current at a given applied potential. The theory gives a simple way to estimate concentrations in crevices in real corrosion situations.

We wish to present a very simple approximate theory for the concentration changes which accompany current flow to an electrode confined in a crevice. The treatment is especially applicable to corrosion along a grain boundary when the sides of the crevice are entirely inert, but with simple modifications it could be used to predict concentration changes in a pit. Following the derivation of equations, experiments using a model crevice are discussed in the light of the theory. This theory differs from the more complicated analyses of concentration changes in crevices by Beck and Grens (1) and by Posey (2) principally in the fact that the sides of the crevice are completely inert.

Theoretical

Consider a crevice of depth l having a thickness w and an arbitrary dimension perpendicular to w and l. The current is assumed to flow only in a direction parallel to the depth, and to be carried by only one ion, for instance, an ion of the metal being dissolved. In each volume element perpendicular to l of thickness dx we have

$$d\phi = I\,dR = \frac{I\rho dx}{A} \qquad [1]$$

in which ϕ is the electrical potential, I is the current flowing in the crevice, R is the resistance of the solution in the crevice, ρ is the resistivity of the solution, and A is the cross-sectional area of the crevice. For dilute solutions the resistivity is given by

$$\rho = \frac{1}{z\mathbf{F}\mu C} \qquad [2]$$

in which z is the valence of the ion which carries the current, $\mathbf{F}$ is Faraday's constant, μ is the ion mobility, and C is the ion concentration. If each volume element is electrically neutral, a very good approximation in most situations of interest (3), then the concentration of the current-carrying ion must be equal to that of the anion (assumed to have equal charge). The concentration of the anion is given by

$$C = C_0 \exp ze\phi/kT \qquad [3]$$

in which C_0 is the concentration of the anion in the bulk of the solution. Introducing the value for C from Eq. [3] and the Einstein relationship $\mu = zDe/kT$ with D the diffusion coefficient, e the electronic charge, k Boltzmann's constant, and T the temperature into Eq. [2] and [1] gives

* Electrochemical Society Active Member.

$$C_o \exp ze\phi/kT \, d\phi = \frac{J \, dx \, kT}{z^2 \, \mathbf{F}eD} \quad [4]$$

in which J is the current density. A solution of Eq. [4] is

$$C = \frac{Jx}{z\mathbf{F}D} + \text{const.} \quad [5]$$

Since $C = C_o$ at $J = 0$ we have from Eq. [5]

$$C - C_o = \frac{Jx}{z\mathbf{F}D} \quad [6]$$

The potential at any point in the crevice can be found by integrating Eq. [4] and noting that $\phi = 0$ at $x = 0$, which gives

$$\phi = \frac{kT}{ze} \ln\left(1 + \frac{Jx}{z\mathbf{F}DC_o}\right) \quad [7]$$

$$= \frac{kT}{ze} \ln\left(1 + \frac{\Delta C}{C_o}\right) \quad [8]$$

where ΔC is the concentration change at the position in question.

Equations [6] and [8], the fundamental equations resulting from the theory, are limited to very dilute solutions in which the ion mobility is not a function of concentration. To a first approximation, however, the equations are useful to concentrations of about molar.

There are two modifications which make the basic equations more useful. The first is to consider the concentration change in the solution just outside the crevice. The same general method for that region, which has approximately cylindrical geometry, leads to the equation

$$\Delta C = \frac{Jw \ln r_2/r}{\pi z\mathbf{F}D} \quad [9]$$

in which r_2 is the radius at which the bulk concentration is reached and r is equal to $w/2$. Equation [8] is valid for the potential in this region, with $\phi = 0$ corresponding to the point where the bulk concentration is reached.

The second modification is useful for total applied potentials large enough so that the concentration reaches a value in excess of molar within the crevice, and the resistivity is no longer represented adequately by Eq. [2]. A crude approximation is to consider that Eq. [6] and [8] are valid to a distance x_1 at which the concentration reaches some value such as molar, and that deeper in the crevice the resistivity of the solution is constant. The value of x_1 is found from Eq. [6] to be

$$x_1 = \frac{z\mathbf{F}D \, \Delta C_{max}}{J} \quad [10]$$

in which ΔC_{max} is the difference in concentration between 1 M/l and the concentration at the mouth of the crevice. The equation for the total potential in the crevice is then

$$\Phi = J \cdot \rho_{max} (1 - x_1) + \frac{kT}{ze} \ln\left(1 + \frac{\Delta C_{max}}{C_o}\right) \quad [11]$$

in which ρ_{max} is the constant resistivity reached deep within the crevice.

Experimental

Sample preparation.—Two types of samples were attempted. First, attempts were made to prepare samples by clamping thin iron foil between optically flat quartz plates; this approach was unsuccessful because electrolyte always penetrated between the foil and the quartz.

The second type of sample, which was more successful, was prepared in the following manner. Optical flats were prepared on pieces of Lucalox,[1] which is a sintered form of Al_2O_3 having theoretical density. The Lucalox pieces were about 2.5 cm² by 0.25 cm thick. A strip 0.1 cm thick was masked off along one edge of the optical flat surface of each piece, and iron was vaporized onto the surface to a thickness of 8000Å. The two pieces were then sintered together at 900°C for 1 hr in hydrogen. A load of about 25 lb was placed on the pieces to promote good contact and sintering. Following the sintering treatment, gold was vaporized onto the end of the sandwich for an electrical contact to the iron. A schematic illustration of the completed sample is shown in Fig. 1. During subsequent experiments, the sides of the sample were coated with stopcock grease to prevent access of the electrolyte to the iron except in the crevice.

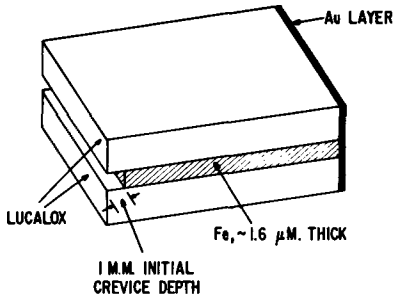

Fig. 1. Schematic of the model crevice

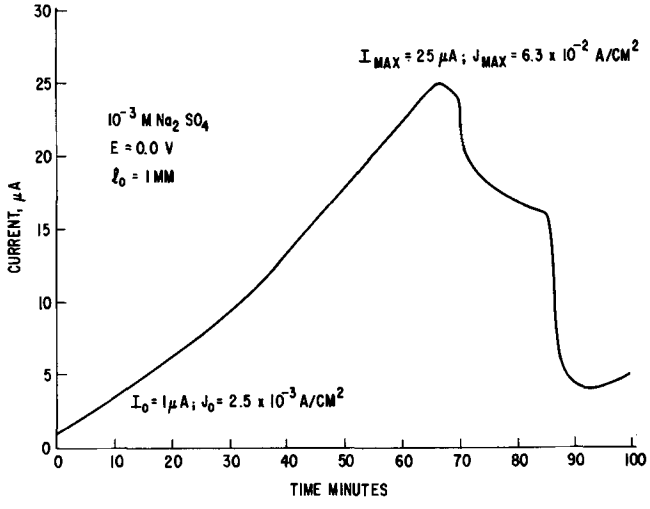

Fig. 2. Results of experiment using 10^{-3}M Na_2SO_4 at 25°C

Potentiostatic anodic polarization experiments.—Polarization experiments were carried out in 10^{-3} M Na_2SO_4 and 10^{-3} M H_2SO_4, using a Wenking Model 66-TA-10 potentiostat. A saturated calomel reference electrode (SCE) was employed with a salt-bridge, Luggin-probe, and Pt counterelectrode. All runs were carried out at room temperature (25°C) in air saturated solutions. Current was measured as a function of time at constant potential. Samples were equilibrated overnight under open-circuit conditions prior to a run.

Results

Figure 2 is a plot of current *vs.* time at an applied potential of 0.0V SCE in 10^{-3} M Na_2SO_4. The experimentally measured initial current was 1 μA, corresponding to an initial current density of 2.5 x 10^{-3} A/cm². The initial current may be calculated from the electrolyte resistivity, the initial crevice depth, the area of the crevice. and the open-circuit potential. In this experiment, the electrolyte resistivity was 5000 ohm-cm and the open-circuit potential was −0.50V. For these conditions, the initial resistance of the elec-

[1] Tradename.

trolyte within the crevice is calculated to be 1.25 x 10^6 ohms and the initial current should have been 0.4 μA.

There are two reasons why the calculated and experimental initial currents may not be in exact agreement. First, some dissolution of the iron may occur while the sample is being equilibrated under open circuit conditions, leading to a decrease of the electrolyte resistance and therefore an increase in the initial current. Second, it is difficult to measure the current during the first few seconds of the run while the applied potential is being adjusted to the desired level. Consequently the calculated value given above may be considered to be in reasonable agreement with the experimental value.

The current was observed to increase steadily for about 1 hr, reaching a maximum value of 25 μA, which corresponds to a current density of about 6.3 x 10^{-2} A/cm^2. The slow increase of current is a consequence of the gradual concentration of the solution in the crevice as the current flow continues. At that point the current was observed to decrease in an irregular manner to a value of 4-5 μA.

From Eq. [3], [8], [9], and [11] the values of concentration and potential at various points in the system were calculated with the following assumptions. The contribution of Na^+ was neglected, since current flow removes it from the crevice; this neglect introduces a small error in the results for the space outside the crevice. The contribution of OH^- was also neglected, since it is present in the bulk solution at a very low concentration. It was assumed that the bulk concentration was reached at $r_2 = 10^{-2}$ cm because of natural convection. With these assumptions, using $z = 2$, $\mathbf{F} \cdot D = 1$, the observed current density (0.063 A/cm^2), $w = 1.6 \cdot 10^{-4}$ cm, $r = 0.8 \cdot 10^{-4}$ cm, and $\rho_{max} = 5$ ohm-cm, the results shown in Table I were obtained.

The theory predicts that the concentration at the bottom of the crevice is greater than 1 M/l and that the potential at that point is −0.105V SCE. For comparison, potentiostatic experiments using 1M Na_2SO_4 solutions and pure iron specimens of various kinds showed that the current density reached values of about 0.15 A/cm^2 at a potential of −0.4V SCE, and then fell to 0.05 A/cm^2 at a potential of −0.2V SCE and remained at that value to +0.25V SCE. These results are in excellent agreement with those from the crevice corrosion experiment. The decrease in current at long times in Fig. 2 may be the result of partial passivation by precipitation of $Fe(OH)_2$ in the crevice.

In order to minimize $Fe(OH)_2$ precipitation further experiments were made using 10^{-3} M H_2SO_4, with the result shown in Fig. 3. In these experiments 2 hr were allowed for the initial equilibration, and the open circuit potential was again −0.5V SCE. In each run the current was still increasing when the run was terminated, but evidently a steady-state was approached. One problem encountered in these experiments is that the crevice depth increases during the run. After each run, the crevice depth was measured optically (the Lucalox is translucent), and the increase in crevice depth was always consistent with the coulometrically integrated current-time curves. Figure 4 presents a photograph of a typical sample after a series of runs in the 10^{-3} M H_2SO_4. It is evident that iron dissolution was relatively uniform along the crevice.

In the experiments of Fig. 3 a potential of −0.2V SCE was used. Calculations like those performed above but using $J = 1.1 \cdot 10^{-1}$ A/cm^2 gave the results shown in Table II.

Numerous experiments using M H_2SO_4 are reported in the literature, and all agree that a current density of about 0.1 A/cm^2 would be expected at a potential of about −0.34V SCE in good agreement with the observed value. It is interesting that an iron wire in the same 10^{-3} M H_2SO_4 solution at −0.2V SCE gave a current density of only 2 x 10^{-3} A/cm^2, an impressive demonstration of the effectiveness of the crevice in increasing the corrosion rate. As with the experiments in Na_2SO_4, the initial current of about 5 μA in Fig. 3 is higher than the calculated value of 1 μA. In the longer crevice (Fig. 3, run 2) the currents are lower as expected.

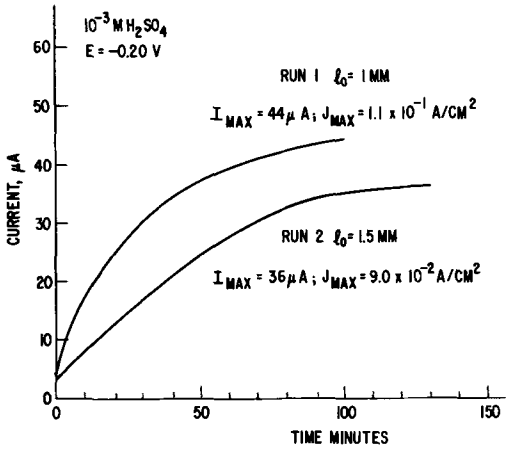

Fig. 3. Results of experiments using 10^{-3}M H_2SO_4 at 25°C

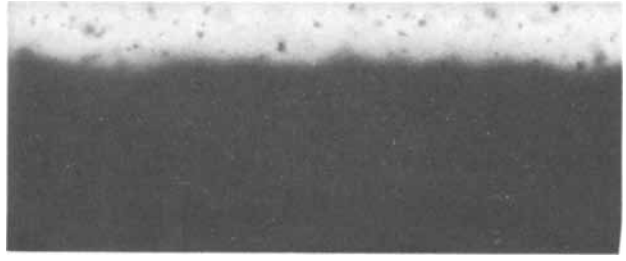

Fig. 4. Photograph of sample after experiments using H_2SO_4; 4X.

Summary

The simple theory for the concentration and potential variation in a crevice makes predictions which are in reasonable accord with experimental results. A consequence of the theory, confirmed by experiments, is that a small potential difference in a crevice can cause a large concentration change and a corresponding large increase in corrosion current at a given applied potential. The theory gives a simple way to estimate concentrations in crevices in real corrosion situations.

Acknowledgment

A conversation with Dr. C. P. Bean was very instrumental in developing the model presented in this paper.

Manuscript submitted Aug. 18, 1969; revised manuscript received ca. Oct. 27, 1969.

Table I. Calculated values for experiment using 10^{-3}M Na_2SO_4

Position	Concentration, M/l	Potential (SCE), V
Bulk	10^{-3}	0
Mouth of crevice	7.8 10^{-3}	−0.028
Position x_1	1.0	−0.091
Bottom of crevice		−0.105

Table II. Calculated values for experiment using 10^{-3}M H_2SO_4

Position	Concentration, M/l	Potential (SCE), V
Bulk	10^{-3}	−0.2
Mouth of crevice	1.4 10^{-2}	−0.235
Position x_1	1.0	−0.290
Bottom of crevice		−0.340

Any discussion of this paper will appear in a Discussion Section to be published in the December 1970 JOURNAL.

REFERENCES

1. T. R. Beck and E. A. Grens II, *This Journal*, **116**, 177 (1969).
2. F. A. Posey, Paper 404 presented at the Montreal Meeting of the Society, Oct. 6-11, 1968.
3. J. Newman, "Advances in Electrochemistry and Electrochemical Engineering," Vol. 5, p. 87, John Wiley & Sons, New York (1967).

Transport Numbers and the Structure of Porous Anodic Films on Aluminum

A. Dekker and A. Middelhoek

N. V. Philips' Gloeilampenfabrieken, Development Laboratory, Zwolle, The Netherlands

ABSTRACT

Experiments are described in which aluminum samples, covered with a porous oxide layer by anodization in oxalic acid, are subsequently re-anodized in boric acid ("forming"). The experimental techniques employed combine standard voltage and current measurements with gravimetric and optical methods for film thickness determination and measurements of the rate of film dissolution. The results show that for a given anodizing electrolyte the porosity depends only on the anodizing voltage and that it decreases with increasing voltage. The growth of the porous films is determined solely by the formation of oxide at the oxide/metal interface. This can be used to define a transport number for the positive ions during anodization, which was found to be $t_+ = 0.33$. During forming in boric acid of a sample already covered with a porous oxide layer some of the oxide is formed in the pores and some at the metal/oxide interface. For this process a transport number $t_+ = 0.24$ was obtained. The average pore diameter, cell diameter, and barrier layer thickness vary linearly with the anodizing voltage, the cell wall thickness being somewhat thinner than the barrier layer.

It is well known that aluminum may be covered with an oxide layer by anodic oxidation. The structure of these anodic films depends markedly on the electrolyte used, particularly on the degree to which it acts as a solvent for the oxide. In a solution containing oxalic acid or other acids which attack the oxide, a porous layer is obtained, whereas in boric acid solution a compact uniform layer is formed. The difference between these two extreme cases is clearly demonstrated by the shape of the voltage *vs.* time curves obtained during growth of the layers at constant anode current density. In oxalic acid the voltage first rises to a relatively low maximum (5-100V), then decreases slightly and approaches a constant value (*e.g.*, Fig. 1). However in boric acid the voltage increases linearly with time, at least until the "sparking voltage" (usually several hundred volts) has been reached. A general review of the subject is given by Young (1).

It is also possible to re-anodize an aluminum sample in boric acid which has been anodized previously in oxalic acid. In fact Dekker and Van Geel (2) used this as a technique to obtain information about the structure of the porous layer laid down initially. According to these authors the pores of the porous layer are filled during the re-anodization process and from the voltage *vs.* time curve obtained at constant current density during this process they deduced a value for the porosity of the original film. This technique has received little further attention in the literature. The interpretation of Dekker and Van Geel has been rejected in the literature (3), but in our opinion without any factual justification. Recently, however, Dunn (4) essentially confirms the pore-filling process.

The present paper deals with experimental results obtained by anodization of aluminum in oxalic acid and subsequent re-anodization in boric acid. In the following the re-anodization in boric acid shall be referred to as "forming;" the term "anodizing" is reserved for the production of a porous layer in oxalic acid. The present study extends that of Dekker and Van Geel by combining the standard current and voltage measurements with optical and gravimetric methods for film thickness determinations and measurements of the rate of film dissolution. The data obtained permit the determination of the porosity of the films produced by anodization, the transport numbers associated with anodization and subsequent forming, and the diameter and density of the pores in porous films.

Key words: anodic oxidation, transport numbers, porosity of aluminum oxide films, Tolansky thickness measurements.

Experimental Evidence for the Pore-Filling Process

In this section we discuss some simple experiments which confirm and extend the results obtained earlier by Dekker and Van Geel. They provide conclusive evidence for the pore-filling mechanism and lead to a model which is used for the interpretation of the results described in the sections that follow. We first describe briefly the procedures and equipment used in these experiments.

Samples

The samples were punched from aluminum foil of 100μ thickness and a purity of 99.98% (impurities in ppm: Cu 26, Si 51, Fe 24, Mg 6). They consisted of a circular area of 50 mm diameter and were provided with a contact strip; it turned out that a constriction in the stem just above the circular area prevented the electrolyte from creeping up. The total anodizable area was 39.0 cm^2. The samples were cleaned by subjecting them to the following sequence of procedures: (*a*) immersion in NaOH (20 g/liter) at 20°C for 9 min; (*b*) rinsing in deionized water at 20°C for 2 min; (*c*) immersion in 48% sulfuric acid at 90°C for 3 min; (*d*) rinsing in deionized water at 20°C for 2 min; (*e*) immersion in a mixture of 950 ml deionized water, 50 ml H_3PO_4 (85%) and 20g CrO_3 at 85°C for 2 min; (*f*) rinsing in deionized water at 20°C for 2 min; (*g*) rins-

ing in alcohol at 20°C for 5 min; and (*h*) drying in a furnace at 50°C for 30 min.

Anodizing

The anodization process was carried out in an oxalic acid solution (80 g/liter) at a constant current, supplied by a constant current generator (maximum variation 1% from 0 to 500V) in a thermostat held constant within 0.1°C. The current generator could be regulated between 100 and 500 mA for voltages between 0 and 1000V. An aluminum plate served as cathode. During the process the voltage (V) across the cell was recorded as a function of time (t) on a Philips line recorder (Type PR 2210 U/21). After anodizing (or forming) the samples were cleaned twice in alcohol at 20°C, the first time for 10 min and the second time for 20 min; alcohol was used rather than water to prevent hydration of the oxide and because of the good solubility of oxalic acid in alcohol. Afterward, the samples were dried in air at 50°C. Since further heating of the samples in air at 450°C for 30 min did not produce a detectable change in weight, the drying procedure was considered satisfactory.

Forming

Forming of a single sample was carried out at a constant current density of 0.38 mA/cm² at 25° ± 0.5°C in an electrolyte prepared as follows. A solution consisting of 27.9g glycol, 24.9g boric acid, and 12.4g ammonia (13*N*) was heated at 140°C until its specific resistivity was about 5000 ohm-cm at 25°C, and diluted with alcohol to give a forming electrolyte with a specific resistivity of approximately 1300 ohm-cm at 25°C.

Results and Discussion

First of all a number of experiments analogous to those performed by Dekker and Van Geel were carried out, *i.e.*, the voltage V was measured as a function of time t during forming with constant current in boric acid of samples that had been anodized previously. Since these results confirmed those of Dekker and Van Geel it may suffice to give one illustrative example. Two samples have been anodized with different current densities J_a and J_b (Fig. 1). The corresponding curves for subsequent forming at equal current densities (Fig. 2) show different initial slopes; the steepest slope is found for the specimen that has been anodized with the highest current density. The first stage in both cases corresponds to the pore-filling

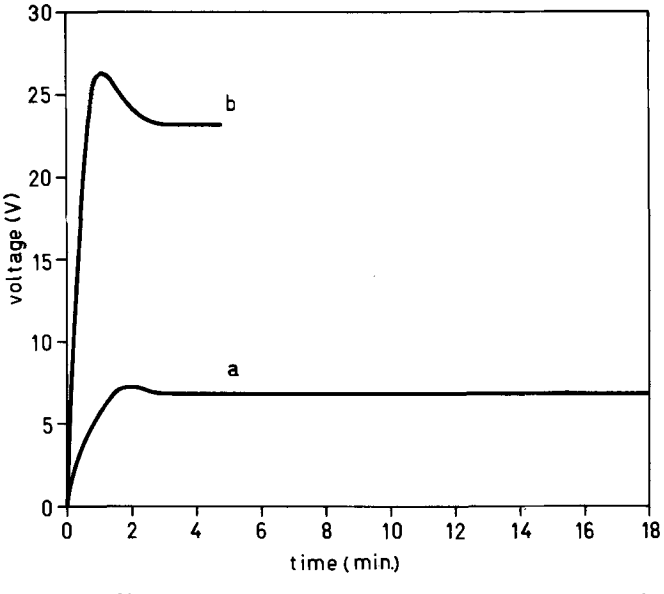

Fig. 1. Voltage vs. time during anodizing in 80 g/l oxalic acid at 20°C. Curve (a) corresponds to an over-all current density J_a = 0.63 mA/cm² for 18 min; curve (b) corresponds to J_b = 2.54 mA/cm² for 4.5 min.

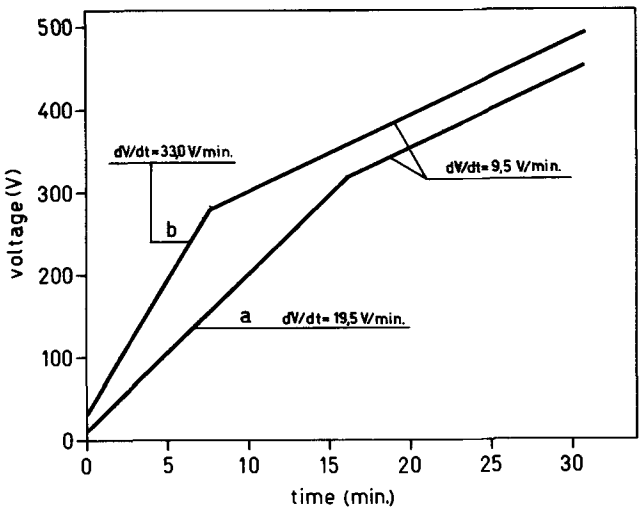

Fig. 2. Voltage vs. time during forming with 0.38 mA/cm² at 25°C after anodizing; curves (a) and (b) refer to the anodizing current densities J_a and J_b of Fig. 1.

mechanism proposed by Dekker and Van Geel. The final slopes are equal to that found for a virgin specimen formed with the same current density. Hence the point where the two straight parts of the V-t curve meet (the "knee-voltage") corresponds to the situation where the pores have been filled completely. Since dV/dt is constant during the pore-filling stage it makes sense to introduce a porosity α_a of the anodized layer defined by the total cross-section of the pores per unit area of the sample. It follows from Fig. 2 that the porosity increases with decreasing anodizing current density. If all the oxide during forming were produced at the pore-base/electrolyte interface, α_a would simply be given by the ratio of the final and initial slopes. However a part of the oxide, as will be shown later, is produced during forming at the metal/oxide interface. This complicates the determination of α_a. The nonzero value of V for $t = 0$ (Fig. 2) results from the presence of a compact barrier layer in the porous films adjacent to the metal; this barrier is built up during the anodizing of the sample (Fig. 1).

A second type of experiment was performed with two samples of which one was anodized for 12 min in oxalic acid with a current density J_a and subsequently for 3 min with another current density J_b, and the other sample was similarly anodized with the same current densities but in reverse order (Fig. 3). The V-t curves recorded during forming (Fig. 4) now consist of three linear stages with slopes that are equal to those encountered in the first type of experiment within the limits of accuracy. From the order in which these slopes occur, one may conclude that the porous layer grows at the metal/oxide interface, *i.e.*, the "old" oxide will be found at the top of the layer.

The anodizing conditions during the second stage may be chosen in such a way that the corresponding porosity α_a approaches unity so that the layer produced during the first stage no longer adheres to the metal. In a typical experiment of this kind a sample was first anodized with a current density of 5.1 mA/cm² during 45 min at 20°C and thereafter with a current density of 0.13 mA/cm² at 40°C. With great care it was possible to obtain in this manner an oxide membrane of about 8 μm thick. This was found to be permeable to a colored liquid (a solution of picric acid in dimethylformamide), which supports the conclusion that such layers are porous. It is interesting to note that w[illegible] heated for 2 hr at 640°C, its weight decreased by only 1.4%, implying that the degree of hydration of the membrane is very low [see also Bernard and Randall (5)]. Subsequent boiling in deionized water for 3 min

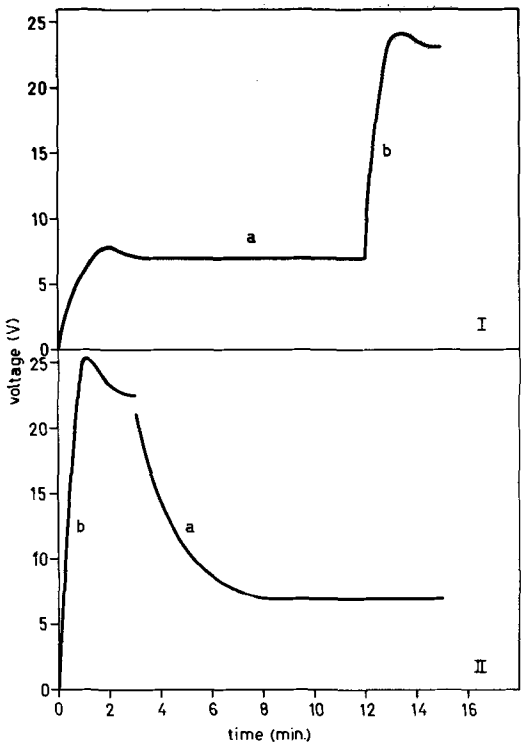

Fig. 3. Voltage *vs.* time during anodizing in 80 g/l oxalic acid at 20°C. I refers to an anodizing current density $J_a = 0.63$ mA/cm^2 applied for 12 min and, subsequently, $J_b = 2.54$ mA/cm^2 for 3 min. II corresponds to the reverse sequence.

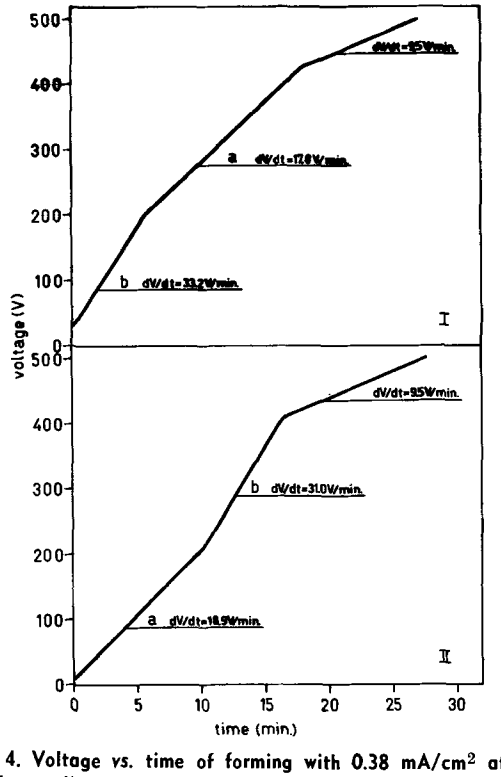

Fig. 4. Voltage *vs.* time of forming with 0.38 mA/cm^2 at 25°C after the anodizing procedures I and II of Fig. 3.

increased the weight by 11.6%; this water could be removed easily by heating. One may thus conclude that the anodized layers are porous and contain originally relatively little water, in contrast to the opinion of Murphy and Michelson (6).

Similar information as referred to above concerning the structure of porous layers can be obtained by current rather than voltage measurements during forming. Such measurements have been carried out in particular with a "duo-circuit" in which two samples are formed in parallel in boric acid with a constant total current; one of the samples a virgin aluminum specimen and the other anodized previously in oxalic acid. For this system we then measured the current drawn by the virgin specimen, $I_f(t)$, the current drawn by the anodized specimen, $I_{a,f}(t)$, and the voltage $V(t)$ across the cell during the forming process. Typical results are shown in Fig. 5. We can distinguish three stages: During the first of forming stage (from $t = 0$ to $t = t_a$) only the virgin sample draws current. For $t = t_a$ the field across the barrier layer of the anodized sample becomes large enough to allow ionic transport and the second stage is reached in which $I_{a,f}$ and I_f remain essentially constant with $I_{a,f} < I_f$. This is consistent with the interpretation that during the second stage the pore-filling mechanism is operative. Near $t = t_b$ the pores are practically filled and the field becomes large enough for the onset of ionic transport through the whole area of the anodized plate; this leads to the final stage in which the samples share the total current equally. The time t_b was found to be proportional to the period of anodization, in agreement with the pore-filling mechanism. The overshoot in the $I_{a,f}(t)$-curve (Fig. 5) near A is a transient effect which is of no further interest to us here. The dip near B in this curve indicates the presence of a constriction in the pores, presumably related to their initiation because the oxide at the top of the layer is produced during the initial stages of the anodization process. For higher anodizing temperatures and/or lower anodizing current densities the constriction is not observed and may even be transformed into an enlargement as a result of the aggressive action of the electrolyte.

Even for thick porous layers, for which the "knee-voltage" of the Dekker-Van Geel technique cannot be determined, the duo-circuit method can be used con-

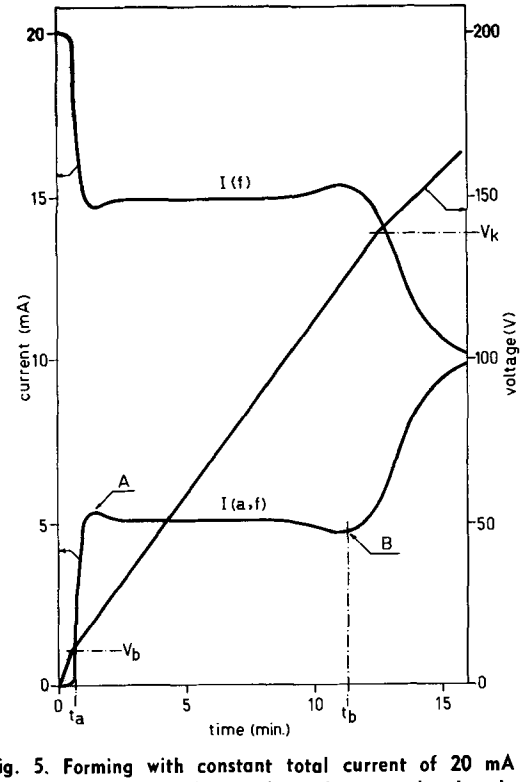

Fig. 5. Forming with constant total current of 20 mA in the "duo-circuit" of a virgin sample and a sample that had been anodized in 80 g/l oxalic acid with 1 mA/cm^2 for 6 min at 15°C. $I_f(t)$ and $I_{a,f}(t)$ represent the currents drawn by the virgin and anodized sample, respectively. The common voltage V is also shown as a function of time, V_k refers to the "knee-voltage" and V_b to the voltage across the barrier layer $t = t_a$.

veniently because it incorporates directly a virgin reference anode.

Model of the Pore-Filling Process

The results described above as well as those reported earlier by Dekker and Van Geel show that during forming in boric acid of a sample covered with a porous oxide layer at least some of the new oxide is formed in the pores. It is evident that this requires transport of positive ions under influence of the electric field from the metal/oxide interface to the pore-base/electrolyte interface. On the other hand, the results do not exclude the possibility that some of the new oxide is formed at the metal/oxide interface as a result of the motion of negative ions. In the next section we shall see that this is actually what happens. The assumption of transport of positive as well as negative ions leads to a schematic model as given in Fig. 6 as a basis for the discussion of the process of forming in boric acid of a sample already covered with a porous layer. Let A_t be the total area of the anodized portion and let A_p represent the total cross section of the pores. The porosity α_a of the porous layer may then be defined as

$$\alpha_a = A_p/A_t \qquad [1]$$

Let $I_{a,f}$ be the current employed during forming and suppose that the pores are only partly filled. The weight of new oxide produced per unit time is then

$$\left(\frac{dw}{dt}\right)_{a,f} = e_{a,f}\,\eta_{a,f}\,I_{a,f} \qquad [2]$$

where $e_{a,f}$ is the electrochemical equivalent of the new oxide and $\eta_{a,f}$ the current efficiency of the process. We may then define a transport number t_+ for the positive ions by

$$t_+ = \frac{\text{weight of new oxide formed in the pores/unit time}}{\text{total weight of new oxide formed/unit time}} \qquad [3a]$$

For simplicity we assume that the density of the oxide formed in the pores, $\rho_{a,f}$ is the same as that formed at the metal/oxide interface.

Using Fig. 6 and Eq. [2], Eq. [3a] becomes

$$t_+ = \rho_{a,f}\,A_p\,(dh_+/dt)/(e\eta)_{a,f}\,I_{a,f} \qquad [3b]$$

Similarly

$$(1 - t_+) = \rho_{a,f}\,A_t\,(dh_-/dt)/(e\eta)_{a,f}\,I_{a,f} \qquad [3c]$$

Solving [3b] and [3c] for the sum $(dh_+/dt + dh_-/dt)$ or $(dh/dt)_{a,f}$, and replacing A_p/A_t by α_a from [1], gives

$$(dh/dt)_{a,f} = \left(\frac{e\eta}{\rho}\right)_{a,f}\frac{I_{a,f}}{A_t}\left[\frac{t_+}{\alpha_a} + (1 - t_+)\right] \qquad [4]$$

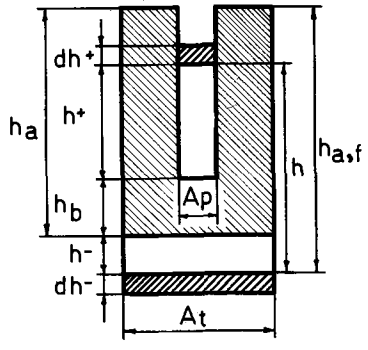

Fig. 6. Schematic picture of forming of an anodized sample in the pore-filling stage. A_p represents the total cross section of all pores in a sample of total area A_t. h_+ and h_- represent the oxide formed in the pores and at the metal side, respectively. h_b represents the thickness of the barrier layer.

For a virgin aluminum sample formed with a current I_f the rate of change of thickness would be given by

$$\left(\frac{dh}{dt}\right)_f = \left(\frac{e\eta}{\rho}\right)_f\frac{I_f}{A_t} \qquad [5]$$

In order to discuss the kind of experiments described above it is convenient to transform from thicknesses to rates of change of voltage across the samples. Thus, let E_f and $E_{a,f}$ represent the effective electric field strengths during forming of the virgin and anodized samples, respectively. Multiplying [4] by $E_{a,f}$ and [5] by E_f, gives the rates of change of voltage, *i.e.*, Eq. [6] and [7].

$$\left(\frac{dV}{dt}\right)_{a,f} = \gamma_{a,f}\frac{I_{a,f}}{A_t}\left[\frac{t_+}{\alpha_a} + (1 - t_+)\right] \qquad [6]$$

$$\left(\frac{dV}{dt}\right)_f = \gamma_f\frac{I_f}{A_t} \qquad [7]$$

where

$$\gamma_{a,f} = \left(\frac{e\eta E}{\rho}\right)_{a,f} \text{ and } \gamma_f = \left(\frac{e\eta E}{\rho}\right)_f \qquad [8]$$

The basic Eq. [6] and [7] can be used to discuss experimental results such as shown in Fig. 2 and Fig. 4 as well as those shown in Fig. 5. For example, the condition required during the second stage of the duo-circuit experiment of Fig. 5 reads

$$\left(\frac{dV}{dt}\right)_{a,f} = \left(\frac{dV}{dt}\right)_f \qquad [9]$$

from which we find for the ratio of the two constant currents

$$\beta \equiv \frac{I_{a,f}}{I_f} = \frac{\gamma}{(t_+/\alpha_a) + (1 - t_+)} \text{ with } \gamma \equiv \gamma_f/\gamma_{a,f} \qquad [10]$$

Solving for t_+ we may write this relation in the following convenient form

$$t_+ = \left(\frac{\alpha_a}{1 - \alpha_a}\right)\left(\frac{\gamma - \beta}{\beta}\right) \qquad [11]$$

From its definition it is clear that γ must be approximately equal to unity, small deviations may arise, for example, from a slight difference between E_f and $E_{a,f}$. In fact, from a rather intricate analysis of experimental results, which we shall not give here, we found $\gamma = 0.98$.

From Eq. [6] and [7] we can also derive an expression for the ratio of the final and initial slopes of a V-t curve during forming of a single anodized plate, such as given in Fig. 2. The final slope must then be identified with $(dV/dt)_f$ and the initial one with $(dV/dt)_{a,f}$. The condition for this type of experiment is expressed by

$$I_{a,f} = I_f \qquad [12]$$

and we find for the "voltage ratio" from [6] and [7]

$$\frac{(dV/dt)_f}{(dV/dt)_{a,f}} = \frac{\gamma}{(t_+/\alpha_a) + (1 - t_+)} = \beta \qquad [13]$$

For the anodizing conditions pertaining to Fig. 5 we actually found a voltage-ratio of 0.33, which is nearly equal to the experimental current-ratio of 0.34, as required by [13]. According to [11] the transport number t_+ can be obtained from experimental values of α_a and β, assuming γ is known or taken equal to unity as a reasonable approximation. We therefore discuss next the determination of α_a.

Determination of the Porosity

The porosity of a porous layer produced by anodization with a current density of 1 mA/cm^2 in 80 g/liter acid at 15°C was determined by gravimetric and optical thickness measurements. The principle of this determination may be explained with reference

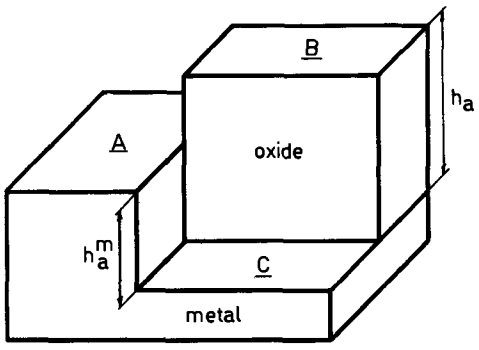

Fig. 7. Schematic view of a partly anodized sample from which part of the oxide has been removed, illustrating the principle of the thickness measurements according to Tolansky.

to Fig. 7 where h_a represents the thickness of the anodized layer and h_a^m the thickness of the metal layer consumed for the anodization. Let W_a and W_a^m represent the corresponding weights per unit over-all area; ρ_a is the density of the oxide (excluding the pores) and ρ_m the density of the metal. Making use of the definition [1] of the porosity α_a we may write

$$dW_a = \rho_a (1 - \alpha_a)\, dh_a \qquad [14]$$

or

$$\alpha_a = 1 - \frac{1}{\rho_a}\frac{dw_a}{dh_a} = 1 - \frac{\rho_m}{\rho_a}\frac{dW_a/dW_a^m}{dh_a/dh_a^m} \qquad [15]$$

The porosity was obtained by measuring the quantities appearing in the last expression.

The densities ρ_a and ρ_m were measured by weighing the anodized samples in air as well as in distilled glycol with a density of 1.1108 g/cm^3 at 20°C and a temperature coefficient of −0.58 mg/cm^3 °C in the region between 15° and 30°C. By repeating this procedure after removal of the oxide in chromic-phosphoric acid the required densities could be found. The results obtained from at least three determinations were

$$\rho_a = 2.96 \pm 0.03 \text{ and } \rho_m = 2.698 \pm 0.003 \text{ g/cm}^3 \qquad [16]$$

The weights W_a and W_a^m were obtained by weighing the samples before anodizing, after anodizing, and after removal of the anodized layer in chromic-phosphoric acid. The results are plotted for a series of experiments in Fig. 8, and we conclude that the so-called "coating ratio"

$$dW_a/dW_a^m = 1.16 \qquad [17]$$

The thickness measurements were carried out by the Tolansky method (7) employing a Leitz Metallux Microscope provided with a sodium light source. Since this method requires very flat surfaces, evaporated aluminum layers on glass were used. For this purpose Corning 7059 glass sheets were cleaned by ultrasonic agitation in isopropylalcohol for 10 min. Afterward they were rinsed in hot isopropylalcohol in a Soxleth apparatus. The substrate was then heated in vacuum for 1 hr at about 350°C to remove adsorbed water in order to obtain good adherence. The aluminum was deposited at about 150°C substrate temperature from a tungsten spiral to a thickness of about 1μ. After anodizing the oxide was removed from one half of the anodized surface in chromic-phosphoric acid. Finally, the whole surface was covered with a thin layer of evaporated aluminum to obtain sufficient reflection. The interference lines were photographed in regions where differences in height occurred. From the shift of the interference lines at a particular step the step height could be determined with an error of a few per cent. The results obtained for various periods of anodization were plotted in the form of a graph of h_a as a function of h_a^m (Fig. 9).

$$dh_a/dh_a^m = 1.21 \qquad [18]$$

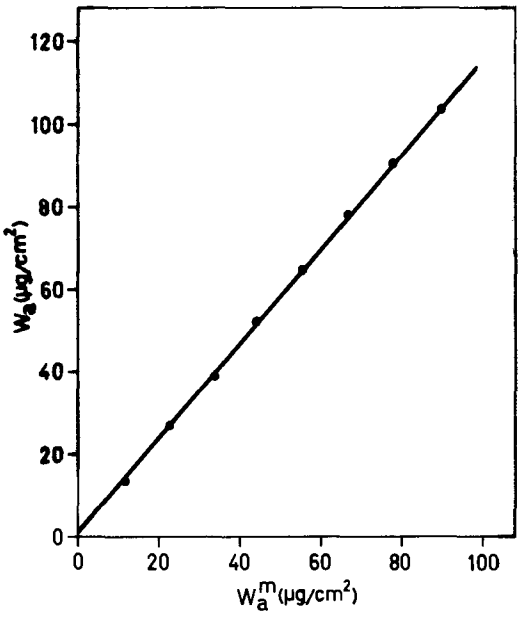

Fig. 8. Weight of anodic oxide (W_a) as a function of the weight of aluminum consumed (W_a^m) for anodization with a current density of 1 mA/cm^2 in 80 g/l oxalic acid at 15°C. The points refer to anodization periods of 2, 4, 6, 8, 10, 12, 14, and 16 min.

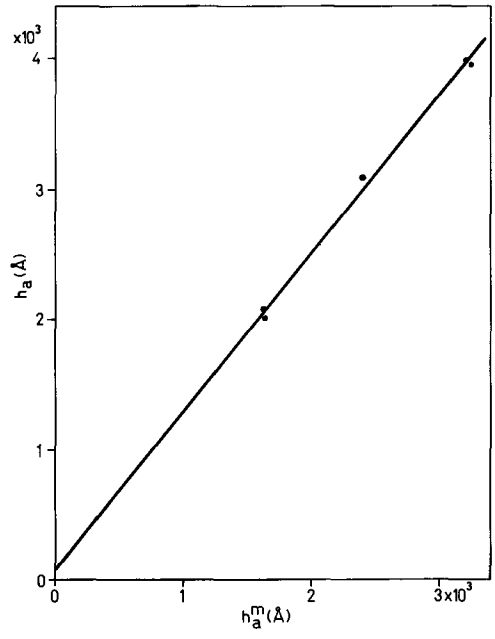

Fig. 9. Height of the oxide film (h_a) as a function of the height of the metal layer consumed (h_a^m), determined by the Tolansky technique for evaporated samples anodized in 80 g/l oxalic acid at 15°C. The points refer to anodization periods of 8, 12, and 16 min.

We may remark that the values found for h_a^m were in good agreement with those calculated from the current density and the period of anodization, assuming a current efficiency $\eta_a = 1$. From the last four formulas we thus obtain for the porosity of the anodized layer, under the experimental conditions used, $\alpha_a = 0.13$.

The porosity can also be obtained from the formula

$$\alpha_a = \frac{h_a - W_a/\rho_a}{h_a - h_b} \qquad [19]$$

which follows immediately from Fig. 6. Using a barrier layer thickness $h_b = 150$Å (as determined in the next section) and the values of h_a and W_a corresponding to an anodizing time of 18 min in Fig. 8 and 9, we

find $\alpha_a = 0.11$. In what follows we shall use

$$\alpha_a = 0.12 \quad [20]$$

The Transport Numbers

From the above information one can calculate the transport number t_+ of the positive ions during forming in boric acid of a sample previously covered with a porous layer. In fact, substituting into expression [11] the value $\beta = 0.34$ (obtained from Fig. 5), $\alpha_a = 0.12$, and $\gamma = 0.98$ one finds $t_+ = 0.26$. A check on this value was obtained as follows. Equation [3] can be changed from weight to volume terms assuming for simplicity that the density of the oxide formed in the pores equals the density of the oxide formed at the metal/oxide interface. Thus from Fig. 6

$$t_+ = \frac{\alpha_a h_+}{\alpha_a h_+ + h_-} \text{ where } \begin{matrix} h_+ = h_a - h_b - (h_{a,f} - h) \\ h_- = h_{a,f} - h_a \end{matrix} \quad [21]$$

For a sample anodized for 16 min with a current density of 1 mA/cm² at 15°C and formed subsequently in boric acid to 395V, the Tolansky technique yielded $h_a = 3930$Å and $h_{a,f} = 5320$Å. The quantities h_b and h were determined by charging the sample before and after forming with a small current density (5 μA/cm²) so that further growth was prevented and a constant voltage was reached. Under these circumstances 1V corresponds to 13.4Å and from the measured voltages we found $h_b = 150$Å and $h = 4870$Å. Substitution into [21] then yields $t_+ = 0.22$. We thus find an average value

$$(t_+)_{\text{forming}} = 0.24 \quad [22]$$

Consequently, the largest fraction of the current during forming of an anodized layer is carried by negative ions, at least under the experimental conditions used.

In recent years several values for the transport number have been reported based on techniques employing some kind of "marker." For example, Davies *et al.* (8) introduced Xe as a marker and reported in one series of experiments with an electrolyte consisting of a solution of borax in glycol and water $t_+ = 0.58$. In another series using an aqueous citrate solution they reported values varying between 0.33 and 0.72. More recently Randall (9) found $t_+ = 0.27$ by employing P^{32} as a marker. The reliability of these results will strongly depend on the absence of interaction of these marker atoms with the environment. It would seem that our method is more direct and, consequently, more reliable than methods using markers.

We shall now discuss the transport number of the positive ions during the anodization process in oxalic acid, *i.e.*, during the formation of the porous layer itself. In this connection it is important to realize that in the stationary period of growth with constant anode current the voltage across the sample remains constant (Fig. 1), *i.e.*, that the distance between the metal/oxide interface and the pore-base/electrolyte interface remains constant. From this we conclude that during anodization the rate of dissolution of oxide at the pore-base/electrolyte interface must just cancel the rate of growth of the barrier layer between the pore-base and metal. Assuming again transport of positive and negative ions, the amount of oxide that dissolves at the pore-base consists of two portions: (*i*) the amount of oxide that would be produced in the pores by that part of the current that is carried by positive ions; and (*ii*) a fraction α_a of the oxide produced at the metal/oxide interface due to transport of negative ions. Consequently, only the fraction $(1 - t_+)(1 - \alpha_a)$ of the anodizing current is effective in producing oxide. Since this newly formed oxide is distributed over a fraction $(1 - \alpha_a)$ of the total area of the sample, the over-all thickness of the anodic oxide layer (h_a in Fig. 7) is determined directly by the transport number $t_- = (1 - t_+)$ of the negative ions. Employing the nomenclature introduced in earlier sections we may thus write for the stationary state during anodization with a current density J

$$\frac{dh_a}{dt} = (1 - t_+)\frac{e_a}{\rho_a}\eta_a J \quad [23]$$

Expressing the current density in terms of the amount of metal consumed during anodization

$$\eta_a J = \frac{\rho_m}{e_m}\frac{dh_a{}^m}{dt} \quad [24]$$

this leads to the relation

$$1 - t_+ = \left(\frac{e_m}{e_a}\right)\left(\frac{\rho_a}{\rho_m}\right)\frac{dh_a}{dh_a{}^m} \quad [25]$$

According to [18] $dh_a/dh_a{}^m = 1.21$ and from [16] we obtain $\rho_a/\rho_m = 1.10$. If we assume that the oxide is pure Al_2O_3 the ratio of the electrochemical equivalent $e_a/e_m = 1.89$ and we find $(1 - t_+) = 0.70$ or $(t_+)_{\text{anodizing}} = 0.30$. However, a titration with $KMnO_4$ showed that the anodized layer contained 3.85% oxalate. This incorporation of foreign material in the oxide would change the effective ratio of the electrochemical equivalents to $e_a/e_m = 1.97$, leading to $(t_+)_{\text{anodizing}} = 0.33$.

In any case, there is some difference between the transport numbers obtained for the anodizing and forming process, indicating some dependence of t_+ on the electrolyte used. Employing the duo-circuit we also found that for given anodizing conditions the current ratio β and the knee voltage V_k (see Fig. 5) depend somewhat on the forming electrolyte used.

Pore Diameter and Pore Density

In this section the structure of porous oxide layers on aluminum is studied in more detail by employing measurements of the porosity α_a as a function of the anodizing voltage V_a and additional information obtained by measurements of the rate of dissolution of the films.

Consider a porous film containing N pores per unit area. With each pore one can associate a "cell" with a diameter D defined by the relation

$$\tfrac{1}{4}\pi N D^2 \equiv 1 \quad [27]$$

Per unit area the total pore area is equal to the porosity α_a and we can define a pore diameter p such that

$$\tfrac{1}{4}\pi N p^2 \equiv \alpha_a \quad [28]$$

In terms of these definitions we have

$$\alpha_a = p^2/D^2 \quad [29]$$

The Dependence of p and D on V_a

An extensive series of measurements of α_a covering a temperature range between 3° and 45°C, a current density range between 0.1 and 20 mA/cm², and a voltage range between 3 and 50V showed that for a given anodizing electrolyte α_a depends only on V_a. For this purpose α_a was determined by substituting into expression [11] or [13] the observed ratio β and taking $t_+ = 0.24$ in accordance with [22]. The results for oxalic acid (80 g/l) and sulfuric acid (63.5 g/l) are shown in Fig. 10. According to [29] these results imply that p/D is also a function of V_a only.

Now, from a study of the geometrical properties of porous anodic films on aluminum, Keller, Hunter, and Robinson (10) arrived at a model in which p, D, and the anodizing voltage V_a satisfy the relation

$$D = 2AV_a + p \quad [30]$$

where A is a constant. Assuming this relation to be correct it is easy to show in combination with [29] that one should have

$$\frac{p}{A} = \frac{2\sqrt{\alpha_a}}{1 - \sqrt{\alpha_a}}V_a \text{ and } \frac{D}{A} = \frac{2}{1 - \sqrt{\alpha_a}}V_a \quad [31]$$

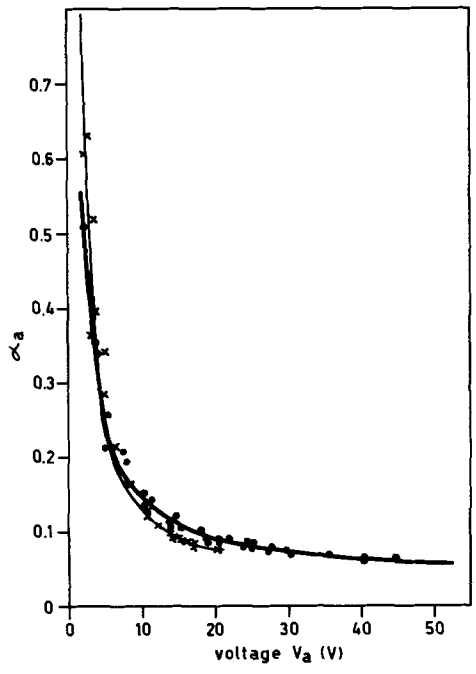

Fig. 10. Porosity α_a as a function of anodizing voltage V_a. The points refer to 80 g/l oxalic acid and the crosses to 63.5 g/l sulfuric acid.

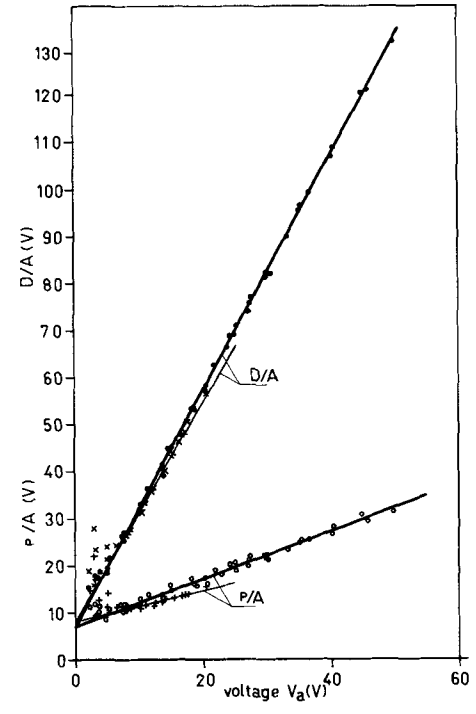

Fig. 11. Quantities p/A and D/A as a function of anodizing voltage. The points and open circles refer to oxalic acid, the crosses and plus signs refer to sulfuric acid.

From a knowledge of α_a as a function of V_a one can thus calculate p/A and D/A as a function of V_a. The results shown in Fig. 11 show that formula [30] indeed applies if both D and p are considered to be linear functions of V_a. The latter result evidently contradicts the conclusion of Keller, Hunter, and Robinson that p is independent of V_a.

Determination of the Pore Diameter and Pore Density

Additional information concerning p and D was obtained by dissolving an anodized layer at constant temperature (25°C) in chromic-phosphoric acid and measuring the reduction in weight as a function of time. Similar experiments have been carried out by Nagayama and Tamura (11). In these experiments it is assumed that there is a constant rate of dissolution $v = -dh/dt$ where h represents the thickness of any part of the oxide surface exposed to the etching solution. A typical result for the change in weight of an anodized sample as a function of the etching time is shown in Fig. 12. There is evidently a rather well-defined time t_R required to dissolve the anodized layer completely. The quantity A introduced in expression [30] pertaining to the Keller-Hunter-Robinson model is clearly related to t_R as follows

$$S \equiv \tfrac{1}{2}(D - p) = vt_R = AV_a \qquad [32]$$

where S represents the cell wall thickness. Once v and t_R are known, A can be obtained and from it p and D can be determined from [31].

The rate of dissolution v was determined as follows: A sample covered with a porous oxide layer was formed in boric acid together with a virgin specimen in the duo-circuit until the knee voltage V_k was reached (see Fig. 5). The pores are then just filled and the thickness of this layer was determined by charging the sample with a small current density (5 μA/cm^2) and measuring the final constant voltage V_m across the sample. Since 1V corresponds to 13.4Å this is an effective method for determining the thickness of the layer. Typical results for the measured voltage V_m as a function of the etching time in chromic-phosphoric acid at 25°C for such layers are presented in Fig. 13 for various anodizing current densities. Since the amount of forming oxide in the pores is relatively small ($\approx$10%), it is assumed that the rates of dissolution so determined are characteristic for the porous layers. Experimental values of v are given in Table I; they depend somewhat on the anodizing current density. From v and t_R we found A = 9.0 Å/V. Values of p and D calculated from [32] and [31] are also given in Table I, together with the current ratio β from which α_a was calculated from [11] assuming t_+ = 0.24. Finally, Table I gives the values of the barrier layer thickness, h_b, which amounts to 10.6Å/V. Note that this is somewhat larger than A, *i.e.*, the barrier layer is somewhat thicker than the cell wall S.

It is of interest to point out that the explicit form of the time-dependence of W_a during etching can also be used to determine p and D. Assuming that the dissolution occurs with the same rate v at the top of the layer, inside the pores and at the base layer we can set up an expression for $W_a(t)$ as follows. With reference to Fig. 6 we may write during etching

$$h_a(t) = h_a(0) - vt \text{ and } p(t) = p(0) + 2vt \qquad [33]$$

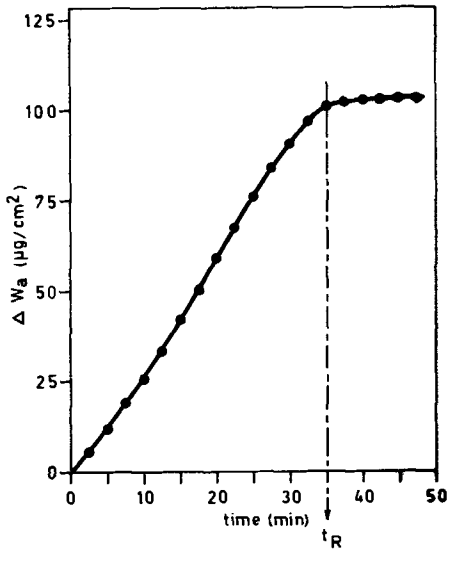

Fig. 12. Change in weight as a function of etching time for a sample anodized with a current density of 1 mA/cm^2 during 16 min.

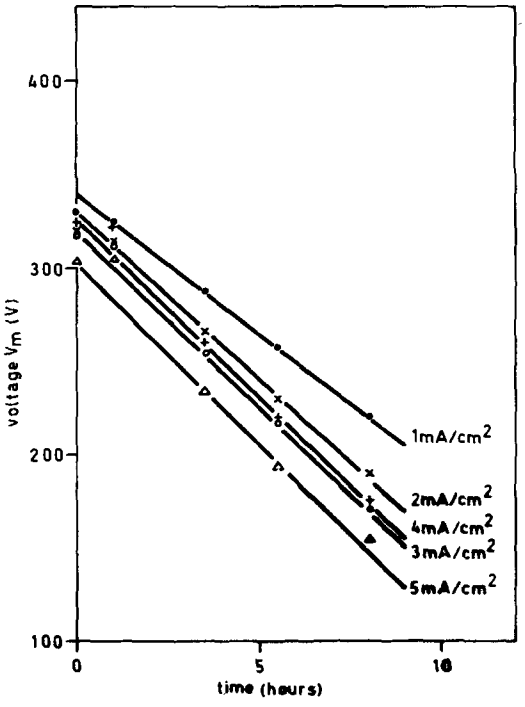

Fig. 13. Measured voltage V_m as a function of dissolution time for sample anodized with various current densities.

where $p(t)$ represents the pore diameter. Let h_p represent the pore depth, *i.e.*, the distance between the top of the oxide layer and the pore base. The weight of the oxide layer per unit area at $t = 0$ is then

$$W_a(0) = \rho_a[h_a(0) - \tfrac{1}{4}N\pi h_p p^2(t)] \quad [34]$$

and after a period t of etching

$$W_a(t) = \rho_a[h_a(0) - vt] - \tfrac{1}{4}\pi N h_p \rho_a[p(0) + 2vt]^2 \quad [35]$$

Note that h_p is constant. Consequently

$$\frac{\Delta W_a}{t} \equiv \frac{W_a(0) - W_a(t)}{t} = \rho_a v[1 + N\pi h_p p(0)] + \rho_a N\pi h_p v^2 t \equiv C + Bt \quad [36]$$

An experimental example of this relationship is shown in Fig. 14 for a sample anodized with a current density of 5 mA/cm². In this case $B = 1.10 \times 10^{-2}$ μg/cm² min² and $C = 0.77$ μg/cm² min. In terms of B and C the original diameter $p(0)$ and the density of pores N are given by

$$p(0) = \left(\frac{C - v\rho_a}{B}\right)v \text{ and } N = \frac{4}{\pi D^2} = \frac{B}{\pi\rho_a h_p v^2} \quad [37]$$

When we calculate $p(0)$ and D by substituting the experimental values for the various quantities into [37] we find, with $h_p = 3260$Å, $p(0) = 282$Å and $D = 930$Å, in good agreement with the corresponding values in Table I for an anodizing current density of 5 mA/cm².

Conclusions

The results obtained above lead to the following conclusions.

(a) Anodic films obtained in oxalic acid are indeed porous in the sense that the pores can be filled by subsequent forming in an electrolyte that does not dissolve the oxide, such as boric acid. The porosity decreases with increasing anodizing current density.

(b) During forming in boric acid of a sample already covered with a porous layer some of the oxide forms at the pore-base/electrolyte interface and some at the metal/oxide interface. This behavior can be used to define a transport number t_+ for the positive ions; under the experimental conditions used it was found that $t_+ = 0.24$. This invalidates the quantitative interpretation of Dekker and Van Geel (2) because these authors tacitly assumed $t_+ = 1$.

(c) The growth of a porous anodic film is determined solely by the formation of oxide at the oxide/metal interface. This can also be used to define a transport number for the anodization process, which was found to be $t_+ = 0.33$.

(d) The average pore diameter, cell diameter, and barrier layer thickness of a porous film vary linearly with the anodizing voltage, the cell wall thickness being somewhat less than the barrier layer thickness. This requires some modification of the Keller-Hunter-Robinson model (10) in which pore diameter is considered independent of the anodizing voltage.

Table I

J (mA/cm²)	V_a (V)	v (Å/min)	β	α_a	p (Å)	D (Å)	h_p (Å)
1	14.1	3.35	0.344	0.116	131	386	150
2	24.1	3.84	0.283	0.089	182	617	251
3	30.9	4.11	0.264	0.082	223	780	332
4	36.2	4.22	0.257	0.078	259	910	379
5	39.7	4.97	0.243	0.074	266	975	429

For the meaning of the symbols, see text.

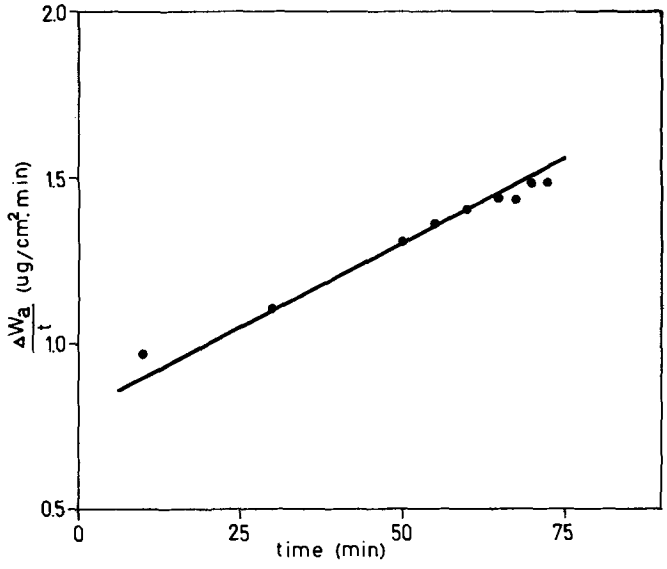

Fig. 14. Quantity $\Delta W_a/t$ as a function of dissolution time in chromic-phosphoric acid of a sample anodized in 80 g/l oxalic acid at 15°C with a current density of 5 mA/cm² during 3.2 min.

Acknowledgments

The authors wish to thank R. Gelsing for supplying the aluminum-coated glass plates and A. Ronteltap for his active part in carrying out much of the experimental work. The authors also express their sincere appreciation to Prof. A. J. Dekker for many valuable discussions during the course of this study.

Manuscript submitted Nov. 6, 1968; revised manuscript received *ca.* Dec. 17, 1969.

Any discussion of this paper will appear in a Discussion Section to be published in the December 1970 JOURNAL.

REFERENCES

1. L. Young, "Anodic Oxide Films," Academic Press, London, New York (1961).
2. A. J. Dekker and W. Ch. van Geel, *Philips Res. Rept.*, 2, 313 (1947).
3. See ref. (1), p. 137.
4. C. G. Dunn, *This Journal*, **115**, 219 (1968).
5. W. J. Bernard and J. J. Randall, Jr., *ibid.*, **107**, 483 (1960).
6. J. R. Murphy and C. E. Michelson, "Proceedings of the Symposium on Anodizing Aluminum, Nottingham University, Sept. 1961," p. 83 ff, Aluminum Development Association, London (1962).

7. S. Tolansky, "Multiple Beam Interferometry of Surfaces and Films," Clarendon Press, Oxford (1948).
8. J. A. Davies, B. Domey, J. P. S. Pringle, and F. Brown, *This Journal*, **112**, 675 (1965).
9. J. J. Randall, *ibid.*, **114**, 560 (1967).
10. F. Keller, M. S. Hunter, and D. L. Robinson, *ibid.*, **100**, 411 (1953).
11. M. Nagayama and K. Tamura, *Electrochim. Acta*, **12**, 1097 (1967).

Anodic Oxidation of Hydrocarbons

T. N. Hartley

Blackburn College of Technology and Design, Blackburn, England

and D. Price

Chemistry Department, University of Salford, Salford, Lancashire, England

ABSTRACT

The anodic oxidation of ethylene in 1.5M sulfuric acid at 80°C has been shown to occur at a gold-coated platinum electrode with a Tafel slope of 0.083V. The effect of variation of the weight of electrodeposited gold and also of temperature were studied. The products were carbon dioxide, acetone, acetaldehyde, and propionaldehyde, the Faradaic efficiency of conversion to carbon dioxide being 20% at 0.79V (*vs.* NHE). The addition of surface active agents to the electrolyte tended to increase the overpotential for ethylene oxidation at platinum and gold electrodes. The effect was particularly pronounced in the case of cetyl pyridinium bromide, probably because of preferential adsorption of bromide ions on the electrodes. Partial anodic oxidation of acetylene in 1.5M sulfuric acid was observed at the gold electrode at 80°C. Much less oxidation was observed for methane and ethane.

In recent years there has been much fundamental research into electro-organic oxidation, particularly with reference to fuel cells. Because of the large numbers of parameters involved (*e.g.*, electrode type, nature of electrolyte, fuel gas, temperature, etc.) much more investigation is required before a comparative picture of the electro-oxidation of hydrocarbons over a reasonably wide range of parameters can be obtained. This work is a study of the anodic oxidation of some simple hydrocarbons.

Experimental

All experiments were carried out in a thermostated Pyrex H-cell, of conventional design, which contained 1.5M sulfuric acid as electrolyte. The anode and cathode compartments were separated by means of a sintered glass disk which prevented diffusion of gases or products between compartments. Connection between the anode and the reference electrode was via a Luggin capillary (1). The reference electrode was mercury-mercurous sulfate in contact with the same 1.5M sulfuric acid electrolyte which was used in the cell. This eliminated any liquid junction potential. The reference electrode was standardized at 20°C against a hydrogen electrode with 1.5M sulfuric acid as electrolyte. The platinum and gold anodes were prepared as electrodeposits, the method of plating being chosen to give a powdery deposit of high surface area (2). Before each run the electrodes were electrically pulsed to remove adsorbed oxygen and organic impurities. Frequent "blank" experiments were used to test for electrode poisoning. When this had become significant, the electrode was stripped and replated.

A 6V lead-acid accumulator was used as a d-c current source, the actual current through the cell being controlled by means of a simple galvanostat. For each run, the anode and cathode compartments were first purged with nitrogen to remove any dissolved oxygen or carbon dioxide. The nitrogen supply to the catholyte was maintained, while that to the anolyte was replaced by hydrocarbon gas bubbled through at about 6-8 cc/min. The rest potential was observed for some 30 min after the hydrocarbon had been admitted. The desired current was then set and the anode potential recorded when a stable potential (potential change less than 10 mV/hr) had been reached. All potentials are expressed *vs.* the normal hydrogen electrode at 20°C.

The Faradaic efficiency for the oxidation of ethylene to carbon dioxide was determined by a titrimetric procedure (3).

The effect of the surface active agents on the anodic oxidation of ethylene was investigated by adding them as a 0.1% w/v solution in the 1.5M sulfuric acid in the anode compartment. The cathode and reference compartments contained 1.5M sulfuric acid only. Blank runs with no surfactant added were carried out before every addition of surfactant to check that the electrodes retained their original activity throughout the experiments.

Reagents.—The methane, ethane, and ethylene were Matheson C.P. grade and the acetylene and nitrogen commercial "oxygen-free" grade. The water used had been previously de-ionized. Sulfuric acid and hydrochloric acid were "Analar" grade and the chlorauric acid was laboratory reagent grade. Mercurous sulfate was anodically generated from mercury and sulfuric acid by the flowing anode method (4). The surface active agents used were anionic-Teepol-610 (Shell Chemicals)—mixture of sodium secondary alkyl sulfates, cationic-cetyl pyridinium bromide (laboratory reagent grade), and nonionic-Nonidet P40 (Shell Chemicals)—an octyl phenol/ethylene oxide condensate.

Results

Anodic oxidation of ethylene at gold electrode.—Figure 1 shows the polarization curve obtained for the oxidation of ethylene in 1.5M sulfuric acid at 80°C at anodes plated with varying quantities of gold. A linear relationship is observed in the approximate region +0.75 to +0.95V. Except in the case of the electrode with the heaviest gold deposit, anode potentials stabilized almost instantaneously in the Tafel region and were independent of changes in ethylene flow rate. Below +0.75V the potentials were slow to stabilize and were very nonlinear. This was attributed to charging of the double layer. The slope of the Tafel region is

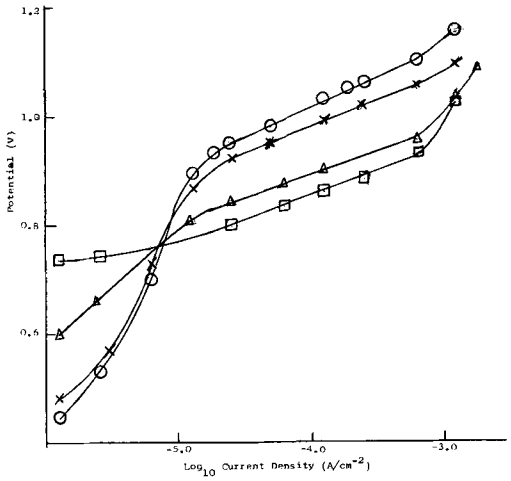

Fig. 1. Current-potential curves for anodic oxidation of ethylene in 1.5M sulfuric acid at 80°C, variation with weight of deposited gold. ○ 0.4375 mg Au cm^{-2}; X 1.5625 mg Au cm^{-2}; △ 4.0375 mg Au cm^{-2}; □ 7.325 mg Au cm^{-2}.

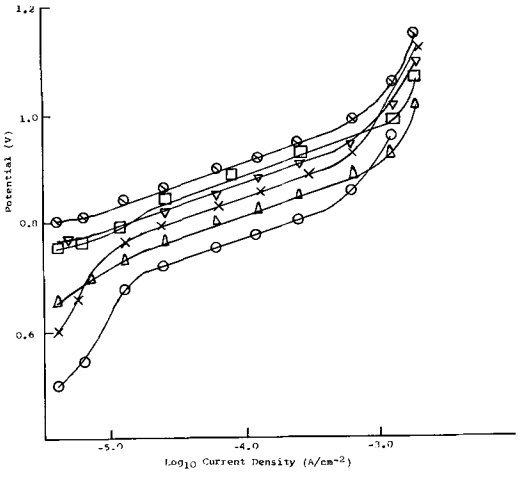

Fig. 3. Current-potential curves for anodic oxidation of ethylene in 1.5M sulfuric acid, effect of temperature. ○ 90°C; △ 70°C; X 60°C; ▽ 50°C; □ 40°C; ⊘ 26°.

0.085V, which corresponds closely to (2.303 RT)/F, at all electrodes except that with the lowest weight of gold, at which it is 0.110V. Figure 2 shows the variation of rest potential with gold coverage.

Polarization curves for ethylene oxidation at the gold electrode at temperatures between 26° and 90°C are shown in Fig. 3. The slope and length of the Tafel lines are independent of temperature within the range investigated, but the Tafel line is displaced toward higher potentials as the temperature is decreased. Calculation of an apparent activation energy for the ethylene oxidation from this data gave a value of 13 kcal $mole^{-1}$. This value will include heats of adsorption of products and reactants as well as the true activation energy which refers to reactants at the electrode surface.

Gas chromatographic analysis, using a hydrogen flame detector, of the anolyte after oxidation of ethylene at the gold anode indicated the presence of propionaldehyde, acetone, and acetaldehyde, the latter two in approximately equal trace amounts. Carbon dioxide was the only product conclusively detected in the effluent gases from the anode compartment. The Faradaic efficiency for the oxidation of ethylene to carbon dioxide at the gold anode was determined as 20%. Figure 4 shows the effect of the presence of three

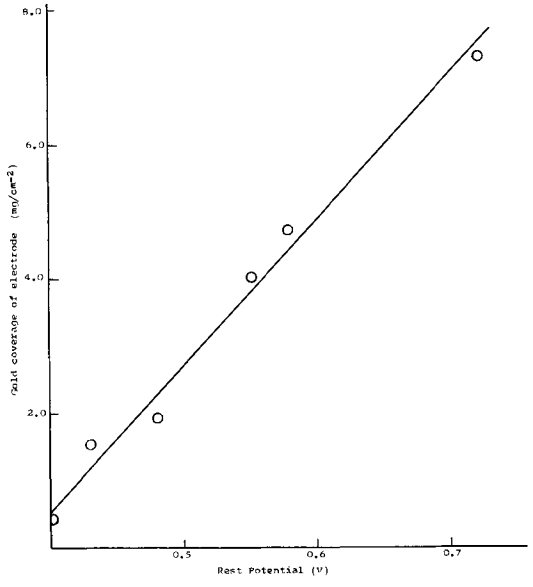

Fig. 2. Variation, with gold coverage, of the rest potential in the presence of ethylene in 1.5M sulfuric acid at 80°C.

different surface active agents on the polarization curves obtained for the anodic oxidation of ethylene at gold and platinum electrodes.

Anodic oxidation of methane, ethane, and acetylene at gold electrode.—Current-potential curves obtained with these gases in 1.5M sulfuric acid with the gold electrode are shown in Fig. 5. The curves for the two saturated hydrocarbons indicate that some oxidation occurred insofar as a short Tafel region can be seen in the 10^{-5} A cm^{-2} region. The acetylene plot shows a Tafel region from 1.25 x 10^{-4} A cm^{-2} to 7.5 x 10^{-3} A cm^{-2}, the slope of the line being 166 mV which corresponds closely to 2(2.303 *RT*)/**F**. Potentials in this region exhibited a slow, continuous oscillation within ±4 mV of the mean value. On completion of the experiment, the anolyte had acquired a golden-yellow color and had an aldehydic odor.

Discussion

The results shown in Fig. 1 confirm that ethylene can be anodically oxidized at gold electrodes. Kuhn *et al.* (5) proposed the following mechanism for this reaction

$$C_2H_4 \rightleftharpoons C_2H_4\ (ads) \qquad [1]$$

$$H_2O \rightleftharpoons OH\ (ads) + H^+ + e \qquad [2]$$

$$C_2H_4\ (ads) + OH\ (ads) \rightarrow -CH_2-O-CH_3\ (ads) \qquad [3]$$

$$-CH_2-OCH_3\ (ads) \xrightarrow{\text{Desorption}} CH_3-C(=O)-H$$

$$-CH_2-OCH_3\ (ads) \xrightarrow{\text{Oxidation}} -CH-CH_2\cdot + H_2O \rightarrow CO_2 \qquad [4]$$

where reaction [3] is rate determining. The results described in this work are consistent with this mechanism. The Tafel slope of 85 mV is associated with a chemical reaction following first charge transfer or following any later charge transfer in which the reactant is at full coverage (6). Substitution of nitrogen for ethylene at the gold anode produced an immediate rapid rise in potential in the Tafel region, whereas at the platinum electrode little change occurred until 10 min after the gas substitution. This supports the view that the rate-determining step at the gold anode involves the species C_2H_4 (ads) [3], while at the platinum anode the slow step is the preceding water discharge reaction [2]. The observed production of aldehydes from the anodic oxidation of ethylene on gold is probably due to the desorption of intermediates from the gold surface, reaction [4]. This reaction should be more rapid at the gold electrode than at a platinum electrode because the strength of a partially covalent bond be-

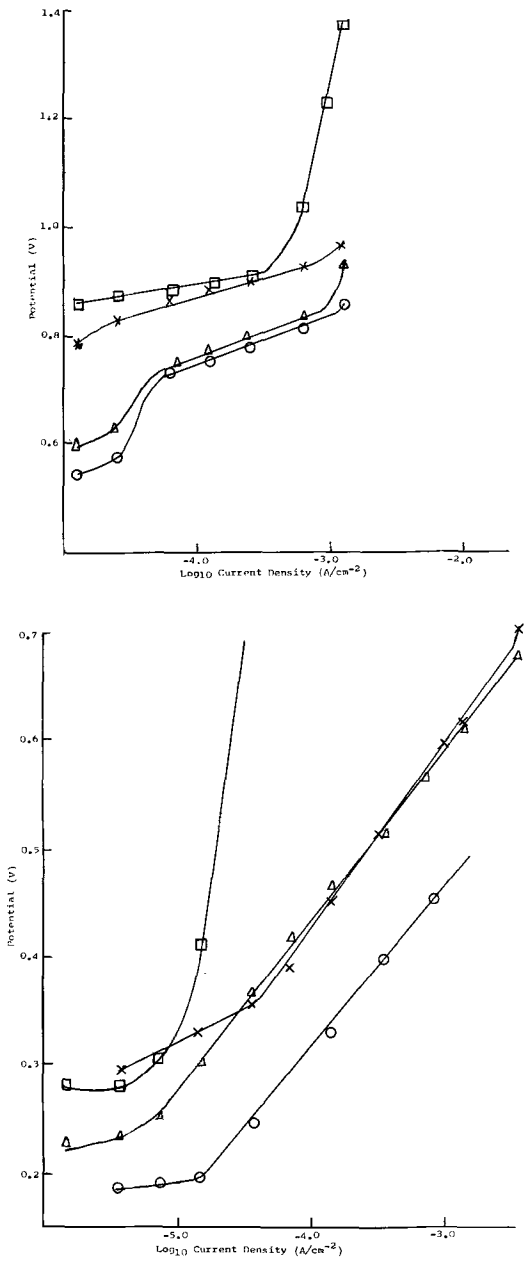

Fig. 4. Effect of surface active agents on current-potential curves for anodic oxidation of ethylene in 1.5M sulfuric acid at 80°C at: (a, top) gold anode; (b, bottom) platinum anode. ○ 1.5M sulfuric acid only; △ 0.1% w/v Nonidet P40 (non-ionic) in 1.5M sulfuric acid; X 0.1% w/v Teepol 610 (anionic) in 1.5M sulfuric acid; □ 0.1% w/v cetyl pyridinium bromide (cationic) in 1.5M sulfuric acid.

tween metal and organic species is about 20 kcal lower for gold than platinum (7).

Passivation of the gold electrode is shown by the continuous increase in potential at higher current densities. This is probably due to retardation of the ethylene oxidation process due to geometric and catalytic retardation effects of oxide formation.

The slopes of the Tafel plots shown in Fig. 1 show that the oxidation of ethylene is little affected by the platinum substrate on which the gold electrode is plated. The displacement of the Tafel line to more positive potentials as the gold coverage decreases (Fig. 2) can be attributed to roughness factor variations. Comparison of the current densities at a single potential indicates that the roughness factor for the high gold weight electrode was approximately fifty times greater than that for the low gold weight electrode. Figure 1 indicates a limiting current density of approximately 10^{-3} A cm^{-2} at which the ethylene oxidation reaction becomes diffusion-controlled. A similar

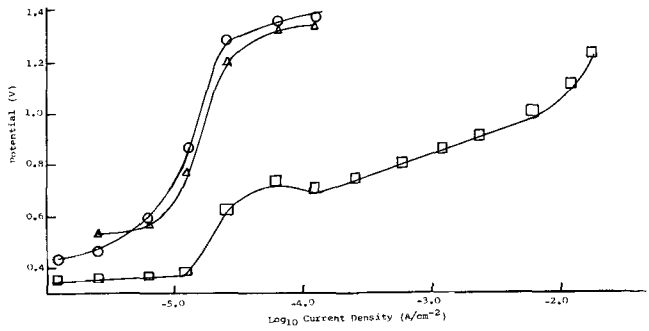

Fig. 5. Current-potential curves for anodic oxidation at gold electrode of various hydrocarbons in 1.5M sulfuric acid at 80°C. □ acetylene; ○ methane; △ ethane.

region has been observed at platinum electrodes (3). A Fick's law calculation indicates that the value lies between 2.6 x 10^{-3} and 0.5 x 10^{-3} A cm^{-2} which is in good agreement with our experimental value. Thus, diffusion control in the limiting current region is due to slowness of transport of sufficient ethylene from the solution to the electrode surface.

Figure 3 shows that the effect of variation of temperature (26° → 90°C) on ethylene oxidation at the gold electrode was merely to displace the linear Tafel regions to higher or lower potentials. The length and slope of the Tafel region was unaffected, showing that anodic oxidation of ethylene on gold can be carried out in the region of ambient temperatures. The value of 13 kcal $mole^{-1}$ obtained for the apparent activation energy for ethylene oxidation at the gold anode is lower than the value of 20 kcal $mole^{-1}$ calculated by Bockris (3) for the oxidation at the platinum electrode. It should be remembered that complete oxidation to carbon dioxide occurs at the platinum electrode whereas, at the gold electrode, oxidation is incomplete. The relationship between this apparent activation energy and the true activation energy at the electrode surface, could well be quite different for the gold than for the platinum electrode because of the greater number, complexity, and variation of absorbed species occurring at the gold surface.

For complete conversion of ethylene to carbon dioxide 12 electrons per molecule are transferred, whereas if only aldehydic compounds are produced the number is 2. In our experiments, using the gold electrode, 20% of the ethylene was oxidized to carbon dioxide. Hence the average number of electrons transferred per molecule of ethylene electro-oxidized was approximately four. The efficiency of the gold electrode as a current-producing device is, therefore, in the region of 30%. Since gold has a similar capital cost to platinum, it would appear that gold is not a practical possibility as an ethylene fuel cell anode, in spite of the reaction having a lower Tafel slope and activation energy compared to the values at the platinum electrode. The temperature effect is of value, however, if the products of the partial oxidation of ethylene are required.

The detection of propionaldehyde, acetaldehyde, and acetone in the electrolyte after anodic oxidation of ethylene is in agreement with a reaction sequence in which the final stage is a branched reaction involving desorption of intermediates to form aldehydes. That partially oxidized products other than acetaldehyde were obtained indicates that the desorption branch of Eq. [4] is an oversimplification. In addition to desorption to produce acetaldehyde, the postulated intermediate —CH_2—O—CH_3 (ads) may undergo further reaction at the gold surface, possibly with adsorbed ethylene, to produce other intermediates containing more carbon atoms.

It is likely that the effects observed when various surfactants were present in the electrolyte, Fig. 4, were due to adsorption of various species at the surface of the electrodes resulting in changes in the effective electrode potentials. Bromide ions are known to be

strongly adsorbed at platinum electrodes (8-10). Vasil'ev and Bogotskii (9) state that the introduction of Cl^-, Br^-, or I^- ions in $10^{-2}N$ concentration will completely inhibit the electrolytic oxidation of an organic substance, an effect which they ascribe to microblocking of the electrode surface. It has also been shown (9) that various organic molecules (aldehydes, carboxylic acids, and high molecular weight alcohols) are adsorbed at a platinum electrode and have an inhibiting effect on the electro-oxidation of ethanol and formic acid.

The polarization curves obtained in the presence of cetyl pyridinium bromide are probably due to the electrostatic attraction between the electrode and bromide ion leading to preferential adsorption of the Br^- ion rather than ethylene. The steeper polarization curve obtained at the platinum electrode indicates that Br^- ion is more strongly absorbed at the platinum than the gold electrodes under the conditions of our experiments.

With the exception of the non-ionic surfactant at the gold electrode, the effect of the anionic and non-ionic compounds is to displace the Tafel lines to more anodic potentials, but without a change in slope. It would appear that the mechanism of ethylene oxidation is not changed by the presence of these agents, but that the number of active sites is reduced probably by blocking due to preferential adsorption of the surfactant molecules.

Figure 5 shows that acetylene is much more strongly oxidized than methane and ethane at the gold anode at 80°C in 1.5M sulfuric acid. The presence of aldehydes in the anolyte indicates that the oxidation is incomplete. The rapid stabilization of potential at low current density observed for acetylene is consistent with the observations of Bianchi (11). Bianchi attributed rest potentials on platinum in the presence of ethane, ethylene, and acetylene to be due to firmly adsorbed acetylene and carbon radicals formed by successive hydrogenation and dehydrogenation of the hydrocarbon. Potentials anodic to the rest potential but less positive than the commencement of the Tafel region were considered due to dehydrogenated carbon radicals whose rate of formation is most rapid in the case of acetylene.

A change in the nature of the species adsorbed at the electrode, in the presence of acetylene, is indicated by the onset of the second region, 1.25×10^{-5} to 1.25×10^{-4} A cm^{-2}, in Fig. 5. The observed Tafel slope of $2(2.303\ RT)/F$ for the acetylene oxidation indicates that the reaction mechanism is different to that for ethylene oxidation (Tafel slope $2.303\ RT/F$). The Tafel slope for the acetylene oxidation suggests that the rate-determining step is a charge transfer reaction. However, Bockris *et al.* (12) state that if the total coverage is linearly dependent on potential, a chemical reaction involving adsorption of one radical as rate-determining step would also give the observed Tafel slope. More experimental data is required to determine the reaction mechanism for the anodic oxidation of acetylene at the gold electrode.

Acknowledgments

We wish to thank the Blackburn College of Technology for research facilities, and Mr. J. G. Sunderland for performing some of the gas-chromatographic analyses.

Manuscript submitted May 9, 1969; revised manuscript received Dec. 3, 1969.

Any discussion of this paper will appear in a Discussion Section to be published in the December 1970 JOURNAL.

REFERENCES

1. P. Delahay, "New Instrumental Methods in Electrochemistry," p. 391, Interscience Publishers, Inc., New York (1954).
2. E. C. Potter, "Electrochemistry, Principles and Applications," p. 286, Cleaver Hulme, London (1956).
3. H. Wroblowa, B. J. Piersma, and J. O'M. Bockris, *J. Electro. Anal. Chem.*, **6**, 401 (1963).
4. J. G. Ives and G. J. Janz, "Reference Electrodes," p. 405, Academic Press, London (1961).
5. A. T. Kuhn, H. Wroblowa, and J. O'M. Bockris, *Trans. Faraday Soc.*, **63**, 1458 (1967).
6. J. W. Johnson, H. Wroblowa, and J. O'M. Bockris, *This Journal*, **111**, 863 (1964).
7. H. Dahms and J. O'M. Bockris, *ibid.*, **111**, 728 (1964).
8. F. C. Anson, *ibid.*, **110**, 436 (1963).
9. Yu. B. Vasil'ev and V. S. Bagotskii, "Fuel Cells—Their Electrochemical Kinetics," p. 77, V. S. Bagotskii and Yu. B. Vasil'ev, Editors, (Translation from Russian), Consultants Bureau, New York (1966).
10. A. H. Taylor and S. B. Brummer, *J. Phys. Chem.*, **72**, 2856 (1968).
11. G. Bianchi, L. De Carlo, and G. Faita, *Chim. Ind.*, **47**, 830 (1965).
12. J. O'M. Bockris, H. Wroblowa, E. Gileadi, and B. J. Piersma, *Trans. Faraday Soc.*, **61**, 2531 (1965).

Photoelectrochemical Processes on Silver-Silver Oxide Electrodes

R. Memming, F. Möllers, and G. Neumann

Philips Zentrallaboratorium GmbH, Laboratorium Hamburg, Germany

ABSTRACT

Oxidation and reduction processes of silver-silver oxide electrodes were studied, especially the influence of light excitation on these processes. The experimental results have shown that light absorption by silver (I) oxide leads to an anodic oxidation to silver (II) oxide. The electrochemical reduction of silver (II) oxide formed during illumination is considerably inhibited. A possible mechanism explaining the photoelectrochemical processes and the inhibition is discussed.

The electrochemical behavior of silver-silver oxide electrodes has been extensively studied during the last two decades because of great interest in its application in high energy batteries. It is well-known that silver is oxidized in two steps (1) using alkaline solutions. It is generally assumed that silver (I) oxide is formed in the first step and silver (II) oxide in a second step. There is still uncertainty about the existence of oxides in which silver apparently has an oxidation state greater than two.

Several authors have found also that the illumination influences the electrochemical properties of a silver electrode. Blocher and Garrett (2) observed a shift of the rest potential during illumination and suggested

that oxide layers are involved in this process. Principally an illumination could lead either to a photodecomposition of the silver (I) oxide followed by a re-oxidation of the silver nuclei or to a further oxidation into silver (II) oxide. Göhr and Breitenstein (3) performed measurements with electrodes produced by evaporating silver on gold substrates. They concluded from their results that photodecomposition is always the primary step. In order to obtain more information about the photochemical reactions we performed corresponding electrochemical investigations with different kinds of silver electrodes.

Experimental

Different types of silver electrodes were used in our experiments: silver sheets, single crystals, and silver film produced by vacuum evaporation or electrolytic deposition. In the latter case (film) a nickel substrate covered with a gold film was used. The silver sheet and single crystals were etched in HNO_3 solution before each measurement.

The experiments were performed in 1*N* KOH saturated with silver (I) oxide. The current-potential curves were measured using a Wenking potentiostat, the electrode potential determined *vs.* a Hg/HgO electrode in 1*N* KOH.

For measuring photocurrents a tungsten lamp (100W) was used as a light source. The full intensity of this lamp was necessary in those cases where products formed during illumination had to be analyzed. In other cases, *e.g.*, measuring the potential dependence or the spectral distribution of the photocurrent itself, considerable changes of the surface layers on the electrode during illumination had to be avoided. Then the intensity was reduced by several orders of magnitude using graded filters, the light was chopped (60 cycles) and the corresponding photocurrent amplified (lock-in amplifier) and displayed on a recorder. In order to distinguish between photocurrents measured at high and low intensities, the latter one (a-c method) will be called "differential photocurrent."

Results and Discussion

As already mentioned in the introduction it is a well-known fact that silver electrodes are readily oxidized during anodic polarization. Sweeping across the corresponding potential range with constant speed two main current peaks could be generally observed (Fig. 1a). As it was proved by several authors (4-6) the first current peak is due to the oxidation of silver to silver (I) oxide ($Ag \rightarrow Ag_2O$) and the second peak to the formation of silver (II) oxide ($Ag_2O \rightarrow AgO$). The corresponding reduction peaks occur during the potential sweep in the cathode direction. The electrode reactions are given by

$$2Ag + 2\,OH^- \rightleftharpoons Ag_2O + H_2O + 2e^- \quad [1]$$

$$Ag_2O + 2\,OH^- \rightleftharpoons 2AgO + H_2O + 2e^- \quad [2]$$

The oxidation from Ag_2O to AgO occurs at a rather high overvoltage (redox potential at +0.47V). Dirkse and co-workers (7) discussed the origin of this overvoltage. Since it is not important for our investigations it will not be used in our paper.

On the other hand the shape of the current-potential curves depend very much on the pretreatment of the electrode. This is especially observed for the first oxidation step $Ag \rightarrow Ag_2O$. In Fig. 1a a typical current-potential behavior is presented (as measured with a silver sheet) after several oxidation-reduction cycles, *i.e.*, after 5 or 6 cycles the shape of such a curve is not changed any more. In the first cycle of a freshly prepared electrode, however, no distinct Ag/Ag_2O peak is visible, only a very weak current peak extending over a much larger potential range was observed. Experiments with other types of electrodes, *e.g.*, Ag single crystals or evaporated films, have shown that different types of electrodes show a different behavior only during the first potential sweeps.

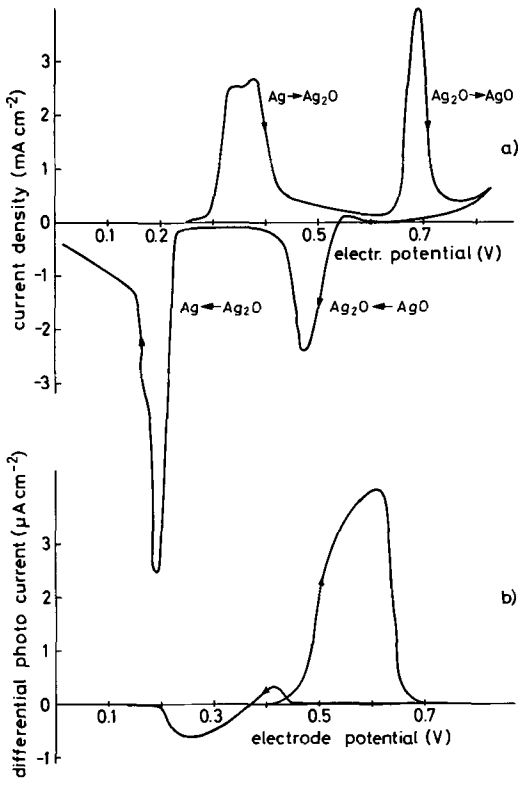

Fig. 1. (a) Interfacial current vs. electrode potential (measured against Hg/HgO in 1*N* KOH) for a silver sheet in 1*N* KOH. Sweeping speed: 50 mV/min. (b) Differential photocurrent vs. electrode potential (measured simultaneously with the curve in (a). [Differential photocurrent is measured during illumination with chopped light of low intensity, *i.e.*, dark current is eliminated.]

As already reported by Göhr (3) the anodic current is increased by illuminating the electrode provided that Ag_2O is present on the electrode surface. We also observed a fast current increase as soon as the light is switched on and a slow decrease within about 10 min as demonstrated in Fig. 2. This result indicates that the Ag_2O film is changed during the illumination. In order to obtain more information on the origin of this photoprocess, we measured the potential dependence of the photocurrent as shown in Fig. 1b, using a differential method as described in the previous section. In this case the light intensity was kept low so that the composition of the Ag_2O layer remained unchanged and

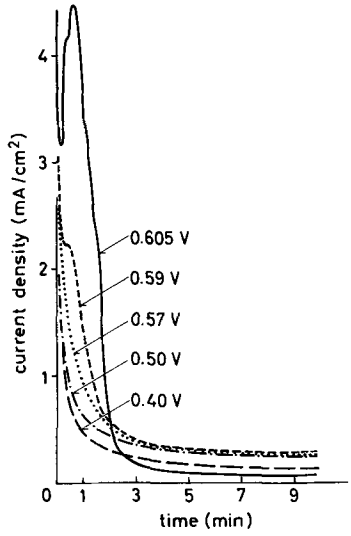

Fig. 2. Interfacial current vs. time during illumination of an Ag/Ag_2O electrode at different electrode potentials. (Electrolyte: 1*N* KOH.)

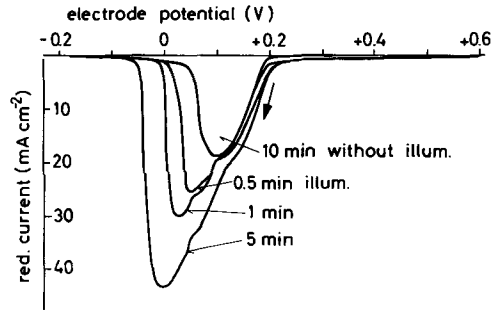

Fig. 3. Reduction (dark) current vs. electrode potential after anodic formation of an Ag_2O layer on the silver (sheet) electrode followed by illumination at $U_E = +0.55V$. The electrode was kept at this potential always for 10 min. In the latter part of this period the electrode was illuminated for a certain time interval as indicated. (Electrolyte: 1*N* KOH.) Sweeping speed: 20 mV/sec.

consequently the differential photocurrent remained constant over a long period of time. This small differential photocurrent was measured independently from the dark current (Fig. 1a).

Comparing Fig. 1a and 1b it is quite obvious that the anodic differential photocurrent sets in as soon as a Ag_2O layer is formed on the electrode, as was reported by Göhr (3). During the potential sweep in the cathodic direction a photocurrent was observed also as soon as the higher oxide (AgO) was reduced to Ag_2O. In this case, however, photocurrents of different signs were found. This result implies that the origin of the photocurrent cannot be explained only by an increase of the electron conductivity within the bulk of Ag_2O.[1] This problem will be discussed later.

As mentioned above, the anodic current increases considerably within a certain potential range during strong illumination and decreases within several minutes (Fig. 2). The main question is what kind of product is formed by light excitation. Göhr (3) explained this process by assuming a decomposition of Ag_2O into silver and oxygen followed by an electrochemical reoxidation of silver nuclei to Ag_2O if the electrode potential is more cathodic than the redox potential[2] of Ag/AgO (= 0.37V on our scale), whereas above this potential the silver nuclei are re-oxidized directly to AgO. In the first case (below 0.37V), however, the decrease of the photocurrent is difficult to understand. This difficulty does not occur if only AgO is formed within the whole potential range. Then the formation of AgO during illumination must not necessarily proceed via photodecomposition. It is also possible that holes are generated within the Ag_2O by light excitation which leads directly to a further oxidation from Ag_2O to AgO.

The existence of AgO after illumination should be very easy to prove since the reduction of AgO to Ag_2O appears as a typical current peak near 0.5V when sweeping toward cathodic potentials (see Fig. 1). We performed corresponding experiments and the results are plotted in Fig. 3. These reduction curves were obtained after having illuminated the electrode at +0.55V for different time intervals. For the illumination we selected an electrode potential (+0.55V) at which the formation of an Ag_2O film is completed and no AgO is formed in the dark. For comparison we also plotted a curve measured after having kept the electrode at the same electrode potential in the dark. Contrary to the assumption that Ag_2O is oxidized to AgO during illumination, the typical current peak AgO → Ag_2O around +0.5V (see Fig. 1a) is not visible in Fig. 3. On the other hand a new current peak around $U_E = 0$ is built up in a potential range where Ag_2O is reduced to Ag. Although the AgO → Ag_2O peak is not visible it may be concluded that the product formed during illumination is at least partly reducible. In order to get information about the origin of this product we checked the charge balance in the oxidation-reduction cycle and studied the composition of the oxide layer using x-ray analysis.

[1] According to Le Blanc and Sachse (8) the conductivity of Ag_2O is of the order of 10^{-8} ohm^{-1} cm^{-1}.

[2] This is a theoretical value determined from the redox potentials Ag/Ag_2O and Ag_2O/AgO.

Composition of Oxide Layers

For measurements of the x-ray diffraction pattern the electrode was separated from the electrolyte following polarization at a certain electrode potential. The validity of this method was tested by studying the diffraction pattern after polarizing the electrode without illumination. In this case we found, as expected, typical signals of an Ag_2O structure after having polarized the electrode around +0.5V, whereas the AgO structure occurred after polarizations above 0.7V. The latter one disappeared again as soon as the AgO was reduced at 0.25V (see Fig. 1a). This is in agreement with the results obtained from the electrochemical oxidation-reduction cycle.

The same AgO pattern was also found after illuminating an Ag_2O film in the potential range 0.30-0.50V, where no AgO was formed in the dark.

According to these results the anodic photocurrent observed during illumination of the Ag_2O layer is only due to the formation of AgO. Obviously this AgO cannot be reduced around 0.5V (see Fig. 3) but only in a more cathodic potential range where normally, *i.e.*, without previous illumination, the reduction of the Ag_2O to Ag occurs.

Charge Balance

The charges consumed during the anodic and cathodic processes were determined as follows (see also Fig. 4): an Ag_2O layer was formed during a potential sweep from −0.2 to +0.5V (sweeping speed 0.1 V/min). Within this potential and time interval the growth of the Ag_2O layer was completed. The charge $Q_{0.1}$ [3] consumed in this process was determined from the corresponding current-time curve. Then the electrode was polarized at a certain potential (between +0.4 and 0.6V) and illuminated (strong light intensity) for 10 min until the photocurrent dropped to a very low level. In this time interval the photocurrent was also recorded and the corresponding charge, Q_L, could be determined. Immediately afterward the illumination was turned off and the electrode was reduced by sweeping back toward cathodic potentials. From the current-time relation we obtained the charge ($Q_{2.1}$) necessary for the reduction of AgO to Ag_2O and the sum of charges necessary for the reduction of Ag_2O to Ag and of the species produced during illumination ($Q_{1.0} + \Delta Q$). The experimental conditions, *i.e.*, the time dependence of light intensity, potential, and current, are shown schematically in Fig. 4.

The charges obtained by this method are plotted in Fig. 5 against the electrode potential U_L at which the electrode was illuminated. As shown in Fig. 5 the sum of all charges consumed during the anodic process ($\Sigma Q_{anod.}$) are within a few per cent identical with those found in the cathodic process ($\Sigma Q_{cath.}$). Since the anodic charges were always slightly larger than the cathodic values we assume that a few per cent of the anodic charge were used for the evolution of oxygen. It should be emphasized that the same amount of charge is lost performing those experiments without any illumination. From this follows

$$\underbrace{[Q_{0.1} + Q_L]}_{\Sigma Q_{anod.}} \approx \underbrace{[Q_{2.1} + (Q_{1.0} + \Delta Q)]}_{\Sigma Q_{cath.}}$$

This result demonstrates clearly that the oxidation products remain on the electrode. In Fig. 5 we also plotted the charges Q_L and $Q_{2.1}$ which were determined separated as outlined above. The additional

[3] The index represents the oxidation state of silver, *i.e.*

$Q_{0.1}$: Ag → Ag_2O $Q_{1.0}$: Ag_2O → Ag
$Q_{1.2}$: Ag_2O → AgO $Q_{2.1}$: AgO → Ag_2O
Q_L = charge consumed during illumination.

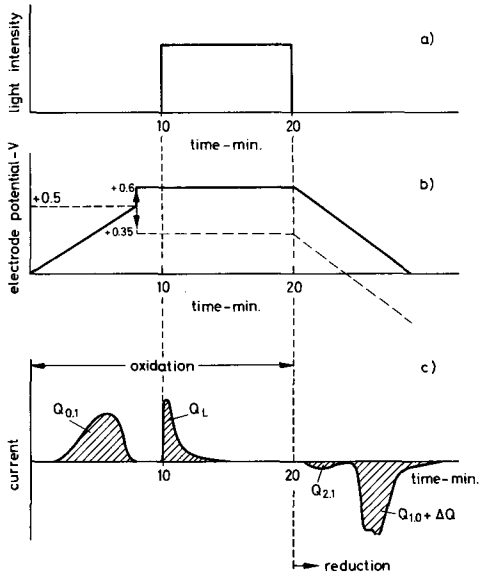

Fig. 4. Schematic presentation for the time dependence of light intensity, electrode potential, and current, applied for determining charges given in Fig. 5 and 6. (For definition of different Q's see footnote 3.)

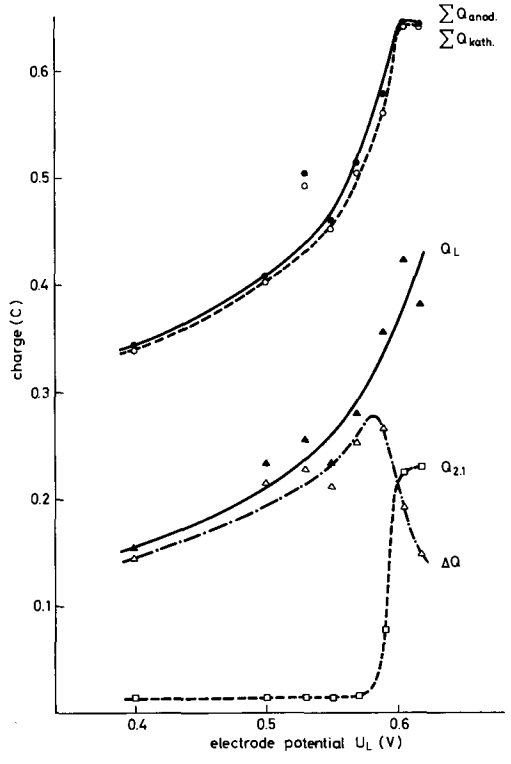

Fig. 5. Charges consumed in different processes *vs.* electrode potential for a silver sheet in 1*N* KOH.

charge ΔQ found in the reduction process after illumination can be calculated according to Fig. 4c using the equation

$$\Delta Q = (Q_{1.0} + \Delta Q) - Q_{0.1}$$

and is plotted in Fig. 5. According to this figure the additional charge ΔQ found during the reduction period after illumination below $U_L = 0.57V$ is practically identical with the charge Q_L consumed during the illumination. Our x-ray measurements show qualitatively that AgO is formed by illuminating an Ag_2O layer at anodic polarization. From this result and from the fact that the anodic charge Q_L consumed during illumination is regained completely during the reduction period ($\Delta Q \approx Q_L$), it has to be concluded that the anodic photocurrent is only due to the oxidation of Ag_2O to AgO. Consequently, photodecomposition has to be excluded. Since no reduction of AgO was found in the potential range (around +0.50V) where it is usually observed after strong anodic oxidation in the dark, the reduction of the AgO formed by light excitation is obviously inhibited. A model for this inhibition will be given in the next section.

On the other hand when illuminating the electrode above $U_L > 0.57V$, the mechanism changes. Now AgO produced above 0.57V is reduced in the potential range where it is also found without illumination, since $Q_{2.1}$ increases (see Fig. 5) whereas ΔQ decreases. The charge Q_L consumed during illumination also rises rapidly. This increase, however, is not equivalent to an increase of the photocurrent itself. This is indicated by the fact that in this case the current did not decay immediately after the light was switched off (after about 20 sec). This also is shown by Fig. 2 (solid line) where a second current peak appears after about 1 min of illumination. Obviously, the oxidation proceeds in this potential range even in the dark after having formed few AgO nuclei during illumination. This illumination potential U_L at which $Q_{2.1}$ increases, could be shifted toward lower values by increasing the light intensity or using thinner Ag_2O layers.

We studied the charge balance with different types of electrodes, silver sheets, single crystals, and evaporated films. In all cases we obtained similar results, *i.e.*

$$\Sigma Q_{anod.} = \Sigma Q_{cath.} \text{ and } \Delta Q \approx Q_L$$

Göhr (3) did not obtain the same result. He observed that $\Sigma Q_{cath.}$ is considerably smaller than $\Sigma Q_{anod.}$. During the reduction period these authors only found a certain percentage of the charge Q_L consumed during illumination. The percentage varies from 0 to 50%. Actually Göhr's model is based on this result: the charges lost in this process Göhr interpreted to be due to the formation of oxygen during photodecomposition.

The question arises, of course, why our results differ from those obtained by Göhr. In connection with this problem it has to be mentioned that Göhr only determined the charge balance with silver layers after many oxidation-reduction cycles. Since we first thought that the pretreatment may be important for the mechanism, we studied several types of electrodes. As mentioned above we found $\Sigma Q_{anod.} = \Sigma Q_{cath.}$ in all cases. Only for rather poor films formed by depositing a thin layer electrolytically is the percentage of charges lost during an oxidation-reduction cycle somewhat larger. In this case, however, the absolute value of Q_L was also much lower than for good electrodes as shown in Fig. 6. We therefore think that the mechanism is identical for all types of electrodes.

Mechanism of Photo-oxidation and Reduction

Measurements of the charge balance have shown that the oxidation products formed in the dark and during illumination are completely reducible. Moreover, it could be concluded from x-ray diffraction measurements that AgO is produced during illumi-

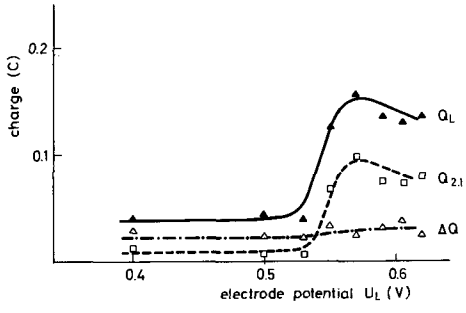

Fig. 6. The same experiment as in Fig. 5 with a thin silver film electrode (0.4μ) deposited on a gold substrate at high evaporation rate in a poor vacuum.

nation. According to our results discussed above the question arises, however, why the reduction of AgO is inhibited if it is produced by illuminating the Ag_2O layer. In order to solve this problem the reaction mechanism itself has to be discussed in more detail.

As reported above, an Ag_2O film is efficiently grown on an Ag electrode above 0.27V. The thickness of this oxide layer depends very much on the pretreatment of the electrode surface. After several oxidation-reduction cycles it reaches about several hundred Angstroms. Basically the film growth is controlled by the ionic conductivity in the oxide itself. The ion transport can proceed by interstitials, lattice vacancies, or pores. Since rather thick oxide layers are formed and since the anodic current decreases rapidly as soon as a certain thickness is obtained, mainly pores must be involved in the transport process.

A further oxidation to AgO occurs at the Ag_2O/electrolyte interface. It is not possible that AgO is formed on the silver itself for thermodynamic reasons. Consequently the oxidation to AgO sets in as soon as the potential at the Ag_2O surface passes a certain value so that some crystal nuclei of AgO are formed. Since the highest electrical field is maintained at surface areas where the original Ag_2O layer is rather thin, the oxidation will mainly proceed within those pores.

As it was proved in the previous sections the electrochemical oxidation from Ag_2O to AgO occurs at lower anodic potentials (see Fig. 1b) when the electrode is illuminated. Since visible light is absorbed by the Ag_2O layer electron-hole pairs are created in Ag_2O by light excitation so that more charge carriers are available for a further electrode process. This phenomenon is very well-known from studies with semiconductor electrodes (9, 10). In general it is observed with this kind of electrodes that, without light excitation, charge transfer processes are practically blocked if minority carriers are involved. Provided that an anodic process proceeds, *e.g.*, via the valence band and not sufficient holes are available at the surface (n-type semiconductor) then the over-all reaction rate is enhanced by formation of holes (minority carriers) during illumination. According to this model we have to assume that in Ag_2O, holes created by light excitation are consumed for further oxidation. This process, however, is only possible in that region of Ag_2O where light is absorbed, *i.e.*, the thickness of an AgO layer depends mainly on the penetration depth of light in the Ag_2O region. In this case deep pores extending further than the penetration depth of light have not much influence on this process. According to its spectral distribution (Fig. 7) the photocurrent is observed below a wavelength of 1.3μ and reaches a maximum at about 0.7μ. Rough absorption measurements have shown that the light absorption in Ag_2O also sets in at about 1.3μ. Since the absorption edge for the higher oxide AgO is even shifted toward the infrared region, AgO also absorbs light around 0.7μ, *i.e.*, AgO formed on the Ag_2O surface screens off the Ag_2O with respect to light excitation.

As we have shown pores extending further into the nonilluminated region of Ag_2O do not affect essentially the oxidation process induced by light. Consequently, we have a discrete layer structure consisting of Ag/Ag_2O/AgO/electrolyte as shown schematically in Fig. 8. This scheme leads also to an interpretation of the inhibition of the cathodic reduction of AgO: since the silver electrode is separated from the AgO by an Ag_2O layer of rather low conductivity the reduction current in a potential region between 0.25-0.5V is relatively small. Obviously, the reduction of AgO can only proceed with a higher rate when the Ag_2O layer is made sufficiently thin by reducing part of it. This model explains the result that, after illumination, the reduction of AgO occurs mainly at more negative potentials, *i.e.*, in this case in the same potential range where the lower oxide Ag_2O is reduced. It should be mentioned again that, in contradiction to the behavior of AgO after illumination, AgO is formed in the dark

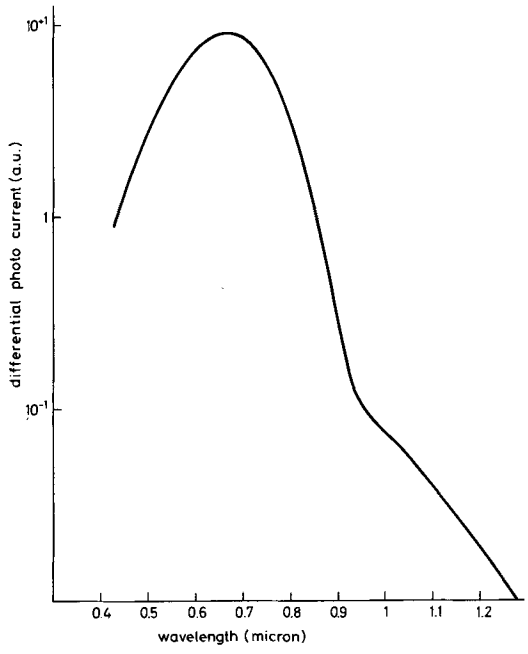

Fig. 7. Spectral distribution of differential photocurrent after formation of an Ag_2O layer on a silver (sheet) electrode. (Electrolyte: 1*N* KOH.)

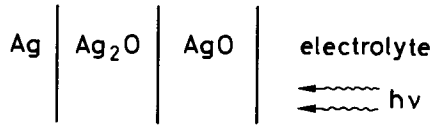

Fig. 8. Schematic structure of a silver-electrolyte interface during and after illumination.

only in those areas (pores) where the Ag_2O layer is rather thin. In this case it is not necessary to reduce some of the Ag_2O prior to the reduction of AgO.

We tried to test this model as follows:

A thin layer (about 0.1μ) of silver was evaporated on a glass plate covered with a conducting transparent SnO_2 layer (see Fig. 9b). Then most of the silver was oxidized electrochemically into Ag_2O. By using such an electrode arrangement with a transparent electrode it is possible to illuminate the Ag_2O from two different directions, through the electrolyte (case I) or through the glass plate (case II). In the first case we would not expect any results different from those ob-

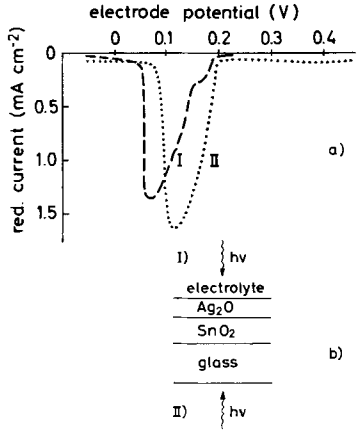

Fig. 9. Reduction current *vs.* electrode potential after anodic formation of an Ag_2O layer on a SnO_2 substrate. These curves were obtained after having illuminated the electrode from two different directions as indicated in the lower part of this figure. (Electrolyte: 1*N* KOH).

tained with solid Ag electrodes. After illumination we observed no reduction of AgO around 0.5V, but only at more cathodic potentials. Following illumination of the Ag_2O from the reverse side (through the glass plate), the reduction of the AgO formed during illumination occurs at more anodic potentials than in the first case, as shown in Fig. 9a. These two experiments differ from each other in so far as the absorption of light within the Ag_2O occurs near the electrolyte if the oxide is illuminated through the electrolyte (case I), whereas the light is absorbed in an oxide region near the SnO_2 layer if the oxide is illuminated through the glass plate (case II). In the latter case AgO is formed in an area adjacent to the silver layer on the SnO_2 surface, *i.e.*, AgO produced in this way is not separated from the Ag by a thick low conducting Ag_2O layer. It should be mentioned, however, that oxidation in this region can only occur if OH^- ions are also available, which may be provided via pores, *i.e.*, the photo-oxidation does occur near the Ag surface but probably only at pores. This argument may also explain the fact that reduction of AgO in case II is still shifted toward cathodic potentials with respect to the reduction following the formation of AgO in the dark.

Potential Dependence of Photocurrent

As mentioned before, an anodic photocurrent was always observed as soon as a thin Ag_2O layer was formed (see Fig. 1). Figure 1b shows the differential photocurrent during growth and reduction of the oxide layers, *i.e.*, Fig. 1b does not really give a defined potential dependence of the differential photocurrent because no equilibrium was achieved. For measuring the potential dependence itself we prepared the Ag_2O layer at first by polarizing the silver electrode at +0.55V for about 10 min. Within this time interval the dark current decreased to a very low value. After having completed the Ag_2O layer in this way we obtained within a certain range a linear dependence between differential photocurrent and electrode potential as shown by curve (a) in Fig. 10. It should be mentioned again that in this experiment also the light intensity was kept so low that further oxidation was negligible. The values of curve (a) were independent of the sweeping direction, *i.e.*, they are stationary values within the potential range 0.22 . . . 0.55V.

According to this result the anodic photo-oxidation, represented by the differential photocurrent in curve (a) in Fig. 10, sets in not only at lower potentials than without illumination but also below the redox potential of Ag_2O/AgO (0.47V). Similar potential shifts were always found with typical semiconductor electrodes (9, 10) and could be explained by the fact that no equilibrium between electrons and holes exists during light excitation. Such a deviation from equilibrium is, of course, relatively large for low conducting materials or if the equilibrium concentration of one type of charge carriers (electrons or holes) is small. Since also in Ag_2O electrons and holes are produced by illumination, at least the density of holes is increased considerably above its equilibrium value in this process.

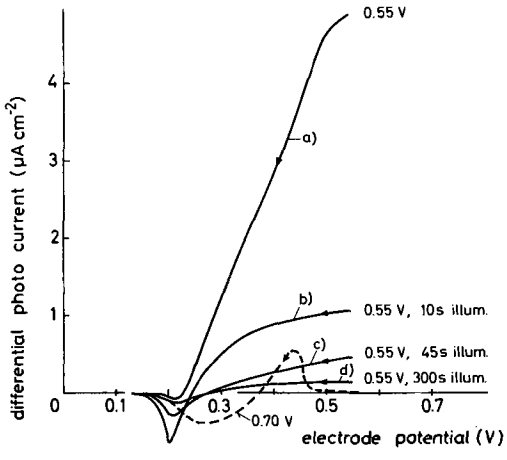

Fig. 10. Differential photocurrent vs. electrode potential after anodic formation of Ag_2O on a silver electrode. (Electrolyte: 1N KOH). (a) Without previous illumination. (b)-(d) After strong illumination at +0.55V. Dotted line: replotted from Fig. 1b.

In further experiments the Ag_2O layer was illuminated with a rather strong light intensity for a certain period of time. As discussed previously, a certain portion of the Ag_2O is transformed into AgO at the Ag_2O/electrolyte interface. Since AgO absorbs visible light, the anodic photocurrents are smaller now as shown by curves (b), (c), and (d) in Fig. 10. In contradiction to the first case [curve (a)], however, a cathodic photocurrent occurs around 0.2V, especially in curve (b). This effect disappears after a long preillumination. This result leads to the conclusion that the reduction process ($AgO \rightarrow Ag_2O$) may be enhanced by light excitation. All differential photocurrents (anodic and cathodic) disappear, however, as soon as the AgO layer filters away too much light.

In the same way the differential photocurrents measured during a complete oxidation-reduction cycle can be interpreted (Fig. 1b). For comparison the photocurrent obtained within the reduction period in Fig. 1b is replotted in Fig. 10 (dotted line).

Conclusion

The experimental results presented in this paper have definitely shown that light absorption by an Ag_2O layer leads directly to anodic oxidation to AgO. It is postulated that holes present in the dark only in negligible concentrations are involved in the oxidation process. Since the over-all reaction rate is controlled by the number of holes at the surface it is considerably enhanced by light excitation. According to our studies with different types of electrodes, the photodecomposition of Ag_2O into silver and oxygen postulated by Göhr (3) has to be excluded.

Moreover, we observed that the reduction of AgO formed during light excitation is inhibited. This result could be interpreted by the fact that this AgO layer was separated from the silver substrate by a rather thick Ag_2O layer of low conductivity. The thickness of the AgO layer is limited by the penetration depth of the exciting light. The inhibition depends slightly on the type of electrode. In the case of very thin porous evaporated silver films the inhibition is somewhat weaker than for silver sheet electrodes.

Acknowledgments

The authors are indebted to Dr. C. W. Berghout, Philips Research Laboratories, Eindhoven, for providing silver single crystals. Thanks are also due to Dr. K. H. Beckmann and Dr. G. Schwandt for stimulating discussions and to Mr. H. Tolle for performing the measurements.

Manuscript submitted Sept. 8, 1969; revised manuscript received ca. Dec. 12, 1969.

Any discussion of this paper will appear in a Discussion Section to be published in the December 1970 JOURNAL.

REFERENCES

1. See, *e.g.*, T. P. Dirkse, *This Journal*, **106**, 453 (1959).
2. J. H. Blocher and A. G. Garrett, *J. Am. Chem. Soc.*, **69**, 1594 (1947).
3. H. Göhr and A. Breitenstein, *Electrochim. Acta*, **13**, 1377 (1968).
4. P. Jones and H. R. Thirsk, *Trans. Faraday Soc.*, **50**, 732 (1954).
5. W. S. Graff and H. H. Stadelmaier, *This Journal*, **105**, 446 (1958).
6. T. P. Dirkse, *ibid.*, **106**, 920 (1959).

7. T. P. Dirkse and G. J. Werkema, *ibid.*, **106**, 88 (1959).
8. M. Le Blanc and N. Sachse, *Phys. Z.*, **32**, 887 (1931).
9. See, e.g., H. Gerischer in "Advances of Electrochemistry and Electrochemical Engineering," Vol. 1, p. 139, P. Delahay, Editor, Interscience Publishers, Inc., New York (1961).
10. R. Memming and G. Schwandt, *Angew. Chem., Intern. Ed. Engl.*, **19**, 833 (1967).

An Unusual 6-Aminopurine Polarographic Wave

Borivoj Janik and Philip J. Elving*

University of Michigan, Ann Arbor, Michigan

ABSTRACT

In addition to a normal four-electron d-c polarographic reduction wave, some 6-amino- and 6-alkylaminopurines, including the biologically important adenine nucleotides, yield a more negative wave of anomalous behavior. The latter wave, which has some of the characteristics of a maximum of the second kind, is primarily due to an enhanced supply of purine as a result of onset of streaming of the solution over the electrode surface; the wave may also involve reduction of the 1,6 C=N bond in the pyrimidine ring which is regenerated by deamination of the initial reduction product. The second d-c polarographic wave of isoguanine is due to catalytic hydrogen evolution. Catalytic hydrogen evolution is a participant in the single voltammetric reduction wave obtained on the HMDE with some derivatives, *e.g.*, adenine and AMP, due to accumulation of reduction product at the electrode surface.

Some 6-amino-substituted purines (1), as well as adenine (6-aminopurine) nucleosides and nucleotides (2) produce at the dropping mercury electrode (DME) under certain conditions, in addition to a normal diffusion-controlled four-electron (4*e*) d-c polarographic reduction wave, a second more negative wave, which can be considered to be unusual or abnormal in the sense that its behavior and current-controlling factors do not follow any common pattern. The few references to such a wave in the literature are mostly in connection with adenine, which is the only 6-substituted purine whose polarographic reduction mechanism and analytical utilization (3-6) have been extensively studied. A postwave, which was eliminated by 0.002% Triton X-100, was observed in adenine solution in *p*H 2-4 chloride and McIlvaine buffers (5, 7). A second wave seen on the background discharge in acidic adenine (8, 9) and adenine 1-N-oxide (10) solutions was ascribed to catalytic hydrogen ion reduction. Whenever the abnormal wave was observed, it was treated as a complicating factor due to its unusual behavior, ill-definition, and interference with the normal wave.

Because of both the intrinsic interest in the odd behavior of the abnormal wave and the necessity of being able to isolate it from and minimize its effect on the normal faradaic wave pattern of the 6-aminopurines, which are among the most important naturally occurring purines as in DNA and RNA, the mechanism of the abnormal wave process was investigated.

Experimental

The chemicals, buffer solutions, apparatus, and procedures were the same as those previously described (1, 2) with the following additions.

Controlled-potential electrolysis was carried out in a three-compartment H-cell, whose main compartment contained a bunch of twelve dropping mercury electrodes as a working cathode, an indicator DME and a 1.0 m*M* adenine solution in *p*H 3.0 McIlvaine buffer. One of the other compartments, which was separated from the main compartment by a Sial No. 4 glass frit, contained a counterplatinum anode in the background solution; the other contained a reference saturated calomel electrode. Nitrogen was bubbled through the main and counterelectrode compartments during electrolysis. A Laboratorni Pristroje LP 60 polarograph and a EZ 2 recorder were used for manual control of potential and for recording of polarographic curves during the course of electrolysis.

Current-time curves were recorded on a Akademie-werkstätten-Berlin GWP 563 polarograph at a chart speed of 10 mm/sec for serial drops from a capillary, whose end was tilted to an angle of 45° (11).

Voltammograms and cyclic voltammograms at the HMDE (hanging mercury dropping electrode) were recorded at polarization rates of 1 to 2 and 100 mV/sec, respectively.

The DME was observed by a laboratory microscope with a 30-fold magnification. Powdered active charcoal was added to the solution examined in an amount just sufficient to indicate streaming of the solution. Accumulation of small bubbles at the capillary orifice indicated hydrogen evolution.

Unless otherwise indicated, measurements were made on 0.5 *M* ionic strength solutions at 25°C.

Abnormal Wave Characteristics

The abnormal wave is generally difficult to define due to its merging with the normal wave and/or background discharge.

Effect of depolarizer nature and concentration.—The abnormal wave has only been observed with purine derivatives having amino or substituted amino groups in the 6-position, *e.g.*, 6-amino- (adenine), 6-methylamino-, 6-hexylamino-, and 6-benzylaminopurines, adenosine-5′-phosphate (AMP), deoxyadenosine-5′-phosphate (dAMP), adenosine-5′-diphosphate (ADP), and adenosine-5′-triphosphate (ATP). 6-Phenylamino- and 6-dimethylaminopurines, adenosine, and deoxyadenosine produce only the normal wave; however, the limiting portion of the latter is often steeply inclined, indicating the presence of an additional faradaic process. Isoguanine (2-hydroxy-6-aminopurine) yields a second more negative wave, whose behavior, as subsequently discussed, differs markedly from that of the abnormal wave. Purine and its 6-methyl- and 6-methoxy- derivatives exhibit no wave in addition to the one or two waves which represent the 4*e* reduction of the 1,6 N=C and 2,3 C=N bonds of the purine ring.

Below 0.1 to 0.2 m*M* depolarizer concentration, the abnormal wave is small and ill-defined, and is usually

* Electrochemical Society Active Member.

seen as an additional contribution on the normal wave limiting portion. With increasing concentration, the abnormal wave height increases relatively more than that of the normal wave; the ratio in pH 3.1 McIlvaine buffer is 1.0, 1.4, and 1.8 in 0.25, 0.50, and 1.00 m*M* adenine, respectively.

Effect of pH, buffer concentration and composition, and ionic strength.—Since the abnormal wave gradually merges with background discharge as the pH decreases or increases, a relatively well-defined limiting portion is usually obtained only between *ca.* pH 2 and 4 to 5 (Fig. 1). The wave exists in a narrower pH region at lower concentrations for some derivatives, *e.g.*, 0.25 m*M* benzylaminopurine exhibits the abnormal wave only in pH 2 chloride buffer.

The half-wave potential, $E_{1/2}$, of the abnormal wave shifts negatively with increasing pH at a rate similar to that of the normal wave for the compound involved (1, 2). Variation of i_l with pH depends on the depolarizer concentration, *e.g.*, i_l increases with increasing pH in 0.50 m*M* solutions and remains practically constant in 0.125 m*M* solutions (Fig. 1). The second isoguanine wave sharply decreases with increasing pH and disappears at *ca.* pH 5; at pH 1, it is about eight times as high as the normal wave.

Formation of the abnormal wave is more favorable in McIlvaine than in acetate buffers, *e.g.*, the wave has been observed in pH 3.9 McIlvaine buffer but not in acetate buffer of the same pH.

In pH 3-4 McIlvaine buffer of 0.1*M* ionic strength, the abnormal wave either is not formed, *e.g.*, below *ca.* 0.5 m*M* adenine, or appears as a nonmeasurable current superposed on the normal wave limiting portion, *e.g.*, adenine and AMP above *ca.* 0.5 and 0.2 m*M*, respectively. With increasing buffer concentration or ionic strength, *e.g.*, on addition of KCl, the abnormal wave gradually increases to a limiting value at ionic strength *ca.* 1; formation of the abnormal wave is less evident with AMP when background concentration is brought up just by adding KCl.

Variation of limiting current with mercury column height.—The variability of plots of i_l *vs.* h, *e.g.*, linear or curved with slopes varying from slightly positive to more or less negative inclination to the h axis, is at least partially due to the ill-definition of the abnormal wave and to the marked change of its shape with h with resulting uncertainty in estimation of i_l. Depending on pH, the abnormal wave more or less merges with background discharge at low h. As h increases, the limiting portion becomes better defined due to a positive shift of the wave, while the background discharge potential does not change. At the same time, the normal wave shifts negatively so that it gradually merges with the abnormal wave; a similar effect occurs when the drop-time is gradually shortened by hitting the capillary.

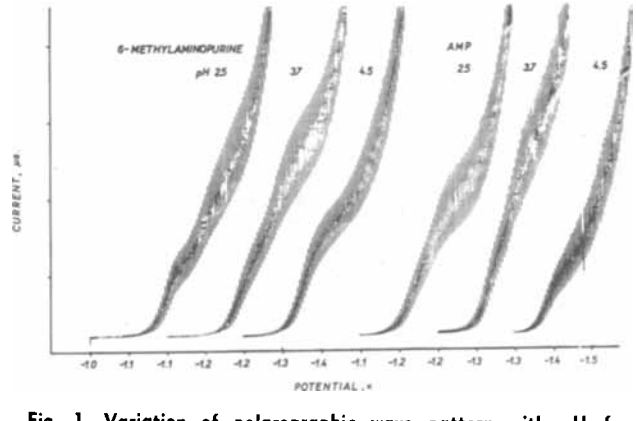

Fig. 1. Variation of polarographic wave pattern with pH for 0.125 mM 6-methylaminopurine and 0.50 mM AMP in McIlvaine buffer (0.5M ionic strength) at 25°C. Current axis: 2.0 μA/division for 6-methylaminopurine and 10 μA/division for AMP.

Effect of temperature.—The temperature coefficient of the abnormal wave in pH 3.0 McIlvaine buffer varies from 4.5 to 9.0% for adenine, 6-methylaminopurine, and AMP, compared to 1.1-2.2% for the normal wave. The abnormal wave is too small at 10°-15° to be measured meaningfully, *e.g.*, in adenine and AMP at 0.5*M* ionic strength, and completely disappears at lower temperatures (Fig. 2), *e.g.*, no indication of it can be seen at 1.5° and 0.1*M* ionic strength.

Effect of surface-active substances.—The abnormal wave given by up to 0.5 m*M* adenine (Fig. 3) and 6-benzylaminopurine is completely eliminated by only 0.0006% Triton X-100. The same is true for other derivatives below *ca.* 0.2 m*M*. At higher depolarizer concentrations, 0.0006% Triton suppresses the abnormal wave by 20-60%, 0.001-0.002% Triton almost completely eliminates it but at the same time decreases the normal wave by 10-20%, and higher Triton concentrations distort the wave shapes. In general, Triton is more effective at higher pH and lower depolarizer concentration, and in such situations where only an additional current is superimposed on the normal wave limiting portion, where the normal and abnormal waves are relatively well separated and where the latter wave merges with the background discharge.

Other surface-active substances are also effective, *e.g.*, less than 0.002% agar completely eliminates the abnormal wave of 0.5 m*M* adenine in pH 3.0 McIlvaine buffer.

Current-time curves.—At potentials on the rising part of the abnormal wave, the parabolic character of the i-t curves on a single drop is gradually distorted as the potential becomes more negative; the distortion, which is pronounced on the limiting portion of the wave, is abrupt with adenine and 6-methylaminopurine and less apparent with AMP.

Microscopic observation of mercury electrodes.—Streaming of the solution past the DME surface is observable at potentials starting at the foot of the abnormal wave, *e.g.*, for adenine, 6-methylaminopurine

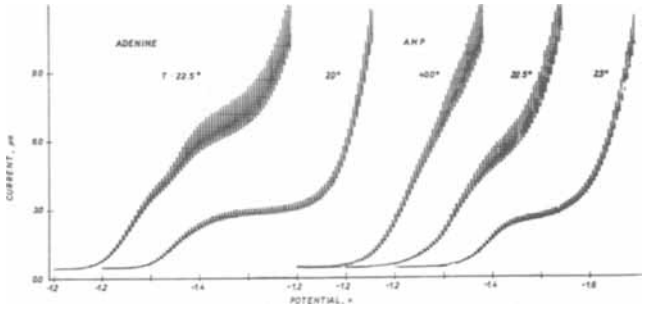

Fig. 2. Effect of temperature on polarographic wave pattern for 0.5 mM adenine and 0.50 mM AMP in pH 3.2 McIlvaine buffer (0.5M ionic strength) at 25°C.

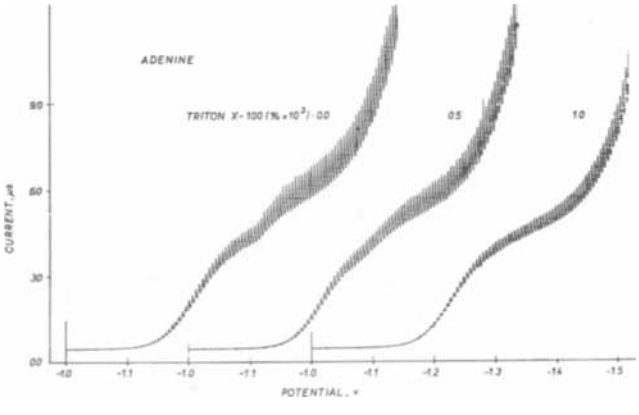

Fig. 3. Effect of Triton X-100 concentration on polarographic wave pattern for 0.25 mM adenine in pH 3.0 McIlvaine buffer (0.5M ionic strength) at 25°C.

and AMP solutions, or, where the abnormal wave is absent, *e.g.*, with adenosine, at the foot of the background discharge. No or only negligible streaming occurs at potentials on the normal and second isoguanine waves. The direction of the streaming is from the bulk solution to the bottom of the DME, over the mercury surface to the top of the drop and from there back to the bulk solution. The streaming is more intense as the potential becomes more negative and diminishes with decreasing h. Addition of 0.002% Triton to 0.5 m*M* adenine at pH 3.0 eliminates the abnormal wave, while the intensity of the streaming is only lowered by a third.

On the hanging mercury drop electrode, HMDE, where only the normal wave appears, streaming does not occur in 0.5 m*M* adenine even at constant potentials on the background discharge.

Hydrogen evolution is not observed at the DME until the background discharge is reached even in saturated, *i.e., ca.* 6 m*M*, solutions of adenine and AMP at pH 2-5, while it occurs on the HMDE at constant potentials at the foot of the normal wave.

Behavior on the HMDE.—Adenine, 6-methylaminopurine, and AMP produce at pH 2.5-4 only a single cathodic wave on single-sweep voltammograms and a single cathodic peak on cyclic voltammograms. $E_{1/2}$ of the wave and E_p of the peak are up to 30 and 100 mV, respectively, more negative than $E_{1/2}$ of the normal DME wave under similar conditions; the difference becomes smaller with decreasing pH. The voltammetric wave is ill-defined due to merging with background discharge; on the second and subsequent runs at the same drop in unstirred solution, $E_{1/2}$ shifts more negatively and the background discharge more positively so that the wave finally disappears. Cyclic voltammograms of isoguanine in pH 2.5 McIlvaine buffer exhibit two peaks, whose E_p are *ca.* 100 mV more negative than $E_{1/2}$ of the corresponding DME waves.

Electrolysis of adenine.—The ratio of the adenine normal and abnormal heights during controlled potential electrolysis at pH 3 at a potential on the crest of the normal wave approximately equals that found for corresponding concentrations in fresh solution. $E_{1/2}$ of the normal wave and, even more so, of the abnormal wave shift more negatively during electrolysis with the abnormal wave consequently merging with background discharge; the potential of the latter may shift up to 30 mV more positively during electrolysis.

Nature of the Electrode Process

The experimental data concerning the nature and origin of the abnormal wave are equivocal in the sense that several possible processes are more or less both supported and refuted. Consequently, decision has to be made on the basis of the relative merits of the evidence and the implications that can be drawn from it.

The possibilities of the abnormal wave being a diffusion-controlled wave or an adsorption postwave involving the oxidized form of the depolarizer are eliminated by the concentration, h, and temperature dependences, and by the i-t curves [*cf.* ref. (12)]; the wave height is several times higher than would be expected for an adsorption wave (12, 13) and the depolarizers are strongly adsorbed only at potentials about 0.7V more positive than those of the reduction (1, 2).

Maximum of the second kind.—Streaming of the solutions as well as the direction of such streaming at the DME at potentials on the abnormal wave strongly indicate that the latter is a maximum of the second kind (13, 14). Corroborative evidence is afforded by the following: (*a*) the wave decreases in height and finally disappears with decreasing ionic strength and buffer concentration, (*b*) the wave height shows a high temperature coefficient, (*c*) surfactants suppress the wave, and (*d*) streaming diminishes on lowering h and does not occur at the HMDE. Two aspects of the behavior of the wave indicate that it may not involve a common maximum of the second kind: (*a*) streaming can continue, only moderately diminished, when the wave is completely suppressed by Triton addition, and (*b*) i_l is not proportional to h. The latter is not too decisive an argument since it is difficult to measure i_l precisely.

Catalytic hydrogen evolution.—Although some features of the abnormal wave support participation of a catalytic hydrogen evolution (15), *e.g.*, location near or on the background discharge, effect of surfactants, increase of wave height with increasing buffer concentration, and shift to more negative potential with increasing pH, the bulk of the evidence is not consistent with an appreciable contribution from a catalytic hydrogen process (13, 15), *e.g.*, the wave shifts to more negative potential with increasing depolarizer concentration and its height increases with increasing pH or is, at least, pH-independent and varies from a fraction to twice that of the normal (4*e*) wave. A catalytic hydrogen wave involving the purine species as participant would normally be expected to decrease with increasing pH and to have a height which is many times that of a corresponding diffusion controlled wave (13, 15), *e.g.*, in pH 3 buffer containing 1 m*M* purine, it would be expected to be several times the height of the 4*e* purine wave; actually, it is only 1.8 times that height. Furthermore, even though the normal adenine wave, due to its behavior, was postulated to contain a catalytic hydrogen component (3), hydrogen evolution was not observed on the DME at potentials more positive than that of the background discharge.

The oxidized and reduced forms of most purine derivatives, as well as the degradation products of the latter, shift the background discharge to more positive potential, *e.g.*, the shift, whose magnitude increases with pH and depolarizer concentration (2, 3), occurs even at pH where the purine derivative is not reduced (1, 2, 3) and in solutions where adenine has been completely electrolyzed (3). The shift, which has been ascribed to catalytic evolution of hydrogen (3), could interfere with the abnormal wave. However, hydrogen evolution seems to be negligible in the abnormal wave at the DME; its presence at the foot of the normal wave at the HMDE is most probably due to accumulation of reduction product at the electrode surface which promotes the catalytic reduction of hydrogen ion and makes the reduction of purine more difficult (13).

The second isoguanine wave, which markedly differs from the abnormal wave, *e.g.*, in having a counterpart on cyclic voltammograms at the HMDE and in exhibiting no streaming at the DME, is probably a catalytic hydrogen wave, as indicated by its being several times higher than the normal wave, decreasing sharply with increasing pH, and being proportional to h.

Deamination reaction.—As previously mentioned, the abnormal wave has been observed only with purines having an amino or substituted amino group in the 6-position. Exhaustive electroreduction of 6-aminopurine (adenine) at a mercury pool electrode is a 6*e* process, involving reduction of the 1,6 and 2,3 double bonds, deamination at the 6-position and reduction of the regenerated 1,6 double bond (3). Since deamination is slower than the electrochemical steps (3, 16), it does not proceed appreciably under polarographic conditions at potentials less negative than the crest of the normal adenine reduction wave (3). However, deamination may be promoted by the electrostatic attraction of the protonated reduction site to the electrode and, consequently, could occur at the more negative potentials, where the abnormal wave is observed. Current resulting from reduction of the regenerated 1,6 C=N bond may thus be involved at the abnormal wave. Moreover, deamination as well as subsequent hydrolysis of the reduction product may result in local concentration and charge gradients and, consequently, in surface tension differences, which, in turn, may

promote streaming of the solution over the DME surface.

Conclusions

The results of exhaustive electrolysis of adenine indicate either that the abnormal wave is associated only with the oxidized form of adenine or that the reduced adenine decomposes sufficiently rapidly that it does not accumulate and, consequently, does not contribute appreciably to the abnormal wave process; degradation products of reduced adenine evidently also do not contribute to the abnormal wave current.

The supply of depolarizer for the abnormal wave process is, therefore, essentially due to an increased transport of the oxidized form of the purine to the DME as a result of streaming at the potentials where the abnormal wave is seen. Simultaneous creation of a depolarizer via a chemical reaction involving restoration of the reducible 1,6 double bond through deamination, may also be a contributing factor in the abnormal wave current.

Although data for the normal purine reduction wave obtained in the presence and absence of the abnormal wave are essentially identical, the proximity of the two waves makes data for the normal wave obtained in absence of the abnormal wave more accurate. Consequently, it is recommended that in future electrochemical studies of 6-aminopurines and their derivatives the complicating presence of the abnormal wave be avoided by the use of low ionic strength solutions and low temperature; an ionic strength of 0.1*M* and temperature below 5°C are recommended.

Alternatively, if it is desired to use solutions of 0.5*M* ionic strength at 25° or the equivalent, the concentration of the electroactive species should not exceed 0.1 m*M*. Thus, in a study (17) of oligonucleotides the abnormal wave was not clearly indicated with ApA, $(Ap)_3A$, and $(Ap)_5A$ and with dinucleotides containing the adenine moiety, apparently due to the low concentrations employed (*ca.* 0.05 m*M*) and to a marked positive shift of background discharge, especially with ApG and GpA.

Acknowledgment

The authors thank J. Volke and M. Heyrovsky of the Heyrovsky Polarographic Institute in Prague for fruitful discussion, and the National Science Foundation and The University of Michigan Cancer Research Institute for helping to support the work described.

Manuscript received Sept. 24, 1969.

Any discussion of this paper will appear in a Discussion Section to be published in the December 1970 JOURNAL.

REFERENCES

1. B. Janik and P. J. Elving, *This Journal*, **116**, 1087 (1969).
2. B. Janik and P. J. Elving, *J. Am. Chem. Soc.*, **92**, 235 (1970).
3. D. L. Smith and P. J. Elving, *ibid.*, **84**, 1412 (1962).
4. M. Brezina and P. Zuman, "Polarography in Medicine, Biochemistry and Pharmacy," p. 338, Interscience Publishers, New York (1958).
5. D. L. Smith and P. J. Elving, *Anal. Chem.*, **34**, 930 (1962).
6. P. J. Elving, W. A. Struck, and D. L. Smith, *Mises Point Chim. Anal. Org. Pharm. Bromatol.*, **14**, 141 (1965).
7. D. L. Smith, Ph.D. Thesis, The University of Michigan, 1962.
8. W. Leyko and H. Panusz, *Bull. soc. sci. lettres Lodz, Classe III*, **5**, No. 2, 1 (1954).
9. W. Leyko and H. Panusz, *Polski tig. lekarski*, **9**, 1057 (1954).
10. C. R. Warner and P. J. Elving, *Collection Czech. Chem. Commun.*, **30**, 4210 (1965).
11. J. Kůta and I. Smoler in "Progress in Polarography," Vol. 1, p. 43, P. Zuman and I. M. Kolthoff, Editors, John Wiley & Sons, New York (1962).
12. L. Meites, "Polarographic Techniques," John Wiley & Sons, New York (1967).
13. J. Heyrovsky and J. Kůta, "Principles of Polarography," Czechoslovak Academy of Sciences, Prague (1965).
14. J. Proszt, V. Cieleszky, and K. Györbiro, "Polarographie," Akademiai Kiado, Budapest (1967).
15. S. G. Mairanovskii, *J. Electroanal. Chem.*, **6**, 77 (1963).
16. A. V. Kotel'nikova and V. V. Solomatina, *Biokhimiya*, **30**, 816 (1965).
17. B. Janik and P. J. Elving, Work in progress.

A Ring-Disk Study of HOBr Formation at Platinum Electrodes in 1.0*M* H_2SO_4

D. C. Johnson*

Department of Chemistry, Iowa State University, Ames, Iowa

and Stanley Bruckenstein*

Department of Chemistry, State University of New York at Buffalo, Buffalo, New York

ABSTRACT

The rotating ring-disk electrode (RRDE) was used to study the oxidation of Br^- at platinum electrodes in 1.0*M* H_2SO_4 supporting electrolyte. In addition to the electrochemical oxidation of Br^- to Br_2 by a convective-diffusion controlled reaction, a small amount of HOBr was produced by oxidation of adsorbed Br^- with concurrent oxidation of the platinum electrode surface. Bromide does not adsorb at an anodized platinum surface, whereas adsorption is very rapid at a reduced platinum surface. The equilibrium surface coverage by Br^- corresponds to a monolayer for bulk concentrations of KBr greater than $4.5 \times 10^{-3}M$.

The purpose of this research was to study the formation of positive oxidation states of bromine at a platinum electrode in 1.0*M* H_2SO_4. No study of such a process is to be found in the literature even though the oxidation of iodine to higher oxidation states at a platinum electrode has been discussed by many authors. A review of this literature is given by Beran and Bruckenstein (1).

Many investigators have studied the Br_2/Br^- couple at platinum electrodes with the primary ob-

* Electrochemical Society Active Member.

jective of determining the electrode mechanism (2-5). The standard reduction potential for the reaction

$$Br_2 + 2e = 2Br^- \quad [1]$$

is +0.841V (*vs.* SCE) (6).

The two most likely higher oxidation states which might be produced in 1.0*M* H_2SO_4 at a platinum electrode appear to be HOBr and BrO_3^- whose standard reduction potentials are (6)

$$HOBr + H^+ + e \rightleftharpoons 1/2\,Br_2 + H_2O, \quad E^\circ = 1.34V \text{ (SCE)} \quad [2]$$

$$HOBr + H^+ + 2e \rightleftharpoons Br^- + H_2O, \quad E^\circ = 1.09V \text{ (SCE)} \quad [3]$$

$$BrO_3^- + 6H^+ + 5e \rightleftharpoons 1/2\,Br_2 + 3H_2O, \quad E^\circ = 1.27V \text{ (SCE)} \quad [4]$$

$$BrO_3^- + 6H^+ + 6e \rightleftharpoons Br^- + 3H_2O, \quad E^\circ = 1.20V \text{ (SCE)} \quad [5]$$

Our experimental results indicate that a limited amount of HOBr can be produced by oxidation of adsorbed bromide at a platinum electrode in 1.0*M* H_2SO_4 via a surface controlled process and that no detectable amounts of BrO_3^- are produced.

Experimental

Instrumentation.—The ring-disk electrode used in this research was constructed by Pine Instruments of Grove City, Pennsylvania. The electrode dimensions are given in Table I of ref. (7) where the electrode is designated as electrode B. For this electrode $\alpha = 0.089$, $\beta^{2/3} = 0.151$, and $N = 0.090$, the area of the disk is 0.470 cm^2.

The four electrode potentiostat was constructed according to a design given previously (8) using an Analog Device 303 Operational Amplifier as the reference potential follower, F-1 in Fig. 1 of ref. (8), and Analog Devices 108 Operational Amplifiers in the remainder of the circuit. Current potential (*I-E*) curves were recorded using an EAI, X-Y-Y', 1130 Variplotter.

Most experimental work was performed at 25° ± 1°C, although the determination of the diffusion coefficient of Br^- in 1.0*M* H_2SO_4 was made at 25.0° ± 0.2°C. Except for instances when bromide was present in the supporting electrolyte, air was removed from the solution with Air Products', high purity (99.999%) nitrogen which was presaturated with H_2O, and a nitrogen atmosphere was maintained above the solution.

The counterelectrode was a platinum wire coil placed in a fritted glass compartment containing 1.0*M* H_2SO_4. The reference electrode was a Beckman, Fiber-Junction, SCE in electrical contact with the solution through a Luggin capillary, containing a saturated KNO_3 solution. The tip of the Luggin capillary was placed about 2 mm from the surface of the rotating electrode, normal to the Teflon between the ring and disk electrodes. All potentials were measured and are reported in volts *vs.* the SCE.

Chemicals.—All chemicals used were Mallinkrodt Analytical Reagent grade. Solutions were prepared using triply distilled water, with the second distillation being from alkaline permanganate solution.

A stock solution of HOBr (approximately 0.2*M*) was prepared according to a procedure similar to those described in ref. (9-11). An excess of Br_2 was added to a mixture of approximately 0.01*M* HNO_3 and silver acetate. The hydrolysis reaction of Br_2 produces Br^- and HOBr, and the reaction is made complete by the precipitation of Br^- as AgBr. The precipitate was separated by filtering and the excess Br_2 removed by bubbling with nitrogen. The presence of HNO_3 aided coagulation and separation of the AgBr precipitate. The HOBr was used approximately 2 hr after preparation.

Notation.—The subscripts d and r to symbols for current, *I*, and potential, *E*, represent the corresponding quantities at the disk and ring electrodes, respectively. The subscript *l*, used with symbols I_d and I_r, signifies that the designated quantity corresponds to the convective-diffusion limited value. The superscripts *a* and c used only with the symbol E_d define the extreme anodic (+) and cathodic (−) disk electrode potentials used in obtaining the particular *I-E* curve. Cathodic current is considered as a positive and anodic current as a negative quantity. All electrical currents are given in microamperes.

Results and Discussion

I_d-E_d curves of Br^-.— Figure 1 shows I_d-E_d curves obtained in a 1.0*M* H_2SO_4-3.3 × 10^{-4}*M* KBr solution. E_d was scanned between $E_d^c = -0.20$V and the E_d^a-value specified until no change in the I_d-E_d curve was observed with continued potential scans. For [KBr] > 1 × 10^{-4}*M*, no change in the *I-E* curve was observed after the second cyclic potential scan. E_d^a was varied from 1.00 to 1.40V by 0.10V increments and a final curve was obtained for $E_d^a = 1.60$V. Three anodic waves were obtained with apparent $E_{1/2}$ values of 0.90V, 1.06V, and 1.24V. These waves are designated A, B, and C, respectively, for discussion purposes. The observed $E_{1/2}$ for wave A of 0.90V is in agreement with data presented in ref. (4) and (12) for the oxidation of Br^- to Br_2 in a similar solution and we conclude that wave A is due to the oxidation of Br^- to Br_2. The small reduction peak, *D*, obtained on the cathodic scan, $E_{peak} = 0.9$V, disappears at faster rotation speeds and/or slower E_d scan rates, and we conclude it is caused by reduction of Br_2 present in the convective-diffusion layer adjacent to the electrode.

The reduction peak E, $E_{peak} = 0.5$V, is also observed in the absence of Br^- (12, 13) and is caused by the electrochemical reduction of the oxidized platinum electrode surface. In Br^--free 1.0*M* H_2SO_4, electrode oxidation occurs if $E_d^a > 0.65$V (12, 13). Figure 1 shows that peak E is obtained in this solution only if $E_d^a > 1.0$V. Hence, electrode oxidation does not occur until the electrode surface concentration of Br^- is zero, *i.e.*, until I_d equals the convective limiting current for Br^- oxidation to Br_2, $I_{d,l}$ ($Br^- \rightarrow Br_2$). As E_d^a increases beyond 1.0V, the height of peak E at 0.5V increases, thus electrochemical oxidation of the platinum disk

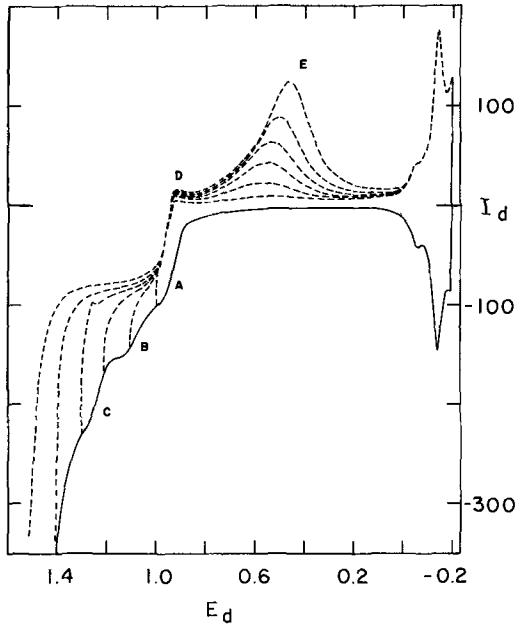

Fig. 1. I_d-E_d *vs.* E_d^a; 1.0*M* H_2SO_4-3.3 x 10^{-4}*M* KBr, 400 rpm, E_d scan rate = 6.0 V min^{-1}, ——— anodic E_d scan, - - - - cathodic E_d scan.

electrode surface occurs concurrently with the processes associated with waves B and C. The inhibition of platinum oxidation by halide ions in acidic media is attributed to halide adsorption at the electrode surface (12, 14).

The shape of the I_d-E_d curves in the potential region $E_d < 0.1$V has been discussed and the cathodic and anodic processes are identified as the formation and dissolution of molecular hydrogen, respectively (12).

I_d-E_d curves were also obtained while holding the electrode stationary, Fig. 2, in 1.0M H_2SO_4-1.0 $\times$ $10^{-3}M$ KBr. The appearance of a reduction peak, F, at 1.15V on the cathodic E_d scan indicates that wave C involves the production of a soluble electroactive species other than Br_2, possibly a higher oxidation state of bromine such as HOBr or BrO_3^-. There is no evidence that wave B corresponds to any reaction other than oxidation of the electrode surface.

I_d-E_d curves were obtained at 400 rpm in the solution used for Fig. 1 as a function of E_d scan rates from 2-10V min^{-1}. These curves showed that, after correcting for double layer charging current, wave A was independent of E_d-scan rate, while the heights of waves B and C increased in approximately a linear manner with increasing E_d scan rate. These results suggest that waves B and C correspond to surface controlled reactions since the magnitude of convective-diffusion limiting currents are independent of E_d scan rate.

I_d-E_d curves were obtained at 400 rpm in a solution identical to that for Fig. 1 for $E_d{}^a = 1.60$V and varying $E_d{}^c$ from -0.20 to $+0.80$V. Differences in the I-E curves in the region of $E_d > 0.80$V obtained for $-0.20\text{V} < E_d{}^c < 0.40\text{V}$ were negligible. For $E_d{}^c > 0.60$V, however, the height of waves B and C decreased. Waves B and C disappeared for $E_d{}^c \geq 0.80$V. Note that for $E_d{}^c \geq 0.80$V, platinum oxide formed at the electrode surface for $E_d > 1.0$V is not reduced during the cathodic portion of the potential cycle. The magnitude of wave A at 1.0V was not affected by variation of $E_d{}^c$. On the basis of these results and the observation in Fig. 1 that $I_d = I_{d,l}$ ($Br^- \rightarrow Br_2$) during the cathodic E_d scan for $1.0 < E_d < 1.4$V, we conclude that the disk electrode reaction resulting in the production of peak F of Fig. 2 is controlled by surface changes at the disk electrode which occur simultaneously with the electrode surface oxidation.

Diffusion coefficient for Br^- *in 1.0M* H_2SO_4.—Values of $I_{d,l}$ ($Br^- \rightarrow Br_2$), wave A, were measured as a function of [KBr] (2, 3, 4, and 5 $\times$ $10^{-4}M$) and rotation speed (400-10,000 rpm) for an E_d scan rate of 0.5V min^{-1}. At this slow scan rate the heights of waves B and C were negligible in comparison to that of wave A. Plots of $I_{d,l}$ *vs.* $\omega^{1/2}$ measured at $E_d = 1.15$V were linear with zero intercepts over the entire range of concentrations. The diffusion coefficient of Br^-, D_{Br^-}, was calculated from each slope using the Levich equation for convective diffusion limited currents (15). The average of 16 slope measurements yielded $D_{Br^-} = (1.58 \pm 0.06) \times 10^{-5}$ cm^2 sec^{-1}.

Ring-disk studies in KBr solutions.—I_r-E_d curves were recorded simultaneously with I_d-E_d curves in 1.0M H_2SO_4-3.3 $\times$ $10^{-4}M$ KBr solution, in the manner described previously (7, 8), for $E_d{}^a = 1.60$V and $E_d{}^c = -0.20$V. E_r was varied from 0.00 to 1.30V by 0.10V increments. I_r-E_d curves for three values of E_r are shown in Fig. 3.

The I_r-E_d curves obtained for $0.20\text{V} \geq E_r \leq 0.70$V were identical, those for $E_r = 0.80$V and 0.90V were identical as were the curves for $1.10\text{V} \leq E_r \leq 1.30$V. I_r-E_d curves obtained for E_r in the vicinity of the $E_{1/2}$ for the reaction described in Eq. [1] varied qualitatively in the expected manner for a slightly irreversible process (16). The I_r-E_d curve obtained for $E_r = 0.10$V and 0.00V were identical to that for $E_r = 0.40$V except that the ring current increased sharply for $E_d > 1.4$V due to the ring electrode reduction of oxygen produced at the disk electrode. The ring current observed at $E_d = 1.10$V for $E_r = 0.40$V results from the reduction of the Br_2 produced at the disk electrode to Br^- (wave A). The experimental collection efficiency at $E_d = 1.1$V calculated from Fig. 3 and the I_d-E_d curve obtained simultaneously, $N_{exp} = -I_r/I_d$, is 0.090 in satisfactory agreement with the theoretical collection efficiency for this electrode.

In Fig. 3, peak P corresponds to a soluble, electrochemically reducible species which was detected at the ring electrode, for $E_r = 0.40$V and 0.80V, coincident with the appearance of wave C at the disk electrode. When the cathodic E_d-scan was reversed at $E_d{}^c = 0.80$V, peak P was not obtained and $I_r = -NI_{d,l}$ ($Br^- \rightarrow Br_2$) for $E_d > 1.0$V on both the anodic and cathodic E_d scans in agreement with results discussed above for wave C at the disk electrode.

For $E_r = 1.20$V, the ring current observed at $E_d < 0.9$V is equal to $\beta^{2/3}$ times $I_{d,l}$ ($Br^- \rightarrow Br_2$) in the absence of complicating reactions at the disk electrode, *e.g.*, Br^- adsorption (16). For $E_d = 1.1$V and $E_r = 1.2$V, $I_r = (\beta^{2/3} - N)$ times $I_{d,l}$ ($Br^- \rightarrow Br_2$) (16).

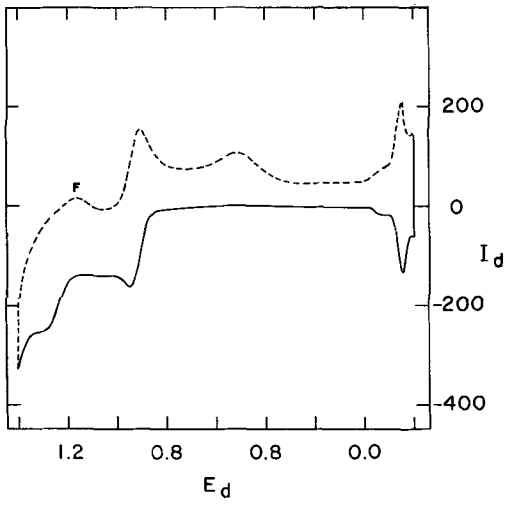

Fig. 2. I_d-E_d; 1.0M H_2SO_4-1.0 x 10^{-3}M KBr, 0 rpm, E_d scan rate = 6.0 V min^{-1}, ——— anodic E_d scan, - - - - cathodic E_d scan.

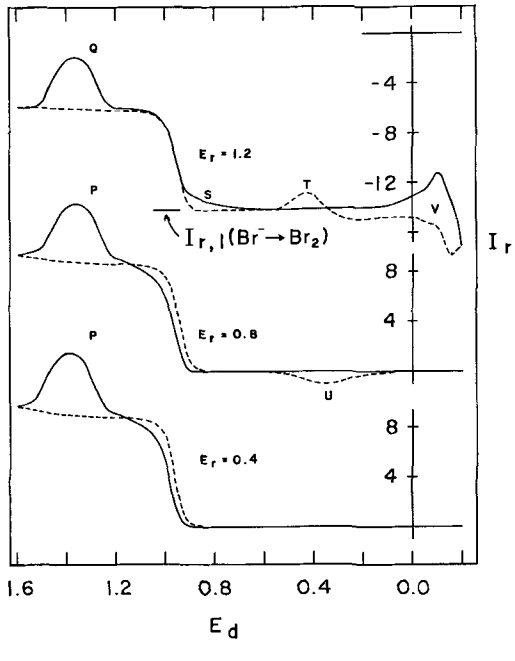

Fig. 3. I_r-E_d *vs.* E_r; 1.0M H_2SO_4-3.3 x 10^{-4}M KBr, 400 rpm, E_d scan rate = 6.0 V min^{-1}, ——— anodic E_d scan, - - - - cathodic E_d scan.

An additional current decrease, peak Q, occurs in this experiment for 1.2V < E_d < 1.5V on the anodic E_d scan (region of wave C). This peak wave was not obtained if $E_d^c \geq 0.80$V.

Figure 2 shows that the electroactive species generated at the disk electrode during wave C is reduced for E_d < 1.2V. Since as stated above, the I_r-E_d curves obtained for E_r = 1.10V and 1.30V are identical, the supposed positive oxidation state of bromine produced at the disk electrode during wave C does not reach the ring electrode during this experiment and undergoes a homogeneous decomposition in the electrode diffusion layer. A reaction sequence which is consistent with the data discussed above pertaining to wave C is

(disk electrode, surface controlled)

$$H_2O + Br^- \rightleftharpoons HOBr + H^+ + 2e \quad [6]$$

and/or

$$H_2O + 1/2Br_2 \rightleftharpoons HOBr + H^+ + e \quad [7]$$

(solution, diffusion layer)

$$HOBr + Br^- + H^+ \rightleftharpoons Br_2 + H_2O \quad [8]$$

(ring electrode)

$$Br_2 + 2e \rightleftharpoons 2Br^- \ (E_r < 0.9V) \quad [9]$$

$$Br^- \rightleftharpoons Br_2 + 2e \ (E_r > 0.9V) \quad [10]$$

The equilibrium constant for reaction [8] has been calculated to be 1.7 × 10^8 (17). Thus, in 1.0*M* H_2SO_4, this reaction lies far to the right at equilibrium. The proposed reaction sequence is consistent with the experimental results shown in Fig. 3 provided reaction [8] is very fast. Eigen and Kustin calculated the rate constant for the hydrolysis of Br_2, the reverse of reaction [8], as 110 sec^{-1} (18). We calculate the rate constant for the forward direction of reaction [8] to be 1.9 × 10^{10} M^{-2} sec^{-1}, fast on the time scale of this experiment.

The above reaction sequence is also in agreement with the results shown in Fig. 2. For E_d > 1.0V, the surface concentration of Br^- is zero and any HOBr present at the electrode surface cannot undergo reaction according to reaction [8] and will subsequently be reduced to Br_2 during the cathodic E_d scan at E_d < 1.2V.

We have excluded the possibility that BrO_3^- is formed as a product of wave C because: (*i*) BrO_3^- does not react rapidly with Br^- in 1.0*M* H_2SO_4 acid to form Br_2, (19), and (*ii*) BrO_3^- is not electrochemically reduced in 1.0*M* H_2SO_4 at potentials more positive than 0.2V in the presence of Br^- or Br_2.

I_d-E_d curves of HOBr *in 1.0M* H_2SO_4.—I_d-E_d curves were obtained for a solution of 1.0*M* H_2SO_4-9 × 10^{-4}*M* HOBr, Fig. 4. These curves show the expected two-step reduction wave corresponding to the one electron reductions of hypobromite to bromine and that of bromine to bromide. HOBr is reduced for E_d < 1.2V, a result which is consistent with our proposal that the product of wave C is HOBr.

I-E curves of Br_2 *in 1.0M* H_2SO_4.—Figure 5 shows a I_d-E_d curve obtained at the stationary disk electrode in 1.0*M* H_2SO_4-2 × 10^{-4}*M* Br_2. The curve shown is the "reproducible" curve observed after five cyclic E_d scans. Again three waves are formed in the anodic region of E_d > 0.8V corresponding to the oxidation of Br^- (produced during the previous cathodic scan) to Br_2, the initiation of platinum surface oxidation and production of HOBr. On the cathodic portion of the E_d scan, peaks are observed for HOBr reduction (E_{peak} = 1.15V), Br_2 reduction (E_{peak} = 0.95V), surface oxide reduction (E_{peak} = 0.50V), and oxygen reduction (E_{peak} = 0.2V). Reversing the potential scan at E_d^c = 0.80V produced a subsequent I_d-E_d curve showing no production or reduction of HOBr, consistent with results considered above.

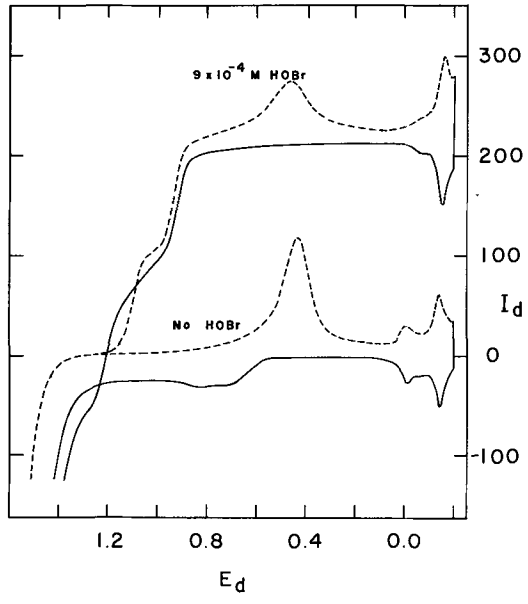

Fig. 4. I_d-E_d; 1.0M H_2SO_4-0M, 9 x 10^{-4}M HOBr, 400 rpm, E_d scan rate = 3.0 V min^{-1}, ——— anodic E_d scan, - - - - cathodic E_d scan.

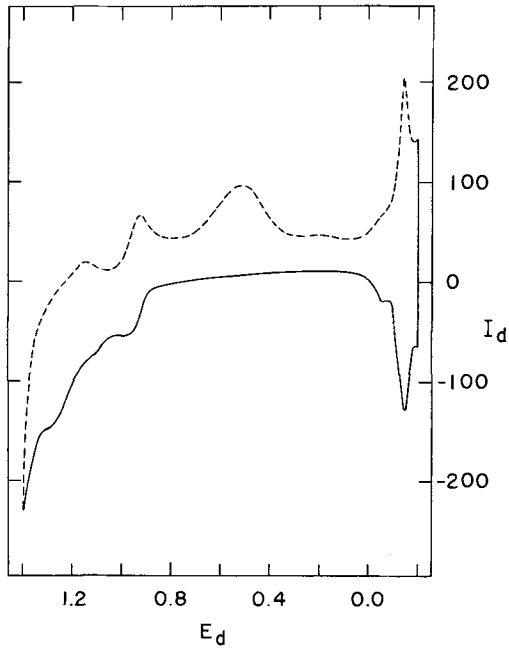

Fig. 5. I_d-E_d; 1.0M H_2SO_4-2 x 10^{-4}M Br_2, 0 rpm, E_d scan rate = 6.0 V min^{-1}, ——— anodic E_d scan, - - - - cathodic E_d scan.

I_r-E_d curves were obtained at 400 rpm in 1.0*M* H_2SO_4-1 × 10^{-4}*M* Br_2 for E_d^a = 1.60V and E_d^c = −0.20V varying E_r from 0.20 to 1.40V by 0.10V increments. I_r-E_d curves for four values of E_r are shown in Fig. 6. The curves recorded for 0.30V ≤ E_r ≤ 0.50V were identical to each other as were those for 0.60V ≤ E_r ≤ 0.80V, those for E_r = 1.0 and 1.1V, and those for E_r > 1.2V. The curve found with E_r = 0.20V showed the reduction of oxygen produced at the disk for E_d > 1.4V.

Note that no ring current peak is observed in the E_d region of wave C for E_r = 1.20V. The absence of peak R is in accord with the proposed reaction sequence, since the bulk concentration of Br^- is zero in this solution. HOBr produced at the disk electrode does not undergo rapid homogeneous reaction in the solution adjacent to the disk electrode, in the absence of Br^-, and will be transported by convective-diffu-

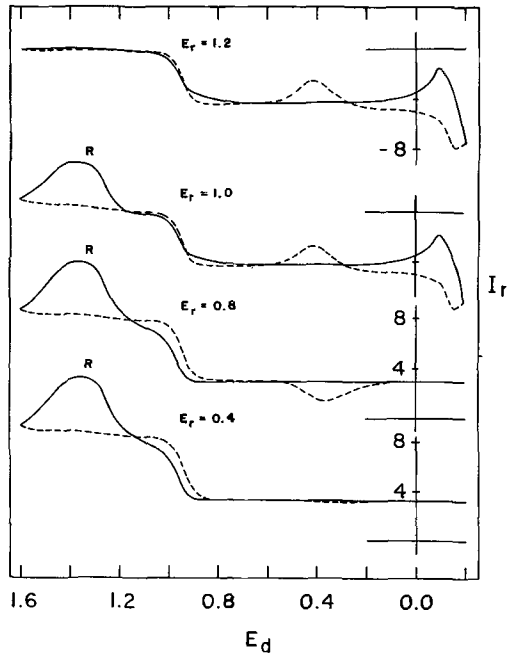

Fig. 6. I_r-E_d vs. E_r; 1.0M H_2SO_4-1 x 10^{-4}M Br_2, 400 rpm E_d scan rate = 6.0 V min^{-1}, ——— anodic E_d scan, - - - - cathodic E_d scan.

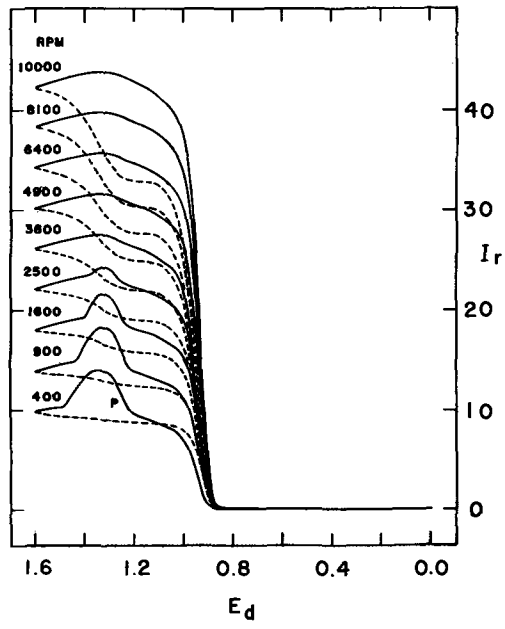

Fig. 7. I_r-E_d vs. rpm; 1.0M H_2SO_4-3.3 x 10^{-4}M KBr, E_d scan rate = 6.0 V min^{-1}, ——— anodic E_d scan, - - - - cathodic E_d scan.

sion to the ring electrode where it will be reduced as peak R.

On the basis of the reaction sequence proposed in the above discussion, it would seem that peak R for the collection of the HOBr at E_r = 0.8V should be twice as great as observed at E_r = 1.0V. The conclusion would follow since at E_r = 1.0V, HOBr is reduced to Br_2 at the ring while for E_r = 0.8V it is reduced to Br^-. Comparison of the areas for peak R obtained at the same time as wave C shows the area at E_r = 0.8V is only about 30% greater than that at E_r = 1.0V. This discrepancy probably arises because Br^- is formed at the ring electrode at E_r = 0.8V and some of the HOBr from the disk reacts with this Br^- to produce Br_2 in the solution adjacent to the ring electrode. The fraction of this Br_2 ultimately collected at the ring electrode will be less than unity, hence the total ring current will be less than that predicted by the disk current and the theoretical collection efficiency.

Effects of variation of electrode rotation speed.—Figure 7 shows I_r-E_d curves obtained in 1.0M H_2SO_4-3.3 x 10^{-4}M KBr for 400 ≤ rpm ≤ 10,000. The ring electrode peak current, P, corresponding to wave C decreases in area with increasing rotation speed. Also the difference between the limiting ring electrode collection current at E_d = 1.1V for the anodic and cathodic E_d scans increases with higher rotation speed. The decrease in the area of peak P and other qualitative changes observed with increased rotation speed were produced at 400 rpm when small (10^{-6}M) increments of Na_2SO_3 were added to the solution. Evidence has been presented previously that the presence of sulfite impurity in sulfuric acid will affect *I-E* curves obtained from Pt electrodes in such solutions (13). Reference (13) also states that the sulfite level slowly increases in a bottle of concentrated sulfuric acid opened repeatedly to the room atmosphere. In this study also, the affects of increased rotation speed, as shown in Fig. 7, were most severe when the electrolyte was prepared from bottles of "old" concentrated sulfuric acid.

Adsorption of Br^-.—Evidence has been given that wave C results in the production of a small amount of HOBr at the disk electrode via a surface controlled reaction that occurs simultaneously with disk electrode surface oxidation. Two possible mechanisms for this reaction are apparent, (*i*) the further oxidation of a portion of the Br_2 produced by the convective-diffusion limited oxidation of Br^- involving a process catalyzed by platinum oxidation, and (*ii*) the oxidation of adsorbed Br^- or Br_2. If the production of HOBr is the result of a surface catalyzed process at active electrode sites, one would expect to see a large effect of E_d scan rate variation on the quantity of HOBr produced during wave C as estimated from the I_r-E_d curves. This prediction follows since oxidation of the platinum surface prevents HOBr formation. Hence, for decreasing scan rates the surface would remain in a "catalytically active" state for a longer time and the amount of HOBr found would be expected to increase. This prediction does not agree with the experimental observation that the amount of HOBr produced is independent of scan rate from 2 to 10 V min^{-1}.

Studies using electrochemical and radiochemical techniques (12, 20-25) have shown that Br^- is strongly adsorbed at platinum surfaces in acidic media. Reference (24) reports that in 1N H_2SO_4 the desorption of Br^- at anodic potentials does not proceed until E > 1.3V (SCE) which is consistent with the observed initial production of HOBr on the anodic E_d scan (Fig. 1, 3, 5). This reference also reports finding bromate in the solution after the desorption process was carried out at E = 2.0V (NHE). HOBr is known to decompose slowly to produce BrO_3^- and Br_2 (10).

The hypothesis that the HOBr stems from the oxidation of adsorbed Br^- can be tested using the ring-disk electrode. For exceedingly large concentrations of KBr the quantity of HOBr produced will be limited by the maximum disk electrode surface coverage by adsorbed Br^-. Simultaneous I_d-E_d and I_r-E_d curves for E_r = 0.60V were obtained at 400 rpm for 2.5 x 10^{-4}M ≤ [KBr] ≤ 6.0 x 10^{-3}M. The area under peak P, Q_p, corresponding to the extra Br_2 collected due to the production of HOBr at the disk electrode and its subsequent reaction according to Eq. [8], increased with increasing [KBr] in the manner shown in Fig. 8. For [KBr] < 1.5 x 10^{-3}M the points lie approximately on a straight line having nearly a zero intercept. For [KBr] > 4.5 x 10^{-3}M, Q_p reached a limiting value of about 27.5 μcoul. Although the convective-diffusion equation has not been solved for this case,

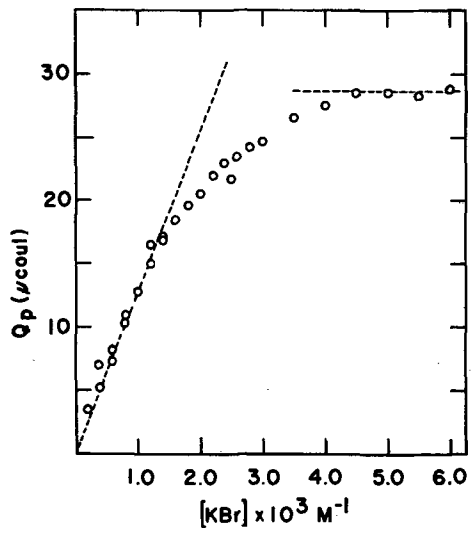

Fig. 8. Q_p vs. KBr; 1.0M H_2SO_4, 400 rpm, E_d scan rate = 6.0 V min^{-1}.

if it is assumed that one molecule of Br_2 is produced in the diffusion layer for each HOBr produced at the disk electrode, and that the fraction of this Br_2 collected at the ring electrode is nearly N_{theory}, the limiting surface coverage of adsorbed Br^- responsible for wave C, Γ, can be calculated as in Eq. [11]. In Eq. [11], n, the number of equivalents per mole for the reduction of Br_2, equals 2.

$$\Gamma = \frac{Q_p}{n(\text{disk area})\, F\, N_{theory}} = \frac{(27.5 \times 10^{-6})}{2(0.470)\,(9.65 \times 10^4)\,(9.0 \times 10^{-2})} \quad [11]$$

$$= 3.4 \times 10^{-9} \text{ g-ions cm}^{-2}$$

Using 1.5×10^{15} atoms cm^{-2} for the atomic packing density for platinum as calculated from the density (26), the surface coverage for an equivalent monolayer is 2.5×10^{-9} g-ions cm^{-2}. Radiotracer studies indicate a surface coverage of 1.3×10^{-9} g-ions cm^{-2} for a $1N$ H_2SO_4-$10^{-3}N$ NaBr solution (24). From Fig. 8, $\Gamma = 1.6 \times 10^{-9}$ g-ions cm^{-2} for $1 \times 10^{-3}M$ KBr. In view of the assumptions made regarding the relation of Q_p to the quantity of HOBr produced at the disk electrode and the inevitable differences in the surface roughness of our electrode and that used in ref. (24), the close agreement between our work and the radiotracer studies may be fortuitous. We conclude, however, that the results given in Fig. 8 are consistent with a mechanism whereby HOBr is produced during wave C at the disk electrode by oxidation of adsorbed Br^-. Furthermore, we conclude that Fig. 8 shows that the limiting value of Q_p corresponds to complete disk electrode surface coverage by adsorbed Br^- for [KBr] $> 4.5 \times 10^{-3}M$.

Examination of the I_d-E_d curves obtained for the various concentrations of KBr in the above experiment revealed that the magnitude of waves B and E remained nearly constant for increasing KBr concentration. Hence, wave B does not correspond to an oxidation of adsorbed Br^- to either the atomic state or a positive oxidation state and we conclude that wave B results only in the oxidation of the platinum electrode surface. Furthermore, the extent of surface oxidation corresponding to wave B is unaffected by the surface coverage with adsorbed Br^-. I_r-E_d curves were obtained, as shown in Fig. 3, for $E_r = 0.80$V. Stopping the anodic E_d scan at 1.10V for times to 30 sec did not result in a significant decrease in the amount of HOBr produced on commencing the anodic E_d scan. Thus, platinum oxide formed at the disk electrode with wave B does not result in a decrease of the disk electrode surface coverage by adsorbed Br^-.

A mechanism for the surface controlled production of HOBr which is consistent with the experimental results discussed above is given in Eq. [12]-[16].

(Oxide-free platinum surface)

$$Pt + Br^- \rightarrow Pt(Br^-_{ads}) \quad [12]$$

$(1.0V < E_d < 1.2V)$

$$Pt(Br^-_{ads}) + H_2O \rightarrow PtO(Br^-_{ads}) + 2H^+ + 2e \quad [13]$$

$$Pt + H_2O \rightarrow PtO + 2H^+ + 2e \quad [14]$$

$(E_d > 1.2V)$

$$PtO(Br^-_{ads}) + H_2O \rightarrow PtO + HOBr + H^+ + 2e \quad [15]$$

$$PtO + H_2O \rightarrow PtO_2 + 2H^+ + 2e \quad [16]$$

The I_r-E_d curve shown in Fig. 3 for $E_r = 1.20$V in the region $E_d < 0.8$V shows effects of Br^- adsorption at the disk electrode. Deviation of I_r from the convective-diffusion limiting value in this E_d region, $I_{r,l}$ ($Br^- \rightarrow Br_2$), will occur due to adsorption and desorption of Br^- at the disk electrode surface. Adsorption of Br^- will result in $I_r > I_{r,l}$ ($Br^- \rightarrow Br_2$) and desorption will result in $I_r < I_{r,l}$ ($Br^- \rightarrow Br_2$). Note that the anodic ring currents are negative quantities. The value of $I_{r,l}$ ($Br^- \rightarrow Br_2$) shown in Fig. 3 was obtained by stopping the E_d scan at $E_d + 0.6$V and letting I_r come to a steady-state value. Areas of deviation from $I_{r,l}$ ($Br^- \rightarrow Br_2$) in Fig. 3 are labelled S, T, U, and V. The interpretation of these waves must also be consistent with the following observations:

1. The reduction of the platinum oxide formed at the disk electrode for $E_d > 1.0$V occurs in the designated E_d region.
2. A small amount of soluble electroactive platinum(II) has been found to be a product of this disk reduction reaction [13] and this platinum(II) species may form bromide complexes (27).
3. The amount of platinum dissolution increases with increased halide concentration (28).
4. Adsorption of bromide at an oxide covered platinum surface is very slow but occurs rapidly following the reduction of the oxide (29).
5. Adsorption of atomic and/or molecular hydrogen competes with bromide adsorption for $E_d < 0.1$V (12).

The I_r-E_d curve for $E_r = 1.2$V in Fig. 3 shows that the adsorption of Br^- at the disk electrode during the cathodic E_d scan for $E_d < 0.9$V is negligible until reduction of the platinum oxide at the disk electrode occurs, $E_d = 0.6$V. The rapid adsorption of Br^- at the reduced disk electrode produces wave T at the ring electrode. This observation is consistent with statement 4 above. I_r-E_d curves were obtained for $E_r = 1.20$V, $E_d{}^c = -0.20$V and $1.0\text{V} \leq E_d{}^a \leq 1.60$V. Wave T was obtained only for $E_d{}^a > 1.2$, region of wave C, even though oxidation of the platinum electrode surface occurs for $1.0\text{V} < E_d < 1.2$V, Fig. 1. This observation is consistent with the hypothesis that HOBr is produced by oxidation of adsorbed Br^- since for $E_d{}^a < 1.2$V no HOBr is produced and no adsorbed Br^- is removed from the disk electrode.

Figure 3 also shows that for $E_r = 0.8$V an anodic peak wave, U, is obtained during the cathodic E_d scan. This, we conclude, is the result of oxidation of a soluble platinum(II) and/or platinum(II) bromide complex species formed at the disk electrode. Comparison of the peak potentials for waves T and U shows that Br^- adsorption occurs prior to the production of the soluble platinum(II) species. These observations are also consistent with the I_r-E_d curves obtained in Br_2 solution and shown in Fig. 6.

For E_d in the "hydrogen region," region V in Fig. 3, Br^- is desorbed on the anodic E_d scan as a result of

the preferential adsorption of atomic and/or molecular hydrogen. On the succeeding anodic E_d scan, the adsorbed hydrogen is ionized and Br^- is again adsorbed. A similar discussion may be given for the observations shown in Fig. 6.

Because of the relatively slow E_d scan rates used in obtaining the I-E curves in Fig. 3 and 5, it is difficult to accurately integrate the I_r *vs.* time in order to attempt a correlation with Q_p. Potential step techniques at a RRDE are useful for the study of adsorption processes (30). Figure 9 shows I_r-t curves obtained in 1.0M H_2SO_4 containing KBr, for E_r = 1.2V, as a result of a E_d step from −0.2 to 0.8V. Figure 9a shows the results for 1.1 × $10^{-3}M$ KBr. Integrating the difference between I_r and $I_{r,l}$ ($Br^- \rightarrow Br_2$) *vs.* time shows that the decrease in Br^- flux to the ring electrode as a result of the E_d step is 7.75 μcoul, *i.e.*, the disk surface coverage by Br^- is 1.9 × 10^{-9} g-ions cm^{-2}. For the same solution, I_r-E_d curves were obtained in a manner identical to that for Fig. 3. The area under wave P, Q_p, was measured to be 13.2 μcoul indicating a disk surface coverage calculated by Eq. [11] of 1.6 × 10^{-9} g-ions cm^{-2}. In view of the lack of theoretical support for a calculation of surface coverage from Q_p, as discussed earlier, we conclude that the results of Fig. 9a shows that sufficient Br^- is adsorbed on the disk electrode surface to account for the production of HOBr during wave C by oxidation of adsorbed Br^-.

Figure 9b shows that for 1.1 × $10^{-4}M$ KBr, the rate of Br^- adsorption at the disk electrode is controlled by the rate of convective-diffusion of Br^- from the bulk solution to the disk electrode surface (30). This was also the case for [KBr] < 1.1 × $10^{-4}M$. This suggested that if the proposed mechanism is correct, variation of the length of time E_d is in a potential region where Br^- adsorption can occur will cause a variation in the amount of HOBr produced during wave C. This would hold provided the disk surface coverage by adsorbed Br^- does not reach the equilibrium value, *i.e.*, very low bulk concentrations of Br^-. Figure 10 shows I_r-E_d curves obtained in the usual manner for E_d^a = 1.6V, E_d^c = 0.0V, and E_r = 0.6V with the exception that the E_d scan was stopped at 0.8V during the anodic scan and held for 0 sec ≤ t ≤ 30 sec before completing the potential cycle. For [KBr] = 0.6 × $10^{-5}M$, Q_p increased in approximately a linear manner with time for t < 25 sec. For t ≥ 25 sec, the disk surface coverage of Br^- reached its equilibrium value for that concentration of KBr. For [KBr] = 1.1 × $10^{-5}M$, equilibrium surface coverage was achieved from t ≥ 10 sec and for [KBr] = 3.3 × $10^{-5}M$, equilibrium coverage was achieved for all t > 0 sec, *i.e.*, within the time required for the normal E_d cycling. These results are in agreement with the proposed mechanism.

Since Br^- adsorption at the platinum disk electrode does not occur until the oxidized surface layer is reduced and since the E_d for the production of HOBr (wave C) is approximately equal to the $E°$ for reaction [3], no conclusion can be drawn from the above data as to whether the oxidation of adsorbed Br^- is catalyzed by oxidation of the platinum electrode surface. The pH dependence of waves A, B, and C is presently being studied in the attempt to answer this question.

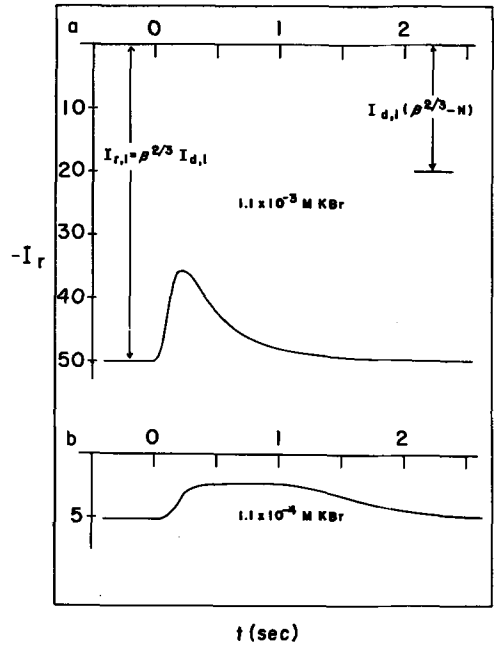

Fig. 9. I_r-time; E_r = 1.20V, 1.0M H_2SO_4-KBr, 400 rpm, E_d step from −0.20 to 0.80V at t = 0 sec.

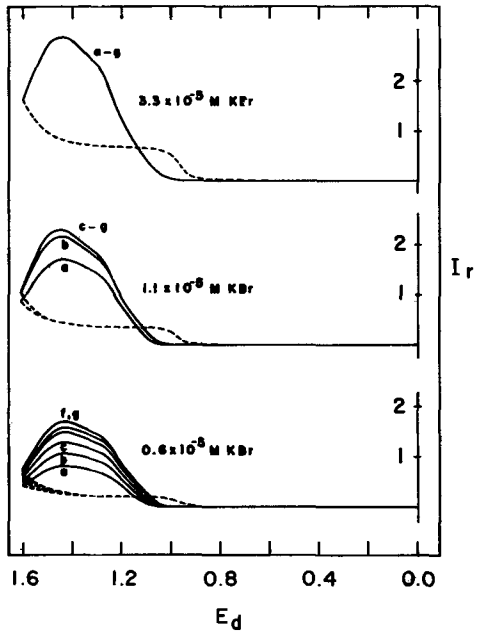

Fig. 10. I_r-E_d *vs.* t for E_d = 0.80V; 1.0M H_2SO_4-(0.6, 1.1, 3.3) x 10^{-5}M KBr, 400 rpm, E_d scan rate = 10.0 V min^{-1}, (a) 0 sec, (b) 5 sec, (c) 10 sec, (d) 15 sec, (e) 20 sec, (f) 25 sec, and (g) 30 sec.

Acknowledgment

Equipment used in this study was purchased with funds supplied by the General Electric Corporation and administered by the Department of Chemistry at Iowa State University.

Manuscript received Oct. 6, 1969.

Any discussion of this paper will appear in a Discussion Section to be published in the December 1970 JOURNAL.

REFERENCES

1. P. Beran and S. Buckenstein, *Anal. Chem.*, **40**, 1044 (1968).
2. J. Llopis and M. Vaquez, *Electrochim. Acta*, **6**, 167, 177 (1962).
3. M. V. Fernandez, *Rev. Real Acad. Cienc. Exact. Fig. Nat. Madrid*, **56**, 513 (1962).
4. T. Mussini, *Chim. Ind.*, **45**, 1075 (1963).
5. G. Faita, G. Fiori, and T. Mussini, *Electrochim. Acta*, **13**, 1765 (1968).
6. W. M. Latimer, "The Oxidation States of Elements and Their Potentials in Aqueous Solutions," Prentice-Hall, Inc., Englewood Cliffs, N. J. (1952).
7. D. C. Johnson, D. T. Napp, and S. Bruckenstein, *Anal. Chem.*, **40**, 482 (1968).
8. D. T. Napp, D. C. Johnson, and S. Bruckenstein, *ibid.*, **39**, 481 (1967).
9. E. A. Shilov and N. P. Kanyaev, *J. Gen. Chem. (USSR)*, **8**, 455 (1938).
10. G. Sourisseau, *Ann. Chim. (Paris)*, **8**, 349 (1953).

11. G. Sourisseau, *Bull. Soc. Chim. France*, **1954**, 45.
12. M. W. Breiter, *Electrochim. Acta*, **8**, 925 (1963).
13. D. C. Johnson, D. T. Napp, and S. Bruckenstein, To be published in *Electrochim. Acta*.
14. A. Kozawa, *J. Electroanal. Chem.*, **8**, 20 (1964).
15. V. G. Levich, "Physicochemical Hydrodynamics," p. 68, Prentice-Hall, Inc., Englewood Cliffs, N. J. (1962).
16. W. J. Albery and S. Bruckenstein, *Trans. Faraday Soc.*, **62**, 1932 (1966).
17. H. A. Liebhofsky, *J. Am. Chem. Soc.*, **61**, 3513 (1939).
18. M. Eigen and K. Kustin, *ibid.*, **84**, 1355 (1962).
19. W. C. Bray and P. R. Davis, *ibid.*, **52**, 1427 (1930).
20. N. A. Balashova, *J. Phys. Chem.*, **207**, 304 (1957).
21. N. A. Balashova, *Wiss. J. Tech. Univ. Dresden*, **12**, 117 (1963).
22. V. E. Kazarinov, *J. Phys. Chem.*, **226**, 167 (1964).
23. N. A. Balashova and V. E. Kazarinov, *Elektrokhimiya*, **1**, 512 (1965).
24. V. E. Kazarinov, *ibid.*, **2**, 1389 (1966).
25. G. N. Mansurov, V. E. Kazarinov, and N. A. Baloshova, *ibid.*, **2**, 1438 (1966).
26. H. A. Laitinen and C. G. Enke, *This Journal*, **107**, 773 (1960).
27. A. T. Hubbard and F. C. Anson, *Anal. Chem.*, **38**, 1887 (1966).
28. V. E. Kazarinov and N. A. Balashova, *Dokl. Akad. Nauk. SSSR*, **134**, 864 (1960).
29. V. E. Kazarinov and N. A. Balashova, *ibid.*, **139**, 641 (1961).
30. S. Bruckenstein and D. T. Napp, *J. Am. Chem. Soc.*, **90**, 6303 (1968).

A Transient Impedance Technique for the Study of Electrode Kinetics

Application to Potentiostatic Methods

Arthur A. Pilla

ESB Incorporated Research Center, Yardley, Pennsylvania

ABSTRACT

A generalized approach to the study of the dynamic behavior of electrochemical systems is presented in terms of the transient impedance technique. It is shown that interpretation of the time domain electrode response to an arbitrary perturbation by conversion of both functions to the frequency domain allows maximum usage of experimental information with minimum ambiguity. Both real and imaginary axis Laplace transformation are used to generate $Z(\sigma)$ and $Z(j\omega)$, respectively. The theoretical and experimental usefulness of both functions is considered in detail and it is shown that a very wide frequency range extending to 10^8 rad/sec may be studied. The basis for the use of aperiodic equivalent circuits to represent active or passive electrodes is considered and sample circuits, rigorously derived, are presented. The equivalent circuit approach is thus generalized and it is shown how their use may constitute shorthand notation for the rigorous solution of the differential equations used to describe a particular electrode model. Application of the transient impedance method to potentiostatic techniques is presented with emphasis on the manner in which this approach allows instrumental errors and artifacts to be markedly reduced, particularly at high frequencies.

The use of time as a variable to study the behavior of electrochemical systems is well-known (1-3). Techniques employing this variable usually involve perturbing the system with supposedly known functions of voltage (4-8), current (9-14), or charge (15-20); *e.g.*, steps or pulses, and observing the corresponding response. The relation of this response to the kinetic processes occurring during the perturbation (or during the relaxation from it) requires data analysis which involves the creation of a physically significant model and subsequent derivation of working equations which may be employed to obtain parameters that describe the mechanism and kinetics of the system under study.

Working equations have been obtained from the original differential equations describing the particular model chosen either by their analytic solution (4, 6, 7, 10-12, 14-18, 20) for certain simple cases or their numerical solution (21-24) for more complex cases. Certain limitations are present in both approaches since the analysis is usually performed in the time domain. One of the major problems in time domain analysis lies in the difficulty with which the total amount of information which is contained in the response function can be obtained (25). Thus, in the cyclic voltammetry technique, one of the most useful diagnostic criteria is the variation of peak current with voltage sweep speed (21). However, while this relation has certainly allowed much information to be gained for certain electrode reaction mechanisms, all of the available information from the total response curve has not been used simply because it is not available in a conveniently usable format. This can result in some ambiguity for complex reactions.

Another problem lies in the fact that the closed form working equations which have been obtained for, *e.g.*, the potential step method, are not readily usable in complete form because of their complexity. Certain approximations are often required for their use, such as measurement at times short (or long) enough so that simple time functions (*e.g.*, $\sqrt{t}$ or $1/\sqrt{t}$) may be obtained. These approximations normally do not allow all of the information content in the response function to be employed. In addition, they place restrictions on data acquisition and often result in some ambiguity in the interpretation of results (26-28). Thus, the time range over which simple functional behavior can be observed may be at such short times that errors in the measurement apparatus (*e.g.*, nonlinearity) can falsify the results. Further, this time interval may be so small that its exact detection could be highly subject to error.

In addition to the above considerations, it has become increasingly apparent that many electrode reactions are more complex with respect to heterogene-

ous reaction steps than had previously been suspected (29-34). Thus, in addition to charge transfer, surface processes such as adsorption may take place. It is, therefore, of increasing importance to obtain information relative to the structure and components of the electrode-electrolyte interphase region (35-36). This means essentially that an attempt should be made to evaluate the double layer capacitance, surface excess and electrode charge in the presence of a faradaic reaction. If the reaction contains heterogeneous steps more complex than charge transfer then the possibility that these may be very rapid, and perhaps also inseparable from the double layer charging process (37-40), places certain severe requirements on both the mode of measurement and data analysis. For example, in these cases, it is no longer acceptable to extrapolate over large time (or frequency) ranges in which measurements were not made to evaluate parameters such as the double layer capacitance (41, 42). This is especially true if measurements were made only over fairly restricted time (or frequency) intervals. It is thus necessary to obtain meaningful data over as wide a time range as possible including the shortest experimentally accessible times.

It is the purpose of this study to present an approach to the interpretation of the pulse response of electrochemical systems such that the concept of pulse impedance may be introduced. It will be shown that this approach generates, for most systems of interest, algebraic equations which are much less ambiguous to interpret than classical time domain expressions, thus eliminating the above-mentioned difficulties to a large extent. In addition, instrumental problems, especially for short time or high frequency measurements, are eliminated.

Theoretical

Time to frequency domain conversion.—Impedance of an electrochemical system can be defined validly only in an appropriate frequency domain (43), because of its vector or phasor properties. Therefore, in order to obtain an impedance function from time domain behavior, it is necessary to convert both the perturbation and response from time functions into frequency functions. This is accomplished normally through the use of a transformation technique which operates on the time variable. One of the most useful techniques which may be employed for this is the Laplace transformation (44). Using this, a time function, $f(t)$, may be transformed to a complex frequency function, $F(s)$, according to

$$F(s) = \int_0^\infty f(t) \exp(-st)\, dt \qquad [1]$$

where s is the Laplace transform variable. The quantity s is a complex number given by $s = \sigma + j\omega$, in which σ is the real and $j\omega$ the imaginary part. The complete function $F(s)$ is thus described by a complex plane in which all absolute values of both σ and $j\omega$ may be employed provided the integral in [1] converges. This plane is known as the complex frequency plane. Examination of the properties of the function $F(s)$ indicates that it is possible to perform the integration along either or both the real and imaginary axes of the complex frequency plane under certain conditions. Thus, considering the real axis ($s = \sigma$), Eq. [1] may be written

$$F(\sigma) = \int_0^\infty f(t) \exp(-\sigma t)\, dt \qquad [2]$$

It is clear that this integral exists when $\sigma > 0$ for any time function which converges when multiplied by $\exp(-\sigma t)$. This includes essentially all time functions of interest in electrode kinetic studies. When [2] is carried out, this will be termed real axis transformation. This type of transformation was first suggested for electrochemical applications by Wijen (45), who considered the current response to a potential step for a diffusion coupled charge transfer reaction. The scope of his approach was, however, somewhat limited in nature since the aspect of impedance was not considered and thus such problems as more complex reactions, double layer charging, or the use of an imperfect potential step (*e.g.*, with finite rise) were not taken into account. Real axis transformation has since been considered by other workers (46, 47), however, essentially their approach has been simply to express some classical faradaic impedance expressions in terms of the complex frequency variables. No attempt was made to generalize the technique in terms of transformation along both axes or to illustrate the enormous advantages in the actual measurement of impedance [see, however, ref. (48)].

In order to see how real axis transformation is actually carried out on an experimental curve, consider Fig. 1. Here the time function is a typical current response to a potential step having finite rise time. The current function, $i(t)$, is multiplied by the exponential function $\exp(-\sigma t)$ shown on Fig. 1. The area under the resulting curve is then equal to the integral defined in [2]. This operation is performed using the total time function (*i.e.*, from $t = 0$) for as many σ values as desired. The resulting quantity, $I(\sigma)$, then expresses the current as a function of the frequency variable σ in radians per second.

If the same operation defined in [2] is performed on the voltage driving function, $V(t)$, the corresponding frequency function $V(\sigma)$ is obtained. Knowledge of both $V(\sigma)$ and $I(\sigma)$ allows the real axis pulse impedance of the system, $Z(\sigma)$, to be defined as

$$Z(\sigma) = V(\sigma)/I(\sigma) \qquad [3]$$

The quantity $Z(\sigma)$ is a real function and as such is the simplest of the impedance functions. To illustrate this, consider an RC series circuit. The real axis impedance of this circuit is given by

$$Z(\sigma) = R + \frac{1}{C\sigma} \qquad [4]$$

This relation may be utilized in the same manner as a normal algebraic equation containing real variables. Thus, the quantities R and C may be obtained simply by plotting $Z(\sigma)$ as a function of $1/\sigma$ as normally would be done for an equation of this type.

In addition to real axis transformation, conversion into the frequency domain by imaginary axis transformation ($s = j\omega$) may be performed. In this case, [1] may be written

$$F(j\omega) = \int_0^\infty f(t) \exp(-j\omega t)\, dt \qquad [5]$$

Equation [5] is the well-known single-sided Fourier transform (49). Inspection of [5] indicates that this integral will converge only for certain time functions. Thus, functions of the type $\exp(-at)$ and $\operatorname{erf}(\sqrt{bt})$ or $\operatorname{erfc}(\sqrt{bt})$ allow [5] to converge when multiplied by $\exp(-j\omega t)$.

Most electrochemical systems respond, in part, according to functions of the type indicated above. How-

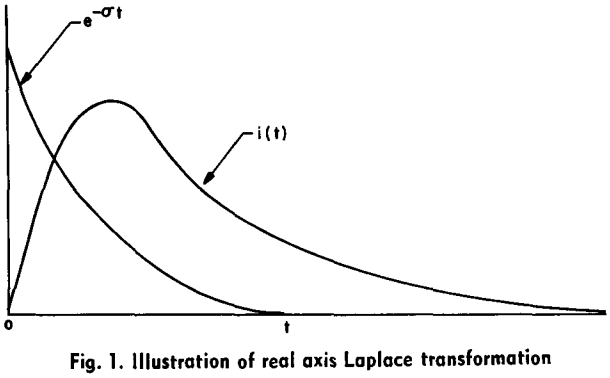

Fig. 1. Illustration of real axis Laplace transformation

ever, the complete time function may contain additive constant terms and it is clear that the integral in [5] will not converge. Use may be made, however, of the fact that imaginary axis transformation actually describes the system behavior in the same manner as if the perturbation were a steady-state sinusoidal function (50). In this case, it is permissible to carry out the complete transformation as described in [1] on the constant portion of $f(t)$ and make the substitution $s = j\omega$ to obtain the result which could have been obtained if [5] could have been employed. If the above is performed, it is now clear that the imaginary axis transformation for a constant A is $A/j\omega$. Therefore, if $f(t) = A + \exp(-at)$, then the complete imaginary axis transformation is obtained by using [5] for $\exp(-at)$ and making the above substitution for A. The complete transformation is then

$$F(j\omega) = \frac{A}{j\omega} + \frac{1}{a + j\omega} \qquad [6]$$

Use of the above procedure enables the pulse behavior of essentially every electrochemical system to be expressed in terms of imaginary axis Laplace transformation.

In order to see how imaginary axis transformation is actually carried out on an experimental curve, it is convenient to rewrite Eq. [5] as

$$F(j\omega) = \int_0^\infty f(t) \cos \omega t \, dt - j \int_0^\infty f(t) \sin \omega t \, dt \qquad [7]$$

in which the complex function $F(j\omega)$ is expressed in terms of its real and imaginary parts. It can be seen that in both cases multiplication of the original time function by a trigonometric function is involved. This is illustrated in Fig. 2. Here, the time function is again the current response, $i(t)$, to a potential step input. This is multiplied from $t = 0$ to the time at which $i \simeq 0$ by a sine (or cosine) function of given frequency, ω. The area under the resulting curve is, as in real axis transformation, equal to the integral defined in [5]. This operation is performed, for both the real and imaginary parts of $F(j\omega)$, for as many ω values as desired. The resulting complex function $I(j\omega)$ is then the total current expressed in terms of the real frequency, ω.

A similar series of operations may be performed on the voltage driving function (in the case of, *e.g.*, the potential step method) to obtain the corresponding complex voltage frequency function, $V(j\omega)$. Knowledge of both $V(j\omega)$ and $I(j\omega)$ allows, similar to the previous case, the imaginary axis pulse impedance of the system, $Z(j\omega)$, to be defined as

$$Z(j\omega) = V(j\omega)/I(j\omega) \qquad [8]$$

In this case, $Z(j\omega)$ is a complex function having both real, $\mathrm{Re}(Z(\omega))$, and imaginary, $\mathrm{Im}(Z(\omega))$, parts and the corresponding phase angle, $\theta(\omega)$. This function is mathematically identical in form to that employed in classical a-c techniques (51-58), where sinusoidal steady-state conditions prevail. It is to be remembered, however, that $Z(\omega)$ in this study is always considered as obtained under nonsinusoidal conditions (*i.e.*, from conversion of both the input and response time domain functions).

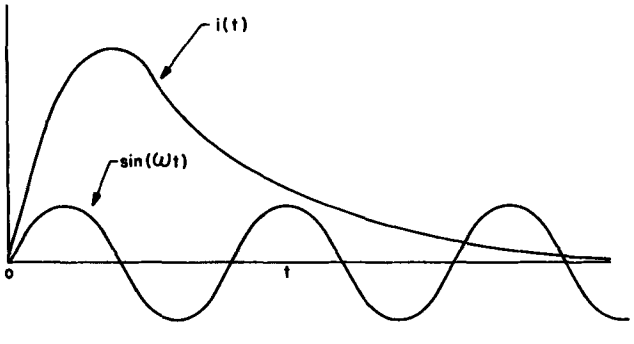

Fig. 2. Illustration of imaginary axis Laplace transformation

Use of $Z(j\omega)$ for the RC series circuit considered for the previous case results in the following complex function

$$Z(j\omega) = R - \frac{j}{C\omega} \qquad [9]$$

In contrast to the simple impedance function obtained above for this case Eq. [4], analysis of Eq. [9] to obtain the quantities R and C requires, as is well-known (57), the use of a complex plane. Among the various approaches using this type of analysis, it is preferable to consider separately, the functional relationships which describe $\mathrm{Re}(Z(\omega))$, $\mathrm{Im}(Z(\omega))$, and $\theta(\omega)$ since this is, in fact, the most sensitive test of whether a given model is valid or not. In terms of Eq. [9], a plot of $\mathrm{Re}(Z(\omega))$ and $\mathrm{Im}(Z(\omega))$ *vs.* $1/\omega$ should result in a horizontal line for the former, the value of which is equal to R, and a straight line for the latter, the slope of which allows C to be obtained. The use of $\theta(\omega)$ is not necessary in this simple case.

It is to be emphasized that obtaining both $Z(\sigma)$ and $Z(j\omega)$ involves operating upon the appropriate time domain functions from $t = 0$ (*e.g.*, along the rise of a potential step). Thus, it is possible to obtain both impedance functions at frequencies as high as 10^8 rad/sec provided the system can be perturbed to such an extent that an observable response is obtained at nanosecond times. In the case of real axis transformation, the use of large σ values heavily weights the short time behavior of $f(t)$ since $\exp(-\sigma t)$ is a very rapidly decaying function in this case. As σ becomes smaller, short time data contributes relatively less to the total integral. Correspondingly, for imaginary axis transformation, large ω values emphasize the short time system response. This is so since the major contribution to the product $f(t) \sin \omega t$ for large ω occurs only in those time intervals during which the value of $f(t)$ changes significantly over one frequency cycle. This means that only small time constants will be observable for relatively large values of ω. Note that, although obtaining $Z(j\omega)$ from pulse measurements results in data identical to that of classical a-c techniques, the requirement that the system actually be perturbed by a sine wave function has been relaxed. In fact, the restriction that the perturbing function be exactly known for either $Z(\sigma)$ or $Z(j\omega)$ is no longer applicable. This is highly significant with respect to experimental measurement especially at high frequencies since the input perturbation and response may be arbitrary functions, even a highly distorted sine wave. In addition, as long as the nonlinearities in the measurement system are the same for both voltage and current functions, the calculation of $Z(\sigma)$ and $Z(j\omega)$ allows their elimination. This will be treated further below.

It can be seen that the use of both real and imaginary axis Laplace transformation on the single time domain response of an electrochemical system and the single time domain driving function, either being of arbitrary form, allows a considerable amount of information to be obtained concerning the impedance of the system. The use of both $Z(\sigma)$ and $Z(j\omega)$ permits four basic functions to be described, the specific functional relationships of which can be used to provide less ambiguity in the elucidation of relatively complex systems.

Aperiodic equivalent circuit interpretation.—The pulse impedance method lends itself quite readily to the description of an electrochemical system by an electrical equivalent circuit containing frequency independent elements (aperiodic equivalent circuit). The use of equivalent circuits as electrical analogs for some electrode reactions is, of course, well-known (51, 52, 54, 58). However, the circuits employed usually con-

tain frequency dependent elements. Little work has been reported concerning the use of aperiodic equivalent circuits. The notable exception is the work of Barker (15) who quite ingeniously, although somewhat empirically, developed aperiodic circuits which describe a variety of electrochemical systems. The use of Laplace transformation to derive the current and voltage frequency behavior of various electrochemical reaction steps allows a great deal of flexibility insofar as the development of a complete model for the particular electrode impedance is concerned. The pulse response of an electrochemical system can then be measured experimentally and $Z(\sigma)$ and $Z(j\omega)$ evaluated with a minimum of *a priori* assumptions necessary concerning the actual mechanism present. Diagnostic criteria, consisting essentially in the determination of the number of time constants and their placement in the appropriate equivalent circuit (topology requirement) can then be employed.

To illustrate this approach, the construction of an aperiodic equivalent circuit will be performed for an electrode at which an adsorption coupled charge transfer faradaic process occurs. It will be assumed at the onset that *a priori* separation may be made of double layer charging current from faradaic current. Thus, the electrode reaction may be considered as a leak across the double layer capacitor, C_d. The general equivalent circuit for this concept is shown in Fig. 3 wherein R_e and Z_F represent the solution resistance and faradaic impedance, respectively. The impedance of this circuit may be written in terms of s, as

$$Z(s) = R_e + \frac{1}{1/Z_F(s) + C_d s} \qquad [10]$$

In general, the complexity of $Z_F(s)$ depends directly on the complexity of the electrode process. It can be shown (59) that one additional time constant must be added to Eq. [10] for every series reaction step, with the exception of charge transfer. Thus, as $Z_F(s)$ becomes more complex, it is increasingly necessary to render experimental conditions such that the time constant representing double layer charging, $R_e C_d$, be independently observable so that it may be appropriately eliminated from the total electrode impedance. This may be performed if a high enough frequency range can be chosen such that the condition $1/Z_F(s) << C_d s$ may be obtained. In this case, Eq. [10] is written

$$Z_F(s) = \frac{1}{C_d s} + R_e \qquad [11]$$

which, in terms of σ and $j\omega$, is given by Eq. [4] and [9], respectively. The general diagnostic criteria for double layer behavior (if separable from the faradaic process) is then, for real axis transformation linearity of $Z(\sigma)$ *vs.* $1/\sigma$, and for imaginary axis transformation linearity in $1/\omega$ for $\mathrm{Im}(Z(\omega))$ and constancy in ω for $\mathrm{Re}(Z(\omega))$. If at least an order of magnitude in frequency range may be obtained for all of these functional relationships, then it may be considered with reasonable assurance that double layer behavior is being observed. This then allows the elimination of one time constant from the general impedance expression (Eq. [10]) unmasking the faradaic impedance for further analysis.

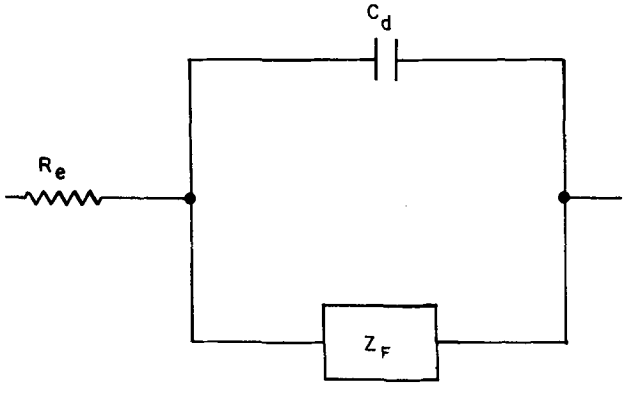

Fig. 3. General aperiodic equivalent circuit for a microelectrode having uniform potential distribution and at which double layer and faradaic processes may be separated.

In order to derive $Z_F(s)$ for a series adsorption coupled charge transfer process the impedance of each of these reaction steps can first be obtained and then appropriately added. The charge transfer impedance may be derived in a straightforward fashion from, *e.g.*, the commonly employed rate equation (60), written in terms of s, as

$$I(s) = I_o \int_o^\infty \exp\left[-\frac{\alpha n\mathbf{F}}{RT} [E(t) - st] \right] - I_o \int_o^\infty \exp\left[\frac{1-\alpha n\mathbf{F}}{RT} [E(t) - st] \right] \qquad [12]$$

where $I(s)$ is the current due to charge transfer; $E(t)$ the overvoltage driving this process; I_o the exchange current density; α the transfer coefficient; the other quantities have their usual significance. This equation, while describing a potential dependent resistor, may be used under certain linear conditions (*i.e.*, low level perturbation) to obtain a simple resistor, R_t. Thus, as $E(t) \to 0$, [12] may be written

$$\frac{E(s)}{I(s)} = \frac{1}{I_o} \frac{RT}{n\mathbf{F}} = R_t^{eq} \qquad [13]$$

which is simply the well-known (61) charge transfer resistance under equilibrium conditions. As $E(t)$ becomes relatively large (*e.g.*, the cathodic Tafel region) and when $\Delta E(t) \to 0$, representing a small perturbation from steady-state conditions, Eq. [12] becomes

$$\frac{\Delta E(s)}{\Delta I(s)} = \frac{1}{I_o} \frac{RT}{\alpha n\mathbf{F}} \frac{1}{\exp(\alpha n\mathbf{F}E/RT)} = R_t \qquad [14]$$

which also represents a pure resistor provided that the exponential term remains essentially constant during the perturbation, which is the case if it is of low level. Note that R_t given by Eq. [14] is of lower value than R_t^{eq}, as expected. The above is an illustration of the procedure of linearizing about a steady-state condition which can be applied to the majority of electrochemical reaction steps, allowing potential dependence to be examined in a relatively convenient fashion.

To develop an equivalent circuit for the adsorption process, standard reaction rate consideration may be employed with no *a priori* assumptions concerning the actual kinetics of adsorption (62, 63). Thus, the net adsorption rate, v, can be expressed as

$$v = k\, C_i^a(s) - k^1\, C_i(o,s) \qquad [15]$$

where $C_i^a(s)$ and $C_i(o,s)$ are the complex frequency concentration functions of the adsorbed species, i, and of the same species in solution at the electrode-electrolyte interphase region, respectively, and k and k^1 are adsorption and desorption rate constants, respectively. These quantities may be arbitrary complex functions of C_i^a, C_i, and the number and nature of available adsorption sites. The actual form of k and k^1 depends on the type of adsorption kinetics involved (Langmuir, Frumkin, etc.).

If equilibrium or steady-state conditions are defined as

$$v_o = k\, C_i^a(o) = k^1\, C_i(o,o) \qquad [16]$$

where v_o is the exchange adsorption rate and the concentrations are those before the application of the perturbation ($t = 0$), then the following may be written

$$v = v_o \left[\frac{C_i^a(s)}{C_i^a} - \frac{C_i(o,s)}{C_i} \right] \qquad [17]$$

This relation describes the adsorption process in terms of a departure from equilibrium or steady-state conditions. The first ratio on the r.h.s. of Eq. [17] relates to the change in concentration of the adsorbed species and the second takes into account mass transport of this species in the electrolyte. If mass transport is negligible (as assumed in this simple model) then $C_i(o,s)/C_i = 1$ and Eq. [17] is correspondingly simplified.

The impedance function for adsorption require knowledge of both the current due to adsorption and its potential dependence. The former is given by

$$I_a(s) = n\mathbf{F}\,[v + s\,C_i^a(s)] \qquad [18]$$

which simply states that the frequency dependence of the total adsorption current is the sum of that due to the net adsorption rate, v, and that due to the change in concentration of adsorbed species, $s\,C_i^a(s)$, as a result of the perturbation. The frequency dependence of the voltage function may be obtained from the linearized Nernst equation

$$E_a(s) = \frac{RT}{n\mathbf{F}}\,\Delta C_i^a(s) \qquad [19]$$

where $\Delta C_i^a(s) = (C_i^a(s) - C_i^a)/C_i^a$, representing the relative concentration change of adsorbed species. Using Eq. [18] and [19], the impedance expression for adsorption is then

$$Z_a(s) = \frac{RT}{n^2\mathbf{F}^2}\left[\frac{C_i^a}{s + v_o/C_i^a}\right] \qquad [20]$$

Inspection of Eq. [20] reveals that it is identical to the complex impedance function for an R_a-C_a parallel circuit where R_a and C_a are the equivalent adsorption resistance and capacitance, respectively. Identification of Eq. [20] with the expression for the actual equivalent circuit allows physical significance to be given to the circuit elements. Thus

$$C_a = \frac{n^2\mathbf{F}^2}{RT}\,C_i^a \qquad [21]$$

which states, as is to be expected, that C_a is a measure of the concentration of adsorbed species (analogous to the storage of charge in a capacitor). R_a is given by

$$R_a = \frac{RT}{n^2\mathbf{F}^2}\,\frac{1}{v_o} \qquad [22]$$

indicating that it contains adsorption and desorption rate constants. In general, R_a is relatively large for slow or irreversible adsorption becoming relatively smaller as adsorption rate increases.

In order to construct a complete aperiodic equivalent circuit representing the complex impedance of the electrochemical system described above, it is merely necessary to substitute for Z_F in Fig. 3 the subcircuits derived for both charge transfer and adsorption placed in series. This is shown in Fig. 4. Analysis of both impedance functions for the presence of this circuit is relatively straightforward, particularly when the double layer time constant is able to be isolated. This will be shown below.

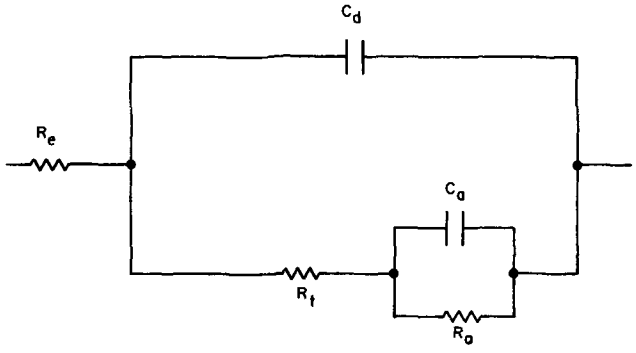

Fig. 4. Aperiodic equivalent circuit for an electrode exhibiting double layer behavior and adsorption coupled charge transfer.

As a specific illustration of the advantage of frequency domain over time domain analysis, a linear diffusion coupled charge transfer process for which the electrolysis conditions are the application of a constant current pulse will be considered. The total current, I_T, is the sum of the faradaic current, I_F, and the double layer charging current, I_C. This condition, which has been generally employed for current step and other relaxation studies (1), implicity assumes that *a priori* separation exists for the double layer and faradaic processes. The total current is then, in terms of s

$$I_T(s) = I_F(s) + I_C(s) \qquad [23]$$

Using the classical definition of capacity charging current, I_C is given by

$$I_C(s) = E(s)\,C_d s \qquad [24]$$

where $E(s)$ is the voltage developed across the double layer. The faradaic current is given by

$$I_F(s) = E(s)/Z_F(s) \qquad [25]$$

The faradaic impedance, $Z_F(s)$, can be constructed by considering that the charge transfer resistance is in series with the diffusion impedance as the model for this process assumes. Thus, $I_F(s)$ is given by, using the linearized rate equation

$$I_F(s) = I_o\left[\frac{C_O(o,s)}{C_O} - \frac{C_R(o,s)}{C_R} - \frac{n\mathbf{F}}{RT}E(s)\right] \qquad [26]$$

in which I_o is the exchange current density for charge transfer; C_O and C_R, the bulk concentrations of the oxidized and reduced species, respectively; $C_O(o,s)$ and $C_R(o,s)$ represent the complex frequency dependence of these concentrations at the electrode surface; and the other symbols have their usual meaning. Inspection of Eq. [26] shows that, in reality, the diffusion impedance, composed of terms due to C_O and C_R, and contained in the concentration ratios, is in series with the charge transfer resistance contained in the last term within the brackets on the r.h.s. of Eq. [26]. (See Eq. [13] for $R_t^{eq.}$)

A specific expression for the concentration ratios in Eq. [26] may be obtained by solving Fick's second law, written in terms of s, for planar diffusion with appropriate boundary conditions for semi-infinite character. The solution is of the form

$$\frac{C_i(o,s)}{C_i} = \frac{I_F(s)}{n\mathbf{F}C\sqrt{D_i}\sqrt{s}} + \frac{1}{s} \qquad [27]$$

in which D_i is the diffusion coefficient of the diffusing species, i. There are as many equations of this type as there are diffusing species. Substitution of Eq. [27] written for C_O and C_R in Eq. [26] gives

$$I_F(s) = \frac{E(s)}{B/\sqrt{s} + RT/n\mathbf{F}\,I_o} \qquad [28]$$

where

$$B = \frac{RT}{n^2\mathbf{F}^2}\left[\frac{1}{C_O\sqrt{D_O}} + \frac{1}{C_R\sqrt{D_R}}\right] \qquad [29]$$

Use of Eq. [24] and [28] allows an expression for $E(t)$ in the time domain to be obtained provided that the form of the current input is known. A true current step would allow $I_T(s)$, Eq. [23], to be written as I_O/s. For this, the simplest of input perturbations, the complete time domain relation for $E(t)$ is given by Eq. [11]

$$E(t) = \frac{I_o}{C_d(a-b)}\left\{\frac{a}{b^2}\left[\exp(b^2t)\,\mathrm{erfc}\,(bt^{1/2}) + \frac{2b\sqrt{t}}{\sqrt{\pi}} - 1\right] - \frac{b}{a^2}\left[\exp(a^2t)\,\mathrm{erfc}\,(at^{1/2}) + \frac{2a\sqrt{t}}{\sqrt{\pi}} - 1\right]\right\} \qquad [30]$$

where

$$\frac{a}{b} = \frac{nFI_oB}{2RT} \pm \left[\frac{n^2F^2I_o^2B^2}{4R^2T^2} - \frac{nF}{RT}\frac{I_o}{C_d} \right]^{1/2} \quad [31]$$

in which B is given by Eq. [20]. As can be seen by Eq. [30], analysis of this system in the time domain involves the manipulation of a relatively complex equation. One approach extensively employed is simplification which requires that measurements be made at short times. This, as stated earlier, allows a more usable $\sqrt{t}$ function to be employed. However, in the case of, *e.g.*, relatively rapid charge transfer kinetics, such short times may be required that the finite rise of the current function can cause considerable error. When this occurs, $I_T(s)$ can no longer be given by I_0/s, but assumes a more complex form thereby adding at least another time constant to a new and even more complex time domain function for $E(t)$. The separation of appropriate kinetic parameters then becomes exceedingly difficult.

The above-mentioned problems are avoided when complex frequency domain analysis is carried out for this system. In this case, the impedance function as given in Eq. [10] may be employed. This normally allows sufficiently high frequencies to be obtained that the double layer time constant may be isolated according to Eq. [11], thus unmasking the faradaic impedance for further analysis. Inspection of Eq. [28] shows that it can be used to obtain $Z_F(s)$. Thus

$$Z_F(s) = \frac{E(s)}{I_F(s)} = \frac{B}{\sqrt{s}} + \frac{nF}{RT}\frac{1}{I_o} \quad [32]$$

in which B is again given by Eq. [29]. The last term on the r.h.s. of Eq. [32] is, as stated earlier, the charge transfer resistance R_t^{eq} (see Eq. [13]). The term $B/\sqrt{s}$, which represents the diffusion impedance, $Z_D(s)$, is identical in form to the imepdance, $Z_L(s)$, of an R_LC_L semi-infinite transmission line. Thus

$$Z_L(s) = \frac{R_L}{C_L}\frac{1}{\sqrt{s}} \quad [33]$$

in which R_L and C_L are the uniformly distributed resistance and capacitance per (arbitrary) unit length of line. The electrochemical equivalence of R_L and C_L can be obtained using the relation $Z_D(s) = Z_L(s)$ and the original partial differential equations describing both diffusion (Fick's second law) and the transmission line. The latter results in $D_i = 1/R_LC_L$. In this manner, R is given by

$$R_L = \frac{RT}{n^2F^2}\frac{1}{C_iD_i} \quad [34]$$

and C_L by

$$C_L = \frac{n^2F^2}{RT}C_i \quad [35]$$

The above discussion indicates that the aperiodic equivalent circuit for planar diffusion is a semi-infinite transmission line. The complete equivalent circuit for this system can thus be constructed as shown in Fig. 5, where the charge transfer impedance, R_t, is in series with the diffusion impedance, Z_D.

Comparison of Eq. [32] with [30] clearly shows that the former is much simpler in form. In addition, exact knowledge of the function for the current input is not required. All of the necessary kinetic constants are readily obtainable from Eq. [32] with no approximations. In the case of real axis transformation, the diagnostic plot is $Z_F(\sigma)$ *vs.* $1/\sqrt{\sigma}$, the intercept of which gives R_t^{eq}, while the slope contains D. Imaginary axis transformation gives the well-known results for $\mathrm{Re}(F(j\omega))$ and $\mathrm{Im}(F(j\omega))$ both of which are linear in $1/\sqrt{\omega}$, having identical slopes containing D_i. The intercept of $\mathrm{Re}(F(j\omega))$ again allows R_t^{eq} to be obtained.

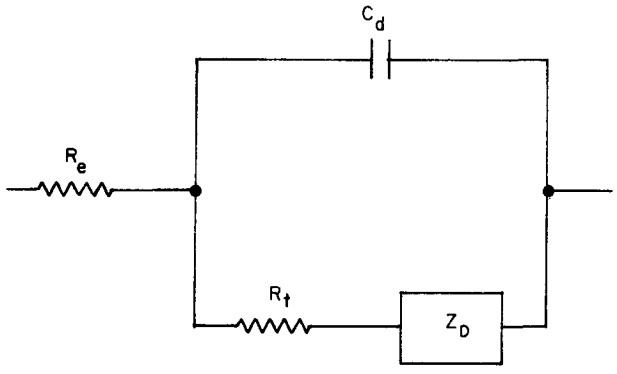

Fig. 5. Aperiodic equivalent circuit for an electrode exhibiting diffusion coupled charge transfer.

The above examples are presented as illustrations of the relative ease with which even a complex electrochemical system may be analyzed using equivalent circuits which may be coupled, if desired, with the pulse impedance approach. The use of aperiodic equivalent circuits allows the representation of the linearized rate expressions for each reaction step by simple frequency independent circuit elements. Once the subcircuits have been established for all of the heterogeneous and homogeneous reaction steps generally encountered in electrochemical reactions, it is relatively simple to construct a complete circuit for specific faradaic processes. To do this, the subcircuits are placed in any series or parallel combination which it is thought adequately represents the electrode reaction under study. In addition, the possibility of obtaining linear behavior at any steady-state condition allows the potential dependence of appropriate circuit elements to be determined, thus facilitating the elucidation of electrode mechanism and kinetics. This approach will be presented in generalized form elsewhere.

It is to be noted that expressing electrode behavior in terms of equivalent circuits does not constitute an empirical approach. The circuits are merely shorthand notation for the rigorous solutions to the several simultaneous differential and partial differential equations needed to describe a particular electrochemical model.

Application to potentiostatic techniques.—The transient impedance approach readily lends itself to potential control methods which offer certain experimental advantages especially with respect to high frequency studies. To illustrate this, the dynamic behavior of a general single amplifier potentiostat will be discussed. Special emphasis is given to the method of elimination of potentiostat parameters thereby allowing only electrochemical quantities to be examined.

The general circuit for single amplifier potential control of an electrode having an arbitrary impedance is given in Fig. 6 wherein the representation of all

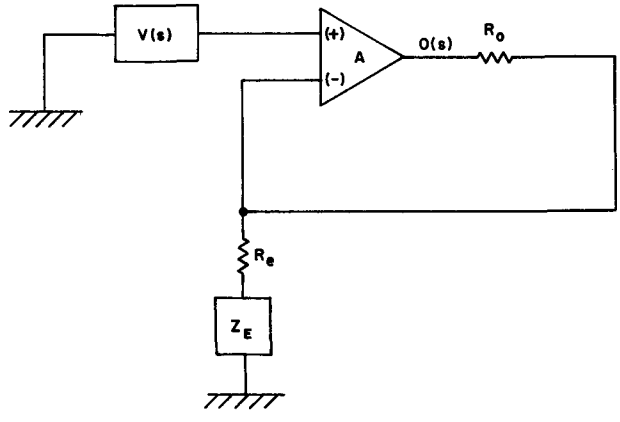

Fig. 6. Block diagram of general potentiostat circuit

functions is made in terms of the Laplace transformation. Here, the output voltage $O(s)$, of the potentiostat, A, is applied to the electrochemical cell, R_e, Z_E, through R_o, which represents the output impedance of A, the counterelectrode impedance, and a current measuring resistor, if present. The driving perturbation, $V(s)$, appears across the electrochemical cell as $E(s)$.

To describe the behavior of the potentiostat-electrolytic cell mentioned above in a quantitative manner, it is sufficient to consider the transfer function of the complete system. This function is defined as the ratio of the transform of the output voltage, $O(s)$, to that of the input voltage, $V(s)$. This ratio is given by

$$\frac{O(s)}{V(s)} = \frac{G(s)}{1 + G(s)\,H(s)} \qquad [36]$$

where $G(s)$ is the open loop gain function of the potentiostat and $H(s)$ is the function representing the fraction of the output voltage which is fed back to the input of the potentiostat. The potentiostat gain function determines, to a large extent, the fidelity with which it can reproduce the driving function, $V(s)$, across its control points as $E(s)$. This is especially important when it is desired to make measurements at short times. Thus, for maximum perturbation and response signal amplitude at, *e.g.*, nanosecond times, the potentiostat should be able to respond to a step function such that meaningful measurements may be obtained at these times. Optimum gain functions for high speed applications have been discussed elsewhere (64). Briefly, however, the ideal potentiostat would be characterized by $G(s) = K$, where K is the open loop d-c gain (usually greater than 1000). Unfortunately, all potentiostats presently available have a finite rise time and, as such, cannot be described by the simple function given above. In order to adequately describe a finite rise potentiostat, a first order gain function of the type

$$G(s) = \frac{K}{s\tau + 1} \qquad [37]$$

must be employed. Equation [37] clearly indicates, if τ is known, the time or frequency at which the potentiostat itself will have sufficient gain for observable response. To illustrate the generality of the potentiostatic transient impedance approach, no *a priori* assumptions will be made concerning the actual form of $G(s)$. It is to be borne in mind, however, that $G(s)$ must allow a signal of sufficient amplitude to be observed at the shortest times compatible with the highest frequencies desired to be obtained by real or imaginary axis transformation.

The function $H(s)$ is simply the ratio of the output voltage appearing across the potentiostat control points to the total output voltage. Thus, for the system described in Fig. 6, $H(s)$ is given by

$$H(s) = \frac{R_e + Z_E(s)}{R_o + R_e + Z_E(s)} \qquad [38]$$

The transfer function is then obtained using [36] and [38]

$$\frac{O(s)}{V(s)} = \frac{[R_o + R_e + Z_E(s)]G(s)}{R_o + R_e + Z_E(s) + [R_e + Z_E(s)]G(s)} \qquad [39]$$

This relation may be employed to derive all of the functions needed to develop an expression for the transient impedance of an electrochemical system when a potentiostat is employed. Note that no *a priori* assumptions have been made concerning the electrode impedance, $Z_E(s)$. Thus, the nature of the electrode impedance has neither been considered nor will it affect the results.

To obtain an impedance expression $Z(s)$ usable for the evaluation of electrochemical parameters knowledge of $E(s)$ and the total output current, $i(s)$, is necessary. $E(s)$ is given by

$$E(s) = O(s) - i(s)R_o \qquad [40]$$

from which, using [39]

$$\frac{E(s)}{V(s)} = \frac{[R_e + Z_E(s)]G(s)}{[R_e + Z_E(s)][G(s) + 1] + R_o} \qquad [41]$$

Examination of Eq. [41] indicates that it is, in reality, an expression for the ideality ratio of the potentiostat. Thus, a perfect potentiostat would have $E(s)/V(s) = 1$. Departure from unity is caused by both $G(s)$ and R_o. Reduction of R_o by, *e.g.*, proper cell design and elimination of current measuring resistors in the negative feedback loop effectively reduces potentiostat rise time. In addition, the smallest value of τ (see Eq. [37]), also reduces potentiostat rise time.

The total output current is given by

$$i(s) = \frac{O(s)}{R_o + R_e + Z_E(s)} \qquad [42]$$

from which, using [39]

$$\frac{i(s)}{V(s)} = \frac{G(s)}{[R_e + Z_E(s)][G(s) + 1] + R_o} \qquad [43]$$

Division of Eq. [41] by Eq. [43] allows the impedance expression to be obtained. The result is

$$Z(s) = E(s)/i(s) = R_e + Z_E(s) \qquad [44]$$

Inspection of Eq. [44] indicates that both $G(s)$ and R_o have been eliminated and that $Z(s)$ is a function only of what appears across the potentiostat control points (*i.e.*, between reference and working electrodes). In this way, the potentiostat characteristics and the impedance of the counterelectrode, current sampling resistors, and wire inductance in the negative feedback loop are not included in the final measurement. The only inductance which may remain is that of the working electrode lead which, in practice, may be reduced to a negligible amount.

It has thus been shown that knowledge of the function $Z(s)$, as defined in Eq. [44], allows the characteristics of the electrochemical system to be isolated from the most troublesome instrumental artifacts when a potentiostat is employed. $Z(s)$ is obtained from both the real and imaginary axis transformation of the voltage appearing across the potentiostat control points, $E(t)$, and the potentiostat output current, $i(t)$. As indicated in the theoretical discussion, both $E(t)$ and $i(t)$ may be obtained at times as close to zero as experimentally feasible. The shortest time at which meaningful results can be obtained is determined, to a large extent by the speed of the potentiostat, *i.e.*, $G(s)$.

Experimental and Results

In order to illustrate and test the transient impedance technique, the general potentiostat circuit shown in Fig. 6 was employed. The specific form of Z_E was initially chosen to be a real electric circuit consisting of a capacitor representing the double layer, C_d, in series with the electrolyte resistance, R_e, as shown in Fig. 7. The potentiostat, A, (Fig. 6), is the ultrafast rise Tacussel Model PIT-20-2A provided with external phase compensation to correctly match the potentiostat with Z_E for fast, smooth and easily measurable response. The step voltage source, $V(s)$, (Fig. 6), is the Monsanto 300A pulse generator which can be correctly mated to the input of the potentiostat through the use of its variable rise and fall times. All voltage

Fig. 7. Equivalent circuit representing double layer behavior only

and current time functions were measured on a Tektronix 556 oscilloscope equipped with two 1A5 preamplifiers. Active probes were used exclusively since the signal is detected at the probe tip at relatively high impedance allowing faithful signal reproduction at rise times as short as 3 nanosec, effectively eliminating the influence of cable length. For those cases in which current could be measured outside the negative feedback loop, two Tektronix P6045 FET probes were employed. When the current measuring resistor was placed inside the negative feedback loop [thus constituting part of R_o, (Fig. 6)], two Tektronix P6046 differential probes were employed. In each case, identical type probes were utilized so that correct signal matching could be maintained. Identical probes could be matched to better than ±5% by appropriate peaking of the high frequency circuits within the respective probe amplifiers to obtain as closely identical pulse shapes from the same signal source as possible. In this way, nonlinearities which may be present in signal measurements are nearly identical for both current and voltage and cancel out of the resulting impedance expression.

Initial experiments were carried out using $R_e = 5$ ohms and $C_d = 0.15$ microfarads. Note that measurements performed on electrical analogs at the times and frequencies attainable in this work require suitable high frequency components. For this reason, only metal film resistors and glass capacitors were used throughout this study. The photograph shown in Fig. 8 illustrates the oscilloscopic recording of current and voltage time traces at 50 nanosec per major horizontal division for the circuit given above. It can be seen from Fig. 8 that an initial voltage or current point at 10 nanosec is readily accessible. As will be seen below, this is sufficient, along with adequate point spacing, to enable frequencies as high as 10^8 rad/sec to be examined.

Both real and imaginary axis transformations were performed by carrying out the mathematical operations in Eq. [2] and [7] numerically using a digital computer (Burroughs 5500 or EAI 640). Complete details of the digital computer calculations will be published elsewhere. Briefly, however, the calculations proceed in the following fashion. Data points in digital form accurately representing the complete experimental time curve are introduced at the beginning of the program and a data check is made to detect errors in transcription, *e.g.*, time voltage or current increment errors. Note here that all data is recorded with a point spacing which corresponds to a maximum of a 10% change in successive points. In practice, when using an oscilloscope, several time overlapping pictures must be obtained to accomplish this. Work is presently underway in this laboratory to directly record data in digital fashion. This will be performed using very fast sample and hold modules to record appropriate spaced initial time points coupled with the single cycle data input mode available on most small computers (such as EAI 640) enabling a data point to be obtained each memory cycle (usually 1 to 1.5 μsec).

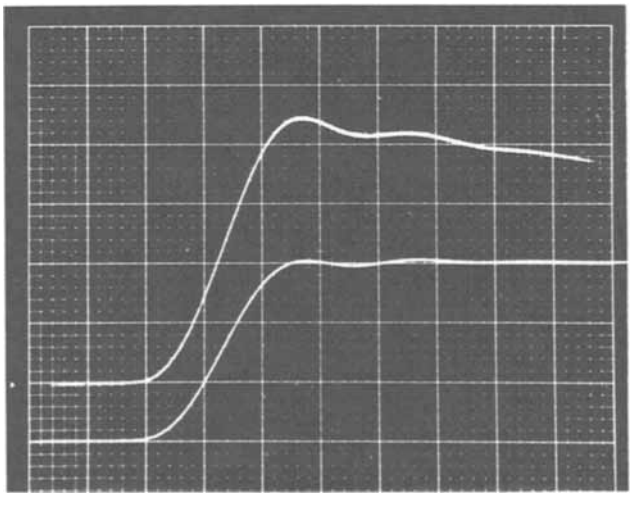

Fig. 8. Actual oscilloscope trace at 50 nanosec per major horizontal division. Lower curve is voltage and upper curve current.

Once the data has been checked, the calculations then proceed, according to the following algorithm in the case of real axis transformation

$$F(\sigma) = \sum_i \left[\frac{[f(t_i+1)e^{-\sigma t_{i+1}} - f(t_i)e^{-\sigma t_i}][t_{i+1} - t_i]}{\ln [f(t_i+1)e^{\sigma t_{i+1}}/f(t_i)e^{\sigma t_i}]} \right] + \frac{f(t_\infty)}{\sigma} \quad [45]$$

where t_i and t_{i+1} represent successive time points; and t_∞ is the time at which the signal achieves steady state, if present. Inspection of Eq. [45] indicates that this integration is carried out by assuming exponential behavior between any two successive data points. The numerical summation is performed for every value of σ desired for all voltage and current points whereupon $Z(\sigma)$ may be evaluated according to Eq. [3].

In the case of imaginary axis transformation, the real and imaginary parts of the time function are evaluated on the basis of Eq. [7]. The alogorithms employed again assume exponential behavior between any two successive data points and are given by, for the real part

$$\mathrm{Re}[F(j\omega)] = \sum_i \frac{1}{a^2+\omega^2} \begin{bmatrix} f(t_{i+1})[a\cos\omega t_{i+1} + \omega \sin \omega t_{i+1}] \\ -f(t_i) \quad [a\cos\omega t_i + \omega \sin \omega t_i] \end{bmatrix} \quad [46]$$

and for the imaginary part

$$\mathrm{Im}[F(j\omega)] = \sum_i \left\{ \frac{1}{a^2+\omega^2} \begin{bmatrix} f(t_{i+1})[a\sin\omega t_{i+1} - \omega \cos \omega t_{i+1}] \\ -f(t_i) \quad [a\sin\omega t_i - \omega \cos \omega t_i] \end{bmatrix} \right\} - \frac{f(t_\infty)}{\omega} \quad [47]$$

where

$$a = \frac{\ln [f(t_{i+1})/f(t_i)]}{t_{(i+1)} - t_i} \quad [48]$$

The summations given in Eq. [46] and [47] are performed for all desired ω values for all voltage and current points from which $Z(j\omega)$ is evaluated by the appropriate division of $V(j\omega)$ and $I(j\omega)$.

It was found that an exponential approximation describing the function between two successive data points was the best possible for both transformations provided that these points are correctly spaced. That this is so can be seen from the fact that, for an electrochemical system which can be described by an aperiodic equivalent circuit, only a single time constant will be predominant over a sufficiently small time interval and a single exponential will, therefore, prevail. Note that the exponential approximation is also valid for diffusion coupled systems exhibiting error function behavior since over relatively small time intervals, this function also behaves exponentially to a very good approximation. An obvious ambiguity in this approach exists for those cases in which two (or more) time constants are essentially identical. In this case, the system will behave as though only one time constant were present over the time interval considered and separation will indeed be difficult. One possible solution to this problem is to vary the initial conditions of the experiment with respect to, *e.g.*, potential and/or concentration, which, in most cases, alters the lumped time constants to widely differing degrees.

One of the major problems in numerical real and imaginary axis transformations as performed in this

study is truncation error which may arise, *e.g.*, in the subtraction of two large numbers. It is therefore important to arrange the steps of the computer program in a sequence designed to minimize this possibility. It is also necessary to have a sufficient number of correctly spaced data points (following the 10% signal variation noted above) over the time region which contribute most heavily to a particular value of σ or ω. If this condition is not met, severe truncation error will also result.

The numerical procedure outlined above was applied to both current and voltage time curves, with initial points being taken at 10 nanosec, obtained for the Re-C_d series circuit mentioned above (Fig. 7). Both $Z(\sigma)$ and $Z(j\omega)$ were then obtained. As indicated by Eq. [4], a plot of $Z(\sigma)$ *vs.* $1/\sigma$ should result in a straight line for this circuit, the slope of which contains C_d while the intercept gives R_e. This plot is shown in Fig. 9 for the highest frequency range attainable in this work (10^8 to 10^6 rad/sec). It can be seen that even at the highest frequency, the results are meaningful and adequately describe the system behavior in terms of Eq. [4]. Maximum error occurs at frequencies above 5 x 10^7 rad/sec and for this system, ranged from ±1% at 5 x 10^7 rad/sec to ±5% at 10^8 rad/sec.

The evaluation of $Z(j\omega)$ for this case allows the examination of its real and imaginary parts as a function of $1/\omega$, according to Eq. [9]. A plot of both of these quantities is shown in Fig. 10 for the frequency range 10^8 to 10^6 rad/sec. It can be seen that expected behavior is observed and, as indicated earlier, provides a rather powerful crosscheck allowing decreased ambiguity in the elucidation of double layer behavior. Maximum error occurs in the frequency interval from 10^7 to 10^8 rad/sec ranging from ±3 to 10%.

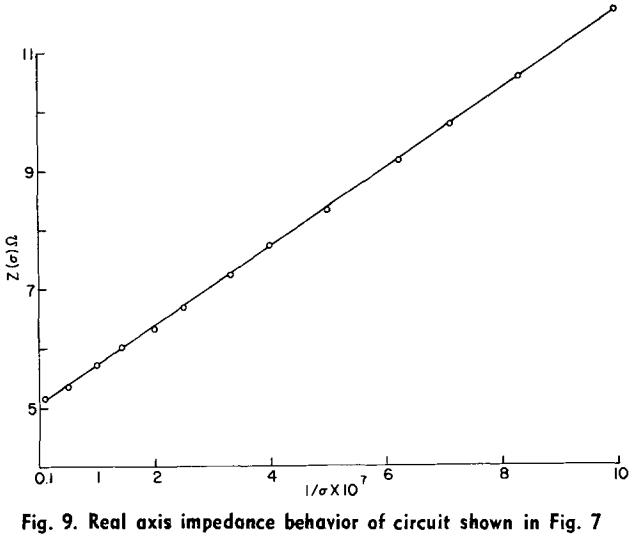

Fig. 9. Real axis impedance behavior of circuit shown in Fig. 7

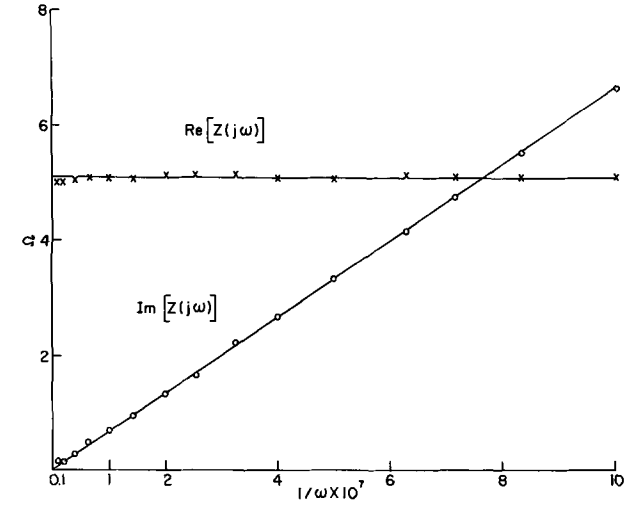

Fig. 10. Imaginary axis impedance behavior of circuit shown in Fig. 7.

In order to more fully test the transformation technique, the equivalent circuit shown in Fig. 4 was examined. This circuit represents, as indicated earlier, an electrode exhibiting double layer behavior along with charge transfer and adsorption, *i.e.*, a system with two time constants The circuit components chosen were R_e = 5 ohms, C_d = 0.15 μF, R_t = 50 ohms, C_a = 1.5 μF, and R_a = 10 kohms. The value of R_a was chosen to be relatively large in order to represent irreversible adsorption for which R_a can then essentially be neglected. An example of this is the hydrogen-platinum system at potentials anodic to the RHE which has recently been studied in this laboratory with the aid of the transient impedance method (65).

The total impedance of this system, in terms of its equivalent circuit (Fig. 4) is given by, neglecting R_a

$$Z(s) = R_e + \frac{R_tC_as + 1}{R_tC_aC_ds^2 + (C_d + C_a)s} \qquad [49]$$

which becomes, at sufficiently high frequencies

$$Z(s) = R_e + \frac{1}{C_ds} \qquad [50]$$

thus illustrating that, for this case, there is a frequency range over which only double layer behavior will be observed (see Eq. [10]). At sufficiently low frequencies, Eq. [49] becomes

$$Z(s) = R_e + \frac{R_tC_a}{C_d + C_a} + \frac{1}{(C_d + C_a)s} \qquad [51]$$

Examination of Eq. [50] and [51] indicates that there are two frequency ranges over which both $Z(\sigma)$ and $Z(j\omega)$ exhibit inverse frequency behavior.

In order to illustrate this, $Z(\sigma)$ was evaluated numerically and diagnostic plots of $Z(\sigma)$ *vs.* $1/\sigma$ are shown in Fig. 11, 12, and 13. Over-all behavior is shown in Fig 11 in the frequency range 10^6 to 10^4 rad/sec which covers the crossover region between only double layer behavior and combined double layer and faradaic behavior. It can already be seen that there is some indication that the system may be diagnosed according to Eq. [50] and [51], however, linearity in $1/\sigma$ is too short in either region to be unambiguous. Figure 12, therefore, shows the high frequency behavior of this system over the range 10^8 to 10^6 rad/sec. The plot is linear over nearly this complete frequency range and allows the evaluation of R_e and C_d which were within ±5% of their known values. Figure 13 shows the low frequency behavior of

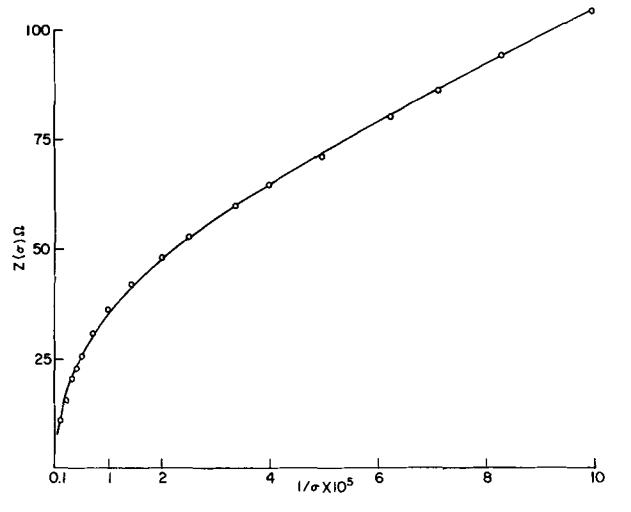

Fig. 11. Over-all real axis impedance behavior of circuit shown in Fig. 4.

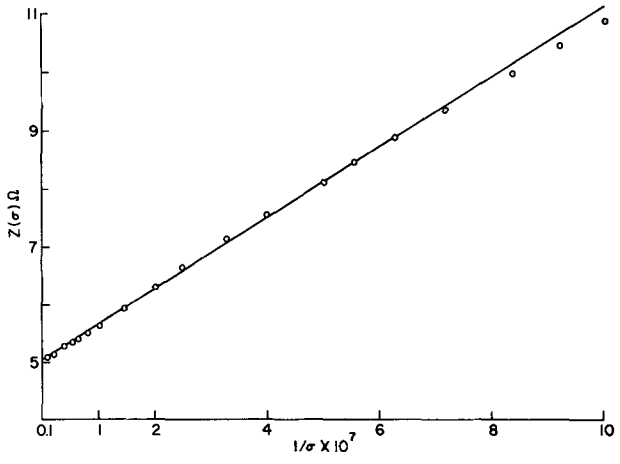

Fig. 12. High frequency real axis impedance behavior of circuit shown in Fig. 4.

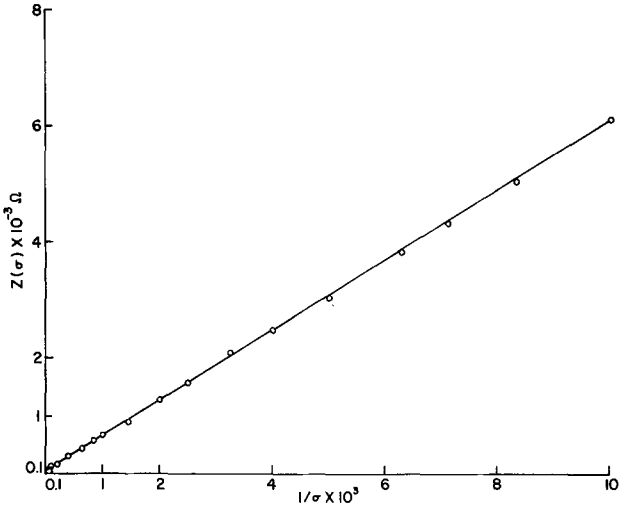

Fig. 13. Low frequency real axis impedance behavior of circuit shown in Fig. 4.

this circuit from 10^4 to 10^2 rad/sec. As can be seen, this plot is again linear in $1/\sigma$ over this frequency range. The values of R_t and C_a calculated from this behavior were within $\pm 5\%$ of their known value. Essentially similar results were obtained for $Z(j\omega)$.

It is to be noted that the time constants of this example were chosen so that double layer behavior can be observed only if relatively high frequencies can be obtained. An electrochemical system exhibiting this behavior is the platinum-hydrogen case (13, 65, 66). Linearity of $Z(\sigma)$ *vs.* $1/\sigma$ in the relatively low frequency range begins at approximately 10^5 rad/sec, normally a high frequency for most impedance studies. Since this plot is a good diagnostic for double layer behavior, it might be assumed that this system did not exhibit adsorption properties, if relatively higher frequencies were not examined. This then illustrates the importance of making frequency studies over as wide a frequency range as possible, especially if adsorption is suspected.

Conclusions

The transient impedance technique presented in this work represents an approach to the study of electrode kinetics which allows the system to be examined using relatively simple algebraic equations with a marked reduction in instrumental errors and artifacts over a relatively wide frequency range. The analysis indicates that meaningful results may be obtained at frequencies as high as 10^8 rad/sec because of the inherent elimination of nearly all instrumental nonlinearities normally encountered at these frequencies. The complete impedance function is generated from time domain data through the use of real and imaginary axis Laplace transformation carried out numerically with the aid of a digital computer. Knowledge of both $Z(\sigma)$ and $Z(j\omega)$ allows considerable cross checking of results once diagnostic plots representing specific types of electrode behavior are available. These criteria may be obtained by the solution of equations describing a particular model in terms of impedance. In this way, both double layer and faradaic behavior (in the presence of each other) may be expressed as relatively simple frequency domain functions as compared with the corresponding time domain functions which, for complex systems, become intractable if, in fact, they can be obtained in closed form at all. In addition, use of the time domain does not allow the inherent simple reduction of instrumental errors. Once the electrode impedance functions have been rigorously derived, they can be identified with aperiodic electrical equivalent circuits for convenience. Thus, circuit elements representing the double layer and faradaic steps such as diffusion, adsorption, charge transfer, etc., can be independently derived and combined in a total equivalent circuit following the particular electrode model chosen. In addition, the variation of these subcircuits with potential can be easily derived if impedance is obtained using small perturbations from steady-state potentials as well as at the equilibrium potential allowing further elucidation of the system under study. It is to be emphasized that the impedance of an electrochemical system must be studied over as wide a frequency range as possible to obtain minimum ambiguity in the interpretation of results. This is especially important when it is desired to evaluate the double layer in the presence of a faradaic reaction, particularly when adsorption or other surface processes may be present.

Acknowledgments

The author sincerely thanks Dr. R. B. Roe and Mr. R. Abramson for their considerable help in establishing the computer programs. Much of this work was performed while the author was at the U.S. Army Electronics Command Research Laboratories, Ft. Monmouth.

Manuscript submitted Oct. 14, 1969; revised manuscript received ca. Dec. 22, 1969.

Any discussion of this paper will appear in a Discussion Section to be published in the December 1970 JOURNAL.

REFERENCES

1. P. Delahay, in "Advances in Electrochemistry and Electrochemical Engineering," Vol. 1, P. Delahay, Editor, Interscience Publishers, Inc., New York (1961).
2. W. H. Reinmuth, *Anal. Chem.*, **36**, 211 (1964); **38**, 270R (1966).
3. A. A. Pilla, *Bull. Soc. Fr. Elec.*, **4**, 24 (1963).
4. H. Gerischer and W. Vielstich, *Z. Physik. Chem.*, **3**, 16 (1955).
5. W. Vielstich and H. Gerischer, *ibid.*, **4**, 10 (1955).
6. W. Vielstich and P. Delahay, *J. Am. Chem. Soc.*, **79**, 1874 (1957).
7. F. C. Anson, *Anal. Chem.*, **38**, 54 (1966).
8. H. A. Laitinen, R. P. Tischer, and D. K. Roe, *This Journal*, **107**, 546 (1960).
9. R. W. Murray and C. N. Reilley, *J. Electroanal. Chem.*, **3**, 182 (1962).
10. H. B. Herman and A. J. Bard, *J. Phys. Chem.*, **70**, 396 (1966).
11. T. Berzins and P. Delahay, *J. Am. Chem. Soc.*, **77**, 6448 (1955).
12. M. Bonnemay, G. Bronoel, E. Levart, and A. A. Pilla, *J. Electroanal. Chem.*, **13**, 44 (1967).
13. M. Rosen, D. R. Flinn, and S. Schuldiner, *This Journal*, **116**, 1112 (1969).
14. R. L. Birke and D. K. Roe, *Anal. Chem.*, **37**, 450, 455 (1965).
15. G. C. Barker, in "Transactions of the Symposium on Electrode Processes," E. Yeager, Editor, John Wiley and Sons, New York (1961); *Pure Appl. Chem.*, **15**, 239 (1967).
16. P. Delahay, *J. Phys. Chem.*, **16**, 2204 (1962).

17. W. H. Reinmuth and C. E. Wilson, *Anal. Chem.*, **34**, 1159 (1962).
18. F. C. Anson, *ibid.*, **38**, 1924 (1966).
19. S. Schuldiner and C. H. Presbrey, *This Journal*, **111**, 457 (1964).
20. W. D. Weir and C. G. Enke, *J. Phys. Chem.*, 275, 280 (1967).
21. R. S. Nicholson and I. Shain, *Anal. Chem.*, **36**, 706 (1964); **37**, 178, 190 (1965).
22. R. S. Nicholson, *ibid.*, **37**, 667, 1351 (1965).
23. J. M. Saveant and E. Vianello, *Electrochim. Acta*, **8**, 905 (1963); **12**, 629 (1967).
24. S. W. Feldberg, in "Electroanalytical Chemistry," Vol. 3, A. J. Bard, Editor, Marcel-Dekker, New York (1969).
25. G. Lauer, R. Abel, and F. C. Anson, *Anal. Chem.*, **39**, 765 (1967).
26. D. J. Kooijman and J. H. Sluyters, *J. Electroanal. Chem.*, **13**, 152 (1967).
27. D. J. Kooijman, *ibid.*, **18**, 81 (1968).
28. K. J. Oldham and R. A. Osteryoung, *ibid.*, **11**, 397 (1966).
29. B. Timmer, M. Sluyters-Rehbach, and J. H. Sluyters, *ibid.*, **15**, 343 (1967).
30. G. C. Barker and F. A. Bolzan, *Z. Anal. Chem.*, **216**, 215 (1966).
31. F. C. Anson, J. H. Christie, and R. A. Osteryoung, *J. Electroanal. Chem.*, **13**, 343 (1967).
32. F. C. Anson and D. J. Barclay, *Anal. Chem.*, **40**, 1791 (1968).
33. D. J. Barclay and F. C. Anson, *This Journal*, **116**, 438 (1969).
34. Z. Kowalski and F. C. Anson, *ibid.*, **116**, 1208 (1969).
35. D. M. Mohilner, in "Electroanalytical Chemistry," Vol. 1, A. J. Bard, Editor, Marcel-Dekker, New York (1966).
36. P. Delahay, "Double Layer and Electrode Kinetics," p. 197, Interscience Publishers, Inc., New York (1965).
37. P. Delahay, *This Journal*, **113**, 967 (1966).
38. K. Holub, G. Tessari, and P. Delahay, *J. Phys. Chem.*, **71**, 2612 (1967).
39. H. A. Laitinen and J. E. B. Randles, *Trans. Faraday Soc.*, **51**, 54 (1955).
40. A. M. Baticle and F. Perdu, *J. Electroanal. Chem.*, **12**, 15 (1966).
41. R. de Levie, *Electrochim. Acta*, **10**, 395 (1965).
42. J. H. Sluyters, *Rec. Trav. Chim.*, **79**, 1092 (1960).
43. M. E. Van Valkenburg, "Network Analysis," p. 228, Prentice Hall, Inc., Englewood Cliffs, N. J. (1964).
44. D. K. Cheng, "Analysis of Linear Systems," p. 155, Addison-Wesley, Inc. (1959).
45. M. D. Wijnen, *Rec. Trav. Chim.*, **79**, 1203 (1960).
46. A. A. Pilla, D.Sc. Thesis, Univ. of Paris, 1965.
47. E. Levart and E. Poirier d'Ange d'Orsay, *J. Electroanal. Chem.*, **19**, 335 (1968).
48. A. A. Pilla and R. Abramson, Communication presented at the Austin, Texas, A.C.S. Meeting, 1968.
49. D. K. Cheng, "Analysis of Linear Systems," p. 142, Addison-Wesley, Inc. (1959).
50. M. E. Van Valkenberg, "Network Analysis," p. 331, Prentice Hall, Inc., Englewood Cliffs, N. J. (1964).
51. B. Breyer and H. H. Bauer, "Alternating Current Polarography and Tensammetry," Intersciences Publishers, Inc., New York (1963).
52. D. C. Grahame, *This Journal*, **99**, 370C (1952).
53. P. Dolin and B. V. Ershler, *Acta Physicochim, U.R.S.S.*, **13**, 747 (1940).
54. J. E. B. Randles, *Disc. Faraday Soc.*, **1**, 11 (1947).
55. H. Gerischer, *Z. Physik. Chem.*, **198**, 286 (1951).
56. T. Berzins and P. Delahay, *Z. Elektrochem.*, **59**, 792 (1955).
57. M. Sluyters-Rehbach and J. H. Sluyters, *Rec. Trav. Chim.*, **82**, 525 (1963).
58. D. E. Smith, in "Electroanalytical Chemistry," Vol. 1, A. J. Bard, Editor, Marcel Dekker, New York (1966).
59. A. A. Pilla, Communication presented at the A.I.Ch.E. National Meeting, St. Louis (1968).
60. H. Eyring, S. Glasstone, and K. J. Laidler, *J. Chem. Phys.*, **7**, 1053 (1939).
61. K. J. Vetter, "Electrochemical Kinetics," Academic Press, New York (1967).
62. H. Gerischer, *Z. Physik. Chem.*, **201**, 55 (1952).
63. (a) P. Delahay and D. M. Mohilner, *J. Am. Chem. Soc.*, **84**, 4247 (1962).
(b) A. N. Frumkin and V. I. Melik-Gaikazyan, *Dokl. Akad. Nauk SSSR*, **77**, 855 (1951).
(c) W. Lorenz, *Z. Elektrochem.*, **60**, 507 (1956); **62**, 192 (1958); *Naturwissenschaften*, **43**, 197 (1956).
64. A. A. Pilla, R. B. Roe, and C. C. Herrman, *This Journal*, **116**, 1105 (1969).
65. A. A. Pilla, J. A. Christopulos, and G. J. DiMasi, Paper 235 presented at the New York Meeting of the Society, May 5-9, 1969.
66. R. Payne, *J. Electroanal. Chem.*, **19**, 1 (1968).

The Absence of a Detectable Potential-Dependence of the Transfer Coefficient in the Cr^{+3}/Cr^{+2} Reaction

Fred C. Anson,* Nancy Rathjen, and Robert D. Frisbee

Gates and Crellin Laboratories of Chemistry, California Institute of Technology, Pasadena, California

ABSTRACT

The rate of reduction of Cr^{+3} at mercury electrodes has been measured polarographically in an extensive series of electrolytes to search for the potential dependence of the transfer coefficient recently reported (2) for this reaction. No clear evidence of such a potential dependence was found and it is concluded that unavoidable propagation of experimental errors coupled with uncertainties in Frumkin double-layer corrections prevent detection of the predicted potential dependence.

The first systematic study specifically intended to test the prediction of Marcus (1) that the transfer coefficient, α, should show a potential-dependence was described recently by Parsons and Passeron (2). On the basis of their polarographic measurements of the Cr^{+3}/Cr^{+2} electrode reaction they concluded "that there is clear evidence for the existence of the variation of the transfer coefficient with overpotential, and the magnitude of this effect is in agreement with the theoretical prediction within experimental error." This paper has been widely cited because it appeared to offer a very satisfactory confirmation of an important aspect of the Marcus theory.

With the intention of examining the effect of the composition of the supporting electrolyte on the poten-

* Electrochemical Society Active Member.

tial-dependence of α, we undertook a series of polarographic experiments with the Cr^{+2}/Cr^{+3} reaction to extend the work of Parsons and Passeron which was confined to a single concentration ($\mu = 0.5$) of a single electrolyte ($NaClO_4$). We began by attempting to duplicate the results of Parsons and Passeron but were not able to do so. A large number of additional experiments was performed in a search for the source of this discrepancy and some of the results of these experiments are reported here. Our conclusion is that in none of the cases studied is a clear potential dependence of α evident. The unavoidable propagation of experimental errors during the usual conversion of polarographic i/i_d values to rates, and of rates at various potentials to transfer coefficients, results in such large uncertainties that any potential dependence of α is hidden by the theoretical and experimental errors.

Experimental

A water-jacketed polarographic H-cell was employed with a mercury pool serving as the auxiliary electrode. The reference electrode compartment contained supporting electrolyte and the reference electrode was a commercially available saturated calomel electrode in which the KCl electrolyte was replaced with NaCl to prevent the precipitation of $KClO_4$ in the fiber junction. Such dilute solutions of Cr(III) were employed (0.1-0.5 mM) that ohmic drops in the cell were always negligible. The DME (dropping mercury electrode) had a natural drop time of 5.5 sec at −800 mV; drops were not mechanically dislodged.

Solutions were scrupulously deoxygenated by means of a nitrogen stream that passed through copper turnings at 450°C, and a V^{+2} washing tower. Reagent grade salts were used without further purification. The sodium perchlorate solution was prepared from $HClO_4$ and NaOH. The Cr^{+3} solutions were prepared by weighing out crystals of $Cr(ClO_4)_3$ prepared by the reduction of an acidic solution of CrO_3 with H_2O_2, heating to destroy excess peroxide, and concentrating the solution by evaporation until crystals formed. Treatment of supporting electrolytes with prepurified charcoal produced no changes in subsequent polarograms.

Current-potential curves were obtained manually by adjusting the potential of the DME with a solid state operational amplifier-based polarograph and recording the resulting current for several drops with a high precision undamped pen and ink recorder. The potential was then changed by 10 mV and the process repeated. The maximum currents at the end of drop life were used in analyzing the polarograms by means of the Oldham-Parry formula (3) for approximating the Koutecky function (4).

Data analysis.—The polarographic currents recorded at the end of drop life were corrected for the residual current and the ratio, i/i_d, of the current at each potential to the diffusion current was calculated.

In a number of the supporting electrolytes studied the polarographic wave was shifted to the vicinity of the standard potential of the Cr^{+2}/Cr^{+3} couple so that it became quasi-reversible. In such cases, the observed i/i_d ratio was corrected for the back reaction, *i.e.*, Cr^{+2} oxidation, according to Eq. [1]

$$\left(\frac{i}{i_d}\right)_{corr} = \left(\frac{i}{i_d}\right)_{obs}\left[1 + \left(\frac{D_{Cr^{+3}}}{D_{Cr^{+2}}}\right)^{1/2} \exp\left[f(E - E^0)\right]\right] \quad [1]$$

where $(i/i_d)_{corr}$ is the corrected value of the ratio, $(i/i_d)_{obs}$ the experimentally observed ratio, $D_{Cr^{+3}}$ and $D_{Cr^{+2}}$ are the diffusion coefficients of Cr^{+3} and Cr^{+2}, E is the electrode potential, E^0 is the standard potential of the Cr^{+3}/Cr^{+2} couple (−0.65V *vs.* SCE), and $f = F/RT$. When Frumkin double-layer corrections were being applied ($E - \phi_2$) was substituted for E in Eq. [1], where ϕ_2 is the potential at the outer Helmholtz plane. According to the data of Cornelissen (5) $D_{Cr^{+3}} = 5.6 \times 10^{-6}$ cm^2 sec^{-1}, $D_{Cr^{+2}} = 7.9 \times 10^{-6}$ cm^2 sec^{-1}, and $(D_{Cr^{+3}}/D_{Cr^{+2}})^{1/2} = 0.84$. The resulting values of $(i/i_d)_{corr}$ were then substituted into the formula of Oldham and Parry (3) to obtain values of the rate of the electrode reaction at each potential.

The sets of data relating logarithm of rate to potential were used to prepare Tafel plots by fitting with a standard least squares computer program to Eq. [2]

$$\ln \lambda = a_0 + a_1 (E - E^0) \quad [2]$$

where λ is proportional to the rate of the reaction at electrode potential E and $a_1 = -\alpha F/RT$. The apparent value of the transfer coefficient, α, was calculated from the resulting value of a_1.

To test for a potential dependence in α the same data were also fitted by least squares to Eq. [3]

$$\ln \lambda = a_0 + a_1 (E - E^0) + a_2 (E - E^0)^2 \quad [3]$$

The resulting value of a_2 expresses the potential dependence of the transfer coefficient. Equations [2] and [3] differ slightly from the corresponding equations employed by Parsons and Passeron (2) to evaluate the same parameters. They used the overvoltage, η, *i.e.*, the difference between the electrode potential and its equilibrium value in the Cr^{+2}-Cr^{+3} mixtures employed, rather than $(E - E^0)$, the difference between the electrode potential and the standard potential for the couple. According to the Marcus theory (1) $(E - E^0)$, not η, is the independent variable that should be used. However, the error introduced by the use of η instead of $(E - E^0)$ was probably not too large since the Cr^{+2}-Cr^{+3} mixtures employed by Parsons and Passeron covered only a small range of equilibrium potentials which were all fairly close to E^0 (6).

Maxima.—The Cr^{+3} reduction wave tended to develop a pronounced maximum when lower concentrations of supporting electrolyte were employed. This problem could be partially circumvented by employing low concentrations of Cr^{+3} (0.1-0.5 mM) but the maxima appeared in all electrolytes if the ionic strength was decreased sufficiently. This difficulty imposed the lower limit on the supporting electrolyte concentrations that could be employed.

Less severe problems with maxima were also encountered at ionic strengths of 0.5-1M if the Cr^{+3} concentration exceeded about 1.5 mM. Not infrequently the pen and ink recording of the individual current-time curves gave no clear indication of the presence of erratic behavior attributable to maxima, but the collection of current-potential points became harder to reproduce from run to run. Under these circumstances the individual current-time curves were not completely identical from drop to drop when they were inspected in detail by means of an oscilloscope. We concluded that concentrations of Cr^{+3} above 1 mM were to be avoided to prevent errors arising from incipient maxima. Similar behavior has also been reported by Cornelissen (5).

Parsons and Passeron (2) do not specify the concentrations of Cr^{+2} and Cr^{+3} they employed but if values as large as 2-5 mM were used (7), it seems quite likely that their data could have been affected by the presence of inconspicuous maxima.

pH effects.—Parsons and Passeron adjusted the pH of their solutions to 3.4 with $HClO_4$ but employed no buffering agent. A pH value as high as 3.4 seems somewhat dangerous because of the extent of hydrolysis of Cr^{+3} that would result [the hydrolysis constant for Cr^{+3} is $K = 10^{-4}$ M (8)]. An especially worrying point is the question of the pH prevailing at the electrode surface during the reduction of Cr(III). At a pH of 3.4 and a total Cr(III) concentration of 2 mM the concentration of $CrOH^{+2}$ and H^+ are equal. The hydroxide ion liberated by reduction of $CrOH^{+2}$ (Cr^{+2} is unhydrolyzed at pH 3.4) will cause the pH at the electrode surface to become greater than 3.4 and the nature and

charge of the Cr(III) species being reduced will change. To test these suspicions a series of polarograms were recorded for 0.5 mM Cr(III) in a 0.5*F* $NaClO_4$ supporting electrolyte having *p*H values from 2.0 to 4.0. The result was that the polarograms for *p*H values of 2.0, 2.5, and 3.0 were essentially identical. At *p*H 3.5 the individual current-time curves were becoming less reproducible from drop to drop and at *p*H 4.0 the current-time curves displayed very erratic behavior. The erratic current-time behavior becomes more severe as the Cr(III) concentration is raised so that data obtained by Parsons and Passeron (2) at *p*H 3.4 with Cr(III) concentrations of 2 mM and higher would very likely have suffered from the same difficulties. To avoid this source of error in the present experiments we adjusted all solutions to *p*H 2.0 with perchloric acid and used Cr(III) concentrations of 0.5 mM or less.

Corrections for the double layer.—Frumkin double-layer corrections were applied to some of the data by application of Eq. [4] and [5] as is explained in the section on Results and Discussion. For perchlorate electrolytes the values of ϕ_2 required for the Frumkin correction were obtained by interpolation from the data of Payne (9) for the corresponding concentration of perchloric acid or from the data of Wroblowa *et al.* (10) for sodium perchlorate. For iodide electrolytes, the data of Grahame (11) and Breiter, Kleinerman, and Delahay (12) were used, and for bromide electrolytes, the data of Lawrence, Parsons, and Payne (13). The specific adsorption of chloride is so slight at the potentials where Cr^{+3} is reduced (14) that the data for sodium fluoride were employed with the potassium chloride electrolyte.

For the lanthanum chloride electrolytes the Joshi-Parsons equation (15) was used to calculate values of ϕ_2 as a function of q^m, the charge on the electrode, assuming the absence of specific adsorption. Next, Russell's tables (16) were used to evaluate the electrode potential, *E*, which would give the same values of q^m in sodium fluoride solutions having concentrations equal to the ionic strength of the lanthanum chloride solution. The values of ϕ_2' corresponding to these values of *E'* were then used to calculate the electrode potentials corresponding to the initially calculated values of ϕ_2 for the lanthanum chloride solution. That is, at constant q^m, $E = E' - (\phi_2 - \phi_2')$, where *E* is the electrode potential and ϕ_2 the potential at the outer Helmholtz plane, in a lanthanum chloride solution and *E'* and ϕ_2' are the corresponding quantities in a sodium fluoride solution of the same ionic strength.

Results and Discussion

Polarograms for 0.5 mM Cr^{+3} in 0.5M $NaClO_4$-0.01M $HClO_4$ were obtained for comparison with the data of Parsons and Passeron (2). Contrary to the behavior they reported, we observed rather straight Tafel plots before Frumkin double-layer corrections were applied, and when the data were forcibly fit to a quadratic relation, Eq. [3], by a standard least square computer program the "goodness of fit," as measured by the *F*-level (17), decreased markedly, and the coefficient, a_2, of the term in $(E - E^0)^2$ had the opposite sign from that reported in ref. (2). Figure 1 shows a typical Tafel plot and compares it with the plot that is predicted by the coefficients given by Parsons and Passeron (2). The same discrepancy was also obtained in a variety of other supporting electrolytes. As is shown in Table I, which summarizes the data obtained, only in lithium perchlorate electrolytes did the coefficient a_2 in Eq. [3] become less than zero. And even in this case, the *F*-levels resulting from the quadratic fit were so low that it is of doubtful significance.

Polarograms resembling more closely those that Parsons and Passeron apparently obtained did result when the *p*H was raised to 3.5, or if the Cr(III) was obtained from older stock solutions which contained substantial amounts of Cr(III)-polymers as indicated by the ratio of their absorptions at 260 and 230 nm (18).

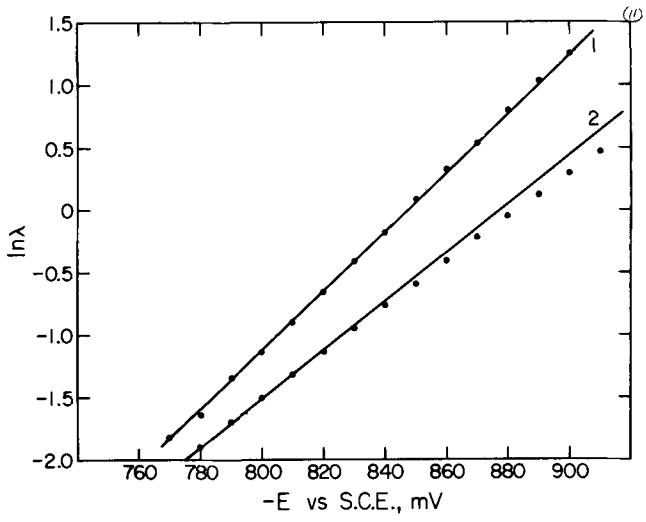

Fig. 1. Tafel plots for reduction of Cr^{+3} in 0.5M $NaClO_4$. Curve 1, Data from the present work; curve 2, data calculated from the parameters given in (2).

It seems likely, therefore, that the solutions used by Parsons and Passeron contained hydrolyzed Cr(III) species which produced Tafel plots unrepresentative of the behavior of monomeric Cr^{+3} ion.

The theoretical prediction that the transfer coefficient should show a potential dependence (1) remains, however, and it was of interest to see if any such dependence could be found in the data obtained with solutions containing only monomeric, Cr^{+3} ions. To do so requires that Frumkin double-layer corrections be applied to the data because the uncorrected data show an apparent potential-dependence of α which has the opposite sign from that predicted by the Marcus theory (1). This behavior does not necessarily throw doubt on the theory because the expected double-layer effects act in the opposite direction to that predicted for the potential dependence of α, *i.e.*, the apparent transfer coefficient before the double-layer correction is applied increases as the potential becomes more negative.

The data were, therefore, re-examined by fitting them via least squares to the equations

$$\ln \lambda + ZF\phi_2 = b_0 + b_1 (E - E^0 - \phi_2) \qquad [4]$$

and

$$\ln \lambda + ZF\phi_2 = b_0 + b_1 (E - E^0 - \phi_2) + b_2(E - E^0 - \phi_2)^2 \qquad [5]$$

where *Z* is the average charge of the Cr(III) in the bulk of the solution, account being taken of any ion pairing between Cr^{+3} and the anions of the supporting electrolyte, ϕ_2 is the potential at the outer Helmholtz plane, and λ, *E*, and E^0 have the same significance as in Eq. [2]. The coefficients b_0, b_1, and b_2 were evaluated by means of least-squares fit of the data to Eq. [4] or [5]. The results of this procedure are also shown in Table I. In all cases, applying the double-layer corrections produced decreases in *F*-levels and increases in the standard errors of the coefficients resulting from the linear least-squares fit. For the quadratic fit the double-layer corrections produced no clear trend in standard errors or *F*-levels (Table I) but in every case the sign of the coefficient of the term in E^2 remained positive. Thus, within the limits set by the uncertainties in the double-layer corrections, the data show no evidence of a potential dependence in the transfer coefficient. We do not regard these results as demonstrating the absence of any potential dependence in α. Rather what has become clear is that much more precise rate measurements, as well as more accurate Frumkin double-layer corrections, will be required before a judgment can be reached.

The last point can be emphasized by examining the errors inherent in any polarographic evaluation of the

Table I. Parameters resulting from least-squares fitting of rate data to linear or quadratic Tafel plots

Supporting electrolyte	Range of $\lvert E - E^0 \rvert$ covered, mV	Before Frumkin correction applied: Linear fit, Eq. [2] α	Std. error	F-level × 10^{-3}	Quadratic fit, Eq. [3] F-level × 10^{-3}	$-\frac{RT}{F}a_1$	Std. error	$\frac{2RT}{F}a_2$	Std. error	Z^a
0.5M $NaClO_4$	110-240	0.60	0.005	29	0.029	0.50	0.02	0.59	0.11	3
0.5M $NaClO_4$	110-240	0.60	0.005	29	0.029	0.50	0.02	0.59	0.11	3
1.0M $NaClO_4$	130-260	0.55	0.002	14	0.0023	0.48	0.04	0.33	0.21	3
1.0M $NaClO_4$	130-260	0.55	0.002	14	0.0023	0.48	0.04	0.33	0.21	3
Parsons-Passeron	100-250					0.53		−0.34		
0.5M KCl	100-260	0.57	0.001	8.3	0.09	0.38	0.02	0.85	0.10	2.13
0.5M KBr	90-240	0.52	0.007	8.1	0.16	0.35	0.01	1.0	0.08	
1.0M KBr	110-270	0.48	0.004	13	0.19	0.35	0.01	0.71	0.05	2.12
0.5M KI	20-190	0.43	0.007	3.5	0.070	0.31	0.01	1.12	0.13	
0.5M $LiClO_4$	100-210	0.73	0.004	31	0.0002	0.75	0.04	−0.13	0.28	3
1.0M $LiClO_4$	130-240	0.69	0.006	13	0.014	0.87	0.05	−0.98	0.26	3
0.08M $CsClO_4$	50-210	0.63	0.005	24	0.0014	0.61	0.02	0.16	0.17	
0.0883M (μ = 0.5) $LaCl_3$	150-280	0.60	0.003	40	0.016	0.50	0.02	0.45	0.11	2.24
0.1666M (μ = 1.0) $LaCl_3$	170-310	0.57	0.002	68	0.003	0.53	0.03	0.18	0.11	2.13

[a] Calculated from reported (18) or estimated (24) ion pairing constants.
[b] Double-layer data unavailable for this electrolyte.
[c] Apparent specific catalysis by adsorbed iodide prevented meaningful calculations. See text.

rate of irreversible electrode reactions: The standard procedure involves measurements of instantaneous or average currents at small potential intervals on the rising portion of the wave. These current measurements, normalized by division by the diffusion current, are then usually converted to a parameter proportional to the rate constant of the reaction by means of the tabulated conversion tables of Koutecky (4). Recently, Oldham and Parry (3) devised a simple algebraic formula which comes very close to matching the Koutecky tabulation and has the advantage of being a continuous function. Using the Oldham-Parry formula, the equation relating the rate of a one-electron, irreversible cathodic electrode reaction to the experimentally determined ratio of i/i_d becomes

$$\lambda = K\left(\frac{0.4X(3-X)}{1-X}\right)\exp\left[-\alpha f(E-E^0)\right] \quad [6]$$

where λ is proportional to the rate of the electrode reaction, $X = i/i_d$, K represents a combination of experimental constants, $f = F/RT$, E is the electrode potential, and E^0 the standard potential of the redox couple. The transfer coefficient, α, is assumed to be independent of potential. If the only experimental error in the polarographic measurements is assumed to reside in the evaluation of the current, then it can be shown that the error in $\ln\lambda$ resulting from an error, ΔX, in X is given by

$$\Delta \ln\lambda = \left(\frac{1}{X} - \frac{1}{3-X} + \frac{1}{1-X}\right)\Delta X \quad [7]$$

The values of X are confined to the interval from zero to unity and measurements typically cover the range 0.1-0.9. Within this range the first factor on the r.h.s. of [7] varies from a maximum of 10.8 (at $X = 0.1$) to a minimum of 3.6 (at $X = 0.5$). Thus, if current measurements are made with a precision of, say, 1%, and potential measurements are free of error, the values of $\ln\lambda$ are established with a precision of only *ca.* 4-10%.

This uncertainty is increased further when the values of $\ln\lambda$ are used to evaluate the coefficient of $(E - E^0)^2$ in Eq. [3]

$$a_2 = \frac{\ln\lambda - a_0 - a_1(E-E^0)}{(E-E^0)^2} \quad [8]$$

If the maximum value of $(E - E^0)$ attained in the experiment is 0.25V, as in the experiments of Parsons and Passeron (2), a 5% uncertainty in $\ln\lambda$ results in a minimum uncertainty of *ca.* 80% in the value of a_2. When double-layer corrections are introduced (by using Eq. [5] to evaluate the coefficient b_2) the resulting uncertainties in b_2 are even larger. Thus, the limits of error reported by Parsons and Passeron for their values of b_2, *i.e.*, *ca.* ±30%, seem unduly optimistic. When the combined uncertainties arising from the limited precision of polarographic rate measurements and simple Frumkin double-layer corrections are considered it is difficult to see how any polarographically measured reaction rate at values of $(E - E^0)$ less than about 1V could be expected to give reliable estimates of the value of b_2 in Eq. [5]. The same general limitation would apply to the recent proposal of Mohilner (19) that experimental searches for potential-dependent transfer coefficients might be more fruitful with intrinsically faster reactions than Cr^{+3}/Cr^{+2} because the absolute value of b_2 would be larger. To do so would require rate measurements much more precise than are achievable polarographically because the attainable values of $(E - E^0)$ would necessarily be smaller due to present experimental limits on the fastest rates which can be measured. The uncertainty introduced into the values of b_2 because of the small size of the $(E - E^0)^2$ term can be overcome in principle (19), but only by achieving a precision in the measurement of the electrode reaction rate considerably better than any that has been attained up to now.

As pointed out by Parsons and Passeron (2), an independent estimate of the magnitude of the potential dependence of the transfer coefficient predicted by the Marcus theory can be obtained from Eq. [9] and [10] (1)

$$k_s \cong 10^4 \exp\left[\frac{-\Delta G^{0\ddagger}}{RT}\right] \quad [9]$$

$$-2\frac{RT}{F}b_2 = \frac{F}{8\Delta G^{0\ddagger}} \quad [10]$$

where k_s and $\Delta G^{0\ddagger}$ are, respectively, the rate constant and free energy of activation of the reaction at E^0. After double layer corrections are applied, most of the values for k_s in Table II are close to $10^{-6.1}$. This value and Eq. [9] give a value of about 14 kcal for $\Delta G^{0\ddagger}$ which leads to a predicted value of $-0.20\ V^{-1}$ for the coefficient $2\ RT/F\ b_2$. Coefficients having much larger absolute values than this resulted when most of the present data were forcibly fit to a quadratic equation but the coefficients had the wrong sign and the standard errors increased greatly (Table I). The fact that data which fit a normal linear Tafel plot very closely can, nevertheless, produce quadratic coefficients which equal or exceed those predicted by the Marcus theory, further emphasizes the need for increased precision in data employed to test this aspect of the theory.

Comments on the data summarized in Table I.—A few features of the data in Table I deserve special comment. The double-layer data of Wroblowa *et al.* (10) and Payne (9) give discrepant values of ϕ_2 but very similar values of $\partial\phi_2/\partial E$. This accounts for the fact that very similar values of α result from the linear fit after double-layer correction using either set of ϕ_2 *vs.* E data.

Table I (Cont.)

After Frumkin correction applied								
Linear fit, Eq. [4]			Quadratic fit, Eq. [5]					
α	Std. error $\times 10^3$	F-level $\times 10^{-3}$	F-level $\times 10^{-6}$	$-\frac{RT}{F}b_1$	Std. error $\times 10^2$	$\frac{2RT}{F}b_2$	Std. error	Remarks
0.47	0.005	7.3	0.029	0.35	0.02	0.96	0.18	ϕ_2 data from (10)
0.45	0.005	7.4	0.029	0.35	0.02	0.91	0.17	ϕ_2 data from (9)
0.48	0.005	8.1	0.004	0.40	0.04	0.47	0.25	ϕ_2 data from (10)
0.43	0.005	7.1	0.0046	0.34	0.03	0.50	0.23	ϕ_2 data from (9)
				0.40		−0.26		$\frac{\partial\phi_2}{\partial E}$ from (9)
0.42	0.02	1.8	0.055	0.13	0.02	1.9	0.12	ϕ_2 data from (16)[b]
0.53	0.003	43	0.073	0.46	0.007	0.40	0.05	ϕ_2 data from (13)[c]
0.58	0.004	20	0.00073	0.55	0.03	+0.12	0.14	ϕ_2 data from (9)
0.58	0.006	11	0.0096	0.71	0.04	−0.86	0.28	ϕ_2 data from (9)[b]
0.54	0.004	17	0.038	0.41	0.02	0.73	0.12	ϕ_2 values calculated as explained in text
0.53	0.007	5.8	0.0020	0.42	0.08	0.51	0.36	

On the basis of the corrected rate data in Table II, however, there seems some basis for preferring the data of Payne (9) to that of Wroblowa *et al.* (10).

For KBr, the value of α resulting from the linear fit is greater after the Frumkin correction is applied, while the contrary is true with the other electrolytes. This difference results from the fact that $\partial\phi_2/\partial E$ in 1M bromide is negative instead of positive, as in the other electrolytes.

Adequate double-layer data were available to apply the Frumkin correction in the case of 0.5M KI (11, 12). However, the Cr^{+3}-reduction is greatly catalyzed by iodide adsorption as is indicated by the smaller values of $E - E^0$ at which the wave occurs. In fact, some non-Frumkin type of catalysis appears to be involved because the observed cathodic currents occur at potentials where net anodic currents are calculated to flow if the usual Frumkin correction and back-reaction correction are applied.

The two $LaCl_3$ supporting electrolytes were used to assess the importance of matching the size and charge of the supporting electrolyte ions to those of the reactant ion, as advocated by Asada *et al.* (20). Extremely linear Tafel plots were obtained both before and after the Frumkin correction but comparable behavior was also obtained with $NaClO_4$ and $LiClO_4$ electrolytes after the Frumkin correction was applied. A clearer test is posed if the values of the standard rate constant for the electrode reaction calculated from the Frumkin correction are compared. This comparison is shown in Table II from which it appears that the standard Frumkin correction leads to a reasonably constant value of the rate constant in all of the electrolytes examined except for KCl. In particular, the $LaCl_3$ electrolytes do not yield values which differ significantly from those for $NaClO_4$ or KBr. Thus, the restrictions on suitable supporting electrolytes suggested by Asada *et al.* (20) for accurate application of the Frumkin correction do not appear to apply to the Cr^{+3}/Cr^{+2} reaction. This observation, coupled with the recent discovery (21, 22) that the apparent failure of simple diffuse layer theory in mixed electrolytes, as reported by Joshi and Parsons (15), resulted from an error in the data analysis, suggests that the effective planes of closest approach for ions of differing size and charge may not be as incongruent as has been imagined (23).

Table II. Standard rate constants before and after double-layer correction

log k_s ($E = -650$ mV *vs.* SCE)

Electrolyte	Before Frumkin correction	Z^0	After Frumkin correction	
0.5M $NaClO_4$	−5.09	3	−6.89	ϕ_2 data from (10)
0.5M $NaClO_4$	−5.09	3	−6.11	ϕ_2 data from (9)
1.0M $NaClO_4$	−5.10	3	−6.55	ϕ_2 data from (10)
1.0M $NaClO_4$	−5.10	3	−6.14	ϕ_2 data from (9)
0.5M $NaClO_4$ (Parsons-Passeron)	−5.15	3		
0.5M KCl	−5.07	2.13	−5.67	
0.5M KBr	−4.77		[a]	
1.0M KBr	−4.87	2.12	−6.15	
0.5M KI	−4.01		[b]	
0.5M $LiClO_4$	−5.19	3	−6.42	ϕ_2 data from (9)
1.0M $LiClO_4$	−5.44	3	−6.41	ϕ_2 data from (9)
0.08M $CsClO_4$	−4.67		[a]	
0.0833M (μ = 0.5) $LaCl_3$	−5.19	2.24	−6.13	
0.1666M (μ = 1.0) $LaCl_3$	−5.58	2.13	−6.11	

[a] ϕ_2 values not available for this electrolyte.
[b] Apparent specific catalysis by adsorbed iodide prevented meaningful calculation of the "standard" rate constant.

Acknowledgments

Dr. Richard Payne kindly offered his unpublished double-layer data for $HClO_4$ solutions. Roger Abel supplied valuable assistance with the computer programs used for the least-squares fitting of the data. This work was supported by the National Science Foundation. It is Contribution No. 3981 of the Gates and Crellin Laboratories of Chemistry, California Institute of Technology.

Manuscript submitted Nov. 18, 1969; revised manuscript received *ca.* Dec. 16, 1969.

Any discussion of this paper will appear in a Discussion Section to be published in the December 1970 JOURNAL.

REFERENCES

1. R. A. Marcus, *J. Chem. Phys.*, **43**, 679 (1965).
2. R. Parsons and E. Passeron, *J. Electroanal. Chem.*, **12**, 524 (1966).
3. K. B. Oldham and E. P. Parry, *Anal. Chem.*, **40**, 65 (1968).
4. J. Koutecky, *Collect. Czech. Chem. Commun.*, **18**, 597 (1953).
5. R. Cornelissen, Thesis, Free University of Brussels, 1962.
6. R. Parsons, Private communication.
7. In a private communication Dr. Passeron stated that concentrations of Cr^{+3} in this range were employed in the experiments reported in ref. (2).
8. K. Emerson and W. M. Garven, *J. Inorg. Nucl. Chem.*, **11**, 309 (1959).
9. R. Payne, Unpublished data.
10. H. Wroblowa, Z. Kovac, and J. O'M. Bockris, *Trans. Faraday Soc.*, **61**, 1523 (1965).
11. D. C. Grahame, *J. Am. Chem. Soc.*, **80**, 4201 (1958).
12. M. Breiter, M. Kleinerman, and P. Delahay, *ibid.*, **80**, 5115 (1958).
13. J. Lawrence, R. Parsons, and R. Payne, *J. Electroanal. Chem.*, **16**, 193 (1968).
14. M. A. V. Devanathan, *Trans. Faraday Soc.*, **50**, 384 (1954).
15. K. M. Joshi and R. Parsons, *Electrochim. Acta*, **4**, 129 (1961).
16. C. D. Russell, *J. Electroanal. Chem.*, **6**, 486 (1963).
17. N. R. Draper and H. Smith, "Applied Regression Analysis," Chap. 1, John Wiley & Sons, Inc., New York (1966).
18. C. Posthmus and E. L. King, *J. Phys. Chem.*, **59**, 1208 (1955).
19. D. M. Mohilner, *J. Phys. Chem.*, **73**, 2652 (1969).
20. K. Asada, P. Delahay, and A. K. Sundaram, *J. Am. Chem. Soc.*, **83**, 3396 (1961).
21. R. Parsons and S. Trasatti, *Trans. Faraday Soc.*, **65**, 3314 (1969).

22. F. C. Anson, R. F. Martin, and C. Yarnitzky, J. Phys. Chem., 73, 1835 (1969).
23. D. M. Mohilner in "Electroanalytical Chemistry," Vol. 1, p. 397, A. J. Bard, Editor, M. Dekker, Inc., New York (1966).
24. F. Basolo and R. G. Pearson, "Mechanisms of Inorganic Reactions," p. 37, John Wiley & Sons, Inc., New York (1967).

Electrochemical Reduction of Chromate in the Presence of Nickel Chloride in Molten Lithium Chloride-Potassium Chloride Eutectic

Branko Popov[1] and H. A. Laitinen*

Department of Chemistry and Chemical Engineering, University of Illinois, Urbana, Illinois

ABSTRACT

Chronopotentiometry of chromate in the presence of $NiCl_2$ in molten LiCl-KCl eutectic reveals a diffusion controlled, three electron reduction step. In the presence of excess $NiCl_2$, chromate is reduced at -0.35V *vs.* Pt(II)/Pt reference electrode and the electroactive species responsible for the chronopotentiometric wave is estimated to have a diffusion coefficient of $1.06 \cdot 10^{-5}$ cm^2 sec^{-1} at 450°C. The stoichiometry of the reduction product depends mainly on the temperature at which the deposit is formed. At 500°C the deposit approaches the composition $LiNi_2CrO_4$. X-ray powder diffraction shows the deposit to be a single compound with a face centered cubic lattice. The length of the unit cell edge is estimated to be 4.14Å. At 1400°C a weight loss of the deposit is observed. X-ray powder diffraction shows the presence of two phases, which are identified as NiO and $NiCr_2O_4$. The weight loss is attributed to volatization of Li_2O.

Laitinen and Propp (1) have shown that the electrochemical reduction product of K_2CrO_4 in LiCl-KCl eutectic containing dissolved $MgCl_2$ is a single unstoichiometric compound of formula $Li_xMg_yCrO_4$, where $x + 2y = 5$. The values of x and y depended on the conditions of the electrolysis, namely current density, temperature, and the molar ratio of Mg(II) to Cr(VI) dissolved in the melt. Typical values of x ranged between 0.3 and 0.5.

Hanck (2) observed that the reduction of chromate in the presence of Zn(II) was shifted from -1.0V *vs.* Pt(II)/Pt reference to -0.5V. Analysis of the deposit indicated the composition to be $LiZn_2CrO_4$. The stoichiometry of the compound was not affected by the electrolysis conditions.

The present investigation was undertaken to determine whether the reduction of K_2CrO_4 is affected by the presence of $NiCl_2$ and to establish the composition of the reduction product. Spectrophotometric measurements failed to indicate any interaction between Ni(II) and chromate in the melt (3). Ni(II) is known to exist as stable chlorocomplexes (4) in chloride melts, and it was of interest to determine whether any chloride is contained in the deposit. Also the reduction potential of Ni(II) lies about 0.2V below that of chromate in the absence of divalent ions and it was of interest to determine whether the deposition of metallic nickel could be avoided.

Experimental

Apparatus.—A Hevi-Duty MK 3012-S vertical split tube furnace (Hevi-Duty Electric Company, Watertown, Wisconsin) was utilized in this work. The temperature sensing element was a chromel alumel thermocouple (Onega Engineering, Inc., Springdale, Connecticut). All experiments were made at 450°C except as noted.

A Sargent Model IV coulometric current source was used for the electrolytic preparation of the electrode deposits. The constant current source for the chronopotentiometric studies has been described previously (1).

A Tektronix 503 oscilloscope served to record chronopotentiograms and to monitor the potential of the working electrode continuously during the preparation of the electrode deposits. The Pyrex cell and envelope have been described previously (5).

Electrodes.—The Pt indicator electrode used in this study has been previously described (6). The electrode had a geometric area of 0.5 cm^2 and was constructed so the glass metal seal was always kept above the level of the melt. The Pt(II)/Pt reference electrode was constructed as described by Ferguson (8).

The platinum gauze electrodes used to prepare samples of the film, as well as the carbon electrode which served as the counterelectrode in all electrochemical investigations in the melt, were constructed as described by Propp (1).

Chemicals.—All chemicals used in this study were reagent grade. Potassium chromate (J. T. Baker Chemical Company, Phillipsburg, New Jersey) was vacuum dried at 150°C before use. Anhydrous $NiCl_2$ was prepared by heating the hexahydrate (J. T. Baker Chemical Company) in vacuum to 180°C over a three day period. Analysis indicated it to be 99.3% pure.

The LiCl-KCl eutectic was obtained from Anderson Physics Laboratories, Inc., Champaign, Illinois. The method of purification has been described (7).

Solid chemicals were added to the melt by means of a small glass spoon. A blanket of argon was kept over the melt at all times to exclude oxygen and water vapor. The purification train used in purifying the argon has been described (8).

Experimental techniques.—Samples of the electrode deposit resulting from the reduction of chromate in the presence of $NiCl_2$ were obtained by constant current electrolysis using platinum gauze electrodes. The gauze electrodes were cleaned in boiling $HClO_4$, rinsed with distilled water, dried at 120°C for 16 hr, and weighed before their insertion into the molten salt solution. After electrolysis the gauze electrodes were

* Electrochemical Society Active Member.
[1] Present address: Faculty of Engineering, University of Skopje, Skopje, Yugoslavia.

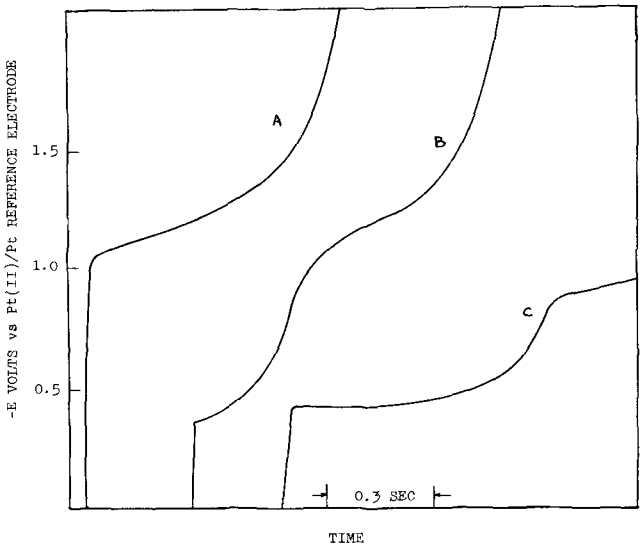

Fig. 1. Effect of nickel chloride concentration on reduction of chromate. 1.56 x 10^{-2}M K_2CrO_4. A. No $NiCl_2$; B. 7.29 x 10^{-3}M $NiCl_2$; C. 3.28 x 10^{-2}M $NiCl_2$.

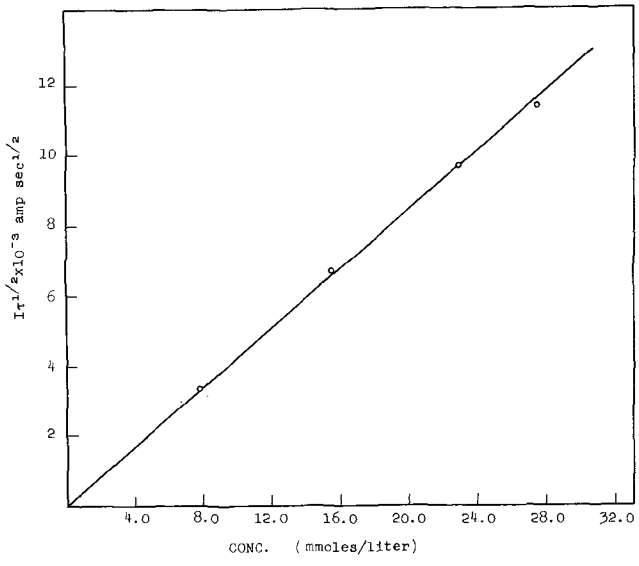

Fig. 2. Dependence of $I \cdot \tau^{1/2}$ on concentration of K_2CrO_4. 0.5 cm^2 Pt flag electrode. $C_{NiCl_2}/C_{K_2CrO_4} > 2.1$.

washed with deionized water, dried at 120°C, and reweighed. The electrode deposits were dissolved in boiling 72% perchloric acid. The nickel content of the deposit was determined by an EDTA titration using a murexide indicator. The method chosen for the chromium determination is a modification of that of Meier, Myers, and Swift (9). The procedure used has been previously described (1). Lithium was quantitatively determined by flame photometry.

Results and Discussion

Chronopotentiometry of K_2CrO_4-$NiCl_2$-LiCl-KCl *systems.*—The effect of Ni(II) on the reduction of chromate was demonstrated by successively increasing the concentration of Ni(II) at constant chromate concentration. Figure 1 shows that at a Ni(II) concentration of 7.29 · $10^{-3}M$, two transitions were obtained: one at 0.35V *vs.* Pt(II)/Pt reference and the other at −1.0V. Additional increases in the nickel concentration caused the wave at −0.35V to grow larger. At a sufficiently high Ni(II)/Cr(VI) concentration ratio (2.1), the wave at −1.0V disappeared but a new wave appeared at approximately −0.85V which corresponds to the reduction of Ni(II). Further increase in the Ni(II) concentration had no influence on the first reduction step. This can be seen from the fact that identical transition times were obtained for 1.56 x $10^{-2}M$ K_2CrO_4 solution containing 3.28 x $10^{-2}M$ $NiCl_2$ and for one containing 5.6 x $10^{-2}M$ $NiCl_2$.

According to the Sand equation the product of $I\tau^{1/2}$ is independent of I for a semi-infinite linear diffusion controlled process. The dependence of $I\ \tau^{1/2}$ on I is demonstrated in Table I for the reduction of K_2CrO_4

Table I. Chronopotentiometry of K_2CrO_4 in the presence of $NiCl_2$

$E_\tau/4 = -0.35V$		Area of the Pt flag = 0.5 cm^2			
$C_{K_2CrO_4}$ (M)	C_{NiCl_2} (M)	i (mA)	$\tau^{1/2}$ ($sec^{1/2}$)	$i\tau^{1/2}$ (A $sec^{1/2}$)	$i\tau^{1/2}/C$ (A $sec^{1/2}$ cm^3 $mole^{-1}$)
7.8×10^{-3}	1.34×10^{-2}	6.625	0.497	3.29×10^{-3}	422
		5.0	0.665	3.25×10^{-3}	426
		4.0	0.850	3.40×10^{-3}	439
		3.33	1.00	3.33×10^{-3}	427
		2.0	1.605	3.20×10^{-3}	410
1.56×10^{-2}	5.67×10^{-2}	8.33	0.80	6.664×10^{-3}	426
		10.0	0.656	6.56×10^{-3}	427
		12.5	0.53	6.63×10^{-3}	424
2.30×10^{-2}	5.67×10^{-2}	12.5	0.775	9.68×10^{-3}	421
		16.7	0.565	9.50×10^{-3}	412
		18.94	0.490	9.77×10^{-3}	425
2.75×10^{-2}	5.67×10^{-2}	14.3	0.79	11.3×10^{-3}	411
		16.7	0.67	11.25×10^{-3}	410
		18.94	0.566	11.30×10^{-3}	411

in the range of 7.8 x $10^{-3}M$ to 2.75 x $10^{-2}M$. The results indicate that the reduction of chromate in the presence of Ni(II) is diffusion controlled over the time interval investigated. Using $n = 3$ from the controlled current coulometry, a value of 4.19 ± 0.010 · 10^2 A $sec^{1/2}$ cm^3 mol^{-1} for the transition time constant and 0.5 cm^2 for the area of the electrode, we calculate $D = 1.06 \pm 0.06 \cdot 10^{-5}$ cm^2 sec^{-1} for the chromate reduction in the presence of Ni(II) at 450°C. From the slope in Fig. 2 (plot of $I \cdot \tau^{1/2}$ *vs.* C) the same value for the diffusion coefficient was obtained.

In order to establish the chemical composition of the electrode deposit, samples of the deposit, which had been prepared by constant current electrolysis over a wide range of preparative conditions were analyzed. To guard against the deposition of metallic nickel, the potential of the working electrode never was allowed to become more cathodic than −0.35 *vs.* Pt(II)/Pt. The influence of temperature, current density, and molar ratio of Ni(II) to Cr(VI) on the deposit composition was studied.

While holding the current density and the Ni(II) to Cr(VI) ratio constant, a series of deposits was prepared at 400°, 450°, and 500°C. The results of chemical analyses of these deposits are shown in Table II. From this table one can see that Li(I) content increases and the Ni(II) content correspondingly decreases as the temperature of the molten salt bath is increased. Table II also shows that the sum of the weight percentages of the three oxides, NiO, Li_2O, and Cr_2O_3 is very close to 100%, indicating that the chromium in the deposit is in the +3 oxidation state, and that no chloride or potassium ion is present. The absence of chloride in the deposit requires that the nickel chlorocomplex dissociate before the Ni(II) is incorporated into the deposit. That such a dissociation occurs rapidly enough to prevent inclusion of chloride in the deposit is remarkable. From Table II it is also obvious that in spite of the fact that the reduction potential of Ni(II) lies about 0.2V below that of chromate in the absence of divalent metal ions, no evi-

Table II. Composition of electrode deposit as function of temperature

$C_{K_2CrO_4} = 0.052M$			$C_{NiCl_2} = 0.198M$		
Temperature (°C)	Wt % Li_2O	Wt % NiO	Wt % Cr_2O_3	Total %	Formula
400	3.75	66.8	31.90	102.0	$Li_{0.60}Ni_{2.10}CrO_{3.91}$
450	4.09	64.5	30.60	99.2	$Li_{0.68}Ni_{2.12}CrO_{3.96}$
500	5.10	64.0	31.90	101.0	$Li_{0.88}Ni_{2.03}CrO_{3.96}$

dence to the deposition of metallic nickel was obtained. The empirical formula which best describes the deposit composition is $Li_xNi_yCrO_4$. As was observed by Propp (1) in his study of the $MgCl_2$-K_2CrO_4 system, $x + 2y = 5$ indicating that no oxide is lost during the electrolysis. At high temperature the deposit approaches the composition $LiNi_2CrO_4$.

Table III indicates that there is only a small change in the composition of the electrode deposit on changing the molar ratio of Ni(II) to Cr(VI). There is a slight decrease in Li(I) content and an accompanying increase in Ni(II) content as the molar ratio of Ni(II) to Cr(VI) is increased. The effect of current density on the composition of the electrode deposit on holding the temperature and the molar ratio of Ni(II) to Cr(VI) constant was observed and is indicated in Table IV. Current density in the range 1-10 mA/cm^2 does not appear to be a significant factor in determining the chemical composition of the electrode deposit.

X-ray powder diffraction studies.—Table V indicates that the deposit is a single compound with a face centered cubic lattice. The length of the unit cell edge is estimated to be 4.14Å.

Thermal stability of electrode deposit.—A sample of deposit, while still on the platinum gauze electrode, was heated in air and in an argon atmosphere to 1000°C for a period of 48 hr. Weight losses were only 0.5% in argon and 0.04% in air. Chemical analyses on the heated samples were in agreement with the previous analyses of unheated samples The heated samples contained 3.87% Li_2O, 66.7% NiO, and 37.50% Cr_2O_3 corresponding to the empirical formula $Li_{0.60}Ni_{2.11}CrO_{3.91}$. The x-ray powder pattern of the deposit appeared to change slightly after heating to temperatures above 950°C. The original face centered cubic lines appeared to shift to give larger "d" spacings and diffuse lines were observed at 4.788 and 2.494Å.

A powdered sample of the deposit was heated to 1430°C in an air atmosphere. The x-ray diffraction pattern of the heated sample is shown in Table VI.

The pattern shows the presence of two phases; a diamond cubic phase with a unit cell edge of 8.305Å and a face centered cubic phase with a unit cell edge of 4.169Å. The face centered cubic phase corresponds reasonably well to NiO (a = 4.176Å) and the diamond cubic phase to $NiCr_2O_4$ (a = 8.32Å). No lines were observed which could be assigned to the unheated nickel compound or to pure Li_2O.

Chemical analyses of the electrode deposit heated to 1400°C are in agreement with x-ray data. The deposit contained 67.01% NiO, 32.3% Cr_2O_3, and no Li_2O, which corresponds to the empirical formula $Ni_{2.11}CrO_{3.61}$.

The empirical formula of an unheated sample was found to be $Li_{0.7}Ni_{2.10}CrO_4$. If the Li_2O is lost during heating, the remainder of the compound must have the empirical formula $Ni_{2.10}CrO_{3.6}$ which is in agreement with chemical analyses of the heated sample.

Table III. Composition of electrode deposit as function of $NiCl_2$ concentration

Temperature = 450°C			I = 1.26 mA/cm^2
$C_{K_2CrO_4}$, M	C_{NiCl_2}, M	Total Wt %	Formula
0.078	0.152	100.1	$Li_{0.71}Ni_{2.08}CrO_{3.94}$
0.068	0.225	99.8	$Li_{0.62}Ni_{2.10}CrO_{3.94}$
0.058	0.312	99.1	$Li_{0.62}Ni_{2.12}CrO_{3.94}$
0.056	0.481	99.0	$Li_{0.62}Ni_{2.18}CrO_{3.98}$

Table IV. Effect of current density on composition of electrode deposit

$C_{K_2CrO_4}$ = 0.0482 M	C_{NiCl_2} = 0.124M	Temperature = 450°C
I, mA/cm^2	Total Wt %	Formula
1.21	99.2	$Li_{0.66}Ni_{2.18}CrO_{3.95}$
2.82	99.2	$Li_{0.63}Ni_{2.19}CrO_{4.00}$
4.31	98.5	$Li_{0.58}Ni_{2.20}CrO_{3.99}$
9.82	98.9	$Li_{0.58}Ni_{2.19}CrO_{3.98}$

Table V. X-ray data for electrode deposit

d(Å)	I/I_o	hkl	a(Å)
2.3840	60	111	4.129
2.0657	100	200	4.137
1.4622	60	220	4.136
1.2476	30	311	4.178
1.1957	20	222	4.1403
1.0352	10	400	4.141

Table VI. X-ray powder pattern of electrode deposit heated to 1430°C

d(Å)	I/I_o
4.7533	10
2.9180	15
2.493	100
*2.4024	60
*2.0798	40
2.0650	20
1.6960	30
1.5938	80
*1.4730	20
1.4696	100
1.2635	10
*1.2599	25
1.207	10
1.0798	10

* Face centered cubic lines.

Manuscript submitted Sept. 23, 1969; revised manuscript received *ca.* Dec. 1, 1969.

Any discussion of this paper will appear in a Discussion Section to be published in the December 1970 JOURNAL.

REFERENCES

1. H. A. Laitinen and J. H. Propp, *Anal. Chem.*, **41**, 645 (1969).
2. K. W. Hanck, Ph.D. Thesis, University of Illinois, (1969).
3. K. W. Hanck, Personal communication, unpublished results.
4. J. Brynestad, C. R. Boston, and G. P. Smith, *J. Chem. Phys.*, **47**, 3179 (1967).
5. H. A. Laitinen and W. S. Ferguson, *Anal. Chem.*, **29**, 4 (1957).
6. H. A. Laitinen and R. D. Bankert, *ibid.*, **39**, 1790 (1967).
7. H. A. Laitinen, R. S. Tisher, and D. K. Roe, *This Journal*, **107**, 546 (1960).
8. W. S. Ferguson, Ph.D. Thesis, University of Illinois (1956).
9. D. J. Meier, R. T. Myers, and E. H. Swift, *J. Am. Chem. Soc.*, **71**, 2340 (1949).

The Electrochemical Reduction of Meta-Dinitrobenzene in Dimethylsulfoxide

John S. Dunning† and Douglas N. Bennion*

School of Engineering and Applied Science, University of California, Los Angeles, California

ABSTRACT

The electrochemical reduction of meta-dinitrobenzene (m-DNB) in solutions of dimethylsulfoxide was studied on platinum electrodes. The rotating disk electrode and the potential step technique were used. The diffusion coefficient of m-DNB in the electrolyte solution was found to be 6.15 x 10^{-6} cm^2/sec. The kinematic viscosity of the test solutions was also determined. The electrochemical reduction in the absence of a proton donor takes place in two steps which correspond to the formation and reduction of the m-DNB radical anion. When a proton donor is added, homogeneous reaction takes place with the radical anion in the solution near the electrode resulting in an effective increase in the number of electrons transferred to four. This corresponds to the reduction to m-nitrophenylhydroxylamine.

The electrochemical reduction of organic compounds in various media has been investigated by numerous workers. In the absence of proton donors, Hoijtink *et al.* (1) found that the chief steps in the reduction of hydrocarbons could be described as follows

$$R + e^- \rightleftharpoons R^- \qquad [I]$$

$$R^- + e^- \rightarrow R^= \qquad [II]$$

The first reaction is the formation of a radical anion by a reversible one electron transfer. The second reaction is the reduction of the radical anion. Reaction [II] occurs at more negative potentials than reaction [I], giving rise to two wave behavior on a dropping mercury electrode polarogram.

The product of reaction [I] may also diffuse into the bulk of the solution and react with a hydrogen ion to form RH which then may dimerize or disproportionate. This would serve to reduce the observed number of electrons below 2.0 for the second wave because all R^- produced by reaction [I] would not be available for reaction [II]. $R^=$ will also diffuse into solution to react eventually with hydrogen ions to form RH_2. In addition, $R^=$ may undergo reaction in the solvent to produce a species which is electroactive at more positive potentials than those of reaction [II]. Such behavior would increase the effective number of electrons transferred in the second step. Observation of exactly two electrons for the second step is rather unlikely as a result of these competing reaction sequences.

If a proton donor is present in the solution, the nature of the reduction process becomes quite complicated and many types of behavior can be displayed. Given and Peover (2), on investigation of the reduction of aromatic hydrocarbons and carbonyl compounds in dimethylformamide, found that five different types or classes of behavior resulted from the addition of phenol and benzoic acid. The major difference between classes is whether the protonation occurs with the R, R^-, or $R^=$ species and the potential at which further reduction takes place.

Kolthoff and Reddy (3) have reported that the reduction of benzoquinone and quinhydrone in 0.1M tetraethylammonium perchlorate (TEAP) solutions in dimethylsulfoxide (DMSO) gave two waves. The first corresponds to a one electron reversible step, while the second wave corresponds to an irreversible addition of, effectively, less than one electron. This is just reactions [I] and [II]. On addition of hydrochloric acid, the second wave shifted to more positive potentials. They suggest that the $R^=$ radical anion is protonated, shifting the second reduction to a more positive potential.

Kemula and Sioda (4) have reported the polarographic behavior of two nitrocompounds in dimethylformamide (DMF). They found that the addition of benzoic acid to a nitrosobenzene solution with $NaNO_3$ as a supporting electrolyte caused the appearance of a new wave at potentials less negative than the first wave. This can be explained as protonation of the reactant, R, which can then react at a more positive potential than R. The addition of benzoic acid to nitrobenzene solution caused an increase in the height of the first wave to the height of the second wave observed in the absence of benzoic acid. The conclusions of Kemula and Sioda were that the reduction of the aromatic nitro-group was a four electron reaction in the presence of a proton donor, and the first step in absence of the proton donor represented the one electron formation of the free radical anion.

In a later study, Kemula and Sioda (5) reported the visible spectrum of the nitrobenzene free radical anion. Geske and Maki (6) have used ESR spectroscopy to observe the electrochemical generation of nitrobenzene free radicals.

Cadle, Tice, and Chambers (7) have studied the reduction of several aromatic nitrocompounds as a function of the proton donor in solutions of acetonitrile, DMSO, propylene carbonate, and DMF. They found that certain proton donors (trichloroacetic acid, o-phthalic acid, and others) caused new waves to appear at potentials more positive than the wave for the formation of the radical anion. Proton donors such as benzoic acid, phenol, hydroquinone, and water at low concentrations did not produce the behavior. It was also found that the reduction of p-chloronitrobenzene in o-phthalic acid solutions of acetonitrile resulted in an effective transfer of three to four electrons. It was also found that four moles of acid were used per mole of p-chloronitrobenzene. This suggests the formation of chlorophenyl-hydroxylamine, which was found by subsequent analysis of the reaction products. P, p dichloro-azoxybenzene was also found, indicating that there are at least two paths through which the reduction can proceed. It is interesting to note that the complete reduction to the aniline, involving six electrons and six hydrogen ions, was not observed. Apparently, in these particular systems, the phenylhydroxylamine is resistant to further reduction and only four electrons are transferred for each nitro-group.

The purpose of the present study was to determine the number of electrons transferred in the reduction, on a platinum electrode, of meta-dinitrobenzene (m-DNB) in DMSO in the presence and absence of a proton donor, ammonium perchlorate. Two independent electrochemical methods were used for the deter-

* Electrochemical Society Active Member.
† Electrochemical Society Student Member.

minations. These were the rotating disk technique and the potential step technique.

In order to use the techniques proposed, determinations of the diffusion coefficient of m-DNB and the kinematic viscosity of the test solutions had to be made.

The potential step technique, involving the solution of the semi-infinite spherical diffusion equation, has been described by Delahay (8). The equation for the time-dependent limiting current is

$$i = n\mathbf{F}AD^{1/2}\ C^{o}\frac{1}{\pi^{1/2}t^{1/2}} + n\mathbf{F}ADC^{o}\frac{1}{r_0} \qquad [1]$$

where n = number of electrons transferred/mole of active species, $\mathbf{F}$ = Faraday's constant, A = area of electrode, D = diffusion coefficient of the active species, C^o = bulk concentration of the active species, t = time from the start of electrolysis, and r_0 = the radius of the spherical electrode.

By measuring the current-time relationship after imposition of a potential step, the number of electrons transferred can be calculated.

The rotating disk technique has been described by Levich (9) and Riddiford (10). Newman (11) has shown that the limiting current on the rotating disk can be given by

$$i_{lim} = \frac{0.554\ n\mathbf{F}D^{2/3}\ \nu^{-1/6}\ \omega^{1/2}\ C^{o}A}{0.8934(1 + 0.298\ Sc^{-1/3} + 0.14514\ Sc^{-3/4})} \qquad [2]$$

where n, $\mathbf{F}$, D, C^o, and A have the same meanings as for the potential step case and ν = kinematic viscosity of the test solution, ω = rotation speed of the disk, and Sc = Schmidt number for the system.

By measuring the limiting current as a function of rotation speed, the number of electrons transferred can be calculated from Eq. [2].

Experimental

Diffusion coefficient.—The diaphragm cell method of Stokes (12) was used to determine the diffusion coefficient of m-DNB in the electrolyte solutions of 0.1M TEAP in DMSO. The glass cell (13) was a vertical tube separated into two compartments by a sintered glass diaphragm and fitted with glass encased magnetic stirring bars for each compartment. The diaphragm was 10 mm in diameter and 3 mm thick with a pore size of 10 to 15μ. During experimental runs, a water bath maintained the temperature at 25.0° ± 0.1°C. Calibration was done with 0.1*N* KCl in water in the lower compartment and redistilled water in the upper compartment. Analysis of the calibrating solutions was done by precipitating the chloride ion as AgCl and weighing. The durations of the calibration runs varied from 175 to 7180 min. The average cell constant was $\beta = 6.19\ cm^{-2}$ with an average deviation of 9.2%.

Two runs were made to determine the unknown diffusion coefficient. The runs were 5840 and 8225 min in length and measured the diffusion coefficient in the concentration range between infinite dilution and 0.05M m-DNB in DMSO. Concentrations of m-DNB were determined by comparing absorbance at 420 mμ with that of known standard solutions. A Beckman Model DU spectrophotometer with slit width set at 0.22 mm was used for this purpose.

Kinematic viscosity.—The kinematic viscosity of m-DNB solutions in 0.1M TEAP-DMSO was measured as a function of concentration. A Cannon Ubbelohde Semi-Micro viscometer was used. It was calibrated to have a constant of 0.003910 centistokes/sec. Measurements were done in a constant temperature oil bath at 24.2°C.

Potential step.—The potential step cell (13) was a glass cylinder containing 190 ml of solution and sealed from the atmosphere. The working electrode was a sphere with an area of $8.55 \times 10^{-2}\ cm^2$ formed by melting the tip of a piece of platinum wire in an oxygen-gas flame. The electrode was sealed into a thin Pyrex glass tube for insertion into the cell. The counterelectrode (also used as a reference) was a cylinder of platinum screen which surrounded the working electrode at a distance of about 1.5 cm. The potential was set between the working and counterelectrodes with an Anotrol Model 4100 Research Potential Controller. Current was measured as a function of time from the application of the potential step by a Tektronix 545-A oscilloscope fitted with a Polaroid camera. The oscilloscope measured the voltage drop across a General Radio precision decade resistor. Potentials of −1.8 and −2.3V were applied to the working electrode to investigate the two waves in the reduction of m-DNB. Preliminary, slow potential sweeps indicated that these potentials are well into the limiting current region for the respective reactions. This was confirmed by adjusting the potential ±0.1V without any observed change in results. Total observed times of electrolysis were less than 2.0 sec from the application of the potential step. The supporting electrolyte was 0.1M TEAP in all cases.

Rotating disk.—The rotating disk electrode equipment (13) consisted of a variable speed motor which drove a rotating shaft by means of pulleys. The motor, bearings, and electrode mountings were constructed so that vibration was minimized. The working electrode was a cross section of platinum wire 0.258 cm in diameter which was force fitted through a Teflon shaft of 3 cm diameter. The surface of the electrode was carefully machined to eliminate wobble and the face was polished to a mirror surface on No. 00 emery paper.

The platinum working electrode was cleaned with a saturated solution of ferrous sulfate in sulfuric acid. It was washed with distilled water and rinsed with the test solution before each run. Between experimental runs, the electrode was carefully repolished with a soft tissue. The cell was washed and dried whenever a fresh solution was being used.

The current through the cell was controlled by a Heathkit Model IP-32 regulated power supply which supplied power through a Clarostat power resistor decade box in series with the cell. A Keithly Model 610B electrometer was used to measure the potential and a Simpson Model 262 volt-ohm-milliammeter measured the current.

The potential was measured *vs.* a saturated Ag/$AgClO_4$, DMSO reference electrode (13) or in some cases *vs.* the counterelectrode. Since the platinum counterelectrode's area was 3000 times the area of the working electrode it was effectively at a fixed potential and performed the same as the Ag/$AgClO_4$ electrode.

Current potential curves were generated for speeds between 200 and 1200 rpm and for concentrations of m-DNB from 0.01 to 0.04M. In all cases the supporting electrolyte was 0.1M tetraethylammonium perchlorate.

The effects of water content on the results of the rotating disk experiments were examined. Distilled DMSO with water content below 100 ppm, as determined by Karl Fischer titration, was used in a sealed cell under a dry nitrogen atmosphere. The m-DNB was recrystallized three times from methanol and the melting point was determined to be 89°C, which is in good agreement with the literature values. The tetraethylammonium perchlorate and ammonium perchlorate used were dried in a vacuum oven for 24 hr at 80°-100°C.

It was found that increasing the water content of the DMSO up to 0.2% did not change the results of the experiments. This is illustrated by Fig. 8 and 9 in which the m-DNB concentration of 0.02*M* represents the data found using a nitrogen blanketed closed cell and the other points represent the results obtained with the reaction vessel open to the atmosphere. These tests were done at ambient (22°-24°C) temperatures.

In addition to the above study, the effect of adding NH_4^+ as ammonium perchlorate was investigated. For these measurements, a 0.02*M* m-DNB solution was used at a rotation speed of 300 rpm. Limiting currents were

recorded as a function of the concentration of the ammonium ion.

Results

Diffusion coefficient.—The results of the two experiments to determine the diffusion coefficient of m-DNB in the solution of 0.1*M* TEAP-DMSO are summarized in Table I.

A simple analysis of the above data indicates some discrepancies for run No. 1. The volumes of the two compartments were determined by filling with water and weighing. They were 25.6 cm^3 for the bottom compartment and 25.7 cm^3 for the top compartment. Using these volumes, it is possible to calculate any one of the four concentrations in Table I from the other three. This can be done by means of the following molar balance

$$C^f_t V_t - C^i_t V_t = C^i_b V_b - C^f_b V_b \qquad [3]$$

The results of the first experimental run do not satisfy Eq. [3]. Because of this discrepancy the second run was undertaken. Run No. 2 gave much better agreement with Eq. [3] and yielded a diffusion coefficient of 6.49 x 10^{-6} cm^2/sec. The value of C^f (top) seems to be in error in run No. 1. This value was discounted and a "corrected" final dilute concentration of 0.0018M was calculated from Eq. [3]. The resulting diffusion coefficient was 5.81 x 10^{-6} cm^2/sec. The mean value of the two runs, used to analyze the electrochemical experiments, was D = 6.15 x 10^{-6} cm^2/sec ±10%. This leads to a discrepancy of ±4% in the value of $D^{2/3}$ used in the rotating disk experiments for determining the number of electrons.

Stokes (12) has reported that accuracies of better than 1% can be obtained with the diaphragm cell technique. In this study deviations of up to 10% were found among the various calibration runs and in the final determination of the unknown diffusion coefficient. It is believed that the main cause of this error was the blockage of some of the pores in the diaphragm by air bubbles. Although the solutions were deaerated by evacuation with an aspirator water pump, some bubble formation was noted as the solution was sucked through the diaphragm to start the experiment. The compartments were refilled before the runs were started, but there is a possibility that some air was still trapped in the diaphragm. This would cause the cell "constant" to be different for different experimental runs, possibly enough to account for the observed discrepancies.

Kinematic viscosity.—The efflux times for flow from the viscometer test section were recorded at each concentration of m-DNB. The results of these measurements are summarized in Table II for various concentrations of m-DNB in 0.1M TEAP-DMSO solutions.

Potential step.—The application of a potential step caused a soluble red product to appear at the platinum sphere electrode. The product was slightly less dense than the 0.1M TEAP-DMSO solution, *i.e.*, it streamed to the surface of the cell. If no m-DNB was present in the cell, the red substance did not appear.

Figures 1 and 2 are plots of the observed current *vs.* the inverse of the square root of the time from the application of the potential step. Figure 1 data result from the application of −1.8V *vs.* the counterelectrode and corresponds to the first step in the reduction of m-DNB. Figure 2 data represent the second step in the reduction due to a −2.7V potential step. It is clear that, for times between 0.2 and 2.0 sec, the plots are linear and pass through the origin for each concentration investigated. Figure 3 shows the dependence of the slopes of Fig. 1 and 2 on the bulk concentration of m-DNB. This is in agreement with Eq. [1] and in-

Table I. Initial and final concentrations in top and bottom compartments of the diffusion cell for two runs

Run No.	Time (min)	C^i top (molar)	C^f top (molar)	C^i bottom (molar)	C^f bottom (molar)
1	5840	0	0.0042	0.0381	0.0363
2	8225	0	0.0075	0.0500	0.0430

Table II. Viscosity of m-DNB in 0.1M TEAP-DMSO solution

Temperature = 24.2°C	
Conc. m-DNB	ν (Centistokes)
0.00	1.958, 1.954, 1.961
0.01*M*	1.989, 1.982, 1.985
0.02*M*	2.008, 2.012, 2.018
0.04*M*	2.037, 2.045, 2.037

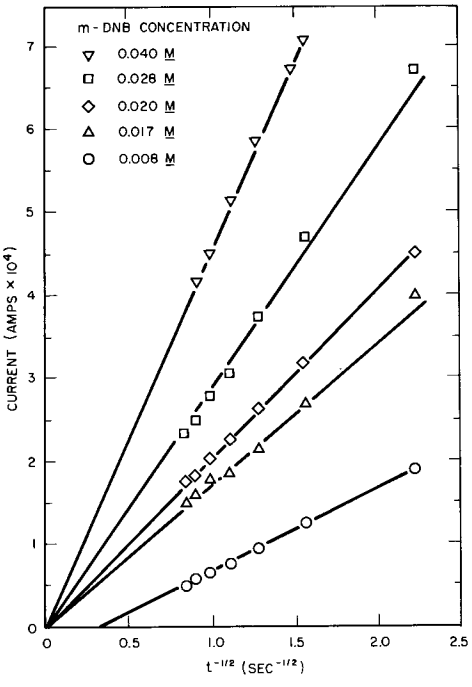

Fig. 1. Current *vs.* time$^{-1/2}$ for 1st wave reduction of m-DNB in DMSO in the absence of proton donors from the potential step method.

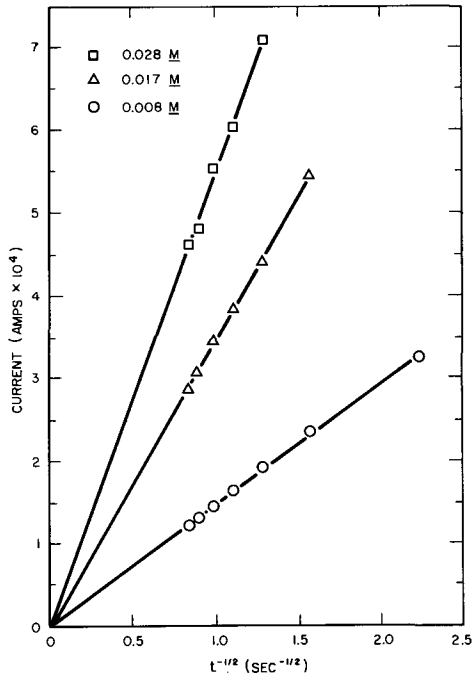

Fig. 2. Current *vs.* time$^{-1/2}$ for 2nd wave reduction of m-DNB in DMSO in the absence of proton donors from the potential step method.

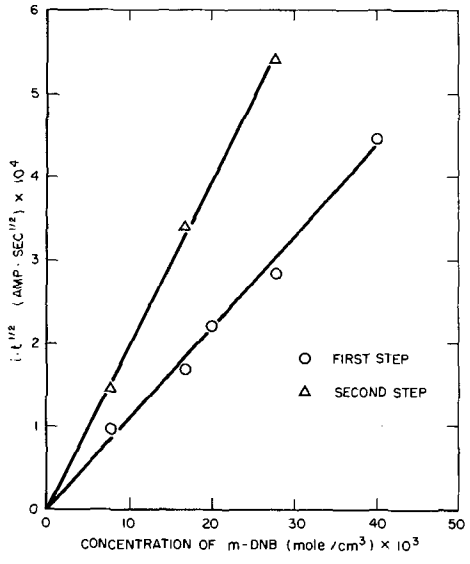

Fig. 3. Concentration dependence of the quantity $i \cdot t^{1/2}$ for 1st and 2nd waves in reduction of m-DNB in the absence of proton donors from the potential step method.

dicates that the desired diffusion controlled process has been attained under the conditions of these experiments. From Eq. [1], the slopes of the lines in Fig. 3, and the diffusion experiment results, the number of electrons transferred in the first and second steps were calculated to be 0.95 ± 0.1 and 1.71 ± 0.1, respectively.

Rotating disk electrode.—Passage of current through the rotating disk produced a red product identical to that observed in the potential step experiments. Figure 4 shows the dependence of the voltage on current for the galvanostatic reduction of 0.02M m-DNB in the 0.1M TEAP-DMSO solution. The voltage was measured *vs.* the $Ag/AgClO_4$ reference electrode. Two steps in the reduction are clearly visible and are marked by limiting currents at 27 and 46 μA, respectively.

Figure 5 shows the voltage-current curves for four rotation speeds in 0.0381M m-DNB. The potentials in this case are measured *vs.* the platinum counterelectrode. The voltage drop due to solution resistance has not been subtracted from the data. It can be seen that the limiting currents for the two waves increase with rotation speed. The dependence of the limiting currents for the first and second waves on the square root of rotation speed is shown in Fig. 6 and 7. The effect of different concentrations of m-DNB is shown in Fig. 8 and 9. The linear nature of Fig. 6 through 9 is consistent with Eq. [2]. From the data and Eq. [2] the effective numbers of electrons were calculated to be 1.01 ± 0.1 for the first wave and 1.76 ± 0.1 for the second wave.

When ammonium perchlorate was added to the solution, the characteristic red color of the first step product began to fade. At higher ammonium perchlorate concentrations the red color was not observed at all. The reduction of the ammonium ion appeared to interfere with the second wave of the m-DNB reduction. (This is apparently hydrogen evolution, although cur-

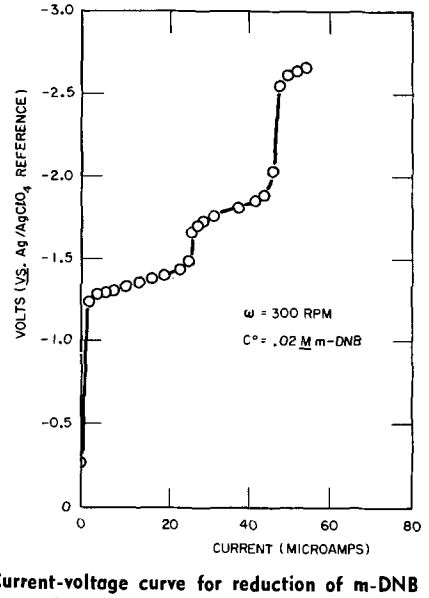

Fig. 4. Current-voltage curve for reduction of m-DNB in the absence of proton donors on the rotating disk electrode.

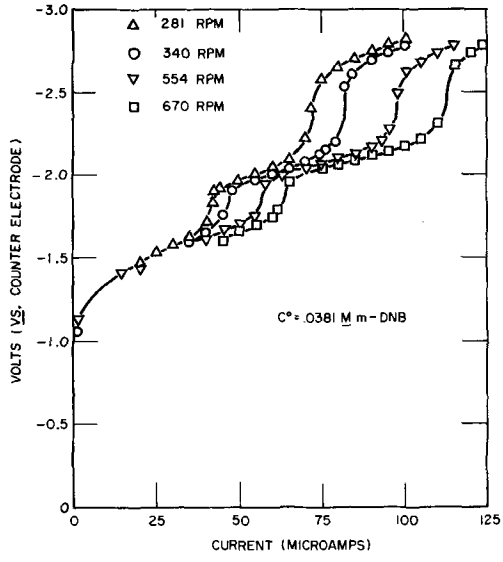

Fig. 5. Current-voltage curves as a function of rotation speed for m-DNB in DMSO in the absence of proton donors.

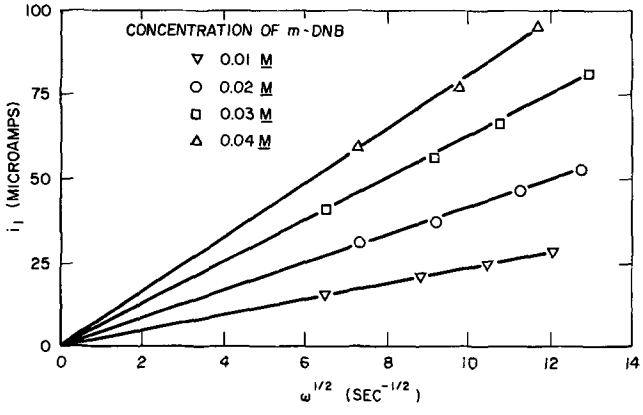

Fig. 6. Limiting current dependence on $\omega^{1/2}$ for 1st wave in the absence of proton donors.

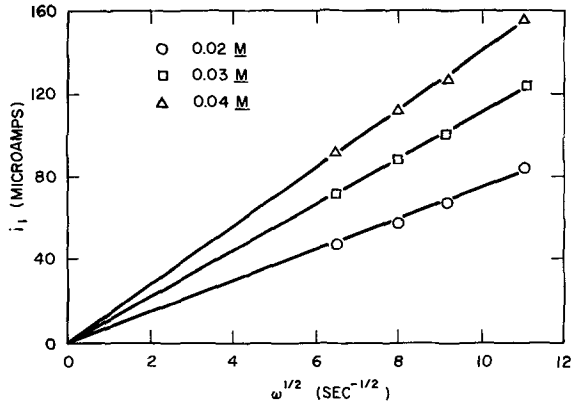

Fig. 7. Limiting current dependence on $\omega^{1/2}$ for 2nd wave in the absence of proton donors.

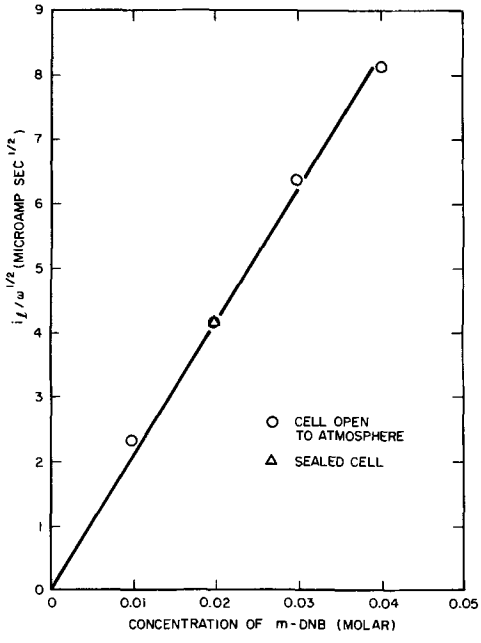

Fig. 8. Dependence of $i_l/\omega^{1/2}$ on concentration of m-DNB in the absence of proton donors. First wave.

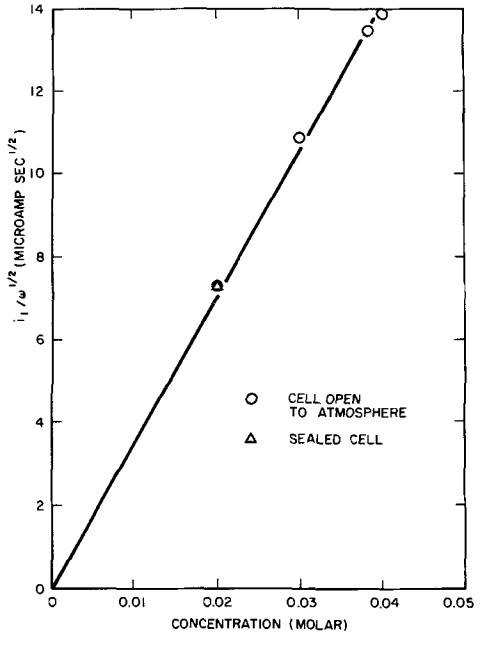

Fig. 9. Dependence of $i_l/\omega^{1/2}$ on concentration of m-DNB in the absence of proton donors. Second wave.

rents were too small to create hydrogen bubble evolution.) Because of the interference, the effect of NH_4^+ addition on the first wave only was considered in this study.

The addition of the NH_4^+ ion to the test solutions had a marked effect on the limiting currents observed. The quantity R_d is defined as the ratio of the concentration of the ammonium perchlorate to the concentration of m-DNB in solution. In these experiments the m-DNB concentration was held constant at 0.02M while the NH_4^+ ion concentration was increased by adding ammonium perchlorate. The rotation speed was held constant at 300 rpm. Figure 10 shows the effect of increasing R_d on the reduction of m-DNB. As R_d is increased, the limiting current also increases. Figure 11 shows the effect of increasing R_d on the limiting current of the first wave. At values of R_d below approximately three, the limiting current is proportional to R_d. Above this value, the limiting current is insensitive to R_d.

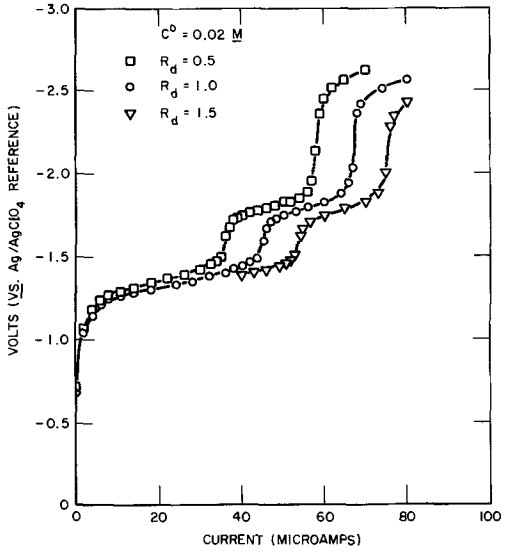

Fig. 10. Current-voltage curves for m-DNB reduction as a function of proton donor concentration.

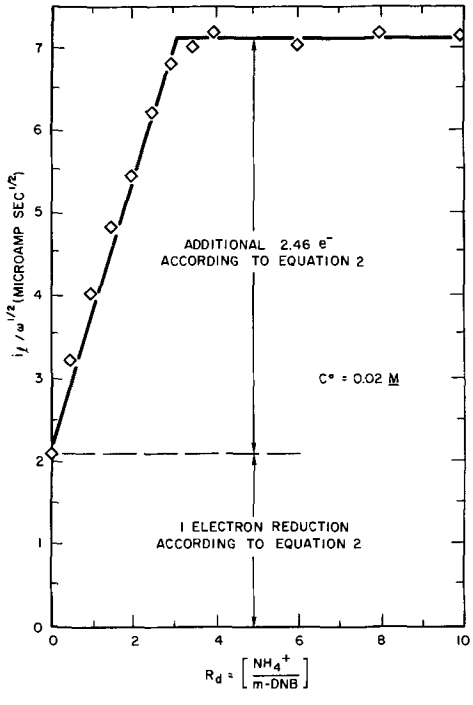

Fig. 11. Effect of addition of ammonium perchlorate on the 1st wave reduction of m-DNB in DMSO.

Discussion

The results of both the potential step and rotating disk experiments are summarized in Table III. They indicate that the reduction of m-DNB in 0.1M TEAP-DMSO solutions occurs in two steps. The first step results from a single electron transfer. This suggests the formation of the m-DNB radical anion. The second step adds an effective 0.75 electrons to the radical anion produced by the first step.

Kemula and Sioda (4) found for nitrobenzene that the second wave height of the reduction in DMF was less than proportional to the concentration of nitrobenzene at concentrations greater than 3.5 x 10^{-4}M. In all probability, considering the general reaction scheme

Table III. Number of electrons transferred in the absence of proton donors for m-DNB reduction in DMSO

Rotating disk	1.01 ± 0.1	1.76 ± 0.1
Potential step	0.95 ± 0.1	1.71 ± 0.1

of Hoijtink (14), the second wave involves the reduction of the radical anion to the di-negative state. The fact that less than one electron is involved is not surprising. The radical anion may be destroyed by side reactions in solution which prevent it from reacting electrochemically. On the other hand, a reaction mechanism recently proposed by Grieg and Rogers (17) in the reduction of trifluoromethyl substituted nitrobenzene suggests that an electroactive nitroso compound may be formed by the action of the solvent (or of residual water) on the dianion. This would increase the effective number of electrons transferred. It is proposed that a mixture of these effects occurs here, with the destruction of the radical anion being dominant.

The effect of the addition of ammonium perchlorate on the reduction of m-DNB appears to correspond to the behavior reported by Given and Peover (2) as class C. This involves the protonation of the radical anion formed by the first electron transfer. The first reduction step in the absence of a proton donor produced a red product. This corresponds to the formation of the m-DNB radical anion, or perhaps a product of the decomposition of the radical anion after formation. If the radical anion disappears by reaction in solution on addition of proton donors, one would expect the color to disappear also. The observed loss of red color on addition of ammonium ions is considered evidence that a reaction, such as protonation, occurs.

A detailed mechanism corresponding to class C behavior of Given and Peover was proposed by Koopmann and Gerischer (15) for the reduction of nitrobenzene in weakly alkaline aqueous solutions. By extension of their mechanism to the present case, the reduction of m-DNB may take place as follows:

I. A single electron step at the electrode which takes place four times

$$4\,\phi\begin{matrix}NO_2\\NO_2\end{matrix} + 4e^- = 4\left(\cdot\phi\begin{matrix}NO_2^-\\NO_2\end{matrix}\right)$$

II. A reaction in solution with the ammonium ion

$$4\left(\cdot\phi\begin{matrix}NO_2^-\\NO_2\end{matrix}\right) + 3NH_4^+ \xrightarrow{k} \phi\begin{matrix}NHOH\\NO_2\end{matrix} + 3\phi\begin{matrix}NO_2\\NO_2\end{matrix} + 3NH_3 + OH^-$$

The over-all reaction is

III. $$\phi\begin{matrix}NO_2\\NO_2\end{matrix} + 3NH_4^+ + 4e^- = \phi\begin{matrix}NHOH\\NO_2\end{matrix} + 3NH_3 + OH^-$$

Reaction III predicts that the stoichiometric ratio of NH_4^+ ions to m-DNB in the solution is 3 to 1. Experimentally, this is confirmed by Fig. 11 which shows the current increasing with NH_4^+ concentration to the point where the 3 to 1 ratio is reached. At this point the ammonium ion concentration no longer limits the current and the current becomes independent of the NH_4^+ concentration.

Equation [2], which was used to predict the number of electrons transferred as a function of the limiting current, was derived for the case in which no chemical reactions were taking place in solution. Reaction II represents just such a reaction and, consequently, Eq. [2] must be modified to account for this. In order to do this, the convective diffusion equations for the species of interest must be solved. If C_1 represents m-DNB concentration and C_2 the radical anion concentration, these equations become

$$\frac{dC_1}{dt} = 0 = D\frac{d^2C_1}{dx^2} - v_x\frac{dC_1}{dx} + \frac{3}{4}kC_2$$

$$\frac{dC_2}{dt} = 0 = D\frac{d^2C_2}{dx^2} - v_x\frac{dC_2}{dx} - kC_2$$

where v_x is the hydrodynamic velocity in the x direction (*i.e.*, perpendicular to the electrode). The boundary conditions are

at $x = 0$, the electrode surface

$$C_1 = 0 \qquad \text{(limiting current condition)}$$

and

$$\frac{dC_1}{dx} = -\frac{dC_2}{dx} \qquad \text{(assuming equal diffusion coefficients)}$$

at $x = \infty$

$$C_1 = C^0 \qquad \text{(bulk concentration of m-DNB)}$$
$$C_2 = 0$$

In addition, the flux of the active species at the electrode surface must be compatible with the observed value of limiting current. This final condition enables the calculation of the rate constant k for reaction II, assuming this is an irreversible reaction. The above equations were solved numerically using an IBM 360/75 computer using the technique of Newman (16). A parabolic form of the velocity profile at the rotating disk surface given by Levich as

$$v_x = -0.51\,\omega^{3/2}\,\nu^{-1/2}\,x^2$$

was used along with the measured values of ν, D, ω, and the limiting current. A rate constant of $k = 336$ sec^{-1} with concentrations expressed in units of moles/cm^3 was found to give good agreement with the observed limiting currents. Almost identical results were obtained (13) using a simpler stagnant diffusion layer model with the layer thickness, δ, calculated from Levich's (9) equation for the mass transfer boundary layer thickness at a rotating disk. It is possible, therefore, to obtain a wave height corresponding to only 3.46 electrons instead of 4 by consideration of the kinetics of a regenerative reaction producing electro-active m-DNB within the diffusion layer. This explanation is also consistent with the observed ratio of 3 proton donors for each m-DNB molecule.

Alternate explanations can be arrived at by proposing competing, parallel reaction sequences. For example, the presence of azoxybenzene as a product in the reduction of nitro compounds have been reported (7, 17, 18). This reaction sequence consumes only three electrons per mole of nitro compound. If this reaction occurs in parallel with a 4 electron sequence, an over-all or effective 3.46 electron reaction results if 54% of the M-DNB reacts through the 3 electron sequence. For our case, this possibility does not clearly explain the observed proton to m-DNB ratio. However, the data thus far cannot definitely establish one mechanism or the other.

Chambers and Adams (19) have suggested a mechanism in which the OH^- ion product further reacts with the dinitrobenzene compound to form a phenol. If all of the OH^- ions reacted in this manner at the electrode, it would have the effect of reducing the over-all electrons transferred to 2 per nitro group reacting. Our data precludes this. If the reaction occurred only partly and in the diffusion layer, its effect is to change slightly the interpretation of the reaction rate constant, k. Since the OH^- concentration will be very small, it seems unlikely that this contribution is large, however.

Acknowledgment

This work was supported by the U. S. Naval Weapons Center, Corona, California, under Contract No. N123-(62738) 57439 A.

Manuscript submitted Aug. 19, 1969; revised manuscript received *ca.* Dec. 16, 1969.

Any discussion of this paper will appear in a Discussion Section to be published in the December 1970 JOURNAL.

REFERENCES

1. G. J. Hoijtink, J. van Schooten, E. de Boer, and W. Aalbersberg, *Rec. Trav. Chim.*, **73**, 355 (1954).
2. P. H. Given and M. E. Peover, *J. Chem. Soc., London*, 385-393 (1960).

3. I. M. Kolthoff and T. B. Reddy, *This Journal*, **108**, 980 (1961).
4. W. Kemula and R. Sioda, *Bull. Acad. Polon. Sci. Ser. Sci. Chim.*, **10**, 107 (1962).
5. W. Kemula and R. Sioda, *Nature*, **197**, 588 (1963).
6. D. H. Geske and A. M. Maki, *J. Am. Chem. Soc.*, **82**, 2671 (1960).
7. S. H. Cadle, Paul R. Tice, and James Q. Chambers, *J. Phys. Chem.*, **71**, 3517 (1967).
8. Paul Delahay, "New Instrumental Methods in Electrochemistry," Interscience Publishers, Inc., New York (1954).
9. Veniamin G. Levich, "Physicochemical Hydrodynamics," Prentice Hall, Englewood Cliffs, New Jersey (1962).
10. A. C. Riddiford, "Advances in Electrochemistry and Electrochemical Engineering," Vol. 4, 47-116, Interscience Publishers, Inc., New York (1966).
11. John Newman, *J. Phys. Chem.*, **70**, 1327 (1966).
12. R. H. Stokes, *J. Am. Chem. Soc.*, **72**, 763 (1950).
13. John S. Dunning, "The Electrochemical Reduction of Meta-Dinitrobenzene in Dimethylsulfoxide," M.S. Thesis, University of California, Los Angeles, June 1968.
14. G. J. Hoijtink, *Rec. Trav. Chim.*, **73**, 895 (1954).
15. R. Koopmann and H. Gerischer, *Ber. Bunsen. Phys. Chem.*, **70**, 127 (1966).
16. John Newman, *Ind. and Engr. Chem. Fund.*, **7**, 514 (1968).
17. W. N. Grieg and J. W. Rogers, *J. Am. Chem. Soc.*, **91**, 5495 (1969).
18. R. F. Fogle, E. T. Seo, and H. P. Silverman, "Voltametric Studies of Nonaqueous Systems," Tech. Report ECOM-02464-F, U.S. Army Electronic Command, December 1967.
19. J. Q. Chambers and R. N. Adams, *J. Electronal. Chem.*, **9**, 400 (1965).

Rotating Ring-Disk Study of the Silver Electrode in Alkaline Solution

B. Miller*

Bell Telephone Laboratories, Inc., Murray Hill, New Jersey

ABSTRACT

Rotating ring-disk electrodes have been used for observing the soluble products on charge and discharge of potential or current controlled silver disks in 1.0-10.1M KOH and 1.0M NaOH. Limits on the solubility of higher valent silver species corresponding to AgO formation and the oxygen evolution region are given. The relative surface concentration of Ag(I) for all disk conditions has been measured and related to existing solubility data, the polarization characteristics of silver, and the reaction mechanisms.

The current-potential characteristics of silver electrodes in alkaline solution and the solubility of the oxide phases have been extensively investigated, particularly since both these aspects are critical in determining the service of secondary cells incorporating a silver positive. The purpose of the present work is to seek a direct correlation of polarization and solubility behavior by simultaneous measurement of the parameters of a charge-discharge cycle and the concomitant distribution of species between the electrode and the contacting solution phase. This may be accomplished by application of the rotating ring-disk technique (1-3) which permits quantitative assessment of the electrode/solution mass balance through use of the detecting surface (ring) concurrent with recording of the current-potential-time behavior of the silver test electrode (disk).

In the present case, potentiostatically controlled rings allow distinguishing silver (I) from higher states formed in the soluble phase by the disk reaction. With a known system collection efficiency, as defined by the ring-disk geometry (4), the fraction of disk anodic current going into film formation at any time (or cumulatively) may be obtained (5). Where complications due to multiple oxidation states exist, as in regions of transition from one oxide phase to another, the split-ring disk approach (5-7), which adds a second equivalent detecting surface to treat the increased number of variables, is of value. In such cases, with the appropriate separation of redox potentials that exists for the different silver oxides, the concentrations of soluble silver (I) and higher valent silver species, as well as the amount of film, can be obtained. Identification of oxidation state by split-ring limiting current ratios independent of actual collection efficiencies is feasible, as previously shown for the related copper system in alkaline solution (5).

* Electrochemical Society Active Member.

Studies on the solubility of bulk Ag_2O and AgO are of relevance both to the elucidation of the electrode mechanisms and to the understanding of the practical cell which is affected by transport of soluble silver species to the (zinc) negative and their subsequent reduction. With the ring-disk electrode it becomes readily practical to examine the solubility as a function of the state of the silver electrode with possible implications, therefore, for specifying optimal operating conditions with respect to this factor in a battery. Earlier data on the solubility of Ag_2O (8, 9) were extended by Amlie and Ruetschi (10) through the KOH concentrations of interest in the operating cell and indicate a maximum at about 6*N* KOH. Data of Pleskov and Kabanov (11), obtained by a rotating disk method, and of Kovba and Balashova (12), taken through radioactive tracer techniques, both show a gradual levelling of Ag_2O solubility with increasing hydroxide concentration but no intermediate maximum.

The composition of the soluble silver (I) species was suggested as AgO^- or its equivalent, $Ag(OH)_2^-$, by the earlier workers (8, 9) from the linearity of the solubility of Ag_2O with $[OH^-]$ at lower hydroxide concentrations. A later proposal that the chief form is $[Ag_3O(OH)_2]^-$ (11) was challenged by Sillén *et al.* (13) who found evidence only for mononuclear complexes in up to 11.5M KOH, further concluding that $Ag(OH)_2^-$ is predominate to at least 5M KOH, above which other species such as $Ag(OH)_3^{-2}$ may perhaps occur, though there was no positive evidence for them.

The situation for AgO has been confused by the experimental fact that the apparent solubilities of AgO and Ag_2O in terms of total silver in solution nearly coincide (14). Amlie and Ruetschi (10) and Pleskov (15) have shown by polarographic techniques that higher valent silver species are essentially absent, less than 10^{-6}M concentration (10), in electrolyte equilibrated with AgO. The expectation (16, 17) of a higher

solubility for AgO than Ag_2O because of the higher oxidation state (a more acidic oxide) does not necessarily follow because of the now accumulated evidence [see ref. (18) for review] that solid AgO is a Ag(I)-Ag(III) compound. Reaction sequences (17) based on the assumption that AgO is really soluble but disappears rapidly have had little experimental basis. The ring-disk method, which makes it feasible to determine higher valent silver and/or its monovalent decomposition products in the solution phase contacting an AgO disk, offers a ready test of such schemes.

Experimental

The rotating ring and split-ring disk mechanical (19) and electronic (7) systems, as employed in this laboratory, have been described elsewhere. The electrodes involved in the present study were fashioned as split-ring disks according to the procedure previously outlined (7). Shorting of the split-rings gives the equivalent of a conventional ring-disk and was the configuration normally used in this work. Where ring current measurements for different potentials were accumulated in pairs by use of the split-ring, this will not be differentiated from the shorted, conventional manner unless specific use is made of the ratio of the currents. Silver disks with either graphite or gold split-rings were employed; the dimensions were disk radius 0.238 cm, inner ring radius 0.262 cm, and outer ring radius 0.321 cm (disk area 0.178 cm^2). The insulating gaps forming the split-ring reduced the calculated collection efficiency (4) by 1-2% (0.1 mm gap), yielding a theoretical ring-current/disk-current ratio for an equal number of electrons transferred at ring and disk of about 0.16_5 per half-ring. Surface polishing of the electrodes was completed on Linde A (0.3μ) alumina.

KOH solutions were prepared directly from the reagent grade for 1.0-10.1M and determined by titration. The cell was modified from an earlier design (6) to an all-glass version with an auxiliary electrode compartment separated by a fritted disk. A saturated calomel electrode (SCE) was used as reference, terminating a capillary-tip bridge to which it was sealed with a standard taper joint, effectively preventing chloride contamination within the experimental time scale (6). Nitrogen was passed continuously into the solution. Experiments were carried out at 23°C.

The previously described operational amplifier circuitry (7) permits galvanostatic or potentiostatic control of the silver disk under conditions of constant, stepped, or linearly time swept values of either controlled variable, while fixed potentials on the half rings are maintained. The latter were normally held at potentials corresponding to limiting currents for reduction of all silver species to silver metal or of only higher valent silver species to silver (I), as determined from experimental disk current-potential cycles.

Displays were fed from the operational amplifier circuitry into a Honeywell 580 XYY' recorder. For the study of solubility through ring currents, when a steady-state flux of disk material was achieved, the outputs from the amplifiers measuring current were occasionally directly read from a Hewlett-Packard 3430A digital voltmeter.

Results and Discussion

Potential sweep experiments.—The controlled potential cycling of a freshly polished silver disk electrode from a totally reduced condition to oxygen evolution on AgO and immediately back is shown in Fig. 1, with the anodic and cathodic sweeps separated for clarity. The right-hand points of the separated traces actually coincide in time. Accompanying the disk traces are simultaneously measured limiting ring-currents for two potentials; −0.2V for the reduction of all soluble silver species to metal and +0.2V for the reduction of higher valent species to Ag(I). It is to be noted that the ring-current scale is 200 times more sensitive than that of the disk, reflecting the disk film-

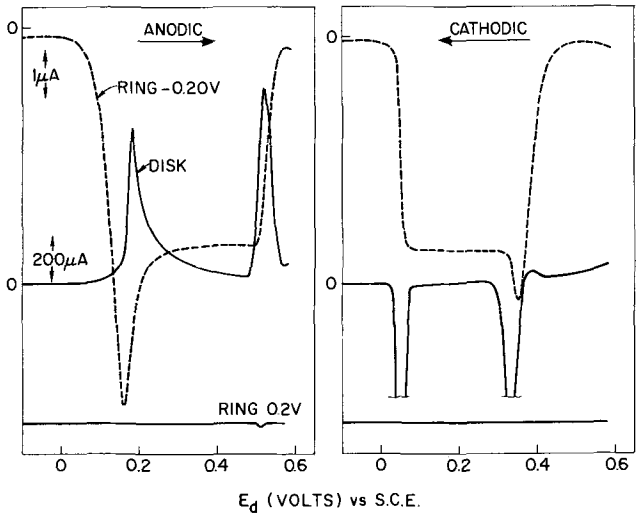

Fig. 1. 5 mV/sec potential sweep at 1000 rpm of freshly polished silver disk with graphite split ring in 1N KOH. Anodic scan (left) followed immediately by cathodic scan (right) with ring monitoring at −0.20 and +0.20V *vs.* SCE. Ring current scales both 1 μA per indicated length, disk current 200 μA per same unit. Anodic currents (ring or disk) increase upward, cathodic downward.

ing processes that limit transport to the ring. This can be further seen in the fact that disk current-potential curves for stationary disks are not distinguishable from those on rotated electrodes. In the disk behavior may be seen the successive formation of Ag_2O and AgO and the corresponding two-step reduction of the oxides. This result for a freshly polished surface is essentially repeated on cycling, except that the first anodic peak ($Ag \rightarrow Ag_2O$) at the disk and the resultant cathodic ring current (−0.2V) may be broadened or, more usually, show a second peak or more complex structure superimposed on the major transition. This effect, which typically develops after the polished surface has been electrochemically oxidized and reduced once, is shown along with additional effects due to higher hydroxide concentrations in the superimposed (as recorded) anodic and cathodic sweeps in 6.24M KOH of Fig. 2.

The cathodic ring current for reduction of all species to silver metal becomes constant independent of potential after the initial single or structured peak of disk current on anodization (Fig. 1 and 2) and remains so until the disk reaction reaches the $Ag_2O \rightarrow AgO$ stage. If the scan is stopped in the peak region, the ring-current decays to this constant, potential invariant, value. During the $Ag_2O \rightarrow AgO$ disk transition this ring current for total reduction declines to a minimum associated with the minimum disk current (conversion to AgO surface). If the anodic scan were continued, the cathodic ring current at potentials in the −0.15 and −0.20V region would increase because of oxygen evolution at the disk and its interfering reduction at the ring. The ring current at the AgO disk minimum current increases with hydroxide concentration and with the accompanying shift of oxygen evolution closer to the point of AgO formation; but at no hydroxide concentration up to the 10.1M limit studied does the ring current at the AgO minimum become equal to that from an Ag_2O electrode. In the concentrated hydroxide solutions the current at the ring, when set at potentials for reduction to the metal as negative as the −0.20V *vs.* SCE of Fig. 1, shows a sharp peak at the end of the disk potential independent plateau before the decline to the AgO minimum. If the ring potential is moved 50-100 mV more positive, still giving a limiting current for Ag(I) → Ag(O), this peak is drastically reduced, indicating that it is due to oxygen being generated before efficient nucleation of AgO in concentrated base and not to higher valent silver or its decomposition products. The potential region involved

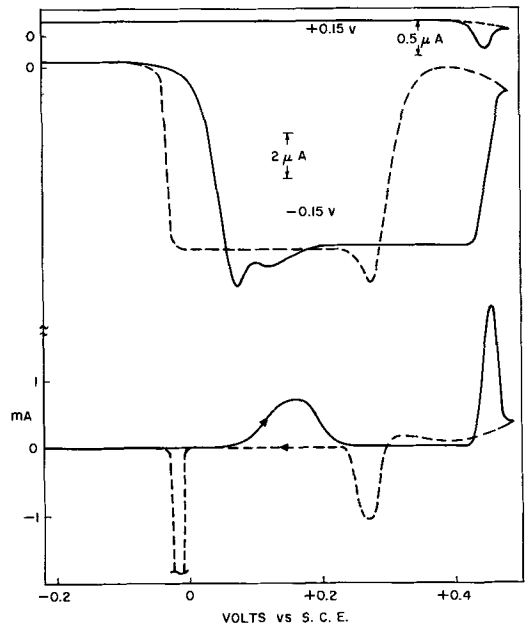

Fig. 2. Superimposed potential sweeps (anodic, solid line, followed by cathodic, dashed line) of previously cycled electrode. Scan rate 5 mV/sec at 1000 rpm in 6.24*N* KOH. Ring current (upper traces) sensitivities at +0.15 and −0.15V are 0.5 and 2 μA per indicated markers, respectively. Left axis shows disk current (lowest trace).

at the ring corresponds to much less than four electron reduction of oxygen, being just on the rising current portion of the reduction curve of the latter, much below the limiting current values.

In Fig. 1 and 2, the rings held positive of Ag(I) reduction but negative of AgO reduction show only residual current until the $Ag_2O \rightarrow AgO$ transformation. Corresponding to this latter process is a ring current peak that increases with hydroxide concentration from only about 1/50 of the value of the ring cathodic plateau current in 1M hydroxide for a Ag_2O covered disk (Fig. 1) up to approximately ¼ of the plateau current in 10.1M KOH. From the relative heights, about 1:30, of the same two ring currents in the intermediate 6.24M electrolyte in Fig. 2, the formation of higher valent soluble species increases appreciably in concentrated base. However, these reduction current peaks for higher valent species are maximum values detected during a transient process. On the completed AgO surface beyond the peak, the current is substantially less.

On the cathodic sweep, the disk current first rises slightly in the anodic direction (Fig. 1 or 2) before the well-defined peak for AgO reduction. The anodic current apparently represents a net corrosion reaction to Ag(I) occurring below the potential of AgO formation whose self-discharge also contributes to a Ag(I) flux. This conclusion with respect to the product is substantiated by the fact that the cathodic ring current at −0.20 or −0.15V begins to increase during this anodic region at the disk, followed by a maximum as the AgO disk reduction proceeds and the net disk current is cathodic. Thereafter a value independent of disk potential is reached exactly equal to that found in the anodic sweep for the Ag_2O region. As the second disk reduction step strips the electrode to metal, the ring current returns to the residual value. The final reduction at the disk is always extremely narrow with no structure, in spite of the varying shape of the $Ag \rightarrow Ag_2O$ step on a polished or cycle-produced surface. During the disk sweeps both conversions, $Ag \rightarrow Ag_2O$ and $AgO \rightarrow Ag_2O$, result in transient supersaturation peaks for Ag(I) at the ring, followed by identical equilibrium levels of ring current from Ag_2O coated disks. Further substantiation of this interpretation will be shown later.

The ring held positive of Ag(I) reduction detects essentially nothing on the disk cathodic sweep (upper trace of Fig. 2 especially). Only in very high hydroxide concentrations, like 10.1M, is there a distinguishable ring current level before AgO reduction, yet only about ¼ the peak found in the anodic sweep which, as noted, was itself only about ¼ of the $Ag(I) \rightarrow Ag(O)$ ring plateau current. Considering equal numbers of electrons transferred in the corresponding ring reactions ($II \rightarrow I$ and $I \rightarrow O$), this suggests even in 10.1M KOH the solubility of AgO is only about 1/16 of that of Ag_2O.

Thus, for the entire range of KOH concentration studied, the $Ag_2O \rightarrow AgO$ step produces a surface from which a much lower level of soluble species is apparently found, as evidenced by the drop of the ring currents for reduction to metal and the low currents produced for reduction to +1. The fact that both these currents are low with respect to the plateau ring current from Ag_2O demonstrates that a solubility mechanism for AgO of a high dissolution rate followed by a very fast, in-transit decomposition of higher valent species to Ag(I) cannot be operative. This is simply ruled out by the more negative ring-potential result, where Ag(I), generated in a post-electrode reaction, would also be counted. The absence of any such appreciable current in Fig. 1 and 2, which are representative of all the solutions examined, shows this mechanism to be a minimal factor. One possible argument for an actual high AgO solubility in spite of these facts would be that the rate of dissolution of AgO is very slow and responsible for the low ring currents. Contradicting this thesis is the low degree of supersaturation seen in the ring current trace at −0.15 or −0.20V for the initiation of the AgO transition at the disk. For an appreciable solubility, *i.e.*, a moderate K_{sp}, to obtain with an assumed small dissolution rate K_{diss}, the precipitation rate, K_{ppt}, would necessarily be correspondingly small since $K_{sp} = K_{diss}/K_{ppt}$. This argument thus predicts a distinct supersaturation for AgO formation in contradiction to experiment.

The ring-disk evidence in the AgO solubility question corresponds well to the conclusions of Amlie and Ruetschi (10) and Pleskov and Kabanov (11) that a bulk AgO saturated solution contains micromolar or less levels of a higher oxidation state. It further proves for the electrolytically formed surface that this is certainly not the result of fast solution decomposition nor very probably the result of slow equilibrium. Since the half-life necessary for a higher oxidation state decomposing in transit from disk to ring not to be detected is of the order of milliseconds, the technique used here is more likely to find detectable concentrations than conventional microelectrode inspection of an equilibrated solution of KOH and solid AgO. The measured levels of ring currents for the AgO surface may be converted to disk surface concentrations of higher valent silver by using an approximate estimate at 1000 rpm rotation speed of a disk current density equivalent of about 0.5 mA/cm²/mM soluble silver from the Levich equation parameters (29). On this basis the detected transient peaks correspond to a few micromolar higher valent silver at 1M KOH [compare 180 micromolar Ag_2O solubility (10)]. In 10.1M KOH, from the ring current at +0.15V on formed AgO surfaces, the disk surface concentration of higher valent silver (calculated as +2) is in the range of 25 μM, or better than one order of magnitude down from the Ag_2O equilibrium silver data (10) of 440 μM.

A more severe test of the conclusion from the disk potential sweeps that the current from a continuous Ag_2O surface is disk-potential independent comes from the results of potential steps within this region as shown in Fig. 3. In this experiment the disk and ring are allowed to equilibrate, with the ring held at −0.20V (unchanged throughout) and the disk at +0.25V (Ag_2O surface). The disk is stepped 100 mV positive until nearly equilibrated, then back, with a second cycle of this kind also shown. The ring response

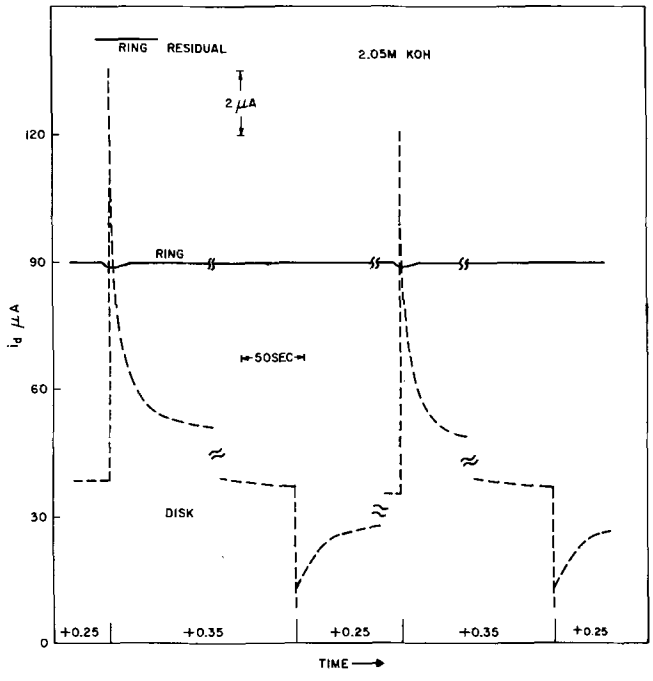

Fig. 3. Potential steps at silver disk between +0.25 and +0.35V vs. SCE with ring current monitored at a constant −0.20V. Steps occur at bars on time axis; disk current left axis. 2.05M KOH, graphite ring, 1000 rpm. 2 μA ring and 50 sec time markers are indicated.

is essentially zero, while the disk traces indicate sharp pulses corresponding to step direction and a very slow recovery to what is eventually a steady-state, potential-independent value. The results indicate that the ring current under the experimental conditions is a function only of the solubility of the oxide film on the disk. The effect at the disk is a thickening (positive step) or thinning (negative step) of the Ag_2O film with a slow attainment of the current level corresponding to the steady-state replacement of the dissolving film. The steady-state values of the ring-current disk-current ratio are in satisfactory agreement with the 0.33 calculated collection efficiency of the shorted half-rings, with uncertainty lying mostly in the slight slow drift of the disk current around an equilibrium value. This is probably due, from the appearance of Fig. 3, to a very small, long-term variation in the control potential.

The above conclusions may be compared to those of Oshe and Kabanov (20, 21) for similar experiments on zinc electrodes in hydroxide solutions. For a zinc disk, the limiting current for zinc ion reduction at the ring for anodic disk currents resulting from small positive potential steps at potentials somewhat positive of initial passivation is that given by the geometric collection efficiency. At quite positive potentials with respect to the open circuited zinc couple, the ring current has only a small sensitivity to disk change, nearing that of the silver case. The behavior exhibited by the Ag_2O-filmed electrode is apparently approached by zinc oxides under the latter conditions, but at less positive potentials, the thinner solid phase acts either partly or entirely as a potential dependent barrier to dissolution of underlying zinc. The insulating silver oxide phase represents a classically simple chemical-dissolution-limited passivity, and this aspect will be quantitatively examined later.

Although solid AgO contains nonequivalent silver atoms and is formulated as the Ag(I) Ag(III) mixed oxide, it is also well-established (22) that AgO yields divalent silver on dissolution in mineral acids. This behavior has been rationalized (23) by the equilibrium (24) $Ag(III)\ O^+ + Ag(I)^+ + 2H^+ \rightleftarrows 2\ Ag(II)^{+2} + H_2O$. It is therefore of interest to examine the number of electrons transferred in the oxidation of Ag(I) ion to AgO. Immediate coulometric distinction between the schemes

$$2\ [Ag(I) \rightarrow Ag(II) + e] \qquad [1a]$$

$$2\ Ag(II) \xrightarrow{OH^-} Ag^{I}\ (OAg^{III}O) \qquad [1b]$$

and

$$Ag(I) \rightarrow Ag(III) + 2e \qquad [2a]$$

$$Ag(I) + Ag(III) \xrightarrow{OH^-} Ag^{I}\ (OAg^{III}O) \qquad [2b]$$

cannot be made since the ratio of Ag(I) reacted to electrons transferred is the same in both if [2b] is very rapid and quantitative. The first scheme implies that the origin of Ag(III) is coupled with the formation of AgO; effectively a solid state disproportionation yields the more stable, mixed valent silver oxide rather than a true $Ag^{II}O$. The second path suggests that only half the Ag(I) is oxidized and precipitates an equivalent amount of Ag(I). No mechanistic detail other than distinguishing whether the nonequivalence of the silver atoms originates in the electron transfer process (scheme [2]) or not (scheme [1]) is to be implied. For example, the process of Ag(I) oxidation by adsorbed OH· radicals (from $OH^- \rightarrow OH\cdot_{ads} + e$) as $Ag(I) + OH\cdot \rightarrow AgO + H^+$ (25) is coulometrically a scheme [1] process in its implications for the behavior of all +1 silver ions reaching the surface at appropriate potentials.

Experimentally, the oxidation of soluble Ag(I) produced at the disk was examined by using the split-ring version of the potential sweeps already described, with one half-ring held at −0.20V and the other at potentials positive of the AgO disk peak. The reducing half-ring has the known one electron reaction $Ag(I) \rightarrow Ag(O)$ and the simultaneous current at the second half-ring for the oxidation of an equal Ag(I) flux can thus be compared. Graphite half-rings operated independently at −0.20V give Ag_2O plateau currents (as in Fig. 1 and 2) within 1% of each other. However, with either a gold or graphite split ring at potentials up to considerable oxygen evolution, no anodic current was found during a disk sweep except for an increasing anodic residual (oxygen, surface oxides) current, while the −0.20V half-ring was showing the expected curve. If the half-ring connections were then reversed, though, so that the silver plated half-ring from the −0.20V operation instead of clean gold or graphite was made about +0.50V *vs.* SCE, an anodic trace, reduced by a constant factor from being an anodic mirror image of the −0.20V cathodic currents, was found during the disk anodic sweep.

The above result implies that oxidation of $Ag(OH)_2^-$ occurs readily only on a previously AgO nucleated surface. Since ring deposition is not radially uniform and the constant factor mentioned was variable between runs, the experiment was repeated with an all-silver split-ring disk electrode produced by plating the graphite split-rings from a cyanide bath formulated from reagent purity materials. The result achieved is shown in Fig. 4, with an anodic half-ring potential of +0.51V. The two half-ring traces above residual currents are effectively reflections of each other, but the measured anodic/cathodic plateau ratio obtained is 0.93. The anodic current is measured above a residual of height comparable to the Ag_2O solubility current, and further positive shifts of potential beyond about +0.52V to be sure of reaching a limiting-current condition are restricted by the stability of the background.

The best interpretation of the results is that the actual ratio of electrons is unity and the direct electrode oxidation product of all the Ag(I) is Ag(II) which is subsequently incorporated into the AgO solid. This result is independent of rotation speed variation. While the 50% $Ag(I) \rightarrow Ag(III) + 2e$ conversion scheme [2] cannot be ruled out, it is rather difficult to visualize a limiting current process with quantitative precipitation of AgO from equal surface concentrations of oxi-

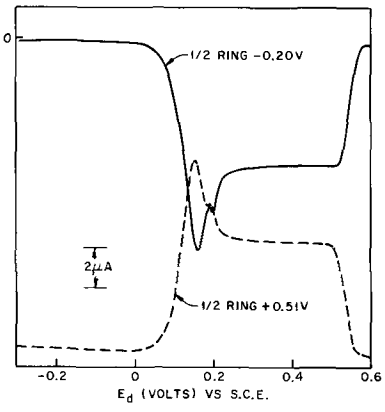

Fig. 4. Half-ring currents during silver disk anodic potential sweep (10 mV/sec at 4000 rpm). Silver-plated graphite half-rings held at −0.20 and +0.51V *vs.* SCE, with the same current sensitivity in 1*N* NaOH. The zero current level of the positive half-ring is below the area of the figure (see text).

dized Ag(I) (Ag(III)) and precipitant Ag(I). This would be necessary for the ring current to be equivalent to one electron per Ag(I) in the flux generated at the disk. In acid solutions, the oxidation of Ag(I) has also been identified as a one electron reaction using the ring-disk electrode technique (26) under conditions where all silver species are soluble. Interpretation of these latter data as a direct Ag(I) → Ag(III) electron transfer process is even more unlikely than in the alkaline case because the complex clathrate solids (18) are not involved and an extremely stable I-III solution complex would have to be invoked.

Constant current and linear current sweep experiments.—Galvanostatic charge and discharge conditions have been applied in most silver electrode studies. Earlier work on the potential-time or coulomb behavior has been reviewed by Dirkse (27). In the present study these aspects can be discussed in terms of the ring-current indications of the concentrations of soluble species, with the results of the previous section's potential sweeps also in mind. A representative potential-time plot for a disk, here anodized in 6.24M KOH at 1.87 mA/cm², is shown in Fig. 5, together with the ring current for reduction back to metal (−0.20V). The current was reversed to cathodic at the disk just as the potential began to rise sharply to oxygen evolution. The cathodic part of the cycle is carried through here beyond the disk potential shift from the "AgO" level to the "Ag_2O" level, as is familiar in the operation of the silver positive. The ring current trace at +0.15 or 0.2V, shown in the potential sweeps, is not included here simply because almost no soluble higher valent

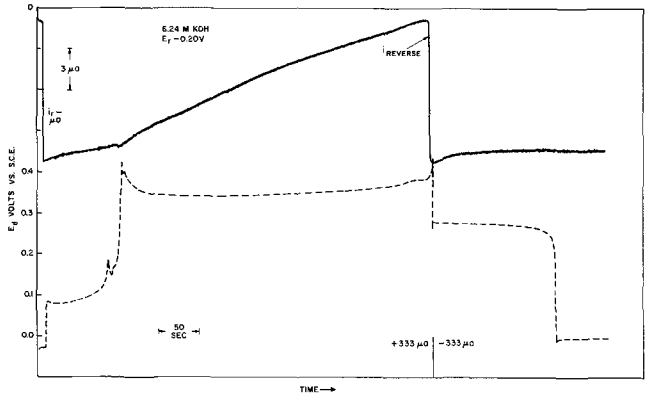

Fig. 5. Lower trace: potential (E_d) *vs.* time trace of disk anodized at 1.87 mA/cm² with current reversal at indicated point. 1000 rpm in 6.24M KOH, 50 sec time marker indicated. Upper trace: ring current at −0.20V, residual zero at upper left. 3 μA marker near left axis indicates sensitivity.

material is detected. For example, the ring current at 0.15V found in the AgO region on charge in 1M hydroxide is indistinguishable from that in the Ag_2O region within the <0.02 μA noise level of the trace.

The disk potential traces, on initiation of anodic current, show typically a small overshoot of potential and a shallow minimum at about the middle of the Ag_2O transition when the electrode is well stripped of oxide before starting. Otherwise, the overshoot and minimum are absent. At the end of the Ag_2O step the potential shows the characteristic large overshoot to nucleation of the AgO phase. A small, premature potential rise is shown on the trace in Fig. 5 before the major AgO shift. This feature was sometimes absent and varied from run to run but with no corresponding variation in the ring current trace, which is shown exactly as recorded. The AgO potential plateau was longer than the Ag_2O step for every concentration of hydroxide and current level studied, a well-known characteristic of these conversions and independent of the rotation of the disk. After the current was reversed at the point of potential rise to oxygen evolution, the equally characteristic shorter discharge plateau at the AgO potential is seen. The rest of the discharge (not shown) extends normally to a 90% or more recovery of the coulombs of charge.

The ring current for reduction to silver shows an initial peak on disk anodization. With higher current densities, the peak has a much more accentuated maximum and a more rapid following decay than that shown in Fig. 5. The ring current declines to a value at the point of the AgO transition that is equal to the plateau ring current in a potential sweep with the same KOH concentration and rotation speed. The galvanostatic experiment indicates an Ag(I) concentration in excess of Ag_2O solubility, presumably because of supersaturation in pores. This continues up to the point of complete coverage of the surface with Ag_2O (equilibrium solubility indicated by the ring current), and this is identified with the initiation of AgO formation. The ring current declines after the potential shift to the AgO level in an almost coulombically linear manner to a minimum nearly equal to the residual value at the point of the potential jump to oxygen evolution. The ring-current decline is actually a little faster than the coulomb equivalent, and this is accentuated as the hydroxide concentration is lowered. The current is due throughout the AgO step to Ag_2O remaining on the surface. This is confirmed by the absence of any current level greater than the minimum shown for a −0.20V ring for a ring held at a more positive potential detecting only higher oxidation states. The actual current at any stage presumably corresponds to the fractional surface coverage by the lower oxide.

In contrast to the Ag_2O → AgO surface conversion, the reverse disk process produces a (Ag(I)) supersaturation peak at the ring and forms an Ag_2O covered film from the beginning of the cathodic current application. Also of interest is the ring behavior in the transition to the Ag_2O level during which the disk potential falls sharply more than 0.25V; the current is completely unaltered by this change. The ring current remains at a constant level until some small nonuniformity of the over-all formation and stripping leads to a drop in ring-measured Ag(I) before the final potential fall (not shown in Fig. 5). Even in this region, the ring current recovers to the previous constant value on open circuiting the disk until discharge is very nearly complete.

The ring trace in the conversion of Ag_2O → AgO shows that for practical battery purposes the amount of soluble silver is minimized by maintaining the positive at full charge. The current reversal shows the discharging cell produces Ag_2O solubility levels immediately. Disk electrodes open circuited at the point of oxygen evolution show gradual increases of ring current to that of the Ag_2O solubility level by self-discharge and further corrosion of underlying silver to +1 as the passive film thins. A net anodic current

must therefore be passed to retain the AgO surface and a minimum soluble material state. Ag(I) ions already in solution will also be slowly deposited as AgO under these conditions.

Supersaturation levels of $Ag(OH)_2^-$ have been shown in both potentiodynamic and galvanostatic formation of Ag_2O on silver and AgO. A further clear demonstration of this process may be obtained from linear current scan studies. If a critical surface concentration of $Ag(OH)_2^-$ must be reached to initiate the nucleation of a solid phase, then −0.2V ring current disk current plots up to that point should be linear with slopes corresponding to the collection efficiency. The experimental results with the disk potential also monitored are shown in Fig. 6. A linear region with a slope in good agreement with the calculated value (0.315 and 0.33, respectively) is obtained. At i_r of about 11 μA, the ring current ceases to increase linearly with disk current and subsequently goes through a maximum, declining (off the disk current scale of the plot) to the equilibrium solubility value (12 μA) just before AgO formation is reached. Allowing for concentration of KOH changes, the monitored disk potential in Fig. 6 shows an Ag/Ag_2O potential corresponding to the initial stage of reaction in the potential sweeps of Fig. 1 and 2. The detectable supersaturation levels in linear current or potential sweeps or constant current anodization vary with the particular conditions, but a factor of nearly two times the solubility is about as high as has been observed. Other systems, $Cu/Cu(OH)_2$ (5) or $Pb/PbSO_4$ (26) for example, exhibit ring-measured relative supersaturations more than an order of magnitude higher than Ag/Ag_2O. The same recovery of totally dissolved Ag(I) on current scans to the point of critical supersaturation has been shown for the reaction AgO → Ag_2O when the i_r/i_d slopes are taken at disk potentials negative enough of the open circuit value that self-discharge processes do not contribute appreciably to the ring current.

Charge capacity-rotation speed and current levels.— When a film forms at a disk in the ring-disk system, the disk coulombic capacity (quantity of film) and the ring currents measuring the instantaneous flux of soluble species during the filming process have a different sensitivity to some of the experimental variables. It would be predicted, for example, that ring currents observed on discharge (Fig. 5) depend systematically on rotation speed (*vide infra*) but that the anodized film layer thickness (coulombic capacity) would be little dependent on stirring in a system of low film solubility. These factors are examined in a series of cycles with fixed rotation speed and varied disk current (Fig. 7) and fixed current and varied rotation speed (Fig. 8).

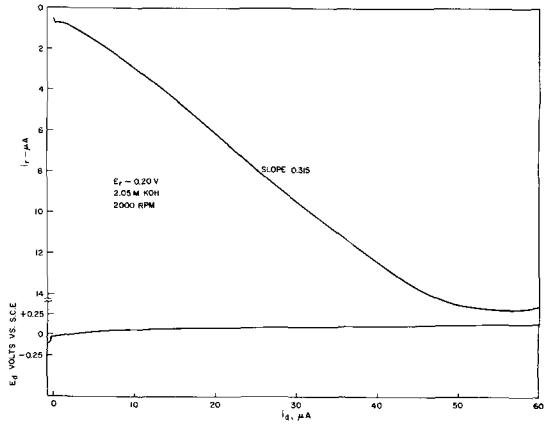

Fig. 6. Lower trace: disk potential *vs.* disk current during 0.1 μA/sec linear current sweep at 2000 rpm in 2.05M KOH. Upper trace: ring current at −0.20V during i_d scan with $\frac{\Delta i_r}{\Delta i_d}$ slope at 0.315 in linear region.

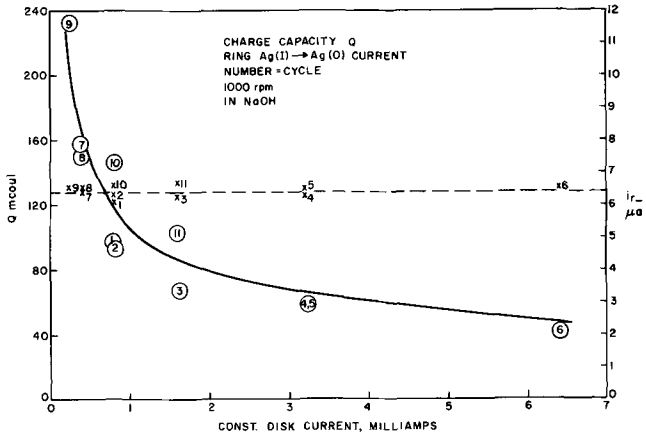

Fig. 7. Solid line: charge capacity, Q, plotted *vs.* constant disk current for cycles of silver disk in 1*N* NaOH at 1000 rpm. Number in points indicates the cycle. Dashed line: ring current, i_r−, at −0.20V for Ag_2O surface (see text) with cycle number indicated.

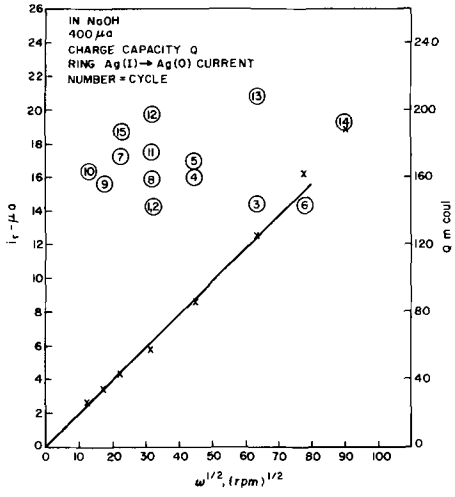

Fig. 8. Circled points are charge capacity, Q, plotted *vs.* $\omega^{1/2}$ for constant 400 μA cycles in 1*N* NaOH, cycles as numbered. Solid line is ring current, i_r−, at −0.20V for Ag_2O surface (see text), with all points at given ω averaged.

The charge capacity, *Q*, is taken as the number of millicoulombs passed in going from silver to the point of the potential excursion to oxygen evolution. Any other measure of capacity would give equivalent trends for the present purposes. For each point a complete cycle is run with current reversed as in Fig. 5. The ring currents for Ag(I) → Ag(O) are taken from the discharge, although the value at the point of the Ag_2O → AgO transition on charge is equivalent. The declining slope of ring current for short oxidation times (down to 6 sec) is so steep at that point, however, that experimentally the stable value on discharge is more reproducible and certain of measure. In both Fig. 7 and 8, the numbers on the points represent the number of the cycle. It is clear from Fig. 7 that the ring current is independent of the current density at the disk for a constant rotation speed. On the other hand, the coulombic capacity is decreased by more than a factor of five for a current density increase from 1.4 to 36 mA/cm², the extremes of measurement. Additionally, the capacity increases slowly in the course of cycling and roughening.

In Fig. 8 it is seen that at constant disk current the charge capacity is essentially independent of rotation speed but tends to increase with cycling. The ring current is a linear function of the square root of the rotation speed and is constant within experimental error for each series of cycles at the given speed. The same results would obtain for any other fixed current density. The essential independence of capacity and rotation speed is a reflection of this small amount of

solubilized material relative to the total coulombs of charge, seen also in the fact that the disk potential-time-current behavior is nearly the same at all speeds. Also, the larger proportion of charge is delivered at the AgO level, and this stage produces ring currents less than the Ag_2O values in Fig. 7 and 8.

Solubility and diffusion coefficients from ring measurements.—The above evidence has amply indicated that the ring current from a Ag_2O-surfaced disk is determined by the solubility of that phase. Placing this on a quantitative basis requires combining a simple model for the dissolution rate with the Levich transport parameters for the system. The dissolution rate of ionic crystals is ideally dependent only on the transport of solute ions by diffusion through a layer of thickness δ (28), assuming that the solution remains saturated at the surface. This is well-supported by both the time-constancy of the ring current and its independence of disk potential. The equivalent disk current for dissolution into a silver-free KOH electrolyte is given by

$$i_d = \frac{n \mathbf{F} A C_s D}{\delta}$$

where n, $\mathbf{F}$, and A are the number of electrons transferred per silver atom (=1), the Faraday, and the disk area, respectively. C_s is the equilibrium solubility of Ag_2O in terms of silver ion, D is the diffusion coefficient of the dissolving silver species (presumed to be $Ag(OH)_2^-$), and δ is the thickness of the diffusion layer. For the rotating disk, Levich (29) found $\delta = K D^{1/3} \nu^{1/6} \omega^{-1/2}$, with K a constant, $\nu^{1/6}$ the kinematic viscosity, and ω the rotation speed. Substitution gives the Levich equation

$$i_d = K_n \mathbf{F} A C_s D^{2/3} \nu^{-1/6} \omega^{1/2}$$

in its usual form except that it is expressed for boundary conditions of $C_{Ag(OH)_2^-} = C_s$ at $x = 0$ (the electrode surface) and $C_{Ag(OH)_2^-} = 0$ at $x = \infty$ instead of the more usual, reverse situation of deposition at the disk from a saturated solution of Ag_2O.

Since $i_{r-} = N i_d$, where i_{r-} is the limiting ring current for the Ag(I) → Ag(O) reaction and N is the geometric collection efficiency, the relation between the two measured parameters i_{r-} and $\omega^{1/2}$ may be expressed as

$$\frac{i_{r-}}{\omega^{1/2}} = (K_n \mathbf{F} A N) D^{2/3} \nu^{-1/6} C_s$$

The data shown already in Fig. 8 have verified the square root relationship. Extension of measurements to cover the range of KOH concentrations from 1.00 to 10.1M is shown in Fig. 9. For these measurements, the disk was potentiostatically held in the Ag_2O region

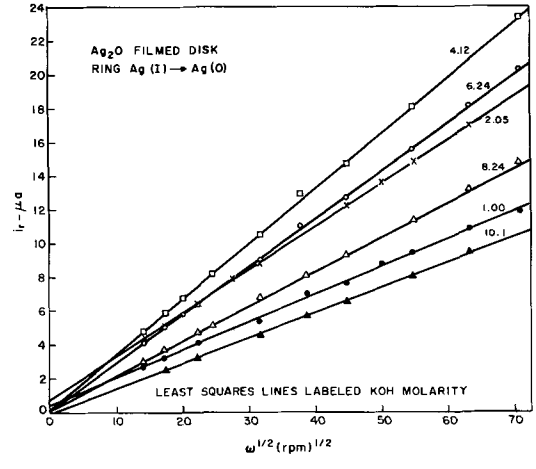

Fig. 9. Plot of ring current, i_{r-}, for the Ag(I) → Ag(O) ring reaction from a potentiostatically held, Ag_2O-filmed disk *vs.* $\omega^{1/2}$. KOH molarity labeled on corresponding line.

and the ring current read for various rotation speeds at −0.20V. The lines are drawn with slopes and intercepts obtained from a least squares treatment and are of higher precision than those obtainable by the techniques outlined for Fig. 8 which involves many cycles of the electrodes. Equivalent data have also been obtained by anodizing the silver disk to an Ag_2O film and then measuring the ring current with the disk at open circuit, replacing the Ag_2O as required. Of particular interest in Fig. 9 is the maximum in the slope as a function of the KOH concentration, 4.12M yielding the highest value of $i_{r-}/\omega^{1/2}$. This maximum is suggestive of the solubility data of Amlie and Ruetschi (10), but the product $D^{2/3} \nu^{-1/6}$, which also determines the slope, changes considerably from 1 → 10M KOH and must be accounted for prior to conclusions regarding the shape of C_s *vs.* KOH concentration.

Two equivalent approaches were utilized. In the first, constancy of the $D\eta$ product (η = viscosity) was assumed for the KOH concentration range involved and a corrected $i_{r-}/\omega^{1/2}$ *vs.* KOH molarity curve was compared to the solubility curve (10). In the second, the solubility data of Amlie and Ruetschi were taken and the $D\eta$ and D values calculated, checking the constancy of the former and comparing the latter to the available data of Pleskov and Kabanov (11). The conclusion of Sillén *et al.* (13) that $Ag(OH)_2^-$ is the only species for which there is evidence supports testing the $D\eta$ assumption.

With $D\eta$ first taken as constant, the Levich product $D^{2/3} \nu^{-1/6}$ is proportional to $\eta^{-2/3} (d/\eta)^{1/6} = \eta^{-5/6} d^{1/6}$, the density, d, being obtainable from Akerlof and Bender (30). Viscosities were interpolated from the data of Klochka and Gadneva (31) and McIntyre (32). Table I gives the values of $\eta^{-5/6} d^{1/6}$ normalized to 1.00 at 1.00M KOH.

The solubility data of Amlie and Ruetschi are plotted in the upper dashed curve in Fig. 10 with the right-hand axis giving the silver concentrations. The left-hand axis has been plotted with the solubility in 1.00M KOH normalized to unity. The lower dashed line represents the solubility data normalized by multiplication by the factors of Table I and thus represents a predicted curve for the normalized experimental $i_{r-}/\omega^{1/2}$ slopes of Fig. 9. The experimental values from Fig. 9 will yield the solid line in Fig. 10, which is in satisfactory agreement with the predicted. The value denoted by the square datum is from the slope of a $i_d/N\omega^{1/2}$ plot for a 6.24M KOH solution equilibrated overnight with solid Ag_2O, where i_d is the cathodic limiting current for the reduction of Ag(I) at the silver disk. The small deviation of the point from the two lines is in the direction of incomplete saturation. The agreement of the predicted and measured curves, if not a fortuitous product of the assumptions, suggests that the maximum of Ag_2O solubility (10) at around 6M KOH is correct rather than the monotonic variation found by other workers (11, 12).

With the Amlie and Ruetschi solubility data and literature values of ν substituted in the expression for ring current, the diffusion coefficients and $D\eta$ product were calculated and are plotted in Fig. 11 along with the existing four D determinations of Pleskov and Kabanov (11). The present data give D's ranging from 8.6 x 10^{-6} cm²/sec (1M) to 2.3 x 10^{-6} cm²/sec (10.1M). The Schmidt number ν/D varies from about 1,100 to 11,000 over this range. Applying the nearly exact

Table I. Values of $\eta^{-5/6} d^{1/6}$

M KOH	$\eta^{-5/6} d^{1/6}$ (normalized)
1.00	1.00
2.05	0.91
4.12	0.74
6.24	0.59
8.24	0.47
10.1	0.37

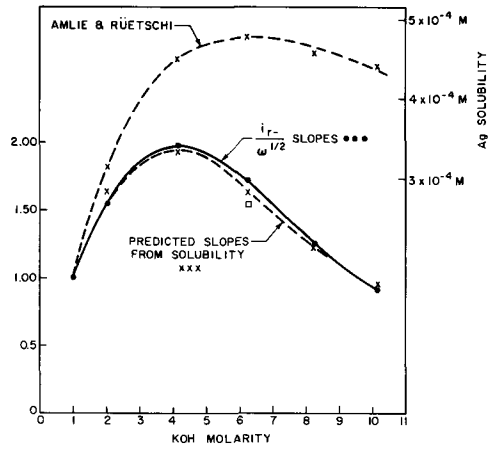

Fig. 10. Upper dashed line is solubility of Ag_2O (right hand axis) vs. KOH molarity, also normalized to unity at 1M KOH (left hand axis). Lower dashed line is upper curve corrected by factors of Table I. Solid line is plot of normalized slopes from Fig. 9 vs. KOH molarity. Point shown as □ is described in text.

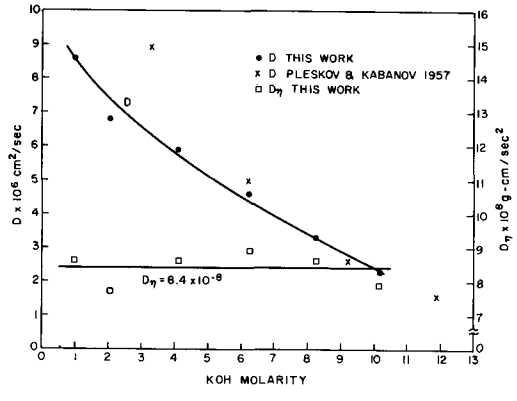

Fig. 11. ● line is D vs. KOH molarity, this work. x points are data for D of Pleskov and Kabanov (11). □ line is $D\eta$ product vs. KOH molarity, this work.

numerical solution of Newman (33) instead of the Levich equation, the D value range would be 9.0 to 2.3 x 10^{-6} cm^2/sec. Either set of values is in appreciable disagreement with Pleskov and Kabanov only at their lowest concentration point. The Pleskov and Kabanov values were obtained for cathodic disk currents in determinatively prepared Ag_2O solutions and the Levich equation. Their solubility determinations, which do not show a maximum, were made by multiplying the ratio of disk current for a saturated solution to that from the known solutions by the known concentration.

The $D\eta$ product is constant within experimental error at 8.4 x 10^{-8} g cm/sec^2. From rotating disk reduction studies in the 2-8M KOH concentration range Davis, Horvath, and Tobias (34) found 13 x 10^{-8} g cm/sec^2 for oxygen. The present data are best consistent with an interpretation of the solubility of Ag_2O passing through a maximum and the soluble species being $Ag(OH_2)^-$ (or some other single formula) in major proportion throughout the KOH range studied.

Examination for Ag(III).—The formation of a relatively soluble Ag(III) species by high current density (70 mA/cm^2) anodization of a silver sheet has been reported recently by Cohen and Atkinson (35). The solubility of this ion, identified by the authors as $Ag(OH)_4^-$, was found to be 2-5 times greater than that of $Ag(OH)_2^-$ in the 1-10M KOH studied in the present work. All controlled potential sweep and constant current curves described to this point were carried only to the region of the minimum of disk current in AgO formation or to the corresponding point of transition to oxygen evolution. For these experiments, when carried further in the anodic direction, a small transient peak at the ring is obtained for the reduction of an almost immediately insoluble product at the disk, the potentials for reduction being kept positive of these responsive to oxygen. The described behavior is similar to that noted for copper in hydroxide solutions which was interpreted as due to transient Cu(III) formation and generation of oxygen on the higher oxide (5). Such a transient oxide conversion is also suggested from resistivity measurements (36).

The current density of the Cohen and Atkinson experiment yields profuse oxygen generation. At a ring-disk electrode, in spite of rotation, bubbles collect and have the effect of lowering the ring current to some fraction of its normal, collection efficiency value. This is readily seen by switching back to an Ag_2O surface and observing the change in the well-defined Ag(I) → Ag(O) ring current level. Thus, quantitative measurements with appreciable oxygen generation currents flowing (visible bubbles) are not feasible without a correction for the effect. The cell used, however, is also equipped with an L-shaped glass tube with medicine dropper bulb which directs a jet of electrolyte across the plane of the spinning disk, removing bubbles. Recovery of the ring response is noted and a reasonable estimate of the unperturbed current can be made.

In experiments under both potential sweep and constant current control, with ring potentials corresponding to reduction to a metallic silver surface, no further appreciable silver species is detectable even at 70 mA/cm^2 and with allowance for the above bubble effects. For example, in 4.12M KOH, when the anodic current at the disk was increased in stages to 80 mA/cm^2, the ring current at 0.00V *vs.* SCE increased to no more than 1 μA higher than that at the minimum in the AgO surface conversion. At 1000 rpm, an Ag_2O disk surface produces limiting current at the ring of 10 μA, though the 0.00V potential yields about 2.5 μA. The solubility curve of Cohen and Atkinson (35) suggests that more than 50 μA should have been measured in the 80 mA/cm^2 experiment, considering that the ring potential is such as to yield > 2 and < 3 electrons, according to their work. Uncompensated resistance effects between reference and working electrodes are in a direction to shift the ring potential more negative with increasing anodic current and thereby to be further certain of not missing any Ag(III) species.

From the ring-disk electrode experiments it must be concluded that there is no appreciable solubility of an Ag(III) species from a strongly oxidized silver disk. Other citations of Ag_2O_3 (37, 38) emphasize its difficulty of formation and instability, and the present experiments are suggestive only of a further incorporation of oxygen into the surface with possibly a small amount of Ag(III) being formed at the point of free oxygen evolution. The experimental discrepancy with the Cohen and Atkinson paper remains currently unresolved.

Summary

From the perspective of ring-current measurements, the anodic-cathodic cycling of a silver electrode may be described as the following. On either controlled-potential sweep or constant-current anodization of silver, Ag_2O is formed through a dissolution-precipitation process involving a supersaturation approaching a detectable maximum of two times the solubility. Actual capacity losses by dissolution and not recoverable on cycling depend on current levels, sweep rates, hydroxide concentrations, and convective diffusion or other transport, but the mechanism will follow for all kinds of silver electrodes. At constant disk current, the ring current does not reach an equilibrium level until the disk Ag_2O → AgO transition. This implies that the film does not become uniform until that point, with the excess solubility coming from unblocked (pore) silver surface, as was also concluded from resistance studies

(36). The thickness of the film at the $Ag_2O \rightarrow AgO$ transition is primarily dependent on current density. In the potential sweep or step formation of the Ag_2O film, the initially higher currents at the ring drop to the equilibrium solubility level of the formed surface. Film thickness depends on potential, reaching the value at which transport across it is equal to the dissolution rate. Shifts in potential, once the film is formed, alter only the thickness of the film, not the dissolution rate. Quantitative studies of the relation of ring current to growth processes, nucleation, and surface coverage remain to be done.

The formation of AgO, seen particularly clearly in the constant current studies, occurs through the volume of the anodized layer with the nuclei on the surface completely converged at the point of the potential rise to oxygen evolution. The surface coverage by AgO increases faster than the coulombs passed, more so at lower KOH concentrations. On reduction, the surface is almost immediately covered with Ag_2O with a supersaturation indicating an initial dissolution-precipitation mechanism. On increasing the thickness of the resistive Ag_2O layer to some value at which the conversion rate of AgO cannot be maintained, the potential shifts to the level at which elementary silver can be formed. The corresponding drop in resistance (36), however, is not accompanied by any surface change; the ring current does not respond indicating the maintenance of a Ag_2O surface until the end of discharge.

The solubility curve for Ag_2O obtained on the basis of the Levich equation, ring currents and a constant Walden product assumption support a maximum in the solubility as a function of KOH concentration. The solubility of AgO is less than that of Ag_2O throughout the hydroxide range of 1-10.1M KOH. The only evidence for a higher oxidation state in solution even at current densities to 70 mA/cm^2 is the transient formations of an additional reducible species which gives a decaying pulse of current at the ring at the initiation of oxygen evolution, as also suggested in resistance studies (36). Higher levels of Ag(III) generation (35), other than the transient presumably due to Ag_2O_3 are not supported by ring evidence.

Acknowledgment

The author is indebted to Dr. P. C. Milner for numerous discussions and critical comments during the course of this work.

Manuscript submitted July 29, 1969; revised manuscript received *ca.* Nov. 26, 1969. This was Paper 201 presented at the Montreal Meeting of the Society, Oct. 6-11, 1968.

Any discussion of this paper will appear in a Discussion Section to be published in the December 1970 JOURNAL.

REFERENCES

1. A. N. Frumkin and L. N. Nekrasov, *Doklady Akad. Nauk. SSSR*, **126**, 115 (1959).
2. A. N. Frumkin, L. N. Nekrasov, V. Levich, and Ju. Ivanov, *J. Electroanal. Chem.*, **1**, 84 (1959).
3. L. N. Nekrasov and N. P. Berezina, *Doklady Akad. Nauk. SSSR*, **142**, 855 (1962).
4. W. J. Albery and S. Bruckenstein, *Trans. Faraday Soc.*, **62**, 1920 (1966).
5. B. Miller, *This Journal*, **116**, 1675 (1969).
6. B. Miller and R. E. Visco, *This Journal*, **115**, 251 (1968).
7. B. Miller, *This Journal*, **116**, 1675 (1969).
8. H. L. Johnston, F. Cuta, and A. B. Garrett, *J. Am. Chem. Soc.*, **55**, 2311 (1933); **56**, 1250 (1934).
9. E. Laue, *Z. Anorg. Allgem. Chem.*, **165**, 325 (1927).
10. R. F. Amlie and P. Ruetschi, *This Journal*, **108**, 813 (1961).
11. Y. V. Pleskov and B. N. Kabanov, *Zhur. Neorg. Khim.*, **2**, 1807 (1957).
12. L. D. Kovba and N. A. Balashova, *ibid.*, **4**, 225 (1959).
13. P. J. Antikainen, S. Hietanen, and L. G. Sillén *Acta Chem. Scand.*, **14**, 95 (1960).
14. T. P. Dirkse and B. J. Wiers, *This Journal*, **106**, 284 (1959).
15. Y. V. Pleskov, *Doklady Akad. Nauk. SSSR*, **117**, 645 (1959).
16. T. P. Dirkse, *This Journal*, **106**, 453 (1959).
17. T. P. Dirkse, L. A. Vander Lugt, and H. Schnyders, *J. Inorg. Nucl. Chem.*, **25**, 859 (1963).
18. M. B Robin and P. Day, in "Advances in Inorganic and Radiochemistry," Vol. 10, p. 247, Academic Press, New York (1967).
19. R. H. Sonner, B. Miller, and R. E. Visco, *Anal. Chem.*, **41**, 1498 (1969).
20. A. I. Oshe, Y. Y. Kulyavik, T. I. Popova, and B. N. Kabanov, *Elektrokhimiya*, **2**, 1485 (1966).
21. A. I. Oshe and B. N. Kabanov, *Zashchita Metallov*, **4**, 260 (1968).
22. J. A. McMillan, *Chem. Rev.*, **62**, 65 (1962).
23. G. L. Cohen and G. Atkinson, *Inorg. Chem.*, **3**, 1741 (1964).
24. A. A. Noyes, J. L. Hoard, and K. S. Pitzer, *J. Am. Chem. Soc.*, **57**, 1221 (1935).
25. M. Fleischmann, D. J. Lax, and H. R. Thirsk, *Trans. Faraday Soc.*, **64**, 3137 (1968).
26. B. Miller, Unpublished data.
27. T. P. Dirkse, *This Journal*, **106**, 453 (1959).
28. A. A. Noyes and W. R. Whitney, *Z. physik. Chem.*, **23**, 689 (1897).
29. V. G. Levich, "Physicochemical Hydrodynamics," Chap. VI, Prentice-Hall, Englewood Cliffs, New Jersey (1966).
30. G. Akerlof and P. Bender, *J. Am. Chem. Soc.*, **63**, 1085 (1941).
31. M. A. Klochko and M. M. Godneva, *Zhur. Neorg. Chem.*, **4**, 2127 (1959).
32. J. D. E. McIntyre, Private communication.
33. J. Newman, *J. Phys. Chem.*, **70**, 1327 (1966).
34. R. E. Davis, G. L. Horvath, and C. W. Tobias, *Electrochim. Acta*, **12**, 287 (1967).
35. G. L. Cohen and G. Atkinson, *This Journal*, **115**, 1237 (1968).
36. B. D. Cahan, J. B. Ockerman, R. F. Amlie, and P. Ruetschi, *ibid.*, **107**, 725 (1960).
37. E. J. Casey and W. J. Moroz, *Can. J. Chem.*, **43**, 1199 (1965).
38. G. Z. Kazakevich, I. E. Yablokova, and V. S. Bagotskii, *Elektrokhimiya*, **2**, 1055 (1966).

Correction

In the paper "Mechanisms and Kinetics of H_2 Dissociation and Open-Circuit Accumulation of H Atoms During the Formation of the Equilibrium H_2/H^+ Electrode on Platinum" by Murray Rosen and Sigmund Schuldiner which appeared in the January issue of the Journal [**117**(1)35-43 (1970)] curves 3 and 4 in Fig. 5 have been misplaced. The proper potential *vs.* time representation of these curves are in the corrected Fig. 5 shown here.

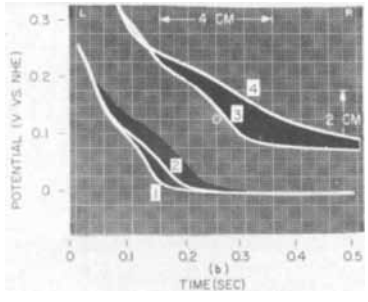

Fig. 5. Oscilloscope traces for potential *vs.* time relation of h.a.r. For Case ●, trace 1; Case ○, trace 2; Case ▲, trace 3; Case △, trace 4. See Symbols.

Study of the Behavior of Ethylene Carbonate as a Nonaqueous Battery Solvent

Gianfranco Pistoia, Mario De Rossi, and Bruno Scrosati*

Istituto Elettrotecnico, Università di Roma, Rome, Italy

In recent years propylene carbonate (PC) has been the solvent most used in the efforts to realize high energy nonaqueous batteries (1). Prototypes of batteries using this solvent have been already constructed (2, 3).

Ethylene carbonate (EC) has some favorable physical properties with respect to PC, such as higher dielectric constant and lower viscosity (see Table I), which have encouraged a detailed study on the possibility of its use in a nonaqueous system. In this paper preliminary results of this study are reported.

The main factor which may have so far limited the investigations on EC as a useful solvent in nonaqueous cells could be its solid state at room temperature. Nevertheless this could represent a remarkable benefit in realizing a thermal battery in which eventual self discharge processes would be greatly reduced. Furthermore, due to the high molal lowering of freezing point of EC (5.5°C), it is also possible to have liquid solutions at room temperature by choosing suitable electrolytes.

Since there is a lack of data about the properties of EC solutions of the salts generally used in organic solvent batteries, such as KPF_6, KCNS, $LiClO_4$ and so on, it seemed useful to acquire all the necessary basic information before examining the behavior of a cell using an electrolytic EC solution.

Purification of the solvent.—EC, reagent grade, was distilled twice on CaO under vacuum at 75°C to avoid decomposition. The analysis of the purified solvent was made by gas chromatography on a Cromosorb W column packed with Carbowax 1500 (8%) at 120°C, using flame ionization detection and helium as a carrier gas. The major impurities were ethylene glycol (10 ppm) and a not yet identified organic substance having a boiling point close to that of ethylene glycol (70 ppm). Other organic impurities were less than 5 ppm.

The water content was estimated to be about 15 ppm by the Karl Fischer method using a radiometer apparatus. The specific conductivity was determined to be $7 \cdot 10^{-7}$ ohm^{-1} cm^{-1} at 40°C and the freezing point 36.2°C, in agreement with the data reported by Seward and Vieira (4).

Preparation of the solutions.—The salts, all reagent grade, were dried under vacuum. The manipulation of the products and the preparation of the solutions were done in a dry box under argon atmosphere.

* Electrochemical Society Active Member.

Table II. Solubilities (g/100g solution) of selected salts at various temperatures in EC

Temperature, °C	KPF_6	KCNS	$LiClO_4$	$(CH_3)_4NBr$	KBF_4	LiCl
25	17.0	27.1	26.1			
30	17.6	27.4	26.3			
35	18.3	27.7	26.6			
40	18.8	28.0	26.9	0.09	0.04	0.83

Solubility.—The salts generally used in PC and similar solvents as electrolytes for battery purposes were: KCNS, $(CH_3)_4NBr$, LiCl, KPF_6, KBF_4, and $LiClO_4$.

The solubility of KCNS at various temperatures and of $(CH_3)_4NBr$ and LiCl at 40°C was determined volumetrically using a method previously described (5).

The solubility of KPF_6 and $LiClO_4$ at various temperatures and of KBF_4 at 40°C, was determined by an evaporation technique. Known amounts of supernatants from saturated solution were slowly dried in an oven and the residual salt weighed until constancy was reached.

Both the volumetric and the evaporation techniques have been tested dissolving known amounts of salts in EC. The accuracy was of the order of 1-2%. The solubility values are reported in Table II.

Specific conductivity.—The specific conductivity of most soluble salts in EC, among those investigated, was measured at 25.00° ± 0.02°C by a Tinsley bridge, Type 4896.

Concentrated solutions of each salt in EC were progressively diluted to measure conductivity at various concentrations.

The specific conductivities of the electrolytic solutions in EC are greater than those of the corresponding solutions in PC, as shown in Table III. The values are of the order of $1 \cdot 10^{-2}$ ohm^{-1} cm^{-1} in spite of the high value of the dielectric constant and the relatively low value of the viscosity of the solvent. As it has already been emphasized in the case of solutions of alkali halides in formamide and its derivatives (5-7), the presence in nonaqueous solutions, even at high dielectric constant, of nonconducting species (pairwise

Table I. Physical properties of ethylene carbonate (EC) and propylene carbonate (PC)

Solvent	Melting point, °C	Dielectric constant	Viscosity, cP	Specific conductivity, ohm^{-1} cm^{-1}	Density, g/cm^3
EC	36.2	89.1(40°C)[a] 95.3(25°C)[a]	1.9(40°C)[b]	7.10^{-7}(40°C)	1.323(40°C)[b]
PC	−49[b]	64.4(25C°)[b]	2.5(25°C)[c] 2.3(40°C)[c]	2.10^{-7}(25°C)[b]	1.198(25°C)[c]

[a] See ref (4).
[b] See ref. (1).
[c] Yung-Chi Wu and H. Friedman, *J. Phys. Chem.*, 70, 501 (1966).

Table III. Maximum specific conductivity ($ohm^{-1}\ cm^{-1} \cdot 10^3$) of various salts in EC and PC at 25°C

	PC	EC
KCNS	8.9 (1.5N)[a]	11.84 (11.3M; 1.6N)
KPF_6	6.8 (0.5N)[b]	11.32 (1.0M; 1.2N)
$LiClO_4$	5.6 (1.0N)[c]	7.87 (0.85M; 0.89N)

[a] J. Chilton, E. Duffek, and A. Reed, Final Report, Contr. NAS W-11, April 1961.
[b] A. Lyall, H. Seiger, and J. Orshich, Tech. Rept., AFAPL-TR-68-71, July 1968.
[c] R. Keller, J. Foster, and J. Sullivan, Rept. NASA CR-72106, Sept. 1966.

and higher than pairwise association) causes conductivity values, at high concentrations, much lower than those obtainable in aqueous solutions. This remains one of the problems in the use of organic electrolytes in batteries.

Lowering of the freezing point.—The molal lowering of the freezing point of EC has been determined by using urea solutions. The average value of two different sets of measurements is 5.5°C. This high value justifies the possibility of having liquid solutions of KCNS or KPF_6 or $LiClO_4$ in EC at room temperature.

Compatibility of electrode and solvent.—It is very important to determine the behavior of the solvent with respect to high reactive electrodes such as magnesium and lithium.

A Mg electrode (1.4g) was dipped at 25°C in a solution 0.85M $LiClO_4$ in EC (5g). After 24 hr the concentration of Mg^{2+} ions in solution was polarographically detected to be 100 ppm.

A lithium foil was dipped for 7 days in a similar $LiClO_4$-EC solution and neither gas evolution nor physical changes of the metal surface were observed.

In conclusion the solvent does not seem to significantly attack magnesium or lithium.

Half cell potentials.—Lithium electrode.—As pointed out by Elliott and co-workers (8), the behavior of metallic electrodes in organic solutions is greatly influenced by the electrolyte used in connection with both the open circuit and under load potential.

In this work lithium potentials have been measured in EC solutions of KPF_6, KCNS, and $LiClO_4$, respectively, using a platinum foil as counterelectrode and a silver foil as reference electrode.

Silver was used as a reference electrode instead of Ag/AgCl because of the possible deterioration of the latter in PC solutions (9) and because a poised silver reference electrode has been reported elsewhere (10, 11). In the present investigation the stability of the silver electrode was ±0.03 mV during repeated polarization experiments. This stability was sufficient for the purpose of this work. For greater reproducibility in other work involving lithium electrodes and electrolytes containing lithium ions, a lithium reference electrode may be preferred (12).

The concentration of the solutions used for the polarization runs were those corresponding to the maximum conductivity, *i.e.*, KCNS 1.3M, KPF_6 1.0M, $LiClO_4$ 0.85M. Lithium rod, 99.9% pure, was reduced in a dry box under argon atmosphere in foils of 2 cm^2 of surface for each side.

Figure 1 shows polarization (reported as the difference between the OCV and the voltage at the indicated current density) *vs.* current density, for the lithium electrode in the three solutions. Lithium shows the best behavior in the $LiClO_4$ solution. In comparison the behavior of the same electrode in a solution 1M $LiClO_4$ in PC is also shown,

Figure 2 shows polarization-time curves at constant current density (10 mA/cm^2) for the lithium electrode in the three solutions. These curves were obtained after the polarization runs and show good stability of the lithium electrode.

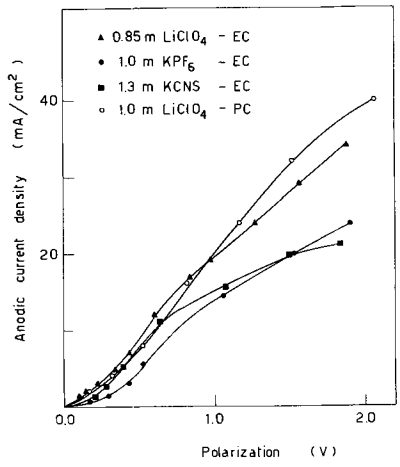

Fig. 1. Polarization of lithium anodes in various electrolytic EC solutions at room temperature and after a 3 min hold on the indicated current density. The PC solution polarization curve is taken from Elliott and co-workers (9).

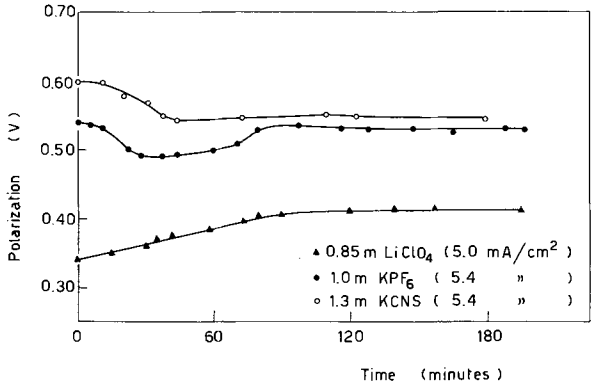

Fig. 2. Polarization-time behavior of lithium anodes at 10 mA/cm^2 in various electrolytic EC solutions at room temperature.

CuF_2 *electrode.*—The CuF_2 electrode has been chosen for preliminary investigations in EC electrolytic solutions, since it is the cathode most widely used in primary organic batteries (13). The solubility of CuF_2, polarographically determined to be 0.009 mol/kg solv. at 25°C in a solution 0.85M $LiClO_4$ in EC, is of the same order of magnitude as that found in $LiClO_4$-PC solutions (13).

The electrode has been prepared with a technique similar to that described by Boden and co-workers (14). A powder made of CuF (85%), graphite (10%) and polyethylene (5%) was dissolved in hot toluene and the paste obtained was spread on a copper net. After drying in an oven at a temperature of 45°-55°C, the electrode was heated for 10 min at 90°C and then compacted at a pressure of 2500 kg/cm^2 for 3 min.

The initial OCV of the CuF_2 electrode *vs.* an Ag reference electrode in a solution 0.85M $LiClO_4$ in EC is 0.35-0.40V. The polarization curve of CuF_2 in the same solution is shown in Fig. 3. The behavior of the electrode under forced discharge is not very satisfactory since, even at low current densities (*i.e.*, current densities greater than 0.6 mA/cm^2), it acquires negative potentials *vs.* Ag. At the end of the polarization run, the OCV of the electrode did not recover and stabilized on values of the order of ±0.03V *vs.* Ag. Similar behavior has been found in $LiClO_4$-PC solutions (9).

Battery test.—As a final test for the utilization of EC electrolytic solutions in the development of nonaqueous battery in this program, the following cell was considered

$$Li/LiClO_4/CuF_2, Cu \quad [1]$$

EC

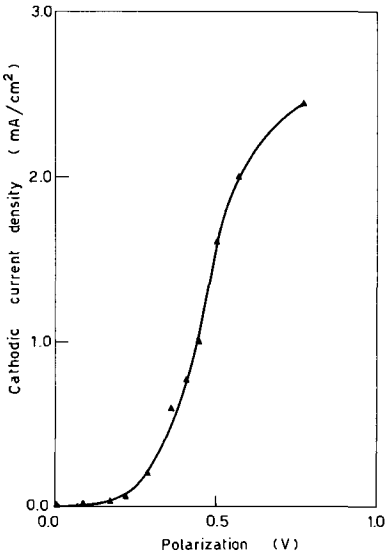

Fig. 3. Polarization curve of the CuF_2 electrode in 0.85M $LiClO_4$-EC at room temperature.

The structure of the cell was essentially a CuF_2 cathode between two lithium anodes and the construction details are reported in Table IV. The OCV is 3.4V at room temperature.

Figure 4 shows typical discharge curves of cell [1] at room temperature and at various current densities. The capacity of cell [1] is limited by the utilization coefficient of the CuF_2 electrode which is on the average 10% (1.5V endpoint), comparable with that found by Jasinski for a similar electrode in $LiClO_4$-PC solutions (15).

Attempts to recharge cell [1] were made. The cell was charged at 4-5 mA/cm² and at a voltage of 3.85-3.90V and submitted to few charge-discharge cycles without showing appreciable changes in its performances. Since the successful use of CuF_2 in secondary battery has not yet been accomplished (13), the rechargeability shown by cell [1] could tentatively be explained by the occurrence of the anodic reaction

$$Cu + 2ClO_4^- \longrightarrow Cu(ClO_4)_2 + 2e$$

We have tried to prove this mechanism by charging and discharging the cell

$$Li/LiClO_4/Cu, C \qquad [2]$$
$$EC$$

at the same condition as cell [1].

After charging, cell [2] showed the same OCV obtained with cell [1] but very short times of discharge. Furthermore, the OCV of the charged cell [2] continuously dropped with time.

Another possible explanation of the apparent rechargeability shown by cell [1] could be a certain

Table IV. Characteristics of cell [1]

Anode: lithium foil 99.9% (4.3 cm² each side).
Cathode: CuF_2 85%, graphite 10%, polyethylene 5% (4.3 cm² each side).
Cell a: 0.86 total grams on a copper net support.
Cell b. 0.68 total grams on a copper net support.
Separator: fiber glass 0.3 mm thick.
Electrolyte $LiClO_4$ 9% (0.85M) in EC.

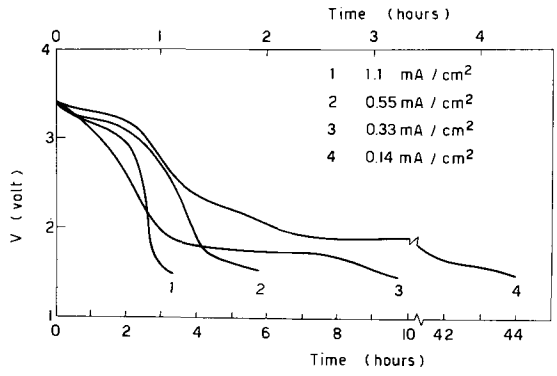

Fig. 4. Typical discharge curves of cell [1] at various current densities and at room temperature. Curves 1 and 2 refer to upper scale and to cell a, curves 3 and 4 refer to lower scale and to cell b (see Table IV).

reactivation of the cathode which could allow the utilization of undischarged CuF_2.

Conclusions

The above reported evidence indicates that EC is a useful solvent for nonaqueous battery development investigations.

Performance of cell [1] could be appreciably improved by using a different separator, by optimizing the preparation of the cathode used or by changing to a more effective positive electrode. This is, however, outside the scope of the present research and will be the object of future work.

Manuscript submitted Aug. 19, 1969; revised manuscript received Dec. 31, 1969. This work was sponsored by the Consiglio Nazionale delle Ricerche, under Contract No. 115/0860/1894.

Any discussion of this paper will appear in a Discussion Section to be published in the December 1970 JOURNAL.

REFERENCES

1. R. Jasinski, "High Energy Batteries," p. 133, Plenum Press, New York (1967).
2. C. Shair, H. Seiger, and A. Lyall, "Proceeding of the Electric Automobile Symposium," p. 152, Santa Clara Valley Engineers' Council, 1967.
3. H. Bauman, Report No. APL-TDR-64-59, AD 601 128, May 1964.
4. R. Seward and E. Vieira, *J. Phys. Chem.*, **62**, 127 (1958).
5. M. L. Berardelli, G. Pistoia, and A. M. Polcaro, *Ric. Sci.*, **38**, 814 (1968).
6. G. Pistoia, G. Pecci, and B. Scrosati, *ibid.*, **37**, 1167 (1967).
7. G. Pistoia and B. Scrosati, *ibid.*, **37**, 1173 (1967).
8. W. Elliott, J. Huff, R. Adler, and W. Towle, *Proc. Ann. Power Sources Cont.*, May 1966.
9. W. Elliott, J. Huff, G. Simons, G. McDonald, J. Jamrozy, and W. Towle, Seventh Quarterly Report, April 1966, Contract NAS-3-6015.
10. K. Hill and R. Selim, Final Report, August 1965, Contract NAS-3-2780; R. Selim, K. Hill and M. Rao, Final Report, February 1965, Contract NAS-3-6017.
11. M. Rao, *This Journal*, **114**, 13 (1967).
12. B. Burrows and R. Jasinski, *ibid.*, **115**, 365 (1968).
13. K. Braeuer and J. Harvey, "Organic Electrolyte High Energy Density Batteries," AD 654813.
14. D. Boden, H. Buhner, and V. Spera, Final Report, Contract DA-28-043-AMC-01394(E), July 1966.
15. R. Jasinski and B. Burrows, *This Journal*, **116**, 422 (1969).

Determination of Optical Constants and Growth Rates of Anodic Alumina by Ellipsometry

R. M. Goldstein, R. J. Lederich, and F. W. Leonhard[1]

McDonnell Research Laboratories, McDonnell Douglas Corporation, St. Louis, Missouri

An ellipsometric study of alumina anodic films formed in aqueous ammonium pentaborate (0.125M) and ammonium pentaborate-ethylene glycol (34% weight of salt) electrolytes has been made.

Briefly, the experimental procedure consisted of mechanically polishing aluminum disks of 99.99% purity and 7.90 cm^2 in area and then electropolishing them at 0°C in an electrolyte composed of 100 ml distilled water, 200 ml nitric acid, 300 ml of 85% phosphoric acid, and 400 ml glacial acetic acid. The aluminum disks (the backside masked) are anodized in a cell consisting of a platinum foil cathode, the disk as anode (separation of 7 cm), another electrode in common with the anode to measure potential drop across the electrolyte and the aqueous ammonium pentaborate (AAP) or ammonium pentaborate-ethylene glycol (AP-EG) solution as electrolyte which is stirred and heated or cooled to 50° or 5°C by a constant temperature bath (Blue M). A constant current density of 0.3 mA/cm^2 is used in all the anodization, and the anodization voltage is monitored on a high impedance (1 Mohm) recorder. An ellipsometer (Gaertner L119) is used, and measurements are made at 6328Å at an angle of 70°. The detector is a photomultiplier (EMI 9502B) coupled to a lock-in amplifier (Ithaco 353) and chopper. The disks are measured for their zero point (*i.e.*, clean substrate) after electropolishing, and the oxide thickness is measured immediately after anodization.

The method used in determining optical constants and thickness values for the anodic alumina film is a standard [for example, ref. (1)] and involves obtaining a best fit of the experimental ellipsometric parameters ψ and Δ to those calculated by the computer program of McCrackin and Colson (2). The parameters ψ and Δ are defined by $\tan \psi = (R_p/R_s) \cdot (E_s/E_p)$ and $\Delta = (\beta_p - \beta_s)_{\text{reflected}} - (\beta_p - \beta_s)_{\text{incident}}$ where E_s and E_p are the amplitudes of the incident beam, R_s and R_p are the amplitudes of the reflected beam, β_s and β_p are phase angles, and where the subscripts s and p refer to the resolution of the light into two components; p is light with the electric vector in the plane of incidence, and s is light with the electric vector perpendicular to the plane of incidence. Figure 1 shows this fit for the oxide films formed in AAP electrolyte at 5°C and gives the optical constants as $n = 1.65 \pm 0.02$, $k = 0.0$. Similarly, Fig. 2 shows that the optical constants for the anodic oxide films formed in the AP-EG solution at 5° and 50°C are $n = 1.67 \pm 0.02$, $k = 0.0$. These values are in good agreement with Barrett (3) who obtained values of $n = 1.66$, $k = 0.0$ for aluminum anodized in 3% ammonium tartrate electrolyte. The oxide thickness values obtained by use of Fig. 1 and 2 have been plotted as a function of forming voltage in Fig. 3. The forming voltage is defined here as the applied voltage corrected for electrolyte drop and the reversible potential for oxide formation. We find that at a current density of 0.3 mA/cm^2 the growth rate for the AAP (5°C) is 12.2 Å/V, while for the AP-EG the growth rate is 11.5 Å/V at 5°C and 13.3 Å/V at 50°C. Previous studies (4, 5) with these electrolytes have indicated growth rates comparable to the results reported here.

[1] Present address; Department of Electrical Engineering, University of Missouri, Columbia, Missouri.

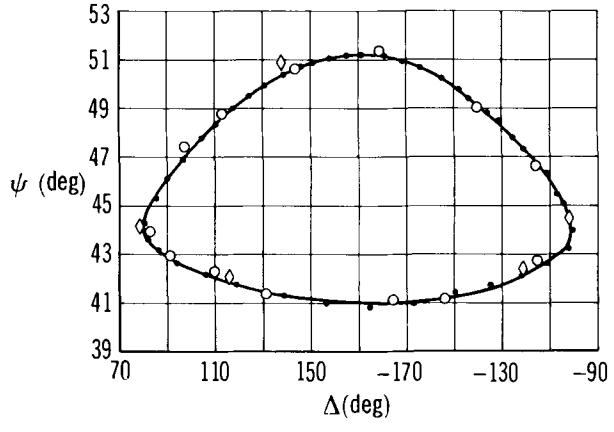

Fig. 1. Ellipsometric data for alumina in AAP at 5°C. ●, n = 1.65, k = 0; ○, experimental points (first cycle); ◇, experimental points (second cycle).

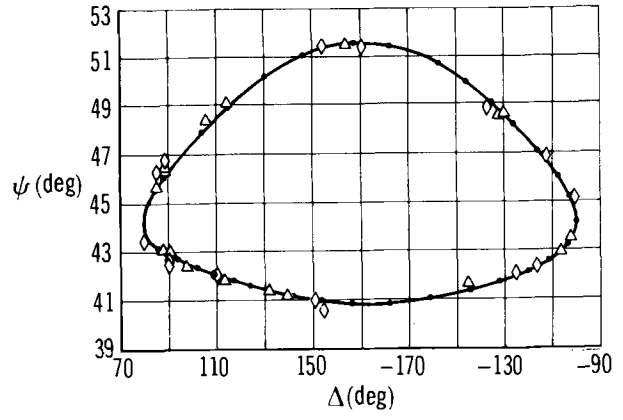

Fig. 2. Ellipsometric data for alumina formed in AP-EG at 5° and 50°C. ●, n = 1.67, k = 0; △, 5°C (first and second cycle); ◇, 50°C (first and second cycle).

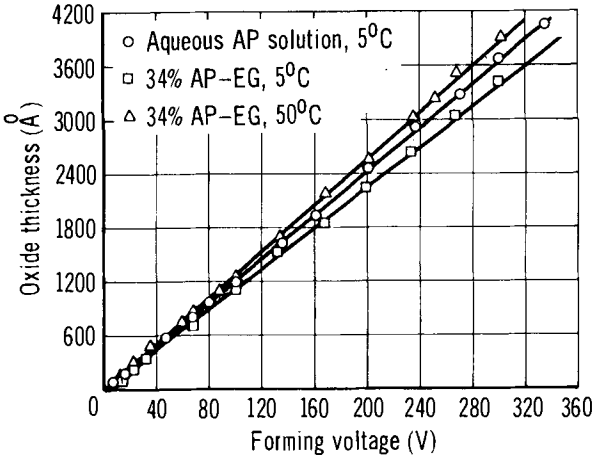

Fig. 3. Oxide thickness as a function of forming voltage

Acknowledgments

The authors wish to acknowledge the assistance of S. C. Wigginton and T. Brennan in this study. This research was conducted under the McDonnell Douglas Independent Research and Development Program.

Manuscript submitted Sept. 24, 1969; revised manuscript received *ca.* Dec. 5, 1969.

Any discussion of this paper will appear in a Discussion Section to be published in the December 1970 JOURNAL.

REFERENCES

1. L. Young and F. G. R. Zobel, *This Journal*, **113**, 277 (1966).
2. F. McCrackin and J. Colson, Nat. Bur. Std. Tech. Note 242 (1969).
3. M. A. Barrett, "Ellipsometry in the Measurements of Surface and Thin Films, Symposium Proceedings, Washington, D. C.," Published by the National Bureau of Standards (1964).
4. W. J. Bernard and J. W. Cook, *This Journal*, **106**, 643 (1959).
5. R. W. Santway and R. S. Alwitt, Extended Abstracts 32, New York Meeting of the Society, May 4-9, 1969.

Chronopotentiometric Measurements of Chemical Reaction Rates

III. On the Finite Difference Approach to the ECE Mechanism

Henry N. Blount[1] and Harvey B. Herman*,[2]

Department of Chemistry, The University of Georgia, Athens, Georgia

Current reversal chronopotentiometry has been applied to kinetic studies of the ECE mechanism (1, 2). This reaction scheme may be represented by

$$A + n_1e^- \rightarrow B \qquad |E_{A/B}| \qquad [1]$$

$$B \xrightarrow{k} C \qquad [2]$$

$$C + n_2e^- \rightarrow D \qquad |E_{C/D}| < |E_{A/B}| \qquad [3]$$

during the forward electrolysis, and by

$$B - n_3e^- \rightarrow E \qquad |E_{E/B}| \qquad [4]$$

$$C + n_2e^- \rightarrow D \qquad |E_{C/D}| < |E_{E/B}| \qquad [5]$$

during the reverse electrolysis. In the case where $n_1 = n_3$ and A = E (*e.g.*, the *p*-nitrosophenol system), the Laplace transform solution of the partial differential equations describing the electrochemical system is exact (1). However, in the case where $n_1 \neq n_3$ and A $\neq$ E (*e.g.*, the *p*-nitrophenol system), the published solution is approximate [see Appendix, ref. (1)].

The technique of finite difference calculations has been shown to be valuable in the solving of the partial differential equations describing electrochemical behavior (3-7), and in particular those related to the ECE mechanism.

It is the purpose of this work to apply the finite difference approach to the heretofore approximate current reversal chronopotentiometric treatment of the ECE mechanism. Moreover, the effect of an oxidation-reduction equilibrium between the E/B and C/D couples (Eq. [4] and [5]) as proposed by Feldberg *et al.* (4, 6) is considered from two different points of view.

Experimental

Current reversal chronopotentiometric data were obtained in the manner already described (2). Measurements were made at 25.0°C in 20 v/o (volume per cent) aqueous ethanol maintained at a pH of 4.92 by an equimolar acetic acid/sodium acetate buffer system, $C_{HA} = 1.0M$, with total ionic strength adjusted to one molar with potassium nitrate. The *p*-nitrophenol (PNO_2P) was obtained as the indicator from Eastman Organic Chemicals and was used as received. Current reversal chronopotentiometric data were corrected for spherical diffusion and adsorption effects by the perturbation treatment of Deron and Laitinen (8).

Finite difference calculations were performed with an IBM System 360/65 computer. A central difference boundary condition was employed and is fully described elsewhere (9).

Results and Discussion

ECE mechanism.—Current reversal chronopotentiometric working curves for the ECE mechanism were determined for the case where $n_1 \neq n_2 = n_3$ (*i.e.*, the PNO_2P case) using both the approximate Laplace transform (L.T.) solution and the exact finite difference (F.D.) solution. These working curves shown in Fig. 1 coalesce at very large and very small values of kt_f. They are, however, significantly different in the region $-1 < \log (kt_f) < +1$ which is the region of paramount interest. The validity of the finite difference treatment was demonstrated by the fact that this approach gave rise to the same result that was obtained through the use of the exact Laplace transform solution in the case where $n_1 = n_2 = n_3$, the *p*-nitrosophenol (PNP) case.

Values of the rate constant for the dehydration of *p*-hydroxyphenyl-hydroxylamine, the product of the first reduction step in the electrolysis of PNO_2P (1),

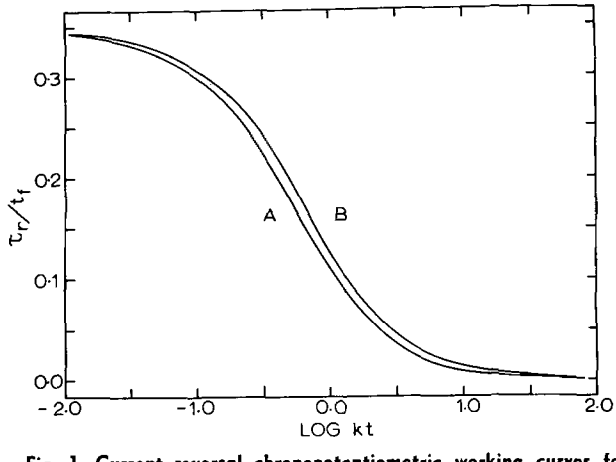

Fig. 1. Current reversal chronopotentiometric working curves for the ECE mechanism, $n_1 = 2n_2 = 2n_3$, A $\neq$ E, $i_{ox} = \frac{1}{2}i_{red}$. Curve A: Evaluated by the "exact" finite difference solution. Curve B: Evaluated by the "approximate" Laplace transformation solution.

* Electrochemical Society Active Member.

[1] Present address: Department of Chemistry, Case Western Reserve University, Cleveland, Ohio 44106.

[2] Permanent address: Department of Chemistry, The University of North Carolina at Greensboro, Greensboro, North Carolina 27412.

Key words: chronopotentiometry, ECE mechanism, digital simulation.

Table I. Results of current reversal chronopotentiometric determinations of the rate constant for the reaction of the reduction product of PNO_2P using the finite difference ECE working curves

HMDE radius = 4.8 × 10^{-2} cm, T = 25.0°C, pH = 4.92 in 20 v/o aqueous ethanol. All data corrected for adsorption and spherical diffusion effects, $i_{ox} = \frac{1}{2} i_{red}$.

A. 1.0 m*M* PNO_2P			B. 5.0 m*M* PNO_2P			C. 10.0 m*M* PNO_2P		
t_f(sec)	τ_r/t_f	k(sec^{-1})	t_f(sec)	τ_r/t_f	k(sec^{-1})	t_f(sec)	τ_r/t_f	k(sec^{-1})
0.541	0.244	0.40	0.218	0.292	0.39	0.246	0.282	0.46
1.15	0.184	0.40	0.617	0.233	0.41	0.393	0.253	0.48
3.40	0.092	0.34	1.26	0.177	0.38	1.02	0.192	0.41
4.60	0.067	0.37	2.87	0.105	0.36	2.56	0.109	0.38
			6.19	0.052	0.34	6.93	0.030	0.39
	Average = 0.38 ± 0.03			Average = 0.38 ± 0.03			Average = 0.42 ± 0.04	

were determined from current reversal chronopotentiometric data. Kinetic results obtained at various levels of PNO_2P concentration using the "exact" working curve are shown in Table I. Also, the data of Herman and Bard [ref. (1), Table IV-B] were re-evaluated using this exact working curve. The results of this re-evaluation are summarized in Table II. The values of the rate constant obtained both in the present work and through the proper treatment of the Herman-Bard data are in good agreement with other workers' measurements of this parameter (2, 10) determined under the same experimental conditions. The results shown in Table II clearly demonstrate the difference between the approximate and exact solutions of the partial differential equations describing the system. As was the case in the earlier work (1), it is not possible to assess the accuracy of the experimentally determined kinetic parameter without prior knowledge of this quantity.

Nuances of the ECE mechanism.—Hawley and Feldberg (4) have considered the effects of "nuances" of the ECE mechanism (*i.e.*, perturbations by the E/B-C/D redox equilibrium) on the measured rated constant for the intervening chemical reaction. These workers have shown that the chronoamperometric working curves are severely altered by such nuances (4). The effects of such perturbations on current reversal chronopotentiometric working curves were yet to be determined.

In order to qualitatively see the effects of this redox nuance, the simpler PNP system where $n_1 = n_3$ and A = E will be used as a model. Consider, in addition to Eq. [1-5], the following

$$A + D \underset{k_b}{\overset{k_f}{\rightleftharpoons}} B + C \qquad [6]$$

where k_f/k_b may also be represented by the equilibrium constant, K, since

$$\frac{k_f}{k_b} = \frac{[B]\,[C]}{[A]\,[D]} = K \qquad [7]$$

Heretofore, current reversal chronopotentiometric treatments of the ECE mechanism (1, 2) have not taken into account the possibility of the reaction given by Eq. [6] and have thereby forced the value of the equilibrium constant given by Eq. [7] to be $K = 0/0$ (4). Since Eq. [3] indicates that the reduction of C occurs more easily than that of A, the observed chronopotentiometric behavior may be represented by Fig. 2(a).

In the case where the nuance reaction given by Eq. [6] is occurring and the value of the equilibrium constant is very small ($K << 1$), the qualitative picture shown in Fig. 2(a) is again valid since this situation corresponds to $|E_{C/D}| << |E_{A/B}|$.

At the other extreme is the situation where $|E_{C/D}| >> |E_{A/B}|$ which corresponds to a very large

Table II. Comparison of current reversal chronopotentiometric kinetic data obtained using Laplace transformation (1) and finite difference ECE working curves

Data of Herman and Bard (1) for 1.8 m*M* PNO_2P, T = 24.8°C in 20 v/o aqueous ethanol, pH = 4.9, HMDE area = 3.6 × 10^{-2} cm². See ref. (1), Table IV-B.

	Method					
	L.T.		L.T., corrected*		F.D., corrected**	
t_f(sec)	τ_r/t_f	k(sec^{-1})	τ_r/t_f	k(sec^{-1})	τ_r/t_f	k(sec^{-1})
0.690	0.220	0.54	0.232	0.46	0.232	0.38
0.870	0.190	0.60	0.201	0.53	0.201	0.43
0.930	0.178	0.62	0.189	0.56	0.189	0.45
3.16	0.078	0.54	0.087	0.49	0.087	0.39
4.20	0.071	0.45	0.081	0.40	0.081	0.32
Averages:		0.55 ± 0.07		0.49 ± 0.06		0.39 ± 0.05

* Data of Herman and Bard (1) as corrected for spherical diffusion effects (8). Kinetic parameters evaluated from Laplace transform working curve (1).

** Data of Herman and Bard (1) as corrected for spherical diffusion effects (8). Kinetic parameters evaluated from finite difference working curve (see text).

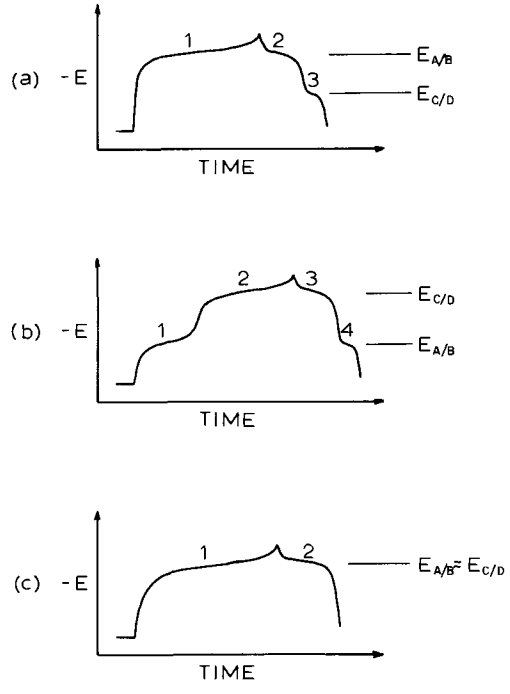

Fig. 2. Qualitative chronopotentiometric ECE behavior showing the effects of a redox nuance. Transition times are not to scale.

Curve	K	Time region	Principle electrode reactions
2(a)	$K<<1$	1	A→B, C→D
		2	B→A, C→D
		3	B→A, D→C
2(b)	$K>>1$	1	A→B,
		2	A→B, C→D
		3	A→B, D→C
		4	B→A, D→C
2(c)	$K\approx1$	1	A→B, C→D
		2	B→A, D→C

value of the nuance equilibrium constant. The chronopotentiometric behavior of this case may be qualitatively represented by Fig. 2(b).

The intermediate case where $|E_{A/B}| \approx |E_{C/D}|$ is the most difficult to treat experimentally. The chronopotentiometric behavior representing this situation is shown in Fig. 2(c).

A major problem which arises in the current reversal chronopotentiometric treatment of a nuance-perturbed ECE system is that of adopting a consistent convention of defining "forward" and "reverse" transition times which will be valid for all values of the equilibrium constant. In the cases where $K << 1$ and $K >> 1$, this consideration is relatively straightforward. However, when $K \approx 1$, a transition corresponding to a single entity is imperceptible. One may choose to treat the total forward and total reverse times given by regions 1 and 2, respectively, in Fig. 2(c).[3] Experimentally, this method is most straightforward. Alternatively, one could adopt the convention of defining transition time as that for the $A \rightleftarrows B$ process and then either (*i*) use pretransition current reversal such that the forward electrolysis time is less than that required for the $A \rightarrow B$ process, or (*ii*) follow the surface concentration of A and B with a spectral technique such as internal reflection spectrometry (11, 12).

There are two possible approaches to the formulation of the equations describing the ECE system in the case of redox nuances. The first involves the use of various values of the equilibrium constant, K, as was done by Feldberg *et al.*, in the chronoamperometric treatment of the problem (4, 6). In the finite difference representation of this approach, diffusion of all species is allowed to take place for one time unit, then equilibrium is forced to be maintained through imposition of the conditions specified by K in Eq. [7]. Following application of the "central difference" boundary condition (9), the entire process is repeated for subsequent units of time. In this approach, the calculations must be handled differently in each of several cases, namely where $K < 1$, $K = 1$, and $K > 1$.

A second approach involves the use of the individual rate constants k_f and k_b as defined in Eq. [7] rather than the equilibrium constant, K. From Eq. [1-3] and [7], one may write the following diffusion equations with appropriate kinetic perturbations

$$\frac{\partial C_A}{\partial t} = D\frac{\partial^2 C_A}{\partial x^2} - k_f[A][D] + k_b[B][C] \quad [8]$$

$$\frac{\partial C_B}{\partial t} = D\frac{\partial^2 C_B}{\partial x^2} - k[B] + k_f[A][D] - k_b[B][C] \quad [9]$$

$$\frac{\partial C_C}{\partial t} = D\frac{\partial^2 C_C}{\partial x^2} + k[B] + k_f[A][D] - k_b[B][C] \quad [10]$$

$$\frac{\partial C_D}{\partial t} = D\frac{\partial^2 C_D}{\partial x^2} - k_f[A][D] + k_b[B][C] \quad [11]$$

The above equations completely describe the diffusion and homogeneous chemical reactions involving all species present in solution. Hence in a given time unit, the finite difference program need only treat diffusion with appropriate kinetic complications as described by Eq. [8-11] and boundary conditions. This singular treatment is valid for all values of the equilibrium constant, K, as defined by Eq. [7]. If the magnitudes of k_f and k_b are chosen such that the products of these rate constants times their corresponding concentration terms are large compared to the product $k[B]$, then the effect of maintaining the redox equilibrium in solution is realized. Moreover, if the chemical system under consideration involves a nonequilibrium redox perturbation, then this fact is easily represented through appropriate choice of k_f and k_b.

The validity of this latter "kinetic" approach has been established through the chronoamperometric treatment of the ECE nuance and comparison of these results with those obtained by Hawley and Feldberg (4) who used the "equilibrium" approach to the problem. The results of the two treatments are indistinguishable over the entire range of K or k_f/k_b when the kinetic approach is applied under conditions where equilibrium is maintained.

The equilibrium nuance approach has been applied to the current reversal chronopotentiometric treatment of the ECE mechanism. Participation in the reaction scheme by the A/B-C/D redox nuance has a marked effect on the current reversal chronopotentiometric working curves both in the case where the total forward and total reverse times are considered (Fig. 3) and in the case where the current is reversed when the surface concentration of A approaches zero. In the latter case, the reverse transition time is taken when the surface concentration of B approaches zero (Fig. 4).

In the limit of very small values of the equilibrium constant, the behavior is that of an ECC scheme, those reactions being

$$(E) \quad A + n_1e^- \rightarrow B \quad [12]$$

$$(C) \quad B \xrightarrow{k} C \quad [13]$$

$$(C) \quad A + D \overset{K}{\rightleftarrows} B + C \quad [14]$$

where $K << 1$. In the limit of very large values of the equilibrium constant, the system exhibits apparent EC behavior, namely

$$(E) \quad A + n_1e^- \rightarrow B \quad [15]$$

$$(C) \quad B \xrightarrow{K} C \quad [16]$$

$$(NR) \quad A + D \overset{K}{\rightleftarrows} B + C \quad [17]$$

where $K >> 1$ and NR indicates no appreciable reaction of B and C. These limits were correctly suggested by Hawley and Feldberg (4), although the chronopotentiometric approach was not treated in that work.

It is possible to formulate the exact expression for the boundary conditions in both limiting cases because the surface concentration of C is zero in the ECC

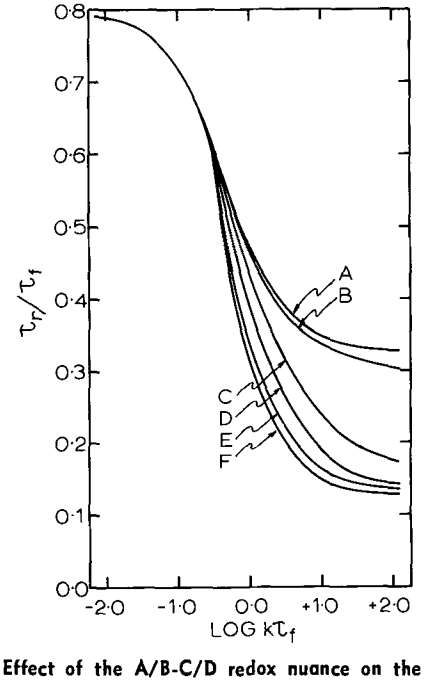

Fig. 3. Effect of the A/B-C/D redox nuance on the current reversal chronopotentiometric working curve for the PNP system where the total forward and total reverse times are considered. These results are for $i_f = 2i_r$ at a plane electrode. The equilibrium constant is defined in Eq. [7]. A: $K \leq 10^{-5}$. B: $K = 10^{-3}$. C: $K = 10^{-1}$. D: $K = 9 \times 10^{-1}$. E: $K = 10^{1}$. F: $K \geq 10^{3}$.

[3] The authors acknowledge the helpful criticism of a reviewer who suggested this particular appproach.

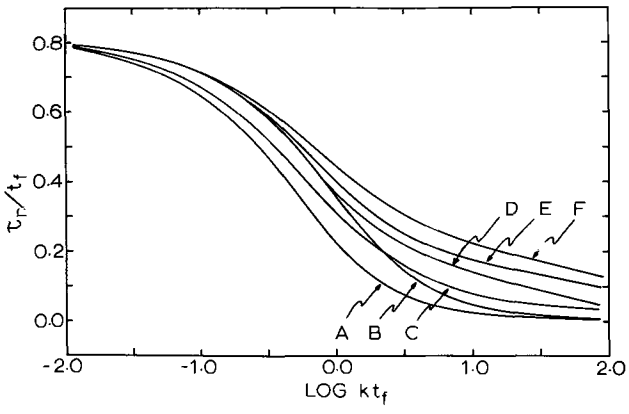

Fig. 4. Effect of the A/B-C/D redox nuance on the current reversal chronopotentiometric working curve for the PNP system where the current is reversed when the surface concentration of A approaches zero and the reverse transition time is taken when the surface concentration of B approaches zero (both 0.1% of initial concentration of A). These results are for $i_f = 2i_r$ at a plane electrode. The equilibrium constant is defined in Eq. [7]. A: ECC working curve as well as all $K \leq 10^{-5}$. B: EC working curve as well as all $K \geq 10^{3}$. C: $K = 10^{-3}$. D: $K = 10^{1}$. E: $K = 9 \times 10^{-1}$. F: $K = 10^{-1}$.

scheme and the flux of C is zero in the EC scheme. An iterative procedure was necessary to calculate the surface concentration and flux of C for intermediate values of K. Convergence was found to be very rapid.

The boundary value problem involved in the kinetic nuance approach is indeed complex. This boundary condition could conceivably be applied in two ways: through the use of heterogeneous rate expressions or through the use of equilibrium arguments at the electrode surface and the iterative procedure described above. Neither approach was attempted in this work.

Other workers have evaluated nuance participation effects on current reversal chronopotentiometric working curves in the limiting case of $K = 0$, and their results (13) are in agreement with those of this study. Although some chemical systems show nuance participation in their ECE behavior (6), it is apparent from electrochemical results (1, 14), curve B in Fig. 4, and the Laplace transform ECE working curve (1) that such participation is imperceptible in the case of the PNP system.

Acknowledgment

This work was supported in part by grants from the Petroleum Research Fund (No. 488-G2) and the National Science Foundation (No. GP-6596).

Manuscript submitted Oct. 23, 1969; revised manuscript received *ca.* Jan. 5, 1970.

Any discussion of this paper will appear in a Discussion Section to be published in the December 1970 JOURNAL.

REFERENCES

1. H. B. Herman and A. J. Bard, *J. Phys. Chem.*, **70**, 396 (1966).
2. H. N. Blount and H. B. Herman, *ibid.*, **72**, 3006 (1968).
3. S. W. Feldberg and C. Auerbach, *Anal. Chem.*, **36**, 505 (1964).
4. M. D. Hawley and S. W. Feldberg, *J. Phys. Chem.*, **70**, 3459 (1966).
5. S. W. Feldberg, *J. Am. Chem. Soc.*, **88**, 390 (1966).
6. R. N. Adams, M. D. Hawley, and S. W. Feldberg, *J. Phys. Chem.*, **71**, 851 (1967).
7. J. W. Strojek, T. Kuwana, and S. W. Feldberg, *J. Am. Chem. Soc.*, **90**, 1353 (1968).
8. S. Deron and H. A. Laitinen, *Anal. Chem.*, **38**, 1290 (1966).
9. H. B. Herman and J. C. Guynn, Submitted for publication.
10. R. S. Nicholson, J. M. Wilson, and M. L. Olmstead, *Anal. Chem.*, **38**, 542 (1966).
11. W. N. Hansen, T. Kuwana, and R. A. Osteryoung, *ibid.*, **38**, 1810 (1966).
12. N. Winograd and T. Kuwana, *J. Electroanal. Chem.*, **23**, 333 (1969).
13. S. W. Feldberg, Private communication, 1965.
14. R. S. Nicholson and I. Shain, *Anal. Chem.*, **37**, 190 (1965).

Ohmic Potential Measured by Interrupter Techniques

John Newman

Inorganic Materials Research Division, Lawrence Radiation Laboratory, and Department of Chemical Engineering, University of California, Berkeley, California

Interruption of the current is used frequently to assess the magnitude of the ohmic potential drop which is included in the measurement of electrode potentials during the passage of current. The value so measured corresponds to the primary current distribution in the electrode system being studied.

When the current is interrupted, the double-layer capacity is left charged at the value prevailing locally. This double-layer capacity may then be discharged by means of a faradaic reaction. The time constant for this decay of charge may be approximated by

$$\tau_1 = RTC/\mathbf{F}i_0 \qquad [1]$$

For an exchange current density i_0 of 1 mA/cm^2 and a double-layer capacity, C, of 20 μF/cm^2, this equation yields $\tau_1 = 0.51$ msec at 25°C. The electrode potential may subsequently shift by decay of the concentration overpotential.

Immediately after the current is interrupted, the current density is not necessarily zero everywhere. If the double layer was nonuniformly charged, current will flow through the solution from one part of the double layer to another in an attempt to make the state of charge uniform. A characteristic time for this process is

$$\tau_2 = r_0 C/\kappa \qquad [2]$$

where r_0 is a length characteristic of the electrode. The value $\tau_2 = 0.5$ msec is obtained for $r_0 = 0.25$ cm, $C = 20$ μF/cm^2, and a solution conductivity of 0.01 mho/cm. For an ideally polarizable electrode, this process will take precedence over decay by a faradaic reaction and in at least one case obscured observation of double-layer relaxation at such an electrode (1, 2).

Let us ignore for the moment the concentration overpotential. A nonuniformly charged double layer is associated with a nonuniform ohmic potential drop during the passage of current. In such a case, what ohmic potential drop is measured by an interrupter technique? It must be some average value which does not prevail everywhere on the electrode. Since, on interruption, the double-layer capacity remains charged, the potential just outside the double layer (relative to the reference electrode) changes by a uniform amount over the entire surface of the electrode. Hence, independent of the current-density distribution prevailing before interruption, the current density changes by amounts which

correspond to a primary distribution, and the observed ohmic drop measured by the interruption corresponds to this distribution. (Here the thickness of the double layer is taken to be small compared to the size of the electrode, a condition which is unlikely to be violated. This allows the double layer to be treated as part of the boundary, being characterized locally by its surface charge density and faradaic current density.)

A rotating disk electrode can be used to illustrate this general conclusion. The current and potential distributions have been worked out under steady conditions (3), and the frequency dispersion in capacity measurements has recently been treated (4) for a disk electrode embedded in a large insulating plane. The potential Φ_0 just outside the double layer can be represented by a series in Legendre polynomials

$$\frac{ZF}{RT}\Phi_0 = \sum_{n=0}^{\infty} B_n P_{2n}(\eta) \qquad [3]$$

where $\eta = \sqrt{1 - (r/r_0)^2}$. (To be consistent with ref. (3), the coefficient ZF/RT has been introduced; it will cancel out shortly.) By means of the orthogonal property of the Legendre polynomials, the coefficients B_n can be expressed as

$$B_n = (4n + 1)\frac{ZF}{RT}\int_0^1 \Phi_0(\eta)P_{2n}(\eta)\,d\eta \qquad [4]$$

In particular, the first coefficient B_0 can be related to the total current flowing to the disk

$$B_0 = \frac{ZF}{RT}\int_0^1 \Phi_0(\eta)\,d\eta = \frac{ZF}{RT}\,\frac{I}{4r_0\kappa} \qquad [5]$$

Let quantities after interruption be denoted by primes. Then, since the double-layer charge does not change instantaneously on interruption

$$\Phi_0' = \Phi_0 - \Delta\Phi$$

where $\Delta\Phi$ is constant over the disk and represents the ohmic drop measured by the interrupter technique. The value of B_0' must be zero since the total current is now zero. Hence

$$B_0' = 0 = \frac{ZF}{RT}\int_0^1 (\Phi_0 - \Delta\Phi)\,d\eta = \frac{ZF}{RT}\left(\frac{I}{4r_0\kappa} - \Delta\Phi\right) \qquad [6]$$

Thus $\Delta\Phi = I/4r_0\kappa$. The change in potential and the resistance $\Delta\Phi/I$ measured by the interrupter technique correspond to the primary current distribution (5). Suitable allowance can be made for the position of the reference electrode probe (5), and the conclusion also remains valid for other electrode geometries. (Except for B_0, the other B_n's will not change at the instant of interruption, that is, $B_n' = B_n$ for $n = 1, 2, \ldots$.)

It may be noted that the current distribution will approximate the primary distribution when the concentration and surface overpotentials are small compared to the ohmic drop. In this case, the interrupter may yield the desired value of the ohmic drop. On the other hand, when the current distribution is more nearly uniform, the ohmic drop will not be large compared to the overpotential, and the interrupter may still yield results of satisfactory accuracy.

Of course, the value measured by current interruption will correspond to the ohmic potential drop to some point on the electrode surface. On the basis of Fig. 1 of ref. (3), one can estimate that this point will be about 80% of the way from the center to edge of the disk. At this point the current density will be approximately equal to the average current density, and errors associated with the nonuniform current density and potential distributions at the disk will largely cancel if one associates the average current density with the ohmic drop measured by the interrupter technique.

The concentration overpotential will complicate the picture slightly. With an excess of supporting electrolyte, conductivity variations probably make a negligible contribution to the ohmic drop. For discharge of an ion from a binary electrolyte, this contribution is larger but can be estimated separately. The observed ohmic drop would not correspond exactly to the primary resistance in this case.

McIntyre and Peck (6) recently perfected a short-time interrupter for use under potentiostatic conditions. For a rotating disk electrode, the ohmic resistance was observed to be independent of current. This should be expected in view of the analysis presented here. It would be desirable to compare their value with one estimated from the disk radius and the solution conductivity, with due allowance for the placement of the reference electrode and the size of the insulating disk in which the electrode was embedded.

Acknowledgment

This work was supported by the United States Atomic Energy Commission.

Manuscript received Nov. 17, 1969.

Any discussion of this paper will appear in a Discussion Section to be published in the December 1970 JOURNAL.

REFERENCES

1. Fred C. Anson, Robert F. Martin, and Chaim Yarnitzky, *J. Phys. Chem.*, **73**, 1835 (1969).
2. John Newman, *ibid.*, **73**, 1843 (1969).
3. John Newman, *This Journal*, **113**, 1235 (1966).
4. John Newman, *ibid.*, **117**, 198 (1970).
5. John Newman, *ibid.*, **113**, 501 (1966).
6. J. D. E. McIntyre and W. F. Peck, Jr., *ibid.*

Brief Communications

Cuprous Halide and Cuprous Sulfide as Electrolytes in Galvanic Cells

R. Routie, P. Taxil, and J. Mahenc

Institut du Génie Chimique et Laboratoire d'Electrochimie, Faculté des Sciences de Toulouse, Toulouse, France

Among the different types of solid electrolyte galvanic cells, Foley (1) has recently considered several cases of solid electrolytes using Ag^+, Cl^-, Na^+, and H^+ transport.

The purpose of this communication is to give an account of the use of cuprous halide and cuprous sulfide in the galvanic cell (at 400°C)

$$Cu\text{-}CuI\text{-}Cu_2S\text{-}S(liq)\text{-}Pt$$

the arrangement of which is the same as in Lehovec and Broder's cell (2) with AgI and Ag_2S as solid electrolytes at about 200°C.

Favorable conditions for a solid-component battery able to produce a high current density result from the particular lattice structure of cuprous halide and cuprous sulfide. Wagner (3) has defined the various types of conductivity occurring in such solid materials. The current, in cuprous sulfide, is carried by Cu^+ ions as well by electronic holes: the electronic conductivity is assumed to depend on the deviations of ideal stoichiometry and is calculated as a function of the ratio copper/sulfur (4). The conductivity in CuI is exclusively due to Cu^+ ions, the transport number of Cu being very close to unity. However, cuprous halide is essentially an ionic conductor (about 1 $ohm^{-1} \cdot cm^{-1}$), between 380° and 450°C, when submitted to a polarizing potential of less than 0.3V: at higher potentials a p-type conduction appears in addition to the ionic conduction (5). In CuI and Cu_2S, high conductivity is a consequence of the lattice structure: the anions (I^- or $S^=$) are bound to fixed lattice positions [large size and extremely low diffusivity (6)] whereas, according to x-ray investigations (7), the cations (Cu^+) are virtually distributed at random among a larger number of nearly equivalent lattice sites.

In the cell under consideration, CuI is inserted to avoid electronic conductance. It is in fact a genuine electrolyte.

Cuprous sulfide was prepared at about 450°C by reaction of copper with sulfur vapor in a glass tube filled with argon. The product was then compressed to obtain cylindrical pellets 12 mm in diameter and 6 mm thick.

Pellets of 99.99% pure copper and cuprous halide (3 mm thick) were used to assemble the cell in a Pyrex glass vessel (Fig. 1). Sufficient electrical contacts, between the different solids, were secured by applying a slight pressure by means of a compressed steel spring. The choice of the thickness of the different solid phases was made in order to avoid crushing the cell.

All the experiments were conducted in an atmosphere of purified argon in an electrical furnace at 400°C.

To obtain current density *vs.* voltage curves, a current of appropriate intensity was drawn from the cell by inserting a platinum load between the cuprous halide and cuprous sulfide pellets (Fig. 1).

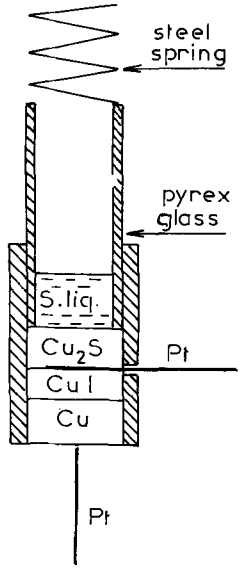

Fig. 1. Experimental cell Cu-CuI-Cu_2S-S(liq)-Pt

Results

In the absence of an external connection, the open circuit voltage of the cell Cu-CuI-Cu_2S-S(liq)-Pt is 0.450V at 400°C. At this potential (higher than 0.3V) a transfer of electrons and copper ions occurs internally, within the cuprous halide, by means of partial electronic conduction. Furthermore, the cuprous sulfide in equilibrium with liquid sulfur (or sulfur vapor) has, at 400°C, a relatively important electronic conductivity. The life of the battery under open circuit conditions (shelf life) is therefore determined by the progress of the cell reaction (formation of Cu_2S) and by the weights of copper and sulfur present in the cell. The shelf life of this cell, at operating temperature, is however considerable (several days) and the internal current is always very small compared to the external current.

The electrical performance of the cell is reported in terms of current density *vs.* voltage curves for operation at constant current, and is shown in Fig. 2.

Within a few seconds after the circuit is switched off, the voltage drops swiftly as a result of internal resistance, polarization and interface resistance occurring in this cell.

During roughly the first 50 min, the voltage decreases parabolically as a function of time; the voltage is given by

$$U = A - B\sqrt{t}$$

$$\text{with} \begin{cases} A = 450 - 1.08I \\ B = 8.10^{-2}I \end{cases}$$

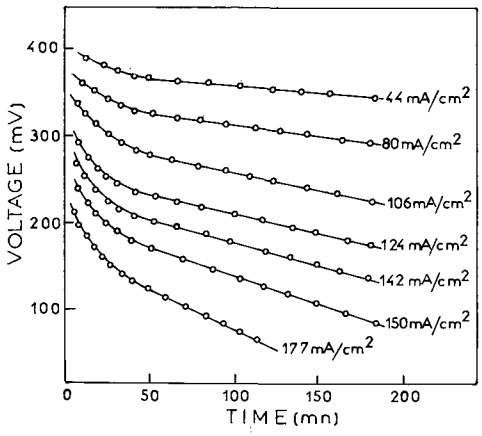

Fig. 2. Current density vs. voltage curves

U and A are expressed in mV; t in min; I in mA/cm^2; and B in mV/min$^{1/2}$.

After this transition state, the voltage decreases as a linear function of the time

$$U = C - Dt$$

$$\text{with} \begin{cases} C = 450 - 1.58I \\ D = 4.10^{-3}I \end{cases}$$

C is expressed in mV and D in mV/min.

The decrease of the voltage appears to be related to the increase in thickness of the product of the cell reaction, *i.e.*, cuprous sulfide. The existence of two different steps for the electrochemical sulfurization of copper (parabolic step and linear step) also conforms with the observations of Mrowec (8) on the copper tarnishing reaction in a sulfur atmosphere, when the product of the reaction is sufficiently thick. The parabolic sulfurization time is also about 50 min. The copper diffusion, within cuprous sulfide, results from a concentration gradient: cuprous sulfide not being an ideal stoichiometric crystal. The diffusion constant is 3.10^{-5} cm^2/sec according to Mrowec and 10^{-5} cm^2/sec according to Wehefritz (9).

Manuscript submitted Nov. 5, 1969; revised manuscript received Dec. 9, 1969.

Any discussion of this paper will appear in a Discussion Section to be published in the December 1970 JOURNAL.

REFERENCES

1. R. T. Foley, *This Journal*, **116**, 130 (1969).
2. K. Lehovec and J. Broder, *ibid.*, **101**, 208 (1954).
3. J. B. Wagner and C. Wagner, *J. Chem. Phys.*, **26**, 1602 (1957).
4. S. Miyatani and Y. Svzuki, *J. Fac. Sci. Niigata, Univ. Ser. I*, 1 (1953).
5. S. Miyatani and Y. Svzuki, *ibid.*, 11 (1953). J. B. Wagner and C. Wagner, *J. Chem. Phys.*, **26**, 1597 (1957).
6. H. Braune and O. Kahn, *Z. Physik. Chem.*, **331**, 157 (1936).
7. P. Rahlfs, *ibid.*, **331**, 157 (1936).
8. I. Bartkowicz, E. Fryt, and Mrowec, *Bull. Acad. Sci. Pol.*, **16**, 5, 263 (1968).
9. V. Wehefritz, *Z. Physik. Chem.*, **26**, 339 (1960).

Electrogenerative Chlorination

Stanley H. Langer* and Sergei Yurchak

Chemical Engineering Department, University of Wisconsin, Madison, Wisconsin

To-date, few direct organic electrogenerative (1) processes have been reported or investigated to any appreciable extent; systems involving migrating anions other than hydroxyl ions would be of particular interest. (We define electrogenerative processes as those in which two or more materials react at electrodes in a manner such that favorable thermodynamic factors drive the reaction, a useful product is produced, and by-product electricity is generated.) We report here the electrogenerative chlorination process in which chlorine and olefin are reacted with the assistance of catalytic electrodes and suitable electrolyte under favorable conditions to give dichloroalkanes and chlorohydrin in varying amounts with accompanying generation of electrical current. Chlorine is reduced at the cathode to chloride ions which are transported through the electrolyte to the anode, where they combine with ethylene to form reaction products and electrons which are conducted through an external circuit to the cathode for reaction with more chlorine. The chlorine gas and unsaturated hydrocarbon are introduced into cathode and anode chambers which are separated by the electrolyte barrier phase bounded by suitable gas permeable electrodes. Both electrodes operate at a positive potential relative to the standard hydrogen electrode under favorable thermodynamic influence. Chlorination rate and potential of the over-all cell can be varied and adjusted with the external resistive circuit (1).

Observed cell reactions, based on product analysis, may be represented generally as

$$\text{Cathode:} \quad Cl_2 + 2e \rightarrow 2Cl^- \qquad [1]$$

$$Cl^-(\text{cathode}) \rightarrow Cl^-(\text{anode}) \qquad [2]$$

* Electrochemical Society Active Member.

$$\text{Anode:} \quad RCH{=}CHR' + 2Cl^- \rightarrow \underset{\displaystyle Cl}{\overset{\displaystyle |}{RCH}}\!\!-\!\!\underset{\displaystyle Cl}{\overset{\displaystyle |}{CHR'}} + 2e \qquad [3]$$

or

$$RCH{=}CHR' + 2Cl^- + H_2O \rightarrow \underset{\displaystyle Cl}{\overset{\displaystyle |}{RCH}}\!\!-\!\!\underset{\displaystyle OH}{\overset{\displaystyle |}{CHR'}} + HCl + 2e \qquad [4]$$

For ethylene, electrogenerative chlorination requires no external power source and differs further from conventional electrochemical chlorination with aqueous electrolyte [reviews in ref. (2) and (3)] in that no significant amount of ethylene glycol is formed in the electrolyte (4, 5).

The free electrolyte phase of our study was generally acidic. In most cases, 2M aqueous potassium chloride was employed but 2M NaCl—1M $HClO_4$ electrolyte did not significantly alter cell performance. The molded gas permeable, electrolyte impermeable LAA-1 platinum black-polytetrafluoroethylene electrodes which confined the electrolyte were of a commercial type[1] and have been described in the literature (6). They were supported on 50-mesh tantalum screen. Carbon-polytetrafluoroethylene electrodes were unsupported. Exposed electrode area was 5.1 cm^2. Cell construction was similar to that of Landi *et al.* (6) except that only Teflon and Viton contacted the hydrocarbon and its reaction product. Electrolyte was static. Design of our gas handling system enabled the chlorination cell to be operated with gas flow or as a closed static system with gas circulation by a Teflon-

[1] Pertinent literature is available through the Commercial Development Division of American Cyanamid Company, Wayne, New Jersey.

Table I. Electrogenerative chlorination

Hydrocarbon	T = ca. 23°C, 2M KCl electrolyte Anode catalyst,[a] mg/cm²	Open circuit voltage, V	Calculated[b] open circuit, V	Vat 4 mA/cm²
Ethylene	Pt, 9	0.81	0.77[c]	0.1
Ethylene	Pt, 9-C	0.80	0.77[c]	0.07
Ethylene	Carbon-C	0.08	0.77[c]	—
Propylene	Pt, 9	0.79	0.76	0.14
Cyclopropane	Pt, 9	0.09	0.31	0.02

[a] Cathode catalyst is Pt, 9 mg/cm² except where C appears after hyphen, when it is carbon.
[b] Based on estimated free energies of formation from group contributions, O. A. Hougen, K. M. Watson, and R. A. Ragatz, "Chemical Process Principles", Vol. 2, Chap. 25, 2nd Ed., John Wiley & Sons, Inc., New York, (1959).
[c] Liquid 1,2-dichloroethane, E° = 0.69 for gaseous dichloroethane.

glass pump. Current generated by the cell was coulometrically equivalent to the chlorine consumed.[2] Typical operating data for several hydrocarbon gases under flow conditions are shown in Table I.

Open circuit potentials are surprisingly close to calculated values, based on free energies of formation, for operable cells despite the fact that these cells generally are not considered to be reversible. The absence of carbon catalytic activity for the reaction of interest at the anode is reflected in a low open circuit potential and operating current. However, carbon electrodes are operable as the cathode. The low open circuit potential for cyclopropane could reflect the weak adsorption of that material (7, 8), especially in the presence of specifically adsorbed chloride ion (9, 10). This cell would appear to be essentially a chlorine concentration cell since no chlorinated product was found. However, with electrogenerative hydrogenation, cyclopropane more nearly resembles olefins with respect to open circuit potentials and current production (1). In the chlorination process, it would seem that our catalyst does not position reactants on the surface in a manner resembling the transition state so that the thermodynamic driving force is brought to bear on the reaction.

At 22°C, the measured potential of the Cl_2/Cl^- electrode in 2M KCl is +1.11V *vs.* the saturated calomel electrode in the current density range 0 to 13 mA/cm² (close to the standard potential of +1.36V for the chlorine electrode); therefore, the bulk of the polarization occurs at the anode. Liquid junction potentials and other corrections would be expected to be small under these conditions.

Since chlorination occurs at potentials significantly lower than the reversible potential for the oxidation of chloride ions, it would appear that the organic molecule participates in the electron transfer reaction. Quantitative determination by gas chromatography of the yield of 1,2-dichloroethane relative to the amount of ethylene reacted as a function of anode potential showed a strong dependence (in a flow system) that has not been previously reported. At an anode potential of +1.05V, a 90% yield was observed while at 1.24V this had diminished to 40%.

Gas chromatographic analysis of the electrolytes by conversion of the aqueous solutions to trimethylsilyl ethers and hexamethyldisiloxane with hexamethyldisilazane (11, 12) and a trace of HCl showed the presence of only 1, 2-chlorohydrin compounds, no glycols being detected. It would seem then that reaction is initiated with formation of $C_2H_4Cl_{adsorbed}$ which can react further by alternate routes.

One would hope that by suitable combination of catalyst, electrolyte, and potential it might be possible to increase control of the product of reaction of olefins and chlorine under electrogenerative conditions. With this in mind, we are investigating these reactions further.

[2] We found it necessary to correct the chlorine gas volume changes at the cathode for small constant losses through the cell gasketing. Only trace quantities of 1,2-dichloroethane were observed on open-circuit at the anode, well below that expected on the basis of chlorine losses.

Acknowledgment

We are grateful to the Wisconsin Alumni Research Foundation and Shell Oil Company for support of this work.

Manuscript submitted Nov. 24, 1969.

Any discussion of this paper will appear in a Discussion Section to be published in the December 1970 JOURNAL.

REFERENCES

1. S. H. Langer and H. P. Landi, *J. Am. Chem. Soc.*, **85**, 3043 (1963); **86**, 4694 (1964).
2. A. P. Tomilov, *Uspekhi Khim.*, **30**, 1462 (1962).
3. M. J. Allen, "Organic Electrode Processes," chap. 8, Reinhold Publishing Corp., New York (1958).
4. S. Bhattacharyya, M. Muthahna, and A. Patankar, *J. Sci. Ind. Res. (India)*, **11.B**, 371 (1952).
5. M. A. Kalinin and V. V. Stender, *J. Appl. Chem. (USSR)*, **19**, 1045 (1946). *C. A.*, **41**, 4767b (1947).
6. H. P. Landi, J. D. Voorhies, W. A. Barber, Preprints of Papers, Biennial Fuel Cell Symposium preprints, p. 12, American Chemical Society, Sept. 10, 1967. "Advances in Chemistry Series," in press, A.C.S.
7. G. C. Bond, "Catalysis by Metals," pp. 271-274, Academic Press, New York (1962).
8. J. Newham, *Chem. Rev.*, **63**, 123 (1963).
9. For many references see J. S. Mayell and S. H. Langer, *J. Electroanal. Chem.*, **1**, 299 (1964); *Electrochim. Acta*, **9**, 1411 (1964).
10. P. Delahay, "Double Layer and Electrode Kinetics," pp. 131-135, Interscience, New York (1965).
11. S. H. Langer, S. Connell, and I. Wender, *J. Org. Chem.*, **23**, 50 (1958).
12. S. H. Langer, R. A. Friedel, I. Wender, and A. G. Sharkey, Jr., *Anal. Chem.*, **30**, 1353 (1958).

High Activity Silver Electrodeposited from Silver Chloride

Y. J. van der Meulen[1] and F. A. Kröger*

Department of Materials Science, University of Southern California, Los Angeles, California

In the course of experiments on the electronic conductivity of silver chloride (1), the emf of the cell C, Cl_2 (1 atm) |AgCl|Ag was measured. The chlorine electrode consisted of high purity carbon in a 1 atm chlorine ambient. The silver electrode consisted either of pure Ag-foil (4*N*) or of silver deposited by slow electrolysis of the silver chloride crystal at 390°C with a field $\leq$ 150 mV/cm at current densities $\leq$ 5 mA cm^{-2}. Cells with the former type of electrode gave an emf reproducible within 1 mV and independent of time, its value corresponding reasonably closely to the tabulated value of the free enthalpy of the reaction $\frac{1}{2}Cl_2 + Ag \rightarrow AgCl$ (Fig. 1).[2] In the cells with the electrodeposited

* Electrochemical Society Active Member.
[1] On leave of absence from Utrecht State University, Utrecht, The Netherlands.

[2] A slightly larger value, E (392°C) = 951 mV, $dE/dt = 5.8 \times 10^{-4}$ V/°C, was reported by Reinhold (2).

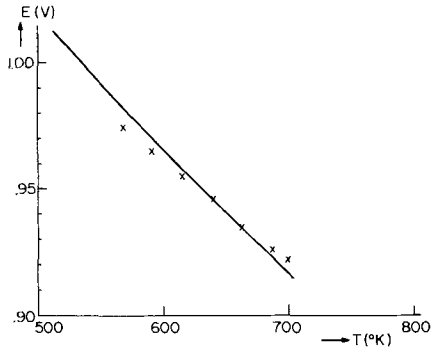

Fig. 1. EMF = $f(T)$ as measured for the cell C, Cl_2 (1 atm) |AgCl|Ag (foil) (individual points) compared with values calculated from thermodynamic data (drawn line).

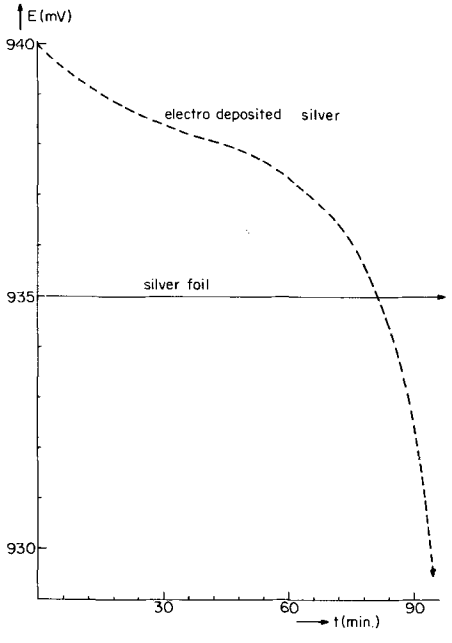

Fig. 2. EMF = $f(t)$ at 390°C for silver foil and electrodeposited silver in the cell C, Cl_2 (1 atm) |AgCl|Ag. The deposition took place on platinum at approximately 2 x 10^{-3} A cm^{-2}. Total amount deposited was approximately 0.20 mg Ag.

silver electrodes, however, the emf measured immediately after termination of the electrolysis changed with time and was initially higher than when silver foil was used (Fig. 2). The result was the same for electrodeposition of silver by electrolysis of ultra pure AgCl containing (5 to 10) x 10^{-6} divalent impurities, mainly Cd, and of AgCl doped with 3 x 10^{-5} Cd. The more slowly the electrolysis was carried out, the more closely the emf approached the value found with the foil. If it is accepted that the emf measured with the foil electrode represents the standard equilibrium value corresponding to the reaction between silver at $a_{Ag} = 1$ and $P_{Cl_2} = 1$ atm, the excess emf with electrodeposited silver could be due to one of the following effects: (*i*) effect due to preferential plating out of less noble impurities, (*ii*) polarization of the AgCl, (*iii*) formation of Cl_2 at $P_{Cl_2} > (P_{Cl_2})_{\text{established}}$, and (*iv*) formation of Ag with activity > 1.

Possibility (*i*) is unlikely, in the first place because of the purity of the AgCl used, in the second place because impurities giving a higher emf would need a higher voltage to be deposited, and therefore preferential deposition is not to be expected.

Possibility (*ii*) is unlikely because of the small overvoltage used in the electrolysis. An internal silver activity > 1 is only to be expected as long as Ag has not nucleated. In such a situation internal excess activities corresponding to 1 mV were observed for the plating of silver from Ag_2S at 400°C (3); this overvoltage dropped to zero with a relaxation time of ≈1 min when nucleation took place.

Possibility (*iii*) may possibly occur for $(P_{Cl_2})_{\text{established}} < 1$ atm if inert gas is present, but is unlikely for $(P_{Cl_2})_{\text{established}} = 1$ atm. The observed overvoltage would correspond to a chlorine pressure $P_{Cl_2} = \exp(\Delta E/kT)$ which for ΔE = 7-8 mV as measured for silver and chlorine discharged at 390°C on carbon, leads to P_{Cl_2} = 1.18-1.23 atm. Since chlorine is evolved at the AgCl-carbon interface, its escape involves diffusion along the interface or through the carbon; and therefore a certain overpressure may be built up during the electrolysis. It is doubtful, however, that this overpressure may be as high as 0.18-0.23 atm under the conditions of the experiment, and it is certainly unlikely that this overpressure would remain over a period of 1 hr, particularly since chlorine is continuously consumed by the chlorination of silver (see below). This then leaves only possibility (*iv*) open as an explanation for the excess emf, the effect being due to the high activity of the deposited silver. Now $a_{Ag} = \exp(\Delta E/kT)$, and for silver deposited on carbon at 390°C where ΔE = 7-8 mV, a_{Ag} = 1.18-1.23.

Silver deposited on platinum[3] gave values of ΔE up to 4 mV, corresponding to a silver activity a_{Ag} = 1.11. Thus the silver is more nearly normal. The emf, however, decreased initially more rapidly than with the Ag/C electrode. This effect is attributed to the diffusion of Ag into the platinum during electrolysis and out of the platinum during the emf measurements (4). Measurements of this kind provide us with a sensitive tool to study the properties of electrodeposited metals as a function of deposition conditions.

ΔG, and thus also ΔE, is related to the dimensions of the surface structure, points or rims. For spherical particles this relation is $\Delta G = 3\gamma V/r$ where γ is the surface energy, V the molar volume, and r the radius. With $\gamma \approx$ 2.5-4 x 10^{-4} cal cm^{-2}, and V = 10 cm^3, ΔE = 5 mV corresponds to $r \approx 0.1\mu$ which is not unacceptable.

The decrease of the emf with time and the final drop after 90 min is due to the consumption of silver of the electrode by reaction with chlorine at the other side. This occurs even when no measurements are made, its rate being limited by ambipolar diffusion of $Ag_i^{\cdot}$ or V'_{Ag} and electrons or holes through the AgCl. In this process the contact between the silver and the crystal is lost. That this is actually the mechanism is shown by the fact that application of a pressure on the electrode, temporarily re-establishes the contact Ag-AgCl and therewith the emf. The gradual lowering of the emf with time in the initial period is due to the preferential consumption of the silver with the highest activity.

Manuscript submitted Sept. 11, 1969; revised manuscript received *ca.* Jan. 2, 1970. This work was supported by the Directorate of Chemical Sciences, Air Force Office of Scientific Research under Contract AF-AFOSR-68-1405.

Any discussion of this paper will appear in a Discussion Section to be published in the December 1970 JOURNAL.

[3] When working with a platinum electrode care was taken to keep the voltage on the cell from dropping below 600 mV, in order to prevent chlorination of the platinum itself.

REFERENCES

1. Y. J. van der Meulen and F. A. Kröger, *This Journal*, **117**, 69 (1970).
2. H. Reinhold, *Z. Anorg. Chem.*, **171**, 181 (1928).
3. H. Schmalzried and C. Wagner, *Trans. AIME*, **227**, 539 (1963).
4. D. O. Raleigh and H. R. Rowe, *This Journal*, **116**, 40 (1969).

JOURNAL OF THE ELECTROCHEMICAL SOCIETY

SOLID STATE SCIENCE

APRIL 1970

Low Temperature Oxidation (24° to 200°C) and Krypton Adsorption Studies on Polycrystalline and Single Crystal Iron Surfaces

M. J. Graham, S. I. Ali,[1] and M. Cohen*

Division of Chemistry, National Research Council of Canada, Ottawa, Ontario, Canada

ABSTRACT

Rates of oxidation of polycrystalline, (110), and (112) surfaces of iron have been measured at 24°, 100°, and 200°C by a manometric method using an initial oxygen pressure of about 1.3 x 10^{-2} Torr. At the lower temperatures the relative rates of oxidation are found to be polycrystalline, (110), and (112) in decreasing order. At 200°C the different single crystal surfaces oxidize at essentially the same rate. Logarithmic rate laws are obeyed reasonably well for oxidations up to 200°C, at which point the oxidation rate, after a time, obeys a parabolic law. Using this parabolic rate constant for the oxidation of polycrystalline iron at 200°C, together with previous microbalance data for the low pressure oxidation of iron at 350° and 400°C (1), an activation energy of 32 kcal. $mole^{-1}$ is found for the formation of magnetite on iron. Surface areas of polycrystalline and (112) surfaces have been measured before and after oxidation using the BET method, employing krypton adsorption at 77°K. It is found that the number of surface sites for the adsorption of krypton is dependent on the nature of the adsorbent surface.

Recent work in this laboratory has considered the oxidation of iron in low oxygen pressures at 350° and 400°C (1) and 450°-500°C (2). The microbalance used in this work was inadequate for kinetic measurements at low temperatures and in order to extend the study of magnetite formation to 200°C and below a manometric system was designed. The apparatus could also be used for surface area measurements. This paper reports the kinetics of magnetite formation between room temperature and 200°C, correlating the 200°C results with the microbalance work (1), and also discusses the effect of an oxide film on monolayer krypton adsorption.

Experimental

Material and surface preparation.—Ferrovac E iron, analyzed to contain the following impurity concentrations (in ppm); Mn, 1; Si, 10; Ni, 10; Al, 10; Cu, 10; Co, 5; Cr, 5; C, 70; N, 20; O, 200 was used. Single crystals of known orientations were produced from this 0.02 cm thick material by strain annealing.

Polycrystalline iron coupons, 4-5 cm x 1 cm were degreased, abraded with 600 grit silicon carbide, and electropolished for 1 min in a 95% glacial acetic acid-5% perchloric acid (70%) solution (3). The specimens were then annealed in vacuum at 700°C for 2 hr and re-electropolished for a further minute. The single crystals were also electropolished before use.

Oxidation apparatus.—The oxidation apparatus is shown schematically in Fig. 1. A Pirani gauge was used to follow the kinetics of oxidation by measuring the change in oxygen pressure with time (at constant volume). With the exception of glass pressure gauges and specimen chamber the apparatus was all metal. Hoke diaphragm seal valves (denoted by S in Fig. 1) were silver soldered directly into stainless steel couplings and Varian flanges, minimizing the apparatus volume by eliminating interconnecting tubing. After an overnight bake at 200°C, pressures better than 10^{-7} Torr were measured by the ion pump.

The walls of the Pirani and reference tubes were maintained at constant temperature by immersing the tubes in an ice-water bath. The Pirani was calibrated against a Decker Model 306 Differential Pressure Gauge which had a sensitivity of 0.187 V $Torr^{-1}$ found by previous calibration against a McLeod gauge. The response of the Pirani gauge was found to be linear up to an oxygen pressure approaching 4 x 10^{-2} Torr, with a calibration of 1.61V $Torr^{-1}$ for oxygen. An oxy-

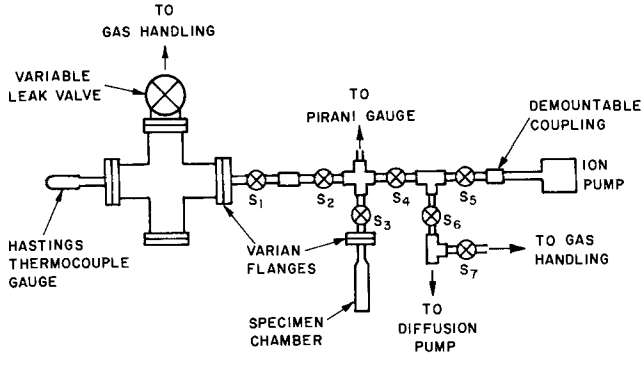

Fig. 1. Oxidation apparatus

* Electrochemical Society Active Member.
[1] Former Post-doctorate Research Fellow.

gen uptake causing the Pirani balance to change by 1 mV was equivalent to a mean thickness of $\frac{3.72}{SA}$ Å Fe_3O_4, where SA is the specimen surface area.

The working volume of the system, *i.e.*, volume enclosed by valves S_2 and S_4, was found to be 50.0 ml and the volume enclosed by S_2, S_3, and S_4 equal to 24.0 ml. The small doser between S_1 and S_2 contained an approximate volume of 3.6 ml.

The specimen chamber was rectangular in shape with internal dimensions of 7.0 x 1.3 x 0.2 cm. The chamber was joined to a Kovar seal which was argon-arc welded into a Varian flange.

Oxidation procedure.—After the system had cooled following an overnight bake and when the pressure was about 1 x 10^{-7} Torr, the specimen air-formed oxide film was reduced with hydrogen at about 4 Torr pressure for 1 hr at 570°C. In order to maintain a H_2O:H_2 ratio as low as possible, the system was evacuated and refilled with fresh hydrogen four times during the hour.

After the hydrogen was removed, the specimen was cooled by lowering the furnace, then reheated under continuous pumping, and maintained at the oxidation temperature for half an hour before admitting oxygen. The temperature gradient of the oxidation furnace over the length of the specimen was ±2° at 200°C.

In all experiments the initial oxygen pressure used was about 1.3 x 10^{-2} Torr. The change in pressure, read on a 50 mV recorder range, measured the uptake of oxygen by the specimen as the oxidation progressed. When the oxygen pressure had fallen by about 40% another dose was added to re-establish the initial pressure.

Surface area measurements.—Surface areas of both hydrogen-reduced and oxidized specimens were measured in an all glass system which was similar in design to the apparatus described above.

After the specimen had cooled to room temperature and the system was thoroughly evacuated, the specimen chamber was immersed in a liquid nitrogen bath to a fixed level, which was maintained constant throughout the experiment. The temperature was allowed to stabilize for 15 min before krypton was admitted and the equilibrium pressure read after a steady state had been reached. Four or five equilibrium measurements taken in a relative pressure range of 0.01-0.1 were sufficient for determining the area. From the equilibrium pressures and initial dose sizes, the volume of krypton adsorbed by the specimen may be found after applying a dead space correction obtained by measurement in the absence of a specimen. The values of the equilibrium pressure were corrected for the thermal transpiration effect using the expression of Bennett and Tompkins (4).

The number of krypton adatoms in a monolayer, N_m, was calculated from the standard BET equation. Knowing N_m and a value of the cross-sectional area of krypton, the surface area may be determined.

Electron diffraction.—Reflection electron diffraction observations were carried out at 50 kV to identify the oxide phases present. After oxidation, the specimens were cooled rapidly to room temperature in the oxidizing atmosphere and transferred to the diffraction apparatus. Following oxidations at 200°C and below, only Fe_3O_4[2] was observed; epitaxial relationships agreed with those reported in the literature, *e.g.*, ref. (5). Specimens oxidized at 260°-400°C for krypton adsorption studies showed α-Fe_2O_3 as well.

Results

Kinetic data.—The early stages of oxidation of polycrystalline iron at a series of temperatures from 24°-200°C are shown in Fig. 2. (Oxide thicknesses are calculated by assuming a roughness factor of 1.) It is observed that the oxidation proceeds in two stages:

[2] A cubic oxide comprising probably both Fe_3O_4 and γ-Fe_2O_3.

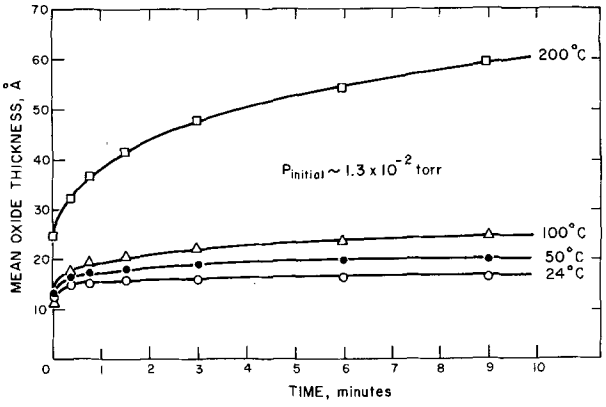

Fig. 2. Early stages of low temperature oxidation of polycrystalline iron.

(*a*) an initial instantaneous oxidation, followed by (*b*) a sharp transition to a period of much lower oxidation rate. The oxide thickness at the turnover of the kinetic curves is dependent on the temperature and also on metal substrate orientation as is seen from Fig. 3, 4, and 5 where the rates of oxidation of polycrystalline, (110), and (112) surfaces of iron at 24°, 100°, and 200°C are shown.

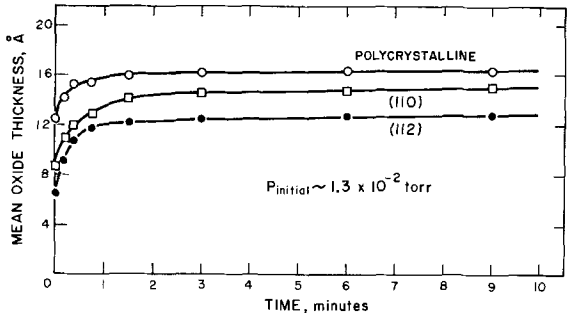

Fig. 3. Oxidation of polycrystalline, (110), and (112) iron surfaces at 24°C.

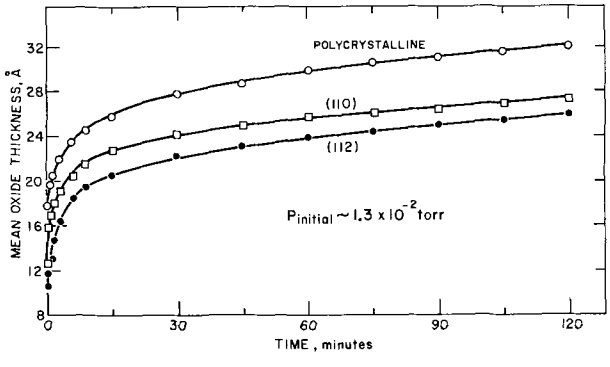

Fig. 4. Oxidation of polycrystalline, (110), and (112) iron surfaces at 100°C.

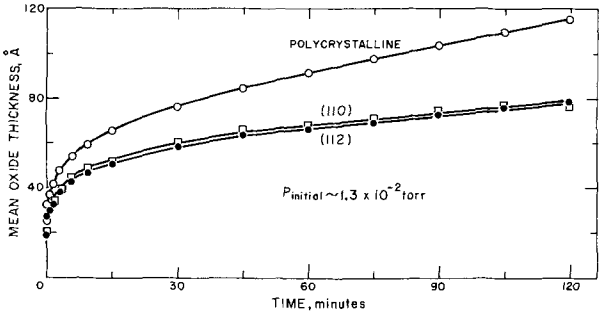

Fig. 5. Oxidation of polycrystalline, (110), and (112) iron surfaces at 200°C.

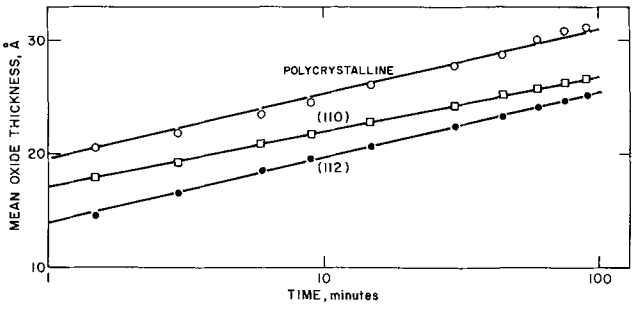

Fig. 6. Logarithmic plot of data from oxidation of polycrystalline, (110), and (112) iron surfaces at 100°C.

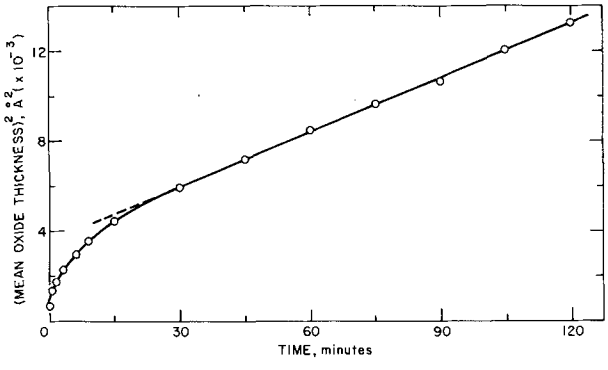

Fig. 7. Parabolic plot of data from oxidation of polycrystalline iron at 200°C.

Oxidations at 24° and 100°C followed a logarithmic rate law of the form $x = A \ln t + B$ (x = film thickness, t = time) reasonably well and the logarithmic plot for the oxidation of various surfaces of iron at 100°C is shown in Fig. 6. At 200°C, the results for the first 20 min of oxidation fit a logarithmic plot after which time the data is best represented by a parabolic plot, as shown in Fig. 7 for polycrystalline iron.

Surface area measurements.—In the BET equation a value of 3.0 Torr was used for the vapor pressure of krypton at 77°K. Having evaluated the monolayer coverage, from the slope of the BET plot, a value for the cross-sectional area of krypton is required in order to determine the surface area. It is becoming increasingly more certain that physically adsorbed atoms are held on surface sites and not adsorbed in a close-packed array, and so the cross-sectional area of, *e.g.*, krypton will be determined by the site density of the particular adsorbent used. Cross-sectional areas, σ, for krypton adsorbed on iron, derived by Brennan and Graham from coverages based on site adsorption (6) are as follows:

Polycrystalline: $\sigma(\text{Kr}) = 17.9\text{Å}^2$
(112) plane : $\sigma(\text{Kr}) = 20.0\text{Å}^2$
(100) plane : $\sigma(\text{Kr}) = 16.4\text{Å}^2$
(110) plane : $\sigma(\text{Kr}) = 17.4\text{Å}^2$

the polycrystalline value of 17.9Å² being the mean value of the cross-sectional area of krypton on the three major low index planes listed above. The appropriate σ values have been used to calculate the surface areas of hydrogen reduced specimens given in Table I. [The above values compare with a commonly used one of $\sigma(\text{Kr}) = 19.5\text{Å}^2$ (7).]

Table I. Surface areas of polycrystalline and (112) iron specimens

Surface orientation	BET surface area (cm²)	Geometric area (cm²)	Roughness factor
Polycrystalline	15.6	12.6	1.2
(112)	15.0	11.2	1.3

Each area measurement was repeated 3 or 4 times and the values were reproducible to an accuracy of ~8-10%. (The reduction in monolayer capacity for krypton of a surface after oxidation will be considered in the discussion.)

Discussion

Kinetics.—It has been found, using a variety of experimental techniques, that the room temperature oxidation of iron involves an initial rapid chemisorption process followed by a slow approach to a mean film thickness of around 10-30Å (8-12), the value depending on surface pretreatment, oxygen pressure, time of exposure, etc. The present result of a thickness of 17±0.5Å after 10 min of oxidation of polycrystalline iron is in keeping with previous findings. Oxide thicknesses after oxidation for 2 hr at 100° and 200°C, viz., 30±2Å and 120±8Å (mean of two separate experiments) are in good agreement with those reported by Gulbransen (8) and Winterbottom (9).

The relative rates of oxidation at 24° and 100°C are found to be polycrystalline, (110) and (112) in decreasing order (Fig. 3 and 4). At 200°C the polycrystalline material again oxidizes at a faster rate than either the (110) or (112) face, but now both single crystals oxidize at essentially the same rate (Fig. 5). The anisotropy of oxidation is probably related to a varying oxide grain size or subgrain size with metal orientation. The smaller the oxide grain size, the higher the oxidation rate because of the presence of more leakage paths for easy diffusion. At higher temperatures where α-Fe_2O_3 is observed, the rate of oxidation will also depend on the rate of nucleation of α-Fe_2O_3 to form a continuous layer (1, 13, 14).

The present oxidation results at 24° and 100°C (and for the first 20 min of oxidation at 200°C) appeared to fit a direct logarithmic plot better than an inverse logarithmic plot, although after about 60 min, the experimental points, particularly for room temperature oxidation, did begin to deviate from a direct logarithmic plot and fitted equally well an inverse logarithmic dependency. As the data do not permit unequivocal rate law interpretation, it is not considered useful to speculate on the particular mechanism of this thin film oxidation (15-18).

The rate constant for the parabolic region of the oxidation at 200°C (from Fig. 7) is compared in Table II with parabolic rate constants determined in a previous study (1) for the initial oxidation of polycrystalline Ferrovac E iron at 350° and 400°C at about the same pressure of 10^{-2} Torr. It should be emphasized that the rate constants refer to the formation of magnetite alone; from electron diffraction studies no α-Fe_2O_3 was detected during these parabolic periods.

An Arrhenius plot of the parabolic rate constants given in Table II is shown in Fig. 8. Here it is observed that the present data at 200°C correlates well with the previous microbalance work, and the resulting activation energy for the formation of magnetite on iron in the temperature range 200°-400°C is found to be 32 kcal. mole^{-1}. This is higher than the approximate value reported previously using data obtained at only 350° and 400°C (1).

Reduction in surface sites following oxidation.—Krypton adsorption measurements on clean metal (prior oxide hydrogen reduced) and oxide covered polycrystalline and (112) iron surfaces show that following oxidation, the number of krypton atoms ad-

Table II. Parabolic rate constants for the oxidation of iron to magnetite at 200°, 350°, and 400°C

Temperature, °C	Pressure, Torr	K_p, g² cm⁻⁴ sec⁻¹
200	1.3×10^{-2}	2.8×10^{-16}
350	1×10^{-2}	1.3×10^{-12}
400	1×10^{-2}	5.5×10^{-12}

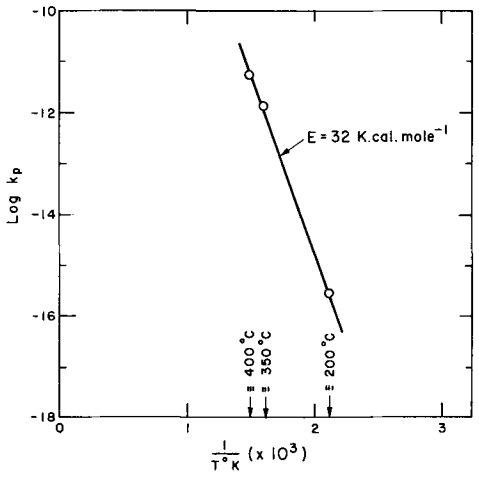

Fig. 8. Logarithm of parabolic rate constant for oxidation at 200°, 350°, and 400°C plotted against (absolute temperature)$^{-1}$. Data at 200°C from this work; data at 350° and 400°C from the microbalance work of Graham and Cohen (1).

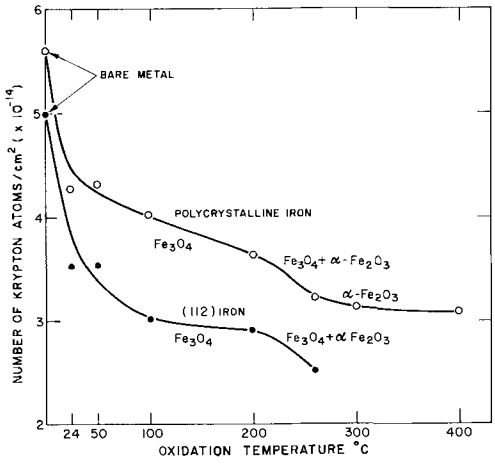

Fig. 9. Reduction in site density for the adsorption of krypton on oxide films formed at various temperatures.

sorbed in a monolayer is reduced. Workers using evaporated metal films find the monolayer capacity of a surface is nearly always lowered by the presence of a chemisorbed layer. The most probable explanation is that following oxidation or chemisorption, the number of surface sites for krypton adsorption has been reduced.

This reduction in site density on oxide films formed at various temperatures is shown in Fig. 9. The reference point for the number of krypton atoms adsorbed per square centimeter (using the "real" surface area) of bare metal is $1/\sigma$, the values of the cross-sectional area of krypton used were those given earlier. In Fig. 9 it is observed that the number of krypton atoms required to complete a monolayer not only changes from a bare metal to an oxidized surface but also depends on the particular oxide formed; αFe_2O_3 appears to provide fewer surface sites than Fe_3O_4. The cross-sectional area of an adsorbate is probably controlled by the site density of the adsorbent and thus would be expected to change as the nature of the adsorbent surface is changed.

Manuscript submitted Sept. 18, 1969; revised manuscript received *ca.* Dec. 19, 1969.

Any discussion of this paper will appear in a Discussion Section to be published in the December 1970 JOURNAL.

REFERENCES

1. M. J. Graham and M. Cohen, *This Journal*, **116**, 1430 (1969).
2. R. J. Hussey and M. Cohen, Unpublished results.
3. P. B. Sewell, C. D. Stockbridge, and M. Cohen, *Can. J. Chem.*, **37**, 1813 (1959).
4. M. J. Bennett and F. C. Tompkins, *Trans. Faraday Soc.*, **53**, 185 (1957).
5. P. B. Sewell and M. Cohen, *This Journal*, **111**, 508 (1964).
6. D. Brennan and M. J. Graham, *Phil. Trans. Roy. Soc. London*, **A258**, 41 (1965).
7. R. A. Beebe, J. B. Beckwith, and J. M. Honig, *J. Am. Chem. Soc.*, **67**, 1554 (1945).
8. E. A. Gulbransen, *Trans. Electrochem. Soc.*, **81**, 327 (1942).
9. A. B. Winterbottom, *J. Iron Steel Inst.*, **9**, (1950).
10. J. Kruger and H. T. Yolken, *Corrosion*, **20**, 29 (1964).
11. M. W. Roberts, *Trans. Faraday Soc.*, **57**, 99 (1961).
12. P. Hancock and J. E. O. Mayne, *J. Chem. Soc.*, **1958**, 4167.
13. W. E. Boggs, R. H. Kachik, and G. E. Pellissier, *This Journal*, **114**, 32 (1967).
14. N. Ramasubramanian, P. B. Sewell, and M. Cohen, *ibid.*, **115**, 12 (1968).
15. K. Hauffe and B. Ilshner, *Z. Electrochem.*, **58**, 382 (1954).
16. N. Cabrera and N. F. Mott, *Rept. Progr. Phys.*, **12**, 163 (1949).
17. T. B. Grimley and B. M. W. Trapnell, *Proc. Roy Soc.*, **A234**, 405 (1956).
18. H. H. Uhlig, *Acta Met.*, **4**, 541 (1956).

Etch Patterns on Zone-Refined Fe

M. E. Straumanis* and C. D. Kim

Graduate Center for Materials Research and Department of Metallurgical Engineering of the University of Missouri-Rolla, Rolla, Missouri

ABSTRACT

Upon dissolution of zone-refined Fe in strong acids, mainly three kinds of corrosion patterns were observed in the crystallites of the sections. Regardless of the acids, the {110} plane always appeared on the three patterns in the form of smooth and even steps, ledges, or facets. The {112}, {122}, and {123} planes were also developed but to a much lesser degree. The {100} and {111} planes were not observed because grains of the respective orientation were missing on the sections. Attempts were made to explain the formation of the planes by taking into consideration the reticular density of the planes and the frequency of their appearance. The theoretical relative corrosion rates of the separate crystallographic planes were estimated. The trend obtained agreed with the observed rates.

Zone-refined iron is attacked only slightly even by strong acids. As a result, in contrast to a previous investigation where a fine crystalline Fe was used (1), characteristic etch patterns appeared on the polycrystalline sample, each grain showing an array of steps, ledges, and facets. The surface was also highly resistive to atmospheric corrosion.

Etch patterns on single Fe crystals (2, 3), kinetics of dissolution of Fe whiskers (4), potentials (5), and anodic dissolution rates of separate crystal planes (6) were investigated previously. However, no reports on angular measurements between the ledges produced on single crystallites of an iron sample by the action of strong acids could be found. The aim of this study was, therefore, to determine the indices of the faces developed on separate grains during corrosion of zone-refined Fe in several acids and to compare the results with those of other investigators who worked, *e.g.*, with single crystal spheres and plates (2,3,6).

The luster of the etched samples originates not only from the strongly reflecting ledges on each grain, but also from other, usually weaker reflecting step systems. If these systems are within the same crystallographic zone, the angles between them can be measured with an optical goniometer. As the wide and shiny steps (see *e.g.*, Fig. 4) are easily indexed (see below), the indices of the other faces of the same zone can be determined from the angles optically measured, the bright steps serving as reference planes.

Samples and Technique

High-purity zone-refined Fe was obtained from Battelle Memorial Institute. The main impurities in ppm were: Ni, 20; Al, 15; Ca, 10; Si, 10; C, 9; P, 9; Cu 7; and other elements in still smaller amounts. The Fe rods were sliced into pieces of about 5 mm thick, and each slice was ground and polished. The specimens, 1-5 cm^2 in surface area, were deeply etched using as solutions concentrated HCl, 1.5*N* HNO_3, 2*N* H_2SO_4, aqua regia (25%), and concentrated HF (48%). Two hours produced an etch pattern in concentrated HCl, whereas several days were required to obtain the same pattern in 2*N* H_2SO_4. Etching in each solvent was continued until the grain boundaries were clearly resolved.

As the Fe rods consisted mainly of large crystallites (2-5 mm in diameter), their orientation could be determined from Laue back-reflection patterns (Fe radiation, sample-to-film distance, 3 cm). The strong reflections were read with the aid of the respective Greninger (-Bond) chart, plotted into Wulff's stereonet and the indices found in the usual way (7, 8).

To determine the indices of the brightest, most reflective planes developed by etching (Fig. 4) on each grain of the sample, the latter was mounted on the head of an optical goniometer and so adjusted that the reflective steps of the grain became perpendicular to the goniometer vertical circle axis, which, in turn, was parallel to the x-ray beam.

With the goniometer head and the adjusted sample now in the Laue camera, the indices of the surface of the parallel steps could easily be found. Minor optical reflections, *e.g.*, the sides of the steps with larger area, were determined in the same way. This procedure of investigating grain after grain was continued on several sections of the polished and etched Fe samples.

Results

Figure 1, representing a unit triangle of a standard (001) stereographic projection, shows a random orientation distribution of the grains.

The etch patterns on each grain were similar to each other although various etchants were used. However, only concentrated HCl produced very clean surfaces with a shining metallic luster. Samples treated with H_2SO_4 and HF were covered with a layer of whitish-gray salts, and those etched with HNO_3 and aqua regia partly exhibited a brown oxide film. Nevertheless, the surface structure of all the grains on the sections was generally similar.

Three major corrosion patterns could be distinguished: (*i*) a set of grooves running nearly parallel across the grains (Fig. 2); (*ii*) triangles or pyramids (Fig. 3); and (*iii*) irregular but shiny ledges running roughly parallel to each other (Fig. 4). Evidently the formation of these etch patterns depended on the degree of inclination of some crystallographic planes within the grains to the surface of the sample.

All of the Laue patterns obtained from the larger area facets of different grains, etched with various

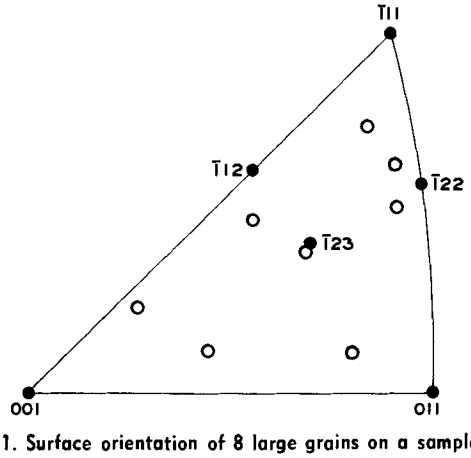

Fig. 1. Surface orientation of 8 large grains on a sample of zone-refined Fe.

* Electrochemical Society Active Member.

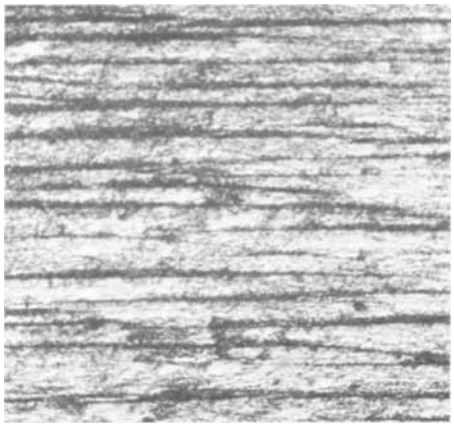

Fig. 2. Crystallite of zone-refined Fe. Etchant: conc. HCl, 12 hr. 150X.

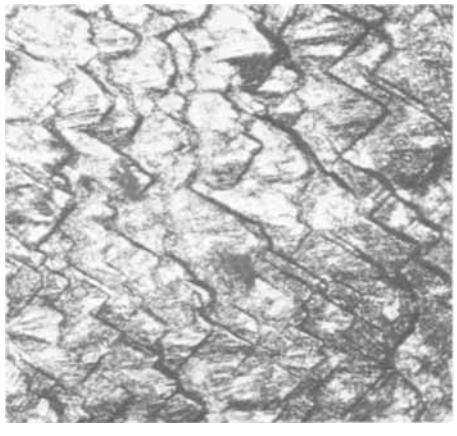

Fig 3. Ditto. Triangles and set of parallel short dark lines on another grain. 150X.

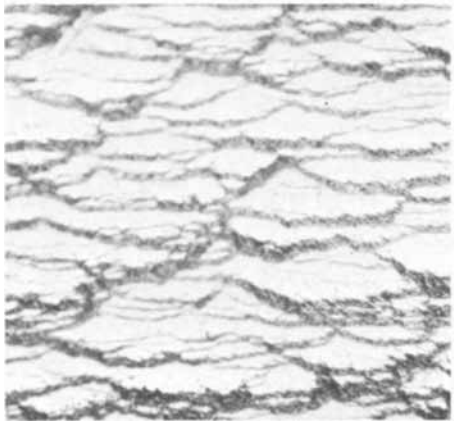

Fig. 4. Ditto. Irregular ledges roughly parallel to each other. 320X.

acids, were indexed. The orientation of these facets is shown by their projections (Fig. 5).

In HF the grains were covered with a layer of corrosion products too thick for goniometric examination. No attempts were made to study these specimens.

Figure 5 clearly shows that the indices of the larger reflecting areas were (in HCl): 6 close to (011), 4 to ($\bar{1}22$), and one to ($\bar{1}23$). In aqua regia: 6 close to (011), 1 to ($\bar{1}22$). In H_2SO_4: 5 close to (011), and in HNO_3: 5 close to (011) and 2 to ($\bar{1}22$). The planes mentioned are not in the ideal positions of (011), ($\bar{1}22$), and ($\bar{1}23$) because the planes formed due to corrosion are never smooth and large enough to produce sharp signals from each crystallite in the goniometer during the setting procedure.

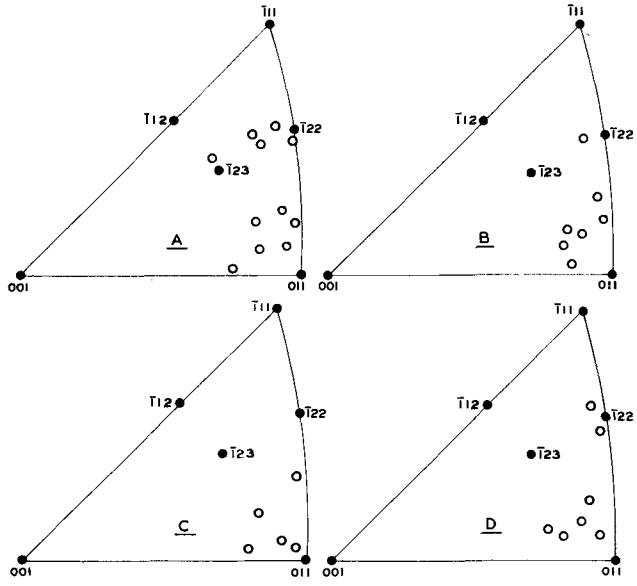

Fig. 5. Orientations of the best defined facets on the grains of Fe samples etched with various acids: A, conc. HCl (10 grains); B, 25% aqua regia (7 grains); C, 2*N* H_2SO_4 (5 grains); D, 1.5*N* HNO_3 (7 grains); full circles, ideal planes; open circles, planes determined.

In addition, there were a series of other weaker optical reflections, the respective planes inaccessible to the x-ray technique. The optical goniometer was a useful tool here.

The angles between the reflections on crystallites showing the etch pattern, Fig. 2, were measured normal to the striations. Surprisingly enough, no new planes were found (Fig. 6).

To obtain as many reflections as possible on grains with etch pattern, Fig. 3, the vertical circle (carrying the sample) was also rotated: at each 5° interval the corroded surface of a certain grain was scanned by turning the horizontal circle. However, the reflecting planes were all the same, but in addition there were weak reflections from {112} and {123}.

Etch pattern 3 (Fig. 4) was investigated in the same way. Very strong reflections from the {011} planes and weak ones from {122} were obtained.

Generally, only the {110} plane appeared as a main facet on the corrosion patterns of zone-refined Fe; the other planes were much smaller in extent and dissolved faster in the acids used.

Discussion

Since the Fe used for the etching experiments was very pure, no significant local corrosion ensued. The corrosion patterns observed are, therefore, a consequence of the reaction of the acids with the body centered structure of crystalline Fe. Such a possibility is deduced from the very slow attack of carbonyl Fe by acids (1) and by the recent facts that the four acids in agreement with Buck and Leidheiser (2, 3), produced in essence the same corrosion patterns (see Fig. 2, 3, and 4) and the planes

$$\{110\},\ \{112\},\ \{122\},\ \text{and}\ \{123\} \qquad [1]$$

This corrosion form of Fe can be compared with that calculated for a body centered crystal (in equilibrium with its vapor) by Kossel and Stranski (9-12)

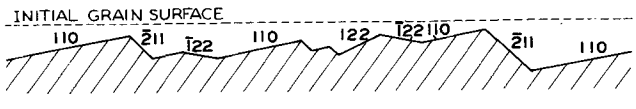

Fig. 6. Planes measured on a crystallite of Fig. 2 with striations within the vertical axis of the horizontal circle of the optical goniometer. Section perpendicular to the striations.

{110}, {100}, {112}, and {111} [2]

whereby the appearance of other planes is not excluded.

The explanation as to why in series [1] the {100} and {111} planes are missing is that none of the grains on the sections were close to these orientations (Fig. 1). On the other hand the (110)-planes are not mentioned, *e.g.*, by Buck and Leidheiser. Thus, there are considerable differences between the theoretical equilibrium form [2] and the corrosion form obtained with Armco Fe or L-steel (2, 3), but there are minor ones between [2] and [1].

However, series [2] can also be obtained, if one assumes that the most stable planes in a homopolar crystal are those with the highest reticular density. The sequence of planes with decreasing relative density, *s*, is then

(110), (100), (112), (111), (123), (122) [3]

s, as listed in Table I, was obtained from both purely geometrical considerations and by calculation from

$$s \sim 1/(h^2 + k^2 + l^2)^{1/2} \quad [4]$$

where *h*, *k*, and *l* are the x-ray indices of a body-centered structure (13).

Thus, the experimental corrosion form [1], would agree with the theoretical form [2] or [3] if the (001) and (111) planes had been in the section areas of the Fe samples.

A further question is which of the planes of form [3] would appear as dots and which would produce larger areas during attack by strong acids? Only estimates can be made, and for this purpose the frequency of appearance of various planes (multiplicity factor, *m*, in x-ray analysis) has to be considered. Assume that the (001)-plane of some crystallites is inclined to the surface of the sample and an etchant is applied. The latter will remove the atoms from the surface and penetrate into the depth of the respective crystallite. But on its way, before reaching the next sound $(00\bar{1})$-plane it will meet one of the high reticular density (101)-planes which occur more frequently ($m = 12$, see Table I) than the (100)-planes with $m = 6$.

The corrosive process, therefore, will be blocked by such planes and penetrate laterally and parallel to them to produce a stairlike structure across the *grains* with (110) as main broad faces and with {112}, {221}, and others as narrow lateral ones (see, *e.g.*, Fig. 4 and 6). Even the {hkl} planes, such as {123} will appear. However, if a (001)-plane is parallel to the sample surface, it may remain during corrosion. The same pertains to the (111)-plane, which is corroded, according to Buck and Leidheiser (2, 3), faster than (001), evidently because of the lower reticular density (Table I).

The relative velocity of corrosion, *V*, of various crystallographic planes can also be estimated, assuming that the rate is proportional to the multiplicity, *m*, of the respective dissolving planes and inversely proportional to the reticular density *s*. This operation will also reduce the corrosion rates of the various planes to the same surface area

$$V = km/s \quad [5]$$

Thus a plane will dissolve faster, the more equivalent directions available to the etchant: the corrosion process on a (001)-plane spreads in 5 directions (or 6, if undermining occurs); on a {110}-plane—in 6 to 12 directions and on {123} or generally {hkl}—in at least 24 directions (up to 48 during undermining), etc. The latter face will, therefore, produce a much higher corrosion rate than (100). This statement is confirmed by the results of Buck and Leidheiser (3). No extensive faces will be developed, only small dots, because of the various inclinations of the {123} planes to the sample surface. A development of larger {123} reflecting planes thus becomes impossible: due to the increased rate of dissolution, corrosion resistive planes, *e.g.*, (101) will be reached soon and steps will develop as already described.

The theoretical maximum *m/s* values are summarized in Table I, the next column showing the relative rates. In the last column rate ratios, as obtained with Fe whiskers by Shemenski *et al.* (4), are given for comparison. Although objections can be raised against this method of calculating rate ratios, the trend does agree with the experimental data obtained by several authors for various kinds of Fe in different solvents (2, 3, 4, 6). Calculated rate ratios for the {hhl} and {hkl} planes are too high because the highest *m* values were taken. Furthermore, ion diffusion rates would limit the velocity of corrosion. On the other hand oxidizers, such as $K_2S_2O_8$ would increase the low rates. The presence of impurities in appreciable amounts would distort the over-all picture. Taking these factors into consideration, the agreement between the theoretical and experimental rate ratios for various crystallographic planes should be regarded as very satisfactory, explaining why the corrosion rate depends on the crystallographic direction, at least for pure Fe.

Table I. Relative reticular density, *s*, of some planes of b.c. metals. Multiplicity factor, *m*, and relative corrosion rates, *m/s*

Plane	*s*	*m*	*m/s*	*m/s**	*m/s* exp.**
100	1.000	6	6	1	1
110	1.412	12	8.5	1.42	2.41
111	0.577	8	13.9	2.32	3.51
112	0.816	24	29.4	4.90	—
122	0.334	24	71.9	11.96	—
123	0.535	48	89.7	14.96	2-4.8†

* Corrosion rate of {100} is assumed to be 1.
** According to Shemenski *et al.* (4) for Fe whiskers in 1*N* H_2SO_4 + 0.2*N* $K_2S_2O_8$.
† Buck and Leidheiser (3) for steel in boiling 0.2M citric acid.

Acknowledgments

Thanks are expressed to the Office of Naval Research for the funds provided, to Dr. W. J. James, Director of the Graduate Center for Materials Research, and to Dr. A. A. Khan for useful discussion.

Manuscript submitted June 27, 1969; revised manuscript received November 21, 1969. This paper is Contribution 68 from the Graduate Center for Materials Research.

Any discussion of this paper will appear in a Discussion Section to be published in the December 1970 JOURNAL.

REFERENCES

1. M. Centnerszwer and M. E. Straumanis, *Z. physik. Chem.*, **A162**, 94 (1932).
2. W. R. Buck and H. Leidheiser, Jr., *Z. Elektrochem.*, **59**, 748 (1955).
3. W. R. Buck and H. Leidheiser, Jr., *This Journal*, **104**, 474 (1957).
4. R. M. Shemenski, F. H. Beck, and M. G. Fontana, *J. Appl. Phys.*, **36**, 3909 (1965).
5. F. N. Speller, "Corrosion, Causes and Prevention," p. 79, McGraw Hill Book Co., New York (1926).
6. H. J. Engell, *Arch. Eisenhüttenw.*, **26**, 393 (1955).
7. A. B. Greninger, *Z. Krist.*, **91**, 424 (1935); *Trans. Met. Soc. AIME*, **117**, 61 (1935).
8. See, *e.g.* B. D. Cullity, "Elements of X-ray Diffraction," Addison-Wesley, Reading, Mass. (1956).
9. W. Kossel, *Nachr. Ges. Wiss, Göttingen*, Mathphysik. Klasse **1927**, 135.
10. I. N. Stranski, *Z. physik. Chem.*, **A136**, 259 (1928).
11. I. N. Stranski and R. Kaischew, *Z. Krist.*, **78**, 373 (1931).
12. B. Honigmann, "Gleichgewichts-und Wachstumsformen," pp. 10 and 116, D. Steinkopff, Darmstadt (1958).
13. F. C. Phillips, "An Introduction to Crystallography," p. 245, J. Wiley & Sons, Inc., New York (1966).

Films of Oil Oxidation Products on Copper

G. W. Poling*[1]

Research and Technical Department, Texaco, Inc., Beacon, New York

ABSTRACT

Films formed on metallic copper catalyzing the low temperature oxidation of pure hydrocarbon liquids and insulating oils were analyzed using reflectance infrared spectroscopy. Onset of rapid air oxidation of n-decane, p-cymene, mineral oil, and a low aromatic content transformer oil at 90°-100°C coincided with the appearance and rapid growth of copper oxalate films on the copper. Cuprous oxide and copper carboxylate species appeared earlier on the copper surfaces but these were not related directly to the autoxidation process. Addition of oxalic acid impurity to mineral oil both increased its power factor and reacted with the copper to form copper oxalate films. Oxalic acid appeared to be an important product in the oxidative deterioration of paraffinic hydrocarbons and insulating oils. Rapid air oxidation of decalin produced copper nitrate reaction products on the copper surfaces. No oxalate was detected. Addition of 1-H benzotriazole to an insulating oil effectively inhibited corrosion of the copper by forming a film of copper benzotriazolate on the copper. Such films retarded the catalytic action of the copper in oxidation of the oil.

Exposure to metallic copper catalyzes the low temperature, liquid-phase oxidation of many oils. For example, transformer oils, exposed to air in the presence of copper and other metals suffer accelerated oxidation. Formation of species such as peroxides, aldehydes, and organic acids causes corrosive attack of the windings and other exposed metals and leads to earlier breakdown of the dielectric. Accelerated tests of the oxidation stabilities of these oils often make use of the catalytic action of copper. One convenient test employs periodic measurement of the d-c conductivity (converted to power factor) of an oil at 95°C exposed to air and copper for several days (1).

In the absence of so-called copper "passivating" additives the oxidation of the oil is usually governed by the copper in solution (2-4). If corrosion of the metallic copper source is inhibited sufficiently, the surface reactions or heterogeneous mechanisms can become rate controlling. Krieger (5) found that dissolution of Cu_2O films normally present on metallic copper, provided the main source of the soluble copper. Freshly reduced copper surfaces did not exert a catalytic action. Adding copper corrosion inhibitors (called "passivators" in insulating oil usage) to the oil could also make the heterogeneous reactions controlling (6). Some inhibitors served a dual function in also chelating the soluble copper to act as "metal deactivators" (4, 6).

Previous studies of the role of copper during the oxidation of oils have focused attention mainly on the changes in composition of the oil phase. Melchiore and Mills (4) found a correlation between increasing power factors and increasing carbonyl contents of degrading transformer oils. Power factor measurements (see Experimental section) provided sensitive tests of the extent of oxidation of their oils. These and other authors have also reported that varnish-like deposits covered the surfaces of the metallic copper catalysts after prolonged oxidation of the oils. To our knowledge, no prior attempts have been made to analyze these thin reaction product films. Knowledge of their composition and structure should aid in understanding the mechanism of the catalytic action of the copper and how to prevent it.

This paper reports infrared multiple reflectance spectroscopic studies of reaction products formed on copper mirrors used as oil oxidation catalysts. Supplemental tests on the oil phase included: power factor measurements, hydroperoxide (ROOH) titrations, and gas chromatographic analysis for other oxidation products. Oxidation tests were conducted usually at 90°-100°C by bubbling air or oxygen for several hundred hours through oil containing the copper mirror catalysts. Periodically, the mirrors were removed from the hydrocarbon, washed in n-pentane, air dryed, and their reflectance spectra recorded. Results are reported for the oxidation of n-decane, decalin, p-cymene, white mineral oil, and several commercial transformer oils. Reflection spectra from the copper mirrors often changed dramatically during the course of an oxidation test. Initial reaction product films usually consisted of thin films (< 100Å) of copper soaps $(RCOO^-)^2Cu^{++}$ on top of thin Cu_2O films. No significant increases in power factor occurred during the appearance and growth of these products. Onset of rapid oxidation of n-decane, p-cymene, and mineral oil was paralleled by formation and rapid growth of copper oxalate (CuC_2O_4) films on the copper. The copper oxalate films often attained thicknesses in excess of 400Å after prolonged oxidation. No copper oxalate was detected from the oxidation of the naphthene decalin. Instead, after several hundred hours of oxidation, formation of copper nitrate ($Cu(NO_3)_2$) films paralleled a sharp increase in power factor.

Addition of benzotriazole ($C_6H_4N_3H$), an effective copper corrosion inhibitor, to the oil produced protective films on the copper and prolonged the low power factor life of an insulating oil.

Experimental

Recording spectra of films.—Spectra of thin films formed on the copper-mirror "catalysts" were recorded from 230 to 4000 cm^{-1} on a Beckman IR-12 spectrophotometer using multiple reflectance accessory optics. Details of this accessory have been provided in a previous paper (7). These optics provided seven reflections at 73° increase from two planar sample mirrors (76 x 38 x 3 mm and 51 x 38 x 3 mm). Use of these multiple reflections increased sensitivity to record absorption of the infrared by thin semitransparent films on the mirror surfaces. A wire-grid polarizer was installed in the monochromator section of the spectrophotometer. This was oriented to transmit the component of light parallel to the plane of incidence of the light at the sample mirrors to further enhance sensitivity (7). Similar optics with "clean" copper mirrors were installed in the reference beam of the IR-12 double beam spectrophotometer. This maintained optical balance and enabled spectra of films on the sample mirrors to be recorded differentially.

Absorption band intensities in the reflectance spectra were measured in terms of ΔR, the fractional change in reflectivity at a band maximum, *i.e.*, $\Delta R = (R_o - R)/R_o$

* Electrochemical Society Active Member.
[1] Present address: Department of Mineral Engineering, University of British Columbia, Vancouver, British Columbia, Canada.

where R_0 = reflectivity in absence of a film; R = reflectivity at band maximum. ΔR values as low as *ca.* 0.0005 could be measured reproducibly. Film thicknesses were calculated using the formula (8)

$$d_A \simeq \frac{(6.38 \times 10^5 N_1^3)}{\nu K_1} \Delta R$$

(for 73° incidence angle of the parallel component) where N_1 = refractive index of the film material; K_1 = absorption constant of the film = $\alpha\lambda/4\pi$; where α = absorption coefficient in cm^{-1} and λ = wavelength of light in cm; ν = band position in cm^{-1}.

Values of K_1 were determined from reference transmission spectra of analogous compounds. Refractive indices were taken from the literature (9). Both represent approximations of the appropriate K_1 and N_1 values for the thin films on copper. Previous similar studies (10,11) in which film thicknesses were checked interferometrically have indicated that errors in the infrared spectroscopic values should be less than 10%. Spectra of films as thin as one monomolecular layer could be recorded using this technique.

Materials and procedures.—Copper mirrors were prepared by electropolishing plates milled from OFHC copper (99.95% Cu) in a 1:1 mixture of H_3PO_4:H_2O as electrolyte (12,13). The freshly polished plates were washed in distilled water, 10% H_3PO_4, boiling distilled water, and finally methanol to ensure that no phosphate was retained on the mirror surfaces (14, 15). Since these mirrors contacted air they were covered rapidly by Cu_2O films 10-20Å thick (12).

The n-decane was Philips Research grade; p-cymene (p-isopropyl toluene) was Eastman White Label; decalin (decahydronaphthalene) was a mixture of cis and trans forms; and the mineral oil was Squibb-Nujol which was composed of 38.4% naphthenic carbon and 61.6% paraffinic carbon with a molecular weight of *ca.* 450. Three different commercial transformer oils were tested. The aromatic, naphthenic, and paraffinic carbon contents of these three oils were respectively: A, 12.5, 42.7, and 44.8%; B, 15.1, 35.5, and 49.4%; and C, 1.9, 50.8, and 47.3% Transformer oil C was reported to also contain about 0.3% of a phenolic-type oxidation inhibitor.

Oil oxidation tests were conducted with the copper mirrors fully immersed in 100-200 ml of the oil at 90°-100°C contained in a tubular glass flask *ca.* 4.5 cm diameter by 20 cm long. Each flask had a 40 mm viton-A o-ring joint at the top to provide access for the mirrors. A gas bubbler tube extended to the bottom of the flask. When testing volatile hydrocarbons, a water-cooled reflux condenser was fitted to the top closure of each flask.

The copper mirrors were removed periodically from the oil, rinsed in n-pentane, air dried, and their IR reflectance spectra recorded. At the same time the power factor of the oil was measured at 95°C using ASTM procedure D-924. Power factor (P.F.) is related to the resistivity (R) of the oil by the equation P.F. = $1/\sqrt{(2\pi f\ CR)^2 + 1}$ where f = frequency, Hz, and C is capacitance. Hydroperoxide contents were determined by $S_2O_3^=$ titrations (16). Tests were continued for several days until high levels of power factor (*i.e.*, P.F. > 5%) were attained.

Results and Discussion

Oxidation of mineral oil.—Argon, CO_2 and air purging.—Figure 1 shows four reflection spectra taken from a sequence of 13 that were recorded during 1884 hr of oxidation of Nujol oil at 90°C. In this test the oil was purged first with argon gas for 141 hr, second with CO_2 for 890 hr, and third with air for 853 hr. The spectra shown in Fig. 1 were selected to illustrate the dramatic changes that occurred in the composition of the reaction product films on the copper mirrors. These spectra were replotted from spectra recorded on a 0-1.0 absorbance mode so that band intensities can be compared directly. In early stages of film growth,

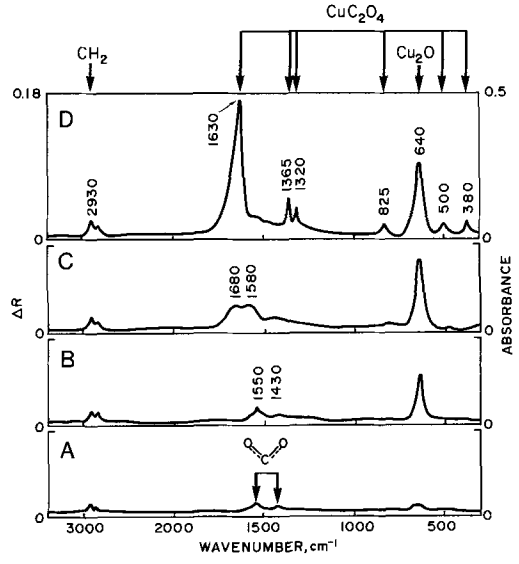

Fig. 1. Reflection spectra from copper exposed to mineral oil at 90°C. A, After 302 hr (141 hr with argon purging +161 hr CO_2); B, 1031 hr (+729 hr CO_2); C, 1225 hr (+194 hr air); D, 1884 hr (+659 hr air).

spectra were also recorded in an expanded per cent transmission mode (up to 25x). This resulted in greater sensitivity to characterize these thin films than is indicated by Fig. 1A, for example. Background reflectance spectra of freshly electropolished copper mirrors were flat and featureless from 4000 to 230 cm^{-1}. Absence of an infrared band characteristic of the air-formed Cu_2O films was due to the fact that spectra were recorded differentially. Nearly identical sets of copper mirrors were present initially in both sample and reference beams. Assignments of the characteristic bands are shown at the top of Fig. 1. These assignments are based on reference to transmission spectra of pure copper compounds (17-20) and on other independent analyses described later.

Figure 2 shows how the intensities (ΔR's) of some of the characteristic IR bands and the power factor of the Nujol changed during the 1884-hr exposure. During the initial 141-hr argon purged exposure, thin films consisting of the equivalent of about one monolayer of a copper carboxylate (R — C  Cu) formed on the Cu (see spectrum A of Fig. 1). During the subsequent 890-hr CO_2-purged exposure, the copper carboxylate films grew to a thickness of ~200Å (Fig. 1B). This was accompanied by growth of relatively thick (~800Å) Cu_2O films on the copper as evidenced by the 640 cm^{-1} Cu_2O band in spectrum B of Fig. 1 (10). One possible

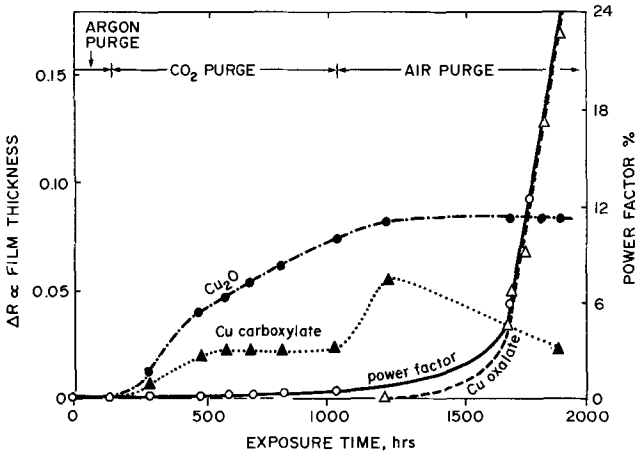

Fig. 2. Change in composition of film on copper and mineral oil power factor with time.

Table I. Copper catalyzed oxidation of oxygen-purged Nujol at 90°C

Oxidation time-hr	Hydroperoxide, m/o	Power factor % at 95°C	Spectra of reaction product films on copper*
0	0.17	0.05	Clean copper†
285	—	0.05	Copper soap (~10Å)
622	0.97	0.05	Copper soap and carboxylic acid‡
832	8.1	0.13	Copper soap and carboxylic acid + CuC_2O_4
1161	16.4	7.75	Mostly CuC_2O_4 (~70Å)

* These films remained on the copper after rinsing in pentane.
† Clean copper ≡ Cu covered only by 10-20Å of air-formed Cu_2O.
‡ Films exhibited: 3400 cm^{-1} O—H; 1710 cm^{-1} acid >C=O; 1440-1390 cm^{-1} C—O or O—H bands.

explanation for the growth of thick Cu_2O films might be the disproportionation of a CO_2 corrosion product such as $Cu(HCO_3)_2$, *i.e.*, $Cu(HCO_3)_2 \rightarrow Cu_2O - Cu + H_2O + 2CO_2$. Copper bicarbonate is formed readily in the presence of small amounts of water and oxygen (22). Neither air nor oxygen purging of the hydrocarbons resulted in formation of such thick Cu_2O films on the copper. The power factor of the Nujol remained low (<0.5%) throughout the initial 1031 hr of exposure.

On changing to an air purge, after 1031-hr exposure, the Cu soap films thickened and a new C=O band appeared at 1680 cm^{-1} (see spectrum C of Fig. 1). After about 700 hr of air purge the power factor increased rapidly. This deterioration was paralled by the formation and rapid growth of copper oxalate (CuC_2O_4) on the copper mirrors (see Fig. 2). At the end of the 1884 hr of exposure, the mirror surface had a varnish-like appearance. The copper oxalate was identified by: (*i*) appearance of new, highly characteristic infrared bands at 1630, 1365, 1320, 825, ~500, 380, and 285 cm^{-1}. These corresponded closely to reference transmission spectra of bulk copper oxalate (18-20); (*ii*) reflection electron diffraction patterns from the copper mirrors; (*iii*) solvation in water ≃ 3 mg/100 cc at 25°C but insolubility in most organic solvents; (*iv*) spot test analyses for oxalate in aqueous extracts of the films. The copper oxalate films were calculated to be about 220Å thick at the end of the 1884-hr exposure (see spectrum D of Fig. 1). Figure 2 indicates that the copper oxalate was the only surface species that was related directly to the autoxidation of the Nujol.

Oxygen purging.—A test similar to that described above but using an oxygen purge produced similar results. When the oil began to oxidize appreciably, as indicated by increased power factor and hydroperoxide contents, copper oxalate again appeared and grew on the copper mirrors. Results are summarized in Table I. One notable difference between these and the above results was that with oxygen purging the Cu_2O films did not thicken appreciably during the 1161 hr of exposure. Figure 2 indicates that in the previous test, most of the Cu_2O film growth occurred during the CO_2 purging period.

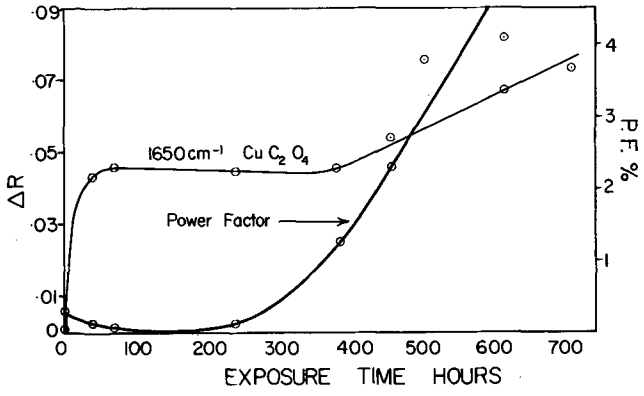

Fig. 3. Effect of adding 0.01 w/o oxalic acid to mineral oil

With oxalic acid addition.—The copper oxalate films described previously were believed derived from an oxalic acid oxidation product in the oil. A test was therefore conducted on Nujol containing 0.01 w/o (weight per cent) of oxalic acid to test the effects of this impurity on both power factor and film composition. Results are shown in Fig. 3. This small addition of oxalic acid increased the 95°C power factor from 0.05 for pure unoxidized Nujol to 0.28. After about 70 hr of oxidation at 90°C using air purging, the power factor had returned to 0.07, which was close to its original value. Part of the oxalic acid impurity had been converted to copper oxalate films approximately 55Å thick on the copper mirrors. These oxalate films did not then grow thicker until the Nujol began to oxidize appreciably after about 300 hr.

The 55Å thick copper oxalate films covering the 108.5 cm^2 area of the copper mirrors accounted for only a fraction of the 0.01 w/o oxalic acid addition. Other reactions involving the reducing property or decomposition of oxalic acid probably also contributed to the consumption of the acid impurity as such during the 70 hr of exposure. The above test did show, however, that both the power factor and film composition were sensitive to the oxalic acid impurity.

Oxidation of n-decane.—The copper catalyzed oxidation of n-decane was studied to compare the behavior of a pure, normal paraffin with the above results on Nujol, a mixture of naphthenic and paraffinic hydrocarbons. In this test, the copper mirrors were exposed to air-saturated n-decane at *ca.* 95°C for a total time of 2516 hr. Reflection spectra were recorded from the copper mirrors at 14 different stages in this exposure. Results of some of these and other analyses are summarized in Table II. Power factors were recorded with the decane at 25°C rather than the standard 95°C to minimize the fire hazard. This made the power factor relatively insensitive to the onset of severe oxidation (21).

Spectra A and B of Fig. 4 illustrate the dramatic changes that occurred in the films on the copper mirrors from 1990 to 2516 hr exposure, respectively. Spec-

Table II. Copper-catalyzed 95°C air oxidation of n-decane

Exposure, hr	Power factor at 25°C	Hydroperoxide,* m/o	GC analysis,† m/o			IR spectra of films on Cu	
			Ketone	Alcohol	Ester	Composition	Thickness, Å
0	0.07	—	—	—	—	Clean Cu	—
194	0.26	—	—	—	—	Cu^{++} soap	10
356	0.3	—	—	—	—	Cu^{++} soap + CuC_2O_4	20
656	0.4	0.53	0.5	0.2	0.1	Mostly CuC_2O_4	32
965	0.4	0.70	—	—	—	Mostly CuC_2O_4	33
1105	0.5	0.84	—	—	—	Mostly CuC_2O_4	33
1487	0.5	1.31	—	—	—	Mostly CuC_2O_4	42
1990	0.5	2.0	—	—	—	Mostly CuC_2O_4	50
2516	~1	1.1	3.2	0.8	1.0	CuC_2O_4 + ester	~500

* By S_2O_3 = titration.
† GC = gas chromatographic.

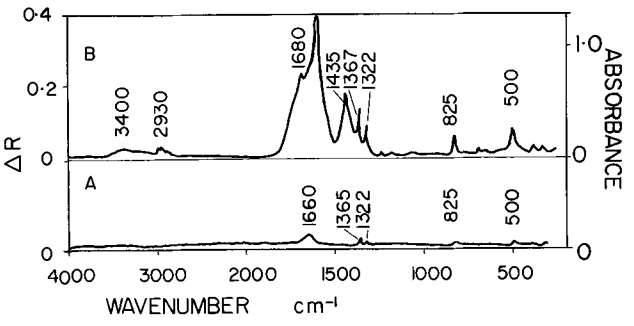

Fig. 4. Reflection spectra from copper exposed to air-saturated n-decane at 95°C for: A, 1990 hr; B, 2516 hr.

tra recorded from ca. 600 to 1990 hr exposure were all similar to spectrum A of Fig. 4. These identified the main constituent of the thin reaction product films as copper oxalate. In spite of this appearance of oxalate, oxidation of the decane appeared to progress slowly up to the last 60-70 hr of this test. While the decane was still clear and colorless at 2450-hr exposure, at the end of 2516 hr it had a blue-green hue and sludge was visible at the bottom of the flask. In addition, the copper oxalate had thickened rapidly to about 500Å during this last exposure period. This result was based on the intensities of the copper oxalate bands at 1650, 1365, 1322, 825, and 500 cm^{-1} in spectrum B of Fig. 4. Although this spectrum identified the majority of the film as copper oxalate, additional bands at 3400, 2960, 2930, 2860, 1680, and 1435 cm^{-1} were attributed to the presence of ketone and ester products as well. Decomposition of hydroperoxide probably provided these products. Table II indicates that the hydroperoxide content of the decane fell appreciably during this last exposure period. Results in Table II and Fig. 4 show that rapid growth in thickness of the copper oxalate film coincide with the onset of rapid or autocatalytic oxidation of the decane.

Oxidation of decalin.—Decalin (decahydronaphthalene) was selected for study to analyze films formed on copper by the oxidation of a naphthenic hydrocarbon. The copper mirrors were exposed for a total of 346 hr to air-saturated decalin at 90°C. Results are summarized in Table III. Reflection spectra from the copper mirrors recorded after A, 20 hr; B, 226 hr; and C, 346 hr are shown in Fig. 5. These spectra illustrate the pronounced changes that occurred in the composition of the reaction product films during this test. Thin films of Cu soap that formed during the first few days of exposure exhibited spectra similar to Fig. 5A. Additional bands that appeared in spectra of the 114 and 226-hr films were assigned tentatively to amide or covalent nitrate complexes (Fig. 5B).

The hydroperoxide content and power factor of the decalin increased slowly and almost linearly for 226 hr of exposure. Both then exhibited a sharp increase in the last 120 hr of exposure and a relatively thick film of copper nitrate appeared on the copper. Bands at 1435, 1335, 1045, and 815 in spectrum C of Fig. 5 were attributed to the copper nitrate (17, 18). Treatment of the filmed mirrors in solvents such as $CHCl_3$ and CH_3CN had no effect on these IR absorption bands

Table III. Copper-catalyzed 90°C air oxidation of decalin

Exposure, hr	Power factor at 95°C	Hydroperoxide, m/o	IR spectra of film: Composition	IR spectra of film: Approximate thickness, Å
0	0.13	—	Clean Cu	0
20	0.14	0.18	Cu^{++} soap	40
42	1.5	0.58	Cu^{++} soap	50
114	3.2	2.9	Cu^{++} soap + amide or nitride	80
226	7.9	7.2	Same	120
346	25+	12.5	Same + $Cu(NO_3)_2$	~300

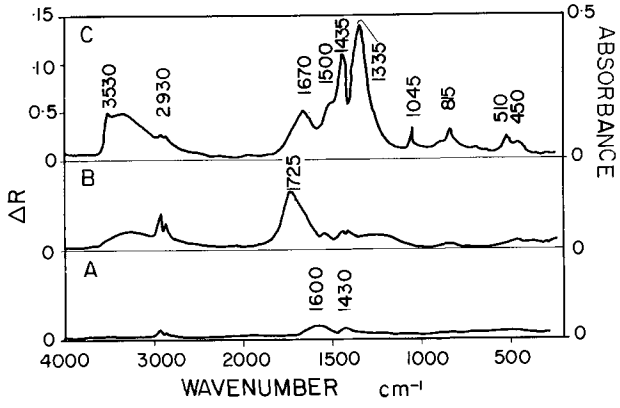

Fig. 5. Reflection spectra from copper exposed to air-saturated decalin at 90°C for: A, 20 hr; B, 226 hr; C, 346 hr.

but water extracted the species responsible for them. Chemical analysis of the aqueous extract confirmed the presence of copper nitrate. No oxalate was detected in these films. This is in contrast to results of the previous tests. The only source for the nitrate found in this test appeared to be fixation of nitrogen from the air purge. Further study is necessary to explain this unexpected result.

Oxidation of p-cymene (p-isopropyl toluene).—Air-saturated p-cymene ($p\text{-}CH_3C_6H_4CH(CH_3)_2$) was oxidized for a total of 334 hr at 90°C. After 330 hr, severe oxidation of the aromatic hydrocarbon began and was accompanied by growth of copper oxalate films (~100Å thick) on the exposed copper mirrors. In addition to copper oxalate, the reaction product films exhibited weak aliphatic C-H bands. No aromatic C-H bands were detected in the films. During this test the hydroperoxide content increased from 0.3 to 2.0 m/o (mole per cent) and the power factor attained a final high value of 8.3%.

Oxidation of commercial insulating oils.—Transformer oils A and B were of similar composition in terms of their aromatic, napthenic, and paraffinic carbon contents. In 90°C, air-saturated oxidation tests of these oils, the initial thin product films formed on the copper-catalyst mirrors consisted primarily of copper carboxylates. After rapid oxidation had occurred, films exhibiting spectra similar to that shown in Fig. 6A had formed on the copper mirrors. This spectrum was recorded after 158-hr exposure of copper mirrors to transformer oil-A. By this time the power factor had risen from an initial value of ca. 0.1% to a high value of ca. 5%. The main bands in spectrum A are believed due to copper bicarbonate present at a film thickness of several hundred angstroms. Although no reference spectrum of copper bicarbonate was found in the literature, the similarity of Fig. 6A to spectra of other bicarbonates gives some credance to this interpretation. This product was insoluble in several organic solvents but dissolved readily in water to leave

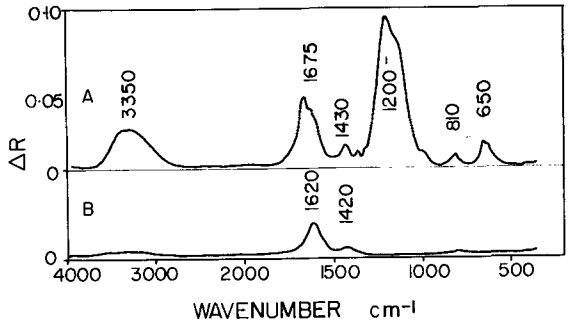

Fig. 6. Reflection spectra from copper exposed to air-saturated transformer oil-A at 90°C for: A, 158 hr; B, after extraction of film in H_2O.

the underlying copper soap films exhibiting spectrum B of Fig. 6. No copper oxalate was detected in these films.

Blending of 0.01 w/o of an effective copper corrosion inhibitor, benzotriazole ($C_6H_5N_3$), into these transformer oils resulted in major improvements in their oxidation stabilities. For example, inhibited transformer oil-A exhibited a power factor of about 1% after 140 hr exposure instead of 5-7% which was typical without this additive. Reflectance spectra from the copper mirrors showed that the benzotriazole had reacted with the copper "catalyst" to form highly protective films of copper benzotriazolate (11). These spectra indicated that the protective films formed quickly. They attained a thickness of *ca.* 90Å after 1-hr and 200Å after *ca.* 140-hr exposure.

Oxidation tests on the low aromatic content transformer oil-C differed significantly. This oil resisted severe oxidation, with air-purging at 95°C, for over 1000 hr. During this period the usual thin films of copper carboxylate were formed on the copper mirrors. After 1200 hr, the oil was oxidized severely and copper oxalate made up a major proportion of the relatively thick films formed on the copper.

Conclusions

Onset of severe air oxidation of several hydrocarbons was accompanied by the formation of highly characteristic reaction product films on the surface of exposed metallic copper catalysts. Infrared multiple reflection spectra provided a sensitive means for analyzing both the composition and thickness of these films.

Paraffinic hydrocarbons generated copper oxalate films on copper when they began to autoxidize appreciably. These copper oxalate films appear to result from reaction of the copper (+ Cu_2O) surfaces with oxalic acid oxidation products generated in the liquid phase. In addition, the power factor of an insulating oil was found to be sensitive to the presence of small amounts of oxalic acid impurity. For example, addition of 0.01 w/o oxalic acid to mineral oil increased its 95°C power factor by approximately 5 times (*i.e.*, from 0.05 to 0.28%). Data in the literature indicated that other expected oxidation products such as monocarboxylic acids exert much smaller effects (21). In addition, the lower the molecular weight of these acids the larger their effect on the power factor. These results suggest that generation of oxalic acid plays an important role in the oxidative deterioration of insulating oils of low aromatic content. This infrared spectroscopic study provides what appears to be the first evidence for the production of such species during such low temperature (< 100°C) oxidations. The concentrating action of scavenging oxalic acid from the liquid phase by the copper mirrors probably contributed significantly to our detection of oxalic acid derivatives.

Evidence on the mechanism of the formation of oxalic acid is still lacking. Reaction of CO_2 gas with an oxidation product like formic acid appears to be ruled out by the observation that oxalate films were formed using pure oxygen purging conditions.

Manuscript submitted Oct. 20, 1969; revised manuscript received *ca.* Nov. 28, 1969.

Any discussion of this paper will appear in a Discussion Section to be published in the December 1970 JOURNAL.

REFERENCES

1. ASTM Test designation D-924.
2. F. Morton and R. T. T. Bell, *J. Inst. Petrol.*, **44**, 268 (1958).
3. C. N. Thompson, *ibid.*, **44**, 295 (1958).
4. J. J. Melchiore and I. W. Mills, *This Journal*, **112**, 390 (1965).
5. M. Krieger, *Proc. 12th Session CIGRE*, Vol. 1, Paris (1948).
6. J. C. Wood Mallock, H. Steiner, and L. G. Wood, *J. Inst. Petrol.*, **44**, 320 (1958).
7. G. W. Poling, *This Journal*, **114**, 1209 (1967).
8. S. A. Francis and A. H. Ellison, *J. Opt. Soc. Amer.*, **49**, 131 (1959).
9. "Handbook of Chemistry and Physics."
10. G. W. Poling, *This Journal*, **116**, 958 (1969).
11. G. W. Poling, To be published in *Corrosion Science*.
12. J. A. Allen, *Trans. Faraday Soc.*, **48**, 273 (1952).
13. W. J. McG. Tegart, "The Electrolytic and Chemical Polishing of Metals," Pergamon Press, Inc., New York (1959).
14. N. H. Simpson and N. Hackerman, *This Journal*, **102**, 660 (1955).
15. F. W. Young, J. V. Cathcart, and A. T. Gwathmey, *Acta. Met.*, **4**, 145 (1956).
16. A. I. Vogel, "A Text-book of Quantitative Inorganic Analysis," Longmans (1961).
17. L. J. Bellamy, "The Infrared Spectra of Complex Molecules," Methuen and Co. Ltd., London (1958).
18. K. Nakamoto, "Infrared Spectra of Inorganic and Coordination Compounds," J. Wiley & Sons, Inc., New York (1962).
19. Sadtler Catalog (Spectra cards) Samuel P. Sadtler and Son Inc., 2100 Arch St., Philadelphia, Pa.
20. Coblentz Society, Standard Spectra Catalog.
21. A. Von Hippel, "Dielectric Materials and Applications," p. 156, John Wiley & Sons, Inc., New York (1954).
22. D. J. G. Ives and A. E. Rawson, *This Journal*, **109**, 447 (1962).

Reactively Sputtered Silicon Oxynitride as a Dielectric Material for Metal-Insulator-Metal Capacitors

R. I. Frank[1] and W. L. Moberg

Sperry Rand Research Center, Sudbury, Massachusetts

ABSTRACT

Silicon oxynitride was formed by rf reactive sputtering of silicon in mixtures of N_2 + N_2O. The dependence of dielectric constant, etch rate, breakdown strength, and IR transmittance on the N_2O concentration in the plasma was determined. Five to ten per cent N_2O gave an average breakdown strength of 1.1 x 10^7 V/cm for metal-insulator-metal capacitors having molybdenum electrodes. The other capacitor parameters were also measured. An explanation of the high breakdown strengths in these capacitors is suggested.

The properties of rf reactively sputtered silicon nitride and silicon oxynitride have been studied as part of a program to investigate new dielectric materials for use in passive components in integrated circuits, particularly for metal-insulator-metal (MIM) capacitors. Silicon nitride was investigated because of its compatibility with integrated circuits and because its higher dielectric constant and higher dielectric strength promised a greater capacitance per unit area than sputtered silicon dioxide (1). Sputtering was used

[1] Raytheon Company, Equipment Division, 528 Boston Post Road, Sudbury, Massachusetts.

because it is a low-temperature process which permits deposition over existing metallization, such as bottom capacitor electrodes and interconnection patterns. The reactive sputtering approach was chosen because of the high-purity silicon source material available and the possibility of varying the composition of the deposited film by controlling the composition of the reactant gas. Finally, rf sputtering was selected because of the superior film properties that had been obtained in comparison with d-c sputtering (2).

Since the low etch rate of pure silicon nitride (3) makes it a difficult material to process in integrated circuit work by direct etching (4), an investigation was undertaken to determine whether the addition of an oxygen-bearing species to the reactant gas would form a silicon oxynitride which would have properties intermediate between those of pure oxide and nitride. This would result in the desired increase in etch rate and in a less desirable, but unavoidable, decrease in dielectric constant compared to pure nitride. It was, in fact, found that the etch rate in 7:1 buffered HF could be increased from 20 Å/min for pure silicon nitride to 200 Å/min with a decrease in dielectric constant of no more than 20%. Thus, a reasonably fast etch rate was achieved, while a substantial advantage in dielectric constant over pure silicon dioxide was still retained. At the same time, a substantial increase over pure silicon nitride in both breakdown strength and yield of capacitors was obtained, greatly increasing the usefulness of this material in integrated circuit applications.

Experimental

Equipment and procedure.—The sputtering system was a CVC AST 100 Plasma Vac Unit with AST 200 rf dielectric sputtering accessory. This system uses an auxiliary filament as a source of electrons to sustain the discharge at low pressures and an external magnet to confine the plasma. A vertical geometry was used for the target and substrate, with the silicon target supported by a rod extending from the rf feedthrough and screwed into an aluminum disk bonded to the back of the silicon. Sputtering of aluminum from this disk was prevented by clamping a silicon backup plate against the rear of the target. This plate had a hollowed-out recess to fit over the aluminum disk, as shown in Fig. 1. The target was a 3-in. diameter by ⅛-in. thick high-purity polycrystalline silicon disk. A 5-in. diameter Pyrex tube enclosed the target and the electron beam traveling upward from the auxiliary filament. It also served to confine the discharge and the deposition of sputtered materials. A rotating substrate holder was placed just outside this tube at a distance of 2½ in. from the target. This holder was a circular plate that held six 1-in. diameter silicon wafers by means of spring-loaded clips. An electrically isolated shield with a hole opposite each wafer was used over the front of the substrate holder to prevent deposition onto adjacent wafers during sputtering. By depositing onto a single wafer and then rotating the next wafer into position, a number of sputtering conditions could be investigated in a single pumpdown.

The substrate plate was electrically isolated and could be biased to a particular voltage during sputtering. It had a heater and thermocouple, with the leads brought out through a slip-ring arrangement. A schematic of the fixturing is shown in Fig. 2, and details of the substrate assembly are shown in Fig. 3 and 4.

The vacuum system had an oil diffusion pump with a liquid nitrogen cold trap. A pressure of 2×10^{-7} Torr was reached before the sputtering gas was admitted. The vacuum-tight gas inlet system was stainless steel and Pyrex. The gas manifold is seen in Fig. 5 along with an over-all view of the vacuum system. For sputtering, nitrous oxide (N_2O) was first admitted and the pressure was set by the ion gauge, since the flow rate was usually too small to register on a flow meter. Ni-

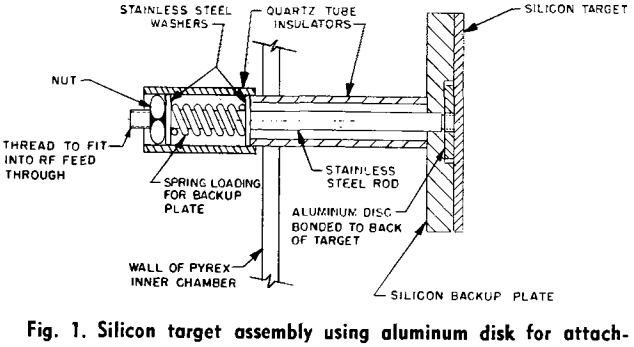

Fig. 1. Silicon target assembly using aluminum disk for attachment.

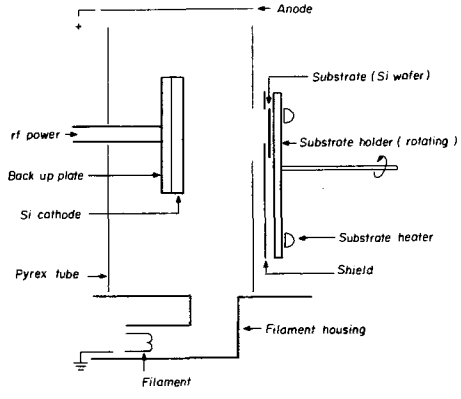

Fig. 2. Schematic of fixturing in sputtering system

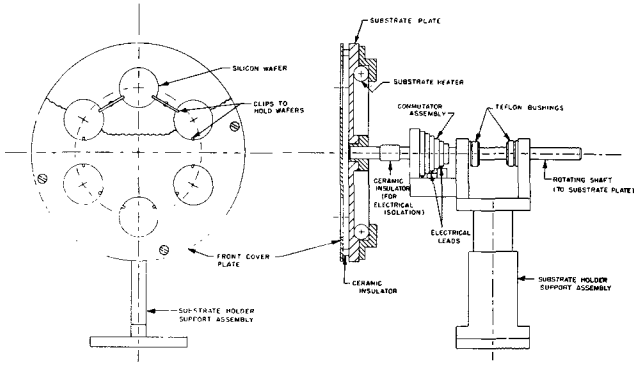

Fig. 3. Rotating substrate holder

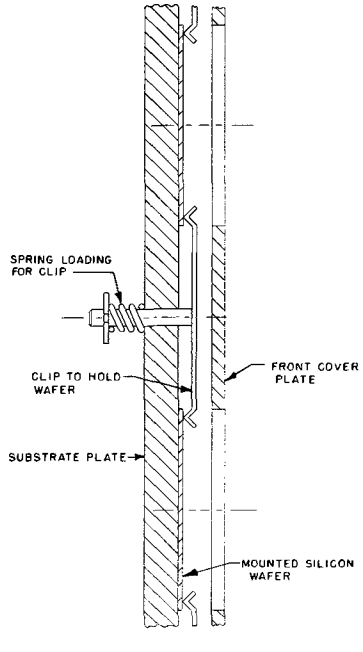

Fig. 4. Detail showing wafer mounted on substrate holder

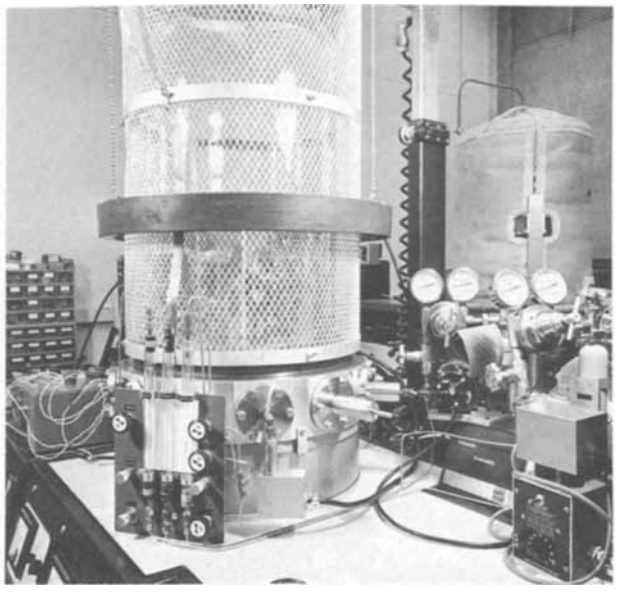

Fig. 5. Over-all view of vacuum system showing gas manifold

trogen was then admitted to give a total pressure of 3μ. Ion gauge readings were checked periodically during a run. The nitrogen was analyzed research-grade gas containing less than 1 ppm of impurities. The oxynitride was formed by the addition of nitrous oxide rather than oxygen to the sputtering gas. This permitted the use of larger quantities of the additive gas, and made the mixing of the reactant gases easier to control. For instance, sputtering in a mixture of 5% oxygen and 95% nitrogen was found to be sufficient to shift the IR absorption maximum of the silicon oxynitride from the 12μ location obtained with 100% N_2, to 9.3μ, which is characteristic of pure SiO_2. Over 20% of N_2O in N_2 was necessary to cause the same IR shift. The N_2O was mass spectrometer analyzed and found to contain 20 ppm argon as the only detectable impurity. The flow rate used was 15 standard cc/min, which was chosen to be as large as possible without causing excessive forepressure, in order to reduce the effect of outgassing from the fixturing and chamber walls during sputtering.

Measurement procedures.—This section describes the measurements made and the methods used for measuring.

Thickness.—Since this is a basic measurement required in the determination of etch rate, dielectric constant, and breakdown strength, its accuracy is of the utmost importance. In order to determine thickness, a portion of a silicon wafer with a sputtered dielectric layer was coated with black wax, and the wafer was immersed in buffered HF until the sputtered deposit was completely removed from the unwaxed portion. The height of the step resulting from this procedure was then equal to the thickness of the sputtered deposit. After removal of the wax and after coating the wafer with silver, the step height was determined by the Tolansky method of multiple beam interferometry, which gives the film thickness to within $\pm$ 50 to 100Å. A typical film thickness was 1500Å.

Etch rate.—The etch rate of the dielectric film is perhaps the most sensitive method of detecting slight changes in film structure or composition. Etch rate was determined by measuring the time required to etch completely through the dielectric layer to the bare silicon underneath, as detected by the sudden change in wettability which occurs when the bare silicon surface is exposed. An etchant of 7:1 buffered HF was used for all measurements. This etchant was prepared by dissolving 1 lb of NH_4F in 680 cc of water, and then adding 100 cc of this solution to 15 cc of water.

Infrared transmission spectrum.—IR transmission measurements give an absorption spectrum associated with film composition and structure. In the case of silicon nitride a single broad band is obtained at $\approx$ 12.0μ, while for SiO_2 a sharp band at 9.3μ is obtained. Intermediate compositions give bands between these two values. IR measurements were done routinely on all samples using a Perkin-Elmer dual-beam IR spectrophotometer. Bare silicon was used in the reference beam, and nitride coated silicon was used for the sample.

Dielectric constant—This quantity is determined from the capacitance, electrode area, and nitride thickness using the usual formula (5) $K = TC/\epsilon_0 A$, where K = delectric constant, T = thickness, C = capacitance, A = electrode area, and $\epsilon_0 = 8.85 \times 10^{-12}$ F/m. The capacitance was determined on a Wayne-Kerr or Boonton bridge, which together covered the frequency range from 100 Hz to 1 MHz. The electrode area was measured by photographing the electrode with a calibrated scale, and the thickness was determined as described above.

Breakdown strength.—This measurement was made with the wafer on a movable stage which allowed a set of probes to be brought into contact with each capacitor in succession. To determine breakdown, the I-V trace on a Tektronix 575 curve tracer was observed. The voltage was gradually increased from zero until either the current trace went suddenly off scale, indicating the device had broken down, or until the current through the capacitor (typical area 175 square mils) reached 0.05 mA. At this current level, the I-V trace was so steep that the voltage remained nearly constant to complete breakdown. A typical I-V trace from this measurement is shown in Fig. 6.

I-V measurements.—I-V measurements were made using a Cary vibrating reed electrometer for currents between 10^{-14} and 10^{-9}A and a Hewlett-Packard 425 A microvoltammeter for currents between 10^{-9} and 10^{-4} A.

Types of structures used for dielectric measurements.—Bare 1 ohm-cm n-type silicon wafers were used as substrates for determining physical properties such as etch rate, thickness, and infrared absorption spectra of the oxynitride films. For electrical measurements and capacitor studies the substrates were first coated with a sputtered or pyrolytic oxynitride layer, and were then metallized in a vacuum system. For general electrical measurements, the oxynitride was deposited over this continuous metal film, which served as a common bottom electrode. The top electrodes were 15 mil diameter metal dots formed by etching a second evaporated layer. A schematic of this structure is shown in Fig. 7. In addition, capacitors suitable for mounting on headers were made by etching individual electrodes in the bottom metal layer, followed by oxynitride deposition and top electrode deposition. It was then necessary to etch windows through the dielectric in order to make contact to the bottom electrodes. The capacitors mounted on headers could be used for high frequency measurements and the determination of the temperature coefficient of

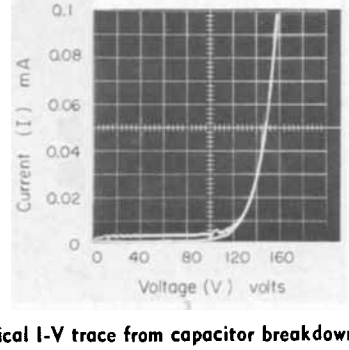

Fig. 6. Typical I-V trace from capacitor breakdown measurement

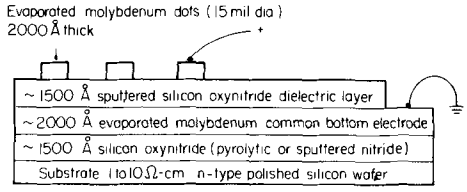

Fig. 7. Schematic of MIM structure with a common bottom electrode.

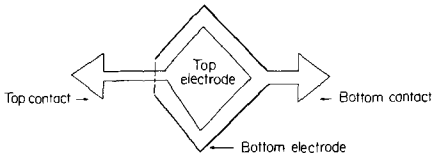

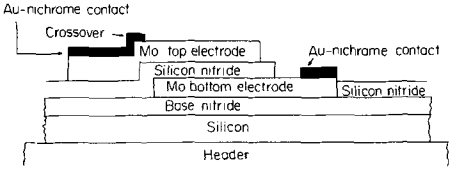

Fig. 8. MIM capacitor structure used for devices to be mounted on headers.

capacitance. A schematic of this structure is shown in Fig. 8.

Results and Discussion

Electrode materials.—The properties of Al, Mo, Ni, Cr, Au, and Pt were investigated for use as both top and bottom electrode materials. The best results were obtained with Mo, with Al and Cr second best. In addition, silicon was tested as a bottom electrode material by depositing the oxynitride directly onto bare silicon substrates. Poor adherence of metal to dielectric and low breakdown strength were encountered with Au, Pt, and Ni. Molybdenum for both top and bottom electrodes gave breakdown strengths higher by about a factor of 1.5 over Al-Al or Mo-Al structures. The breakdown strength of Mo-Si MIS capacitors biased so that the voltage drop across the dielectric was the same as that of Mo-Mo structures. Molybdenum as a top electrode gave about 10% greater capacitance, and hence a higher effective dielectric constant than other materials used as top electrodes. This was found to be independent of the bottom electrode material. In addition, Mo is hard, durable, and highly adherent to silicon oxynitride, and its bulk resistivity is only twice that of Al. The Mo was deposited by electron beam evaporation.

Contacts.—A contact material was necessary in capacitors that were to be mounted on headers, since gold wires could not be attached directly to Mo. In addition, the Mo was not electrically continuous at the point where the top electrode crossed over the bottom electrode, so that the contact material had to be extended onto this crossover as shown in Fig. 8. Gold was used for the contact material, but, since it did not adhere well to Mo during processing, a nichrome interlayer was used to provide adherence. This gold-nichrome layer was adherent and provided electrical continuity at the crossover.

Effect of substrate preparation.—The effect of substrate preparation on breakdown strength was very pronounced. This seemed to be a joint effect of both smoothness and cleanliness. In the case of MIM capacitors with Mo bottom electrodes, a much higher breakdown strength was obtained with the common bottom electrode structure than with the structure having individual bottom electrodes. Since the only difference in the fabrication method between the two structures was in the photoresist work done to form the individual bottom electrodes, contamination from this step must have been responsible for the difference in breakdown strength. It was found that the breakdown strength of the individual electrode structure could be increased by either reverse sputtering of the bottom electrodes after photoresist processing or by the deposition of the bottom electrodes through a metal mask, thus avoiding all photoresist work on the bottom electrodes.

Substrate smoothness as defined by the absence of any points of light in dark field illumination also had a strong effect on breakdown. Even devices with a common bottom electrode would show a poorer yield when prepared on poor substrate material. Best results were obtained on substrates which had been etched in HCl gas at 1200°C. These substrates had the best appearance under dark field illumination, considerably better than those cleaned by even the most elaborate wet chemical procedures.

Dielectric properties as a function of N_2O concentration in the sputtering gas.—Measurements of the electrical and physical properties of the sputtered silicon oxynitride films were carried out as described before over a range of N_2O concentrations in nitrogen varying from 0 to 20%. In addition, silicon dioxide was sputtered in a plasma consisting of 50% O_2 in argon in order to obtain a comparison with the N_2O data. Each type of measurement was carried out on 5-10 wafers sputtered under the same conditions, and the results were then averaged. Electrical measurements were made on 50-100 capacitors randomly distributed over each wafer.

The results of these measurements are shown in Table I. The first column, for etch rate, shows a value of 20 Å/min for "pure" silicon nitride, which is in general agreement with that obtained by other workers (6). This value is not as low as the value of 10 Å/min obtained in this laboratory for pyrolytically grown silicon nitride, indicating that the sputtered nitride has a "looser" structure than the pyrolytic nitride. The etch rate values increase monotonically with increasing per cent of N_2O until a value of 1300 Å/min is reached for the 50% O_2 addition, which is somewhat higher than that obtained for thermally grown silicon dioxide.

The second column shows that the IR absorption maximum also changes monotonically from the value for pure silicon nitride to the value for pure silicon dioxide. The location of the IR absorption maximum for sputtered silicon nitride agrees with that for pyrolytic nitride, which indicates the greater sensitivity of etch rate in comparison with IR measurements for detecting slight changes in film structure. Figure 9 shows a series of IR absorption curves for various N_2O concentrations. The next column, for breakdown field, will be discussed separately and in more detail in the following sections.

Measurements for dielectric constant are shown in column four and in Fig. 10. These measurements were

Table I. Effect of N_2O additions on the dielectric properties of silicon oxynitride films

% N_2O	Etch rate, Å/min	IR absorption, maximum (μ)	Breakdown field,* V/cm × 10^6	Dielectric constant, at 1 kHz	Figure of merit
0	20	12.1	6.0	9.1	5.4
1	42	12.0	6.9	8.7	6.0
3	143	11.8	9.3	8.3	7.7
4	167	11.2	10.1	7.2	7.3
5	225	11.0	10.1	6.8	6.9
7	305	10.7	10.1	6.1	6.2
10	587	10.1	10.9	5.3	5.8
20	1180	9.6	8.3	4.0	3.3
(50% O_2, 50% Ar)	1300	9.3	8.0	3.9	3.1

* At the center of higher peak on breakdown distribution curve for MIM capacitor (see Fig. 11).

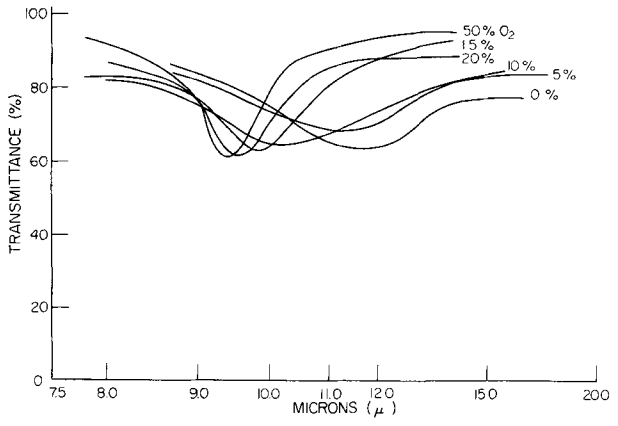

Fig. 9. Infrared transmission spectrum of sputtered silicon oxynitride as a function of N_2O% in the sputtering gas.

made with molybdenum for both top and bottom electrodes. As mentioned above, the use of molybdenum as a top electrode material gives a higher capacitance and therefore a higher effective dielectric constant than other materials, which accounts for the rather high dielectric constant of 9.1 for pure silicon nitride. The last value in the column, 3.9, agrees closely with that for thermally grown silicon dioxide.

The last column gives the usual figure of merit for capacitors, which is based on the product of dielectric constant and dielectric strength. It is proportional to the maximum capacitance per unit area obtainable with a given dielectric material. The maximum in the figure of merit which occurs for 3% N_2O addition is due to the high dielectric strength at this point. Normally the dielectric having the largest figure of merit would be the most desirable choice for thin film capacitors. However, the effect of capacitor yield is not fully taken into account in the figure of merit, and since yield is of the utmost importance in integrated circuit applications, the better choice is actually the oxynitride made with 5% N_2O addition, as discussed below.

Breakdown strength and yield of capacitors.—While most properties change monotonically with increasing N_2O concentration, the dielectric strength and breakdown strength distribution or capacitor yield, are exceptions and have a maximum in the range of 5-10% N_2O. Here yield is defined as the percentage of dots breaking down within a given range of the most probable breakdown, as determined from a breakdown distribution plot. Figure 11 shows a set of such plots for N_2O concentrations of between 0 and 20% of the reactant gas. The data were obtained from devices having a Mo common bottom electrode and 15 mil diameter Mo dots for top electrodes. To construct these curves the

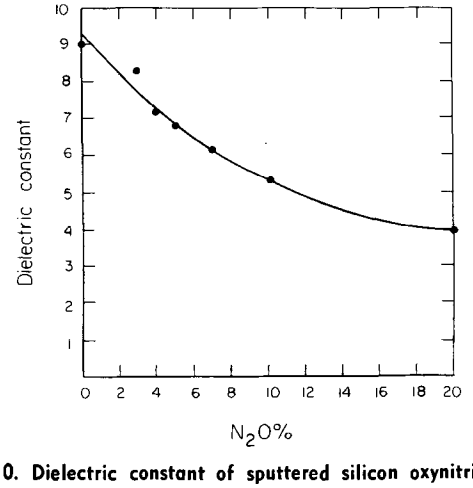

Fig. 10. Dielectric constant of sputtered silicon oxynitride as a function of per cent of N_2O in the sputtering gas.

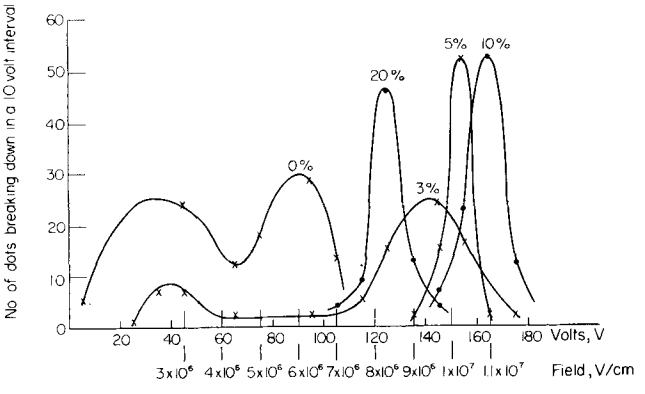

Fig. 11. Effect of N_2O additions on the breakdown voltage distribution curves for MIM capacitors. (Dielectric thickness 1500Å, Mo top and bottom electrodes.)

number of dots breaking down in a particular 10V range is plotted *vs.* the midpoint of that range, and a smooth curve is then drawn through these points. Each curve is based on a sample of 50-100 dots taken at random over the wafer. The curves show the striking effect of the different N_2O additions. The curves for the 0% N_2O addition show a characteristic double-peak structure, which probably indicates the presence of two distinct breakdown mechanisms. The lower peak occurs at a field of $\approx 3 \times 10^6$ V/cm, and the upper peak at $\approx 6 \times 10^6$ V/cm. At 3% N_2O addition the lower peak has decreased substantially in height, while the upper peak has shifted to much higher fields of $\approx 9 \times 10^6$ V/cm. For 5 and 10% N_2O additions, the lower peak has vanished[2] and the upper peak is narrow and is shifted to still higher fields. For N_2O additions in excess of 15% the single-peaked distribution curves remain, but become somewhat broader, and the breakdown field at the peak decreases to about 9×10^6 V/cm. The curve for 20% N_2O illustrates this behavior. A sharply peaked distribution curve means a high capacitor yield will be obtained. For use as capacitors in integrated circuits, the lowest N_2O percentage giving both a high yield and dielectric constant, *i.e.* N_2O additions of 4-5%, are most desirable.

Other dielectric measurements.—High-frequency measurements of capacitance and loss tangent were made on devices with individual molybdenum top and bottom electrodes, which had a dielectric sputtered in the presence of 5% N_2O added to the nitrogen. These capacitors were mounted on TO-5 headers. The loss tangent of these devices was 0.003 at 1 kHz, 0.0015 at 10 kHz, and 0.01 at 1 MHz. These low frequency losses are quite small compared to other thin film capacitors, and the increase at 1 MHz was due to losses in the electrodes (7). The dielectric constant changed by only 3% in going from 100 Hz to 1 MHz. The temperature coefficient of capacitance is + 150 ppm/°C between 25° and 125°C at 1 and 10 kHz. Thus, the measurements show these devices to have highly desirable properties as thin film capacitors.

I-V measurements on MIS samples with 5% N_2O addition showed ohmic conduction to fields of $\approx 1 \times 10^6$ V/cm, followed by a relationship of the form $I \propto \exp(\text{const } V^{1/2})$ all the way to breakdown. Typical currents through a 15 mil diameter dot were 10^{-12} A at a field of 1×10^6 V/cm and 200 μA at 1.2×10^7 V/cm. There was only a slight polarity dependence, which with the observed I-V relationship probably indicates a bulk limited Poole-Frenkel conduction mechanism (8).

Observations on breakdown processes in silicon oxynitride.—Molybdenum top electrodes of devices with high breakdown voltage were observed through a microscope. As the applied field was gradually increased to about 5×10^6 V/cm, tiny sparks appeared at

[2] Sometimes a few capacitors break down at low voltages, but they are a very small fraction of those which have higher voltage breakdowns.

random across the surface. During this time, momentary current spikes were superimposed on the I-V trace of the device. If the voltage remained at this value, the sparking gradually decreased and stopped. When the sparking ceased, so did the current spikes. At this point, the initially smooth electrode surface exhibited tiny pits. The observed sparking therefore represented localized breakdown which burned away the molybdenum at faults in the dielectric. The striking result, however, was the fact that after the sparks had disappeared, the field could be increased typically to a value of 10^7 V/cm until the whole molybdenum electrode disintegrated at once. In contrast, other electrodes, such as gold and platinum, exhibited a general breakdown at the lower fields that resulted only in the onset of sparking with molybdenum electrodes.

As Table I indicates, the high ultimate breakdown voltage was observed only with molybdenum, and then only with silicon nitride containing a particular range of N_2O concentrations. This suggests that there exists a fortunate combination of molybdenum and silicon oxynitride that results in the rapid consumption of molybdenum when heated. This reaction of the molybdenum is so rapid that the localized electrical breakdown process is terminated before it can affect the surrounding dielectric. This termination must be due to removal of the field over the dielectric at the localized regions where the molybdenum electrode is burned away. The high breakdown strength of Mo-silicon oxynitride capacitors thus results from the self-healing action of this particular electrode-dielectric combination. For other electrode material-silicon oxynitride combinations, the electrode is apparently not consumed rapidly enough to prevent lateral (probably thermal) propagation of the breakdown process leading to premature distruction of the capacitor.

Summary

The rf reactive sputtering of Si in 5% N_2O + 95% N_2 mixtures yields a silicon oxynitride with many desirable properties for use in integrated circuit applications. Principally, these are high breakdown strength, high yield, a dielectric constant of 6.8, and an etch rate of $\approx$ 200 Å/min. Due to the increased breakdown and dielectric constant, the maximum capacitance per unit area is about 2.5 times that of sputtered silicon dioxide. In relation to pure silicon nitride (0% N_2O) the most striking features are the increased etch rate, increased breakdown strength, and high yield as shown by the sharply peaked breakdown distribution curve.

Acknowledgment

The authors wish to thank Drs. Frank A. Sewell, Jr., and H. A. R. Wegener for helpful discussions and suggestions. This work was supported in part under Rome Air Development Center Contract No. F30602-67-C-0223.

Manuscript received Nov. 21, 1968; delay in publication was incurred by clearance delay. This was Paper 484 presented at the Montreal Meeting, Oct. 6-11, 1968.

Any discussion of this paper will appear in a Discussion Section to be published in the December 1970 JOURNAL.

REFERENCES

1. A. R. Janus and G. A. Shirn, Symposium on the Deposition of Thin Films by Sputtering, co-sponsored by University of Rochester and CVC, June 9, 1966.
2. A. R. Janus and G. A. Shirn, *This Journal*, **113**, 212C (1966).
3. S. M. Hu and L. V. Gregor, *ibid.*, **114**, 828 (1967).
4. G. H. Scheer, W. Van Gelder, V. E. Hauser, and P. F. Schmidt, 1966 IEEE International Electron Devices Meeting, Washington, D. C.
5. N. H. Frank, "Introduction to Electricity and Optics," 2nd Ed., p. 240, McGraw-Hill Book Co., New York (1950).
6. L. V. Gregor, Study of Silicon Nitride as a Dielectric Material for Microelectronic Applications, Interim Report No. 1, Contract No. AF 33(615)-5326, Air Force Avionics Laboratory, November 1966.
7. F. S. Maddocks and R. E. Thun, *This Journal*, **109**, 101 (1962).
8. D. A. Vermilyea, *Acta Met.*, **2**, 347 (1954).

Mechanism of Heterogeneous Deposition of Thin Film Rutile

R. N. Ghoshtagore

Westinghouse Research Laboratories, Pittsburgh, Pennsylvania

ABSTRACT

The kinetics of rutile (TiO_2) thin film deposition on silicon from the reaction $TiCl_4 + O_2 \rightarrow TiO_2 + Cl_2$ has been studied over a range of temperature (673°-1320°K), titanium tetrachloride partial pressure (2.9×10^{-2} to 9.28×10^{-1} Torr), and oxygen partial presure (2.5×10^{-1} to 760 Torr) in a horizontal flow system with a rf-heated susceptor. Between 673° and 1120°K the reaction has been found to proceed by a Rideal-Eley mechanism with the surface reaction rate constant (k_s) following the relationship $k_s = 4.9 \times 10^3 \exp(-0.775 \pm 0.044\ eV/kT)$, over a range of partial pressures and flow rates. Homogeneous reaction becomes appreciable above 1120°K.

The vast influence of solid surfaces on reaction kinetics has been the subject of catalysis for more than a century. But a detailed understanding of the molecular mechanism of such interactions requires a knowledge of chemical reaction equilibria and kinetics, vapor pressures of all the participating species, fluid dynamics of the system, and the adsorption and desorption characteristics (including surface diffusion) of all the chemical entities. So few of these quantities are known for most systems that a complete theoretical and/or experimental analysis of most chemical vapor deposition reactions becomes almost impossible. However, several guidelines are available in this direction.

Chemical vapor deposition under large supersaturations or chemical driving force, is controlled by growth, producing a fine-grained, roughly random deposit (1), with growth rates tending to approach a maximum as fixed by the slowest (rate determining) process. Under low supersaturations (fixed by vapor-

phase mass transport) nucleation can become rate-controlling, preferred-orientation deposits can form (epitaxy or oriented growth), and growth rates can be less than the maximum.

Titanium dioxide thin films are currently the subject of many investigations (2-5) since their potentially high dielectric constants would be of value in numerous applications. Since very little is known about the kinetics and mechanism of chemical vapor deposition of TiO_2 film (6, 7) from the system $TiCl_4 + O_2 \rightarrow TiO_2 + Cl_2$, this paper reports some measurements designed to elucidate such information. The polycrystalline films prepared have the rutile structure (8). Detailed examination of the structural and electrical properties of these films has been made, and the results will be communicated in future publications.

Experimental Technique

The experiments utilize the chemical reaction between titanium tetrachloride and oxygen on a heated substrate in a conventional horizontal quartz tube "silicon epitaxial" reactor at atmospheric pressure (9). Purified titanium tetrachloride (prepared by multiple distillation of 99.995% pure material) in thermostat-held quartz bottles is used as a titanium source bubbler through which a carrier gas of ultrapure argon or ultrapure oxygen (Matheson) is passed at a controlled rate. This gas (saturated with $TiCl_4$ vapor) is then mixed with additional ultrapure oxygen and/or argon through a set of calibrated flowmeters, liquid traps, and filters and the mixture reacted on a quartz encapsulated high purity graphite susceptor heated by rf induction. The over-all reaction can be described by

$$TiCl_4(g) + O_2(g) \rightleftharpoons TiO_2(\text{rutile})(s) + 2Cl_2(g) \quad [1]$$

Free energy changes (ΔF) for this reaction, calculated from known thermochemical data (10), are −33.0, −30.3, −27.7, and −25.2 kcal/mole at 700°, 900°, 1100°, and 1300°K, respectively.

Single crystal silicon wafers (15-20 mils thick) of (111), (100), and (110) orientations, obtained from Texas Instruments, were lapped, polished in Linde B, and then chemically etched in 15:5:3 HNO_3:HAc:HF to a mirror finish by the supplier. Substrates for TiO_2 deposition were prepared by scribing 5 mm squares out of these wafers. The substrates were then degreased by boiling in trichloroethylene and acetone and chemically polished in 15:5:3 HNO_3:HAc:HF to remove about 5-10μ of surface layer. The substrates were then blown dry in dry nitrogen, mounted on the susceptor, and baked for 20-30 min in ultrapure hydrogen at 900°-1000°C to remove any residual oxide film (11).

The reactor atmosphere is then flushed with ultrapure argon and the substrate temperature is adjusted, the temperature being monitored with an optical pyrometer [corrected for absorption by the quartz tube wall, reactor atmosphere, and substrate emissivity (12)] and/or an infrared radiation pyrometer. Titanium tetrachloride vapor in the carrier gas is then passed into the reactor (after prolonged purging to vent), argon flow is discontinued and mainline ultrapure oxygen is introduced at a predetermined flow rate. The deposits and substrates are then pushed off the susceptor at regular time intervals with a quartz push rod and the deposition rate is determined from an average of 16-18 samples run for 8-9 different time periods. Film thicknesses were determined by reference to an ellipsometrically calibrated color chart. The temperature of titanium tetrachloride was maintained at 25° ± 0.5°C and that of the substrates to ±5°C.

Results

The kinetics of the polycrystalline rutile film growth reported in this section was independent of substrate orientation [(100), (110), or (111)], resistivity level (0.01-30 ohm cm), and resistivity type (8) (arsenic and phosphorus-doped n-type or boron-doped p-type). So, no mention of these factors will be necessary in the following.

Flow rate relationships.—Dependence of rutile thin film growth rates on the total gas flow rate is shown in Fig. 1(a) and 1(b). The slope of the mass transfer controlled region (where the growth rate is a function of the flow rate) approximates the theoretical value (13) of 1/2 at all p_{TiCl_4} and at temperatures at or below 1100°K. Deposition rates could not be determined at very low flow rates because of nonuniformity of deposition (apparently controlled by nucleation). Apparent slope of > 1/2 at 1205° and 1320°K will be discussed in a later section. At all temperatures and p_{TiCl_4} (p_{O_2} = 1 atm) the surface reaction rate (as measured from the growth rate) attain a constant value at high flow rates. Boundary layer theory predicts that under such circumstances the gas-phase mass-transfer coefficient is much higher than the surface-reaction rate constant and the reaction kinetics is controlled by an activated process (adsorption, desorption, or surface reaction). Figure 2 shows a plot of the maximum p_{TiCl_4} that can be used to attain an activated process control of the heterogeneous reaction as a function of total flow rate at constant p_{O_2} of 1 atm. At any temperature under 1100°K they can be described by the relationship

$$V = C/p_{TiCl_4} \quad [2]$$

where V is the minimum flow rate and C is a tempera-

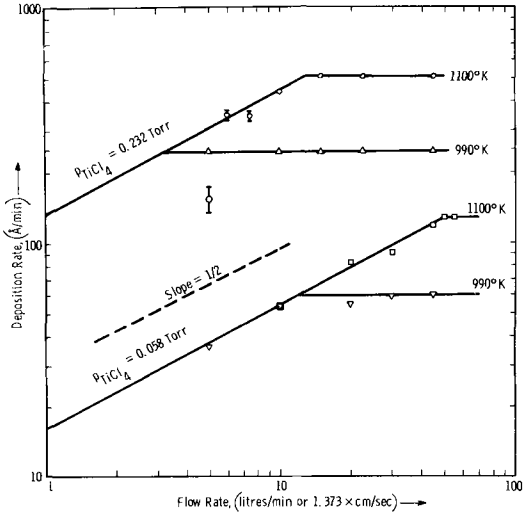

Fig. 1a

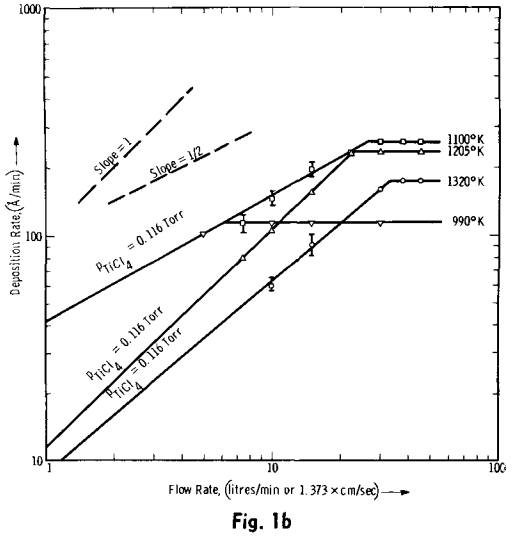

Fig. 1b

Fig. 1. Flow rate dependence of rutile deposition rate on silicon in 54 mm ID horizontal quartz tube epitaxial reactor at different substrate temperatures and titanium tetrachloride partial pressures, and a fixed oxygen partial pressure of 1 atm (susceptor dimensions: 43 x 13 x 150 mm).

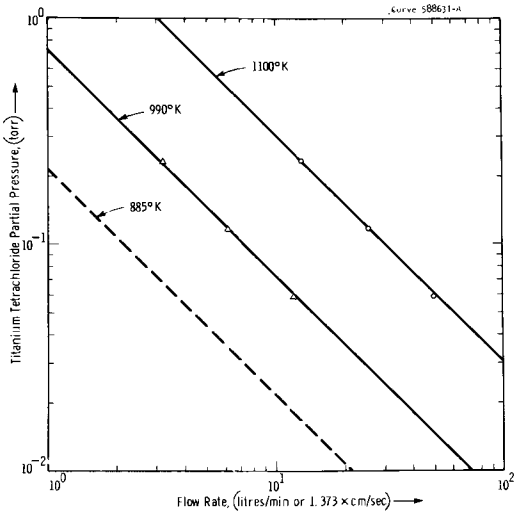

Fig. 2. Maximum titanium tetrachloride partial pressure for activated rutile deposition on silicon as a function of average gas flow rate at different temperatures (oxygen partial pressure ≅ 1 atm).

ture-dependent constant. No attempt was made to obtain such a relationship at higher temperatures because as can be seen from Fig. 1(b) they do not follow such a simple model.

Reactant partial pressure relationships.—Deposition rates of the rutile thin film as a function of p_{TiCl_4} is shown in Fig. 3 at different substrate temperatures and at a fixed p_{O_2} of 1 atm. At each of these temperatures the total flow rate was maintained such that the deposition rate was independent of the flow rate (*cf.* Fig. 1 and 2) at each p_{TiCl_4} used. As is evident from Fig. 3 the surface reaction is of first order with respect to titanium tetrachloride at or under 1100°K. But at 1205° and 1320°K the apparent reaction order is more than one and is a function of temperature.

The surface reaction rates (as measured from deposition rates) as a function of p_{O_2} at different but constant p_{TiCl_4} is shown in Fig. 4 at two temperatures where the reaction is of first order with respect to titanium tetrachloride. The reaction is of one-half order at low oxygen partial pressures, but becomes zero order above a minimum p_{O_2} whose value increases with increasing p_{TiCl_4} as shown in Fig. 5. All these data were obtained at or above a total flow rate extrapolated from Fig. 2 using ultrapure argon as diluent. Since the data of Fig. 1 were obtained for p_{O_2} = 1 atm, their validity at low p_{O_2} was verified and found to hold. As can be seen from Fig. 5, within the

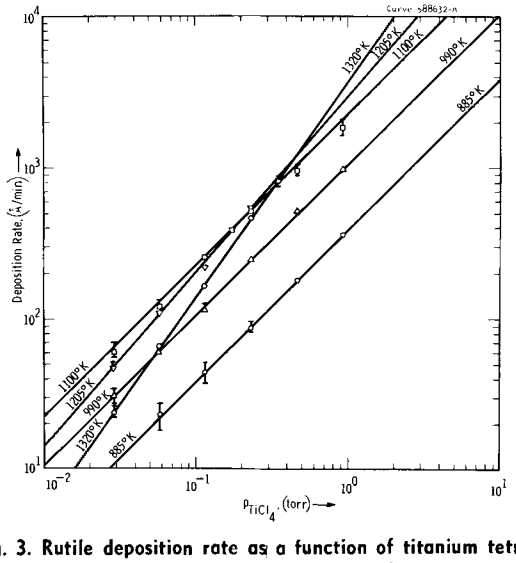

Fig. 3. Rutile deposition rate as a function of titanium tetrachloride partial pressure at different temperatures (oxygen partial pressure ≅ 1 atm).

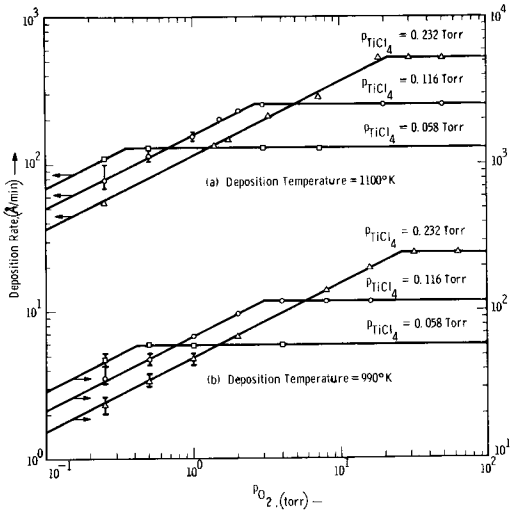

Fig. 4. Oxygen partial pressure dependence of rutile deposition rate at different titanium tetrachloride partial pressures.

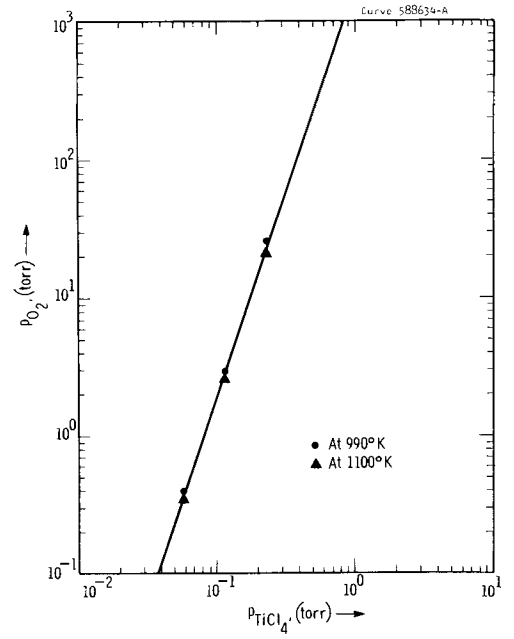

Fig. 5. Minimum oxygen partial pressure required for zero order (with respect to oxygen) activated rutile deposition at different titanium tetrachloride partial pressures.

range of experimental accuracy, the minimum p_{O_2} required for oxygen pressure independent deposition rate at any p_{TiCl_4} is independent of temperature (below 1100°K). This can be described by the equation

$$p_{O_2} = 1.8 \times 10^3 \, (p_{TiCl_4})^3 \qquad [3]$$

where the partial pressures are expressed in millimeter Hg. It can be noted from Fig. 5 that the maximum p_{TiCl_4} for 1 atm of total pressure is of the order of 7.6×10^{-1} Torr. This explains why the data of Fig. 3 could not be determined at higher p_{TiCl_4}.

Temperature coefficient of the heterogeneous reaction.—Deposition rates are plotted as a function of inverse absolute substrate temperature in Fig. 6. These data represent the rates of the rate-determining activated process because the volume flow was maintained at or above the value where the growth rate is independent of flow rate. At 850° ± 5°C the film growth rate attained a maximum at each of the p_{TiCl_4} values used. Surface deposition rates in units of molecules $TiO_2/cm^2/sec$ shown in the left ordinate of Fig. 6 was calculated from the determined deposition rate and theoretical density of 4.26 for rutile. The surface reac-

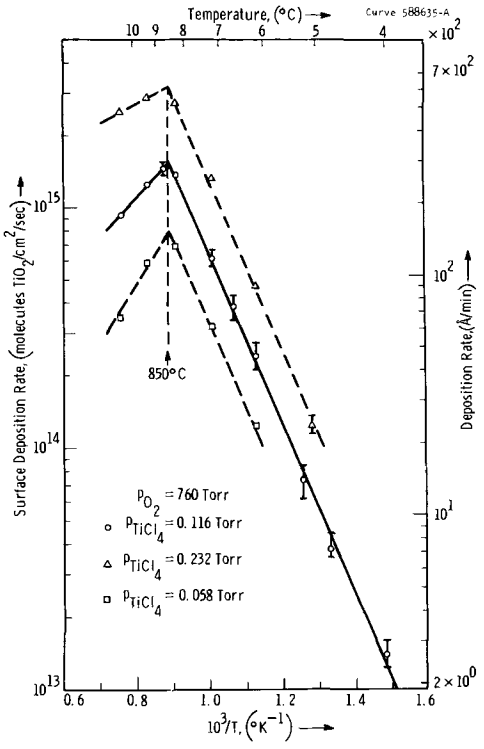

Fig. 6. Temperature dependence of rutile deposition rate at 1 atm of oxygen partial pressure and different titanium tetrachloride partial pressures.

tion rate constants were calculated from the data of Fig. 6 using the relationship

$$G = \frac{C_G}{N} k_s \qquad [4]$$

where G is the growth rate in cm/sec, C_G is the titanium tetrachloride gas phase concentration in molecules/cm³, N is the number of TiO_2 molecules per unit volume of the film, and k_s is the surface reaction rate constant (cm/sec). These data for k_s are shown in Fig. 7 as a function of absolute substrate temperature and below 850° ± 5°C can be represented by the equation

$$k_s = 4.9 \times 10^3 \exp(-0.775 \pm 0.044\ \text{eV}/kT)\ \text{cm/sec} \qquad [5]$$

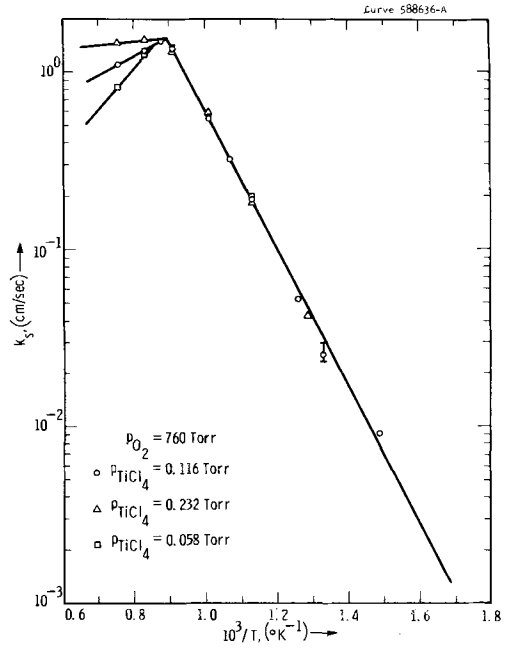

Fig. 7. Arrhenius plot of the surface reaction rate constant

This activation energy of 0.775 ± 0.044 eV/molecule agrees with that for the velocity of reaction (0.796 eV) determined by Antipov *et al.* (6). The reasons for the invalidity of Eq. [5] above 850°C will be discussed later.

Reaction efficiency.—Fractional efficiency (E) of this heterogeneous reaction at any temperature and p_{TiCl_4} (p_{O_2} = 1 atm) can be calculated from the equation

$$E = \frac{G}{C_G V} \qquad [6]$$

where G is the film deposition rate in moles TiO_2/cm²/sec, C_G is the gas phase $TiCl_4$ concentration in moles/cm³, and V is the average calculated (from reactor cross-section) gas velocity in cm/sec. These data are shown in Fig. 8. Below 850°C all these lines (at different p_{TiCl_4}) have a slope of 0.65 eV. At any temperature below 850°C the efficiency increases proportionally with p_{TiCl_4} at fixed p_{O_2} of 1 atm. This explains why these data are not comparable with those of Antipov *et al.* (6) and Shchegrov (7), neither of whom published p_{TiCl_4} data of their experiments. The fact that the efficiency of the heterogeneous reaction decreases with increasing temperature at any p_{TiCl_4} is consistent with the fact that the equilibrium constant of the reaction represented by Eq. [1] [calculated from the available thermochemical data (10)] also decreases with increasing temperature.

Discussion

Reaction behavior below 850°C.—It is generally accepted that a gaseous reaction involving two species on a solid surface involves the following steps: (*i*) diffusion of reactants to the surface, (*ii*) adsorption of one or both of the reactants on the surface, (*iii*) surface reaction preceded by surface diffusion and formation of activated complex, (*iv*) desorption of gaseous products with or without some surface migration, and (*v*) diffusion of products away from the surface. The following reasons will let one exclude steps (*i*) and (*v*) as the rate-controlling mechanism in this system:

(*1*) Steps (*i*) and (*v*) are not activated processes whereas the rate studied was that for an activated process. To be certain that the studied rate was that of an activated process the value of the average boundary layer thickness was calculated from a completely mass-transfer controlled model and found to be very much higher than that calculated from fluid dynamic

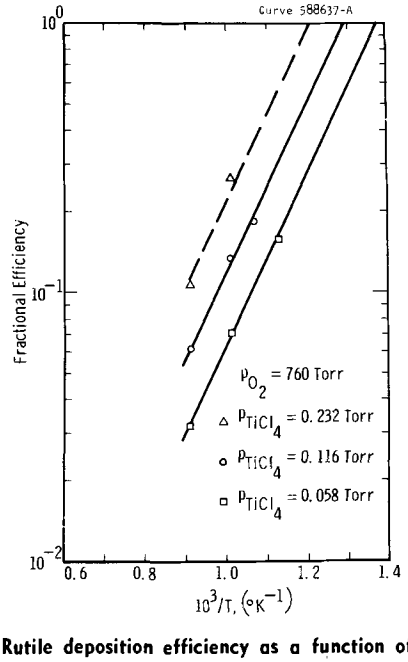

Fig. 8. Rutile deposition efficiency as a function of temperature at different titanium tetrachloride partial pressures.

relationships. Moreover, the determined deposition rate was found to vary exponentially with inverse absolute temperature and not with 1.5-2.0 power of temperature.

(*II*) The value of activation energy of surface reaction rate constant (Eq. [5]) is too high to be that of diffusion in the gas phase.

Surface diffusion and desorption of the gaseous product chlorine (step *iv*) also appears to be very unlikely as a rate-limiting step because:

(*a*) chlorine is not known to be strongly adsorbed on either silicon or rutile;

(*b*) at any temperature the calculated p_{Cl_2} (from thermodynamic K_p, the stoichiometric Eq. [1] and the condition that $p_{O_2} + p_{TiCl_4} + p_{Cl_2} = 1$ atm) is 3 to 4 orders of magnitude higher than that in the immediate vicinity of the surface (calculated from the efficiency of reaction and gas phase p_{TiCl_4}) and so the concentration of chlorine is almost negligible;

(*c*) chlorine introduced into the reactor with the reactants (at about the same concentration as $TiCl_4$) had no detectable effect on the deposition rate.

Now, of the two remaining possible rate-controlling steps [steps (*ii*) and (*iii*)] there are two broad possibilities:

(*a*) Langmuir-Hinshelwood Mechanism. In this mechanism the reaction occurs between both the species adsorbed on adjacent sites with considerable competition for the adsorption sites.

(*b*) Rideal-Eley Mechanism. Here the reaction occurs between an adsorbed species and a gaseous species without any competition for the adsorption sites.

The major distinguishing feature of these two mechanisms is that in the former the rate (R) will pass through a maximum as the partial pressure of either reactant is varied, whereas in the latter the rate will reach a limiting value when the partial pressure of one of the reactants is varied (which is the one that is adsorbed). It has been shown before that

$$R \propto (p_{O_2})^{1/2} (p_{TiCl_4}) \quad [7]$$

at low p_{O_2} and all p_{TiCl_4}, whereas

$$R \propto p_{TiCl_4} \quad [8]$$

at high p_{O_2} (depending on p_{TiCl_4}) and all p_{TiCl_4}. Since the surface reaction rate is proportional to adsorption it is clear that Rideal-Eley mechanism is operating with atomic oxygen as the chemisorbed species and molecular $TiCl_4$ colliding on the surface from the gas phase. The fact that at any temperature p_{O_2} required to saturate the surface and follow Eq. [8] increases more than proportionally with p_{TiCl_4} can be explained by considering the unknown equilibrium: O_2(gas) → O(chemisorbed).

For a closer examination of other possible intermediate species that may be involved in the reaction and the nature of the surface reaction the following facts are noted:

(*i*) $TiCl_4$ is only a dimer in the liquid (14) and so can be expected to be virtually unassociated in the gas phase at high temperatures.

(*ii*) Available thermodynamic data (10) indicate the equilibrium concentrations of TiCl, $TiCl_2$, and $TiCl_3$ above 400°C to be 7-10 orders of magnitude less than that of $TiCl_4$.

(*iii*) $TiOCl_2$ is not an intermediate product in this reaction (7). This was reverified during this study using a very sensitive technique due to Fowles *et al.* (15) and found to hold.

(*iv*) The deposition rates reported here were at high supersaturations and growth-controlled region, and the deposition rate and preferred deposit orientations were substrate orientation independent.

(*v*) ESR studies show the presence of both charged and uncharged adsorbed oxygen atoms on TiO_2 (16-18).

(*vi*) No silicon oxide could be detected at the film-substrate interface (IR spectroscopy).

Combining this information with the Rideal-Eley mechanism a detailed atomic mechanism can be pictured. After the supersaturation-controlled initial nucleation on silicon, atomic oxygen (charged or uncharged, dissociation after adsorption or adsorption of dissociated molecules) is chemisorbed on titanium sites only. During the collision process of gaseous $TiCl_4$ molecules with these chemisorbed oxygen atoms titanium-oxygen linkage must be formed for tetrahedrally bonded titanium of $TiCl_4$ to be incorporated in octahedral configuration in bulk rutile. These configurational changes of $TiCl_4$ in catalyzing organic reactions have been discussed in the literature (19). Subsequent reaction of such bonded $TiCl_4$ with the surface oxygen atom in the adjacent site produces rutile (which can chemisorb more atomic oxygen) and removes chlorine atoms (ultimately as molecules). However, there does not seem to be any clear reason for producing rutile form of TiO_2 exclusively by this system in contrast to other known systems producing anatase (2). From this atomic mechanism it appears that the surface reaction is the rate-controlling step in this heterogeneous reaction (at high p_{O_2}).

Reaction behavior above 850°C.—In discussing the reaction behavior above 850°C it should first be pointed out that the recorded rate at these temperatures were also of some activated process or processes. The major abnormalities of the reaction at these temperatures are listed below.

(*i*) In the mass transfer control range (Fig. 1) the slope of the apparent reaction rate as a function of flow rate is more than one-half, *i.e.*, less apparent deposition rate than would be predicted by vapor phase mass transport.

(*ii*) At fixed p_{O_2} (= 1 atm) and temperature more than proportional amount of TiO_2 is deposited with increasing p_{TiCl_4} (Fig. 3).

(*iii*) At fixed p_{O_2} (= 1 atm) the drop in the apparent surface reaction rate as a function of $1/T$ is slower the higher the p_{TiCl_4} (Fig. 6 and 7).

It is clear now that a process which decreases the effective p_{TiCl_4} is involved. The probabilities are (*a*) sudden change in chemisorption rate of atomic oxygen, (*b*) depletion of p_{TiCl_4} by reaction on the reactor tube wall, and (*c*) depletion of p_{TiCl_4} by homogeneous reaction. Since such sharp change (as shown in Fig. 6) in the adsorption of a gas on a solid surface is not known for any system and hardly any TiO_2 deposit is found on the reactor tube wall above 850°C, the first two possibilities appear improbable. Moreover, since the homogeneous reaction at any temperature and high p_{O_2} (zero order range) will consume a fixed fraction of $TiCl_4$, the more is the input p_{TiCl_4} the more is the unreacted p_{TiCl_4} available for surface reaction. Thus homogeneous reaction becomes quite appreciable and can account for all the anomalous behavior of the reaction above 850°C, including the disparity of the behavior of Arrhenius plots of Antipov *et al.* (6) and those reported in this study (Fig. 6 and 7). Since Antipov *et al.* (6) designed their experiments to determine the total reaction rate of Eq. [1], they could not distinguish the fraction of the reaction that proceeded by adsorption on the solid (TiO_2) surface.

Conclusions

The heterogeneous reaction of titanium tetrachloride and oxygen on silicon surface proceeds by Rideal-Eley mechanism. Atomic oxygen is chemisorbed on the titanium sites of the initial rutile nuclei and molecular $TiCl_4$ reacts with this oxygen from the gas phase. This explains why the reaction is first order with respect to $TiCl_4$ and one-half order with respect to oxygen up to 850°C. No intermediate chemical species like TiCl, $TiCl_2$, $TiCl_3$, and $TiOCl_2$ seem to be involved. Above 850°C the Arrhenius relationship does not hold because of the appreciable consumption of titanium tetrachloride by the homogeneous gas phase reaction. Because of very low chemisorption rate of atomic

oxygen on rutile at high temperatures a larger amount of oxygen is required (for maximum possible rate at any temperature) than indicated by the stoichiometric equation.

Acknowledgments

The author wishes to acknowledge Dr. J. E. Johnson and P. Rai-Choudhury for many helpful suggestions and discussions. Expert experimental help from R. F. Yut is gratefully acknowledged.

Manuscript submitted Aug. 18, 1969; revised manuscript received *ca.* Dec. 1, 1969.

Any discussion of this paper will appear in a Discussion Section to be published in the December 1970 JOURNAL.

REFERENCES

1. R. D. Gretz, in "Vapor Deposition," pp. 149-190, C. F. Powell, J. H. Oxley, and J. M. Blocher, Jr., Editors, John Wiley & Sons, New York (1966).
2. M. Yokozawa, H. Iwasa, and I. Teramoto, *Japan. J. Appl. Phys.*, **7**, 96 (1968).
3. A. E. Fuersanger, *Proc. IEEE*, **52**, 1463 (1964).
4. F. Huber, *This Journal*, **115**, 203 (1968).
5. D. R. Harbison and H. L. Taylor, in "Thin Film Dielectrics," pp. 254-278, F. Vratny, Editor, The Electrochemical Society, New York (1969).
6. I. V. Antipov, B. G. Koshunov, and L. M. Gofman, *J. Appl. Chem. (USSR)*, **40**(1), 9 (1967).
7. L. N. Shchegrov, *Ural. Politekh. Inst. im S. M. Kirova*, **1960**(96), 82; *Titan i Ego Splavy, Akad. Nauk SSSR, Inst. Met.*, **1961**(5), 211.
8. R. N. Ghoshtagore and A. J. Noreika, To be published.
9. E. F. Cave and B. R. Czorny, *RCA Rev.*, **24**, 523 (1963); T. L. Chu, J. R. Szedon, and G. A. Gruber, *Trans. Met. Soc. AIME*, **242**, 532 (1968).
10. JANAF Interim Thermochemical Tables, Dow Chemical Company, Midland, Michigan, Dec. 31, 1960.
11. H. D. Hagstrum, *J. Appl. Phys.*, **32**, 1020 (1961); J. J. Lander and J. Morrison, *ibid.*, **33**, 2089 (1962); F. Jona, *Appl. Phys. Letters*, **6**, 205 (1965).
12. F. G. Allen, *J. Appl. Phys.*, **28**, 1510 (1957).
13. H. Schlichting, in "Boundary Layer Theory," Chap. 7, 4th Ed., McGraw-Hill, New York (1960).
14. J. E. Griffiths, *J. Chem. Phys.*, **49**(2), 642 (1968).
15. G. W. A. Fowles, D. F. Lewis, and R. A. Walton, *J. Chem. Soc. (A)*, **1968**, 1468.
16. P. F. Cornaz, J. H. C. van Hooff, F. J. Pluijm, and G. C. A. Schuit, *Discussions Faraday Soc.*, **1966** (41), 290.
17. D. Iyengar, M. Codell, J. Karra, and J. Turkevich, *ibid.*, **1966** (41), 323.
18. G. C. A. Schuit, *ibid.*, **1966**, (41), 326.
19. P. Cossee, *Trans. Faraday Soc.*, **58**, 1226 (1962); *J. Catalysis*, **3**, 80 (1964); *Tetrahedron Letters*, **17**, 12 (1960); *J. Catalysis*, **3**, 99 (1964).

The Solidus Boundary in the GaP-InP Pseudobinary System

L. M. Foster* and J. E. Scardefield

IBM Research Division, Yorktown Heights, New York

ABSTRACT

The solidus boundary in the GaP-InP system was determined by a technique which uses the electron microprobe to analyze the solid phase of compositions equilibrated in the solid-liquid phase field. The boundary shows the substantial positive deviation from ideal behavior found in a number of other analogous III-V systems. Vegard's law for the relation between lattice parameter and composition holds for this system.

$Ga_xIn_{1-x}P$ is one of the systems that is currently being investigated for p-n junction electroluminescence. Hilsum (1) pointed out the possibility of achieving direct band-to-band transitions up to about 2 eV in energy in compositions of this material that contained substantial amounts of InP. Lorenz *et al.* (2) showed experimentally that direct gap character actually is preserved up to about $x = 0.8$, where band-to-band transitions up to about 2.2 eV at room temperature should be possible.

GaP-InP forms a series of solid solutions over the entire composition range, and a T-x diagram similar in general character to those of GaSb-InSb, InSb-AlSb, GaSb-AlSb, InAs-GaAs, InSb-InAs, and InP-InAs is expected (3). It is desirable to know the details of the T-x diagram in order to explore the possibility of single crystal growth from the melt.

Panish (4) has determined the liquidus in the GaP-InP pseudobinary system. The melting points of the end products, InP and GaP, are known from the literature. In the present study the solidus over the entire range of mixed crystals was determined to complete the diagram.

Experimental

Previously, the solidus boundaries of similar systems were generally determined in one of two ways (3). In the first method, finely ground mechanical mixtures or rapidly quenched two-phase ingots are annealed at progressively higher temperatures until complete homogenization is achieved, as evidenced by an x-ray pattern showing only a single phase, then the melting point of the mixed crystal is measured. This method was first employed by Stohr and Klemm (5) to establish that miscibility existed over the complete range of compositions in the Ge-Si system.

In the second method, an intimately mixed, two-phase charge is equilibrated at a temperature that is above the solidus but below the liquidus, then it is rapidly quenched. The composition of the solid phase is then found by determining its lattice parameter and comparing this with the values of the lattice parameter obtained as a function of composition for single-phase alloys that are prepared separately by the first method (or by assuming that Vegard's law holds without experimental verification). This method was employed by Woolley and Lees (6) to determine pseudobinary diagrams with InSb as one component, and has been discussed in detail by Woolley and Smith (7).

We have employed a modification of this technique to determine the solidus in the GaP-InP system. In our case, the quenched, two-phase mixture that had been equilibrated above the solidus was analyzed with the electron microprobe. This provided a direct de-

* Electrochemical Society Active Member.

termination of the composition of the solid phase and circumvented the additional step of preparing homogenized samples for x-ray analysis.

The sample was in the form of a pellet pressed from a finely ground GaP-InP powder mixture with the aid of a fugitive binder. After outgassing to remove the binder, the pellet was sealed in a quartz capsule with a minimum of free space so that the phosphorus loss during dissociation of the sample on melting would not significantly change the composition of the charge. At temperatures below 1200°C the capsule had sufficient strength to contain the phosphorus pressure arising from decomposition of the charge. For higher temperatures, the capsule was backed by a graphite container. For very high temperatures it is desirable to contain the pellet in a separate alumina container to prevent contact with the quartz. This is essential for the study of the reactive systems, InAs-AlAs and InP-AlP, for which the same assembly is being used (8). The assembly is shown in Fig. 1.

The composition of the starting mix for a particular temperature was chosen to be approximately along the straight line connecting the melting points of the two terminal compounds. This assured very roughly equal amounts of liquid and solid at equilibrium.

The charge was held at the chosen temperature for one week. The initial experiments showed that equilibrium had been achieved in that time. No survey was made to determine whether a shorter time would have been adequate. After the holding period, the capsule was removed rapidly from the furnace. It was established that the equilibrated solid could be readily distinguished from the quenched liquid when this procedure was followed and that a more rapid quench was not necessary.

The sintered pellet was sectioned approximately through the center and lapped with 3μ grit. For the electron microprobe analysis, an 0.8μ beam was moved across the lapped surface in 10μ steps. Pure GaP and InP standards were included, and the usual corrections for absorption and atomic number were made. Ga, In, and P counts were taken. Ga and In were considered to offer the greatest precision and over-all compositions based on one agreed to within ± 5% with those based on the other.

Results and Discussion

The success of this technique depends entirely on whether equilibrium is indeed achieved, and, if so, whether the equilibrium solid can be clearly distinguished from the nonequilibrium quenched liquid. The micrographs in Fig. 2 of three representative samples show that the liquid and solid can be clearly distinguished. The top sample was the more typical and shows a mosaic structure with large grains of the solid separated by the fine-particle quenched liquid. The center sample shows an unusual case where much of the solid is found in one large grain situated near one edge of the pellet, possibly as a result of a very slight temperature gradient. For the bottom sample, the initial composition was inadvertently very near the

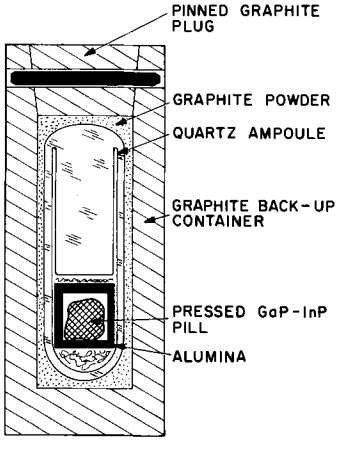

Fig. 1. Assembly for containing pellet of reaction charge at high temperature and pressure.

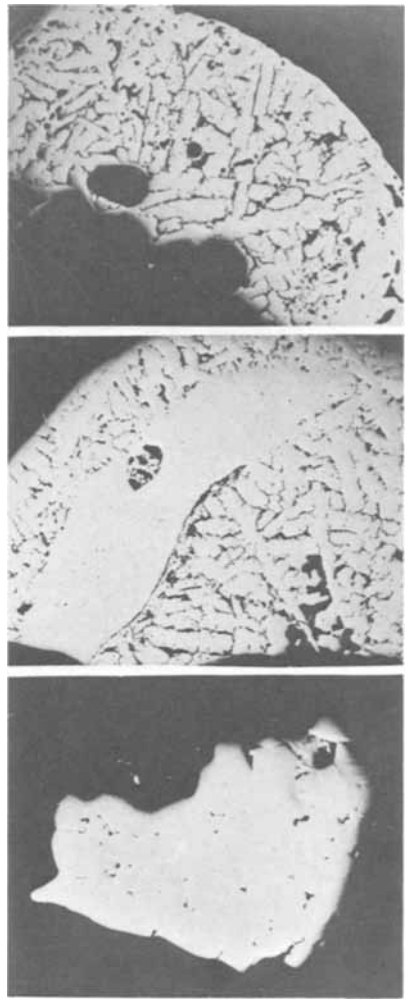

Fig. 2. Photomicrographs of three homogenized GaP-InP charges (Magnification 10X).

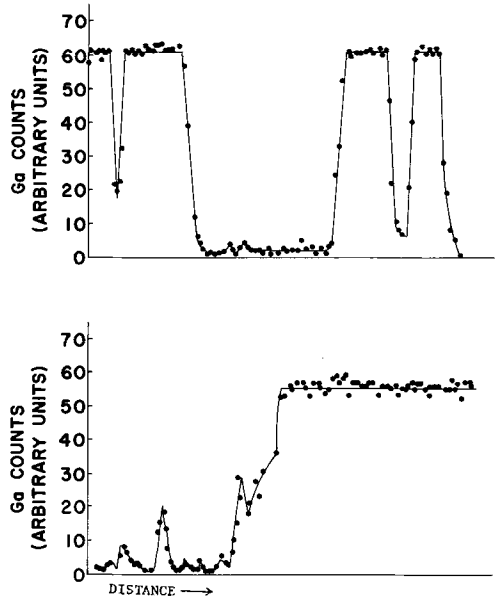

Fig. 3. Representative electron microprobe data for the top and center samples of Fig. 2.

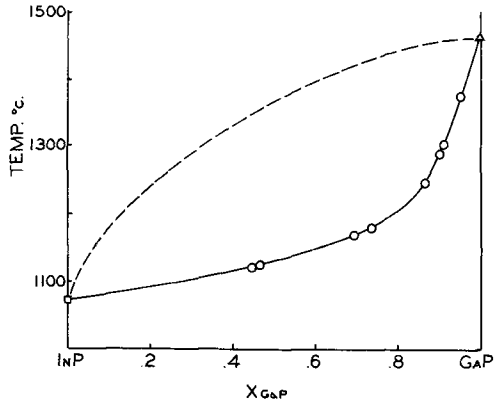

Fig. 4. GaP-InP phase diagram. ○ This work, △ Richman (11), □ Koster and Ulrich (9), — — — Panish (4).

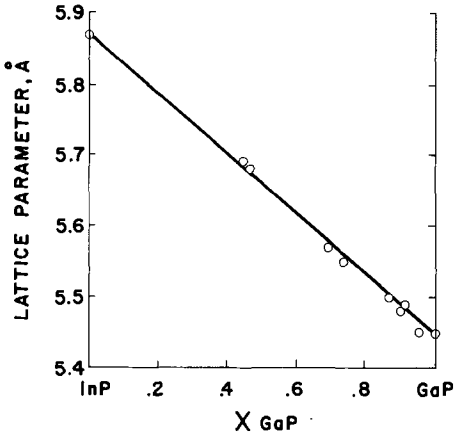

Fig. 5. Lattice parameter vs. composition for GaP-InP system

solidus boundary so only a small amount of liquid remained between the solid grains.

Criteria for equilibrium are that the phase richest in GaP must be the equilibrium solid, and the individual grains of this phase must be of constant composition across their entire breadth. That these criteria were met is evident from Fig. 3, which shows the microprobe data for part of the two top samples of Fig. 2. The top trace shows an excursion across four prominent arms of the structure and the indium-rich quenched liquid in between. The bottom trace shows an approach along an indium-rich valley and arrival at the large equilibrated grain where the composition remained constant within the precision of the method for its entire width of about 1000μ (100 data points). A sufficient excursion was made across each of the eight samples of the series to ensure that a number of plateaus were included in the data, and that no regions more rich in GaP than the plateaus existed.

The data are shown in Fig. 4. The InP melting point of 1070°C was taken from Koster and Ulrich (9). This agreed within ± 2 degrees with the recent determination by Panish and Arthur (10). The melting point for GaP of 1465°C was taken from Richman (11). The liquidus curve shown by the dashed line was determined by Panish (4) and is included in Fig. 4 to complete the diagram.

The dependence of the lattice parameter on composition was determined on the same series of samples by making powder x-ray patterns from the finely ground pellets. A typical pattern consisted of discrete reflections corresponding to the smallest parameter (highest GaP content) phase, followed at larger angle by broad bands of close-spaced reflections from the nonhomogeneous, In-rich, quenched liquid. The results are shown in Fig. 5. It is seen that Vegard's law is followed within the precision of the x-ray data on these samples, which were not ideally suited to x-ray work because of the large amount of second phase present.

Acknowledgment

The authors are indebted to Messrs. J. D. Kuptsis and J. Angilello for the electron microprobe and x-ray analyses, respectively; and to Mr. R. J. Chicotka for supplying the InP.

Manuscript submitted Nov. 7, 1969; revised manuscript received Jan. 19, 1970.

Any discussion of this paper will appear in a Discussion Section to be published in the December 1970 JOURNAL.

REFERENCES

1. C. Hilsum, *Proc. Seventh Internat. Conf. Phys. Semiconductors, Paris*, p. 1127 (1964).
2. M. R. Lorenz, W. Reuter, W. P. Dumke, R. J. Chicotka, G. D. Pettit, and J. M. Woodall, *Appl. Phys. Letters*, **13**, 421 (1968).
3. For a summary of data and individual references, see R. K. Willardson and H. L. Goering, "Compound Semiconductors," Vol. 1, Reinhold (1962).
4. M. B. Panish, Bell Telephone Laboratories, Private communication. Submitted to *J. of Chemical Thermodynamics*.
5. H. Stohr and W. Klemm, *Z. anorg. Chem.*, **241**, 305 (1935).
6. J. C. Woolley and D. G. Lees, *J. Less Common Metals*, **1**, 192 (1959).
7. J. C. Woolley and B. A. Smith, *Proc. Phys. Soc. (London)*, **72**, 214 (1958).
8. To be published.
9. W. Koster and W. Ulrich, *Z. Metallk.*, **49**, 365 (1958).
10. M. B. Panish and J. R. Arthur, Bell Telephone Laboratories, Private communication. Submitted to *J. of Chemical Thermodynamics*.
11. D. Richman, *J. Phys. Chem. Solids*, **24**, 1131 (1963).

Insulating Films on Ni-Fe-Mo Alloy Powders by Fluorination

J. H. Swisher, F. Schrey, P. K. Gallagher, and E. O. Fuchs

Bell Telephone Laboratories, Incorporated, Murray Hill, New Jersey

ABSTRACT

A new method has been developed to produce insulating films on Ni-Fe-Mo alloy (permalloy) powders by fluorination. The method consists of passing argon-fluorine gas mixtures through a fluidized bed of the powder at 350°C. Magnetic permeability and electrical resistivity data are given for bars pressed from the powders. Film thicknesses of 0.6μ or greater are required to obtain pinhole-free films on the powders; however, high resistivities are obtained with thinner films by subsequently oxidizing portions of the particle surfaces exposed by the pinholes. With an improvement in the stress-relief annealing procedure, this method would be competitive with the presently used $Mg(OH)_2$-Na_2SiO_3 coating process for inductance coils.

Magnetic alloy powders which have been coated with an insulating film and pressed into toroids are used commercially in inductance coils. For one widely used coil, an 81% Ni, 17% Fe, and 2% Mo alloy powder (2 Mo permalloy) is coated with a magnesium hydroxide-sodium silicate insulating film. The powder is first produced from cast ingots using a grain-boundary embrittlement technique. Sulfur is added to the liquid alloy, and a grain-boundary sulfide network forms during hot rolling which causes the grains to break apart. The insulation is applied as an aqueous slurry and dried by baking. Talc and zinc stearate are added to the slurry to facilitate pressing the powders into cores. The processing procedures are described in greater detail by Harendza-Harinxma (1). Improvements in coating technology are needed for miniaturization of the coils, higher permeability, better process control, and lower cost.

Flaschen and Garn (2) used fluorination as a means of forming insulating coatings on aluminum and copper. Resistivities of the order of 10^{14} ohm-cm were obtained for AlF_3 and CuF_2 films; however, the films were hygroscopic and tended to oxidize at 500°C (AlF_3) and 250°C (CuF_2).

Nickel and its alloys are used as container materials for handling fluorinating agents because nonhygroscopic, protective NiF_2 films are formed when nickel is exposed to fluorine. Cannon *et al.* (3) review previous studies on the fluorination of nickel and copper alloys and also present additional data on the passivation reactions. The literature on the fluorination of nickel alloys led us to believe that adherent, insulating films could be formed on molybdenum permalloy powder by direct reaction in a fluidized bed reactor. In pursuing this idea, films of several thicknesses were formed by varying the fluorination time and temperature and the fluorine partial pressure. Resistivity and permeability measurements on pressed bars were used to characterize the properties of the materials.

Experimental

The permalloy powder was taken from a commercial lot of material produced by the Western Electric Company, Chicago. These powders are screened to pass a 120 mesh sieve (125μ screen opening). The average particle size is about 40μ. A sample of powder insulated with a $Mg(OH)_2$-Na_2SiO_3 coating was obtained from the same supplier. This sample served primarily as a comparison standard for the fluorinated materials.

Figure 1 shows a schematic diagram of the reactor used for fluorinating the powders. The dimensions of the inside of the reaction chamber were 4 cm diameter by 4 cm high. Nickel was used in all parts of the reactor exposed to fluorine. Argon-fluorine gas mixtures were passed through a preheating coil, then through a porous nickel frit with a 75μ pore diameter. The reactor was contained in a vertical resistance furnace. A thermocouple in the furnace was used to control the furnace temperature, and another thermocouple inserted through the cover plate in the reactor was used to monitor the temperature of the sample The temperatures used for fluorination were in the range from 200° to 450°C. Most of the treatments were done at 350°C, with reaction times ranging from 15 min to 8 hr.

The usual procedure was to add 100g of powder to the reactor with nitrogen flowing through the system. A gas flow rate of 1 liter/min was used. This flow rate was sufficient to maintain movement in the bed of particles; however, the density of the particles was too great to fluidize the bed in the usual sense. For most of the work, mixtures of 10% F_2 in Ar were prepared by metering the individual gases. Undiluted fluorine and premixed cylinders of 1 and 5% F_2 in Ar were used in a few experiments. The fluorine was 99% pure. The sum of the impurity concentrations of HF and CO_2 was 0.4%, the sum of the N_2 and O_2 concentrations was 0.5%, and CF_4 was present at the ppm level. The only purification step used was passage of the fluorine through an NaF trap to remove HF.

Commercially, the insulated powders are pressed into toroids of various sizes at a pressure of 200,000

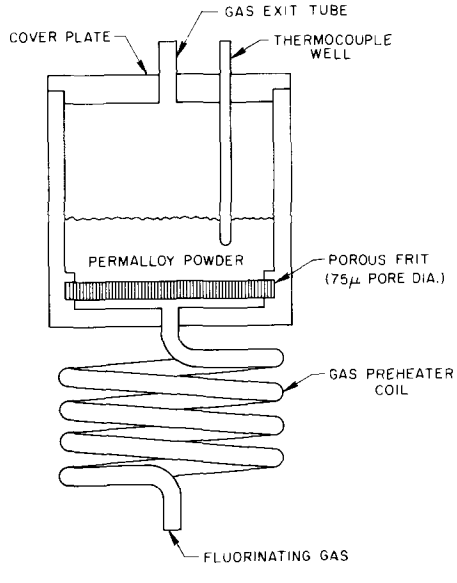

Fig. 1. Fluidized bed reactor

psi. The pressed cores are stress relieved in a forming gas atmosphere at 625°C. The magnetic permeability of the annealed cores is determined from an a-c inductance measurement. The quality of the insulation is determined by winding the cores with copper wire and measuring the eddy current losses in the material.

Facilities were not readily available to obtain the same data on the fluorinated samples, so the following method was devised to determine the quality of the experimental materials. Rectangular bars, 0.25 x 0.25 x 4.3 cm, were pressed from the powder at 100,000 psi. The permeability was determined from a d-c measurement, using a balanced solenoid and a Lowell Electronics DC Hysteresigraph. The electrical resistivity of the pressed bars was measured with an ohmmeter when the resistivity was sufficiently low. For higher resistivity values, a 500V d-c bridge was used.

Stress-relief annealing of the bars insulated by fluorination proved to be an important step in the processing. Heating the bars in a reducing or an inert gas atmosphere to 625°C resulted in loss of fluorine from the samples by reduction or vaporization. Annealing in air at 625°C resulted in partial conversion of the fluoride to oxide. While breakdown of the insulation did not occur during air annealing, the permeability of the material could not be increased, which was the purpose of the annealing step. The most satisfactory procedure proved to be encapsulation of the bars under vacuum in quartz tubing with a small amount of CuF_2 added to the capsules. The capsules were then annealed at 625°C for 2 hr. The commercial analogue of encapsulation would be bell jar annealing.

The fluorine content of the treated powders was determined by measuring the weight loss of samples after hydrogen reduction of the fluoride film. The method consisted of passing hydrogen over the specimens in a controlled-atmosphere tube furnace for 2 hr at 650°C. Under these conditions, the fluoride is readily reduced by hydrogen to form HF, which is continuously swept from the furnace. No additional weight loss was observed when the specimens were held for longer times. The fluorine content obtained for one sample was cross-checked with a magnetic moment measurement using a pendulum magnetometer and also with a wet chemical analysis. The magnetic moment measurement yielded a fluorine content about 10% greater than by the weight loss method, and the wet chemical analysis gave a fluorine content about 15% greater. The weight loss method was adopted because it was considered sufficiently accurate for the present purpose, and it was the most convenient to use.

Results

A metallographic study of the permalloy powders insulated both by fluorination and with the standard 0.3μ $Mg(OH)_2$-Na_2SiO_3 coating was made by Bennett (4). Two scanning electron micrographs obtained from this study are reproduced in Fig. 2. Figure 2(a) was obtained from a purposely mixed sample of uninsulated and oxide-insulated powders. At the beam potential of 2 kV, the insulated particle appears much darker than the uninsulated particles. The dark spots on the surfaces of the uninsulated particles are presumed to be sulfide and/or oxide inclusions which were present at grain boundaries in the original ingots. It is this second phase material at grain boundaries that causes the ingots to disintegrate into fragments during the final stage of rolling.

Figure 2(b) was obtained from a powder sample treated in an Ar plus 10% F_2 mixture at 350°C for 2 hr. There appeared to be fluoride crystal growth swirls on the particles, meaning that the fluoride films are not uniform in thickness; however, there was complete coverage of the metal surfaces, at least under these fluorinating conditions.

The results of an initial series of experiments are listed in Table I. The gas composition was Ar plus 10% F_2 and the reaction time was 2 hr. Direct comparisons should not be made between the permeability values given in Table I and values obtained on commercially processed powder cores. Differences in the magnetic test methods, powder compaction pressures, and other processing procedures lead to large differences in the permeability values obtained. A comparison was made on the oxide-coated material using the two processing and test methods. The permeability was about four times higher by the a-c inductance test on cores pressed at 200,000 psi than by our d-c method on bars pressed at 100,000 psi. When the same comparison was made on fluoride-coated material, the difference was about a factor of three.

The film thicknesses in Table I were computed by considering the particles to have a uniform diameter of

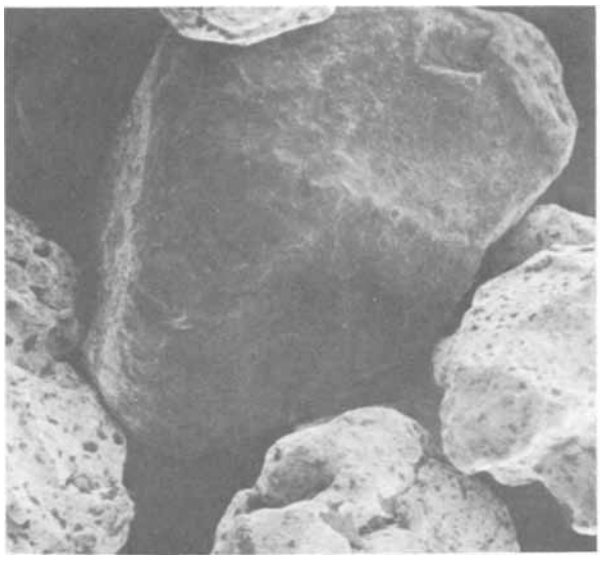

Fig. 2a. Scanning electron micrograph of a mixture of oxide-insulated (dark) and uninsulated (light) permalloy powders. X425.

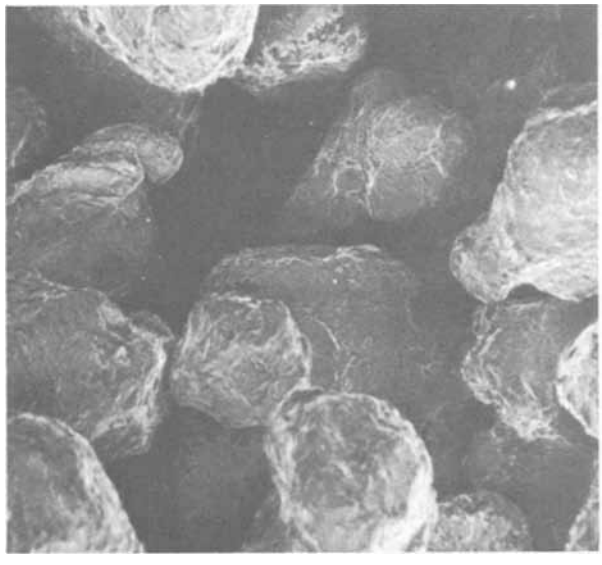

Fig. 2b. Scanning electron micrograph of permalloy powder fluorinated in Ar + 10 pct F_2 at 350°C for 2 hr. X400.

Table I. Properties of pressed bars of powders fluorinated for 2 hr in Ar + 10% F_2 at various temperatures

Furnace temp, °C	Effective permeability, μ_e	Resistivity, ohm-cm	F_2, w/o	Computed film thickness, μ
200	—	<0.03	0.15	0.05
280	26.5	0.08	0.25	0.09
300	22.2	5.0	0.68	0.24
350	15.3	1.3×10^9	2.02	0.72
450	Reaction strongly exothermic			

40μ. The fluoride film was assumed to be (Ni, Fe)F_2 and to have a density of 4.4 g/cm^3. (NiF_2 has a density of 4.6 g/cm^3, and FeF_2 has a density of 4.1 g/cm^3.) By dissolving the fluoride film from the surfaces of one powder sample in boiling water and chemically analyzing for Ni, Fe, and Mo, the ratio of Ni to Fe in the fluoride was found to be 3.12 (weight basis). The corresponding ratio for the starting alloy was 4.77, so some enrichment of iron in the fluoride phase occurred. No molybdenum was detected in the fluoride, which is understandable in view of the high vapor pressure of MoF_6.

Examination of the data in Table I leads to the conclusion that the rate of fluorination is strongly temperature dependent. The rate was fast, but still controllable at 350°C. At higher temperatures, the exothermic nature of the reaction led to temperature excursions in the sample of more than 200°C. At 350°C there was an initial increase of about 30°C during the first few minutes of exposure, then the temperature in the bed decreased slowly and approached the temperature of the furnace. In all subsequent experiments, the furnace temperature was maintained at 350°C.

Data are plotted in Fig. 3 which show the computed film thickness as a function of the square root of reaction time. The rate during the first hour is essentially parabolic and is presumed to be controlled by diffusion through an adherent film. At longer times, a gradual acceleration occurs which is attributed to a loss of adherency of the film. Although the diffusing species in NiF_2 is known to be the fluoride ion (5), interdiffusion of metal and fluoride ions may occur in (Ni, Fe)F_2 films. The observation that the Ni to Fe ratio in the fluoride differs from the ratio in the underlying metal is an indication that interdiffusion may be occurring.

Figure 3 shows data relating the permeability of pressed bars, both before and after annealing in quartz capsules, to the computed film thickness. Corresponding values are plotted for material insulated with a $Mg(OH)_2$-Na_2SiO_3 coating. The film thickness in the oxide-coated material is taken to be 0.32μ (6). The limiting permeability obtainable in the pressed bars is 39.7, which is the value obtained when uninsulated powder is pressed and annealed. In Fig. 4, the permeabilty of the fluorinated specimens can be seen to decrease in a regular manner with increasing film thickness.

The theoretical permeability of pressed powder cores is given by the following equation (6).

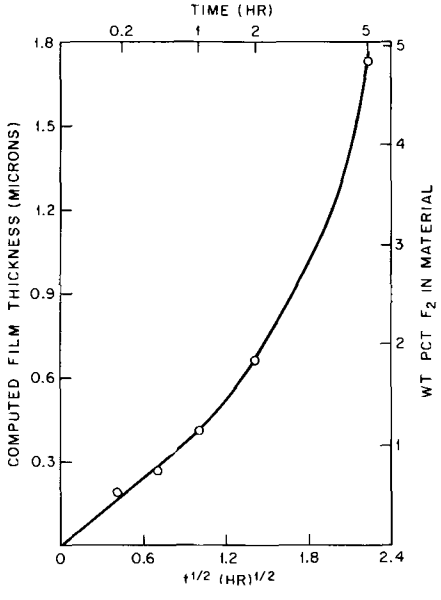

Fig. 3. Film thickness vs. time plot for fluorination of permalloy powder in Ar + 10% F_2 at 350°C.

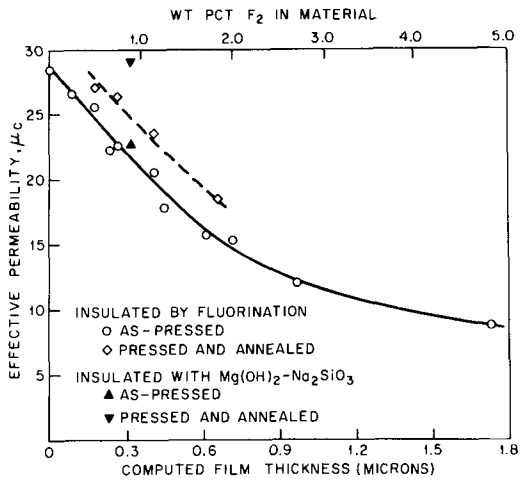

Fig. 4. Permeability of pressed bars of insulated permalloy powder as a function of film thickness.

$$\mu_c = \frac{\mu}{\tau(\mu - 1) + 1} \qquad [1]$$

where μ_c is the effective permeability of the core, μ is the permeability of the magnetic particles, and τ is the ratio of the length of the flux path through the "air gaps" to the total length of the magnetic circuit. Here "air gap" includes both the insulating film and voids in the pressed material. Higher permeabilities can be achieved by decreasing the air gap and by annealing the compacts to increase the permeability of the particles. Greater compaction pressures and thinner insulating films both decrease the air gap and increase the effective permeability.

Notice in Fig. 4 that while the as-pressed permeability of the oxide- and fluoride-coated materials are nearly the same for the same film thickness, the oxide-coated material is somewhat better after annealing. The reasons for this difference are not obvious. One possibility is that the fluoride film thickens during annealing, due to oxygen or fluorine pickup within the capsule.

In Fig. 5, data are plotted which show the variation of the electrical resistivity of pressed bars with film thickness. In the range of film thicknesses from 0 to 0.6μ, the logarithm of the resistivity increases approximately linearly with film thickness. While this behavior can be rationalized qualitatively in terms of

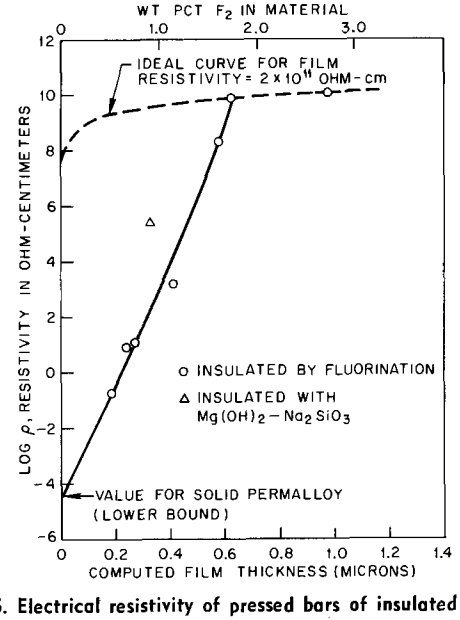

Fig. 5. Electrical resistivity of pressed bars of insulated permalloy powder as a function of film thickness.

variations in charge-carrier concentrations across the film, the results of other experiments demonstrated that pinholes and other defects to a large degree limited the resistivities obtained in the thinner films. When thin fluoride films were formed on permalloy strip specimens and gold spots evaporated onto the fluoride films, electrical continuity between the gold spots and the underlying metal was observed. It was also found that the resistivity of pressed bars in which the fluoride film thickness was 0.2-0.4μ could be increased by about three orders of magnitude by air baking the bars at 400°C for 5 hr. Thus, by oxidizing the base metal under the pinholes in the film, resistivity values were obtained which were about the same as for the $Mg(OH)_2$-Na_2SiO_3 insulated material with the same film thickness. There was no measurable change in the permeability of the materials after this heat treatment.

Referring again to Fig. 5, when the film thickness increased from 0.6 to 1.0μ, the resistivity increased by a much smaller amount, indicating that conduction through pinholes was no longer important. An approximate calculation based on these data yielded a fluoride film resistivity of 2 x 10^{11} ohm-cm. The estimated uncertainty in this value is half an order of magnitude. For films thicker than 1μ, the resistivity decreased somewhat, due presumably to the loss of adherence of the thicker films to the metal particles. This effect was also mentioned in connection with the results shown in Fig. 3. Using a value of 2 x 10^{11} ohm-cm for the fluoride resistivity, the ideal curve in Fig. 5 was computed for pinhole-free insulation on the powders.

Discussion

Fluorination as a means of insulating permalloy powder offers some advantages over the presently used process of forming a complex oxide film by applying an aqueous slurry to the particles and removing the water from the slurry by heating. A fluorination process is simpler, more direct, and should in principle lead to lower costs and better process control. Fluorinated powders can also be pressed into dense and strong toroids without the use of pressing aids. There are some limitations, however, which must be overcome before a fluorination process can be considered better than the presently used commercial process. Among these limitations are defects present in the films of the desired thickness and the difficulty of annealing the parts after pressing.

The advantages of forming defect-free fluoride films on the powders are apparent if we examine the ideal resistivity curve in Fig. 5. A 0.1μ defect-free film should result in a resistivity of 10^9 ohm-cm in the pressed material, which is about four orders of magnitude higher than in the presently used 0.3μ oxide insulation. With this reduction in film thickness from 0.3 to 0.1μ, the permeability would be increased by a factor of three from Eq. [1], if the "air gap" were reduced by the same factor.

The safety hazard in fluorination processes, particularly when fluorine gas is used, is another factor of importance. While undiluted fluorine reacts vigorously and sometimes explosively with nearly all substances the same reactions often occur at controllable rates when fluorine is diluted with an inert gas. In our experiments at 350°C, the fluorination of permalloy powder could not be controlled when undiluted fluorine was used. With 10% F_2 in Ar, the fluorination reaction was easily controlled as long as the 350°C operating temperature was not exceeded. By diluting further to 5% F_2 in Ar, no noticeable change in the reaction rate was evident. (Some of the points in Fig. 4 and 5 were obtained using 5% F_2 in Ar.) When 1% F_2 in Ar was used, the reaction rate was still appreciable, although slower by approximately a factor of two. Based on these data, dilution of the fluorine by a factor of approximately one to one-hundred is recommended for large-scale processing because of safety considerations.

Fluorination of permalloy powder can be achieved without using fluorine gas. A weaker fluorinating agent such as NH_4F can also be used. A few experiments were performed to demonstrate that fluoride films are formed when permalloy is exposed to NH_4F. Solid NH_4F and permalloy powder samples were placed in adjacent boats in the hot zone of a horizontal tube furnace at 350°C. The vapor pressure of NH_4F is appreciable at this temperature. Helium was passed over the NH_4F, then over the permalloy sample. Insulating fluoride films were formed on the permalloy samples in this way, although a more elaborate technique was needed to coat the particles uniformly. A better technique might have been to insulate the particles in a two-stage fluidized bed reactor, the first stage to introduce NH_4F into a carrier gas and the second stage to react NH_4F in the gas with the permalloy sample. In both the NH_4F and the direct fluorination experiments, an alternative method would have been to drop the powder through a furnace chamber with the fluorinating gas flowing upward through the chamber.

Thus far the discussion has been limited to materials for powder cores. Permalloy is also used in tape-wound cores, high quality transformer laminations, and as the soft magnetic component in twistor wire. There is no reason why fluorination could not be used to form insulating films required for these applications. Here a fluorination process might be more attractive than for powder cores because annealing could be done before insulating the material.

Summary

Molybdenum permalloy powders were successfully insulated by direct reaction with argon-fluorine gas mixtures. Permeability and electrical resistivity data were obtained on bars pressed from powders insulated under various fluorinating conditions. The magnetic and electrical properties were comparable to but not better than properties obtained commercially with an oxide-coating process. The potential advantages of a fluorination process are simplicity, better control over properties, and possibly lower cost. The disadvantages are handling problems associated with fluorinating agents and the difficulty of annealing without breakdown of the insulation.

Acknowledgments

The authors wish to thank Messrs. J. P. McKune for providing the powder samples, R. C. Sherwood for the magnetic moment measurement, G. L. Link for helpful discussions, and T. D. Schlabach for reviewing the manuscript.

Manuscript submitted Aug. 6, 1969; revised manuscript received ca. Dec. 19, 1969.

Any discussion of this paper will appear in a Discussion Section to be published in the December 1970 JOURNAL.

REFERENCES

1. A. J. Harendza-Harinxma, *Western Electric Engr.*, **8**, 10 (1964).
2. S. S. Flaschen and P. D. Garn, *J. Am. Ceram. Soc.*, **42**, 641 (1959).
3. W. A. Cannon, S. K. Asunmaa, W. D. English, and N. A. Tiner, *Trans. Met. Soc. AIME*, **242**, 1635 (1968).
4. J. E. Bennett, Bell Telephone Labs., Inc., Columbus, Ohio, 1969.
5. R. L. Larry, J. Fischer, W. H. Gunther, *This Journal*, **110**, 346 (1963).
6. C. D. Owens, "Stability Characteristics of Molybdenum Permalloy Powder Cores," Monograph No. 2576, Bell Telephone Labs., Inc., Murray Hill, N. J. (1956).

Single Crystal Growth of Titanium Carbide by Chemical Vapor Deposition

Takehiko Takahashi,* Kohzoh Sugiyama, and Hideaki Itoh

Department of Applied Chemistry, Faculty of Engineering, Nagoya University, Nagoya, Japan

ABSTRACT

Various forms of titanium carbide crystals were deposited on graphite substrates from the vapor phase consisting of hydrogen, titanium tetrachloride, and a hydrocarbon in the temperature range of 1200°-1350°C. The correlations between the crystal morphology and the growth conditions (temperature, gas flow-rates, concentrations, impurities, etc.) were investigated. The decomposition of the hydrocarbon was found to play an important role on the growth process. By x-ray diffraction, it was concluded that the growth direction of these crystals was mainly <111> although sometimes kinked toward <1$\bar{1}$1>. The growth mechanism of the single crystal was further studied by observation of the etching figures of the cross section which showed hexagonal growth layers. Finally the tensile strength of needle or pillar crystals was measured and a linear relation (on log-log scale only) was confirmed between the diameter and the strength.

Titanium carbide, one of the typical interstitial compounds having a high melting point of 3250°C and Vicker's hardness of 3200 kg/mm^2, has been well-known as a super-hard and refractory material. Boule single crystals of titanium carbide have been prepared by the Arc-Verneuil process and many studies have been made on its crystal structure and physical properties (1-4). Few papers, however, have been published on the preparation of needle or whisker forms of the single crystal from vapor phase, except a brief report by Hertl (5) who obtained fibrous titanium carbide from TiO_2 and colloidal carbon in a chlorine atmosphere.

The purpose of this investigation was to deposit needle, whisker, pillar, or polyhedron single crystals at least several millimeters long and to investigate the growth reaction, crystal morphology, and growth mechanism. In discussing the crystal growth process, the theory on whisker growth of Wagner *et al.* (6) was instructive as well as the experimental study on silicon carbide (7) and boron carbide whiskers (8). The extrapolated values of the tensile strength may be compared with published values of other whisker materials.

Experimental

The schematic diagram of the experimental apparatus is illustrated in Fig. 1. Titanium carbide single crystal was prepared according to the reaction: $TiCl_4 + C_xH_y + H_2 \rightarrow TiC + HCl + C_mN_n$, where C_xH_y was propane in this experiment. The reaction was performed in a horizontal quartz tube, the inside diameter of which was about 35 mm. A cylindrical graphite tube (50 mm in length, 30-32 and 10-23 mm in outside and inside diameters, respectively) was placed at the center of the tube, and served as the substrate for deposition of titanium carbide. The tube was heated by induction. Titanium tetrachloride (bp 136.5°C) was introduced into the hydrogen stream by means of a bubbling-type saturator, maintained at 90°C. The gas flow rates of dried hydrogen and propane were measured with a flow meter. After precleaning the reaction tube with hydrogen, the flow of mixed gases of titanium tetrachloride, hydrogen, and propane was initiated. It was necessary to keep the gas mixture at 90°-100°C by cooling water at the inlet which was 20-50 mm in front of the surface of the graphite substrate to prevent the propane from decomposing excessively due to radiation from the heated graphite. The substrate temperature was measured through the glass window W_1 with a photopyrometer and the growth process was observed through the other glass window W_2. Impurities such as Au, Pd, H_2PtCl_6, HgCl, $MnCl_2$, $Mn(NO_3)$, $AgNO_3$, Na_2SO_4, etc., were incorporated into the graphite and the impurity effect on the crystal growth was investigated.

The morphology of each single crystal was observed through the microscope. The deposits were identified by x-ray diffractometer and the growth directions were determined by the Laue method. The cross section of needle and pillar crystals was etched in hot concentrated nitric acid for 5 min, after abrading the surface.

The fracture strength along the crystal axis was measured by the buoyancy method, whereby the crystal was fixed at both ends on copper supports, one of which was connected to a buoy via thin tungsten wire and was loaded continuously in tension by draining the water which sustained the buoy.

Results

Growth conditions.—The conditions for single crystal growth were investigated as a function of temperature, gas flow rate, and the shape of the graphite substrate in the reaction tube. The temperature dependence was noteworthy; when the temperature of the substrate was below 1200°C, a thin film of titanium carbide (9) was coated on the surface, and when above 1400°C, polycrystals were deposited rapidly. In this experiment, the single crystal growth was studied in detail in the temperature range of 1200°-1400°C. Figure 2 shows the influence of temperature and the propane gas flow rate on the crystal growth, when the hydrogen gas flow rate was 4.0-8.0 cc/sec (linear velocity 27.5-55.0 cm/sec in the graphite tube). It should be noted from Fig. 2 that a suitable temperature range for single crystal growth is from 1240°-1280°C. Using a

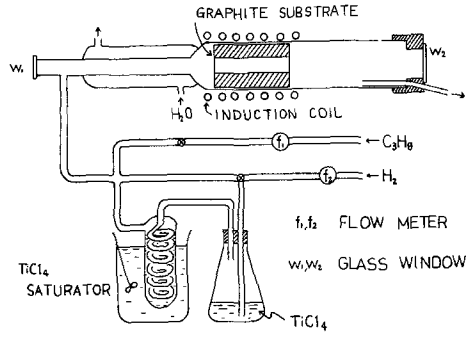

Fig. 1. Schematic diagram of the experimental apparatus

* Electrochemical Society Active Member.

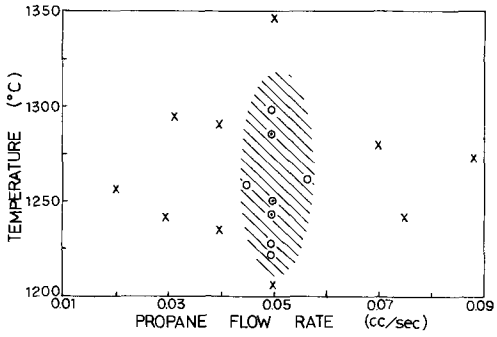

Fig. 2. Influence of temperature and propane gas flow rate on crystal growth.

propane gas flow rate of 0.05 cc/sec [0.8 m/o (mole per cent)] is essential. The influence of hydrogen gas flow rate and temperature on the crystal morphology is shown in Fig. 3 at a fixed propane gas flow rate of 0.05 cc/sec. Needle or whisker crystals were found to deposit at a relatively high flow rate of about 7.7 cc/sec (53.1 cm/sec), while pillar crystals were deposited at a lower flow rate of 6.2 cc/sec (43.8 cm/sec), and polyhedron crystals at a higher temperature range of 1250°-1300°C. These experimental data were obtained when the inside diameter of substrate was 10 mm. As the inside diameter decreased a number of needle crystals 6-7 mm long were deposited, but it was difficult to obtain reproducible data.

Crystal morphology.—Figures 4 and 5 show the needle crystals observed from two different directions. They occur in radiating clusters, apparently from a single nucleus. The initial growth rate is from 5 to 7 mm/hr, but the rate decreases abruptly in 60-80 min. This seems to show that the growth region of needles is limited to the thin gas film over the graphite surface, because some long needles kink toward the appropriate atmosphere at the tip. Whiskers from 2 to 12μ in diameter were observed together with fine needles at a higher linear flow rate of hydrogen gas (Fig. 6 and 7). A few pillar single crystals, shown in Fig. 8, grow in different directions from a single nucleus just like the needle crystals. These are from 30 to 50μ in diameter and from 1 to 5 mm in length, but the growth rate is lower than that of needles. One pillar crystal is magnified in Fig. 9, where the side plane of the hexagonal prism and the tip of the truncated pyramid are observed. Each side has a smooth plane and a metal gloss, except for a special case described later. Polyhedron crystals grown for several hours in a high temperature range, have a different sort of mor-

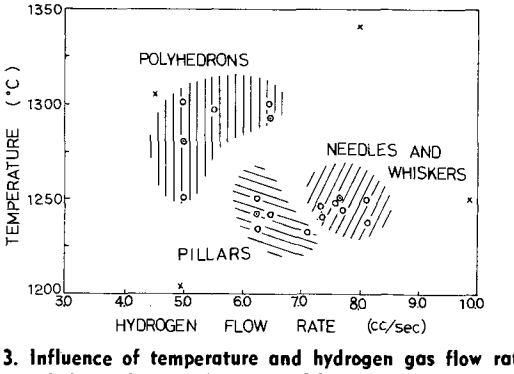

Fig. 3. Influence of temperature and hydrogen gas flow rate on crystal morphology. (Propane flow rate of 0.05 cc/sec.)

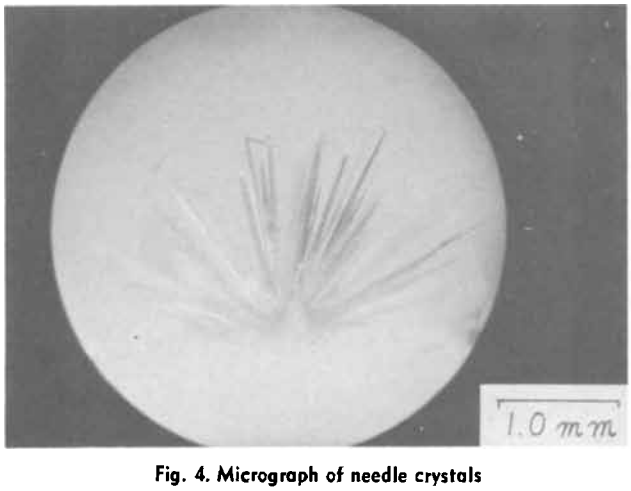

Fig. 4. Micrograph of needle crystals

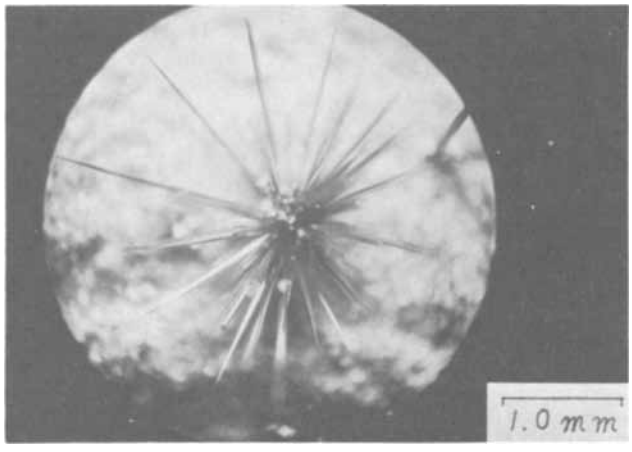

Fig. 5. Micrograph of needle crystals

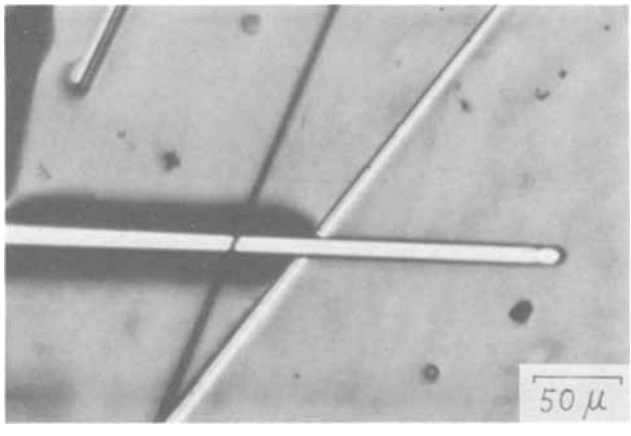

Fig. 6. Micrograph of whiskers (temperature, 1240°C)

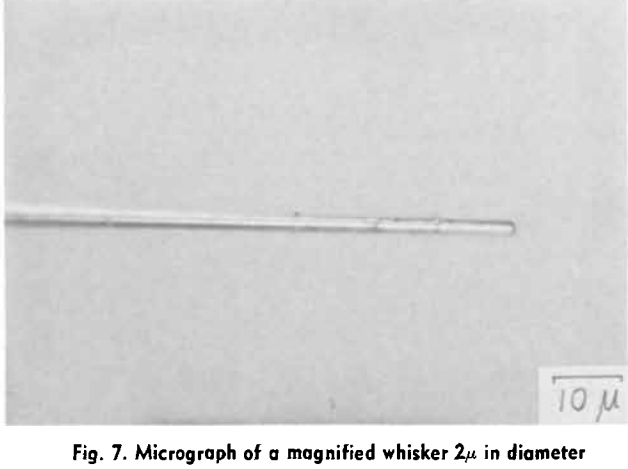

Fig. 7. Micrograph of a magnified whisker 2μ in diameter

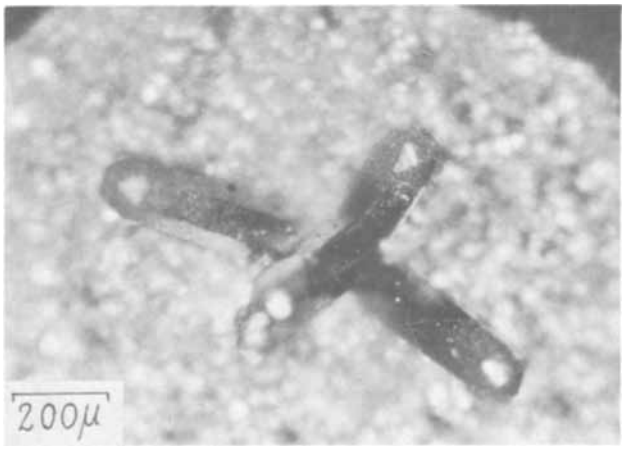

Fig. 8. Micrograph of a few pillar crystals

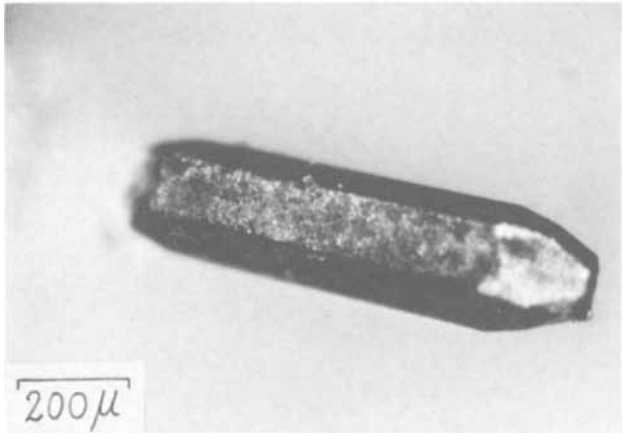

Fig. 9. Micrograph of a magnified pillar crystal like an hexagonal prism.

phology, for example, hexahedron or octahedron. Figure 10 shows the polyhedron crystals, whose tips are octagonal pyramids, and they grow large enough to become adjacent to each other.

Growth direction.—After the identification with the titanium carbide ASTM card, the growth direction was determined by the Laue method. X-ray beam from a molybdenum target was radiated on a needle or pillar crystal mounted vertically on the goniometer head. Figure 11 (a and b) are Laue photographs taken

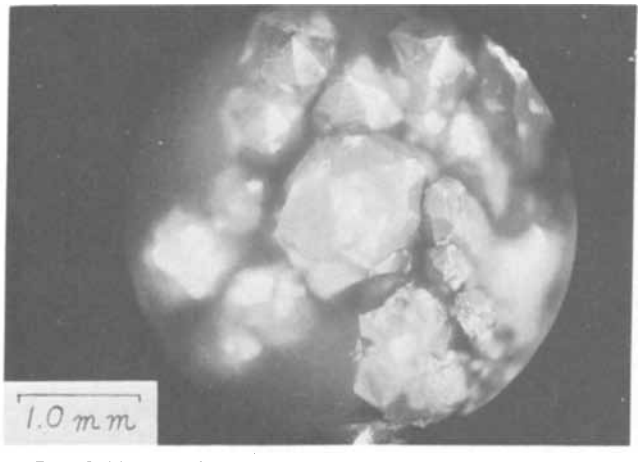

Fig. 10. Micrograph of polyhedron crystals (temperature, 1320°C)

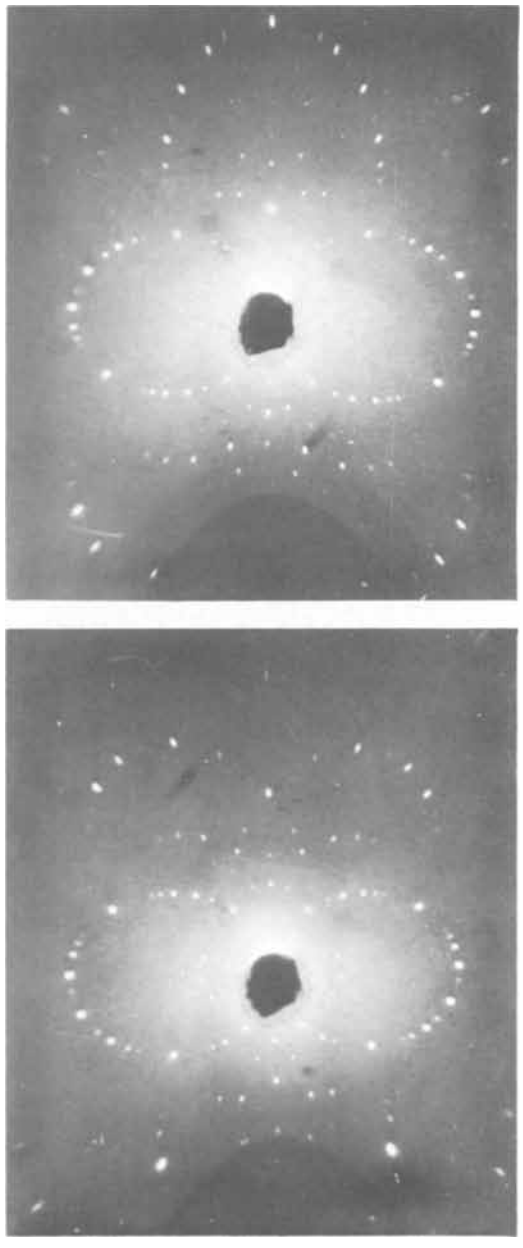

Fig. 11. Laue photographs (target, molybdenum; exposure, 40 kV, 15 mA, 90 min; crystal-to-film distance, 16 mm). (a) Laue spots with a mirror symmetry, radiated from a given direction, (b) Laue spots from a rotated direction by 60° around the axis.

from a given position (a), and from the rotated position by 60° (b). It is suggested from the two mirror symmetries in the figures that <111> is the growth direction, since titanium carbide has a NaCl type crystal structure. Therefore, each side of the hexagonal prism observed in Fig. 9 is apparently (110). Figure 12 shows the kinking of needle crystals described above, and the measured angle of the kinked tip to the original direction <111> is about 108°, so that the kinking direction is assigned the same form $<1\bar{1}1>$.

Etching figure and growth steps.—Etching of the cross section in hot concentrated nitric acid reveals the growth layers shown in Fig. 13 and 14. Figure 13 shows the etching figure of a needle crystal, where the nearly circular growth layers are observed. On the other hand, there are regular hexagonal growth layers in Fig. 14, which show the etching figure of a pillar crystal. Each side of the hexagon is found to correspond to the (110) plane indexed previously. At the center of the cross section, there is a circular projected part about 10μ in both figures, which is difficult to etch.

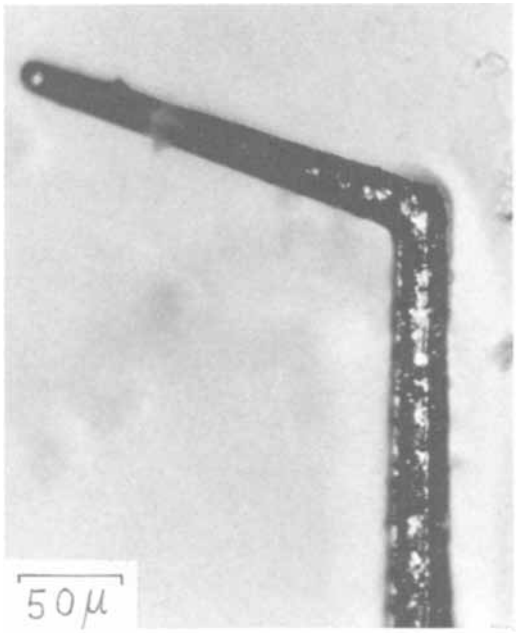

Fig. 12. Micrograph of a kinked needle crystal

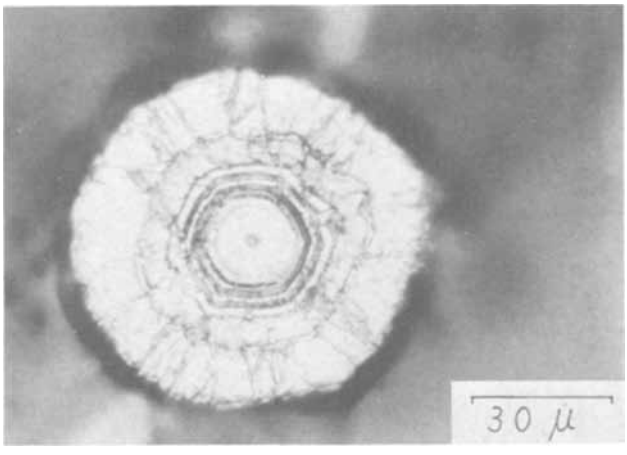

Fig. 13. Etching figure on the cross section of a needle crystal

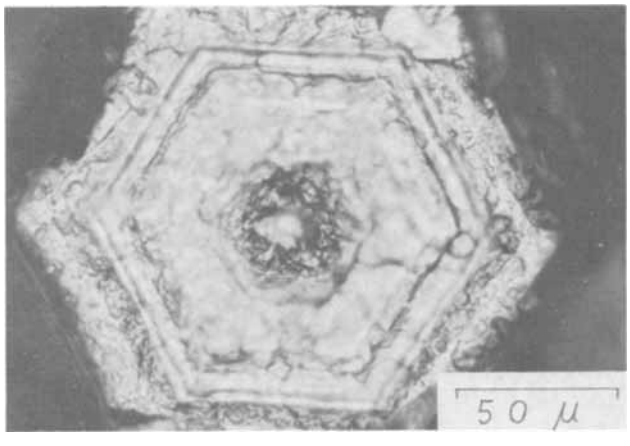

Fig. 14. Etching figure on the cross section of a pillar crystal

Continuous large growth steps were observed on the side of a pillar crystal (Fig. 15 and 16 magnified) and each step has a secondary step at the edge. Figure 17 shows a few irregular and larger growth steps for a crystal grown at the higher temperature range.

Impurity effect.—Though it was difficult to get an exact quantitative knowledge about the impurity effect, we could establish the difference of deposition rate by incorporating a few kinds of impurities into various parts of the graphite substrate. For example, manganese nitrate shows a positive effect on the crystal growth, as shown in Fig. 18. It was found similarly that Au, Pt, Pd, Ag, etc., represented positive effects, while Cu, Fe, Co, Zn, etc., showed negative effects.

Tensile strength.—The fracture strength *vs.* the diameter of needle or pillar crystals is plotted on logarithmic scales in Fig. 19. A linear relation can be seen from Fig. 19. The extrapolated value to 5μ is about 1000 kg/mm^2. The tensile strength of titanium carbide whiskers, therefore, is estimated to exceed that of iron (250 kg/mm^2), sapphire (350 kg/mm^2), and alumina (560 kg/mm^2) for the same diameter (10).

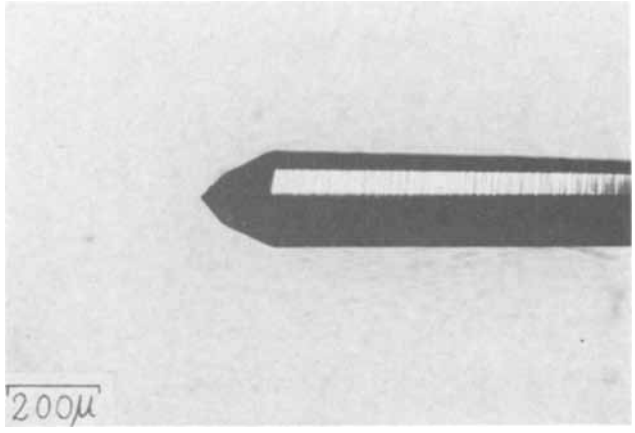

Fig. 15. Micrograph of continuous large growth steps of a pillar crystal.

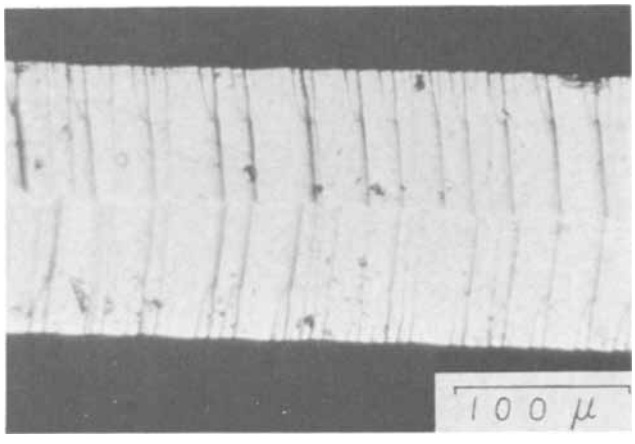

Fig. 16. Micrograph of magnified large growth steps followed by the secondary steps.

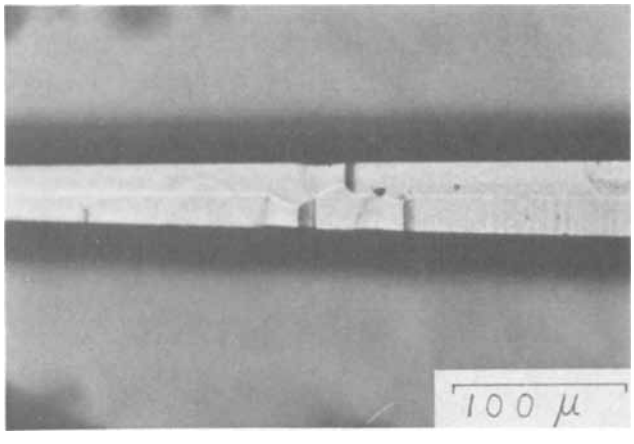

Fig. 17. Micrograph of a few irregular larger growth steps

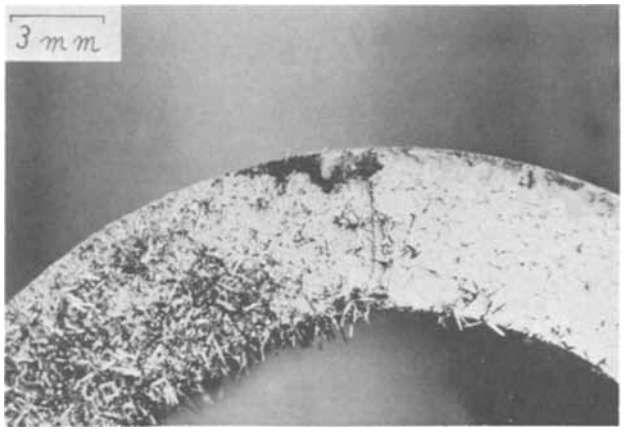

Fig. 18. Impurity effect on the graphite substrate incorporated with manganese nitrate (left side), and no impurity (right side).

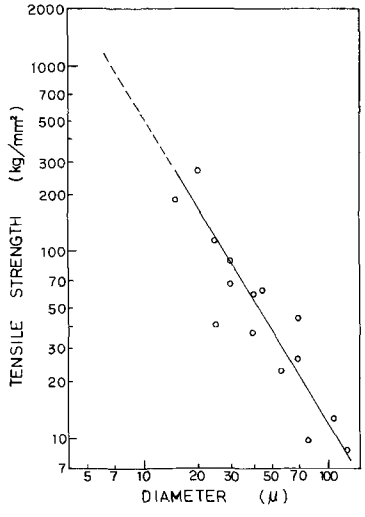

Fig. 19. Fracture tensile strength vs. diameter of needle or pillar crystals.

Discussion

Vapor phase reaction and crystal morphology.—The fact that the propane gas flow rate of 0.05 cc/sec (0.8 m/o) and cooling of gas mixture at 90°-100°C were essential for growth of a single crystal, means the decomposition reaction of hydrocarbon play an important part in the formation of titanium carbide single crystals. This suggestion seems to be supported by the study of Pearce (11) who discussed the reaction mechanism and concluded the initial formation of pyrocarbon is important rather than the reduction of the halide to elemental titanium. An appropriate temperature distribution and gas diffusion process in the reaction tube should be employed to provide pyrocarbon on the surface of the graphite substrate. In addition, a constant supersaturation at the growth tip should be maintained to obtain a given crystal morphology as described by Gatti (8). When the inside diameter of the cylinder is large, for example, it is difficult to introduce the proper quantity of pyrocarbon while keeping the temperature of the atmosphere constant. Consequently the reproducibility decreases. However, with small inside diameters, the linear flow rate of hydrogen gas is higher, making it easier to grow a fine whisker, as shown in Fig. 3.

Growth mechanism.—Observations of the etching figures (Fig. 13 and 14) suggest differences in the growth mechanism between the center and the circumference. It is convenient to describe two steps; one is the whisker growth and the other is the side growth of the needle or whisker crystals. Through microscopic observations, however, small globules could not be found at the tip of the whisker or needle crystals. Also impurities were not always essential for whisker growth as indicated before. So it is not acceptable to explain whisker growth by V.L.S. mechanism (12). More detailed investigations on the microstructure and the impurity effect should be made to learn the mechanism of whisker growth.

The growth layers in Fig. 13 and 14 suggest the variations of chemical composition. The growth steps in Fig. 15 and 16 show that the lateral growth rate increases when bunched growth steps pass through any side. Therefore we conclude the pillar crystals grow by the movement of steps on the side simultaneously with the tip growth, while in the case of the needle crystals, the side growth is a little slower than the tip growth.

Conclusion

Single crystals of titanium carbide were grown from the vapor phase in the temperature range of 1200°-1350°C. It was found that the gas flow rate or the shape and the impurities of the substrate greatly affected the crystal morphology. Above all, the contribution of propane gas flow rate was so remarkable that the decomposition of propane gas was considered to define strictly the growth range of single crystals.

Polyhedron crystals were deposited in the high temperature range, and have smooth and glossy planes on the crystal surface. Pillar crystals grew gradually as hexagonal prisms, while needle crystals grew rapidly from a growth nucleus. Whisker crystals about 3μ in diameter were observed among them. The growth direction of needle or pillar crystals was found to be <111> by the Laue method and the kinking direction was $<\bar{1}11>$.

Etched hexagonal growth layers, the large growth steps, and impurity effects suggested that the tip growth of whiskers was followed by the movement of growth steps on the side.

From the linear relation between the strength and the diameter, the tensile strength of 1000 kg/mm^2 was estimated at 5μ in diameter. Titanium carbide whiskers, are worthy of note, as a material having superior high tensile strength, as well as the other mechanical properties.

Manuscript submitted Sept. 8, 1969; revised manuscript received *ca.* Dec. 16, 1969.

Any discussion of this paper will appear in a Discussion Section to be published in the December 1970 JOURNAL.

REFERENCES

1. Wendell S. Williams, *J. Appl. Phys.*, **32**, 552 (1961).
2. G. E. Hollox and R. E. Smallman, *ibid.*, **37**, 818 (1966).
3. J. Venables, *Phys. Status Solidi*, **15**, 313 (1966).
4. F. W. Vahldick, *J. Less-Common Metals*, **12**, 429 (1967).
5. W. Hertl, *J. Am. Ceram. Soc.*, **50**, 630 (1967).
6. R. S. Wagner, W. C. Ellis, K. A. Jackson, and S. M. Arnold, *J. Appl. Phys.*, **35**, 2993 (1964).
7. M. J. Noone and J. P. Roberts, *Nature*, **212**, 71 (1966).
8. A. Gatti, C. Mancuso, E. Feingold, and R. Mehan, *J. Phys. Chem. Solids, Suppl.*, 317 (1967).
9. T. Takahashi, K. Sugiyama, and K. Tomita, *This Journal*, **114**, 1230 (1967).
10. R. L. Mehan and W. H. Sutton, *AIAA J.*, **4**, 1889 (1966).
11. M. L. Pearce and R. W. Marek, *J. Am. Ceram. Soc.*, **51**, 84 (1968).
12. R. S. Wagner and W. C. Eills, *Appl. Phys. Letters*, **4**, 89 (1964).

Structure and Electrical Properties of $FeO-P_2O_5$ Glasses

D. L. Kinser

Vanderbilt University, Nashville, Tennessee

ABSTRACT

Dielectric loss measurements, d-c conductivity, and transmission electron microscopic observations were made on thermally treated $55FeO-45P_2O$ (mole fraction) glasses. The results of this study indicate that this glass is partially devitrified after low temperature treatments. This dispersed crystalline phase gives rise to Maxwell-Wagner-Sillars heterogeneous dielectric dispersions similar to those previously attributed to electron hopping resonance in these glasses.

The electrical properties of $FeO-P_2O_5$ glasses have been investigated by Hansen (1). He has reported the d-c conductivity behavior of a $55FeO-45P_2O_5$ glass with varying $Fe^{3+}/Fe^{3+} + Fe^{2+}$ ratio, with a minimum at equal concentrations. Hansen *et al.* (2) have also reported a dielectric dispersion in three iron phosphate glasses with different $Fe^{3+}/Fe^{3+} + Fe^{2+}$ ratios. These dielectric relaxation peaks were tentatively attributed to resonance of the hopping electrons between ferrous and ferric sites. His x-ray and transmission electron microscope investigations of these glasses revealed no evidence of crystalline phases or liquid-liquid separation after annealing at 500°C.

Previous work by the present author (3) in sodium phosphate-vanadium pentoxide glasses has shown the appearance of dielectric losses with thermal treatments that cause small amounts of crystallization. Marked changes in the d-c conductivity due to thermal treatment were also reported in vanadium glasses by Hamblen *et al.* (4).

The present paper presents results of dielectric measurements on a $55FeO-45P_2O_5$ glass with different thermal treatments. A dielectric loss peak in the audio frequency range has been shown to appear concurrently with the formation of crystals that were observed by transmission electron microscopy. The dielectric loss, d-c conductivity, and transmission electron microscopy were correlated using heterogeneous dielectric models.

Experimental Procedure

Glasses examined in this study were prepared from reagent grade Fe_2O_3 and P_2O_5, melted 1 hr at 1300°C in platinum exposed to air in an electric furnace. The glass was poured in a steel mold that yielded samples approximately 17 mm diameter and 5 mm thick. All samples were annealed 1 hr at 300°C and air-cooled.

Samples used for electrical measurements were thermally treated, then polished to approximately 3 mm final thickness. After polishing, gold electrodes were vapor deposited in a guard-ring configuration. Alternating current electrical measurements were conducted in a specially designed environmental chamber that allowed atmosphere and temperature control during measurements.

Alternating current electrical measurements were accomplished using conventional audio and radio frequency transformer ratio-arm bridges. Direct current measurements were conducted in a guarded configuration using a conventional electrometer with an applied field of approximately 2 V/mm.

Samples for transmission electron microscopy were prepared from glass buttons, cast, and thermally treated as above. The samples were mechanically cut to approximately 0.3 mm thick and 3 mm in diameter. The outer annulus of approximately 1 mm width was then masked with a lacquer stop and the sample was placed in a boiling solution of equal parts HCl and H_2O. The sample was left in this solution until a "dimple" developed, then etching was stopped, and the outer masking ring was removed with acetone. The dimpled sample was then placed in the same solution and held by the outer ring with tweezers. As the first hole developed within the dimple, the sample was removed and washed in distilled H_2O. The samples were then placed in a Philips EM-300 electron microscope and examined by conventional techniques. No conducting layer was necessary to prevent charging as is required in silicate glasses. This is apparently the result of the electronic conductivity and lack of polarization in these glasses.

Each of the thermally treated glasses was also examined in a Debye-Scherrer x-ray diffraction camera.

Results

Electrical.—The d-c resistivity-inverse temperature dependence of each of the thermally treated glasses is shown in Fig. 1. The resistivity shows a subtle decrease with the 1-hr thermal treatments up to 500°C. Comparison of the d-c conductivity after annealing at 500°C with Hansen's data indicates that the $Fe^{3+}/Fe^{3+} + Fe^{2+}$ ion ratio is 0.12. Thermal treatments of 1 hr at temperatures of 600°, 700°, and 800°C cause pronounced increases in resistivity. Results of the dielectric measurements are given in Fig. 2, 3, 4, and 5 in the form

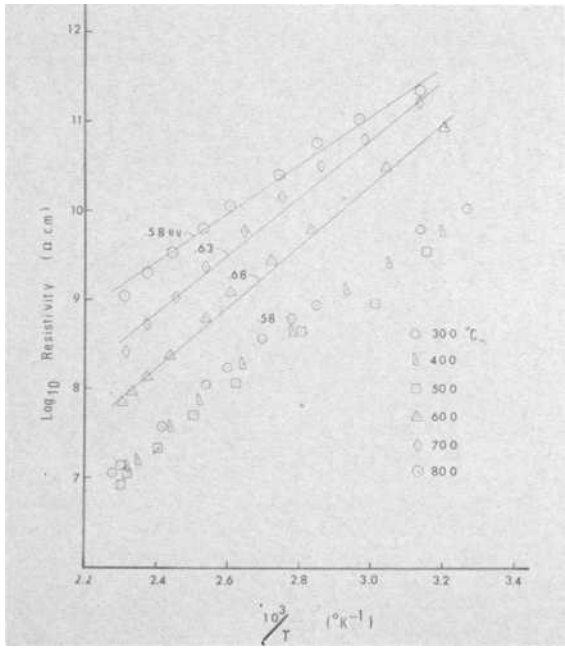

Fig. 1. D-C resistivity as a function of inverse temperature after noted thermal treatments of 1 hr duration.

* Electrochemical Society Active Member.

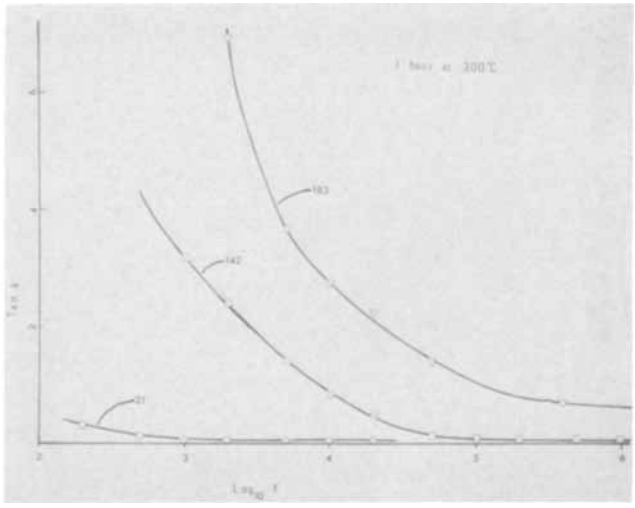

Fig. 2. Loss tangent as a function of $\log_{10}$ of frequency for $55FeO-45P_2O_5$ glass thermally treated 1 hr at 300°C. Measurement temperatures noted on curves in °C.

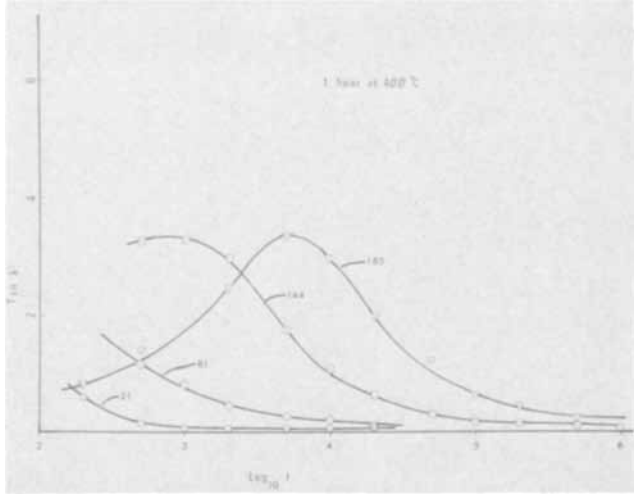

Fig. 3. Loss tangent as a function of $\log_{10}$ of frequency for $55FeO-45P_2O_5$ glass thermally treated 1 hr at 400°C. Measurement temperatures noted on curves in °C.

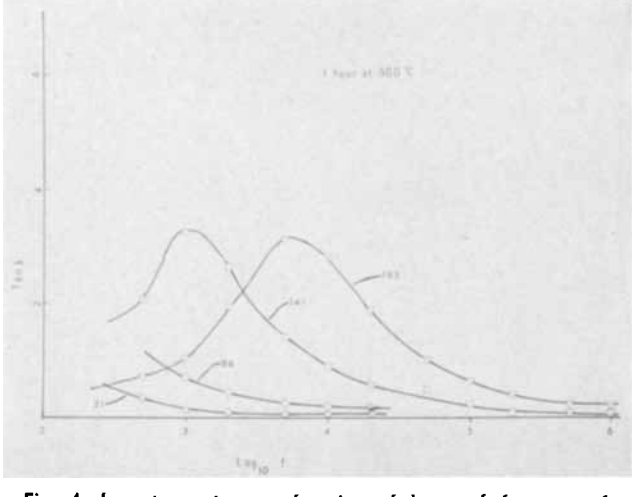

Fig. 4. Loss tangent as a function of $\log_{10}$ of frequency for $55FeO-45P_2O_5$ glass thermally treated 1 hr at 500°C. Measurement temperatures noted on curves in °C.

of tan δ_{Total} as a function of frequency. The d-c contributions were not subtracted because the resistivity is so large as to make this unnecessary. Samples treated for 1 hr at 300°C (Fig. 2) show that no resolved loss peak appears in the frequency range 10^2 to 10^6 Hz. After a 1-hr treatment at 400°C (Fig. 3), a broad loss peak appears. A similar, but somewhat sharper, loss peak also appears in the sample treated 1 hr at 500°C (Fig. 4). A 1-hr thermal treatment at 600°C (Fig. 5) yields a sample free of loss peaks in the 10^2-10^6 Hz frequency range. Thermal treatment for 1 hr at 700°C gives loss behavior indistinguishable from Fig. 5.

Microscopy.—Optical microscopy of samples thermally treated in the same manner as the electrical samples shows crystals approximately 0.1 mm diameter in the 700°C samples and approximately 100μ in diameter in the 600°C samples, but no crystals in the samples treated at lower temperatures.

Transmission electron microscopy of the samples thermally treated 1 hr at 500°C (Fig. 6) shows a fine dispersion of crystals of elongate morphology, 20,000-50,000Å in length and volume fraction probably less than 1%. Electron micrographs of the samples thermally treated 1 hr at 400°C show (Fig. 7) a still finer dispersion of elongated crystals, 5,000-10,000Å in length and volume fraction indistinguishable from the 500°C sample. Transmission electron micrography of the sample thermally treated 1 hr at 300°C shows no resolvable crystals (probably <50Å) and no evidence of liquid-liquid separation. The glass-glass phase separation could be present, but undetected, because the separated amorphous phases would have nearly equivalent electron scattering behavior.

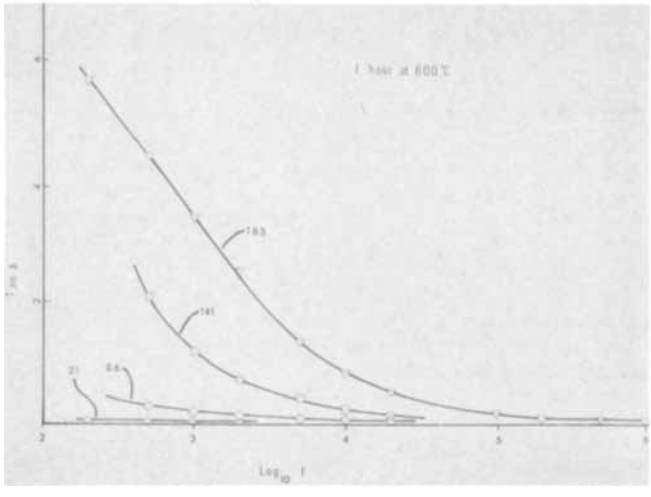

Fig. 5. Loss tangent as a function of $\log_{10}$ of frequency for $55FeO-45P_2O_5$ glass thermally treated 1 hr at 600°C. Measurement temperatures noted on curves in °C.

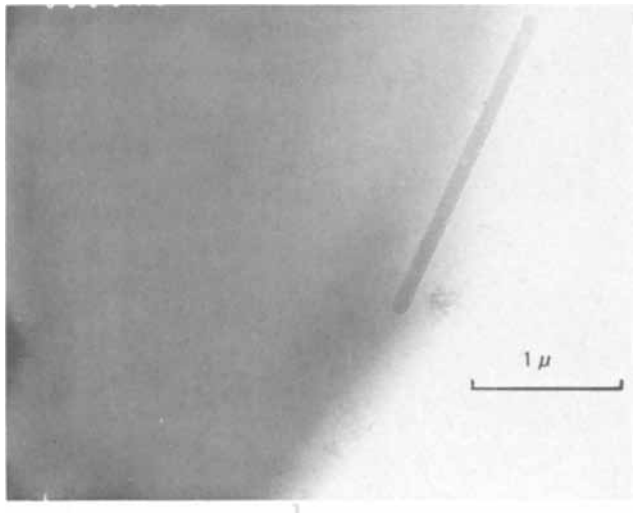

Fig. 6. Transmission electron micrograph of $55FeO-45P_2O_5$ glass after thermal treatment of 1 hr at 500°C.

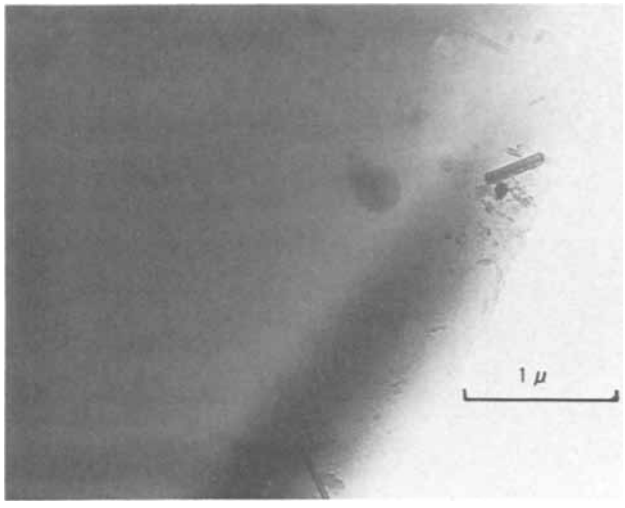

Fig. 7. Transmission electron micrograph of $55FeO-45P_2O_5$ glass after thermal treatment of 1 hr at 400°C.

The Debye-Scherrer technique shows crystals after 1 hr at 600° and 700°C. These crystals have been tentatively identified as $Fe_3(PO_4)_2$, although several lines are shifted as if solution of either FeO or P_2O_5 were present in the crystal.

Discussion

The resistivity decrease with thermal treatment temperature up to 500°C indicates that the matrix of the material is becoming a better conductor. There are two possible explanations of this observation. The first is that the increasing annealing temperature is decreasing the volume of the material and the ferrous-ferric ions are coming closer together. As the material is an electronic conductor, this approach would increase the conductivity. The second, and more probable, explanation is that the crystals observed after low temperature treatment are preferentially formed from ferrous ions, leaving the matrix relatively richer in ferric ion, thus increasing the conductivity according to Hansen's (1) observations.

After the higher temperature treatment, however, the opposite effect occurs, in that the dispersed crystals preferentially incorporate ferric ions, leaving the matrix depleted in ferric ions. The dispersed conducting phases do not contribute to the d-c conductivity because they are not contiguous; hence, no high conductivity path exists. The activation energies noted in Fig. 1 do not change appreciably with thermal treatment and compare favorably with previous results. The small deviation from linearity is also in agreement with previous results.

The Maxwell-Wagner-Sillars (5-7) heterogeneous dielectric analysis indicates that a highly conducting dispersed phase gives rise to dielectric dispersion. Conditions which give rise to this type of loss appear to be present in these materials after 400° and 500°C thermal treatments. The microscopic results indicate that the glass after a 300°C thermal treatment is homogeneous and no dielectric dispersion is observed in glasses so treated. After thermal treatments at either 400° or 500°C, a finely dispersed crystalline phase is observed in these glasses. As these crystals appear, a dielectric dispersion also appears in these crystal-glass materials. It seems that the crystalline phase is more conductive than the matrix phase, although no independent conductivity data for the crystals are available. Thermal treatments at higher temperatures (600°C and above) yield a very few large crystals which, because of their number, do not lead to observable losses.

In summary, it can be said that the dielectric loss behavior of the glasses examined in this work is consistent with partial devitrification during thermal treatments which have been previously used as annealing treatments. This result is confirmed by transmission electron microscopy, dielectric loss behavior, and d-c resistivity data.

It also appears likely that the dielectric relaxation behavior observed by Hansen in glasses of $Fe^{3+}/Fe^{3+} + Fe^{2+}$ ratios of 0.793, 0.465, and 0.147 can be attributed to similar preferential segregation in a crystalline phase.

Conclusions

1. Dielectric losses observed in $55FeO-45P_2O_5$ glasses can be attributed to Maxwell-Wagner-Sillars heterogeneous loss mechanisms, rather than the electron hopping resonance between Fe^{3+}-Fe^{2+} ion sites previously proposed.

2. The assumption of preferential segregation of a particular oxidation state of transition metal ion is necessary to explain the pronounced d-c conductivity changes observed in this glass. It is probable that similar behavior in other semiconducting transition metal oxide glasses results from similar segregation.

Acknowledgments

The author would like to acknowledge the aid of Mr. A. Dozier in experimental work and Dr. L. Wilson in parts of the analysis. The financial support of the U.S. Department of Defense under the THEMIS Program Contract No. DAAD-05-69-C-0043 is also gratefully acknowledged.

Manuscript submitted Sept. 24, 1969; revised manuscript received Dec. 1, 1969. This paper was presented at the International Commission on Glass Annual Meeting, Toronto, Sept. 11, 1969.

Any discussion of this paper will appear in a Discussion Section to be published in the December 1970 JOURNAL.

REFERENCES

1. K. W. Hansen, *This Journal*, **112**, 994 (1965).
2. K. W. Hansen and M. T. Splann, *ibid.*, **113**, 895 (1966).
3. D. L. Kinser, A. E. Clark, and L. L. Hench, Abstr. ACS 70th Annual Meeting, *Bull. Am. Ceram. Soc.*, April, 1969, p. 398.
4. P. P. Hamblen, R. A. Weidel, and G. E. Blair, *J. Am. Ceram. Soc.*, **46**, 499 (1963).
5. J. C. Maxwell, "Electricity and Magnetism," Vol. 1, p. 328, Clarendon Press, London (1892).
6. K. W. Wagner, *Arch. Elektrotech.*, **2**, 371 (1914).
7. R. W. Sillars, *J. Inst. Elec. Engrs. (London)*, **80**, 378 (1937).

Dielectric Properties of Crystalline Gamma-Al_2O_3 Formed on Dilute Al-Cu Alloys

A. J. Brock

Metals Research Laboratories, Olin Corporation, New Haven, Connecticut

At temperatures of 425°C and above pure aluminum oxidizes to form films consisting of both amorphous and crystalline γ-Al_2O_3 (1). The outer amorphous component grows by outward diffusion of aluminum ions whereas the crystalline phase grows as a series of expanding cylinders at the amorphous oxide-metal interface by the inward migration of oxygen ions through the amorphous film. The parabolic rate constant for amorphous oxide formation has a high-temperature sensitivity, 54 kcal/mol, and is independent of the presence of underlying crystals of oxide. The crystalline oxide appears to offer little or no resistance to the egress of aluminum ions.

Saunders and Pryor (2) determined an activation energy of 19.1 kcal/mol for the parabolic growth of γ-Al_2O_3 on copper-3% Al-2% Si in the temperature range 450°-740°C. These γ-Al_2O_3 films were crystalline at higher temperatures and had excellent protective properties. The pre-exponential constant, A, in the Arrhenius equation for the formation of amorphous γ-Al_2O_3 on pure aluminum below 525°C was around 2×10^8 times greater than for the formation of the structurally similar films of alumina on the copper alloy. Since the A value was considered by the authors to represent the number of cation diffusion paths in the oxide, they concluded that copper ions occupied vacant cation sites in the defect cation lattice of γ-Al_2O_3, hence decreasing the rate of outward diffusion of aluminum ions. Since the number of copper ions retained in the oxide increased with increasing temperature, reduced temperature sensitivity together with low growth rate resulted.

To throw further light on this phenomenon the dielectric characteristics of crystalline γ-Al_2O_3 formed on high-purity aluminum and on an aluminum-0.1% Cu alloy were determined. The composition of the metals is shown below.

The aluminum-0.1% Cu alloy was solution treated at 500°C for 8 hr in high vacuum and quenched in still water.

Specimens were etched for 15 min in 0.5N NaOH solution at 25°C, rinsed, immersed for 1 sec in 50% HNO_3 at 85°C, rinsed in distilled water and methanol, and stored in a desiccator for 24 hr. The specimens were oxidized in 76 Torr oxygen for 72 hr at 500°C. Such a procedure results in an oxide containing both crystalline and amorphous γ-Al_2O_3 with crystalline oxide coverage being essentially complete. This is evident from the transmission electron micrographs of the oxides stripped from the metals (Fig. 1).

Gravimetric experiments (Fig. 2) permit calculation of the total weight and, hence, the total thickness of

Table I. Composition of aluminum and aluminum-0.1% Cu alloy

Nominal composition	Cu	Fe	Si
Al	<0.0005	0.0027	0.0005
Al-0.1% Cu	0.095	0.0018	0.0005

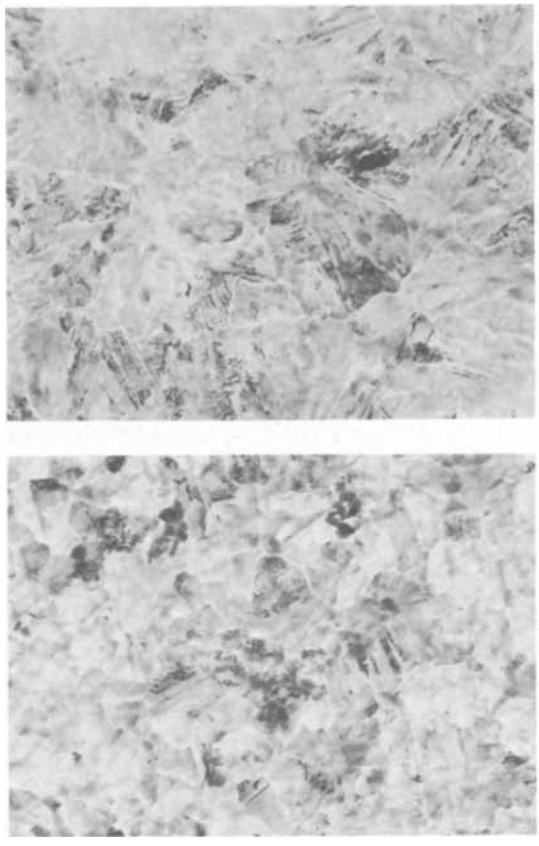

Fig. 1. Transmission electron micrographs of oxide films formed on (a) (top) Aluminum, and (b) (bottom) aluminum-0.1% copper alloy after oxidation for 72 hr at 500°C in 76 Torr oxygen. 16,000X.

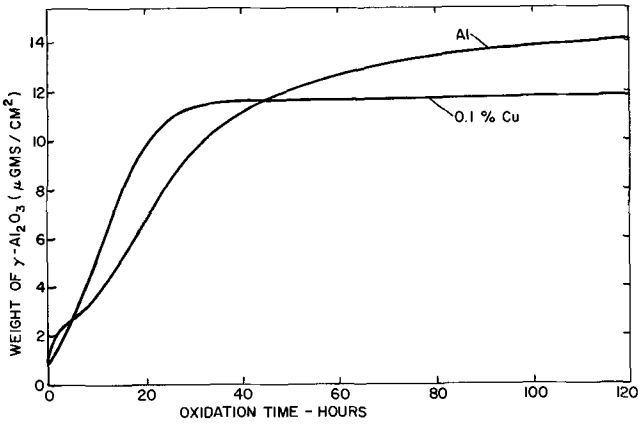

Fig. 2. Relationship between weight of γ-Al_2O_3 formed on aluminum and aluminum-0.1% copper alloy to time of oxidation in 76 Torr dry oxygen at 500°C.

oxide formed on pure aluminum after 72 hr at 500°C. Previous work on pure aluminum (1) showed that the crystalline layer was 217Å thick. Subtraction of this from the total thickness of oxide results in the thickness of amorphous oxide which was 128Å. When such a duplex film is thinned to a maximum degree in sodium chromate solution (3) the equivalent series capacitance increases to a steady value. This value, together with the equivalent series capacitance of the unthinned oxide, permits calculation of the thickness of amorphous oxide dissolved (the solution will not dissolve crystalline oxide) and hence the thickness of amorphous oxide when thinning has been completed. Results for pure aluminum are contained in Table II.

The thickness of crystalline oxide formed on Al-0.1% Cu alloy was measured directly by shadowing the inner suface of a stripped oxide film and yielded a value of 130Å. Gravimetric experiments (Fig. 2) permit calculation of the amorphous film thickness after oxidation for 72 hr at 500°C which was 151Å. Similar thinning experiments established the thickness of the amorphous oxide present on Al-0.1% Cu alloy after thinning in chromate solution to be 23Å (Table II).

The equivalent parallel resistance and equivalent series capacitance measurements made at 1 kHz on duplex films that had been fully thinned in chromate solution, with corrections being made for the residual amorphous film which remained (Table II), permits calculation of the resistivities (resistance/thickness) and apparent dielectric constants of the γ-Al_2O_3 formed on aluminum and Al-0.1% Cu alloy. These results are shown in Table III.

The dielectric properties of the crystalline γ-Al_2O_3 formed on the Al-0.1% Cu alloy are virtually identical to those of amorphous γ-Al_2O_3 whereas the crystalline oxide formed on pure Al is an extremely poor and lossy dielectric. It seems unlikely that these results can be explained in terms of the faults present in the crystals since the crystals formed on Al and Al-0.1% Cu alloy are visually faulted to the same degree (Fig. 1). Accordingly, the high apparent dielectric constant of the crystalline alumina formed on pure aluminum most likely results from the relatively large numbers of defects (vacant cation sites) in the cation lattice (2-2/3 per unit cell at stoichiometry). Such an effect has previously been observed by Gray (4) on introducing large numbers of defects into bulk rutile, and by Pryor (5) on introducing fluoride ions into amorphous γ-Al_2O_3. Since these cation vacancies will be preferred sites for aluminum ion diffusion the greater their number the lower will be the ionic resistance.

Table II. Initial thickness, thickness removed and final thickness of amorphous γ-Al_2O_3 formed on Al and Al-0.1% Cu alloy

Alloy	Initial thickness, A	Thickness removed, A	Final thickness, A
Al	128	113	15
Al-0.1% Cu	151	128	23

Table III. Thickness and dielectric properties of crystalline γ-Al_2O_3 formed on aluminum and aluminum-0.1% Cu alloy

Alloy	Capacitance at 1kHz, μF/cm^2	Thickness, A	Apparent dielectric constant	Resistivity at 1kHz, ohm-cm
Al	4.54	217	117	4.6×10^7
Al-0.1% Cu	0.554	130	9.2	3.5×10^9

Copper ions entering the crystalline oxide will have a strong tendency to associate with these vacant sites particularly since both Cu_2O and CuO form spinels with γ-Al_2O_3 (6, 7). Consequently, the preferred paths for cation migration will be decreased in number thereby explaining the increased resistance of the crystalline oxide formed on Al-0.1% Cu alloy. This result is in complete agreement with the recent work of Saunders and Pryor (2). Furthermore, since the number of cation vacancies is decreased by doping with copper ions a more normal dielectric constant is to be expected.

Resistance measurements at 1 kHz are generally taken to reflect the presence of both electronic and ionic defects in γ-Al_2O_3. Accordingly, in the present experiments and at relatively large film thicknesses, the loss measurements at 1 kHz appear more sensitive to changes in ionic conductivity than electronic conductivity since the latter must have increased due to the presence of electrons in the oxide required to preserve electrical neutrality.

Further evidence that the ionic resistance of the crystalline oxide is increased by addition of copper ions is seen from the rates of oxidation of the two metals at 500°C presented in Fig. 2. After oxidation for about 60 hr, where crystalline coverage is substantially complete, the slope of the weight gain-time curve for oxide formation on Al-0.1% Cu alloy is considerably less than that for oxide formation on high-purity aluminum. Since these slopes represent the rate of amorphous oxide formation on both alloys, when crystalline coverage is complete, the low rate on the Al-0.1% Cu alloy is due to the crystalline oxide affording additional substantial resistance to the egress of aluminum ions because its dielectric properties are similar to those of the amorphous oxide. This is in distinction to pure aluminum where the crystals of γ-Al_2O_3 are so lossy as to present no significant barrier to the passage of aluminum ions.

Acknowledgments

The author wishes to thank the Aluminum Division of the Olin Corporation for their support of this work and for their permission to publish the results.

Manuscript submitted Oct. 3, 1969; revised manuscript received *ca.* Dec. 12, 1969.

Any discussion of this paper will appear in a Discussion Section to be published in the December 1970 JOURNAL.

REFERENCES

1. A. F. Beck, M. A. Heine, E. J. Caule, and M. J. Pryor, *Corrosion Sci.*, **7**, 1 (1967).
2. S. R. J. Saunders and M. J. Pryor, *This Journal*, **115**, 1037 (1968).
3. M. A. Heine and M. J. Pryor, *ibid.*, **110**, 1205 (1963).
4. T. J. Gray, Private communication.
5. A. F. Beck, M. A. Heine, D. S. Keir, D. Van Rooyen, and M. J. Pryor, *Corrosion Sci.*, **2**, 133 (1962).
6. G. Holgersson, *Z. Anorg. Chem.*, **204**, 381 (1932).
7. Hahn and Lorent, *Z. Anorg. Allgem. Chem.*, **279**, 241 (1955).

Variation of the Optical Energy Gap with Composition in MnSe-CdSe Solid Solutions

Heribert Wiedemeier and A. Gary Sigai[1]

Department of Chemistry, Rensselaer Polytechnic Institute, Troy, New York

Increasing attention has been directed toward the investigation of alloy semiconductors, particularly with respect to the variation in energy gap with composition in pseudo-binary solid solutions. Studies of such alloys of II-VI, IV-VI, and III-V compounds show that the change in energy gap with composition is essentially linear in some cases [*e.g.*, ZnS_xSe_{1-x} (1), $PbSe_xTe_{1-x}$ (2), $Zn_xCd_{1-x}S$ (3)] and sublinear in others [*e.g.*, $Ga_xIn_{1-x}Sb$ (4)]; in some cases there is even a minimum in energy gap [*e.g.*, $ZnSe_xTe_{1-x}$ (1)].

The compounds MnSe and CdSe have the NaCl (cubic) and wurtzite (hexagonal) structure, respectively. The temperature-composition phase diagram of the pseudo-binary $Mn_xCd_{1-x}Se$ system (5, 6) includes a cubic one-phase region between 0 and 10 m/o (mole per cent) CdSe and a hexagonal one-phase region between 50 and 100 m/o CdSe, separated by a two-phase region. The present work deals with transmittance measurements on single crystals and reflectance measurements on powders of solid solutions in the MnSe-CdSe system to determine the variation in energy gap with composition. Measurements have been performed on samples in both the cubic and hexagonal one-phase regions.

Experimental

Preparation of materials.—The compounds MnSe and CdSe were synthesized from high-purity elements by vapor transport reactions (7) with iodine as the transporting agent. Powdered mixtures of various mole ratios of the pure compounds were thoroughly mixed, pressed into pellets at a pressure of 13.5 Kbar, and sealed under a vacuum of 10^{-6} Torr or less in outgassed quartz ampules. The CdSe-rich mixtures were annealed for several one-week periods at 500°C, the MnSe-rich mixtures for similar periods at 1100°C. To insure homogeneity of the solid solutions, the samples were powdered and repressed after each annealing period until the lattice parameters remained constant. Single crystals of MnSe (8) and of CdSe were prepared by vapor transport reaction; single crystals of two hexagonal solid solutions were grown by sublimation of annealed powder samples in evacuated quartz ampules at 960°C in a temperature gradient of less than 10°C. Crystals of several millimeter edge length were obtained in the form of platelets and columns. The as-grown faces of the MnSe crystals were (111) planes, and those of the CdSe and solid solution crystals were (0001) planes, as determined by the Laue back-reflection technique.

Analysis.—Quantitative chemical analysis of the pure compounds by EDTA titration (9) revealed that both materials were stoichiometric within the limits of experimental error (Cd (exp.) = 58.60%, Cd (calc.) = 58.74%; Mn (exp.) = 40.96%, Mn (calc.) = 41.03%). On the basis of radioactive tracer studies by Schäfer and Odenbach (10), the amount of iodine incorporated into the transported material is estimated to be less than 10^{-2} m/o. Emission spectrographic analysis of the compounds gave the following metal impurities in ppm by weight: Si(6-60), Cs(30-300), Mg(3-30), Fe(3-30), Al(15-150), Ca(10-100), Cu(6-60). Debye-Scherrer x-ray diffraction studies were carried out using a 114.59 mm camera and Ni-filtered CuKα-radiation to determine lattice parameters for the pure compounds and solid solutions. The final composition of the solid solutions as confirmed by lattice parameters agreed with the nominal weights of MnSe and CdSe used within the limits of experimental error. The linear dependence of lattice parameter on composition was established previously (6) and yielded the equations $a_o = 5.462 + 0.202 \cdot N$ (for the MnSe-rich cubic phase) and $a_o = 4.173 + 0.124 \cdot N$, $c_o = 6.822 + 0.193 \cdot N$ (for the CdSe-rich hexagonal phase), where N is the mole fraction of CdSe.

Reflectance measurements.—In the absence of single crystal platelets sufficiently large for transmittance measurements over the entire range of solid solution, the diffuse reflectance of microcrystalline powders was used to provide a relative measure of the absorption. This method has been fully described by Fochs (11). The intensity of the diffusely reflected light from the powdered sample on a 3.5 cm diameter disk was measured with a Beckman DU Spectrophotometer. Magnesium carbonate was used as a reference. Diffuse reflectance spectra for several $Mn_xCd_{1-x}Se$ solid solutions are shown in Fig. 1, where the per cent diffuse reflectance is plotted against wavelength. The curves possess a region of relatively constant reflectivity at the shorter wavelength end since the particles are completely absorbing. With increasing wavelength the absorption coefficient decreases, leading to multiple reflections and refractions in the powder and to a net increase in the diffuse reflectivity. When the absorption coefficient is very low, the reflectivity may approach unity. The energy gap was calculated from the wavelength at the intersection of the straight-line extrapolations above and below the short-wavelength knee of the curve. Fochs (11) and Godik and Ormont (12) have shown that this method of evaluation yields

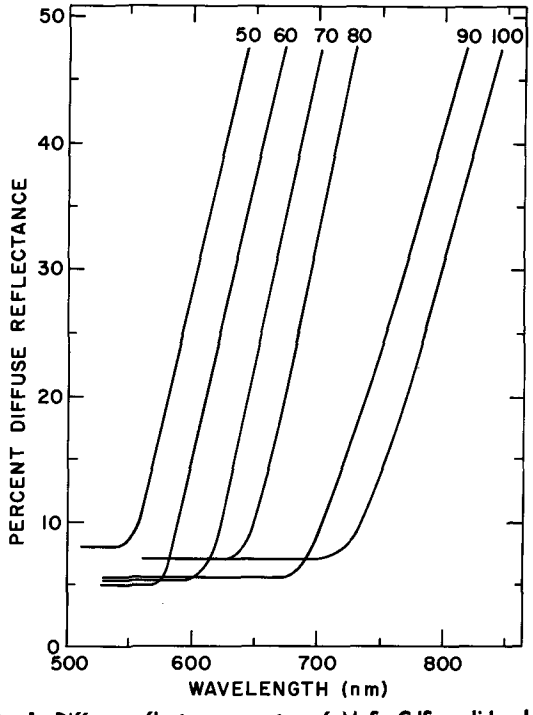

Fig. 1. Diffuse reflectance spectra of MnSe-CdSe solid solutions. Figures indicate m/o CdSe.

[1] Present address: RCA Laboratories, Princeton, New Jersey.

Key words: linear variation, optical energy gap, MnSe-CdSe solid solutions, transmittance and reflectance measurements.

an accuracy of 1-2% and does not depend critically on the particle size of the powder.

Transmittance measurements.—Measurements of the transmittance (I/I_0) were made on single crystal platelets of CdSe, two hexagonal solid solutions and MnSe, all grown from the vapor phase. A Cary recording spectrophotometer Model 14R was used. The incident light was perpendicular to the faces of the crystal platelets, and the degree of inherent polarization of the instrument was between 15 and 30% (13) in the wavelength range of interest. The energy gap was determined from the wavelength given by the intersection of the extrapolated linear portion of the steeply descending transmittance curve with the wavelength axis. The uncertainty in the wavelength intercepts is estimated to be less than ±10 nm.

Results and Discussion

The compositions, lattice parameters, colors, and energy gaps of the investigated materials are summarized in Table I. The variation of the energy gap with composition for the one-phase regions of the MnSe-CdSe system is shown in Fig. 2. It is seen that there is a linear dependence of the energy gap on composition in the CdSe-rich hexagonal one-phase region up to the phase boundary at 50 m/o CdSe. The relationship can be expressed by the equation

$$E_G = 2.78 - 1.08 \cdot N \qquad [1]$$

where N is the mole fraction of CdSe and E_G is given in eV. CdSe is known to have a direct band transition (14); the linear variation of the band gap could indicate (15) that the solid solutions might also have direct gaps.

The value of the energy gap for pure CdSe obtained from reflectance measurements (1.70 eV) is identical with values obtained from transmittance measurements on three CdSe (0001)-platelets of different thickness (1.70 eV, with light partially polarized perpendicular to the c-axis). These results are in reasonable agreement with the value found by Keller and Pettit (16) (1.72 eV, with light polarized perpendicular to the c-axis). The slight disparity is probably due to different experimental conditions.

Qualitative thermoelectric measurements on CdSe platelets indicate n-type conductivity in agreement with previous observations (17). This is usually explained by the selenium deficiency of CdSe, since the entire homogeneity range of CdSe apparently lies on the Cd-rich side of the stoichiometric composition (17). Thermoelectric measurements on solid solution single crystals with 50 and 60 m/o CdSe, respectively, also indicated n-type conductivity.

Reflectance measurements on polycrystalline powders of pure MnSe and solid solution samples containing 10 m/o CdSe yielded energy gap values of 2.00 and 1.94 eV, respectively. Preliminary investigation of transmittance measurements on single crystal platelets of MnSe indicated an extrapolated absorption edge at 680 nm (1.8 eV). An energy gap value for MnSe of 2.5 eV was reported by Lawson and Nielsen (18) with no indication of the experimental technique used. Makovetskii and Sirota (19) obtained a value of 0.7 eV from measurements of the electrical conductivity as a function of temperature on sintered polycrystalline powders of MnSe. Since the MnSe spectrum is complicated by transitions within the d-levels of manganese, similar to the situation found for MnS (20, 21), a detailed analysis of the low temperature spectrum of MnSe will be necessary in order to determine unambiguously the fundamental absorption edge. For this reason the data reported for MnSe can be regarded as only preliminary.

Table I. Lattice parameters, colors, and room temperature energy gaps for MnSe, CdSe, and their solid solutions

Bulk composition, m/o CdSe	Lattice constant (Å)* a_0	c_0	Color	λ_{edge}, nm	Energy gap,† eV
0	5.462		Brown-Black	620	2.00
10	5.483		Brown-Black	640	1.94
50	4.236	6.919	Orange-Red	555	2.23
60	4.247	6.938	Crimson-Red	585	2.12
70	4.261	6.958	Red-Violet	605	2.05
80	4.272	6.973	Black	645	1.92
90	4.285	6.997	Black	695	1.78
100	4.298	7.016	Black	730	1.70

* The error limits for a_0 are ±0.001Å in the cubic phase (0 and 10 m/o CdSe), and ±0.001 and ±0.003Å for a_0 and c_0, respectively, in the wurtzite phase.

† From reflectance measurements; the uncertainty in the energy gap is estimated not to be greater than 1-2%.

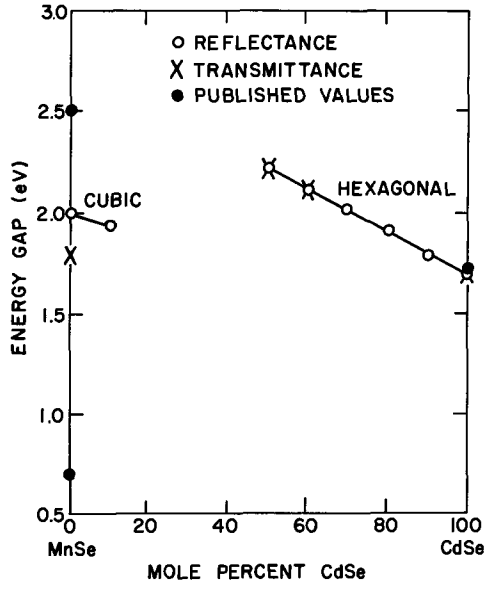

Fig. 2. Energy gap as a function of composition in the cubic and hexagonal one-phase regions of the MnSe-CdSe system.

Acknowledgments

The authors wish to acknowledge the support of this work by the National Aeronautics and Space Administration, by the National Science Foundation, and partially by the Xerox Corporation.

Manuscript submitted June 17, 1969; revised manuscript received ca. Jan. 7, 1970. This paper is based in part on a thesis submitted by one of the authors (A.G.S.) to the Graduate School of Rensselaer Polytechnic Institute in partial fulfillment of the requirements for a Ph.D. degree.

Any discussion of this paper will appear in a Discussion Section to be published in the December 1970 JOURNAL.

REFERENCES

1. S. Larach, R. E. Shrader, and C. F. Stocker, *Phys. Rev.*, **108**, 587 (1957).
2. W. W. Scanlon, *J. Phys. Chem. Solids*, **8**, 423 (1959).
3. J. H. Gisolf, *Physica*, **6**, 84 (1939).
4. J. C. Woolley, S. A. Evans, and C. M. Gillett, *Proc. Phys. Soc.*, **74**, 244 (1959).
5. W. R. Cook, Jr., *J. Am. Ceram. Soc.*, **51**, 518 (1968).
6. H. Wiedemeier and A. G. Sigai, "Phase Studies in the Solid Region of the MnSe-CdSe System," to be published elsewhere.
7. H. Schäfer, "Chemical Transport Reactions," Academic Press, New York (1964).
8. H. Wiedemeier and A. G. Sigai, *J. Cryst. Growth*, **6**, 67 (1969).
9. H. Flaschka, *Chem. Anal.*, **42**, 56 (1953).
10. H. Schäfer and H. Odenbach, *Z. Anorg. Allg. Chem.*, **346**, 127 (1966).
11. P. D. Fochs, *Proc. Phys. Soc. (London)*, **69B**, 70 (1956).
12. E. E. Godik and B. F. Ormont, *Sov. Phys.-Solid State*, **2**, 2680 (1961).
13. M. E. Hills, A. L. Olsen, and L. W. Nichols, *Appl. Opt.*, **7**, 1437 (1968).

14. M. Aven and J. S. Prener, "Physics and Chemistry of II-VI Compounds," Chap. 1, p. 53, John Wiley & Sons, Inc., New York (1967).
15. H. Reiss, "Progress in Solid-State Chemistry," Vol. 1, p. 277, Pergamon Press, New York (1964).
16. S. P. Keller and G. D. Pettit, *Phys. Rev.*, **120**, 1974 (1960).
17. H. Reiss, "Progress in Solid-State Chemistry," Vol. 2, p. 249, Pergamon Press, New York (1965).
18. W. Lawson and S. Nielsen, "Preparation of Single Crystals," p. 243, Butterworths Scientific Publications, London (1958).
19. G. Makovetskii and N. Sirota, *Dokl. Akad. Nauk. Belorussk SSR*, **9**, 85 (1965).
20. D. Huffman, R. Wild, and J. Callaway, *J. Phys. Soc. Japan*, **21**, 623 (1966).
21. H. Wiedemeier and A. Khan, Unpublished results.

Preparation of Thin Silicon Crystals by Electrochemical Thinning of Epitaxially Grown Structures

H. J. A. van Dijk and J. de Jonge

Philips Research Laboratories, N. V. Philips' Gloeilampenfabrieken, Eindhoven-Netherlands

The availability of large area, thin silicon crystals on insulating substrates would increase the possibilities of design and fabrication of semiconductor devices. Silicon on sapphire may be one approach to this subject. Another way to obtain single crystals thinner than 20μ with areas larger than 1 cm^2 consists of controlled thinning of lapped wafers by mechanical or chemical means. Mechanical thinning is not an easy way. Machines used for this work are mechanically complicated because of the need of precise thickness and plane-parallelism control. Equally thinning of wafers by chemical etching requires a good control of the etching conditions to realize a preset and uniform thickness over larger areas. The preparation of thin silicon crystals by selective electrochemical etching of suitable epitaxial structures is described in this paper. The system is designed to be self-controlling; the etching process stops automatically at a preset thickness without the need of highly controlled etching conditions. Crystals with thicknesses of 0.5-20μ and as large as 10 cm^2 can be made easily in routine operations.

The anodic dissolution of silicon has been studied by numerous workers (1). We investigated the anodic dissolution rate of plate-shaped silicon single crystals in some detail, using a 5% solution of hydrofluoric acid in water as an electrolyte. In Fig. 1, schematically, the current density of the silicon anodes is plotted *vs.* the applied potential. Since the current density is related to the dissolution rate of silicon, it can be seen that p-type and heavily doped n-type material can be dissolved, whereas n-type silicon does not dissolve at sufficiently low voltages. It should therefore be possible to separate n$^+$- or p-type regions from n-regions by electrochemical dissolution. This principle was evaluated to obtain high quality thin crystals starting from suitable epitaxially grown structures.

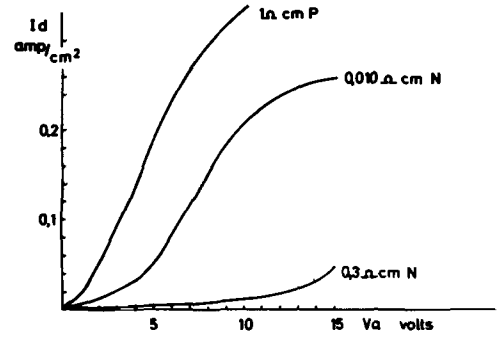

Fig. 1. Current density *vs.* applied potential of silicon anodes in 5% HF.

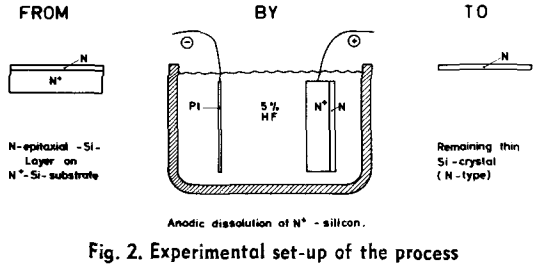

Fig. 2. Experimental set-up of the process

Experimental Technique

The experimental set up is shown schematically in Fig. 2. On a heavily doped n-type substrate with a specific resistance of less than 0.015 ohm-cm an n-type layer is grown epitaxially with a specific resistance higher than 0.3 ohm-cm. The epitaxial wafer is mounted face down on a glass plate with beeswax. The anode contact is made by pressing a platinum strip on the n$^+$-side of the wafer close to its edge. The wafer is immersed completely in the electrolyte and the n$^+$ substrate is dissolved anodically using a current density of about 150 mA/cm^2. The dissolution process stops at those areas where the n-epitaxial layer becomes exposed to the electrolyte. A thin, plate-shaped crystal is left.

In order to prevent the formation of isolated n$^+$-islands (residues of substrate material) on the remaining n-layer, the substrate is bevelled prior to etching in such a way that it is somewhat thinner at the area remote from the anode contact. This bevelling operation is not a critical process step and can be done by hand lapping. To prevent any etching of the epitaxial layer as soon as it is exposed to the electrolyte some precautions must be taken. Mechanical damage of the epilayer, the presence of hole-injecting structures as well as excessive heating and exposure to light should be avoided. Hence the electrolyte is kept at room temperature, and the etching is performed in total darkness.

Often, after electrochemical etching, the newly exposed crystal surface has a dull appearance due to a thin deposit ($<0.1\mu$) of unknown composition. A treatment with a slow-working etch (*e.g.*, a solution containing HF, acetic acid and some $KMnO_4$) results in a smooth and shiny surface. It may be clear that thickness variations of the thin crystals prepared by this technique only depend on the thickness control during the epitaxial growth.

The preparation of thin, p-type crystals is possible by this technique starting from n$^+$np-structures. After mounting on a glass plate with wax (with the p-type zone adjacent to the glass) the n$^+$ substrate is dissolved anodically. The n-type intermediate layer acts as the etching-stop. This n-type layer, which can be very thin, can be etched away chemically. A con-

venient way to prepare thin p-type crystals is to start with an epitaxially grown p-type layer with a specific resistivity higher than 0.5 ohm-cm on a n^+-substrate. The substrate is dissolved anodically, leaving a thin p-type crystal with a very thin n-type layer adjacent to the former substrate side.

Also thin n-type silicon crystals with a thin n^+-base (total thickness, *e.g.*, 10μ) can be prepared with this technique starting with multilayer epitaxial structures of suitable geometry and doping levels. Both n^+ (substrate) nn^+n and n^+ (substrate) pn^+n-structures can be used. After the substrate has been dissolved electrochemically the n- or p-type layer can be etched away chemically leaving the overlying thin crystal with n^+n-structure. The chemical etching is not a critical process and can be carried out in the conventional way.

The selective electrochemical etching process outlined above may contribute to silicon device and circuit technology in various ways. One possibility is first to carry out all necessary diffusions, metallizations etc. on the epitaxial silicon wafers followed by the removal of the substrate by electrochemical etching. MOS transistors and other devices with "vertical" junctions have been prepared. The preparation of targets for silicon-vidicon-TV pick-up tubes is possible with this technique. Thin membranes of single crystalline silicon showed excellent properties for the preparation of pressure sensitive devices for medical and other purposes.

Acknowledgment

Acknowledgment is given to E. Kooi and M. J. J. Theunissen for their stimulating discussions and to L. A. H. v. Hoof for his outstanding experimental help.

Manuscript submitted Oct. 6, 1969; revised manuscript received *ca.* Dec. 4, 1969. This was a Recent News Paper presented at the Montreal Meeting, Oct. 6-11, 1968.

Any discussion of this paper will appear in a Discussion Section to be published in the December 1970 JOURNAL.

REFERENCE

1. A. Uhlir, *Bell Syst. Tech. J.*, **35**, 333 (1956); D. R. Turner, *This Journal*, **105**, 402 (1958); D. R. Turner, *ibid.*, **107**, 810 (1960); R. Memming *et al.*, *Surface Sci.*, **4**, 109 (1966).

The Effect of Gas Concentrations in the Diffusion of Silicon from a Phosphine Source

James S. Kesperis

U. S. Army Electronics Command, Electronic Components Laboratory, Integrated Electronics Division, Fort Monmouth, New Jersey

The use of the gas phosphine (PH_3) as a diffusion source for silicon was originally presented by Donovan and Smith (1). These workers pointed out that adjustment of the diluted phosphine concentration in a nitrogen carrier gas containing very low O_2 concentrations offered a means of creating a local P_2O_5 diffusion source in a predictable manner. There has been, however, no discussion in the literature of those process and control factors whch determine the utility of the process as a practical and applicable technology. In the present paper, the experimental results on the effect of O_2 and PH_3 concentrations on sheet resistance (r_p), phosphosilicate glass growth, and process control are presented in a range pertinent to the fabrication of npn-bipolar based integrated circuits, and more specifically to the fabrication of emitter and other high conductivity areas of such circuits.

Experimental

In all cases, diffusion depositions were carried out in a Thermco furnace with a 20-in. thermal zone flat to ±1°C. Depositions were made with the silicon mounted horizontally on the diffusion boat. The phosphine source is commercially prepared as a 1% diluted mixture in argon. An analysis by infrared spectroscopy provides the specific concentration. The phosphine was injected through a quartz vane which terminated in the 55 mm diffusion tube at a point corresponding to a temperature of 625°C. Brooks Instrument Corporation flow meters, with calibrated graduations for argon, were used to monitor the phosphine flow rate in relation to the source tank analysis. Directly calibrated N_2 and O_2 flow meters of similar type were used. The meters were kept in a cabinet at a temperature of 80° ± 2°F. It was assumed that the flow meters exhausted into an open tube diffusion reactor (atmospheric pressure). N_2 and O_2 were injected at the rear of the tube. Half of the total N_2 flow was coinjected with the PH_3 through the vane. One-inch diameter wafers were used, the orientation was (111), and the resistivity was p-type, 1 ohm-cm ±10%. The same total flow rate, 1700 cc/min was used in all cases. With the exception of the data on the dependence of sheet resistance on temperature, all depositions were made for 20 min. A deposition was initiated by inserting the wafers in a nitrogen flow. After a stabilization period of 1 min, the proper amount of oxygen is introduced for a period of 1 min. The phosphine is then turned on for the deposition period. O_2 and N_2 are allowed to flow for an additional minute after the PH_3 is turned off. The O_2 is turned off and the wafers are left in a nitrogen flow for an additional minute before pull-out.

It should be noted that in practice, diffusion runs are made in tubes which are maintained in a "doped" condition. All runs in this study were made only after the tube had received a minimum of 1 hr predoping during the day of the run under conditions of 1500 ppm PH_3 and 35% O_2. Observations on the behavior of the tube itself as an absorber or emitter of P_2O_5 have been described (2). For the flow concentrations and dynamics in the present study, tube predoping was found to have a negligible effect in the sheet resistance range of interest, and successive emitter fabrication runs showed indistinguishable spreads in r_p between wafers within a run and on a run-to-run basis. The fact that the tube itself acts as a source means that a phosphorous-containing oxide is formed on the silicon surface during the 2-min interval in the furnace prior to the introduction of the phosphine source so that an immediate diffusion source exists for the silicon.

Effect of O_2 and PH_3 Concentrations

In Fig. 1, r_p is plotted against the PH_3 concentration for oxygen concentrations ranging from 1.5 to 70.6%

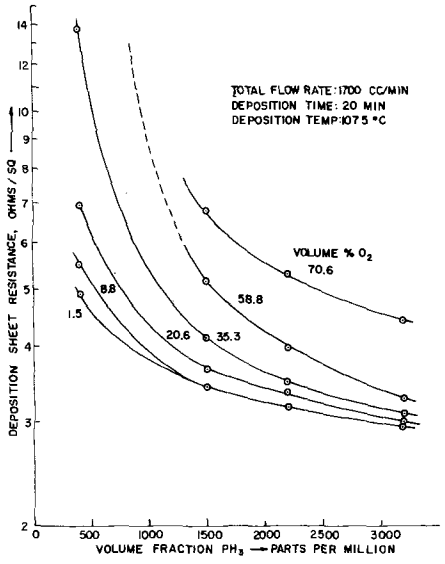

Fig. 1. Variation of r_p with volume fraction PH_3

by volume. Each point represents an averaging of eight independent runs made under the indicated conditions. All curves, with the possible exception of the one with 70.6% O_2, converge with increasing PH_3 concentration. The rate of change of sheet resistance decreases as the PH_3 concentration increases. Process saturation, however, when defined as zero change in r_p with change in PH_3 concentration, is not reached even at 3200 ppm PH_3.

A change in oxygen concentration, from 1.5 to 8.8% produces no significant r_p change for 1500 ppm PH_3 or more. Above 8.8% O_2 the change in r_p with per cent O_2 change increases with increasing oxygen. The effect of increasing O_2 concentration, important from a process control viewpoint, is to produce increasingly rapid r_p changes as the phosphine concentration decreases, the effect being maximum at high oxygen concentrations and at low phosphine concentrations.

In Fig. 2, the same r_p data are plotted in terms of equal volume fraction ratios (cc PH_3/cc O_2) against r_p with cc PH_3 as the parameter. Here it can be seen that equal volume concentrations do not produce equal sheet resistances. The r_p values depend on the PH_3 flow rate, and the curves shift upward and to the left

Table I. Sheet resistance control
(values in ohms/square, ± extreme variation)

	ppm PH_3			
% O_2	420	1500	2200	3200
1.5	4.94 ± 1.9%	3.45 ± 0.8%	3.17 ± 0.7%	2.95 ± 0.5%
8.8	5.51 ± 3.7%	3.45 ± 1.0%	3.20 ± 1.1%	2.95 ± 1.0%
20.6	6.97 ± 3.2%	3.66 ± 1.9%	3.37 ± 1.8%	2.99 ± 0.7%
35.3	10.70 ± 3.2%	4.15 ± 2.0%	3.51 ± 1.7%	3.10 ± 1.8%
58.8	—	5.19 ± 5.3%	3.97 ± 4.0%	3.28 ± 2.2%
70.6	—	6.78 ± 5.0%	5.33 ± 4.6%	4.44 ± 2.8%

with closer spacing as PH_3 saturation of r_p is approached. Furthermore, it is obvious that r_p decreases as the concentration of both reactants (O_2 and PH_3) is increased.

Process Reproducibility

The reproducibility of the process increases generally as r_p goes toward saturation with respect to either PH_3 or O_2 concentration. In Table I, the average sheet resistance of eight runs for each point is listed together with the variation of the measured extremes about their mean in per cent. It can be seen that for ppm PH_3 = 1500 and % O_2 = 35.3, the maximum variation is ±2%. The process is uncontrollable with 58.8 and 70.6% O_2 at 420 ppm PH_3 for the indicated conditions of time, temperature, and total flow rate.

Phosphosilicate Glass

The formation of a phosphosilicate oxide (glass) during the deposition process appears to be essential for controllable diffusion with this process. Attempts to utilize the thermal cracking of PH_3 in a nonoxidizing atmosphere

$$2\,PH_3 \xrightarrow[440°C]{\Delta} 3H_2 + 2P \qquad [1]$$

for diffusion temperatures of 1000°-1100°C gave erratic results while causing damage to the silicon surface. No controllable conversion to n-type resulted in the reducing atmosphere, although localized conversion was observed. Frequently, random pitting resulted, suggesting enhanced reactions at surface defect sites. At all times heavy deposits of phosphorus were observed at both the back and exit ends of the reaction tube. In the presence of oxygen, the general dependence of glass thickness on O_2 and PH_3 concentration can be seen in Fig. 3. In this figure, the indicated points were determined by interference techniques to establish the order and by very careful matching and

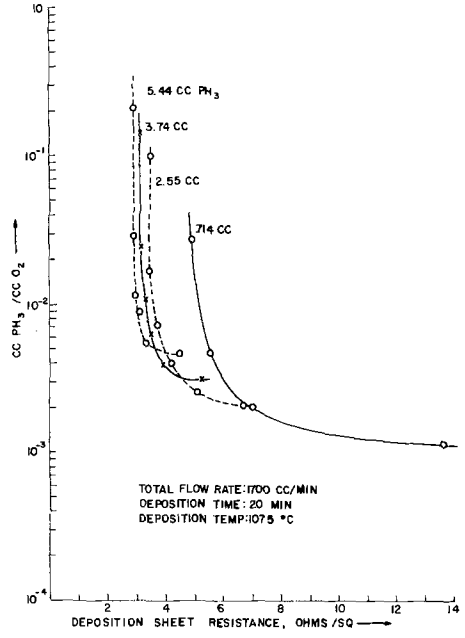

Fig. 2. Variation of r_p with the volume ratio PH_3/O_2

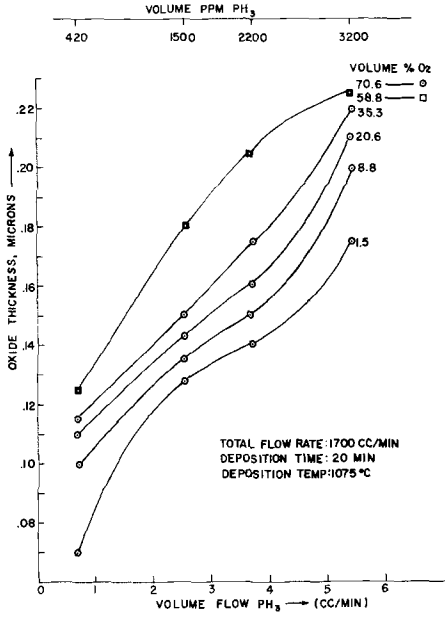

Fig. 3. Dependence of oxide thickness on volume fraction PH_3

interpolation-approximation between established interference colors using actual calibrated oxidized silicon samples. (In addition, this approximation involves an undetermined error in absolute oxide thickness because of differences in the indices of refraction of the doped oxides and that of pure SiO_2.) The thickness can be seen to increase with both PH_3 and oxygen concentrations. Changes from 58.8 to 70.6% O_2 produced no detectable color change for any given PH_3 concentration, and the convexity (above 1500 ppm PH_3) of this curve is in contradistinction to the others in the figure, suggesting that the glass growth rate mechanism differs at high oxygen concentrations. Assuming the correctness of the curve shapes in Fig. 4, there is no simple quantitative relationship between growth rate and either O_2 or PH_3 concentrations. There are several possible reactions involved in the deposition process which can determine both phosphorus source availability and glass growth rate.

For low oxygen concentrations, Donovan and Smith have postulated reactions [1], [2], and [3].

$$4P + 5\,O_2 \rightarrow 2P_2O_5 \qquad [2]$$

$$2P_2O_5 + 5Si \rightarrow 5SiO_2 + 4P \qquad [3]$$

The last [3] reaction involves the localized reduction of a P_2O_5 source by the silicon, with the growth of a SiO_2-P_x glass phase from which diffusion takes place. In the present study, water was consistently observed at the exit port of the diffusion tube, with the amount condensed heaviest at 3200 ppm PH_3. This suggests that for the dynamic tube conditions the P_2O_5 source is maintained by

$$2PH_3 + 3\,O_2 \rightarrow P_2O_5 + 3H_2O \qquad [4]$$

In the presence of excess O_2 or H_2O from [4], an increased oxidation rate of silicon would limit the direct reduction of P_2O_5 by the silicon as postulated by [3]. However, for any fixed O_2 concentration, an increase in PH_3 produces a thicker oxide and a lower sheet resistance (Fig. 1 and 3) suggesting the incorporation of more available phosphorus in the growing glass which acts as the diffusion source. On the other hand, with constant PH_3, increases in O_2 concentration generally yield an increased glass thickness with an increase in sheet resistance throughout most of the experimental range, suggesting for this range source limitation in which diffusion determines the phosphorus availability to the silicon.

Temperature Dependence of r_p

An expression for r_p as a function of average mobility (μ), surface concentration (N_s) deposition time (t_p), and an exponential thermal dependence of the diffusion constant D_o is given by the following for constant source conditions

$$r_p = (\sqrt{\pi}/2\; q\mu \sqrt{D_o t_p})\,(1/N_s)\; e^{E/2KT} \qquad [5]$$

If N_s and μ show small variations over the temperature range, then a semilog plot of the data should result as shown in Fig. 4. The above dependency has been observed for various deposition systems, for example $POCl_3$, BBr_3 (2), and P_2O_5-CaO (3) among others. Phosphine depositions made for 1 hr in this study showed reasonable agreement with respect to sheet resistance and activation energy with the P_2O_5-CaO closed box depositions of Mackintosh (3) in the same temperature range.

The points on curve 4 were made under conditions of 35% O_2 and 1500 ppm PH_3 for 1 hr in the temperature range of 975°-1100°C. Three independent runs were made at each temperature and averaged. No point group showed a maximum spread of greater than 2%. It was found impossible to construct such a curve at 70.6% O_2 because of poor control at temperatures below 1075°C with 1500 ppm PH_3. One hour r_p values of 2.08 ohms/sq with 1.5% O_2 and 1500 ppm at 1075°C, and 4.20 ohms/sq with 8.8% O_2 and 1500 ppm at 1000°C have been reproducibly obtained, suggesting that lines of approximately the same slope lying below the 35% O_2 curve can be readily obtained for lower oxygen concentrations. Extrapolation, however, to lower temperatures for any fixed condition should not be made; and the relationship should be established empirically for desired conditions of time, concentrations, and total flow rate, first to establish the reproducibility and second to determine inflection points to increased slope, which limited experiments in this study have shown to occur at temperatures below 1000°C.

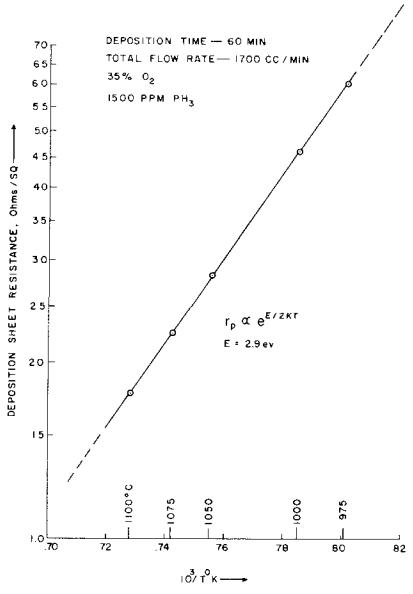

Fig. 4. Thermal dependence of r_p

Discussion

The phosphine process, with its requirement for an oxidizing atmosphere and its dependence on the transport of a P_2O_5 source to the silicon surface for diffusion of phosphorus, is similar to the well-known solid P_2O_5 and liquid $POCl_3$ source processes. The formation of water is unique with the PH_3-O_2 system, but bears no parallel to the deleterious effect of moisture on the control of sheet resistance with the P_2O_5 source, since with this system the P_2O_5 species is locally and controllably created within the diffusion tube in the vapor state.

The control of the process is excellent, particularly in the sheet resistance range of interest in this study, and maximum control is obtained when the process is performed at near saturation conditions of r_p. For 20-min deposition times, the use of the 35% O_2, 1500 ppm PH_3 process has yielded a 4.19 ohms/sq ± 2.5% (2-sigma) variation in 140 test wafers used to monitor emitter deposition runs during IC and bipolar fabrication. From Table I, it can be inferred that this control would be even tighter for the more saturated conditions of lower O_2 and higher PH_3 concentrations.

The uniformity and predictability of oxide color is excellent and surpasses that observed for equivalent $POCl_3$ and P_2O_5 depositions. Visual perfection and lack of microscopic defects is invariably obtained with occasional nonuniformity observed only where the oxide thickness was less than 1250Å (values for 420 ppm PH_3). This oxide thickness increases with the PH_3 flow rate (and the volume concentration) for any fixed experimental oxygen volume concentration. The thickness also increases with oxygen concentration for fixed PH_3 concentrations up to ≈ 60% O_2. In terms of volume ratios, the oxide thickness increases with (cc PH_3/cc O_2) for constant oxygen concentration and decreases for constant PH_3 concentration for oxygen concentrations less than 60%.

It can be seen that for a given time and temperature, this process uniquely permits selection from a wide range of controllable emitter sheet resistances and

oxide thicknesses by variation of the phosphine or oxygen concentrations. This permits two degrees of freedom over the variation of temperature conventionally used with other sources. Operational simplicity is a further advantage; the desired rates are set by flow meter, the process can be readily automated, and there is no source preparation or reservoir maintenance involved. The process is completely compatible with the fabrication of silicon integrated circuits. The fact of water formation and the possibility of PH_3-Ar commercial source contamination adversely affecting the electronic quality of the device or the final SiO_2 layer has been examined through the fabrication of high-gain bipolars. These devices, using phosphine-deposited emitters with areas as high as 3 square mils and with the deposition oxide retained, have exhibited gains of 1,000 with VCB = 0 at a collector current of 1 μA. The collector currents were exponential with qV_{BE}/KT from at least 100 pA to a few milliamperes, while the base currents varied with exp qV_{BE}/nKT with $n = 1.2$ at a V_{BE} corresponding to a collector current of 1 μA. Conventional wet/dry oxidation techniques were used for the original thermal oxide.

Acknowledgment

Mr. J. Schweitzer, USAECOM, provided considerable assistance in diffusion and evaluation. Mr. R. S. Yatsko, now with ERC, NASA, made important contributions in the initial investigation of gas diffusion processes at Fort Monmouth which were accelerated by helpful discussions with G. Strull and R. M. McLouski (4) of Westinghouse.

Manuscript submitted Sept. 12, 1969; revised manuscript received *ca.* Jan. 12, 1970.

Any discussion of this paper will appear in a Discussion Section to be published in the December 1970 JOURNAL.

REFERENCES

1. R. P. Donovan and A. M. Smith, Paper 150 presented at the New York Meeting of the Society, Sept. 29-Oct. 3, 1963.
2. R. M. Burger and R. P. Donovan, "Fundamentals of Silicon Integrated Device Technology," Vol. 1, Prentice-Hall, Inc., Englewood Cliffs, N. J. (1967).
3. I. M. Mackintosh, *This Journal*, **110**, 392 (1962).
4. R. M. McLouski, "Investigation and Development in the Diffusion of Gaseous Impurities into Silicon," Final Rpt., Project GADS, NAS 5-2755, NASA-Goddard, March 1965.

Brief Communication

Oxygen X-Ray Emission Band Shifts Applied to the Characterization of Transition Metal Oxide Surface Layers

H. B. Krause,[1] G. A. Savanick, and E. W. White

Materials Research Laboratory, The Pennsylvania State University, University Park, Pennsylvania

In the course of a research program on metallic corrosion an investigation was undertaken to determine the feasibility of employing shifts in the oxygen x-ray emission band to characterize structurally and chemically the thin, often amorphous, oxide layers that form when a metal corrodes. The first results of this research were reported by Gigl, Savanick, and White (1), who observed shifts in the aluminum x-ray emission band (Al Kβ) and the oxygen x-ray emission band (O Kα) and used these shifts to characterize thin corrosion layers on aluminum.

This note demonstrates that shifts in the O Kα band can be used to characterize oxide films on transition metals. Prior to experimentation on thin films it was necessary to investigate the oxygen x-ray band shifts with chemical variations of the emitter, using bulk samples of known composition.

Three series of transition metal oxides (Ti, Mn, and Fe) were included in this study. The oxide standards were in powder form and were prepared by drying from suspension onto polished carbon rods (¼ in. diameter) after being ground under alcohol.

The oxygen x-ray emission bands were recorded with an Applied Research Laboratories electron probe microanalyzer model EMX, equipped with a flow proportional counter. A clinochlore crystal (2d=28.39A) was used to disperse the oxygen x-ray emission bands. Baun and White (2) have described clinochlore and demonstrated that it is particularly well suited for the x-ray spectrometry of oxygen.

An accelerating voltage of 20 keV was selected and the sample current was adjusted to 0.1 μA resulting in peak O Kα count rates of 100-350 cps. A large (100μ) electron beam diameter was used to minimize beam damage in the specimen. The peaks were scanned at approximately 0.03 Å/min. Scans were repeated in triplicate from three areas of each sample. Peak positions were measured by extrapolating the line of midchords to the peak intensity. All wavelength measurements were made with respect to the O Kα from quartz (α-SiO_2). This quartz peak was arbitrarily assigned a wavelength of 23.60Å.

The data presented (Fig. 1 and 2) demonstrate that the magnitude of the shifts in the oxygen x-ray emission bands is a continuous function of the metal to oxygen ratio of the emitter. A plot of the position of the peaks for a series of manganese oxides of different chemical compositions is presented in Fig. 1, along with similar data for a titanium oxide series. Figure 2 shows the O Kα wavelength shifts with changing oxidization state of the cations in a series of iron oxides. In all these three series the peaks shift toward shorter wavelength with increasing oxidation.

These plots demonstrate that the cation valence of these transition metal oxides can be determined from measurements of the O Kα wavelength. These data for the titanium oxides corroborate the findings of Fischer and Baun (3) who published a figure showing a progressive shift in the intensity maximum of the oxygen band in the series TiO-Ti_2O_3-TiO_2. The oxygen band shift technique was applied to a thin (0.5μ) oxide layer prepared by heating a polycrystalline iron bar

[1] Present address: Physics Department, Northern Illinois University, De Kalb, Illinois.

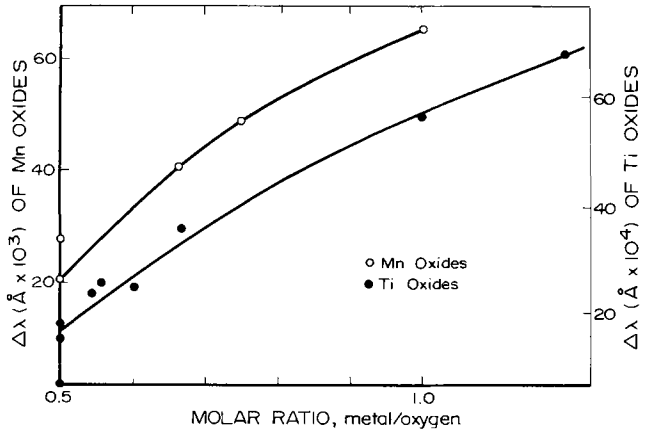

Fig. 1. Shifts in the position of the oxygen emission band for a series of manganese and titanium oxides as a function of the metal to oxygen ratio.

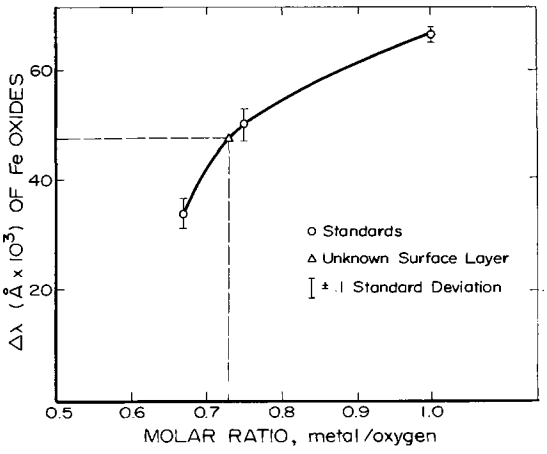

Fig. 2. Oxygen band positions for a series of iron oxide standards and an unknown surface layer.

at 290°C under a pressure of 20,000 psi for 16 hr. The oxide existed as a blue surface layer and was positively identified as Fe_3O_4 by x-ray diffraction. Figure 2 shows that the wavelength of the O Kα band emitted from the blue oxide is essentially the same as that measured from Fe_3O_4 and is significantly different from the wavelengths of FeO and Fe_2O_3. Thus, thin iron oxide films can be identified with reference to oxygen shift data.

Oxide films thicker than 100Å can be investigated by this technique free of interference from the metallic substrate. The oxide films need not be crystalline or of uniform thickness.

Acknowledgment

Financial support for this work was provided by the Office of Naval Research under contract number NR-032-502. The authors would like to thank P. D. Gigl who provided the iron oxide surface layer.

Manuscript received Nov. 24, 1969.

Any discussion of this paper will appear in a Discussion Section to be published in the December 1970 JOURNAL.

REFERENCES

1. P. D. Gigl, G. A. Savanick, and E. W. White, *This Journal*, **117**, 15 (1970).
2. W. L. Baun and E. W. White, *Anal. Chem.*, **41**, 831 (1969).
3. D. W. Fischer and W. L. Baun, *J. Appl. Phys.*, **39**, 4757 (1968).

JOURNAL OF THE ELECTROCHEMICAL SOCIETY

ELECTROCHEMICAL TECHNOLOGY

APRIL 1970

Lithium/Silver Chloride Button Cells

Glenn M. Cook

Research & Development Laboratories, Sprague Electric Company, North Adams, Massachusetts

ABSTRACT

The operating parameters for a laboratory model Li/AgCl button cell are presented. The cell voltage is given as a function of current density over a temperature range from −55° to +125°C. Cathode utilization is 90% at 0.46 mA/cm² at room temperature. Cell life for these rudimentary cells is estimated for several temperatures. These studies indicate that the Li/AgCl cell has properties which differ considerably from those of existing commercial systems and which permit it to satisfy new power requirements.

Over the past several years, many workers have directed their efforts toward the development of various nonaqueous battery systems (1). It is the purpose of this paper to examine the temperature dependence of the shelf life and operating characteristics of cells based on the system, $Li/LiAlCl_4$, PC/AgCl, Ag [PC = propylene carbonate (2)].

The nonaqueous Li/AgCl cell has certain advantages and certain disadvantages. The advantages are:

1. The high cell voltage allows the use of fewer cells in a battery.
2. The operating temperature range is very wide.
3. The low temperature performance is good.

The disadvantages are:

1. The cells must be fabricated under an inert atmosphere and the solvent carefully distilled (3, 4).
2. The high electrolyte resistance restricts the usage of these cells to low rate applications.
3. The present shelf life is low, roughly equivalent to that of Leclanché cells.

Results

The three-piece polypropylene cell case used for these studies is illustrated in Fig. 1. The internal dimensions are 15 mm in diameter by 13 mm high. The cells were fabricated in a controlled-atmosphere dry box containing less than 1 ppm water or oxygen in the vapor phase. The cathode compartment is filled with about 1g of a silver chloride-acetylene black mix. The anode consists of 1/3g of lithium metal, which makes the cells cathode limited. About 4 cc of a $LiAlCl_4$-PC electrolyte, saturated with LiCl, was used. The over-all cell weight was 10g and the open-circuit voltage was 2.84V.

Some precautions were taken with the preparation of the electrolyte. These included the use of freshly distilled PC with a water content of about 40 ppm, the slow dissolution of $LiAlCl_4$ to prevent overheating, and electrolyte storage in the presence of lithium. All of the necessary manipulations were carried out in a dry box. This electrolyte was found to have a $[Cl^-]$ activity which permits the formation of $AgCl_2^-$ to a concentration of 10^{-4} molar. This was determined by using procedures similar to those of Butler (4). Some cell anodes were found to have very small quantities of silver on them. The presence of silver is not unexpected, and the small quantities observed validate the low concentration of $AgCl_2^-$ calculated above.

Cell polarization.—The term cell polarization, as used here, is the sum of all factors causing a reduction in cell voltage from the open-circuit potential. For convenience, the figures give the cell voltage rather than the polarization. This is done in order to provide a measure of cell output which is needed to determine its suitability for a particular use.

The first important cell polarization effect is its increase with increasing current density and decreasing temperature. The data shown in Fig. 2, which gives the cell voltage *vs.* current density as a function

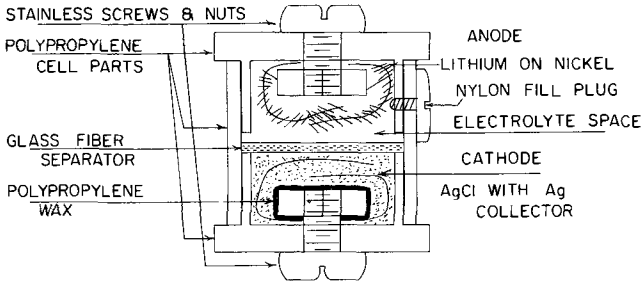

Fig. 1. Construction detail of Li/AgCl button cells

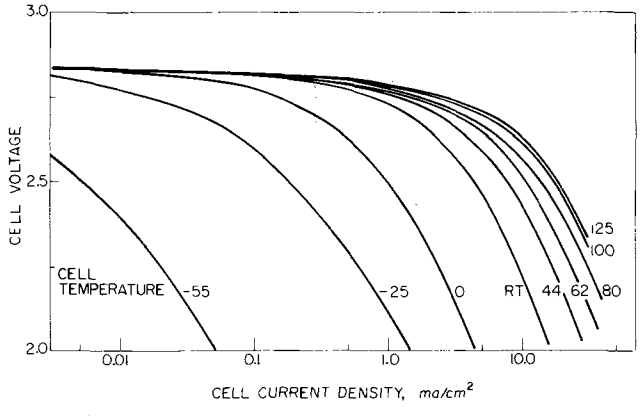

Fig. 2. Cell voltage *vs.* current density of fresh cells at various temperatures, °C.

of cell temperature, were obtained as the average for two fresh cells at each temperature. The smooth curves were obtained by drawing them through the average of all data points. Three current densities per decade were selected and the current held constant for 1 min prior to recording the cell voltage. The current was then stepped to the next value. Data were obtained for both increasing and decreasing currents. No data were obtained beyond 30 mA/cm^2 or below a cell voltage of 2V.

Two hours were allowed for the cells to reach thermal equilibrium prior to testing. Identical results were obtained when the cells were retested after an additional stand of 2 hr at temperature.

The curves for the lower temperatures are somewhat distorted as compared to those obtained at higher temperatures. The internal resistance of the Li/AgCl cells is higher than that of existing systems because of the use of the low-conductivity, nonaqueous electrolyte. As a result, heating effects are of greater importance.

The variation of cell current with inverse temperature at constant cell voltage yields some information regarding the source of cell polarization. Figure 3 is such a representation for a voltage drop of 10% from OCV. Similar plots can be made for other amounts of cell polarization from the data in Fig. 2. If such plots are made, it is found that the cell polarization arises from *IR* losses, concentration effects, and chemical polarization. The first two of these factors are expected to vary with temperature in the same manner as the electrolyte conductivity. At high temperatures the rate of reaction, cell current, is roughly proportional to electrolyte conductivity with only a small polarization attributable to chemical polarization. At lower temperatures, there appears to be an increase in chemical polarization as determined by the methods of Gorbachev (5). No specific values were determined since the cells were not identical, but only similar to one another.

The other important cell polarization effect is its increase with the increase in the extent or depth of discharge. All systems show a decreasing cell voltage as the discharge continues (6). The more constant the cell voltage throughout the discharge, the higher is the "quality" of the system as a power source. Figure 4 compares the Li/AgCl cell voltage-time characteristics with those of three important commercial systems (6-8). All of the characteristics are for cells of similar structure, the button or cylindrical dry cell configuration. The 100 hr rate was chosen since the cell polarization of the Li/AgCl cell is quite good at the 100 hr rate. It would be expected to be even better at a lower rate.

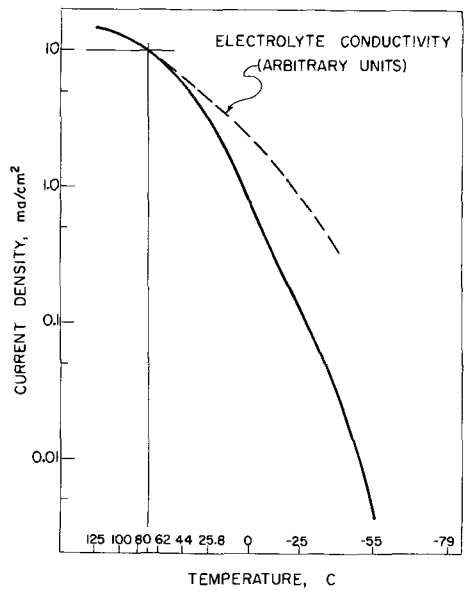

Fig. 3. Comparison of electrolyte conductance with current density as a function of temperature. The current is obtained at a 10% drop in cell voltage from OCV.

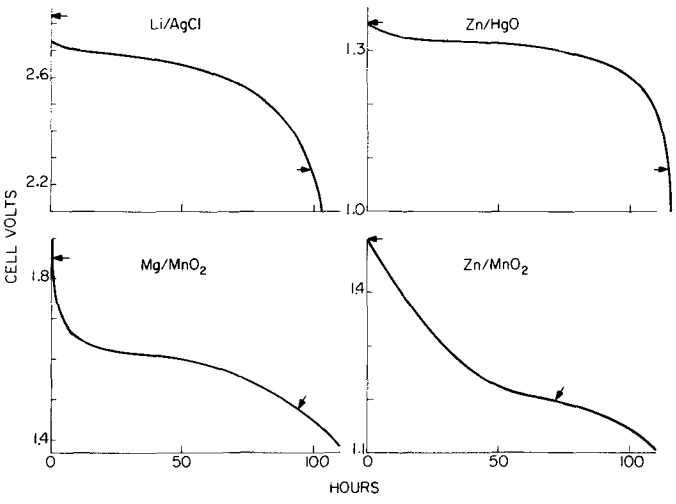

Fig. 4. A comparison of the cell voltage of four systems discharged at comparable rates. Arrows indicate OCV and 0.8 OCV.

Cell capacity.—The theoretical cell capacity is the number of ampere-hour equivalents corresponding to the amount of active material used in the limiting electrode. For this study, the working or true cell capacity is defined as the value of i x t obtained at a voltage greater than 80% of the initial closed-circuit voltage. Therefore, the true capacity is a function of the current density and the temperature of operation. This dependence is not easily described. However, experimental results of commercial mercury and Leclanché cells have successfully been illustrated as approximately linear on log-log plots of discharge time *vs.* current density (8). Figure 5 treats the data for Li/AgCl cells in this manner over a wide temperature range. The measured capacities achieved from 10 to 90% of that theoretically obtainable from the cathode. The discharge times corresponding to 25, 50, and 100% of theoretical capacity are indicated for convenience. Figure 6 compares the Zn/HgO cell with the Li/AgCl cell at 0°C. The mercury cell has a stronger dependence on current density. Figure 7 illustrates the variation in the current density to produce 100% capacity as a function of temperature. The performance of the mercury cell falls rapidly with a decrease in temperature. The current density in the silver cell is low but decreases only very slowly with a decrease in temperature. As a result, the Li/AgCl cell outperforms the mercury cell at temperatures lower than —5°C at all current densities.

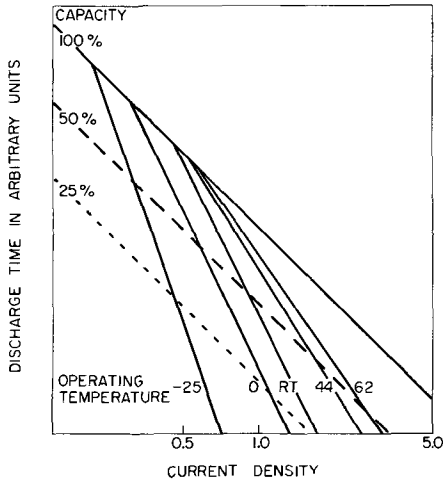

Fig. 5. Cell capacity as a function of current density at several operating temperatures, °C.

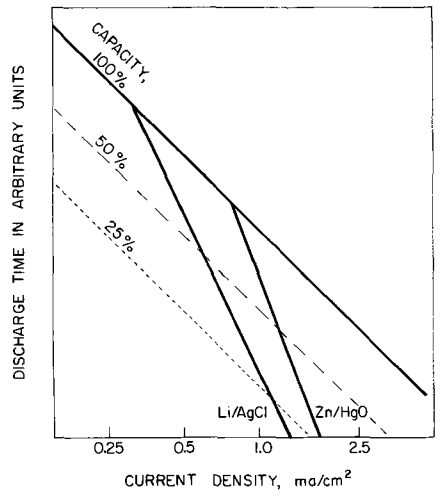

Fig. 6. Comparison of the current density dependence of cell capacity for the Zn/HgO and Li/AgCl button cells at 0°C.

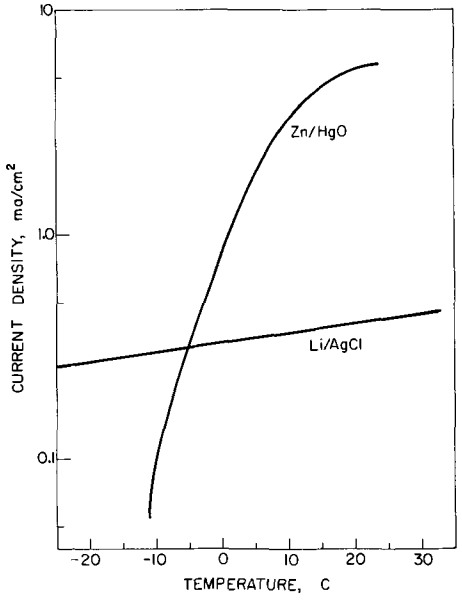

Fig. 7. Maximum current density possible for achieving 100% capacity as a function of temperature.

Cell life.—The shelf life of a battery is an important parameter. However, in new cell systems it is impractical to depend on such long-term tests to provide direction for a development program. Accelerated testing is the only way in which data can be obtained rapidly enough to be of use.

The shelf life data of commercial systems have been presented as linear plots with the logarithm of the life *vs.* the reciprocal absolute temperature (9). In other words, the degradation process behaves as though it is activation controlled. In this way, it is possible to estimate the room-temperature life from high-temperature data. It is not the purpose of this work to prove the validity of this procedure. One of the uncertainties in this procedure is that the degradation mechanism may be a function of temperature, so that the slope of the curve does not remain constant. For this reason, it is preferable to obtain data as near to the use temperature as possible.

These extrapolative procedures often do not yield results rapidly enough. Further acceleration of the testing and lower-temperature data can be obtained from the time variation of the rate of discharge at a given cell voltage. Since flat parallel electrodes are used, the capacity as well as the rate of discharge can be arbitrarily assumed to be proportional to the area or quantity of available active material. Under this assumption, a plot of log i_o/i_t *vs.* time should be linear for a first order reaction (where i_o is the initial current and i_t is the current at time, t). Under the experimental conditions of this study, this assumption seems to hold true as illustrated in Fig. 8. The actual cell discharge capacity was checked in several cases and found to be in substantial agreement with this concept. In this way, it is possible to extrapolate data to obtain a life to some predetermined capacity remaining in the cell, such as 10% of the original working capacity. Data obtained in this manner are given in Fig. 9. The end of cell life is at 10% of the original capacity.

The actual cell capacity was measured for a group of cells stored at 62°C. Cells were periodically removed from storage, then discharged at room temperature. Cells stored for a short time gave a very *long* extrapolated life. As the storage time became longer, the rate of degradation increased as indicated by both i_t and actual cell capacity. It may be possible that poor construction techniques lead to seal problems which result in a short life through electrolyte loss.

The extrapolation to room temperature is not obvious. For lack of a better method, the slope of the lines given in Fig. 9 is the same as that obtained by other workers for the degradation of aqueous batteries. These results indicate a room-temperature life of 1.3-4.0 yr with a possible maximum as large as 7.8 yr. The

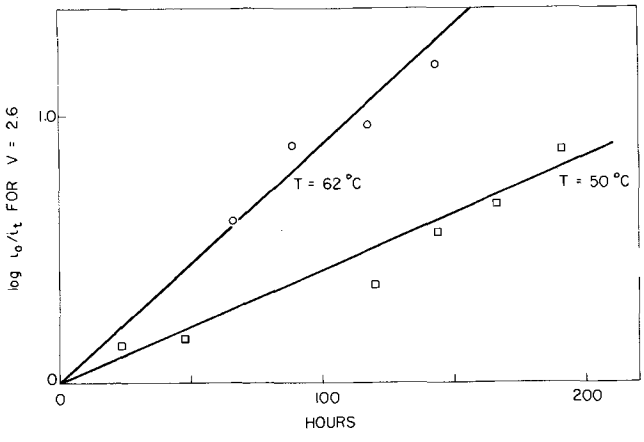

Fig. 8. Cell degradation data, for cells at two temperatures.

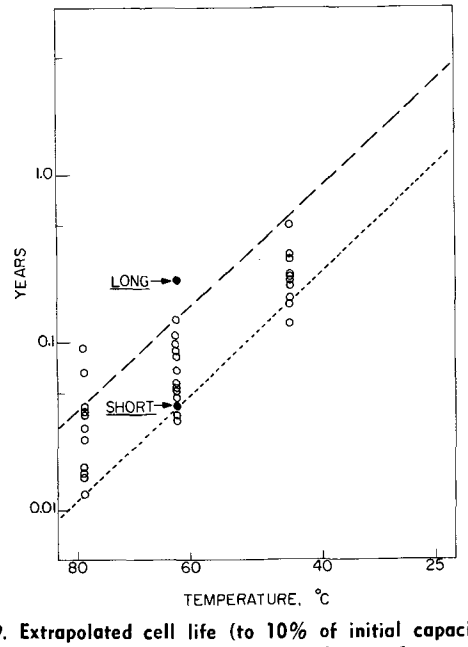

Fig. 9. Extrapolated cell life (to 10% of initial capacity) as a function of storage temperature. Solid circles are for a cell which initially degraded very slowly to yield *long* then rapidly to yield the over-all value labeled *short*.

last figure is estimated from the *long* life extrapolated from 62°C.

The life of these crude laboratory cells is actually quite good and approximately equivalent to the life of standard Leclanché cells.

Discussion

The operating parameters of most cell systems are given in terms of expected usage. With a new system, this is not quite possible since a use is not established. The testing that has been done and is reported here gives an indication of possible uses. These are limited, to some degree, by the fact that the results presented in the preceding paragraphs are for a single rudimentary button cell design. The size and capacity of this cell is roughly that of the PX-14 2.7V mercury battery.

The operating characteristics of these cells are different from any existing cell systems and thus have different possible applications. These Li/AgCl button cells are expected to be useful in low rate (C/100) applications where a wide operating temperature range and good voltage regulation is required. At low temperatures and rates, the discharge characteristics are competitive with Zn/HgO button cells. In addition, the higher cell voltage permits the fabrication of smaller, high-reliability multicell batteries. To estimate the possibility for using the Li/AgCl system as a power source, these properties can be compared with the required properties. Basically, the Li/AgCl cell is not a replacement for all applications of any existing battery. It has certain operating characteristics that present batteries lack. It is a new system which can fill some old, as well as some new, requirements.

Acknowledgment

The author thanks Mr. H. A. DeGrenier for his help in obtaining the experimental data presented in this paper.

Manuscript submitted Aug. 27, 1969; revised manuscript received Dec. 18, 1969.

Any discussion of this paper will appear in a Discussion Section to be published in the December 1970 JOURNAL.

REFERENCES

1. R. Jasinski, *Electrochem. Technol.*, **6**, 28 (1968).
2. (a) J. E. Chilton and G. M. Cook, Tech. Rpt. No. ASD-TDR-62-837 (1962).
   (b) H. F. Bauman *et al.*, Tech. Rpt. No. RTC-TDR-53-4083 (1963).
   (c) J. E. Chilton, Jr., *et al.*, Tech. Rpt. No. AFAPL TR-64-147 (1964).
3. R. Jasinski and S. Kirkland, *Anal. Chem.*, **39**, 1663 (1967).
4. J. Butler, *ibid.*, **39**, 1799 (1967).
5. S. V. Gorbachev, *Soviet Electrochem., Proc. Conf. Electrochem., (English Transl.), 4th, Moscow, 1956*, **1**, 63 (1961).
6. Eveready Battery Applications and Engineering Data.
7. Battery Corp. of America Data Sheet.
8. Burgess Engineering Manual.
9. E. Willihnganz, Paper 25 presented at Electrochem. Soc. Meeting, Chicago, Oct. 15-19, 1967.

Chemical Vapor Deposition of Silicate Glasses for Use with Silicon Devices

I. Deposition Techniques

Werner Kern* and Richard C. Heim[1]

David Sarnoff Research Center, RCA Corporation, Princeton, New Jersey

ABSTRACT

Compositions synthesized include borosilicates, phosphosilicates, aluminosilicates, aluminoborosilicates, and some zinc glasses. The compositions containing aluminum or zinc were prepared by simultaneous oxidation of the hydrides and trimethyl aluminum or diethyl zinc vapor. The deposition temperatures were in the 300°-500°C range. The effects of system variables on the deposition rate and composition of borosilicate films obtained from silane, diborane, and oxygen were examined in detail. Variables investigated included carrier gas and hydride flow rates, silane/diborane and oxygen/hydride ratios, deposition time and temperature, and reactor geometry.

The need to protect semiconductor devices from humid or corrosive environment is well recognized in the manufacturing of transistors and integrated circuits. Conventionally, a passivating layer of thermally grown silicon dioxide has been used to stabilize devices, but its molecular network structure is not sufficiently impervious to contaminants, and the thermal expansion mismatch with the substrate limits the layer thickness. The devices must therefore be sealed in hermetic enclosures. A more desirable packaging technology is based on the sealing of semiconductor device wafers with an impervious dielectric layer so that hermetic enclosures are no longer required. Chemical vapor deposition of silicate glasses is an attractive approach toward this objective. Glass films of suitable composition and high purity can be deposited at relatively low substrate temperatures, the film thickness can be readily controlled, and the films conform to the surface contours of a substrate.

Both organic and inorganic source materials can serve for the chemical vapor synthesis of silicate glasses. Eversteijn (1) deposited aluminosilicate films from tetraethyl siloxane and tri-isobutyl aluminum in oxygen at 400°C. Mayer, Kern, and Goldsmith (2) utilized simultaneous pyrolytic oxidation of tetraethyl siloxane and trimethyl borate or trimethyl phosphate to form borosilicate or phosphosilicate films at 730°C. The synthesis of lead silicate and lead borosilicate glasses with excellent passivating properties was achieved by incorporating tetraethyl lead in the vapor mixture, followed by a thermal densification treatment of the films. Low deposition rates, toxicity, and other shortcomings of the organic systems led us to investigate low-temperature hydride reactions based

* Electrochemical Society Active Member.
[1] Present address: Kasper Instruments, Incorporated, Santa Clara, California.

on the silane oxidation system originally described by Goldsmith and Kern (3). The incorporation of diborane or phosphine leads to borosilicate or phosphosilicate films, respectively. Ternary glass compositions were synthesized by simultaneous gas phase oxidation of silane, diborane, and either trimethyl aluminum leading to aluminoborosilicates, or diethyl zinc leading to zinc borosilicates. The binary borosilicates synthesized from the hydrides and oxygen were found particularly well suited for glassing of silicon devices; this system will therefore be discussed in some detail. The properties of these various glasses will be described in Part II (4) of this paper.

Experimental

Reactants and carrier gases.—Semiconductor-grade silane, diborane, and phosphine, in concentrations of 4-8 vol % in argon (The Matheson Company, Inc.) were used as starting materials. Mass spectrographic gas analysis served to establish the exact gas compositions; the results are shown in Table I. Trimethyl aluminum and diethyl zinc (Ethyl Corporation) of commercial purity were used for preparing the glasses containing aluminum or zinc. The purity of the oxygen was 99.9% and that of nitrogen was 99.998%. The nitrogen and oxygen were passed through a submicron range final filter before entering the flow meters.

Gas distributing system.—A schematic of the gas handling system is shown in Fig. 1. For clarity, the nitrogen-flush for each of the hydride lines has been omitted. The system is operated nominally at atmospheric pressure, but provision is made for pumping out gas lines initially, and for flushing them with nitrogen prior to start-up. A small volume of liquid metal alkyl is drawn from the storage cylinder into a constant temperature bubbler, *e.g.* 25°C, through which nitrogen is passed to carry alkyl vapor to the reaction chamber. Final mixing of the gases is accomplished by turbulence and convection in the deposition chamber.

Deposition apparatus.—The deposition apparatus consists essentially of a heated gear assembly which rotates the substrates in planetary fashion. A commercial high-temperature hotplate with thermostatic control is used to attain substrate temperatures up to 500°C. An opening between the glass chamber and the hotplate surface serves as exhaust. The apparatus is capable of reproducibly depositing uniform films simultaneously on three semiconductor substrate wafers of up to 1.5 in. diameter. A complete description of the equipment has been published previously (5).

General deposition procedure.—The deposition processes were optimized for obtaining various glass compositions, but the general procedure can be summarized as follows. The substrate wafers placed on the cold pedestals are introduced in the preheated, nitrogen-purged chamber. Thermal equilibration of the rotating wafers is attained within 5 min. Diluted silane is introduced first, followed by the oxygen 20 sec later. This sequence of introduction of the substrates and the gases is designed to minimize oxidation of the metal in the case of metallized device wafers. For synthesizing borosilicates, diborane is introduced next. If the diborane were introduced before sufficient oxygen was present in the deposition chamber, oxygen-deficient films could form. The introduction of phosphine or of metal alkyls is less critical with respect to the oxygen excess. For synthesizing ternary compositions, the alkyls are added to the gas stream subsequent to the introduction of the hydrides. Layer structures can be made homogeneous, graded, or abrupt by suitable adjustment of the appropriate gas stream(s). The deposition is terminated by reversing the gas flow sequence.

Fixed test conditions for parameter studies.—The evaluation was based on the deposition rate, the thickness uniformity, several dielectric properties, and the chemical composition of 1μ thick films deposited on silicon.

The fixed conditions for the borosilicate system were as follows: 1—mechanically polished silicon wafers (111-oriented, 10 ohm-cm p-type, 0.015 in. thick) were used as substrates; 2—the temperature at the wafer surface was held at 450° ± 3°C; 3—a hydride mixture corresponding to 22.5 m/o (mole per cent) B_2H_6 and 77.5 m/o SiH_4 was metered, yielding a borosilicate composition of approximately 17 m/o B_2O_3. 4—the oxygen/hydride volume ratio was 40:1; 5—the nitrogen/hydride volume ratio, 530:1; 6—the exit opening of the reaction chamber was 1 mm; 7—the reactive gas flowrates were chosen to yield intermediate deposition rates in the range of 1400-1800 Å min^{-1} and were kept constant within each experiment; 8—the deposition was started and terminated by briefly lifting the reaction chamber during the start of the gas introduction and before shutting off the gases. This procedure avoids formation of the initial and final thin silicon dioxide layers that would complicate the film analysis.

Rate of film deposition.—Film deposition does not begin immediately upon introduction of the reactive gases but it is delayed for a period that depends on the deposition conditions and the substrate surface. Timing of the deposition was therefore started at the precise moment a tan interference-colored deposit appeared on the surfaces of the substrate wafers. For films having a refractive index close to 1.5, this color represents a thickness of approximately 500Å, which was taken into account in the calculation of deposition

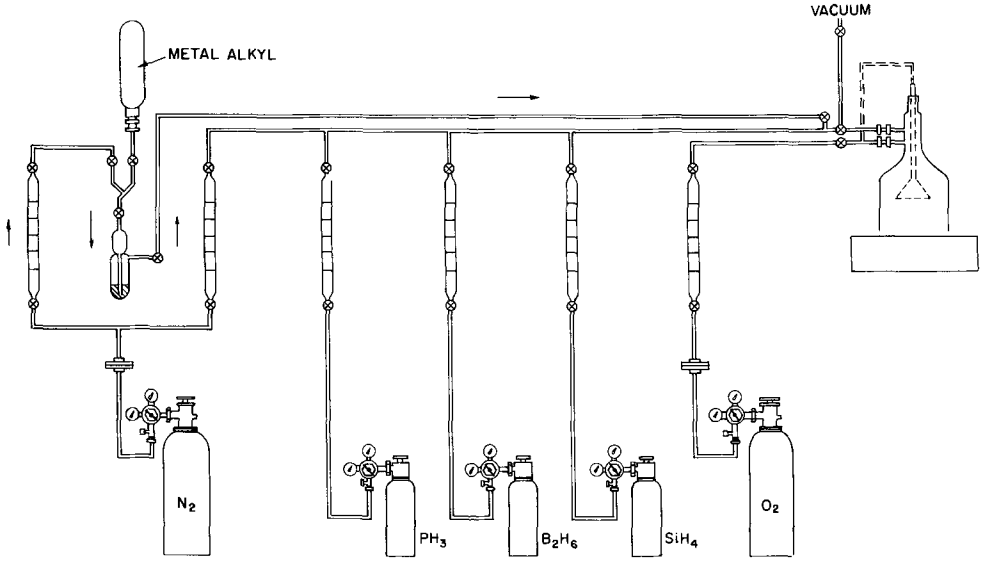

Fig. 1. Schematic of gas regulating and distributing system for chemical vapor glassing.

rates. The exact thickness and composition of the films were determined by methods described in the second paper of this series (4).

Chemical Vapor Deposition of Borosilicate Glasses

Deposition Rate and Borosilicate Composition as a Function of System Variables

Hydride flow rates.—Within certain limits of hydride and nitrogen inputs, the glass deposition rate is directly proportional to the silane-diborane gas flow rates. The linear range of the deposition rate extends up to a flow rate of 11 cm^3 undiluted hydride per minute, where a film deposition rate of 3200 Å min^{-1} is obtained. The reaction yield of vitreous borosilicate glass product on the sample and metal surfaces within the deposition chamber averages about 20%. The remainder forms a powdery deposit on the walls of the reactor or passes out with the exhaust gases. It will be shown later that the yield of vitreous product can be substantially increased by operating at different temperatures and flow rates. If the hydride flow rates are increased beyond 11 cm^3 min^{-1}, the deposition rates under the present conditions tend to level off, but the glass properties and film uniformity are not affected appreciably. For example, doubling the gas flow to 22 cm^3 min^{-1} yields a deposition rate of 3640 Å min^{-1}, an increase of barely 20%.

Nitrogen flow rate.—The main purpose of the nitrogen is to dilute the reactive gases to a safe concentration. The oxidation of the hydride is so vigorous that even at a concentration of only 1.6% silane-diborane in nitrogen the reaction proceeds with a bluish flame when mixed with excess oxygen (32:1). Dilution to 1.2% or below allows the reaction to take place without flame. The concentration in the present test series was 0.17%. As seen from Fig. 2, insufficient dilution of the hydride mixture with nitrogen depresses the rate of deposition. The rates begin to level off at nitrogen flow rates of about 2000 cm^3 min^{-1}; some additional increase is attained by extending the nitrogen flow rate beyond the maximum in Fig. 2 to 4000 cm^3 min^{-1}. Still higher flows impede the deposition rate and lead to nonuniform films.

Silane-to-diborane ratio.—The ratio of silane/diborane is the primary factor that determines the chemical composition of the resulting glass films, provided a large stoichiometric excess of oxygen is present. Figure 3 presents a correlation of the hydride composition with the resulting film composition at the substrate temperature of 450°C. The dashed line indicates the relationship expected on a stoichiometric basis. The boron content in the glass was determined by dissolving the films in hydrofluoric acid and reacting the BF_4^- complex with N-methylthionine (6). The colored complex was extracted and measured spectrophotometrically (7, 8). The precision of each coordinate point in Fig. 3 is defined by the X-Y spread drawn.

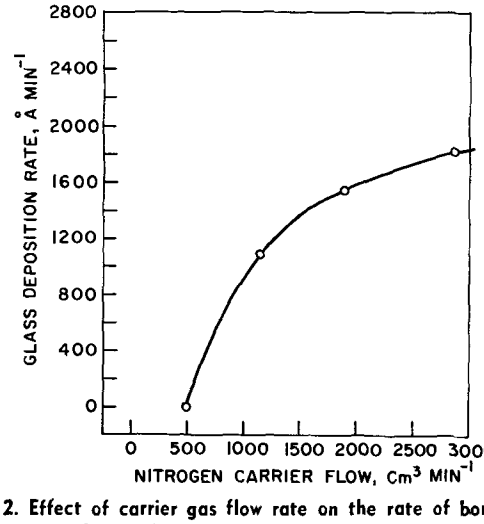

Fig. 2. Effect of carrier gas flow rate on the rate of borosilicate film deposition for the diborane-silane system.

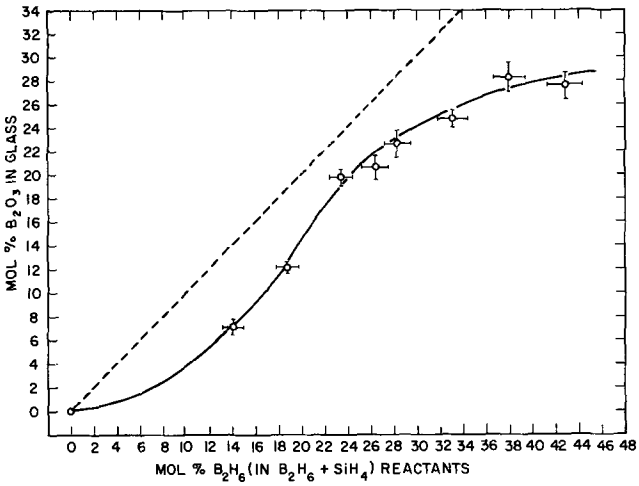

Fig. 3. Glass composition as a function of the hydride composition from which the borosilicates were synthesized at 450°C.

Oxygen-to-hydride ratio.—Based on the stoichiometric reactions of the hydrides with oxygen to form the oxides and water as products, the stoichiometric ratio of oxygen to hydride required for our silane plus diborane mixture is 2.25. In practice, a much larger ratio is required to prevent the formation of the oxygen-deficient films. The composition of such films has not been determined with certainty, but they are poorly insulating and are insoluble in hydrofluoric acid, have a high refractive index, and show no infrared absorption bands in the B-O, B-O-Si, or Si-O regions of 2.5-15μ. Figure 4 indicates that constancy in deposition rate and film composition is attained at ratios beyond 20, a 9-fold stoichiometric excess. It should be pointed out that this graph was obtained for the particular system conditions stated. (For example, borosilicates were obtained at oxygen ratios close to stoichiometry at 400°C under different gas flow and reaction chamber conditions, but the B_2O_3 content in these films was abnormally high.)

Deposition time.—The increase of glass film thickness with deposition time was tested up to a thickness of 42μ (deposition period of 4½ hr) and found to be linear. The deposit on the wall of the reactor was allowed to accumulate during this test and had no measurable effect on the glass composition.

Substrate temperature.—The effect of temperature on the rate of film deposition is presented graphically

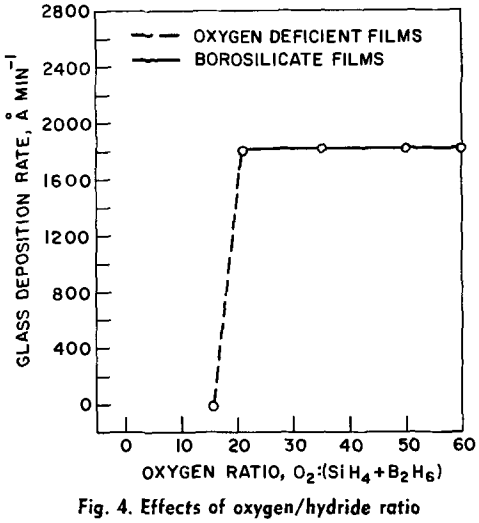

Fig. 4. Effects of oxygen/hydride ratio

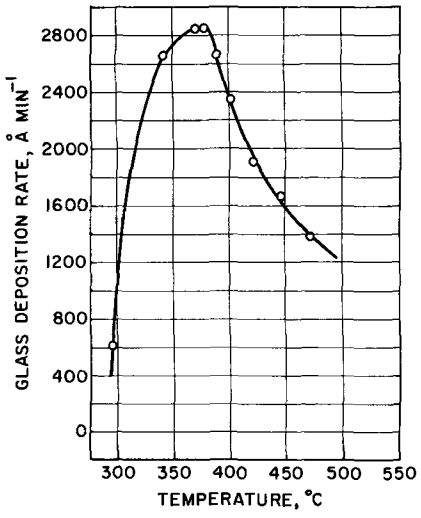

Fig. 5. Film deposition rate vs. substrate temperature

in Fig. 5. A plot (not shown here) of the log deposition rate *vs.* the reciprocal, absolute temperature reveals that the curve is a composite of two straight lines. Borosilicate films begin to deposit at a substrate temperature of about 280°C. The rate of deposition increases steeply with increasing temperature, levels off at about 370°, and drops steeply as the temperature is increased above 375° because of homogeneous gas phase nucleation. The rate of deposition on the walls of the reactor is thereby increased, competing with the formation of glassy borosilicate films on the substrate surface.

The deposition temperature also affects the film composition (Fig. 6). Up to 375°C, the boron oxide content in the glass increases rapidly; above this temperature, the change with increasing temperature is much smaller. Raising the temperature from 400° to 425° increases the boron oxide content about 4%. The temperature of 450° is least sensitive, and would be a desirable one from the standpoint of glass composition control. However, the rates attainable at the lower temperatures are so much greater that a compromise of 400° is usually employed.

The specifically marked data points in Fig. 6 were obtained by using a premixed diborane-silane-argon

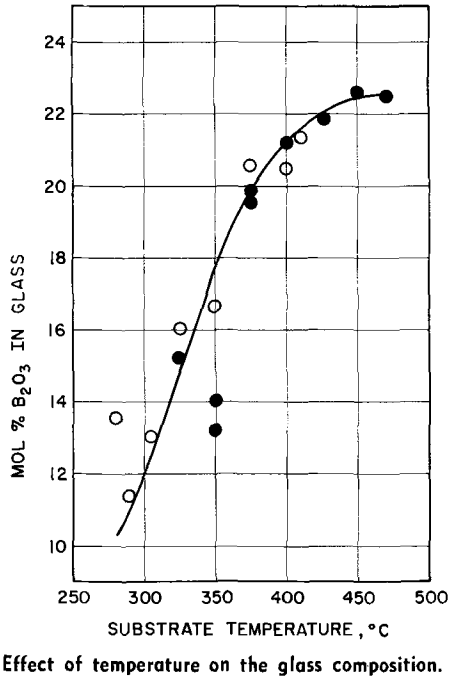

Fig. 6. Effect of temperature on the glass composition. The solid data points were obtained from a premixed diborane-silane mixture.

Table I. Results of mass spectrographic analysis of silane and diborane sources

Diluted gas	Cylinder	Supplier	Elapsed time to analysis, weeks	Silicon hydrides				Boron hydrides				Diluent gases			Reactive gases		
				SiH_4	Si_2H_6	$(CH_3)_2SiH_2$	Total as* "SiH_4"	B_2H_6	B_4H_{10}	B_5H_9	Total as** "B_2H_6"	Ar	N_2	He	H_2	O_2	CO_2
Silane	A	M	31	4.3	0.0040	—	4.308	—	—	—	—	72	19.6	—	3.6	<0.004	0.0130
Diborane	B	AR	136	—	—	—	—	3.9	0.026	—	3.95	52	4.6	33	6.0	0.17	0.15
Silane	C	M	10	7.8	0.0020	—	7.804	—	—	—	—	85	5.6	—	1.48	<0.004	0.0022
Diborane	D	AR	31	—	—	—	—	6.4	0.21	—	6.82	89[d]	1.00	<0.001	3.8	<0.001	0.005
Silane	E	M	0	7.4	0.0030	—	7.406	—	—	—	—	92[d]	0.03	—	<0.35	<0.03	<0.001
Diborane	F	M	0	—	—	—	—	5.4	0.40	0.04	6.30	92[d]	0.0080	—	1.9	0.0018	<0.016
Silane	G	M	0	7.3	0.0020	0.0035	7.308	—	—	—	—	92[d]	<0.30	—	0.26	<0.30	<0.001
Diborane	H	M	0	—	—	—	—	3.8	0.018	0.0009	3.838	96[d]	0.043	—	0.43	<0.0004	<0.002

M—Matheson Company, Inc.
AR—Air Reduction.
* "Silicon" concentration in gas = SiH_4 concentration.
** "Boron" concentration in gas = twice B_2H_6 concentration.
The mass spectrographic analyses were carried out by Gollob Analytical Service, Inc. (Gases A-D) and by the Matheson Company, Inc. (Gases E-H). All concentrations are expressed as vol %. The gas samples were scanned by mass spectrographic analysis from mass 2 through mass 100 and no other constituents were detected. The detection threshold for most constituents is 0.001% or better. "d" means by difference.

gas source to guarantee uniformity in the hydride ratio. The mixture contained a slightly higher diborane concentration than used normally, yielding a glass composition with 22.5 m/o B_2O_3 at 450°C; this composition was matched by the separate source mixture.

Deposit on reactor wall.—Three types of oxide product are formed: 1—a glassy borosilicate film on the heated substrate and the metal hotplate surfaces; 2— a white powdery deposit on the inside glass walls of the reactor and the glass support ring; and 3—colloidal oxide particles in the reaction exhaust gases. To increase the yield of glassy product and to avoid contamination of the glass films, the formation of powdery product should be minimized. The build-up of wall deposit was measured both by the time required for the chamber to become translucent by visual observation, and by weighing the wall deposit in the reactor.

Table II lists the effects of three critical system variables on the deposition rate on the walls: 1—temperature of substrate; 2—temperature of reactor wall; and 3—flow rate of carrier gas. The data are presented in terms of stoichiometric yield of glassy substrate deposit and of deposit on the reactor wall. An estimate of the time for the reaction chamber to become translucent is also listed. The theoretical 100% value was calculated from the following chemical reactions, the hydride flow rates used, and a glass density of 2.1 g cm^{-3}:

$$SiH_{4(g)} + 2\,O_{2(g)} \rightarrow SiO_{2(s)} + 2H_2O_{(g)}$$

and

$$B_2H_{6(g)} + 3\,O_{2(g)} \rightarrow B_2O_{3(s)} + 3H_2O_{(g)}$$

It was assumed that the reaction proceeded to completion and that the entire exposed surface area of the heated sample stage was uniformly glass coated with the film thickness measured on the silicon wafers. The data in Table II indicate that lowering the temperature increases the yield of the glassy deposit and decreases the powdery deposit on the reactor wall. If the reactor walls are purposely heated, nearly all of the product deposits on the walls as a glassy layer. Water cooling the wall slightly increases the product yield on the substrate while slightly decreasing that on the wall. The best combination is a lowered substrate temperature and an increased flow rate of carrier gas without deliberately modifying the temperature of the reactor walls. The major portion of product now deposits as uniform glass coating on the substrate surface.

Reactor geometry.—The geometry of the reactor influences the flow patterns in the gas stream. Several different reaction chambers were tested in addition to the standard bell-shaped reactor.[2] These include chambers with modified neck curvature, cylindrical shapes, bottle and deflected designs, and reactors with provisions for either water cooling or heating of the vessel walls. The effects of these variations are minor. However, the nonrestrictive concentric gas exit design of the present chambers was found superior to tubular or slotted openings with respect to deposit uniformity and deposition rate. The spacing between the reaction chamber and the hot stage affects the rate of film deposition to some extent. The rate decreases 7%/mm increase of the opening.

Nature of substrate.—The nature of the substrate surface has a marked effect on the induction period for film growth. The differences can be measured by simultaneously depositing a thin (*e.g.*, 2000Å) glass film on differently treated substrates and comparing the film thicknesses on the samples. For example, an HF-etched polished silicon surface has a short induction time, whereas thermally grown silica or silicon nitride layers have longer times.

Preferred combination of deposition conditions.—Based on the results of this study, a favorable combination of conditions was formulated for the deposition of borosilicate films for our apparatus. A substrate temperature of 400°C and a hydride mixture yielding a glass having 17 ± 1 m/o B_2O_3 were chosen. The hydride mixture satisfying this condition corresponds to 24 m/o B_2H_6 and 76 m/o SiH_4. An oxygen/hydride volume ratio of 25:1 was chosen, and a nitrogen/hydride volume ratio of approximately 400:1. The gas flow rates were adjusted to yield deposition rates in the range of 2000-3000 Å min^{-1}.

Stability of Silane and Diborane Sources

Separate hydride sources.—The stability during storage of diluted silane and diluted diborane was evaluated so that reproducible glass compositions could be prepared. As seen from Table I, variable fractions of higher hydrides of boron and silicon were detected in each of these mixtures, necessitating proper corrections of the gas concentrations by assuming complete oxidation of the higher hydrides. The composition of borosilicate films deposited after various periods of storage but otherwise identical conditions from stoichiometrically equivalent mixtures of these gases has shown that silane and diborane, both in argon at concentrations up to 8 vol %, are reasonably stable at room temperature over a period of at least 10 months (Table III).

Silane plus diborane mixtures.—Premixed gas sources consisting of silane, diborane, and argon would simplify the control of the gas flow rates and assure a uniform composition. Stability studies conducted in our laboratory in connection with doped oxides deposited from silane plus diborane mixtures have shown variable degrees of instability, generally

[2] Photographs were shown in a previous paper (5).

Table II. Coating on substrate and coating on reactor wall as a function of three system variables

Test No.	Definition	Substrate temperature, °C	Reactor wall temperature, °C		Carrier flow rate, cm^3 N_2 min^{-1}	Translucency time, min	Distribution of deposits, % of stoichiometry Substrate	Wall	Total
1	Standard	450	Neck Center Bottom	100 140 220	2900	4	16	35	51
2	Low-substrate temperature	375	Neck Center Bottom	100 120 175	2900	6	35	13	48
3	High-wall temperature	450	400-450		2900	>>20	3	119[a,b]	122[a]
4	Low-wall temperature	450	~25		2900	4	21	30	51
5	Low-wall and substrate temperature	375	~25		2900	4	32	31	63
6	High N_2 carrier gas flow	450	Neck Center Bottom	100 140 220	6200	>20	15[c]	46	61
7	Low-substrate temperature and intermediate N_2 carrier gas flow	375	Neck Center Bottom	100 140 175	4000	8	35	4	39

[a] Excess not accounted for.
[b] Clear, glassy wall deposit (all other wall deposits are powdery).
[c] Nonuniform deposit.

Table III. Comparison of borosilicate compositions synthesized from various silane and diborane sources

Elapsed time before or after gas analysis, weeks	Cylinder*	Hydride component	Number of film samples analyzed	Composition ratio** Product / Reactants
−4	A	SiH_4	8	1.000 (Standard curve, Fig. 3)
−4	B	B_2H_6		
2	E	SiH_4	4	1.204 ± 0.020
2	F	B_2H_6		
15	C	SiH_4	3	1.002 ± 0.025
15	D	B_2H_6		
38	A	SiH_4	2	1.000 ± 0.000
38	B	B_2H_6		

* Reference to Table I.
** "Reactants" = The boron content of various gas mixtures prepared during deposition by flow metering the gases at equivalent rates.
"Product" = The boron content of the gas mixture that corresponds to the borosilicate composition obtained. These glass compositions were determined by infrared spectroscopic analysis. The correlation was made by means of Fig. 3.
1.000 indicates a perfect correlation.

on the order of 5% decrease in the diborane content per month (9). In the present investigation, glass films were deposited from a mixture containing 6 vol % SiH_4 and 1.3 vol % B_2H_6 in argon (Precision Gas Company) over a period of 6 months. The mixture had high concentration of disilane (600 ppm as compared to normally 30 ppm) and a slightly increased amount of higher boranes. The glass composition deposited initially and after 3 months showed a boron decrease of 7%. After 5 months of gas storage, it had decreased by an average of 11%, and after 6 months, by 13%. The magnitude of these decreases should not adversely affect the glass composition if the mixture is used within a period of a few months. There is no question that argon-diluted diborane mixed with silane is less stable than without silane, which may cause diborane to polymerize to higher boranes that have a low vapor pressure. These would remain in the cylinder causing the gas to decrease in boron content as polymerization continues. Trace impurities may have an inhibiting or catalyzing effect on this reaction; consequently, it is recommended that the highest gas purity available be used and the concentrations of higher silanes and boranes be held to a minimum.

Chemical Vapor Deposition of Other Silicate Glasses

Several other binary and ternary silicate compositions were synthesized from the hydrides with and without metal alkyls. The effects of important deposition parameters on the film composition are summarized below.

Phosphosilicates and Phosphoborosilicates

Films of phosphosilicates were deposited from nitrogen-diluted silane, phosphine, and oxygen, analogous to the borosilicates from silane and diborane. Incorporating diborane in the gas mixture yielded phosphoborosilicate with a composition similar to that expected from the separately deposited binary glasses.

Phosphosilicate films deposited at 400°C from a mixture containing 0.93 vol % PH_3 and 9.08 vol % SiH_4 in argon, at an oxygen/hydride ratio of 12:1, contained 4.7 m/o (10 w/o) P_2O_5. The composition corresponds very closely to the 4.6 m/o expected from the chemical equation based on oxide and water formation. At concentrations up to 5 m/o P_2O_5, the reaction at 400°C proceeds stoichiometrically, but at higher phosphine ratios the phosphorus oxide content in the glass does not increase proportionately. The composition of glasses in the range of 5-10 m/o P_2O_5 is not affected markedly by changes in deposition temperatures of 325°-475°C and oxygen/hydride ratios of 4-24. For example, films prepared at 325° and an oxygen/hydride ratio of 4:1, and films deposited at 475°, ratio of 24:1, had a chemical composition agreeing within 10%. It can generalized that the phosphine-silane system is affected by deposition parameters to a lesser extent than the diborane-silane system. Furthermore, the chemical stability of phosphine on storage is much better than that of diborane; phosphine diluted with argon, or mixtures of phosphine-silane-argon, were found to be stable over periods of at least 1 yr (9).

Aluminosilicates and Aluminoborosilicates

Films of aluminum oxide were obtained from trimethyl aluminum vapor and oxygen at various temperatures (10). Incorporating nitrogen-diluted trimethyl aluminum vapor in the mixture of silane and oxygen, or of silane-diborane-oxygen, yielded aluminosilicates or aluminoborosilicates, respectively. Reaction conditions similar to those employed for binary borosilicate formation were used.

Trimethyl aluminum was selected from aluminum alkyl compounds because of the large aluminum-to-organic ratio, its relatively high vapor pressure which allows liquid alkyl source to be used at room temperature, and the high reactivity of the compound permitting relatively low deposition temperatures. The nitrogen carrying the alkyl vapor should be introduced in the diborane-silane-nitrogen stream just before it enters the reaction chamber to prevent possible condensation of aluminum borohydride in the gas lines. Controlled oxidation of the alkyl-hydride mixture was carried out by introducing oxygen in the reaction chamber as for the binary borosilicate depositions at substrate temperatures of 450° or 475°C. A large stoichiometric excess of oxygen and a relatively high temperature promote complete oxidation of the organic constituents to carbon dioxide and water with the formation of aluminum oxide according to the over-all reaction

$$Al_2(CH_3)_{6(g)} + 24\,O_{2(g)} \rightarrow Al_2O_{3(s)} + 6CO_{2(g)} + 9H_2O_{(g)}$$

Zinc Silicates and Zinc Borosilicates

Vitreous films of zinc oxide, zinc silicates, and zinc borosilicates were prepared analogously to the alumino-glasses. Diethyl zinc vapor was introduced to the system with nitrogen carrier gas from a liquid source bubbler. Zinc oxide films were deposited from diethyl zinc vapor and oxygen at 275°C. The soft film deposits could be hardened by a heat treatment in air at 600°C. Zinc silicates were deposited on silicon substrates at 450°C from diethyl zinc, silane, and a large excess of oxygen with nitrogen as diluent gas. Zinc borosilicates were prepared by adding diborane to the gas stream. These films were deposited at a rate of 800 Å min^{-1}.

Conclusions

The reaction of hydrides, or mixtures of hydrides and metal alkyl vapors, with oxygen at 275°-475°C in a special rotary reactor, has been optimized for the deposition of glass films. Reactants were silane, diborane, phosphine, trimethyl aluminum, diethyl zinc, and oxygen. Nitrogen and argon were the carrier gases. Glass compositions synthesized include borosilicates, phosphosilicates, aluminosilicates, zinc silicates, aluminoborosilicates, and zinc borosilicates.

The deposition parameters for binary borosilicates synthesized from silane, diborane, and oxygen have been discussed in detail. Conclusions of particular importance are: 1—To prevent spontaneous ignition, nitrogen should be added to the reaction mixture to dilute the hydride concentration to 1% or less. 2—The molar boron/silicon ratio in the deposited films is lower than that in the reactant gas. 3—The oxygen/hydride ratio should be at least 20:1 to assure complete oxidation of the hydrides. 4—Starting at 280°C, the deposition rate of borosilicate films increases steeply as the substrate temperature is increased to 375°. The rate declines with a further temperature increase because of the formation of powdery deposits

on the reactor walls. 5—The deposition temperature also affects the composition of the glass films, the boron content in the glass decreasing with decreasing temperatures, especially below 400°C. 6—Borosilicate glasses with a high silica content that are difficult to prepare homogeneously by conventional ceramic techniques (because of their high viscosity and liquidus temperature) can be readily prepared.

For phosphosilicate films containing up to 5 m/o P_2O_5, the deposition from silane, phosphine, and oxygen at 400°C proceeds stoichiometrically, but at higher concentrations the yield of phosphorus oxide diminishes.

The simultaneous gas phase oxidation at 450°-475°C of trimethyl aluminum or diethyl zinc vapor with the silane or silane-diborane yielded aluminosilicate, zinc silicate, aluminoborosilicate, or zinc borosilicate compositions.

A thermal densification is required to approach bulk glass properties. The effects of this treatment are discussed in Part II (4) of this series, together with an evaluation of chemical, dielectric, thermal, and optical properties of the films.

Acknowledgments

We thank especially George F. Stockdale, Larry K. Baker, and Eugene R. Skaw, for independently testing and verifying the chemical vapor glassing technology described in this paper, and James A. Amick for critically reviewing the results and the manuscript. We are also indebted to Bernard L. Goydish for the chemical analyses of glass compositions.

Manuscript submitted May 16, 1969; revised manuscript received Jan. 5, 1970. This was Paper 92 presented at the Boston Meeting, May 5-9, 1968.

Any discussion of this paper will appear in a Discussion Section to be published in the December 1970 JOURNAL.

REFERENCES

1. F. C. Eversteijn, *Philips Res. Repts.*, **21**, 379 (1966).
2. "Surface Passivation Techniques for Compound Solid State Devices," AF33(657)-11615, Interim Tech. Doc. Prog. Rep. No. 1-4, 6/1/63 to 5/31/64; Techn. Rep. AFAL-TR-75-213, 1965; Proj. 4460, Task 446002, Res. & Technol. Div., Air Force Syst. Comm., Wright-Patterson Air Force Base, Ohio.
3. N. Goldsmith and W. Kern, *RCA Rev.*, **28**, 153 (1967).
4. W. Kern and R. C. Heim, *This Journal*, **117**, 568 (1970).
5. W. Kern, *RCA Rev.*, **29**, 525 (1968).
6. L. C. Pasztor and J. D. Bode, *Anal. Chem.*, **32**, 1530 (1960).
7. L. C. Pasztor and J. D. Bode, *Anal. Chim. Acta*, **24**, 467 (1961).
8. B. L. Goydish, RCA Laboratories, Personal communication.
9. A. W. Fisher and J. A. Amick, *RCA Rev.*, **29**, 549 (1968).
10. W. Kern, To be published.

Chemical Vapor Deposition of Silicate Glasses for Use with Silicon Devices

II. Film Properties

Werner Kern* and Richard C. Heim[1]

David Sarnoff Research Center, RCA Corporation, Princeton, New Jersey

ABSTRACT

Chemical, dielectric, thermal, and optical properties of glass films synthesized by chemical vapor reactions from the hydrides are discussed. The binary borosilicate glasses deposited at low temperature from silane, diborane, and oxygen require a thermal densification to approach bulk glass properties. The rate of densification in the temperature range of 770°-800°C is very rapid but water vapor has an accelerating influence, allowing densification at reasonable rates at temperatures as low as 450°C. The thermal expansion match with silicon was sufficiently close to allow the crack-free coating of wafers with 12μ of glass. Borosilicate films of 5μ thickness on silicon withstood severe thermal shock, temperature cycling, moisture penetration, and corrosion resistance tests. Densified borosilicate of typical compositions had a dielectric constant of 3.8-4.1 and a dissipation factor at 10^3 Hz of 0.10-0.15. The d-c dielectric field strength sustained by MIS capacitors made from 1μ thick densified films measured before and after a 1-yr exposure to room air, was 6 to 8 x 10^6 V cm^{-1}. The properties of vapor-deposited phosphosilicate glasses and of glasses containing the oxides of aluminum and zinc are briefly described.

This paper is concerned with the properties of glass films deposited by chemical vapor reaction from hydrides and oxygen by the methods presented in Part I of this series (1). Particular emphasis is placed on binary borosilicate glass compositions synthesized from silane, diborane, and oxygen at 400°-450°C. This type of glass is well suited for glassing silicon device wafers.

Experimental

Film thickness.—Approximate thicknesses of less than 1μ were estimated from the interference color of the films on polished silicon, using the known colors for SiO_2 (2) and taking into account changes of the refractive index of the various glasses. Precision measurements of films up to 2μ were made by multiple-beam interferometry (3) of samples in which a step in the glass was etched followed by overcoating with an opaque metal film (4); the accuracy was typically ±100Å. Much thicker layers were cross-sectioned and measured directly under a Leitz microscope using a calibrated filar eye piece.

Film composition.—Except for the borosilicate glasses, the chemical composition of the films was determined by standard microchemical techniques (1).

* Electrochemical Society Active Member.
[1] Present address: Kasper Instruments, Santa Clara, California.

Routine composition measurements of the borosilicate films were carried out by infrared absorbance. The analysis is based on the ratio of the net intensities of two characteristic main absorption bands, one for B-O and one for Si-O. The absorbance ratios of a series of primary standards of deposited borosilicate films were correlated with the compositions obtained by chemical analysis to establish a calibration curve. Details of the method were presented elsewhere (5).

Film etch rate and density.—The determination of the etch rate was carried out by a technique previously described (6). The measurements were made at 25.0° ± 0.1°C with etchants including hydrofluoric acid of various concentrations, ammonium fluoride buffered HF (454g NH_4F, 654 cm^3 H_2O dist., 163 cm^3 HF 49%), and P-etch (7).

The film density was calculated from thickness, weight, and surface area measurements using 5-10μ thick glass films deposited on 1.25 in. diameter polished silicon wafers. A microbalance (Mettler Type M-5) was used for the weight determinations.

Index of refraction and infrared absorption.—The refractive indices of 1μ thick films were determined interferometrically by reflection spectrophotometry (8) in the visible wavelength region using a double-beam grating spectrophotometer (Beckman Model DB-6).

Infrared measurements were used not only for determining the film composition but also for comparing spectral shifts caused by structural and chemical changes during densification and corrosion tests. Polished high-resistivity silicon wafers of constant and high infrared transmission were used as substrates. Half of each wafer was stripped of its coating and placed in the reference beam of the spectrophotometer (Perkin-Elmer Model 137 B) to cancel possible substrate effects.

Dielectric properties.—One-micron thick glass films were deposited on low-resistivity polished silicon wafers. Circular top electrodes of 0.014 in. diameter aluminum were vacuum-evaporated on these films to form parallel plate capacitors. Capacitance and dissipation factor measurements were made with a capacitance bridge (General Radio Company Model 716-C) at 10^3 Hz. Measurements were made on at least six capacitors per sample to obtain reliable average values.

The d-c dielectric strength of the films was measured by connecting the capacitors so that the silicon was at positive potential to obtain the true dielectric strength of the glass (9). The tests were carried out at 15% relative humidity and 21°C. The voltage was raised in increments to a current of 1 na leakage. The results reported are the arithmetic means of the breakdown field values sustained by 10 different capacitors on the same wafer.

Glass densification treatments.—Densification of the films was conducted in a quartz tube furnace. The ambient gases consisted of high-purity nitrogen or argon, or room air. Water vapor generated from deionized and distilled water in a quartz vessel was used for low-temperature densification.

Properties of Vapor-Deposited Borosilicate Glasses

Film etch rates.—The isothermal etch rate of borosilicates is a characteristic function of the boron oxide content of the glass and the etchant composition. The etch rate in aqueous hydrofluoric acid increases with increasing boron oxide content of the glass as shown in Fig. 1. Etch rates for the same samples after thermal densification are also shown for comparison. The boron content of the hydride mixture can be correlated with the boron content of the glass by means of Fig. 3 presented in Part I of this paper (1). A semilog plot of etch rates as a function of the boric oxide in the glass obtained by this (nonlinear) relation is shown in Fig. 2 for the concentration range 0-30 m/o, (mole per cent) B_2O_3.

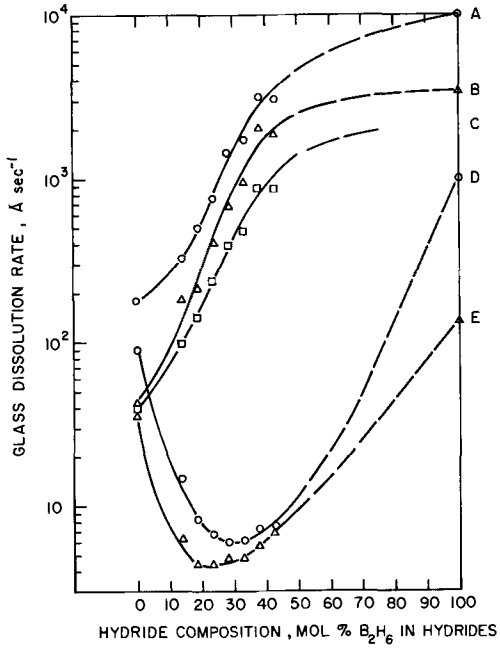

Fig. 1. Etch rate of borosilicate films as functions of the hydride composition from which they were deposited, densification conditions, and etchant. A—Approximate etch rates for films as deposited at 450°C, dilute HF etchant (1 vol 49% HF: 2 vol H_2O). B—Densified 5 min 770°C, Ar; HF etchant (1 vol 49% HF: 2 vol H_2O). C—Densified 5 min 770°C, air; HF etchant (1 vol 49% HF: 2 vol H_2O). D—As-deposited at 450°C, HF-buffer etchant. E—Densified 5 min 770°C, Ar; HF-buffer etchant.

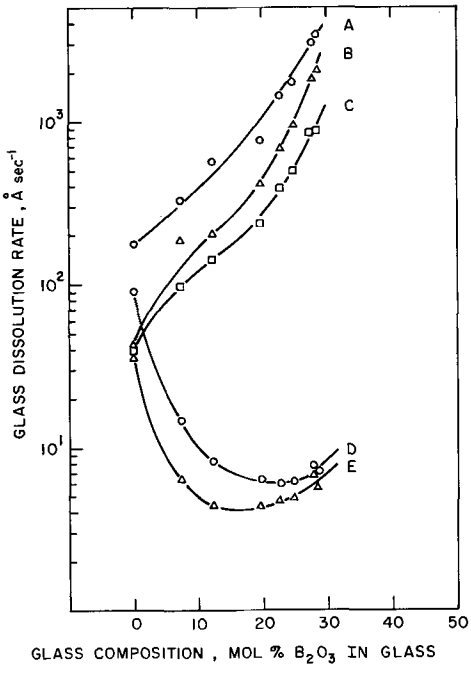

Fig. 2. Etch rate of borosilicate films as functions of glass composition, densification conditions, and etchant. A—Approximate etch rate for films as deposited at 450°C, dilute HF etchant (1 vol 49% HF: 2 vol H_2O). B—Densified 5 min 770°C, Ar; HF etchant (1 vol 49% HF: 2 vol H_2O). C—Densified 5 min 770°C, air; HF etchant (1 vol 49% HF: 2 vol H_2O). D—As-deposited at 450°C, HF-buffer etchant. E—Densified 5 min at 770°C, Ar; HF-buffer etchant.

Different HF-water compositions lead to different etch rates, but the slopes of the curves are similar. P-etch (7), a composition of diluted HF containing some HNO_3, also yields similar slopes. Thermal densification lowers the film etch rates without greatly altering the slope of the curves. The rates of the densified films are similar to those obtained with borosilicate

bulk glasses of comparable composition. The etch rate of a borosilicate glass can therefore serve as a rapid test for estimating its boron content.

The etch rate in buffered HF decreases as the boron oxide content is increased, apparently because of a lowered reactivity of this etchant toward Si-O-B bonds. The increase in etch rate beyond the 20-23 m/o B_2O_3 composition appears to be caused by free B_2O_3. Vapor synthesized borosilicate compositions containing more than approximately 25 m/o B_2O_3 tend to devitrify and may be soluble in boiling water before and after densification at 800°C.

Corrosion resistance.—Thermally densified borosilicate film deposits of standard composition, or compositions containing a lower concentration of boron oxide, were found by infrared analysis to be stable, insoluble, and corrosion resistant even under the following conditions: 1—exposure to cold concentrated HCl, concentrated H_2SO_4; 2—chromic/sulfuric acid at 125°C; 3—sulfuric acid/hydrogen peroxide at 125°C; and 4—boiling deionized and distilled water for 1 hr. The last treatment is a particularly severe stability test for glass films (10). The borosilicates withstood all treatments without change except for a small amount of reversible OH-uptake during the boiling water treatment. Microscopic examination of borosilicate layers containing up to 19 m/o B_2O_3 that had been exposed for 144 hr to 95% relative humidity at 95°C showed no signs of devitrification or other defect formation in both the undensified and the densified states.

Film density.—A 5μ thick borosilicate film deposited at 400°C contained 18 m/o B_2O_3 and had a density of 2.25 g cm^{-3}. Densification in argon at 800°C for 20 min proceeded without detectable loss in weight, while the layer thickness decreased by several per cent. Since there was no loss in weight, the changes observed represent a molecular compaction or densification effect. As expected, the density decreases as the boron oxide content of the glass increases. A sample of a 7μ thick borosilicate film deposited at 375°C contained 20 m/o B_2O_3 and lost no weight on densification at 800°C. The density of this film after heat treatment was 2.24 g cm^{-3}. The density values agree with those for bulk borosilicate glasses of comparable composition.

Resistance to moisture penetration.—The moisture resistance of glass layers was tested by exposing "uncanned" glassed transistors to high humidity at elevated temperature and monitoring critical electrical parameters. Silicon planar npn transistors with a primary passivating layer of thermal SiO_2 and metallized with vapor deposited tungsten (11) were used as test vehicles. The device wafers were coated with 5μ of the borosilicate glass, followed by densification at 770°C, photoresisting, and chemical etching to expose the bonding pads and grid lines for scribing. The device pellets were mounted by conventional techniques on headers, and wire bonded (11). Each transistor was protected mechanically with a topless metal can. Two types of tests were conducted to check for moisture resistance: 1—Exposure to 95% relative humidity at 70°C for periods up to 150 hr followed by 30 min drying in room air. The moisture-sensitive collector-base leakage current (I_{CBO} at −10V d.c., in the low nanoamp range) was monitored. 2—Operating life stress tests at 95% relative humidity and 70°C for 680 hr at periodically increasing power levels. The parameter monitored was V_{BE}, the forward bias potential of the emitter junction required to maintain the rated power dissipation. This test was carried out at high temperature (heat from ambient and heat generated at the collector junction) under reverse bias and at high humidity. The electrical stability observed demonstrated clearly that no moisture had penetrated through the films under these test conditions.

Thermal and structural strength properties.—An important requirement for achieving high-quality glass-to-substrate seals is the absence of stresses that would lead to cracks or other defects. A glass composition with an average coefficient of thermal expansion close to that of the substrate should yield a stress-free system. Actually, a slightly lower coefficient for the glass is preferable to force it under compressive stress, thereby increasing its mechanical strength considerably. In addition to stresses associated with mismatches in thermal expansion, stresses are introduced during the process of film deposition. The total stresses of the various glass compositions were compared empirically observing the maximum layer thickness that could be built up on polished silicon wafers without forming microcracks. The films were deposited at 450°C at rates of 650-1000 Å min^{-1} and analyzed chemically as described earlier. The results presented in Table I indicate that the thermal expansion and contraction match of the glass/silicon system improve with increasing boric oxide content, as expected. The standard composition containing 17 m/o B_2O_3 yielded crack-free layers of approximately 12μ. Compositions much richer in B_2O_3 permit the build-up of substantially thicker layers, but the stability of these boron-rich glasses is poor.

The maximum thickness of crack-free glass obtainable is influenced by the surface area of the substrate. Layers of standard borosilicate were deposited on silicon wafer sections of approximately 1 cm^2. Layers as thick as 54μ were found free of cracks before and after densification at 800°C.

The softening temperatures were measured semiquantitatively by determining the temperature at which two pieces of a glass-coated silicon wafer would fuse under pressures on the order of a few hundred pounds per square inch. The softening temperature was in the range of 800°-850°C for borosilicates of standard composition. It should be noted that a few hundred Angstroms of a SiO_2 layer over the glass are sufficient to prevent fusion.

Thermal shock tests were conducted as follows: Silicon wafers coated with a 5μ layer of glass were cycled from a dry ice-acetone slurry at −65°C to boiling water and back, allowing equilibration periods of 30 sec. Similar tests were also run using liquid nitrogen (−196°C) and boiling water. Microscopic examination at 1000-fold magnification showed that no cracks or other defects formed during these stress tests. When glassed silicon wafers were deliberately fractured, the glass did not separate from the silicon even though silicon fragments tore out of the silicon substrate.

Effects of film densification.—As a general rule, the properties of dielectric films deposited at low temperature can be significantly improved by a heat treatment which densifies the film structure and relieves lattice stresses introduced during deposition. The rate of densification is dependent on both temperature and ambient. Pliskin and Lehman (7) found water vapor to be particularly effective for densifying silicon dioxide films deposited from organo-oxysilanes. Effects of thermal densification of silicon dioxide films from silane (12, 13) and of a variety of glass films synthesized from organic reactants (14) were discussed

Table I. Maximum thicknesses of coherent borosilicate films on silicon wafers as a function of glass composition

B_2O_3 content m/o	B_2O_3 content w/o	Film thickness in microns: Free of cracks	Film thickness in microns: Beginning crack formation
0*	0*	2.2	~2.5
11.8	13.4	~4	4.8
15.2	17.1	<10.8	<10.8
16.8	19.0	~12	13.2
25.5	28.5	~21	23
32.5	36.8	>13	>13

* Silicon dioxide deposited from silane and oxygen under similar conditions.

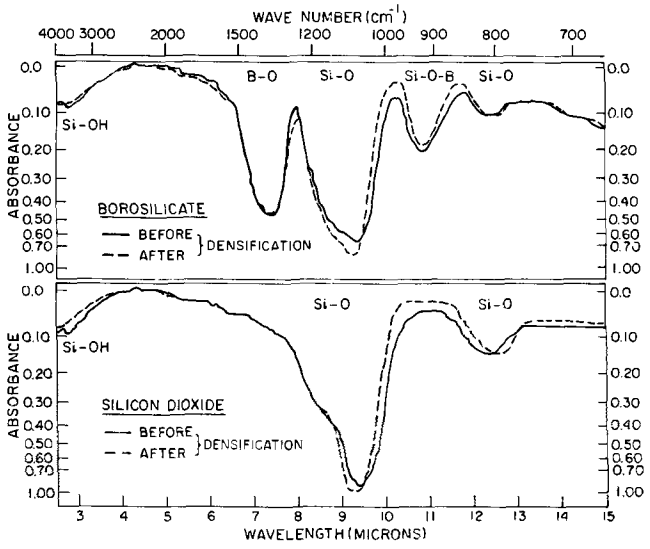

Fig. 3. Comparative *IR* absorption spectra of vapor-deposited borosilicate and silica films as-deposited at 450°C and after densification at 800°C in air for 10 min.

previously. The silicate glasses described in the present paper can be densified similarly.

The etch rate data presented in Fig. 1 and 2 are for films as deposited at 450°C and also after densification at 770°C for 5 min in pure argon or in nondried room air. No data for buffered etch were taken for the borosilicate samples densified in air, but the etch rate value for SiO_2 previously reported (12) was 21% lower than for the same sample densified in argon, indicating a generally increased effectiveness of air. The major decrease of the film etch rates at temperatures from 770° to 800°C takes place within the first 5 min of heat treatment. Further decreases proceed at a slow logarithmic rate which is accelerated by water vapor in the ambient as reported in a separate paper (5). This accelerating effect is much more pronounced at lower temperatures. For example, nearly complete densification of a standard borosilicate composition can be achieved in steam at 450°C in about 5 hr, whereas dry ambients would require extremely long periods at this temperature (5). Densification conditions compatible with a particular device structure and metallization can therefore be chosen. The accumulative effects of progressive densification of the films are also manifested in changes of the infrared absorption bands and in the dielectric properties, as shown below.

Infrared absorption.—The infrared spectrum of a typical borosilicate film before and after densification at 800°C is presented in Fig. 3 and compared with the spectrum of a silicon dioxide film deposited from silane. The dominant absorbance maximum between the wavelengths of 9.2 and 9.4μ in each curve, and the smaller peak of 12.4μ, are caused by the Si-O stretching vibration. The peak at 10.85μ in the borosilicate spectra indicates the Si-O-B stretching vibration, and that at 7.4μ, the B-O stretching. The ratio of the absorbance maxima for the 7μ B-O peak and the 9μ Si-O peak was found to be related to the glass composition and was utilized for quantitative analysis. The minor peak at 2.7μ is caused by O-H stretching and disappears during the densification. Other effects of densification for both types of films are an increase in the absorbance intensity of the Si-O major peak and its shift toward shorter wavelengths, similar to SiO_2 films deposited from other source materials (7). It is significant that the absorbance intensity of the B-O peak remains constant, indicating that no loss of B_2O_3 occurs during the heat treatment of the glass films.

Index of refraction.—Films prepared under a variety of deposition conditions were tested before and after densification. Similar to other film properties, the refractive index was relatively independent of deposition conditions for a given glass composition. Typical borosilicate films measured in the 5000-6000Å wavelength region before and after densification, had a refractive index of 1.42-1.43. The refractive index increased toward the shorter wavelength region, the behavior normally observed for glasses.

Dielectric properties.—Dielectric properties of 1μ thick borosilicate films deposited under various conditions were evaluated before and after heat treatment at 800°C in air. The vapor compositions were adjusted to yield glasses containing between 17 and 19 m/o B_2O_3, regardless of the deposition conditions. The results presented in Table II indicate that the dielectric properties are not influenced greatly by these variations.

The dielectric constant for densified films was similar to that of a pure borosilicate bulk glass consisting of 22.1 m/o B_2O_3 and 77.9 m/o SiO_2, which has a value of 4.05 for the frequency range 10^2 to 3 x 10^9 at 25°C (15). The same borosilicate bulk glass has a dissipation factor of 0.086 (most commercial borosilicate glasses containing minor additional components have much higher values) (15). Some loss tangent measurements were also made in the rf range; vapor-deposited and densified borosilicate films of standard composition had a dissipation factor of approximately 1.3% when tested at 2 x 10^9 Hz at 23°C (16). The d-c electrical field strength sustained by MIS capacitors made from various as-deposited 1μ thick films ranged from 6 to 10 x 10^6 V cm^{-1} but decreased substantially on sample storage in room air over a period of 1 yr, whereas capacitors made from the densified films remained perfectly stable. The dielectric breakdown potential measured at a leakage current at 1 na ranged from 650 to 800V (normalized to 10,000Å film thickness), corresponding to 6.5-8.0 x 10^6 V cm^{-1}. The films deposited at 400° and 450°C showed distinct improvements in dielectric strength compared to those formed at 375°C.

The instability in dielectric strength noted above is explained as follows. Undensified borosilicates lose boric oxide on storage. The residual film has, therefore, a lower density which causes a decrease in the

Table II. Dielectric properties of borosilicate films* as a function of deposition conditions and heat treatment

Substrate temp, °C	Oxygen/ hydride ratio	Film deposition rate, Å min^{-1}	Dielectric constant K at 24°C, $f = 10^3$ Hz		% Decrease of b	Dissipation factor % D at 24°C, $f = 10^3$ Hz		% Decrease of b	Maximum dielectric strength 10^6 V cm^{-1}		Capacitor yield, %**	
			a	b		a	b		a	b	a	b
375	15:1	3100	5.53	4.07	26	0.46	0.12	74	#	6.45	100	100
375	50:1	3100	5.41	3.94	27	0.45	0.12	73	#	6.89	100	100
375	15:1	5000	5.25	3.87	26	0.36	0.12	67	#	6.96	100	100
400	15:1	3300	5.29	3.96	25	0.21	0.15	29	#	7.70	100	100
450	15:1	1700	5.21	3.81	27	0.31	0.10	68	#	7.95†	100	100

* Containing 17-19 m/o B_2O_3.
[a] Film, as deposited.
[b] Film, heat-treated 20 min at 800°C in air.
** Capacitors tested for shorts (10 devices measured/sample).
† Film thickness only 8600Å (all others 9400-10,000Å).
# Unstable: original values were at least as high as those in (b), but decreased on storage in room air over a period of 1 yr.

Table III. Dielectric properties, etch rates, and infrared absorbance of typical films* of phosphosilicate, aluminosilicate, and aluminoborosilicate

Film property	Phosphosilicate as dep.	Phosphosilicate densif.	Phosphosilicate as dep.	Phosphosilicate densif.	Aluminosilicate as dep.	Aluminosilicate densif.	Aluminoborosilicate as dep.	Aluminoborosilicate densif.
Film composition								
m/o P_2O_5	6.1		8.6		0		0	
m/o Al_2O_3	0		0		11.1		~11	
m/o B_2O_3	0		0		0		12	
m/o SiO_2 (by difference)	93.9		91.4		89.9		77	
Film thickness, μ	0.89		0.85		0.90		0.99	
Dielectric constant, K	3.9	4.0	3.7	3.6	5.4	4.1	4.9	3.8
Change of K on densification, %		2.6		−2.7		−24		−22
Dielectric breakdown, kV	0.85	0.70	0.90	0.70	0.65	0.60	0.80	0.75
Sustained voltage test (80% of breakdown voltage, 15 min at 25°C) failures		0		0		0		0
Stability of dielectric strength (after 3 yr storage, dry air, 23°C)								
V at 1 na	672	584	700	902	<300	706	320	603
V at 10 na	878	664	675	706	<300	812	400	759
Etch rate in buffered HF, Å sec^{-1}	98	82	93	90	62	33	11.2	7.2
Change of etch rate on densification, %		−16		−3.2		−47		−36
IR absorbance maxima, wavelength								
P-O stretching, μ	7.60	7.55	7.60	7.55				
Si-O stretching, μ	9.18	9.07	9.14	9.07	9.30	9.24	9.29	9.23
Si-O confirmation, μ	12.30	12.50	12.50	12.35	12.35	12.30	12.46	12.35
B-O stretching, μ							7.18	7.26
B-O-Si stretching, μ							10.93	10.95
Not assigned definitely, μ					10.92	—		

* These films were deposited at 475°C as described previously (1). Densification was carried out at 770°C in an argon atmosphere for 20 min.

dielectric strength. The loss of B_2O_3 is slow, but can be detected over a period of time by infrared analysis.

Phosphosilicates

The effects on the film composition of variations in the silane/phosphine/oxygen ratio at deposition temperatures from 325° to 475°C were described in Part I (1) of this series. A summary of dielectric properties, etch rates, and infrared absorbance of two typical phosphosilicate films as-deposited at 475°C and after densification at 770°C in argon is presented in Table III.

The most remarkable differences between the phosphosilicates and all other silicates tested are: 1—the absence of marked changes of the dielectric constant on densification, 2—the long-term stability in dielectric strength of both densified and undensified films, and 3—the much smaller decrease of the etch rate after densification. In the more selective P-etch, etch rate changes are more pronounced than in buffered-HF, and the etch rate increases sharply with increasing P_2O_5 content.

Infrared spectra of a phosphosilicate film before and after densification are presented in Fig. 4. The Si-O band in the 9μ region is much broader than that observed for SiO_2 (Fig. 3) and shifts on densification toward shorter wavelength to a greater extent, probably because of a phosphorus-induced increase in polymerization of SiO_4 tetrahedra (17, 18). A second pronounced change on densification (particularly for films deposited at 325°C) is the large increase of absorbance of the P-O band in contrast to the B-O band in borosilicates.

Eleven-micron thick phosphosilicate layers containing 4.65 m/o P_2O_5 and deposited at 400°C on silicon substrates were weighed before and after heat treatment at 800°C in argon. As for borosilicates, no weight loss was detectable on densification. The surface of the glass at this thickness was nodular but the thermal expansion matched silicon sufficiently well to prevent cracking of the films when deposited on wafers. Phosphosilicate compositions containing 13 m/o P_2O_5 were deposited in 25μ thick layers without cracking. Thinner layers of 5μ had a grainy microstructure and exhibited a grayish appearance, whereas films less than 1μ thick were similar to deposited oxide films in appearance.

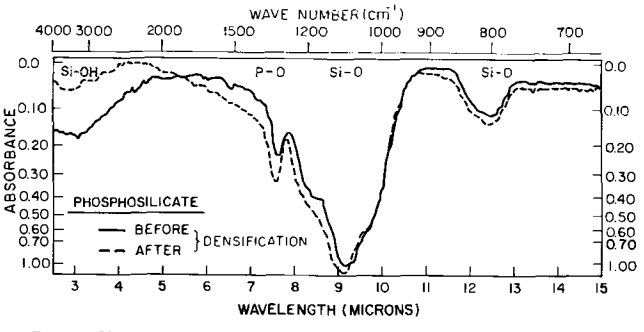

Fig. 4. *IR* absorption spectra of a vapor-deposited phosphosilicate film as-deposited at 475°C and after densification at 770°C in argon for 20 min.

The chemical stability of phosphosilicate films toward moisture at elevated temperature is generally poor because of their inherent hygroscopic nature. For device glassing, phosphosilicates should therefore be used only in conjunction with a more stable outer layer.

Aluminosilicate and Aluminoborosilicates

Aluminosilicate films deposited from silane, trimethyl aluminum, and oxygen at 475°C (1) contained up to 11 m/o Al_2O_3. Properties of a typical aluminosilicate film are shown in Table III. The infrared absorption spectrum was similar to that of SiO_2 films deposited was 8 x 10^6 V cm^{-1} and remained stable over weak absorption maximum noticeable in undensified films in the region of 10.8-11μ.

The incorporation of trimethyl aluminum in the silane-diborane-oxygen reaction mixture did not markedly affect the borosilicate composition. Films deposited at 450°C at a rate of 600 Å min^{-1} consisted typically of 1.5 m/o Al_2O_3, 18 m/o B_2O_3, and 80.5 m/o SiO_2. Layers of 12μ thickness were deposited on silicon without cracking. Properties of a film with a higher alumina content and deposited at 475°C are included in Table III. The dielectric properties, etch rates, and infrared absorption characteristics of these films as-deposited and after densification in argon were very similar to those of binary borosilicates of the same boron content. Microscopic examination of undensified and densified films of aluminosilicates and aluminoborosilicates that had been exposed to 95% relative humidity at 95°C for 144 hr showed no devitrification or other changes. Life tests with transistors as described for borosilicates but employing 5μ of densified aluminoborosilicate withstood moisture penetration tests (680 hr exposure to 95% relative humidity at 70°C).

Zinc Silicates and Zinc Borosilicates

These films were deposited from the appropriate hydride(s), diethyl zinc vapor, and oxygen (1). The

etch rate of zinc silicate films in buffered HF solution was similar to that of silane-deposited SiO_2 films. Crack-free films of 2μ thickness were deposited; crack formation set in at 4μ. Infrared absorption spectra were similar to those for deposited SiO_2 except for the presence of an absorption peak at 10.8μ, which is probably due to Si-OH bending similar to that observed in evaporated SiO_2 films (7). Layers of 1μ thickness withstood dielectric breakdown potentials of greater than 400V.

Crack-free zinc borosilicate films of 4μ thickness were obtained on silicon wafers; line cracks began to set in at 9μ. Etch rates and infrared band positions were very similar to those for binary borosilicates of comparable boron content. As for zinc silicates, the dielectric breakdown potential of 1μ thick film was in excess of 400V.

Conclusions

Important properties of borosilicate films prepared by chemical vapor reaction of silane and diborane with oxygen have been evaluated. The thermal expansion and contraction match with silicon of compositions of typically 17 m/o B_2O_3 are sufficiently good to allow the crack-free build-up of several-micron thick glass layers suitable for glassing of silicon devices. A thermal densification treatment is essential to produce stable films of optimum properties; water vapor accelerates the rate of densification significantly, particularly at low temperatures. The dielectric properties of borosilicate films deposited under a variety of conditions were found to be relatively independent of deposition parameters. For densified films of glasses containing 17-19 m/o B_2O_3, the dielectric values are as follows: dielectric constant, 3.8-4.1; dissipation factor, 0.10-0.15; d-c dielectric breakdown field strength sustained, 6-8 x 10^6 V cm^{-1}. The electrical stability on life testing of borosilicate glassed planar transistors indicates that the glass layer was effective in preventing moisture penetration. Several-micron thick densified borosilicate films are smooth, uniform, transparent, free of cracks or crazing, resist moisture penetration, and are well suited for silicon device glassing.

The ratios of absorbance of the B-O and the Si-O infrared absorption maxima are related to the glass composition and have been utilized for quantitative film composition analysis. The etch rate of borosilicates in specific etchants is a characteristic function of the boron oxide content and can be utilized to check the approximate glass composition. In aqueous HF solutions or in P-etch, the etch rate increases exponentially with increasing boron oxide. In buffered HF, it decreases steeply to a minimum and then increases rapidly with increasing boron oxide concentration due to free B_2O_3. Densification of the films at temperatures from 450° to 800°C lowers the etch rates markedly, indicating an increase of the apparent film density. Densification of borosilicates at 800°C proceeds without weight loss and leads to densities comparable to borosilicate bulk glasses.

The dielectric constant of phosphosilicate films chemically vapor deposited from silane, phosphine, and oxygen did not change on densification, in contrast to all other vapor-synthesized silicate films. The sustained dielectric breakdown field of films as deposited was 8 x 10^6 V cm^{-1} and remained stable over 3 yr of storage in air at room temperature. Phosphosilicates require a protective top layer because of their hygroscopic nature. The properties of silicate glasses containing the oxides of aluminum or zinc showed no distinct advantages over the simpler binary borosilicates.

Manuscript submitted May 16, 1969; revised manuscript received Jan. 5, 1970. This was Paper 92 presented at the Boston Meeting, May 5-9, 1968.

Any discussion of this paper will appear in a Discussion Section to be published in the December 1970 JOURNAL.

REFERENCES

1. W. Kern and R. C. Heim, *This Journal*, **117**, 562 (1970).
2. W. A. Pliskin and E. E. Conrad, *IBM J. Res. Develop.*, **8**, 43 (1964).
3. S. Tolansky, "Multibeam Interferometry of Surfaces and Films," Clarendon Press, Oxford (1948).
4. G. R. Booker and C. E. Benjamin, *This Journal*, **109**, 1206 (1962).
5. W. Kern, *ibid.*, **116**, 251C, RNP 372 (1969).
6. W. Kern, *RCA Rev.*, **29**, 557 (1968).
7. W. A. Pliskin and H. S. Lehman, *This Journal*, **112**, 1013 (1965).
8. E. A. Corl and H. Wimpfheimer, *Solid State Electron.*, **7**, 755 (1964).
9. F. L. Worthing, *This Journal*, **115**, 88 (1968).
10. W. A. Pliskin, *Proc. IEEE*, **52**, 1468 (1964).
11. J. A. Amick and J. Shaw, Paper presented at Electrochem. Soc. Meeting, Detroit, Oct. 5-9, 1969.
12. N. Goldsmith and W. Kern, *RCA Rev.*, **28**, 153 (1967).
13. B. Swaroop, *This Journal*, **115**, 239C, Abs. 481 (1968).
14. "Surface Passivation Techniques for Compound Solid State Devices," AF33 (657)-11615. Interim Tech. Doc. Prog. Rep. No. 1-4, 6/1/63 to 5/31/64; Techn. Rep. AFAL-TR-75-213, 1965; Proj. 4460, Task 446002, Res. & Technol. Div., Air Force Syst. Comm., Wright-Patterson Air Force Base, Ohio.
15. "Dielectric Materials and Applications," A. R. von-Hippel, Editor, pp. 309, 310, John Wiley & Sons, New York (1954).
16. "Uhf Film Integrated Circuits," M. Caulton *et al.*, Rep. No. 1, Contract No. DAAB07-68-C-2096, OSD-1366, Nov. 1968, U.S. Army Electronics, Fort Monmouth, N. J.
17. F. Matossi and H. Krueger, *Z. Physik.*, **99**, 1 (1936).
18. W. A. Pliskin, *Appl. Phys. Letters*, **7**, 158 (1965).

Technical Note

The Development of a Primary Nonaqueous Lithium/Mercuric Fluoride Cell

S. Lerner and H. N. Seiger*

Electrochemical Research Laboratory, Gulton Industries, Incorporated, Metuchen, New Jersey

The purpose of this program was to investigate the lithium/mercuric fluoride system. This communication describes our efforts to make the HgF_2/Hg electrode dischargeable to a signficant extent in a nonaqueous electrolyte. The theoretical watthours/in.^{3} (59) and watthours/lb (343) for the Li/HgF_2 system compare favorably to those of the Ag/Zn system (61 whr/in.^{3} and 195 whr/lb). In addition, the theoretical open-circuit voltage of 3.4V is more than twice that of Ag/Zn (1.60V).

Because of the dearth of information about such systems, the approach chosen was based on previous experience with the lithium/nickel fluoride nonaqueous system (1).

Preparation of Electrodes

Mercuric fluoride was purchased commercially from Alfa Inorganics, Incorporated. Each shipment of HgF_2 was analyzed for purity by x-ray diffraction. Lithium metal was purchased as a dispersion in mineral oil from Foote Mineral, Incorporated.

The mercuric fluoride electrodes were prepared by pasting a mixture of HgF_2, UCET acetylene black, silver powder, and Microthene on an expanded Monel screen. The UCET is present as a conductive diluent, as the HgF_2 is not conductive. The silver is present to prevent electrode poisoning by amalgamating with the mercury formed as a discharge product. The Microthene is a microporous polyethylene used as a binder. After pasting, the electrodes were heated to 110°C to allow the binder to flow.

The lithium anodes were prepared by pasting lithium in a mineral oil dispersion onto an expanded nickel screen. The pasted screen was pressed in an inert atmosphere to produce a uniform electrode. Prior to constructing a cell, the dispersion oil was removed by leaching in hexane.

The electrolyte chosen after investigations of a number of possible solvent-solute pairs was propylene carbonate-phenyl trimethyl ammonium hexafluorophosphate.

Cell Testing

Cells were constructed using lithium anodes, cathodes of composition 54% HgF_2, 18% Ag, 18% UCET,

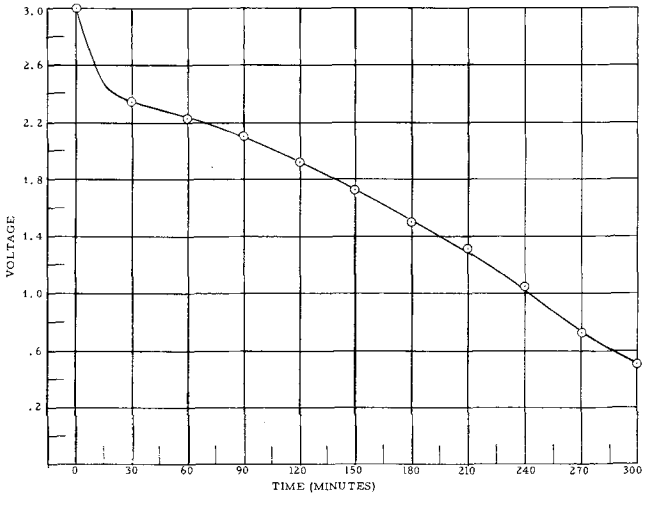

Fig. 2. C/6 discharge curve—HgF_2/Li cell—electrolyte PC/$PTMAPF_6$—54% HgF_2/18% Ag/18% C/10% binder (10 mA = 2 mA/cm^2).

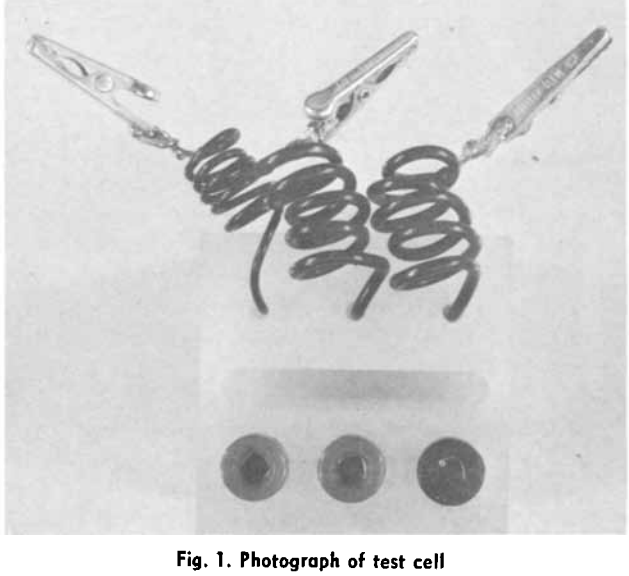

Fig. 1. Photograph of test cell

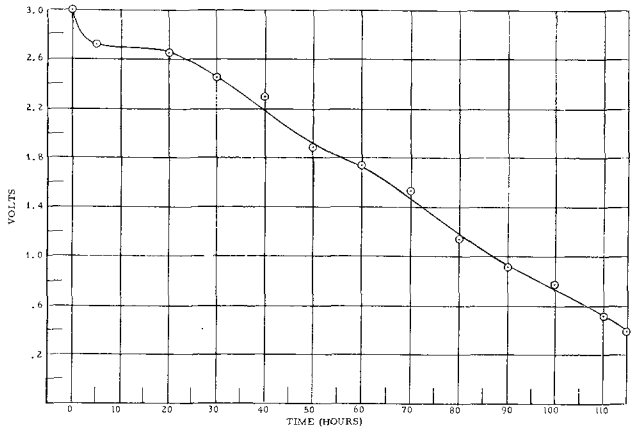

Fig. 3. C/150 discharge curve—HgF_2/Li cell—electrolyte PC/$PTMAPF_6$—54% HgF_2/18% Ag/18% C/10% binder (0.4 mA = 0.08 mA/cm^2).

* Electrochemical Society Active Member.
Key words: primary batteries, nonaqueous cells, lithium, mercuric fluoride, lithium/mercuric fluoride system.

and 10% Microthene binder, and an electrolyte consisting of a saturated solution of phenyl trimethyl ammonium hexafluorophosphate in propylene carbonate. The test cell block is shown in Fig. 1. The electrodes are placed in the slot and connections are made to the positive, negative, and reference electrodes. The jacks allow connection to an external recorder. Typical discharges of cells of this type are shown in Fig. 2 and 3. Figure 2 is a C/6 discharge (10 mA or 2 mA/cm^2) in which the cell delivered 41% of its theoretical capacity at an average voltage of 1.66V. Figure 3 is a discharge at the 150 hr rate (0.4 mA or 0.08 mA/cm^2) in which the cell delivered 39% of its theoretical capacity. The average cell voltage for the entire discharge was 1.6V.

Later analysis showed the material to be about 50% HgF_2 and 50% HgO. Based on the HgF_2 content, discharge showed about 80% utilization of theoretical capacity. Qualitatively, self-discharge occurs to a significant extent over a 2-week period.

Conclusions

The goal of this program was to prepare a mercuric fluoride electrode, dischargeable in a nonaqueous medium.

The work described in this communication indicates that a HgF_2 primary electrode can be prepared which yields a ramped shape voltage characteristic averaging 1.6V at discharge rates of C/6 or lower, and is about 80% efficient based on a two-electron change after correcting for the HgF_2 content. It has also been found that the electrode polarization is, to a large measure, electrolyte dependent. Also, the addition of silver to the electrode markedly increases the voltage level on discharge. We believe this is due to amalgamation of the Hg as it forms, more so than to an increase of conductivity.

Manuscript submitted Aug. 7, 1969; revised manuscript received Dec. 18, 1969.

Any discussion of this paper will appear in a Discussion Section to be published in the December 1970 JOURNAL.

REFERENCE

1. A. E. Lyall and H. N. Seiger, "Nonaqueous Lithium/Nickel Halide Batteries"; Proceedings First IECEC Conference, Los Angeles (1966).

Errata

In the paper "A New Fast-Charging Power Source" by P. Bro and N. Marincic which appeared on pp. 131-134 of the January 1970 issue of the JOURNAL, Vol. 117, No. 1, the charging rates were printed as °C. In each case, these should be read without the degree sign.

In the paper "A Calorimetric Study of the Electroless Deposition of Nickel" by J.-P. Randin and H. E. Hintermann which was published on pp. 160-167 of the February 1970 issue of the JOURNAL, Vol. 117, No. 2, in reactions [9], [11], and [12], p. 163, the coefficient $\left(\frac{b}{2a}/a\right)$ should be read $\left(\frac{b-2a}{a}\right)$.

JOURNAL OF THE ELECTROCHEMICAL SOCIETY

REVIEWS AND NEWS — JANUARY 1970

Report of the Electrolytic Industries for the Year 1968[1]

Robert R. Dukes*

Leonard Construction Company, Chicago, Illinois

Robert G. Milner*

Union Carbide Corporation, Parma Technical Center, Cleveland, Ohio

A. Electrical Energy

1. U. S. Generation.—In 1968, the electrical utility industry of the United States scored records in production, generating capability, construction expenditures, sales, and revenues. Production by the industry was 1326 billion kwhr; the increase of 114 billion kwhr over 1967 represented an increase of 9.4%. Further large gains are anticipated for 1969 (1).

The total United States electrical power system capacity at the end of 1968 was 293,366 Mw, of which the major portion, 226,293 Mw or 77.1%, was obtained from fossil fuel. Contributing factors to the large proportion of fossil fuel plants are reductions in the cost for transporting coal, and construction of mine-mouth plants (2).

Hydroelectric power continued as the second most important, but declining, source of the total U.S. power supply. Conventional hydroelectric plants account for 51,161 Mw or 17.6% of the total capability. This amounts to only 26% of the estimated resources available. Yet the lack of suitable-size hydro installations handicaps future growth of water power. Opposing this trend is the advent of "pumped-storage" stations. For the first time, pumped-storage statistics have been separated from conventional hydroelectric production figures. While the number of conventional hydro plants continues to dwindle each year, the development of sites for the pumped-storage capacity is growing (3).

2. Nuclear Power.—Nuclear energy did not make the operational gains in 1968 that were expected. Just 380 Mw were added according to the data from the Federal Power Commission. As a result, the total of 2817 Mw nuclear-fueled generation in commercial operation amounts to only 1% of the total electrical power system capability. This is the same relative position as a year ago.

Industry, however, is planning increasing reliance on nuclear generation. It is expected that nearly 35% of future expansion installations will be of this variety. Orders for delivery through 1974 approximated 60-65,000 Mw of nuclear-fueled capacity. Reportedly over 70 units are involved, of 500-1100 Mw size. Only 10% of this capacity is expected to produce by the end of 1970 (3).

The total additions to U.S. power generation are listed:

Generation additions in megawatts

Prime mover	Added 1968	Planned for: 1969	1970	1971	1972	Total additions planned
Hydro	2,493	1,757	1,723	1,461	3,915	8,856
Pumped storage	818	400	—	1,020	9,730	11,150
Fossil steam	15,839	18,941	16,952	20,698	38,967	95,588
Nuclear steam	805	2,885	6,873	8,065	44,444	62,267
Internal combustion	345	267	60	47	522	896
Gas turbine	2,495	4,107	2,261	256	666	7,290
Total	22,795	28,357	27,869	31,547	98,244	186,017

3. D-C Power Transmission.—Utility networks added 18,452 circuit miles of 23 kV and over, high-voltage power lines in fiscal 1968. This was an increase of 19% over 1967.

Construction continued on the intertie system linking the Pacific Northwest and the Southwest. Two legs are 500 kV a-c lines, already in operation. A third leg will be an 825 mile, 800 kV, d-c line from the Dalles Substation on the Columbia River to the Sylmar substation in Los Angeles. The fourth line, also 800 kV d.c., extends from Dalles to Hoover Dam. Both d-c lines are capable of delivering 1350 Mw and will reach completion in 1969 and 1972, respectively. When complete, the entire system can transfer 4 million kw of power in either direction (3).

B. Chlorine-Caustic Soda

1. Production.—The production of chlorine increased last year to a new record of 8,460,000 tons in the United States, according to the preliminary figures of The Chlorine Institute, Inc (4). This is an increase of about 10.7% over the 1967 production of chlorine gas. In Canada, gas production also reached a new high of 775,500 tons, up about 10.4% over the preceding year. Average annual growth rate during the period 1959-1968 in the U.S. has been 7¾%.

During 1968, the U.S. daily chlorine capacity jumped 1852 tons, or about 8%. During the same period, Canadian capacity grew by 197 tons, or about 8.6%. The increased U.S. and Canadian capacity in 1968 stemmed from four new and seven expanded chlor-alkali plants, somewhat fewer than for the previous year, and despite three plant shutdowns.

Despite the availability of additional production facilities, U.S. manufacturers in 1968 operated at average monthly rates of 96.4% of capacity, while Canadian manufacturers operated at 89.7%.

At the end of the year, caustic soda was in tight supply. Although the growth rate for caustic is not projected to be as great as that for chlorine, it is

[1] This report is sponsored by the Industrial Electrolytic Division of The Electrochemical Society. Formerly it was known as the "Chlor-Alkali Report," but since 1963 it has been expanded to include other electrolytic industries although it remains primarily a summary of production and developments in the chlor-alkali industry.

The material presented herein has been gathered from many sources, as noted in the References, and does not necessarily represent the opinions of the authors.

* Electrochemical Society Active Member.

anticipated that any future oversupply of caustic soda will be solved by shifting the markets between soda ash and caustic soda. Caustic soda has already replaced soda ash in aluminum potlines, and it may accomplish a similar replacement in the glass industry (5).

2. Expansions.—The Chlorine Institute estimates that, by the end of 1969, projects now under way will increase current U.S. daily capacity of 25,090 tons by more than 2700 tons. Combined U.S. and Canadian annual capacity should reach 10,667,000 tons by the year's end.

Recent changes and announced plans for capacity changes are shown below (6, 7):

Company & location	Type of cell	Capacity, tons/day	Completion date
(a) Shutdown			
Monsanto, Sauget, Mo.	Hooker Diaphragm		Jan. 1969
Monsanto, Anniston, Ala.	DeNora Mercury		May 1969
(b) Production Started			
Alcoa, Point Comfort, Texas	DeNora Mercury	230	April 1968
Allied Chemical Corp., Baton Rouge, La.	Hooker S-4 Diaphragm	500	4th Quarter 1968
Allied Chemical Corp., Syracuse, N. Y.	Hooker S-4 Diaphragm	150	4th Quarter 1968
Dow Chemical of Canada Ltd., Fort Saskatchewan, Alberta	Dow Diaphragm	300	4th Quarter 1968
Hooker Chemical Corp., Taft, La.	Hooker S-4 Diaphragm	140	?
Olin Mathieson Chemical Corp., Charleston, Tenn.	Olin E-812 Mercury	300	Mid-1968
Olin Mathieson Chemical Corp., Saltville, Va.	Olin E-812 Mercury	?	1st Quarter
Reactive Metals, Inc., Ashtabula, Ohio	Downs	50% exp.	Portion mid-1968
Vulcan Materials Co., Newark, N. J.	Hooker Diaphragm	100% exp.	2nd Quarter 1968
(c) Building or Planned			
American Magnesium, Snyder, Texas	Magnesium Cells		Portion 1969 Bal. over 1970
Canso Chemicals Ltd., Abercrombie, Nova Scotia	ICI Mercury		1st Quarter 1970
Consolidated Chemicals, Jamaica		500	1970
Dow Chemical Co., Pittsburgh, Calif.	Dow Mercury	450	Mid-1970
Dryden Chemicals Ltd., Brandon, Manitoba	Dryden Diaphragm	60	2nd Quarter 1969
GAF Corp., Linden, N. J.	BASF-Krebs Mercury	250	3rd Quarter 1969
Interprovincial Cooperative Ltd., Saskatoon, Saskatchewan	Kureha HD-4 Mercury	70 exp.	1st Quarter 1969
Kaiser Aluminum & Chemical Corp., Gramercy, La.	Hooker S3B Diaphragm	300 exp.	May 1969
National Lead, Magnesium Div., Salt Lake City, Utah (Near Grantsville)	Magnesium Cells	360	1971
PPG Industries, Lake Charles, La.	DeNora Mercury	600	1st Quarter 1969
PPG Industries, Puerto Rico	DeNora Mercury	500	1971
Stauffer Chemical Corp., St. Gabriel, La.	Uhde Mercury	500	1st Quarter 1970
Velsicol, Memphis, Tenn.	Hooker S-4 Diaphragm		2nd Quarter 1969
Wyandotte Chemicals Corp., Geismar, La.	Hooker S-4B Diaphragm	350	April 1969

The greatest single end-use for chlorine is as a bleaching agent by pulp and paper mills, accounting for about 17% of all chlorine consumption, and the rate of growth of this usage is about as fast as the average of all the other uses.

The major growth market for chlorine is in the production of vinyl chloride. It was estimated that more than 10% of the 1968 chlorine production was used for vinyl chloride production as compared to less than 9% in 1964, and the share going into monomer production will increase even more, since PVC output rose 15% in 1968 and is still moving up (8).

3. New Developments.—a. Pricing. In the last quarter of 1968, a price hike of $4/ton of chlorine was announced, which brought the price of chlorine in bulk tank-car quantities to $73-$74/ton (8).

b. Mercury. The chlor-alkali industry continued to be the largest user of mercury, with significant increases this year in pharmaceutical and mildew-proofing paint applications. Use of mercury in catalysts dropped.

Mine production of 25,600 flasks was up 8% over 1967, and secondary production increased 35%. In addition, the General Services Administration contributed to the supply by continuing to release surplus mercury at the average rate of 1700 flasks/month. In the first nine months of the year this amounted to 15,175 flasks, but the stock was expected to be exhausted in early 1969. Ninety per cent of the domestic production was realized from California and Nevada, with the remainder from Alaska, Arizona, Idaho, Oregon, Texas, and Washington. Primary production was valued at $13.9 million.

Imports of mercury decreased 12%, though world output remained about constant. Turkey began expanding its production, and Cominco's Pinchi Lake mine in British Columbia commenced production slated to reach 20,000 flasks/yr.

The estimated average U.S. price was $542/flask in 1968, compared with $489 for 1967 and $342 for the 1962-1966 five-year period (9).

Diamond Shamrock began production of mercury in Texas in a plant having an initial capacity of 2000 flasks/yr. This company is also involved in development work in Alaska where, with Hydrametals Corp., it is evaluating a high-grade cinnabar deposit (10).

C. Other Alkalis and Electrolytic Processes

1. Caustic Potash.—Preliminary production figures for caustic potash show an increase of about 8% to almost 178,000 tons in 1968 (11). The price for flake and liquid remained steady during 1968 (12).

Canadian natural potash production continued to rise, and, for the companies with production facilities in both New Mexico and Saskatchewan, there is strong commercial justification for increasing output at the latter at the expense of New Mexico (13).

2. Soda Ash.—Natural and synthetic sodium carbonate (soda ash) production was 2.0 (14) and 4.42 million (15) tons, respectively, in 1968. The bulk of the U.S. natural production came from the Green River formation in Wyoming, with smaller amounts from dry lake beds in California.

While the quantity of natural soda ash rose about 16% over the 1967 figure, the value of this production increased only 12%. Year-end bulk price was $1.55-$1.60/cwt; bagged price was $2.05-$2.15 in hundred-pound paper bags.

According to *British Chemical Engineering*, disproportionately rising chlorine consumption and the attendant caustic excess has spurred design of an improved "electrolyser" by Czech researchers. The outmoded Hargreaves/Bird unit (introduction of carbon dioxide on the cathode side of a diaphragm cell to convert hydroxide to soda) has been modified to a vertical cell with a deposited diaphragm, and graphite anodes. The hydroxyl ions are mostly converted to carbonate ions and this catholyte processed to the final product by a second-stage carbonation in towers. An 80% conversion with a current efficiency of 93-95% is reported (16).

3. Sodium Chlorate.—United States production of sodium chlorate in 1968 was 166,925 tons. This is about an 11% increase over the 1967 figure, larger than the 8% growth rate previously predicted (17). This growth rate is expected to continue with the Penn-Olin completed expansion to 31,000 tons/yr, and the Hooker and the American Potash expansions planned for early 1970 which will add 34,000 tons/yr to industry capacity (18).

The price of drummed chlorate gradually increased to $190/ton by the end of 1968 (19).

4. Sodium.—The projected production of sodium metal, based on the first nine months of 1968, shows a drop of about 5%: 156,000 tons for 1968 compared to 163,000 tons in 1967. Actual figures through September list 116,819 tons produced. Brick price continued most

of the year (20) at $0.225/lb, but ended the year (19) selling for $0.24/lb; fused prices, in the 18,000-lb lots were $0.225/lb at year's end.

The largest use of sodium is by far (over 80%) for the lead alkyl business; tetra-ethyl-lead and tetra-methyl-lead. Of the several possible new markets for sodium, the brightest appears to be NACON (Simplex Wire & Cable and Union Carbide Corp.) Corp.'s metallic sodium polyethylene-clad electrical cable (21). A number are on test in low-voltage applications, and the next target is high-voltage cable. Other possibilities include liquid sodium as a coolant in nuclear power stations, and as a reducing agent in the manufacture of titanium sponge.

5. Aluminum.—Production of primary aluminum in the United States in 1968 continued at near capacity for most of the year but dropped slightly to 3.25 million short tons, partly because of a midyear strike at the two leading producers (22).

Apparent consumption of aluminum in 1968 increased slightly to about 4.1 million tons. The slight decrease in primary aluminum production was offset by an increase in imports, in purchases from surplus Government stocks, and a decrease in producers' stocks. Secondary aluminum production capacity increases at existing installations were made by addition of new potlines at:

Anaconda Aluminum Co., Columbia Falls, Mont.
Consolidated Aluminum Corp., New Johnsonville, Tenn.
Intalco Aluminum Corp., Bellingham, Wash.
Kaiser Aluminum & Chemical Corp., Tacoma, Wash.
Reynolds Metals Co., Longview, Wash.

New plants are being built by:

Eastalco Aluminum Co., Frederick Co., Md.
Gulf Coast Aluminum Corp., Lake Charles, La.
National Southwire Aluminum Co., Hawesville, Ky.
Northwest Aluminum Co., Inc., Warrenton, Ore.
Revere Copper & Brass Co., Scottsdale, Ala.

The total Canadian production in 1968 was approximately 994,500 tons. It is expected that the production will increase about 10% in 1969 (23, 24).

6. Magnesium.—Apparent consumption of magnesium in 1968 was estimated at 103,000 tons. A midyear shortage caused a severe stock depletion coupled with an increase in net exports. Only 3600 tons of magnesium were imported in the January to September period *vs.* exports of 14,000 tons. In October, however, legislation enacted permitting the General Services Administration to offer 55,000 short tons of magnesium from the national stockpile yielded only acceptable bids for 2600 tons. Thus it would appear the midyear shortage had been alleviated (25).

Domestic production of primary magnesium in 1968 was 97,000 short tons, or about the same as 1967. Secondary magnesium recovery, too, was similar to 1967, totaling 13,000 tons this year.

Dow Chemical Co. plants at both Freeport and Velasco, Texas, operated at capacity, producing magnesium from seawater; Alabama Metallurgical Corp. continued production from dolomite at Selma, Ala.; and Titanium Metals Corp. of America at Henderson, Nev., manufactured magnesium for titanium production. As reported last year, American Magnesium Corp. began construction of a 30,000-tons/yr plant at Snyder, Texas. By mid-1969, 10,000 tons of annual capacity should be operable. This facility will use magnesium chloride obtained from underground brines (26).

Northwest Magnesite Co. permanently shut down their operation of magnesite production at Chewelah, Wash. It was reported that FMC planned to discontinue operation of its magnesium oxide plant at Newark, Calif., if no buyer was found by the end of the year. Regarding the Magnesium Project (of National Lead Co., Magnesium Division) at Great Salt Lake, plans are moving forward to operate a 45,000-tons/yr electrolysis plant for magnesium metal (and 81,000 tons/yr of *liquid chlorine*). A major step for MP cost considerations was realized when the Utah Public Service Commission ordered Utah Power and Light Co. to begin negotiations which would supply the project with 3.1 mil power on an uninterruptable basis. Pilot operations at Henderson have produced about 20 tons of magnesium metal for development purposes (27).

Increasing use of the BOF in the steel industry has reduced the per unit requirements for magnesium refractories. Accordingly, continuing the trend started in 1966, production and demand of refractories fell again in 1968.

Dominion Magnesium, Ltd., the only primary magnesium producer in Canada, shipped almost 22,200,000 lb in 1968 as compared to 19,550,000 lb in 1967. The demand is expected to continue strong in 1969 (28).

7. Manganese.—A reduction in import duties for manganese ferroalloys and metal was experienced in 1968, together with continuing soft ore prices. Domestic production of manganese ore, ore concentrate, and nodules—containing 35% or more manganese continued to be insignificant compared to consumption, while both domestic consumption and imports showed little change from those of the preceding year. Australia's new Groote Eylandt deposits became a major supplier of manganese ore for both local consumption and export (29).

Domestic ore consumption was expected to be approximately 2.4 million tons, which is roughly the same as that for each of the two previous years. Foote Mineral Co.'s large new electrolytic manganese metal plant went on stream in May 1968 at New Johnsonville, Tenn.

American Metal Market quotations for manganese ore containing 46-48% manganese dropped 1¢ early in February to $0.59-$0.63 nominal, per long ton unit, c.i.f. eastern seaboard and Gulf ports. Manganese ore prices in all markets remained poor from the standpoint of suppliers. Effective October 21, the price of standard electrolytic manganese metal was cut to $0.266/lb from $0.2985. Reductions were made in other grades of electrolytic metal.

8. Beryllium.—For the fourth consecutive year, the consumption of beryllium in the U.S. increased. General imports of beryl during the January to September period of this year totaled 3486 tons, valued at $2,323,639 at foreign ports. Domestically, Colorado and South Dakota produced small quantities of hand-sorted beryl, but production data are confidential. The Brush Beryllium Co., and Kawecki Berylco Industries (Beryllium Corp. and Kawecki Chemical Co. merger) processed hand-sorted beryl, and electrorefined beryllium was made by Beryllium Metals and Chemical Corp.

Government inventories at midyear showed 28,244 tons of beryl, containing 11% BeO; 7387 tons of Beryllium copper-master alloy; and 229 tons beryllium metal. The General Services Administration sold 16,857 short ton units (stu) of beryllium oxide in September at $50.16-$53.27/stu. The same quality was offered for sale by the GSA at the end of 1968 (30).

In June, Albert Hayward (Assistant Director of Defense Engineering and Research) stated that, in order to guarantee a supply of beryllium metal for defense, the Government may consider subsidizing research in beryllium production or possibly even direct aid to producers. A Government report on sources and fabricating capability, supposedly due in October, was to determine Government action (31).

9. Chromium.—The United States continued to rely exclusively on imports for its chromite requirements. For the first nine months, the metallurgical industry consumed 634,000 short tons of chromite in producing 287,026 tons of chromium alloys, while the refractory and chemical industries consumed 249,000 and 150,000 tons, respectively (32).

Industrial inventory of chromite on September 30 was 26% lower than at the beginning of the year as the

three consuming industries reported significant decreases in stocks.

General Services Administration under a long-range disposal program placed on order for future delivery 99,031 short dry tons of metallurgical chromite. This brought the total for the program to 678,920 tons. During the first 11 months of the year, industry took delivery of 131,220 tons. In October and again in November, an additional 183,680 tons of metallurgical grade chromite were offered for sale on a competitive bid basis. All bids were rejected for both offerings. The material is now available for sale on a negotiated basis.

In November, GSA offered for sale on a competitive bid basis approximately 22,000 tons of chemical-grade chromite. (No acceptable bids were received.) Industry has shown no interest in purchasing this material over the past three years.

Price of metallurgical-grade chromite continued to increase owing to United Nations economic sanctions against Southern Rhodesia, one of the principal suppliers of domestic requirements prior to 1967. The price of Russian (54-56% Cr_2O_3, 4-1 chromium to iron ratio) chromite per long ton was quoted at \$30.50—\$33.00 in 1967, \$36.50—\$40.00 in 1968, and \$45.50—\$49.20 for 1969 delivery. The price of Turkish ore followed a similar pattern.

10. Titanium.—Titanium sponge (refined ore) metal consumption dropped appreciably from 20,000 tons in 1967 to less than 15,000 tons this year. Sponge production decreased 25%, due partly to a strike at Reactive Metals Inc. (owned by U.S. Steel Corp. and National Distillers & Chemical Corp.), Ashtabula, Ohio, plant, and partly resulting from decreased demand. Through September, general imports (including some scrap) decreased about one third. There were no sales of titanium sponge metal from the Government stockpile during 1968. At the end of the year, 99.3% purity titanium sponge metal sold for \$1.32/lb; Japanese sponge metal was quoted at \$1.25/lb.

The slump in the use of titanium is almost wholly due to cutbacks in aerospace programs, which take about 90% of the total U.S. output (33). Principally, these were reductions in federal spending caused by tighter budgets and the stretch-out of the supersonic transport (SST) program (34). In an effort to bolster the sagging market, Titanium Metals Corp. of America (owned by Allegheny Ludlum Steel Corp. and National Lead Co.) cut its prices on sheet, strip, and plate by about 20-30% in August (35). It is hoped the price reductions will make the strong-but-light and anticorrosive qualities of titanium more attractive to construction and chemical industries. Commercially pure sheet and strip (in 4000-lb lots, F.O.B. customer plant) dropped to \$3.45/lb; alloy, \$6.00-\$9.90; plate HR, commercially pure, \$3.00; alloy, \$3.25-\$4.85.

Domestic production and imports of ilmenite both rose significantly. Consumption of ilmenite, chiefly used for making titanium pigment, remained nearly constant. December prices for domestic ilmenite of 60% TiO_2 content ranged from \$30-\$35/short ton; imported ilmenite of 54% TiO_2 content \$20-\$21/long ton or \$1-\$3/long ton less than in December 1967.

Due to cessation of production in July by M&T Chemicals, sole U. S. producer, domestic output of rutile was less than a third of what it was in 1967. Rutile imports were also lower. Demand for rutile, used in making pigment and metal, increased again this year, but not so much as in the last few years. In December 1968 imported rutile of 96% TiO_2 content was \$121-\$125/short ton, or \$2-\$4/ton more than last year (36).

11. Lithium, Cesium, and Rubidium.—The production of lithium minerals and lithium carbonate derived from natural sources was higher in both quantity and value than the previous year.

The processors of lithium raw materials to lithium primary products were Foote Mineral Co. at Sunbright, Va., and Silver Peak, Nev.; American Potash & Chemical Corp., at Trona, Calif.; and Lithium Corp. of America, Inc., at Bessemer City, N.C. Production data were not available for publication (37).

Some quoted prices for lithium products are: lithium metal—100-lb lots, delivered, \$8.00/lb; lithium carbonate—drums, car lots, ton lots, delivered, \$0.445/lb; and lithium chloride, anhydrous, car lots, ton lots, delivered, \$0.85-\$0.87/lb. (19).

Production and prices of cesium and rubidium in 1968 were about the same as in 1967 (38).

12. Copper. The industry-wide copper strike, which began July 15, 1967, continued through the first quarter of 1968 and resulted in a reduction of mine copper output again for the year of 1968. The 1968 total was 1,199,000 tons, a reduction of 16% from the 1,429,000 ton high established in 1966; the monthly output, however, based on the last nine months of 1968 was 123,000 tons which exceeded the 119,000 tons per month figure for 1966 (39).

Smelter production from domestic and foreign primary materials was listed, respectively, at 890,000 and 220,000 tons for the first ten months in 1968, compared to 1,127,570 and 298,250 tons in 1966. The consumption of refined copper also declined for the second straight year, to 1,860,000 tons; this represents a decrease of 4% from 1967 to 21% from 1966. Imports of refined copper and blister copper were up, estimated at 400,000 and 300,000 tons, respectively, over the 1967 values of 330,000 and 269,000 tons. Exports of refined copper were 280,000 tons, or about the same as 1966, after a drop of 159,000 tons in 1967.

Stocks of refined copper rose at primary refineries, totaling 48,000 tons; inventories and unrefined copper also rose slightly to 272,000 tons by the end of 1968.

In April, major copper producers raised the price to \$0.42/lb (from \$0.38). Copper scrap, at a U.S. high of \$0.48/lb in February, fell with the resumption of production to \$0.30/lb in May and leveled out at \$0.33/lb as the year progressed. The London Metal Exchange, similarly, quoted wire bar at a high of \$0.90 which declined to \$0.58 by December.

13. Nickel.—Great activity in the exploration for, and development of, nickel deposits throughout the world, coupled with virtually universal production increases, featured the industry in 1968. Supplies remained tight, however, despite the fact that no marked gain in domestic consumption was registered. The producer price remained unchanged amid rumors of an increase in the offing and differing opinion as to its probable timing (40).

Domestic production of primary nickel from domestic ore was 13,050 short tons, contained in ferronickel. In addition to this production, there was expected to be approximately 1000 tons as a by-product of copper refining and 25,000 tons from secondary sources.

Consumption in the United States at approximately 170,000 tons, as estimated from nine months' data, was at approximately the same level as that of the preceding year—still down from the high of 1966.

The producer price for cathodes remained at \$0.94/lb, F.O.B. shipping point, while ferronickel remained at \$0.915/lb, same basis. *Metals Week* quotations for merchants' or dealers' cathodes had dropped by December to \$1.55-\$1.65/lb, delivered, from \$1.95-\$2.05 at the start of the year.

Imports were expected to approximate 150,000 tons of contained nickel with exports at the previous year's level of approximately 32,000 tons gross weight.

World production of nickel increased approximately 553,000 tons with higher production credited for each of the important producing countries. Exploration and development were vigorously pursued around the world.

In Canada, The International Nickel Co. of Canada Ltd. announced that construction was to start immediately on an \$85-million refinery at Copper Cliff, Ontario. Also in Canada, Falconbridge Nickel Mines Ltd. brought two new mines into production, and

Sherritt Gordon Mines Ltd. was constructing a $2-million pilot plant for testing lateritic ores from the Philippines and elsewhere.

Both Falconbridge and International Nickel proceeded with plans designed to lead to eventual production from lateritic deposits in the Dominican Republic and Guatemala, respectively.

Plans for underdeveloped lateritic deposits of the Philippines, Indonesia, New Caledonia, and elsewhere advanced as did development of the Australian sulfide deposits.

14. Zinc.—The increased smelter output and the continued high imports consumed in 1968 were responsible for a substantial recovery in the domestic zinc industry. Despite work loss at some locations due to strikes, smelter production this year rose 6% to 1,070,000 tons, nearly equaling the all-time 1966 high of 1,108,000 tons. The production of pigments, compounds, and galvanizing by direct use of concentrates increased about 9% to 124,000 tons of contained zinc. Projected general imports of zinc will reach all-time highs, approximately equaling the 1943 ore value of 539,000 tons and the slab figure of 278,000 tons attained in 1966.

Despite the 1968 surge, U.S. mine production of zinc dropped for the third straight year; the 526,000-ton yield was the smallest since 1963. Fifty-three per cent of the total came from Tennessee, New York, Idaho, and Colorado, in ranking order.

Prime Western grade zinc on the East St. Louis market held steady for the year at $0.135/lb. The London Metal Exchange price varied a few tenths of a cent during the year, and was $0.119 in October (41).

D. Developments of Interest

1. Vanadium Refining.—The Bureau of Mines Metallurgy Research Laboratory has developed an electrolytic cell process for refining vanadium to 99.99% purity for breeder reactor use. The process uses a molten salt electrolyte containing vanadium chloride. The anode is a cylindrical double basket containing 99.5% pure vanadium briquettes, and the current passed through the cells deposits the high-purity metal on a central cathode of molybdenum (42).

2. Dimensionally Stable Anode (DSA).—A development of major interest to the $500-million/yr chlorine/caustic soda industry came this year with the announcement by Diamond Shamrock Corp. (Cleveland, Ohio) and Oronzio De Nora Impianti Elettrochimicici (Milan, Italy) of a dimensionally stable anode (DSA). The anode is made domestically by Diamond's subsidiary, Electrode Corp. (formerly Permelec Corp.) which holds exclusive rights to produce, lease, and service the new anode in the U.S. and Canada and Mexico. De Nora is making the DSA in Italy. Monsanto, long the agent marketing de Nora cells in North America, will continue on this role.

The DSA is basically an expanded titanium sheet having a thin coating of a mixture of several conductive metallic oxides. The new anode is said to stay on stream twice as long as the conventional graphite anode. At this time, servicing is required which consists of recoating the titanium substrate with the unidentified metallic oxides formulation. Although the coating remains company-confidential, ruthenium oxide is thought to be one of the components (43).

The advantage attributed to a dimensionally stable anode would be the constant anode-cathode gap. It is reported that cells using the DSA operate at 0.8V less than graphite. Such a condition reduces power losses, and power is the largest single operation expense.

A cell containing these electrodes is reported to operate at 50% higher current density, increase cell productive capacity by 50%, reduce electrical power requirements by 10-20%, and require less mercury initially. It is also expected to operate with less mercury loss per ton of chlorine produced (44).

3. Great Salt Lake.—The Utah Land Board, three years ago, determined to grant nonexclusive rights to extract the dissolved salts contained in Great Salt Lake. In the intervening period, two projects have grown to major significance: (*a*) Lithium Corp.-Salzdetfurth A.G.'s "Great Salt Lake Minerals and Chemicals Corp." and (*b*) National Lead Co.-Magnesium Division's "Magnesium Project." Neither complex will be fully operable before 1970 (27).

The Great Salt Lake Minerals and Chemical Corp. is facing a total expenditure exceeding $30 million for a solar evaporation (completion spring 1968) and lithium and salts recovery complex. The "Magnesium Project" outlay, in the order of $50 million over the next two years it is reported, will encompass an electrolysis plant, a gypsum plant, and other unspecified salts recovery plants.

Recovery of salts other than sodium chloride is complicated by the unique composition (relatively high SO_4 content) and strength of Great Salt Lake brine. Sea water runs about 3.5% dissolved salt; G.S.L. analyses 27%: typically 70% NaCl, 14% $MgCl_2$, 12% Na_2SO_4 and 4% KCl plus important small concentrations of bromine (100 ppm) and lithium (40 ppm). The Lake covers 1000 square miles and is reported to be the biggest source of low-cost K_2SO_4 in the world, in addition to the boon to chemical production of magnesium, lithium, and the other salts.

Manuscript received July 22, 1969. This report was presented at the Industrial Electrolytic Division Luncheon at the New York Meeting, May 4-9, 1969.

Any discussion of this report will appear in a Discussion Section to be published in the December 1970 JOURNAL.

REFERENCES

1. Robert H. Gerdes, President, Edison Electric Institute.
2. *Electrical World*, **171**, 79 (1969).
3. Federal Power Commission, Annual Report, Fiscal Year 1968.
4. Frederick O. Gilbert, President, Chlorine Institute.
5. *C & E News*, p. 73, March 10, 1969.
6. *Chemical Week*, p. 29, Feb. 17, 1969.
7. Chlorine Institute.
8. *Chemical Week*, p. 52, Feb. 22, 1969.
9. Mineral Industry Surveys, U.S. Dept. of the Interior Annual Preliminary, "Mercury in 1968."
10. *C&E News*, p. 45, March 4, 1968.
11. Current Industrial Census Inorganic Chemicals and Gases, U.S. Dept. of Commerce, Bureau of the Census.
12. *Oil Paint & Drug Reporter*, Dec. 30, 1968.
13. *Phosphorus and Potassium*, p. 36, Jan./Feb. 1969.
14. Mineral Industry Surveys, U.S. Dept. of the Interior, Annual Preliminary, "Sodium Compounds in 1968."
15. Current Industrial Census, Inorganic Chemicals and Gases, U.S. Dept. of Commerce, Bureau of the Census.
16. *Brit. Chem. Eng.*, p. 1655, Dec. 1968.
17. Current Industrial Census, Inorganic Chemicals and Gases, U.S. Dept. of Commerce, Bureau of the Census.
18. *Chemical Week*, p. 43, March 9, 1968.
19. *Oil, Paint & Drug Reporter*, Dec. 30, 1968.
20. *Ibid.*, Aug. 19, 1968.
21. *Power*, p. 72, Sept. 1968.
22. Mineral Industry Surveys, U.S. Dept. of the Interior, Annual Preliminary, "Aluminum and Bauxite in 1968."
23. Aluminum Co. of Canada, Ltd., Verbal communication.
24. Canadian British Aluminum, Ltd., Verbal communication.
25. Mineral Industry Surveys, U.S. Dept. of the Interior, Annual Preliminary, "Magnesium and Magnesium Compounds in 1968.
26. U.S. Industrial Outlook, U.S. Dept. of Commerce.
27. *Chem. Eng.*, p. 106, June 17, 1968.
28. Dominion Magnesium, Ltd., Verbal communication.
29. Mineral Industry Surveys, U.S. Dept. of the Interior, Annual Preliminary, "Manganese in 1968."

30. *Ibid.*, "Beryllium in 1968."
31. *Chemical Week*, p. 36, June 22, 1968.
32. Mineral Industry Surveys, U.S. Dept. of the Interior, Annual Preliminary, "Chromium in 1968."
33. *C&E News*, p. 23, June 17, 1968.
34. *Business Week*, p. 81, Aug. 10, 1968.
35. *The Iron Age*, p. 67, Aug. 8 1968.
36. Mineral Industry Surveys, U.S. Dept. of the Interior, Annual Preliminary, "Titanium in 1968."
37. *Ibid.*, "Lithium in 1968."
38. *Ibid.*, "Cesium and Rubidium in 1968."
39. *Ibid.*, "Copper in 1968."
40. *Ibid.*, "Nickel in 1968."
41. *Ibid.*, "Zinc in 1968."
42. *C&E News*, p. 43, March 11, 1968.
43. *Chemical Week*, p. 40, Feb. 16, 1969.
44. *C&E News*, p. 13, March 17, 1968.

Future Meetings

Los Angeles, California,
May 10, 11, 12, 13, 14, and 15, 1970
Headquarters at Biltmore Hotel

★ ★ ★ ★ ★

Atlantic City, New Jersey,
October 4, 5, 6, 7, 8, and 9, 1970
Headquarters at Chalfonte Haddon Hall

★ ★ ★ ★ ★

Washington, D. C.,
May 9, 10, 11, 12, 13, and 14, 1971
Headquarters at Sheraton Park Hotel

★ ★ ★ ★ ★

Cleveland, Ohio,
October 3, 4, 5, 6, 7, and 8, 1971
Headquarters at Sheraton Cleveland Hotel

★ ★ ★ ★ ★

Houston, Texas,
May 7, 8, 9, 10, 11, and 12, 1972
Headquarters at the Shamrock Hilton

★ ★ ★ ★ ★

Miami Beach, Florida,
October 8, 9, 10, 11, 12, and 13, 1972
Headquarters at Fontainebleau Hotel

JOURNAL OF THE ELECTROCHEMICAL SOCIETY

REVIEWS AND NEWS — FEBRUARY 1970

Techniques for Melt-Growth of Luminescent Semiconductor Crystals under Pressure[1]

A. G. Fischer*

RCA Laboratories, Princeton, New Jersey

ABSTRACT

Wide-bandgap III-V and II-VI binary semiconductor crystals can be grown from the melt by a variety of methods, all requiring pressure. The necessary apparatus, from the simple to the sophisticated, has been investigated. Methods using resistance or rf heating, unsupported or supported ampoules of several materials, without or with high-pressure autoclave, under inert or active gas pressure, and the required control systems, are described. A broad description of the liquid encapsulation method is given, and construction details are contained in the figures. Special attention is given to the growth of gallium phosphide crystals and to the preparation of the starting material from the elements.

Compounds like ZnS [mp 1830°C (1)], ZnSe [mp 1515°C (2)], CdS [mp 1475°C (1)], ZnTe [mp 1300°C (3)], and GaP [mp 1470°C (4)] decompose into their volatile components far below their melting points so that crystals can be grown from the melt only under pressure. Since large crystals can be grown from the melt faster and hence more inexpensively than by other methods, the need for initially costly pressure equipment is no longer a major deterrent.

As usual in many fields, the long period of dormancy in which only a few devoted enthusiasts do the exploratory work, without much response, is over for crystal growth from the melt under pressure. Recently it became the focus of attention. This was caused by the coincidence of an industrial need for GaP crystals for electroluminescent diodes, triggered by the achievement of high efficiency in the visible, and the achievement of large GaP single crystals made by pulling through a boric oxide blanket under pressure.

Many of the results described here are scattered in government contract and conference reports so that a review of this increasingly important field is now timely. The results of other workers in this field are included. Most of the methods described below have actually been tested by us, so that their advantages and disadvantages can be related with authority.

The paper is organized by describing the techniques in sequence of increasing complexity and refinement, which coincides frequently with the chronological order of their conception. Since materials synthesis is closely intermeshed with crystal growth, the synthesis methods are not described separately, but within the proper context. We treat Bridgman and Czochralski methods under high inert gas pressure and under cation or anion vapor pressure, the necessary equipment, control systems as they become necessary, and material synthesis from the elements. Since it is of prime importance now, we describe in detail crystal growth using liquid encapsulation, published by Metz, Miller and Mazelsky (5) in 1962, applied to GaP first by Bass and Oliver (6) at SERL, and amplified by our own results (7).

The paper contains, besides numerous new scientific results, practical experiences and technological innovations, especially in the figures. The paper is confined to *techniques and methods;* properties of the prepared crystals have been and will be described elsewhere.

Resistance Heater Methods

Bridgman growth under high inert gas pressure.— Tiede and Schleede (8) found that ZnS and CdS could be melted by retarding the decomposition with high nitrogen pressure. We found this method to work only for II-VI compounds, where cation and anion are similar in volatility. With III-V compounds, the metal has hardly any vapor pressure and thus is retained in the crucible, whereas the anion escapes. GaN and InN decompose even under 200 atm of N_2 pressure. Due to the stability of the N_2-molecule, nitrogen behaves like an inert gas in this case.

To repulse the emanating vapors effectively, the pressure of the inert atmosphere should be as high as possible; more than 100 atm are usually applied for ZnS and CdS. The atmosphere at the melt surface should be still, not turbulent, which precludes crystal pulling because of strong thermal drafts at the open meniscus of the melt. The crucible should be covered by a lid.

After examining other possible constructions (1, 9), we found that the most advantageous graphite tube furnace, suitable for 2200°C max and 200 atm, is the one shown in Fig. 1 (10, 11). In this furnace, a straight, high-density carbon tube, which can be tapered in its wall thickness along its length at will to influence the thermal gradient, is clamped and contacted at one end by a packing of compressed graphite granules to allow for thermal expansion and contraction. The autoclave lid is one electrode, the bottom vessel the other. Since only 12V max are needed, the pressure gasket seal also acts as an electrical insulator. For

[1] The research reported in this paper was sponsored in part by the Air Force Cambridge Research Laboratories, Office of Aerospace Research, under Contract Numbers AF19 (604) 8018 and AF19 (628)-3866; and RCA Laboratories, Princeton, New Jersey.

* Electrochemical Society Active Member.

Key words: crystal growth, semiconductor crystals, liquid encapsulation.

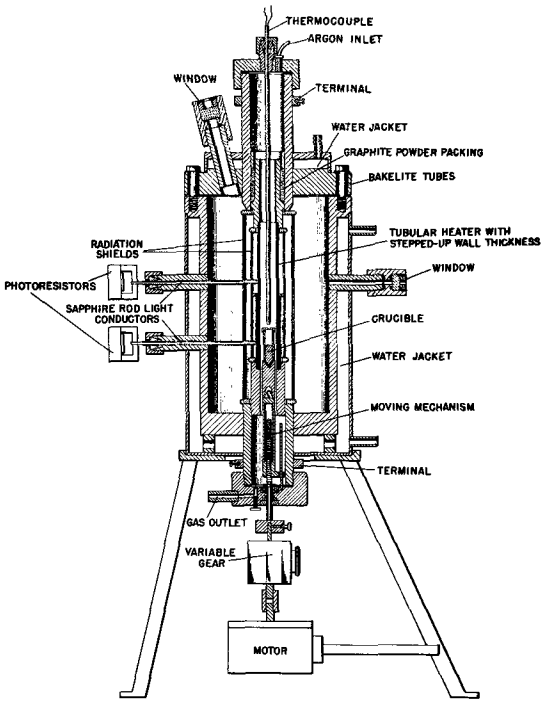

Fig. 1. Carbon-tube furnace (12V, 2000A) for up to 2200°C, 250 atm. The carbon tube with stepped-up wall thickness and radiation shields is held by granular carbon packings at the ends.

reasons of purity, use of carbon or molybdenum cylinders as radiation baffles is preferable to granular ceramic insulation (12). Other graphite furnaces using delicate double-wall graphite tubes or double helixes, with contacts at the same side, are not as rugged and flexible in use.

Corrosive vapors from the melt attack thermocouples; smoke and thermal schlieren in the compressed, dense gas make the use of optical pyrometers inaccurate. Therefore, the temperature is sensed best with a sapphire rod light conductor (10), as shown in Fig. 1. Stabilization of the input power against line voltage fluctuations[2] is advantageous in all crystal growth equipment described. For this particular furnace, temperature control was *via* saturable reactor and step-down transformer, using a proportional controller. To allow accurate control by the sluggish big saturable reactor, load inertia had to be increased by using a thick-walled, cylindrical graphite radiation baffle, not shown in the figure. (To prevent oscillations, a control system must be able to respond faster than the process to be controlled.) A simple electromechanical melting-point detector (12) was found to be very useful.

Crystals of all wide-gap II-VI compounds are now being grown successfully by this method at many places.

The capillary-tipped ampoule method for ZnTe.— ZnTe has a relatively low melting temperature and decomposition pressure, but the starting material usually contains a slight, hard-to-remove excess of tellurium. The ZnTe therefore develops a higher pressure when it is sealed into a quartz ampoule than its true stoichiometric decomposition pressure, which is 1.9 atm.[3] This leads to thermoplastic expansion of the ampoule.

[2] Automatic voltage regulator, General Radio Company, Concord, Massachusetts.

[3] This value is higher than the published value of 0.6 atm obtained by extrapolation from measurements at lower temperature. We determined it by lowering the pressure over a liquid-encapsulated melt (*see* later in this article) until the melt started fuming violently. The corresponding values for ZnSe (2.2 atm), and for CdS (3.2 atm), also differ from published values. ZnS could not be measured by this method due to rapid volatilization of the encapsulant at 1830°C.

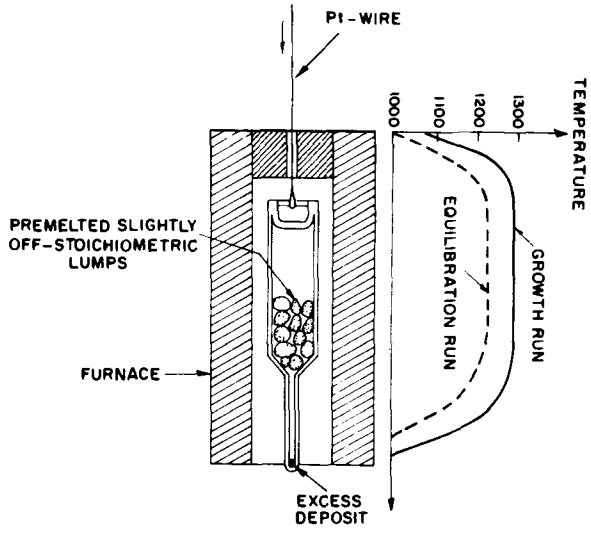

Fig. 2. Melting of ZnTe in unsupported quartz ampoules with capillary cold trap to remove excess components.

It was found that ZnTe crystals can be grown from the melt in unsupported quartz ampoules if the ampoules have a capillary extension which protrudes from the furnace into the cold, where it is closed (13). This cold capillary traps the excess volatile component and then seals itself (Fig. 2). This simple method is applicable to other similar compounds.

The "soft ampoule" method.—In order to control the stoichiometric composition of the growing crystal, one has to apply excess cation or anion pressure. This requires a gas-tight container which is inert at temperatures of about 1500°C, where compounds such as GaP, ZnSe or CdS melt.

A quartz or borosilicate (Vycor) ampoule, even when thermoplastic at the melting point of the compound, serves as a gastight inert vessel. By letting the internal decomposition pressure drive it against a tight-fitting graphite enclosure which counteracts the mechanical forces (14) (*see* Fig. 3), many atmospheres of pressure can be sustained. This method works for ZnSe and CdS, and has been used recently in modified form for GaP (15).

It was found earlier (14) that, during the initial heating of a compound to the melting point, the internal pressure could be high while the ampoule is still brittle, leading to ampoule failure. This can be prevented by heating the ampoule very fast, so that it reaches its softening temperature while the charge is still relatively cool, and therefore, does not exert its full decomposition pressure. This method is simple but limits the time of growth runs to a few hours due to gradual divitrification of the quartz, unless alkali contamination is carefully avoided (26).

Preparing II-VI compounds from the elements.— The II-VI compound materials can be purchased as chemically prepared fluffy powders.[4] Particle size can be enlarged by firing in hydrogen. But if one melts such densified powders, the volume of the final ingot is still only about 1/5 of the original powder, leaving too much unused crucible space.

As compared to the customary laborious synthesis of polycrystalline chunks from the elements by vapor reaction in sealed ampoules, the following method is much simpler and yields compact slugs which can be made exactly to fit the crucible that is later used for single-crystal growth.

The spectroscopically pure elements are reacted in a small "bomb" (Fig. 4) which is pressurized with full

[4] For instance from General Electric Company, 1099 Ivanhoe Rd., Cleveland 10, Ohio.

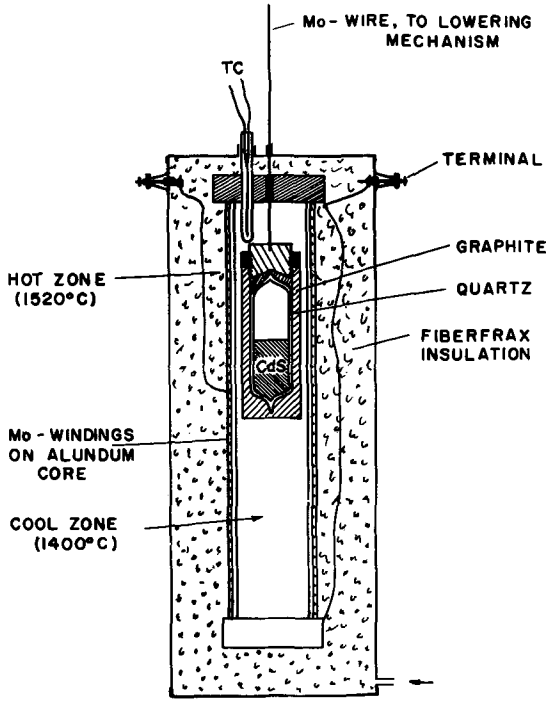

Fig. 3. Growth of CdS by "soft ampoule" method also applicable for ZnSe and GaP.

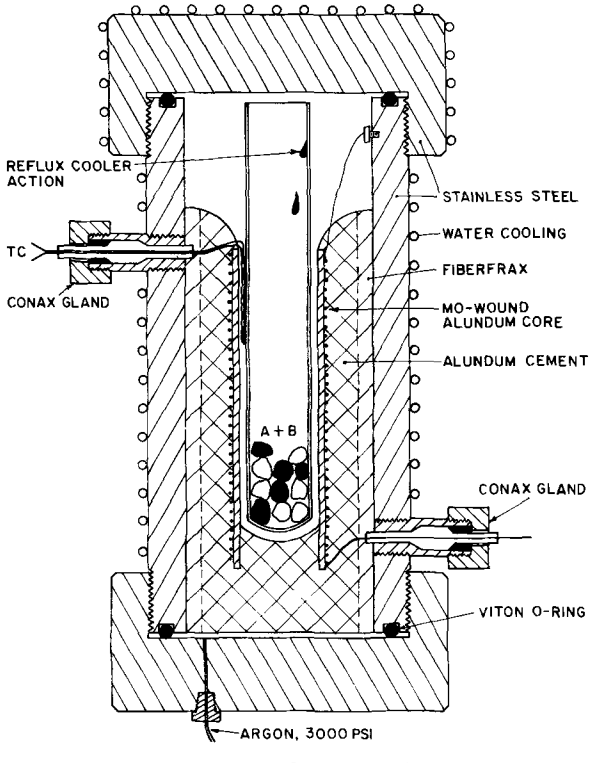

Fig. 4. Bomb for synthesis of polycrystalline II-VI ingots from the elements.

tank pressure of argon (250 atm) (11). When the Mo-wound heater is slowly warmed to the melting point of the compound, the pressure rises to about 400 atm by thermal expansion of the gas. The mixed pieces of the elements, even if they should react strongly exothermically, cannot create a shock wave, due to the inert atmosphere slowing down the rate of the reaction. The upper end of the quartz tube reaches out of the furnace into the colder part of the bomb, acting as a trap and "reflux" cooler. Since some anion vapor is usually lost, one adds more than needed at the beginning.

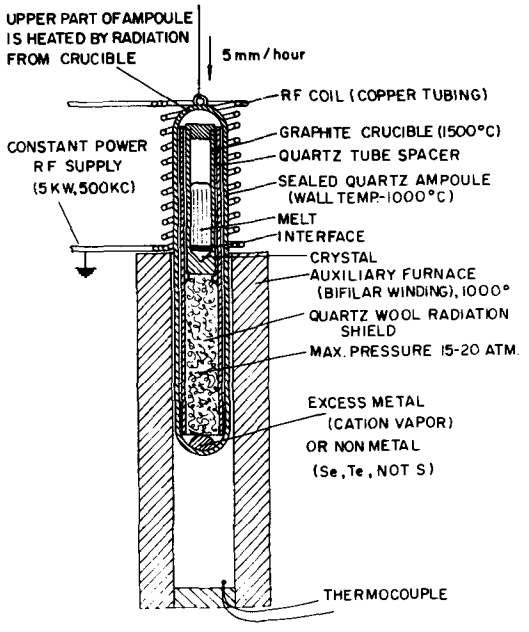

Fig. 5. RF Bridgman growth under controlled atmosphere in unsupported quartz ampoule.

All II-VI compounds can be synthesized quite easily in this way, including ZnS. For the III-V compounds, especially the phosphides, better methods are described later.

Induction Heater Methods

Vertical and horizontal Bridgman method in unsupported quartz ampoules.—Induction heating can be more advantageous than resistance heating because it allows one to heat a graphite crucible to a very high temperature *inside* a quartz ampoule, whereas the ampoule itself can be kept below its weakening temperature. Standard-wall quartz tubes of 1-in. OD can stand 30 atm of pressure up to 1000°C. However, safety shields should be used for protection of the operator.

In the arrangement shown in Fig. 5, the lower, cooler part of the ampoule extends into a wire-wound heater which is bifilarly wound (two parallel helixes connected at one end, with both terminals at the other end) as are all wire-wound resistance heaters located near rf coils, to prevent rf coupling. It contains the excess cation or anion material which provides the required vapor pressure. The upper, hotter part receives an experimentally adjusted amount of radiative heat from the graphite susceptor inside (13). The temperature of this part can be roughly checked with "Tempilstik" thermocrayons.[5]

To melt-grow ZnS and CdS, a sulfur atmosphere cannot be used with porous carbon susceptors because of CS_2 formation which leads to explosions (10, 16). Vitreous carbon is more inert, but the growth runs still must be short. Much better results are obtained by melting II-VI compounds under their metal vapors. In this way, ZnS, CdS, and ZnSe can be prepared highly n-type and with high mobility (10) (especially with additional aluminum doping) in a one-step process, in contrast to other methods which require after-firing of the crystal submerged in a cation metal melt.

This method can also be used for horizontal zone melting (16). For example, silver impurities have been effectively swept to one end of a ZnSe ingot, rendering it weakly p-type (17).

Vertical Bridgman growth in pressure-relieved ampoules.—To remove the explosion hazard of quartz ampoules, the decomposition pressure inside the ampoule, which reaches a dangerous magnitude in the preparation of GaP (35 atm), can be balanced by external gas pressure in a steel autoclave.

[5] Tempilstik Corporation, New York, N. Y.

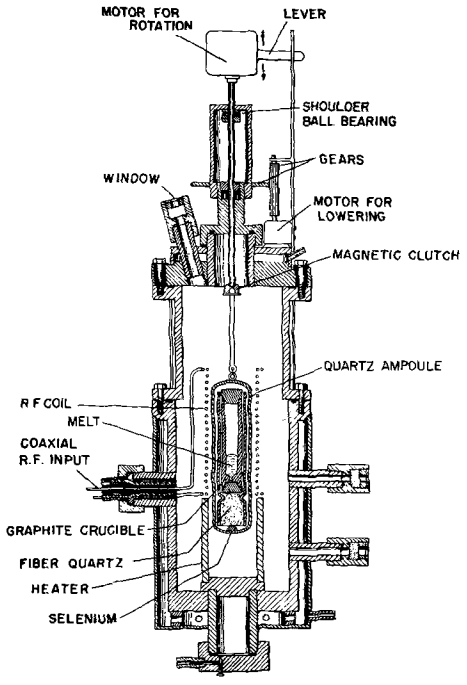

Fig. 6. RF Bridgman growth of ZnSe in pressure-compensated sealed ampoule in steel autoclave. Note the coaxial rf input.

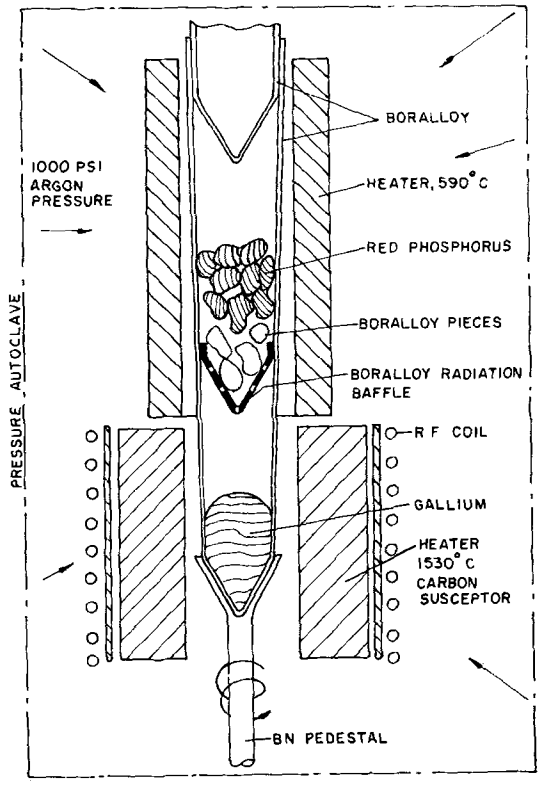

Fig. 7. GaP synthesis and crystal growth in a demountable pyrolytic BN ampoule.

An rf work coil placed inside a thick-walled steel vessel does not lead to significant power losses if 2-3 in. of clearance is maintained. The water-cooled rf leads should be brought through the steel walls coaxially if magnetic steel walls and/or frequencies above 1 megacycle are used. For nonmagnetic (stainless steel) walls, which are preferable for cleanliness, and for frequencies of 500 kilocycles or lower, simple straight parallel feedthroughs with Teflon bushings[6] are sufficient.

This vertical Bridgman method (Fig. 6) has been successfully used for ZnSe crystal growth (10, 17, 18) and is applicable to GaP growth under P pressure.

In order to simplify this method and do away with ampoule pumping and sealing, a demountable, reusable ampoule with a ground joint can be used (17). The internal atmosphere communicates with the external pressurized gas (which, for this reason, must be of ultrahigh purity) through a capillary which is heated to prevent clogging. The crystal grows, in the case of ZnSe for example, in an argon-selenium atmosphere. This method has the additional advantage that the added argon pressure prevents bubbling of the solidifying melt caused by exudation of the excess anion concentration of the melt at the interface, which is frequently observed in pure anion atmospheres. The disadvantage is, of course, that some anion vapor escapes through the capillary and contaminates the autoclave; this can be minimized by trapping it on a nearby cold surface.

For melt-growth of GaP we found early (10) that boron nitride containers are desirable since BN does not react with GaP (19). "Boralloy" pyrolytic BN crucibles[7] are ideal since they are very pure and can be reused almost indefinitely because the GaP does not stick to the walls. For II-VI compounds, vitreous carbon[8] makes an excellent container material.

This growth method, in conjunction with Boralloy containers, has yielded the most economical method for GaP synthesis and crystal growth (*see* Fig. 7). Pure gallium and red phosphorus[9] are placed in a long conical Boralloy crucible, separated by a perforated radiation baffle, as shown. The crucible is closed by a loosely fitting Boralloy lid, made intentionally nonfitting by a piece of red phosphorus which volatilizes subsequently. The whole system is pumped, filled, and pressurized with argon to 75 atm. The gallium is heated to 1500°C and the phosphorus to 590°C, corresponding to 40 atm of phosphorus pressure. The red phosphorus is quite stable and decomposes only very gradually to attain its thermal equilibrium pressure.

After the GaP has formed, the Boralloy crucible is slowly cooled, or lowered into a cooler zone, for Bridgman-type crystallization. The thin and flexible Boralloy container does not exert mechanical strain on the crystal by differential thermal expansion. After this, the system is shut off and depressurized. The GaP crystal falls right out of the inverted Boralloy crucible. This is a one-step operation which can be fully automated, with no contamination by silicon (which occurs by contact with quartz) or carbon (if a carbon rf susceptor in a phosphorus atmosphere is used), and all parts can be reused indefinitely.

In all of these methods, the necessary rf power setting for reaching the melting point must be determined in a preliminary "dry" run where a thermocouple is inserted into the crucible. Tungsten-rhenium thermocouples[10] are most suitable, even though they drift somewhat due to contamination. This effect is much stronger in platinum-rhodium thermocouples which are very sensitive to phosphorus.

During the actual run, one usually relies on the constancy of the generator output which is sensed *via* rf pickup coil and "thermocross" tube[11] (Fig. 8), or grid-dip meter. An additive combination of thermocouple temperature signal and rf pickup signal proved to give even better constancy (20) (better than ± 1°C). Very small loads (thimble-sized crucibles) require fast-responding control systems using thyristors or thyratrons in the rf power supply (20), whereas larger (about pound-sized) loads can be conveniently controlled with customary, sluggish saturable reactor systems in the line power supply. For medium-sized loads, such as for a crucible of 200g weight, it is bet-

[6] "Conax Glands," manufactured by Conax Corporation, Buffalo, New York.
[7] Union Carbide Corporation, New York, N. Y.
[8] Beckwith Carbon Company, Van Nuys, California.
[9] Gallium: Alusuisse, Metals, Inc., Fort Lee, N. J. Phosphorus: Mitsubishi International Corp., New York, N. Y.
[10] Engelhard Industries, Inc., Newark, New Jersey.
[11] RCA tube No. 1946.

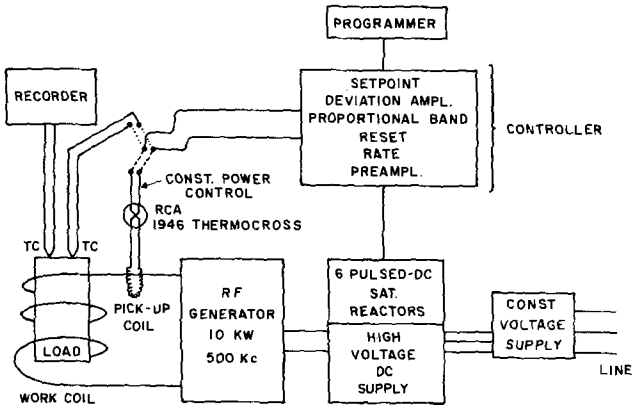

Fig. 8. Complete control system for rf generator. It can be switched from the thermocouple signal input to power signal input.

ter to use small fast-responding presaturated saturable reactors in the pulsed d.c. of the high-voltage line to the rf tubes,[12] presently still more reliable than SCR's, rather than a bulky reactor in the line voltage supply. Temperature control systems employing fast smooth all-electronic signal transfer[13] are inexpensive and preferable to jerky electromechanical systems.

Czochralski-type pulling under pressure.—Gremmelmeier-type pulling (21) under pressure in sealed quartz ampoules, with force transfer by rotating magnets, requires rather accurate bucking of the internal decomposition pressure by external autoclave pressure to prevent explosions or inplosions (10). The slow attainment of the equilibrium phosphorus vapor pressure over red phosphorus necessitates a differential manometer (10), but this adds further complication. There are other additional reasons which make this method unduly difficult. In addition to the auxiliary heaters to maintain the vapor pressure, one needs additional heaters to keep the viewing windows unfogged, since visibility is mandatory for crystal pulling. Furthermore, for pulling II-VI compounds, atmospheres consisting of the group VI vapors cannot be used because S, Se, and Te vapors are opaque (10). If one attempts to grow under cation vapor pressure, the required temperatures to reach the proper vapor pressures are above 700°C, where the magnets become very weak. Instead of the Gremmelmeier-type, one must use demountable ampoules with precision-sealed rotating quartz shafts (Fig. 9) (10), with elaborate baffle shields to prevent sticking by formation of deposits. Such systems have been built, and much effort was spent to pull GaP crystals under phosphorus pressure using a magnetic pulling apparatus (25), with only partial success, due to these complications. However, in the perspective of this paper, the method illustrated in Fig. 9 is presently the only one which would permit *pulling* of II-VI crystals, for which no suitable encapsulants (*see* later) are available as yet.

Crystal Growth Using Liquid Encapsulation (L.E.)

Czochralski pulling.—Crystal pulling using an oriented seed is undoubtedly the best crystal growth method. By placing a liquid blanket of molten boric oxide on top of the semiconductor melt and applying inert gas pressure exceeding the decomposition pressure, melt decomposition and escape of vapors can be prevented in an elegant and simple way, making auxiliary heaters and ampoule enclosures unnecessary (5, 6, 22). Now crystal pulling under pressure through the vitreous viscous blanket is possible. At 1500°C, the B_2O_3 evaporates only very slowly, so that crystal growth runs extending over many hours are possible. The loss of phosphorus is very slight. The boric oxide glass blanket is also beneficial in reducing the temperature loss of the melt surface, and by dampening oscillations of the melt meniscus caused by external vibrations.

[12] McDowell Electronics Company, Metuchen, New Jersey.
[13] Electronic Control Systems, Inc., Fairmont, West Virginia.

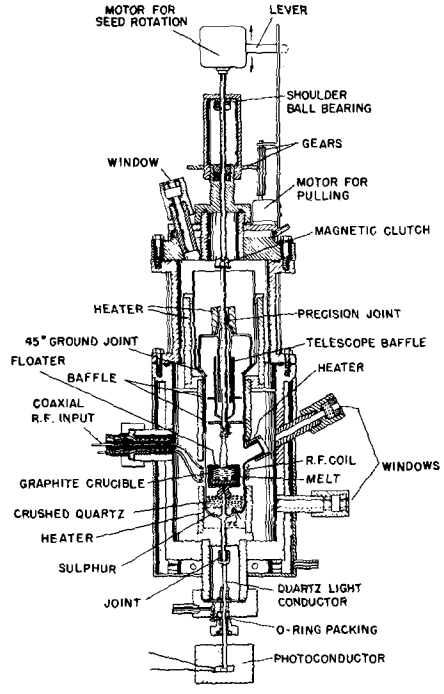

Fig. 9. Pressure puller using close-fitting rotating shaft

Temperature control at the beginning of the run is very critical. If the melting temperature is exceeded too far, the melt starts fuming and becomes metal-rich. This inevitably leads to polycrystallinity. To reduce this risk, the inert gas pressure should be as high as possible. We use 75 atm for GaP.

At present, boric oxide* seems to be the only practical encapsulant. It must be vacuum-dried for 24 hr at 1200°C (6). To be suitable, an encapsulant must wet the crucible, otherwise vapors will escape through the annular slot at the crucible wall (7, 10). Proposed molten salts such as BaF_2 (22) do not wet carbon or BN; they wet quartz, but heavily attack it. Also, these molten salts are "pervious" blankets for II-VI compounds because they are solvents for the melt (7, 10). Since they are not vitreous, they drip off the seed near the interface and hence do not protect the pulled crystal. In thick layers such molten salts may be usable for Bridgman growth, provided they do not contaminate or dope the melt with their constituents.

The boron contamination of III-V melts from B_2O_3 is below the ppm range. However, II-VI melts pick up about 300 ppm of boron (7). ZnSe can be pulled (7), but II-VI pulling is much harder than III-V crystal pulling due to the miscibility of molten B_2O_3 with the II-VI melt. New encapsulants may have to be found for satisfactory II-VI pulling.

Our equipment for L. E. pulling is shown in Fig. 10 and 11.[14] The system can be run in a normal laboratory, with direct personal control and viewing, as opposed to commercial systems which require remote-control, closed-circuit television viewing, and special, explosion-protected buildings.

It is important to start with a GaP polycrystalline ingot which fills the crucible solidly, for the following reason: If one starts with a crucible filled with irregularly shaped chunks, too much boric oxide is needed to fill the crevices and to cover the tops of the highest chunks to prevent the escape of phosphorus. When the GaP finally melts, the resultant B_2O_3 layer is too thick for easy pulling, since visibility through this layer gradually deteriorates due to emerging excess gallium

[14] Built at a total cost of $12,000, including the controls shown in Fig. 8 and the rf generator (only 8 kw are needed with proper impedance matching).

* Ultrapure B_2O_3, United Minerals & Chemical Co., New York, N. Y.

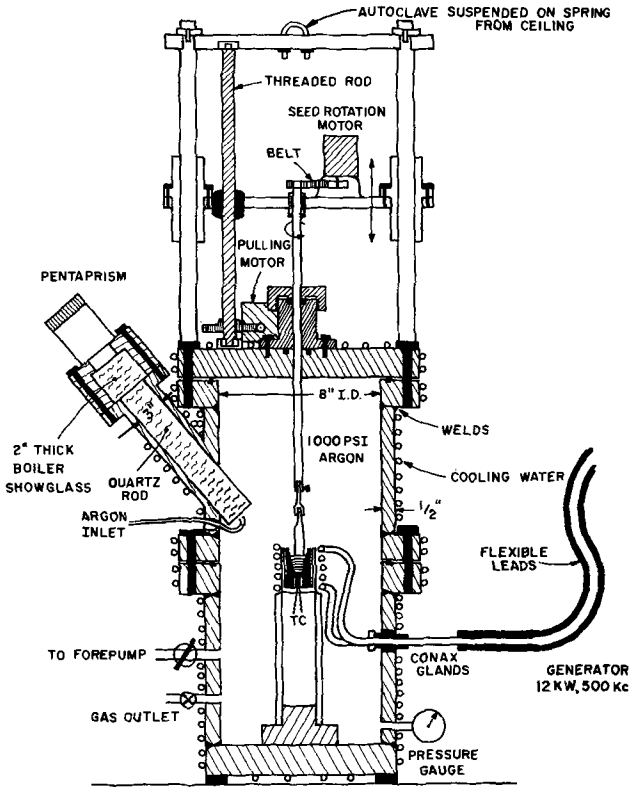

Fig. 10. Apparatus for liquid encapsulation-pulling under 1000 psi (75 atm) pressure, with direct viewing. The quartz rod eliminates most of the optical turbulence and is self-defogging. Vibrations have been minimized by rubber-mounting the motors and by hoisting the autoclave on a spring.

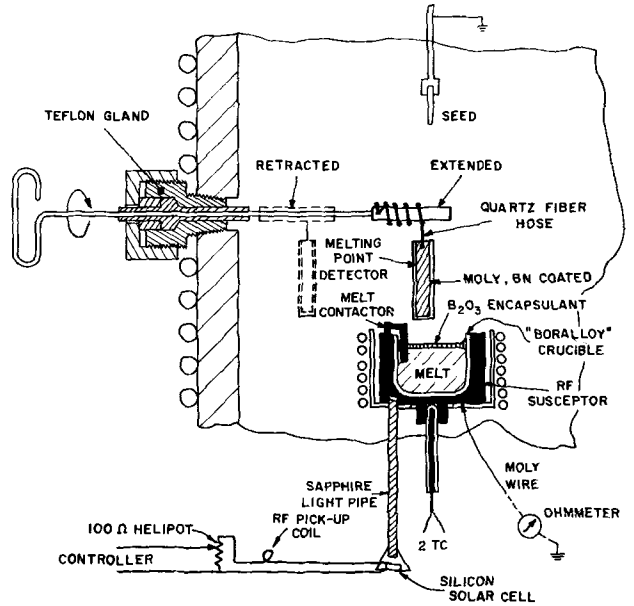

Fig. 11. Crucible arrangement and accessories for liquid encapsulation pulling. Note retractable melting point detector and electro-optic temperature sensor combined with rf power signal pickup for control. Temperature is measured by W-Re thermocouples. Contact between seed and melt is monitored by an ohmmeter.

which forms gallium subborate dispersed in the B_2O_3. One can then see the pulled part of the crystal only minutes later, when it emerges from the encapsulant layer. In general, the layer should not be thicker than 3/8 in. We therefore found it advantageous to synthesize a solid ingot in the same type of crucible from which the crystal is pulled later on. Demountable reusable equipment capable of producing sound, stoichiometric GaP ingots of 80g weight is shown in Fig. 12.

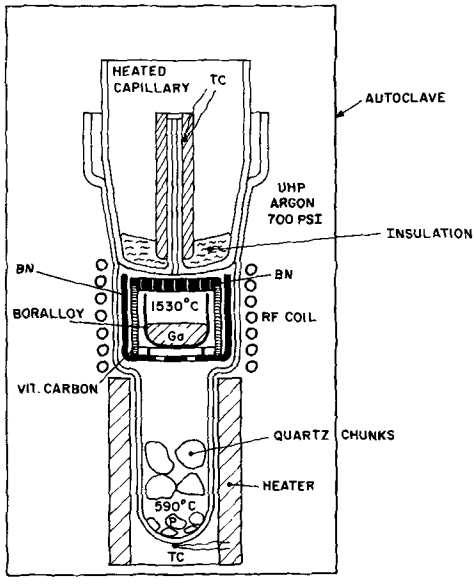

Fig. 12. Demountable setup for synthesis of GaP ingots

The temperature control problem presents here a new difficulty. One must take great care to prevent the runaway effect, which is much more serious here than in normal crystal pulling, due to the high temperature, and due to the limitation of visibility through the B_2O_3 layer. If one wants the crystal to become thicker, the increasing crystal size draws more heat from the melt, thereby cooling it, so that in the extreme case the whole melt solidifies. On the other hand, if one wants the crystal to become thinner, for instance for forming a neck at the beginning of growth to eliminate twins, the thinner crystal draws less heat from the melt; if the power input remains constant, the melt temperature increases, until the crystal is interrupted.

Maximum use of the "reset" function of the 3-action controller makes melt temperature more independent of heat demand. This is preferable to simply keeping input power constant. Instead of a thermocouple, a sapphire rod light conductor (10) which pipes the visible heat radiation into a silicon solar cell is very sensitive for controlling, due to the T^4 dependence of radiation intensity. One can combine this signal with a signal from the rf output power pickup sensor (Fig. 11), in varying proportions.

Liquid encapsulation Bridgman growth.—The previously described L. E. pulling method, though a great advance over previous methods, requires highly skilled manpower and does not yield a good crystal every time. L. E. Bridgman growth, although it usually does not yield oriented crystals, is more economical since it can be fully automated. Compared to the method described before (see under Vertical Bridgman growth in pressure-relieved ampoules), however, it does not permit synthesis and growth in one run, and the GaP crystal cannot be so easily removed from the Boralloy crucible since the B_2O_3 pulls off a thin BN skin each time.

Liquid encapsulation zone leveling.—The growth of mixed arsenide-phosphide or sulfo-selenide crystals (which are of interest for electroluminescence) from the melt by horizontal zone leveling was formerly impossible because one could not provide the correct pressurized anion vapor atmosphere mixture. This difficulty can now be overcome easily by covering a long horizontal boat containing the alloy with B_2O_3, applying inert gas pressure, and zoning in an autoclave (7).

Liquid encapsulation floating zone growth.—Frosch and Derick (23) have already reported crucible-free floating zone growth of GaP. By embedding the initially polycrystalline GaP rod in a B_2O_3-melt, one can use the buoyancy to grow a thicker crystal than with-

out the liquid encapsulation. Despite this, it is clear that this interesting method (24) poses no advantages at present.

Summary and Conclusion

Melt-growth of crystals under pressure from decomposable materials has come of age, especially for the important wide-gap III-V and II-VI materials. A synopsis of available methods reveals that, for obtaining GaP single crystals, liquid encapsulation (L.E.) pulling is the most elegant method. However, a new unified synthesis and Bridgman growth method in Boralloy containers may be more economical. L.E. pulling of II-VI crystals is more difficult and must probably await a more suitable encapsulant than B_2O_3 before its widespread application. For II-VI materials, the various Bridgman methods using component vapor or inert gas pressure for the suppression of decomposition can be employed.

For all of these methods, the requisite technologies and most suitable methods have been investigated, evaluated, and described.

Acknowledgments

I wish to thank the numerous colleagues who contributed to this program, and the referees who helped to improve this manuscript, especially C. J. Nuese.

Manuscript submitted Aug. 12, 1969; revised manuscript received Nov. 3, 1969.

Any discussion of this paper will appear in a Discussion Section to be published in the December 1970 JOURNAL.

REFERENCES

1. A. Addamiano and P. A. Dell, *J. Phys. Chem.*, **61**, 1020, 1253 (1967).
2. A. G. Fischer, *This Journal*, **106**, 878 (1959).
3. J. N. Carides and A. G. Fischer, *Solid State Comm.*, **2**, 217 (1964).
4. D. Richman, *J. Phys. Chem. Solids*, **24**, 1131 (1963); M. Rubenstein, Electrochem. Soc. Abstracts, **11**, 129 (1962).
5. E. P. A. Metz, R. C. Miller, and R. Mazelsky, *J. Appl. Phys.*, **33**, 2016 (1962).
6. S. J. Bass and P. E. Oliver, *J. Crystal Growth*, **3**, 286 (1968).
7. A. G. Fischer and T. V. Pruss, Am. Committee for Crystal Growth (ACCG) Conf., Gaithersburg, Aug. 11, 1969.
8. E. Tiede and A. Schleede, *Ber. dt. Chem. Ges.*, **53B**, 1717 (1921).
9. *See, e.g.*, W. E. Medcalf and R. H. Fahrig, *This Journal*, **105**, 719 (1958).
10. A. G. Fischer, Extended Abstract No. 53, Electrochem. Soc. Meeting, Pittsburgh, Pa, April 15-18, 1963; and Final Report, AFCRL-63-526, Contract AF 19 (604) 8018. Note: Contract report copies can be ordered from Clearing House for Scientific and Technical Information, Springfield, Va. 22151, or, by contractors, from DDC, Cameron Station, Alexandria, Va. 22314.
11. A. G. Fischer, Report No. 1, AFCRL 360 (1961), Contract AF 19 (604) 8018.
12. A. G. Fischer, *Z. Naturforsch.*, **13a**, 105 (1958).
13. A. G. Fischer, Final Report, AFCRL-67-0005 (1966), Contract No. AF 19 (628) 3866.
14. A. G. Fischer, U.S. Pat. 3,033,659 (1962).
15. S. E. Blum and R. J. Chicotca, *This Journal*, **115**, 298 (1968).
16. A. G. Fischer, *Bull. Am. Phys. Soc.*, II **6**, 17 (1961).
17. A. G. Fischer, Report No. 2, AFCRL-62-588 (1962), Contract AF 19 (628) 3866.
18. A. G. Fischer, Reports No. 2 and 3, AFCRL 721 and 979 (1961), Contract AF 19 (604) 8018.
19. C. C. Wang, M. Cardona, and A. G. Fischer, *RCA Rev.*, **25**, 159 (1964).
20. A. G. Fischer, U.S. Pat. 3,177,336 (1965).
21. R. Gremmelmeier, *Z. Naturforsch.*, **11a**, 511 (1956).
22. J. B. Mullin, B. W. Straughan, and W. S. Brickell, *J. Phys. Chem. Solids*, **26**, 782 (1965).
23. C. J. Frosch and L. Derick, *This Journal*. **108**, 251 (1961).
24. Prof. Schieber, Hebrew Univ., Jerusalem, Personal communication.
25. L. R. Weisberg *et. al*, Contract AF19 (604) 6152, AFCRL-62-540.
26. W. C. Holton, R. K. Watts, and R. D. Stinedurf, *J. Crystal Growth*, **6**, 97 (1969).

Reports on ECS Summer Assistance Awards and Weston Fellowship Award for 1969

During the summer of 1969, the following graduate students received $800 each, representing three Summer Assistance Awards of The Electrochemical Society.

Larry R. Faulkner, Harvard University, Cambridge, Mass., was awarded the Edward Weston Fellowship.

Lucien Papouchado, The University of Kansas, Lawrence, Kan., was designated recipient of the Colin Garfield Fink Fellowship.

Kathryn R. Bullock, Northwestern University, Evanston, Ill., received the ECS Summer Fellowship Award.

The Summer Assistance Award is made "without regard to sex, citizenship, race, location, or financial need to a fellow or teaching assistant pursuing work between the degree of B.S. and Ph.D. on a subject in a field of interest to The Electrochemical Society." It is intended to cover a period during which the recipient has no financial support for the continuance of his work.

The Edward Weston Summer Fellowship Report

A summary of Mr. Faulkner's report is given below.

Magnetic Field Effects on Some Fluid-Solution Processes Involving Anthracene Triplets and Their Relevance to the Mechanism of Electrogenerated Chemiluminescence

Over the past few years, a fairly substantial research effort has been directed toward a greater understanding of a novel group of chemiluminescent electron-transfer reactions (1-4). As an example, a typical reaction of this type might involve the homogeneous one-electron oxidation of the rubrene radical anion in some nonaqueous solvent such as N,N-dimethylformamide. When one carries out this reaction, one often observes the emission of light having the same spectral distribution as the fluorescence of rubrene. Moreover, one observes the same emission if one reduces the radical cation of rubrene in a homogeneous reaction using some suitable reductant (5). Several studies have shown that this kind of chemiluminescent electron-transfer reaction is common among aromatic hydrocarbons and their derivatives and also among several heterocycles (2, 6-8). Since the reactants are most easily generated and studied electrochemically, this phenomenon has become known as "electrogenerated chemiluminescence" (ECL).

The investigations which have been carried out thus far with these organic systems strongly suggest that excited molecular electronic states are populated directly in the redox step. That is, the results indicate that excited states are actually intermediates in these redox reactions. Since electron-transfer reactions are fundamental to all of chemistry, the discovery that excited states participate in the transfer in some cases raises questions of substance to many different fields, such as the study of quenching mechanisms of excited states and the study of electron-transfer in biological systems. Thus it is not surprising that investigators working in this area have sought to understand the more intimate details of this reaction and its mechanism.

Highlights for Los Angeles Meeting

The Electrochemical Society Lecture

Dr. Leo Brewer, Professor of Chemistry and Head of the Inorganic Materials Research Division of the Lawrence Radiation Laboratory at the University of California in Berkeley, has been selected to deliver the ECS Lecture, choosing as his topic "Electrons —The Universal Glue." It will be presented at the Plenary Session of the 137th ECS National Meeting in Los Angeles, California, on Monday, May 11th, at 9:00 A.M.

Dr. Brewer attended California Institute of Technology and received his B.S. in 1940. He attended the University of California, Berkeley and received his Ph.D. in 1943. He then became a Research Associate, Manhattan District Project, University of California, Berkeley. In 1946 he was appointed assistant professor, University of California, in 1950 associate professor, and in 1955 he became professor of chemistry. Since 1961 he is also Head of the Inorganic Materials Research Division of the Lawrence Radiation Laboratory. He became a member of the Natural Academy of Sciences in 1959. A frequent invited speaker at national and international meetings such as the International Congress of Pure and Applied Chemistry, Paris, 1957, he has delivered honorary lectures at universities throughout the country.

Dr. Brewer is an inorganic physical chemist of international stature who, by introducing the discipline of modern high-temperature chemistry over 15 years ago and most recently formulating an alloy theory for the transition metals, has advanced the understanding of the behavior of materials in areas most in need of improvement. He has systematically attacked important chemical problems at high and very high temperatures by experimental and theoretical means. His approach includes an unusual array of techniques from the arsenal of modern chemistry, physics, and metallurgy, combined with a great imagination and a keen judgment of critical factors.

Dr. Brewer is keenly interested in communicating the most advanced scientific results to his students and those concerned with the application of this knowledge to practical problems. Very interested in the education of our youth, he has been actively engaged in the reform of high school science curricula in California.

Some of the national awards received are: Guggenheim Fellow, Oxford, 1950-1951; Leo Hendrick Baekeland Medal, ACS, 1953; E. O. Lawrence Memorial Award of the AES, 1961.

Dr. Leo Brewer

Banquet Speaker

Dr. William H. Pickering, Director of the Jet Propulsion Laboratory, California Institute of Technology, Pasadena, California will be the guest speaker at the Annual Banquet of the 137th ECS National Meeting in Los Angeles on Tuesday, May 12th at 6:30 P.M. His topic will be "Exploring the Solar System."

For over a decade since the launching of the Soviet earth satellite Sputnik in late 1957, Dr. Pickering has been devising, developing, and supervising significant space and satellite programs for military and civilian agencies of the United States Government. Under his direction, the U. S. lunar and planetary missions, RANGER, MARINER, and SURVEYOR were planned, developed, and carried out at JPL.

In December 1962 the MARINER II spacecraft successfully completed a fly-by mission of the planet Venus, culminating a 109-day journey of over 180.2 million miles. This date marks the birth of the interplanetary age, indicating the first time that man penetrated the depths of space to the vicinity of another planet and obtained first-hand information. In July 1964, the spectacular flight of RANGER VII radioed to earth 4,316 high-resolution pictures of the lunar surface of the moon which proved to be 2,000 times better than those produced by the best earth-based telescopes. Again, in February and March of 1965, RANGERS VIII and IX successfully photographed still other selected areas of the moon.

In July 1965 after a 228-day journey of over 325 million miles, the first close-up pictures of another planet (Mars) were obtained by the MARINER IV spacecraft.

In June 1966 the SURVEYOR I spacecraft, built under the technical direction of JPL, landed gently on the surface of the moon after a near-perfect 63-1/2 hour flight. Over a period of 42 days, SURVEYOR received and acted upon approximately 120,000 commands from the earth and returned over 11,000 pictures of which the first 144 were relayed "live" through commercial television and Early Bird satellite to the nation and to Europe.

Dr. Pickering was born in Wellington, New Zealand. He attended Canterbury College, University of New Zealand, before leaving for the United States to continue his studies at the California Institute of Technology. He received his B.S. degree in Electrical Engineering in 1932, his M.S. in 1933, and his Ph.D. in Physics in 1936. He then joined the Caltech faculty as an instructor in electrical engineering and was appointed, successively, assistant professor, associate professor, and in 1946 professor in electrical engineering. In 1954 he was appointed Director of the Jet Propulsion Laboratory.

Dr. Pickering is a member of the National Academy of Sciences and a Charter Member of the National Academy of Engineering. He is past president of the International Astronautical Federation; an Honorary Fellow and Past President of the American Institute of Aeronautics and Astronautics; a Fellow of the Institute of Electrical and Electronic Engineers; the American Academy of Arts and Sciences; and the American Association for the Advancement of Science. He is a member of the International Astronautics Academy; the American Association of University Professors; the American Geophysical Union; and the Royal Society of New Zealand. He is an Honorary Fellow of the British

(Continued on page 156C)

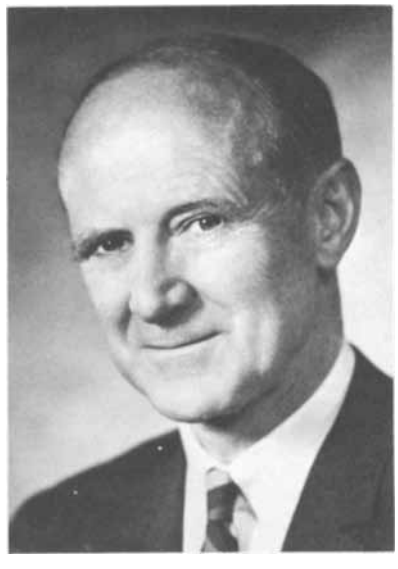

Dr. William H. Pickering

sense. Since I was doing a lot of translating in other languages for the boys here, I thought I'd better get the Russian, too."

Dr. Frary, the man of science, found no conflict between religion and science. He considered religion the single most important factor in a man's life, saying: "A man is hired for his character and ability, and religion builds character."

Today, technicians at Alcoa Research Laboratories have the opportunity to start or continue their education with tuition loans from the Francis C. Frary Educational Fund. He established the fund with the $1000 he was awarded with the Acheson Medal of The Electrochemical Society.

About retirement, Dr. Frary said: "My main argument for retirement is that when a man gets to a certain age he should move along and let some of the young man have their shot."

Until they moved to the nearby Presbyterian Home, a grandfather clock, in the family since 1788, stood on the stair landing in the Frary home. Dr. Frary's study was an alcove with an antique desk and a wall of French windows looking out on his apple trees.

Said his wife Alice: "The trees got exactly five sprays a year and a spring pruning—and every pruning wound got a dab of aluminum paint. He loved to travel and work with his hands. He even built a fallout shelter downstairs. He never had enough time to read. And he had a passion for fruit. But, above all, work was his gospel."

NEWS ITEM

Mathers Lectureship Established at Indiana University

A lectureship in chemistry, honoring Dr. Frank C. Mathers, professor of chemistry at Indiana University, has been set up through an anonymous donation from a former student of Dr. Mathers. Recognizing Dr. Mathers' productivity as a research chemist, the lectureship was established to present discussions of their research by noted chemists. The first holder of the lectureship is John S. Griffin, professor of chemistry at Indiana University, who will give a series of four lectures during the 1970 spring semester.

Dr. Mathers has continued to work regularly in his Indiana University research laboratory since his retirement 20 years ago. when he had served on the faculty 47 years. Many of his former students have advanced to top-level positions in industry and as educators.

His principal research interest has been in electrochemistry, especially electroplating. He is credited with many improvements in technique in this field. During World War I, he discovered a workable method of preparing fluorine gas. Fluorine produced by his method was used at Oak Ridge National Laboratory in the processing of uranium for atomic reactors.

Born on a Monroe County farm in 1881, Dr. Mathers received his A.B. and his M.A. degrees at Indiana University, and his Ph.D. from Cornell University. He returned to Indiana University as an assistant professor, advancing to associate professor in 1913 and professor in 1923. He was interim chairman of the Department of Chemistry in 1946-1947.

Dr. Mathers was President of The Electrochemical Society in 1940-1941 and has published many articles in the JOURNAL. In 1959 he became an honorary member.

Notice to Members

April 1 is Cut-Off Date

Your attention is called to Article III, Section 9 of the Society Constitution which states: "Any member delinquent in dues after April 1 of each year shall no longer receive the Society's publications, and will not be allowed to vote in any Society election until such dues are paid. All members in arrears for one year after the first of April shall lose their membership status and can be reinstated only by action of the Board of Directors." Members who have not sent in 1970 payments were mailed a second notice in March and are urged to make payment promptly in order to avoid delay in receipt of the JOURNAL.

POSITIONS AVAILABLE

Please address replies to the box number shown, c/o The Electrochemical Society, Inc., 30 East 42 St., New York, N.Y. 10017.

Solid State Chemist Physicist or Metallurgist sought to take part in government sponsored project in major east coast university. Required is interest in theoretical and calculatory work diffusion in solids. Reply Box B-52.

Applications invited for Research Team in Electrochemistry to be built up on Campus East Coast University. Good background in modern electrode kinetics, practical knowledge in electronic instrumentation is advantage. Hiring at **Technician B.S.** and **Ph.D. level group leader** intended. Apply Box B-53.

Book Reviewers Needed

The Electrochemical Soceity needs competent individuals to review books for the Journal.

Any Society member who wishes to volunteer his services should send his name, address, and field of competence to the attention of the Book Review Editor, Dr. Julius Klerer, c/o The Electrochemical Society, 30 East 42 Street, New York, N. Y. 10017.

ADVERTISER'S INDEX

Bell Telephone Laboratories 145C

Brinkmann Instruments 153C

Foote Mineral Company 151C

Great Lakes Carbon Corp., Graphite Products Division .....Cover 2

Matheson Gas Products, A Division of Will Ross, Inc. 155C

Plenum Publishing Corp. 155C

Princeton Applied Research Corp. 141C

Unitron Instrument Co. 152C

POSITIONS WANTED

Please address replies to the box number shown, c/o The Electrochemical Society, Inc., 30 East 42 St., New York, N.Y. 10017.

Materials and Process Engineer—M.Chem.E. with 25 years diversified aerospace industrial experience in oceanography, corrosion problems, material failure analysis, contamination studies, printed circuits, Klystron tubes, electrodeposition, electrochemistry, electroforming, supervisory, technical service, patents granted, papers published. Seeks position in technical or administration areas. Available immediately. Reply Box C-30.

Department Head—Ph.D. 1953, Physical-Inorganic Chemist, Age 41. Unusually broad basic and applied research experience. Heavy administrative responsibilities. Electrodeposition, physical properties, corrosion, friction, wear and lubrication, electrical contacts, materials research. Honors, awards, 50 publications and patents. Mid-twenties. Reply Box C-31.

Solid State Scientist—PhD 1970—Research on surface preparation and characterization including etching processes, thin film formation, defect characterization and device fabrication. Seeks R & D or teaching position. Publications. Resume available. Reply Box C-32.

Solid State Chemist/Physicist—Ph.D. Solid State Sciences 1970, Ph.D. Physics 1968. Specialized in Characterization and properties using electron microprobe, scanning electron microscope, X-ray, etc. Cathodoluminescence thesis. Desire challenging position in materials characterization and properties. Age 26. Reply Box C-33.

(Continued from page 148C)

Interplanetary Society and an Honorary Member of the New Zealand Institution of Engineers.

In 1965 Dr. Pickering was awarded the NASA Distinguished Service Medal by President Lyndon B. Johnson. He has also received the Army Distinguished Civilian Service Medal; the Columbus Gold Medal; the Robert H. Goddard Memorial Trophy; the Crozier Gold Medal; the Spirit of St. Louis Medal; the Italian Order of Merit; and has been honored many times nationally and internationally for his scientific contributions leading to the conquest of space.

JOURNAL OF THE ELECTROCHEMICAL SOCIETY

ELECTROCHEMICAL SCIENCE

MAY 1970

ES

Polarization Characteristics of a Cupric Chloride Cathode in a Lewis Acid Organic Electrolyte

M. Eisenberg,* R. E. Kuppinger, and K. M. Wong

Electrochimica Corporation, Menlo Park, California

ABSTRACT

The polarization characteristics of copper-cupric chloride electrodes in Lewis acid-type organic electrolytes, using propylene carbonate as an aprotic solvent, were studied. Two experimental techniques were used: a multireference polarization cell (MRP) and a rotating disk electrode (RDE). For the latter, a range of rotational velocities from 25 to 2000 rpm was covered. Following elimination or accounting for concentration polarization, the remaining polarization is considered to be attributable not only to charge transfer steps, but also to chemical steps such as a slow dissolution of the cupric chloride crystal in this electrode of the second kind. Apparent exchange current density values in the range of 3-6 x 10^{-5} A/cm^2 have been determined for the reduction of $CuCl_2$ to copper.

The interest in high energy battery systems employing organic nonaqueous electrolyte with aprotic solvents has focused attention on metal halides as cathode materials (1). Little is known about the polarization behavior of electrodes of this type in Lewis acid-type electrolytes in cyclic ester solvents such as propylene carbonate. The purpose of this study was to develop and adopt two techniques for a steady-state determination of the polarization characteristics of metal halide electrodes in nonaqueous media, and as an initial study to determine the cathodic polarization of a copper-cupric chloride electrode in LiCl-$AlCl_3$-propylene carbonate electrolyte.

Apparatus and Experimental Procedure

Cathodic polarization of copper-cupric chloride electrodes has been determined by the use of two galvanostatic methods in which the steady-state polarization is achieved at successively increased levels of current density. One of the methods is based on the employment of a cell with a precise, uniform geometry and equipped with a multiplicity of sidewall reference electrodes (MRP cell); the other is based on the use of the rotating disk electrode in a closed system cell specifically developed for work with nonaqueous electrolytes.

Multireference polarization cell (MRP cell).—The MRP cell was designed as a symmetrical cell of cylindrical uniform cross section in which the working electrode (under investigation) is located centrally between two auxiliary electrodes, completing the basic cell. A schematic presentation of this cell is shown in Fig. 1. Figure 2 shows an exploded view of the cell components. The uniform cylindrical geometry of the cell, the mounting of the electrodes to the accurately machined polypropylene sections of the cell, and the

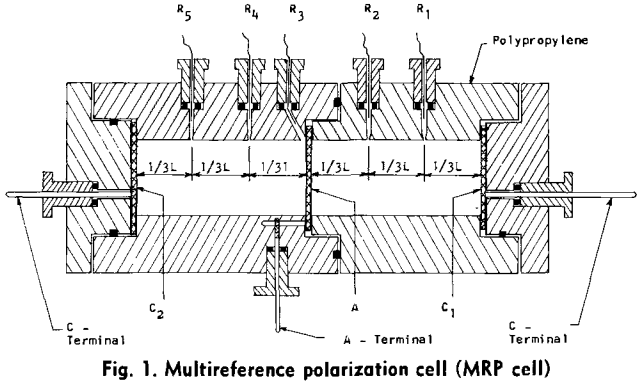

Fig. 1. Multireference polarization cell (MRP cell)

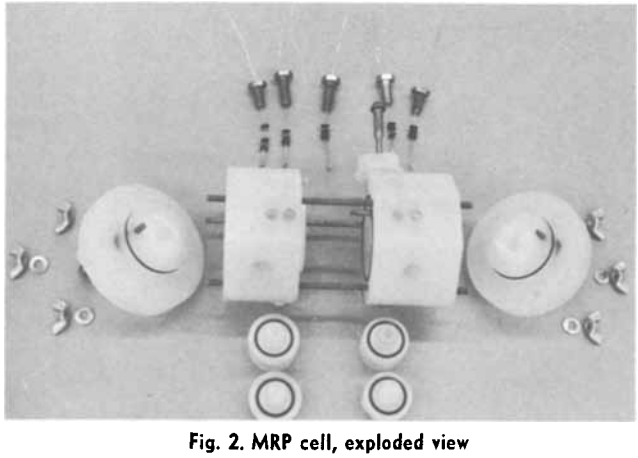

Fig. 2. MRP cell, exploded view

* Electrochemical Society Active Member.

equidistant position of the electrode under study between the two auxiliary electrodes provides a uniform primary current distribution at the surface of the electrode.

Several silver-silver chloride reference electrodes are located at precise distances, on both sides, from the plane of the electrode under study. The capillary leading to each reference electrode compartment is built into the side wall of the polypropylene cell without any protrusions or indentations; thus, the primary current distribution remains undisturbed, and there are no shielding effects commonly involved in kinetic work where protruding glass capillaries are used. The location of the capillary openings for references R_1, R_2, R_4, and R_5 (see Fig. 1) is such as to divide each half-cell compartment exactly into 1/3 lengths. Thus a measurement of the emf while current is passing through the cell between references R_1 and R_2, or R_4 and R_5 provides a direct value for the iR-drop involved for the distance 1/3 L.

There are several different ways in which the MRP cell can be employed for galvanostatic polarization studies. As can be seen in Fig. 1, it is possible to omit an electrode in position, *A*, place the working electrode under study, *e.g.*, in position C_2, place a suitable counterelectrode in position C_1, thus spacing current from one end of the cell to the other end. Through the use of reference electrodes R_5, R_4, and R_3 obtaining and carrying out measurements between the working electrode, C_2 and reference R_5, as well as between the other references, the extrapolative method may be used to correct for the iR drop included in the measurement between C_2 and R_5, since the same iR drop is involved in the distance C_2-R_5 as in the distance R_5-R_4.

It is also possible to employ the cell by placing the electrode under investigation in the center and employ the two end electrodes as counterelectrodes. In this case, a balanced polarizing circuit is employed to assure that the same amount of current flows to both sides of the electrode under investigation. This is illustrated in Fig. 3. It should be noted that in this case, by the use of reference electrode R_3, which is connected by means of a 45° capillary directly to the face of the working electrode (or a similar reference electrode R_6 on the other side), it is possible to reduce the iR drop involved in the measurement to a very small value, depending on how small and properly machined the capillary is. At the same time, if the diagonal capillary R_3 is small, it indeed comes very close to the surface of electrode A.

The polarization of the central electrode, A can be determined by employing all references, R_3, R_4, and R_5. It should be noted that the potential difference between R_3 and R_4 includes not only the iR drop, but also the effects of any concentration changes at the surface of the working electrode. Thus, the measurement employing reference, R_3, offers the means for assessing reasonably closely the effects of concentration polarization. Consequently, another way to express activation polarization is offered by the relation

$$\Delta E_{act} = (AR_4)_{net} - \Delta(R_5R_4)_{net} - [\Delta(R_4R_3) - \Delta(R_5R_4)] \quad [1]$$

where the last term in the square bracket represents the major portion of concentration polarization component, ΔE_{conc} (depending on the accuracy of the R_3 location). In the experimental studies reported here, the method expressed by Eq. [1] was employed. Lithium electrodes were used as counter-working electrodes to avoid any gas or undesirable by-product generation which would disturb the experiment.

The silver-silver chloride reference electrodes were constructed of silver wires, 0.020 in. diameter, terminating with a small loop. The wires were carefully cleaned to remove any surface oxides and coated with silver chloride by dipping in a melt of AgCl. The reference electrodes were equilibrated by immersion in the electrolyte prior to insertion into the reference electrode compartments of the MRP cell. The cell was assembled and filled with electrolyte in an argon drybox. It was then removed from the drybox and used in the normal laboratory environment. A Keithley Model 621 electrometer and a Hewlett-Packard Model 405CR digital voltmeter were used for the emf measurements. During the run a current was set and emf measurements performed until steady state was achieved. Subsequently, a larger current density level was set. During the run, reference to reference emf measurements were taken at several current values.

Rotating disk electrode.—In order to work with nonaqueous electrolyte systems under exclusion of air and moisture, a special housing was constructed for the rotating disk electrode using polypropylene materials which are inert to the cyclic esters, and a gastight construction with "O" rings for the top and bottom plates of the cell. The cell has a large ID (6.35 cm) to accommodate a variety of rotating disk diameters. A schematic diagram of the cross section of the cell is shown in Fig. 4. The diagram illustrates the relative positions of the rotating disk electrode (RDE) and of the Luggin capillary leading to an Ag/AgCl reference electrode. The distance of the tip of the capillary, which is in the same plane as the RDE from the

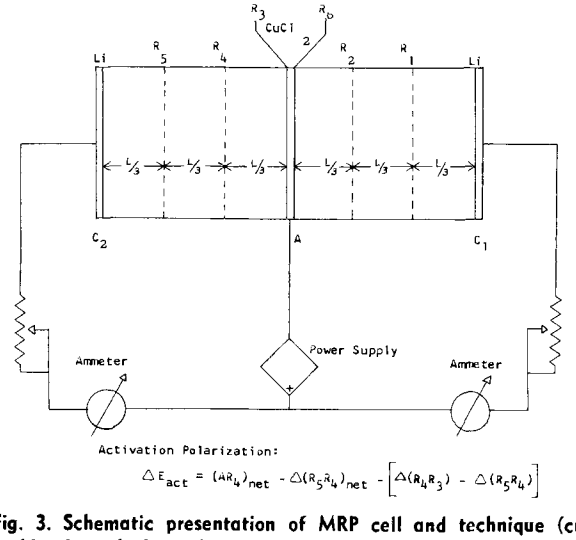

Fig. 3. Schematic presentation of MRP cell and technique (cupric chloride cathode in the center).

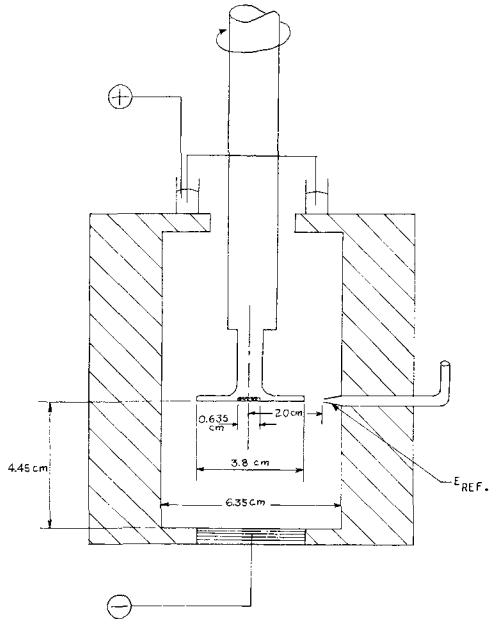

Fig. 4. Schematic diagram of RDE electrode

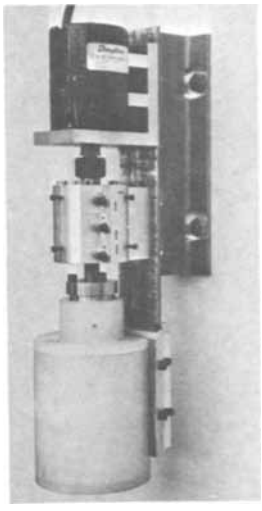

Fig. 5. Rotating disk electrode, assembled

access of the latter, is an important parameter since it affects the iR drop through the solution included in the steady-state measurement. Figure 5 shows the assembled cell in operation in the normal laboratory environment following its assembly inside an argon drybox. A mercury well is employed on top of the cell to provide both electrical contact to the RDE and a seal from the air atmosphere. The emf measurements between the RDE and the Ag/AgCl reference electrode (prepared similarly to those for the MRP cell) were made with a Keithley Model 621 electrometer and with a Hewlett-Packard Model 405CR d-c digital voltmeter. The RDE cell is constructed in such a way that the distance between the center of the active area of the RDE and the tip of the Luggin capillary can be adjusted over a range of values. For these experiments this radial distance was set at 0.635 cm, and the radius of the active area of the electrode was $R_0 = 0.318$ cm. Thus, the surface area of the RDE was 3.16 cm^2.

The elimination of the iR drop between the working electrode and the Luggin capillary tip of the reference electrode is an important matter for consideration, especially due to the relatively lower conductivity of the electrolyte employed. Under favorable experimental circumstances, it is possible to obtain the value of the resistance involved by experimental means, such as the use of an interruptor and an analysis of the emf decay trace obtained on an interruption of the current. Efforts to employ an interruptor consisting of a mercury wetted Reed relay activated by an oscilloscope (Tektronix 535) sweep pulse were not successful in obtaining the iR drop at a fixed current load, because of the surface resistance of the copper chloride layer on the electroformed electrode. Different values were obtained depending on the thickness of the electroformed layer. For this reason, the method of calculation of the iR drop in the cell developed by Newman and Hsueh (2) was employed, using an experimentally determined value of the specific conductivity of the electrolyte, K. When the Luggin capillaries are located in the plane of the RDE, their relation can be expressed as

$$R = \frac{\tan^{-1}\lambda_o}{2\pi r_o K} = \frac{0.523}{K} = 102.0 \qquad [2]$$

where

$$\lambda_o = \sqrt{\frac{r}{r_o} - 1} \text{ at } z = 0$$

and the values applicable to this study are:

K = specific conductivity (5.13×10^{-3} mhos/cm^2)
r_o = radius of disk electrode (0.318 cm)
r = radial distance to Luggin capillary of reference electrode (0.635 cm)

Using the resistance value $R = 102$ ohms, the iR drops were calculated for each level of current density employed during the polarization run and subtracted to obtain net total polarization values.

The experimental procedure consisted of fixing a given rotational speed, obtaining the open-circuit emf difference between the copper-copper chloride RDE, and the Ag/AgCl reference electrode. Subsequently, a given current density was applied, held constant until steady state was achieved, and the emf determined at each level. Three levels of rotational velocity were employed throughout this study: 25, 300, and 2000 rpm. The rotational speed was determined by using a magnetic pickup, sensing the passage of a small magnet attached to the rotating shaft. The speed of the electrode, driven by a d-c series motor (1/5 hp), was controlled by a d-c regulated power supply (Power Designs Inc. Model 5015-S).

Electrolyte and electrode preparation.—The electrolyte was prepared from propylene carbonate (Jefferson Chemical Company), twice vacuum distilled at 50 mm of mercury and a temperature of 150°C. Anhydrous aluminum chloride (Matheson, Coleman and Bell) was dissolved in it to yield a molality of 0.8*M*. Lithium chloride (J. T. Baker), additionally dried in a vacuum oven overnight at 150°C, was added to yield a molality of 0.7*M*. At the LiCl:$AlCl_3$ ratio of 0.7:0.8, the solution is essentially saturated in respect to LiCl. The solution was stored in a glass stoppered Erlenmeyer inside an argon drybox. The physical properties of this electrolyte were determined by conventional methods to be as follows

Specific conductivity: 25°C
$K = 5.13 \times 10^{-3}$ mhos/cm (± 0.1)
Viscosity: $\mu = 4.05$ Hz
Density: $d = 1.243$ g/cc
Kinematic viscosity: $\nu = 3.25 \times 10^{-2}$ cm^2/sec

As far as the copper-cupric chloride cathode is concerned, it was deemed necessary to employ a simple, essentially nonporous electrode in which only the species copper and cupric chloride would be present. Initial efforts to paste a suspension of anhydrous cupric chloride in acetone onto a copper foil were unsuccessful, since poor adhesion resulted after drying of the electrode. It was consequently decided to prepare the electrode by anodic electroforming of a surface layer of $CuCl_2$ in an organic electrolyte essentially of the same nature as the electrolyte in which the electrode is to be studied. This approach was found successful and the final procedure adopted consisted of cleaning a copper foil (0.015 in. thick) to remove oxides, rinsing with acetone and subsequently with propylene carbonate, and then electroforming by making the foil anodic in a 1.5*M* $AlCl_3$ solution in propylene carbonate, using platinum electrodes and applying a current density of 0.5 mA/cm^2 for time periods of 24-48 hr. These electrodes, in the form of a circular disk of the proper diameter, could then be inserted into the MRP cell in such a way that an active surface area of 4 cm^2 presented itself to the electrolyte inside the MRP cell.

For the RDE studies, the electrode was prepared by subjecting the exposed and cleaned end of the solid copper electrode-rotor to the same electroforming treatment. Care was taken to provide a sufficient amount of electroformed cupric chloride to cover the consumption occurring during the cathodic polarization runs and provide for a safe margin.

While the electroformed cathodes represent the basic approach taken in this study, it was of some interest to investigate the comparative behavior of a porous pressed electrode. These could only be studied in the MRP cell, since a reliable attachment of a pressed layer to the rotor electrode of the RDE cell could not be achieved. The pressed electrode for the MRP cell was prepared to provide an equimolar ratio of Cu-metal and $CuCl_2$. This corresponded to a weight per cent ratio of 67% $CuCl_2$ and 32% Cu, to which 1% (by weight) of a polyethylene binder was added. The copper was added as a metal powder (No. MD 151). The $CuCl_2$ (J. T. Baker) was dehydrated by treatment

Table I. Sample calculation of ΔE_{act} (run 16, Fig. 6) according to Eq. [1]

1 Current density, mA/cm²	2 $(AR)_{4\,net}$, V	3 $\Delta(R_5R_4)_{net}$, V	4 $\Delta(R_1R_3)_{net}$, V	5 $[\Delta(R_1R_3)_{net} - \Delta(R_5R_4)_{net}]$, V	6 ΔE_{act}, V
0.15	0.107	0.029	0.033	0.004	0.074
0.25	0.179	0.044	0.058	0.014	0.121
0.50	0.312	0.070	0.106	0.036	0.206
1.25	0.592	0.164	0.237	0.073	0.355
3.00	1.485	0.436	0.587	0.151	0.898

with thionyl chloride and vacuum oven removal (at 150°C) of SO_2 and HCl by-products. Electrodes 0.035 in. thick were produced by pressing this mixture onto a 24-mesh copper screen. The resulting volume porosity was 26%.

The counterelectrodes employed in both the MRP and the RDE cells were lithium pressed to a nickel foil.

Results

MRP cell studies.—A sample calculation for the activation polarization, ΔE_{act}, using Eq. [1] is given in Table I. As discussed previously, to the extent that R_3 is small and accurately located, the bracketed expression given in column 5 of Table I represents all or a major portion of the concentration polarization. This polarization remains small at lower current densities and reaches 14.4% (0.15V out of a total of 1.049V) at an apparent current density of 3 mA/cm². A comparison of column 3 (which expresses the iR-drop involved in the polarization measurement of column 2) and of columns 5 and 6 serves to give an appreciation of the importance of iR corrections and concentration polarization corrections for the accuracy of a Tafel plot. With an appreciation of these limitations, Eq. [1] appears to offer a reasonable approach to a determination of net electrode polarization.

The results for electroformed copper-copper chloride cathodes are shown in Fig. 6 in the form of a Tafel plot. Four runs are presented, each with a fresh electrode; two for the cathode positioned in the center of the cell, and two for the cathode positioned at one end. The polarization, expressed in the form of activation polarization, was calculated from Eq. [1], or an equivalent form of it. The curve in Fig. 6 was drawn through the points for the cathode position in the center of the cell, since these results were somewhat more reproducible. It may be noted, however, that for the other two runs the polarization values are only slightly higher. It should be noted from the data that a straight Tafel line would only apply over a limited range of current density values (approximately up to 1 mA/cm²).

The results for the pressed (26% porous) electrodes are given in Fig. 7 which shows independent runs; two

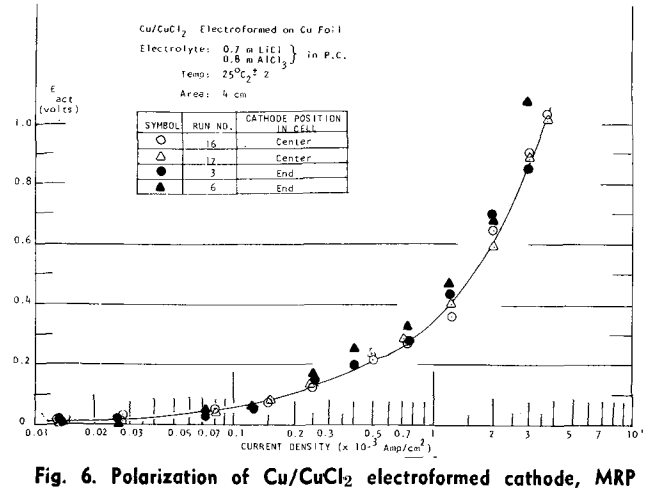

Fig. 6. Polarization of $Cu/CuCl_2$ electroformed cathode, MRP cell.

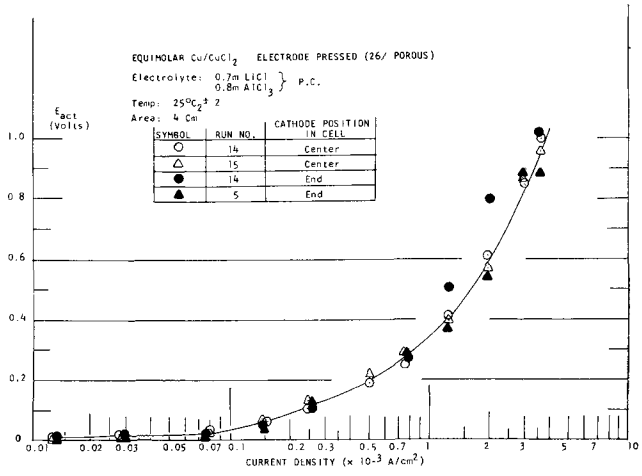

Fig. 7. Polarization of the pressed $Cu/CuCl_2$ cathode, MRP cell

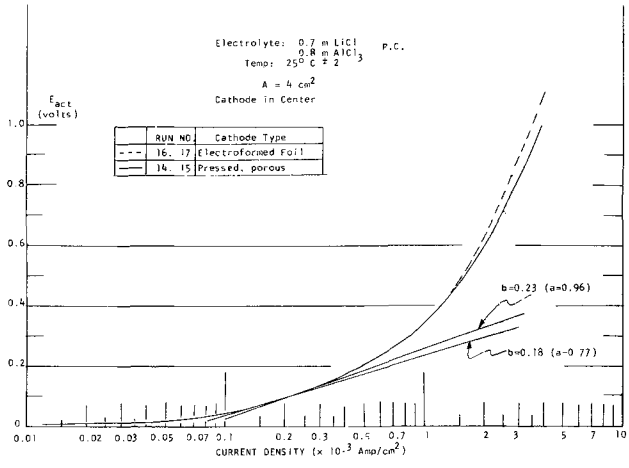

Fig. 8. Comparison of electroformed and pressed $Cu/CuCl_2$ cathode polarization, MRP cell.

for the cathode position in the center, and two for the end of the cell. Here, again, the runs with the electrode in the center are more reproducible and, consequently, the line was drawn through these data. However, in general, the results are in agreement for both electrode positions in the cell. A comparison of the results obtained for the two types of cathodes is shown in Fig. 8. The relatively close agreement of the results was at first considered surprising, since a lower polarization for the same apparent current density was expected for the pressed electrode. The results indicate that the porosity of the pressed electrode, produced in this case at a pressure of 6 tons/in.², must have been of the same order of magnitude as the natural porosity of the $CuCl_2$ layer on the surface of the anodically formed electrode. In the current density range of 0.1-0.5 mA/cm², Tafel slopes in the range $b = 0.18$ to $b = 0.23$ appeared to be applicable. However, deviation from linearity for current density of 1 mA/cm² or above, was significant. It should be remembered that the polarization values as plotted in Fig. 8 are already those obtained after subtraction of the concentration polarization component represented by the bracketed expression of Eq. [1]. As can be seen from the sample data shown in Table II, this concentration polarization (columns 2a and 2b) is subtracted from the total polarization (columns 1a and 1b) before the activation polarization, ΔE_{act} (columns 3a and 3b) is plotted in the figure. It should be noted that the concentration polarization values (columns 2a and 2b) for the two types of electrodes do not agree too well for a given current density. However, this may be due to the drift of the reference electrode potential which often occurred during a run. Such references

Table II. Sample data from the MRP cell studies

Current density, mA/cm²	Electroformed foil (Run 16) Total polar., 1a	ΔE_{conc}, 2a	ΔE_{act}, 3a	Pressed electrode (Run 14) Total polar., 1b	ΔE_{conc}, 2b	ΔE_{act}, 3b
0.25	0.135	0.014	0.121	0.119	0.009	0.110
0.5	0.242	0.036	0.206	0.202	0.013	0.189
1.25	0.428	0.073	0.355	0.457	0.041	0.416
2.00	0.754	0.103	0.651	0.683	0.068	0.615
3.00	1.049	0.151	0.898	0.946	0.104	0.842

had to be replaced from time to time. The difference may also, however, be due to the different natures of the electrode and its effect on the surface concentration of the chloride ion (see discussion in next section).

RDE cell studies.—The polarization values obtained in the RDE cell after the iR correction formally still contain a mass transfer or concentration polarization component. There is no direct way for its assessment, the way this could be done in the MRP cell. However, it can be readily estimated that for an electrode process which is productive, rather than consumptive (*i.e.*, in which a concentration build-up occurs at the interface; in this case, a build-up of Cl^- ions or $AlCl_4^-$ ions), concentration polarization is usually negligibly small. Furthermore, it should be noted that in the RDE cell the diffusional mass transport is practically of a radial nature (considering the small size of the electrode compared to the shape of the electrolyte volume in the cell). Thus, a more uniform steady state is produced in the RDE cell than in the case of the stationary electrodes in the MRP cell.

Figure 9 shows the total polarization (iR free) obtained for two runs at 25 rpm. Unlike the MRP cell, the data here are in agreement with the Tafel line over a wider range of current densities. Both curves in Fig. 9 give a slope of $b = 0.18$, although somewhat different a values have resulted. The results at 300 rpm (Fig. 10) are, again, not completely reproducible, but they fall within a fairly narrow range of slopes of $b = 0.18$-0.23. The same can be said about the results obtained at 2000 rpm (Fig. 11) where, however, one run yielded significantly higher values of the constant, a. It may be interesting to know that by comparing the results of Fig. 9, 10, and 11, increased rotational velocity did not diminish the total polarization. This, indirectly, verifies the previously discussed estimate of negligible concentration polarization in the MRP cell results.

Discussion

It is interesting to compare the RDE cell results with those of the MRP cell. It can be seen in Fig. 8 for the straight lines with slopes $b = 0.18$ and $b = 0.23$

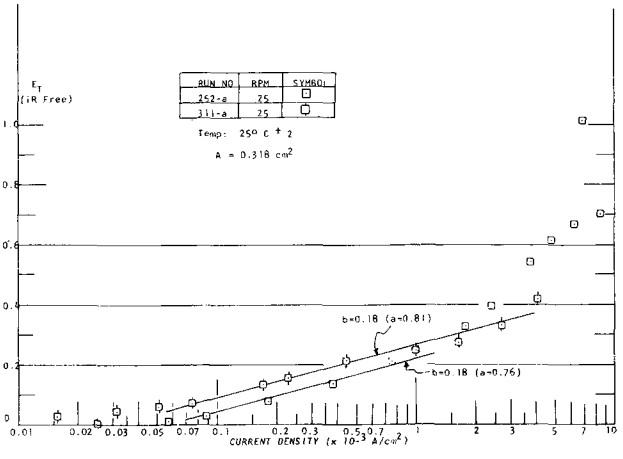

Fig. 9. Total polarization of $Cu/CuCl_2$ electroformed cathode in the RDE at 25 rpm.

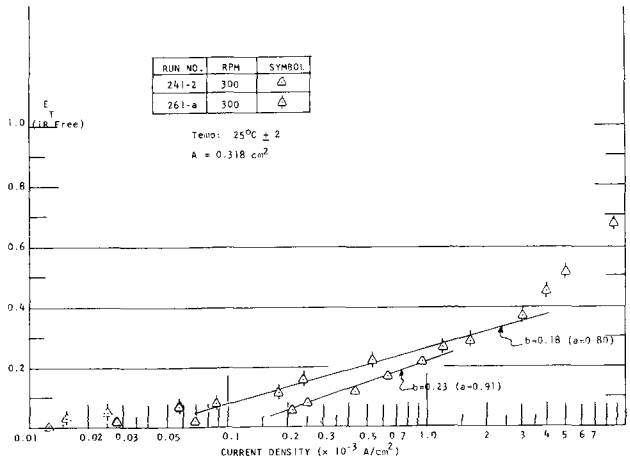

Fig. 10. Total polarization of $Cu/CuCl_2$ electroformed cathode in the RDE at 300 rpm.

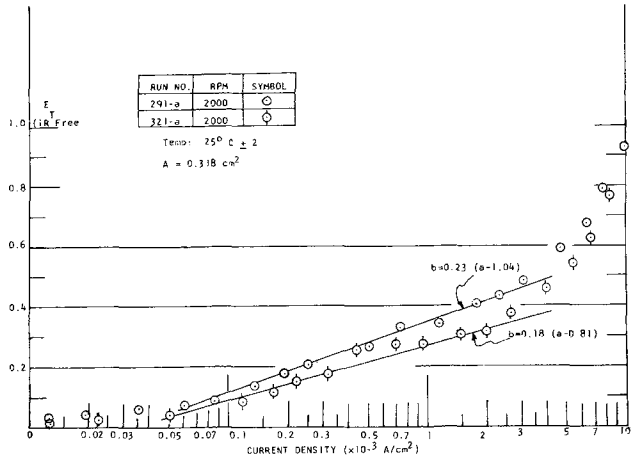

Fig. 11. Total polarizaton of $Cu/CuCl_2$ electroformed cathode in the RDE at 2000 rpm.

(and with a range of a-values bracketing the results of the RDE cell) that fair agreement is obtained in the lower ranges of current density, but serious deviation of linearity is indicated for the MRP cell above 0.5 mA/cm², while linearity is preserved for the RDE cell data up to 4 or 5 mA/cm². This indicates that possibly ohmic effects resulting in a resistance type polarization are important for the stationary cathode in the MRP cell, and that these effects can become very significant. For instance, at 3 mA/cm², Fig. 10 indicates a polarization of the order of 0.35V for the RDE cell. The corresponding value for the MRP cell is 0.84V (see Fig. 8). In light of the fact that the MRP cell method already subtracts the bulk solution concentration polarization, this large typical difference can only be attributed to ohmic effects on the surface of the cathode itself, as may result from a possible crystallization of lithium chloride as the discharge of $CuCl_2$ (and consequently, local build-up of chloride ions) proceeds in the electrolyte layer immediately adjacent to the cathode and already saturated in respect to LiCl. Another possibility is that the larger polarization is not due to an ohmic effect, but to a "reaction polarization" associated with an increased resistance to the dissolution of $CuCl_2$ which may be a chemical step preceding the charge transfer step in the over-all kinetics (see discussion further). In any event, the MRP cell should not be employed for appreciable current densities and in runs with prolonged duration. On the other hand, the RDE cell, with a small electrode area compared to a large volume of electrolyte and with a uniform and high rate of mass transfer, is conducive to obtaining overvoltage data free of resistance polarization components associated

with partial or total surface coverage by lithium chloride, or any other species which may be involved in the mechanism.

The over-all reaction in the discharge of the cupric chloride electrode can obviously be stated as

$$CuCl_{2(s)} + 2e^- \rightarrow Cu^0_{(s)} + 2Cl^- \qquad [3]$$

This is an electrode of the second kind, the kinetic treatment of which is complex, since the over-all process involves not only charge transfer, but also several chemical reactions. Not only is a solid phase $CuCl_2$ involved, but also the possibility of complex ion formations which the cupric or cuprous state of the copper may enter into with Cl^- ions or with Lewis-acid ions, $AlCl_4^-$. A theoretical treatment of electrodes of this general type involves, according to Jaenicke (4, 5) and Vetter (6), the reaction velocity of the chemical step, namely, the dissolution of the ionic crystal immediately at the phase boundary with the metal conductor (here, $CuCl_2$) prior to the charge transfer step in the following scheme

$$\begin{aligned} &1.\ Cu^{++}(\text{crystal}) + 4Cl^- \rightleftharpoons [CuCl_4]^{-2}{}_{\text{soln.}} \\ &2.\ [CuCl_4]^{-2}{}_{\text{soln.}} \rightleftharpoons Cu^0 + 4Cl^- + 2e^- \end{aligned} \qquad [4]$$

In reactions of this type the rate-determining step is usually the first one. This has, of course, not yet been established specifically for the reaction investigated here. As far as step 2 is concerned, it may in reality consist of two sequential steps, namely, a reduction, first, of Cu^{++} to the cuprous state, and then to the metallic state. The possibility of further interactions between the Cu^{++} state and Cu^0 state may also need consideration.

In this first study an elucidation of the detailed mechanism was not undertaken. From a realization of the complexity of the kinetics, the limited theoretical significance of an over-all exchange current density, i_o, and of the transfer coefficient, α, is appreciated. These values should be regarded as apparent values. On the other hand, from the point of view of an assessment of over-all reversibility of the processes involved, their calculations appear to be of interest. The values as obtained from the individual methods and under specific conditions are given in Table III.

The effective or apparent exchange current density, i_o, would appear to be predominantly of the order 6×10^{-5} A/cm^2 for the results of the MRP cell, and predominantly of the order of 3×10^{-5} A/cm^2 for the RDE cell. A statement of these effective values amounts to a statement that the electrochemical reduction of $CuCl_2$ in the organic electrolyte under study does not proceed very reversibly and that the predominant mode of polarization one can expect would be activation polarization, by which we mean all modes of polarization other than that attributable to mass transfer resistance in the electrolyte. Obviously, when the geometric relationship in the cell, the quantity of available electrolyte, and a limited rate of mass transfer of the chloride ion away from the surface of the $Cu/CuCl_2$ cathode, combined with an appreciable build-up of surface crystallization of lithium chloride (or of other possible compounds in the particular electrolyte, *e.g.*, $LiAlCl_4$), an appreciable component of resistance polarization or of "reaction polarization" associated with inhibition of step 1 may result, as was clearly demonstrated by the results of the MRP cell, compared to those of the RDE cell. In the discharge of a galvanic cell, where the limitations of mass transfer may be even more severe than they were in the MRP cell, the importance of this phenomenon must be fully appreciated.

Table III. Values from individual methods, under specific conditions

	Slope b	a	App. trans coefficient, α	App. exchange curr. density, i_o, A/cm^2
MRP cell	0.18	0.77	0.164	5.3×10^{-5}
	0.23	0.96	0.128	6.75×10^{-5}
RDE	0.18	0.76	0.164	6.02×10^{-5}
25 rpm	0.18	0.81	0.164	3.16×10^{-5}
RDE	0.18	0.80	0.164	3.6×10^{-5}
300 rpm	0.23	0.91	0.128	11.2×10^{-5}
RDE	0.18	0.81	0.164	3.16×10^{-5}
2000 rpm	0.23	1.04	0.128	3.02×10^{-5}

Manuscript submitted Jan. 16, 1968; final revised manuscript received Jan. 15, 1970. This was Paper 6 presented at the Chicago Meeting of the Society, Oct. 15-19, 1967.

Any discussion of this paper will appear in a Discussion Section to be published in the December 1970 JOURNAL.

REFERENCES

1. R. E. Kuppinger and M. Eisenberg, Paper 54 presented at the Philadelphia Meeting of the Society, Oct. 9-14, 1966.
2. L. Hsueh, MS Thesis, U.C., Berkeley, UCRL 16607 (Jan. 1966).
3. D. P Gregory and A. C. Riddiford, *J. Chem. Soc.*, **1956**, 3756.
4. W. Jaenicke, *Z. Elektrochem.*, **56**, 473 (1952)
5. W. Jaenicke and M. Haase, *ibid.*, **63**, 521 (1959).
6. K. J. Vetter, "Elektrochemische Kinetik," Springer Verlag, p. 573, *et seq.* (1961).

Charge Acceptance of the Cadmium-Cadmium Hydroxide Electrode at Low Temperatures

Y. Okinaka* and C. M. Whitehurst

Bell Telephone Laboratories, Incorporated, Murray Hill, New Jersey

ABSTRACT

Premature hydrogen evolution occurs when a discharged cadmium hydroxide electrode is brought to a low temperature and charged at a moderate rate. It was found that, in addition to various other known factors, the discharge rate and the temperature during discharge just prior to the temperature lowering greatly affect the charge acceptance in the first low temperature charge. Light and electron microscopic examination and BET surface area measurement showed that the cadmium hydroxide crystals formed at lower discharge rates and at higher temperatures are larger in size and more difficult to reduce. The results are interpreted on the basis of the mechanism involving a soluble intermediate species in both the charging and the discharging reactions. X-ray and electron diffraction analyses of the cadmium hydroxide crystals formed on discharge in 6.9*N* KOH at temperatures below $-18°C$ showed the presence of γ-$Cd(OH)_2$ in addition to the ordinary β-$Cd(OH)_2$. Electrodes containing γ-$Cd(OH)_2$ have a greater low-temperature charge acceptability than those containing β-$Cd(OH)_2$ alone.

When a sealed nickel-cadmium battery is brought to a low temperature in the discharged state and charged, hydrogen gas may evolve from the negative electrode before the positive electrode is fully charged (1). Since the rate of hydrogen recombination in the cell is practically negligible, it accumulates on repeating the low-temperature charge and eventually leads to a high internal pressure and a failure due to explosion. This is one of the serious limitations in the applicability of sealed nickel-cadmium batteries.

Gottlieb (2) made an extensive investigation of various factors affecting the charge acceptance of the negative cadmium hydroxide electrode and found that the charge acceptance decreases with increasing charge rate, decreasing temperature during the charge, and increasing temperature during the preceding charge-discharge cycles. He interpreted these results on the assumption that larger and/or more perfect cadmium hydroxide crystals are formed on discharge at higher temperatures and they are difficult to reduce on charge at lower temperatures and at higher rates. Popat and Rubin (3) reported experimental results similar in some respects to Gottlieb's, but they proposed an entirely different interpretation. It was postulated by them and Rubin (4) that "active" and "inactive" forms of cadmium hydroxide are formed during discharge, and they are reduced at different potentials on charge.

The main purpose of this communication is to present experimental evidence supporting Gottlieb's assumption and showing that there is a close correlation between the low-temperature charge acceptance and the size of the cadmium hydroxide crystals. Experimental results are also presented showing that, in addition to the three factors studied by Gottlieb, the discharge rate and the temperature during the discharge immediately preceding the low-temperature charge have a profound effect on the size of cadmium hydroxide crystals formed and, consequently, on the charge acceptance in the first low temperature charge. An incidental finding made during the course of this investigation was that γ-$Cd(OH)_2$, the monoclinic modification, is formed preferentially on discharge at lower temperatures rather than β-$Cd(OH)_2$, the ordinary hexagonal modification.

* Electrochemical Society Active Member.

Key words: cadmium, cadmium hydroxide, battery, nickel-cadmium battery.

Experimental Methods

All experiments were performed in flooded cells with 6.9M KOH. The cadmium hydroxide impregnated sintered nickel plate electrodes had a theoretical capacity ranging from 543 to 575 mA·hr. Their dimensions were approximately $5.6 \times 2.5 \times 0.076$ cm. The electrodes were prepared by a vacuum impregnation method consisting of impregnation in 4M $Cd(NO_3)_2$, reduction in hot 25% KOH, washing, and drying in nitrogen. This sequence was repeated five times. The electrodes were then subjected to eleven forming charge-discharge cycles at various currents. After final full discharge they were washed, dried, and stored under nitrogen atmosphere. The test cell contained one cadmium electrode, two nickel sheet counterelectrodes, and a 6.9M KOH salt bridge connecting the cell to a Hg/HgO (6.9M KOH) reference electrode. In each experiment, the cadmium electrode was first "conditioned" by repeating the following cycle three times: charge at 200 mA with approximately 50% overcharge and then a full discharge to -0.5V against the reference electrode at the same current. Finally the electrode was charged fully at 200 mA before it was subjected to a study of various experimental variables. This conditioning was carried out at room temperature.

Optical photomicrographs were taken with polarized light with a Unitron Metallograph BNX-11 using a xenon illuminator. Electron photomicrographs were obtained on specimens prepared by transferring cadmium hydroxide crystals from the electrode surface to a collodion film. X-ray diffraction data were obtained by using CuK_α radiation. Electron diffraction analysis was made by Ladd Research Industries, Inc., Burlington, Vermont, on carbon replicas prepared from collodion film specimens. BET surface area measurements were made by Numec Instruments and Controls Corporation, Monroeville, Pennsylvania, using an Orr surface-area pore-volume analyzer. Krypton was used as the adsorbate. The samples were degassed at 50°C for 24 hr.

Results and Discussion

To illustrate the problem, a potential-time curve obtained on charge and discharge at $-18°C$ is compared in Fig. 1 with the curve obtained at 25°C before the temperature lowering. Both curves were obtained at a constant current of 200 mA. It is seen that the

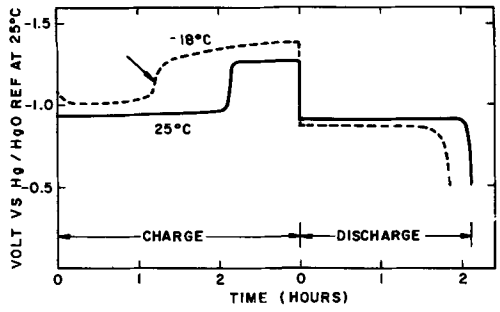

Fig. 1. Charge-discharge curves of cadmium hydroxide electrode at 25° and at —18°C after discharge at 25°C.

rise in potential at —18°C toward the hydrogen evolution range occurs after only about 60% of the 25°C discharge capacity is returned to the electrode. The arrow sign indicates where the gas bubble formation begins to become visible. The term "charge acceptance" is defined here as the ratio of the charge that the electrode accepted before this point to the charge capacity found in the discharge prior to the lowering of temperature. It is true that the charging reaction at the low temperature continues after the potential has reached the hydrogen evolution region, as is evidenced by the fact that the capacity found on the subsequent discharge was considerable greater than the charge that the electrode accepted before the onset of hydrogen evolution. However, it is the charge acceptance defined above that is important in sealed nickel-cadmium batteries because no hydrogen gas can be permitted to accumulate. Two distinct plateaus on potential-time curves, which were reported by Popat and Rubin (3) and Rubin (4) and attributed by them to the reduction of "active" and "inactive" cadmium hydroxides, were not observed under our experimental conditions.

In the previous study, Gottlieb (2) mentioned that the charge acceptance at low temperatures is not affected by the current used for the preceding cycles at a higher temperature. We found the contrary to be true, *i.e.*, the low-temperature charge acceptance is greatly affected by the magnitude of the current used for the discharge prior to the charge. Results are shown in Fig. 2. The experiments were carried out in the following manner. After the conditioning cycles described in the preceding section, the cell was placed in a bath maintained at a desired temperature and, after temperature equilibration, discharged fully to —0.5V at a specific rate. The test electrode was then removed from the cell, and a small portion of it was cut off for microscopic and other examination purposes, while the remainder of the electrode was immediately placed back into the cell. The cell was then transferred into a —18°C bath and, after a 2-hr open-circuit stand, charged at the C/2 rate. The charging current was adjusted on the basis of the capacity found in the preceding discharge appropriate correction having been made for that portion of the electrode which had been cut off. The reproducibility of the charge acceptance measurement was found to be about ±4% for the discharge rates of C/2 and C/20 at room temperature. This is indicated by the vertical lines on the two points in Fig. 2.

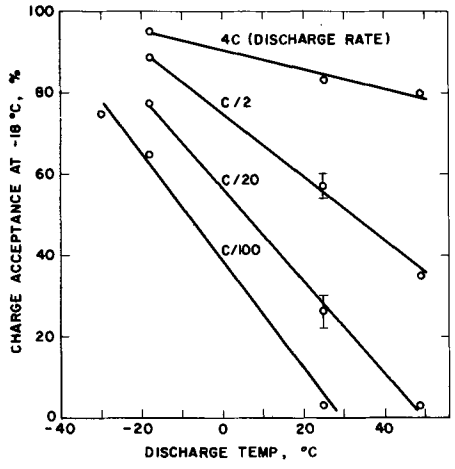

Fig. 2. Charge acceptance of cadmium hydroxide electrodes at —18°C at C/2 after discharging at various rates and temperatures. Small vertical lines indicate the reproducibility of measurement.

Figure 2 shows that the low-temperature charge acceptance is higher after the electrode is discharged at higher rates and at lower temperatures. The charge acceptance values were found to be independent of the extent of loading of the electrode with the active material in the range between 75 mA·hr/plate and 896 mA·hr/plate. On the other hand, it is striking that the charge acceptance varies from almost 0 to 100% depending on the conditions during discharge. It is of interest to note in Fig. 2 that the charge acceptance found when the electrode was first discharged at —30°C and then charged after raising the temperature to —18°C was greater than the value found when both discharge and charge were carried out at the same temperature of —18°C.

These results can be accounted for qualitatively on the basis of the mechanism involving a soluble intermediate species in both the discharging and the charging reactions. In the potential range of interest, these reactions may be represented by the following simple equations (5, 6)

Discharge:

$$Cd + 3\,OH^- \rightarrow Cd(OH)_3^- + 2e^- \quad [1]$$

$$Cd(OH)_3^- \rightarrow Cd(OH)_2 + OH^- \quad [2]$$

Charge:

$$Cd(OH)_2 + OH^- \rightarrow Cd(OH)_3^- \quad [3]$$

$$Cd(OH)_3^- + 2e^- \rightarrow Cd + 3\,OH^- \quad [4]$$

There is some evidence indicating that anodically produced cadmium hydroxide crystals can also be reduced directly without going through the soluble intermediate (6). It will be shown in this paper that all experimental results described here can be accounted for without depending on a direct reduction mechanism. The dissolution-precipitation mechanism for the discharge reaction [1] and [2] predicts the size of $Cd(OH)_2$ crystals to be larger when they are formed at lower discharge rates. The reasoning is as follows. At lower discharge rates the rate of formation of the soluble complex $Cd(OH)_3^-$ is slower, and this should cause the precipitation reaction [2] to proceed more slowly from a more dilute, and hence less supersaturated solution. As a general rule, it is known that particles of crystalline precipitates formed from more dilute solutions are larger in size (7). The dissolution-precipitation mechanism also predicts that larger $Cd(OH)_2$ crystals should form on discharge at higher temperatures, because the degree of supersaturation of the electrolyte with the soluble complex $Cd(OH)_3^-$ should be less at higher temperatures owing to an increased solubility. This predicted relation between the crystal size and the discharge conditions has been substantiated experimentally, as will be described in the subsequent section. From considerations of surface area effects in conjunction with the solution-reduction mechanism [3] and [4], it can easily be understood why large $Cd(OH)_2$ crystals yield a poor charge acceptance. This mechanism also predicts that for a given electrode with $Cd(OH)_2$ crystals of a given size, the charge acceptance should decrease with increasing charging current and with decreasing charging temperature. These relations have been found experimentally by Gottlieb (2).

Size and shape of $Cd(OH)_2$ *crystals.*—A large number of electron and optical photomicrographs were taken in order to establish the effect of discharge rate

and temperature on the size of cadmium hydroxide crystals. Some examples of transmission electron photomicrographs of actual crystals (dark areas) are reproduced in Fig. 3. Although the crystal size in each plate varies over a wide range, it is clearly seen that the crystals formed at C/20 are much larger on the average than those formed at C/2. It is also seen that the crystals formed at higher temperatures are larger. The crystals produced at C/100 were so large that they were very clearly observable under the light microscope (see Fig. 4).

In both photomicrographs it is seen that the electrodes discharged at −18° and at −30°C contained long, needle-shaped crystals, while the crystals in the electrodes discharged at higher temperatures were all hexagonal and flat. X-ray and electron diffraction analyses showed conclusively that the needlelike crystals are γ-$Cd(OH)_2$, the monoclinic modification (8), while the normal hexagonal ones are β-$Cd(OH)_2$. Typical x-ray diffraction intensity diagrams are shown in Fig. 5. It is seen that no lines corresponding to γ-$Cd(OH)_2$ appeared in the pattern obtained with the electrode discharged at 25°C, while the electrodes discharged at −18° and at −30°C showed many distinct lines corresponding to γ-$Cd(OH)_2$. It is also apparent that more γ-$Cd(OH)_2$ formed at −30° than at −18°C. This is clearly seen also from the light photomicrographs shown in Fig. 4. γ-$Cd(OH)_2$ was identified in all electrodes discharged at −18°C regardless of the rate of discharge (4C to C/100).

Recently, Breiter and Vedder (9) reported that γ-$Cd(OH)_2$ was identified on solid polycrystalline cadmium electrodes oxidized in 1M and 5M KOH at room temperature. In 6.9M KOH and with sintered-plate type electrodes, we found no γ-$Cd(OH)_2$ at room temperature and also at 49°C at all discharge rates studied. In 1M KOH, however, a large number of γ-$Cd(OH)_2$ crystals were formed even at room temperature. As already reported by Breiter and Vedder, γ-$Cd(OH)_2$ is unstable and slowly converted to β-$Cd(OH)_2$ on open-circuit stand in contact with KOH. The conversion is, however, quite slow at room temperature. For example, the appearance of the electrode surface discharged at C/100 at −30°C (Fig. 4, top) did not change appreciably after 10 days' open-circuit stand at room temperature. At 49°C, however, the conversion was considerably accelerated, and no γ-$Cd(OH)_2$ remained only after 3 days' open-circuit stand.

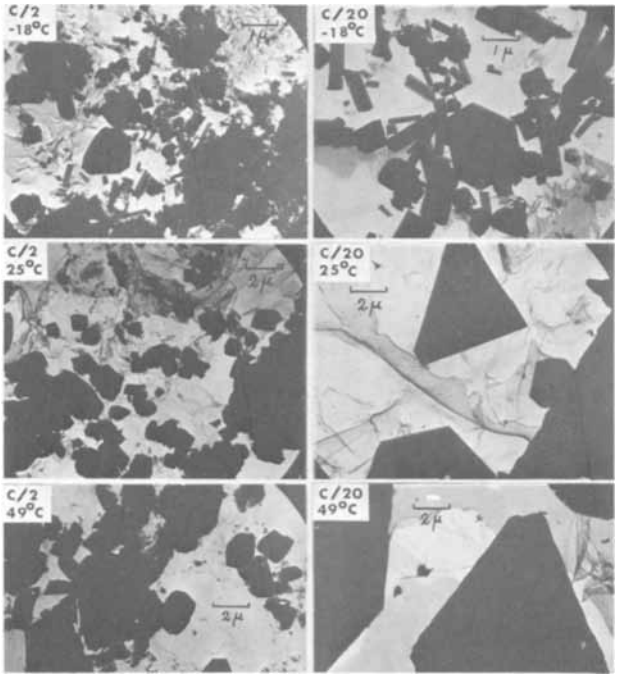

Fig. 3. Transmission electron photomicrographs of $Cd(OH)_2$ crystals formed at various temperatures and discharge rates.

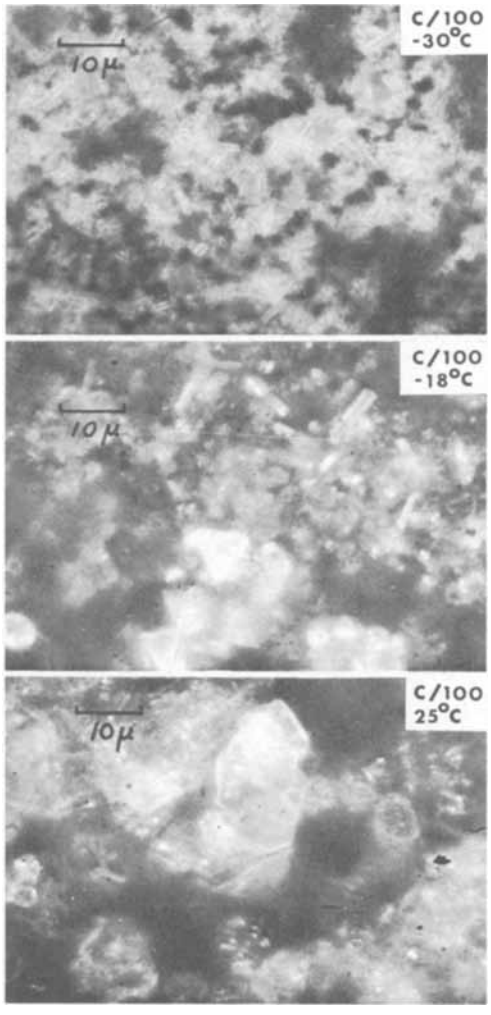

Fig. 4. Optical photomicrographs of $Cd(OH)_2$ crystals formed at the discharge rate of C/100 at various temperatures. Magnification 750 X

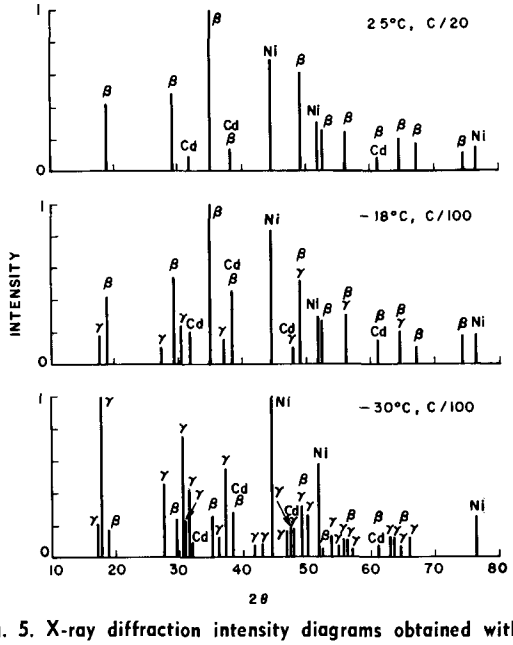

Fig. 5. X-ray diffraction intensity diagrams obtained with electrodes discharged at rates and temperatures shown.

BET surface area.—The information obtained by the microscopic observation pertains only to the surface of the electrode, and there is no assurance that the same relation between crystal size and charge accept-

ance holds for the crystals within the pores of the electrode. Measurement of the total surface area by the BET method should provide a means of comparing the size of crystals within the electrodes. With some samples brown coloration apparently due to the oxidation of undischarged cadmium occurred under the degassing conditions used (50°C, 24 hr). The data for such samples were discarded. In Fig. 6 the charge acceptance at −18°C is plotted against the BET surface area for only those samples which showed no discoloration. The surface area is expressed per gram of the electrode and not of the cadmium hydroxide crystals, since the contribution of cadmium metal particles left undischarged to the total surface area did not vary very much from electrode to electrode. The discharge capacity of all of the electrodes for which the BET measurement was made ranged approximately from 75 to 90% of the theoretical capacity. Thus, the trend shown in Fig. 6 is believed to be attributable to cadmium hydroxide crystals.

It is seen that at constant temperatures (25° and −18°C) the surface area and the charge acceptance were both smaller for electrodes discharged at lower rates. Also, the surface area of the electrode discharged at C/20 at 49° was less than that of the electrode discharged at 25°C at the same rate. The observed effect of discharge rate and temperature on the surface area parallels that on the crystal size, and undoubtedly the general conclusion drawn from the microscopic observation holds also for the crystals within the electrode.

It is significant to note in Fig. 6 that the electrodes discharged at −18° and −30°C had a considerably smaller surface area than those discharged at 25°C and yet exhibited a good charge acceptability. It appears that γ-$Cd(OH)_2$ is more readily chargeable than β-$Cd(OH)_2$ for the same surface area. Breiter and Vedder's experiments with a solid cadmium electrode also indicated that γ-$Cd(OH)_2$ is more easily reduced than β (9). In practical sealed cells, however, there seems to be no way of utilizing the favorable characteristics of γ-$Cd(OH)_2$ because of its instability at higher temperatures. With an electrode containing both β- and γ-phases, it was found that γ-$Cd(OH)_2$ crystals were all converted into the β-form after only a few 50% depth charge-discharge cycles at room temperature. It has been suggested that the active and inactive cadmium hydroxides postulated by Rubin (4) might correspond to the γ- and β-forms. With electrodes containing both γ- and β-$Cd(OH)_2$, however, we failed to observe such two separate potential plateaus as reported by Rubin.

As already described by Gottlieb (2), the greatly reduced charge acceptance is observed only in the first charge after temperature lowering. If the electrode is continuously cycled at the low temperature, the charge acceptance in the second and subsequent charge cycles becomes almost normal. This can be expected from the crystal size effect, because the $Cd(OH)_2$ crystals formed on the second and subsequent cycles should be small since these cycles are carried out at the low temperature. The formation of γ-$Cd(OH)_2$ may also be responsible for the increased charge acceptance.

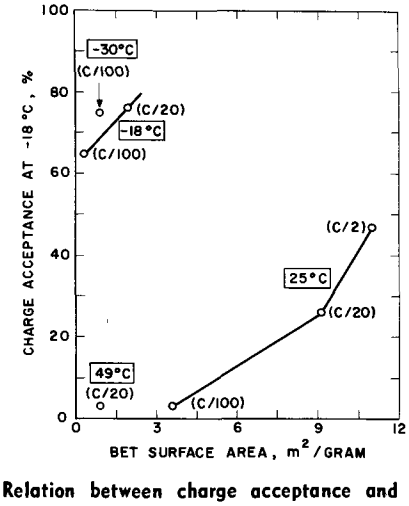

Fig. 6. Relation between charge acceptance and BET surface area. Temperatures and rates shown refer to discharge conditions.

Effect of partial cycles.—All experimental results discussed in the previous sections were obtained with electrodes discharged completely following a full charge. In sealed nickel-cadmium cells, the cadmium hydroxide electrode is not cycled in this fashion but only partially cycled, because the cells are constructed with a large excess capacity in the negative electrode. Effects of such partial cycles on the low-temperature charge acceptance were studied to simulate more closely the conditions encountered by sealed cells. Results are tabulated in Table I. In these experiments, electrodes previously charged completely at the C/2 rate were first discharged at C/20 (exp. 1 to 4) or C/2 (exp. 5 to 8), charged at C/2 until 50% of the discharge capacity was returned, and then fully discharged at various rates. This partial cycle was given at room temperature and only once except for exp. 2, in which 9 partial cycles were given. After the final full discharge, the cells were left on open circuit in a bath maintained at −18°C for 2 hr and charged at the C/2 rate.

The results of exp. 1 to 4 show that under these conditions, the charge acceptance is determined by the rate used for the initial discharge prior to the partial cycle (C/20) rather than the discharge rate used in the partial cycle. These results can be explained in the following manner. Suppose that the size of the $Cd(OH)_2$ crystals formed after the initial C/20 discharge was distributed according to a certain distribution law, for example, the normal law. On partial charge, the size of each crystal must have decreased regardless of the extent of the charge and the "tightness" (the magnitude of the standard deviation) of the distribution, whereas the total number of crystals may or may not have decreased depending on these two factors. Under the present experimental conditions, the total number of crystals appears to have remained essentially unchanged before and after the partial charge, and the $Cd(OH)_2$ crystals of reduced size which existed at the end of the partial charge appear to have grown back to the initial size on completion of the final discharge. This explains the fact that the charge acceptance observed after the partial cycle was nearly the same as that found after the full, straight C/20 discharge. The observed independence of the charge acceptance on the discharge rate used in the partial cycle probably indicates that no new nuclei were formed during the final discharge.

The same explanation applies also to exp. 5 and 6, in which the initial discharge was carried out at C/2. When the final discharge rate used in the partial cycle was very low as compared to the rate used for the initial discharge (exp. 7 and 8), the charge acceptance was considerably lower than that observed after

Table I. Effect of partial cycle (50%) at room temperature on charge acceptance at −18°C (Charge acceptance measured at C/2 rate)

Exp. No.	Rate used for full discharge prior to partial cycle	Partial cycle: Charge rate	Partial cycle: Discharge rate	Charge acceptance found, %: After partial cycle	Charge acceptance found, %: Without partial cycle
1	C/20	C/2	C/2	25	26
2	C/20	C/2	C/2 (9 cycles)	20	
3	C/20	C/2	C/26	33	
4	C/20	C/2	C/50	22	
5	C/2	C/2	C/2	51	57
6	C/2	C/2	C/25	53	
7	C/2	C/2	C/46	37	
8	C/2	C/2	C/100	3	

a straight, full discharge at C/2. This result appears to indicate that the very low rate discharge caused the small crystals initially formed at C/2 to either agglomerate or grow into large crystals.

All results listed in Table I were obtained after 50% depth partial cycles. If the depth of partial cycle is increased sufficiently when the initial discharge rate is low and the final discharge rate is high (*e.g.*, in exp. 1), a better charge acceptance is expected because of the possibility of forming small new nuclei during the final high rate discharge. Experimentally, this was found to occur, but the effect was relatively small until the depth of partial cycle was increased to about 90%. For example, the charge acceptance measured after an 87% partial cycle (C/20 full initial discharge, 87% charge at C/2, and full discharge at C/2) was found to be 36% as compared to 25% after a half depth cycle and 57% after a full depth cycle.

Practical significance of crystal size effect.—Practical significance of various experimental results described here can be summarized as follows:

1. The low-temperature charge acceptance of the negative electrode in sealed cells containing a large excess negative capacity is determined by the size of the excess cadmium hydroxide crystals, and no significant improvement in charge acceptance can be expected by high rate cycles. Consequently, sealed cells should be constructed using negative electrodes with small cadmium hydroxide crystals. Fast rate, low-temperature forming cycles should help produce small crystals.
2. Even if the negative electrode initially contains small crystals, they grow large on open-circuit stand by recrystallization. Since the rate of recrystallization is slower at lower temperatures, cells should be stored at a low temperature if they are not to be used for an extended period of time.
3. Cells in the charged state should not be left on open circuit for a long time, because the charged positive electrode self-discharges slowly to give off oxygen, and the latter discharges the negative electrode at a slow rate, which leads to the formation of large $Cd(OH)_2$ crystals.
4. Extremely low rate discharge should be avoided. This produces large $Cd(OH)_2$ crystals and possibly agglomerates of small crystals.
5. If conditions permit, temperature should be lowered when the cell is in the fully charged state rather than in the discharged state, so that the first operation at the low temperature becomes a discharge and not a charge.

Conclusion

There is little doubt that the size and the structure of $Cd(OH)_2$ crystals play an important role in determining the low-temperature charge acceptance of cadmium hydroxide electrodes. A number of experimental results can be accounted for in terms of these effects in conjunction with the reaction mechanism involving a soluble intermediate species in both the charging and the discharging reactions. However, it cannot be stated that the crystal size and structure effect explains all results. For example, we observed that the charge acceptance decreases to some extent with increasing number of charge-discharge cycles given to the electrode prior to the low temperature charge. This may be due to a redistribution of the active material within the electrode which is known to occur as a result of use (10). More complete understanding of the phenomenon would require a further investigation.

Acknowledgment

The authors are indebted to D. R. Turner and P. C. Milner for suggestions and discussions, and to Miss S. E. Koonce and F. B. Koch for their help in electron microscopy and x-ray diffraction studies.

Manuscript submitted July 28, 1969; revised manuscript received *ca.* Dec. 15, 1969.

This was Paper 50 presented at the Chicago Meeting of the Society, Oct. 15-20, 1967.

Any discussion of this paper will appear in a Discussion Section to be published in the December 1970 JOURNAL.

REFERENCES

1. M. H. Gottlieb and T. H. Willis, *Electrochem. Technol.*, **4**, 515 (1966).
2. M. H. Gottlieb, *ibid.*, **5**, 12 (1967).
3. P. V. Popat and E. J. Rubin, Abstract 47 in Extended Abstracts of Papers Presented at the Philadelphia Meeting of the Society, Oct. 9-14, 1966.
4. E. J. Rubin, Abstract 51 in Extended Abstracts of Papers Presented at the Chicago Meeting of the Society, Oct. 15-19, 1967.
5. P. C. Milner and U. B. Thomas, in "Advances in Electrochemistry and Electrochemical Engineering," C. W. Tobias, Editor, Vol. 5, Interscience Publishers, New York, 1967.
6. Y. Okinaka, *This Journal*, **117**, 289 (1970).
7. See, for example, I. M. Kolthoff and E. B. Sandell, "Textbook of Quantitative Inorganic Analysis," Chap. VII, The Macmillan Co., New York (1952).
8. P. M. de Wolff, *Acta Cryst.*, **21**, 432 (1966).
9. M. W. Breiter and W. Vedder, *Trans. Faraday Soc.*, **63**, 1042 (1967).
10. E. Lifshin and J. L. Weininger, *Electrochem. Technol.*, **5**, 5 (1967).

The Effect of Lead Ions on the Dissolution and Deposition Characteristics of a Zinc Single Crystal in 6*N* KOH

F. Mansfeld*[1] and S. Gilman*

National Aeronautics and Space Administration, Electronics Research Center, Cambridge, Massachusetts

ABSTRACT

Dissolution of the basal plane of single crystal zinc and deposition of zinc on the same material in alkaline solutions in the presence of 10^{-4}M lead ion, has been studied using *in situ* microscopy and the scanning electron microscope (SEM). It was found that in the presence of lead ions, most of the surface was protected against dissolution when polarized as much as 100 mV positive to the rest potential. Dissolution occurs initially in the form of a limited number of hexagonal etch pits that grow in size and number with time. The pits appear to correspond to sites of macroscopic crystalline imperfection.

In the absence of Pb ions, deposition of Zn on the basal plane of a zinc crystal tends toward epitaxial growth at low overpotentials. In the presence of Pb ions, at both high and low overpotentials, Zn deposition tends to initiate mainly at the few sites not protected by the microscopically smooth Pb film. At high overpotentials, growth tends to be cylindrical and microcrystalline, rather than dendritic. It is shown that, under the present conditions, no increase in the cathodic current is to be expected with increase of time.

The alkaline zinc electrode is encountered in several commercial and proposed aqueous battery devices. Its attractiveness as a uniquely high-energy anode material (for aqueous systems) is diminished by such concomitant problems as poor quality of the electrodeposit (secondary battery application) and corrosion of zinc. The use of additives incorporated into the anode, or dissolved in solution, has been proposed over the years and evaluated empirically. Most of the research effort in this area has been concentrated at industrial laboratories.

The use of Pb and Sn ion additions to the electrolyte as suggested earlier by Kudryavtsev is quoted in (1). The use of Pb ions was again investigated by Oxley and Fleischmann (2) who found that the deposit adherency on polycrystalline Zn increased when lead acetate was added at an optimum concentration of 0.5 g/l to a solution of 43% KOH, 1.13M in zinc ions. The reason for the influence of lead on deposit adherency was unclear.

Recently Bockris *et al.* (3) claimed that "the presence of 10^{-4} molar lead completely suppresses dendrites." This conclusion was reached, however, only from the change of the total current density with time without microscopical observation of the actual deposit.

At this laboratory an investigation of the effect of additives, especially lead, on dissolution and deposition characteristics of single crystal zinc has been carried out using the light microscope in a way similar to Powers' experiments (4, 5) and the scanning electron microscope as demonstrated by Naybour (6, 7). Powers studied deposition of zinc on the basal plane of a single crystal of zinc and on polycrystalline material (4) and, with Breiter (5), dissolution and passivation of the basal plane. Naybour investigated the effect of substrate orientation on growth (6) as well as the effect of electrolyte flow on the morphology of zinc deposits (7). Both optical methods have not been used previously in investigations of the effects of additives.

The effect of metal cations, anions and neutral molecules on the hydrogen evolution rate of polycrystalline zinc in 6*N* KOH and rate of hydrogen evolution of Zn-Pb and Zn-Al alloys will be reported in a separate paper. (12).

* Electrochemical Society Active Member.
[1] Present address: North American Rockwell, Thousand Oaks, California 91360.

Experimental

The zinc electrodes were obtained by cleavage from single crystal rods grown from 99.9995% pure zinc. The crystal was cooled to liquid nitrogen temperature and then cleaved and rewarmed in a drybox under argon. The cell used for microscopic observation under polarization was similar to that used by Powers (4), with the only significant modification being to the window of the optical coverglass. The coverglass was fused to the Pyrex sleeve thereby avoiding the use of adhesives which dissolve more or less rapidly in KOH. The reference electrode was a zinc rod (99.95%), the counterelectrode was gold foil. The zinc electrode potential was controlled by a Tacussell potentiostat and monitored by a Keithley electrometer. The current was recorded on a Moseley strip-chart recorder. The microscope was by Reichert, Austria, used mainly with Nomarski interference contrast.

The solution of 6*N* KOH + 20 g/l ZnO was made up from reagent grade KOH and bidistilled water using a quartz still and ZnO, "pure" (99.9%). Lead was added in the form of the acetate salt in a concentration of 1 x 10^{-4}M. Previous experiments with addition of 10^{-4}M acetic acid had shown that the acetate ion has no effect on deposition characteristics.

Results

Anodic dissolution.—In the investigation of the effect of lead on anodic dissolution of the basal plane of zinc, a constant potential of +75 or +100 mV *vs.* zinc in the same solution was applied after the specimen had been in contact with the solution for 5 min. In the absence of lead the surface changes in the same way as on cathodic deposition (4), the difference of course being dissolution of the surface. This indicates that dissolution and deposition occur at the same sites, probably screw dislocations. After about 60 sec one observes pits in the form of hexagonal pyramids (Fig. 1). These hexagonal pits cannot be observed with dark field methods and are consequently not visible in the paper of Powers and Breiter (5), (Fig. 2). Addition of 10^{-4}M lead to the electrolyte does not result in a perceptible coating of lead on the zinc surface (*c.f.*,

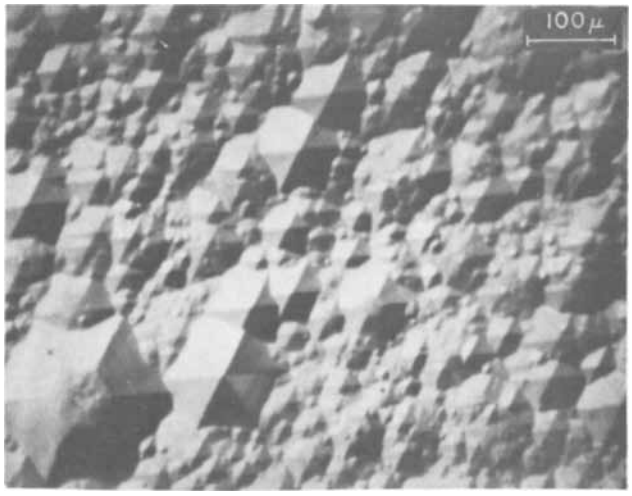

Fig. 1. Anodic dissolution of zinc, (0001) plane at +100 mV in 6*N* KOH + 20 g/l ZnO after 60 sec. Nomarski Interference Contrast (NIC), 110X.

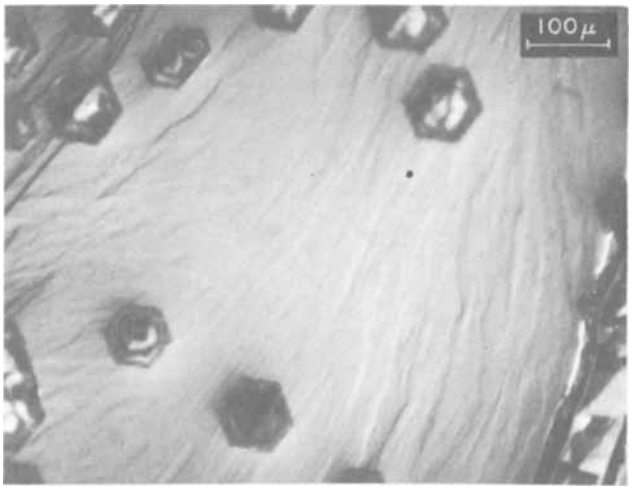

Fig. 2. Anodic dissolution of zinc, (0001) plane at +100 mV in 6*N* KOH + 20 g/l ZnO + 10^{-4}M PbAc after 240 sec. NIC, 110X.

Fig. 2), but does have a profound effect on the anodic dissolution characteristics. After applying the anodic potential hexagonal pits are observed which grow in size and number (Fig. 2). They are very numerous at more macroscopic defects of the crystal such as cracks introduced by cleavage (see right corner of Fig. 2). This difference in dissolution is also reflected in the different change of current with time (Fig. 3). With no additions, the current rises sharply and then decays; with additions, it increases slowly with the number

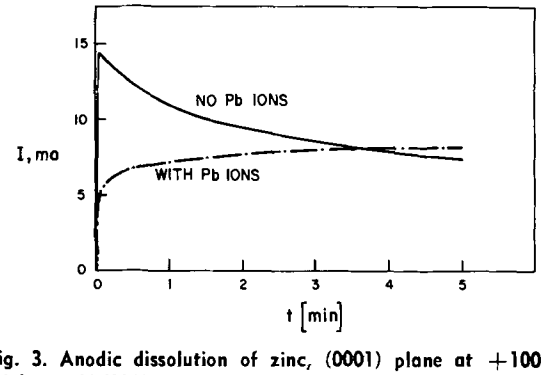

Fig. 3. Anodic dissolution of zinc, (0001) plane at +100 mV. Solid line, 6*N* KOH + 20 g/l ZnO; dashed line, 6*N* KOH + 20 g/l ZnO + 10^{-4}M PbAc. Geometric area of electrode = 0.178 cm^2.

and size of pits. Observation with the scanning electron microscope (SEM) shows that the pits are shallow, have a flat bottom and stepped sides (Fig. 4). The sides of all pits are parallel to [11$\bar{2}$0]. These pits occur probably on sites with macroscopic damage or irregularities of the crystal as can be seen from Fig. 5. The crystal was left at the open-circuit potential for 2 hr. A number of hexagonal pits were observed; they were

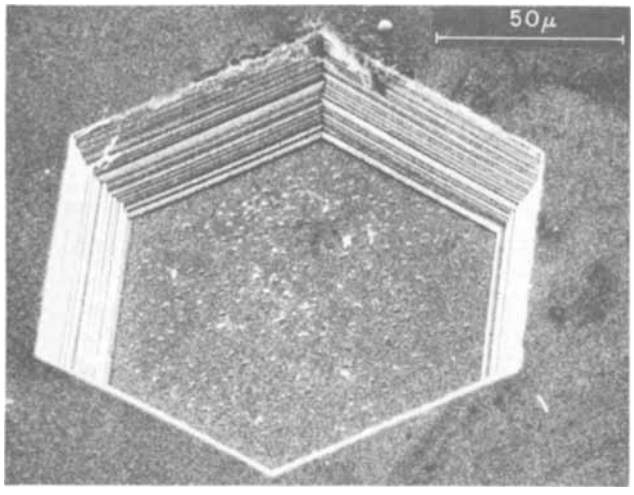

Fig. 4. Pit produced in experiment of Fig. 2 after 300 sec scanning electron microscope (SEM), 480X, 45°.

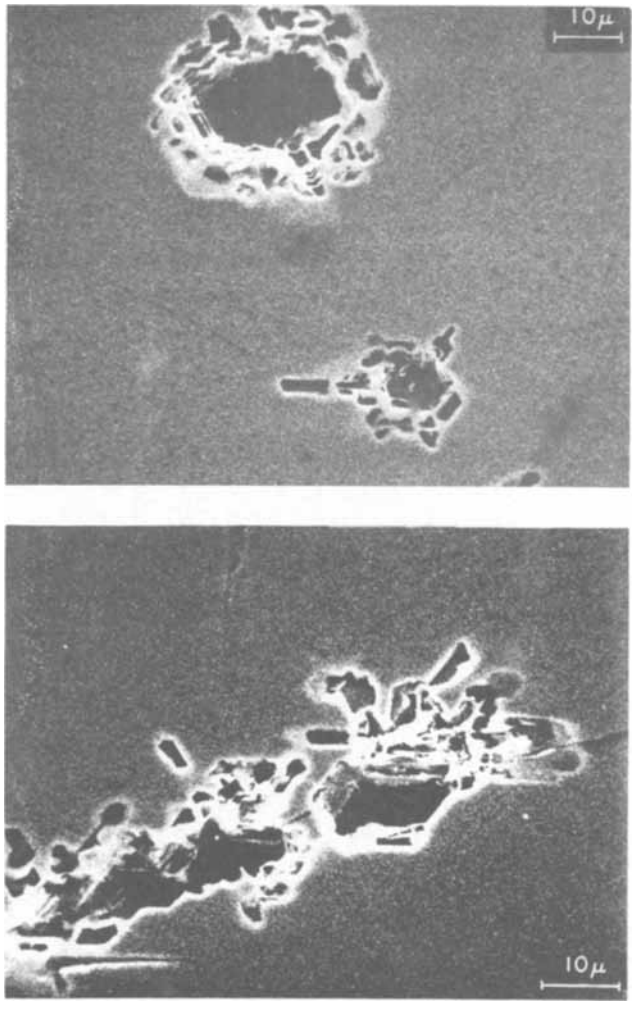

Fig. 5. Pits formed at the corrosion potential after 2 hr in 6*N* KOH + 10^{-4}M PbAc. SEM. (a) (top) 840X; (b) (bottom) 1000X.

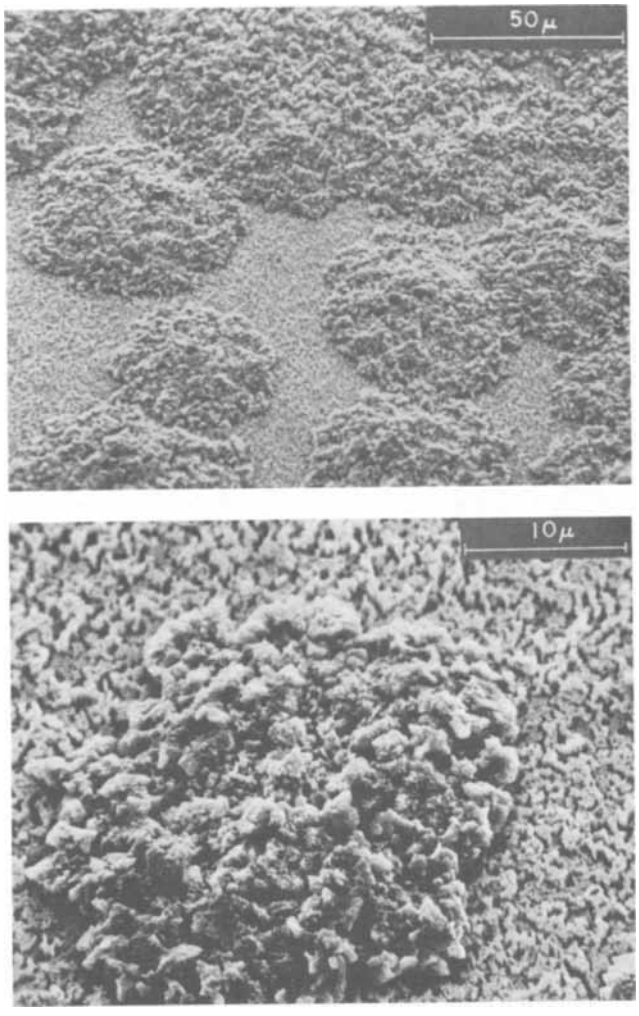

Fig. 6. Deposit at —100 mV from 6*N* KOH + 20 g/l ZnO + 10^{-4}M PbAc after 617 sec, SEM, 45°. (a) (top) 500X; (b) (bottom) 2080X.

concentrated at cracks in the surface like the one in Fig. 5b. These macroscopic defects serve as anodes, where zinc dissolves, while Pb (and hydrogen) plate out on the cathodes.

Cathodic deposition.—Cathodic deposition on the basal plane of zinc was carried out from a solution of 6*N* KOH + 20 g/l ZnO with or without additions of 10^{-4}M lead acetate at potentials of —100 or —200 mV *vs.* zinc in the same solution. The results without additions of lead were the same as already shown by Powers (4): at —100 mV the deposit was in the form of pyramids, the number of which declines with time as the more active pyramids cover the less active ones. No classical dendrites were observed at this potential even after 1 hr of plating, although a number of small protrusions were observed.[2] At —200 mV the number of growth centers was much larger and after a short time dendrites with side branches occurred. If the potential is held at —100 mV for about 30 min and then changed to —200 mV, a large number of new growth centers appear on the sides of the previously formed pyramids. After some time dendrites are observed. If the potential is brought back to —100 mV after 1 or 2 min at —200 mV, the growth centers formed at —200 mV disappear while the pyramids continue to grow.

The effect of lead additions is shown in Fig. 6 for deposition at —100 mV. It can be seen from Fig. 6a that two different types of deposit are obtained: little bumps or hills consisting of many little crystallites and flat areas consisting of a very large number of pipes growing perpendicular to the surface. Figure 6b shows both types at a higher magnification.

Figure 7 shows the deposit at —200 mV from the same solution. The deposit is completely different from that obtained in the absence of lead (classical dendrites), it reminds one of corals. The deposit consists of a very large number of crystallites, the structure of the protrusions and of the flat areas of the surface seem to be the same. Figure 7c is a magnification of one of the flat areas. The depression corresponds to blockage of deposition by a hydrogen bubble. In order to obtain additional information about the effect of lead additions, an experiment was conducted with

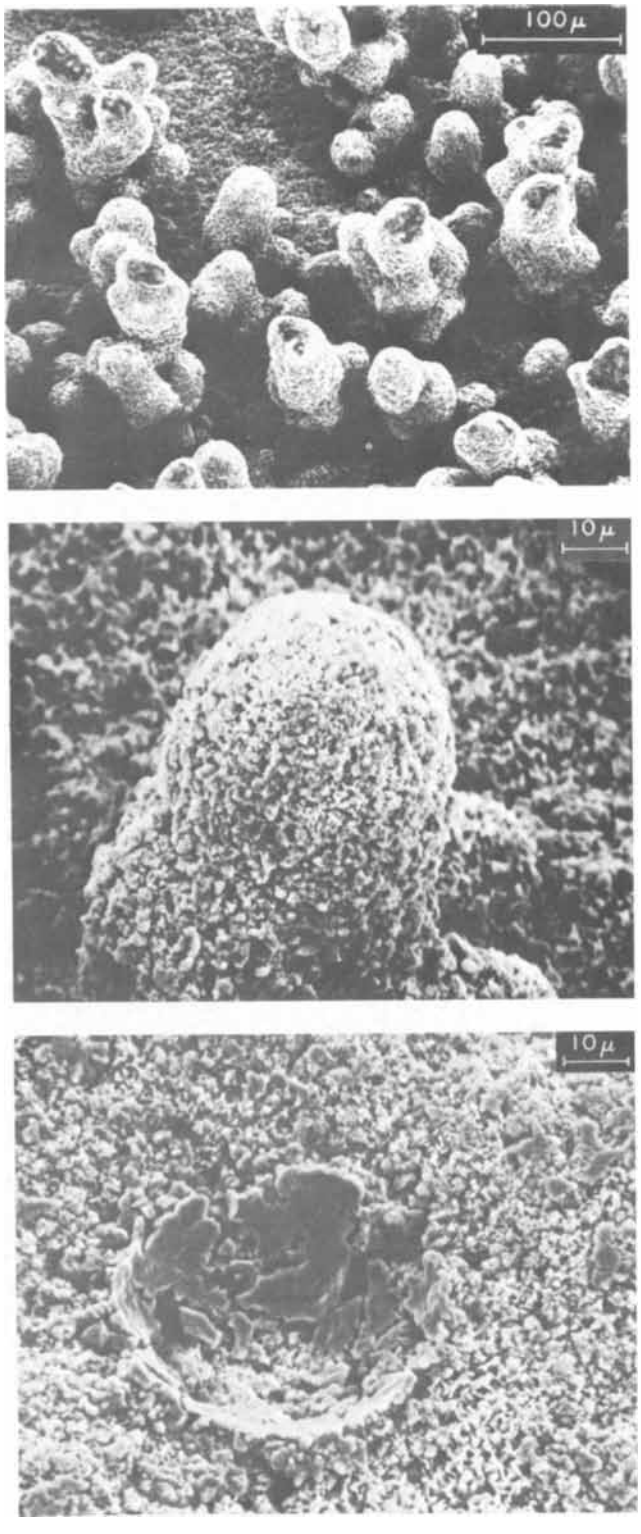

Fig. 7. Deposit at —200 mV from 6*N* KOH + 20 g/l ZnO + 10^{-4}M PbAc after 3600 sec, SEM, 45°. (a) (top) 180X; (b) (center) and (c) (bottom) 800X.

[2] The nature of these protrusions has been studied in more detail in (13).

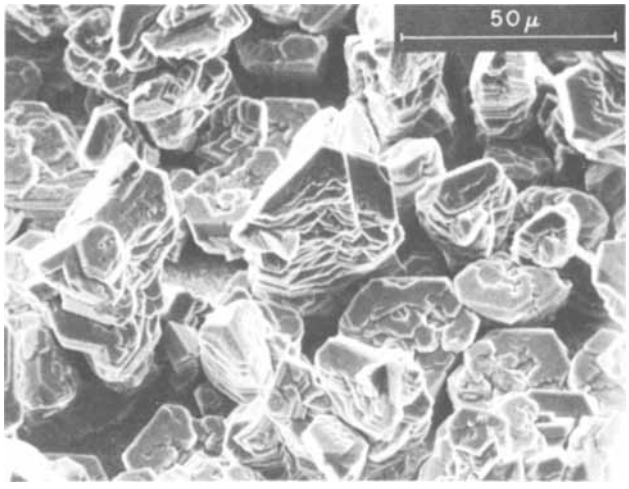

Fig. 8. Deposit at −100 mV: 60 sec in 6*N* KOH + 20 g/l ZnO + 10^{-4}M PbAc, followed by 3600 sec in 6*N* KOH + 20 g/l ZnO, SEM, 45°. 560X.

deposition at −100 mV for 1 min in a solution containing 10^{-4}M of lead, followed by additional deposition in lead-free solution. Figure 8 shows the deposit obtained at −100 mV after 1 hr of plating in the latter solution. The deposit is different from that obtained with addition of lead ions; it is similar to the protrusions observed in lead-free solutions after longer plating times (13). The protrusions are clearly crystalline with layer growth parallel to the surface but also with planes having an angle to the main crystallographic axis (center of Fig. 8).

Experiments where deposition at −100 mV in 6*N* KOH and 20 g/l ZnO was followed by deposition in the same solution with addition of lead ions produced deposits very similar to the ones shown in Fig. 6. The flat areas of the surface are again covered with pipe-shaped growths of varying length (Fig. 9). Deposition at −200 mV produced deposits similar to the ones shown in Fig. 7.

Discussion

Our results clearly show that the addition of lead ions to a solution of KOH containing zincate strongly affects anodic dissolution of the basal plane of a zinc single crystal and deposition of zinc on the same specimen. Without an externally applied potential, a microscopically smooth lead coating is deposited on the zinc surface while zinc dissolves on the anodic sites, which are thought to be major defects of the crystal (Fig. 4). If an anodic potential is applied, the crystal only dissolves at these latter sites, the other sites, which are active during dissolution in lead-free solutions (Fig. 1), are blocked and protected by lead. The pits observed after dissolution for 5 min are all rather shallow and all seem to have the same width. They are oriented with their edges parallel to $[11\bar{2}0]$ which implies that $(11\bar{2}0)$ dissolves faster than $(10\bar{1}0)$ and this in turn faster than (0001), in parallel with increasing packing density. Ashton and Hepworth (8) came to the same conclusion by measuring anodic polarization curves on the (0001), $(10\bar{1}0)$, and $(11\bar{2}0)$ plane of zinc in 0.5 NaOH.

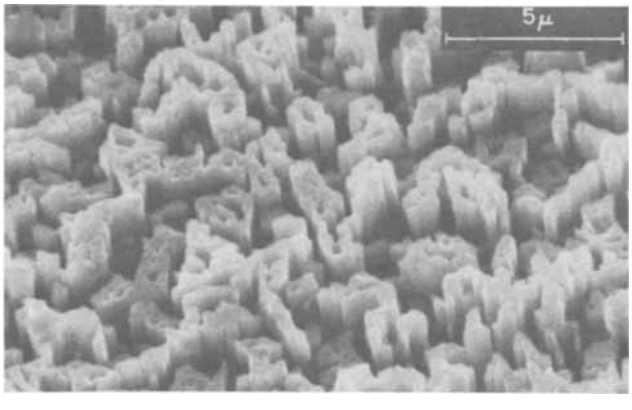

Fig. 9. Deposit at −100 mV: 150 sec in 6*N* KOH + 20 g/l ZnO followed by 1200 sec in 6*N* KOH + 20 g/l ZnO + 10^{-4}M PbAc, SEM, 45°. 4600X.

The results of deposition in lead-free solutions suggest that at the less negative potential (−100 mV) and lower deposition currents, the zinc particles diffuse on the surface to growth sites leading to pyramid growth. At more negative potentials (−200 mV) and higher deposition currents, the rate of arrival of zincate ions is higher than the rate of diffusion to growth sites, the zinc adatoms "inhibiting" their own diffusion. This results in dendritic growth. The results obtained by switching the potential from −100 to −200 mV (new nuclei, dendritic growth) and switching from −100 to −200 mV and after a short time back to −100 mV (disappearance of nuclei formed at −200 mV) support this scheme.

From our observations of the anodic dissolution of zinc in the presence of lead it follows that most of the sites for dissolution are blocked by lead. If it can be assumed that the sites for deposition and dissolution are the same, namely screw dislocations (9), then one would expect that growth on these sites is also blocked by lead. In addition it is possible that the presence of lead changes deposition characteristics from the crystallographic form of dendrites (according to Naybour (7) both tip and side branches of a dendrite grow in the $[11\bar{2}0]$ direction, the main stem and the side branches being monocrystalline) to protrusions which are no longer monocrystalline but consist of a large number of small crystals. In fact, the results of Fig. 6 and 7 show that parts of the surface are inactive for growth; the areas of larger growth consist of a large number of very small crystallites. The results of Fig. 8 show indeed that lead blocks parts of the surface, subsequent growth in lead-free solution exhibits crystalline growth again, the deposit growing mainly in the vertical direction, while large areas remain active. The nature of the sites for growth under these conditions is not known, but it seems possible that the same physical defects (or impurity centers) that act as anodes on dissolution in the presence of lead act as growth sites in deposition. Vaughan and Pick (10) assumed that copper nucleation sites were impurity centers, physical defects acting as preferred sites for impurity segregation. Although Naybour (6) showed that the number of surface defects on a zinc crystal was less than the number of growth sites, conditions are different in the present case where more surface defects are produced through local action currents. Figure 7 also shows that no classical dendrites are obtained when lead is present in the solution most likely due to incorporation of lead. There seems to be no major difference in the structure of the deposit at −100 and −200 mV in solution containing lead (Fig. 6b and 7b), the little bumps growing to larger protrusions with time under diffusion control. The nature of the pipe-like structure in Fig. 6 and Fig. 9 is not known at the present.

The conclusion of Bockris *et al.* (3) that lead addition suppresses dendrites is correct only in so far as the protrusion is not a monocrystal anymore but consists of many small crystallites. The lack of a parabolic increase of current with time as observed in (3) might be due to a lack of dependency of the diffusion current upon a radius of curvature of the substrate (11) in the case of lead additions, growth probably being linear-diffusion controlled for the type of protrusions shown in Fig. 7. A parabolic or exponential increase of current with time as observed by Bockris and co-workers (3, 11) seems questionable, however, since it was not observed by Powers (4) and in the present work in solutions free of lead ions. It could

result from the special preparation of the electrodes in (11) which consist of zinc electrodeposited on small Pt spheres and which are quite different from the much larger (0.495 cm^2) single crystal plane used in (4) and the present work. It should be remembered also that the parabolic increase of current with time in the treatment of Bockris *et al.* (11) results from the assumption that dendrite initiation is continuous, but from Naybour's (6) work it seems that dendrite initiation is instantaneous.

The small increase of current with time while dendrites grow in lead-free solutions observed in (4) and the present work results most likely only from an increase in total area as the dendrites penetrate the diffusion layer. In the presence of lead the current does not change appreciably after about 60 sec of deposition at −200 mV. The protrusions produced in this experiment have a cylindrical shape and grow perpendicular to the base contrary to real dendrites. From Table I which gives some average parameters of those protrusions it can be seen that the largest protrusions have reached a length comparable to the thickness of the diffusion layer, which is calculated to be 0.03 to 0.003 cm by using a limiting c.d. of 35 mA/cm^2 and a value of the diffusion coefficient of 2×10^{-5} to 2×10^{-6} cm^2 sec^{-1} (2). It follows that no substantial increase in area and therefore in current is expected as protrusions grow.

Conclusion

The presence of small amounts of lead ions in an alkaline solution markedly changes the anodic dissolution behavior of the basal plane of zinc by blocking most of the active sites for dissolution. Its presence also changes deposition characteristics from monocrystalline dendrites to protrusions consisting of many small crystals while large parts of the surface are inactive for deposition. It is concluded that, in the presence of lead, dissolution and deposition occurs at more macroscopic physical defects of the crystal.

It is possible that other metal ions which have a reversible potential sufficiently more noble than zinc act in a similar way. It is not entirely clear at the present how the above results apply to secondary batteries. The change in deposit morphology is certainly beneficial since no sharp dendrites result which would penetrate separators. It remains to determine what happens to the lead additions through cycling of a battery. The beneficial effect of lead ions in the electrolyte or lead alloyed in small amounts to zinc on hydrogen evolution will be reported in a separate paper (12).

Table I. Typical parameters for protrusions in experiment Fig. 7

Height	$(1.6 \pm 0.1) \times 10^{-2}$ cm
Radius	$(2.0 \pm 0.2) \times 10^{-3}$ cm
Particles/cm^2	$(1.5 \pm 0.2) \times 10^{4}$

Acknowledgment

One of the authors (F.M.) wishes to acknowledge support under a National Academy of Sciences Research Associateship. Scanning electron micrographs were taken with the help of Mr. J. Herman of Professor Ogilvie's laboratory, Massachusetts Institute of Technology. We are grateful to Mr. A. Pinella for metallurgical services and for helpful discussions, and to Dr. R. W. Powers for providing drawings of the Teflon cell used in light microscopy.

Manuscript submitted Oct. 8, 1969; revised manuscript received Jan. 19, 1970.

Any discussion of this paper will appear in a Discussion Section to be published in the December 1970 JOURNAL.

REFERENCES

1. J. E. Oxley, NASA Contract Report NASA CR-377, Contract NAS 5-3908, February 1966.
2. J. E. Oxley and C. W. Fleischmann, Quarterly Report No. 3, NASA Contract No. NAS 5-9591, March 1966.
3. J. O'M. Bockris, J. W. Diggle, and A. Damjanovic, First Quarterly Report to NASA, Contract NGR 39-010-002, 1-1-69 to 3-31-69.
4. R. W. Powers, *Electrochem. Technol.*, **5**, 429 (1967).
5. R. W. Powers and M. W. Breiter, *This Journal*, **116**, 719 (1969).
6. R. D. Naybour, *Electrochim. Acta*, **13**, 763 (1968).
7. R. D. Naybour, *This Journal*, **116**, 520 (1969).
8. R. F. Ashton and M. F. Hepworth, *Corrosion*, **24**, 50 (1968).
9. H. Gerischer and R. P. Fischer, *Z. Elektrochem.*, **61**, 1159 (1957).
10. F. B. Vaughan and H. J. Pick, *Electrochim. Acta*, **2**, 179 (1960).
11. J. W. Diggle, A. R. Despic, and J. O'M. Bockris, Paper 375 presented at the Montreal Meeting of the Society, Oct. 6-11, 1968.
12. F. Mansfeld and S. Gilman, submitted for publication in *This Journal*.
13. F. Mansfeld and S. Gilman, Short communication, in preparation.

Direct Current-Voltage Characteristics of Calcia Stabilized Zirconia with Porous Platinum Electrodes

Hiroaki Yanagida,[1] R. J. Brook,[2] and F. A. Kröger*

University of Southern California, Los Angeles, California

ABSTRACT

The direct current-voltage characteristics of symmetrical cells Pt, O_2(I), $|Zr_{0.85}Ca_{0.15}O_{1.85}|$Pt, O_2(II), with pO_2(I) = pO_2(II), were measured at 560°C under oxygen pressures from 1 to 10^{-20} atm. The characteristics were nonohmic, the deviation from ohmic law being mainly due to the potential drop at the cathode interface between the solid electrolyte and the gas ambient. The characteristics consist of two parts. The first is characterized by a marked oxygen pressure dependence and is observed at voltages lower than approximately 2V (weak polarization). In this range, the rate-determining process is the diffusion of oxygen atoms (resulting from dissociation of O_2 or H_2O) through the platinum of the Pt paste electrode. The second part of the characteristic is almost independent of the oxygen pressure and is observed at voltages higher than approximately 2V (strong polarization). Here the rate-determining step is the process in which neutral oxygen atoms, adsorbed at the cathode surface of the electrolyte, combine with effectively neutral oxygen vacancies V_O^x, (oxygen ion vacancies which have trapped two electrons) to form a normal O^{2-} lattice ion (O_O^x). This process utilizes the part of the electrolyte surface not in contact with the platinum, but close to points where the platinum makes contact, and involves migration of electrons from the platinum over the surface of the electrolyte.

Stabilized zirconia with the composition $Zr_{0.85}Ca_{0.15}O_{1.85}$ crystallizes in the CaF_2 structure (1, 2) and contains 7.5% extrinsic vacant oxygen sites (2, 3). The electrical conduction at high temperature in air or oxygen is ionic in nature and is due to the migration of oxygen ions by a vacancy mechanism (2-4). The vacancies involved are oxygen ion vacancies with an effective charge +2, $V_O^{\cdot\cdot}$ (5). At lower oxygen pressures, however, electronic conduction sets in (2, 5, 6). An ionic transference number t_i is defined by

$$t_i = \sigma_i/(\sigma_i + \sigma_e) \qquad [1]$$

where σ_i is the ionic and σ_e the electronic conductivity. The value of the oxygen pressure at which this transference number is 0.5 is a function of temperature (2, 6) and varies from sample to sample (4). Typical values of $(pO_2)_{0.5}$ for stabilized zirconia of the composition given above are 10^{-42} atm at 560°C, 10^{-32} atm at 800°C, 10^{-26} atm at 940°C (2). A galvanic cell with platinum electrodes and stabilized zirconia as a solid electrolyte operated with different oxygen pressures at the two sides, gives an open circuit emf E_{open} given by (2, 7)

$$E_{open} \equiv E_{II} - E_I = \frac{1}{4F}\int_I^{II} t_i(\mu O_2)\, d\,\mu O_2 = \frac{RT}{4F}\int_I^{II} t_i\,(pO_2)\, d \ln pO_2 \qquad [2]$$

where $\mu O_2 = RT \ln pO_2$. The cell can be used as a fuel cell or a solid-state battery (8) and also as an oxygen pressure monitor (7).

The emf arises as a consequence of the simultaneous migration of ionic and electronic defects. In the stationary state, the total electrical current carried by these defects at open-circuit voltage must be zero, and therefore the electronic current j_e and the ionic current j_i must be equal and opposite

$$J = j_e + j_i = 0 \text{ or } j_e = -j_i \neq 0 \text{ at } V = E_{open} \qquad [3]$$

The ionic current is stopped by the application of a voltage E_{stop} (9, 10) given by

$$E_{stop} = \frac{1}{4F}[\mu O_2(II) - \mu O_2(I)] \qquad [4]$$

Since $t_i \leq 1$ comparison of [2] and [4] shows that

$$E_{stop} \geqq E_{open} \qquad [5]$$

Application of a voltage higher than E_{stop} causes oxygen ions to move through the electrolyte from the lower oxygen pressure side toward the higher pressure side, and thus oxygen gas is pumped from the side of lower oxygen pressure to the side of high oxygen pressure (11-13). The oxygen pump not only pumps O_2, but can also decompose H_2O (11) and CO_2 (13). If ionic currents flow, and as seen above this is true in all cases unless $V = E_{stop}$, the chemical potential of oxygen in the electrolyte at the cathode surface (where oxygen is taken up) is lower than that of its gas ambient, and the chemical potential of oxygen in the electrolyte at the anode surface (where oxygen gas is evolved) is higher than that of its gas ambient. These potential drops, if appreciable, must be expected to reduce the accuracy of oxygen pressure monitor cells and the efficiency of fuel cells or oxygen pump cells. Their presence is indicated by the nonohmic character of the current-voltage characteristics; such nonohmic effects have been observed with several ionic conductors (12-15). It is the purpose of the present study to investigate the current-voltage characteristics of calcia stabilized zirconia in order to gain insight into the processes taking place at the electrodes. In this study, mainly symmetrical cells with pO_2(I) = pO_2(II) and $J = 0$ at $E_{stop} = 0 = E_{open}$ have been used. This was done to avoid possible complications arising from the ionic current inside the electrolyte in asymmetrical cells at $J = 0$ [see (3)]. Asymmetrical cells were only used to separate the effects of anodic and cathodic potential drops. The oxygen pressure of the gas ambient under which the measurements were made was between 10^{-20} and 1 atm.

* Electrochemical Society Active Member.
[1] Present address: Department of Industrial Chemistry, University of Tokyo, Hongo, Tokyo, Japan.
[2] Present address: British Atomic Energy Authority, Harwell, England.

Experimental Procedures

Sample preparation.—Zirconium dioxide was made by slow calcination of zirconium tetra-acetyl-acetate (supplied by Matheson Coleman and Bell Company) at 800°C in air. Major impurities present in the acetate were [in weight per cent (w/o)]: 0.15 SiO_2, 0.005 Fe_2O_3, 0.003 Al_2O_3, 0.003 MgO, 0.003 TiO_2, 0.004 (Na_2O + K_2O). The ignition loss was 71.23 w/o. Calcium carbonate supplied by Mallinckrodt was used as a source of calcia. For this, the maximum limits of major impurities, given in weight per cent, are: 0.10 Na, 0.10 Sr, 0.02 Mg, 0.01 K, 0.005 Ba. Zirconium dioxide and calcium carbonate powders were weighed to give the composition (0.15 CaO + 0.85 ZrO_2), mixed in an agate mortar for 2 hr, and pressed to pellets. The pellets were heated in dry Argon gas at 1900°C for 2 hr in an induction furnace with a graphite crucible. The pellets as fired showed a brown color. The color disappeared on heat-treatment in air at 800°C. X-ray analysis showed the diffraction pattern of the fluorite structure only. The pellets in their final state were 1 mm thick and 10 mm in diameter.

Experimental set-up.—The specimen, whose characteristic was to be studied, was kept in a stabilized zirconia tube through which a carrier gas (5 ml/sec) containing various amounts of oxygen was circulated. The experimental set-up is shown schematically in Fig. 1. Nitrogen gas was used as the carrier gas and was found to contain $\approx 10^{-4}$ oxygen as an impurity. In addition water vapor was present. The oxygen content was varied by passing the gas through an oxygen pump cell consisting of stabilized zirconia as a solid electrolyte with platinum paste electrodes (11-13). The oxygen pressure was reduced by applying to the pump cell, operated at 670°C, a voltage higher than E_{stop} corresponding to the two oxygen pressures, $pO_2(I) \approx 10^{-4}$ atm (N_2) and $pO_2(II) \approx 0.2$ atm (air). The oxygen pressure was increased by applying a voltage smaller than E_{stop}. To reduce the amount of water vapor in the gas ambient around the test specimen, a liquid nitrogen cold trap was used with the trap usually at position A. Some measurements were carried out without the trap to find the effects of water vapor.

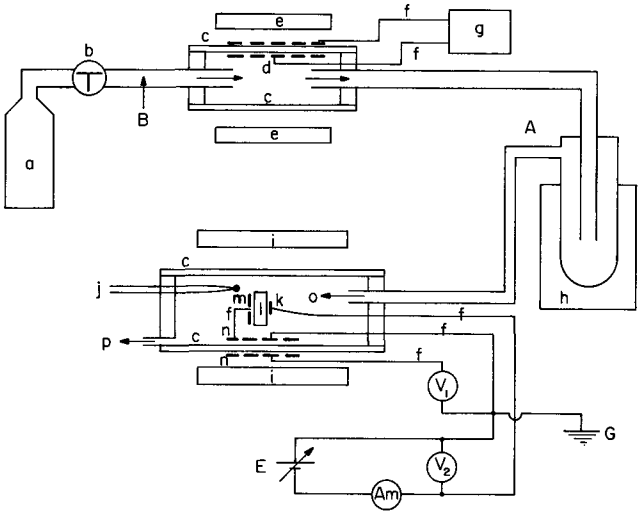

Fig. 1. Experimental set-up. a, inert gas bottle; b, cock and flow meter; c, stabilized zirconia tube; d, platinum paste electrodes for oxygen pump; e, oxygen pump furnace; f, platinum leads; g, d-c power supply for oxygen pump; h, liquid nitrogen cold trap; i, furnace for *I-V* characteristic measurements; j, thermocouple; k, platinum paste cathode; l, test specimen; m, platinum paste anode; n, platinum paste electrodes for oxygen pressure monitoring; o, gas input; p, gas outlet; V_1, volt meter for oxygen pressure monitoring (Cary 31); V_2, volt meter for *I-V* characteristic measurements (Cary 31); Am, d-c power supply and voltage regulator; G, ground; A, position of the liquid nitrogen trap used in most of the experiment; B, alternative position of the cold trap.

Some measurements were also done with the trap at position B rather than at A. The oxygen pressure around the specimen was monitored by a zirconia cell using the wall of a commercial Zircoa B grade stabilized zirconia tube with the composition $(ZrO_2)_{0.90}(CaO)_{0.10}$ as the electrolyte.

The test specimen was provided with platinum paste electrodes at the two sides. The platinum paste was prepared using a submicron platinum powder and an organic suspending medium. At one side the paste covered much of the surface specimen (5-20 mm^2); at the other side the electrode had an area of ≤ 1 mm^2. Contact to the electrodes was made by spring loaded platinum wires (0.01 in. diameter) which were dipped in platinum paste prior to their application to the electrodes.

The specimen with electrodes and contacts in place was heated to 800°C for about ½ hr in order to remove the organic material and to sinter partially the platinum powder. The microscopic configuration of the contact is shown schematically in Fig. 2. The platinum has a spongelike structure with interconnected gas channels. It makes direct contact with the zirconia over part of the surface, leaving a gas-zirconia contact over the remaining surface area. Lines where the triple contact platinum-zirconia-gas occurs are indicated by T. Usually only half of the characteristic will be reported, *viz.*, that half for which the small area electrode is the cathode.

The voltage differences between the electrodes of the oxygen pressure monitor cell and between those of the test specimen (pellet) were measured with a vibrating reed electrometer (Cary 31, Applied Physics Corporation). The current through the specimen was measured with the aid of a Keithley 610B multipurpose electrometer. The voltage applied over the specimen was changed with a voltage divider, Dekavider DV-412 (Electro-Measurements, Inc.). A Burgess 5156 (Clevite Corporation) dry battery was used as a direct current source. Most of the measurements were carried out at 560°C, a temperature chosen to be high enough to keep the resistance at a reasonable level, but low enough to reduce F center migration from the cathode into the electrolyte which complicates the analysis.

In one instance, measurements were made on an asymmetric cell, *i.e.*, where $pO_2(I) = 10^{-20}$ atm and $pO_2(II) = 0.2$ atm. For this experiment, the sample was cemented to the end of a zirconia tube and placed in a furnace containing an air atmosphere. The interior of the tube was filled with flowing nitrogen which had been purified to $pO_2 = 10^{-20}$ atm by the zirconia pump, this value being measured by the open-circuit emf of the sample itself. Paste electrodes and platinum wire contact probes were used for this experiment in the same way as described above for the symmetric cells, except in that both electrodes were of the same area ~ 1 mm^2.

Minimum oxygen pressures around the test specimen.—The lowest oxygen pressure monitored near the test specimen was 10^{-20} atm at 560°C. This is well above the values (16) monitored within the oxygen pump cell itself (11). The pressure increase is due to

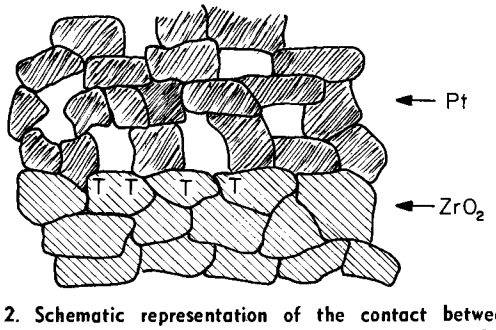

Fig. 2. Schematic representation of the contact between the electrolyte and a sintered Pt contact made by sintering Pt paste at 800°C.

leakage through the wall or release of oxygen from the wall of the glass tube connecting the pump to the measuring vessel. An alternative experimental arrangement with the cold trap at the position B in Fig. 1 gave pressures in the measuring cell well above those found with the trap in the usual position A. The difference is due to the buffering action of hydrogen (11). If water vapor present in the tank nitrogen is still present when the gas enters the pump cell (*i.e.*, the set-up with the trap at A), the water is decomposed with the formation of an equivalent amount of hydrogen. Drying the gas at A then removes most of the residual water and leads to a certain value of the water-hydrogen pressure ratio $(pH_2O/pH_2)_A$. On the other hand, with the cold trap in position B, the water is largely removed before the gas enters the cell, and therefore the amount of H_2 that can be formed is largely reduced. This leads to a higher value of the water-hydrogen pressure ratio $(pH_2O/pH_2)_B$. If no leakage would occur, each would give rise to an oxygen pressure given by the ratio

$$pO_2^{1/2} = K_{H_2O} pH_2O/pH_2 \qquad [6]$$

with $(pO_2)_A < (pO_2)_B$. Moreover, leakage of oxygen occurs and this will have a much stronger effect if the H_2 pressure is low (case of position B) than if it is high (case of position A). As a result, the value of pO_2 finally measured in the monitor cell is again smaller in case A than in case B.

Experimental Results and Discussions

Hysteresis.—If at a given oxygen pressure the current is measured as a function of applied voltage, first increasing the voltage from zero to 6V at a rate of 1 v/min, and then decreasing it to zero at the same rate, hysteresis is observed. Figure 3 shows the result for a measurement with the cell in air. Both the decrease of current wtih time (4, 9, 17) and the increase of current with time (9, 11) were previously reported. The hysteresis, however, has not been satisfactorily explained (9). The present authors believe that the increase is due to the injection of F centers into the electrolyte from the cathode at voltages ≧2V, and that the decrease is due to the time required for the completion of polarization or, if it is after a considerable number of F centers have been formed, the time required for these centers to disappear. The most reproducible curves were obtained with measurements taken during the decrease of the applied voltage from 6 to 0V at a rate of 1 V/min (the solid curve in Fig. 3) after the voltage had been increased from 0 to 6V beforehand at the same rate and held at 6V for half a minute. The times involved are supposed to be long enough to build up space charges characteristic of polarization, but are still short enough to keep F centers, formed at the cathode at high voltages, from drifting into the electrolyte to an appreciable extent. From here on, only the characteristics obtained according to this schedule will be discussed.

Oxygen pressure dependence of the direct-current vs. voltage characteristics.—Some examples of current-voltage characteristics measured at various oxygen pressures are shown in Fig. 4. It is seen that variation of the oxygen pressure affects the characteristic in different ways. At $V > 2V$ the current slightly decreases with increasing oxygen pressure in the range $10^{-14.5}$ to $10^{-4.3}$ atm and hardly changes with the oxygen pressure in the range $pO_2 > 10^{-4.3}$ atm. This behavior is more easily seen from a plot of the slope of the *I-V* characteristic, *i.e*, the dynamic conductance $(\partial I/\partial V)$, as a function of applied voltage. The inverse of this derivative, $(\partial V/\partial I)$, is of the dimension of a resistance and is called dynamic resistance. Figure 5 shows the relation between $(\partial V/\partial I)$ and applied voltage for various oxygen pressures. The effect of oxygen pressure upon the dynamic resistance is strongest where applied voltage is zero, and weakest at voltages higher than 2V. This behavior suggests that the characteristic is determined by two different mechanisms, the effect of one being dominant at $V < 2V$, the other being dominant at voltages >2V.

A difference in mechanism is also indicated by a difference in the effect of the presence of water vapor (Fig. 6). The effect of a variation in pH_2O is seen only at low O_2 pressures where oxygen atoms are present mainly as water molecules, and at $V < 2V$; at higher voltages there is practically no effect.

Finally the time dependence in the high and low voltage regions is different: the current at high voltages increases with time probably as a result of the occurrence of electronic conduction, increasing when F centers formed at the cathode drift into the electrolyte. That at low voltages tends to decrease.

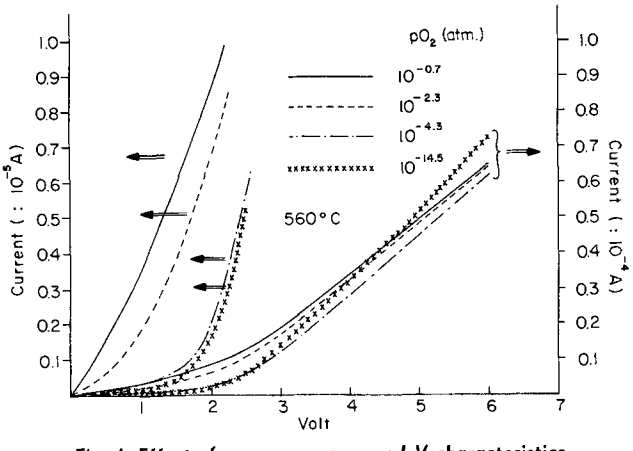

Fig. 4. Effect of oxygen pressure on *I-V* characteristics

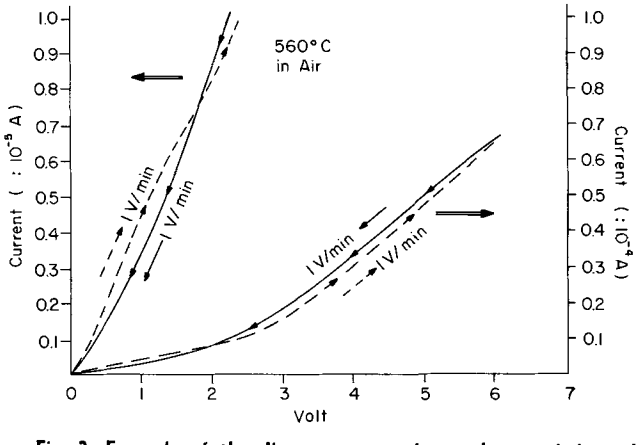

Fig. 3. Example of the direct current-voltage characteristic and hysteresis.

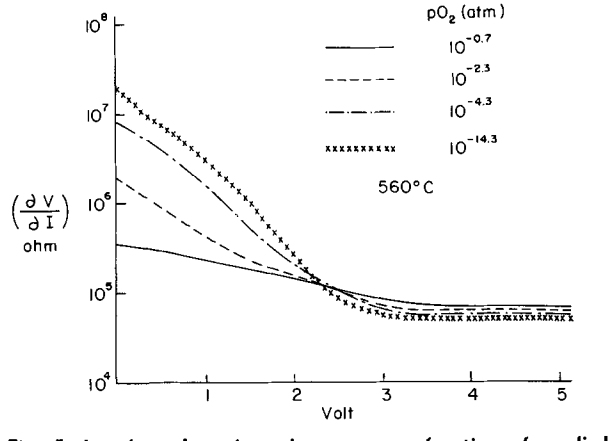

Fig. 5. Interface dynamic resistance as a function of applied voltage and oxygen pressure.

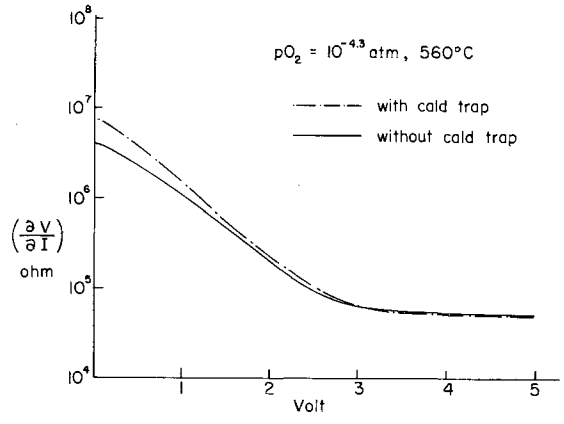

Fig. 6. Effect of water vapor on the dynamic resistance as a function of voltage.

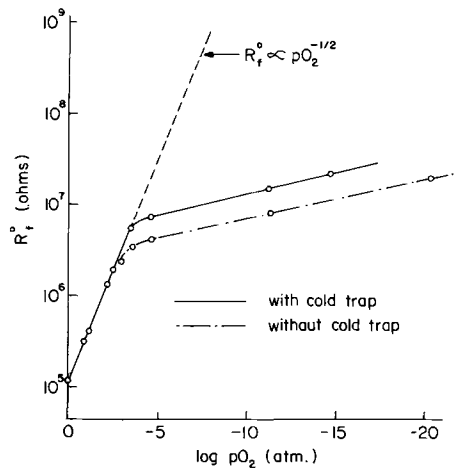

Fig. 7. R_f^0 as a function of oxygen pressure ($R_b = 5 \times 10^5$ ohm)

Low voltage section of the characteristic.—Dynamic resistance at zero volts.—Since the test specimen was operated with the same oxygen pressures at the two sides, E_{stop} as given by [4] is zero. Since no ionic current occurs when the applied voltage is E_{stop}, no potential drop can be present at the electrolyte-gas ambient interfaces. Furthermore, since the applied voltage is zero in this case, there is no oxygen chemical potential drop across the electrolyte.

The equivalent circuit consists of three resistances in series: one, R_c represents the resistance between the electrolyte and its gas ambient at the cathode side, the second, R_b, the bulk resistance of the electrolyte, and the third, R_a, the resistance between the ambient and the solid electrolyte at the anode side interface. The relation

$$\left(\frac{\partial V}{\partial I}\right)_{V=0} = R_b^0 + R_c^0 + R_a^0 \qquad [7]$$

holds, where the superscript 0 indicates that the applied voltage is zero. Or, introducing the total interface resistance R_f, defined by

$$R_f^0 = R_c^0 + R_a^0 \qquad [8]$$

and noting that R_b is ohmic so that $R_b^0 \equiv R_b$, [7] can be written

$$\left(\frac{\partial V}{\partial I}\right)_{V=0} = R_b + R_f^0 \qquad [9]$$

The resistance across the electrolyte is practically independent of oxygen pressure since the concentration of anion vacancies responsible for ionic conduction is fixed and determined by the calcium oxide content; also the electronic contribution to the conductivity across the electrolyte is hardly measurable in the oxygen pressure range 1 to 10^{-20} atm covered in this study, so that $t_i \approx 1$. Hence, the change in the dynamic resistance $(\partial V/\partial I)_{V=0}$ with pO_2 must be mainly due to a change in the interface resistance R_f^0. Equation [9] tells us that if a constant ($=R_b$) is subtracted from the observed dynamic resistances, the residue should be the R_f^0, which is a function pO_2. Trial and error shows that a plot of log R_f^0 *vs.* log pO_2 is linear for the oxygen pressure range from 10^{-4} atm up to 1 atm if $R_b = 5 \times 10^5$ ohms; the line has a slope of $-\frac{1}{2}$, indicating that $R_f^0 \propto pO_2^{-1/2}$ (Fig. 7). The value of R_b found in this manner should be compared with reported values for the resistivity of stabilized zirconia. According to Kingery *et al.* (3), $\rho(560°C) \approx 2.9 \times 10^4$ ohm cm. For a sample thickness, t, of ≈ 1 mm, a gross cathode contact area, S_g, of ≈ 1 mm^2, an anode area of 5 mm^2, and thus for an effective cross section of the conduction path of $S_{eff} = (5 - 1)/\ln 5 = 2.5$ mm^2, the calculated value of the bulk resistance $\left(\rho \frac{t}{S_{eff}}\right)$ is 1.16×10^5 ohms. The fact that the characteristic leads to a slightly larger value may be due to the fact that the actual contact area for the low voltage mechanism, S_L, is less than S_g. For $S_L/S_g = 1/4.3$, the two resistance values agree. This phenomenon, described here in terms of S_L and S_g has been discussed elsewhere (19) in terms of a "constriction resistance."

The plot of log R_f^0 *vs.* log pO_2 shown in Fig. 7 has a sharp change in slope near $pO_2 = 10^{-4}$ atm, indicating that R_f^0 is only weakly dependent on the oxygen pressure for $pO_2 < 10^{-4}$ atm. This sharp change in behavior requires a distinction between R_f^0 for high and for low oxygen pressure, *i.e.*, between $R_{f,h}^0$ and $R_{f,l}^0$. Comparison of the results of experiments with and without the liquid nitrogen cold trap (*i.e.*, with gas of the same oxygen pressure but containing different amounts of water vapor) shows that $R_{f,l}^0$ is variable, but $R_{f,h}^0$ is not affected. This indicates that $R_{f,h}^0$ involves oxygen atoms deriving from O_2 molecules, but that $R_{f,l}^0$ involves oxygen atoms deriving from buffer molecules, *e.g.*, H_2O or CO_2 (in the present case probably the former). It indicates also that we are dealing with a different rate-limiting process. We shall deal with the oxygen process and with the water process below.

The relative importance of the two terms, R_c^0 and R_a^0, may be shown by noting that a change in the gross anode surface area from 5 to 20 mm^2 did not give any alteration of the observed characteristics whereas changing the cathode area did alter the behavior. This indicates that R_f^0 is determined mainly by R_c^0: it is mainly the cathodic processes that determine the current-voltage characteristics. Consequently

$$R_f^0 \approx R_c^0 \qquad [10]$$

and

$$R_c^0 >> R_a^0 \qquad [11]$$

The same feature is indicated by a comparison of the *I-V* characteristic of an asymmetrical cell, for which $pO_2(I) = 10^{-20.0}$ atm and $pO_2(II) = 0.2$ atm, with the *I-V* characteristics of symmetrical cells operated at these two pressures. As shown in Fig. 8, the section of the asymmetrical characteristic for $V > E_{open}$ (curve 1a) where the electrode at the low pO_2 side is the cathode, is almost identical with the symmetrical characteristic for $pO_2 = 10^{-20.0}$ atm (curve 2) if the latter is shifted by E_{open} (curve 2). Similarly the section of the asymmetric characteristic for $V < E_{open}$ (curve 1b) where the electrode at the high pO_2 side is the cathode, is almost identical with the characteristic of the symmetrical cell having $pO_2 = 0.2$ atm (curve 3) similarly shifted (curve 3'). Thus the gas present at the cathode (negative relative to E_{open}) determines the shape of the characteristic.

If the cathode process determines R_f^0, the pressure dependence of R_f^0 mainly arises from the pressure dependence of R_c^0. Since $R = C^{-1}$, where C is the conductance, the pO_2^{-n} dependence of R_c^0 corresponds to the following relation for the conductance C_c^0 at the cathode side interface

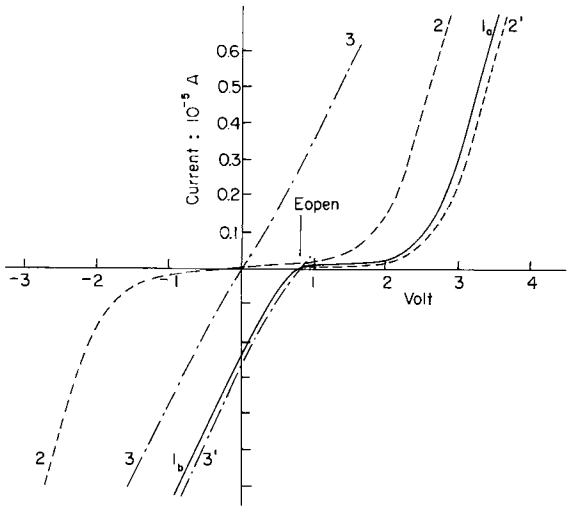

Fig. 8. Comparison of the *I-V* characteristic of an asymmetrical cell with those of symmetrical cells. 1_a, asymmetrical characteristic for $V \geqq E_o$ (E_o = 810 mV, at 560°C, $pO_2(I) = 10^{-20.0}$ atm and $pO_2(II) = 10^{-0.7}$ atm); 1_b, asymmetrical characteristic for $V \leqq E_o$; 2, symmetrical characteristic for $pO_2 = 10^{-20.0}$ atm; 2', 2 shifted to the right by 810 mV; 3, symmetrical characteristic for $pO_2 = 10^{-0.7}$ atm; 3', 3 shifted to the right by 810 mV.

$$C_c^0 = \frac{1}{R_c^0} \propto pO_2^n \qquad [12]$$

where $n = \frac{1}{2}$ at high oxygen pressures and $n \approx 0$ at low oxygen pressures. The conductance is given by

$$C_c^0 = \left(\frac{\partial I}{\partial V}\right)_{V=0} \qquad [13]$$

The current I is given by the number of O^{2-} ions formed per second from $O_2(g)$ or $H_2O(g)$ at the cathode and transferred to the solid electrolyte (15). This may happen in various ways, each involving a number of steps, one of which is the rate-determining one.

Determination of the rate-limiting step: $pO_2 >> pH_2O$.—At relatively high oxygen pressures, when $pO_2 >> pH_2O$, the over-all cathode process consists of the dissociation and ionization of oxygen and its incorporation into the zirconia

$$\tfrac{1}{2}\,O_2(g) + 2e^-(Pt) \rightarrow O^=(ZrO_2) \qquad [14]$$

It has been argued (13) that since species in three phases are involved in this process, it has to occur at a triple contact where these three phases meet (Fig. 2,T). It should be understood, however, that this triple contact is one-dimensional and cannot carry any current. Although the actual process will occur more or less close to T, it must take place across a two-dimensional surface, *e.g.*, an area either at the Pt side or at the zirconia side (or at both sides) of T. In the first case the process must involve diffusion of an oxygen species through or over the platinum; in the latter case it must involve electron diffusion from the Pt at T over the free zirconia surface. It is proposed that the first mechanism is responsible for the low-voltage behavior and that the second mechanism accounts for the high-voltage behavior. We shall now proceed with a discussion of the former. The following steps, indicated schematically in Fig. 12 are supposed to be involved.

$$\tfrac{1}{2}\,O_2(g) \rightleftarrows \tfrac{1}{2}\,O_2(Pt/g) \qquad [15]$$

$$\tfrac{1}{2}\,O_2(Pt/g) \rightleftarrows O(Pt/g) \qquad [16]$$

$$O(Pt/g) \rightarrow O(Pt/ZrO_2) \qquad [17]$$

$$O(Pt/ZrO_2) + V_O{}^{\cdot\cdot} \rightleftarrows O_O{}^x + 2h^{\cdot} \qquad [18]$$

$$2e^-(Pt) + 2h^{\cdot} \rightleftarrows 0 \qquad [19]$$

Here $O_2(Pt/g)$ are oxygen molecules adsorbed at the interfaces between the platinum crystals and the gas phase either at the outer surface of the paste electrode or inside the platinum sponge; $e^-(Pt)$ are electrons of the platinum, with energies corresponding to its Fermi surface; $O(Pt/g)$ are oxygen atoms in the platinum at the platinum-gas interface (the formation of charged forms of oxygen in the platinum, *e.g.*, O^- or $O^=$, is not energetically favored), $O(Pt/ZrO_2)$ are oxygen atoms in the platinum near the Pt, ZrO_2 interface, $V_O{}^{\cdot\cdot}$ are the oxygen ion vacancies present in the zirconia at a concentration given by that of calcia (2, 3), $O_O{}^x$ is the structure element symbol for a normal $O^=$ ion in the zirconia, and $h^{\cdot}$ are electron holes formed in the ZrO_2 surface by solution of the oxygen atoms from the platinum.

Each of the steps in the reaction sequence must be considered as a possible rate-limiting step. To treat them in turn, reaction [15] represents access of the oxygen gas to the platinum surface and could be the rate-limiting step if diffusion of oxygen molecules through a boundary layer were slow. The oxygen flux would then be

$$J_O = \frac{2D'}{\eta}\,[pO_2(g) - pO_2(Pt/g)] \qquad [20a]$$

where η is the boundary layer thickness and D' the diffusion coefficient for oxygen in the boundary layer.

By an analysis similar to that used in the next section, it can be shown that this leads to an equation for the interface resistance of the form

$$R_f{}^0 = \frac{RT}{4\mathbf{F}B'}\,pO_2{}^{-1}(g) \qquad [20b]$$

where **F** is the Faraday and B' is a constant (cf. Eq. [35]). The resistance thus varies linearly with $pO_2{}^{-1}(g)$ whereas the experimental observations (Fig. 7) vary with $pO_2{}^{-\frac{1}{2}}(g)$. Thus [15], which has been recognized in the literature (19) as a possibly important rate-limiting process (gas phase polarization), is not the rate-controlling step in any of the present experiments.

In a similar manner, reaction [16] can be eliminated as a rate-limiting step since it also shows a conductance proportional to $pO_2(g)$. Of all the reactions, only [17] and [18] have the required $pO_2{}^{\frac{1}{2}}$ dependence through the equilibrium of [16] combined with [17]. Of these two, [18] has no voltage dependence since the activity of $V_O{}^{\cdot\cdot}$ may be considered constant as determined by the calcium concentration. If the current capable of being given by [18] is greater than $I_b = V/R_b$ given by the ohmic bulk resistance, R_b, and this must be expected to occur close to the origin of the *I-V* curve where I_b is small, the over-all current must be limited by R_b and be independent of pO_2. On the other hand, if the current given by [18] is the smaller one so that [18] becomes the rate-limiting step it leads to a voltage independent current $I_m \propto pO_2{}^{\frac{1}{2}}$. The resulting *I-V* characteristic near the origin would be as shown in Fig. 9. The experimental results in the present work show, however, that in the area where the dynamic resistance is proportional to $pO_2{}^{-\frac{1}{2}}$, the current near $V = 0$ is dependent on both $pO_2{}^{\frac{1}{2}}$ and V. Therefore [18] cannot be rate limiting, and [17] is indicated as the rate-determining step.

Low voltage I-V characteristic for $pO_2 >> pH_2O$.—The fact that [17] is the rate-determining step leads to an expression for $(\partial V/\partial I)_{V=0}$ which may be compared with the data. As mentioned earlier, in any situation in which ionic current flows, *i.e.*, where $V \neq E_{stop}$, the chemical potential of oxygen at the cathode surface of the electrolyte is lower than that of its gas ambient. For $pO_2(I) = pO_2(II)$ as holds for the cells investigated in the present study, and in accordance with the experimental results which indicate that the cathode resistance $R_c >> R_a$ the anodic resistance, the variation of the chemical potential of oxygen through

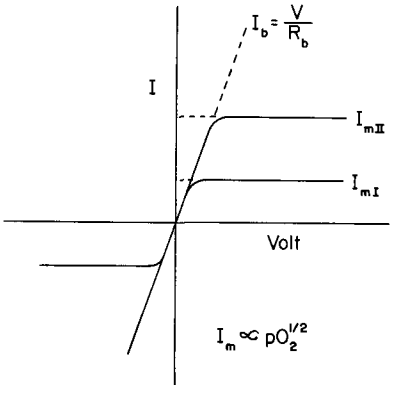

Fig. 9. Schematic diagram for the case where the process [18] would be the rate-determining step. It would be expected that $(\partial V/\partial I)_{V=0} = R_b$ near the origin; $I_m \propto pO_2^{1/2}$.

the cells can be shown schematically as in Fig. 10. As shown, the drop in μO_2 at the cathode is much larger than the increase in μO_2 at the anode: $\mu O_2(g) - \mu O_2(c) >> \mu O_2(a) - \mu O_2(g)$

$$\Delta\mu O_2 = \mu O_2(a) - \mu O_2(c) \approx \mu O_2(g) - \mu O_2(c)$$

The induced potential difference $\Delta\mu O_2$ over the electrolyte represents an emf

$$E_{a-c} \approx E_{g-c} = \frac{\Delta\mu O_2}{4F} \qquad [21]$$

which is almost of the magnitude and sign to stop the migration of ions under the influence of the outer field. The ionic conduction processes may be represented by the equivalent circuit (Fig. 11). The limitation of electronic conduction may be represented by a resistance, R_e, parallel to the others which represent the resistance to ionic conduction. In this equivalent circuit, the polarization emf (21) works over the resistance $R_f \approx R_c$. Since there is practically no electronic conduction under the conditions of the experiments, $R_e \approx \infty$. A small ionic current is kept going if the applied voltage is larger than the polarization voltage (21)

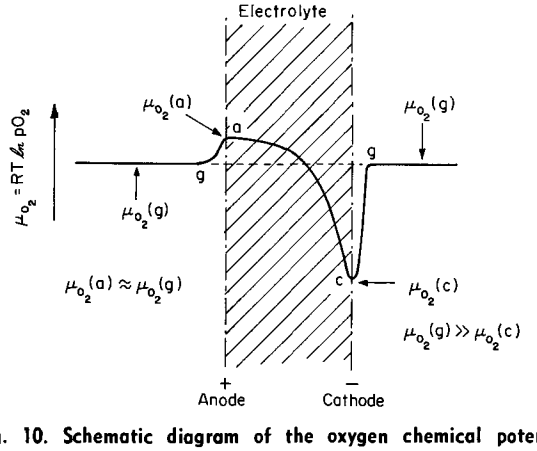

Fig. 10. Schematic diagram of the oxygen chemical potential across the circuit (electrode-electrolyte) if ionic current flows.

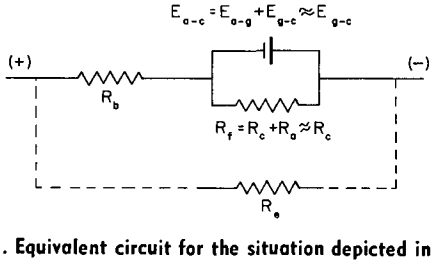

Fig. 11. Equivalent circuit for the situation depicted in Fig. 10

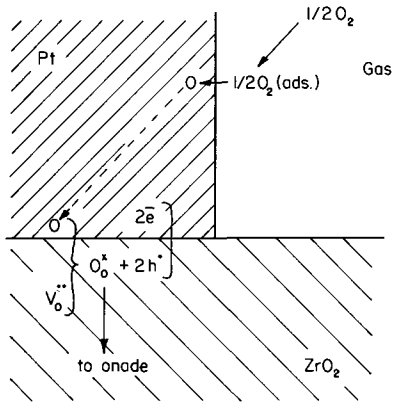

Fig. 12. Reaction steps in the low-voltage mechanism. The dotted line indicates the rate-controlling step.

$$V = I \cdot R_b + E_{a-c} \qquad [22]$$

$$E_{a-c} = \frac{RT}{4F} \ln \frac{pO_2(a)}{pO_2(c)} = \frac{RT}{4F} \ln \frac{pO_2(g)}{pO_2(c)} \qquad [23]$$

If [17] is the rate-determining step, the rate is given by a diffusion flux equation

$$J_O = D \frac{\partial}{\partial x} [O(Pt)] \qquad [24]$$

where D is the diffusion constant of O atoms for diffusion through the platinum from the Pt/gas surface to the Pt/ZrO_2 interface along any of the paths pp', qq', rr', tt' in Fig. 13; it may include diffusion along the Pt/ZrO_2 interface (path Ts in Fig. 13) but not diffusion along the Pt/gas interface (p → q → r → t → T), since the latter would be effected faster by a diffusion of O_2 molecules through the gas phase. (This is true in particular in pure oxygen where concentration gradients cannot occur, and since there is no indication of a change in mechanism on going from pure oxygen to inert gas-O_2 mixtures, the same appears to hold for operation in these mixtures also. Gas diffusion of O_2, if rate determining, would also give a rate $\propto pO_2$.)

The maximum contact area for the proposed process is the total area S of the Pt/ZrO_2 interfaces (wT in Fig. 13). As we saw in the section on Dynamic resistance at zero voltage, the contact area for the low voltage mechanism $S_L \approx (1/4.3)S_g$. The total ZrO_2 surface becomes accessible only if the ZrO_2 becomes sufficiently conductive at its surface to transport electrons from the platinum over the ZrO_2 surface.

Assuming a linear gradient, [24] can be changed to

$$J_O = \frac{D}{\partial}\{[O(Pt/g)] - [O(Pt/ZrO_2)]\} \qquad [25]$$

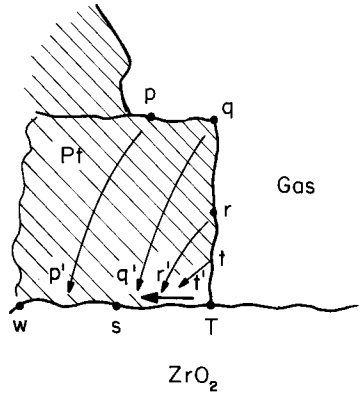

Fig. 13. Various diffusion paths for O in Pt

Here ∂ is the effective length of the diffusion path, *i.e.*, in Fig. 13, the appropriate average of the lengths of paths pp' to tt'.

The equilibrium for [15] and [16] leads to

$$[O(Pt/g)] = K_1 pO_2^{1/2}(g) \quad [26]$$

and one can also write (Fig. 10)

$$[O(Pt/ZrO_2)] = K_1 pO_2^{1/2}(Pt/ZrO_2) \equiv K_1 pO_2^{1/2}(c) \quad [27]$$

Consequently

$$J_O = \frac{D}{\partial} K_1 \{pO_2^{1/2}(g) - pO_2^{1/2}(c)\} \quad [28]$$

At the interface Pt/ZrO_2, O atoms are transformed into $O^=$ ions by reaction [18]. Therefore the particle current [28] ultimately represents an equivalent electrical current through the ZrO_2 of

$$I_h = 2\mathbf{F}S_L J_O \quad [29]$$

Here S_L is the effective area of the Pt/ZrO_2 interface, **F** is the Faraday, and the subscripts h and L are used to indicate respectively relatively high O_2 pressure ($pO_2 >> pH_2O$) and a low voltage. Combining [29] with [22], [23], and [28], we find

$$V = I_h R_b + \frac{RT}{4\mathbf{F}} \ln pO_2(g)/pO_2(c) \quad [30]$$

and

$$I_h = 2\mathbf{F}S_L \frac{D}{\partial} K_1 \{pO_2^{1/2}(g) - pO_2^{1/2}(c)\} = B\{pO_2^{1/2}(g) - pO_2^{1/2}(c)\} \quad [31]$$

where

$$B = 2\mathbf{F}S_L(D/\partial)K_1 \quad [32]$$

Eliminating $pO_2(c)$ from [30] and [31] we get

$$V = I_h R_b + \frac{RT}{4\mathbf{F}} [\ln pO_2(g) - 2 \ln \{pO_2^{1/2}(g) - I_h/B\}] \quad [33]$$

and, by differentiation

$$\frac{\partial V}{\partial I} = R_b + \frac{RT}{2\mathbf{F}B} \{pO_2^{1/2}(g) - I_h/B\}^{-1} \quad [34]$$

or, for zero voltage where $I_h = 0$

$$\left(\frac{\partial V}{\partial I}\right)_{V=0} = R_b + \frac{RT}{2\mathbf{F}B} pO_2^{-1/2}(g) \quad [35]$$

This is just the form observed for R_f^0 at $pO_2 > 10^{-4}$ atm (Fig. 7). The current by this mechanism cannot exceed a limiting value given by [31] with $pO_2(c) = 0$, *i.e.*

$$(I_h)_{lim} = BpO_2^{1/2}(g) \quad [36]$$

This limiting value is approached when $V \to \infty$; $\partial V/\partial I$ as given by [34] approaches ∞, or $\partial I/\partial V$ approaches zero. In the present experiments the saturation level is not reached, a different mechanism with a larger current taking over at large voltages. This new mechanism is discussed below.

Low-voltage characteristic for $pO_2 << pH_2O$.—At lower oxygen pressures and in an incompletely dried gas where $pO_2 < pH_2O$, oxygen atoms are present mainly in the form of water molecules, and the O atoms in the platinum will be mainly formed from these. The successive steps of the entire cathodic process are then

$$H_2O(g) \to H_2O(g/Pt) \quad [37]$$

$$H_2O(g/Pt) \rightleftarrows H_2O(Pt/g) \quad [38]$$

$$H_2O(Pt/g) \rightleftarrows O(Pt/g) + H_2\uparrow \quad [39]$$

followed by [17]-[19]. The fact that the voltage dependence of the current is similar to that in the O_2 governed case and different from the dependence shown in Fig. 9 suggests that we are again dealing with a diffusion controlled process. If it is assumed that [17] is again the rate-limiting step, then the concentration of O(Pt/g) depends on the activity of H_2O and H_2 through [38] and [39] and the current may be represented by

$$I_l = 2\mathbf{F}S_L \frac{D}{\partial} K_2 \left[\frac{pH_2O}{pH_2}(g) - \frac{pH_2O}{pH_2}(c)\right] \quad [40]$$

K_2 being the equilibrium constant of [38] and [39] combined. But since $pH_2O/pH_2 = K_{H_2O}pO_2^{1/2}$, this would make I_l again $\propto pO_2^{1/2}$, whereas a much weaker dependence was observed (see Fig. 7). Thus [17] cannot be the rate-limiting step. The observed behavior is found if diffusion across a boundary layer in the gas phase, *i.e.*, [37], is the rate-limiting process. This leads to a current

$$I_l = 2\mathbf{F}K_3 \{pH_2O(g) - pH_2O(g/Pt)\} \quad [41]$$

dependent on pH_2O in the gas and pH_2O at the gas-Pt surface, the latter depending on the applied field in a manner similar to that found for $O(Pt/ZrO_2)$ in the oxygen governed case.

The weak pO_2 dependence seen in Fig. 7 is at least qualitatively explained by the way in which pH_2O is linked to pO_2, in that a lowering of pO_2 results from the decomposition of H_2O with the formation of H_2. Thus a decrease of pO_2 is tied to a decrease of pH_2O and increase of pH_2. But whereas pO_2 is determined by pH_2O/pH_2, the rate of [37] depends on pH_2O alone, and the latter may vary only slightly while the former varies considerably. However, a quantitative fit on the basis of this model with $(K_{H_2O})_{560°C} = 7.6 \times 10^{12}$ atm$^{1/2}$ is not obtained, and further experiments with well-defined buffer mixtures are required to clarify the mechanism operating in this range.

High-voltage section of the characteristic.—At voltages above 2V a new mechanism becomes operative. It might be assumed that the change in mechanism is due to a change from ionic conduction, dominant at low voltages, to electronic conduction at high voltages. This, however, cannot be the case. The electronic conductivity σ_e and the concentration of free electrons [e'] in calcia stabilized zirconia vary with the oxygen pressure as (2, 6)

$$\sigma_e \propto [e'] \propto pO_2^{-1/4} \quad [42]$$

whereas the high-voltage conductivity $(\partial I/\partial V)_H$ is practically independent of pO_2. Thus apparently the current remains largely ionic. This conclusion is also supported by the fact that the dynamic resistance, $(\partial V/\partial I)_H$, shown in Fig. 5 and 6, has a value of 5-8 x 10^4 ohms which is close to the value 1.16 x 10^5 ohms calculated on the basis of the published ionic conductivity (3) and the dimensions of the cell, assuming the cathode electrode to be active over its whole surface. The following mechanism is proposed.

As shown in Fig. 10, the chemical potential of oxygen at the cathode surface of the ZrO_2 (point c) is lower than that of the gas ambient. This is the result of the slow process at the interface and represents polarization. Although a certain amount of polarization takes place at all voltages, its extent increases with applied voltage. Increasing the strength of polarization results in a lowering of μO_2 at point c. Since the concentration of electronic defects is related to pO_2 by [42], types of oxygen vacancies different from the ones present under normal conditions can be formed

$$V_O^{\cdot\cdot} + e^- \rightleftarrows V_O^{\cdot} \quad [43]$$

$$V_O^{\cdot} + e^- \rightleftarrows V_O^{x} \quad [44]$$

where $V_O^{\cdot}$ and V_O^{x} are oxygen ion vacancies with one and two trapped electrons respectively. Once V_O^{x} vacancies are present, it is possible for the oxygen adsorbed at the surface of the ZrO_2 to enter the lattice directly by the reaction

$$O(ZrO_2/g) + V_O^x \rightarrow O_O^x \quad [45]$$

The O_O^x can then pass to the anode.

This model relies on having V_O^x close to the ZrO_2-gas interface. Since the polarization occurs at the platinum cathode, the V_O^x occurs initially at that point and diffuses away with longer times of polarization as shown in Fig. 14. As a result of the sideways diffusion of the F-centers (V_O^x), path a in Fig. 14, the free ZrO_2 surface next to the platinum becomes electronically conductive and becomes available to the adsorbed oxygen for the reaction of Eq. [45].

The spreading of an area with increased, probably electronic, conductivity has been observed by Kleitz (13). Also, inspection of samples used in the present work revealed F-centers (a purple coloration) over the entire contact area if the samples were subjected to voltages >6V. The high voltage characteristic is time dependent, with current increasing with time; this is predicted by the model (*i*) because F-centers diffuse into the zirconia away from the interface (path b in Fig. 14) causing some electronic conduction in the bulk (this is the effect that was minimized in the design of the experiments; section on Experimental set-up), and (*ii*) because the sideways diffusion increases the surface area that can take part in the O transport of Eq. [45] (the distance vT in Fig. 14 increases with time). In the present experiments the maximum sideways diffusion path length is of the order of the radius of the platinum particles, *i.e.*, small relative to the thickness of the sample. Therefore, a state is very quickly reached where the entire free surface is active. From then on the only time dependence is due to process (*i*).

Once the entire free surface area is available for reaction [45], the sequence of processes involved in the incorporation of oxygen is (Fig. 15)

$$\tfrac{1}{2}O_2(g) \rightleftarrows \tfrac{1}{2}O_2(ZrO_2/g) \quad [46a]$$

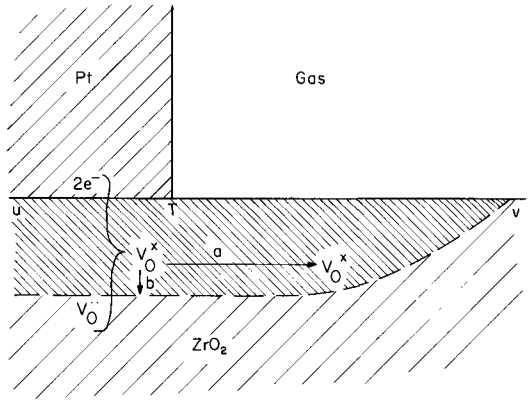

Fig. 14. Diffusion of F-centers away from the platinum electrode region into the zirconia.

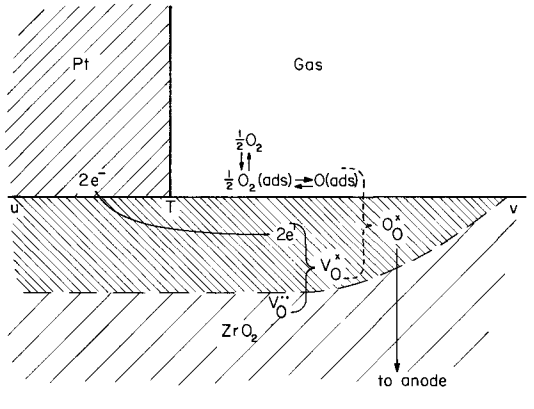

Fig. 15. Reaction steps for the high-voltage mechanism. The dashed lines indicate the rate-controlling step.

$$\tfrac{1}{2}O_2(ZrO_2/g) \rightarrow O(ZrO_2/g) \quad [46b]$$

$$2e^-(Pt) \rightarrow 2e'(ZrO_2) \quad [47a]$$

$$2e'(ZrO_2) + V_O^{\cdot\cdot} \rightarrow V_O^x \quad [47b]$$

together with reaction [45]. The rate-controlling step in this sequence can be determined in much the same way as for the low voltage case. Experimentally, the high voltage characteristic is voltage dependent but not oxygen pressure dependent. Since [46a] and [46b] and [47a] are oxygen pressure dependent, and [47b] is voltage independent, the indication is that [45] is the rate-controlling step.

The oxygen pressure independence of reaction [45] may be shown as follows. The number of neutral oxygen atoms adsorbed on the zirconia surface is

$$O(ads)_H = K_4 S_H p{O_2}^{1/2}(g) \quad [48]$$

where K_4 is the equilibrium constant of [46a] and [46b] combined, and S_H is the effective surface area for the mechanism. The concentration of V_O^x vacancies is given by [43], [44], with equilibrium constants K_5, K_6, and [42]

$$[V_O^x(c)] = K_5 K_6 [V_O^{\cdot\cdot}] p{O_2}^{-1/2}(c) \quad [49]$$

The current generated by the high voltage mechanism with [45] as the rate-limiting step is equivalent to the number of O_O^x lattice ions formed per second

$$I_H = 2F\frac{dO_O^x}{dt} = 2F A S_H [V_O^x] O(ads) \quad [50]$$

where A is the rate constant for reaction [45]. Using [48] and [49]

$$I_H = C\,[pO_2(g)/pO_2(c)]^{1/2} \quad [51]$$

with $C = 2F A K_4 K_5 K_6 S_H [V_O^{\cdot\cdot}]$. Or using [23]

$$I_H = C \exp\frac{2F}{RT} E_{a-c} \quad [52]$$

From [22] and [52]

$$V = I_H R_b + \frac{RT}{2F} \ln (I_H/C) \quad [53]$$

and

$$\frac{\partial V}{\partial I_H} = R_b + \frac{RT}{2F} I_H^{-1} \quad [54]$$

These expressions do not contain pO_2 and thus give the required independence from oxygen pressure. They also represent a voltage dependent current as required. The dynamic resistance [54] approaches R_b with increasing current, *i.e.*, at large voltages, as is observed (Fig. 5 and 6).

Since the bulk resistivity of the electrolyte, ρ_b, is independent of voltage, the bulk resistance applicable to the low voltage mechanism is

$$R_{b,L} = \rho_b \frac{y}{S_L}$$

and the bulk resistance applicable to the high voltage mechanism is

$$R_{b,H} = \rho_b \frac{y}{S_H}$$

where y is the sample thickness, and S_L, S_H are the active contact areas appropriate to the two mechanisms. From above, $R_{b,L} = 5 \times 10^5$ ohms, and from Fig. 5 and 6, $R_{b,H} \approx 2 \times 10^5$ ohms. Thus, as an approximate figure

$$\frac{S_H}{S_L} \approx 2.5$$

or in other words, the platinum crystals physically cover about 30% of the zirconia surface "covered" by the paste.

Transition from the low- to the high-voltage mechanism.—Although we have spoken about low-voltage and a high-voltage mechanism with a transition at $\approx$ 2V, in reality both mechanisms occur at all voltages: only the ratio in which they contribute varies. The total ionic current is the sum of the current generated by the two mechanisms, *i.e.*, that from the low voltage mechanism, I_L, and that from the high voltage mechanism, I_H. Then

$$I = I_L + I_H \qquad [55]$$

I_L in turn involves two types of oxygen atom source, one at high oxygen pressures, I_h, and one at low oxygen pressures, I_l. These are given by [31] and [41]. Then

$$I_L = I_h + I_l \qquad [56]$$

Consequences of the proposed models.—The models proposed here have been developed on the basis of experiments on moderately sintered Pt-paste contacts. They are sufficiently general, however, to be applied to other types of contacts and contact configurations, *e.g.*, Pt, Au, and Ag point contacts as used by Kleitz (13), evaporated or sputtered Pt contacts as used by Heyne (9) and Karapachev *et al.* (18). The oxygen dominated low-voltage regime was found to depend on diffusion of O through the platinum and was characterized by a diffusion coefficient D and an effective thickness ∂. As shown in [32]-[34], the resistance is greater than the bulk electrolyte resistance and is proportional to ∂ as long as ∂ is not too small; a decrease of ∂ will decrease the resistance until a constant resistance R_b is reached. For large ∂, the resistance is quasi-ohmic but polarization occurs; for small ∂, the resistance is truly ohmic, and no polarization occurs. The conclusions only hold if other rate-limiting steps are avoided.

Absence of polarization with thin sputtered Pt cathodes and the occurrence of polarization with thicker Pt layers was actually observed by Heyne (9). An increase of the current, attributable to a decrease of the effective diffusion path, was observed by Karapachev *et al.* (18) in experiments in which they made scratches in evaporated Pt layers, thus creating 3-phase boundaries with small effective ∂. In terms of Fig. 13, the unscratched layer corresponds to $\partial \approx$ pp', while the scratched one reduces ∂ to the average of pp'-tt'. An almost ohmic characteristic was also found by Yuan *et al.* (11) who used a thinly spread paste cathode in pumping experiments.

An investigation of the electrode characteristics in the O_2 dominated low-voltage range should show a material dependence through the solubility of O and its diffusion constant. This may account for the differences observed between Pt, Au, and Ag point contacts (13). The high-voltage mechanism was based on the utilization of free ZrO_2 surface. Therefore, a cathode geometry which reduces the free surface area (*e.g.*, evaporated or sputtered platinum) should suppress the current based on this mechanism and may make an increase in current due to electronic conduction (characterized by a $pO_2^{-1/4}$ dependence) observable.

A transition from a low- to a high-voltage mechanism has been observed by others, *e.g.*, Kleitz (13) and Guillou *et al.* (15). These authors used point contacts and therefore must have observed ionic effects of the type discussed here. Experiments with porous cathodes as employed in the present investigation but with zirconia doped with donors (5) should show a high-voltage mechanism as discussed in the present paper, but setting in at a lower voltage. The discussion given so far applies to densely sintered zirconia. With porous zirconia other models become possible in which oxygen may reach the Pt/ZrO_2 interface by diffusion as O_2 through the pores in the zirconia. This as the rate limiting step would lead to a current $\propto pO_2$.

Determination of transference numbers by polarization techniques.—It is interesting to consider in the light of the results presented in this paper, the use of polarization experiments to determine the extent of electronic conduction in stabilized zirconia. In the technique of Vest and Tallan (4), the time dependence of the voltage needed to drive a constant current across the sample is measured, and the electronic transport number obtained from the relation

$$t_e = \frac{E(0)}{E(\infty)} \qquad [57]$$

where $E(0)$ is the voltage at time = 0, and $E(\infty)$ is that at time = ∞. This relation is as pointed out, valid only when the electrodes are blocking to the passage of oxygen. With the electrodes used in the present paper, blocking behavior was not observed, and values of t_e deduced from the time effects would not be correct; that Vest and Tallan were able to observe isolated electronic conduction may well be due to their use of "fluxed" platinum paste electrodes, *i.e.*, electrodes with a glass additive used to improve adhesion. The presence of the glass would seem to improve the blocking effect of the electrode, presumably by sealing gas permeation channels and thus increasing ∂ in Eq. [25]; at any rate the different behavior with at first sight similar (both Pt) electrodes, emphasizes the need to consider the details of electrode structure when interpreting observations of electrical behavior in largely ionic conductors.

Summary

The direct current-voltage characteristics of cells Pt, O_2/(Zr, Ca) O_2/Pt, O_2 with the same oxygen pressures at both sides were measured at 560°C under oxygen pressures ranging from 1 to 10^{-20} atm. The characteristics were markedly nonohmic and showed two distinct regions. One, at voltages <2V shows an oxygen pressure dependence, the conductance varying as $pO_2^{1/2}$ as long as O_2 is the major O-containing species; a weaker pO_2 dependence is found if H_2O is the main O-containing species. The rate-determining step for the O_2 case is the diffusion of O atoms through the platinum of the electrode. The high-voltage region shows practically no pO_2 dependence. Here the rate-limiting step is the combination of O atoms adsorbed at the ZrO_2 gas interface with V_O^x formed as a result of polarization.

The importance of the electrode material and the electrode geometry is stressed.

Acknowledgment

This work was supported by the Directorate of Chemical Science, Air Force Office of Scientific Research under Contract AF-AFOSR-68-1405.

Manuscript submitted Aug. 22, 1969; revised manuscript received *ca.* Jan. 21, 1970.

Any discussion of this paper will appear in a Discussion Section to be published in the December 1970 JOURNAL.

REFERENCES

1. R. C. Garvie, *J. Am. Ceram. Soc.*, **51,** [10], 553 (1968).
2. Hermann Schmalzried, *Z. Elektrochem.*, **66** [7], 575 (1962).
3. W. D. Kingery, James Pappis, M. E. Doty, and D. C Hill, *J. Am. Ceram. Soc.*, **42** [8], 393 (1959).
4. R. W. Vest and N. M. Tallan, *J. Appl. Phys.*, **36** [2], 543 (1965).
5. F. A. Kröger, *J. Am. Ceram. Soc.*, **49** [4], 215 (1966).
6. J. W Patterson, E. C. Bogren, and R. A. Rapp, *This Journal*, **114** [7], 752 (1967).
7. G. G. Charette and S. N. Flengas, *ibid.*, **115** [8], 796 (1968).
8. D. P. Clark and R. E. Meridith, *Electrochem. Technol.*, **5** [9/10], 446 (1967).
9. L. Heyne, "Ionic Conductivity in Oxides," pp. 149-164 of "Mass Transport in Oxides," J. B. Wachtman, Editor, National Bureau of Standards, Special Publication No. 296 (1968).
10. F. A. Kröger, *Proc. Brit. Ceram. Soc.*, **1**, July, p. 167 (1964).

11. Daniel Yuan and F. A. Kröger, *This Journal*, **116**, [5], 594 (1969).
12. J. Besson, C. Deportes, and M. Kleitz, Brevet Francais, No. Provisoire 128-327 (Nov., 1967).
13. M. Kleitz, "Electrode Reactions in Solid Oxide Electrolytes," Thesis, University of Grenoble (May, 1968).
14. C. J. Devane and E. L. Holverson, *J. Appl. Phys.*, **38** [13], 5421 (1967).
15. M. Guillou, J. Millet, and S. Palous, *Electrochim. Acta*, **13** [6], 1411 (1968).
16. Hiroaki Yanagida, cited in ref. (11) as private communication. To be published elsewhere.
17. D. W. Strickler and W. G. Carlson, *J. Am. Ceram. Soc.*, **47** [3], 120 (1964).
18. S. V. Karapachev and A. T. Filyaev, *Elektrokhimiya*, **2** [11], 1330 (1966).
19. C. S. Tedmon, Jr., H. S. Spacil, and S. P. Mitoff, *This Journal*, **116** [9], 1170 (1969).

Electrodeless Electrolysis

Abner Brenner* and John L. Sligh, Jr.*

National Bureau of Standards, Washington, D. C.

ABSTRACT

Solid ionic conductors and fused salts were electrolyzed without contact of solid electrical leads. The current was carried to the materials to be electrolyzed either by means of electrons emitted by a hot filament or by a glow discharge. The materials were made the separating wall between the anode and cathode compartments of an apparatus constructed of glass or fused silica. Electrolysis of glass produced a white opaque material which did not seem to differ chemically from the original glass. Dendrites of several metals were obtained in the glow discharge electrolysis of fused salts. The results of the latter process resembled conventional electrolysis with metal electrodes and was not similar to the glow discharge electrolysis of aqueous electrolytes.

In electrodeposition or electrolysis as ordinarily practiced, the electrodes are metals or graphite, and the products of electrolysis form at the interface between the electrode and the electrolyte. Most of the data of electrolysis have been obtained with the use of such electrodes, and their characteristics have entered into the theories. Thus, the cathode provides a pathway by means of which electrons can flow to the electrolyte-cathode interface. However, the electric current is conducted by other kinds of systems, such as the electron beam and rarified gases; and the question arises as to whether electrochemical reaction will occur with such systems in contact with an electrolyte.

The purpose of this investigation was to call attention to prior work that showed that electrolysis could be accomplished without the use of conventional electrodes and to explore further the variety of unconventional ways in which electrolysis could be accomplished.

Electrolysis in the absence of the conventional electrode-electrolyte interface will in this paper be called, for brevity, "electrodeless electrolysis," although it is recognized that the electron beam, rarified gas, or other conducting phase in contact with the electrolyte is performing the function of the conventional electrode.

The subject of electrodeless electrolysis has not previously been unified in the literature as a single topic or branch of electrochemistry. For that reason the introductory part of this paper has been amplified beyond the customary scope of an introduction, so as to present a survey of the field. We define electrodeless electrolysis as the occurrence of an electrochemical reaction, such as those resulting in deposition of metal or evolution of gas, at locations in the system which are remote from the metallic conductors which bring the current to the system. Electrodeless electrolysis has been observed in a variety of experiments, and the nature and, hence, the explanation of the phenomena, are not necessarily the same for all. Probably the first example of electrodeless electrolysis was that reported by Grotthuss (1) in 1819 who passed a current through a crack in a glass vessel which was wet on both sides by a silver nitrate solution. Silver separated out in the vicinity of the crack. The phenomena was studied in detail by Braun (2) in 1891 who gave it the name electrostenolysis. Metal deposition or evidence of a chemical reaction also was observed by a number of electrochemists at an organic membrane, such as a pig bladder or at an inorganic membrane, such as copper ferrocyanide, on the passage of current through systems consisting of a membrane separating solutions of heavy metal salts:

Anode/salt solution//membrane//salt solution/cathode

Electrostenolysis differed from deposition at membranes in that the former required 20V or more, whereas the latter process occurred with the low voltages used in ordinary electrodeposition. The subject of the electrolytic processes at membranes has been capably reviewed and discussed by Söllner (3) and, thus, there is no need for further treatment here.

Electrodeless electrolysis of an entirely different kind occurred with the glow discharge above an aqueous solution. The phenomenon was first reported by Gubkin in 1887 (4). In an evacuated vessel containing an electrolyte (and water vapor) he passed a current between an electrode suspended in the vapor and an electrode situated beneath the surface of the electrolyte. A potential of several hundred volts was required. This phenomena was studied in some detail by several workers some 50 or 60 years later [(5), no attempt is made here to give a complete bibliography of glow discharge electrolysis].

Glow discharge electrolysis is very different from conventional electrolysis. Either reduction (for example, of permanganate ion) or oxidation (for example, of ferrous ion) can occur and the yield may be several times greater than that expected from Faraday's law. Furthermore, in some experiments it makes little difference whether the anode or cathode is placed in the electrolyte (5b) (the other electrode being in the space above the electrolyte) or whether direct or alternating current is used. The separation of metal was reported in two instances (5a, 5c), but this seems to be a rare occurrence and the observations are open to question. One explanation of the glow discharge electrolysis is that water vapor is decomposed in the

* Electrochemical Society Active Member.

Key words: electrolysis, electrodeless electrolysis, glow discharge, electrolysis of fused salts, electrolysis of glass, electron beam electrolysis.

discharge into free radicals which then react with the dissolved salt.

Although the term "glow discharge electrolysis" has been used almost invariably in the literature as the name of the phenomena described in the preceding paragraph, it is unlikely that the phenomena involve the mechanism of conventional electrolysis. Hence, the use of the word "electrolysis" in connection with the action of the glow discharge of aqueous solutions is a little unfortunate.

Couch and Brenner (6a) observed a green corona above a copper solution and a blue corona above an indium solution with the glow discharge. Sastry (6b) observed similarly colored corona with some other salt solutions but not with fused salts. He concluded that the presence of water was necessary and that the decomposition of water vapor into free radicals in the cathode fall was involved in the mechanism.

A very different type of electrodeless electrolysis was described by Burt in 1925 (7a, 7b) and by Selenyi (7c) in 1927. They placed an ordinary (evacuated type) light bulb in a bath of fused sodium nitrate in which a wire was placed and served as anode. The filament of the lamp was made incandescent by passage of an a-c current. Then a d-c potential was placed between the wire serving as anode in the sodium nitrate and the filament, which was made negative. Current passed through the glass bulb and pure sodium collected on the upper cool walls of the interior of the bulb. The yield was exactly in accordance with Faraday's law. The explanation of the phenomena was that sodium ions migrated through the bulb from the sodium nitrate and were discharged on the inner surface of the bulb by the stream of electrons from the hot filament.

We have extended electron beam electrolysis to materials other than glass; this work is described in a subsequent section. The fused salt bath, which presumably served as a source of sodium ions, we found not to be an essential part of the experiment, as electrolysis could be performed with the bulb immersed in distilled water instead of fused sodium nitrate or with the electrical contact established through copper, plated on the outside of the bulb. Thus, the glass was actually electrolyzed to yield sodium.

The systems described in the previous examples of electrodeless electrolysis all possessed a sharp discontinuity between an electrolyte and another phase, for example, between a membrane and an electrolyte or between a gaseous phase and an electrolyte. Milicka (8) described an unusual example of electrodeless electrolysis in which both phases were aqueous. In a U-tube a concentrated solution of potassium iodide was placed and above it, in one limb, distilled water was placed. Current was passed through the liquids in the U-tube, and iodine was observed to separate out at the interface between the two liquids. Substitution of copper sulfate for the iodide resulted in the deposition of copper or copper hydroxide at the interface. Milicka stated that these experiments were well known to the earlier electrochemists, but gave no reference.

Since nothing in the current theories of electrolysis would lead one to expect electrolysis to occur at the boundary of two aqueous liquids, we attempted to verify the report. In our experiment the amount of iodine was very slight, and it was necessary to introduce starch into the liquids to make its presence visible. A blue color did occur on passing a current of 50 mA at about 1000V through the column. It appeared to form chiefly next to the wall of the glass tube. It is likely that the phenomenon is not as simple as it seems, and the presence of the glass wall may be essential to the electrolysis.

The most recent example of electrodeless electrolysis was described by Palit (9) in 1968. He observed that gas collected in a salt bridge which was used to connect a vessel of catholyte to a vessel of anolyte. The gas began to appear after about 6 hr of electrolysis, and the composition of the gas ranged from 60% to 90% oxygen. The formation of the gas was attributed to the production of charged water molecules which migrated away from the electrodes and reacted with either hydroxyl or hydrogen ions.

Our experiments on electrodeless electrolysis which are described below deal mainly with the electrolysis of solid materials and fused salts. Aqueous solutions were not involved. The phase contacting the material to be electrolyzed was a partial vacuum ranging from about 1.0 to 10^{-5} Torr/(133 to 0.00133 N/m^2). It will be noted that in some of these experiments materials have been electrolyzed almost in free space, as the only electrical contact with the specimen was an electron beam and/or a gas at low pressure.

Electron Beam Electrolysis

Apparatus and procedure.—A schematic diagram of the apparatus is shown in Fig. 1. It is taken from U.S. Patent 3,366,562 in which it is fully described. The apparatus consisted of a glass envelope, 10 and 12, which was provided with a large port, 17, for evacuation by an oil diffusion pump, 18, and with vacuum-tight seals, 20, 21, and 28, for introducing the electrical leads, 26 and 30. The tungsten filament, 25, was heated by alternating current and could carry up to 17A. The specimen to be electrolyzed took a number of forms, but for some of the work it was a solid, cast around the end of the anode lead and was placed in the top of the holder shaped like a long stem funnel. The latter was made from fused silica or mullite. The stem of the holder protruded through a vacuum-tight seal to the outside and served both as a conduit for the positive lead and to prevent short circuiting of the latter by the electron beam. The voltage for electrolysis was applied between the tungsten filament, 25, and the positive lead, 30. The pressure in the vessel was about 10^{-5} Torr.

The solid materials which were electrolyzed had to be heated to attain a conductivity sufficient for electrolysis. For example, glass required about 400°C and selected ceramics still higher temperatures. In some experiments the tungsten filament was placed only a centimeter or two distant from the electrolyte, and the heat from the filament was sufficient to raise the temperature of the electrolyte to a point that it became conducting. However, this was not adequate for

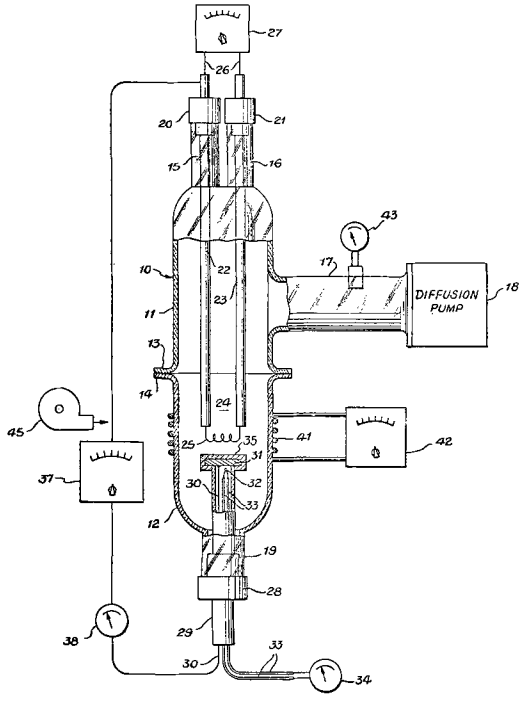

Fig. 1. Diagram of apparatus for electron beam electrolysis. Figure taken from U.S. Pat. No. 3,366,562. The numbers refer to the description in the patent.

some materials, and it was necessary to use a noninductively wound resistance heater which was placed inside of the glass envelope around the solid electrolyte. Heating by induction with a metal susceptor placed around the electrolyte was not successful, as the magnetic field of the induction coil apparently dispersed the stream of electrons and no current could be made to pass through the system.

In a typical experiment the apparatus was pumped down to 10^{-5} Torr and as a check on the system the high voltage, 1000-1500V d.c., was applied between filament and the positive lead with the resistance heater off. The absence of current flow was evidence that there was no electrical leakage. The heating element was next energized to make the solid conductive. As the latter became hot, current began to flow. Usually the current was held below 50 mA as a higher current (and a higher voltage) occasionally caused perforation of the specimen, in which case all the current flowed through the pore and electrolysis ceased.

The main difficulty with electron beam electrolysis was establishing a good electrical connection between the anode lead and the solid electrolyte. A solid metallic connection was unsatisfactory. A number of methods were evaluated using glass as a representative solid electrolyte. In the electrolysis of glass it was well known before 1900 that solid contacts were unsatisfactory, but that molten salts or sodium amalgam could be used. Markin (10) showed that the difficulty with solid electrodes was that the contact that it made with a solid electrolyte occurred only at isolated points and resulted in a very high local current density. This caused either arcing through or the formation of dendrites, which soon extended through the solid and shorted the electrodes.

In Burts' light bulb experiment the anode lead to the glass was a fused salt. However, this is not generally applicable, because so few materials are readily obtainable in the form of a bulb. We, therefore, gave up the attempts to find a suitable solid positive contact and turned to conduction through a rarified gas to establish the electrical contact with the electrolyte. This subject is treated in a later section of this paper.

Materials for electrolysis.—Preparation of a solid electrolyte in a shape suitable for electrodeless electrolysis, whether by electron beam or by the glow discharge method, was a difficulty that we did not completely overcome. In these methods of electrolysis high voltages had to be used because even the heated solid materials were not very conductive. Consequently, the slightest pore which traversed a solid electrolyte allowed the circuit to be completed without passage of current through the electrolyte. Solid electrolytes made by fusing a salt and allowing it to solidify all seemed to have cracks. Very slow cooling, particularly in a metal container made of foil, helped to eliminate some of the stresses arising from contraction on cooling. However, to obtain a sound disk of a salt, it seemed that cutting a slice from a single crystal was the only solution. The solid materials which could be obtained readily for electrolysis, therefore, were silver chloride, which is plastic at room temperature, glass, ceramic materials commercially available in the form of plates or impervious tubes closed at one end, and single crystals.

Results of experiments with electron beam electrolysis.—In our apparatus the "light bulb" experiment of Burt was easily carried out as follows. A glass test tube filled with an easily fusible salt mixture was placed near the tungsten filament. The open end of the tube extended through a vacuum-tight seal to the outside. The positive lead was inside of the test tube. Under these circumstances the outside wall of the glass tube was exposed to the electron beam and readily electrolyzed. The sodium could not be collected because it was spread as a mist or film over the extensive inner surface of the chamber. However, the film was dissolved in water and titrated. The alkalinity corresponded to over 90% of the amount of sodium predicted by Faraday's law.

A similar experiment with a mullite tube resulted in the formation of a dark layer on the outside of the tube, but the nature of the transformation was not investigated.

In other experiments the arrangement shown in Fig. 1 was used, which involved direct contact of the materials with the positive metallic lead. Copper and nickel dendrites were obtained from their chlorides which had been melted with potassium chloride and cooled. Silver dendrites were obtained from solid silver chloride. The deposition occurred on the surface facing the heated filament, and dendrites extended into the body of the solid. Here is a clear instance of an electron beam acting as a cathode exactly as would be expected of a metal or any other electronically conducting cathode, *i.e.*, the dendrites formed at the cathode-electrolyte interface and grew into the electrolyte.

In one experiment solid sodium tetraborate was electrolyzed, but the heat of the filament and the IR drop caused the salt to melt, and consequently the experiment was actually electrolysis of the fused salt. At the conclusion of the experiment a lump of transparent boric oxide was found on top of the melt; the sodium liberated by the electrolysis had volatilized. Materials which normally did not electrolyze, also did not undergo electrolysis with the electron beam. For example, molybdenum disulfide, which is an electronic conductor, did not undergo any observable change in the electron beam experiment.

Glow Discharge Electrolysis of Solid Electrolytes

Development of process, apparatus, and procedure.—The difficulty of obtaining a satisfactory electrical contact of the positive lead to the solid electrolyte in electron beam electrolysis led to the investigation of glow discharge electrolysis. The first experiment was a hybrid type of electrolysis—a modification of the one with a glass tube described earlier. In that experiment the outside surface of the tube was exposed to the electron beam for electrolysis; the inside contained a molten salt for making a good electrical connection to the positive lead wire. In the modified experiment with glow discharge the fused salt was not used. Instead, the interior of the tube was evacuated to a low pressure at which a good glow discharge occurred. The path of the current thus went from the positive lead through the rarified gas to the inside wall of the glass tube, and finally through the wall to the electron beam. Satisfactory operation of the glow discharge as a positive lead to the solid electrolyte suggested using the glow discharge also on the outside wall of the glass tube to carry the current instead of the electron beam. Thus, in essence, a body would be electrolyzed without any palpable contact with metallic electrical connections.

The first experiment in which the glow discharge was used to make electrical contact to both sides of a glass wall was performed with simple equipment. A 96% silica glass[1] tube about 5 cm in diameter and 75 cm in length served as one electrode chamber. At one end of the tube was a connection to a vacuum pump and a graphite electrode which passed through a vacuum-tight seal. The other electrode chamber was simply a long glass test tube about 2.5 cm in diameter which extended into the larger tube through a vacuum-tight seal. This smaller tube likewise was provided with a graphite electrode and a vacuum connection. The central part of the apparatus was heated by a tube furnace to 400°-500°C. On placing a potential of about 1400V across the two graphite electrodes (both vessels being evacuated to between 0.1 and 1.0 Torr) a glow discharge occurred and a current of about 40 mA flowed. The path of the current was from one graphite electrode, through the rarified gas,

[1] Vycor, Registered TM, Corning Glass Works.

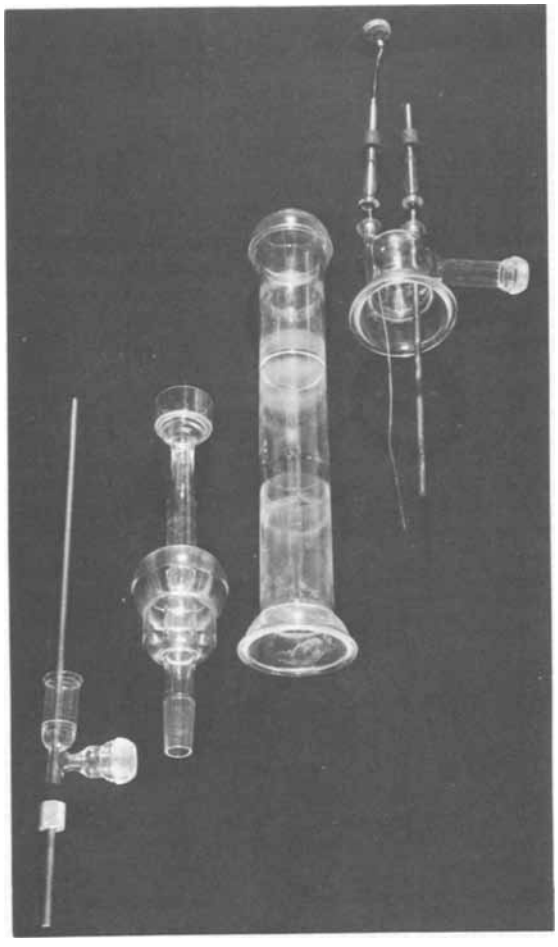

Fig. 2. Disassembled apparatus for glow discharge electrolysis

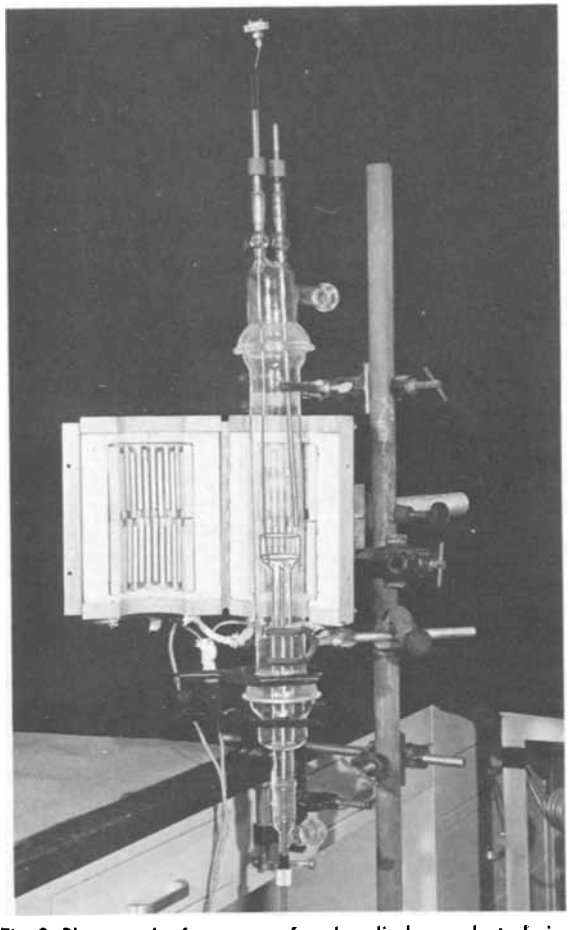

Fig. 3. Photograph of apparatus for glow discharge electrolysis

through the glass wall and through rarified gas on the other side to the other graphite electrode. The appearance of the glass after electrolysis was similar to that of the tube electrolyzed by the hybrid glow discharge-electron beam procedure described in the preceding paragraph.

The next step in the development of the apparatus was to provide for the electrolysis of solid materials in the form of a slab or disk because, as already mentioned, we had difficulty in obtaining materials in the form of a thin-walled tube (1-3 mm thick). The apparatus which was designed is shown disassembled in Fig. 2 and assembled in Fig. 3. It was essentially a modification of the electron beam apparatus with the filament and the positive lead replaced by a graphite rod.

The main envelope was again a silica glass tube about 6 cm in diameter with spherical joints at each end. The glass fixture which was attached to the upper end of the envelope carried a side tube for attachment to an ordinary vacuum pump (a high vacuum was not necessary) and two tubulations which were provided with vacuum-tight seals. One tubulation carried a graphite rod (6 mm in diameter) which served as an electrode and the other carried a sheathed thermocouple, about 1.5 mm in diameter. The glass fixture attached to the lower end of the envelope also was provided with a side tube for connection to a vacuum pump and a vacuum-tight seal for a graphite electrode.

The part of the apparatus which needs further elaboration is the funnel shaped part which projected upward to about the middle of the main chamber. It is shown schematically in Fig. 4. It was made of fused silica, and it was integral with the lower fixture, just described. It may be noted that, by closing the mouth of the funnel with a disk, the apparatus became divided into two chambers, the large outer

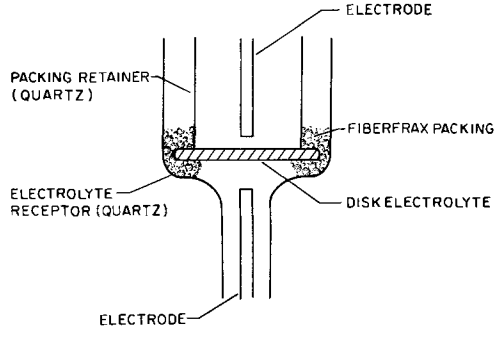

Fig. 4. Diagram of funnel shaped holder of electrolyte in glow discharge electrolysis.

chamber and the smaller chamber consisting of the fused silica funnel.

As with electron beam electrolysis, one of the most significant problems was to prevent short circuiting by flow of current between the edges of the disk and the mouth of the funnel. The key to the solution of the problem was the observation that the glow discharge would not penetrate through a tortuous path, even though it was porous enough for gas to flow through. For example, powdered magnesium oxide (which is a good insulator even at elevated temperatures) packed in a tube so as to make a compact about 1 cm thick prevented the glow discharge. A fibrous mineral material[2] was also satisfactory and easier to use. To prevent leakage around the disk of solid electrolyte, which was inserted into the mouth of the funnel, the fibrous mineral was packed underneath the outer perimeter of the disk and around its sides so as to fill the space between the disk and the funnel wall. To still further increase the length of the tortuous path, a fused silica cylinder was placed on the sur-

[2] Fiberfrax, Registered TM, Carborundum Company.

face of the disk and fibrous mineral packed around it, as shown in the diagram, Fig. 4. This arrangement prevented current from leaking, even up to an applied potential of 6000V.

The packing was useful also for preventing electrical leakage between the electrodes via the tubing connected to the vacuum pump. The vacuum connections at the top and bottom of the apparatus were connected to a T-joint which led to the vacuum pump. In some instances the discharge took the path of going from one side tube, through the rubber tubing and the T-connection to the other side tube, thus, effectively short-circuiting the flow of current through the disk. This short-circuiting was prevented by packing fibrous material lightly in the tubing between the T-joint and the apparatus. The glow discharge was thereby discouraged from traversing this path.

In the first experiments the residual air sustained the glow discharge. Replacement of the residual air by argon (at low pressure) was found necessary in the electrolysis of silver chloride, because otherwise the silver formed was oxidized to silver oxide. In most experiments, therefore, argon was introduced through a tube which ended in the vicinity of the disk. The flow of gas was controlled simply by manipulating a screw clamp on the rubber tubing and observing the bubbling of the gas as it flowed through oil in a U-tube. Argon gave a glow discharge over a wider range of pressure than air, namely, between 0.05 and 8 Torr at a voltage between 1000 and 3000.

In comparison with electron beam electrolysis, the glow discharge experiments were much easier to perform because (*i*) a higher pressure was satisfactory (as much as 1.0 Torr could be used as compared to less than 10^{-4} Torr for the electron beam process), (*ii*) contamination from a filament was eliminated (in the electron beam procedure some tungsten evaporated from the filament); (*iii*) short circuiting between the cathode and anode chambers was minimized.

Usually an electrolysis current of about 25 mA was desired. This required from 1000 to 3000V. Heating of the specimen was necessary to obtain sufficient conductivity for passage of current, and the tube furnace used is shown in Fig. 3. It permitted a temperature of about 800°C to be obtained, but this temperature was inadequate for obtaining conductivity of some ceramics.

The source of voltage in the glow discharge experiments was a commercial instrument which delivered a maximum of 30 kV at 35 mA. During the glow discharge experiments, particularly those in which a gas flowed through the system, regulation of the pressure was necessary. This was accomplished by a commercial electronic instrument which had a thermocouple type of pressure gauge as a sensing device. The instrument automatically turned the vacuum pump on and off so as to keep the pressure between two prescribed limits, for example, between 0.1 and 0.2 Torr.

Results of experiments with solid electrolytes.— Silver chloride was the electrolyte which we used for exploring the variables of operation and the modifications of equipment. Silver chloride is easily melted, gives a sound ingot on solidification, and is plastic, so that it does not develop pores and cracks. In electrolysis, the side facing the negative lead became covered with silver. On long electrolysis (an hour or more) silver dendrites eventually grew through the disk and shorted out the flow of current through the silver chloride. Silver iodide electrolyzed similarly to silver chloride. In a quantitative experiment, we found that the silver chloride disk lost weight about equal to the amount of chlorine that should have been liberated on the basis of Faraday's law. No silver was observed on the anode side unless the experiment was run long enough for the dendrites formed on the cathode side to penetrate completely through the electrolyte. This further demonstrates that the process which occurred was truly an electrolysis between plasma electrodes and not a thermal decomposition. We believe this to be the first reported example of an electrolysis between two gas plasma electrodes.

The most interesting results were obtained with the electrolysis of glass. In an electrolysis performed (as described earlier) with a fused salt bath serving as the anode connection, the glass did not change its appearance, even though sodium was liberated.

In the electrolysis of glass with the glow discharge (or with the glow discharge on one side and the electron beam on the other, as in an earlier section) the side of the glass facing the cathode became dull and developed some blisters, while the side toward the anode developed an opaque white layer which readily flaked off, as shown in Fig. 5. The chemistry of the change was not elucidated, as the opaque material gave an x-ray pattern similar to that of the original glass and the content of silica in the materials seemed to be almost the same as that in the original glass. The dramatic change in the appearance of the glass on electrolysis warrants further investigation.

Thin disks of some titanates, such as barium titanate which were initially light yellow in color became brown or black on electrolysis, the discoloration occurring throughout the thickness of the disk. The disk also became electrically conductive. A similar phenomenon resulted on heating a disk of the titanate to 700°C in an atmosphere of hydrogen.

Several other materials in the form of disks sawed from a single crystal were electrolyzed and, although they changed in appearance, no clear evidence was obtained of the nature of the chemical change. It is thought that in some of these instances, the conductivity of the material was too low at the temperature of the experiment, and that the flow of current may have been through pores or cracks which developed as a result of thermal shock. A single crystal disk of sodium chloride became opaque on the side facing the cathode and a thin white film deposited on the surface of the containing vessel. The film gave an alkaline reaction and probably was derived from vaporized sodium. Similar results were obtained with a disk of potassium bromide. Calcium fluoride did not allow enough current to pass, even at 750°C, to permit an adequate amount of electrolysis for qualitative examination.

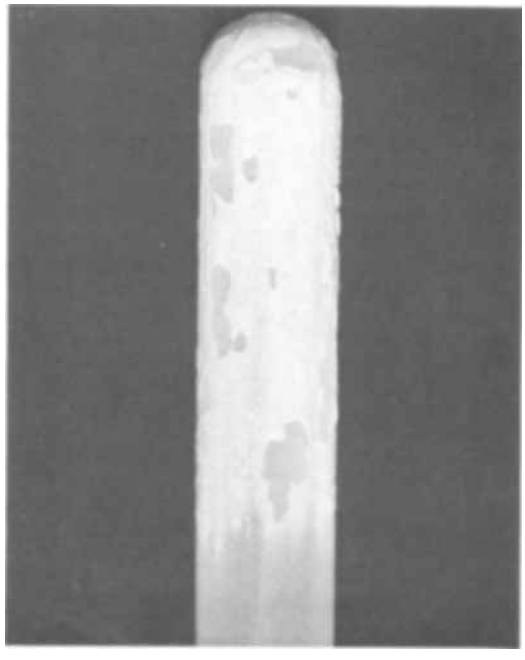

Fig. 5. Glass test tube electrolyzed by the glow discharge method.

Glow Discharge Electrolysis of Fused Salts

Background.—It was pointed out in the introduction and survey that the glow discharge electrolysis of aqueous solutions differed from conventional electrolysis with metal electrodes in that the products were not those usually obtained (metals were seldom reported as having been deposited) and the yields were several times greater than those expected on the basis of Faraday's law. This kind of electrolysis involves complexities in the vapor phase. By contrast the glow discharge electrolysis of fused salts is simpler, resembling conventional electrolysis in products formed and their yields. The fact that the current is conducted to the molten electrolyte by a gas at low pressure instead of metal conductors appears to make no difference in the results, except that reaction or alloying of the product with a metallic electrode can be avoided.

Of the various types of electrodeless electrolysis which have been described, the glow discharge electrolysis of fused salts was the process most easily performed and seems to be the one most likely to have any practicable use.

Apparatus.—The most obvious kind of apparatus to use for the glow discharge electrolysis of fused salts is a U-tube, such as shown in Fig. 6. The tube was made of glass or fused silica. The fused salt, B, was contained in the bend of the U-tube and was separated into two portions by the porous diaphragm, D. The U-tube was constructed with a considerably reduced diameter at the bend, which was occupied by the fused salt (diameter at the bend about 2 mm), so as to restrict the amount of melt electrolyzed to about 1 or 2 ml. This was necessary because the amount of metal formed in electrolysis was small (amounting to 10-50 mg in a typical experiment) and, consequently, was very difficult to recover from a large mass of fused salt. After each experiment, the U-tube was sawed through at the diaphragm in order to separate the cathode and anode compartment and make possible the working up of the salt for the products of electrolysis.

Most of the experiments in fused salt electrolysis were done with the simple apparatus shown in Fig. 7. Since in all of the experiments the main interest was in the metal deposit, the cathode chamber, A, was made small, and it was immersed in a larger amount of fused salt, B. The chamber A was introduced empty into the test tube C at the beginning of an experiment. On lowering the chamber into the melt, the latter entered through the porous disk D. The purpose of the disk was to filter the fused melt which was to be electrolyzed and to prevent loss of products which formed

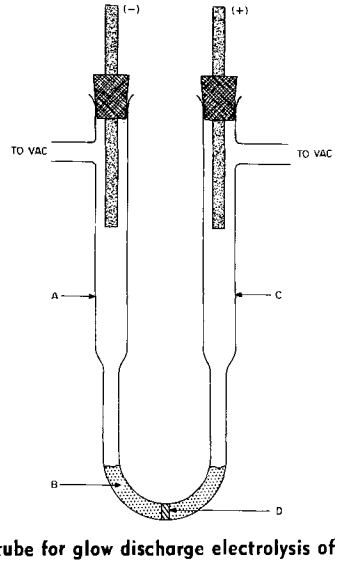

Fig. 6. U-tube for glow discharge electrolysis of fused salts

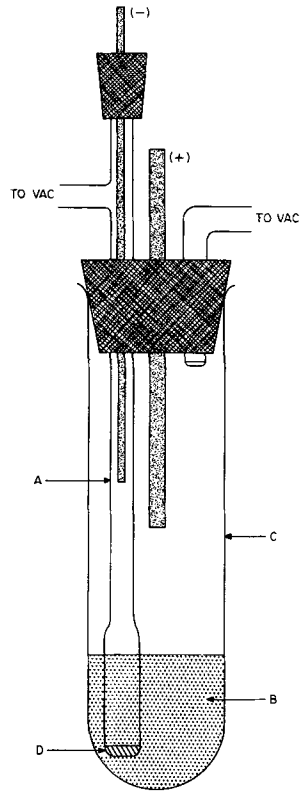

Fig. 7. Apparatus with a test tube envelope for the glow discharge electrolysis of fused salts.

in A during electrolysis. At the conclusion of the electrolysis, the chamber A was removed and the molten salt allowed to drain out. The chamber was then sawed through a short distance above the frit so as to expedite the collection of the product.

In all of the experiments the degree of vacuum was the same as that used for the glow discharge electrolysis of solid electrolytes. Care had to be taken in evacuating the vessel to prevent an inequality in pressure from forcing the melt completely from one chamber into the other.

In these experiments the phenomena in the anode chamber were not investigated and were not of concern, particularly since the diaphragm prevented any products from the anode compartment from entering the cathode compartment. Therefore, in most experiments a metallic anode was used is the anode chamber instead of a glow discharge. However, in at least one experiment, the electrolysis of molten silver chloride, the glow discharge was used in both chambers to demonstrate that solid electrodes were not essential.

Results of experiments with fused salts.—The glow discharge electrolysis of fused cupric chloride in potassium chloride yielded no deposit, probably because the electrolysis resulted only in a reduction of cupric ion to cuprous. The electrolysis of molten cuprous chloride at first also yielded no deposit. However, it was surmised that the presence of a small concentration of cupric ion was responsible for this failure. The molten cuprous chloride (in potassium chloride melt) was then treated with copper powder in the anode compartment prior to the electrolysis and then forced through the porous diaphragm in the cathode compartment. A yield of copper dendrites was obtained in the cathode compartment on electrolysis.

Silver chloride was electrolyzed in the U-tube without difficulty. After electrolysis, the solidified melt was obtained in the form of a rod after breaking away the glass tubing. On compressing the plastic chloride into a thin, transparent sheet, silver dendrites were readily visible, as shown in Fig. 8. The yield was roughly in accord with Faraday's law.

Tin dendrites were obtained from stannous chloride, cobalt dendrites from cobalt chloride, and nickel dendrites from nickel chloride. These products were separated from the solidified melts by dissolving the latter with water.

In the electrolysis of magnesium chloride, small, shining crystals collected in the tube above the level of the melt, thus indicating that the metal had been liberated at the surface of the melt as a vapor and had then subsequently condensed on the cooler portion of the apparatus.

Conclusion

This investigation of electrodeless electrolysis is only of an exploratory nature. The glow discharge electrolysis of ceramics and solid materials warrants further investigation. We suggest that the apparatus be designed to permit the ceramic electrolyte to be heated to much higher temperatures than we used, in order to promote a higher conductivity. If vessels could be constructed of a transparent, high melting material like yttrium oxide (mp 2410°C), the work would be greatly facilitated. Further work is in order to explain the curious change produced in glass on electrolysis.

The high voltages required for electron beam or glow discharge electrolysis militates against their use for any but a highly specialized application. The residual electrical conduction imparted to ceramics by the glow discharge electrolysis might be of some practicable use. The glow discharge electrolysis of fused salts might be of advantage in a situation in which the contamination of the deposit by a metallic cathode could not be permitted.

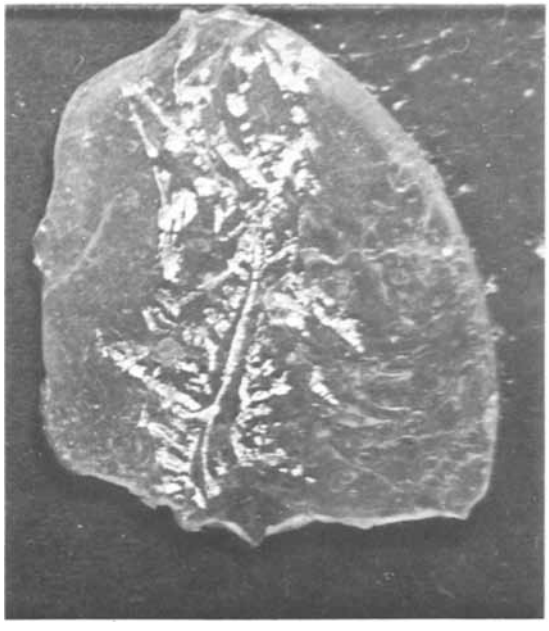

Fig. 8. Dendrites of silver in silver chloride which had been electrolyzed in the fused state.

The main interest in these exploratory experiments in electrodeless electrolysis, however, is in calling for a broader understanding of electrochemical phenomena by calling attention to the wide variety of situations in which chemical changes can be produced by the electric current.

To generalize as to the common denominator underlying all these curious examples of electrolysis, it seems that the presence of a metallic conductor is not it. Rather it seems that the essential factors are (assuming the presence of at least one ionic conductor) that the two materials in contact be different phases (gas, liquid, solid) and /or differ greatly in electrical conductivity.

Acknowledgment

The authors wish to express appreciation for the financial support of this research by the National Aeronautics and Space Administration under Contract No. R-09-022-052.

Manuscript submitted Aug. 1, 1969; revised manuscript received Jan. 8, 1970. This was Paper 153 presented at the Detroit Meeting of the Society, Oct. 5-9, 1969.

Any discussion of this paper will appear in a Discussion Section to be published in the December 1970 JOURNAL.

REFERENCES

1. Grotthuss, *Ann. Physik* (Gilbert), **61,** 65 (1819).
2. F. Braun, *ibid.*, **278,** 450 (1891); *ibid.*, **280,** 471 (1891); *ibid.*, **280,** 501 (1891).
3. K. Söllner, *Z. Elektrochem.*, **35,** 789 (1929).
4. J. Gubkin, *Ann. Physik*, **268,** 114 (1887).
5a. O. M. Corbino, *Atti Accad. Lincei*, **5** [6], 377 (1927).
5b. A. Klemenc, *Chimia*, **6,** 177 (1952).
5c. A. Klemenc and W. Kohl, *Monatsh. Chem.*, **84,** 498 (1953).
5d. M. Haissinsky and A. Coche, *J. Chim. Phys.*, **51,** 581 (1954).
5e. A. Banege-Nia, *Compt. rend.*, **245,** 1421 (1957).
5f. A. R. Denaro and A. Hickling, *This Journal*, **105,** 265 (1958).
5g. A. Hickling and M. D. Ingram, *Trans. Faraday Soc.*, **60,** 783 (1964).
5h. K. O. Hough and A. R. Denaro, *J. Sci. Instr.*, **43** [7], 488 (1966).
5i. A. R. Denaro and P. A. Owens, *Electrochim. Acta*, **13,** [2], 157 (1968).
6a. D. E. Couch and A. Brenner, *This Journal*, **106,** 628 (1959).
6b. B. S. R. Sastry, *J. Electroanal. Chem.*, **10** [3], 248 (1965).
7a. R. C. Burt, *J. Opt. Soc. Am.*, **11,** 87 (1925).
7b. R. C. Burt, U.S. Pat. 1,776,993, Sept. 30, 1930.
7c. P. Selenyi, *Ann. Phys.*, **84,** 111 (1927); **85,** 643 (1928).
8. L. Milicka, *Z. Physik. Chem.*, **210,** 23 (1959).
9. S. R. Palit, *J. Indian Chem. Soc.*, **45** [3], 286 (1968).
10. B. I. Markin, *J. Gen. Chem. USSR* (English Trans. of Consultants Bureau) **22,** 1137 (1952).

Current Distribution During the Electrodeposition of Gold

H. Y. Cheh

Bell Telephone Laboratories, Incorporated, Murray Hill, New Jersey

ABSTRACT

The phenomenon of macro- and microcurrent distribution in plating systems is studied. At high current densities where mass transport of the reacting species is rate controlling, the plating process will yield relatively uniform macro- but nonuniform microcurrent distribution. At low current densities where depletion of the reacting species is negligible, relatively uniform micro- but nonuniform macrocurrent distribution will be observed. The effect of surface roughness and current density on the microcurrent distribution of gold plated from a citrate bath is studied experimentally. The microcurrent distribution is found to improve considerably by reducing the surface roughness and by performing the deposition process at a lower current density. Due to the low gold content of most gold baths, practical gold plating is performed under conditions where mass transport limitations of the reacting species are significant.

The electrodeposition of gold is becoming increasingly important due to its wide applications in electronics equipment. The purpose in plating a thin layer of gold over certain parts of a substrate surface is to protect the parts from corrosion, reduce the electrical contact resistance, or provide a conducting path between devices. More uniform deposition both on a macro- and microscale and deposits with lower porosity and better mechanical properties are the goals pursued by the modern plating industry.

In this paper, the current distribution of a gold plating system is considered. The theoretical aspects of macro- and microcurrent distributions concerning systems involving only one electrochemical reaction are first examined. The conclusions from these considerations can be applied to many practical plating systems. Experimental observations on the microcurrent distribution of gold plated from a citrate gold bath are then reported.

Phenomenological Description of Macro- and Microcurrent Distribution

A typical linear dimension for a microprofile on a surface is in the order of 50μ whereas the linear dimension for a macroprofile is about 1000μ or larger. Transition between micro- and macrodimensions occurs between these limits. These definitions are somewhat arbitrary. The dimension of micro- *vs.* macroprofiles suggested here falls in the range used by most electroplaters. A rigorous definition can be established from the concept of the diffusion layer thickness. This will be treated in a later section.

Many investigators have found that a fundamental difference of current distribution occurs on macro- and microprofiles. For instance, Meyer (1) and Gardam (2) found that, in acid copper bath, uniform plating into the pores of the basis metal occurred although the macrocurrent distribution was poor. In a cyanide copper bath, the filling of microgrooves was poor whereas the macrocurrent distribution was relatively uniform. Reinhard (3), Foulke and Kardos (4), and Kardos (5) all found that the microcurrent distribution for all baths became less uniform with increasing current density. It is well known to electroplaters that (6), as a common rule, in the absence of a leveling agent, a bath having relatively uniform macrocurrent distribution generally has nonuniform microcurrent distribution and *vice versa*.

Fundamental Transport Processes in Plating Systems

A general theory of current distribution on electrodes is based on a consideration of the phenomenological theory of transport processes in electrochemical systems. The fundamental transport equations in dilute solutions have been discussed in detail by Levich (7) and more recently by Newman (8). Application of these equations has followed two main courses. At low current densities where change of concentration near the electrode-solution interface can be neglected, the transport equations reduce to the Laplace equation (9)

$$\nabla^2\phi = 0 \qquad [1]$$

and the current density is given by

$$\vec{i} = -\kappa\nabla\phi \qquad [2]$$

where ϕ is the potential in the solution, $\vec{i}$ is the current density vector, and κ is the electrical conductivity of the solution. An extensive review of the solution of the Laplace equation for electrochemical systems has been completed by Fleck (10). At high current densities and when electrical migration is neglected, the mass transport of the reacting species becomes rate controlling and the transport equations reduce to the convective diffusion equation (9)

$$\frac{\partial c_i}{\partial t} + \vec{v}\cdot\nabla c_i = \nabla\cdot(D_i\nabla c_i) \qquad [3]$$

and

$$\vec{i} = -z_i\mathbf{F}D_i\nabla c_i \qquad [4]$$

where c_i, D_i, z_i are the concentration, differential diffusion coefficient, and valency of species i, $\vec{v}$ is the fluid velocity, and **F** is the Faraday constant. Methods of solving the convective diffusion equation have been treated in detail by Levich (7).

These two limiting cases play an important role in electroplating. The application to the phenomenon of macro- and microcurrent distribution is given below.

Application to the Phenomenon of Macro- and Microcurrent Distribution

An important parameter used in systems where mass transport is slow is the Nernst diffusion layer thickness δ_N. For a single electrode reaction, it is defined by

$$i = -z_i\mathbf{F}D_i\left(\frac{\partial c_i}{\partial y}\right)_{\text{at electrode}} \equiv z_i\mathbf{F}D_i\frac{c_{iB} - c_{iI}}{\delta_N} \qquad [5]$$

where y is a distance coordinate normal to the electrode surface, c_{iB} and c_{iI} are the concentration of the reacting species i in the bulk and at the interface, respectively. δ_N is a function of Reynolds number and Schmidt number in forced convection systems and a

Key words: electrodeposition, current distribution, gold.

function of Grashof number and Schmidt number in free convection systems (11). Typical values of δ_N in gently stirred solutions range from 50 to 100μ (12). δ_N can be used conveniently to establish an operational definition of macro- and microprofiles (4, 5, 14). When the linear dimension of a surface profile is in the same range or slightly smaller than δ_N, the profile is considered to be microscopic. When the linear dimension is at least one order of magnitude larger than δ_N, the profile becomes macroscopic. Since δ_N depends on both the flow condition and physical properties of the system, the dimension of macro- and microprofiles varies accordingly. The local variation of δ_N determines the characteristics of local mass transport. For instance, a faster transport results from a thinner diffusion layer. Consequently, from the standpoint of mass transport, microprofiles are "rough" whereas macroprofiles are "smooth." On the other hand, when mass transport of the reacting species is not rate controlling, ohmic drop in the solution and electrode overpotential at the interface are the important parameters to consider. Let us now examine the two cases.

Ohmic drop and electrode overpotential controlling.—This is the case where low current density is applied. The concentration gradient of the reacting species at the interface is negligible. On a macroprofile, the effect of ohmic drop in the solution is predominant in determining the current distribution. Primary current distribution results when electrode overpotential is negligible. The current distribution depends only on geometrical factors concerning the electrochemical cell and electrode arrangements. On a microprofile, the effect of ohmic drop in the solution is outweighed by the electrode overpotential at the interface. The microcurrent distribution is governed by the secondary current distribution. A linear electrode overpotential-current density relation exists when the electrode overpotential is small

$$i = \frac{i_0 n\mathbf{F}}{RT}\eta \qquad [6]$$

where i_0 is the exchange current density for the reaction, n is the number of electrons transferred for the reaction, η is the electrode overpotential, R is the gas constant, and T is the absolute temperature. The current distribution depends on the same geometrical factors as to the primary current distribution and, in addition, to the dimensionless parameter (9, 13) $(L/\kappa)(di/d\eta)$ where L is a characteristic length of the microprofile. For large cathodic overpotentials, the electrode overpotential-current density relation is given by the Tafel equation

$$\eta = -\frac{RT}{(1-\alpha)n\mathbf{F}}[\ln(-i) - \ln i_0] \qquad [7]$$

where α is the transfer coefficient. The current distribution now depends on the parameter (9, 13) $|i_{avg}|(1-\alpha)n\mathbf{F}L/RT\kappa$, where i_{avg} is the average current density. It has been confirmed in numerous cases (14, 15) that, at low current densities, the secondary current distribution on a microprofile is uniform due to the high overpotential of the deposition reactions and the high conductivity of most plating baths. This is the reason for the statement (6) "a bath of poor macrocurrent distribution has good microcurrent distribution."

Mass transport controlling.—At high current densities when mass transport of the reacting species becomes rate controlling, the Nernst diffusion layer thickness is the most important parameter to consider. A relatively uniform distribution of current is seen on the macroprofile due to the uniform thickness of the Nernst diffusion layer over the profile whereas the local variation of the diffusion layer thickness over the microprofile is responsible for the poor microcurrent distribution. Of course, current distribution can be highly nonuniform at electrode edges. For instance, the theoretical current density is infinite at the leading edge of a flat plate in the direction of electrolyte flow (16). Therefore, the above statement is only valid at regions where both the momentum and the diffusion boundary layers are fully developed.

For most plating baths, the metal ion concentration is so high that the two limiting cases can readily be distinguished and consequently lead to the interesting observation of macro- and microcurrent distribution. However, the gold content in a gold plating bath is usually so low (approximately 10-20 g/l) that under most operating conditions, the process is influenced by both electrode potential, ohmic drop and mass transport. To study the applicability of the above theoretical considerations, experimental investigation on the microcurrent distribution of a gold plating system was carried out.

Experimental

Electrolyte.—The Ehrhardt acid citrate bath (17) which contained 21.3 g/l potassium gold cyanide and 50 g/l ammonium citrate (dibasic) was chosen for these experiments. At 60°C, the *p*H of the bath was 5 and the conductivity of the bath was 0.063 ohm^{-1} cm^{-1} measured by a conductivity bridge which supplied 1000 Hz bridge current.

Electrodes.—Two types of cathodes were used to study the effect of the dimension and geometry of surface inhomogeneities. Electroformed nickel with a wavy surface of amplitude approximately 25μ and polished planar OFHC copper plates were chosen to study the microcurrent distribution. The surface area for both electrodes was 1 cm^2. Three identical V-shaped grooves, 2.5 mm apart, were cut into the copper plates. The angles of the grooves were 30°, 60°, and 90°, and the groove depths were approximately 50, 125, and 250μ. The anode was a platinum coil.

Experimental procedures.—Prior to plating, both the nickel and the copper electrodes were cleaned and degreased using acetone and trichloroethylene, respectively. The copper electrodes were then bright-dipped for approximately 10 sec in a solution containing 250 ml H_2SO_4, 125 ml HNO_3, 4 ml HCl, and 250 ml water. Both electrodes were then rinsed with distilled water. The plating cell was cylindrical in shape with a volume of 200 ml. For each plating, 150 ml of the citrate gold solution was used. Oxygen-free nitrogen was bubbled through the solution for 30 min prior to electrolysis, and a nitrogen atmosphere was maintained above the solution during electrolysis. No stirring was applied. The plating was performed at 60°C. The applied cathodic current density was 2, 4, and 6 mA/cm^2. The limiting current density for gold deposition in this experiment was found to be 6.3 mA/cm^2. The Tafel slope for the system was measured under galvanostatic condition using a rotating disk electrode at a constant rotational speed of 1730 rpm. The value was found to be 130 mV at 60°C. Depending on the depths of these grooves and the current density used, the duration of electrolysis was varied between 1 to 6 hr for optimum observation. To protect the gold surface for sectioning, approximately 12μ of Watts nickel was plated over the gold coating.

These electrodes were then mounted in epoxy, sectioned, polished, and etched in an equivolume mixture of acetic acid, nitric acid, and phosphoric acid. The microcurrent distribution of the citrate gold was determined by microscopic examination.

Results

Typical results from photomicrographs are shown in Fig. 1 to Fig. 5. They can be summarized as follows:

1. The microcurrent distribution is relatively uniform on the electroformed nickel electrode.

2. On the copper electrode, the microcurrent distribution becomes less uniform at increasing cathodic current densities and sharpening V-angles.

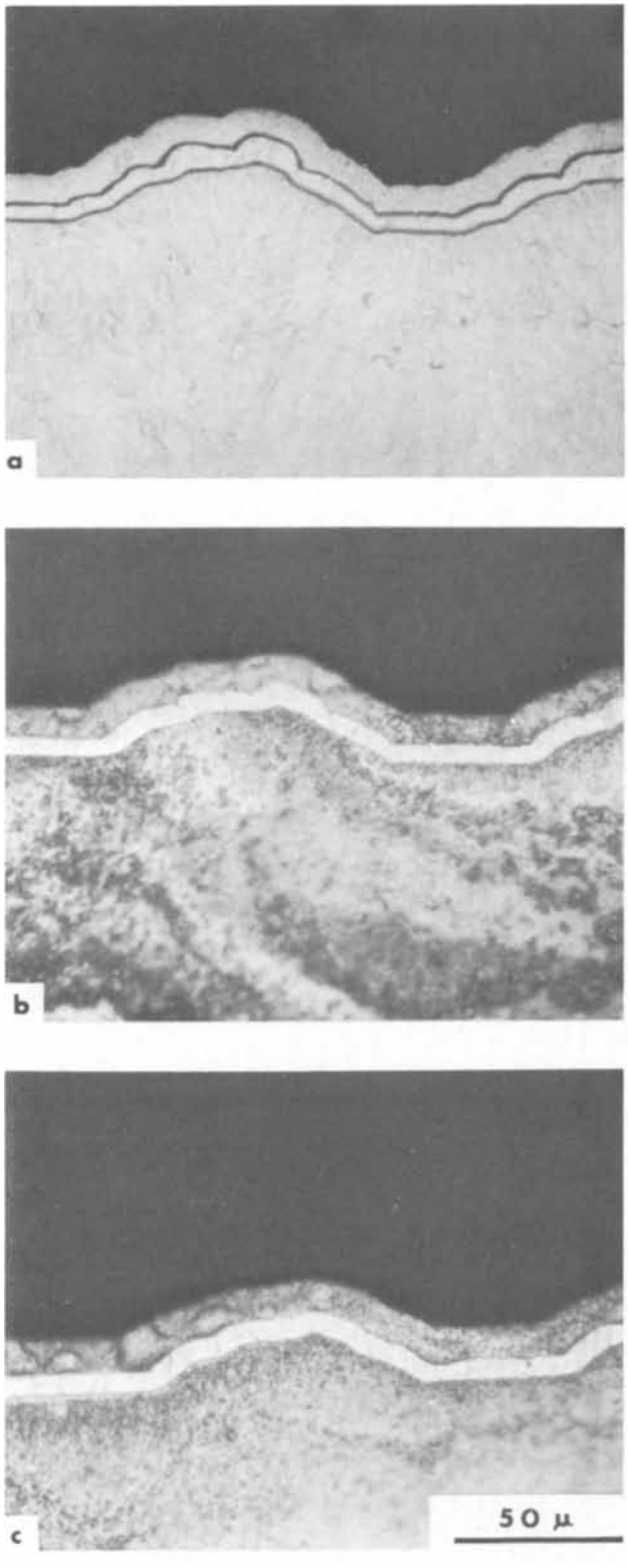

Fig. 1. Photomicrographs of gold deposits on nickel substrates with wavy surfaces: (a) 2 mA/cm^2; (b) 4 mA/cm^2; (c) 6 mA/cm^2.

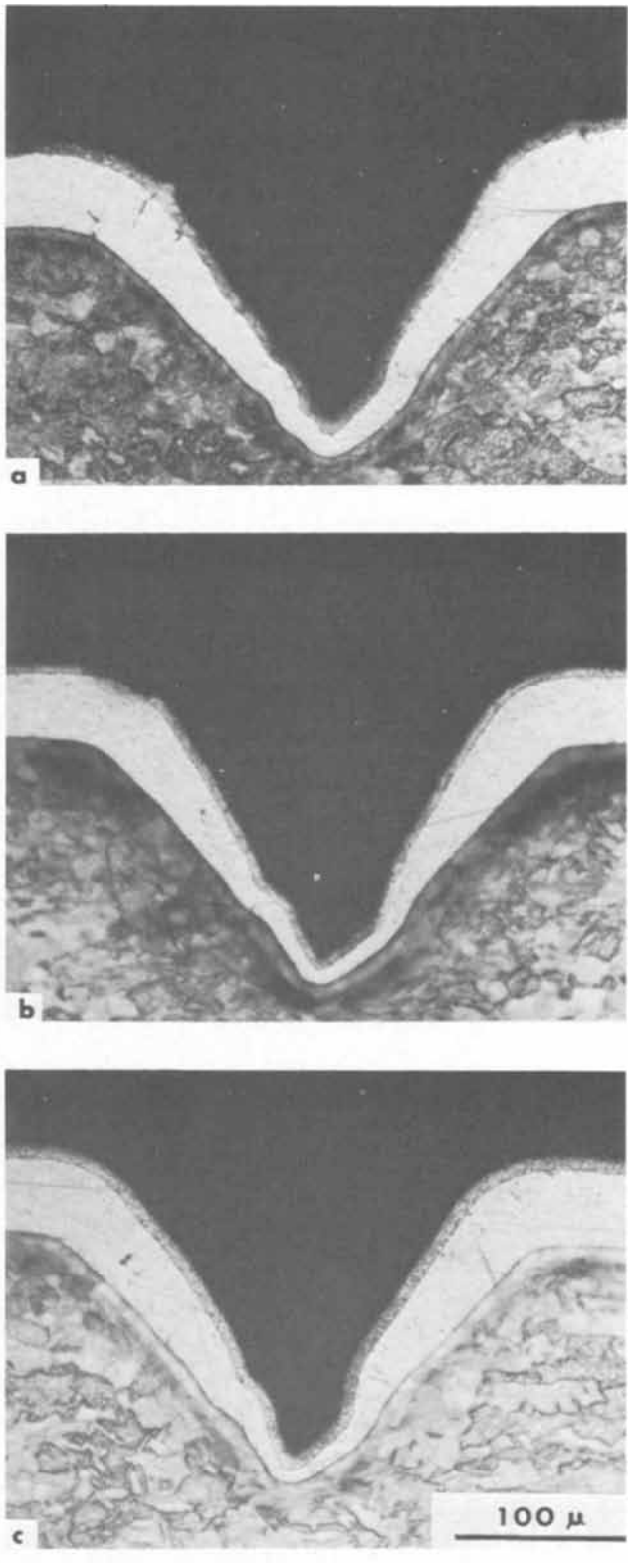

Fig. 2. Photomicrographs of gold deposits on copper substrates with triangular grooves: (a) 2 mA/cm^2; (b) 4 mA/cm^2; (c) 6 mA/cm^2.

3. On the copper electrode, the microcurrent distribution becomes less uniform at increasing groove depth.

Quantitative information on the microcurrent distribution of citrate gold plating are plotted in Fig. 6 to Fig. 8. The current distribution is represented by a gold plating thickness ratio h_1/h_2 where h_1 is the average deposit thickness on a planar surface and h_2 is the thickness at the bottom of a triangular groove. Geometrical factors used in these figures are the groove depth d and groove angle θ, and the operating variable chosen here is the current density.

Discussion

It has been concluded that the secondary current distribution depends heavily on the dimensions and geometry of the surface profile that is being plated. It is, therefore, not surprising to find that, on electro-

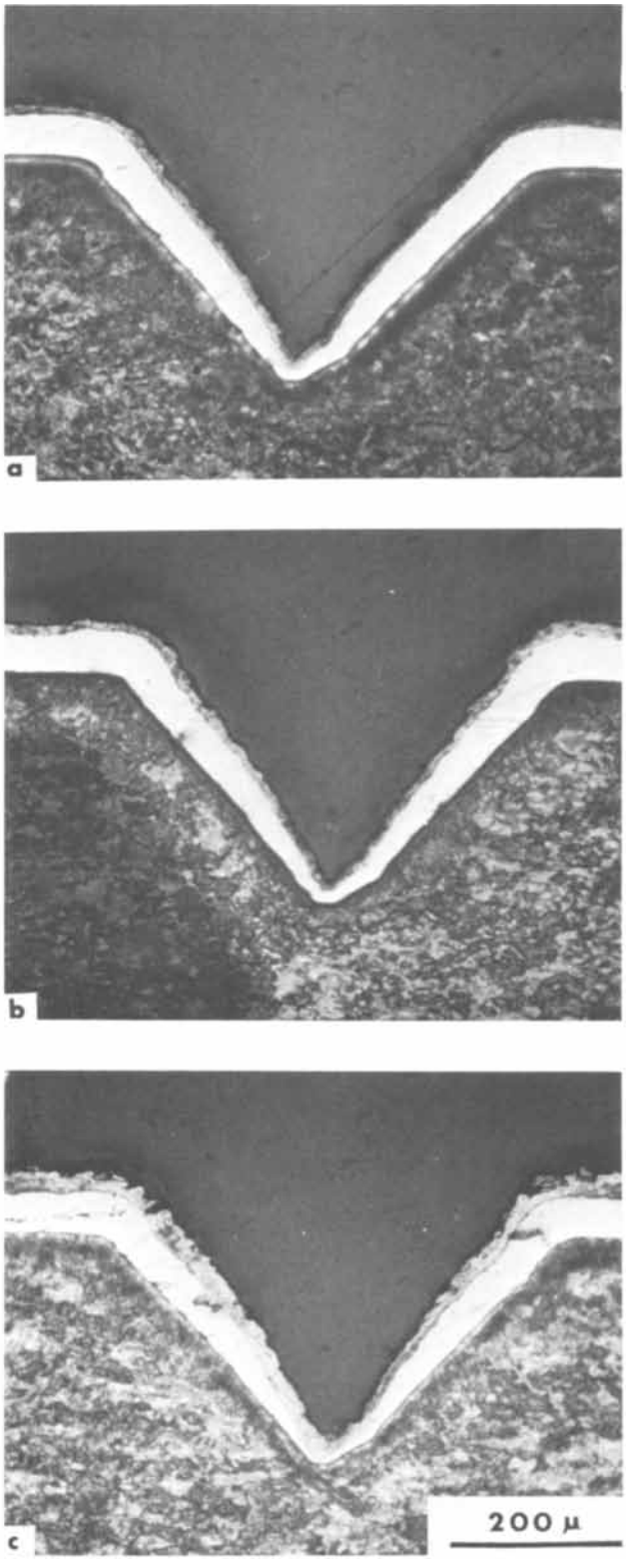

Fig. 3. Photomicrographs of gold deposits on copper substrates with triangular grooves: (a) 2 mA/cm^2; (b) 4 mA/cm^2; (c) 6 mA/cm^2.

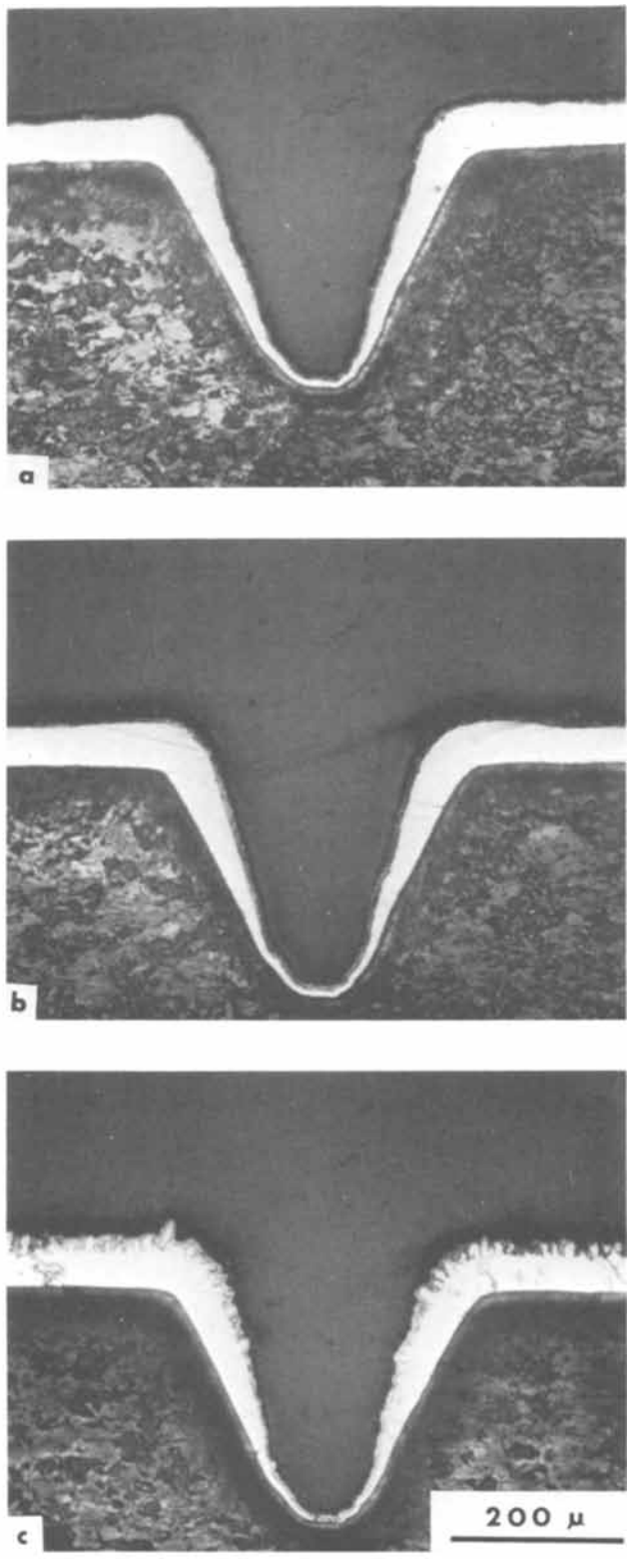

Fig. 4. Photomicrographs of gold deposits on copper substrates with triangular grooves: (a) 2 mA/cm^2; (b) 4 mA/cm^2; (c) 6 mA/cm^2.

formed nickel surface which is relatively smooth, the microcurrent distribution is rather uniform.

At increasing cathodic current densities, the process becomes increasingly mass transport limited and consequently, the microcurrent distribution becomes less uniform. At the limiting current density, gassing is observed at the electrode. The deposit becomes incoherent and frequently rough or powdery.

Wagner (18) has calculated theoretically the secondary current distribution on a triangular wave surface when the counterelectrode is far removed from the working electrode. The geometrical parameter is shown to be 1/2 (cos $\theta/2$/sin $\theta/2$) where θ is the angle between the two adjacent sides of the triangle. For linear polarization,

$$\frac{i_p - i_r}{i_{avg}} = \frac{L}{\kappa}\frac{di}{d\eta}\frac{1}{2}\frac{\cos\theta/2}{\sin\theta/2} \qquad [8]$$

whereas for Tafel polarization

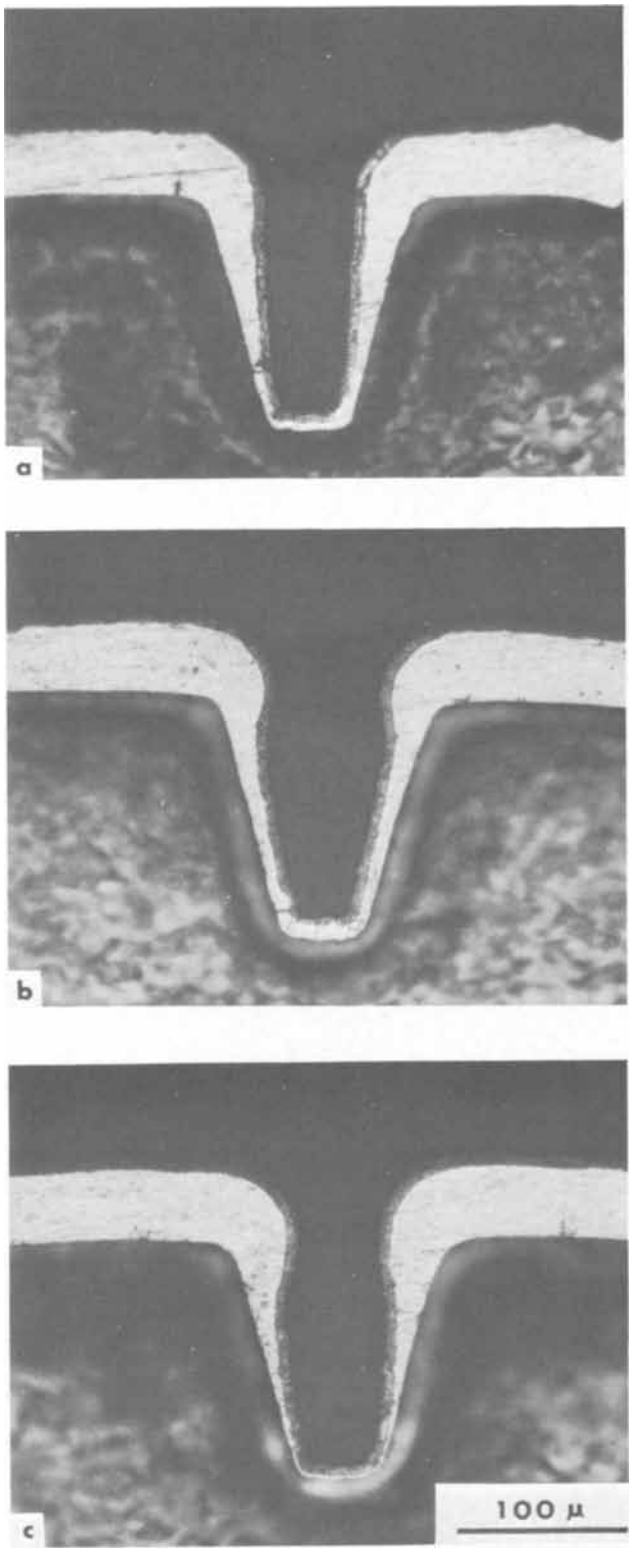

Fig. 5. Photomicrographs of gold deposits on copper substrates with triangular grooves: (a) 2 mA/cm^2; (b) 4 mA/cm^2; (c) 6 mA/cm^2.

$$\ln \frac{i_p}{i_r} = \frac{|i_{avg}| L(1-\alpha)n\mathbf{F}}{\kappa RT} \frac{1}{2} \frac{\cos \theta/2}{\sin \theta/2} \qquad [9]$$

where i_p is the current density at the peak, i_r is the current density at the recess, and L is the distance between two adjacent peaks. Varying θ from 90° to 30°, the geometrical parameter increases by approximately a factor of ten. Therefore, the microcurrent distribution is very sensitive to the value of this angle. This conclusion is also amply demonstrated in the present investigation as shown in Fig. 6-8.

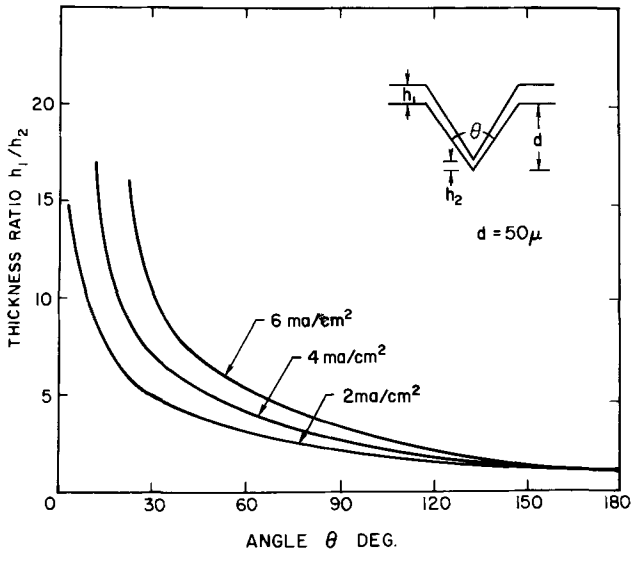

Fig. 6. Microcurrent distribution of gold deposits on copper substrates.

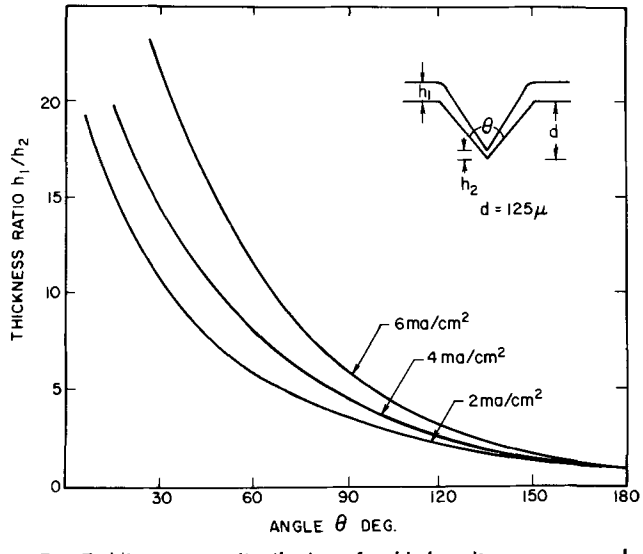

Fig. 7. Microcurrent distribution of gold deposits on copper substrates.

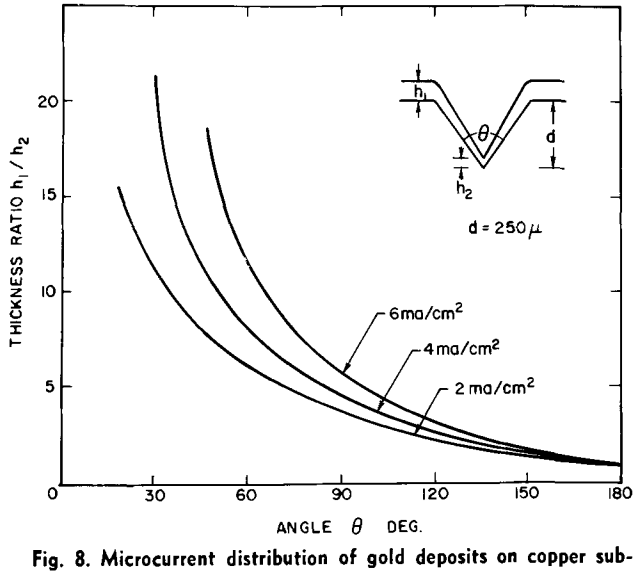

Fig. 8. Microcurrent distribution of gold deposits on copper substrates.

Considering the effect of groove depth from these figures, a significant increase in the thickness ratio is seen when groove depth is increased from 50 to 125μ but less change is found from 125 to 250μ. This can be explained by a consideration of the mass transfer aspect. Using the limiting current density of 6.3 mA/cm^2 and assuming the diffusion coefficient of gold ion as 9 x 10^{-6} cm^2/sec, δ_N is calculated from Eq. [5] to be 100μ. The difference between the diffusion path is, therefore, greater when d is changed from 50 to 125μ than from 125 to 250μ. Ignoring the effect of electrical migration, the interfacial concentration of gold ion is 10 g/l at a cathodic current density of 2 mA/cm^2 and 5.7 g/l at 4 mA/cm^2. Comparing these values to the bulk concentration of gold (15 g/l), it is seen that even at 2 mA/cm^2, the effect of mass transport is appreciable. It is therefore concluded that for most gold baths, due to the low gold content, the plating process is performed under conditions where mass transport limitations cannot be ignored.

Conclusions

Theoretical aspects of macro- and microcurrent distribution are presented. Two operating regimes for plating systems are established. At low current densities where concentration gradients near the electrode-solution interface can be neglected, a plating bath with no leveling agents will have relatively uniform microcurrent distribution but nonuniform macrocurrent distribution. At high current densities where mass transport of the reacting species is rate controlling, the plating bath will have nonuniform microcurrent distribution but relatively uniform macrocurrent distribution.

Quantitative information on the microcurrent distribution of a citrate gold plating system have been obtained. Effect of surface roughness as well as operating conditions such as metal concentration and current density on the current distribution has been established. It is also confirmed that most gold plating systems are operated under conditions where the effect of mass transport of the reacting species cannot be neglected.

In order to improve the microcurrent distribution, reduction of surface roughness and application of low current densities are both essential. An alternative approach will be either to search for suitable leveling agents or to raise the gold content of the bath thereby reducing the mass transfer controlling effect on microcurrent distribution.

Acknowledgment

The author wishes to thank D. R. Turner for his interest and encouragement during the course of this work.

Manuscript submitted Aug. 20, 1969; revised manuscript received Dec. 18, 1969.

Any discussion of this paper will appear in the Discussion Section to be published in the December 1970 JOURNAL.

List of Symbols

c_i, Concentration of species i, moles/cm^3
c_{iB}, c_{iI}, Concentration of species i in the bulk and at the interface, respectively, moles/cm^3
D_i, Differential diffusion coefficient of species i, cm^2/sec
d, Depth of a triangular grove, cm
$\mathbf{F}$, Faraday's constant, coulomb/equiv
h_1, h_2, Deposit thickness on a planar surface and at the recess of a triangular groove, respectively, cm
$\vec{i}, i$, Current density vector and measured current density, A/cm^2
i_{avg}, i_p, i_r, Average current density, current density at the peak and current density at the recess of a triangular wave surface, A/cm^2
i_o, Exchange current density, A/cm^2
L, A characteristic length, cm
L, Wave length of a triangular wave, cm
n, Number of electrons transferred in a reaction
R, Gas constant, joule/mole °K
T, Temperature, °K
$\vec{v}$, Fluid velocity, cm/sec
y, Distance normal from electrode, cm
z_i, Valency of species i
α, Transfer coefficient in polarization equation
δ_N, Nernst diffusion layer thickness, cm
η, Electrode overpotential, V
κ, Conductivity, mho/cm
ϕ, Electrostatic potential, V

REFERENCES

1. W. R. Meyer, *Proc. Am. Electroplaters' Soc.*, **23,** 116 (1935).
2. G. E. Gardam, *J. Electrodepositors' Tech. Soc.*, **22,** 155 (1947).
3. C. E. Reinhard, *Proc. Am. Electroplaters' Soc.*, **37,** 171 (1950).
4. D. G. Foulke and O. Kardos, *ibid.*, **43,** 172 (1956).
5. O. Kardos, *ibid.*, **43,** 18 (1956).
6. E. Raub and K. Müller, "Fundamentals of Metal Deposition," Elsevier, Amsterdam, (1967).
7. V. G. Levich, "Physicochemical Hydrodynamics," Prentice Hall, Englewood Cliffs, N. J. (1962).
8. J. Newman, "Transport Process in Electrolytic Solutions," C. W. Tobias, Editor, Advances in Electrochem. and Electrochem. Eng., **5,** 87 (1967).
9. J. Newman, *Ind. Eng. Chem.*, **60** [4], 12 (1968).
10. R. N. Fleck, "Numerical Evaluation of Current Distribution in Electrochemical Systems," M. S. Thesis, University of California, Berkeley, 1964.
11. N. Ibl, *Electrochim. Acta*, **1,** 117 (1959).
12. N. Ibl, *Chem.-Ing.—Tech.*, **35,** 353 (1963).
13. T. P. Hoar and J. N. Agar, *Discussions Faraday Soc.*, **1,** 162 (1947).
14. O. Kardos and D. G. Foulke, "Applications of Mass Transfer Theory: Electrodeposition on Small Scale Profiles," C. W. Tobias, Editor, Advances in Electrochem. and Electrochem. Eng., **2,** 145 (1962).
15. N. Ibl, "Diffusion Layers; Influence on Mass Transport on the Structure of Electrolytic Deposits," Protection Against Corrosion by Metal Finishing, Zürich, Forster Verlag A. G., p. 48 (1966).
16. C. W. Tobias and R. G. Hickman, *Z. Physik. Chem.* (Leipzig), **229,** 145 (1965).
17. R. A. Ehrhardt, *Proc. Am. Electroplaters' Soc.*, **47,** 78 (1960).
18. C. Wagner, *This Journal*, **98,** 116 (1951).

Electroless Deposition of Certain Metal Oxides

I. Alpha-PbO_2

W. Mindt*[1]

Bell Telephone Laboratories, Incorporated, Murray Hill, New Jersey

ABSTRACT

Electroless deposition of α-PbO_2 films by oxidation of lead(II) acetate with peroxydisulfate is described. Investigations into the mechanism of this reaction show it to be a mixed electrolytic process with the two partial reactions $Pb^{++} + 2H_2O \rightarrow \alpha\text{-}PbO_2 + 4H^+ + 2e^-$ and $S_2O_8^= + 2e^- \rightarrow 2SO_4^=$. The variation of mixed potential and growth rate with the *p*H of the electrolyte is studied and interpreted in terms of the *p*H dependence of both partial reactions. A mechanism of the reduction of $S_2O_8^=$ at PbO_2 is proposed.

The anodic oxidation of some metal ions in aqueous solutions leads under certain conditions to the deposition of an oxide at the anode, according to the electrode reaction

$$mMe^{z+} + nH_2O \rightarrow Me_mO_n + 2nH^+ + (2n - mz)e^- \quad [1]$$

(in acid solutions). Some well-known examples are the systems Pb^{++}/PbO_2, Mn^{++}/MnO_2, $Ni^{++}/$"NiO_2", Tl^+/Tl_2O_3 and Ag^+/AgO. If the oxidation of the metal ion is carried out as a controlled heterogeneous reaction by a suitable oxidizing agent instead of an external electrical current, the deposition of the metal oxide can be called "electroless" in analogy to the corresponding process known for metals.[2] In general, the conditions under which electroless deposition of metal oxides is possible are equivalent to those for metals: The oxidizing agent must have, of course, a higher redox potential than the equilibrium potential of reaction [1], and its reduction at the metal oxide must be kinetically possible. The reduced species should be soluble in the electrolyte and should not interfere with the anodic process, *e.g.*, due to adsorption at the metal oxide. Nucleation of the metal oxide in the solution should be prevented since this results in an uncontrolled precipitation. Finally, since oxidation and reduction steps occur at different locations, charge transport within the metal oxide must be possible, *i.e.*, the metal oxide has to be an electrical conductor.

In the present work some systems are investigated in which these conditions are fulfilled. In the first part, deposition of α-PbO_2 is described. Films of this oxide are of interest for use as counterelectrodes in solid valve metal oxide capacitors, since they have a considerably higher conductivity than MnO_2 films which are used so far, and capacitors with PbO_2 coatings show similar self-healing properties (2, 3).

The oxidizing agent used in our experiments is peroxydisulfate (persulfate). The studied over-all reaction is

$$Pb^{++} + 2H_2O + S_2O_8^= \rightarrow \alpha\text{-}PbO_2 + 4H^+ + 2SO_4^= \quad [2]$$

This reaction was described earlier by Rüetschi and Cahan (4). The authors obtained α-PbO_2 as precipitate from solution by a homogeneous reaction. Occasionally, the formation of PbO_2 films at the walls of the glass beakers in which the reaction was carried out was observed (5); however, this effect was not further studied. In the experiments described here, reaction [2] was carried out heterogeneously on PbO_2 substrates under conditions where no precipitation of PbO_2 in the solution occurred.

It is of some practical interest to be able to deposit adherent α-PbO_2 films on insulating substrates. In electroless metal deposition, this is usually accomplished by treating the substrate surface in such a way that it acts as catalyzer during the deposition of an initial metal layer. We did not investigate an equivalent procedure of surface activation. As an alternative method, an initial PbO_2 layer of a few hundred angstroms was precipitated from solution by catalyzing reaction [2] with Ag^+, as will be described in the experimental part. Further growth of PbO_2 was carried out by electroless deposition. α-PbO_2 films obtained in this way showed good adherence up to a thickness of 1μ on various substrates, such as glass, quartz, ceramics, or Ta_2O_5.

Experimental

All experiments were carried out in a supporting electrolyte of M $NH_4C_2H_3O_2$ which was prepared from 30% NH_4OH and glacial acetic acid (both Baker "electronic grade"). Lead acetate was added to this solution in the form of PbO (Fisher "certified") and an equivalent amount of acetic acid. In most experiments, a concentration of lead acetate of 50 mM was used. $S_2O_8^=$ was added from a freshly prepared aqueous solution of ammonium persulfate (Fisher "certified") which was brought to the *p*H of the studied solution by addition of NH_4OH.

The PbO_2 electrodes used for the current/potential measurements were prepared by anodic deposition of a *ca.* 0.5μ thick layer on a 0.25 cm^2 Pt electrode. The deposition was carried out immediately before each measurement in the same electrolyte, applying a current density of 0.5 mA/cm^2. Weight measurements of the deposited PbO_2 were carried out on electrodes of larger surface area to achieve a higher accuracy. For this purpose, 3 x 1 in. glass slides were used, on which an initial layer of 500Å PbO_2 was precipitated in the following way: Glass slides were exposed in a vertical position to a solution prepared by mixing 100 ml of 50 mM lead acetate dissolved in M $NH_4C_2H_3O_2$ with 100 ml of 2M $(NH_4)_2S_2O_8$, both brought to a *p*H of 6. To this solution, $AgNO_3$ was added as catalyst in a concentration of 5 x 10^{-5}M. After an induction time of about 15 min, the solution turned slowly brown, and after 45 to 90 min, a continuous film of 500Å PbO_2 was precipitated on the glass slides. After washing with distilled water and drying at room temperature, the slides were used for the weight and open-circuit potential measurements. Results of these measurements should be, of course, independent of the way in which the initial PbO_2 layer was obtained. This was confirmed by experiments carried out on 20 cm^2 Pt elec-

* Electrochemical Society Active Member.
[1] Present address: C/O F. Hoffmann-La Roche and Company, CH 4002 Basel, Postfach, Switzerland.
[2] Electroless deposition of a metal oxide is known so far only in the case of MnO_2. Films of this oxide are deposited by reduction of MnO_4^- (1). It is, however, doubtful if the term "electroless" can be applied to this process, since it is precipitation from solution rather than a controlled heterogeneous reaction.

trodes, on which PbO_2 was electrodeposited, as well as by using glass substrates on which PbO_2 was deposited by hydrolysis of lead tetraacetate as described by Robinson (2).

The potential/current measurements were carried out potentiostatically, using a 1*N* calomel reference electrode (NCE) and a Pt counterelectrode. Stationary conditions were achieved after a few minutes at low current densities (< 10 $\mu A/cm^2$) and after several seconds at higher current densities. The electrolyte was stirred. All experiments were carried out at 25°C.

Results

In Fig. 1, stationary current/potential curves are shown which demonstrate that the nature of the deposition is a mixed electrolytic process. Curve 1 was obtained in a solution of 50 mM lead acetate in M $NH_4C_2H_3O_2$ at *p*H 8.5. In this solution, where the lead ions are solubilized by complexing with acetate, the anodic reaction is

$$Pb^{++} + 2H_2O \rightarrow \alpha PbO_2 + 4H^+ + 2e^- \qquad [3]$$

with cathodic currents, PbO_2 is reduced to a lower oxide. Curve 2 was obtained after addition of 50 mM ammonium persulfate to the above solution. The net current results from the superposition of reaction [3] and the reduction of $S_2O_8^=$

$$S_2O_8^= + 2e^- \rightarrow 2SO_4^= \qquad [4]$$

By subtraction of curve 1 from curve 2, the partial current voltage curve of reaction [4] is obtained (curve 3). At open circuit, deposition of PbO_2 occurs at the mixed potential U_m with the partial current density i_d. Independent determinations of i_d by weight measurements of the deposited PbO_2 give the same result. This can be seen in Fig. 2 which shows i_d and U_m as a function of *p*H. The electrolyte was again 50 mM lead acetate and 50 mM ammonium persulfate in M ammonium acetate. The *p*H was varied between 5 and 10 by addition of $HC_2H_3O_2$ or NH_4OH, respectively. i_d was determined from the stationary anodic current at the potential U_m in the absence of $S_2O_8^=$ as described before as well as by weight measurements. The results of both methods were reproducible with deviations not larger than 10%. A current density of 1 mA/cm^2 corresponds to a deposition rate of 760 Å/min. The deposition current increases with *p*H, following the relationship

$$\log i_d = \text{const} + 0.81\, pH \qquad [5]$$

U_m was determined on PbO_2 films deposited on Pt and on glass substrates. With increasing *p*H, U_m shifts in negative direction by (59 ± 5) mV per *p*H unit.

The observed *p*H dependence of i_d and U_m results from influences of both anodic and cathodic reactions.

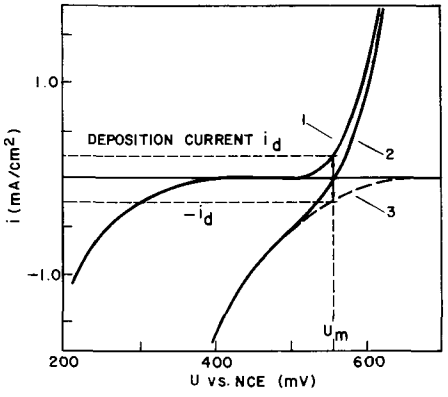

Fig. 1. Stationary current/potential curves at PbO_2 electrode. Curve 1, anodic partial reaction [3], measured in a solution of 50 mM lead acetate in 1M ammonium acetate at *p*H 8.5; curve 2, over-all reaction [3] + [4], measured after addition of 50 mM ammonium persulfate; curve 3, cathodic partial reaction [4], calculated by subtraction of curve 1 from curve 2.

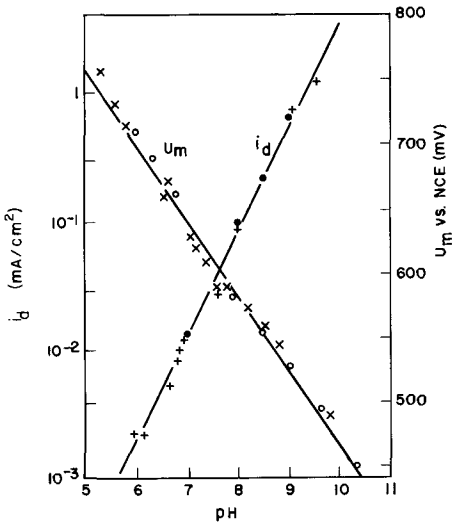

Fig. 2. Deposition current i_d and mixed potential U_m as function of *p*H. Electrolyte: 50 mM lead acetate + 50 mM ammonium persulfate in 1M ammonium acetate. ●, i_d from current at U_m in absence of $S_2O_8^=$; +, i_d from weight measurements; o, U_m at PbO_2 deposited on platinum; x, U_m at PbO_2 deposited on glass (1 mA/cm^2 corresponds to 760 Å/min).

This becomes evident from Fig. 3 in which the partial current/potential curves of the two reactions are plotted at different *p*H values. The anodic curves were determined in a solution of 50 mM lead acetate in M ammonium acetate. The *p*H was varied as before. The reduction of $S_2O_8^=$ could not be studied in a similar way in a solution containing $(NH_4)_2S_2O_8$ only. Under this condition, the PbO_2 electrode turned slowly into a passivated state, and the current measurements were irreproducible. It is assumed that this is the effect of adsorption of the reaction product, $SO_4^=$. Apparently, the PbO_2 surface which is freshly formed during the deposition shows a different behavior with regard to the kinetics of the $S_2O_8^=$ reduction. The partial current/potential curves of the $S_2O_8^=$ reduction near U_m were determined from the difference between the currents of the Pb^{++} oxidation and the over-all reaction [2] as described for Fig. 1. The intersections between anodic and cathodic curves at the same *p*H represent open-circuit conditions (zero net current), *i.e.*, give the values of i_d and U_m. The dotted line is obtained from the experimental data of i_d and U_m in Fig. 2. The log i/U curves of the Pb^{++} oxidation approach at higher current densities and low *p*H a Tafel slope of 118 mV which is expected for this reaction if the trans-

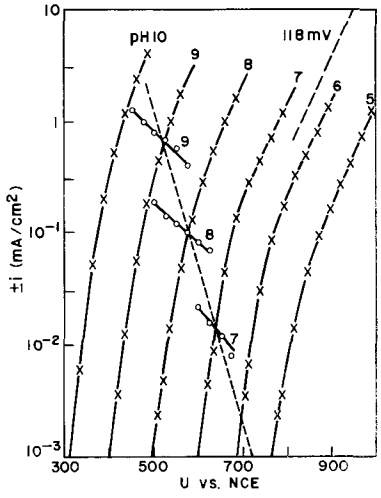

Fig. 3. Partial current/potential curves at various *p*H. x, anodic reaction [2]; o, cathodic reaction [4]; dotted line, i_d *vs.* U_m from data in Fig. 2.

fer coefficient α is 0.5. In the region studied here (dotted line), the slopes are generally smaller. The Tafel slopes of the reduction of $S_2O_8^=$ vary between 210 and 270 mV, corresponding to transfer coefficients between 0.28 and 0.22. The low transfer coefficient is typical for this reaction, *e.g.*, a value of $\alpha = 0.32$ was obtained by Müller (6) in alkaline solutions at Pt electrodes.

In Fig. 4, the partial cathodic current is plotted as a function of the $S_2O_8^=$ concentration at constant electrode potentials. This experiment was carried out again in a solution of 50 mM lead acetate in 1M $NH_4C_2H_3O_2$, to which $(NH_4)_2S_2O_8$ was added from a 2M aqueous solution. The pH was kept constant at 8.50. At low concentrations, the current is proportional to the square root of the persulfate concentration indicating a reaction order of 0.5 for the $S_2O_8^=$ ion. The deviation from linearity at higher concentrations is probably the effect of the presence of $SO_4^=$ ions which seem to inhibit the reaction. This assumption is supported by the fact that an addition of 0.1M $(NH_4)_2SO_4$ to the solution results in a decrease of the current to nearly zero.

Properties of the PbO_2 *films.*—The electron diffraction pattern of the PbO_2 films deposited on glass substrates showed only lines of the α-modification. There was no evidence for the presence of lower lead oxides. In some cases, the crystallites had a slight orientation with the (100)-plane parallel to the substrate as is observed also on electrodeposited α-PbO_2 (7). The crystallite size of a 5000Å thick film deposited at pH 8 is about 2000Å as determined by electron microscopy.

The electrical properties are, in general, similar to those of electrodeposited α-PbO_2 (8). Hall effect measurements showed that the carrier density is about 10^{21} cm^{-3} and is nearly independent of the pH at which the films were deposited. There is, however, an effect on the resistivity with increasing pH, *e.g.*, a 5000Å thick film deposited at pH 7 had a resistivity of 2×10^{-3} ohm cm, whereas at pH 10 a resistivity of 3×10^{-2} ohm cm was obtained.

Discussion

The result that the deposition occurs at the rate expected from the stationary current potential relations indicates that the deposition is a pure electrochemical process, *i.e.*, that no "chemical" deposition due to a reaction without charge exchange at the interface is involved. The deposition rate is controlled by the potential U_m which is a function of the composition of the electrolyte.

The variation of U_m with pH was found to be linear in the studied pH region with a slope of −59 mV/pH. An interpretation of this result is difficult since it arises from a complex pH dependence of the current potential relations of both partial reactions, as was seen in Fig. 3. In the following, the origins of the pH dependence of the two reactions are discussed.

The drift of the anodic current potential curves with pH is mainly the effect of the variation of the equilibrium potential of the anodic reaction. The equilibrium potential of reaction [3] is

$$U_o = 1.450 - 0.0296 \log (Pb^{++}) - 0.1183\, pH \quad [6]$$

Measurements of the open-circuit potential of a PbO_2 electrode in a solution of 50 mM lead acetate in 1M ammonium acetate are shown in Fig. 5 (dotted line). The variation with pH is linear and has a slope of −90 mV/pH instead of −118 mV/pH which would be expected for reaction [3]. Better agreement with this result would be given by the reaction

$$Pb(OH)^+ + H_2O \rightleftharpoons PbO_2 + 3H^+ + 2e^- \quad [7]$$

with

$$U_o = 1.270 - 0.0296 \log [Pb(OH)^+] - 0.0887\, pH \quad [8]$$

It is, however, not certain what composition the lead acetate complex has in this solution. The assumption that a complex of the type $Pb(OH)(C_2H_3O_2)_n^{(n-1)-}$ exists is not unreasonable, since $Pb(OH)^+$, respectively $Pb_4(OH)_4^{4+}$, is the hydrolyzed form stable in this pH region in perchlorate medium according to Olin (12). It should be mentioned that the absolute values of the open-circuit potentials in Fig. 5 cannot be compared with the calculated equilibrium potentials, since no liquid junction potentials and activity coefficients have been taken into account. The fact that the deviation is as high as 150 mV indicates that the activity coefficient of lead(II) in this solution is very low.

Besides the pH dependence of the equilibrium potential, there is also an effect of the pH on the rate of the anodic reaction, as can be seen in Fig. 3. At higher pH, the current potential curves are steeper. It is unlikely that this is an effect of an increase of the exchange current of reaction [3], since the influence of the reverse current should be negligible at overpotentials more than about 120 mV. It may be suggested that the mechanism of the reaction changes at higher pH, possibly due to the formation of $Pb(OH)_2$ or a complex of this with acetate.

The result that the cathodic curves are pH dependent is at first surprising, since $S_2O_8^=$ as well as the reaction product $SO_4^=$ are almost completely dissociated in the studied pH region. The mechanism of the $S_2O_8^=$ reduction on platinum electrodes in alkaline solution, as proposed by Müller (6)

$$S_2O_8^= \rightleftharpoons (2SO_4^{-\cdot})_{ads} \quad [9]$$

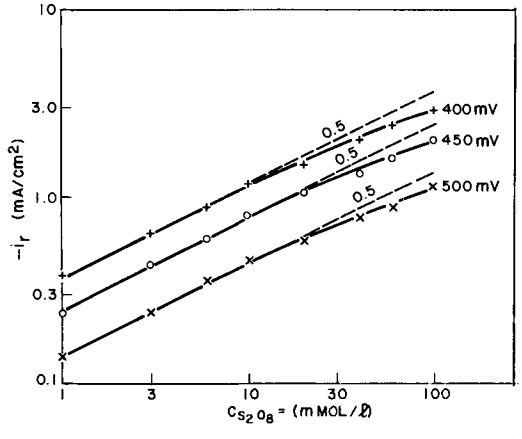

Fig. 4. Partial current of $S_2O_8^=$ reduction at PbO_2 *vs.* concentration of $S_2O_8^=$. Electrolyte: 50 mM lead acetate + x mM ammonium persulfate in 1M ammonium acetate, pH 8.50.

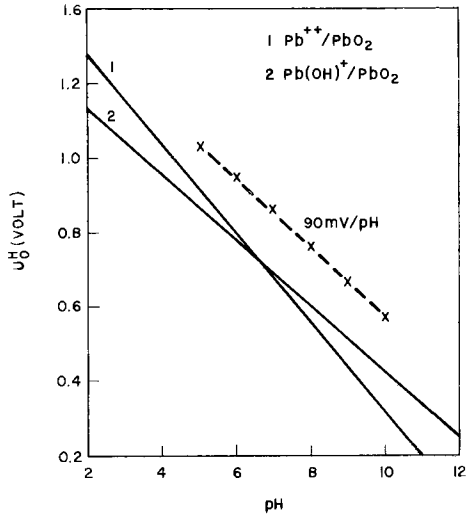

Fig. 5. Equilibrium potentials calculated from thermodynamic data (9) *vs.* pH. x, open-circuit potentials of PbO_2 electrodes measured in a solution of 50 mM lead acetate in 1M ammonium acetate.

$$2(SO_4^-)_{ads} + 2e^- \rightarrow 2SO_4^= \quad [10]$$

does also not explain the pH dependence found here. It has been proposed by several authors (10) that the sulfate radical is converted to the OH· radical, according to

$$SO_4^- + H_2O \rightleftharpoons OH\cdot + SO_4^= + H^+ \quad [11a]$$

or

$$SO_4^- + OH^- \rightleftharpoons OH\cdot + SO_4^= \quad [11b]$$

Recent investigations on the photolysis of persulfate ions (11) showed that between pH 8.5 and 10.8 the stability of the SO_4^- radical decreases rapidly, indicating the existence of a pH dependent equilibrium like Eq. [11]. Although the path of the conversion of SO_4^- into OH· is not yet clarified, the following mechanism of the reduction of $S_2O_8^=$ at PbO_2 can be proposed

$$S_2O_8^= \rightleftharpoons 2SO_4^-{}_{ads} \quad [9]$$

$$2SO_4^-{}_{ads} + 2\,OH^- \rightleftharpoons 2\,OH\cdot_{ads} + 2SO_4^= \quad [11]$$

$$2\,OH\cdot_{ads} + 2e^- \rightarrow 2\,OH^- \quad [12]$$

The steady-state conditions for $SO_4^-{}_{ads}$ and $OH\cdot_{ads}$ are

$$\frac{d[SO_4^-]}{dt} = 2k_9\,[S_2O_8^=] - k_9'\,[SO_4^-]^2 - k_{11}\,[SO_4^-][OH^-] + k_{11}'\,[SO_4^=][OH\cdot] = 0 \quad [13]$$

$$\frac{d[OH\cdot]}{dt} = k_{11}\,[SO_4^-][OH^-] - k_{11}'\,[SO_4^=][OH\cdot] - k_{12}\,[OH\cdot] = 0 \quad [14]$$

and

$$i = \mathbf{F}\,k_{12}\,[OH\cdot] \quad [15]$$

Assuming that the equilibrium of reaction [11] is on the left side in the studied pH region, $k_{11}'/k_{11} >> 1$, and that $k_{12} << k_{11}'$, the following relation is obtained for the current at a constant potential

$$i = -\mathbf{F}\frac{k_{11}\,k_{12}}{k_{11}'}\sqrt{2\frac{k_9}{k_9'}}\frac{[OH^-][S_2O_8^=]^{1/2}}{[SO_4^=]} \quad [16]$$

This result is in agreement with the reaction order of 0.5 found for the $S_2O_8^=$ ion at low concentrations (Fig. 4). Furthermore, it gives an explanation for the pH dependence of reaction [4], although the experimental data in Fig. 3 are not sufficient to determine if the reaction order of OH^- is actually one. Finally, Eq. [16] shows that an increase of the sulfate ion concentration will decrease the current. This was also observed in the experiments; however, a passivation of the PbO_2 surface by formation of lead(II) sulfate may have a similar effect.

Acknowledgments

The author would like to thank U. B. Thomas and P. C. Milner for their interest in this work and many helpful discussions. He is also indebted to H. C. Montgomery for the provision of facilities for the Hall effect measurements and to G. W. Kammlott for carrying out the electron diffraction and electron microscopic studies.

Manuscript submitted Sept. 30, 1969; revised manuscript received Jan. 9, 1970.

Any discussion of this paper will appear in a Discussion Section to be published in the December 1970 JOURNAL.

REFERENCES

1. R. W. Berry, P. M. Hall, and M. T. Harris, "Thin Film Technology," p. 388, D. van Nostrand Co., Inc., Princeton, (1968).
2. P. Robinson, U.S. Pat. 3,066,247, Nov. 27, 1962.
3. W. Mindt, G. I. Parisi, Patent pending.
4. P. Rüetschi and B. Cahan, *This Journal*, **104**, 406 (1957).
5. B. Cahan, Private communication.
6. L. Müller, *J. Electroanal. Chem.*, **13**, 275 (1967).
7. A. T. Zaslavskii and S. S. Tolkachev, *Z. Fiz. Khim., SSSR*, **26**, 743 (1952).
8. W. Mindt, *This Journal*, **116**, 1076 (1969).
9. "Selected Values of Chemical Thermodynamic Properties," National Bureau of Standards Circular 500, Part 1, p. 158 (1961).
10. D. A. House, *Chem. Rev.*, **62**, 185 (1962), review article.
11. L. Dogliotti and E. Hayon, *J. Phys. Chem.*, **71**, 2511 (1967).
12. A. Olin, *Acta Chem. Scand.*, **14**, 126, 814 (1960).

Electrochemical Behavior of Selenium and Tellurium in Fused LiCl-KCl Eutectic

F. G. Bodewig and James A. Plambeck***

Department of Chemistry, University of Alberta, Edmonton, Alberta, Canada

ABSTRACT

Liquid selenium has been reduced coulometrically in fused LiCl-KCl eutectic at 400°C. Nernstian behavior is observed for the cell C,Se(1)/$Se^=$, LiCl-KCl//Pt^{++},LiCl-KCl/Pt. The standard potentials of the selenium/selenide couple at 450°C with respect to the appropriate standard platinum reference electrode are −1.141, −1.172, and −1.252V on the molar, molal, and mole fraction scales, respectively. Voltammetric studies showed an anodic wave at +0.05V ascribed to $2Se + 2Cl^- \rightarrow Se_2Cl_2(g) + 2e^-$ and a cathodic wave at −1.07V ascribed to $Se + 2e^- \rightarrow Se^=$. For tellurium an anodic wave at −0.15V is ascribed to Te → Te(II) + $2e^-$ and a cathodic one at −1.40V to the plating of lithium into tellurium; the formation of free telluride does not appear to occur. The standard potential for the couple Te(II)/Te is estimated at −0.1V.

A recent publication from this laboratory (1) reported the electrochemical behavior of sulfide in the fused LiCl-KCl eutectic. The present paper extends this study to selenium and tellurium.

The literature on selenium and tellurium in fused salt media is scanty. Verdieck and Yntema (2) measured the deposition potential of tellurium from solutions of tellurium dioxide in fused $AlCl_3$-NaCl-KCl at 218°C. The solid electrolyte cells Ag(s)/AgI(s)/Ag in Te or Se have been investigated by Kiukkola and

** Electrochemical Society Active Member.
* Electrochemical Society Student Member.

Wagner (3). Foster and Liu (4) employed the cell $Li_3Bi(s)$, Li in Bi(l)/LiCl-LiF/Li in Te(l), Li_2Te to obtain the free energy of formation of Li_2Te by emf measurements, and a similar cell has been used in the Bi-Te system by Liu and Angus (5). Selenium and tellurium have been used as cathode materials in secondary cells with fused salt electrolytes at Argonne National Laboratory (6, 7).

Experimental

Apparatus.—Potentials were measured with a digital voltmeter (Model 3440A, Hewlett-Packard). Coulometric generations employed a Model IV Coulometric Current Source (E. H. Sargent and Company). An Anotrol Model 4100 Potential Controller was used for voltammetric investigations.

A Lindberg Hevi-Duty Model 54381A furnace with a Model 59344 temperature controller was employed. Temperatures were measured with a chromel-alumel thermocouple calibrated at the melting point of zinc.

The electrolytic cell was essentially the same as described previously (8).

Solvent.—The preparation of the LiCl-KCl eutectic solvent (59.5 m/o LiCl, mp 352°C) has been described previously (1).

Chemicals.—Reagent grade LiCl (Fisher Scientific Company) and KCl (Fisher Scientific Company or Shawinigan Chemicals) were used. Selenium (99.99%) was obtained in ¼ x 2 in. rods from A. D. Mackay, Inc. Tellurium (99.999%) was obtained from Atomergic Chemetals Company. Graphite electrodes were Special Spectroscopic Electrodes ⅛ in. in diameter (National Carbon Company). Argon was dried by passage through a magnesium perchlorate column and two traps cooled by a dry ice-acetone bath.

Electrodes.—A reference electrode based on the Pt(II)/Pt couple (about 0.03M) was generated coulometrically for each experiment by anodization of a coil of platinum wire.

The selenium electrode consisted of a small Pyrex cup (7 mm diameter, 5 mm long) containing pieces of selenium. Contact with the selenium (liquid at operating temperature) was made with a graphite rod attached to Nichrome leads well above the melt level. The Pyrex cup rested on the bottom of the isolation compartment and was totally immersed in the melt.

The tellurium electrodes were made by melting lumps of tellurium in a 4 mm Pyrex tube under argon. A tungsten wire was inserted into the liquid tellurium which was then allowed to solidify. The electrode was removed by carefully breaking the glass.

A graphite rod in an isolation compartment was used as the counterelectrode.

Procedure.—The crucible containing the frozen eutectic, isolation compartments, and electrodes was placed inside the outer glass jacket of the electrolytic cell which could be connected to a vacuum pump. Transfers of frozen eutectic to the crucible were made inside a dry box under nitrogen. The outer jacket was closed to the atmosphere by means of a Pyrex cap connected to it with a 75 mm O-ring joint. On this cap were blown five 14/20 ground-glass joints which were used to insert a thermocouple, an argon inlet tube, and the electrodes. The isolation compartments were made of 10 mm Pyrex sealing tubes with 10-20μ frits (D porosity; Ace Glass Inc.) The temperature of the cell was slowly raised to 370°C under vacuum in order to dry the glass equipment and electrodes before fusion of the eutectic. After fusion of the eutectic, argon was introduced and bubbled through the melt during all experiments. The compartments were allowed to fill with eutectic during a period of 8-10 hr. The selenium or tellurium was added as a final step. Ionic species were generated by anodization or cathodization of the selenium or tellurium. The cells were operated at 400° ± 2°C to minimize loss of volatile materials from the melt, which was still the most serious problem encountered in the investigation.

Electrode potentials were measured against the platinum reference electrode and corrected to the Pt(II), 1.0 *M*/Pt standard molar platinum electrode (SMPE) of Laitinen and Liu (9); they are reported in conformance with the IUPAC "Stockholm" sign convention. The thermoelectric potential of the graphite and leads was measured as +10 mV with respect to platinum. It was essentially invariant with temperature from 400° to 450°. The potentials were corrected for this effect. They were then converted from 400° to 450°C using the experimentally determined potential-temperature relationships (see below) and the actual temperature of each potential measurement. The amount of solvent in each isolation compartment was determined by a potentiometric chloride titration; when necessary, selenide was removed by acidification (in a hood). The concentrations of $Se^=$ and Pt^{++} were determined from the coulombs passed and solvent volume (9). The least-square calculations were done on the University of Alberta IBM/360 computer, and copies of the programs used are available in the thesis of one of the authors (F.G.B.).

The voltammetric procedure was as described previously (1).

Results

Voltammetric results.—The voltammetric curves obtained for selenium and tellurium are shown in Fig. 1, denoted respectively by triangles and circles. In the absence of selenium and tellurium, the only electrochemical phenomena observed are anodic chlorine evolution (+0.3V) and cathodic lithium deposition (>−2.1V) as in previous work (1, 9).

The cathodic branch observed with selenium is ascribed to $Se(l) + 2e^- \rightarrow Se^=$. A red-brown color was observed leaving the electrode until the entire compartment contents were colored when cathodic current was passed. Extrapolation of the linear part of the curve to zero current gave −1.07 ± 0.02V for the "decomposition" potential, in good agreement with the potentiometric results given below. The anodic wave is ascribed to $2Se(l) + 2Cl^- \rightarrow Se_2Cl_2(g) + 2e^-$, analogous to the reaction $2S(l) + 2Cl^- \rightarrow S_2Cl_2(g) + 2e^-$ observed previously (1). The "decomposition" potential was +0.05 ± 0.02V. Colorless gas bubbles were observed forming on the electrode at this potential and leaving the melt. No attempt was made to trap the gas since Se_2Cl_2 is reported as unstable at considerably lower temperatures than those employed here. Stable potentials could not be obtained, as is expected when the species produced electrochemically volatilizes from the melt.

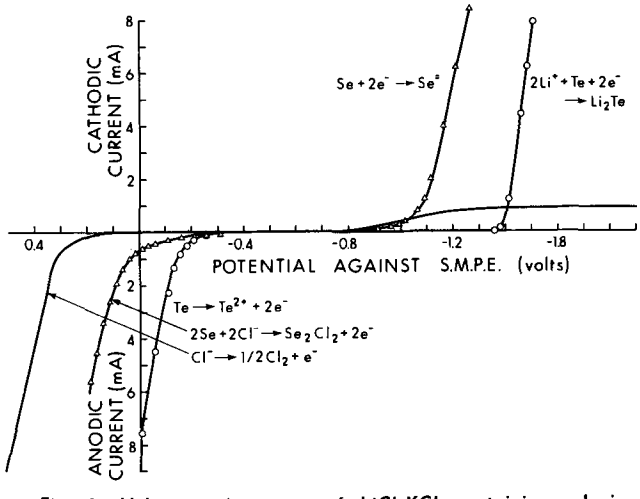

Fig. 1. Voltammetric curves of LiCl-KCl containing selenium (triangles) or tellurium (circles). Temperature 400°C, reference potential SMPE. Area of selenium pool approximately 0.4 cm^2, of tellurium rod 1.1 cm^2. Voltammetric curve of pure melt on graphite electrode is line without symbols.

Voltammetric curves were also taken with selenium electrodes in compartments in which selenide had been generated. Two typical curves are shown in Fig. 2. Identical straight lines were always obtained regardless of the direction of voltage change as long as precautions were taken to prevent significant changes in the ion concentration between measurements. These precautions included stirring and, when necessary, oxidation or reduction such that the zero current potential remained within 3 mV of its original value. The slope of these lines was approximately 15 ohms and represents the cell resistance. These curves show the $Se/Se^{=}$ couple to be reversible in this solvent system.

The cathodic branch observed with tellurium (Fig. 1) is ascribed to the formation of stable lithium-tellurium intermetallic compounds whose limiting composition is Li_2Te (4); the reaction written as $Te(s) + 2Li^+ + 2e^- \rightarrow Li_2Te(s)$ is probably an oversimplification. The potential characteristic of this reaction was -1.40 ± 0.02V. Liquid alloys were observed to form on the tellurium rod on cathodization beyond this potential. Such alloy formation on cathodization has been observed in previous studies of the Li-Te system (4, 10). The anodic wave is ascribed to $Te \rightarrow Te(II) + 2e^-$. An orange-brown color was observed leaving the electrode upon anodization. The "decomposition" potential for this reaction was -0.15 ± 0.03V, in good agreement with the potentiometric measurements given below.

Potentiometry of selenium.—Three complete experiments, each involving multiple cells, were carried out with new compartments, electrodes, and eutectic charge used in each. A total of 52 data points were taken at 400° ± 2°C. For each point, the emf became constant, within 0.5 mV, 30-90 min after completion of coulometric reduction of selenium and stirring. The potential was thereafter constant, within 1 mV, over several hours.

The effect of temperature on the emf was determined in several experiments over the temperature range 380°-420°C, with both increasing and decreasing temperature. The measured potential was, for a fixed selenide concentration, linearly dependent on temperature. A plot of $\Delta E/\Delta T$ against the logarithm of the molar concentration (as moles $Se^{=}$/liter of eutectic at 450°C) was linear (Fig. 3). Least square analysis of this plot gives $\Delta E/\Delta T = +0.123 \log [Se^{=}] - 0.510$ mV/°C, with a relative standard error of 6% in the slope and 1.5% in the intercept, for the temperature dependence of the cell (−)C, Se(l)/$Se^{=}$, LiCl-KCl// Pt(II), LiCl-KCl/Pt (+). This equation is identical to that obtained for the analogous sulfide cell (1) within experimental error. It was used to extrapolate all measured potentials to 450°C. This temperature is accepted as standard for potential measurements in this fused salt system [(11), and references cited therein].

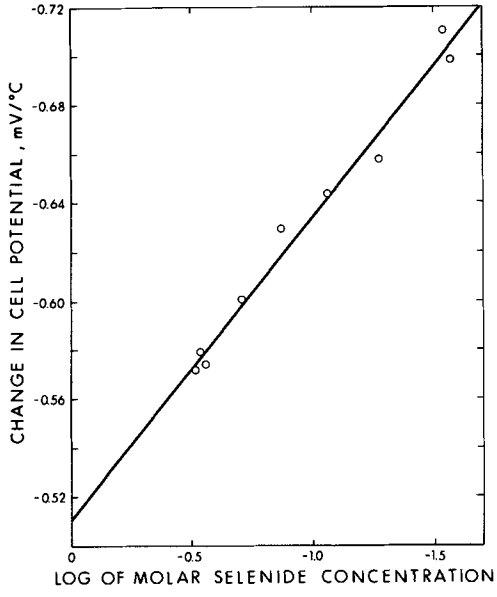

Fig. 3. Temperature dependence of potential as a function of selenide ion concentration. Line is that given by least-squares analysis. Temperature range 380°-420°C.

These extrapolated potentials gave linear Nernst plots over the concentration range 0.015-0.35M selenide. A typical plot of potentials against the logarithm of selenide concentration (Fig. 4) shows that Henry's law is obeyed over the concentration range studied. A summary of all runs is given in Table I; the original data are available in the thesis of F.G.B. Least square analysis of all points gave a standard potential of -1.141V for the Se(l)/$Se^{=}$ couple (molarity scale) at 450°C, with a standard error of 0.002V. This corresponds to values of -1.172 and -1.252V, with the same standard error, on the molality and mole fraction scales, respectively (11), all potentials being with respect to the appropriate standard platinum electrode. The slope of the Nernst plot was -0.0660 V/log unit with a standard error of 0.0014, corresponding to 2.17 ± 0.05 electrons taking part in the reaction. This is in agreement with the theoretical value of 2 expected for $Se + 2e^- \rightarrow Se^{=}$.

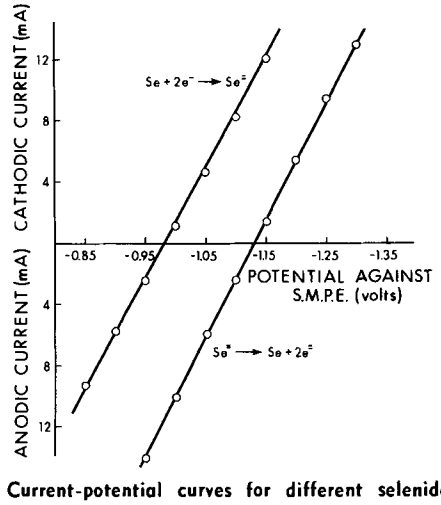

Fig. 2. Current-potential curves for different selenide concentrations in the same compartment. Reference potential SMPE, temperature 400°C.

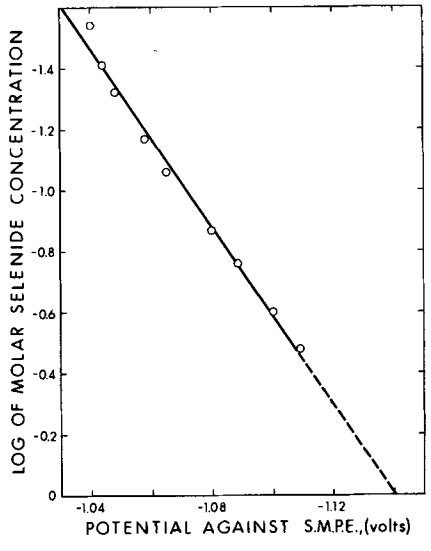

Fig. 4. Electromotive force of selenide electrode (vs. SMPE) as a function of selenide concentration in a typical run, showing obedience to Henry's law. Temperature (extrapolated) 450°C.

Table I. Standard emf determinations for the $Se/Se^{=}$ couple*

Selenide molarity	No. of points	$E_M°$, V	Standard deviation, mV	Exper. n
0.015-0.10	7	−1.136	2.6	2.22
0.024-0.24	9	−1.141	1.1	2.27
0.018-0.16	9	−1.144	1.2	2.21
0.029-0.32	9	−1.143	2.4	2.08
0.029-0.33	9	−1.140	2.8	2.10
0.039-0.35	9	−1.143	2.3	2.10
Least square analysis of all points	52	−1.141	1.5	2.17

* Values corrected to 450°C and SMPE; each entry is a separate compartment, the first being run 1, the next two being run 2, and the remainder being run 3.

Stable potentials could not be obtained on anodization of selenium electrodes, for the reasons discussed above.

Potentiometry of tellurium.—Attempts were made to measure the standard potential of the $Te(s)/Te^{=}$ couple. These attempts were unsuccessful because the solubility of "Li_2Te" in the LiCl-KCl eutectic in the presence of excess tellurium is very low; even an attempt to produce $2 \times 10^{-3}M$ $Te^{=}$ resulted in the formation of liquid on the surface of the tellurium electrode. The potentials obtained in this manner were quite stable. They correspond, after correction for reference electrode, to those observed by Foster and Liu (4) for very tellurium-rich alloys of lithium and tellurium in a similar system, and therefore cannot be considered as true tellurium/telluride electrode potentials.

Anodization of tellurium produced an orange-brown solution. Long needles of tellurium were observed extending from the electrode. The potentials measured were unstable, however, and drifted in the negative direction continuously after anodization was completed. At the same time, the color of the solution slowly disappeared. A yellow powder sometimes condensed in the cooler top of the isolation compartment. This behavior would be expected if a volatile species such as $TeCl_2$ (bp 327°C) escaped from solution at 400°. The experiment was repeated at 375°, but the species formed still volatilized from solution.

Attempts to produce meaningful Nernst plots from the potential data for this system were unsuccessful. The slope varied between 0.067 and 0.134 V/log unit. Since 0.033 V/log unit would be expected for a four-electron process, the ionic species produced should be Te(II) rather than Te(IV). From these plots and the voltammetric curves the standard potential (molarity scale) of the Te(II)/Te(s) couple is estimated as -0.10 ± 0.03V, placing it between Rh(III)/Rh and Ir(III)/Ir couples in this medium (11). Attempts to further oxidize the Te(II) species at a graphite electrode were unsuccessful.

Discussion

The potential between selenium and lithium electrodes, using literature data for lithium (11) and the result of the present study for selenium, is 2.2V at 450°C. This is in good agreement with the open-circuit potentials of 2.3-2.4V obtained from the Li/Se secondary cell between 350° and 400°C (7) and implies that at nearly full charge the selenium electrode potential of that cell may well be determined by soluble $Se^{=}$ in the electrolyte rather than electrode composition. The free energy of the reaction $2Se(l) + Cl_2 \rightarrow Se_2Cl_2(g)$ can be estimated as −11 kcal/mole from the voltammetric curves. No literature data could be found with which to compare this value; it seems reasonable, however, as it is similar to that for the formation of gaseous S_2Cl_2 (1).

The Li/Te secondary cell is reported (4, 6) to have an open-circuit voltage of 1.7-1.8V which is in agreement with the value of 1.9V obtained from the voltammetric curves of the present study.

There is a significant point raised in the present work related to lithium-chalcogen cells. Clearly, a soluble selenide species determines the potential of the selenium electrode under the conditions of the present study. Such a species, whether $Se^{=}$ or Li_2Se, can be expected to be present in Li/Se cells (6) and to diffuse to the lithium electrode if cell construction so permits. This will lead to reduced cell efficiency and eventual cell failure. The problem appears less significant in the Li/Te system due to lower solubility of the species produced.

Acknowledgment

The authors are grateful to the National Research Council of Canada for financial assistance in the form of an Operating Grant (to J.A.P.). This paper is taken from the thesis of one of the authors (F.G.B.) submitted to the Faculty of Graduate Studies, University of Alberta, in partial fulfilment of the requirements for the Ph.D. degree.

Manuscript submitted Sept. 29, 1969; revised manuscript received Dec. 20, 1969.

Any discussion of this paper will appear in a Discussion Section to be published in the December 1970 JOURNAL.

REFERENCES

1. F. G. Bodewig and J. A. Plambeck, *This Journal*, **116**, 607 (1969).
2. R. G. Verdieck and L. F. Yntema, *J. Phys. Chem.*, **48**, 268 (1944).
3. K. Kiukkola and C. Wagner, *This Journal*, **104**, 379 (1957).
4. M. S. Foster and C. C. Liu, *J. Phys. Chem.*, **70**, 950 (1966).
5. C. C. Liu and J. C. Angus, *This Journal*, **116**, 1054 (1969).
6. H. Shimotake, G. L. Rogers, and E. J. Cairns, Paper 18 presented at the Chicago Meeting of the Society, Oct. 15-19, 1967; Extended Abstracts of the Battery Div., J-1, **12**, 42 (1967).
7. H. Shimotake and E. J. Cairns, Paper 282 presented at the Boston Meeting of the Society, May 5-9, 1968.
8. H. A. Laitinen and J. A. Plambeck, *J. Am. Chem. Soc.*, **87**, 1202 (1965).
9. H. A. Laitinen and C. H. Liu, *ibid.*, **80**, 1015 (1958).
10. J. A. Plambeck and C. C. Liu, Unpublished data.
11. J. A. Plambeck, *J. Chem. Eng. Data*, **12**, 77 (1967).

Kinetics of the Hydrogen Evolution Reaction on Titanium

N. T. Thomas* and Ken Nobe*

School of Engineering and Applied Science, University of California, Los Angeles, California

ABSTRACT

The kinetics of the hydrogen evolution reaction on titanium in sulfuric acid solutions between pH 0.25 to 2.25 have been investigated. The Tafel slope of the HER was 150 mV at all pH values, and the electrochemical reaction order was 0.6 with respect to the hydrogen ions. The corrosion potential varied negligibly with pH; $(\partial \log i_{corr}/\partial \text{ pH}) = -0.57$; $(\partial \log i_o/\partial \text{ pH}) = -0.23$. If it is assumed that a thin incipient oxide film covers the surface of active titanium, a mechanism for the HER based on Temkin adsorption behavior, electrochemical desorption as the rate-determining electrode reaction step, and the dual barrier model is consistent with the experimental results.

There have been a number of investigations of the hydrogen evolution reaction (HER) on titanium in aqueous solutions. However, a mechanistic study of the HER on titanium has not been reported thus far.

Hackerman and Hall (1) reported an HER Tafel relationship of $\eta' = 1.30 + 0.154 \log i$, volts, for titanium in sodium chloride solutions. Straumanis *et al.* (2) and Andreeva (3) obtained HER Tafel slopes of 175 and 160 mV for titanium in 0.5*N* and 40% H_2SO_4, respectively. Kolotyrkin and Petrov (4) observed the Tafel behavior of $\eta' = 0.82 + 0.135 \log i$, volts, and a first order dependence on the concentration of hydrogen ions for the HER on titanium in sulfuric acid solutions. Petrenko (5) and Artemova (6) obtained Tafel relationships of $\eta' = 0.97 + 0.119 \log i$ and $\eta' = 0.97 + 0.135 \log i$, volts, for titanium in 2*N* H_2SO_4, respectively.

This work is an investigation of the kinetics and mechanism of the HER on titanium in sulfuric acid solutions of pH ranging from 0.25 to 2.25 at room temperature. Experimental details have been given elsewhere (7).

Results

Figure 1 shows the results of the cathodic polarization of titanium in sulfuric acid solutions. The HER Tafel slope was 150 mV for all pH values. It should be observed that deviations from the Tafel behavior occurred at about −1.0V *vs.* SCE for all pH values. At more active potentials, the current density was greater than the value obtained by extrapolating the Tafel line. This behavior suggests the possible commencement of a second reduction process.

As shown in Table I, the corrosion potential did not vary significantly with the pH. The corrosion current at each pH was determined by extrapolating the Tafel line to the corrosion potential. These values and the exchange current densities are also given in Table I.

Figure 2 is a cross plot of the data in Fig. 1. The log i *vs.* pH lines at constant potential ψ, in the Tafel region, are all parallel with slope

$$\left(\frac{\partial \log i}{\partial \text{pH}}\right)_{\psi} = -0.60 \qquad [1]$$

Similarly, the ψ *vs.* pH lines at constant current i, in the Tafel region, are all parallel as shown in Fig. 3. The slopes were

$$\left(\frac{\partial \psi}{\partial \text{pH}}\right)_{i} = -90 \text{ mV} \qquad [2]$$

Figure 4 gives the dependence of the corrosion current on the pH of the solution and shows that

$$\frac{\partial \log i_{corr}}{\partial \text{pH}} = -0.57 \qquad [3]$$

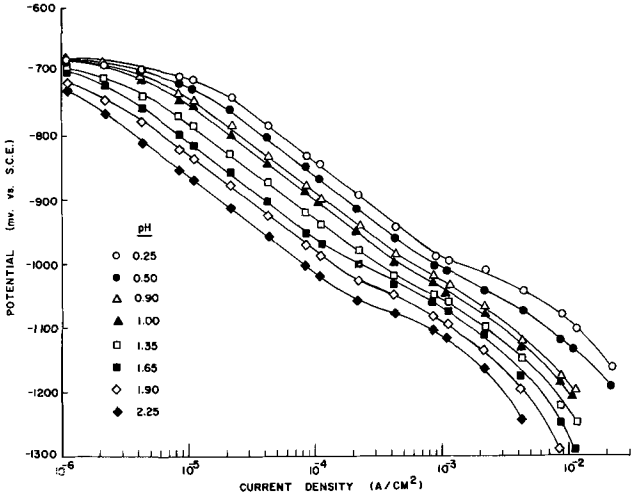

Fig. 1. Cathodic polarization curves of titanium in H_2SO_4

The dependence of the exchange current of the HER on the pH is given in Fig. 5 and shows that

$$\frac{\partial \log i_o}{\partial \text{pH}} = -0.23 \qquad [4]$$

Values of the Tafel slopes and the exchange current densities for the HER obtained in this investigation are comparable to the values reported by other investigators (1, 2, 4-6). The corrosion rates are in reasonable agreement with the values reported by Millaway (8).

In the Tafel region, the rate of the HER can be expressed as

$$i = k a_{H^+}{}^n \exp\left(\frac{-\alpha F \psi}{RT}\right) \qquad [5]$$

where k is the rate constant, a_{H^+} is the activity of the hydrogen ions, α is the over-all transfer coefficient, and n is the electrochemical reaction order with respect to the hydrogen ions. The over-all transfer coefficient, $\alpha = 0.4$, is determined from the cathodic Tafel slope of 150 mV. The slope of the curves in Fig. 2

Table I. Cathodic parameters of titanium in H_2SO_4

pH	Active corrosion potential, mV *vs.* SCE	Tafel slope, mV	Corrosion current, μA/cm²	Exchange current, μA/cm² × 10³	$R_p \times 10^{-3}$, ohm-cm²
0.25	−680 ± 10	150	9.0 ± 0.7	15.4 ± 1.2	4.0 ± 0.5
0.50	−675	150	6.0	13.5	5.7
0.90	−670	150	3.4	11.5	8.0
1.00	−665	150	2.9	10.5	11.0
1.35	−678	150	2.0	8.8	14.0
1.65	−675	150	1.4	7.5	23.0
1.90	−680	150	1.0	6.5	34.0
2.25	−685	150	0.6	5.5	51.0

* Electrochemical Society Active Member.

Key words: hydrogen evolution, titanium, kinetics, corrosion, Temkin isotherm, dual-barrier.

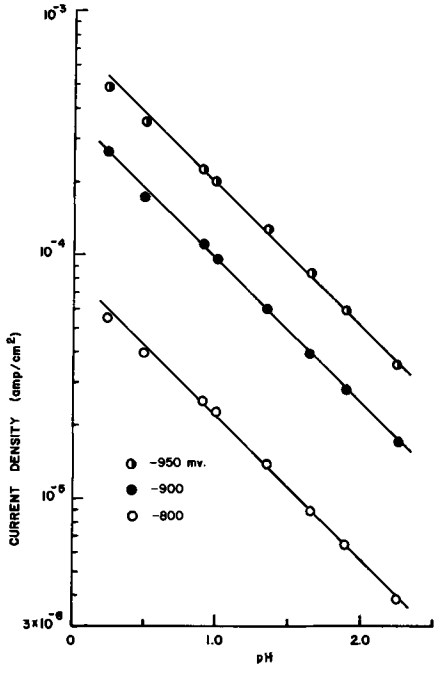

Fig. 2. Plot of logarithm of current density *vs.* pH in the Tafel region of the HER.

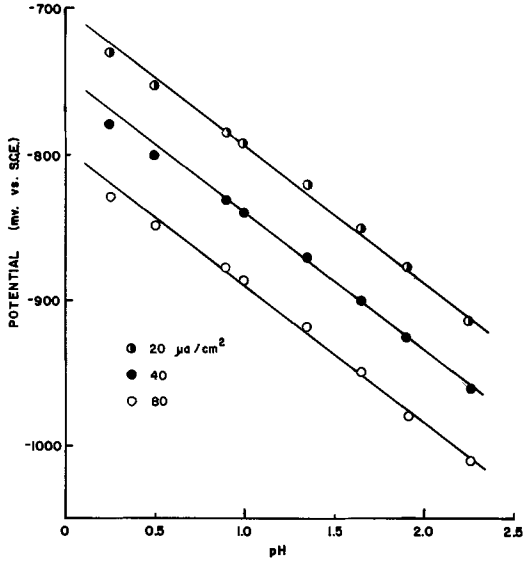

Fig. 3. Plot of potential *vs.* pH in the Tafel region of the HER

gives the reaction order

$$n = -\left(\frac{\partial \log i}{\partial pH}\right)_{\psi} = 0.60 \qquad [6]$$

Equation [5] shows that $(\partial\psi/\partial pH)_i = -2.303\ RT/\mathbf{F}$ $n/\alpha = -90$ mV which agrees with the experimental value of Eq [2]. The equation for the exchange current density can be obtained from Eq. [5]

$$i_o = k a_{H^+}{}^n \exp\left(\frac{-\alpha \mathbf{F}\psi_o}{RT}\right) \qquad [7]$$

It follows from Eq. [7] and the Nernst equation, $\psi_o = -2.303\ RT/\mathbf{F} \log a_{H+}$ that $i_o = k a_{H^+}{}^{n-\alpha}$. Thus

$$\frac{\partial \log i_o}{\partial pH} = -0.20 \qquad [8]$$

which is in good agreement with Eq. [4]. The equation for the corrosion current can also be obtained from Eq. [5]

$$i_{corr} = k a_{H^+}{}^n \exp\left(\frac{-\alpha \mathbf{F}\psi_{corr}}{RT}\right) \qquad [9]$$

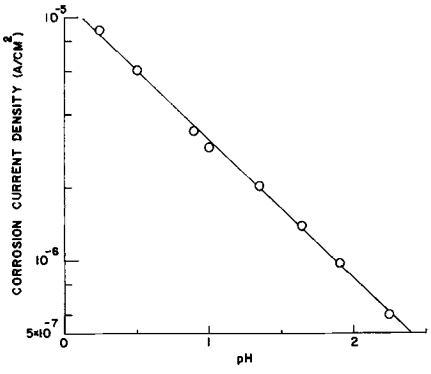

Fig. 4. Dependence of corrosion current on pH

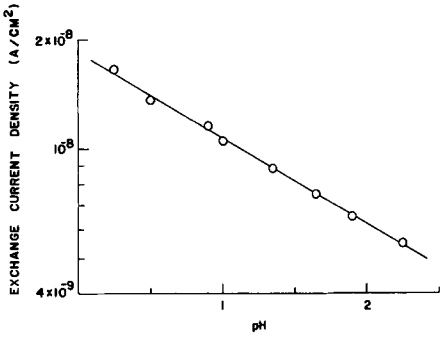

Fig. 5. Dependence of the HER exchange current on pH

From Eq. [9], the pH dependence of the corrosion current can be determined

$$\frac{\partial \log i_{corr}}{\partial pH} = -n + \frac{\alpha \mathbf{F}}{2.3RT}\left(\frac{\partial \psi_{corr}}{\partial pH}\right) \qquad [10]$$

Since it has been shown that $\partial\psi_{corr}/\partial pH \approx 0$

$$\frac{\partial \log i_{corr}}{\partial pH} \approx -n = -0.60 \qquad [11]$$

and this value agrees well with Eq. [3].

Since a single anodic process and a single cathodic process can describe the corrosion of titanium in sulfuric acid, the polarization current can be expressed as

$$i = i_{corr}\left[\exp\left(\frac{\alpha_a \mathbf{F}\eta}{RT}\right) - \exp\left(\frac{-\alpha_c \mathbf{F}\eta}{RT}\right)\right] \qquad [12]$$

where α_a and α_c are the over-all transfer coefficients of the anodic and cathodic processes, respectively, and $\eta = \psi - \psi_{corr}$. From Eq. [12] the relation between the polarization resistance, R_p, and the corrosion rate, i_{corr}, can be determined (9)

$$R_p = \left(\frac{\partial \eta}{\partial i}\right)_{\eta \to 0} = \frac{RT}{i_{corr}(\alpha_a + \alpha_c)\mathbf{F}} \qquad [13]$$

Figure 6 shows a linear plot of $(\psi - \psi_{corr})$ *vs.* the applied current for titanium in sulfuric acid of various pH values. The slope of each curve is the polarization resistance which is given in Table I. A plot of log R_p *vs.* log i_{corr} is shown in Fig. 7. It is seen that a slope of -1 correlated the data well. The polarization resistance-corrosion current values were comparable to those values obtained for a number of different metals as shown in Fig. 5 of ref. (10).

The $R_p - i_{corr}$ data and $\alpha_c = 0.40$ indicates that $\alpha_a = 0.44$. Thus, an anodic Tafel slope of 136 mV for titanium electrodissolution can be estimated.

Equation [5] can be expressed as

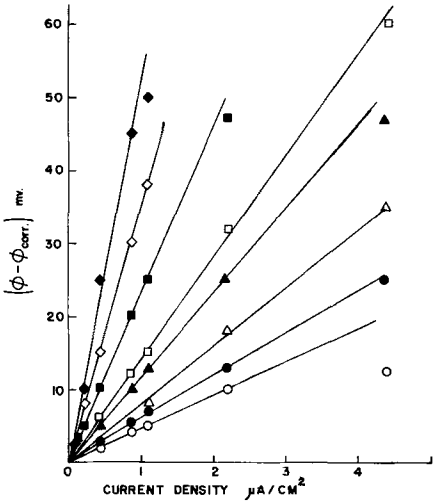

Fig. 6. Linear plot of (ψ—ψ_{corr}) vs. current density. Same symbols as in Fig. 1.

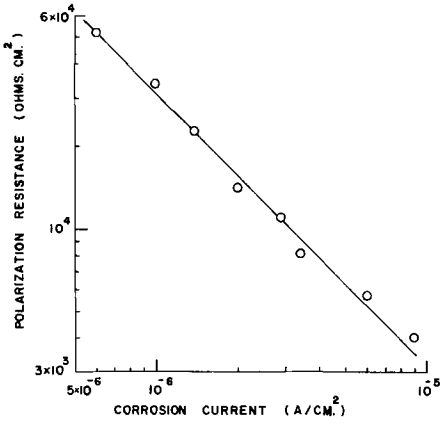

Fig. 7. Log. polarization resistance (ohm cm^2) vs. log corrosion current (A/cm^{-2}).

$$i_{corr} = k a_{H^+}{}^n \exp\left(\frac{-\alpha_c \mathbf{F} \psi_{corr}}{RT}\right) \quad [14]$$

Equations [13] and [14] can be used to express the pH dependence of the polarization resistance as shown in Eq. [15]

$$\frac{\partial \log R_p}{\partial pH} = n + \frac{\alpha_c \mathbf{F}}{2.303\, RT}\left(\frac{\partial \psi_{corr}}{\partial pH}\right) \quad [15]$$

Since it has been shown that $\partial\psi_{corr}/\partial pH \approx 0$

$$\frac{\partial \log R_p}{\partial pH} \approx n = 0.60 \quad [16]$$

Figure 8 shows a plot of log R_p vs. pH. The slope of the straight line which best fits the experimental points is 0.57 and agrees well with Eq. [16]. The slope of Fig. 8 is also consistent with the results given in Eq. [3]. The above analysis has shown that the experimental results of this investigation are self-consistent.

The rate of the HER on titanium in sulfuric acid between pH 0.25 to 2.25 can be expressed by the equation

$$i = k a_{H^+}{}^{0.6} \exp\left(\frac{-0.40 \mathbf{F} \psi}{RT}\right) \quad [17]$$

Figure 9 shows the results of the measurements of the differential capacitance of titanium in pH 0.25 solutions as a function of potential. At potentials more negative than the active corrosion potential, the capacitance decreased with decrease in potential. A minimum capacitance value is attained at approximately

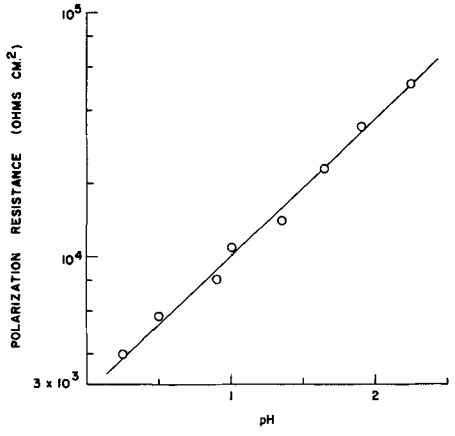

Fig. 8. Dependence of the polarization resistance on pH

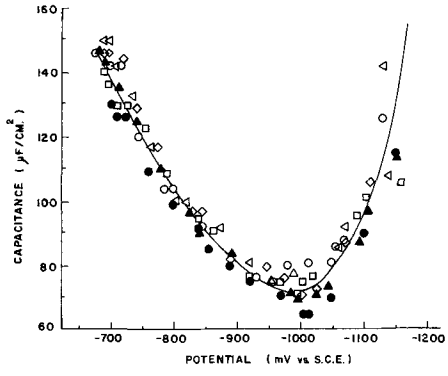

Fig. 9. Differential capacitance of titanium in 1N H_2SO_4 as a function of potential.

−1.0V. The capacitance increased again with further decrease in potential.

Discussion

The reaction steps in the HER which are generally considered are Eq. [18], [19], and [20]:

$$H^+ + e^- \rightarrow H_{ads} \quad [18]$$

and

$$H^+ + H_{ads} + e^- \rightarrow H_2 \quad [19]$$

or

$$H_{ads} + H_{ads} \rightarrow H_2 \quad [20]$$

A detailed account of the mechanisms of the HER on metals, assuming the applicability of the Langmuir isotherm for the adsorption of hydrogen atoms, is given by Bockris (11). Parsons (12), Thomas (13), and Conway and Salomon (14) have considered the kinetics of the HER using the Temkin isotherm for the adsorbed hydrogen atoms.

The experiments of Tomashov *et al.* (15) show that a mixed oxide film of TiO_2 and Ti_2O_3 is present on the surface of passive titanium. The thermodynamic data of these oxides indicate their possible presence even on active titanium in the Tafel region of the HER

$$Ti + 2H_2O = TiO_2 + 4H^+ + 4e^-; \quad \psi^o = -1.100\text{V } vs.\text{ SCE} \quad [21]$$

and

$$2Ti + 3H_2O = Ti_2O_3 + 6H^+ + 6e^-; \quad \psi^o = -1.405\text{V } vs.\text{ SCE} \quad [22]$$

The presence of other titanium oxides are also possible in the HER Tafel region, and it is surmised that in this region a thin oxide film is always present on the surface of titanium.

Meyer (16) has utilized a dual barrier model to develop electrode kinetic equations for metals covered with thin oxide films. Meyer (16, 17) and Posey *et al.* (18) interpreted the kinetics of reduction reactions on

zirconium and passive steel, respectively, in terms of the dual barrier model. MacDonald and Conway (19) used this model to analyze the kinetics of the oxygen evolution reaction on gold. The electrode reaction rates for this model are dependent on the potential across the oxide film, ψ_f, and across the double layer in the electrolyte, ψ_d. Thus

$$\psi = \psi_f + \psi_d \quad [23]$$

The rate of electron transport through the thin oxide film can be described by Eq. [24]

$$i = k_f \exp\left(\frac{-\alpha_f \mathbf{F}\psi_f}{RT}\right) \quad [24]$$

where α_f is the transfer coefficient for the electromigration of electrons in the film and k_f is the film rate constant. It is assumed that the charge transfer across the film and the electrolyte double layer are both rate determining. Analysis has shown that experimental data is consistent with the electrochemical desorption step, Eq. [19], as the rate-determining step for the HER and with Temkin behavior for adsorbed hydrogen atoms. For this case

$$i = k' a_{H^+}^{(1+\beta)} \exp\left(-\frac{2\beta \mathbf{F}\psi_d}{RT}\right) \quad [25]$$

Equations [24] and [25] lead to Eq. [26]

$$i = k'' a_{H^+}^{\frac{(1+\beta)\alpha_f}{2\beta+\alpha_f}} \exp\left[-\frac{2\beta\alpha_f \mathbf{F}\psi}{(2\beta+\alpha_f)RT}\right] \quad [26]$$

Expressions for the reaction order and the HER Tafel slope can be determined from Eq. [26]

$$n = \frac{(1+\beta)\alpha_f}{2\beta+\alpha_f} \quad [27]$$

$$\frac{\partial\psi}{\partial \log i} = -2.303\frac{RT}{\mathbf{F}}\frac{(2\beta+\alpha_f)}{2\beta\alpha_f} \quad [28]$$

By substituting the experimental values, $n = 0.60$ and $\partial\psi/\partial \log i = 150$ mV, one obtains $\alpha_f = 0.67$ and $\beta = 0.5$. These derived values indicate that a mechanism consistent with the experimental results of the HER on titanium in sulfuric acid can be based on Temkin adsorption, electrochemical desorption as the rate-determining electrode reaction step, and the dual barrier model.

Bockris and Srinivasan (20) present a plot of log i_o of the HER *vs.* the work function of metals. This plot shows that the metals fall into three groups, those with high hydrogen overpotentials, medium hydrogen overpotentials, and low hydrogen overpotentials. The rate-determining step for the HER on these three groups of metals was ascribed to be ion discharge, electrochemical desorption, and recombination, respectively. This correlation shows that titanium is included in the medium hydrogen overpotential group, that is, the electrochemical desorption step is the rate-determining step which is in accord with the analysis of the experimental results of this work. In the present study, the values of log i_o for the HER on titanium in H_2SO_4 were between -7.8 to -8.3 for solutions of *p*H between 0.25 and 2.25 which is in good agreement with the data used in the correlation reported by Bockris and Srinivasan (20).

It was observed in the polarization of titanium in sulfuric acid that, at approximately -1.0V, deviations from Tafel behavior commenced with an anomalous increase in the cathodic current. A possible explanation of this phenomenon is the complete reduction of the incipient oxide film at this potential and the subsequent hydrogen ion discharge on oxide-free titanium. This interpretation seems to be in accord with the results of Beck (21) who reported that the rate of the HER on an oxide-free titanium surface in 12M HCl was greater than on an oxide-covered surface.

A second feasible explanation of the nonlinearity in the ψ-log i curve is the possible titanium hydride formation from the hydrated oxides Ti_2O_3 and TiO_2, at about -1.0V, as indicated by calculations based on thermodynamic data obtained from Pourbaix (22, 23)

$$Ti_2O_3 + 10H^+ + 10e^- = 2TiH_2 + 3H_2O; \quad \psi^o = -1.027\text{V } vs.\text{ SCE} \quad [29]$$

$$TiO_2 + 6H^+ + 6e^- = TiH_2 + 2H_2O; \quad \psi^o = -0.910\text{V } vs.\text{ SCE} \quad [30]$$

It should be noted that Pourbaix's calculations (22) were based on the standard free energy of formation of titanium hydride reported by Baymakov and Lebedev (24), ΔG_f^o (TiH_2) = 10.00 kcal/mole. On the other hand, thermodynamic data reported by Stalinski and Bieganski (25) indicate a value, ΔG_f^o (TiH_2) = -20.6 kcal/mole. Based on the latter value, the standard potentials of TiH_2 formation from Ti_2O_3 and TiO_2 are as follows

$$Ti_2O_3/TiH_2;\ \psi^o = -0.764\text{V } vs.\text{ SCE} \quad [31]$$

$$TiO_2/TiH_2;\ \psi^o = -0.692\text{V } vs.\text{ SCE} \quad [32]$$

It is also seen that, at approximately -1.0V, a minimum in the differential capacitance of titanium in 1*N* H_2SO_4 occurred as shown in Fig. 9. The potential of zero charge of titanium, -942 mV *vs.* SCE, was calculated from the work function by Petrenko (5). At present, no significance is attached to this apparent agreement between the potential of the capacitance minimum and the calculated potential of zero charge.

Acknowledgment

This work is part of a continuing University of California program in sea water desalination.

Manuscript submitted Aug. 22, 1969; revised manuscript received Jan. 5, 1970.

Any discussion of this paper will appear in a Discussion Section to be published in the December 1970 JOURNAL.

LIST OF SYMBOLS

a_{H^+},	hydrogen ion activity
$\mathbf{F}$,	Faraday constant
i,	current density, A/cm^2
i_o,	exchange current density for HER, A/cm^2
i_{corr},	corrosion current density, A/cm^2
k,	rate constant in Eq. [5]
k',	rate constant in Eq. [25]
k'',	rate constant in Eq. [26]
k_f,	film rate constant in Eq. [24]
n,	electrochemical reaction order with respect to hydrogen ion
R,	gas constant
R_p,	polarization resistance, ohm cm^2
T,	absolute temperature, °K
α,	over-all charge transfer coefficient
α_a,	anodic charge transfer coefficient
α_c,	cathodic charge transfer coefficient
α_f,	charge transfer coefficient for electromigration of electrons in film
β,	charge transfer coefficient for electrochemical desorption step, Eq. [19]
η,	($\psi - \psi_{corr}$), V
η',	hydrogen overpotential ($\psi - \psi_o$), V
ψ_{corr},	corrosion potential, V
ψ_o,	equilibrium potential for HER, V
ψ^o,	standard electrode potential, V
ψ_d,	potential across double layer
ψ_f,	potential across oxide film

REFERENCES

1. N. Hackerman and C. D. Hall, *This Journal*, **101**, 321 (1954).
2. M. E. Straumanis, S. T. Shih, and A. W. Schlecten, *J. Phy. Chem.*, **59**, 317 (1955).
3. V. V. Andreeva and V. I. Kazarin, *Proc. Acad. Sci. USSR, Phy. Chem. Sec.*, **121**, 577 (1958).
4. Ya. M. Kolotyrkin and P. S. Petrov, *Zhur. Fiz. Kim.*, **31**, 659 (1957).
5. A. T. Petrenko, *Russ. J. Phy. Chem.*, **36**, 815 (1962).

6. V. M. Artremova, *Soviet Electrochem.*, **3**, 1089 (1967).
7. N. T. Thomas and Ken Nobe, *This Journal*, **116**, 1748 (1969).
8. E. E. Millaway, *Mater. Protec.*, **8**, 16 (1965).
9. M. Stern and A. L. Geary *This Journal*, **104**, 56 (1957).
10. M. Stern and E. Weisert, *Proc. Am. Soc. Testing Mat.*, **59**, 1280 (1959).
11. J. O'M. Bockris, "Modern Aspects of Electrochemistry," Vol. 1, Chap. 4 Butterworth, London (1954).
12. R. Parsons, *Trans. Faraday Soc.*, **54**, 1053 (1958).
13. J. G. N. Thomas, *ibid.*, **57**, 1603 (1961).
14. B. E. Conway and M. Salomon, *Electrochim. Acta*, **9**, 1599 (1964).
15. N. D. Tomashov, R. M. Al'tovskii, and M. Ya. Kushnerev, *Proc. Acad. Sci. USSR, Phy. Chem. Sec.*, **141**, 927 (1961).
16. R. E. Meyer, *This Journal*, **107**, 847 (1960).
17. R. E. Meyer, *ibid.*, **110**, 167 (1963).
18. F. A. Posey, G. H. Cartledge, and R. P. Yaffe, *ibid.*, **106**, 582 (1959).
19. J. J. MacDonald and B. E. Conway, *Proc. Roy. Soc.*, **A269**, 419 (1962).
20. J. O'M. Bockris and S. Srinivasan, *J. Electroanal. Chem.*, **11**, 350 (1966).
21. T. R. Beck, *This Journal*, **15**, 890 (1968).
22. M. Pourbaix, Cebelcor report, R. T. 146, May 1968.
23. M. Pourbaix, "Atlas of Electrochemical Equilibria in Aqueous Solutions," pp. 213-22, Pergamon Press, New York (1966).
24. Y. V. Baymakov and O. A. Bieganski, U. S. Dept. of Commerce Report AD 613.519, MT 64-317 (1966).
25. B. Stalinski and Z. Bieganski, *Bull. Acad. Polanaise Sci.*, **X**, 247 (1962).

Specular Reflection Studies of Gold Electrodes *in situ*

T. Takamura, K. Takamura, W. Nippe, and E. Yeager*

Department of Chemistry, Case Western Reserve University, Cleveland, Ohio

ABSTRACT

Multiple specular reflection has been used to examine the gold electrode in acid and alkaline solutions. Reflectivity-potential and linear sweep voltammetry curves have been recorded simultaneously. The wavelength dependence indicates that reflectivity changes with potential arise principally because of the interaction of the d-c electric field at the interface with the internal photoelectric effect in gold corresponding to a 5d → 6s band transition. The results demonstrate that multiple specular reflection techniques are particularly well suited to *in situ* studies of the specific adsorption of ions, the formation of mono- and polylayer oxides, and the Faraday adsorption of ions such as lead and cadmium to form monolayers of these metals on gold.

Substantial interest has been expressed by electrochemists recently in the use of optical techniques for the examination *in situ* of electrode-solution interfaces. Ellipsometry and reflectance measurements have received the principal attention.

The purpose of this publication is to demonstrate how a simple multiple specular reflection technique can be used to obtain interesting information concerning adsorption phenomena, oxide formation, and the electronic properties of metal electrode surfaces. McIntyre (1) also has called attention to the suitability of specular reflection methods for *in situ* studies of adsorption and the formation of various layers. Holden and Ullman (2) have used specular reflectance to study anodic film formation interferometrically. Walter (3, 4) has used a grazing-angle specular reflection technique for *in situ* examination of electrode surfaces.

Gold electrodes were chosen for study not only because of their importance to electrochemistry but also because of the marked wavelength dependence of reflectance in the visible portion of the spectrum. An internal photoelectric effect (5-7) involving a 5d → 6s band transition ($L_{32} \rightarrow L_2$) leads to an edge in the optical reflectivity at approximately 2.3 eV or 5500Å. This transition should be sensitive to the interaction of surface orbitals with adsorbed species and the electric field at the interface. The plasmon excitation in gold is at ~8 eV, far in the vacuum ultraviolet.

Apparatus and Experimental Procedure

The measurement cell (Fig. 1) consisted of two flat gold electrodes mounted parallel with a 2-mm separation and backed by glass plates. These electrodes were connected in parallel and a third gold electrode (E in Fig. 1) was used as the counterelectrode in a compartment separated from the main compartment by a fritted glass disk. The potential of the parallel working electrodes was measured relative to a saturated calomel electrode in a separate vessel connected by a Luggin capillary whose tip was placed near the center of the parallel gold working electrodes but outside of the optical path. This arrangement is satisfactory provided the current density on the working electrodes is sufficiently small for no appreciable ohmic drop to occur in the electrolyte between them. Such was true for all of the work reported here with the exception of the cathodic peak associated with oxide reduction.

This cell was not gas tight and hence should be considered a preliminary model. Air-saturated solutions were used rather than having the solutions contaminated with some unknown amount of O_2 from the air. The electrolyte solutions were prepared from

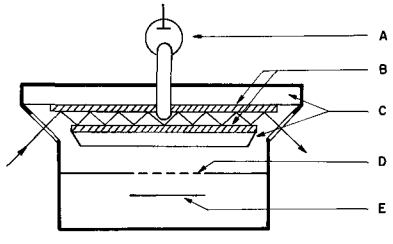

Fig. 1. Schematic diagram of specular reflection electrochemical cell. A, reference electrode (SCE): B, gold plates (working electrode).

* Electrochemical Society Active Member.

high-purity reagent grade chemicals and triply distilled water. The $HClO_4$ and H_2SO_4 solutions were pre-electrolyzed with gold electrodes. The NaOH solutions were not pre-electrolyzed and hence were contaminated with iron and other species.

The flat gold plates used as working electrodes were 99.99% pure, 0.5 mm thick, 25 mm high, and about 40 mm in length. They were polished on a flat glass plate with 5μ alumina grinding powder followed by 0.3μ chromic oxide grinding powder. After final polishing, the plates were cleaned with acetone, hot sodium hydroxide-ethanol mixture, and pure concentrated nitric acid, and finally rinsed with triply distilled water.

A monochromatic beam from a Beckmann DU spectrophotometer with a tungsten source was passed through the optically flat cell windows (Fig. 1) into the electrolyte and externally reflected approximately 20 times between the working electrodes at an angle of incidence near 50°. The reflected light was detected by a photomultiplier (RCA 1P28) and the signal then amplified with a chopper amplifier (Beckmann Model 5800) and fed to an X-Y plotter (Mosley Model 7000A) on which was also displayed the potential of the parallel gold electrodes *vs.* the reference electrode. The linearity of the photomultiplier-amplifier system with respect to optical intensity was checked by comparison with the detection-readout system ordinarily used with the Beckmann DU spectrophotometer. No polarizer was used in the optical system, but after a few specular reflections from the gold the light became plane polarized perpendicular to the plane of incidence.

Linear sweep cyclic voltammetry curves were recorded simultaneously on a second X-Y plotter in the usual manner with a Wenking potentiostat and Hewlett-Packard function generator (Model 3300A) at voltage sweep rates normally between 33 and 100 mV/sec. All potentials in this paper are relative to the saturated calomel reference electrode. The temperature was 22°-23°C.

Results

A typical reflectivity-potential curve at 5400Å and corresponding linear sweep voltammetry curve are given in Fig. 2 for a 0.2*M* $HClO_4$ solution. Small variations occur in the reflectivity and reflectivity dependence on potential from sample to sample, depending on the quality of the surface finish, but the shapes of the curves are invariant. Specific adsorption effects should be relatively small in this solution. The reflectivity-potential curve consists of two regions: linear characterized by slight hysteresis; and nonlinear corresponding to formation of an oxide layer and characterized by large hysteresis. Formation of stable gold oxide begins at about +1.1V on the anodic sweep branch (8-12) and at the same potential the reflectivity begins to decrease rapidly. The over-all decrease in Fig. 2 amounts to about 1% per single reflection. During the reverse potential sweep the reflectivity remains constant until the oxide layer starts to be reduced at about 1.0V. The large peak in the cathodic sweep in the voltammetry curve at 0.98V is attributed to the reduction of the oxide. Similar reflectivity-potential curves were obtained at all wavelengths (4800-8000Å) in both $HClO_4$ and H_2SO_4 solutions, although at wavelengths longer than 6000Å the plots showed some curvature in the region from 0 to 1.0V.

In Fig. 3 are superimposed the curves for the potential dependence of charge and reflectivity changes associated with formation and reduction of the oxide layer in 0.2*M* $HClO_4$. The charge-potential curve was obtained by integrating the voltammetry curve of Fig. 2. The reflectivity changes plotted in this figure correspond to the difference between the observed relative reflectivity in Fig. 2 and the value obtained by a linear extrapolation of the reflectivity change-potential curve recorded while scanning anodically in the potential range 0-1.0V. The two curves, including the hysteresis effects, correlate fairly well providing further evidence of the formation of the oxide layer and the attending reflectivity changes. At more anodic potentials in Fig. 3, the oxide layer is certainly more than a monolayer. Curves similar to those given in Fig. 3 have been obtained in 0.5*M* NaOH. Both the reflectivity and charge curves in Fig. 3 may be somewhat distorted by IR drop within the solution and nonuniform current distribution on the electrode surfaces.

The reflectivity change-potential curve in Fig. 3 resembles corresponding plots of the relative amplitude and phase retardation *vs.* potential obtained by Sirohi and Genshaw (12) from ellipsometric measurements on gold at 5500 and 6328Å in acid solutions at potential steps of 0.1V.

The relationship between the change in reflectivity and the extent of oxidation of the surface has been further examined by recording simultaneously the change in reflectivity and the charge passed as a function of time when the potential is stepped from a value just below that at which oxide starts to form (0.96V) to a value sufficient to form a multilayer oxide (*e.g.*, 1.20V). The plots of the change in reflectivity *vs.* charge associated with formation of oxide indicate two linear regions (Fig. 4) with the change in slope occurring at ~500 μcoul/cm^2, which probably corresponds to the completion of monolayer coverage.

The reflectivity-potential and voltammetry curves for an alkaline solution are shown in Fig. 5. The presence of oxygen in the solution contributed waves associated with the O_2-HO_2^- couple in the anodic and cathodic sweeps at potentials in the range 0 to −0.20V. The hysteresis in this potential range is probably caused by this couple. In contrast to the results in acid solution at wavelengths shorter than 6000Å, the non-oxide portion of the reflectivity-potential curve in NaOH solution is no longer characterized by a single linear region but rather appears to consist of two approximately linear portions intersecting at about −0.40V for the sweep in either the anodic or cathodic direction. This potential value corresponds to the point

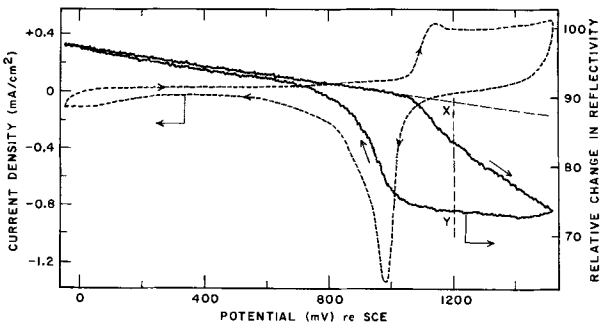

Fig. 2. Relative reflectivity change-potential (—) and current-potential (- -) curves of the gold electrode in 0.2M $HClO_4$ at 22°C. Potential sweep rate, 108 mV/sec; wavelength, 5400Å; electrode area, 23 cm^2; incident angle, 50°.

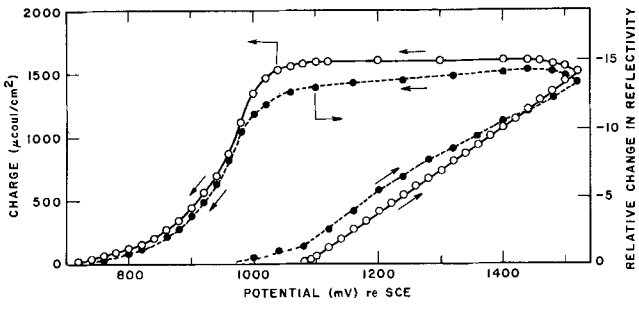

Fig. 3. Relative reflectivity change-potential (—●—) and charge-potential (—○—) curves for the formation of gold oxide layer obtained in 0.2M $HClO_4$. Conditions same as for Fig. 2.

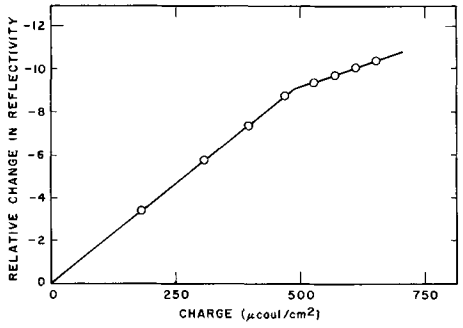

Fig. 4. Relative reflectivity changes *vs.* charge associated with oxide formation in 0.1M H_2SO_4 at 22°C. Wavelength, 6750Å; potential, +1.20V re SCE.

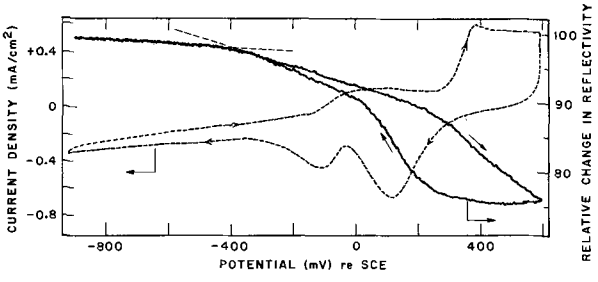

Fig. 5. Relative change in reflectivity-potential (—) and current-potential (- -) curves of gold in 0.5M NaOH at 22°C. Potential sweep rate, 104 mV/sec; wavelength, 5400Å; exposed electrode area, 23 cm^2; incident angle, 50°; number of reflections, 18.

of zero charge (pzc) reported by Eyring and co-workers (13) for gold in NaOH solutions. According to these workers, the pzc for gold in the 0.2*M* $HClO_4$ solutions used for the measurements in Fig. 2 is approximately −0.05V which is more cathodic than the voltage regions scanned in this figure.

To obtain further information on the relation of the reflectivity to the pzc, iodide ions were added to 0.5*M* NaOH solution (Fig. 6). The specific adsorption of I^- shifts the pzc to more negative values. The potential (E_A) of the intersection of the two linear portions of the reflectivity-potential curves is likewise shifted. A plot of E_A *vs.* log C_{I^-} is given in Fig. 6. Linearity is expected on the basis of the Esin-Markov effect (14). Three points in the semilog plot in Fig. 6 fall on a straight line with a slope of −0.060V/decade.

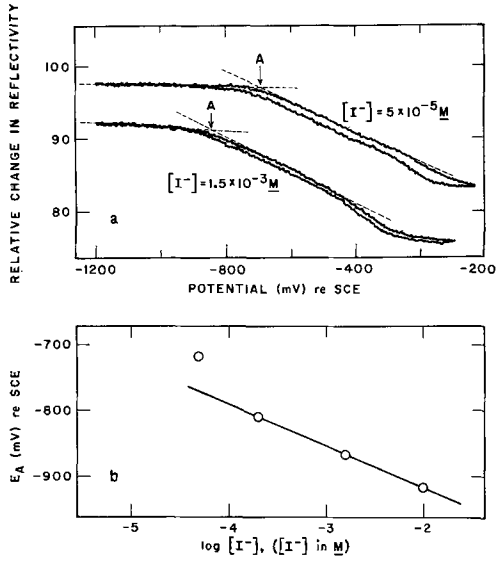

Fig. 6. Effect of iodide ions on the reflectivity-potential curves of gold: (a) in 0.5M NaOH and the shift of the potential of intersection of the two linear regions (E_A) with iodide concentration (b). Wavelength, 5600Å; other conditions same as in Fig. 5.

Some of the small hysteresis observed in Fig. 6 may be associated with the slow adsorption-desorption of I^-.

The sensitivity of the reflectivity curves to the pzc and specific ionic adsorption cannot be readily explained on the basis of the dependence of the reflectivity on the refractive index of the ionic double layer. The calculations of Stedman (15) and Prostak and Hansen (16) have shown that such effects should be too small to cause changes in the reflectivity of the magnitude observed in the present work.

The adsorption of ions on the electrode surface, however, can produce changes in the charge on the metal surface and the penetration of the electric field into the surface of the metal. These in turn would lead to changes in the carrier concentration in the surface of the metal as well as to changes in the photon energies required for the 5d → 6s band transition. Both of the effects would produce a change in the complex refractive index and hence the reflectivity of the interface.

The wavelength dependence of the reflectivity at various potentials provides further insight into the mechanism by which reflectivity changes with change in electrode potential. The wavelength dependence of the reflectivity, however, could not be recorded directly at given electrode potentials because the intensity of the light reaching the photomultiplier changes far too rapidly with wavelength after the large number of reflections involved in the present system. Consequently the wavelength dependence of the slopes of the reflectivity-potential curves has been examined instead. In Fig. 7 are plotted the relative rates of change of the reflectivity with respect to potential expressed in per cent $[(100/R)\ (dR/dE)]$ evaluated at 0.27V and +0.70V at 0.2*M* $HClO_4$. The slopes are the same at these two potentials for $\lambda \leq 5500$Å since the reflectivity-potential plot is linear in this region. Also plotted in this figure is the change in reflectivity associated with the formation of the oxide at a potential of +1.20V (taken as the distance X-Y in Fig. 2). The maxima in all three curves occur at 5500Å where the reflectivity of gold changes rapidly due to the 5d → 6s band transition (see insert drawing in Fig. 7). This implies that the maximum in these curves is caused by the rapid change in reflectivity of the gold. Feinleib (17), using an a-c modulation technique obtained a peak at the same wavelength in his electrochemical reflectance studies of gold. The slopes plotted in Fig. 7 correspond to the a-c signal obtained by Feinleib, who used a modulation potential of 2V which probably encompassed the linear region of Fig. 2, the oxide region, and perhaps the H_2 evolution region. Thus the quantitative significance of his results is in doubt.

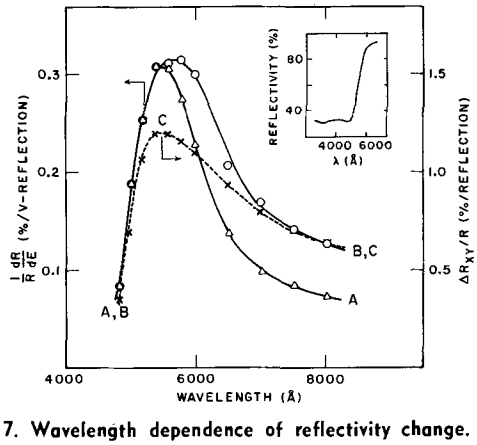

Fig. 7. Wavelength dependence of reflectivity change. Curve A, $(1/R)\ (dR/dE)$ at $E = +0.27$V re SCE. Curve B, $(1/R)\ (dR/dE)$ at $E = +0.78$V re SCE. Curve C, relative reflectivity change (X-Y in Fig. 2) for oxide formation. Conditions same as for Fig. 2. Insert figure, reflectivity of gold in air (17).

The relative slope *vs.* wavelength plot for +0.27V in Fig. 7 indicates that the effects of potential become relatively small at wavelengths remote from the maximum. Even when these relative slopes are converted to absolute values by multiplying by the absolute reflectivity, the absolute slope for +0.27V still passes through a pronounced maximum at 5500Å. This means that the principal effect of changing the electrode potential on the reflectivity-wavelength curve at potentials from 0 to ~+0.4V is to translate the curve along the wavelength scale with the change in reflectivity negligible at wavelengths shorter than the threshold for the 5d → 6s band transition. The direction of the shift along the wavelength scale indicates that the photon energies required for the transition become lower with increasing anodic potential. Such a decrease in the minimum photon energy required for this transition is in accord with the idea that the transition is from the top of the 5d band to the Fermi level and that the top of the 5d level bends upward (higher energy) at the surface, while the Fermi level is relatively invariant.

Prostak and Hansen (16) calculated the change in reflectivity for the gold-electrolyte (1*M* KCl) interface assuming a 0.5Å thick surface layer in the metal phase in which the optical constants have been modified by an amount equivalent to a photon energy of 0.1 eV due to penetration of the electric field into the metal. By applying Maxwell's equations to a three-layer structure, these authors obtain a change in reflectivity (100 $\Delta R/R$) at normal incidence of 0.07% at 5500Å, compared with a value of $(1/R)dR/dE = 0.3\%/$ V per reflection observed at this wavelength in the present work at an angle of incidence of 50° for an applied potential +0.27V. The four-fold discrepancy is not surprising since the comparison is valid only if the penetration depth is 0.5Å and 10% of the change in applied potential occurs within this layer, aside from the difference in angle of incidence. The calculated change in reflectivity should be larger for a deeper penetration and for a larger electric field within the metal. Therefore, the experimental values appear reasonable in terms of a model involving the penetration of the field into the metal to a depth of the order of 1Å.

The shift in the slope of the linear portion of the reflectivity-potential curve associated with passing through the pzc can be explained on the basis of a change in the fraction of the applied electric field which penetrates into the metal surface. Such a change in the distribution of the potential at the interface is certainly to be expected when the ions predominating in the plane of closest approach to the electrode surface are changed from anions to cations and the solvent dipoles at the interface probably reorient.

The maximum in the curve in Fig. 7 corresponding to the reflectivity change for the oxide can be interpreted in terms of a shift in the threshold frequency of the 5d → 6s band transition resulting from the interaction of the oxide ions with the surface orbitals of the metal. An alternate view of the same phenomenon is that the local field produced by the oxide ions penetrates into the metal phase thus shifting the threshold frequency of the 5d → 6s transition. The decrease in reflectivity caused by the oxide, however, persists at longer wavelengths (see Fig. 7) and hence the reflectivity is decreased by some other mechanism at longer wavelengths. One possibility is a change in carrier concentration and mobility in the surface layers of the metal due to the local field of the oxide ions.

Various workers (12, 18-20) have proposed that the chemisorption of an oxygen species; *i.e.*, AuO or AuOH, occurs on gold at potentials more cathodic than those of oxide layer formation. Sirohi and Genshaw (12) have explained the changes in phase retardation and amplitude in their ellipsometric studies of gold at relatively cathodic potentials in terms of the chemisorption of an oxygen species, which modifies the optical constants of the metal phase. Without some kind of relatively slow adsorption-desorption process, these authors find it difficult to explain the observed time dependence.

Unfortunately the present results do not provide strong evidence for or against such chemisorption at potentials cathodic to the oxide region although it may cause the curvature noted in the reflectivity-potential curves in the potential range +0.3 to 1.0V at $\lambda > 6000$Å. Why this curvature is not evident at shorter wavelengths remains to be explained.

The Faradaic adsorption of lead and cadmium on the gold electrodes has been examined using the present apparatus. Lead or cadmium ions strongly adsorb on gold at far more positive potentials than the standard electrode potentials of these ions (21, 22). Reflectivity-potential and current-potential curves for gold in 0.2*M* $HClO_4$ containing 5 x 10^{-4} *M* Pb^{2+} are shown in Fig. 8. The Faradaic adsorption and desorption peaks for Pb occur at +0.10V in the voltammetry curve. The surface concentration of adsorbed Pb estimated from the area under the voltammetry peaks corresponds to 400 μcoul/cm^2, providing further evidence for monolayer formation. The reflectivity-potential curve shows a marked change on adsorption or desorption of the lead atoms and is quite wavelength-dependent (Fig. 9). At shorter wavelengths, *e.g.*, 5000Å, the reflectivity increases on the formation of the Pb monolayer, whereas at longer wavelengths, *e.g.*, 7500Å, the reflectivity decreases. A similar situation has been found with cadmium (Fig. 9).

The wavelength dependence of the change in reflectivity attending the formation of lead and cadmium monolayers remains to be explained but is not sur-

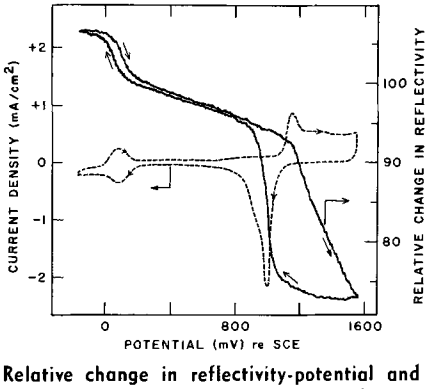

Fig. 8. Relative change in reflectivity-potential and current-potential curves for gold in the presence of Pb^{+2} ions. Electrolyte: 5 x 10^{-4}M Pb^{2+} + 0.2M $HClO_4$. Potential sweep rate, 105 mV/sec; wavelength, 5200Å; other conditions same as for Fig. 6.

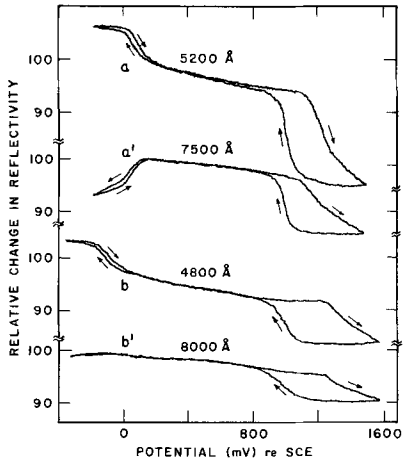

Fig. 9. Relative change in reflectivity-potential curves at various wavelengths in the absence of Pb^{2+} or Cd^{2+}. Electrolyte: curves a, a'; 5x10^{-4}M Pb^{2+} + 0.2M $HClO_4$. Curves b, b'; 1x10^{-3}M Cd^{2+} + 0.2M $HClO_4$. Potential sweep rate, 105 mV/sec; other conditions same as for Fig. 2.

prising since a monolayer of foreign metal atoms on the gold surface has specific electronic and hence optical properties. This wavelength dependence should provide an important tool in studying the electronic properties of such monolayers.

The work reported here is preliminary. It has demonstrated, however, that specular reflection techniques can be used to: (*i*) establish the point of zero charge for solid metal electrodes, (*ii*) follow adsorption and desorption, and (*iii*) obtain information concerning the surface electronic properties of metal electrodes and the penetration of the electric field into the metal phase.

Acknowledgment

The authors are pleased to acknowledge the support of this research by the U.S. Office of Naval Research.

Manuscript submitted Oct. 17, 1969; revised manuscript received *ca.* Dec. 22, 1969. This was Paper 257A presented at the New York Meeting of the Society, May 4-9, 1969.

Any discussion of this paper will appear in a Discussion Section to be published in the December 1970 JOURNAL.

REFERENCES

1. J. D. McIntyre, Paper 232 presented at the New York Meeting of the Society, 135th National Meeting, Electrochemical Society, May 4-9, 1969; Extended Abstracts, pp. 578-579.
2. B. J. Holden and F. G. Ullman, Papers 52, *ibid.*; Extended Abstracts, pp. 61-4.
3. D. C. Walter, *Can. J. Chem.*, **45**, 807 (1967).
4. D. C. Walter, *Anal. Chem.*, **39**, 896 (1967).
5. R. Zallen in "Optical Properties and Electrical Structures of Metals and Alloys," p. 164, F. Abeles, Editor, John Wiley and Sons, Inc., New York (1966).
6. D. Beaglehale and T. J. Hendrickson, *Phys. Rev. Letters*, **22**, 133 (1969).
7. A. Mooradian, *ibid.*, **22**, 185 (1969).
8. F. G. Will and C. A. Knorr, *Z. Electrochem.*, **64**, 270 (1960).
9. H. A. Laitinen and M. S. Chao, *This Journal*, **108**, 726 (1961).
10. S. B. Brummer and A. C. Makrides, *ibid.*, **111**, 1122 (1964).
11. G. Gruneberg, *Electrochim. Acta*, **10**, 339 (1965).
12. R. S. Sirohi and M. A. Genshaw, *This Journal*, **116**, 910 (1969).
13. D. D. Bode, T. N. Anderson, and H. Eyring, *J. Phys. Chem.*, **71**, 792 (1967). See also, G. M. Schmid and N. Hackerman, *This Journal*, **109**, 243 (1962); M. Green and H. Dahms, *ibid.*, **110**, 466 (1963).
14. O. A. Esin and B. F. Markov, *Acta Physiochim. URSS*, **10**, 353 (1939).
15. M. Stedman, *Chem. Phys. Letters*, **2**, 457 (1968).
16. A. Prostak and W. N. Hansen, *Phys. Rev.* **160**, 600 (1967).
17. J. Feinleib, *Phys. Rev. Letters*, **16**, 1200 (1966).
18. J. P. Hoare, *This Journal*, **110**, 245 (1963).
19. J. P. Hoare, *Electrochim. Acta*, **9**, 1289 (1964).
20. G. M. Schmid and R. N. O'Brien, *This Journal*, **111**, 832 (1964).
21. E. Schmidt and H. R. Gygax, *J. Electroanalyt. Chem.*, **13**, 378 (1967); **14**, 126 (1967).
22. E. Schmidt, Paper B5, 19th Meeting of CITCE, Detroit, September 1968; Extended Abstracts, pp. 43-46.

Galvanostatic Overpotential Transients and Electrocrystallization Processes on Copper Single Crystals in Solutions of Cupric Perchlorate

L. H. Jenkins*

Solid State Division, Oak Ridge National Laboratory, Oak Ridge, Tennessee

ABSTRACT

Overpotential transients have been measured on copper single crystal surfaces oriented (100), (110), (111), and (321) undergoing galvanostatic dissolution or deposition in acidic solutions of $Cu(ClO_4)_2$. In the current density range 1-400 $\mu A/cm^2$ it is shown that maximum values observed in overvoltage-time relationships respond to analytical treatment. For the (100) and (110) the anodic and cathodic overpotential maxima *vs.* current density relationships were symmetric about the equilibrium point, but not for the (111) and (321). From plots of certain functions of overvoltage maxima *vs.* current density, orientation sensitive quantities similar to exchange current densities could be calculated. At the low and intermediate current densities it was established that a "deposition anomaly" was observed on all orientations. Deposited material did not seem to occupy crystal lattice positions, and moreover, affected subsequent anodic overpotential-time relationships in a manner related to the extent of the deposition. *In situ* photomicrography and goniometric observations were used to determine the orientations and rates of facet development on the various surfaces when subjected to long term deposition or dissolution, and these results are discussed in terms of the relative ease of movement of monatomic steps over the various orientations. A model is proposed of a sequence of events on the surface and in the diffusion layer which provides a self-consistent explanation of all the experimental data.

The behavior of copper serving as electrodes in acidic solutions of cupric perchlorate have previously been studied by Piontelli, Poli, and Serravalle (1) and by Bockris and Enyo (2). Among other things, both studies attempted to relate kinetic parameters of the systems to structural characteristics of various electrode surfaces. Also, Shanefield and Lighty (3) have observed the changes in growth forms on copper (100) surfaces produced by electrodeposition from cupric perchlorate solutions containing various impurities.

The report of Piontelli *et al.* concerned data for copper single crystal surfaces oriented (100), (110), and (111) in which the "quasi-steady" overvoltages observed under galvanostatic conditions at current

* Electrochemical Society Active Member.

densities of ~ 1-10 mA/cm^2 were orientation dependent. Anodic and cathodic data were not symmetric about the equilibrium point for any one orientation, nor were the relative differences between orientations the same for anodic and cathodic processes. Employing spherical electrodes ~ 0.1 cm in diameter, Bockris and Enyo determined kinetic parameters for surfaces prepared by melting in helium or by electrodeposition. In ~ 0.1M $Cu(ClO_4)_2$ at current densities $\gtrsim$ 10 mA/cm^2 the data indicated charge transfer to be the rate-controlling step, but it was suggested that at lower current densities surface diffusion was the slow process. Certain differences observed between the two types of electrodes were thought to arise from differences in dislocation densities.

Data such as these indicate that perhaps the determination of pertinent kinetic parameters at current densities lower than those studied previously would, when augmented by observations of changes in surface structure resulting from long-term dissolution or deposition, yield information regarding the effects of structure on the reactivity of a metal surface. Obviously there are many other relevant reports in the literature concerning the behavior of copper electrodes in solutions of copper ions. As a matter of fact, data regarding systems of copper sulfate far exceed that related to perchlorates. However, the work previously cited regarding the latter provides an adequate basis to discuss the research reported here, and similar work in sulfate systems which is currently being prepared for publication will provide opportunity later for discussion of other systems.

Materials.—Preferentially oriented cylindrical copper single crystal slugs approximately 25 mm diameter x 100 mm were grown in this laboratory by seeding 99.999+% metal from the melt in graphite crucibles. From such crystals coin-shaped specimens ~ 7 x 25 mm were cut with an acid string saw, and the flat surface chemically polished on a soft cloth polishing wheel using an aqueous solution containing $CuCl_2$, HCl, and H_3PO_4. Finally, the crystals were electropolished in a copper-containing phosphoric acid bath, rinsed in dilute phosphoric acid, and washed in distilled water. [Details of these procedures have been published previously (4, 5).] The manipulations introduced no new dislocations into the crystals, and the average dislocation density in as-grown material was ~ 5 x 10^4-10^6 cm^{-2}. The large surfaces prepared in this manner were not absolutely flat, but rather contained a few gentle undulations such that the average orientation was within ± 0.1° of that desired.

Solutions of $Cu(ClO_4)_2$ were prepared from doubly recrystallized material and stored in rack reservoirs in the manner previously described (6). All solutions used in this study were 0.20M in $Cu(ClO_4)_2$ with pH adjusted to ~ 1 by addition of $HClO_4$. When introduced into the Teflon cells they were free of dissolved oxygen, under an atmosphere of hydrogen, and in equilibrium with polycrystalline metallic copper. Ultrapure grade (99.999+%) tank hydrogen was passed through a platinum catalytic purification system and then through magnesium perchlorate drying towers before using.

Experimental methods.—Two types of reaction cells were used. One type, illustrated in Fig. 1, was used to obtain galvanostatic current-potential data. The apparatus consisted of a large brass support plate with a flat surface and an O-ring groove. On this was mounted a pipe flange-type reaction flask cover with fine ground face and standard taper outer joints. A shallow dish of Teflon sat within this enclosure. Four ports with thin, beveled lips in the bottom of the Teflon dish provided for isolation of the crystal orientation of interest. The copper specimens were pressed against the lips of the port and held in place by gentle pressure from the mounting screws in the manner shown. The diameter of the ports was such that 2 cm^2 geometric

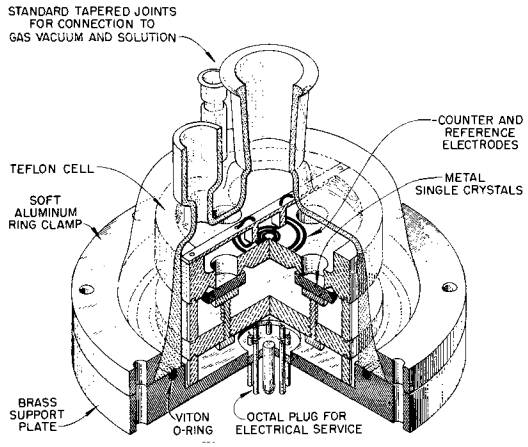

Fig. 1. Cell for isolating single orientations and determining current-overpotential characteristics.

area of each crystal surface was exposed to the solution. Infrequently, crystals of different orientation were mounted in each of the four available ports. Usually only three orientations were used in order to obtain duplicate data for one of them. Polycrystalline copper wires suspended from a cross member over the dish served as counter and reference electrodes. Electrical access was provided through a vacuum tight octal plug welded in the brass support plate. After the crystals were mounted and appropriate electrical connections made, the flask cover was placed over the dish and secured to the plate by a ring clamp. The entire apparatus was then attached to the solution flask and hydrogen and vacuum lines on a mounting rack. Usually a glass electrode inserted through the small standard taper port served as an auxiliary reference electrode. After repeated evacuation and flushing with hydrogen over a period of at least two days, solution was admitted to the system. Appropriate stopcocks were then closed, the entire system detached from the rack, and placed in an air bath maintained at 23.00° ± 0.02°C and which was surrounded by a Faraday cage. Potential measurements were made with either vibrating reed electrometers or a Philbrick P-2 operational amplifier, and data were recorded either on a strip chart recorder or by photography of oscilloscope traces, respectively.

The second type of reaction cell is shown in Fig. 2. The main body of the cell was machined from 99.99+% copper. After the viewing glass was attached, an electropolished crystal was mounted and pressed against the lower Viton O-ring. (Since all O-rings contacted the solution, they previously had been soaked for many hours in hot solutions of the same composition as the test solution.) Solution was introduced to the system through the small side port in the main body of the

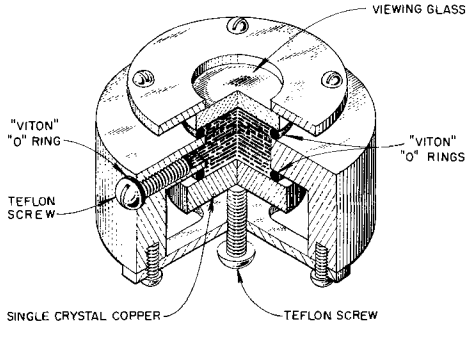

Electrolytic Cell for Microscopic Observation.

Fig. 2. Cell permitting microscopic observation and time-lapse photomicrography of surfaces. Main cell body of 4/9s copper serves as counterelectrode.

cell with the aid of a pipette drawn to a needle tip capillary. Obviously, it was impossible to maintain an inert atmosphere within the cell while filling the system. Because of this, the solutions used in the 2-ml capacity cells were not free of dissolved oxygen, nor certainly were they initially at equilibrium with copper metal. As in the previous cell, 2 cm^2 geometric surface area of the crystal was exposed to the solution. The cell was filled to the top of the port such that insertion of the closure screw with O-ring seal caused overflow and prevented entrapment of air within the system. After filling and sealing, the cell was set aside for a period of at least two weeks so that equilibrium could be established. The cell was then placed on a microscope stage, and using the body of the cell as a counterelectrode, changes in single crystal surface structures due to dissolution or deposition process concomitant with the passage of current through the system were observed and recorded by time lapse photomicrography. A few systems were closed with a Teflon screw which contained a polycrystalline copper wire sealed through its length to serve as a reference electrode, but usually no attempts were made to measure potentials within these cells. All the data discussed here were obtained under galvanostatic conditions. The current source was a dry cell pack, and current flow was regulated by fixed in-line resistors with resistance values very large compared with those of the various cells.

In all cases when the reaction cells were opened, crystals were examined and photographed under the microscope. Orientations of surface facets were determined with a two-circle reflection goniometer. In instances in which deposition had been to an extent great enough to make the observations valid, Laue back reflection x-ray techniques were used to establish the orientation of the deposited metal.

Experimental Results

Changes in surface structure.—Using the copper body cells, observations were made on surfaces oriented (100), (110), (111), and (321). Data were taken at constant currents of 4, 40, and 400 $\mu A/cm^2$ original surface area for all orientations during both dissolution and deposition, and a few observations were made at other current densities also. Under any given combination of experimental conditions the changes observed in a surface structure were reproducible. Data always were obtained from duplicate systems, and in many cases from triplicate, so that the results discussed below derive from more than 60 different crystals. In all cases tested, deposits were single-crystalline and oriented like the substrate.

(100).—Under all experimental conditions dissolution of the (100) was completely uniform and regular, and resulted in the formation of square pits. Figure 3 shows that rapid removal produced a more regular and well-defined pit than removal of a like amount of material at a lower rate. At lower current densities sides of pits were less well defined and apparently relatively more material was removed by motion of steps over the original surface than at higher current densities. Nevertheless, in general, such differences were of degree rather than kind.

By comparison, deposition on the (100), although accompanied by the formation of four-sided pyramids, did not occur in as regular and uniform a manner. At higher current densities pyramids of a uniform size developed, but at current densities $\lesssim$ 100 $\mu A/cm^2$ (although initial deposition and growth occurred uniformly) some pyramids soon began to develop at a much greater rate than others. A few of these larger pyramids, appearing dark to the viewer, had sides $\sim$ 22° from the (100), but they were outnumbered approximately 10:1 by the lighter appearing large kind with sides $\sim$ 8° from the original surface. The number of large pyramids, both light and dark, comprised less than 1% of the total number on the surface. However, initial deposition occurred uniformly, and the formation of large pyramids seemed apparently a random fluctuation. As a first approximation, growth rates of topographic features were linear in time. Deposition growth forms occurred in an even less uniform manner at 4 $\mu A/cm^2$. Again, although nucleation of small pyramids apparently occurred over the entire surface, random large growths began to develop. At this low current density much of the material seems to have been deposited by step motion over the original surface, similar to the case for dissolution, for the volume of material contained in the pyramids was calculated to be only $\sim$ 20% of the total deposited.

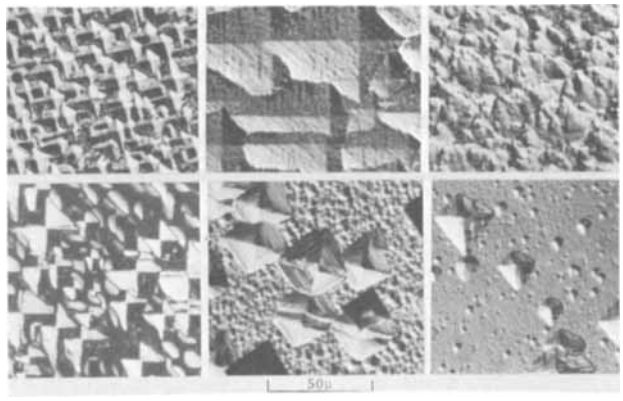

Fig. 3. Structures developed on (100) due to long-term galvanostatic processes. Upper photographs represent features developed by anodic process after removal of the equivalent of $\sim$ 4.5 coulombs cm^{-2} at current densities (left to right) of 4000, 40, and 4 $\mu A\ cm^{-2}$, respectively. Lower photographs after deposition equivalent to $\sim$ 1.0 coulombs cm^{-2} at (left to right) 400, 40, and 4 $\mu A\ cm^{-2}$.

Facets formed by both pyramids and pits always were oriented along <100> zones, and no facets on any other zones were ever obtained under the stated conditions. As in the case previously reported (7) pit bottoms always were within $\sim$ 5° of the original (100), but as indicated above, deposition-formed facets exhibited more varied orientations.

(110).—Structures developed on the (110) were very similar under all conditions. Reaction always occurred in a uniform manner and invariably resulted in the formation of a well-defined series of sharp-topped ridges separated by equally sharp-bottomed valleys, as illustrated in Fig. 4. Ridge sides were never formed other than along the <100> zone, and faceting was more or less continuous along this zone out to $\sim$ 40° from the (110).

(111).—The (111) also seemed to react in a completely uniform manner. Either dissolution or deposition apparently occurred by the removal of material at submicroscopic steps on the surface. In early stages, these

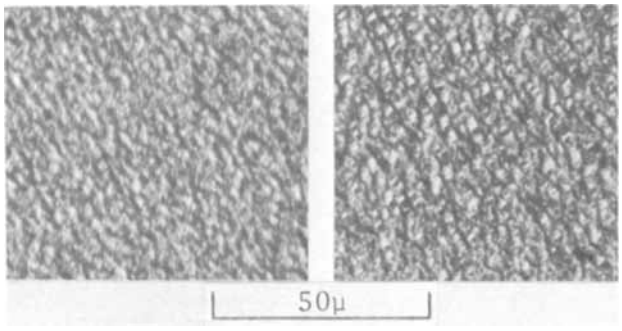

Fig. 4. Typical structures developed on the (110), left, and (321) right. Former shown after dissolution of $\sim$1.5 coulombs cm^{-2} at 4 $\mu A\ cm^{-2}$, and the latter after equivalent deposition at 400 $\mu A\ cm^{-2}$.

steps interacted to form small ledges of such great density that the entire surface appeared roughened. As the process continued, small ledges interacted to form large ledges separated by apparently flat (111) surfaces, such that the surface appeared as smooth over local areas as at initiation of reaction. Figure 5 is a series of photomicrographs, some taken *in situ* of the same area, which illustrates this process. The large ledges formed in all cases were, of course, highly faceted.

(321).—This surface also seemed to react in a uniform manner with no appreciable difference in the facets produced by dissolution or deposition. A great deal of (111) faceting was always observed (see Fig. 4), and this was accompanied by the development of companion facets along the two <100> zones, such that nonsymmetrical, triangular shaped pits or pyramids were formed. At high current densities facets developed along these zones approached within 4° of the (100). At lower current densities faceting along the <100> zones tended to be further removed from the (100) and nearer the (210).

Potential vs. time data.—Data obtained in the Teflon cells at all current densities (1-400 μA/cm^2), both anodic and cathodic, and on all four orientations studied revealed that potential *vs.* time curves of working electrodes exhibited maxima generally of the shape observed by Roiter *et al.* (8) on zinc single crystals in solutions of zinc sulfate. However, one important difference must be noted: The times to formation of the maxima reported here are much too long (generally by an order of magnitude) to be associated with charging of the double layer. True steady-state overpotentials could not be established on any of the crystals, in that, following establishment of a maximum value, if the current passed long enough, the measured overpotential gradually decreased. Ultimately microscopic changes in surface structure could be observed without a true steady state being established, although pseudo-steady states frequently were observed shortly after maxima were established. Figure 6 illustrates typical potential-time curves of overvoltages for the orientations studied. The excellent reproducibility of the values of the potential maxima, as well as times to formation, for successive anodic pulses is clearly indicated. Cathodic overpotential-time relationships were equally reproducible. As shown, excellent agreement between the absolute values of anodic and cathodic maxima were obtained, although at current densities $\lesssim$ 100 μA/cm^2 slightly longer times were often required to establish the latter. Note also at the lower current density shown the post-maximum overvoltage-time relationship is quite different in the anodic and cathodic cases. At higher current densities times to formation of maxima were approximately equal for both processes, but again over-all overvoltage-time relationships were not precisely similar.

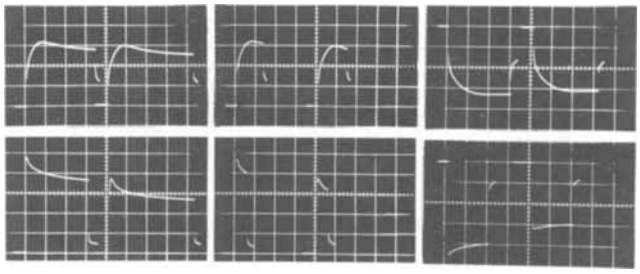

Fig. 6. Oscilloscope traces of "normal" overpotential-time relationships. Top row all at 30 μA/cm^2, 5 mV/div vertical scale, 2 sec/div horizontal scale, from left to right: anodic (110), (321); anodic (110), (321); cathodic (110), (321). Bottom row all at 150 μA/cm^2, 10 mV/div vertical scale, 1 sec/div horizontal scale, from left to right: anodic (100), (111); anodic (100), (111); cathodic (100), (111).

The most interesting feature of the deposition process was its effect upon a subsequent anodic pulse. Overvoltage-time relationships were altered drastically for an anodic process which had been preceded by a cathodic pulse. [Similar phenomena have been observed on other single crystalline material (9).] This is illustrated in Fig. 7 which, when compared with Fig. 6, shows that such anodic maxima can take much longer to become established than under postanodic conditions. Also, the absolute values of these overpotential maxima are greatly reduced at higher current densities, and in all cases the entire overvoltage-time relationship is altered. Interestingly enough, only very slight differences were observed between postanodic and postcathodic overpotential-time relationships during deposition, and the value of a cathodic overpotential maximum rarely showed noticeable effects of previous electrode processes. Due to excessively long decay times following cathodic current interruption, an exhaustive study of postdeposition cathodic overpotential-time relationships was not undertaken. These observations will be of considerable significance in later discussions concerning interpretation of all the data.

The extent of this postdeposition anomaly was dependent on the current density, deposition time, orientation of the surface to some extent, and the time lapse

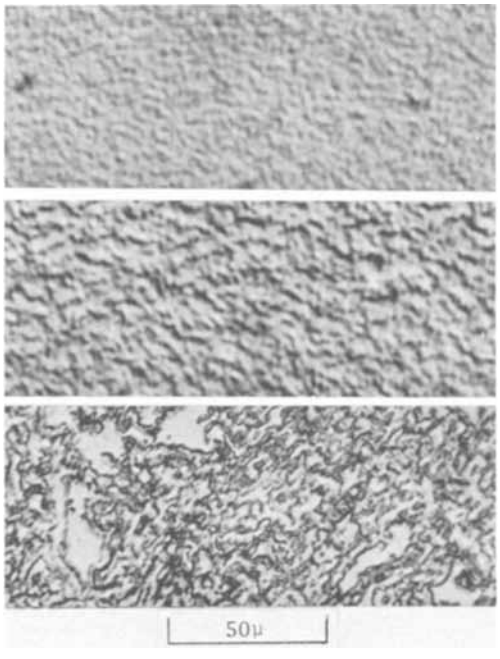

Fig. 5. A (111) surface undergoing dissolution at 400 μA/cm^{-2}. Top and middle are *in situ* views of the same area after 6- and 15-min reaction, respectively. Lack of definition is due to the difficulty of lighting and focusing through the cell and solution. Bottom illustrates a view of the same crystal after removal from the cell following 1 hr of reaction.

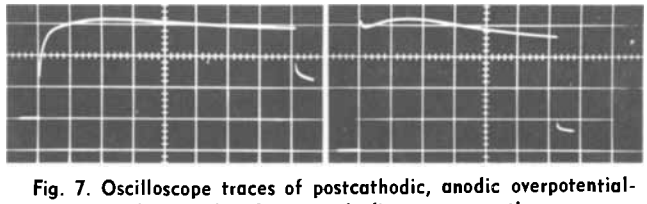

Fig. 7. Oscilloscope traces of postcathodic, anodic overpotential-time relationships ½ hr after a cathodic process at the same current density. Left: (110) at 30 μA/cm^2, 5 mV/div vertical scale, 2 sec/div horizontal scale. Right: (100) at 150 μA/cm^2, 10 mV/div vertical scale, 1 sec/div horizontal scale. Compare with extreme left trace, top and bottom, respectively, of Fig. 6.

between deposition and subsequent dissolution. The effect was more pronounced at low current densities, < 25 $\mu A/cm^2$, than at high, > 150 $\mu A/cm^2$. Consequently, effects of deposition time were also more pronounced at lower current densities. In general, low current density deposition, as indicated in Fig. 8, increased the time to formation of the succeeding anodic maximum by an amount proportional to the extent of deposition. At current densities > 200 $\mu A/cm^2$ even slight deposition effects were not detectable after periods more than one hour. At extremely low current densities, < 5 $\mu A/cm^2$, the effect could be observed for periods of many hours.

Other ambiguous potential-time relationships were observed. Whether the electrode supported an anodic or cathodic process at higher current densities, about 10 min were required to re-establish equilibrium potential after the flow of current was interrupted. However, at low current densities recovery time was much longer. For example, a current of 300 $\mu A/cm^2$ flowing for 1 sec typically would establish an overvoltage maximum near 50 mV in $\sim$ 0.03 sec, and would regain rest potential within 10 min following current interruption. After 60 sec at 5 $\mu A/cm^2$ (equal charge passed) a maximum typically would not have yet been established, the observed overvoltage would not have exceeded $\sim$ 10 mV, and still it could require hours for the rest potential to become re-established. Therefore, it appears that the rate of potential decay was not directly related to the absolute value of the observed overvoltage, nor, in a simple manner, to the quantity of current flowing. In general, recovery time following a cathodic process would exceed that following an exactly similar anodic pulse.

Current potential data.—At this point it is important that it be understood that, unless otherwise indicated, the overpotentials quoted in the presentations which follow are always values of the postanodic maxima. That is to say, every cathodic pulse applied in systems in which current-potential characteristics were being determined was followed by an anodic pulse of equivalent magnitude and duration. This latter pulse was disregarded, and equilibrium allowed to become established in the system. Only then was the next electrode process of interest initiated and data recorded.

Figure 9 illustrates the current-potential relationships obtained on the various surface orientations in this study. The following experimental observations are shown by the figure: (*i*) The curves for (100) and (110) are symmetrical about zero current and overpotential. (*ii*) While it is not obvious from this figure,

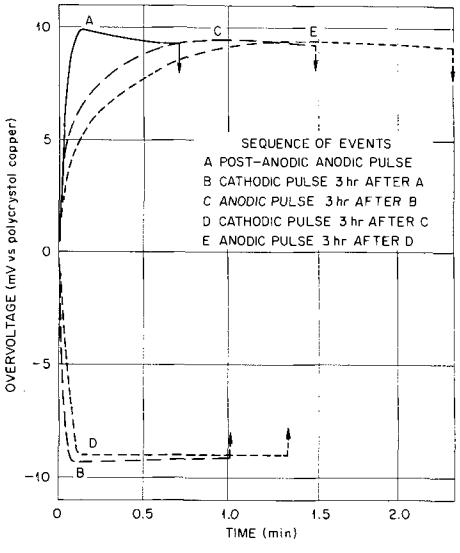

Fig. 8. Effects of deposition on overvoltage-time relationships on the copper (321) orientation at 15 $\mu A/cm^2$.

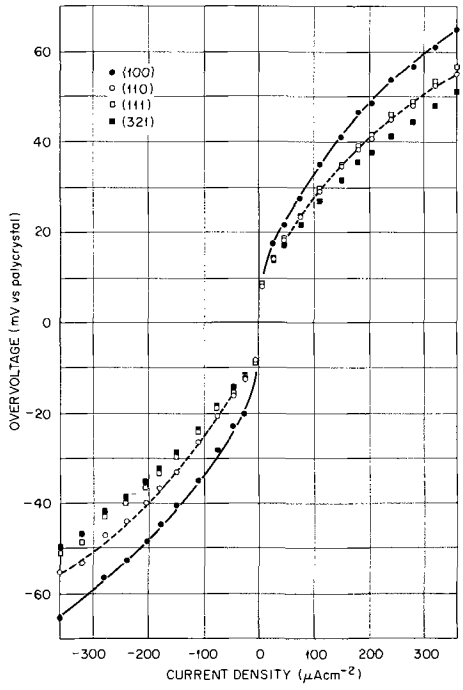

Fig. 9. Overvoltage maxima for variously oriented copper single crystals as a function of current density in solutions of 0.2M $Cu(ClO_4)_2$ and $HClO_4$ (pH $\sim$ 1) at 23°C.

the (321) data are not exactly symmetric about zero. (*iii*) The (111) data are obviously asymmetric in that at any given current density the absolute value of the cathodic maximum is smaller than that of its anodic counterpart. (*iv*) At any current density the absolute value of the overvoltage associated with the process was a function of crystal orientation, increasing in the order (321) $<$ (110) $<$ (100). The (111) obviously cannot be included in this generalization because of the asymmetric character of the data. (*v*) Since the step densities on the (100), (110), and (111) must be approximately equal and much smaller than that of the (321), measured overvoltage maxima are independent of the surface step density.

Discussion

Surface structure.—The classic model of electrocrystallization processes assumes that, after crossing the double layer and undergoing stepwise discharge, atoms ultimately are incorporated into the crystal lattice at kink sites on steps. Whether this is accomplished by diffusion of adatoms over the surface to steps or by direct action at step and/or kink sites, deposition or dissolution ultimately may be described as occurring by the "motion of steps" over the crystal surface, and use of the phrase here does not imply a choice as to the mechanistic detail. Sources of steps are crystal edges, dislocations, new steps nucleated during the processes, and departures from close-packed arrangements due to crystal orientation. It is difficult to assess the exact number of steps arising from dislocations, but if it is assumed that all dislocations have a screw component and that an equal distribution of dislocations of equal and opposite sign exists, the maximum number of steps generated by dislocations should be of the order of the square root of the dislocation density. On the other hand, a misorientation of only $\sim$ 0.1° from a close-packed arrangement will produce $\sim$ 10^5 steps cm^{-1}. It is readily seen that, since the surfaces used in this study could not be prepared with orientations better than $\pm$ 0.1°, the density of orientation related steps was approximately two orders of magnitude greater than that produced by the maximum dislocation density, $\sim$ 10^6 cm^{-2}. Furthermore, although apparently it is not generally recognized, the major

source of steps on a large number of noncleaved metal surfaces employed in studying electrocrystallization phenomena is just such slight misorientations. One other fact is most helpful in discussing the structures developed on the surfaces reported here: Young and Hulett (10) have demonstrated that steps on a copper (111) surface arising from misorientations of $\sim 0.1°$ can sustain a current density as great as 10 mA/cm^2 over long periods of time without nucleation of new steps becoming necessary. This is a current density two orders of magnitude greater than the highest employed in these studies.

It could be assumed that facets developed on (321) surfaces are the end products of complex step interactions and reflect more of the nature of such interactions than of the model substrate supporting the steps. On the other hand the interaction on the (111) of steps to form ledges, which in time aggregated to form larger ledges separated by apparently flat (111), does indicate something of the nature of that orientation. First it is clear that bunched steps constitute a reasonably stable array. Their rapid rates of formation suggest material is as easily added or removed on this surface from such an array as from the initial configuration. Ledges formed are large enough to be considered discreet areas of orientation other than (111), which in turn suggests that step motion over the (111) occurs with some difficulty. At lower current densities on the (100) observations clearly indicated a large portion of the process had to be sustained by step motion since all material was not accountable by pit or pyramid formation. However, as kinetic demands increased, it appears step motion was insufficient to support the reaction, and facets over which steps could move with greater facility were formed. The absolute failure ever to develop facets within $\sim 5°$ of the (100) would indicate that step motion over this orientation is most difficult of any orientation studied. The same type of argument can be used to explain formation of a ridge-valley structure on the (110). In summary, it is proposed that facet development on close-packed orientations is a consequence of the relative difficulty with which steps move over such surfaces. However, facets of close-packed arrangements can be developed as a result of step motion on surfaces with large step densities, such as (321), since the latter contain components of the former within their structure. As a consequence of this argument it must be concluded that, once facets are developed on a surface, little reaction occurs on the areas covered by low index facets, and the surface is in a true sense no longer acting in a uniform manner.

The fact that regardless of initial orientation a large proportion of the total facets formed were oriented along <100> zones suggest that steps move along the <100> zone with relative ease. The low angle facets developed on (100) indicate that the degree of faceting is related to the rate of the surface process in that only those facets necessary to support the reaction are formed. This proposal is substantiated by the observation that at high current densities facets on the (321) formed orientations near the (100), while those formed at lower current densities were further removed from the (100) along the two <100> zones.

Finally, it should be stated there was no evidence that the defect structure of the copper crystals played a significant role in crystal growth or dissolution. Even the pits and pyramids on the (100) could not be related to the crystal defect density.

Overpotential-time data.—Before discussing the overpotential-time data, it is helpful to consider the entire system in the manner employed by Bertocci (11). Although he treated steady-state conditions, the concepts should be applicable to transient processes. Three reactions must be considered: a redox reaction

$$Cu^+ \rightleftarrows Cu^{++} + e \qquad \text{(i)}$$

the reaction between adatoms and cuprous ions

$$A \rightleftarrows Cu^+ + e \qquad \text{(ii)}$$

and the exchange of adatoms with the metal lattice

$$M \rightleftarrows A \qquad \text{(iii)}$$

Bertocci, in treating the general case, assumed the concentration of adatoms always to be the equilibrium value so considerations here are a bit less specific. At any rate, however, it can be shown that the equilibrium potential can be expressed as

$$E_{eq} = E^{o}_{Cu^+/Cu^{2+}} + \frac{RT}{F} \ln \frac{(a_{Cu^{2+}})_{eq}}{(a_{Cu^+})_{eq}} = E^{o}_{A/Cu^+} + \frac{RT}{F} \ln \frac{(a_{Cu^+})_{eq}}{(a_A)_{eq}} \qquad [1]$$

and that when activities of the various species at the interface depart from equilibrium values, the potential of the electrode may be expressed as a sum of the reversible potential of the pertinent reaction and the overvoltage for that reaction

$$E = E_{Cu^+/Cu^{2+},\,rev} + \eta_i = E_{A/Cu^+,\,rev} + \eta_{ii} \qquad [2]$$

Using the notation that $E_i \equiv E_{Cu^+/Cu^{2+},\,rev}$, etc., it follows that

$$E_i - E_{eq} = \frac{RT}{F} \ln \frac{(a_{Cu^{2+}}) \times (a_{Cu^+})_{eq}}{(a_{Cu^{2+}})_{eq} \times (a_{Cu^+})} \qquad [3]$$

$$E_{ii} - E_{eq} = \frac{RT}{F} \ln \frac{(a_{Cu^+}) \times (a_A)_{eq}}{(a_{Cu^+})_{eq} \times (a_A)} \qquad [4]$$

Since electrocrystallization processes must be associated with reaction (iii), the electrocrystallization overvoltage, will be noted as η_{iii}. It has been defined by Vetter (12) as

$$\eta_{iii} \equiv \frac{RT}{F} \ln \frac{(a_A)_{eq}}{(a_A)} \qquad [5]$$

Note that this expression for η_{iii} is contained in Eq. [4] so that also

$$E_{ii} - E_{eq} = \frac{RT}{F} \ln \frac{(a_{Cu^+})}{(a_{Cu^+})_{eq}} + \eta_{iii} \qquad [6]$$

Still following the method of Bertocci it can be shown from Eq. [2], [3], [4], and [5] that, since

$$E - E_{eq} \equiv \eta \qquad [7]$$

$$\eta = \frac{RT}{F} \ln \frac{(a_{Cu^{2+}}) \times (a_{Cu^+})_{eq}}{(a_{Cu^{2+}})_{eq} \times (a_{Cu^+})} + \eta_i = \frac{RT}{F} \ln \frac{(a_{Cu^+}) \times (a_A)_{eq}}{(a_{Cu^+})_{eq} \times (a_A)} + \eta_{ii} \qquad [8]$$

and that

$$2\eta = \frac{RT}{F} \ln \frac{(a_{Cu^{2+}}) \times (a_A)_{eq}}{(a_{Cu^{2+}})_{eq} \times (a_A)} + \eta_i + \eta_{ii} = \frac{RT}{F} \ln \frac{(a_{Cu^{2+}})}{(a_{Cu^{2+}})_{eq}} + \eta_i + \eta_{ii} + \eta_{iii} \qquad [9]$$

Among others, Bertocci considered the special case in which $2\eta = \eta_i$. He pointed out such circumstances required that $(a_{Cu^{2+}}) = (a_{Cu^{2+}})_{eq}$ and that reaction (ii) occur completely reversibly (that is $\eta_{ii} = 0$). These requirements also were those necessary for Bockris and Enyo to interpret their data obtained under conditions of charge transfer control. However, Eq. [8] indicated such circumstances also require that $(a_A) = (a_A)_{eq}$, a limitation which would seem obtainable only if, under the stated conditions, adatoms are indistinguishable from those occupying lattice sites, and therefore, that the adatom concentration equal the number

of surface lattice sites. This relationship will be explored more fully in discussions which follow.

Bertocci's model can be used to explore situations in which charge transfer is not the rate-controlling process, and it is necessary that this be done, for Bockris and Enyo also clearly demonstrated that the redox reaction could not be rate limiting under the experimental conditions reported here. It could be thought, for example, that premaxima overvoltage transients resulted solely from the occurrence of the redox reaction within the diffusion layer without a net flux of material across the interface prior to the establishment of maxima. Since the equilibrium constant for the reaction, $Cu^{o} + Cu^{++} \leftrightarrows 2Cu^{+}$, is approximately 10^{-6} (13), it can readily be demonstrated there were sufficient cuprous ions within the diffusion layer to support the necessary current. This mechanism dictates that, during the time of the premaximum transients, reactions (ii) and (iii) do not occur. From the data of others it is only reasonable to assume that also $(a_{Cu^{2+}}) = (a_{Cu^{2+}})_{eq}$. However, a consequence of the mechanism is that concentrations of cuprous ions in the diffusion layer are smaller than at equilibrium for anodic processes and larger for cathodic. The second portion of Eq. [8] reveals that such circumstances require either that anodic processes exhibit negative overpotentials or $\eta_{ii} \neq 0$. Since either choice is unacceptable the proposed mechanism must be considered most implausible. Moreover, it does not aid in understanding the deposition anomaly. However, as is indicated below, this situation related to cuprous ion activities within the diffusion layer is permissible if surface adion concentrations depart from the equilibrium value.

All the time dependent characteristics of overpotentials reported here cannot be explained on the basis of the classic model of adatom diffusion over the surface to steps where they eventually can be incorporated into the crystal lattice. The data are easier understood if it is assumed that surface diffusion coefficients are much smaller than those for similar processes in solutions. Also, it is necessary to make one alteration in the assumptions generally made regarding the classic model: It will not be assumed that exchange of adatoms at steps occurs more rapidly than other surface processes, but rather that the action is hindered in some manner, and a barrier to exchange exists.

The formation of maxima, the dependence of the rate of decay of overpotential on the current density prior to opening the circuit and on the total charge passed, as well as the inverse relationship between current density and total charge passed at overpotential maxima formation suggest the following interpretation of the data. On closing a circuit at a higher current density the initial current was carried largely without reaction at steps. As the surface concentration of adatoms changed rapidly from the equilibrium value, other necessary events occurred such that the conditions required for steps to act as sources or sinks for adatoms were established. Thereafter, reaction began to occur at steps, and continued reaction produced gradual changes in surface adion concentrations toward the equilibrium value in efforts to establish desired steady-state concentrations. However, under the given experimental conditions, the net flux of adatoms at steps was such that the theoretical steady-state surface adion concentration was slow in being established since most of the adatom flux at steps served largely to support the net reaction rather than to change the average surface concentration of the species. (As will be seen later, it is also proposed that voltage-time relationships are influenced by events occurring at the metal-solution interface.) Obviously such a mechanism assumes the occurrence of time-dependent phenomena. Consequently, if it is assumed that at higher current densities overvoltage maxima were formed before significant reaction occurred at steps, premaxima current flow can be expressed in terms of adion activities

$$(a_A)_{eq} - (a_A)_t = kit/\mathbf{F} \qquad [10]$$

where (a_A) = activity of surface adions at equilibrium or time, t, as designated,

i = current density,
k = fraction of the total current carried by adion reaction,
$\mathbf{F}$ = the Faraday.

By combining Eq. [5] and [10] one obtains the expression

$$\exp(-z\mathbf{F}\eta_{iii}/RT) + kit/\mathbf{F}(a_A)_{eq} = 1 \qquad [11]$$

Consequently, the shape of premaxima portions of overvoltage-time curves at higher current densities should reflect the indicated relationship between overvoltage and time. For the few conditions tested, this was found to be the case, but effects of orientation, current density, polarity, etc., were such that additional studies of these phenomena are being conducted. Shapes of postmaxima portions of overvoltage-time curves should be a complex function of, among other things, the rate of change of surface adion concentration toward equilibrium values, events in the diffusion layer, and changes in surface structures produced by the process under observation. The absolute values of maxima resulting from such a reaction mechanism could, as experimentally observed, be independent of the surface step density, although postmaxima overvoltage-time relationships should not necessarily be.

The failure to establish a true steady-state potential at higher current densities over reasonable times suggests the time required for such an event is of the order of that for significant alterations in initial surface structure. Data shown in Fig. 10 clearly indicate that "normal," postanodic maxima were established before the equivalent of a monolayer of copper had reacted. The high current density data suggest that the equilibrium concentration of adatoms is at least two orders of magnitude less than the total number of lattice sites, if as previously suggested, the initial current flow was largely supported without reaction at steps.

Such a mechanism also accounts satisfactorily for the more rapid establishment of equilibrium conditions following termination of high current density pulses as compared with low decay rates of overpotential

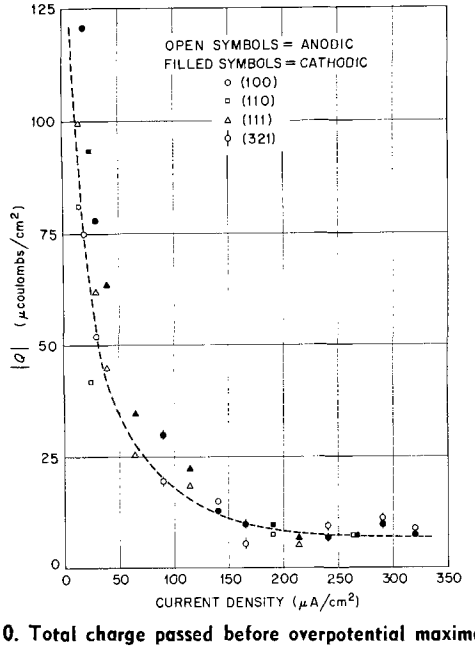

Fig. 10. Total charge passed before overpotential maxima formed on different orientations as a function of current density.

after low current density processes. On interruption of large currents, the potential for a short time, although rapidly decaying, was still sufficient to exceed the barrier to exchange at steps such that they still could act as sources or sinks for adatoms. During this time the total number of adatoms approached the equilibrium value, and additional time was required only for the proper equilibrium distribution to become established.

Anodic pulses at low current densities apparently followed the same general pattern. However, the data in Fig. 9 and 10 suggest that at current densities $\lesssim 25$ $\mu A/cm^2$ "normal" anodic maxima were formed by a current flow supported extensively by reaction at steps. Otherwise, the surface adatom concentration would have been so depleted that much higher overpotentials should have been observed. Also, since early, premaxima stages of current flow were accompanied by a slow monotonic increase in overpotential at low current densities, it would appear that at least a portion of the barrier to reaction at steps was indeed due to the occurrence of some sort of time dependent phenomena. The extremely slow rate of decay to equilibrium potential following interruption of a low current density pulse suggests that related processes at steps also were dependent on the overpotential. On interruption of small anodic currents, overpotentials during decay apparently were of such a relatively small magnitude that the barrier to reaction at steps was not exceeded sufficiently to produce adatoms at a rate necessary to satisfy rapidly the equilibrium requirements. Therefore, rates of potential decay during open circuit following low current density anodic processes were slower because they reflected the rate of production of adatoms at steps rather than, as at higher current densities, attainment of an equilibrium distribution by an adequate adion concentration. It will be seen that cathodic processes at low current densities can be understood on the basis of the same general model, although slight, but significant, alterations must be made.

Since Piontelli (14), as well as others, questions the validity of overpotential maxima and generally attributes their existence to the presence of impurities, perhaps some comments on the systems reported here would be useful. Admittedly neither the data of others obtained at higher current densities nor present theories of electrocrystallization phenomena are too helpful in assessing these results. It seems highly unlikely they can be dismissed as an impurity effect because it is difficult to propose a model of surface processes involving impurities which accounts satisfactorily for all the experimental results reported here.

At this point it is informative to discuss in some detail a part of the data reported by Bockris and Enyo (2). Although they were concerned primarily with the determination of kinetic parameters for copper electrodes exposed to various acidic solutions of different copper salts under conditions such that charge transfer was the slow process, only that portion of the data gathered when such conditions were not met ($i \lesssim 10$ mA/cm^2) is considered here. As much as is possible reference is made only to data concerned with cupric perchlorate systems. However, unless specifically excluded by the authors, it is assumed their general remarks drawn from all the data apply equally to perchlorate solutions. Using spherical copper electrodes they obtained different current-overpotential relationships for electrodes prepared by melting in helium and others of similar origin which were subjected to electrodeposition before use. In general, electrodes of the latter type acted in a much more consistent and understandable manner. For example, cathodic Tafel behavior was obtained for the latter, but not the former type, and values of anodic overpotentials gathered from the two kinds of electrodes did not agree completely. It was proposed that such behavior resulted from the different surface properties of the electrodes. They suggested that electrodes melted in helium contained an oxide film which, on exposure to acidic solutions, dissolved to expose a "new (clean) copper surface" on which the exchange current density would be expected to be greater than on a surface formed by electrodeposition. Further, they assumed a dislocation density of $\sim 10^9$ cm^2 for the former type and that of the latter to be greater, and concluded, therefore, that because electrodes melted in helium had this lower density of growth sites a surface process (diffusion) could become rate determining. It was also concluded that, at the lower current densities studied, surface diffusion was the rate-controlling step on both types of surfaces, which also helped explain the observation that rise times of overpotentials were greater than expected and differed for the two types of electrodes, as well as in anodic and cathodic cases for a single type.

The surface processes suggested by Bockris and Enyo are not unreasonable, but more credible alternatives do exist. From considerations of elementary geometry it can be shown that surfaces of spherical copper electrodes must have an average step density of $\sim 10^7$ cm^{-1} due solely to the intersection of crystallographic planes by the circumference of the sphere. Since, as previously discussed, the number of steps generated by dislocations intersecting a surface surely cannot exceed the square root of the dislocation density, defect related steps on the electrodes of Bockris and Enyo most probably did not number more than $\sim 10^5$ cm^{-1}. Therefore, growth sites produced by electrode geometry far outnumbered those associated with line defects in both types of electrodes, and it appears highly improbable that surface diffusion processes were affected to any significant extent by dislocations present in either type of electrode. Since average step densities on the two electrodes must have been approximately equal, it is much more reasonable to assume that differences measured on the two surfaces were not related to the average number of steps, but rather to the arrangement and distribution of this number of steps due to the different methods of surface preparation. This suggestion is compatible with the changes they observed on "new (clean)" helium-melted surfaces as more data was gathered on them. Presumably the net reaction on such electrodes in time would produce a surface similar to that resulting from electrodeposition, which, because of the method of preparation (15), surely must have consisted of ledges, facets, etc., formed by the bunching of steps.

It is not the primary purpose of this discussion to argue whether the interpretation presented here for the data of Bockris and Enyo is preferable to that of the authors, but rather to demonstrate that data gathered by others under entirely different conditions than those described in this report can reasonably be interpreted in a manner to lend support to the argument that a surface can yield vastly different current-potential and potential-time characteristics depending upon the arrangement of steps on that surface. The surfaces reported in this study upon which current-potential data were gathered contained steps distributed, as previously indicated, in a more or less continuous manner. The reactions performed on these surfaces were conducted at such low rates that the initial step distribution was changed very little during the course of the measurements, and it is certain these data are representative of structures quite different from those of Piontelli *et al.* and Bockris and Enyo. Therefore, it is not surprising that apparently little correlation can be made between any of these experimental results.

Before attempting an analytical treatment of observed overpotential maxima, it would be informative to discuss the data illustrated in Fig. 9 in more gen-

eral terms. It is conceivable that current-potential data for (100), (110), and (111) alone could support an argument that the differences observed on different orientations were related to the relative ease of direct reaction at steps on these orientations. However, the similarity of cathodic data for (321) and (111) preclude the possibility of direct discharge at steps on these orientations, since under such conditions the magnitude of the overvoltages should be proportional to the orientation related step densities which are $\sim 10^7$ and 10^5/cm, respectively. Moreover, the nearly perfect symmetry of the anodic and cathodic branches of the (321) data indicates that the mechanism also is not operable during dissolution from the (321). Then because of their relationships to the (321) and to each other [relative differences between (100) and (110) are greater than between (110) and (321)] and because of their perfect symmetry in anodic and cathodic branches, the (100) and (110) also appear unlikely to react by such a mechanism.

In considering the possibility of nucleation phenomena occurring, it is helpful again to compare cathodic data for the (321) and (111) with their structures. While the idealized (111) is a familiar structure, the ball model of a fcc (321) is perhaps not so well known. The model shows that 40% of the atoms on this surface are located along continuously kinked steps, and on the average, of course, a step occurs every 2½ atom rows. The only "nucleus" capable of existence on the model surface would be a long chain of single atoms at the half position between steps. Placement in any other lattice position would constitute direct growth at steps. Although a real crystal surface most surely does not have that of the idealized model, the arrangement must be such that $\sim$ 40% of the atoms, on the average, represent a kink stepped arrangement. Otherwise, the real surface area of the (321) would have to increase due to formation of preferred orientations, an occurrence which has previously been shown not to happen (5). Therefore, regardless of the real structure of the (321), the similarity of its cathodic current-potential maxima to those of the (111) argue against nucleation as a major event on these surfaces. It would seem then that data concerning the current-potential maxima relationships do not offer any objections to the modified model of surface processes previously proposed.

It does appear strange, however, that overpotential-current relationships should show such a pronounced orientation effect but apparently be free from any influence of step density. This is especially true in view of the relationship between current and step densities derived from the theoreies of electrocrystallization overvoltage. Several authors have considered surfaces from which material is added or removed by step motion, and they have arrived at expressions which relate step density to the average current density and overpotential. Bertocci *et al.* (16) have discussed these models and have shown that it is possible that a proportionality between step and current densities could be observed for misorientations an order of magnitude greater than those of surfaces used in these studies. However, all such models assume that adatom exchange at steps is unhindered. Because of this and also because effects obviously related to crystal orientation were observed, it is unreasonable to conclude that overvoltage characteristics reported here are unrelated to electrocrystallization phenomena. This argument is strengthened further by treating the data for (100) and (110) as indicated in Fig. 11. That similar results are not obtained by treating (321) and (111) data in this manner is demonstrated in Fig. 12. The assumption of indicated values for certain parameters leads to a slight misfit for (321) and a gross misfit for (111) data. Figure 13 shows that a better fit for the (111) is obtained if the value of α is assumed to be 0.46 for this orientation. The slight misfit observed for (321) data suggests an

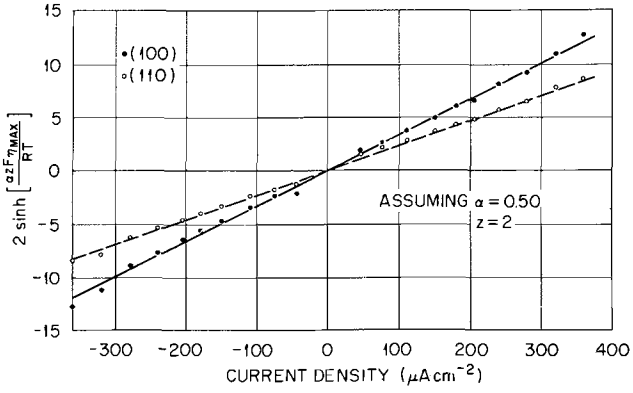

Fig. 11. Relationships between overpotential maxima and current densities on the (100) and (110) at 23°C in 0.2M $Cu(ClO_4)_2$ + $HClO_4$ (pH ~ 1).

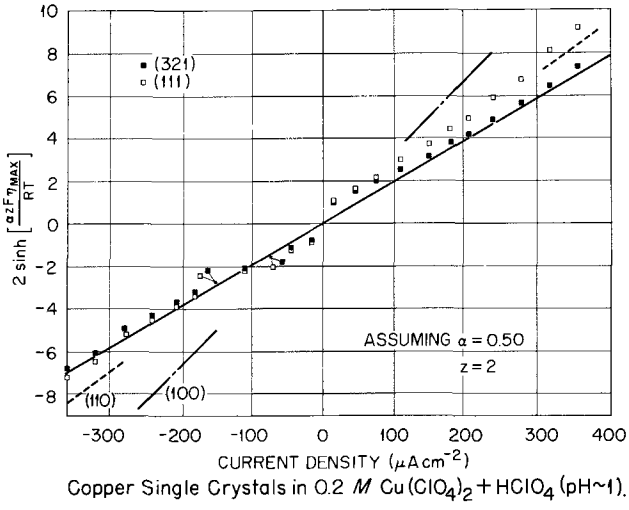

Fig. 12. Relationships between overpotential maxima and current densities on the (111) and (321) if same parameters assumed which permit proper fitting of (100) and (110) data.

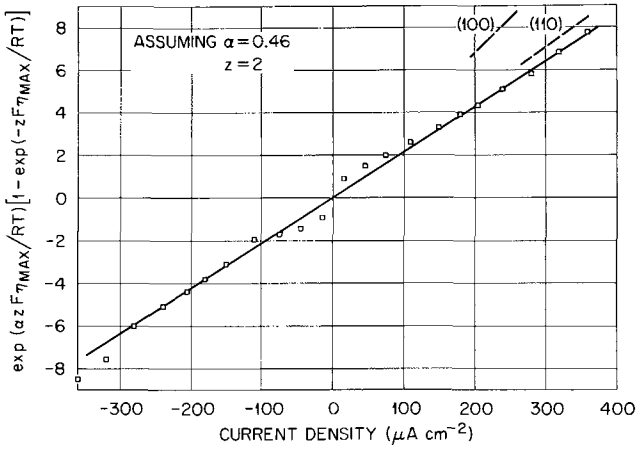

Fig. 13. Relationships between overpotential maxima and current densities on the (111) at 23°C in 0.2M $Cu(ClO_4)_2$ + $HClO_4$ (pH ~ 1) at indicated values assumed for α and Z.

α value of $\sim$ 0.49 for this surface, and further calculations are judged to be not worthwhile. From such plots it is readily seen that the relationship between values of overpotential maxima and the current flowing in the system can be described by the expression

$$i = K\left\{\exp\left[\frac{\alpha z\mathbf{F}\eta_*}{RT}\right] - \exp\left[\frac{-(1-\alpha)z\mathbf{F}\eta_*}{RT}\right]\right\} \quad [12]$$

where η_* = value of overpotential maximum
α = an orientation sensitive transfer coefficient having the values (100) and (110) = 0.50; (321) = 0.49; (111) = 0.46.
z = a factor relating the electrocrystallization overvoltage to the measured overvoltage.
K = a pre-exponential function having the dimensions of current density. The orientation dependent values measured from the slopes of the lines in Fig. 11, 12, and 13 are: (100) = 30; (110) = 40; (111) = 45; (321) = 50 $\mu A/cm^2$
i = current density.

The remaining terms have the significance previously indicated.

Previously it has been postulated that premaxima currents were accompanied by changes in surface adatom concentrations without concomitant action at steps. This is, of course, in agreement with the requirements that surface adatom concentrations be less than the equilibrium value during anodic processes when $\eta_{iii} \neq 0$. A cursory examination of Eq. [9] reveals that data of others regarding $(a_{Cu^{2+}})$ and η_{ii} define conditions such that $2\eta = \eta_i + \eta_{iii}$. The preceding analytical treatment of current-overpotential maxima data requires that $\eta_{iii} = 2\eta$. Therefore, it is necessary to determine conditions under which η_i can approach zero, and to decide if those conditions can be established. Again referring to Eq. [8] and considering the anodic case, it is obvious that η_i can approach the limiting zero value only under the circumstances previously discussed when $(a_{Cu^+})_{eq} > (a_{Cu^+})$. This, in turn, is permissible in the specific case considered when $(a_A)_{eq} > (a_A)$. Therefore, it appears the analytical treatment is reasonable in terms of a model reaction sequence which requires that $(a_{Cu^{2+}}) = (a_{Cu^{2+}})_{eq}$, $\eta_{ii} = 0$, $\eta_i \rightarrow 0$, and that reaction (i) occur within the diffusion layer at a rate greater than reaction (iii) occurs on the surface during the time of the transient. Apparently voltage time characteristics resulted from complicated interactions due to these latter two reactions, and in view of such processes even the twin maxima often observed during postcathodic anodic transients illustrated in Fig. 7 seem reasonable and comprehensible.

At current densities higher than those reported here it would appear that $\eta_i >> 0$ and $\eta_{iii} < 2\eta$. Eventually at still higher current densities the conditions become established whereby, as reported by others, $\eta_{iii} = 0$ and $\eta_i = 2\eta$. It is interesting to note that the data of Piontelli *et al.* were obtained in just this transitional range of current densities where it is suggested that the relationship between η_i and η changes with current density.

Figures 11 to 13 indicate that overpotential values obtained at current densities $\lesssim$ 100 $\mu A/cm^{-2}$ do not agree with the proposed mechanism and treatment as well as those obtained at higher current densities. However, this effect is consistent with the assumption that maxima occurring under the former conditions were not established before significant reaction had occurred at steps. The significance of the pre-exponential constants determined for each orientation depends on the validity of the suggested model of events on the surface and in the diffusion layer. If the proposals advanced to explain the experimental observations are correct, and if the adatom concentrations at equilibrium are about equal on all orientations, then K values could closely approximate the values of the exchange current density of adatoms and ions in solution. It is interesting to compare them with the value of 20 $\mu A\ cm^{-2}$ obtained by Roiter *et al.* (8) on single crystalline zinc in zinc sulfate solutions. Anodic and cathodic maxima were symmetric about the equilibrium point in the zinc system, and it was determined that observed values of maxima depended upon the nature of the preceding electrode process. Unfortunately, no reference is made to the orientation(s?) of zinc crystals used in the study so analogies regarding orientations cannot be drawn. Obviously K values are lower by factors of $\sim$ 200 than the exchange current densities determined by Bockris and Enyo under conditions of charge transfer control. However, as previously noted, such experimental conditions require that adatoms and metal atoms be indistinguishable, a condition not demanded of the systems reported here. This suggests the possibility that excessive removal rates so alter copper surfaces that measurements determined thereon are concerned with surfaces of marked physical differences, in the sense of geometric arrangements, adsorbed species, identity of nearest neighbors, etc., from those on which removal rates are low enough that a surface process may be rate controlling.

Anomalous deposition effects.—The previous treatment accounts in a self-consistent manner for most of the experimental phenomena mentioned earlier, but it still must be shown that the proposed model accommodates equally well the observed effects of deposition on a succeeding dissolution process. If material is incorporated into the metal lattice at steps, it must become identified with, and indistinguishable from, the rest of the crystal. Therefore, no "deposition effect" should be observed following such a process. By the same token, if nucleation occurred and the deposit formed over the old substrate, only the new steps bounding deposits should serve as possible sources of different effects since material bounded by the steps should be identical with the substrate. However, data shown in Fig. 9 indicate that the deposition process was independent of step density in the range $\sim 10^5$-10^7 cm^{-1} since almost identical cathodic branches of current-overpotential data were obtained for the (321) and (111). Therefore, it is difficult to believe that nucleation phenomena could account for the observed deposition anomaly. A reasonable alternative is suggested by the shapes of anodic overpotential-time curves of the type illustrated in Fig. 8. If, as proposed, the shape of low current density "normal" anodic overpotential-time curves reflect both reaction at steps as well as depletion of surface adatoms, then the relationships between cathodic and subsequent postcathodic, anodic curves indicate that material deposited at low and intermediate current densities had more the characteristics of adatoms than of the crystalline substrate. (Although it is not to be assumed that the process is completely independent of the substrate.) Moreover, these characteristics were retained over long periods of time. Therefore, it is suggested that much of the material deposited at low current densities over relatively short periods of time did not occupy half-crystal positions, and in this sense could not be distinguished from adatoms. Since, as indicated in Fig. 8, the anomaly could be observed for the total deposit equivalent to much more than a monolayer of material, such deposits probably have extremely open structures with high vacancy concentrations. This is equivalent to proposing that under these conditions crystal growth occurred more or less by direct addition of atoms at random sites, with little subsequent surface diffusion. While conceptually the idea lacks a certain appeal, it appears that, following a low current density cathodic process, the observed smaller values of anodic maxima and increases in times to establishment can be explained on the basis of an increased concentration of adatom-like material under conditions of "pseudo-equilibrium."

A further indication of the differences in dissolution and deposition processes at low and intermediate current densities is seen by comparing the post-maxima shapes of overpotential-time curves of Fig. 6. Such dif-

ferences were more difficult to detect at current densities in excess of ~ 200 $\mu A/cm^2$, and with the exception of the (111) and possibly the (100), at higher current densities overpotential-time relationships were almost precisely similar for anodic and cathodic processes at the same current density on any one orientation.

A somewhat more quantitative discussion of the deposition anomaly is possible. The data in Fig. 10 show clearly that "normal" maxima for both anodic and cathodic processes at the indicated current densities were established on all orientations well before the equivalent of a monolayer of copper had reacted. But as indicated in Fig. 8 the deposition effect was not restricted to the charge passed in establishing a maximum, but rather to the total amount of material deposited. The highest current density at which it was established that ensuing anodic maxima formed only when the total previous deposit had been removed was 160 $\mu A/cm^2$. Six hours following depositions lasting 1 min at this current density, dissolution produced anodic maxima only after one minute at the same current density. ("Normal" anodic maxima under such conditions were established in ~ 0.1 sec on all orientations and had larger absolute values than observed in postcathodic instances.) These depositions corresponded approximately to the equivalent of 15 atom layers. At lower current densities the largest deposit which was precisely duplicated in a succeeding anodic overvoltage-time to maximum curve corresponded to ~ 50 atom layers. Neither of the examples cited here were established as limiting cases, nor indeed were any of the limiting conditions precisely defined. However, it was observed that at current densities $\gtrsim$ 200 $\mu A/cm^2$ the effect diminished as the current density increased, and a relationship between the total amount of deposit and the amount removed at the time of anodic maximum formation could not be established at higher current densities.

A most intriguing aspect of the overpotential data is that the (321) and (111) have nearly identical cathodic but quite different anodic branches. Previously it has been pointed out that, as illustrated in Fig. 6, on any orientation postmaxima anodic and cathodic overpotential-time relationships are not always identical for any one reaction rate, even at the highest current densities studied. This indicates that immediately after the maximum change in adion concentration had been established, subsequent surface events were not precisely equivalent for dissolution and deposition. The suggested model of reaction seems suitable for anodic processes, but further discussion is required in the cathodic case. The relative step densities on the (321) and (111) suggest that the lack of symmetry in the (111) overpotential data resulted from lower values for cathodic processes rather than excessively high values for the anodic. If so, it was not diffusion over the surface which limited the maximum cathodic overpotential developed on the (111), otherwise the (321) surfaces would not have produced data identical to that obtained for the (111). At higher current densities it is possible that unusual growth processes might have occurred on the (111). It could be that diffusion was such a relatively slow process that growth was accomplished on the flat surface areas rather than by diffusion to step sites. However, there is insufficient evidence to suggest nucleation processes occurred, and furthermore, by analogy to observations on all orientations at low current densities, it seems preferable to think of growth on the (111) as being accomplished by rather ill-defined methods which produced atom layers with a very high vacancy content.

A more plausible reason for the asymmetric behavior of the (111) and (321) could be a consequence of the fact that the (111) is the close packed plane in copper. In face-centered cubic systems such as copper the close packed planes are stacked in the sequence ABCABC-AB . . ., etc., but it is not at all certain that adatoms on a (111) area are restricted to sites representing proper crystal sequential orders. So while there are two types of geometrically similar sites available to adatoms on this surface, in terms of permanent occupancy of such sites one of them is crystallographically improper. Growth occurring in such unsuitable arrays, rather than by movement of crystallographically correct steps over the surface, could have been responsible for the asymmetric behavior observed. The slight asymmetric property of the (321) data emphasizes the fact that a tremendously high step density was incapable of causing complete obliteration of this effect, and that perhaps it is indeed an intrinsic property of the close-packed arrangement. Therefore, it is not at all certain that the "deposition anomaly" observed on all orientations at lower current densities did not also occur undetected on all orientations at higher current densities. It is possible that diffusion over any orientation was relatively so difficult that initial growth at all the current densities reported here occurred in such a way that structures with very high vacancy content always were formed.

Manuscript submitted Jan. 27, 1969; revised manuscript received *ca.* Dec. 24, 1969. The data reported here were presented in part as Paper 110 at the Washington Meeting, Oct. 11-15, 1964, and in part as Paper 72 at the Philadelphia Meeting, Oct. 9-14, 1966. The research on this paper was sponsored by the USAEC under contract with Union Carbide Corporation.

Any discussion of this paper will appear in a Discussion Section to be published in the December 1970 JOURNAL.

REFERENCES

1. R. Piontelli, G. Poli, and G. Serravalle, *"Transactions of the Symposium on Electrode Processes,"* E. Yeager, Editor, John Wiley & Sons, New York (1961).
2. J. O'M. Bockris and M. Enyo, *Trans. Faraday Soc.*, **58,** 1187 (1962).
3. D. Shanefield and P. Lighty, *This Journal,* **110,** 973 (1963).
4. F. W. Young, Jr. and T. Wilson, *Rev. Sci. Inst.,* **32,** 559 (1961).
5. L. H. Jenkins and U. Bertocci, *This Journal,* **112,** 517 (1965).
6. L. H. Jenkins and J. Stiegler, *ibid.,* **109,** 467 (1962).
7. L. H. Jenkins, *ibid.,* **113,** 75 (1966).
8. W. Roiter *et al., Acta Physicochem. USSR,* **10,** 845 (1939).
9. W. Krebs and D. Roe, *This Journal,* **114,** 892 (1967).
10. F. W. Young, Jr. and L. D. Hulett, Jr., "Metal Surfaces," W. Robertson *et al.,* Editors, Am. Soc. for Metals, Metals Park, Ohio (1963).
11. U. Bertocci, *Electrochim. Acta,* **11,** 1261 (1966).
12. K. J. Vetter, "Electrochemical Kinetics," Academic Press, New York (1967).
13. F. Fenwick, *J. Am. Chem. Soc.,* **48,** 860 (1926).
14. R. Piontelli, *Electrochimica Metallorum,* **1,** 5 (1966).
15. J. O'M. Bockris *et al., J. Sci. Inst.,* **33,** 400 (1956).
16. U. Bertocci, L. D. Hulett, Jr., L. H. Jenkins, and F. W. Young, Jr., "Reactivity of Solids," J. W. Mitchell *et al.,* Editors, Wiley-Interscience, New York (1969).

Oxygen Reduction on Active Platinum in 85% Orthophosphoric Acid

A. J. Appleby*

Institute of Gas Technology, Chicago, Illinois

ABSTRACT

The oxygen reduction reaction on platinum that has been anodized, followed by reduction at 500 mV, has been studied in 85% orthophosphoric acid over a wide temperature range. This anodized platinum surface is more active for oxygen reduction than annealed reduced platinum in the 850-950 mV potential range and has a higher Tafel slope (1.79 $RT/\mathbf{F}$ at 25°C, compared to 1.04 $RT/\mathbf{F}$ for the annealed surface). Activation energy at the reversible potential is 14.9 ± 1.5 kcal. It is suggested that the rate-determining step on this surface is

$$S + O_2 + H^+ + e^- \rightarrow SO_2H$$

under conditions in which the adsorption of the product is close to Langmuirian. Hydrogen peroxide is *not* appreciably involved in the reduction mechanism. These results are interpreted in terms of the surface structure of the electrode after oxide reduction.

It is well-known that platinum that has been freshly anodized behaves as a more effective catalytic surface for a wide range of electrochemical processes. This effect has been explained by Kolthoff and Nightingale (1) and by Davis (2) as being due to facilitated electron transfer from the oxidized platinum surface by an oxygen-bridge mechanism. Other workers, on the other hand, have argued that a chemical mechanism is responsible in which reagents react directly with the oxidized surface, which is unstable under reducing conditions (3, 4).

Anson (5) considered that platinum that has been oxidized then reduced by a redox system is covered by a thin, platinized layer, and behaves as a specially active surface. This argument is supported by the observation that marked roughening of the surface occurs under a-c conditions (6). However, Gilman (7) has shown that only a small increase in area is produced by one polarization cycle, and this is true only if reduction of the oxidized surface is rapid. An alternative explanation was advanced by Feldberg, Enke, and Bricker (8) who attributed the enhanced activity of oxidized and reduced platinum to an adsorbed layer of PtOH.

In general, no special increase in activity other than that which may be attributed to impurity adsorption (9, 10) is observed by pulsing platinum to 1.6V (11). Under these conditions, approximately one monolayer of adsorbed oxygen on the platinum surface is involved (12). At higher potentials, more than one monolayer of oxide may form (13-15).

In this paper, the reduction of oxygen in 85% orthophosphoric acid is studied on reduced platinum that has been previously anodized at high potentials. Kinetics and mechanism on this active surface are compared with those occurring on a reduced, annealed platinum surface (10).

Results are interpreted in terms of surface modification due to partial reduction of the oxide layer, with the formation of a strained lattice containing dissolved oxygen and with a high density of surface defects (16).

Experimental

The all-silica cell in which the experiments were carried out has been described in a previous publication (17). The working electrode consisted either of one of a number of 1-cm² platinum foils suspended from wires, or of the disk of a rotating ring-disk electrode. Electrodes (zone-refined grade, nominal 99.999% purity) were degreased and washed in concentrated HCl, conductivity water, and the electrolyte itself before use. The reference electrode was a dual bubbling hydrogen system equipped with a Luggin capillary. Hydrogen for the reference electrode and oxygen or oxygen-nitrogen mixtures (reproducibly mixed to the required P_{O_2} by capillary flowmeters) were led to the cell via presaturators. All measurements throughout this work were carried out by conventional galvanostatic methods, although with the ring-disk electrode a potentiostat was used. The latter electrode was used to study the formation of hydrogen peroxide intermediates in the reaction and to obtain polarization data over a longer activation-controlled range.

The electrolyte was purified by treatment with hydrogen peroxide in a manner previously described (17). All potentials throughout this paper are expressed relative to the bubbling hydrogen electrode in the same solution (HRE potentials).

Electrode pretreatment.—Electrodes were anodized at a potential of 2V HRE for 2 min and were then allowed to reduce galvanostatically at a current density of 20 μA/cm² until the potential reached 500 mV. Following this treatment the cathodic galvanostatic current was switched off and the electrode was allowed to attain its equilibrium rest potential.

Rest potentials.—Rest potentials of the electrodes were approximately 990-1010 mV. The values were not significantly temperature dependent; initial experiments, carried out by adding small quantities of analytical grade 85% orthophosphoric acid to the pure electrolyte, established that small traces of impurities resulted in lowered values.

Tafel plots were obtained as soon as the electrode had reached an open-circuit potential whose value had changed by less than 5 mV in the previous 2 min. It was noted, however, that the potentials of electrodes left on open circuit slowly rose over a period of hours to a maximum of 1020-1030 mV.

Tafel plots.—Galvanostatic Tafel plots were made using a conventional battery-operated, high impedance circuit allowing sufficient time (up to 5 min at low current density, 1-2 min at higher current density) for equilibrium to be reached at each point. Steady-state readings were taken when the potential changed by less than 2 mV in the previous interval of 1 min. Plots were obtained in this way at 25.1°, 52.1°, 76.1°, 95.9°, 116.0°, and 136.1°C (Fig. 1). In general, they could be traced forward and backward with very little hysteresis.

Each potential-log current plot shows a gently sloping region extending from the rest potential, followed

* Electrochemical Society Active Member.

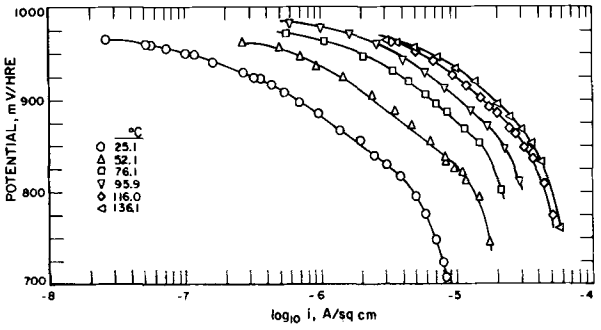

Fig. 1. Galvanostatic Tafel plots of oxygen reduction on active platinum, temperature dependence.

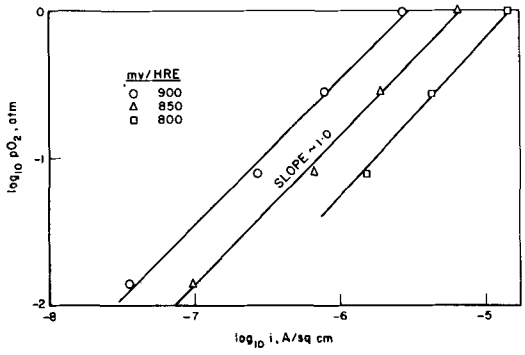

Fig. 2. Effect of oxygen partial pressure on polarization at 52.1°C

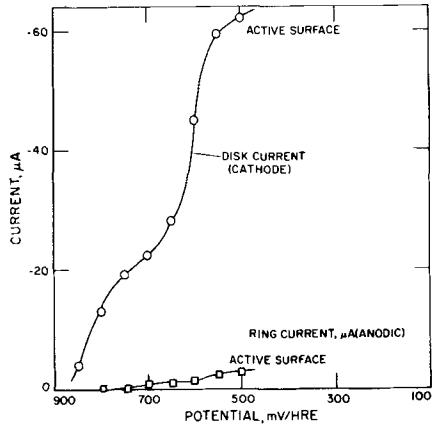

Fig. 3. Ring-disk electrode data, 4840 rpm at 76.1°C

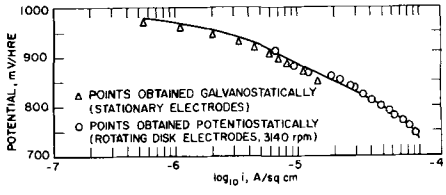

Fig. 4. Tafel plot at 76.1°C on active platinum: stationary and rotating disk electrode data.

by a Tafel region starting at about 925 mV. The Tafel slopes and $1/\alpha$ values at each temperature studied are given in Table I. In addition, Table I contains exchange current values obtained by extrapolating the Tafel line to the calculated reversible potential at each temperature (assuming $P_{O_2} = 1$ and $P_{H_2} = 1\text{-}p$ atm, where p is the water vapor pressure above phosphoric acid).

In each case the experimentally obtained exchange current has been corrected to 1 atm oxygen partial pressure assuming a first order mechanism (see below).

Order of reaction for oxygen.—A series of Tafel plots was made at different oxygen partial pressures. At the lower partial pressures it was necessary to wait for some time to elapse before the first point was taken to allow oxygen evolved during electrode pretreatment by anodizing to disperse before reproducible results could be obtained. Tafel plots at four oxygen partial pressures on active platinum electrodes at 52.1°C have been previously published (18). A log-log plot of polarization data in the Tafel range of these plots is shown in Fig. 2, which indicates that the chemical reaction order for oxygen reduction is unity.

Hydrogen peroxide.—A rotating ring-disk electrode was used to determine the percentage of hydrogen peroxide produced, either as the end product of a parallel mechanism or as an intermediate in the overall process of oxygen reduction to water. In these experiments the disk electrode was prepared by anodizing followed by reduction in the same way as the platinum foil working electrodes referred to previously. The lightly platinized ring of the electrode was maintained at a constant potential of 1.3V HRE; at this potential hydrogen peroxide oxidation is diffusion controlled. Experiments were carried out at 76.1° and 116.0°C in 85% orthophosphoric acid purified by hydrogen peroxide treatment. Disk current and the corresponding anodic ring current were determined at various cathodic potentials applied to the disk by means of a potentiostatic circuit. A typical reduction wave for oxygen at 76.0°C is shown on Fig. 3, for a rotational velocity of 4840 rpm. Unlike the corresponding case on oxide-free annealed platinum (10), little effect of impurity adsorption on oxygen reduction kinetics in the double layer region was noted.[1] At 76.1°C, small quantities of hydrogen peroxide were detected at the electrode ring. The collection factor of the electrode used was 35%; on this basis hydrogen peroxide accounted for less than 10% of the total reaction product or detectable intermediate. At the same temperature on annealed oxide-free platinum, hydrogen peroxide accounted for a greater proportion, approximately 16% of the total product or intermediate. At 116°C, no hydrogen peroxide could be detected at the ring when the disk was in the "active" state.

The ring disk electrode at 3140 rpm was used to confirm the Tafel slope at 76.1°C over a greater range than was possible in the electrolyte stirred by gas bubbling. At this rotation speed, the linear Tafel range at the electrode was increased by approximately a further decade. Figure 4 shows that there is good agreement between the Tafel slope for platinum foil electrodes under stirring by gas bubbling and a rotating disk electrode at a high rate of hydrodynamic stirring.

Activation energy.—Figure 5 shows an Arrhenius plot of the extrapolated i_0 values (corrected for oxygen partial pressure). Activation energy at the reversible potential on this basis is about 14.9 ± 1.5 kcal (10), and the value on active platinum is close to that observed on oxidized platinum (13.1 kcal) (17).

The higher temperature i_0 values lie somewhat off the line; this is probably due to the uncertainty in measuring the Tafel slope (assumed to be about 125 mV/decade) at the higher temperatures.

Table I. Kinetic data for oxygen reduction on active platinum in 85% orthophosphoric acid

Temp, °C	i_0, A/cm² (atm O_2)	Tafel slope, mV/decade	$1/\alpha$
25.1	2.7×10^{-10}	106	1.79
52.1	3.4×10^{-9}	119	1.85
76.1	1.5×10^{-8}	120	1.76
95.9	4.0×10^{-8}	124	1.69
116.0	1.2×10^{-7}	125	1.62
136.1	2.8×10^{-7}	125	1.52

[1] This deactivation is attributed by Bockris *et al.* (19) to $H_2PO_4^-$ ion adsorption.

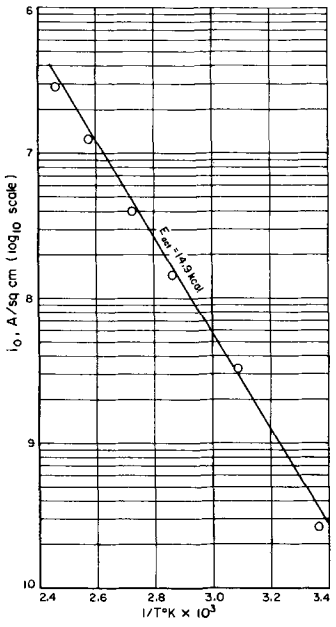

Fig. 5. Arrhenius plot of extrapolated exchange currents for oxygen reduction on active platinum in 85% orthophosphoric acid.

Discussion

Nature of the active platinum surface.—Platinum which has been anodized at high potential has on its surface a phase oxide film at least two monolayers thick (13-15). In addition, the outer layers of the platinum lattice appear to contain "dermasorbed" oxygen, that is, oxygen dissolved in the first two or three atomic layers of the platinum. Evidence for the existence of the latter type of dissolved oxygen has been given by Schuldiner and Warner (20), and is implicit in the observation that the anodic charge in galvanostatic transients is always greater than the cathodic charge in the platinum oxidation reduction cycle. The evidence for this has been reviewed by Vetter (21) and Hoare (22). This observation has been explained by Gilman (23) in terms of an impurity oxidation reaction contributing to the anodic current, by Laitinen and Enke (14) in terms of oxygen evolution in the anodic cycle, and by Vetter and Berndt (24) in terms of a cathodic mechanism involving a 2-electron reduction of the oxide film so that hydrogen peroxide was the end product rather than water. The latter reaction is unlikely, in view of the ring-disk electrode data of Frumkin *et al.* (25), which indicated that no detectable hydrogen peroxide was produced during oxide-film reduction on platinum. Equally, the first two explanations are unlikely as the same phenomenon is observed under conditions of high purity (additionally oxidation of many species is strongly inhibited on oxidized platinum) (26) and oxygen evolution is not normally apparent at low potentials, at which this effect is still observed.

Feldberg *et al.* (8) offer an explanation for this phenomenon in terms of a partial reduction of the platinum oxide film [which consists of PtO (27) if the potential of the electrode is not greater than about 1.8V] to PtOH, on the assumption that the reduction of this compound is highly irreversible. This is difficult to accept on kinetic grounds, and it is hard to see how an oxide film some monolayers thick can be exactly half reduced to a PtOH film with the same thickness.

A previous publication (10) has described the kinetics of oxygen reduction on a platinum surface prepared by electrochemical reduction to remove any residue oxide followed by anodic and cathodic pulsing (at a maximum anodic potential of 1.2-1.5V) to produce a surface free of adsorbed capillary-active impurities. If PtOH is the end product of the reduction of the PtO produced in the anodic pulse, it would be expected that the electrode surface would be covered with a monolayer of this material. The surface produced by this treatment is, however, kinetically similar to platinum pretreated by hydrogen reduction at 500°C. The latter surface is unlikely to carry any oxidized platinum; in addition, it is hard to see how radicals such as O_2H or O can be adsorbed on a surface bearing a monolayer of a similar species (OH) and still obey a Temkin-type adsorption isotherm, in which the heat of adsorption of species of similar electronegativity (for example, OH, O, O_2H) falls off as the total coverage increases (28). This isotherm accurately applies only at intermediate coverages ($0.2 < \theta < 0.8$); at $\theta \rightarrow 0$ or 1, adsorption is Langmuirian. Hence, with a coverage of —OH close to unity, the adsorption isotherm for O or O_2H would be expected to be also Langmuirian.

It seems reasonable to assume that the charge imbalance in anodic and cathodic galvanostatic transients is caused by diffusion of oxide ions into the first few monolayers of the platinum lattice (20) where they become inaccessible for reduction. Because of the high energy of the platinum lattice containing interstitial oxygen, it is energetically difficult for the oxygen to diffuse out through the reduced outer one or two monolayers of platinum. The latter are envisaged to be, therefore, situated on top of a disordered highly strained lattice of Pt-O alloy, so that the surface after oxide reduction is a high-energy, randomly oriented platinum layer containing numerous vacancies and lattice defects.

It is interesting to note that the "active" surface is not produced by pulsing to 1.5V, where only one monolayer of reducible oxide is involved (12). It is necessary to strongly oxidize the surface by anodizing at high potential, followed by reduction at about 600-700 mV to remove the superficial reducible oxide layer. The disordered surface containing dissolved oxygen thus produced is not particularly stable, but is more stable than would be expected for a very lightly platinized surface, of the type suggested by Anson (5).

As Feldberg *et al.* (8) have shown, the active surface degrades very slowly above 700 mV, but is reduced relatively quickly to give a normal annealed platinum surface at 300 mV. It seems likely that the nitric-acid-treated platinum surface reported by Hoare (29) is a similar high-energy surface containing dissolved oxide ions.

Mechanism of Reaction on the Active Surface

The principal kinetic characteristics of the active surface are: (*i*) first order reduction of oxygen, and (*ii*) Tafel slopes of 1.79 *RT*/**F** to 1.54 *RT*/**F**, depending on temperature. In addition, the surface is more active than annealed, oxide-free platinum, less affected by impurities, and produces less hydrogen peroxide.

On normal (annealed) platinum the Tafel slope is *RT*/**F**, and oxygen reduction is first order. It has been shown that this is consistent with the rate-determining step (10, 11)

$$SO_2 + H^+ + e^- \rightarrow SO_2H$$

in which it is assumed that the adsorption of SO_2H follows the Temkin isotherm. This is justified on the following grounds. The rate equation for the above reaction is

$$i = \theta' k\mathbf{F} \exp(-\beta\mathbf{F}V/RT - \beta r\theta/RT)$$

where β is a symmetry factor, θ' is the coverage of molecular oxygen, θ is the total coverage of similar oxygenated compounds (—O, —OH, and —O_2H) on the electrode surface, r is the change in heat of absorption for unit change in θ, and k is the specific rate constant. **F**, *R*, and *T* have their usual meanings. Only the adsorption of the product of the reaction follows the Temkin isotherm; the observation that oxygen reduction is first order implies that $pO_2 \propto \theta'$; that is, a

Langmuir isotherm (at low coverage) operates for the reactant (10).

Assuming that the oxidation products of water (—O and —OH) are in equilibrium on the electrode, and their adsorption obeys a Frumkin isotherm (Temkin approximation in the coverage range $0.2 < \theta < 0.8$) then it can be shown in this interval of θ (30)

$$\partial V/\partial\theta = \frac{r}{\mathbf{F}}$$

and $\mathbf{F}V = r\,\theta$ (29)

Hence

$$i \propto pO_2 \exp(-\mathbf{F}V/RT)$$

Damjanovic and Brusic (11) have also shown that this treatment is consistent with their observed pH dependence.

In principle, the oxygen electrode on oxide-free platinum behaves like a normal charge transfer process with a Tafel slope $2RT/\mathbf{F}$, which is progressively poisoned (*i.e.*, the rate constant decreases) by the increasing surface coverage of the oxidation products of water with increasing potential. The reduction reaction on the active surface apparently involves the same rate-determining step taking place under conditions of increased heat of adsorption of the reaction intermediate ($—O_2H$),[2] thus accounting for the increased rates, and where this effective poisoning (fall in rate constant due to change in heat of adsorption with coverage) is less apparent. We must postulate that the adsorption isotherm of O_2H is more nearly Langmuirian on the "active" surface.

If we consider a surface with a high proportion of lattice defects, it is probable that the range of energy distributions at individual defects is not too wide. On this basis, with only a small number of sites that are active at any time, approximately Langmuir conditions of adsorption at relatively low coverage are possible. The effect of $O^=$ within the lattice must not be discounted. If the Temkin isotherm on the annealed surface is caused by an induced heterogeneity effect, due to dipole interaction at the surface, then the effect of lattice oxygen may be to reduce these interactions and allow a more Langmuirian isotherm to operate.

The activation energy on the reduced annealed surface was previously determined to be approximately 22.9 kcal at the reversible potential (10). This figure contains a heat of adsorption term due to fall in bond-strength of reaction intermediates as —O coverage on the electrode rises with potential. For this reason, it is more legitimate to compare activation energies for the two surfaces at a potential where coverage by adsorbed —O is low, rather than at the reversible potential. On this basis, the difference in activation energy at about 800 mV ($\eta \sim -400$ mV) is (22.9-14.9) $-$ $(\alpha_1 - \alpha_2)\,\eta\mathbf{F}$ kcal, where α_1 and α_2 are the mean transfer coefficients on each surface. With $\alpha_1 \sim 1.0$ and $\alpha_2 \sim 0.59$, this difference amounts to approximately 2.5 kcal. If one assumes that the total increase in surface energy is equivalent to about one surface defect for every ten surface atoms, then it is possible to account for most of the activation energy decrease on this basis. If a platinum atom at a defect has extra energy available for bonding equal to 4 available Pt-Pt bonds, then the excess energy of each site (compared with normal platinum) is about 4 $Ls/6$ where Ls is the latent heat of sublimation of platinum. On the basis of Pauling's equation (31) for the strengths of polar bonds, the increase in bond strength of the reaction intermediate at each site will be approximately

$$\frac{1}{2}\,\frac{4Ls}{6} \sim 40 \text{ kcal/mole}$$

The net increase in bond strength over the whole surface will thus be about 4 kcal. If one assumes that the change in activation energy will be given by $\beta \times 4$ kcal where β is a symmetry factor, a change of 2 kcal might be expected, with $\beta = 1/2$.

It is also likely that the electronic work function at a defect site is not canceling, *i.e.*, it appears in the over-all rate equation. This possibility has been discussed by Damjanovic, Setty, and Bockris (32). Hence, if the electronic work function is lower at defects, an additional reduction in the activation energy may be expected.

[2] This also explains the lower proportion of H_2O_2 detected in comparison with that at the annealed oxide-free surface (10).

Conclusion

The "active" surface of platinum is kinetically different from a normal annealed platinum surface prepared by reduction. This may be attributed to the effect of dermasorbed oxygen (20) within the first few layers of the lattice, and to a high degree of surface disorder. Since the structure of the surface is not stable, eventual rearrangement and recrystallization take place with the production of a platinum surface with normal properties. The method of activation by anodizing and reducing is consequently not a promising method for long-time improvement in the electrocatalytic properties of the substrate.

Acknowledgment

The author wishes to thank the sponsors of the TARGET fuel cell program and Pratt & Whitney Aircraft Division of United Aircraft Corp. for permission to publish this work. The help of members of IGT in the preparation of this publication is also greatly appreciated.

Manuscript submitted Oct. 31, 1969; revised manuscript received *ca.* Feb. 3, 1970.

Any discussion of this paper will appear in a Discussion Section to be published in the December 1970 JOURNAL.

REFERENCES

1. I. M. Kolthoff and E. R. Nightingale, *Anal. Chim. Acta*, **17**, 329 (1957).
2. D. G. Davis, *Talanta*, **3**, 335 (1960).
3. K. I. Rozenthal and V. I. Veselovskii, *Zh. Fiz. Khim.*, **27**, 1163 (1953).
4. T. I. Borisova and V. I. Veselovskii, *ibid.*, **27**, 1195 (1953).
5. F. C. Anson, *Anal. Chem.*, **33**, 934 (1961).
6. F. C. Anson and D. M. King, *ibid.*, **34**, 362 (1962).
7. S. Gilman, *J. Electroanal. Chem.*, **9**, 276 (1965).
8. S. W. Feldberg, C. G. Enke, and C. E. Bricker, *This Journal*, **110**, 826 (1963).
9. S. D. James, *ibid.*, **114**, 1113 (1967).
10. A. J. Appleby, *ibid.*, **117**, 328 (1970).
11. A. Damjanovic and V. Brusic, *Electrochim. Acta*, **12**, 615 (1967).
12. W. Bold and M. Breiter, *ibid.*, **5**, 145 (1961).
13. A. K. N. Reddy, M. Genshaw, and J. O'M. Bockris, *J. Electroanal. Chem.*, **8**, 406 (1964).
14. H. A. Laitinen and C. G. Enke, *This Journal*, **107**, 773 (1960).
15. D. Gilroy and B. E. Conway, *Can. J. Chem.*, **46**, 875 (1968).
16. H. Dietz and H. Gohr, *Electrochim. Acta*, **8**, 343 (1963).
17. A. J. Appleby, *J. Electroanal. Chem.*, **24**, 97 (1970).
18. A. J. Appleby and A. Borucka, *This Journal*, **116**, 1212 (1969).
19. J. O'M. Bockris, Cahan, and Stoner, *Chem. Instrumentation*, **1**, 273 (1969).
20. S. Schuldiner and T. B. Warner, *This Journal*, **112**, 212 (1965).
21. K. J. Vetter, "Elecktrochemische Kinetik," pp. 500-506, Springer, Berlin (1961).
22. J. P. Hoare, "The Electrochemistry of Oxygen," pp. 24-26, Interscience Publishers, New York (1968).
23. S. Gilman, *Electrochim. Acta*, **9**, 1025 (1964).
24. K. J. Vetter and D. Berndt, *Z. Elektrochem.*, **62**, 378 (1964).
25. A. N. Frumkin, E. I. Krushcheva, M. R Tarasevich, and N. A. Shumilova, *Elektrokhimiya*, **1**, 17 (1965).
26. J. O'M. Bockris and H. Wroblowa, *J. Electroanal. Chem.*, **2**, 428 (1964).

27. J. P. Hoare, *ibid.*, **12**, 260 (1966).
28. B. E. Conway and E. Gileadi, *Trans. Faraday Soc. London*, **58**, 2493 (1962).
29. J. P. Hoare, *This Journal*, **112**, 849 (1965).
30. H. Wroblowa, M. L. B. Rao, A. Damjanovic, and J. O'M. Bockris, *J. Electroanal. Chem.*, **15**, 139 (1967).
31. L. Pauling, "The Nature of The Chemical Bond," 3rd ed., pp. 88-91, Cornell University Press, Ithaca, N. Y. (1960).
32. A. Damjanovic, T. H. V. Setty, and J. O'M. Bockris, *This Journal*, **113**, 429 (1966).

Technical Notes

Zinc-dichromate High Power Primary Cell

Gianfranco Pistoia and Bruno Scrosati*

Istituto Elettrotecnico, Universitá di Roma, Rome, Italy

It is known that the electrochemical cells so far developed, at high discharge current drains, *i.e.*, current densities greater than 0.15 A/cm^2, generally have the characteristic of showing an appreciable voltage drop at the electrodes. This makes it impossible to obtain high specific power values, *i.e.*, power densities greater than 0.25 W/cm^2, with such systems.

The characteristics necessary in an electrochemical system for the development of a high power cell, *i.e.*, a cell capable of tolerating high discharge rates, are in essence: (*a*) high values of open circuit potential (OCV), (*b*) very low internal resistance to ensure that IR drops through the cell are almost negligible, and (*c*) very low electrode polarizations even at high discharge rates.

None of the high power cells based on metallic anodes and halogens as cathodes, such as Mg/Cl_2 (1), Zn/Cl_2 (2), and Mg/Br_2 (3) has all these characteristics. In these systems, in order to dissolve the halogens, it is necessary to use electrolytes containing halide salts, such as NaCl and NaBr (1), $CaCl_2$ and $ZnCl_2$ (2), and $MgBr_2$ (3), which do not possess high specific conductivities. This results in an appreciable voltage drop under discharge and, consequently in the impossibility of obtaining high power values. Furthermore, the necessity of a continuous supply to the positive electrode of the gaseous or liquid halogen from a separate container creates enormous problems as far as both materials and techniques are concerned. Finally the high cost and the use of substances which are dangerously toxic makes this type of cell limited in its application.

It would seem more practical to use, as a cathode, a couple in which the oxidized form is present on the electrode support, as in the Zn/KIO_3 (4) and Zn/AgO (5) systems, or, alternatively, in solution. The latter has some advantage over the former, since it does not require preformation of the cathode, as it is sufficient to provide an inert electrode, such as graphite, at whose surface the oxidized species may be reduced.

One of the cells which works with a liquid depolarizer is the zinc-dichromate cell. This cell is an old concept and could in principle be discharged at high current drains (6). On the other hand the cell, in its old construction, presents serious disadvantages, such as electrode polarizations and very short shelf life, which have so far prevented its use for high power purposes. These disadvantages can be overcome by recirculating the electrolyte through the electrodes, choosing the best electrolyte concentration and working temperature and by careful design of the cell. Using a similar technique, Crowley *et al.* were able to realize a high rate performance cell based on a Mg/CrO_3 system having a recirculating acidic electrolyte (7).

In this work the characteristics and the performance of an improved zinc-dichromate cell are reported.

Experimental

Choice of electrolyte.—Before arriving at the system Zn/$Na_2Cr_2O_7$ in acidic solution, several other possible cathodic couples for the development of high power cells, were taken into consideration. Among these were

$S_2O_8^{2-}/SO_4^{2-}$	$E° = 2.01$V
Co^{3+}/Co^{+2}	$E° = 1.81$V
MnO_4^-/Mn^{2+}	$E° = 1.69$V
Ce^{4+}/Ce^{3+}	$E° = 1.61$V

The respective voltage under load of cells using each of these systems coupled with a zinc anode and in sulfuric solution was, at best, about 1V for current densities of the order of 0.05 A/cm^2.

More encouraging results were obtained with systems utilizing the $Cr_2O_7^{2-}/Cr^{3+}$ couple and therefore attention was focused on this cathodic material. The characteristics of the zinc-dichromate system were thoroughly studied, particularly as far as the composition of the electrolyte and its recirculation procedure through the electrodes were concerned.

It is known that the formal potential of the $Cr_2O_7^{2-}/Cr^{3+}$ couple varies widely with the nature and the concentration of the acid (8). In HCl and $HClO_4$ solutions, especially when dilute, the formal potential is considerably lower than in H_2SO_4 solutions. It was noted that progressively increasing the H_2SO_4 concentration up to 4.5M [32 w/o (weight per cent)] the OCV of the zinc-dichromate system correspondingly increases to a value very close to the 2.12V expected from the formal potentials of the two electrodes.

Also the dichromate concentration plays an important role especially as far as the oxidation reaction rate is concerned (9). It is known that in acidic solution the following equilibria are present

$$HCrO_4^- \rightleftharpoons H^+ + CrO_4^{2-}$$

$$2HCrO_4^- \rightleftharpoons H_2O + Cr_2O_7^{2-}$$

It appears that the most active ion in the oxidation process is $Cr_2O_7^{2-}$ which predominates at high concentrations (8). It follows that the use of concentrated dichromate solutions is necessary in order to obtain the high reaction rates that are essential to realize an electrochemical system able to work at high current drains.

* Electrochemical Society Active Member.

Several tests were performed with the system Zn/$K_2Cr_2O_7$ using a 32 w/o H_2SO_4 aqueous solution and with a $K_2Cr_2O_7$ concentration increasing from 3 to 10g for 100g of sulfuric solution. The cell performance improvement was consistent with the concentration increase. Potassium dichromate, however, is not very soluble and it was not possible to reach a concentration higher than 10 w/o of the salt in the sulfuric solution. Since sodium dichromate has greater solubility, the Zn/$Na_2Cr_2O_7$ system was examined, with the dichromate concentration increasing from 10 to 20 w/o. Since concentrations higher than 15 w/o did not improve the cell performance significantly, the solution H_2SO_4 32 w/o and $Na_2Cr_2O_7$ 15 w/o in water, was chosen as the optimum electrolyte solution.

Cell structure.—A possible cell structure is shown in Fig. 1. This cell essentially consists of a circular amalgamated zinc plate forming the anode which faces the cathode, a circular graphite plate. The surface of each electrode is 50 cm^2 and the distance between them 0.2 cm.

The electrodes are kept at the desired distance by an inert support on which are located both the inlet and the outlet for the recirculating electrolyte. The system is sealed by the external casing and by gasket rings. The cell performance improves with the temperature increase of the solution. In order to avoid an external heat source, an initial working temperature has been chosen that could be obtained simply by mixing the $Na_2Cr_2O_7$ aqueous solution with the sulfuric acid before the activation of the cell. For this purpose the sulfuric acid and the dichromate solutions are kept in two separate containers (Fig. 2). By this procedure it is possible to obtain a temperature of 75°C and an electrolytic conductivity of 0.97 $ohm^{-1} \cdot cm^{-1}$ compared with 0.66 at 20°C.

At the moment of the cell activation, known amounts of the two solutions are released and mixed together

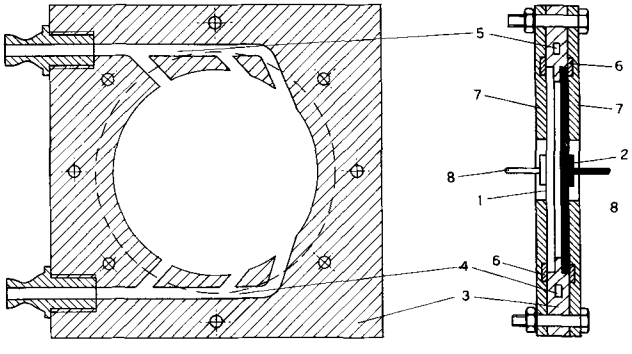

Fig. 1. Cell structure: 1, zinc plate; 2, graphite plate; 3, electrode support; 4, electrolyte inlet; 5, electrolyte outlet; 6, gasket rings; 7, external case; 8, external contacts.

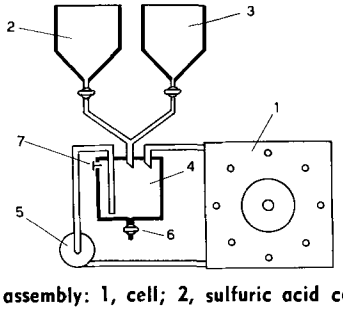

Fig. 2. Cell assembly: 1, cell; 2, sulfuric acid container; 3, dichromate container; 4, mixing container; 5, pump; 6, exhausted solution outlet; 7, valve.

Table I. Performance of the cell Zn/H_2SO_4 (32%), $Na_2Cr_2O_7$(15%)/C

Average working temperature; 60°C; OCV: 2.10-2.12V; electrode surface: 50 cm^2; electrode separation 0.2 cm.

Current density ($A/cm^2 \cdot 100$)	Average voltage at electrodes (V)	Power ($W/cm^2 \cdot 100$)	Time of discharge (min)
1.6	1.88	3.0	50
8.0	1.83	14.6	25
13.6	1.76	23.9	10
20.0	1.64	32.8	10
30.0	1.59	47.7	8
40.0	1.54	61.6	5
44.0	1.41	62.0	4
48.0	1.22	58.5	4
50.0	1.00	50.0	3

in a third container situated below. By means of a pump, the electrolyte is then continuously recycled between the electrodes. The electrolyte inlets are designed so as to ensure a uniform distribution of the liquid on the plates. At the end of the cell operation the exhausted electrolyte is eliminated from the mixing container by an outlet at the bottom of the container itself. In this way the contact between electrodes and solution is restricted solely to the period when the cell is operative. Consequently, self discharge processes are minimized. A value in the upper part of the container eliminates the possibility of any pressure build-up.

The electrolyte recirculation is extremely convenient for this type of cell, because allowing a continuous renewal of the liquid layer in contact with the electrode surfaces avoids accumulation of reaction products in the vicinity of the electrodes.

Results

The performance of the cell is reported in Table I, from which it can be seen that the values of the voltage under load remain sufficiently high even at high discharge current densities. This is due both to the very low value of the internal resistance, calculated as 0.004 ohm at the working temperature, and to the rapid renewal of the electrolytic solution. The first characteristic makes the IR drop almost negligible and the second avoids serious concentration polarization effects.

Figures 3 and 4 show the performance of this cell compared with those based on the most common system so far developed for operation at high current density rates. It can be seen that the cell is able to furnish current and power density values twice as great as those of the Mg/Br_2 cell (3) which to date has been considered the best of the high power cells operating for the periods of time shown in Table I. For instance with the zinc-dichromate cell it is possible to obtain

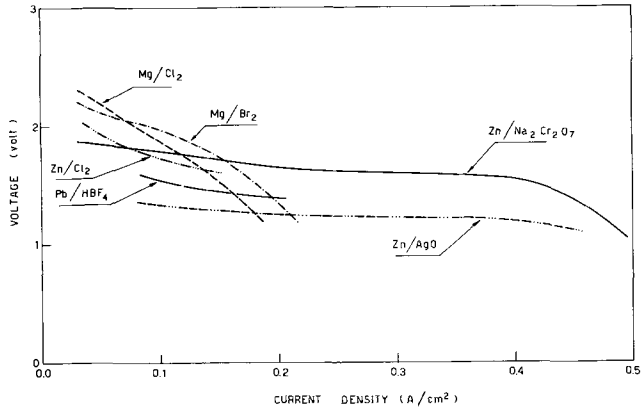

Fig. 3. Voltage-current density for the zinc/dichromate and other batteries at high drain rates. Data related to Zn/AgO and Pb/HBF_4 systems were obtained in pulse condition (10). For data related to Mg/Cl_2, Zn/Cl_2, and Mg/Br_2 see ref. (1), (2), (3), respectively.

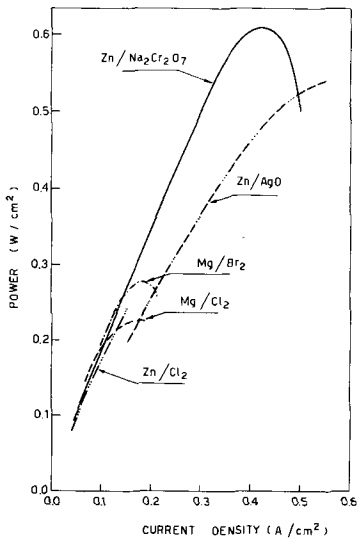

Fig. 4. Power-current density curve for the zinc-dichromate and other batteries at high drain rates. Data related to the Zn/AgO are obtained in pulse condition (10). For data related to Mg/Cl_2, Zn/Cl_2, and Mg/Br_2 see ref. (1), (2), (3), respectively.

a maximum power density value of about 0.62 W/cm² at 0.44 A/cm², while the Mg/Br_2 cell gives a maximum value of 0.28 W/cm² at 0.19 A/cm².

No attempt has yet been made on optimizing the volume and the weight of the cell and therefore no W/g or W/cm³ values are here reported.

The low cost of manufacture, the safety, and the simplicity of use represent other important advantages of the zinc-dichromate cell over the metal-halogens type.

Acknowledgment

This work was sponsored by the Consiglio Nazionale delle Ricerche under Contract No. 115/0860.0.1894.

Manuscript submitted Nov. 3, 1969; revised manuscript received Jan. 16, 1970. This was Paper 45 presented at the Detroit Meeting of the Society, Oct. 5-9, 1969.

Any discussion of this paper will appear in a Discussion Section to be published in the December 1970 JOURNAL.

REFERENCES

1. R. Blue, N. Sweeny, and M. Neipert, U.S. Pat. 3,019,279 Jan. 30, 1962.
2. P. Howard, *This Journal*, **99**, 206C (1952).
3. M. Neipert and R. Carr, U.S. Pat. 3,134,968, May 26, 1964.
4. J. Jones and A. Arranaga, *This Journal*, **115**, 435 (1968).
5. R. Jasinski, "High Energy Batteries," p. 269, Plenum Press, New York (1967).
6. L. Jumeau, "Piles et Accumulateurs Électriques," p. 37, A. Colin, Paris (1941).
7. C. Crowley, W. Langdon, D. Louzos, and J. Conolly, U.S. Pat. 2,921,111, Feb. 2, 1953.
8. H. A. Laitinen, "Chemical Analysis," p. 441, McGraw-Hill Book Co., New York (1960).
9. F. H. Westheimer, *Chem. Rev.*, **45**, 419 (1949).
10. See ref. (5), p. 211.

Electrode Overvoltages in Molten Fluorides
The Corrosion of Zirconium Electrodes in Molten KHF_2

S. Pizzini*,[1], G. Sternheim

Euratom CCR, Materials Department, Petten, North Holland

In the previous papers (1, 2) dealing with the evolution of hydrogen at bright Pt electrodes as well as in a paper of this series (3) dealing with the corrosion of aluminum electrodes in KHF_2 melts, it was shown that in anhydrous melts or in melts where the water contamination is lower than about 0.1% by weight, the limiting current for the cathodic evolution of hydrogen and accordingly, the corrosion current of aluminum, is negligibly small. Indeed, it has been felt that the cathodic deposition of the refractory metals from KHF_2 melts should be feasible if the solubility of the fluorides of the refractory metals in KHF_2 melts is sufficiently high or if the diffusion coefficient of the cations is high enough at the relatively low working temperatures. In order to obtain preliminary information on this subject, zirconium was chosen as a test material and corrosion as well as polarization experiments on zirconium electrodes were carried out.

A flanged copper cell with Viton gaskets [a slightly modified version of the graphite cells described in ref. (2)] was used. As before, Teflon was used as a container for the melt and a graphite ring as the auxiliary electrode. KHF_2, twice-crystallized in water-10% ethanol mixtures and dried under vacuum, was used.

Pure anhydrous nitrogen gas was used as cover gas to minimize the contamination of the melt. Electrodes of known geometrical dimensions (about 1 cm²) were mechanically polished, rinsed with ethanol, and then used for corrosion or polarization measurements. The electrodes used for corrosion experiments were quickly extracted from the melt and cleaned in ethanol in an ultrasonic bath. Overvoltage measurements were carried out by the galvanostatic method, as previously described (1-3). As reference electrode, an iso-electrodic zirconium or a hydrogen electrode was used. The voltage of a cell constituted by a hydrogen electrode and a zirconium electrode is about −500 mV. The solubility of ZrF_4 (added to the melt after being previously dried under vacuum) is of the order of 2×10^{-3} moles/liter at 250°C.

Figure 1 shows the ϵ *vs.* current density plot for the cathodic polarization of zirconium electrodes. From this figure one recognizes the presence of a limiting current at about 1×10^{-2} A/cm² and of small plateau at about −1700 mV.

Inspection of the electrode, after polarizing it at about −2000 mV, revealed the presence of a film of potassium metal. When anodically polarized, the electrode eventually passivates. In Fig. 2 the results of different corrosion experiments (at different cathodic polarizing currents) are reported. The experimental value of $i°_K$, the corrosion current under conditions of spontaneous corrosion, equals 3.96×10^{-2} A/cm² (average of 20 experiments). The corresponding mean square deviation is quite large (1.22×10^{-2} A/cm²), thus indicating poorly reproducible surface conditions.

* Electrochemical Society Active Member.
[1] Present address: Istituto di Elettrochimica e Metallurgia dell' Università, via G. Venezian 21, Milano, Italy.

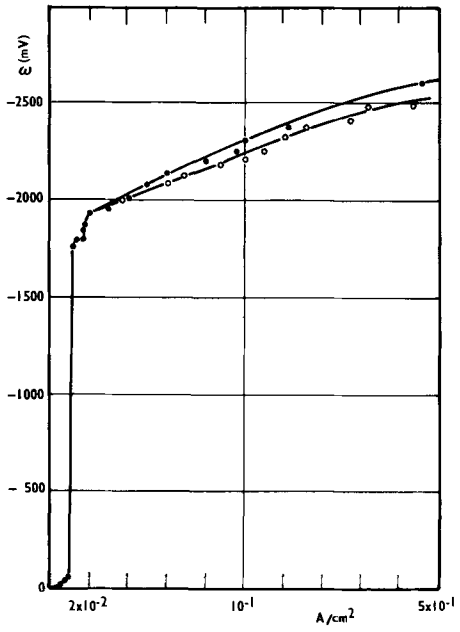

Fig. 1. ϵ *vs.* current density plot for the cathodic polarization of zirconium electrodes in KHF_2 melts. Temperature, 250°C, zirconium reference electrode.

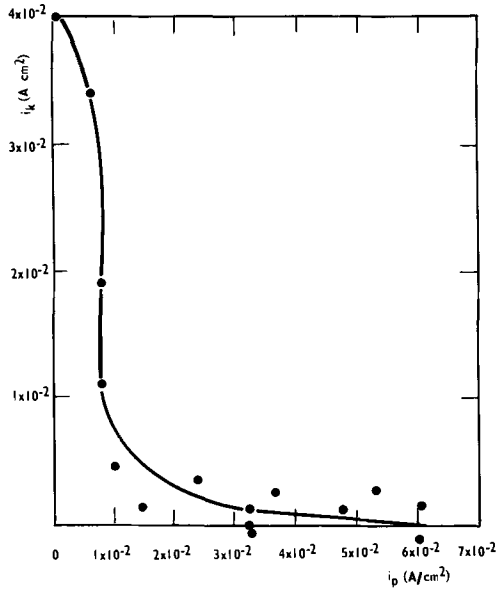

Fig. 2. Weight changes *vs.* polarization current plots for the cathodic polarization of zirconium electrodes in KHF_4 melts. Temperature, 250°C. Weight changes are expressed in terms of corrosion current.

Figures 1 and 2 show that the corrosion rate is greatly reduced and eventually suppressed at voltages between −1700 and −2500 mV. It appears, however, that when the corrosion rate is zeroed, a discharge of potassium takes place. (The negligibly small weight increase observed at the highest cathodic polarization could, however, indicate simultaneous discharge of Zr and K). The zirconium deposition rate is, however, insignificant for any technological application. As this behavior is similar to that of aluminum in the same melt (3), discussion of these present experimental results could be carried out by analogy with the aluminum case, when considering zirconium as a corrosion electrode.

Figure 3 is a picture of the possible reactions which occur at such a corrosion electrode, when the cathodic reactions are supposed to be, according to our previous papers (1, 2), the reactions

$$(\alpha)\ HF + e \rightarrow \tfrac{1}{2}H_2 + F^-$$

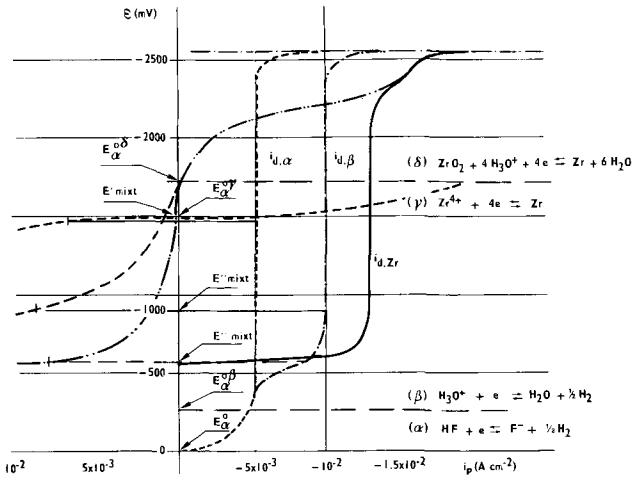

Fig. 3. Schematic diagram of the partial anodic and cathodic reactions at a zirconium electrode in steady state corrosion conditions.

and

$$(\beta)\ H_3O^+ + e \rightarrow \tfrac{1}{2}H_2 + H_2O$$

both of which are diffusion limited. In the case of (β) reaction it has been demonstrated that the limiting current is a function of the water content (1). The overvoltage *vs.* the current density (c.d.) curves for (α) and (β) reactions, reported in Fig. 3 correspond to that measured at Pt electrodes in KHF_2 melts containing water; although the overvoltage for the H_2 discharge could be very different at the Zr electrode, the value of the limiting current must be the same in melts of the same composition.

In the same figure, a guess is also made for the shape of the overvoltage *vs.* c.d. for the possible anodic reactions

$$(\gamma)\ Zr \rightleftharpoons Zr^{4+} + 4e$$

and [see also ref. (4) for the same reaction in aqueous solutions]

$$(\delta)\ Zr + 6H_2O \rightleftharpoons ZrO_2 + 4H_3O^+ + 4e$$

Reaction (γ), whose standard potential (indicated in Fig. 3 as $E_\alpha^{\circ\gamma}$) has been calculated (5) from the free energy of the reaction

$$Zr + 4HF = ZrF_4 + 2H_2 \quad \Delta G^{250°C} = -151.9 \text{ kcal/mole} \quad [1]$$

for a melt saturated in KF as well as in ZrF_4,[2] should account for the free corrosion of zirconium, when the partial cathodic reaction is reaction (α)

$$(\alpha)\ HF + e \rightarrow \tfrac{1}{2}H_2 + F^-$$

Reaction (δ), whose standard potential (indicated in Fig. 3 as $E_\alpha^{\circ\delta}$) has been calculated from the free energy value of the reaction

$$Zr + 2H_2O = ZrO_2 + 2H_2 \quad \Delta G^{250°C} = -132.2 \text{ kcal/mole} \quad [2]$$

is the usual expression for the half cell reaction of an oxide electrode (6).

In Fig. 3 the ϵ *vs.* i_P curves for reactions (γ) and (δ) have been drawn (as dotted and dashed lines) in a manner that supposes the absence of effects of overvoltages for reaction (γ)[3] and a strong hindering (due to the presence of a ZrO_2 layer, possibly nonstoichiometric) of reaction (δ).

Although reaction [1] is apparently thermodynamically favored, reaction [2] should occur as soon as

[2] The possible formation of zirconium hydride has not been accounted for, inasmuch as this effect may be considered as a slight reduction of the thermodynamic activity of zirconium metal.

[3] This condition, based on the assumption that zirconium is a "normal metal" with an exchange current of the order of 10^{-2} A/cm², is, however, unessential for the treatment which follows.

the accumulation of metal cations and water near to the electrode leads to supersaturation and consequent precipitation of the sparingly soluble ZrO_2.

In the same figure different possible values of the mixed potential of the corrosion electrode have been indicated, which only depend on the shape of the anodic overvoltage curve for reactions (γ) and (δ). Reactions (α) and (β) in fact occur under conditions of diffusion-limited current. If it is supposed that reaction (γ) occurs, coupled with reaction (β), then the value of the mixed potential E'_{mixt} closely corresponds to the E_α^γ value and the corrosion current i°_K can be calculated from the known value of $i_{d,\beta}$ as (3)

$$i^\circ_K = i_{d,\beta}$$

Figure 3, where the curves of Fig. 1 (solid lines) are replotted by recognizing that the inflection at −1750 mV corresponds to the zirconium deposition plateau and that the plateau at −2000 mV corresponds to potassium deposition, shows, however, that the potential which the electrode takes under current-less conditions (*i.e.*, E'''_{mixt}) is definitely more anodic than that corresponding to the E'_{mixt} value. Moreover, the corrosion current takes a value

$$i^\circ_K = 3\, i_{d,\beta} = 3\, i_{d,Zr}$$

(where $i_{d,Zr}$ is the cathodic limiting current measured at the Zr electrode, see Fig. 1) if we consider that the average content of water of a KHF_2 bath after the treatments used for the present experiments corresponds to a limiting current for the (β) reaction of about 1.3 x 10^{-2} A/cm² (1, 2).

From the ϵ *vs.* current density curves for the anodic polarization of a zirconium electrode reported in Fig. 3, it appears that the present experimental behavior is well accounted for, if one assumes that the electrode works according to reactions (δ) and (β), *i.e.*, as a covering layer electrode.

When considering a stationary film thickness of the order of 100Å or less [as results from the extrapolation of the data of ref. (4) to a formation voltage corresponding to the overvoltage of the partial anodic reaction (δ)] and ambipolar migration in the semiconducting[4] layer, more insight into the corrosion mechanism could be gained by using the phase-scheme of Fig. 4 for a Zr, ZrO_2 electrode. Here the electrode is represented as a "Korrosion Deckschicht Elektrode" according to Lange (9) and it is supposed that the rate-determining step for the corrosion reaction is the diffusion of H_3O^+ across the diffusion layer. Mobility of Zr^{4+} and O^{--} in the ZrO_2 film does not imply that we assume the migration of ions as a volume process via lattice defects; faults, dislocations, and grain boundaries are alternative paths (10, 11).

From Fig. 4 it is apparent that reactions (γ) and (β), subdivided in the elementary reaction steps and written as

$$(\pi + Zr^{4+} - \text{transf.} + \theta)\underset{I}{Zr^{4+}} \rightarrow \underset{II}{Zr^{4+}}$$

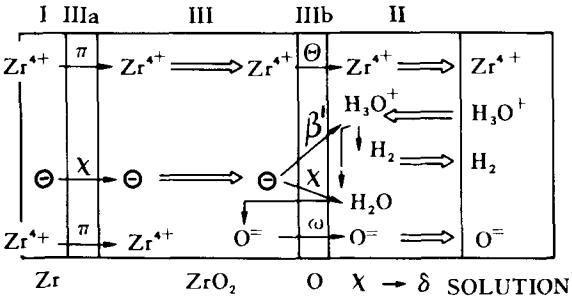

Fig. 4. Phase scheme of a "Korrosion Deckschicht Elektrode." The metal phase is indicated with I, the oxide phase with III, and the solution phase with II. δ indicates the thickness of the diffusion layer. Other Greek symbols indicate, as in the previous paper (3), reactions taking place at the interfaces IIIa and IIIb.

and

$$(\chi + e\text{-transf.} + \beta')\ \underset{II}{H_3O^+} + \underset{I}{e} \rightarrow \underset{II}{H_2O} + \underset{II}{\tfrac{1}{2}H_2}$$

(where Zr^{4+} — transf. and *e*-transf. indicate the mass and charge transfer processes across the ZrO_2 phase) occur simultaneously at a rate which equals the limiting current of β reaction.

If the coupling of reactions (γ) and (β) were the unique process responsible for the corrosion reaction, then the corrosion current i°_K should equal the value of the limiting current $i_{d,\beta}$. This is not apparently the case, because of the side reaction with H_2O, which is a product of reaction (β) and reacts with Zr according to the partial reactions

$$(\chi + e\text{-transf.} + \chi')\ \underset{II}{H_2O} + \underset{I}{2e} \rightarrow \underset{III}{O^=} + \underset{II}{H_2}$$

and

$$(\pi)\ \underset{I}{Zr^{4+}} \rightarrow \underset{III}{Zr^{4+}}$$

and occur as well with a maximum rate which equals the $i_{d,\beta}$ value. In steady state conditions we have therefore

$$i^\circ_K = i_{d,\beta} + 2\, i_{d,\beta}$$

which is a figure very close to the experimental value. This result confirms the proposed model and suggests as a reasonable explanation for the observed codeposition of Zr and K, the permanence (see Fig. 3) of a ZrO_2 layer [with the overvoltage associated with the polarization of the electrode according to reaction (δ)] at voltages higher than the discharge potential of Zr according to reaction (γ).

Nomenclature

E^j_α	Potential of an electrode j, *vs.* a hydrogen electrode whose reaction is α
ϵ	Electrical potential difference measured at the terminals of the tensiometric cell
i_P	Polarizing current A/cm²
i_d	Diffusion limiting current
i°_K	Corrosion current, A/cm², when external current is zero
i_K	Corrosion current, A/cm²
$_I Me^{z+} = {}_I Me - Z_I e$	

Subscripts I, II, III indicate the metal, solution, and oxide phases, respectively.

APPENDIX

In this paper the symbols for the electrode reactions have been written according to our previous papers (1-3) and the nomenclature used is a slightly modified version of the Lange and Göhr symbolism (6).

The arbitrary zero of the potential scale of Fig. 3 is the potential of the reaction (α) for hydrogen at 1 atm and HF at 39.8 mm Hg, which is the equilibrium pressure of a melt of KHF_2 at 250°C saturated with KF.

The potential of reaction (β) is calculated according to ref. (1) by taking into account the free energy of the reaction

$$H_2O + HF \rightleftarrows H_3O^+ + F^-$$

($\Delta G \simeq 9000$ cal/mole at 250°C) and corresponds, for H_2O at 1 atm and HF at the equilibrium partial pressure, to −263 mV.

Acknowledgments

The authors are greatly indebted to Dr. J. H. Westbrook for his valuable suggestions.

Manuscript submitted March 14, 1969; revised manuscript received Dec. 22, 1969. This was Paper 202 presented at the New York Meeting of the Society May 4-9, 1969.

Any discussion of this paper will appear in a Discussion Section to be published in the December 1970 JOURNAL.

[4] S. Aronson (8) quotes, at temperatures around 500°C, an ionic transport number of 0.35.

REFERENCES

1. S. Pizzini, G. B. Barbi, and G. Sternheim, *Electrochim. Acta*, **8**, 227 (1963).

2. S. Pizzini and A. Magistris, *ibid.*, **9**, 1189 (1964).
3. S. Pizzini, A. Magistris, and G. Sternheim, *Corr. Sci.*, **4**, 345 (1964).
4. G. C. Willis, G. B. Adams, and P. Van Ryssel-berghe, *Electrochim. Acta* **9**, 79 (1964); **9**, 93 (1964).
5. Janaf Thermochemical Tables, Clearinghouse (1965).
6. K. J. Vetter, "Elektrochemische Kinetik," Springer, Berlin (1961).
7. T. Smith, *This Journal*, **112**, 560 (1965).
8. S. Aronson, *ibid.*, **108**, 312 (1961).
9. F. Lange and H. Göhr, "Thermodynamische Elektrochemie," Hütig Verlag, Heidelberg (1962).
10. R. Cox and C. Roy, AECL-2350, October 1965.
11. E. A. Gulbransen and K. F. Andrew, *Trans. AIME*, **209**, 394 (1957).

On the Electrical Analog Circuit for the Study of Metal Solution Interfaces by the Square Wave Technique for Capacitance Measurements

R. G. Barradas*

Department of Chemistry, Carleton University, Ottawa, Ontario, Canada

and E. M. L. Valeriote*

Department of Physical Chemistry, University of Bristol, Bristol, England

In an earlier paper (1) we evaluated the technique for capacitance measurements published by McMullen and Hackerman (2) and reported that capacity *vs.* potential (*C. vs. E*) curves change in using different values of R_s [see ref. (1)]. At that time the maximum possible values of R_s were used and we argued that there was some empiricism in assuming the electrical analog of the metal-solution interface. In a subsequent communication (3) we suggested an experimental improvement in the electrode assembly to minimize the problems due to R_s. However, on further reconsideration, the following electrical analysis is now offered by way of an appendix as a more plausible explanation of some of the anomalies observed. Referring to McMullen and Hackerman's analysis and nomenclature of time-potential curves it is not necessary to assume that $R_p = \infty$ (see Fig. 1). It is to be noted that R_p should, in principle, be more rigorously represented by the complex faradaic impedance (Z_f). The representation of a faradaic process by a simple resistor (R_p) is somewhat restrictive with respect to *a priori* separation of this process from double layer charging. The exact form of Z_f depends on the model for the faradaic process. In the limiting case, when Z_f approaches infinity, the same conclusions will be reached. Hence, one could alternately replace R_p by Z_f throughout this paper, and subsequently R by Z (see Eq. [13]), where $Z = (R_s + R_c)Z_f/R_s + R_c + Z_f$, but this appears to be a less desirable choice because it would involve mixing complex quantities with purely real or imaginary ones. However, this simple treatment is limited to near ideally polarizable electrodes, where negligible faradaic processes occur, such as the hanging mercury drop electrode (3) for which the assumption that Z_f approaches infinity renders the model depicted in Fig. 1 to be valid.

If $R_c = 0$ as stated in case I [ref. (2)]

$$E_c = \frac{R_p E_i}{R_p + R_s}\left[1 - \left(\frac{\exp[-R_p + R_s]\,t}{R_p R_s C^1}\right)\right] \quad [1]$$

If the period of the square wave $\tau << \dfrac{R_p R_s C^1}{(R_p + R_s)}$ the exponential term in Eq. [1] can be linearized to give $E_c = E_i t/R_s C^1$. Following McMullen and Hackerman's analysis [case III in ref. (2)] when $R_c = 0$ one obtains

$$E_x = iR_c + E_i t/R_s C^1 \quad [2]$$

as a correct equation for E_x (the observed signal) for each half-cycle obtained on the oscilloscope. The slope of the observed linear oscilloscope trace is then given by

$$dE_x/dt = R_c\ di/dt + E_i/R_s C^1 \quad [3]$$

The first term on the right hand side of Eq. [3] is not independent of the parameters in the second term and may not be negligible in comparison. The negligence of $R_c\ di/dt$ is therefore questionable.

To investigate this point more rigorously, the circuit analysis should be carried out with the initial condition that R_c could take any value (except infinity). Assuming that R_p and R_s are finite, application of Kirchoff's laws yields the following equations

$$E_i = iR_s + E_x \quad [4]$$

$$E_x = E_c + iR_c \quad [5]$$

$$E_c = i_p\ R_p \quad [6]$$

$$dE_c/dt = i_c/C^1 \quad [7]$$

$$i = i_p + i_c \quad [8]$$

Solving Eq. [4] and [5] gives

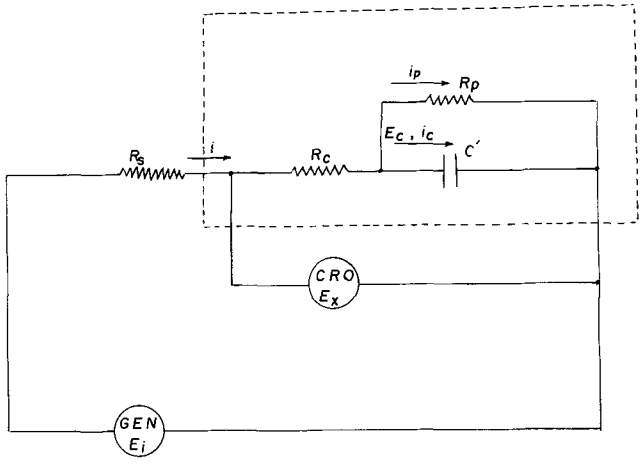

Fig. 1. Electrical analog circuit with the addition of GEN (generator) and CRO (oscilloscope) symbols.

* Electrochemical Society Active Member.

$$E_x = E_c\left(\frac{R_s}{R_s + R_c}\right) + E_i\left(\frac{R_c}{R_s + R_c}\right) \quad [9]$$

and

$$E_i = (R_s + R_c)i + E_c \quad [10]$$

From Eq. [6] and [8]

$$E_c = R_p(i - i_c) \quad [11]$$

Combination of the differentials of [10] and [11], and recalling that E_i is constant during each half cycle

$$dE_i = 0 = (R_p + R_s + R_c)di - R_p\, di_c \quad [12]$$

Integrating the right hand side of Eq. [12] using the boundary condition that at $t = 0$, $E_c = 0$; it follows from Eq. [4] and [5] that $(E_i)_{t=0} = i/(R_s + R_c)$. Setting

$$\underline{R} = (R_s + R_c)\, R_p/R_s + R_c + R_p \quad [13]$$

yields:

$$i_c = \frac{R_s + R_c}{\underline{R}}\left[i - \frac{E_i}{R_s + R_c} \right] \quad \text{and}$$

$$\frac{di_c}{dt} = \frac{R_s + R_c}{\underline{R}} \cdot \frac{di}{dt} \quad [14]$$

Combining Eq. [7] with [14] and the differential of [10] then results in

$$\frac{di_c}{i_c} = \frac{-dt}{\underline{R}C^1} \quad [15]$$

Integration of [15] from $i_c = E_i/(R_s + R_c)$ to i_c and $t = 0$ to $t = t$, and taking the exponentials of the resulting expression, one obtains

$$i_c = \frac{E_i}{R_s + R_c} \exp(-t/\underline{R}C^1) \quad [16]$$

Substitution of [16] into Eq. [7], and integrating, on substitution into Eq. [9] leads to

$$E_x = \frac{E_i}{R_s + R_c}\left\{ \frac{R_s\underline{R}}{R_sR_c}\left[1 - \exp\left(-t/\underline{R}C^1\right)\right] + R_c \right\} \quad [17]$$

t is always $\leq \tau/2$ during a half cycle, hence at large enough frequencies so that $t \leq \tau/2 << RC^1$ the exponential in [17] can be linearized to give

$$E_x = \frac{E_iR_c}{R_s + R_c} + \frac{E_iR_s}{(R_s + R_c)^2} \cdot \frac{t}{C^1} \quad [18]$$

the condition under which linearization can be made equivalent to $\tau/2 << C^1(R_s + R_c)$, since $\underline{R} \to R_s + R_c$ as $R_p \to \infty$. This condition is realized to a good approximation as long as no faradaic process occurs. It is to be noted from Eq. [18] that as long as the wave is linear, the form of E_x is independent of the value of R_p. The slope of the output wave is given by

$$\frac{dE_x}{dt} = \frac{E_i}{C^1} \cdot \frac{R_x}{(R_s + R_c)^2} \quad [19]$$

or

$$C = \frac{C^1}{A} = \frac{E_iR_s}{A(R_s + R_c)^2} \cdot \frac{1}{(dE_x/dt)} \quad [20]$$

where A is the electrode area and C is the differential capacity. If $R_c << R_s$ then

$$C = \frac{E_i}{AR_s(dE_x/dt)} \quad [21]$$

Equation [21] is not dissimilar in essence from the one ultimately arrived at by McMullen and Hackerman (2). However, when R_c becomes significant compared to R_s, Eq. [21] will give values of C which are greater than those obtained from the more accurate Eq. [20] because $R_s/(R_s + R_c)^2$ is $< 1/R_s$ for $R_c > 0$. This analysis goes a long way toward explaining the anomalous dependence of capacities on R_s reported in ref. (1). Examination of Fig. 2, 3, and 4 in ref. (1) suggests that a potential shift is also occurring. An assumption that R_c changes as a function of potential alone could not explain the difference between cathodic and anodic branches for small values of R_s. In all likelihood, it is more probable that for small values of R_s it is reasonable to consider that there is some undesirable faradaic reaction occurring in the case of the large Hg pool electrode (5 cm^2), but the faradaic process should be minimal if not insignificant with the use of a hanging Hg electrode [ref. (1)]. R_c may well vary as a function of potential if it is not to be regarded as purely the electrolyte resistance. In any case, it is possible to incorporate the nonelectrolyte component of R_c into a term such as Z_f if R_p is replaced by it; thereby making R_c the electrolyte resistance only (6). The anomalies for large R_s values (implying constant current conditions) appears in all probability to be solely due to departure from constant current conditions at given potential if a faradaic process was occurring, in which case the simple model shown in Fig. 1 would be invalid unless the form of Z_f and its coupling with the charging impedance were considered as mentioned earlier. The present model is not intended, as stated previously, to cover such a case and the technique is not meant to be used under such conditions. Considering the availability of many other more accurate methods for determining capacitance data from slopes of oscilloscope traces [see *e.g.*, ref. (4) and (5)] the technique as published by McMullen and Hackerman (2) does not appear to warrant further complicated theoretical considerations. McMullen and Hackerman's objective was meant for a specialized application, namely to obtain electrode surface area measurements where no faradaic processes occur. The technique could indeed be useful under either constant current or constant voltage conditions.

Acknowledgment

Financial support from the National Research Council of Canada is gratefully acknowledged. We are also indebted to Professor R. S. C. Cobbold of the University of Toronto for helpful discussions.

Manuscript submitted Sept. 15, 1969; revised manuscript received *ca.* Dec. 24, 1969.

Any discussion of this paper will appear in a Discussion Section to be published in the December 1970 JOURNAL.

REFERENCES

1. R. G. Barradas and E. M. L. Valeriote, *This Journal*, **112**, 1043 (1965).
2. J. J. McMullen and N. Hackerman, *ibid.*, **106**, 341 (1959).
3. R. G. Barradas and E. M. L. Valeriote, *ibid.*, **114**, 593 (1967).
4. J. W. Hayes and C. N. Reilley, *Anal. Chem.*, **37**, 1322 (1965).
5. E. R. Brown, T. G. McCord, D. E. Smith, and D. D. DeFord, *ibid.*, **38**, 1119 (1966).
6. B. B. Damaskin, "The Principles of Current Methods for the Study of Electrochemical Reactions," pp. 68 and 73, McGraw-Hill Book Co., New York (1967).

A Simple Cell and Reference Electrode for Voltammetry in Alkaline Melts

E. Banks,* C. W. Fleischmann,*,[1] and L. Meites[2]

Department of Chemistry, Polytechnic Institute of Brooklyn, Brooklyn, New York

Various techniques are used to provide conductance between two or more otherwise isolated compartments of an electrolytic cell. For molten salt studies, isolation of the compartments is usually accomplished by fritted glass, porous silica disks, or asbestos plugs. Examples are given in recent reviews (1-4). These materials, however, are severely attacked by alkaline melts. For use in such melts, particularly those of the alkali tungstates, a simple, inexpensive, and easily constructed two-compartment cell was designed. This cell employed commercial laboratory porcelain as a nonporous conductive separator between the working and reference half-cell compartments.

Sodium glasses have been employed as conductive separators in molten salts (5, 6), but the use of glass limits work to below 500°C. Labrie and Lamb (7), however, developed a reference electrode employing the Ag/Ag(I) couple in which a sodium-containing porcelain separator was used in melts up to 900°C. These workers also demonstrated the feasibility of commercial porcelain as a separator.

Reference half-cells reversible to oxygen have been employed in oxide-containing melts (1-4), but because they are inconvenient, they have not been recommended (3) for use in fused-salt voltammetry. A large Pt electrode is frequently employed as a reference for voltammetry in melts (1-4), but since it had not been demonstrated that such an electrode is well poised in tungstate melts, a metal, metal ion couple was preferred. The Ag/Ag(I) couple has been used as a reference in a number of melts (1-4), and Ag/Ag_2WO_4 was found to be a successful half-cell for use as a reference with the present cell design.

The Ag_2WO_4 used in these studies was prepared by precipitation from aqueous solutions. A filterable precipitate was obtained by mixing together *0.1-0.2F* solutions of reagent-grade $AgNO_3$ and Na_2WO_4 and allowing the precipitate to digest, overnight, in the dark. The precipitate was washed several times with water, then acetone, and dried in air.

The cell is illustrated in Fig. 1. A 5-ml Coors porcelain crucible served both as the container for the Ag/Ag_2WO_4 reference half-cell and as the conductive septum. This crucible was placed in a 10-ml porcelain tray along with the study melt. For improved conductance, the area of the crucible in contact with the melt was increased by placing the crucible on a loose platform of alumina tubes or rods. The resistance between the reference and working electrodes was determined for each cell by means of an a-c bridge so that the recorded voltammograms could be corrected for the potential drop across the porcelain.

Reproducibility of the potential of a Ag/Ag_2WO_4 half-cell was determined to be ±10 mV from the potentials of nine cells of the composition

$$Ag/Ag_2WO_4//Na_2WO_4//Ag_2WO_4/Ag$$

Potentials were measured at 750°C with the cells under argon. A second measurement on some cells was made after 3 hr to establish the extent of the potential drift with time. Table I records the potential of cells prepared as follows: Cells 1 through 4, constructed from freshly synthesized Ag_2WO_4 and previously unused Ag-wire electrodes; Cells 5 and 6, one half-cell was prepared from Ag_2WO_4 recovered from a previous reference compartment; and in cells 8 and 9, new and previously used silver wires were opposed. In cell 7, one porcelain crucible was of more recent manufacture than the other (8).

Ag/Ag_2WO_4 half-cells are polarized only about 5 mV at 100 mA/cm² (750°C) as shown by an extrapolation of the current-voltage data in Fig. 2 to that current density. This figure gives the total polarization of the anodic and cathodic reactions at two silver wire electrodes immersed in silver tungstate. The polarization at each electrode may be taken to be 2-3 mV at 100 mA/cm² assuming that the anodic and cathodic contributions to the total polarization are equal. This assumption is supported by voltammograms obtained at silver microelectrodes in Ag_2WO_4 which did show equivalent anodic and cathodic polarizations.

Since most voltammetric studies employ a small study electrode (*e.g.*, a 1-mm diameter Pt bead), the current density at the reference would be of the order of 1 mA/cm². Such a current density would give rise to negligible polarization as may be read from Fig. 2.

* Electrochemical Society Active Member.

[1] Present address: Mallory Battery Company, Tarrytown, New York.

[2] Present address: Clarkson College of Technology, Potsdam, New York.

Key words: fused salt voltammetry cell; silver-silver tungstate reference, voltammetry fused Cd(II) tungstate.

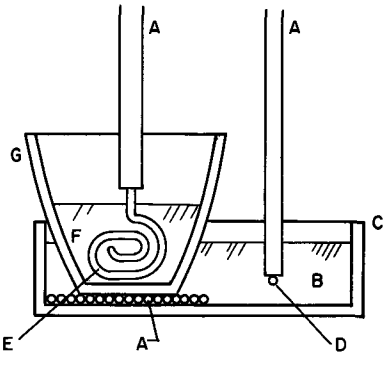

Fig. 1. Two-compartment cell for voltammetry. A, alumina tubing; B, study melt; C, 10-ml porcelain dish; D, study electrode; E, silver wire; F, Ag_2WO_4; G, 5-ml porcelain crucible.

Table I. Potentials of cells: $Ag/Ag_2WO_4//Na_2WO_4//Ag_2WO_4/Ag$, 750°C

Full-cell No.	Potential[a] of cell, V	Potential of cell, V after 3 hr	Description of cell[b]
1	0.00619	—	Both half cells were constructed from freshly synthesized Ag_2WO_4 and previously unused Ag-wire electrodes.
2	0.0148	0.0094	
3	0.00376	—	
4	0.000496	0.00175	
5	0.0388	—	One half-cell was prepared from Ag_2WO_4 recovered from a previously reference compartment.
6	0.00923	0.00845	
7	0.00150	—	New and previously used silver wires were opposed.
8	0.00507	0.0004	
9	0.0033	—	One crucible was of more recent manufacture than the other.

[a] Polarity always selected to give positive cell potentials.

[b] Otherwise as for Full-cell No. 1-4.

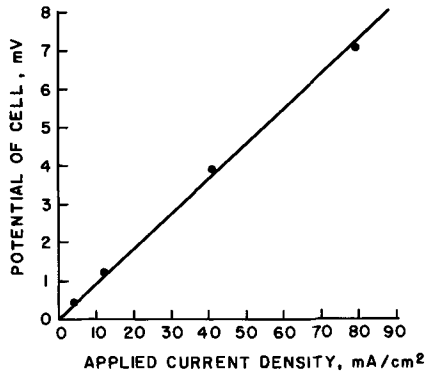

Fig. 2. Current-voltage data for two Ag electrodes in Ag_2WO_4, 750°C. Constant current applied in increasing steps; potential read after 30 sec.

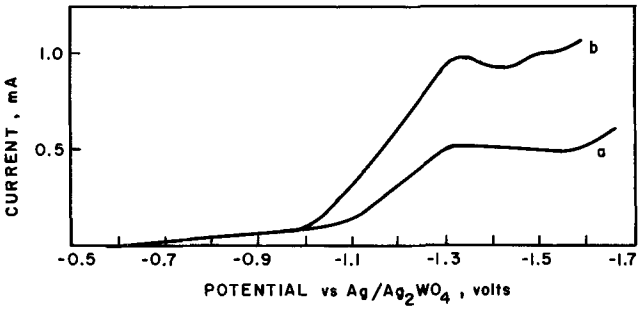

Fig. 3. Voltammograms for Pt bead (0.03 cm^2 area) in Na_2WO_4 containing: (a) 0.2 m/o Cd(II), (b) 0.4 m/o Cd(II), 750°C. Sweep rate, —250 mV/min.

The cell shown in Fig. 1 was employed to study the reduction of WO_3 and simple cations from alkali tungstate melts. As an illustration, Fig. 3 presents voltammograms obtained for the reduction of 0.2 and 0.4 m/o (mole per cent) Cd(II) from Na_2WO_4, 750°, at a Pt bead (0.03 cm^2 area).

This cell design was also employed for synthesis. For electrosynthesis at constant current when it is not desired to monitor the potential of the study electrode, any suitable couple may be employed on the other side of the porcelain membrane. As an example, tungsten bronzes were electrodeposited from polytungstate melts and a suitable anodic reaction on the other side of the porcelain was the electro-oxidation of alkali tungstate at Pt.

Acknowledgment

Special thanks are due to the National Aeronautics and Space Administration for support given under the NASA Predoctoral Traineeship Program. This paper is abstracted in part from a dissertation submitted by one of us (C.W.F.) to the Polytechnic Institute of Brooklyn in partial fulfillment of requirements for a Ph.D. degree (Chemistry).

Manuscript received Aug. 6, 1969.

Any discussion of this paper will appear in a Discussion Section to be published in the December 1970 JOURNAL.

REFERENCES

1. A. D. Graves, G. J. Hills, and D. Inman, "Advances in Electrochemistry and Electrochemical Engineering," Vol. 4, p. 117, P. Delahay, Editor, Interscience (John Wiley), New York (1965).
2. Iu. K. Delimarskii and B. F. Markov, "Electrochemistry of Fused Salts," Sigma Press, Washington, D.C. (1961).
3. C. H. Liu, K. E. Johnson, and H. A. Laitinen, "Molten Salt Chemistry," p. 681, M. Blander, Editor, Interscience (John Wiley), New York (1964).
4. R. W. Laity, in "Reference Electrodes," p. 524, D. J. G. Ives and G. J. Janz, Editors, Academic Press, New York (1961).
5. J. O'M. Bockris, G. J. Hills, D. Inman, and L. Young, *J. Sci. Instr.*, **33**, 438 (1956).
6. K. Hauffe and A. L. Vierk, *Z. Electrochem.*, **53**, 151 (1949).
7. R. J. Labrie and V. A. Lamb, *This Journal*, **106**, 895 (1959).
8. C. S. Ryland, Sales Manager, Chemical Porcelain Products Division, Coors Porcelain Co., Private communication.

JOURNAL OF THE ELECTROCHEMICAL SOCIETY

SOLID STATE SCIENCE

MAY 1970

Factors Affecting the Growth of Porous Anodic Oxide Films on Zirconium

B. Cox*

Chalk River Nuclear Laboratories, Atomic Energy of Canada Limited, Chalk River, Ontario, Canada

ABSTRACT

Although anodization of zirconium and its alloys generally results in the formation of barrier-type films, porous anodic oxide films can be produced in some electrolytes and by some preparation techniques. A survey of common electrolytes reveals that those containing nitrate, chromate, dichromate, and phosphate ions commonly lead to porous anodic films. An electron microscope study of the films produced in these electrolytes, and others giving barrier-type films, has shown that no single explanation fits all instances of porous film formation. While incorporation of the electrolyte anion in the oxide may be the primary factor influencing the formation of porous oxide films, it appears to operate primarily by affecting the local transport of oxygen ions through the films. This effect may be achieved by influencing the crystallization of the oxide during growth so that in some instances local oxidation and cracking occur at grain boundaries, while in other instances it leads to the general development of a porous structure.

Zirconium and Zircaloy-2 readily form barrier-type anodic oxide films in a wide range of electrolytes (1-4), including gaseous plasmas (5). A few instances of the formation of thick porous anodic films have been reported, generally associated with anodization at high voltages in solutions containing the nitrate ion (1, 6). We have found that porous films can be formed even at low voltages and have used such films in testing a porosimeter designed to measure pore sizes in zirconia films *in situ* (7, 8).

It was found that the capacitance, and especially the resistance, of even the barrier-type oxide films was much less than would be predicted from optical measurements of the oxide thickness and previous measurements of the resistivity of zirconia films using dry metallic contacts (9, 10). This effect was most pronounced for Zircaloy-2, an alloy containing small second phase particles, but was also present with the batch of crystal-bar zirconium used in our experiments.

It appeared that there might be a whole spectrum of degrees of porosity from electrolyte to electrolyte, and we set out to study this possibility and to correlate the effect with observable variations in the ionic transport process through the oxide film.

Experimental

Paddle shaped specimens, with 2 x 2 cm blades, were cut from one sheet of crystal-bar zirconium (Be) and one of Zircaloy-2 (Bh). Analyses of these batches of material are listed in Table I. The specimens were chemically polished in mixed nitric/hydrofluoric acids, washed in water and alcohol, and weighed prior to and after anodization.

Anodization was carried out either by the stepwise constant voltage technique, holding for different predetermined times in the range 0.5-100 min at each voltage step or by the constant current technique with applied currents between 1.0 and 5.0 mA/cm^2 and a predetermined final voltage. The electrolytes used were "normal" solutions of the following in water: H_2SO_4, Na_2SO_4, HNO_3, NH_4NO_3, KNO_3, KNO_2, KOH, NH_4OH, $K_3Fe(CN)_6$, $K_2Cr_2O_7$, $KCrO_4$, tartaric, lactic, formic, oxalic, acetic, and citric acids; saturated solutions of potassium persulfate, ammonium borate, and boric acid; 2% ammonium borate in ethylene glycol; 0.5M NH_4NO_3 in ethylene glycol; 85% phosphoric acid; a

Table I. Analysis of crystal-bar zirconium and Zircaloy-2 batches

Element	Crystal-bar Zirconium (Be), ppm	Zircaloy-2 (Bh), ppm
Al	<25	<40
B	<0.2	<0.2
C	35	80
Ca	10	—
Cd	<0.3	<0.2
Co	<5	<5
Cr	20	0.09*
Cu	<25	<20
Fe	80	0.14*
H	2	10
Hf	75	60
Mg	<10	<10
Mn	<10	<10
Mo	<10	—
N	12	20
Na	<10	—
Nb	<100	—
Ni	<10	0.05*
O	<5	1000
Pb	<40	—
Si	<40	70
Sn	<10	1.45*
Ta	<200	<200
Ti	<20	<20
V	<5	—
W	<25	—
Zn	<50	—

* Weight per cent.

* Electrochemical Society Active Member.

Key words: zirconium alloys, oxidation, anodization, oxide films, morphology, electron microscopy.

1:2:3 mixture of water, oxalic acid, and ethylene glycol, and a complex solution recommended by workers at Oak Ridge National Laboratory (4).

At the final anodization voltage and time the d-c source was disconnected and the leakage rates of the films determined by plotting the voltage decay on a high speed recorder. The anodic oxide surface was examined by optical microscopy, replica electron microscopy, and scanning electron microscopy. The metal-oxide interface was examined with the scanning electron microscope. The electrical properties of the films were determined with a GR1680A automatic impedance bridge during immersion in a molar ammonium nitrate solution; capacitative and resistive components (based on a parallel equivalent circuit) were followed as a function of immersion time. Measurements were also made using mercury and Viking alloy LS232 liquid metal contacts (8), and in a mercury porosimeter designed to measure pore sizes in insulating oxide films (7).

The "optical thickness" of the oxide films was determined by comparing the interference colors of the oxide on individual metal grains with a calibration strip prepared using the data of Wilkins (11) and checked with a spectrophotometer. The refractive index of the films was assumed to be insensitive to the forming electrolyte. The insensitivity of the refractive index to the forming electrolyte was demonstrated by Wilkins (3) for a limited range of electrolytes, and has been generally assumed to hold for all electrolytes by other investigators (4, 12). The "capacitative thickness" was determined from the capacitative component of the a-c impedance of the specimen, assuming the oxide to be effectively a parallel sided slab of dielectric. Average current efficiencies were determined from the optical thickness and the time taken to reach the final voltage. Instantaneous current efficiencies were calculated from the slope of the voltage/time plot on the assumption that the formation rate (Å/V) was constant throughout the period of film growth.

Results

Electrical measurements.—Selected measurements of optical thickness and impedance of the oxide films are presented in Table II to demonstrate the variations in the behavior observed in the various electrolytes. Further details may be obtained from the author. The oxide formation rates (based on the optical thickness of the oxide) for those electrolytes where sufficient specimens were anodized to give a meaningful average are quoted in Table III in comparison with other published values for which the formation method is known. Porous oxides could be detected electrically either by following the change in capacitance of a specimen with time after immersion in an aqueous electrolyte (Fig. 1) or by comparing the apparent thickness indicated by liquid metal and aqueous electrolytic contacts [see Ref. (8), Fig. 19]. The much greater degree of porosity of the films formed in NH_4NO_3 than in H_2SO_4 could be readily seen from the separation of the curves of apparent thickness measured in an aqueous electrolyte and in mercury. The capacitative thickness of apparently nonporous films is plotted against their optical thickness in Fig 2.

The degree of porosity of the other anodic films was also estimated from a comparison of the apparent oxide thickness measured with mercury, LS232, and an aqueous electrolyte as contacts (Table II). A consistently higher apparent thickness in the liquid metals

Table II. Properties of anodic oxide films formed on zirconium and Zircaloy-2

Specimen No.	Forming electrolyte	Final voltage, V	Forming method*	Optical thickness, Å	Impedance 1/C, cm²/μF Hg	LS232	NH_4NO_3	Specific resistance, ohm × 10^8 Hg	LS232	NH_4NO_3	Comments
Zirconium specimens											
Be 95	$KCrO_4$	25	C	500-650	3.83	3.34	2.97	34.8	28	13.2	See Fig. 5 and 6
Be 153	Na_2SO_4	25	C	300-650	3.48	2.80	2.72	40.0	26	15.2	
Be 154	Citric	25	C	300-650	4.08	4.09	2.68	51.8	21	12.7	
Be 155	NH_4NO_3	25	C	300-650	4.51	3.68	2.98	12.4	39-0.002	10.7	
Be 24	KNO_2	156	V	3350	—	17.3	16.4	—	62	60	Increasing flaws or porosity in the oxide
Be 34	KOH	144	V	3820	—	21.2	19.6	—	185	11.7	
Be 23	H_2SO_4	144	V	3350	—	19.5	17.5	—	55	42	
Be 31	ORNL	125	V	2400	—	13.4	8.6	—	49	3.89	
Be 40	NH_4NO_3	112	V	gray	313	177	8.0				
Zircaloy-2 specimens											
Bh 257	Amm. Bor.	25	C	500	3.49	3.17	3.14	64.1	15	9.54	Apparent order of increasing flaws or porosity
Bh 265	Na_2SO_4	25	C	375	3.32	3.00	2.97	7.29	40	20.4	
Bh 330	$K_2S_2O_8$	25	C	400	3.81	3.25	3.36	59.0	38	20.0	
Bh 258	$K_2Cr_2O_7$	25	C	550	5.39	6.04	4.23	5.79	53	12.4	
Bh 266	H_3PO_4	25	C	575	9.66	10.13	2.51	50.5	29	10.3	
Bh 238	NH_4NO_3	25	C	500-1400	11.5	16.2	2.44	37.3	160	1.46	
Bh 320	KOH	100	V	2550	—	13.0	12.14	—	72	39.2	Increasing flaws or porosity in the oxide
Bh 321	KNO_2	100	V	2660	32.4	15.0	12.85	0.015	47	36.7	
Bh 249	H_2SO_4	98	V	1990	11.7	12.7	9.69				
Bh 354	ORNL	100	V	1930	18.6	10.7	2.59	0.025	99	0.08	
Bh 227	NH_4NO_3	96	V	~4000	121	70	5.86				

* Forming method: V = constant voltage; C = constant current.

Table III. Formation rates of anodic oxide films on zirconium and Zircaloy-2

Electrolyte	Formation method	Formation rate, Å/V	Reference
0.5M H_2SO_4	Stepwise constant voltage, <5 min decay/step	16.8	This work
0.5M H_2SO_4	Stepwise constant voltage, 1-2 hr/step	22	This work
0.5M H_2SO_4	Stepwise constant voltage, >24 hr/step	25.5-29	This work
0.1M H_2SO_4	Stepwise constant voltage, decay to 0.2 mA/cm²	16.9	Wilkins (3)
1.0M KOH	Stepwise constant voltage, ~5 min decay/step	22.2	This work
1.0M KOH	Constant current 1.0 mA/cm², no decay	21.1	This work
1% KOH	Constant current 10 mA/cm², decay to 0.2 mA/cm²	26.5	Wilkins (3)
1% NaOH	Constant current 10 mA/cm², decay to 0.2 mA/cm²	25.3	Wanklyn (13)
ORNL solution	Stepwise constant voltage, ~5 min decay/step	16.3	This work
ORNL solution	Constant current, 1.0 mA/cm²	15.0	This work
ORNL solution	Constant voltage, 30 sec decay	14.5	Banter (4)
Sat. amm. borate	Stepwise constant voltage, ~5 min decay/step	19.5	This work
Sat. amm. borate	Stepwise constant voltage, ~1 hr decay/step	20.0	This work
Sat. amm. borate	Stepwise constant voltage, >24 hr decay/step	~30	This work
Sat. amm. borate	Stepwise constant voltage, decay to 0.2 mA/cm²	22	Wanklyn (13)
Sodium borate/ boric acid	Stepwise constant voltage, 5 min-1 hr decay	27	Salomon (14)

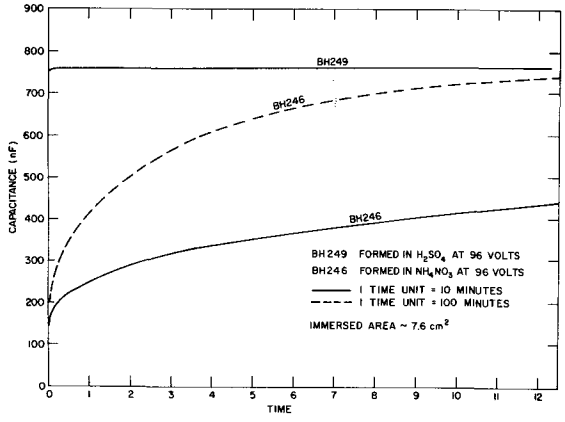

Fig. 1. Comparison of impedance vs. immersion time curves for porous and nonporous anodic oxide showing equality of barrier layer oxide thickness for both specimens.

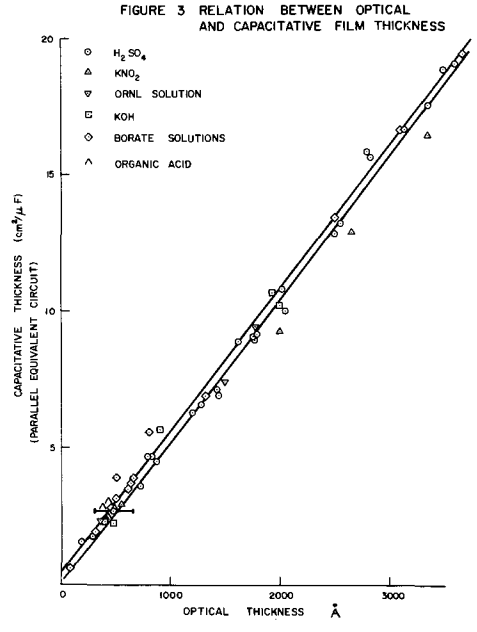

Fig. 2. Relation between optical and capacitative oxide thickness for films formed in various electrolytes.

is indicative of the total oxide thickness, while the final apparent thickness in ammonium nitrate measures the barrier thickness. The sizes of the flaws present in some films have been determined using a mercury porosimeter (Fig. 3) and the results can be correlated with the observed defects seen by electron microscopy [see Ref. (7) for details].

During forming at constant current the characteristic plateau (13) in the voltage-time curve was often observed. The duration of this plateau varied enormously with the electrolyte being used and in any given electrolyte was always longer for Zircaloy-2 specimens than for zirconium specimens. During the plateau localized oxygen evolution could be observed at a number of sites. Anodization was attempted initially at ~1 mA/cm² for all specimens; in some instances the current had to be increased as much as a factor of five before the plateau could be passed. The current was returned to 1 mA/cm² once film growth resumed. Typical examples of the shapes of the constant current curves for Zircaloy-2 are shown in Fig. 4, and for zirconium in Fig. 5. The voltage decay curves were obtained for zirconium and Zircaloy-2 specimens after formation at constant current. Examples are shown in Fig. 6. The decay currents of specimens formed at constant voltage in different electrolytes were also measured [see Ref. (8), Fig. 24].

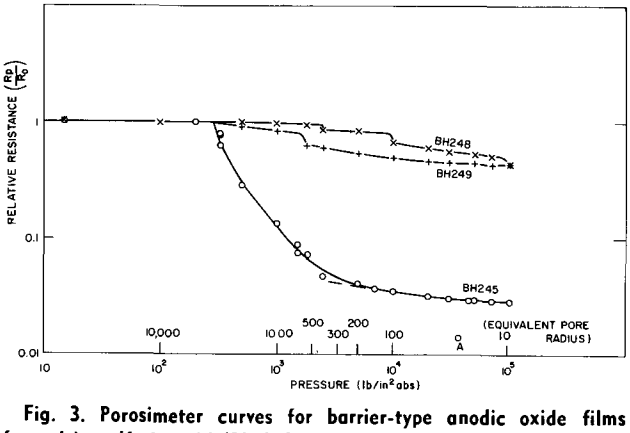

Fig. 3. Porosimeter curves for barrier-type anodic oxide films formed in sulfuric acid (Bh 248, Bh 249) and a porous anodic film formed in ammonium nitrate (Bh 245).

Visual observations.—Observation of the specimens in the optical microscope showed that (for most electrolytes) the interference colors were uniform over the zirconium matrix. Large intermetallic particles were clearly different in interference color from the surrounding matrix, but in most instances were too small for the film thickness on the intermetallics to be determined in the optical microscope, or even to estimate whether it was greater or less than the surrounding oxide thickness. Electrolytes giving porous oxide films commonly yield irregular interference colors, and some other electrolytes reproducibly gave local variations in oxide thickness.

Examination of the specimens with the electron microscope and scanning electron microscope showed that most anodic films, especially on Zircaloy-2, contained a number of flaws, even when they would be classified as good barrier-type oxide films from an examination of the electrical measurements. These flaws fell into a few characteristic types (illustrated by Fig. 7-9) which appeared commonly in a number of solutions and in the case of cracking at grain boundaries became more prominent with increasing oxide thickness.

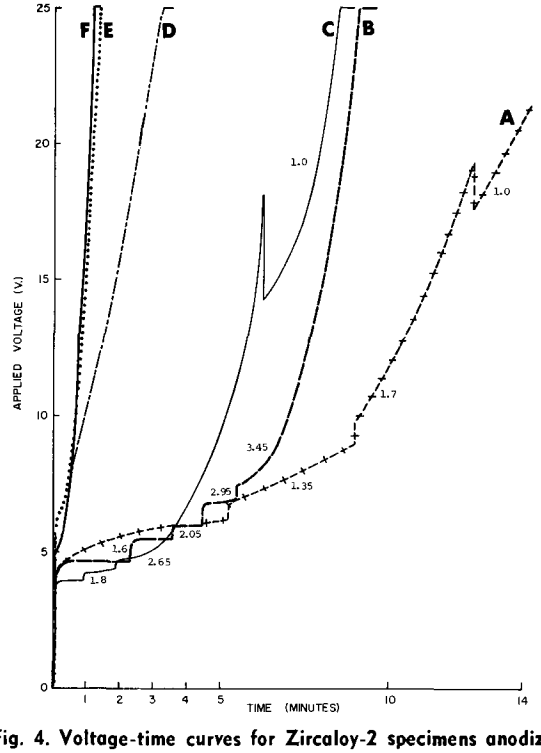

Fig. 4. Voltage-time curves for Zircaloy-2 specimens anodized in organic acid electrolytes. Numbers by curves indicate current density where this was increased above 1 mA/cm² to overcome the plateau in the anodization curve. Specimens anodized in (a) citric acid, (b) tartartic acid, (c) oxalic acid, (d) lactic acid, (e) acetic acid, (f) formic acid.

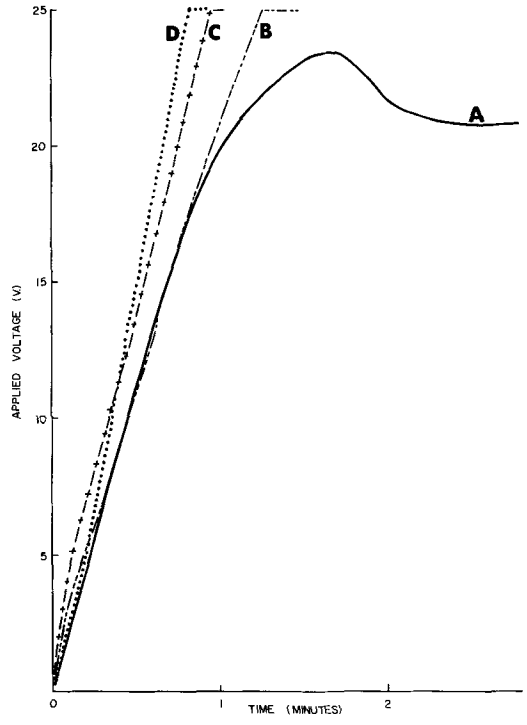

Fig. 5. Constant current anodization of unalloyed zirconium at 1 mA/cm². Specimens anodized in (a) $KCrO_4$, (b) NH_4NO_3, (c) citric acid, (d) Na_2SO_4.

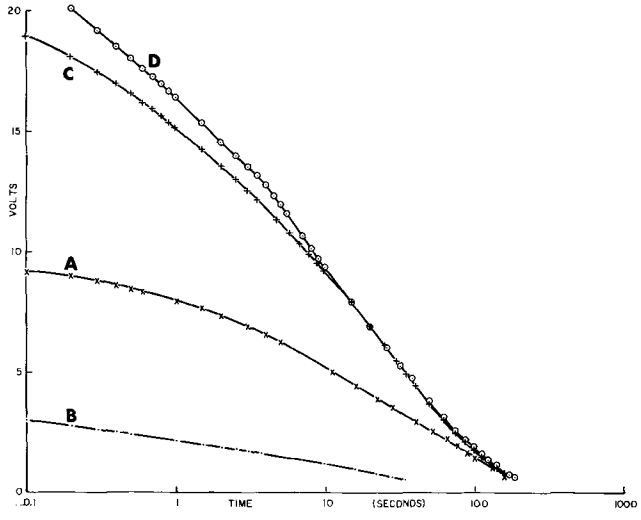

Fig. 6. Decay of the formation voltage for specimens of unalloyed zirconium shown in Fig. 5. (a) $KCrO_4$, (b) NH_4NO_3, (c) citric acid, (d) Na_2SO_4.

However, the phenomena which were studied in most detail were those leading to more severe breakdown of the oxide and to generally porous oxide films. These can be divided into three different types of failure.

1. Formation of thicker oxide along grain boundaries and around intermetallic particles leading to cracking along grain boundaries and ultimately to spalling of the oxide (see Fig. 10-12).
2. Local formation of patches of thicker rough oxide eventually leading to spalling (Fig. 13 and 14).
3. Formation of generally porous oxide films which continue to grow considerably in thickness when held at the forming voltage (Fig. 15-17).

Transmission electron microscopy of stripped oxide films from selected specimens formed in sulfate, hydroxide, tartrate, and nitrate electrolytes showed unique features associated with the films formed in nitrate. In bright and dark field illumination the

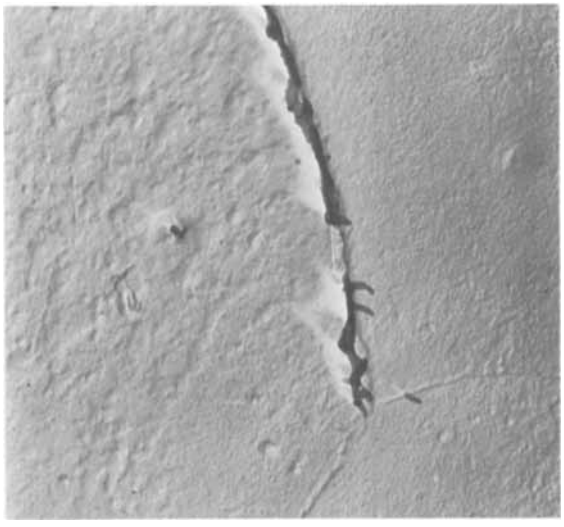

Fig. 7. Cracks forming along prior metal grain boundaries in anodic oxide film formed in sulfuric acid specimen (Bh 249, 96 V). X 20,000.

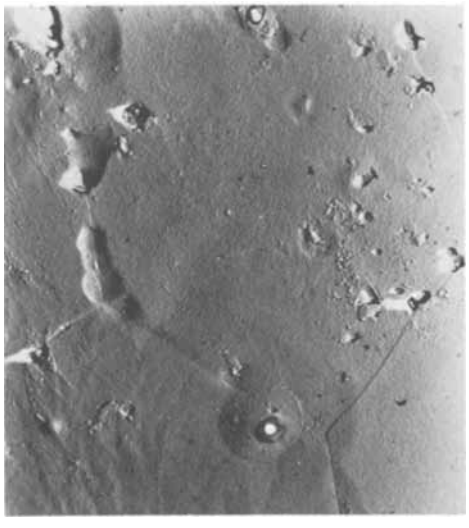

Fig. 8. Minor flaws produced by cracking of anodic oxide around intermetallic particles in a Zircaloy-2 specimen anodized in ammonium borate (Specimen Bh 306, 18 V). X 5000.

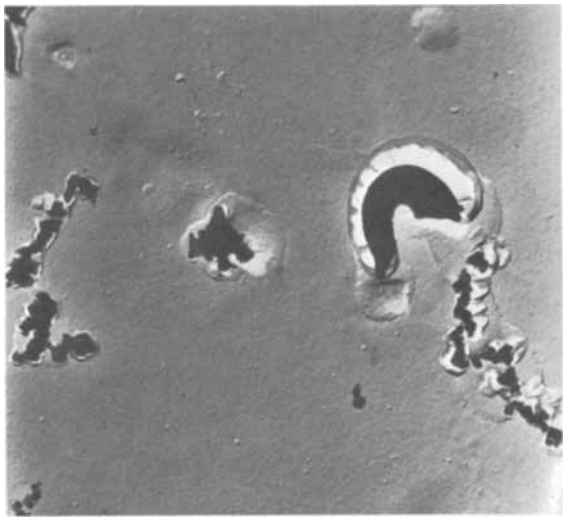

Fig. 9. Small areas of poorly adherent thicker oxide detached from specimen, anodized in ORNL solution, by the replication technique (Specimen Bh 319, 100 V). X 20,000.

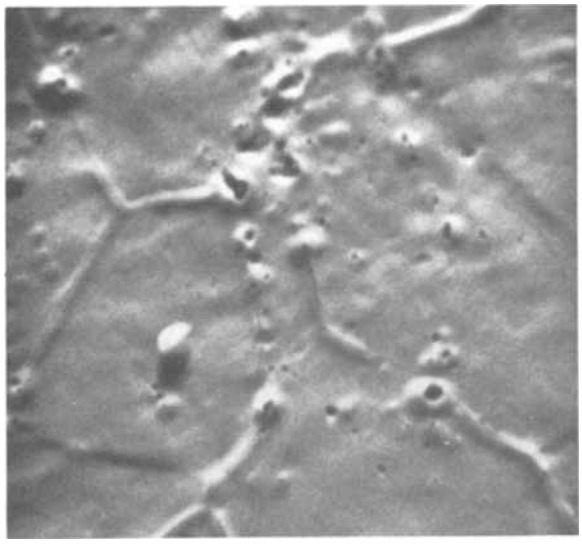

Fig. 10. Scanning electron micrograph showing later stages of development of thick oxide ridges along prior metal grain boundaries. Cracks in oxide are now visible along some boundaries (Specimen Bh 249, 96 V in H_2SO_4). X 2000.

Fig. 11. More advanced stage of growth in sulfuric acid of grain boundary ridges of thick anodic oxide (Specimen Bh 315, 132 V). SEM X 10,000.

crystallite size was clearly smaller in the nitrate films compared with films formed in the other three electrolytes (Fig. 18). In addition to being larger the crystallites were also less distorted in the barrier-type films. In the nitrate films the thickness varied in an irregular fashion not evident in the other oxides, and small thin patches, which might be the early stage of pore development, could be seen (Fig. 19). The diffraction patterns, from basal planes of the zirconium matrix, showed that the nitrate film was also unique in being essentially all monoclinic ZrO_2, whereas the other films had large percentages of cubic ZrO_2 ($\geq$75%) and only traces of the monoclinic phase (Fig. 20). There were differences between the barrier-type films in the randomness of the distribution of the cubic oxide crystallites. In some instances, especially tartaric acid, the crystallites were almost random, giving rise to complete rings (Fig. 21), whereas in the other barrier-type oxides the crystallites were highly oriented.

Fig. 12. Local oxide spalling as result of formation of thicker oxide along grain boundaries. X 1000. (Photo-emission electron micrograph).

Fig. 13. Uneven growth of anodic oxide films in potassium chromate solution, X 10,000.

Scanning electron microscopy of the oxide/metal interfaces of anodic oxide films showed that considerable roughness of the interface was present for oxides known from other measurements to be porous (Fig.

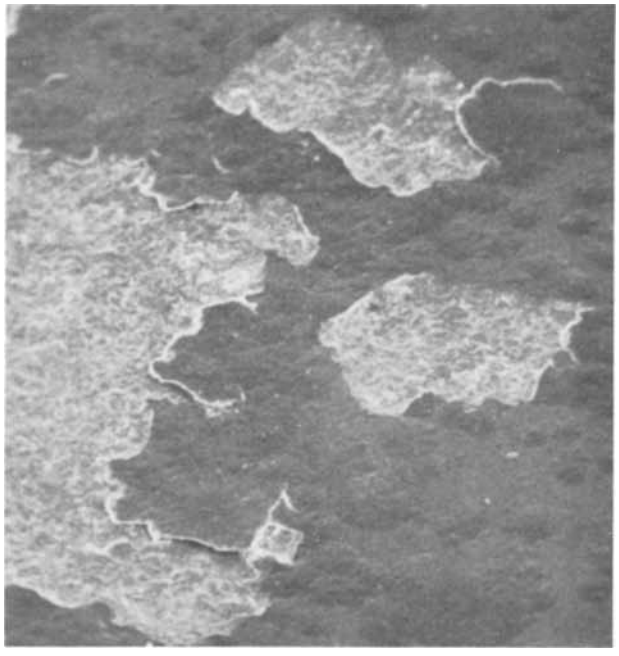

Fig. 14. Spalling of oxide resulting from multiplication and coalescence of areas of thick oxide formed in potassium chromate. X 100.

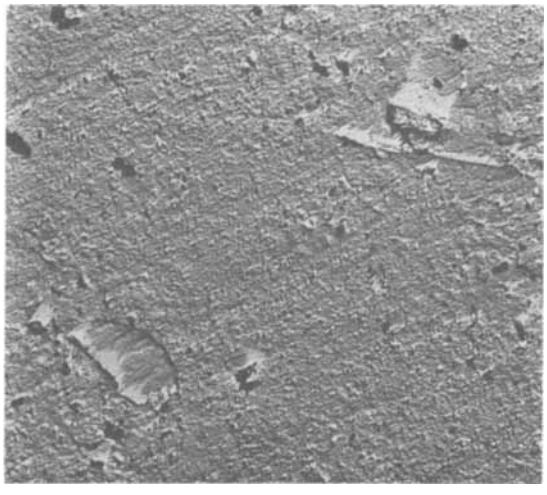

Fig. 15. Intermediate stage in development of pore network in oxide formed in ammonium nitrate (Specimen Bh 312, 18 V, 5 min). X 5000.

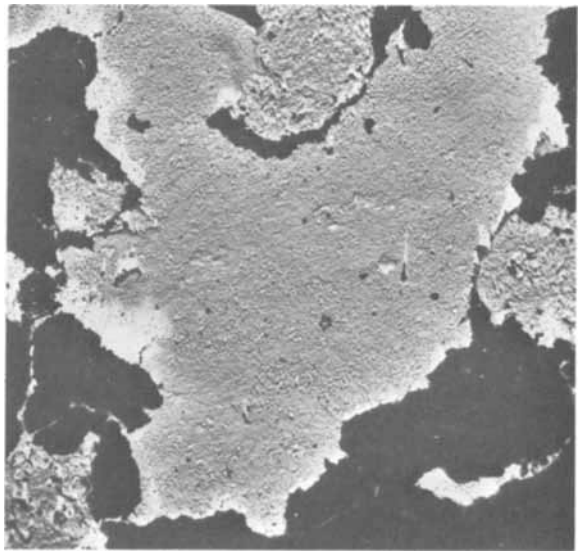

Fig. 16. Oxide spalling at a later stage in formation of thick porous oxide in ammonium nitrate (Specimen Bh 246 96 V). X 5000.

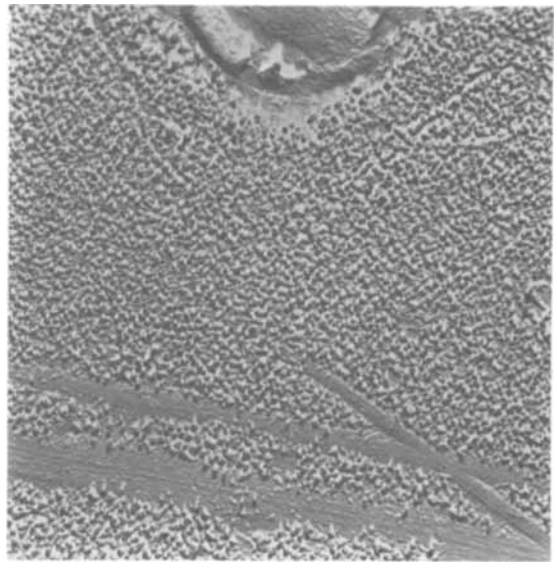

Fig. 17. Uniform pore network in anodic oxide formed in phosphoric acid (Specimen Bh 266, 25 V). X 20,000. N.B. absence of porous oxide along residual scratches.

22), whereas the interfaces of barrier-type films were generally smooth except in the vicinity of second phase particles.

Discussion

Identification of porous oxide films from electrical measurements.—A study of the impedance measurements (*e.g.*, Table II) shows that porous oxide films result for specimens formed in solutions containing the nitrate ion (NH_4NO_3, HNO_3, KNO_3) and phosphoric acid. The mode of formation has some influence on the results, however. Zircaloy-2 specimens formed at constant voltage or constant current showed little difference in the relative thickness indicated by liquid metal and aqueous contacts (*c.f.*, specimens Bh 225, 328, and 329), whereas for crystal-bar zirconium, films formed at constant current showed less evidence of porosity than those formed at constant voltage. This conclusion from the impedance measurements was confirmed by electron microscopy. The oxide surface on the zirconium specimen was found to be uneven, but not obviously porous. This conclusion might have been different had the specimen been held at the final voltage for some time after forming at constant current, if the increase in porosity found for Zircaloy-2 specimens held at constant voltage for increasing lengths of time is indicative of general behavior (Fig. 15-17).

Oxide films formed on Zircaloy-2 in chromate and dichromate solutions showed extensive areas of breakdown. There was correspondingly less evidence for breakdown on a zirconium specimen formed in potassium chromate solution at constant current, than for a comparable Zircaloy-2 specimen both from impedance measurements and electron microscopy.

Films formed in most other electrolytes showed relatively small differences between apparent thickness measurements in liquid metals and aqueous electrolytes. Of the former the measurements in LS232 are the more reliable because of its better ability to wet zirconia (8). Of those showing major differences between the impedance with aqueous and liquid metal contacts (a factor of two or more differences in apparent thickness in NH_4NO_3 and LS232) porosity, or other major flaws, were confirmed by electron microscopy and porosimetry only for films formed in phosphoric and sulfuric acids. Differences less than a factor of two can probably be explained on the basis of a

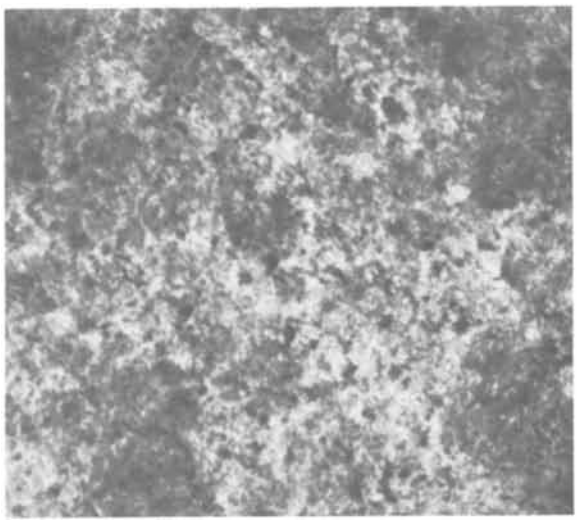

Fig. 18a

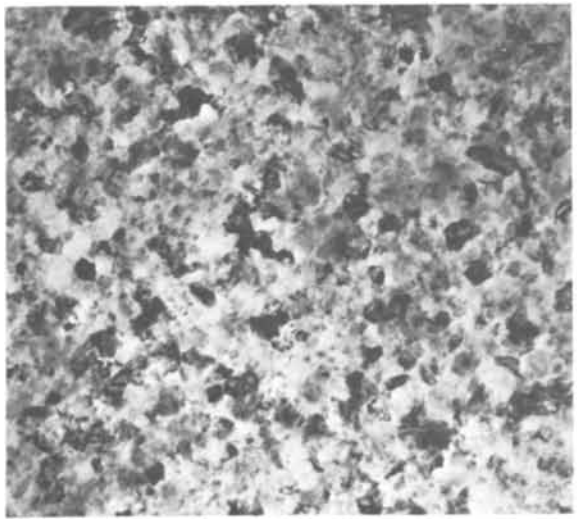

Fig. 18b

Fig. 18. Transmission electron micrographs of anodic oxide films (a) formed in ammonium nitrate (Bh 224); (b) formed in potassium hydroxide (Bh 308). X 75,000.

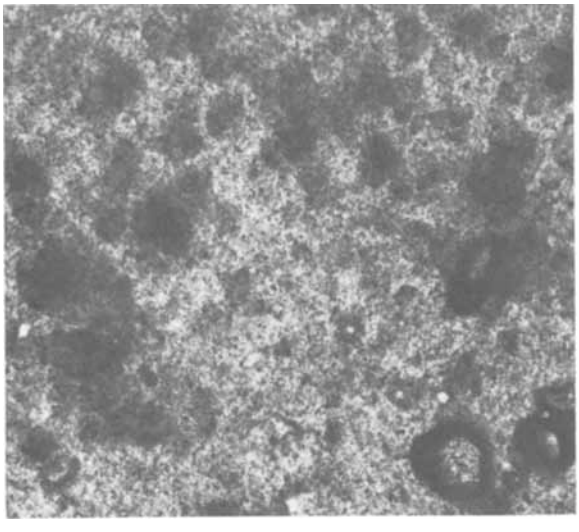

Fig. 19. Cellular structure developing in anodic oxide formed in ammonium nitrate. X 20,000.

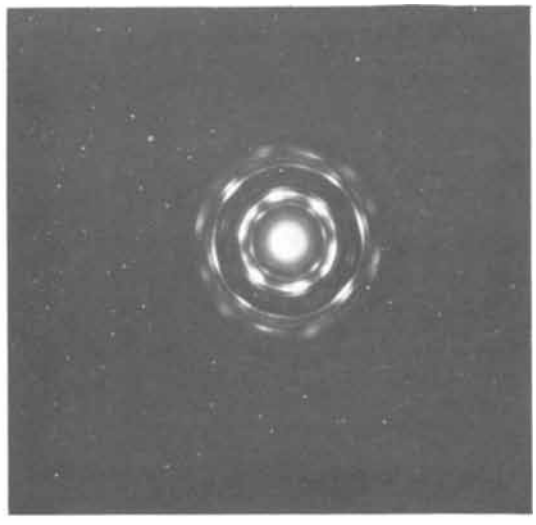

Fig. 20a

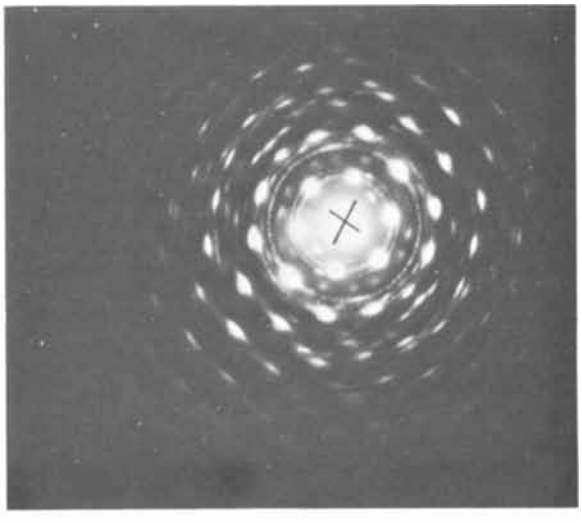

Fig. 20b

Fig. 20. Diffraction patterns from oxide formed (a) in ammonium nitrate (Bh 224), (b) in potassium hydroxide (Bh 308).

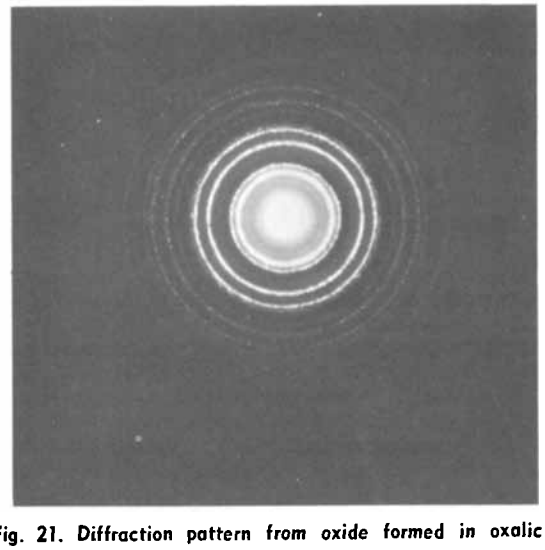

Fig. 21. Diffraction pattern from oxide formed in oxalic acid (Bh 263).

number of small flaws associated with the intermetallic particles.

Banter (4) has demonstrated for zirconium that in many electrolytes the anion is incorporated into the anodic film. However, with the exception of the organic acids, the other electrolytes for which he demonstrated this phenomenon were ones which we have found to yield porous or cracked oxide films. Thus, it

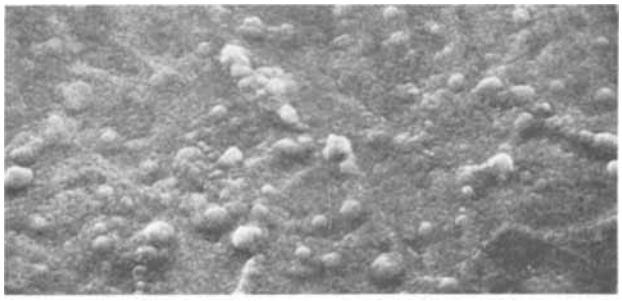

Fig. 22. Oxide metal interface of thick porous anodic oxide film formed in ammonium nitrate (Bh 247, 97 V).

is possible that anions from the electrolyte adsorbed in the porous structure rather than incorporated into the oxide lattice led to many of his observations. Nevertheless, it seems likely that anions from most if not all electrolytes are incorporated into nonporous anodic oxides (12, 15), but at levels generally below the level of detection of the methods employed by Banter.

That the incorporation of anions does not lead to any major change in the physical properties of the oxide formed is shown by the small spread of the impedance/thickness data for relatively defect free oxides in Fig. 2. The phosphate films for which Banter observed the outer layers dissolving faster than the inner ones were likely also to have been porous (Fig. 17) and the dissolution may have been due to this porosity rather than to the incorporation of a larger fraction of phosphate ions into the oxide lattice in the outer regions of the film. Absorbed phosphate would almost certainly have been more highly concentrated within the porous layer than within the inner "barrier-type" film, thus leading to the possible misinterpretation of the observations.

Current decay curves and leakage currents.—The formation of porous anodic films could also be detected in the current decay curves for specimens formed at constant voltage. An essentially constant (but fluctuating) current was observed for specimens forming porous films. Cracking and breakdown of the film can be distinguished from this process as they usually lead to discontinuous increases in the forming current. The rate of decay of the current during forming does not seem to be indicative of the quality of the final film as determined from a-c impedance measurements. Presumably the size of this current (which is probably mainly electronic at long decay times) measures the effectiveness with which the intermetallic particles are anodized, although no correlation could be found with the apparent thickness of the oxide on the intermetallic particles in those instances where this could be estimated.

Unusually high decay currents were observed for films formed in KOH. This current represents mainly oxygen evolution at intermetallic sites and might be thought to be due to lack of film formation on these intermetallics. However, electrical measurements on these films did not show them to be of significantly lower resistance than other films which did not yield such high leakage currents. The high decay currents in KOH also explain the apparent difference between our values for the formation rate in KOH (Table III) and those quoted by Wilkins (3, 11). Our specimens were held at each voltage step for a constant time whereas Wilkins' were held until a predetermined leakage current (0.2 mA/cm^2) was reached. Our data suggest that this would represent a long time at each voltage step and would be expected to yield a higher formation rate in Å/V. The good agreement when equivalent formation methods are compared is shown by the results in sulfuric acid. Wilkins' technique is equivalent to a decay time of about 1 min at each voltage, and therefore the formation rates are very close for the two equivalent conditions.

During formation at constant current, breakdown of the type observed in chromate and dichromate reveals itself as a failure of the voltage to continue to rise (Fig. 5). This feature is not observed with specimens forming porous films in nitrate or phosphate solution. These, and other, films show the normal arrest in the anodic growth curve (1, 16) at about 5V, at the current densities used here.

The height and length of this arrest varied from 3.7-6.3V and from a few seconds effectively to infinity depending on the electrolyte. In any given electrolyte the height was also a function of the current density. Extrapolation of our curves of "plateau" height *vs.* current density to the current densities of Adams *et al.* (16) gives good agreement with their data. Observation of local oxygen evolution during this plateau together with other data suggests that the plateau is caused by the presence of second phase particles in the zirconium matrix. The plateau is commonly very small or absent for unalloyed zirconium except at very low current densities, or for roughly abraded surfaces (16) where embedded abrasive particles may substitute for the intermetallic particles in Zircaloy-2.

The variation from electrolyte to electrolyte in the length of the plateau, and the current density needed to exceed it, is presumably a measure of the ability of each electrolyte to form a nonconducting film on the intermetallic particles. In Zircaloy-2 these are either Zr-Fe-Ni or Zr-Fe-Cr phases and the critical step may be the formation of an oxide film other than ZrO_2 on these particles. The big variation in the length of the plateau for different organic acids is surprising in this context since little difference would be expected in the ability of lactic, tartaric, and citric acids (for instance) to oxidize the intermetallic particles.

For unalloyed zirconium a clear distinction was found in leakage rate for porous and nonporous oxide films (Fig. 6). This distinction was not apparent with anodic films formed on Zircaloy-2, showing that in the latter instance the properties of the oxide formed on the intermetallic particles were more important in determining the leakage rate of the oxide than the porosity of the oxide formed on the majority of the surface. That this conclusion is reasonable may be judged from the fact that the porous oxide films all apparently have a barrier-layer at the oxide-metal interface, as judged from impedance measurements during immersion (Fig. 1). The intermetallic particles are large enough to short-circuit the whole oxide if the oxide over them is very thin, cracked, or more conducting (electronically) than that on the matrix. Further confirmation of this explanation may be provided by the apparent correlation between the leakage rate (estimated from the residual voltage after 10 sec) and the average current efficiency for formation (indicated by the time to reach 25V) for most of the specimens where no change in current density was needed to exceed the plateau (Table IV). Since most of the time taken to reach 25V was required to overcome the effect of the intermetallic particles the second of the above quantities probably measures the efficiency with which these particles are oxidized in a particular electrolyte.

Electron microscope studies.—Unlike anodic oxide films on many other valve metals, those formed on zirconium and its alloys are essentially microcrystalline (17) and bear a striking resemblance in the transmission electron microscope to thin thermal oxide films formed at ~300°C (18). Although marker studies using rare gas atoms indicated that the moving species during anodization is oxygen (19); the oxides used by Davies *et al.* were formed in nitrate solution and were therefore probably porous. Thus, electrolyte could have migrated past the markers via the pores. Further studies by Whitton using charged marker ions and oxides formed in borate solution have confirmed that the migrating species is oxygen but that migration is not through the bulk of the lattice

Table IV. Current efficiency and leakage rate of specimens anodized to 25V

Specimen	Electrolyte	Optical thickness (Å) Matrix	Optical thickness (Å) Intermetallics	Current efficiency (%) at ~1 mA/cm² Average	Current efficiency (%) at ~1 mA/cm² Final	Leakage rate (residual voltage at time) 1.0 sec	Leakage rate (residual voltage at time) 10 sec
Bh 257	Amm. borate	500	200	22.6	40.0	—	—
Bh 258	$K_2Cr_2O_7$	550	—	Breakdown occurred			
Bh 259	$KCrO_4$	550	—	before reaching 25V			
Bh 260	Amm. borate	500	200	—	—	—	—
Bh 261	Tartaric	425	—	0*	54.3	—	—
Bh 262	Lactic	425	—	34.8	30.2	2.2	1.25
Bh 263	Oxalic	375	825	0	30.0	—	—
Bh 264	Citric	475	—	0	15.2	—	—
Bh 265	Na_2SO_4	375	—	50.4	84.0	3.8	1.90
Bh 266	H_3PO_4	575	—	0	61.3	—	—
Bh 267	1:2:3/H_2O/HOx/Gly	290	600	29.1	~100	2.45	1.52
Bh 268	Amm. bor/E. Gly	250	600	High	80.0		
Bh 269	NH_4NO_3/E. Gly	1100-3000	—	>87	~100	5.4	2.2
Bh 325	Acetic	430	—	82	~100	4.9	1.4
Bh 326	$K_3Fe(CN)_6$	500	—	59.7	70.0	2.5	0.5
Bh 328	NH_4NO_3	500-1400	—	>78	>80	3.3	1.1
Bh 329	NH_4NO_3	550-1600	—	>83	>80	3.3	1.05
Bh 330	$K_2S_2O_7$	400	—	50.0	100	2.8	0.8
Bh 331	Formic	200	—	43.5	61.8	3.1	1.4

* Specimens showing zero current efficiency did not anodize beyond the plateau at 1 mA/cm². Leakage rates are not shown for these specimens.

(15). Thus, since the latter films were probably nonporous, it appears that in anodic films, as in thermal films (20), the oxygen transport process is via the boundaries between the oxide crystallites (or any residual amorphous material between the crystallites) rather than through the bulk of the oxide lattice.

The various processes by which irregular or porous oxide films are formed in different electrolytes are thought to be related to the effect of incorporated electrolyte ions on the crystallization or recrystallization of the oxide film. Thus, transmission microscopy has shown that crystallite size and degree of orientation are affected by the electrolyte used. These effects are most readily seen in the enhanced oxidation and ultimate cracking (perhaps) due to local stresses observed at grain boundaries in sulfuric acid, and to a lesser extent in potassium nitrite. The effect of such cracks on dielectric loss in films formed in sulfuric acid has already been reported by Young (21). Disorder at grain boundaries might be expected to lead to variations in the density of easy diffusion paths and locally enhanced oxidation via local modifications in the field strength in the oxide. That this phenomenon is infrequent during anodic oxidation presumably indicates a normally greater degree of order at crystallite boundaries in anodic films than is present in thermal oxide films so that locally enhanced anodic oxidation at grain boundaries is the exception rather than the rule. The observation that barrier-type films are predominantly cubic ZrO_2, would be expected to lead to less lattice disorder in crystallite boundaries than in thermal oxide films which are predominantly monoclinic.

The electron microscope study of films formed in nitrate, phosphate, and dichromate solutions shows that the porosity originates in the growth of films having relatively rough outer and inner interfaces, and apparently associated with a high percentage of monoclinic ZrO_2 in the film. In nitrate and phosphate solutions these rough films cover virtually the whole surface, and eventually develop a network of pores. Thicker films do not form along residual scratches in the metal, which can often be seen in the optical microscope because the interference color film over them is of normal thickness (8). Presumably the distorted nature of the underlying metal prevents the formation of the thicker films at these points, although the precise reason for this is not clear. Perhaps the cold work in the surface causes the formation of cubic oxide at these sites, and this inhibits the development of roughness and porosity.

It is concluded therefore that electrolytes, which lead to the formation of porous oxides, modify the crystallization of the oxide thus permitting the development of a thick and ultimately porous oxide. The cell structure (such as it is) in the thick films formed in nitrate solutions seems to develop from a pattern of crystallization which occurs in the first few seconds of formation (Fig. 19). The manner in which the pore structure develops from this has not been elucidated. Penetration of the electrolyte into the pores and the development of a columnar crystallite structure would permit this growth process to continue. In chromate and dichromate solutions the course followed seems to be basically the same, but becomes irregular on a small scale. This leads to small local patches of thicker oxide which eventually crack and spall, presumably due to the more severe local stresses in these films than in the nitrate or phosphate films.

Previous studies of the crystal structure of anodic oxide films on zirconium by x-ray and glancing angle electron diffraction (22-25) have been unable to agree on the relative proportions of cubic, monoclinic, and amorphous oxide in the film formed in different electrolytes. Previous studies of anodic films by transmission electron microscopy have stopped short of attempted interpretations of the diffraction patterns (17).

The basic processes relating the changes in oxide morphology to the effect of the incorporated ions and changes in the crystallization process require a detailed study of the films by transmission electron microscopy. This is currently in progress but is beyond the scope of the present work.

Conclusion

A survey of the anodization of zirconium alloys in a number of electrolytes has shown that (using a forming method involving long holds at constant voltage) porous anodic films can be formed in solutions containing nitrate, chromate, dichromate, and phosphate ions. Flaws formed at intermetallic particles and by cracking of the oxide along grain boundaries are also prevalent being worst in sulfuric acid of the electrolytes tested here, but being found to a greater or lesser extent in most of the electrolytes yielding barrier-type films.

In the electrolytes yielding porous films the precise mechanism of their formation is apparently different for each electrolyte, however the underlying mechanism is believed to be associated with the incorporation of anions into the oxide and their effect on the crystallization of the oxide during anodization.

Acknowledgments

The author is indebted to R. A. Ploc for the transmission electron microscopy quoted here. This forms part of a broader study of the structure of anodic oxide films on zirconium alloys which is still in progress. The photo-emission electron microscopy was kindly performed by Balzer's Ltd. (see Fig. 12).

Manuscript submitted Oct. 7, 1969; revised manuscript received *ca.* Jan. 26, 1970. This was Paper 30 presented at the New York Meeting of the Society, May 4-9, 1969.

Any discussion of this paper will appear in a Discussion Section to be published in the December 1970 JOURNAL.

REFERENCES

1. R. D. Misch and bibliography in "Metallurgy of Zirconium," pp. 663-677, Lustman and Kerze, Editors, McGraw-Hill Book Co., New York (1955).
2. L. Young, "Anodic Oxide Films," Academic Press Inc., New York and London (1961).
3. N. J. M. Wilkins, *This Journal*, **109**, 998 (1962).
4. J. C. Banter, *ibid.*, **114**, 508 (1967).
5. N. Ramasubramanian, Atomic Energy of Canada Limited, Unpublished results.
6. I. L. Rosenfeld, E. N. Lantseva, and E. I. Kalinina, *Russ. J. Phys. Chem.*, **34**, 473 (1960).
7. B. Cox, *J. Nucl. Mater.*, **27**, 1 (1968).
8. B. Cox, Atomic Energy of Canada Limited, Report AECL-2668.
9. D. K. Dawson and R. H. Creamer, *Brit. J. Appl. Phys.*, **16**, 1943 (1965).
10. B. Cox and D. L. Speirs, Atomic Energy of Canada Limited, Report AECL-2704.
11. N. J. M. Wilkins, UKAEA Report AERE-R4666 (1964); *Corrosion Sci.*, **4**, 17 (1964); **5**, 3 (1965).
12. G. T. Rogers, P. H. G. Draper, and S. S. Wood, *Electrochim. Acta*, **13**, 251 (1968).
13. C. F. Britton, J. V. Arthurs, and J. N. Wanklyn, UK Report, AERE-4702.
14. R. E. Salomon, W. M. Graven, and G. B. Adams Jr., *J. Chem. Phys.*, **32**, 310 (1960).
15. J. L. Whitton, *This Journal*, **115**, 58 (1968).
16. G. B. Adams Jr., T. S. Lee, S. M. Draganov, and P. Van Rysselberghe, *ibid.*, **105**, 660 (1958).
17. J. N. Wanklyn, "Corrosion of Zirconium Alloys," ASTM, STP 368, pp. 58-75 (1964).
18. R. A. Ploc, *J. Nucl. Mater.*, **28**, 48 (1968).
19. J. A. Davies, B. Domeij, J. P. S. Pringle, and F. Brown, *This Journal*, **112**, 675 (1965).
20. B. Cox, *J. Nucl. Mater.*, **31**, 48 (1969).
21. L. Young, *Trans. Faraday Soc.*, **55**, 842 (1959).
22. P. H. S. Draper and J. Harvey, *Acta Met.*, **111**, 873 (1963).
23. R. K. Hart, D. I. C. Thesis, Imperial College, London (1951).
24. I. S. Kerr, Ph.D. Thesis, University of London (1955).
25. R. D. Misch and W. E. Ruther, *This Journal*, **100**, 531 (1953).

Reactions Caused by Additive Coloration of Tl^+- and Pb^{+2}-Doped KCl

L. Ben-Dor, A. Glasner, and A. Zudkevitz

Department of Inorganic and Analytical Chemistry, The Hebrew University, Jerusalem, Israel

ABSTRACT

Additive coloration of KCl doped with Tl^+ may reduce the substitute $-Tl^+$ ions to Tl^0 neutral centers or to negative "Tl^-" complex centers. In the case of Pb^{+2}-doped KCl, an intermediate Pb^+ and a Pb^0 netural center are formed.

Tl^+-Doped Alkali Halides

The spectra of Tl^+-doped alkali halides is well understood (1-1c) and is thought to be directly connected with electron excitations confined to the impurity ion. Additive coloration performed by heating the crystal in vacuum or low nitrogen pressure, in alkali metal vapor as well as radiative coloration, performed by x-rays or γ-rays, of the doped alkali halides have been studied (2-4), but attention was paid mainly to the effect of the impurity on F-center formation.

In the case of KBr, Tamai (5) observed the formation of two distinct bands on additive coloration by potassium vapor: a Tl neutral center (TNC) peaking at 4.1 eV (310 nm) and a Tl complex center (TCC) peaking at 3.1 eV (400 nm). The nomenclature adopted had been used earlier (2). The TNC is supposed to be a Tl^+ ion associated with one F center, and the TCC a Tl^+ ion associated with two F centers.

The formation of Tl^0 as well as Tl^{+2} in KCl as a result of low-temperature γ-irradiation was studied (6). Coloration by irradiation causes both reducing and oxidizing processes. The elucidation of the resulting absorption spectra is complicated because of the simultaneous formation of a variety of V, F, and impurity centers. Also, the species thus formed are highly excited and labile, disappearing on warming above liquid nitrogen temperature. In contrast, additive coloration forms only reduced centers, which are stable to heat- and bleaching-treatments in general. It seemed advisable to carry out a further investigation to check the new "reduced-only" color centers formed and possibly confirm the existence of a negatively charged TCC center in other alkali halides besides KBr.

Pb^{+2}-Doped Alkali Halides

The absorption of Pb^{+2}-doped alkali halides, unlike the Tl^+-doped salts, is attributed solely to charge transfer transitions (7). The existence of Pb^{+2}-cation vacancy complexes has been reported by many investigators (8-10). In studies of X-irradiated NaCl doped with Pb^{2+}, a gray coloration caused by Pb^0 (11) and an "atomary" lead center (12), peaking at 254 nm, were reported. Low-temperature colorability of doped KCl was also studied (13, 14), but no attention was given to uv impurity bands formed thereby. In this work, the reduced species formed on additive coloration are more closely defined.

Experimental Section

All chemicals used, KCl, TlCl, $PbCl_2$, were J. T. Baker Analyzed Reagents. Single crystals were grown by the Stockbarger method, and additive coloration was performed both in Pyrex (550°C) and in nickel (700°C) (16) containers at a pressure of ~50 Torr nitrogen. The optical absorption was recorded on a Perkin-Elmer Model 137 uv spectrophotometer, working in the double beam mode. A special holder with 1 mm slit was used in the sample beam of the spectrophotometer, so that a 1-2 mm thick crystal plate, cleaved from the center of the colored single crystal (13 mm on the edge), could be moved in front of the beam. In this manner the spectrum of a desired region of the crystal plate could be recorded at various distances from the exposed surface. The spectra were taken at room temperature.

Results and Discussion

A KCl crystal containing 0.01-0.05 m/o (mole per cent) Tl^+ did not show F absorption on coloration as

the high impurity concentration acted as an efficient trap for electrons. Crystals containing less than 0.001 m/o Tl^+ were easily colored and showed a distinct band peaking at 290 nm, besides the well-defined F band (Fig. 1). The additively colored crystal plates cleaved from the center of the colored cube exhibited three distinct areas [cf. ref. (2)]: an outer bluish F-zone about 2.5 mm wide, a brown-yellow zone containing the reduced center (290 nm), and an innermost colorless zone containing the unreacted Tl^+ ions. The same crystals, when colored for longer periods (2 hr instead of 1 hr) and/or at higher nitrogen pressure (100 Torr instead of 50 Torr), or in the presence of thallium chloride powder added to the coloring vessel, showed another previously unobserved band peaking at 345 nm (Fig. 2). It was found that the center responsible for this latter band is formed mainly in the outer zone, overlapping the F zone, of the crystal. On the other hand, the center responsible for the 290 nm band is found in the inner square of the crystal plate, 4.5-5 mm deep inside the face exposed to the coloring alkali metal vapor. The 247 nm A band of the Tl^+ ions survives in the interior colorless square (Fig. 3). Following former nomenclature, we wish to identify the 290 nm band as being due to TNC and the 345 nm as a TCC, reasoning that the doubly reduced TCC is formed only under drastic reducing conditions in the outer zone, where the concentration of electrons is highest. Comparing the centers observed in KBr by Tamai (5) with those found by us:

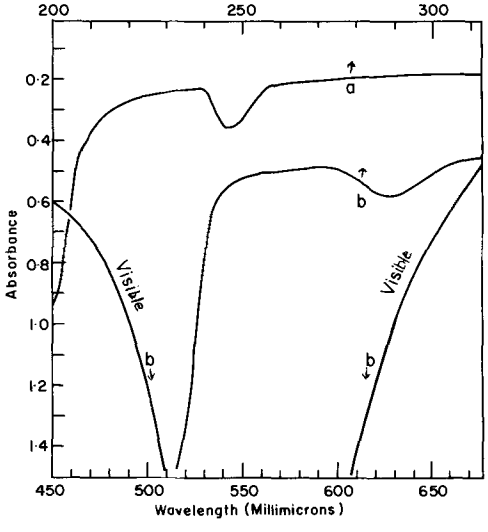

Fig. 1. Absorption spectra of Tl^+ doped KCl: (a) before coloration, (b) after additive coloration (1 hr, 700°C, 50 Torr nitrogen).

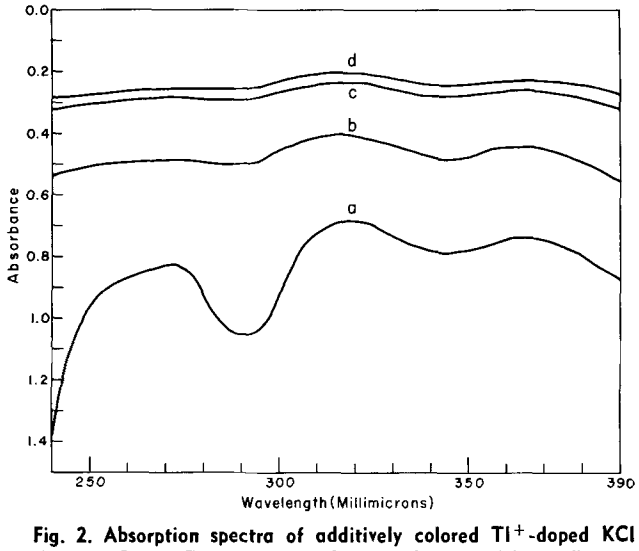

Fig. 2. Absorption spectra of additively colored Tl^+-doped KCl (2 hr, 550°C, 100 Torr nitrogen). Spectra shown in (a) to (d) were taken in progressively inner parts of the crystal.

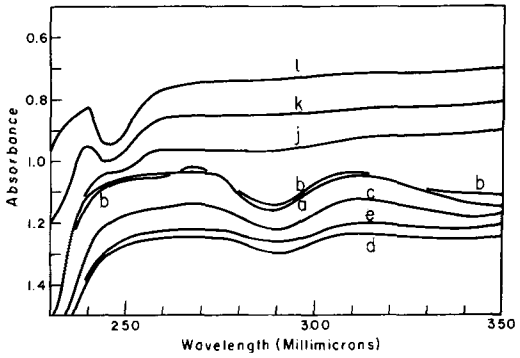

Fig. 3. Absorption spectra of additively colored Tl^+-doped KCl (conditions of coloration as in Fig. 2). Spectra shown in (a) to (d) were taken at ½ mm distances from the exposed face. Spectra (e)-(i) were omitted for clarity; (j)-(l) show spectra to 6 mm from the face.

	TNC, eV	TCC, eV
KCl	~4.3	3.6
KBr	4.0	3.1

one observes a shift in the same direction and similar magnitude when changing the matrix from KBr to KCl.

Delbecq *et al.* (6) identified a Tl^0 center in low-temperature γ-irradiated KCl, showing a weak band at ~300 nm, as well as a comparatively stronger band peaking at 380 nm, and three other extremely weak bands peaking in the visible and near IR regions. All these bands are attributed to Tl^0 centers on the basis of an analogy with the well-established Ag^0 center (17). The authors point out (7) that the 380 nm absorption is associated with a transition from the $^2P_{1/2}$ ground state to a $^2S_{1/2}$ resonant level in the conduction band. This latter excited level may be unstable at high temperatures. On the other hand, the 290 nm band prominent in our spectra may be due to a transition in the Tl^0 center from the ground state completely up to the conduction band. Thus, in the additively colored crystals only a single absorption band in the uv, arising from the Tl^0 center, was observed.

The 345 nm band produced only under more drastic conditions of coloration is attributed to a negative thallium complex, *i.e.*, a substitute Tl^0 atom associated with an F center. The Tl^0 center first produced carries an effective negative charge making its association with an anion vacancy highly probable. Under the drastic coloring conditions this associate could then capture a second electron to produce the negative complex center.

KCl single crystals containing 0.025-0.05% Pb^{+2}, as grown, showed besides the characteristic 273 nm Pb^{+2} band an absorption band at 325 nm (Fig. 4). This 325 nm band was also observed in concentrated KCl solutions containing ~100 ppm Pb^{+2} ions. Crystals absorbing in this region invariably had a yellow coloration, reminiscent of the yellow-brown coloration appearing in Tl^+ as well as in Zn^{+2}, Cd^{+2}, or Hg^{+2} doped (15) KCl crystals when additively colored. In all these cases the characteristic absorption band causing the yellow-brown coloration was attributed to the formation of neutral atomic species. Hence we suggest that, in the case of lead-doped crystals, dispersed neutral species appear to be formed by reduction in the melt, or by a photochemical decomposition, during crystal growth

$$PbCl_2 \rightarrow Pb^0 + Cl_2$$

Hence the 325 nm band is attributed to an atomary Pb^0-center. On the other hand, the gray coloration ob-

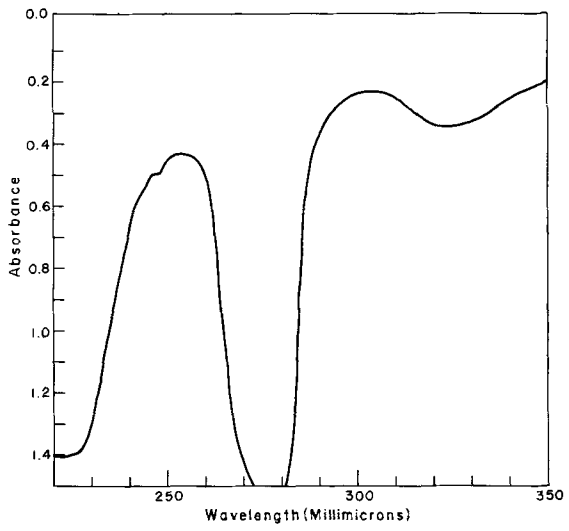

Fig. 4. Absorption spectra of Pb^{+2}-doped KCl after growth (the kink at ~250 nm should be disregarded).

served by Schulman *et al.* (11) in NaCl is indicative of colloidal lead aggregates.

On additive coloration of the Pb^{+2}-doped KCl, a further band, not well resolved, situated at ~254 nm, was obtained (Fig. 5). Since this band is different from the one described above, 325 nm, attributed to Pb^{o}, and since the crystal had neither a yellow nor a gray coloration, it must be due to another intermediary reduced species, viz., Pb^{+} center.

The Pb^{2+}-doped crystals were further studied by irradiative coloration at r.t., and it was found that with very low doping concentration (0.002 m/o Pb^{+2}), F centers are formed, but the presence of any other band is hardly discernable, although the characteristic Pb^{+2} band at 273 nm diminishes in intensity. Optical bleaching by direct sunlight renders the crystals colorless, and on further heat-treatment for 2 hr in a closed ampoule at ~200°C, the previously observed 254 nm band is formed. We claim, in accordance with Schulman *et al.* (11), that irradiation causes the formation of Pb^{o} centers (in low concentration not discernable in the spectrum) as well as immobile oxidizing species such as holes. During heat-treatment the Pb^{o} centers are partly reoxidized, causing the appearance of the band at 254 nm. This center, formed both by a reduction (additive coloration) and by an oxidizing process, could only be a Pb^{+} center.

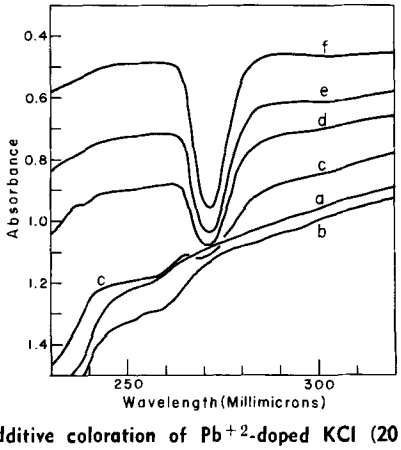

Fig. 5. Additive coloration of Pb^{+2}-doped KCl (20 hr, 550°C, 100 Torr nitrogen). Spectra shown in (a) to (f) were taken in progressively inner parts of the crystal. Note weak 254 nm band in outer parts, its disappearance toward the interior with the simultaneous appearance of the Pb^{+2} band (273 nm).

In summary, both Tl^{+} and Pb^{+2} substituted in KCl crystals act as electron traps; therefore crystals containing high concentrations of these ions do not color, *i.e.*, no F centers are formed either on irradiation or treatment with alkali metal vapor. In each case a maximum of two electrons per impurity ion may be trapped, but the impurity ions prefer to be reduced to the neutral atomary state.

In moderately doped KCl crystals the following centers were observed and may be identified as follows:

Tl^{o} (290 nm), Tl^{o}-F center complex	(345 nm)
Pb^{+} (254 nm), Pb^{o}	(325 nm)

The position of the bands is indicated in parentheses. Our results in the case of Tl^{+}-doped KCl are similar to those of Tamai (5) with KBr, but the models attributed to the respective centers are different, as shown above.

The apparent discrepancy between low-temperature irradiative coloration (6) and the results obtained on additive coloration of Tl^{+}-doped KCl is explained.

Of all the cation impurities studied, to date, only thallium was found to form a complex center formed from an association of Tl^{o} (neutral) with an F center. In the case of Pb^{2+}-doped KCl, the reduced species formed are most probably Pb^{+} and Pb^{o} centers. The 254 nm band is thus identified as a monovalent Pb^{+} center, rather than an "atomary" center as had been casually suggested (12) in the case of NaCl crystals.

Manuscript received Oct. 20, 1969; revised manuscript received *ca.* Jan. 15, 1970. This paper is based on the M.Sc. Thesis of one of the authors (A.Z.) (1965).

Any discussion of this paper will appear in a Discussion Section to be published in the December 1970 JOURNAL.

REFERENCES

1. F. Seitz, *J. Chem. Phys.*, **6**, 150 (1938).
1a. R. S. Knox, *Phys. Rev.*, **115**, 1095 (1959).
1b. J. E. A. Alderson, *Phys. Stat. Sol.*, **7**, 21 (1964).
1c. A. Fukuda, *J. Phys. Soc. Japan*, **26**, 1006 (1969); **27**, 96 (1969).
2. O. Stasiw, *Gött. Nachr.*, 1 (1936).
3. T. G. Castner and W. Känzig, *J. Phys. Chem. Solids*, **3**, 178 (1957).
4. J. J. Markham and H. N. Hersh, *J. Chem. Phys.*, **32**, 1885 (1960).
5. T. Tamai, *J. Phys. Soc. Japan*, **16**, 2463 (1961).
6. C. J. Delbecq, A. K. Ghosh, and P. H. Yuster, *Phys. Rev.*, **151**, 599 (1966); **154**, 797 (1967).
7. J. H. Schulman and W. D. Compton, "Color Centers in Solids," Pergamon Press, London, New York (1962).
8. E. Berstein, J. W. Davisson, and N. Seler, *Phys. Rev.*, **96**, 819 (1954).
9. R. A. Eppler and H. G. Drickamer, *J. Phys. Chem. Solids*, **15**, 112 (1960).
10. W. J. Fredericks and A. B. Scott, *J. Chem. Phys.*, **28**, 249 (1958).
11. J. H. Schulman, R. J. Ginther, and C. C. Klick, *J. Opt. Soc. Am.*, **40**, 854 (1963).
12. L. V. Grigoruk and I. Ya. Melik-Gaikazyan, *Optika i Spektros.*, **15**, 394 (1963).
13. W. A. Sibley, E. Sonder, and C. T. Butler, *Phys. Rev.*, **136**, A537 (1964).
14. E. Sonder and W. A. Sibley, *ibid.*, **140**, A539 (1965).
15. L. Ben-Dor, A. Glasner, and S. Zolotov, *Phys. Stat. Sol.*, **18**, 593 (1966).
16. C. Z. van Doorn, *Rev. Sci. Inst.*, **32**, 755 (1961).
17. C. J. Delbecq, W. Hayes, M. C. M. O'Brien, and P. H. Yuster, *Proc. Roy. Soc. (London)*, **271**, 243 (1963).

Physical and Electrical Investigations on Silicon Epitaxial Layers on Sapphire Substrates

J. Mercier

Section Physique des Couches Minces,
Laboratoire d'Electrostatique et de Physique du Métal, Grenoble-Gare, France

ABSTRACT

X-ray microdiffraction and special IR spectrometry techniques are used to explain the peculiarities of electrical properties of silicon thin films on sapphire substrates. Taking into account an autodoping effect due to the transfer of aluminum from the substrate into the layer, an optimum epitaxial temperature is observed. The results are interpreted in terms of misoriented regions, which are related to the presence of various Si-O bonds, the nature and the amount of which are dependent on the epitaxial temperature. It is concluded that chemical interactions between the substrate and the layer are more effective than crystallographic effects in determining the particular electrical properties of these silicon layers.

The need for physical methods is especially strong in the field of heteroepitaxy studies. This need does not arise from the number of the preparation steps, but from the intricate nature of the physical parameters involved in the process. The electrical characteristics, so useful with respect to the applications of these layers, give no physical insight. Furthermore they often involve long, sometimes destructive steps before measurements.

For these reasons, x-ray diffraction methods and IR spectrometry techniques complement the conventional electrical methods, in order to characterize thin silicon films grown by pyrolysis of silane, in hydrogen, on single crystal sapphire.

The aim of this study is an attempt to answer the following question: what are the relative contributions of fundamental factors and of incidental ones, inherent to the fact that the film properties are different from those of bulk material? The discrimination between these factors lies in the ability to improve the incidental ones, while the fundamental ones can only be optimized.

Experimental Conditions

Following Matare's general analysis presented in his excellent review paper (1), we can state some fundamental factors, optimizing in principle the experimental conditions:

1. High crystalline quality, Al_2O_3 ingots are used: they are Czochralski grown, and various tests confirm this quality (etching techniques, Borrmann effect).

2. The orientation $(01\bar{1}2)$ of the substrates gives two related advantages: (*a*) a nonpreferential *in situ* etching with H_2 at high temperature (1300°C), and (*b*) a quasi-systematic epitaxy of Si (100) as determined by x-ray and electron diffraction methods.

3. The substrate, 500 μm, and film, 5 μm, thick are chosen to minimize the strain of the layers.

4. Stresses are also avoided by a slow cooling rate after epitaxy ($\sim$ 100°/min).

5. The residual contamination level is low. With quite identical process conditions, silicon homoepitaxy is performed in the range 1000°-1200°C (2). Layers 5 μm thick are grown with N-type conductivity: when on 5-10 ohm cm P-type substrates, the layers resistivities are >100 ohm cm, and when on 0.01 ohm cm Sb doped substrates, the impurity concentration is less than 10^{14} cm^{-3}, at 1150°C.

6. The flow conditions (H_2 as a carrier gas, silane prediluted in H_2) have been determined to get low supersaturations required for epitaxy. The mean growth rate is 0.1 μm/min at 1100°C.

Electrical Results

The mean value results are shown in Fig. 1. Two processes have been used: process A, in which a chemical treatment of the substrate by hot phosphoric acid prior to insertion in the reactor is employed; and process B, without this chemical treatment. In any case, no intentional doping is performed.

From Fig. 1a, it follows that P-type doping occurs in the higher range of temperature, whatever the process, but N-type layers are grown at low temperatures, with the A process only.

Figure 1b gives the variation of Hall mobility with the epitaxial temperature. In the experimental range, a maximum value occurs at some optimum temperature (say T_0 = 1100°C). But if the sensitivity is far less in the A process than in the B process, the maximum value in the former case is slightly less than in the latter one.

Figure 1c gives another picture of this last result. If, instead of absolute values, a quality factor, F expressed as follows

$$F = \frac{\text{Hall mobility (film)}}{\text{Hall mobility (bulk for the same type and conc.)}}$$

is used, the difference between both processes disappears. We note that F increases with T_{epi} and reaches 50-60% at T_0.

Using a MOS structure, the majority carrier concentration (N_S) and the minority carrier lifetime (τ_S) near the free surface of the film (3, 4) has been measured.

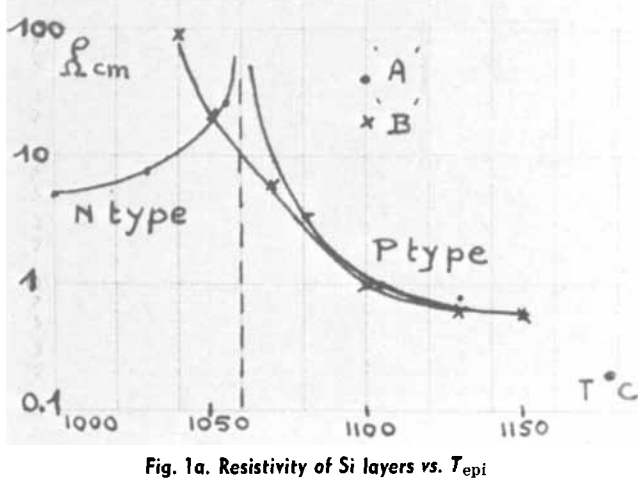

Fig. 1a. Resistivity of Si layers vs. T_{epi}

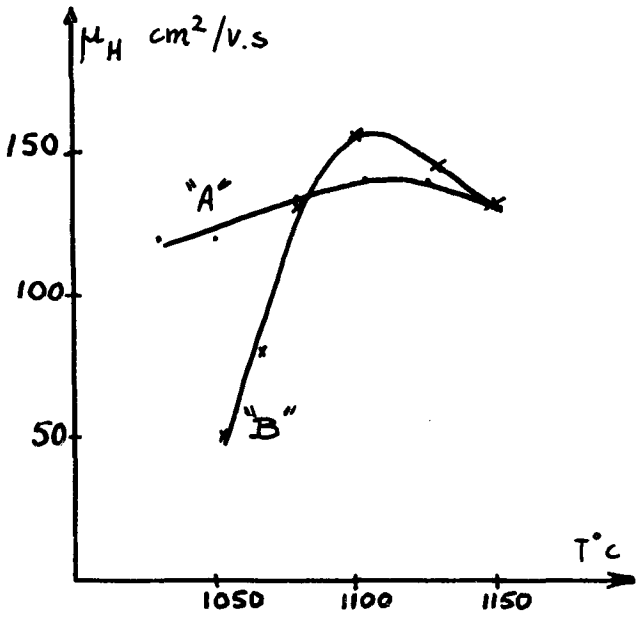

Fig. 1b. Hall mobility vs. T_{epi}

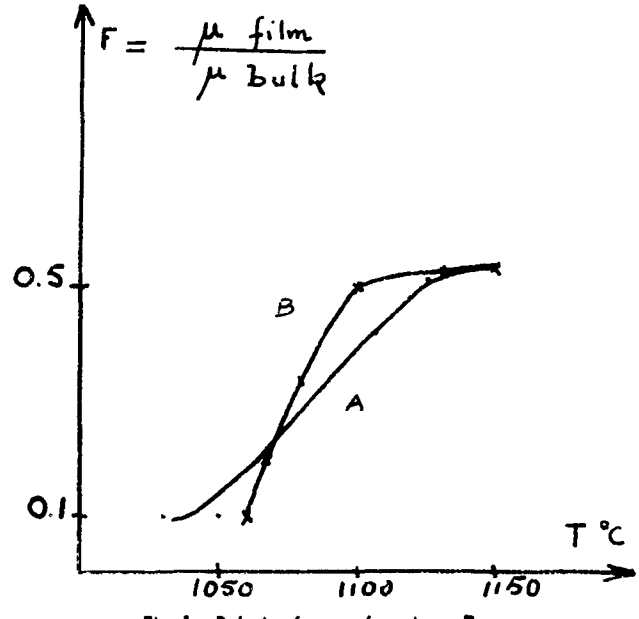

Fig. 1c. Relative factor of merit vs. T_{epi}

The variation of τ_s and its apparently high maximum value, when compared to other results (5) have been noted. The results are given in Table I.

Furthermore, some N-type layers were subjected to short time moderately high temperature, H_2 atmosphere treatments. For example, a 10 ohm cm N-type layer after 5 min at 1100°C turns to 150 ohm cm P-type. This change could not be explained in terms of usual dopant's diffusion. That it occurs only with H_2 atmosphere seems to indicate interfacial electrical states similar to those reported in ref. (6).

Table I. Electrical characteristics of Si layers

T_{epi}	Type	ρ, ohm cm	N_S, cm^{-3}	τ_S(ns)	Nature of oxide
1030	N	7.6	3.3×10^{15}	90	Pyrolitic
1055	N	23.8	1.1	7	Pyrolitic
1080	P	3.5	8.0	4	Anodic
1105	P	1	7.0	45	Anodic
1150	P	0.55	1.1×10^{16}	3	Anodic

Discussion

Some of these results can be now interpreted.

1. It has been ascertained by (7, 8) that Al from the substrate gives rise to P-type autodoping. The exact mechanism involved has not been clearly demonstrated. But from the variation of the layer resistivities, it seems reasonable to suppose that the N-type contamination is due to phosphorous residues after etching. This contamination has thus no other reason, but is inherent with the difficulties involved in the chemical surface preparation of the substrates. This result is to be compared with more subtle interfacial contamination effects (9). As a consequence, P-type layers grown at high temperature in the A process conditions are certainly electrically compensated. This explains the slightly lower maximum value of μ_f for the A process than for the B process (Fig. 1b).

2. The observed reduction of mobility (expressed by F) being independent of the type and doping level, it is plausible to explain in terms of structure defect the limitations at low temperature. This assumption must be checked by specific methods (discussed later). On the other hand, the decrease of mobility values in the higher temperature range can be attributed to impurity defects, the level of which increases with temperature.

X-ray Surface Topography

In the analysis of structural defect limitations, the first step to be considered is the state of preparation of the substrate surface. Reflection techniques as schematically described in Fig. 2 are used (10). Plate and sample under study are simultaneously moved to explore the whole surface, the resolution is fairly good (10μ).

Figure 3 shows a well polished substrate, and Fig. 4a presents a poorly polished one. An optical examination would have given in either case a very flat appearance. Then the same last wafer, after subjection to an H_2 treatment at 1300°C is seen in Fig. 4b. The efficiency of this treatment is demonstrated by the removal of

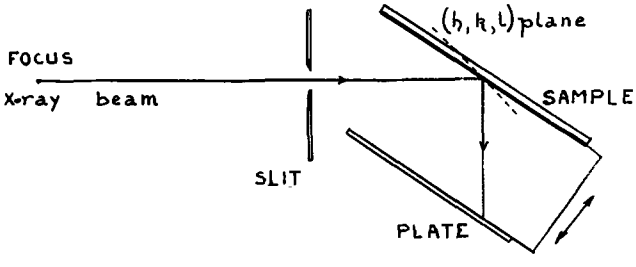

Fig. 2. X-ray surface topography arrangement

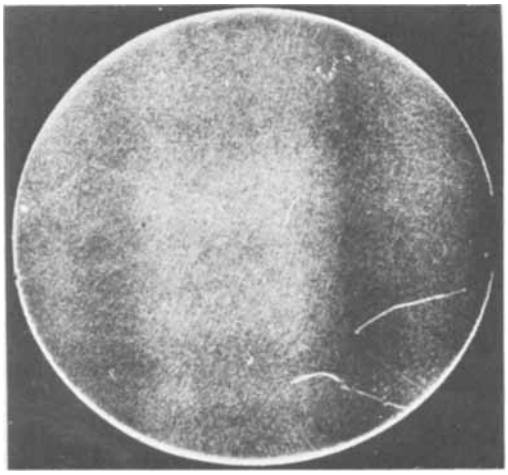

Fig. 3. X-ray surface topography of a well polished Al_2O_3 substrate.

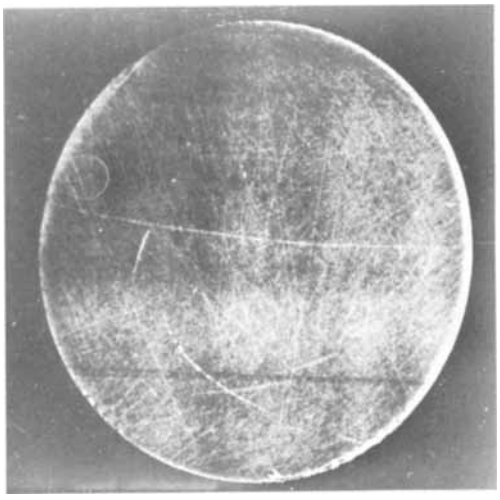

Fig. 4a. X-ray surface topography of a poorly polished Al_2O_3 substrate before H_2 treatment.

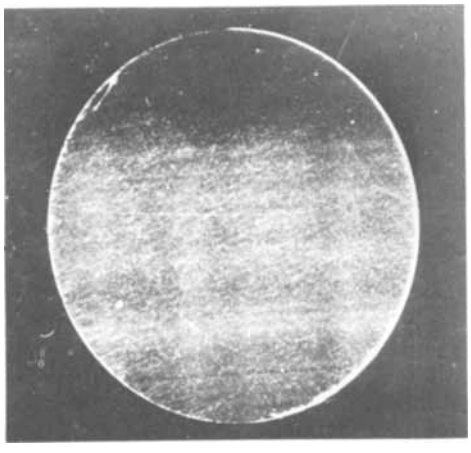

Fig. 4b. X-ray surface topography of a poorly polished Al_2O_3 substrate after H_2 treatment.

fine scratches and the smoothing of dislocation lines. Some preferential etching is indicated by the [100] direction as seen in Fig. 5, which is a G x 10 part of that substrate. This direction has been spotted with the [$0\bar{2}1$] reference direction. This last one is the intersection of the (3.2.4) reflecting plane with the (01.2) plane.

From these results, one may say that, in spite of difficulties, mechanical and gaseous polishing give good surfaces for epitaxy.

After growing a silicon layer, it is possible, with a proper choice of film thickness to investigate during the same experiment the free surface of the silicon film and the silicon-substrate interface (obviously with different reflecting planes: for Si (440) is convenient). Generally no structure is seen. But Fig. 6a (silicon surface) and Fig. 6b (interface) are special cases: the structures' replica is apparent (see the right corner

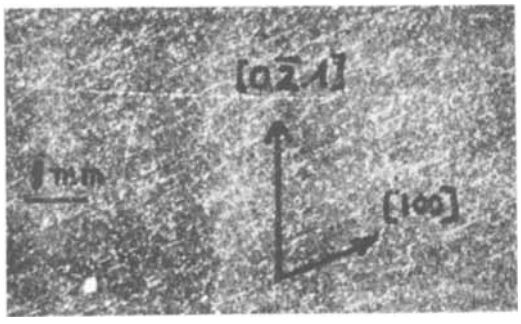

Fig. 5. Part (G x 10) of that wafer

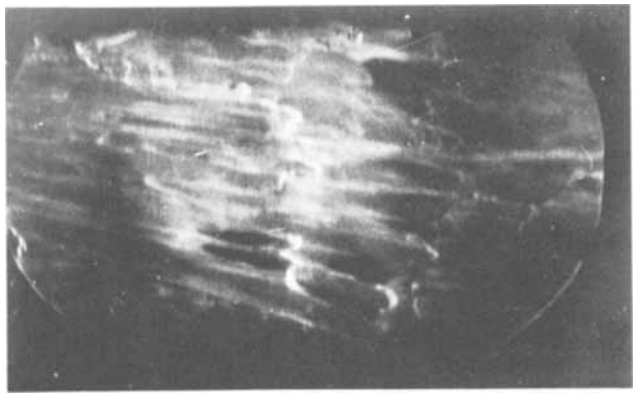

Fig. 6a. X-ray surface topography of the silicon film free surface

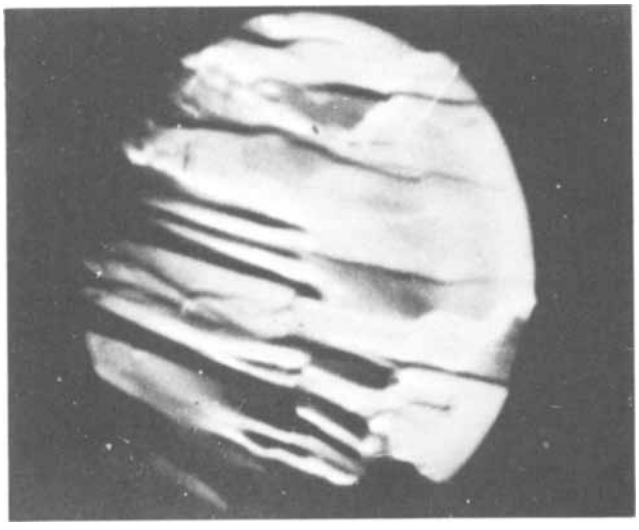

Fig. 6b. X-ray surface topography of the Si-Al_2O_3 interface

down). As these structures are visible only if a rapid cooling rate after epitaxy takes place, it may be concluded that the contrast is due to thermal stresses both in the silicon film and in the substrate.

Assessment of Crystalline Quality of Films

The x-ray diffraction method is a powerful technique for this aim, its interesting features are: (*i*) nondestructive, (*ii*) analysis of net planes in the film and not only of the surface structure, and (*iii*), semiquantitative: the diffracted intensities are comparative estimates of this quality.

Table II shows relative intensities of the Cu $K\alpha_1$ radiation, diffracted on various planes for six layers (D 1 to 6), deposited at different temperatures.

The (400) plane-reflection corresponds to the predominant (100) orientation of Si films. Regardless of the position of the x-ray spot (2 x 5 mm^2) on the surface, and whatever the sample under study, this intensity is constant and is the strongest one. It will be taken as a reference, with a value of 10^6 in arbitrary unit.

The (200) plane-reflection does not normally satisfy the Bragg condition, unless some planes are missing.

Table II. Relative intensities of x-ray diffracted beam

T_{epi}, °C →	1030	1055	1080	1105	1125	1150
Plane:						
(400)	10^6	10^6	10^6	10^6	10^6	10^6
(200)	1.6×10^3	10^4	1.2×10^5	<40*	1.4×10^4	400
(220)	2×10^3	200	<40	<40	2.8×10^3	200

* 40 is the (relative) detection limit.

This means that stacking faults are present in the layers and the given figures are indicative of their density. It must be noticed that the reported values are maximum ones, for the intensity varies from place to place.

The (220) plane-reflection, which has been reported by others (11) is due to an epitaxial defect orientation (110). Its intensity is uniform for a given film.

The stressed layers as shown in Fig. 6 were (110) mono-oriented.

In conclusion, the comparison of figures in Table II, gives an optimum temperature from both the point of view of stacking fault and of misorientation densities. This temperature is the same one as for mobility values.

Substrate Layer Chemical Interactions

That chemical interaction occurs at the initial stages of the heteroepitaxial process is ascertained with a simple experiment: the selective removal of the epitaxial layer leaves a disturbed Al_2O_3 surface (12) which is not observed solely due to an H_2 heat treatment.

It has generally been assumed that heteroepitaxy occurs in this specific case, by the way of a substitution for Al atoms by Si atoms (13). A reducing action of Si itself seems to have been demonstrated (14-16) in vacuum deposition. However, these authors agree that a very low supersaturation gives this etching effect, and this condition is not generally met in normal deposition conditions. In fact, this would not allow the reversible reaction

$$2Si + Al_2O_3 \rightleftarrows 2SiO + Al_2O$$

to take place but, the following reactions

$$Si + Al_2O_3 \rightleftarrows SiO_2 + Al_2O$$

$$SiO_2 + H_2 \rightleftarrows SiO + H_2O$$

involving less silicon but also the presence of H_2 would be favored due to the extremely dry atmosphere of the experimental conditions.

In any case, however, two consequences of this reactivity are expected: (*i*) the association between the epitaxial condition and the presence of Al in the layer, and (*ii*) the introduction of various Si-O bonds at the film-substrate interface, and probably in the layer itself, due to the high solubility of oxygen in silicon.

Infrared Spectroscopy

In order to check these two points, we have conducted experiments in infrared spectroscopy.

Infrared interferences in the range 1.5-7μ are used for layer thickness measurement. But absorption lines, characteristic of specific chemical bonds are well known. For Si-O bonds they lie in the 700-1400 cm^{-1} range, and for Si-Al the optically excited line is 560 cm^{-1} (0.067 eV) (see the special references at the end of this article).

The use of IR spectrometry however gives rise to two main difficulties with respect to: (*i*) selectivity to avoid interfering effects of the substrate, and (*ii*) sensitivity due to the small amount of Si, containing a low impurity concentration (from a chemical point of view).

The attenuated total reflection method in an arrangement first proposed by Harrick (17) using multiple reflections, has been devised for this purpose. The principle is given in Fig 7. A monochromatic light of the proper wavelength hits a prism in optical contact with the sample. With a suitable refractive index of this prism, a total reflection condition is obtained, and light transfers some part of its energy to a certain depth inside the absorbing medium (Si) (18).

Experimental difficulties, with the optical contact, the low transmittance (<20%), the need for a compensating circuit in the reference beam, add to the theoretical difficulties in the interpretation of the results.

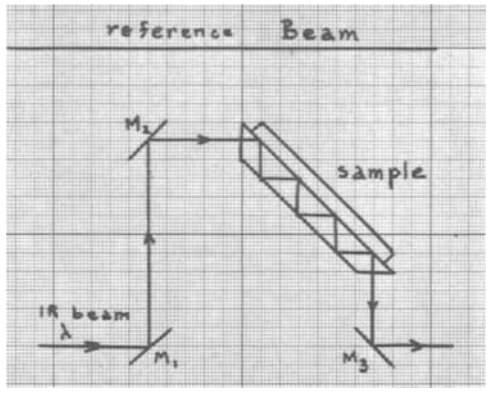

Fig. 7. Attenuated total reflection arrangement

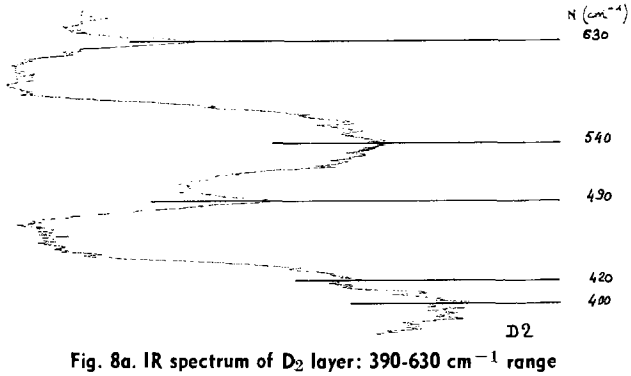

Fig. 8a. IR spectrum of D_2 layer: 390-630 cm^{-1} range

For example, difficulties inherent to the method are: (*a*) shift toward long wavelengths, (*b*) attenuation of short λ bands, and (*c*) reduction of spectrum contrast.

For the moment, only qualitative results are given in Table III. Some spectra are given for the D_2 and D_1 layers (Fig. 8 and 9) and an Al_2O_3 substrate (Fig. 10).

Discussion

1. The Si-Al bond is detected in all epitaxial layers, whatever the epi temperature process and therefore electrical type of the layer.

2. Various Si-O bonds are found, the nature and the amount of which depend on the epi temperature. No apparent continuous transition between amorphous poly- and monocrystalline forms is found when increasing T_{epi}. But for the same optimum T as before,

Table III. IR absorption spectra of Si films (10)

Wave No. cm^{-1} N	T_{epi}, °C: 1030	1055	1080	1105	1125	1150	Sub-strate	Reference
	Sample: D_1	D_2	D_3	D_4	D_5	D_6		
390	+	+	+	+	+	+	+	Al_2O_3
420-430		+	+		+		+	Al_2O_3
450-470				+	+	+		?
490	+	+	+		+	+	+	Al_2O_3
510			+	+			+	?
530-560	+	+		+	+	+		Al in Si
630	+	+	+	+	+	+		SiO (amorphous) at 620, but also Al_2O_3
700-720			+		+			
760	+	+						
780-820	+		+	+		+		α Quartz
865-895	+							SiO_2 (crystalline)
940		+		+	+			SiO_2 (vitreous)
985	+		+					
1015	+							Si-O
1050-1080		+	+		+	+		
1110-1160	+		+		+	+		α Quartz
1220-1280	+	+	+			+		α Quartz
1385						+		SiO_2 (polycrystalline)

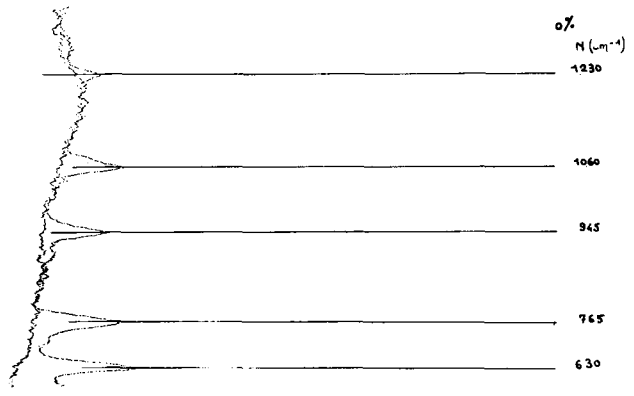

Fig. 8b. IR spectrum of D_2 layer: 630-1400 cm^{-1} range

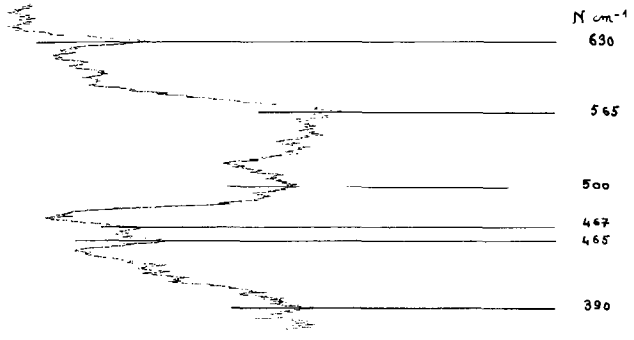

Fig. 9a. IR spectrum of D_4 layer: 390-630 cm^{-1} range

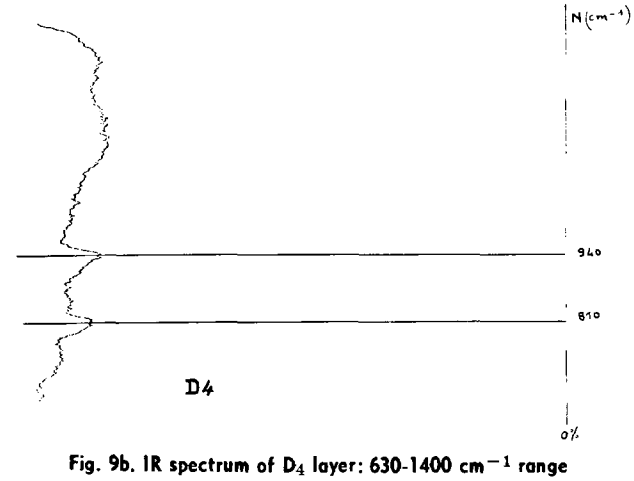

Fig. 9b. IR spectrum of D_4 layer: 630-1400 cm^{-1} range

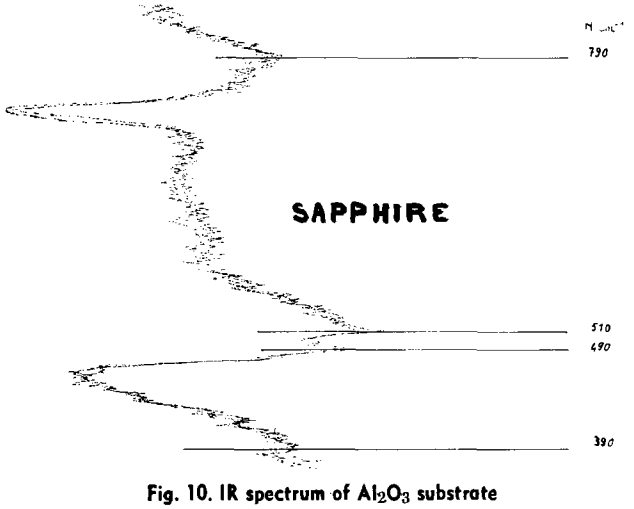

Fig. 10. IR spectrum of Al_2O_3 substrate

(*a*) the number of absorption lines is minimum, and (*b*) no amorphous SiO and SiO_2 quartz bonds are present in this layer.

Quartz as a separate phase might have its own orientation, quite independently of the substrate and as a result misorientation effects could be ascribed to its presence.

To resolve an objection against the preceding discussion, we have performed the same experiment on N/N^+ homoepitaxial silicon layers without finding any evidence of Si-O and Si-Al bonding. This removes the possible influence of impurities in silane itself.

Conclusion

Even in our optimized conditions, imperfections are always present in heteroepitaxial Si layers. The optimum range of epitaxial temperatures, around 1100°C, has been found for the majority carrier mobility and has been correlated to crystalline quality from x-ray diffraction methods. IR spectrometry has pointed out the outstanding influence of chemical bonds in explaining most of the layer properties. This conclusion does not mean that crystallographic defects are not of great importance, but it seems that their effects are essentially indirect, due to interaction between dislocations and impurities for example.

Acknowledgments

This work is partly supported by the French Délégation Générale à la Recherche Scientifique and by the French Centre National de la Recherche Scientifique. The author thanks these Administrations for permission to publish. I am grateful to Professor L. Neel for allowing this work and to Dr. B. K. Chakraverty for valuable discussions. It is a pleasure to thank Dr. G. Blet and his group of the L.R.B.G. of Thomson-Houston for his contribution to physical measurements. Without his help, I would not have so rapidly demonstrated the possibilities of infrared techniques in such studies. I also thank Mr. Jund of the C.S.F. laboratory for performing special electrical measurements.

Manuscript submitted June 18, 1969; revised manuscript received *ca.* Jan. 14, 1970. This was Recent News Paper 343 presented at the New York Meeting of the Society, May 4-9, 1969

Any discussion of this paper will appear in a Discussion Section to be published in the December 1970 JOURNAL.

REFERENCES

1. H. F. Matare, "Semiconductor Silicon," R. R. Haberecht and E. L. Kern Editors, Joint Symposium, New York Meeting of the Society, 249 (1969).
2. J. Mercier, 3rd International "Mikroelektronik Tagung," Münich (Nov. 1968), R. Oldenburg, Editor.
3. C. Jund and R. Poirier, *Solid State Electron.*, **9**, 315 (1966).
4. S. R. Hofstein, *I.E.E.E. Trans. Electron Devices*, **ED12**, 104 (1965).
5. F. P. Heiman, *ibid.*, **ED14**, 781 (1967).
6. J. Olmstead *et al.*, *ibid.*, **ED12**, 104 (1965).
7. D. J. Dumin and P. H Robinson, *This Journal*, **113**, 469 (1966).
8. J. Mercier, *Rev. Phys. Appl.*, **3**, 127 (1968).
9. F. P. Heiman, *Appl. Phys. Letters*, **11**, 132 (1967).
10. G. Blet, Private communication.
11. D. J. Dumin, *J. Appl. Phys.*, **38**, 1909 (1967).
12. R. Nolder and I. Cadoff, *Trans. Met. Soc.* AIME, **233**, 549 (1965).
13. J. L. Fraimbault, Thesis, Grenoble University, July 1967.
14. J. D. Filby, *This Journal*, **113**, 1085 (1966).
15. G. W. Cullen, Private communication.
16. S. J. Strepkoff, Thesis, Caen University, May 1968.
17. N. J. Harrick, *Phys. Rev. Letters*, **4**, 124 (1960).
18. J. Fahrenfort, *Spectrachim. Acta*, **17**, 698 (1961).
19. G. Blet, Unpublished results, PV No. 201.

Special References for the IR Study

N (cm^{-1})	*Reference*
390	Alumina (Sadtler—ref. Y 172 S) P. T. Sarjeant and R. Roy (*J. Appl. Phys.*, p. 4541, Oct. 1967) give 378
490	P. T. Sarjeant gives 440 and 485
540-560	Near 0.067 eV optical level Al/Si T. S. Moss, "Optical Properties of Semiconductors" [Butterworths, p. 123 (1961)], C. B. Collins [*Phys. Rev.*, **108**, 1049 (1957)], W. Kohn [*Solid State Phys.*, **5**, 257 (1957)], Hrostoroski and Kayser [*J. Phys. Chem. Solids*, **4**, 48, 315 (1958)]
584	P. T. Sarjeant and R. Roy [*J. Appl. Phys.*, p. 4541 (Oct. 1967)]
630	Sadtler, P. T. Sarjeant, and P. T. Sarjeant and R. Roy 620:SiO_2 amorphous (Desoto Chemical Coatings) L. C Afpemow and J. T. Vandeberg
800	B_3 line of α quartz (Plyler), E. K. Plyler [*Phys. Rev.* (2) **33**-1929-48]
777-828-809	Reflection lines α quartz B. D. Saskena [*Proc. Indian Acad. Sci.*, **A12**, 93-139 (1940); *ibid.*, **A22**, 379-182 (1945)]
790	SiO_2 Sadtler Y 1695
820	SiO_2 crystalline (Desoto Chemical Coatings 4663)
940	Silica glass (Gmelin 935) D. G. Drummond [*Nature*, **134**, 739 (1934)]
1010	SiO (Gmelin, p. 266, gives 1001) G. Hass and C. D. Salzberg [*J. Opt. Soc. Am.*, **44**, 181 (1954)]
1110	SiO_2 α quartz B_4 line (Gmelin and E. K. Plyler)
1260	2nd line twin β_4 α quartz Mean value 1220-1285
1375	Mean value 1320-1400 (Gmelin) A. H. Pfund and Silverman [*Phys. Rev.* (2), **39**, 64 (1932)], A. S. Barker, Jr., [*Phys. Rev.*, **132**, 1473 (1963)] studied the spectrum *vs.* orientation and surface state of alumina

The Role of Damage in the Annealing Characteristics of Ion Implanted Si

Billy L. Crowder

IBM T. J. Watson Research Center, Yorktown Heights, New York

ABSTRACT

Carrier concentration profiles are presented for Si which has been implanted with a low (3 x 10^{13} cm^{-2}), intermediate (3 x 10^{14} cm^{-2}) or high (8 x 10^{15} cm^{-2}) dose of 280 keV P^{31} ions at room temperature and subjected to a 30 min post implantation anneal in the temperature range 550°-850°C. The annealing behavior of these samples is correlated with the amount of damage produced by the room temperature implantation. If a continuous amorphous region is present, ions within this region become electrically active and uncompensated during the epitaxial recrystallization of the layer between 550° and 600°C. These results are generalized to provide a model for the annealing characteristics observed for room temperature and elevated temperature ion implanted Si layers.

Ion implantation doping of silicon at or near room temperature has been shown to produce gross structural defects consisting of amorphous (or highly disordered) regions along the path of the ion (1). Theoretical estimates of the spatial distribution of damage in "amorphous" Si have indicated that the average projected range of the ions is somewhat larger than the average damage depth and that the straggling in these quantities are comparable (2, 3). Recent experimental observations confirm these estimates for implantations of P, As, B, and Si into Si (4). Annealing is required to remove such gross lattice damage and to achieve the desired electrical activity of the implanted dopant. Previous investigations of the dose dependence of the annealing characteristics of Si doped with P or As by room temperature ion implantation have indicated a minimum in the number of carriers per implanted ion as a function of the number of implanted ions in the temperature range 500°-700°C (5, 6). The purpose of this investigation is to demonstrate that this minimum is due to three factors: (*i*) the damage distribution lies closer to the surface than the implanted ion distribution (4), (*ii*) the compensating centers remaining after the annealing of the damage clusters are thermally stable up to temperatures characteristic of diffusion processes in Si (4), and (*iii*) a continuous amorphous layer, if present, recrystallizes epitaxially onto the underlying substrate at 500°-600°C (1).

Experimental

Implantation was accomplished with a Cockcroft-Walton accelerator capable of operation to 300 kV. The P ions were obtained from gaseous PF_5. The ion beam was focused, mass analyzed magnetically, and electrostatically scanned uniformly over a 4 cm^2 area. The total dose was obtained by integrating the current from the samples. Dose rates were typically 1 μamp cm^{-2}. Accurate target alignment was not available since the beam sweep was over approximately $\pm$ 1°.

The Si substrates were <100> wafers cut from Czochralski-grown crystals, which were boron-doped and 1 ohm-cm resistivity. The substrates were lapped and chemically polished. Contact areas were diffused with As prior to implantation to facilitate good electrical contact to the implanted region.

The electrical evaluation of ion implanted layers was accomplished by Hall effect and sheet resistivity measurements on van der Pauw configurations in conjunction with removal of Si layers by anodic oxidation and HF stripping. This technique has been fully described by Mayer *et al* (7). The details of our experiments have been covered in a previous publication and will not be repeated here (8)

Experimental Results

Table I summarizes the electrical properties observed for Si implanted with 280 keV P^{31} ions at a low, inter-

Table I. Summary of electrical properties of Si implanted with 280 keV P^{31}

Dose (cm^{-2})	Annealing temperature[a] (°C)	Sheet resistivity (ohm/□)	n_s[b] (cm^{-2})	n_s[c] (cm^{-2})
3×10^{13}	550	2800	0.4×10^{13}	0.4×10^{13}
	600	680	1.6×10^{13}	2.4×10^{13}
	850	480	2.2×10^{13}	3.2×10^{13}
3×10^{14}	550	2400	0.05×10^{14}	0.07×10^{14}
	600	500	0.4×10^{14}	0.6×10^{14}
	700	175	1.3×10^{14}	2.0×10^{14}
	850	150	2.0×10^{14}	2.6×10^{14}
8×10^{15}	550	14	6.4×10^{15}	—
	600	13.6	6.7×10^{15}	7.6×10^{15}
	850	13.4	6.2×10^{15}	7.2×10^{15}

[a] Samples annealed after ion implantation for 30 min in a nitrogen atmosphere.
[b] Effective number of carriers cm^{-2} determined from the sheet Hall coefficient of the entire implanted layer.
[c] The total number of carriers cm^{-2} obtained by integrating over the distribution obtained by the anodic oxidation and HF stripping procedure in conjunction with sheet Hall coefficient and sheet resistivity measurements.

mediate, and high dose and subjected to annealing for 30 min at the temperature given in column 2. In column 4, the effective number of carriers cm^{-2} as determined from the sheet Hall coefficient of the implanted layer is presented. This number is less than the true number of carriers cm^{-2} (presented in column 5 and obtained from stripping experiments) due to the fact that it represents a weighted average which favors higher mobility carriers (7). The utilization of the implanted P ions (*i.e.*, the ratio of carriers observed to P implanted), presented in Table II, exhibits the minimum observed by previous authors (5, 6).

The depth distribution of carriers for Si implanted with P^{31} and annealed at various temperatures for 30 min are given in Fig. 1 (3×10^{13} P cm^{-2}), Fig. 2 (3×10^{14} cm^{-2}), and Fig. 3 (8×10^{15} cm^{-2}). In Fig. 3, the total P atom profile [obtained by neutron activation analysis as described in ref. (9)] is also shown. The carrier concentration after an 850°C anneal (not shown in the figure) corresponds closely to this total P profile [see ref. (8)]. It should be emphasized that no appreciable differences were observed between the total P profile obtained by neutron activation analysis for samples which were not annealed and samples which were annealed at 850°C for 30 min; *i.e.*, no appreciable diffusion occurs as a result of the annealing step (9). The low dose implant (Fig. 1) exhibits a large "tail" which is due to partially channeled P ions. As the damage produced during the course of the implantation is increased, channeling of P ions is eventually curtailed (10). Channeled P ions contribute less to the profile for the intermediate dose (3×10^{14} cm^{-2}, Fig. 2) than to that for the low dose. For the high dose implant, ions which have partially channeled represent only a small fraction of the implanted dose (Fig. 3).

The Hall mobility observed in Si implanted with 3×10^{14} cm^{-2} 280 keV P ions (see Fig. 2 for profiles) are presented in Fig. 4 as a function of the observed carrier concentration. After a high temperature anneal (850°C), the mobility of the implanted layer is comparable to that observed for bulk Si, as previously observed for well annealed ion implanted layers by Baron *et al.* (11). At lower annealing temperatures, where most of the implanted P ions are not electrically active and uncompensated, the observed mobility is lower for layers within approximately 0.5μ of the surface, presumably because of the presence of charged compensating species. Similar behavior was observed for the Hall mobility in the low dose implants (3×10^{13} cm^{-2}) in that the mobility after a 550°C anneal was lower than that observed in uncompensated bulk Si, for layers within 0.5μ of the surface.

The surface of the substrate implanted with 8×10^{15} P ions cm^{-2} exhibited the "milky" appearance characteristic of amorphous Si. The depth of this amorphous region was determined to be 0.5μ by interference fringes observed in the optical absorption spectrum of a similarly implanted wafer (12). The surface still exhibited the milky appearance after annealing at 550°C for 30 min, but the depth of the amorphous layer was only 0.1μ. This observation is consistent with the epitaxial regrowth onto the crystalline substrate previously reported (1). Annealing for 30 min at 600°C

Table II. Utilization factor for Si implanted with 280 keV P^{31}

Dose (cm^{-2})	Utilization factor[a] 550°C	600°C	700°C	850°C
3×10^{13}	0.13	0.8	~1[b]	1
3×10^{14}	0.02	0.2	0.7	0.9
8×10^{15}	~1[b]	1.0	~1[b]	0.9

[a] The utilization factor (defined as the total number of carriers observed to the number of P ions implanted) is given as a function of the temperature at which the sample was annealed for 30 min.
[b] These values are obtained from the effective number of carriers cm^{-2} (rather than the total number of carriers cm^{-2}), estimating the profile correction from the data given at temperatures for which wafers were stripped and profiled.

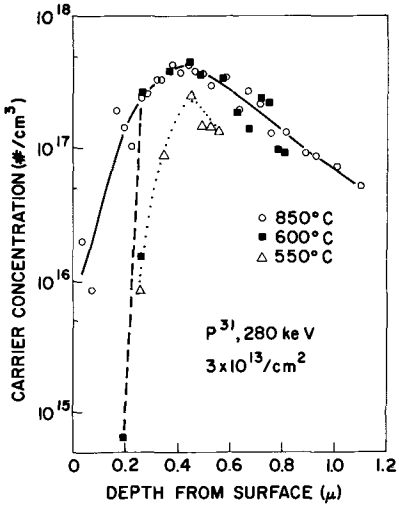

Fig. 1. Carrier concentration profile of <100> Si implanted with 3×10^{13} cm^{-2} 280 keV P^{31}. Samples were annealed for 30 min at 550°C (open triangles), 600°C (closed squares), or 850°C (open circles).

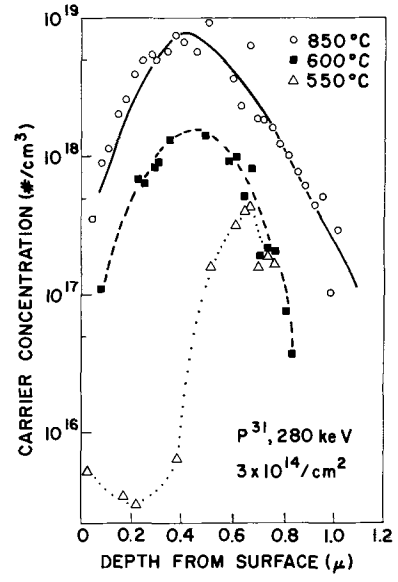

Fig. 2. Carrier concentration profile of <100> Si implanted with 3×10^{14} cm^{-2} 280 keV P^{31}. Samples were annealed for 30 min at 550°C (triangles), 600°C (squares), or 850°C (circles).

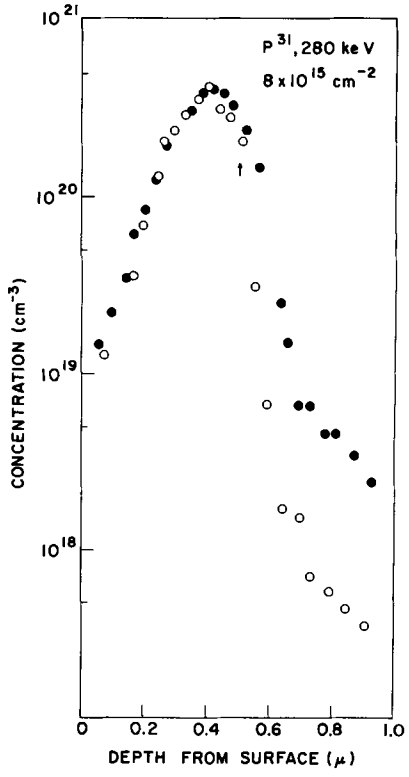

Fig. 3. Concentration profile of <100> Si implanted with 8 x 10^{15} cm^{-2} 280 keV P^{31}. Closed circles represent total P concentration as determined by neutron activation analysis. Open circles represent carrier concentration observed after a 30 min anneal at 600°C. Arrow marks depth of continuous amorphous region present after implantation and before annealing.

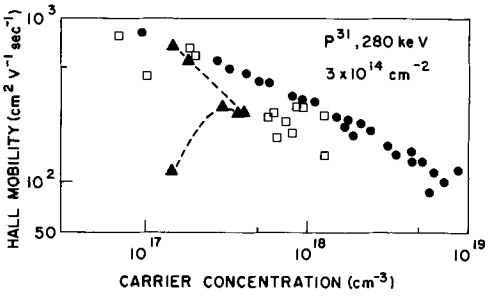

Fig. 4. Hall mobility of Si ion-implanted layers as a function of observed carrier concentration of the layer. Carrier concentration profiles of these samples are given in Fig. 3. Samples were annealed for 30 min at 550°C (triangles), 600°C (open squares), or 850°C (circles).

was sufficient to eliminate this milky appearance. These results may explain the higher annealing temperatures reported for P-implanted layers by Davies, who employed a four point probe (*i.e.*, contacting only the high resistance surface layer) to measure resistivity (13).

Discussion of Results

In a study of the electrical properties of Si implanted with 400 keV P ions, Gibson *et al.* observed essentially complete annealing at temperatures as low as 550°C for low dose (1 x 10^{13} cm^{-2}) and high dose (1 x 10^{15} cm^{-2}) implantations in a random direction (14). These authors did not report on intermediate doses, but the results of the previous section indicate that for such doses only a fraction of the implanted P ions are electrically active and uncompensated after a 550°C anneal for 30 min, in spite of the fact that the gross lattice damage produced by low dose implants anneals below 400°C (15).

Experimental investigations on the spatial distribution of damage in Si produced by P ions in the energy range 70-280 keV show that the ratio of the average damage depth (*i.e.*, the depth from the surface at which the peak in the damage distribution profile occurs) to the average projected range of the P ions (R_p) is between 0.6 and 0.7 [ref. (4)]. For 280 keV P implantations considered here, the maximum damage density occurs at 0.24-0.28μ. Since the damage increases with increasing ion dose, the amount of damage in the spatial region in which most of the P ions lie is much greater for a dose of 3 x 10^{14} cm^{-2} than for 3 x 10^{13} cm^{-2}. These factors are clearly reflected in both the profile of carrier concentration after a 550°C anneal in Fig. 1 and 2 and the low mobilities observed for carriers in this region of highest damage density. An analogous situation is observed for implantations conducted at temperatures above 400°C, where gross lattice damage anneals during implantation. Thermally stable defects remain after the annealing of isolated damage clusters, whether annealing occurs during or after implantation. The density of these defects in the vicinity of the ion distribution is higher for higher doses. Higher temperatures, at which diffusion processes can eliminate such compensating centers, are required to achieve a large fraction of the implanted ions electrically active and uncompensated.

In the case of a high dose which produces a continuous amorphous region, the annealing behavior is markedly different. After a 600°C anneal, the carrier concentration profile corresponds closely to the implanted P ion profile (Fig. 3) to a depth of 0.5μ and the Hall mobility is that expected for bulk Si of comparable doping. Beyond this point, the carrier concentration is markedly lower than the P concentration. Since most of the implanted P ions lie within 0.5μ of the surface, a 600°C anneal results in nearly complete utilization of the implanted P (Table I). The process of epitaxial regrowth of the amorphous region onto the underlying crystalline Si substrate provides a mechanism for the incorporation of most of the P atoms substitutionally and the elimination of any compensating defect centers. Annealing at 550°C also results in nearly complete utilization of the implanted P, even though the surface is still amorphous. As shown earlier, the depth of the amorphous region after a 550°C anneal is only 0.1 to 0.13μ so that most of the P ions lie within recrystallized Si. The diffused contact areas serve to make good electrical contact to this "buried" conducting region.

Similar results are obtained for high dose As implantations, as presented in Fig. 5. The depth of the continuous amorphous region was determined to be 0.35 to 0.36μ [stripping and visual observation; interference fringes (12)] as shown by the arrow. Arsenic ions which are within 0.35μ of the surface (*i.e.*, within the amorphous region) become electrically active and uncompensated after a 550°C anneal for 30 min.

In the high dose P and As implantations, the distribution of ions which lie just beyond the boundary of the amorphous layer produced by room temperature implantation are located in a region of relatively high damage density, thus requiring temperatures characteristic of diffusion processes in Si in order to become uncompensated and electrically active.

Summary

The fact that the damage distribution lies closer to the surface than the ion distribution giving rise to the damage has been shown to have interesting consequences in the low temperature annealing behavior of room temperature implantations of P into Si. These results can be generalized as follows:

1. At a sufficiently low dose, the damage density is so low in the region where the bulk of the ion distribution lies that a large fraction of the implanted species

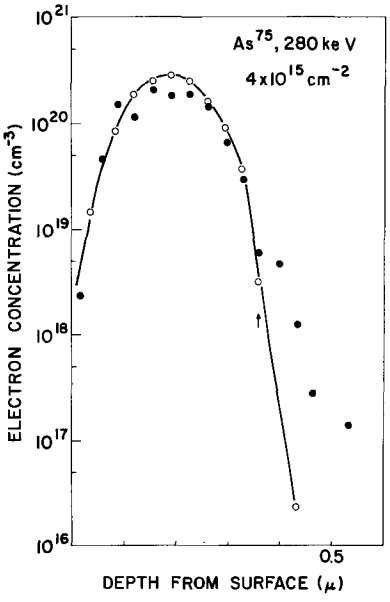

Fig. 5. Carrier concentration profile of <100> Si implanted with As^{75}, 280 keV, 4 x 10^{15} cm^{-2}. Samples were annealed for 30 min at 550°C (open circles) or 800°C (closed circles). Arrow marks depth of continuous amorphous Si region present after implantation and before annealing.

are electrically active and uncompensated after a low temperature anneal, as observed, *e.g.*, for P implants by Gibson *et al.* (14) and for low dose B implants by Seidel and MacRae (16).

2. As the dose is increased, the amount of damage in the region occupied by the ion distribution increases. A fraction of the damage centers which remain after the gross lattice damage has annealed are thermally stable to temperatures characteristic of those at which diffusion processes can occur (4). When this fraction of compensating defects is comparable to or exceeds the ion concentration, high temperatures are required to achieve a high degree of electrical activity in the implanted layer. These observations apply for the situation where annealing is accomplished during implantation as well as low temperature implantations followed by a post implantation anneal. Such behavior has been noted for B, P, and As implantations by a number of authors [see, *e.g.*, ref. (9) and (16)].

3. If the dose is sufficiently high and the temperature sufficiently low to allow the formation of a continuous amorphous region overlapping the ion distribution, the epitaxial regrowth of this amorphous region "sweeps out" the compensating defects and the ions within this regrown region are electrically active and uncompensated. At a given temperature, light ions require a higher dose to produce this amorphous layer than heavy ions, as shown, *e.g.*, for room temperature implantations of P or As (6). For a given ion, lower doses are required at lower temperatures, as demonstrated for B implantations into Si by Davies (13). The required dose may approach a limiting value at sufficiently low temperatures.

Acknowledgments

The author gratefully acknowledges the capable technical assistance of W. N. Hammer, N. A. Penebre, and R. A. Fiorio.

Manuscript submitted Oct. 13, 1969; revised manuscript received *ca.* Dec. 26, 1969.

Any discussion of this paper will appear in a Discussion Section to be published in the December 1970 JOURNAL.

REFERENCES

1. R. S. Nelson and D. J. Mazey, "International Conference on Applications of Ion Beams to Semiconductor Technology," 1967, Grenoble, France, p. 337.
2. P. Sigmund and J. Sanders, *ibid.*, p. 215.
3. P. V. Pavlov, D. I. Tetel'baum, E. I. Zorin, and V. I. Aleksev, *Soviet Phys.-Solid State (English Transl.)*, **8**, 2141 (1967).
4. B. L. Crowder, To be published.
5. V. K. Vasil'ev, E. I. Zorin, P. V. Pavlov, and D. I. Tetel'baum, *Soviet Phys-Solid State (English Transl.)*, **9**, 1503 (1968).
6. B. L. Crowder and F. F. Morehead, *Appl. Phys. Letters*, **14**, 313 (1969).
7. J. W. Mayer, O. J. Marsh, G. A. Shifrin, and R. Baron, *Can. J. Phys.*, **45**, 4073 (1967).
8. B. L. Crowder and J. M. Fairfield, *This Journal*, **117**, 363 (1970).
9. J. M. Fairfield and B. L. Crowder, *Trans. Met. Soc. AIME*, **245**, 469 (1969).
10. K. E. Manchester, *This Journal*, **115**, 656 (1968).
11. R. Baron, G. A. Shifrin, O. J. Marsh, and J. W. Mayer, *J. Appl. Phys.*, **40**, 3702 (1969).
12. B. L. Crowder, R. S. Title, M. H. Brodsky, and G. D. Pettit, *Appl. Phys. Letters*, 16 (1970).
13. E. Davies, *Appl. Phys. Letters*, **14**, 227 (1969).
14. W. M. Gibson, F. W. Martin, R. Stensgaard, F. Palmgren Jensen, N. I. Meyer, G. Galster, A. Johansen, and J. S. Olsen, *Can. J. Phys.*, **46**, 675 (1968).
15. J. A. Davies, J. Denhertog, L. Eriksson, and J. W. Mayer, *ibid.*, **45**, 4053 (1967).

Ionic Instabilities in Pyrolytically Deposited SiO_2 Films

P. M. Dunbar[1] and J. R. Hauser

North Carolina State University, Raleigh, North Carolina

ABSTRACT

Forms of ionic instability in pyrolytic SiO_2 layers are investigated through movements of the flat band voltage. The films were in the thickness range of 1000Å, deposited at 725°C, and annealed at 800°C in a steam atmosphere. As deposited, the films exhibited the presence of both positive and negative charge. This charge was also found to be highly mobile. The annealed films exhibited only positive ionic charge but high flat band voltages with instability present only after long term bias.

The process of pyrolytic deposition has become quite widely used in semiconductor device fabrication. Basically, the process concerns the deposition of thin insulator films such as SiO_2 for both diffusion and electrical insulation. Some of the initial work with this process was performed by Jordan (1) in his attempt to apply the process as a suitable method for diffusion masking on germanium. Klerer (2, 3) expanded on Jordan's work and studied the chemical

[1] Present address: Howard University, Washington, D. C. 20001.

reactions involved in a pyrolytic deposition. Other evaluations showed densified pyrolytic films to be quite comparable to thermally grown SiO_2. However, ionic instability usually occurred in the films. These instabilities have been noted briefly (4), and this present work expands on this problem.

Experimental Techniques and Results

The apparatus used in this work was similar to that used by Jordan (1). A diagram of the complete system is shown in Fig. 1. This system allows the three basic operations of purging, deposition, and annealing in a steam atmosphere. The nitrogen purge takes place prior to any deposition and while the furnace is heating or cooling. When the slice obtained proper temperature, the deposition was initiated by introducing nitrogen into the bubbler which contains liquid tetraethyoxysilane. The tetraethyoxysilane was standard reagent grade material. This flow rate and the purge rate can be controlled by flowmeters 1 and 2. The bubbler was held at 32°C in order to regulate the absorption rate of the tetraethyoxysilane into the nitrogen carrier. This allowed an improvement in repeatability by excluding room temperature as a process parameter. The substrates used were n-type silicon slices. The resistivity was in the 10 ohm-cm range, and the crystal orientation was [100]. The slices were approximately 3 cm in length by 1.5 cm in width.

The substrates were stored in methyl alcohol prior to deposition, and placed wet into a 200°C furnace at the outset of a run. The system was then purged with a nitrogen flow rate of 1.0 l/min for about 15 min. When proper temperature was reached, deposition was begun by diverting 0.5 l/min of nitrogen through the tetraethyoxysilane while allowing 0.5 l/min of nitrogen to flow freely into the furnace, giving a total deposition flow rate of 1.0 l/min. This combination yielded the best results, because a higher or lower rate through the bubbler detracted from the uniformity of the films. At the end of the desired deposition time, the bubbler flow was cut off and the purge flow of 1.0 l/min was returned. After allowing 2 min for the system to clear of tetraethyoxysilane vapors, the power to the furnace was shut off. The slice was then removed after the temperature dropped to 300°C. Deposition temperatures were in the 700°C range with deposition rates of 60 to 160 Å/min. This range of deposition rates had no detectable effect on the stability results.

The resulting films were clear in appearance and the thicknesses, estimated from the film color, were in the 1000Å range. Although the films suffered from a thickness nonuniformity in the range of 20%, the region over which metal was evaporated had no more than a 5% variation. The annealed films were processed identically except that a 15 min steam treatment at 800°C was included.

To fabricate the capacitors, 17 mil diameter dots were evaporated onto the slice. Both gold and aluminum were used, but the metal thickness was 4000Å throughout. Electrical contact was made to these devices with a probing technique.

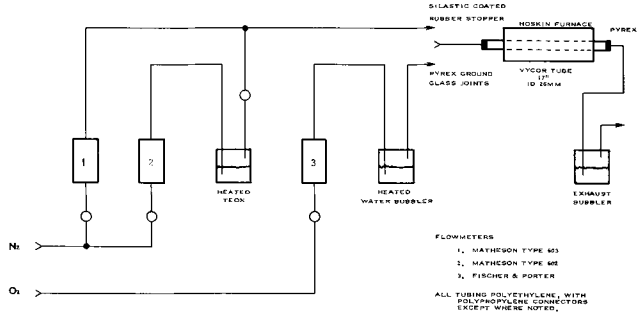

Fig. 1. Apparatus for pyrolytic deposition of thin insulating films

Evaluation

Studies of these devices showed the steam annealed films to be quite similar to thermal oxides with respect to dielectric strength and structural qualities such as pinhole characteristics. Although the unannealed devices had both high leakage currents and pinhole counts, the breakdown strength of all the devices were in the 10^7 V/cm range. The relative permeativity values were quite scattered, but generally were 20% higher than in thermal oxides.

It is known that pyrolytic oxides obtained from tetraethyoxysilane can contain considerable concentrations of impurities which can dope the silicon either p- or n-type. No doping effect on the silicon was noted for the temperatures and times used in the present work. The possible presence of a p-type layer was checked by etching the oxide from several wafers after testing and checking for the conductivity type which remained n-type. Similar deposits on p-type wafers of about 10 ohm·cm resistivity have also failed to show the presence of a thin n-type layer due to diffusion from the pyrolytic oxide during the temperatures and time employed in this work.

The apparatus used to determine the capacitance *vs.* voltage characteristics involved a standard capacitance bridge outfitted so that the voltage could be automatically swept across the device. A block diagram of this system is shown in Fig. 2. A 50 msec ramp voltage from the oscilloscope was used to sweep the device voltage. The ramp was 50V in height but the beginning and end points could be adjusted by means of the series bias. The scope could be triggered externally or allowed to free run, depending on the mode of sweep voltage desired. Comparisons of the curve shifts were made by photographs of the scope face.

The initial curves were obtained by single sweeps of the ramp voltage across the device. After the initial curve was obtained, the ramp voltage was allowed to free run across the device for several thousand cycles to detect any rapid movements of the curve. The bridge was then disconnected, and a 9V d-c bias was connected across the device for a 4-hr period with the metal positive. At the end of this time, the battery was disconnected and the bridge reconnected, and another "initial" curve was obtained. As before, the ramp was then set on free run to detect any rapid changes. This was then repeated for the opposite polarity for the 4-hr bias.

The need to bias the ramp voltage resulted from the need to sweep the device voltage in a bipolar method. This bias, however, resulted in a d-c component of voltage placed across the device whenever a sweep was made. Although this d-c component had no detectable effect in the single sweep mode, the effect was quite appreciable during the free run time. The voltages applied to the devices during the free running mode are shown in Fig. 3. Typical initial curves for both types of devices are shown in Fig. 4 and 5. The flat band voltage for this oxide thickness and substrate doping occurred when C/C_{max} was in the order of 0.7. These curves depict the movements somewhat typical of unstable oxides. Note however, that the unannealed films exhibited positive flat band voltages after negative stress. This indicates the presence of a fairly large negative charge density in the layer.

Note also, that after annealing in a steam atmosphere the effect of this negative charge could also explain the low flat band voltage of the unannealed films

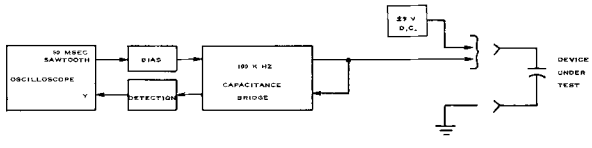

Fig. 2. Capacitance *vs.* voltage apparatus

A. Ramp voltage employed after negative stress.

B. Ramp voltage employed after positive stress.

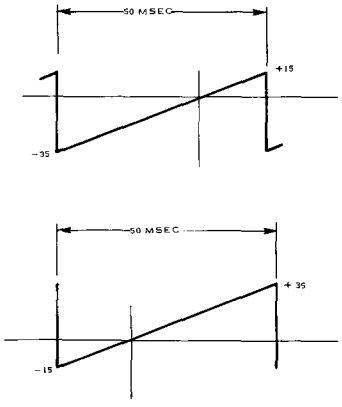

Fig. 3. Sweep voltage

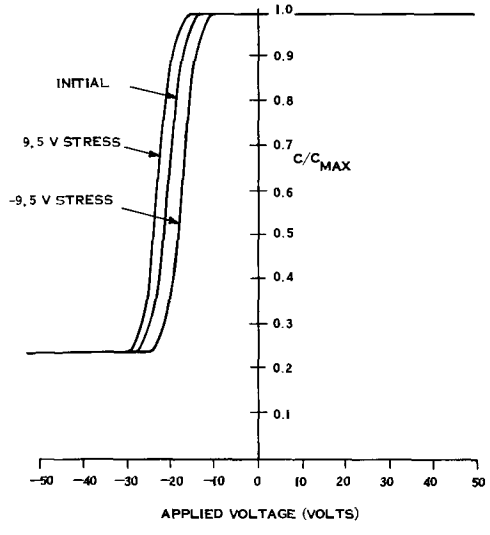

Fig. 4. Capacitance vs. voltage for annealed devices before and after stress.

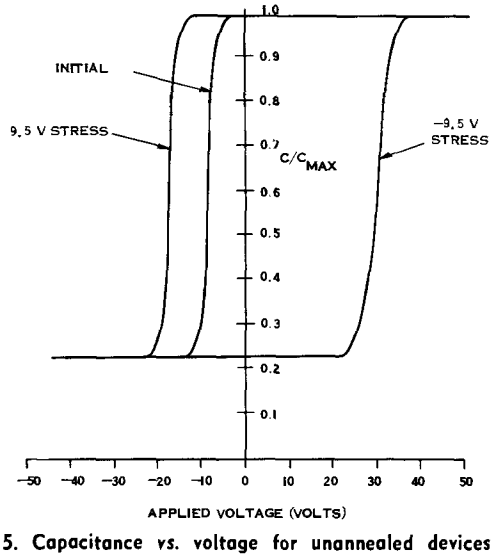

Fig. 5. Capacitance vs. voltage for unannealed devices before and after stress.

as compared to the annealed films, since the negative charge would counteract any positive charge present in the layer, thus lowering the flat band voltage. Since the annealing seems to eradicate these charge centers, the counteracting effect would not be present in the annealed films, allowing the now free positive charge to raise the flat band voltage. The positive charge and its related high flat band voltage could, of course, have been caused by a contamination entering at some point in the process; however, the apparent nulling of the negative charge by annealing suggests that this negative charge is inherent in the unannealed pyrolytically deposited SiO_2 films.

Another major difference between the annealed and unannealed devices was exhibited when the sweep voltage was set to free run in order to detect any rapid movements. The unannealed devices, as shown in Fig. 6 and 7, exhibited a very rapid flat band movement, indicative of a highly mobile charge species. Two factors indicate that the mobile charge causing this is the negative charge. Primarily, this type of rapid hysteresis was not present after annealing. This, when coupled to the indication that the negative charge was eliminated by annealing points to this charge as the cause of the rapid shifts.

A close examination of the rapid instability also indicates that negative charges can explain the rapid shifts in flat band voltage. Note that after positive stress, the positive charge would be near the SiO_2-Si interface, having a more pronounced effect in V_{FB} than the negative charges which are at the SiO_2-metal interface. The d-c component of the free running sweep, then would move the negative charges to the SiO_2-Si interface but the positive charges would remain comparatively unmoved, thus counteracting the negative charge movement, slowing down any hysteresis effects. The case of negative stress points this out in somewhat more dramatic fashion. After stress, the positive charge is now at the metal-SiO_2 interface,

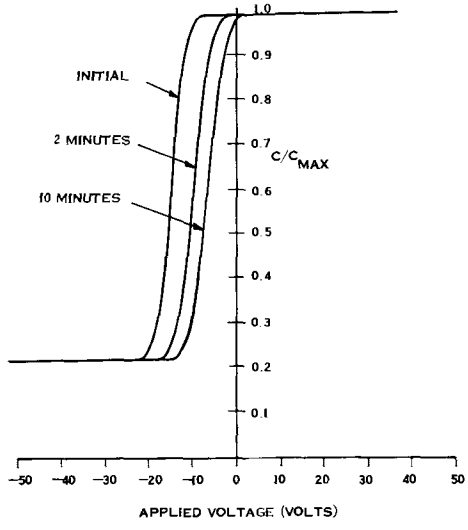

Fig. 6. Capacitance vs. voltage showing rapid charge movement after positive stress in unannealed devices.

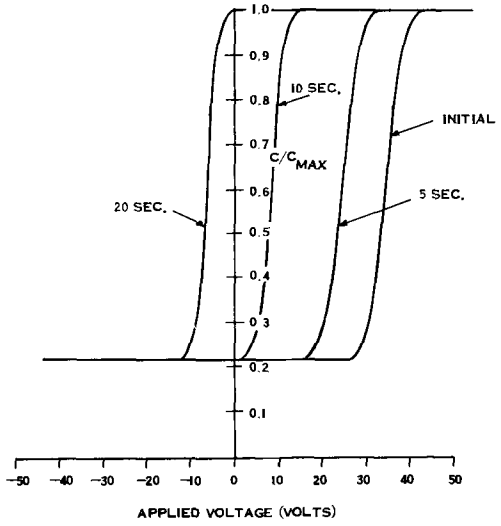

Fig. 7. Capacitance vs. voltage showing rapid charge movement after negative stress in unannealed devices.

where it has little effect on V_{FB}, and the negative charge, now at the SiO_2-Si interface, is the controlling factor. So, when the free run component occurs, this negative charge now moves rapidly to the metal-SiO_2 interface, lowering the V_{FB} just as rapidly, causing the rapid movement as seen in Fig. 7.

These results, however, were somewhat scattered. Although the characteristics shown in Fig. 6 and 7 were quite typical, the speed of the movements varied widely, indicating a somewhat unpredictable mobility of the negative charge. Another factor of note is that these rapid changes did not occur until after the devices were put under a long term bias.

Summary and Conclusions

Stability studies showed the films to be unstable with high flat band voltage as compared to good thermally grown oxides. Both the annealed and unannealed films exhibited the effects of charge movement indicative of positive ionic charge in the oxide layer. The unannealed devices indicated the presence of both positive and negative charge in the oxide layer.

The presence of the negative total charge in the oxide differs from that of thermal oxides where positive ionic charges are observed. The origin of the negative charge can only be speculated on at this point. Ionic instabilities in SiO_2 have been studied in considerable detail (5, 6). The rapid movement of the negative charges in the present study would require, however, a much larger mobility than has previously been reported for ions. Hofstein (7) has reported on a hydrogen ion trapping instability in SiO_2 which gives times more consistent with the rapid shifts observed in this work. The hydrogen ion, however, is a positive charge whereas the present observations indicate a rapid movement of negative charges. The negative charges may in fact be just electronic motion within the pyrolytic SiO_2 layer. A thin higher quality thermal oxide at the silicon interface could prevent the electrons from flowing out of the pyrolytic oxide into the silicon, resulting in their accumulation at the pyrolytic-thermal oxide interface.

The improvement in the C-V shifts following annealing in a stream atmosphere appear to be due largely to the elimination of the rapid negative charge movements within the oxide. The steam annealing process can have two effects on the insulating layer. Previous work (2-4) has indicated this process results in a densification of the pyrolytic oxide films. Also, there is likely some increase in the thickness of the thermal oxide between the silicon and the pyrolytic oxide. Both of these processes may contribute to the improved electrical properties following annealing.

Manuscript received May 3, 1969; revised manuscript received ca. Jan. 26, 1970.

Any discussion of this paper will appear in a Discussion Section to be published in the December 1970 JOURNAL.

REFERENCES

1. E. L. Jordan, *This Journal*, **108**, 478 (1961).
2. J. Klerer, *ibid.*, **108**, 1070 (1961).
3. J. Klerer, *ibid.*, **112**, 503 (1965).
4. J. Oroschnik and J. Kraitchman, *ibid.*, **115**, 649 (1968).
5. W. Leighton, *IEEE Proc.*, **55**, 214 (1967).
6. E. H. Snow *et al.*, *J. Appl. Phys.* **36**, 1664 (1965).
7. S. R. Hofstein, *IEEE Trans. Electron Devices*, **ED-13**, 222 (1966).

Water Contamination in Thermal Oxide on Silicon

G. L. Holmberg,[1] A. B. Kuper,[2] and F. D. Miraldi

School of Engineering, Case Western Reserve University, Cleveland, Ohio

ABSTRACT

Wet-grown, baked 5400Å films were controllably hydrated in tritiated-water vapor under conditions approximating device operation (50°-250°C, 0.25-8 hr, 25-400 Torr water vapor pressure). Fast penetration and fast outdiffusion suggest a micropore diffusion mechanism. This conclusion is supported by a low diffusion activation energy (0.3 eV) and exponential profiles in the bulk oxide. Strong surface peaking of the hydrogen tracer in both indiffusion and outdiffusion is attributed to surface energy lowering (Gibbs effect). "Water" under these conditions gave negligible MOS ΔQ_{ox} or ΔQ_{is} even with a hydrogen concentration of 5×10^{18} cm^{-3} at the silicon. Sodium contamination gave an order higher water entry rate. Water, likewise, increased sodium entry rate and charge production by the sodium.

Water has long been considered a serious contaminant in oxide-passivated silicon planar devices. Since it is not possible to eliminate it in device manufacture or, except by hermetic sealing, in device use, it is desirable to study its effects under likely contamination conditions.

In previous studies (1, 2), fused silica was hydrated at high temperatures (600°-1200°C) to measure the diffusion coefficient and the activation energy for water diffusion in silica. The same studies indicated that water interacted with bridging oxygens to form silanol (Si-OH) groups on entering the silica.

Oxides on silicon have been grown in tritiated steam at 1000°C (3, 4). The diffusion coefficient (3, 4) and activation energy (3) determined from bakeout were comparable to those determined for water diffusion in fused silica, but bakeout data were not taken below 500°C. Only one study (5) has produced a hydrogen profile associated with water contamination; the sample was contaminated by boiling in tritiated water.

Electrical effects of water contamination in thermal oxide on silicon have been studied. Water has been shown (6) to promote channel conduction on p-type surfaces. Water under certain conditions is believed (5, 7) to act as a positively charged species, probably due to formation of H^+ ions. Water also acts to annihilate interface states (8-10) and is known to increase dielectric loss in bulk silica (11). Water introduced during oxidation appears to have no charge associated with it as evidenced by the fact that the hydrogen in

[1] Present address: 3508 Wilson St., Fairfax, Virginia 22030.
[2] On leave 1969-1970 to Electrical Engineering, Technion, Haifa, Israel.

tritiated-steam grown oxides (3, 4) did not redistribute under bias-temperature stress.

Since data were not available on the diffusion of water in silica below 600°C, we had to extrapolate fused-silica data to the lower temperatures of interest in our work. The validity of the extrapolation from 600°C is questionable; in addition, significant differences exist between the oxide and bulk silica. The oxide is very thin and therefore may be dominated by surface effects. It is under large compressive stress, contains concentration gradients of silicon and oxygen, and has a different thermal history than the fused silica; in particular, the oxide film is formed below its softening point. Evidence recently summarized (12) also suggests a micropore structure in the oxide.

A number of experiments have demonstrated the interaction of water with sodium in silica. Increased sodium transport in the presence of water (13) and increased wet oxidation rates in the presence of sodium (12) have been shown. Sodium is thought to release hydrogen (5) in the oxide. Glass corrosion studies indicate (14) that water can release sodium in silica.

In our study, oxides were hydrated in tritiated-water vapor under controlled conditions approximating device operating conditions. Sets of hydrogen profiles were developed with time, temperature, and water vapor pressure as parameters. Outdiffusion and other experiments further characterized the hydration. Models are presented for the hydration process. MOS measurements of charge and interface-state density were made to assess the electrical effects of the water.

Radioactive sodium and water were diffused together in some samples; profiles and MOS electrical effects were measured to determine interactions between the two diffusants.

Experimental

Samples were 1 or 10 ohm-cm, n-type, {111}-oriented silicon. They were wet-oxygen oxidized in a quartz-tube furnace at 1200°C to a thickness of 5400Å, then baked for 30 min at 1000°C in dry nitrogen.

Hydrations were carried out in the apparatus shown in Fig. 1. The sample cell was a solid aluminum cylinder into the top of which several slots had been milled; the remainder of the apparatus was stainless steel, sealed to the cell by a Viton O-ring. Oxidized wafers were dropped into the slots and held in good thermal contact with the aluminum by means of Teflon strips at their edges. The source vial contained 0.5 cc of tritiated water with specific activity of approximately 250 mc/g. The tubing and valves were wrapped with heating tape and kept well above the temperature of the source vial to prevent water condensation anywhere except in the source vial.

The tritiated-water source vial was valved off while loading the samples. The source vial was then cooled with liquid nitrogen, the source valve opened, and the apparatus evacuated with a mechanical forepump. After evacuation, the source valve was closed, the cell and samples brought to temperature in a thermostated oven, and the source vial thermostated at a temperature corresponding to the desired water vapor pressure.

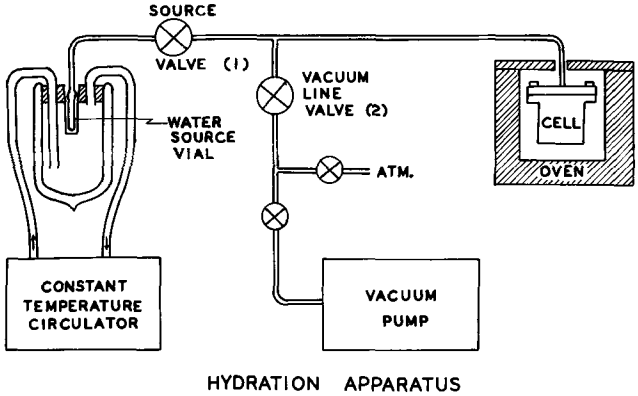

HYDRATION APPARATUS

Fig. 1. Apparatus for tritiated-water hydrations

When source and samples were at the proper temperature, the vacuum line valve was closed, the source valve opened, and timing started. At the end of the desired hydration time, these operations were reversed to recondense the water into the source vial and to remove the samples.

An experiment was done to test pressure equilibration. With a glass plate in place of the sample cell, it was found that water immediately condensed onto the glass on opening the source valve. A calculation confirmed that pressure in the apparatus should equilibrate within a second after opening the source valve. Thus we felt it unnecessary to have a manometer in the system, and pressures are based on source vial temperature.

The apparatus allowed close control of hydration conditions. Accuracy and precision of temperature were within 1°C, pressure was within 1%, and time was accurate within a few seconds. Also, the cell allowed several samples to be loaded simultaneously and exposed to identical hydration conditions.

Samples were etched in dilute HF and the etchants were liquid-scintillation counted. Since the efficiency of liquid scintillation counting is degraded by large amounts of aqueous material in the solution, an apparatus was built to minimize etchant volume. The apparatus allowed etching with 0.5 cc of acid and rinsing in 1 cc of water with good reproducibility.

Samples were washed in water before sectioning to exchange off adsorbed tritiated water from the surface and thus to avoid contaminating the first section with adsorbed activity. Samples were also washed between sections to avoid cross-contamination between adjacent sections.

The etchant was neutralized with calcium hydroxide, then solubilized with a xylene-PBD mixture by means of Beckman Biosolve BS-3 solubilizer. Counting was done in a Picker Ansitron II liquid scintillation counter. Counting efficiency was approximately 25% and background about 25 counts per minute. Sufficiently long counts were taken to keep one-sigma counting errors below 5%.

Counting efficiency was determined by counting a standard along with the etchants. The standard had the same chemical composition as the unknowns, and its activity was known to ±3%. Accuracy of relative concentrations (for profile shapes or for comparisons of profiles) was equal to the 5% counting error. However, uncertainty in the specific activity of the tritiated water in the source vial limited accuracy of absolute hydrogen concentrations to about 20%.

Sodium-water interactions were studied with a $Na^{22}Cl$ tracer. Samples were either baked or else equilibrated with a wet ambient (nitrogen, 95°C dew point) at 800°C. They were next contaminated by dipping them into a methanol solution of the tracer and air drying them. The samples were then sandwiched between two bare silicon wafers to minimize sodium evaporation during the diffusion and were diffused in a tube furnace. The dry (baked) oxides were diffused in a dry nitrogen ambient and the wet oxides in a wet (95°C dew point) nitrogen ambient.

The sodium-contaminated samples were sectioned in dilute HF. The etchant was gamma scintillation counted with a 4 x 4 in. NaI(Tl) crystal and a multichannel analyzer. A counting standard (±3%) was again used.

Some samples were diffused both with $Na^{22}Cl$ and with tritiated water. These samples were etched like other hydrated samples and liquid scintillation counted. Two analysis channels were set up on the liquid scintillation counter to count the two isotopes in the presence of each other. Counting efficiencies and the interferences of the isotopes on each other were determined from counting standards. Sodium concentrations were also checked by gamma scintillation counting.

Aluminum dots were evaporated onto some of the samples, and 1-MHz C-V curves were run. Room temperature flatband voltage was used to measure fixed charge in the oxide. Interface state density was measured by the Gray-Brown (15) technique of determining the shift in flatband voltage between room temperature and liquid nitrogen temperature.

Hydration Results

A typical hydration profile is shown in Fig. 2. The profile is made up of three regions: at the air interface is a sharp spike of hydrogen; in the bulk oxide the profile is rather flat; at the silicon interface there is a slight peak with a dip just before the peak. The spike at the air interface is present in all profiles, the peak and dip at the silicon only in some profiles. This profile and others to be presented are simply drawn through the data points and represent no theoretical fit.

Figure 3 shows the time development of the hydration profile at constant temperature and pressure (hydration time was the time during which tritiated water vapor was actually in contact with the samples). The spike at the air interface is present in all profiles. In the bulk oxide the profile is roughly exponential (*i.e.*, linear on the semilog plot). The effect of increasing hydration time is to fill and flatten the profile in the bulk oxide. Concentration in the oxide near the air interface increases with increasing hydration time, but penetration of the spike remains roughly constant.

For 15-min hydrations, not shown in the figure, the hydration profile is nonreproducible and shows anomalous peaking near the silicon. Even for the profiles shown, however, the penetration is much faster than expected. A diffusion coefficient estimated from the profiles in Fig. 3 is 10^{-13} cm²/sec, more than an order larger than estimated by extrapolating fused silica hydration data (1) from 600°C.

The effect of hydration temperature at constant time and pressure is shown in Fig. 4. The effect of increasing hydration temperature is similar to the effect of increasing hydration time. The profile fills and flattens in the bulk, and the surface spike rises in amplitude at constant penetration.

The anomalous peaking in the 50° and 100°C profiles is similar to that at short times. It appears that there is some defect in the oxide which interacts with

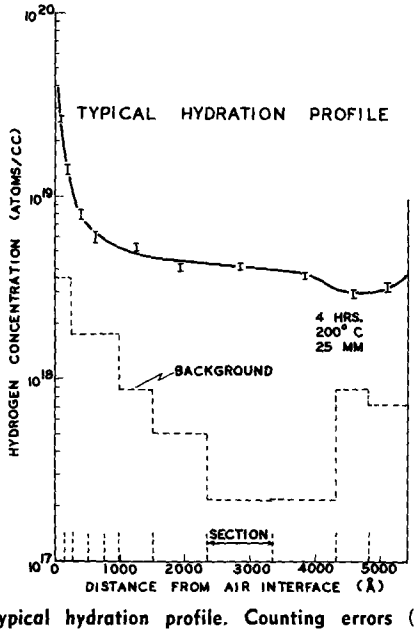

Fig. 2. Typical hydration profile. Counting errors ($\pm 1\sigma$) are shown by error bars. Concentration equivalent of counting background is represented by dashed curve and sectioning by vertical dashed lines. Reproducibility on individual data points was about ±10% from sample to sample.

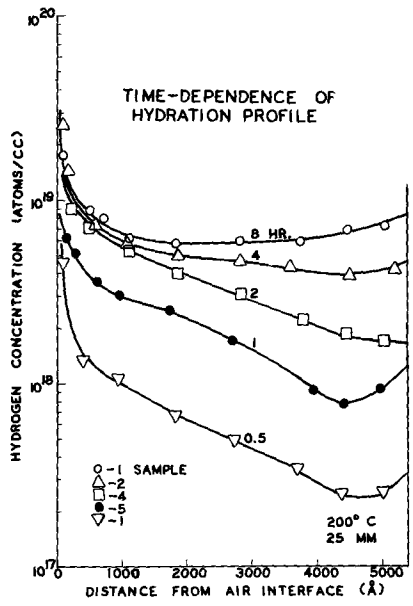

Fig. 3. Time development of hydration profile at constant temperature and pressure. Profiles are in reasonable agreement with Hofstein's (5) profile for a dry oxide. Data are averages of one or more samples, as indicated.

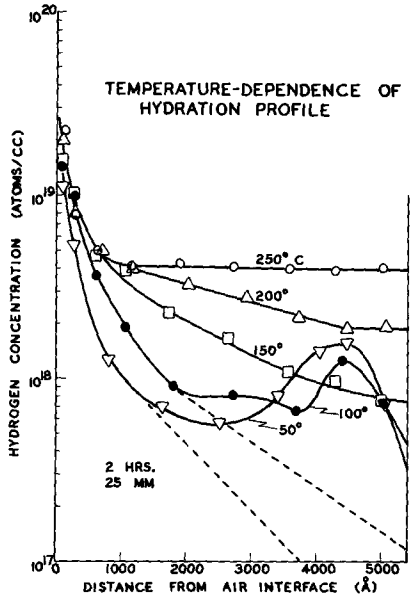

Fig. 4. Effect of temperature on hydration profile at constant time and pressure. Anomalous peaking at low temperature is similar to that seen for short times. Activation energy for diffusion was about 0.3 eV.

the "water" and then saturates. At higher temperatures (or longer times) the hydrogen profile levels itself out.

For error-function profiles, either the total hydrogen in the oxide (N) or the intercept (x) of the profile with a given concentration level should have the same temperature dependence as $D^{1/2}$ (D is the diffusion coefficient). Although the profiles are not actually error functions, Arrhenius plots were made for N and x (from Fig. 4) and the slope used to approximate the energy dependence of $D^{1/2}$. The former method estimated an activation energy of 0.25 eV for D (0.13 eV for $D^{1/2}$), and the latter gave 0.3 eV.

An activation energy of 0.3 eV is less than half of the activation energies found for fused silica hydration (1, 2), steam oxidation (16), or wet-oxygen oxidation (17) of silicon, or for outdiffusion of water from steam-grown oxides (3). The low activation energy suggests that hydration rates could be appreciable at room temperature.

The effect of hydration pressure is shown in Fig. 5. Increase in pressure shifts the hydration profile uniformly to higher concentrations. Concentration of hydrogen in the oxide varies as the square root of hydration pressure, as expected from fused silica hydration data (1, 2), which indicates the breakup of the water molecule into two independently diffusing fragments on entering the oxide. The square root pressure dependence throughout the oxide implies that little of the hydrogen tracer exists as water molecules in the oxide.

Several experiments were done to characterize the hydrogen surface spike. As shown in Fig. 3-5, the amplitude of the spike increased with time, temperature, and pressure with no significant increase in penetration. It was considered possible that the surface region of the oxide was different from the remainder of the oxide, possibly due to local stress-relief.

In order to test this hypothesis, 1000Å of oxide was etched from the surface. The etched oxide and an unetched oxide were then hydrated together for 4 hr. The surface spike was still present in the oxide which had been etched before hydration. The same result was obtained in the same experiment with a 1-hr hydration.

It was also considered possible that the spike was an experimental artifact. As mentioned previously, the sample surface was thoroughly washed before the first section was taken in order that adsorbed surface activity not be contained in the first section, thus making its concentration incorrectly high. Also, samples were soaked overnight in concentrated HCl and washed overnight in running water with no noticeable effect on the spike. Thus, the spike was apparently actually present in the oxide surface region.

An outdiffusion experiment was done to characterize further both the surface spike and the bulk diffusion mechanism. Three samples were hydrated simultaneously. One was etched immediately as a control (profile A in Fig. 6) and showed good agreement with other samples hydrated previously under the same conditions.

A second sample was vacuum-baked after hydration. After baking, it had the profile shown as profile B in Fig. 6. Note that roughly half of the hydrogen outdiffused in 4 hr at 200°C. Extrapolation of bake-out data for tritiated-steam grown oxides (3) would give a negligible outdiffusion rate at 200°C. This suggests that water diffused at 200°C is incorporated differently into the oxide than it is incorporated during a steam oxidation.

The first 1250Å of the third sample was sectioned (profile C in Fig. 6). This profile agreed well with the profile in the surface region of the control. We assume

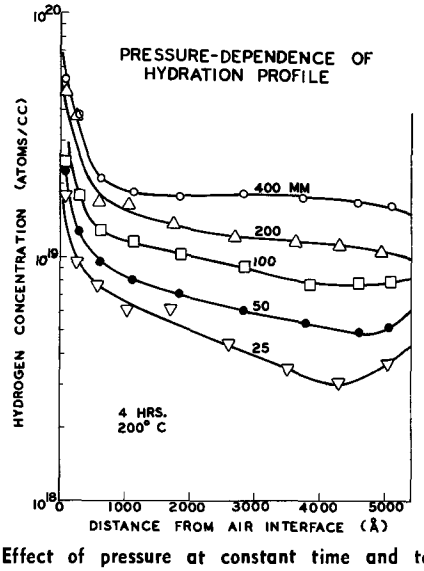

Fig. 5. Effect of pressure at constant time and temperature. Concentration varied as square root of pressure.

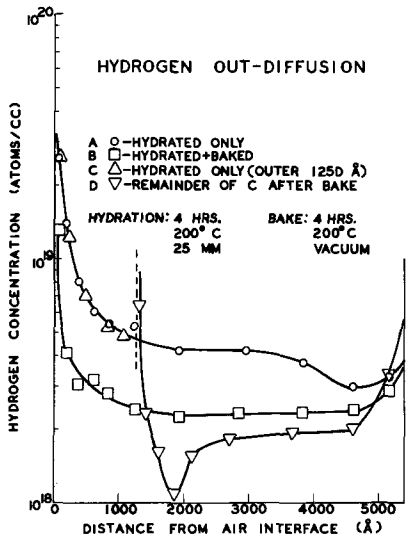

Fig. 6. Outdiffusion behavior of hydrated oxides

that the remainder of the profile in this sample was similar to that in the control. After vacuum baking, the partially etched sample had the profile shown as profile D in Fig. 6. Again the outdiffusion rate is large. Of greater significance, however, is the fact that the surface spike reformed in the outdiffusion. In fact, the dip in the profile just beyond the spike suggests that hydrogen was preferentially segregated from this region into the surface region.

It should perhaps be emphasized that these results were obtained on single samples, and reproducibility was therefore not checked. Similar results have, however, been obtained (18) for a similar outdiffusion experiment with sodium in an oxide film.

There were essentially no MOS electrical effects from hydrations at 200°C or below, even though hydrogen concentrations as high as 5×10^{18} cm^{-3} were measured at the silicon. Room-temperature flatband voltage showed a positive shift of about 1V (4×10^{10} electrons cm^{-2}), attributed to annealing. No measurable change in interface state density was observed. Annihilation of states was complete for hydrations at 800°C, however, suggesting that temperature is important to the annihilation.

Interpretation of Results

To interpret the hydration data two models are considered, one for bulk oxide profiles, one for the surface spike.

In bulk oxide, hydration is characterized by fast in- and outdiffusion, exponential profiles, low activation energy, and anomalous peaking for "gentle" hydrations (as in Fig. 4, 50° and 100°C). It is possible that extrapolation from high temperature data underestimates the diffusion coefficient. This would explain "fast" penetration. However, it would not explain the anomalous peaking, nor the fact that the profile does not have the expected error-function shape.

A model in which the oxide is assumed to contain a network of micropores could explain the observations. A "network of micropores" as used here does not mean actual pinholes through the oxide. Rather it means an interconnected network of small (probably a few atom diameters) disturbed regions which have a somewhat higher diffusivity than the bulk oxide. Such a model for oxide structure has been previously suggested (12).

We considered diffusion in such a micropored structure to be analogous to grain boundary diffusion and applied Fisher's (19) diffusion model to the hydration data. In Fisher's treatment, the diffusant is considered to penetrate very quickly along the high diffusivity path and then to side-diffuse. The model predicts exponential profiles, as observed, and appears consistent with the fast diffusion, low activation energy, and even the anomalous peaking which was observed.

Such a high diffusivity path would, of course, show up most strongly at low temperatures where bulk diffusion is slow. At high temperatures, such as in steam oxidations, bulk diffusion would be expected to dominate, as has been observed (3, 4, 17).

Several explanations were considered for the surface spike. We first thought that the spike represented a second, slower-diffusing hydrogen species. However, the shape of the spike and the change in amplitude with no penetration change were not consistent with this interpretation.

Surface rate limitation would give the observed behavior of the spike for indiffusions. However, it could not explain reformation of the spike from a flat profile in outdiffusion.

The remaining possibility was enhanced solubility in the surface region, either electrically or chemically caused. Electrical binding was rejected since no evidence was found of charge associated with the "water."

In keeping with the micropore model, it was considered possible that the surface region had a higher pore density and therefore retained more water than the bulk oxide. However, to explain the experiments in which the oxide surface was etched before in- and outdiffusion, it would be necessary to assume that the heavily pored region reformed in hours at 200°C.

The model which we favor has recently been described in papers on near-surface effects in metal-metal diffusions (20, 21) and is referred to as the Gibbs effect. In a diffusion system such as water-silica, where the reaction between the diffusant and the host matrix is exothermic, segregation of the diffusant near the surface of the host matrix leads to lowering of surface free energy. Thus, water segregates near the surface of the oxide simply because this lowers the energy of the system. The penetration of the spike in our profiles (a few hundred angstroms) is in good agreement with the penetration in the profiles shown in ref. (21).

With this model it would be expected that surface concentration would rise with bulk concentration, as observed. The constant penetration and the shape of the spike are reasonable. The reformation of the spike in outdiffusion would be expected.

Sodium-Water Interactions

Sodium chloride was diffused wet and dry as previously described, and sodium distributions and their electrical effects were measured. Although the diffusion length was orders greater than the oxide thickness (11) for dry diffusions at 600°C, profiles were steeply falling and diffusion time (1 to 60 min) had little effect on the profile. It appeared that the sodium was being preferentially segregated in the surface region of the oxide. This segregation could possibly be explained again by the Gibbs effect (20, 21). An alternative explanation, given by Fowkes and Burgess (18), is a surface layer of negative oxide ions which attract the sodium ions and bind them near the surface.

In wet diffusions the profile showed a definite development with time, *i.e.*, a filling and flattening with increasing time. Furthermore, profiles for wet diffusions peaked at the silicon, which has been associated with image charge in the silicon (22). Profiles for 1 hr wet and dry diffusions are shown in Fig. 7. In addition to the other differences noted between wet and dry diffusions, the water had the effect of significantly increasing the quantity of sodium transported. Such an effect has been previously noted (13).

Electrically, a definite sodium-water interaction is also seen. Charge production in the silicon is shown in Fig. 8 as a function of diffusion time. In dry diffusions at 600°C charge buildup was slow as expected from the sodium profiles. At 800°C charge buildup also behaved as expected [the decrease for long diffusion times has been attributed to anion compensation (23)].

Charge buildup in the wet diffusions, however, was very rapid. This is expected from the larger amount of sodium transported in the wet diffusions. However,

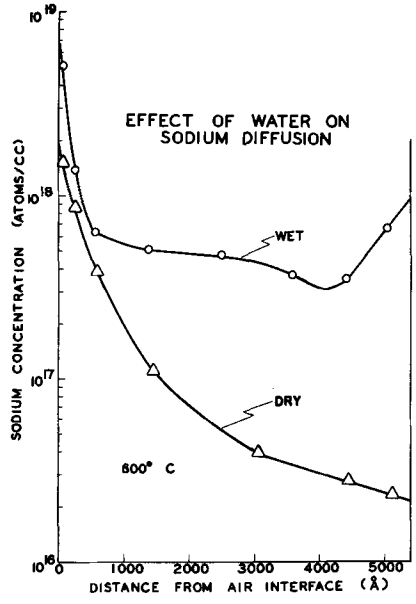

Fig. 7. Comparison of sodium profiles for 1-hr wet and dry diffusions of $Na^{22}Cl$ at 600°C.

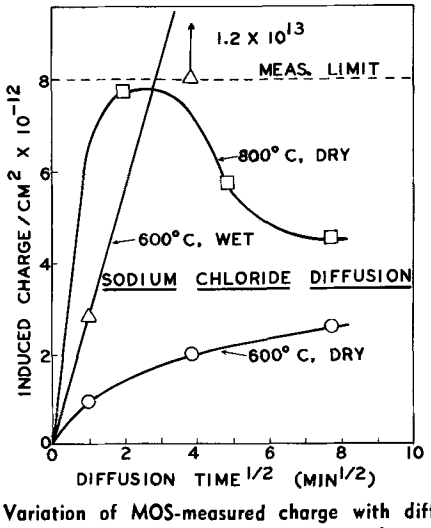

Fig. 8. Variation of MOS-measured charge with diffusion time for NaCl. Wet diffusions at 800°C gave charge beyond measurement limit for all diffusion times.

the larger sodium transport alone does not appear sufficient to explain the magnitude of charge production. The same amount of sodium can easily be transported in a dry diffusion (by increasing diffusion temperature, for example) as was transported in these wet diffusions without producing as large a charge (22). This implies that water enhances the charge production of sodium. The mechanism of such enhancement has not been ascertained.

It was noted in the wet diffusions that the sample coverplates were oxidized several times faster where they were in contact with the contaminated samples than they were on areas remote from the contamination (the covers were larger than the samples). Since the water in the wet nitrogen ambient was necessarily the oxidant, this observation implied that sodium also enhanced the transport of water into the oxide. Such sodium-enhanced oxidation has been previously observed (12) and could possibly be explained by Charles' (14) proposed mechanism for the sodium-enhanced corrosion of silica.

The hypothesis that sodium enhanced the water transport was directly checked in a 200°C hydration. Sodium-contaminated and uncontaminated samples were hydrated together and sectioned. The profiles are shown in Fig. 9. The sodium level in the contaminated

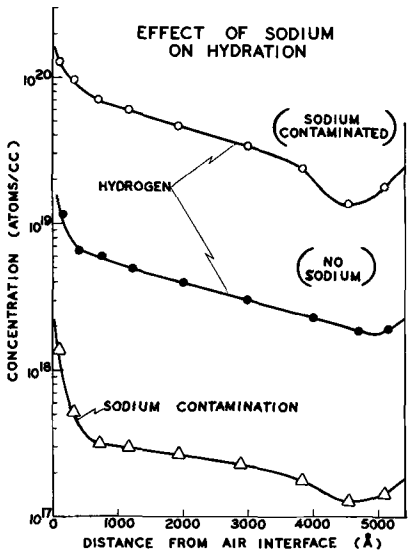

Fig. 9. Effect of sodium contamination on hydration at 200°C. Lowest profile represents sodium contamination in contaminated samples. Other profiles are hydration profiles in uncontaminated and contaminated samples, respectively.

oxides was rather low, a few times normal residual levels. However, this small amount of sodium was sufficient to increase "water" transport by roughly an order of magnitude as shown by the hydrogen profiles for contaminated and for uncontaminated oxides.

Electrically, however, water still appeared to have no effect at 200°C, even in a sodium-contaminated oxide. Room-temperature flatband voltage and interface state density were measured on samples after sodium diffusion. Hydration of these samples had no measurable effect on interface state density and gave the same slight positive shift of room-temperature flatband voltage as noted in hydration of clean oxides.

Summary

1. At "device" temperatures (200°C) hydration of a thermal oxide appears to occur via micropores; this may help to elucidate the structure of the oxide.

2. The diffusing species is not known, but water molecules separate into two independently diffusing fragments on entering the oxide.

3. Peaking of hydrogen in the surface region of the oxide is characteristic of the water-silica system and is explained by the Gibbs effect (surface energy lowering).

4. Water enhances sodium transport and positive charge production at moderate temperatures (600°-800°C).

5. Sodium enhances water transport at "device" temperatures (200°C).

6. At the device temperatures of interest in this study, diffused water has negligible effect on silicon surface potential or on interface-state density.

Acknowledgments

This work was supported by Grant NGR 36-003-067, NASA Electronics Research Center, Cambridge, Massachusetts. We gratefully acknowledge the contributions of Professors A. H. Heuer and E. T. Yon, as well as those of C. J. Slabinski, H. P. Caban-Zeda, and J. Hoel in experimental assistance and helpful advice. This paper was submitted by one of us (G.L.H.) in partial fulfillment of requirements for the Ph.D. degree in Engineering to Case Western Reserve University.

Manuscript submitted June 27, 1969; revised manuscript received Jan. 5, 1970. This was Paper 113 presented at the New York Meeting of the Society, May 4-9, 1969.

Any discussion of this paper will appear in a Discussion Section to be published in the December 1970 JOURNAL.

REFERENCES

1. A. J. Moulson and J. P. Roberts, *Trans. Faraday Soc.*, **57**, 1208 (1961).
2. T. Drury and J. P. Roberts, *Phys. Chem. Glasses*, **4**, 79 (1963).
3. P. J. Burkhardt, *This Journal*, **114**, 196 (1967).
4. T. E. Burgess and F. M. Fowkes, *ibid.*, **113**, 63C (1965).
5. S. R. Hofstein, *I.E.E.E. Trans. Electron Devices*, **ED-14**, 749 (1967).
6. A. B. Kuper and E. H. Nicollian, *This Journal*, **112**, 528 (1965).
7. S. R. Hofstein, *I.E.E.E. Trans. Electron Devices*, **ED-13**, 222 (1966).
8. E. H. Nicollian and A. Goetzberger, *Appl. Phys. Letters*, **7**, 216 (1965).
9. E. Kooi, *Philips Res. Rept.*, **21**, 477 (1966).
10. D. M. Brown and P. V. Gray, *This Journal*, **115**, 760 (1968).
11. A. E. Owen and R. W. Douglas, *J. Soc. Glass Tech.*, **43**, 159 (1959).
12. A. G. Revesz and K. H. Zaininger, *R. C. A. Rev.*, **29**, 22 (Mar. 1968).
13. T. E. Burgess *et al.*, *This Journal*, **116**, 1005 (1969).
14. R. J. Charles, *J. Appl. Phys.*, **29**, 1549 (1958).
15. P. V. Gray and D. M. Brown, *Appl. Phys. Letters*, **8**, 31 (1966).
16. V. A. Pliskin, *IBM J. Res. Develop.*, **10**, 198 (1966).
17. B. E. Deal and A. S. Grove, *J. Appl. Phys.*, **36**, 3770 (1965).
18. F. M. Fowkes and T. E. Burgess, *Surface Sci.*, **13**, 184 (1969).
19. J. C. Fisher, *J. Appl. Phys.*, **22**, 74 (1951).
20. T. S. Lundy and R. A. Padgett, *Trans. Met. Soc. AIME*, **242**, 1897 (1968).
21. A. J. Mortlock, *ibid.*, **242**, 1963 (1968).
22. E. Yon, W. H. Ko, and A. B. Kuper, *I.E.E.E. Trans. Electron Devices*, **ED-13**, 276 (1966).
23. A. B. Kuper, C. J. Slabinski, and E. T. Yon, *Phys. Failure Electron.*, **5**, 232 (RADC 1967); also A. B. Kuper, *Surface Sci.*, **13**, 172 (1969).

Epitaxial GaAs Kinetic Studies: {001} Orientation

Don W. Shaw*

Texas Instruments, Incorporated, Dallas, Texas

ABSTRACT

Gallium arsenide deposition rate studies were conducted with an open tube, chloride transport system which permitted independent control of the reactant input partial pressures. A recording microbalance was adapted to the deposition apparatus so that the epitaxial growth rates could be continuously measured during the actual deposition process. At low temperatures and high reactant partial pressures the process appears to be kinetically controlled. The rate then becomes inversely proportional to the gallium monochloride partial pressure and may indicate the presence of a competitive adsorption process. At high temperatures and low partial pressures the rates may be described in terms of a "quasi-equilibrium" model where a fraction of the incoming gas stream equilibrates with the condensed phase.

Studies of the influence of substrate temperature on GaAs epitaxial growth rates in the $Ga/HCl/As/H_2$ system have indicated that at low temperatures the process operates under kinetic control (1). Under such conditions the growth rate is independent of the total gas flow rate but is strongly dependent on the crystallographic orientation of the substrate. In addition the rate increases rapidly with increasing substrate temperature contrary to the behavior predicted from thermodynamic considerations. The epitaxial growth rates as well as the electrical characteristics of the deposits are also known to be significantly influenced by the composition of the vapor from which the layers are grown (2, 3). These facts indicate the utility of a detailed investigation of the influence of the gas phase composition on the kinetics of GaAs epitaxial growth.

Kinetic studies in gas flow systems are often limited by lack of precision of the rate data. Usually the studies are conducted by deposition for a fixed time period with subsequent measurement of the layer thickness. Although this approach is straightforward, it is time consuming and relatively imprecise. Implicit in its use is the assumption that the deposition rate is constant over the time interval used for deposition of the layer. An effort was made in the present investigation to eliminate these problems by use of an apparatus which permitted continuous measurement of the epitaxial growth rate as the layer was being deposited. This consisted of a recording microbalance adapted to the epitaxial deposition system. By suspension of the substrate crystal from one arm of the microbalance, the weight of the crystal was continuously measured. The details of this approach are described in the following section.

Experimental

Under proper conditions the growth of GaAs from a $GaCl/As_4/HCl/H_2$ ambient is a surface catalyzed process (1). This is a critical requirement to the study of epitaxial growth kinetics since it permits growth on the substrate only. Extraneous growth on the tube walls or the substrate holder would greatly complicate the results due to depletion of the gas stream of reactants. Obviously, if the epitaxial growth rate is to be obtained by continuous gravimetric measurements of the crystal, extraneous growth on the specimen hangdown and support must be eliminated. The GaAs system to be described meets these requirements, particularly if a small excess of HCl is added to the reactant gas phase (1).

The experimental apparatus is illustrated in Fig. 1. It consists principally of two parts: a microbalance, from one arm of which the specimen is suspended, and the fused silica reactor assembly. The microbalance is a Cahn RG Electrobalance (Cahn Instrument Company, Paramount, California) which uses the null balance principle. As the specimen weight changes, the deflection of the beam from its equilibrium point is detected. Attached to this beam is a coil positioned in a magnetic field. As the beam is deflected, a current is applied to the coil which restores the beam to the equilibrium position. From the measured current the specimen weight is obtained. Ideally, the balance is sensitive to 0.1 μg with a maximum capacity of 1g. As the specimen weight changes, it does not move vertically within the reaction apparatus. Consequently the length of the flat profile region of the furnace is minimized. The temperature variation over the length of the substrate crystal was found to be $< 2°C$. Both the weight and growth or etch rates are continuously measured. The latter data are obtained by electronically differentiating the balance output with time using a Cahn Mark II Time Derivative Computer. Usually the rate was displayed on one channel of a dual pen recorder, while the variable under study (temperature, partial pressure, etc.) was displaced simultaneously on the other channel. The noise level for both the rate and the weight outputs was minimized by electronic filtering.

The materials employed in construction of the balance mechanism are not inert to the corrosive gases used in deposition. Consequently, it was necessary to protect the balance by use of a hydrogen counterflow. This flow entered the center arm of the balance chamber, passed over the balance mechanism, and then flowed downward. The protective hydrogen flow rate

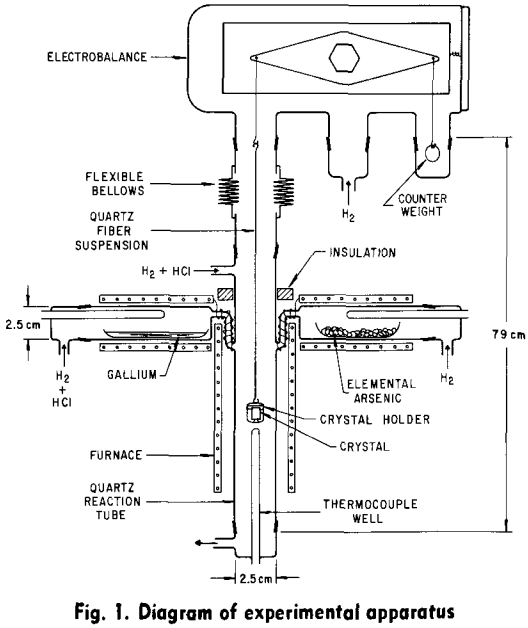

Fig. 1. Diagram of experimental apparatus

* Electrochemical Society Active Member.

amounted to one half of the total flow rate passing over the specimen. Coupling of the balance chamber to the actual epitaxial apparatus was achieved with a flexible Teflon bellows attached to the standard taper joints with heat shrinkable tubing. Initially a fused silica tube was used in the coupling, but mating of fused silica tapers between the balance chamber, deposition apparatus, and the coupling tube required very precise axial alignment. The use of a flexible Teflon bellows eliminated this problem.

Specimen removal and replacement was accomplished by movement of the balance chamber while the deposition apparatus was held in a fixed position. In this case the balance chamber was mounted on a rack and pinion device which permitted vertical movement. In addition, the balance chamber and mount could be translated in the horizontal direction. In order to change samples, the balance was moved upward, thus detaching it from the coupling tube. The hangdown fibers were unhooked at the opening and the balance then shifted horizontally. Finally, the lower hangdown fiber was extracted together with the specimen. The reverse procedure was followed in loading a new specimen.

Gaseous gallium monochloride and arsenic were the reactants. As mentioned earlier, some hydrogen chloride was added to retard nucleation and growth of extraneous material on the specimen hangdown or the tube walls. Gallium monochloride is formed by reaction of HCl with liquid gallium at 925°C. Earlier experiments (1) showed that the reaction goes essentially to completion at temperatures as low as 900°C. Thus the gallium monochloride input partial pressure was calculated from the total flow rate, the H_2-HCl flow rate over the gallium source, and the HCl partial pressure in the latter flow. Experimentally the gallium monochloride partial pressure was varied by changing the HCl partial pressure in the gas stream passing over the gallium source. This HCl partial pressure as well as that entering the tube as free HCl were continuously monitored with thermistor type thermal conductivity cells. Pure H_2 flowed through the reference sides of these cells. The arsenic input was obtained by passing hydrogen over elemental arsenic. The arsenic partial pressure was empirically determined from independent measurements of arsenic weight loss as a function of temperature. The same carrier gas flow rate over the arsenic source was used for all experiments, and the arsenic partial pressure was varied by changing the arsenic source temperature. All temperatures were monitored with thermocouples inside fused silica tubes. The thermocouple measuring the substrate temperature extended to just below the suspended substrate. Furnace profiles permitted determination of the actual substrate temperature from the thermocouple reading. Kanthal wound resistance furnaces were used throughout. Since gallium monochloride is unstable at low temperatures, it was necessary to prevent the gas temperature from falling below the substrate temperature between the gallium source and the substrate. Failure to do so would result in premature disproportionation of GaCl. This was prevented by heating the GaCl inlet tube with resistance wire wound as shown in Fig. 1.

The flow rates measured at room temperature were as follows:

Protective H_2 flow through balance chamber	300 ml/min
H_2-HCl flow over Ga source	100 ml/min
H_2-HCl flow—free HCl input	100 ml/min
H_2 flow over arsenic source	100 ml/min

Since the GaAs epitaxial growth rate is often dependent on the substrate orientation, under the experimental conditions it was necessary to expose essentially only one surface orientation to growth. For the {001} orientation used in this study this was achieved by using very thin specimens polished on both sides. Typical substrate dimensions were 1 × 1 × 0.02 cm. The slices were cleaved into squares, which exposed very smooth {110} sides. This resulted in 96% of the geometrical surface area being the {001} orientation while the remainder was {110} [which is typically a slower growing orientation (4)]. The samples were supported in a sample basket constructed of fused silica fibers. This was suspended from the balance by a fused silica hangdown fiber 125 μm in diameter. Usually, the sensitivity of the apparatus was determined by the noise level, which resulted from mechanical vibrations, thermal effects, or the aerodynamic drag (5) exerted on the specimen and the hangdown by the flowing gas. The latter is very significant, although not so severe as to prevent successful results. A change in the total flow rate results in an immediate change in the zero position of the balance. However, if the flow is held constant the drag is constant and the new zero position remains stable. For epitaxial kinetic studies a precise determination of the actual weight is unnecessary. Only the rate of change is important; thus zero shifts due to the gas flow effects are of little significance since they do not result in long term drifts. Under typical experimental conditions a change in rate of 0.005 mg/min may be detected. For a 2 cm^2 GaAs specimen, this corresponds to a change in rate of 0.275 μm/hr, which exceeds the sensitivity of the usual rate determination methods in open flow systems.

The rate-partial pressure experiments were conducted in such a manner as to gain simultaneously information concerning the sensitivity of the growth rate to temperature and reactant partial pressure. This was accomplished by very slowly cooling the substrate at a fixed gas phase composition. The deposition rate, as determined from the balance output, was plotted on one axis of an x-y recorder, while the output of the substrate thermocouple was measured on the other. This, in effect, yielded a rate-temperature plot for a given gas composition. The partial pressure of one of the reactants would then be changed and the experiment repeated. This would be continued until the rate-temperature curves were obtained for a range of reactant partial pressures. Isothermal sections from these curves yielded the rate-partial pressure curves for any desired temperature in the experimental range studied. Usually the previous deposit was removed by *in situ* etching between cycles so that each cycle represented growth on a similar surface. Since the weight gain during a temperature cycle represented the deposit thickness, the amount necessary for removal by etching between cycles was always known. After etching, at the beginning of each new cycle, an isothermal, steady-state growth rate was established before cooling to minimize effects of variations in the initial growth rates due to the freshly vapor etched surface.

Results

Figure 2, which was constructed from x-y plots of rate *vs.* thermocouple reading, summarizes the influence of deposition temperature on the {001} growth rate. Several curves are illustrated, each representing a different arsenic partial pressure. Constant values of the GaCl and HCl partial pressures were maintained for all runs. In general shape, the curves agree with the preliminary results reported in ref. (1), which were obtained by a set of fixed time depositions at various temperatures. Previous evidence (1) identifies the low-temperature regions, where the rate increases with increasing temperature, as kinetically or surface limited regions. Here the rate is limited principally by a relatively slow surface step which might be an adsorption or desorption process or an actual surface reaction. At higher temperatures each curve passes through a maximum, beyond which the rate begins to decrease with further increases in temperature. Figure 2 shows that the actual value of the temperature, T_{max}, where the maximum rate is observed, is a function of the arsenic partial pressure.

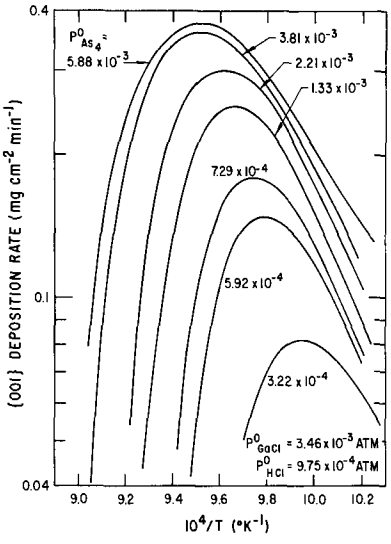

Fig. 2. Growth rate as a function of reciprocal temperature at several arsenic input partial pressures in atmospheres.

A similar set of rate *vs.* $1/T$ curves at various gallium monochloride partial pressures is given in Fig. 3. For these experiments the arsenic and hydrogen chloride partial pressures were held constant. Again the same basic curve shape is observed. As in Fig. 2, the value of T_{max} is a function of the gas phase composition. Apparent activation energies measured in the kinetic regions exhibit good agreement among the various runs and yield an average value of 48.7 ± 3.5 kcal/mole. No dependence of the activation energy on gas phase composition was evident.

If the deposition temperature is continually reduced, a point is ultimately reached at which the growth rate actually passes through a minimum. Additional temperature reductions result in an apparently increasing growth rate. Termination of the experiment after the temperature had been reduced below the minimum and examination of the crystal and its support revealed that extraneous GaAs deposits were beginning to form on the fused silica crystal support and hangdown fiber. Thus the apparent increase in growth rate was the result of the increased surface area and weight which accompanied the nucleation of these extraneous deposits. As the substrate temperature is lowered in the kinetic region, the growth rate decreases, even though the gas phase supersaturation is increasing, due to a reduction in the rate of some activated surface process. This will continue until the supersaturation exceeds the critical value necessary for nucleation on fused silica; then an apparent rate increase would be observed with our technique for rate measurement. The earlier stages of this effect are apparent in Fig. 3 for the curves corresponding to the three highest gallium monochloride partial pressures. Although this particular experiment was not extended so far as to produce an actual minimum in rate, a decrease in slope of the curves is evident at very low temperatures. The decrease occurs at higher temperatures as the gallium monochloride partial pressure is increased since the critical value of gas phase supersaturation is reached at higher temperatures.

Figure 4 illustrates the influence of the arsenic initial partial pressure on the deposition rate at several selected temperatures. At low temperatures the plots are nearly linear (on a log-log scale) with relatively small slopes. At intermediate temperatures the low partial pressure region exhibits an increased slope. This slope becomes characteristic of the entire curve at high temperatures. These plots are actually isothermal sections from Fig. 2. Comparison of Fig. 2 and 4 reveals that the regions where the rate is most sensitive to arsenic partial pressure variations, *i.e.*, at low arsenic partial pressures and high temperatures, correspond to regions of Fig. 2 where the growth rate decreases with increasing temperature. This illustrates the value of obtaining the rate-partial pressure data at several temperatures. Certainly, erroneous conclusions would be obtained if rate-partial pressure variations were interpreted in terms of a kinetic model when at low partial pressures the rate is no longer kinetically limited. For example, only the high partial pressure points of the 754° curve in Fig. 4 actually correspond to the kinetically limited region.

Interesting results are obtained when the growth rate is plotted as a function of the gallium monochloride partial pressure. This is shown in Fig. 5 where the curves for several deposition temperatures are given. It is apparent that, at least at the lower temperatures, the rate passes through a maximum with increasing gallium monochloride partial pressure. As in the preceding case, it is important to identify those portions of these curves which correspond to the kinetically limited region. Again this may be ascertained by comparison with Fig. 3. Although there might be a small region of the ascending portions of the curves in Fig. 4 which represent kinetic control, only the descending regions beyond the maximum definitely correspond to the activated regions in Fig. 3. Although not shown in Fig. 5, the growth rates actually

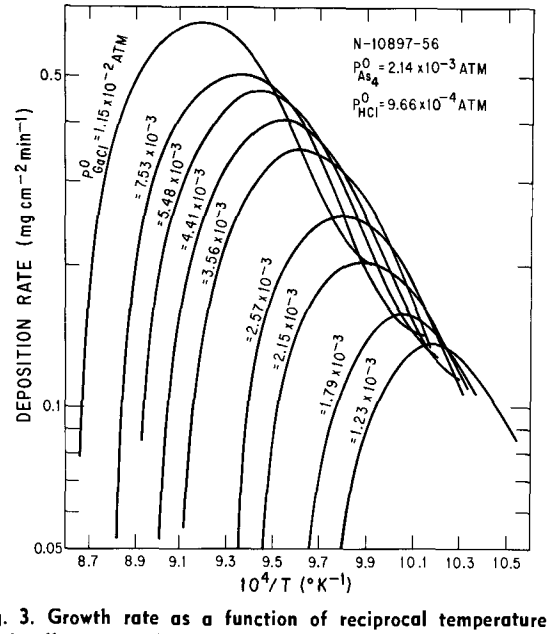

Fig. 3. Growth rate as a function of reciprocal temperature at several gallium monochloride input partial pressures in atmospheres.

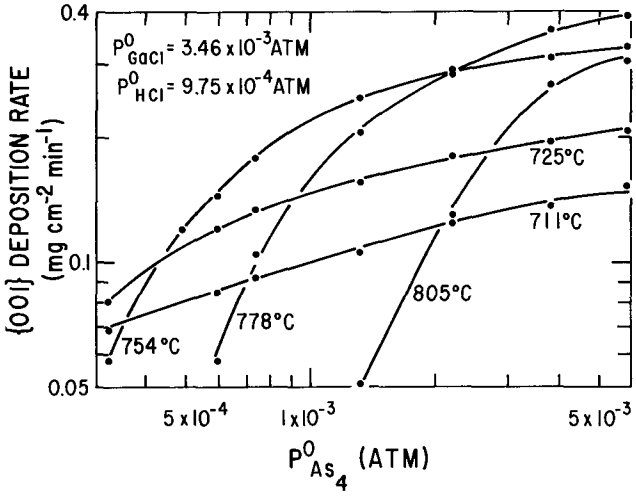

Fig. 4. Growth rate as a function of arsenic input partial pressure for several substrate temperatures.

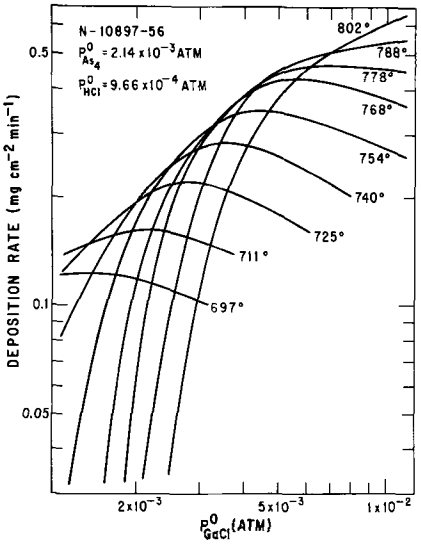

Fig. 5. Growth rate as a function of gallium monochloride input partial pressure for several substrate temperatures.

pass through a minimum at high partial pressures considerably in excess of the value for the rate maximum. This is due to two-dimensional nucleation on the fused silica hangdown fiber which results in extraneous growth as previously mentioned. Since this is independent of the single crystal epitaxial growth, such data will be excluded from the discussion. The results shown in Fig. 4 and 5 correspond only to conditions where growth is confined to the substrate crystal.

In general the results may be summarized in terms of two unique growth regions. The first region, which corresponds to low partial pressures and high temperatures, is characterized by rates which decrease with increasing temperature and increase when the partial pressure of one reactant is increased while holding the other constant. In the second region, the rate increases with increasing temperature and with increasing arsenic partial pressure, but actually decreases when the other reactant, gallium monochloride, is increased.

Discussion

As previously stated, the low-temperature region where the rate increases with increasing temperature is believed to represent a region where the process operates under kinetic control. This interpretation is supported by the following evidence: (*i*) The deposition rate exhibits a strong orientation dependence (4). (*ii*) An exponential temperature dependence is observed which is contrary to that predicted from equilibrium considerations (1). (*iii*) The rate is independent of the total gas flow rate (1). Having now established the influence of reactant partial pressures on the growth rate in this kinetically controlled region, it is of interest to examine the possibilities of extracting information concerning the nature of the slow surface process. The process might be adsorption of either reactant species, some surface reaction between adsorbed species, or desorption of the products.

The inverse dependence of the rate on the gallium monochloride partial pressure may indicate a competitive adsorption process whereby GaCl competes with arsenic for adsorption sites. Consider, for example, that As_4 is in gas phase equilibrium with As_2 which in turn is adsorbed dissociatively on the {001} surface. If GaCl should compete for these sites, perhaps by attraction of the Cl portion of the molecule to the surface, the amount of surface available for arsenic adsorption would be reduced. By assuming a Langmuir type adsorption process, the fraction of the surface covered by arsenic atoms could be expressed by the following equation

$$\theta_{As} = \frac{\beta_{As_2}{}^{1/2} P_{As_2}{}^{1/2}}{(1 + \beta_{As_2}{}^{1/2} P_{As_2}{}^{1/2} + \beta_{GaCl} P_{GaCl})} \quad [1]$$

where β_{As_2} and β_{GaCl} represent the Langmuir adsorption coefficients for the subscripted species. If the rate-limiting process involves a reaction of adsorbed arsenic atoms, then the rate may significantly begin to decrease with increasing gallium monochloride partial pressures when

$$\beta_{GaCl} P_{GaCl} > 1 + \beta_{As_2}{}^{1/2} P_{As_2}{}^{1/2} \quad [2]$$

Actually, several different rate-limiting surface processes may be imagined which involve adsorbed arsenic atoms. General rate expressions were derived for many of these processes in an attempt to describe the actual growth mechanism in the kinetic region. However, the resulting equations all involve several undetermined constants. Although many of the rate expressions appear to agree with the experimental results, the undetermined constants precluded identification of which if any of the mechanisms was the most valid. Consequently, one cannot determine the true nature of the rate-limiting process in the region of kinetic control. However, a competitive adsorption process between arsenic and gallium monochloride for the arsenic adsorption sites can qualitatively account for the experimental observations.

The high temperature-low partial pressure regions where the rate exhibits a negative temperature dependence could be due to an activated etching process which becomes significant at higher temperatures. However, this is unlikely since earlier results (1) indicated that the orientation dependence diminishes markedly in this region. Another possibility is that, at high temperatures or low partial pressures, the entire gas stream approaches equilibrium with the condensed phase. In order to investigate this possibility, equilibrium calculations were carried out for conditions which corresponded to our experiments. In these calculations, the composition of a mixture was determined which represented the minimum free energy of the system subject to the mass balance constraints. Thermodynamic values employed in the calculations were taken from Day's (6) compilation. However, comparison of the experimental rates described earlier with the calculated values revealed a large discrepancy. Yet when the two results were plotted, the curve shapes were very similar, particularly in the regions of high temperatures and low reactant partial pressures.

Sedgwick (7) described a method for treating silicon epitaxial deposition in which a "quasi-equilibrium" is assumed. In this case, only a fraction of the incoming gas stream equilibrates with the condensed phase, while the remainder passes by unreacted. Silvestri (8) has successfully applied this approach to germanium deposition from $GeCl_4$ and H_2. Actually the quasi-equilibrium approach is very similar to models which assume diffusion control, where all diffusing species have the same diffusion coefficients and the rate is determined by the difference between the bulk stream partial pressure of a given species and its equilibrium value at the crystal surface.

According to Sedgwick, the deposition rate for a process operating in the quasi-equilibrium mode may be expressed as

$$D = J \cdot \alpha \cdot \beta \quad [3]$$

where J is the flux of the species being deposited, α is a theoretical efficiency factor which represents the fraction of the flux which would be deposited if complete equilibrium were achieved between the entire gas stream and the substrate, and β is the fraction of the incoming gas stream which actually equilibrates with the condensed substrate. For the case where the entire gas stream equilibrates with the condensed phase, β is unity. However, for the quasi-equilibrium case, β is less than unity and is a highly geometry dependent factor.

Calculations of the factor $J \cdot \alpha$ were made for portions of the data shown in Fig. 2 through 5. The factor β was then estimated by assuming that the quasi-equilibrium approach was valid at 740°C and the lowest gallium monochloride partial pressure (1.23×10^{-3} atm) shown in Fig. 5. A value of $\beta = 0.093$ was obtained. This value was assumed to remain constant for all the experimental conditions described since the same geometry and linear gas stream velocity were used throughout the study. It should be noted that β should be only weakly dependent on temperature. Using the above mentioned value of β, theoretical curves for the dependence of the deposition rate on the arsenic and gallium monochloride initial partial pressures were determined. These curves, together with points representing the experimental results, are shown in Fig. 6 and 7. The same value of β was used in construction of the curves for both figures.

Very poor agreement between the theoretical and experimental values is obtained at low temperatures, but, as the deposition temperature is increased, the agreement becomes better. Very good agreement is obtained at 768°C at the lower partial pressure values. Comparison of Fig. 6 and 7 with Fig. 2 and 4 reveals that deviations between the experimental and calculated values become significant when the data falls in the activated regions or where the process begins to operate under kinetic control. However, in the high temperature-low partial pressure regions good agreement is apparent, indicating that the quasi-equilibrium model is applicable in the region. The value of $\beta = 0.093$ for the GaAs system may be compared with a value of 0.3 obtained for Ge deposition (8) and the range of values from 0.03 to 0.30 for Si deposition (7).

In summary, with the present system, GaAs can be deposited epitaxially under two unique regimes depending on the temperature and reactant partial pressures. At low temperatures and high reactant partial pressures the GaAs deposition rate is limited by some surface process. The rate is then inversely dependent on the gallium monochloride partial pressure and may indicate a competitive adsorption process between gallium monochloride and arsenic. With lower partial pressures and high deposition temperatures, the rate behavior agrees well with a quasi-equilibrium model.

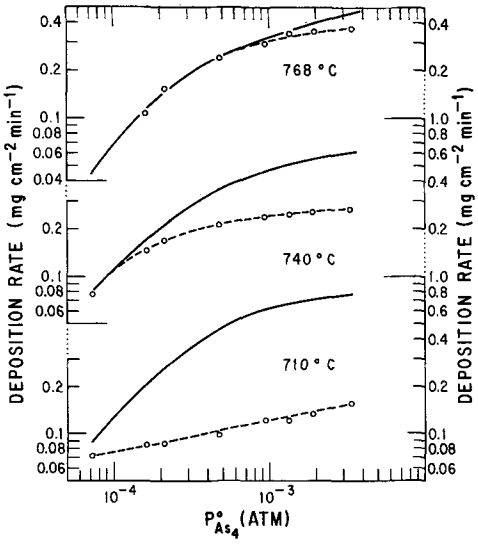

Fig. 6. Theoretical curves of rate as a function of arsenic input partial pressure. Open circles represent experimental data. Ordinate scales on each side of the figure correspond to 710°, 740°, and 768° in ascending order.

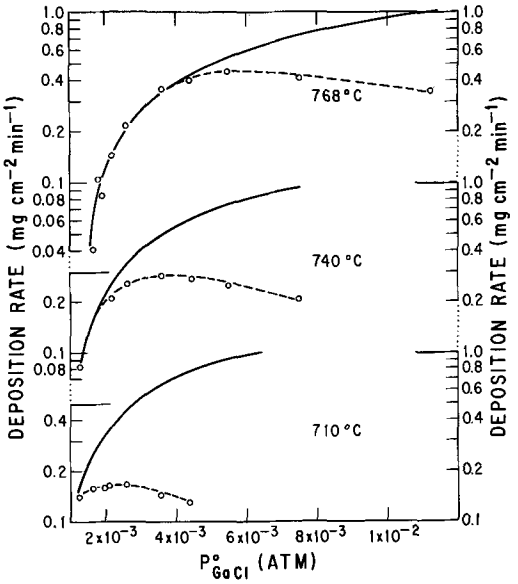

Fig. 7. Theoretical curves of rate as a function of gallium monochloride input partial pressure. Open circles represent experimental data. Ordinate scales on each side of the figure correspond to 710°, 740°, and 768° in ascending order.

These two types of deposition should be accompanied by differences in surface morphologies and electrical characteristics. For example, Silvestri (8) has observed that smooth surfaces are obtained when Ge is deposited under conditions corresponding to the quasi-equilibrium case, while structured surfaces predominate when surface limitations are significant. Differences in the electrical characteristics may also be observed since growth in the high temperature region occurs under conditions which more closely approach equilibrium than in the low temperature kinetically controlled region. Such differences will be the subject of future studies.

Acknowledgments

Appreciation is expressed to Miss Carolyn Banks for her assistance with the experimental work. In addition, the author wishes to thank Drs. L. G. Bailey and B. G. Secrest for their interest and several stimulating discussions.

Manuscript submitted Oct. 27, 1968; revised manuscript received Jan. 27, 1970. This was Paper 172 presented in part at the Detroit Meeting of the Society, Oct. 5-9, 1969.

Any discussion of this paper will appear in a Discussion Section to be published in the December 1970 JOURNAL.

REFERENCES

1. D. W. Shaw, *This Journal*, **115**, 405 (1968).
2. R. E. Ewing and P. E. Greene, *ibid.*, **111**, 1266 (1964).
3. D. W. Shaw, R. W. Conrad, E. W. Mehal, and O. W. Wilson, 1966 Inter. Symp. on GaAs, Inst. of Physics and the Physical Society Conf. Series No. 3, 10-15.
4. D. W. Shaw, 1968 Inter. Symp. on GaAs, Inst. of Physics and the Physical Society Conf. Series No. 6, 50-54.
5. L. Cahn and H. Schultz, *Anal. Chem.*, **35**, 1729 (1963).
6. G. F. Day, "Heterojunction Device Concepts" prepared for Air Force Avionics Laboratory, Contract AF 33(615)1988, Varian Associates, September 1966.
7. T. O. Sedgwick, *This Journal*, **111**, 1381 (1964).
8. V. J. Silvestri, *ibid.*, **116**, 81 (1969).

The Theory of Anomalous Diffusion in Solids Near Diffusant Saturation Concentrations: Example–Phosphorus in Silicon

P. E. Bakeman, Jr.

Rensselaer Research Corporation, Troy, New York

and J. M. Borrego

Electrophysics Division, Rensselaer Polytechnic Institute, Troy, New York

ABSTRACT

This paper presents a diffusion theory for the diffusion of impurities which exhibit solid solubility saturation. The theory is based on a simple assumption for impurity atom interaction which yields a self-consistent result for the diffusion constant and chemical potential of the impurity. The theory predicts the diffusion constant of the diffusing species to be: $D' = D(C_{max} + C)/(C_{max} - C)$, where D is the low level diffusion constant, C is the impurity concentration, and C_{max} is the saturation impurity concentration. The theory is compared with available experimental data on the diffusion of phosphorus in silicon. The theory and experiment are in excellent agreement.

It is the purpose of this paper to advance a theory of diffusion which is capable of explaining the anomalous diffusion behavior observed in the diffusion of impurities which exhibit solid solubility saturation, such as phosphorus diffusing in silicon. The assumption is made that atoms of the diffusing species do interact with each other during diffusion as opposed to the assumption that they move independently, which is implicit in deriving Fick's first law. The rationale for the atomic interaction assumption is presented and the assumed interaction is expressed both phenomenologically and as a term in the chemical potential equation.

A recent communication (1) evaluates the effect of ambipolar or field aided diffusion of impurities in silicon and concludes that this effect is insufficient to cause experimentally observed diffusion anomalies. In fact, it can be shown that ambipolar diffusion effects can account for a maximum increase in D, the impurity diffusion constant, by a factor of 2 in semiconductors if Maxwell-Boltzmann statistics are used (2). In the degenerate case, Shockley (3) has evaluated the ambipolar diffusion effect using Fermi statistics and derived the relation

$$\frac{D^*}{D} = 1 + \left(\frac{\pi}{6}\right)^{1/3}\left(\frac{N_d}{N_c}\right)^{2/3} \qquad [1]$$

This correction still cannot explain the experimentally observed diffusion phenomena.

Theory

Let us derive a one dimensional expression for the impurity atom flux density as a function of concentration and concentration gradient. In the classical derivation, which yields Fick's first law, the following assumptions are made (4).

1. The impurity atoms move in discrete jumps (length = α) with a jump frequency Γ (jumps/sec) which is a function of neither concentration nor concentration gradient.
2. Each impurity atom moves at random independent of other diffusing impurity atoms.

The second assumption indicates that there is an equal probability of an impurity atom, at plane x, jumping in the $+x$ and $-x$ directions on any given jump. Thus, the probability, $P(+,x)$, that it jumps in the $+x$ direction is 1/2 and, similarly, the probability, $P(-,x)$, that it jumps in the $-x$ direction is 1/2. By definition

$$P(+,x) + P(-,x) = 1 \qquad [2]$$

These assumptions yield the result that (4)

$$D = 1/2\ \Gamma\alpha^2 \qquad [3]$$

Let us change assumption 2 to account for impurity atom interaction as follows:

2'. Each impurity atom moves at random to available sites within the host material. Also assume that the total concentration of impurity cannot exceed C_{max}.

The effect of the new assumption is to change the values of $P(+,x)$ and $P(-,x)$ so that they are no longer equal, but their sum is still unity.

The probabilities $P(+,x)$ and $P(-,x)$ are mathematically determined by counting the density of empty sites in planes $x + \alpha$ and $x - \alpha$. Since we have assumed that the impurity atom will diffuse into any empty site with equal probability

$$\frac{P(+,x)}{P(-,x)} = \frac{N_{max} - N(x+\alpha)}{N_{max} - N(x-\alpha)} \qquad [4]$$

where N_{max} = maximum density of impurity in an atomic plane; $N(x)$ = density of impurity atoms in atomic plane at x (number/cm^2); and α = spacing of atomic planes.

Combining Eq. [2] and [4] yields the values of $P(+,x)$ and $P(-,x)$

$$P(+,x) = \frac{N_{max} - N(x+\alpha)}{[N_{max} - N(x+\alpha)] + [N_{max} - N(x-\alpha)]} \qquad [5a]$$

$$P(-,x) = \frac{N_{max} - N(x-\alpha)}{[N_{max} - N(x+\alpha)] + [N_{max} - N(x-\alpha)]} \qquad [5b]$$

Referring to Fig. 1, we calculate the atom flux density $J(x)$ across plane x. The net flux equals the number of impurity atoms flowing from plane $x - \alpha/2$ to plane $x + \alpha/2$ minus those moving from $x + \alpha/2$ to $x - \alpha/2$

$$J = N\left(x - \frac{\alpha}{2}\right) P\left(+, x - \frac{\alpha}{2}\right)\Gamma - N\left(x + \frac{\alpha}{2}\right) P\left(-, x + \frac{\alpha}{2}\right)\Gamma \qquad [6]$$

where Γ = impurity jump frequency.

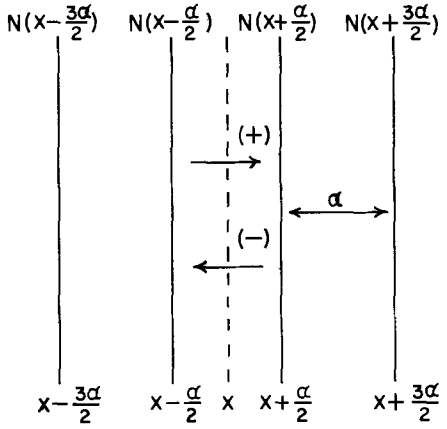

Fig. 1. Atomic flux density across plane x

By transforming the value of x in Eq. [5a] and [5b], we find

$$P\left(+, x-\frac{\alpha}{2}\right) = \frac{N_{max} - N\left(x+\frac{\alpha}{2}\right)}{\left[N_{max} - N\left(x+\frac{\alpha}{2}\right)\right] + \left[N_{max} - N\left(x-\frac{3\alpha}{2}\right)\right]} \quad [7a]$$

$$P\left(-, x+\frac{\alpha}{2}\right) = \frac{N_{max} - N\left(x-\frac{\alpha}{2}\right)}{\left[N_{max} - N\left(x-\frac{\alpha}{2}\right)\right] + \left[N_{max} - N\left(x+\frac{3\alpha}{2}\right)\right]} \quad [7b]$$

The relationship between area concentration, $N(x)$, and volume concentration, $C(x)$ is

$$N(x) = C(x)\,\alpha \quad [8]$$

Combining Eq. [6] through [8] yields

$$J = -1/2\,\Gamma\alpha^2 \frac{dC(x)}{dx} \frac{C_{max}^2 - C(x)^2 + \left(\frac{\alpha}{2}\frac{dC(x)}{dx}\right)^2}{[C_{max} - C(x)]^2 - \left(\frac{\alpha}{2}\frac{dC(x)}{dx}\right)^2} \quad [9]$$

but

$$\frac{\alpha}{2}\frac{dC(x)}{dx} << C_{max} - C(x) \quad [10]$$

therefore

$$J = -\tfrac{1}{2}\Gamma\alpha^2 \frac{dC(x)}{dx}\frac{C_{max} + C(x)}{C_{max} - C(x)} \quad [11]$$

Thus, from Eq. [3] and [11], the effective diffusion constant D', is a function of concentration and equals

$$D' = D\frac{C_{max} + C(x)}{C_{max} - C(x)} \quad [12]$$

where, D = the impurity diffusion constant at low impurity concentrations. Equation [12] shows that the diffusion constant, D', of an impurity in a material is a function of the actual concentration of the impurity relative to its saturation concentration. At low concentrations [$C(x) << C_{max}$] the impurity diffusion constant equals D and is independent of concentration; at high impurity levels Eq. [12] must be used to calculate D' as a function of concentration.

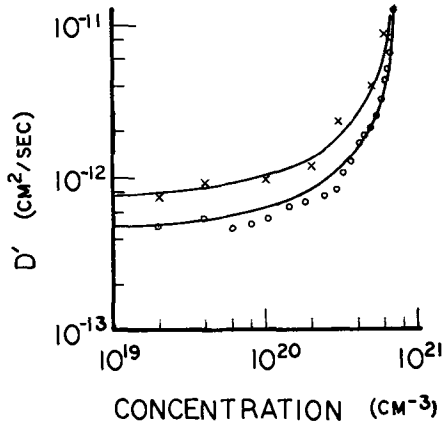

Fig. 2. Diffusion constant, D', of phosphorus in silicon as a function of phosphorus concentration. Data points are experimental measurement of two samples diffused at 1050°C for 30 min each, from Tannenbaum (5). Curves are as calculated from Eq. [12] using $D = 7.4 \times 10^{-13}$ cm²/sec and $C_{max} = 7.4 \times 10^{20}$ cm^{-3} (upper) and $D = 4.8 \times 10^{-13}$ cm²/sec and $C_{max} = 7.7 \times 10^{20}$ cm^{-3} (lower).

It should be noted that Eq. [12] can be derived using the random-walk approach to diffusion theory (7) and the directional jump probabilities presented in Eq. [5a] and [5b].

Discussion

Figure 2 is a graph of effective diffusion constant *vs.* impurity concentration for the diffusion of phosphorus in silicon. The data points were obtained by Tannenbaum (5) from experimental radioactive tracer data of two diffusion runs under identical conditions. The upper and lower curves are calculated from the theory presented herein using values for D of 7.4 and 4.8 x 10^{-13} cm²/sec and for C_{max} of 7.4 and 7.7 x 10^{20} atom/cm³, respectively. It can be seen that the theory and experiment show remarkable agreement. Similar experimental verification can be shown using recent experimental data by Vick and Whittle (6) for the diffusion of boron in silicon.

The chemical potential for an impurity in a solid with the assumption of no impurity atom interaction is

$$\phi = +kT \ln C(x) + \text{constant} \quad [13]$$

It can be shown from Eq. [12] that the chemical potential in the system based on assumption 2′ is

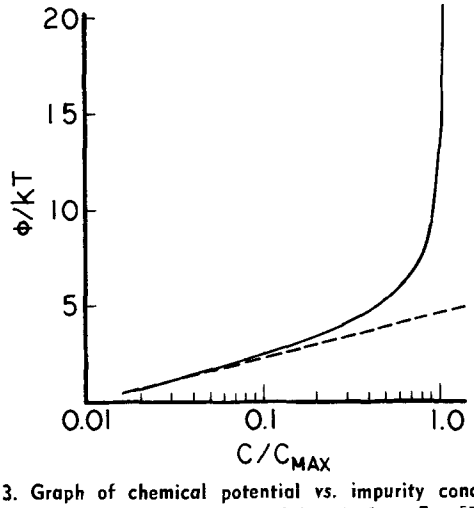

Fig. 3. Graph of chemical potential *vs.* impurity concentration for the two diffusion theories. Dotted line is from Eq. [13]. Solid line, corrected for impurity atom interaction, is from Eq. [14].

$$\phi = +kT \ln \frac{C(x)}{\left[1 - \frac{C(x)}{C_{max}}\right]^2} + \text{constant} \quad [14]$$

These equations are plotted in Fig. 3. The abrupt rise in ϕ' at $C = C_{max}$ is precisely what is required of an impurity for it to exhibit a maximum solid solubility at a concentraton C_{max}.

Acknowledgment

The authors wish to thank Dr. H. B. Huntington for his assistance in reviewing the manuscript.

Manuscript submitted Aug. 29, 1969; revised manuscript received ca. Jan. 5, 1970.

Any discussion of this paper will appear in a Discussion Section to be published in the December 1970 JOURNAL.

REFERENCES

1. D. P. Kennedy, *Proc. IEEE (Letters)*, **57**, 1202 (June 1969).
2. F. M. Smits, *Proc. IRE*, **46**, 1049 (1958).
3. W. Shockley, *J. Appl. Phys. (Letters)*, **32**, 1402 (July 1961).
4. P. G. Shewmon, "Diffusion in Solids," pp. 41-42, McGraw-Hill Book Co., New York (1963).
5. E. Tannenbaum, *Solid-State Electron.*, **2**, 123 (1961).
6. G. L. Vick and K. M. Whittle, *This Journal*, **116**, 1142 (1969).
7. J. R. Manning, "Diffusion Kinetics for Atoms In Crystals," D. Van Nostrand Co., Inc. (1968).

New Data on Basic Lead Sulfates

H. W. Billhardt[1]

Mineralogisches Institut der Universität (TH), Karlsruhe, Germany

ABSTRACT

High-temperature x-ray and DTA investigations of the lead oxide-lead sulfate system confirmed the phase relations established by Esdayle and Lander. In order to elucidate discrepancies in the literature and to insure positive identification of the three basic lead sulfates $PbO \cdot PbSO_4$, β-$2PbO \cdot PbSO_4$, and $4PbO \cdot PbSO_4$, single crystals were prepared and investigated by several x-ray techniques. Indexed x-ray powder data, cell parameters, and also IR-absorption spectra are presented. A high-temperature x-ray pattern is given for α-$2PbO \cdot PbSO_4$.

During the investigation of lead silicate sulfate glasses and their crystallization products, the well-known system PbO-SO_3 (1-6) was re-investigated. Discrepancies were found between the x-ray data given in previous papers and those obtained from our own measurements. In order to insure positive identification of all basic lead sulfates, single crystals were prepared and investigated by means of several x-ray techniques. IR-absorption spectra were also recorded.

Pure PbO and $PbSO_4$ were used for the preparation of the basic lead sulfates. The oxides in stoichiometric relation were fused in Pt crucibles, taking into account the loss caused by evaporation. To protect the Pt crucible from reaction with Pb a small amount of NH_4NO_3 was added to the sample in order to get an oxidizing atmosphere [Merker and Wondratschek (7)] and then the batch was heated very slowly. A serious attack of the crucibles by Pb-rich melts was never observed. After each preparation the Pt crucibles were cleaned by a soda-borax melt. The loss of Pt was always less than 1 mg.

In the lead oxide-lead sulfate system, the monobasic, the α- and β-dibasic and the tetrabasic lead sulfate are the only phases which are observed. The phase diagram established by Esdaile (3) and Lander (4) has been confirmed (Fig. 1). It stands in strict contradiction to the newly published paper of Margulis and Kopylov (6). Our repeated DTA-analyses and high-temperature x-ray measurements under different heating and cooling rates, revealed that the diagram given by Margulis and Kopylov is based on systems not in equilibrium and on cooling-curves with retarded crystallization effects and should, therefore, be rejected.

Monobasic Lead Sulfate

Monobasic lead sulfate obtained by slow cooling of a $PbO \cdot PbSO_4$ melt in Pt crucibles was found to be identical with the mineral lanarkite. The crystallographic space group is C2/m and the monoclinic cell parameters tabulated in Table I are in close agreement with the data of lanarkite described by Richmond and Wolfe (8) and Binnie (9). The cell parameters presented in this paper are the result of refinement of the x-ray powder data in Table II (AEG-Guinier camera, $CuK\alpha_1$-radiation, intensities photometrically measured) with the help of a least-squares computer procedure.

Dibasic Lead Sulfate

Dibasic lead sulfate exists in two modifications (3, 10). High-temperature x-ray investigations (Nonius-Guinier camera) revealed that this compound is unstable below about 640°C and decomposes at this temperature to mono- and tetrabasic lead sulfate. This decomposition takes place very slowly. Even at cooling rates of 10°C/hr, α-$2PbO \cdot PbSO_4$ is stable down to 450°C and then it forms metastable β-$2PbO \cdot PbSO_4$.

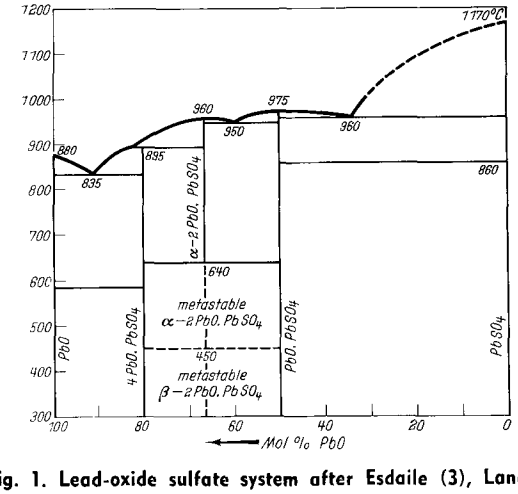

Fig. 1. Lead-oxide sulfate system after Esdaile (3), Lander (4), and the author's measurements.

[1] Present address: Forschungsinstitut der Zementindustrie, Düsseldorf-Nord, Germany.

Table I. Single-crystal data of $PbO \cdot PbSO_4$ and lanarkite

	$PbO \cdot PbSO_4$	Lanarkite	
	Present work	Binnie	Richmond and Wolfe
Probable space group	C2/m	C2/m	C2/m
a in Å	13.753 ± 0.02	13.75 ± 0.04	13.73
b in Å	5.697 ± 0.02	5.68 ± 0.02	5.68
c in Å	7.064 ± 0.02	7.05 ± 0.02	7.07
β in °	115.9 ± 0.2	116.2 ± 0.2	116°13′
V in Å³	498	494	495
z	4	4	4
ρ calc. in g/cm³	7.02	7.08	7.07
ρ meas.	7.08 ± 0.1	6.92	

Table II. Indexed x-ray pattern of monobasic lead sulfate

I/I_o	$d_{meas.}$	$d_{comp.}$	h k l	I/I_o	$d_{meas.}$	$d_{comp.}$	h k l
25	6.31	6.36	0 0 1	15	2.228	2.230	$\bar{6}$ 0 2
25	6.14	6.19	2 0 0	4	2.190	2.192	$\bar{4}$ 2 1
20	5.85	5.90	$\bar{2}$ 0 1			2.214	$\bar{2}$ 2 2
10	5.14	5.17	1 1 0	6	2.167	2.169	$\bar{3}$ 1 3
45	4.40	4.43	$\bar{1}$ 1 1	10	2.120	2.121	0 2 2
20	3.69	3.70	1 1 1			2.119	0 0 3
15	3.50	3.51	$\bar{3}$ 1 1	5	2.100	2.100	$\bar{1}$ 1 3
80	3.34	3.34	3 1 0			2.096	4 2 0
20	3.18	3.18	0 0 2	20	2.063	2.062	6 0 0
		3.093	4 0 0	30	2.048	2.050	$\bar{4}$ 2 2
100	2.957	2.959	$\bar{1}$ 1 2	5	1.967	1.968	6 0 3
		2.952	$\bar{4}$ 0 2	5	1.910	1.909	5 1 1
50	2.860	2.863	$\bar{3}$ 1 2	25	1.849	1.850	4 0 2
4	2.844	2.848	0 2 0			1.848	2 2 2
7	2.603	2.603	3 1 1	15	1.835	1.835	$\bar{4}$ 2 1
7	2.585	2.587	2 2 0	5	1.828	1.832	$\bar{7}$ 1 1
7	2.563	2.566	$\bar{2}$ 2 1	4	1.810	1.809	$\bar{2}$ 2 3
20	2.473	2.474	$\bar{5}$ 1 1	5	1.778	1.777	$\bar{6}$ 2 1
25	2.429	2.429	2 0 2	7	1.760	1.759	$\bar{4}$ 0 4
10	2.400	2.400	$\bar{4}$ 0 1	8	1.757	1.756	$\bar{6}$ 2 2
5	2.354	2.343	$\bar{5}$ 1 2	5	1.749	1.750	6 0 1
8	2.339	2.342	$\bar{2}$ 0 3	20	1.726	1.725	3 3 0
15	2.271	2.270	5 1 0	10	1.682	1.681	$\bar{8}$ 0 1
5	2.254	2.257	2 2 1	15	1.671	1.671	6 2 0

This low-temperature modification has the monoclinic space group $P2_1/m$ or $P2_1$, in agreement with Boivin, Thomas, and Tridot (10), but we could not confirm all the cell parameters given by these authors (a = 7.814Å, b = 5.803Å, c = 8.035Å, β = 102.64°, ρ_{calc} = 6.98 g/cm³, ρ_{exp} = 7.08 g/cm³). Our repeated density measurements and x-ray single-crystal investigations led to the following cell parameters: a = 8.06 ± 0.02Å, b = 5.79 ± 0.02Å, c = 7.17_5 ± 0.02Å, and β = 103°C ± 0.02°.

The calculated density is 7.63 g/cm³, assuming two formula weights per unit cell. This density is close to our experimentally determined density of 7.6 ± 0.05 g/cm³. The β-$2PbO \cdot PbSO_4$ single crystals are twinned about a twofold [101] rotation axis or a $(10\bar{1})$ twin plane. The angle between a_1^* of the one cell and c_2^* of the other cell is about 8.4 ± 0.3°.

DTA-heating curves and high-temperature x-ray measurements reveal that the metastable β low-temperature modification exists up to about 450°C and then decomposes to mono- and tetrabasic lead sulfate. At or above 640°C, $2PbO \cdot PbSO_4$ recrystallizes from the two basic lead sulfates, but now in the α-form. It is remarkable that the inflection point at 640°C is not strictly

Table III. X-ray powder diffraction of α-$2PbO \cdot PbSO_4$ at 700°C

I/I_o	d, Å	I/I_o	d, Å
10	7.56	20	2.996
15	6.00	3	2.82
4	4.84	5	2.728
10	4.74	6	2.712
10	4.27	6	2.583
3	3.78	15	2.427
100	3.21	20	2.354
30	3.16	12	2.184
12	3.13	10	2.139
60	3.06	5	2.002

Table IV. Indexed x-ray pattern of β-dibasic lead sulfate

I/I_o	$d_{meas.}$	$d_{comp.}$	h k l
20	7.85	7.86	1 0 0
2	6.99	6.99	0 0 1
10	5.92	5.93	$\bar{1}$ 0 1
7	4.74	4.72	1 0 1
2	4.64	4.66	1 1 0
7	4.46	4.46	0 1 1
5	4.13	4.14	$\bar{1}$ 1 1
7	3.80	3.81	$\bar{2}$ 0 1
10	3.67	3.66	1 1 1
2	3.50	3.50	$\bar{1}$ 0 2
2	3.49	3.495	0 0 2
100	3.25	3.25	2 1 0
2	3.18	3.18	$\bar{2}$ 1 1
75	3.00	2.995	$\bar{1}$ 1 2
	2.991	2.993	0 1 2
30	2.971	2.963	$\bar{2}$ 0 2
20	2.952	2.957	1 0 2
60	2.894	2.896	0 2 0
10	2.767	2.758	2 1 1
10	2.713	2.717	1 2 0
8	2.631	2.633	1 1 2
7	2.471	2.468	1 2 1
2	2.414	2.414	$\bar{3}$ 1 1
20	2.387	2.386	3 1 0
25	2.375	2.367	$\bar{3}$ 0 2
20	2.357	2.361	2 0 2
25	2.300	2.305	$\bar{2}$ 2 1
4	2.231	2.231	$\bar{1}$ 2 2
		2.230	0 2 2
6	2.206	2.206	$\bar{1}$ 1 3
3	2.199	2.191	$\bar{3}$ 1 2
3	2.184	2.186	2 1 2
3	2.166	2.162	0 1 3
4	2.135	2.129	3 1 1
7	2.123	2.127	$\bar{2}$ 2 1
25	2.074	2.071	$\bar{2}$ 2 2
20	2.067	2.069	1 2 2
20	1.966	1.964	$\bar{4}$ 0 0
10	1.899	1.901	$\bar{4}$ 1 1
		1.901	3 0 2

Table V. Indexed x-ray pattern of tetrabasic lead sulfate

I/I_o	$d_{meas.}$	$d_{comp.}$	h k l
15	8.30	8.17	1 1 0
8	7.37	7.31	0 0 1
8	6.21	6.20	0 1 1
7	5.77	5.83	0 2 0
		5.72	2 0 0
7	5.43	5.42	1 1 1
2	5.17	5.14	2 1 0
2	4.47	4.48	$\bar{2}$ 0 1
2	4.26	4.25	$\bar{1}$ 2 1
2	3.48	3.49	0 1 2
3	3.44	3.43	0 3 1
4	3.32	3.32	1 1 2
8	3.28	3.28	1 3 1
100	3.22	3.23	3 1 1
3	3.21	3.21	$\bar{2}$ 3 0
80	3.10	3.10	$\bar{2}$ 0 2
		3.099	0 2 2
80	3.06	3.06	$\bar{2}$ 0 2
5	3.01	3.00	$\bar{1}$ 2 2
3	2.962	2.962	$\bar{2}$ 1 2
3	2.940	2.939	$\bar{3}$ 2 1
3	2.924	2.918	0 4 0
55	2.880	2.862	4 0 0
2	2.838	2.826	1 4 0
3	2.716	2.711	2 2 2
90	2.665	2.664	0 3 2
2	2.646	2.651	$\bar{4}$ 0 1
8	2.601	2.600	$\bar{1}$ 3 2
		2.598	2 4 0
6	2.572	2.568	4 2 0
5	2.558	2.557	3 1 2
2	2.394	2.391	$\bar{3}$ 2 2
2	2.342	2.343	$\bar{1}$ 1 3
2	2.328	2.330	1 1 3
4	2.319	2.317	3 4 0
2	2.293	2.286	1 5 0
2	2.279	2.280	$\bar{0}$ 4 2
2	2.262	2.268	$\bar{4}$ 0 2
2	2.257	2.255	$\bar{2}$ 0 3
4	2.241	2.240	$\bar{1}$ 4 2
		2.238	4 0 2
3	2.228	2.227	$\bar{4}$ 1 2
3	2.212	2.213	$\bar{1}$ 2 3
5	2.199	2.198	4 1 2
4	2.189	2.190	4 3 1
2	2.149	2.155	$\bar{5}$ 1 1
4	2.130	2.130	5 2 0
3	2.113	2.115	$\bar{4}$ 2 2
4	2.065	2.066	0 3 3

Table VI. IR-absorption spectra of lead sulfates

SO_4^{2-}	$PbSO_4$	$PbO \cdot PbSO_4$	β-$2PbO \cdot PbSO_4$	$4PbO \cdot PbSO_4$
(Siebert)		311 cm^{-1} st	345-365 cm^{-1}	350 cm^{-1} st (b)
		367 m (b)	387 st	
			397 st	390 sh
		420 st		437 (b)
ν_2: 451 cm^{-1}		454 sh	453 sh	460 m
				471 m
			520 st	
ν_4: 613	595 st	599 st	605 st	600 st
		607 sh (?)	613 st	610 st
				615 sh
ν_1: 981	900-1200	900-1200	955 st	960 m
	(max. at	(max. at 1066)		1050 st (b)
	1030-1090)		1050 st	1100 sh
ν_3: 1104			1146 st	1133 m

reversible at normal cooling rates and may be easily overlooked.

The transformation of α-$2PbO \cdot PbSO_4$ (which is metastable below 640°C) to the β-form occurs even during quenching at 450°C. The high-temperature x-ray data of α-$2PbO \cdot PbSO_4$, recorded in Table III, are similar to those of β-$2PbO \cdot PbSO_4$. In order to index these data, further high-temperature single-crystal investigations are necessary and are planned.

Tetrabasic Lead Sulfate

Zimkina and Shchemelev (11) gave for tetrabasic lead sulfate the following rhombic, pseudotetragonal crystal data: a = 11.5Å, b = 11.7Å, and c = 7.3Å, obtained from electron diffraction patterns. Pinsker and Farmakovskaya (12) determined the hexagonal cell parameters a = 8.98Å and c = 24.8Å. The material had been obtained by deposition from an aqueous suspension by dusting it through a silk screen. The data of Pinsker and Farmakovskaya (12) are similar to those of a basic lead carbonate $2PbCO_3 \cdot Pb(OH)_2$ described by Cowley (13).

In the course of our investigation, it was possible to synthesize the incongruently melting compound $4PbO \cdot PbSO_4$ in large single crystals out of a ternary silicate sulfate melt having the over-all composition 60 m/o (mol per cent) PbO, 15 m/o $PbSO_4$, and 25 m/o $PbSiO_3$. Oscillation, Weissenberg, and precession photographs revealed that the data of Zimkina and Shchemelev (11) are only approximate. The new cell dimensions are: Probable space group: $P2_1/a$ and a = 11.443 ± 0.02Å, b = 11.666 ± 0.02Å, c = 7.316 ± 0.02Å, and β = 90.82 ± 0.2°. The calculated density is 8.13_5 g/cm^3, assuming the number of formula weights per unit cell, Z = 4. The experimental density is 8.1 ± 0.1 g/cm^3. With these cell parameters, the powder diffraction pattern in Table V could be indexed completely. We have never observed the hexagonal modification of $4PbO \cdot PbSO_4$ described by Pinsker *et al.* (12), nor any other basic lead sulfate with hexagonal cell parameters.

The $4PbO \cdot PbSO_4$ data in Table V has, like the other basic lead sulfates in Tables II and IV, many more d-values than the (unindexed) ASTM-cards 6-0275, 308, 382, 388; 2-1276 and 12-775. Furthermore, the differing intensities reveal that possibly the ASTM-cards are based on samples which were not free of texture.

The IR-absorption data of all basic lead sulfates are collected in Table VI. They are compared with those of $PbSO_4$, anglesite, and those of the free SO_4^{2-} anion (14). The typical SO_4^{2-} absorption bands appear in all basic lead sulfates, but they show relatively large splitting (*e.g.*, $\nu 4$) which indicates that the SO_4^{2-} ion in the basic lead sulfates has lower site-symmetry than in lead sulfate.

Acknowledgments

The author expresses his thanks to Professor Dr. H. Wondratschek for his interest and support of this work. He is grateful to Dr. G. Weitz and Dr. W. E. Klee (Mineralogisches Institut der Universität Karlsruhe) for many helpful discussions.

Manuscript submitted Sept. 8, 1969; revised manuscript received *ca.* Dec. 29, 1969.

Any discussion of this paper will appear in a Discussion Section to be published in the December 1970 JOURNAL.

REFERENCES

1. F. M. Jäger and H. C. Germs, *Z. anorg. allgem. Chem.*, **119**, 152 (1921).
2. G. L. Clark, J. N. Mrgudich, and N. C. Schieltz, *ibid.*, **229**, 401 (1936).
3. J. D. Esdaile, *This Journal*, **113**, 71 (1966).
4. J. J. Lander, *ibid.*, **95**, 174 (1949).
5. H. H. Kellogg and S. K. Basu, *Trans. Met. Soc. AIME*, **218**, 70 (1960).
6. E. V. Margulis and N. I. Kopylov, *Russ. J. Inorg. Chem. (English Transl.)*, **9**, 423 (1964).
7. L. Merker and H. Wondratschek, *Glastech. Ber., Sonderband*, **30**, 473 (1957).
8. W. E. Richmond and C. W. Wolfe, *Amer. Mineralogist*, **23**, 799 (1938).
9. W. P. Binnie, *Acta Cryst.*, **4**, 471 (1951).
10. J.-C. Boivin, D. Thomas, and G. Tridot, *Compt. Rend.*, Ser. C, **267**, 532 (1968).
11. T. M. Zimkina and V. N. Shchemelev, *Fiz. Tverd. Tela Akad. Nauk SSSR*, **2**, 1646 (1960) [Solid-State Physics, Acad. Sci., USSR, **2**, 1489 (1960)].
12. G. Z. Pinsker and G. J. Farmakovskaya, *Kristallografiya*, **6**, 268 (1961).
13. J. M. Cowley, *Acta Cryst.*, **9**, 391 (1956).
14. H. Siebert, "Anwendung der Schwingungsspektroskopie in der Anorganische Chemie," p. 68, Springer Verlag, Berlin, (1966).

The Deposition of Molybdenum and Tungsten Films from Vapor Decomposition of Carbonyls

L. H. Kaplan

IBM Components Division, East Fishkill Laboratory, Hopewell Junction, New York

and F. M. d'Heurle

IBM Thomas J. Watson Research Center, Yorktown Heights, New York

ABSTRACT

Molybdenum and tungsten films formed by the pyrolytic decomposition of the respective carbonyls were investigated to determine their usefulness as conductors in microcircuit devices. The relations between deposition variables (such as pressure of carbonyls, pressure of the carrier gas, rate of gas flow, and substrate temperature) and deposition parameters (such as rate of film growth) or film properties (such as resistivity) were studied. The effects of carrier gas substitution on molybdenum film resistivity were determined. At a carbonyl pressure of 0.001 Torr, a hydrogen pressure of 0.01 Torr, a gas flow of 12 std cc/min, and a substrate temperature of 500°C, molybdenum films were deposited with a resistivity close to that of bulk (5.6 μohm cm), at a rate of 3.7 Å/sec. In molybdenum films deposited at lower substrate temperatures the resistivity increased, presumably because of increased carbon within the films. The resistivity of tungsten film is always greater than the resistivity of Mo films deposited under equivalent conditions. The lowest resistivity achieved in a tungsten film was approximately twice the value for bulk tungsten (5.5 μohm cm). The structures of both molybdenum and tungsten films deposited under conditions that favored the formation of films with the lowest resistivities were examined by x-ray diffraction as well as replica electron microscope techniques. Measured lattice parameters, when corrected for independently determined stress, were approximately equal to the parameters reported for pure molybdenum and tungsten. In all tungsten films studied, tensile stresses were found, but in molybdenum films the stresses were tensile for substrate temperatures greater than 500°C and compressive for lower temperatures.

Molybdenum and tungsten are potentially interesting materials for semiconductor device applications because of their relative inertness, high-temperature stability, satisfactory electrical resistivity, low thermal expansion coefficients, and good etching properties. Since damage to the semiconductor surface should be minimal during deposition of metal interconnections, chemical vapor deposition is preferable to sputtering or electron-bombardment evaporation. Of several ways to vapor-deposit molybdenum and tungsten, the most attractive are hydrogen reduction of metal halides and thermal decomposition of carbonyls. The latter process has the advantage of a starting material that is a fairly inert, volatile solid, which allows a relatively simple system design. It does, however, require operation at reduced pressure, in contrast to halide reductions (1-6), which usually proceed at atmospheric pressure.

In the pioneering study of molybdenum and tungsten carbonyl decomposition by Lander and Germer (7, 8) the main emphasis was placed on the mechanical properties of thick coatings used to protect bearing surfaces against wear. Electrical properties were not considered and deposition rates were not systematically studied. A general article on carbonyl metallurgy by Carlton and Goldberger (9) considers thermodynamics and kinetics. Carlton and Oxley (10) have determined the kinetics of iron carbonyl decomposition. Matyuskenko *et al.* (11) have investigated the morphology of molybdenum and tungsten films deposited via carbonyl decomposition. More recently, Cuomo (12) has described preliminary work on molybdenum and tungsten films formed from their respective carbonyls.

In the present work, the carbonyl decomposition process was characterized with regard to deposition rate and to properties (resistivity, stress, orientation, grain size) of the films produced. The effects were investigated of varying the parameters (temperature, pressure, and rate of gas flow) and of modifying the chemistry of the system. A specific aim of some of these experiments was to reduce carbon in molybdenum films.

Apparatus and Method

All films were deposited as follows in an apparatus shown schematically in Fig. 1. The apparatus consisted of a diffusion-pumped vacuum system 1 connected to a vertical reactor tube 2. A cylindrical molybdenum susceptor 3, supported and rotated from below, was heated inductively through use of a coil mounted outside the tube. The substrate, generally an oxidized silicon wafer, was placed on the susceptor and was perpendicular to the direction of the incoming gas. The gas (hydrogen or other carrier gas at reduced pressure, containing a known partial pressure of metal carbonyl) entered through the top of the tube. The carbonyl pressure was established by regulating the temperature of solid carbonyl in a reser-

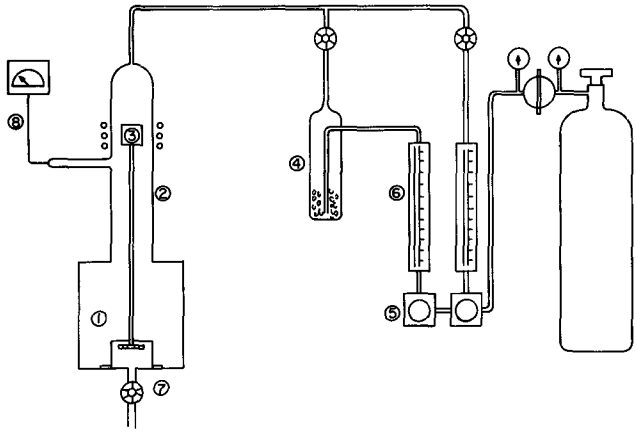

Fig. 1. Schematic drawing of apparatus used for film deposition

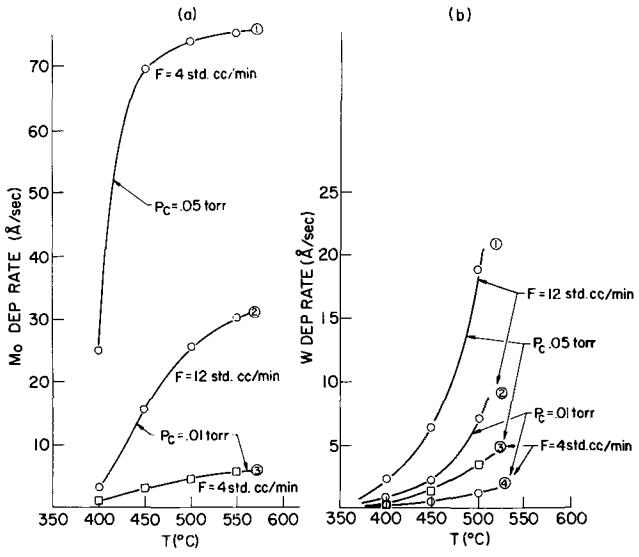

Fig. 2. Rate of metal deposition vs. deposition temperature. a. P_H = 0.07 Torr; b. P_H = 0.23 Torr.

voir 4 through which the carrier gas passed. This reservoir (shown in the diagram as a single chamber) consisted of a superheated carbonyl source followed by an equilibrating chamber maintained at the desired temperature. The rate of flow was regulated by a needle valve 5 and calibrated flow meter 6. Pressure in the tube was determined by setting the vacuum valve 7 and was read by a calibrated Pirani gauge 8.

The temperature of the molybdenum susceptor was read from a thermocouple rigidly fastened to it. The substrate was thermally coupled to the susceptor by a layer of liquid gallium which maintained susceptor and substrate at essentially identical temperatures. To prevent reaction between the gallium and the molybdenum susceptor, the upper surface of the susceptor was coated with reactively sputtered silicon nitride. The hydrogen and argon (Matheson research grade, 99.995% pure, with nitrogen the main impurity) were used without further purification. The molybdenum carbonyl (99.5% purity)[1] was found by emission spectroscopy to contain less than 0.01% metallic contaminants.

Typically, film deposition would begin with evacuating the reactor tube to a pressure of 2 x 10^{-5} Torr. Carrier gas was then admitted through a by-pass at low flow rate and pressure, while the substrate temperature was raised to the desired point. The carrier gas was then allowed to flow through the carbonyl powder and into the reactor at the desired flow rate, while the vacuum valve was used to adjust reactor pressure. After the desired deposition time, gas flow and heat were turned off, and the substrate was cooled to room temperature, while carrier gas flow was maintained. The most important process parameters that could be varied independently were substrate temperature, carbonyl partial pressure, carrier gas pressure, and carrier gas flow rate. Each significantly affected the rate of deposition, but deposition temperature appeared to affect the resistivity of the films formed most significantly.

Thickness measurements were made with a Talysurf instrument and/or a Tolanski interferometer. Film resistivities were derived from resistance measurements obtained from a linear four-point probe and a Keithley 503 milliohmeter. A qualitative evaluation of film adhesion was obtained by means of the so-called "Scotch-tape test."

Results and Discussion

Process rate studies.—Figure 2a and b show the effect of substrate temperature on deposition rates of Mo and W, respectively, for several typical sets of operating parameters. Although the conditions for the two metals were not fully equivalent, it may be noted that deposition rates for Mo were higher than those for W. As the deposition temperature is increased, the deposition rate tends to rise sharply at first but then levels off at high temperatures. However, the leveling off effect shown by the Mo rate curve at higher temperatures is not exhibited by the W curves. Additional results have shown that for deposition temperatures lower than 400°C, the rates of growth of Mo films appear to increase slightly with decreasing temperatures. A maximum in deposition rate is reached at about 300°C. Since this unexpected increase in deposition rate occurs under conditions where molybdenum carbide rather than molybdenum films are obtained, it is likely due precisely to the formation of molybdenum carbide. At temperatures below 300°C the rate of deposition falls rapidly to zero.

The effect of carbonyl partial pressure P_c on deposition rate is shown in Fig. 3a and b for Mo and W, respectively, for various conditions of temperature and flow. In all cases approximate linearity is observed in the initial portions of the curves, generally followed by a leveled-off portion. The importance of carrier gas flow rate F, at constant P_c and total pressure, in determining the rate of Mo and W deposition is clearly shown in Fig. 4a and b, for low and high levels of temperature and carbonyl pressure.

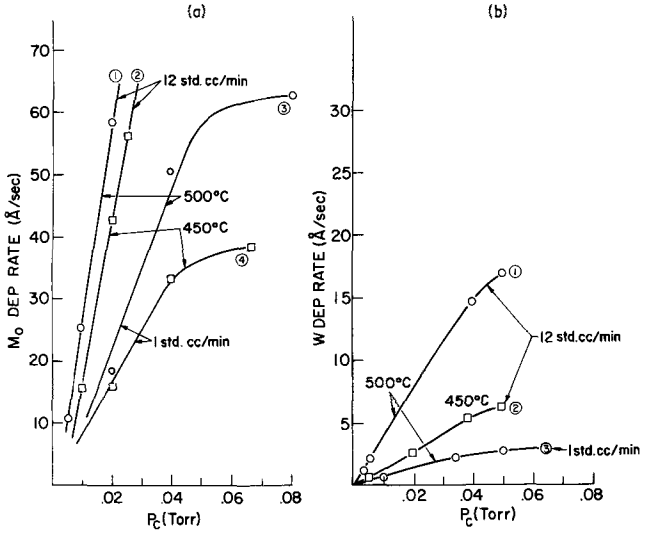

Fig. 3. Rate of metal deposition vs. carbonyl partial pressure. a. P_H = 0.07 Torr; b. P_H = 0.23 Torr.

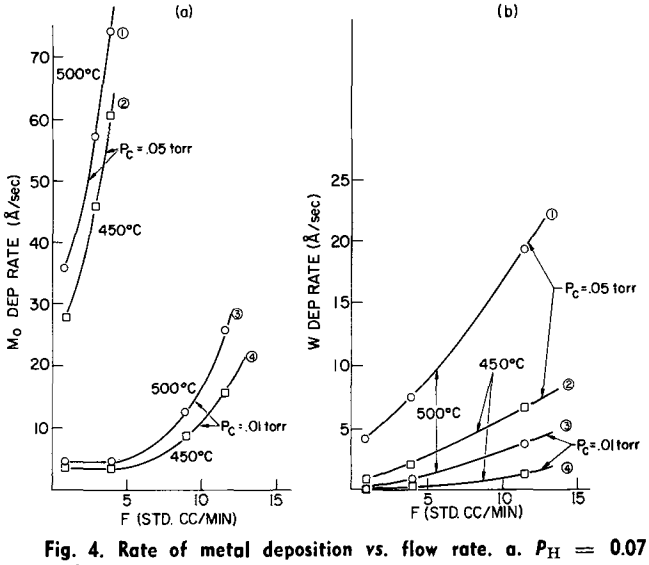

Fig. 4. Rate of metal deposition vs. flow rate. a. P_H = 0.07 Torr; b. P_H = 0.23 Torr.

[1] Purchased from Gallard-Schlesinger Chemical Manufacturing Corporation, Carle Place, New York.

In vapor decomposition processes such as those considered here, two mechanisms are generally expected to play a rate-controlling role: (*i*) the chemical decomposition of the carbonyl, and (*ii*) gaseous diffusion of carbonyl vapor to the deposition surface. Also, in this latter diffusion mechanism one should include the diffusion of by-products, in this case CO, away from the same surface.

The individual processes should each exhibit a different temperature dependence. Thus, as the temperature is raised, the rate of the chemical decomposition will increase as exp $(-Q/kT)$ (where Q is the activation energy), while the rate of a gaseous diffusion will vary only as the $\sqrt{T}$ (13). Hence, while the carbonyl decomposition might be the rate-limiting step at some lower temperature range (here, apparently 200°-400°C), the diffusion steps would limit the rate at higher temperatures.

It should also be noted that an experimental limitation can be caused by the carbonyl depletion of the gas at high deposition rates. A quick calculation indicates that under the deposition conditions used here, such a depletion effect contributes to the leveling-off in the deposition rates recorded in curves 1 and 2 of Fig. 2a.

The shape of the curves (deposition rate *vs.* carbonyl pressure) in Fig. 3 suggests that gaseous diffusion of carbonyl molecules to the substrate surface is rate-limiting. The rate of such diffusion should be linear with carbonyl concentration until the concentration becomes high enough that diffusion is no longer the slowest process. At higher carbonyl pressure the over-all rate should be much less affected by pressure, and the curves should level off.

The effect of flow rates on the rate of deposition is shown in Fig. 4. The curves do not extrapolate to a deposition rate of 0 at 0 flow rate. This undoubtedly reflects the diffusion of carbonyl vapor from the source to the reactor. The approximate proportionality observed between deposition rate and pressure (at equal temperature) at the lowest flow rates substantiates this point. The more than linearly increasing variation of deposition rate at high flow rate in curves 3 and 4 of Fig. 4a remains unexplained.

From the temperature dependence as shown in Fig. 2, one may attempt to calculate an over-all activation energy for the reactions. The form of these curves indicates that, in the case of Mo, carbonyl decomposition is rate-limiting only at the lower temperature ranges. Figure 5 shows an Arrhenius-type plot of the rate/temperature data for a typical set of conditions (0.05 Torr of Mo $(CO)_6$ flowing at 0.9 std. cc/min). For Mo $(CO)_6$ an activation energy of 23 kcal/mole was found, while the corresponding value for W $(CO)_6$ was 18 kcal/mole. These figures are roughly in the same range as the value of 14 kcal/mole reported (14) for the decomposition of nickel carbonyl, Ni $(CO)_4$.

Lander and Germer (7) found that Mo deposition on an iron surface stops totally when the temperature is lowered to 160°C. In the course of this study, a similar behavior was found to occur at temperatures which varied with choice of substrate surfaces. In each case, the expected exponential decay of deposition rate with temperature was interrupted by a sudden cutoff of deposition. In order to initiate deposition at temperatures in the range immediately above the cutoff, it was found necessary to raise the system pressure to several Torr for a few seconds. Once deposition began, pressure could be lowered to the desired level (usually about 0.01 Torr) and deposition continued. Minimum Mo deposition temperatures were established for oxidized silicon surfaces, as well as for various polymer surfaces. On SiO_2, Mo deposition cuts off between 180° and 170°C. On oxidized silicon wafers coated with AZ1350, a photosensitive varnish used in semiconductor technology,[2] deposition does not occur below 210°C. Although not all deposition parameters were studied for all cases, it was found that the cutoff temperature for SiO_2 surfaces was not significantly dependent upon carbonyl pressure or flow rate.

[2] Distributed by the Shipley Corporation, Wellesley, Massachusetts.

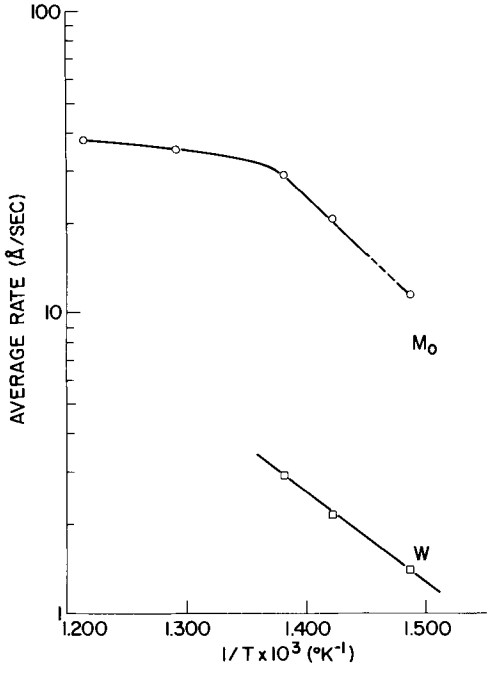

Fig. 5. Log (rate) vs. 1/T

Film properties.—Adherence.—Adherence of films to a substrate is a function of two types of opposing forces. One arises from the bonding between film and substrate and the other from the state of stress of the film. If the stresses in the film are effectively independent of film thickness, adhesion will decrease with increasing film thickness because of the increased shearing force at the film-substrate interface. On the other hand, the increase in film adhesion usually observed with increasing temperature of deposition may be attributed to the formation of chemical bonds between substrate and film material. In general, films formed above 500°C were perfectly adherent. Molybdenum films with thicknesses of 13,000Å or less deposited at 450°C were satisfactory according to the "Scotch-tape test." The Mo films deposited at lower temperatures were unsatisfactory. The same finding is essentially true for tungsten films of the same thickness.

To obtain adherent films in the lower temperature ranges so that other film properties might be evaluated, several potentially useful methods were developed. The addition during the first minute of deposition of a partial pressure (1-2 Torr) of an oxidizing gas (O_2 or H_2O) greatly improved adhesion to SiO_2 surfaces and allowed deposition temperatures as low as 325°C. Similarly low temperatures were made practical by first depositing at a very low rate (0.1-1.0 Å/sec) up to a thickness of several hundred angstroms. Deposition at normal rates following this step yielded adherent films at substrate temperatures as low as 325°C. Adherence of films depends strongly on the nature of the substrate surface. Ultrathin coatings (*e.g.*, 100Å) of AZ1350, or other photosensitive varnishes, on the oxidized silicon wafers allowed deposition of adherent Mo films at all substrate temperatures down to the 210°C cutoff temperature. Aside from the effects of such coatings, no relationship between film adhesion and substrate preparation procedures could be established.

Electrical resistivity.—The resistivity of metal films is of paramount importance for most microelectronic applications. The most probable cause for high resistivities in the films produced by carbonyl decomposition is the incorporation of carbon into the metal struc-

Table I. Resistivity and carbon content for various deposition conditions

Carrier gas	Deposition Temperature, °C	Rate, Å/sec	P_{H_2O}, mm	Resistivity, μohm cm	Carbon content, ppm
H_2	430	5	0	28	4400
H_2	480	5	0	10.1	2800
CO_2	480	5	0	9.5	1600
H_2	480	5	0.0003	8.8	1100
H_2	430	5	0.0003	9.0	1100
Ar	480	5	0	9.0	1000
H_2	500	5	0.0003	6.2	700
H_2	530	5	0	5.8	700
H_2	480	0.8	0	5.8	<260

ture either as interstitial atoms or in the form of a finely divided carbide. Such a cause/effect relationship is strongly suggested by the data in Table I. Here, the average carbon content, obtained by chemical analysis (oxidation followed by micro-gas-analysis), is listed with average resistivity for various deposition conditions, including the presence of water vapor in the plating gas. A good correlation between carbon content and resistivity is evident.

Figure 6a and b show the effect of deposition temperature on resistivity for films of Mo and W formed via carbonyl decomposition. It may be noted that resistivity of films deposited in the high range of substrate temperature is essentially invariant with temperature. For any given pressure and flow conditions, however, there will be some substrate temperature below which the resistivities of deposited films are found to increase. In fact, a decrease of 50°C in substrate temperature in this range can cause the resistivity of the resultant film to be 10-100 times as high as that of films formed at higher temperatures. Indications are that resistivity may level off again for still lower deposition temperatures. However, diffraction studies indicate that a carbide phase is deposited at such temperatures.

The dramatic effect of deposition temperature on resistivity of the deposited films shown in Fig. 6 can be explained, at least qualitatively, in terms of the thermodynamics of the CO/CO_2 equilibrium. When thermodynamic equilibrium is assumed, the ratio of carbon to metal deposited in the films can be derived from a consideration of the following reactions

$$M(CO)_6 = M + 6\,CO \qquad [1]$$

$$C + CO_2 = 2\,CO \qquad [2]$$

Clearly, the number of moles of deposited carbon will be equal to the number of moles of CO_2. From the knowledge of the equilibrium constant K for Eq. [2] one may then calculate the ratio of moles of deposited carbon to moles of deposited metal. This is expressed by the relation

$$\frac{n_m}{n_c} = \frac{K}{6} \cdot \frac{1}{P_{CO}} + \frac{1}{3} \qquad [3]$$

where n_m and n_c are the numbers of moles of deposited metal and carbon, respectively. Calculated values of the ratio n_c/n_m, together with values of K (15) as a function of T are listed in Table II. At least in the lower concentration range, n_c/n_m should be linear with resistivity. The values of CO pressure used were obtained by assuming a carbonyl pressure of 0.0076 mm (a typical pressure here) and using the derived relationship

$$P_{CO} = \frac{K}{4}\left(-1 \pm \sqrt{1 + 48\ P_c/K}\right) \qquad [4]$$

It is apparent that an increasingly sharp rise in the ratio n_c/n_m is to be expected as the deposition temperature is lowered. In practice, as is seen in Fig. 6, this effect reaches noticeable proportions below 450°C in molybdenum and generally below about 500° for tungsten.

Table II. Calculated deposition of carbon in films as function of temperature
(For $P_c = 7.6 \times 10^{-3}$ mm $= 10^{-5}$ atm)

Temperature, °C	Equilibrium constant, $K = p_{CO}^2/P_{CO_2}$	P_{CO}, atm	n_m/n_c	n_c/n_m, $\times 10^6$
800	10.0	6.23×10^{-5}	9.95×10^5	1
750	2.98	5.96×10^{-5}	2.96×10^6	3
700	1.01	6.06×10^{-5}	1.02×10^7	10
650	0.347	6.07×10^{-5}	3.52×10^4	28
600	0.079	5.99×10^{-5}	7.90×10^3	127
550	0.019	5.98×10^{-5}	1890.0	552
500	3.7×10^{-3}	6.01×10^{-5}	369.0	2,710
450	5.6×10^{-4}	5.07×10^{-5}	47.6	21,000
400	9.2×10^{-5}	3.45×10^{-5}	5.60	179,000

Although no correlation between resistivity and any one deposition parameter other than deposition temperature was established, the resistivity of molybdenum films was found to change with deposition rate, as illustrated in Fig. 7. These films were deposited on substrates at 400°C and had relatively high resistivities. Results obtained with films deposited at 500°C might be expected to show a similar relationship between resistivity and rate. However, because the resistivities of such films were so close to bulk value, they were almost indistinguishable. The more sensitive parameter of resistivity ratio ($\rho_{\text{room temperature}}/\rho_{\text{liquid } N_2}$) was used in an attempt to discover a relation-

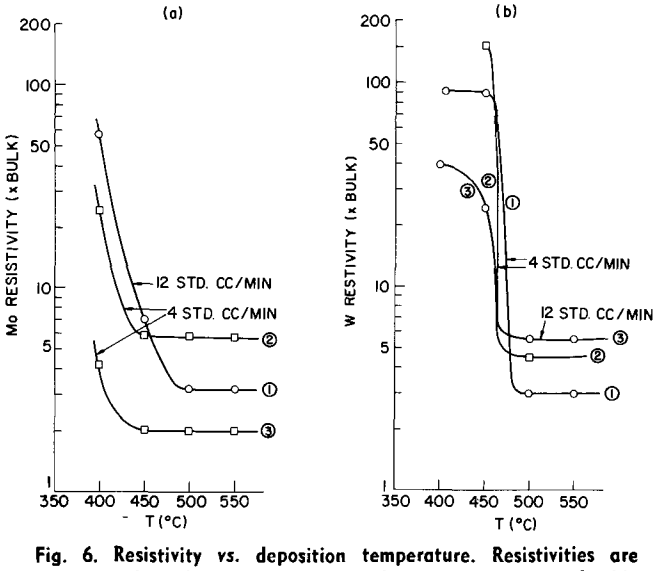

Fig. 6. Resistivity vs. deposition temperature. Resistivities are given as number of times bulk value, taken as 5.7 μohm cm for Mo and 5.5 μohm cm for W. a. $P_H = 0.074$ Torr; b. $P_H = 0.23$ Torr.

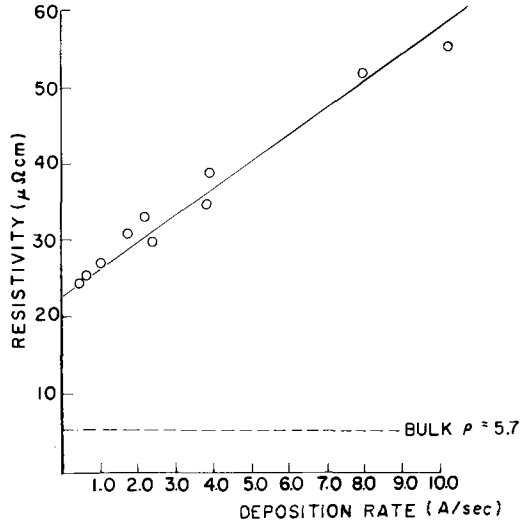

Fig. 7. Resistivity vs. deposition rate

ship between the resistivity and rate of growth of films deposited at 500°C, but no clear-cut relation was found. The dependence of resistivity on deposition rate, observed in films deposited at 400°C, is possibly explained by the physical incorporation of adsorbed carbon-containing molecules (CO and CO_2) into the growing film. If the rate of deposition is high enough that an adsorbed biproduct molecule is covered before it can move away, the molecule will become an impurity in the film. Lower rates of deposition might allow a greater portion of biproduct molecules to escape before entrapment and thus yield films with lower resistivity.

An investigation aimed at determining the optimum deposition parameters for molybdenum films deposited at the lowest possible substrate temperature, but still displaying a resistivity of approximately 6 μohm cm (close to that of pure bulk molybdenum), yielded the following results: substrate temperature 500°C, carbonyl pressure 0.001 Torr, hydrogen pressure 0.01 Torr, rate of gas flow 12 std. cc/min, rate of film growth 3.7 Å/sec. Attempts to obtain films with as low resistivities, but deposited at lower substrate temperatures, were all unsuccessful.

Some alloys of Mo and W were formed by simultaneous decomposition of the two carbonyls in appropriate molar ratios. Alloys prepared from such mixtures containing 0, 2, 5, 10, and 50% W had resistivities of 6.9, 7.3, 7.7, 8.6, and 14.7 μohm cm. Experience with chromium impurities in certain batches of molybdenum carbonyl in this work indicated that Cr exerts a deleterious influence on the resistivity of Mo films. This effect, which appears quite large, may be partly due to the formation of chromium carbide.

Structure, orientation, and stress.—Films deposited at different substrate temperatures were examined by the usual replica electron microscopy technique and by x-ray diffraction. In some instances, the stresses in the films were determined by the "wafer bending technique," (16) in which stresses are evaluated from the optically determined bow imparted to the underlying silicon substrate.

Measurements made on an XRD-5 diffractometer with a Cu target yielded information about structure, preferred orientation, and particle size; and through lattice parameter (17) determination (with an accuracy of ± 0.0015Å) gave values for the homogeneous film stresses. Strains measured from lattice parameter measurements were correlated with stresses determined by optical means, according to the formula

$$\epsilon_z = \frac{2\nu}{E}\sigma_x \qquad [5]$$

where ϵ_z is the strain normal to the surface of the film, ν is the Poisson ratio, E the modulus of elasticity, and σ_x is the homogeneous film stress in the direction parallel to the film surface. The values (18) of ν and E are 0.32 and 3.2 x 10^{12} dynes/cm^2, respectively, for pure molybdenum.

For tungsten $E = 3.5 \times 10^{12}$ dynes/cm^2, and $\nu = 0.27$, from the listed values (19) of E and G, the modulus of rigidity. The diffraction line broadening was partitioned into two parts, respectively proportional to $1/\cos\theta$ and $\tan\theta$, which yielded values of particle size and heterogeneous film stresses. A few samples were also examined by electron diffraction.

Molybdenum films used for structural studies were deposited under conditions that produced films with the lowest value of film resistivity obtained. The carbonyl pressure was 0.0015 Torr, hydrogen pressure 0.01 Torr, and rate of gas flow 12 std. cc/min; only the substrate temperature was varied for the different film depositions.

The residual stresses measured by optical means at room temperature were tensile for films deposited at high substrate temperatures (1.5 to 2 x 10^9 dynes/cm^2, 580°C) and compressive, with quite high values, for films deposited at lower substrate temperatures. Compressive stress values of 2 x 10^9 dynes/cm^2, 1.3 x 10^{10} dynes/cm^2, and as high as 2.3 x 10^{10} dynes/cm^2 were determined for films deposited at substrate temperatures of 530°, 480°, and 430°C, respectively.

Figure 8 shows the surface topography of a film deposited at 580°C, as shown by the microscope. X-ray diffraction indicates that such a film has a very strong (100) orientation. The lattice parameter measured on a similar film was found to be 3.1456Å, and 3.1468Å after correction for a film stress of 2 x 10^9 dynes/cm^2. (The listed lattice parameter (20) is 3.1466Å for pure molybdenum.) The particle size, from x-ray measurements, was $\sim$ 2500Å in a direction normal to the film surface. If one assumes that Fig. 8 gives a good indication of the grain size in a direction parallel to the film surface, it would appear that the grain structure is approximately equiaxed. Values of heterogeneous stresses, approximately ± 3.5 x 10^9 dynes/cm^2, appear quite high.

Figure 9 is an electron micrograph of a replica taken from a 5000Å thick film of molybdenum deposited at a substrate temperature of 530°C. This film showed a mixed (100)-(211) orientation, with the (211) part predominant. The combination of orientations, as well as an apparently smaller grain size, probably accounts for the more complex surface aspect displayed in Fig. 9 as compared with Fig. 8. The high lattice-parameter value, measured as 3.1490Å (corresponding to 3.1475Å after correction for a stress of 2.3 x 10^9 dynes/cm^2) corroborates indications that the film is in a state of compressive stress. Diffraction-determined grain size and heterogeneous stress values are about equal to those reported above for a film deposited at 580°C. Film orientations do not correspond to those observed by Lander and Germer (7) who reported mostly (111) orientations.

Films deposited at a substrate temperature of 480° and 430°C displayed nondistinctive surface structures on examination by electron microscopy.

When films deposited at a substrate temperature of 480°C were studied by x-ray diffraction, strong (211) and (111) peaks were obtained, while (200) peaks were either absent or extremely weak. The lattice parameter of one such film was 3.1562Å, or 3.1480Å after correction for a compressive stress of 1.3 x 10^{10} dynes/cm^2. The diffraction peaks were quite wide. If

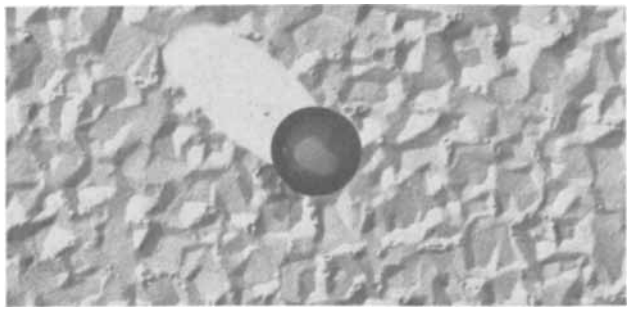

Fig. 8. Electron micrograph of a molybdenum film, 9000Å thick, deposited at a substrate temperature of 580°C. The latex ball has a diameter of 5000Å (as on the other photographs).

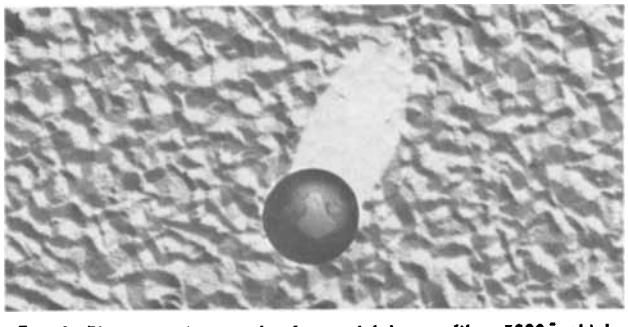

Fig. 9. Electron micrograph of a molybdenum film, 5000Å thick, deposited at a substrate temperature of 530°C.

one assumes, as was found in films deposited at higher temperatures, that the line broadening can be partitioned equally between grain size and heterogeneous stress effects, the grain size would be of the order of 600Å and the heterogeneous stress approximately $\pm 5.5 \times 10^9$ dynes/cm^2.

Several films were deposited at a substrate temperature of 430°C. Unfortunately, because of poor adhesion and other difficulties, these had to be used independently for optical stress measurements and for x-ray studies. A compressive stress with a magnitude of 2.3×10^{10} dynes/cm^2 was observed in one of these films. This apparently corresponds to a lattice parameter of 3.1622Å determined in a similar film with a (100) orientation, which would give a value of 3.1477Å after correction for stress. However, most films deposited under similar conditions appeared to have a random orientation and a lattice parameter of 3.1510Å. This latter value would fit quite well with a stress value of 3.6×10^9 dynes/cm^2 which was also measured in a film deposited at 430°C under identical conditions. It was not possible to determine the cause of the two orientations and of the relation between film stress and film orientation. In all of these films, regardless of substrate temperature during deposition, the lattice parameters (after correction for stress), agree within the accuracy of these measurements with the lattice parameter of pure molybdenum. Impurities, therefore, do not contribute significantly to the lattice parameter of the films.

When the substrate temperature during deposition is below 400°C, molybdenum carbide films rather than molybdenum metal films are obtained. The transition between deposition temperatures that correspond to molybdenum films and those that correspond to molybdenum carbide films occurs rather sharply at about 400°C. Only in films deposited at this temperature were diffraction lines characteristic of molybdenum and molybdenum carbide obtained simultaneously. Films deposited at 415°C appeared to be essentially "pure" molybdenum and films deposited at 370°C "pure" carbide. This value of the transition temperature appears in rough agreement with the one that can be extrapolated from the work of Lander and Germer. In spite of rather strong preferred orientations in carbide films, enough diffraction peaks were obtained to establish that the carbide phase is the cubic form reported by the same authors.

Molybdenum carbide films deposited at substrate temperatures of 375°C or below had very strong (100) orientations, although in films deposited at 300°C this orientation was somewhat less pronounced. Figure 10 is an electron micrograph of a replica taken from a 5000Å film deposited at 345°C. The apparent grain size is commensurate with a value of 1200Å determined in a similar film by x-ray diffraction. In general, carbide films had remarkably sharp diffraction lines, indicating that grain size did not decrease much below 1000Å and that heterogeneity either of stress or composition was limited. The lattice parameter, which seems to increase with decreasing temperature of deposition, may be influenced by lack of carbon stoichiometry. Values of 4.136, 4.146, and 4.160Å were found for films deposited at 370°, 350°, and 300°C, respectively.

For purposes of structural examination, tungsten films were deposited at a carbonyl pressure of 0.002 mm, at a hydrogen pressure of 0.01 mm, at a flow rate of 12 std. cc/min, and at substrate temperatures of 450°, 400°, 350°, and 300°C. X-ray diffraction examination of the films showed that all of them were "pure" tungsten, without detectable carbide lines. These results were confirmed by electron diffraction for the films deposited at 450°, 400°, and 300°C. Thus, as previously observed by Lander and Germer, the tendency to form carbides is much less in tungsten films than in molybdenum films. The film deposited at 450°C had a (100) orientation, while the others were randomly oriented. For both tungsten and molybdenum films, higher temperatures of deposition favor (100) orientations. However, for equal temperatures of deposition, tungsten films show tensile stress, whereas molybdenum films show compressive stresses. From two tungsten films deposited at 400°C, the value of the tensile stress was found to be $4.6 \pm 1 \times 10^9$ dynes/cm^2. In a film deposited at 450°C the lattice parameter was 3.1616Å, which, when compared with a lattice parameter of 3.1650Å for pure tungsten (21), corresponds to a tensile stress of 5.3×10^9 dynes/cm^2. Diffraction line broadening showed the film had heterogeneous stresses of $\pm 4 \times 10^9$ dynes/cm^2 and a particle size of 1200Å. Comparison of this value with the apparent grain size of the same film in Fig. 11 indicates that the structure might be slightly columnar.

The stress level in the tungsten films is approximately twice the 2.6×10^9 dynes/cm^2 value that would be expected on the basis of differential contraction between tungsten and silicon, for films deposited at about 400°C. It appears, therefore, that the films are deposited with intrinsic tensile stresses. The molybdenum films, however, display compressive stresses, which probably are due to carbide precipitation.

Effects of gaseous additions and substitutions.—Since low resistivity is desired for conducting films in microelectronic devices, different techniques were used to try to decrease the resistivity of molybdenum films. Generally speaking, the aim was to improve the resistivity by decreasing the carbon incorporated in the films during deposition.

Addition of water vapor and hydrogen sulfide to carrier gas.—The removal of carbon from metals, according to the reaction

$$H_2O + C = H_2 + CO \qquad [6]$$

is well established. However, excessive concentrations of H_2O in a system could lead to oxidation of the host material, according to a reaction such as

$$Mo + 3\,H_2O = MoO_3 + 3H_2 \qquad [7]$$

which would be expected to deleteriously affect the resistivity. Hence, with increasing water vapor, the resistivity passes through a minimum. In fact, the oxidation of Mo by mixtures of H_2 and H_2O is thermodynamically favored up to 800°C for the minimum

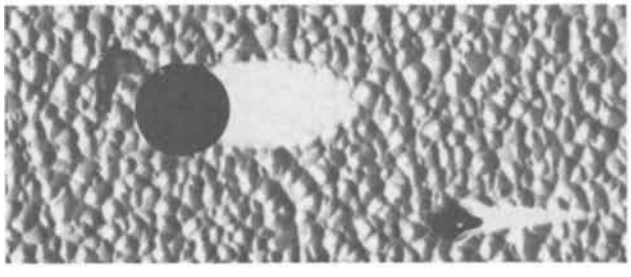

Fig. 10. Electron micrograph of a molybdenum carbide film, 5500Å thick, deposited at a substrate temperature of 345°C.

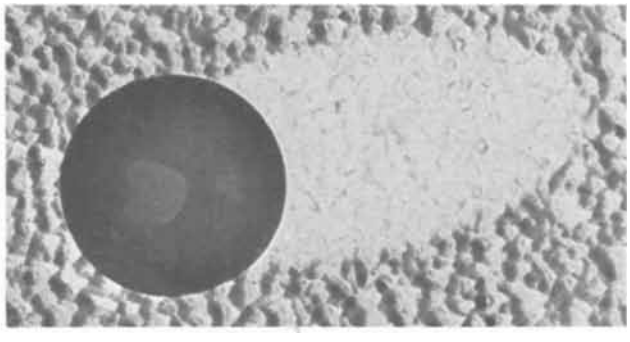

Fig. 11. Electron micrograph of a tungsten film, 3000Å thick, deposited at a substrate temperature of 450°C.

H_2O/H_2 ratio (0.01) used in this work. Calculations indicate that an H_2O/H_2 ratio at 2×10^{-6} is just oxidizing at 400°C. These calculations were based on the data of Glassner (22) for MoO_3 ($\Delta F = -157$ kcal/mol at 300°K and -115 kcal/mol at 800°K) and for MoO_2 ($\Delta F = -116$ kcal/mol at 300°K and -89 kcal/mol at 800°K) and on the method described in Darken and Gurry (23). [The substantial disagreement between this value and the 0.062 mentioned by Lander and Germer (7) probably is due to their use of unreliable data for the free energies of formation of the two molybdenum oxides.] Results of experiments on adding water vapor to the hydrogen carrier gas are shown in Fig. 12. Although resistivity improved substantially at low deposition temperatures, where resistivity values generally are high, very little improvement occurred in films deposited at 500°C, which had a resistivity close to that of bulk molybdenum even when deposited without added water vapor. To determine whether reaction [6] plays a significant role in the resistivity of films deposited in the presence of water vapor, several films deposited at a substrate temperature of 480°C (with water vapor pressure of 0.001-0.002 Torr) were subsequently annealed in hydrogen at 600°C. This treatment had no effect on the resistivity of the films. It is possible that the negative result is due to the difficulty in reaching equilibrium at this comparatively low temperature for molybdenum.

Removal of carbon by H_2S could be envisaged according to the following reaction

$$2H_2S + C = 2H_2 + CS_2 \qquad [8]$$

Although such a reaction is not thermodynamically favored, under equilibrium conditions, decreases in the carbon content of molybdenum films deposited in the presence of H_2S were reported by Lander and Germer (7).

Results obtained here indicate that although the addition of H_2S produces a substantial decrease in resistivity at a deposition temperature of 350°C, no advantage is gained for deposition at 500°C. In fact, it has been observed that even extremely small concentrations of H_2S cause the resistivity to rise for films deposited at this temperature.

Substitution of argon or carbon dioxide for hydrogen. —The water-carbon reaction of Eq. [6] suggests another means for reducing the carbon content in these films. When hydrogen is used as a carrier gas, it tends to drive this reaction to the left, causing carbon to form by the reduction of the CO biproduct from the carbonyl decomposition. Hence, substitution of an inert gas such as Ar might be expected to reduce carbon content. Figure 13 compares the electrical resistivity of films made with H_2 with that of films made with Ar carrier gases at various temperatures.

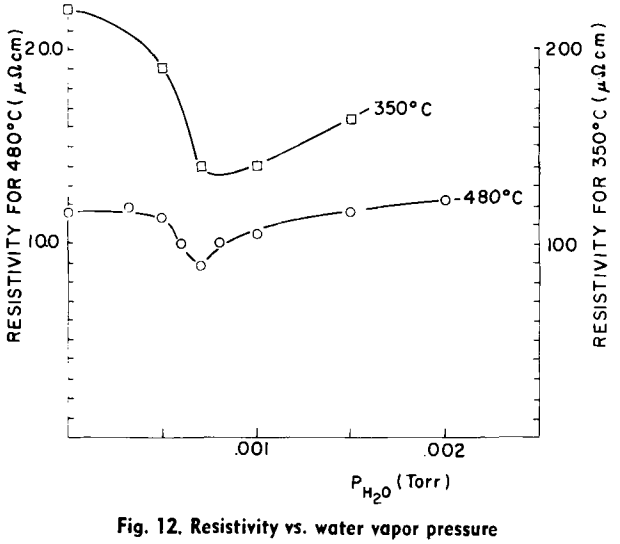

Fig. 12. Resistivity vs. water vapor pressure

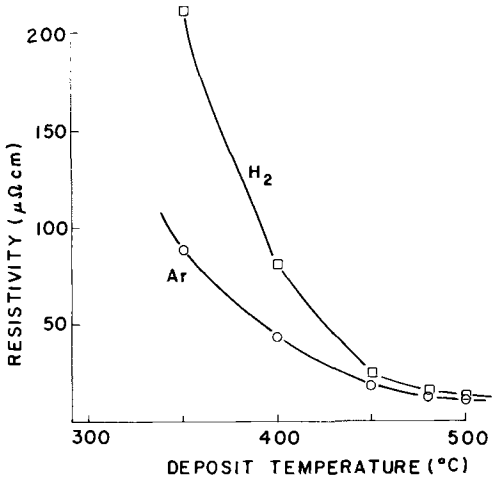

Fig. 13. Resistivity vs. deposition temperature for two carrier gases.

Although at low deposition temperatures the carrier gas substitution has a definite advantage, improvement falls off rapidly with increasing temperature. Carbon analysis of films deposited at 480°C shows no substantial differences in carbon content when the carrier gas is changed.

The disproportionation of carbon monoxide, shown in Eq. [2] to be a likely source of carbon in the films, theoretically should be reversed by an increase in concentration of CO_2. As in the case of water, however, too much CO_2 can constitute an oxidizing atmosphere and react with the depositing metal M, according to the reaction

$$M + 3\,CO_2 = MO_3 + 3\,CO \qquad [9]$$

It was to be expected then that pure CO_2 carrier gas would lead to large resistivities. A mixture of CO_2 and H_2 might minimize both oxide and carbon impurities. Figure 14 shows resistivity as a function of mole fraction of H_2 in the carrier gas for films deposited at 400°C. A minimum is evident in the region of 30 m/o (mole per cent) H_2.

Conclusions

Molybdenum films with a resistivity approaching the bulk value can be deposited from decomposition of molybdenum carbonyl at temperatures of 500°C, or above, and at growth rates of 3-4 Å/sec. At lower deposition temperatures films with bulk resistivity cannot be obtained, presumably because of carbon incorporation within the films, as evidenced by the correlation between film resistivity and carbon content.

In molybdenum films the stress changes from a tensile value of 1.5-2 x 10^9 dynes/cm^2 for films deposited at 580°C to a compressive value of 2.3 x 10^{10} dynes/cm^2 for films deposited at 430°C. In tungsten films deposited in a similar range of temperatures,

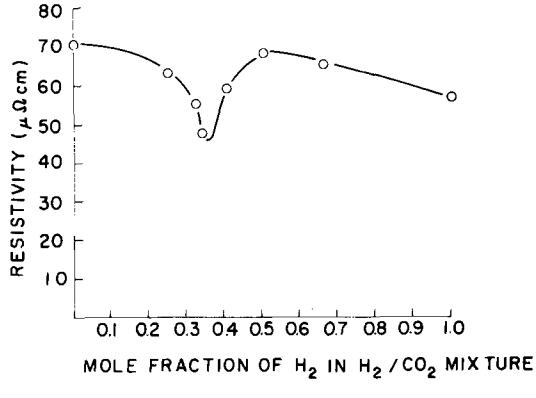

Fig. 14. Resistivity vs. mole fraction of H_2 in H_2/CO_2 mixtures

only tensile stresses were observed, with a value of 4.6 x 10^9 dynes/cm^2 for a film deposited at 400°C. This difference between tungsten and molybdenum films is probably related to the formation of a carbide phase, which was found to form much more readily in molybdenum than in tungsten.

Attempts to produce films with low resistivity by making chemical deposition conditions more oxidizing were most successful at deposition temperatures of about 400°C. However, the improvements obtained were not sufficient to reduce resistivity to values approaching bulk value. Additions of water vapor, hydrogen sulfide, carbon dioxide, and argon to hydrogen, and various combinations of these were not effective in the temperature range of 450°-500°C, where the unmodified carbonyl decomposition in hydrogen gives films with resistivities of 1.5-2 times bulk value. Thus it must be concluded that production of molybdenum films with bulk resistivity by carbonyl decomposition at substrate temperatures below 500°C is unlikely.

Acknowledgments

The authors are pleased to acknowledge the help of Mr. W. C. Metzger who accomplished most of the experimental work involved in depositing the films and in making the stress determinations. Mr. C. Aliotta made the replicas and obtained the electron micrographs. Comments by T. Sedgwick were extremely helpful.

Manuscript received Oct. 2, 1969.

Any discussion of this paper will appear in a Discussion Section to be published in the December 1970 JOURNAL.

REFERENCES

1. W. J. Childs *et al., Trans. ASM,* **43,** 105 (1951).
2. S. T. Wlodek and J. Wulff, *This Journal,* **107,** 565 (1960).
3. S. H. Smiley, D. C. Brater, and H. L. Kaufman, *J. Metals,* **17,** 605 (1965).
4. G. Kano *et al., J. Appl. Phys.,* **37,** 2985 (1966).
5. J. G. Donaldson and H. Kenworthy, U.S. Dept. of Interior, Bureau of Mines, Report 6853 (1966).
6. G. F. Wakefield, *This Journal,* **116,** 5 (1969).
7. J. J. Lander and L. H. Germer, *Trans. Met. Soc.-AIME,* **175,** 648 (1948).
8. J. J. Lander, U.S. Patent 2,690,980 (October 1954).
9. H. E. Carlton and W. M. Goldberger, *J. Metals,* **17,** 611 (1965).
10. H. E. Carlton and J. H. Oxley, *A.I.Ch.J.,* **11,** 79 (1965).
11. N. J. Matyushenko, A. A. Rozen, and V. V. Sagalovich, *Fiz. Metal. Metalloved.,* **21,** 403 (1966).
12. J. J. Cuomo, To be published.
13. S. Dushman, "Scientific Foundations of Vacuum Techniques," pp. 10 and 74, John Wiley & Sons, Inc., New York (1949).
14. R. K. Chan and R. McIntosh, *Can. J. Chem.,* **40,** 845 (1962).
15. J. B. Austin and M. J. Day, *Ind. Eng. Chem.,* **33,** 23 (1941).
16. R. Glang, R. Holmwood, and R. L. Rosenfeld, *Rev. Sci. Instr.,* **36,** 7 (1965).
17. F. d'Heurle, *Trans. Met. Soc.-AIME,* **236,** 314 (1966).
18. H. R. Clauser, "The Encyclopedia of Engineering Materials and Processes," p. 430, Reinhold Publishing Corp., New York, (1963).
19. *Ibid,* p. 686.
20. W. P. Pearson, "A Handbook of Lattice Spacings and Structure of Metals and Alloys," p. 752, Pergamon Press, New York (1963).
21. *Ibid.,* pp. 884-885.
22. A. Glassner, "Thermochemical Properties of Oxides, Fluorides and Chlorides," Argonne National Laboratory, Contract W 31-109-eng-38 (1957), L.C. 58-62015.
23. L. S. Darken and R. W. Gurry, "Physical Chemistry of Metals," p. 349, McGraw-Hill Book Co., Inc., New York (1953).

The Ga-GaP-GaAs Ternary Phase Diagram

G. A. Antypas

Varian Associates, Palo Alto, California

ABSTRACT

The ternary phase diagram of Ga-GaP-GaAs has been calculated using Darken's quadratic formalism for a ternary liquid in equilibrium with a regular solid solution. Liquidus isotherms have been calculated from 900° to 1450°C in 50°C increments. GaP distribution curves have also been calculated for 0.95, 0.9, 0.8, 0.7, 0.6, 0.5, 0.4, 0.3, and 0.1 mole fraction of GaP. The calculated ternary and pseudobinary phase diagrams are in excellent agreement with available experimental data.

Since it was demonstrated that the GaP-GaAs system forms continuous solid solutions (1) the system has attracted great attention, primarily because a portion of the system has a bandgap corresponding to the visible region of the spectrum. Initially, the GaAs-GaP crystals were prepared by vapor transport techniques, using AsH_3 and PH_3 as the source materials (2). It has been demonstrated, however, that III-V compounds grown from solution have a lower native defect density (3) and in general have more efficient radiative recombination properties. Thus an understanding of the thermodynamic properties of both the liquid and solid solutions is necessary for establishing optimum growth conditions. The model to be presented has already been applied to the In-Ga-As and Ga-As-Sb (4) systems where it gave excellent agreement with available experimental data. It can also be applied to all III-V ternary solids forming continuous solid solutions.

Phase Equilibria of III-V Ternary Compounds

Ternary-phase diagrams of III-V compounds have been calculated using the quasi-chemical equilibrium treatment (5) and the regular solution treatment (6). In computing the conditions for equilibrium between a ternary liquid solution A, B, C (Ga, P, As) and a pseudobinary solid solution AB-AC (GaP-GaAs), Stringfellow and Greene (5) derived the following equations

$$\ln \gamma_{AB}x = \ln 4N_AN_B + \ln (\gamma_A\gamma_B/\gamma_A^{STC}\gamma_B^{STC}) + \Delta S^F_{AB}(T^F_{AB} - T)/RT$$
$$\ln \gamma_{AC}(1-x) = \ln 4N_AN_C + \ln (\gamma_A\gamma_C/\gamma_A^{STC}\gamma_C^{STC}) + \Delta S^F_{AC}(T^F_{AC} - T)/RT \quad [1]$$

where γ_{AB} and γ_{AC} are the activity coefficients of AB and AC in the solid solution, x is the mole fraction of AB, N_i and γ_i (i = A, B, C,) are the atom fraction and

activity coefficient of i in the liquid solution, respectively, γ_i^{STC} is the activity coefficient of N_i at the stoichiometric composition, ΔS^F_{AB} is the entropy of fusion of AB, T^F_{AB} is the temperature of fusion of AB, R is the universal gas constant, and T is the temperature in °K.

Under the restriction

$$N_A + N_B + N_C = 1 \qquad [2]$$

Eq. [1] can be solved numerically on a computer to yield two sets of curves, one describing the liquidus isotherms and the other describing the solidus isoconcentration curves of the system.

In previous investigations the activity coefficients were determined by the quasi-chemical equilibrium (5) approach and by considering the ternary liquid as a strictly regular solution (6). In the present communication, however, the determination of the activity coefficient in the liquid phase is based on Darken's quadratic representation, which for a binary liquid is

$$\ln \gamma_A = \alpha_{AB} N_B^2$$
$$\ln (\gamma_B/\gamma^0_B) = \alpha_{AB}(-2N_B + N_B^2) \qquad [3]$$

where A is the solvent and B is the solute, γ^0_B is the activity coefficient of B at infinite dilution, and α_{AB} is the interaction parameter of the system. Equation [2] reduces to that describing a regular solution if $\ln \gamma^0_B = \alpha_{AB}$. This formalism has been satisfactorily applied by Darken (7) and Turkdogan and Darken (8) to a number of liquid metallic solutions for concentration of up to 60%. This formalism is consistent with the Gibbs-Duhem equation and satisfies Raoult's and Henry's laws as the limiting cases. The quadratic formalism was also extended by Darken (9) to ternary systems, which results in activity coefficients given by

$$\begin{aligned}
\ln\gamma_A &= \alpha_{AB}N_B^2 + \alpha_{AC}N_C^2 + (\alpha_{AB} + \alpha_{AC} - \alpha_{BC})N_BN_C \\
\ln(\gamma_B/\gamma^0_B) &= -2\alpha_{AB}N_B + (\alpha_{BC} - \alpha_{AB} - \alpha_{AC})N_C \\
&\quad + \alpha_{AB}N_B^2 + \alpha_{AC}N_C^2 + (\alpha_{AB} + \alpha_{AC} - \alpha_{BC})N_BN_C \\
\ln(\gamma_C/\gamma^0_C) &= -2\alpha_{AC}N_C + (\alpha_{BC} - \alpha_{AB} - \alpha_{AC})N_B \\
&\quad + \alpha_{AB}N_B^2 + \alpha_{AC}N_C^2 + (\alpha_{AB} + \alpha_{AC} - \alpha_{BC})N_BN_C
\end{aligned} \qquad [4]$$

where component A is the solvent and components B and C are the solutes, γ^0_C is the activity coefficient of component C at infinite dilution, and α_{i-j} are the interaction energies of the various binary systems. The above formalism is also consistent with the Gibbs-Duhem equation, and furthermore it reduces to the binary quadratic formalism as one of the solutes in the ternary approaches infinite dilution.

The solid solution in equilibrium with the ternary liquid was assumed to be regular, *i.e.*, $\Delta F^{xs} = \alpha_{AB\text{-}AC}x(1 - x)$, where $\alpha_{AB\text{-}AC}$ is the interaction energy and x is the mole fraction of one of the components in the solid. The activity coefficients are thus given by

$$\ln \gamma_{AB} = \alpha_{AB\text{-}AC}(1 - x)^2$$
$$\ln \gamma_{AC} = \alpha_{AB\text{-}AC}x^2 \qquad [5]$$

Substituting Eq. [4] and [5] in Eq. [1] the ternary phase diagram can be calculated numerically to yield the liquidus and solid distribution curves.

Calculation of the Ga-GaP-GaAs Phase Diagram

The parameters necessary in calculating the ternary phase diagram are the temperatures T^F and entropies ΔS^F of fusion of the III-V compounds and the interaction parameters α_{AB}, α_{AC}, α_{BC}, and $\alpha_{AB\text{-}AC}$. T^F and ΔS^F for GaP and GaAs can be obtained directly from the literature and are shown in Table I. Vieland (10) has used regular solution theory to calculate the liquidus of III-V compounds. The interaction parameter obtained from such a treatment is

$$\alpha = \frac{\Delta S^F (T - T^F)\,[1 + R/\Delta S^F \ln 1/4x(1 - x)]}{2(x - 0.5)^2} \qquad [6]$$

Table I. List of thermodynamic parameters used in calculating the Ga-GaP-GaAs phase diagram

	GaP	GaAs	As-P	GaP-GaAs
α (cal/mole)	7900-7.00 T (11)	−3.7 T (12)	2000	1000
ΔS^F (eu)	15 (11)	16.64 (12)	—	—
T^F (°C)	1470	1238	—	—

where x is the column V element in solution. For a regular solution α should be independent of temperature and composition. Thurmond (11), however, demonstrated that for GaAs and GaP α is a linear function of temperature given by

$$\alpha_{GaAs} = 9960 - 11.15\ T$$
$$\alpha_{GaP} = 7900 - 7.00\ T \qquad [7]$$

When the interaction parameter α is divided by RT so that it will be thermodynamically consistent with Darken's formulation it takes the form of

$$\omega = \frac{\mathcal{L}}{RT} - \frac{\mathcal{S}}{R} \qquad [8]$$

which is of the form derived by Turkdogan and Darken (8), where $\mathcal{L}$ and $\mathcal{S}$ have the units of enthalpy and entropy, respectively.

In calculating α_{GaAs}, Thurmond assumed a ΔS^F_{GaAs} value of 14.0 eu. Arthur (12) pointed out that when a recently measured value for ΔS^F_{GaAs} of 16.64 eu is used, then

$$\alpha_{GaAs} = 5160 - 9.16\ T$$

Arthur has also calculated the activity coefficient of As from As vapor pressure measurements, and using a regular solution treatment found that the interaction parameter is accurately given by

$$\alpha_{GaAs} = -3.7\ T$$

The interaction parameter of the As-P system was calculated to be 2000 cal/mole by fitting the liquidus curve to a regular solution model and comparing it to available experimental data (13). Similarly, the interaction parameter of the GaP-GaAs system was determined by fitting the solidus to recently published data of the GaP-GaAs pseudobinary (14). Calculations performed by Moon (15) on GaP-GaAs were in good agreement for $\alpha_{GaP\text{-}GaAs} = 1000$ cal/mole.

Figure 1 represents the calculated ternary phase diagram. Solid lines represent the liquidus isotherms from 900° to 1450°C by 50°C increments, while dotted lines represent GaP isoconcentration curves at 0.95, 0.9, 0.8,

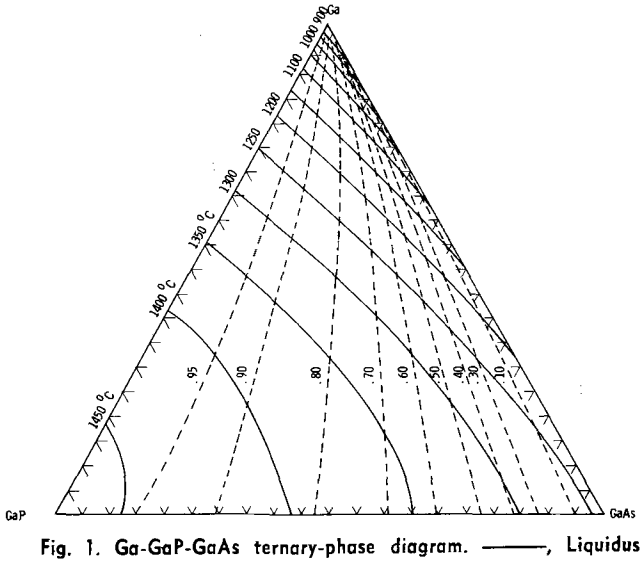

Fig. 1. Ga-GaP-GaAs ternary-phase diagram. ———, Liquidus isotherms, - - - - -, GaP isoconcentrations curves.

0.7, 0.6, 0.5, 0.4, 0.3, and 0.1 mole fraction of GaP. The pseudobinary obtained from Fig. 1 is shown on Fig. 2 along with available experimental data (14). Figures 3, 4, and 5 compare the experimental results reported by Thurmond for the GaAs and GaP compounds, and by Panish (16) for the Ga-GaP-GaAs solution growth and solution epitaxy results. Figure 3 is a portion of Fig. 1, plotted in cartesian coordinates, showing the

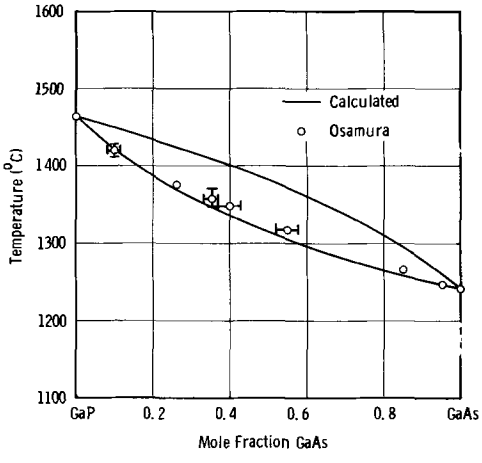

Fig. 2. GaP-GaAs pseudobinary-phase diagram

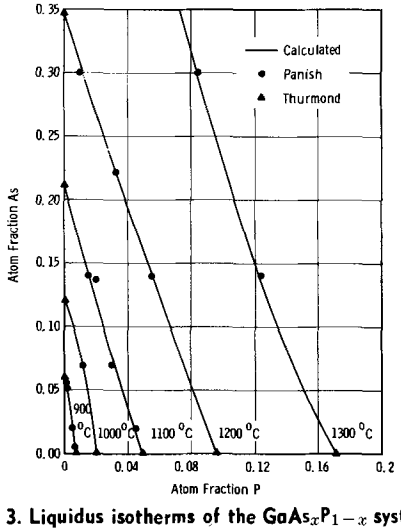

Fig. 3. Liquidus isotherms of the $GaAs_xP_{1-x}$ system

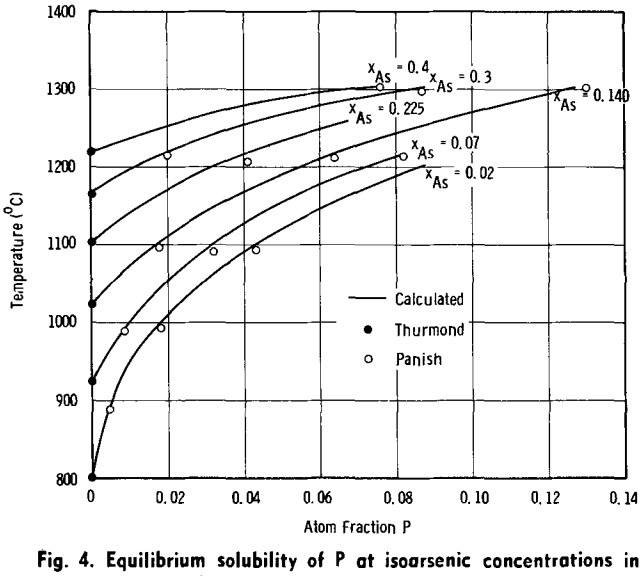

Fig. 4. Equilibrium solubility of P at isoarsenic concentrations in the ternary liquid solution.

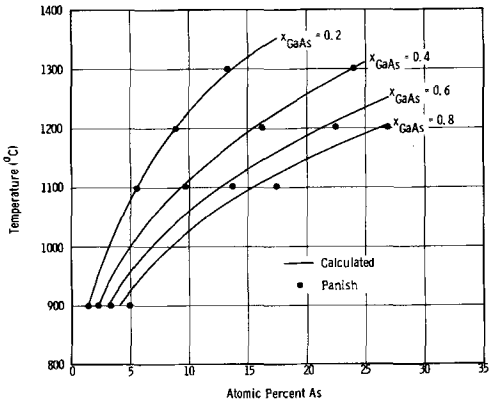

Fig. 5. GaAs isoconcentration curves plotted as a function of temperature and As concentration in the melt.

equilibrium solubility of P as a function of the As concentration in the melt for 900°, 1000°, 1100°, 1200°, and 1300°C isotherms. Excellent agreement is obtained between calculated and experimental results. Figure 4 also shows a portion of the ternary-phase diagram in greater detail, on which the solubility of P is plotted as a function of temperature at isoarsenic concentrations. Figure 5 represents the distribution of GaAs in equilibrium with the ternary melt as a function of the As present in the liquid solution. The distribution coefficient is defined by

$$D = \frac{\gamma_{GaP}}{\gamma_{GaAs}} \frac{x_{GaAs}/x_{As}}{x_{GaP}/x_P}$$

where γ_{GaAs}, x_{GaAs}, and x_{As} are the activity coefficient of GaAs in the solid solution, the GaAs mole fraction, and the atom fraction of As in the liquid solution, respectively. For the 1100°C isotherm, D varied between 0.13 for $x_P = 0.045$ and 0.27 for $x_P = 0.002$.

Conclusions

It has been shown that ternary phase diagrams of III-V compounds calculated by Darken's phenomenological quadratic formalism are in excellent agreement with available experimental data. The parameters used in calculating the Ga-GaP-GaAs phase diagram were either directly obtained from the literature, or were obtained by fitting the model to available experimental data. Although this model is derived to describe the solution in the vicinity of the major component (in solution epitaxy and solution growth of GaP_xAs_{1-x} in the vicinity of the Ga corner of the ternary diagram), the agreement between the calculated and experimental results of the pseudobinary phase diagram indicate that the quadratic formalism accurately describes the ternary phase diagram of Ga-GaP-GaAs for concentration of up to 50%.

Manuscript submitted Oct. 30, 1969; revised manuscript received Dec. 18, 1969.

Any discussion of this paper will appear in a Discussion Section to be published in the December 1970 JOURNAL.

REFERENCES

1. N. A. Goryunova, "The Chemistry of Diamond-Like Semiconductors," Chapman and Hall Ltd. (1965).
2. J. J. Tietjen and J. A. Amick, *This Journal*, **113**, 724 (1966).
3. C. S. Kang and P. E. Greene, *Appl. Phys. Letters*, **11**, 171 (1967).
4. G. A. Antypas and L. W. James, Accepted for publication in *J. Appl. Phys.*, 1970.
5. G. B. Stringfellow and P. E. Greene, *J. Phys. Chem. Solids*, **30**, 1779 (1969).
6. M. Ilegems and G. L. Pearson, "Proceedings of the Second International Symposium on GaAs," C. I. Pedersen, Editor, p. 3, Institute of Physics and the Physical Society, London (1969).

7. L. S. Darken, *Trans. Met. Soc. AIME*, **239**, 80 (1967).
8. E. T. Turkdogan and L. S. Darken, *ibid.*, **242**, 1997 (1968).
9. L. S. Darken, *ibid.*, **239**, 90 (1967).
10. L. J. Vieland, *Acta Met.*, **11**, 137 (1963).
11. C. D. Thurmond, *J. Phys. Chem. Solids*, **26**, 798 (1965).
12. J. R. Arthur, *ibid.*, **28**, 2257 (1967).
13. M. Hansen, "Constitution of Binary Alloys," McGraw-Hill Book Co., New York (1958).
14. K. Osamura and Y. Murakami, *Japan J. Appl. Phys.*, **8**, 967 (1969).
15. R. L. Moon, Private communication.
16. M. B. Panish, *J. Phys. Chem. Solids*, **30**, 1083 (1969).

Properties of Aluminum Oxide Obtained by Hydrolysis of $AlCl_3$

T. Tsujide, S. Nakanuma,* and Y. Ikushima

IC Division, Nippon Electric Company, Tokyo, Japan

ABSTRACT

A study has been made of aluminum oxide films prepared by the hydrolysis of mixtures of $AlCl_3$, H_2, and CO_2. Positive shifts of the flat band voltage of the MAS structure occur independently of the polarity and type of the applied bias when this is higher than a critical voltage. This phenomenon can be explained by electron injection and trapping. The trapped electrons have a long lifetime, but are excited by radiation such as x-rays and electron beam without introduction of damage.

One of the most important processes in the fabrication of semiconductor devices is the passivation of the semiconductor surface. For this purpose, various dielectric films have been examined, among which the most studied has been thermally grown silicon dioxide, because of its ease of preparation. Unfortunately, it exhibits instabilities such as shifts in device characteristics due to the migration of impurities, especially Na ions through the oxide at elevated temperatures under bias conditions (1) and degradation of device characteristics under irradiation environments (2); more demanding requirements have therefore led to the need for insulating films superior to this oxide.

It is a reflection of such requirements that recently silicon nitride and aluminum oxide have been receiving a great deal of attention. These materials were found to have properties superior to silicon dioxide films, in that the ion migration effect has been shown to be sufficiently negligible that they may be used as a barrier for contamination (3, 4), making it possible to fabricate capless devices. In addition, they have a high radiation resistance (5, 6). However, silicon nitride has some disadvantages of high surface charge density and crack generation during subsequent heat-treatment. On the other hand, it has been reported that aluminum oxide makes the silicon surface more p-type due to the negative charge (7, 8). This is pertinent to the fabrication of insulated gate field effect transistors with low threshold voltage as well as n-channel enhancement mode devices. Moreover, there are several applications of the aluminum oxide such as a diffusion mask, passivating film for bipolar type devices, and other new structures.

There are various methods for formation of aluminum oxide: pyrolysis of organic compounds such as $Al(C_3H_7O)_3$ (3, 9) and $Al(C_2H_5O)_3$ (10), anodization of aluminum in oxygen plasma (11), reactive evaporation (12), and reactive sputtering (13, 14). The films obtained by the above methods are structureless, *i.e.*, amorphous, but some of these aluminum oxide films have instabilities under thermal stress which are found to be reduced by post annealing at temperatures as low as 400°C. On the other hand, deposition of polycrystalline aluminum oxide films on silicon by the hydrolysis of $AlCl_3$ at about 800°C was reported by Nigh (15) and Doo and Tsang (16). The properties of such polycrystalline films, namely refractive index, etch rate, infrared absorption, and dielectric constant, have been studied by us as a function of deposition conditions, and the MAS (metal-aluminum oxide-silicon) structures have been used to evaluate the electrical properties of the Si-Al_2O_3 interface. All of these results are discussed here.

* Electrochemical Society Active Member.

Experimental

The system used for the deposition of aluminum oxide films on silicon wafers was similar to that reported by Nigh (15) in which H_2O vapor, formed by the reaction of CO_2 with hydrogen, hydrolyzes $AlCl_3$ vapor. All deposition runs were carried out using the following conditions: the flow rates of CO_2, hydrogen saturated with $AlCl_3$ vapor and make-up hydrogen were 326 cc/min, 2 l/min, and 20 l/min, respectively, and the temperature of the silicon wafers was measured by means of an optical pyrometer and was kept at 850°C. The deposition rate of aluminum oxide was approximately 70 Å/min. The silicon wafers with (100) orientation and resistivities of $3 \sim 5$ ohm-cm, either p-type or n-type, were mechanically-chemically polished and carefully cleaned. The cleaning procedure involved rinses in trichlorethylene and acetone using ultrasonic agitation immediately prior to the deposition.

The refractive index and the thickness of the aluminum oxide films were measured by ellipsometry. The etch rate was determined by measuring thickness after each successive etching.

For the evaluation of the electrical properties of the aluminum oxide films and the Si-Al_2O_3 interface, the MAS structure was constructed by the deposition of aluminum oxide on silicon, followed by the evaporation of aluminum electrodes of 1 mm diameter and mounting on TO-5 headers. The C-V characteristics of the MAS structure were measured at 1 MHz. From the area of the electrode, the thickness of the film, and the capacitance of the MAS structure under accumulation conditions the dielectric constant was obtained. The I-V characteristics of the aluminum oxide were also measured by the same MAS structure using a Keithley electrometer in order to analyze the conduction mechanism in the aluminum oxide.

Results

Ellipsometric measurements on the aluminum oxide yielded values for the relative permittivity of $7.6 \sim 7.8$. These are consistent with 7.6 for the film obtained by anodization in oxygen plasma (11), but are less than

those of 8.9 ~ 9.3 (15) and 11 (17) for the films formed by the hydrolysis of $AlCl_3$.

The dielectric strength measured using the MAS structure was found to depend on the polarity of the applied voltage. When positive voltage was applied to the Al electrode, dielectric breakdown occurred at fields of $6 \sim 7 \times 10^6$ and $8 \sim 9 \times 10^6$ V/cm at room and liquid nitrogen temperature, respectively, while for negative polarity it occurred with time dependence, *i.e.*, when a somewhat lower field than $1.1 \sim 1.2 \times 10^7$ V/cm was applied for a few minutes, a thermal current fluctuation of nA order was observed and finally the film underwent breakdown. Similar phenomena have been observed for steam-grown silicon dioxide films, though the polarity dependence was opposite (18).

Figure 1 shows the capacitance-voltage characteristics of an Al_2O_3 film of 1200Å in thickness on n-type silicon substrate at three different temperatures, −196°, 25°, and 250°C. It should be noted that this unit has a nearly zero flat band voltage at room temperature in coincidence with the ideal MIS diode characteristic; the C-V curve shifts in the positive voltage direction at liquid nitrogen temperature and in the negative direction at 250°C. The MAS structure with p-type silicon, however, showed the opposite shifts to that with n-type silicon, indicating that fast surface states exist in the energy gap of silicon. These shifts can be explained by the existence of acceptor- and donor-type surface states near the band edge of the conduction and valence bands, respectively, as reported by Gray and Brown (19) for the thermal grown oxide film. With decreasing temperature down to liquid nitrogen temperature the acceptor-type states above the room temperature Fermi level are filled with electrons so as to make the surface of the silicon more p-type. The amount of scatter in the flat band voltages at room temperature is in the range $0 \sim 0.5$V for n-type silicon and $0.4 \sim 3.0$V for p-type. These positive flat band voltages imply that negative charges of $10^9 \sim 10^{11}$ electron charges/cm^2 exist either at the Si-Al_2O_3 interface or within the Al_2O_3 film. The origin of the negative charge has been explained in terms of the existence of negative ions in the Al_2O_3 film (10), but the negative charge reported here is believed to be due to electrons, as will be discussed later.

The MAS structure exhibited an interesting behavior in that the C-V curves shifted in the positive direction after application of voltages higher than a critical voltage, below which the C-V curves are very stable and reproducible. This positive shift occurred independently of the polarity and type of the bias, such as +d.c., −d.c., a.c., and pulse. Figures 2(a) and 2(b) show the effects of positive and negative bias, respectively, applied to the metal electrode on the C-V

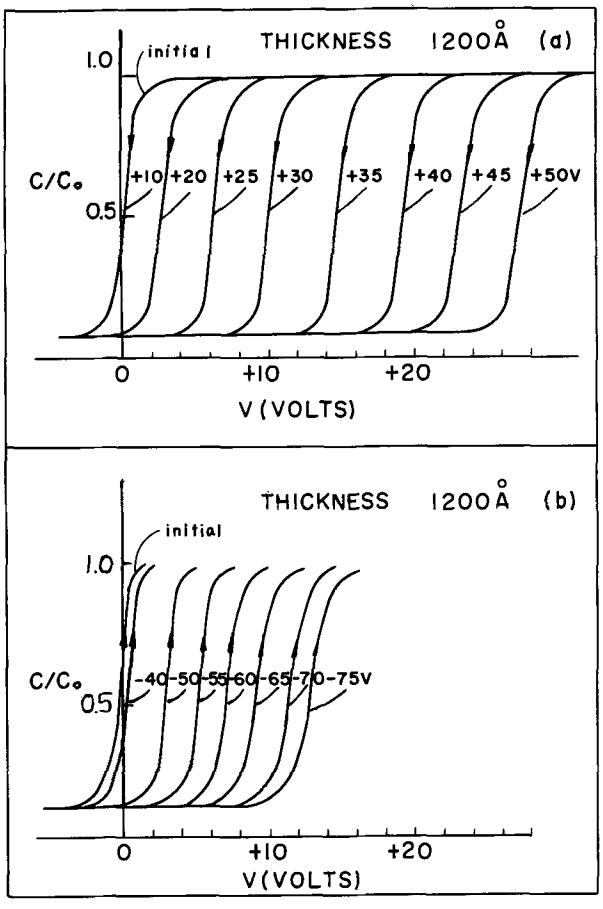

Fig. 2. Capacitance-voltage characteristics after application of various voltages to the Al electrode at room temperature for 1 min: (a) the effect of positive bias; (b) the effect of negative bias.

characteristics of the MAS structure with an Al_2O_3 film of 1200Å in thickness. These curves were taken after application of the bias indicated in the figures at room temperature for 1 min. Figure 3 shows the voltage shifts *vs.* the applied bias, where the critical voltages for the negative and positive bias were +15 and −40V, respectively. With positive bias, voltage shifts continue to increase linearly with applied bias until dielectric breakdown occurs, while with negative voltage linear positive shifts above the negative critical voltage followed by a decrease of the positive shifts are observed. This decrease is always accompanied by increasing current through the aluminum oxide film, which will be discussed later. Such positive shifts were also observed at liquid nitrogen temperature as shown

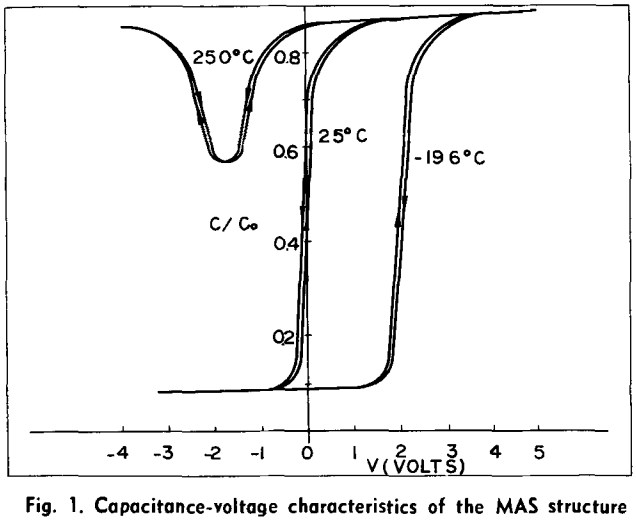

Fig. 1. Capacitance-voltage characteristics of the MAS structure at −196°, 25°, and 256°C, 3 ohm-cm n-type silicon substrate.

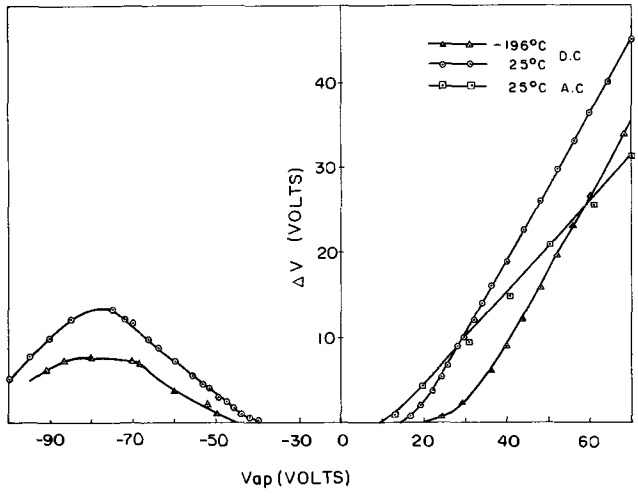

Fig. 3. Relationship between positive shift ΔV and applied voltage (d.c. and a.c., 50 Hz) at room and liquid nitrogen temperature. A-C bias shows peak value; initial flat band voltage is +0.2V.

in Fig. 3, but the lower the temperature, the higher are the critical voltages.

Figure 4 shows the change in the positive shifts when the negative bias is applied to the MAS structure after the positive shifts caused by the positive bias, and when positive bias is applied after the positive shifts by the negative bias. This means that the shifted voltages are kept constant to the same values when the voltage is reversed.

The time dependence of the positive shifts in the C-V characteristics of a typical sample with a 1200Å aluminum oxide film at room temperature for bias values of +40 and −60V is shown in Fig. 5. Although there seems to be a broad distribution of time constant, saturation was observed about 100 min after the application of the bias in both cases. The decay of the shift was studied as a function of film thickness, temperature, and polarity of the applied bias and the results are shown in Fig. 6 and 7. Figure 6 shows a typical decay curve of the positive shift at room temperature, where the shift was caused by application of +100V for 1 min to the MAS structure with a 2400Å aluminum oxide film. An initial decrease of the shift is followed by a very slow decay, where it takes 10^{14} hr to decay by a half of the shift. Figure 7 shows decay curves of the MAS structure with a 1200Å aluminum oxide film at several temperatures, the shifts of which were caused by the application of positive bias as well as negative bias, where samples having nearly the same values of the shift were used. Apparently the decays consist of two parts; 1, a rapid decay for the first several minutes especially for the samples with the shift caused by a positive bias, which compares with the initial rapid increase of the shift shown in Fig. 5 and has considerably large temperature and polarity dependencies; 2, a subsequent slow decay which is in proportion to the logarithm of time, the temperature dependence of which is less sensitive than that of the rapid decay and the slope of which is larger for the positive bias than the negative bias.

Figure 8(a) and (b) show the effect of x-rays on C-V characteristics of the as-grown MAS structure

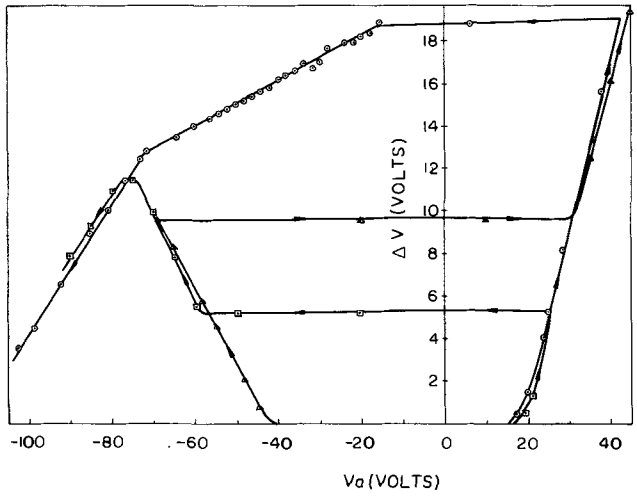

Fig. 4. Dependence of positive voltage shift ΔV of MAS structure with previous bias history on subsequent voltage applications.

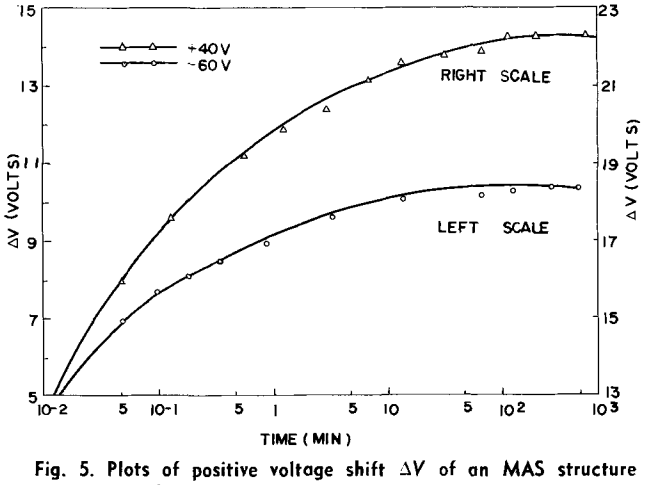

Fig. 5. Plots of positive voltage shift ΔV of an MAS structure with initial flat-band voltage of +0.2V.

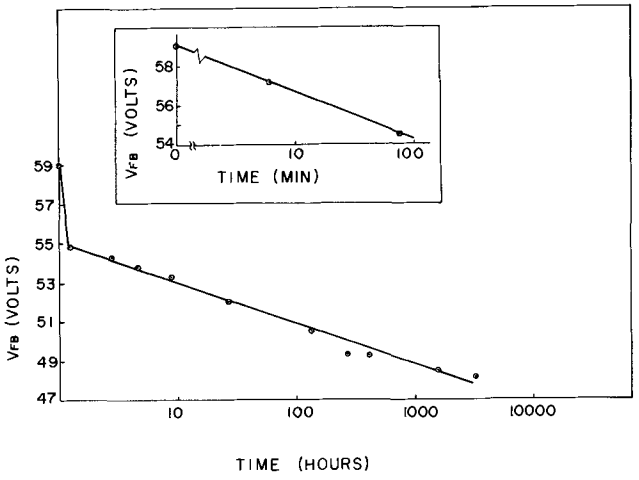

Fig. 6. Decay of positive shift of flat-band voltage with time at room temperature. Insert illustrates initial decay. Film thickness is 2400Å, and p-type silicon substrate is used.

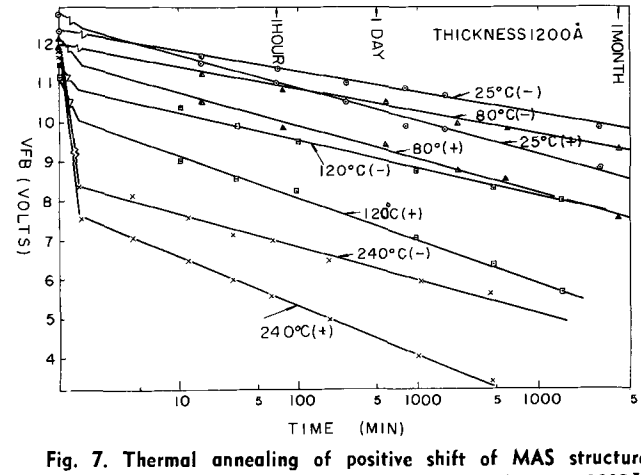

Fig. 7. Thermal annealing of positive shift of MAS structure with initial flat band voltages of +0.2V. Film thickness is 1200Å, and 3 ohm-cm n-type silicon substrate is used.

Figure 8(a) and (b) show the effect of x-rays on C-V characteristics of the as-grown MAS structure

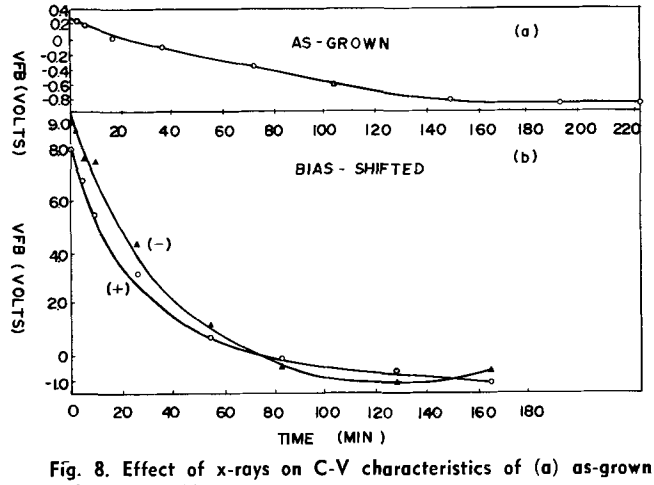

Fig. 8. Effect of x-rays on C-V characteristics of (a) as-grown and (b) shifted MAS structure.

and the shifted one, respectively, where x-rays from a copper target tube operated at 25 kV and 2 mA were irradiated through the aluminum electrode at a distance of 5 cm. No difference of the decay constants for the shift by positive bias and by negative bias was observed. Logarithm of flat-band voltage *vs.* radiation time gave a straight line, indicating exponential decay. The shapes of the C-V curves before and after irradiation were unchanged and an MAS structure which had been returned to the initial state by irradiation with x-rays or an electron beam showed the same positive shift on application of bias greater than the critical voltage as it did in the first place.

In addition to the large positive shifts for the MAS structure, a very slight C-V hysteresis of the order of 0.05V was observed, as shown in Fig. 1, which at room temperature occurred in the same direction of shift as that due to ion migration or polarization, but in the opposite direction at liquid nitrogen temperature. This was also observed on the positive shifted C-V curve with the same order of the hysteresis, that is, this is independent of the positive shift.

A time dependence of the I-V characteristics of the MAS structure was observed. When the applied voltage exceeds the critical voltage above which the positive shift of the C-V curve occurs, the current through the aluminum oxide film decreases gradually for 15 min or longer, then reaches a steady state. An additional I-V measurement of this MAS structure gave lower currents than the previous ones regardless of the polarity. Below the critical voltage, neither a time dependence nor a polarity dependence of the I-V characteristic was observed with ohmic currents in the picoampere range.

Figure 9 shows a typical I-V characteristic of the MAS structure with a 1400Å aluminum oxide film for positive and negative bias, where each point indicates the current measured 20 min after application of the bias. At higher voltages than the critical voltage, the current increases exponentially with the square root of the applied voltage over several decades of current.

The temperature dependence of the current through aluminum oxide films is shown in Fig. 10 and 11.

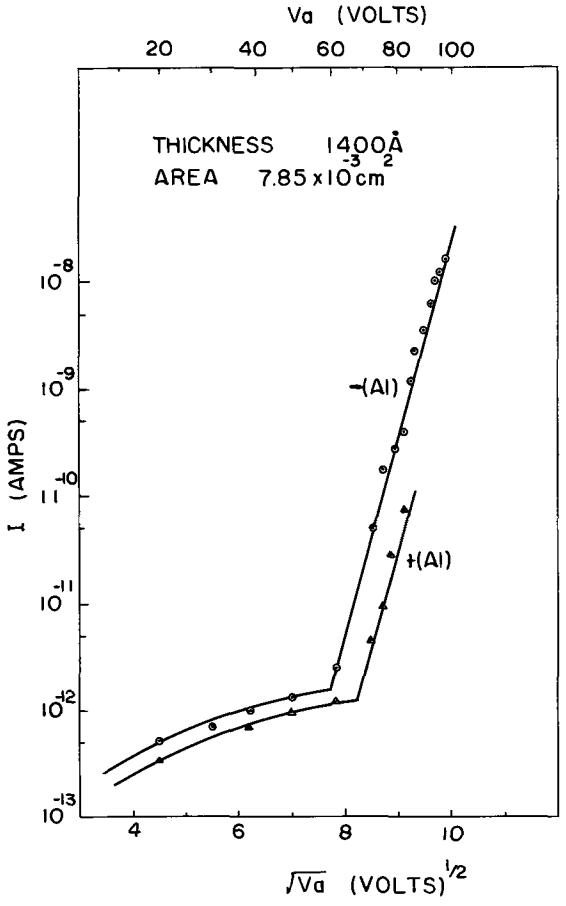

Fig. 9. Current *vs.* square root of applied voltage for both polarities at room temperature for MAS structure with 1400Å aluminum oxide film and electrode area of 7.85×10^{-3} cm^2. Positive bias is applied after measurement of I-V characteristic with negative bias.

Discussion

Positive shifts by bias voltages have been reported in MIS structures with insulators such as phosphosilicate glass (20), silicon nitride (21, 22), and reactively sputtered aluminum oxide (12) by several workers. Those of the phosphosilicate glass, the silicon nitride, and the aluminum oxide have been explained in terms of polarization of the glass, injection of electrons, and mobile negative ions, respectively. The aluminum oxide in this work shows a different type of positive shift, that is, the positive shifts occur independently of the type and polarity of the applied bias such as +d.c., −d.c., a.c., and pulse, and are observed in the same direction even at liquid nitrogen temperature. This means that these shifts are neither due to ionic transport nor to ionic polarization, but to electronic phenomena. Therefore, the positive shifts of the aluminum oxide are based on a different origin than those for the reactively sputtered aluminum oxide because ionic migration is quite improbable at liquid nitrogen temperature. These shifts can be explained by electron trapping in the aluminum oxide as follows: when a positive bias is applied to the MAS structure, electrons are injected from the semiconductor into the aluminum oxide by tunneling (23) and some of them are trapped in trapping states. This injection needs some energy which results in the critical field as reported in silicon nitride by Deal *et al.* (22). However, when a negative bias is applied, electrons are injected from the metal to the aluminum oxide to cause the positive shifts. Similar explanations have been proposed for sputtered silicon nitride, although the

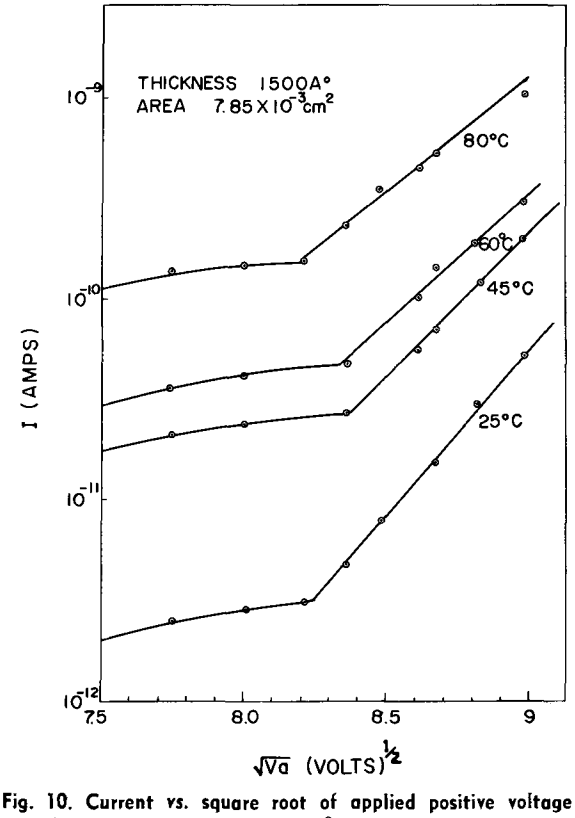

Fig. 10. Current *vs.* square root of applied positive voltage at four different temperatures with 1500Å aluminum oxide.

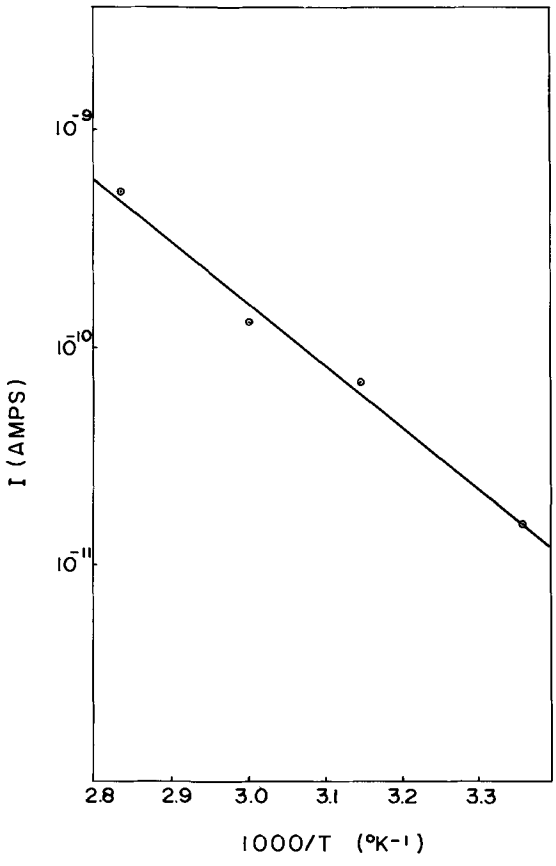

Fig. 11. Current vs. $1/T$ at voltage of + 75V in Fig. 10

carriers injected were holes rather than electrons (24). As the electron trapping near Si-Al_2O_3 interface is efficient, it takes more energy to trap electrons at negative than at positive bias. This model for the positive shifts is supported (*i*) by the fact that the positive shifts by negative bias decay more slowly and have smaller initial decay than those by positive bias as shown in Fig. 7, that is, the trapped electrons near the interface are more easily released than those away from the interface; and (*ii*) by the fact that the trapped electrons by negative bias as well as by positive bias can be excited by radiation such as x-rays and electron beam without introduction of damage. Although several radiation effects have been reported and explained by radiation damage in MIS structures (25), with the excitation of trapped electrons the drift due to the built-in field in the aluminum oxide is responsible for the exponential decay of the positive shifts by x-rays, as shown in Fig. 9.

The decrease of the positive shifts by higher negative bias as shown in Fig. 3 is always accompanied by an exponential increase of the current through the aluminum oxide, so that this is due to the release of trapped electrons by the rapid increase in current. A similar decrease was reported for a MOS structure with three different SiO_2 films (26).

The aluminum oxide film used in this work did not show any distinguishable change in its electrical properties when it was heated below the deposition temperature. Further, under bias temperature stress of the MAS structure, no appreciable change was observed in its flat band voltage below a critical voltage at the temperature of the bias temperature stress.

The critical voltage for the positive shifts is temperature dependent. As shown in Fig. 3, the critical voltages increase with decreasing temperature with negative bias as well as with positive bias because of the increase of the barrier height for injection.

The initial decay of the positive shifts with a strong temperature dependence as shown in Fig. 7 is also explained by the barrier height lowering at elevated temperature. The decay of the positive shifts depends on the distribution of trapped electrons, so the application of higher negative voltage after positive shift by a positive bias produces a redistribution of trapped electrons, that is, the trapped electrons near the interface are easily released to the semiconductor. Therefore, positive shifts thus obtained are more stable than those by the positive bias alone. Similar redistribution occurs when positive shifted MAS structures are exposed to x-rays and electron beams.

On the other hand, the time dependence of I-V characteristics previously mentioned can be interpreted by the change of space charge distribution due to electron injection. This is closely related to the time dependence of the C-V characteristics. This means that the electric field in the aluminum oxide has a spatial distribution due to the electron injection, particularly, near the Si-Al_2O_3 interface. This is one of the reasons why we describe the positive shifts as a function of applied voltage rather than electric field.

The I-V characteristics obtained in this work are very similar to those reported by Sze for silicon nitride (27) due to hopping of thermally excited electrons from one isolated state to another at lower voltages. Assuming the rapid increase in current as internal Schottky or Poole-Frenkel current, a static dielectric constant of 3.4 is obtained which is in approximate agreement with the square of the refractive index of 1.78. Furthermore, from the slope of ln I *vs.* $1/T$, an activation energy of 1.3 eV is obtained which is to be compared with 1.3 and 1.5 eV for Si_3N_4 obtained for the $SiCl_4$-NH_3 system and the SiH_4-NH_3-H_2 system (28), respectively.

The MNOS structure has been extensively investigated for memory devices (29). This MAS structure also has been utilized for the fabrication of a read-only memory (30) consisting of MAS FET's, which can be written by electron injection from the semiconductor as well as from the metal. The amount of current through the Al_2O_3 film is 2 orders smaller than that through Si_3N_4 films and, as can be seen from Fig. 8, both the positive-shifted MAS structure and the as-grown one are very stable between ±20V which corresponds to an electric field of 2×10^6 V/cm.

Conclusions

The properties of aluminum oxide films prepared by the hydrolysis of $AlCl_3$ have been evaluated by using a MAS structure. The positive shifts of the flat band voltages of the MAS structure occur independently of the polarity and type of the applied bias when this is higher than a critical voltage, under which the MAS structure has stable C-V characteristics. These positive shifts can be explained by electron injection and trapping in the aluminum oxide. The trapped electrons persist for a long time before discharge. However, they can be excited by radiation such as x-rays and electron beams without damage to the MAS structure and, as they drift and discharge, the positive shift decays exponentially. These aluminum oxide films are suited for the insulator in nonvolatile field-effect memory devices.

Acknowledgments

The authors wish to thank Drs. A. Ohuchi, S. Tsuneki, Y. Matsukura, Y. Haneta, and K. Kobayashi for many stimulating discussions. Thanks are also due to Messrs. S. Konno and M. Nakagiri for their assistance with the experimental work.

Manuscript received Nov. 10, 1969; revised manuscript received Jan. 20, 1970.

Any discussion of this paper will appear in a Discussion Section to be published in the December 1970 JOURNAL.

REFERENCES

1. S. R. Hofstein, *Solid-State Electronics*, **10**, 657 (1967).
2. E. H. Snow, A. S. Grove, and D. J. Fitzgerald, *Proc. IEEE*, **55**, 1168 (1967).

3. N. C. Tombs, H. A. Wegener, R. Newman, B. T. Kenny, and A. J. Coppola, *ibid.*, **54**, 87 (1966).
4. S. K. Tung and R. E. Caffrey, Paper 477 presented at the Montreal Meeting of the Society, Oct. 6-11, 1968.
5. A. G. Holmes-Siedle and K. H. Zaininger, *Solid State Tech.*, **12**, 40 (1969).
6. K. H. Zaininger and A. S. Waxman, *IEEE Trans.*, **ED-16**, 333 (1969).
7. J. A. Aboaf, *This Journal*, **114**, 948 (1967).
8. H. Matsushita and Y. Koga, Paper 90 presented at the Boston Meeting of the Society, May 5-9, 1968.
9. S. Krongelb, *This Journal*, **116**, 1583 (1969).
10. S. Nishimatsu, T. Tokuyama, and M. Matsushita, Paper 480 presented at the Montreal Meeting of the Society, Oct. 6-11, 1968.
11. A. Waxman and K. H. Zaininger, *Appl. Phys. Letters*, **12**, 109 (1968).
12. E. Ferrieu and B. Pruniaux, *This Journal*, **116**, 1008 (1969).
13. R. G. Frieser, *ibid.*, **113**, 357 (1966).
14. T. Tanaka and S. Iwauchi, *Japan J. Appl. Phys.*, **7**, 1420 (1968).
15. H. E. Nigh, Paper 476 presented at the Montreal Meeting of the Society, Oct. 6-11, 1968.
16. V. Y. Doo and P. J. Tsang, Paper 16 presented at the New York Meeting of the Society, May 4-9, 1969.
17. H. Teshima, Y. Tarui, and T. Matsuoka, Inst. Electronics Comm. Engrs. Japan Mtg. Oct. p. 765 (1967).
18. F. L. Worthing, *This Journal*, **115**, 88 (1968).
19. P. V. Gray and D. M. Brown, *Appl. Phys. Letters*, **15**, 31 (1966).
20. E. H. Snow and B. E. Deal, *This Journal*, **113**, 264 (1966).
21. S. M. Hu, *ibid.*, **113**, 693 (1966).
22. B. E. Deal, P. J. Fleming, and P. L. Castro, *ibid.*, **115**, 300 (1968).
23. E. P. Herman and G. Warfield, *IEEE Trans.*, **ED-12**, 167 (1965).
24. S. M. Hu, D. R. Kerr, and L. V. Gregor, *Appl. Phys. Letters*, **10**, 97 (1967).
25. J. P. Mitchell, *IEEE*, **ED-14**, 764 (1967).
26. K. Kobayashi and Y. Haneta, Japan Appl. Phys. Soc. Fall Mtg. (1969).
27. S. M. Sze, *J. Appl. Phys.*, **38**, 2951 (1967).
28. G. A. Brown, W. C. Robinette, Jr., and H. G. Carlson, *This Journal*, **115**, 948 (1968).
29. E. C. Ross and J. T. Wallmark, *RCA Rev.*, **30**, 366 (1969).
30. S. Nakanuma, T. Tsujide, R. Igarashi, K. Onoda, T. Wada, and M. Nakagiri, IEEE International Solid-State Circuits Conference, Session VI (6.2), (1970).

Technical Notes

Divalent Rare Earth Activated 96% SiO_2 Glass

A. Wachtel

Westinghouse Electric Corporation, Bloomfield, New Jersey

Doping of porous 96% silica glass (1, 2) with organic dyes or transition metal ions, the latter followed by heat-treatment, is a well-known process for the preparation of color filters (3). Claffy, Ginther, and Arnold (4) reported on Ce, Sm, Mn, and Cu activated phosphors based on this material.

The present note describes the fluorescence of the divalent rare earths Eu^{2+}, Yb^{2+}, and Sm^{2+}, which is obtained only if Al^{3+} is also present. The glasses are therefore related to the high-SiO_2 form ("Phosphor I") of aluminosilicates which was described in an earlier publication (5), the principal differences in composition being only the B^{3+} content and the lower Al^{3+} content of the glasses.

The purpose of this note is twofold: (*i*) it shows that the effect of B^{3+} provides additional evidence concerning the nature of the Eu^{2+} activator center (5), and (*ii*) it attempts to explain the large effect of particle size on the spectral energy distribution of the Eu^{2+} emission in terms of optical cascade energy transfer.

Experimental

The raw material consisted of Corning No. 7930 glass ("thirsty Vycor") which contained 6.9×10^{-3} g atoms Al/mole. In the few instances where Al-free glass was required (Al = 0 points in Fig. 2), a raw material was prepared, in this laboratory, from 55 w/o (weight per cent) SiO_2-10 w/o Na_2O-35 w/o B_2O_3 glass by annealing at 575°C for 20 hr, and leaching in dilute HCl. The glasses were activated by impregnating with aqueous $RE^{3+}(NO_3)_3 + Al(NO_3)_3$ solutions of appropriate concentrations, followed by firing in a reducing atmosphere.

Fluorescence intensity of Eu-activated glass was measured by use of an integrating sphere in which specimens were excited through a 254 nm transmitting interference filter. Measurements were also taken on ground samples, using conventional powder plaques for which the intensity of 254 nm excitation was standardized with $CaWO_4$:Pb, NBS No. 1026. The detector used was the Spectra Brightness Spot Meter[1] set on "blue" ($\bar{z}$ sensitivity). Emission and excitation spectra were obtained as described by Thornton (6).

Results and Discussion

Figure 1 shows fluorescence intensity as a function of Eu for low or high Al concentrations. The former represent samples not intentionally doped with Al, *i.e.*, containing 6.9×10^{-3} Al/mole. The latter were prepared by impregnation, at 95°C, with fused salt mixtures $Al(NO_3)_3 \cdot 9H_2O + Eu(NO_3)_3 \cdot 6H_2O$. While fluorescence intensities of the samples prior to and after grinding are measured differently and are therefore not directly comparable, it can be seen that in both cases, maxima occur near 4×10^{-4} and 5×10^{-3} Eu. At approximately three times higher Eu concentrations, the samples acquired a yellow body color caused by a broad absorption band which is otherwise not present. At still higher Eu concentrations, the glasses devitrified. Note that the fluorescence intensity of unground specimens is highest at low Al and Eu concentrations, while the opposite holds true for powders.

Figure 2 shows fluorescence intensity, at three Eu concentrations, as a function of Al up to the highest

[1] Photo Research Corporation, Hollywood, California.

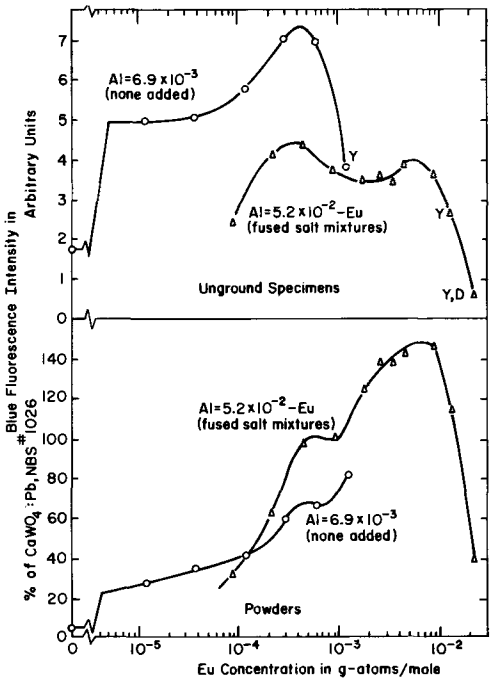

Fig. 1. Fluorescence intensity of 96% SiO_2 glass as a function of Eu^{2+} concentration. Y, yellow discoloration; D, devitrification.

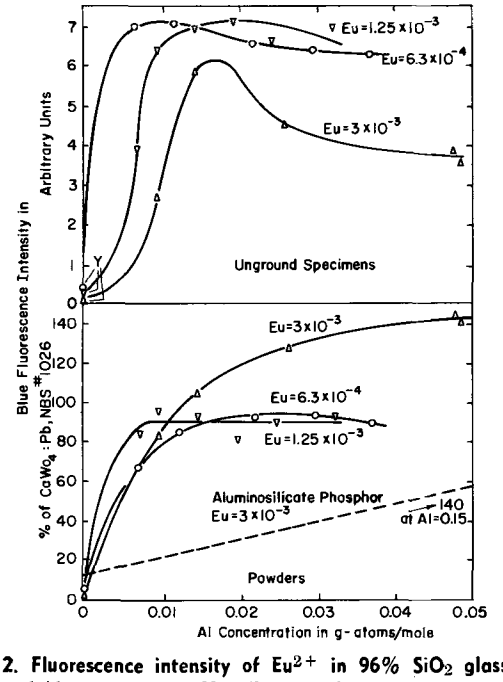

Fig. 2. Fluorescence intensity of Eu^{2+} in 96% SiO_2 glass as a function of Al concentration. Y, yellow discoloration.

attainable with the fused salt mixtures. In contrast to phosphors with varying Eu concentration (Fig. 1), single maxima are obtained; however, we note again that grinding shifts these to higher doping levels. The actual fluorescence intensity of powders prepared with 3×10^{-3} Eu becomes comparable to that of aluminosilicate phosphor I (5). It can be seen that in the powdered glasses, this fluorescence intensity level is obtained at somewhat less than 5×10^{-2} Al/mole, *i.e.*, at three times lower Al concentration than in the aluminosilicate phosphor,[2] and the shape of the curve suggests that at still higher Al concentrations, it would not be appreciably increased. At lower Eu concentrations, maximum fluorescence intensity in powders is obtained within the concentration range employed, but again, the fluorescence increases rapidly with increasing Al concentration. At Al = 0, the data were obtained on samples prepared with the Al-free raw material. These samples were essentially nonluminescent and showed a yellow body color even at the lowest Eu concentration.

A search for crystalline inclusions (mullite) which, in the case of the aluminosilicate phosphor, were proposed to be instrumental in the luminescence process, was unsuccessful. Even highly doped glasses failed to show distinct x-ray reflections or revealed significant inhomogeneities in electronphotomicrographs taken by transmission through thin edges.

The principal differences between the present glasses and the aluminosilicate phosphor, therefore, are the B^{3+} content of the glasses, and the lower Al^{3+} concentration which is required to produce the same fluorescence intensity observed in the aluminosilicate phosphor. The relatively large Eu^{2+} ion is a network modifier and therefore occupies interstitial sites. Charge compensation of network modifiers in silicate glasses by Al^{3+} or B^{3+} leads to formation of network forming (substitutional) $[AlO_4]$ or $[BO_4]$ tetrahedra (7-9). Each Eu^{2+} ion then requires two M^{3+} according to $2M^{3+} + Eu^{2+} = 2Si^{4+}$. The present experimental evidence, however, indicates that the activator center involves network modifying (interstitial) $[AlO_6]$ groups. This evidence may be summarized as follows: (*i*) Boron does not give rise to Eu^{2+} luminescence. Unlike Al^{3+}, it enters the SiO_2 network only substitutionally, an excess over low-valence modifiers forming triangularly coordinated $[BO_3]$ groups (9, 10). It is likely, therefore, that Eu^{2+} charge-compensated by substitutional Al^{3+}, is also nonluminescent. (*ii*) At low concentrations, Al^{3+} normally tends to occupy substitutional sites; in the presence of B^{3+}; however, some of the Al is displaced into interstitial sites (11, 12). The more rapid rise of fluorescence intensity with Al concentration in the (B-containing) glasses, as compared with the aluminosilicate phosphor, can therefore be explained by the more rapid rise in concentration of interstitial Al. (*iii*) Even in the glasses, maximum fluorescence intensity obtains at Al/Eu ratios which are substantially higher than the 2/1 ratio suggested by charge compensation. Again, such excess Al is known to occupy interstitial sites (9, 12, 13).

These arguments suggest that the luminescence center in the (homogeneous) glasses is basically no different from that proposed for the heterogeneous aluminosilicate phosphor in which Eu^{2+} replaces Al^{3+} at a mullite surface, and is charge compensated by Si^{4+} at the adjacent amorphous SiO_2 phase (5). In both cases, Al is a cation, and only the size of $[AlO_6]$ aggregates and the degree of crystalline order of interstitial aluminosilicates is different.

Emission spectra consist of bands with widths at half maximum averaging 77.1 nm in unground, and 75.6 nm in ground glasses. Variations in Eu concentration primarily affect the peak emission wavelengths as seen in Fig. 3. This figure shows the same low and high Al series shown in Fig. 1. In both cases, it can be seen that at high as well as low Eu concentrations, the emission spectra are independent of particle size. At moderate Eu concentrations, however, differences become pronounced, particularly in the high Al glasses. At 2.7×10^{-3} Eu, this difference is at a maximum of 10 nm. A displacement of the emission band is also observed by shifting the excitation of powders to longer wavelengths, as shown in Table I. Here it can be seen that in going from 254 to 405 nm excitation, the emission peak is shifted to longer wavelengths by 15.6 nm. The table also shows that the width at half maximum does not decrease (as expected by lack of emission below 405 nm), but actually increases by 2.2 nm.

Figure 4 shows the emission of the 2.7×10^{-3} Eu glass under 254 nm excitation. The excitabilities of the

[2] In ref. (5), Al was expressed as Al_2O_3 with the optimum at 0.075, *i.e.*, 0.15 Al.

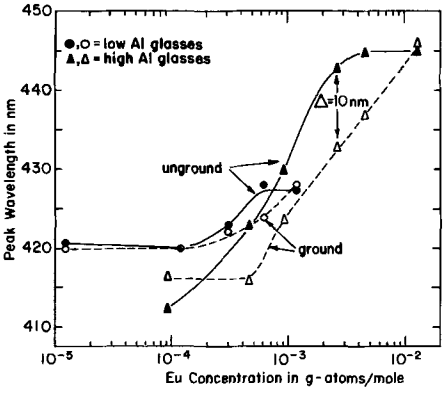

Fig. 3. Peak emission wavelength of 96% SiO_2 glass, under 254 nm excitation, as a function of Eu^{2+} concentration.

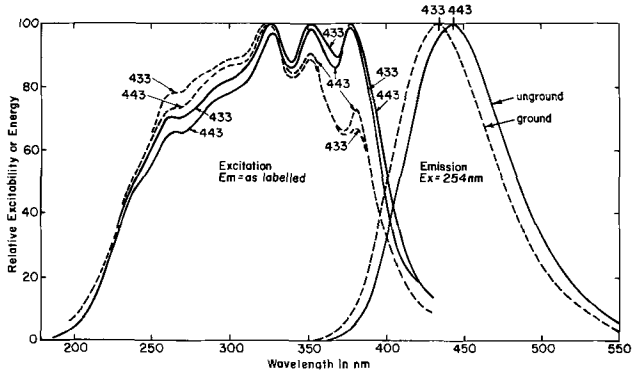

Fig. 4. 254 nm—excited emission spectra, and excitation spectra of 96% SiO_2 glass containing 2.7 x 10^{-3} Eu^{2+}/mole. Numbers in figure denote wavelength of measured emission.

two peak emission wavelengths, shown by the numbers in the figure, are also included. The relative heights of these are seen to vary with the observed emission wavelengths in the direction one would expect, and even more strongly with the particle size. In the latter case, the displacement is in the direction of greater excitability of powders at shorter wavelengths.

The 10 nm shift to longer wavelengths of the emission of the unground glass, as compared to that of the powder, is not due to self-absorption alone, since the emission band width is not narrower. It is therefore caused by excitation energy at longer wavelengths which is present in addition to the 254 nm radiation employed. Figure 4 shows that this energy originates from the 254 nm-excited emission of the glass, and that radiation near 400 nm (the center of overlap between the excitation and emission spectra) is primarily responsible for this process. Since pure 405 nm excitation of the powder caused a shift of 15.6 nm (Table I), it follows that in the present case, the shift should be smaller. The observed value of 10 nm, therefore, indicates that about 2/3 of the emission of the unground glass originates from optical cascade energy transfer. A detailed treatment of powder-optical processes which contribute to the present discussion is given by Melamed (14).

Table I. Emission properties of powdered 96% SiO_2 glass doped with 4.9 x 10^{-2} Al^{3+} and 2.7 x 10^{-3} Eu^{2+}

Excitation wavelength, nm	Emission peak wavelength, nm	Emission width at half maximum nm
254	433.0	76.0
365	435.5	75.2
405	448.6	78.2

96% silica glass (as well as the aluminosilicate phosphor) can also be activated by Yb^{2+} or Sm^{2+}, although these elements proved to be more difficult to reduce to the divalent state than Eu. Figure 5 shows excitation and emission spectra of an unground specimen of glass doped with 4.4 x 10^{-3} Al + 2.2 x 10^{-3} Yb/mole and fired in H_2 for 20 hr. The excitation spectrum, taken with Hg lines, is corrected for equal quanta of exciting radiation, but may contain more detail than indicated in Fig. 5. Nevertheless, it appears that there may be four excitation bands in addition to the pronounced increase in excitability towards short wavelengths. The broad emission band is unproportionally high on the short wavelength side, and therefore may consist of a number of unresolved bands. Figure 6a shows excitation and emission spectra of a glass doped with 4.4 x 10^{-3} Al + 2.2 x 10^{-3} Sm, fired in air, and Fig. 6b shows the same glass fired in H_2 for 20 hr. The excitation spectra in Fig. 6a and 6b were taken with a continuous source of uv, and are also corrected for equal quanta of exciting radiation. It can be seen that at 77K, neither the excitation nor the emission spectra of Sm^{2+} are significantly better resolved, although the vibronic side bands are markedly decreased. In this respect, the emission line widths of Sm^{2+} in the glasses differ from those in many crystalline matrices (15-19) where usually, broad bands are observed at room temperature. It should also be noted that the emission of the H_2-fired glass includes weak lines at 602 and 649 nm due to Sm^{3+}; with 254 nm excitation (not shown) these are considerably enhanced. This is caused by incomplete reduction in spite of the prolonged firing, and due to the relatively high reduction potential of Sm (20). For this reason, optimum doping with Sm (or Yb) is somewhat higher than with Eu, and detailed measurements of fluorescence as a function of actual Sm^{2+} or Yb^{2+} concentration have not been carried out.

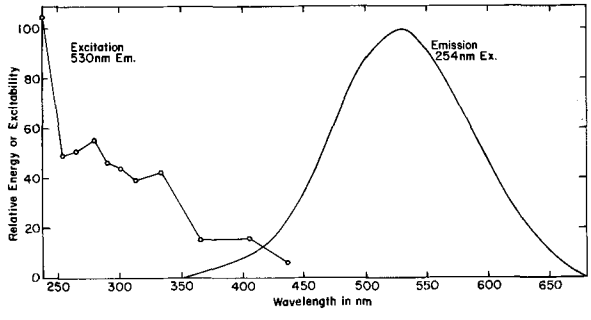

Fig. 5. Excitation and emission spectra of 96% SiO_2 glass doped with 4.4 x 10^{-3} Al + 2.2 x 10^{-3} Yb/mole, fired in H_2 at 1150°C for 20 hr.

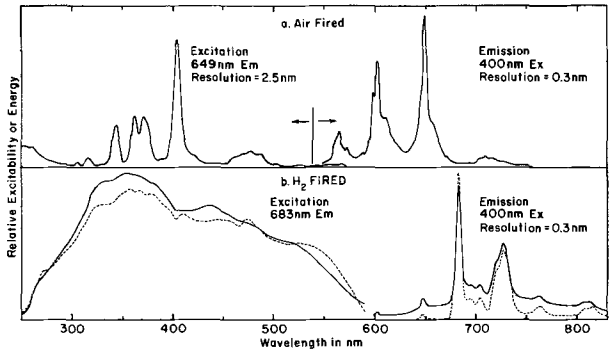

Fig. 6. Excitation and emission spectra of 96% SiO_2 glass doped with 4.4 x 10^{-3} Al + 2.2 x 10^{-3} Sm/mole; a, fired in air at 1150°C for 3 hr; b, fired in H_2 at 1150°C for 20 hr. Solid lines = spectra at room temperature; broken lines = spectra at 77K.

Acknowledgments

The writer wishes to thank Miss I. Walinski for sample preparation and measurements, and W. A. Thornton, N. T. Melamed, W. B. White, and C. Hirayama for spectra and helpful discussions. E. P. Riedel kindly determined the spectra of the Sm activated glasses.

Manuscript submitted June 30, 1969; revised manuscript received *ca.* Jan. 26, 1970. This was Paper 87 presented at the New York Meeting of the Society, May 4-9, 1969.

Any discussion of this paper will appear in a Discussion Section to be published in the December 1970 JOURNAL.

REFERENCES

1. H. P. Hood and M. E. Nordberg, U.S. Pat. 2,106,744, Feb. 1, 1938; 2,215,039, Sept. 17, 1940; 2,221,709, Nov. 12, 1940; 2,286,275, June 16, 1942.
2. K. Kühne and W. Skatulla, *Silikattechnik*, **10**, 105 (1959).
3. M. E. Nordberg and H. E. Rumenapp, U.S. Pat. 2,303,756, Dec. 1, 1942; 2,315,329, March 30, 1943; 2,340,013, Jan. 25, 1944; 2,355,746, Aug. 15, 1944; and H. P. Hood and M. E. Nordberg, U.S. Pat. 2,315,329, March 30, 1943.
4. R. J. Ginther, J. H. Schulman, and G. W. Arnold, Extended Abstract 26, New York, Meeting of the Society May 4-9, 1959.
5. A. Wachtel, *This Journal*, **116**, 61 (1969).
6. W. A. Thornton, *ibid.*, **116**, 286 (1969).
7. R. H. Doramus, *Phys. Chem. Glasses*, **10**, 28 (1969).
8. M. W. Safford and A. Silverman, *J. Am. Ceram. Soc.*, **30**, 203 (1947).
9. A. A. Appen, The Structure of Glass, Proc. All-Union Conf. Glassy State, Leningrad (1953). Consultants Bureau Trans. pp. 75-82 (1958).
10. Tosio Abe, *J. Am. Ceram. Soc.*, **35**, 284 (1952).
11. E. I. Galant, The Structure of Glass, Proc. All-Union Conf. Glassy State, Leningrad (1953). Consultants Bureau Trans. pp. 451-3 (1960).
12. N. I. Vlasova, E. I. Galant, and A. A. Kefeli, *ibid.*, Vol. 2, pp. 327-30 (1960).
13. Sook Lee and P. J. Bray, *Phys Chem. Glasses*, **3**, 37 (1962).
14. N. T. Melamed, *J. Appl. Phys.*, **34**, 500 (1963).
15. G. H. Dieke and R. Sarup, *J. Chem. Phys.*, **36**, 371 (1962).
16. A. W. Smith, *Appl. Optics*, **3**, 147 (1964).
17. J. P. Axe and P. P. Sorokin, *Phys. Rev.*, **130**, 945 (1963).
18. V. H. Konyukhov, V. M. Marchenko, and A. M. Prokhorov, *Opt. and Spectros*, **20**, 299 (1966).
19. B. I. Bykovskii and V. F. Pisarenko, *ibid.*, **26**, 271 (1969).
20. W. Noddak and A. Brukl, *Angew. Chem.*, **50**, 362 (1937).

Beryllium as an Acceptor in Silicon

E. A. Taft and R. O. Carlson

General Electric Research and Development Center, Schenectady, New York

The high oxygen content of Czochralski grown silicon crystals is well known (1), and some study has been made of the reactions of group III acceptors with this oxygen (2). The high free energy of formation and great thermal stability of BeO is also well established (3). The possibility of beryllium combining with oxygen in liquid or solid silicon to form a stable, electrically inactive impurity led to our investigation.

Experimental

Beryllium has been added to 500 ohm-cm silicon to be pulled from quartz crucibles. Single-crystal material was difficult to grow by this method because of nucleation from oxides on the melt surface, but specimens which could be studied were obtained. A beryllia crucible was also found to be suitable for use in pulling doped single-crystal silicon. However, the reaction of molten silicon with the crucible wall supplied the dopants, and the amount of dopant obtained could not be controlled. Also beryllium was diffused into oxygen-containing n-type and p-type silicon wafers at 1170°C for times up to 16 hr. It was found that consistent results could be obtained only if the beryllium metal was not directly exposed to the quartz walls of the furnace. The silicon test sample was, therefore, enclosed with beryllium in a cavity of silicon while the diffusion proceeded. In addition, float-zoned crystal of 1 ohm-cm beryllium doped oxygen-free silicon was made available by R. J. Mulligan. These variously doped crystals were then studied in infrared absorption, resistivity, Hall effect, and heat treatment.

Results

The oxygen content of undoped silicon crystals pulled from small quartz crucibles is typically 10^{18} atoms/cm^3. The oxygen is readily determined by infrared absorption (1). Beryllium doped crystals pulled from similar quartz crucibles typically contained 10^{17} atoms/cm^3 of oxygen, a moderate reduction. There is possibly some gettering of oxygen by beryllium in the melt, but, more likely, the formation of a beryllium silicate on the quartz crucible wall reduced the reaction rate of molten silicon with quartz. Crystals pulled from beryllia crucibles were found to contain oxygen in amounts comparable to that found for the beryllium doped crystals pulled from quartz crucibles. This oxygen level does not approach the concentrations of 10^{15} atoms/cm^3 found in float zoned silicon.

The distribution coefficient, k, of Be in silicon was obtained for a number of crystals pulled from quartz crucibles. The impurity concentration, C_S, of acceptors was obtained from traveling probe resistivity data at room temperature (4). (Most of the acceptors are ionized at the low concentrations obtained.) C_S is plotted against the atom fraction, g, of the initial charge solidified in a pulled crystal in Fig. 1. The curve $C_S = kC_L/1 - g$ contains the initial concentration, $C_L = 3.2 \times 10^{19}$ atoms/cm^3 of beryllium in the liquid obtained from the initial weighed charges of beryllium and silicon. For best fit to the points, k was selected at 1.3×10^{-4}. The consistency in results for several crystals measured, and the excellent fit to the curve, indicate that the dopant losses during the crystal growth were not significant. All crystals were "p" type showing values between 1.3 and 1.6×10^{-4} for k.

N-type silicon of 50 ohm-cm and of 0.06 ohm-cm was converted to p-type after Be was diffused at 1170°C for up to 16 hr, indicating the acceptor nature of the Be center. As the resistivity of these crystals was no longer changing with time of diffusion, the silicon appeared to be saturated with Be after this treatment. The resistivity *vs.* temperature for one of these crystals, Be 3, is shown in Fig. 2. Also in this figure are the data for K-97, a Be-doped crystal pulled from a quartz crucible. These p-type crystals prepared by different methods show the same deep-lying acceptor level of Be. The carrier concentration derived from Hall effect data for these same two crystals is given in

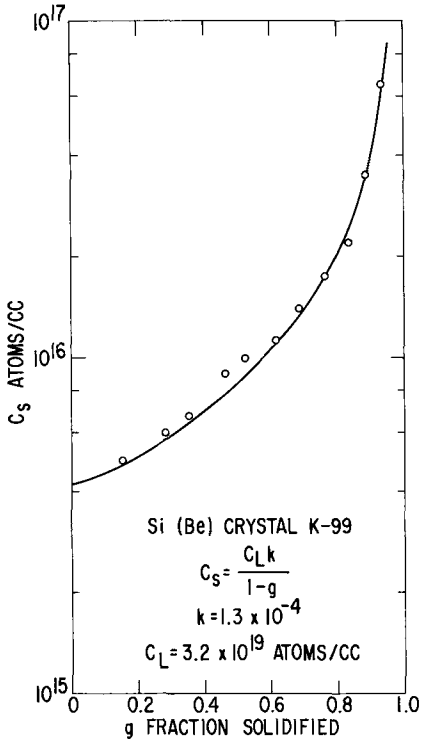

Fig. 1. Distribution coefficient of beryllium in silicon; k is chosen for best fit to the data points.

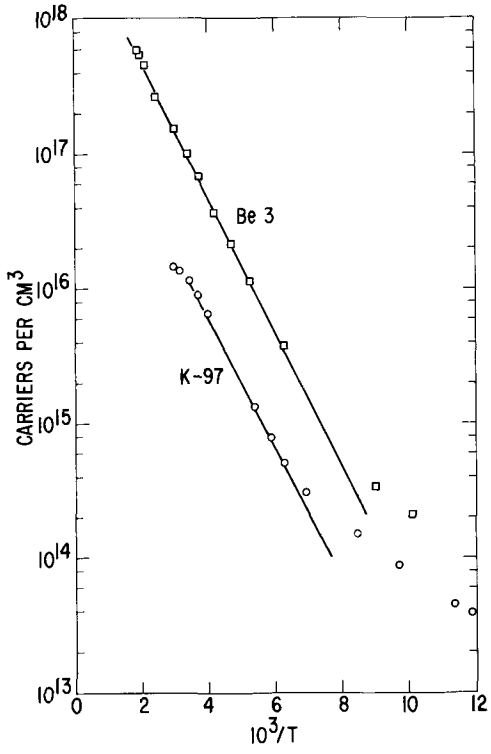

Fig. 3. Temperature variation of hole concentration in beryllium doped silicon derived from Hall effect data.

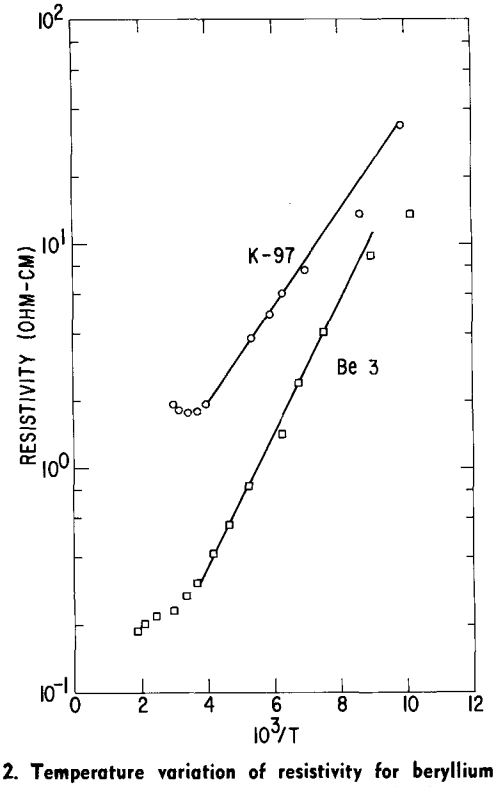

Fig. 2. Temperature variation of resistivity for beryllium doped silicon. K-97 is a grown crystal containing Be; Be 3 is a Be diffused silicon sample.

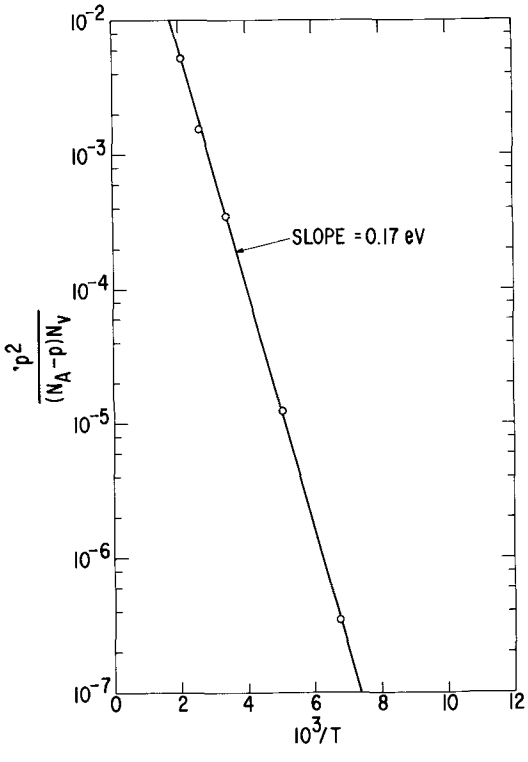

Fig. 4. Acceptor level determination from Hall effect data using corrections for total acceptor sites and for temperature variation of valence band density of states.

Fig. 3. A room-temperature mobility of 230 $cm^2\ V^{-1}\ sec^{-1}$ with an exponential temperature dependence of -2.4 for Be 3 shows that this crystal exhibits reasonable behavior for doped silicon. K-97 also exhibits normal mobility values.

Further analysis of the Hall effect data, such as that used by Hutson (5), yields the curve of Fig. 4. All crystals analyzed were similar in showing an activation energy of 0.17 eV for the Be acceptor center. Following Hutson, the intercept of Fig. 4 can be used to estimate the degeneracy of the Be center. As Fig. 4 was derived from a crystal with $< 10^{14}$ donor centers, compensation was negligible and the simpler equation is used.

$$\frac{p^2}{(N_A - p)N_V} = \left(\frac{m}{m}\right)^{*3/2} D^{-1} \exp\left(\frac{-E_o}{kT}\right)$$

The intercept is 0.25, $(m/m)^{*3/2}$ is 0.45 for holes in silicon leaving a degeneracy factor $D = 1.8$ or closely 2.

The possibility that Be contributes two levels in silicon has been considered but not investigated. The chemically similar element, zinc, is known to give two levels (6). If beryllium is considered to be a well-behaved solute in silicon, the distribution coefficient can be used to estimate the solid solubility at any temperature (7). Our coefficient of 1.3×10^{-4} would give an equilibrium concentration of 5×10^{17} Be atoms/cm^3 at 1170°C. As the data of the diffused sample Be 3 of Fig. 3 do not show a saturation of carriers, the room-temperature value has been utilized. Assuming an acceptor level of 0.17 eV in silicon, the number of acceptors needed to get the 10^{17}/cm^3 room-temperature carriers observed in Fig. 3 is calculated in the usual textbook approach. The value of 1.2×10^{18}/cm^3 acceptors obtained is higher than, but in reasonable agreement with, the value obtained from the distribution coefficient. Our data are not considered to be of sufficient accuracy to deduce an arguable meaning, such as two energy levels, from these differences in acceptor concentration.

Further trying to take advantage of the affinity of beryllium for oxygen, some of the crystals were subjected to heat treatment at 1000°C. The crystals contained initially 10^{16} atoms/cm^3 of Be and 10^{17} atoms of O_2 as determined from resistivity and from infrared absorption, respectively. The room-temperature resistivity of the samples rose by a factor of over 100 after only a few hours of heating. The Be was no longer active electrically and only background impurities of $< 10^{14}$/cm^3 were in evidence. The oxygen content changed little, if at all, but the oxygen was of course in great excess relative to the beryllium. A short heat treatment at 1300°C did not return the resistivity to the original value as is the case for the more usual dopants upon interaction with dissolved oxygen (8). The beryllium was thus not available for redissolution (9). In this case, it is not clear whether the Be actually left the crystal by means of diffusion to the surface or whether a Be-O combination is too tightly bound to be dissociated to any extent at 1300°C.

A 2 mm thick piece of oxygen-free beryllium doped ($\sim 10^{16}$/cm^3) crystal was heated in argon at 1050°C for 1 hr. The room-temperature resistivity doubled after this treatment, the Be presumably going to the surface to react with the surface oxide. From this result, we have an estimate of the diffusion coefficient of Be in silicon at 1050°C of $\sim 10^{-7}$ cm^2/sec. In this case, it is clear that the Be is leaving the silicon and not reacting with dissolved oxygen as could be expected with the pulled crystal samples. Diffusion or clustering of O_2 is not significant for these short times and low temperatures.

To sum up, beryllium in silicon is a fast diffuser giving an acceptor level at 0.17 eV. The distribution coefficient is 1.3×10^{-4}. A Be-O combination has not been observed.

Acknowledgment

We wish to acknowledge the interest and encouragement of the late F. H. Horn who suggested this study.

Manuscript submitted Sept. 23, 1969; revised manuscript submitted Jan. 28, 1970. This was a Recent News Paper presented at the New York Meeting of the Society, May 4-9, 1969.

Any discussion of this paper will appear in a Discussion Section to be published in the December 1970 JOURNAL.

REFERENCES

1. W. Kaiser and P. H. Keck, *J. Appl. Phys.*, **28**, 822 (1957).
2. C. S. Fuller, F. H. Doleiden, and Katherine Wolfstein, *Phys. Chem. Solids*, **13**, 187 (1960).
3. D. W. White, Jr., and J. E. Burke, "The Metal Beryllium," p. 599, The American Society for Metals, Cleveland, Ohio (1955).
4. J. C. Irvin, *Bell System Tech. J.*, **41**, 387 (1962).
5. A. R. Hutson, *Phys. Rev.*, **108**, 222 (1957).
6. R. O. Carlson, *ibid.*, **108**, 1390 (1957).
7. R. N. Hall, *J. Phys. Chem. Solids*, **3**, 63 (1957).
8. C. S. Fuller and F. H. Doleiden, *J. Appl. Phys.*, **29**, 1264 (1958).
9. J. B. Robertson, *Bull. Am. Phys. Soc.*, **13**, 1475 (1968).

Selected Area Electron Diffraction Study of α-Fe_2O_3 Platelet Growths Twinned on Twist Grain Boundaries

In this paper by R. L. Tallman and E. A. Gulbransen which appeared in the February 1970 issue of the Journal, the diffraction patterns in Fig. 3 and 4 on page 252 were completely obscured by snow-storm-like additions.

Figures 3 and 4 are shown below as they should be.

Fig. 3

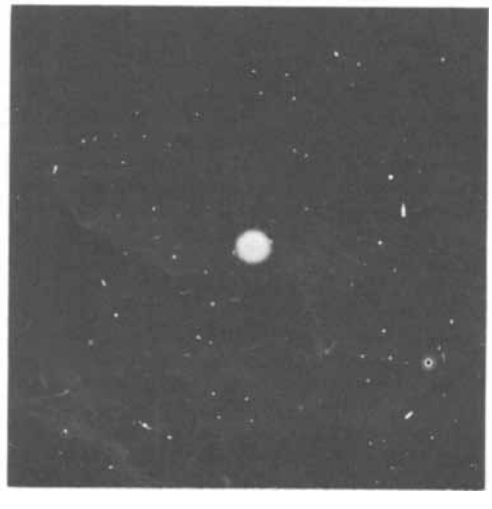

Fig. 4

JOURNAL OF THE ELECTROCHEMICAL SOCIETY

ELECTROCHEMICAL TECHNOLOGY

MAY 1970

High-Surface-Area Electrodeposited Aluminum

Richard J. Roethlein

Research and Development Laboratories, Sprague Electric Company, North Adams, Massachusetts

ABSTRACT

Aluminum was electrodeposited from a nonaqueous organic hydride electrolyte, $AlCl_3$ and $LiAlH_4$ in ethyl ether, which produced aluminum deposits ranging from smooth compact to rough and highly porous. Formation of high-surface-area Al substrates has been obtained by the application of high current densities. High-capacity values are explained on the basis of fine particle formation incurred under these plating conditions. Current-voltage curves for the anodic and cathodic reaction are indicative of a diffusion-controlled process.

The preparation of high-surface-area aluminum electrodes for electrolytic capacitors has always been a major concern in order to obtain the maximum capacitance values per unit geometric area or volume. Increasing the surface area of aluminum has been done for the most part either by chemical or electrolytic etching. Recently, however, large surface gains have been reported (1) through the electrodeposition of aluminum.

By means of an organic aluminum plating solution (2) and varying current density, aluminum dendritic growths have been reported to produce a surface gain factor over smooth aluminum of one to two orders of magnitude, depending on the formation voltage of the sample. Due to the possible advantages such a method may have in producing high-surface-area aluminum substrates, an investigation was undertaken to determine the feasibility of electrodepositing aluminum.

The formation of dense compact aluminum deposits has received considerable attention in the literature (2-7); however, highly dispersed porous aluminum deposits which would produce maximum surface roughness have been avoided. Parameters were therefore studied which would affect the nature of the aluminum deposit and tend to produce high-capacitance values. Electroplating was carried out in a nonaqueous electrolyte on aluminum wire electrodes.

Experimental

Due to the detrimental effects moisture has on aluminum plating baths, all experiments were carried out in a dry box containing an atmosphere consisting of 9 parts N_2 and 1 part H_2. Reagent-grade anhydrous materials used in the plating solutions were weighed inside of the dry box to avoid contact with water vapor in the atmosphere. The aluminum plating bath was an organic electrolyte (5, 6) which was operable at room temperature and consisted of an ethyl ether solution of 3M $AlCl_3$ and 0.4M $LiAlH_4$. The addition of anhydrous ether to the alkali halides must be done slowly, otherwise foaming and undesirable side reactions occur which affect properties of the plating solution. The plating cell consisted of a cylindrical Pyrex glass vessel 6 in. in length formed from a 60/50 joint; the top portion consisted of an array of equally spaced 10/30 joints which served as inlet ports for the study, reference, and counter electrodes. The study electrode was a section of 47 mil diameter aluminum wire, 99.99% purity, which was sealed to a section of Pyrex tubing by means of heat shrinkable Flo-tite[1] Teflon[2] tubing. The aluminum electrode, with an exposed geometric area of approximately 0.5 cm^2, could then be adjusted in the plating cell by means of a 10/30 Teflon gland. The counterelectrode consisted of a spiral section of either aluminum or platinum wire which provided an even current distribution on the study electrode. A Luggin capillary was sealed to one of the 10/30 joints into which a section of platinum wire was inserted which served as the reference electrode.

Aluminum electrodes were precleaned by the following sequence: immersion into acetone, rinsed, concentrated solution of 85% H_3PO_4-15% HNO_3 at 85°C for 2 min, rinsed, 1N-NaOH 2 min, rinsed, then dried at 90°C. After immersion into the plating solution, it was necessary to preanodize the electrode at a high current density, 200 mA/cm^2, for about 1 min; failure to preanodize the electrode in the plating solution produced nonadherent deposits. After anodization was complete, the current was immediately reversed to the appropriate cathodic plating current.

Both capacitance and RC product values were measured with a conventional a-c bridge having a few millivolts' signal. The electrodeposited wire was suspended in a cylindrical glass tube, the sides of which were lined with a platinum black counterelectrode. The measuring electrolyte had a resistivity of 12 ohm-cm and was used previously by Burger and Cheseldine (8). Oxide formations were carried out in a solution of 17% ammonium pentaborate in ethylene glycol. Values of the capacity measured at "zero voltage" were taken on the unformed wire which has a thin natural oxide on its surface.

Results

The use of this organic aluminate plating solution provides uniform adherent electrodeposits of Al and has the added advantage of being operable at room temperature. Conductometric studies (9) have shown that an ethereal solution of $AlCl_3$ will increase in conductivity with addition of $LiAlH_4$ up to approximately 17% equivalence. The formation of ionized species,

[1] Trade-mark, Pope Scientific Company.
[2] Trade-mark, Du Pont Corporation.

$Al_2Cl_5^+ + AlH_4^-$, has been postulated to produce this conductivity maximum; further addition of the hydride causes a destruction of the ionic species and lowering of the conductivity. A contrary view has been held by several authors (13, 14) in that the presence of excess $AlCl_3$, or the formation of $AlHCl_2$ or trichlorodialane $AlH_2Cl \cdot AlHCl_2$ is considered more favorable. Recent studies (15) have postulated the existence of several chemical species present in the plating solution and the possibility that the plating current is carried by three or four different ions. They conclude that an anion containing hydride exists and that the Li etherate is the principal current-carrying ion. The exact nature of the ionic species in solution has still, however, not been definitely proved.

In the presence of moisture, oxygen, and carbon dioxide the bath rapidly deteriorates; hydrogen gas is liberated at both electrodes during electrolysis, but to a much greater extent at the anode. Brenner (6) concluded that the bath was not regenerative due to a different ionic species formed during the dissolution of aluminum. More extensive studies (15) of bath life, extending over an 8 month period, have shown that the Al anode does dissolve to some extent in a manner which replaces the deposited aluminum. We have found that reproducible plating results can be maintained by a periodic addition of solid $AlCl_3$ and $LiAlH_4$ to the plating solution.

Surface roughness of the electrodeposited material can be varied to a considerable extent by variations in the plating current density. Generally, a current density less than 50 mA/cm² tends to give a smooth deposit. As the current density is increased the deposits tend to become nodular, and for values greater than 100 mA/cm² dendritic growth becomes rapid. At current density values greater than 300 mA/cm², a black powdery-like deposit forms on the electrode surface. Values of the capacity showed a large variation with changes in the surface morphology of the electrodeposited aluminum.

A series of aluminum electrodes having an apparent geometric area of 0.5 cm² were electroplated at various cathodic current densities both at constant cathodic charge (Q), and also for varying periods of time with current density constant. For electrodes plated at current densities ranging from 50 to 300 mA/cm², capacity measurements taken at zero formation voltage fell into a limited range from 4 to 15 μfd/cm². Depending on the amount of charge passed, deposit thickness for these electrodes ranged from 1 to 10 mils, the thicker deposits exhibiting the higher capacity values.

Larger values of the capacity were not realized until the plating current density was increased to values greater than 300 mA/cm². At these extremely high current densities, a black deposit forms on the electrode surface accompanied by gas evolution. Capacity measurements gave values in excess of 150 μfd/cm² on the unformed wire, and plots of the reciprocal of capacity *vs.* formation voltage were linear (Fig. 1). Microscopic inspection of the dark deposit at magnifications up to 500X show the growth of crystals. Spectrographic comparison of the electrodeposited material and an Al wire showed traces of B, Si, Fe, and Cu to be present in both samples. Lithium, which is one of the constituents of the plating solution, was not detected in the sample of electrodeposited aluminum using a method accurate to 10 ppm. Photomicrographs taken on a cross section of an Al wire that was electroplated at a current density of 500 mA/cm² for 7 min are shown in Fig. 2. The photos show that electrodeposited material consists of a highly porous deposit, 3-4 mils in thickness, containing dendritic growths of varying diameter.

Figure 3 is a plot of capacity/cm² *vs.* formation voltage comparing the results we obtained for a wire electrodeposited at 300 mA/cm² for 5 min with that reported by Muhlhausser (1). In the low-voltage region, <10V, Muhlhausser's data indicate a considerable increase in capacitance over what we have found on

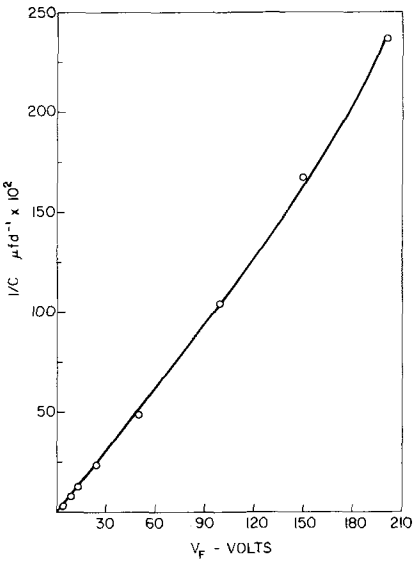

Fig. 1. Reciprocal capacity vs. formation voltage: electrodeposited Al, 300 mA/cm², 5 min.

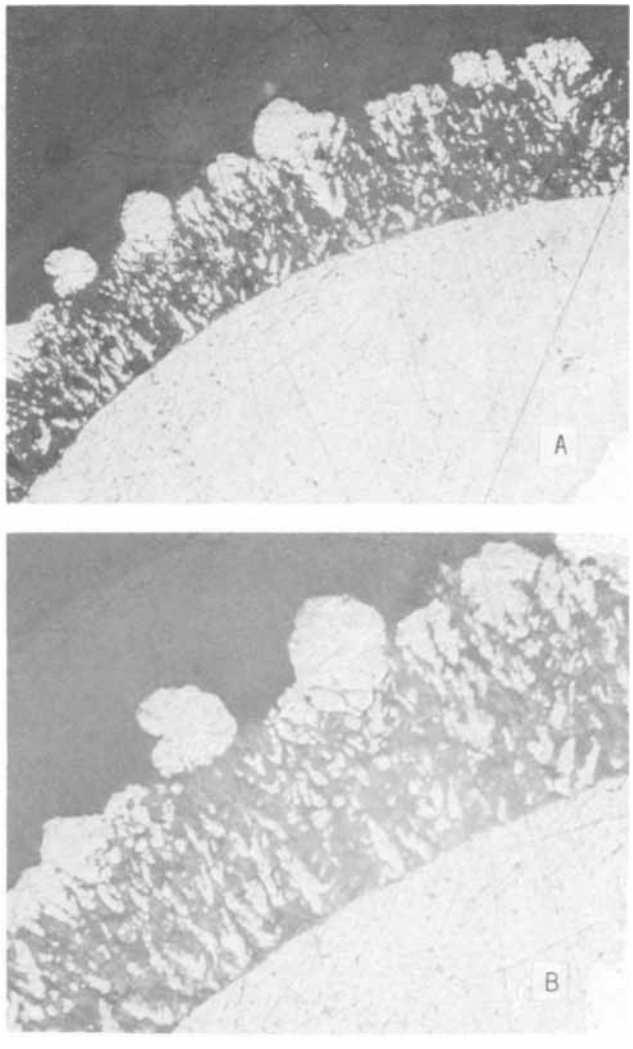

Fig. 2. Photomicrographs of electrodeposited Al plating. Conditions: 500 mA/cm², 7 min. Magnification (A) 200X, (B) 385X.

electrodeposited wires; at higher formation voltages, the capacities he reports are considerably less than what we have observed.

The capacity of unformed wire was studied for Al deposits obtained at several high current densities for varying periods of time. Figure 4 indicates a sharp rise in capacitance with the amount of Al deposited

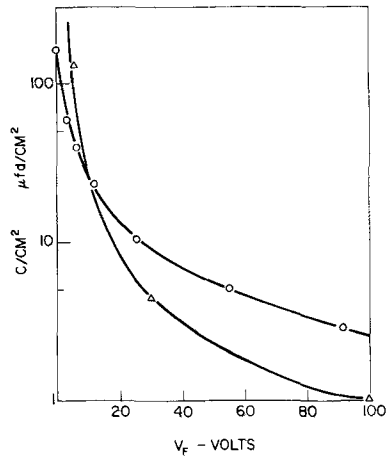

Fig. 3. Comparison of capacity/cm² for various Al structures. ○—Electrodeposited wire, 300 mA/cm², 5 min. △—Muhlhausser's data, 8 mA/cm², 30 min; 60 mA/cm², 1.5 min; 15 mA/cm², 30 min.

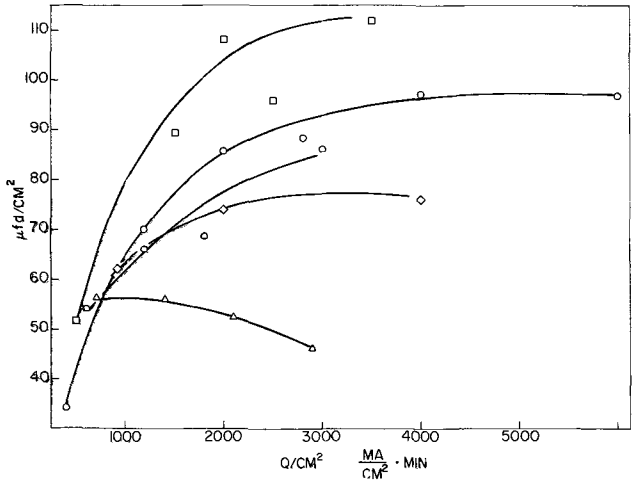

Fig. 4. Variation of capacitance for electrodeposits obtained at different current densities and total charge. Plating current density, mA/cm: ◇—300, ○—400, □—500, ⌓—600, △—700; zero formation voltage.

which tends to level off as the charge increases. The capacity also seems to be a function of the plating current density, the highest values being obtained for a current density the order of 500 mA/cm². The lower capacity values obtained at higher plating current density are due to a lack of adherence of the depositing material which becomes increasingly worse as the current density is raised. Adherence of the electrodeposited Al at high current density can be somewhat enhanced if a periodic short current reversal is applied during the plating sequence, *e.g.* 5 sec anodic/60 sec cathodic. During current reversal, the species formed could be aluminum hydride (16).

Values of the capacity measured as a function of formation voltage for three different deposit thicknesses (Fig. 5) indicate less of a capacity loss is incurred at higher formation voltages for thicker electrodeposits of aluminum. This does not contradict the previous findings, for if the samples used in Fig. 4 were formed at a higher formation voltage a more linear rise in capacity with charge increase would be observed.

Steady-state current voltage curves for the deposition and dissolution of aluminum were taken galvanostatically, potential differences being measured between the study electrode and a platinum reference electrode. A linear relationship exists between current and potential for both the anodic and cathodic electrode process; polarization values are similar to

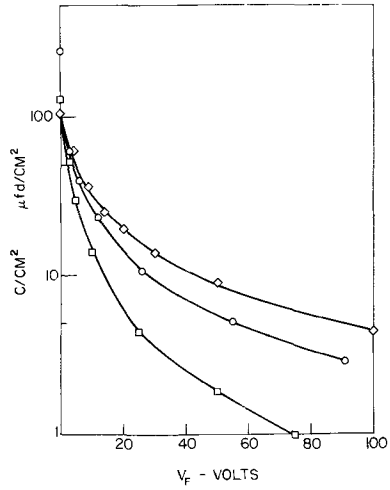

Fig. 5. Capacity/cm² vs. formation voltage as a function of deposit thickness. ◇—9 mils, 300 mA/cm², 20 min; ○—3 mils, 300 mA/cm², 5 min; □—1 mil, 300 mA/cm², 1 min.

those reported by Hayashi (10). A semilog plot, Fig. 6, gives a low value of the slope for the linear portion of the curve between 5 and 10 mV/decade. The low value of the slope eliminates the possibility of activation control and indicates that the reaction is most probably diffusion controlled. Measurements of the difference in potential between the extended linear portion of the curve and the potential observed at a certain current density gave a constant value for the resistance, $\Delta E/I$, over the range of currents studied. Although the shape of the curve indicates a limiting current region, most of the polarization is due to an ohmic drop incurred through the electrolyte. This is further emphasized by the small decrease in polarization that was observed when the electrolyte was stirred. For the concentrations used in these experiments, a true limiting current is not observed until current densities from 200 to 300 mA/cm² are reached.

Discussion

Since the largest capacity increases were observed for aluminum electrodeposits obtained at high current densities, the discussion is concerned mainly with that region of the experimental results. The formation of very fine crystals or powder metals by electrolysis is well known in the powder metallurgy industry, and these forms have been prepared from a wide variety of metals in both aqueous and nonaqueous systems (11). These deposits often appear black because of the very small size of the particles. The structure of these deposits depends strongly on the formation of new nuclei and the rate of growth of the already existing crystals. If the rate of nucleation is

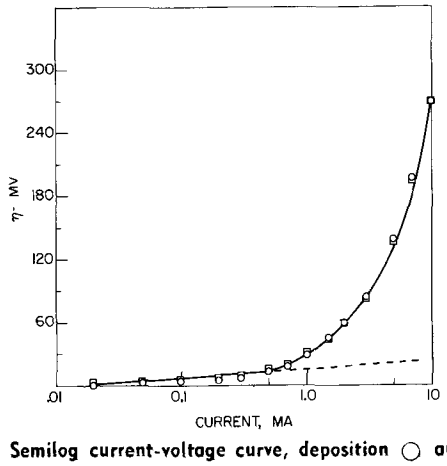

Fig. 6. Semilog current-voltage curve, deposition ○ and dissolution □ of Al.

large and crystal growth is inhibited, the formation rate of powder metals will be increased. Those factors that tend to reduce interfacial concentration, such as increased current density or decreasing metal ion concentration, will favor a high nucleation rate. As the concentration of metal ions in solution approaches zero, at limiting current, the onset of powder deposition begins.

We have observed experimentally that, upon application of a current sufficiently high to cause powder deposition, a black deposit does not begin to form until after a few seconds' time have elapsed. This lag is due to the time necessary to reduce the concentration of Al ions to near zero at the electrode solution interface. Initially, a bright metal deposits on the electrode but, as the concentration of Al ions at the interface approaches zero, a black powder begins to form. Consequently, those factors (current density, temperature, rate of stirring) that influence mass transport phenomena influence the formation of both powder deposition and particle size. After the onset of a black powdery deposition, we have observed that for current densities between 300-500 mA/cm^2 the deposits tend to become metallic again after several minutes of plating. This is probably due to an increase in the surface area of the electrode which in turn reduces the true current density. Thus, the Al ion concentration at the surface is increased favoring the deposition of larger metallic aluminum particles. This view is supported by the photomicrographs in Fig. 2 which show that larger particles tend to grow as the thickness of the electrodeposit increases.

The aluminum deposits we have studied in this work which have exhibited high capacities are a combination of very fine black Al particles overgrown by a porous dendritic deposit. Aluminum deposits grown at current density below the formation of powdered Al exhibit capacities that are an order of magnitude lower even though they are dendritic in nature and of the same or greater thickness. Capacity measurements for the deposition of copper (12) have also shown that a steep rise in capacity occurs with the onset of powder formation at limiting current.

The adhesion of these powder deposits is favorable for current densities below approximately 500 mA/cm^2; for higher current density values, the black particles fall off the electrode easily. It is therefore necessary to maintain a current density in the region where the particles will adhere to the aluminum substrate; this can be enhanced to some extent by a periodic reversal of current for a short duration.

Conclusions

1. A nonaqueous organic plating solution has been used successfully in electrodepositing aluminum to obtain high-surface-area Al electrodes.
2. The increased capacity values observed for these deposits have been related to the formation of fine black Al crystals which are obtained in the region of limiting current density.
3. Current-voltage curves indicate that the electrodeposition of Al from this electrolyte is probably diffusion controlled.

Acknowledgments

The author wishes to thank Drs. Robert S. Alwitt and Glenn M. Cook for their advice and help during the course of this project.

Manuscript submitted Oct. 28, 1969; revised manuscript received Feb. 3, 1970.

Any discussion of this paper will appear in a Discussion Section to be published in the December 1970 JOURNAL.

REFERENCES

1. M. Muhlhausser, *Electrochem. Technol.*, **6**, 183 (1968).
2. K. Ziegler and H. Lehmkuhl, *Z. Anorg. Allgem. Chem.*, **283**, 414 (1956).
3. W. J. Kroll, *Trans. Electrochem. Soc.*, **87**, 551 (1945).
4. K. H. Hurley, and T. P. Wier, U.S. Pat. 2,446,349, Aug. 3, 1948; *This Journal*, **98**, 204 (1951).
5. D. E. Couch and A. Brenner, *This Journal*, **99**, 234 (1952).
6. J. H. Connor and A. Brenner, *ibid.*, **103**, 657 (1956).
7. A. L. Levinskas and A. Yu. Simanauichus, *Electrokhimiya*, **2**, 200 (1966).
8. F. Burger and D. Cheseldine, 1st Semiannual Report, Contract DRB9596-S3811 Defense Research Board (Canada) (1964).
9. G. Evans, J. Kennedy, Jr., and F. DelGreco, *J. Inorg. Nucl. Chem.*, **4**, 40 (1957).
10. T. Hayashi and T. Ishida, *Bull. Univ. Osaka Pref., Ser. A*, **7**, 43 (1959).
11. N. Ibl, *Advan. Electrochem. Electrochem. Eng.*, **2**, 49 (1962).
12. M. Loshkarlv, A. Ozerov, and N. Kudrautsev, *Zhur. Priklad. Khim.*, **22**, 294 (1949); *Chem. Abs.*, **43**, 5674g (1949).
13. Yu. M. Kessler, N. M. Alpatova, and O. R. Osipov, *Russian Chem. Rev.*, **33**, No. 3, 119 (1964).
14. E. C. Ashby and J. Prather, *J. Am. Chem. Soc.*, **88**, 729 (1966).
15. F. A. Clay, W. B. Harding, and C. J. Stimetz, *Plating*, **56**, 1027 (1969).
16. *Russian Chem. Rev.*, **57**, No. 2, 99 (1968).

Electrodeposition of Resin

S. Mercouris and W. F. Graydon

Department of Chemical Engineering and Applied Chemistry, University of Toronto, Toronto, Ontario, Canada

ABSTRACT

The electrodeposition, under constant voltage, of an emulsion of a polyacrylic resin is studied. The coulombic yield of the process is examined at different voltages and for different deposition times. The coating is analyzed for iron, and the iron content/coulombs relationship was found to be linear. An addition of a small amount of Cl^- in the bath highly increased the iron content of the coating. The role of the electrodissolved anodic metal is examined by comparative deposition on steel and platinum. The water content of the coating was studied and the "gassing" effect at the anode was related to the resistance of the resulting film.

Electrocoating, as a method of applying primers or finishes on metalic surfaces, has attained wide application in recent years. Several patents cover the use of different electrocoating baths and conditions of deposition. However, in spite of the numerous publications in this field, the actual mechanism of the electrodeposition process is not yet clearly understood, and the continuous operation of the electrocoating tanks still involves many problems.

The composition of an electropainting bath is very complex. It may consist of resin, pigment, extenders, and a crosslinking agent as well as other compounds

which give specific properties to the coating. All those constituents must be deposited at the same rate or special care must be taken to keep the composition of the bath constant. The problem is solved mainly by special formulation of the bath, so that equal rates of deposition are attained.

Due to the complexity of the electropainting bath, and the fact that a knowledge of behavior under simple conditions is a prerequisite to the understanding of complex technological problems, a relatively simpler system of an emulsion of a polyacrylic resin was studied. Moreover, the resin undergoes all the reactions leading to the deposition of the paint. The resin was solubilized in water by use of triethylamine and the suspended particles of the emulsions were aggregates of polymeric molecules charged by the ionization of some carboxyl groups of the molecules located on the surface of the particle.

Tawn and Berry (1) discussed the application of the theories of Pauli and Helmholtz to the above systems and they stressed the difficulties in studying them in terms of fundamental physicochemical properties alone. Following their ideas in the present work, the relationship among some of the less fundamental variables of the electrodeposition process was studied. The rest of the variables had to be kept constant and this caused some problems when the degree of dispersion was to be kept constant. In the emulsion of the resin, there is a wide distribution of particle sizes and size/charge ratios. This distribution cannot be exactly reproduced and, even for a given solution, changes with time. This difficulty can be easily overcome in many cases by taking all the measurements within a short time interval, but nothing can be done in the case where the concentration of the resin is the independent variable. The dependent variable then does not depend only on the given concentration, but also on the degree of dispersion of the prepared emulsions. Consequently, a higher variance is expected.

This can be clearly demonstrated in Fig. 5. Each point of the three lines is the mean of two measurements with a mean deviation less than 1% and all the points of each line come from measurements taken in a short time interval. However, the repetition of the same experiment, using the same emulsion on three different days, produces three distinct curves and this must be attributed to the change in the degree of dispersion of the emulsion since all the other variables can be considered reproducible.

Electrode reactions.—The species moving toward the anode by the applied electrical field are negatively charged colloidal particles of resin (colloid-R) COO^- and OH^-. It is generally accepted that the deposition is not due to the immediate discharge of the colloidal particles at the anode, and the main arguments are as follows:

1. Deposition can take place on diaphragms interposed between the anode and the emulsion which do not permit immediate contact between the colloidal particles and the anode [Fink and Feinleib (2)].
2. If deposition were due to immediate discharge of the particles, we would not be able to explain the deposition after the first layer is formed, since the particles cannot reach the anode any more [Finn and Mell (3)].
3. Tawn and Berry (1) reported a delay period before deposition could be observed and a progressive increase of the concentration of resin in the film adjacent to the anode (dipped film) during this period. This cannot be explained if the particles are immediately discharged and deposited.
4. Immediate discharge of the particles should be followed by a Kolbe Electrolytic Synthesis producing a condensation of the resin ions with an evolution of carbon dioxide. Gloyer, Hart, and Cutforth (4) have not detected either carbon dioxide evolution at the anode or significant reduction in acid value of the deposited resin.

It is generally accepted in literature that deposition is due to the following reactions.

$$(\text{Colloid-R})\text{COO}^- \xrightarrow{Fe^{2+}} [(\text{Colloid-R})\text{COO}]_2\text{Fe} \quad [1]$$

$$(\text{Colloid-R})\text{COO}^- \xrightarrow{H^+} (\text{Colloid-R})\text{COOH} \quad [2]$$

Fe^{2+} come from electrodissolution of the anode, and H^+ come from a local drop of the pH after the discharge and consequent removal of the OH^-.

Fink and Feinlieb (2) and, later, Olsen (5) proved that the iron is dissolved in the form of Fe^{2+} by adding thiocyanate or ferricyanide ions in the bath. The same was proved in this work more quantitatively by analyzing the coating for Fe^{2+} and Fe^{3+}.

May and Smith (6) tried to calculate the ratio of the amounts deposited, according to reactions [1] and [2], from the ratio of the electrical charges involved in each of them. The number of coulombs used for reaction [1] was calculated from the amount of iron determined by analysis of the coating. The charges involved in reaction [2] were calculated from the weight of the deposited coating and the acid number of the resin. The sum of the two numbers, as above calculated, was less than the total number of coulombs used for the deposition. They called this difference "unaccounted current."

Results and Discussion

Iron content of the coating.—A spectrophotometric method was used to analyze the coating for iron after dissolution with alcohol. The iron was determined in alcoholic solutions and in the presence of the resin. The number of coulombs used for the deposition was calculated from the area under the current/time curve obtained by the use of a recorder.

The lower curve of Fig. 2 shows the weight deposited *vs.* coulombs relationship, for different deposition times. A straight line, followed by a downward curve at higher deposition times (*i.e.*, beyond 4 min), is obtained. The slope of the straight line represents the coulombic yield of the deposition. A very small increase of the coulombic yield was observed with increasing concentration of the bath and a number 8-12 mg/coulomb was obtained for concentrations of 2-12% solids.

The amount of iron *vs.* the number of coulombs relationship for different times of deposition is linear as shown in Fig. 1. Since the coulombic yield is constant for different deposition times, a constant concentration of iron for different deposition times must be concluded. This concentration of iron was calculated to be of the order of 0.006%; the bath had a concentration of 2% solids. The relationship between the amount of iron and coulombs was also found to be linear for a solution of 12% solids and a similar iron concentration was calculated.

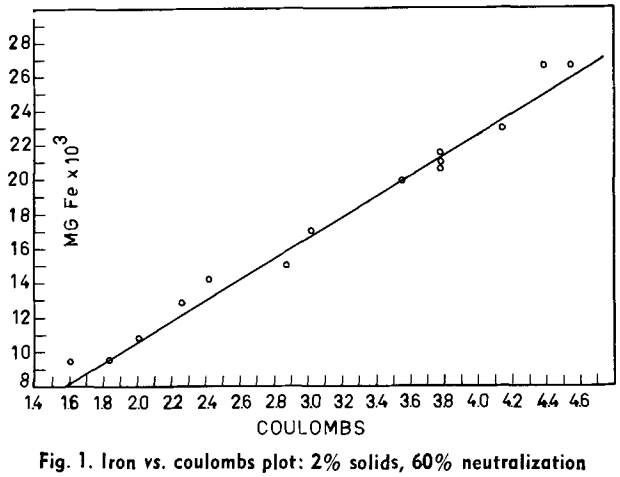

Fig. 1. Iron *vs.* coulombs plot: 2% solids, 60% neutralization

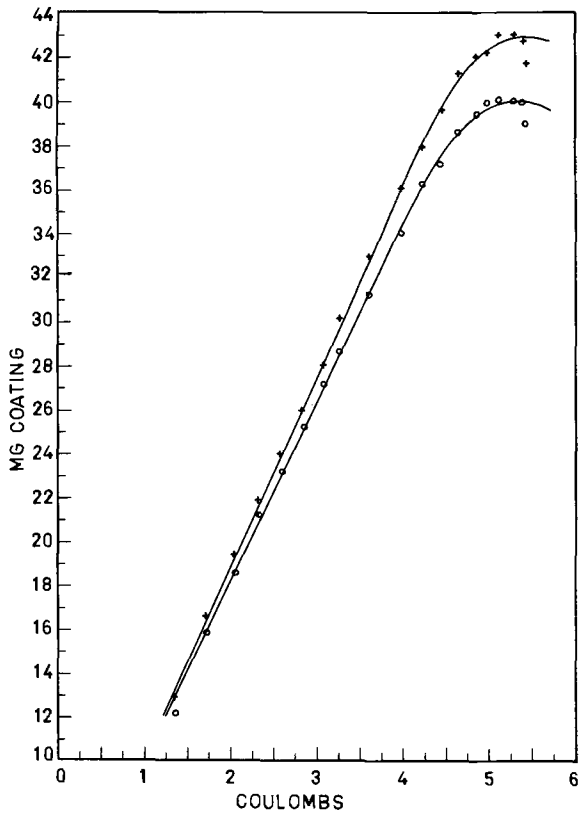

Fig. 2. Weight vs. coulombs plot: 2% solids, 60% neutralization. ○, Weight of baked coating; +, weight of unbaked coating.

The effect of the contamination of the bath with foreign anions was studied by adding a small amount of NaCl (50 mg/liter). The iron/coulombs relationship was again linear, but the concentration of iron was highly increased from 0.006 to 2%. The high concentration of iron is quite evident by the brown color of the coatings obtained.

Comparative deposition on iron and platinum was studied under identical conditions. The rates of deposition were found to be the same and identical coulombic yields were obtained. The equality of the coulombic yields is demonstrated in Table I. A pair comparison of the tabulated values must be considered (Fe-Pt), since the values for each pair are the result of experiments conducted under identical conditions (in a short time interval).

Role of iron in the electrodeposition process.—The percentage of the total current used to dissolve the iron can be calculated from the previous data. Table II shows the results for different runs.

Table I. Comparison of the coulombic yields for deposition on Fe and Pt

Conditions: 2% solids (+ 50 mg NaCl/liter)
60% neutralization
110V
3 min deposition time

Run No.	Coulombic yield Fe	Pt
1	8.24	8.30
2	7.83	7.61
3	7.25	7.55

Table II. Percentage of coulombs used to dissolve the iron

	% Coulombs for iron
2% solids, 60% neutralization	2.07
12% solids, 60% neutralization	1.86
2% solids, 35% neutralization	3.37
2% solids (+ 50 mg/liter NaCl), 60% neutralization	72.8

The percentage of the current used for the iron dissolution seems to be independent of the concentration and has a higher value for a lower degree of neutralization.

From the acid number of the resin and the weight of the coating, the percentage of the current used to deposit the resin, according to reaction [2], can be calculated. This method of calculation, however, is not correct for the following reasons. The emulsion used for the electrodepositions consists of colloidal particles formed by aggregates of polymeric molecules. The charge of the particles is due to ionization of some carboxyl groups of molecules which are at the surface of the particle. However, there is a large number of other carboxyl groups which, being in the mass of the particle, are not ionized. Consequently, they do not take part in the electrodeposition reactions, but are deposited because of the deposition of the whole particle.

Tawn and Berry (1) represented the deposited species in the form

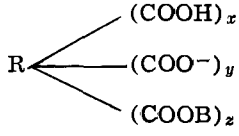

where B represents the neutralizing base.

x, y, and z can have different values depending on the ionization constants of the carboxyl groups and the base. Water insolubility or coagulation will result from an increase in the value of x, with a corresponding decrease in y, and will also be promoted by loss of base, *i.e.* fall in z. The above discussion shows that a particle can be deposited even when some of the carboxyl groups are still ionized or are neutralized with an equivalent amount of base.

It would be expected, thus, that by adding the percentage of the current used to dissolve the iron plus the percentage of the current calculated by counting all the carboxyl groups of the resin a number much higher than 100 would be obtained.

This was not verified by the experiments for they gave a sum much lower than 100. The difference from 100 is the unaccounted current reported by May and Smith (6).

Using an average value for the coulombic yield equal to 10, the percentage of the coulombs for the resin is calculated as being equal to 19. The unaccounted current, having been calculated equal to 79%, shows a very bad efficiency for reactions [1] and [2].

In the case of the bath contaminated with chlorides, the percentage of electrochemical equivalents for the iron was found equal to 72.8 (Table II). This is much higher than the percentage of the electrochemical equivalents of the resin calculated in the previous paragraph. That means that the amount of iron in the coating is much higher than the one required from the stoichiometry of reaction [1], even if we assume that this is the only deposition reaction. Consequently, questions arise as to the form in which the rest of the iron exists in the coating.

The results shown in Table I proving equal coulombic yields for deposition on iron and platinum cannot be explained by the previous theory. In the case of deposition on platinum, a large amount of current is used to discharge the chlorine ions producing chlorine gas. This amount of current does not result in any deposition. In the case of deposition on iron, the discharged chlorine ions dissolve the anode, producing iron ions, which deposit a certain amount of resin. Consequently, a higher coulombic yield for deposition on iron would be expected.

Sullivan (7) explains the existence of iron in the coating as being due to the formation of stable iron oxides by the reaction of the ferrous and ferric ions with the hydroxyl ions traveling toward the anode.

$$Fe^{+2} + 2\,OH^- \rightarrow Fe(OH)_2 \qquad [3]$$

$$Fe^{+3} + 3\,OH^- \rightarrow Fe(OH)_3 \qquad [4]$$

The main reaction explaining the deposition of resin in all cases is reaction [5].

$$(\text{Colloid} - \text{R})\text{COO}^- + \text{H}^+ \rightleftarrows (\text{Colloid} - \text{R})\text{COOH} \quad [5]$$

This reaction must be considered as having the form of equilibrium, and deposition occurs when $[(\text{Colloid}-\text{R})\text{COO}^-]\,[\text{H}^+] > k$, where k is the ionization constant of the resin. The drop of the *p*H close to the anode cannot be local, as often reported in literature, and a concentration gradient from the anode up to the bulk of the solution must be considered. Due to this concentration gradient, a large number of H^+ do not take part in the deposition reactions but are transferred to the bulk of the solution. This is a possible explanation of the "unaccounted current" since the current used to produce the above H^+ does not lead to any deposition.

Tawn and Berry (1) reported a higher concentration for the resin in the dipped film. An immediate discharge of the particles, as was already discussed, cannot be accepted. Consequently, a similar concentration gradient to H^+ for resin must be considered.

The delay period reported by Tawn and Berry (1) can be explained as the time required for the above two concentration gradients to build up. Deposition starts when the product $[(\text{Colloid-R})\text{COO}^-]\,[\text{H}^+]$ becomes greater than k. This also explains the progressive increase of the concentration of resin in the dipped film during the delay period reported by the same authors and the decrease of the delay period with an increase of the applied voltage reported by Yeates (8). The higher the voltage, the faster the formation of the two concentration gradients.

Finally, the curvature of the weight/coulombs curve after a long time of deposition, shown in Fig. 2, can be explained by the above proposed scheme. After a long time of deposition, the anode is almost isolated and there is a large potential drop through the film. The remaining potential difference is not sufficient to maintain the above concentration gradients. Thus, $[(\text{Colloid-R})\text{COO}^-]\,[\text{H}^+] < k$, and dissolution of the film occurs instead of deposition.

Water content of the coating.—The investigations of the water content of the film and the gassing effect, which will be discussed later, are of great technological importance since the studied variables are directly related to such qualities of the coating produced as appearance and resistance. For example, the higher the water content of the film, the higher the possibility of getting pinholes in the coating because of the escape of water bubbles during the baking process.

The water content of the film was calculated as the difference between the weight of a baked and an unbaked film under identical conditions. The unbaked film was dried by putting it in a desiccator under vacuum conditions.

Figure 2 shows the weight/coulombs plot of the baked and unbaked film for different times of deposition for a 2%-solids bath. It is interesting to note that even the weight of the unbaked film changes linearly with the number of coulombs. A problem arising here is that the difference in the weight of the unbaked and baked film, which gives the amount of water in the film, can be of similar magnitude as the variance of the distributions of the two numbers used for the subtraction. Consequently a great variance for the distribution of the water content is expected, making the results inconclusive.

The above problem was solved by drawing the regression lines and taking the differences between corresponding points. Each point of the regression line represents the mean of the distribution of the individual measurements, whose variance is eliminated in this way. A large number of points were used for the construction of the two regression lines in order to have a higher degree of confidence.

The values of the water content of the film at different times of deposition were calculated from Fig. 2.

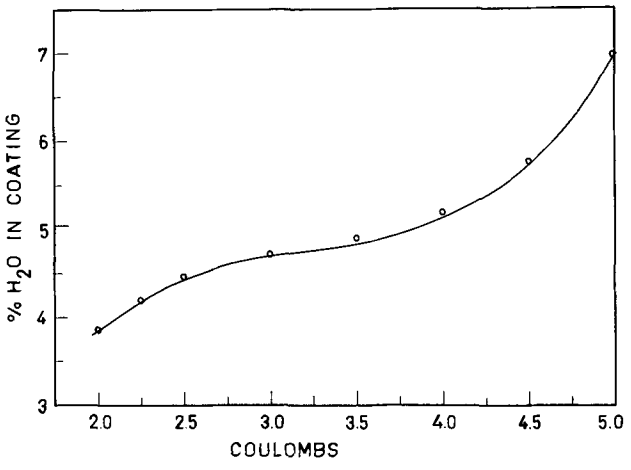

Fig. 3. Water content *vs.* coulombs plot: 2% solids, 60% neutralization.

The plot of the water content *vs.* the number of coulombs is shown in Fig. 3. An increase in the water content of the coating is observed with an increase in the number of coulombs at different deposition times.

The same work was repeated using a 12%-solids bath. The same increase of the water content was observed with increasing deposition time, but the actual numbers were higher (almost double).

The conclusion from the above results is that a film with lower water content can be obtained by using a lower concentration of resin and a shorter deposition time.

Gassing effect.—Tasker and Taylor (9) and, more recently, Curtis, Pugh, and Taylor (10) reported a peak in their resistance of the film/weight deposited plots. The experiment was conducted under constant current conditions. They examined the film with the aid of a microscope and proved that the peak occurred at the point at which the film originally laid down disrupted in order to allow the trapped anodic gas to escape.

Similar peaks were observed in the current/time curves under constant voltage conditions, as shown in Fig. 4. The peaks are inverted since the current is inversely proportional to the resistance.

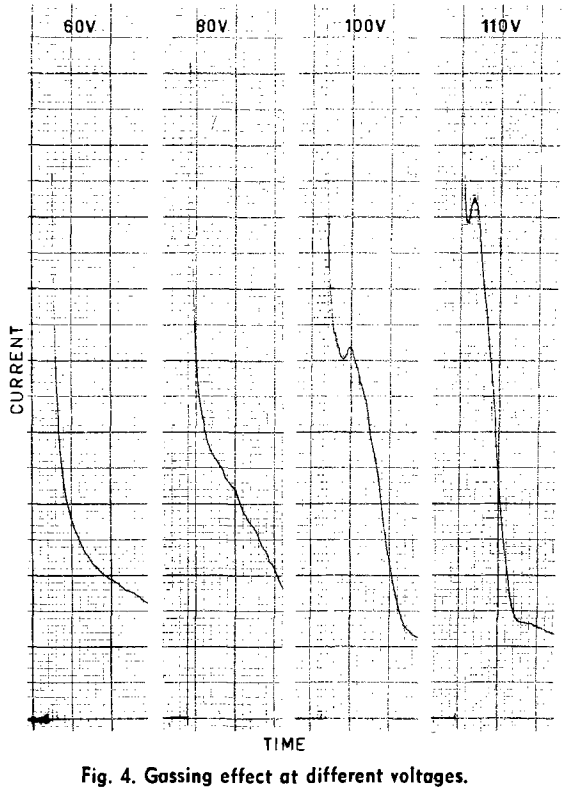

Fig. 4. Gassing effect at different voltages.

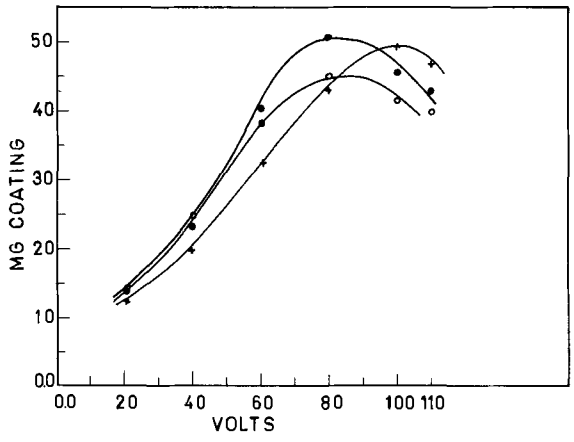

Fig. 5. Weight vs. voltage for 3 min deposition time: 4% solids, 60% neutralization. ○, First day; ●, second day; +, third day.

In Fig. 5, the weight of coating is plotted *vs.* the corresponding voltage of deposition for 3 min deposition time. The three curves represent three runs at three different days. An almost linear increase for each curve is observed followed by a curvature at 80-110V. This curvature of the weight/voltage plots starts almost at the same voltage at which the resistance "peaking" starts to appear. Possibly, there is a connection between the two phenomena.

After about 90V, a higher voltage deposits a lower weight for the same deposition time (3 min). That means that the higher the voltage, the higher the resistance of the deposited film. This can be considered a justification for the high voltages used in technical applications (100-300V). In the above experiment, a 4%-solids solution was used. For lower concentrations the above gassing effect was not observed, whereas for higher concentrations it was even more clearly evident (Fig. 5).

Conclusions

The coulombic yield of the electrodeposition was found to be constant for different voltages and at different deposition times. Almost constant coulombic yield was found for different concentrations of resin and for deposition on different metals. The iron content of the film, for deposition on steel, was proved to be almost constant for different concentrations of resin and different deposition times.

The electrochemical current used to dissolve the iron was proved to be a small percentage of the total current. The iron content of the film and the percentage of the total current used to dissolve the iron were highly increased after a small contamination of the bath with chlorides. The role of the ferrous and ferric ions in the electrodeposition reactions is not as yet clearly understood. More work must be done in order to elucidate the exact form of iron in the coating.

A small amount of water was found in the film. This increases with deposition time and is higher for higher concentrations of resin.

A rupture of the film due to the escape of trapped anodic gas was observed at a certain time during the deposition. This rupture occurred for higher concentrations and voltages greater than 80. In addition, an increase in the resistance of the film obtained was observed with a voltage greater than 80.

Manuscript received Sept. 29, 1969.

Any discussion of this paper will appear in a Discussion Section to be published in the December 1970 JOURNAL.

REFERENCES

1. A. R. H. Tawn and J. R. Berry, *J. Oil Colour Chemists' Assoc.*, **48**, 790 (1965).
2. C. G. Fink and M. Feileib, *J. (and Trans.) Electrochem. Soc.*, **94**, 309 (1948).
3. S. R. Finn and C. C. Mell, *J. Oil Colour Chemists' Assoc.*, **47**, 219 (1964).
4. S. W. Gloyer, D. P. Hart, and R. E. Cutforth, *Off. Digest J. Paint. Technol. and Eng.*, **37**, No. 481, 113 (1965).
5. D. A. Olsen, *J. Paint Technology*, **38**, No. 499, 429 (1966).
6. C. A. May and G. Smith, *ibid.*, **40**, No. 526, 494 (1968).
7. M. R. Sullivan, *ibid.*, **38**, No. 499, 424 (1966).
8. R. L. Yeates, "Electropainting," Robert Draper Ltd. (1966).
9. L. Tasker and J. R. Taylor, *J. Oil Colour Chemists' Assoc.*, **48**, No. 2, 121 (1965).
10. W. B. Curtis, J. A. Pugh, and J. R. Taylor, *Chem. Ind. (London)*, **1967**, 1858.

Preparation and Evaluation of Spreading Resistance Probe Tip

E. F. Gorey, C. P. Schneider, and M. R. Poponiak

IBM Components Division, East Fishkill Facility, Hopewell Junction, New York

ABSTRACT

The spreading resistance technique used to evaluate various types of silicon structures is dependent primarily on the probe point. Data are presented on point preparation and loading of different point materials. A method for preparation and evaluation of point characteristics for effective use on thin silicon structures is described.

The spreading resistance technique (1-3) is the most versatile technique used to characterize impurity profiles of multilayered structures.

An improved spreading resistance probe (4) which utilized balance beam probe arms, weight loading, and controlled velocity of impact emphasized contact reproducibility as one of its most important parameters. It has been implied in the previous papers that a spreading resistance probe will function properly if a particular type of probe point is used.

The most critical part of the technique is the probe point. It must have the capability of making thousands of measurements without deteriorating and must maintain certain characteristics that make it useful in measuring both n- and p-type silicon structures.

This paper describes a method of preparing and evaluating a probe point for its use in the spreading resistance technique.

Probe Point Characteristics

A good probe point has the following characteristics: the effective penetration of the probe into the silicon surface must be kept to a minimum, and the spreading resistance measured in the forward and reverse

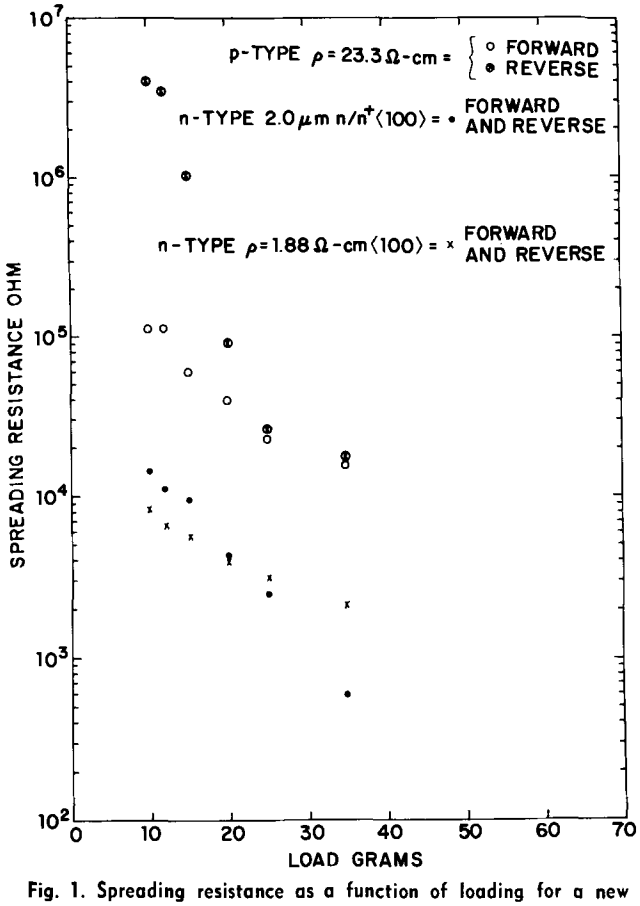

Fig. 1. Spreading resistance as a function of loading for a new K-75 point as received from vendor.

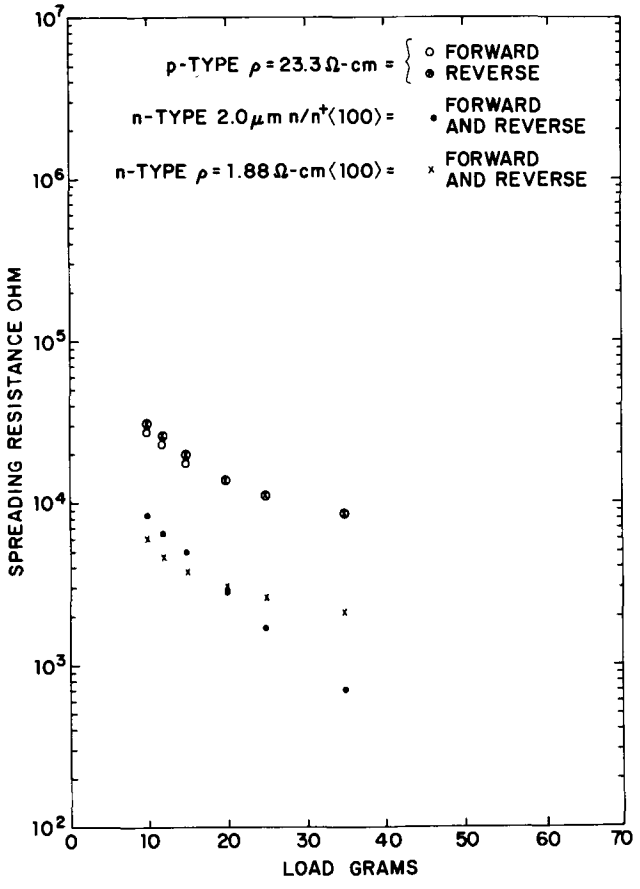

Fig. 2. Spreading resistance as a function of loading for a K-75 point prepared by 3 sec abrasion.

direction of current must not differ by more than 5% of the average. Experimental data indicate that a probe can function on n-type silicon but can give inconsistent results on p-type.

An experiment designed to study these characteristics and the behavior of n- and p-type silicon wafers was performed on 3 wafers. A 23.3 ohm-cm p-type mechanical polished bulk wafer was used to indicate when good contact was achieved. Good contact exists when the spreading resistance in the forward and reverse direction of current is within 5% of the average. A 1.88 ohm-cm n-type bulk wafer was used as a control wafer. A 3.0 ohm-cm n-type epitaxial layer of 2.0 μm thickness on a 0.001 ohm-cm n-type substrate was used to indicate effective probe penetration. In the range of loading where the ratio of the spreading resistances of the epitaxial wafer to the n-type bulk wafer remains constant, no effective penetration is considered to exist.

Spreading resistance was plotted as a function of probe point loading. All measurements were made utilizing the spreading resistance apparatus described in Ref. (4). Figures 1 through 4 show the results obtained from tungsten-ruthenium probe points with tip radius of 0.0007 in.

Figure 1 represents the results of a point as received from the vendor.[1] From 10 to 15g loads, bad contact is made on the p-type wafer. Good contact is made on both n-type wafers and no effective penetration exists. At 20g, the ratio of the two n-type wafers now changes and effective probe penetration is observed. The difference between the forward and reverse spreading resistance from the average on the p-type sample is 40%. Greater effective probe penetration of the epitaxial layer and good contact on the p-type wafer is observed at 25g loading. Deep effective penetration of the thin epitaxial layer and good contact on the p-type wafer was observed at 35g loading. From results obtained, it can be seen that at no one loading of the probe point did the point exhibit good contact and no effective penetration.

The probe in Fig. 2 was prepared by an abrasive blasting of 3 sec. The spreading resistance probe point is prepared by an abrasive blasting technique in the following manner. A series of probe points to be prepared are positioned in a holder with their points exposed. An air abrasive unit is then used to abrade the point with 27.5 μm aluminum oxide with a 50 psi pressure. The unit has a 1/16 in. nozzle orifice.

The nozzle of the unit is placed approximately 1 in. from the probe points. After abrading, each probe is immersed in trichlorethylene for 5 min. The probes are then wiped with cotton swabs saturated with acetone. This procedure gives the probe tips the proper finish to make good contact to the sample.

It was evident that the abrasive blasting technique changes the results significantly. Good contact was made on the p-type wafer with only 10g loading. This probe point will operate properly if used between 10-15g loading.

Figure 3 shows the results of abrading for 5 sec. Effective penetration starts at 15g. The probe point represented in Fig. 4 was the result of abrasion for 10 sec. In Fig. 3 and 4, the tips exhibited large spikes due to the abrasion which caused deep effective penetration.

Figure 5 shows the results of an osmium alloy probe point with a tip radius of 0.0007 in.[2] Effective penetration did not occur until 35g, but poor contact was made to the p-type wafer. This point will not meet all the requirements of a good point. Figure 6 represents a ruthenium alloy probe point with a tip radius of 0.0007 in.[3] which exhibited characteristics similar to the osmium point.

A convenient method to insure a good probe point is as follows. Measurements are made on 3 wafers: No. 1, a thin ($\sim$ 2.0 μm thick) n-type epitaxial layer of

[1] Fidelitone K-75 PIVOT, tungsten ruthenium alloy.

[2] Fidelitone #741 PIVOT, osmium alloy.

[3] Fidelitone #347 PIVOT, ruthenium alloy.

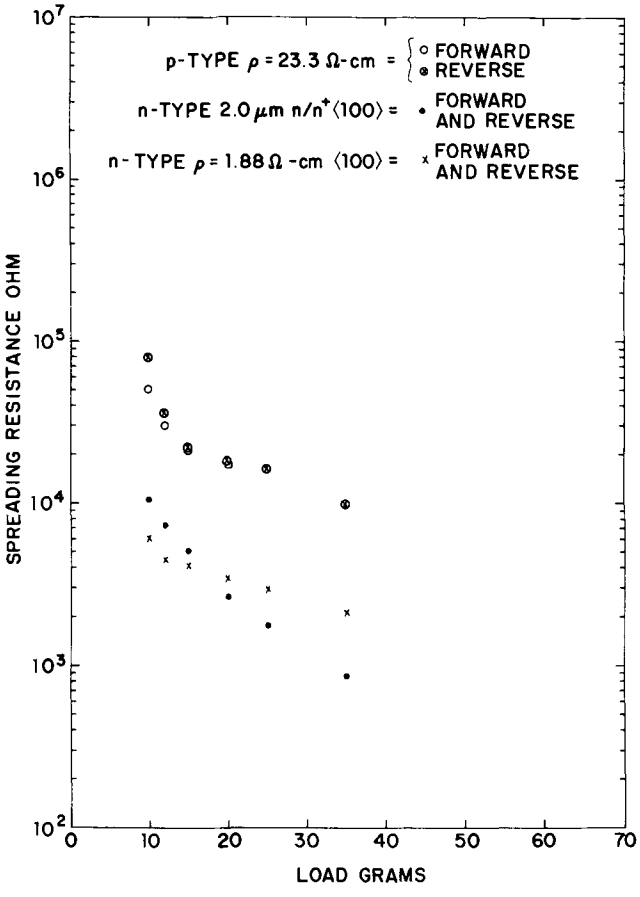

Fig. 3. Spreading resistance as a function of loading for a K-75 point prepared by 5 sec abrasion.

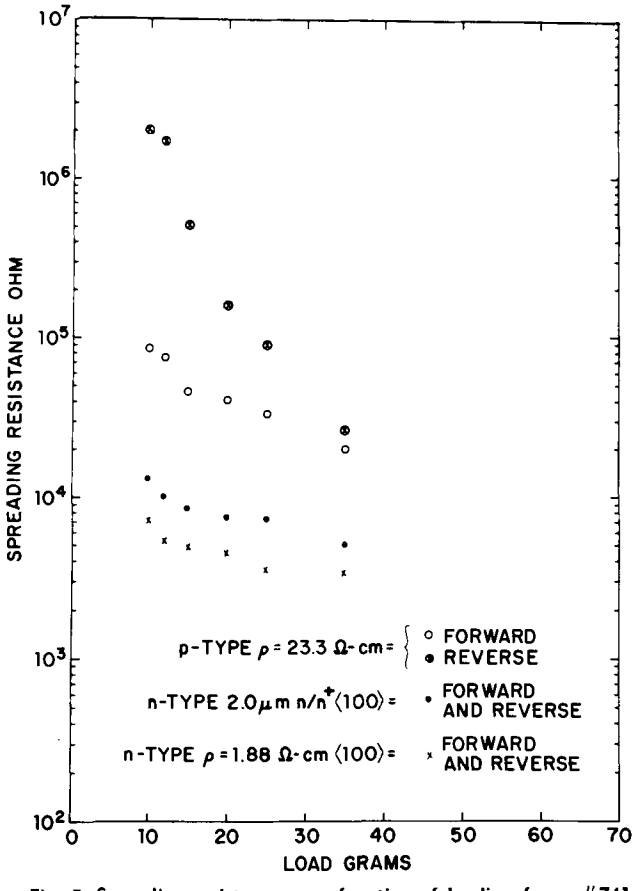

Fig. 5. Spreading resistance as a function of loading for a #741 osmium alloy point.

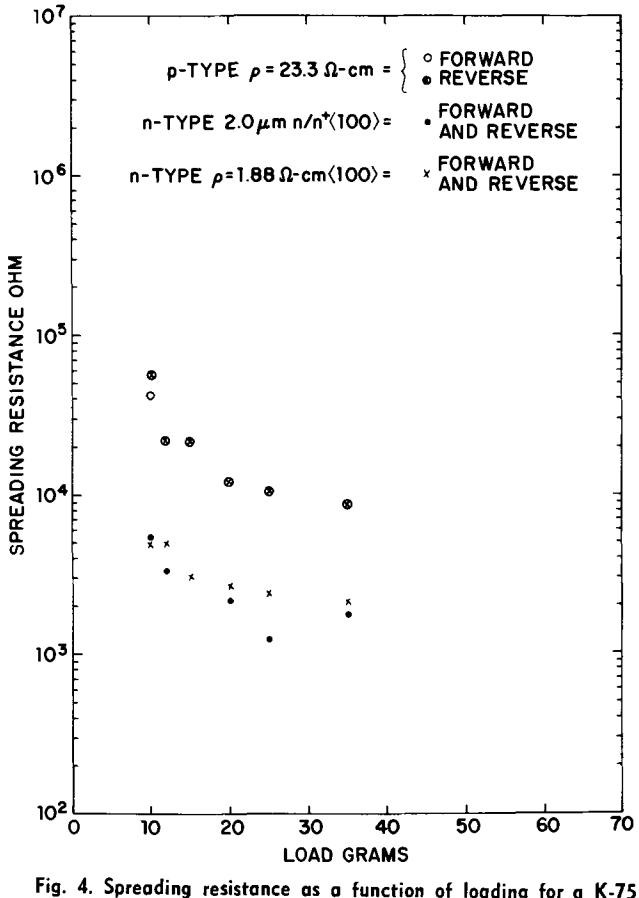

Fig. 4. Spreading resistance as a function of loading for a K-75 point prepared by 10 sec abrasion.

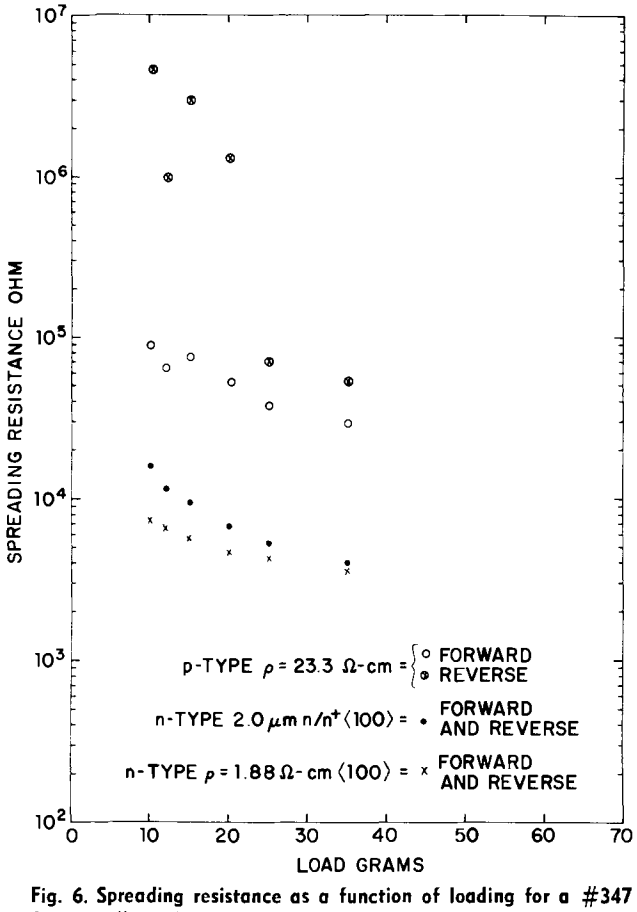

Fig. 6. Spreading resistance as a function of loading for a #347 ruthenium alloy point.

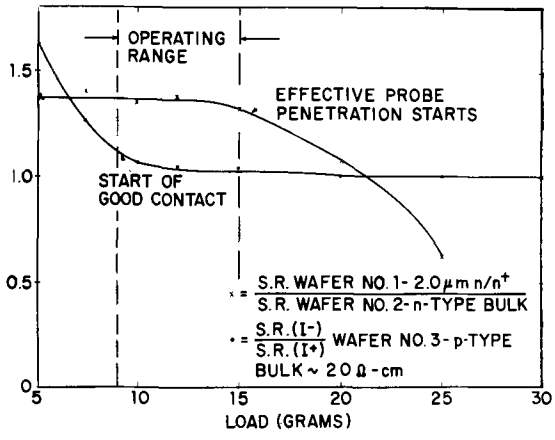

Fig. 7. Ratios of spreading resistances of n/n+ to n-type bulk wafers and spreading resistances in the reverse direction to the forward direction of current as a function of loading for a typical prepared K-75 probe point.

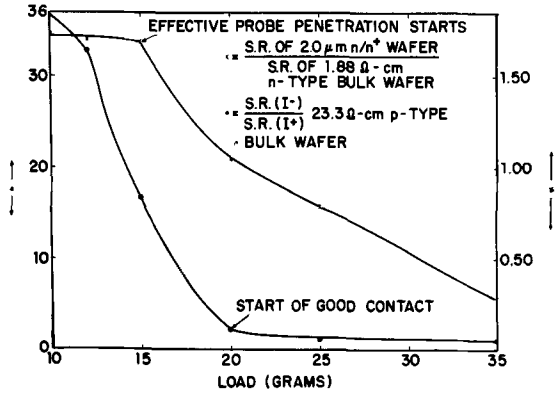

Fig. 8. Ratios of spreading resistances of n/n+ to n-type bulk wafers and spreading resistances in the reverse direction to the forward direction of current as a function of loading for an unprepared K-75 probe point.

some ρ on an N+ substrate exhibiting a certain spreading resistance; No. 2, an n-type bulk wafer with approximately the same spreading resistance as wafer 1; and No. 3, a p-type mechanical polished bulk wafer of ~ 20.0 ohm-cm. Starting with a probe point loading of 5.0g, the ratios of the spreading resistances of the n/n+ wafer to the n-type bulk and the spreading resistances in the reverse direction of current to the forward direction of current of the p-type wafer are plotted as a function of loading.

Figure 7 represents a probe point which will be operable in the range of 9-15g loading. The selection of the load for proper operation is limited to the regions where both ratios have a slope of 0. For comparison, Fig. 8 presents the same ratios for the probe point used in Fig. 1. In this case, the regions where the slopes are 0 do not coincide for any loading of the probe point indicating that the point cannot be used effectively in a spreading resistance apparatus.

At this point, the loading should be set at the midpoint of the operating range. Previous experience indicated that final conditioning of the point required repeated use under operating conditions to insure stability. Experimental data showed that a minimum of 250 measurement cycles are required to stabilize the probe point. Stabilization is a wearing-in process that removes probe point spikes that are not strong enough to withstand repeated operations. These manifest themselves by rapid changes in the spreading resistance.

Figure 9 is a test profile of a n/n+ epitaxial wafer. The wafer was beveled at a 1° angle and spreading resistance was measured on the bevel at intervals of

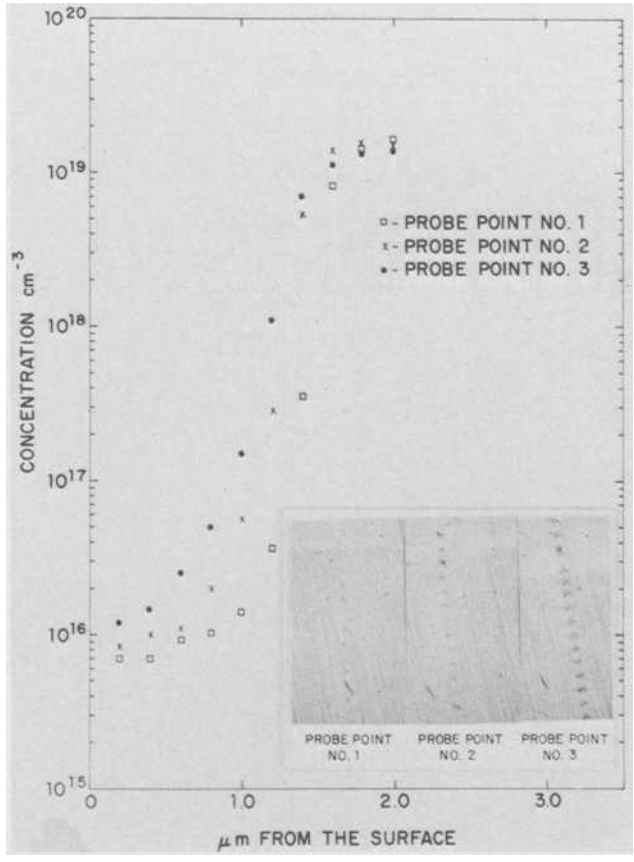

Fig. 9. Concentration *vs.* depth profile of a thin n/n+ epitaxial layer measured with three different K-75 probe points.

0.0005 in. resulting in depth increments of 0.20 μm. Three probe points, using the apparatus described in Ref. (4), were used to determine concentration *vs.* depth profiles. Probe point 1 was considered to have minimal effective penetration and probes No. 2 and 3 had increasing effective penetration, respectively. Visual inspection of the photographs of the three points' indentations on the bevel corroborate this finding. Probe point No. 1 was the only probe that would qualify as a good point using the method described previously.

Discussion

The method has been developed that produces probe points to be used in the measurement of spreading resistance of silicon with good precision. The requirements that a probe point must have are little effective penetration and good contact. A probe point with, and only with, these characteristics enables concentration *vs.* depth profiles of thin layers of any type structure to be measured.

Acknowledgments

The authors wish to acknowledge the help of Mr. P. A. Schumann, Jr., for his helpful discussions in preparation of this paper and Mr. P. Amato for some of the experimental data presented in this paper.

Manuscript submitted Sept. 15, 1969; revised manuscript received Jan. 26, 1970. This was a Late News Paper presented at the New York Meeting, May 4-9, 1969.

Any discussion of this paper will appear in a Discussion Section to be published in the December 1970 JOURNAL.

REFERENCES

1. R. G. Mazur and D. H. Dickey, *This Journal*, **113**, 255 (1966).
2. E. E. Gardner, "Symposium on Manufacturing In-Process Control and Measuring Techniques for Semiconductors," Phoenix, March 9-11, 1966.

3. E. E. Gardner, P. A. Schumann, and E. F. Gorey, "Measurement Techniques for Thin Films," p. 258, B. Schwartz and N. Schwartz, Editors, The Electrochem. Soc. (1967).

4. J. M. Adley, M. R. Poponiak, C. P. Schneider, P. A. Schumann, and A. H. Tong, Paper 324 presented at Electrochem. Soc. Meeting, New York, May 4-9, 1969.

Technical Note

Electrical Properties of Flash Evaporated Thin Film CdSe-CdTe Alloys

Tung H. Weng

School of Engineering, Oakland University, Rochester, Michigan

The work described in this paper was undertaken to determine the feasibility of forming thin film solid solutions of CdSe and CdTe by means of flash evaporation techniques and evaluate their electrical properties. One of the outstanding features of this alloy is the continuous variation of energy band gap and electrical properties with the composition of the constituent compounds. This means that a semiconductor with specific properties can be prepared simply by changing the composition. Such a wide range of properties would undoubtedly widen the scope of application which could not be achieved otherwise with a simple compound semiconductor.

Film preparation.—The apparatus used for flash evaporation is similar to that suggested by Müller (1), but with different design in the part of the powder feeder assembly as shown in Fig. 1. Instead of using mechanical vibration as in Müller's system, the powder is fed into the evaporator by a relay-operated plunger. When the relay is energized or de-energized by a variable square wave generator, the plunger strikes the reservoir so that the powder falls through a small opening located at the bottom of the reservoir into the funnel of the evaporator. This method provides a continuous and uniform rate of feeding which is essential if a homogeneous film with the original composition is to be obtained. One of the advantages of this system is that the rate of feed, and hence the rate of deposition, can be easily controlled by merely changing the frequency of the generator when the other physical settings, such as the diameter of the opening and the weight of the plunger, remain unchanged. This is desirable because it provides a simple means for controlling the crystalline structure as well as the properties of the deposit which is known to depend heavily on the deposition rate.

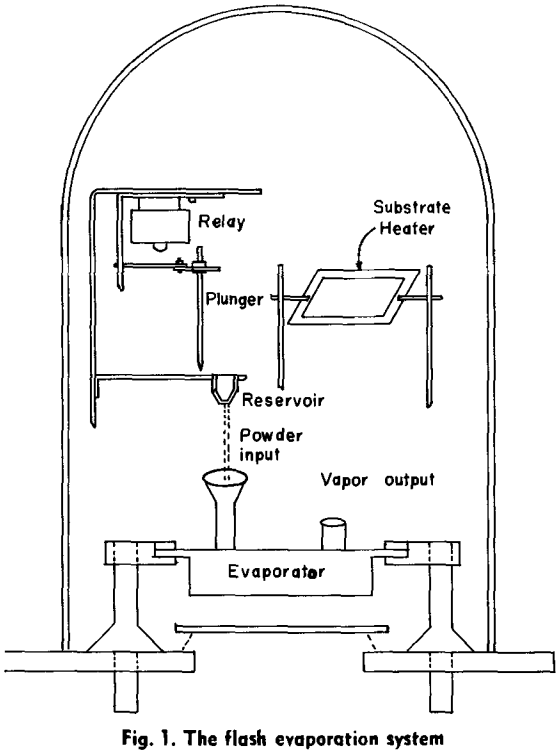

Fig. 1. The flash evaporation system

A folded molybdenum sheet was used as substrate heater. The glass substrate was inserted between the two sheets and clamped to the heater by metal screws. A Chromel-Alumel thermocouple for measurement of substrate temperature was placed adjacent to the substrate heater and made direct contact to the glass. The substrate was located about 8 in. from the evaporator with the hope that such a large distance between substrate and evaporator would minimize the heating effect generated by the heat radiating from the evaporator and produce a uniform thickness of the deposit. The vacuum system used is a 4 in. diffusion pump system with a liquid nitrogen trap. The pressure was maintained at 5×10^{-6} Torr during the entire evaporation. The evaporator which was designed specifically for the flash evaporation of compound semiconductors was kept at 1200°C. This assures a rapid and complete evaporation of each grain of the CdSe-CdTe powder which reaches the heater source.

CdSe and CdTe powders having a purity of 99.999% were supplied by Semi-elements, Inc. These powders were well mixed and sieved through a 0.088 mm opening before being put into the reservoir of the powder feeder assembly. For a given physical setting of the assembly, the rate of feed was approximately 10 mg/min which produced a 5 Å/sec deposition rate. A lower rate was also used, but the film resistivity was substantially higher than those obtained at 5 Å/sec. This is presumed to be caused by the absorption of oxygen during the crystal growth even though the vacuum pressure was in the 10^{-6} Torr range. In order to obtain a wide range of solid solutions, the composition used in this investigation varied from 10 to 90% of CdSe by weight. The substrates used were Corning's Type 7059 glass with dimensions of 3 in. x 1 in. x 0.048 in. Microslides with the same dimensions as the 7059

glass were also used. It was found that no significant difference in the characteristics of the deposited films was observed when these two types of glasses were interchanged. The substrates were cleaned, baked, and preheated to the designated temperature before evaporation took place. A set of four films with different substrate temperatures ranging from 50° to 200°C was prepared at a single pump down. This was intended to reveal the properties of the films as a function of the substrate temperature without being affected by other parameters which could conceivably have a pronounced effect on the properties of the deposits. A lower substrate temperature could not be obtained because of the heat radiating from the evaporator even with the substrate located far from the heater source. At higher substrate temperatures, however, the film resistivity was so high that the electrical measurement became increasingly difficult to perform and in many cases a thicker film could not be obtained. This is believed to be due to either re-evaporation or to a low sticking coefficient at a higher temperature.

Film properties.—The lattice type and constants of the CdSe-CdTe films were determined using x-ray diffraction. The diffractometer patterns were taken at room temperature and the output showed a single peak with a Bragg angle which varied with the composition of the constituent compounds. No trace of either CdSe or CdTe was detected regardless of their composition and preparation conditions. Since the as-deposited films showed a strong preferred orientation which would not give the information needed for an accurate result, the diffraction of randomly oriented powder was then performed. This was done by first stripping the films from their substrates and then pulverizing them before x-ray data were taken. Based on diffraction from various [hkl] planes, it was possible to determine their crystal type and lattice parameters rather accurately. The results are tabulated in Table I, and are similar to those obtained by Stucks and Farrell (2) for pure CdSe-CdTe alloys. The film containing 50 w/o (weight per cent) of CdTe could not be positively identified. This presumably was due to the presence of both hexagonal and cubic structures as reported elsewhere (2). There were no notable changes between the interplanar distance for a given composition when the substrate temperature was changed from 50° to 200°C. The relative intensity distributions for the powdered CdSe-CdTe alloys were estimated by measuring the peak heights directly on the diffractometer tracings. These data showed that the intensities for [002] (hex.) and [111] (cubic) directions are stronger than other reflections. These were also the preferred orientations of the films as deposited where a single peak was observed.

Table I. Lattice type and constants of thin film CdSe-CdTe alloys

Percentage of CdSe in CdSe-CdTe alloys	Hexagonal structure a Å	c Å	Cubic structure a Å
100	4.290	7.010	
75	4.352	7.146	
60	4.390	7.200	
50			
40			6.301
25			6.336
10			6.387
0			6.471

The carrier mobility and conductivity of CdSe-CdTe films with thickness of about 2000Å were determined using the Hall effect measurements. The dimensions of the Hall sample were 3/16 in. x ⅜ in. with evaporated indium films as ohmic contacts. All films regardless of their composition were N-type with carrier mobility and concentration varying with both composition and substrate temperature. In general, both mobility and carrier density decreased with increasing substrate temperature and varied appreciably from one set of films to another. Since reproducible properties of these films cannot be obtained without strict control of the preparation conditions, no attempt was made to pin down their electrical properties as a function of the preparation conditions. However, the mobilities of the films containing 25-50 w/o of CdSe prepared at the substrate temperature around 50°C were in the vicinity of 30 cm^2/V-sec. This figure is comparable to those of pure CdSe films (3).

On the basis of experimental results, one concludes that the flash evaporation technique can indeed be used to form polycrystalline thin film solid solutions of CdSe and CdTe and similar alloys (4). This technique offers simplicity and could be easily adopted for epitaxial growth of these alloys onto various single-crystal substrates, provided that suitable growth condition could be established. One of the immediate applications of these thin film alloys is in the area of thin film transistors. These have been fabricated successfully (5) and showed similar characteristics as CdSe and CdTe insofar as the stability and frequency response are concerned.

Manuscript submitted Sept. 10, 1969; revised manuscript received *ca.* Jan. 26, 1970. This was Paper 179 presented at the Detroit Meeting, Oct. 5-9, 1969.

Any discussion of this paper will appear in a Discussion Section to be published in the December 1970 JOURNAL.

REFERENCES

1. E. K. Müller, *J. Appl. Phys.*, **35**, 580 (1964).
2. A. D. Stuckes and G. Farrell, *J. Phys. Chem. Solids*, **25**, 477 (1964).
3. F. V. Shallcross, *RCA Review*, **24**, 676 (1963).
4. Tung H. Weng and H. J. Yu, *Solid-State Electron.*, **12**, (1969).
5. Tung H. Weng, *Proc. IEEE*, **57**, 1780 (1969).

Brief Communication

Porosity in Electrodeposited Gold-Alumina Alloys

E. S. Chen and F. K. Sautter

U. S. Army Watervliet Arsenal, Watervliet, New York

Porosity is an important factor which affects the properties of all materials. In recent years, the emphasis of many investigations was on the effect of ductility (3, 4) of materials. However, it is frequently overlooked that test materials inherently contain pores as a consequence of the fabrication process. This is

alloys regardless of whether the manufacturing process is one of powder technique or electroforming. This report presents the results of a study on the porosity in electroformed Au-Al_2O_3 alloys before and after high-temperature heat treatment and the attending implications of porosity in the creep strength of these alloys.

Experimental

Electrodeposited Au-Al_2O_3 alloys were prepared from solutions containing

$KAu(CN)_2$	10 g/liter
KCN	10 g/liter
α-Al_2O_3 (1.0μ)	2-25 g/liter

using the techniques reported by Sautter (5). The plating was conducted at a pH of 10.5, current density of 3.5 mA/cm^2, and temperature of 60°C using pure gold as soluble anodes and electropolished copper tubings, 0.4 cm diameter, as cathodes. The solutions were agitated by Teflon-coated magnetic stirrers. Only one plate was prepared from each solution. For a cathode with a total surface area of 10 cm^2, the thickness of the deposit was on the average 180μ after 16 hr of plating. Tubular Au-Al_2O_3 alloy samples are obtained on removing the copper substrate by dissolution in 50% HNO_3.

The porosity in our electroformed alloys was studied through density measurements since such studies are commonly used to measure residual porosity in sintered materials and are also applicable to studying porosity in dispersion-hardened alloys (6). The density of Au-Al_2O_3 samples weighing 1.5g each were determined with an immersion technique using an analytical balance with a sensitivity of 0.1 mg. The immersion solution was doubly distilled water with added Triton X-100 surfactant to lower the surface tension to 35 dynes/cm thereby reducing solution damping effects. The precision of the density measurements is better than ±0.03 g/cm^3. The density for each sample was determined at room temperature before and after annealing for 1 hr at 1000°C in air. The Al_2O_3 content in the alloy specimens was determined gravimetrically.

In the course of preparing the alloy samples for density measurements, the observation was made that all annealed samples show permanent length increases. This unique behavior in the electrodeposited Au-Al_2O_3 alloys was further investigated with a Leitz dilatometer, using a heating rate of 2°C/min.

Results

Typical results of the density measurements as a function of Al_2O_3 content are shown in Fig. 1. The upper curve shows the density of the as-plated alloy to be a linear function of oxide volume per cent (v/o) and that the measured densities would superimpose on the theoretical values (not illustrated) predicted by the rule of mixtures using the densities of pure gold and aluminum oxide as 19.3 and 3.97 g/cc, respectively. The lower curve shows the effect of the heat treatment. The initial decrease in density is very pronounced up to an oxide concentration of 1.5 v/o at which point the density appears to vary linearly with further increases in oxide content. Figure 2 shows the expansion behavior typical of the Au-Al_2O_3 alloys tested. The curve shows the linear expansion *vs.* temperature of an alloy specimen 1.0 cm long containing 10.5 v/o 1μ Al_2O_3 particles against a 5.0 cm pure gold reference. Distinct discontinuities in the expansion-temperature curve were observed at 240°, 330°, and 450°C, indicating the release of different gas impurities from the metal matrix as well as adsorbed impurities from the surface of the oxide particles. Impurity analysis using mass spectrometry showed that the composition of the evolved gas was mainly hydrogen and water and that gas evolution commences at about 300°C.

Discussion

The difference between the densities of the plated alloys before and after heat treatment can be attributed to the presence of adsorbed impurities on the surface of the oxide particles. These impurities may be water, hydroxyl groups, or organic additives present in the plating electrolyte and are codeposited with the

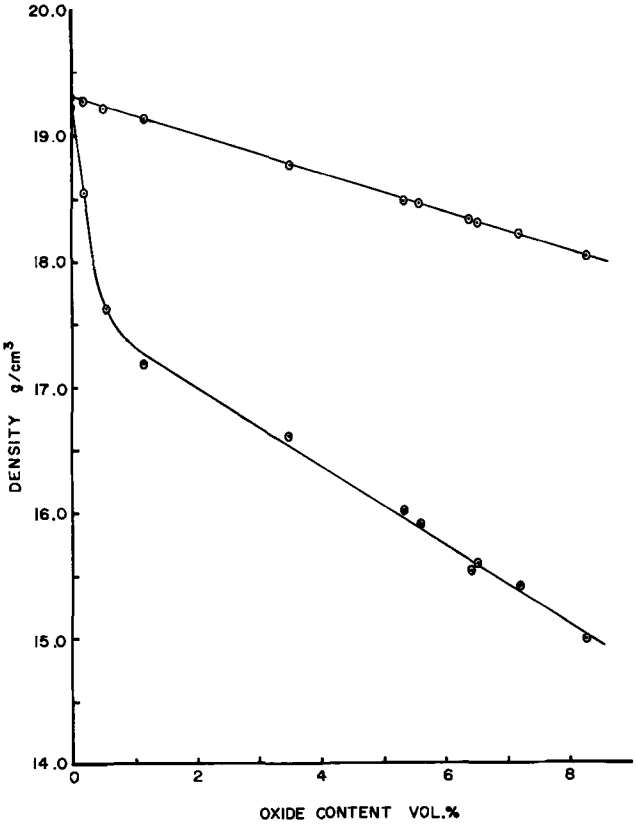

Fig. 1. Density as a function of volume per cent oxide in Au-Al_2O_3 (1.0μ) alloys. (Upper curve—as-plated alloys; lower curve—annealed alloys, 1 hr at 1000°C.)

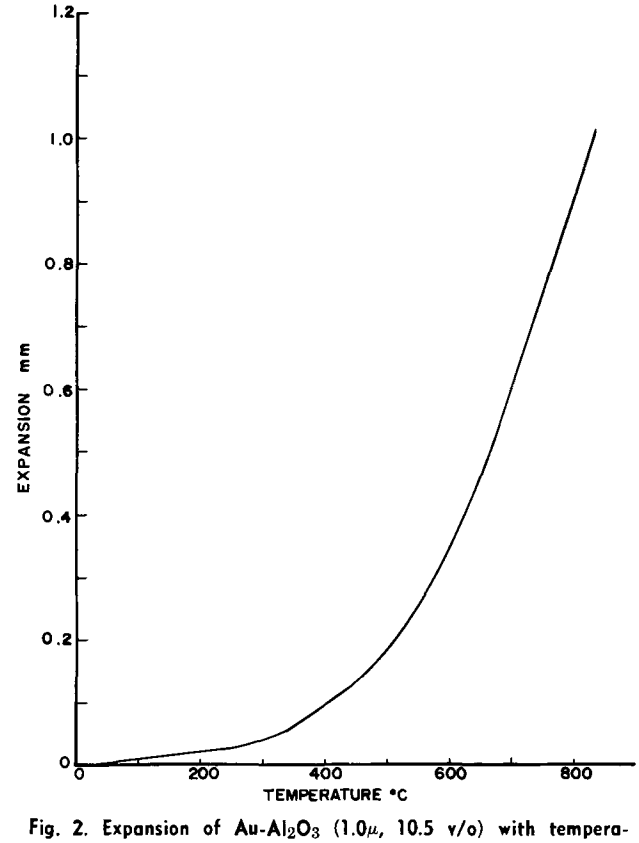

Fig. 2. Expansion of Au-Al_2O_3 (1.0μ, 10.5 v/o) with temperature for a heating rate of 2°C/min.

oxide particles. It has been calculated that an adsorbed monolayer on powders with a specific surface area of 100 m^2/g represents an impurity level of 5-10 v/o (7). The adsorbed monolayer occupies little volume in the condensed state. As such, the as-plated density should not deviate from the theoretical value; however, gasification of the impurities at high temperatures introduces porosity resulting in a subsequent decrease in alloy density. A simple calculation can illustrate this point more clearly. Consider an alloy sample containing 8 v/o oxide that is annealed at 950°C. The 1μ Al_2O_3 powder has an estimated specific surface area of 2 m^2/g. At 950°C, the gasified impurities build up sufficient pressure to cause irreversible deformation in the alloy. The resulting pore volume can be estimated by neglecting the effects of surface energy and assuming the ideal gas law holds. Using the pressure $P = 72$ psi or 4.9 atm which is the stress at zero strain (threshold stress for creep deformation) for a gold alloy containing 8 v/o oxide (8), $T = 1223$°K, $R = 82$ cc atm/°mole and 0.00016/18 moles of water, the pore volume is estimated to be 0.18 cc or 18 v/o. This compares favorably with our experimental value of 16.4 v/o measured at a slightly higher temperature of 1000°C. In view of the crude nature of the foregoing calculation, the significance of the illustration should not be attached to the agreement obtained but rather to the probability of pore formation proceeding in this manner. The initial sharp decrease in density of the heat-treated alloys is difficult to interpret without further investigation; however, one possible explanation is that should the relative degree of oxide particle agglomeration in the plating solution be greater when the solution is less concentrated in oxide, the resulting electrodeposit will also contain more agglomerated particles. Because occluded electrolyte is more prevalent in the agglomerated case, such system will show more porosity when the alloys are heat treated. Optical microscopic examination of polished alloy specimens indicates that a difference in degree of agglomeration does exist in the electrodeposits prepared from plating solutions of varying oxide concentrations. To eliminate the effects of particle agglomeration entirely, we are currently conducting experiments whereby electrodeposits are prepared under ultrasonic agitation to achieve optimum oxide dispersion.

The amount of porosity in the electrodeposited Au-Al_2O_3 alloys as calculated from our density measurements was as high as 16.5 v/o. A similar but smaller increase in porosity was observed after heat treatment of extruded and drawn Au-Al_2O_3 samples prepared by powder metallurgy. Furthermore, we have qualitatively studied alloy samples which were heat treated to produce porosity followed by cold working, extruding, and wire drawing whereby the density approached 99.9% of the theoretical value only to find that subsequent annealing will restore the porosity. This effect is a consequence of residual gases which can be eliminated only by completely melting the sample. In terms of high-temperature properties, the important criterion is therefore no longer the nucleation but the growth of existing pores that will determine the creep strength of these dispersion strengthened alloys. The presence of nonassociated pores anchored by uniformly distributed oxide particles will require creep deformation to be accompanied by the growth of these pores. Thus any gaseous impurities which can lower the internal metal surface energy must also be considered. The gasification of impurities, particularly that of water, at the indicated temperatures is in general agreement with the findings of other investigators (9), who deduced that surface hydration does occur on suitable parts of the α-Al_2O_3 surface and that ignition to 400°C results in the dehydration of physically bound water, while ignition above 400°C eliminates chemically bound water. Additional work is in progress using differential thermal analysis techniques to gain insight on the dehydration and gasification of adsorbed impurities in these alloys.

Manuscript submitted Aug. 29, 1969; revised manuscript received Jan. 28, 1970.

Any discussion of this paper will appear in a Discussion Section to be published in the December 1970 JOURNAL.

REFERENCES

1. D. Hull and D. E. Rimmer, *Phil. Mag.*, **4**, 673 (1959).
2. R. C. Boettner and W. D. Robertson, *Trans. AIME*, **221**, 613 (1961).
3. J. O. Stiegler, K. Farrell, B. T. M. Lok, and H. E. McCoy, *Trans. ASM*, **60**, 494 (1967).
4. H. Kellerer and G. Piatti, *J. Matls. Sci.*, **3**, 222 (1968).
5. F. K. Sautter, "Electrodeposition of Au-Al_2O_3 Alloys," Tech. Report WVT-RR-6321, Dec. 1963.
6. P. Bonnet, H. Kellerer, G. Piatti, and H. W. Schleicher, *Scripta Met.*, **2**, 689 (1968).
7. R. K. Stringer, C. E. Warble, and L. S. Williams, "Kinetics of Reaction in Ionic Systems," Material Science Research, Vol. 4, p. 74, Plenum Press (1969).
8. F. K. Sautter and E. S. Chen, "Oxide Dispersion Strengthening, Metallurgical Society Conferences," Vol. 47, p. 495, Gordon and Breach (1968).
9. D. J. O'Connor, P. G. Johansen, and A. S. Buchanan, *Trans. Faraday Soc.*, **52**, 229 (1956).

JOURNAL OF THE ELECTROCHEMICAL SOCIETY

ELECTROCHEMICAL SCIENCE

JUNE 1970

The Proton Diffusion Coefficient for the Nickel Hydroxide Electrode

D. M. MacArthur*

Bell Telephone Laboratories, Incorporated, Murray Hill, New Jersey

ABSTRACT

The diffusion coefficient for protons moving in the hydrated nickel hydroxide lattice has been determined using a potential step technique. It was found to have the value about 3.1 x 10^{-10} cm^2 sec^{-1} during charging and 4.6 x 10^{-11} cm^2 sec^{-1} during discharging for the nickel hydroxide structure usually found in the nickel electrode of the nickel-cadmium battery. The temperature dependence of the coefficient has been determined, and it has been concluded that the proton moves in the lattice by thermal diffusion. The enthalpy of diffusion was found to be 2.2 kcal deg^{-1} $mole^{-1}$ during charging and 2.3 kcal deg^{-1} $mole^{-1}$ during discharging of the electrode.

In previous work (1) the approximate diffusion coefficient for proton diffusion during oxidation of an α nickel hydroxide[1] electrode was found by a potential sweep technique. This procedure required the use of a semi-infinite diffusion model which entailed extrapolation from the experimental data. In the present work a new approach was used. A potential step was applied to the electrode and the data were analyzed using a finite diffusion model. Values of the diffusion coefficient for α and β nickel hydroxide during oxidation and reduction have been determined. The coefficient for β nickel hydroxide has also been found as a function of temperature.

Theoretical Considerations

The oxidation of the nickel hydroxide electrode is believed to proceed by a reversible one electron transfer step at the nickel ion site in the nickel hydroxide lattice. This produces a Ni^{III} ion and releases a proton. The proton diffuses from the oxidation site to the electrode-electrolyte interface where it reacts with an hydroxyl ion to form a water molecule. Electron conduction through the lattice is believed to be rapid in comparison to the rate of proton diffusion. It is also assumed that charge balance is maintained in the lattice at all times.

For the purposes of a quantitative description of the diffusion process we regard the initial concentration of protons in the lattice as constant at the value C° through the depth of the film and zero everywhere else. This is illustrated in Fig. 1. The electrodes used in this work were planar and therefore the diffusion problem is one dimensional.

This problem is the familiar heat transfer problem and has the solution (2)

$$C = \frac{4C^\circ}{\pi} \sum_{n=0}^{\infty} \frac{(-1)^n}{2n+1} \exp - \left\{ \frac{D(2n+1)^2\pi^2 t}{4h^2} \right\} \cos \frac{(2n+1)\pi x}{2h} \qquad [1]$$

where D is the diffusion coefficient and t is the time from the start of the diffusion process.

The experimentally measured quantity is the current as a function of time. This is expressed as

$$i_{diff} = n_e \mathbf{F} A D \left(\frac{\partial C}{\partial x} \right)_{x=h} \qquad [2]$$

$$i_{diff} = \frac{n_e \mathbf{F} A D 2C^\circ}{h} \sum_{n=0}^{\infty} \exp \left[- \frac{D\pi^2(2n+1)^2 t}{4h^2} \right] \qquad [3]$$

where n_e is the number of positive charges on the diffusion species, $\mathbf{F}$ is the Faraday, and A is the area of the electrode. A semilog plot of Eq. [3] is shown in Fig. 2 for typical values of D and h. This series, Eq. [3], which is valid for the finite boundary value problem, converges rapidly even for small times if the ratio D/h^2 is sufficiently large. C° is assumed to be equal to the concentration of nickel sites in the nickel hydroxide lattice, since one proton is released at each nickel site, and is expressed in mole/cm^3. It is found by dividing the molecular weight by the density of the nickel hydroxide layer. The molecular weight used in the calculations was that for α-$Ni(OH)_2 \cdot 2/3\ H_2O$ and the density was the x-ray value (4) for this material (2.5 g/cm^3).

In order to determine the diffusion coefficient D, the value of the diffusion length h must be known. This

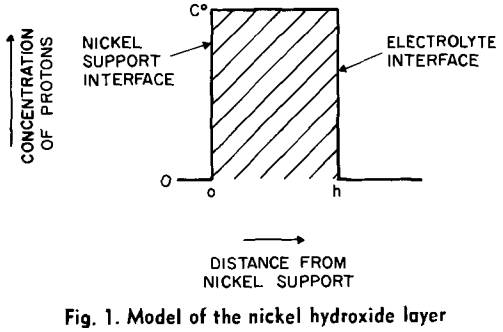

Fig. 1. Model of the nickel hydroxide layer

* Electrochemical Society Active Member.

[1] See ref. (1) for an explanation of the use of α and β.

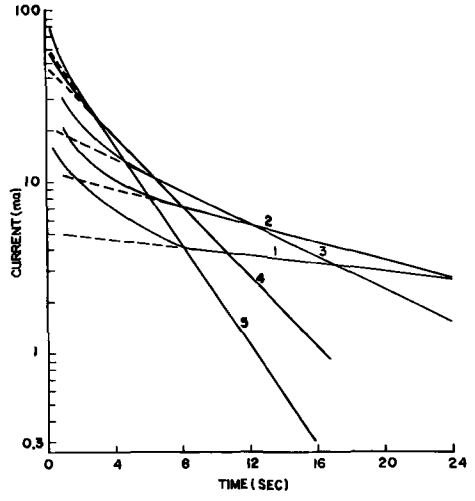

Fig. 2. Calculated diffusion currents $h = 1.0 \times 10^{-4}$ cm curve 1, $D = 1 \times 10^{-10}$; 2, $D = 2.5 \times 10^{-10}$; 3, $D = 5 \times 10^{-10}$; 4, $D = 1 \times 10^{-9}$; 5, $D = 1.5 \times 10^{-9}$.

may be found by noting that for sufficiently long times only the term with $n = 0$ in the summation of Eq. [3] will be significant and on extrapolating to zero time the current intercept has the value $n_e\mathbf{F}AD2C^\circ/h$ in which all the variables are known except D/h. The ratio of the slope of the straight line (on a semilog plot) in this region to the intercept has the value $\pi^2/8n_e\mathbf{F}AC^\circ$ $(1/h)$ and therefore

$$h(\text{cm}) = 5.318 \times 10^{-4} \times \frac{\text{intercept (A/cm}^2\text{)}}{\text{slope (sec}^{-1}\text{)}} \quad [4]$$

As a check on the results h may then be compared to the thickness of the film.

The thickness (l) of the film may be found from the expression

$$l = \frac{ItM}{n\mathbf{F}d} \quad [5]$$

where I is the current used to electroprecipitate the film, t the time of deposition, M the molecular weight of α nickel hydroxide, $n\mathbf{F}$ the number of electrons transferred per mole of nickel hydroxide deposited, and d the density of nickel hydroxide. A current deposition efficiency of 100% is assumed in the calculation. This has been found to be true for films of the thickness used in this work.

The total current measured upon the application of a potential step to the electrode is the sum of the diffusion current and the current required to charge the double layer at the electrolyte interface. This is expressed as

$$i = i_{\text{diff}} + i_{\text{cap}} = i_{\text{diff}} + C\left(\frac{dE}{dt}\right)$$

$$= i_{\text{diff}} + \frac{E_2 - E_1}{R} \exp - \left\{\frac{t}{RC}\right\}$$

where the symbols have the following meaning: E_1 is the starting potential of the electrode; E_2 is the potential to which it is shifted; C is the surface capacitance per unit area; and R is the uncompensated resistance between the reference and working electrodes of the electrolysis cell. We note that corrections for surface capacitance are important if D/h^2 and $1/RC$ are comparable. The value of D/h^2 lies between 10^{-1} and 10^{-2} sec^{-1}.[2] The surface capacitance of the nickel electrode is unusually large (5). The uncompensated resistance in the working electrode circuit is small however so that for typical values of the capacitance and resistance (3000 μf/cm^2 and 0.1 ohm), $1/RC$ is about 3000 sec^{-1}, four orders of magnitude larger than D/h^2, and the capacitance correction will be insignificant.

[2] From the experimental results.

Two possible mechanisms for the diffusion process are:

1. The proton may jump from one oxygen ion in the lattice to another as it diffuses toward the electrolyte interface. This hopping process is expected to have an appreciable activation energy since partial chemical bonds must be broken. As a result, this diffusion process will have a considerable temperature dependence. For instance, if the activation energy is 23 kcal/mole as given by Feitknecht and coauthors (3) at temperatures above 100°C, then the rate of the reaction room temperature quadruples for a 10°C rise in temperature.

2. Once released the proton may simply diffuse without any further chemical interaction with the lattice. This process is expected to have a small temperature dependence.

Besides these two extreme examples there is the possibility of intermediate processes some of which could include hydrogen bonding. It is evident, however, that the temperature dependence of the rate can give some insight into the physical nature of the diffusion process.

Experimental

The electrolysis cell has been described elsewhere (1). The working electrode was a film of hydrated nickel hydroxide electrochemically precipitated onto a 1 cm^2 disk of high-purity Inco 270 nickel that had been hand-polished with several grades of emery paper, the last being 4/0, washed with 10% HCl, and rinsed with distilled water immediately before the precipitation step. The electrochemical precipitation step consisted of immersing the electrode (wet with distilled water) into a beaker of 0.5M reagent $Ni(NO_3)_2$ solution and making it cathodic at a current density of 2 mA/cm^2 for 4 min. It was removed, washed with running tap water and distilled water, and then (still wet) placed in the electrolysis cell which contained about 300 ml of solution.

In earlier work (1) it had been found that the diffusion coefficient was independent of the concentration of electrolyte. In this work all measurements were made in 1M KOH (except where 1M LiOH was used). This solution was chosen because the electrode was more stable in the dilute solutions yet the solution was sufficiently concentrated that concentration polarization effects would be minimized.

The diffusion coefficient was determined by applying a potential step to a Wenking fast rise time model 61RS potentiostat and measuring the current as a function of time. Electronic compensation for solution resistance between the working electrode and the reference electrode was incorporated into the circuit. The potential step function was applied through a summing operational amplifier to the potentiostat. The base potential could be preset to any value.

Current was determined by measuring the voltage drop across a precision 5-ohm resistor in the working electrode circuit. It was recorded on either a Tektronix 564 oscilloscope (short times) or a Houston Instruments HR95 X-Y recorder (longer times).

For the diffusion experiments the electrolysis cell was immersed in a water bath which was held at constant temperature ± 0.1°C. The reference electrode, Hg/HgO (1M KOH), was at room temperature (25°C) for all experiments. Junction potentials for the solutions at different temperatures were considered small enough to be neglected.

The procedure for preparing the electrodes for the potential step experiments was to cycle the electrode three times in the solution using a potential scan. For the α nickel hydroxide experiments the electrode was then used immediately. To prepare the β structure the electrode was subsequently held at 0 volts (*vs.* Hg/HgO) for 16 to 24 hr and then potential stepped.

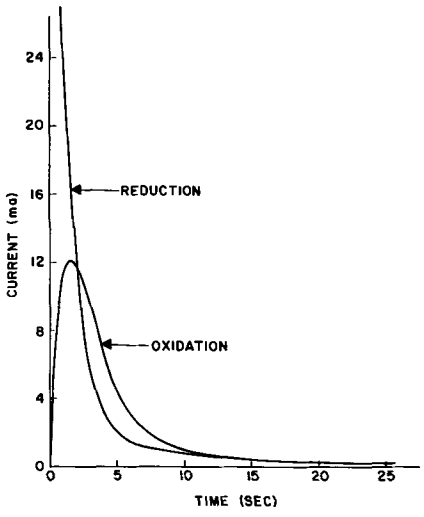

Fig. 3. Typical diffusion currents found on stepping the β nickel hydroxide electrode (40°C).

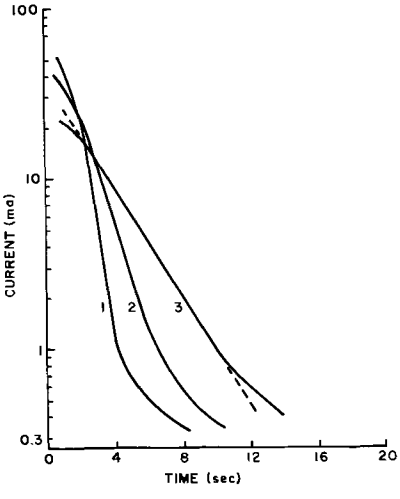

Fig. 4. Dependence of the oxidation currents on the potential of the applied step, β nickel hydroxide. Initial potential was 0.25V stepped to 0.51 (curve 1) to 0.49 (curve 2) to 0.475V (curve 3).

Results and Discussion

A typical plot of the current during stepped charge and discharge of a β nickel hydroxide electrode is illustrated in Fig. 3.[3] During charge (oxidation) of the electrode, the current increases over a period of about 2 sec before it begins to show the exponential decay. This behavior is unexpected. It may be that the poor conductivity of the reduced material limits the current flow until enough oxidized material has been produced to provide sufficient conductivity. On the other hand the current in the first second during reduction is larger than expected. This phenomenon may be related to the unusually large surface capacitance observed for this electrode and may reflect a surface layer in a higher state of oxidation than the bulk material.

The semilogarithmic plots of the oxidation and reduction currents are shown in Fig. 4 and 5, respectively. These may be compared to the curves in Fig. 2. The results agree with the theory in all respects except two. (*a*) A dependence of the oxidation current on the height of the potential step was found, and (*b*) the current during reduction was smaller than expected at long times.

The potential dependence of the oxidation current is shown in Fig. 4. The curve had the longest linear section for the smallest applied potential step. The higher potential step functions apparently were introducing added complications, perhaps from the formation of a higher surface oxidation state and from the competing oxygen evolution reaction. It was decided, therefore, that the data at the lower potentials were more representative of the conditions used to derive Eq. [3], and these were used in the calculations.

[3] Data plotted on the graph have been corrected for the residual oxygen evolution current.

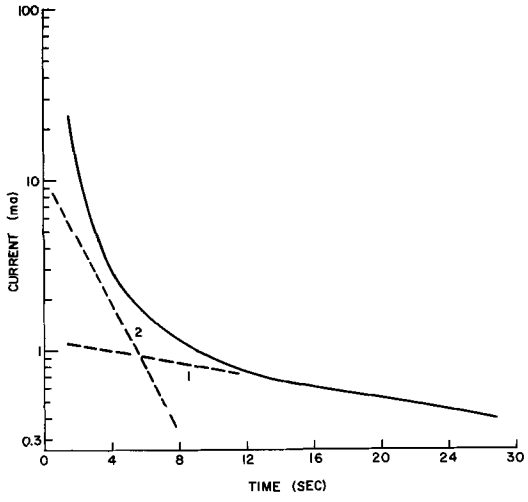

Fig. 5. Typical reduction current. Initial potential was 0.52V stepped to 0.36V.

The low currents observed on reduction suggested that a two step process occurs on reduction. Initially a rapid reduction was thought to occur and then a slower diffusion limited process. Examination of Eq. [3] reveals that the second term of the expansion has a coefficient in the exponential that is nine times larger than the coefficient in the first term. That is, the line representing the second term (line 2 in Fig. 5) should have a slope nine times greater than the line representing the first term (line 1). It was found that in all cases the slope of line 2 was in the range 8-10 times the slope of line 1 suggesting that there is no change in the diffusion process. Unless the initial reduction were very rapid it would probably be detected by this procedure. A more likely explanation for the failure of all the material to reduce in the time of the experiment now appears to be the formation of a poorly conducting layer as suggested in a previous paper (1). The currents on reduction were independent of the size of the potential step.

The diffusion lengths and diffusion coefficients found from the various experiments are included in Tables I and II. It was found that the diffusion length was consistently about 0.55 x 10^{-4} cm during oxidation and 0.15 x 10^{-4} cm during reduction. These values may be compared to the calculated (Eq. [5]) film thickness of 1.0 x 10^{-4} cm. This value is calculated assuming uniform planar distribution of the active material. This is not likely to be the case and surface

Table I. Values obtained during oxidation

Structure	Temp, °C	Intercept, A x 10^{-3}	Slope, sec^{-1}	h, cm x 10^{-4}	D	D^* $cm^2\ sec^{-1}$ x 10^{-9}
α	25	28	0.268	0.56	0.36	0.33
α	40	38	0.364	0.56	0.45	0.45
α	55	55	0.405	0.72	0.85	0.50
β	25	27.5	0.256	0.57	0.34	0.31
β	40	30	0.326	0.49	0.32	0.40
β	55	38.5	0.362	0.56	0.46	0.44
β (lost capacity)	70	17	0.176	0.51	0.19	0.22
β (LiOH electrolyte)	25	27.5	0.335	0.44	0.26	0.41
				Avg. 0.55		

* Calculated with h = 0.55 x 10^{-4} cm.

Table II. Values obtained during reduction

Structure	Temp, °C	Intercept, A × 10^{-3}	Slope, sec^{-1}	h, cm × 10^{-4}	D cm^2 sec^{-1} × 10^{-10}	D* cm^2 sec^{-1} × 10^{-10}
α	25	1.40	0.058	0.13	0.039	0.71
β	25	1.20	0.038	0.17	0.043	0.46
β	40	1.17	0.041	0.15	0.038	0.50
β	55	1.26	0.048	0.14	0.038	0.59
β	70	1.14	0.056	0.11	0.027	0.69
β (LiOH electrolyte)	25	0.85	0.050	0.090	0.017	0.61

* Calculated with $h = 0.55 \times 10^{-4}$ cm.

irregularities would be expected to result in shorter diffusion paths. A diffusion path of about one half the estimated film thickness, as found during oxidation, is reasonable. The smaller diffusion length found during reduction comes from the small reduction currents and is probably in error since it appears unreasonable that the diffusion length should change on going from oxidation to reduction. For this reason it appears preferable to use the diffusion length found on oxidation in the reduction calculations. The last column in Table I and II lists the diffusion coefficients found using the average diffusion length of 0.55×10^{-4} cm. At room temperature the coefficient on oxidation is about one seventh of the value found previously (1). This is satisfactory agreement since the earlier value was considered to be only an order of magnitude estimate.

Oxidation currents for an α nickel hydroxide electrode at three potentials are shown in Fig. 6. The dependence on the height of the potential step was similar to that for β nickel hydroxide, but more pronounced. As before, the reduction current was not dependent on the size of the potential step. The diffusion coefficient found for the α nickel hydroxide was not greatly different from that found for the β structure suggesting that the proton diffusion process is not dependent on the amount of water of constitution in the structures.

The diffusion coefficient found for the electrodes cycled in LiOH electrolyte also was not appreciably different from the other values. This experiment was done because of Tuomi's (5) description of a lithium nickelate phase that forms on cycling in the lithium electrolyte.

The temperature dependence of the diffusion coefficient for β nickel hydroxide is plotted in Fig. 7. These values were obtained on a single electrode because the temperature variation was so small that it did not greatly exceed random variation among the electrodes.[4]

[4] This appeared to be a result of changes in the structure of the electrodes as they aged at the different temperatures. The conversion from α to β $Ni(OH)_2$ was so rapid in fact at the higher temperatures that it was impossible to take measurements on α $Ni(OH)_2$.

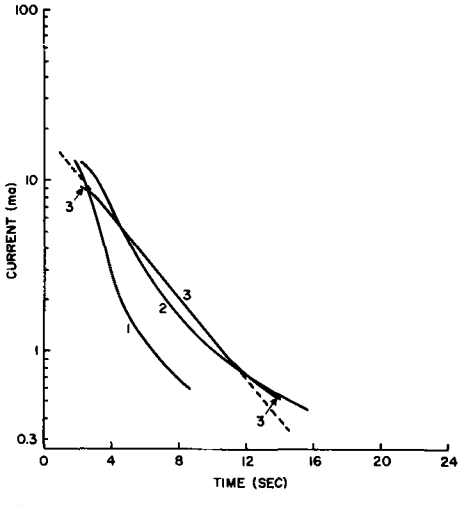

Fig. 6. Oxidation currents for α nickel hydroxide at 40°C. Initial potential 0.25V stepped to 0.50 (curve 1) to 0.48 (curve 2) to 0.46V (curve 3).

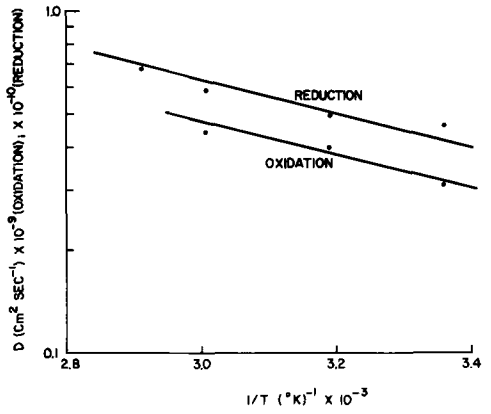

Fig. 7. Temperature dependence of the oxidation and reduction diffusion coefficients.

Electrodes were aged at 40°C by cycling them several times and then potentiostating them at 0 volt *vs.* Hg/HgO for about 24 hr. The first measurement following this procedure invariably showed a diffusion coefficient much lower than normal. This possibly is the result of excessive dehydration of the electrode during the forced discharge. The second and subsequent measurements however were reproducible and consistent. Measurements were taken on the same electrode in the order 40°, 25°, 55°, and 70°C with a 2-hr stand at each temperature for equilibration. This time period apparently was short enough that further structural changes did not take place since the measurements gave consistent results.

A least squares fit was used to draw the lines in Fig. 7. From the slope of the lines and using the expression

$$D = D_o \exp \frac{-\Delta H}{RT}$$

the enthalpy of diffusion (ΔH) for the protons diffusing in oxidized material (charging process) was 2.2 kcal deg^{-1} $mole^{-1}$ and for protons diffusing in reduced material (discharging process) was 2.3 kcal deg^{-1} $mole^{-1}$. The respective values for D_o were found to be 1.3×10^{-8} and 1.9×10^{-9} cm^2 sec^{-1}. The small temperature dependence of the diffusion coefficient clearly demonstrates that the protons move through the lattice by a simple diffusion process rather than by a jumping from one oxygen atom to the next.

Feitknecht (3) and coauthors measured the diffusion coefficient of protons in the $Ni(OH)_2$ lattice by a radiotracer technique. They found that, at temperatures above 100°C, the enthalpy of diffusion was about 23 kcal deg^{-1} $mole^{-1}$ and D_o was about 2×10^{-7} cm^2 sec^{-1} although the latter value could be wrong by several orders of magnitude since the data showed considerable scatter. These values were obtained by measuring the rate of exchange of hydrogen with water vapor. When they tried to measure the rate of exchange with water at lower temperatures, they found no temperature dependence. (It may be that the discrepancy in the results arises from a change in mechanism which generates the proton defects.) These authors clearly were measuring ΔH_f which is the sum of the enthalpy of formation of a proton defect and the enthalpy of diffusion of the proton. In the present experiments only the enthalpy of diffusion was measured since the electrode reaction generated the proton defects.

Acknowledgments

The author would like to express his appreciation to D. R. Turner, Y. Okinaka, and particularly P. C. Milner for helpful suggestions.

Manuscript received Dec. 16, 1969. This was Paper 175 presented at the Boston Meeting of the Society, May 6-9, 1968.

Any discussion of this paper will appear in a Discussion Section to be published in the December 1970 JOURNAL.

REFERENCES

1. D. M. MacArthur, *This Journal*, **117**, 422 (1970).
2. Carslow and Jaeger, "Conduction of Heat in Solids," 2nd ed., p. 97, Oxford (1959).
3. W. Feitknecht, A. Wyttenback, and W. Buser, Proc. 4th Internat'l. Symp. on Reactivity of Solids, p. 234, Amsterdam (1960).
4. Y. I. Tur'yan and A. I. Tsinman, *Rus. J. Phys. Chem.*, **36**, 212 (1962).
5. D. Tuomi, *This Journal*, **112**, 1 (1965).

An Ellipsometric Study of Surface Films on Copper Electrodes Undergoing Electropolishing

M. Novak,[1] A. K. N. Reddy,[2] and H. Wroblowa[3]

Electrochemistry Laboratory, University of Pennsylvania, Philadelphia, Pennsylvania

ABSTRACT

Simultaneous current-potential and *in situ* steady-state ellipsometric measurements were carried out in order to study the electropolishing of vertical copper electrodes in a 65% aqueous solution of phosphoric acid. A technique was developed for displacing the visible, viscous film with glycerol and examining whether a second film was sandwiched between the copper surface and the viscous film. By using this technique, it was demonstrated that the electropolishing process involves the formation of two films on the electrode: (*i*) an adherent sandwiched solid film at least 40Å in thickness, and (*ii*) a displaceable viscous layer of highly concentrated electrolyte about 2000-3500Å thick. The solid film was either completely or partially destroyed when the electrode undergoing polishing was removed from the electrolyte, washed, and dried.

Theories concerning the mechanism of electropolishing of metals [cf. Hoar (1) and Jacquet (2) for reviews] have invoked the presence of either one or two layers in the immediate vicinity of the electrode. In the case of metals forming colored ions, a viscous liquid layer can be detected visually. This viscous liquid layer has been considered to be in contact with film-free metal (3-6), with metal covered with an adsorbed layer of oxygen or anions (7-9), or with metal covered with oxide or salt layers varying in thickness from about one monolayer to several tens of angstroms (10-21), according to the references quoted. This controversial situation has arisen most probably because the particular *in situ* methods used hitherto (impedance measurements, coulometry, current-potential curves) are not capable of yielding direct evidence about the thickness and nature of the film or films present. Direct methods such as electron diffraction suffer from a distinct disadvantage because they necessitate removal of the electrode from solution, followed by washing and drying.

What is required, therefore, is a technique which permits direct and *in situ* examination of the surface of an electrode undergoing electropolishing. Since the technique of ellipsometry is such a direct and *in situ* technique, it was used to study the electropolishing of copper.

Experimental

Procedure.—The copper electrode was mounted in a Teflon block, polished mechanically, rinsed with distilled and conductivity water, and placed vertically in the 65% phosphoric acid saturated with Cu^{++} ions. It was then potentiostated at the desired potential, until steady-state values were obtained for current (i) relative phase retardation (Δ), and relative amplitude reduction (ψ). The same steady-state values of the above parameters were obtained when the electrode was first potentiostated in the etching region of potentials to ensure a film-free metal surface, and then brought to the desired potential. The latter procedure, however, requires much longer periods of time, because the surface becomes rougher during dissolution and time is needed to smooth it in the region of potentials corresponding to polishing.

The presence of the viscous liquid film introduces an experimental difficulty which comes in the way of establishing the existence of a second film sandwiched between the metal and the liquid layer and of determining the nature and thickness of this sandwiched film. Thus, it is not clear whether the Δ and ψ values recorded from an *in situ* examination of the electrode are contributed to by one or two films. Under these circumstances, the following experimental procedure was adopted: (*i*) after the attainment of steady-state polishing conditions and the recording of the i, Δ, and ψ values, the electrolyte was displaced by an organic liquid of surface tension lower than that of the electrolyte; (*ii*) during this replacement of the electrolyte, the electrode was held potentiostated at the same potential as in the presence of the electrolyte. The following were the results of this procedure: first, the viscous liquid film present during electropolishing was removed; second, the inert organic liquid effectively stopped the anodic current without cessation of potential control; third, at no stage does the electrode become exposed to the atmosphere. Consequently, it may be assumed that after replacement of the electrolyte with the organic liquid, the viscous liquid film has been removed without destroying or altering any underlying film which may be present. In this "frozen" condition, the electrode was subject to ellipsometric measurements.[4]

The organic liquid usually used was glycerol. At several potential values the whole experiment was re-

[1] Present address: Chemistry Division, Academy of Sciences, Budapest, Hungary.

[2] Present address: Department of Inorganic and Physical Chemistry, Indian Institute of Science, Bangalore-12, India.

[3] Present address: Institute for Direct Energy Conversion, University of Pennsylvania, Philadelphia, Pennsylvania 19104.

[4] Since the experimental procedures adopted here permit ellipsometric measurements to be made in the presence and absence of the viscous layer, it is not necessary to make an *a priori* assumption that the viscous layer is liquid in nature. Even if it were a film of loose precipitate, the present experimental approach would still be valid.

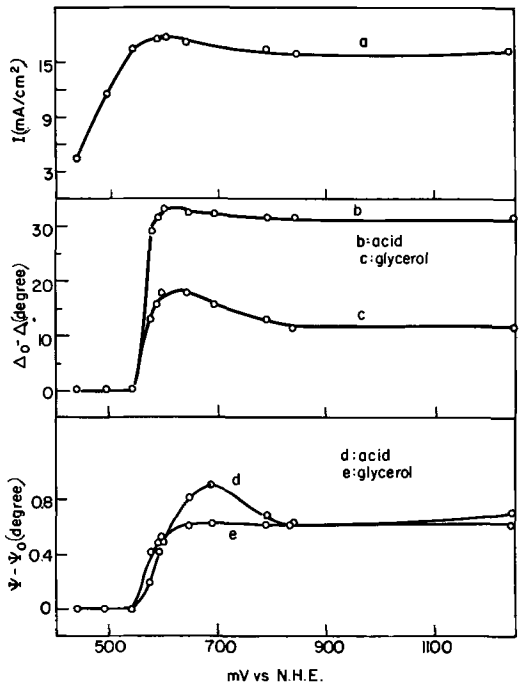

Fig. 1a. Steady-state current-potential relation; Fig. 1b. decrease of Δ with potential: b, for the total film, c, for the adherent film; Fig. 1c. decrease of ψ with potential: d, for the total film, e, for the adherent film.

peated using two new electrodes with two other organic materials: glycol and ethyl-octanol. Within the experimental error, the results obtained were identical with those in glycerol. It follows, therefore, that the same layer (be it the assumed viscous liquid layer, or a precipitated loose film) was removed by the displacing action of the organic fluids.

A new electrode-electrolyte system was used for each potential at which measurements were carried out.

Materials.—Polycrystalline blocks of Cu cut out of 99.9% pure Cu; 85% Baker phosphoric acid A.R.; Baker's Spectroscopically pure glycerol; Baker A. R. glycol; Airco FD ethyl-octanol; Baker A. R. copper oxide; conductivity water were used in experiments.

Apparatus.—1. Ellipsometer: D. C. Rudolf & Sons, Inc., Model 437-200E was used with the adjustable polarizer and analyzer positions and a fixed quarter-wave plate set between the polarizer and metal surface at $-45°$ to the plane of incidence. The source of light was a zirconium arc, followed by a mercury green filter (λ = 5461Å). Suitable corrections were made for nonnormal incidence of light. Accuracy of measurements was 0.05°. Reproducibility of results in the polishing region was $\pm 0.1°$.

2. Electrometer: Keithley, 610A.

3. Potentiostat: Wenking, 1A output current.

4. The cell (5 x 5 x 2.5 cm) was made of synthetic fused quartz with optically flat and homogeneous walls. Electrodes used were a saturated calomel reference electrode and a bright Pt sheet as a counterelectrode.

Results

The potential-dependence of the steady-state current density i, of $\Delta° - \Delta$,[5] and of $\psi - \psi°$ values is shown in Fig. 1a. (top), b (center), c (bottom), respectively. Curves b and d correspond to results obtained in phosphoric acid, curves c and e to results obtained after replacement of the electrolyte with glycerol. The angles of incidence, ϕ_1, were 69.34° and 70.04° in phosphoric acid and glycerol, respectively.

[5] $\Delta°$ and $\psi°$ refer to the values for reflection from a film-free metal surface in the particular medium under discussion.

Analysis of Results and Discussion

Qualitative description of the electrode surface at various potentials.—In the potential region up to 540 mV (*vs.* NHE), there is dissolution of the copper electrode (*cf.* the anodic current of Fig. 1a) without any change in Δ and ψ (*cf.* Fig. 1b and 1c). Since Δ and ψ remain at the values $\Delta°$ and $\psi°$, characteristic of a film-free copper surface, it must be concluded that there is no film formation in this domain of the current-potential curve which is known to be associated with visible etching and not with electropolishing. It is of significance to the technique of ellipsometry that the changes in Δ and ψ which may result from roughening of the surface during etching are less than the measurement accuracy of 0.05°.

In the range of potentials between 540 and 590 mV, four observations should be stressed: (*i*) there is an arrest in the current-potential curve (Fig. 1a); (*ii*) there is a visible brightening of the surface of the copper electrode; (*iii*) there is an abrupt change in the optical parameters (Fig. 1b and 1c), particularly in Δ which decreases by about 30° in the phosphoric acid electrolyte; and (*iv*) the change in Δ decreases by about 17° to about 13° after replacing the electrolyte with glycerol. Observations (*i*) and (*ii*) are customarily associated with the onset of the electropolishing process; observation (*iii*) must be interpreted in terms of the formation of one or two films necessary for electropolishing, and observation (*iv*) indicates that even after removal of some loose, nonadherent layer (either a viscous liquid layer or a loose precipitate), the electrode is covered with an adherent film. Thus, even without a quantitative analysis of the ellipsometric data, the present experiments have established that the electropolishing process is associated with the formation of two films, a loose, displaceable film and a second film adhering to the electrode.

The variation of Δ and ψ between about 540 and 840 mV (curves c and e) shows that the properties of the adherent sandwiched film undergo changes. These properties, however, remain constant from 840 to about 1300 mV, as indicated by the constancy of Δ and ψ.[6]

Quantitative characterization of films on copper electrodes undergoing electropolishing.—Adherent film on the electrode.—The experimental values of Δ and ψ obtained for each potential were compared with the sets of Δ and ψ values calculated by the IBM 7040 computer programmed with the exact equation for reflection from the film covered surface

$$\tan \psi \, e^{i\Delta} = R^p/R^s \qquad [1]$$

where

$$R^v = \frac{r_{12}^v + r_{23}^v e^{-i\delta}}{1 + r_{12}^v r_{23}^v e^{-i\delta}}$$

where v = p (parallel) or s (vertical) component of the polarized light, r's are Fresnel's reflection coefficients; subscripts 1, 2, 3 correspond to the bulk liquid medium, film and metal, respectively; $\delta = 4\pi \bar{n}_2 \cos \bar{\phi}_2 L/\lambda$

$\bar{n}_2$ = $(n_2 + i\kappa)$ = complex refractive index of film
n_2 = real part of the refractive index of the film
κ = absorption coefficient
$\bar{\phi}_2$ = angle of refraction in the film
L = film thickness
λ = wavelength *in vacuo* of the incident light (5461Å).

The value of $\bar{\phi}_2$ was expressed as a function of $\bar{n}_2$ by means of Snell's law included in the computer program

$$\sin \bar{\phi}_2 = n_1/\bar{n}_2) \sin \phi_1$$

[6] No experimental points are shown in the figure for the latter potential range, since all the measurements carried out in this range (in about ~50 mV intervals) practically coincided with each other and are denoted on nomograms and in Table I by No. 8.

where n_1 = refractive index of glycerol = 1.466; ϕ_1 = angle of incidence = 70.04°.

Since the two measurable quantities, Δ and ψ, are related to three unknown properties, L, n_2, and κ, of the film by two equations only, an infinite number of solutions are possible. Nevertheless, by adopting the procedure described below, the lower limit of film thickness at each potential was obtained without any assumptions and solely from the ellipsometric data.

Nomograms of n and κ were plotted on the $\Delta - \psi$ plane for various constant values of film thickness L. An example of a nomogram for a film thickness of 55Å is given in Fig. 2. In these nomograms, the "iso-κ" lines run from top to bottom and are bounded by the $\kappa = 0$ line at the extreme right. Since negative values of κ are physically meaningless, this 55Å nomogram must be considered inapplicable to experimental $\Delta - \psi$ points falling outside (*i.e.*, to the right of) the boundary defined by the $\kappa = 0$ line. To illustrate this argument, points 5, 6, and 8 have been inserted in Fig. 2 to show that they cannot correspond to $\kappa \geqq 0$ values, and that, therefore, they cannot be interpreted with the 55Å nomogram. Fortunately, such points (*e.g.*, 5, 6, and 8 of Fig. 2) can be made to fall within the $\kappa \geqq 0$ domain by trying nomograms for other film thickness. This is because the $\kappa = 0$ lines shift with increasing thickness toward the right, *i.e.*, toward higher ψ values (Fig. 3). Thus, experimental points lying to the right of the $\kappa = 0$ line in a nomogram for a particular thickness, L, must correspond to a film of a thickness $L' > L$. By applying nomograms for various thicknesses to the experimental $\Delta - \psi$ points obtained at various potentials, the lower limits of the thickness of the adherent sandwiched film were determined as a function of the relative potential of the electrode undergoing electropolishing (cf. Fig. 4).

It is of significance to the mechanism of electropolishing that, at a potential of only 40 mV more positive than 540 mV (which marks the limit of the etching region), the film formed on the surface of the electrode undergoing electropolishing has a thickness of not less than 40Å. This film which is sandwiched between the electrode and the viscous film persists on the electrode up to the potential of 1300 mV at which potential it has a thickness of not less than 55Å. Thus it must consist of a multilayer solid phase.

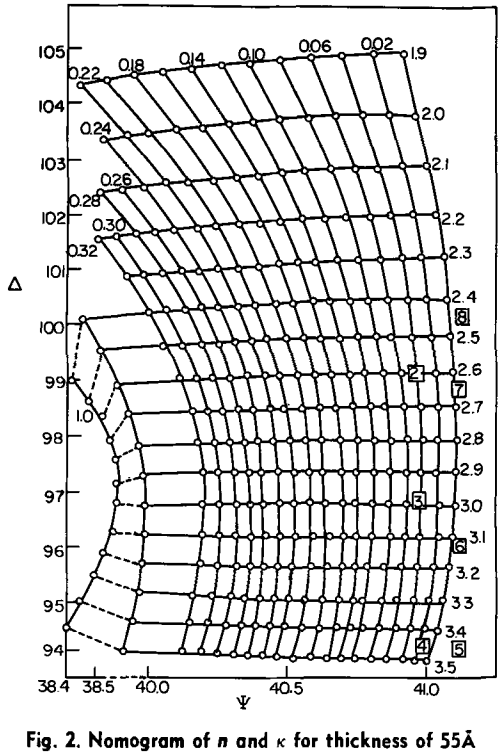

Fig. 2. Nomogram of n and κ for thickness of 55Å

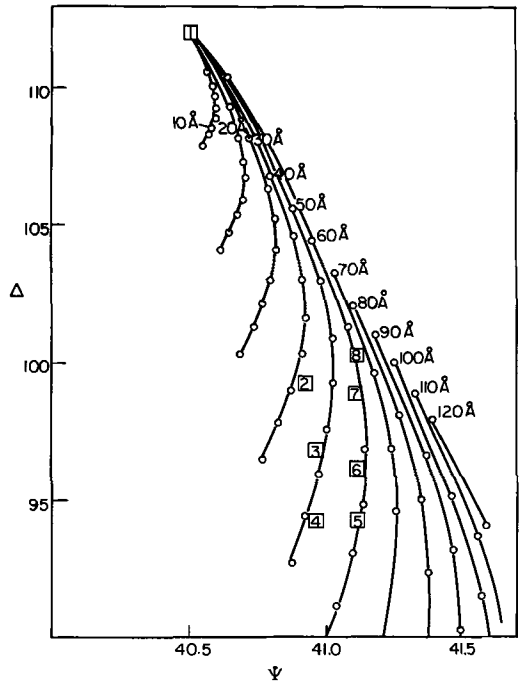

Fig. 3. Nomogram of $\kappa = 0$ lines for varying thicknesses of the film.

To advance from a determination of the lower limit of thickness of the sandwiched film to a characterization of its thickness and properties (*i.e.*, to a determination of the values of L, n_2, and κ), certain assumptions and additional arguments must be invoked.

The compounds constituting the solid film are most probably oxides or phosphates of copper. The refractive indices of copper oxides and phosphates are 2.7-2.8 (22) and 1.8 to 1.9,[7] respectively. These values are for bulk compounds, but one would not expect the values for a film to be lower. Hence, the refractive index of the sandwiched film can be argued to be not less than 1.8. It was found, however, that nomograms for thickness greater than 120Å force the experimental $\Delta - \psi$ points to correspond to films with a refractive index less than 1.8. In this way, it can be taken that the upper limit of the thickness of the sandwiched film is 120Å.

By restricting the thickness of the sandwiched film to a lower limit of 40Å and an upper limit of 120Å, the experimental $\Delta - \psi$ results were further analyzed in the following way. Using the nomogram for a particular thickness, the n_2 and κ values corresponding to a particular $\Delta - \psi$ point (obtained at a particular potential) were noted down. (It is obvious, for example, that the $\Delta - \psi$ point 2 in Fig. 2 corresponds to $n_2 = 2.6$ and $\kappa = 0.04$ in the 55Å nomogram.) For this same $\Delta - \psi$ point, the procedure was repeated with nomograms for different thicknesses. When a similar approach was adopted for all the experimental $\Delta - \psi$ points, Table I was constructed. From this table, it is seen that a particular $\Delta - \psi$ point corresponds to n_2 and κ values which are constrained to lie within certain limits. From these limits and the variation of the limits with potential, the following conclusions can be drawn.

1. In the potential range 0.580-0.840V, the absorption coefficient κ of the sandwiched film would have to change with potential if the refractive index is assumed constant and the film refractive index would have to vary with potential, if κ is assumed constant. Hence, either the refractive index or the absorption coefficient or both of them change with increasing anodic potential in the range just mentioned. That is, between 0.580 and 0.840V, the sandwiched film undergoes structural changes.

[7] Calculated from the Lorentz-Lorenz equation for $Cu(H_2PO_4)_2$.

Table I. Refractive indices and absorption coefficients as a function of thickness and potential

No.	2		3		4		5		6		7		8	
V (mV)	0.580		0.590		0.610		0.640		0.685		0.785		0.840-1.300	
L, Å	n_2	κ	n_2	κ	n_2	κ	n_2	κ	n_2	κ	n_2	κ	n_2	κ
40	3.1	0.00	—	—	—	—	—	—	—	—	—	—	—	—
45	2.9	0.02	—	—	—	—	—	—	—	—	—	—	—	—
50	2.7	0.04	3.2	0.00	—	—	—	—	—	—	—	—	—	—
55	2.6	0.04	3.0	0.04	3.5	0.02	3.3	0.00	3.1	0.00	2.6	0.00	2.4	0.00
60	2.4	0.06	2.8	0.05	3.2	0.04	3.2	0.01	2.9	0.01	2.5	0.01	2.3	0.00
70	2.2	0.05	2.5	0.06	2.8	0.07	2.8	0.04	2.6	0.04	2.3	0.02	2.1	0.01
80	2.1	0.05	2.3	0.06	2.6	0.08	2.6	0.06	2.3	0.04	2.1	0.02	2.0	0.02
90	2.0	0.04	2.2	0.05	2.4	0.08	2.4	0.06	2.2	0.04	2.0	0.02	1.9	0.01
100	1.9	0.04	2.1	0.05	2.3	0.08	2.3	0.06	2.1	0.04	2.0	0.02	1.9	0.01
120	1.8	0.03	1.9	0.04	2.1	0.06	2.1	0.05	2.0	0.04	1.9	0.02	1.8	0.01

2. The absorption coefficient of the final film (0.840-1.300V) has a very low value between zero and 0.02. The κ values at the potential 0.785V are also limited to this range.

3. The final film has a refractive index limited to the 1.8-2.4 range, indicating that it consists of copper phosphate or of a "mixture" of the latter and cuprous oxide (n_{Cu_2O} = 2.7-2.8 (22), $n_{Cu(H_2PO_4)_2}$ = 1.8-1.9).[8]

4. Winterbottom (23) quotes the value of κ_{Cu_2O} as 0.0086, obtained by measuring the attenuation of light (5451Å) by thin cuprous oxide disks. Thus, if the sandwiched solid film consists of phosphates with refractive index 1.8-1.9, its adsorption coefficient would be (*cf.* Table I) 0.01; and if it consists of cuprous oxide, its absorption coefficient would be 0.0086. Any mixture of the phosphate and oxide would most probably have an absorption coefficient of the same magnitude, *i.e.*, κ = 0.01.

It can be assumed, therefore, that $\kappa \leq 0.01$ and that higher values of κ can be rejected. This conclusion is supported by the electrochemical evidence contained in the current-potential curve (Fig. 1). Whereas the current-potential curve for electropolishing resembles that generally observed for anodic passivation in the initial rise of current with increasing anodic potential followed by a fall to a plateau in which the current is virtually independent of current, the plateau current for electropolishing ($\sim$ mA/cm^{-2}) is orders of magnitude greater than the plateau current ($\sim \mu$A/cm^{-2}) for passivation. In both cases, the potential is not sufficiently anodic for significant oxygen evolution to occur; hence the current must be utilized by some other process. If the solid film is an electronic conductor, as implied by Bockris *et al.* (24), then ionic transport through this film becomes prohibitively difficult, *i.e.*, the metal dissolution current becomes negligible. The large dissolution currents passing during electropolishing may, therefore, be taken to mean that the sandwiched solid film is not an electronic conductor, but an ionic conductor, in which case it would have an absorption coefficient very close to zero unless it is absorbing the 5461Å light used in the ellipsometer.

Since, in the light of these arguments, the absorption coefficient can be assigned a value ≤ 0.01, the thickness and refractive index of the solid film on the electrode surface can be assigned values as shown in Fig. 4. This is the best possible solution to the ellipsometric problem of recovering unique values of the thickness, refractive index, and absorption coefficient from the measurement of Δ and ψ in the absence of independent and direct knowledge of one of the three unknowns. It must be stressed, however, that no uncertainty exists with regard to the lower limit of thickness of the solid film which has been established to be 40-55Å.

Mention must be made at this stage of the fact that sensitive non-*in situ* methods, *e.g.*, electron diffraction, do not reveal the presence of this thick (40-55Å) film of copper phosphate/oxide on the electrode. To resolve this contradiction, the following experiment was performed. A copper electrode was immersed in the 65% phosphoric electrolyte and potentiostated at a potential of 1V until the polishing current assumed a steady value. Instead of displacing the electrolyte with glycerol and revealing a solid film of 60Å on the electrode, the latter was removed from the electrolyte, washed, dried, and then subjected to ellipsometric measurements in air. The thickness of the film did not exceed 20Å. This indicates that the 60Å solid film on the electrode does not survive the treatment of removal from the electrolyte, washing, and drying: it is either completely destroyed with the $<$ 20Å film being the result of atmospheric oxidation of a bared copper surface or it is partially dissolved with the $<$ 20Å film being a residue of the thick electropolishing film. It is understandable, therefore, that electron diffraction examination of a copper electrode removed from the polishing solution, washed with water and then with isopropyl alcohol, and dried, reveals the existence of a very thin ($< \sim$ 10Å) film of copper oxide. Thus, non-*in situ* methods used without special precautions designed to preserve the solid film on the electrode cannot lead to an elucidation of the electropolishing process.

Displaceable, nonadherent film.—An attempt to assess the properties of the viscous layer, displaceable by organic material, was made using a double film computer program (25) and an IBM 7090 computer. For both the first film on the copper surface and the second film, the value of κ was assumed to be zero.

The solutions for the experimental $\Delta - \psi$ values obtained in phosphoric acid fell into two distinct types. The first type of solution corresponds to a thin (0-10Å) internal film on the copper surface and an external film of about 60Å thickness and refractive index ~3, inconsistent with the 40-55Å lower limit of thickness previously established. In contrast, the second type of solution indicated an internal sandwiched film of about 40-70Å thick with a refractive index within the >2.4-3.6 range; this is virtually the same range of thickness as that established for the solid film observed on the electrode surface after displacing the external film.

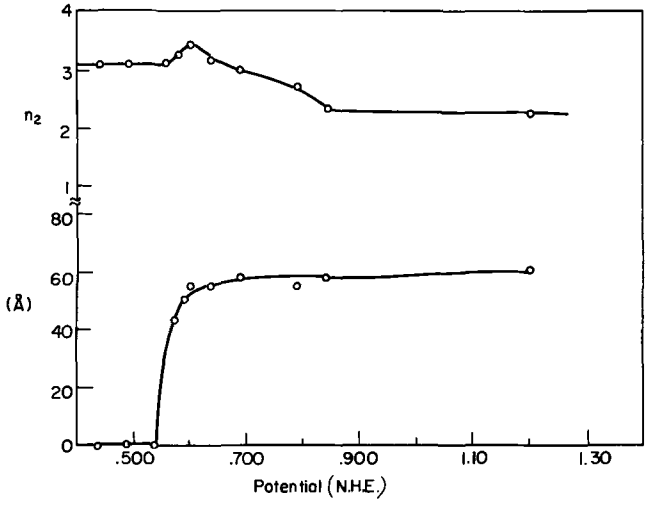

Fig. 4. Refractive index (n_2) and thickness (Å) of the adherent film as a function of potential, assuming the lowest limit of the film's thickness.

[8] *Cf.* footnote 7.

The range of n_2 includes the values corresponding to the latter film. The double-film computer program assumes that the films are sharply defined; in other words, it assumes that, at the external film-electrolyte interface, there is a discontinuous change in the refractive index. It is reasonable, however, to expect that, instead of a sharp interface, there is in fact an interphasial region in which the refractive index changes smoothly from a value characteristic of the displaceable film to one characteristic of the bulk electrolyte. If one ignores the existence of an interphasial region and considers a sharply defined displaceable film, then the second type of solution for the experimental $\Delta - \psi$ values indicates a film which has a thickness of 2000-3500Å and a refractive index very close to that of the bulk electrolyte. In other words, the ellipsometric measurements indicate that the displaceable layer observed during electropolishing is a thick, liquid film and not a loose precipitate.

The mechanism of electropolishing.—The present results support the views of Hoar (11), according to which the polishing can occur only if the metal dissolves randomly, and not preferentially as happens during the etching process. This randomness can be ensured only by dissolution of the metal into random vacancies arriving at the metal surface. Thus, polishing can occur only if a film is formed at the surface, through which cationic vacancies created at the film-electrolyte interface by the film's dissolution can migrate to the metal surface and accept the dissolving metal ions. (In molten salts, electropolishing could occur without a presence of such a film, since random holes are already present in the electrolyte itself.)

The film existing in the region 0.840-1.300V does not change its properties, nor thickness with potential, as evidenced by the constancy of Δ and ψ values (cf. Fig. 1 and 2). This fact contradicts the interpretation of impedance measurements given by Hoar (1), according to which the film's thickness increases linearly with potential. This, according to Hoar (1), was due to the fact that the rate of ionic migration through the film, v_m, has to be equal in the steady state to the rate of film's dissolution. The latter, being diffusion-limited, is constant and potential independent, and thus v_M must be potential-independent. Since v_M is proportional to the field across the film, $X = v/L$, it can be constant only if the film's thickness increases linearly with potential.

However, it seems that the vacancy mechanism of metal dissolution may lead to a different conclusion.

Since on arrival at the metal-film interface cationic vacancies are immediately filled in the fast process of metal dissolution into them, their concentration at the metal-film interface is always equal to zero and thus metal dissolves under limiting conditions determined by the rate of creation of vacancies at the film-solution interface, *i.e.*, by the rate of the film dissolution, which is potential-independent.

Thus in the potential region where the properties of the film remain constant with increasing potential (in this case, 0.840-1.3V), its thickness would also remain constant, since the film cannot be formed at the metal-film interface faster than it dissolves into the electrolyte.

The above suggestion, according to which the mechanism of electropolishing is that proposed by Hoar (1), however with a different rate-determining step, requires further verification in view of contradictory experimental findings, *i.e.*, thickness of the film (*a*) increasing with potential, as found by impedance measurements (1), or (*b*) constant, as found by ellipsometric evidence.

Acknowledgments

Financial support for this work by U. S. Army Electronics Command, Fort Monmouth, N. J., Contract DA-36-039-Sc-88921, is gratefully acknowledged.

The authors also wish to express their thanks to Professor J. O'M. Bockris for suggesting the topic of this work.

Manuscript submitted Sept. 24, 1969; revised manuscript received Feb. 12, 1970.

Any discussion of this paper will appear in a Discussion Section to be published in the December 1970 JOURNAL.

REFERENCES

1. T. P. Hoar, "Modern Aspects of Electrochemistry," Vol. 2, p. 262, Butterworths Scientific Publications, London (1959).
2. P. Jacquet, *Metal Rev.*, **1**, 157 (1956).
3. V. I. Leiner, "Electrolytic Polishing and Etching of Metals," (Russian), p. 37, Litizdat, Moskva (1947).
4. J. A. Allen, *Trans. Faraday Soc.*, **48**, 273 (1952).
5. N. Finch, Proc. Third Intern. Conf. on Electrodeposition, p. 43, London, 1947.
6. N. Frisby, *Compt. Rend.* **224**, 1003 (1947).
7. P. V. Shtigolev, "Electrochemical and Chemical Etching of Nickels," p. 10, Moskva (1959).
8. E. Darmois, T. Epelboin, and D. Amine, *Compt. Rend.*, **231**, 1222 (1950).
9. P. Brouillet and T. Epelboin, *Rev. Inst.*, **51**, 693 (1954).
10. P. Bouillon, Y. Bouillon-Nyssen, and A. Delplancke, *Bull., Soc. Chim. Belges*, **65**, 245 (1956).
11. T. P. Hoar and J. A. S. Mowat, *Nature*, **165**, 64 (1950).
12. R. Piontelli, *Met. Ital.*, 1950.
13. T. P. Hoar and T. W. Farthing, *Nature*, **169**, 324 (1952).
14. M. Cole and T. P. Hoar, Proc. 8th Meeting CITCE, India 1956, p. 158, Butterworths, London, (1956).
15. N. Moore, *Ann. Physk.*, **33**, 133 (1938)
16. E. Nelson, *Phys. Rev.*, **57**, 559 (1940).
17. Knauert, Leise, and Raettier, *Z. Physik*, **122**, 24 (1944).
18. E. C. Williams, J. M. A. Barrett, *This Journal*, **103**, 363 (1956).
19. N. P. Fedotiev and S. Ya. Grilibec, *Zhur. Prik. Khim.*, **30**, 643 (1957).
20. A. T. Turashev and G. S. Vozdvizhenskii, *Dokl. Akad. Nauk, SSSR*, **114**, 358 (1957).
21. A. K. N. Reddy and J. O'M. Bockris, *Natl. Bur. Std. Misc. Publ.*, **256**, 229 (1964).
22. Gmelin, Handbook 60.
23. A. B. Winterbottom, Det. Kgl. Norske Videnskobers Selskobs Skrifter (1955), 1.
24. J. O'M. Bockris, A. K. N. Reddy, and M. G. B. Rao, *This Journal*, **113**, 1133 (1966).
25. NBS Technical Reports, No. 242.

Film Formation and Reduction on Zinc Electrodes in Concentrated Potassium Hydroxide Solutions

M. W. Breiter*

General Electric Research and Development Center, Schenectady, New York

ABSTRACT

Anodic films were formed under potentiostatic conditions at three characteristic potentials in unstirred 6M KOH + 0.25M ZnO at 25°C on polycrystalline zinc electrodes, arranged either in a horizontal or vertical position. The film formation was followed as a function of time by determining the charge equivalent of the films by a method employing cathodic potential sweeps at 0.33 mV/sec. At each of the potentials, film formation occurred more rapidly on the horizontal than on the vertical electrode. The efficiency of film formation decreased from values above 50% at 250 sec to values around 20% on the horizontal electrodes. It stayed below 6% for the vertical electrodes.

The formation of anodic films on horizontal zinc electrodes was recently studied (1) in concentrated potassium hydroxide solutions either by taking photomicrographs of the electrode surface *in situ* at different potentials during a slow anodic voltage sweep or by measuring the two components of the electrode impedance with a small signal of superimposed 1000 Hz a.c. In agreement with earlier investigations (2-4), the course of the passivation was found to depend strongly on the convective conditions in the electrolyte near the zinc electrode. A loose, flocculent film, designated as type I, formed by precipitation from a supersaturated zincate solution near the surface in the absence of stirring. When the conditions of supersaturation were largely removed by stirring, the formation of a thin, more compact film, designated as type II, could be observed. The type II film, which is considered responsible for the passivation of the zinc electrode, appears to grow directly at the surface rather than by precipitation. It was also detected (5) beneath the type I film on horizontal electrodes in unstirred solutions. The different shape of voltammetric current-potential curves, measured on horizontal or vertical electrodes in unstirred solutions, was attributed to the influence of the convective conditions. While both type I and II film are produced in the absence of stirring on horizontal electrodes, the formation of type II film is predominant on these electrodes in stirred solutions and on vertical electrodes in unstirred solutions because of the effect (6) of natural convection.

New results concerning the formation of anodic films at constant potential are presented in this communication. Three characteristic potentials (−1.3V, −1.1V, −0.90V *vs.* an Hg/HgO reference electrode in 6M KOH) were chosen for the study. The potentials of −1.3 and −1.1V are close to the potentials of peaks in voltammetric current-potential curves on horizontal electrodes and vertical electrodes respectively of polycrystalline zinc in unstirred 6M KOH + 0.25M ZnO at 20° ± 1°C. The potential of −0.9V is located in the passive region. The film formation was followed by determining the charge Q_{Film} required for the reduction of the film. The efficiency of film formation was obtained from the ratio Q_{Film}/Q_{total}. Here Q_{total} designates the anodic charge consumed at constant potential U in time t.

Experimental conditions differ greatly from those of the recent coulogravimetric investigation (7) of the zinc electrode in potassium hydroxide. With regard to previous work on anodic films at zinc electrodes, the reader is referred to the comprehensive bibliography in ref (1).

Experimental Procedure

The electrodes were cut from rolled zinc sheet, designated as Mix 60 by the New Jersey Zinc Company, with a purity of 99.99%. They were polished by dipping them for a short time in concentrated nitric acid. Polishing was followed by a thorough rinsing in a stream of distilled water. The electrodes were mounted and immediately put into the vessel. They stayed at open circuit for 30 min in 6M KOH + 0.25M ZnO, saturated previously with purified nitrogen, before the desired potential was applied by the potentiostat. Nitrogen flowed at a large rate above the solution during the measurements. Throughout the study the electrode potential was measured against and is referred to a mercury-mercuric oxide electrode in 6M KOH. The solutions were prepared from reagent grade chemicals and distilled water. They were either made up freshly before the experiments or stored under argon with the exclusion of air.

The Teflon polymer vessel with the vertical arrangement of the electrode was described (1, 8) previously. The apparent surface area was 0.79 cm^2. For the horizontal arrangement the zinc electrode was pressed against a Teflon polymer block with a rectangular hole (2.5 cm long, 1 cm wide, 3 cm high) by a suitable Teflon polymer holder. The rectangular hole served as test electrode compartment and was connected with the counterelectrode compartment by another hole, drilled into the Teflon polymer block at a distance of 2 cm from the electrode surface. Visual observation of the electrode surface was feasible. A fine hole in the block, 0.05 cm from the surface, led to a separate reference electrode compartment. The counterelectrode was a hydrogen-diffusion electrode of the Niedrach-Alford type (9). It was verified that, under anodic polarization, the potential of the diffusion electrode did not differ by more than 0.1V from the value in the absence of polarization. Since platinum does not dissolve (10) at such potentials in alkaline solutions, side effects (11) originating from traces of platinum in the electrolytic solution were eliminated.

After applying a potential step by turning the switch of the Wenking 6 ITRS potentiostat, the anodic current was measured as a function of time on the meter of the instrument. The first reliable measurement of the current was feasible after about 10 sec. It took several seconds in the case of large initial currents before a constant potential was established. The procedure proved satisfactory since long-time experiments were involved. Short-time recording of the current during potentiostatic potential steps is worthless since the changing iR_{El} drop distorts the attempted potential step.

After the desired time of anodic polarization the potentiostat was turned off, leaving the zinc electrode at open circuit. The electrode potential became more negative and reached values close to −1.33V within 30 sec. The potentiometer of the potentiostat was adjusted to the value of the open-circuit potential. Po-

*Electrochemical Society Active Member.

tentiostatic control was turned on again, and a cathodic voltage sweep at 0.33 mV/sec, supplied by the Type 255 Exact function generator, was started by the manual triggering of the generator. The time required for the operations between the switching-off of the anodic polarization and the start of the voltage sweep was always 130-150 sec. The voltammetric I-U curves were recorded on a Mosley Model 136A X-Y recorder.

After the zinc electrode reached a potential at which hydrogen evolution was indicated by the current-potential curve, the potentiostatic circuit was disconnected. The open-circuit potential of the test electrode moved to values close to −1.36V. The potentiometer of the potentiostat was adjusted to this value. Potentiostatic control was switched on, and a second cathodic sweep was applied at 0.33 mV/sec. A time of about 150 sec elapsed between the stopping of the first cathodic sweep and the start of the second one.

The zinc electrode was removed from the vessel at the end of the second cathodic sweep. The procedure (anodic polarization, open circuit, first cathodic sweep, open circuit, second cathodic sweep) was always started with a fresh, chemipolished electrode.

Experimental Results

The anodic current density i is plotted as a function of time for the horizontal and vertical electrodes at the different potentials in Fig. 1 and Fig. 2. A double logarithmic plot was chosen to accommodate most of the data.

Some of the voltammetric i-U curves obtained in the described manner on horizontal electrodes are shown in Fig. 3. The solid curves on the left side of Fig. 3 were measured after an anodic polarization of 250 sec and the curves on the right side after 4500 sec at −1.3, −1.1, and −0.9V, respectively. The dotted curves result from the second cathodic sweep on the respective electrode (a' after a, etc.). Voltammetric curves on the vertical electrodes are similar to curves

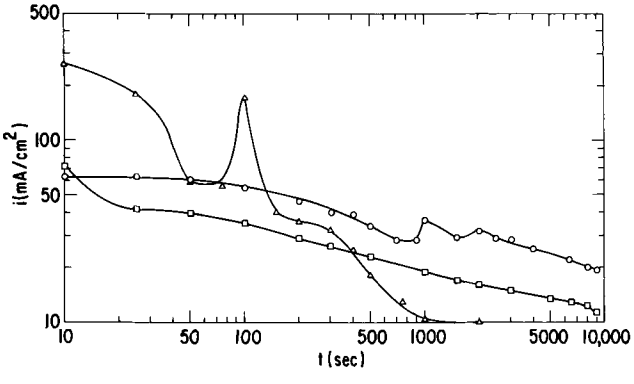

Fig. 1. Current density during the oxidation of horizontal zinc electrodes at −1.3V (○), −1.1V (△), and −0.9V (□).

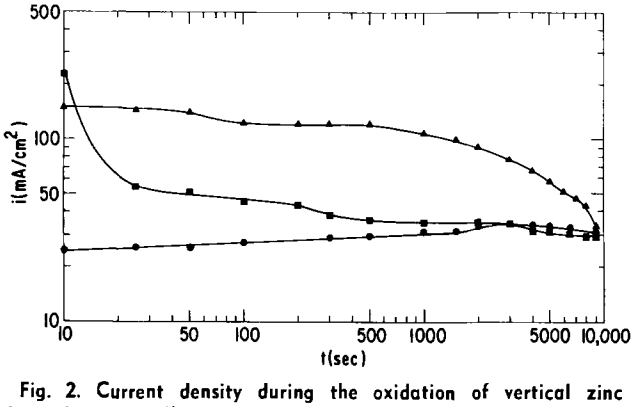

Fig. 2. Current density during the oxidation of vertical zinc electrodes at −1.3V (●), −1.1V (▲), and −0.9V (■).

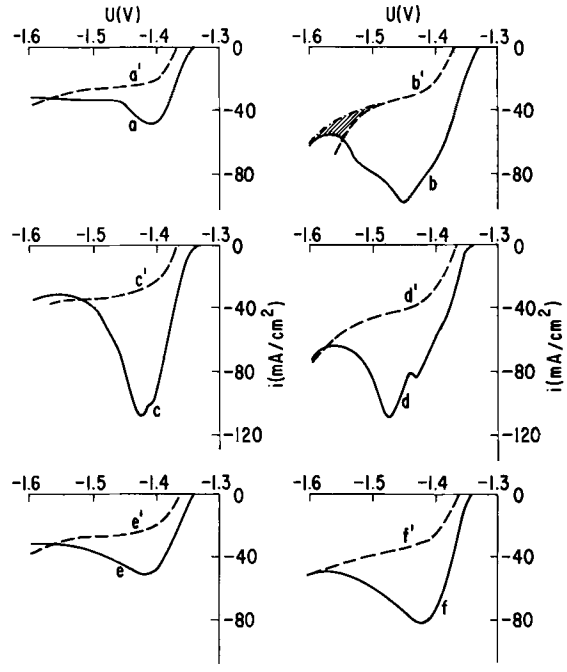

Fig. 3. Voltammetric *i-U* curves obtained at 0.33 mV/sec during cathodic sweeps after anodic polarization at −1.3V (a,b), −1.1V (c,d), −0.9V (e,f) for 250 sec (a,c,e) or 4500 sec (b,d,f) on the horizontal electrode. Dotted curves resulted from the second sweep on the respective reduced electrode.

a and e. The dotted curves, especially at shorter times of anodic polarization, are closer to the solid curves on vertical than on horizontal electrodes.

The charge Q_{Film} for the reduction of the film on the zinc electrode was evaluated in an approximate way

$$Q_{\text{Film}} = \int_{U_1}^{U_3} i\,dt - \int_{U_2}^{U_3} i\,dt \qquad [1]$$

Here U_1 and U_2 designate the starting potentials for the first and second cathodic sweep. U_3 is the potential where the solid and dotted curve intersect. The Q_{Film} values are plotted in Fig. 4 as a function of time of anodic polarization for the three different potentials. Open symbols belong to measurements on horizontal electrodes. Solid symbols refer to measurements on vertical electrodes. The Q_{Film} values were found equal to zero within the error limits for the different times of oxidation of the vertical electrode at −1.3V. The total charge consumed during time t of anodic polarization of the zinc electrode at constant potential was

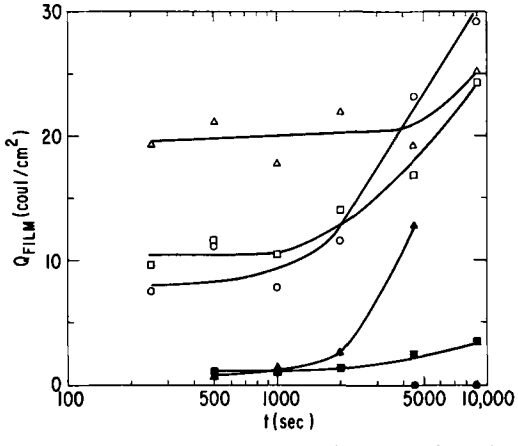

Fig. 4. Charges for the reduction of films, formed anodically on horizontal (○, △, □) and vertical (●, ▲, ■) electrodes as a function of time of anodic polarization. ○, ●, −1.3V; △, ▲, −1.1V; □, ■, −0.9V.

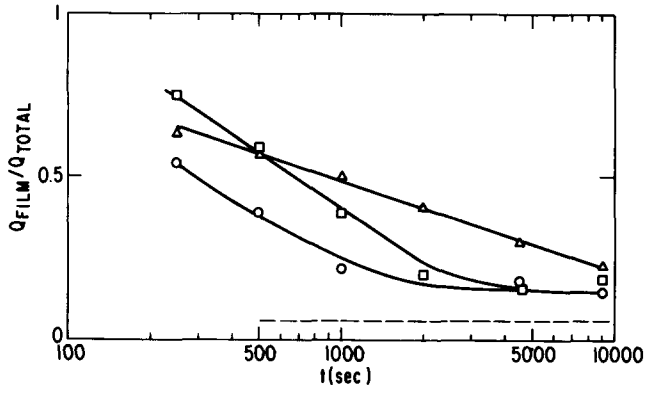

Fig. 5. Efficiency of film formation as a function of time for the horizontal electrodes (○: −1.3V, △: −1.1V, □: −0.9V). The efficiency stayed below 6% for the vertical electrodes.

determined by graphical integration of the i-t curves in a linear plot

$$Q_{\text{total}}(U,t) = \int_0^t i(\tau)d\tau \qquad [2]$$

The ratio $Q_{\text{Film}}/Q_{\text{total}}$ of the charges represents the efficiency of film formation and is plotted in Fig. 5 by open symbols for the horizontal electrode as a function of oxidation time. Here Q_{total} and Q_{Film} are values that result from three successive measurements. Since the error in the determination of Q_{Film} values is large, only the upper limit of 6% is shown for the ratio $Q_{\text{Film}}/Q_{\text{total}}$ on vertical electrodes in Fig. 5.

Discussion

General features of film formation.—The formation of anodic films and of dissolved zincate occur simultaneously at constant potential. The i-t curves display peaks within relatively narrow time intervals and steps in somewhat larger intervals (see Fig. 1 and Fig. 2). In agreement with previous results (1) this behavior is ascribed to the nonuniform film formation. Visual observation of the horizontal electrodes confirmed that the films started to grow in distinct patches on certain parts of the surface. The patches spread over the surface with time and grew in thickness. The initial patches appeared after shorter times when the potential became less negative. Wide vertical pores leading to uncovered areas of the zinc surface were visible as bright spots for at least 1000 sec.

The film formed at −1.3V on horizontal electrodes looked dark and sometimes contained white stripes in contrast to its whitish appearance (1) on the (0001) plane of zinc single crystals. Since it possessed the same properties (flocculence, loose adherence) as the type I film on the (0001) plane otherwise, the film at −1.3V is designated as type I film for polycrystalline surfaces. It forms by precipitation from the supersaturated zincate solution near the electrode surface.

At −0.9V a large part of the surface of the horizontal electrode assumed a goldish look after 200 sec. The goldish look darkened in the first 1000 sec. The formation of the compact type II film is observed. Patches of a grayish film, possibly type I film, appeared on top of the goldish film after about 1000 sec and spread with time.

The horizontal and vertical electrodes display a different long-time behavior. The current at a given potential decreases more rapidly with time on the horizontal electrode than on the vertical electrode (see Fig. 1 and Fig. 2). The different behavior will be correlated to the film formation in the discussion of Fig. 5. Since a steady-state current is not reached at constant potential on the zinc electrodes after 9000 sec, the shape of anodic current-potential curves on zinc in concentrated potassium hydroxide solutions depends strongly on the time intervals in which the potential is changed from one value to the next one.

Reduction of the film and determination of Q_{Film}.—The following processes may occur simultaneously during a cathodic potential sweep, starting at −1.33V after the preceding polarization of the zinc electrode at −1.3, −1.1, or −0.9V:

1. Reduction of the film.
2. Deposition of zinc from 6M KOH + 0.25M ZnO.
3. Hydrogen evolution.

Attempts to eliminate the zinc deposition by carrying out the reduction in 6M KOH failed because the loosely adherent type I film was partly removed from the surface during the replacement of 6M KOH + 0.25M ZnO by 6M KOH. Fast potential sweeps proved (12) useful for the determination of adsorbed carbonaceous species in the presence of large bulk concentrations of fuel on smooth platinum metal electrodes. However, the anodic films possess a porous structure on zinc. The application of fast sweeps or galvanostatic pulses would introduce additional problems because of the poor response (13) of porous systems.

The technique used in this investigation was already described under Experimental Procedure. It is based on a number of assumptions:

(*A*) After the film formation the specimen is at open circuit for 130-150 sec before the cathodic sweep is initiated. Autoreduction during this time has to be small.

(*B*) The charge consumed by the processes 2 and 3 is the same during the first and second cathodic sweep.

The error introduced by assumption *A* is not large for porous films (type I) on top of solid films (type II) because the processes which occur inside the pores are slow. Reduction of the type II film which was formed on vertical electrodes in 6M KOH takes place with a noticeable shift of the peak of the reduction wave toward more negative potentials with increasing sweep rate. The reduction of type II film is a hindered process, leading to a relatively small rate of autoreduction at open circuit within 130-150 sec. While assumption (*B*) is not strictly fulfilled, its application leads to acceptable errors in the present study for the following reasons.

(*a*) After short times of anodic polarization ($t \leq$ 250 sec) the dotted curves coincide within the experimental reproducibility with the curves of the first cathodic sweep, started at the open-circuit potential on fresh zinc electrodes in the horizontal or vertical arrangement. The maximum contribution of process 2 which is controlled by mass transport at $U < -1.4$V is given by curves a', c', and e' in Fig. 3 for a flat surface. The solid and the dotted curves are reasonably close on horizontal or vertical electrodes at potentials more negative than the potential U_{in} at which they intersect. Thus the position of the intersection which is largely determined by process 3 is not critical.

(*b*) The area under the dotted curve, as defined by the second integral in Eq. [1], increases with the time of anodic polarization for $t > 250$ sec (compare curves b', d', f' in Fig. 3). This increase reflects the fact that the zinc electrode became porous. The shape of the dotted curve did not change when the time between the end of the first cathodic sweep and the start of the second cathodic sweep was increased from 150 to 1000 sec. Thus each of the dotted curves represents the maximum contribution of process 2 at $U \leq -1.5$V on the porous electrode in question. The position of the intersection was not critical after anodic polarization at −1.1 and −0.9V on the horizontal electrode (see curve d' and d and curves f' and f in Fig. 3) because of the reasonable closeness of solid and dotted curve. The ascending branches of the dotted and solid curves at $U < -1.5$V were not found close any more on horizontal electrodes after larger times of anodic polarization at −1.3V. Hydrogen evolution starts earlier during the second sweep (see curve b' in Fig. 3) than

during the first sweep (curve b). The possible error may be estimated and is indicated by the shaded area between curves b and b' in Fig. 3. It is not large. A similar reasoning applies to the results on vertical electrodes whenever the solid and dotted curves are not reasonably close at $U < U_{in}$.

The error in the determination of Q_{Film} was estimated to be less than 10% for horizontal electrodes. Since the reproducibility is worse, this appears satisfactory for horizontal electrodes. For vertical electrodes, the error is larger than 10% because the anodic film is thin in most cases. Since an error estimate is difficult, the respective results on the vertical electrodes are of a more qualitative nature.

The solid curves c, b, and d in Fig. 3 display peaks. These peaks are connected with the reduction of the film since they are not eliminated by the point-wise subtraction of curve c' from curve c for instance. More about the origin of the peaks is not known at present.

Efficiency of film formation.—The points, representing the charge Q_{Film} at a given potential as a function of time of anodic polarization, scatter considerably in Fig. 4. The scattering reflects the fact that the film does not grow in a reproducible way on the different electrodes. It is less noticeable for the vertical electrodes because the same scale was used as for the horizontal electrodes.

In general Q_{Film} (U, t) is larger for the horizontal electrodes than for the vertical ones. The charge Q_{Film} increases with time in agreement with the visual observations on horizontal electrodes. When removing vertical electrodes after anodic polarization at −1.1V, preferential attack by big etch pits in the upper half of the circular surface was noticed. A wide hole shaped like a bird's wing penetrated the whole electrode (thickness 0.5 mm) after 9000 sec. The sudden increase of Q_{Film} with time between 1000 and 4500 sec at −1.1V may reflect preferential film formation in etch pits where the natural convection is not so strong than on the rest of the vertical surface.

The ratio Q_{Film}/Q_{total} decreases with time at each of the three potentials and reaches values between 0.15 and 0.23 after 9000 sec on the horizontal electrodes. The charge for zincate production is much larger than that for film formation. On the vertical electrodes the ratio Q_{Film}/Q_{total} remained below 0.06. Only this maximum value is indicated by the dotted line in Fig. 5 for the vertical electrodes.

More than 90% of the total current on vertical electrodes goes into zincate formation. The decrease of the net current with time at −1.1 and −0.9V (see Fig. 2) is largely due to an inhibition of the zincate production by the anodic film on vertical electrodes. A similar conclusion may be drawn at −1.1 and −0.9V for the horizontal electrodes at times between 2000 and 9000 sec (see Fig. 5). It is likely that the decrease of the rate of zincate production is caused by the gradual closing of pores when the films grow thicker with time. The peaks in the i-t curves result from the sudden opening and closing of pores. The gradual disappearance of the bright spots which reflect the presence of wide vertical pores ending at the metal surface, confirms the role of wide pores.

Manuscript submitted Nov. 20, 1969; revised manuscript received *ca.* Feb. 5, 1970. This was Paper 334 presented at the Los Angeles Meeting of the Society, May 10-15, 1970.

Any discussion of this paper will appear in a Discussion Section to be published in the December 1970 JOURNAL.

REFERENCES

1. R. W. Powers and M. W. Breiter, *This Journal,* **116,** 719 (1969).
2. M. Eisenberg, H. F. Bauman, and D. M. Brettner, *ibid.,* **108,** 909 (1961).
3. N. A. Hampson and M. J. Tarbox, *ibid.,* **110,** 95 (1963).
4. N. A. Hampson, M. J. Tarbox, J. T. Lilley, and J. P. G. Farr, *Electrochem. Technol.,* **2,** 309 (1964).
5. R. W. Powers, *This Journal,* In review.
6. N. Ibl, "Advances in Electrochemistry and Electrochemical Engineering," Vol. 2, Chap. III, P. Delahay and Ch. W. Tobias, Editors, Interscience Publishers, New York (1962).
7. A. Langer and E. A. Pantier, *This Journal,* **115,** 990 (1968).
8. M. W. Breiter, *Electrochim. Acta,* In print.
9. L. W. Niedrach and H. R. Alford, *This Journal,* **112,** 117 (1965).
10. P. Malachesky, R. Jasinski, and B. Burrows, *ibid.,* **114,** 1104 (1967).
11. R. Thacker, *Electrochim. Acta,* **14,** 433 (1969).
12. M. Breiter, "Electrochemical Processes in Fuel Cells," Chap. IX, Springer Verlag, New York (1969).
13. R. DeLevie, "Advances in Electrochemistry," Vol. 6, p. 329 P. Delahay, Editor, Interscience Publishers, New York (1967).

Electrolytic Determination of Porosity in Gold Electroplates

I. Corrosion Potential Measurements

Ronald J. Morrissey*

Research Division, AMP Incorporated, Harrisburg, Pennsylvania

ABSTRACT

The porosities of gold electroplates on copper may be determined by measuring the corrosion potentials of the specimens *vs.* a suitable reference electrode in an electrolyte which serves as a mild corrodant for the exposed basis metal. The corrosion potentials of gold-plated copper specimens in 0.1M NH_4Cl electrolyte are shown to vary with the exposed area fraction of copper according to an expression derived by Stern. It is possible to calibrate the technique so that values of the exposed basis metal area fraction in electroplated specimens can be estimated to a reasonable approximation. The method is simple and offers very high sensitivity, particularly at low porosities. Operational considerations and sources of error are discussed.

Chemical and electrographic test procedures for the determination of porosity in electrodeposits have been reviewed and evaluated in the literature (1-4). Such procedures are in most cases destructive and in general have not proven highly suitable for process control applications. Electrolytic techniques offer the promise of rapid and relatively nondestructive means of determining electroplate porosities with great sensitivity. Such techniques have therefore been of considerable interest.

In 1938, Hoar (5) suggested that the corrosion potential of a specimen coated with a porous electroplate could serve to indicate the degree of porosity. In 1951, Shome and Evans (6) reported the determination of porosities in electrodeposits of nickel and cobalt on steel by measuring the cell currents (leakage currents) passed when the specimens were connected, in an electrolyte of 3% NaCl plus 0.1% Rochelle salt, to a large copper gauze which served as an auxiliary cathode. No reference electrode was used. They reasoned that, if the copper gauze were made sufficiently large, the cell current would be limited only by the rate of anodic dissolution and would therefore be directly proportional to the exposed area of bare steel. This technique was subsequently extended by Ehrhardt (7) with the addition of an external power supply with which the potential between the specimen and the auxiliary cathode could be controlled. Again, no reference electrode was employed. Using an electrolyte of 5% H_2SO_4, and with a potential of 0.75V maintained between the specimen and the auxiliary cathode, Ehrhardt measured porosities in gold electroplates on copper. A variation of the leakage-current technique has been employed by Kamm, Willey, and co-workers (8) to determine the continuity of the iron-tin alloy layer in electrolytic tinplates on steel.

Clarke and Britton (9) considered the pore channels in an electrodeposit as an array of minute electrical resistances in parallel, and devised a technique for estimating the sum of these resistances (and hence, a measure of the porosity of the electrodeposit) by measuring the slope dV/dI of the anodic polarization curve of the specimen at potentials within approximately 100 mV of the corrosion potential. These authors also noted that the corrosion potentials of electroplated specimens appeared to vary with the porosity of the electrodeposit, but did not pursue the matter further. Using an electrolyte of 5% Na_2SO_4 plus 0.1% Rochelle salt, Clarke and Leeds (10) have applied the dV/dI technique to measurements of the porosities of gold electroplates on copper.

Relation of the Corrosion Potential to Electrodeposit Porosity

A series of experiments was undertaken to investigate the possible usefulness of corrosion potential measurements for determining porosity in gold electroplates on copper. OFHC copper sheet of 1 mm thickness was stamped to form a series of circular coupons of 25 mm diameter, each having a small punched tab at one edge. The geometric surface area of each specimen thus formed was 10.8 cm^2. Following stamping, the specimens were cleaned, degreased, and then rack-plated with Temperex HD gold[1] to a thickness of 100 μin. (2.54μ). Temperex HD is an unbrightened gold which yields deposits with a density approaching the bulk density of pure gold. Following plating, the specimens were rinsed in demineralized water, dried, and retained in a desiccator over dried silica gel prior to testing.

Corrosion potentials of the plated specimens were determined *vs.* that of a saturated calomel reference electrode in a solution of 0.1M KCl. A Pyrex resin kettle of 2 liters capacity served as the reaction vessel. This was fitted with a Plexiglas cap through which the electrodes could be immersed into the bath. Experiments were performed at room temperature, which varied from 22°-25°C. Solutions were made up using demineralized, boiled water, the specific resistance of which was typically 140,000-160,000 ohms. Analytical Reagent grade chemicals were employed throughout.

The reference electrode employed was a Beckman No. 39170 saturated calomel electrode having a fiber junction. For convenience, this was located in the electrolyte bath at a distance of 5 cm from the test specimen, which was itself suspended in the electrolyte by means of a 99.99% gold wire.[2] It had been shown in previous work (9) that the position of the reference electrode is of negligible influence in determining corrosion potentials of specimens coated with porous electrodeposits. Prior to each experiment, the potential of the saturated calomel electrode was checked against that of a Beckman No. 41236 silver-silver chloride electrode which was reserved as a standard.

Potentials were determined using a Keithley Model 610A electrometer. The output of this instrument was relayed to a strip-chart recorder, so that slow changes in the observed emf could be discerned easily. It was

* Electrochemical Society Active Member.

Key words: electroplates, porosity, porosity testing, galvanic cells, gold, copper, corrosion potential.

[1] Sel-Rex Corporation, Nutley, New Jersey.

[2] Obtained from the Sigmund Cohn Corporation.

noted that after a gold-plated copper specimen was immersed in the electrolyte its potential, measured *vs.* that of the reference electrode, would drift for a period of 10-30 min in a generally negative direction until a steady value was attained. The steady values, once attained, were observed to be stable for periods of several hours duration. It was further found that on repeated testing of the same sample the steady corrosion potentials observed were ordinarily reproducible to within ±2 mV.

Further experiments were conducted to obtain comparative indications of porosity in electroplated specimens from corrosion potential measurements and also by means of the ammonium persulfate—ammonium hydroxide etch technique described by Frant (11). Corrosion potentials of gold-plated OFHC copper specimens prepared as outlined previously were determined *vs.* SCE in 0.1M KCl solution. Following this, the specimens were rinsed in demineralized water, dried, and then individually subjected to the ammonium persulfate-ammonium hydroxide etch technique, the apparent porosities being indicated as parts per million of cupric ion in the resulting solutions. In order to minimize undermining of the gold platings by the rather aggressive etchant, etching times were restricted to 5 min/specimen. Analysis of the resulting solutions was performed by emission spectrography, using a rotating disk technique with radio-frequency spark excitation.

The results of this series of experiments are shown plotted in Fig. 1. It was found that the steady-state corrosion potentials obtained for the specimens in 0.1M KCl solution were proportional to the logarithms of their apparent porosities as determined by the chemical etch technique. Agreement of the experimental points to the line in Fig. 1 was found to be within the limits of precision of the emission spectrographic technique employed. Porosity in these specimens was found to occur most prominently at rack marks (thinly plated areas) in the area of the punched tab. These tended to be rather irregular among the various specimens, accounting for the observed dispersion in porosity values obtained.

Relation of the Corrosion Potential to Basis Metal Area Fraction

Experimental Considerations

The evidence of Fig. 1 leads one to speculate that the corrosion potentials of gold-plated copper specimens might perhaps be related to the logarithm of the exposed area or area fraction of copper. This is not without precedent. Stern (12) had shown that for binary galvanic couples controlled by activation polarization the corrosion potential was given by

$$\eta_{corr} = -\frac{E_A\beta_C}{\beta_A+\beta_C} - \frac{\beta_A\beta_C}{\beta_A+\beta_C}\log A_A i_{o_A} + \frac{\beta_A\beta_C}{\beta_A+\beta_C}\log A_C i_{o_C} \quad [1]$$

where η_{corr} is the corrosion potential of the couple, measured with respect to the equilibrium potential of pure cathode material in the same electrolyte, which is taken as zero. E_A is the corrosion potential of pure anode material in the electrolyte, again measured with respect to the equilibrium potential of pure cathode material taken as zero. β_A and β_C are the Tafel slopes of the logarithmic polarization curves for the anodic and cathodic processes, respectively. A_A and A_C are the respective area fractions of anode and cathode materials in the actual couple (such that $A_A + A_C = 1$), and i_{o_A} and i_{o_C} are the exchange current densities for the anodic and cathodic processes.

Here we may note that for a given base metal-noble metal couple in a given corrodant bath, the electrochemical parameters E_A, β_C, β_A, i_{o_C} and i_{o_A}, as well as the equilibrium potential of pure cathode material, are constants. Further, for the case of base metal specimens coated with noble metal electroplates of moderate to low porosity, $A_C >> A_A$. In this case, A_C approaches unity, and the term in ($\log A_C i_{o_C}$) may be considered a constant. It thus becomes possible to rearrange expression [1], combining and substituting terms to obtain a simplified expression of the form

$$V_{corr} = K_1 - K_2 \log A_A \quad [2]$$

where V_{corr} is the corrosion potential as measured *vs.* a suitable reference electrode, K_2 is equal to ($\beta_A\beta_C/\beta_A+\beta_C$), and K_1 incorporates the remaining constant terms resulting from the rearrangement of expression [1].

Establishment of Calibration Curves

Experiments were undertaken to determine the change in corrosion potential with basis metal area fraction in galvanically connected gold-copper couples of known geometric area relationships. 1 mm gold sheet of 99.9% purity[3] was stamped to form a circular coupon of 25 mm diameter, having a small punched tab at one edge. This was used as the gold specimen in all determinations. Its geometric gross surface area was 10.8 cm^2. Prior to each experiment, this specimen was cleaned by rinsing in acetone, soaking for 30 min in 1.0M HCl, and then rinsing with demineralized water. The specimen was then suspended in the electrolyte by means of a 99.99% gold wire.[2]

Formvar-insulated copper wire in No. 20, No. 30, and No. 36 gauge sizes[4] and in No. 47 gauge size[5] was chemically stripped and cut into short lengths. The cut ends were then ground approximately flat on an abrasive wheel. Spectrographic analysis indicated that these samples were of 99.99+% purity. Prior to each experiment, the copper specimen was cleaned by rinsing with acetone, soaking for 30 min in 1.0M NH_4Cl, and rinsing with demineralized water. The specimen was then suspended in the electrolyte by means of an adapter attached to the shaft of a micrometer head which could be mounted in the cap of the reaction vessel. Electrical contact to the copper specimen was effected by means of a lead connected to the micrometer barrel. Use of this arrangement allowed the immersed area of copper to be varied, during the course of a given experiment, over several orders of magnitude. The immersed area of gold was maintained constant at 10.8 cm^2 in all experiments.

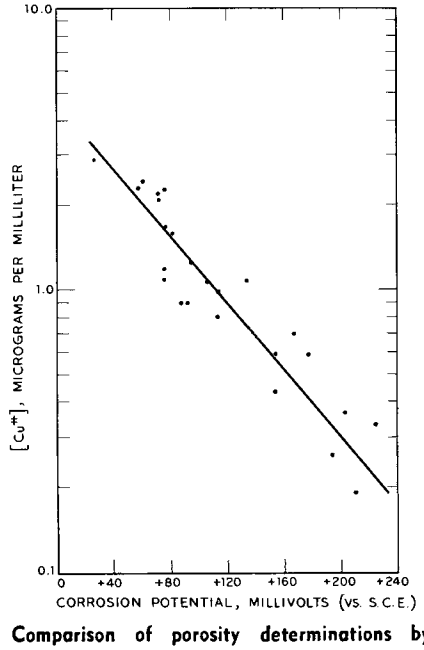

Fig. 1. Comparison of porosity determinations by corrosion potential and chemical etch techniques.

[3] Obtained from Handy and Harman, Inc.
[4] Obtained from Consolidated Wire Company.
[5] Obtained from Bridgeport Insulated Wire Company.

Some representative plots of measured corrosion potential (*vs.* SCE) *vs.* immersed area fraction of copper for gold-copper couples in 0.1M KCl solution are shown in Fig. 2. Figure 2 summarizes the results of two experiments, one using a No. 20 copper wire specimen and the other using a No. 36 copper wire specimen. The area fractions shown here are calculated on the basis of geometric areas. In determining the true immersed areas, one must consider the surface roughness factors of the various specimens. For purposes of this work, we have assumed that the roughness factor for a given wire specimen should be fairly consistent along its length. The straightness of the plots obtained would appear to indicate that this is true. The continuity of the plots obtained using No. 20 and No. 36 copper wire specimens would indicate that the surface roughnesses of these two specimens were comparable.

Deviations from linearity are observed in Fig. 2 at both large and small values of the immersed copper area fraction. At large copper area fractions, this is in accordance with the expression [1], for then (log $A_C i_{oC}$) can no longer be considered a constant. At small area fractions of copper, the deviations are caused experimentally by withdrawal of the wire specimen through the topmost layers of the electrolyte, giving rise to differential aeration and other interface effects at the meniscus. These effects can be eliminated by the use of metallographically mounted and sectioned wire specimens, or alternatively by the use of wire specimens which have been heavily gold plated and then perpendicularly sectioned according to the method of Ehrhardt (7). Additionally, the range of measurement may be extended by the use of a larger gold specimen and/or finer copper wire specimens.

Prolonged immersion in 0.1M KCl solution produces a visible film on copper. While this did not appear to affect the corrosion potentials of gold-copper couples, further experiments were performed using 0.1M NH_4Cl electrolyte, which exhibits a slight solvency for copper oxides. A plot of corrosion potential *vs.* immersed area fraction of copper for gold-copper couples in this electrolyte is shown in Fig. 3. The two lowermost points in this illustration were obtained using No. 47 copper wire specimens which were plated with Temperex HD gold to a thickness of 1 mil (25.4μ) and then perpendicularly sectioned so as to expose only the cross-sectional area of the copper wire substrate. Each such specimen, after cleaning by brief immersion

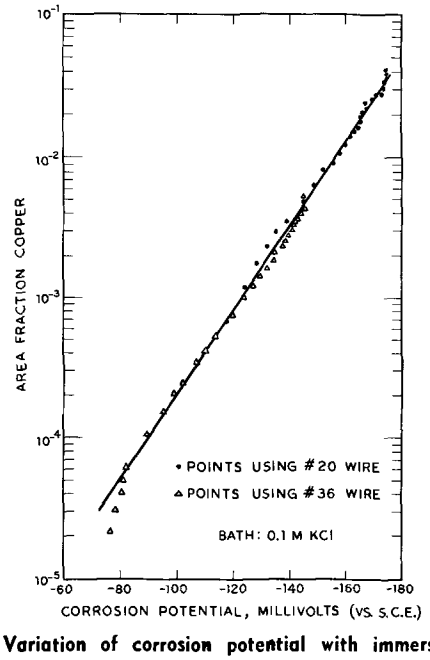

Fig. 2. Variation of corrosion potential with immersed copper area fraction.

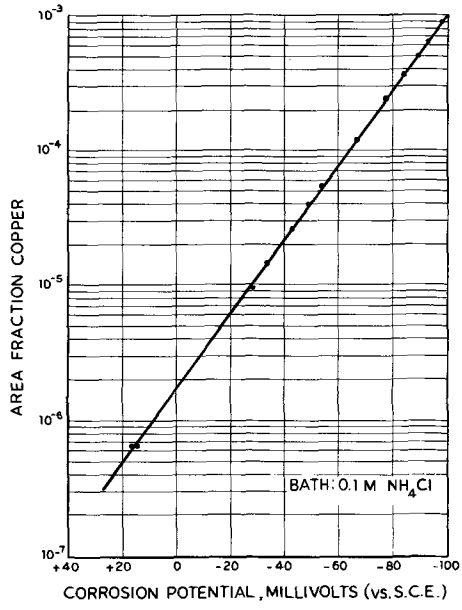

Fig. 3. Variation of corrosion potential with immersed copper area fraction.

in 6M HCl and rinsing in demineralized water, was introduced into the electrolyte via the micrometer device and immersed to a depth of 1 cm. Coupling of the plated and sectioned wire to the gold specimen and determination of the corrosion potential of the couple were then accomplished as previously outlined. In this fashion, interface effects were successfully avoided. The remainder of the data points in Fig. 3 were obtained using a bare No. 47 copper wire specimen prepared and immersed as outlined previously. The slope K_2 of this plot, calculated using common logarithms, is 0.0357V. This is in excellent agreement with the value of 0.0329V calculated for K_2 from the observed values for β_C of gold (0.0935V) and β_A of copper (0.0507V) in this electrolyte. The slope of Fig. 2 is 0.0335V, indicating that the Tafel slopes of gold and copper in 0.1M KCl solution are probably quite similar to those obtained in 0.1M NH_4Cl.

The range of measurement in Fig. 3 is extended by two orders of magnitude from that of Fig. 2. It was noted that corrosion potentials of gold-copper couples of a given immersed area fraction of copper in 0.1M NH_4Cl solution were more positive by approximately 25 mV than those of corresponding couples in 0.1M KCl solution.

Validation of the Calibration Curves

The expression [1] was derived for the case of binary galvanic couples controlled by activation polarization. It would thus be expected that the curves shown in Fig. 2 and 3 could serve as calibration curves for specimens coated with porous electrodeposits only if conditions were such that the effects of concentration and resistance polarization are small, and that accumulation of solid corrosion products in the pore channels is minimized or prevented entirely.

Two series of experiments were performed in an attempt to assess the validity of the calibration curves for specimens coated with porous electrodeposits. The first such series involved an attempt to simulate a porous specimen, again using a gold-plated copper wire. A No. 47 copper wire (diameter = 0.003 cm) was heavily plated with Temperex HD gold, the final diameter after plating being 0.0089 cm. The plated wire specimen was then perpendicularly sectioned, mounted in the micrometer device, cleaned as outlined previously, and immersed into the electrolyte. The corrosion potential of the plated wire specimen was then determined *vs.* SCE at various depths of immersion in the 0.1M NH_4Cl test electrolyte, and indicated

values of the immersed copper area fraction (obtained from the corrosion potentials by reference to Fig. 3) were compared to the values calculated geometrically from the immersion depths and the known cross-sectional parameters. Pertinent data are shown in Table I.

Agreement between the indicated and calculated values of the immersed copper area fraction was excellent at small values of the area fraction, becoming poorer as the specimen was progressively withdrawn from the electrolyte. Microscopic examination of the specimen at 25X magnification immediately after the experiment revealed that the copper wire substrate had been etched back slightly during the course of the experiment. It is felt that the deviations observed in the final readings may have been due in part to crystallographic changes occurring at the copper surface during etching, or to concentration polarization and diffusion effects arising from partial entrapment of soluble corrosion products within the confines of the gold tubulus thus formed. Additionally, withdrawal of the specimen through the topmost layers of the electrolyte would be expected to introduce differential aeration and other interface effects such as had been experienced in preparation of the calibration curves. Throughout the range investigated, agreement between the indicated and calculated values of A_A was within a factor of two.

The second series of experiments involved measuring the change in corrosion potential occurring when a copper specimen coated with a porous gold electroplate was galvanically coupled, in a solution of 0.1M NH_4Cl, to a large plate of pure gold and then decoupled, so that the exposed area fraction of copper, whatever its value, could be varied by a constant and calculable factor. The specimens employed were small OFHC copper electrical terminals, each of 2.5 cm^2 gross geometric surface area. These were barrel plated in small lots with Temperex HD gold to thicknesses of 100, 200, and 400 μin. (2.54, 5.08, and 10.16μ). In addition, several circular OFHC copper coupons of 25 mm diameter similar to those previously described were rack-plated with Temperex HD gold to a thickness of 50 μin. (1.27μ). These specimens each had a gross geometric surface area of 10.8 cm^2, but again owing to the incidence of rack marks in the area of the punched tab, this area was not immersed in the test electrolyte. The total immersed geometric surface area of each of these specimens was calculated to be 10.2 cm^2.

The gold specimen employed was a rectangular panel of 99.9% purity having a gross geometric surface area of 102.09 cm^2. This was then plated with Temperex HD gold to a thickness of 200 μin. so as to give it a smooth matte surface finish approximately comparable to that of the plated copper test specimens. Cleaning and preparation of this specimen was accomplished as previously indicated.

The experimental procedure was as follows. After cleaning, the gold panel was suspended in the 0.1M NH_4Cl test electrolyte by means of a 99.99% gold wire. Its corrosion potential was then determined *vs.* SCE. Typically, this was in the range +0.200 to +0.215V. The test specimen was then suspended in the electrolyte by means of a 99.99% gold wire and connected shuntwise to the gold panel and the electrometer voltmeter. The corrosion potential of the coupled specimens was then determined, after which the gold panel was decoupled from the specimen and the electrometer, and the corrosion potential of the test specimen alone was determined.

For the plated electrical terminals, coupling to the gold panel produces an increase in gross gold surface area by a factor of approximately 42. Since the exposed area of base copper is unchanged, its effective area fraction is diminished by the same factor. Inspection of Fig. 3 reveals that a change in A_A of this magnitude would yield a change in corrosion potential of approximately 59 mV. For the circular coupons, the change in effective copper area fraction is by a factor of approximately 11. Again from Fig. 3, the change in corrosion potential corresponding to such a change in effective area fraction is approximately 39 mV. The results of this series of experiments are shown in Table II.

In all cases, changes in corrosion potential observed in these experiments are equal to, or quite close to, the predicted values. The effect of increasing thickness of gold plating appears to be negligible in the range investigated, which is taken to indicate that in this range the effects of concentration and resistance polarization are small. Interestingly, the rack-plated coupons of 50 μin. gold thickness show less apparent porosity than the barrel-plated terminals of 200 μin. gold thickness. This is attributed both to the different conditions of plating and to the more complex shape of the barrel-plated terminals, which have significantly greater lengths of edge in relation to their surface areas than do the circular coupons.

The results of these series of experiments are felt to indicate that the corrosion potentials of gold-plated copper specimens in 0.1M NH_4Cl electrolyte are adequately described by an expression of the form of Eq. [2], and that calibration curves of the type shown in Fig. 2 and 3 can be employed to obtain the apparent basis metal area fraction of such specimens to a reasonable approximation, probably within a factor of two or smaller.

Factors Affecting Corrosion Potentials

The corrosion potentials of gold-plated copper specimens in 0.1M NH_4Cl solution are affected both by the *p*H of the electrolyte and by accumulation of cupric ions at concentrations in excess of 4×10^{-6}M. Figure 4 shows the effect of electrolyte *p*H on the corrosion potential of a gold-plated copper specimen in 0.1M NH_4Cl. In this experiment, the corrosion potential of an OFHC copper electrical terminal (area = 2.5 cm^2) plated with 200 μin. of Temperex HD gold was determined *vs.* SCE in a bath of 500 ml of 0.1M NH_4Cl. A 5 ml aliquot of 1.0M HCl was then added to the electrolyte, and the solution back-titrated in small steps with 1.0M NH_4OH. Solution *p*H was monitored using an Instrumentation Laboratory, Inc. Model 175 *p*H meter. The effect of electrolyte *p*H on the corrosion potentials of gold-plated copper specimens in this system is of the order of 10 mV per *p*H unit, which is relatively small.

The effect of cupric ion accumulation on the corrosion potential of a gold-plated copper specimen in 0.1M NH_4Cl solution is shown in Fig. 5. In this experiment,

Table I. Comparison of indicated and calculated values of immersed copper area fraction

Copper cross-sectional area = 7.06×10^{-6} cm^2

Immersion depth, cm	Immersed gold area, cm^2	V_{corr}, *vs.* SCE	A_A indicated	A_A calculated
1.720	0.0483	−0.067	1.25×10^{-4}	1.46×10^{-4}
1.105	0.0311	−0.072	1.7×10^{-4}	2.26×10^{-4}
0.851	0.0240	−0.0755	2.1×10^{-4}	2.94×10^{-4}
0.597	0.0169	−0.0805	3.0×10^{-4}	4.18×10^{-4}
0.343	0.0098	−0.084	3.7×10^{-4}	7.20×10^{-4}

Table II. Corrosion potentials of gold-plated copper specimens in 0.1M NH_4Cl

Specimen area, cm^2	Gold thickness, μin.	V_{corr} (*vs.* SCE) Coupled	Uncoupled	ΔV_{corr}
2.5	400	+0.177	+0.122	0.055
2.5	400	+0.163	+0.104	0.059
2.5	200	+0.124	+0.060	0.064
2.5	200	+0.115	+0.055	0.060
2.5	100	+0.117	+0.063	0.054
2.5	100	+0.095	+0.036	0.059
10.2	50	+0.125	+0.084	0.041
10.2	50	+0.123	+0.084	0.039

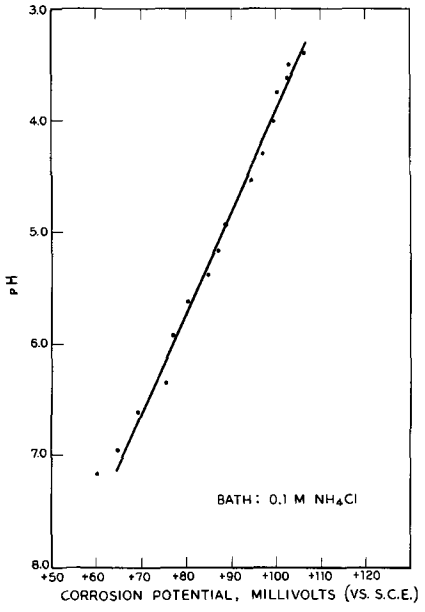

Fig. 4. Effect of electrolyte pH on corrosion potential

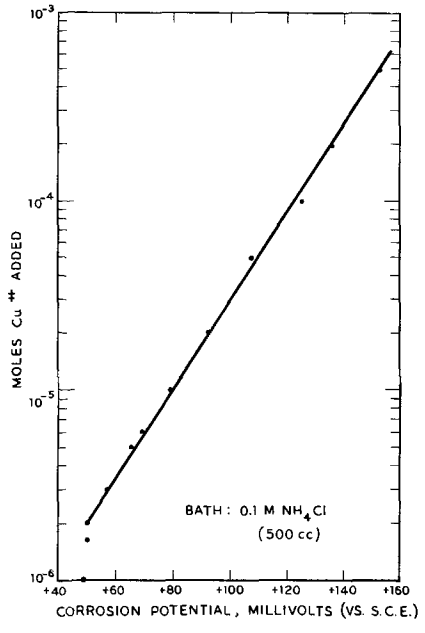

Fig. 5. Effect of cupric ion accumulation on corrosion potential

the corrosion potential of a circular OFHC copper coupon (area = 10.8 cm^2) plated with 100 μin. of Temperex HD gold was determined *vs.* SCE in a bath of 500 ml of 0.1M NH_4Cl. The bath was then titrated in small increments with 0.1M $CuCl_2$. No effect on the corrosion potential was noted until the indicated cupric ion concentration exceeded 4 x 10^{-6}M, after which the corrosion potential was observed to shift in a positive direction by approximately 43 mV per order of magnitude of cupric ion concentration. Due to the very limited solubility of cuprous salts in water, titrations involving cuprous ion were not attempted.

Provided that the electrolyte is changed at reasonable intervals, there would appear to be little danger of erroneous corrosion potential readings due to cupric ion accumulation in the bath. Assuming an exposed copper surface area of 10^{-5} cm^2 per test specimen and a steady corrosion current density of 1 mA/cm^2 of exposed copper (a value obtained from polarization resistance determinations in this electrolyte), it can be calculated that testing of several thousand specimens for periods of 1 hr each would be required to raise the cupric ion concentration of one liter of 0.1M NH_4Cl from zero to 10^{-6}M.

Parallel experiments were conducted in which the corrosion potentials of gold-plated copper specimens in 0.1M NH_4Cl electrolyte were monitored during titration of the electrolyte with solutions of 0.01M $NiCl_2$ and 0.01M $ZnCl_2$. No effect on the corrosion potentials was observed. It is conceivable that under proper conditions such a system might be calibrated to serve as a specific-ion electrode for cations of the basis metal.

Discussion

The corrosion potential technique represents a particularly simple means for determining electroplate porosities, and it would seem likely that with a suitable choice of electrolyte the method should prove applicable to a fairly wide variety of noble metal electroplates on base metal substrates. Less obviously, perhaps, inspection of Fig. 2 and 3 reveals that the sensitivity ($\Delta V_{corr}/\Delta A_A$) of the technique increases as A_A decreases. As far as is known, this feature is unique, and it would appear that for gold electroplates of low porosity on copper the method represents the most sensitive liquid-phase test technique yet devised. With a proper choice of the test electrolyte, the method is relatively nondestructive. From polarization resistance measurements, the corrosion current densities of gold-plated copper specimens in 0.1M NH_4Cl electrolyte are calculated to be of the order of 1 mA/cm^2 of exposed copper.

Limitations in applicability of the method as a porosity test are encountered at both large and small values of A_A. Regarding the upper limit, it was shown previously that in preparing the calibration curves of Fig. 2 and 3, deviations from linearity were observed at values of A_A larger than about 10^{-2}. The value of A_A at which deviations from linearity are first noted in the calibration curve represents the upper limit of A_A for which the approximate expression [2] is applicable to the system under investigation. At values of A_A larger than this, the method fails rapidly. A plot of corrosion potential *vs.* A_A yields, according to the general expression [1], an S-shaped trace, the center of which, in the systems examined in this work, is found experimentally to be quite flat. Thus, for gold-copper couples in 0.1M NH_4Cl solution, variation of A_A in the range of 5-95% or so is accompanied by only a negligibly small change in the corrosion potential, and in this range the method fails entirely.

In the lower limit, it has been shown by previous authors (13, 14) that liquid reagents often do not penetrate very fine or very deep pores in electrodeposits. This effect represents a limitation in detectability inherent in any porosity test method employing a liquid phase. The addition of a surfactant to the test electrolyte might serve to alleviate this effect somewhat, although Clarke and Britton (14) reported no significant improvement in pore penetration in similar experiments employing a surfactant.

Specific experiments have not been performed in this work to determine the effect of dissolved oxygen on the corrosion potentials of gold-copper couples. In the bulk solution, one might infer from the results of Fig. 4 that the magnitude of this effect would probably be rather small. In the topmost layers of the electrolyte, however, and particularly at the meniscus, the situation is complicated by the possibility of oxygen and other interface effects occurring simultaneously. It was mentioned previously that with certain refinements in specimen preparation techniques it is possible to avoid these latter effects in establishing calibration curves, and this was done in the preparation of Fig. 3.

Finally, it is noted that the time required after immersion of a plated specimen until a steady corrosion potential is achieved varies with the apparent porosity of the electroplate and with the chemical reactivity of the electrolyte employed. In 0.1M NH_4Cl solution,

equilibration times are of the order of 10-100 min, being generally greatest for specimens of lowest apparent porosity. The use of a more aggressive electrolyte, such as a solution of 0.05M H_2SO_4 + 0.1M NaCl, reduces equilibration times to the order of 1-2 min. This latter electrolyte has been found suitable for porosity determinations in gold electroplates on nickel as well as on copper, but the corrosion rates of the plated specimens are rather high. It has been pointed out in review that the addition of a surfactant to the test electrolyte might affect a significant reduction in equilibration times. Further work in these areas is indicated.

Summary

A method is presented for the determination of electroplate porosity by measuring the corrosion potential of the plated specimen *vs.* a suitable reference electrode in an electrolyte which serves as a mild corrodant to the exposed basis metal. It is shown that for gold-plated copper specimens in 0.1M NH_4Cl electrolyte the corrosion potential varies with the exposed area fraction of copper according to an expression derived by Stern. It is possible to calibrate the technique so that the exposed basis metal area fractions of plated specimens can be estimated to a reasonable approximation. Porosity values obtained from corrosion potential determinations are in fairly good agreement with those obtained using a chemical etch technique described by Frant.

The corrosion potential technique offers the advantages of great simplicity and very high sensitivity, particularly at low porosities. The corrosion potentials of gold-plated copper specimens in 0.1M NH_4Cl electrolyte are affected by the pH of the electrolyte and by accumulation of cupric ions at concentrations in excess of 4×10^{-6}M. In common with other liquid-phase porosity test techniques, a limitation in detectability is imposed by the ability of the electrolyte to penetrate very fine or very deep pores.

Manuscript submitted Nov. 24, 1969; revised manuscript received Feb. 23, 1970.

Any discussion of this paper will appear in a Discussion Section to be published in the December 1970 JOURNAL.

List of Symbols

η_{corr}	Corrosion potential of a galvanic couple as measured with respect to the equilibrium potential of pure cathode material in the same electrolyte (V).
E_A	Corrosion potential of pure anodic material as measured with respect to the equilibrium potential of pure cathode material in the same electrolyte (V).
V_{corr}	Corrosion potential of a galvanic couple as measured with respect to a known reference electrode (V).
β_C	Cathodic Tafel slope (V).
β_A	Anodic Tafel slope (V).
i_{oC}	Cathodic exchange current density (A/cm²).
i_{oA}	Anodic exchange current density (A/cm²).
A_C	Cathode area function (dimensionless).
A_A	Anodic area fraction (dimensionless).

REFERENCES

1. N. Thon, *Proc. Amer. Electroplaters' Soc.*, **36**, 241 (1949).
2. H. H. Uhlig, Editor, "The Corrosion Handbook," pp. 953 ff, John Wiley & Sons, Inc., New York (1948).
3. H. W. Hermance and H. V. Wadlow, *Symposium on Rapid Methods for the Identification of Metals*, ASTM Special Technical Publication No. 98, A.S.T.M., Philadelphia, 1950, pp. 12 ff.
4. F. I. Nobel, B. D. Ostrow, and D. W. Thomson, *Plating*, **52**, 1001 (1965).
5. T. P. Hoar, *J. Electrodepositors' Tech. Soc.*, **14**, 42 (1938).
6. S. C. Shome and U. R. Evans, *ibid.*, **27**, 45 (1951).
7. R. A. Ehrhardt, *Proc. Amer. Electroplaters' Soc.*, **47**, 78 (1960).
8. G. G. Kamm, A. R. Willey, R. E. Beese, and J. L. Krickl, *Corrosion*, **17**, 84t (1961).
9. M. Clarke and S. C. Britton, *Trans. Inst. Met. Finishing*, **36**, 58 (1958).
10. M. Clarke and J. M. Leeds, *ibid.*, **43**, 50 (1965).
11. M. S. Frant, *This Journal*, **108**, 774 (1961).
12. M. Stern, *Corrosion*, **14**, 329t (1958).
13. F. Ogburn, D. W. Ernst, and W. H. Roberts, *Plating*, **46**, 1052 (1959).
14. M. Clarke and S. C. Britton, *Trans. Inst. Met. Finishing*, **37**, 110 (1960).

An Interrupter Technique for Measuring the Uncompensated Resistance of Electrode Reactions under Potentiostatic Control

J. D. E. McIntyre* and W. F. Peck, Jr.

Bell Telephone Laboratories, Incorporated, Murray Hill, New Jersey

ABSTRACT

A simple interrupter technique is described which permits the uncompensated resistance, R_u, in an electrochemical cell to be measured while the test electrode is under potentiostatic control. The ohmic potential drop, IR_u, can be monitored continuously as a function of the cell current, I, the d-c bias potential, and/or time.

In studies of the kinetics of electrode processes by modern potentiostatic techniques, a loss of control of the electrode potential can result from the ohmic potential drop associated with the flow of cell current, I, through the "uncompensated resistance" of the system (1). This uncompensated resistance, R_u, consists of the resistance of the electrolyte between the working electrode and the equipotential surface in the solution at which the Luggin capillary tip of the reference electrode is situated. It includes as well the resistance of the electrode itself and that of the lead connecting it to the potentiostat.

In measurements made with a constant or slowly varying d-c bias potential, the ohmic potential drop, IR_u, produces a distortion of the steady-state current-voltage (I-E) curves which, if uncorrected, will yield erroneous values of the characteristic kinetic parameters of the electrode reaction. The effects are even more serious for transient techniques such as rapid linear-scan or cyclic voltammetry since the I-E curves

* Electrochemical Society Active Member.

are further distorted by alteration of the voltage scan rate. In a-c measurements, the series combination of R_u and the double-layer capacity, C_{dl}, produces a phase shift between the actual electrode potential and the applied modulating voltage.

Several methods have been devised to correct for these undesirable effects. These include: (*i*) direct measurement of R_u by a-c bridge (2) or potential- or current-pulse techniques (3, 4) and subsequent correction of steady-state *I-E* curves; (*ii*) direct compensation by use of a resistance-bridge (5) or phase-reverter (6) circuits; (*iii*) direct compensation by means of positive feedback circuits (7-11); (*iv*) correction via electronic simulation and subtraction (12). The a-c bridge method is very accurate and properly takes into account the effects of shielding by the reference electrode probe; it is somewhat inconvenient to use. Positive feedback circuits automatically compensate for the ohmic potential drop, regardless of the magnitude of the current passed through the cell. The correct feedback setting can only be made, however, when there is negligible current flow through the cell. If the current distribution is nonuniform or varies with applied potential, the compensation is then only approximately correct. This method also fails when R_u changes with time as is the case for the dropping mercury electrode (DME). Further difficulties arise when cells with appreciable stray capacitance to ground are employed. In this case the additional phase shift can cause the potentiostat to burst into oscillation at a degree of positive feedback well below that required to compensate properly for R_u. For certain types of cells, overcompensation is possible (13).

Interrupter techniques, although widely used in the past to measure resistive overpotentials in galvanostatic experiments (14), have not been commonly employed for measurements on electrodes under potentiostatic control. For solid electrodes, they offer the possibility of measuring R_u and the ohmic potential drop directly as a function of applied potential. Changes in R_u can be ascribed to a variation of the current distribution on the surface or to the formation or removal of a surface film. In polarography, the variation in R_u can be detected as the mercury drop grows with time. When positive feedback circuitry is employed, the interrupter provides a convenient check on the degree of feedback required to compensate the ohmic potential drop correctly. In the present communication we describe the use of a simple potentiostatic interrupter technique which monitors IR_u continuously during the recording of a steady-state *I-E* curve.

Potentiostatic Interrupter Circuit

Figure 1 illustrates the circuit employed to interrupt the cell current momentarily. This circuit is a simple adaptation of a novel high-speed electronic switch devised by Warner and Schuldiner (15) to change from potentiostatic to galvanostatic control. In the present modification, the cell current is momentarily interrupted by applying a pulse of a few microseconds duration to the potentiostat input. The sign and magnitude of this pulse are such that the output of the control amplifier is driven to a voltage level sufficient to reverse-bias the diode, D1, connected in series with the counterelectrode. When the diode becomes nonconducting, the cell is isolated from the potentiostat control amplifier and is effectively "open-circuited." The voltage follower, *V*, detects the instantaneous change in potential, ΔE, caused by the removal of the ohmic potential drop, IR_u. This instantaneous change is followed by a much slower decay due to the discharge of C_{dl} through the Faradaic impedance of the electrode reaction. Knowing the cell current, *I*, and the potential change, ΔE, corresponding to the applied d-c bias potential, the value of R_u can be determined as a function of potential and/or time.

At the end of the pulse, diode D1 is restored to a conducting state, current flows again through the cell,

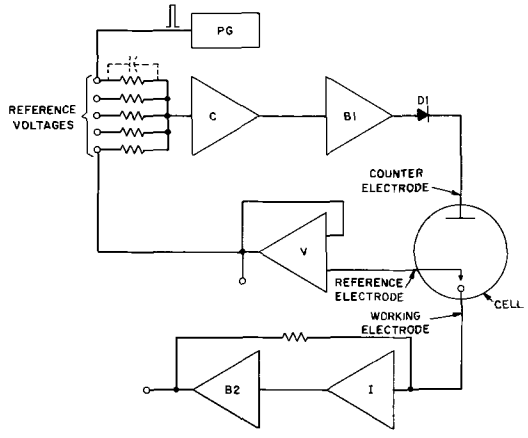

Fig. 1. Electrochemical cell and potentiostat with interrupter: C,I, Philbrick P45A operational amplifiers; V, Philbrick P25 operational amplifier; B1,B2, Booster amplifiers; D1, Western Electric 458A diode; PG, Tektronix Type 114 pulse generator.

and the potentiostat regains control. If the voltage pulse is sufficiently short, the decay of the electrode potential within its duration is very small, and the steady-state conditions of the reaction are not perturbed.

Faster "switch-off" times can be obtained by injecting a voltage pulse directly at the input of the booster amplifier, B1, as shown in Fig. 2. Amplifiers B1 and B2 consist of complementary pairs of npn and pnp transistors connected in a common emitter configuration (16) illustrated in Fig. 3. With this method, the pulse

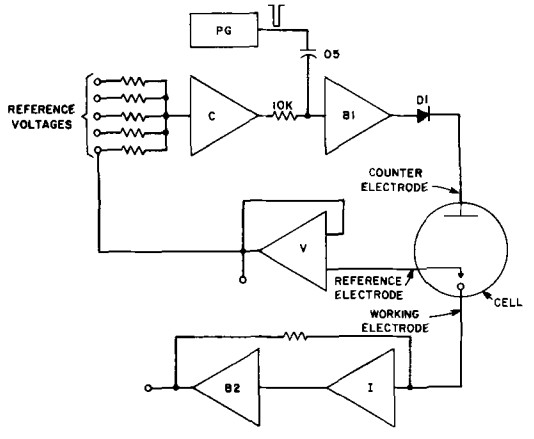

Fig. 2. Electrochemical cell and potentiostat with interrupter. Components are the same as in Fig. 1. Injection of pulse at input of B1 gives faster switch-off and recovery times.

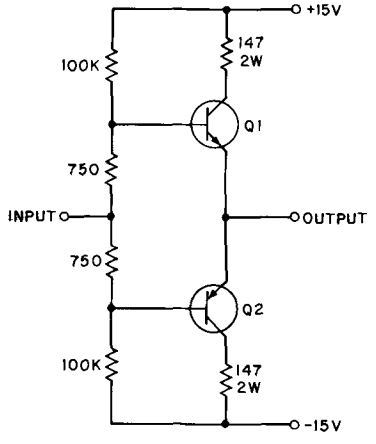

Fig. 3. Transistor booster amplifier: Q1, Western Electric 30A (npn); Q2, Western Electric 31A (pnp).

used must be larger and of polarity opposite to that employed with the circuit of Fig. 1. The pulse generator is isolated from the output of operational amplifier C by a blocking capacitor and series resistor.

The principal advantage of the second method is that the "switch-off" time is not dependent on the rise time of the summing amplifier. During the voltage pulse, the output voltage of "off-balance" amplifier C rises in an attempt to restore current through the cell. The output voltage of C thus remains positive and sufficiently high to restore D1 to its forward-biased state instantaneously when the pulse is removed. The potentiostat "recovery" time is thus shortened.

Anodic currents can be interrupted by a simple reversal of the diode and pulse-voltage polarity. The performance of the circuit of Fig. 2 is discussed below.

Circuit performance.—Figure 4 illustrates a network which simulates impedances found in a working electrochemical cell. Figure 5 shows the form of the potential relaxation observed at the output of voltage follower V when, with $R_u = 20$ ohms, a "cathodic" d-c current of 10.0 mA flowing through this circuit is interrupted by applying to the input of B1 a negative-going pulse of *ca.* −5V amplitude and 5 μsec duration. The initial rapid fall in potential represents the switch-off time of the system, *ca.* 0.2 μsec. The bottom flat section of the waveform represents the potential at point Y (Fig. 4), which decays with a time constant of 400 μsec. At the end of the pulse, the voltage at X rises rapidly, overshooting its initial value, and then decays back to its steady-state level. By substituting for R_u a series of standard resistors ranging from 1 to 100 ohms, it was ascertained that the value of the uncompensated resistance could be determined by this method with an accuracy of ~1%. To achieve this accuracy, the pulse repetition frequency must be low enough to allow amplifier ringing to decay completely after each pulse is applied.

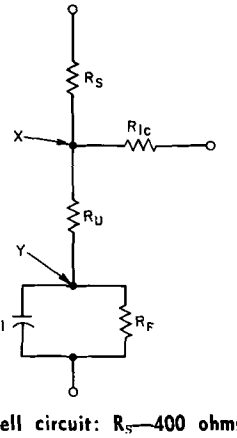

Fig. 4. Equivalent cell circuit: R_s—400 ohms; R_{lc}—20 kohms; C_{dl}—4 μF; R_F—100 ohms.

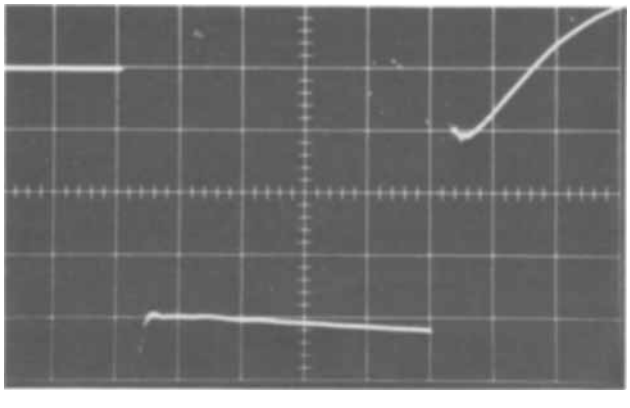

Fig. 5. Potential-relaxation waveform for equivalent cell circuit: I—10.0 mA, R_u—20.0 ohms; Y-axis, 50 mV/div; X-axis—1 μsec/div.

Figure 6 shows the form of the potential-relaxation waveform observed with an actual electrochemical cell. The working electrode was a gold rotating-disk electrode (RDE) of 0.32 cm^2 area immersed in oxygen-saturated 0.1*N* KOH. The platinum counterelectrode was isolated in a separate compartment by a fritted-glass disk, while the Hg/HgO reference electrode was isolated by a Teflon stop-cock. To avoid disturbance of the hydrodynamic streamlines at the RDE, the tip of the Luggin capillary was positioned *ca.* 0.75 cm below its surface. With the bias potential and rotational speed adjusted to give a limiting current of 1.00 mA, the value of the uncompensated resistance in this cell was found to be 17 ohms.

Although the design of this cell is far from optimal for rapid transient measurements, the switch-off time of this system is only 0.2 μsec. Best results are obtained by minimizing the length and capacitance of the shielded coaxial cable connecting the reference electrode to the voltage-follower input of the potentiostat. The effects of cable capacitance can be reduced by using a guard circuit to hold the shield at the same potential as the inner conductor, *i.e.*, at the reference electrode potential. This is conveniently accomplished by using a BNC connector with an isolated "ground" terminal (Dage Electric Co., Inc., Franklin, Ind., Model No. 4890-1) driven by the voltage-follower output. A significant reduction in recovery time and increased electronic stability was obtained by use of an auxiliary platinum-wire counterelectrode, positioned within a few centimeters of the working electrode and a.c.-coupled through a capacitor to the potentiostat output. This electrode affords a low-impedance by-pass path for transient currents and reduces the over-all time constant of the system. The response time of the system is the same regardless of whether or not the current follower is used. To avoid attenuation of the waveform amplitude, the resistance of the reference electrode probe arm should be made as small as possible. Luggin capillaries with closed isolating stop-cocks tend to act as low-pass filters for electrical signals.

No effect of the current interruption is observable in the recordings of the steady-state *I-E* curves measured with an RDE if the pulses are short and the time interval between pulses is longer than the sum of the pulse duration and the recovery time. Pulse durations of 5-10 μsec and a pulse repetition frequency of 0.1-1 kHz are generally suitable. The method can be used in a single-shot mode if a storage oscilloscope is employed.

The value of IR_u can also be monitored continuously as the direct current is altered. In Fig. 7, the vertical distance between the two traces represents the value of IR_u in the electrochemical cell; distance along the horizontal axis corresponds to the cathodic direct current flowing through this network. The diagonal trace in this photograph was formed by repeatedly interrupting the direct current as the latter was slowly

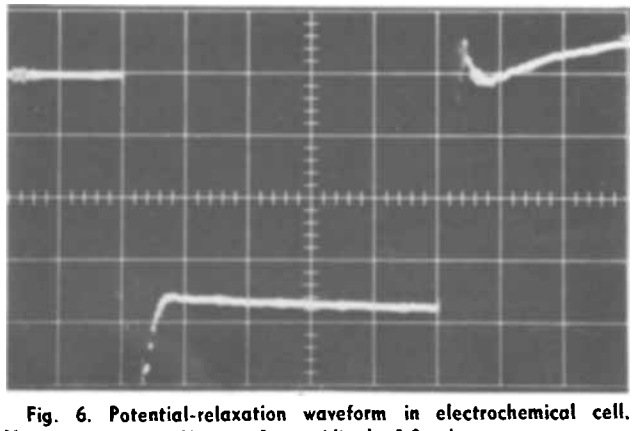

Fig. 6. Potential-relaxation waveform in electrochemical cell. Y-axis—5 mV/div; X-axis—1 μsec/div. I—1.0 mA.

varied from 0 to 1 mA. The oscilloscope beam intensity was simultaneously enhanced for the duration of each current interruption. Only the "flat" sections of the voltage pulses at the output of follower V exhibit sufficient intensity on the oscilloscope screen to register on the film. The slow variation in the d-c electrode potential is not recorded if the oscilloscope is a.c.-coupled to the output of V. A convenient horizontal reference trace is then obtained as shown in Fig. 7. At low current levels ($\sim$100 μA), the forward-biased diode resistance is too high for the potentiostat to maintain proper control and oscillation occurs. The instability of the potentiostat at low currents precludes the use of this technique at present for monitoring R_u in polarographic studies.

Discussion

The potentiostatic interrupter technique described in the preceding sections is particularly useful in studies of the kinetics of electrode reactions by the RDE method. Relatively high current densities can be attained with this method at high disk angular velocities. Since it is not desirable to position the reference electrode probe close to the surface of the RDE, ohmic potential drops can easily amount to 50-100 mV in solutions of moderately good conductivity (*e.g.*, 0.1M). The distortion of the steady-state I-E curves can readily be removed by analog simulation (12) or when the experimental data are subjected to computer analysis.

When appreciable overpotentials exist at the electrode surface due to activation or concentration polarization, the current distribution differs significantly from the primary distribution determined by the spreading resistance of the electrode (16). The equipotential contours in the electrolyte close to the electrode surface are distorted to force a higher current flow to the center of the disk. For electrode potentials in the limiting current region, the current distribution on the disk is uniform. The potential at the disk center is then 27% higher than the uniform surface potential associated with the primary current distribution, while the potential at the disk periphery is 18% lower. An intermediate situation exists when there is appreciable activation polarization. The possibility arises, therefore, of detecting a nonuniform current distribution by means of the potentiostatic interrupter technique.

In an experimental test, the value of R_u was measured at the quarter, half, and three-quarter wave points and in the limiting-current region of the steady-state I-E curve for oxygen reduction on a gold RDE. The probe tip was positioned 0.75 cm below the RDE surface. The value of R_u was observed to be constant over the entire I-E curve within the experimental precision of the measurements (*ca.* 2%). This apparent constancy of R_u is shown by the linearity of the diagonal trace of Fig. 7, which was obtained by continuously monitoring the values of IR_u and I as the potential was scanned through the wave.

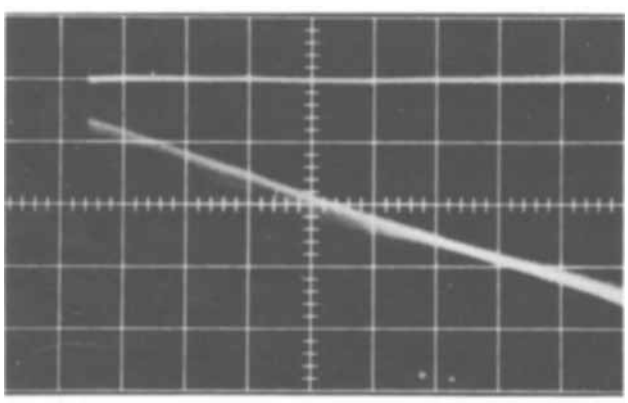

Fig. 7. Variation of ohmic potential drop in electrochemical cell with current. Y-axis—5 mV/div; X-axis—0.1 mA/div.

The observed constancy of R_u in the above experiment cannot, however, be taken as evidence of a uniform current distribution throughout the entire I-E curve. For the two extreme cases of the primary current distribution (uniform potential in the solution at the outer boundary of the diffusion layer) and the limiting-current distribution (uniform current density on the disk), significant differences in the measured ohmic potential drop to the center of the disk can only be detected when the probe tip is located at a distance within *ca.* 0.5 r_o of the disk surface, where r_o is the radius of the disk (17, 18). For the 0.25 in. diameter electrode employed, this would necessitate placing the probe tip at a distance less than 1.5 mm below the disk. This separation is independent of the electrolyte conductivity and so small as to cause distortion of the hydrodynamic and electrical current streamlines by geometric screening. Further, instability of the control system is likely to result when R_u becomes very small (19). In order to detect nonuniform current distribution on an RDE by this method, use of a large diameter disk ($r_o \geq 0.5$ in.) is indicated.

A second phenomenon will prevent detection of any alteration in R_u, however. Newman (20) has pointed out that if the potential across the surface is not uniform, the double-layer capacity is nonuniformly charged. When the direct current is interrupted, a transient current flows through the electrolyte from one section of the disk to another until the surface potential and charge become uniform. The relaxation time for this process is

$$\tau = r_o C/\kappa$$

where C is the specific double-layer capacity and κ is the specific conductivity of the electrolyte. With $r_o = 0.125$ in., $C \approx 20$ F cm^{-2} and κ (0.1N KOH) $= 0.024$ ohm^{-1} cm^{-1}, we have $\tau \approx 0.3$ msec, a time much longer than the duration of the interrupter pulse. As a result, the initial potential drop corresponds to the value of R_u associated with the primary current distribution, regardless of the actual current distribution on the disk before interruption. It is also this value of R_u which is measured by rapid pulse and high-frequency a-c methods as well as by positive feedback circuitry. The interrupter technique offers certain advantages over pulse or sinusoidal a-c methods since the latter require an accurate measurement of the transient current and are sensitive to the value of C_{dl} and the rise times of the pulse generator and potentiostat. The interrupter technique is not sensitive to these factors and requires only an accurate measurement of the d-c cell current.

Very brief current interruption times must be employed if perturbation of fast electrode reactions is to be avoided. With fast-rise potentiostats, amplifier ringing persists for 1 μsec or less. Interruption times of 5-10 μsec are then of sufficient length to permit the ohmic potential drop to be determined. The shorter the interruption time, the more rapid is the recovery of the potentiostat. Perturbation times associated with the voltage and current pulse methods are in general considerably longer. Interrupter measurements can only be made, of course, when there is an appreciable direct current flowing through the cell. This procedure should also be useful for potentiostats having relatively slow response times.

Acknowledgment

The authors wish to express their thanks to Dr. John Newman for helpful discussions.

Manuscript submitted July 1, 1969; revised manuscript received *ca.* Feb. 2, 1970.

Any discussion of this paper will appear in a Discussion Section to be published in the December 1970 JOURNAL.

REFERENCES
1. K. B. Oldham, *J. Electroanal. Chem.*, **11**, 171 (1966).
2. B. R. Sundheim, *This Journal*, **115**, 158 (1968).
3. C. C. Krischer and R. A. Osteryoung, *ibid.*, **112**, 735 (1965).
4. W. F. Mindt and H. Gerischer, Private communication.
5. T. Berzins and P. Delahay, *J. Am. Chem. Soc.*, **77**, 6448 (1955).
6. D. J. Kooijman and J. H. Sluyters, *Electrochim. Acta*, **11**, 1147 (1966).
7. G. L. Booman and W. B. Holbrook, *Anal. Chem.*, **35**, 1793 (1963).
8. G. Lauer and R. A. Osteryoung, *ibid.*, **38**, 1106 (1966).
9. E. R. Brown, T. G. McCord, D. E. Smith, and D. D. DeFord, *ibid.*, **38**, 1119 (1966).
10. J. D. E. McIntyre and W. F. Peck, Jr., Paper 96 presented at the Cleveland Meeting of the Society, May 5, 1966.
11. P. C. Milner and C. G. Enke, Private communication.
12. J. W. Hayes and C. N. Reilly, *Anal. Chem.*, **37**, 1322 (1965).
13. A Bewick, *Electrochim. Acta*, **13**, 285 (1968).
14. T. B. Warner and S. Schuldiner, *This Journal*, **114**, 359 (1967).
15. Department of the Army Technical Manual TM 11-690, "Basic Theory and Application of Transistors," p. 133, Headquarters, Department of the Army, Washington 25, D.C. (1959).
16. J. Newman, *This Journal*, **113**, 501 (1966); *ibid.*, **115**, 1235 (1966); *ibid.*, **114**, 239 (1967).
17. D. H. Angell, T. Dickinson, and R. Greef, *Electrochim. Acta*, **8**, 887 (1965).
18. J. Newman, Private communication.
19. G. L. Booman and W. B. Holbrook, *Anal. Chem.*, **37**, 795 (1965).
20. J. Newman, *This Journal*, **117**, 507 (1970).

Effect of Overpotential on the Temperature Dependence of the Electrolytic Hydrogen-Deuterium Separation Factor on Platinum

M. Hammerli, J. P. Mislan, and W. J. Olmstead

Atomic Energy of Canada Limited, General Chemistry Branch, Chalk River Nuclear Laboratories, Chalk River, Ontario, Canada

ABSTRACT

The temperature dependence of the electrolytic hydrogen-deuterium separation factor, S_D, was studied on bright platinum bead electrodes as a function of overpotential in 1.2*N* HCl-10% D_2O over the temperature range of 2°-80°C. As expected, S_D decreased with increasing temperature at a given overpotential. At each temperature, S_D increased as the overpotential corrected for *IR*-drop, η_{corr}, increased from $|-25$ mV$|$ to about $|-300$ mV$|$; from -300 mV to about -500 mV, the experimental limit, (which corresponds to $\eta_{appl} = 1.2$V) S_D remained constant within the ±5% reproducibility of the measurements. This behavior is attributed to a possible change in the mechanism of the hydrogen evolution reaction as $|\eta|$ is increased. The temperature coefficient of S_D is independent of η_{corr} within the experimental error. The Arrhenius activation energy difference between the hydrogen-deuterium and the hydrogen producing reactions, ΔE_A, is positive; ΔE_A decreases as $|\eta_{corr}|$ increases, but reaches a plateau value for $\eta_{corr} \geq |-300$ mV$|$. Conversely, the Arrhenius pre-exponential factor ratio, A_{H_2}/A_{HD}, increases over the same range of overpotentials before reaching a plateau value for $\eta_{corr} \geq |-300$ mV$|$. Comparison with published work is made.

The electrolytic hydrogen-deuterium separation factor, S_D, is defined as the atomic ratio of hydrogen to deuterium in the evolved gas divided by the atomic ratio of hydrogen to deuterium in the electrolyte. S_D has been studied as a function of temperature by several workers (1-5) on different cathode metals and in different electrolytes, usually with the aim of elucidating the mechanism of the much studied hydrogen evolution reaction. These studies were all carried out using constant current.

More recently, some workers have investigated the electrolytic hydrogen-deuterium separation factor as a function of the overpotential (6-10). As previously reported (11) we have studied S_D on bright platinum bead electrodes in 1.2*N* HCl-10% D_2O electrolyte as a function of the applied as well as the corrected overpotential, the latter quantity being equal to the applied overpotential minus the ohmic potential drop (henceforth called the *IR*-drop) due to the electrolyte resistance between the tip of the Luggin capillary and the cathode. It was clearly demonstrated that S_D is a function of the corrected overpotential under carefully controlled experimental conditions.

The present work was undertaken to determine if the temperature dependence of S_D was a function of the corrected overpotential, and to see if the Arrhenius activation energy difference for the H_2 and HD producing reactions was comparable to the theoretical maximum predicted by Rowland (1) on the basis of free atom reactions. It was also hoped that the Arrhenius pre-exponential factor ratio would possibly indicate the presence or absence of proton tunneling (12-15).

The Arrhenius factors may be evaluated from a temperature study of S_D as follows. In relatively dilute deuterium solutions (up to about 10% D_2O) the main species which undergo reduction in 1.2*N* HCl are H_3O^+ and H_2DO^+, and the main products are H_2 and HD. On this basis, Conway and Salomon (16, 17) have shown that

$$S_D = \left(\frac{D}{H}\right)_s \cdot 2\frac{[H_3O^+]}{[H_2DO^+]} \cdot \frac{f_{H_2DO^+}}{f_{H_3O^+}} \cdot \frac{f_{H_2}^{\dagger}}{f_{HD}^{\dagger}} \quad [1]$$

for the slow atomic hydrogen recombination or cata-

Key words: hydrogen, deuterium, separation factor, isotope separation, effect of temperature on, electrolysis, water, heavy water.

lytic mechanism (16) *viz.*

$$\left.\begin{aligned} &M-H+M-H \rightarrow H_2 \\ &M-H+M-D \rightarrow HD \end{aligned}\right\} \quad [2]$$

where M denotes the metal adsorption site for H or D and

$$S_D = \left(\frac{D}{H}\right)_s \cdot \frac{[H_3O^+]}{[H_2DO^+]} \cdot \frac{f_{H_2DO^+}}{f_{H_3O^+}} \cdot \frac{f_{H_2}^{\dagger}}{f_{HD}^{\dagger}} \quad [3]$$

for the slow atom-ion or electrochemical mechanism (16) *viz.*

$$\left.\begin{aligned} &M-H+H_3O^+ + e \rightarrow M + H_2O + H_2 \\ &M-D+H_3O^+ + e \rightarrow M + H_2O + DH \\ &M-H+H_2DO^+ + e \rightarrow M + H_2O + HD \end{aligned}\right\} \quad [4]$$

and for the slow proton discharge mechanism (17) *viz.*

$$\left.\begin{aligned} &M + H_3O^+ + e \rightarrow MH + H_2O \\ &M + H_2DO^+ + e \rightarrow MD + H_2O \end{aligned}\right\} \quad [5]$$

In Eq. [1] and [3], $(D/H)_s$ is the atom ratio of deuterium to hydrogen in the bulk solution (1.111 for 10% by volume D_2O), $[H_3O^+]/[H_2DO^+]$ is the concentration ratio of the H_3O^+ and H_2DO^+ ions in the solution, and the f-terms represent the appropriate partition functions of the indicated species, *e.g.*, $f_{H_2}^{\dagger}$ is the partition function for the activated complex leading to H_2 production. Since

$$k_{H_2}/k_{HD} = f_{H_2DO^+} f_{H_2}^{\dagger}/f_{H_3O^+} f_{HD}^{\dagger} \quad [6]$$

then Eq. [1] and [3] become

$$S_D = \left(\frac{D}{H}\right)_s 2\frac{[H_3O^+]}{[H_2DO^+]}\frac{k_{H_2}}{k_{HD}} \quad [7]$$

and

$$S_D = \left(\frac{D}{H}\right)_s \frac{[H_3O^+]}{[H_2DO^+]}\frac{k_{H_2}}{k_{HD}} \quad [8]$$

respectively; k_{H_2} and k_{HD} are the electrochemical rate constants for the H_2 and HD producing reactions respectively. Equations [7] and [8] can further be simplified, since

$$\left(\frac{D}{H}\right)_s = \frac{[HDO]}{2[H_2O] + [HDO]} \doteqdot \frac{[HDO]}{2[H_2O]} \quad [9]$$

i.e., $2[H_2O] >> [HDO]$. Therefore

$$S_D \doteqdot K_b\, k_{H_2}/k_{HD} \quad [10]$$

for the slow atomic hydrogen recombination mechanism, and

$$S_D \doteqdot K_b\, k_{H_2}/2\, k_{HD} \quad [11]$$

for the slow atom-ion and the slow proton discharge mechanisms, where K_b is the equilibrium constant for the reaction

$$H_2O + H_2DO^+ \rightleftharpoons HDO + H_3O^+ \quad [12]$$

i.e.

$$K_b = f_{HDO}\, f_{H_3O^+}/f_{H_2O}\, f_{H_2DO^+} \quad [13]$$

K_b can be evaluated from the partition function ratios as will be shown later, and therefore k_{H_2}/k_{HD} may be calculated once S_D has been measured. Using the well-known Arrhenius equation for the rate constant we obtain

$$\log_{10}\frac{k_{H_2}}{k_{HD}} = \log_{10}\frac{A_{H_2}}{A_{HD}} + \frac{\Delta E_A}{2.3\,RT} \quad [14]$$

after taking logarithms to the base 10. In Eq. [14], A_{H_2} and A_{HD} are the Arrhenius pre-exponential factors for the H_2 and HD producing reactions, respectively. The Arrhenius activation energy difference, ΔE_A, is defined as

$$\Delta E = E_A^{HD} - E_A^{H_2} \quad [15]$$

where E_A^{HD} and $E_A^{H_2}$ are the Arrhenius activation energies for the HD and H_2 producing reactions respectively. R and T have their usual significance. Both A_{H_2}/A_{HD} and ΔE_A are readily evaluated from a plot of $\log_{10}(k_{H_2}/k_{HD})$ *vs.* T^{-1} in the usual manner.

Experimental

The cell.—The cell and its operation for separation factor measurements have been described in detail in a previous paper (11). The following changes in the procedures reported there were made:

All data were obtained using the hydrogen reference electrode situated about 20 cm from the cathode and the smooth platinum bead cathodes described in (11). The reference electrode was effectively placed 1 mm from the cathode by means of a Luggin capillary. The pretreatment of the cathodes (geometric surface area $\simeq$0.06 cm^2) was changed for some experiments by eliminating the extraction of the cathode with warm electrolyte overnight in a Soxhelet extractor. For these experiments, the cathodes were placed in the cell as soon as possible after the hydrogen reduction step. No change in the reproducibility of the results was noted. On the contrary, the number of runs which produced spurious results decreased significantly to the point where only about one in twenty experiments had to be abandoned.

The second change involved the hydrogen reduction step of the cathode pretreatment. Instead of evacuating the oven before the cathode was allowed to cool to room temperature, the hydrogen atmosphere was maintained in the oven while the cathode cooled. In order to remove any hydrogen sorbed on the cathode, the assembly was evacuated for several hours to 10^{-6} mm Hg. This change did not affect the reproducibility or the absolute value of S_D measurements. All other procedures remained as described in (11) for the platinum bead cathodes, including the leaching-distillation pretreatment of the cell.

Anode.—The anode consisted of a strip of platinum gauze, 15 cm long and 4.5 cm wide (Johnson, Matthey and Mallory Unimesh No. Q2050, 48 mesh x 0.006 in.). This strip was wound into a roll, 0.5 cm in diameter and 4.5 cm wide, to which a platinum wire, 0.127 cm in diameter, was fastened at one end.

Chemicals.—The 1.2N HCl-10% D_2O electrolyte was prepared as described previously (11). The specific conductance of this electrolyte was 0.399 ohms^{-1} cm^{-1}.

Potential control.—For most of the results reported here, the applied overpotential, η_{appl}, was controlled by manually adjusting the current supplied by a galvanostat (Northeast Scientific Corporation, Model RI-234) to the cell while monitoring the reference electrode-cathode potential difference on a digital voltmeter (Fairchild, Model 7050). The current density based on the geometric surface area of the cathode varied from about 2 mA cm^{-2} at $\eta_{appl} = -25$ mV to about 3 A cm^{-2} at $\eta_{appl} = -1.0$V.

In practice, electrolysis was allowed to proceed until the current reached a steady state before the evolved hydrogen isotopes were collected for a separation factor measurement. A few minutes were necessary before this steady state was reached; once reached only minor, if any, current adjustments were found necessary to keep the desired applied overpotential constant during an electrolysis which lasted anywhere from 1 to 60 min depending on the applied overpotential. This procedure was found necessary because we have not yet been able to design a satisfactory transistor switch for obtaining IR-drop measurements using a potentiostat for potential control. Furthermore, it became apparent, as will be shown, that IR-drop measurements should accompany S_D measurements. The above procedure together with a transistor switch designed in our laboratory permitted the acquisition of *IR*-drop data immediately after a separation factor

determination. In fact, the electrolysis was terminated with the *IR*-drop meaasurement.

For comparison, however, some results based on potentiostatic control of η_{appl} as outlined previously (11) are included.

Temperature control.—The temperature of the cell was controlled to ±0.1°C by a circulating water bath. To prevent excessive liquid carry-over into the gas collection system during collection of the gas mixture (liberated hydrogen isotopes and argon sweep gas) a water cooled condenser was fitted onto the cathode compartment head. The temperature was monitored during several experiments by means of a platinum-10% rhodium 90% platinum thermocouple, placed about 2 mm from the cathode.

H/D *analyses.*—All gas samples were analyzed in triplicate on a CEC (Consolidated Electrodynamics Corporation) Model 21-130 mass spectrometer with a reproducibility better than ±1% in the H/D ratio.

IR-drop measurement.—To measure the *IR*-drop between the tip of the Luggin capillary and the working electrode a switch with an extremely rapid break time is ideal. The point where the potential decay due to double layer discharge and/or Faradaic discharge begin and where the *IR*-drop ends can then be readily determined. Existing solutions to this type of problem have generally involved mercury-wetted relays that have extremely rapid break times, but whose operate times of about 3-6 msec make it difficult to reduce switch times below 1 msec.

The switch used (Fig. 1) operates on a single pulse or continuous mode with a toggle frequency of about 5 MHz over the current range 0-800 mA and potential range 0-60V. The theoretical frequency response of the switch is 250 MHz which corresponds to a break time of 4 nsec. The practical response was about 200 nsec in the circuit shown schematically in Fig. 1.

Operation of the circuit depends on the fact that one state of the bistable or flip-flop circuit consisting of C_1, C_2, D_1, D_2, and E_3 turns on the transistors, Q_1 and Q_2, and the other state of the bistable circuit turns them off. When the transistors are conducting, the current source is short circuited to ground, but diodes D_3, since they will then be back biased, prevent the cell from also being short circuited. When the transistors are not conducting, current readily flows through the cell because diodes D_3 are then forward biased. In theory, micrologic elements E_1 and E_2 are not required, but in practice were found necessary to drive Q_1 and Q_2 completely to ground. E_1 and E_2 thus serve as buffer elements and ensure that enough current is supplied to Q_1 and Q_2. The micrologic elements are powered by two mercury batteries in series (B_1 and B_2) *i.e.*, by 2.7V. R_1 serves to isolate the bistable from the pulse generator.

The bistable was triggered by a Datapulse Type 101 pulse generator which is particularly suitable because it has a variable delay line built into one output channel. Thus, the Tektronix Type 581 oscilloscope with a Type 1A1 plug-in (rise time = 13 nsec at a sensitivity of 5 mV/division) could be triggered first and the applied overpotential recorded on the first part of the oscillogram before the current to the cell was switched with the delayed pulse to the bistable. The next pulse turns the transistor off and current to the cell is restored.

By operating the switch in the single pulse mode, it was possible to measure the *IR*-drop with a 1 μsec/division sweep rate and to terminate a given electrolysis simultaneously.

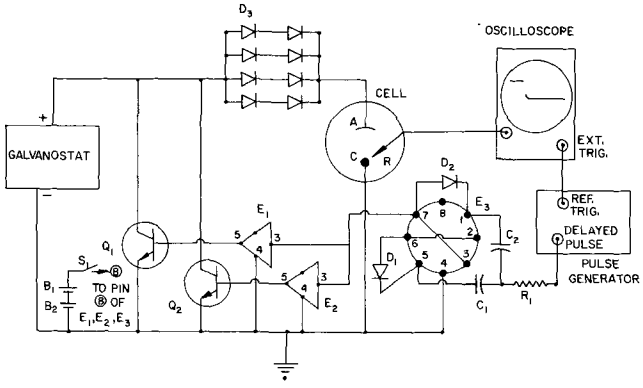

Fig. 1. Schematic of transistor switch, electrolysis cell and instruments used in *IR*-drop measurement. A, anode; C, cathode; R, reference electrode; B_1, B_2, 1.35V mercury batteries Type RM12R; C_1, C_2, 220 μμf capacitors; D_1, D_2, D_3, Type FD700 diodes; E_1, E_2, micrologic elements Type μl 900; E_3, micrologic element Type μl 914; Q_1, Q_2, transistors Type 2N2219; R_1, 68 kohm resistor; S_1, power switch.

Results and Discussion

S_D as a Function of η_{appl} and T.—The main result of our experiments concerning the effect of temperature on the relation between the separation factor, S_D, and η_{appl} on platinum electrodes immersed in 1.2*N* HCl-10% D_2O aqueous electrolyte, is that, as the temperature is increased from 2° to 80°C, the separation factor decreases fairly evenly over the range of applied overpotentials, $|-50\text{ mV}| \leq \eta_{appl} \leq |-1200\text{ mV}|$. Figure 2 shows this effect of temperature on the dependence of S_D on η_{appl} where η_{appl} was controlled potentiostatically (closed symbols), and where η_{appl} was controlled by manually adjusting the current output from a galvanostat (open symbols) as described in the experimental section. Within experimental error both methods produced the same values. The potentiostatic results at 25°C (closed circles) are those reported previously (11). All the results in Fig. 2 are within a ±5% reproducibility range, although the reproducibility was poorest at 2°C, possibly due to a greater influence of impurity sorption effects at the electrode-electrolyte interface. It is also interesting to note that on several occasions considerable dissolution of platinum occurred at the anode at 80°C and when platinum ions were allowed to reach the cathode where they were readily plated out, the separation factor decreased; at the same time the results became much less reproducible. Such results were discarded.

That S_D appears to decrease as $\eta_{appl} \geqq |-500\text{ mV}|$ for the 2° results we believe is due to local heating of the cathode and/or the electrolyte immediately adjacent to it. An increase in the effective temperature

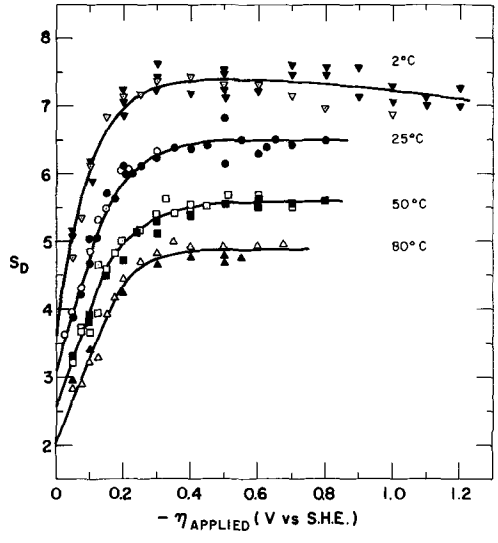

Fig. 2. Temperature dependence of the H/D separation factor as a function of the applied overpotential. Open symbols refer to galvanostatic control of the applied overpotential; closed symbols refer to potentiostatic control of the applied overpotential.

of 7°C can account for the observed drop in S_D from 7.35 at the maximum to 7.05 or about 4%, and in any case is within the limit of the reproducibility of the measurements. Nevertheless, it should be pointed out that a temperature measurement within about 2 mm of the cathode only showed an increase in temperature of a few tenths of a degree over the entire range of η_{appl}.

IR-drop measurements.—A typical oscillograph of the *IR*-drop between the cathode and the Luggin capillary is shown in Fig. 3. The *IR*-drop was measured from the horizontal line at the top, representing η_{appl} just before the anode-cathode circuit was broken, to the lower curve extrapolated back to where the potential difference fell. The small oscillations in the lower line are due to internal reflections in the coaxial lead cables which were kept as short as possible to minimize this effect. A 1 μsec/division sweep rate was used for all *IR*-drop measurements reported here. In this way *IR*-drops were readily measured at the end of an electrolysis to within ±3% for a given electrode in a given aliquot of electrolyte.

The *IR*-drop results are summarized in Fig. 4 in which η_{corr} is plotted as a function of η_{appl}. Because the results at different temperatures correspond to different cathode-Luggin capillary distances (about 1 mm), different cathodes, and different aliquots of electrolyte, some variation in the *IR*-drop would be expected. Evidently this variation is sufficiently large to mask completely the expected decrease in the *IR*-drop with increasing temperature due to an increase in conductivity of the electrolyte. Nevertheless, Fig. 4 clearly shows the importance of the *IR*-drop corrections at $\eta_{appl} \geq |-75\ mV|$ since these corrections approach 50% at $\eta_{appl} = -1000$ mV.

The effect of the *IR*-drop on the reproducibility of the separation factor-overpotential relationship is illustrated in Fig. 5 in which the closed and open triangles represent the applied and corrected overpotentials respectively. The importance of obtaining an *IR*-drop measurement for each specific S_D determination is shown clearly by the points 7 and 8 for example; for both, $\eta_{appl} = -300$ mV but $\eta_{corr} = -200$ mV and -150 mV, respectively. With the appropriate *IR*-drop correction, both S_D values fall on the smooth curve well within the estimated experimental error; as a function of the applied overpotential, they differ by about 7%. Points 1 and 2 further illustrate the advantage of obtaining *IR*-drop measurements coincident with S_D determinations as in this case the order in the magnitudes of the respective overpotentials is reversed when the *IR*-drop corrections are applied.

Although the *IR*-drop correction can be large, its effect on the dependence of S_D on overpotential is relatively small as seen in Fig. 6 (cf. Fig. 2) because S_D reaches a plateau. In Fig. 6 for reasons already stated, the 2°C curve is treated according to the dotted line.

Calculation of K_b.—Before the Arrhenius parameters can be obtained it is necessary to evaluate K_b (see Eq. [13] and *cf.* Eq. [10], [11], and [14]) as follows:

By applying the rule of the geometric mean (18) it can be shown that

$$f_{H_2DO^+}/f_{H_3O^+} = 3(f_{D_3O^+}/f_{H_3O^+})^{1/3} \qquad [16]$$

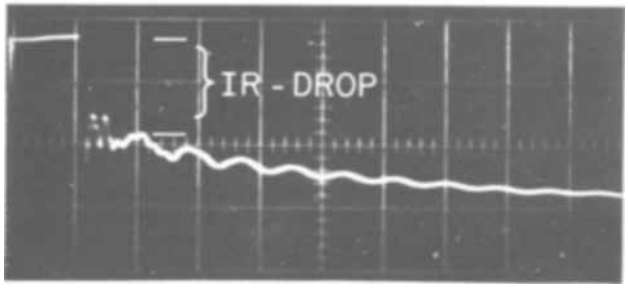

Fig. 3. Oscillograph of IR-drop for $\eta_{appl} = -680$ mV using the galvanostat; *IR*-drop = 300 mV and $\eta_{corr} = -380$ mV; ordinate = 200 mV/division; abscissa = 1 μsec/division.

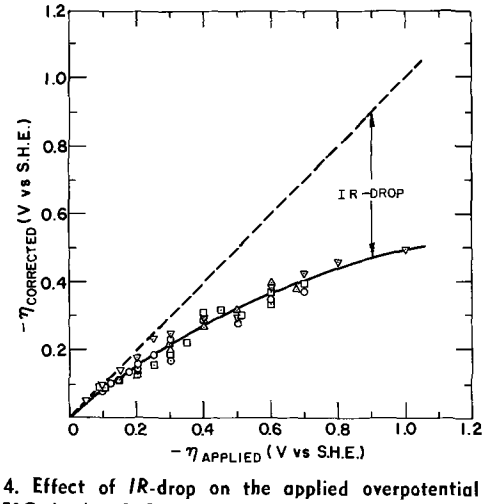

Fig. 4. Effect of *IR*-drop on the applied overpotential at 2°C (▽), 25°C (○), 50°C (□), and 80°C (△), respectively; ----, slope = 1.

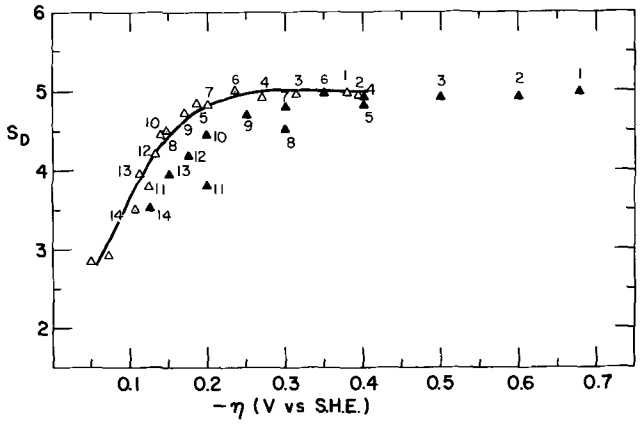

Fig. 5. Effect of *IR*-drop on the reproducibility of the H/D separation factor-overpotential relationship for 80°C. △, corrected for IR-drop; ▲, not corrected for IR-drop. Corresponding pairs of points have the same number.

Calculation of K_b (see Eq. [13] and *cf.* Eq. [10], [11], and [14]) as follows:

By applying the rule of the geometric mean (18) it can be shown that

$$f_{H_2DO^+}/f_{H_3O^+} = 3(f_{D_3O^+}/f_{H_3O^+})^{1/3} \qquad [16]$$

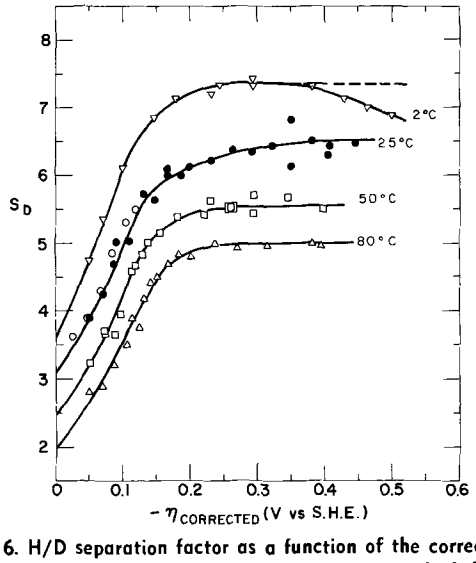

Fig. 6. H/D separation factor as a function of the corrected overpotential. Open symbols refer to galvanostatic control of the applied overpotential; closed symbols refer to potentiostatic control of the applied overpotential.

Table I. Evaluation of K_b for the reaction
$HDO + H_3O^+ \rightleftharpoons H_2O + H_2DO^+$

t°C	$(f_{D_3O^+}/f_{H_3O^+})$ [a]	$(f_{H_2DO^+}/f_{H_3O^+})$	(f_{D_2O}/f_{H_2O}) [a]	(f_{HDO}/f_{H_2O})	K_b
0	41.035	103.476	2550.9	97.933	0.9464
2	—	—	—	—	0.9436[b]
25	18.267	79.008	1394.2	72.400	0.9164
50	9.075	62.577	842.58	56.283	0.8994
75	4.910	50.991	550.46	45.493	0.8922
80	—	—	—	—	0.8915[c]

[a] Ref. (19).
[b] Interpolated.
[c] Extrapolated.

McIntyre and Salomon (19) have calculated f_{D3O+}/f_{H3O+} as well as f_{D2O}/f_{H2O} for the liquid phase as a function of temperature. Now consider the equilibrium

$$D_2O + H_2O \rightleftharpoons 2HDO \qquad [17]$$

for which the equilibrium constant for the liquid phase, K_w, is

$$K_w = f^2_{HDO}/f_{H2O}f_{D2O} \qquad [18]$$

so that

$$f_{HDO}/f_{H2O} = (K_w f_{D2O}/f_{H2O})^{1/2} \qquad [19]$$

K_w has recently been measured (20, 21) as a function of temperature. We have used $K_w = 3.76$ over our temperature range (2°-80°C) since the temperature dependence of K_w was found to be within the experimental error of the measurements (20). The values of K_b at 2° and 80°C were obtained by interpolating and extrapolating McIntyre and Salomon's data (19) for the temperature range 0°-75°C, respectively. The data are summarized in Table I.

Arrhenius parameters.—The Arrhenius plot for the activation energy difference between the hydrogen and the hydrogen-deuterium producing reactions[1] is shown in Fig. 7 as a function of the overpotential. Although the estimated errors are large (about ±10% for $\eta = 0$ and ±8% for the others) they are not shown in the interest of clarity. From the graph, it is obvious (*a*) that the positive slope, corresponding to a positive activation energy difference, becomes smaller as the cathodic overpotential increases and (*b*) that for $\eta_{corr} \geq |-300$ mV|, this difference remains constant. These facts are shown more clearly in Fig. 8 which is essentially a plot of the slopes of the lines in Fig. 7 as a function of η_{corr}.

Since the activation energy difference is positive and decreases as $|\eta_{corr}|$ increases, then, according to Eq. [15], the activation energy for the evolution of HD must be larger than that for the evolution of H_2 as expected, but must be decreasing relatively as $|\eta_{corr}|$ increases until $\eta_{corr} \geq |-300$ mV| where the activation energy difference becomes independent of overpotential. On the basis of the activation energy difference, therefore, S_D would be expected to decrease as $|\eta|$ is increased up to about |−300 mV| (see Eq. [10], [11], and [14]). Experimentally, the reverse is true. The explanation lies in the Arrhenius pre-exponential factor ratio.

If we extrapolate the curves in Fig. 7 to zero, *i.e.*, infinite temperature, we can estimate the behavior of the Arrhenius pre-exponential factor ratio, A_{H_2}/A_{HD}, for the H_2 and HD producing reactions, respectively, as a function of the corrected overpotential. As Fig. 9 shows, the pre-exponential factor ratio increases in an analogous manner as S_D itself. This increase more than offsets the tendency of the activation energy difference to decrease S_D as $|\eta|$ is increased, the net result being that S_D increases as $|\eta|$ increases up to about |−300 mV| for each temperature studied.

[1] For electrolytes of 10% D_2O content or less, the amount of D_2 liberated is negligible compared to HD.

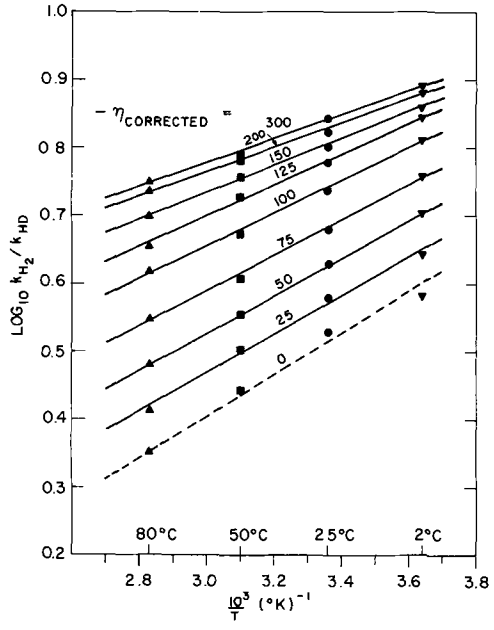

Fig. 7. Arrhenius plot as a function of the corrected overpotential on bright platinum bead electrodes in 1.2*N* HCl-10% D_2O for the temperature range 2°-80°C. - - - -, based on values of S_D extrapolated in Fig. 6.

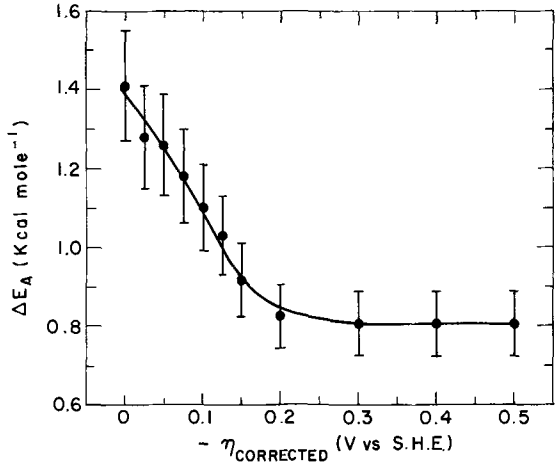

Fig. 8. Plot of the Arrhenius activation energy difference between the HD and the H_2 producing reactions as a function of the corrected overpotential (see Eq. [15]).

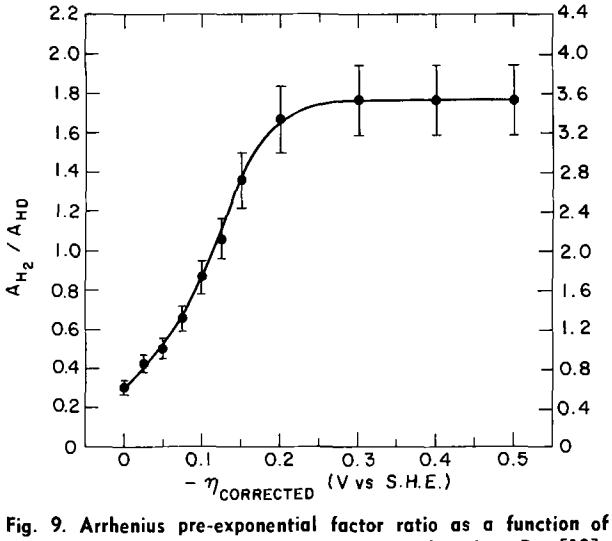

Fig. 9. Arrhenius pre-exponential factor ratio as a function of the corrected overpotential. Left-hand ordinate based on Eq. [10]; right-hand ordinate based on Eq. [11].

The fact that A_{H_2}/A_{HD} is less than unity for $0 \leq |\eta| \leq 110$ mV (see Fig. 9) based on the slow H-recombination mechanism and for $0 \leq |\eta| \leq 50$ mV based on the slow atom-ion and discharge mechanisms, may be interpreted as evidence for some proton tunneling in the proton discharge step according to Christov's theory (15). But in these overpotential regions the Tafel slope at 25°C (11) is −29 mV which conflicts with Conway's (12) theoretical prediction that the Tafel slope should be anomalously large (2 to 3) if proton tunneling is significant. We have found such high Tafel slopes (11), but for $|\eta| \geq 150$ mV where $A_{H_2}/A_{HD} > 1$ for which it is not necessary to invoke quantum effects. However, the authors do not intend to discuss the merits of the various proton tunneling theories; for this purpose the reader is referred to ref. (22).

Comparison with published results.—The fact that S_D increases as $|\eta|$ is increased and then reaches a plateau for each temperature studied may be due to a change in the mechanism, a change in the rate-determining step, or both (23). Our results at 25°C compare favorably with the theoretical calculations that include proton tunneling corrections (24). For 25°C Bockris and Srinivasan obtained $S_D = 3.0$ for the slow proton discharge followed by fast H-recombination mechanism while for the fast proton discharge followed by slow atom-ion desorption mechanism, $S_D = 5.5$. The experimental values are 3.2 ± 0.3 and 6.5 ±0.33 at $\eta = 0$ and $\eta > |-300$ mV|, respectively.

However, if we assume proton tunneling is absent, then it is possible to assign at least one other mechanism (24) for $\eta \to 0$. This mechanism is linked proton discharge-atom-ion desorption with either rate determining for which $(S_D)_{calc.} = 3.4$ based on 100% coulombic energy for all interactions and 3.6 based on 20% coulombic energy for M-H and H^+-OH_2, and 15% for H-H interactions. But, whether one argues for or against proton tunneling, a change in the mechanism as the cathodic overpotential is increased can account for the observed dependence of S_D on η.

Alternatively, the Tafel slope of −29 mV for $|\eta| \leq 75$ mV (11) has been attributed to slow H-recombination (25, 26), and this conclusion has been supported by Salomon and Conway's calculations (16). The fact that our Tafel slope approached $-\infty$ where S_D reached a plateau (11) may be indicative of a rate-controlling H-recombination step under Langmuir type adsorption when the hydrogen coverage approaches unity (26). Thus we have presumably explained the Tafel behavior based on a single mechanism and rate-determining step over an overpotential range where S_D about doubles before reaching a plateau. Therefore it is necessary to assume that the change in S_D results from changes in the relative adsorption-combination rates leading to H_2 and HD, respectively, as a function of total coverage of H and D which must be potential dependent to explain the results. This hypothesis is difficult to accept under Langmuir adsorption conditions where the adsorption energy is assumed to be independent of coverage. Tafel slopes alone may therefore be misleading in determining the mechanism of the hydrogen evolution reaction.

Within the experimental error of the measurements the temperature coefficient, dS_D/dT, of S_D is independent of η_{corr} as well as temperature. These results are presented in Table II along with those of Walton and Wolfenden (5) and those of Raman *et al.* (2) for alkaline solutions. The agreement between the three sets of results is good in view of the large errors and the different experimental conditions used. Our results suggest that perhaps dS_D/dT decreases as the temperature increases while those of Raman *et al.* suggest just the opposite. In both cases, the trends are within the experimental errors themselves. Although both the Arrhenius activation energy difference and the ratio of the pre-exponential factors are functions of η_{corr}, the net effect on the temperature coefficient is negligible since these dependencies are in opposite directions.

Table II. Comparison of temperature coefficients of S_D on platinum

Electrolyte	Temperature range, °C	$\frac{\Delta S_D}{\Delta T}$, deg^{-1}	Ref.
0.2 to 0.5N H_2SO_4 30 to 50 vol % D_2O	20-85	−0.028	(5)
1.2N HCl	2-25	−0.041 ± 0.019	This work
10 vol % D_2O	25-50	−0.030 ± 0.008	
	50-80	−0.019 ± 0.007	
15% KOH	30-40	−0.027	
10 vol % D_2O	40-50	−0.028	(2)
	50-60	−0.039	

Our results can be described by the following limit lines

$$k_{H_2}/k_{HD} = 0.30 \exp(1380 \text{ cal}/RT) \text{ at } \eta = 0, \text{ and}$$
$$k_{H_2}/k_{HD} = 1.77 \exp(815 \text{ cal}/RT) \text{ at } |\eta| \geq 300 \text{ mV}$$

based on the slow H-recombination mechanism (Eq. [10])

$$k_{H_2}/k_{HD} = 0.61 \exp(1380 \text{ cal}/RT) \text{ at } \eta = 0, \text{ and}$$
$$k_{H_2}/k_{HD} = 3.54 \exp(815 \text{ cal}/RT) \text{ at } |\eta| \geq 300 \text{ mV}$$

based on the slow atom-ion and proton discharge mechanisms (Eq. [11]). If we assume that K_b is about one (see Table I) over the whole temperature range, then the above limit lines for the slow H-recombination mechanism may be compared with Rowland's theoretical datum (maximum S_D) line 1 based on the postulate of free atoms at the electrode-electrolyte interface, and given by the expression: $S_D = 0.53 \exp(1840/RT)$. Certainly at the higher cathodic overpotentials our experimental activation energy difference is smaller than Rowland's theoretical one. Also, the theoretical value of the pre-exponential factor ratio is included in the experimental ones for the slow H-recombination mechanism but not for the slow atom-ion and proton discharge mechanisms.

Finally, it should be mentioned that our results at all temperatures disagree with those of Bockris *et al.* (23) at room temperature for the H/T separation factor, S_T. These authors claim that S_T on platinum in 1.0*N* HCl is independent of overpotential in the range −45 to −190 mV. This is precisely the range where S_D varies the most according to our results. Roy (3) found a linear correlation between the H/D, H/*T*, and D/*T* separation factors in alkaline solution on iron cathodes in good agreement with the theoretical predictions of Bigeleisen (27). Intuitively, it seems reasonable to expect a similar relationship for acid solutions and platinum cathodes since separation factors are ratios and not absolute quantities. To explain this discrepancy we have to assume that their electrode surfaces and/or experimental techniques were radically different from ours. It is difficult to assess this possibility since Bockris *et al.* give no experimental details or references for their HCl results on platinum.

Conclusions

1. Carefully controlled experiments yield reproducible (±5%) S_D values on smooth platinum electrodes in 1.2*N* HCl-10% D_2O.

2. In our system, *IR*-drops at a given applied overpotential could vary with time on the same electrode in the same aliquot of electrolyte. The reason for this behavior is not clear. Accordingly, the *IR*-drop was measured for each individual S_D determination.

3. The Arrhenius parameters are a function of overpotential. Agreement between our Arrhenius parameters and the theoretical ones based on Rowland's theory (1) is not too good. The pre-exponential factor ratio, A_{H_2}/A_{HD}, was less than unity for small cathodic overpotentials which may be indicative of some proton tunneling.

4. Experimentally, S_D increased as the cathodic overpotential was increased, and then reached a plateau at about $|\eta| \geqq 300$ mV at all temperatures. This behavior is best interpreted on the basis of theoretical calculations (24), as indicative of a change in the mechanism from slow proton discharge followed by fast H-recombination at $\eta \doteqdot 0$ to fast proton discharge followed by slow atom-ion desorption.

5. Within the experimental error dS_D/dT is independent of overpotential as well as temperature and agrees with other work.

Acknowledgments

The authors remain indebted to Dr. M. Salomon for many helpful criticisms of the manuscript. They are also most grateful to Mr. E. B. Selkirk who designed the transistor switch and to Mr. J. G. Wesanko who constructed the electrolysis cell.

Manuscript submitted Sept. 8, 1969; revised manuscript received *ca.* Feb. 11, 1970.

Any discussion of this paper will appear in a Discussion Section to be published in the December 1970 JOURNAL.

List of Symbols

S_D,	electrolytic hydrogen-deuterium separation factor
$(D/H)_s$,	atomic ratio of deuterium to hydrogen in the bulk solution
f_n,	partition function of species n
$f_n^\dagger$,	partition function of the activated complex n
k_{H_2}, k_{HD},	over-all electrochemical rate constants for the H_2 and HD producing reactions, respectively
K_b, K_w,	equilibrium constants defined by Eq. [13] and [18], respectively
A_{H_2}, A_{HD},	Arrhenius pre-exponential factors for the H_2 and HD producing reactions, respectively
ΔE_A,	Arrhenius activation energy difference between the HD and H_2 producing reactions
$E_A^{H_2}$,	Arrhenius activation energy for the H_2 producing reaction
E_A^{HD},	Arrhenius activation energy for the HD producing reaction
R,	gas constant
T,	absolute temperature
η_{appl},	applied overpotential with respect to the standard hydrogen electrode
η_{corr},	applied overpotential minus the ohmic potential drop between the tip of the Luggin capillary and the cathode
$\Delta S_D/\Delta T$,	experimental change in the electrolytic hydrogen-deuterium separation factor over a finite temperature range

REFERENCES

1. P. R. Rowland, *Nature*, **218**, 945 (1968).
2. M. S. Raman, R. Kumar, and R. L. Datta, *Z. Naturforsch.*, **18a**, 347 (1963).
3. L. P. Roy, *Can. J. Chem.*, **40**, 1452 (1962).
4. J. Brun and Th. Varberg, *Kgl. Norske Videnskab. Selskabs. Forh.*, **26**, 19 (1953) [*C.A.* 49: 11468e].
5. H. F. Walton and J. H. Wolfenden, *Trans. Faraday Soc.*, 34, 436 (1938).
6. G. P. Lewis and P. Ruetschi, *J. Phys. Chem.*, **66**, 1487 (1962).
7. W. Vielstich, T. H. Schuchardt, and M. Von Stackelberg, *Z. Elektrochem.*, **67**, 645 (1963).
8. H. von Buttlar, W. Vielstich, and H. Barth, *ibid.*, **67**, 650 (1963).
9. M. Salomon and B. E. Conway, *J. Phys. Chem.*, **68**, 2009 (1964).
10. T. Yokoyama, *J. Res. Inst. Catalysis, Hokkaido Univ.*, **15**, 84 (1967).
11. H. Hammerli, J. P. Mislan, and W. J. Olmstead, *This Journal*, **116**, 779 (1969).
12. B. E. Conway, *Can. J. Chem.*, **37**, 178 (1959).
13. M. Salomon and B. E. Conway, *Discussions Faraday Soc.*, **39**, 223 (1965).
14. J. O'M. Bockris and D. B. Matthews, *J. Chem. Phys.*, **44**, 298 (1966).
15. St. G. Christov, *Electrochim. Acta*, **4**, 306 (1961).
16. M. Salomon and B. E. Conway, *Z. Elektrochem.*, **69**, 669 (1965).
17. B. E. Conway and M. Salomon, *ibid.*, **68**, 331 (1964).
18. C. G. Swain, R. F. W. Bader, and E. R. Thornton, *Tetrahedron*, **10**, 200 (1960).
19. J. D. E. McIntyre and M. Salomon, *J. Phys. Chem.*, **72**, 2431 (1968).
20. J. Friedman and V. J. Shiner, Jr., *J. Chem. Phys.*, **44**, 4639 (1966).
21. J. W. Pyper, R. S. Newbury, and G. W. Barton, Jr., *ibid.*, **46**, 2253 (1967).
22. General Discussion, *Discussion Faraday Soc.*, **39**, 253 (1965).
23. J. O'M. Bockris, E. Gileadi, and R. Haynes, *J. Electroanal. Chem.*, **19**, 446 (1968).
24. J. O'M. Bockris and S. Srinivasan, *Electrochim. Acta.*, **9**, 31 (1964).
25. J. O'M. Bockris and A. M. Azzam, *Trans. Faraday Soc.*, **48**, 145 (1952).
26. B. E. Conway and M. Salomon, *Electrochim. Acta*, **9**, 1599 (1964).
27. J. Biegeleisen, Tritium Phys. Biol. Sci., Proc. Symp., Vienna, Austria, 1961; **1**, 161 (Pub. 1962) [*C.A.* 57: 11901a].

Oxidation and Adsorption of Ammonia on a Platinized Platinum Electrode

Kazuo Sasaki and Yoshiro Hisatomi

Department of Applied Chemistry, Hiroshima University, Hiroshima, Japan

ABSTRACT

The electro-oxidation and adsorption of ammonia in aqueous alkaline solution on a platinized platinum electrode has been investigated by using the potentiodynamic technique. For comparison, the oxidation of hydroxylamine as well as potassium nitrite was also studied. It was concluded that the primary step of ammonia oxidation involves one electron. The primary product was relatively stable, indicating that the rate-determining step is one of the later steps of the net reaction. Pavela's method was used in conjunction with the potentiodynamic technique to study the adsorption of ammonia. The adsorption was found to be in accord with Temkin's isotherm, and the surface coverage of adsorbed ammonia was found to be about 0.3 at saturation.

It is generally accepted that many organic amino compounds adsorbed on a metal surface inhibit corrosion (1). Little is known, however, about the adsorption of ammonia, the simplest amino compound, on a metal surface from aqueous phase. In the present paper, the oxidation and adsorption of ammonia on a platinized platinum electrode in a potassium hydroxide solution has been studied.

Experimental Description

Aqueous 1M potassium hydroxide solution was the base solution throughout the experiments. All reagents were used without further purification. A cylindrical glass cell with a volume of 50 ml was used as the electrolytic cell. Electrodes were platinized platinum wires. In contrast to the ordinary cell system, a dummy electrode of a size similar to the working electrode was installed to start the potential sweep from any desired potential (Fig. 1).

In an actual experiment, the potentiostat was connected initially to the dummy electrode, and the potential sweep was run with this electrode. When the potential of the dummy electrode reached the desired value, the circuit was switched rapidly to the working electrode by a relay, leaving the dummy electrode at open circuit.

Measurements usually were made at 20°C. Potential values in this paper are referred to a "dynamic hydrogen electrode" (2) in 1M potassium hydroxide solution. Solutions were deaerated by bubbling nitrogen.

In order to determine the amount of ammonia adsorbed, Pavela's method (3) was used in conjunction with the potentiodynamic technique. The working electrode was first subjected to alternate cathodic and anodic polarization in the base solution to clean the surface. This pretreatment was continued until the shape of the current-potential curve no longer changed. The sweep was finally stopped at 0.5V in an anodic half cycle, where the electrode surface is free from both adsorbed hydrogen and oxygen. The electrode thus obtained was immersed in a solution containing the adsorbent. After a given time, the electrode was withdrawn from this bath and washed to minimize the amount of adhering solution. After washing, the test electrode was put into the electrolytic cell containing fresh base solution in order to study the electrochemical behavior of the ad-species.

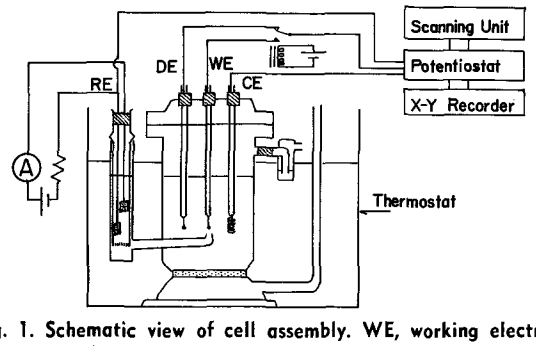

Fig. 1. Schematic view of cell assembly. WE, working electrode; RE, reference electrode; CE, counterelectrode; DE, dummy electrode.

The amount of adsorbed species was determined from the difference between the anodic charges which were obtained from current-potential curves measured with and without adsorption. After transferring the test electrode from the adsorption bath to the electrolytic cell, three kinds of potential sweeps were employed: (*i*) sweep started at 0.5V toward more positive potentials, (*ii*) sweep started at 0.5V toward more negative potentials, and (*iii*) anodic sweep started, with the aid of the dummy electrode, from the negative end of the hydrogen wave at 0.15V.

Using sweep (*i*), it was possible to find the total charge required to oxidize the adsorbed species. From sweep (*ii*) information on the oxidation state of the adsorbed species was gathered. Finally, with the aid of sweep (*iii*), the surface coverage of the adsorbed species was obtained from the decrease of the hydrogen wave. In actual experiments, combinations or modifications of these three sweeps were frequently employed.

After studying the effect of the washing time on the anodic stripping of adsorbed ammonia, the washing procedure was standardized as follows. After drawing the electrode out of the adsorption bath it was washed for 1 min by pouring a large quantity of the base solution over it and then rinsed for 2 min in a fresh base solution stirred with nitrogen.

Results and Discussion

Anodic oxidation of ammonia.—Cyclic current-potential curves in solutions with and without ammonia are shown in Fig. 2. An anodic current peak (Pa) appears prior to the formation of platinum surface oxide, and a sharp cathodic current peak (Pc1) appears in the potential range of hydrogen adsorption in the presence of ammonia. In contrast to the regular curve in solutions containing no ammonia (dashed line), the cathodic current peak for the reduction of platinum surface oxide is suppressed significantly by the presence of ammonia. The current peaks at Pa and Pc1 were found not only with ammonia but also with solutions containing either hydroxylamine (Fig. 4) or potassium nitrite (Fig. 5). Both peaks, Pa and Pc1, were proportional to the square root of the sweep rate indicating that the rate of reaction at these potentials is limited by diffusion (4).

Current-potential curves obtained at various potentials of sweep reversal are shown in Fig. 3. It is inter-

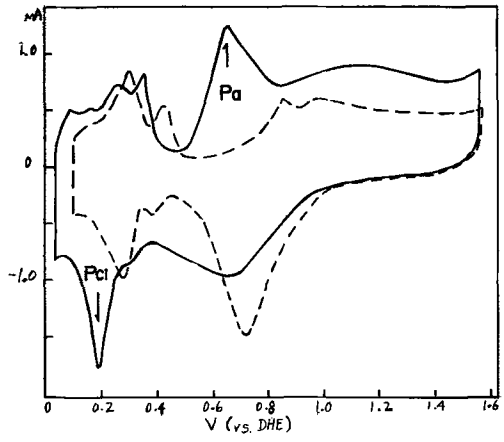

Fig. 2. Cyclic current-potential curves with and without ammonia. Solid line, with solution containing $1x10^{-2}$M ammonia; dashed line, 1N KOH base solution; sweep rate, 50 mv/sec.

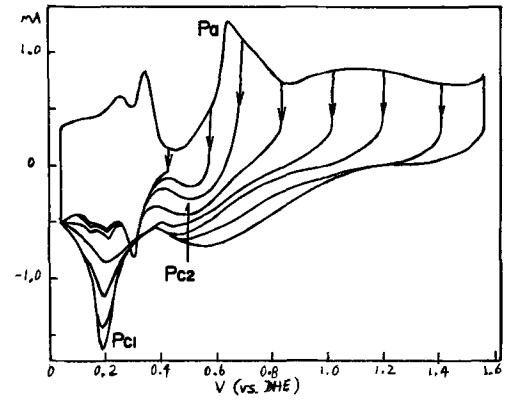

Fig. 3. Cyclic current-potential curves at various potentials of sweep reversal. Concentration of ammonia, $1x10^{-2}$M; sweep rate, 50 mV/sec.

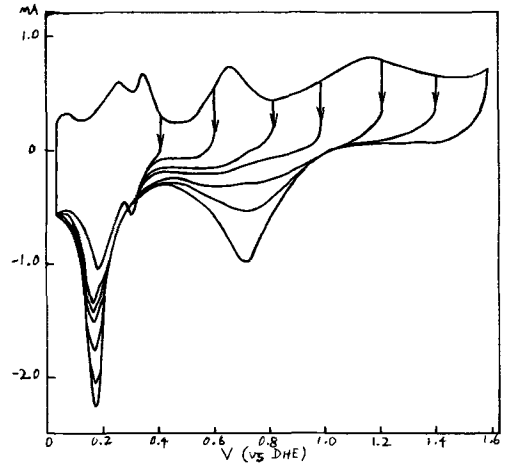

Fig. 4. Cyclic current-potential curves in a hydroxylamine solution. Hydroxylamine, $1x10^{-2}$M; sweep rate, 50 mV/sec.

esting to note that a characteristic cathodic peak, Pc2, is observed. Although this peak is not particularly sharp, it is suggested that the peak represents the reverse reaction of the one at Pa. This is illustrated in Fig. 6. The cathodic and anodic potentials of sweep reversal were fixed at 0.55 and 0.75V, respectively, in the potential range of Pa. The quantities of electricity during the anodic and cathodic half cycles changed with the sweep rate. The ratio of these two quantities, $Q(Pa)/Q(Pc2)$, decreased from 4.45 at 25 mV/sec to 1.25 at 200 mV/sec, suggesting that the ratio converges to unity at higher sweep rates. Values of the charge ratio are given in the caption of Fig. 6.

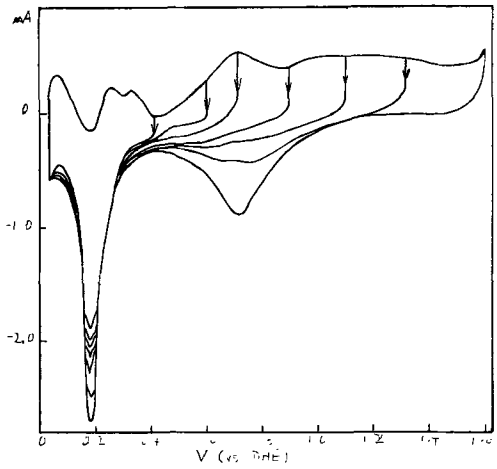

Fig. 5. Cyclic current-potential curves in a potassium nitric solution. Potassium nitric, $1x10^{-2}$M; sweep rate, 50 mV/sec.

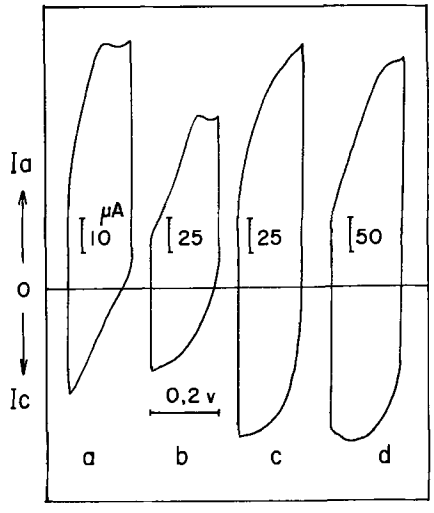

Fig. 6. Cyclic current-potential curves in an ammonia solution when cycle was repeated in potential range of Pa at various sweep rates. Area of electrode estimated from hydrogen wave was 5.45 cm^2. Concentration of ammonia was $5x10^{-3}$M. Sweep rates were 25, 50, 100, and 200 mV/sec for curves a, b, c, and d, respectively. Corresponding values of charge ratio, Qa/Qc, were 4.45, 1.93, 1.55, and 1.23, respectively.

The peak, Pc2, was characteristic of ammonia solution. When hydroxylamine or potassium nitrite were used instead of ammonia, the cathodic peak corresponding to Pc2 was no longer present (Fig. 4 and 5). This is more clearly illustrated in Fig. 7[1] where the effect of sweep rate on the shape of current-potential curves in a hydroxylamine solution is shown. In contrast to ammonia, the primary oxidation product of hydroxylamine undergoes further oxidation and no cathodic current is observed at sweep rates lower than 100 mV/sec. In addition, the peak height of the cathodic current in the hydrogen wave, Pc1, increased markedly with increasing potential of reversal (see Fig. 3). The cathodic current in this region was also observed as a strong peak with solutions containing either hydroxylamine or potassium nitrite (Fig. 4 and 5). With solutions of hydroxylamine, the peak was found even when a cathodic sweep was started from the positive end of the hydrogen wave, where hydroxylamine could not be oxidized to any degree. Several conclusions can be drawn from these observations:

[1] Although the electrode used to obtain the results in Fig. 6 and 7 was the same, having a geometric area of 0.014 cm^2, the real areas were different from each other owing to the aging of platinum black. The roughness factors of the electrode surface estimated from the hydrogen wave were 418 and 57.4 for the experiments of Fig. 6 and 7, respectively.

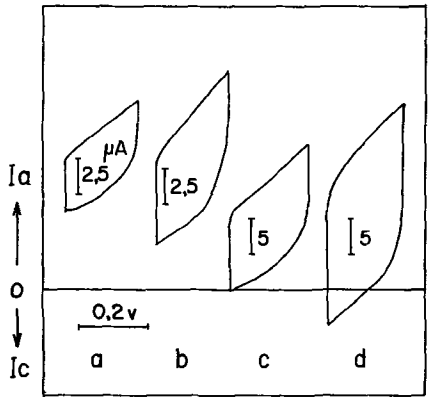

Fig. 7. Cyclic current-potential curves in a hydroxylamine solution at various sweep rates. Sweep range was fixed in potential range of Pa. Concentration of hydroxylamine, 5.10^{-3}M. Sweep rates were 25, 50, 100, and 200 mV/sec for curves a, b, c, and d, respectively. Area of electrode, 0.803 cm^2.

(*i*) The oxidation of ammonia is not complete, and some intermediates such as hydroxylamine or nitrite are produced partly and diffuse into the solution under the condition of cyclic voltammetry. (*ii*) Hydroxylamine as well as nitrite anion are reduced at potentials of the hydrogen region. (*iii*) The species responsible for the reaction at Pc2 is different from hydroxylamine, which is the reduction product of ammonia by a two-electron process; it is more likely to be an intermediate produced from ammonia by a one-electron process.

If the species responsible for Pc2 is the one-electron product then the charge ratio, $Q(\text{Pa})/Q(\text{Pc2})$, should vary, depending on the stability of the Pc2 species. The ratio must become larger than two when the Pc2 species is relatively unstable because the successive steps proceed at a faster rate than the initial one-electron step. The results summarized in Fig. 6 show that the ratio is less than two when the sweep rate exceeds 50 mV/sec and approaches unity. An extrapolation indicated that the ratio becomes unity when the sweep rate exceeded 400 mV/sec, suggesting that the life time of the primary oxidation product is in the order of 1 sec.

Undoubtedly, however, the primary product is not extremely stable, and actual oxidation proceeds further. Nitrogen was evolved when the oxidation was subjected to a prolonged treatment even at the potential range of Pa. Katan and Galiotto (6) and Wynveen (7) established the following net reaction

$$NH_3 + 3\,OH^- \rightarrow 1/2N_2 + 3H_2O + 3e$$

Based mainly on the analogy to the gas phase reaction, Oswin and Salomon (5) proposed the following sequence of reactions

$$NH_3 + M + OH^- \rightleftarrows M - NH_2 + H_2O + e \quad [1]$$

$$M - NH_2 + OH^- \rightarrow M = NH + H_2O + e \quad [2]$$

$$M = NH + OH^- \rightarrow M \equiv N + H_2O + e \quad [3]$$

$$M \equiv N + M \equiv N \rightarrow 2M + N_2 \quad [4]$$

According to this mechanism, reaction [2] is rate determining, and the primary step [1] is in quasi-equilibrium. This is in accordance with the present results.

Adsorption of ammonia.—When the cyclic potential sweeps were applied in solutions containing ammonia, the current peak corresponding to the oxidation of ammonia was always greater in the first sweep than the successive cycles. Probably this indicates that a finite amount of ammonia adsorbed on the platinum surface during the waiting time before the measurements. In order to confirm this, a series of experiments based on Pavela's method were conducted. Adsorption was carried out in a separate bath containing different concentrations of ammonia, and the stripping was carried out in a fresh base solution.

A typical example of the anodic stripping of adsorbed ammonia is shown in Fig. 8 by the curve represented by the solid line. The presence of adsorbed ammonia is clearly indicated by an anodic current peak located in the potential region of Pa and also by a decrease of the height of the hydrogen waves. The anodic peak was found unaffected by agitating the stripping solution with nitrogen. The peak disappeared, however, during an anodic sweep preceded by a cathodic one in stirred solution. This fact suggests that the adsorbed species was not ammonia itself, but had a certain oxidation state which could be reduced cathodically to ammonia.

It was found that the adsorption is proportional to the logarithm of the adsorption time. Adsorption was, in accordance with Temkin's isotherm, also proportional to the logarithm of the concentration of ammonia in the adsorption bath. As evident from Fig. 9, the maximal coverage (saturation) is observed at 10^{-4} to 10^{-3}M. The amount of adsorbed ammonia was approximately 78 $\mu coul/cm^2$ at saturation, and this corresponds to a fractional coverage of 0.3.

As shown in Fig. 8, the decrease of the area under the hydrogen wave is almost equal to the area of Pa. This indicates that the oxidation of the ad-species requires one electron per site.

In order to see the composition of the ad-species in more detail, the charge required for the cathodic reduction (Qc) of the ad-species was compared with that required for the anodic stripping (Qa). If the reaction sequence proposed by Oswin and Salomon is assumed to be correct, the following values of Qa/Qc can be expected for the respective intermediates

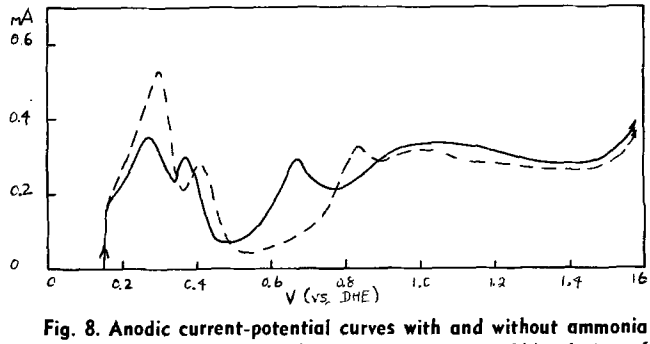

Fig. 8. Anodic current-potential curves with and without ammonia adsorption. Solid line, after 10 min adsorption in a 1M solution of ammonia. Dashed line, after 10 min immersion in a fresh base solution.

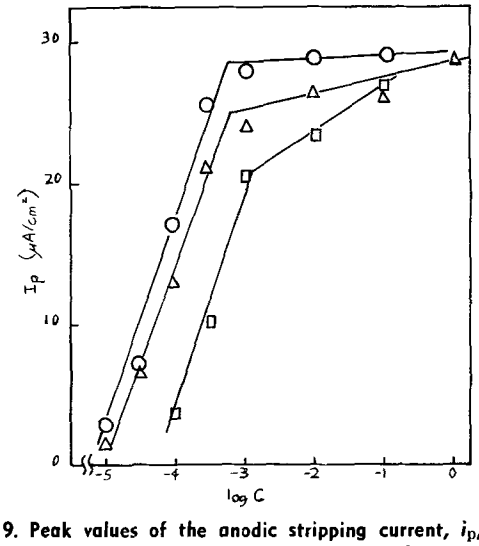

Fig. 9. Peak values of the anodic stripping current, i_p, vs. logarithm of concentration of ammonia in adsorption bath. Duration of adsorption treatment: □, 1 min; △, 5 min; and ○, 10 min.

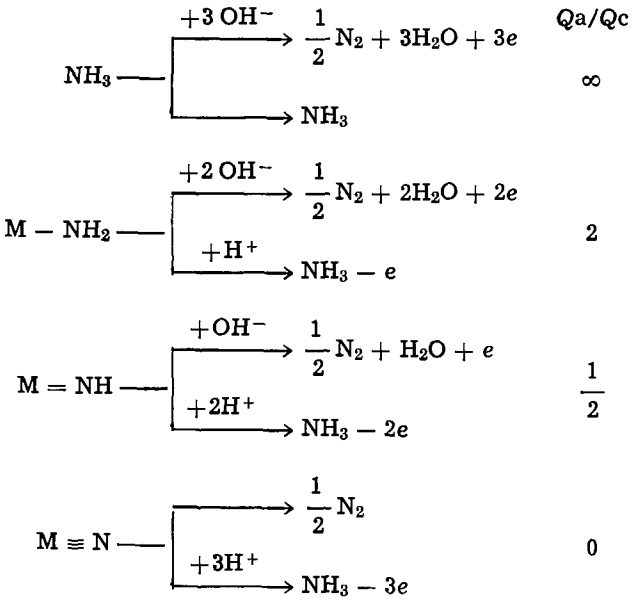

Actual values observed with ammonia were scattered from 1/2 to unity, and with hydroxylamine the values were from 1/5 to 1/2. Probably the actual composition is a mixture of these species. Furthermore, the presence of some oxygenated ad-species, which have often been reported in the case of organic compounds (8)[2] may not be ignored.

Effect of surface oxide on adsorption of ammonia.— In order to see the effect of the electrode potential on the composition of the ad-species, the following experiments were carried out. The test electrode was previously oxidized in the base solution at a given constant potential. In addition, the same potential was also applied to the test electrode during the time of adsorption.

The potential sweep in the stripping experiment was started in the cathodic direction from the potential at which the adsorption was carried out. Several examples of the current-potential curves are shown in Fig. 10. The sharp rise of anodic current at the starting point (see curves A and B) was found to represent the oxidation of sites on the platinum surface neither covered adsorbents nor the surface oxide. Similarly, the narrow cathodic current peak in curve C represents the rapid reduction of the surface oxide. The curves in Fig. 10 demonstrate that the cathodic current peak for the reduction of the surface oxide decreased with the decrease of the potential at which the adsorption took place. The oxidation peak during the subsequent anodic sweep increases in the sequence A, B, C. Figure 11 represents results of the same type in which the potential of the adsorption was at 0.9V and the duration of the adsorption was varied. The increase of the cathodic current at about 0.5V is pronounced for longer times of adsorption.

It is concluded from these results that ammonia still adsorbs on the platinum surface even at the potential where the surface oxide forms. The ad-species accumulates and the surface oxide diminishes at least at the potential of 0.9V. The appearance of the characteristic peak, Pc2 in Fig. 10 and 11, suggests that the major part of the ad-species consists of the same species as the primary product of the anodic oxidation. At higher potentials, however, the adsorbed amount decreases with increasing potential, indicating that species with higher oxidation state are unstable on the surface.

[2] Hydration of reacting species was not considered in the mechanism expressed by Eq. [1]-[4]. Both ammonia and hydroxylamine exhibit a cathodic current peak at Pc1, where the nitrite anion is reduced, and the peak becomes larger with increasing anodic potential of reversal. This seems to suggest the formation of some oxygenated compounds.

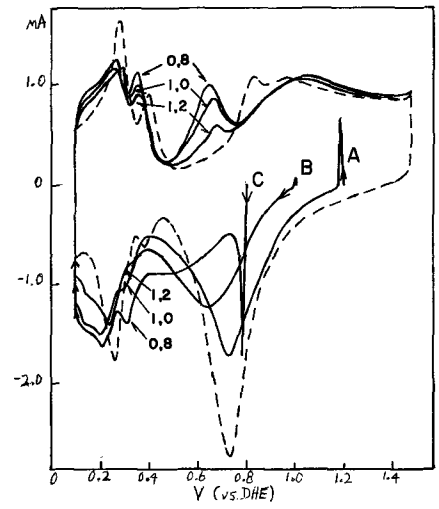

Fig. 10. Influence of electrode potential during adsorption. Numerical figures attached to each curve indicate electrode potential at which adsorption was carried out. Dashed curve represents current-potential curve observed in base solution. Concentration of ammonia in adsorption bath, 2×10^{-3}M. Sweep rate, 50 mV/sec.

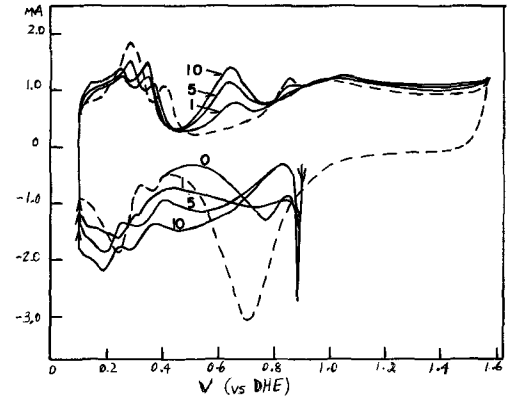

Fig. 11. Influence of adsorption time on stripping current. Adsorption was carried out at a constant potential of 0.9V. Numbers indicate time in minutes.

Summary

The anodic oxidation and adsorption of ammonia in alkaline solutions have been studied on a platinized platinum electrode. Ammonia is anodically oxidized at about 0.65V in 1M potassium hydroxide solutions. The rate of oxidation was, as a whole, diffusion limited. Under the condition of cyclic voltammetry, it was found that the primary product of the anodic oxidation is relatively stable. The life time was estimated to be in the order of 1 sec. When hydroxylamine was examined in place of ammonia, a stable intermediate was not detected. These results are in accordance with the mechanisms reported previously.

Adsorption was studied by employing Pavela's method. It was found that ammonia adsorbs on a platinum surface in accord with Temkin's isotherm and that the surface coverage is about 0.3 at saturation. It is suggested that the major species in the ad-layer is the primary product of ammonia oxidation.

Manuscript submitted Sept. 2, 1969; revised manuscript received Jan. 30, 1970.

Any discussion of this paper will appear in a Discussion Section to be published in the December 1970 JOURNAL.

REFERENCES

1. F. M. Donahue, A. Akiyama, and K. Nobe, *This Journal*, **114**, 1006 (1967).
2. J. Giner, *ibid.*, **111**, 376 (1964).
3. T. O. Pavela, *Ann. Acad. Sci. Fenn., Ser. II, A.*

Chem., 59 (1954).
4. P. Delahay, "New Instrumental Methods in Electrochemistry," p. 119, Interscience Publishers, New York (1964).
5. H. G. Oswin and M. Salomon, *Can. J. Chem.*, **41**, 1686 (1963).
6. T. Katan and R. J. Galiotto, *This Journal*, **110**, 1022 (1963).
7. Wynveen, "Fuel Cells," Vol. II, p. 153, Reinhold Publishing Co., New York (1963).
8. S. B. Brummer and M. J. Turner, *J. Phys. Chem.*, **71**, 2825, 2838, 3494, 3902 (1967).

The Mechanism of the Cadmium Electrode

K. E. Heusler and L. Gaiser

Max-Planck-Institut für Metallforschung, Stuttgart, Germany

ABSTRACT

Measurements of current-potential curves with solid cadmium in solutions of cadmium perchlorate and barium perchlorate under stationary and transient conditions indicate that the electrode reaction proceeds via two consecutive charge transfer steps with adsorbed monovalent cadmium as the intermediate. The rate constants and their dependence on potential and coverage were calculated from the experiments.

The kinetics of dissolution and deposition of solid cadmium in sulfate solutions has been investigated by Lorenz (1, 2). Results were in apparent agreement with the assumption that the rate-determining step is the charge-transfer reaction of Cd^{2+}-ions with a charge-transfer valence $z = 2$ and a cathodic transfer coefficient $\alpha = 0.45$. The results have been quoted as a clear verification of the theoretical relationships derived for such a simple transfer reaction (3, 4). However, the verification may have been only accidental due to the limited experimental evidence.

A mechanism involving two consecutive transfer reactions cannot be excluded, namely

$$Cd^{2+} + e \underset{k_1^+}{\overset{k_1^-}{\rightleftharpoons}} Cd_{ad}^{+} \qquad [1]$$

$$Cd_{ad}^{+} + e \underset{k_2^+}{\overset{k_2^-}{\rightleftharpoons}} Cd \qquad [2]$$

Indeed, an analogous mechanism with monovalent metal in the adsorbed state has been deduced from the kinetics of the solid zinc electrode in perchlorate solutions (5). Furthermore, measurements (6-12) at cadmium amalgam electrodes that yielded transfer coefficients close to $\alpha = 0.25$ assuming $z = 2$ point toward the mechanism [1], [2]. In addition, Lorenz (2) found $\alpha = 0.25$ from measurements of transition times for the deposition of solid cadmium at high current densities.

In an attempt to achieve a clearer understanding of the mechanism of the cadmium electrode, the present study focused experimentally on measurements of current-potential curves over a potential range greater than 0.5V, variation of the concentration of cadmium salt at constant ionic strength of the solution between 0 and 1.3M, and measurements of the time dependence of the polarization. It is significant that all the experimental facts on the kinetics of the cadmium electrode from the present investigation as well as those of Lorenz (1, 2) are consistent with the consecutive mechanism [1], [2]. Thus, a theoretical treatment of an electrode reaction with two consecutive charge-transfer steps is developed taking into account adsorption of the intermediate by generalizing the approach of Gerischer and Mehl (13). The treatment includes earlier considerations (3, 14-16) of the consecutive mechanism as limiting cases.

Experimental

The electrodes were made from cadmium wire with $<$ 1 ppm of metallic impurities. The wire was insulated with Teflon except for the part which served as the electrode. The nearly hemispherical electrodes with an area of about 1 mm^2 were renewed by heating the Teflon to about 200°C, pulling out the wire, and breaking it with tweezers without touching the electrode region. The electrode contained only very few grains. The reference electrode for fast pulse polarizations and the counterelectrode were made from the same cadmium wire. The potential of the reference electrode was measured against a saturated calomel electrode (SCE) at room temperature. A saturated sodium chloride solution separated the potassium chloride from the perchlorate solutions in the cell.

Perchlorate was chosen because this anion does not form complexes with the cadmium ion. Moreover the activity of the cadmium salt can be made much higher than for example in sulfate solutions, and no specific interaction of the anion with the metal surface is expected. The supporting electrolyte usually was a 1M barium perchlorate solution prepared from A. R. grade barium hydroxide, perchloric acid and water triply distilled from a dilute potassium permanganate solution. By adding a 1M cadmium sulfate solution, barium ions were partially replaced by cadmium ions. The solutions were centrifugated in order to remove barium sulfate. The ionic strength was kept constant (with the exception of the 1.3M cadmium perchlorate solution). Usually the solutions were slightly acidic at $pH = 2$ to 4. Sodium perchlorate solutions were also used in some experiments.

Measurements were performed at 0°C in a cell forming a loop in which the solution was rapidly circulated with a magnetic stirrer. The working electrode was polarized under galvanostatic or potentiostatic conditions. A pulse generator and a potentiostat with rise times $\leq 10^{-7}$ sec were used. The pulse heights and the signals from the electrode were measured with a dual-beam oscilloscope.

Results

Current-potential curves were obtained by polarizing the cadmium electrode from its rest potential or equilibrium potential to other potentials by potentiostatic pulses. After switching on the pulse, a current transient with an almost potential-independent decay time of $\tau' \lesssim 15$ μsec was observed. This decay corresponds to the charging of the double layer capacity (17, 18) of 20 to 30 $\mu F/cm^2$ through the effective electrolyte resistance $R_E \leq 0.55$ ohm cm^2 between the working electrode and the reference electrode. Values of C_D and R_E were measured independently by applying constant current pulses and observing the po-

tential transients. All the potentials given below are corrected for $R_E \cdot j$ using the respective experimental values of the electrolyte resistance and of the current density.

The double layer capacity did not change with the height of the current pulse. When hydrogen evolution was the only faradaic process, the transients were well described by the relationship of Roiter *et al.* (3, 19, 20). No significant frequency dispersion of C_D has been observed which might be caused by the roughness of the electrodes (21).

When dissolution or deposition of cadmium occurred, under potentiostatic conditions a slower current transient followed after the first transient. The characteristic time, τ, of the slower transient was in the order of 10^{-3} to 10^{-5} sec depending on experimental conditions. The limit for the separation of the two transients experimentally is given by the condition that $\tau' < \tau$. After the decay of the second transient the current remained constant for times of about 100τ. If the duration of the pulse was made longer than about 100τ, the current increased until a new steady state was attained.

Such long polarization was found to change the effective surface area, leaving the mechanism of the electrode reaction unaltered. These changes of the effective surface area are produced by depositing or dissolving layers of cadmium with an average thickness of the order of 1 μm. The steady-state surface morphology is finally determined by processes of positive or negative crystallization (22, 23), that in this paper will not be discussed further.

On the other hand, current-potential curves measured at times $3\tau < t < 100\tau$ correspond to steady states of the electrode reaction on a surface of constant morphology. In Fig. 1, steady-state current potential curves are shown for different cadmium salt concentrations. The potentials at zero current were found to shift by $\partial\epsilon/\partial \log c_{Cd2+} = 27$ mV/decade indicating that the equilibrium between cadmium and cadmium ions was established. The equilibrium was not appreciably disturbed by hydrogen evolution at $pH \geqq 3$ and $c_{Cd2+} \geqq 10^{-3}$M. Current-potential curves did not change with the pH-value of the solution. The anodic curve was independent of the cadmium salt concentration at overvoltages >60 mV. At high current densities a constant Tafel slope of about 108 mV/decade was found for both anodic and cathodic polarizations.

The reaction order, y_{Cd2+}, with respect to the cadmium ions was obtained from current-potential curves in solutions containing various concentrations of cadmium salt. An approximate value $y_{Cd2+} = 1$ was taken from those parts of the cathodic curves in which the currents were much smaller than the current limited by the diffusion of cadmium ions but much higher than the exchange current at the equilibrium potential. After correcting for diffusion polarization which yielded substantial contributions only for $c_{Cd2+} < 0.1$M, the more exact currents of Fig. 2 were obtained. Within the limits of reproducibility, the reaction order was found to be $y_{Cd2+} = 1.0$ for $c_{Cd2+} < 10^{-1}$M, but for $c_{Cd2+} > 10^{-1}$M the reaction order appeared to drop to about $y_{Cd2+} \approx 0.85$. There was no dependence of the dissolution rate of cadmium on the concentration of cadmium salt.

The anodic current-potential curve was measured down to very low current densities in solutions free of cadmium salt. The low current densities changed more rapidly with the potential than the high current densities. Tafel lines with slopes of 40-50 mV/decade may be assigned to the experimental points shown in Fig. 3. The cathodic Tafel lines in Fig. 3 with a slope of

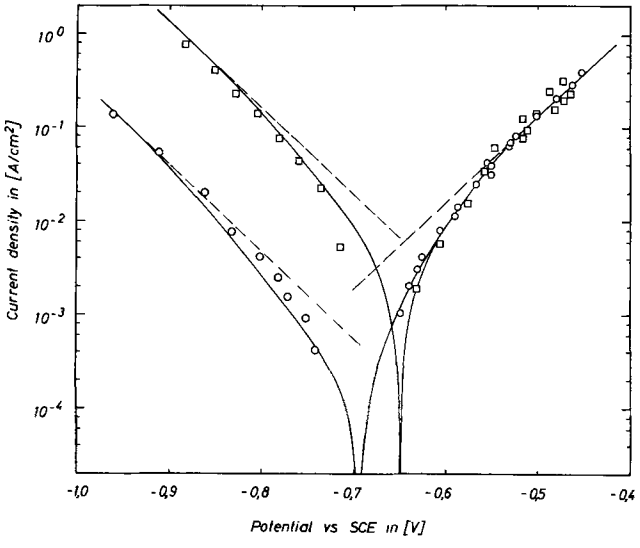

Fig. 1. Current-potential curves in the steady state of the electrode reaction.

(○) 0.0089M $Cd(ClO_4)_2$ + 1.0M $Ba(ClO_4)_2$

(□) 0.45M $Cd(ClO_4)_2$ + 0.55M $Ba(ClO_4)_2$

at pH ≈ 2.5 and 0°C.

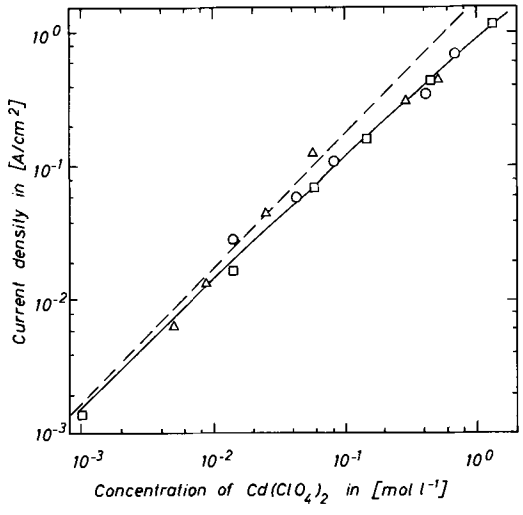

Fig. 2. Current densities for deposition of cadmium at different concentrations of $Cd(ClO_4)_2$ in solutions containing $Ba(ClO_4)_2$ to maintain a constant ionic strength, at $\epsilon = -0.85$V vs. SCE and 0°C. Each symbol corresponds to a run with a particular electrode.

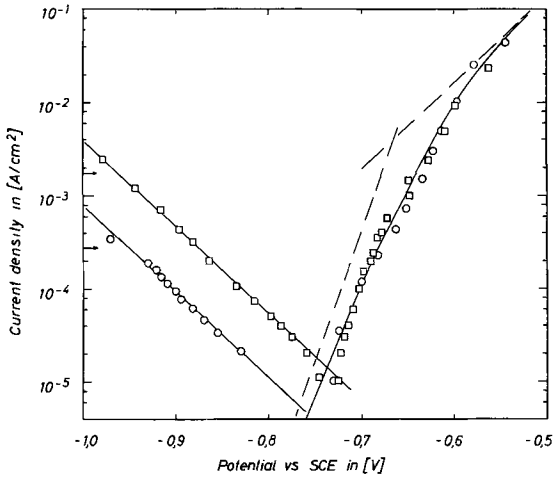

Fig. 3. Steady-state current-potential curves in 1M $NaClO_4$ and $HClO_4$ to render (○) pH = 2.4, and (□) pH = 1.6, at 0°C. Arrows indicate diffusion limited current densities of hydrogen evolution.

about 115 mV/decade are due to hydrogen evolution with the rate being nearly proportional to the hydrogen ion activity.

For a quantitative analysis of the potentiostatic transients following the charging of the double layer the differences between the current densities, $j(t)$, at different times and the stationary current density, $j(\infty)$, were plotted logarithmically against the time as shown in Fig. 4. An exponential decrease of the excess current density, $j(t) - j(\infty)$, with time was only observed when $j(t)$ differed from $j(\infty)$ by 10% or less. The current decay was faster than exponential for large excess current densities. The effect is not caused by interference with the charging of the double layer, since it was observed even when the decay was very slow. It was also present for small excess current densities for which no significant corrections due to the electrolyte resistance, R_E, were necessary. Actually, any correction for $R_E \cdot j$ would enhance the effect.

For both cathodic and anodic overpotentials the stationary state was approached from higher current densities. The characteristic times, τ, taken from the final exponential decay of the excess current density on the cathodic side decreased for more negative potentials and on the anodic side for more positive potentials by about 108 mV/decade. The times of decay were measured at overvoltages between about 0.1 and 0.25V in a region where corrections due to the reverse reaction, to concentration polarization, ohmic drop, and interference with the charging of the double layer capacity were rather small. The dependence of the cathodic times of decay at constant potential upon the concentration of cadmium salt are plotted in Fig. 5 on a double logarithmic scale. The decay times decreased almost proportional to the cadmium perchlorate concentration.

At low cadmium perchlorate concentrations the charging of the double layer capacity was so much faster than the subsequent decay of the current that the faradaic currents at times $t \to 0$ after changing the potential could be measured. The corresponding transient current-potential curves were found to be symmetrical with respect to the equilibrium potential. The transient exchange current densities were about 0.5 A/cm². The absolute accuracy of such large values is low due to the high $R_E \cdot j$-correction. However, it was possible to compare the transient exchange current densities for different cadmium perchlorate concentrations by measuring at the same electrode without changing the geometry. A very small concentration dependence of the transient exchange current densities was observed as shown in Fig. 7.

Discussion

Considering the steady-state current-potential curves, Vetter (3) has given the following individually sufficient criteria for the appearance of consecutive charge transfer reactions: (a) extrapolation of the anodic and cathodic Tafel lines toward the equilibrium potential leads to two different current densities; (b) the Tafel line changes its slope $\partial\epsilon/\partial \ln j$ from a small value at low overvoltages to a large value at high overvoltages; and (c) the sum of the apparent anodic and the cathodic transfer coefficients $\alpha' = RT\partial/n\mathbf{F}\partial\epsilon$ does not add up to the number n of electrons transferred in the over-all reaction (15), *e.g.*, $n = 2$ for the cadmium electrode. The experiments show that not only one but all three criteria are fulfilled, except for specific experimental conditions. Thus, it is safe to conclude that a consecutive mechanism is operating. Additional information on the mechanism may be derived from the following theoretical treatment.

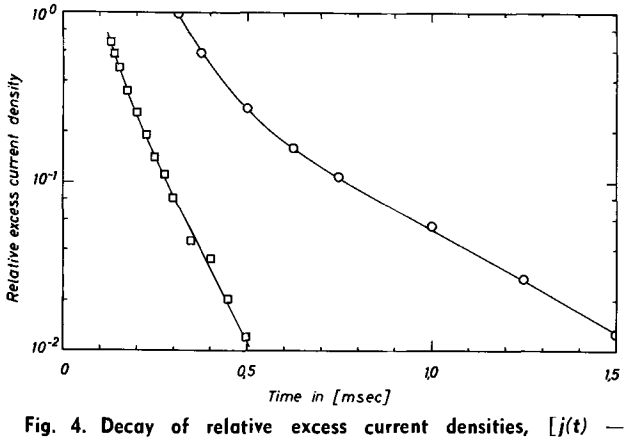

Fig. 4. Decay of relative excess current densities, $[j(t) - j(\infty)]/j(\infty)$, with time after switching from the equilibrium potential to negative overvoltages. (○), $\epsilon = -0.895$V vs. SCE in 0.014M $Cd(ClO_4)_2$ + 0.99M $Ba(ClO_4)_2$, (□), $\epsilon = -0.848$V vs. SCE in 0.15M $Cd(ClO_4)_2$ + 0.85M $Ba(ClO_4)_2$.

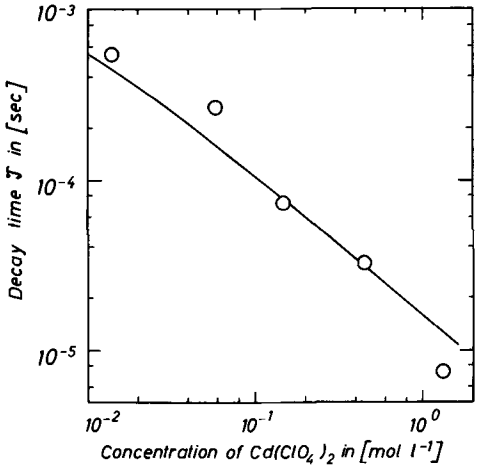

Fig. 5. Cathodic decay times at $\epsilon = -0.85$V vs. SCE as a function of the concentration of $Cd(ClO_4)_2$ in solutions of constant ionic strength at 0°C.

A consistent quantitative interpretation of the experiments is impossible without considering the adsorption of the intermediate. In deriving the following general relationships it is taken into account that the monovalent cadmium can only exist in the adsorbed state. The rates of the charge transfer reactions [1] and [2] in terms of current densities are given by

$$j_1 = k_1^+(\epsilon) \cdot f(\theta) - k_1^-(\epsilon) \cdot a_{Cd2+} \cdot g(\theta) \quad [3]$$

and

$$j_2 = k_2^+(\epsilon) \cdot g(\theta) - k_2^-(\epsilon) \cdot f(\theta) \quad [4]$$

with the rate constants $k_{1,2}^+(\epsilon) = k_{1,2}^+ \cdot \exp[\alpha_{1,2}\mathbf{F}\epsilon/RT]$ and $k_{1,2}^-(\epsilon) = k_{1,2}^- \cdot \exp[-(1-\alpha_{1,2})\mathbf{F}\epsilon/RT]$ and the transfer coefficients α_1, α_2 of the two steps [1] and [2]. The potential ϵ refers to a constant reference electrode like the SCE.

The influence of the relative surface coverage, θ, by the intermediate on the rates is expressed by the functions

$$f(\theta) = \theta \cdot \exp[-b(1-\theta)] \quad [5]$$

and

$$g(\theta) = (1-\theta) \cdot \exp[-a\theta] \quad [6]$$

The desorption of monovalent cadmium proceeds at a rate proportional to the coverage θ. It is assumed, consequently, that the rate of adsorption is proportional to the part $(1-\theta)$ of the surface not yet covered. Another effect to be considered is the dependence of the rate constants upon coverage. To a first approximation, there is a linear dependence of the activation energies of the charge-transfer reactions on the coverage as suggested by Temkin (24). For the activation energy E_a of adsorption one writes

$$E_a = E_a^0 + a\,RT\,\theta \quad [7]$$

and for the activation energy E_d of desorption

$$E_d = E_d^0 + b\,RT\,(1-\theta) \quad [8]$$

There are two reactions of adsorption, anodic reaction [2] and cathodic reaction [1]. It is assumed that [7] holds for both reactions with the same potential-independent interaction coefficient, a. The analogous assumption concerning the coefficient, b, follows from the fact that the coefficient, $A = a + b$, must be independent of the particular reactions [1] or [2], because A describes a thermodynamic quantity, namely, the change of the adsorption enthalpy with coverage at the equilibrium of the cadmium electrode.

The rates of dissolution or deposition of cadmium are given by

$$j = j_1 + j_2 \qquad [9]$$

The stationary state is characterized by $j_1 = j_2$. After elimination of either $f(\theta)$ or $g(\theta)$ two equivalent equations for the steady state current density, $j(\infty)$, are obtained

$$j(\infty) = 2\,g(\theta) \cdot \frac{k_1^+(\epsilon) \cdot k_2^+(\epsilon) - k_1^-(\epsilon) \cdot k_2^-(\epsilon) \cdot a_{Cd2+}}{k_1^+(\epsilon) + k_2^-(\epsilon)} \qquad [10]$$

and

$$j(\infty) = 2\,f(\theta) \cdot \frac{k_1^+(\epsilon) \cdot k_2^+(\epsilon) - k_1^-(\epsilon) \cdot k_2^-(\epsilon) \cdot a_{Cd2+}}{k_1^-(\epsilon) \cdot a_{Cd2+} + k_2^+(\epsilon)} \qquad [11]$$

The adsorption isotherm describing the dependence of the steady-state coverage on potential and cadmium ion activity follows from [5], [6], [10], and [11]

$$\frac{\theta}{1-\theta} \exp\left[a\theta - b(1-\theta)\right] = \frac{k_1^-(\epsilon) \cdot a_{Cd2+} + k_2^+(\epsilon)}{k_1^+(\epsilon) + k_2^-(\epsilon)} \qquad [12]$$

At large positive potentials both anodic rate constants become much larger than the cathodic rate constants. Then, as one can easily show, the potential dependence of the rate is given by $\partial/\partial = RT/\alpha_1\mathbf{F}$ if $k_1^+(\epsilon) << k_2^+(\epsilon)$ or by $\partial/\partial = RT/\alpha_2\mathbf{F}$, if $k_1^+(\epsilon) >> k_2^+(\epsilon)$. For $k_1^+(\epsilon) \approx k_2^+(\epsilon)$ and $\alpha_1 \neq \alpha_2$ the slope of the Tafel line depends on the potential. Analogously, at large negative potentials the Tafel slope is $\partial\epsilon/\partial \ln j_- = RT/(1-\alpha_1)\mathbf{F}$ for $k_1^-(\epsilon)\,a_{Cd2+} >> k_2^-(\epsilon)$ and $\partial\epsilon/\partial \ln j_- = RT/(1-\alpha_2)\mathbf{F}$ for $k_1^-(\epsilon)a_{Cd2+} << k_2^-(\epsilon)$. The earlier statement (3, 14, 15) that the Tafel slopes at high overvoltages are determined by the transfer coefficients of the respective preceding reaction step does not hold when considering adsorbed intermediates. Experimentally, it was found that $\partial \ln j_\pm/\partial = 2\mathbf{F}/\mathrm{RT}$ on both the cathodic and anodic sides. One concludes that $\alpha_1 = \alpha_2 = 0.5$ within the limits of experimental accuracy of at least $\pm 10\%$.

If at $a_{Cd2+} \to 0$ the cathodic current density for the deposition of cadmium becomes negligible, at negative potentials $k_2^-(\epsilon)$ must become large compared to $k_1^+(\epsilon)$. In this case, the equilibrium [2] is not appreciably disturbed by the anodic dissolution of cadmium; the coverage, θ, depends strongly on the potential; and the Tafel slope is $\partial\epsilon/\partial \ln j_+ = RT/(1+\alpha)\mathbf{F}$. This behavior is in good agreement with the anodic current-potential curve of Fig. 3.

On the other hand, it follows from [12] that for $a_{Cd2+} \to 0$ the coverage approaches $\theta_- \to 0$ at negative potentials, and therefore $g(\theta_-) \to 1$. As long as the activity of cadmium ions is small enough, $[1 - g(\theta_-)] << 1$, and the current density, j_-, at constant potential stays proportional to the activity, a_{Cd2+}, as is deduced from [10]. The current density, j_-, increases less than proportional to the activity of cadmium ions as soon as $g(\theta_-)$ deviates from unity appreciably. For very high activities the coverage may approach its limiting value $\theta_- \to 1$, or $[1 - f(\theta_-)] << 1$. Under this condition, the rate of deposition is independent of the activity, a_{Cd2+}, according to [11].

The activities and the concentrations of the cadmium ions are proportional to each other, since the experiments were done at constant ionic strength and since the activity coefficients of cadmium perchlorate and barium perchlorate solutions are nearly equal. For the purpose of the following numerical calculations it suffices to refer to concentrations.

From the measurements at low concentrations Fig. 2 yields the rate constant $k_1^- = j_-(\infty)/2c_{Cd2+}$. Extrapolating to high cadmium salt concentrations, one obtains $g(\theta_-) = j_-(\infty)/2k_1^- \cdot c_{Cd2+}$. At the highest concentration $c_{Cd2+} = 1.3\mathrm{M}$ a value of $g(\theta_-) \approx 0.5$ was found. A definite value of the interaction coefficient, a, cannot be calculated from such small deviations of $g(\theta_-)$ from unity. One finds that, qualitatively, $k_2^- > k_1^- \cdot c_{Cd2+}$ up to the highest concentrations.

An important step in calculating the six unknown parameters a, b, $k_{1,2}^\pm$, is the consideration of the dependence of the cathodic decay times on the concentration, c_{Cd2+}, shown in Fig. 5. Generally, the transient currents flowing after switching from the equilibrium potential to another constant potential are given by [9] inserting [3] and [4] and the change of coverage with time which may be calculated from [13]

$$Q \cdot d\theta/dt = \left[k_1^-(\epsilon) \cdot a_{Cd2+} + k_2^+(\epsilon)\right] g(\theta) - \left[k_1^+(\epsilon) + k_2^-(\epsilon)\right] f(\theta) \qquad [13]$$

where Q is the charge necessary to cover the bare cadmium surface completely with monovalent cadmium. Equation [13] describes how the steady state of [12] is approached from the equilibrium coverage θ_0 at $t \to 0$. Due to the complicated nature of the functions $f(\theta)$ and $g(\theta)$ an exponential decay of the current is generally not to be expected. The decay should be faster than exponential as long as θ changes rapidly at small times after a potential step. Such a behavior was observed experimentally. However, if either θ or $(1-\theta)$ are close to unity or if θ is close to its steady-state value, the variation of the exponential terms of [5] and [6] with θ can be neglected. The coverage then changes, as if the isotherm were of the Langmuir-type. The excess current densities decay almost exponentially according to the solution derived by Gerischer and Mehl (13)

$$\frac{j(t) - j(\infty)}{j^* - j(\infty)} = \exp -\frac{t}{\tau} \qquad [14]$$

The current density, j^*, is obtained by extrapolation to $t \to 0$ of the exponential decay, but it is not the true transient current density for $t \to 0$. The decay time, τ, is given by

$$Q/\tau \approx \left[k_1^-(\epsilon) \cdot a_{Cd2+} + k_2^+(\epsilon)\right] \exp\left[-a\theta\right] + \left[k_1^+(\epsilon) + k_2^-(\epsilon)\right] \exp\left[-b(1-\theta)\right] \qquad [15]$$

In [15], the rate constants are corrected for their dependence on the coverage. By definition, the rate constants, k_1^+ and k_2^-, correspond to $\theta = 1$ and the rate constants, k_1^- and k_2^+, to $\theta = 0$.

The reciprocal, cathodic and anodic decay times at high overvoltages were found to change with the potential in the same way as the rate constants, in agreement with [15]. Decay times are determined by the fastest of the rate constants. Cathodic decay times are expected to be independent of the activity, a_{Cd2+}, at low activities and proportional to the activity at high activities. From Fig. 5, it follows that $k_1^-(\epsilon) \cdot c_{Cd2+} \cdot \exp\left[-a\theta\right]$ apparently surpasses $k_2^-(\epsilon) \cdot \exp\left[-b(1-\theta)\right]$ even at relatively low concentrations, c_{Cd2+}. On the other hand, rather small deviations of $g(\theta_-)$ from unity are calculated from Fig. 2. Both the experiments of Fig. 2 and 5 are compatible, only if $b > a$. However, a whole set of interaction coefficients does agree with the two experiments almost equally well.

The ambiguity is completely removed by considering the interdependence of the cathodic and the anodic rate constants. Thermodynamics requires $k_1^+(\epsilon) \cdot$

$k_2^+(\epsilon) = k_1^-(\epsilon) \cdot k_2^-(\epsilon) \cdot a_{Cd2+}$ at the equilibrium potential, $\epsilon = \epsilon_o$. A second condition to be fulfilled is that from its constant value at positive potentials, $f(\theta_+)$ must begin to drop rapidly as soon as the potential gets more negative than about $\epsilon = -0.6$V *vs.* SCE, because of the increasing steepness of the anodic current-potential curves shown in Fig. 1 and 3. The two conditions can be fulfilled with a well-defined pair of interaction coefficients only. The selection of a pair of interaction coefficients with a large value of $A = a + b$ leads to a large rate constant, k_2^-, and a large product, $k_1^+(\epsilon_o) \cdot k_2^+(\epsilon_o)$. From the Tafel line at high anodic overvoltages and constant coverage, θ_+, the individual values of $k_1^+(\epsilon)$ and $k_2^+(\epsilon)$ are obtained. In the case of too large values of A, the calculated anodic current-potential curves are found to increase their slope at too negative potentials.

By successive approximation the parameters for optimal description of the experiments were obtained. The resulting interaction coefficients are $a = 0$ and $b = 10$. This indicates that the lateral interaction of the adsorbed monovalent cadmium only affects the activation energy of desorption. The rate constants at $\epsilon = -0.7$V *vs.* SCE are $k_1^+ = 10^{-3}$ [A/cm^2], $k_1^- = 38$ [A cm/mol], $k_2^+ = 1.7$ [A/cm^2], and $k_2^- = 8.0$ [A/cm^2]. Using these parameters the solid lines in Fig. 1, 2, 3, and 5 were calculated.

With slightly more divergent interaction coefficients such as $a = -1$ and $b = 12$, a good fit of the concentration dependence of the cathodic decay times is also obtained. However, the rate constants are left almost unchanged by such small changes, and there is very little effect on the general form of the current-potential curves.

The current-potential curves measured by Lorenz (2) for overvoltages <0.1V coincide with the calculated curves as well as the measurements in Fig. 1. However, the current densities observed in the earlier work are displaced to lower current densities by a factor of about two. This may be due to an inhibiting effect of the sulfate solutions as compared to the perchlorate solutions (11). The inhibiting effect of sulfate should be even larger than just estimated: the measurements of Lorenz (2) were performed at 20°C, the present ones at 0°C. According to the present results, the apparent symmetry of the current potential curves at potentials between $\epsilon = -0.6$V and $\epsilon = -0.8$V *vs.* SCE is due to the similar influences of k_2^- on the anodic rate and of k_2^+ on the cathodic rate.

From the rate constants one may evaluate the coverage as a function of the potential using (12). The coverage changes between the potential independent values, θ_+ at very positive potentials, and θ_- at very negative potentials, with the equilibrium coverage, θ_o, in between. The coverages, θ_- and θ_o, depend on the concentration of cadmium perchlorate as shown in Fig. 6. The coverage, θ_-, is almost proportional to the concentration for $\theta_- < 0.1$ corresponding to $c_{Cd2+} < 10^{-2}$M. The equilibrium coverage is almost proportional to the logarithm of the concentration in the range plotted in Fig. 6. The coverage, θ_+, naturally is independent of the concentration and has a value close to unity because $k_1^+ << k_2^+$. From the equilibrium coverage, the steady-state exchange current densities, $j_o(\infty)$, were calculated using [16]

$$j_o(\infty) = 2 f(\theta_o) \frac{k_1^+(\epsilon_o) \cdot k_2^+(\epsilon_o)}{k_1^-(\epsilon_o) \cdot a_{Cd2+} + k_2^+(\epsilon_o)} \quad [16]$$

or any other of the four equivalent equations to be derived from [10] and [11] for $j(\infty) = 0$. In Fig. 7, the steady-state exchange current densities are plotted as a function of the concentration, c_{Cd2+}, along with Lorenz's experimental results (2) derived from the equilibrium polarization resistance. The slopes of the two lines are exactly the same. The displacement by a constant factor is the result of the different experimental conditions, as mentioned above.

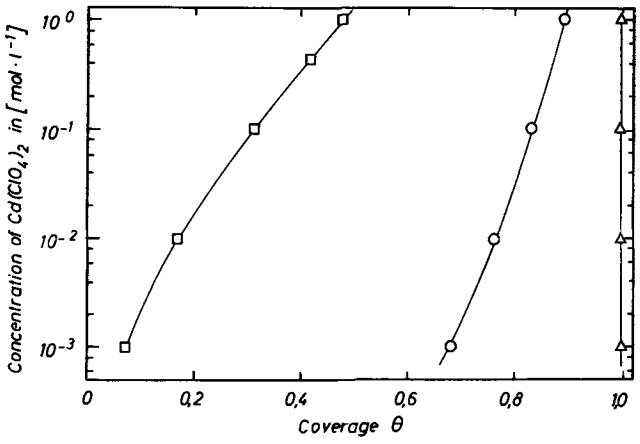

Fig. 6. Relative coverages with adsorbed monovalent cadmium, [△], at very positive potentials, θ_+; [□], at very negative potentials, θ_-, and [○], at equilibrium, θ_o, calculated from the experiments for different concentrations of $Cd(ClO_4)_2$.

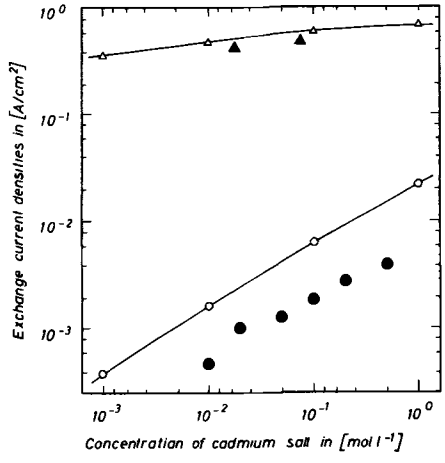

Fig. 7. Steady-state and transient exchange current densities, $j_o(\infty)$ and $j_o(0)$, for different concentrations of cadmium salt at constant ionic strength. [○], $j_o(\infty)$; [△], $j_o(0)$ calculated from the experiments; and [▲], $j_o(0)$ by direct measurements in perchlorate solutions at 0°C; [●], $j_o(\infty)$ from measurements of the equilibrium polarization resistance by Lorenz (2) in solutions containing $CdSO_4$ + 1.5M K_2SO_4 at 20°C.

At the equilibrium of the cadmium electrode the two steps [1] and [2] with two different exchange current densities are also in equilibrium. The exchange current densities of each step are obtained from [3] and [4] with $j_1 = 0$ or $j_2 = 0$. By comparison with [16] one deduces the relationship

$$2/j_o(\infty) = (1/j_{1,o}) + (1/j_{2,o}) \quad [17]$$

Under transient conditions, $j_1 \neq j_2$, but [9] is still valid. A transient current-potential curve measured for the time $t \to 0$ after switching from the equilibrium potential to other potentials should yield Tafel lines with a slope of 2 RT/F at high overvoltages. The extrapolation of the anodic and cathodic Tafel lines to the equilibrium potential should lead to a common transient exchange current density which is the sum of the exchange current densities of the two steps

$$j_o(0) = j_{1,o} + j_{2,o} \quad [18]$$

The transient exchange current densities are determined by the fastest step. On the other hand, the steady-state exchange current densities are determined by the slowest step. Since $j_{2,o}$ exceeds $j_{1,o}$ for all possible concentrations, c_{Cd2+}, the transient current densities are always larger than the steady-state current densities. Such a behavior is not generally expected but more probable than $j(0) < j(\infty)$, because

$$\frac{j(0)}{j(\infty)} = \frac{1}{2}\left[\frac{f(\theta_o)}{f(\theta_\pm)} + \frac{g(\theta_o)}{g(\theta_\pm)}\right] \quad [19]$$

as derived earlier (5). The transient exchange current densities obtained by direct measurement and indirectly by calculation from the other experiments are in excellent agreement, which can be considered as another proof for the validity of the proposed mechanism.

The first order rate constants of step [2] in both directions of the reaction are always larger than the rate constants of step [1] even at the highest cadmium perchlorate concentrations. Therefore, one might consider step [1] to be rate determining. This does not mean that step [2] is always in equilibrium. At high overvoltages the respective reverse reactions of both steps do not have any influence on the rate of the overall reaction. Although the rate constants of step [2] are relatively high, the electronic interaction between the cadmium metal and the adsorbed monovalent cadmium is still very weak. The kinetics can be explained with transfer coefficients of $\alpha = 0.5$ for both steps and with a well-defined monovalent intermediate. Therefore, the monovalent cadmium with the center of its charge in the Helmholtz layer must be separated from the metal. The obvious model is to assume that the monovalent cadmium is bound to the metal by a water bridge. Thus, step [2] is a metal/ion reaction (3) with the charge being transferred by the metal ion. On the other hand, step [1] is a typical redox reaction with electrons carrying the charge across the Helmholtz layer.

The comparatively low rate constants of step [1] may be assigned to drastic differences in the solvation sheets of cadmium ions in the solution and of adsorbed monovalent cadmium, according to the theory of redox reactions recently reviewed by Levich (25). Therefore, one may suppose that only small rearrangements of the solvation sheets of the completely discharged metal in the surface and of the adsorbed monovalent metal are left for the further reaction of step [2] resulting in a relatively large rate.

Acknowledgments

Financial support by the "Arbeitsgemeinschaft Korrosion" is gratefully acknowledged. The authors are indebted to Mrs. Ch. Hertel for reliable assistance during the experimental work.

Manuscript submitted Oct. 2, 1969; revised manuscript received Feb. 9, 1970.

Any discussion of this paper will appear in a Discussion Section to be published in the December 1970 JOURNAL.

LIST OF SYMBOLS

α,	transfer coefficient
a, b,	interaction coefficients
ART,	(with $A = a + b$) change of adsorption enthalpy between zero and full coverage with the intermediate
C_D,	double layer capacity
ϵ,	potential *vs.* SCE
$f(\theta), g(\theta)$,	functions of relative coverage
j,	current density
$j(\infty)$,	steady-state c.d.
$j_o(\infty)$,	steady-state exchange c.d.
$j(t)$,	transient c.d.
$j(0)$,	transient c.d. for time $t \to 0$
$j_o(0)$,	transient exchange c.d. at the equilibrium potential ϵ_0
k^-, k^+,	cathodic and anodic rate constants
R_E,	effective resistance of the electrolyte between reference electrode and working electrode
τ,	decay time
θ,	relative coverage of the surface with the intermediate
θ_o,	relative coverage at equilibrium
θ_-, θ_+,	relative coverage at high negative and positive overvoltages
y,	reaction order
z,	charge-transfer valence

REFERENCES

1. W. Lorenz, *Naturwiss.*, **40**, 578 (1953).
2. W. Lorenz, *Z. Elektrochem., Ber. Bunsenges. Physik Chem.*, **58**, 912 (1954).
3. K. J. Vetter, "Electrochemical Kinetics," Academic Press, New York (1967).
4. P. Delahay, "Double Layer and Electrode Kinetics," Interscience, Inc., New York (1965).
5. L. Gaiser and K. E. Heusler, *Electrochim. Acta*, In press.
6. H. Gerischer, *Z. Elektrochem., Ber. Bunsenges. Physik Chem.*, **57**, 604 (1953).
7. T. Berzins and P. Delahay, *J. Am. Chem. Soc.*, **77**, 6448 (1955).
8. W. Vielstich and P. Delahay, *J. Am. Chem. Soc.*, **79**, 1874 (1957).
9. J. E. B. Randles, "Electrode Processes," p. 209, E. Yeager, Editor, John Wiley & Co., Inc., New York (1961).
10. B. Lovrečček and N. Marinčic, *Electrochim. Acta*, **11**, 237 (1966).
11. D. J. Kooijman and J. H. Sluyters, *ibid.*, **12**, 693 (1967).
12. N. A. Hampson and D. Larkin, *J. Electroanal. Chem. Interfacial Electrochem.*, **18**, 401 (1968).
13. H. Gerischer and W. Mehl, *Z. Elektrochem., Ber. Bunsenges. Physik. Chem.*, **59**, 1049 (1955).
14. R. M. Hurd, *This Journal*, **109**, 327 (1962).
15. V. V. Losev and V. V. Gorodetskii, *Elektrokhimyia*, **3**, 1061 (1967).
16. J. H. Plonski, *This Journal*, **116**, 944 (1969).
17. N. A. Hampson and D. A. Larkin, *ibid.*, **114**, 933 (1967).
18. V. Ya. Bartenev, E. S. Sevastyanov, and D. I. Leikis, *Elektrokhimia*, **4**, 745 (1968).
19. W. A. Roiter, W. A. Juza, and E. S. Polujan, *Acta physicochim. USSR*, **10**, 389 (1939).
20. W. A. Roiter, E. S. Polujan, and W. A. Juza, *ibid.*, **10**, 845 (1939).
21. R. de Levie, "Advances in Electrochemistry and Electrochemical Engineering," P. Delahay and Ch. W. Tobias, Editors, Vol. 6, p. 389, Interscience, New York (1967).
22. R. Piontelli, G. Poli, and G. Serravalle, "Electrode Processes," p. 80, E. Yeager, Editor, John Wiley & Sons, Inc., New York (1961).
23. M. Fleischmann and H. R. Thirsk, "Advances in Electrochemistry and Electrochemical Engineering," P. Delahay and Ch. W. Tobias, Editors, Vol. 3, p. 123, Interscience, New York (1963).
24. M. Y. Temkin, *Russ. J. Phys. Chem.*, **14**, 1153 (1940); **15**, 296 (1941).
25. V. G. Levich, "Advances in Electrochemistry and Electrochemical Engineering," Vol. 4, p. 249, P. Delahay, Editor, Interscience, New York (1965).

Film Formation on Copper and Alpha Brass in Aqueous Cupric-Ammonia Systems

L. H. Jenkins* and R. B. Durham

Solid State Division, Oak Ridge National Laboratory, Oak Ridge, Tennessee

ABSTRACT

Reaction rates of single crystalline copper and α-brass surfaces exposed to solutions of $Cu(NH_3)_x(OH)_2$ in ~15M aqueous ammonia have been investigated. Composition of the precipitated films formed on the surfaces was investigated and attempts made to correlate film texture and composition with the mode of attack on the metal surfaces. An estimate of the activity coefficient of NH_3 in concentrated aqueous NH_4OH could be made from the copper system data, and it is shown that film formation on brass occurred outside the limits defined in a general model of relative interfacial concentrations in the system. Also, it was observed that a thin film developed on α-brass prior to tarnish formation. Nonhomogenous breakdown of this initial film, which was more protective than the tarnish layer, occurred by means other than mechanical rupture. Some applications of the data to stress related corrosion phenomena are discussed.

Ammoniacal solutions of copper sulfate have been employed by Mattson (1), Forty and Humble (2), and McEvily and Bond (3) to investigate stress related corrosion phenomena of α-brass. The tendency of such solutions slowly to form precipitates over long periods of time somewhat affected the reproducibility of experimental results and introduces some uncertainty and difficulty in attempts to understand associated chemical phenomena. To circumvent this difficulty, Pugh, Montague, and Westwood (4) used solutions of $Cu(NH_3)_x(OH)_2$ in either 15M or 1M aqueous NH_3 in studying the role of aqueous complex ions of copper in the cracking of α-brass. Further studies by Pugh and Westwood (5) in 15M aqueous ammonia containing predominantly $Cu(NH_3)_5(OH)_2$ were interpreted to indicate two mechanisms of stress corrosion cracking, one in the presence of a tarnish layer and another in its absence. Also, they concluded that behavior was strongly influenced by the concentration of the complex cupric ion $Cu(NH_3)_5^{++}$. Recently Bertocci (6) proposed a model reaction mechanism whereby the reaction rates observed by Pugh *et al.* were explained in terms of enhanced transport of the oxidizing agent across the diffusion layer. The model assumed that immediately at the metal-solution interface the total concentration of cupric species was zero, having all been reduced to cuprous by the act of oxidizing the metal. In the case of copper metal in the systems reported here the cuprous concentration at the interface would be simply twice that of the bulk cupric concentration. For brass, the relative concentrations of zinc and cuprous ions at the interface would be determined by the composition of the alloy. However, uncertainties still exist regarding the exact nature of the films observed by Pugh and co-workers and the relationships between structure of the substrate, composition of the films, and composition of the solution. The following report concerns data collected in attempts to define these relationships.

Experimental Data

Materials and methods.—All data reported here were collected on coin shaped single crystalline metal specimens approximately 2.5 cm diameter x 0.7 cm thick. Prior to use the copper specimens were electropolished in an acid copper phosphate bath and rinsed in dilute solutions of H_3PO_4. Crystals of α-brass [70 w/o (weight per cent) Cu-30 Zn] were chemically polished using a solution after Mitchell (7) on a flat, soft cloth surface. Following rinsing, washing, and drying, the flat, polished surfaces were then spring-mounted with gentle pressure to a Viton O-ring of 1.6 cm ID at the end of a glass tube of the same dimensions. In this manner the orientation to be studied was isolated within a container and also served as the bottom of the chamber into which the test solution was introduced. The glass tube was ~ 15 cm long.

Solutions of varying copper content were prepared by dissolving Cu_2O in air-saturated aqueous solutions of ~ 15M NH_3. The air served to oxidize the cuprous ions to cupric so that the final test solutions consisted of air saturated solutions of soluble complex cupric hydroxides: $Cu(NH_3)_x(OH)_2$. Most observations were recorded in systems initially containing either 0.95, 1.90, or 3.80 g/l total copper (0.015, 0.03, 0.06M and hereafter referred to as test solutions II, III, and IV, respectively). However, some data also were obtained from ammoniacal solutions 0.015M in $Cu(NH_3)_x(OH)_2$ and 0.09M in KOH (hereafter referred to as test solution IIa). In all experiments the volume of test solution was 15 ml so that, following introduction of solution into the chamber formed by the metal surface and glass cylinder and closing the open tube end, a volume of air equal approximately to that of the solution was enclosed within the system.

At the conclusion of the tests, solutions were decanted and analyzed by spectrophotometric means for metal content. Sample surfaces were rinsed in distilled water and dried carefully in a gentle air stream in a manner which would not disturb any films present on the surface. Surfaces were then examined and photomicrographs taken. In some cases films cracked on drying revealing the substrate such that it was possible to measure average film thickness directly. (In a few instances the thickness of semitransparent, very thin films also could be measured.) The films were then dissolved in solutions of 50% by volume aqueous ethylenediamine, which subsequently were analyzed for metal content and the results correlated with measured film thicknesses. The clean metal substrate was then examined and again photomicrography used to record the observations. Films were stripped from certain other representative samples and examined by electron diffraction techniques in order to establish more accurately the components of films formed in typical solutions.

Copper metal-ammonia systems.—Compositions of test solutions II, III, and IV are within the limits of concentrations termed ranges II, III, and IV, respectively, by Pugh and Westwood (5), who reported the following observations for α-brass reacting under an

* Electrochemical Society Active Member.

applied stress within these ranges of concentration: In range II fracture occurred in both a trans- and intercrystalline manner after the formation of a brown, loosely adherent film. In range III failure occurred before visible surface films were formed. Range IV specimens were coated with the characteristic tarnish layer, and fracture was largely intercrystalline.

Test solutions II, IIa, III, and IV were used in the manner previously described to study the effects of solution composition and crystallographic orientation on the rate of dissolution of copper as a result of the following reactions

$$Cu(NH_3)_x^{+2} + Cu^o \overset{NH_3}{\leftrightarrows} 2Cu(NH_3)_2^+ \quad [1]$$

$$2Cu(NH_3)_2^+ + 1/2\,O_2 + H_2O \overset{NH_3}{\leftrightarrows} 2Cu(NH_3)_x^{+2} + 2\,OH^- \quad [2]$$

Although often thick by microscopic standards, from an analytical viewpoint the total material contained in a film over a copper substrate in all cases was insignificant as compared with the total material removed from the specimens and dissolved in the solution in which the film formed. Therefore, the rate of increase of copper in solutions shown in Fig. 1 indicates that the rate of weight loss of copper single crystals was independent of both crystal orientation and composition of the test solutions. The latter observation was unexpected for while, in general, films were not detected on copper in type II test solutions, exposure to solutions IIa, III, and IV caused immediate film formation.

In type II test solutions film formation was observed only after the copper content of the solution had increased to ~ 2 g/l (after ~ 90 hr reaction) due to the occurrence of reactions [1] and [2]. The onset of precipitation at this concentration suggested a means of estimating the activity coefficient of NH_3 in these systems. Although the equilibrium constant for the reaction

$$Cu^{++} + Cu^o \leftrightarrows 2Cu^+ \quad [3]$$

is $\sim 10^{-6}$, the stability constants for cuprous and cupric ammonia complexes is such that equilibrium is established in solutions of concentrated NH_3 only when reaction [3] is shifted almost completely to the right. In a series of experiments equilibria were established in different solutions initially containing varying amounts of $Cu(NH_3)_x(OH)_2$ in ~ 15M aqueous NH_3 exposed to copper metal in a closed system. It was determined that the limit of Cu_2O solubility (shown by the presence of a "tarnish" film at equilibrium) and

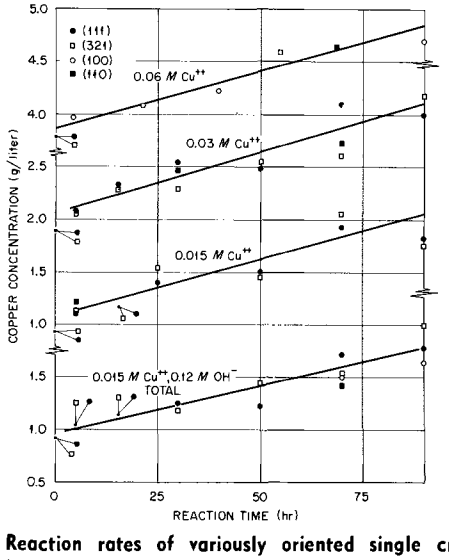

Fig. 1. Reaction rates of variously oriented single crystalline copper surfaces as a function of exposure time and solution composition in cupric-ammonia solutions.

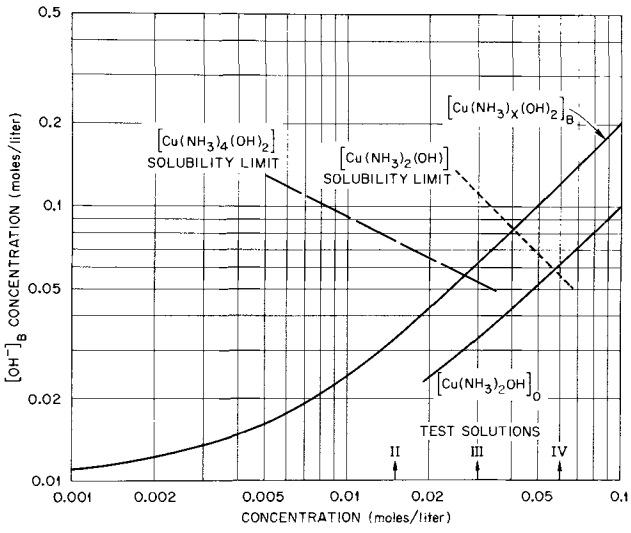

Fig. 2. Hydroxyl ion concentration in ~ 15M aqueous ammonia shown as a function of the concentration of $Cu(NH_3)_x(OH)_2$ in the system. Compositions of test solution types II, III, and IV also are indicated. Subscripts "B" and "O" refer to bulk and interfacial concentrations, respectively, when a copper surface is exposed to the solutions. Values of $[Cu(NH_3)_2OH]_0$ are calculated, of course, and are simply twice the corresponding bulk cupric concentrations.

the complete conversion of all cupric ions to cuprous (as demonstrated by the change from the characteristic deep blue color of cupric ammonia complexes to the colorless cuprous form) occurred simultaneously only in solutions initially containing ~ 1.90 g/l (0.03M) copper as soluble $Cu(NH_3)_x(OH)_2$. Therefore, the solubility limit of $Cu(NH_3)_2OH$ in ~ 15M aqueous ammonia was ~ 0.06M.

Using this value it is possible to estimate the activity coefficient for NH_3 in these concentrated systems: From the relationship

$$\frac{[NH_3]}{[OH^-]} = [NH_4^+]\ 5.5 \times 10^4 \ ^1 \quad [4]$$

it is readily seen that any contribution to the total hydroxyl ion concentration from the NH_4OH inevitably present must be small compared with the ~ 0.06M concentration associated with the cuprous complex, and may be neglected at this concentration. Then assuming that at this composition activity coefficients for all components other than NH_3 are unity, from the relationship

$$[Cu^+]\,[OH^-] = 1.26 \times 10^{-15} \quad [5]$$

and the stability constant of the cuprous ammonia complex

$$[NH_3]^2 = \frac{[Cu(NH_3)_2^+]}{[Cu^+]} \times 1.38 \times 10^{-11} \quad [6]$$

an activity coefficient of ~ 0.4 can be calculated for NH_3 in ~ 15M aqueous ammonia.

Using this value in Eq. [4] it is possible to determine the relationship illustrated in Fig. 2 between the total hydroxyl ion concentration, due to the presence of NH_4OH as well as $Cu(NH_3)_x(OH)_2$, and the concentration of the latter dissolved in concentrated aqueous ammonia. It is seen that at concentrations of $Cu(NH_3)_x(OH)_2 \gtrsim$ 0.03M practically all hydroxyl ions are furnished by the copper salt, while at lower concentration of the cupric complex significant contribution is made by the ammonium hydroxide present in the system. Figure 2 also illustrated another interesting feature of these solutions. From the relationships

$$[Cu^{+2}]\,[OH^-]^2 = 1.52 \times 10^{-20} \quad [7]$$

[1] See ref. (8) for the origin of all constants quoted here.

and

$$\frac{[Cu^{++}]\,[NH_3]^4}{[Cu(NH_3)_4{}^{++}]} = 2.35 \times 10^{-13} \qquad [8]$$

by using the previously indicated values for activity coefficients, it is possible to calculate the solubility limit of $Cu(NH_3)_4(OH)_2$ in the system. The figure shows that in ~ 15M aqueous NH_3 the solubility of $Cu(NH_3)_4(OH)_2$ could not exceed ~ 0.027M. Therefore, the primary effect of the formation of a $Cu(NH_3)_5{}^{++}$ complex ion, which Pugh *et al.* (4) reported to be the predominant complex cupric species in these systems, is to increase the total amount of copper which can be dissolved in such solutions. The calculations show that a saturated solution of $Cu(NH_3)_4(OH)_2$ could not generate sufficient cuprous ions at a copper interface to exceed the solubility of $Cu(NH_3)_2OH$ and form a tarnish film.

Also, the solubility limit of $Cu(NH_3)_2OH$ calculated from [5] and [6] is shown, as well as the maximum possible concentration of this species at a copper metal-solution interface when it is assumed that, as in the model proposed by Bertocci, at the interface all cupric ions have been converted to cuprous by the occurrence of reaction [1]. The calculations indicate that for interfacial concentrations which correspond to $Cu(NH_3)_x{}^{+2}$ bulk concentrations greater than ~0.028M, solubility of $Cu(NH_3)_2OH$ should be exceeded at the metal solution interface. This is in excellent agreement with the observed onset of film formation whenever the concentration of the cupric complex increased to ~ 0.03M in type II test solutions. Further agreement was indicated by immediate film formation on copper specimens when exposed to solution types IIa and III. The bulk hydroxyl ion concentration in the former solution totaled 0.12M and the cupric complex 0.015M. Using 0.4 for the activity coefficient of NH_3, Eq. [5] and [6] can be used to show that concentrations are such that conditions are established in which the solubility of $Cu(NH_3)_2(OH)$ is just exceeded at a copper metal interface immediately upon immersion in either type IIa or III solutions. Type IV solutions, of course, produced a great excess of cuprous species at the interface over that necessary to exceed the solubility of $Cu(NH_3)_2OH$.

Despite differences in composition, the type, as well as the rate, of film growth on copper surfaces was precisely the same in these three test solutions. In early growth stages (< ~ 15 hr exposure) a semitransparent film was formed through which features of the substrate often could be seen. The film appeared brown when wet, but a mottled green-yellow-red when dry. It was firmly adherent, compact, and possibly bore some epitaxial relationship to the single crystal substrate. After longer reaction times the films appeared blue-black when wet, and only slightly lighter in color when dried. Average film thicknesses gradually increased from ~ 2μ at 30 hr to ~ 8μ at 50 hr, although film growth did not always occur in a uniform manner for occasionally some areas were covered by a slightly thicker film than others. When dried the black film occasionally cracked or flaked away from the metal surface, and infrequently wet films did not adhere well to the substrate. Chemical analysis of the early tarnish film indicated it to be extremely porous, containing only about 20% of the theoretically possible Cu_2O. After still longer reaction times (50-90 hr) the films did not undergo further changes in appearances; nor did they grow much thicker, for the thickest films measured only ~ 10μ after 90 hr reaction. However, they did become much more dense and compact, and analysis revealed these films contained ~ 80% of the Cu_2O theoretically possible. Also, they adhered quite firmly to the substrate.

Electron diffraction measurements revealed that in all cases the films consisted primarily of Cu_2O. It seems, therefore, that differences in appearances, color, etc., arose from causes other than major differences in composition. No effects of orientation on film types were detected. However, for any given set of conditions, films on the copper (111) adhered better than on other orientations, although only slightly better than on the (100).

Reaction in type II solutions produced metal surfaces free of visible films, but greatly etched and faceted as illustrated in Fig. 3. Removal of equal amounts of material in type III solutions through thick oxide films on the surfaces resulted in a much more uniformly attacked surface substrate, as is also illustrated. Furthermore, the greater the supersaturation of CuOH produced at the interface, the more uniform was the surface attack as is illustrated in the figure. The appearance of the (100) substrate after prolonged reaction in the two types of test solution not shown in Fig. 3 are illustrated in Fig. 4. It is clear that test solutions III and IIa react in a very similar manner, but do not cause as uniform an attack as observed with type IV solutions.

The influence of oxide formation on reaction at a twin boundary is shown in Fig. 5. Since, as previously noted, reaction rates were the same in all test solutions, the different reaction times illustrated in Fig. 5 are directly proportional to the amount of material removed. Note that less material was removed preferentially at the boundary in every case where reaction occurred through a thick film covering the surface. Only after 70 hr in test solution III was boundary attack equivalent to that after only 2 hr in type II solution. To examine further the effects of grain boundaries on reactivities, polycrystalline copper specimens also were exposed to the test solutions. Typical results are illustrated in Fig. 6. Attack in type II solutions produced the normally heavily etched surface containing pits, etc., but type III solutions caused drastic alterations in surface appearances. As illustrated, in the latter case certain areas apparently reacted very little while others reacted to a greater extent. Comparison of these two illustrated surfaces indicated little relationship between grain boundary structure and the reactive areas on the film-covered polycrystal surface, although possibly the least reacted areas originally resulted from an epitaxial relationship between the film and substrate. On the illustrated surface obtained in type III solutions the areas of deepest attack were ~ 5μ, and as shown, reaction in these areas was more or less uniform on a large scale and no deep crevices or other evidence of preferential grain boundary attack was observed.

Brass-cupric ammonia systems.—With the exception of a few samples ~ 9° from the (111), the data were obtained from α-brass surfaces oriented (111). At the termination of reaction, solutions were analyzed for both copper and zinc content. In solution types II, IIa, III, and IV there was an initial decrease in copper content of the solutions so that part of the film concomitantly developed on the brass surface formed from copper initially in solution; and although the presence of zinc in solution could be detected, the zinc analysis was not sufficiently sensitive at low concentrations to conclude that its increase corresponded to the decrease in copper content. Therefore, little comparison can be made of the initial rates of reaction with those of copper, nor of the ratio of zinc/copper concentrations in solution. However, as reactions proceeded, the bulk copper concentrations in solution increased such that original concentrations were exceeded, and of course zinc concentrations increased with time.

When exposed to test solutions II, IIa, III, and IV films immediately began to form and grow on the brass surfaces. (It should be recalled that films on copper surfaces exposed to test solution II were not observed until after about 90 hr reaction time when the composi-

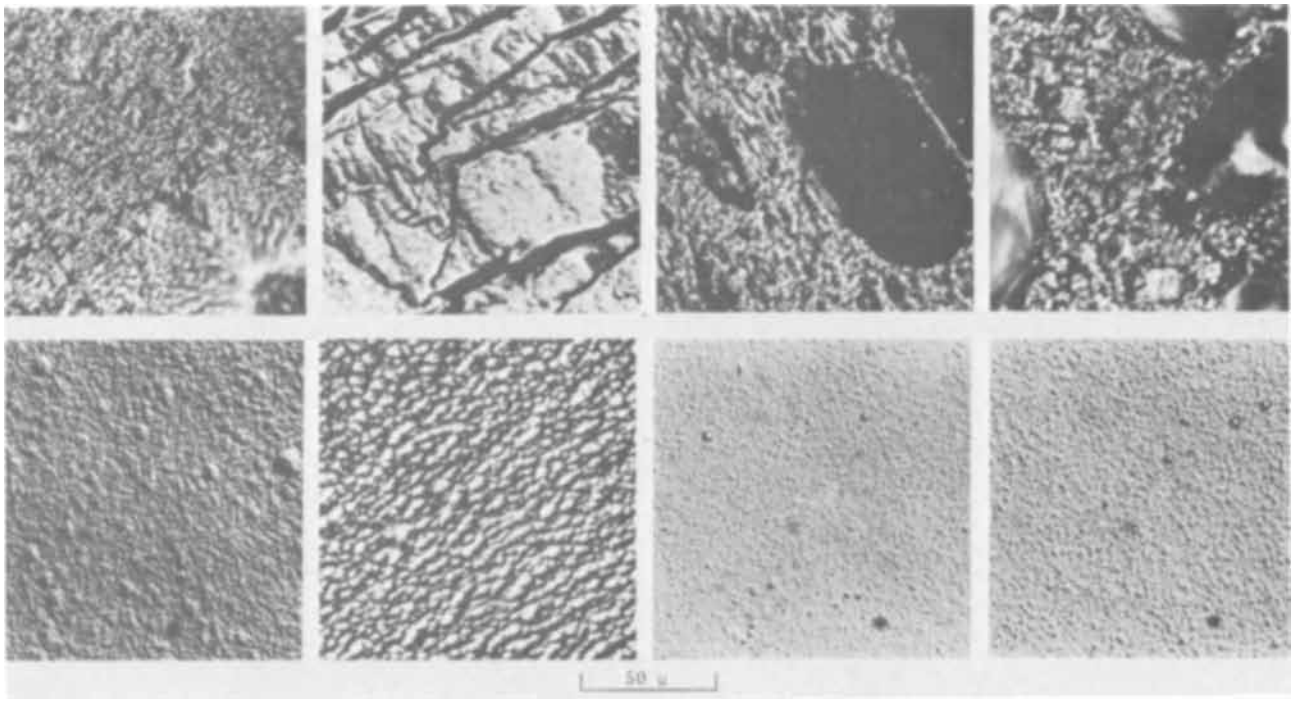

Fig. 3. Effects of orientation and solution composition on surface appearances. Top left to right: (111), (321), (110), and (100) after 90 hr exposure to type II solutions without visible film formation. Bottom illustrates the same orientations as above, but are photographs of metal substrates after "tarnish" film removed following 90 hr reaction in type III solutions for the (111) and (321), and the same length of exposure to type IV solutions for the (110) and (100). Although surfaces were film covered during the entire exposure to type III and IV solution, approximately the same amount of material had been removed from each of the eight surfaces illustrated.

tion of the solution had changed to approximately that of type III test solutions.) Like the copper systems, the rate and type of film growth on brass was approximately the same in all these test solutions. In the earliest stages ($< \sim 2$ hr) a relatively thin, more-or-less transparent film through which features of the substrated were discernible formed over the surface in an apparently homogenous manner. Interference colors were seen, and the film appeared firmly attached to the substrate. At exposure times greater than 2 hr it became obvious that further reaction did not proceed in a uniform manner over the entire surface. On portions of the surface the film appeared relatively unchanged from earlier appearances, but in other areas the film became opaque and darkened to a brown hue. When completely freed of all films it could be observed that the areas under dark film patches were more deeply etched than those portions of the surface which had been covered by the transparent film. With time the brown areas of the film changed to a dark blue-black color, and the regions covered by dark film islands increased at the expense of the less reactive areas under the thin transparent film. After approximately 70 hr, the mottled appearance vanished as the surfaces were entirely covered with the familiar "tarnish" film. But even on removal of the tarnish film formed during 70 or more hours reaction time, examination of the substrate revealed that attack had occurred in the described manner, for although all areas had reacted extensively, some had reacted to a much greater extent than others. All these observations are illustrated in Fig. 7 which shows the growth of island areas and concomitant changes in the structure of the substrate.

Direct measurements of tarnish film thicknesses could not be made. However, in general they appeared to fill the etched crater containing them and not to protrude significantly above the surface covered by the transparent film. Since the thicker films were contained in what was effectively an enormous etch

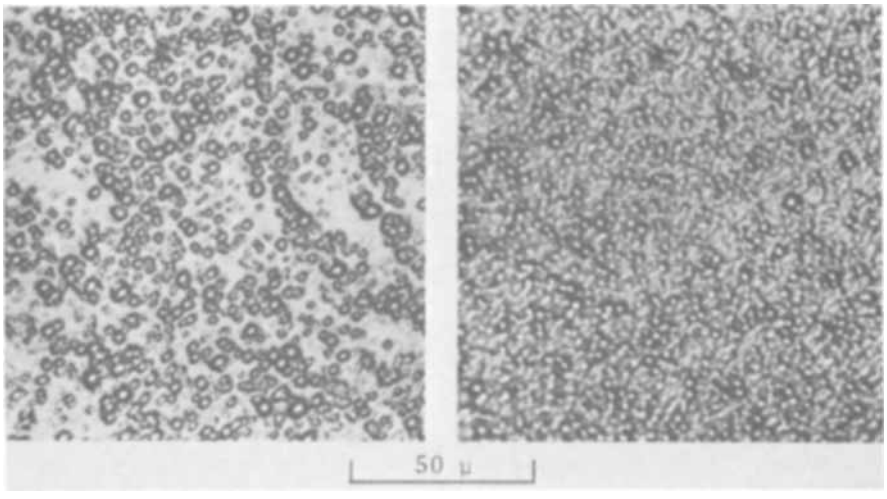

Fig. 4. Metal substrates of (100) after film removed following 90 hr reaction in solution type IIa (left) and III (right). Total reaction at these surfaces was the same as for those illustrated in Fig. 3.

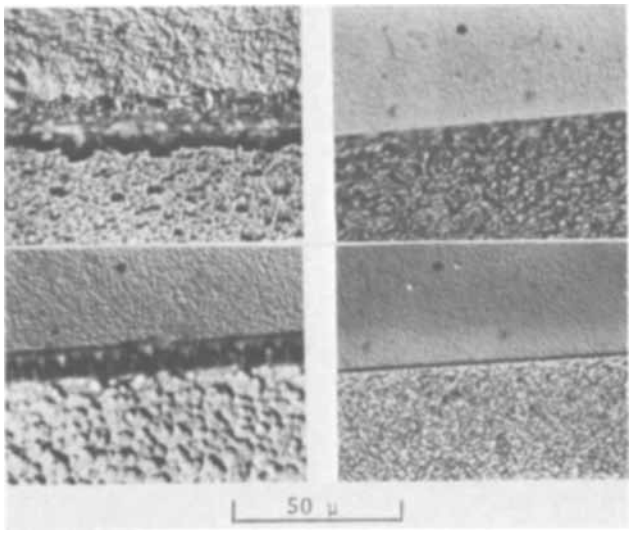

Fig. 5. Effects of reaction time, orientation, and solution composition on a bicrystal surface. In each photograph the top surface illustrated is a (111) and the bottom a (511). Top left: after 2 hr in type II solution without visible film formation; top right; metal substrate following film stripping after 2 hr reaction in type III solution; bottom left: metal substrate following film stripping after 70 hr in type III solution; bottom right: metal substrate following film stripping after 15 hr reaction in type IV solution.

pit with extremely rough and irregular features, they appeared reasonably adherent. Certainly once the tarnish film had developed over the entire surface the films appeared extremely compact and adherent.

Electron diffraction was used to establish that the tarnish films consisted of Cu_2O, ZnO, and Cu. Whether the slight traces of copper metal detected had their origin in the metal or in the solution is not known. However, the former is considered more likely since analysis indicated the tarnish films to be $\sim$ 80% Cu_2O and 20% ZnO so that no evidence for selective zinc dissolution was found in thick films. The traces of metallic copper possibly were inclusions of metal detached with the film during the stripping process.

In order to confirm the observations of Pugh and Westwood that film formation occurred in $\sim$ 15M aqueous ammonia with $Cu(NH_3)_x(OH)_2$ concentrations less than $\sim$ 0.01M, brass specimens were exposed to concentrated solutions of ammonia 0.005M and 0.007M in the soluble cupric hydroxide complex. Film formation was observed on surfaces in these solutions within 2 hr, and after 4 hr the unmistakable beginnings of nonhomogenous attack of the type illustrated in Fig. 7 were observed.

Discussion

At this point it is interesting to use Bertocci's model for interfacial and diffusion layer processes to construct a diagram of the bulk and interfacial concentrations of various components in a system of α-brass (70% Cu-30% Zn) reacting in cupric-ammonia systems. The results are shown in Fig. 8. For purposes of comparison, the corresponding concentration ranges of Pugh and Westwood are also indicated on the graph. The solubility limits of cuprous and zinc species are shown, as are their calculated maxima interfacial concentrations. Zinc relationships were calculated from the values

$$[H^+]^2\,[ZnO_2^{2-}] = 10^{-29} \qquad [9]$$

$$[Zn^{2+}]\,[OH^-]^2 = 10^{-17} \qquad [10]$$

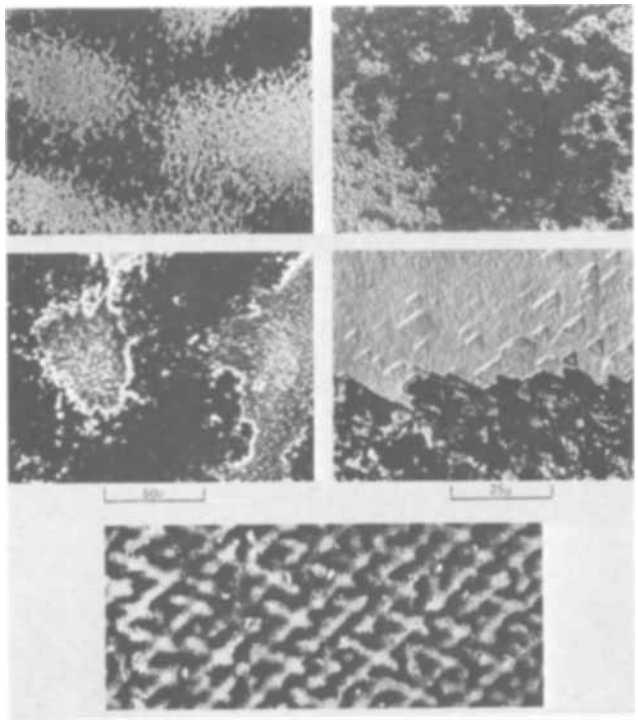

Fig. 7. α-brass surfaces oriented (111) after exposure to various test solutions. Top: after 4 hr in test solutions containing 0.005 g/l Cu (1/3 type II solution concentration), film covered surface (left), and substrate after film dissolved (right), magnifications as indicated. The dark aspect of the film is due to the presence of the "brown" appearing oxide. The substrate appears dark even when the brown film is removed because vestiges of the film remain and also because the area is heavily faceted. Middle: after 20 hr in type IV solution; surface illustrated at left was completely film covered and dark areas correspond to tarnish film, the lighter to the thin semitransparent film; the substrate after the film was dissolved away is illustrated at the right, and the highly local nature of the attack is emphasized. The bottom photograph is a low magnification picture of a brass substrate (originally completely covered with "tarnish" after 90 hr in type II solution) following dissolution of the film in aqueous ethylenediamine. The dark areas reflect the heavy faceting underlying the thick tarnish, the light areas reacted much less extensively. Note the geometric nature of the attack on this unstressed surface oriented $\sim$ 9° from the (111).

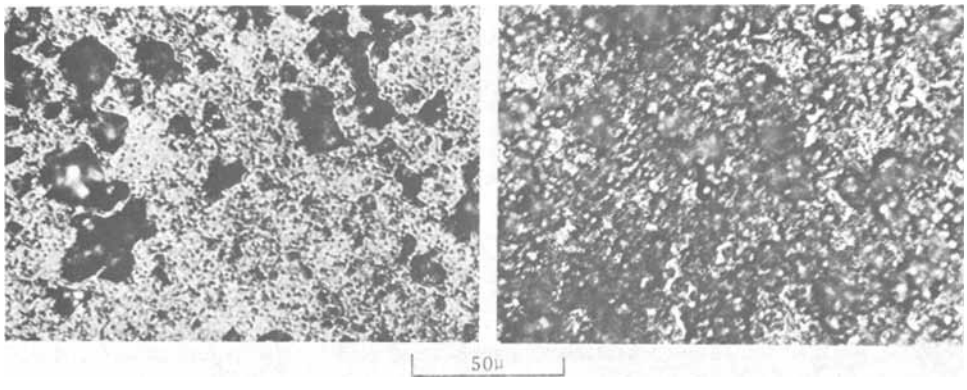

Fig. 6. Polycrystalline copper surfaces after 5 hr exposure to type II solution (left) and 70 hr to type III (right).

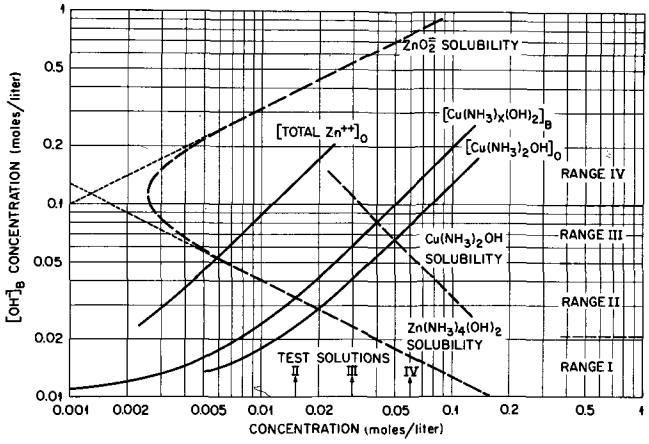

Fig. 8. Concentrations and solubility limits of various species in systems of α-brass exposed to solutions of ~ 15M aqueous ammonia containing the indicated concentrations of $Cu(NH_3)_x(OH)_2$. The subscripts B and O refer respectively to bulk concentration and those at the α-brass-solution interface.

$$\frac{[Zn^{2+}]\,[NH_3]^4}{[Zn(NH_3)_4{}^{2+}]} = 10^{-9} \qquad [11]$$

As Bertocci pointed out, Zn exhibits a solubility minimum in the system due to its existence in solution in two forms. However, note that under the conditions reported here, as well as those of Pugh and Westwood, zincate ions could not have been formed in quantities sufficient to alter interfacial hydroxyl ion concentrations to any significant extent. According to the model, complete reduction of cupric ions to cuprous produces zinc and cuprous ions at the interface in quantities proportional to the composition of the brass. The calculations shown in Fig. 8 indicate $Zn(OH)_2$ should precipitate slightly before the solubility of CuOH was exceeded. Moreover, they also indicate that no precipitate should form at the interface until the bulk concentration of $Cu(NH_3)_x(OH)_2$ exceeded ~ 0.025M (test solution type III; Pugh and Westwood range III). Since film formation on α-brass is reported here, as well as by Pugh and Westwood, at much lower bulk cupric complex concentrations, it is apparent that experimental observations in α-brass systems do not agree with the proposed model.

It could be assumed that initial reaction occurred by the selective oxidation of zinc without dissolution of copper from the metal, and that cupric ions in solution were reduced to the metallic state. Such an occurrence would produce the maximum possible interfacial zinc ion concentration in that it would exactly equal the bulk cupric ion concentration. Even so, Fig. 8 shows $Zn(OH)_2$ should not precipitate at cupric ion concentrations less than ~ 0.015M, although film formation was observed at concentrations smaller by a factor of three. Despite this discrepancy, the values of the constants used in [9], [10], and [11] probably are not sufficiently accurate to justify absolute rejection of the possibility of initial selective zinc oxidation.

The most obvious reason for film formation on single crystalline α-brass surfaces outside the limits established by Bertocci's model could be assumed to result from locally higher concentrations than allowed in the model which presupposes a uniform attack. Such events might account satisfactorily for thick films over reactive regions, but not for the thin films always observed over the remaining surface areas. At any rate it is apparent that Bertocci's model of interfacial phenomena adequately defines suitable conditions for film growth to occur, but it does not define the limiting conditions for film formation in the α-brass system. Moreover, it should be realized that the model has limited application to the systems reported here and to those of Pugh and Westwood since in deriving the model consideration was restricted to conditions in which films were not formed.

The rather periodic occurrence of areas of excess reactivity over the surface of brass single crystals (see Fig. 7) suggests that such areas did not develop because of the defect structure of the substrate or film. Surface appearances imply that the initial semitransparent film on brass was essentially of a protective nature. Apparently at random locations on the surface the film was penetrated, and further reaction of a highly local nature occurred in these areas. Meanwhile, nearby areas reacted to a very limited extent. Obviously the more reactive areas were influenced by the orientation of the brass since reaction proceeded along preferred crystallographic directions. The data do not suggest that the passive areas played an active role in the dissolution process, and it is highly doubtful that reduction of cupric ions, for example, occurred at these locations. Had this happened the tarnish film should have grown at these sites immediately on exposure to the more concentrated type IV solutions since the solubility of $Cu(NH_3)_2(OH)$ would have been exceeded at the interface. As this did not occur, it seems reasonable to suppose that, due to the fact Cu_2O is a p-type and ZnO an n-type semiconductor, perhaps the thin oxide films covering brass were composed of a mixture of these two oxides such that electron conduction became difficult.

Application to Stress-Corrosion Phenomena

While all the data reported here were gathered from unstressed specimens, the observations do have some applicability to similar systems in which stress related phenomena were observed, particularly those of Pugh and Westwood. The chemical system of Forty and Humble and of McEvily and Bond was slightly different from that employed in these studies, but the chemistry of films formed in all these systems is sufficiently similar to give some validity to reasonable comparisons.

Information from both copper and brass systems indicates that the dark, tarnish film is of a protective, but not of a passivating nature. On copper the reaction rate was not hindered by the formation of very thick oxide layers, and clearly the tarnish on brass formed over the more reactive areas. This is not to conclude that the thin passive films on brass differed greatly in composition from the tarnish film. While this might well be true, it could not be demonstrated, and comparison with films over copper serves as a reminder of the possibility that the differences could have been only of density and texture.

Since brown films on α-brass actually only represent the early stages of tarnish film formation, it appears highly unlikely that "brown" and "tarnish" films functioned in different manners during stress-corrosion processes in the studies Pugh and Westwood conducted in concentrated aqueous ammonia. Tarnish formation seems primarily indicative of the breakdown of an initial passive film and a reaction rate sufficient to permit more rapid film growth. Then, since highly local attack was observed on these unstressed brass surfaces, it appears that mechanical rupture of the tarnish film in similar stressed systems is a sufficient, but not a necessary, condition for nonuniform reaction to occur. As a matter of fact, the observations reported here would suggest that in the absence of truly passive films there is little effect of substrate structure, and that interfacial processes conductive to tarnish formation are not compatible with those necessary to maintain the passive film on α-brass. Of course this does not invalidate the observations of others indicating a relationship between cracks generated in the tarnish film by flexing and subsequent attack and crack formation in the brass substrate. Even if no other effects were obtained by

such procedures, the beneficial influence on reaction rates by diffusion in solution contained within a crack rather than through an amorphous oxide film is apparent. Also, McEvily and Bond have pointed out that although Forty and Humble's specimens were deformed to such an extent that slip bands were formed, while such massive deformation was certainly sufficient to establish a correspondence between cracks in the tarnish and in the metal substrate, cracking of the metal could occur at much lower stresses.

Occurrence of reaction on unstressed single crystal brass surfaces in an enhanced manner along <110> crystallographic directions, as illustrated in Fig. 7, suggests an explanation for inter- or transgranular cracking in these systems. If solution composition is such that extensive reaction occurs before a film is formed, it is reasonable to expect a certain degree of intergranular attack as a result of enhanced reactivity at grain boundaries. Conversely, if solution compositions are such that films are formed immediately, transgranular cracking should increase as selective attack at grain boundaries is decreased and the structure of individual metallic grains becomes more important. As a matter of fact, a reasonable argument can be made that it is not always necessary to postulate surface layer embrittlement and film rupture associated with applied stress to understand stress related corrosion phenomena. As on the unstressed specimens reported here, film penetration (without mechanical rupture) could occur on stressed specimens in a random manner. Reaction progressing along preferred directions occasionally could encounter dislocation pile-ups. Alternatively, film penetration could occur coincidentally through unstressed film covering areas of dislocation pile-ups in the metal substrate.

Conclusions

1. Reaction rates at copper surfaces were independent of the presence, thickness, or appearances of films formed on the metal surfaces.

2. The activity coefficient for NH_3 in 15M aqueous ammonia is $\sim$ 0.4.

3. The significance of $Cu(NH_3)_5^{2+}$ formation in concentrated aqueous ammonia apparently is to permit greater total cupric complex concentrations than can be achieved with the less soluble $Cu(NH_3)_4^{2+}$ form.

4. Visible films formed on copper surfaces always consisted primarily of Cu_2O, even though vastly different in appearances due to conditions of formation and growth.

5. The model proposed by Bertocci for diffusion layer phenomena and interfacial concentrations is useful in defining conditions for film growth, although not necessarily the limiting conditions for film formation.

6. A thin, colorless film formed on α-brass acted as a truly passive film, but tarnish films were not as protective. The composition of the passive film could not be determined, but tarnish films were composed primarily of Cu_2O and ZnO in approximately the proportions the metals were contained in the brass specimens.

7. Mechanical rupture was not a necessary condition for penetration of the passive film in α-brass. Once film breakdown had occurred, highly local reaction proceeded along crystallographically preferred directions in unstressed specimens.

Manuscript received June 24, 1969. Research was sponsored by the USAEC under contract with Union Carbide Corporation.

Any discussion of this paper will appear in a Discussion Section to be published in the December 1970 JOURNAL.

REFERENCES

1. E. Mattsson, *Electrochim. Acta*, **3**, 279 (1961).
2. A. J. Forty and P. Humble, *Phil. Mag.*, **8**, 247 (1963).
3. A. J. McEvily, Jr., and A. P. Bond, *This Journal*, **112**, 131 (1965).
4. E. N. Pugh, W. G. Montague, and A. R. C. Westwood, *Trans. Am. Soc. Metals*, **58**, 665 (1965).
5. E. N. Pugh and A. R. C. Westwood, *Phil. Mag.*, **13**, 167 (1966).
6. U. Bertocci, *Electrochim. Metallorum*, **3**, 275 (1968).
7. J. W. Mitchell *et al.*, *Can. J. Phys.*, **45**, 453 (1967).
8. J. Bjerrum *et al.*, "Stability Constants, Part II: Inorganic Ligands," The Chemical Society, London (1958).

On the Correspondence between Electrochemical and Chemical Accelerated Pitting Corrosion Tests

B. E. Wilde* and E. Williams

Applied Research Laboratory, United States Steel Corporation, Monroeville, Pennsylvania

ABSTRACT

For some years now, many workers have been active in the development of a stainless steel that is resistant to pitting and crevice corrosion in halide media. Electrochemical techniques combined with statistical multiple-regression analysis have beeen used to derive a relationship between pitting susceptibility and chemical composition. Recent publications in the literature have suggested, however, that the use of electrochemical accelerated tests for pitting corrosion studies leads to erroneous conclusions about the pitting susceptibility of alloys. This paper describes the results of a program designed to investigate the above reports and firmly establish whether indeed electrochemical techniques can be used as valid accelerated tests in pitting-corrosion studies.

Extensive experimental investigation in 1*M* sodium chloride on Type 430 stainless steel have shown an excellent correlation between electrochemical and chemical techniques, both in visually observed pitting susceptibility and metal weight loss data. Further, data obtained in 1*M* sodium chloride containing different dissolved gases have indicated why other authors failed to obtain any correspondence between electrochemical and chemical accelerated pitting tests. Values of the critical breakdown potential were found to vary from -0.035 V_{SCE} to -0.185 V_{SCE} for the same steel in 1*M* NaCl saturated with oxygen and hydrogen, respectively.

Controlled potential chemical tests have shown, that although pitting can occur at potentials active to the breakdown potential, the corrosion potential in a given redox system rises to values more noble than this latter potential, as a necessary prerequisite for pit initiation.

Electrochemical techniques have been used extensively in the study of passivity breakdown and the development of alloys resistant to pitting corrosion. Brennert (1), Mahla and Nielson (2), and Kolotyrkin (3) have employed measurements of the "critical breakdown potential for passivity," E_c, to predict the resistance of alloys to pitting corrosion in halide media. Streicher (4) has successfully employed an electrolytic test to assess the pitting resistance of a number of alloys to chloride containing environments. The unique feature in these techniques is that they greatly accelerate the corrosion process, and thereby greatly facilitate laboratory studies (5-13). We have used the breakdown technique in our laboratory as a screening tool in alloy development programs, on the premise that, if we can raise E_c (by alloy chemistry changes) to potentials more noble than the corrosion potential of the alloy in the intended environment, we would get no pitting.

Recently, however, articles have appeared in the literature in which the validity of using E_c as an index of pitting corrosion in the above manner, has been questioned. France and Greene (14) report a lack of correlation between electrochemical and chemical exposure tests on AISI Type 430 stainless steel and zirconium in halide media. These authors argue that an electrostatic build-up of aggressive chloride ions at the metal interface occurs during electrochemical polarization, which does not necessarily occur at a freely corroding interface thereby leading to differing behavior. Steigerwald (15) has reported that although E_c relates to pitting performance in some manner, he has observed pitting to propagate at potentials active to E_c, for Fe/Cr alloys in acidified $FeCl_3$.

In view of the apparent conflict between the above reports and numerous laboratory tests, we undertook a study to demonstrate the correspondence between accelerated electrochemical and chemical pitting tests, no attempt being made to extend this correspondence to long term corrosion behavior. This paper describes the results of this study and an attempt to explain the discrepancies noted above.

Materials and Experimental Work

Effort was made as far as possible to duplicate the conditions reported by France and Greene (14) to be certain that the experimental technique was not a variable. Cylindrical electrodes of AISI 430 and 304 stainless steel were machined (0.25 in. diameter by 0.75 in. long) from solution-annealed stock having the composition shown in Table I. The electrodes were abraded through 2.0 emery paper, washed in detergent, rinsed in distilled water, and dried. Polarization experiments were conducted in a glass cell with bright-platinum

* Electrochemical Society Active Member.

Table I. Chemical compositions of steels used in this study

Composition, w/o

Designation	C	Si	Mn	P	S	Cr	Ni	Cu	Mo	W
AISI Type 430 stainless steel	0.094	0.32	0.56	0.026	0.01	16.35	0.17	0.08	0.02	ND
AISI Type 304 stainless steel	0.079	0.56	1.33	0.027	0.034	18.1	8.22	0.22	0.36	ND
AISI Type 316 stainless steel	0.08	0.40	1.7	0.036	0.018	17.2	11.6	0.2	2.2	ND
Carpenter 20 Cb3	0.027	0.39	0.37	0.016	0.004	20.56	33.71	3.38	2.24	ND
Incoloy 825	0.028	0.27	0.71	0.002	0.004	21.1	42.60	2.0	3.13	ND
Hastelloy C	0.06	0.73	0.67	0.007	0.005	15.44	56.27	ND	13.6	5.2

ND = Not determined.

auxiliary electrodes. The specimens were mounted on a Stern-Mackrides-type holder (16).

The corrodent was reagent grade 1*M* sodium chloride, dissolved in distilled water (6.3 meg ohm cm^{-1}), to give a final *p*H of 6.3 at 25°C. Tests were conducted under thermostatic control at 25° ± 1°C. All potentials were measured with reference to a saturated calomel electrode connected to the cell with a Luggin Haber probe. No effort was made to correct for liquid junction potentials. Polarization measurements were conducted potentiodynamically by using equipment and procedures described elsewhere (17, 18) at a sweep rate of 0.600 V/hr similar to the traverse rate used by France and Greene in their step technique. The continuous scan procedure was adopted in the interests of better reproducibility (18).

Accelerated chemical exposure tests were conducted in: (*a*) 1*M* sodium chloride solution containing 178 g/l $K_4Fe(CN)_6$ and 2.23 g/l $K_3Fe(CN)_6$ to give a final corrosion potential at −0.100 V_{SCE} on a Type 430 stainless steel electrode, (*b*) the standard "ferric chloride test" (19), that is, 108 g/l $FeCl_3 \cdot 6H_2O$, with the *p*H adjusted to 0.9 with HCl.

All solutions, unless otherwise stated, were saturated with hydrogen gas at a flow rate of 1.5 l/min, giving a dissolved oxygen content of 0.076 ppm.

Results and Discussion

Polarization measurements and environmental variables.—Potentiodynamic anodic polarization curves for the two steels in hydrogen saturated 1*M* sodium chloride are shown in Fig. 1. The electrolyte volume in each test was regulated to 600 ml, and the curves were constructed by exposing the specimen to the corrodent for 60 min, followed by scanning in the noble direction. In contrast to data reported elsewhere (14) no active-passive transitions were observed, and the corrosion potentials on Type 430 stainless steel were slightly more noble having a value of −0.492 V_{SCE}. Clear breakdown potentials were observed however on both steels, the value on Type 430 stainless steel coinciding closely with that published previously (14), (−0.185V). The value of E_c on Type 304 stainless steel was −0.050 V_{SCE}. Prolonged exposure to potentials more noble than E_c resulted in severe pitting corrosion, as shown in Fig. 2. Although not shown in Fig. 2, no evidence of crevice corrosion was observed on any sample, and each polarization curve was reproducible to ± 10 mV with respect to E_c on repeat runs.

Since previous accelerated chemical test data were obtained using oxygen as the oxidizer (14), anodic polarization curves were obtained for the two steels in oxygen saturated 1*M* sodium chloride, at a flow rate of 1.5 l/min, to see if the oxidizer affected the passive state. Typical curves are shown in Fig. 3, from which

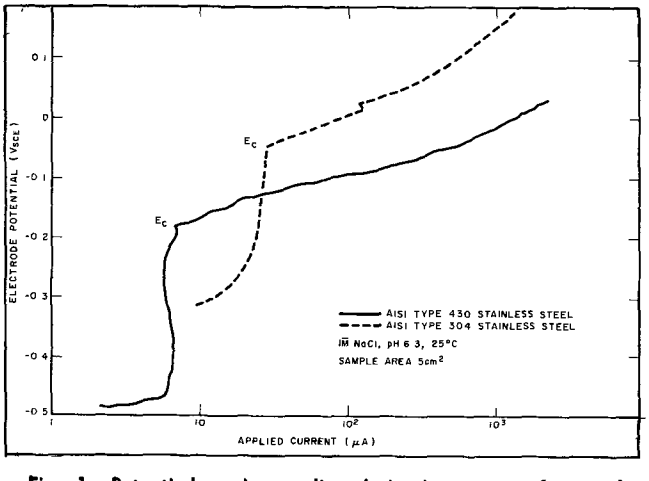

Fig. 1. Potentiodynamic anodic-polarization curves for steels exposed to hydrogen-saturated 1M NaCl sweep rate, 0.600 V/hr.

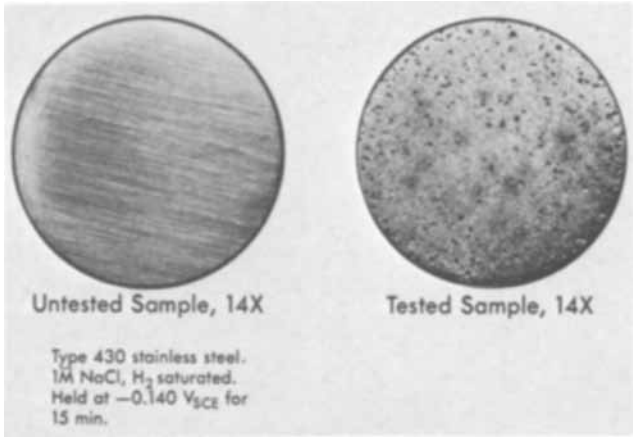

Fig. 2. Macrophotographs of AISI Type 430 stainless steel samples before and after polarization at potentials noble to E_c.

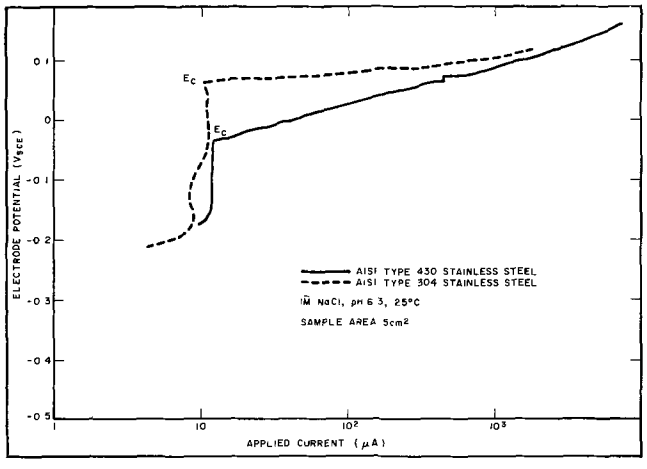

Fig. 3. Potentiodynamic anodic-polarization curves for steels exposed to oxygen-saturated 1M NaCl sweep rate, 0.600 V/hr.

it is clear that both steels evidenced a value of E_c considerably more noble than that recorded in hydrogen saturated solutions. It is interesting to note that the passive current for Type 430 stainless steel is not significantly affected by the presence of oxygen in the electrolyte, whereas that for Type 304 stainless steel is decreased. In view of the influence of oxygen on E_c, several other gases were used during polarization to see if any effect could be noted. The results of these experiments have been reported elsewhere (20), but are briefly summarized in Table II. It is evident from Table II, that E_c varies considerably with the nature of the stirring gas, which we treat as significant and not experimental artifacts in view of the stated reproducibility of our curves. Since nitrogen and argon are nonionic and do not participate in any electrode process, we do not at this time have any explanation of the effect. We might suggest however, that these gases may be involved in an adsorption process on the surface and, in this way, impede the adsorption of chloride ions that appears to be necessary for pit

Table II. Variation in E_c with the nature of the dissolved gases (20) in 1M NaCl at 25°C

Gas	$\frac{E_c}{V_{SCE}}$ Type 430 stainless steel	Type 304 stainless steel
Hydrogen	−0.185	−0.050
Nitrogen	−0.130	−0.020
Argon	−0.100	0.050
Oxygen	−0.035	0.065

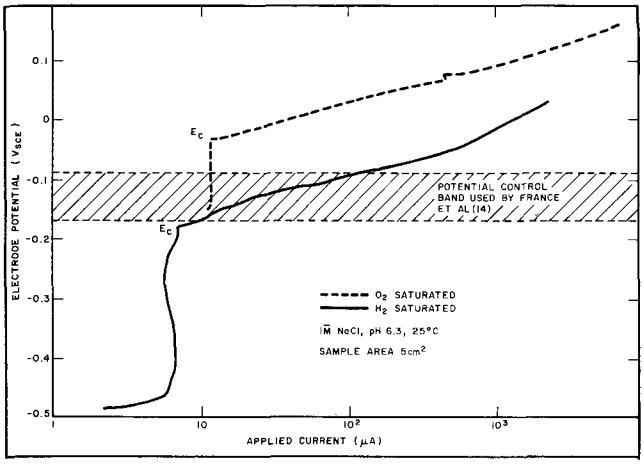

Fig. 4. Semischematic presentation of why previous authors (14) failed to pit AISI Type 430 stainless steel in chemical pitting tests with oxygen.

initiation (4, 21) to a degree varying with the nature of the gas. The important fact, however, is that E_c is not a unique function of alloy composition and is dependent markedly on environmental variables.

To explore the possible dynamic nature of this effect a Type 430 stainless steel was exposed to a solution of oxygen saturated 1*M* sodium chloride. The steady-state corrosion potential, E_{corr}, was -0.140 V_{SCE} in close agreement with that observed previously (14). Although on the basis of E_c obtained in hydrogenated solutions the sample should have pitted, no pitting was observed over a period of 100 hr. The sample was then connected to a potentiostat, and the applied potential regulated at -0.140 V_{SCE} for a further 100 hr, over which time no pitting was observed. At this point, without interrupting the applied potential, the oxygen flow was stopped and replaced by hydrogen at 1.50 l/min, and after 16 hr pronounced pitting occurred with a rapid increase in applied anodic current. These data clearly indicate the protective influence of oxygen with regard to passivity breakdown, and also that this influence can be destroyed merely by aspirating oxygen out of solution with hydrogen. Further they indicate the extreme caution which must be exercised when using breakdown data to predict pitting corrosion susceptibility.

On the basis of the above data, we can satisfactorily explain the reasons why France and Greene (14) did not get any correspondence between electrochemical and chemical accelerated pitting tests for Type 430 stainless steel as summarized in Fig. 4. It will be shown in a following section, that when controlled potential chemical tests are conducted with an oxidizer that does not interact with the passive film on the sample, complete agreement between the tests is obtained.

Accelerated chemical exposure tests.—The breakdown potentials of a series of alloys was determined, as previously described, in nitrogen-saturated 1*M* sodium chloride. The alloys were so chosen as to have a wide range of values of E_c, as shown in Table III. Each alloy was exposed to the "standard ferric chloride test" (19), for periods of 20 and 72 hr. Sheet specimens, (0.060 x 1 x 3 in.) were exposed, suspended in the solution by Teflon tape threaded through a hole in the top of the sample. At the same time, electrodes of each material were immersed and the potential/time behavior recorded. This corrodent contains chloride ions at a normality of 1.185 and is therefore similar to the 1*M* sodium chloride used to determine E_c, except that the redox potential on bright platinum was 0.555 V_{SCE} due to the presence of trivalent iron. In this solution, alloys whose corrosion potential went more noble than the breakdown potential should evidence pit initiation. Visual inspection after 20 and 72 hr indicated all the alloys had pitted except Hastelloy C as shown in Fig. 5. The potential transients are shown in Fig. 6, and are characterized by a relatively rapid (over 15 min) increase in E_{corr} to values between 0.220 and 0.525 V_{SCE}. On all samples except Hastelloy C, the corrosion potential then decreased in an oscillatory manner to values often much more active than E_c, and in certain cases to values approaching those reported by Steigerwald (15) on similar material, *e.g.*, -0.150 V_{SCE} for the 18 w/o Cr Type 304 stainless steel, and -0.300 V_{SCE} for

Table III. Experimental data on alloys used in chemical pitting tests in aqueous ferric chloride

Alloy designation	E_c (in 1*M* NaCl + N_2) V_{SCE}	Corrosion potential during test V_{SCE} Maximum	Minimum
Type 430 stainless steel	−0.130	0.230	−0.310
Type 304 stainless steel	−0.020	0.280	−0.140
Type 316 stainless steel	0.100	0.385	0.090
Carpenter 20 Cb	0.500	0.520	0.120
Incoloy 825	0.525	0.530	0.180
Hastelloy C	>0.900	0.530	0.530

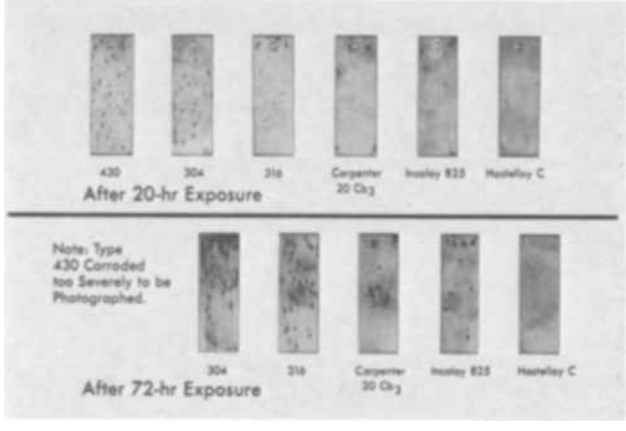

Fig. 5. Photographs of samples removed from the ferric chloride test indicating complete correlation with predictions of pitting susceptibility based on E_c.

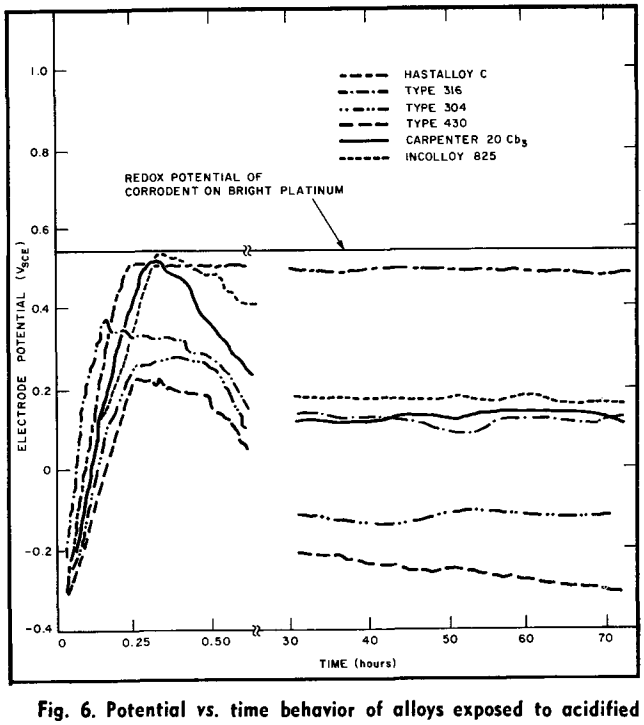

Fig. 6. Potential vs. time behavior of alloys exposed to acidified $FeCl_3$ solution.

the 17 w/o Cr Type 430 stainless steel. It is clear from inspection of Fig. 6 and Table III, that pitting did indeed occur at potentials more active than E_c for Types 304 and 430 stainless steel. However, it should be noted that at small times, all the samples except Hastelloy C, exhibited corrosion potentials more noble than their respective E_c and would therefore be expected to initiate pits. The initial passivation process, where the E_{corr} increases to values close to the solution redox potential, can be quite rapid as shown in the next section, where pit initiation occurred in less than 60 sec after immersion, followed by propagation at potentials more active than E_c, thus, both confirming and explaining Steigerwald's finding.

To further emphasize this point that E_c relates specifically to the pit initiation process and not to the propagation process, a series of controlled potential measurements were made. A schematic of a typical "cyclic" polarization curve (22) for Type 430 stainless steel in nitrogenated 3.5 w/o NaCl is shown in Fig. 7, to indicate the potential regions where pits once initiated, will propagate. Pits were initiated anodically at potentials noble to E_c in area A, then the applied potential was switched to those shown in areas B and C. It was clear that propagation occurred in area B, (*i.e.*, active to E_c) over a period of 100 hr, whereas no propagation was noted in area C. Pourbaix (22) has used such plots to develop the concept of the "protection potential E_p," which represents the potential more active than which pit propagation cannot be sustained and repassivation occurs.

From the above data, two significant factors emerge: (*i*) that there is complete correspondence in predictions of pitting susceptibility between electrochemical polarization data and exposure data obtained in an accelerated chemical test, and (*ii*) that although pitting corrosion can be sustained at potentials active to E_c, a necessary prerequisite in this process is that the corrosion potential of the sample at some time must become more noble than E_c to initiate pits. This latter process can occur quite rapidly in solutions of oxidizers and may be missed if a continuous potential check is not made, leading to the erroneous conclusion that pitting corrosion can initiate at potentials active to E_c.

Controlled potential chemical pitting tests.—It was shown above that oxygen stabilized the passive state with regard to breakdown by chloride ions, *e.g.*, values of E_c obtained in oxygenated solutions were considerably more noble than those obtained in hydrogenated solutions. On this basis it is understandable why no correspondence was obtained between controlled potential pitting tests conducted potentiostatically in H_2 saturated solutions and with oxygen as the oxidizer (14) in 1*M* sodium chloride solutions. To demonstrate further the correspondence between electrochemical and chemical pitting tests, a Type 430 stainless steel sample was exposed to a hydrogen saturated solution of 1*M* NaCl containing $K_4Fe(CN)_6$ and $K_3Fe(CN)_6$ to give a corrosion potential of -0.100 V_{SCE}. Selection of the ferro- and ferricyanide salts for a redox system was made on the premise that being large anions they would be less likely than oxygen to be involved in adsorption processes which stabilized the passive state. Within 60 sec after immersion, pit nuclei were clearly visible because the Fe^{2+} corrosion product formed a patch of "Prussian blue" at the pit site, as reported by Stoffel *et al.* (22). Continued exposure resulted in an oscillatory shift of E_{corr} in the active direction as observed in the $FeCl_3$ tests. Equivalent tests on the same material, conducted potentiostatically at -0.1 V_{SCE} in hydrogen saturated 1*M* sodium chloride, resulted in distinct pit nuclei after approximately 45 sec. These tests were conducted for 24 hr and a comparison made of the weight loss behavior and general appearance in both the electrochemical and chemical test. These data are shown in Table IV, from which it is seen that excellent agreement was observed between both tests.

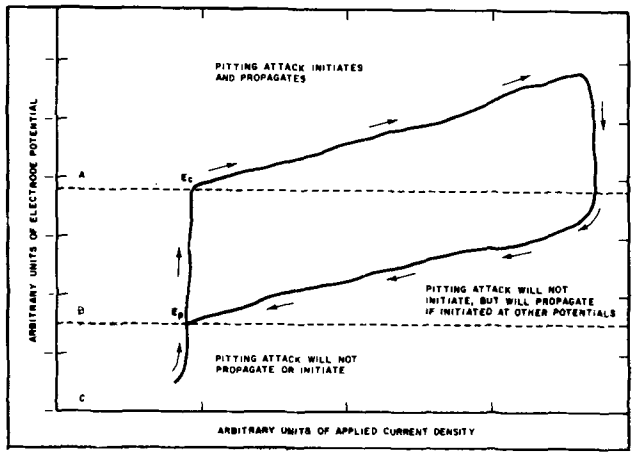

Fig. 7. Schematic presentation of data to support the argument that pit propagation can continue at potentials more active than E_c.

Table IV. Weight-loss data on AISI Type 430 stainless steel after electrochemical and chemical corrosion tests

	Type of test	
	1*M* NaCl	
	Electrochemical + 1*M* NaCl in H_2O +	$[Fe(CN)_6]^{4-}$ $[Fe(CN)_6]^{3-}$
Solution temperature	25° ± 1°C	25° ± 1°C
Exposure time	24 hr	24 hr
Specimen potential	-0.100 V_{SCE}	-0.100 V_{SCE}
Corrosion rate (mpy)	96.4	128
Initial pH	6.3	6.7
Final pH	8.3	6.9
Type of corrosion	Pitting	Pitting

Conclusions

Evidence has been presented which demonstrates the complete correspondence between the pitting corrosion behavior of Type 430 stainless steel in accelerated electrochemical and chemical tests. On the basis of polarization measurements and controlled potential corrosion studies, discrepancies previously reported between the two test methods can be satisfactorily explained.

The specific relation of the critical breakdown potential to pit initiation and not to pit propagation has been demonstrated, along with confirmation of the previously reported fact that pit propagation may proceed at potentials active to the breakdown potential.

It has been shown that extreme caution must be used when utilizing E_c as an index of pitting corrosion susceptibility, since the absolute magnitude of E_c has been demonstrated to vary not only with the well-documented environmental and experimental variables, but also with the nature of the gases dissolved in the corrodent.

Manuscript received Oct. 23, 1969.

Any discussion of this paper will appear in a Discussion Section to be published in the December 1970 JOURNAL.

REFERENCES

1. S. Brennert, *J. Iron Steel Inst.*, **135**, 101 (1937).
2. E. M. Mahla and N. A. Nielsen, *Trans. Electrochem. Soc.*, **89**, 167 (1946).
3. Ya. M. Kolotyrkin, *This Journal*, **108**, 209 (1961).
4. M. A. Streicher, *ibid.*, **103**, 375 (1956).
5. W. Schwenk, *Corrosion*, **20**, 129t (1964).
6. J. Horvath and H. H. Uhlig, *This Journal*, **115**, 791 (1968).
7. H. P. Leckie and H. H. Uhlig, *ibid.*, **113**, 1262 (1966).

8. V. Hospadaruk and J. V. Petrocelli, *ibid.*, **113**, 878 (1966).
9. M. Pourbaix, L. Klimzack-Mathieiu, Ch. Mertens, J. Meunier, Cl Vanleugenhaghe, L. deMunck, L. Laureys, L. Neelemans, and M. Warzee, *Corrosion Sci.*, **3**, 239 (1963).
10. Ya. M. Kolotyrkin, "First International Congress on Metallic Corrosion," p. 10, Butterworths, London (1962).
11. Ya. M. Kolotyrkin, *Corrosion*, **19**, 261t (1963).
12. T. P. Hoar, D. C. Mears, and G. P. Rothwell, *Corrosion Sci.*, **5**, 279 (1965).
13. D. E. Davies and M. M. Lotlikar, *Brit. Corros. J.*, **1**, 149 (1966).
14. W. D. France and N. D. Greene, *Corrosion*, **26**, 1 (1970).
15. R. F. Steigerwald, *ibid.*, **22**, 107, (1966).
16. M. Stern and A. C. Makrides, *This Journal*, **107**, 782 (1960).
17. B. E. Wilde and N. D. Greene, *Corrosion*, **25**, 300 (1969).
18. W. D. Henry and B. E. Wilde, *ibid.*, **25**, 515 (1969).
19. H. A. Smith *Metal Progr.*, **33**, 596 (1938).
20. B. E. Wilde and E. Williams, *This Journal*, **116**, 1539 (1969).
21. E. Brauns and W. Schwenk, *Archiv. Eisenhuttenw.*, **32**, 387 (1961).
22. M. Pourbaix, Private communication, CEBELCOR, Brussels, Belgium.
23. H. Stoffels and W. Schwenk, *Werkstoffe u. Korrosion*, **12**, 493 (1961).

Technical Notes

Diffusion Coefficients in Propylene Carbonate, Dimethyl Formamide, Acetonitrile, and Methyl Formate

J. M. Sullivan,[1] D. C. Hanson, and R. Keller*

Rocketdyne, A Division of North American Rockwell Corporation, Canoga Park, California

Diffusion coefficients in aprotic solvents are of interest for estimates of transport limitations in nonaqueous lithium batteries. Integral diffusion coefficients of $LiClO_4$ and some other solutes were measured in four aprotic solvents, and viscosity data were obtained.

The solvents propylene carbonate (PC), dimethyl formamide (DMF), and acetonitrile (AN) were distilled, and were analyzed by a vapor phase chromatographic technique employing a Porapak Q column. Solvent batches were used that contained 40 ± 20 ppm water and less than 60 ppm organic impurities according to this analysis; impurity contents were somewhat higher in the case of methyl formate (MF), namely, about 100 ppm water and 500 ppm methanol.

High grade commercial products were analyzed and used without further purification as solutes, except for vacuum drying of the lithium compounds. Lithium hexafluoroarsenate was supplied in a methyl formate stock solution by Honeywell's Livingston Electronic Laboratory, Montgomeryville, Pennsylvania.

A method that involves determining the weight change of a porous disk filled with the solution to be tested was employed for measuring diffusion coefficients. This method is described in detail in ref. (1) and was first used by Schulze (2). It has been revived by Wall *et al.* who studied its application to measure diffusion coefficients for aqueous electrolyte solutions (3), diffusion coefficients of polymers in aqueous environment (4), and in various nonaqeuous solutions (5). In this present work, the method has been applied to measure diffusion coefficients in aprotic electrolyte systems.

A porous disk was filled with the solution to be studied and suspended in a large volume of pure solvent. The apparent weight is measured as a function of time, and an average or integral diffusion coefficient, D, determined from equation

$$\log[W(t) - W(\infty)] = \alpha Dt + b \qquad [1]$$

where $W(t)$ is the apparent weight of the suspended disk at time t, and $W(\infty)$ the weight after equilibrium has been reached; α is an apparatus constant.

The recommended Micro-Porous Filter Disks (2-in. diameter, ¼-in. thick, porosity No. 10) were obtained from the Selas Corporation of America. They were evacuated, filled with the solution to be studied, and allowed to soak overnight. Each disk was suspended by a fine wire from the arm of an analytical balance in about 1½ liters of pure solvent. The solvent container was placed in a constant temperature mineral oil bath maintained at 25.00° ± 0.02°C. A flow of nitrogen was swept over the solvent. An aqueous 1.5M KCl solution was used for the determination of the frit constant α [in accordance with ref (1), the differential diffusion constant for one-half of the initial KCl concentration in the frit was employed, *i.e.*, $D = 1.87 \times 10^{-5}$ cm^2 sec^{-1} at 25°C].

The results of diffusion coefficient measurements are given in Table I; the estimated accuracy is 1-2%.

Viscosities were determined by a conventional technique involving measurement of the efflux time of the solutions through a capillary. Results are given in Table II.

There was direct correlation between the diffusion coefficient and the solvent viscosity. If the products of these two values, $D \times \eta_{(solvent)}$, are formed, they deviate not more than ±16% from the average for the reported values (the consistency is significantly smaller if the viscosity of the solution rather than of

Table I. Diffusion coefficients in aprotic solvents at 25°C

Electrolyte	Diffusion coefficient, cm^2 sec^{-1}
1M $LiClO_4$/PC	2.58×10^{-6}
0.7M LiCl + 1M $AlCl_3$/PC	3.04×10^{-6}
1M $LiClO_4$/DMF	7.29×10^{-6}
1M LiCl/DMF	5.87×10^{-6}
1M $LiClO_4$/AN	1.71×10^{-5}
1M $LiClO_4$/MF	1.68×10^{-5}
1.1M $LiAsF_6$/MF	1.54×10^{-5}

* Electrochemical Society Active Member.
[1] Present address: Fundamental Research Branch, Tennessee Valley Authority, Muscle Shoals, Alabama.

Table II. Viscosities of aprotic solvents and solutions at 25°C

Solution (solvent)	Viscosity, millipoises
PC	24.8
1M $LiClO_4$/PC	70.8
DMF	7.93
1M $LiClO_4$/DMF	18.9
AN	3.36
1M $LiClO_4$/AN	6.60
MF	3.38
1.1M $LiAsF_6$/MF	8.06

the solvent is considered). It may be tentatively suggested to estimate diffusion coefficients for other, similar solutions based on the solvent viscosity. It should be noted, however, that the values given here were all for solutes containing lithium ions at a concentration of 1M; diffusion coefficients of other solutes which do not contain the strongly solvated lithium ion with its low ion mobility are expected to be somewhat greater. The diffusion coefficient of 1M LiCl/DMF, incidentally, is believed to be slightly lower than the diffusion coefficient for 1M $LiClO_4$/DMF because of ion pair formation.

Acknowledgments

This work was supported by the NASA Lewis Research Center, under Contract NAS3-8521. The efforts of Dr. J. N. Foster in analyzing starting materials are gratefully acknowledged.

Manuscript submitted June 16, 1969; revised manuscript received Feb. 5, 1970.

Any discussion of this paper will appear in a Discussion Section to be published in the December 1970 JOURNAL.

REFERENCES

1. D. P. Shoemaker and C. W. Garland, "Experiments in Physical Chemistry," p. 156, McGraw-Hill Book Co., New York (1962).
2. G. Schulze, *Z. physik. Chem.*, **89**, 168 (1914).
3. F. T. Wall, P. F. Grieger, and C. W. Childer, *J. Am. Chem. Soc.*, **74**, 3562 (1952).
4. F. T. Wall and C. W. Childer, *ibid.*, **75**, 6340 (1953).
5. G. B. Taylor and F. T. Wall, *ibid.*, **75**, 3550 (1953).

Liquidus Curves for Aluminum Cell Electrolyte

V. Representation by Regression Equations

E. W. Dewing*

Alcan Research and Development Limited, Arvida, Quebec, Canada

Previous reports from this laboratory (1-4) have given liquidus curves for a wide range of aluminum reduction cell electrolytes based on cryolite. The object of this note is to rationalize the results in the form of equations which may be used to predict the freezing point of any composition likely to be encountered in practice.

The typical pseudo-binary diagram for the system (cryolite + additives)-alumina shows a cryolite liquidus and an α-alumina liquidus meeting in a eutectic. For small additions of all additives except NaF and AlF_3 (the constituents of cryolite) the lowering of freezing point of cryolite should be linear and additive; for higher concentrations nonlinear terms may need to be introduced in order to obtain a good fit. For NaF and AlF_3 the linear terms are absent (since the freezing point is a maximum at the cryolite composition and small additions do not affect it) and only squared and higher order terms are needed. The equation for the cryolite liquidus to be tried is thus of the type

$$t = t_o + a(Al_2O_3) + b(Al_2O_3)^2 + c(CaF_2) + d(CaF_2)^2$$

$$+ e(CaF_2)(AlF_3) + f(AlF_3)^2 + \ldots\ldots\ldots\ldots$$

where (Al_2O_3), etc., represent weight per cent (w/o). [Note that (AlF_3) and (NaF) are quantities in excess of the cryolite composition and not total quantities.]

The unknown constants t_o, a , b, etc., in this equation were determined by a step-wise least-squares regression analysis program which accepted only those terms which were statistically significant. Most of the higher order terms were rejected. Three separate equations were generated; one for the normal range of cell operation (CaF_2 up to 12 w/o, AlF_3 up to 16.67%), one for the additives NaF, AlF_3, Al_2O_3, CaF_2, MgF_2, Li_3AlF_6, and NaCl to a maximum freezing point depression of 100°, and the third for depressions of up to 200°. The respective standard deviations of the experimental values from the equations are 2.1° (51 points), 2.9° (112 points), and 3.5° (133 points). Since the experimental accuracy is certainly not better than 1° this is satisfactory. Table I shows the coefficients in the equations.

Developing an equation for the alumina branch of the liquidus has to be done on empirical grounds since the concentrations are high and there is no useful limiting law to act as a guide. After several trials a general power series of the type

$$t = t_o + a(AlF_3) + b(Al_2O_3) + c(AlF_3)(Al_2O_3) + d(Al_2O_3)^2 + \ldots$$

was used. No terms in (NaF) were employed since, if it is present in any substantial amount, β-Al_2O_3 instead of α-Al_2O_3 is the stable phase.

The earlier experimental values (1-3) were obtained by visual observation of the onset of crystallization, while later ones (4) were obtained by an

Table I. Equations for the cryolite liquidus

	Eq. [1]	Eq. [2]	Eq. [3]
Restrictions	$(CaF_2) \leq 12$ w/o $(AlF_3) \leq 16.67$ w/o	$(CaF_2) \leq 15$ w/o Liquidus ≥ 909°C	$(CaF_2) \leq 15$ w/o Liquidus ≥ 809°C
Term	Coefficients		
$(NaF)^2$	—	−0.1474	−0.1604
$(NaF)^3$	—	+0.00205	+0.00248
$(AlF_3)^2$	−0.117	−0.1453	−0.1633
$(AlF_3)^4$	−0.000296	−0.000194	−0.000169
(Al_2O_3)	−6.646	−7.088	−7.204
$(Al_2O_3)^2$	+0.168	+0.214	+0.209
(CaF_2)	−2.853	−2.898	−2.990
(MgF_2)	—	−5.167	−5.307
(Li_3AlF_6)	—	−4.652	−4.900
(NaCl)	—	−4.786	−4.916
Constant	1010.6	1011.7	1013.5
Standard deviation	2.11°C	2.85°C	3.48°C
No. of exptl. points	51	112	133

Note: Concentrations, *e.g.*, (CaF_2) are in weight per cent (w/o). (NaF) and (AlF_3) are excess quantities and do not include that contained either in the Na_3AlF_6 or in Li_3AlF_6.

* Electrochemical Society Active Member.

Key words: cryolite, liquidus temperature, alumina, aluminum fluoride, sodium fluoride, calcium fluoride, lithium fluoride, magnesium fluoride, sodium chloride, freezing point, aluminum cell electrolyte.

Table II. Equation for the alumina liquidus

Restrictions	Liquidus $\leq$ 1010°C $AlF_3 \leq$ 15 w/o $CaF_2 \leq$ 15 w/o $MgF_2 \leq$ 15 w/o $Li_3AlF_6 \leq$ 25 w/o NaCl $\leq$ 20 w/o
Term	Coefficient
$(AlF_3))$	−3.063
(Al_2O_3)	14.250
(CaF_2)	3.404
(Li_3AlF_6)	−0.9282
(AlF_3) (Al_2O_3)	0.4814
(MgF_2) (Al_2O_3)	0.8143
(Li_3AlF_6) (Al_2O_3)	0.4116
(NaCl) (Al_2O_3)	0.3782
(CaF_2) (Al_2O_3)	0.3301
Constant	826.5

Standard deviation, 5.25°C (4.2°C for normal range)
No. of exptl. points, 125 (58 in normal range)

equilibration method and gave higher temperatures for a given composition. To clarify the picture more equilibration measurements were made in the Na_3AlF_6-Al_2O_3 system and in the Na_3AlF_6-AlF_3-CaF_2-Al_2O_3 system. In the course of the regression analysis it was shown that the equilibration results were higher than the visual ones by 16°, with a standard error of ±1.2°. There was no indication that the difference varied with composition, and all the old results have been corrected upward by that amount.

Only one set of coefficients was generated to cover the whole range of composition; it gave a standard deviation of 5.3°C (125 points) or 4.2°C for the 58 points in the normal range of composition (Table II). The accuracy is poorer than for the cryolite liquidus; this is partly because the experimental methods are not so precise and partly because of the inadequate form of the equation used.

Several points call for comment:

1. Since the correction of 16° has been applied to the visual results, the equations given here are more accurate than the diagrams in the original papers (1-3).
2. The possible importance of various combination terms, *e.g.* (AlF_3) (MgF_2), has not been assessed since no results were available in which those constituents were added simultaneously. No data from other sources have been used. This is not to imply that they are inferior, but simply because of the danger that, if systematic differences between sources do exist, the regression analysis is liable to attribute them to the effect of the combination of additives. Since the combination terms are in general not very important it has been considered safer to ignore them than to risk having them seriously distorted.
3. With the aid of these equations computer programs can readily be written to determine liquidus and eutectic temperatures for a given composition, alumina solubilities for a given composition and temperature, etc.

Acknowledgment

It is a pleasure to acknowledge numerous valuable discussions with Dr. E. A. Hollingshead.

Manuscript received Jan. 12, 1970.

Any discussion of this paper will appear in a Discussion Section to be published in the December 1970 JOURNAL.

REFERENCES

1. N. W. F. Phillips, R. H. Singleton, and E. A. Hollingshead, *This Journal*, **102**, 648 (1955).
2. N. W. F Phillips, R. H. Singleton, and E. A. Hollingshead, *ibid.*, **102**, 690 (1955).
3. Anne Fenerty and E. A. Hollingshead, *ibid.*, **107**, 993 (1960).
4. D. A. Chin and E. A. Hollingshead, *ibid.*, **113**, 736 (1966).

The Standard Potential of the Silver-Silver Chloride Electrode in N-Methylformamide at 25°C

M. L. Berardelli, G. Pecci, and B. Scrosati*

Istituto Elettrotecnico, Università di Roma, Rome, Italy

In the last few years there has been a renewed interest in nonaqueous solvents because of their use to develop high energy battery systems. Particular attention has been focused on the amides and their alkyl derivatives.

The values of standard potential of reference electrodes in formamide (1-6), dimethylformamide (7), dimethylacetamide (8), and N-methylacetamide (9), have been reported.

In this work we extended the series to report the behavior of the silver-silver chloride electrode in N-methylformamide (NMF) at 25°C with respect to the standard hydrogen electrode using the following cell

$$Pt, H_2 \mid HCl\ (m)\ in\ NMF \mid AgCl, Ag \qquad [1]$$

N-methylformamide (NMF) (C. Erba RP product) was purified by storing it over CaO for two days and then by fractional distillation under reduced pressure. The final product had a specific conductance of 3×10^{-6} ohm^{-1} cm^{-1} in good agreement with the value reported in the literature (10).

The HCl gas was obtained by dropping concentrated H_2SO_4 on reagent grade NaCl and passing the evolved gas first through concentrated H_2SO_4 and finally through two traps at dry ice temperature.

The solutions used in cell [1] were prepared by passing HCl gas into NMF. The concentration of HCl was determined according to the technique described by Berardelli, Pistoia, and Polcaro (11).

The cell was an all-glass type of the design recommended by Ives and Janz (12). Particular care was taken in the preparation of the silver-silver chloride electrodes since their behavior in NMF depends to a great extent on the method and accuracy of preparation. The thermal electrolytic type electrodes, prepared according to the procedure described by Ives and Janz (12), were not reproducible in NMF. For the electrolytic type of electrodes, prepared by the method described by Brown (13) and Ives and Janz (12), the adherence of the AgCl films was very poor in NMF, and therefore the electrodes failed in short periods of time, as was previously found by Case and Parsons (14). Apparently the anodically formed silver chloride layer is easily dissolved by the solvent.

In this work the silver-silver chloride electrodes were of the thermal type, prepared according to the method described by Keston (15) and Ives and Janz (12). This method, when properly used, yields elec-

* Active Electrochemical Society Member.
Key words: silver-silver chloride electrode, standard potential in nonaqueous solvent, N-methylformamide.

trodes which possess remarkable advantages over the electrolytic types, *i.e.*, less sensitivity to light and the absence of any occlusion or absorption of electrolyte during the preparation (12). This circumstance becomes very important for electrodes to be used in amides which can be decomposed by traces of water, the amide decomposition being catalyzed by hydrogen chloride (16). The electrodes were made by covering a platinum spiral of about 1.5 mm diameter, sealed in a glass tube, with a paste of 90% Ag_2O and 10% $AgClO_3$, to form a sphere of about 4 mm diameter. The electrodes were slowly heated to 100° and then to 650°C and maintained for about a half-hour at this temperature. The electrodes were then cooled slowly in the furnace (12). The preheating up to 100°C is critical and was made slowly to avoid crackings on the surface of the electrodes. The coating of the sphere by the paste, and the subsequent heating cycle were repeated until the surface of the electrode was completely uniform. The electrodes were stored in NMF and rinsed several times in the cell solutions before use. The silver-silver chloride electrodes, prepared and stored as described, were stable and reproducible in NMF for several hours, showing bias potentials of 0.1 mV or less. Hydrogen electrodes were prepared in the usual manner (12).

The emf measurements were made at 25.00° ± 0.05°C by a differential Keithley 662 voltmeter. EMF readings were taken 30 min after starting the hydrogen flow. The time to achieve equilibrium was about 3 hr, and was considered to have been obtained when the emf's remained constant, generally within ± 0.0005V, for 2 or more hours. Readings taken 24 hr later gave emf's 0.007-0.008V higher than the equilibrium values. This slow increase of the emf with time is probably due to a slight decomposition of the NMF solvent by traces of water when the cell remained for long periods of time in the water thermostatic bath. This reaction, which is catalyzed by hydrogen chloride, has been already observed in the case of emf determinations in formamide by Mandel and Delcroly (1) and by Agarwal and Nayak (2).

The emf's of cell [1], corrected to unit fugacity of H_2, are given in Table I, column 2, as a function of HCl molality. The molal standard potential of the silver, silver chloride electrode at 25°C was determined by plotting the function E' *vs.* the HCl molality m where E' is given by the equation

$$E' = E + \frac{2(2.303)\,RT}{F} \times \log m - \frac{2(2.303)\,RT}{F}\alpha\sqrt{m}$$

$$= E^\circ - \frac{2(2.303)\,RT}{F}\beta m \quad [2]$$

where the Debye-Hückel constant α for NMF at 25°C is 0.159 calculated using for the dielectric constant of NMF the value 171 reported by Weeda and Somsen (17).

Figure 1 shows the values of E' *vs.* the HCl molality. Extrapolation to zero molality by the method of least squares gives the standard potential of the Ag,AgCl electrode in NMF at 25°C, as $E^\circ = +0.208 \pm 0.003$V

Table I. Emf data at 25°C

m, HCl	E, V	E', V	$\gamma_\pm$
0.0100	0.450	0.211	0.979
0.0122	0.434	0.206	0.978
0.0213	0.406	0.206	0.980
0.0238	0.408	0.213	0.981
0.0319	0.378	0.198	0.984
0.0365	0.378	0.204	0.987
0.0388	0.373	0.202	0.988
0.0396	0.373	0.203	0.989
0.0461	0.368	0.206	0.993
0.0541	0.360	0.206	0.999
0.0684	0.347	0.204	1.011

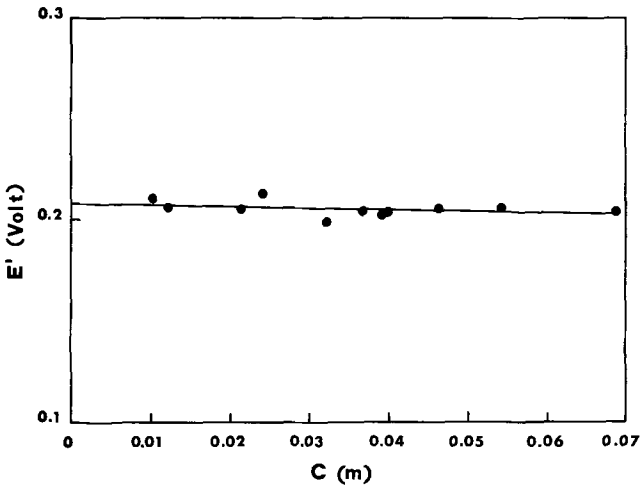

Fig. 1. E' as a function of HCl molality at 25°C

(Gibbs-Stockholm-I.U.P.A.C. convention). The decomposition of the solvent, which may occur to a different extent in each case, even in the freshly prepared solutions, is probably responsible for the scatter of the experimental points.

The best fit of the data corresponds to a straight line with a slope of −0.08 comparable with the −0.03 value found for a similar plot in N-methylacetamide (9). The value of β in Eq. [2] is then 0.676.

The mean molal activity coefficient $\gamma_\pm$ of HCl in NMF at 25°C may be calculated by the equation

$$\log \gamma_\pm = -\alpha\sqrt{m} + \beta m \quad [3]$$

Values of $\gamma_\pm$ obtained from Eq. [3] are listed in Table I.

Studies on the properties of the silver-silver chloride and other reference electrodes in other nonaqueous solvents are in progress in this laboratory.

Acknowledgment

This work was sponsored by the Consiglio Nazionale delle Ricerche under contract C.N.R. No. 115/0860/1894.

LIST OF SYMBOLS

E = potential (V)
E° = standard potential (V)
R = universal gas constant (Joule/mole-deg)
T = absolute temperature (°K)
F = Faraday's constant (coulomb/equiv.)
m = molality (moles/1000g solvent)
α, β = Debye-Hückel constants
$\gamma_\pm$ = mean ion activity coefficient

Manuscript submitted Nov. 10, 1969; revised manuscript received March 9, 1970.

Any discussion of this paper will appear in a Discussion Section to be published in the December 1970 JOURNAL.

REFERENCES

1. M. Mandel and P. Decroly, *Nature*, **182**, 794 (1958).
2. R. K. Agarwal and B. Nayak, *J. Phys. Chem.*, **70**, 2568 (1966); *ibid.*, **71**, 2062 (1967).
3. R. W. C. Broadbank, S. Dhabanandana, K. W. Morcom, and B. L. Muju, *Trans. Faraday Soc.*, **64**, 3311 (1968).
4. T. Pavlopoulos and H. Strehlow, *Z Physik. Chem.*, **2**, 89 (1954).
5. R. W. C. Broadbank, B. L. Muju, and K. W. Morcom, *Trans. Faraday Soc.*, **64**, 3318 (1968).
6. M. De Rossi, G. Pecci, and B. Scrosati, *Ric. Sci.*, **37**, 342 (1967).
7. G. P. Kumar and D. A. Pantony, "Polarography 1964," Vol. 2, p. 1061, Macmillan, London (1966).
8. B. Scrosati, G. Pecci, and G. Pistoia, *This Journal*, **115**, 506 (1968).
9. L. R. Dawson, R. C. Sheridan, and H. C. Eckstrom, *J. Phys. Chem.*, **65**, 1829 (1968).

10. G. Iohari and P. Tewari, *ibid.*, **69**, 3167 (1965).
11. M. L. Berardelli, G. Pistoia, and A. M. Polcaro, *Ric. Sci.*, **38**, 814 (1968).
12. D. J. G. Ives and G. J. Janz, "Reference Electrodes," Academic Press, New York (1961).
13. A. S. Brown, *J. Am. Chem. Soc.*, **56**, 646 (1934).
14. B. Case and R. Parson, *Trans. Faraday Soc.*, **63**, 1224 (1967).
15. A. S. Keston, *J. Am. Chem. Soc.*, **57**, 1671 (1935).
16. V. Kreibel and K. Holst, *ibid.*, **60**, 2976 (1938).
17. L. Weeda and G. Somsen, *Recueil*, **86**, 263 (1967).

Surface Active Agents as Corrosion Inhibitors for Aluminum

D. A. Vermilyea, J. F. Brown, Jr., and D. R. Ochar

General Electric Company, Schenectady, New York

Recent studies (1, 2) of the reaction between aluminum and water have shown that the mechanism involves the formation of amorphous Al_2O_3, the dissolution of the Al_2O_3 to form soluble species, and the precipitation of AlOOH from the solution. The AlOOH layer provides deposition sites close to the surface for dissolved species and hence allows the reaction to proceed at a high rate despite the very low solubility of Al_2O_3 in neutral solutions. Inorganic inhibitors function by becoming adsorbed on the oxide and preventing the nucleation and growth of the hydroxide layer (2).

This report is concerned with the use of several surface active agents as inhibitors. It is found that the most effective inhibitors are those which contain a strongly inhibiting inorganic group attached to a hydrocarbon. At least one of these is a better inhibitor, especially in acid solutions, than any of the inorganic ions previously studied.

Experimental

Previous studies (1, 2) showed that substances which retarded the attack of water on anodic Al_2O_3 films were corrosion inhibitors for aluminum, and the majority of the work reported here involved such anodic films. Anodic Al_2O_3 films were formed on evaporated aluminum films at 175V in a 1% ammonium borate solution at 25°C; the exact formation technique has been described in an earlier report (1). The principal means of measuring the rate of attack on the Al_2O_3 films was the measurement of electrical capacitance, although infrared absorption measurements and weight changes were also employed. All techniques have been fully described previously (1, 2).

The reaction medium was usually a solution containing the inhibitor at 10^{-3} M/1 or 0.01 v/o with the *p*H adjusted to 5 by additions of NaOH or $HClO_4$. A *p*H of 5 was selected because tests showed maximum inhibition at that pH. Some of the surface active agents used were proprietary compounds obtained from General Aniline and Film Corporation. Table I contains a list of such compounds and a description of their composition. Dodecyl acid phosphate was obtained from Hooker Chemical Corporation as an approximately equimolar mixture of monoalkyl and dialkyl phosphates. We found that part of this mixture was insoluble and separated the soluble part by repeatedly heating an aqueous slurry to 100°C, filtering, cooling to 5°C, and refiltering. We assume that the dialkyl derivative was more insoluble and that we retained mainly the monoalkyl phosphate. After this treatment the solution was entirely clear at 100°C. Of the other compounds tested some were obtained from chemical suppliers and some were made in our laboratory using standard techniques.

Table I. Proprietary surface active agents

Designation	Type	Description
Gafac RS-710	Anionic	Sodium salt of complex phosphate ester
Igepal CO-880	Nonionic	Nonylphenoxypoly (ethyleneoxyethanol)
Katapol VP-532	Cationic	Polyoxyethylated alkylamine

Results

Figures 1 and 2 show the capacitance data as a function of time. The initial change of capacitance is usually a decrease both because of a change of dielectric constant of the oxide on heating and because of the deposition of a layer of organic material on the surface. As the Al_2O_3 film is dissolved the capacitance increases. In order to avoid a sign change and to be able to plot data on a logarithmic scale we have added 2.0 to each measured change of AC^{-1} (area times reciprocal capacitance). In order to express changes of AC^{-1} in angstrom units of Al_2O_3 it is only necessary to multiply by 80. Large errors may result from such calculations when the change in capacitance is small.

The data of Fig. 1 show that nonionic and cationic substances are less effective than anionic substances. The Al_2O_3 film is probably slightly positive to its point of zero charge at *p*H 5, so that anions tend to be more strongly attracted. The nonionic CO-880 becomes more effective with time, probably due to entrapment in pores of the AlOOH layer.

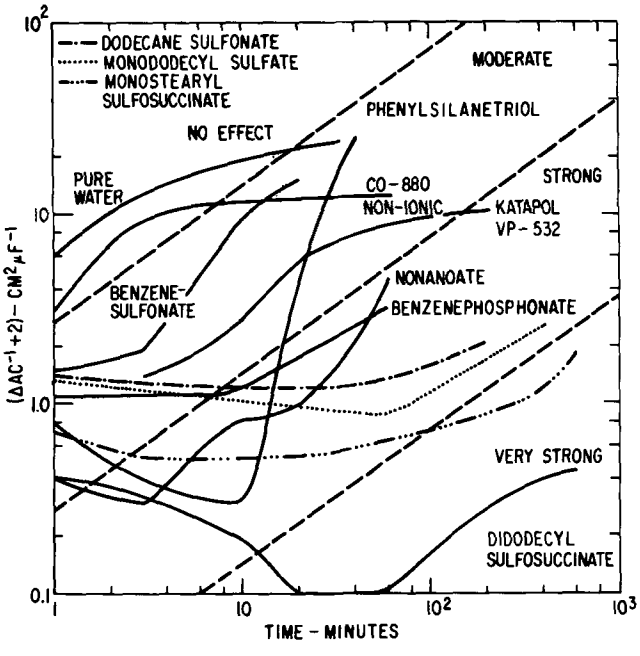

Fig. 1. Capacitance changes during reaction of anodic Al_2O_3 films with boiling solutions of various inhibitors at *p*H 5.

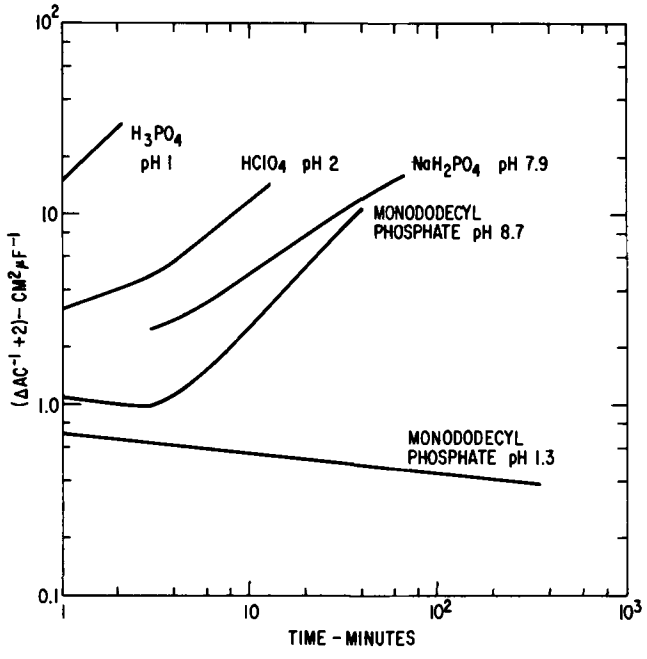

Fig. 2. Capacitance changes during reaction of anodic Al_2O_3 films with boiling solutions at various pH.

The anionic inhibitors all produced more or less hydrophobic surfaces on the Al_2O_3, showing that the ions were oriented with the inorganic group next to the oxide. The best inhibitors gave surfaces that were extremely hydrophobic. A comparison of data for benzenesulfonate and benzenephosphonate shows that the phosphonate group is much more effective than the sulfonate group. The comparison of data from straight chain hydrocarbon surface active agents shows that the order of effectiveness is $PO_4^{-3} > SO_4^{-2} > COO^{-1}$. With monododecyl phosphate and Gafac RS-710 at pH 5 no detectable attack on the oxide film occurs, and the data are not plotted in Fig. 1. Absence of attack was verified by infrared, which showed that the Al_2O_3 absorption was unchanged. An idea of the effectiveness of monododecyl phosphate ion can be obtained from Fig. 2, where results at lower pH are plotted. At pH 1.3 monododecyl phosphate entirely prevents attack on the oxide, while inorganic acids readily dissolve the Al_2O_3 (see $HClO_4$, Fig. 2) and phosphoric acid itself attacks the film at an even greater rate. Monododecyl phosphate is not effective at high pH, however, perhaps in part because the surface charge on the oxide changes sign as the pH is increased.

A few of these substances produced rather thick layers on the surface; all such substances were phosphates. At pH 5 Gafac RS-710, monododecyl phosphate, and monolinolenyl phosphate produced hydrophobic layers which resulted in large capacitance decreases (ΔAC^{-1} about 10). If it is assumed that the dielectric constant of the deposited material is 2, then such capacitance changes are equivalent to a layer roughly 200Å thick, so that multilayer films are evidently deposited. Infrared measurements confirmed the presence of aliphatic C-H on the surface. Such films could not be removed with organic solvents, but were slowly removed (in about one day) on exposure to pure water at 100°C, so that "permanent" protection by deposition of such a layer was not possible.

The phenylsilanetriol, produced *in situ* by the addition of an acetone solution of phenyltrichlorosilanetriol, was very effective for the first 10 min, producing an extremely hydrophobic surface, but apparently soon disappeared from the solution and hence ceased to protect. A second specimen treated in the same solution behaved as it would have in pure water. Possibly the silanetriol became attached to the surface of the vessel, or it may have undergone polycondensation (3).

Discussion

We believe that a reasonable interpretation of our data is that anionic surface active agents become attached to the Al_2O_3 surface by the inorganic group, forming a hydrophobic surface, preventing access of water to the surface and hence preventing dissolution of the Al_2O_3 and precipitation of AlOOH. The nature of the inorganic group is of primary importance, and phosphate, the most effective inorganic inhibitor, is also the most effective inorganic group in anionic surface active agents. Silicate is similarly effective as long as it remains in solution. Sulfate, while only weakly effective alone, becomes very effective when present attached to an organic molecule. The result with monododecyl phosphate at pH 1.3 confirms that these compounds can often be very much more effective than the inorganic ion itself.

We were not able to obtain anionic surface active agents based on other strongly inhibitive inorganic anions such as arsenate, periodiate, tungstate, sulfite, phosphite, tellurate, vanadate, antimonate, and selenate. It would be very interesting to synthesize and test such substances.

Acknowledgments

Conversations with W. Vedder and L. V. Interrante are gratefully acknowledged.

Manuscript received Feb. 6, 1970.

Any discussion of this paper will appear in a Discussion Section to be published in the December 1970 JOURNAL.

REFERENCES

1. W. Vedder and D. A. Vermilyea, *Trans. Faraday Soc.*, **554**, 561 (1969).
2. D. A. Vermilyea and W. Vedder, General Electric Memo MO-68-0551 (April 1968); to be published in *Trans. Faraday Soc.*
3. J. F. Brown, Jr., *J. Am. Chem. Soc.*, **87**, 4317 (1965).

The Discussion Section which usually is published in this issue of the Journal will appear in the July 1970 issue.

JOURNAL OF THE ELECTROCHEMICAL SOCIETY

SOLID STATE SCIENCE

JUNE 1970

SSS

Vapor Deposition and Etching Open Tube Kinetics under Diffusion Controlled Conditions

F. A. Kuznetsov and V. I. Belyi

Institute of Inorganic Chemistry,
Siberian Department of the Academy of Sciences of the USSR, Novosibirsk, USSR

ABSTRACT

A quantitative method for treating chemical deposition and etching open tube processes is described. The method is based on the gas dynamic theory of boundary layer and on the similarity of mass- and heat-transfer phenomena. For the conditions Le=Sc=Pr=1, the equation for the rate of the process is

$$R_t = \rho_e u_e b S t$$

This equation is applied for the calculation of the rate of Ge and Si crystals deposition and etching. A good agreement of calculated and experimental values is obtained.

Chemical decomposition and etching in gas or vapor streams, the so-called open tube method, is often used for semiconductor crystal and device technology. As has been frequently pointed out in the literature, the best conditions for both chemical deposition of epitaxial layers and chemical vapor etching of single crystals in flowing systems at high temperatures correspond to diffusion control in the vapor phase.

Some analytical methods based on one-dimensional diffusion model have been used for calculation of the rate of these processes (1, 2). While useful for evaluation of the average rate, these methods could not take into account a very important feature: changing of the local rate of the deposition or etching along the direction of the gas stream. This nonuniformity of local rates very often can be observed in chemical vapor growth and etching processes and reflects nonuniformity of conditions of mass transfer along the gas flow direction.

In our calculations we have tried to make use of a method based on a model for the laminar boundary layer commonly employed in gas dynamic problems (3).

Let us consider a scheme of the boundary layer over a flat plate which is created as a result of chemical reaction between the plate and a gas stream parallel to it (Fig. 1). L on Fig. 1 is the length of the plate. Thickness of the boundary layer, schematically depicted by the curve OB, is the distance $\delta(x)$ along the direction normal to the plate surface, where the main change in gas species concentration, due to reaction at the plate, takes place. $\delta(x)$ is increasing along the direction of gas flow and is equal to zero at the front edge of the plate.

Mathematical expressions used for describing mass transfer across the boundary layer become much simpler if the interaction between the gas flow and plate is considered as transfer of the plate substance, E, from the solid phase to the gaseous solution or *vice versa*, and the concentration of the plate material E in gas phase is expressed by weight fraction, K, which can be calculated as

$$K = \frac{\sum_i P_i L_i A}{\sum_\lambda P_\lambda M_\lambda} \qquad [1]$$

where P_i is the partial pressure of i gaseous species containing the plate material atoms, L_i is a number of these atoms in i species, A is atomic weight of the plate substance, P_λ is the partial pressure of any gaseous species, and M_λ is the molecular weight of these species. We will assume below that the concentration of E just near the plate surface, K_w, is constant and equal to the equilibrium one, $K_w = K_{eq}$.

The concentration of E at the upper limit of boundary layer (OB curve) and above, K_e, is equal to that of initial gaseous solution.

The vector diagram on Fig. 1 shows variation of the concentration across the boundary layer along the y-axis.

Mass transfer at any point inside the boundary layer can be described by the following equation

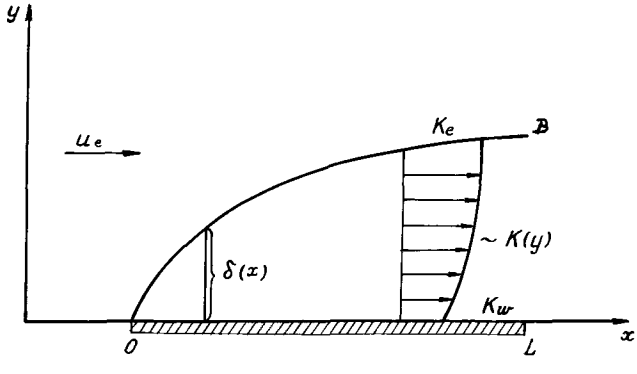

Fig. 1. Scheme of the boundary layer.

$$\rho u \frac{\partial K}{\partial x} + \rho v \frac{\partial K}{\partial y} = \frac{\partial}{\partial y}\left(\rho D \frac{\partial K}{\partial y} \right) \quad [2]$$

where ρ is gas mixture density, D is the diffusion coefficient, and u and v are components of the linear velocity of the gas stream in perpendicular and parallel directions in respect to the plate surface plane.

When integrated for the region of the boundary layer adjacent to the plane surface for a distance where a magnitude of the derivative $\partial K/\partial x$ becomes very close to zero, Eq. [2] gives

$$(\rho v)_w = (\rho v K)_w - \left(\rho D \frac{\partial K}{\partial y} \right)_w \quad [3]$$

where the subscript, w, indicates values corresponding to the region described above. Subscript, e, denotes parameters of the main flow outside the boundary layer.

The left-hand side of Eq. [3] is the mass flux of E per unit area in the direction normal to the plate surface. It is equal, evidently, to the local rate, R_t, of a heterogeneous process at steady state. The right-hand side is composed of two terms corresponding, respectively, to convective and diffusion contributions to the over-all rate.

Dependence of R_t on K_e, K_w, D, temperature and linear velocity of a gas stream, u_e, can, in principle, be obtained by the integration of Eq. [3].

The problem will be simplified if one considers the similarity theory for mass, heat, and momentum transfer phenomena. For this, we recall first that in flowing systems of the type considered in this paper, not only concentration but thermal and momentum boundary layers are formed over the surface of the plate. Without going into great detail, we may recall[1] that under the condition[2]

$$Le = Pr = Sc = 1 \quad [4]$$

all of these three layers have the same shape. That is to say, the thicknesses of the layers are equal to one another at any distance along the gas stream.

Under condition [4], concentration, enthalpy, and momentum fields over the plate are similar, and differential equations for diffusion, energy, and momentum all have the same form (as Eq. [2] does) (4). The similarity of the concentration and the enthalpy fields enables us to write

$$\frac{K - K_w}{K_e - K_w} = \frac{h - h_w}{h_e - h_w} \quad [5]$$

where h is steady motion enthalpy.

Equation [3] can be rearranged by substituting the derivative $(\partial K/\partial y)$ obtained from Eq. [5] by differentiating with respect to y.

By employing a usual expression for the Stanton number

$$St = \frac{1}{\rho_e u_e (h_e - h_w)} \left(\rho_e a \frac{\partial h}{\partial y} \right)_w \quad [6]$$

and remembering that $D/a = Le = 1$, one can transform Eq. [3] into

$$(\rho v)_w = \frac{(K_e - K_w)}{1 - K_w} \cdot \rho_e \cdot u_e \cdot St \quad [7]$$

Replacing $(\rho v)_w$ by R_t, the processes rate (per unit area), and the dimensionless ratio $(K_e - K_w)/(1 - K_w)$ by b, the mass transfer parameter, one can finally write

$$R_t = \rho_e \cdot u_e \cdot b \cdot St \quad [8]$$

One can see that the last equation consists only of values not too difficult to estimate.[3] The Stanton number used in Eq. [8] can be presented as a function of other dimensionless parameters, the Reynolds and the Prandtl numbers

$$St = f(Re, Pr) \quad [9]$$

Specific form of the relationship depends on geometry of the flowing system.

Assuming similarity of the viscous and enthalpy fields, one can use the following expression for the Stanton number for the case of parallel streamlining of flat surfaces (5)

$$St = 0.322\ Re_{(x)}^{-1/2}\ Pr^{-2/3} \quad [10]$$

Here a magnitude of St varies along the stream direction due to coordinate dependence of $Re_{(x)}$

$$Re_{(x)} = \frac{u_e x}{\nu} \quad [11]$$

where x is a distance along the plate equal to zero at the front edge of the plate. Thus, Eq. [8] with St given by Eq. [10] enables local rates of the process to be calculated.

An average value of the process rate can be calculated from Eq. [8] by employing for the Stanton number

$$St = 0.664\ Re_{(L)}^{-1/2} \cdot Pr^{-2/3} \quad [12]$$

where $Re_{(L)}$ is to be calculated from Eq. [11] by using L, the whole length of the plate, in place of x.

For a case of normal flow, with respect to the surface, the Stanton number magnitude is to be obtained (6) from

$$St = 0.47 \cdot Re_{(L/2)}^{-1/2}\ Pr^{-2/3} \quad [13]$$

where $Re_{(L/2)} = u_e \cdot (L/2)/\nu$. L is the width of the plate.

If a cold gas mixture reacts with a hot substrate (i.e., a substrate which is R.F. heated), an empirical coefficient $(T_w/T_e)^{-0.11}$ should be introduced (8) in Eq. [8]. This results in

$$R_t = \rho_e u_e b\ St \left(\frac{T_w}{T_e} \right)^{-0.11} \quad [14]$$

where T_w and T_e are plate and incoming gas stream temperatures, respectively. Values of density, ρ_e, and velocity, u_e, are now those in the incoming gas stream.

We have assumed so far that the surface concentration, K_w, is equal to the equilibrium one, K_{eq}. This makes the mass-transfer parameter, b, used in Eq. [8] and [14] easy to calculate. In cases where surface kinetic limitations are not negligible, this approach becomes unworkable, and the real surface concentration should be taken into calculation.

In general, this problem is very complicated, but for first order surface processes it can be solved. In this case, a relationship including both surface kinetic and mass-transfer limitation has the following form (7)

$$R_t = \frac{k \cdot \beta}{k + \beta} P_e \quad [15]$$

where k is surface reaction rate constant, β is the mass-transfer coefficient, and P_e is a partial pressure of gaseous species reacting with the surface in the main flow (outside the concentration boundary layer).

For practical use of Eq. [15], the rate constant, k, must be known. The mass-transfer coefficient, β, can be calculated as follows: rate of a process under purely diffusion controlled conditions can be described by the equation

$$R_t = \beta (P_e - P_{eq}) \quad [16]$$

where P_{eq} is the equilibrium pressure of the species of interest. Another expression for R_t is, for example, Eq. [8]. Combining Eq. [8] and [16], we obtain

$$\beta = \frac{\rho_e u_e b\ St}{P_e - P_{eq}} \quad [17]$$

[1] For more detail, see, for example (3, 4).

[2] $Le = a/D$ is the Lewis number (a is the thermal diffusivity), $Pr = \nu/a$ is the Prandtl number (ν is the kinematic viscosity), $Sc = \nu/D$ is the Schmidt number.

[3] An example of calculation based on Eq. [8] is given in the Appendix.

Table I. Systems considered and experimental conditions

System	Kind of process	Position of substrate*	Thermal conditions	Temperature interval, °C	Velocity of gas stream cm·sec^{-1}	Eq. used for calc	Ref.
Ge-H_2-I_2	Etch	↓ ↓	Isotherm	800-900	10.9-11.9	[8], [12]	(9)
Ge-H_2-I_2	Etch	↓ ↓	Isotherm	550-750	11025.5-13705.0	[15]	(10)
Ge-H_2-I_2	Etch	⟶|	Isotherm	800-900	18.3-19.8	[8], [13]	our data
Ge-H_2-Br_2	Etch	⟶|	Isotherm	800-900	43.3	[8], [13]	our data (11)
Ge-H_2-Br_2	Etch	↓ ↓	Isotherm	600-900	37.2-43.3	[8], [15]	our data (11)
Si-H_2-I_2	Growth	⟶|	Nonisotherm	1100-1200	1.4-5.6	[14]	(12)
Si-H_2-Cl_2	Growth	↓ ↓	Nonisotherm	1250-1300	32.7	[14]	(1)
Ge-H_2-Cl_2	Growth	⟶|	Nonisotherm	800-900	1.5 at −850°C	[14]	our data (13)

* ↓ ↓ denotes parallel position of the plate surface in respect to direction of gas stream, ⟶| corresponds to the perpendicular position.

Equations [8], [14], and [15] have been employed for a number of semiconductor crystal vapor growth and etch rate calculations. The calculations were performed for processes for which experimental kinetic data were obtained in our investigations or were available in the literature.

Table I contains information about systems considered and experimental conditions taken into consideration. Figures 2a and 2b give a comparison of calculated and experimental data for etching and growth processes, respectively. Logarithmic coordinates are used because of considerable variation of the rate values of different processes.

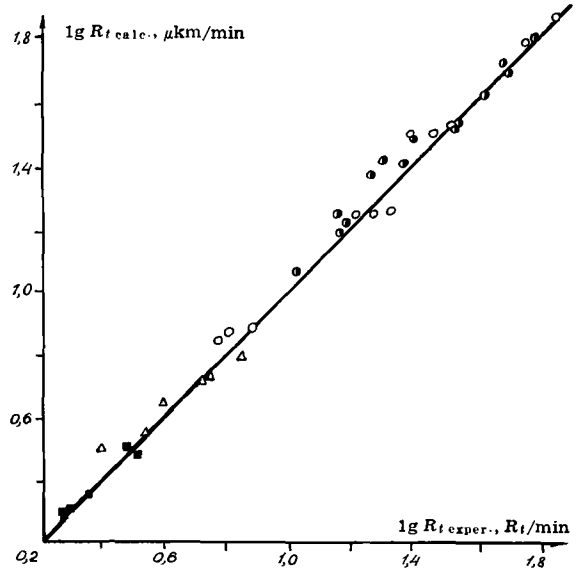

Fig. 2a

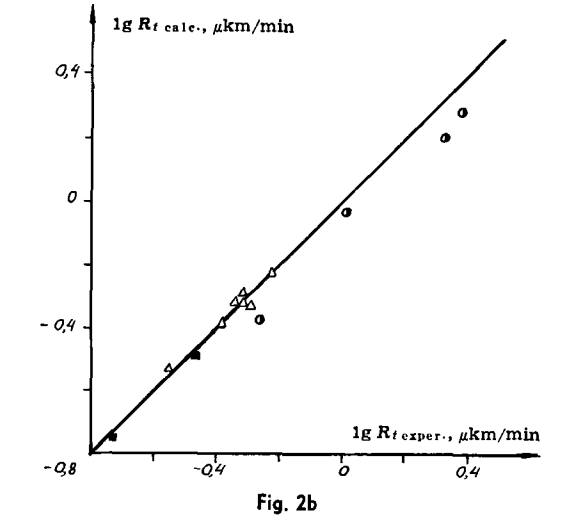

Fig. 2b

Fig. 2. Comparison of calculated and experimental rates: *(a)* Etching processes: ◑, our data (11), ○, Reisman and Berkenblit (9), △, Reisman and Berkenblit (10), ■, our data presented in the Appendix. *(b)* Growing processes: ◑, Shephard (1), △, Seki and Araki (12), ■, our data (13).

As can be seen, agreement is quite satisfactory. The difference between calculated and experimental results in the majority of the cases is not greater than 5-10%. Thus it can be concluded that for the processes considered, the method described above gives accuracy commensurate with the reproducibility of experimental results. Because of a number of simplifying restrictions used the method cannot, unfortunately, be regarded as a universal one, and experimental control should be undertaken for a few points when one employs the method for any particular process.

Manuscript submitted Nov. 18, 1968; revised manuscript received Feb. 18, 1970. This was Paper 76 presented at the Boston Meeting of the Society, May 5-9, 1968.

Any discussion of this paper will appear in a Discussion Section to be published in the December 1970 JOURNAL.

APPENDIX

1. Physical parameters of gas phase are calculated under the assumption that it can be considered as a perfect gas mixture.

Density, ρ_e, (g · cm^{-3}) of a gas mixture can be obtained from

$$\rho_e = \sum_i n_i \rho_i$$

where n_i is the mole fraction of i species and ρ_i is its density.

Gas stream velocity, u_e, (cm · sec^{-1}) is calculated from

$$u_e = \frac{V_{To}}{S} \frac{T_{sub.}}{T_o}$$

where V_{To} is the flow rate (cm^3 · sec^{-1}) (measured at temperature T_o, °K), S is the cross section of a reactor (cm^2), and $T_{sub.}$ is temperature in the reaction zone.

Kinematic viscosity of a gas mixture, V, (cm^2 · sec^{-1}) is obtained from

$$\nu = \frac{1}{\sum_i n_i/\nu_i}$$

where ν_i is the viscosity of i gaseous species at pressure equal to its partial pressure in the mixture.

An example of calculation based on Eq. [8] is shown here for the case of Ge etching with H_2 + HI mixture. Our experimental results obtained for this process in a horizontal reactor with the substrate perpendicular to the gas flow direction have been used for comparison with calculated data.

Table II. Equilibrium partial pressure of gaseous species

P_H / P_I	Gaseous species	Partial pressure, atm 800°C	850°C	900°C
151.1	GeI_2	$2.08 \cdot 10^{-3}$	$2.09 \cdot 10^{-3}$	$2.10 \cdot 10^{-3}$
	HI	$8.50 \cdot 10^{-3}$	$8.59 \cdot 10^{-3}$	$8.68 \cdot 10^{-3}$
	H_2	$9.89 \cdot 10^{-1}$	$9.89 \cdot 10^{-1}$	$9.89 \cdot 10^{-1}$
48.4	GeI_2	$1.04 \cdot 10^{-2}$	$1.04 \cdot 10^{-2}$	$1.04 \cdot 10^{-2}$
	HI	$1.91 \cdot 10^{-2}$	$1.89 \cdot 10^{-2}$	$1.88 \cdot 10^{-2}$
	H_2	$9.69 \cdot 10^{-1}$	$9.69 \cdot 10^{-1}$	$9.69 \cdot 10^{-1}$

Table III. Calculated values of several parameters

P_H/P_I	Temperature, °K	$\rho \cdot 10^5$ (g · cm^{-3})	u_e cm · sec^{-1}	ν cm^2 · sec^{-1}	$Re_{L/2}$	$Re_{L/2}^{1/2}$	St	$K_w \cdot 10^2$	$b \cdot 10^2$	R_t calc μmk · min^{-1}	R_t exper. μmk · min^{-1}
151.1	800	4.10	18.3	7.40	0.98	0.99	0.55	3.98	4.21	1.85	1.74
	850	3.90	18.9	8.00	0.95	0.97	0.56	4.03	4.19	1.94	1.79
	900	3.80	19.8	8.60	0.92	0.96	0.57	4.04	4.20	1.99	1.86
48.4	800	7.80	18.3	5.20	1.41	1.19	0.46	9.69	10.8	7.80	8.21
	850	7.60	18.9	5.70	1.34	1.16	0.47	9.70	10.7	8.05	8.50
	900	7.30	19.8	6.10	1.30	1.14	0.48	9.75	10.7	8.35	9.10

Values of the system parameters, used both in the experimental study and in calculations, were the following

$$S = 0.785 \text{ cm}^2, \quad V_{H_2} = 235 \text{ cm}^3 \cdot \text{min}^{-1} \text{ (at 300°K)}$$

$$V_{HI} = \frac{2 V_{H_2} \cdot P_{I_2}}{760 - P_{I_2}} \text{ cm}^3 \cdot \text{min}^{-1} \text{ (here } P_{I_2} \text{ is V.P. of iodine at the I source)}$$

$$V_{To} \text{ (total)} = V_{H_2(To)} + V_{HI(To)}, \frac{L}{2} = 0.4 \text{ cm}$$

Table II shows computed equilibrium partial pressure of gaseous species for two values of hydrogen to iodine ratio, P_H/P_I, used both in the experiment and calculations. These data were employed for surface concentration, K_w, and parameter b calculations.

The parameter b was calculated from relationship $b = (K_e - K_w)/(1 - K_w)$. For the process under consideration $K_e = 0$ because the incoming gas mixture does not contain germanium compounds.

It has been assumed that the process at 800°-900°C is purely diffusion controlled so that the surface pressures could be considered as equilibrium ones.

Table III presents calculated values of several parameters used in the rate of process calculation. Value of the Pr needed for the St number calculation was taken equal to 0.8 as for diatomic gas mixtures. The last two columns show calculated and experimental values of the rate of process.

REFERENCES

1. W. H. Shephard, *This Journal*, **112**, 988 (1965).
2. J. J. Grossman, *ibid.*, **110**, 1065 (1963).
3. L. Lees in "Combustion and Propulsion Third AGARO Colloquium," New Jersey 1958.
4. E. R. Eckert and R. M. Drake, "Heat and Mass Transfer, New York (1959).
5. V. S. Avduevski, Fundamentals of the Heat Transfer in Aviation and Rocket Technique. Oborongiz 1960 (in Russian).
6. V. K. Fedorov, *J. Engrg. Phys.*, **N2**, 198 (1965) (in Russian).
7. D. A. Frank-Kamenetski, "Diffusion and Heat Transfer in Chemical Kinetics," Academic Press of USSR (1968).
8. S. S. Kutateladze, Fundamentals of the Heat Transfer. Mashgiz (1962) (in Russian).
9. A. Reisman and M. Berkenblit, *This Journal*, **112**, 812 (1965).
10. A. Reisman and M. Berkenblit, *ibid.*, **113**, 140 (1966).
11. V. I. Belyi and F. A. Kuznetsov, *Izv. Sibirsk. Otd. Akad. Nauk. SSSR* (Chem. Ser.) **2**, 1, 68 (1967).
12. H. Seki and T. Araki, *Japan. J. Appl. Phys.*, **4**, 645 (1965).
13. V. S. Kravtchenko, A. A. Andreeva, and F. A. Kuznetsov, in "Physics of Semiconductors" (collection of articles) p. 109, Siberian Dept. of Academ. of Sci. Press., Novosibirsk, 1968.
14. S. Bretshnaider, Properties of Gases and Liquids, Chemistry 1968 (in Russian).

Buckling of Anodic Coatings

R. J. Block

Department of Chemical Engineering and Materials Science, The University of Oklahoma, Norman, Oklahoma

ABSTRACT

Anodic coatings on aluminum substrates undergoing tensile deformation have been observed to buckle. In general, buckling is a result of circumferential shrinkage of the surface. The buckling process is discussed, and an expression for the surface shrinkage of single crystals deforming on one slip system is derived.

The behavior of anodized coatings on aluminum undergoing plastic deformation has been studied by a number of investigators (1-3). However, one of the several mechanisms by which the coating accommodates the deformation of the substrate has not been described in the literature. Edeleanu and Law (4) and Bubar and Vermilyea (5) presented micrographs which showed buckling of anodic coatings but did not discuss the process.

Experimental

The present experiments consisted of extending monocrystals and polycrystalline aluminum wire in 0.4M boric acid solution brought to a pH of 5.5 with ammonium hydroxide. The aluminum had been electropolished, stripped of residual films, and both anodized and extended in the boric acid. The treatments produced barrier-type anodic coatings.

Results

Thick coatings accommodate deformation of the substrate by circumferential cracking after about 2% extension (6) and later by longitudinal buckling as shown in Fig. 1. Buckling is evidenced by the short vertical structures shown in the figure. The interference fringes apparent at each of the buckles indicate that the coating has indeed been lifted from the substrate. Figure 2 is a micrograph of an anodized polycrystalline wire showing buckling of the coating in one grain and general circumferential cracking. It should be noted that here as with the single crystal, both cracking and buckling are independent of slip plane traces in the substrate. A coating of intermediate thickness, 420Å, sometimes cracked along slip plane traces as shown in Fig. 3. When this occurred, short circumferential cracks were always associated with

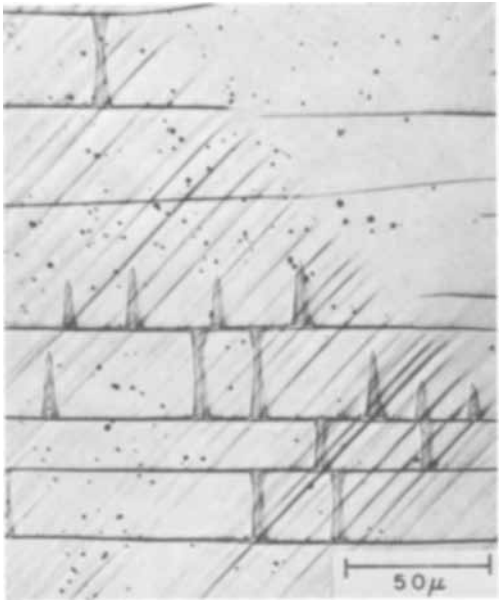

Fig. 1. Aluminum single crystal anodized at 90V and extended 14%. Tensile axis is parallel to vertical direction. Cracks in coating run horizontally. Wide vertical structures resulted from buckling of coating. Slip lines in matrix and in a kink band are visible beneath coating.

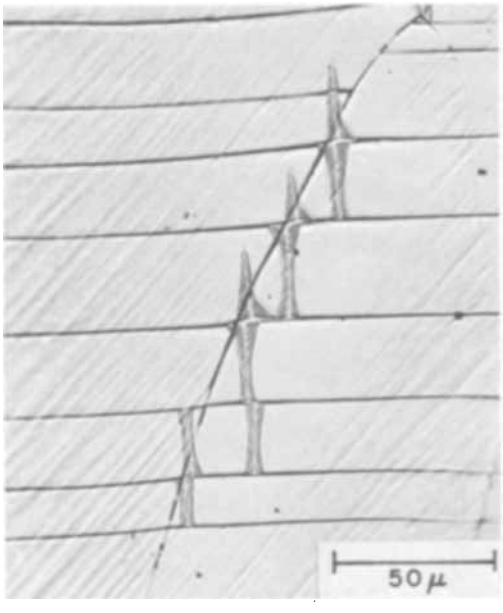

Fig. 2. Polycrystalline aluminum wire anodized at 90V and extended 3.7%. Extension was sufficient to cause general cracking of coating. However, buckling occurred only in isolated grains and at a few regions of singularity such as grain boundary shown.

the sites where buckling had occurred. Very thin coatings (approximately 100Å) showed only slip plane traces and were never observed to buckle. Presumably, their adherence exceeds their ability to support a significant load. The following discussion considers the behavior of thick coatings as illustrated in Fig. 1.

Discussion

Cracking of anodic coatings.—It is obvious that circumferential cracking results from substrate extension which is too great to be accommodated by the coating. The equivalent situation has been discussed by Edeleanu and Law (4) who invoked an interfacial slip mechanism to allow for stress relief between cracks

Fig. 3. Aluminum single crystal anodized at 30V and extended 11%. Cracks in coating formed along some of slip plane traces. In addition short circumferential cracks can be observed where buckling has occurred.

in the coating. Recently Grosskruetz and McNeil (7) also discussed the case of regularly spaced cracking of brittle coatings. There is some evidence from the present work that detachment of the coating ahead of the propagating crack permits partial stress relaxation in the coating.

Buckling of anodic coatings.—Buckling of the coating is due to shrinkage in the circumference of the substrate which results from extension. With specimens which should deform homogeneously, such as heavily cold worked wires, the circumferential shrinkage which produces buckling may be calculated directly from the extension, using a constant volume approximation. As the result of an experiment using as-swaged wire anodized at 90V, it was found that a circumferential shrinkage of 3.2% was required to initiate buckling of the coating. The problem of calculating the surface shrinkage of monocrystals deforming on a single slip system may also be solved in a fairly direct manner.

Surface shrinkage during single slip.—During single slip an initially circular specimen cross section becomes elliptical. According to the analysis of Schmid and Boas (8) the major axis of the ellipse is generally greater than the original specimen diameter while the minor axis is obviously reduced. Figure 4 represents this change in cross sectional shape, where R, the radius of the circle, is one half the original diameter, A is the major semiaxis of the ellipse, and B is the minor semiaxis. Assuming a coating on the specimen surface is broken into short cylindrical sections by circumferential cracks, then a point, (x, y), on the original surface at an angle, θ_0, to the major axis, becomes the point, (x', y'), at the angle θ_1 on the deformed crystal surface. The ratios of the axes, A/R and B/R, are p_1 and p_2 respectively, where p_1 and p_2 are the positive roots of Schmid and Boas' equation

$$p^4 + p^2\left[\frac{2\cos(\lambda_0 - \lambda_1)\sin\lambda_1}{\sin\lambda_0} + \frac{\sin^2(\lambda_0 - \lambda_1)}{\sin^2\chi_0}\right] + \frac{\sin^2\lambda_1}{\sin^2\lambda_0} = 0 \quad [1]$$

and λ_0 and λ_1 are the angles between the tensile axis and slip direction before and after extension and χ_0 is the angle the tensile axis makes with the slip plane. The transformation of a point on the circle to the cor-

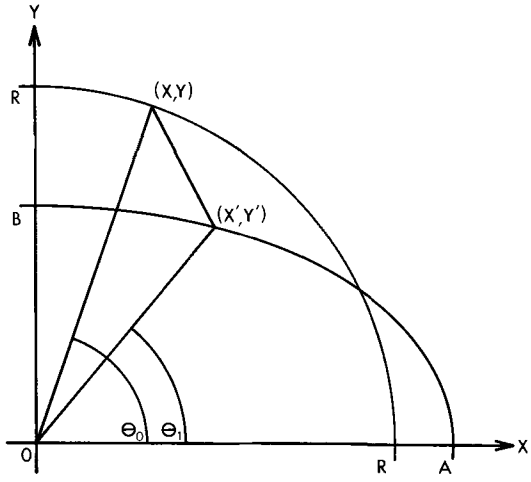

Fig. 4. Change in cross section of a cylindrical specimen undergoing single slip, diagram shows displacement of a point on surface of coating.

responding point on the ellipse is given by

$$x' = p_1 x \quad [2]$$

and

$$y' = p_2 y \quad [3]$$

From the equation of the circle and the transformation equations one obtains

$$dy = -\cot\ \theta_0\ dx \quad [4]$$

$$dx' = p_1 dx \quad [5]$$

and

$$dy' = -p_2 \cot\ \theta_0\ dx \quad [6]$$

The perimeter elements of the circle and the ellipse, dS_c and dS_e, are obtained from

$$dS_c^2 = dx^2 + dy^2 \quad [7]$$

and

$$dS_e^2 = dx'^2 + dy'^2 \quad [8]$$

Substituting in the above one obtains for the ratio of perimeter elements at a point on the circle and the corresponding point on the ellipse

$$\frac{dS_e}{dS_c} = \left[\frac{p_1^2 + p_2^2 \cot^2 \theta_0}{1 + \cot^2 \theta_0} \right]^{1/2} \quad [9]$$

One may now consider a few specific cases. When θ_0 is zero, the perimeter ratio, dS_e/dS_c, is p_2 and $0 \leq p_2 \leq 1$. The surface shrinkage, $1 - (dS_e/dS_c)$, always will be positive. When θ_0 is 90°, the perimeter ratio becomes p_1, where $1 \leq p_1 < (\sin \lambda_0 / \sin \chi_0)$. In this case the surface shrinkage is always zero or negative implying an expansion of the surface during deformation. Due to the limitations on the extent of single slip, one could expect only about 5% as the practical upper limit to circumferential surface expansion. This will be obtained for orientations of the tensile axis near [122].

For a given tensile extension there will be a point on the perimeter which has undergone neither shrinkage nor expansion. The angle, θ_1^*, to that point on the elliptical cross section is given by

$$\theta_1^* = \tan^{-1} \left[\frac{p_2}{p_1} \left(\frac{1 - p_2^2}{p_1^2 - 1} \right)^{1/2} \right] \quad [10]$$

A final case which might be worth noting is obtained when the crystal orientation is such that the tension axis, slip direction, and slip plane normal are coplanar, *i.e.*, $\lambda_0 = \chi_0$. Then the equation yielding the perimeter ratio assumes a particularly convenient form

$$\frac{dS_e}{dS_c} = \left[\frac{1 + \left(\frac{1}{1+\delta} \right)^2 \cot^2 \theta_0}{1 + \cot^2 \theta_0} \right]^{1/2} \quad [11]$$

where δ is the tensile extension.

The shrinkage at a point on the surface is thus a function of the extension and its direction relative to the slip vector for a crystal of a given orientation. In general the perimeter shrinkage increases from approximately zero for points near the surface through which pure edge dislocations exit the crystal, to its maximum near points on the surface through which pure screws egress.

Figures 5 and 6 illustrate the extremes in the behavior of the coating which was observed at various positions on a crystal in which $\lambda_0 \approx \chi_0$. The specimen shown had been deformed well into stage II, however, the regions associated with the "edge" and "screw" surfaces are still clearly defined. Longitudinal buckling characteristic of proximity to the "screw" face (Fig. 1 and 5) is never observed near the edge surface. In contrast, the appearance of the edge surface is shown in Fig. 6. Here, the coating has become detached and raised as a result of conjugate slip on planes whose

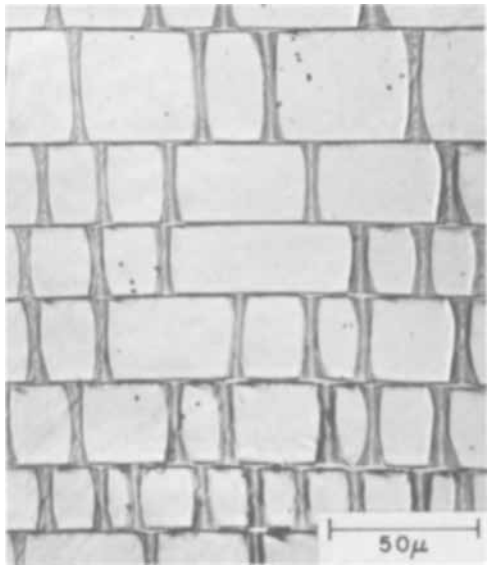

Fig. 5. Film buckling on "screw" surface of aluminum single crystal shown in Fig. 1.

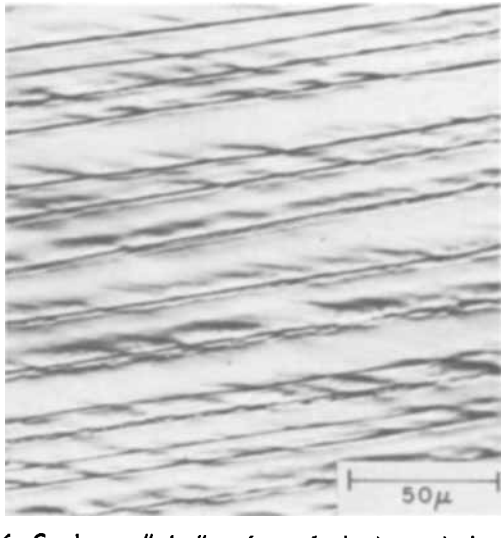

Fig. 6. Cracks on "edge" surface of aluminum single crystal shown in Fig. 1. Film has been lifted as a result of shear on intersecting slip planes, however, no buckling of coating has occurred.

traces intersect cracks which have formed earlier in the deformation. This phenomenon has already been described in the literature (4).

Acknowledgments

The author wishes to express his gratitude to Dr. J. H. Christensen for the many valuable discussions during the preparation of this paper, and to Mr. Parviz Mehdizadeh who prepared the specimens. This work was sponsored by the U.S. Atomic Energy Commission (Contract AT-(40-1)-3401) whose support is gratefully acknowledged.

Manuscript received Jan. 12, 1970.

Any discussion of this paper will appear in a Discussion Section to be published in the December 1970 JOURNAL.

REFERENCES

1. H. L. Logan, *J. Res. Natl. Bur. Std.*, **48**, 99 (1952).
2. D. H. Bradhurst and J. S. Ll. Leach, *This Journal*, **113**, 1245 (1966).
3. S. F. Bubar and D. A. Vermilyea, *ibid.*, **114**, 882 (1967).
4. C. Edeleanu and T. J. Law, *Phil. Mag.*, **7**, 573 (1962).
5. S. F. Bubar and D. A. Vermilyea, *This Journal*, **113**, 892 (1966).
6. D. H. Bradhurst and J. S. Ll. Leach, *Trans. Brit. Ceram. Soc.*, **63**, 793 (1963).
7. J. C. Grosskruetz and M. B. McNeil, *J. Appl. Phys.*, **40**, 355 (1969).
8. E. Schmid and W. Boas, "Plasticity of Crystals," pp. 60-63, Chapman and Hall (1968).

Photosensitization of Terbium Fluorescence by Europium in CaF_2

Robert L. Amster[1]

Bayside Research Center of General Telephone & Electronics Laboratories Incorporated, Bayside, New York

ABSTRACT

Eu^{2+} sensitizes the fluorescence of Tb^{3+} in CaF_2. Furthermore, Tb^{3+} emission is sensitized by energy transfer from Eu^{3+}-O^{2-} complexes which possess intense broad ultraviolet absorption bands. The energy transfer from Eu^{2+} to Tb^{3+} is believed to occur by means of an exchange mechanism.

The fluorescence peak of Eu^{2+} in calcium fluoride is observed at 430 nm ($\sim$ 23,200 cm^{-1}) and corresponds to a transition from the lowest $4f^65d$ level, designated as $^8P_{5/2}$ or $4f^6(^7F_0)5d$ (e_g), to the $^8S_{7/2}$ ground state (1-6). When CaF_2 is activated with Tb^{3+}, an absorption line is observed at 487 nm ($\sim$ 20,500 cm^{-1}) which corresponds to the Tb^{3+} $^7F_6 \rightarrow {}^5D_4$ transition (7). An energy separation of only 2700 cm^{-1} between these Eu^{2+} and Tb^{3+} transitions suggests that one might observe nonradiative energy transfer from Eu^{2+} to Tb^{3+} in CaF_2. This nonradiative process would probably occur via a nonresonant transfer similar to that discussed by Van Uitert and Johnson (8). In such a case, the approximately 2700 cm^{-1} difference in energy between the ionic transitions would be transferred either to the ground state multiplet of a second Tb^{3+} ion or would be converted into lattice energy.

Nelson and co-workers (9) have observed energy transfer from Eu^{2+} to Tb^{3+} in fused silica. In silica containing only Tb^{3+}, the authors observed that 260 nm excitation yielded terbium fluorescence from both the $^5D_3$ and $^5D_4$ levels. When silica was doubly activated with Eu^{2+} and Tb^{3+}, they observed Tb^{3+} emission from only the $^5D_4$ level. They, therefore, concluded that Eu^{2+} selectively transferred energy to the $^5D_4$ level of Tb^{3+}.

In the present investigation CaF_2 has been doubly activated with Eu^{2+} and Tb^{3+}. Radiationless energy transfer from Eu^{2+} and within $(Eu^{3+}, Tb^{3+}, -O_2)^{2+}$ complexes to Tb^{3+} has been inferred. The results are discussed and models for the transfer processes are derived.

Experimental

The rare earth trihalides used were obtained from the Lindsay Division of American Potash Company and were reported to be 99.95% pure with respect to rare earth content. Calcium fluoride was Fisher Certified Reagent Grade. CaF_2:Eu^{2+}, CaF_2:Tb^{3+}, and CaF_2:Eu^{2+}, Tb^{3+} were produced by blending anhydrous EuF_3 and TbF_3 as required with CaF_2 and heating these mixtures for 2 hr at 1050°C in a hydrogen atmosphere. The starting materials were contained in alumina boats or crucibles and were held in a quartz tube through which hydrogen was continuously passed. The quartz tube, in turn, was inserted into a tube furnace initially heated to 500°C. The Eu^{2+} concentration in CaF_2:Eu^{2+} was varied between 0.001 and 0.035 g-atom/mole CaF_2. For the CaF_2:Tb^{3+}, the terbium concentration was generally 0.064 g-atom/mole CaF_2. In CaF_2:Eu^{2+}, Tb^{3+}, the Eu^{2+} concentrations were in the range 0.0025 to 0.05 g-atom/mole CaF_2 while Tb^{3+} concentrations ranged from 0.004 to 0.10 g-atom/mole CaF_2.

The emission and excitation spectra obtained were corrected in terms of energy *vs.* wavelength using a technique previously reported (10).

Results

The emission and excitation spectra of CaF_2:0.035 Eu^{2+} are shown in Fig. 1. Excitation at 390 nm yields a broad band fluorescence with a maximum at 430 nm. Excitation bands correspond to direct absorption by Eu^{2+}. Eu^{3+} emission is observed above 500 nm indicating that europium is incompletely converted to the divalent form even under strong reducing conditions. The relative emission intensities over a range of europium concentrations are as follows:

Eu^{2+} concentration, g-atom/mole CaF_2	Relative intensity of Eu^{2+} fluorescence
0.001	100
0.006	93
0.01	50
0.035	33

It is obvious from the data that increasing Eu^{2+} concentration in the range studied results in quenching of the divalent europium fluorescence.

[1] Present address: Harris, Upham & Company, Inc., New York, New York 10005.

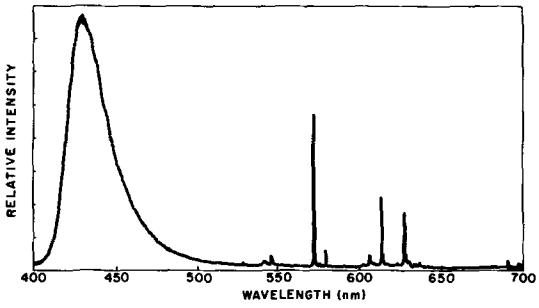

Fig. 1a. Emission spectrum of CaF_2:0.035Eu^{2+} excited at 390 nm.

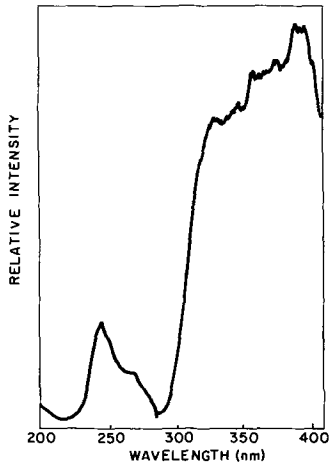

Fig. 1b. Excitation spectrum of CaF_2:0.035Eu^{2+} for emission at 430 nm.

CaF_2:Tb^{3+} emits very weak fluorescence from the $^5D_4$ level when excited with ultraviolet radiation; the most intense emission is observed at 542 nm corresponding to a $^5D_4 \rightarrow {}^7F_5$ transition (Fig. 2a). The excitation spectrum (Fig. 2b) consists of a number of sharp lines between 300 and 400 nm characteristic of Tb^{3+} absorption and a band extending from 300 nm into the far ultraviolet. The latter band corresponds to the absorption of Tb^{3+} from the $4f^8$ to $4f^75d$ configuration (11) plus contributions from OH^- and O^{2-} ions (12) which are present as a result of the initial presence of adsorbed water on the calcium fluoride. Oxide ion serves to charge compensate the excess positive charge introduced into the CaF_2 lattice when Tb^{3+} replaces a Ca^{2+} ion (13).

When CaF_2:Eu^{2+}, Tb^{3+} was excited by 390 nm radiation, Eu^{2+} emission was observed near 436 nm (Fig. 3a) corresponding to a shift of about 6 nm to longer wavelength relative to the emission from CaF_2:Eu^{2+}. (Although this shift is not apparent in the reduced figures, the shift is real, reproducible, and is readily observed in original spectra.) Intense terbium fluorescence was observed corresponding to emission from the $^5D_4$ level. The excitation spectra for both Eu^{2+}

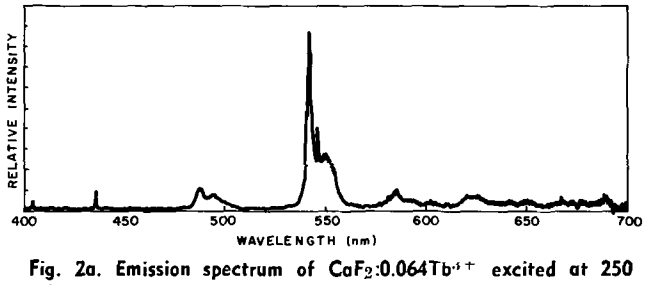

Fig. 2a. Emission spectrum of CaF_2:0.064Tb^{3+} excited at 250 nm; high gain.

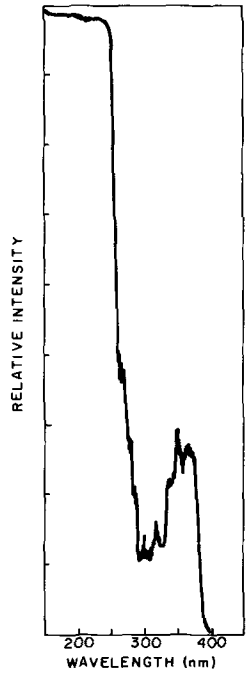

Fig. 2b. Excitation spectrum of CaF_2:0.064Tb^{3+} for emission at 541 nm; high gain.

and Tb^{3+} emission possess a broad band with a maximum near 390 nm corresponding to Eu^{2+} absorption (Fig. 3b). The fine structure of this band is similar for both CaF_2:Eu^{2+} and CaF_2:Eu^{2+}, Tb^{3+} and may be

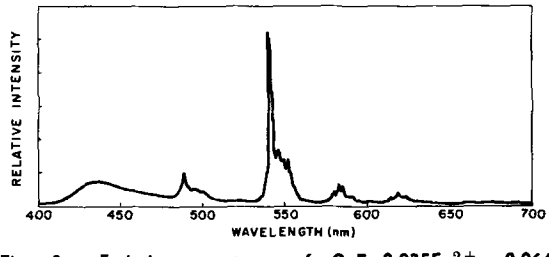

Fig. 3a. Emission spectrum of CaF_2:0.035Eu^{2+}, 0.064Tb^{3+} excited at 390 nm.

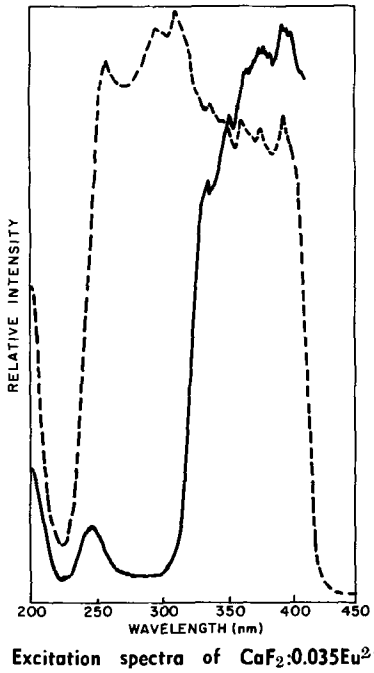

Fig. 3b. Excitation spectra of CaF_2:0.035Eu^{2+}, 0.064Tb^{3+}; solid line corresponds to emission at 436 nm, dashed line to emission at 541 nm.

identified with transitions from the $^8S_{7/2}$ ground state to crystal field split sublevels of the excited $^8P_{5/2}$ state of Eu^{2+}. Although direct excitation of Tb^{3+} ions in CaF_2:Eu^{2+}, Tb^{3+} undoubtedly occurs, the Tb^{3+} excitation lines are probably obscured by the intense broad bands observed in the 200-400 nm region. A comparison of emission spectra of CaF_2:0.035 Eu^{2+}, 0.064Tb^{3+} with CaF_2:0.035 Eu^{2+} (Fig. 4) indicates that addition of Tb^{3+} to CaF_2:Eu^{2+} results in appreciable quenching of the entire Eu^{2+} fluorescence band. Furthermore, the presence of Eu^{2+} in CaF_2:Eu^{2+}, Tb^{3+} leads to considerable enhancement of Tb^{3+} emission relative to that in CaF_2:Tb^{3+} (Fig. 4). It is evident that nonradiative energy transfer occurs from Eu^{2+} to Tb^{3+} ions. Since the Tb^{3+} $^7F_6 \rightarrow {}^5D_4$ absorption is quite weak, the enhancement of terbium emission by addition of Eu^{2+} cannot be ascribed to a radiative transfer process. Rare earth ion concentrations of several mole per cent are required for the observation of $Eu^{2+} \rightarrow Tb^{3+}$ energy transfer. This indicates that short-range interactions are involved in the transfer process and suggests the possibility that the transfer occurs via an exchange mechanism (14).

In addition to the 390 nm band, the excitation spectrum for Tb^{3+} emission contains an intense structured band peaking at 310 nm (Fig. 3b). In a paper (10) concerning the emission and excitation spectra for CaF_2:Eu^{3+}, a similarly broad fluorescence excitation band was identified as a Eu^{3+}-O^{2-} charge transfer band. This was in turn associated with a $(Eu_2\text{-}O_2)^{2+}$ complex in which two nearest neighbor Eu^{3+} ions were bridged by two oxide ions. The oxide ions served to compensate the excess positive charges of trivalent europium substituted for divalent calcium in CaF_2. Forrester and McLaughlin (15) have proposed similar pair formation for Tm^{3+} in CaF_2: they concluded that Tm^{3+} ion pairs are bridged by two charge compensating O^{2-} ions when CaF_2 is reacted with Tm_2O_3. Eu^{3+} emission has been observed in CaF_2:Eu^{3+}, Tb^{3+} indicating that trivalent europium is present in this material. It is possible then that $(Eu^{3+}\text{-}O^{2-})_2{}^{2+}$ complexes and $(Eu^{3+}, Tb^{3+}\text{-}O^{2-})_2{}^{2+}$ complexes exist in CaF_2:Eu^{2+}, Tb^{3+}; the oxide ions would have been formed during reaction upon the high-temperature hydrolysis of the calcium fluoride with previously adsorbed water (13). The 310 nm band observed in the Tb^{3+} fluorescence excitation spectrum of CaF_2:Eu^{2+}, Tb^{3+} may be ascribed to charge transfer absorption by Eu^{3+}-O^{2-} in $(Eu^{3+}, Tb^{3+}\text{-}O^{2-})^{2+}$ followed by an intracomplex energy transfer with subsequent Tb^{3+} emission. That this band is not observed in the Eu^{2+} fluorescence excitation spectrum would indicate that either oxide ion bridged Eu^{3+}-Eu^{2+} complexes do not form or that there is no energy transfer within such complexes that can lead to Eu^{2+} emission.

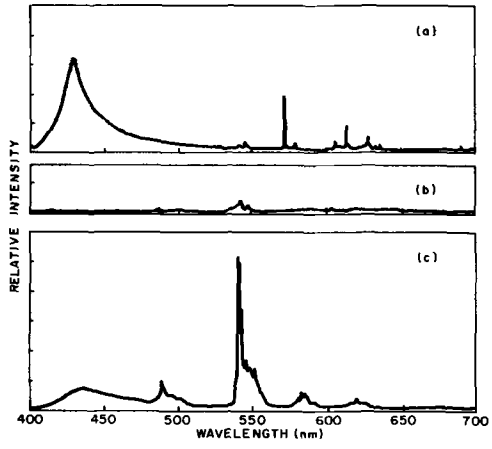

Fig. 4a. Emission spectrum of CaF_2:0.035Eu^{2+} excited at 390 nm; Fig. 4b. emission spectrum of CaF_2:0.064Tb^{3+} excited at 250 nm, all spectra recorded under identical conditions; Fig. 4c. emission spectrum of CaF_2:0.035Eu^{2+}, 0.064Tb^{3+}, excited at 390 nm.

Two alternative explanations may be given for the appearance of the 310 nm Tb^{3+} excitation band. It is known that the wavelength positions of divalent europium absorption bands are sensitive to the Eu^{2+} environment and may be observed near 300 nm. Thus, the 310 nm band might be ascribed to a Eu^{2+} ion in a lattice site differing somewhat from that of Eu^{2+} which is excited at 390 nm. One may assume that such Eu^{2+} ions, although transferring energy to Tb^{3+} ions, would yield some fluorescence like the Eu^{2+} ions absorbing at 390 nm. However, as noted previously the excitation spectrum for the only observed Eu^{2+} emission contains no 310 nm excitation band. It is, therefore, considered unlikely that the 310 nm band is a result of Eu^{2+} absorption.

The second alternate explanation for the 310 nm band is that it should be ascribed to the $4f^8 \rightarrow 4f^75d$ absorption in Tb^{3+} which is shifted to lower energy by the addition of europium (Eu^{2+} or Eu^{3+}) to CaF_2:Tb^{3+}. In no case has there ever been reported a Tb^{3+} f $\rightarrow$ d transition band in the 300 nm region. It appears quite unlikely that the presence of europium should have such an unusual effect on Tb^{3+} as to produce such a large shift in f $\rightarrow$ d absorption band wavelength. Additional support for the identification of the 310 nm excitation as a band associated with europium are the results of two other studies (17). In one case there was observed a 310 nm excitation band for Tb^{3+} fluorescence in $CaO\cdot 6Al_2O_3$:Eu^{2+}, Tb^{3+} and in another case for Mn^{2+} emission in $K_2O\cdot 6Al_2O_3$:Eu^{2+}, Mn^{2+}. In both studies the band was not observed when europium was not present. Clearly, this suggests that the 310 nm band is not to be identified with Tb^{3+} f $\rightarrow$ d absorption.

There is further precedent for associating the 310 nm band with Eu^{3+}-O^{2-} charge transfer. The presence of an oxide ion in the immediate vicinity of Eu^{3+} has given rise to charge transfer bands in the absorption and fluorescence excitation spectra of several activated materials. Blasse and Bril (18) have observed broad uv bands in the fluorescence excitation spectra of $NaGdO_2$:Eu^{3+} which they attribute to charge transfer from O^{2-} to Eu^{3+}. Similarly, Jørgensen (19) developed a theoretically founded explanation for such bands for Eu^{3+} in basic oxide solvents. It is reasonable to ascribe a similar identification to the 310 nm excitation band in CaF_2:Eu^{2+}, Tb^{3+}.

It must be recalled here that earlier studies reported nonradiative energy transfer from Tb^{3+} to Eu^{3+} in oxyanion salts (20). The transfer was considered to arise from a long-range electric dipole-electric dipole interaction. In the present study, the author explicitly suggests that the Eu^{3+}-Tb^{3+} interaction is short range and actually takes place via an intracomplex energy transfer. This is quite distinct from the earlier work where isolated Tb^{3+} ions were reported transferring to Eu^{3+}. One can best look on the transfer process in CaF_2 as arising from an absorption of energy by a $(Eu^{3+}, Tb^{3+}\text{-}O_2{}^{2-})^{2+}$ complex with the absorbed energy initially localized at a Eu^{3+}-O^{2-} band. The energy is subsequently relocalized at the Tb^{3+} ion by an intracomplex migration with resultant Tb^{3+} emission. In its simplest form, it is the Eu^{3+}-O^{2-} pair which is considered as the sensitizer of Tb^{3+}. Since it possesses an energy above ground (corresponding to 310 nm) greater than the $^7F_J \rightarrow {}^5D_4$ separation of Tb^{3+} it is possible for the $(Eu^{3+}\text{-}O^{2-})^+$ to Tb^{3+} transfer to occur. It must be repeated that such a model is in no way inconsistent with long range energy transfer from Tb^{3+} to Eu^{3+} in other host lattices.

Conclusion

It has been shown that Tb^{3+} emission can be photosensitized by nonradiative energy transfer from Eu^{2+} in CaF_2. It is further suggested that the appearance of

a 310 nm band in the Tb^{3+} excitation spectrum for $CaF_2:Eu^{2+}, Tb^{3+}$ indicates that energy can be absorbed by a $(Eu^{3+}, Tb^{3+}\text{-}O_2{}^{-2})^{2+}$ complex with the energy eventually becoming localized at the Tb^{3+} ion with resultant Tb^{3+} fluorescence. Such a model is supported by observations and is not inconsistent with earlier work where Tb^{3+} to Eu^{3+} energy transfer was reported.

Acknowledgment

The author gratefully acknowledges helpful and stimulating discussions with F. C. Palilla, S. Natansohn, and O. Sovers and thanks C. S. Wiggins for obtaining emission and excitation spectra.

Manuscript submitted Aug. 25, 1969; revised manuscript received *ca.* March 3, 1970.

Any discussion of this paper will appear in a Discussion Section to be published in the December 1970 JOURNAL.

REFERENCES

1. Y. R. Shen, *Phys. Rev.*, **134**, A661 (1964).
2. Y. R. Shen and N. Bloembergen, *ibid.*, **133**, A515 (1964).
3. J. C. Suits, B. E. Argyle, and M. J. Freiser, *J. Appl. Phys.*, **37**, 1391 (1966).
4. M. J. Freiser, S. Methfessel, and F. Holtzberg, *ibid.*, **39**, 900 (1968).
5. W. A. Runciman and C. V. Stager, *J. Chem. Phys.*, **38**, 279 (1963).
6. A. A. Kaplyanskii and A. K. Przhevuskii, *Opt. Spectry.*, **19**, 331 (1965).
7. N. Rabbiner, *J. Opt. Soc. Amer.*, **55**, 436 (1965).
8. L. G. Van Uitert and L. F. Johnson, *J. Chem. Phys.*, **44**, 3514 (1966).
9. W. F. Nelson *et al.*, Physics of Non-Crystalline Solids, Proc. of Int. Conf. Delft, p. 625, July 1964.
10. R. L. Amster and C. S. Wiggins, *This Journal*, **116**, 68 (1969).
11. E. Loh, *Phys. Rev.*, **147**, 332 (1966).
12. J. Rolfe, F. R. Lipsett, and W. J. King, *ibid.*, **123**, 447 (1961).
13. J. Sierro, *J. Chem. Phys.*, **34**, 2183 (1961).
14. D. L. Dexter, *ibid.*, **21**, 836 (1953).
15. P. A. Forrester and S. D. McLaughlin, *Phys. Rev.*, **138A**, 1682 (1965).
16. A. A. Kaplyanskii and P. P. Feofilov, *Optics and Spectros.*, **13**, 129 (1962).
17. R. L. Amster, Proceedings 7th Rare Earth Conference, San Diego, California, October 1968.
18. G. Blasse and A. Bril, *Solid State Communic.*, **4**, 373 (1966).
19. C. K. Jorgensen, *Molecular Phys.*, **5**, 271 (1962).
20. L. G. Van Uitert, E. F. Dearborn, and H. M. Marcos, *Appl. Phys. Letters*, **9**, 255 (1966).

Photoluminescence of ZnS:TbF_3 Thin Films

Y. S. Chen, J. C. Burgiel, and D. Kahng

Bell Telephone Laboratories, Incorporated, Murray Hill, New Jersey

ABSTRACT

Photoluminescence from ZnS:TbF_3 evaporated films of approximately 1μ thick has been studied at room temperature as a function of the fluoride concentration. The excitation or pumping wavelength varies from 4880 to 2600Å, while the Tb^{3+} ($^5D_4 \rightarrow {}^7F_5$) emission transition at 5425Å is monitored at the output. For pumping photon energies below the ZnS forbidden gap, the excitation spectra resemble that of the pure TbF_3 film or single crystal. For this case, the conversion efficiency with 4880Å ($^7F_6 \rightarrow {}^5D_4$) pumping in samples that contain 0.86% TbF_3 is close to 100% as compared to 0.8% for pure TbF_3. With pumping energies above the ZnS gap, photoluminescence presumably due to energy transfer from electron-hole pairs has also been observed; however, such a process yields conversion efficiency generally in the 10^{-5}-10^{-6} range. These results support the model that electroluminescence in devices using similar films arises from direct excitation of Tb^{3+} levels by hot electrons as proposed by one of the authors.

The subject of photoluminescence (PL) in solids has been widely studied for the purpose of understanding impurity levels, energy transfer mechanisms, the effect of crystal field on transitions, as well as electroluminescent (EL) device mechanisms. In recent years, rare earth ions have been introduced into a number of host lattices (1), since it is possible to obtain emission lines corresponding to the orbital transitions of these ions. More recently, Anderson (2, 3) and also Razi and Anderson (4) reported EL and PL results of trivalent rare earth Tb^{3+} ion in ZnS single crystals. They have shown that the energy transfer mechanism is similar to that of the ZnS:Mn system (5), namely, resonant energy transfer resulting from electron-hole pair recombinations.

In this paper, we report the room temperature PL results of a new material system in which the rare earth fluoride molecules are incorporated within a host lattice. The particular system studied in this work is ZnS:TbF_3 thin films. Such films have been used in EL devices reported by one of us elsewhere (6). Our main purpose is to study the energy transfer mechanisms together with the efficiencies of such processes. We have also studied the emission and excitation spectra as a function of the fluoride concentration. A brief discussion is given at the end of this paper to relate the PL results to the proposed model for EL given in ref. (6).

Experimental

The system used for measuring the photoluminescence is given in Fig. 1. The excitation source consists of a 900W d-c Xe arc lamp, a 90-cycle chopper, and a Bausch & Lomb high intensity grating monochromator with interchangeable u.v. and visible gratings. The resolution used for excitation is 100Å.

The critical part of the system is the parabolic reflector in the sample chamber. The excitation beam travels through the window at the center of the reflector and is focused on the sample, which at the same time is positioned at the focal point of the reflector such that the PL signal generated can be efficiently collected. A Spex 3/4 meter spectrometer is used to analyze the PL spectra (resolution used is 10Å). Filters of appropriate characteristics were placed at the exit slits of the two monochromators to minimize the presence of scattered light from the excitation source.

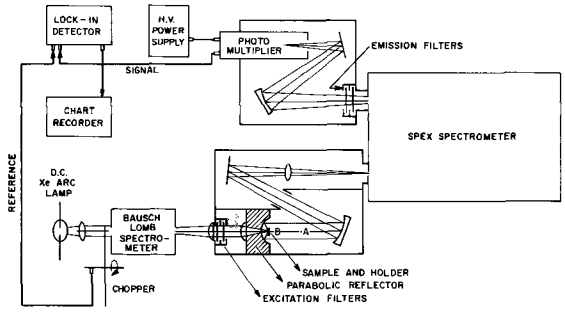

Fig. 1. Experimental setup for photoluminescence measurement

Sample preparation.—To determine quantitatively the conversion efficiency (defined as power emitted over power absorbed) of the PL signal generated in a thin luminescent film, it is necessary to know the excitation spectrum characteristic to the material and to know how much of the excitation power can be coupled to the film in the presence of interference phenomena. The problem of interference can be avoided by matching the indices of refraction of the film and the substrate which should be very thick and have slightly nonparallel surfaces. Such a sample geometry is depicted in Fig. 2. The aluminum mirror on the back of the substrate is provided to maximize the coupling between excitation and emission and to make sure that the reflected portion of the excitation beam can escape through the window in the parabolic reflector without suffering scattering onto the wall of the reflector.

We have prepared thin film samples of TbF_3 [n = 1.57 in the visible (7)] on quartz [n = 1.5 in the visible (8)] substrates and also thin film samples of ZnS [n = 2.3 at 5000Å (9)] with various TbF_3 concentration on $KTaO_3$ [n = 2.3 at 5000Å (10)] substrates. The samples were all prepared by evaporation or co-evaporation near 1000°C from separate sources onto a cold substrate. The optical properties of the thin TbF_3 film were found to be very close to that of the bulk TbF_3 single crystal. The concentration of TbF_3 in ZnS was determined by x-ray fluorescence and chemical analysis on the Tb content. The film thicknesses were determined optically (9).

PL efficiency and absolute power measurement.—To measure the absolute excitation and PL power, the following experimental steps were taken:

i. The power of the excitation beam, P_{ex}, was directly measured by a calibrated thermopile placed at B (see Fig. 1).

ii. The same excitation beam after a known amount of attenuation, X1, was measured by a photomultiplier (EMI No. 9558Q with S-20 response) placed at A in Fig. 1. The signal strength is $S(\lambda_{ex}, \Delta\lambda_{ex})$, where λ_{ex} is the wavelength of the excitation beam and $\Delta\lambda_{ex}$ is the bandwidth.

iii. The PL signal is measured by the same PM with a sample placed at B. The signal strength is $S(\lambda_o, \Delta\lambda_o)$, where λ_o is the emission wavelength and $\Delta\lambda_o$ is the bandwidth formed by appropriate filters. These filters attenuate the signal by X2. We have chosen $\Delta\lambda_o$ to embody the strongest line of the Tb^{3+} emission, namely the $^5D_4 \rightarrow {}^7F_5$ transition near 5450Å. Furthermore, since we are dealing the inner orbital transition of the rare earth ion, the emission spectra remain essentially fixed with respect to the variation of excitation wavelength and the total power content of emission is therefore proportional to the power content within $\Delta\lambda_o$.

iv. The proportionality contant, C, was determined by (*a*) taking the emission spectrum, (*b*) correcting the spectrum with the spectral response of the PM, (c) integrating out the areas of the entire spectrum and that within $\Delta\lambda_o$ and, finally (*d*) the ratio of the two areas is then the constant C.

v. The total power content of emission is then

$$P_{PL} = \frac{S(\lambda_o, \Delta\lambda_o) \cdot X1}{S(\lambda_{ex}, \Delta\lambda_{ex}) \cdot X2} \cdot P_{ex} \cdot C \cdot \epsilon$$

where ϵ is the relative PM response at λ_{ex} and λ_o (with $\Delta\lambda_{ex}$, $\Delta\lambda_o << \lambda_{ex}$, λ_o). The accuracy of the absolute power measurement was held to within ± 10%.

To determine the conversion efficiency of PL it is necessary to know the amount of power absorbed in the film. Such information is available from the absorption spectrum of TbF_3 single crystal, the ZnS reflection and transmission data above the energy gap, and the concentration of TbF_3 in ZnS.

In the weakly absorbing films such as TbF_3 pumped between 2500 and 4900Å and ZnS pumped well below the ZnS gap ($\lambda > 3600$Å), the relative amount of power absorbed can be expressed as (the sample geometry is given in Fig. 2)

$$\frac{\Delta I}{I} = \alpha \cdot 2d \qquad [1]$$

if

$$\alpha d << 1$$

and

$$\alpha d << \frac{1}{R} - 1$$

where I is the intensity of the incident light, ΔI is the loss of incident light due to the absorption, α is the absorption coefficient of the film, d is its thickness and R is the air-sample interface reflectivity and is equal to $([1 - n]/[1 + n])^2$ with n being the refractive index of the film (and the substrate). The substrate is assumed to be nonabsorbing in Eq. [1]. In Eq. [1], we have ignored the loss of the incident light due to the finite scattering in the film; this step is justified as long as the scattering process does not contribute to the emission process.

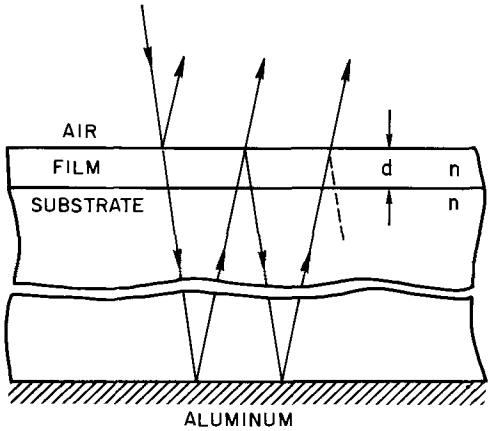

Fig. 2. Sample geometry used in photoluminescence measurement

Results

Three samples were investigated in this work: a TbF_3 film of 0.825μ in thickness, and ZnS:TbF_3 (3.3% and 0.86%) films of 1.17 and 1.66μ in thickness, respectively. The PL spectrum of a TbF_3 single crystal and those of the film samples under 2840Å pumping are given in Fig. 3. Notice that the fine structures appear in the spectrum of the TbF_3 crystal only. Understandably, excess strain and lack of symmetry in the film would cause the line broadening. To compare the results of PL in these film samples the $^5D_4 \rightarrow {}^7F_5$ (5300-5600Å) transition was monitored, while the excitation wavelength was varied from 2600 to 4880Å. This range of wavelength spans across the band edge of ZnS (~ 3200Å). No emission was observed under the excitation of 4700-3800Å; this means that the energy loss of the excitation beam due to the inevitable finite scat-

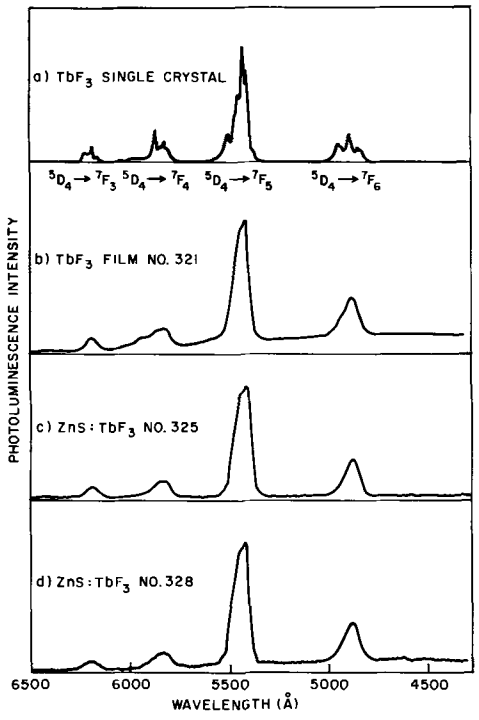

Fig. 3. Photoluminescence spectra at RT pumped with 2840Å light. (a) TbF_3 single crystal, (b) TbF_3 film 0.825μ thick (No. 321), (c) ZnS:TbF_3 (3.3%) film 1.17μ thick (No. 325), and (d) ZnS:TbF_3 (0.86%) film 1.66μ thick (No. 328).

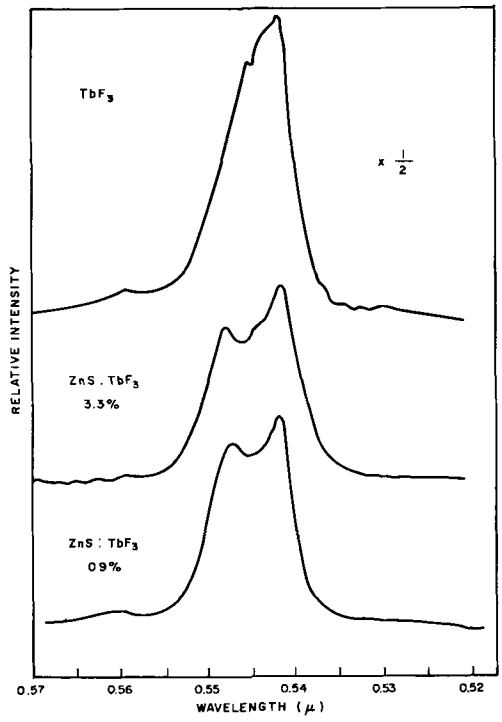

Fig. 4. Room temperature photoluminescence spectra near 5500Å of TbF_3, ZnS:TbF_3 (3.3%), and ZnS:TbF_3 (0.86%) films pumped at 4880Å.

tering in the film is not coupled to any energy transfer mechanism leading to the excitation (and the emission) of the Tb^{3+} ions. Thus the scattering loss, if any, can be treated the same as the reflection loss and can be ignored in the efficiency calculation of the energy transfer mechanisms. The results are given in Table I (columns I to III).

The 4880Å pumping was chosen in order to detect the direct excitation of Tb^{3+} in ZnS:TbF_3 as it is possible to have the combination of $^7F_6 \rightarrow {}^5D_4$ ($\sim$ 4880Å) up and $^5D_4 \rightarrow {}^7F_5$ down transitions. It is important to notice that the host ZnS at this wavelength is non-absorbing. The PL spectra of the film samples near 5500Å with 4880Å pumping are given in Fig. 4. Notice there is some difference between that of TbF_3 and those of ZnS:TbF_3; this difference could be due to the effect of host crystal field on the incorporated molecular centers.

The absorption band of the $^7F_6 \rightarrow {}^5D_4$ transition in TbF_3 single crystal has a bandwidth of 100Å and the absorption coefficient at the peak was measured to be 10 cm^{-1}. From Eq. [1] we have found the conversion efficiency for TbF_3 with 4880Å pumping is 0.8%. Under the assumption that the absorption by TbF_3 centers is proportional to the concentration and is independent of the medium in which they are situated (11), it was further found that the conversion efficiencies with 4880Å pumping are 12 and 32% for the 3.3 and 0.86% doped samples, respectively. These observed data clearly indicate the existence of a strong concentration quenching of the Tb^{3+} $^5D_4 \rightarrow {}^7F$ emission.

Notice that the power conversion efficiency of PL by direct excitation is near unity at a concentration level [$\sim$ 1 m/o (mole per cent)] much higher than the reported solid solubility of bare Tb^{3+} in ZnS ($\sim$0.01 m/o) (2, 12).

The conversion efficiencies for pumping above the ZnS gap are typically 10^{-5}-10^{-6}, as shown in column V of Table I. This is because the absorption coefficient α is typically of the order of 10^5 cm^{-1} in ZnS. In other words, most of the pumping energy is consumed to create electron-hole pairs. It is of interest to see if there exists, while pumping above the ZnS gap, a mechanism to transfer energy from the electron-hole pair recombination to the excitation of TbF_3 centers in addition to the direct excitation intrinsic to these centers. Such a mechanism can be referred to as lattice-coupled excitation. To investigate this, it is necessary to know the penetration depth δ ($= 1/\alpha$) of incident light into the ZnS film and the measured values are given in column IV of Table I. The value of δ determines the volume in which the energy transfer due to the direct excitation takes place. The ratio $\mathcal{R}$ of PL due to lattice coupled excitation over that from direct excitation can be defined as

Table I. Efficiency calculation of energy transfer mechanisms

I Excitation wavelength, A	II Xe source, mW	III PL (nw) TbF_3, No. 321	III PL (nw) ZnS, No. 325	III PL (nw) ZnS, No. 328	IV δ, ZnS, μ	V Efficiency η No. 321	V Efficiency η No. 325	V Efficiency η No. 328	VI $\mathcal{R}$ No. 325	VI $\mathcal{R}$ No. 328
4880	1.84	6.4	4.3	4.3	2d	0.008	0.12	0.32	0	0
3740	0.95	19.2	4.3	5.8	0.85		5.7×10^{-6}	7.5×10^{-6}	~0	~0
3520	1.06	21.8	5.0	6.0	0.167		5.4×10^{-6}	7.1×10^{-6}	4.0	5.0
3310	1.06	7.5	7.8	7.4	0.096		8.7×10^{-6}	9.2×10^{-6}	38	35
3180	1.06	8.0	10.0	8.7	0.087		1.2×10^{-5}	10^{-5}	50	45
3030	1.03	7.7	13.0	12.0	0.077		1.6×10^{-5}	1.5×10^{-5}	77	72
2840	0.796	12.6	16.5	14.0	0.064		2.6×10^{-5}	2.2×10^{-5}	72	63
2600	0.354	9.3	12.0	13.5	0.041		4.1×10^{-5}	4.7×10^{-5}	110	130
Film thickness d, μ		0.825	1.17	1.66						
TbF_3 concentration, m/o		100	3.3	0.86						

$$\mathcal{R} = \left[\frac{PL_{ZnS}(\lambda)}{PL_{ZnS}(\lambda_o)} \cdot \frac{2d}{\delta}\right] \Big/ \left[\frac{PL_{TbF_3}(\lambda)}{PL_{TbF_3}(\lambda_o)}\right] - 1 \quad [2]$$

where $PL_{ZnS}(\lambda)$ and $PL_{TbF3}(\lambda)$ are the PL intensities pumped above ZnS energy gap, $\lambda_o = 4880$Å, and d is the thickness of ZnS:TbF_3 film. The results are given in column VI of Table I. Indeed there exists some noticeable lattice coupled excitation although only 10^{-5} of the excitation energy is converted into PL. Furthermore, the sudden increase of $\mathcal{R}$ near 3300Å is further evidence that lattice coupled excitation takes place. The absolute magnitude of $\mathcal{R}$ was found to vary slightly from sample to sample because of variations in the competing nonradiative processes.

Discussion

Our results can be summarized as follows:

1. The molecular center, TbF_3, in ZnS can be pumped directly and efficiently at levels below the energy gap of ZnS. This is true presumably for any host lattice and any rare earth fluoride dopant. The conversion efficiency, which is enhanced greatly in a dilute system, can be close to 100%.

2. The same centers can be excited via energy transfer from electron-hole recombination if pumped at energies above the forbidden gap of the host lattice. The efficiency for this process (lattice coupled excitation) is very poor and is in the range of 10^{-5}-10^{-6}.

There is very little data in the literature concerning PL in thin films to compare with our results. Efficiency of resonant transfer in ZnS:Ag powder sample has been reported as high as 21% (13) and rare-earth ions in a tungstate system gives efficiency near 1% (1).

When the ZnS:TbF_3 film is used in the electroluminescence device as described in ref. (6), the external power efficiency is about 10^{-4} (corresponding to an internal efficiency of $\sim 10^{-3}$ due largely to total internal reflection). The ionization coefficients for pair production in insulating ZnS single crystals and films, using conventional methods (14), were found by us to be 5×10^2 cm^{-1} at 10^5 V/cm and less than 10^4 cm^{-1} at 10^6 V/cm. Therefore, the efficiency for pair production from the injected carriers in the EL device is at best 5×10^{-2} for a 1000Å ZnS:TbF_3 film. The over-all power efficiency of EL emission, if lattice coupled excitation is the dominant mode, would be at best in the range of 10^{-6}-10^{-7}, which is clearly too small compared to the observed value. On the other hand, if the Tb^{3+} ions in ZnS:TbF_3 are impact excited directly, one would merely require an impact excitation coefficient of 200 cm^{-1} at 10^6 V/cm for these centers to achieve the observed efficiency in the EL devices. Thus we believe, from our PL results, direct impact excitation of the Tb^{3+} ions in ZnS:TbF_3 films is indeed the most likely mechanism for observed electroluminescence as proposed by one of the authors (6).

Acknowledgments

The authors wish to thank M. V. DePaolis for designing the PL sample chamber and many other technical assistances. They are also indebted to E. W. Chase for preparing the samples and to S. M. Vincent for analyzing the fluoride concentrations of the ZnS:TbF_3 samples.

Manuscript submitted Nov. 7, 1969; revised manuscript received Feb. 25, 1970.

Any discussion of this paper will appear in a Discussion Section to be published in the December 1970 JOURNAL.

REFERENCES

1. L. G. Van Uitert and R. R. Soden, *J. Chem. Phys.*, **33**, 567, (1960); and also L. G. Van Uitert, "Luminescence of Inorganic Solids," p. 465, P. Goldberg, Editor, Academic Press, Inc., New York (1966).
2. W. W. Anderson, *Phys. Rev.*, **136**, A556 (1964).
3. W. W. Anderson, S. Razi, and D. J. Walsh, *J. Chem. Phys.*, **43**, 1153 (1965).
4. S. Razi and W. W. Anderson, *Trans. Met. Soc. AIME*, **239**, 350 (1967).
5. W. W. Piper and F. E. Williams, "Solid State Physics," vol. 6, p. 129, F. Seitz and D. Turnbull, Editors, Academic Press, Inc., New York (1958).
6. D. Kahng *Appl. Phys. Letters*, **13**, 210 1968; the devices are reported in detail by E. W. Chase, R. T. Hepplewhite, D. C. Krupka, and D. Kahng, *J. Appl. Phys.*, **40**, 2512 (1969).
7. "Progress in the Science and Technology of the Rare Earths," p. 102, L. Eyring, Editor, Pergamon Press, Oxford, (1966).
8. "American Institute of Physics Handbook," p. 6-25, D. E. Gray, Editor, McGraw-Hill Book Co., Inc. New York (1963).
9. J. C. Burgiel, Y. S. Chen, F. Vratny, and G. Smolinsky, *This Journal*, **115**, 723 (1968).
10. S. H. Wemple *Phys. Rev.*, **137**, A1575 (1965).
11. The problem of localized centers in a dielectric medium is treated by D. L. Dexter in "Solid State Physics," Vol. 6, p. 360, Academic Press, New York (1958). The absorption cross section σ is proportional to $\left[(E_{eff}/E_o)^2 \frac{1}{n}\right]$ or $\frac{(n^2+2)^2}{9n}$ for a cubic or an isotropic medium. Since it is difficult to estimate $[E_{eff}/E_o]^2$ for pure TbF_3, which is noncubic, we have assumed here σ of TbF_3 centers is independent of the medium in which they are situated.
12. H. H. Woodbury, "Physics and Chemistry of II-VI Compounds," p. 230, M. Aven and J. S. Prener, Editors, John Wiley & Sons, New York (1967).
13. A. Bril, "Luminescence of Organic and Inorganic Materials," p. 479, H. P. Kallmann and G. M. Spruch, Editors, John Wiley & Sons, New York (1962).
14. A. G. Chynoweth and K. G. McKay, *Phys. Rev.*, **108**, 29 (1957).

Some Aspects of Optical Measurement of Luminescence

W. A. Thornton

Advanced Development Department, Lamp Division,
Westinghouse Electric Corporation, Bloomfield, New Jersey

ABSTRACT

Five aspects, all of which lead toward simplification of measurement, are discussed. It is shown that: (*I*) Slit width and resolution have no effect on the proper measurement of a line-plus-continuum spectrum; *i.e.*, the proper energy ratios are obtained independent of resolution as long as point-by-point analysis is used. (*II*) Calculated chromaticity of line-plus-continuum spectra such as those of fluorescent lamps is constant to ½% for slit width (line width at half-maximum) as great as 15 nm. Simpler analysis of lines as triangular area is as accurate and precise. (*III*) Differences in calculated characteristics of line-emitting phosphors are negligible at slit widths up to at least 8 nm. (IV) Spectrum broadening by nonzero slit width amounts, for example, to 1-2% for a slit-width/band-width ratio of 0.2. (V) A rough method of fluorescent lamp analysis by unequal slits and 10 nm intervals results in chromaticity accurate to 1% or better.

Accurate optical measurement of the spectral energy distribution (SED) of lamps or phosphors is at best difficult, particularly when line emission, or line emissions plus continuum, are present. Five aspects of such measurement are discussed, with the objectives of simplification without loss of necessary accuracy and of clarifying the advantages and validity of certain simplifying procedures.

Dispersing instruments used for analyzing the spectral energy distribution of a light source, as a function of wavelength, generally allow variation of resolution, usually by adjustment of the width of one or more slits at focal planes in the instrument. In this paper, resolution is specified as the width in nanometers, at half-height, of the apparent SED of actual line emission of zero width. For example, the 436 nm emission line from a mercury vapor discharge serves reasonably well as a source by which to measure the resolution, thus defined, of a dispersing instrument. Many research problems in luminescence require the best resolution attainable; that is the narrowest possible apparent SED of actual line emission. The reader is reminded that there are, however, numerous and important problems in luminescence for which excellent resolution is not only not required, but of no actual advantage, and thus in fact wasteful of time and effort in analysis. Examples are chromaticity, lumen output, and color rendering index of lamps, and chromaticity, quantum efficiency, mean wavelength, and luminosity of the emission of phosphors. The determination of most of these characteristics requires only moderate resolution simply because the tristimulus or color matching functions of human vision are involved multiplicatively, and these functions are comparatively structureless. Analysis of the SEDs of lamps or phosphor emission is simpler the broader the resolution of the dispersing instrument used; that is, the necessary sampling interval in point-by-point analysis becomes larger the broader the resolution, and fewer points suffice to analyze a given spectrum. One of the central considerations of this paper is the influence of this breadth on accuracy of analysis.

Effect of Slit Width or Resolution on Proper Measurement of a Line-Plus-Continuum Spectrum

It has been suggested by some that whether or not one obtains the proper relationship between the energy contents, for example, of a narrow line and of a continuum present in the same spectrum, depends on the slit width and resolution of the instrument used. The purpose of this section is to show that there is no basis for this proposal, and that in fact there is no range nor combination of slit widths (resolution) which in itself causes error.[1] We assume throughout that point-by-point analysis of experimental spectra is performed, in the manner now used by NBS (1), and that the attempt is not made as in past years (2, 3) to use some sort of relationship between peak heights and pass-bands.

Slit widths much smaller than the width of any component of the spectrum.—In this case, the spectrum of the source will be laid down in the exit plane with its correct spectral energy distribution. Scanning by an exit slit of the same width as the entrance slit, or larger or smaller, will yield the correct spectral energy distribution as long as the width of either slit is very small compared to the structure of the spectrum, as assumed. Hence the integrated energy in any component of the spectrum will bear the proper relationship to the integrated energy in any other component.

Slit widths much larger than the width of some component(s) of the spectrum.—Assume an actual spectral distribution, as shown in Fig. 1A, consisting of a broad continuum and a superposed very sharp

[1] Of course, one must retain sufficient resolution not to introduce significant errors due to wavelength-dependent correction factors, but this is a separate consideration, and such correction curves are also comparatively structureless.

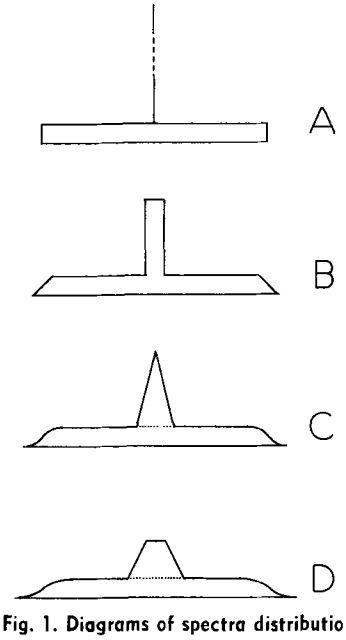

Fig. 1. Diagrams of spectra distribution

line of arbitrary height (intensity); the abscissa in Fig. 1A can be considered to be linear in wavelength, but in the following figures the abscissa will represent only the direction along which dispersion takes place, and the ordinates will represent proportional intensity in some units.

Figure 1B represents the way the spectrum of Fig. 1A is laid down in the exit plane by a dispersing instrument with entrance slit equal to one division. The entrance slit, however wide, is assumed to be filled with diffuse radiation, or at least that it and the entrance aperture are filled; any other arrangement will introduce source geometry as a factor, although it will be shown later that this is also unimportant to the question at hand. Note that the abscissa of Fig. 1B is no longer simply in wavelength units since the one-division-wide pedestal atop the continuum now represents essentially a single wavelength. Figure 1B indicates that the spectrum consists of 12 units in the continuum and 4 units in the line, and the question is, "Does this ratio apparently change with slit width?" Figure 1C represents the apparent spectral distribution as the spectrum 1B is scanned by an exit slit equal to one division. The "gain" convention used throughout this section is that when the exit slit is filled by and only by the continuum the output signal is equal to the actual intensity of the continuum. The continuum-line ratio remains 3 for this condition of equal slits. Figure 1D represents the apparent spectral distribution as the spectrum 1B is scanned by an exit slit equal to two divisions. The continuum-line ratio remains 3 for this condition of unequal slits.

The inference is that a slit width much wider than the width of the line emission in a line-continuum spectrum nonetheless yields the correct proportion of integrated energies in the line and continuum; again it is clear that entrance and exit slit widths need not be equal.

Slit widths comparable to the width of some component(s) of the spectrum.—It could be assumed that if no trouble arises in the cases given in the two previous sections that all should be well in the case of comparable widths also, and this is shown by the following. Let Fig. 2E represent an actual spectral energy distribution consisting of a continuum (20 units) and a "line" (4 units) which is two units wide at its base. If the entrance slit is two divisions wide, Fig. 2F represents the way the actual spectrum of Fig. 2E will be laid down in the exit plane; the 20/4 area ratio of course still holds. Figure 2G represents the apparent spectral distribution as the spectrum 2F is scanned by an exit slit equal to two divisions. The shaded areas were plotted on a larger scale and were found equal to one part in 300. This is taken as proof that slit widths comparable to line widths can still, in themselves, cause no error in point-by-point analysis of areas under the different components. One additional case was considered: that where slit width is several times line width. Again, Fig. 3H represents the actual distribution, Fig. 3J the distribution in the exit plane by a four-division entrance slit, and Fig. 3K the result of scanning 3J with a four-division exit slit. The area ratios are the same in H, J, and K. No problem exists within the scope of this discussion in obtaining the proper intensity relationship between "line" emission and a continuum in the same spectrum. It is suggested that the reader convince himself by drawing and integrating areas in the manner of Fig. 1-3. Since it has been shown that entrance and exit slit widths need not be equal, and it is apparent that failure to fill the entrance aperture will not affect the layout of the spectrum in the exit plane, it follows that it is irrelevant how the source radiation is introduced into the instrument.

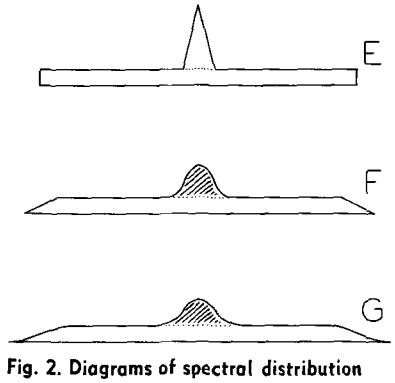

Fig. 2. Diagrams of spectral distribution

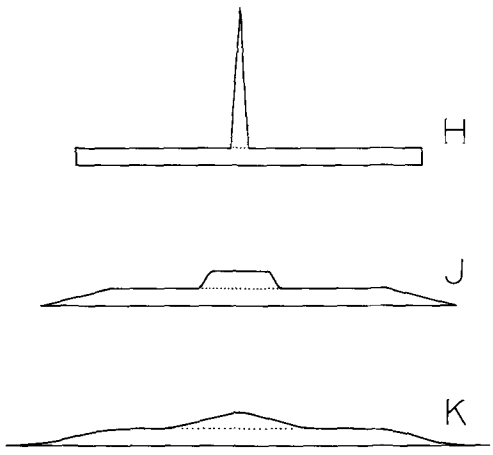

Fig. 3. Diagrams of spectral distribution

An experimental verification was done by analysis of a 365 nm mercury line superposed on the continuum due to calcium tungstate phosphor; the same ratio of energies in the line and continuum was obtained, within experimental error, over an 8X range of slit width (1.5-12 nm width at half-maximum of the apparent SED of the 365 nm Hg line).

Fluorescent Lamp Chromaticity vs. Slit Width and Method of Analysis of SED

A method for determining chromaticity of fluorescent lamps, which is both as simple and as accurate as possible, is of course needed wherever lamp color is rigidly specified. The usual colorimeter has a long history of difficult, if not excruciating, problems mainly because its good precision is limited to light sources which are very similar indeed in SED to the carefully calibrated standard lamp which must ordinarily be used. Therefore, NBS in September 1965 (1) changed "from a visual to a spectroradiometric basis for calibrating fluorescent lamp chromaticity coordinates." That is, lamp chromaticity would henceforth be determined from the SED of the lamp. The NBS method is a point-by-point (wavelength-by-wavelength) comparison of fluorescent lamp output to that of a standard incandescent lamp. The NBS paper (1) by Hammond quotes the following errors:

Repeatability of x and y by new method[2,3]:	0.002
Agreement with old method:	0.003
Range of values by three laboratories[3]:	0.004

On this basis, "the NBS therefore has decided that the accuracy of the spectroradiometric measurements is now sufficient to permit the calibration of fluorescent-lamp chromaticity standards from such measurements" (1).

A brief comparison of experimental procedure follows. NBS: Wavelength-by-wavelength comparison of outputs of unknown fluorescent and standard incan-

[2] NBS, GE, and Durotest are the three laboratories quoted as using the new method.

[3] A more recent NBS fluorescent lamp round robin (analysis completed in September 1969) showed an average deviation in x and y among five laboratories of 0.0025.

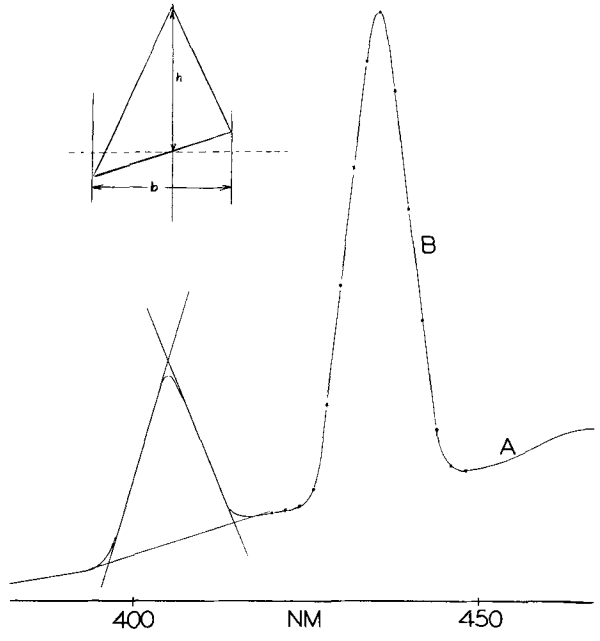

Fig. 4. Portion of SED of 40W 3500K white lamp

descent lamps. Here: Run raw SED, correct, and calculate by computer from stored data from standard incandescent lamp. Measurement time: NBS: About 40 min. Here: About 40 sec. Both: Accept light from a short section of the fluorescent lamp. Here: Also can use an integrating enclosure containing both fluorescent lamp and incandescent standard (only one of which is operating at one time) and from which the monochromator samples the integrated emission. Both: Entrance and exit slits equal; passband equal to about 6 nm, normally. Both: use EMI 9558 photomultiplier and anode amperes less than 10^{-6}.

Our method of analysis is illustrated in Fig. 4, which is a portion of the raw SED of a 40W 3500K White lamp, using 3 mm slits, which lead to a line width at half maximum of roughly 9 nm. The objective was to see (*a*) whether calculated chromaticity of a particular lamp varied with slit width or (*b*) whether the line emission was analyzed as areas of the triangles or point-by-point analysis, at various wavelength intervals, over the trace of the line emission. Both methods are illustrated in Fig. 4. When the mercury line emission was measured as triangular[4] areas (nm times vertical units), the phosphor emission continuum A was measured at 10 nm intervals. When the line emission was measured point-by-point (as, for example, in 2 nm intervals at B) the continuum was measured at the same or different intervals, as convenient. Obviously it is much simpler to measure the continuum from end to end at large (here 10 nm) wavelength intervals and then to add the triangular areas at the center wavelengths of the mercury lines; it turned out that this is just as accurate as the point-by-point method.

The results are given in Table I. Chromaticity varies by at most 0.002 with (*a*) variation in slit width (resolution) over a factor of five, or (*b*) analysis of mercury lines simplified to triangular areas rather than analyzed point-by-point at sufficiently small intervals, *i.e.*, the two methods pictured in Fig. 4.

It is concluded that any convenient slit width up to a resolution (line width at half-maximum) of at least 15 nm may be used without degrading chromaticity results beyond the 0.002 repeatability level experienced by NBS (1). The simpler triangle method of analysis, which allows measurement of the continuum as a whole and at wide wavelength intervals, and avoids

[4] The reader is reminded that the area of a skew triangle is half the height times the projected base; see sketch in Fig. 4.

Table I. Calculated chromaticity x, y in 1931 CIE color space, of a single 3500K white 40W fluorescent lamp, as a function of method of analysis of lamp SED

	Slit width,* mm	Equivalent resolution, nm	x	y	Method of analysis
1.	1-1	3-3	0.4079	0.3954	Point by point (1 nm**)
2.	3-3	9-9	0.4090	0.3953	Point by point (2 nm**)
3.	5-5	15-15	0 4104	0.3956	Point by point (4 nm**)
4.	1-1	3-3	0.4083	0.3973	Triangles
5.	3-3	9-9	0.4092	0.3954	Triangles
6.	5-5	15-15	0.4081	0.3953	Triangles
7.	2.5-6	7.5-18	0.4054	0.3953	Point by point, all 10 nm

* Entrance slit, then exit slit. Grating monochromator.
** Interval used to analyze mercury lines.

point-by-point analysis of mercury lines, is as accurate and as precise as the latter. This conclusion applies, of course, to SEDs other than those of fluorescent lamps. On the other hand, where great accuracy is called for, as in the case of fluorescent lamp standards, these approximate methods must be used with caution since the presently achieved precision of 0.002 in chromaticity must be improved.

Integrated Optical Characteristics of Line Emitters

Because of their interest in transitions among many discrete, closely spaced energy levels, some researchers like to measure their emission spectra at resolutions at least as high as 0.1-0.3 nm. On the other hand, because such spectra, when they consist of several or many lines, become prohibitively difficult to analyze accurately point-by-point, some workers purposely reduce resolution; this makes analysis simpler, although it is still arduous to analyze, for example, a many-line-emitting phosphor like yttrium oxide:Eu^{3+}.

At the higher resolutions used, even though the spectra are nominally corrected by some device, one has to be content with rather approximate relative line heights and (if two or more lines are unresolved) very little idea of the total energy in a composite group. By reducing resolution and using point-by-point analysis to obtain a rather precisely corrected spectral energy distribution (from which total energy, total photons, total lumens, quantum efficiency, chromaticity, mean wavelength, luminosity, etc. can be calculated), we attain a precision which is of the order of one MPCD (minimum perceptible color difference) in chromaticity, for example.

The question is: How much accuracy is forfeited by reducing resolution to this extent? That is, will the broadened SEDs give appreciably different, and erroneous, values of chromaticity, lumen output in blends, and the like? The SED of yttrium oxide:Eu^{3+} (YOE) was simplified to three lines as indicated in Fig. 5. Then this SED was altered by broadening the lines to Gaussian energy distributions 8 nm wide at half-height. Total energy under the SEDs remained constant, although this is not indicated in Fig. 5. Chromaticity, mean wavelength, and luminosity factor were computed for the SEDs. They were then combined by computer in blends with other phosphors and lumen output and color rendering index computed.

Table II lists chromaticity x, y, mean wavelength $\bar{\lambda}$ in nm, luminosity factor η, total lumen output of the blend including discharge in a 40W LPMV fluorescent lamp, color rendering index, and correlated color temperature of the blend SEDs. These tabulated quantities differ, for the most part, by two parts per thousand or less. In the case of chromaticity, the difference amounts to less than one minimum perceptible color difference.

It is concluded that the differences in calculated characteristics of SEDs of a single line-emitting phos-

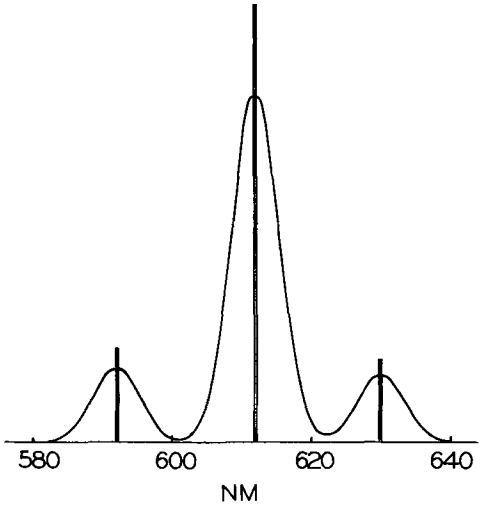

Fig. 5. Simplified SED of yttrium oxide:Eu^{3+}

phor, or of a complete lamp containing that phosphor in a blend, are completely negligible if resolution in terms of half-width in nanometers falls in the range 0-8 nm.

SED Broadening by Finite Slit Width

The true "natural" width of line or band emission is always apparently somewhat broadened by the use of nonzero slit width. It is sometimes useful to know the magnitude of this apparent broadening given the resolution of the dispersing instrument, either to know whether the apparent broadening is appreciable, or to be able to correct for it and thus obtain the true width of the emission.

Given a Gaussian distribution as the model SED, calculations were made of the apparent broadening by entrance and exit slits of various widths, both equal and unequal. The procedure was the same as that used in the section on Effect of Slit Width; the Gaussian distribution was scanned by a slit (pass-band) of a given width in units of the abscissa, the resulting "signal" was plotted and that distribution scanned again by a slit of the same or different width (pass-band). The width at half-maximum of the final distribution was then compared to that of the original distribution. The results for equal slits are plotted in Fig. 6 as fractional apparent increase in band width *vs.* the ratio of slit width (*i.e.*, equivalent resolution in wavelength units) to true band width. A range of ratios from about 0.02 to about 2.0 was covered. For example, the cross in Fig. 6 might represent a slit width of 8 nm (that is, a resolution equivalent to a broadening of line emission to 8 nm width at half maximum; this might result from an actual slit width of 2-3 nm in a given monochromator) analyzing an SED like that of zinc silicate:Mn of 40 nm width at half-maximum true band width. Thus the ratio will be 0.2, and we can expect a broadening of less than 2%. At very high ratios (broad slits, narrow emission) the broadening will be equal to the slit width, both in units of the true emission width; hence the asymptote of slope unity. Experimentally, at least for the monochromators[5] used in the present work,

[6] 500 mm, concave mirror, reflection grating.

Table II. Characteristics of the phosphor SEDs alone and in blends

Line width, nm	x	y	$\bar{\lambda}$	η	Blend L_0 (%)	Blend CRI	Blend CCT
0	0.6591	0.3406	611.4	0.4877	100.1	77.7	4062K
8	0.6580	0.3417	611.4	0.4881	100.0	77.8	4068K
	0.005	0.002	(1 MPCD)				

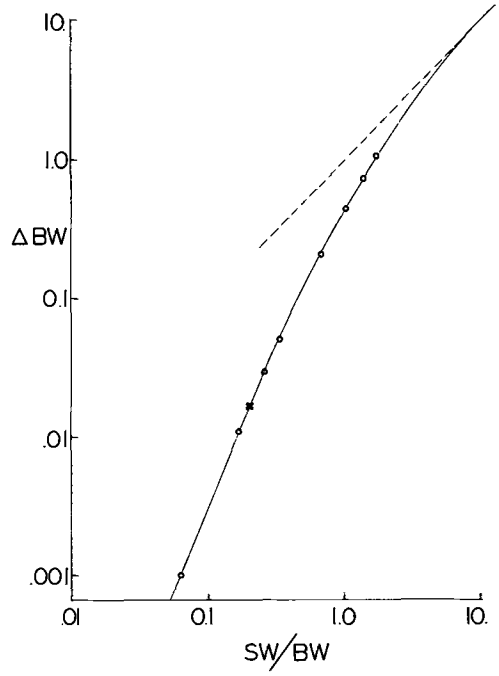

Fig. 6. Results for equal slits plotted as fractional apparent increase in band width *vs.* ratio of slit width to true band width.

observed broadening due to slit width is always less than predicted, presumably because other factors slightly broaden the apparent SED and prevent determination of the exact "true" width even at very small slit widths. Unequal slits cause broadening relatively 10-20% greater than that due to equal slits of the average value, but much less than that due to equal slits of the greater value.

Rough Method of Analysis of Fluorescent Lamps

The line emission of fluorescent lamps is a little work to analyze even if triangular areas are substituted for the lines as discussed in the section on Fluorescent Lamp Chromaticity. Slits can be widened so as to smear the SED to the point where 10 nm intervals are sufficiently closely spaced to sample adequately the SED. It happens, however, that the more important visible mercury line emissions fall near 5 nm multiples in wavelength. Hence it seemed likely that a certain choice of unequal slit widths would cause these line emissions to appear as trapezoids with corners falling

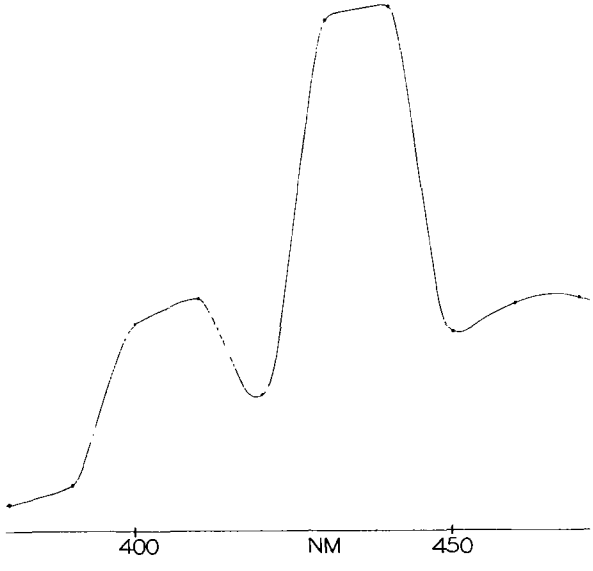

Fig. 7. SED of white (3500K) Standard fluorescent lamp

approximately at 10 nm multiples. In this way, 10 nm intervals would be expected to lead to more accurate evaluation of fluorescent lamp SEDs than if the necessarily greater broadening by wider, equal slits were resorted to.

Figure 7 is the SED of the same White (3500K) Standard fluorescent lamp, obtained with unequal equivalent slit widths (resolutions) of about 10 and 20 nm, corresponding roughly to 3 and 6 mm slits in the monochromator used. Calculated characteristics analyzed at 10 nm intervals are compared in Table I to those of the same lamp measured in the more conventional manner with equal slit widths and analyzed in narrow intervals or by the use of triangular areas as already described. Actually, since the computer can as easily use 10 nm intervals such as 401, 411, 421, etc., the mercury lines could be considered as centering on 366, 406, 436, 546, 576 nm and an even more accurate trapezoidal trace could be obtained for each line. This was not done here.

Conclusion

Even this rough approximation to the true fluorescent lamp SED, allowing simpler analysis than the triangle method, leads to a difference of about 0.004 in x and no detectable difference in y. Presumably a bit more finesse would allow even this simplest method to provide the 0.002 accuracy obtained by more difficult procedures.

Acknowledgment

It is a pleasure to thank E. Chen for help with the analysis and computer work.

Manuscript submitted Sept. 12, 1969; revised manuscript received Nov. 18, 1969. This was Paper 57 presented at the New York Meeting of the Society, May 4-9, 1969.

Any discussion of this paper will appear in a Discussion Section to be published in the December 1970 JOURNAL.

REFERENCES

1. H. K. Hammond, Spectroradiometric Calibration of Fluorescent-Lamp Chromaticity Standards, Document No. 5, USCOMM-NBS-DC, 1965.
2. W. G. Rudy, *App. Opt.*, **4**, 1484 (1965).
3. S. T. Henderson and M. B. Halstead, *Brit. J. App. Phys.*, **3**, 255 (1952).

The Glazing of Vacuum-Evaporated Gold-Chromium Films with a Lead-Containing Glass at 775°C

R. H. Buck[1]

United Kingdom Atomic Energy Authority, Aldermaston, Berkshire, England

ABSTRACT

The glazing of vacuum-evaporated gold-chromium duplex films on alumina substrates at 775°C using a lead-containing glass has been investigated. This process forms a part in the construction of a multilayer hybrid circuit. A detailed examination of a unique glazing defect using electron beam analytical facilities has led to the identification of a fine needlelike deposit associated with the defect as single crystals of the compound Pb_2CrO_5.

Examination of the other characteristic features of the defect, a central black spot and a porous gold film, has involved a study of the thermal stability of gold-chromium duplex films under nonglazing and glazing conditions. From the nonglazing experiments it is concluded that the chromium content of the needlelike deposit results from grain boundary diffusion of chromium through the gold film to be followed by oxidation at the gold/air interface during the heating cycle of the glazing schedule. The resistivity changes observed to occur in Au-Cr films at 400°C appear qualitatively consistent with this view. The cohesion and adhesion of gold chromium films of various thickness ratios were found to be maintained or improved after heating at 775°C for 2 hr. Glazing the as-deposited film gives rise to attack of the gold film by the lead constituent of the glass causing the black spot and a porous gold film.

In order to accommodate the high density circuitry required to meet the future needs of the computer industry it has been found necessary to adopt a multilayer structure comprising a ceramic substrate base with alternating planes of electrical conductors interspersed with glass or polymer insulating layers (1, 2). This approach, involving the use of commercially available materials as far as possible, poses novel problems in the construction of reliable arrays. Quite often situations are met, that rarely, if ever, have occurred in the more traditional applications of these materials, *e.g.*, the ability to be able to glaze over gold conductors with the requirements of the glaze layer to be more stringent electrically and in geometry than has been demanded hitherto.

Vacuum evaporation of the metal, followed by conventional photoresist and etching techniques, may be used to define the conductor geometry closely. Thus the question of the stability of the evaporated conductor arises if it is to be subjected to the temperatures and times involved in the glazing schedule. Contemporary applications of vacuum-deposited metal usually limit its use to low temperatures (generally below 200°C) and smooth substrate surfaces, *e.g.*, as metallization for active devices, thin-film circuitry on glass substrates and in optics. Less is understood and known about its use and properties at temperatures in the range 700°-800°C and on rougher surfaces. Therefore part of the investigation described below is to gain information on the behavior of vacuum-deposited metal films at high temperatures and the effect, if any, of the glazing process on them.

Experimental

In order to examine the effect of glazing, test specimens were prepared according to the procedure

[1] Present address: 9 Three Acre Road, Newbury, Berkshire, England.

Table I. Analysis of the glass F1169

Oxide	PbO	SiO_2	B_2O_3	Li_2O	ZrO_2	Al_2O_3	CdO	ZnO	TiO_2
w/o	54.7	30.0	4.2	1.5	2.3	1.9	3.5	1.0	1.0

adopted in constructing one part of a multilayered module.

Chromium was first evaporated onto a 2 x 1 in. alumina substrate to give a layer 300-400Å in thickness. The substrate material was AlSiMag 772 from the American Lava Corporation and had a 10 μin. CLA surface roughness (Talysurf measurement). This was followed by evaporation of a layer of gold, 5000-6000Å thick, from a molybdenum boat. A layer of glass, whose compositional analysis is presented in Table I, was subsequently screen-printed over the gold to give a pinhole-free, smooth, clear, layer 50μ thick after firing. The glass was obtained from C. E. Ramsden Company Ltd., of Stoke-on-Trent, and was designated F1169. It is a high lead silicate glass, not normally used in commercial glazing operations but in more specialized applications requiring a low working temperature and good flow properties. It was incorporated, as supplied, into a commercial screen-printing vehicle available from Blythe Colours Ltd., also of Stoke-on-Trent, to form a paste. The glaze-firing schedule involved placing the specimen in a muffle furnace at room temperature, raising its temperature to about 775°C and, after holding at this temperature for 1½ hr, allowing the furnace to cool to room temperature before withdrawing the specimen.

On examination of the substrate it was usually found that crawling back of the glaze had occurred at the edges and, on some substrates, circular, nonglazed regions appeared on firing. Figure 1 shows part of a substrate exhibiting this effect. Obviously this layer would not meet the demands of an acceptable insulating layer since the gold conductor layer is left bare. The majority of the areas have a black spot in the center suggesting that this is associated with the nonwetting behavior.

As this particular commercial glass possessed properties (3) that were otherwise very desirable for the construction of the multilayered circuit such as good flow properties leading to very smooth surfaces for subsequent conductor deposition, and as an alternative would not be easily available, it was decided to investigate the cause of this defect in more detail in an effort to understand and perhaps avoid its occurrence.

Examination of the defect.—The characteristic features of one of the areas illustrated in Fig. 1 is shown in Fig. 2 in greater detail. Long thin needles of approximately equal length may be seen radiating out from the black central spot like the spokes of a wheel. For the purpose of clarification these characteristic features may be described as the following: (*a*) the needles; (*b*) the black spot; (*c*) the gold film. The detailed investigation of these features, taken individually, was possible with the aid of electron beam, as well as optical, analytical techniques. The interrelationship of these features became clearer as the investigation proceeded.

Fig. 1. Nonwetted areas of a glazed gold-covered alumina substrate. 3.3X.

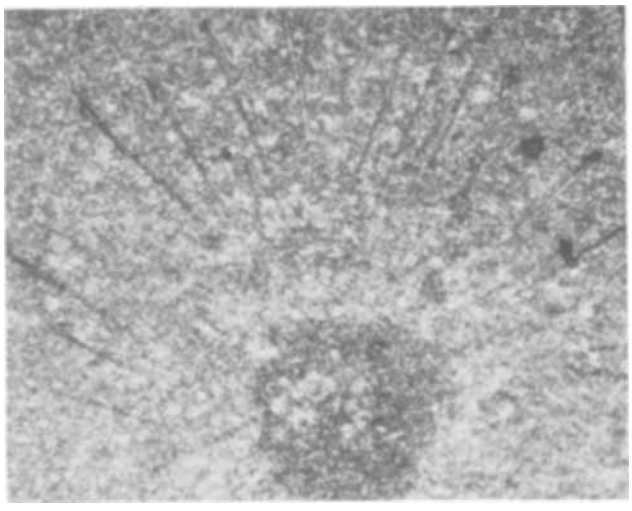

Fig. 2. Microscopical features of the majority of the nonwetted areas shown in Fig. 1. *ca.* 100X.

The needles.—The needles are very regular in shape. Figure 3 shows the needles enlarged. In the example of Fig. 2 they are about 0.4 mm long, between 2-6μ wide and 1-2μ high. That they were a precipitate lying on top of the gold film was proved by scratching them with the tip of a lightly loaded microhardness indenter and exposing the gold film underneath. They were found in regions wherever the glaze had crawled back, *e.g.*, at the edges of the substrate, and were oriented roughly perpendicular to the edge of the retreating glaze. When viewed in white light in a microscope they appeared red in color. In order to obtain more detailed information the electron beam microprobe and electron diffraction were used.

Microprobe examination.—Accurate microprobe analysis of the needles is complicated by their small dimensions and their shape above the level of the gold film (4). The probe is not normally used for such thin specimens, and a special technique was developed to keep the penetration depth of the electron beam in the specimen to a minimum by the use of low beam accelerating voltages. In addition, a traversing technique was adopted to ensure that x-rays from the needles only and not from their surroundings were analyzed since the needles were comparable in width to the electron beam spot size. Qualitative analysis was

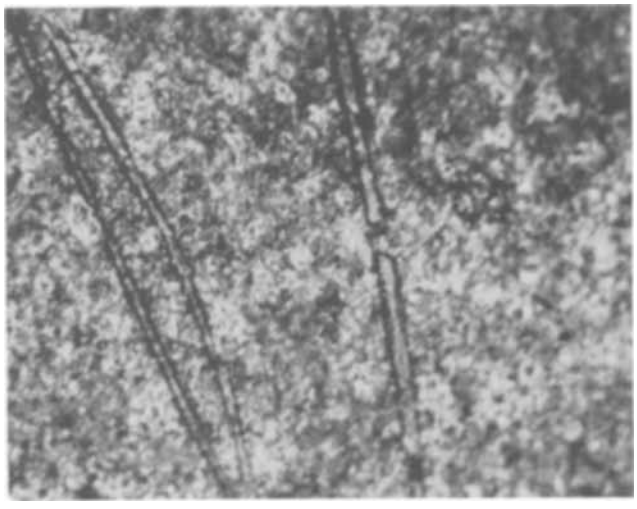

Fig. 3. Needlelike precipitates of Fig. 2. 360X

performed to determine what elements were present, as well as quantitative analysis to determine the amount of each element present in the needles.

After applying the usual corrections to the raw count data the final result was that the needles contained 70.4 w/o Pb and 9.2 w/o Cr and, as no other elements were found, the rest was presumed to be oxygen. Figure 4 shows the most recent PbO-Cr_2O_3 phase diagram (5) which gives all the possible compositions between pure lead oxide and chromium oxide. These are Pb_5CrO_8, Pb_3CrO_6, and Pb_2CrO_5. The latter compound, to judge from its melting point, may be the most stable. The compositional data gave good agreement with a compound of the formula Pb_2CrO_5.

Electron diffraction.—To confirm the above result, the needles were extracted using plastic replicas and analyzed by electron diffraction. It was necessary before extraction to dissolve the gold film in the vicinity of the needles using an etchant based on iodine and potassium iodide to lessen the adherence of the needles. The etchant did not appear to attack them chemically. The result was to show that the needles were of one composition, were crystalline (and not a glass for example), and were single crystals.

The electron diffraction pattern correlated well with x-ray data from the monoclinic compound Pb_2CrO_5, prepared by the direct fusion of PbO and $PbCrO_4$ in the correct proportions (6).

Needle pattern.—The reasons why the needles in the defect areas should adopt the pattern described are interesting, and perhaps not too much importance should be placed on the fact that they generally appear perpendicular to the glaze edge.

From microscopical studies of the needles in the circular defect areas and at the edge of the substrate, there did not appear to be any correlation between the orientation of the individual needles and the retreating glaze edge. That the needles appear as radiating out from the centers of the spots may only be a consequence of the initial growth nuclei being formed in or near the central black spot region when the glaze is beginning to crawl back from that area. If the nuclei are randomly oriented, needle growth can proceed in all directions out from the black spot center. The circle of glass outlining the defect gives the pattern of needles the appearance of spokes.

Similarly, where the glaze edge was straight, *i.e.*, at the substrate edges, a small but sufficient number of needles were found to lie parallel to the edge, to assume that the needles are the result of growth from randomly oriented nuclei.

The black spot.—Figure 5 is an optical micrograph of the black spot region taken with transmitted light. The black, opaque islands are of practically pure gold. Microprobe analysis could detect only very small amounts of Cr in the islands (of the order of 1/10 of 1% by weight) and no lead. A transparent section of a needle overlies this area.

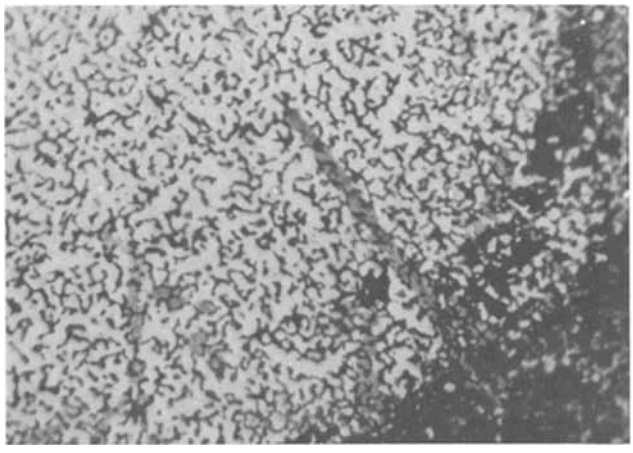

Fig. 5. Micrograph of a spot by transmitted light. 332X

Observations by scanning electron microscopy (SEM) showed that the islands possessed smooth, rounded forms, suggesting that, at some stage in the glazing process, the gold metallization had coalesced and may have been part of a molten system. In this manner, breakup of the gold film had occurred leading to the formation of the black spots which, in turn, became responsible for the nonglazing of the gold film at these points.

The interisland material, which is colored black, is probably a very thin interaction layer on the alumina substrate. It was bereft of gold, but seemed to be electrically conducting to judge from its behavior on microprobing since it allowed analysis of the islands without causing charging-up effects.

The gold film.—The gold film was examined in places where it was exposed, using SEM, and compared with the duplex film in the as-deposited state and after subjecting the film to the heat-treatment involved in the glaze firing schedule but without the presence of glaze.

The as-deposited films merely replicate the underlying alumina surface. In Fig. 6, on top of the individual alumina grains the gold film is smooth because the underlying grains themselves have smooth as-fired surfaces. The gold surface shown in Fig. 7, however, is very roughened as the result of the glazing treatment and contains pores of micron size.

That lead-containing glasses may attack gold and cause the roughened appearance is probable for, in the manufacture of ruby glasses (7), gold salts are dissolved in high-lead glasses. There is also the possibility that metallic lead, freed during the heating portion

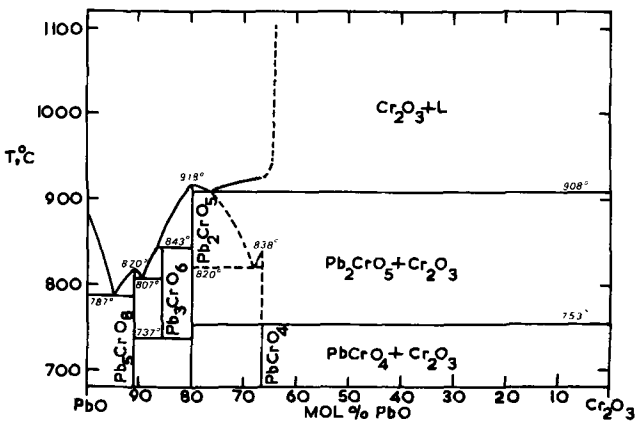

Fig. 4. PbO-Cr_2O_3 phase diagram (4)

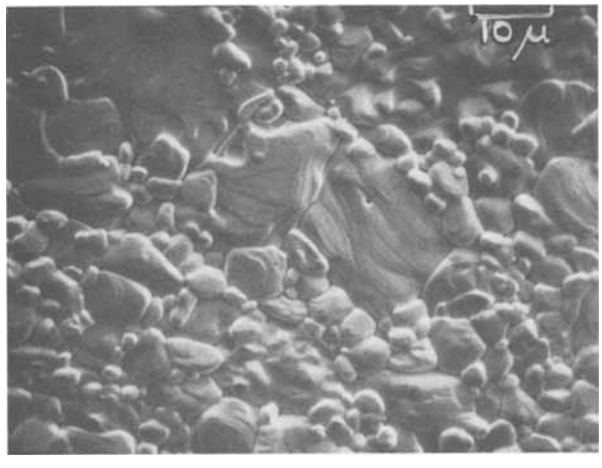

Fig. 6. Stereoscan micrograph of the gold-covered substrate surface.

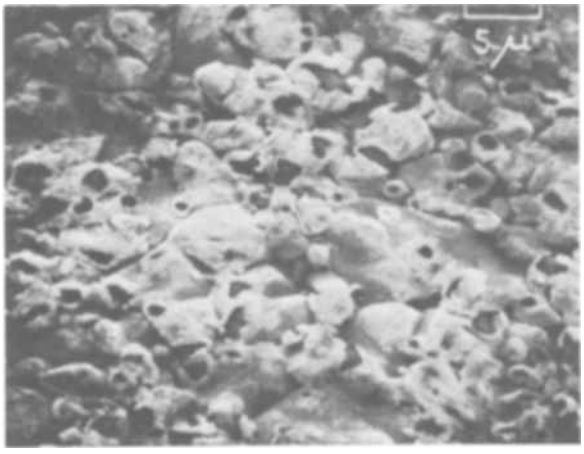

Fig. 7. Gold-covered alumina substrate surface after glazing showing porosity and roughening of the surface.

of the glazing cycle by reducing atmospheres that may be present, *e.g.*, due to carbonization of the screen-printing vehicle, will also attack the gold.

In a separate investigation (8), however, no lead particles could be found in the glass after firing. The glass was etched for various times, and any particles in the glaze were extracted using carbon replicas and examined by electron microscopy and diffraction.

Effect of heat-treatment on duplex gold-chromium films.—SEM and electron microscopy were used to examine the duplex films that had been heat-treated in air as for glazing but without the presence of glass. A visible change in the appearance of the gold surface takes place after heat-treating at 775°C in that the surface darkens. In contrast, the unglazed areas on a glass-coated specimen appear as gold or green-gold. Figure 8 shows a direct view of the surface. The film is not porous as after glazing. There are no black spot defects, and it remains adherent as shown on the basis of a simple "Scotch Tape" test. There is a network pattern visible on the gold within the areas encompassed by the underlying alumina grains whose meshes have similar dimensions to grain size one would expect (9) for a film of this thickness (of the order of a micron diameter). It suggests that chromium has reached the surface by grain boundary diffusion through the gold and is removed from solid solution in the gold by oxidation at the gold/air interface. The network we thus

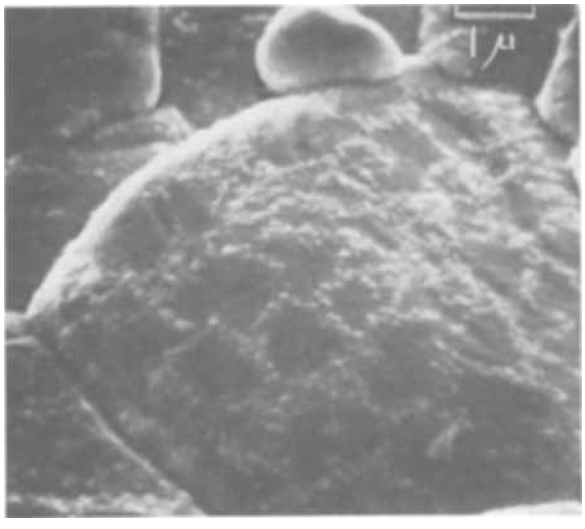

Fig. 8. Gold-chromium film after heat treatment at 775°C in air. A network pattern is visible on the smooth surface of the coated alumina grain.

Table II. Adhesion of gold/chromium films of different thicknesses on alumina substrates before and after heat-treatment at 775°C for 2 hr

Specimen No.	Gold thickness,* Å	Chromium thickness,* Å	Ratio Au/Cr	Adhesion As-deposited	Adhesion After heat-treatment	Appearance
1	800	500	1.6	Yes	Yes	Green
2	2500	250	10	Partial	Yes	Darkened Gold
3	4500	300	15	No	Yes	Darkened Gold
4	6000	400	15	Yes	Yes	Darkened Gold
5	4000	150	27	No	Yes	Darkened Gold
6	3000	100	30	Yes	Yes	Darkened Gold

* Using a "Talystep" machine, the thicknesses were measured by employing concurrent deposition onto glass slides.

observe is formed by a pattern of chromium oxide nuclei outlining the gold grain boundaries.

The results obtained by testing for adhesion by the Scotch Tape test after heat-treatment at 775°C for 2 hr are shown in Table II for various gold/chromium thickness ratios.

Two significant conclusions may be drawn from these results: for all specimens the gold film remained adherent and coherent and the heat-treatment leads to an improvement in adhesion where previously the gold had not, or only partially, shown adherence. The green appearance of specimen 1 was obviously due to the oxidation of the chromium content of the film which was high.

Evidence of chromium being transported completely through the gold film is provided by the results of Bingham *et al.* (10) and Schnable and Keen (11) who measured change of the resistance of heated gold films on glass substrates with time. Figure 9 shows some of Bingham's results for films of different total thicknesses heated at 400°C. In each case the thickness of chromium was 400Å. The independent measurements of Whitcomb *et al.* (12) for films of different gold/chromium ratios baked at 450°C have been added, and tentative curves have been drawn through the few experimental points shown. The greatest changes in resistance occur within the first 4 hr at temperature, and the initial and final resistance values after periods of time greater than 12 hr are identical. The former behavior is qualitatively consistent with two competing processes: one involving the increase in resistance due to penetration of chromium atoms into the gold lattice and the other involving a decrease in resistance due to withdrawal of chromium atoms from the gold by oxidation at the gold surface. The similarity in the initial and final

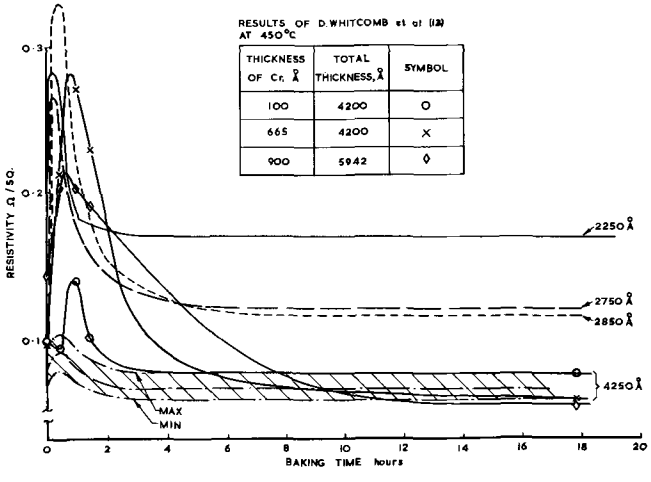

Fig. 9. Changes in resistivity of gold-chromium duplex films of varying gold thicknesses with time at 400°C (9). The result of Whitcomb *et al.* (12) for films of differing gold-chromium thickness ratio, baked at 450°C have been superimposed.

resistance values reflects the fact that these measurements have been made on virtually pure gold. In line with this argument, careful measurements made with the electron microprobe analyzer in the course of this work also failed to detect any chromium in the exposed gold film of the glazed samples.

Whitcomb *et al.* (12) noticed that the thickness of the chromium underlay affected the change with time of the resistivity. This has been made more obvious by plotting his results in Fig. 9. On the basis of the present description this dependence would arise simply because more chromium is available as a source material for diffusion through the gold overlay, followed by oxidation at the gold surface.

An alternative mechanism giving rise to the observed pattern is possible if it is assumed that bulk diffusion of chromium occurs with nucleation of the oxidized chromium at the gold grain boundaries. However, the work of Kenrick (13, 14) would seem to indicate the importance of the grain boundary in the transport of chromium atoms to the surface of the gold at lower temperatures than those used with present work. He examined films annealed up to 300°C on glass substrates and found evidence of early topographical changes at the gold grain boundaries due to chromium transport.

In bulk metals, grain boundary diffusion plays a significant part in the diffusive transfer of material at low temperatures, *i.e.*, below about 0.6 T_M where T_M is the absolute melting point of the metal. During glazing it probably occurs during the heating up period. Hence the grain pattern is established early on in the process and persists even at the peak glazing temperature of 775°C (0.78 T_M). This implies that stress-relieving processes such as grain growth and secondary recrystallization may have been inhibited by the presence of the chromium in the grain boundaries of the gold. Some evidence for this viewpoint comes from investigations of monolithic films where it has been found (15, 16) that grain boundary self-diffusion plays an important part in stress relief by acting to produce hillock growth. Modification of the grain boundaries, *e.g.*, by alloying, leads to modification of the mode of hillock growth.

Discussion

As a result of the investigation of the features of the defect, the needles, the gold film, and the black spot, the relationship between these features may now be established.

Having concluded that the needles are single crystals of a lead-chromium-oxygen compound we are now in a position to see how they were formed. During heating of the duplex film chromium diffuses through the gold film, primarily by a grain boundary mechanism. Since the specimen is fired in air oxygen is present at the surface, and lead results from reduction of the lead glass. The reacting species combine to form the most stable compound of the PbO-chromium oxide system, Pb_2CrO_5, which is solid at the glazing temperature. The reactants are brought together by transport over the surface of the exposed gold film.

The formation of the needles may then be visualized as a two-dimensional precipitation process with the reactants present at the gold surface. It is necessary to propose a nucleation and growth mechanism to account for the small number of nuclei present coupled with a fast growth rate in certain crystallographic directions in order to produce needles. Low supersaturations produce small numbers of nuclei. It can arise in this case since only small amounts of chromium are present in relation to the other elements, lead and oxygen. The high growth rate directions and reasons why these are preferred, however, may be resolved by studies of the structure of Pb_2CrO_5 which are presently being carried out (6) and will be reported on later.

The establishment of chromium as present in a concentrated form in the needles brings additional proof of the diffusion of Cr through the film and its removal at the surface. Given this knowledge alone, the practical consequences may have been expected to be twofold: (*a*) the conductivity of gold film conductors in a multilayer assembly remain substantially the same before and after heat-treatment, and (*b*) some loss of adhesion of the gold film to the alumina substrate may result.

The former consequence is advantageous, and successful working multilayer modules having the designed electrical properties have been produced using glasses other than F1169 (1). Contrary to the expectation (*b*), there is no noticeable lack of adhesion of the gold films after heating to 775°C in air for 2 hr without the glass layer. In fact the adhesion is enhanced. This treatment gives rise to the network pattern of chromium oxide. The duplex film remains intact and adherent even though this heat-treatment would be generally expected to be severe for such a film. Microns-thick, single-layer gold films, for example, on a metal surface such as cobalt are reported to coalesce completely on heating in vacuo at 400°C (17). The apparently remarkable ability of chromium in maintaining the adherence of a gold film even after heating in air has also been noted by Haq, Behrndt, and Kobin (18) who examined the adhesion of Au/Ta, Au/Si, Au/Ge, and Au/Cr combinations. They observe that "in contrast to all other systems, Au/Cr combinations exhibit no noticeable deterioration of adhesion, even after heat treatment at 450°C in air for several hours . . . ." A major contributing factor in the high-temperature stability of the duplex film must therefore be the presence of the chromium in maintaining both the adherence and coherence of the gold film.

On the other hand, when the glass coating is applied, black spots appear and the gold film becomes porous. Coalescence of the gold film to produce the black spots occurs before or during the time the glass is molten, since it is only possible for crawling back of the glass to take place at this time.

In the case of the film porosity, as with the formation of the black spots, it is difficult to isolate any one cause as solely responsible on the basis of the work described. The porosity in the film is not only present in the area of the defect, but extends over the whole of the metal film on the substrate. In the study of the etching behavior of this glass (8) it was noticed under the glass layer as well as adjacent to it in an area of coated substrate which, deliberately, had not been glazed.

In view of the fact that the lead constituent of lead glasses may easily be reduced to elemental lead and attack the gold film it was attempted to simulate this process by vacuum-depositing stripes of lead, 1 cm wide and 1μ thick, on to alumina substrates which had been precoated with gold-chromium layers of the thicknesses used in this work and subjecting these substrates to the glazing heat treatment schedule. A roughened porous film with the gold or green-gold appearance typically seen on substrates that had been glazed, resulted with isolated areas where the gold film had coalesced and produced black spots similar to those observed in the center of the glazing defect. These experiments provide some evidence that the film is capable of being attacked chemically by any lead that may be present during glazing. In addition, the attack is likely to be aided by any stresses in the film arising from thermal mismatch and chromium diffusion as already discussed.

The glaze defect is thus seen to be due to the break-up of the gold film at isolated, random points to form a surface discontinuity in the form of the black spot. The presence of the spot, which may be formed during

heating of the film or at the peak glazing temperature, especially if free lead is formed by reduction in the glaze, is at once made obvious by the crawling back of the molten glass.

The crawling back of glaze at surface discontinuities such as edges, steps, and holes is a well-known phenomenon in the practice of glazing and it is not always easy to define the causes (19). The amount of crawling depends largely on the wetting of the substrate by the glass, and in some of the samples used in this study where the glass had covered both gold and alumina on the same substrate, the crawling back was always more pronounced on gold. This effect above all precluded the use of this glass as a glaze insulator over patterned gold conductors where there were many gold/substrate discontinuities.

Conclusions

The pursuit of the reasons for the hitherto unexplained and unique type of defect arising on glazing gold-chromium duplex films was justified by producing a better understanding of the materials and processes involved, *e.g.*, of glasses and glazing and the interaction with processes affecting the stability of duplex thin films.

The obvious conclusion that this and allied glasses may not be employed in the glazing of patterned gold films has been drawn exclusively from a detailed examination of the defects where the small dimensions of the characteristic features, a deposit of red needles arranged around a central black spot region and a porous film, required the use of electron-beam analytical tools.

The red needles were found to be single crystals of the compound Pb_2CrO_5. The formation of their pattern in the defect has been described as a two-dimensional precipitation process with the reactants present at the gold surface.

The duplex gold-chromium films employed can withstand heating at the time and temperature required for the glazing process. The presence of the lead-glass, however, degrades the film by giving rise to isolated regions (black spots) where the glass does not adhere and a porous film. Attack by the lead glass of a stressed film appears responsible for this behavior.

Although the glaze adhered well to the gold it tended to be sensitive to surface discontinuities. The presence of these was exaggerated by pronounced crawling back of the glaze. In this manner the formation of the black spot regions by coalescence of the gold film caused the circular defects to appear in the glaze.

Acknowledgment

This work is part of a project supported by the Ministry of Technology, Electronics Division. Discussions with K. C. Bingham of International Computers Ltd., who kindly supplied some of the specimens, and the assistance of the Electron Optics Section of UKAEA, Aldermaston, are gratefully acknowledged.

Manuscript submitted, Nov. 24, 1969; revised manuscript received Feb. 16, 1970.

Any discussion of this paper will appear in a Discussion Section to be published in the December 1970 JOURNAL.

REFERENCES

1. K. C. Bingham, *Microelectronics and Reliability*, **7**, 155 (1968).
2. R. G. Loasby, *Microelectronics*, **2**, 12 (1969).
3. R. H. Buck, "Glazing Defects in the Construction of Multilayer Circuitry for Computers," AWRE 'O' Series Report (HMSO), 024/69.
4. R. H. Buck and G. Lawrence, "Microprobe Analysis of a Unique Glazing Defect", In preparation.
5. T. Negas, *J. Am. Ceram. Soc.*, **51**, 716 (1968).
6. R. H. Buck, C. R. Ruckman, and R. T. W Morrison, "Structure and X-ray Parameters of Pb_2CrO_5," In Preparation.
7. W. A. Weyl, "Coloured Glasses," Dawson's of Pall Mall (London) (1959).
8. R. H. Buck, "The Etching of Precise Patterns of Holes in Glass Layers," AWRE 'O' Series Report (HMSO), 035/69.
9. I. Watts, BSIRA, Chislehurst, UK, Private communication.
10. K. C. Bingham, International Computers Ltd., Stevenage, UK, Private communication.
11. G. L. Schnable and R. S. Keen, "Study of Contact Failures in Semiconductor Devices," RADC-TR-66-165, Final Report (1966).
12. D. Whitcomb *et al.*, "Advanced Technology of Interconnections in Microelectronics", (Motorola Inc.), NASA-CR-85011, 1966-1967, p. 20.
13. P. S. Kenrick, *Nature*, **217**, 1249 (1968).
14. P. S. Kenrick, *Microelectronics*, **2**, 32 (1969).
15. A. D. Paddock and J. R. Black, "Hillock Formation on Aluminum Thin Films," In review.
16. W. B. Pennebaker, *J. Appl. Phys.*, **40**, 394 (1969).
17. J. P. Foster and R. J. Reynik, *This Journal*, **115**, 812 (1968).
18. K. E. Haq, K. H. Behrndt, and Ilse Kobin, *J. Vac. Sci. Technol.*, **6**, 148 (1969).
19. J. R. Taylor, Ramsden Glass Co., Stoke-on-Trent, UK, Private communication.

Phosphorus Diffusion in Silicon Using Phosphine

Y. W. Hsueh*

General Instrument Corporation, Microelectronics Division, Hicksville, New York

ABSTRACT

A study of phosphorus diffusion into silicon has been made by using an open tube diffusion system and phosphine in nitrogen as the impurity source. For constant doping gas and oxygen concentrations, the sheet resistance and junction depth were exponential functions of the reciprocal of absolute temperature. A linear relationship was obtained between junction depth and the square root of the diffusion time. Also, the experimental results showed the independence of mean conductivity, ($\bar{\sigma} \equiv 1/x_j\rho_s$) with diffusion time and temperature. The diffusion coefficient for phosphorus in silicon was calculated to be $6 \times 10^{-6} \exp(-1.90/kT)\,cm^2/sec$.

Phosphorus is used extensively as an n-type impurity material in silicon semiconductor device technology. Generally, open tube systems have been adopted for the diffusion process because of their operational simplicity over sealed tube diffusion methods. The impurity sources have usually been red phosphorus, phosphorus pentoxide (P_2O_5), or phosphorus oxychloride ($POCl_3$) (1).

As mentioned in a previous paper (2), the disadvantages of solid or liquid source diffusion systems are the control of the dopant concentration in the car-

* Electrochemical Society Active Member.

rier gas, difficulty in maintenance due to the complexity of the diffusion system, and reproducibility of results. For instance, Nassibian and Whiting (3) pointed out that the surface concentration could be increased by three orders of magnitude by raising the source temperature of red phosphorus from 260° to 320°C. Similarly, if $POCl_3$ is used as the diffusion source, the product of sheet resistance and surface concentration should be vapor pressure dependent. Nassibian's results showed that a change in source temperature from 20° to 28°C increased the surface concentration by a factor of two while the sheet resistance decreased by about 70%. It is therefore preferable to use a gas phase source, with known impurity concentration, if it gives increased reproducibility in the diffusion process.

The phosphine system has been discussed previously by Smith and Donovan (4), McLouski (5), and Heynes and van Loon (6). This paper describes the diffusion system characteristics and the process parameters in detail. Special emphasis is placed on more shallow diffusion processes than those reported in other published results.

Experimental Procedure

The diffusion system and material preparation were similar to those reported in a previous paper (2). A 50 mm diameter quartz tube was connected to a stainless steel gas supply system. The silicon wafers were (111) oriented, 10-40 ohm-cm p-type, boron doped, and mechanically and chemically polished. The doping gas was 1% phosphine in argon. Nitrogen was used as the carrier gas.

The sheet resistance was measured by the four point probe technique, and the average value was taken of several measurements made on each slice. The variation across a slice and from slice to slice in a single batch was less than 5% unless otherwise specified. Usually, the sheet resistance variation in either case was within 2%.

For calculations, the impurity distribution was assumed to follow the complementary error function distribution for the deposition process, and the Gaussian distribution for redistribution. The surface concentration was calculated by using Irvin's curves (7) after the junction depth was obtained by the standard angle lapping and staining method.

Result and Discussion

Diffusion system.—Oxygen is used in the phosphine diffusion process to provide phosphorus as the local diffusion source at the material surface according to the equations

$$2PH_3 \xrightarrow{450°C} 2P + 3H_2 \qquad [1]$$

$$2PH_3 + 4\,O_2 \longrightarrow P_2O_5 + 3H_2O \qquad [2]$$

In the absence of oxygen, reddish phosphorus appeared on the tube wall as a result of the reaction shown in Eq. [1]. In this case, it was found that the diffusion of phosphorus did not occur. However, when oxygen was used in the system, the phosphine was reduced to P_2O_5, and this acted as the local diffusion source. The diffusion mechanism was therefore similar to a system using P_2O_5 or $POCl_3$. Additional empirical analysis showed that large variations in deposition sheet resistance occurred when the concentration of phosphine in the carrier gas was less than 200 ppm. Also, abnormally high concentrations of phosphine caused phosphite precipitation, and the formation of electrically inactive phosphorus was detected. A fixed value of 300 ppm for phosphine concentration was used for all the following experimental work.

Oxygen was detrimental to the process only when present in high concentrations. No phosphorus deposition was observed on the system end cap even when the oxygen concentration was as low as 0.3%. Also for a given diffusion temperature, the diffusion parameters were not appreciably affected by variations in oxygen concentration between 0.5 and 4%. However, the sheet resistance increased by a factor of 2 when the oxygen concentration was increased from 4 to 8%, and the rate of increase of sheet resistance with oxygen concentration was very rapid for oxygen concentrations above 8%. The high sheet resistance obtained with high oxygen concentrations was caused by an apparent decrease in diffusion rate. Excessive growth of silicon dioxide in high oxygen concentrations partially masked the diffusion of phosphorus. For this reason, an oxygen concentration of 1% was used for these experiments.

Variations in total gas flow rate will give nonuniform deposition, and it was empirically determined that a total flow rate between 1100 and 1400 cc/min gave the best uniformity for this system. In addition, it was observed that other variations in sheet resistance sometimes occurred. These variations could not be correlated with low diffusion temperatures, low phosphine concentration processes, or diffusion times, and they were independent of surface concentration. This effect was eventually attributed to depletion of phosphorus from the heavily doped diffusion tube and was investigated experimentally.

The tube was saturated with phosphorus by a continuous phosphine flow. The phosphine supply was then turned off and wafers were then inserted for given periods of time. The sheet resistances obtained are shown in Fig. 1. The top curve shows the variation in sheet resistance for the wafer near the gas inlet, while the bottom curve indicates the average sheet resistance of wafers 12 in. further along the tube. The sheet resistance for wafers near the gas inlet was much higher than for those further down the tube, as predicted. The surface concentrations obtained were approximately 10^{20} at./cm^3 for a 1-hr period.

In addition, an experiment was carried out to investigate the rate of depletion of phosphorus from the tube. First, the sheet resistance was measured on wafers diffused for a given period of time after predoping the tube for 40 min. Second, material was diffused under identical conditions except for a delay of 45 min between the tube doping cycle and the diffusion process. The results showed a 35% difference in measured sheet resistance for the two processes. It can therefore be concluded that, the background doping from the tube must be taken into account in order to obtain good

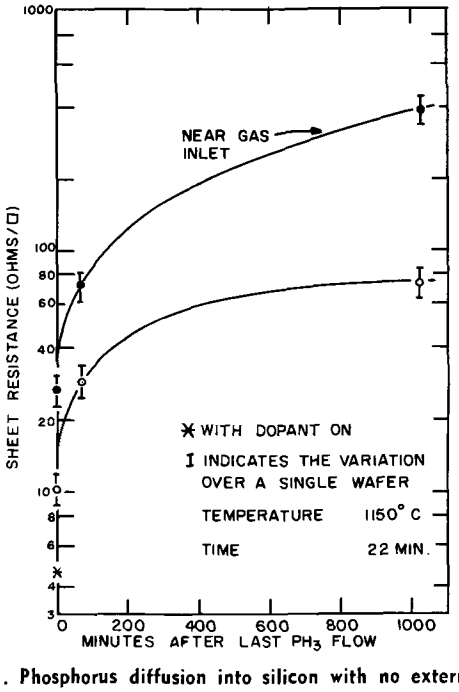

Fig. 1. Phosphorus diffusion into silicon with no external source fed into the diffusion system.

control over the diffusion process. It has been found that predoping of the tube for half an hour at the beginning of a working day is sufficient for high concentration processes, *i.e.*, $>10^{19}$ at./cc. Appropriate time intervals can be determined empirically for low surface concentration processes.

Diffusion time and temperature.—The relationship obtained between diffusion time and sheet resistance is shown in Fig. 2. The sheet resistance decreases slowly as the deposition time increases. For low temperatures and short deposition times, these values can fluctuate as described previously.

In Fig. 3, sheet resistance is shown as a function of the reciprocal of absolute temperature. The gradients of these curves are approximately constant for temperatures above 1000°C, but below 1000°C they increase as the temperature decreases. It has been shown (2) that sheet resistance can be expressed by the following equation

$$\rho_s = C \exp\left(\frac{E}{2kT}\right) \qquad [3]$$

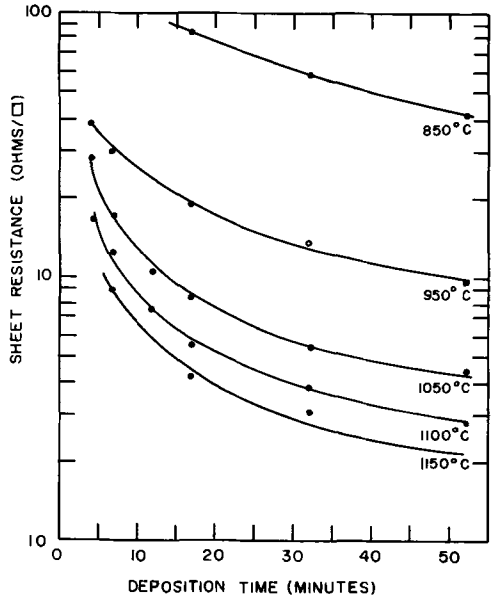

Fig. 2. Sheet resistance as a function of deposition time

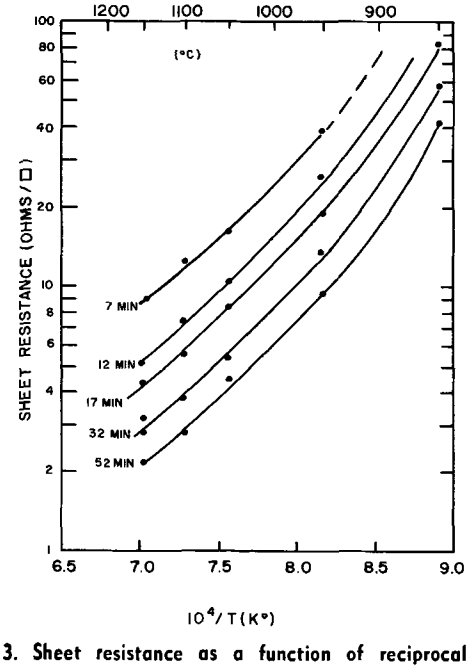

Fig. 3. Sheet resistance as a function of reciprocal absolute temperature.

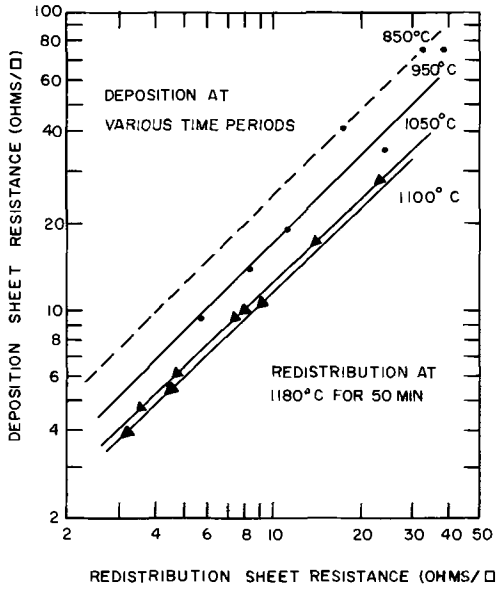

Fig. 4. Relationship between deposition and redistribution sheet resistances.

where E is the activation energy in eV, k is the Boltzmann constant, and

$$C = \frac{1}{q\mu}\frac{1}{2N_0}\left(\frac{\pi}{tD_0}\right)^{1/2} = \text{constant}$$

Thus, it is possible to determine the activation energy, E, from results shown in Fig. 3. This was calculated to be 2.11 eV in the temperature range 1000°-1150°C, 2.71 eV at 950°C, and 5.84 eV at 850°C. This temperature dependency of activation energy appears to be connected to the maximum solid solubility (8) of phosphorus at a given temperature. However, values for the activation energy calculated here are less than those obtained by MacKintosh, (9), and far less than those shown in Fuller's (10) results. This may mean that the activation energy depends on the oxidation rate at the silicon surface since the diffusion rate here was partially retarded.

Figure 4 shows that a straight line relationship exists between deposition and redistribution sheet resistance over the whole experimental range. This agrees with the results reported by MacKintosh (9) in which a closed tube system and a phosphorus pentoxide source were used.

The linear relationship in Fig. 4 can be expressed by

$$\rho_{dep} = a(\rho)^{b}{}_{redist} \qquad [4]$$

where a and b are constants for a given set of diffusion parameters. The values of a and b for various diffused temperatures were calculated and listed in Table I. These were again different from the values quoted by MacKintosh (9). Allowing for experimental error, the index b can be assumed to be unity. The constant a, therefore, becomes the ratio between deposition and redistribution sheet resistances. Apparently, this is temperature dependent up to 1000°C and is directly related to the solid solubility of phosphorus in silicon.

No apparent variation in the redistribution process was observed for different oxidizing conditions. Typical

Table I. Values of a and b for diffused temperatures

Temperature, °C	a	b	Remark
850	2.62	0.985	Present work
950	1.74	0.987	a was calculated using b_{av}
1050	1.32	0.952	b_{av} = 0.97
1200 and 1300	2.80	1.30	Ref. (9)
			$N_b = 5 \times 10^{14}$ and 10^{17} at./cm³

Table II. Results

Deposition sheet resistance, ohms/□	Redistribution					
	Temp, °C	Time, min	Cond.	Oxide, KÅ (approx.)	ρ_s, ohm/□	X_j, μ
11.5	1180	30	Wet	6.7	9.1	3.3
			Dry	1.5	9.2	3.0-3.3
10.7	1180	60	Wet	10	8.3	4.2
			Dry	3	8.4	3.9-4.2

results are listed in Table II. The junction depth after deposition was 1.0μ. The process normally involves the removal of the phosphorus glass by etching prior to redistribution. For nonetched wafers, the final oxide thickness was approximately 5% thicker and the sheet resistance 5-10% lower than for etched wafers, while the measured junction depths were almost equivalent. The similarity of these results can be explained by the high segregation coefficient (11) of phosphorus in silicon dioxide causing phosphorus to accumulate at the silicon-silicon dioxide interface. The depletion of phosphorus caused by the oxidation process must therefore be negligible compared with the total amount of diffused impurity.

Although the silicon dioxide growth rate under wet redistribution conditions is much faster than the growth rate in dry conditions, the faster diffusion rate of phosphorus under wet conditions must compensate for the added depletion which occurs. The difference between the two redistribution processes for shallow diffusion requirements is negligible.

Junction depth and surface concentration.—Junction depth is usually a function of diffusion time for constant process conditions. For constant diffusion temperature and carrier gas impurity concentration, a linear relationship was obtained between junction depth and the square root of diffusion time. The results for temperatures in the range 850°-1150°C are given in Fig. 5. Extrapolation of the curves for diffusion temperatures of 850°, 950°, and 1050°C gives a positive intercept for deposition time at zero junction depth. This infers that the maximum solid solubility limit is not obtained immediately, and the time lapse for the diffusion process to begin is approximately 1 min.

The diffusion equation states that

$$N(x_j, t) = N_0 \operatorname{erfc}\left(\frac{x_j}{2(Dt)^{1/2}}\right) \qquad [5]$$

where $N(x_j, t)$ is the concentration at a depth x_j and time t; (in this case the background concentration N_b); N_0 the surface concentration; x_j the diffusion junction depth; t the diffusion time; and D the diffusion coefficient of phosphorus in silicon. Therefore the curves in Fig. 5 represent a constant surface concentration diffusion condition, and the gradient of each curve is given by $2(D)^{1/2}\ \operatorname{erfc}^{-1}\ (N_b/N_0)$.

By using Irvin's curves, the surface concentrations were estimated from the sheet resistance and junction

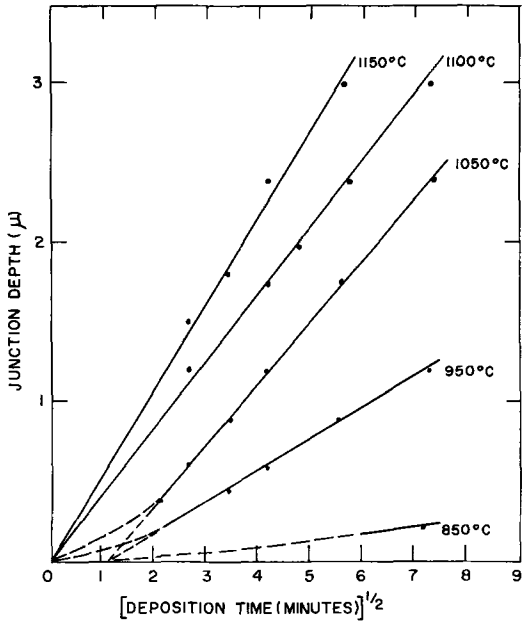

Fig. 5. Relationship between the junction depth and square root of time for various diffusion temperatures.

depth measurements. The results are temperature dependent and are listed in Table III. The surface concentrations obtained are higher than those reported by MacKintosh, and a correspondingly higher value for the solid solubility of phosphorus in silicon is therefore obtained. However, difficulty in measuring shallow junction depths accurately means that results for short diffusion times or low diffusion temperatures are liable to large errors.

Diffusion coefficient.—The diffusion process was assumed to follow the complementary error function except for those processes in which a redistribution step was used. The diffusion coefficient calculated on this model is useful for practical purposes. Some typical values are shown in Table III. The diffusion coefficient was also plotted against the reciprocal of absolute temperature. These results are shown in Fig. 6. Some previously published data are also included. For low diffusion temperatures, a large error can be introduced into these results by the inaccuracy in measuring shallow junction depths. The activation energy for the phosphine process based on a wide range of results is 1.90 ± 0.13 eV.

Assuming a value of 1.90 eV for the activation energy, the diffusion coefficient can be calculated from the following expression

$$D = 6 \times 10^{-6} \exp\left(\frac{-1.90}{kT}\right) \text{ cm}^2/\text{sec} \qquad [6]$$

The values obtained for D_0 are smaller than those re-

Table III. Results

Temp, °C	Time, (t), min.	Sheet resistance, ρ_s (ohm/□)	$\rho_s t^{1/2}$	Junction depth, x_j, μ	$\frac{1}{x_j \rho_s}$, ohm^{-1} cm^{-1}	Surface concentration, N_0, 10^{20} at./cc	Calculated diffusion coefficient, D, 10^{-14} cm^2/sec
850	52	41.0	295	0.3	820	7.0	6.2
950	17	19.2	79	0.6	880	7.7	7.7
950	32	13.7	77.5	0.9	813	7.0	9.0
950	52	9.6	69	1.2	867	7.6	10.0
1050	4.5	28.0	59	0.4	890	8.2	12.4
1050	12	10.0	34.6	0.9	1110	10.0	23.6
1050	17	8.4	34.6	1.2	990	10.0	30.0
1050	32	5.5	31.1	1.8	1030	10.0	36.0
1050	52	4.6	33.2	2.4	907	8.4	39.0
1100	17	5.6	23	1.8	990	10.0	67.0
1100	32	3.9	22	2.4	1060	10.0	63.0
1100	52	2.9	21	3.0	1150	10.0	61.0
1150	17	4.2	17.3	2.4	990	10.0	120.0
1150	32	3.3	18.6	3.0	1010	10.0	100.0

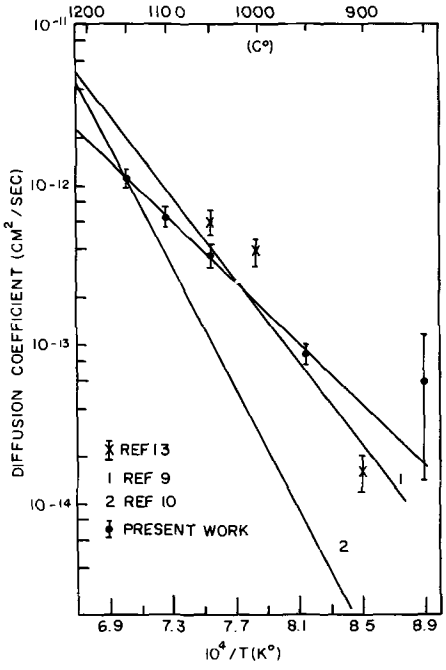

Fig. 6. Diffusion coefficient of phosphorus in silicon using phosphine.

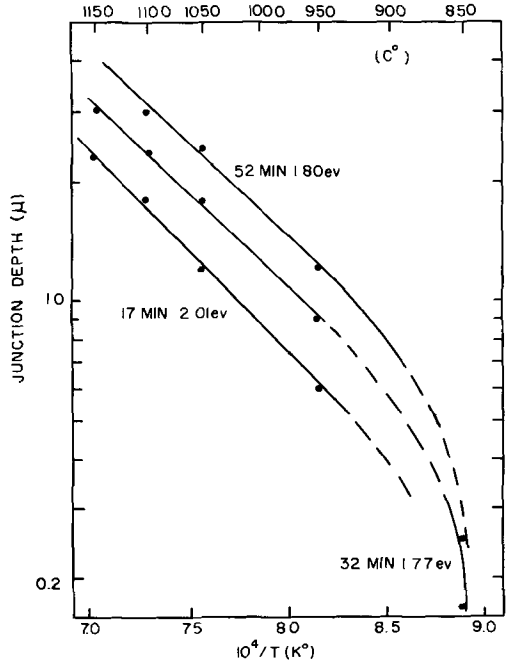

Fig. 7. Diffusion junction depth as a function of reciprocal absolute temperature.

ported by Fuller. Values for D_0 are very sensitive to activation energy, and the activation energies of 3.7 and 2.4 eV obtained by Fuller and MacKintosh respectively are higher than those obtained here.

From Eq. [5] and the expression $D = D_0 \exp(-E/kT)$, the junction depth can be expressed by

$$x_j = C' \exp(-E/2kT) \quad [7]$$

where $C' = 2(D_0 t)^{1/2} \operatorname{erfc}^{-1}(N_b/N_0)$. This is constant if the diffusion time t, background concentration N_b, and surface concentration N_0 are kept constant. Figure 7 plots ln x_j against $1/T$. The activation energy based on the data from this figure varied from 1.77 to 2.01 eV. These values increase rapidly as the diffusion temperature decreases. The relatively close agreement between the three calculated values for the activation energy verifies the consistency of the results presented in this work.

From Eq. [3] and [7], it can be shown that the product of sheet resistance and junction depth is time and diffusion temperature independent. The data shown in Table III agree quite well with this conclusion except for very short diffusion times and shallow junction processes.

Conclusion

The results obtained for a phosphorus diffusion process based on phosphine showed that the junction depth and sheet resistance varied exponentially with reciprocal temperature, the junction depth varied with the square root of time, and the sheet resistance varied with the inverse of square root of time. Also, the product of sheet resistance and junction depth was independent of diffusion time and temperature. The activation energy for the process was calculated to be 1.90 eV. These results are based on the assumption that the diffusion process follows a complementary error function distribution.

Acknowledgments

The author is very grateful to Dr. J. B. Preece for his stimulating discussions and critical revision of the manuscripts and also to Mr. W. J. Dautzenberg for his valuable suggestion and discussion.

Work on this paper was performed at the Molecular Electronics Division, Westinghouse Electric Corporation.

Manuscript submitted April 14, 1969; revised manuscript received Feb. 16, 1970.

Any discussion of this paper will appear in a Discussion Section to be published in the December 1970 JOURNAL.

REFERENCES

1. Research Triangle Institute, Integrated Silicon Device Technology, Vol. IV. Diffusion. Durham, N.C., Feb. 1964, Ad 603-716.
2. Y. W. Hsueh, *Electrochem. Techol.*, **6**, 361 (1968).
3. A. G. Nassibian and G. Whiting, *Solid-State Electron*, **8**, 843 (1965).
4. R. P. Donovan and A. M. Smith, Paper 150 presented at the New York Meeting of the Society, Sept. 29-Oct. 3, 1963.
5. R. M. McLouski, Private communication.
6. M. S. R. Heynes and P. G. G. van Loon, Paper 92 presented at the Dallas Meeting of the Society, May 7-12, 1967.
7. J. C. Irvin, *Bell System Tech. J.*, **41**, 387 (1962).
8. F. A. Trumbore, *ibid.*, **39**, 205 (1960).
9. J. MacKintosh, *This Journal*, **109**, 392 (1962).
10. C. S. Fuller and J. A. Ditzenberger, *J. Appl. Phys.* **27**, 544 (1956).
11. A. S. Grove, O. Leistiko, and C. T. Sah, *ibid.*, **35**, 2695 (1964).
12. K. H. Nicholas, *Solid-State Electron.*, **9**, 35 (1966).
13. E. Tannebaum, *ibid.*, **2**, 123 (1961).

Dopant Transfer in Heteroepitaxial Si Layers on Sapphire Substrates

J. Mercier

Section Physique des Couches Minces,
Laboratoire d'Electrostatique et de Physique du Métal, Grenoble, Gare, France

ABSTRACT

The contribution of hydrogen only to the impurity redistribution in heteroepitaxial silicon layers is analyzed. It is clearly demonstrated that a chemical reaction between H_2 and the sapphire substrate occurs at high temperature. Unequivocal evidence of the aluminum transfer is given. The rear of the substrate is the prevailing dopant source during the over-all process in our experiments.

P-type autodoping in epitaxial silicon layers, grown on sapphire substrates by pyrolysis of silane, has been reported extensively (1-7).

However, the understanding of this redistribution process is somewhat obscured by the following conditions:

1. Various doping sources are potentially possible. Their location, as well as their chemical nature, must be considered because the exact redistribution process depends on them.

2. The physical properties of the layers depend not only on the impurity concentration we wish to determine, but also on the high crystalline defect density that they contain. This affects to a large extent, for example, the carrier mobility and the impurities diffusion coefficient (2).

The major p-type dopant introduced in these layers is aluminum. It can obviously be supplied by the sapphire substrate, but it may be freed by a physical (outdiffusion) or a chemical process (reduction), and the physical location of the dopant source may be the rear or the front of the sapphire substrate. If a chemical reaction is assumed, the reducing species may be hydrogen or silane itself (8).

All these difficulties lead us to a separate analysis of the influence of the various chemical species involved. We began with hydrogen, but this does not imply that it has the prevailing effect on the redistribution process. Nevertheless, it fulfills several functions in the over-all process, which may take part in this autodoping. It is not only used as a carrier gas but also as a chemical agent. It has been proven that high-temperature prefiring of the substrate in hydrogen after mechanical polishing is the most reliable way to remove work damage. Figure 1 shows an x-ray surface topography of a $(01\bar{1}2)$ oriented substrate after such a heat-treatment. The crystalline quality is good, but preferred etching along [100] is clearly seen. This result can be considered as direct evidence of a chemical surface reaction between hydrogen and the sapphire substrate. The following reaction has been suggested (1)

$$Al_2O_3 + 2H_2 \rightleftarrows Al_2\overset{\nearrow}{O} + 2H_2\overset{\nearrow}{O}$$

Other steps may give rise to such a chemical reaction. Hydrogen remains in direct contact with sapphire (*a*) before complete coverage of the upper surface is achieved, and (*b*) during the growth step, with the rear face, which is only ground, not polished, to afford better thermal contact, and which allows the penetration of hydrogen. It must also be remembered that the temperature there is higher than anywhere else.

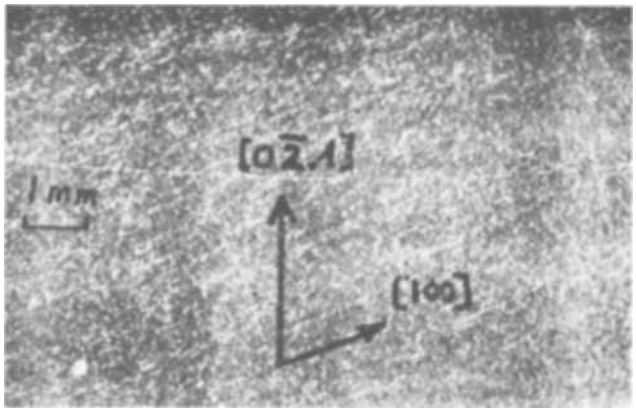

Fig. 1. X-ray surface topography of the sapphire substrate after H_2 etching at 1300°C.

Experimental Conditions

At any time, hydrogen flows in the reaction chamber. Unless otherwise specified, only heat-treatment in hydrogen in the reactor is performed on two kinds of substrates. Under normal conditions, the substrate has two bare faces, but for the sake of comparison some substrates are covered on their backside by a 10-μm thick, polycrystalline silicon layer. This layer has a p-type conductivity of the order of 0.1 ohm^{-1} cm^{-1}, but no conclusion can be drawn about its impurity concentration because of the unknown mobility.

Preliminary experiments must ascertain: (*a*) a sufficiently low residual contamination level from the system, afforded by the tubing, carrier gas or susceptor used. In fact, heat-treatment in H_2, of a lightly doped silicon wafer (5 to 10 ohm-cm n-type) at 1300°C, has no detectable effect on the conductivity type or resistivity of this sample. (*b*) The purity of the silane itself. It can be checked by growing an epitaxial silicon film on a silicon substrate of the same characteristics as indicated above. The layer resistivity is currently higher than 100 ohm-cm n-type, with this undoped silane.

In the following experiments, in order to remove the uncertainty arising from the influence of structure imperfections on the properties of these heteroepitaxial layers, a bulk silicon substrate is used as a check sample of the autodoping. Its initial characteristics are known, for example, the relation between resistivity and impurity concentration (9), the impurity diffusion constant (10). This wafer lies on the upper surface of the sapphire substrate. If its conductivity is n-type, the autodoping, when it occurs, can be measured by the characteristics (conductivity $\bar{\sigma}$ and diffusion depth x_j) of a p-type diffused layer produced at its surface.

Experimental Results

Heat-treatment with sapphire substrates only.—At a given temperature, when an inversion layer occurs in the n-type silicon sample, we have found that the layer

Table I. Dopant transfer from the substrate

T, °C	Back coating	Inversion	$\bar{\sigma}$, ohm^{-1} cm^{-1}	C_S, cm^{-3}	X_j, μm	λ, μm	D, cm^2/s
1050	Yes	No	—	—	—	—	—
	No	Yes	0.3	1.6×10^{16}	1.0	0.67	8.5×10^{-13}
1100	No	Yes	1.7	2×10^{17}	2.6	1.25	1.75×10^{-12}
	Yes	Yes	1.2	1×10^{17}	2.1	1.05	1.5×10^{-12}
1150	No	Yes	4.0	8×10^{17}	5.3	2.2	6.7×10^{-12}
	Yes	Yes	2.2	2.7×10^{17}	5.0	2.1	6.0×10^{-12}

Table II. Dopant transfer from sapphire with an epi layer

Epi layer type	Inversion	$\bar{\sigma}$, ohm^{-1} cm^{-1}	C_S, cm^{-3}	X_j μm	λ, μm	D, cm^2/s
p	Yes	1.5	1.5×10^{17}	1.4	0.67	1.2×10^{-12}
n	Yes	0.8	6×16^{16}	0.8	0.41	4.5×10^{-13}

depth x_j increased with time, as

$$x_j \propto \sqrt{t}$$

This means that some diffusion process occurs. Therefore we can deduce from Irvin's curves (9) the surface concentration C_S of the diffused layer, when x_j, the initial impurity concentration C_B, and the layer conductivity, $\bar{\sigma}$, are measured.

Assuming an ERFC profile, we determine the diffusion length λ and the diffusion coefficient D of the assumed dopant impurity from: $\lambda = 2\sqrt{Dt}$ (Table I).

The autodoping level (C_S) increases as T increases.

The back coating of the substrate reduces this level for a given set of conditions, so much so that at 1050°C no inversion layer is observed.

The calculated D have nearly the same values, whether the substrate is back coated or not. This result is consistent with the reasonable assumption that the same impurity is involved in both cases.

Using an Arrhenius plot of log D *vs.* $1/T$ (°K) and comparing with published results for B and Al in bulk silicon (10), it can be deduced unambiguously that aluminum is the transferred dopant by such an interaction, involving only hydrogen and sapphire.

No doubt such a situation is met at least for the prefiring treatment which supplies a large quantity of aluminum.

Impurity transfer from a substrate covered with an epitaxial silicon layer.—In order to test a possible barrier effect of an epitaxial layer against the impurity transfer, the same heat-treatments are performed, at a given temperature, $T = 1100$°C, but using a sapphire substrate on the upper surface of which an epitaxial silicon layer was previously grown.

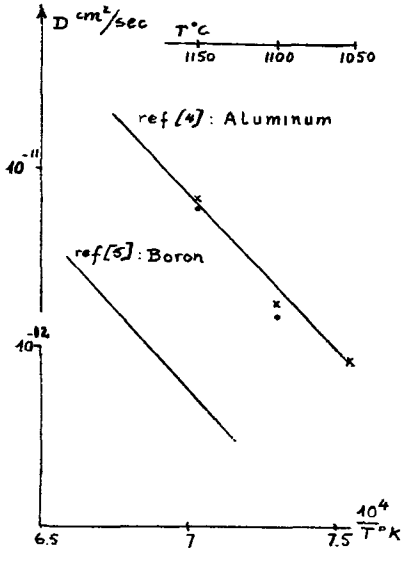

Fig. 2. Plot of log D (cm^2/sec) *vs.* $10^4/T$(°K). Solid curves, ref (10); experimental points: x unprotected substrate, o back coated substrate.

The comparison is made with two layers, (*a*) a 10 μm thick — 0.7 ohm-cm p-type layer (autodoped), and (*b*) a 6 μm thick — 8.7 ohm-cm n-type (deliberately doped with phosphorus) (Table II).

A somewhat surprising result is the occurrence of a diffused p-type layer, regardless of the epitaxial silicon conductivity type. This can be explained by (*a*) an electrical compensation existing in the n-type layer, which should contain phosphorus and aluminum; this result is reported elsewhere (11), and (*b*) a prevailing contribution of the rear of the substrate.

Both reasons are likely to be true because (*a*) on the one hand the high resistivity of the n-type layer may be the result of two large impurity concentrations of opposite type, but having two different transfer characteristics, and (*b*) on the other hand, the diffused layers have similar properties, for the same experimental conditions but for the presence of an epi layer, as it is apparent from Table III, gathering the comparative experiments reported in Tables I and II (at 1100°C, no back coating p-type layers).

The slightly smaller values in case II can account for some barrier effect, but the order of magnitude being the same, this indicates the importance of the rear surface.

It is therefore not surprising to find a fairly good agreement between the calculated diffusion coefficient when a p-type layer is involved. On the contrary, with the n-type layer the discrepancy is noticeable. The likely occurrence of phosphorus and aluminum diffusion precludes the validity of the assumptions made in the calculation of D.

Dopant transfer during growth.—The purpose of this experiment is to determine quantitatively the differences in the redistribution conditions during a heat-treatment or an actual epitaxy process.

The growth temperature is again $T = 1100$°C which is our optimum temperature (12), and we compare the properties of layers of different thicknesses (Table IV). Usually this layer thickness is of the order of 5 μm (reference conditions). Co is the impurity surface concentration in the layer. It is deduced from MOS capacitance measurements (13).

Table III. Comparison of diffused layer characteristics, heat-treatment $T = 1100$°C, no back coating

Condition	$\bar{\sigma}$, ohm^{-1} cm^{-1}	C_S, cm^{-3}	X_j, μm
I	1.7	2×10^{17}	2.6
II	1.5	1.5×10^{17}	1.4

Table IV. Autodoping in epitaxial growth at $T = 1100°C$

Back coating	Thickness, μm	ρ, ohm-cm	Co, cm^{-3}
No	5.2	0.7	7×10^{15}
No	1.5	0.135	1.5×10^{17}
Yes	1.4	0.64	3×10^{16}

Obviously, and this constitutes a weakness of our reasoning, the doping is not characterized by the same properties when growth or heat-treatment conditions are considered. But it is interesting to notice that Co has the same order of magnitude for thinner layers, as the surface concentration C_S of the diffused layer (1 to 2 x 10^{17} cm^{-3}) for the heat-treatment experiment.

The dependence of the layer resistivity on its thickness is apparent.

The contribution of the rear surface is also confirmed by a comparison of results on ρ and Co.

Some semiquantitative results can be deduced from the preceding figures, about the carrier mobility. Assuming (*a*) a weak dependence on the impurity concentration of this mobility for a given layer, and (*b*) a direct relation between the mean impurity concentration in the layer and Co, we can introduce a mean carrier mobility $\bar{\mu}$ taking into account the dependence on the layer depth of the electrical characteristics and write

$$\bar{\mu} \propto (\rho\ Co)^{-1}$$

Using the subscripts 1, 2, 3 for the three cases reported in Table IV, we have approximately

$$\frac{\bar{\mu}_1}{4} \simeq \frac{\bar{\mu}_2}{1} \simeq \frac{\bar{\mu}_3}{1}$$

We generally find for $\bar{\mu}_1 \sim$ 150-200 cm^2/V sec [measured values (12)] and therefore obtain

$$\bar{\mu}_2 \sim \bar{\mu}_3 \sim 40\text{-}50\ \text{cm}^2/\text{V sec}$$

It can be seen, comparing these results with measured (not calculated) figures reported by (7), that for thin layers, we get the same order of magnitude for $\bar{\mu}$ and $\bar{\mu}$ is weakly dependent on the impurity concentration. This implies reasonably that the mobility figures are limited for thinner layers rather by crystalline defects than by impurities.

Interesting experimental observations are made during the silicon growth on a back coated substrate.

In general, when silicon deposition begins, a decrease of the surface temperature (read with an optical pyrometer on the wafer) is observed, until a steady-state value is reached. But for a given set of conditions (H_2 flow, temperature), the transient time as well as the magnitude of this temperature decrease are different when protected or unprotected substrates are used. For example the following figures are typical

Substrate	Uncoated	Back coated
Transient time, min	5	1
$-\Delta T$, °C	30	10

Furthermore, the magnitude of the temperature gradient, observed between the edge and the center of the wafer during the steady state is reduced from 30° to 10°C, respectively.

All these observations are obviously related to the different thermal behavior of α Al_2O_3 and Si (infrared absorption, thermal conduction). It can be assumed, and we are now studying this point, that different nucleation conditions are achieved in both cases.

Conclusion

From the above, the following conclusions can be drawn:

1. Hydrogen is a powerful transport agent for aluminum. The need for a high-temperature gaseous etching of the sapphire substrates in H_2 makes a certain redistribution in the layers unavoidable.
2. The rear surface of the substrate is a prevailing doping source for aluminum during the prefiring stage as well as during the epitaxy process itself.
3. The back coating of the substrate offers a partial solution against the dopant transfer into the epitaxial layers.

Acknowledgments

This work is supported by the French Délégation Générale à la Recherche Scientifique and the Centre National de la Recherche Scientifique. The author thanks these organizations for permission to publish and expresses his gratitude to Professor L. Neel who allowed this work to be done in his laboratory.

Manuscript submitted Sept. 8, 1969; revised manuscript received *ca.* Feb. 12, 1970.

Any discussion of this paper will appear in a Discussion Section to be published in the December 1970 JOURNAL.

REFERENCES

1. H. M. Manasevit *et al.*, Trans. Metal. Soc., AIME, **233**, 540 (1965).
2. D. J. Dumin and P. H. Robinson, *This Journal*, **113**, 465 (1966).
3. D. J. Dumin, *J. Appl. Phys.*, **38**, 1909 (1967).
4. P. B. Hart, *et al.*, *Brit. J. Appl. Phys.*, **18**, 1389 (1967).
5. D. J. Dumin and P. H. Robinson, *J. Appl. Phys.*, **39**, 2759 (1968).
6. J. Mercier, *Rev. Phys. Appl.*, **3**, 127 (1968).
7. D. J. Dumin and P. H. Robinson, *J. Crystal. Growth*, **3.4**, 214 (1968).
8. J. D. Filby, *This Journal*, **113**, 1085 (1966).
9. J. C. Irvin, *Bell Sys. Tech. J.*, **41**, 387 (1962).
10. "Fundamental of Si Integrated Device Technology," R. M. Burger and R. P. Donovan, Editors, Vol. 1, Prentice Hall (1967).
11. J. Mercier, To be published.
12. J. Mercier and C. R. Colloque, Microélectronique Toulouse, March 1969.
13. A. Goetzberger, *Bell Syst. Tech. J.*, **45**, 1097 (1966).
14. D. J. Dumin, *Rev. Sci. Inst.*, **38**, 1107 (1967).

Analysis of the High Temperature Electrical Properties of Wustite

M. S. Seltzer and A. Z. Hed

Metal Science Group, Battelle Memorial Institute, Columbus Laboratories, Columbus, Ohio

ABSTRACT

A model is proposed to interpret the electrical conductivity and the Seebeck coefficient of wüstite. The methods for evaluating the concentration of charge carriers as a function of temperature and oxygen partial pressure were developed earlier from an analysis of thermogravimetric data. A hopping type mechanism of conduction is assumed. Thus, the mobility of the charge carriers is proportional to the jump probability which is assumed to be influenced by two factors. These are a blocking factor, which renders a fraction of the sites neighboring a charge carrier unavailable for occupancy, and a self-screening parameter which partially negates the blocking.

In a previous publication (1) the deviation from stoichiometry of wüstite has been computed on the basis of a defect structure model involving complex defects. The defects were assumed to be composed of two iron vacancies on octahedral sites and an iron interstitial on a tetrahedral site.

The model enables one to calculate the concentration of free charge carriers and therefore the electrical conductivity and the Seebeck coefficient. As is shown below, however, a straightforward calculation does not yield the observed experimental values obtained for the electrical conductivity. Furthermore, no model exists which can explain the observed change in sign of the Seebeck coefficient, Q.

In this paper we present an attempt to analyze the experimental data on the basis of the model proposed in ref. (1), with the inclusion of some parameters affecting the mobility of the charge carriers at high concentrations. Since these parameters affect the probabilities of occupancy of sites, they affect the Seebeck coefficient by changing the density of available states.

Vallet and Raccah (2) have proposed that their thermogravimetric data and high temperature x-ray studies of $Fe_{1-x}O$ may be explained only by assuming three different phases in the wüstite homogeneity range. In a recent publication, Fender and Riley (3) suggest that the high temperature electrolytic cell studies of the thermodynamic properties of $Fe_{1-x}O$ within the compound homogeneity range supports the existence of three different phases in wüstite. It has been proposed that the occurrence of different phases are due to differences in the ordering of the defects. The identification of these phases is, however, still an open question and is based on the fact that plots of emf values *vs.* temperature at constant composition consist of three linear regions. Rizzo *et al.* (4) have recently made similar measurements and have found a simple nonlinear relation over the whole range. The problem can be reduced simply to the question of whether these data are best fit by three different straight lines with different slopes or a single nonlinear line. We show in the following that a rather simple model can account for the nonlinearity of the observed properties at high temperature.

It has been suggested (6) that the negative thermal emf observed for wüstite at high deviations from stoichiometry is due to the appearance of negative charge carriers. This suggestion cannot be accepted as may be seen below.

The conductivity, σ, of a solid can be calculated from the general formula $\sigma = (n\mu_n + p\mu_p)\, e$, where n and p are the respective concentrations of negative and positive charge carriers, μ_n and μ_p their respective mobilities, and e their charge. At a given temperature p and n are related by $p \cdot n = n_i^2$, where n_i is an intrinsic concentration. It can be shown (5) that if positive and negative charge carriers participate in the conduction, a minimum in the isothermal conductivity occurs when $n\mu_n = p\mu_p$. Also, the transition from positive to negative thermal emf should occur at p/n ratios very close to $n/p = \mu_p/\mu_n$, or near the same concentration where minimum conductivity is observed.

No minimum in the isothermal conductivity of wüstite has been reported when the composition is changed from $Fe_{0.95}O$ to $Fe_{0.84}O$. This indicates that the condition $n\mu_n = p\mu_p$, is never attained. We therefore conclude that the model proposed by Hillegas (6) cannot account for the observed electrical conductivity in wüstite. To further substantiate the argument that only positive charge carriers contribute to the conductivity, consider the fact that the conductivity increases monotonically with increasing deviation from stoichiometry, even when the thermal emf changes sign. If, as Hillegas suggests, the decrease in thermal emf is due to the appearance of negative charge carriers, the conductivity should decrease throughout the minimum rather than increase.

We therefore assume that only one type of charge carrier, namely, holes, are contributing to the conductivity. The conductivity then is given by

$$\sigma = pe\mu_p \qquad [1]$$

To calculate the conductivity it is necessary to compute p, the concentration of holes. In ref. (1) it was suggested that the defects consist of the following complex ($V_{Fe}Fe_iV_{Fe}$), *i.e.*, two iron vacancies associated with an iron interstitial. The creation and ionization of these defects may be written as

$$Fe_{Fe} + V_i + \frac{1}{2}O_2 = Fe_c^x + O_O \qquad [2]$$

$$Fe_{Fe} + Fe_c^x = Fe_c' + Fe_{Fe} \cdot e^+ \qquad [3]$$

Fe_c^x and Fe_c' are neutral and singly ionized complex defects respectively, where the prime refers to negative charge, V_i represents an interstitial (tetrahedral) site available for occupancy by the complex defect, and Fe_{Fe} is a divalent Fe atom on a normal site (octahedral), $Fe_{Fe} \cdot e^+$ is an Fe^{+++} ion on an octahedral site with one extra electron hole (a trivalent iron cation), and O_O is an oxygen ion on an oxygen lattice site.

With the neutrality condition

$$p = [Fe_{Fe} \cdot e^+] = [Fe_c'] \qquad [4]$$

and expressing the concentration of the defects in molar fraction y, the deviation from stoichiometry, is given by

$$y = [Fe_c^x] + [Fe_c'] = \alpha + \beta \qquad [5]$$

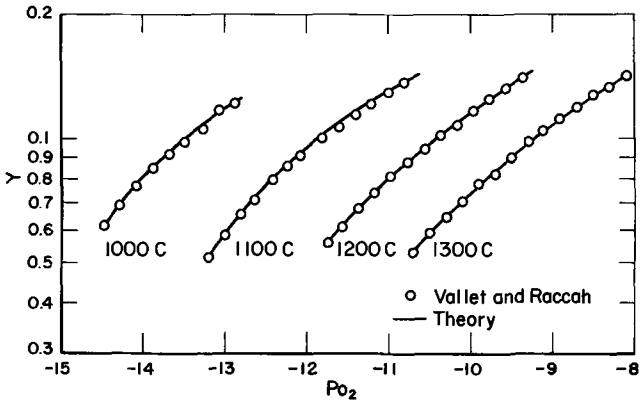

Fig. 1. Nonstoichiometry in wustite, y in $Fe_{1-y}O$, as a function of temperature and partial pressure of oxygen. Experimental results after Vallet and Raccah (2).

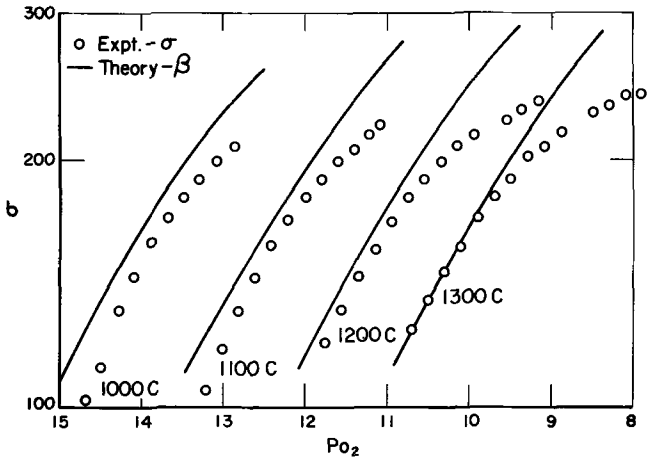

Fig. 2. Electrical conductivity as a function of oxygen partial pressure for several temperatures. Solid lines are obtained using Eq. [1]. Experimental data is after Hillegas (6).

where α is the concentration of unionized complex defects and β is a concentration of ionized defects and is also equal to p, the concentration of free charge carriers.

Due to the large concentration of defects, the concentration of regular octahedral sites and of empty tetrahedral sites cannot be assumed to be constant. It has been shown in ref. (1) that

$$[Fe_{Fe}] = 1 - \beta - 2y \qquad [6a]$$

and

$$[V_i] = 2 - 7y \qquad [6b]$$

With these values for the activities of octahedral sites and tetrahedral sites, the law of mass action applied to Eq. [2] and [3] yields

$$y - \beta = K_1 (2 - 7y)(1 - \beta - 2y)\, p_{O_2}^{-1/2} \qquad [7]$$

and

$$\beta^2 = K_i (y - \beta)(1 - \beta - 2y) \qquad [8]$$

Solving these equations, we obtain for β

$$\beta = \frac{-K_i(1 - y) \pm [K_i^2(1 - 3y)^2 + 4K_i y(1 - 2y)]^{1/2}}{2(1 - K_i)} \qquad [9]$$

and for p_{O_2}

$$p_{O_2} = \left[\frac{K_1 (1 - 2y - \beta)(2 - 7y)}{y - \beta} \right]^{-2} \qquad [10]$$

These equations have been solved numerically in ref. (1).[1] With the expressions $K_1 = 1.75 \times 10^{-9} \exp(79{,}400/RT)$ and $K_i = 0.13 \times 10^2 \exp(-17{,}900/RT)$ we calculated the deviation from stoichiometry as a function of p_{O_2}. The results are presented in Fig. 1 with the experimental results of Vallet and Raccah (2). Excellent agreement of theory with experiment is apparent. The values of β as a function of temperature and oxygen partial pressure were then used to calculate the conductivity using Eq. [1]. The mobility is assumed to be a constant of temperature and is calculated from the conductivity at the smallest deviation from stoichiometry separately at each temperature. The conductivity at all y has been calculated from these values of μ, and the results are shown in Fig. 2. We see that the conductivity as calculated deviates markedly from the measured conductivity even at relatively small values of y. This is not surprising since the concentration of charge carriers is extremely high and one would expect that the mobility would be a function of this concentration.

From the experimental results and the known concentration of charge carriers one can, however, estimate an approximate value for the mobility $\mu \cong 1$ cm²/V sec.[2] Such a small mobility is typical of solids where small polaron hopping is the operative mode of conduction (7). In this case the mobility is proportional to the jump probability of a charge carrier from site to site. If the concentration of charge carriers is very high, it is highly probable that one of the nearest neighbor sites will already be occupied by a charge and therefore hopping to this site will be prohibited. The probability of a jump will therefore be decreased by a factor $1 - \gamma\beta$, where γ represents a blocking parameter describing the availability of sites for charge motion. This term is similar to the blocking term on the tetrahedral site (Eq. [6b]), and we assume that each octahedral site occupied by a charge carrier blocks half the neighboring octahedral sites and its own site. Therefore, γ is equal to 4 in our calculations. Since the concentration of charge carriers is extremely large, it is quite probable that some of the blocked sites calculated in this manner are blocked twice. To allow for this effect we tried to accommodate in the model different screening parameters. Usually, self screening is proportional to the 1/2 or 2/3 power of the concentration of charge carriers. We found the former to better fit the results and we therefore used 1/2 for calculating the conductivity. The following expression for the mobility is therefore used

$$\mu = \mu_0 \beta^{1/2} (1 - 4\beta) \exp \frac{-E_a}{kT} \qquad [11]$$

The activation energy E_a is the heat of motion for the charge carriers themselves and it has been taken to be 0.01 eV. This is determined from the temperature dependence of the lowest conductivity values at each temperature where the influence of the blocking parameters is minimal. Also the deviation from stoichiometry at this part of the phase diagram does not change much with temperature and is about 5%. Using Eq. [1] and [11] the conductivity has been calculated. The results of these calculations are shown in Fig. 3 and are compared with the experimental results of Hillegas (6). Apart from a slight decrease in the conductivity with increasing concentration of charge carriers at the high oxygen pressure part of the phase, the fit of the calculated σ with the experimental values is very good. Later we discuss possible sources for the deviations at high concentrations of charge carriers.

One would like, however, to check the validity of the model proposed here on an independent set of experimental results. The Seebeck coefficient may serve

[1] Unfortunately, in ref. (1) a typographical error occurred in the pre-exponential values of K_1 and K_i; furthermore, to obtain better agreement with thermogravimetric results, the constants have been slightly varied in the present work.

[2] At the temperatures in question, this value alone is not by itself a sufficient consideration to apply the hopping model. Measurement at lower temperatures suggests, however, a mobility which strongly decreases with temperature and on this basis the hopping assumption is made.

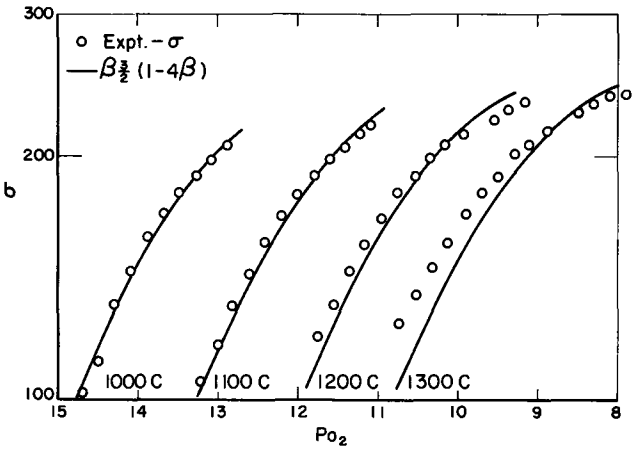

Fig. 3. Electrical conductivity as a function of oxygen partial pressure for several temperatures. Solid lines are obtained using Eq. [1] and [11]. Experimental data is after Hillegas (6).

as a tool for this purpose since it is, theoretically, simply related to the concentration of charge carriers.

The Seebeck coefficient is given by the expression

$$Q = \frac{k}{e}\left\{ \ln\frac{N_v}{c} + A \right\} \qquad [12]$$

where N_v is the density of states, c the concentration of charge carriers, and A a kinetic term. When the charge carriers are localized, N_v is assumed to be the concentration of available sites. From our discussion above this should be $N_v = \beta^{1/2}(1 - 4\beta)$. With $c = \beta$, we therefore obtain for Q

$$Q = \frac{k}{e}\left\{ \ln\frac{(1-4\beta)}{\beta^{1/2}} + A \right\} \qquad [13]$$

In Fig. 4 we plotted these values together with the experimental results of Hillegas (6). The kinetic term here equals −0.89. It is seen that good correlation is found between the experimental results and the theoretical curves which were obtained from the same model used to explain the conductivity data. A possible explanation of the negative kinetic term is presented below.

Discussion

We have presented here a model which has been used to interpret three sets of experimental data which are dependent on temperature and oxygen pressure. These data are deviation from stoichiometry, the electrical conductivity, and the Seebeck coefficient. The parameters of the theory are K_l and K_i which are temperature dependent in a well-determined way, and the blocking and screening effects.

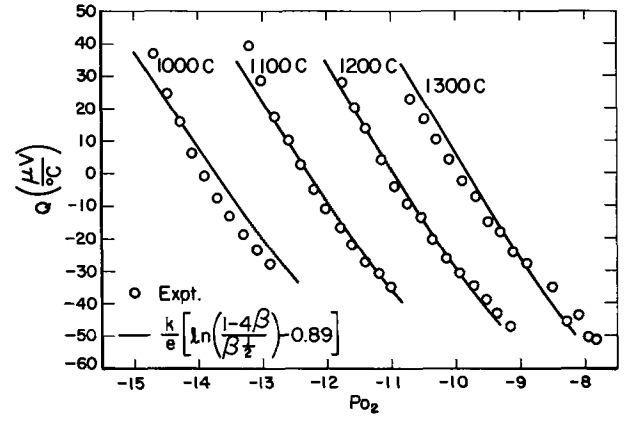

Fig. 4. Seebeck coefficient as a function of oxygen partial pressure for several temperatures. Solid lines are obtained using Eq. [13]. Experimental data is after Hillegas (6).

The blocking and screening parameters have been chosen in a manner consistent with physical reality. K_l and K_i were determined to fit the experimental thermogravimetric data alone. K_l was determined from the deviations from stoichiometry at low values of y, while K_i was estimated from the high y portions of the phase diagram. The fact that a very good fit for three independent experimental variables obtained over a wide range of temperatures and oxygen partial pressures, could be calculated using parameters derived to fit a single set of values,[3] points up the fact that the defect structure proposed and the form of the mobility bear a close relation to the actual properties of wüstite.

One of the conclusions from this treatment is that the nonlinearity observed in thermogravimetric data obtained using solid state electrolytic cells and in measurements of electrical conductivity does not warrant the introduction of three different phases in wüstite. This does not rule out the possibility of the existence of a long-range order as discussed by Koch and Cohen (8). However the macroscopic properties of wüstite would be influenced only to a minor degree even if such a long-range order did indeed exist.

The model presented here does have, however, some intrinsic limitations. We have seen that at very high concentrations of charge carriers the theoretically obtained values of the conductivity do deviate from the experimental ones. Assuming that the experimental values are correct one asks himself where the theory could be improved to account for these deviations. The parameters K_l and K_i and their temperature dependence have been calculated using the experimental thermogravimetric data. K_i however determines the ratios of β to y. (It describes the ionization of the complex defects.) The thermogravimetric data are by their nature less accurate than electrical conductivity data and less sensitive to K_i. Slight changes in K_i could influence the calculated conductivity to a larger degree than the deviation from stoichiometry. It is possible, therefore, that a better value of K_i could improve the theoretical values of the conductivity.

It is not impossible, however, that the screening coefficient $\beta^{1/2}$ changes slightly with β itself. We tested this idea, and for high β a screening coefficient $\beta^{2/3}$ does fit the results better than $\beta^{1/2}$. This would be a plausible result since the concentrations of charge carriers do increase by a factor of 3. Such a procedure will, however, render the relative simplicity of the model useless, and may involve the fitting of the experimental results to theory with too many parameters.

The exact form of the kinetic term in the Seebeck coefficient is still uncertain. Heikes *et al.* (9) show that for hopping charge carriers $A = \beta E_\mu/kT$ with $\beta = 1$ or $0 < \beta < 1$. To our knowledge no theoretical work predicts $\beta < 0$.

This behavior has, however, been observed before in CoO (10) and the question arises as to whether or not this is a general property. One speculation to explain this peculiar effect is that we have here a case of a "negative phonon drag." The A term in the thermoelectric power describes the temperature dependence of the scattering mechanism in the transport of charge carriers. In most cases, this is also the temperature dependence of the mobility. The phonon drag is however associated with an anisotropic scattering of phonons by the charge carriers, yielding an extra thermal energy in the direction of the charge motion. In the case of hopping, the charge motion is phonon assisted and one could interpret this as scattering of electrons by phonons and therefore a lowering of the thermal energy

[3] It should be noted that the fact that the temperature dependence of K_l and K_i must be of a given form does limit the choice of parameters, and a good agreement of the theoretical value to the thermogravimetric data is by itself a good indication of the usefulness of the model chosen.

of the system in the direction of motion. The occurrence of this negative A term in CoO, in some spinels, and in wüstite warrants a deeper theoretical study of this effect. It may be noted in this context that 0.89 is approximately E_μ/kT in this temperature range, and this also is very similar to the expression observed in CoO.

Acknowledgments

The authors are grateful to Dr. Hillegas and Professor J. B. Wagner for supplying us with their detailed experimental results.

Manuscript submitted Dec. 11, 1969; revised manuscript received *ca.* Feb. 23, 1970.

Any discussion of this paper will appear in a Discussion Section to be published in the December 1970 JOURNAL.

REFERENCES

1. P. Kofstad and A. Z. Hed, *This Journal*, **115**, 102 (1968).
2. P. Vallet and P. Raccah, *Mem. Sci. Rev. Met.*, **62**, 1 (1965).
3. B. E. F. Fender and F. D. Riley, *J. Phys. Chem. Solids*, **30**, 793 (1969).
4. F. Rizzo and J. V. Smith, *J. Phys. Chem.*, **72**, 485 (1968).
5. J. H. Becker and H. P. R. Frederikse, *J. Appl. Phys. Supp.*, **33**, 447 (1962).
6. W. J Hillegas, Jr, Ph. D. Thesis, Northwestern University, June 1968.
7. T. Holstein, *Ann. Phys. (N.Y.)*, **8**, 343 (1959).
8. F. Koch and J. B. Cohen, *Acta Cryst.*, **325**, 275 (1969).
9. R. R. Heikes, A. A. Muradudin, and R. C. Miller, *Ann. Phys. (Paris)*, **8**, 733 (1963).
10. B. Fisher and D. S. Tannhauser, *J. Chem. Phys.*, **44**, 1663 (1966).

Technical Note

Heats of Fusion of the $A_2^{V}B_3^{VI}$ Compounds

As_2S_3, As_2Se_3, As_2Te_3, and Sb_2S_3

M. B. Myers and E. J. Felty

Research Laboratories, Xerox Corporation, Rochester, New York

The nonoxide group V-VI, A_2B_3 compounds are of interest because of their semiconducting and photoconductive properties. Further, the particular compounds of the present study are in a very interesting class of materials referred to as chalcogenide glass formers. Because the active interest in these materials is a relatively recent one, there are little data with respect to their thermodynamic properties. This paper reports measurements of the heats of fusion and the corresponding melting points for As_2S_3, As_2Se_3, As_2Te_3, and Sb_2S_3.

Experimental

The materials were prepared by reaction of Gallard Schlesinger 99.9999% pure elemental components in silica glass ampoules at 600°C for 24 hr and air cooling to room temperature. The As_2Te_3 and Sb_2S_3 melts crystallized on cooling, whereas As_2S_3 and As_2Se_3 formed glasses. Suitable As_2Se_3 crystals were prepared from the glassy material by sublimation in sealed silica glass ampoules. Difficulty in obtaining completely crystalline As_2S_3 necessitated the use of natural crystals of the mineral orpiment.

The identity of the compounds was checked by x-ray diffraction, and the stoichiometry of their major constituents was determined to be within ± 1.0 a/o (atomic per cent) of the desired composition by electron microprobe analysis. The absence of any observable eutectic reactions during the thermal analyses further verified the accuracy of the compound compositions.

Calorimetric determinations were carried out with two different types of apparatus depending on the melting temperature of the compound. A Perkin-Elmer DSC-1B differential scanning calorimeter (1, 2) was employed in the analyses on As_2S_3, As_2Se_3, and As_2Te_3, whereas, the calorimeter accessory (3) for the Du Pont 900 DTA was used for Sb_2S_3.

The Perkin-Elmer calorimeter read out temperatures were corrected by calibrating the instrument using the melting points (4) of In, Sn, Pb, Zn, Cd, and Te. The Du Pont instrument potentiometrically recorded temperature with chromel-alumel thermocouples, and calibration with appropriate melting points indicated no additional corrections were required. The accuracy of the temperature measurement is ± 1°C. However, the uncertainty of the melting points is greater as indicated because of the difficulty in discerning the exact onset of melting. A comparative analysis on materials with well established melting points indicated a preference for an extrapolated onset technique for the DTA and a point of first departure from baseline for the DSC-1B.

The heats of fusion were determined by a comparison of the areas of the melting endotherms of the unknowns to those of standards with melting peaks in the same temperature range. The areas of the melting peaks were enclosed by drawing a straight line from the point of first departure from the baseline of the thermogram trace to the point of return. The area of each endotherm was measured ten times with a planimeter, and ten analyses were made on each unknown and standard.

The standard employed for the As_2S_3 determination was Pb, and the standard for the As_2Se_3 and As_2Te_3 determinations was Zn. These calibrations were checked by employing them for the measurements of the heats of fusion of Cd and Te. Comparison of the mean values of these determinations with literature values indicates a difference of 2.0 and 3.6%, respectively. The primary calibrant for the determination on Sb_2S_3 with the Du Pont apparatus was Bi_2Te_3. Because of the marked temperature dependence of the calibration factor in the temperature range of interest, the

Table I. Melting points, heats of fusion, and entropies of fusion of $A_2^VB_3^{VI}$ Compounds

Compound	Melting point, °C		ΔH fusion kcal/g at. (kcal/mole)		ΔS fusion cal/g at.° (cal/mole°)	
	Present study	Literature	Present study	Literature	Present study	Literature
As_2S_3	~315	307 (7)	1.37 ± 0.06 (6.85 ± 0.30)	0.91 (7)	2.33 (11.65)	1.6 (7)
As_2Se_3	368 ± 4.0	360 (12)	1.95 ± 0.06 (9.75 ± 0.30)		3.04 (15.20)	
As_2Te_3	374 ± 1.0	362 (13)	2.67 ± 0.07 (13.35 ± 0.35)		4.13 (20.65)	
Sb_2S_3	549 ± 4.0	547 (8)	2.29 ± 0.12 (11.45 ± 0.60)	1.12 (8)	2.79 (13.95)	1.37 (8)

secondary calibrants Cd, Zn, and Te were employed to establish a temperature coefficient for the factor. The error in the determination of the heat of fusion of Sb_2S_3 with the calibration is approximately 5%.

The heating rates for all of the analyses were 10°C/min, and depending on the gram-atomic weight of the sample, 1-10 mg of material were analyzed. The sample holders employed were Perkin-Elmer sealable aluminum containers for volatile samples. The inhibition of free vaporization was most important for As_2Te_3 and Sb_2S_3 near the melting point. Reaction with the sample container was only noted for Sb_2S_3 and was eliminated by forming a thicker oxide coating on the container by anodization.

Discussion and Results

The heats of fusion, melting temperatures, and computed entropies ($\Delta S_f = \Delta H_f/T_f$) obtained in this investigation are summarized in Table I and are compared in Fig. 1 with the literature values for Sb_2Se_3 (5), Bi_2S_3 (5), Sb_2Te_3 (6), and Bi_2Te_3 (6). The literature values for ΔH_f of As_2S_3 (7) and Sb_2S_3 (8) were determined by the pressure dependence of the melting point and by cryoscopic measurements, respectively. Comparison with the values of this study indicates fair agreement for As_2S_3 and poor agreement for Sb_2S_3. The determination of ΔH_f by cryoscopy requires assumptions concerning the nature of the liquid solution which are difficult to verify. It is believed that the calorimetrically determined value of the present study is the more accurate parameter for Sb_2S_3.

There is a great deal of experimental evidence indicating that ΔH_f is proportional to T_f for certain classes of crystal structures (9, 10). However, a constant entropy relationship between ΔH_f and T_f is not found for any of the groups of isostructural compounds appearing in Fig. 1. This lack of proportionality is also demonstrated for the isostructural elements Se and Te (8) included in Fig. 1 for comparison.

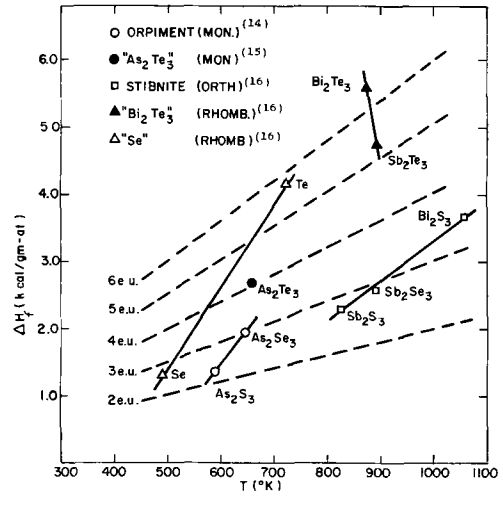

Fig. 1. Relationship between the heat of fusion and thermodynamic melting point. The isostructural compounds, connected by solid lines, are identified as to structural type in the upper left quadrant of the diagram. The broken lines indicate constant entropy values.

In order to evaluate the relative differences quantitatively in the entropy of fusion for these compounds, all the sources of entropy change require consideration. These contributions can arise from the volume change, molecular orientation randomization, and random mixing of elemental components. The importance of these factors vary according to the degree of dissociation of the compound in the melt.

Unfortunately, neither the ΔV_f nor detailed structural information of the melts are available to assess their relative contributions to ΔS_f. However, it is possible to qualitatively relate the differences in ΔS_f to variations in the constitution of the melt by comparing the ΔS_f's with the change in cohesive energy with fusion. The change in cohesive energy is assumed to be reflected by the ratio of the gram-atomic heat of fusion to the gram-atomic heat of atomization. The heats of atomization are not experimentally available; however, they can be estimated (11) from

$$\Delta H_a = 1/5\,[-\Delta H^\circ_{F(A_2B_3)} + 2\Delta H_a^\circ{}_{(A)} + 3\Delta H_a^\circ{}_{(B)}]$$

where ΔH°_F is the heat of formation of the compound, and ΔH_a° is the heat of atomization of the elements.

The data in Fig. 2 do indicate for both isostructural groupings and for these A_2B_3 compounds in general that the increase in the entropy of fusion is associated with a greater relaxation of bonding energy on fusion. This observation suggests that the progressive increases in the ΔS_f's observed in Fig. 2 are associated with greater structural change on fusion. The resulting melts would be characterized by increased dissociation and randomization. This trend is consistent with the observed decrease in glass forming tendencies and melt viscosities found for the higher gram-atomic weight compounds.

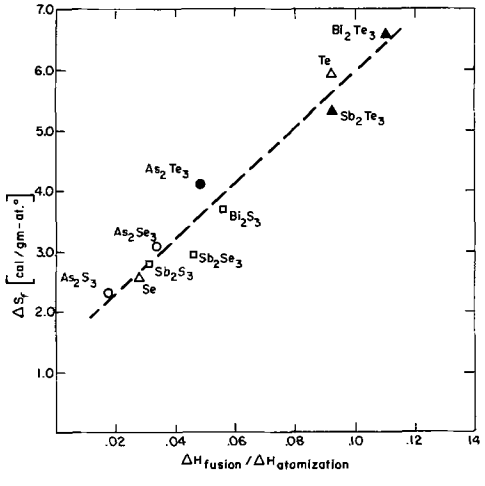

Fig. 2. Relationship between ΔS_f and the decrease in average bonding energy. Isostructural compounds are denoted as in Fig. 1.

Acknowledgment

The authors wish to express their appreciation to J. O'Neill for his excellent help in the experimental work.

Manuscript submitted Jan. 7, 1969; revised manuscript received Feb. 9, 1970.

Any discussion of this paper will appear in a Discussion Section to be published in the December 1970 JOURNAL.

REFERENCES

1. E. S. Watson, M. J. O'Neill, J. Justin, and N. Brenner, *Anal. Chem.*, **36**, 1233 (1964).
2. A. Gray, "Analytical Calorimetry," R. S. Porter and J. F. Johnson, Editors, Plenum Press, New York (1968).
3. S. L. Boersma, *J. Am. Ceram. Soc.*, **38**, 281 (1955).
4. American Institute of Physics Handbook, McGraw-Hill Publishing Co., Inc. New York (1963).
5. A. C. Glatz and K. Cordo, *J. Phys. Chem.*, **70**, 3757 (1966).
6. B. W. Howlett, S. Misra, and M. B. Bever, *Trans. AIME*, **230**, 1367 (1967).
7. V. A. Kirkmskii, A. P. Ryaposov, and V. g. Yakushev, *Bull. Acad. Sci., USSR, Inorg. Materials*, **3**, 1931 (1967).
8. Circular 500, NBS (1952).
9. O. Kubaschewski, E. L. Evans, and C. B. Alcock, "Metallurgical Thermochemistry," 4th ed. pp. 213-214, Pergamon Press Inc., New York (1967).
10. B. Chalmers, "Principles of Solidification," p. 41, John Wiley & Sons, Inc., New York (1964).
11. R. L. Myuller, "Solid State Chemistry," Z. U. Borisova, Editor, Consultants Bureau, New York (1966).
12. S. A. Dembovskii, *Russ. J. Inorg. Chem.*, **7**, 1454 (1952).
13. M. Hansen, "Constitution of Binary Alloys," McGraw-Hill, New York (1958).
14. N. Moromoto, *In, J.*, **1**, 160 (1954).
15. G. J. Carron, *Acta Cryst.*, **16**, 338 (1963).
16. R. Wycoff, "Crystal Structures," *1* and *2*, Interscience, New York (1963) and (1964).

The Discussion Section which usually is published in this issue of the Journal will appear in the July 1970 issue.

JOURNAL OF THE ELECTROCHEMICAL SOCIETY

ELECTROCHEMICAL TECHNOLOGY

JUNE 1970

Changes in the State of the Zinc Anode during Discharge of Leclanche Dry Batteries

K. Miyazaki*

Mitsui Mining and Smelting Company, Central Research Laboratories, Mitaka-shi, Tokyo, Japan

ABSTRACT

Microanalytical and x-ray diffraction examination of cross-sectional areas of discharged zinc anodes has been carried out together with the measurement of the extent of metal dissolution using typical fabricated zinc cans. The behavior of zinc as a dry cell anode, including the generation of discharge products, is very dependent on the degree of discharge and the capacity, even for batteries incorporating identical anodes. Manganese occurrence at the zinc-electrolyte interface is observed in particular cases of discharge. This is associated with the generation of enlarged micropores in the MnO_2 particles contained in the cathode cake.

This paper deals with an experimental study of zinc anode behavior in actual Leclanché dry cells. It is ordinarily recognized that the reaction of zinc anodes during discharge in Leclanché cells exhibits the following general features: (*a*) dissolution of the metal, (*b*) change in the crystalline orientation, and (*c*) generation of discharge products. However, these changes seem to have been overlooked in many cases, partly because a major portion of the technology in this field has long been in a border area between the zinc supplier and the dry cell producer and partly because the zinc is the "consumed electrode" and therefore provides few opportunities for investigation.

In recent years, much attention has been devoted to the nature of the zinc anode and its participation in some electrode processes. Among the basic studies on zinc behavior, McMurdie (1) related the discharge products including $ZnCl_2 \cdot 4Zn(OH)_2$, and $ZnCl_2 \cdot 2NH_3$. Cahoon (2) mentioned the occurrence of $ZnCl_2 \cdot 2NH_3$ and $ZnCl_2 \cdot 4NH_3$, and Drotchmann (3) and Bell (4) discussed the corrosion problem of the zinc plate in the Leclanché electrolyte. Most of the published data, however, have been limited to discussions of the results of rather "static experiments" with test pieces immersed in cell electrolytes, and a recalculation is required when applying them to the characterization of zinc anodes with "dynamic discharge reactions" in actual dry cells. It is often observed that the behavior of zinc in actual dry cell service deviates significantly from what might be expected from a separate immersion test with zinc pieces.

Because of the importance of the contribution of zinc ions to Leclanché dry cell reactions as seen in the previous work (5), an effort has been made in the present paper to observe where, and to what extent, the zinc anode will react to function as the counter-electrode of the MnO_2 during discharge of a Leclanché cell. It is well known that the cathode cake and paste formulation has a major influence on zinc anode performance; even with the same species of zinc anode, the performance of cells is largely governed by the way they are made. In the present study, utilizing this phenomenon and selecting some of the parameters in cell fabrication, a number of laboratory dry cells were constructed with a typical impact-extruded zinc can. These cells, prepared with several modifications, were then discharged on heavy and light loads. The resultant anodes have been examined by means of x-ray diffraction and electron probe microanalysis. The purpose here is to reveal how the three general features, (*a*), (*b*), and (*c*), mentioned above manifest themselves with a typical fabricated zinc can under actual service conditions and how they are described in terms of discharge characteristics of the cell.

Experimental

Anode zinc can.—A typical impact-extruded zinc can for commercial D-size cells in Japan was used for constructing the test cells. The weight was 14g and the chemical analysis was: Fe 0.01%, Pb 0.12%, Cd 0.06%, Cu 0.004%, and Zn the balance. This can was manufactured through the three main steps according to the common practice; *i.e.*, (i) metal ingot before rolling, (ii) "coins" obtained from the rolled sheet and ready for impact-extrusion, and (iii) impact-extruded can.

Figure 1 shows the x-ray diffraction pattern for each stage. At stage (i), the most intense peak was (101) being characteristic of the metallic zinc. The relative intensities of the (002) and (004) peaks became stronger at stage (ii), showing that the hexagonal zinc unit cells had slipped along the basal planes (6) through the rolling operation. After impact-extrusion, at the final stage (iii), the (002) peak remained stronger and the (103) peak was also intensified, while the (004) peak was comparatively reduced.

Construction of the cells.—The standard formulation in the previous work (5) was used in constructing laboratory cells with the above zinc cans. To provide a series of varied discharge characteristics, the following parameters were selected and varied; the source and activity of manganese dioxide, mixing ratios in the cathode mix, pH of the electrolyte, aging time of the mix, wrapping and unwrapping of cathode bobbin, and

* Electrochemical Society Active Member.

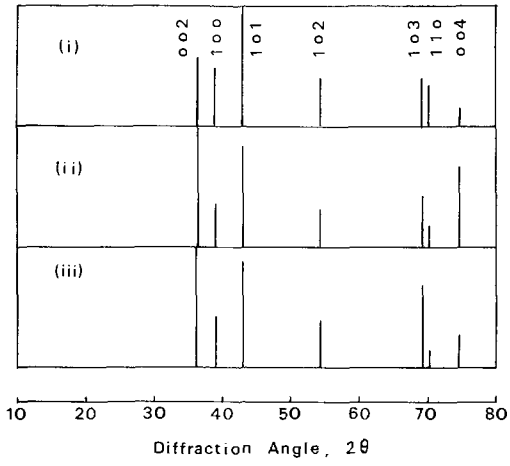

Fig. 1. X-ray diffraction examination of the zinc can at the main production stages: (i) the zinc ingot, (ii) rolled sheet, and (iii) impact-extruded can.

composition of the paste, thus giving 20 kinds of experimental fabrication processes. Mercury was always added to the paste in the form of $HgCl_2$ solution. Forty experimental cells in all, two cells for each fabrication, were obtained. They were hand pressed, containing 22g of manganese dioxide per cell.

In terms of present-day technology, our formulation and fabrication are probably outdated and perhaps naive. However, they did give us first-hand experience with some of the basic qualities of zinc when functioning as anode in actual working dry cells.

Discharge of the cells.—The two cells for each formulation were discharged, one on a relatively heavy load, 4 ohms for 30 min/day and 5 days a week, and the other on a relatively light load, 40 ohms for 4 hr/day and 5 days a week, to a cut-off voltage of 0.75V, respectively. Intermittent discharges were employed considering the fact that the daily usage of dry batteries is mostly intermittent.

Separation of discharged zinc anodes.—The discharged dry batteries were disassembled and the residual zinc anodes were separated, quickly rinsed with water, and then with acetone. Acetone facilitated the removal of the water and was itself removed at 20°C in air.

Care was exercised in removing some of the constituent materials of the residual cell, including the paste, from the consumed zinc electrode. Preliminary tests showed that the residual materials were removed from the developed anode surface by the brief rinse with water, and the film of zinc compounds formed on the immediate interior wall was satisfactorily stable and not affected by this treatment if the water was successively replaced with a volatile solvent such as acetone. Acetone was conveniently employed because it readily escaped from the surface at the room temperature of 20°C without any harmful effect to the consumed electrode.

When the rinsing procedure was not followed after disassembling the discharged dry cells, three undesirable effects took place: (i) the weight of the residual zinc anode was erroneous due to the wet paste, (ii) the bulk of the paste adhering to the electrode dried during the x-ray examination process and secondary compounds were formed other than the primary discharge products to be examined, and (iii) the wet paste interfered with mounting the specimen in the resin matrix used for the EPMA device and with examining it under the electron bombardment in vacuo.

There still remains a problem that this separation procedure may not be entirely satisfactory for a soluble discharge product such as polyammines, if any. However, the scope of the present study does not attempt to cover all the discharge products occurring in the cell, but concentrates on the changes in the state of the impact-extruded zinc metal from x-ray aspects. Among several ways tested for paste removal, the procedure described above was the best for the purpose of the present study.

Examination of discharged zinc anodes.—The discharged zinc anodes were examined as follows: (i) decrease in weight as an approximate measure of zinc dissolution, (ii) x-ray diffraction pattern of the developed interior surface using Cu K_α radiation for discharge products, and (iii) electron probe microanalysis for the Zn, Pb, and Mn distribution across vertical sections by scanning for the individual characteristic K_α x-rays.

Among the elements indicated in the chemical analysis of the zinc anode, Cd, Fe, and Cu were too small in amounts to be examined with the EPMA method, their images being overshadowed with the level of background. On the other hand, mercury which had been added to the paste in the form of $HgCl_2$ during assembly could be observed because it formed a layer of amalgam on the interior surface of the zinc anode.

In the case of Hg examination, however, the L_α ray instead of the K_α was employed due to the fact that the maximum accelerating voltage of the EPMA device with a LiF spectrum crystal was 50 kV, while the excitation voltage for Hg K_α ray is about 83 kV and that for Hg L_α is about 15 kV. Care was also extended to examine the background intensity of the Hg L_α image, because it was different from the one in the conventional cases of K_α images. A usual practice in the EPMA technique was followed in this case; a slight shift in the detecting angle from the wavelength of the Hg $L_{\alpha 1}$ ray, which is 1.23863Å, provided the background intensity of the Hg $L_{\alpha 1}$ itself, there being no interfering elements in the specimen that correspond to any wavelength in the shifted range.

The counting sensitivity of the x-ray detector of the microanalyzer was adjusted higher for the Pb, Mn, and Hg elements by a factor of 100 than for Zn because of their minor amounts. The other EPMA conditions were similar to the one described in the previous work (5).

Pore distribution measurement for MnO_2.—Pore size distributions were measured for the MnO_2 before and after discharge to determine changes that occurred as it functioned as a source of Mn^{+2} ions during discharge. The Barrett, Joyner, and Halenda method was used on the basis of nitrogen gas adsorption-desorption curves in a range of $p/p_o = 0.03$ to 0.97 obtained with a BET apparatus.

Results and Discussion

Dissolution of zinc.—The decrease in weight of the anode during discharge *vs.* the discharge hours are plotted in Fig. 2 and 3. The zinc anode dissolved in a larger quantity during the light discharge than during the heavy. The dissolution of the zinc is observed to be approximately proportional to the discharge duration in the former case, while not in the latter.

Changes in x-ray diffraction pattern.—The 40 residual zinc cans obtained, 20 each from the heavy and the light discharges, were roughly classified into four types of x-ray diffraction patterns as shown in Fig. 4. After the heavy discharge there was observed either a type that produced a number of the peaks of $ZnCl_2 \cdot 4Zn(OH)_2$ [Fig. 4(a)] or of $ZnCl_2 \cdot 2NH_3$ (b). After the light discharge, the zinc anode mainly produced the basic chloride rather than the diammine and the degree of generation was in some cases small (c), and in other cases considerable (d). While type (d) retained some of the stronger residual peaks of zinc, type (c) on the contrary possessed only smaller peaks of the metal.

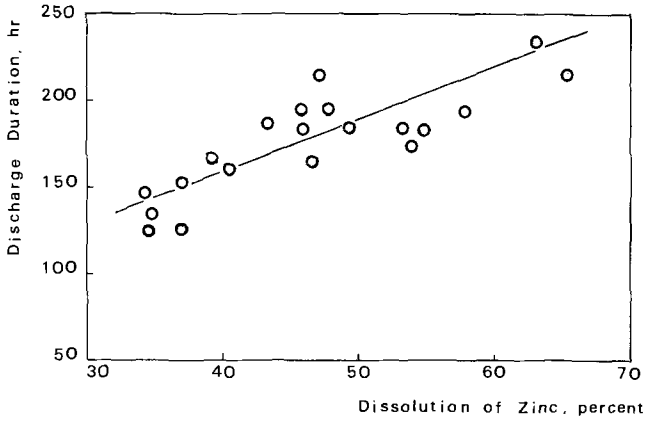

Fig. 2. Relationship between discharge duration and dissolution of zinc during the light discharge.

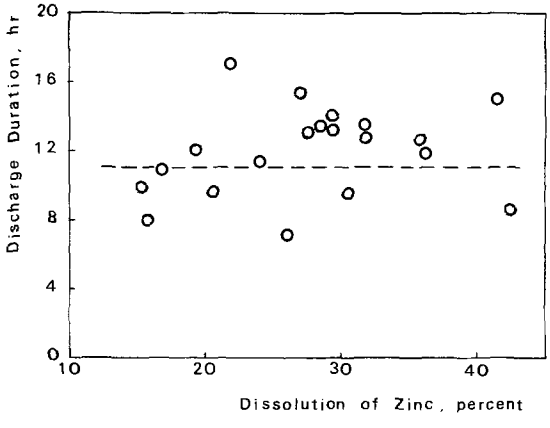

Fig. 3. Discharge duration vs. dissolution of zinc during the heavy discharge.

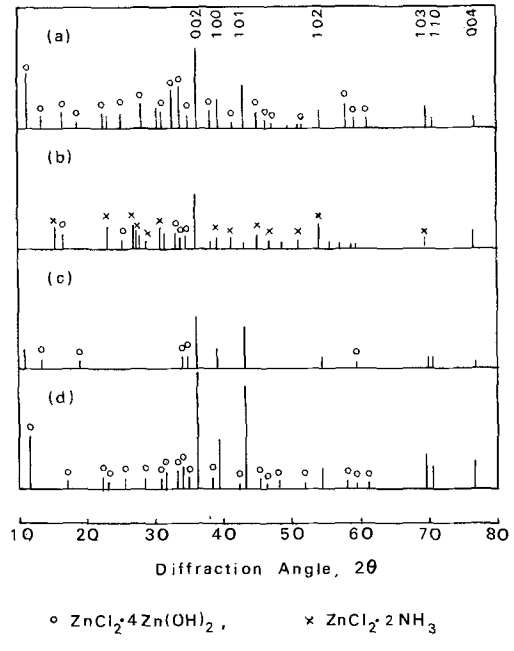

Fig. 4. Typical x-ray diffraction pattern of the zinc can after discharge: (a) and (b) after the heavy discharge, and (c) and (d) after the light discharge.

Figure 5 shows that the reduction of the intensity of the (002) peak is an approximate indication of the light discharge duration. It follows from Fig. 2 and 5 that the closest packed plane may be comparatively insensitive to dissolution during discharge, just analogous to the cases of heterogeneous catalysis with some metals where the closest packed planes are also

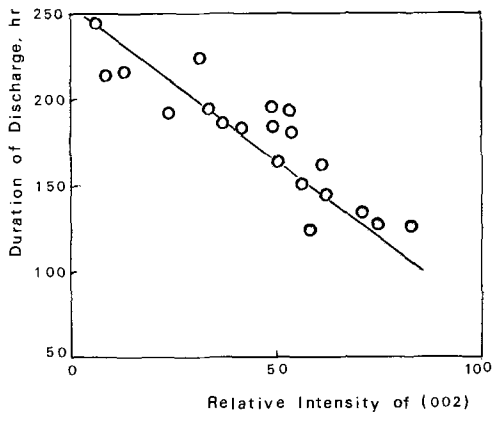

Fig. 5. A parallelism between the light discharge duration and the reduction of intensity of the (002) peak of the zinc anode after discharge.

the most inactive (7). This change was not pronounced in the case of the heavy discharge, probably because many other mechanical stresses would exist latent in the fabricated zinc can. Effects of these may overlap those of crystal orientation in determining changes during high rate drainage. Figure 6 is another indication that the basal planes of the hexagonal zinc lattice (00n), where n = 2 and 4 in the diffraction diagram of Fig. 1 (iii), are slower in the metal dissolution during the light discharge.

Discharge products and performance of dry cells.— An arbitrary rating for the degrees of generation of $ZnCl_2 \cdot 4Zn(OH)_2$ and of $ZnCl_2 \cdot 2NH_3$ was made on the basis of x-ray diffraction charts obtained with the residual zinc anodes. Five ratings were assigned from 1 through 5 for the basic chloride—for instance, the ones such as (a) in Fig. 4 were rated 5, while those such as (b) or (c) were 1. The diammine generation was likewise rated from zero through 3, being zero because a few examples did not produce any appreciable amount of the diammine as in the cases of (a), (c), and (d) in Fig. 4.

Figure 7 was obtained in this way showing that the more the zinc anode dissolved during the light discharge, the less basic chloride was generated. This observation indicates that the migration of zinc ions from the anode penetrates far into the cathode containing MnO_2 during discharge with the better performing batteries. It is therefore implied that most of the zinc precipitating as the basic chloride may come from the zinc chloride in the electrolyte and not from the zinc anode.

Figure 8 shows how the diammine generation is related to the initial voltage of cells; the lower the initial voltage, the more the diammine was generated during the discharge. If the ammonia radical to constitute the diammine is liberated by the oxidation reaction of ammonium ions (8, 9) at an initial stage of

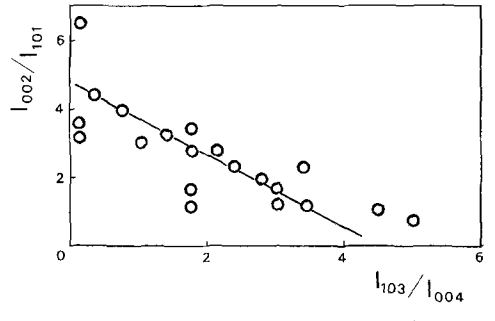

Fig. 6. Relationship between I_{002}/I_{101} vs. I_{103}/I_{004}, two specific intensity ratios of x-ray diffraction peaks, for residual zinc anodes after the light discharge.

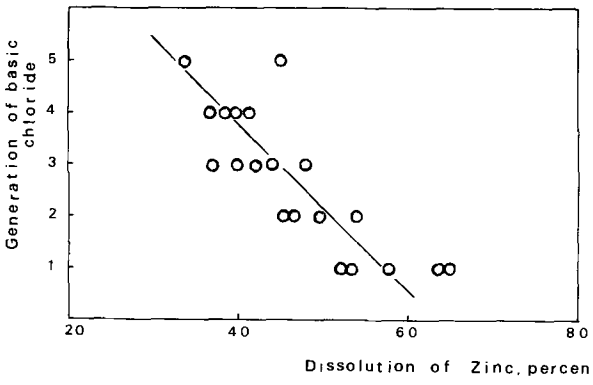

Fig. 7. Metal dissolution from the anode during the light discharge *vs.* the basic chloride generation.

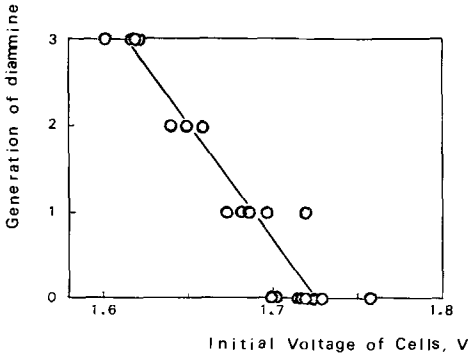

Fig. 8. Diammine generation during the heavy discharge *vs.* the initial voltage of cells.

discharge, the depolarizing power of MnO_2 may more or less participate in giving the relationship in Fig. 8.

$$2MnO_2 + 2NH_4^+ + 2e \rightarrow Mn_2O_3 \cdot H_2O + 2NH_3 \quad [1]$$

$$ZnCl_2 + 2NH_3 \rightarrow ZnCl_2 \cdot 2NH_3 \quad [2]$$

When the MnO_2 used is highly oxidative and its initial voltage is high, an excessive amount of ammonia may be supplied by Eq. [1], and the polyammines can be successively formed through the capture of the ammonia as follows (9, 10).

$$ZnCl_2 \cdot 2NH_3 + 2NH_3 \rightarrow ZnCl_2 \cdot 4NH_3 \quad [3]$$

$$ZnCl_2 \cdot 4NH_3 + nNH_3 \rightarrow ZnCl_2 \cdot (4 + n)NH_3 \quad [4]$$

The polyammines thus formed are rather soluble in a weakly alkaline atmosphere in the Leclanché cathode bobbin during discharge (8, 9, 11). However, when the MnO_2 used is mild in its activity and of low initial voltage, the liberation of ammonia at the initial stage of discharge may be low and just enough for the formation of the diammine; thus, the transformation of diammine to the polyammines may be limited in this case.

The relationship such as plotted in Fig. 8 was not found after the light discharge, probably due to a possible dissolution or transformation of the diammine, if any occurred, during the longer periods of discharge.

Transverse section of zinc anodes before and after discharge.—Figure 9 is a vertically sectioned area of zinc anode before discharge typically observed with the EPMA technique, while Fig. 10 and 11 show typical transverse aspects after the heavy and the light discharges, respectively.

It is interesting to note in Fig. 9(b) and (c) that the lead, which is usually alloyed with the zinc in a small quantity in order to improve the fabrication properties of the metal (12), is distributed in a rather homogeneous fashion together with the zinc base across the transverse section of the can wall. Figure 9(d) for

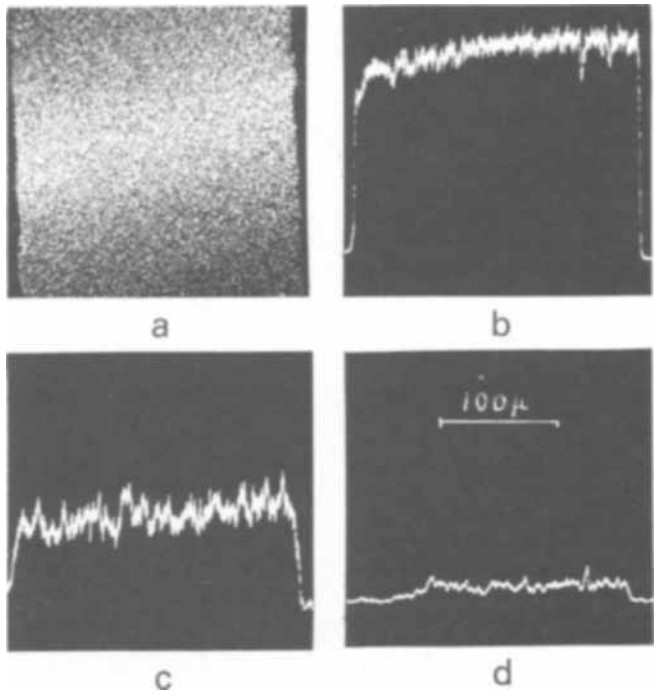

Fig. 9. Typical EPMA images from a vertically sectioned zinc anode before discharge: (a) Zn K_α distribution image, (b) Zn, (c) Pb, and (d) Mn line profiles.

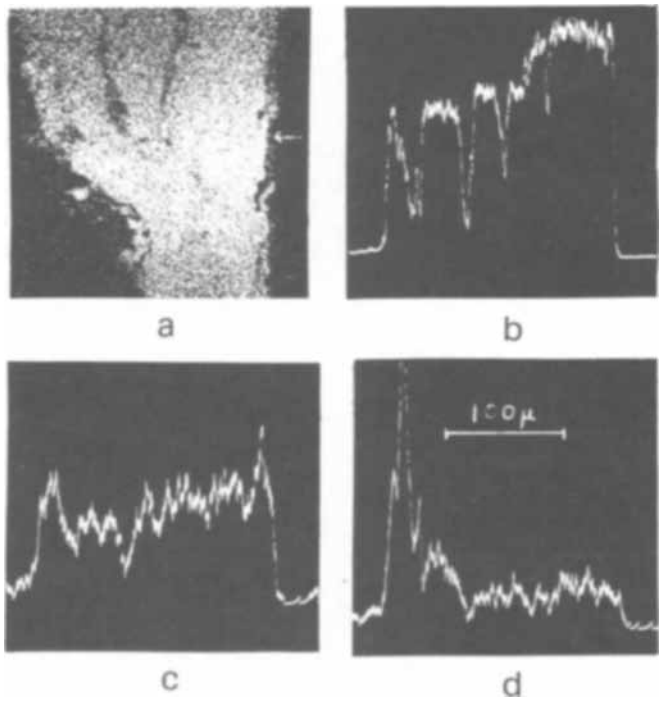

Fig. 10. Typical EPMA images from a vertically sectioned zinc anode after the heavy discharge: (a) Zn K_α distribution image, (b) Zn, (c) Pb, and (d) Mn line profiles.

manganese, although not an additive element to the zinc, was photographed as a blank test of the line profile for observing the movement of this element from MnO_2 after discharge.

After the heavy discharge, it is seen from Fig. 10(a) of the Zn K_α distribution image that the inside of the can (to the left side of the photograph) has been irregularly corroded as a result of the discharge. The line profiles for Zn, Pb, and Mn were obtained across the can at the position indicated with an arrow in Fig. 10(a) and are shown in Fig. 10(b), (c), and (d).

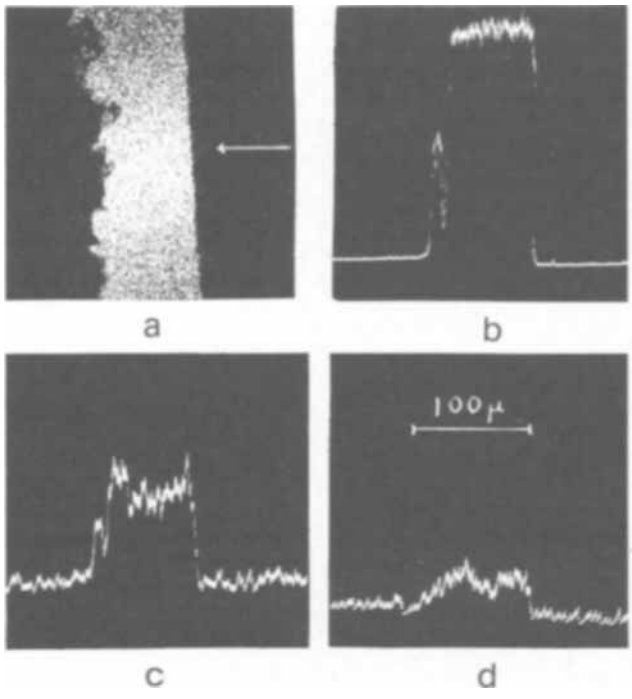

Fig. 11. Typical EPMA images from a vertically sectioned zinc anode after the light discharge: (a) Zn K_α distribution image, (b) Zn, (c) Pb, and (d) Mn line profiles.

A diluted zinc distribution toward the left side in (b) indicates that this element in this region may exist as a compound such as $ZnCl_2 \cdot 4Zn(OH)_2$ or $ZnCl_2 \cdot 2NH_3$ and not as the metal. Although the lead in (c) has come to distribute in a lightly zigzag pattern, a notable local concentration has not occurred.

The manganese line profile in (d), however, possesses an intense peak at the inside of the residual anode after the heavy discharge showing a local deposition of this element. This indicates that the manganese, which was practically absent before discharge as shown in Fig. 9(c), has moved onto this area during the discharge from the anode cake—the only manganese source across the electrolyte paste of the cell.

In the case of the light discharge, the situation is quite different from Fig. 10 as shown in Fig. 11, where the zinc seems to have dissolved rather homogeneously [(a) and (b)]. The lead shows no particular segregation along the transverse region (c) as in the case of the heavy discharge. It is interesting to note that no significant manganese occurrence is seen at the inside wall of the residual anode here (d), except that the background pattern somewhat differs depending on the metal zone and the surrounding resin matrix. It is generally observed as shown in (c) that the thickness of the residual can has become thinner in the light discharge than in the heavy.

Figure 12 shows the mercury line profiles, (a), (b), and (c), together with the backgrounds, (d), (e), and (f), where the pair (a) and (d) is a transversal section before discharge, (b) and (e) the one after the heavy discharge, and (c) and (f) after the light discharge, respectively. The line profiles were obtained with the 1.23863Å Hg $L_{\alpha 1}$ ray. As for the backgrounds, the continuous x-rays at a slightly longer wavelength by 0.016Å from the wavelength of Hg $L_{\alpha 1}$ ray were used by shifting the detecting angle of the microanalyzer by 30 min in angle from the position for the Hg $L_{\alpha 1}$. In this case, overlap of several other elements such as Ge, Sm, W, Yb, Xe, Re, Sb, and Tm would have to be taken into consideration if any of them were present in the specimen, because they could radiate their own characteristic x-rays in the range of 0.016Å shifted from 1.23863Å. However, it is most improbable that these

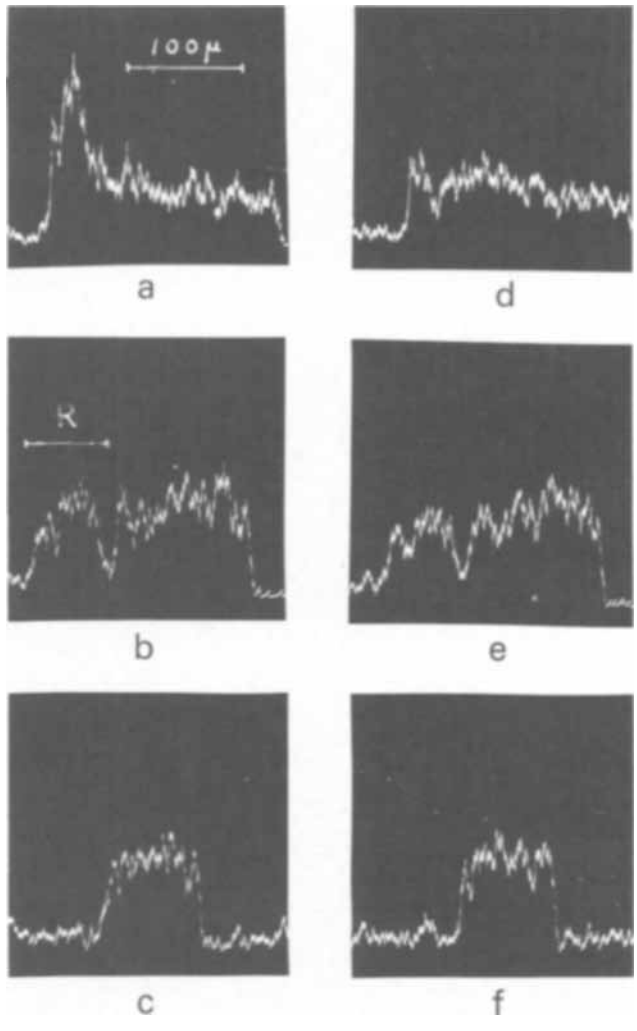

Fig. 12. Typical line profiles of Hg from a vertically sectioned zinc anode before and after discharge: (a) Hg $L_{\alpha 1}$ line profile before discharge with background image (d), (b) Hg $L_{\alpha 1}$ line profile after the heavy discharge with background image (e), and (c) Hg $L_{\alpha 1}$ line profile after the light discharge with background image (f), respectively.

elements exist to any extent in the zinc can used. Therefore, the images of the continuous x-rays taken by means of this technique [(d), (e), and (f)] secures the level of background for the mercury line profiles [(a), (b), and (c)] in Fig. 12.

In Fig. 12(a) and (d), it is observed that mercury was present in the anode wall in the order of 70-80μ deep from the inner surface which was in contact with the electrolyte before discharge. It is to be noted from Fig. 12(b) and (e) that the intensity of the Hg line profile of the region "R" is slightly higher than that of its background, which actually shows that a very small portion of mercury is retained in the discharge products on the surface during the heavy discharge. This is not the case during the light discharge [(c) and (f)]. It is indicated in general that the amalgamated film of the anode dissolved during an earlier period of discharge and the outer electrode regions having no mercury were left at the later stages of discharge.

Migration of manganese onto the zinc anode.—To consider the source of the above manganese deposit, although its chemical formula has not yet been established due to the small amount, the pore size distribution after discharge was measured for the MnO_2 particles taken from the discharged anode mixes of the cells corresponding to Fig. 10 and 11. As illustrated in Fig. 13, the heavily discharged MnO_2 possessed a dis-

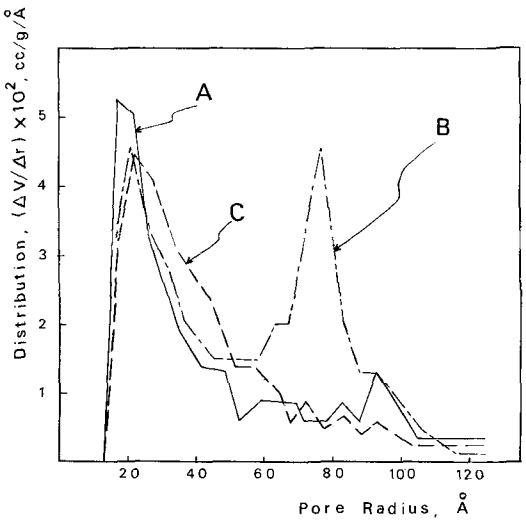

Fig. 13. Shifts in pore distribution in the typical MnO_2 after discharges: (A) before discharge, (B) after the heavy discharge, and (C) after the light discharge, where the X-axis represents the pore size in Angstroms and the Y-axis the distribution of pores expressed in terms of cc/g/Å by using the Barrett, Joyner, and Halenda equation.

tinctly double-headed pore distribution curve (B), one around 20Å and the other around 80Å in size. The initial pore openings distributed around 20Å before discharge (A), and this situation did not change much after the light discharge, only a minute enlargement of the average pore diameter having occurred (C). It should be pointed out that the additional pore openings around 80Å were generated to contribute to the heavy discharge output from the surface region of the MnO_2 particles, while the light discharge proceeded gradually along the paths of initial micropores of the interior. Many earlier workers (13-15) described the formation of Mn^{+2} ions as one of the discharge products of MnO_2. It has been shown here that a part of the Mn^{+2} ions formed can be transported across the dry cell compartments to reach the anode surface, particularly in the case of the heavy discharge.

The above observation will also be understood from the result of the preceding work (5) in which the discharge of MnO_2 particles was found to proceed through two processes, one from the surface and the other along the micropores or cleavages inside of the particles. At the same time, it is to be noted that the movement of the two ions, zinc and manganese, may extend to a greater distance toward their opposing electrodes during discharge of dry cells than has hitherto been expected.

Summary and Conclusions

Experimental study of the behavior of the zinc anode has shown that the mode and extent of its reactions are closely related to battery performance in actual service. The zinc anode dissolved to a greater extent during the light discharge than during the heavy. During the light discharge, the dissolution of the zinc was observed to be approximately proportional to the discharge duration, and the amount of zinc that dissolved was related inversely to the amount of the basic chloride, $ZnCl_2 \cdot 4Zn(OH)_2$ that formed. Although the anodes before use exhibited an intense (002) orientation, the intensity of this peak was reduced by an amount proportional to the light discharge hours. During the heavy discharge, a generation of the diammine, $ZnCl_2 \cdot 2NH_3$, was characteristic when the initial voltage of the dry battery was low. Before discharge, mercury was seen to be present in the anode to a depth of about 70-80μ from the inner surface which had been in contact with the cell electrolyte. It was observed that the inside wall of the anode with the amalgamated film dissolved at an early stage of discharge and the outer electrode regions having no mercury were left after discharge. Manganese ions were observed to have partly migrated from the cathode onto the anode just as the zinc did from the anode to the cathode. The heavy discharge produced additional pores in the MnO_2 that were larger in diameter than the original micropores. It is implied from a technical point of view that developing means of facilitating the mutual transportation of these ions during discharge will be one of the major concerns for improving the discharge performance of Leclanché dry batteries.

Acknowledgments

The author wishes to thank his colleagues, N. Sasaki, for the x-ray diffraction, T. Kobayashi, for the electron probe microanalysis, and M. Yamamoto, for helpful discussions during the course of this investigation.

Manuscript submitted Oct. 29, 1969; revised manuscript received *ca.* March 3, 1970.

Any discussion of this paper will appear in a Discussion Section to be published in the December 1970 JOURNAL.

REFERENCES

1. H. F. McMurdie, *Trans. Electrochem. Soc.*, **86**, 313 (1944).
2. N. C. Cahoon, *ibid.*, **92**, 159 (1947).
3. C. Drotschmann, *Batterien*, **17**, 510 (1963).
4. G. S. Bell, *Electrochim. Acta*, **13**, 2197 (1968).
5. K. Miyazaki, *This Journal*, **116**, 1469 (1969).
6. C. H. Mathewson, "Zinc," p. 413, Reinhold Publishing Corp., New York (1959).
7. G. Okamoto, *Sci. Paper Inst. Phys. Chem. Res.*, **29**, 223 (1936).
8. N. C. Cahoon and G. W. Heise, *This Journal*, **94**, 214 (1948).
9. T. Hirai and M. Fukuda, *Denki Kagaku*, **29**, 794 (1961).
10. T. Takahashi and K. Sasaki, *ibid.*, **25**, 118 (1957).
11. K. Sasaki, "Denchi Handbook," p. 239, Denki Shoin, Tokyo (1964).
12. K. Sasaki, *ibid.*, p. 279.
13. J. M. Cowley and A. Walkley, *Nature*, **161**, 173 (1948).
14. D. T. Ferrel, Jr., and W. C. Vosburgh, *This Journal*, **98**, 334 (1951).
15. A. M. Chreitzberg, D. R. Allenson, and W. C. Vosburgh, *ibid.*, **102**, 557 (1955).

Effect of Atmospheric Exposure on the Contact Resistance of Selected Tin Alloys

Sidney L. Phillips[*,1,2] **and Christian E. Johnson**

National Bureau of Standards, Washington, D. C.

ABSTRACT

Atmospheric exposure of plated specimens in a rural outdoor location showed that both tin-zinc and tin-cadmium alloy coatings on steel maintained a lower contact resistance than did equal thicknesses of tin, tin-lead, or tin-antimony alloys. After exposure for over 2 months, the contact resistances under a 50g load for 5-38 μm thicknesses of tin-zinc and tin-cadmium ranged between 10-100 mohms, although both coatings rapidly lost their luster. The tin-lead alloy maintained the lowest contact resistance of all the coatings tested, although it failed to provide corrosion protection as good as equal thicknesses of tin-zinc or tin-cadmium.

The metal coatings plated onto the structural materials used in the electronics industry sometimes have a dual function (1). On one hand, the coating must provide corrosion protection to the basis metal when exposed to a variety of atmospheric conditions. In addition, the same coating may also be required to present a low contact impedance when joined to another metal which is acting as an electrical conductor. Ficchi has discussed in detail the importance of good electrical bonding between structural surfaces both to provide low impedance paths to ground, and to prevent the accumulation of undesirable static charges at poorly conducting interfaces (1). From the viewpoint of machine design, a low impedance across a region of contact between conductors will also permit joined parts to be considered as a continuous conductor so that calculations can be simplified. In the present work, we report the results of a study which was focused on finding metal coatings that could be plated onto structural steel and meet these two criteria.

Work has been reported on the atmospheric corrosion of metals that were evaluated for use as coatings on the separable electrical conductors used in the electronics industry (2-8). These studies were primarily concerned with metals and alloys that would maintain low interfacial resistances under conditions of sliding contact between the metal parts. It was found that, if the load exceeds about 25g, such metals as gold, tin, rhodium, platinum, and tin-lead alloy maintain contact resistances in the range 1-10 mohms under a variety of exposure conditions for several years (2-5). The precious metals do not appear to be economically feasible either singly or in a duplex coating for structural materials, so that tin or tin-lead alloy would be of greater interest. For this reason, the work described here centers mainly around tin and some selected tin alloy coatings.

Experimental

In the present work, the conditions of exposure included both indoor and outdoor atmospheric exposure and the water-sulfur accelerated aging test (4). The criterion used to rank the various coatings was the change in electrical contact resistance when the metals were exposed to various environments. The measurements of contact resistance were carried out using a procedure similar to that reported in other work (2-8). Of interest also was the degree of rust products observed on the surface of the various coatings, and qualitative observations are included here.

* Electrochemical Society Active Member.

[1] Research Associate from International Business Machines Corporation, at the National Bureau of Standards, Washington, D. C., 1968-1969.

[2] Permanent address: Systems Development Division, International Business Machines Corporation, San Jose, California.

Key words: corrosion, contact resistance, metal plating.

Contact resistance of tin and selected tin alloy coatings.—As noted, tin or tin-lead alloy coatings will maintain contact resistance values in the low milliohm range under a variety of environmental conditions, provided the load exceeds about 50g (4, 5). In addition to the published data on tin and tin-lead alloy, we were able to obtain similar measurements on alloy specimens of tin with cadmium, nickel, and zinc which were kindly furnished by The Tin Research Institute. For the most part, these specimens had been plated in the 1950's and were then stored under different conditions in their laboratory. The various coatings which they furnished together with coating thicknesses, storage conditions, and contact resistance are recorded in Table I. Included also in this table are data obtained for a specimen of tin-zinc which had been plated onto steel by M&T Chemicals, Incorporated, and gold and nickel coated specimens which had been plated at the National Bureau of Standards.

From this table, it can be seen that only the tin-nickel alloy consistently gave the highest and least reproducible readings under all aging conditions. In addition, contact resistance values were less reproducible and comparatively higher for tin-zinc alloy specimens which were passivated with chromic acid prior to storing. This effect can no doubt be traced to the presence of a poorly conducting film on the alloy surface which is difficult to shear so that the formation of metal-to-metal conducting paths is prevented (9). Some of the specimens had been stored in a washroom for 1 yr prior to further storage in the laboratory. In this case, the washroom had an atmosphere which was usually humid and polluted by the gases from the flue of a gas-fired water heater. The pollutants were not identified, but the result was to cause a marked increase in the contact resistance of the exposed samples. Nonetheless, the specimens plated with the tin-zinc alloy coating still gave much lower values than the tin-nickel alloy which had been exposed in a similar manner.

It should be noted that the relatively low values obtained for the tin, tin-zinc, and tin-cadmium alloys are due almost entirely to the softness of the coatings (5). If the load exceeds about 0.1g, the probe tip can shear through surface films and make contact with metal beneath the film so that the measured resistance is lowered considerably (9). Some surface rearrangement took place on the soft coatings when the measurements were made in this work, because shiny spots were observed on an otherwise matte finish at the circle of contact between the probe tip and the plated metal.

In addition to the contact resistance, the current flow through plated finishes at radio frequencies is of interest for electronic applications (1, 10). Contact imped-

Table I. Contact resistance measurements[c] of coated steel specimens from The Tin Research Institute. Applied load, 50g

Coating composition	Coating thickness, μm	Year plated	[a]Contact resistance, milliohms	[b]Resistance ratio	Remarks
Gold	3.8	1967	2.3 ± 0.2	—	Plated by NBS.
Tin	25	1953	2.0 ± 0.3	1.0	Stored in laboratory.
75 Tin-25 cadmium	25	1953	3.3 ± 0.6	1.4	Stored in laboratory.
50 Tin-50 cadmium	25	1953	3.1 ± 1.2	1.3	Stored in laboratory.
Tin-zinc	25	1953	4.3 ± 0.9	1.7	Stored in laboratory.
Tin-zinc	7.6	1964	2.3 ± 0.2	1.0	Stored in laboratory.
Tin-zinc	13	1952	40 ± 30	20	Chromic acid passivated.
Tin-zinc	13	1952	*	*	Chromic acid passivated; washroom 1 yr.
Tin-zinc	13	1952	8.6 ± 4.1	3.7	Polished. Stored in laboratory.
Tin-zinc	13	1952	51 ± 35	22	Polished. Wash room 1 yr.
Tin-zinc	13	1956	2.0 ± 0.1	1.0	Handled. Stored in laboratory.
Tin-zinc	18	1968	3.2 ± 0.7	1.5	Plated by M&T. Stored in laboratory.
Tin-nickel	25	1956	4400 ± 2600	1900	Stored in laboratory.
Tin-nickel	30	1958	235 ± 150	100	Stored in laboratory.
Tin-nickel	25	1962	135 ± 50	60	Stored in laboratory.
Tin-nickel	30	1958	170 ± 40	75	Stored in laboratory.
Tin-nickel	10	1955	$>10^6$	∞	Wash room 1 yr.
Tin-nickel	10	1955	$>10^6$	∞	Fingerprinted, then exposed in open laboratory for 1 yr.
Nickel	50	1967	40 ± 17	17	Stored in laboratory.

[a] Average and average deviation of 6-10 determinations.
[b] Ratio of measured contact resistance to that of gold.
[c] Measurements were made at NBS in 1968.
* Surface severely discolored and pitted. Nonuniformity prevented meaningful data.

Table II. Contact impedance of coated steel specimens from The Tin Research Institute. 15° Measurement obtained by rotating probe tip 15° under a 25g load

Specimen	Contact impedance, milliohms, at frequency indicated											
	10 kHz initial	+15°	100 kHz initial	+15°	500 kHz initial	+15°	1 MHz initial	+15°	10 MHz initial	+15°	30 MHz initial	+15°
100Sn	4.5	3.8	3.9	2.4	7.9	7.2	13.4	13.0	109	109	295	295
75Sn-25Cd	3.0	4.2	3.0	3.5	6.5	6.6	10.3	10.1	77	77	207	205
50Sn-50Cd	3.8	2.6	3.0	2.6	6.2	6.1	10.2	10.2	82	82	220	220
Sn-Zn	6.8	5.7	6.4	5.5	9.2	8.6	12.5	12.2	70	70	185	185
Sn-Zn	3.7	2.5	3.1	2.5	6.6	6.1	10.4	10	71	71	189	189
Sn-Zn	4.5	3.6	5.1	2.7	7.8	5.7	11.4	9.6	75	74	200	197
Sn-Zn	923	20	915	20	920	22	925	24	900	75	840	190
Sn-Zn	7.0	4.2	7.0	4.0	10.0	7.8	14.0	12.0	26.5	26.5	223	223
Sn-Zn	4.5	4.0	4.1	3.5	5.9	5.9	7.5	7.8	8.9	18	17	36
Sn-Zn	39	4.2	40	4.2	42	15.2	44	18	81	70	187	178
Sn-Ni	2570	800	2520	800	2510	800	2520	800	2440	775	2220	793
Sn-Ni	238	121	230	121	233	124	235	128	242	147	273	222
Sn-Ni	7050	830	7650	830	7900	840	7900	835	8000	820	8100	800
Sn-Ni	4400	4400	4300	4350	4300	4350	4300	4350	4100	4100	3700	2730
Sn-Ni	250	63	247	63	250	67	252	69	261	110	305	213

ance measurements covering the frequency range 10 kHz to 30 MHz were obtained on specimens selected from Table I, and results are recorded in Table II. The presence of poorly conducting films was demonstrated by rotation of the probe tip under a sufficient load during contact, which had the effect of shearing through surface films so that metal-to-metal contact was established (4, 9). In the present work, the probe was rotated 15° and the usual result was a lowering of the contact impedance as shown in Table II. The decrease in contact impedance was especially marked for the specimen coated with tin-zinc alloy, which had been polished and stored in the washroom before final laboratory storage. The initial contact impedance fell between 840-923 mohms as compared with 20-190 mohms after rotation. Similar decreases were also obtained for all but one of the specimens coated with tin-nickel alloy, thus showing an important difference between sliding and static modes of electrical contact.

Other alloys of tin with bismuth and antimony were prepared by melting and mixing the pure metals under an argon atmosphere, and contact resistance values were obtained before and after atmospheric exposure tests including the sulfur-water accelerated aging test (3, 4). Although the alloy surfaces were discolored after exposure, the contact resistance values were only 4-20 mohms.

Based on the above results, it was concluded that tin and some tin alloys could provide corrosion protection to steel while also maintaining a low contact impedance under various conditions of exposure. Tin, and selected tin alloys were plated onto steel specimens for investigation in the atmospheric tests.

Preparation and plating of test specimens.—The test specimens were cut from sheets of cold rolled No. 3 finish steel, SAE 1010, one side of which had been polished bright, with a No. 4 temper. Each specimen was numbered near one corner using a steel die, and a narrow strip was cut halfway across the top, then turned over at a right angle to serve as a hanger (11). A hole was drilled in the center of this hanger, and the specimen was screwed to a plating rack. The rack held ten 3.4 x 7.6 x 0.09 cm specimens arranged in two rows of five each. The specimens were cleansed using conventional electrolytic methods, rinsed and washed with water, and finally dipped into 10% hydrochloric acid. The absence of a water break after this last dip was taken as the criterion for a clean metal surface.

Plating followed conventional procedures, with both the bath formulations and the plating conditions used being based on published data (12, 13). For each coating, three thicknesses were plated to include the ranges 2-5, 7-12, and 20-39 μm. Before exposing to the atmosphere, the surface of each specimen was finished by manually polishing with wet 600 grit silicon carbide paper. The hanger then was cut out of each specimen, and the area around the cut was painted over with stopoff lacquer.

Atmospheric exposure.—Individual specimens were placed in position on porcelain knob insulators screwed into place at predetermined positions on an aluminum

Table III. Effect of outdoor exposure on the electrical contact resistance and appearance of coated steel specimens

Key to letter rankings: A. No visible rust to the unaided eye. B. Slight rust. C. Some rust. D. Better than 50% of surface covered by rust.

Coating	Thickness, μm	[a]Contact resistance in milliohms Days exposed 0	7	24	35	65	Appearance Days exposed 3	10	17	24	35	40	65
Stannate tin	5	2.1	4.6	$>10^6$	—	—	D	D	D	D	—	—	—
	13	1.0	1.3	2-10	$>10^6$	—	A	A	A	B	C	C	D
	38	1.2	1.4	3-10	35	10^2-10^6	A	A	A	A	B	B	B
Bright tin	2.5	1.3	30	10^3	$>10^6$	—	D	D	D	D	D	D	—
	10	1.1	2.0	3-10	10^3	$>10^6$	C	C	C	C	D	D	D
	28	1.0	1.5	3-10	10-20	$>10^6$	B	B	B	B	B	C	D
[b]80% Tin	5	1.8	2.2	3-5	5-10	10-100	A	A	A	A	A	A	A
20% Zinc	13	1.9	2.5	3-5	5-10	20-30	A	A	A	A	A	A	A
	38	1.3	1.7	3-5	5-10	10-30	A	A	A	A	A	A	A
[b]67% Tin	2.5	1.1	10^2-10^3	$>10^6$	—	—	D	D	D	—	—	—	—
33% Lead	10	1.0	1.4	2-5	2-5	2-10	C	C	C	C	C	C	D
	33	1.0	1.0	2-5	2-5	2-5	A	A	B	B	B	B	B
[b]80% Tin	2.5	2.1	4.2	$>10^6$	—	—	B	C	D	—	—	—	—
20% Cadmium	13	1.5	2.3	5-10	10-20	10^2-10^3	A	A	A	A	A	A	A
	38	1.0	1.5	3-10	10-20	10-50	A	A	A	A	A	A	A
[b]Tin-antimony	2.5	Not exposed.											
(0.4% Sb)	10	1.5	2.2	10-50	10^3	$>10^6$	B	B	B	C	D	D	D
	28	1.5	1.4	5-10	5-10	10^2-10^4	A	B	B	B	B	C	C

[a] Average or range of six readings. [b] Composition determined by chemical analysis.

rack (11). The knobs held the specimens about 2 cm above the aluminum frame so that there was no metal-to-metal contact that could result in formation of an electrolytic cell. To minimize stress corrosion, the specimens were free to move slightly, but they could not be dislodged by a strong wind or a sharp blow. For outdoor exposure, the rack was inclined at about a 45° angle from the horizontal, and the specimens were placed so that the edge with the lacquer pointed down. The specimens undergoing exposure indoors were not inclined and lay flat in a horizontal plane. Both sets of specimens were observed at intervals to follow the effects of corrosion, and to measure any changes in contact resistance.

After 65 days of exposure indoors, there was neither a significant change in contact resistance nor observable rust products on any of the specimens. After the same length of exposure outdoors, only the three specimens coated with tin-zinc and the two specimens coated with the thicker tin-cadmium did not show any significant rust products. These outdoor specimens were tarnished so that the original metallic luster was replaced by a dull grayish color, while all the other specimens showed surface rust products. As might be expected, the amount of surface rust products was less marked for the specimens with thicker plated coatings.

The data obtained from the outdoors exposure test are given in Table III, where observations with the unaided eye of the extent of corrosion, and measurements of the contact resistance, are recorded as a function of time. Included also in this table are the times when corrosion was initially observed, and the times at which corrosion or corrosion products were judged to cover better than 50% of the surface of the metal coating. Rusting around the edges was discounted somewhat when recording data for this table, and a greater weight was assigned to the extent of rusting away from the edges. The enhanced corrosion caused by accumulation of moisture at points where contact was made between the edges of the specimen and the porcelain knobs was also discounted to some extent. Measurements of the contact resistance were discontinued on specimens which showed rust and rust stains over better than 50% of the surface. In these cases, values of the contact resistance depended on the portion of the surface which made contact with the probe tip, and the readings ranged between low milliohms and high ohms.

The specimens coated with tin-zinc alloy and those coated with the two thickest tin-cadmium alloy have been the outstanding performers in the outdoor exposure tests. While the surfaces of these specimens were dulled and covered by oxide films and particulate matter such as dust, there was no visible rust on the surface, including the edges and places where contact was made with the porcelain knobs. Three weeks after the original specimens were exposed, 2.5 μm thick coatings of both the tin-zinc and tin-cadmium alloys were exposed outdoors along with duplicates of the other three thicknesses of tin-zinc. In agreement with the earlier results, the 2.5 μm tin-cadmium coating showed appreciable rust within 7-10 days. On the other hand, the 2.5 μm coating of tin-zinc did not show any environmental effects for about 30 days, after which slight rusting around the edges and at a spot on the surface was observed. On the basis of these results, the tin-zinc alloy coating has provided somewhat better corrosion protection to steel when exposed outdoors than has the tin-cadmium coating. For both coatings, the contact resistance was less than 10 mohms on surfaces not covered by rust or rust products.

From measurements of the contact resistance of the specimens obtained from The Tin Research Institute, results of the water-sulfur environmental tests, and the exposure data obtained to date, we conclude that tin-zinc and tin-cadmium alloy coatings will best maintain a low contact resistance for long periods of time.

Acknowledgments

The Tin Research Institute furnished the steel specimens coated with tin alloys, and M&T Chemicals, Incorporated, furnished a tin-zinc coated specimen. Abner Brenner, Vernon Lamb, Eugene Damm, and Fielding Ogburn provided guidance during the course of the project, and Art Bunch furnished the contact impedance measurements.

Manuscript submitted Oct. 31, 1969; revised manuscript received *ca.* Feb. 20, 1970.

Any discussion of this paper will appear in a Discussion Section to be published in the December 1970 JOURNAL.

REFERENCES

1. R. F. Ficchi, "Electrical Interference," p. 29, Hayden Book Co., Inc., New York (1964).
2. U. B. Thomas, Intern. Res. Symposium on Electric Contact Phenomena, Univ. of Maine, Orono, Maine (1961).
3. R. F. Walton, *Plating*, **53**, 209 (1966).
4. R. V. Chiarenzelli, *Proc. Eng. Seminar on Electrical Contacts, Univ. of Maine, Orono, Maine* (1965); *ibid.* (1966).
5. K. G. Compton and R. G. Baker, *ibid.*, Penn. State Univ., University Park, Pa. (1960).
6. M. Antler, *Plating*, **53**, 1431 (1966).

7. H. C. Angus; *Trans. Inst. Met. Finishing*, **39**, 20 (1962).
8. R. Holm, "Electric Contacts," 4th Ed., Springer-Verlag, New York (1967).
9. M. Cocks, *Proc. Phys. Soc., London*, **B67**, 238 (1954).
10. A. M. Fowler, *Plating*, **55**, 1277 (1968).
11. W. Blum, P. W. C. Strausser, and A. Brenner, *J. Res. Nat. Bur. Std.*, **13**, 331 (1934).
12. A. Brenner, "Electrodeposition of Alloys," Academic Press, London and New York (1963).
13. "Electrodeposition of Alloys," V. A. Averkin, Editor, Office of Technical Services, U.S. Dept. of Commerce, Washington, D.C. (1964) (English Translation).

The Structure of Ferric Compounds Introduced into Layers of Electrolytically Formed Aluminum Oxides

Z. Alexan, M. Bornaz, A. Calusaru, G. Filoti, A. Gelberg, and E. Romas

Institute of Atomic Physics, Bucharest, Rumania

ABSTRACT

By means of Mössbauer effect, x-ray, and infrared methods, we have studied samples of electrolytically formed aluminum oxide in which a ferric compound was introduced by immersion in ferric chloride solution. Two kinds of thin films were obtained: (*a*) with brown color and (*b*) with yellow color. At room temperature, both samples show a quadrupole splitting. At liquid nitrogen temperature, the Mössbauer spectrum has two lines in the first case and six in the second. After heating at 673°K, the spectra of both samples were taken at 77°K. They display a magnetic splitting, but the effective field value is different for each sample. The characteristic parameters of the spectra show that the ferric compounds are not in a simple oxyhydroxide form on the aluminum oxide surface, but that some combination with aluminum oxide had occurred.

The method of electrolytic oxidation is particularly important in the case of aluminum (1) due to the properties of Al_2O_3 layers formed on the metal surface, which have a high adhesion and an expansion coefficient close to that of metallic aluminum. The improvement of the properties of aluminum oxide would be of practical importance due to the large-scale use of electrolytic oxidation of aluminum in industry. By extension of chemical combinations, particularly the combination of aluminum oxide with nickel oxide, new properties can be obtained, *e.g.* higher compactness, increased endurance to external agents, or a new color. The purpose of the present work is to study the iron and aluminum oxide combination from the standpoints of both preparation method and chemical structure. Structure studies were made using Mössbauer spectroscopy of ^{57}Fe.

Experimental

In the case of aluminum and iron oxide layer preparation, we can distinguish two stages: (*a*) electrolytic oxidation leading to Al_2O_3 layers and (*b*) aluminum oxide combination with ferric compounds.

1. The aluminum oxidation was carried out using a classical method (2); the electrolyte was 30% H_2SO_4 solution at room temperature, 2 A/dm^2 current density, and an oxidation time of 30 min. The aluminum foil of 0.1 mm thickness had a purity of 99.99%.

2. The aluminum oxide combination with ferric compounds was carried out by immersion of the oxide layer in a ferric chloride solution. The anodic oxide was first washed in distilled water, in concentrated ammonia, and again in distilled water. A ferric chloride concentration of 100 g/liter was employed, at 98°C, with an immersion time of 1 min for each sample. The *p*H of this solution was not controlled, but neither $FeCl_3$ concentration nor solution *p*H caused differences in results.

Two kinds of layers can be obtained by this procedure: one yellow and the second brown, but it was not possible to establish the experimental conditions needed to obtain only one or the other.

3. Measuring techniques. The x-ray spectra were measured using conventional apparatus, the Mössbauer spectra were obtained by means of a sinusoidal velocity drive (3), and the infrared spectra with a Zeiss spectrometer. The ^{57}Co source was embedded in a copper lattice. The thermal treatment was carried out in a Pt Mössbauer oven. The temperature was maintained at 673° ± 2°K. The spectra at 80°K were recorded by means of a simple nitrogen cryostat.

Results

X-ray diffraction.—The aluminum oxide layers containing ferric compounds were scraped from the aluminum support and the powder was analyzed by x-ray diffraction using the Debye-Scherrer method. The 11 lines were compared with data from literature (4). Their structure was found to be close to that of β-FeOOH, γ-FeOOH, or α-Fe_2O_3 structure, because all these forms of iron compounds give similar patterns. Therefore, we can conclude that x-ray diffraction cannot give a reliable answer concerning the chemical structure of the layers.

Mössbauer spectra.—The Mössbauer spectra were taken of both yellow and brown samples at the treatment temperatures, *viz.* 80°, 298°, and 673°K. The temperature of 673°K was the upper limit for treatment due to the aluminum backing.

The brown sample spectra show a quadrupole splitting both at room and 80°K temperature before thermal treatment, and display a magnetic splitting at 80°K after thermal treatment (Fig. 1, a and e).

The yellow sample at 80°K shows a magnetic splitting both before and after thermal treatment, but at room temperature shows only a quadrupole splitting (Fig. 2, a and e). Each thermal treatment was carried out for 1 hr.

Infrared spectra.—In order to establish more precisely the composition of ferric compounds in the aluminum oxide layers, we recorded the infrared spectra for both yellow and brown samples. In Fig. 3, a comparison is made between infrared spectra of β-FeOOH

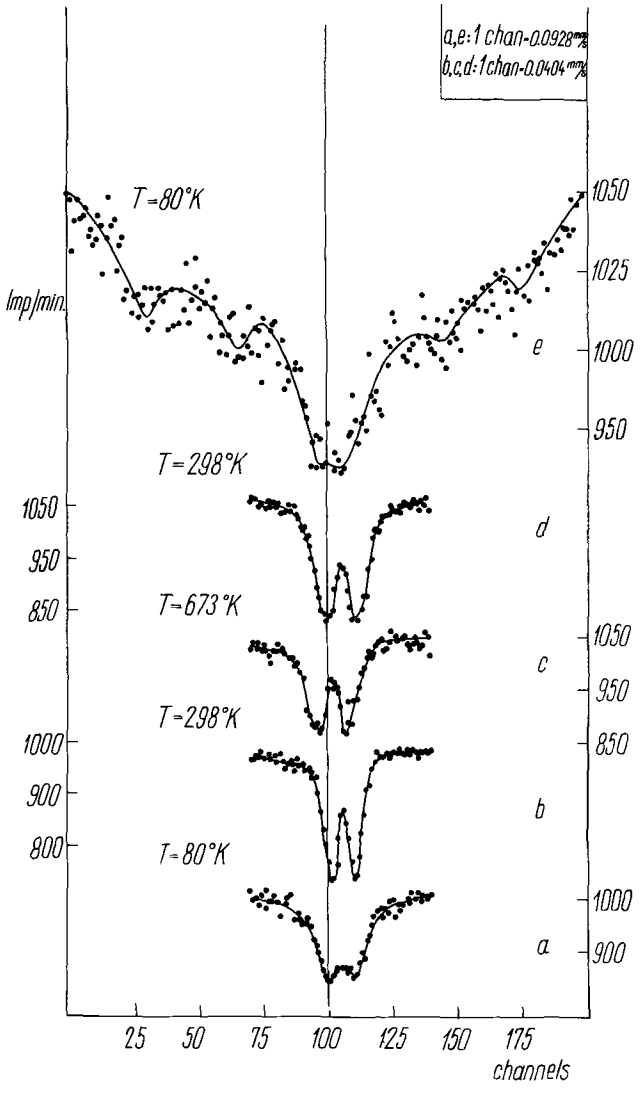

Fig. 1. Mössbauer spectra of brown sample (A)

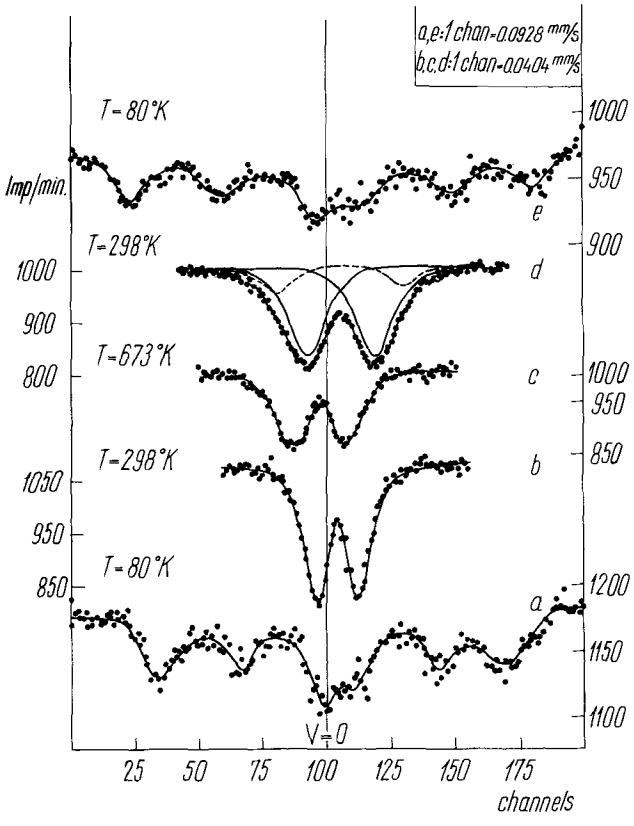

Fig. 2. Mössbauer spectra of yellow sample (B)

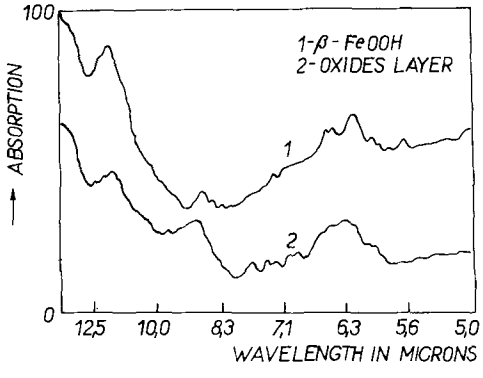

Fig. 3. Infrared spectra of both brown and γ-FeOOH samples

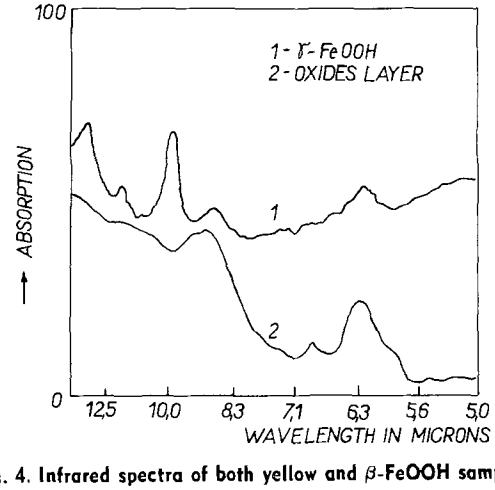

Fig. 4. Infrared spectra of both yellow and β-FeOOH samples

and of the yellow sample. There is some degree of correspondence between these substances and it seems reasonable to propose that the yellow sample is a β-FeOOH compound. These results agree well with the Mössbauer spectra. The peaks corresponding to the oxide layer are more flattened owing to the presence of aluminum oxide in the sample.

The same comparison between infrared spectra of γ-FeOOH and the brown sample is given in Fig. 4. It is possible to observe some peaks in both spectra at the same wavelength, for instance at 8.9 and 6.2μ, but there are other peaks existing in the spectra of the γ-FeOOH sample only. This fact may indicate some analogies in the structure of both compounds. However, it seems difficult to conclude that the samples are identical.

Discussion

The ferric compounds, formed by immersion of aluminum oxide layers into ferric chloride, could either be an iron compound by itself or a chemical combination between iron and aluminum oxides. These possibilities may be described by the following reactions:

$$2\,FeCl_3 + y\,Al_2O_3 + z\,H_2O = (Fe_2O_3)_x\,(H_2O)_z\,(\text{ads.})\,(Al_2O_3)_{y-x} + 2x\,AlCl_3 \quad [1]$$

$$2\,FeCl_3 + y\,Al_2O_3 + z\,H_2O = (Fe_2O_3)_x\,(Al_2O_3)_{y-x}\,(H_2O)_z + 2x\,AlCl_3 \quad [2]$$

The problem is to establish which type of compound is formed.

As it was shown, x-ray diffraction cannot distinguish between several iron oxides and oxyhydroxides, so that other methods had to be used in order to decide which of the two reactions takes place in our case. Mössbauer spectroscopy is able to establish the structure of compounds with general formula FeOOH or Fe_2O_3. In the

Table I

Brown sample (A)

No.	Sample	Temp, °K	Quadrupole splitting, mm/sec	Magnetic splitting, mm/sec	Isomer shift, mm/sec
1	Untreated	77	0.666		+0.333
2	Untreated	298	0.666		+0.444
3	During the treatment	673	0.852		+0.130
4	Treated	298	0.852		+0.426
5	Treated	77		14.12	+0.06

Table II

Yellow sample (B)

No.	Sample	Temp, °K	Quadrupole splitting, mm/sec	Magnetic splitting, mm/sec	Isomer shift, mm/sec
1	Untreated	77		13.42	+0.045
2	Untreated	298	0.603		+0.175
3	During the treatment	673	0.616		−0.121
4	Treated	298	1.050 2.178		+0.222 +0.202
5	Treated	77		15.73	+0.15

case of FeOOH type combinations (5), the α-form presents magnetic splitting both at room temperature and at 110°K, the β-form shows a quadrupole splitting at room temperature and a magnetic one at 110°K, and the γ-form displays at both room temperature and at 110°K only a quadrupole splitting. Obviously, the corresponding Mössbauer spectra indicate characteristic values for both quadrupole splitting and isomer shift.

It seems at first sight from the Mössbauer spectra that the brown sample belongs to a compound of γ-FeOOH. The spectra at both room and 80°K temperatures present a quadrupole splitting, but their characteristic values were different from literature values. Indeed, the infrared spectra show that the brown sample is not identical to γ-FeOOH. In this case, it may be possible that a combination between γ-FeOOH and Al_2O_3, as indicated by the second proposed reaction, is formed. The formation of such a compound explains the difference of the quadrupole splitting and isomer shift between the present spectra (Table I) and the other known data (5). After thermal treatment, the resulting compound had completely new characteristics which were considerably different from those of the initial compound.

The yellow sample, without thermal treatment, presents a 80°K spectrum with a Zeeman splitting superimposed on a quadrupole spectrum. At room temperature, only a quadrupole splitting is left with a value different from that of the brown compound.

The values of the quadrupole splitting both at room and 80°K temperature differ from the values corresponding to β-FeOOH by about 15-20% (Table II).

The infrared spectra (Fig. 3) show a close analogy between β-FeOOH and the yellow sample. In this case, no combination with Al_2O_3 is formed, the ferric compound being adsorbed only on the aluminum oxide surface.

After thermal treatment, the spectra are strongly different from the corresponding one obtained with untreated samples (Fig. 2, d and e). The room-temperature spectra (Fig 2d) of the two wide lines can be decomposed in two doublets. The quadrupole splitting values are larger than those obtained before treatment. At 80°K, there also was an increase in the distance between the extreme lines *vs.* the same spectrum taken before the thermal treatment: Fig. 2a.

In addition, the yellow sample was subjected, for 16 hr, to thermal treatment to see if it was transformed into α-Fe_2O_3 configuration (7). This treatment brought about no modification of the structure, and this is additional proof that the spectrum corresponds to a more complicated compound.

Manuscript submitted Sept. 29, 1969; revised manuscript received *ca.* March 2, 1970.

Any discussion of this paper will appear in a Discussion Section to be published in the December 1970 JOURNAL.

REFERENCES

1. L. Young, "Anodic Oxide Films," Academic Press, London and New York (1961).
2. J. Salauze, "Traité de Galvanoplastie," Dunod, Paris (1957).
3. M. Bornaz, G. Filoti, A. Gelberg, V. Grabari, and C. Nistor, *Nucl. Instr. Methods*, **40**, 61 (1966).
4. ASTM—Tables.
5. T. Takada, M. Kiyama, Y. Bando, T. Nakamura, M. Shiga, T. Shiujo, N. Yamamoto, Y. Endoh, and H. Takaki, *J. Phys. Japan* **19**, 1744 (1964).
6. W. Kündig H. Bömmel, G. Constabaris, and R. H. Lindquist, *Phys. Rev.*, **142**, 327 (1966).
7. I. Dézsi, L. Keszthelyi, D. Kulgawczuk, B. Molnar, and N. A. Eissa, *Phys. Status Solidi*, **22**, 617 (1967).

Gold-Alloy Electrodeposits—Phase and Microstructural Changes Induced by Heat Treatment as Revealed by X-Rays

A. F. Mohrnheim

Metallurgical Research and X-Ray Laboratory, University of Rhode Island, Kingston, Rhode Island

ABSTRACT

Changes in composition and microstructure of gold-alloy electrodeposits caused by thermal treatment at relatively low temperatures, 100°-500°C, are revealed by semiquantitative x-ray diffraction analysis. The metallurgical characteristics of gold-nickel and gold-cobalt plates deviate from known equilibria shown by the temperature-composition or phase diagrams of the thermally alloyed systems. The plates as deposited are essentially single phase, metastable supersaturated, solid solutions. Thermal treatment of the Au-Ni plate causes precipitation of a Ni-rich phase; the precipitates of the Au-Co plate are practically pure, allotropic modifications of Co.

In general, electroplaters are concerned with: (*a*) the composition of the plating bath, (*b*) the conditions of the electrodeposition process, and (*c*) the resulting chemical and physical properties of the metal deposit. This report deals exclusively with the metallic structure of the deposit which naturally determines its physical properties. The bath and the process are not dealt with in detail because the plates were submitted as plated from proprietory baths containing metal chelates. We believe that such baths can be bought from a number of supply sources. Of course, no guarantee can be given that similar baths will reproduce exactly what has been found from the intensive study of electroplates from three commercially available bath formulations.

Previous Investigations

In a recent comprehensive treatise on electrodeposition of alloys by Brenner (1), it is stated: "The only reference to the structure of (gold-nickel) electrodeposited alloy is that of Raub (2). His x-ray diffraction examination showed that in alloys containing up to 6% nickel the lattice constant of gold was unchanged and that of nickel was expanded about 2%. Apparently the alloy was not a single phase like the equilibrium thermal diagram."

Our x-ray study leads to different conclusions. This difference, however, does not prove that these previous findings are erroneous since they were obtained from alloys plated from baths of different composition. Russian investigators (3) have reported that cobalt does not codeposit with gold. "However, Raub and Bihlmeier (4), mentioned obtaining deposits that contained from 0.4 to 0.8% of cobalt. Since there is some doubt that the deposit contained cobalt, their hardness must be attributed to their small grain size and perhaps to the presence of inclusions (1)."

Results of our x-ray studies, obtained from samples plated in baths containing complexing agents, differ from the above and were published in a preliminary detailed research report (5). Additional analytical data and supporting facts are presented in the following. The previous paper also reported observations and a semiquantitative analysis of preferred orientation in Au electrodeposits which, therefore, are not further discussed.

Theory

The angular position of x-ray diffraction peaks or lines (2θ-degrees), as expressed in Bragg's law, is a function of the interplanar spacing. Using this law and basic space relations, the lattice parameter, a (edge length of unit cell), can be computed. Since a varies in solid solutions (S.S.) with the concentration of the solute, changes in a can be related to changes in phase composition induced by heat treatment. Using Vegard's fundamental law (6), information can be gained about phase equilibria and phase changes by precipitation from supersaturated S.S. Vegard's law states that, in continuous S.S. of ionic salts, the lattice parameter of the solution is directly proportional to the atomic per cent (a/o) of solute present. Though this relationship is not strictly obeyed by metallic S.S., it is widely used for comparison. Complicating factors, limitations, and supporting evidence justifying the application of this method in this work are discussed later.

Changes in angular 2θ position and in the shape or profile of the x-ray diffraction peak caused by heat treatment can be interpreted as changes in the sample's microstructure. This is true because the height and breadth (width) of a recorded peak is influenced by residual microstresses, fine particle (grain) size smaller than 10^{-5} cm, and lattice imperfections. By systematically following changes in height and breadth of a diffraction peak due to heat treatment, the temperature range where recovery or grain growth occurs can be determined by plotting sample temperature *vs.* x-ray diffraction data.

Samples

Each of the Au electroplated specimens investigated measures 5 x 2.5 x 0.3 cm with a highly reflective surface on one side only. This side has been used for x-ray measurements. The samples as received have a Au deposit of about 10 μm (0.4 mils) electroplated on pure Cu mostly with a Ni interliner electroplated on top of the Cu surface before the Au deposition.

The electroplates have been deposited from three different commercial baths (7). Acidic bath A deposited bright, industrially pure Au with little Co. Acidic bath B deposited bright, industrially pure Au with little Ni. Both baths are operated at 32°C (90°F) with agitation, at 5 A/ft^2 current density, having 7.5 g/liter (1 oz/gal) Au with Co or Ni chelates and brighteners as additives. Bath C, a low cyanide bath (pH 8-10), deposits a bright Au deposit with about 1 w/o Ag and is operated under the same conditions as the other baths except at a slightly higher bath temperature, 38°C.

Since deposits from the Au-Ag bath, as previously reported (5), do not show changes in angular position of the diffraction peak nor in the peak profile due to heat treatment, they have been used as a control and for comparison. X-ray data for plates from this bath are shown in this article only in the "as-plated" condition.

In order to investigate the possible influence of the Cu substrate on the deposit, one Au-Co sample has been plated directly on the Cu without a Ni interliner. This sample indeed behaves differently due to early diffusion of the Cu atoms into the Au alloy plate at a relatively low-temperature heat treatment, as is shown later.

Experimental Procedures

The Au-plated samples have been treated and investigated as shown in the stepwise scheme below:

1. Scan samples as received.
2. Heat samples in air for a certain time in an oven at constant temperature.
3. Cool samples in air to room temperature (R.T.).
4. After cooling, scan samples and record x-ray diffraction peak on strip chart.
5. Compare peak profile and derive characteristic data before and after every heat treatment.
6. If there are changes in peak location and/or profile, reheat to the same temperature extending the time of thermal exposure.
7. If no further change is observed by the last treatment, increase the temperature, heat for a certain time, and repeat from No. 3 above.
8. Record and evaluate all changes, plot temperature *vs.* x-ray data, and find the temperature where the changes are most pronounced.

The time duration for the 1st heat treatment at a certain temperature had been 1 hr; most of the 2nd treatments at this temperature were 2 hr duration, that is, a total of 3 hr at the same temperature. If no distinct changes were observed after the last heat treatment, the experiments were continued at the next higher temperatures. The chosen temperatures (R.T., 100°, 175°, 200°, 240°, and 380°C) have been based on preliminary experiments and the ranges of available heating ovens. Slightly different temperature intervals, as will be indicated, have been chosen for duplicating experiments with other samples of Au-alloy plates.

Methods of Analysis

The *ideal* x-ray diffraction pattern of pure Au powder (8) has been considered the standard for comparing samples. A pure Au powder which has been prepared by the author and the Au-Ag deposit from bath C were found to produce almost identical diffraction patterns in contrast to the Au-Co and Au-Ni electroplates. All samples have been scanned under the same x-ray operating condition.

The diffraction patterns of the Au alloy electroplates as received, when compared with the standards, show striking differences of relative peak intensity [based on the strongest diffraction (111) of pure Au, $I/I_1 = 100\%$], peak profile (height and width), and peak location (diffraction angle, 2θ).

Significant differences in x-ray line characteristics between standards and Au-alloy deposits can be interpreted by differences in microstructure and in chemical composition, as is discussed later.

A definite proof of the presence of the alloying elements in the deposits has been obtained by the detection of the characteristic fluorescent radiation of Co and Ni recorded by conventional x-ray spectrographic techniques. For the detection of Ni in the deposit, the possible contributing Ni radiation from the Ni underplate and Ni impurities in the x-ray tube have been checked and are found to be insignificant in comparison with the intense Ni radiation from the electroplate.

The applied instrumental conditions for the x-ray diffraction analysis are shown in the Appendix. For control purposes, the whole x-ray diffraction pattern has been recorded on a strip chart. For expediency and reasons discussed later, the semiquantitative data for the (422) diffraction peak have been selected for tabulating and plotting the relatively large effects due to phase and microstructural changes caused by heat treatment.

Control measurements have been indicating satisfactory alignment and functioning of the x-ray equipment; they also confirm the assumed purity of the standards used. The approximate lattice parameter, a, as derived from the measured diffraction angle 2θ of the (422) peak has been compared with the *precise* parameter for pure Au powder, $a_0 = 4.0786$Å (Angstroms, 10^{-8} cm). The (422) diffraction angle of the pure Au electroplate and of the powder both show $a = 4.078$Å. The third decimal figure obtained by this method is usually considered unreliable but has been checked and verified by more precise methods as will be shown and discussed in detail.

The procedure for the semiquantitative x-ray analysis of the (422) peak of Au before and after each heat treatment was as follows:

1. Record the (422) peak on the strip chart.
2. Locate the approximate peak maximum on the chart.
3. Define 2θ by finding I max, maximum intensity (in c/sec = pulse counts per second), by counting for 1 min at three selected points near the peak. For broad peaks, determine the apex by fitting a parabola through the selected points (9).
4. Establish on the chart a base line with a ruler by joining the beginning and the end of the peak. Measure h max (in cm) and b (peak breadth) at ½ h max (in cm).
5. Count *I.I.* (integrated intensity), a measure of the area under the peak (in counts, c).
6. Tabulate the obtained data and plot temperatures *vs.* x-ray measurements.

The experimental method described above of measuring the changes in lattice parameter, a, is fairly easy. Simply by selection of a high angle line on the pattern, one usually obtains an accuracy of 0.01Å or about 0.4%. Most of the thermal effects observed in the following experiments are larger. In order to check on the method and the significance of the data obtained, several experiments have been duplicated using the time-consuming measurements of several high reflection angles and determining a for each line by assigning the proper wavelength and employing an electronic computer. By plotting the obtained values of a against $\cos^2\theta$ and extrapolating the curve to $\cos^2\theta = 0$, the "precise" a_0 is obtained. The accuracy is thus increased to 0.001Å, or about 0.04%. The extrapolation has been carried out by applying the method of least squares, that is, an objective, analytical method of finding the line which best fits the data. Most data shown in this report carry five decimal figures for computation only. The extrapolated a_0 (Tables IV, V, and VI) shows the fourth decimal figure in parenthesis for rounding a_0 to three significant figures, *i.e.*, 10^{-3}Å $= 10^{-11}$ cm.

As will be shown, the refined method of determining a_0 does not invalidate the first simple experimental method but confirms the first approximations by the addition of more significant figures.

Effects of Experiments

For convenient comparison, the scanned diffraction peaks have been traced from the back of the chart paper and superimposed, in order to show the difference between the original profile of the diffraction peak and its shape after heat treatment at different temperatures (Fig. 1-3). The peaks have been traced after those heat treatments that show significant changes in peak location and profile. Heating at 100°C for 2 more hr does not produce further changes. After heating for 1 hr at 175°C, further changes are observed and measured [Fig. 1(a) and 2(a)]. The effects of heat treatment at higher temperatures are shown in Fig. 1(b), 2(b), and 3.

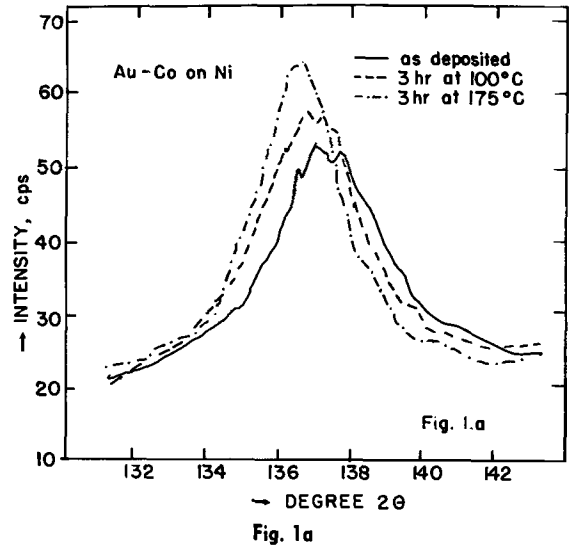

Fig. 1a

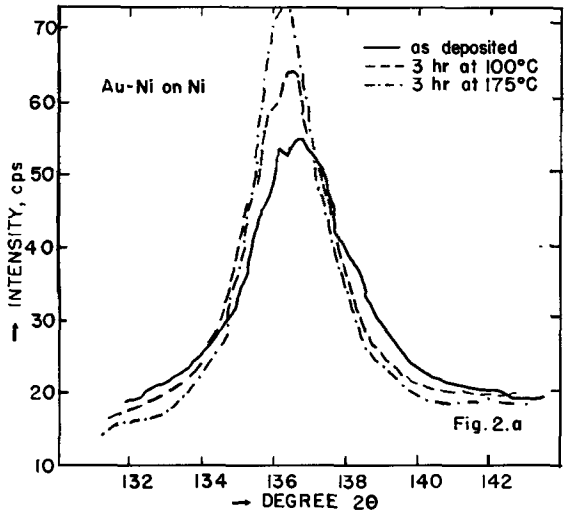

Fig. 2a

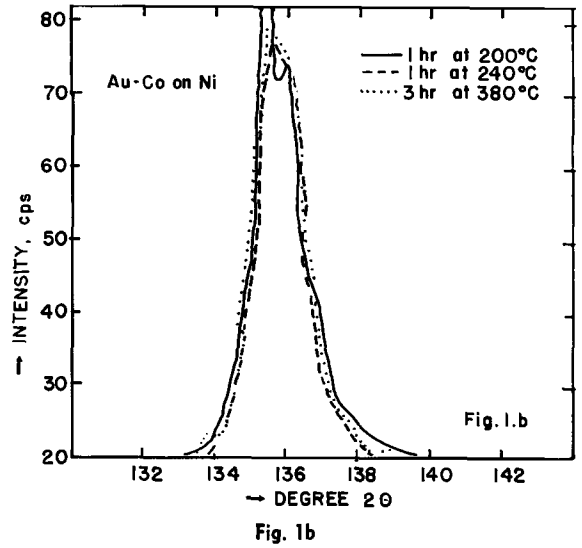

Fig. 1b

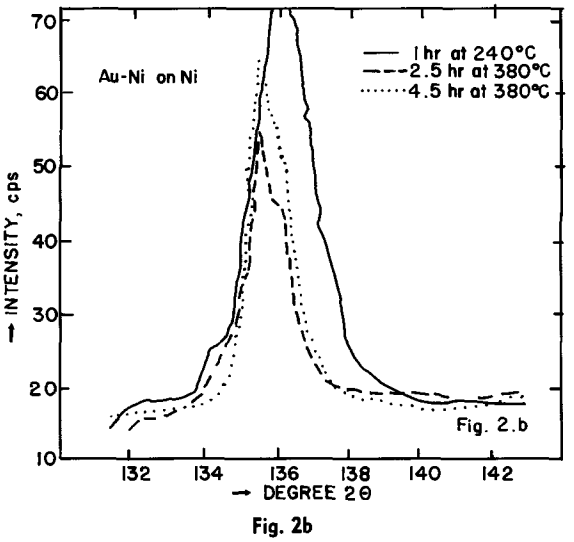

Fig. 2b

Fig. 1 (a and b). Heat treatment of Au-alloy electroplates. Superimposed (422) XRD peaks recorded after shown durations at temperatures.

Fig. 2 (a and b). Heat treatment of Au-alloy electroplates. Superimposed (422) XRD peaks recorded after shown durations at temperatures.

Comparison of the peak profiles from heat-treated Au-Co on Cu, having no Ni interliner (Fig. 3) with Au-Co on Ni [Fig. 1(b)] reveals obvious differences due to Cu diffusion and Au-Co-Cu alloying which is discussed later.

The XRD (x-ray diffraction) measurements (Tables I and II) show an angular shift of the (422) peak induced by heat treatment for four different Au-alloy samples. The corresponding, increasing parameter, a, expresses lattice growth. When heat-treating temperature is plotted *vs.* a, then rate changes in growth are indicated by the slope changes of the four curves (Fig. 4). Au-Co on Cu, having no Ni interliner (Sample No. 1) shows a considerable increase in a by heat treatment at 175° and 200°C, similar to the other samples. After heat treatment at 380°C, its cell edge, a, decreases drastically. Diffusion of the Cu atoms from the substrate at 240°C interferes with the growth of a. At this temperature, the Au color of the sample surface is changed to deep blue. At 380°C, the deep blue changes first to brick red (cuprous oxide, Cu_2O) and then to black (cupric oxide, CuO).

Sample No. 2, Au-Co on Ni, shows a distinct and steep increase of a at 200°C when it becomes practically equal to the a of pure Au. Like sample No. 1, this sample turns pale blue at 240°C and deep blue at 380°C; it does not turn red at 380°C. The slight surface oxidation can be wiped off.

Table I. Heat treatment of Au-Co electroplates—XRD measurements of angle 2θ for (422), Cu Kα, and derived uncorrected lattice parameter, a

Treatment	Sample No. 1 (on Cu) 2θ	a, Å	Sample No. 2 (on Ni) 2θ		a, Å
As plated	137.4	4.054	136.7		4.063
175°C	136.8	4.062	136.4		4.068
200°C	136.5	4.066	135.4	α_1	4.078
240°C	136.6	4.065	135.4	α_1	4.078
380°C	139.8	4.021	135.4	α_1	4.078

Table II. As Table I for Au-Ni on Ni

Treatment	Sample No. 3 2θ		a, A	Treatment	Sample No. 4 2θ		a, A
As plated	136.6		4.065	As plated	137.3		4.055
100°C	136.5		4.066	100°C	136.9		4.060
175°C	136.1		4.072	150°C	136.6		4.065
200°C	136.1		4.072	200°C	—		—
240°C	135.4	α_1	4.079	250°C	136.2		4.070
380°C	135.4	α_1	4.079	300°C	135.8	α_1	4.073
				350°C	135.6	α_1	4.076
				400°C	135.4	α_1	4.078

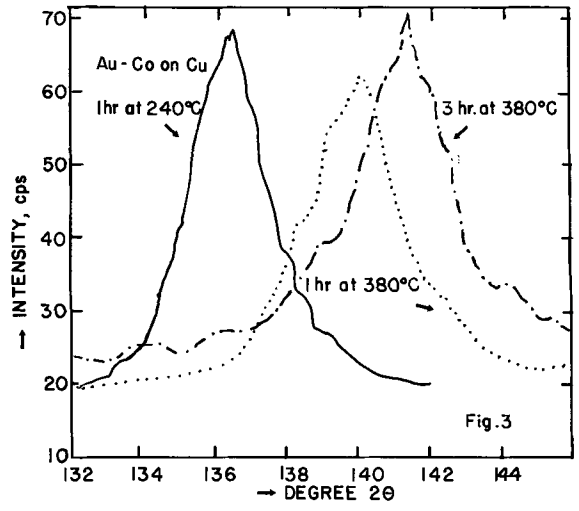

Fig. 3. Heat treatment of Au-alloy electroplates. Superimposed (422) XRD peaks recorded after shown durations at temperatures.

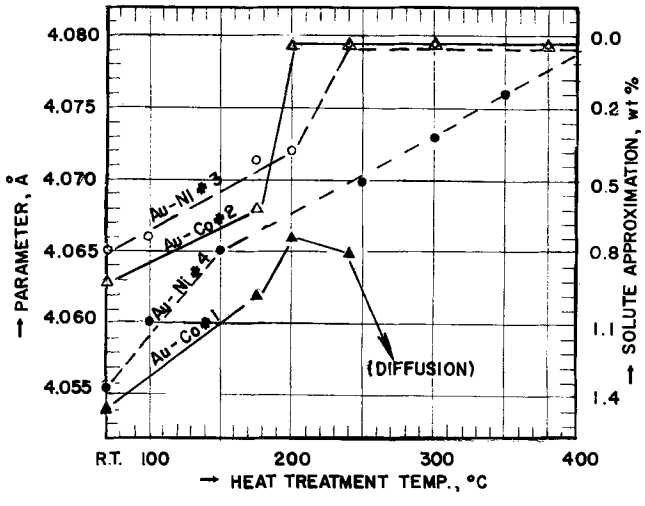

Fig. 4. Growth of lattice parameter with heat treatment of four Au alloy electroplates. For orientation, the concurrent change in concentration of the alloying element in S.S. is shown at the right ordinate. Sample No. 1, having no Ni interliner, breaks down at 240°C.

All samples differ in a in the condition "as plated." Samples No. 3 and 4 (both Au-Ni on Ni) also show a distinct difference in the growth rate of a. Similar to sample No. 2, sample No. 3 shows a steep growth of a up to the value of pure Au, except at a higher temperature (240°C). In contrast, the a of sample No. 4 with a relatively small initial value (more Ni atoms in the Au lattice) increases a rather rapidly at the temperatures 100° and 170°C, and then grows uniformly at 250°, 300°, and 350°C. Finally, a reaches the value of pure Au at 400°C. Further heat treatment for 1 hr at 450°C does not produce further change in a. The color of the Au-Ni samples turns gray (250°C), then increasingly dark (300°, 350°, 400°C) to almost black (450°C) because of increasing surface oxidation and diffusion.

The measured changes in peak profile as induced by heat treatment of samples No. 3 and 4 are expressed as *I.I.*, I max, h max, and b at 1/2 h max (Table III). Their plots against heat-treating temperatures (Fig. 5) show the rate of changes; most curves show distinct differences between the peak characteristics "as plated" and after heat treatment at 100°C. Up to and including heat treatment at 175°C, the rate of change of the slope of the curves is rather gradual. However, at 200°C, the Au-Co sample changes its peak profile drastically. No further large changes in peak profile can be observed after further heat treatment.

Table III. Changes in profile characteristic of the XRD peak (422) of Au-alloy electroplates induced by heat treatment

Treatment	*I.I.*, c	I max, c/s	h max, cm	b at ½ h max, cm
	Au-Co Sample No. 2			
As plated	4000	32	7.8	3.8
100°C	4000	34	8.6	3.6
175°C	4300	37	10.5	2.0
200°C	4600	79	15.3	1.9
240°C	4700	82	15.3	2.0
380°C	4600	75	15.3	2.1
	Au-Ni Sample No. 3			
As plated	4500	42	8.7	3.8
100°C	4600	49	11.8	2.8
175°C	4650	61	14.2	2.8
200°C	4700	62	14.7	2.5
240°C	4500	62	14.1	2.4
380°C	2700	60	12.5	1.6

Slope changes of the Au-Ni sample are not quite as steep as with the Au-Co sample. The peak breadth, b at ½ h max, drops distinctly at 100°C and decreases then rather uniformly. Maximum peak height is observed at 200°C. At 380°C, the peak characteristic of this sample becomes quite similar to that of pure Au standards (not shown).

Duplicate and control data for different Au-alloy electroplates and heat treatments (Tables IV and V) have been plotted, graphically extrapolated (Fig. 6 and 7), and analyzed by the method of least squares. As an example and for orientation, the four XRD peaks of the Au-Co "as plated" (Table IV) render a_0 = 4.051Å, shown by the intercept of the lowest dashed curve (Fig. 6), the slope = 0.0034 and the drift constant = 0.00014; the latter is a measure of the total systematic error involved in this determination.

Au-Co on Ni shows that a_0 has become largest and close to "pure" Au at 450°C. The considerable decrease of a_0 at 500°C suggests alloying of the Au-Co plate with atoms from the substrate by the process of diffusion. The same effect but at a lower temperature (400°C) is observed with the samples Au-Co without Ni interliner. Similarly, the control measurements for a_0 of Au-Ni alloy and pure Au electroplate support the

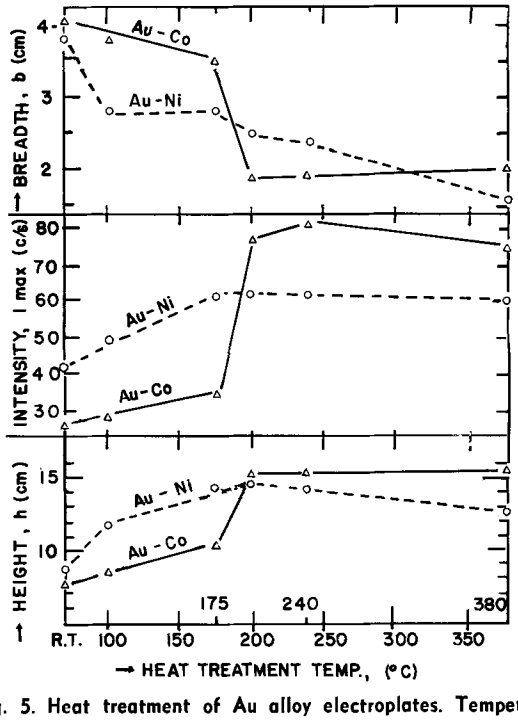

Fig. 5. Heat treatment of Au alloy electroplates. Temperatures *vs.* (422) XRD peak characteristics.

Table IV. Heat treatment of 2 Au-Co electroplates—XRD data and derived "precise" lattice parameter

Treatment	hkl	2θ		cos² θ	a, Å	a_0, Å
			Au-Co on Ni			
As plated	331	112.0		0.31269	4.05315	
	420	116.6		0.27612	4.05205	
	422	137.6		0.13078	4.05072	
	511	162.0	α_1	0.02447	4.05225	4.051(4)
300°C	420	115.6		0.28396	4.07415	
	422	136.1		0.13973	4.07173	
	511	159.0	α_1	0.03321	4.07054	4.069(9)
400°C	420	115.6		0.28396	4.07415	
	422	136.0		0.14034	4.07318	
	511	158.7	α_1	0.03416	4.07253	4.073(0)
450°C	331	110.9		0.32168	4.07975	
	420	115.4		0.28733	4.07864	
	422	135.5		0.14338	4.07704	4.077(8)
500°C	420	116.5		0.27691	4.05424	Note, plate destruction by diffusion
	422	137.3		0.13255	4.05152	
			Au-Co on Cu			
400°C	331	111.8		0.31432	4.05796	
	420	116.4		0.27769	4.05644	
	422	137.3		0.13255	4.05486	
	511	161.4		0.02611	4.05565	4.054(8)—Diffusion

Table V. As Table IV for Au-Ni alloy and, for comparison, for a pure Au electrodeposit

Treatment	hkl	2θ		cos² θ	a, Å	a_0, Å
			Au-Ni on Ni			
As plated	311	111.7		0.31513	4.06036	
	420	116.3		0.27846	4.05863	
	422	137.0		0.13432	4.05900	
	511	161.4	α_1	0.02611	4.05565	4.056(0)
300°C	331	111.0		0.32081	4.07731	
	420	115.5		0.28474	4.07638	
	422	135.9		0.14093	4.07459	
	511	159.1		0.03290	4.07324	4.072(7)
400°C	422	135.8		0.14154	4.07604	
	511	158.4		0.03511	4.07788	4.078(5)
450°C	331	110.9		0.32163	4.07978	
	420	115.1		0.28790	4.08542	
	422	135.7		0.14215	4.07749	4.074(6)
			"Pure" Au			
As plated	331	110.7		0.32326	4.08469	
	420	115.2		0.28711	4.08314	
	422	135.2	α_1	0.14521	4.08141	
	511	157.7	α_1	0.03740	4.07938	4.078(8)

previous findings observed by measuring semiquantitatively the shifts of the (422) diffraction peak only.

The growth of a_0 from the "as-plated" condition to the a_0 of practically pure Au by heat treatment can be explained, according to Vegard's law, by a concurrent decrease of solute content. Figure 4 shows corresponding, derived, approximate percentages of solute in S.S.

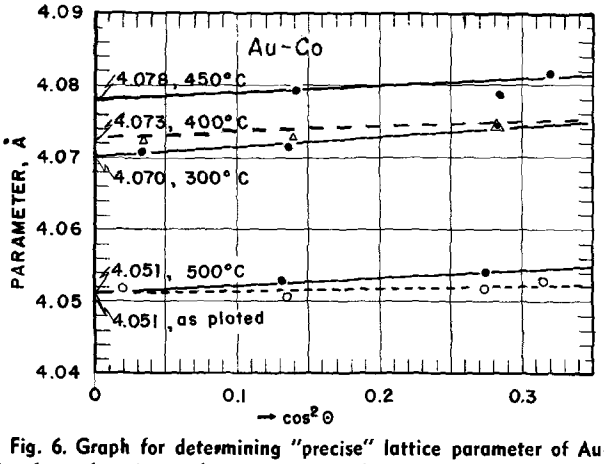

Fig. 6. Graph for determining "precise" lattice parameter of Au-Co electrodeposit as plated and after different heat treatment.

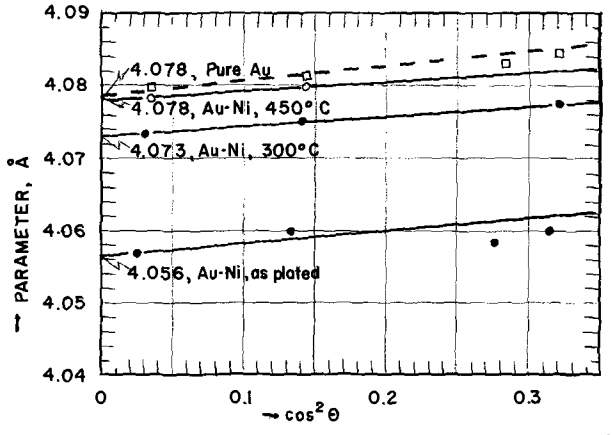

Fig. 7. As Fig. 5 for Au-Ni electroplate. The square symbols show measured data for a pure Au deposit, for orientation.

Vegard's Law and Atomic Absorption Analysis

The concentration of the solute, that is, Co and Ni in S.S. of the Au-alloy electroplates, as derived from the unit cell parameter, a_0 (Tables IV and V), as mentioned before, is based on the assumption that Vegard's law holds. Deviation from Vegard's law when it occurs is usually greatest about the middle of the composition-lattice parameter diagram. Since this study is concerned only with small amounts of alloying elements, a linear relationship between a/o and a can be assumed for approximating the solute content in the Au-alloy plate.

In order to check the x-ray computation of a and the applicability of Vegard's law for approximating the alloying element content in the plate, the electrodeposits were stripped and Co and Ni determined by AA (atomic absorption) analysis. While the results differ between plates, reasonable agreement is found for the same sample between AA analysis and the results from a measurements and computations. The x-ray computation and Vegard's law, of course, are based on the assumption that the alloying element in the "as-plated" Au alloy is present in a single-phase, supersaturated, substitutional S.S. which is discussed later.

Results and Discussion

The analysis of the semiquantitative XRD data (Table III) shows increasing h max and decreasing b at ½ h max; that is, "recovery of profile broadening" by heat treatment of the samples (Fig. 5). The peak profile approaches the appearance of the relatively high and narrow peak of pure Au standards. Small profile changes have been observed after heat treatment for 1 hr at 100°C. The progressive peak recovery by sharpening and narrowing of the profile is practically completed after heat treatment for 1 hr at 200°C for Au-Co and at 240°C for Au-Ni. Extra peak width, according to x-ray theory, could be caused by very fine particle or grain size smaller than 10^{-5} cm, lattice defects (dislocations), and/or microstrains. The *I.I.* (area under the peak) does not change much during heat treatment except for Au-Ni after the last treatment (Table III).

The steep slope changes of the curves with the concurrent minimum of b at ½ h max for Au-Co and the maxima for I max and h max (Fig. 5) suggest that the heat treatment causes gradual recovery from lattice faults, relief from microstrains (stresses), and/or grain growth. Though the latter is possible, it seems less likely since the beginning of the profile change for these "alloys" was observed at the relatively low temperature of 100°C, and no steep profile changes occur at 200° or 240°C. Also, x-ray back-reflection photographs of the samples after heat treatment at 400°C do not show Laue spots (10) which would indicate coarse grain growth.

Since heat treatment increases a to the value of pure Au, the alloying elements are assumed to have been codeposited in S.S. with the Au and to be precipitated by heat treatment as a separate phase. Under favorable conditions, one might expect to find diffraction peaks from the precipitated phase. By careful search for new diffraction lines as evidence for the precipitation, weak additional peaks were detected after heat treatment at 400°C. The analysis of the XRD measurements by the method of least squares (Table VI) and Vegard's law suggest a FCC, Ni-rich S.S. containing 97 a/o Ni. This value is in good agreement with the composition of the thermal alloy at equilibrium, 96 a/o Ni at 450°C, as determined by Wise (11).

Similarly, the Au-Co plate after heat treatment at 450°C shows six additional diffraction peaks. Their x-ray data (Table VII) suggest that the two allotropic forms of Co are present; that is, beta Co (FCC) which is said to be stable above 450°C (10), and the alpha or epsilon Co (HCP) which is said to be stable at lower temperatures (12). The derived $a = 3.549$Å for the Co beta precipitate is practically equal to pure Co, $a_0 = 3.552$Å, that is, containing little or no Au in S.S. This finding is also in good agreement with the known constitutional diagram for the binary system Au-Co at equilibrium (13). Attempts to discern precipitates under the microscope were unsuccessful.

Shifts in angular position of the peaks, in general, can be caused by applied uniaxial macrostrains, lattice imperfections, and/or change in lattice parameter. The following circumstantial evidence points to the latter:

(a) AA analysis of the stripped Au alloy plates for Co and Ni content check satisfactorily with the results from the x-ray determinations, that is, the computed alloying content derived from a_0 of the sample as plated and Vegard's law, suggesting that the Au alloy as plated consists of a single-phase S.S.

(b) The recorded diffraction pattern of the samples as plated shows only peaks for the Au-rich S.S.; no other peaks for the alloying elements can be detected. After prolonged heat treatment, however, several weak additional peaks can be positively identified as deriving from precipitated phases. This suggests that the plates as deposited are single-phase, supersaturated S.S. and that equilibrium is produced by precipitation caused by the heat treatment.

(c) During heat treatment, a of the samples increases to the value of pure Au and, excluding diffusion, remains constant upon further heat treatment (Fig. 4). This suggests that the originally supersaturated S.S. as plated approaches equilibrium as a result of heat treatment and that the phase mixture in the electroplate thus becomes stable (13).

Conclusions

1. The Au-alloy plates contain Co and Ni, respectively, as proven by x-ray spectrographic analysis.

Table VI. Precipitate in Au-Ni electroplate after heat treatment at 400°C—XRD measurements and derived lattice parameter, a_0

2θ (deg)		hkl	$\cos^2\theta$	a,Å	a_0,Å
74.6		220	—		
92.3		311	0.43993	3.54547	
120.9		400	0.24323	3.54464	
153.0	α_1	420	0.05450	3.54256	3.542(4)

Table VII. Precipitate in Au-Co electroplate after heat treatment at 400°C—XRD measurements and lattice parameter approximation

Measurements 2θ, deg	I/I_1	hkl	Co-phase	a, Å
42.2	w	100	α (HCP)	—
47.7	m	002	α	—
51.5	vw	200	β (FCC)	3.55
84.5	m	100	α	—
92.2	w	311	β	3.548
97.6	m	222	β	3.549

2. The alloying elements in the plates as deposited are in a single-phase, Au-rich metastable S.S. which is affected by heat treatment for 1 hr at 100°C.

3. The alloying element content varies between plates as approximated by Vegard's law and checked by AA analysis.

4. For Au-Co, the phase equilibrium is approached by heat treatment at 200°C. Nearly pure α- and β-Co is precipitated from the primary supersaturated S.S., thus forming a phase mixture where almost pure Au is the matrix.

5. For Au-Ni, the phase equilibrium is approached by heat treatment for 1 hr at 240°C. A secondary phase is precipitated from the primary supersaturated S.S., thus forming a two-phase alloy. The precipitate is a Ni-rich S.S., about 96 a/o Ni, in an almost pure Au matrix.

6. Recovery of the x-ray diffraction peak profile begins at 100°C and continues as temperature increases. This peak recovery is most pronounced for Au-Co and is practically completed after heat treatment for 1 hr at 200°C. The changes can be considered as caused by recovery from microstructural lattice defects in the plate, relief from residual microstrains (stresses), and/or possible grain growth.

7. Discoloring of the Au alloy plates after heat treatment for 1 hr at 240°C indicates surface oxidation.

8. Alloying by the process of solid-state diffusion of Cu from the substrate when there is no Ni interliner is shown by the x-ray data after heat treatment for 1 hr at 200°C; that is, before surface oxidation can be observed.

9. The noble character of the Au deposit surfaces is obviously lost after heat treatment in air for 1 hr at 380°C.

Acknowledgments

Thanks are due to Dr. Edward A. Parker, Vice President of Technic, Incorporated, Cranston, Rhode Island, for stimulating discussions and for supplying the samples, and to Mr. Tarek El Heneidy, research assistant, for making the measurements.

Manuscript submitted Sept. 12, 1969; revised manuscript received *ca.* Dec. 19, 1969.

Any discussion of this paper will appear in a Discussion Section to be published in the December 1970 JOURNAL.

REFERENCES

1. A. Brenner, "Electrodeposition of Alloys," Vol. 2, p. 247, Academic Press, New York (1963).
2. E. Raub, *Z. Electrochem.*, **55**, 146 (1951), and *Metalloberflaeche*, **7A**, 17 (1953).
3. N. P. Fedot'ev, N. P. Ostromouva, and Vyacheslavov, *Zh. Prikl. Khim*, **27**, 489 (1954); *ibid.*, **29**, 489 (1956). N. P. Fedot'ev, P.M. Vyacheslavov, N. P. Ostromouva, and S. Ya. Griliklas, *Legakaya Prom.*, **17**, 43 (1957).
4. E. Raub and K. Bihlmeier, *Mitt. Forschungsinst. Probieramts Edelmetalle, Staatl. Hoehere Fachschule Schwaeb. Gmuend*, **11**, 59 (1957).
5. A. F. Mohrnheim, *Metalloberflaeche*, **20**, 464 (1966).
6. B. D. Cullity, "Elements of X-Ray Diffraction," p. 352, Addison-Wesley Publishing Co., Reading, Mass. (1959).
7. U.S. Pat. No. 3,149,057 and 3,149,058 (Sept. 1964).
8. "ASTM-Powder Diffraction File," No. 4-784, American Society for Testing and Materials, Philadelphia, Pa.
9. D. P. Koistinen and R. E. Marburger, *ASM Trans.*, **51**, 537 (1959).
10. A. Taylor, "X-Ray Metallography," p. 333, John Wiley & Sons, Inc., New York (1961).
11. E. M. Wise, *Trans. AIME*, **83**, 384 (1929).
12. See Ref. No. (8), card No. 5-0727.
13. M. Hansen and K. Anderko, "Constitution of Binary Alloys," 2nd Ed., McGraw-Hill Book Co., New York (1958).

APPENDIX

The equipment and the instrumental conditions used for the x-ray diffraction analysis were: General Electric XRD-5; tube target Cu; take-off angle 4°; 23.5 kVp; 15 mA; beam slit 3°; Soller slit MR; detector slit 0.1°; Ni filter, 2 X 0.00035 in.; counter tube SPG-6 (Xenon); chart range 100 Hz; time constant 2.0 sec, linear response; scan 2°/min; chart speed 30 in./hr.

An Optical Study of Cathodic Hydrogen Evolution in High-Rate Electrolysis

Dieter Landolt,*,[1] Raul Acosta,* Rolf H. Muller,* and Charles W. Tobias*

Inorganic Materials Research Division, Lawrence Radiation Laboratory and Department of Chemical Engineering, University of California, Berkeley, California

ABSTRACT

Hydrogen bubbles evolved cathodically under conditions encountered in electrochemical machining have been studied by stop-motion photography. Constant current densities up to 150 A/cm^2 and flow rates up to 2500 cm/sec have been employed with an experimental flow channel of 0.5 mm gap width. The observed bubble size decreased strongly with increasing flow rate and increased with increasing current density. At flow rates above 800 cm/sec, the bubble size was always below 20μ, the smallest diameter resolved by the optical arrangement used. Less gas was evolved in nitrate than in chloride electrolytes under otherwise identical conditions. The hydrogen bubbles were usually confirmed to a region near the cathode. Voltage oscillations and electric breakdown coincided with the appearance of a new type of bubble.

In electrochemical machining, metals are dissolved anodically at current densities in the order of 100 A/cm^2 or higher. Hydrogen gas is formed cathodically and must be transported away from the reaction zone by the electrolyte stream. This hydrogen may affect the electrolytic process in several ways: It may increase the ohmic resistance of the electrolyte, resulting in higher cell voltage and different local current distribution. It may be oxidized at the anode and, thus, decrease the current efficiency of the metal dissolution process. It may form a continuous gas blanket at the cathode and, thus, lead to sparking. It may accumulate in large bubbles, which extend over the entire interelectrode gap, and, thus, drastically affect mass-transfer conditions at the anode. In order to obtain a better understanding of the relative importance of such phenomena, a photographic study of cathodically generated gas bubbles was initiated. During the course of this pursuit, somewhat related work has appeared in the literature (1, 2). In the present investigation, a more sophisticated optical arrangement has been employed and a better control and wider range of critical variables, such as current density and flow velocity, have been employed in addition to the use of a well-defined flow system.

Experimental Technique

The apparatus used has been described before (3). It consisted of a rectangular flow channel cell of 8 mm width and 0.5 mm height. Its sidewalls were made of flat glass plates, which provided for the optical observation of the interelectrode gap. The total channel length was 8.5 cm; the center of the electrodes was positioned 1 cm from the downstream end. The design of the flow cell provided for fully developed velocity profiles at the electrodes. Flow rates up to 2500 cm/sec were employed, corresponding to inlet pressures in the order of 10 atm. Since most of the pressure drop occurs in the entrance length of the flow channel, the absolute pressure at the electrodes, even at the highest flow rate employed, was only about 2 atm. Although under these conditions the effect of pressure on the gas volume has to be taken into account, at flow rates up to 1000 cm/sec, where most observations were made, the absolute pressure at the electrodes was only 1 to 1.3 atm, and its effect on bubble size was negligible within the accuracy of the present measurements. The copper electrodes were 3.17 mm long in the flow direction and 0.53 mm wide. Before experiments, the electrode surfaces were mechanically polished with 1μ diamond paste, cleaned with aqueous detergent and acetone, and degreased by hydrogen evolution in aqueous caustic.

The optical arrangement is shown schematically in Fig. 1.[2] A commercial flash light source (A) of 0.5μ sec flash duration[3] was used for illumination of the gas bubbles generated in the flow cell (B) in transmitted light mode. A camera (H) with open shutter and high speed film[4] was attached to a microscope tube containing a 2x objective (C) (f = 48 mm, N.A. = 0.08) and a 10x eyepiece (E). A small circular aperture (D) of 1.6 mm diameter, located in the rear focal plane of the objective (C) served as a telecentric stop (4). The purpose of this device is to avoid variations in the apparent size of bubbles due to differing distances from the objective and to increase the depth of field. Unfortunately, the telecentric stop also reduces the speed and resolution of the objective, the latter being about 20μ. In order to obtain a photographic distinction between the electrode surface and an adjacent, dense

*Electrochemical Society Active Member.

[1] Present address: University of California, Department of Engineering, Los Angeles, California.

[2] Design considerations of the optical system are discussed elsewhere in more detail.

[3] EG & G 594 microflash.

[4] Kodak SO 340.

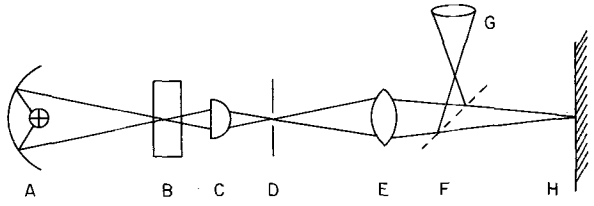

Fig. 1. Optical arrangement for high-speed photography of gas bubbles: A—light source (flash), B—flow channel cell, C—microscope objective, D—telecentric stop, E—microscope eyepiece, F—beam splitting prism, G—magnifier for visual observation, H—camera film plane.

layer of gas bubbles, a pre-exposure in the absence of bubbles was made at reduced light intensity. In a typical experimental run, constant current was applied to the cell for a short period of time by switching the output of a constant current supply[5] from a dummy circuit to the cell circuit. A mercury relay, actuated by a pulse generator, was used for the switching. The circuit also served to trigger the flash light source after a preset time, which was chosen to correspond to the passage of 12 coulombs/cm^2. The current was switched back to the dummy load automatically after the total passage of 15 coulombs/cm^2. The charge passed between the start of an experiment and the moment the picture was taken resulted in the evolution of about 1.5 cm^3 hydrogen (1 atm, 298°K) per cm^2 electrode. This was considered sufficient to establish steady-state conditions with respect to gas evolution. During the experiments, current and potentials were recorded by means of a light beam oscillograph.

Experimental Results

Bubble size.—Typical photographs obtained in 2*N* KCl solution at different flow rates and current densities are given in Fig. 2 to 4. Figure 2 illustrates the influence of flow rate and cathode orientation on bubble size for a current density of 50 A/cm^2. An estimate of the size distribution of the bubbles for the same experiments is given in Fig. 5. These distributions were obtained by measuring the diameter of all the bubbles which were individually discernible in the whole interelectrode gap, and determining the fraction in each size bracket of 25μ width. The quantitative validity of the distributions given in Fig. 5 is limited for several reasons: (*a*) The number of measured gas bubbles (27-60) represent only part of the total gas volume, and the differentiation between discernible and not discernible bubbles is subject to personal interpretation. (*b*) The variability of results in successive experiments probably requires a more sophisticated statistical evaluation. (c) Bubbles close to the cathode surface were usually not individually discernible and could, therefore, not be included in the count. (*d*) Bubbles smaller than 20μ in diameter were below the optical resolution. Qualitatively, however, Fig. 5 illustrates not only the order of magnitude of cathodically generated bubbles, but it also shows the decrease in size with increasing flow rates: the median bubble diameters are 99, 69, and 35μ for flow rates of 100, 200, and 400 cm/sec, respectively. It should also be noted that, at the lower flow rates (below 400 cm/sec), a few large bubbles often existed in addition to a large number of smaller ones. It was observed during the experiments that these large bubbles were sticking to the cathode surface for prolonged periods of time while the smaller bubbles detached from areas in between. Figure 5 also shows that the orientation of the cathode, *i.e.* whether it is facing up or down, has no systematic effect on size distribution, except at the lowest flow rate.

Figure 3 illustrates gas evolution at high flow rates. The size of the generated bubbles decreases rapidly with increasing velocity in this range and the size distribution becomes narrower, so that the previously

[5] Electronic measurements C-618.

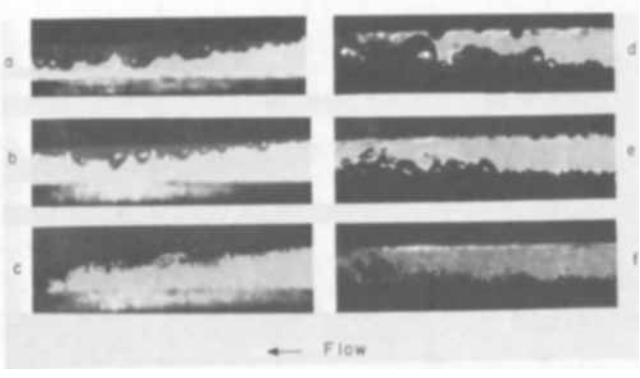

Fig. 2—Influence of flow rate and cathode orientation on gas evolution in 2*N* KCl. Current density 50 A/cm^2, electrode gap 0.5 mm: a—flow rate 100 cm/sec cathode facing down, b—flow rate 200 cm/sec cathode facing down, c—flow rate 400 cm/sec cathode facing down, d—flow rate 100 cm/sec cathode facing up, e—flow rate 200 cm/sec cathode facing up, f—flow rate 400 cm/sec cathode facing up.

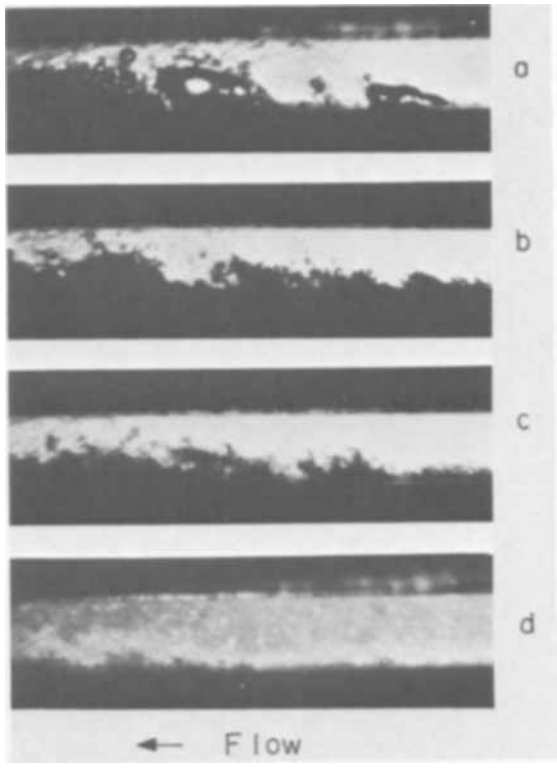

Fig. 3. Influence of flow rate on cathodic gas evolution in 2*N* KCl. Current density 100 A/cm^2, cathode facing up: a—flow rate 400 cm/sec, b—flow rate 600 cm/sec, c—flow rate 1000 cm/sec, d—flow rate 2500 cm/sec.

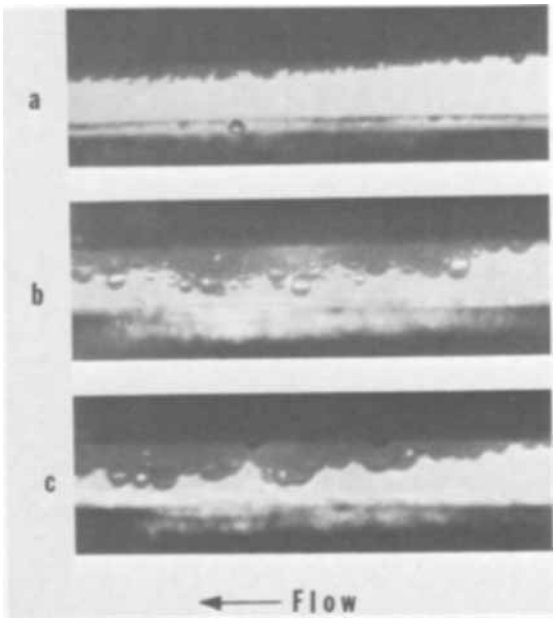

Fig. 4. Influence of current density on cathodic gas evolution in 2*N* KCl. Flow rate 100 cm/sec, cathode facing down: a—current density = 5 A/cm^2, b—current density = 20 A/cm^2, c—current density = 50 A/cm^2.

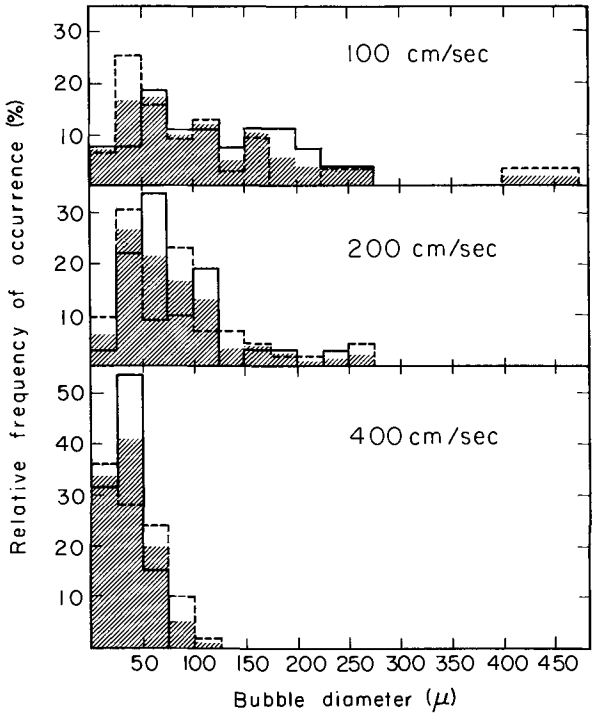

Fig. 5. Distribution of cathodic gas bubble diameters in 2N KCl. 50 A/cm²; 100, 200, and 400 cm/sec. Total number of bubbles measured 31, 43, and 50, respectively, for cathode facing up (- - -) and 27, 32, and 60, respectively, for cathode facing down (———). (Counts incomplete in range 0-25μ, due to lack of resolution below 20μ.)

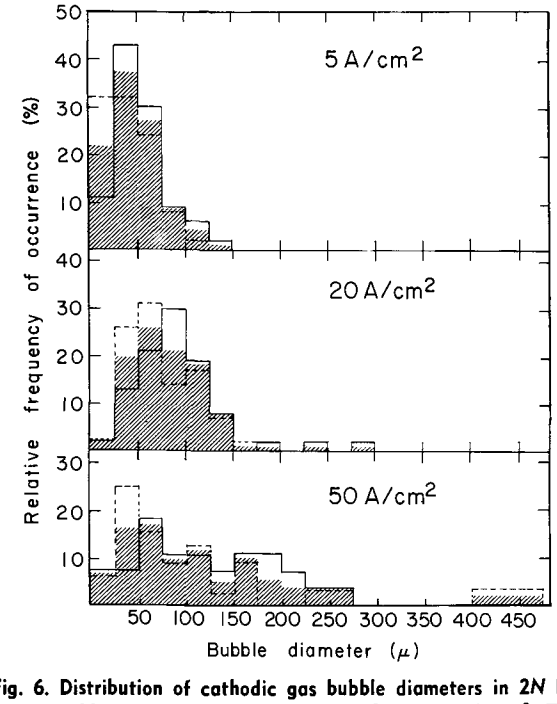

Fig. 6. Distribution of cathodic gas bubble diameters in 2N KCl. Flow rate 100 cm/sec, current density 5, 20, and 50 A/cm². Total number of bubbles measured 47, 47, and 31, respectively, for cathode facing up (- - -) and 37, 42, and 27, respectively, for cathode facing down (———). (Counts incomplete in range 0-25μ, due to lack of resolution below 20μ.)

observed coexistence of few large bubbles with smaller ones disappears. At flow rates of 800 cm/sec or higher, all individual bubbles were too small (below 20μ) to be resolved photographically.

The effect of current density on bubble size is illustrated in Fig. 4 and 6. A clear increase in bubble size is observed with increasing current density under otherwise identical conditions: the median bubble diameters are 56, 78, and 99μ for current densities of 5, 20, and 50 A/cm², respectively. These observations are in marked contrast to findings reported by Venczel (5), who studied gas evolution at vertical electrodes in stagnant solutions and reported a decrease in bubble size with increasing current density. The discrepancy might possibly be explained by the different modes of convection. A bubble may be assumed to detach from the surface when external forces, such as gravity or friction with the moving liquid, become larger than the normal component of the surface tension. Since in a stagnant solution the rate of stirring is increased when more gas is generated, higher current densities may lead to an earlier detachment of gas bubbles. In our experiments, on the other hand, local stirring was mainly due to the hydrodynamic flow and was, therefore, almost independent of current density. A decrease, rather than an increase, in bubble size with increasing current density would also be expected from the work of Kabanov and Frumkin (6). They showed that the contact angle, which determines the normal component of surface tension, depends on electrode potential. For very slow hydrogen evolution on mercury, smaller contact angles and, hence, smaller bubbles were observed at increasingly negative potentials.

Force balances have been applied to the prediction of bubble size in forced convection boiling (7). Such a force balance for an individual bubble may be formulated as

$$F_\sigma = F_i + F_b \qquad [1]$$

where F_σ is the surface tension force which holds the bubble on the electrode, F_i is the inertia force of the electrolyte acting on the bubble, and F_b is the buoyancy force of the bubble. The latter can be neglected at high flow velocities. According to Tong (7), a model of this kind predicts a decrease in bubble size with the square of the flow velocity. Such a dependence is at least qualitatively consistent with the present results. Relation [1] does, however, not account for the influence of current density and the wide distribution of bubble diameters observed at low flow rates. This distribution is at least partly due to the fact that the presence of other bubbles on the surface leads to locally varying flow conditions. Considering the fact that not even the dynamics of a single bubble growing in a laminar velocity field has been analyzed, no attempt has been made here to give a more detailed account of the vastly more complex case of multiple bubble dynamics in turbulent flow. Additional experimental studies should include the time dependence of bubble growth for a more detailed description of gas evolution under the present conditions in turbulent flow. Glas and Westwater (8) have investigated electrochemical gas evolution in stagnant solutions by high-speed cinematography. They found two growth stages: an early rapid growth period, associated with bubble diameters of up to about 50μ, followed by a slow period. Theoretical aspects of growth mechanisms have been discussed by Cheh (9), who applied mass transfer considerations to predict growth rates in the slow (asymptotic) growth period. No theoretical models exist at present which predict growth rate in the rapid growth period. Since, in our study, the bubble size was often smaller than 50μ, growth rate and residence time on the cathode surface could not be estimated on theoretical grounds.

Thickness of two-phase region.—Figures 2-4 illustrate the observation that the gas bubbles are not dispersed uniformly throughout the gap, but usually occupy a region near the cathode. At flow rates above 100 cm/sec, the thickness of this two-phase region is the same whether the cathode faces up or down. This behavior is to be expected, since at higher flow rates a gas bubble, unless it is very large, is swept away from the interelectrode gap too fast to be affected by

buoyancy. From Stoke's law, which may be applied to bubbles of less than 1 mm diameter (10), the steady-state velocity due to buoyancy can be described by Eq. [2]

$$v = \frac{g \rho d^2}{18\eta} \qquad [2]$$

where g = gravitational constant, ρ = difference in density of gas and liquid, d = bubble diameter, η = viscosity of liquid. Assuming an electrolyte flow velocity of 400 cm/sec and a bubble diameter of 50μ, the vertical distance traveled by the bubble due to gravity during the time needed to pass over a 3 mm long electrode is only 1.2μ.

In order to account for the observed thickness of the two-phase region, unusually high velocities perpendicular to the flow direction are required. In Fig. 3c for example (100 A/cm^2, 1000 cm/sec), bubbles are found up to a distance of approximately 0.3 mm from the cathode surface. A bubble moving steadily outward from the leading edge of the electrode would need an average velocity perpendicular to the cathode of 100 cm/sec to reach this position at the downstream end of the electrode. This motion away from the cathode surface is aided by the turbulence in the liquid. Such an effect is suggested by the irregular shape of the two-phase region, which can show large variations in local thickness (Fig. 3). It is interesting to note, however, that the average thickness seems to increase little downstream from the middle of the cathode. If turbulent mixing were the only mechanism determining the spreading of the two-phase region, we would rather expect a steady increase of its average thickness in the flow direction. It is, therefore, possible that other mechanisms contribute to the dispersion of gas bubbles. An example is the "rapid fire mechanism" mentioned by Glas and Westwater (8), who observed that in stagnant solution bubbles were frequently ejected from the electrode at a high velocity. This phenomenon is, at present, not well understood. The relatively smaller increase of the two-phase region in the downstream part might also be ascribed to a lower current density in this region, caused by the higher gas fraction and the associated higher ohmic resistance in the electrolyte. Dissolution of gas in the electrolyte furnishes another possible explanation for the same phenomenon. Indeed, a simple estimation shows that, under most conditions, all the gas generated could be dissolved in the total electrolyte volume passing through the gap. For example, assuming a current density of 100 A/cm^2, 8 x 10^{-6} moles of hydrogen are produced per second in our cell, while, at a flow rate of 1000 cm/sec, 40 cm^3 of electrolyte are flowing through it. A homogeneous dissolution of all the generated hydrogen would result in a concentration of 2 x 10^{-4} moles/liter, which is of the same order as the saturation concentration of hydrogen in potassium chloride solutions (11). However, the direct dissolution of all cathodically generated gas without the formation of bubbles is, in general, not likely because the concentration gradients available under typical flow conditions are too small to account for the transport of dissolved hydrogen by convective diffusion. This is the case even under the assumption of a 1000-fold supersaturation at the electrode surface.

A rapid dissolution of initially formed gas bubbles could provide an alternate route to a homogeneous solution. This process would also affect the measured gas bubble diameters. Such a redissolution of gas bubbles would be similar to the behavior of vapor bubbles generated in a supercooled liquid under forced convection. Gunther (12) has shown that such bubbles became smaller and eventually disappeared upon moving downstream. The time required to dissolve 50% of the volume of a bubble of 50μ diameter can be estimated as follows: If we assume saturation concentration of the gas at the gas-liquid interface under constant pressure, and zero gas concentration in the bulk solution, the concentration difference driving force will be given by the saturation concentration, say 5 x 10^{-4} moles/liter. For a constant mass flux per unit area of a spherical bubble, the decrease in volume may then be expressed by Eq. [3]

$$\frac{dV}{dt} = -A\, k\, C_{sat}\, V^{2/3} \qquad [3]$$

with $A = (RT/P)\ 4\pi\ (3/4\pi)^{2/3}$, C_{sat} = saturation concentration, k = mass transfer coefficient (cm/sec), V = bubble volume. Integration leads to Eq. [4]

$$3(V^{1/3} - V_o^{1/3}) = A\, k\, C_{sat}\, t \qquad [4]$$

where V_o = initial bubble volume. The time $t_{1/2}$ in which the volume is reduced to ½ V_o is

$$t_{1/2} = \frac{2.38\, V_o^{1/3}}{A\, k\, C_{sat}} \qquad [5]$$

With an arbitrarily assumed mass transfer coefficient of 10^{-1} cm/sec,[6] one obtains $t_{1/2} \approx 1$ sec for 1 atm, 298°K. This time is almost four orders of magnitude larger than the residence time of a bubble moving at 1000 cm/sec between the electrodes (3 x 10^{-4} sec). The redissolution of gas is, therefore, too slow to produce a homogeneous gas solution within the length of the present electrode gap or even to affect measurably the diameter of bubbles in our photographs.

Influence of electrolyte.—Figure 7 illustrates the surprising observation that less gas was produced at the cathode in KNO_3 than in KCl solutions, under otherwise identical conditions. The relative volume of the two-phase region in the interelectrode gap, shown in Fig. 8, has been obtained by planimetry of the areas occupied by the dispersed gas in the photographs. Since the solubility of hydrogen is about the same in both electrolytes (11), the observed difference must be due to other than differences in solubility. For example, the same amount of hydrogen could appear to be smaller in nitrate solutions due to a more finely dispersed form. A more likely explanation is that, due to the reduction of nitrate at the cathode, only part of the current is used for hydrogen evolution. In the present flow apparatus, the total amount of evolved hydrogen could not be determined, but some experiments were performed in stagnant solutions of KNO_3 and KCl at 5 A/cm^2. They confirmed that a much smaller volume of hydrogen was produced in nitrate than in chloride solution. A quantitative investigation of cathodic reactions in nitrate solutions has been initiated. The effect of different electrolytes on the amount of cathodically formed gas was further investigated by use of chlorate and sulfate solutions. Both the photographs taken in the flow system and the volumetric measure-

[6] Since the relative motion between bubble and solution is not known, the mass transfer coefficient k has to be assumed arbitrarily. The value chosen is a maximum guess. It corresponds to the figure estimated for the electrode-solution interface at the highest flow rates employed (3).

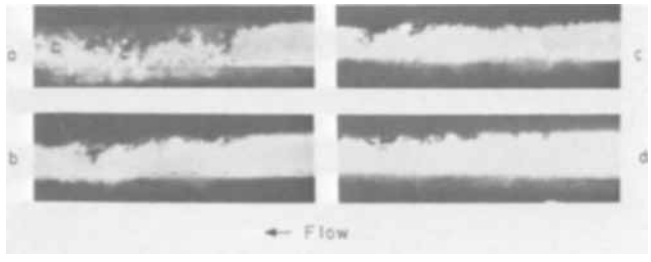

Fig. 7. Cathodic gas evolution at 100 A/cm^2 in 2N KNO_3 and 2N KCl, cathode facing down: a—KCl, flow rate 400 cm/sec; b—KCl, flow rate 800 cm/sec; c—KNO_3, flow rate 400 cm/sec; d—KNO_3, flow rate 800 cm/sec.

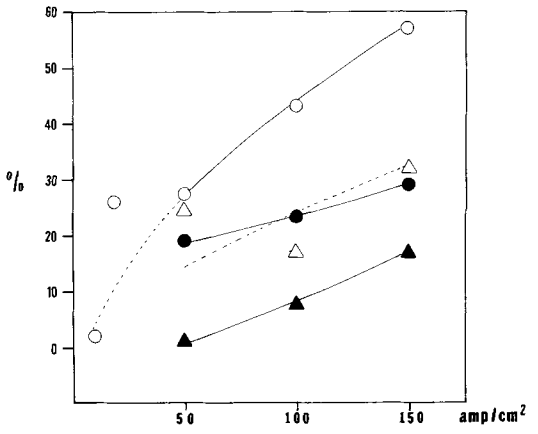

Fig. 8. Apparent volume fraction of interelectrode gap occupied by two-phase region (gas-electrolyte mixture): ○—2*N* KCl, 400 cm/sec; ●—2*N* KCl, 800 cm/sec; △—2*N* KNO_3, 400 cm/sec; ▲—2*N* KNO_3, 800 cm/sec.

ments in stagnant solutions indicated that, within the experimental accuracy, the same amount of gas was generated in these electrolytes as in the chloride solution.

Potential measurements under high current density conditions are dominated by large ohmic drops in the electrolyte between the working electrode and the tip of the reference electrode capillary (3). The apparent cathode potentials, thus determined at constant current density, provide an indirect measure of electrolyte conductivity and, consequently, gas volume fraction. Apparent cathode potential measurements are given in Fig. 9. It can be seen that a rapid increase of potential with decreasing flow rate, indicating the presence of a substantial volume fraction of gas in the electrode gap, occurs at a higher flow rate in chloride than in nitrate solutions. This shift is consistent with the evolution of a larger gas volume in the first electrolyte.

Discussion

Ohmic resistance.—Since one of the purposes of this study was to define the effect of cathodically generated gas on the electrolyte resistance, the question remains under which conditions this effect is significant. For the controlled current operation of these experiments, an increase in the ohmic resistance of the electrolyte results in an increase in over-all cell voltage. A marked increase in cell voltage, which is observed with decreasing flow rate in 2*N* KCl (Fig. 10), can be attributed primarily to cathodic phenomena, since anode potentials did not vary by more than 1-4V for different flow rates. This increase in cell voltage occurs at flow rates which rise with increasing current density and parallels the onset of voltage fluctuations. Although the qualitative influence of gas bubbles on cell voltage is thus strongly indicated, it has not been possible to derive a simple quantitative relation between the gas volume fraction and the cell voltage, which would hold for different current densities. The difficulty may, in part, be due to the fact that the gas was not homogeneously dispersed, neither in the direction normal nor parallel to the electrodes. The bubbles which have been observed to stick to the cathode surface at flow rates below 400 cm/sec further complicate the situation. Cole and Hopenfeld (1) have also investigated the influence of gas bubbles on cell voltage under ECM conditions. They accounted for the effect of the dispersed gas on the ohmic resistance of the electrolyte by using a relation given by De La Rue and Tobias (13). By making certain simplifying assumptions about the two-phase region and by adjusting one empirical parameter, they obtained agreement between theoretical and experimental results. The present study suggests, however, that such a simple treatment is not valid for the range of conditions employed here.

Sparking.—The formation of continuous gas blankets on vertical wire electrodes in sulfuric acid, at current densities of 6-8 A/cm², has been described by Kellogg (14). The formation of his gas blanket coincided with a drastic increase in surface temperature and a sharp drop in current. A similar phenomenon also is known to occur in heat transfer under forced convection conditions, where formation of vapor films leads to a sharp reduction in heat flux (burn out, critical heat flux) (15). It was, therefore, of interest to see whether, under ECM conditions, similar gas films are formed and whether they may lead to sparking and electrical breakdown. As long as a sufficiently high flow rate was maintained, no such phenomena were observed in the present experiments, even at current densities much higher than those employed by Kellogg. Upon decreasing the flow rate, however, large voltage fluctuations and eventual sparking occurred. These fluctuations, indicated by the broken lines in Fig. 10, soon became so large as to impede any measurement upon further re-

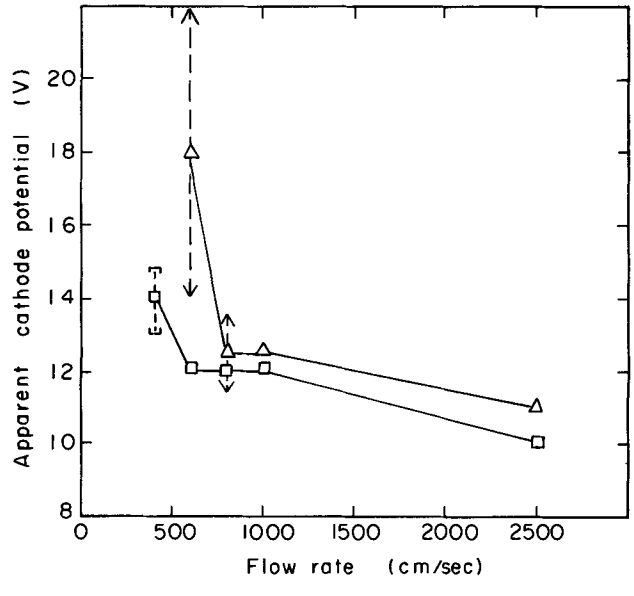

Fig. 9. Effect of gas evolution in different electrolytes on apparent cathode potentials, measured *vs.* sat. calomel with capillary upstream from the electrode. Current density 100 A/cm², cathode facing up. △—2*N* KCl, □—2*N* KNO_3. - - - amplitude range of voltage fluctuations.

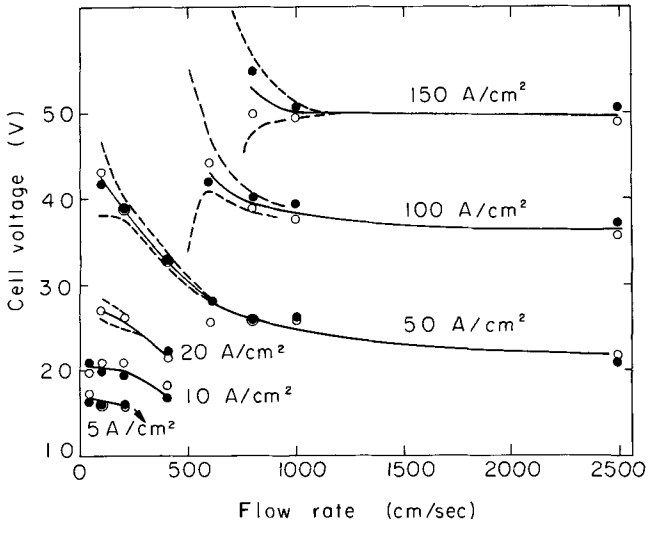

Fig. 10. Effect of gas evolution in 2*N* KCl at different current densities on cell voltage: ●—cathode facing down; ○—cathode facing up; - - -, amplitude range of voltage fluctuations.

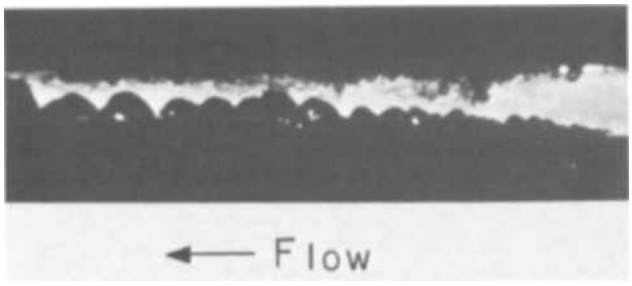

Fig. 11. Anodic dissolution products generated in 2*N* $NaClO_3$ at 50 A/cm² and 100 cm/sec. Cathode facing up.

duction of flow rate. A close parallelism between oscillations in cathode potential and cell voltage confirmed the cathodic origin of the oscillations. The onset of these fluctuations coincided with the appearance of a different type of gas bubble characterized by a large size and odd shape. Picture (a) in Fig. 3 is typical for this situation. It appears that, under these conditions, small individual bubbles are no longer generated and continuous gas pockets may cover a sizeable fraction of the cathode surface. Although an actual sparking event could not be photographed, it is possible that such a breakdown coincides with an instantaneous complete coverage of the cathode. The gas volume fraction, at which uncontrolled fluctuations set in, has been estimated on the basis of current density and flow rate (neglecting gas dissolution) to be approximately 0.2 at 100 and 150 A/cm².

Anode reactions.—Voltage oscillations in constant current electrolysis may also originate at the anode. While a detailed discussion of such phenomena is beyond the scope of the present report, it is interesting to note that the anodic oscillations have been observed under certain conditions with several electrolytes, most notably sodium chlorate. Figures 12a to c illustrate how the anodic contribution to fluctuations in over-all cell voltage U increases in the electrolyte series, chloride, nitrate, chlorate, while the cathodic contribution remains about the same (except for a slight reduction in nitrate, due to the smaller gas volume). Of particular interest are the usually well behaved periodic oscillations which originate at the anode (as indicated by the apparent anode potential e_A in Fig. 12c) in chlorate solution. The frequency of these oscillations depended primarily on current density and was only slightly

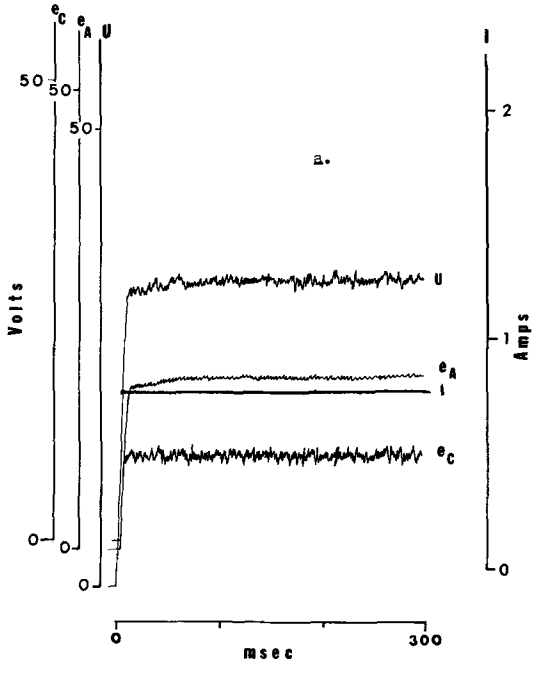

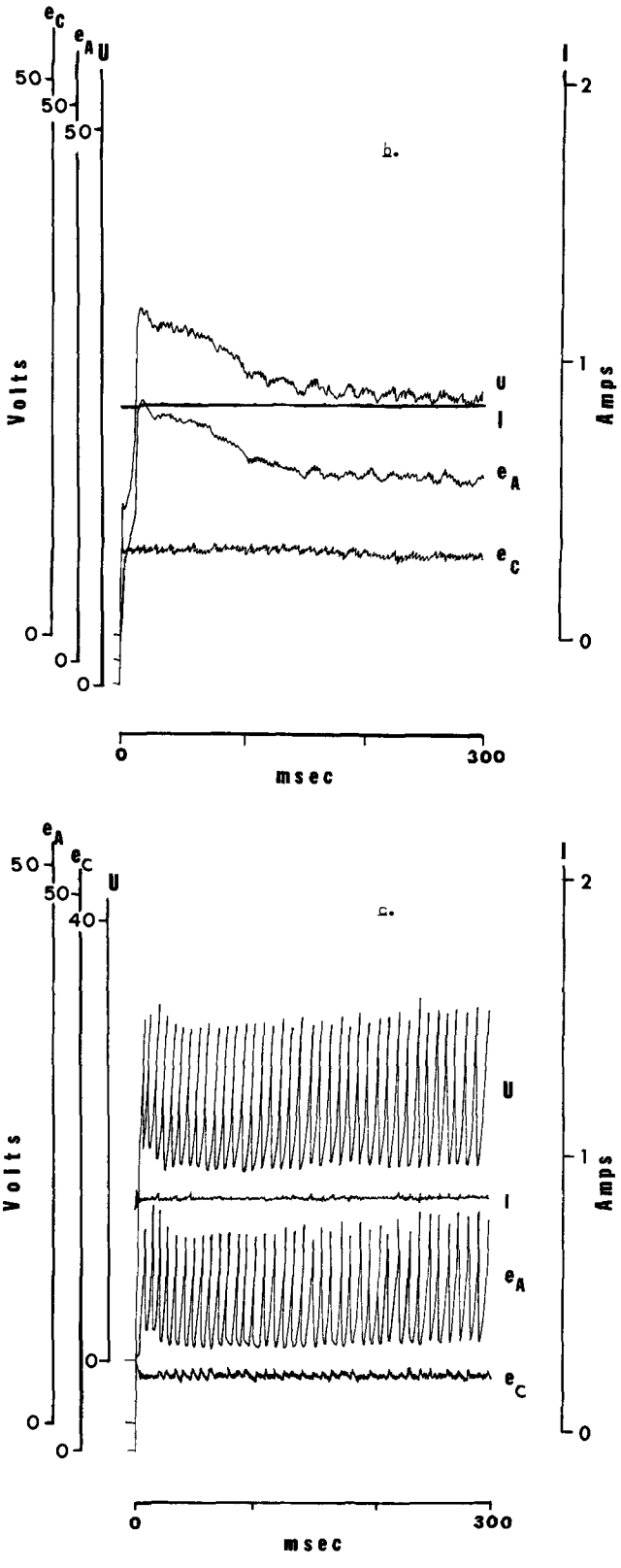

Fig. 12. Typical recorder traces of cell voltage U, current I, apparent anode potential e_A, and apparent cathode potential e_C; 50 A/cm², 400 cm/sec. a—2*N* KCl, b—2*N* KNO_3, c—2*N* $NaClO_3$.

affected by changes in flow rate. Typical frequencies were 130 and 300 Hz at 50 and 100 A/cm², respectively. The voltage fluctuations which originate at the cathode were irregular. Their frequency was much higher (mostly over 2000 Hz) and the amplitude depended strongly on flow rate as well as current density. Periodic phenomena at the anode can be related to the formation of solid films (3, 16), and Fig. 11 shows indeed how solid dissolution products are being re-

moved from the anode surface (together with a small amount of gas). Similar, but less pronounced, shedding of solid reaction products has been observed in sulfate and nitrate solutions.

The photographic pictures obtained in this study also demonstrate that, under the conditions of a previous investigation of anodic phenomena (3), gas bubbles were usually confined to the vicinity of the cathode. In view of the low solubility of hydrogen gas, it can be concluded that any fraction of the total anodic current possibly used for the oxidation of hydrogen has been negligible. The distribution of gas bubbles in the interelectrode gap gave no indication of the occurrence of plug flow phenomena, which could drastically affect mass transfer at the anode.

Summary and Conclusions

The present study was aimed at providing visual information on cathodic gas evolution during high rate metal dissolution, in order to determine the importance of cathodic phenomena on ohmic electrolyte resistance, anode reactions, and sparking. Qualitative rather than quantitative conclusions can be drawn from the results obtained in a flow channel cell with short electrodes.

1. The size of cathodically generated gas bubbles depends on current density as well as flow rate. At flow rates above 400 cm/sec, only very small (few microns in diameter) or no recognizable bubbles were generated.

2. A substantially smaller gas evolution in nitrate than in chloride solutions has been observed. It indicates the occurrence of cathodic reactions other than hydrogen evolution in the former solution.

3. The influence of cathodically generated gas bubbles on the ohmic cell resistance was very small at flow rates above approximately 1000 cm/sec for all current densities employed (up to 150 A/cm^2). At lower flow rates, this influence can be substantial. Models which are based on a uniformly distributed two-phase region and, among other simplifications, neglect the residence time of gas bubbles on the cathode surface, did not predict valid cell voltages.

4. No plug flow phenomena seem to have been induced by the gas evolution under the conditions employed in the present study.

5. The influence of cathodic gas evolution on anodic processes such as mass transfer and current efficiency was usually very small.

6. At insufficient flow rates, strong fluctuations in cell voltages were observed, which coincided with the formation of gas patches at the cathode and which eventually led to electric breakdown. The effect was more pronounced in chloride than nitrate solutions, in agreement with the fact that less gas was generated in the latter solutions under otherwise identical conditions.

7. In the absence of a theoretical model describing even the most simple single bubble dynamics in a flow field, additional experimental observations are needed to gain even a qualitative insight into the factors which determine growth, detachment, and dispersion of gas bubbles generated at high current densities and electrolyte flow rates in narrow gaps.

Acknowledgment

This work was conducted under the auspices of the U.S. Atomic Energy Commission.

Manuscript received Jan. 12, 1970.

Any discussion of this paper will appear in a Discussion Section to be published in the December 1970 JOURNAL.

REFERENCES

1. J. Hopenfeld and R. R. Cole, *J. Eng. Ind.*, **88**, 455 (1966).
2. J. Hopenfeld and R. R. Cole, *ibid.*, **91**, 755 (1969).
3. D. Landolt, R. H. Muller, and C. W. Tobias, *This Journal*, **116**, 1384 (1969).
4. G. H. Cook, in "Applied Optics and Optical Engineering," R. Kingslake, Editor, Vol. 3, p. 118, John Wiley & Sons, New York (1965).
5. J. Venzcel, Ph.D. Thesis No. 3019, ETH, Zurich (1961).
6. B. Kabanov and A. Frumkin, *Z. Phys. Chem.*, **A165**, 433 (1933).
7. L. S. Tong, "Boiling Heat Transfer and Two Phase Flow," p. 138, John Wiley & Sons, New York (1965).
8. J. P. Glas and J. W. Westwater, *Intern. J. Heat Mass Transfer*, **7**, 1427 (1964).
9. H. Y. Cheh, Ph.D. Thesis, Univ. of California, Berkeley; UCRL-17324 (1967).
10. F. H. H. Valentin, "Absorption in Gas Liquid Dispersions," E. F. N. Spon, Ltd., London (1967).
11. International Critical Tables, **3**, 272 (1929).
12. F. C. Gunther, *Trans. ASME*, **73**, 115 (1961).
13. R. E. De La Rue and C. W. Tobias, *This Journal*, **106**, 827 (1959).
14. H. H. Kellogg, *ibid.*, **97**, 133 (1930).
15. S. Levy, in "Lecture Series on Boiling and Two Phase Flow for Heat Transfer Engineers," H. A. Johnson, Editor, p. 81, Univ. of California Extension, Berkeley and Los Angeles (1965).
16. K. Kinoshita, Ph.D. Thesis, Univ. of California, Berkeley; UCRL-19051, Sept. 1969.

Technical Note

Capacitor Discharge Current for Thin-Film Alloy Deposition

Herman E. Austen

Process Research & Development, The National Cash Register Company, Dayton, Ohio

There are numerous articles in the literature on the use of thin films (less than 1000Å) of iron-nickel alloy for computer memories (1-5). These thin-film memory elements switch either by Néel wall movement or, preferably, coherent rotation. The rotational switch is faster and switching time is inversely proportional to the difference of the applied field and the coercive force.

Thin films of iron-nickel have been produced by sputtering, vacuum deposition, and electrodeposition.

Maintaining a constant composition from initial deposit to final thickness is difficult in electrodeposition of thin films because equilibrium conditions must be established in the cathode film and this requires an appreciable time. In the thinnest films (~ 500Å, or less), the total thickness may be deposited by the time equilibrium has been reached. The resultant change in composition will exert an appreciable influence on magnetic properties up to 1000Å, or more, thickness (15-17).

Several investigators have analyzed deposits as a function of thickness and have tried to obtain uniformity by the use of varying currents instead of direct current (6-14). Improvement has been obtained but none of the methods have produced a constant composition.

A method is herein described for varying the current to obtain a nearly constant coercive force from initial deposit to any desired thickness. In plots of coercive force *vs.* thickness using constant current, it had been found that the coercive force increased logarithmically with decreasing thickness. Various investigators had made analyses of thin deposits of iron-nickel (6-8), showing a similar increase in iron concentration of the deposit with decreasing thickness.

Since increasing the current density increases the nickel concentration, it was felt that a current which started high and decayed logarithmically to some d-c value would counteract the composition change. The curves of composition *vs.* thickness, or time, are similar to the decay current of a capacitor through a resistor. Although it has been shown that composition varies as $t^{-1/2}$ (14), for the short times involved in deposition of very thin films, variation of the current with log t is probably a close enough approximation and can be more easily obtained. The effect of such a current on the magnetic properties of iron-nickel deposits was investigated.

The simplest form of circuit is a power supply, capacitor, and DPDT switch as shown in Fig. 1(a). However, there is little flexibility in this circuit. One which provides for plating various thicknesses on cathodes of various configurations and sizes is shown in Fig. 1(b).

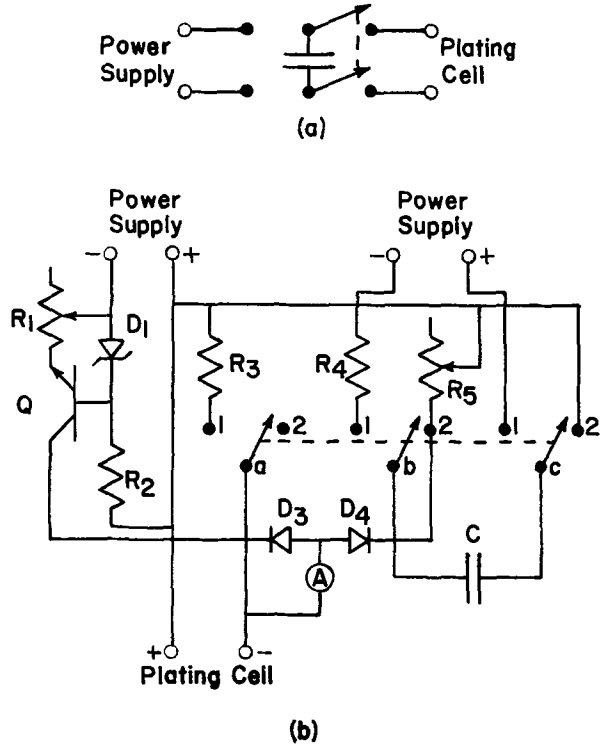

Fig. 1. Capacitor discharge circuits: (a) simplest form; (b) as used in experimental work.

Table I. Circuit values used in obtaining Fig. 2

R_1	500 ohms
R_2	750
R_3	22
R_4	22
R_5	5
D_1	V_z – 7.5V
C	0.35f
Plating cell impedance	300 ohms

Resistors R_1 and R_2, transistor Q, and Zener diode D_1 form an adjustable constant current circuit for the d-c plating current. When the gang switch is in position 1, the resistor R_3 acts as a load and allows presetting of the current and also acts to provide a bias against solution potential when the cathode is being placed in the solution. Also, with the switch in position 1, the capacitor is being charged through the current limiting resistor R_4.

When the switch is thrown to position 2, the capacitor is connected to the plating cell and resistor R_5 in parallel. Diode D_3 prevents capacitor current from flowing into the constant current circuit and, when the current from the capacitor drops to the preset constant direct current, the current flow comes from the constant current part of the circuit and diode D_4 prevents this current from flowing into the capacitor part of the circuit. Resistor R_5 adjusts the rate of decay of the capacitor. The resistance of R_5 is much less than the impedance of the plating cell and the capacitor charge is much larger than that required to deposit the iron-nickel. These conditions allow some variation in plating resistances without appreciable effect on the capacitor discharge time.

The values of the components as used for depositing on samples 1.8 cm in diameter are shown in Table I. Both power supplies provided 15V. These adjustments for optimum results were found by trial and error, using magnetic properties as the criteria. Undoubtedly, the optimum values of these components will vary with solution composition, temperature, and other operating variables. Satisfactory methods of analysis were not available and the samples were complicated as to analysis because the iron-nickel was deposited over a nonmagnetic chemical nickel deposit on a platinum substrate.

A composition of approximately 20% iron-80% nickel was assumed when a low coercive force and nearly zero magnetostriction were obtained. The shape of the

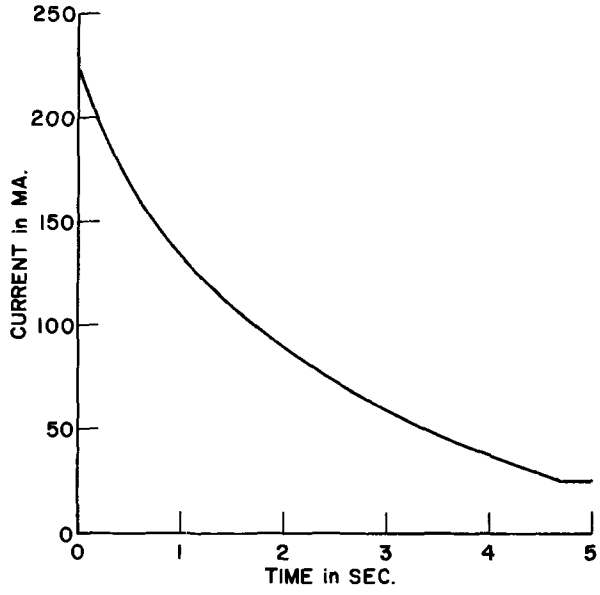

Fig. 2. Typical capacitor discharge current to a d-c level

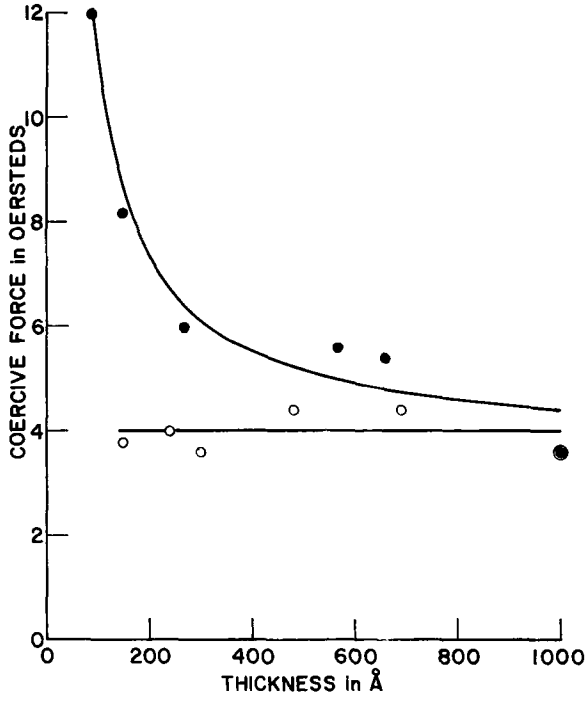

Fig. 3. Comparison of coercive force of d.c. and capacitor discharge plated films: ●, d.c.; ○, capacitor discharge.

hysteresis loop also suggested a constant composition when the sides were straight and the knees square. A typical current-time curve is shown in Fig. 2.

A comparison of coercive force *vs.* thickness curves for d-c plated samples and capacitor discharge plated samples is shown in Fig. 3. These samples were deposited on a platinum foil substrate which was stripped and re-used so that the epitaxial effect was the same for each sample. Also, a plating solution volume of 2 liters was used so that compositional, impurity, and pH variations were minimized. The platinum was not bright and thus a higher coercive force was obtained than would have been the case on a mirror-smooth substrate. On smooth copper, a coercive force of 5 oersteds was obtained at a thickness of only 65Å and an iron-nickel-molybdenum film deposited on copper had a coercive force of 4.5 oersteds at only 13Å thickness. These thicknesses were estimated from flux densities and charge used in deposition.

Experiments with pulsed current, a-c superimposed on d-c, and an initial high voltage strike have shown the capacitor discharge to be much better in obtaining the desired uniformity of thin-film deposits.

Manuscript submitted Sept. 19, 1969; revised manuscript received *ca.* Feb. 25, 1970.

Any discussion of this paper will appear in a Discussion Section to be published in the December 1970 JOURNAL.

REFERENCES

1. R. J. Petschauer, *IEEE Trans. on Magnetics*, **MAG-1**, 185 (1965).
2. P. D. Barker and E. J. Torok, *J. Appl. Phys.*, **37**, 1363 (1966).
3. J. E. Eide, *ibid.*, **37**, 1365 (1966).
4. Hsu Chang, *ibid.*, **38**, 1203 (1967).
5. John H. Kefalas, *IEEE Trans. on Magnetics*, **MAG-3**, 135 (1967).
6. G. H. Cockett and E. S. Spencer-Timms, *This Journal*, **108**, 906 (1961).
7. M. E. Henstock and E. S. Spencer-Timms, *Trans. Inst. Metal Finishing*, **40**, Pt. 4, 179 (1963).
8. W. O. Freitag, J. S. Mathias, and G. DiGuilio, *This Journal*, **111**, 35 (1964).
9. R. Girard, *J. Appl. Phys.*, **38**, 1423 (1967).
10. J. M. Brownlow, *ibid.*, **38**, 1440 (1967).
11. W. D. Doyle, *ibid.*, **38**, 1441 (1967).
12. Zlata Kovac, Paper presented at the Montreal Meeting of The Society, Oct. 6-11, 1968.
13. Harold B. Shukovsky and Thomas P. Turnbull, *IEEE Trans. on Magnetics*, **MAG-4**, 59 (1968).
14. H. Dahms, *Electrochem. Technol.*, **5**, 448 (1967).
15. D. O. Smith, *J. Appl. Phys.*, **29**, 264 (1958).
16. I. W. Wolf, *ibid.*, **33**, 1152S (1962).
17. Fred E. Luborsky, *IEEE Trans. on Magnetics*, **MAG-4**, 19 (1968).

The Discussion Section which usually is published in this issue of the Journal will appear in the July 1970 issue.

JOURNAL OF THE ELECTROCHEMICAL SOCIETY

ELECTROCHEMICAL SCIENCE

JULY 1970

Some Aspects of the Mechanism of the Anodic Dissolution of Zinc in Sulfamic Acid-Formamide Solutions

I. A. Menzies, G. W. Marshall, D. Gearey, and G. B. Griffin

Corrosion Laboratories, Department of Chemical Engineering, University of Manchester Institute of Science and Technology, Manchester, England

ABSTRACT

The anodic behavior of zinc has been studied in sulfamic acid-formamide solutions as a function of sulfamic acid concentration, temperature, and water content of solutions. It has been shown that anodic polarization curves for Zn are typical of polishing systems, and it has been found that linear relationships exist between limiting current densities and the reciprocal viscosities of the solutions. The processes in solution are controlled by diffusion of cations or of solvent species. Film formation occurs at the onset of polishing as shown by a-c impedance studies, and this film is either highly soluble or unstable in the presence of considerable amounts of water. The over-all conclusion is that the mechanisms of polishing in sulfamic acid-formamide solutions are in agreement with those proposed by Hoar for anodic polishing in other environments.

The present work is a continuation of previous studies (1-3) of the anodic behavior of metals in organic electrolyte solutions. It has been shown that Fe, Cd, Sn, Ti, Zn, Pb, Ag can be electropolished in 1M sulfamic acid-formamide solutions and that typical anodic polarization curves are obtained under potentiostatic conditions. Furthermore similar, although less clearly defined, cell polarization curves have been obtained under galvanostatic conditions. However, these studies have been of a general nature, and the mechanisms involved in such anodic processes have not been examined in any great detail. Zinc appeared to be one of the more stable systems and hence perhaps the most promising of metals for such studies, and in the present work the role of sulfamic acid concentration, solution temperature, and the effects of water additions have been studied in relation to the anodic behavior of zinc in formamide. Alternating current measurements have also been made to study general aspects of the etching-polishing transition in this system.

Experimental

General techniques for the handling of anhydrous organic electrolyte solutions have been described elsewhere (1, 3) as have many of the experimental procedures. Only essential information will be given here.

Materials and polarization studies.—Formamide was purified by the method of Verhock (4) and had a specific conductance of 2 x 10^{-4} ohm^{-1} cm^{-1} at 25°C. Microanalytical grade sulfamic acid was used without further purification after storage in a vacuum desiccator. Zinc of 6*N* purity was used as the anode throughout. Zinc sulfamate hydrate was prepared by the reaction of zinc carbonate and sulfamic acid, the Zn sulfamate being crystallized out of the filtrate by evaporation of the solution under reduced pressure at 40°-50°C.

The cell used for polarization measurements has been described elsewhere (1, 3). The working electrode was placed between two Ta counterelectrodes, and the potential of the working electrode was measured against a $Cd/CdCl_2$ electrode in a KCl (satd.)-formamide solution prepared as described by Pavlopoulos and Strehlow (5) and contained in a separate compartment. The working electrode was a zinc rod machined to fit tightly into PTFE tubing so as to expose approx. 0.75 cm^2. The PTFE tube was fitted tightly into a glass tube and the Zn connected to a copper wire via a mercury contact as described previously (3). The Zn electrodes were prepared metallographically to 600 grade SiC paper, vapor degreased, etched in 10% HNO_3, and washed in distilled water, then formamide before use.

The polarization curves were measured galvanostatically using an electronically stabilized galvanostat (E.M. Wareham Measuring Instruments Ltd., Type C 220) having a variable output of up to 1A at 80V. A Millivac d-c Multimeter (Type MV 77B) was used to measure the potential between reference and working electrodes. During polarization measurements the galvanostatic current was increased in a stepwise manner (2.5-7.5 mA) and the potential of the working electrode determined 15s after each step. All measurements were carried out at 25° ± 0.1°C.

Measurement of solution densities and viscosities at 25° ± 0.1°C.—Densities were determined using a graduated pycnometer of 5 ml size, and viscosities were determined using British Standard U-tube viscometers sizes A and B. Double distilled water boiled for 30 min and quickly cooled immediately before use was used for calibration of both the pycnometers and U-tube viscometers, and the measurements of densities and viscosities were made in accordance with the Institute of Petroleum standard methods (6). For cali-

bration purposes the density and viscosity of water were taken to be 0.99704 g/cm³ and 0.8937 cp at 25°C, respectively (7).

A-C impedance measurements.—The bridge network is shown in Fig. 1. The 10 kHz sine wave input was controlled at 10 mV amplitude to prevent interference with the d-c process. A screened and balanced transformer input (T_1) was used, the supply thus being balanced to earth. The resistive ratio arms R_1, R_2 were maintained at equal values if possible to maintain best the advantages of the balanced input. The unknown was measured as a series resistance/capacitance combination.

The d.c. was applied across the diagonal of the bridge to avoid any possibility of shunting the a.c. from the unknown; a battery supply was used in order to minimize noise and earthing problems. A choke in the d-c circuit blocked a-c from d-c circuit when the bridge was unbalanced and the capacitor C_b blocked the d-c path through the diagonal. Bridge imbalance was detected with a tuned amplifier coupled to the bridge through the screened transformer T_2.

A special electrode was constructed for a-c measurements (Fig. 2). A strip of Zn, ~1 mm², was soldered to the end of the copper connecting wire and the specimen sealed into the glass tube with Araldite. Before use the base of the electrode was ground flat exposing ~1 mm² of metal surface to the electrolyte. The electrode was lightly pickled in 10 v/o HNO_3, washed and dried with acetone in a stream of warm air before use. This electrode was made the anode and surrounded by a large Ta cathode. The prepared anode was lowered into the solution in the cell in an atmosphere of dry oxygen-free nitrogen and the bridge balanced alternately for resistance and capacitance. Various current densities were then applied (0.1-1.0 mA/mm²) and the corresponding resistance and capacitance recorded.

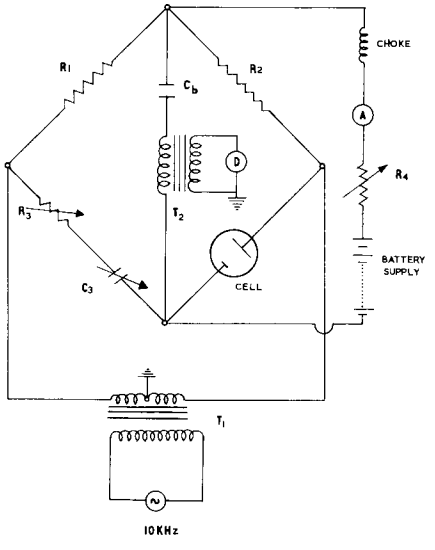

Fig. 1. Bridge circuit for a-c measurements: R_1, R_2, resistive ratio arms; R_3, C_3, variable resistance and capacitance boxes; T_1 screened and balanced transformer; T_2 screened transformer; A ammeter (100 mA); R_4 variable resistor (for current control); D tuned amplifier.

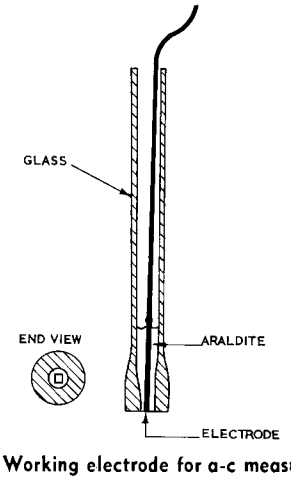

Fig. 2. Working electrode for a-c measurements

Results

Density and viscosity measurements.—The densities and viscosities of the solutions used in the present investigation are given, with other data, in Tables I-III. The viscosities of solutions of sulfamic acid in formamide varied with sulfamic acid concentration in accordance with the expression $\log \eta = \log \eta_o + Zc$ where η and η_o are the kinematic viscosities of the solution and pure formamide, respectively, c is the concentration of sulfamic acid in moles/liter, and Z is a constant (Fig. 3.). It is also clear that there was a change in the slope of the function at concentration of 0.6-0.7M w.r.t. sulfamic acid (curve A). In sulfamic acid-formamide-water solutions similar relationships hold in formamide solutions with water concentrations up to 5M and in solutions containing >50 v/o water, *i.e.*, >26M, curve B.

Anodic polarization of zinc in sulfamic acid-formamide solutions.—The overpotential-current density relationships obtained in sulfamic acid-formamide solutions all exhibited reasonably well-defined limiting current densities. Typical curves are shown in Fig. 4; the values of the limiting current densities are given in Table I. In general the reproducibility of the curves and the limiting current densities was excellent (±2%), but at high overpotentials corresponding to the upper end of the limiting current density plateaus some scatter was observed. This made accurate measurement of the overpotential range corresponding to the limiting current density somewhat difficult. It is however clear that the overpotential range corre-

Table I. Densities, viscosities, and polarization data for the anodic dissolution of Zn in sulfamic acid-formamide solutions at 25°C

Sulfamic acid conc. (M)	Density, g. cm⁻³	Viscosity, cp	I_{lim}, mA/cm²	Voltage range corr. to I_{lim} (V)
0	1.139	3.350		
0.10	1.142	3.401	100	21
0.25	1.148	3.607	70	32
0.50	1.153	3.858	66	24
0.75	1.165	4.349	60	30
1.0	1.177	4.918	53	33
2.6 (sat.)	1.260	11.520	28	60

Table II. Densities, viscosities, and polarization data for the anodic dissolution of Zn in 1M sulfamic acid-formamide-water solution at 25°C

Water conc. m/l	Density, g. cm⁻³	Viscosity, cp	I_{lim}, mA/cm²	Voltage range corr. to I_{lim} (V)
4.07	1.170	3.418	85	28
7.24	1.169	3.091	96	20
10.41	1.164	2.687	115	17.5
15.68	1.157	2.179	188	12.5
26.83	1.153	1.604	322	9.0
31.96	1.126	1.396	428	—
37.39	1.111	1.251	—	—

Table III. Densities, viscosities and polarization data for the anodic dissolution of Zn in 1M-sulfamic acid-formamide solution 8.1M wrt water at 25°C

Zn sulfamate hydrate conc. (M)	Density, g. cm⁻³	Viscosity, cp	I_{lim}, mA/cm²
0.063	1.170	3.096	110
0.125	1.177	3.493	110
0.188	1.187	3.726	100

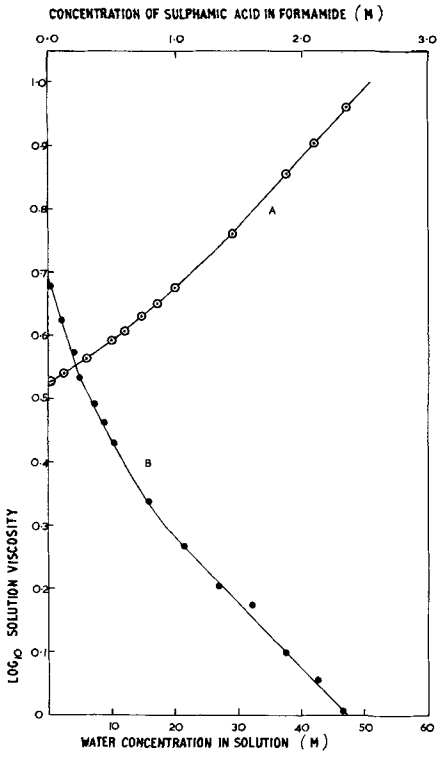

Fig. 3. Relationship between concentration and solution viscosity at 25°C (A) sulfamic acid in formamide, (B) H_2O concentration in 1M sulfamic acid-formamide solutions.

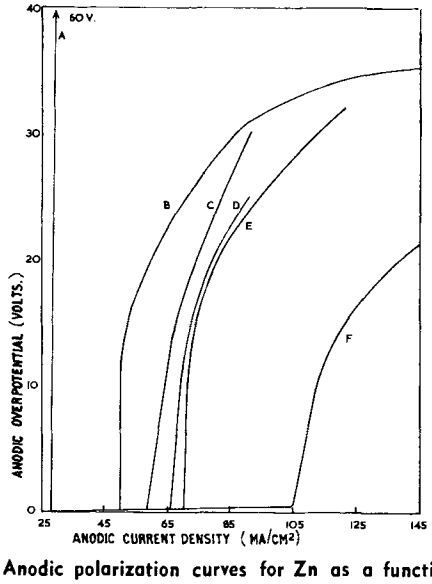

Fig. 4. Anodic polarization curves for Zn as a function of sulfamic acid concentration at 25°C: A, 2.6M; B, 1.0M; C, 0.75M; D, 0.5M; E, 0.25M; F, 0.1M.

sponding to the limiting current density increased with increasing sulfamic acid concentration from ~22V in 0.1M solutions to ~60V in 2.6M solutions. The limiting current density (Table I) decreased with increasing sulfamic acid concentrations, *i.e.*, with increasing solution viscosity. In fact (Fig. 5) there was a linear relationship between the limiting current density and the reciprocal of viscosity for sulfamic acid concentrations of from 0.25 to 2.6M.

The polarization curves obtained in 1M sulfamic acid-formamide solutions were similar at higher temperatures to curve B in Fig. 4 except that at 55°C there was a greater increase in current density with potential for potentials >7V than at other temperatures. The limiting current density increased with increasing temperature, and again there was a linear relationship

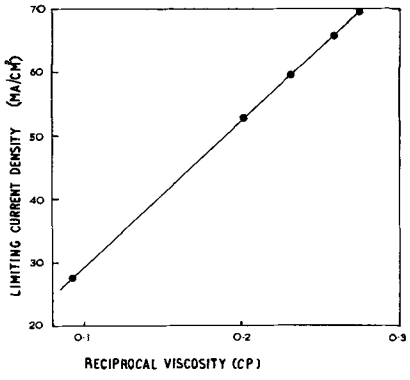

Fig. 5. Relationship between limiting current density and reciprocal viscosity as a function of sulfamic acid concentration at 25°C.

between limiting current density and reciprocal viscosity (curve A, Fig. 6).

Anodic polarization of zinc in 1M sulfamic acid-formamide-water solutions at 25°C.—The overpotential-current density curves obtained in 1M HSO_3NH_2-formamide solutions containing various proportions of water are shown in Fig. 7 and 8. The limiting current density was well defined at water concentrations up to ~31.9M (Fig. 7) whereas at higher water concentrations the limiting current density became decreasingly well defined as the water concentration increased. In general etching was observed at all current densities below the limiting current density and bright polishing at current densities equal to or greater than the limiting current density in solutions where these were reasonably well defined. It is clear from Table II that the solution viscosity decreased with increasing water concentration and this coincided with an increase in the observed values of limiting current density. For water concentrations up to 10.4M there was a linear relationship between the limiting current density and the reciprocal of solution viscosity (Fig. 8). This relationship did not however hold for higher water concentrations.

Anodic polarization of zinc in a 1M sulfamic acid-formamide-water (8.1M) solution at 25°C with Zn sulfamate additions.—Zinc sulfamate hydrate was not readily soluble in this solution and less so in sulfamic acid-formamide solutions in the absence of water. Hence only a limited investigation was carried out.

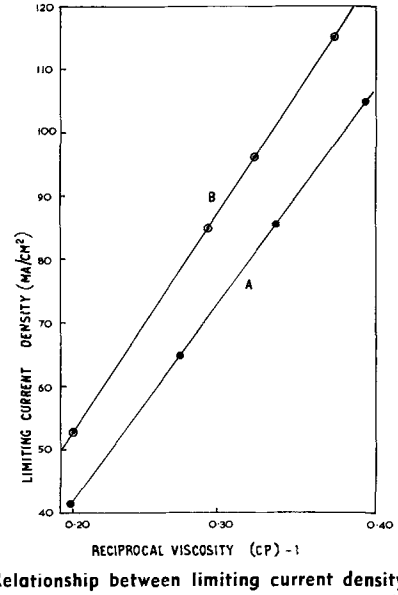

Fig. 6. Relationship between limiting current density and reciprocal viscosity as a function of (A) temperature and (B) water concentration in 1M sulfamic acid-formamide solutions.

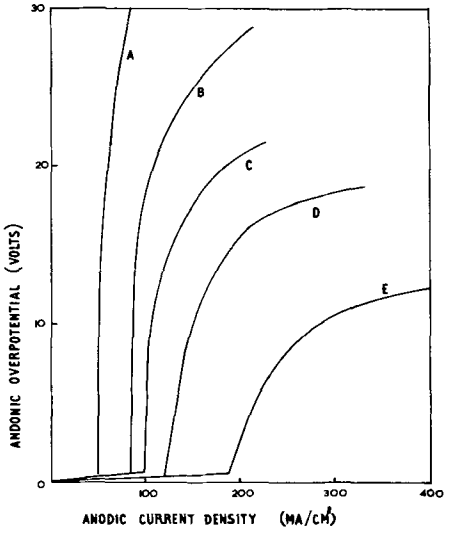

Fig. 7. Anodic polarization curves for Zn in 1M sulfamic acid-formamide-water solutions at 25°C as a function of water concentration: A, no H_2O; B, 4.07M; C, 8.1M; D, 10.4M; E. 15.7M.

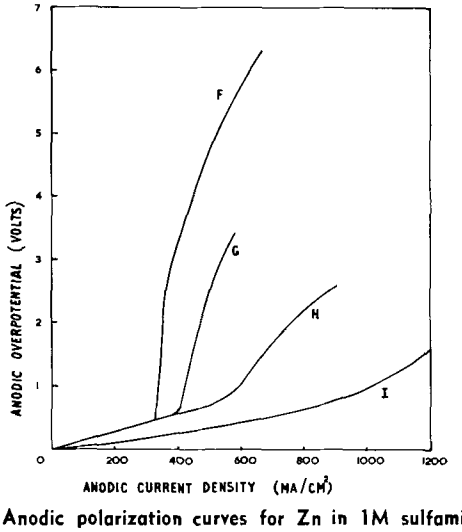

Fig. 8. Anodic polarization curves for Zn in 1M sulfamic acid-formamide-water solutions at 25°C as a function of water concentration: F, 26.8M; G, 31.9M; H, 37.4M; I, H_2O only.

The polarization curves were all similar to the corresponding curve in the absence of Zn sulfamate additions (C in Fig. 7) and showed well-defined limiting current densities typical of electropolishing systems. Again etching and polishing of zinc occurred in the appropriate regions of the curves. As can be seen in Table III, the solution viscosity increased with increasing zinc sulfamate concentration. This may have caused the decrease in the limiting current densities observed at higher sulfamate concentrations. However there appears to be relatively little effect of Zn ion concentration.

A-C impedance measurements in 1M sulfamic acid-formamide solutions at 25°C.—The variation of resistance and capacitance (measured as a SERIES combination) with current density is shown in Fig. 9A, 9B. Increase in current density toward i_{lim} resulted in small changes in resistance (a few per cent in the zero current value of 3.5 ohm cm²) and approximately a fivefold increase in capacity to 50 μF/cm² as the potential controlled conditions in the interphase changed. For current densities greater than i_{lim} the resistance and capacitance changed rapidly (<1 sec) to R values of 180 ohm cm² and C values of 0.2 μF/cm².

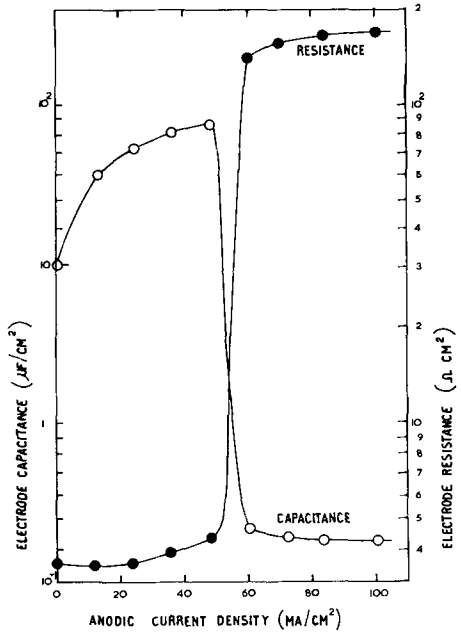

Fig. 9. Electrode resistance and capacitance as a function of current density during anodic polarization at 25°C in 1M sulfamic acid-formamide solutions: A, resistance; B, capacitance.

Interpretation and Discussion

The present results are an extension of previous studies of electropolishing (1-3, 8) and give a more detailed picture of a number of aspects.

The diffusional nature of the limiting currents is indicated by the linear $i_{lim}v \cdot 1/\eta$ relationship on varying the viscosity either by change of temperature (curve A, Fig. 6) or of sulfamic acid concentration (Fig. 5). Water content also affected viscosity and resulted in a linear $i_{lim}v \cdot 1/\eta$ relationship (curve B, Fig. 6) for water concentrations <10M where i_{lim} was still well defined. At higher water contents i_{lim} was ill defined probably due to increased solubility of the solid products of the dissolution reaction or to the water taking over as "acceptor" as discussed later.

The exact nature of the diffusing species is less certain. The values of i_{lim} obtained in this work are at the lower end of those found in aqueous polishing solutions (20 mA/cm²-several A/cm²) and this is in agreement with the larger solvodynamic unit expected in formamide. The over-all diffusion coefficient is nevertheless of the same order of magnitude as in aqueous solutions, and this suggests strongly that the diffusing species is a relatively simple species and is not a complex polymerized structure.

The diffusional situation appears then to be analogous to that in other environments reviewed by Hoar (9). Briefly, limiting currents are controlled either by (*i*) diffusion of metal ions away from the electrode surface the surface metal ion concentration $(M^+)_s$ being controlled by precipitation of a solid compound or (*ii*) diffusion of "acceptor" species (10-12) from the bulk solution.

The absence of effect of metal ion concentration (Table III), except in a possible viscosity effect, on i_{lim} might be thought to eliminate metal ion diffusion. However the diffusional flux is proportional to the concentration gradient $[(M^+)_s - (M^+)_b]/\delta$ where $(M^+)_b$ is the metal ion concentration in the bulk solution and δ is the diffusional layer thickness. If the maximum value of $(M^+)_b << (M^+)_s$ change in $(M^+)_b$ will not affect i_{lim}.

This might result from a high degree of supersaturation in the interphase (it seems likely that high field conditions in the double layer would encourage this) or simply from a rather soluble solid reaction product which permits a high value of $(M^+)_s$ before precipitation. An attempt was made, in the present work, to in-

vestigate the latter possibility and at the same time the variation of i_{lim} with $(M^+)_b$ by using a likely solid product zinc sulfamate as the source of $(M^+)_b$. Unfortunately only the hydrate salt was available, and its solubility was limited. Although little effect of i_{lim} with $(M^+)_b$ was noted this cannot be considered conclusive evidence against metal ion diffusion control of i_{lim}. It is intended to use anhydrous sulfamate and also other sources of metal ion to investigate this problem further; other sources of metal ion will of course entail introduction of foreign anions whose effect will need to be monitored.

The lack of effect of sulfamate ion bulk concentration $(sulf)_b$ on i_{lim} except as a viscosity effect (Fig. 5) does appear to eliminate sulfamate ion diffusion, because the diffusional flux would be approximately proportional to $(sulf)_b$ which is directly controlled. Other "acceptors" are available however which could control metal ion dissolution; the solvent itself either as a neutral species or as $HCO\ NH^-$ might be so involved. Such a mechanism could be correlated with the destruction of i_{lim} by water addition at higher concentrations (Fig. 8) as the faster diffusing water takes over the acceptor role. Thus although the diffusional nature of the limiting currents is clear, the diffusing species cannot be conclusively identified from a study of the limiting current behavior.

Perhaps the outstanding feature of the experimental results is the extremely high anode potentials (up to 60V) obtained. The appearance of these high potentials is accompanied by a rapid rise in a-c resistance and corresponding drop in series capacitance (Fig. 9). The resistance value is considerably larger than typical resistance measured in aqueous solutions (~100 ohm. cm^2 compared with ~10 ohm cm^2). It is considered that these observations can only be explained in terms of solid film formation for the following reasons:

1. The very rapid rise in a-c resistance and anode potential at currents of the order if i_{lim} is not typical of diffusion layer build up.
2. The fall in series capacitance is indicative of a thin film (~ several hundred Å).

Formation of a relatively thick viscous layer would be expected to result in a resistive increase only. The two cases are illustrated schematically below.

this results in R values ~400 ohm cm^2 and C values ~0.1 $\mu F/cm^2$ in the parallel mode. Using $C = (\epsilon/4\pi t)$ esu (9×10^{11} esu = 1F) where ϵ is the dielectric constant and t is film thickness and assuming $\epsilon = 10$ the value for $t \approx 10^{-5}$ cm.

3. If the resistance increase were due to a viscous layer in the region 0.05 cm thick (a typical probe/surface distance) the specific resistance would need to be 10,000 ohm cm^{-1}. Walton (13) measured specific resistances of simulated anodic diffusion layers in copper ion/phosphoric acid/glycerol solutions and found a maximum value of only 133 ohm cm^{-1}.

Epelboin *et al.* (14, 15) have also reported high anode potentials during Al polishing in ethanolic solutions of Mg $(ClO_4)_2$. They suggest a close packed anhydrous layer of adsorbed ClO_4^- ions to account for the high potentials. This appears unlikely. If specifically adsorbed layers were responsible for such potentials, then the phenomenon would have been observed in the numerous studies of the effect of specific adsorption on double layer structure (16). Hoar (9) has also criticized the close-packed layer idea on account of its lack of lateral stability.

It is considered more likely that the high anode potentials are simply a result of a more resistive than normal solid film, about 1000Å in thickness as indicated by the a-c impedance measurements. Further impedance measurements with potentiostatic control of the direct component are planned to confirm this hypothesis. The Zn system is ideal for such an investigation because of the large voltage and the high film impedances. The exact nature of the film also awaits further results.

The anodic behavior of zinc in these solutions can then be explained on the solid film theory of polishing (9, 17); a solid film in close contact with the metal surface suppresses etching by ensuring that random vacancies occur at the metal/film interface. This film is more resistive than normal aqueous polishing films. High anode potentials are a direct result of this resistance. The over-all process of dissolution is diffusion controlled in the solution phase. The nature of the diffusing species is uncertain. It is possible to combine the inward diffusion of an "acceptor" species with the film theory in a very similar way to the more conventional metal ion diffusion from the surface. A

PATHS

10 kHz. No film. Faradaic paths of minor importance. Impedance becomes series combination of solution resistance and double layer capacitance.

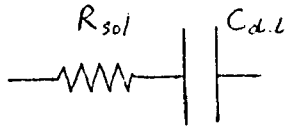

Thickish viscous layer. Capacitive impedance >> resistive impedance across layer. Layer appears as resistance only. Change in series resistance only.

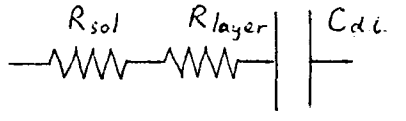

Thin solid film. Capacitive and resistive impedances of film are reasonable alternative paths. Change in total series R and C expected.

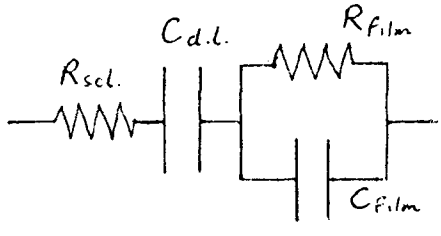

Moreover, in the present case, the film impedance is considerably larger that the other impedances, *i.e.*, solution resistance and double layer capacitance, and impedance measured can sensibly be attributed to the film. Series/parallel transformation is necessary to identify the resistive and capacitive film components—

choice between the two diffusion mechanisms (*i*) solvent diffusion from the bulk solution and (*ii*) metal ion diffusion from the surface cannot therefore be made at this stage. Water additions probably increase the film solubility or stability thus reducing anode potentials attainable and also decrease solution viscosity

resulting in an increase in i_{lim} values. The work of Epelboin (14, 18) in which refrigeration of the electrode increased the anodic potentials suggests that an increase in i_{lim} might in itself be responsible for film breakdown as a result of increased Joule (i^2R) heating. The effect of decreasing sulfamate concentration (Fig. 4) in increasing i_{lim} and decreasing the anode voltages can be similarly explained.

Acknowledgments

The authors wish to thank Professor T. K. Ross for the provision of research facilities and the Science Research Council for their support and interest in this work.

Manuscript received Jan. 20, 1970.

Any discussion of this paper will appear in a Discussion Section to be published in the June 1971 JOURNAL.

REFERENCES

1. I. A. Menzies, D. N. Bulin, and G. W. Marshall, *Trans. Inst. Metal Finish.*, **45**, 122 (1967).
2. I. A. Menzies and A. F. Averill, *Electrochim. Acta*, **13**, 807 (1968).
3. I. A. Menzies, G. W. Marshall, and G. B. Griffin, *Corrosion Sci.*, **9**, 287 (1969).
4. F. H. Verhock, *J. Am. Chem. Soc.*, **52**, 2693 (1930).
5. T. Pavlopoulos and H. Strehlow, *Z. phys. Chem.*, **2**, 89 (1954).
6. Standard Methods of Testing Petroleum Products, Institute of Petroleum (1951).
7. Handbook of Chemistry and Physics, 41st Ed., Cleveland, Chemical Rubber Publishing Co. (1959).
8. A. J. Johnson and L. L. Shreir, *Corrosion Sci.*, **5**, 269 (1965).
9. T. P. Hoar, "Modern Aspects of Electrochemistry," p. 262, J. O'M Bockris, Editor, Vol. 2, Butterworth, London.
10. M. Halfawy, *Experimentia*, **7**, 175 (1951).
11. J. Edwards, *This Journal*, **100**, 189C (1953).
12. C. Wagner, *ibid.*, **101**, 225 (1954).
13. H. F. Walton, *ibid.*, **97**, 219 (1950).
14. I. Epelboin, *Galvanotechnik u Oberflächenschutz*, **8**, 247 (1967).
15. E. Darmois and M. I. Epelboin, *Bull Soc. Franc. Des Electricians*, **4** (Ser 7), 344 (1954).
16. P. Delahay, "Double Layer and Electrode Kinetics," Interscience Publishers, Inc,. New York (1966).
17. T. P. Hoar, D. C .Mears, and G. P. Rothwell, *Corrosion Sci.*, **5**, 279 (1965).
18. M. Garreau and I. Epelboin, *J. Chim. Phys.*, (11-12), 1515 (1966).

Electrical Properties of Manganese Dioxide and Manganese Sesquioxide

P. H. Klose*, [1]

Union Carbide Corporation, Electronics Division, Greenville, South Carolina

ABSTRACT

Measurements of electrical properties of MnO_2 and Mn_2O_3 were carried out on material obtained by pyrolysis of $Mn(NO_3)_2$. From resistivity data, it is proposed that the conduction process is due to oxygen forming a donor level at 0.044 eV. In Mn_2O_3, oxygen vacancies might be acting as an acceptor level with an activation energy of 0.30 eV. Resistivity measurements were used to establish the MnO_2-Mn_2O_3 transition temperature at 545°C. The Hall mobility of MnO_2 was measured at 25°C. For resistivities of 0.1-100 ohm-cm, the mobility depends on the resistivity. This was taken as an indication that impurity scattering is the dominating process in this region. The voltage-current characteristic was measured for samples from 0.1 to 10^5 ohm-cm. The material showed ohmic behavior for fields from 10 mV/cm to 100 V/cm. The Seebeck coefficient was investigated over the temperature range 25°-125°C. A response of 0.6 mV/°C was found in high-resistivity n-type MnO_2, and 0.37 mV/°C in p-type Mn_2O_3.

The electrical properties of MnO_2 have been investigated previously by several experimenters. A survey of the results reported in the literature suggested that material preparation as well as type and technique of the measurements on MnO_2 might have affected the result, thus leading to apparent contradictions. Sasaki and Kojima (1), Glicksman and Moorehouse (2), and Brenet (3) measured the electrical resistivity of MnO_2 samples which were obtained by pressing pellets out of ground MnO_2 powder. The values reported for the resistivity ranged from about 30 to 300 ohm-cm. Bhide and Damle (4) investigated the properties of MnO_2 samples cut from naturally occurring pyrolusite. In their work the values quoted for the resistivity ranged from about 10 to 1000 ohm-cm. An entirely new approach to the preparation of experimental samples of MnO_2 was chosen by Wiley and Knight (5). Their samples were prepared by pyrolytic decomposition of chemically pure $Mn(NO_3)_2$. (A process commonly used to form the counterelectrode in tantalum capacitors). Wiley and Knight report a resistivity of about 0.1 ohm-cm for their material. In addition to the resistivity measurements by the above authors the differential thermal analysis of the MnO_2-Mn_2O_3 system carried out by Kozawa (6) offered an interpretation of the system from an entirely different point of view. His results indicated the possible existence of a low-temperature phase transition as well as the well-known high-temperature phase transition for MnO_2-Mn_2O_3 at about 580°C. Furthermore his results show a difference in the high-temperature phase transition temperature for pyrolusite which Kozawa refers to as β-MnO_2 and electrolytically formed MnO_2 which he designates γ-MnO_2. With the ample but divergent results reported in the literature the experimental work reported in this paper was, therefore, undertaken in an effort to find answers to some of the questions posed by the earlier experimental results.

Experimental

Sample preparation.—The experimental samples were produced by following the technique suggested

* Electrochemical Society Active Member.
[1] Present address: Energy Conversion Devices, Incorporated, Troy, Michigan.
Key words: resistivity, Seebeck coefficient, Hall coefficient.

by Wiley and Knight. Reagent grade manganous nitrate solution (50%) was pyrolized in a Pyrex test tube. The tube was filled repeatedly until a sufficiently thick layer had formed on the bottom of the tube. It was noted that the geometry of the test tube, *i.e.*, the ratio of diameter to the depth, affected the porosity of the deposit. To explore this effect material was pyrolized under various conditions by changing the geometry of the container. At the one extreme the container consisted of a flat dish which was repeatedly moistened with $Mn(NO_3)_2$ and then returned to the pyrolysis temperature. The other extreme condition was generated by carrying out the pyrolysis in a Pyrex vessel enclosed in an autoclave. This condition might be encountered on the inside of the porous structure of a tantalum capacitor. A small hole was provided in the autoclave to permit escape of the water vapor and other reaction gases. The reaction rate and the vent hole were adjusted so that only a small pressure gradient existed between the inside and the outside of the autoclave. Following the time schedule of Wiley and Knight sufficient reaction time was allowed in all cases to continue pyrolysis until the resistivity of the material became constant. The material was then cut with a carborundum saw in the shape of a rectangular parallelepiped with the approximate dimensions of 2 x 5 x 20 mm. Samples used for density measurements were mounted on a fixture and ground with 600 mesh alumina to a dimensional accuracy of about 1%. To obtain the different resistivities used in the various measurements high density ($\approx$4.7 g/cm^2) samples were baked for 16 hr in air. This period was found sufficient to establish resistivity equilibrium in all cases. Several different techniques had to be used to apply electrical contacts to the samples to accommodate the requirements of the various measurements. In the temperature range from $-50°$ to 125°C the resistivity was measured by applying small dots of silver paint to the side of the parallelepiped. These dots served as voltage probes. Silver paint was also used for the large current contacts at both ends of the sample. Between 125° and 625°C large area carbon pressure contacts held in place by tungsten springs gave reproducible and noise free results.

To measure the Seebeck coefficient the hot junction was formed by a lead point contact of about 0.1 mm^2. The cold junction consisted of a large area water-cooled lead contact. Silicone oil was used to improve the thermal coupling between the lead and the sample.

Density

The theoretical density of MnO_2 is given as $\rho = 5.026$ g/cm^3 (7). In their experiments Wiley and co-workers prepared essentially void-free MnO_2 with a density of 4.0 g/cm^3 by pyrolizing $Mn(NO_3)_2$. In an attempt to reproduce this result in our laboratory it became apparent that the shape of the reaction tube affected the resistivity and density of the end product. Repeated filling of a flat dish, *e.g.*, produced material with a density of 2.5 g/cm^3 and a resistivity of about 1 to 10 ohm-cm. If the pyrolysis was carried out at the same temperature as before but inside a standard Pyrex test tube, the density increased to about 4.0 g/cm^3 and the resistivity was reduced to 0.1 ohm-cm. The partial pressure of the reaction products over the solid was further increased by placing the Pyrex tube into a steel autoclave. The vent hole in the autoclave was adjusted to permit escape of water and other gases so as to generate only a small pressure differential inside the autoclave. Again the test tube was filled repeatedly until a sufficient amount of MnO_2 was collected at the bottom of the tube. The material pyrolyzed in the autoclave had a density of 4.7 g/cm^3 $\pm$1% and a resistivity of 0.0028 ohm-cm. From these results it appears that the partial pressure of the reaction products has a strong effect on the resistivity and the density of MnO_2. Since the complex pyrolysis process would require considerable more experimentation than could be carried out in connection with this work it was, therefore, only regarded as a tool to prepare suitable samples.

Resistivity and Activation Energy

The temperature dependence of the resistivity of MnO_2 has been investigated previously from various points of view (1-3). Our objective was to find regions of extrinsic, intrinsic, and mixed conduction in MnO_2 and Mn_2O_3 and, if posible, to identify the impurity associated with the activation energy of the resistivity. Assumptions about the structure and the stoichiometry of MnO_2 and Mn_2O_3 produced in our laboratory are based on the gravimetric and structure analysis reported by Wiley and Knight (5). As starting material for the resistivity measurements in most cases MnO_2 with a density between 4.0 and 4.7 g/cm^3 was selected. The oxygen content of the sample was gradually reduced by baking the material in air. A holding time of 30 min at the baking temperature was found to be sufficient to establish the oxygen equilibrium in the specimen as indicated by the resistivity. A family of resistivity *vs.* temperature curves generated by heating a sample (curve 1) to 450°C (curve 2), 525°C (curve 3), 540°C (curve 4), and 541°C (curve 5) is shown in Fig. 1. The temperature range of $-50°$-125°C was selected so that the temperature dependence of the resistivity could be expressed by the equation $\rho = \rho_0 \exp -\Delta E/kT$. Curve 1 was measured on the sample in the "as pyrolized" or "unbaked" condition. As the resistivity was increased through baking at successively higher temperatures the activation energy calculated from the slope of the resistivity curve went through a maximum of $\Delta E = 0.044$ eV at a room temperature resistivity of 0.5 ohm-cm. Curve 5 clearly deviates from an exponential dependence on inverse temperature. At this resistivity the impurity level seems to be exhausted, and mixed conduction arising from extrinsic plus intrinsic carriers determines the shape of the resistivity *vs.* temperature curve. For this resistivity (100 ohm-cm) Wiley and Knight give an oxygen to manganese ratio of 1.96. Further loss of oxygen by baking the sample at 542° $\pm$ 5°C results in a drastic change in structure (6), resistivity (5), and activation energy. No intermediate region could be found within the experimental accuracy of setting the baking temperature. The resistivity changes by about three orders of magnitude from 10^2 ohm-cm (MnO_2) to 10^5 ohm-cm Mn_2O_3. The activation energy for the impurity level in Mn_2O_3 as calculated from the temperature dependence of the resistivity is $\Delta E = 0.30$ eV. The two curves shown in Fig. 2 were obtained by heating the material to 542°C (6) and 545°C (7), respectively. At the low-temperature side of the graph the presence of another, much lower energy level may be noted. Measurements of the Seebeck coefficient indicated that conduction in Mn_2O_3

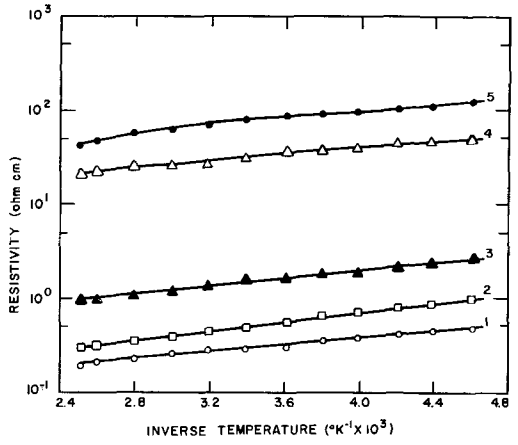

Fig. 1. Temperature dependence of the resistivity of MnO_2 for various anneal temperatures. Curve 1 represents a typical sample in the "as pyrolyzed" state. Samples 2 through 5 are heated in air at 450°, 525°, 540°, and 541°C, respectively.

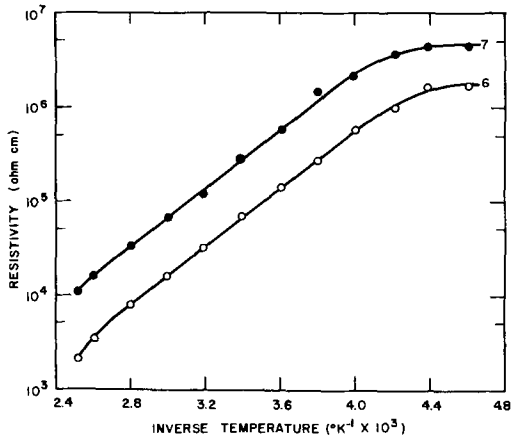

Fig. 2. Temperature dependence of the resistivity of Mn_2O_3 heated in air at 542°C, 6, and 545°C, 7.

is p-type. Apparently in Mn_2O_3 the observed impurity level is again controlled by the oxygen concentration, but in this case acting as acceptor. In the next experiment the intrinsic part of the temperature dependence of the resistivity was explored. Figure 3 shows resistivity measurements taken in the temperature region from 25° to 625°C. Material produced in the autoclave was used in this experiment. The sample had an initial resistivity of 0.0028 ohm-cm and an activation energy $\Delta E = 0.0066$ eV. The resistivity *vs.* temperature curves shown in Fig. 3 were obtained by continuously recording resistivity as a function of temperature as the sample was alternately heated and cooled. The temperature indicated on the various curves represents the maximum temperature to which the sample has been exposed. At this temperature the sample was held for 30 min to establish equilibrium before being cooled down again. The heating and cooling rate was kept linear at about 10°C/min. The slope of the high-temperature portion of the high resistivity MnO_2 sample was used to calculate the energy gap of the MnO_2 lattice $E_g = 0.37$ eV. Similarly for Mn_2O_3

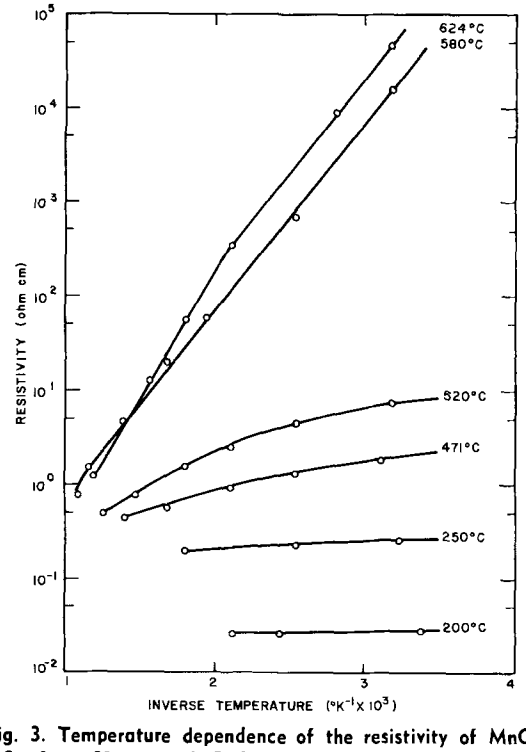

Fig. 3. Temperature dependence of the resistivity of MnO_2 and Mn_2O_3 from 23° to 650°C. The individual curves were recorded during the cooling cycle after each 30-min heat-treatment at the various temperatures indicated on the graph.

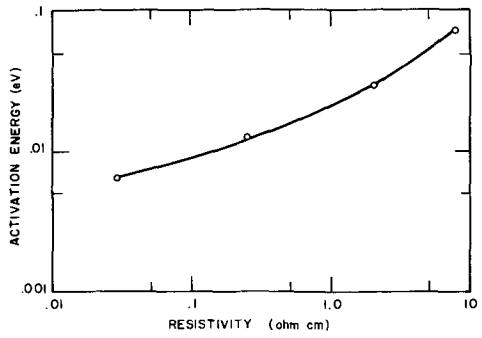

Fig. 4. Activation energy of MnO_2 as a function of the resistivity at 23°C. The activation energy was calculated from the resistivity in the temperature interval 57°-225°C.

$E_g = 1.08$ eV is found. The "growth" of the intrinsic region in Mn_2O_3 can be observed as the maximum anneal temperature of the sample is changed from 580° to 624°C (Fig. 3).

In the extrinsic-intrinsic region, a gradual increase in the activation energy as a function of resistivity is noted. This feature we believe is generally found in semiconductors. The temperature where it is observed depends on the material and the doping level. Resistivity measurements on gallium doped germanium reported by Fritzsche (8), *e.g.*, show this gradual change of the "activation energy" in the temperature region from 3° to 10°K. For every particular system a graph can be prepared which relates resistivity and activation energy in the appropriate temperature region. Hence it becomes possible to find the resistivity without knowledge of the geometry by measuring the temperature dependence of the resistance. Figure 4 shows the results for the MnO_2 system in the temperature interval 57°-225°C. Previously reported measurements which have been carried out over this temperature range roughly follow this relationship, *i.e.*, higher resistivity samples also tended to have higher activation energy.

It is interesting to note the close agreement between the high resistivity MnO_2 sample shown in Fig. 1 and the equivalent sample in Fig. 3. Both are of the order of 10 ohm-cm although one sample had an initial resistivity of 0.0028 ohm-cm and the other an initial resistivity of 0.2 ohm-cm.

In addition to the positive resistivity changes generated by heating MnO_2 in air at relatively high temperature a negative change of resistivity was consistently observed during the first heating cycle of a virginal sample to a temperature of about 120°C. This decrease in the resistivity of MnO_2 is usually of the order of 5-10% and is accompanied by a decrease in the activation energy as well.

Results of differential thermal analysis of the MnO_2-Mn_2O_3 system reported by Kozawa (6) indicate the possibility of a phase change at this temperature.

Hall Mobility

Results of Hall measurements reported by Das (9) established MnO_2 as an n-type semiconductor with a Hall mobility of the order of 10 cm²/V sec. Our measurements were carried out on MnO_2 samples with resistivities ranging from 0.23 to 115 ohm-cm. The temperature was kept constant at 23°C. The magnetic field was 1900 gauss. Results are summarized in Table I. The strong dependence of the Hall mobility on the re-

Table I. Hall coefficient of MnO_2 as a function of anneal temperature

Hall coefficient cm³/coul	Resistivity, ohm-cm	Hall mobility, cm²/V sec	Anneal temp, °C
−0.95	0.23	4.2	250
−2.6	0.63	4.1	350
−10.2	0.70	14.5	475
-2.4×10^3	115	21.0	540

sistivity leads to the conclusion that impurity scattering is most likely the dominant scattering mechanism in this temperature range. From the results we can estimate the intrinsic carrier concentrations. Using $\rho_i = (2\ n_i e_i \mu_H)^{-1}$ where ρ_i, n_i, e_i, and μ_H are the intrinsic resistivity, carrier concentration, electronic charge, and Hall mobility, respectively, we find $n_i = 8 \times 10^{14}$ cm^{-3}.

Voltage Current Characteristics

Bhide and Damle in their extensive work (4) with MnO_2 measured the V-I characteristic of naturally occurring pyrolusite. Their results showed an exponential relationship $I = C \exp. V$. In our measurement, as before, the material was prepared by pyrolysis of $Mn(NO_3)_2$. It was found that pressure contacts of tungsten or carbon lead to an exponential V-I characteristic as observed by Bhide and Damle.

However, the material showed ohmic behavior if large area silver paint contacts were applied to the samples. Figure 5 shows the results of these measurements. The electric field was varied from 10 mV/cm to 100 V/cm. The various curves shown in Fig. 5 represent samples of different resistivities obtained, as before, by baking in air. The deviation from linearity observed on one of the samples at fields higher than 20 V/cm is probably due to heating of the sample. Since the current density is considerably higher for the low-resistivity samples, it seems possible that this condition, compounded by an inhomogeneity in the material could give rise to undesirable heating effects or other nonohmic behavior of reversible and irreversible nature.

Seebeck Coefficient

Since the measurement of the Hall coefficient proved to be experimentally quite difficult for the high resistivity Mn_2O_3 material, the Seebeck coefficient and resistivity were measured on the samples covering this range of resistivities to establish the sign of the carrier and also to define better the temperature regions of extrinsic, intrinsic and mixed conduction. In Fig. 6 the Seebeck voltage is graphed as a function of the temperature differential of MnO_2 and Mn_2O_3. The results were obtained by holding the cold junction constant at 14°C while the hot junction was varied from 14° to 125°C. Trace 1 is typical for MnO_2 in the virginal state (as pyrolyzed). Traces 2 through 5 were measured on MnO_2 after heating in air to 525°, 535°, 540°, and 541°C, respectively. This group represents MnO_2 with decreasing oxygen content down to a ratio of oxygen to manganese of about 1.96. Traces 6 and 7 are intrinsic and high resistivity Mn_2O_3 obtained at baking temperatures

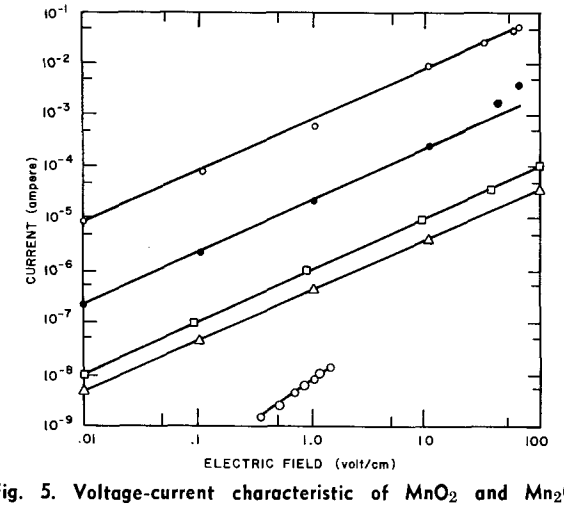

Fig. 5. Voltage-current characteristic of MnO_2 and Mn_2O_3. Curves 1, 2, and 3 are MnO_2 with resistivities of 0.4, 0.7, and 100 ohm-cm; curve 4 is typical for Mn_2O_3 with a resistivity of 10^5 ohm-cm. The short piece of V-I curve at the bottom of the graph shows a typical result of an earlier investigation (4).

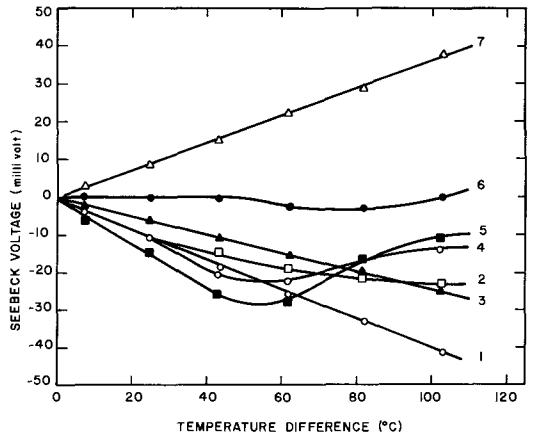

Fig. 6. The Seebeck voltage of MnO_2 and Mn_2O_3 in the temperature interval 14°-125°C. Curve 1 is typical for MnO_2 as pyrolyzed; curves 2 through 5 are obtained by heating MnO_2 at 525°, 535°, 540°, and 541°C. Curves 6 and 7 are Mn_2O_3 obtained by heat-treatment of MnO_2 at 542° and 545°C, respectively.

of 542° and 545°C, respectively. We note that the Seebeck coefficient reaches a maximum of −0.6 mV/°C in MnO_2 with a room temperature resistivity of about 50 ohm-cm. The Seebeck coefficient goes to zero at about 70°C and then turns positive in the region dominated by intrinsic conduction. From this one might conclude that the hole mobility is equal or greater than the electron mobility as has been observed in other semiconductors. Trace 2 and 3 represent an intermediate condition which does not seem to fit the over-all pattern. It seems possible that inhomogeneity of the oxygen concentration at the surface of the material gave rise to the anomalous behavior. Trace 6 indicates essentially zero Seebeck coefficient over the entire temperature range. From resistivity measurements we conclude that this material is already Mn_2O_3. Further baking at 545°C clearly establishes the p-type conduction shown in trace 7 with a Seebeck coefficient of +0.37 mV/°C.

Discussion

Wiley and co-workers have shown that high density low resistivity MnO_2 can be produced by pyrolysis of manganous nitrate. The material produced in the autoclave in connection with our work reinforces their findings. By varying the geometry of the reaction vessel we were able to observe extreme conditions which might be considered analogous to the condition commonly encountered in the manufacture of tantalum capacitors. Pyrolysis in the autoclave simulates the conditions found on the inside of the porous structure of a capacitor; pyrolysis in the flat dish relates to the condition on the outside skin. The many orders of magnitude of difference in the resistivity found in our measurements are expected to have a strong effect on the dissipation factor and the frequency response of such a device. Through the measurements of the electrical resistivity as a function of temperature it became evident that the activation energy is a sensitive tool suitable to distinguish between MnO_2 and Mn_2O_3 as long as the appropriate temperature range is selected. In the region of mixed conduction, *i.e.*, near room temperature and above, the variation of the resistivity *vs.* temperature slope might be helpful in finding the resistivity without knowledge of the geometry; this is a useful technique to monitor the pyrolysis process. From the measurements of the resistivity of MnO_2 in the extrinsic region it appears that loss of oxygen through baking gradually creates a sufficient number of vacancies in the lattice until it shifts to the Mn_2O_3 configuration. We find that, while the resistivity increases, the Hall mobility also shows an increase. This might be an indication that oxygen acting as an impurity is the major contributing factor to the scatter-

ing process in this temperature region. The activation energy $\Delta E = 0.044$ eV found in MnO_2 is tentatively ascribed to oxygen acting as a donor. The acceptor level found in Mn_2O_3 with activation energy $\Delta E = 0.30$ eV also was found to be controlled by the oxygen concentration. However, since further reduction of Mn_2O_3 finally leads to MnO with low p-type resistivity one might be inclined to associate this level with manganese vacancies. Further work in this area is needed to answer these questions. The apparent difference between the ohmic V-I characteristic of MnO_2 measured in this laboratory and the exponential dependence found for pyrolusite by Bhide *et al.* are most likely due to the large area silver contacts used in our experiment. In addition, however, one must consider the possibility that naturally occurring pyrolusite has different electrical properties than the MnO_2 prepared by pyrolysis of $Mn(NO_3)_2$ solution. Kozawa in his work on differential thermal analysis of pyrolusite and electrolytically prepared MnO_2 finds that pyrolusite has its phase transitions at a higher temperature than the MnO_2 prepared by electrolysis. The MnO_2-Mn_2O_3 phase transition temperature (545°C) found by Wiley using the gravimetric technique is in agreement with Kozawa's findings for electrolytic MnO_2. Since the transition temperature established by the resistivity measurement in this laboratory are also in agreement with Kozawa's results we are inclined to follow the suggestion of Kozawa to treat pyrolusite as a separate phase of MnO_2 produced by other than natural means. Our measurements of the Seebeck coefficient are essentially in agreement with the results published earlier by Das (9). Since the measurements reported here cover a large range of resistivity for MnO_2 as well as Mn_2O_3 the results can be used to assign temperature regions where extrinsic, intrinsic, and mixed conduction are to be found.

Although the foregoing information helps to clarify many aspects of the published information on the resistivity and activation energy of MnO_2 and Mn_2O_3, more work is needed to establish without doubt the origin of the impurity levels in MnO_2 and Mn_2O_3.

Acknowledgments

It is a pleasure to acknowledge the help and advice of Dr. J. Piper, of Union Carbide Corporation, and of Dr. E. Fagen and Mr. R. Neale, of Energy Conversion Devices, Inc., in the preparation of this manuscript. The author also wishes to acknowledge gratefully the help of Mrs. Ruth Skinner in the preparation of the material and in carrying out many of the electrical measurements.

Manuscript submitted June 6, 1969; revised manuscript received April 1, 1970.

Any discussion of this paper will appear in a Discussion Section to be published in the June 1971 JOURNAL.

REFERENCES

1. K. Sasaki and K. Kojima, *J. Electrochem. Soc., Japan*, **22**, 564 (1954).
2. R. Glicksman and C. K. Moorehouse, *This Journal*, **103**, 149 (1956).
3. J. Brenet, *Schwiezer Archiv., Agnew. Wiss. U. Tech.*, **26** [1], 10 (1960).
4. V. G. Bhide and R. V. Damle, *Physica*, **26**, 33 (1960).
5. J. S. Wiley and H. T. Knight, *This Journal*, **111**, 656, (1964).
6. A. Kozawa, *ibid.*, **106**, 79 (1959).
7. Hand Book of Chemistry and Physics, 42nd edit. (1962).
8. H. Fritzsche, *Phys. Rev.*, **99**, 406 (1955).
9. J. N. Das, *Z. Physik*, **151**, 345 (1958).

Anodization of Tantalum Over the Temperature Range 0° to 250°C

R. J. Dreiner* and T. B. Tripp

Research and Development Center, Sprague Electric Company, North Adams, Massachusetts

ABSTRACT

Tantalum was anodized at constant current in an aqueous electrolyte over the temperature range 0°-250°C. The voltage build-up was linear up to a voltage at which crystallization of the oxide occurred. The "crystallization voltage" decreased with increasing temperature. The change of the voltage build-up rates (dV/dt) with temperature was not compatible with the single barrier law for high field ionic conduction. In spite of the extended temperature range, it was not possible to distinguish between ionic current (i)-field (F) relations of the form $\ln i \propto F^{1/2}$ and $\ln i \propto F + F^2$. Current efficiencies were determined from charge and optical film thickness. The current efficiencies were (a) essentially constant up to a formation temperature of about 170°C and (b) decreased by about 30% between 170° and 250°C. Capacitance and loss angle of "equal charge" films increased with anodization temperatures higher than about 180°C. Oxygen dissolution in the tantalum substrate was suggested as the likely cause.

In recent literature (1-6) the three equations

$$i = i_1 \exp [(q\,a\,F - W_1)/kT] \quad [1]$$

$$i = i_2 \exp [(\gamma\sqrt{F} - W_2)/kT] \quad [2]$$

$$i = i_3 \exp [(q\,\alpha + \beta F)F - W_3)/kT] \quad [3]$$

have been applied to describe the field, F, dependence of the ionic current, i, during anodic oxide growth. Equation [1] expresses that a single barrier of width, $2a$, and height, W, is rate determining. The charge on the moving ion is q and the action of the electric field on the ion reduces the barrier height by $q \cdot a \cdot F$. The model (2) that the potential energy of an ion due to the applied field is modified by the coulomb attraction of large trapping centers within the oxide, leads to Eq. [2], which is similar to the Schottky relation for the field supported emission of electrons from metals. The exponent of the third equation is quadratic in the field. Christov and Ikonopisov (7) showed that the quadratic term arises if it is assumed that the applied

* Electrochemical Society Active Member.

field does not only modify the barrier height, but also shifts its position.

Combining Eq. [1], [2], or [3] with Faraday's law

$$d = \eta\lambda \int_o^t i^* dt \qquad [4]$$

yields the following relations for the voltage build-up rate (dV/dt) during constant current anodization

$$\frac{dV}{dt} = \eta\lambda i^* \left[\frac{W_1}{qa} + \frac{k \ln (i^*/i_1)}{qa} \cdot T \right] \qquad [5]$$

$$\frac{dV}{dt} = \eta\lambda i^* \left[\frac{W_2}{\gamma} + \frac{k \ln (i^*/i_2)}{\gamma} \cdot T \right] \qquad [6]$$

$$\frac{dV}{dt} = \eta\lambda i^* \left[-\frac{\alpha}{2\beta} \pm \frac{W_3 + kT \ln (i^*/i_3)}{\alpha\beta} \right] \qquad [7]$$

where d is the oxide film thickness. λ is equal to the ratio of the equivalent weight of tantalum oxide over the product of the Faraday number, the density of Ta_2O_5, and the area of the sample. The ionic current, i, and the external current, i^* are related as $i = \eta i^*$. The current efficiency, η, has been assumed to be independent of time, but might depend on temperature. The current efficiency has been neglected in the log terms. This can readily be done since the pre-exponential terms, i_1, i_2, i_3, which are of the order of 10^8 A/cm^2 (1, 2, 5), are much larger than i^* and because the current efficiency is not affected strongly enough by temperature as will be shown.

Plots of (dV/dt) and the square root of (dV/dt) *vs.* temperature should allow a distinction between the single barrier relation or the Schottky type Eq. [2]. No such straightforward evaluation is possible if Eq. [3] is valid. The exponents of Eq. [1] and [3] are parts of a series expansion of the exponent of Eq. [2], as shown in the Appendix. It is, therefore, rather difficult to distinguish between these three relations, which will become clear from the following.

The investigation of the high field ionic conduction during the anodization of tantalum in aqueous electrolytes is restricted to a limited field range and, if no special equipment is used, to a limited temperature range as well. The field changes by only about 30% if, at constant temperature, the formation current density is varied from 1 μA/cm^2 to 10 mA/cm^2. The upper current limit more or less assures that no excessive or uncontrolled heating of the sample occurs, and the lower limit is essentially set by time. It takes, for instance, about 10^3 sec to grow an oxide layer of 5Å on tantalum if the formation current is 1 μA/cm^2. Furthermore, at these low current levels the ionic current is not necessarily equal to the externally applied one, since the electronic current through the oxide may become an appreciable fraction of the total. Normally, the temperature range is set by the freezing and boiling points of the aqueous electrolyte, which is used when one wants to minimize incorporations of anions in the anodic oxide film (8). The formation field changes, again only by about 30%, if the temperature is varied between 0° and 100°C during anodizations at a constant current.

Individual values of the voltage build-up rate (dV/dt) can be determined quite accurately from constant current anodizations, but the scatter from sample to sample is such that it is almost impossible to make the necessary distinction in the trend of (dV/dt) over the temperature range 0°-100°C. The following should give an indication of the experimental accuracy needed to distinguish, *e.g.*, between Eq. [1] and [3]. Values for (dV/dt) were calculated at 10°C intervals between 0° and 100°C using Eq. [3] and the constants reported by Young (1). An equation of the form $(dV/dt) = a + bT$ was fitted to these points by least square analysis and (dV/dt) values were determined over the temperature range 0°-250°C, using this linear relationship. The data from this linear approximation are compared with values predicted by Eq. [3] and Young's constants in Table I. The percentage column in Table I is an indication of the experimental accuracy needed in order to distinguish between the linear approximation, which would mean that Eq. [1] is valid and Eq. [3]. Between 0° and 100°C, the precision has to be better than 1%, and to our knowledge this has not been achieved with voltage build-up measurements.

Table I. Comparison of calculated voltage build-up rates

Temp, °C	A (dV/dt)* in V/sec	B (dV/dt)** in V/sec	(A-B)·100/A in %
0	0.372	0.370	0.5
50	0.328	0.329	0.3
100	0.290	0.288	0.7
150	0.257	0.248	3.5
200	0.226	0.207	8.4
250	0.198	0.166	16.2

* Calculated using Eq. [3] and Young's data.
** Linear approximation.

The results of a study by Draper and Jacobs (5) are of interest in connection with this discussion. These authors anodized Ta in 0.1*N* H_2SO_4 [0°-100°C], 100% H_2SO_4 [2°-50°C], and 40% H_2SO_4 [−65°-90°C] over the temperature ranges indicated in the brackets. They found (*i*) agreement with the single barrier theory, Eq. [1], when evaluating the data obtained from experiments over the smaller temperature ranges and (*ii*) deviations from Eq. [1] over the larger temperature range of about 150°C. The latter result could have been influenced by anion incorporation which is known to depend on formation temperature and electrolyte concentration.

In this work, the temperature range of anodizing tantalum in dilute aqueous electrolytes was extended up to 250°C by using an autoclave. In addition to reporting new data, which were obtained from the anodizations of tantalum in an aqueous electrolyte above 100°C, an attempt is made to distinguish between the ionic current-field relations.

Experimental

Samples were cut from 99.9% pure 10 mil tantalum sheet, and 70 mil diameter tantalum wire was spot welded to the tabs. The foils were degreased, electropolished in a 9:1 by volume mixture of concentrated nitric acid and HF, and then vacuum annealed at 2100°C, $<10^{-4}$ Torr. Just prior to use, each sample was immersed for 5 sec in 48% HF and thoroughly rinsed with distilled water.

The anodization cell was constructed from 303 stainless steel, and its configuration is shown schematically in Fig. 1. Electrical contact to the foil was made with

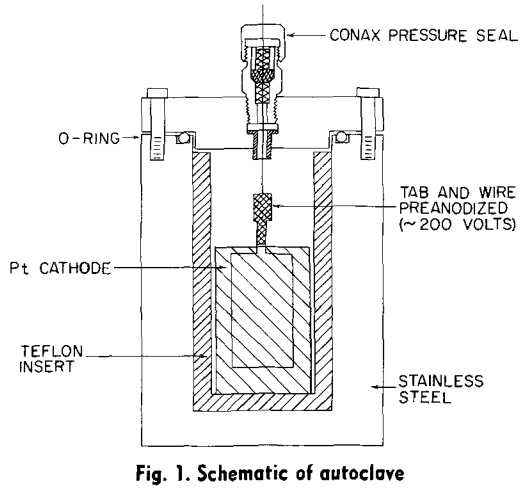

Fig. 1. Schematic of autoclave

the tantalum wire, which passed through a Connex PL power lead pressure seal. This seal is so designed that the wire is only in contact with Teflon and ceramic sleeves, thus assuring good electrical insulation from the cell. The tab of the foil and the wire were preanodized to 200V or higher if necessary. The 0.01M K_2SO_4 electrolyte was contained in a Teflon cup and was stirred with a Teflon covered magnetic stirring bar. The cathode was platinum foil. The cell was placed in a temperature-controlled, vertical tube furnace and rested on a stirring hot plate. The temperature of the cell was measured with a Chromel-alumel thermocouple, which was inserted into a small diameter hole drilled into the wall of the cell. The temperature of the system was at equilibrium for at least 15 min prior to a formation. As indicated by the thermocouple, the temperature fluctuated less than 1° during this period and the subsequent anodization.

All anodizations were carried out at a constant current density of 1.0 mA/cm^2. The voltage build-up was monitored with a Keithley 610-A Electrometer combined with an Esterline-Angus Recorder. Capacitance and loss angle were measured at 120 cps in a 40 w/o (weight per cent) H_2SO_4 solution at 25°C. The time of measurement after anodization varied from ½ to 3 hr depending on the anodization temperature and the corresponding time necessary to cool the cell to room temperature. The thickness and refractive index of the anodic oxide films were estimated by ellipsometry using the mercury line of wavelength 5461Å.

Results

A typical voltage-time curve, which was recorded during a constant current anodization at 214°C, is shown in Fig. 2. As seen, the voltage rose linearly with time to a peak voltage, V^*, then declined by ΔV^* to a minimum and after that increased again to a higher plateau. This higher voltage plateau was associated with film breakdown, since oscillations were observed in the voltage time recording. The period between the moment when the voltage reached V^* and the time when the potential again attained this value, during the second voltage rise, was designated t^*. Some values for V^*, t^* and ΔV^* are compiled in Table II. No data are listed for anodizations at temperatures below 100°C, since severe breakdowns occurred in the oxide film at the air-electrolyte interface. It was not possible to preanodize the tabs of the tantalum samples to sufficiently high voltages and, therefore, the breakdowns could not be prevented.

Similar voltage time curves as in Fig. 2 have been reported by Lakhiani and Shreir (9), who investigated the anodic oxidation of niobium over the temperature range 25°-95°C. These authors found, using electron diffraction, that films formed at 90°C to the lower voltage plateau or beyond were crystalline. Furthermore, electron micrographs revealed (*i*) that the niobium oxide films started to crack at the peak voltage V^* and (*ii*) that crystalline Nb_2O_5 appeared underneath the amorphous oxide on further anodization.

Table II. Effect of formation temperature on the peak voltage, V^*, which is related to the onset of oxide crystallization. See Fig. 2 for explanation of t^* and ΔV^*.

Form. temp, °C	V^*, V	t^*, min	ΔV^*, V
102	373	—	—
112	333	—	30.0
125	285	>60	25.0
150	179	—	—
175	110	~14	12.0
190	87	~13	7.0
200	75	—	5.0
214	73	~10	3.5
223	71	~8	2.5
250	63	—	1.5

The tantalum samples, which had been anodized to the start of the lower voltage plateau, did not exhibit the usual bright and uniform interference colors over the whole sample area. Inspection under the microscope indicated small regions which looked similar to the ones described by Vermilyea (10) as "crystalline areas." These crystalline regions covered the whole area of samples which had been formed beyond the lower voltage plateau. Therefore, it is thought that the lower plateau is caused by the crystallization of the oxide film and that crystalline tantalum oxide is formed when samples are anodized to higher voltages.

Most of the tantalum samples were anodized by passing a constant charge of 3.33 coul, which corresponded to a formation time of 180 sec. Within this period, the potential rose to about 36V during formations at 250°C. Even at this temperature, this is well below the peak voltage V^*, see Table II, which is related to the onset of crystallization. To limit the formation times to 180 sec assured that no or only very little crystallization occurred at the higher formation temperatures during this time period.

The capacitances and loss angles of the samples were measured at 120 Hz and are plotted *vs.* the formation temperature in Fig. 3. As seen, there is a significant increase in the dielectric parameters of films grown

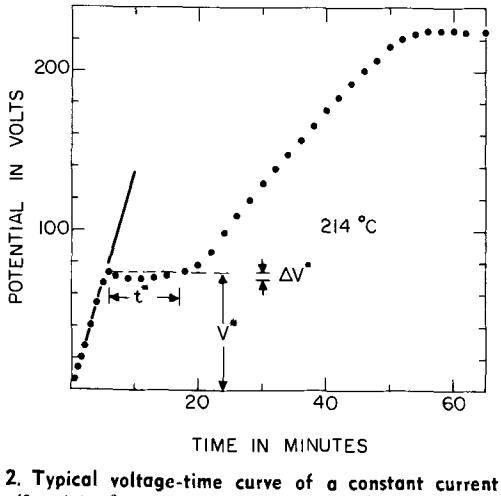

Fig. 2. Typical voltage-time curve of a constant current anodization (1 mA/cm^2) of tantalum at 214°C in 0.01M K_2SO_4 electrolyte.

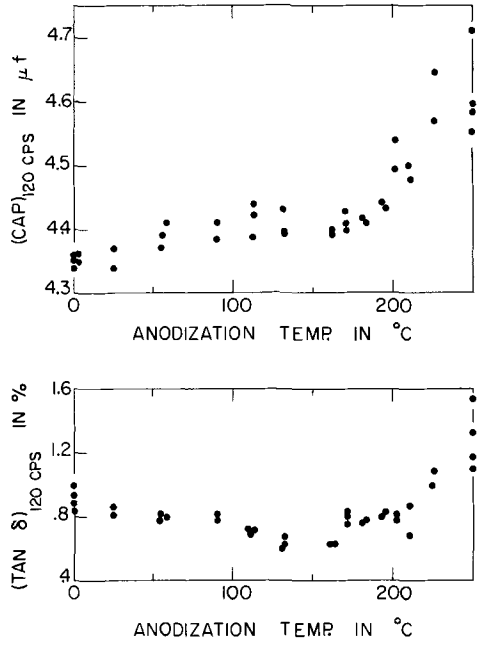

Fig. 3. Variation of capacitance and loss angle with anodization temperature. Measurements were made in 40% H_2SO_4 electrolyte at 25°C.

above about 180°C. It has been shown by Smyth *et al.* (11) (*i*) that the tantalum substrate extracts oxygen from the anodic oxide film when annealed at temperatures of 200°C and higher, and (*ii*) that the oxygen deficient layer adjacent to the tantalum substrate causes capacitance and loss angle to increase. The anodic growth of tantalum oxide occurs at the metal-oxide and oxide-electrolyte interfaces, since both the oxygen and metal ions are mobile (12). The dissolution of oxygen in the tantalum substrate during high-temperature anodizations should result in a lower current efficiency, but not cause an oxygen deficient oxide layer, as the oxygen is replenished by the formation process. However, the anodization cell did not cool down rapidly after formations had been terminated, and maybe the sample remained sufficiently long at a high enough temperature for some additional oxygen to dissolve in the tantalum substrate. This would cause an oxygen deficient layer located at the tantalum-tantalum oxide interface and thus give rise to higher capacitances and loss angles.

Voltage build-up rates (dV/dt) were determined from least square lines through voltage-time data evaluated from the recorder plots at 10-sec intervals over the first 180 sec of the formations. The variation of the voltage build-up rates with temperature is shown in Fig. 4. The data would be very well represented by a straight line over the first 100°C, but deviations from linearity are apparent when the fit is made over the entire temperature range. This then excludes Eq. [1], the single barrier relation. The solid line in Fig. 4 was calculated using Young's (1) data, which were obtained from runs at various current densities over the temperature range 0°-94°C. Young (1) found it justified to take the current efficiency as being equal to unity. The excellent agreement between the extrapolated curve of Young's data and our experimental results might, therefore, suggest that the current efficiency was unity over the whole temperature range 0°-250°C. However, this was not necessarily the case, as will be shown later.

We have plotted the square root of the voltage build-up rate *vs.* the formation temperature and from the least square analysis we obtained.

$$\sqrt{dV/dt} = (0.786 \pm 0.006) - (0.660 \pm 0.007)10^{-3}T \quad [8]$$

with T in °K. The correlation coefficient, which is one for a perfect linear relation, was 0.997. From the intercept at $T = 0$, we calculated 0.33 x 10^4 $(V/cm)^{1/2}$ for the ratio (W_2/γ), which compares very favorably with 0.335 x 10^4 $(V/cm)^{1/2}$ as reported by Young and Zobel (2). Hence, the data are represented very well by the Schottky-type Eq. [2]. On the other hand, the results are also in very good agreement with Eq. [3], as seen by the excellent fit of the calculated curve to the experimental data in Fig. 4. Thus, we were unable to distinguish between the ionic current field relations 2 and 3 in spite of the extended temperature range.

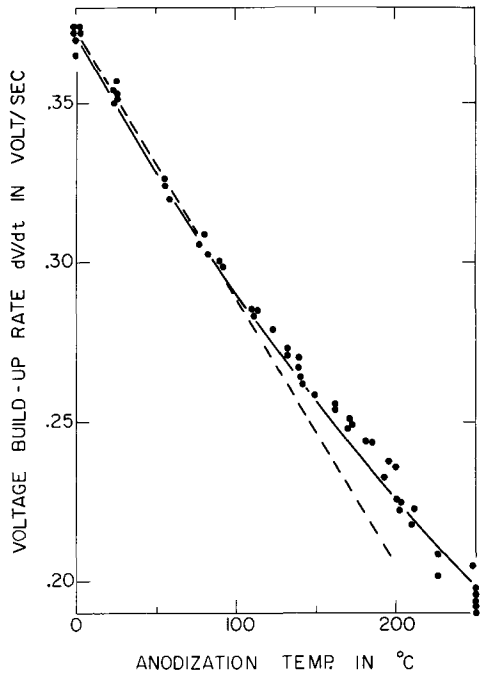

Fig. 4. Change in voltage build-up rate *(dV/dt)* with anodization temperature. Solid line was calculated using quadratic relation and Young's (1) data. Dashed line is least square fit to the 0°-100°C data.

The optical film thicknesses were determined assuming a homogeneous oxide layer from ellipsometer measurements, which were made under two angles of incidence. Results are summarized in Table III for a sample anodized at 202°C. The computer determined approximate values of the refractive index and the film thickness from analyzer and polarizer readings, designated (exp.) in Table III. Next, the exact analyzer and polarizer positions (calc. in table) were calculated using the refractive index and the film thickness previously determined. Then, the computer tried to minimize the differences (*a*) between the film thickness obtained from different angles of incidence and (*b*) between the experimental and calculated analyzer and polarizer positions. For the case demonstrated in Table III, the refractive index of 2.55 and the average film thickness of 891Å were selected.

Film thickness and refractive indices, obtained in this way, were plotted *vs.* anodization temperatures in Fig. 5 and 6. Both quantities are quite independent of anodization temperature up to about 170°C, and over this range the refractive index compares well with the one reported by Young (14). Above 170°C, the thickness of the "equal charge" films decreased and the refractive index increased. The colors of the "equal charge" films were compared with a color gauge con-

Table III. Results of ellipsometer measurements with a sample anodized at 202°C

Angle of incidence, deg.	Refr. index, n	Film thickness, D, Å	Δ (D), Å	Analyzer (A) (exp.), deg.	Analyzer (A) (calc.), deg.	Δ (A), deg.	Polarizer (P) (exp.), deg.	Polarizer (P) (calc.), deg.	Δ (P), deg.
50	2.50	918	11	35.88	35.47	0.41	227.37	227.36	0.01
70		907		20.72	20.24	0.48	239.79	239.79	—
50	2.55	894	6	35.88	35.52	0.36	227.37	227.36	0.01
70		888		20.72	20.34	0.38	239.79	239.79	—
50	2.60	870	16	35.88	35.58	0.30	227.37	227.37	—
70		854		20.72	20.44	0.28	239.79	239.79	—

Optical constants of Ta—substrate: $N_2 = 3.30$; $K_2 = 2.24$ (Young).

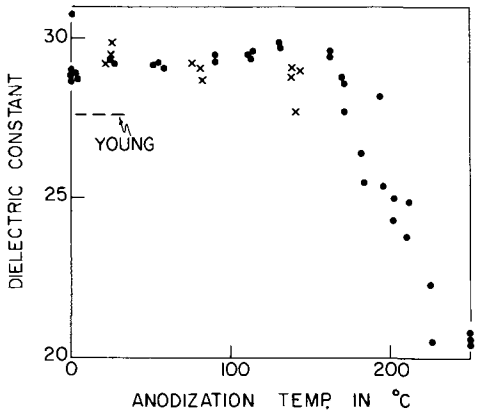

Fig. 5. Optical film thickness as a function of anodization temperature. Oxide films were formed to an equal charge of 3.33 coul (•) and 90V (x).

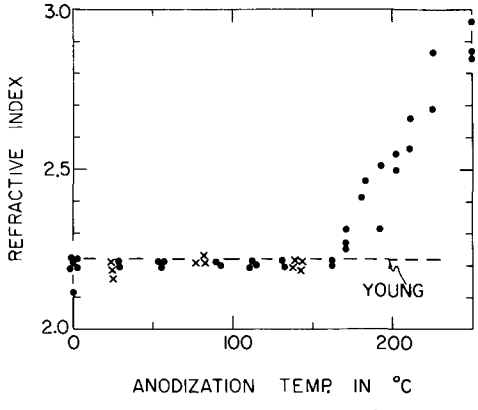

Fig. 6. Effect of anodization temperature on the refractive index of oxide films formed to equal 3.33 coul charge (•) and 90V (x).

sisting of tantalum samples, which had been anodized to different voltages (in steps of 5V) at 34°C. The color variation between films formed at room temperature and at 250°C was small and corresponded to a potential difference of about 5V. The optical path, the product of thickness times refractive index, should, therefore, be approximately the same. This is the case as may be estimated from Fig. 5 and 6.

The rise of the refractive index with anodization temperature is not understood. Masing *et al.* (13) reported that the index increased by about 0.06% per 10°C rise of formation temperature. This was observed over the range 0°-100°C. The effect is too small to explain the steep rise of the refractive index of about 180°C, Fig. 6. Values for the index of some crystalline modifications of Ta_2O_5 are quoted by Young (14), and none exceed 2.37. Hence, the increase of the refractive index is unlikely to have been caused by some crystallization of the oxide, which might have occurred during higher temperature anodizations without affecting the voltage build-up. Regardless of anodization temperature, the same optical constants of the tantalum substrate were used for the evaluation of the ellipsometric data. It was speculated that these parameters were not true constants over the whole temperature range, but the following test indicated otherwise. Using the same optical constants for the substrate, the average optical thickness of four films anodized at room temperature remained unchanged after annealing in air at 200°C for 1 hr and after an additional 1-hr annealing in air at 300°C.

Thinner films and, therefore, lower current efficiencies are caused by oxygen dissolution in Ta substrate as has been discussed earlier. Current efficiencies (η) were calculated from Eq. [4] and are plotted *vs.* formation temperature in Fig. 7. It was assumed that the film density was uniform and independent of tempera-

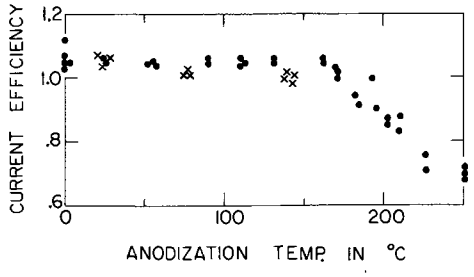

Fig. 7. Variation of current efficiency with anodization temperature of equal 3.33 coul charge (•) and 90V (x) formations.

ture. The efficiencies were approximately constant up to about 170°C. The average value was 1.04. A value larger than unity is partially due to the fact that the optical thickness includes the air-oxide film. Furthermore, the density (here 7.93 g/cm^3) (14) and sample area enters into the calculations of η and their combined uncertainty is hardly less than 4%.

The dielectric constant was calculated from optical thicknesses and capacitances and, as seen from Fig. 8, its value dropped drastically above anodization temperatures of 180°C.

The temperature dependence of the voltage build-up rates (dV/dt) has to be adjusted if the current efficiencies vary with temperature. This was done and Fig. 9 shows that up to ~170°C, the produce of voltage build-up rate times reciprocal current efficiency is not

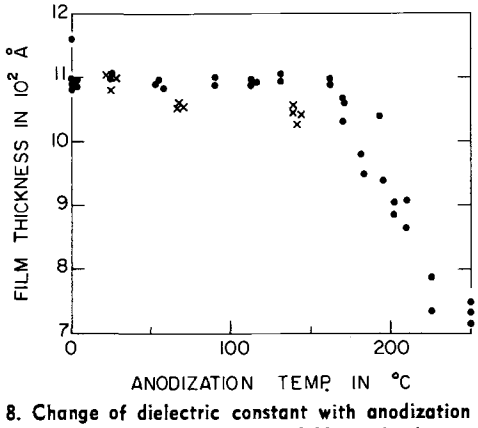

Fig. 8. Change of dielectric constant with anodization temperature. Oxide films formed to equal 3.33 coul charge (•) and 90V (x).

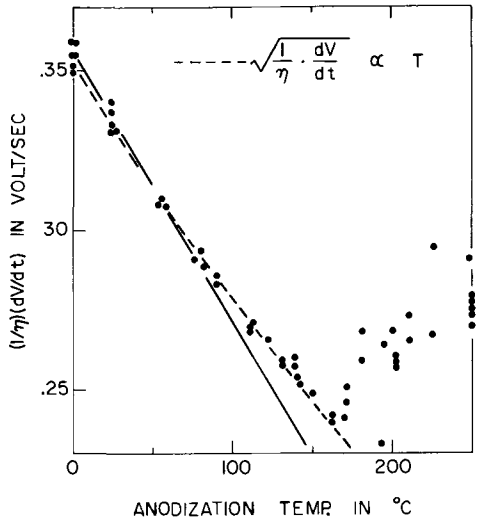

Fig. 9. Change of the adjusted voltage build-up rate $(1/\eta)(dV/dt)$ with anodization temperature. (η) is the current efficiency. Solid line is a linear approximation through the low-temperature points.

a linear function of anodization temperature. The broken line was calculated from the equation

$$\sqrt{(1/\eta)\,(dV/dt} = (0.770 \pm 0.066) - (0.646 \pm 0.099) \cdot 10^3 \cdot T \quad [9]$$

which was obtained from least square analysis. T is in degrees Kelvin. Equation [9] indicates that the Schottky-type current field relation is valid over the range 0°-~170°C. However, as shown in the Appendix, the difference between relations [2] and [3] is rather small and, therefore, the data are equally well represented by the current-field relation of which the exponent is quadratic in the field. The increase of the adjusted voltage build-up rates $(1/\eta)\,(dV/dt)$ with anodization temperatures above about 170°C implies that the formation field rose with temperature. It is not known why this should be the case.

Summary

Tantalum was anodized at a constant current of 1 mA/cm² in an aqueous electrolyte over the temperature range 0° to 250°C. The initial voltage build-up was linear. The linear range was limited essentially by crystallization of the oxide film, which occurred at lower voltages as the temperature increased. The change of the voltage build-up rates (dV/dt) with temperature was not compatible with the single barrier law for high field ionic conduction. In spite of the extended temperature range, it was not possible to distinguish between ionic current (i)—field F relations of the form $\ln i \propto F^{1/2}$ and $\ln i \propto F + F^2$. A reason for this was discussed. However, a recent publication by Dignam and Gibbs (15) showed (i) that there is extensive theoretical justification for the quadratic field term and (ii) that a statistical analysis of available experimental data arrived at a smallest standard deviation when the quadratic field term was included.

Current efficiencies were determined from charge and optical film thickness. The current efficiencies were (a) essentially constant up to a formation temperature of about 170°C and (b) decreased by about 30% between 170° and 250°C.

Capacitance and loss angle of "equal charge" films increased with formation temperatures higher than about 180°C. Oxygen dissolution in the tantalum substrate was suggested as the likely cause.

Acknowledgments

The authors gratefully acknowledge the contributions of Dr. M. Ghezzo and Mr. E. Burdick with respect to the ellipsometric measurements. Dr. Ghezzo set up the computer program for the evaluation.

APPENDIX

Expanding the square root term in the exponent of Eq. [2] and neglecting higher terms than the cubic one yields

$$F^{1/2} = F_o^{1/2} + \frac{1}{2} F_o^{-1/2} (F - F_o) - \frac{1}{8} F_o^{-3/2} (F - F_o)^2 + \frac{1}{16} F_o^{-5/2} (F - F_o)^3$$

Let the first three terms on the right side be $f(F)$. The error is of the order of the third term if $F^{1/2}$ is replaced by $f(F)$ and the relative error is

$$[F^{1/2} - f(F)]/F_o^{1/2} \simeq (F - F_o)^3/16\, F_o^3$$

The voltage build-up rate (dV/dt) is directly proportional to the field during constant current anodizations. With the following values from Fig. 4 ($T = 0$°C, $dV/dt = 0.373$ V/sec and $T = 125$°C, $dV/dt = 0.273$ V/sec) one obtains for the relative error: 0.31×10^{-2}. This means the maximum error is about 0.3% if, over the whole temperature range of 250°C, the square root term is replaced by a quadratic relation. Thus, within this limit, Eq. [2] can be expressed in the form of Eq. [3], with the constants adjusted accordingly.

Manuscript received Dec. 18, 1969. This was Paper 31 presented at the New York Meeting of the Society, May 4-9, 1969.

Any discussion of this paper will appear in a Discussion Section to be published in the June 1971 JOURNAL.

REFERENCES

1. L. Young, *Proc. Roy. Soc.*, **A258**, 496 (1960).
2. L. Young and F. G. R. Zobel, *This Journal*, **113**, 277 (1966).
3. M. J. Dignam and D. Goad, *ibid.*, **113**, 382 (1966).
4. W. J. Bernard and J. W. Cook, *ibid.*, **106**, 643 (1959).
5. P. H. G. Draper and P. W. M. Jacobs, *Trans. Faraday Soc.*, **59**, 2895 (1963).
6. R. Dreiner, *This Journal*, **111**, 1350 (1964).
7. S. G. Christov and S. Ikonopisov, *ibid.*, **116**, 56 (1969).
8. J. J. Randall, W. J. Bernard, and R. R. Wilkinson, *Electrochim. Acta*, **10**, 183 (1965).
9. D. M. Lakhiani and L. L. Shreir, *Nature*, **188**, 49 (1960).
10. D. A. Vermilyea, *This Journal*, **102**, 207 (1955).
11. D. M. Smyth, G. A. Shirn, and T. B. Tripp, *ibid.*, **110**, 1264 (1963).
12. J. A. Davies, B. Domeij, J. P. S. Pringle, and F. Brown, *ibid.*, **112**, 675 (1965).
13. L. Masing, J. E. Orme, and L. Young, *ibid.*, **108**, 428 (1961).
14. L. Young, "Anodic Oxide Films," p. 82, Academic Press, London and New York (1961).
15. M. J. Dignam and D. B. Gibbs, *J. Phys. Chem. Solids*, **30**, 375 (1969).

The Nucleation, Growth, and Structure of Electroless Copper Deposits

Richard Sard*

Bell Telephone Laboratories, Incorporated, Murray Hill, New Jersey

ABSTRACT

An electron microscopic investigation has revealed that the electroless deposition of copper occurs by repeated three-dimensional nucleation at catalytic sites on a substrate. The nature of the catalytic sites formed by immersion in the standard stannous and palladium chloride solutions was observed and found to influence the structure of the subsequently deposited metal. Initially, copper nuclei about 25Å in diameter form aggregates an order of magnitude larger. As the autocatalytic reduction reaction continues the aggregates increase in size until they become energetically unstable; then recrystallization occurs. The resulting continuous copper films exhibit a heterogeneous microstructure with grain size variations of more than an order of magnitude and also numerous twin faults.

There exists at present a considerable and rapidly growing interest in the electroless deposition of metallic films onto nonconducting substrates. Although many chemical systems for metal deposition have been developed (1), relatively little is known about the mechanisms which govern the behavior of these complex systems. Recently, however, some progress toward this goal has been made by Okinaka (2) and Paunovic (3) who employed electrochemical methods to study the kinetics of the electroless copper plating reaction.

An important property of electroless systems is their ability to deposit metals selectively. This property, which depends critically on the structure of the sensitized substrate, has been demonstrated by Sharp (4), who desensitized portions of a surface with u.v. radiation, and also by Turner (5), who used a printing technique to apply a sensitizer selectively.

A fundamental aspect of this type of deposition, about which very little is known, concerns the basic structural mechanisms responsible for the nucleation and growth of metallic films. These factors are important because they will ultimately determine the properties and consequently the technological usefulness of the films. Interest in magnetic thin films has led to several studies dealing with the structure of electroless nickel (6-8) and cobalt (9-12) deposits that were chemically reduced from solutions containing hypophosphite. However, there appears to be virtually no data available on the growth and structure of other electroless deposits including copper, which is of considerable technological importance. Also, there is very little direct evidence (6, 9) concerning the structures which exist prior to the formation of a continuous metal deposit. One reason for this lack of direct evidence is that electron microscopes capable of resolving information on the order of 10Å are needed. While such instruments are available, they have not yet been employed to study the process of electroless deposition.

The present study has been primarily concerned with the nucleation and growth of electroless copper deposits. However, some of the results, particularly those pertaining to the sensitization and activation treatments which precede metal deposition, are undoubtedly of a more general nature and can therefore be applied to other electroless deposition systems.

Experimental

Four aspects of the over-all process of electroless deposition were investigated: first, the influence of the substrate; second, the sensitization of the substrate with stannous chloride; third, the activation of the sensitized substrate with palladium chloride; finally, the deposition of a metallic copper film. The formulations of the various solutions are given in Table I. Initially, solutions were prepared using distilled water of conventional purity. Subsequently, however, deposition experiments were carried out with a higher regard for purity. For example, these experiments were conducted in a laminar flow work station and solutions were prepared with water[1] that was twice distilled in a quartz apparatus. The water used for the rinsing operations after each stage of the process was of the same type used for solution preparation. Reagent grade chemicals were used without further purification.

The electron microscopic techniques which were used to investigate the structures present at each

[1] An analysis carried out by D. L. Malm, of Bell Telephone Laboratories, using spark source mass spectroscopy indicated that this water contained from 1 to 10 atomic ppm of total residual impurities.

Table I. Solution formulations

Constituents	Quantity	Concentration
Sensitization*		
A. $SnCl_2 \cdot 2H_2O$	16 g/l	0.07 M
Conc. HCl	30 ml/l	0.82 M
B. $SnCl_2 \cdot 2H_2O$	30 g/l	0.13 M
Conc. HCl	10 ml/l	0.27 M
Activation*		
A. $PdCl_2$	0.1 g/l	0.0006 M
Conc. HCl	8 ml/l	0.22 M
B. $PdCl_2$	0.75 g/l	0.004 M
Conc. HCl	10 ml/l	0.27 M
Electroless Copper		
A. Saubestre's solution (22)	170 g/l	0.60 M
$KNaC_4H_4O_6 \cdot 4H_2O$ (Rochelle salt)	50 g/l	1.25 M
NaOH	35 g/l	0.14 M
$CuSO_4 \cdot 5H_2O$	30 g/l	0.28 M
EDTA	10 g/l	0.03 M
Immediately prior to use five parts of this solution are combined with one part HCHO (37%).		
B. Okinaka's methanol solution (23)		
Part 1		
$CuSO_4 \cdot 5H_2O$	10 g/l	0.04 M
HCHO (37%)	60 ml/l	0.78 M
CH_3OH	300 ml/l	30%
Part 2		
NaOH	40 g/l	1.0 M
$KNaC_4H_4O_6 \cdot 4H_2O$ (Rochelle salt)	28 g/l	0.1 M
Parts 1 and 2 are mixed in equal volumes prior to use.		

* Based on Bergstrom's patent (21).

* Electrochemical Society Active Member.
Key words: electroless deposition, copper, nucleation and growth, structure of thin films, electron microscopy.

stage of the process were bright-field and dark-field imaging combined with selected-area electron diffraction, as well as direct carbon or two-stage surface replicas shadowed with a Pt-Pd alloy. These investigations were carried out with a Siemens Elmiskop instrument operated at 100 kV.

In order to study the initial stages of the process, prior to the formation of a continuous, self-supporting deposit, an electron-transparent substrate is required. Evaporated carbon films, about 200 to 400Å thick, were used, and suitable substrates were prepared by conventional techniques employing either plastic-coated microscope grids or glass slides as the original substrate materials.

Continuous copper films, 500-1000Å thick, were deposited onto glass slides, evaporated carbon, Kapton (a polyimide film), and freshly cleaved mica substrates. The structures of these films were studied by the electron microscopic techniques mentioned previously, which required stripping of the deposits from all but the carbon substrates. Continuous copper deposits were also examined by reflection electron diffraction while they were still adherent to their substrates in order to determine whether the different substrates exerted any influence on their orientation and structure.

Results and Discussion

Sensitization.—Evaporated carbon substrates were immersed in stannous chloride solutions, rinsed in distilled water, dried, and examined electron microscopically.[2] It was found that the product of this sensitization treatment exists as particulate matter on an extremely fine scale. Particles of the order of 10Å were resolved, and these tended to agglomerate into dense clumps an order of magnitude larger. High resolution bright-field and dark-field micrographs which illustrate these results are shown in Fig. 1a and 1b, respectively.

Figure 1a represents the structure present after immersion of a carbon substrate for 3 sec in stannous chloride solution A. The darker regions are in diffraction contrast and correspond to the deposited material. These regions appear to be clumps that are about 100-250Å in size and are comprised of smaller particles about 25Å in size. The coverage in this field of view is apparently less than 25%. In dark-field micrographs at higher magnifications (Fig. 1b) the smallest resolvable particles are approximately 10-20Å in size. Images of this type reveal only a portion of the deposited material as most of the diffracted electrons are stopped by the objective aperture.

The electron diffraction pattern shown is Fig. 2 is typical of those observed after sensitization in either solution for periods up to 1 min and water rinsing. This pattern corresponds to the oxide phase, SnO_2 (ASTM Data Card 5-0467). The analysis[3] of numerous similar diffraction patterns confirmed this result. It is important to remember, however, that these experiments were not performed *in situ* and the deposits were exposed to an air environment for at least 10 min prior to examination, during which time oxidation undoubtedly occurred.

The breadths of diffraction lines, as determined from microdensitometer traces, yielded an independent calculation of the particle size. Both the integral breadth and the peak width at half maximum were determined from several typical patterns. Breadths of 1 to 2 x 10^{-3} radians were found, which correspond to calculated values of the particle sizes in the range from about 30 to 15Å, to a first approximation (14).

[2] One series of these experiments was carried out in collaboration with R. D. Heidenreich using a modified Siemens Elmiskop that is capable of 2Å resolution under optimum conditions (13). It is unlikely, however, that features smaller than 10Å could be resolved in the present samples due to the background "noise" from the substrates.

[3] These measurements were facilitated by graphically recording many of the patterns with a Jarrell Ash microdensitometer. Evaporated TlCl was used for a calibration standard.

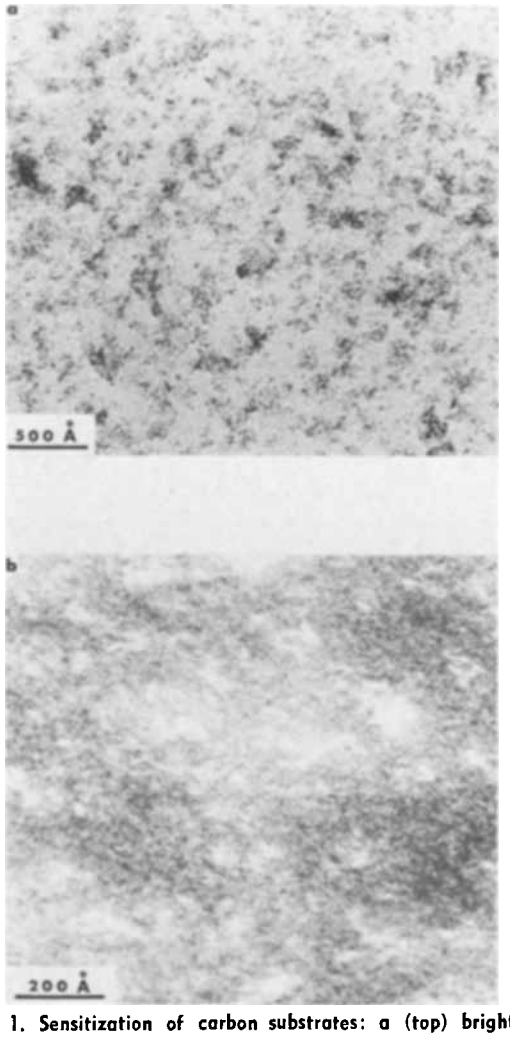

Fig. 1. Sensitization of carbon substrates: a (top) bright-field image, 3 sec in $SnCl_2$-A; b (bottom) dark-field image, 10 sec in $SnCl_2$-B.

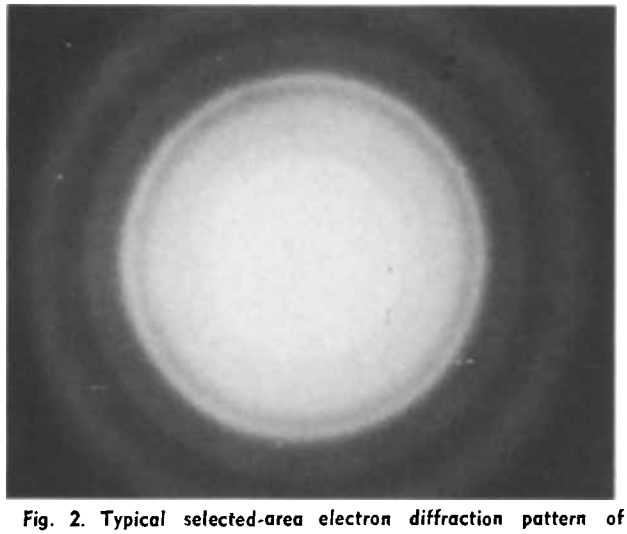

Fig. 2. Typical selected-area electron diffraction pattern of sensitized carbon substrate.

Increasing either the concentration of stannous chloride or the immersion time resulted in an increased coverage of the adsorbed sensitizing species. However, on a microscopic scale the coverage was heterogeneous, particularly when distilled water of ordinary purity was used. The results obtained from high-purity solutions showed a marked improvement with respect to uniformity and reproducibility. Figure 3 illustrates the effect of increasing the immersion time from 5 to 30 sec, as coverage increases from ap-

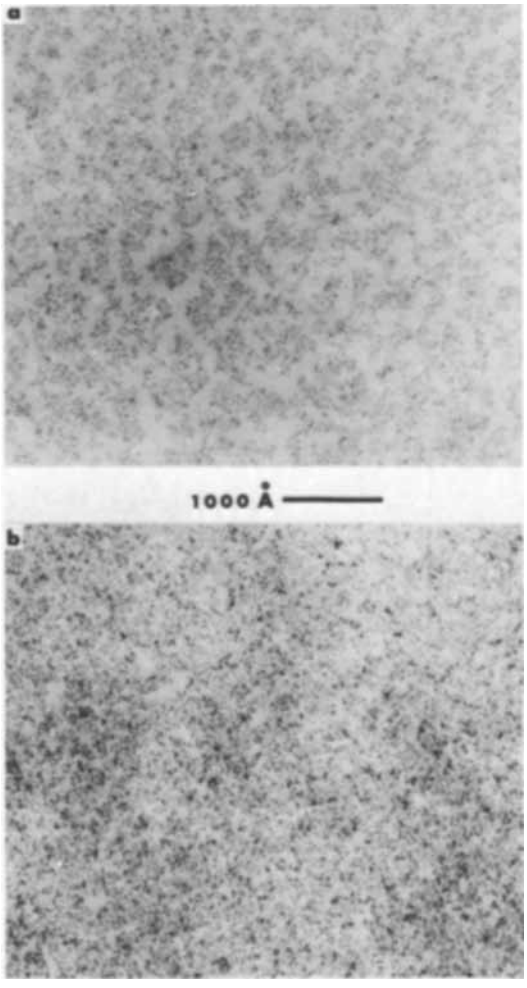

Fig. 3. Effect of time on sensitization of carbon substrates in $SnCl_2$-A (high purity): a (top) 5 sec immersion, b (bottom) 30 sec immersion.

proximately 30 to 75%. Although these fields of view are representative and appear to have uniform coverage, the results must be considered qualitative as other samples subjected to similar treatments occasionally exhibited different configurations. Hence, a considerable amount of statistical data would have to be obtained and analyzed, together with measurements on a more macroscopic scale, in order to describe and interpret the adsorption kinetics of this system quantitatively.

The above results confirm some of the deductions which were made recently by other workers who have studied the nucleation, growth, and structure of electroless nickel (6) and cobalt (9, 10) deposits. Marton and Schlesinger (6) were unable to resolve the products of stannous chloride sensitization, prior to activation and nickel deposition. By extrapolating a plot of particle size *vs.* time (back to $t = 0$) for growing Ni-P islands, assuming a constant microscopic growth rate, the catalytic sites were estimated to be less than 10Å in diameter. On the basis of the present results, it appears that the most important sites for further nucleation and growth are the densest regions of the deposit.

Several important aspects regarding the sensitization with stannous chloride solutions require further study. Although the presence of SnO_2 is indicated by electron diffraction, this analytical method is obviously not well suited to a direct study of hydrolyzed species and therefore cannot identify which of the many possible (15,16) stannous or stannous chlorohydroxides, oxyhydroxides, or hydrated oxides forms at the surface. In this regard, the *p*H at the surface is an important factor which has been found (4) to determine which compounds are formed. Recent work by Sharp and co-workers (4) has shown that tin must be present as Sn^{+2} and not Sn^{+4}, otherwise activation and electroless deposition will not occur. Diffraction patterns indicating the presence of the bivalent oxide, $(SnO)_{16}O$ (ASTM Data Card 13-111) were observed on samples subjected to a very mild rinse, *i.e.*, 10 sec immersion without turbulence. Although no systematic study of rinsing was conducted, this treatment influenced the structure observed during activation and electroless deposition.

Activation.—A surface containing only an adsorbed sensitizer is inactive in an electroless solution(17). Hence, the presence of a suitable catalyst is essential if that surface is to receive an electroless deposit. Palladium chloride solutions are most frequently used to provide the catalyst. The reaction mechanism for this process is generally thought (24) to be: $Sn^{+2} + Pd^{+2} \rightarrow Pd^0 + Sn^{+4}$, which means that the adsorbed stannous ions provide the sites and electrons for the adsorbing palladium ions. When excess sensitizer is dragged through into $PdCl_2$ solutions due to inadequate rinsing, the reduction to metallic Pd occurs adjacent to the interface and in the bulk of the solution. In such cases, metallic Pd particles, 50-100Å in size, become adsorbed on the surface. The set of arrows shown in Fig. 4 refers to corresponding regions in bright and dark-field micrographs where these particles are clearly seen.

The manner in which rinsing was carried out after the sensitization and activation treatments was found to affect the configuration of the adsorbed material. In contrast to the previous results for relatively mild rinsing by immersion, the structure shown in Fig. 5

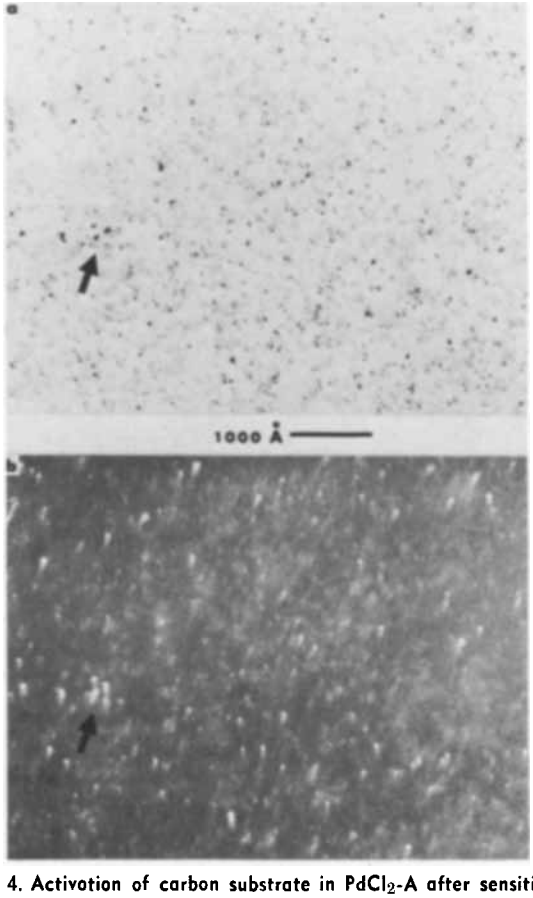

Fig. 4. Activation of carbon substrate in $PdCl_2$-A after sensitization in $SnCl_2$-A (high purity, 5 sec each) with incomplete rinse. Arrows indicate Pd particles. a (top) Bright-field image; b (bottom) dark-field image of same region.

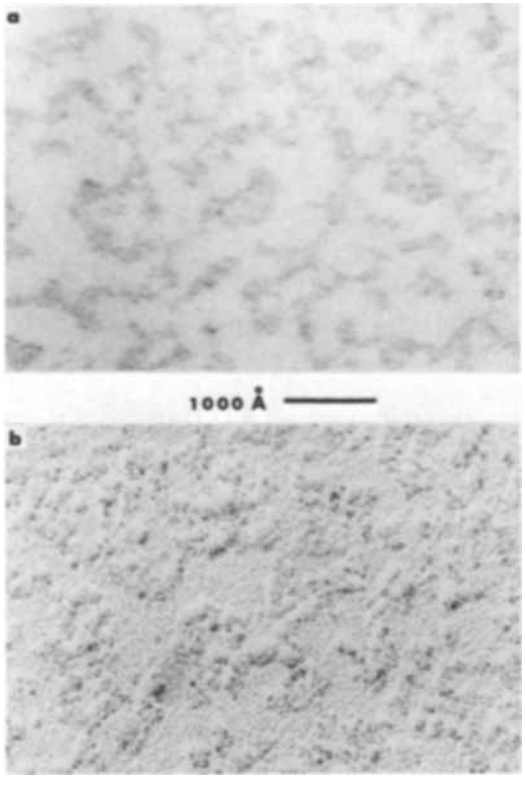

Fig. 5. Effect of severe agitation during rinsing of carbon-coated glass substrate. Sensitization and activation for 30 sec each in $SnCl_2$-A and $PdCl_2$-A. a (top) Bright-field image, b (bottom) shadowed, carbon replica showing surface morphology.

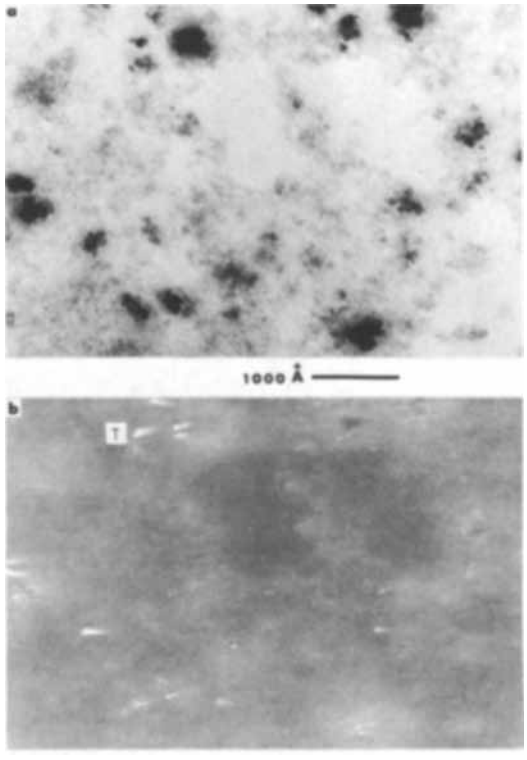

Fig. 6. The initial stage of copper deposition after 3 sec in solution A. Carbon substrate sensitized and activated for 3 sec each in $SnCl_2$-A and $PdCl_2$-A. Twinned crystallite denoted by "T." a (top) Bright-field image, b (bottom) dark-field image of same region.

resulted from a more severe rinse, *i.e.*, holding the carbon-coated glass substrate under running distilled water. The transmission micrograph in Fig. 5a indicates that the active material covers only a relatively small fraction of the surface in an island network. The morphology of this structure is visible in carbon replicas (Fig. 5b). Based on the shadowing geometry and Fig. 5b, these islands are estimated to be approximately 40Å in elevation.

The structures and diffraction patterns observed after activation of sensitized surfaces that received adequate rinsing were quite similar to those obtained prior to the activation treatment. The network-like clumps of adsorbed sensitizer persisted and the diffraction patterns became more diffuse which suggests that the activation process consists of the adsorption of very small amounts (probably less than about 20Å) of Pd onto the sensitized regions. Direct evidence of metallic Pd in diffraction patterns of these samples was observed when electron-beam induced recrystallization resulted in particles 100-150Å in size. Also, regions exhibiting dense coverage frequently gave diffraction patterns with extra lines corresponding to PdO.

The following qualitative results on the effect of the deposition variables were obtained. Increased concentration (solution B) resulted in increased Pd coverage. With respect to activation time, it appeared that most of the sensitized regions became covered after about 10-20 sec and that prolonged immersion had little effect. These effects were only observed when other factors, such as rinsing, did not interfere.

Electroless copper deposition.—The electroless deposition of copper from solution occurs only at catalytic regions on a surface. The initial stage in this process is represented by Fig. 6, which corresponds to a 3-sec immersion in solution A. The copper particles, which appear dark in Fig. 6a, nucleated at the most favorable catalytic sites. These sites correspond to the densest regions of the active material, which appear in gray contrast in Fig. 6a against the lighter, inactive regions on the substrate. It is interesting to note that the copper particles, which range up to about 300Å in size, are not single crystals but consist of aggregates of smaller crystallites. This observation is confirmed by the dark-field micrograph (Fig. 6b), which shows that the larger aggregates contain randomly oriented crystallites that are less than 50Å in diameter. The streaks associated with the bright, diffracting crystallites in Fig. 6b are due to spherical aberration, *i.e.*, the objective aperature was positioned off the optical axis, and are without structural significance. The feature denoted by the letter "T," which consists of two regions in diffraction contrast separated by a small dark band with parallel sides, is believed to represent a twinning fault. The formation of twins during electroless copper deposition is an important part of this process and is discussed below.

As the process continues autocatalytically, copper deposits on the originally formed nuclei. After about 10 sec in solution A, the largest aggregates exceed 500Å in size, yet all of these features consist of smaller crystallites as seen in Fig. 7. Crystallites as small as 25-50Å across are resolved, although some coherently diffracting regions larger than 100Å are plainly visible. Close examination of this as well as numerous similar samples revealed that the twin fault density at this stage is about 10^{10} cm^{-2} which corresponds to approximately 1% of the deposited nuclei. The diffraction patterns obtained from these deposits indicate that the copper is randomly oriented and possesses the lattice parameter of bulk material. It appears, therefore, that the deposition process from solution is random with respect to orientation. Thus, the formation of twin faults can occur whenever adjacent crystallites are in twin orientation across a common {111} boundary.

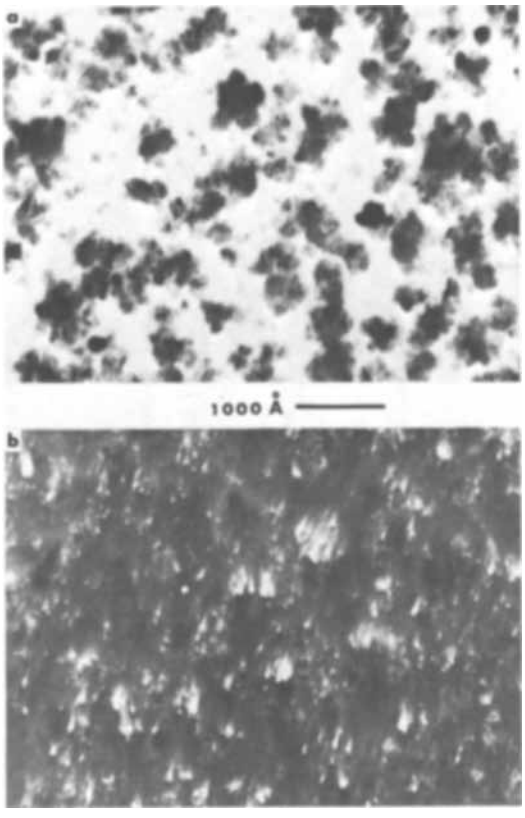

Fig. 7. Copper deposit after 10 sec in solution A. Carbon substrate sensitized and activated for 10 sec each in $SnCl_2$-A and $PdCl_2$-A. a (top) Bright-field image, b (bottom) dark-field image of same region.

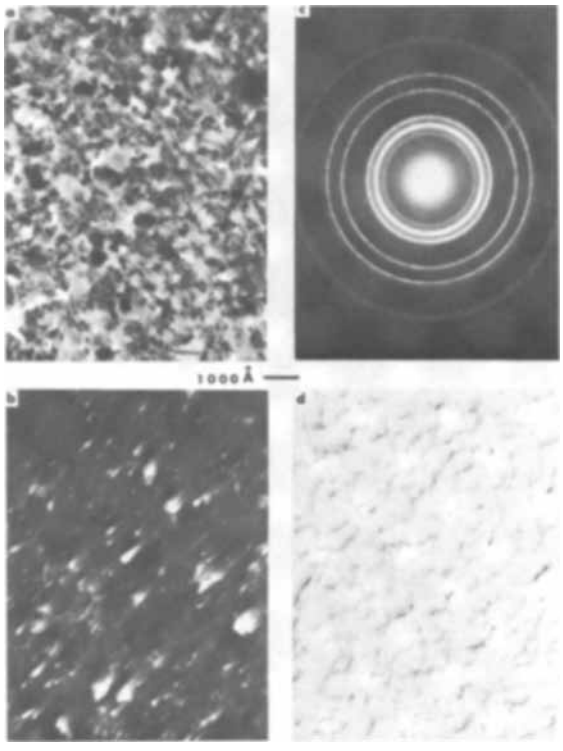

Fig. 8. Continuous copper deposit formed in solution A after pretreatment equivalent to that of Fig. 5. a, Bright-field image; b, dark-field image of same region; c, selected area diffraction pattern characteristic of copper and Cu_2O; d, shadowed, carbon replica of surface.

Several important aspects of the electroless deposition of continuous films are illustrated in Fig. 8, which represents the structure formed when an activated substrate similar to Fig. 5 was plated for 1 min in solution A. The bright and dark-field pair of transmission micrographs (Fig. 8a and 8b, respectively) reveal that the grain size of this structure varies by more than an order of magnitude. The largest grains are 800-1000Å across, which corresponds to the estimated film thickness. It is noted that these larger grains tend to form continuous chains that are separated by regions consisting of much finer crystallites. The surface morphology of this deposit (Fig. 8d) confirms the existence of large elevated chains separated by regions where the film is thinner. The large-grained regions undoubtedly correspond to the active sites on the substrate where copper deposition originated.

With the exception of the chainlike network of larger grains, the basic structural features that are visible in Fig. 8 were common to all continuous deposits regardless of pretreatment. The microstructures were all qualitatively similar with respect to the grain-size variations and the existence of numerous twin faults. (The parallel fringes which extend across many of the larger grains in Fig. 8a are due to microtwin faults.) Typically, twin fault densities in excess of 10^{10} cm^{-2} were observed.[4] Moreover, all deposits were randomly oriented. This result was determined from transmission patterns (*e.g.*, Fig. 8c) of detached films and confirmed from reflection patterns of deposits still adherent to their substrates. The substrates activated for use in the reflection experiments were glass, freshly cleaved mica, and the polyimide material, Kapton.

The rate of electroless copper deposition is dependent on the nature of the catalytic surface as well as the composition of the solution. Solution A, which is relatively unstable, deposits copper at an average rate of 25 μ/hr (70 Å/sec), whereas solution B, which is more dilute and contains a stabilizer, is slower by a factor of about twenty. Despite this difference, it was found that both solutions yielded deposits with similar structural characteristics. In fact, by altering the catalyst coverage and immersion times it was possible to obtain virtually identical deposits. Figure 9 illustrates this point. The deposit in Fig. 9a received a 5-sec sensitization and activation prior to electroless deposition for 10 sec in solution A. When solution B was used with the same pretreatment relatively few nuclei were deposited and these required several minutes to grow into large aggregates. However, increasing the pretreatment times to 30 sec prior to deposition in solution B for an equivalent duration resulted in the structure shown in Fig. 9b.

Several stages in the development of a copper deposit from solution B when the surface concentration of catalyst is low can be seen in Fig. 10. In these experiments glass slides were used as substrates and ultrasonic agitation during rinsing reduced coverage to between 10 and 20%. The copper deposits together with their evaporated carbon supports were removed from the glass in 10% HF. This treatment accounts for the replicalike effect in Fig. 10a, where the outline of the deposit present at 30 sec is visible although the copper has dissolved and also accounts for the undercutting on the 1-min deposit (Fig. 10b). The other bright-field micrographs in Fig. 10c and 10d represent the structures developed after deposition for 3 and 5 min, respectively. The deposits obtained under these conditions, *i.e.*, low catalyst concentration and stabilized solution, differ from the one in Fig. 9b in that there are fewer aggregates and these grow to several thousand angstroms in size before encountering other similar features. The dark-field image (Fig. 10e) and diffraction pattern (Fig. 10f) confirm that the basic microstructural characteristics of these deposits

[4] Similar twin fault densities have been observed for both single crystal (18) and polycrystalline (19) copper electrodeposits and also for evaporated films (20).

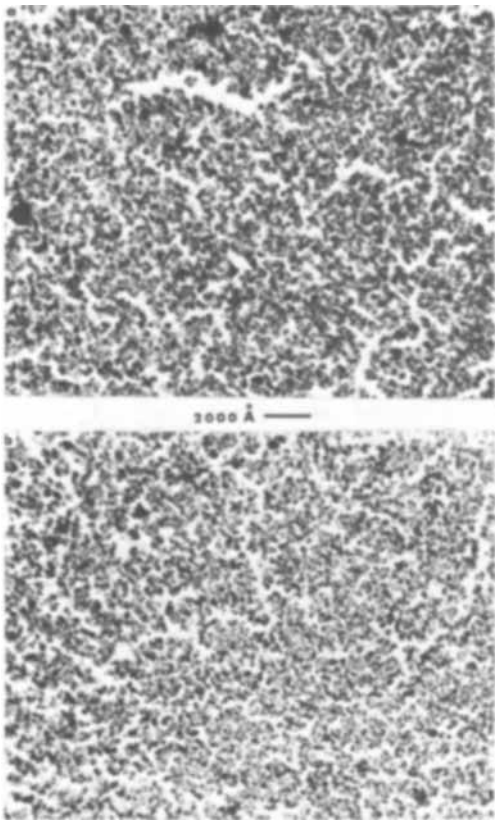

Fig. 9. Discontinuous copper deposits obtained from different solutions on glass substrates. a (top) Solution A, 10 sec after 5 sec each in $SnCl_2$-A and $PdCl_2$-A; b (bottom) solution B, 30 sec after 30 sec each in $SnCl_2$-A and $PdCl_2$-A.

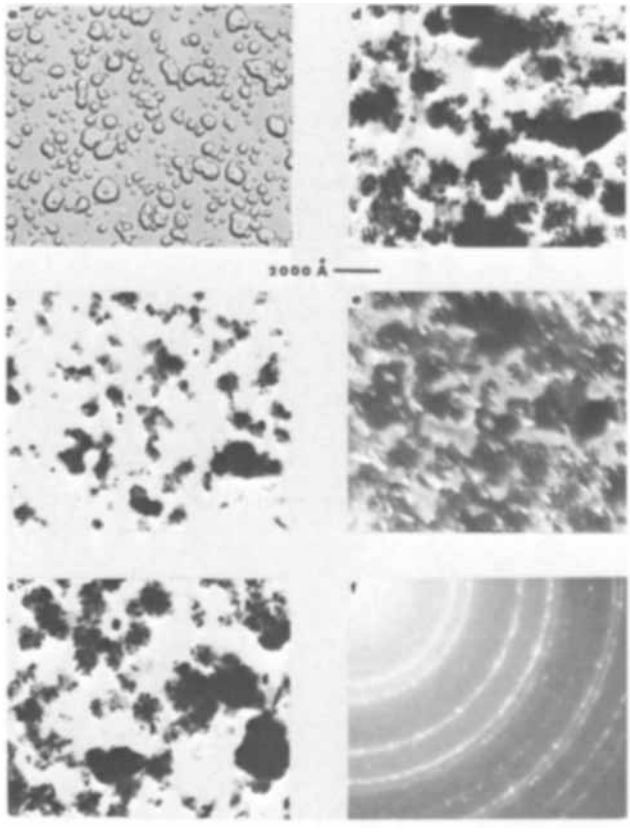

Fig. 10. Several stages in the formation of a copper deposit in solution B on a glass substrate with low catalyst concentration. Sensitization and activation for 30 sec each in $SnCl_2$-A and $PdCl_2$-A with ultrasonic agitation during rinsing. a-d, Bright-field images, 30 sec, 1, 3, and 5 min, respectively; e, dark-field image of region shown in d; f, selected area electron diffraction pattern.

are no different from those discussed previously.

The above results indicate that the structure of continuous electroless copper deposits is a direct consequence of the nucleation and growth phenomena which occur during the initial stages of the process. Initially three-dimensional nucleation occurs at catalytic sites on a surface. These nuclei form aggregates which become larger due to the continued depositon of material from solution until they become energetically unstable. At this stage a recrystallization process occurs which eliminates the interior boundaries and transforms the unstable aggregates into larger, single grains. Therefore, the conventional descriptions of metal deposition processes wherein nucleation is followed by two-dimensional growth via surface diffusion are not applicable to electroless deposition due to the chemical reduction reaction at the surface. The mechanism of this reaction is of great importance and has recently been studied using electrochemical techniques (2, 3). It appears that a detailed understanding of both the physical and the chemical aspects of this complex system will have to be obtained before a complete quantitative description can be given.

Summary

High resolution electron microscopy provides an extremely powerful method for elucidating the structural phenomena associated with the electroless process for metal deposition on nonconducting substrates. Application of this method has resulted in the following description of this process.

The products of the standard stannous chloride sensitization treatment exist as adsorbed clumps of material that are several hundred angstroms across and are comprised of particles 10 to 30Å in size. Activation with palladium chloride results in the adsorption of catalytic material onto the sensitized regions. The configuration of these active regions can be altered by rinsing. This alteration is reflected in the structure of the subsequently deposited metal.

The structural mechanisms which govern the electroless deposition of copper were deduced by following the stepwise development of metallic films. This process proceeds by repeated three-dimensional nucleation from solution at catalytic sites on the surface. The copper nuclei, which are about 25Å in diameter, form aggregates an order of magnitude larger. Since the reduction reaction is autocatalytic, the size of the aggregates increases during growth until they become energetically unstable. Then a recrystallization process takes place and the unstable aggregates are transformed into relatively large grains several hundred angstroms across. Continuous copper films obtained by this process exhibit a heterogeneous microstructure with grain size variations of more than one order of magnitude. This variation is attributed to the repeated nucleation and recrystallization process. These deposits also contain numerous ($>10^{10}cm^{-2}$) twin faults. Twin faults can form whenever adjacent nuclei are in twin orientation and possess a common {111} boundary. This situation apparently occurs quite frequently during the initial stages of the process when the randomly oriented copper nuclei form on the substrate.

An important first step toward the goal of elucidating the physical aspects of electroless copper deposits has been achieved. However, a more quantitative description encompassing both the physical and chemical aspects of the system is urgently needed.

Acknowledgment

Thanks are due to R. D. Heidenreich who made the electron microscope facilities available to the author and also assisted in the high resolution study of the sensitization process which resulted in Fig. 1a and 1b. The efforts of G. W. Kammlott who obtained the re-

flection diffraction patterns are also acknowledged. Finally, considerable insight regarding the chemistry of the electroless process was provided by Y. Okinaka, who, along with D. R. Turner participated in helpful discussions during the course of this work.

Manuscript submitted Jan. 19, 1970; revised manuscript received March 13, 1970.

Any discussion of this paper will appear in a Discussion Section to be published in the June 1971 JOURNAL.

REFERENCES

1. W. Goldie, "Metallic Coating of Plastics," Electrochemical Publications Ltd., Middlesex, England (1968).
2. Y. Okinaka, Paper 144 presented at the Detroit Meeting of the Society, Oct. 5-9, 1969.
3. M. Paunovic, *Plating*, **55**, 1161 (1968).
4. D. J. Sharp, J. Henrickson, J. D'Amico, and J. Kenney, Paper 136 presented at the Detroit Meeting of the Society, Oct. 5-9, 1969.
5. D. R. Turner, Paper 137 presented at the Detroit Meeting of the Society, Oct. 5-9, 1969.
6. J. P. Marton and M. Schlesinger, *This Journal*, **115**, 16 (1968).
7. M. Schlesinger and J. P. Marton, *J. Phys. Chem. Solids*, **29**, 188 (1968).
8. A. H. Graham, R. W. Lindsay, and H. J. Read, *This Journal*, **112**, 401 (1965).
9. A. S. Frieze, R. Sard, and R. Weil, *ibid.*, **115**, 586 (1968).
10. A. S. Frieze, M. S. Thesis, Stevens Institute of Technology (1966).
11. M. G. Miksic, R. Travieso, A. Arcus, and R. H. Wright, *This Journal*, **113**, 360 (1966)
12. L. Cadorna, P. Cavallotti, and G. Salvago, *Electrochem. Metallorum.*, **1**, 177 (1966).
13. R. D. Heidenreich, W. M. Hess, and L. L. Ban, *J. Appl. Cryst.*, **1**, 1 (1968)
14. See, for example, J. T. Randall, "The Diffraction of X-Rays and Electrons by Amorphous Solids, Liquids and Gases," Chap. 3, John Wiley & Sons, Inc., New York (1934).
15. J. D. Donaldson, *Prog. Inorg. Chem.*, **8**, 287 (1967).
16. J. D. Donaldson and W. Moser, *J. Chem. Soc*, **117**, 835 (1961).
17. W. Goldie, *Plating*, **51**, 1069 (1964).
18. R. Sard and R. Weil, To be published in *Electrochim. Acta.* Paper presented at C.I.T.C.E. Meeting, Detroit, 1968.
19. E. M. Hofer and H. E Hintermann, *This Journal*, **112**, 167 (1965).
20. See, for example, D. W. Pashley, *Advanc. Phys.*, **14**, 327 (1965).
21. I. A. Bergstrom, U. S. Pat. 2,702,253.
22. E. B. Saubestre, *Proc. AES.*, **46**, 264 (1959).
23. Y. Okinaka, Paper in preparation.
24. W. Goldie, *op. cit.*, p. 50.

Electrochemical Method to Measure the Copper Ionic Diffusivity in a Copper Sulfide Scale

A. Etienne

Department of Metallurgy, University of British Columbia, Vancouver, British Columbia

ABSTRACT

Copper sulfides have been grown on a copper anode from an acidic solution saturated with H_2S under a constant current. A theoretical model for the scale growth has been derived for steady-state conditions. From the set of experimental data, the cuprous ionic diffusivity of chalcocite and digenite in the scale have been calculated in the range of temperature from 30° to 73°C. The measured diffusion coefficient of cuprous ion in low chalcocite was found to be

$$D_{Cu+} = 8.1 \times 10^{-3} \exp\left(-\frac{5870}{T}\right) \text{ (cm}^2\text{ sec}^{-1}\text{)}$$

and in low digenite

$$D_{Cu+} = 3.6 \times 10^{-2} \exp\left(-\frac{6100}{T}\right) \text{ (cm}^2\text{ sec}^{-1}\text{)}$$

The calculation of the activation entropy for diffusion in both phases is attempted.

Copper sulfides can be grown on a copper anode from an acidic solution saturated with H_2S. If the operation is conducted at constant current, different sulfide layers of decreasing copper activity are built as the oxidation proceeds. If equilibrium is established, the successive phases should be, according to the phase diagram (1) (Fig. 1): copper, chalcocite, djurleite digenite, covellite, and sulfur. The reaction occurring at the anode is

$$y\text{Cu} + \text{H}_2\text{S} \rightarrow \text{Cu}_y\text{S} + 2\text{H}^+ + 2e$$

The electrochemical potential of such an electrode (Stockholm convention) is given by the following relationship

$$E = E_o - \frac{RT}{2\mathbf{F}} \ln \frac{A_{Cu^y} A_{H_2S}}{A_{Cu_yS} A_{H^+2}} + E_a \qquad [1]$$

The copper activity at the solid-liquid interface reflects the conditions imposed on the system and the transport properties of the scale being built. The sulfide activity is taken as unity. In defined geometric and stirring conditions, under a constant current, the hydrogen sulfide and hydrogen ion activities are constant in the vicinity of the electrode. In steady-state conditions, the activation overvoltage for a given sulfide is a constant. Therefore, the electrode potential variation with time follows the evolution of the copper activity according to the relationship [2] derived from [1].

$$\frac{dE}{dt} = -\frac{RT}{2\mathbf{F}} \frac{d}{dt} \ln A_{Cu^y}$$

$$\frac{dE}{dt} = -y \frac{RT}{2\mathbf{F}} \frac{d}{dt} \ln A_{Cu} \text{ if } y = \text{constant} \qquad [2]$$

If the sulfide scale grows uniformly on the electrode surface, the copper activity at the liquid-solid inter-

Key words: copper sulfides, diffusion coefficient, anodic film.

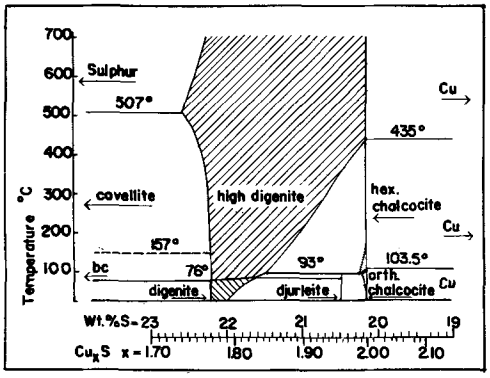

Fig. 1. Portion of the phase diagram of the system Cu-S from Roseboom (1).

face can be directly linked to the transport properties of the sulfide layer.

Theoretical Anode Model

In the copper sulfides, the sulfur ion mobility is considered negligible in comparison with copper ion mobility (2). In the case of high-temperature phases (αCu_2S, βCu_2S) there is experimental evidence (3, 4) to support this. It is also reasonable for the low-temperature phases in view of the relatively large size and associated immobility of the anion.

The copper sulfides have a good electronic conductivity. Chalcocite is a p-type semiconductor, its conductivity increases notably with copper deficiency ($\sigma = 10^{-2} \rightarrow 50$ ohm^{-1} cm^{-1} at room temperature) (5, 6). Digenite and covellite are almost metallic in character ($\sigma = 2 \times 10^4$ ohm^{-1} cm^{-1} at room temperature) (5, 7).

The phenomenological equations for diffusion relate the particle flux to the forces responsible for their motion. If the interaction effects are neglected, unidimensional transport in a two component system in the presence of a low strength electric field can be equated by

$$J_{Cu+} = - M_{Cu+}\left(\frac{d}{dx}\mu_{Cu+} + q_{Cu+}\frac{d}{dx}\Phi \right) \quad [3]$$

$$J_e = - M_e\left(\frac{d}{dx}\mu_e + q_e\frac{d}{dx}\Phi \right) \quad [4]$$

The electrical potential gradient can be derived from Eq. [4] and substituted in Eq. [3].

$$J_{Cu+} - \frac{q_{Cu+}}{q_e}\frac{M_{Cu+}}{M_e}J_e = - M_{Cu+}\left(\frac{d}{dx}\mu_{Cu+} - \frac{q_{Cu+}}{q_e}\frac{d}{dx}\mu_e \right) \quad [5]$$

Chemical potentials of ion and electron are not experimentally accessible values but are related through the measurable quantity, μ_{Cu}

$$\mu_{Cu} = \mu_{Cu+} + \mu_{e-}$$

Equation [5] is then simplified

$$J_{Cu+} + \frac{M_{Cu+}}{M_e}J_e = - M_{Cu+}\frac{d}{dx}\mu_{Cu} \quad [6]$$

As reported earlier, the copper sulfides are electronic conductors, their electronic conductivity being much larger than their ionic conductivity, and Eq. [6] can be reduced to

$$J_{Cu+} = - M_{Cu+}\frac{d}{dx}\mu_{Cu} \quad [7]$$

The Onsager coefficient M_i is directly related to the conductivity, diffusivity, and mobility of the particle i

$$\sigma_i = M_i q_i^2$$

$$\sigma_i = B_i C_i q_i^2$$

$$\sigma_i = \frac{D_i}{RT} C_i q_i^2$$

Equation [7] can be expressed in terms of any of these four parameters.

$$I_{Cu+} = - \frac{\sigma_{Cu+}}{\mathbf{F}}\frac{d}{dx}\mu_{Cu} \quad [8]$$

If the sulfide scale grows uniformly and continuously over the whole electrode surface, the sample thickness at any time is proportional to the number of coulombs passed through the electrolytic cell during that time

$$x - x_o = \frac{I_{Cu+}(t - t_o)}{y\mathbf{F}}\left(\frac{M}{d}\right)_{Cu_yS} \quad [9]$$

Combining Eq. [2], [8], and [9], yields Eq. [10].

$$I_{Cu+}{}^2\frac{1}{2\mathbf{F}}\left(\frac{M}{d}\right)_{Cu_yS} = + \sigma_{Cu+}\frac{dE}{dt} \quad [10]$$

which permits the calculation of the ionic conductivity of the sulfide scale formed under steady-state conditions from the slope of the recording of the electrode potential as a function of time.

Experimental

The anode was made of copper rod (99.995% purity) 0.905 cm in diameter, mounted in acrylic resin (Koldmount), and polished so that only one plane was in contact with the solution. The solution, 0.2M in Na_2SO_4 and 0.2M in H_2SO_4, was saturated by continuously bubbled H_2S. A strong convection pattern was brought about by a magnetic stirrer. The system was held at constant temperature by a regulated water bath. A 21V Ni-Cd battery unit provided current to the system through a set of appropriate resistors. The electrode potential was measured *vs.* a saturated calomel electrode by a Keithley 153 voltmeter which fed the signal to a Sargent SRG recorder.

Series of experiments have been carried out at temperatures between 30° and 73°C (below the digenite transition temperature) and under selected current densities between 1.9×10^{-4} A cm^{-2} and 1.55×10^{-3} A cm^{-2}.

The sulfide layer shows a uniform thickness over the electrode surface (Fig. 2) which ranged from 50 to 380μ depending on experimental conditions and the period of oxidation. The reaction products were identified by x-ray diffraction on a powder sample. The scale

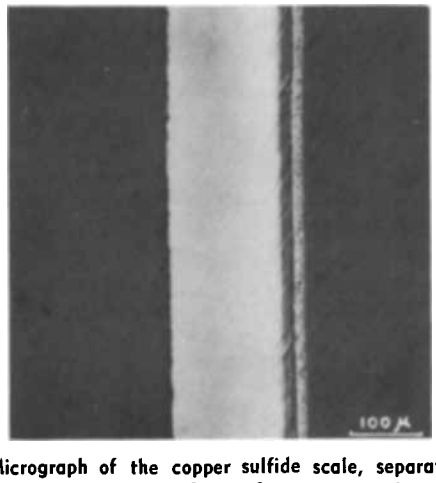

Fig. 2. Micrograph of the copper sulfide scale, separated from its Cu substratum. The Cu-Cu_2S interface was on the right side of the specimen. Digenite and djurleite are the only two phases to remain present. The band structure results from differences in the scale morphology emphasized by polishing.

structure and morphology could not be investigated by microscopy, electron diffraction, or microprobing. The three-sulfide assembly is not in equilibrium, and in the absence of an electric current one phase disappears during the time required for the sample preparation according to the reaction

$$0.8\ Cu_2S + 0.2\ Cu_{1.8}S \rightarrow Cu_{1.96}S$$

Results and Discussions

So far, three sulfides have been identified, chalcocite, djurleite, and digenite. No evidence, either direct or indirect, for the appearance of covellite was obtained in these experiments.

The sulfide growth model, analyzed earlier in this paper, is valid only in steady-state conditions, that is, when the cationic and total electric currents are constant. These conditions are satisfied when the first sulfide layer (Cu_2S) is deposited. The stoichiometry range of low chalcocite is smaller than 0.5% of its copper content (1), and, during Cu_2S formation, the ionic current virtually equals the total electric current (Fig. 3).

When a new sulfide starts to grow on the anode, the copper flux reaching the solid-liquid interface is changed according to the Cu^{++} to Cu^+ ratio in the new phase. If the digenite composition is approximated by $Cu_{1.8}S$ the reaction occurring at the liquid-solid interface at the stage of digenite growth can be represented by Fig. 4 and the correspondingly cationic (I^b_{Cu+}) and electronic ($I_e{}^b$) currents are equal to 90 and 10% respectively of the total current (I). The boundary between two solid phases is characterized by a thermodynamically fixed value of copper activity or electrochemical potential; therefore the potential drop in each sulfide layer is a constant. Consequently, the abrupt change in cuprous current at the onset of growth of a new phase initiates an unsteady-state process during which each sulfide layer adjusts its thickness to the new current conditions. The solid-state transformations accompanying the phase boundary motion are believed to generate stresses in the specimen because the scale always breaks away from the copper before CuS growth is apparent.

So far, the digenite stoichiometry range has been ignored. The digenite composition is reported (1) to extend from $Cu_{1.765}S$ to $Cu_{1.79}S$ at room temperature. Although the Cu poor limit is not affected by temperature, the Cu-rich limit changes to $Cu_{1.83}S$ at 83°C where digenite inverts to high digenite. During the digenite layer growth there is a continuous change in the Cu current flowing through the scale, but this variation is only 1.75% of the total current and is smaller than the accuracy of the measurement method.

From the set of experimental data, the cationic diffusivity of the chalcocite and digenite in the scale has

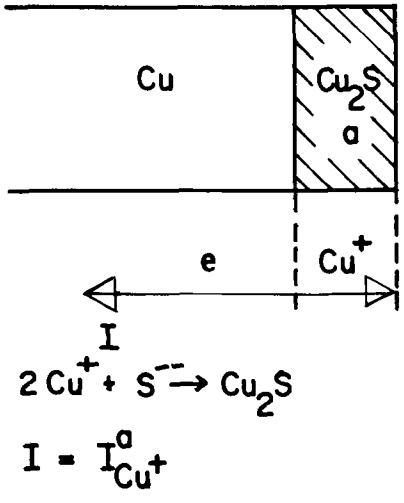

Fig. 3. Model of the Cu_2S film growing on the Cu anode

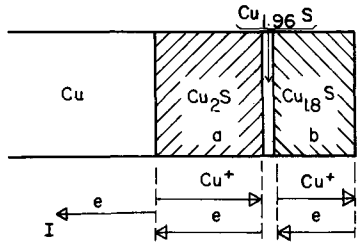

$$1.8\ Cu^+ + S^{--} \longrightarrow Cu_{1.8}S + .2e$$

$$I = I^b_{Cu^+} + I^b_e = I^a_{Cu^+} + I^a_e$$

$$I^b_{Cu^+} = 9I^b_e \qquad I^a_{Cu^+} = I^b_{Cu^+} + X$$

$$I^b_{Cu^+} = .9I \qquad I^a_e = I^b_e - X$$

$$I^b_e = .1I \qquad .1I \geq X \geq 0$$

Fig 4. Model of the copper sulfide scale at the stage of $Cu_{1.8}S$ growth.

been calculated in a range of temperature going from 30° to 73°C. Although djurleite was present in every sample, the ionic conductivity value could not possibly be derived from the experimental curve. This phase probably does not extend over enough atomic layers to allow a steady state to be established.

The measured ionic conductivity of digenite was independent of the current density used. In the chalcocite case, however, there was a current density value above which the experimental results became inconsistent. This limiting current density was increasing sharply with temperature. The dependence of the apparent ionic conductivity on the current density raises the problem of the morphology of the sulfides grown electrolytically.

It is usual practice to classify anodic films into continuous and noncontinuous films. In most of the cases reported in the literature, the distinction between continuous and noncontinuous films is based on the nature of the resistance opposed by the film to the current flow. It is characteristic of noncontinuous film to exhibit an approximately constant and low resistance (a few ohms) to the current flow during the growth of the scale (8). The smooth copper anode and the one plane electrode surface prevent introducing stresses which might lead to the cracking of the film. There is no solid-state transformation when the useful measurements are made, say when steady-state conditions prevail. The film growth is kinetically controlled by the copper ion diffusion through the solid, which mechanism favors the formation of a continuous, uniform scale. A decrease of the ionic strength of the solution (0.1 Na_2SO_4, 0.1 H_2SO_4) did not affect the experimental results.

The measured diffusion coefficient of cuprous ion in low chalcocite was found (Fig. 5) to be

$$D_{Cu+} = 8.1 \times 10^{-3} \exp\left(-\frac{5{,}870}{T}\right) \text{cm}^2\ \text{sec}^{-1}$$

$$D_{Cu+} = 1.1 \times 10^{-10}\ \text{cm}^2\ \text{sec}^{-1} \text{ at } 50°\text{C}$$

The measured diffusion coefficient of cuprous ion in low digenite was found (Fig. 6) to be

$$D_{Cu+} = 3.6 \times 10^{-2} \exp\left(-\frac{6{,}100}{T}\right) \text{cm}^2\ \text{sec}^{-1}$$

$$D_{Cu+} = 2.4 \times 10^{-10}\ \text{cm}^2\ \text{sec}^{-1} \text{ at } 50°\text{C}$$

In the temperature range studied, cuprous ions diffuse about twice as fast in digenite as in chalcocite. The ac-

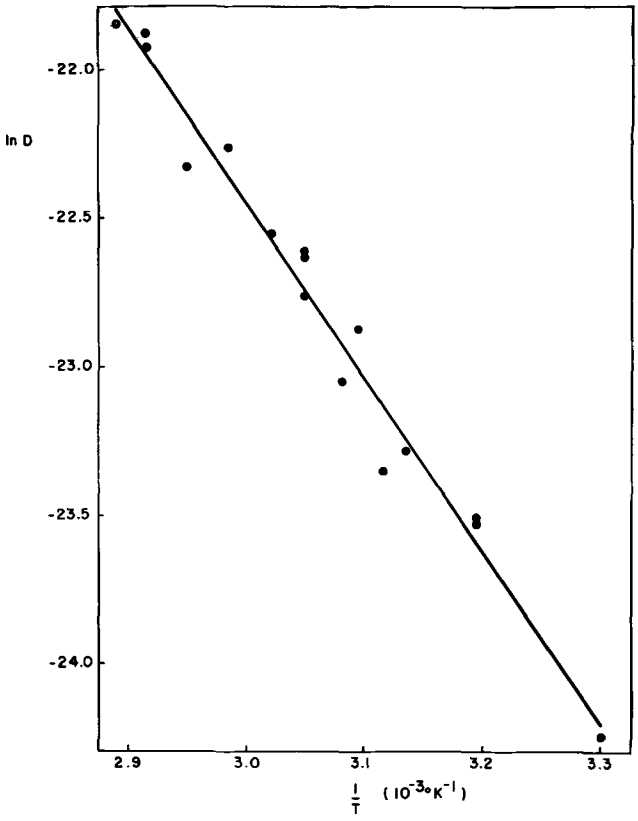

Fig. 5. Temperature dependence of the cuprous ion diffusion coefficient in chalcocite:

$$D_{Cu+} = 8.1 \times 10^{-3} \exp\left(-\frac{5{,}870}{T}\right) (cm^2\,sec^{-1})$$

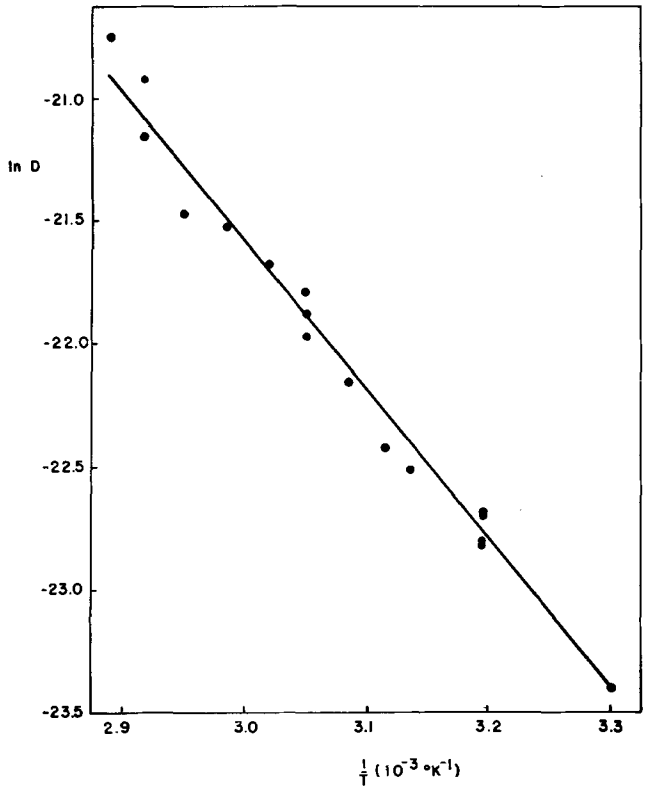

Fig. 6. Temperature dependence of the cuprous ion diffusion coefficient in digenite:

$$D_{Cu+} = 3.6 \times 10^{-2} \exp\left(-\frac{6{,}100}{T}\right) (cm^2\,sec^{-1})$$

tivation energy for diffusion is 11.7 ± 1 kcal mole^{-1} for chalcocite, and 12.1 ± 0.8 kcal mole^{-1} for digenite, respectively.

If an activation entropy for diffusion is to be calculated, the nature and concentration of diffusing defects must be known. The diffusion in ionic type crystals is often associated with the migration of Schottky or Frenkel type defects. X-ray investigations have suggested that in some ionic type crystals metallic ions were distributed virtually at random among a large number of nearly equivalent lattice sites [αAg_2S(9), αAgI(10), αCu_2S(4)]. In the case of low chalcocite and digenite which have relatively ordered copper lattices, an interstitialcy mechanism (the cations being equally mobile) may account for the cuprous ion diffusion. This is supported by the experimental observation that no significant variation of the diffusion coefficient has been observed with deviation from stoichiometry. Therefore, the equation of zeolitic diffusion is applicable (11).

$$D = \lambda^2 \frac{kT}{h} \exp\left(\frac{\Delta S}{R}\right) \exp\left(-\frac{\Delta H}{RT}\right) \quad [11]$$

The activation entropy for diffusion is then 1.9 e.u. for chalcocite and 1.3 e.u. for digenite, respectively. These low values are consistent with a mechanism which introduces little disordering in the lattice.

Conclusion

The thickening of a copper sulfide film on a copper anode at low electric field strength has been accounted for by electrolytic transport in the scale. The diffusion coefficients of cuprous ion in low chalcocite and low digenite have been measured in the temperature range of 30°-73°C during the growth of the anodic film. The phase boundary reactions did not appear to be too irreversible to interfere with these measurements.

Similar processes take place during the direct leaching of chalcocite minerals. This experiment supports the view that solid-state diffusion is a rate-controlling mechanism in the leaching of these minerals (12).

Acknowledgments

The author thanks Dr. E. Peters for his kind assistance throughout this work, and the National Research Council of Canada for awarding a studentship necessary to carry out her research program.

Manuscript submitted Nov. 3, 1969; revised manuscript received March 5, 1970.

Any discussion of this paper will appear in a Discussion Section to be published in the June 1971 JOURNAL.

LIST OF SYMBOLS

A_i,	activity of species i in the electrode vicinity
B_i,	mobility of species i, cm^2·sec^{-1}·J^{-1}
C_i,	concentration of species i, cm^{-3}
D_i,	diffusivity of species i, cm^2·sec^{-1}
d,	specific weight, g cm^{-3}
E,	electrode potential, V (Stockholm convention)
E_o,	standard electrode potential, V
E_a,	activation overpotential, V
$\mathbf{F}$,	Faraday constant, 96,484 A sec·eq^{-1}
h,	Planck constant, 6.62 × 10^{-27} erg sec
I_i,	current density carried by species i, A·cm^{-2}
J_i,	flux of particles i, cm^{-2}·sec^{-1}
k,	Boltzmann constant, 1.380 × 10^{-16} erg·molecule^{-1}·K^{-1}
M_{ii},	M_i Onsager coefficient, cm^{-1}·sec^{-1}·J^{-1}
M,	molecular weight, g.mol^{-1}
q_i,	charge carried by particle i, A·sec
R,	gas constant, 8.31439 J·K^{-1}·mol^{-1}
T,	absolute temperature, °K
t,	time, sec
t_o,	arbitrary reference for time, sec

x, abscissa at time t, cm
x_o, abscissa at time t_o, cm
y, number of copper atoms per sulfur atom in compound Cu_yS
ΔH, activation enthalpy for diffusion, cal. mol^{-1}
ΔS, activation entropy for diffusion, e.u.
ϕ, electrical potential, V
λ, average distance travelled by particle i in one jump, Å $= 10^{-8}$ cm
μ_i, chemical potential of species i, $J \cdot mol^{-1}$
σ_i, partial conductivity due to species i, $ohm^{-1}\ cm^{-1}$

REFERENCES

1. E. Roseboom, Jr., *Econ. Geol.*, **61**, (4), 641 (1966).
2. W. Jost, "Diffusion in Solids, Liquids, Gases," Academic Press Inc., New York (1960).
3. J. Mikulski, S. Mrowec, I. Stronski, T. Werber, *Z. phys. Chem. (Frankfurt) N. F.*, **22**, 20 (1959).
4. V. Wehefritz, *ibid.*, **26**, 359 (1960).
5. L. Eisenmann, *Ann. Phys.*, **10**, 129 (1952).
6. E. Hirahara, *J. Phys. Soc. Japan*, **6**, 422 (1951).
7. T. Kamigaichi, *J. Sci. Hiroshima Univ.*, **A16**, 325 (1952).
8. D. A. Vermilyea, Anodic films, Advances in Electrochemistry and Electrochemical Engineering, P. Delahay and C. W. Tobias, Editors, Interscience Publishers, New York (1963).
9. C. Wagner, *J. Chem. Phys.*, **21**, 1819 (1953).
10. F. A. Kroger, "The Chemistry of Imperfect Crystals," North Holland Publishing Co. (1964).
11. D. M. Barrer, *Trans. Faraday Soc.*, **37**, 590 (1941); **38**, 78 (1942).
12. A. R. Burkin, *Min. Sci. Engng.*, **1**, 4 (1969).

Theory of the Separation in Displacement Electrophoresis

G. Brouwer and G. A. Postema

Philips Research Laboratories, N. V. Philips' Gloeilampenfabrieken, Eindhoven-Netherlands

ABSTRACT

Displacement electrophoresis is a method of separating ions. After completion of this separation a qualitative and quantitative analysis of the sample composition can be made. In this report the separation process is investigated. It is shown that the sample introduces a transient system of homogeneous zones which are finally reduced to zones containing only one component of the sample. Starting from such basic equations as electroneutrality, current-continuity, and conservation of ionic species, equations are derived which permit the calculation of all quantities of interest, such as local field strength, composition of a particular zone, and speed of zone boundaries. In the case of a two-component sample the separation time can be calculated exactly; for the case of a multicomponent sample an approximate expression is given.

Displacement electrophoresis is an analytical technique which separates and orders ions in an electrical field according to their mobilities. A complete analysis of a sample is obtained with this method. If one is interested in, *e.g.*, separation of cations, the sample which has to be analyzed is placed in a column between a leading solution containing cations with a higher mobility than that of any of the cations in the sample, and the trailing solutions containing cations with a lower mobility than that of any of the cations in the sample. Electrodes are placed in the leading and trailing solution, and when an electrical field is applied the separation process starts and the cations move toward the cathode. After some time all cations will have the same counter-ions as these are moving in the opposite direction. Between the leading and trailing solutions the sample components have finally ordered themselves into consecutive zones according to increasing mobilities in the direction of migration. The same principle applies to the separation of anions.

Originally the method was employed as a separation method. In this way Kendall (1-4) in 1925 separated rare earth ions. Vestermark (5) and Eriksson (6) used this technique to isolate and concentrate certain substances from, *e.g.*, beet juice. Martin and Everaerts (7, 8) used its qualities for quantitative analyses. Independently Konstantinov, Fiks, and Oshurkova (9-12) arrived at similar observations.

This article emphasizes the separation process. It is shown that this process is governed by a number of simple equations. In the case of a two-component sample the time required for complete separation can be calculated as a function of the various parameters involved. For a multicomponent sample all quantities of interest can be calculated and an estimate of the separation time can be given.

Key words: boundary velocity, concentration boundary, concentration relations, conservation of ionic species, continuity of current, diffusion, dissociation, electroneutrality, electrophoresis, field-strength relations, heat production, homogeneous zones, ions, ion mobility, ion separation, leading solution, multicomponent sample, qualitative analysis, quantitative analysis, separation boundaries, separation time, trailing solution, transition region.

Theory of the Separation Process

General considerations.—Before application of the electrical field the sample is placed between the leading ion solution A and the trailing solution X. The concentrations of A and X are known; the concentrations of the various components in the sample are unknown

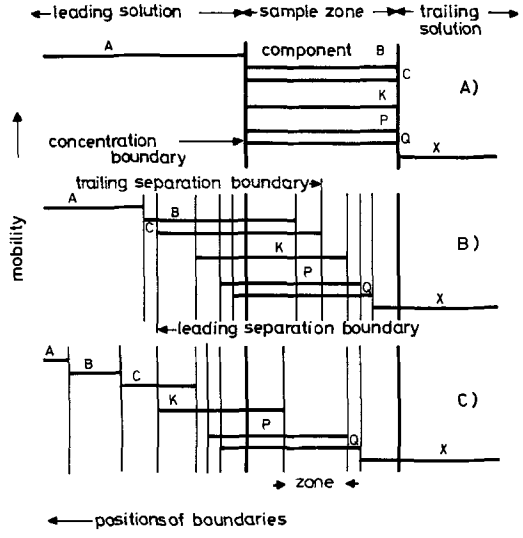

Fig. 1. Development of the zones and the positions of the components at the start (A), after application of the electrical field (B), and after some time has elapsed (C).

but well defined. This situation is schematically represented in Fig. 1A where only one type of ions is considered, say the cations A, B, C, ... K, . . . , P, Q, X. For simplicity it is assumed that there is only one common anionic species Z. The presence of certain ions is indicated by the position of horizontal lines. The levels of these lines indicate the mobilites of the cations. The original sample zone divides the column into three separate regions, marked by heavy vertical lines. After application of a constant current a new situation develops (Fig. 1B). The faster components of the sample have occupied leading positions whereas the slower ones are falling behind. The thin vertical lines represent zone boundaries. These indicate the limits of the sample components and the occurrence of fairly abrupt concentration changes of other sample components. Adjacent to the leading solution a zone is present containing the fastest component only. Heading the trailing solution is a zone containing the slowest sample component. After a sufficient time the number of zones decreases as the tails of the faster components pass the fronts of the slower components (Fig. 1C). Finally the sample components are separated, and consecutive zones containing only one component proceed to the cathode with a uniform speed, characteristic of displacement electrophoresis. As the apparent mobility of an ion is the product of the degree of dissociation of the ion and the mobility at complete dissociation, it will be preferable to choose optimal conditions. In order to control the degree of dissociation of weak electrolytes a particular choice of counter ions must be made. If the sample contains a weak acid the counter ion should be derived from a base, preferably a weak one to limit the hydroxyl ion concentration. Both groups mutually become charged by proton transfer. The degree of dissociation depends on the sum of both pK values. A more detailed treatment is postponed to a future paper.

At a certain stage of the separation a number of homogeneous zones is assumed to be present. A number of interzonal relations can be derived which determine the process completely. When the solvent is at rest, and the uniform field strength of zone j is called E_j (V cm^{-1}), an ion K with a mobility μ_K (cm^2 V^{-1} sec^{-1}) travels at a speed (cm sec^{-1})

$$v_{Kj} = \mu_K E_j \qquad [1]$$

A uniform cross section of the capillary tube results in a constant current density i (A cm^{-2}) in any zone. If the Faraday constant is $\mathbf{F}$ (C g-equiv.$^{-1}$) and the concentration of ion K in zone j is C_{Kj} (g-equiv. cm^{-3}), the following current density equation is valid

$$i/\mathbf{F} = E_j \sum_K (\mu_K + \mu_Z) C_{KJ} \qquad [2]$$

The ions K are neutralized by an equal amount of Z ions; the current contributions of both ions are proportional to the individual mobilities. Within a zone the ions of the same kind move with uniform velocities. In order to retain homogeneity an observer moving with the boundary should see a nondivergent flow of ions. For ions K passing the boundary between zones j and k this leads to

$$C_{Kj}(\mu_K E_j - v_{jk}) = C_{Kk}(\mu_K E_k - v_{jk}) \qquad [3]$$

where v_{jk} is the speed of the boundary between the zones j and k with respect to the solvent. Equation [3] results in

$$v_{jk} = \mu_K(C_{Kj}E_j - C_{Kk}E_k)/(C_{Kj} - C_{Kk}) \qquad [4]$$

There are as many ways to express v_{jk} as there are cationic species. Before any conclusions are drawn from this formula a survey is made of the various possible boundaries.

Types of boundaries.—Two types of boundaries can be distinguished (*a*) the separation boundaries, where one particular component is present on only one side of the boundary, *e.g.*, $C_{Kj} = 0$ and $C_{Kk} \neq 0$; in that case Eq. [4] results in

$$v_{jk} = \mu_K E_k \qquad [5]$$

and (*b*) concentration boundaries, which will be shown to be immobile and where all components are present on both sides. Equation [2] can be applied to zone j as well as to zone k. Subtracting these equations results in

$$\sum_K (\mu_K + \mu_Z)(C_{Kj}E_j - C_{Kk}E_k) = 0 \qquad [6]$$

Provided $v_{jk} \neq 0$ it is legitimate to divide each individual term of the sum [6] by v_{jk}. The assigned way to reduce the resulting expression is to select the particular cation of the term under consideration to evaluate v_{jk} from [4]. Then the following result is obtained

$$\sum_K \alpha_K C_{Kj} = \sum_K \alpha_K C_{Kk} \qquad [7]$$

where

$$\alpha_K = (\mu_K + \mu_Z)/\mu_K \qquad [8]$$

This relation can be applied repeatedly to consecutive zones separated by separation boundaries. As the concentrations of the leading and trailing solutions can be chosen at the beginning of the separation process and the concentrations of components in the sample are arbitrary, Eq. [7] is not satisfied at the original sample boundaries. This leads to the conclusion that these boundaries are immobile as only the condition $v_{jk} = 0$ can invalidate Eq.[7]. From [4] one can derive in this case

$$C_{Kj}/C_{Kk} = E_k/E_j \qquad [9]$$

When the sample is completely separated and the zones contain only one component, Eq. [7] is still valid and permits a quantitative analysis. In this restricted form the relation was given by Kohlrausch (13).

Two types of separation boundaries have to be distinguished: (*a*) the leading separation boundary between consecutive zones where zone j contains the components G, H, ... K, ... P and the following zone k the same but, in addition, the slower component Q; the latter is separated out as it is not transferred from k to j. (*b*) the trailing separation boundary between the zones k and l, in which case zone k contains the components G, H, ... K, ... Q whereas zone l contains the same components with the exception of the fastest ion G, which is separated out. Though Eq. [2], [4], and [9] permit the calculation of all unknown quantities, the elimination problem is tedious. A more convenient approach is given below.

Interzonal field strength relations.—To derive a relation for the ratio of the field strengths on both sides of a separation boundary case (*a*) will be considered first. As $C_{Qj} = 0$ Eq. [3] yields for K = Q

$$v_{jk} = \mu_Q E_k \qquad [10]$$

If we define β_{jk} as

$$\beta_{jk} = E_j/E_k \qquad [11]$$

Eq. [3] results by substituting [10] and [11] in

$$C_{Kj} = C_{Kk}(\mu_K - \mu_Q)/(\mu_K\beta_{jk} - \mu_Q) \qquad [12]$$

When both zones are not separated by an immobile concentration boundary, application of [12] to Eq. [7] results in

$$\sum_{K=G}^{P} \alpha_K C_{Kj} = \sum_{K=G}^{Q} \alpha_K C_{Kk} = \sum_{K=G}^{P} \frac{\alpha_K C_{Kk}(\mu_K - \mu_Q)}{\mu_K\beta_{jk} - \mu_Q} \qquad [13]$$

The last sum can be extended to K = Q because this final term equals zero. Equating the second expression

of [13] and the extended third one leads to

$$(\beta_{jk} - 1) \sum_{K=G}^{Q} \frac{\alpha_K C_{Kk}}{\beta_{jk} - \mu_Q/\mu_K} = 0 \qquad [14]$$

The solution $\beta_{jk} = 1$ has to be ruled out because substitution in [12] renders all concentrations equal except C_Q. This is in violation with Eq. [7] because of an excessive term $\alpha_Q C_{Qk}$. This leads to the restriction $\beta_{jk} < 1$.

Hence [14] results in

$$f(\beta_{jk}) = \sum_{K=G}^{Q} \frac{\alpha_K C_{Kk}}{\beta_{jk} - \mu_Q/\mu_K} = 0 \qquad [15]$$

This is a function from which only one root yields positive concentrations for all values C_{Kj} obtained by inserting C_{Kj} in [12]. From Eq. [12] it follows that for positive values of C_{Kj} the value $\beta_{jk} > \mu_Q/\mu_P$ and therefore

$$\mu_Q/\mu_P < \beta_{jk} < 1 \qquad [16]$$

The qualitative behavior of $f(\beta_{jk})$ is shown in Fig. 2. The function has poles at the values $\beta_{jk} = \mu_Q/\mu_K$. It is evident from the graph that only one root satisfies [15] and [16].

The conditions for a trailing separation boundary when the fastest component is separated out can be derived similarly. When we define

$$\beta_{kl} = E_k/E_l \qquad [17]$$

it results in

$$\sum_{K=G}^{Q} \frac{\alpha_K C_{Kk}}{\mu_G/\mu_K - \beta_{kl}} = 0 \qquad [18]$$

for

$$1 < \beta_{kl} < \mu_G/\mu_H \qquad [19]$$

Starting from a defined zone such as the sample zone all quantities of interest of the preceding one can be calculated. Primarily Eq. [15] determines the field strength ratio and Eq. [12] yields the various concentrations. The zone following the sample zone can be treated in a similar way by application of Eq. [18] and [12]. This process can be repeated until in all the zones all quantities are known. The concentration on opposite sides of a concentration boundary are linked by Eq. [9]. The system is completely determined as all conditions that can be imposed are obeyed. This also justifies the assumption of homogeneous zones. The field strength increases from zone to zone with a possible exception at the immobile boundaries.

Example.—In Fig. 3 the various stages of a separation process are illustrated. In this particular case the solvent is moved with a constant speed equal but opposite to the speed of the leading zone. The positions of various zone boundaries are plotted horizontally and the time vertically. After some time the number of zones is reduced until finally five zones each containing one sample component are formed. The concentration barriers, immobile with respect to the solvent, move backward with the speed of the solvent.

Influence of diffusion.—For discontinuous concentration variations diffusion should be taken into account. Because of the electrical field on the one hand and diffusion on the other hand a steady state is obtained. MacInnes and Longsworth (14) derived a relation for the transition width κ_{KL} (cm) between two zones, one containing only component K and the other one containing only component L in the moving boundary electrophoresis. When the limits of the transition are arbitrarily defined by the extremes

$$-2 \leq \ln (C_K/C_L) \leq 2 \;,\; \kappa_{KL} = \frac{4RT}{F v_{KL}} \frac{\mu_K \mu_L}{(\mu_K - \mu_L)} \qquad [20]$$

where R (J °K^{-1}) is the universal gas constant, T (°K) the absolute temperature, and v_{KL} the speed of the boundary concerned. In experimental conditions κ_{KL} will not exceed a few tenths of a millimeter. This value is comparable to the accuracy with which a boundary can be detected.

Separation time.—In order to evaluate the possibilities of analyzing a sample with the aid of displacement electrophoresis, a reasonable estimate of the separation time must be made. This is done by starting with a case of a two-component system which leads to a simple expression. From this an approximate value can be obtained for multicomponent samples.

In the simplest case the sample contains two components and, moreover, both leading and trailing solutions are adapted to the sample according to Eq. [7]. Therefore no concentration boundaries are required. The solvent is kept immobile. This case is illustrated in Fig. 4A where the positions of the boundaries are plotted along the horizontal axis against time along vertical axis. The original sample length is called λ_1 and the concentrations C_{B1} and C_{C1}. Inspection of Fig. 4A shows that the width of zone BC gradually diminishes as the confining boundaries converge with a differential velocity, given by the product of the local potential gradient and the difference in mobility of the species B and C. As the zone BC is on the verge of disappearing the separation is complete and the time elapsed, τ (sec), is given by

$$\tau = \lambda_1/(\mu_B - \mu_C) E_{BC1} \qquad [21]$$

The above case is merely fortuitous, and a more realistic one can be constructed by concentrating the sample by a factor γ. The sample length has to be reduced by the very same factor when the total amounts of B and C are kept unchanged. Two concentration boundaries appear in this case as is shown in Fig. 4B.

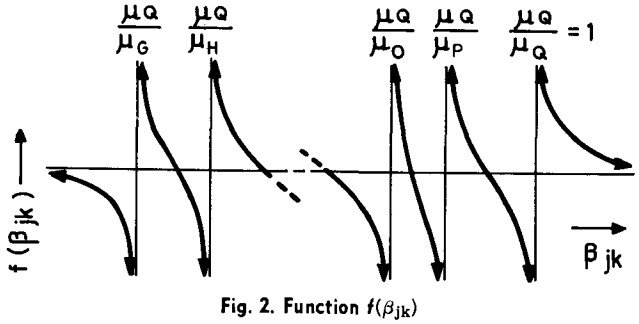

Fig. 2. Function $f(\beta_{jk})$

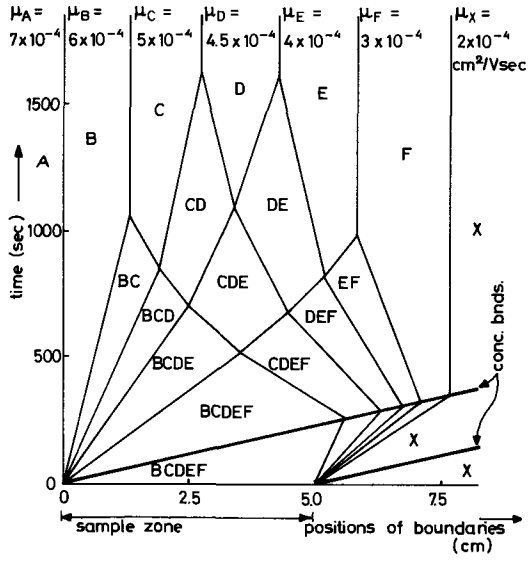

Fig. 3. Development of the various zones in the case of a five-component sample. In this arithmetical example: $C_A = 10^{-5}$ gEq. cm^{-3}, $C_B = C_C = C_D = C_E = C_F = 2.5 \times 10^{-6}$ g-equiv. cm^{-3} in the original sample zone, and $E_A = 30$ V cm^{-1}.

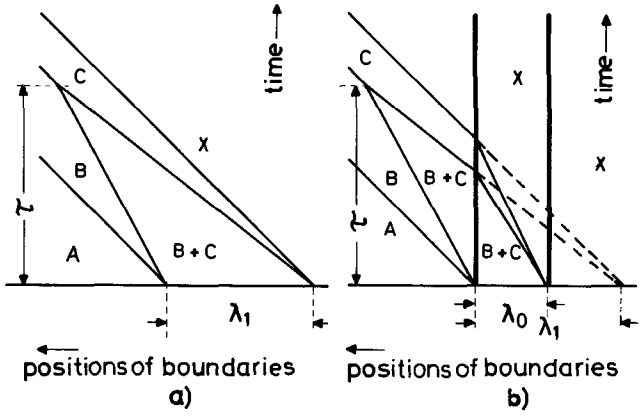

Fig. 4. Diagram of the separation of a two-component sample. Horizontally the positions of the boundaries are plotted, vertically the time. In case (a) the concentrations are all mutually adapted, and case (b) is the general one.

When the same current density is conserved the field strength, E_{BCO}, in the sample is lowered by a factor γ with respect to the previous case or, with respect to the part of the sample zone that has crossed the concentration boundary already. The time required by zone BC to leave the original sample region is the same as before because not only is the distance over which the boundary (BC,C) has to travel reduced by the factor γ, but its velocity as well. For comparison the simplest case is drawn in dashed lines. It can be concluded that the separation time is not affected by concentration boundaries.

A reduction of τ can be achieved by raising the potential gradients. The heat production per unit volume, P_m (W cm^{-3}), occurring in the adapted trailing solution puts a restriction on the system. Long separation times are found when $\mu_B \approx \mu_C \approx \mu$. Optimal conditions have to be chosen in order to limit τ to a reasonable value. Consider an example in which the sample length is λ_O whereas the concentrations are C_{BO} and C_{CO}. When a comparison is made with the adapted quantities the conservation of ionic species requires

$$\lambda_1(C_{B1} + C_{C1}) = \lambda_O(C_{BO} + C_{CO}) \qquad [22]$$

As it was shown that concentration boundaries do not affect the separation time

$$\tau = \lambda_O/(\mu_B - \mu_C)E_{BCO} \qquad [23]$$

Introduction of the zonal conductivities σ_A (ohm^{-1} cm^{-1}), σ_{BCO} and σ_X in Eq. [2] leads to

$$\sigma_A E_A = \sigma_{BCO}E_{BCO} = \sigma E_X = i \qquad [24]$$

As the conductivity is lowest in the adapted trailing zone, the local heat production, P_m, is a limiting factor, given by

$$P_m = \sigma_X E_X^2 \qquad [25]$$

When the system is operated under optimal conditions, it is possible to calculate a close approximation of τ by combining Eq. [8], [9], and [22] through to [25]

$$\tau \approx \lambda_O\sigma_{BCO}\mu_A^{1/2}/(\mu_B - \mu_C)\,(\sigma_A P_m \mu_X)^{1/2} \qquad [26]$$

In this formula all quantities are known with the exception of σ_{BCO}, which can be determined by a conductivity measurement, and $(\mu_B - \mu_C)$. The latter can either be predicted or be considered as a minimum value if the pair is to be separated in the time τ.

In order to arrive at the separation time of a multicomponent sample, a suggestion by Martin (private communication) is followed. Usually the bottleneck of the process is formed by the separation of a single obstinate pair which consumes so much time that the prelude to this stage can be neglected. In that case Eq. [26] again gives a reasonable estimate.

Conclusions

The separation process of displacement electrophoresis can be described adequately by equations for the system of homogeneous zones which are generated from the sample zone. Finally only zones containing one sample component remain, and they move with uniform speed. With the aid of relation [7] their concentration can be calculated as a function of the concentration of the leading electrolyte. In the solvent immobile concentration boundaries are situated at the original boundaries of the sample zone. The column which is preferably capillary, is thus divided into three regions in each of which Eq. [7] is valid. The changes of concentration at the immobile boundaries have a fixed ratio, and Eq. [9] gives the relation between the field strengths on both sides of this boundary. From a zone with known concentrations and field strength the field strength of an adjacent zone can be calculated by applying [15] or [18] and its composition by applying Eq. [12]. By repeating this process the potential gradient and the composition of all occurring zones can be calculated. Boundary speeds follow from [3] while the optimal separation time is given by [26].

Acknowledgment

The authors wish to thank Dr. C. v.d. Stolpe for contributory discussions.

LIST OF SYMBOLS

j,k,l,	zone
A,B, ... Z,	ionic species
A,	ionic species of leading zone
X,	ionic species of trailing zone
Z,	ionic species of common counter ions
B,C, ... Q,	ionic species present in sample
E_j,	potential gradient in zone j, V cm^{-1}
μ_K,	mobility of ionic species K, cm^2 V^{-1} sec^{-1}
v_{Kj}	speed of ion K in zone j, cm sec^{-1}
i,	current density, A cm^{-2}
$\mathbf{F}$,	Faraday constant, C g-equiv.$^{-1}$
C_{Kj},	concentration of ion K in zone j, g-equiv. cm^{-3}
v_{jk},	velocity of boundary between zones j and k, cm sec^{-1}
α,	inverse transport number
β_{jk},	ratio of the field strengths of zones j and k
κ_{KL},	transition width, cm
R,	universal gas constant, J°K^{-1}
T,	absolute temperature, °K
λ,	zone length, cm
τ,	separation time, sec
γ,	reduction factor
σ,	zonal conductivity, ohm^{-1} cm^{-1}
P_m,	maximal heat production per unit volume, W cm^{-3}
pK,	dissociation constant

Manuscript submitted Nov. 12, 1969; revised manuscript received March 3, 1970.

Any discussion of this paper will appear in a Discussion Section to be published in the June 1971 JOURNAL.

REFERENCES

1. J. Kendall and B. L. Clarke, *Proc. Natl. Acad. Sci. USA*, **11**, 393 (1925).
2. J. Kendall and W. West, *J. Am. Chem. Soc.*, **48**, 2619 (1926).
3. J. Kendall, E. Jette, and W. West, *J. Am. Chem. Soc.*, **48**, 3114 (1926).
4. J. Kendall, *Science*, **67**, 163 (1928).
5. A. Vestermark, *Naturw.*, **54**, 470 (1967).
6. G. Eriksson, *Acta Chem. Scand.*, **21**, 2290 (1967).
7. A. J. P. Martin and F. M. Everaerts, *Anal. Chim. Acta*, **38**, 233 (1967).
8. F. M. Everaerts, Thesis, Technical University, Eindhoven (1968).
9. B. P. Konstantinov and V. B. Fiks, *Russ. J. Phys. Chem.* **38**, 1038 (1964).
10. B. P. Konstantinov and O. V. Oshurkova, *Sov.*

Phys. Tech. Phys., **11**, 693 (1966).
11. B. P. Konstantinov and O. V. Oshurkova, *ibid.*, **12**, 1280 (1968).
12. B. P. Konstantinov and O. V. Oshurkova, *Dokl. Akad. Nauk.* USSR, **148**, 1110 (1963).
13. F. Kohlrausch, *Ann. Phys. u. Chem.*, **10**, 4 (1897).
14. D. A. MacInnes and L. G. Longsworth, *Chem. Rev.*, **11**, 171 (1932).

Purification of Potassium Chloride Solutions

Voltammetric Criteria

Murray Rosen,*[1] Henry H. Bauer,*[2] and Philip J. Elving*

The University of Michigan, Ann Arbor, Michigan

ABSTRACT

Impurities of heavy metal and surface-active types can be removed readily from solutions of reagent grade potassium chloride by electrolysis at a graphite electrode; the surface-active material is also largely removed by column chromatography over charcoal. Operational approaches for monitoring the purity are described.

To obtain pure aqueous solutions, *e.g.*, of the alkali metal halides, for electrochemical studies, one may consider purifying the salt, the prepared solution, or even both. Purification of the salt can often be accomplished by growing crystals under carefully controlled conditions or by recrystallization. Purification of the solution would appear to be a more direct approach and, consequently, two procedures based on the types of impurities found in solutions of potassium chloride, are described; these involve column chromatography using charcoal and pre-electrolysis with a graphite electrode.

The purification of alkali metal halides has been frequently discussed in the literature. For example, before applying square wave polarography to solutions that had been pre-electrolyzed at mercury for removal of reducible species, Barker (1) found it necessary to contact these solutions with an inert adsorbent to remove surface-active substances. Berezina and Nikolaeva-Fedorovich (1a) monitored surface-active substances in water purified by various methods through observation of polarographic maxima of the second kind. Recent voltammetric studies of the background current at the pyrolytic graphite electrode (PGE) and the dropping mercury electrode (DME) in aqueous solutions of potassium chloride, revealed the presence of two types of impurities, which were found even in spectroscopic grade KCl. Type I impurity is polarographically active at the DME, *i.e.*, a catalytic peak (Fig. 2) is seen at -1.1V in 0.5*M* KCl solutions between *p*H 0.85 and 3, suggestive of the presence of a surface-active substance; in addition, it seems to be electrochemically reducible. Type II impurities definitely result in faradaic processes, *i.e.*, deposition waves or stripping peaks are seen at the PGE, indicating that they are probably heavy metals.

Removal of the two types of impurities has been investigated in terms of operational tests for the efficiency of the purification process. Since the absence of surface-active impurities is a frequent necessity in electrochemical and other investigations, the results of the present study should be of general interest.

In general, the electrolytic purification procedure is recommended over the charcoal treatment, even for the removal of surface-active impurities in potassium chloride solutions, *e.g.*, *p*H changes and concentration adjustments which generally accompany use of charcoal can be avoided (*c.f.* subsequent discussion). In addition, electrolytic purification can be used *in situ* and can be duplicated more easily in other laboratories. Moreover, the same procedure that is used to purify the solution can often be used to check impurity levels and to repurify the solution, if necessary, without essentially disturbing the main experiment. The electrolytic purification procedure described here is an adaptation of stripping analysis and, therefore, lends itself to quantitative interpretation if desired.

Experimental

Reagents.—Reagent grade hydrochloric acid (du Pont), potassium hydroxide pellets (Baker & Adamson), potassium chloride (J. T. Baker), spectroscopic grade potassium chloride (Hilger), Darco G-60 decolorizing charcoal (Atlas Chemical), and double-distilled water were used. The charcoal was purified as specified by the manufacturer (2); a suspension of it in 2*M* HCl was boiled and then filtered and washed on a Buchner funnel. Nitrogen (oil pumped grade), used for oxygen removal, was passed successively through two gas bubblers containing ammonium vanadate solution reduced by zinc amalgam in hydrochloric acid (3), gas bubblers contain calcium hydroxide solution and, finally, one containing double-distilled water.

Cells.—The working compartment (1.2-liter capacity) of the all-glass unjacketed cell used (Fig. 1) is fitted with a Teflon plug stopcock on the side near the bottom and can be closed with a No. 7 stopper; the two connecting bridges can be closed with No. 00

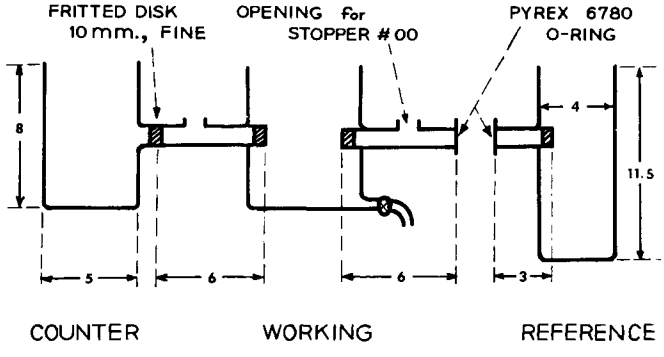

Fig. 1. All-glass three-compartment pre-electrolysis cell. Dimensions shown are in cm. The stopcock on the working compartment is perpendicular to the plane of the drawing.

* Electrochemical Society Active Member.
[1] Present address: Naval Research Laboratory, Washington, D. C.
[2] Present address: University of Kentucky, Lexington, Kentucky.
Key words: aqueous solution purification, electrolysis, heavy metal impurities, potassium chloride purification, purification by electrolysis, purity monitoring by voltammetry, surface-active impurities.

stoppers. The working and counterelectrode compartments, which constitute a single unit, are joined to the reference electrode compartment by clamping the O-ring joints together. This arrangement enables the working cell to be cleaned without affecting the reference electrode.

The connecting bridges, which are bounded by glass-fritted disks and are stoppered to minimize mixing of solutions, are filled with background electrolyte solution when the cell has been assembled. This arrangement minimizes migration of undesired ions between compartments and is essential in preventing mercury ions from diffusing from the reference electrode compartment, *e.g.*, an early observation of an anodic stripping peak just positive of zero volt, when using an ordinary H-cell, was traced to the presence of mercury ions.

Electrodes.—A 1 x 12 in. strip of Grafoil self-bonded tape (Union Carbide), served as the working or purification electrode. Voltammetric analysis of solution purity was done with a shielded electrode (19.6 mm^2) made from pyrolytic graphite rod (General Electric) (4).

Apparatus.—A Sargent Model XV polarograph was used for the polarographic analyses. Voltammetry was carried out with a three-electrode system and operational amplifier circuits (5); voltammograms were recorded on a Moseley 7001A(S) X-Y recorder, using a Model 17106 filter to prevent saturation of the recorder amplifiers by a-c noise (no attenuation of the signal was noted). A Wenking potentiostat (100 mA output) provided the potential control for the pre-electrolysis. The Leeds & Northrup Model 4776 *p*H meter used was standardized with Beckman standard buffer solutions. All potentials were measured and are reported *vs.* the saturated calomel electrode (SCE).

The 1-in. diameter glass column used for chromatography, contained 3 to 24 in. of premoistened, purified charcoal with premoistened angelhair as a filter and plug at the bottom. To aid in replacement of the charcoal, the stem of the column was fitted with a Pyrex 6780 O-ring joint, which was mated to another joint attached to a Teflon stopcock. The solution to be purified is fed from a 2-liter, round-bottom flask joined to the top of the column. The stopcock tip is connected to a suction flask, to which an aspirator is attached.

Results

Type I impurity.—This impurity manifests itself by producing a catalytic wave with a peak at −1.1V at the DME in 0.5*M* KCl solutions of *p*H 1.4; the height of the wave varies between 2 and 45 μA and, for a given sample, reaches a maximum at *p*H 1.5 (Fig. 2). Drop-time (*t*) *vs.* potential (*E*) (electrocapillary) curves show no unusual dips or distortions, neither at the electrocapillary maximum nor at −1.1V.

The fact that the wave is decreased by about 85% on bubbling nitrogen through the solution while the latter is in contact with a mercury pool indicates that the impurity either reacts chemically with mercury or is adsorbed from solution.

Attempts at plotting adsorption isotherms for the impurity on the charcoal used in purification (2) did not yield a reproducible value for *n* in the Freundlich adsorption isotherm. However, the results indicated that at least two stages of charcoal treatment are necessary to remove 85-90% of the impurity. On column chromatography, results were generally as expected, *i.e.*, the longer the charcoal column the purer would be the resulting solution, but a longer time was needed and quite often the *p*H change was greater. Since an exhaustive study of the correlation of all of the possible parameters with solution purity was not attempted, only relative trends can be described. For a 6-in. charcoal column, removal was about 50-60% effective, and the resultant solution had a *p*H of about 8. A 24-in. charcoal column removed nearly 90% of the impurity; however, the resultant solution *p*H was often as high as 10, and generally 2 hr were required to draw two liters of solution through the 24-in. column via the aspirator. Barker (6) also noted that charcoal treatment caused a slight rise in solution *p*H during purification of 0.5*M* KCl.

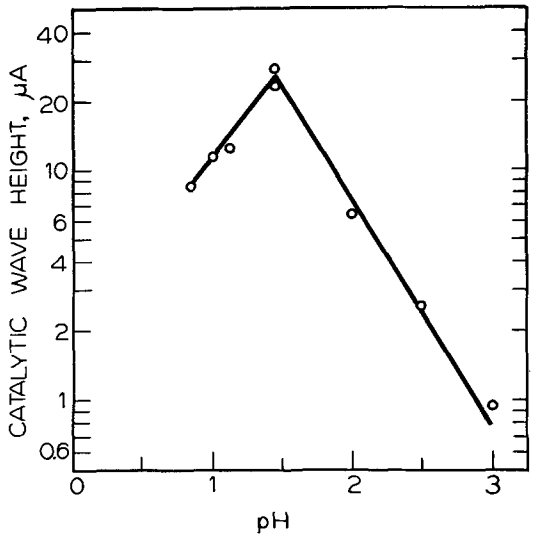

Fig. 2. Variation of catalytic wave height at DME with *p*H in 0.5*M* KCl solution.

Use of charcoal gives, at best, 90% removal of the impurity. Whether this effectiveness could be improved by recycling or by a batch-column arrangement was not tested since the same effectiveness could be achieved by electrolytic purification. It is possible that had Barker (1) used a carbon-type electrode for pre-electrolysis, further "cleaning" would not have been necessary. Since he does mention that his "cleaning" by charcoal treatment was effective in producing solutions in which the double-layer capacitance did not vary by more than 2% in about 20 min, it is possible that the 90% achieved here might have been adequate for his work.

Some exchange process occurs because the *pH* always increases after treatment. Since premoistened charcoal has to be used, the KCl solution to be purified has to be more concentrated than the final desired value, and the solution coming off the column has to be titrated and then diluted to the proper concentration. Another disadvantage in the use of charcoal is that the charcoal itself requires a lengthy and messy purification.

The electrocapillary (*t-E*) curve for a solution of the charcoal-treated material (diluted to 0.5*M* KCl) is not altered but is slightly displaced to lower drop times over the entire potential range.

Type II impurity.—The principal advantage of purification by electrolysis is in being able to plate out impurities on an electrode under conditions duplicating those used for subsequent voltammetric studies themselves.

In preliminary tests, 0.5*M* KCl solutions of *p*H 1.4, 6.4, and 12 were electrolyzed at a 5-mm diameter PGE at −0.8*V* for 10 min; without opening the circuit, the potential was then scanned to a more positive value. The resultant stripping peaks in the potential range of −0.8 to −0.2V. (Fig. 3) were largest at *p*H 1.4, indicating that impurities are most effectively removed at this *p*H. Stripping peaks observed between 0.2 and 0.7V are not due to the presence of the impurities, but are associated with the PGE surface (7).

The procedure for evaluating purity consists, then, essentially of electrolysis for 10 min at −0.8V, followed by scanning to 0.8V. During an electrolytic purification, *ca.* 1 liter of *p*H 1.4 potassium chloride solution is placed in the cell and its initial purity is

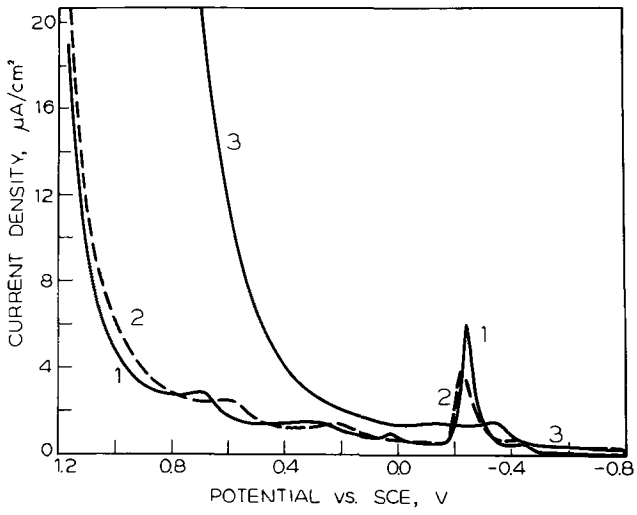

Fig. 3. Voltammograms for evaluating effectiveness of removal of type II impurities from 0.5M KCl solutions of pH 1.4 (curve 1), pH 6.4 (curve 2), and pH 12.7 (curve 3): stripping curves obtained after electrolysis at —0.8V for 10 min.

checked, using the 5-mm diameter PGE. After each 4 hr of electrolysis. the purity is rechecked. If further electrolysis is necessary, the Grafoil in the electrolysis cell is replaced by a fresh piece and the salt-bridge solutions are replaced by electrolyzed solution from the cell. Generally, at least 8 hr are necessary before stripping peaks are no longer observed in a solution-purity test. The electrolytic purification procedure does not appreciably alter the pH of the pH 1.4 solution used, because the amount of hydrogen ion gained or lost in 8 hr would be negligible. Purified solution can be drawn off via the Teflon stopcock whenever needed and brought to the desired pH by addition of acid or base.

Although at least three stripping peaks are observed, there is no way of determining whether any of them result from a type I impurity. Nevertheless, purification by pre-electrolysis also removes about 80 to 90% of the type I impurity, as measured operationally.

Acknowledgments

The authors thank Dr. Glenn Dryhurst, who first demonstrated the presence of the type I impurity, and the Atomic Energy Commission and the National Science Foundation for financial support of the work described.

Manuscript submitted Dec. 22, 1969; revised manuscript received March 9, 1970.

Any discussion of this paper will appear in a Discussion Section to be published in the June 1971 JOURNAL.

REFERENCES

1. G. C. Barker, Atomic Energy Research Establishment, Report C/R 1563, November 27, 1954; *Anal. Chim. Acta*, **18**, 118 (1958).
1a. N. P. Berezina and N. V. Nikolaeva-Fedorovich, *Elektrokhimiya*, **3** (1), 3 (1967) via *Soviet Electrochemistry*, **3**, 1 (1967).
2. Atlas Chemical Industries, "Measuring Adsorptive Capacity of Activated Carbon for Liquid Purification," Publication D-87. Wilmington, Del.
3. I. M. Kolthoff and C. Miller, *J. Am. Chem. Soc.*, **63**, 1013 (1947).
4. P. J. Elving, I. Fried, and W. R. Turner, in "Polarography 1964," pp. 277-97, G. J. Hills, Editor Macmillan, London (1966).
5. D. D. DeFord, 133rd Meeting American Chemical Society, San Francisco, 1958.
6. G. C. Barker, *Analyst*, **77**, 685 (1952).
7. M. Rosen and P. J. Elving, Work in progress.

Mathematical Study of Galvanic Corrosion

Equal Coplanar Anode and Cathode with Unequal Polarization Parameters

E. Kennard and J. T. Waber

Department of Material Science, Northwestern University, Evanston, Illinois

ABSTRACT

This paper gives a theoretical analysis of the distribution of potential and current density on the surface of a coplanar galvanic cell in which the polarization parameters for cathode and anode are unequal. The potential at any point can be represented as a Fourier series, in which the coefficients themselves are infinite series. It is shown that these Fourier coefficients can only be approximated by numerical methods. The potential distribution across the electrode at the electrode/electrolyte interface is shown to be dependent on both the anodic and cathodic polarization parameters and cannot be deduced from the potential distribution occurring when the anodic and cathodic polarization parameters are equal. As the cathodic polarization parameter is increased relative to that of the anode the potential shifts toward the open-circuit anodic voltage and both the potential and current distribution become more uniform. A parameter is suggested which characterizes the "microscopic" or "macroscopic" behavior of the cell. When the ratio between polarization parameters is large the behavior of the cell tends toward either anodic or cathodic control rather than the "mixed" control.

This paper gives a theoretical analysis of the distribution of potential for a galvanic cell in which the anode and cathode lie in the same plane. It is assumed that the slope of the current-potential curves has different values for the anodic and cathodic processes.

The distribution of potential in such a galvanic cell is determined by the current-potential relationship and the conductivity of the electrolyte solution. Wagner (1) formally proposed the name "polarization parameter" to represent the product of the conductivity and the slope of the polarization curve. The polarization parameter has the dimensions of length and it was shown by Waber (2) that the size of the cell in relation to the polarization parameter L could be used to determine whether the cell behaved in a microscopic or macroscopic fashion. In a microscopic cell the polarization parameter is large with respect to a characteristic dimension λ of the cell, and polarization

dominates to the extent that potentials are nearly uniform everywhere in the corroding liquid. If, on the other hand, the cell dimension is much larger than the polarization parameter, then the resistance drop through the electrolyte is controlling; this is a macroscopic cell, with large potential variations throughout the corrodent. The critical dimension λ of the cell is dependent on the configuration of the electrodes and electrolyte. Waber (3) showed that by using a linear approximation to the polarization curve the potential and current distribution could be calculated in terms of the polarization parameter, the equilibrium electrode potentials, and the geometric parameters of the cell. In this work the polarization parameter was assumed to be equal for the anodic and cathodic processes. The present work demonstrates the differences in potential which occur when the anodic and cathodic polarization parameters are unequal.

Description of Cell

In this work the model cell used is shown in Fig. 1. We choose the origin to lie in the plane at the midpoint of the anode. We assume both the anode and cathode to be infinite in the y-direction and of equal width c in the x-direction. The electrodes are covered by an electrolyte which is infinite in the $+z$-direction. A tangent approximation to the potential-current relationship is assumed. Figure 2 is a stylized representation of complex polarization curves such as reported by Ketcham and Haynie (3). Tangent lines are drawn to the polarization curves at some appropriate average current density. The intersections with the ordinate (E_a,E_c) are taken as the anodic and cathodic potentials for zero current. Of course these are in many cases very different from the true values. This method of linearizing a complex problem is equivalent to drawing a tangent to the enthalpy (H) curve for a two-component system in order to find the partial molar heats of mixing of the two components. In analogy one writes either

$$H^\alpha = H^\alpha{}_d + (\partial H/\partial x)\Delta x$$

for the enthalpy, or

$$E^\alpha = E_a + (\partial \Delta E_a/\partial J)J$$

for the polarization.

Mathematical Analysis

The polarized potential $P^*(x,z)$ in the cell must satisfy the two-dimensional Laplace equation

$$\partial^2 P^*/\partial x^2 + \partial^2 P^*/\partial z^2 = 0 \qquad [1]$$

and satisfy the boundary conditions

$$(\partial P^*/\partial x)_{x=0} = (\partial P^*/\partial x)_{x=c} = 0 \qquad [2]$$

$$P^*(x,0) = \begin{cases} E_a + L_a(\partial P^*/\partial z)_{z=0} & \text{for } 0 \leq x \leq c/2 \\ E_c + L_c(\partial P^*/\partial z)_{z=0} & \text{for } c/2 \leq x \leq c \end{cases} \qquad [3]$$

where L_a and L_c represent the anodic and cathodic polarization parameters.

The most general solution of Eq. [1] which satisfies the boundary Eq. [2] and which remains finite as z approaches either zero or infinity is

$$P^*(x,z) = A_0 + \sum_{n=1}^{\infty} A_n \cos(n\pi x/c) \exp(-n\pi z/c) \qquad \text{for } n = 1,2,3\ldots. \qquad [4]$$

The boundary conditions in Eq. [3] are used to determine the coefficients A_n of the series. The problem reduces to obtaining solutions of the infinite set of equations, for which A_i can now be regarded as the variable.

$$A_i = \sum_{j=0}^{\infty}{}' \alpha_{ij}A_j + \beta_i \qquad i = 0,1,2\ldots. \qquad [5]$$

where the prime on the summation indicates that the term $j = i$ is not included. The terms α_{ij} and β_i which enter as elements of the infinite determinant can be summarized as follows

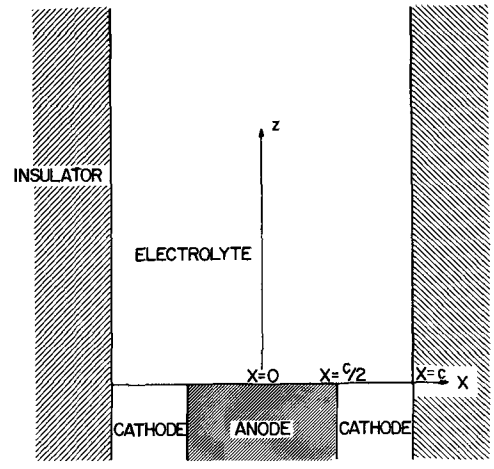

Fig. 1. Geometric arrangement of coplanar electrodes in model cell.

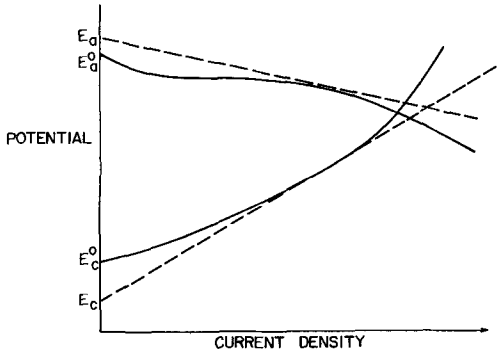

Fig. 2. Tangent approximation to the polarization curves. Extrapolated potentials E_a and E_c are not equal to the open-circuit potentials E_a° and E_c°.

Integers

i	j	Value of α_{ij}	Value of β_i
0	odd ≥ 1	$\alpha_{0j} = \dfrac{2(L_a - L_c)}{(L_a + L_c)} \sin(j\pi/2)$	$\beta_0 = \dfrac{(E_aL_c + E_cL_a)}{L_a + L_c}$
odd	even > 0	$\alpha_{ij} = \dfrac{-iL \sin(i\pi/2) \cos(j\pi/2)}{(a + bi)(j^2 - i^2)}$	$\beta_i = \dfrac{[(E_a/L_a) - (E_c/L_c)] \sin(i\pi/2)}{i(a + bi)}$
even	odd ≥ 1	$\alpha_{ij} = \dfrac{jL \sin(j\pi/2) \cos(i\pi/2)}{(a + bi)(j^2 - i^2)}$	$\beta_i = 0$
odd	odd	$\alpha_{ij} = 0$	
even	even	$\alpha_{ij} = 0$	

where the parameters L, a, and b are defined by

$$L = [(1/L_c) - (1/L_a)]$$

and

$$(a + bi) = \pi/4[(1/L_a) + (1/L_c) + 2i\pi/c]$$

The infinite set of simultaneous equations given by Eq. [5] possesses a unique solution which may be approximated using numerical methods. A discussion of the conditions under which a solution exists and a description of the numerical approximation is given in the Appendix.

The coefficients A_i were evaluated up to A_{100} for given parameters, L_a, L_c, voltages, E_a, E_c, and the electrode width c. The coefficients A were then substituted in Eq. [4] to obtain values for $P^*(x,z)$. The value of 100 was shown to be sufficient to ensure numerical convergence. The current density at the cathode was calculated using the dimensionless parameter

$$C_c(x) = \frac{P^*(x,0) - E_c}{L_c} \cdot \frac{2c}{E_a + E_c} \qquad c/2 \leq x \leq c$$

The anodic current density $C_a(x)$ is similarly defined Eq. [3]. It should be noted that the total current obtained by integrating $C_a(x)$ from 0 to $c/2$ is equal but opposite in sign to the similar integral of $C_c(x)$.

Results

The potential distribution at the electrode surface is shown in Fig. 3. These results were obtained by putting L_a equal to 1 cm and varying L_c from 0.1 to 10 cm. The total width c of the electrode was assumed to be equal to 1.0 cm.

Figure 4 shows the results obtained by setting $L_a = L_c = 10$ cm, and $L_a = L_c = 1$ cm. It is apparent that the behavior of the electrodes with unequal anodic and cathodic polarization parameters cannot be deduced from the separate curves obtained for equal polarization parameters.

Two curves are presented in Fig. 5 which represent the variation of the anodic current parameter $C_a(x)$ over the anode, and the cathodic current parameter $C_c(x)$ over the cathode; namely, the variation in current density as x ranges from 0 to 0.5c and from 0.5c to 1.0c. These two curves are drawn for a fixed value of L_a, namely 1 cm, but for two values of L_c. They illustrate the influence of L_c on the two current density parameters. In such circumstances, the anodic values are relatively uniform even though the cathodic values are not.

In order to assess the uniformity of corrosion attack, it is useful to construct the ratio of maximum to minimum current values. For the anode this is

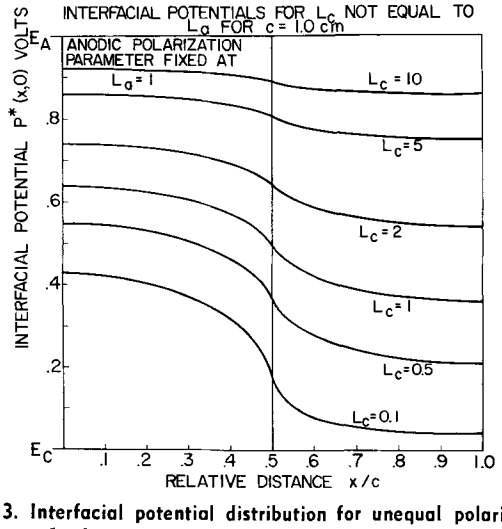

Fig. 3. Interfacial potential distribution for unequal polarization parameters, for $L_a = c = 1$ cm.

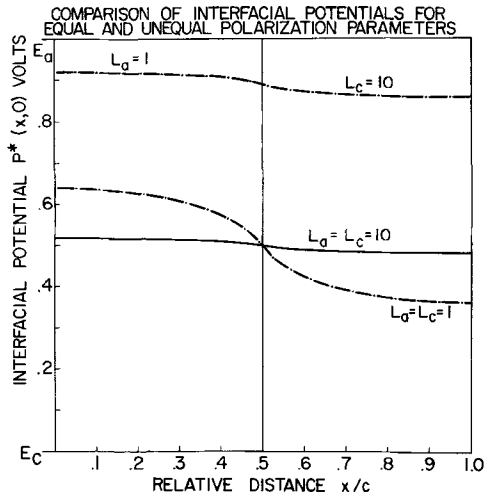

Fig. 4. Comparison of interfacial potential distribution for equal and unequal polarization parameters, presented as a function of (L_a/L_c) for fixed value of c.

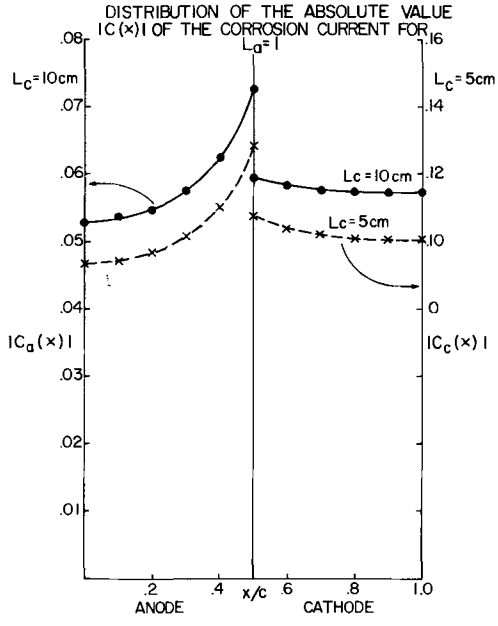

Fig. 5. Anodic and cathodic current densities for unequal polarization parameters, for $c = L_a = 1$ cm. Note that the gradients dC_a/dx and dC_c/dx in the vicinity of $x = c/2$ are inversely proportional to L_a and L_c, respectively.

$$\frac{\max C_a}{\min C_a} = \frac{C_a(x = 0.5c)}{C_a(x = 0)}$$

and similarly for the cathode

$$\frac{\max C_c}{\min C_c} = \frac{C_c(x = 0.5c)}{C_c(x = 1.0c)}$$

These two ratios are plotted as a function of the dimensionless parameter $2c/(L_a + L_c)$ in Fig. 6.

Discussion

In the majority of corrosion experiments one observes that the anodic and cathodic polarization parameters are approximately equal. However, in cases where the anodic reaction is strongly polarized, such as in a passive region, L_a is clearly much larger than L_c. The opposite situation might be encountered when the cathodic reaction is diffusion controlled. The present analysis is directed toward such situations. The question of the "microscopic" or "macroscopic" behavior of corrosion cells cannot be determined by the simple parameter (c/L). It can be seen from Fig. 3

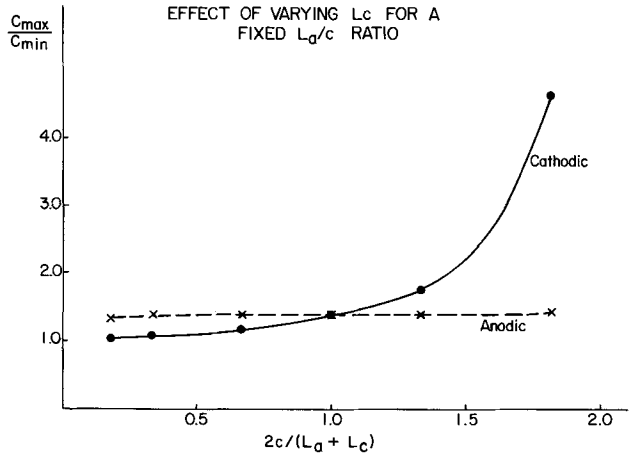

Fig. 6. Variation of the ratio of maximum to minimum current density with the parameter $2c/(L_a + L_c)$. Cathodic current full line, anodic current dashed line, for $c = L_a = 1$ cm. Small values of L_c are on the right-hand side.

that as the difference between the polarization parameters is increased the potential across the electrode becomes more uniform. We may thus replace the parameter (c/L) by $2c/(L_a + L_c)$ as the factor which determines whether the cell will behave "microscopically" or "macroscopically." When this ratio is small, the variation of current densities is small and the potentials are relatively uniform. These are the characteristics of a microscopic cell. In contrast, when the characterizing ratio is large, *i.e.*, when some cell dimension is much larger than both L_a or L_c, the cell can be regarded as "macroscopic." The variation of potential over the interface and the variation in current density is large. The ratio $2c/(L_a + L_c)$ represents what Waber (2) has defined as the characterizing size ratio (λ/L). Hence as the electrolyte is infinite the critical dimension λ is logically the electrode width c. It is reasonable to replace L by the average value $(L_a + L_c)/2$. Figure 6 thus shows that max C_a/min C_a increases rapidly as $2c/(L_a + L_c)$ exceeds unity. Since the total anodic current must be equal to the total cathodic current as L_c/L_a increases the anodic current is forced to decrease because the cathode is more effectively polarized. The net result of this is that there is a shift in both the anodic and cathodic potentials toward the open cell value of E_a and the distribution of potential over both anode and cathode becomes more uniform. This is illustrated in Fig. 3.

From Eq. [4] it can be seen that the potential of the specimen measured by a remote probe, *i.e.*, $P(x,\infty)$, is equal to A_o. The calculations show that A_o is equal to the mean of E_a and E_c for the case where L_a is equal to L_c. However, for $L_a > L_c$, A_o approaches E_c, and for $L_c > L_a$, A_o moves in the opposite direction toward E_a. The potential at a remote point $(z = \infty)$ is independent of x and has been named the potential of the composite electrode by Waber (5). One notes that the composite potential is dependent also on the ratio of the polarization parameters.

APPENDIX

A trial solution of Laplace's equation is

$$P(x,z) = A_o + \sum_{n=1}^{\infty} A_n \cos \frac{n\pi}{c} x \exp - \frac{n\pi}{c} z$$

which will be subject to the three boundary conditions

$$\frac{\partial P}{\partial x} = 0 \qquad \text{at } x = 0 \quad \text{and } x = c \qquad [1A]$$

$$P(x,o) = E_a + L_a \left.\frac{\partial P}{\partial z}\right|_{z=0} \qquad \text{for } 0 \leq x \leq c/2 \quad [2A]$$

$$P(x,o) = E_c + L_c \left.\frac{\partial P}{\partial z}\right|_{z=0} \qquad \text{for } c/2 \leq x \leq c \quad [3A]$$

Having defined $h \equiv \pi/c$, direct substitution of the series into boundary condition [2A] yields for $o \leq x \leq c/2$

$$A_o + \sum_{n=1}^{\infty} A_n \cos nhx = E_a + L_a \sum_{n=1}^{\infty} -nhA_n \cos nhx$$

Multiplying through by $\cos qhx$ (where q is an integer) and integrating with respect to (hx) from 0 to $\pi/2$, we obtain

$$\frac{A_o}{q} \sin (q\pi/2) + Aq\,\pi/4 + \sum_{\substack{n=1 \\ n\neq q}}^{\infty} \frac{A_n}{2} \left[\frac{\sin (n+q)\,\pi/2}{n+q} + \frac{\sin (n-q)\,\pi/2}{n-q} \right] = \frac{E_a}{q} \sin q\,\pi/2 - L_a qh\, A_q\,\pi/4 - L_a \sum_{\substack{n=1 \\ n\neq q}}^{\infty} \frac{A_n}{2} nh \left[\frac{\sin (n+q)\,\pi/2}{n+q} + \frac{\sin (n-q)\,\pi/2}{n-q} \right] \qquad [4A]$$

Similarly substituting into boundary condition [3A] and integrating from $\pi/2$ to π, we obtain

$$-\frac{A_o}{q} \sin q\,\pi/2 + A_q\,\pi/4 - \sum_{\substack{n=1 \\ n\neq q}}^{\infty} \frac{A_n}{2} \left[\frac{\sin (n+q)\,\pi/2}{n+q} + \frac{\sin (n-q)\,\pi/2}{n-q} \right] = -\frac{E_c}{q} \sin q\,\pi/2 + L_c \sum_{\substack{n=1 \\ n\neq q}}^{\infty} \frac{nh}{2} A_n \left[\frac{\sin (n+q)\,\pi/2}{n+q} + \frac{\sin (n-q)\,\pi/2}{n-q} \right] - L_c qh\, A_q \pi/4 \qquad [5A]$$

Dividing [4A] by L_a, [5A] by L_c and adding, one obtains

$$\frac{A_o}{q} \sin q\,\pi/2 \left[\frac{1}{L_a} - \frac{1}{L_c} \right] + (\pi/4)\, A_q \left[\frac{1}{L_a} + \frac{1}{L_c} \right] + \left[\frac{1}{L_a} - \frac{1}{L_c} \right] \sum_{\substack{n=1 \\ n\neq q}}^{\infty} \frac{A_n}{2} \left[\frac{\sin (n+q)\,\pi/2}{n+q} + \frac{\sin (n-q)\,\pi/2}{n-q} \right] = \left[\frac{E_a}{L_a} - \frac{E_c}{L_c} \right] \frac{\sin q\,\pi/2}{q} - A_q (q\,h\pi/2) \qquad [6A]$$

For convenience, let us define two auxiliary factors

$$L \equiv \frac{1}{L_c} - \frac{1}{L_a}$$

$$a + bq \equiv (\pi/4) \left[\frac{1}{L_a} + \frac{1}{L_c} + 2qh \right]$$

Rearranging Eq. [6A] one obtains

$$A_q = \frac{A_o}{q} \frac{\sin q\pi/2}{[a+bq]} L + \frac{L}{[a+bq]} \sum_{\substack{n=1 \\ n\neq q}}^{\infty} \frac{A_n}{2} \left[\frac{\sin (n+q)\,\pi/2}{n+q} + \frac{\sin (n-q)\,\pi/2}{n-q} \right] + \left[\frac{E_a}{L_a} - \frac{E_c}{L_c} \right] \frac{\sin q\,\pi/2}{q[a+bq]} \qquad [7A]$$

Defining the auxiliary function g as $g(n,q) \equiv$

$$\frac{\sin (n+q)\,\pi/2}{n+q} + \frac{\sin (n-q)\,\pi/2}{n-q}$$

The following four possibilities obtain

q	n	
odd	odd	$g(n,q) = 0$
odd	even	$g(n,q) = \frac{2}{n^2 - q^2}(-q \sin q\,\pi/2 \cos n\,\pi/2)$
even	even	$g(n,q) = 0$
even	odd	$g(n,q) = \frac{2}{n^2 - q^2}(n \sin n\,\pi/2 \cos q\,\pi/2)$

Substituting in [7A], we obtain when q is an odd integer

$$A_q = \frac{A_o}{q}\frac{\sin q\,\pi/2}{[a + bq]} \cdot L + \frac{L}{[a + bq]} \sum_{\substack{\text{even} \\ n}} A_n \left[\frac{-q}{n^2 - q^2}\right] \sin q\,\pi/2 \cos n\pi/2 + \left[\frac{E_a}{L_a} - \frac{E_c}{L_c}\right] \frac{\sin q\,\pi/2}{q[a + bq]} \quad [8A]$$

but when q is an even integer

$$A_q = \frac{L}{[a + bq]} \sum_{\substack{\text{odd} \\ n}} A_n \left[\frac{n}{n^2 - q^2}\right] \sin n\,\pi/2 \cos q\,\pi/2 \quad [9A]$$

Returning now to our boundary condition, we can also solve for A_o in the following way

$$0 \leq x \leq c/2$$

$$A_o + \sum_{n=1}^{\infty} A_n \cos nhx = E_a + L_a \sum_{n=1}^{\infty} -nh\, A_n \cos nhx$$

Integrating $P^*(x,0)$ with respect to (hx) from 0 to $\pi/2$

$$A_o\,\pi/2 = E_a\,\pi/2 - L_a h \sum_{n=1}^{\infty} A_n \sin n\,\pi/2 \quad [10A]$$

and separately from $\pi/2$ to π

$$A_o\,\pi/2 - \sum_{n=1}^{\infty} \frac{A_n}{n} \sin n\,\pi/2 = E_c\,\pi/2 + L_c h \sum_{n=1}^{\infty} A_n \sin n\,\pi/2 \quad [11A]$$

Dividing the first of this pair by L_a, and the second by L_c and adding, we obtain

$$A_o = 2/\pi \left(\frac{L_a - L_c}{L_a + L_c}\right) \sum_{\substack{\text{odd} \\ n}} \frac{A_n}{n} \sin (n\,\pi/2) + \left[\frac{E_a}{L_a} + \frac{E_c}{L_c}\right] \frac{L_a L_c}{L_a + L_c} \quad [12A]$$

Now make the variable change, $B_n = nA_n$ for $n = 1,2,\ldots\ldots$ and we obtain from Eq. [8A], [9A], and [12A], an infinite set of linear equations in the variables A_o and B_n which is of the form

$$B_j = \sum_i \alpha_{ij} B_i + \beta_j \quad [13A]$$

Specifically

$$q = 0 \qquad A_o = 2/\pi \left(\frac{L_a - L_c}{L_a + L_c}\right) \sum_{\substack{\text{odd} \\ n}} \frac{B_n}{n^2} \sin n\,\pi/2 + \left[\frac{E_a}{L_a} + \frac{E_c}{L_c}\right] \frac{L_a L_c}{L_a + L_c}$$

q an odd integer

$$B_q = A_o \sin q\,\pi/2 \frac{L}{a + bq} + \frac{Lq}{a + bq} \sum_{\substack{\text{even} \\ n}} \frac{-qB_n}{n(n^2 - q^2)} \sin q\,\pi/2 \cos n\,\pi/2 + \left[\frac{E_a}{L_a} - \frac{E_c}{L_c}\right] \sin \frac{q\,\pi/2}{a + bq} \quad [14A]$$

q an odd integer

$$B_q = \frac{Lq}{a + bq} \sum_{\substack{\text{odd} \\ n}} \frac{B_n}{n^2 - q^2} \sin n\,\pi/2 \cos q\,\pi/2$$

A set of equations of the form [13A] has a unique solution if certain convergency conditions are satisfied (4). These conditions are

$$(a) \quad \sum_i |\alpha_{ij}| < 1 \qquad j = 1,2,\ldots\ldots$$

$$(b) \quad |\beta_j| \leq K\left[1 - \sum_i |\alpha_{ij}|\right] \qquad K > 0$$

If these conditions are satisfied, then it can be shown that a bounded solution of the finite set of N equations

$$B_j = \sum_{i=1}^{N} B_i + \beta_j \quad [15A]$$

which we represent as $\{B_j^N\}$ is an approximation to the solution $\{B_j\}$ in the sense that $\lim_{N \to \infty} \{B_j^N\} = \{B_j\}$ and thus an approximation to B_j can be obtained by solving a finite set of simultaneous equations.

In order to prove the convergence of the equations given by [14A], we must thus consider the infinite sums

$$(i) \quad 2/\pi \left(\frac{L_a - L_c}{L_a + L_c}\right) \sum_{\substack{\text{odd} \\ n}}^{\infty} \left|\frac{1}{n^2}\right|$$

$$(ii) \quad \frac{Lq^2}{a + bq} \sum_{\substack{n \\ \text{even}}}^{\infty} \left|\frac{1}{n(n^2 - q^2)}\right|$$

$$(iii) \quad \frac{Lq}{a + bq} \sum_{\substack{\text{odd} \\ n}}^{\infty} \left|\frac{1}{n^2 - q^2}\right|$$

Considering first (i), it is easily shown that

$$\sum_{\substack{\text{odd} \\ n}} \left|\frac{1}{n^2}\right| = \frac{\pi^2}{8}$$

thus the infinite sum reduces to $\pi/4\ |L_a - L_c/L_a + L_c|$ and this is obviously < 1.

Turning now to Eq. (ii) and (iii), we must consider the infinite sums

$$\frac{q^2 L}{(a + bq)} \sum_{\substack{\text{even} \\ n}} \left|\frac{1}{n(n^2 - q^2)}\right|$$

and

$$\frac{qL}{(a + bq)} \sum_{\substack{\text{odd} \\ n}} \left|\frac{1}{n^2 - q^2}\right|$$

Without detailing the proofs, it can be shown that these sums are equal to

$$\frac{L}{a + bq}\left[1 + \log 2 + \left[1 + \frac{1}{2} + \frac{1}{3} \cdots \frac{2}{q-1}\right] - \left[\frac{1}{q+2} + \frac{1}{q+4} \cdots \frac{1}{2q-1}\right] - \frac{1}{2q}\right]$$

and $\frac{L}{a + bq} \sum_{n=1}^{q} \frac{1}{2n - 1}$, respectively.

It is not possible from these expressions to determine exactly the convergence for any arbitrary values of L_a, L_c, and c.

The convergence was investigated by selecting reasonable values for L_a, L_c, and c and numerically evaluating the expressions. These were found to be less than unity for the values of L_a, L_c, and c quoted in the section on "Results." The expressions were found to take on values greater than unity for either very large or very small ratios of L_a to L_c.

In a similar fashion, the convergence condition (*b*) concerning the magnitude of the free terms b_i was investigated by numerical evaluation. After the convergence conditions were tested in this fashion, the set of Eq. [15A] was solved for $N = 100$, and for given values of L_a, L_c, E_a, E_c, and c. The simultaneous set of equations was solved by direct substitution using a CDC 6400 computer.

Acknowledgment

This research was supported by the National Aeronautics and Space Agency, Washington, and by the Advanced Research Program Agency of the Department of Defense through the Materials Research Center at Northwestern University.

This paper was submitted by one of the authors (E.K.) in partial fulfillment of requirements for the degree of Doctor of Philosophy, Northwestern University.

Manuscript received Oct. 23, 1969; revised manuscript received *ca.* March 13, 1970.

Any discussion of this paper will appear in a Discussion Section to be published in the June 1971 JOURNAL.

REFERENCES

1. C. Wagner, *This Journal*, **98**, 116 (1952).
2. J. T. Waber, *Corrosion*, **13**, 95t (1957).
3. J. T. Waber and M. Rosenbluth, *This Journal*, **102**, 344 (1955).
4. S. J. Ketchum and F. H. Haynie, *Corrosion*, **19**, 242t (1963).
5. L. Kantorovich and V. Krylov, "Approximate Methods of Higher Analysis," Interscience Publishers, Inc., New York (1958).

Electrochemical-Chemical Synthesis of Methylene bis(Aluminum Dichloride)

Edward H. Mottus and Morris R. Ort

Monsanto Company, St. Louis, Missouri and Texas City, Texas, respectively

ABSTRACT

The electrochemical-chemical (EC) synthesis of methylene bis(aluminum dichloride), $Cl_2AlCH_2AlCl_2$, involves electrolysis of dichloromethane solutions using an aluminum anode and a passive cathode in an undivided cell. The aluminum anode is consumed during electrolysis. One gram-atom aluminum is lost per faraday. Suitable electrolytes are $AlCl_3$, $HOAlCl_2$, tetraalkylammonium chlorides, and, in general, salts that are sufficiently soluble in dichloromethane to give conducting solutions. The nature of the reactions and characterization of the products are discussed.

The electrochemical synthesis of organometallics usually involves the electrolysis of organometallic A to produce organometallic B or the reduction of a species

$$\text{(i.e., RX, RCR, } CH_2 = CHCN\text{, etc.)}$$

at a reactive cathode to form the organometallic of the cathode material (1). Some Kolbe reactions are reported to give direct reaction of an organic compound with a reactive anode (2). Chadwick and Kinsella (3) reported the preparation of methylaluminum diiodide by electrolysis of a solution of aluminum triiodide in methyl iodide with aluminum electrodes. We wish to report the EC synthesis of methylene bis(aluminum dichloride) ($Cl_2AlCH_2AlCl_2$) I.

Experimental

Electrolysis cells.—Small-scale electrolyses (100 ml total volume) were carried out in a tubular cell, 4 cm diameter and approximately 25 cm tall. The cell was fitted with ports for electrical leads and a condenser. An opening was provided at the bottom of the cell to allow introduction of gases into the electrolysis solution. The electrodes were constructed from 99.99% aluminum sheet 0.01 in. thick (Consolidated Aluminum Company of Canada) as concentric cylinders. The cathode was 2 in. high x ½ in. diameter, the anode was 2 in. high x 1 in. diameter, and they were held in place with Teflon spacers. In some experiments a platinum cathode was used. Stirring in the cell was with a magnetic stirring bar and by passage of gas through the electrolysis solution.

Larger-scale electrolyses were carried out in a 500 ml cell. In this cell a three-electrode concentric cylinder assembly was used. The dimensions of the cylinders were 1¾, 2¼, and 2¾ in. in diameter and 1 in. high. The inner and outer electrodes were cathodes, and the middle electrode was the anode.

Prior to use, the cell assemblies were dried in an air-circulating oven at 140°C. The cells were assembled hot and cooled under dry nitrogen.

Electrolyte solutions.—*Solvent.*—Dichloromethane (Matheson, Coleman and Bell or Fisher Scientific) was dried by passing through a 3 ft x 1 in. column packed with 3A molecular sieves (Linde).

Method A.—To 400 ml of dichloromethane under nitrogen was added 0.036 ml (0.002 mole) of water. The mixture was stirred until solution was complete and 0.267g (0.002 mole) of sublimed aluminum chloride added. The mixture was stirred overnight to give a clear, yellow solution. The solution was used as prepared or was heated under reflux to drive off by-product HCl.

Method B.—To 400 ml of dichloromethane under nitrogen was added 0.25g (0.002 mole) of ethylaluminum dichloride (Texas Alkyls Inc.). The solution was stirred and 0.036 ml (0.002 mole) of water added. The mixture was stirred overnight to give a clear, yellow solution of $HOAlCl_2$.

Method C.—A mixture of 0.267g (0.002 mole) of sublimed aluminum chloride and 400 ml of dichlorometh-

ane was refluxed under nitrogen overnight to a clear, light-yellow solution.

Methylene bis(aluminum dichloride).—The 500 ml cell was charged with 564g of electrolyte solution containing 5 millimoles/l of electrolyte with a 2.88 Cl^-/Al ratio. The electrolyte solution was saturated with ethylene and electrolyzed for 40 min at 0.5A with a steady-state voltage of 185-195V. Ethylene was continuously bubbled through the cell during electrolysis. After the electrolysis was complete, the solution was transferred to a 500 ml flask under nitrogen. The mixture was refluxed for about 30 min to drive off the excess ethylene and any HCl if present. During the electrolysis 12.21 m**F** of current were passed, and 0.3377g (12.51 mg atom) of aluminum was lost from the anode. This corresponds to 1.03 g atom of Al/**F**. The weight of the cathodes remained unchanged. Weight fractions of the solution were analyzed for Cl^-, Al-C bonds (4), and Al.

Anal. Calcd.—for $Al_2CH_2Cl_4$: Al, 0.10%; Al-C bonds, 12.51 meq; Cl^-, 30.75 meq. Found: Al, 0.09%; Al-C bonds, 12.01, 11.77 meq; Cl^-, 30.00, 30.00 meq.

The above Al and Cl^- analyses include the electrolyte in the solution of I. The chemical yield of I is $\sim$ 100%.

Alkylaluminum chloride etherates.—A RB flask equipped with a magnetic stirring bar and 3-way stopcock was charged with a known quantity of alkylaluminum chloride in dichloromethane or hexane solution. The solution was stirred and an excess of diethyl ether added. The excess ether and solvent were removed by distillation and the last traces of volatiles removed by pumping under 0.1 mm vacuum overnight. The alkylaluminum chloride etherates were diluted approximately 50% with dichloromethane for nmr studies.

Nmr.—The spectra were obtained on either a Varian A-60 or A-56-60. The internal standards were either TMS or dichloromethane. Where dichloromethane was used as the internal standard, the values were converted to TMS reference for comparison.

Results and Discussion

The EC synthesis of I involves the electrolysis of dichloromethane in the presence of an electrolyte at an aluminum anode in an undivided cell. The aluminum anode is consumed during the electrolysis. The over-all reaction is EC since 1g atom of the aluminum anode is consumed per faraday. If the reaction were truly electrochemical, 3 faradays/g atom of aluminum consumed would be required. The following sequence of reactions is postulated to account for the formation of I and by-products.

At cathode:

$$CH_2Cl_2 + e^- \rightarrow Cl^- + ClCH_2\cdot \quad [1]$$

$$CH_2Cl_2 + 2e^- \rightarrow 2Cl^- + CH_2: \quad [2]$$

If [1] is operative, the chloromethyl radical can dimerize.

$$2ClCH_2\cdot \rightarrow ClCH_2CH_2Cl \quad [3]$$

However, [2] is the most probable reaction, and the carbene formed undergoes typical carbene reactions.

$$2CH_2: \rightarrow CH_2 = CH_2 \quad [4]$$

$$CH_2 = CH_2 + CH_2: \rightarrow \begin{matrix} & CH_2 & \\ \diagup & & \diagdown \\ CH_2 & & CH_2 \end{matrix} \quad [5]$$

$$CH_2: + CH_2Cl_2 \rightarrow ClCH_2CH_2Cl \quad [6]$$

At anode

$$Cl^- \rightarrow e^- + Cl\cdot \quad [7]$$

$$Cl\cdot + Al \rightarrow AlCl \quad [8]$$

$$AlCl + CH_2Cl_2 \rightarrow Cl_2AlCH_2Cl \quad [9]$$

$$AlCl + Cl_2AlCH_2Cl \rightarrow \underset{\text{I}}{Cl_2AlCH_2AlCl_2} \quad [10]$$

Reactions [9] and [10] are postulated on the fact that AlCl is electronically analogous to carbene and probably undergoes the same type of reactions as carbene.[1]

The essential features of the anode reactions are, first, the oxidation of chloride to atomic chlorine and, second, the attack of atomic chlorine on the aluminum anode to give aluminum monochloride, the key intermediate in the synthesis of I.

The chemical reaction of aluminum and dichloromethane does not take place under standard conditions. Lehmkuhl and Schäfer (5) reported the synthesis of I in approximately 40% yield by the reaction of dichloromethane with aluminum shot-etched with dibromomethane or by using aluminum tribromide as an initiator.

The reaction in this case was through bromide followed by exchange of chloride for bromide.

The basic reaction sequences presented here are believed to be general and will be further defined by us at a later date.

The conditions used during electrolysis played a large and unique role in the electrochemical synthesis.

If the electrolyses were carried out under nitrogen, Al (6) was deposited at the cathode via

$$AlCl_2^+ + 3e^- \rightarrow Al + 2Cl^- \quad [11]$$

Under these conditions the electrolyte was depleted and the conductance of the cell decreased with time.[2] However, if, under nitrogen, cyclohexene was added to the electrolysis solution, or ethylene was used as the blanketing gas instead of nitrogen, the deposition of Al at the cathode did not occur. Further, the conductance remained high throughout the electrolysis. The role of the olefin must be that of complex formation with the $AlCl_2^+$. Complex of the $AlCl_2$ cation with

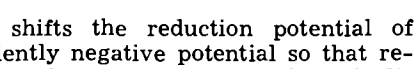

[12]

olefin apparently shifts the reduction potential of $AlCl_2^+$ to a sufficiently negative potential so that reduction of dichloromethane becomes the only cathodic process.

The effect of the use of ethylene *vs.* nitrogen on the cell resistance is shown in Fig. 1. Shown in Fig. 1 are three electrolyses in which only the atmosphere has been changed. The cell resistances were calculated from the voltage and amperage at the experimental points. The sharp increase in cell resistance is immediately reversed by changing the atmosphere in the cell from nitrogen to ethylene (plot 3). Plot 2 shows that by carrying out the electrolysis for approximately 2 hr before the ethylene atmosphere is introduced most of the electrolyte has been depleted. Even though the electrolyte has been largely depleted, the introduction of ethylene has a significant effect on the cell resistance.

The use of ethylene or other olefins during electrolysis did not alter the composition of the product. Decomposition of the product solutions with CH_3OD gave mainly CH_2D_2 whether the electrolyses were carried out under nitrogen or ethylene. Deuterated ethane was never observed as a product of reaction with CH_3OD.

In some of our work the electrolysis was carried out under 6-11 psig ethylene pressure. Mass spectral analysis of gaseous atmosphere after electrolysis showed

[1] The referee questioned whether an attempt had been made to identify the intermediate Cl_2AlCH_2Cl as was postulated in Eq. [9]. The presence of small amounts of Cl_2AlCH_2Cl was indicated by mass spectral analysis of the gases obtained by decomposition of electrolysis solutions containing I with methanol. In all of the decomposition studies 0.5-0.7% CH_3Cl was observed which would only arise from Cl_2AlCH_2Cl. Since the postulated reactions occur at the metal surface the absence of larger amounts of Cl_2AlCH_2Cl is not surprising.

[2] The referee commented on the decline of conductivity under N_2 even though concentration of I was increasing and I is an electrolyte. I is a satisfactory electrolyte only in the presence of olefin. We propose that the olefin promotes ionization of I by complexing with the cationic species.

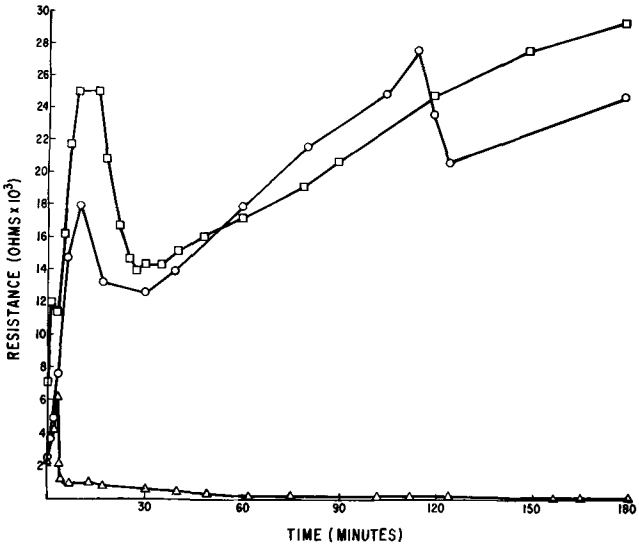

Fig. 1. Effect of ethylene on cell resistance: curve 1, □, electrolysis under nitrogen; curve 2, ○, electrolysis under nitrogen for 114 min, then under ethylene for 66 min; curve 3, △, electrolysis under nitrogen for 3 min, then under ethylene for 177 min.

the predominate product to have a mass of 42. For this specific experiment it was not determined if the product was propylene or cyclopropane. However, in subsequent work (to be reported by us at a later date) on a related reaction, the product with mass of 42 was identified as cyclopropane. By analogy we postulate that the reduction of dichloromethane is a 2-electron reduction to give carbene which adds to ethylene to give cyclopropane (see Eq. [5]).

In most of the studies the electrolyte was either $AlCl_3$ or $HOAlCl_2$, from the reaction of H_2O with $AlCl_3$ or $C_2H_5AlCl_2$. Other electrolytes investigated were tetraethylammonium chloride and manganese chloride. Both these were sufficiently soluble in CH_2Cl_2 to give conducting solutions and allow electrolyses to give I. Solutions of I in CH_2Cl_2 (at 2.5 x 10^{-3} mol/l) were also used as electrolyte.

The nature of product I has been established by decomposition studies, titration, and nmr. Decomposition of electrolysis solutions with CH_3OD yields mainly CH_2D_2, which can only arise from al-CH_2-al species. Titration with iodine yields one —C(Cl)—al— bond per Al lost from anode. Nmr spectrum of the etherate of I was compared with that reported for I prepared by Lehmkuhl and Schäfer. They isolated, characterized, and obtained the nmr spectrum of the dietherate of I. The al-CH_2-al protons were observed at τ, 11.01. When electrochemically prepared I was complexed with ether and the nmr spectrum obtained, two peaks were observed at τ, 11.14 and τ, 10.44. The peak at 11.14 corresponds to the dietherate of I; the one at 10.44 was of unknown origin.

Alkylaluminum chlorides are known to exchange rapidly to give equilibrium mixtures. For example, a solution of methylaluminum dichloride (25%) and dimethylaluminum chloride (75%) shows only a single sharp proton resonance signal both at room temperature and at —60°C (7).

It had been observed in long-term electrolysis that solid products began to precipitate toward the end of the electrolysis. If I underwent exchange reactions and the product of the exchange reaction was a solid, the equilibrium would be altered. Further, by complexing with ether the exchange should be stopped and both products observed by nmr. The exchange reaction is proposed as follows

$$2Cl_2AlCH_2AlCl_2 \rightarrow AlCl_3 + \underset{\text{II}}{Cl_2AlCH_2\overset{Cl}{\overset{|}{A}}lCH_2AlCl_2}(S) \qquad [13]$$

In order to determine if the peak at τ, 10.44 could be assigned to II, a series of alkyl aluminum chloride etherates was prepared in which the Al/CH_2 was varied. The influence of the aluminum on the methylene protons should vary as the Al/CH_2 ratio varies. The results are given in Table I.

In order to eliminate possible differences in the shielding of multiple ether complexing on the same molecule ethylaluminum dichloride, ethylaluminum dichloride etherate, I and I·diethereate were compared. The results are given in Table II.

The results in Table II indicate that the effect of adding ether is additive, and the contribution is the same for each aluminum etherate.

The results given in Table I indicate that the effect of aluminum on adjacent methylene protons is additive, and the peak at τ, 10.44 can probably be assigned to compound II. Further evidence that this assignment is correct is that, as the electrochemically prepared I was allowed to stand, more solids precipitated. When the etherate complex of the solution with an increased amount of solids present was prepared and the nmr spectrum obtained, the peak at τ, 10.44 increased at the expense of the peak at τ, 11.14.

Stable solutions of I in CH_2Cl_2 could be prepared by carrying out a series of electrolyses in which the electrolyte was the solution of I from the previous experiment. These solutions did not deposit solids (11) on standing. It is proposed that $AlCl_3$ or HCl in electrolysis solutions catalyzes the conversion I → II (Eq. [13]). The technique of successive electrolyses provides the means of obtaining solutions of I free from other Al species.

Summary

The electrochemical synthesis of methylene bis(aluminum dichloride) is an EC type involving electrochemical reduction of chloride to atomic chlorine, attack of atomic chlorine on the aluminum anode to yield aluminum monochloride. Reaction of this key intermediate with the solvent, dichloromethane, leads to the product. The cathodic products are postulated to arise from carbene, the two-electron reduction product of dichloromethane.

Manuscript submitted Dec. 29, 1969; revised manuscript received *ca.* March 20, 1970. This was Paper 132 presented at the New York Meeting of the Society, May 4-9, 1969.

Table I. Results

Compound	Al/CH_2 ratio	τ-CH_2Al	δ Shift
$(C_2H_5)_2AlCl\cdot(C_2H_5)_2O$	0.5	9.36	0.54
$C_2H_5AlCl_2\cdot(C_2H_5)_2O$	1	9.90	
$Cl_2AlCH_2\overset{Cl}{\overset{|}{A}}lCH_2AlCl_2\cdot[(C_2H_5)_2O]_3$	1.5	10.44	0.54
$Cl_2AlCH_2AlCl_2\cdot[(C_2H_5)_2O]_2$	2	11.14 (11.01)[5]	0.70

Table II. Results

Compound	τ-CH_2Al	δ Shift	Shift/ether
$C_2H_5AlCl_2$	9.46	0.44	0.44
$C_2H_5AlCl_2\cdot(C_2H_5)_2O$	9.90		
$Cl_2AlCH_2AlCl_2$	10.34	0.80	0.40
$Cl_2AlCH_2AlCl_2\cdot[(C_2H_5)_2O]_2$	11.14		

Any discussion of this paper will appear in a Discussion Section to be published in the June 1971 JOURNAL.

REFERENCES

1. E. M. Martlett, *Ann. N.Y Acad. Sci.*, **125**, 12 (1965).
2. S. Swann, Jr., "Technique of Organic Chemistry," A. Weissberger, Editor, 2nd ed., Vol. II, p. 385, Interscience Publishers, New York (1956); see also ref. (1).
3. J. R. Chadwick and E. Kinsella, *J. Organometal. Chem.*, **4**, 334 (1965).
4. The aluminum carbon bonds were analyzed by the method of S. A. Bartkiewicz and J. W. Robinson, *Anal. Chim. Acta.*, **20**, 326 (1959). The solvent for the iodine was changed from benzene to dichloromethane.
5. H. Lehmkuhl and R. Schäfer, *Tetrahedron Letters*, **21**, 2315 (1966).
6. For these electrolyses a platinum cathode was used, and analyses by XRF of the deposit on the cathode showed the deposit to be aluminum.
7. S. Brownstein, B. C. Smith, G. Erlich, and A. W. Laubengayer, *J. Am. Chem. Soc.*, **82**, 1000 (1960).

Estimation of Molecular Diffusivities in Liquids

R. O'Brien,* D. Quon, and C. R. Darsi

Department of Chemistry, University of Victoria, Victoria, British Columbia, Department of Chemical and Petroleum Engineering, University of Alberta, Edmonton, Alberta, and Chemcell Ltd., Edmonton, Alberta, respectively, Canada

ABSTRACT

A new experimental technique for measuring molecular diffusion through liquids, using microcell interferometry, is described. The main advantage is that an experiment can be performed in a few minutes. Aside from the saving in time, these short runs, which are inherently unsteady state, are more likely to be free of external effects. Concentration profiles are recorded on film at suitable time intervals. By analyzing the semidiscrete form of the diffusion equation and by a suitable linear transformation of the variables denoting the concentration profile, linear relationships are established between the logarithms of these transformed concentrations and time. This permits the determination of the diffusivity with maximum sensitivity. Conventional "least squares" curve fitting techniques are shown to be inadequate for analyzing the data from these experiments.

The present paper is concerned with (*a*) a description of the experimental techniques in which data on transient one-dimensional diffusion in a liquid are obtained by optical methods, and (*b*) a mathematical analysis of these data to determine diffusivities.

Experimental Techniques

The technique to be described involves microcell interferometry. Since a considerable amount of work in the fields of measuring diffusivities has been done in the past with a wide variety of apparatus, it is of some importance to show why a new technique should be introduced. The justification must be that either convenience or accuracy or both are better served.

Most diffusion apparatus in the past (1) has been large, with a long diffusion path, and relatively small concentration gradients. This has led to long experimental elapsed times and, hence, a difficulty in isolating the system from outside perturbations. In these measurements extremely good thermostatting arrangements have been necessary to avoid thermally induced convection, and great care must be taken to avoid mechanical agitation of any kind.

The advantages of the present cell is that experimental results are obtained very quickly, in only a few minutes. Better accuracies are to be expected since the outside perturbations are usually too slow to affect the results.

Furthermore, since the concentration gradient is produced electrochemically, a wide variety of gradients can be selected, including very steep ones, and the diffusion path is short.

Apparatus and procedure.—The main apparatus consists of an interferometer cell, its light source and the recording apparatus, in this case a motion picture camera.

The cell, shown in Fig. 1, has been described in some detail elsewhere (2). Briefly, it consists of a wedge-

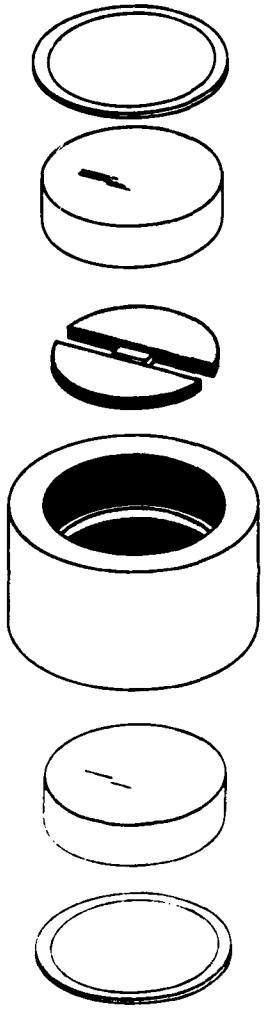

Fig. 1. Interferometric microcell

* Electrochemical Society Active Member.

type interferometer set up as an electrochemical cell. Copper blocks are sandwiched between glass flats which have partially reflecting dichroic coatings on the inner surfaces. Collimated sodium vapor light at near 90° incidence is made to interfere by beam intensity splitting at the reflecting coatings (Fig. 2) and a system of light and dark fringes at a spacing of about 3/mm is produced.

The experiments were carried out at two copper block spacings, 3 mm and 30 mm apart. These blocks, connected to a potential source, acted as parallel-faced horizontal electrodes with the cathode above the anode, separated by 0.1N $CuSO_4$ solution of pH 4.5. The electrical circuit was arranged to give a constant current of about 1 mA/cm^2. After approximately 3 min of electrolysis, the established concentration gradient (as shown by the bends in the interference fringes, Fig. 3) extended toward the center of the cell from both the anode and the cathode but left an unaltered volume of electrolyte in the center. The motion picture camera was started and the current switched off. Previous tests had confirmed that a linear relationship exists between concentration and refractive index. Hence, the shape of the interference fringes corresponds to the concentration profile existing in the cell. Figure 3 shows typical sets of fringes obtained at various times during the course of one run. For that particular magnification, the scale shows the relation between the concentration (in gram-moles/liter) and fringe displacement. Full details on how to interpret these fringes are given elsewhere (2). It was felt more desirable to study the decay portion of the curve, rather than the build-up portion, in order to avoid extraneous electrical effects. Since the camera speed was 8 frames/sec and about 5 min of the concentration gradient decay process were taken, only certain frames were analyzed (about 10). Further, in analyzing the fringes, each of which represents not only a refractive index contour but also a concentration contour, only certain fringes and certain points selected from these fringes were used. In fact, a fringe was selected which appeared to be representative and the same fringe was measured in each frame.

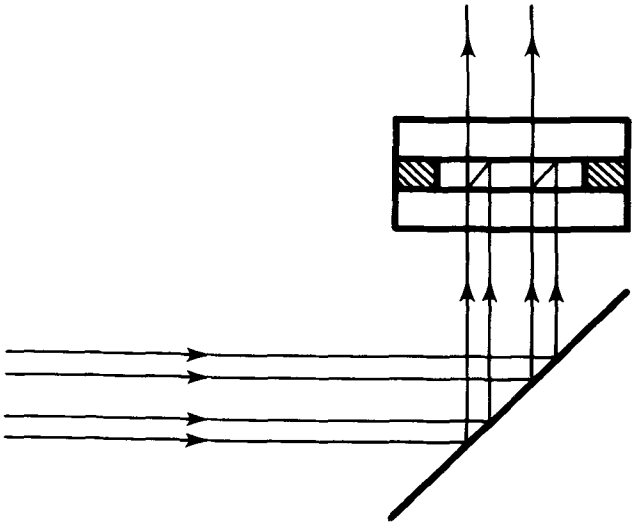

Fig. 2. Schematic diagram of light path

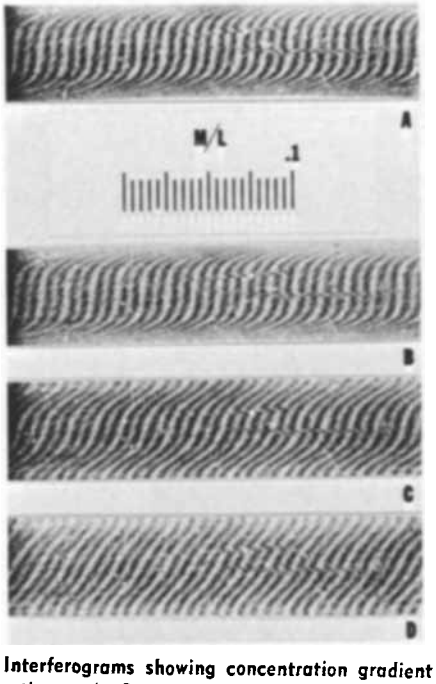

Fig. 3. Interferograms showing concentration gradient relaxation at various times: A, 0 sec; B, 1 sec; C, 60 sec; d, 30 sec.

Two methods of measuring were used. In some cases the fringe was projected on to rectangular coordinate graph paper at about 50X magnification, then sketched in with a pencil and the requisite values obtained by eye. In other cases, the film negative was placed in a flying spot digitalizer and computer punch cards made for various points on the selected fringe. These were then curve fitted on a computer and the values required found from an interpolation routine.

Mathematical Analysis

The general one-dimensional diffusivity equation with no internal source terms, is given by

$$\frac{\partial}{\partial x}\left(D\frac{\partial u}{\partial x}\right) = \phi\frac{\partial u}{\partial t} \qquad \begin{matrix} 0 < x < L \\ 0 < t \end{matrix} \qquad [1]$$

where u is the concentration, x distance, t time, D diffusion coefficient, ϕ the capacity factor, and L cell width.

For a typical boundary condition, one that corresponds to the experiments to be described later, the concentration is constant at the cell center and the gradient is zero at the walls. If the cell walls correspond to $x = 0$ and $x = L$, then these boundary conditions and any arbitrary but known initial condition are described by

$$\frac{\partial u}{\partial x} = 0 \qquad \text{at } x = 0,\ t > 0 \qquad [2]$$

$$u = u_c \qquad \text{at } x = L/2,\ t > 0 \qquad [3]$$

$$u = u_1(x) \qquad \text{at } t = 0,\ 0 < x < L/2 \qquad [4]$$

If D and ϕ are constant then the equation reduces to

$$\alpha\frac{\partial^2 u}{\partial x^2} = \frac{\partial u}{\partial t} \qquad [5]$$

where $\alpha = D/\phi$.

An analytical solution for the above problem is given by Carslaw and Jaeger (3) in the form of an infinite series, as follows

$$u = u_c + \frac{2}{(L/2)}\sum_{n=0}^{\infty}\exp\left[\frac{-\alpha(2n+1)^2\pi^2 t}{4(L/2)^2}\right] \cdot \cos\frac{(2n+1)\pi x}{2(L/2)}\left[\frac{2(L/2)(-1)^n u_c}{(2n+1)\pi} + \int_0^{L/2} u_1(x') \cdot \cos\frac{(2n+1)\pi x'}{2(L/2)} \cdot dx'\right] \qquad [6]$$

where x' is a dummy variable.

If data are available in discrete form, in which u is tabulated at various x's and t's but α itself is unknown, then presumably Eq. [6] can be used to calculate α. The best method appears to be a trial-and-error one, *i.e.*, guess a value of α, calculate u for a given x and t and compare this to the experimental value of u. One

could then use the least squares criterion to get the best fit value of α for the whole set of data. However, attempts to apply this technique to the experimental data from the test cells failed to yield useful results, for reasons which will be discussed later.

We have therefore set up an alternate mathematical model which permits a much more meaningful interpretation of the data. The space derivative in Eq. [5] may be discretized using the grid spacing shown below

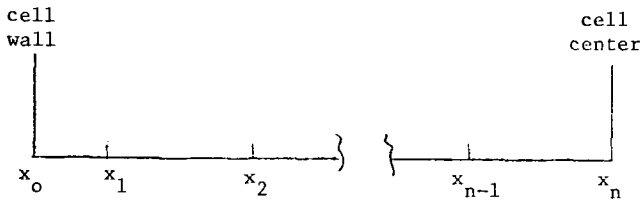

where $x_{i+1} - x_i = \Delta x - h$ a constant $i = 2, \ldots, n$ and $x_1 - x_0 = \Delta x/2 = h/2$

Using central difference approximations, where appropriate

$$\frac{\partial^2 u_1}{\partial x^2} \simeq \frac{u_2 - u_1}{\Delta x^2}$$

$$\frac{\partial^2 u_i}{\partial x^2} \simeq \frac{u_{i-1} - 2u_i + u_{i+1}}{\Delta x^2} \qquad i = 2, \ldots, n-1$$

$$u_n = u_c \qquad [7]$$

This may be written in matrix form as

$$\frac{du}{dt} = \frac{\alpha}{h^2} Ku + b \qquad [8]$$

where u is the concentration vector, K the coefficient matrix, and b the boundary value vector (which is constant in this case).

If the potential vector u happens to fall along one of the characteristic directions of K (as represented by one of its eigenvectors, say u^*), we have the following equation

$$\frac{du^*}{dt} = \frac{\alpha}{h^2} \gamma^* u^* + b \qquad [9]$$

where γ^* is the eigenvalue corresponding to that eigenvector. This essentially decouples the system of equations, permitting a closed form analytical solution of Eq. [8]. Further, since any potential vector can be expressed in terms of the system eigenvectors or characteristic directions, a general solution may be obtained as follows.

Let Q be the matrix whose columns are the unit or normalized eigenvectors of K. By the nature of the equations, the coefficient matrix K is real and symmetric. This means (4) that there are: (*i*) n real eigenvalues and (*ii*) n mutually orthogonal and linearly independent eigenvectors; further, if the eigenvectors are chosen to be of unit length, the vectors are orthonormal. This also means that $Q^{-1} = Q^T$.

Define a new vector v by the equation

$$u = Qv \text{ and } v = Q^{-1}u = Q^T u \qquad [10]$$

Geometrically, the new variables v represent the same variables u with the coordinate system changed from the orthogonal cartesian coordinates to the orthogonal eigenvector system of coordinates. Substituting [10] in [8]

$$\frac{dQv}{dt} = \frac{\alpha}{h^2} KQv + b \qquad [11]$$

Premultiplying [9] by Q^T

$$Q^T Q \frac{dv}{dt} = \frac{\alpha}{h^2} Q^T K Q v + Q^T b \qquad [12]$$

But if Q is the matrix formed by the unit eigenvectors of K, the operation Q^TKQ is a similarity transformation which serves to diagonalize K, and produce a diagonal matrix Λ, whose diagonal elements are the eigenvalues of K (5), *i.e.*

$$Q^T K Q = \Lambda \qquad [13]$$

Also $Q^TQ = I$, the unit matrix; hence, [10] becomes

$$\frac{dv}{dt} = \frac{\alpha}{h^2} \Lambda v + c \qquad [14]$$

where $c = Q^T b$

In expanded form

$$\frac{d}{dt} \begin{bmatrix} v_1 \\ \cdot \\ \cdot \\ \cdot \\ v_n \end{bmatrix} = \frac{\alpha}{h^2} \begin{bmatrix} \lambda_1 & 0 & & \\ 0 & \cdot & & \\ & & \cdot & 0 \\ & & 0 & \lambda_n \end{bmatrix} \begin{bmatrix} v_1 \\ \cdot \\ \cdot \\ \cdot \\ v_n \end{bmatrix} + \begin{bmatrix} c_1 \\ \cdot \\ \cdot \\ \cdot \\ c_n \end{bmatrix} \qquad [15]$$

Each of these individual equations can be written as

$$\frac{dv_i}{dt} = \frac{\alpha}{h^2} \lambda_i v_i + c_i \qquad [16]$$

$$(i = 1, \ldots n)$$

The system of differential equations is now decoupled in terms of the modified variables, and there is no problem in integrating these equations separately.

The solution of [16] is

$$\frac{\lambda_i v_i(t) + c_i}{\lambda_i v_i(0) + c_i} = \exp\left(\frac{\alpha \lambda_i t}{h^2}\right) \qquad [17]$$

where $v_i(0)$ is the value of v_i at $t = 0$. Let the l.h.s. of [17] be referred to as $z_i(t)$ then,

$$z_i(t) = \exp\left(\frac{\alpha \lambda_i t}{h^2}\right) \qquad [18]$$

Therefore, plotting ln $z_i(t)$ *vs.* t should result in a straight line from whose measured slope α can be easily calculated.

Treatment of Experimental Data

Molecular diffusion of copper sulfate in water.—It was observed, as predicted from theoretical considerations, that the concentration at the mid-point of the microcell remained unchanged during the course of the experiments. The cell was divided into two five-point grids on either side of the center line, with the boundary conditions as designated by Eq. [2], [3], and [4].

It has been shown elsewhere (5) that a five-point grid is sufficient to give three-figure accuracy if the input data are known exactly. An appropriate interpolation formula was used to obtain the concentrations at the grid points and various elapsed times which are shown in Table I. The calculated values of $z_i(t)$ are given in Table II.

From the definition of the uncoupled variable vector $v(t)$, Eq. [10], it can be seen that the components $v_i(t)$ of this vector are the scalar products of potential vector $u(t)$ with the individual eigenvectors q_i ($i = 1$ to 5). Geometrically, these may be looked on as the projections of the potential vector $u(t)$ onto the individual eigenvectors q_i. If the initial condition vector u_0 happens to be colinear with one of the eigenvectors q_j, then it follows that v_j would have a finite value whereas the other v_i's ($i \neq j$) will have zero value and will continue to have zero values at subsequent times and these variables will contribute nothing to the analysis of data. In practice, the initial condition vector is "more colinear" with some eigenvectors than

Table I. Experimental data on diffusivity of copper sulfate

Cell width = 3.13 mm; cell temperature = 25°C
Only the results for the low concentration half of the cell are presented here.

Time, sec	Grid point mm from top of cell	Concentration, g moles/l					
		1	2	3	4	5	Center
		2.9877	2.7032	2.4186	2.1341	1.8495	1.5650
0		0.0013	0.0331	0.0442	0.0492	0.0506	0.0494
5		0.0054	0.0332	0.0440	0.0467	0.0480	0.0494
20		0.0079	0.0312	0.0424	0.0463	0.0486	0.0494
40		0.0106	0.0228	0.0413	0.0465	0.0483	0.0494
50		0.0118	0.0280	0.0409	0.0460	0.0481	0.0494
75		0.0145	0.0277	0.0405	0.0459	0.0481	0.0494
100		0.0172	0.0281	0.0381	0.0457	0.0480	0.0494
120		0.0181	0.0281	0.0386	0.0457	0.0476	0.0494
150		0.0208	0.0283	0.0377	0.0444	0.0477	0.0494
200		0.0231	0.0288	0.0369	0.0423	0.0467	0.0494

Table IIA. Eigenvalues and cos θ for various eigenvectors

i	1	2	3	4	5
Cos θ_i*	0.0119	0.1912	0.0458	0.6751	0.7109
λ_i	−3.6825	−2.8308	−1.7153	−0.6903	−0.0810

* θ is the angle between the normalized vectors $u^{(o)}$ and q_i.

Table IIB. Values of transformed variable $z_i(t)$ at various times

Sec \ i	$z_i(t)$				
	1	2	3	4	5
5	0.6910	0.8027	1.0024	0.8200	0.9705
20	0.4583	0.6323	0.7745	0.7667	0.9816
40	0.0936	0.2508	0.5588	0.7201	0.9998
50	0.0791	0.2341	0.5235	0.6745	0.9881
75	−0.0315	0.1080	0.4049	0.6181	0.9557
100	0.2761	0.0844	0.2297	0.5291	0.9399
120	0.1721	0.0021	0.2347	0.5095	0.9239
150	0.0204	0.0092	0.1241	0.4213	0.9001
200	−0.1485	0.0259	0.0956	0.3004	0.8895

the others; this is indicated by the relative magnitudes of the scalar products such as the ones shown in Table IIA.

The variables $z_i(t)$ are functions of $v_i(t)$, and are normalized values of v_i with respect to the initial value $v_i(o)$ and the modified boundary condition vector component c_i (Eq. [17] and [18]). Since these z_i's decay exponentially to zero with time (Eq. [18]), it follows that they are unity in numerical value at zero time, but displacement along the time axis will not affect the determination of α. Some of these z_i's decay faster than the others depending on the numerical value of the corresponding eigenvalue λ^*_i. Referring again to Table IIA, we notice that θ_2 is greater in magnitude than θ_1 or θ_3, but is less than θ_4 and θ_5. Since the eigenvalue λ^*_2 is about 4 times larger than λ^*_4 and about 35 times larger than λ^*_5, it follows that its decay is much faster than of z_4 and z_5. This is clearly seen by the relative size of numbers in Table IIB, columns 2, 4, and 5. The noise in the data has affected the accuracy of numbers in column 2 beyond 40 sec. Presumably, if more data were available between 0 to 30 sec, z_2 could be used along with z_4 and z_5 to calculate D. It must be remembered, however, that v_4 and v_5 (from which z_4 and z_5 were derived) had much better initial values.

These considerations have led us to use z_4 and z_5 only for the estimation of diffusivity of copper sulfate. They were separately fitted to a straight line (Fig. 4). The value of D using z_4 was 0.585 x 10^{-6} cm²/sec; using z_5 it was 0.602 x 10^{-6} cm²/sec. The average value (0.594 x 10^{-6} cm²/sec) is consistent with the reported literature value which ranges from 0.55 to 0.80 x 10^{-6} cm²/sec (6).

In order to compare the proposed procedure with the conventional "least squares" technique, the same data were analyzed, using a trial-and-error search procedure to find the minimum variance by substituting in various values of D, the diffusivity into Eq. [6].

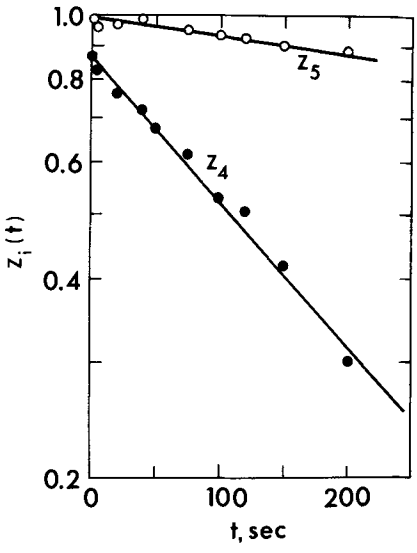

Fig. 4. Relations between transformed concentrations and time

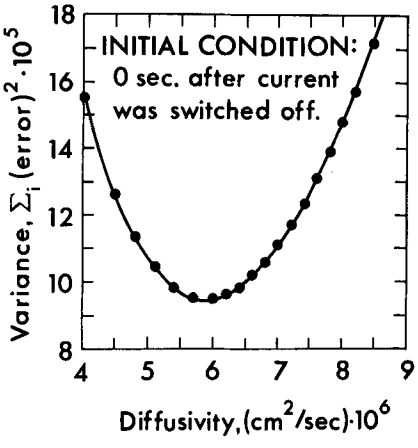

Fig. 5. Least squares analysis, initial condition A

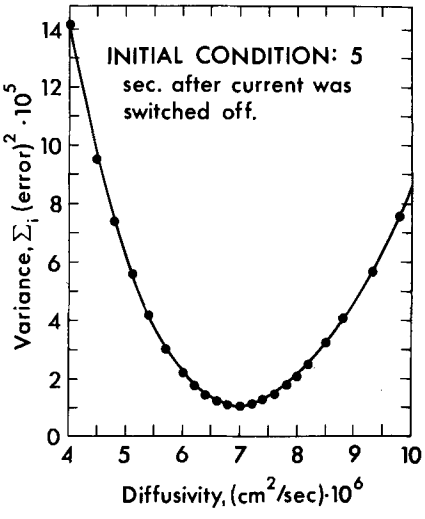

Fig. 6. Least squares analysis, initial condition B

The choice of an initial condition posed a problem; it was finally decided to carry out the calculations for two initial conditions, A and B, corresponding to 0 and 5 sec after the current was switched off. Results are shown in Fig. 5 and 6. As can be seen, it is most difficult to find the "best fit" value of α, the diffusivity, the two curves giving values of α that differ by more than 15%.

Conclusions

1. A combination of microcell interferometry and theoretical analysis provides a new means for rapid and accurate determination of molecular diffusivities in liquids.

2. The procedure outlined here is capable of yielding useful results even from rather "noisy" data. As better light sources and improved microcells are developed, the accuracy should be even better.

3. The "least squares" technique, besides using excessive computing time, failed to yield useful results. The variance, which is a measure of "best fit" is relatively insensitive to the value of α, the diffusivity. Furthermore, the method is predicated on a known initial condition; hence, much weight is placed on the correctness of these conditions. The proposed procedure, on the other hand, places approximately equal weight on all the data, which more truly reflects the experimental conditions.

Manuscript submitted April 24, 1967; revised manuscript received *ca.* March 20, 1970.

Any discussion of this paper will appear in a Discussion Section to be published in the June 1971 JOURNAL.

REFERENCES

1. W. Jost, "Diffusion in Solids, Liquids and Gases," p. 436, Academic Press, New York (1952).
2. R. N. O'Brien, *Rev. Sci. Inst.*, **35**, 803 (1964).
3. H. S. Carslaw and J. D. Jaeger, "Conduction of Heat in Solids," 2nd ed., p 101, Ederendon Press, Oxford (1959).
4. G. Birkhoff and S. MacLane, "A Survey of Modern Algebra," MacMillan Co., New York (1953).
5. C. R. Darsi, and D. Quon, *Can. J. Chem. Eng.*, **44**, 263 (1966).
6. W. G. Eversole, H. M. Kindsvater, and J. D. Peterson, *J. Phy. Chem.*, **46**, 370 (1942).

Ion and Water Transport in Ion Exchange Membranes

J. H. B. George, R. A. Horne,[1] and C. R. Schlaikjer*[2]

Arthur D. Little, Inc., Cambridge, Massachusetts

ABSTRACT

Measurements have been made of the electrical conductivity of cation- and anion-permeable ion exchange membranes (Nepton CR-61 and AR-110) in a number of ionic forms at 10°, 25°, and 40°C and the corresponding Arrhenius activation energies calculated. Conductivity measurements have also been made on free solutions chemically analogous to the membrane systems and on membranes containing two mobile ions. Conductivities in the membrane are much lower than in free solution and the activation energies somewhat higher. In the case of mobile cations, but not anions, there is a very strong charge dependence. The observed conductivity phenomena are interpreted in terms of a general structural retardation of movement as a consequence of the enhanced water structure in the internal solution, and a more specific relaxation arising from the interaction of the mobile ions with the total coulombic field of their environment. Water transport measurements indicate that the ions moving in the membrane carry with them their primary hydration sphere, a sizable fraction of their total coulombic hydration atmosphere, and, especially in the case of larger species, entrained (or electro-osmotic) water as well.

Description of the Resin Systems

The membranes used in the present investigation were cation permeable Nepton CR-61 and anion permeable Nepton AR-110, both manufactured by Ionics, Inc. The manufacturer cooperated by taking particular pains to provide membrane samples as similar as possible with respect to properties such as capacity, water content, cross-linking, etc. The membranes are composed of divinyl-benzene-cross-linked polystyrene resins, the former with sulfonate, the latter with quaternary ammonium charge sites. They are quite highly cross-linked (30%) and, therefore, show relatively little water transport, a desirable feature in electrodialysis. The general aspect of the membrane then is of a porous, hydrophobic resinous matrix containing water and studded with hydrophilic charge sites.

Cross-linked resins sometimes exhibit a sieve effect, that is to say they mechanically exclude ions too large to pass through the available distribution of hole sizes [see Chap. 5 of Helfferich (1)]. Large ions such as $CH_3(CH_2)_2NH_3^+$, $(C_2H_5)_4N^+$, and $(CH_3)_3N(CH_2\phi)^+$ are mobile in the present membranes from which the conclusion can be drawn that there is an ample number of moderately large passages, *i.e.*, with diameters in excess of about 10Å. The "mesh width" of organic ion exchange resins ranges on the average from a few to about 100Å depending on the extent of cross-linking (1), and, inasmuch as the extent of cross-linking in a given membrane is highly variable, these numbers probably can be taken to represent the limits of pore sizes in a membrane. However, movement of species in the internal solution of the resin is not totally without mechanical restraint, thus water transport is markedly higher at low current densities (2) where the ions travel with accompanying water through the larger pores than at high current densities where the ions are forced through the smaller pores as well (3).

The membranes are roughly 30% water by weight. The water content (Table I) shows little dependence on the nature of the mobile ions present. But the water content of the anion permeable membrane appears to be consistently lower than that of the cation permeable membranes. Inasmuch as the relative water content of the cation-*vs.* anion-permeable membranes is just the opposite of what one would expect on the basis of hydration considerations, the difference is probably due to differences in the microgeometry of the two types of membranes and to the greater sul-

* Electrochemical Society Active Member.
[1] Present address: Woods Hole Oceanographic Institution, Woods Hole, Massachusetts.
[2] Present address: P. R. Mallory & Co., Burlington, Massachusetts.

Table I. Water content of ion permeable membranes

Ionic form of membrane	% by Weight of water, mean value
Nepton CR-61	
Li^+	36.9
Na^+	36.5
K^+	35.7
Rb^+	32.2
Cs^+	32.7
NH_4^+	36.0
Tl^+	37.8
Mg^{++}	35.5
Ca^{++}	35.2
Sr^{++}	32.8
Ba^{++}	32.8
La^{+++}	32.5
Nepton AR-110	
F^-	33.8
Cl^-	29.8
Br^-	32.7
I^-	31.2
NO_3^-	30.4
ClO_4^-	30.4
PF_6^-	28.9
$CO_3^=$	25.4
$SO_4^=$	30.2
$Fe(CN)_6^{\equiv}$	29.4

fonate concentration in the cation-permeable membrane than quaternary ammonium concentration in the anion-permeable membrane. The dehydration procedure was a mild one, drying to a constant weight at 110°C; hence these values probably represent only the water held weakly in the membrane. Characteristically colored hydrated ions, such as $Cu(H_2O)_4^{++}$, do not lose their coloration in the membrane on drying by this method; hence they must retain at least some of their waters of hydration. Similarly infrared studies on "dried" membranes in the La^{+++} form revealed quantities of water left. Then too, the membrane itself may retain some of its hydration crust.

The capacity of the cation-permeable membranes is about 1.47 meq/g (wet resin in the Na^+ form) and of the anion-permeable membranes 0.650 meq/g (wet resin of the Cl^- form). Little is known concerning the spatial distribution of the charge sites in the membrane. If coulombic forces dominate when the charge sites are synthesized, one would expect a more or less even spacing in order to achieve maximum charge separation; however, if hydrophobic forces are important, a clustering of charge sites would result. Furthermore the polymer condensation process results in considerable inhomogeneity of the degree of cross-linking, and this in turn also tends to concentrate the charge sites in clusters. The bulk of available evidence indicates that charge sites are usually very unevenly spaced (1). A crude estimate based on the capacities would indicate that on the average the distance between charge sites is of the order of magnitude of 10Å.

In order to avoid electrolyte invasion, in all of the measurements described here, unless otherwise stated, the concentration of the external solution was kept at 0.01*N*. To preserve electrical neutrality the concentration of the mobile ion in the internal solution is determined by the number of oppositely charged sites in the membrane and can therefore be calculated from the membrane's capacity and water content. The concentrations of mobile ions in the internal solution in the membranes thus calculated are about 4 and 2*N* for the cation-permeable and anion-permeable membranes, respectively.

As the concentration of the external solution is increased above 0.05*N*, invasion of the membrane by both ions of the external electrolyte commences. The internal electrolyte concentration becomes roughly proportional to the external concentration, and the proportionality factor increases as the charge of the ion increases, that is to say, the higher the charge of the ion the more readily it invades the membrane (Fig. 1).

Experimental Results

The major part of the experimental effort in the present studies was devoted to the measurement of

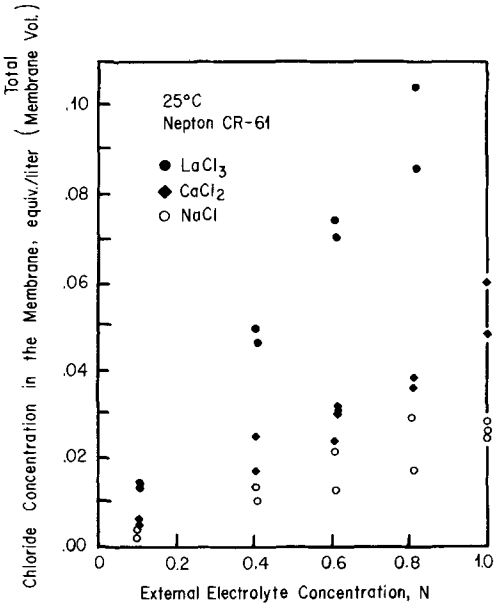

Fig. 1. Invasion of a cation-permeable membrane

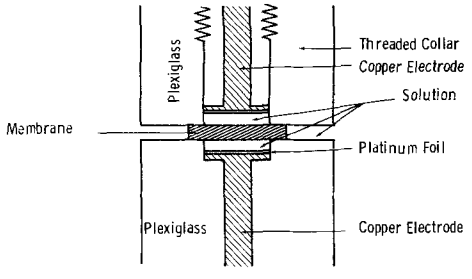

Fig. 2. Membrane conductivity cell

the electrical conductivity of cation- and anion-permeable membranes containing different mobile ions. The conductivity cell used is shown in Fig. 2 with a membrane in place. The electrodes in the cell are parallel disks of platinized platinum. The equivalent circuit of the cell has been discussed by Feates, Ives, and Pryor (4), while further experimental details were given in a previous paper (2). Table II summarizes measured conductivities of the membranes containing

Table II. Electrical conductivities and activation energies of conductance of membranes containing different simple inorganic cations and anions at 25°C

Ion	λ_m, $cm^2\ ohm^{-1}$	λ°_s, $cm^2\ ohm^{-1}$	$E_{a,m}$, kcal/mole	$E^\circ_{a,s}$, kcal/mole	$\lambda^\circ_s/\lambda_m$
Nepton CR-61					
Li^+	2.19[a]	38.68[b]	5.46	4.13	17.7
Na^+	2.82[a]	50.10[b]	5.39	3.87	17.8
K^+	5.31[a]	73 50[b]	3.69	3.47	13.8
Rb^+	3.81[a]	77.81[b]	4.09	3.38	20.4
Cs^+	1.86[a]	77.26[b]	4.15	3.33	41.6
NH_4^+	5.32[a]	73.55[b]	4.69	3.86	13.8
Tl^+	3.04[a]	—	4.73	—	—
Mg^{+2}	0.69[a]	53.05[b]	4.87	3.92	77.0
Ca^{+2}	0.99[a]	59.50[b]	4.46	3.92	60.0
Sr^{+2}	0.84[a]	59.45[b]	4 82	4.04	71.0
Ba^{+2}	0.75[a]	63.63[b]	4.80	4.23	85.0
La^{+3}	0.22[a]	69.75[b]	4.00	4.64	317.0
Nepton AR-110					
F^-	6.40	55.40[b]	4.21	—	8.7
Cl^-	5.62	76.35[b]	4.56	3.57	13.6
Br^-	3.84	78.14[b]	5.30	3.54	20.4
I^-	1.85	76.84[b]	5.55	3.28	41.4
NO_3^-	4.28	71.46[b]	5.25	3.28	16.7
ClO_4^-	1.00	67.36[b]	6.70	3.35	67.4
PF_6^-	0.50	—	4.90	—	—
$CO_3^=$	4.68	—	5.90	—	—
$SO_4^=$	3.90	80.02[b]	5.10	3.90	20.5
$Fe(CN)_6^{\equiv}$	0.11	—	4.90	—	—

[a] From ref (2).
[b] From ref (5).

different mobile ions, λ_m. Also included in Table II are the limiting ionic conductivities of the ions in free solution λ^o_s and the Arrhenius activation energies in the membrane, $E_{a,m}$ calculated from data at 10°, 25°, and 40°C and for the free solution $E^o_{a,s}$ calculated from literature values of λ^o_s.

In order to test for any intrinsic tendency on the part of the species present in the membranes to form ion-pairs, conductivity measurements were made on the following systems which represented solution analogues of the membranes:

SOLUTION ANALOGUES OF THE CATION PERMEABLE MEMBRANE

Li^+
Na^+
K^+
H^+
Mg^{++}
Ca^{++}
Ba^{++}
La^{+++}

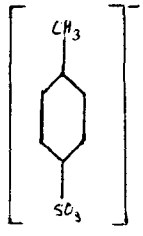

p-toluenesulfonate (PTS)

SOLUTION ANALOGUES OF THE ANION-PERMEABLE MEMBRANE

Cl^-
I^-
$SO_4^=$

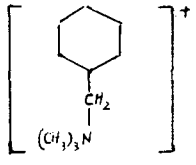

benzyltrimethylammonium (BTMA)

These measurements were made on solutions of concentration ranging from 0.001 to 2.5*N* at 10°, 25°, and 40°C. Some typical plots of the conductance *vs.* the square root of the concentration are shown in Fig. 3, while Table III summarizes measured conductivities and calculates activation energies of conductance of these systems.

The membrane conductivity studies were extended to embrace several series of more complex organic cations and anions and a few ammoniated metallic cations as mobile ions and the results are summarized in Table IV, while the results of studies on mixed electrolyte systems are presented in Fig. 4 and 5.

Table V summarizes the results of water transport measurements in the membranes at three different temperatures. The details of the experimental procedure have been described previously (2).

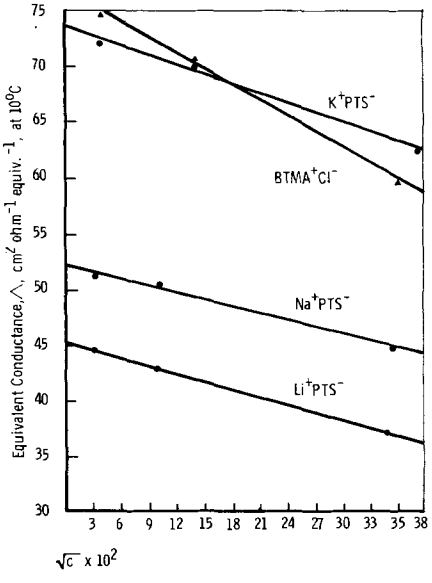

Fig. 3. Concentration dependence of the equivalent conductances of membrane analogue solutions.

Table III. Equivalent conductivity (Λ) and Arrhenius activation energies of conductivity (E_a) of membrane-analogue solutions

Ion	$\Lambda_{10°C}$ cm² ohm⁻¹ eqv⁻¹	$\Lambda_{25°C}$ cm² ohm⁻¹ eqv⁻¹	$\Lambda_{45°C}$ cm² ohm⁻¹ eqv⁻¹	E_a, kcal/mole
p-toluenesulfonates (PTS)				
1.77N H^+	132.5	172.5	211.0	2.4
1.77N Li^+	14.6	22.5	31.0	4.1
1.77N Na^+	20.9	32.0	43.0	3.8
1.77N K^+	35.0	49.1	68.0	3.5
1.77N Mg^{++}		28.4		4.3
1.77N Ca^{++}		24.2		3.6
1.77N Ba^{++}*		23.0		6.1
1.77N La^{+3}*	12.0	16.0	23.0	7.3
benzyltrimethylammonium (BTMA) salts				
0.65N Cl^-	43.0	59.6	72.0	4.2
0.65N I^-		48.0		4.0
0.65N $SO_4^=$		57.8		4.0

* Extrapolated values.

Table IV. Equivalent conductivities of membranes in various ionic forms

Ion	Λ_m cm² ohm⁻¹ equiv⁻¹	$E_{a,m}$ kcal/mole
Nepton CR-61		
$(CH_3)_4N^+$	1.42	—
$(CH_3)NH_3^+$	0.73	—
$(C_2H_5)_4N^+$	0.76	—
$(CH_3)_3N(CH_2-\phi)^+$	0.36	—
1.44*N** n-$C_5H_7NH_3^+$	0.98	6.36
1.42*N* n-$C_4H_9NH_3^+$	0.65	—
1.43*N* n-$C_5H_4NH_3^+$	0.39	—
1.45*N* $^+H_3N(CH_2)_2NH_3^+$	1.59	4.73
1.45*N* $^+H_3N(CH_2)_3NH_3^+$	1.33	—
1.45*N* $^+H_3N(CH_2)_4NH_3^+$	0.93	—
$Cu(H_2O)_4^{++}$	1.19	5.49
$Cu(NH_3)_4^{++}$	0.76	3.89
$Cr(H_2O)_6^{+++}$	0.32	5.13
1.49*N* $Cr(NH_3)_6^{+++}$	0.18	4.50
1.49*N* $Co(NH_3)_6^{+++}$	0.31	9.78
Nepton AR-110		
1.04*N* CH_3COO^-	1.66	6.27
1.04*N* $C_2H_5COO^-$	1.39	—
1.05*N* $C_3H_7COO^-$	1.03	—
1.03*N* $^-OOC\ COO^-$	1.63	5.49
1.04*N* $^-OOC\ CH_2COO^-$	1.34	—
1.04*N* $^-OOC(CH_2)_2COO^-$	1.11	—

* Concentrations are in equiv. per liter of membrane including the organic matrix and the Fiberglas backing material, and solution.

Discussion

The results in Table II present a number of interesting features. The two most striking of these are the great reduction of ionic mobility in the internal as compared to the external solution (last column)

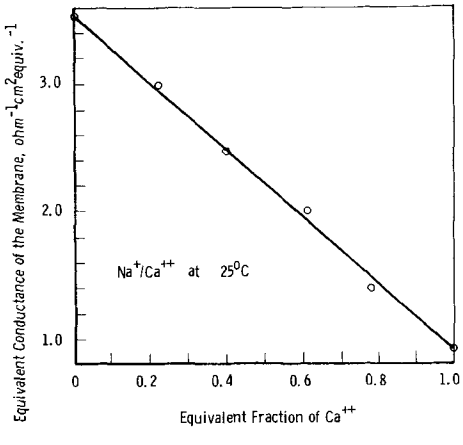

Fig. 4. Conductivity mixture effect in a cation-permeable membrane at 25°C for the system Na^+/Ca^{++}.

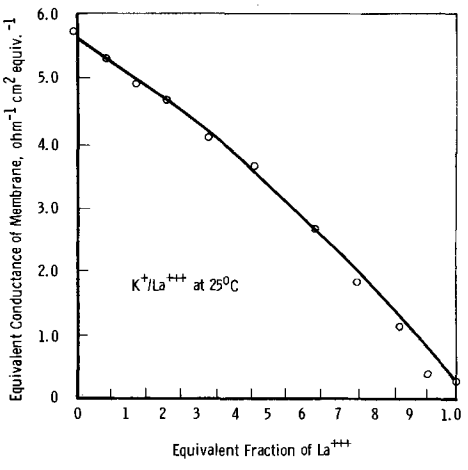

Fig. 5. Conductivity mixture effect in a cation-permeable membrane at 25°C for the system K^+/La^{+3}.

and the strong dependence of cationic mobility in the membrane on charge type. The strong charge dependence has been reported earlier by Heymann and O'Donnell (6), Rosenberg, George, and Potter (7), Spiegler and Coryell (8), and Grubb (9) and is in strong contrast with the free solution where the increase in hydration with increasing charge type tends to compensate for ion size and charge type, and results in surprisingly little variation in conductivities among different ions. The value of λ_m for anions shows no charge dependency and is more variable within a charge type than among charge types. In the case of the halide anions, however, there is a regular decrease in their mobility in the membrane with increasing ion size (crystal radius) and there is also, as might be expected, a regular increase in $E_{a,m}$, the Arrhenius activation energy of conductivity in the membrane. The ratio of the limiting conductivity of the mobile ion in free solution to the conductivity of the membrane containing that ion, λ^o_s/λ_m. is perhaps even more interesting: the value of this ratio is very nearly the same for all monovalent ions, both cations and anions, and for $SO_4^=$, falling in the range of about 14-20. The anions which do not obey this rule, F^-, I^-, and ClO_4^- are all anions which are notoriously eccentric in aqueous solution. presumably because of their peculiar effects on water structure. The only cationic exception to the rule, Cs^+, curiously enough has the same value of λ_s/λ_m as isoelectronic (and also anomalous) I^-, although this could be fortuitous. The doubly charged

Table V. Water transport

Ionic form of membrane	Water transfer, mole/Faraday		
	10°C	25°C	40°C
In Nepton CR-61 (0.2 mA/cm²)[a]			
Ni^+	20.6	16.9 (22)	17.1
Na^+	13.3	14.0 (13)	13.8
K^+	10.7	10.1 (7)	9.7
Rb^+	7.9	7.7	8.1
Cs^+	8.9	8.5 (6)	6.6
NH_4^+	14.4	12.5	14.8
Tl^{+2}	16.4	11.5	6.4
Mg^{+2}	5.5	3.5 (36)	2.5
Ca^{+2}	7.2	6.8	6.4
Sr^{+2}	6.3	4.8 (29)	3.2
Ba^{+2}	5.4	4.5	3.1
La^{+3}	3.9	2.3	2.0
In Nepton AR-110 (0.7 mA/cm²)			
F^-	12.4	11.0 (7)	8.8
Cl^-	5.7	7.3 (5)	6.0
Br^-	5.2	7.0 (5)	4.8
I^-	11.9	11.3	9.7
ClO_4^-	5.0	6.5	7.9
NO_3^-	5.3	4.9 (6)	5.2
PF_6^-	8.3	11.4	11.5
$CO_3^=$	5.5	6.3	6.7
$SO_4^=$	3.3	3.0 (12)	3.4
$Fe(CN)_6^{\equiv}$	−9.4	−10.2	−11.9

[a] From ref. (2).

cations form a second family of similar λ^o_s/λ_m ratios. the value in this instance ranging from 60 to 85. To generalize, the values of λ^o_s/λ_m fall into the ranges of approximately 20.70:300 for singly, doubly, and triply charged cations.

Few systematic tendencies are evident in the activation energies of conductivity in the membrane. The $E_{a,m}$'s for conductivity in anion-permeable membranes tend to be in the majority of cases higher than for cation-permeable membranes, and this probably reflects differences in the mobile ions. As expected, save for a single exception, La^{+3}, the activation energy of conductance in the membrane is always higher than for the mobile ion in free solution. Inasmuch as E_a in free solution tends to decrease with increasing electrolyte concentration (10), the differences between the membrane and a free solution of comparable electrolyte concentration may be even greater.

A comparison of the results in Table II with those in Table III is also revealing. In the case of the monovalent ions the E_a's of the conductivity of the solution analogues of the membrane (Table III) fall between those of the membrane and of the ion in infinitely dilute free solution for both anions and cations. Mg^{++} and $SO_4^=$ are also intermediate. E_a for Ca^{++} PTS falls below the value of $E^o_{a,s}$, while the E_a's for Ba^{++}PTS and La^{+3}PTS fall very appreciably above both the corresponding $E_{a,m}$ and $E^o_{a,s}$. For the PTS solutions λ increases in going from Li^+ to Na^+ to K^+ (Table III) just as it did in the case of the membrane systems (Table II), and in all cases the value for the membrane analogue solutions is intermediate between λ_m and λ^o_s. E_a decreases with decreasing radius of the hydrated ion as expected. Heavily hydrated La^{+3} has a low Λ and a high E_a. Hydration increases with charge type; hence Λ decreases as E_a increases with increasing charge on the ion. Both Λ and especially E_a for BTMA salts show little systematic dependence on the nature of the anion.

Ion pair formation in the internal solution is commonly evoked in order to account for the observed differences between ionic mobilities in resins and in free solution. However, dilute solutions of each of the resin-analogue systems studied obeyed the Onsager limiting law (11), that is to say, plots of equivalent conductivity *vs.* the square root of the concentration were linear in the dilute solution range (Fig. 3). On the basis of this linearity, the conclusion can be drawn that none of the two ion systems examined showed any evidence for appreciable association in free aqueous solution, and from this, inasmuch as, apart from electrolyte concentration effects, there is no good reason for supposing that the dielectric constant is different in the internal than in the external solution, we can further conclude that these studies have given no reason for supposing that there is appreciable ion pair formation in the analogous resin systems. The strong dependence of Donnan exclusion on charge type is thus the consequence of ion field interaction rather than enhanced mobile ion-fixed ion association.

The classical theory of ionic conductivity takes as its model a charged sphere moving through a viscous continuum. As the concentration of electrolyte increases, the ions cease to move independently of one another, and the ion-ion interactions give rise to what is in effect a drag that reduces ion mobility. Hence conductivity equations such as the Onsager-Fuoss equation take the form of the limiting conductance Λ^o, minus subtractive terms for the drag effects.

$$\Lambda = \Lambda^o - (\phi_E + \phi_R)\sqrt{I} \qquad [1]$$

where I is the ionic strength, a concentration dependent parameter. In free aqueous solutions the first subtractive term, ϕ_E, represents the electrophoretic effect, the fact that an ion is moving, not in a stationary medium, but in a medium that is moving as a consequence of the motion (in the opposite direction) of

the waters surrounding the oppositely charge ions. Inasmuch as the charge sites in the membrane are more or less fixed, the movement of the mobile ion in the membrane should not be reduced by this phenomenon, unlike free solution. On the other hand, one might expect the relaxation effect, ϕ_R, to be more important in the membrane than in free solution. This drag effect arises from the restoring force when an ion is displaced in the coulombic field represented by its environment. In the membrane, because of the fixed locations of the charge sites, this field should be more resistant to alteration by the displaced ion than in free solution.

Meares (12) has derived a theoretical expression for the conductivities of ions in resins by consideration of the electrophoretic and relaxation effects. In the case of a resin, unlike free solution, the solvent flow is in the same direction as the movement of mobile ions, and the two effects are opposite. Here we wish to present a closely related but alternative analysis. We prefer to take the view that the immobility of the fixed charge site on the resin matrix makes the electrophoretic effect (ϕ_E in Eq. [1]) negligible[3] and the relaxation effect (ϕ_R) more important, and that the increased relaxational drag and the tightening of water structure in the membrane are the two principal factors responsible for the observed great reduction of ionic mobilities in the membrane as compared to free solution. Therefore, for membranes Eq. [1] can be rewritten

$$\Lambda_m = \Lambda^o_s/A_1 - \phi_{R,m}\sqrt{I} \qquad [2]$$

Since only the mobile ion contributes to the conductivity in the membrane λ^o_s is for the mobile ion only. The constant A_1 is a factor representing the reduction of species mobility by the "abnormal" water structure in the internal solution of the membrane and its value is probably in the neighborhood of 10. Also contained in A_1 is the "dilution" of the resin by the volume occupied by the nonconductive organic matrix. In free solution the relaxation term is given by (5)

$$\phi_{r,s} = \frac{2.8 \times 10^6 |z_1 z_2| q\, \lambda^o_s}{(\epsilon T^{3/2})(1 + \sqrt{q})} \qquad [3]$$

where q is $[|z_1z_2|/|z_1| + |z_2|]\ [(\lambda^o_1 + \lambda^o_2)/(|z_2|\lambda^o_1 + |z_1|\lambda^o_2)]$. Taking the charge of the resin, z_2, to be unity and its conductive parameters to be zero, we arrive at the following approximate expression for relating membrane conductivities to the charge of the mobile ion

$$\Lambda_m = \frac{\lambda^o_s}{10} - A_2 z_1 \sqrt{C(1 + z_1)/2} \qquad [4]$$

where z_1 is the charge of the mobile ion and C is its concentration (about $4N$ in the present case). Using the values in Table II we estimate that A_2 is somewhere in the range 0.8 to 1.2. The value of A_2 in free solution (25°C, $\epsilon = 78$) is 0.785[5] but inasmuch as A_2 contains $\epsilon^{-3/2}$ we expect this constant's value to be higher in the highly concentrated internal solution of the membrane. Thus an equation containing only a water structure factor and a relaxational term enables the semiquantitative estimation of the conductivity of mobile cations of any charge in a cation permeable membrane from the limiting conductivity of the cation in free solution. The calculated values for Λ_m, using $A_1 = 10$ and $A_2 = 1.1$, are 1.7, 2.8, 5.2, 5.6, 5.5, 5.2, 0.03, 0.67, 1.08, and negative [*sic*] for Li^+, Na^+, K^+, Rb^+, Cs^+, NH_4^+, Mg^{++}, Ca^{++}, Sr^{++}, Ba^{++}, and La^{+3}, respectively. Agreement with the observed values in Table II is good for monovalent ions and fair for divalent ions, but more important, Eq. [4] gives the right range of values for singly, doubly, and triply charged cations.

An expression of the form of Eq. [4] is not applicable to the conductivities of anions in anion-permeable membranes for they, as we have seen, exhibit no systematic charge dependency. In the case of anions, size, rather than charge, is clearly the important variable. For the smaller anions a structural retardation factor of a magnitude of 10-15 is still very much in evidence, but as the ion gets as large as Br^- or greater the retardation becomes even more severe as evidenced both by retardation factors of 20 and greater and higher energies of activation. Even more important, the relaxation term has ceased to be significant. This could be due to either the membrane or the mobile ion. The charge sites in cation-permeable membranes are coulombically hydrated whereas those in anion-permeable membranes with their CH_3 groups are hydrophobically hydrated. Generally speaking anions in free solution are less hydrated than cations, *i.e.*, anions interact coulombically more weakly with their environment. One reason for this is that their charge densities tend to be lower. Furthermore it is difficult to increase the charge on an anion without also increasing its size. Polyvalent anions stable in aqueous solutions are for the most part also polyatomic. This increase in size tends to diminish the effect of the increased charge so that anion charge densities are not as variable with charge type as cationic charge densities. The weakened capacity for coulombic interactions in the case of anions could very well greatly diminish the relative importance of the relaxation term.

Of particular current interest is the structural retardation factor, constant A_1 in Eq. [2]. Transport processes in clay minerals are retarded in a manner quite parallel to the present synthetic organic ion exchange materials; the activation energies are increased (and there is little ion-clay interaction contribution) and the apparent viscosity of the internal solution is anomalously high, and these observations have been attributed to a structuring of the water near the mineral surfaces (13, 14). Figure 6 compares schematically the probable differences in water structure in the internal and external solutions. Recently a new water form, "orthowater" has been discovered (15, 16) which reportedly has a viscosity 10 to 15 times that of "normal" water, in very good agreement with the present value of A_1. Whether orthowater and vicinal water (as in the resin) are synonymous or whether the former is peculiar to silica surfaces, which may catalyze its formation, remains to be seen (17).

It might also be noted that the diffusion of Na^+ in a Nepton membrane is 10 times slower than in free, dilute solution (8, 18).

The conductivities of tetra-alkylammonium cations, except for $(CH_3)_4N^+$ whose hydration still has considerable coulombic character (19), are very much lower than those of the simple monovalent ions in Table II; in fact, in the larger members of the series such as $(CH_3)N\text{-}CH_2\phi$ and $n\text{-}C_5H_{11}NH_3^+$ the values are comparable to those for triply-charged inorganic ions (Table II and IV). In addition to the importance

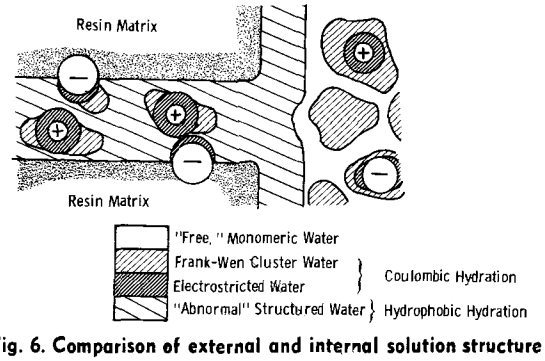

Fig. 6. Comparison of external and internal solution structure

[3] While the fixity of one ion makes the electrophoretic contribution to conduction (*i.e.*, the retardation of the movement of one ion by the oppositely directed movement of the solvent accompanying the second moving oppositely charged ion) negligible, it does not preclude the electrophoretic transport of solvent by the other moving and oppositely charged ion.

of ionic size, hydrophobic hydration may appreciably reduce the mobility of species in the internal solution, an hypothesis supported by the observation that, if these substances are made less hydrophobic by the addition of a second hydrophilic charge group, the conductivity increases so that, although doubly charged simple cations are less conductive than singly charged ones (Table IV), doubly charged diamine cations are much more conductive than isoelectronic singly charged monamines (Table IV) and the activation energies correspondingly lower. Within a given series the conductivity of the membrane decreases with increasing size of the mobile ion as expected.

In free solution the relatively high λ^{o}_{s} of $Co(NH_3)_6^{+++}$ (20) compared to La^{+3} (21) can be attributed to the weaker interaction of the former ion with the surrounding water. In the membrane the situation is reversed, and in the case of Cu(II) and Cr(III) the ammoniated cation is less mobile than the hydrated cation although paradoxically, the $E_{a,m}$'s are lower (Table IV). The reason for these abnormalities is not clear. The possibility of hydrolysis of these trivalent cations in the membrane casts severe doubt on the reality of the values. It is, however, reassuring to note that Λ_m for the trivalent ions of Co and Cr are comparable to the value listed in Table II for La^{+3}.

As before, the organic anions appear on the whole to be more mobile in the membrane than comparable cations, and again the differences between charge types, so obvious in the case of cations, has largely disappeared. The values of Λ_m tend to be lower than for simple anions (Table II) and decrease, as expected, with increasing size.

Mixed electrolytes.—In free aqueous solutions containing more than one electrolyte there are detectable deviations from the Kohlrausch principle of independent ionic mobilities and this "mixture effect" becomes more marked the greater the difference in the mobilities of the like-charged ions. For cations with a common anion Longsworth (22) has shown that the phenomenon depends only on the cations. Horne and Courant (23) have studied the effect of hydrostatic pressure on the mixture effect in free solution, and Mackay and Meares (24) examined the mixture effect for the system Na^+/H^+ in cation-permeable resin at 1 atm. Theoretical analysis of the conductivity of mixed electrolytic solutions (25, 26) predicts a mixture effect arising from the relaxation term. In the light of the apparent importance of relaxation in the internal solution of a membrane in determining ionic mobilities (see above), the conductivity of the asymmetrical systems Na^+/Ca^{++} and K^+/La^{+3} in Nepton CR-61 was examined. For their symmetrical system Na^+/H^+ Mackay and Meares (24) found a downward deviation from linearity, whereas the present results indicate that the Na^+/Ca^{++} system gives a nearly linear dependence of conductance on ionic composition (Fig. 4) and the K^+/La^{+3} system gives an upward deviation from linearity (Fig. 5).

The paper of Mackay and Meares (24), in addition to the mixture effect measurements, is of interest inasmuch as it contains two conclusions very similar to two of the crucial points that have emerged from the present study, namely that (*i*) specific ion pair and ionic association-type interactions are of minor importance, and (*ii*) the effective viscosity in the internal solution is anomalously high.

Water transport.—The question of how much of its hydration atmosphere a moving ion carries with it is of particular significance in desalination technology because the more water the solute transfers, the more difficult will be the separation of solute and solvent.

An ion moving in the internal solution of the membrane carries with it the more tightly bound electrostricted waters of hydration. The primary hydration number is not significantly different in the membrane than in free solution (3rd and 2nd columns, respectively, in Table VI). In addition it may also retain further waters of its total hydration atmosphere. If it is a large ion, water may also be transported as the result of ionic movement by entrainment in the ion's wake and/or by being pushed along the membrane passages in front of the moving ion.

Table VI. Primary hydration numbers of cations in an infinitely swollen sulfonated styrene-type cation exchange resin

[From E. Glueckauf and G. P. Pitt, *Proc. Roy. Soc.* (London), A228, 322 (1955)]

Ion	Hydration Number	
H^+	3.9	4
Li^+	3.3	2-6
Na^+	1.5	2-5
K^+	0.6	1-4
Cs^+	0	0-4
NH_4^+	0.4	0-2
Be^{++}	7.0	4
Mg^{++}	7.0	4-12
Ca^{++}	5.2	4-8
Sr^{++}	4.7	4-10
Ba^{++}	2.0	3-5
Hg^{++}	4.5	5

Even though measurements were made at different current densities, the anions for the most part appear to transport less water than the cations (Table V) which is compatible with the generally greater hydration of cations. Except for Li^+, which is the most heavily hydrated of the alkali metal cations and Rb^+ and Cs^+, the amounts of water carried by all of the ions (multiplying the values of the multicharged ions by their charge) are remarkably similar. Among the anions, F^-, I^-, PF_6^-, and $Fe(CN)_6^{\equiv}$ appear to be exceptional. The hydration of F^- is considerably greater than that of its sister halides, hence the sizable number of waters it transfers is no surprise. Iodide ion, however, is at best only very weakly hydrated. It and PF_6^- may be sufficiently large to transport appreciable water by entrainment or pumping. The present experiments give little quantitative indication of the relative amounts of this electro-osmotic water and water of hydration. The qualitative expectation might be that for smaller ions the latter dominates and for larger ions the former becomes important. However, the situation is complicated by the fact that the most heavily hydrated ions are also commonly the largest. Electro-osmotic water transfer may tend to compensate for hydrated water sheared away as the ions press through the smaller passages.

The water transport value for $Fe(CN)_6^{\equiv}$ is negative, that is to say, the water moves in the direction opposite to that of the anion. This trivalent ion is taken up so strongly by the resin that it converts the membrane from an anion to a cation exchanger analogous to the conversion of a cation to an anion exchanger by Th(IV) complex ions (7) and of an anion exchanger to a cation exchanger by the absorption of oxalate (27). Values in Table V on the right are hydration numbers determined from membrane transport experiments by Rutgers and Hendrikx (28). Agreement is very good in the case of monovalent ions of both types, but they obtained values much higher than the present ones for divalent ions.

Figure 7 compares the temperature dependence of the number of water molecules transported by the alkali metal cations with the number of molecules of water in their total hydration atmospheres in free solution (29). The conclusions that can be drawn from this comparison are: (*i*) the ions in the membrane transport more water molecules than their primary hydration number (tightly bound electrostricted water) but less than their total hydration atmosphere in free solution; (*ii*) inasmuch as Li^+, the most heavily hydrated cation, retains more of its less strongly bound waters in the membrane its water transport has the largest temperature dependence. The other ions, being already stripped of many of their less strongly

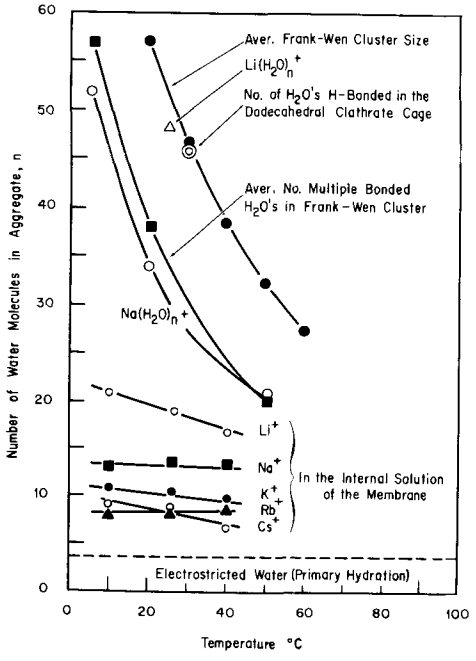

Fig. 7. Comparison of the water transport in the membrane with the total hydration atmosphere of the ions in free solution.

bound waters in the membrane, do not so readily lose further water molecules with increasing temperature.

Acknowledgment

This work was supported in part by the Office of Saline Water, U. S. Department of Interior, Contract No. 14-01-001-962.

Manuscript submitted July 11, 1968; revised manuscript received Jan. 17, 1970. This was Paper 249 presented at the Boston Meeting of the Society, May 5-9, 1968.

Any discussion of this paper will appear in a Discussion Section to be published in the June 1971 JOURNAL.

REFERENCES

1. F. Helfferich, "Ion Exchange," McGraw-Hill Book Co., Inc., New York (1962).
2. J. H. B. George and R. A. Courant, *J. Phys. Chem.*, **71**, 246 (1967)
3. L. Lakshminarayanaiah, *Proc. Indian Acad. Sci.*, **A55**, 200 (1962).
4. F. S. Feates, D. J. G. Ives, and J. H. Pryor, *This Journal*, **103**, 580 (1956).
5. R. A. Robinson and R. H. Stokes, "Electrolyte Solutions," 2nd ed., Butterworths Inc., London (1959).
6. E. Heymann and I. J. O'Donnell, *J. Colloid. Sci.*, **4**, 395 (1949).
7. N. W. Rosenberg, J. H. B. George, and W. D. Porter, *This Journal*, **104**, 111 (1957).
8. K. S. Spiegler and C. D. Coryell, *J. Phys. Chem.*, **57**, 687 (1953).
9. W. T. Grubb, *ibid.*, **63**, 55 (1959).
10. R. A. Horne, *Water Resources Res.*, **1**, 263 (1965).
11. L. Onsager, *Phys. Z.*, **28**, 277 (1927).
12. P. Meares, *J. Polymer Sci.*, **20**, 507 (1956).
13. G. R. Dutt and P. F. Low, *Soil Sci.*, **93**, 195 (1962).
14. R. S. Mokady and P. R. Low, *ibid.*, **105**, 112 (1968)
15. B. V. Deryagin, *Discussion Faraday Soc.*, **42**, 109 (1966).
16. E. R. Lippincott, R. R. Stromberg, W. H. Grant, and G. L. Cessac, *Science*, **164**, 1482 (1969).
17. R. W. Bolander, J. L. Kassner, Jr., and J. T. Zung, *Nature*, **221**, 1233 (1969).
18. D. Richman and H. C. Thomas, *J. Phys. Chem.*, **60**, 237 (1956).
19. R. A. Horne and R. P. Young, *ibid.*, **72**, 1763 (1968).
20. G. S. Hartley and G. W. Donaldson, *Trans. Faraday Soc.*, **33**, 457 (1937).
21. P. N. Spedding, P. E. Porter, and J. M. Wright, *J. Am. Chem. Soc.*, **74**, 2055 (1952).
22. L. G. Longsworth, *ibid.*, **52**, 1897 (1930).
23. R. A. Horne and R. A. Courant, *J. Chem. Soc., (London)*, **1964**, 3548.
24. D. Mackay and P. Meares, *Trans. Faraday Soc.*, **55**, 1221 (1959).
25. L. Onsager and R. M. Fuoss, *J. Phys. Chem.*, **36**, 2639 (1932).
26. L. Onsager and S. K. Kim, *ibid.*, **61**, 215, 1687 (1957)
27. R. A. Horne, R. H. Holm, and M. D. Meyers, *J. Phys. Chem.*, **61**, 1661 (1957).
28. A. J. Rutgers and Y. Hendrikx, *Trans. Faraday Soc.*, **58**, 2184 (1962).
29. R. A. Horne and J. D. Birkett, *Electrochim. Acta*, **12**, 1153 (1957).

Technical Notes

High Conductivity Solid Electrolyte System RbI-AgI

Boone B. Owens*[1] and Gary R. Argue*[2]

Atomics International, A Division of North American Rockwell Corporation, Canoga Park, California

There has been a considerable interest in solid electrolytes because of a large number of potential applications in electrochemical devices. However, such applications have been severely limited by the low conductivity of the available solid electrolytes (1). The conductivities of solid electrolytes at 25°C are in general many orders of magnitude smaller than those of electrolyte solutions, the former values being in the range of 10^{-12} to 10^{-6} (ohm-cm)$^{-1}$. Some progress has been reported in using compressed powders of AgI for which the observed specific conductivity at room temperature was of the order of 10^{-4} (ohm-cm)$^{-1}$ (2, 3). The conductivity of the solid electrolyte Ag_3SI at 25°C was reported to be 10^{-2} (ohm-cm)$^{-1}$ by Reuter and Hardel (4). Subsequent studies pertaining to the electrical conductivity and related devices of Ag_3SI were reported by Reuter and Hardel (5) and by Takahashi and Yamamoto (6-9).

The goal of obtaining solid electrolytes with conductivities (at ambient temperatures) comparable to those of electrolyte solutions was only recently accom-

* Electrochemical Society Active Member.
[1] Present address: Gould Ionics Inc., Canoga Park, California.
[2] Present address: General Telephone & Electronics Laboratories, Inc., Bayside, New York.

Key words: conductivity, $RbAg_4I_5$, rubidium iodide, silver iodide, solid electrolyte.

plished. The solid electrolytes MAg_4I_5 (M = K, Rb, NH_4, and to a limited extent Cs) were reported to have unusually high ionic conductivities (10, 11). The values reported for the electrical conductivities of these materials differ by a factor of two to four. For example, the conductivity at 20°C of KAg_4I_5 was reported to be 0.050 (10) and 0.21 (ohm-cm)$^{-1}$ (11). In the present investigation the conductivity of the RbI-AgI system was investigated in greater detail and, in particular, the conductivity of the intermediate compound $RbAg_4I_5$ was studied.

Experimental

The compounds and intermediate compositions were prepared by the combination reaction

$$RbI + nAgI \rightarrow RbAg_nI_{n+1} \quad [1]$$

where n is the ratio of moles AgI to moles RbI. The indicated product is a single phase at 165°C for n = 0, ½, 4, and ∞, as may be readily deduced from the phase diagram (10). Other values of n yield two-phase products, in accord with the phase diagram. The compositions in the product were readily identified by x-ray diffraction analysis.

Mallinckrodt AgI and Research Organic RbI (99.9%) were used without any further purification. The reactants were melted together and then quenched; this product was then gound, compacted, and annealed under an argon atmosphere at a temperature of 165°C for 16 hr. The pulverizing, compaction, and annealing were repeated once. The annealing permitted any unreacted material to form the desired product and was not carried out to sinter the product *per se*.

The conductivity cells were of the type Ag foil/Ag, $RbAg_4I_5$/electrolyte/Ag,$RbAg_4I_5$/Ag foil in which a ½ in. diameter pellet was clamped between two Ag foil contacts. As indicated above, the pellet consisted of three layers, the two outer layers serving as Ag/Ag^+ contacts to the central electrolyte sample. The electrodes were prepared from intimate mixtures of Ag and $RbAg_4I_5$ containing nominally 20 w/o (weight per cent) of $RbAg_4I_5$. These mixtures were prepared by the *in situ* reduction of Ag_2O in a carbon-$RbAg_4I_5$ matrix to yield the indicated electrode powder. A cell was fabricated from the powdered electrodes and electrolyte samples by placing a ¼g of electrode powder into a ½ in. die, spreading the electrode powder with the piston, adding the electrolyte powder (1-5g), again forming the powder into a right cylinder, and then adding another ¼g of the electrode powder to form the second contact. The powder was then pressed to approximately 10,000 lb to form the pellet cell.

The cells for the composition dependence of the electrical conductivity were fabricated and tested under ambient conditions. Resistance measurements were carried out at 22°C. However, the cells for the temperature dependence of the specific conductivity of $RbAg_4I_5$ were fabricated in a dry box, under Ar atmosphere. The cells were placed in a controlled atmosphere chamber in which the temperature could be regulated to ±2°C. Cell resistances were measured with a 1 kHz conductivity bridge (ESI, Model 250 DA).

The specific conductivity σ was calculated in the conventional manner, from the sample resistance (corrected for contact resistance) and the sample geometry (diameter and length of right cylinder). The bulk density of these $RbAg_4I_5$ pellets at 22°C is 5.30 g/cm^3 as compared to the x-ray density of 5.38 g/cm^3 (13). No correction was applied for the temperature variation of the cell constant.

Results and Discussion

The effect of composition upon the conductivity is shown in Fig. 1 in which σ is plotted *vs.* m/o (mole per cent) AgI. The maximum value of 0.26 (ohm-cm)$^{-1}$ occurs at 80 m/o AgI which is the composition of $RbAg_4I_5$; this demonstrates the usefulness of composition-conductivity curves for phase diagram or possibly solid-state reaction studies (12). Values of 2 x 10^{-4} (ohm-cm)$^{-1}$ were observed for AgI and less than 10^{-8} for RbI and Rb_2AgI_3. The intermediate compositions were polyphase and had the intermediate σ values shown in Fig. 1.

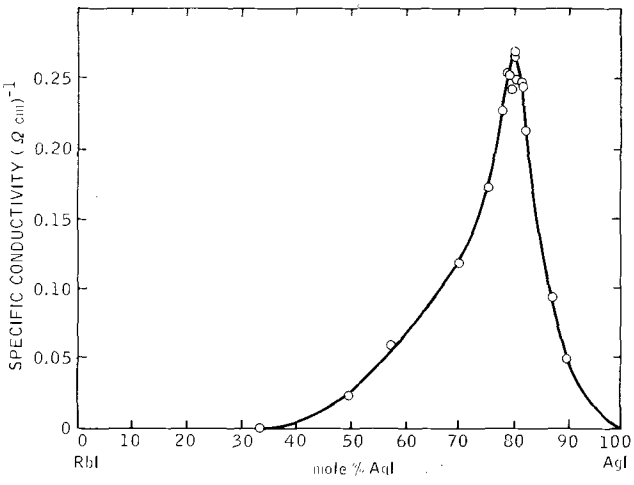

Fig. 1. Electrical conductivity of the system RbI-AgI at 22°C

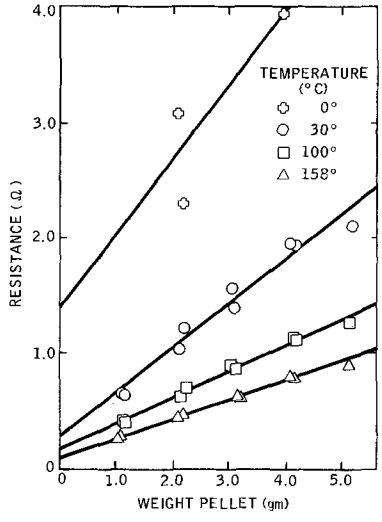

Fig. 2. Resistance of 1.27 cm diameter pressed powder pellets of $RbAg_4I_5$ as functions of sample weight.

The resistances of $RbAg_4I_5$ samples are shown in Fig. 2 for temperature values from 0° to 158°C. The contact resistance values reported in Table I are the intercepts of plots such as those shown in Fig. 2; from the slopes of these linear curves the values for the specific conductivities were calculated. The contact resistance increased considerably at the subambient temperatures, and there was greater scatter in the resistance values.

The Arrhenius plot of the specific conductivity is shown in Fig. 3. The plot is linear from 158° down to

Table I. Specific conductivity of $RbAg_4I_5$

T, °C	Contact resistance, ohm	Specific conductivity (ohm-cm)$^{-1}$
158	0.08	0.68
100	0.16	0.51
30	0.27	0.30
0	1.4	0.18
−55	3.4	0.087
−85	8	0.027

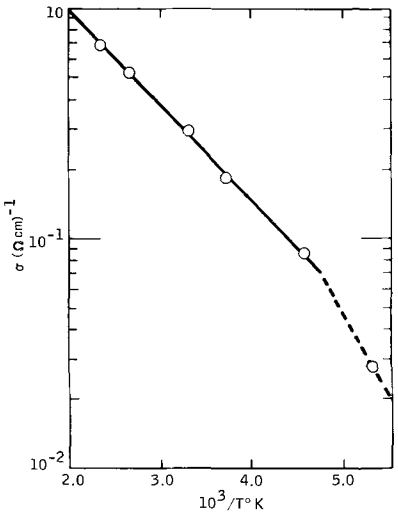

Fig. 3. Arrhenius plot of the electrical conductivity of $RbAg_4I_5$

−55°C; however, the −85°C value deviates from the linear curve. The Arrhenius activation energy for conduction is 1.7 kcal/mole over the temperature interval of at least 158° to −55°C. A low temperature reversible transition in $RbAg_4I_5$ has been observed by Geller (13); the transition temperature has been found to be −65°C, based on both optical measurements (14) and low-temperature calorimetry (15). However, no discontinuity in the conductivity was observed at this temperature although there is a conductance discontinuity at −155°C associated with a second reversible transition (11). The present conductivity values, when combined with prior results for lower temperatures, tentatively indicate that the solid phase existing between −65° and −155°C has an Arrhenius activation energy of 4 kcal/mole, with the approximate slope shown in Fig. 3 by the dashed line. The higher activation energy is associated with a structure in which the silver ions are in a more ordered state than in the highly disordered phase of $RbAg_4I_5$ existent at ambient temperatures (13, 15-17).

The mobile species in $RbAg_4I_5$ is the Ag^+ ion (18), and the low magnitude of the activation energy is consistent with the high ionic conductivity of the salt. The value of 1.7 kcal/mole is also in good agreement with the activation energy for the self-diffusion of Ag^+ ion in $RbAg_4I_5$; Bentle has reported the value of 1.99 kcal/mole (19).

The variations in the conductivity values previously reported for the MAg_4I_5 solid electrolytes (10, 11) are believed to be due to resistance contributions from the electrode contacts, as shown by the present investigation. In addition, the electrical conductivity of single crystal $RbAgI_5$ has been determined by Raleigh who observed a value of 0.268 $(ohm\text{-}cm)^{-1}$ at 24°C, with no orientation dependence (20). The value of σ at 24°C, based on the present investigation is 0.26 $(ohm\text{-}cm)^{-1}$, thus confirming the correlation of the high ionic conductivity of polycrystalline $RbAg_4I_5$ with the structure of the pure single crystal $RbAg_4I_5$ (12). The high mobility of the Ag^+ ion in $RbAg_4I_5$ is an intrinsic property of the pure crystal rather than a result of high surface mobility as has been suggested for powdered AgI (2, 3).

Acknowledgment

The authors wish to acknowledge the assistance of Mr. Louis D. Hermo who carried out many of the measurements.

Manuscript submitted Feb. 3, 1969; revised manuscript received March 6, 1970. This was Paper 280 presented at the Boston Meeting of the Society, May 5-9, 1968.

Any discussion of this paper will appear in a Discussion Section to be published in the June 1971 JOURNAL.

REFERENCES

1. J. N. Mrgudich, "Solid Electrolyte Batteries" in "The Encyclopedia of Electrochemistry," C. A. Hampel, Editor, p. 84, Reinhold Publishing Corp., New York (1964.)
2. J. N. Mrgudich, *This Journal*, **107**, 475 (1960).
3. J. N. Mrgudich, P. J. Bramhall, and J. J. Finnegan, IEEE Transactions on Aerospace and Electronic Systems, Vol. AES-1, No. 3, 290 (1965).
4. B. Reuter and K. Hardel, *Naturwiss.*, **48**, 161 (1961).
5. B. Reuter and K. Hardel, *Z. anorg. u allgem. Chem.*, **340**, 158 (1965).
6. T. Takahashi and O. Yamamoto, *Denki Kagaku*, **32**, 610 (1964).
7. T. Takahashi and O. Yamamoto, *ibid.*, **33**, 346 (1965).
8. T. Takahashi and O. Yamamoto, *Electrochim. Acta*, **11**, 779 (1966).
9. T. Takahashi and O. Yamamoto, *ibid.*, **11**, 911 (1966).
10. (a) J. N. Bradley and P. D. Greene, *Trans. Faraday Soc.*, **62**, 2069 (1966); (b) J. N. Bradley and P. D. Greene, *ibid.*, **63**, 425 (1967).
11. B. B. Owens and G. R. Argue, *Science*, **157**, 308 (1967).
12. J. N. Bradley and P. D. Greene, *Trans. Faraday Soc.*, **63**, 1023 (1967).
13. S. Geller, *Science*, **157**, 310 (1967).
14. S. Geller, Private communication (1967).
15. W. V. Johnston and G. W. Lindberg, Abstracts, 156th National Meeting of the American Chemical Society, Atlantic City, N. J. September 1968, No. PHYS 97.
16. H. Wiedersich and S. Geller, Proc. Inst. on "Chemistry of Extended Defects in Non-Metallic Solids," in press.
17. H. Wiedersich and W. V. Johnston, *J. Phys. Chem. Solids*, **30**, 475 (1969).
18. L. E. Topol and B. B. Owens, *J. Phys. Chem.*, **72**, 2106 (1968).
19. G. G. Bentle, *J. Appl. Phys.*, **39**, 4036 (1968).
20. D. O. Raleigh, *ibid.*, in press.

A Simple Apparatus for Controlling and Measuring Very Low Flow Rates through Porous Electrodes

A. P. Saunders

Institute for Direct Energy Conversion, University of Pennsylvania, Philadelphia, Pennsylvania

Steady-state electrochemical measurements at flow-through porous electrodes require a method of controlling and measuring flow rates which are often less than 10^{-2} ml/sec. A review of the literature failed to produce any information in this area and so a simple apparatus was devised (shown schematically in Fig. 1), based on a well-known method of obtaining a constant level, with which it is possible to maintain a constant (±1%) pressure behind the electrode, enabling mean flow rates through the electrode to be measured with

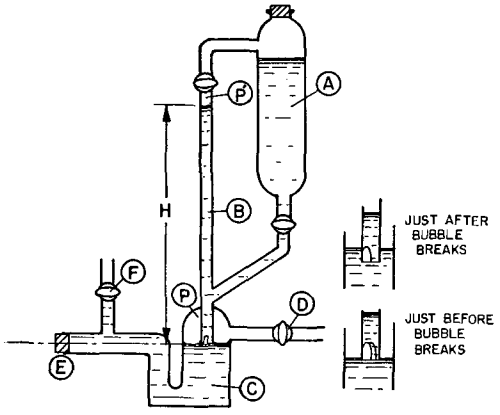

Fig. 1. Apparatus for controlling and measuring flow rates

a precision greater than 99%. A simple level controlling drain tube in the electrochemical cell (not shown) establishes a constant pressure drop across the electrode.

The apparatus, made of Pyrex glass, consists of an electrolyte reservoir (A), communicating via two Teflon stopcocks to an 0.8 cm ID calibrated precision bore tube (B), the bottom of which is notched and projects into the controlled level chamber (C). With the gas inlet (D) closed and the Teflon stopcocks open, electrolyte is flowed into the lower part of the apparatus, air or other chosen atmosphere being vented from the back of the electrode (E) by means of the stopcock (F). When the electrolyte level in (B) reaches a desired level, the Teflon stopcocks are closed and gas at a controlled pressure is admitted through (D), bubbling up the precision tube until an equilibrium is reached when

$$P\text{gas} + P'' = H\sigma g + P'$$

where P'' is a composite of a small head of electrolyte and meniscus forces, σ is the density of the electrolyte, and g is the acceleration due to gravity. Flow of electrolyte through the electrode deforms the annular meniscus in (C), creating a bubble which projects through the notch into the bottom of the precision tube. Eventually the bubble detaches and rises, displacing electrolyte from (B), which restores the level of the meniscus. The volume of ΔH is mainly controlled by the area of the annulus in (C) and the height of the notch. In this case, the two diameters of the annulus are 1.5 and 1 cm, the notch being approximately 5 mm wide and 3.25 mm high.

The system for regulating the gas pressure is shown in Fig. 2. The output (100 mV for a range of 0 to 5 psi) from an Ametek Model 58-5B/A-SS pressure transducer, 1, is varied by a potential divider and fed into a Moseley Model 680 recorder, 2. A limit switch on the recorder operates a solenoid valve, 3, between the gas supply cylinder and the system. As the limit switch has considerable dead band, it was only possible to control the pressure with fluctuations about a mean

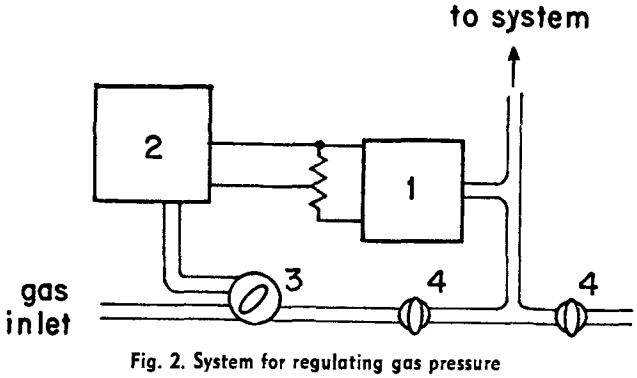

Fig. 2. System for regulating gas pressure

value. Judicial use of the fine needle valves, 4, on the inlet and outlet and the pressure regulator on the gas cylinder, enabled these fluctuations to be reduced to a uniform cycle with a frequency of 8 sec and an amplitude of less than 1% of the applied pressure, which ranged from 2 to 25 cm Hg.

It has been established by observation that just before the addition of electrolyte from (B), the meniscus in (C) falls to a constant level, rising sharply with the entry of electrolyte to a level which varies, corresponding to small variations of less than 5% in ΔH. Flow rates are therefore obtained by combining the volume of ΔH with the period of the meniscus rise in (C) which denotes the volume entering and exiting from the electrolyte at the back of the electrode. The meniscus in (B) occasionally moved slightly upward during the first 1 or 2 min following a level change before arriving at a stable position. In all cases, when measuring ΔH, the final stable position gave flow rates closer to the mean value than if the initial height (before the small upward movement) was used. Precision may be increased by using several successive increments of ΔH (*i.e.*, two, three or four bubbles entering (B)) with one time measurement. The apparatus will operate at the controlled pressure with the Teflon stopcocks open, the reservoir maintaining a constant supply of electrolyte to the electrode. These stopcocks should be closed when measuring flow rate, however, to keep the volume P' small and the apparatus less sensitive to changes in the ambient temperature.

Table I gives typical results using 2M KI electrolyte, and a ΔH of one, two, and three bubbles. Variations in flow rate with temperature (approximately 2%/°C), are clearly seen, the highest precision being obtained when the changes in ambient temperature were small. ΔH was measured with a cathetometer accurate to ±0.005 cm. Using a glass capillary to simulate a porous electrode giving the desired order of flow rate and pressure, measurements have been made with water and 3M KI electrolyte. The liquid was collected and weighed after passing through the capillary, the two methods agreeing to within 1%. The apparatus has been used through the range 2.5×10^{-4} to 1×10^{-2} ml/sec without loss of precision, but a high degree of dexterity is required when making measurements at the higher flow due to a bubble breaking every 30 sec, whereas the long period between bubbles at the low flow rate ($<10^3$ sec) causes some inconvenience. It is recommended, should flow rates in these regions be required, that changes be made in the annulus dimensions and notch height to provide a suitable time per bubble, *i.e.*, reducing the annular area and notch height to give a smaller ΔH at the 10^{-4} ml/sec range.

Should the pore characteristics of (E) be such that a low pressure of gas is required to obtain the desired flow rate, a controlled orifice, *i.e.*, a glass/Teflon needle

Table I. Flowrate measurements of 2M KI at a uniform pressure of 6.3 cm Hg

No. of measurements	T_{mean}, sec	ΔH_{mean}, cm	Mean flowrate, ml/sec × 10^3	Room temp, °C	Bubbles per ΔH
11	181.1	0.603	1.74 ± 2.8%*	21.4 ± 0.1*	1
10	362.2	1.205	1.742 ± 1.24%	21.4 ± 0.1	2
9	543.7	1.808	1.741 ± 0.75%	21.4 ± 0.1	3
8	178.7	0.593	1.74 ± 2.8%	21.3 ± 0.1	1
7	358.5	1.189	1.736 ± 1.1%	21.3 ± 0.1	2
6	538.5	1.784	1.735 ± 0.66%	21.3 ± 0.1	3
14	175.2	0.604	1.81 ± 3.87%	23.4 ± 0.4	1
13	350.6	1.209	1.805 ± 1.95%	23.4 ± 0.4	2
12	526.1	1.813	1.804 ± 1.2%	23.4 ± 0.4	3
12	150.5	0.564	1.96 ± 3%	27.0 ± 0.2	1
12	301.1	1.129	1.963 ± 1.2%	27.0 ± 0.2	2
10	452.8	1.697	1.962 ± 0.7%	27.0 ± 0.2	3

* Maximum deviation.

valve, may be inserted between (C) and (E) to provide a pressure dropping device.

Acknowledgment

The assistance of Mr. R. Welsh is gratefully acknowledged.

Manuscript received Jan. 13, 1970; revised manuscript received April 3, 1970.

Any discussion of this paper will appear in a Discussion Section to be published in the June 1971 JOURNAL.

On the Anisotropy Observed During the Passivation of Nickel Monocrystals

C. J. Mauvais, R. M. Latanision,[1] and A. W. Ruff, Jr.

Metallurgy Division, Institute for Materials Research, National Bureau of Standards, Washington, D. C.

The passivation of polycrystalline nickel electrodes in acid solution has received much attention over the years (1-8). In many of these studies some particulars of the passivation mechanism have been deduced through the measurement of anodic polarization diagrams. It should be recognized, however, that such studies on ordinary polycrystalline specimens yield at best an average measure of processes which undoubtedly occur at different rates on the various exposed crystal faces. Indeed, significant anisotropy has been reported in the anodic dissolution of various metals (9) and in the growth of passive films on iron monocrystals (10).

In this study, we have potentiostatically measured the anodic polarization behavior of nickel surfaces parallel to low index crystallographic planes in 1*N* H_2SO_4 and found that a strong anisotropy occurs in the passive region.

Experimental

The two 99.999% nickel monocrystals used in this study were cut from a semicircular disk ⅛ in. thick × 5/16 in. radius with a [110] axis. Three low index faces {100}, {110}, and {111} were produced by spark machining and then chemically polished in an acetic acid-nitric acid solution to remove any damage. The orientation of each face, determined by the back-reflection Laue method, was within 1.5° of the selected orientation.

Potential measurements were made relative to a saturated calomel electrode by means of a salt bridge-Luggin probe assembly taking suitable precaution to avoid contamination of the electrolyte by Cl^-. The geometrical arrangement of the components of the electrolytic cell was in accord with the recommendations of Greene (11). The 1*N* H_2SO_4 electrolyte was prepared from double-distilled water and reagent grade acid. Steady-state polarization measurements were performed potentiostatically in solutions exposed to air at temperatures of 22°-23°C throughout. In each experiment, only the crystal face of interest was exposed to the solution, the remainder of the specimen being covered with a protective lacquer. There were no indications that the electrolyte penetrated the lacquer and thus complications arising from leakage currents were avoided. A reflection of the crystal symmetry of each surface is shown in the etch figures produced during these experiments, Fig. 1.

Results and Discussion

The anodic polarization behavior is shown for each of the exposed crystal faces in Fig. 2. It is clear that the current density in the passive region was not the same from one crystal plane to the next but decreased in the order: {100} > {110} > {111}. It is of interest to note that the relative rates of gaseous oxidation of the various crystal faces of nickel were reported (12, 13) to be in decreasing order: {100} > {110} > {111} when epitaxial oxide films were formed. In short, the degree of protection provided by the passive film as well as

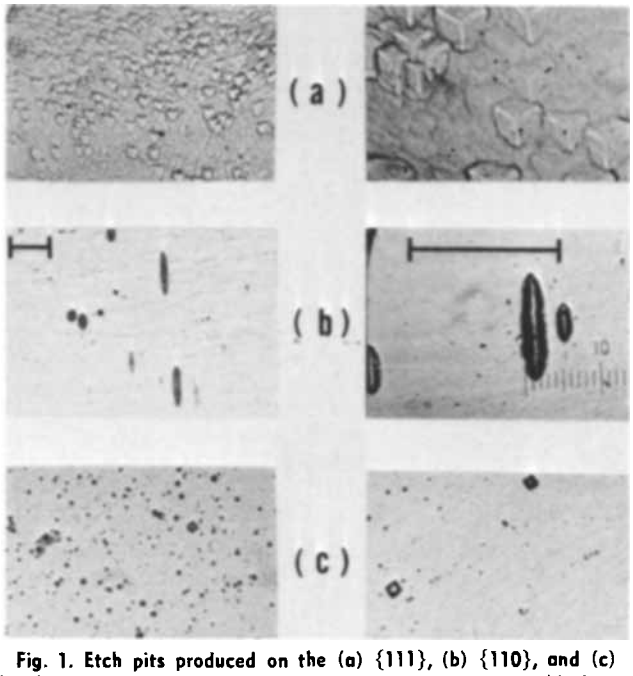

Fig. 1. Etch pits produced on the (a) {111}, (b) {110}, and (c) {100} faces during the anodic polarization experiments. Markers indicate separations of 50 μm.

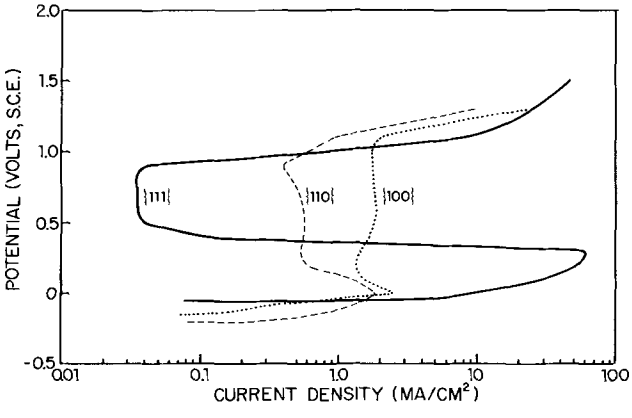

Fig. 2. Anodic polarization diagrams determined potentiostatically for the three low index faces of the nickel monocrystal in 1*N* H_2SO_4 at 22°-23°C.

[1] NAS-NAE-NBS Postdoctoral Research Associate. Present address: RIAS, Martin Marietta Corporation, Baltimore, Maryland 21227.

Key words: polarization, nickel monocrystals, dislocations, passive film, surfaces.

by films developed in gaseous oxidation tends to be a maximum for the {111} face and a minimum for the {100} surface of Ni monocrystals.

Although NiO is generally the only stable oxide formed in air or oxygen (13), it has been suggested that the passive film on Ni in H_2SO_4 is not necessarily NiO, but may be a higher oxide (4) or a composite of oxides (2, 3, 14). Nevertheless, assuming that NiO is formed in at least some early stage of passivation, it should be noted that gaseous oxidation studies (15) have shown the existence of parallel orientations between NiO and Ni for the three low index faces, *i.e.*, {111}NiO||{111}Ni,{110}NiO||{110}Ni, {100}NiO||{100}Ni. Recognizing that the lattice parameters of NiO and Ni are unequal (misfit $\simeq$19%), we suggest that the orientation dependence of passivation observed in this work may be understood in terms of (*i*) the creation of a grid of dislocations at the Ni/NiO interface which accommodates the lattice misfit and (*ii*) boundaries developed within the passive film during its growth.

First, on the basis of Van der Merwe's theoretical treatment of oriented overgrowths (16), we expect that the oxide, when only a few monolayers thick, transforms from a pseudomorphic structure with the lattice parameter of the substrate to the (oriented) oxide structure having essentially the lattice parameter of the bulk oxide, the lattice misfit taken up principally by interfacial dislocations. The geometry and spacing of dislocations in the misfit network are expected to be a function of the orientation of the substrate [see, for example, ref. (17)]. If only pure edge dislocations are formed at the interface, one expects that the separation between the misfit dislocations on {111} is greater than on {100} surfaces. The strain fields of these dislocations may have an important accelerating effect on ionic diffusion and thus on the passivation process.

Second, it is known (15) that NiO occurs in both {111} and {100} orientations on {100}Ni surfaces. The first orientation relation has four different variants depending on the relative <110> orientations in the metal and oxide. If the passive film forms by nucleation over the original metal surface, it seems likely that the film would contain a mixture of the different variants. This would require misfit boundaries in the film oblique to the interface, which would affect the oxidation rate by providing additional rapid diffusion paths through the passive film. By comparison, {110} and {114}NiO orientations occur on the {110}Ni surface leading again to oblique misfit boundaries. Only {111}NiO films have been reported on the {111}Ni surface although two twin-related orientations are possible. The oblique twin boundaries formed in this instance should be less effective in increasing the reaction rate than those expected for the other two Ni orientations. In short, if the degree of protection in the passive region may be related to the availability of short-circuiting reaction paths one expects {111} to be better protected than {100}, as observed.

The present results thus indicate the heretofore neglected importance of considering the crystallography and defect structure of the film and the metal-film interface in understanding the mechanism and kinetics of passivation. Similar contributions to the kinetics of film growth in the gaseous oxidation of Ni and Cu monocrystals have been discussed by Cathcart and co-workers (18, 19).

Acknowledgment

The experiments described herein were performed by C. J. Mauvais as part of the American University Summer Science Participation Program for Secondary School Students. Mr. Mauvais is in his senior year at Bethesda-Chevy Chase High School, Bethesda, Maryland.

It is a pleasure to thank the American University, sponsor of the Summer Research Program, and especially Mrs. Margaret Maury, Associate Director of this program, through whose efforts this collaboration was made possible.

Manuscript submitted Dec. 1, 1969; revised manuscript received March 12, 1970.

Any discussion of this paper will appear in a Discussion Section to be published in the June 1971 JOURNAL.

REFERENCES

1. R. Piontelli and G. Serravalle, *Z. Elektrochem.*, **62**, 759 (1958).
2. G. Okamoto and N. Sato, *Trans. Japan Inst. Metals*, **1**, 16 (1960).
3. N. Sato and G. Okamoto, *This Journal*, **110**, 605 (1963).
4. T. J. Gromoboy and L. L. Shrier, *Electrochim. Acta*, **11**, 895 (1966).
5. J. O'M. Bockris, A. K. N. Reddy, and B. Rao, *This Journal*, **113**, 1133 (1966).
6. R. R. Sayano and K. Nobe, *Corrosion*, **23**, 27 (1967).
7. J. Postlethwaite and L. B. Freese, *ibid.*, **23**, 109 (1967).
8. N. Ya. Bune, *Zashchita Metallov*, **3** [1], 50 (1967).
9. R. Piontelli, in Trans. of the Symposium on Electrode Processes, p. 67, Electrochemical Society, John Wiley & Sons, Inc., New York (1961).
10. J. Kruger, *This Journal*, **114**, 43 (1967).
11. N. D. Greene, "Experimental Electrode Kinetics," Rensselaer Polytechnic Institute (1965).
12. K. R. Lawless, F. W. Young, and A. T. Gwathmey, *J. Chim. Phys.*, **53**, 667 (1956).
13. G. C. Wood, I. G. Wright, and J. M. Ferguson, *Corrosion Sci.*, **5**, 645 (1965).
14. R. M. Latanision and R. W. Staehle, *Acta Met.*, **17**, 307 (1969).
15. A. T. Gwathmey and K. R. Lawless, in "The Surface Chemistry of Metals and Semiconductors," p. 483, John Wiley & Sons, Inc., New York (1960).
16. J. H. van der Merwe, *J. Appl. Phys.*, **34**, 117 and 123 (1963); in "Single Crystal Films," p. 139, Pergamon Press, New York (1964).
17. E. R. Thompson and K. R. Lawless, *Appl. Phys. Letters*, **9** [4], 138 (1966).
18. J. V. Cathcart and G. F. Petersen, *This Journal*, **115**, 595 (1968)
19. J. V. Cathcart, G. F. Petersen, and C. J. Sparks, Jr., *ibid.*, **116**, 664 (1969).

Spectrophotometric Study of Electrogenerated Sulfur-Sulfide Solutions in Fused LiCl-KCl

F. G. Bodewig and James A. Plambeck***

Department of Chemistry, University of Alberta, Edmonton, Alberta, Canada

During electrochemical investigations on chalcogen-chalconide systems in fused LiCl-KCl eutectic carried out in this laboratory (1, 2) it was noticed that a solution containing sulfide ions is blue in color if an excess of sulfur was present as a liquid pool floating on the melt (1). The blue color intensified when more sulfide was added to the solution, but disappeared when the sulfur was pumped off, indicating that it is not due only to a simple sulfide species. It appeared interesting to obtain the spectrum of this species and to investigate whether or not Beer's law is followed when it is generated by cathodization of a sulfur pool.

The spectrum of molten KSCN has been published (3) and the blue color observed has been ascribed to sulfur. An absorbance maximum was observed at 605 mμ between 250° and 450°C and below 250°C an additional one appeared at 415 mμ. The molar absorptivity for the 605 mμ maximum was estimated to be between 16,600 and 30,000.

A spectrum of molten LiCl-KCl eutectic containing sulfur has been published (4), and the blue color of the solution has been attributed to dissolved sulfur. The maximum absorbance was at about 600 mμ between 400° and 600°C. No value for the molar absorptivity was reported.

Experimental

Apparatus.—Spectra were recorded on a Cary Model 14 spectrophotometer. Potentials and currents were measured with a digital voltmeter (Model 3440A, Hewlet-Packard). Two 45V batteries in series were employed as a current source from which currents between 50 and 500 μA were drawn through a resistor network.

The spectrophotometric cell consisted of square Pyrex tubing (Vitro Dynamics) of inside dimensions 22 x 10 mm with a top connected to it by means of a 34/45 ground-glass joint. Four 10/30 ground-glass joints were blown on this top which were used to insert a thermocouple, a gold foil electrode, an isolation compartment with a tungsten electrode, and an inert gas inlet tube. The isolation compartments for the anode were made of Pyrex sealing tubes (5D; Ace Glass Inc.). Part of this cell is shown in Fig. 1. The cell path length was 10 mm.

After several attempts a furnace was constructed that operated satisfactorily and fitted into the Cary sample compartment (Fig. 1). Previously published oven designs (5, 6) did not allow insertion of the relatively large Pyrex cell used in the present study. Problems were also encountered in obtaining the uniform temperature necessary over a melt column of about 5 cm. The present design, which uses a large aluminum cylinder, accomplishes this; the temperature gradient in the unstirred melt was less than 2° over a vertical distance of 5 cm. The temperature of the oven was controlled by a Model 226 2-Mode solid state controller (API Instruments). The regulating thermocouple (not shown in Fig. 1) was placed close to the heating elements.

Materials.—The chemicals used have been described previously (1). Helium was used as inert gas. It was passed through three cold traps cooled with liquid nitrogen; the last cold trap contained activated carbon. After preparation of the melt as described previously (1) it was filtered through a Pyrex frit (B porosity; Ace Glass Inc.) before freezing and storage. A gold foil electrode (Johnson, Matthey & Mallory Ltd.) was used to generate the sulfide from a sulfur pool. The anode consisted of a tungsten spiral in an isolation compartment which prevented mixing of anode and cathode products.

Procedure.—The frozen eutectic was transferred to the cell and allowed to melt under a helium atmosphere. Once molten, the eutectic was again treated with chlorine gas after insertion of the isolation compartment and the Pyrex tube for the thermocouple. After 10-15 min the chlorine was removed by purging with helium which was also passed over the melt during the remainder of the experiment. The sulfide was generated with a gold electrode in a sulfur pool floating on the melt. The current used was about 100 μA. After each coulometric generation the solution was made uniform by stirring it with the isolation compartment. The temperature of the melt was 400° ± 2°C. Spectra were recorded with a scanning speed of 25 Å/sec. The concentration of the sulfide was calculated from the measured current, time of generation, and volume of melt obtained as before from a potentiometric chloride titration (1).

Results and Discussion

The spectrum of the solvent with a sulfur pool floating on it is the lower curve in Fig. 2. The zero

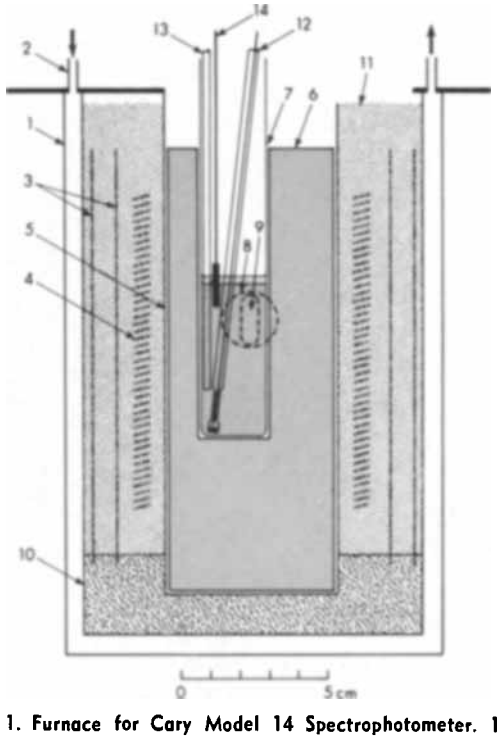

Fig. 1. Furnace for Cary Model 14 Spectrophotometer. 1, Brass water jacket; 2, water inlet and outlet; 3, semicylindrical aluminum reflectors; 4, semicylindrical heating units, parallel, each 290W, length 4 in., ID 2⅜ in. (Fisher Scientific Company); 5, stainless steel crucible, 59 mm diameter; 6, aluminum cylinder, 58 mm diameter; 7, square 22 x 10 mm (ID) Pyrex cell; 8, quartz window in water jacket, 20 mm diameter; 9, opening in aluminum cylinder, 7 x 17 mm; 10, insulation; 11, Pyrex wool; 12, isolation compartment with tungsten electrode; 13, Pyrex tube for thermocouple; 14, gold foil electrode making contact with sulfur pool.

** Electrochemical Society Student Member.
* Electrochemical Society Active Member.

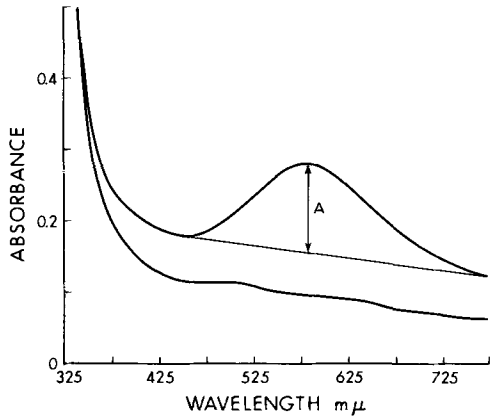

Fig. 2. Absorbance as a function of wavelength. Lower curve, fused LiCl-KCl with sulfur pool floating above it; upper curve; same following coulometric generation of sulfide.

point on the absorbance scale was taken arbitrarily since the reference light beam passed through air. It showed no peaks between 400 and 800 mμ, contrary to an earlier report by Greenberg, Sundheim, and Gruen (4). In the present work no blue color developed when care was taken in the purification of both the melt and the inert gas. Impurities present in the melt might have reduced enough sulfur to have produced the blue color observed in the earlier work (4). The spectrum after coulometric addition of sulfide to the melt is also given in Fig. 2. Only one maximum was observed at 585 mμ, not two as reported earlier (4).

Spectra of solutions with increasing sulfide concentrations were recorded at 400° ± 2°C. The absorbance at 585 mμ was measured as indicated in Fig. 2. For several experiments these absorbances were plotted as a function of time of coulometric sulfide generation at constant current. In all cases the extrapolated lines passed through the origin. This indicates that the linear background line drawn under the upper curve in Fig. 2 is the zero absorbance line. It should be noted that the "zero absorbance" line shifted from that of the solvent plus sulfur when sulfide was added to the solution. This was observed in all experiments.

A typical plot of absorbance as a function of sulfide concentration is shown in Fig. 3. Concentrations up to 2.2 x 10^{-5}M followed Beer's law accurately. Negative deviations occurred at higher concentrations. The cell path was measured as 1.00 cm. From this and the slope of the line of Fig. 3 the molar absorptivity of the absorbing species, calculated as $S^{=}$, was found to be 4600 1 $mole^{-1}$ cm^{-1} for sulfide concentrations up to 2.2 x 10^{-5}M. Lux and Anslinger (3) estimated the molar absorptivity to be 16,600 or higher, but this value was arrived at under the assumption that the absorbing species is S_2. Furthermore, it is not clear how these authors determined the zero absorbance line from which the absorbance was measured. The present value is therefore not strictly comparable with their value, especially in view of the fact that the fused salts used are significantly different.

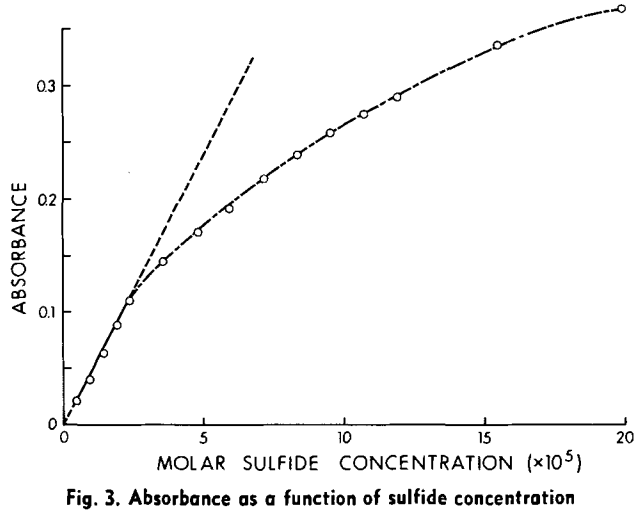

Fig. 3. Absorbance as a function of sulfide concentration

In the course of the present work several pure heavy metal sulfides have been added to the LiCl-KCl eutectic, in which they appeared to be very slightly soluble. These solutions were colorless until after sulfur was also added, when they turned the expected blue. This indicates that spectrophotometric measurements could be used to determine the solubility of metal sulfides in fused salts. However, suitable calibration curves would be required due to the pronounced deviations from Beer's law. Moreover, the solubilities measured would be those of metal sulfides in the presence of excess sulfur and could not *a priori* be assumed to be those which would be observed if the sulfur were not there. In spite of this, and the difficulty of preventing reduction of some of the sulfur by impurities, spectrophotometry may be a more practical approach than coulometry. Coulometric titrations of anodically generated Fe^{++}, Ni^{++}, Co^{++}, and Ag^{+} by reduction of a sulfur pool electrode produced potentiometric titration curves with breaks of 160-400 mV. These breaks consistently occurred a considerable, but not a reproducible, distance before the theoretical equivalence point.

Conclusion

The results reported here confirm the suggestion of our previous paper (1) that this absorption band and the blue color are due to one or more polysulfide species. It cannot be due to either sulfur or sulfide alone. The width of the band and the deviation from Beer's law suggest that multiple species may be involved. The present apparatus, however, permits no variation in the sulfur concentration and we have thus far been unable to test that suggestion.

Acknowledgment

The authors are grateful to the National Research Council of Canada for financial assistance in the form of an Operating Grant (to J.A.P.).

This paper is taken from the thesis of one of the authors (F.G.B.) submitted to the Faculty of Graduate Studies, University of Alberta, in partial fulfillment of the requirements for the Ph.D. degree.

Manuscript submitted Jan. 29, 1970; revised manuscript received March 4, 1970.

Any discussion of this paper will appear in a Discussion Section to be published in the June 1971 JOURNAL.

REFERENCES

1. F. G. Bodewig and J. A. Plambeck, *This Journal*, **116**, 607 (1969).
2. F. G. Bodewig and J. A. Plambeck, *ibid.*, **117**, 618 (1970).
3. H. Lux and H. Anslinger, *Chem. Ber.*, **94**, 1161 (1961).
4. J. Greenberg, B. R. Sundheim, and D. M. Gruen, *J. Chem. Phys.*, **29**, 461 (1958).
5. J. R. Morrey and A. W. Madsen, *Rev. Sci. Instr.*, **32**, 799 (1961).
6. D. M. Gruen, *Quart. Revs*, **19**, 349 (1965)

The Polarization Correction in Conductance Measurements

R. P. T. Tomkins, G. J. Janz,* and E. Andalaft

Rensselaer Polytechnic Institute, Department of Chemistry, Troy, New York

To attain conductance data of highest precision, one finds that extrapolation of the measured resistances as a function of frequency is subject to various approaches and is not well documented in texts or the published literature. Two of the outstanding practices are due to Jones and Christian (1), *i.e.*, a graphical extrapolation based on the Warburg analysis of concentration polarization and to Fuoss (2), who introduced the inverse frequency extrapolation. With the recent increase of interest in nonaqueous electrolytes, where brightly polished or lightly platinized electrodes are generally used, the extrapolation techniques are reoccurring problems. Because of this uncertainty, alternate procedures such as measurements at frequencies up to 100 kHz (3), the use of electrodeless cells (4) and d-c bridge techniques (5, 6) have been used. Features specific for molten salts have recently been discussed elsewhere (7) and will not be mentioned here except to note that the basic problem, an extrapolation to correct for polarization effects, is encountered there as for aqueous and nonaqueous measurements. The conventional a-c conductance technique, nevertheless, is still the most generally and widely used method, largely because of its versatility and relatively simple instrumentation. The present note reports a critical evaluation of the limitations and applicability of the extrapolation procedures in most frequent use, and also redirects attention to the frequency dispersion errors that may arise if a conductance cell is used outside the range for which the calibration standard is applicable.

Experimental.—The purification of sodium iodide and acetonitrile have been described in a previous communication (8). Two Shedlovsky-type cells having constants of 16.8456 and 1.33735 were used for the concentrated and dilute solutions, respectively. The conductances of all solutions were measured with a Jones-Dike (9) a-c conductance bridge and accessories (Leeds & Northrup Company). A variable frequency audio signal generator (Eico, Model 377) and a tuned amplifier and null detector (General Radio, Model 1323-A) were used for the a-c signal and bridge circuit balance. The freqeuncy range was varied from 0.6-10 kHz.

* Electrochemical Society Active Member.

Table III. Comparison of different extrapolation techniques to obtain the polarization free value of the resistance (cell constant = 1.33735; conc = 14.7751 x 10^{-4} mol/l)

Technique	R, ohms	Per cent departure from value obtained graphically
Graphical extrapolation ΔR	5751.4 ±0.5	—
L.S.† to quadratic in f^{-1} σ	5751.5 0.01	0.017
L.S. to linear in f^{-1} σ	5750.4 0.6	0.017
L.S. to quadratic in $f^{-1/2}$ σ	5751.5 0.6	0.017
L.S. to linear in $f^{-1/2}$ σ	5745.6 1.2	0.101

† L.S., least squares analysis; σ, standard deviation.

Results and Discussion

The values of resistance as a function of concentration and applied frequency are in Table I and II. With the low cell constant (Table I), a considerable curvature in a plot of R *vs.* $f^{-1/2}$ is observed, and a satisfactory extrapolation (to infinite frequency, to gain the polarization-free value of R) cannot be advanced with certainty. On the other hand it is found that the graph of R *vs.* f^{-1} is linear; the thus extrapolated values for R at infinite frequency are in Table I. For more concentrated solutions (Table II), the extrapolation R *vs.* $f^{-1/2}$ is satisfactory.

As an alternative approach to gain R at infinite frequency, a least-squares analysis to quadratic or linear

Table I. Variation of measured resistance with frequency at different concentrations of NaI in anhydrous acetonitrile at 25° (cell constant = 1.33735)

f(Hz) \ 10^4C (N)	14.7751	17.9938	27.0081	32.1555	42.7746	59.3252
			Resistance, ohms			
∞	5751.4	4546.9	3090.9	2618.1	2010.6	1485.5
10000	5754.1(0.05)	4549.5(0.06)	3093.6(0.09)	2620.9(0.11)	2013.4(0.14)	1488.4(0.20)
6000	5755.7(0.07)	4551.6(0.10)	3095.5(0.15)	2622.8(0.18)	2015.4(0.24)	1490.1(0.31)
5000	5756.7(0.09)	4552.2(0.12)	3096.4(0.18)	2623.7(0.21)	2016.3(0.28)	1491.1(0.38)
4000	5757.8(0.11)	4553.8(0.15)	3097.7(0.22)	2625.1(0.27)	2017.7(0.35)	1492.8(0.49)
2500	5762.0(0.18)	4557.7(0.24)	3101.8(0.35)	2629.2(0.42)	2021.7(0.55)	1496.8(0.76)

Values in parenthesis indicate the per cent error in the measured value from that obtained by extrapolation to infinite frequency.

Table II. Variation of measured resistance with frequency at different concentrations of NaI in anhydrous acetonitrile at 25° (cell constant = 16.8456)

f(Hz) \ $C_{(N)}$	0.85296	0.52109	0.42221	0.34279	0.30514	0.24998	0.16070	0.13009
				Resistance, ohms				
∞	1345.6	1147.2	840.5	735.4	681.6	604.7	540.7	436.7
10000	1350.7(0.38)	1151.5(0.37)	844.9(0.52)	739.1(0.50)	686.1(0.66)	608.2(0.58)	543.8(0.57)	439.6(0.66)
8000	1351.1(0.41)	1152.2(0.44)	845.4(0.58)	739.5(0.56)	686.7(0.75)	608.7(0.66)	544.3(0.67)	439.9(0.73)
6000	1352.0(0.48)	1152.9(0.50)	846.1(0.67)	740.1(0.64)	687.3(0.84)	609.3(0.76)	544.8(0.76)	440.4(0.85)
5000	1352.7(0.53)	1153.4(0.54)	846.7(0.74)	740.8(0.73)	687.8(0.91)	609.7(0.83)	545.3(0.85)	440.9(0.96)
4000	1353.5(0.59)	1154.2(0.61)	847.6(0.84)	741.2(0.76)	688.8(1.06)	610.3(0.93)	545.0(0.79)	441.3(1.05)
3000	1354.8(0.68)	1155.2(0.72)	848.7(0.98)	742.3(0.94)	689.7(1.19)	611.5(1.12)		

Values in parenthesis indicate the per cent error in the measured value from that obtained by extrapolation to infinite frequency.

equations in f^{-1} was programmed. A comparison of the results with those of the preceding graphical extrapolations is in Table III. The agreement (both for f^{-1}) leaves little to be desired.

It is also informative to examine the results for the "per cent error" if the measurements are limited to one frequency only. Inspection of Table I and II shows that the per cent error depends on factors such as the cell constant, concentration, and frequency. The per cent error, thus introduced, is invariably larger than the limit of error (±0.02%) for meaningful theoretical interpretation of conductance data. It is also seen from Table III that the standard deviation provides a useful guide line for the selection of the "best" extrapolation technique.

An analysis of the frequency dispersion of the resistance, based on the results in Table I and II, is shown in Fig. 1. The curves indicate the limits of the concentration range where the slopes of the resistance-frequency plots are fairly constant when measurements with any one cell are being used over a range of electrolyte concentrations. The concentration dependence of $\Delta R/\Delta f^{-1/2}$ is illustrated in Fig. 2. Slopes A and B show the trends for dilute and concentrated solutions, respectively, whereas slope C is an attempt to curve-fit all the data points.

The equation advanced by Fuoss and Hsia (10) for KCl in water

$$\Lambda = 149.935 - 94.88C^{1/2} + 25.48\ C \ln C + 221 \cdot C^{3/2}$$

is in agreement with the Jones and Bradshaw demal standards at 0.01 and 0.1 within 0.11%, respectively, and is recommended for conductance cell calibrations.

While both Ives (11) and Fuoss (12) have advanced equivalent circuit models for the electrode/solution interface, the interpretation of the polarization correction remains incomplete, and from this viewpoint further discussion is best deferred. To summarize, both the $f^{-1/2}$ and f^{-1} graphical extrapolations are valid procedures providing due cognizance is taken of factors such as the cell constant, concentration, and range of frequencies. That extrapolation which gives a linear fit, or alternately the computer fitted equation having the least standard deviation is the "best" for the polarization correction but the justification remains largely empirical, namely that this is "what works."

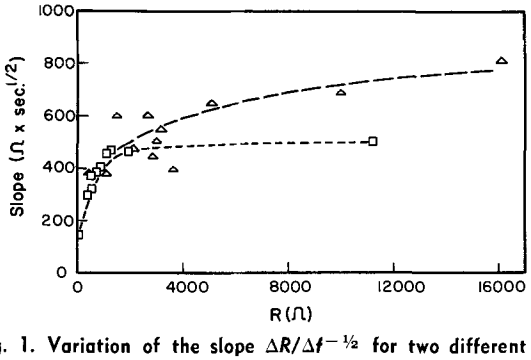

Fig. 1. Variation of the slope $\Delta R/\Delta f^{-1/2}$ for two different conductance cells as a function of R(ohms). △, data from measurements with conductance cell having a cell constant of 1.33735; □, *ibid.*, but cell constant of 16.8465.

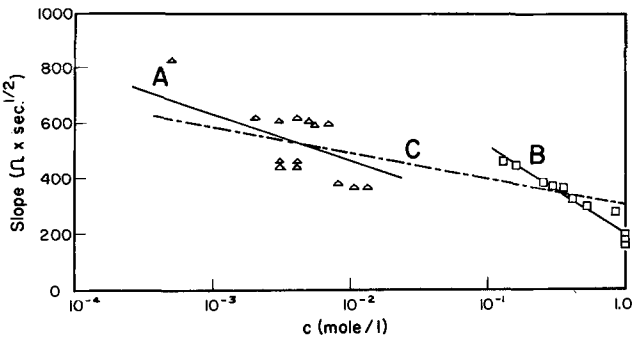

Fig. 2. Variation of the slope $\Delta R/\Delta f^{-1/2}$ with concentration of electrolyte. △, data from measurements with conductance cell with a cell constant of 1.33735; □, *ibid.*, but with cell constant of 16.8465.

Manuscript received Sept. 17, 1969; revised manuscript received Feb. 16, 1970.

Any discussion of this paper will appear in a Discussion Section to be published in the June 1971 JOURNAL.

REFERENCES

1. G. Jones and S. M. Christian, *J. Am. Chem. Soc.*, **57**, 272 (1935).
2. O. V. Brody and R. M. Fuoss, *J. Phys. Chem.*, **60**, 177 (1956).
3. E. R. Buckle and P. E. Tsaoussoglou, *J. Chem. Soc.*, **1964**, 667.
4. G. J. Hills and S. Djordjevic, *Electrochim. Acta*, **13**, 1721 (1968).
5. H. E. Gunning and A. R. Gordon, *J. Chem. Phys.*, **10**, 126 (1942).
6. L. A. King and F. R. Duke, *This Journal*, **111**, 172 (1964)
7. G. D. Robbins, *ibid.*, **116**, 813 (1969).
8. R. P. T. Tomkins, E. Andalaft, and G. J. Janz, *Trans. Faraday Soc.*, **65**, 1906 (1969).
9. P. H. Dike, *Rev. Sci. Instr.*, **2**, 379 (1931).
10. R. M. Fuoss and K. L. Hsia, *Proc. Nat. Acad. Sci. U.S.*, **57**, 1550 (1967).
11. F. S. Feates, D. J. G. Ives, and J. H. Pryor, *This Journal*, **103**, 580 (1956).
12. R. M. Fuoss, Private communication (1966).

DISCUSSION SECTION

This Discussion Section includes discussion of papers appearing in the *Journal of The Electrochemical Society*, Vol. 116, No. 6, 8, 11, and 12, June, August, November, and December 1969.

Epitaxial Growth with Light Irradiation

M. Kumagawa, H. Sunami, and J. Nishizawa[1]
(Not published in the *Journal*)

This will acknowledge the receipt of a paper submitted for publication in this *Journal* entitled "Epitaxial Growth with Light Irradiation" in May 1967.

[1] Research Institute of Electrical Communication, Tohoku University, Sendai, Japan.

The paper was authored by M. Kumagawa, H. Sunami, and J. Nishizawa,[1] and described a technique for the enhancement of the low-temperature epitaxial growth of silicon with the aid of light irradiation. Unfortunately, the paper was not published in this *Journal* primarily because of the difficulty experienced by the authors in describing their work in current *Journal* style English, though the authors do not assent to the reason for rejection. Several months later, another paper was received for publication entitled "Low Temperature Silicon Epitaxy" by R. G. Frieser. By coincidence, the subject matter of this paper was very simi-

lar to that previously submitted by the Japanese authors. Since the paper by Dr. Frieser was well written and entirely acceptable in the opinion of several reviewers, it was published without delay and, of course, appeared before the paper by Kumagawa *et al.*, was completely revised. Those interested in the work of Kumagawa *et al.*, will find it in the November 1968 issue of the *Japanese Journal of Applied Physics.*

Effects of Oxidizable Anion Adsorption on the Anodic Behavior of Platinum

Sigmund Schuldiner (pp. 767-771, Vol. 116. No. 6)

T. Biegler[2]: In a recent series of papers[3-5] culminating in the work under discussion, Schuldiner has promulgated the views that there is negligible coverage of a platinum electrode by oxygen containing species up to at least 1.2V in the presence of hydrogen and 1.6V in the presence of formic acid and that, consequently, the retardation of hydrogen or formic acid oxidation at lower potentials is caused by anion adsorption. In criticizing these conclusions, Vetter and Schultze[6] have given an analysis of the kinetics of the partial reactions involved in the reduction of surface "oxide" by hydrogen or formic acid and have thereby shown the possibility of a steady coverage of "oxide" in the potential region where Schuldiner denies its existence. This appears to be an unnecessarily obscure way of attacking Schuldiner's assertions since the direct evidence for surface oxidation of platinum under these conditions is well established and well documented.

Will and Knorr[7] studied the effect of sweep rate on cyclic linear-sweep voltammograms in the presence of hydrogen. Even at quite low sweep speeds (1.6V sec^{-1}), the current-voltage curve approached the shape obtained in absence of hydrogen showing that formation and reduction of adsorbed oxygen (and hydrogen) layers occur more or less independently of the presence of bulk hydrogen. Direct comparisons of surface oxygen coverages in presence and absence of hydrogen,[8] formic acid,[9] and methanol[10,11] indicate that surface "oxide" formation is only slightly affected by the presence of these oxidizable species. In these cases, cathodic stripping was used to determine adsorbed oxygen and it seems unlikely that the association of the measured cathodic charge with surface "oxide" was in error. Furthermore, on the basis of reflectance measurements, Koch and Scaife[12] concluded that formaldehyde has no significant effect on oxygen coverage on platinum.

The published experimental evidence (the above list is not intended to be exhaustive) for adsorbed oxygen on platinum under these conditions is therefore strong. Nevertheless, in view of the amount of space being devoted to contrary assertions, it seems worthwhile to present a graphic and, I think, unambiguous demonstration of the presence of surface "oxide" during formic acid oxidation. No originality is claimed for the experiment and no quantitative data are extracted from it; indeed, results obtained by analogous methods already appear in the literature[8-11]. A platinum wire electrode in a deoxygenated solution of 1M formic acid, 1M sulfuric acid, is held at 0.18V (*vs.* reversible hydrogen electrode) to produce an "oxide"-free surface, then the potential is stepped to a value ϕ_{ox} for 10 sec after which a fast cathodic sweep (45V sec^{-1}) is started. At this sweep rate, the anodic current due to formic acid oxidation is swamped by the cathodic current

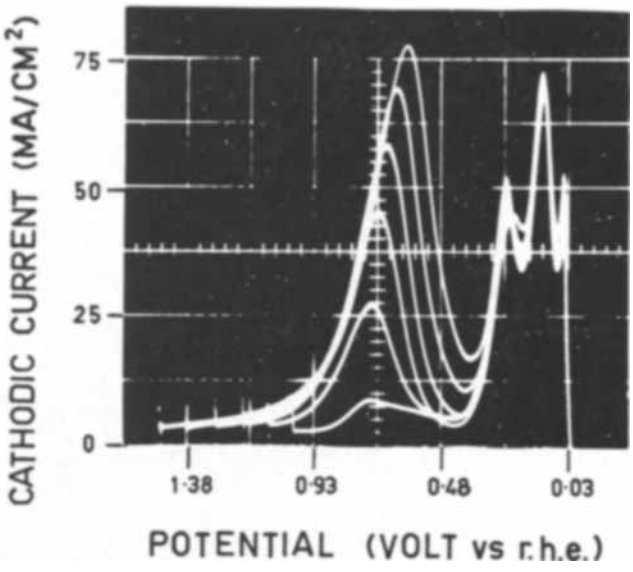

Fig. 1. Cathodic linear sweeps after 10 sec at various potentials in 1M HCOOH, 1M H_2SO_4. From left, curves start at 1.48, 1.38, 1.28, 1.18, 1.08, and 0.98V *vs.* r.h.e. Sweep rate 45V sec^{-1} (5 msec/graticule division).

arising from surface reduction processes. Figure 1 shows a series of sweeps for ϕ_{ox} ranging from 0.98 to 1.48V in 0.1V steps. The curves contain three cathodic peaks. The first increases with increasing ϕ_{ox} and its peak potential shifts cathodically; its behavior is analogous to that found in absence of formic acid[13,14] and it is therefore attributed to "oxide" reduction. The other maxima are the two well-known hydrogen peaks which show only a slight dependence on ϕ_{ox}, mainly due to a small overlap between "oxide" reduction and the first (more anodic) hydrogen peak.

These experimental results and their interpretation in terms of the presence of surface oxygen doubtless conform to the expectations of most electrochemists, especially as the work repeats that done in several other laboratories. Their publication is intended to counteract the wide circulation of incorrect notions concerning the surface behavior of platinum electrodes and to provide a challenge, in the simplest possible form, to explain the cathodic peak around 0.6-0.7V in terms of adsorbed species other than those containing oxygen.

S. Schuldiner: The communications gap between Biegler and myself is due to our very different concepts of the "steady state." Biegler evidently considers that stepping the potential to a given value for 10 sec brings the electrode to its steady-state condition. My measurements in formic acid,[15] formic acid + sulfuric acid,[15] and pure sulfuric acid[16,17] solutions showed that attainment of the steady state in the potential region of interest took many hours. My Fig. 1[15] typifies the current density *vs.* time relation found when a given potential is applied.

Using a rapid anodic charging method, Warner and Schuldiner[18] deposited a monolayer of what was considered to be oxygen atoms, O_{ad}, on a Pt electrode. Under open-circuit conditions, the Pt-O_{ad} reacted with H_2 in the sulfuric acid solution. As the reaction proceeded, a second anodic pulse was applied and the amount of O_{ad} formed to complete the monolayer was taken to be the amount of O_{ad} reacted at the time the second pulse was applied. Knowing the change in potential with time, we were able to determine a re-

[2] C.S.I.R.O., Division of Mineral Chemistry, Port Melbourne, Victoria, Australia.
[3] S. Schuldiner, *This Journal*, **115**, 362 (1968).
[4] S. Schuldiner, *This Journal*, **115**, 897 (1968).
[5] S. Schuldiner, *This Journal*, **116**, 767 (1969).
[6] K. J. Vetter and J. W. Schultze, *This Journal*, **116**, 824 (1969).
[7] F. G. Will and C. A. Knorr, *Z. Elektrochem.*, **64**, 258 (1960).
[8] M. W. Breiter, *Electrochim. Acta*, **7**, 601 (1962).
[9] M. W. Breiter, *Electrochim. Acta*, **8**, 447 (1963).
[10] M. W. Breiter and S. Gilman, *This Journal*, **109**, 622 (1962).
[11] V. S. Bagotzky and Yu. B. Vassilyev, *Electrochim. Acta*, **12**, 1323 (1967).
[12] D. F. A. Koch and D. E. Scaife, *This Journal*, **113**, 302 (1966).
[13] W. Bold and M. W. Breiter, *Electrochim. Acta*, **5**, 145 (1961).
[14] T. Biegler and R. Woods, *J. Electroanal. Chem.*, **20**, 73 (1969).
[15] S. Schuldiner, *This Journal*, **116**, 767 (1969).
[16] S. Schuldiner, *This Journal*, **115**, 362 (1968).
[17] S. Schuldiner, *This Journal*, **115**, 897 (1968).
[18] T. B. Warner and S. Schuldiner, *This Journal*, **115**, 28 (1968).

lation between O_{ad} and potential (Fig. 4[18]). These transient measurements showed that when the potential decayed to about 0.9V the Pt surface was still covered by O_{ad}. However, my data[17] (see Fig. 2[17]) showed that under steady-state conditions at 0.9V only about one half of the adsorption sites on the Pt surface were covered with an adsorbate (which, under these steady-state conditions, I believe to be sulfate ion rather than O_{ad}). Recent work at this Laboratory,[19] also in H_2-saturated sulfuric acid solution further confirms that the amount of O_{ad} which can be deposited on a Pt electrode at potentials above 0.4V was time dependent. In summary, the point is that transient charging to an anodic potential may deposit O_{ad} on the Pt surface but, if the anodic potential is maintained, slow changes occur on the surface which result in a removal of O_{ad} by reaction with H_2 or formic acid and a deposition of sulfate ions.

I should like to point out at this time that charging curves can determine the number of coulombs of charge required to go from one potential to another and that ramp techniques can determine changes in current under potential sweep conditions, but the interpretation of what is occurring on the electrode surface is based more on consensus than on proof.

Concentration Changes in Operating Fuel Cells

T. J. Lundquist, Jr., and W. M. Vogel (pp. 1066-1069, Vol. 116, No. 8)

M. Beltzer[20]: T. J. Lundquist, Jr., and W. M. Vogel found large concentration changes in both strong acid and base electrolytes at high current densities ($\simeq$70 to 150 mA/cm^2) in their fuel cells, contrary to the results of Beltzer.[21] The authors claim that they cannot speculate as to the causes of the discrepancies. I suggest, however, that further analysis by the authors of their own experimental results would reveal the differences to be valid ones. Thus, they should not be considered discrepancies.

The major difference in the experiments of the authors and those of Beltzer lies in the properties of the matrices used. Consequently, it is necessary to examine the properties of matrices and their effect on mass transfer.

Although Lundquist and Vogel correctly state that the steady-state concentration difference (ΔC_∞) depends on matrix geometry, they completely ignore the retarding influence of the matrix to mass transfer. The effective mobility of ions traversing any matrix is invariably less than the mobility in bulk solution.[22-24] This results in larger steady-state concentration differences than would occur if the matrix were absent. This quantity (ΔC_∞) is also markedly dependent on the particular matrix used. For example, the authors used a Johns-Manville fuel cell asbestos matrix. Coleman *et al.*[25] have shown that the same electrode will exhibit substantially different performances when different asbestos matrices are used in the cell. The linear dependence of ΔC_∞ with matrix thickness and the near zero intercept (Fig. 6) certainly substantiates the authors' claim that the concentration gradients are confined solely to the matrix. Consequently, valid comparisons of results of different experimenters can be made only when these effects are accounted for.

Sample calculations using the authors' equations and data show how the particular matrix used can result in different concentration changes in cells operating at comparable current densities and employing essentially identical or similar electrodes.

Table I. Steady-state concentrations in H_2/O_2 cell filled with KOH, no matrix

I [mA/cm^2]	ΔC_∞ [mole/liter]	$(C_a)_\infty$ [mole/liter]	$(C_c)_\infty$ [mole/liter]
0	0	6.80	6.80
72	0.28	6.65	6.93
144	0.56	6.52	7.08

The effective diffusion coefficient of, *e.g.*, hydroxide ion in the matrix, is calculated from the authors' Eq. [7]

$$\Delta C_\infty = in_- l/DqF$$

where ΔC_∞ was determined experimentally, l is the matrix thickness, q the area, and n_- the transport number of hydroxide ion. I have used the authors' value of $n_- = 0.78$, an acceptable value in KOH solutions greater than 3 molar.[26] The relative mobilities of potassium and hydroxide ion in the matrix are most likely similar to that in solution so that the use of this value for the transference number in the matrix is justified.

Using the authors' case of the O_2/H_2 cell filled with 6.8M KOH (Table II), I have calculated an average diffusion coefficient based on the 72 and 144 mA/cm^2 discharge data of $D = 1.13 \times 10^{-5}$ cm^2/sec. The bulk value of D at 60°C is 5.05×10^{-5} cm^2/sec. This value was obtained using the 25°C value estimated by Austin[27] and a conductance activation energy of 2.4 kcal/mole.[28] This activation energy applies to KOH solutions ranging from 3 to 6 molar and is therefore applicable to the range of solutions used by the authors and myself.

Thus, if one did not use a matrix at all, the ΔC_∞ across a laminar section of the bulk solution having the same area and thickness as the matrix would be about only 1/5 of the matrix ΔC_∞. The calculated values of ΔC_∞, $(C_a)_\infty$, and $(C_c)_\infty$, the latter two quantities, the steady-state anolyte and catholyte concentrations in the absence of a matrix are tabulated in Table I of this discussion.

At 144 mA/cm^2 in the absence of a matrix, the concentration decrease in the anolyte would be only 0.28 moles/liter as opposed to 1.3 moles/liter with the matrix. The calculated concentration polarization resulting from this decrease is negligible

$$\eta = 0.066 \log \frac{6.80}{6.52} = 0.001\text{V}$$

This is in accord with the experimental results of Beltzer. Similar considerations apply to the catholyte and to both electrodes in strong acids as well. Negligible concentration polarizations at high current densities in acids and basic electrolytes have been demonstrated by Niedrach[29-30] and others.[31] Niedrach operated an anode at 400 mA/cm^2 in 6M KOH and encountered very little concentration polarization. He, too, did not use a matrix but employed free electrolyte in the interelectrode spacing.

In view of the foregoing, it is difficult to see how the authors can regard the results of others as contrary to theirs, when the differences are authentic ones, and the results of the different experimenters internally consistent.

[19] S. Schuldiner, M. Rosen, and D. R. Flinn, Submitted for publication in *This Journal*.
[20] Esso Research and Engineering Co., Government Research Lab., Linden, N. J.
[21] M. Beltzer, *This Journal*, 114, 1200 (1967).
[22] J. S. Mackie and P. Meares, *Proc. Roy. Soc. (London)*, A232, 498 (1955).
[23] J. A. Lane and J. W. Riggle, *Chem. Eng. Progr. Symp. Ser.*, 55, 127 (1959).
[24] F. Helffrich, "Ion Exchange," p. 348, McGraw-Hill Book Co., New York (1962).
[25] W. P. Coleman, D. Gershberg, J. DiPalma, and R. G. Haldeman, *Proc. Ann. Power Sources Conf.*, 19, 14 (1965).
[26] M. Knobel, D. K. Worcester, and F. B. Briggs, *J. Am. Chem. Soc.*, 45, 77 (1923).
[27] L. G. Austin, "Handbook of Fuel Cell Technology," C. Berger, Editor, p. 141, Prentice Hall Inc. (1968).
[28] M. G. Manvelyan, T. V. Krymoyan, A. G. Eganyan, and A. M. Kocharyan, *Izv. Akad. Nauk Arm. SSR*, 9, 3 (1956).
[29] L. W. Niedrach and H. R. Alford, *This Journal*, 112 117 (1965).
[30] L. W. Niedrach and D. W. McKee, *Proc. Ann. Power Sources Conf.*, 21, 6 (1967).
[31] R. G. Haldeman, W. P. Coleman, S. H. Langer, and W. A. Barber, *Advan. in Chem. Ser.*, 47, 106 (1965).

I have an additional and admittedly minor point to make. The terms membrane and matrix are used interchangeably and the authors are not alone in this misuse of the terms. A membrane is a type of matrix but not all matrices are membranes. The operational definition of a membrane that is commonly accepted is that a membrane is a structure or phase which permits passage of material exclusively by molecular movement; *e.g.*, see Sollner.[32] I can only assume that Lundquist and Vogel did not use a true membrane because they took the trouble to orient the structure in a horizontal position to minimize liquid circulation through the "membrane." They also changed the relative positions of the anode and cathode so that the denser electrolyte (catholyte when KOH was used) is on the bottom. These manipulations would have been unnecessary if the matrix was a true membrane.

J. T. Lundquist, Jr., and W. M. Vogel: The discussion refers primarily to our Eq. [7] which is indeed incorrect if l and q are taken as the thickness and area of the matrix. By mistake, an essential sentence was omitted (not, however, in the Extended Abstract No. 335, ECS Meeting, Montreal 1968); namely, that the tortuosity and porosity of the matrix have to be taken into account. Thus, l and q are not the dimensions of the matrix as given in our Table II but are the latter multiplied by what is commonly called the matrix factor. Since this factor (approximately tortuosity/porosity) cannot be measured directly, we made no use of Eq. [7] *per se* but tested our theory using Eq. [13] which is free of this factor. The ratio of the bulk value for $D = 5.05 \times 10^{-5}$ (cm^2/sec) and the apparent value calculated by Beltzer is actually the matrix factor. This factor (4.4) is entirely reasonable for the kind of matrix used in our study.

We quite agree that if no membrane is used the concentration changes would be much smaller. However, in his original paper (see footnote 21) Beltzer describes his electrodes as being clad with a membrane (caption to Fig. 1 and 2 and other places). We understood this to mean that there was a porous body between the catalyst and the free electrolyte, in which case the discrepancy mentioned in our paper still exists.

Electrocapillary Measurements at the Interface Insulator-Electrolytic Solution

H. Dahms (pp. 1532-1534, Vol. 116, No. 11)

Ikram Morcos[33]: We note with interest the electrocapillary measurements at the insulator-electrolytic solution interface. We believe, however, that the interpretations given by the author are inapplicable for the experimental results. In this regard, we would like to point out the following.

Variation in the polyethylene/electrolytic solution interfacial tension cannot be calculated on the basis of the well-known equation

$$\gamma = \frac{rh\Delta\rho g}{2} \qquad [1]$$

This equation describes the relationship between the capillary rise and surface tension of liquids. The use of this equation for electrocapillary studies of liquid metals is justified because γ in such cases is also the liquid metal/electrolytic solution interfacial tension.

In the work of Dahms, we believe that the variation in the capillary rise of the solution inside the polyethylene tubing results from the variation in the contact angle between the solution and the polyethylene wall. This variation results from variation in the polyethylene/electrolytic solution interfacial tension according to the Young equation

$$\cos\theta = \frac{\gamma_{S/g} - \gamma_{L/s}}{\gamma_{L/g}} \qquad [2]$$

where θ is the contact angle and $\gamma_{S/g}$, $\gamma_{L/s}$, and $\gamma_{L/g}$ are interfacial tensions of the solid/gas, liquid/solid, and liquid/gas interfaces. Electrocapillary studies for solid electrodes based on the Young equation have already been reported in the literature[34-36].

In the case of a capillary tubing, the capillary rise or depression is a function of the contact angle as shown by the more general equation of capillary rise

$$h = \frac{2\gamma\cos\theta}{g\,r\,\Delta\rho} \qquad [3]$$

It has been reported by Zisman[37] that θ for the polyethylene/water system is around 100° and, accordingly, cos θ cannot be omitted from Eq. [3] on the basis of the assumption that the solution completely unwets the polyethylene wall with an angle of 180 as in the case of mercury. Under the effect of an electric field, $\gamma_{L/s}$ in Eq. [2] will decrease (as a result of charging the double layer and adsorption of ions) and, if we assume that $\gamma_{S/g}$ and $\gamma_{L/g}$ remain constant, cos θ should increase. This increase in cos θ should, according to Eq. [3] result in an increase in the capillary rise, h. Because the contact angle is more than 90°, this increase will be a decrease in the capillary depression as shown by Dahms. Again, with the assumption that $\gamma_{L/g}$* is constant, h should, according to Eq. [3], vary linearly with the variations in cos θ.

The use of capillary rise (or depression) *vs.* applied electric field plots to obtain surface charge or surface excess in the case of insulator electrolytic solution requires assuming the validity of Gibbs' equation. While such an equation has been used in the case of an ideally polarizable or reversible electrode,[38] it is questionable that the same applies for the insulator/electrolytic solution interface.

H. Dahms: The comments of I. Morcos appear to be concerned mainly with two points in my treatment of the electrocapillary data: the linear relationship between capillary depression, h, and the surface tension insulator/solution, which I have used, and the applicability of Gibbs' equation for this interface.

As indicated by the title of my communication, the electrocapillarometer which I have described is measuring the voltage dependence of the interfacial tension insulator/electrolytic solution, γ_{SL}. This phenomenon is certainly fundamentally different from the capillary depression or rise in a nonwetting or wetting capillary which is determined by the surface tension solution/gas, γ_{LG}. It can be seen that, independent of the contact angle, θ, there is a direct proportionality between h and γ_{SL}. By combining the general capillary rise equation with the Young equation (Morcos' Eq. [3] and [2]), we obtain

$$h = \frac{2\gamma_{SG}}{r\,\Delta\rho\,g} - \frac{2\gamma_{SL}}{r\,\Delta\rho\,g} \qquad [1']$$

Since only γ_{SL} will vary with the electric field while γ_{SG} remains constant, we can write

$$dh = -\frac{2}{r\,\Delta\rho\,g}\,d\gamma_{SL} \qquad [2']$$

This is the linear relation which I have used to obtain changes of surface tension from changes in capillary depression.

Concerning the applicability of Gibbs' equation, I agree readily that it cannot be directly used to obtain

[32] K. Sollner, *J. Phys. Chem.*, **49**, 47 (1945).
[33] Hydro-Quebec Institute of Research, Montreal, Que., Canada.
[34] I. Morcos and H. Fisher, *J. Electroanal. Chem.*, **17**, 7 (1968).
[35] I. Morcos, *J. Electroanal. Chem.*, **20**, 479 (1969).
[36] A. N. Frumkin, A. Gorodetzkaja, B. Kabanov, and N. Nekrassov, *Phys. Z, Soviet Union*, **1**, 225 (1932).
[37] W. A. Zisman, *Advan. Chem. Ser.*, **43**, 13 (1964).
* $\gamma_{L/g} = \gamma$.
[38] A. N. Frumkin, *Svensk Kem. Tidskr.*, **6**, 77 (1965).

surface charge from γ-voltage plots. For this purpose, the total applied electric field would have to be divided into the field acting across the bulk of the insulator phase and the field acting across the insulator/solution interface. This problem awaits further study. It will be noted that I have, therefore, avoided using Gibbs' equation to obtain surface charge. I think, however, that Gibbs' equation can be applied for obtaining the surface excess of a neutral species, n-butanol in my case, at the interface insulator/electrolytic solution. This treatment is based on the assumption that the voltage across the interface remains constant; *i.e.*, that the voltage distribution between insulator bulk and interface does not change with surface coverage by the neutral species, butanol. I think that this assumption is reasonable. The interface insulator/electrolytic solution can be considered to be an ideally polarizable interface in that there is, by definition, no current flow.

A Preliminary Investigation of Fluidized Bed Electrodes

J. R. Backhurst, J. M. Coulson, F. Goodridge, R. E. Plimley, and M. Fleischmann (pp. 1600-1607, Vol. 116, No. 11)

Richard Prober[39]: The development of fluidized bed electrodes, as reported by Backhurst, Coulson, Goodridge, Plimley, and Fleischmann, should stimulate considerable research interest directed toward optimization of electrode geometry as well as toward exploitation in large-scale electrochemical processes.

A fluidized bed electrode is a type of dispersed electrode, since the electrochemical reactions occur on the surfaces of suspended particles.[40] Heretofore, dispersed electrodes have used particles suspended by agitation or particles flowing as a slurry.[41] Fluidization of a bed of particles provides efficient contacting between the particles and the current feeder, and it consumes less power in suspending particles.

It is noteworthy that the reduction of m-nitrobenzene sulfonic acid on copper cathodes, which Backhurst *et al.* used as a test reaction system, is of the same class of reactions as the earliest application (to my knowledge) of dispersed electrodes.[42]

The data on the distribution of potential within a fluidized bed electrode (Figure 10) do, indeed, indicate that the bed is more effective near the current feeder than at points far away from it. This is evident upon replotting the data with cartesian coordinates in Fig. 10a and 10b. Both curves shown have a change of slope some 1.5-1.7 cm above the base of the bed. Above that point, the curves are linear with slopes that imply an effective resistance of 0.5 ohm cm of bed depth and an effective resistivity of 3.5 ohm-cm (*cf.* 2.5 ohm-cm for 1M sulfuric acid solution at 18°C). Thus, the upper part of the bed seems to be inactive unless the current feeder is located there.

John R. Backhurst: We would like to thank Dr. Prober for his comments on our paper on fluidized bed electrodes. It should be emphasized that we were reporting the preliminary results from this work, and more detailed experimental data has since been obtained. These experimental and theoretical conclusions will be published shortly.

In brief, they indicate, as Dr. Prober suggests, that in any fluidized electrodes of large dimensions in the direction of current flow there are regions of inactivity. However, these are not necessarily located in regions of the bed remote from the feeder. The distribution of activity shows a complex dependency on the many parameters which are used to describe the system; of these, the ratio of particulate to electrolyte conductivity appears at this stage to be most influential. In fact, if the feeder is located at the beginning of the bed away from the counterelectrode, the region of least activity for the reactions investigated so far is located in the center of the bed.

[39] Chemical Engineering Science Division, Case Western Reserve University, Cleveland, Ohio.

[40] R. Prober and J. C. Dygert, Paper 61a, American Institute of Chemical Engineers, 62nd Annual Meeting, Washington, D. C., Nov. 16-20, 1969 (Submitted for publication in *A.I.Ch.E. Journal*).

[41] See, *e.g.*, J. Held and H. Gerischer, *Ber. Bunsengesell. Phys. Chem.*, 67, 921 (1963) or E. Baur, *Z. Elektrochem.*, 39, 162 (1933).

[42] C. F. Boehringer, German Pat. 117,007 (1900).

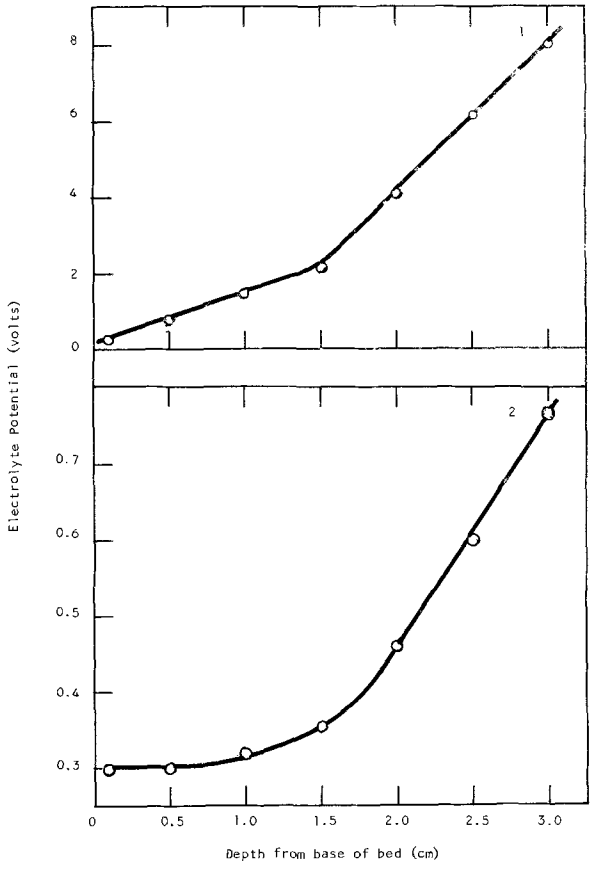

Fig. 10. Distribution of potential in the electrolyte in a fluidized bed electrode (based on data of Backhurst *et al.*). Panel a (upper): feeder near base of bed, current—8.0A, above 1.6 cm slope of curve 1 is 4.1 V/cm. Panel b (lower): feeder about 1.5 cm above base of bed, current—0.7A, above 1.7 cm slope of curve 2 is 0.31 V/cm.

A Reversible Solid-State Battery with $RbAg_4I_5$ as Electrolyte

Mario De Rossi, Gianfranco Pistoia, and Bruno Scrosati (pp. 1642-1646, Vol. 116, No. 12)

Takehiko Takahashi[43]: On page 1643, Dr. De Rossi wrote that the electrolyte (Ag_3SI) cannot be used for battery purposes since it has high electronic conductivity, referring to the review written by Foley.[44]

The transference number of Ag^+ ion in Ag_3SI, t_i, was measured by Takahashi and Yamamoto to be 0.977 or 0.985.[45] But, when the transference number of the electron is small, $1 - t_i$ is not always considered to give an exact value of the electron transference number.

For this reason, Takahashi and Yamamoto also measured the electronic conductivity of Ag_3SI by Wagner's method to obtain 10^{-8} ohm^{-1} cm^{-1} at room temperature,[46] the value of which was, however, different from that obtained by the extrapolated figure of Reuter and Hardel's work ($10^{-4} \sim 10^{-5}$ ohm^{-1} cm^{-1}) as described in Dr. Foley's review.

The exact reason for this discrepancy has not been made clear, but it will be attributed to the preparation

[43] Dept. of Applied Chemistry, Faculty of Engineering, Nagoya University, Nagoya, Japan.

[44] R. T. Foley, *This Journal*, 116, 13C (1969).

[45] Takahashi and Yamamoto, *Electrochim. Acta*, 11, 779 (1966).

[46] Takahashi and Yamamoto, *Electrochim. Acta*, 11, 783 (1966).

procedure of Ag_3SI, the electronic conductivity of which is easily changed by changing the vapor pressure of sulfur when the reaction between AgI and Ag_2S is carried out to synthesize Ag_3SI. Thus, the electronic conductivity of 10^{-8} ohm^{-1} cm^{-1} at room temperature can easily be obtained by using a suitable vapor pressure of sulfur on synthesizing Ag_3SI without any change of ionic conductivity.[47]

Bruno Scrosati: The comment of Prof. Takahashi on this paper does not seem to need a precise answer since this answer is already included in the comment itself. Undoubtedly, some disagreements on the Ag_3SI electronic conductivity do exist in the literature, many of them due to different preparation procedures or to different determination techniques.

As to what the utilization of Ag_3SI as such in a solid state relates to, it may be definitive of the work of Owens and co-workers[48] on the Ag_3SI stability. In this work, it has been clearly proved that this solid electrolyte is not stable in the presence of iodine since it slowly degrades to AgI and S. It follows that the application of Ag_3SI in solid electrolyte cells is quite limited. Only low emf cells could be operative with all the related disadvantages, such as low power density, low emf., and kinetic restrictions.[48]

[47] *Denki-Kagaku*, 22, 610 (1964).

[48] B. Owens, G. R. Argue, I. J. Groce, and L. D. Hermo, *This Journal*, 116, 312 (1969).

JOURNAL OF THE ELECTROCHEMICAL SOCIETY

SOLID STATE SCIENCE

JULY 1970

RF Sputtered Aluminum Oxide Films on Silicon

C. A. T. Salama*

Department of Electrical Engineering, University of Toronto, Toronto, Ontario, Canada

ABSTRACT

The physical and electrical properties of aluminum oxide films deposited on silicon by rf sputtering from an alumina target in an argon atmosphere were investigated as a function of sputtering power density in the range from 0.5 to 3 W/cm^2. The deposition rates ranged from 20 to 80 Å/min. The density, index of refraction, and dielectric constant of the films increased while the etch rate decreased with increasing power density. The surface charge at the aluminum oxide-silicon interface was typically larger than 10^{12} e/cm^2. This charge increased with increasing sputtering power density and could be reduced to 7-8 x 10^{11} e/cm^2 by annealing. The films exhibited trapping instabilities at room temperature but no polarization was observed under bias-temperature stress. The characteristics of composite layers of thermally grown silicon dioxide and sputtered aluminum oxide layers on silicon were also investigated and found to exhibit low surface charge densities, no hysteresis, and a "contact potential" as well as charge stored at the interface between the two insulators.

Dielectric films deposited on semiconductor substrates serve many functions in solid state devices. These functions include masking against diffusion of impurities during the formation of pn junctions, surface passivation, insulation in multilayer interconnections, fabrication of capacitor structures, and insulated-gate field-effect transistors (IGFET).

Amorphous silicon dioxide films have been used extensively in silicon device technology and are still the most commonly used dielectrics. However, silicon dioxide is structurally porous (as indicated by its low density) and permeable to ionic migration which reduce its effectiveness as a passivating layer. These disadvantages have prompted the investigation of other oxide and nitride dielectrics; among these is aluminum oxide.

The interest in aluminum oxide films stems from the following experimental observations: the ionic mobility of impurities (Na^+) is very low in these films (1), their radiation resistance is high compared to silicon dioxide films (2), and their dielectric constant is double that of silicon dioxide (3). These films are also of interest in double layer (SiO_2-Al_2O_3) structures where they act as effective junction seals (4) and also offer a possible method of controlling the threshold voltage of IGFET devices (5) due to the presence of a "contact potential" at the silicon dioxide-aluminum oxide interface.

Aluminum oxide films have been deposited on silicon by various methods. Chemical vapor deposition involving the hydrolysis of aluminum trichloride (6) or pyrolysis of organo-aluminum compounds (7) have been the most commonly used. The films prepared by these methods exhibit interface charge densities in the range 3-10 x 10^{11} cm^{-2} and this charge can be reduced to 1-2 x 10^{11} cm^{-2} when a thermally grown silicon dioxide interlayer is used between the silicon and the aluminum oxide (8). Both positive and negative interface charges have been reported in these films (7-11), the charge being strongly process dependent. DC reactively sputtered (12-14) aluminum oxide films have resulted in extremely low surface charge and surface state densities. Plasma anodized (2, 15) aluminum oxide films have also yielded extremely low surface charge densities. More recently, films have also been prepared by reactive evaporation (16), and yielded results similar to those obtained with chemically deposited films. Relatively little has been reported on the deposition of aluminum oxide by rf sputtering on silicon or other substrates (17, 18).

The purpose of this study is to investigate the physical and electrical properties of aluminum oxide films deposited on silicon by rf sputtering from an aluminum oxide target in an argon atmosphere and to evaluate the suitability of these films as passivating layers on silicon. This study also includes an investigation of the characteristics of sputtered aluminum oxide-thermally grown silicon dioxide double layers on silicon.

Experimental

The rf sputtering apparatus used in this work is shown schematically in Fig. 1. The dielectric target used was a sintered aluminum oxide (99.97%) disk 12.5 cm in diameter and 1 cm thick. It was metallized on one side and bonded using silver epoxy to a flat water-cooled aluminum disk which formed part of the vacuum chamber wall through a system of vacuum seals and an insulating ring. A metal shield surrounded the exposed areas of the water-cooled aluminum disk at a spacing of 0.5 cm in order to prevent sputtering from this region. The substrate supporting configuration was water-cooled.

A conventional rf generator operating at 13.56 MHz was used as the source of power which was coupled to the target electrode through a tunable network which insured matching between the coaxial transmission

* Electrochemical Society Active Member.
Key words: thin film, dielectric, passivation.

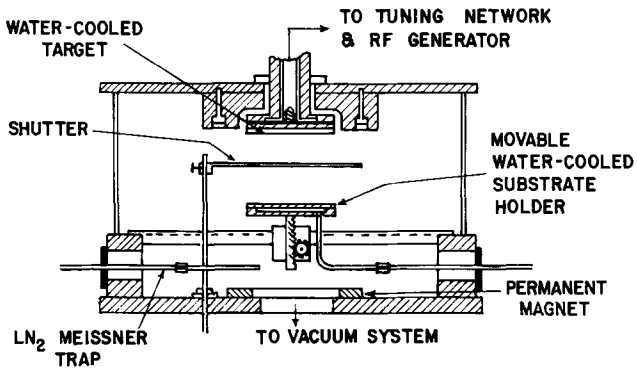

Fig. 1. Schematic diagram of rf sputtering apparatus

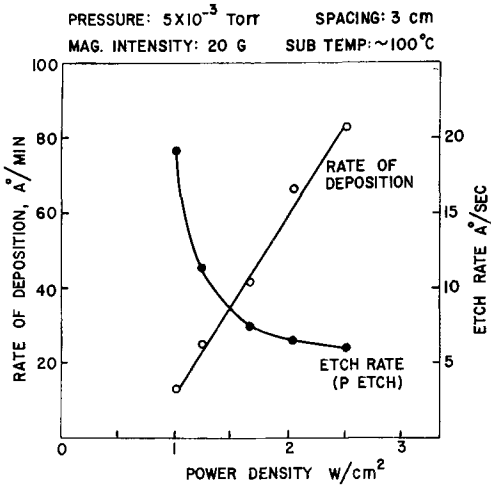

Fig. 2. Effect of power density on deposition and etch rates

line impedance and the sputtering system load impedance. The power delivered to the discharge was measured using a standing-wave power meter. A permanent magnet inside the vacuum system was used to provide a magnetic field (20 gauss) perpendicular to the dielectric target surface. This magnetic field caused a 20% increase in the deposition rate and helped to stabilize and confine the glow to the space between the two electrodes. Ultra high-purity argon (99.999%) was used as the sputtering gas and the pressure during sputtering was monitored by means of a cold cathode gauge. The system was evacuated by a 6 in. oil diffusion pump equipped with a water-cooled baffle and a liquid nitrogen trap. A Meissner trap was also fitted into the 18 in. glass bell jar to improve the ultimate vacuum.

In a typical run, the initial pressure in the system was 4×10^{-7} Torr. Prior to deposition, the target was cleaned by argon ion bombardment (with the substrates shielded) and the system was pumped down again to 4×10^{-7} Torr. Argon was then re-introduced in the system and the oxide deposition carried out under predetermined operating conditions. To minimize gas contamination the pumping system was not throttled during sputtering and liquid ntirogen was used in both traps. The argon pressure was kept at 5-7μ during most of the runs. At this sputtering pressure a 3 cm target to substrate distance was found to be compatible with a self-sustained uniform discharge and satisfactory deposition rates.

The nominal substrate temperature was measured using a thin (0.010 in.) chromel-alumel thermocouple prior to turning on and immediately after extinguishing the glow discharge. In most cases, the silicon slices were held on the substrate holder by means of a thin layer of gallium which provided good thermal contact and allowed deposition at low temperatures (~100°C). Depositions were also carried out with the substrates thermally isolated from the holder. The substrate temperature during these runs did not exceed 200°C and reached equilibrium within a few minutes after the discharge had been turned on (19).

Silicon used in this work was in the form of polished circular slices (Monsanto) 2.5 cm in diameter prepared by the Czochralski method. The dislocation count was specified to be less than 10^3 cm^{-2}. The slices used were n-type phosphorus doped, (111) orientation of approximately 10 and 0.01 ohm-cm resistivities. The high-resistivity slices were used for surface studies and the low-resistivity ones were used for investigations of the dielectric and optical properties of the aluminum oxide films. Prior to aluminum oxide deposition or silicon dioxide growth the polished silicon wafers were degreased, boiled in nitric acid, dipped in hydrofluoric acid, and then rinsed in deionized water. The silicon dioxide growth was carried out at 1100°C in dry oxygen in a horizontal resistively heated furnace provided with a quartz tube and mullite liner. The silicon dioxide was then annealed at the same temperature in nitrogen for 30 min. Both the oxygen and nitrogen gases were obtained from liquid sources.

After deposition the aluminum oxide films were annealed in nitrogen for 30 min at 300°C unless otherwise noted.[1] The heat treatments were restricted to a temperature below 320°C because of the possible occurrence of a new phase of aluminum oxide (γ') above this temperature (20).

The thickness of the films was measured using a Talystep (Taylor-Hobson) capable of ±20Å accuracy. The structure of the films was examined by electron microscopy. The density was determined by a differential weighing technique using a microbalance. The index of refraction was obtained from measurements on the interference pattern in the visible u.v. range by means of a Perkin-Elmer 450 spectrophotometer fitted with a 350 specular reflectance attachment. Knowing the film thickness from Talystep measurements, it was possible to estimate the index of refraction as a function of wavelength (21). The infrared spectra were obtained using a Perkin-Elmer 621 spectrophotometer fitted with two microspecular reflectance attachments.

Most of the electrical evaluations involved MIS (metal-insulator-semiconductor) structures. These were prepared by evaporating aluminum (99.999%) field plates, 1000Å thick, 500μ in diameter over the dielectric through a mask. Aluminum was also evaporated on the bare back-side of the silicon for contact. The evaporations were carried out from a resistively heated tungsten filament in a vacuum of 10^{-6} Torr. Electrical measurements were then carried out as described later in the paper.

Results and Discussion

For rf sputtering of insulating films on semiconductor substrates, the power density affects the rate of deposition, the etch rate, the density, the dielectric constant, the conductivity, and the surface characteristics of the semiconductor-insulator interface (22). Some of these effects will be considered in the following sections.

Physical Properties

The rate of deposition of aluminum oxide films as a function of power density is shown in Fig. 2. The deposition rate is a linear function of power density. The film thickness was uniform within 5% over the whole area of any one slice and films could be deposited over six slices simultaneously with a thickness uniformity of better than 10%. No cracks were observed in films ranging up to 5000Å in thickness.

The etch rate is a sensitive indicator of the structural properties of the film. The P-etch[2] rate for alu-

[1] Annealing at such low temperatures was found to have negligible effect on the densification of the layers.
[2] 15 parts 49% HF; 10 parts 70% HNO_3; 300 parts H_2O.

minum oxide films is shown in Fig. 2 and is seen to increase drastically at low power densities, indicating porous films. This fact was also confirmed by measurements of the density of the films as a function of power density. The low power depositions resulted in lower film densities as shown in Fig. 3. The density ranged from 3.5 g/cm^3 at a power density of 1 W/cm^2 to about 3.8 g/cm^3 at 2.5 W/cm^2.

The films examined by low-angle electron diffraction were found to be amorphous independently of the deposition power densities used in this investigation. The index of refraction of the films was found to increase with increasing power density ranging from 1.55 to 1.65 at 0.5μ. A typical infrared reflectance spectrum for an aluminum oxide film deposited on low-resistivity silicon is shows in Fig. 4. It exhibits a broad peak around 15μ, in general agreement with the data reported for α-aluminum oxide (23). No trace of water could be detected in the films from these infrared measurements. Relatively minor variations were observed in the physical properties of annealed films deposited on substrates held by gallium on the holder and those deposited on substrates thermally isolated from the holder.

Electrical Properties

Metal-aluminum oxide-silicon (MAS) structures.—Dielectric constant.—The dielectric constant of aluminum oxide films sputtered under the conditions described above were obtained from capacitance measurements of 1 kHz using a GR 1650B bridge. The values obtained ranged from 7 at a power density of 1 W/cm^2 to 8.5 at a power density of 2.5 W/cm^2. Values of 8.55 for sputtered aluminum oxide films have been reported by Pratt (18). The low dielectric constant observed at low power density is probably related to the low film density (24). The dissipation factor for these films ranged from 0.01 to 0.004.

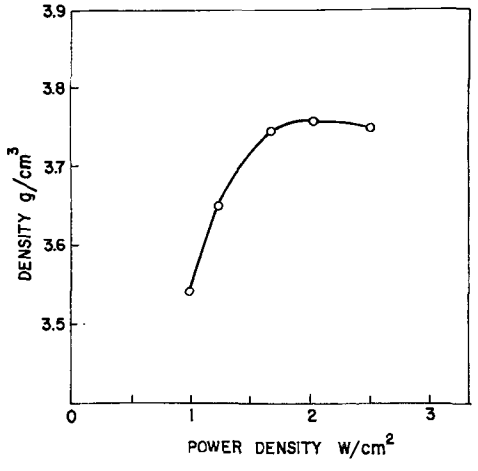

Fig. 3. Film density as a function of deposition power density

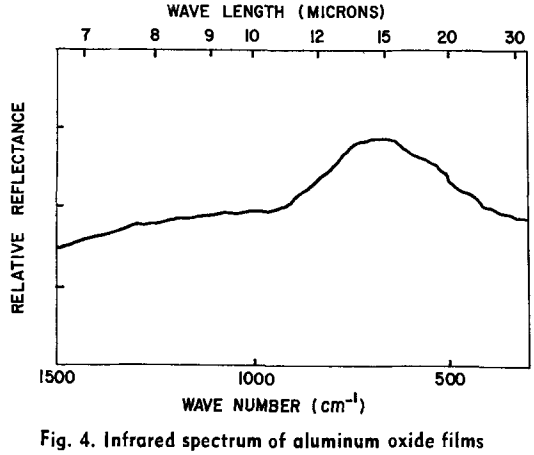

Fig. 4. Infrared spectrum of aluminum oxide films

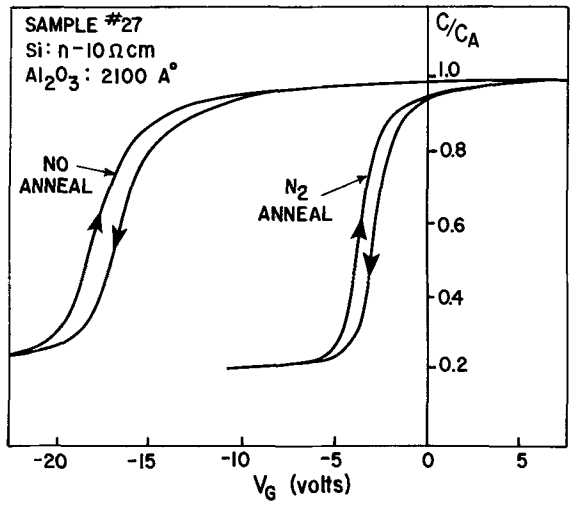

Fig. 5. Capacitance-voltage plots for a MAS device showing the effect of annealing. (C_A = aluminum oxide capacitance per unit area.)

Breakdown field.—The breakdown field of aluminum oxide films was measured by the method described by Worthing (25). A general correlation between power density and breakdown field was not possible and the measured breakdown values ranged fom 2 to 8 x 10^6 V/cm. These values agree with the ones reported by Pratt (18).

Surface charge.—The charge per unit area Q_{SA} stored in the aluminum oxide was determined from the capacitance-voltage characteristics (C-V) of the MAS structure. This method involves the determination of the flat-band voltage V_{FB} of the experimental C-V curve. The charge density Q_{SA} is then related to V_{FB} by the expression[3]:

$$V_{FB} = -Q_{SA}\left[\frac{x_a}{\epsilon_a}\right] + \phi_{MS} \qquad [1]$$

where ϕ_{MS} is the metal-semiconductor work function difference (26), and x_a, ϵ_a are, respectively, the thickness and dielectric constant of the aluminum oxide layer. The capacitance measurements were carried out at 1 MHz using a Boonton 71A capacitance meter.

As mentioned in previous sections, higher deposition power densities result in denser, higher quality films, however, a major detrimental effect in using high power densities is the deterioration of the silicon surface properties. The induced charge was measured as a function of deposition power density prior to annealing of the films. The charge induced was observed to increase with sputtering power density in agreement with the observations of Hu and Gregor (24). When the power density was below 1 W/cm^2 the induced charge was about 10^{12} e/cm^2. At power densities of 2.5 W/cm^2 and above the surface charge was 10^{13} e/cm^2 or larger. In all cases the effective charge stored in the oxide was positive. Annealing at 300°C for 30 min in N_2 prior to electrode deposition was found to reduce this charge in most cases to about 7-8 x 10^{11} e/cm^2. For initial (prior to annealing) charge densities higher than 10^{13} e/cm^2 N_2 annealing was found to have little or no effect and the charge stored in the oxide could not be significantly reduced. Figure 5 shows the C-V characteristics of a MAS sample prior to and after N_2 annealing. The increase in induced charge with increasing deposition power density can be attributed to an increase in the charge stored in the oxide due to structural differences between oxides deposited at various power densities and/or to bombardment induced surface damage during sputtering (24). Since the surface charge after annealing was approximately

[3] The charge Q_{SA} was assumed to be at the silicon-aluminum oxide interface.

constant for power densities below 2.5 W/cm^2, the reduction in surface charge can be due to annealing of radiation damage at the silicon-aluminum oxide interface. However, at higher power densities the surface charge is more likely to be associated with structural changes in the oxide or permanent surface damage which could not be annealed.

The distribution of oxide charge was studied as a function of distance in the oxide. The oxide charge, after annealing, was found to be located predominantly at or near the silicon-aluminum oxide interface. This observation was the result of a series of etching-annealing experiments. Aluminum oxide layers, 2000Å thick, were thinned by etching to produce oxide thicknesses ranging from 500 to 2000Å in several steps. The oxides were then annealed as described previously and the surface charge measured. In all cases the effective surface charge densities were of the order of 7-8 x 10^{11} e/cm^2 independent of oxide thickness. Similar results have been observed in sputtered silicon dioxide films on silicon (27).

A further observation which can be made regarding the C-V plots of Fig. 5 is the difference in the shape of annealed and unannealed samples. The slow transition in the C-V curve for the latter is probably related to a high surface state density which can be reduced by annealing.

Trapping.—Hysteresis is present in the C-V curves shown in Fig. 5. The sense of the hysteresis (flat-band voltage more negative after the maximum negative excursion) indicates charge interchange across the aluminum oxide-silicon interface. Hole emission from the silicon to the insulator or electron emission from traps in the insulator to the silicon could account for the observed sense of the hysteresis (28). An increase in hysteresis was observed when the bias-voltage swing about flat-band was increased. A displacement of the C-V curves was also observed at room temperature after application of a stress field exceeding a threshold of 1-2 x 10^6 V/cm. The direction of this displacement was opposite to that caused by polarization or ion migration and was temperature independent and dependent on previous bias history. Figure 6 shows the effect of stress voltage on the flat-band voltage of a MAS capacitor. Similar results have been observed on silicon nitride (28), (29), and vapor-deposited silicon oxide (30) on silicon. This instability is postulated to be associated with deep trapping centers in the dielectric coupled with charge transfer across the interface region between the dielectric and the semiconductor. The trapping instability and hysteresis could be caused by the presence of a very thin silicon dioxide layer (~20Å) which is usually present on silicon.

Polarization and ion migration.—Polarization and ion migration are characterized by a displacement of the C-V curves in a direction opposite to the polarity of the applied bias when the MAS sample is subjected to bias-temperature stress. The displacement is a function of applied bias and temperature. Annealed aluminum oxide layers were subjected to bias-temperature stress for 10 min at 250°C. The field applied during these experiments was smaller than the threshold field required for trapping (typically 1 x 10^6 V/cm). The resulting voltage shifts were typically less than 1V. Bias-temperature stress experiments with controlled Na^+ contamination indicated that Na^+ did not migrate appreciably through a 1000Å layer of aluminum oxide in agreement with the results of Tung and Caffrey (1). The above experiments indicate that polarization and ion migration in the sputtered films are negligible.

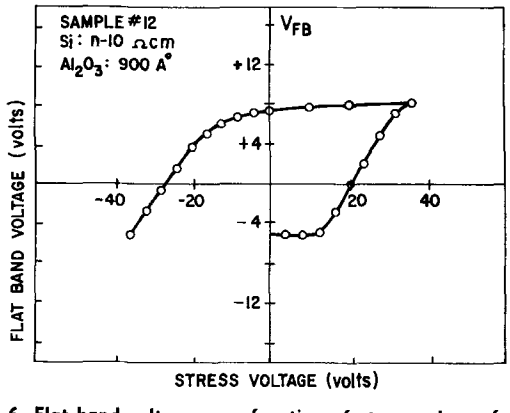

Fig. 6. Flat-band voltage as a function of stress voltage for MAS device.

Metal-aluminum oxide-silicon dioxide-silicon (MAOS) structures.—The electrical characteristics of aluminum oxide-silicon structures discussed above indicate that in spite of the absence of polarization and ion migration, the sputtered aluminum oxide films are not entirely satisfactory for passivation purposes because of the trapping instability associated with the insulator-semiconductor interface. Since thermally grown silicon dioxide on silicon does not exhibit charge instability, the properties of double layers of SiO_2 + Al_2O_3 were investigated.

Characterization of the insulator charge in MAOS structures was performed by C-V techniques. The analysis in this case is slightly complicated by the possible presence of a charge Q_{ii} at the silicon dioxide-aluminum oxide interface and a "contact potential" ϕ_{ii} at the same interface (4, 31). Taking these factors into account the flat-band voltage for the double layer is given by

$$V_{FB} = -Q_{SS}\left[\frac{x_o}{\epsilon_o} + \frac{x_a}{\epsilon_a}\right] - Q_{ii}\left[\frac{x_a}{\epsilon_a}\right] + \phi_{ii} + \phi_{MS} \quad [2]$$

where Q_{SS} is the fixed positive surface charge density at the Si-SiO_2 interface and x_o, ϵ_o are, respectively, the thickness and dielectric constant of the silicon dioxide layer. Distributed charge in the aluminum oxide and silicon dioxide has been neglected in the above equation (32).

In order to investigate the validity of Eq. [2] and to evaluate the magnitude of the various terms in that equation, four sets of samples having 1000Å of thermally grown silicon dioxide with overlayers of aluminum oxide ranging in thickness from 700 to 3000Å were prepared. The aluminum oxide layers were deposited at different power densities (ranging from 1 to 2 W/cm^2) for each set of samples. The double layers were then annealed at 300°C for 30 min in N_2 prior to electrode deposition. Figure 7 shows the C-V characteristics of one of the MAOS test samples. The C-V characteristics of the double layer do not exhibit hysteresis. Trapping is also absent in the double layer

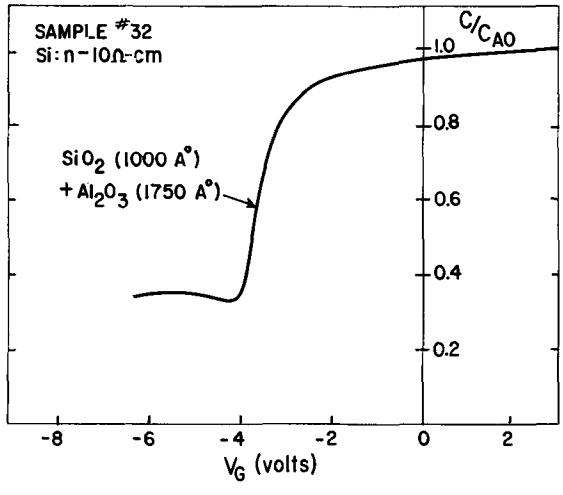

Fig. 7. Capacitance-voltage plot for a MAOS device. (C_{AO} = double-layer dielectric capacitance per unit area.)

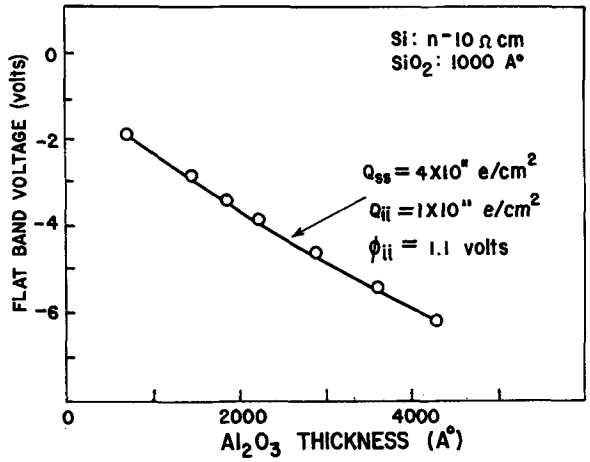

Fig. 8. Flat-band voltage as a function of aluminum oxide thickness in MAOS devices.

even for stress voltages up to the destructive breakdown of the dielectric layer. Similar results have been observed in Si_3N_4-SiO_2 double layers (29). Figure 8 shows a plot of the flat-band voltage of the double layer as a function of the aluminum oxide thickness for one set of samples. The aluminum oxide films in this case were deposited at 1.5 W/cm^2.

The constant parameters in Eq. [2] were estimated by curve fitting and found to be

$$Q_{SS} \sim 4 \times 10^{11} \text{ e/cm}^2 \text{ (positive)}$$

$$Q_{ii} \sim 1 \times 10^{11} \text{ e/cm}^2 \text{ (positive)}$$

$$\phi_{ii} \sim 1.1\text{V}$$

It should be noted that the intercept of the curve with the flat-band voltage axis for zero aluminum oxide thickness is not the value of ϕ_{ii}. This intercept depends on the values of Q_{SS}, x_o, ϵ_o, and ϕ_{MS} (-0.35V in this case). The magnitude of Q_{SS} in the annealed MAOS samples was found to be approximately the same as the one observed in MOS samples when the silicon dioxide was subjected to the same annealing. Wu and Formigoni (27) reported similar results on double layers of silicon dioxide sputtered on thermally oxidized silicon. The charge Q_{ii} was found to be positive for all the samples investigated and increased with increasing power density ranging from 1 x 10^{11} to 4 x 10^{11} e/cm^2. The charge Q_{ii} may be associated with charged traps at the interface. The density of these traps increases with increasing power density thus causing an increase in the stored charge. The origin of ϕ_{ii} is not completely understood (33), and it was found to range from 1 to 1.2V for the samples investigated. Both Q_{ii} and ϕ_{ii} have considerable effect on the threshold of IGFET's and the control of these parameters by deposition or annealing processes[4] may be required before the advantages of the double-layer structure can be fully realized.

Conclusions

Good quality aluminum oxide films can be prepared by rf sputtering of an alumina target in an argon atmosphere. The rate of deposition of the films is in the range 20-80 A/min for power densities ranging from 0.5 to 3 W/cm^2. The films were found to be amorphous and the etch rate, the density, the index of refraction, as well as the dielectric constant, were found to increase with increasing power density. In general, high power sputtering is preferred however, in this case surface charge becomes a problem. The initial surface charge after deposition was found to be larger than 10^{12} e/cm^2. After annealing this charge could be reduced to 7-8 x 10^{11} e/cm^2. The films deposited directly on silicon exhibited trapping instabilities at room temperature, but no polarization was observed under bias-temperature stress. Double layers of thermally grown silicon dioxide and sputtered aluminum oxide exhibited low-surface charge densities, no trapping instabilities, and a "contact potential" as well as charge stored at the interface between the two dielectrics. Both the interface charge and the contact potential were found to be process dependant and both will have to be controlled if full advantage is to be taken of characteristics of the double-layer structure.

[4] For double layers of aluminum oxide-silicon dioxide on silicon, Nigh *et al.* (4) have reported a positive ϕ_{ii} (of approximately the same value as the one reported here) but no Q_{ii}; Nishimatsu *et al.* (10) have reported the presence of both a negative Q_{ii} and a distributed charge in the Al_2O_3 films but no ϕ_{ii}; Kalter *et al.* (31) have reported a positive ϕ_{ii} but not Q_{ii}.

Acknowledgments

This work was supported by the Defence Research Board of Canada (Grant 5566-34) and by the National Research Council of Canada (Grant A-4408). The author wishes to thank Mrs. S. Trettin for assistance in the sample preparations, Dr. J. G. Simmons for use of the Talystep, and Dr. S. Zukotynski for use of the spectrophotometers.

Manuscript submitted Nov. 5, 1969; revised manuscript received Jan. 29, 1970. This was Paper 96 presented, in part, at the Detroit Meeting of the Society, Oct. 5-9, 1969.

Any discussion of this paper will appear in a Discussion Section to be published in the June 1971 JOURNAL.

REFERENCES

1. S. K. Tung and R. E. Caffrey, *This Journal*, **115**, 239C (1968).
2. A. Waxman and K. H. Zaininger, *Appl. Phys. Letters*, **12**, 109 (1968).
3. L. V. Gregor and R. E. Jones, *Solid State Technology*, p. 40, May 1968.
4. H. E. Nigh, J. Stach, and R. M. Jacobs, *IEEE Trans. ED*, **ED-14**, 631 (1967).
5. G. T. Cheney, R. M. Jacobs, H. W. Korb, H. E. Nigh, and J. Stach, *ibid.*, **ED-15**, 410 (1968).
6. S. K. Tung and R. E. Caffrey, *This Journal*, **114**, 275C (1967).
7. J. A. Aboaf, *ibid.*, **114**, 948 (1967).
8. T. L. Chu, *J. Vacuum Sci. Technol.*, **6**, 25 (1969).
9. H. Matsushita and Y. Koga, *This Journal*, **115**, 69C (1968).
10. S. Nishimatsu, T. Tokuyama, and M. Matsushita, *ibid.*, **115**, 239C (1968).
11. V. Y. Doo and P. J. Tsang, *ibid.*, **116**, 117C (1969)
12. R. J. Frieser, *ibid.*, **113**, 357 (1966).
13. T. Tanaka and S. Iwauchi, *Japan J. Appl. Phys.*, **7**, 1420 (1968).
14. K. Nagano, S. Iwauchi, and T. Tanaka, *ibid*, **8**, 277 (1969)
15. K. H. Zaininger and A. S. Waxman, *IEEE Trans. ED*, **ED-16**, 333 (1969).
16. E. Ferrier and B. Pruniaux, *This Journal*, **116**, 1008 (1969).
17. E. Augustine, P. Hall, and R. Rossmeil, *Proc. 5th Microelectronics Symp.*, p. 5D-1 (1966).
18. I. H. Pratt, *Thin Solid Films*, **3**, R23 (1969)
19. P. M. Schaible and L. I. Maissel, *ibid.*, **3**, 277 (1969).
20. A. L. Dragoo and J. J. Diamond, *J. Amer. Ceram. Soc.*, **50**, 568 (1967).
21. F. Reizman and W. Van Gelder, *Solid-State Electron.*, **10**, 625 (1967).
22. J. L. Vossen and J. Y. O'Neill, Jr., *RCA Rev.*, **29**, 149 (1968).
23. A. S. Barker, Jr., *Phys. Rev.*, **132**, 1474 (1963).
24. S. M. Hu and L. V. Gregor, *This Journal*, **114**, 826 (1967).
25. F. L. Worthing, *ibid.*, **115**, 88 (1968).
26. B. E. Deal, E. H. Snow, and C. A. Mead, *J. Phys. Chem. Solids*, **27**, 1873 (1966).
27. S. Y. Wu and N. P. Formigoni, *J. Appl. Phys.*, **39**, 5613 (1968).
28. S. M. Hu, D. R. Kerr, and L. V. Gregor, *Appl. Phys. Letters*, **10**, 97 (1967).
29. T. L. Chu, J. R. Szedon, and C. H. Lee, *Solid-State Electron.*, **10**, 897 (1967).
30. B. E. Deal, P. J. Fleming, and P. L. Castro, *This Journal*, **115**, 300 (1968).
31. H. Kalter, E. Kooi, and J. J. Schatorje, *ibid.*, **116**, 250C (1969).
32. V. Rodriguez and D. Frohman-Bentchowski, *ibid.*, **116**, 290C (1969).
33. L. V. Gregor, *ibid.*, **115**, 238C (1968).

Photoluminescence of Eu(II) Activated $EuAlO_3$

Philip M. Jaffe*

Zenith Radio Corporation, Chicago, Illinois

ABSTRACT

$EuAlO_3$ activated with Eu(II) results in an efficient band emitting uv excited phosphor. From a study of the optical properties of $EuAlO_3$:Eu(III) and $EuAlO_3$:Eu(II) the following conclusions were reached: (*i*) there is little if any emission from Eu(III) because of concentration quenching; (*ii*) other than the trivial radiative energy transfer from Eu(II) to Eu(III) there is little interaction between Eu(II) and Eu(III); (*iii*) the excitation spectrum of Eu(II) emission can be explained in terms of crystal field theory.

In the last few years there has been much interest in divalent and trivalent Eu activated phosphors. This interest has been both theoretical and practical as evidenced by an examination of the recent phosphor literature as, for example, ref. (1) through (8). In these phosphors, other than those reported by McAllister (8), only one oxidation state of Eu was present. McAllister's work was with the complicated (Li, Ba, La, Eu)PO_4 in which Eu(II) and Eu(III) were present, simultaneously. A better phosphor in which to study interactions, if any, between Eu(II) and Eu(III) would appear to be $EuAlO_3$.

$EuAlO_3$ exists in two modifications, perovskite (cubic) and orthorhombic (9). The perovskite structure, which has the general form ABO_3, may be considered to be made up of layers of oxygen atoms (10). The large A ions are located in twelve-fold coordination and the smaller B ions in six-fold coordination. In $EuAlO_3$ the Eu(III) is in the A site. When Eu(II) is formed on reduction of Eu(III) it stays in an A site since no ion migration or rearrangement is necessary for its incorporation into the host lattice as may be necessary with McAllister's phosphors.

Experimental

The phosphors studied here were mixtures containing 80-90% of the cubic $EuAlO_3$, the balance being the orthorhombic modification. X-ray diffraction analysis has shown that $EuAlO_3$ can exist over the range of at least 0.1 g at. of excess Eu or Al using the substitution $Eu_{1\pm x}Al_{1\mp x}O_3$.[1]

The various compositions studied here were prepared by coprecipitating $Al(OH)_3$ and $Eu(OH)_3$ with ammonia from a hot solution of the nitrates. After digesting overnight, the precipitate was filtered, dried at 120°C, triturated, and fired in alumina crucibles at 1250°-1350°C.

Absorption, emission, and excitation spectra were obtained with a Jarrell-Ash ¼ meter monochromator fitted with a motor drive on the grating. The emission spectra were corrected for instrumental errors and for photomultiplier response. The excitation spectra are given relative to fluorescein above 3300Å and sodium salicylate below this wavelength. Absorption spectra were also taken on a Beckman DU spectrophotometer.

Firing in an O_2 atmosphere results in $EuAlO_3$ having a white body color. It is nonluminescent under uv excitation and shows a very weak red line emission under cathode rays. The spectrum consists of three groups of lines located at 589, 592, and 596 nm ($^5D_0 \rightarrow {}^7F_1$); 610, 614, 618, and 626 nm ($^5D_0 \rightarrow {}^7F_2$); and 655nm ($^5D_0 \rightarrow {}^7F_3$), respectively. The dominant line is at 614 nm. Firing in a reducing atmosphere (NH_3 was preferred) resulted in phosphors having a yellow-green band emission and a yellow-green body color. Figure 1 shows the emission spectrum from a typical NH_3 fired $EuAlO_3$ phosphor taken under uv excitation.[2] It consists of a broad band peaking at 510 nm. Examination of the recorded spectrum shows the absence of any line emission but the presence of some line absorption located around 520 to 540 nm.

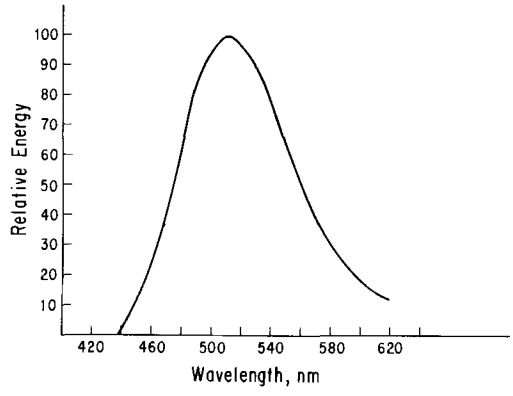

Fig. 1. Spectral distribution of the emission from $EuAlO_3$ fired in ammonia.

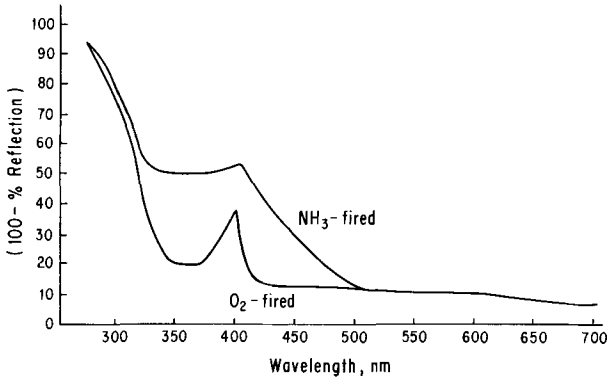

Fig. 2. Absorption spectra of $EuAlO_3$ fired in oxygen and in ammonia.

Figure 2 shows the absorption spectrum of near stoichiometric phosphors fired in O_2 and in NH_3, respectively. The oxygen-fired material shows a strong absorption band below 350 nm and a narrow, weaker band at 405 nm. The NH_3-fired phosphor shows a broad band extending from 330 to about 500 nm with a sharp peak at 405 nm. There is also a slight long wave broadening of the band below 350 nm. Superimposed on the absorption of the O_2- and NH_3-fired samples are several groups of absorption lines located around 360 to 400 nm, 525 to 550 nm, and 590 to 600 nm. These trivalent Eu absorptions are due to the

* Electrochemical Society Active Member.

[1] Increasing the Eu(III) or Al concentration above the stoichiometric 1:1 ratio results in an increase in the lattice parameter, a_o. Above 0.1 g at. Al, Al_2O_3 begins to appear whereas above 0.1 g at. Eu, the orderly lattice expansion of a_o becomes erratic. Firing in NH_3 results in the formation of $Eu(II)Al_2O_4$ at Eu concentrations above 0.1 g at.

[2] This system is difficult to work with and leaves much to be desired in reproducibility. The data presented are the average of several repeat samples.

transitions $^7F_0 \rightarrow {}^5D_{3\text{-}5}$, $^7F_0 \rightarrow {}^5D_1$, and $^7F_{0\text{-}2} \rightarrow {}^5D_0$, respectively. Corresponding lines in the two spectra are of about equal intensity. No absorption lines corresponding to the transitions $^7F_0 \rightarrow {}^5D_2$, 460 to 490 nm, were observed.

Using the substitution $Eu_{1\pm x}Al_{1\mp x}O_3$, samples were prepared over the stability range for excess Eu and Al, *ca.* 0.1 g at. Figure 3 shows the absorption spectrum of samples having $x = 0.1$ Al and 0.1 Eu; also shown for comparison is the spectrum of the near stoichiometric phosphor. Starting with an excess of Eu, increasing Al results in a progressive broadening of the two absorption bands plus an increase in the amplitude of the long wavelength band. The excitation spectra of these three phosphors are shown in Fig. 4. There are three distinct excitation bands located around 350, 310, and 260 nm. There might be a fourth band below 225 nm, but it could not be verified since measurements could not be made below 225 nm. The amplitude of the 310 nm band was invariant relative to the 350 nm peak while that of the 260 nm peak increases with increasing Eu. The brightness of these phosphors as a function of excess Eu or excess Al is shown in Fig. 5 for excitation into the three above-mentioned excitation bands. Starting with excess Eu, for all three excitations a progressive decrease in Eu, *i.e.*, increasing Al, results in a progressive increase in the brightness. In addition, the slope of the curves for 310 nm and 350 nm excitation are the same but different from the slope of the 260 nm excited curve. Incidentally, these phosphors are fairly efficient under 3650Å excitation. For example, the brightness of a good but nonoptimized near stoichiometric phosphor is about 60% of a (ZnCd)S:Ag phosphor of a similar color.

The temperature dependence of a near stoichiometric $EuAlO_3$ phosphor is shown in Fig. 6 for excitation into the three excitation bands. The curves are similar and show a temperature break-point around 200° to 220°K followed by a leveling off around 260° to 300°K.

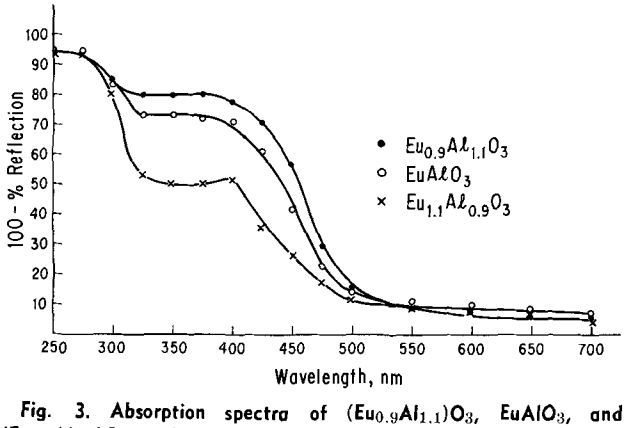

Fig. 3. Absorption spectra of $(Eu_{0.9}Al_{1.1})O_3$, $EuAlO_3$, and $(Eu_{1.1}Al_{0.9})O_3$ fired in ammonia.

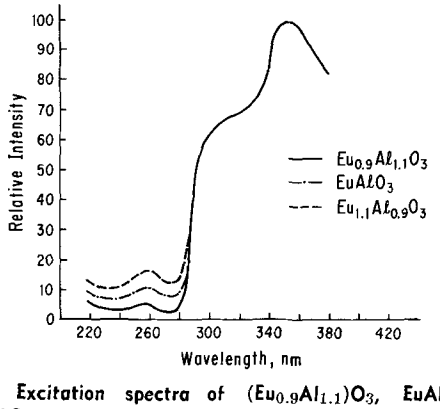

Fig. 4. Excitation spectra of $(Eu_{0.9}Al_{1.1})O_3$, $EuAlO_3$, and $(Eu_{1.1}Al_{0.9})O_3$ fired in ammonia.

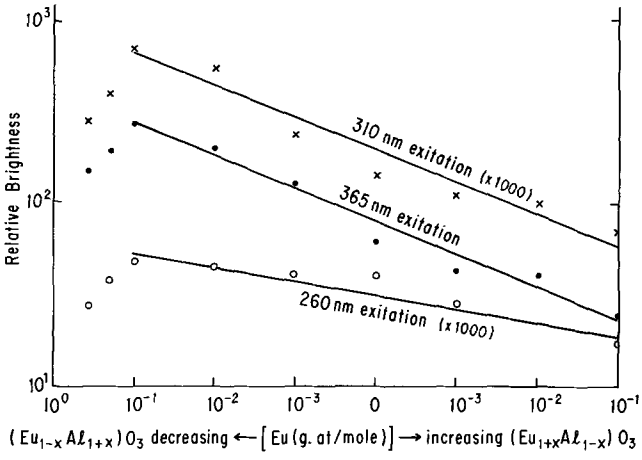

Fig. 5. Effect of an excess or deficiency of Eu on the brightness of $Eu_{1\pm x}Al_{1\mp x}O_3$. The stoichiometric composition is at the zero point on the abscissa. To its right, Eu is increasing; to its left it is decreasing. Excitation into the three excitation bands shown in Fig. 4.

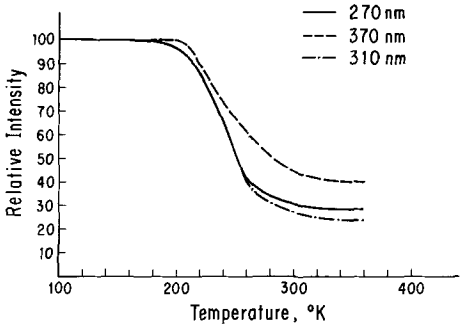

Fig. 6. Temperature dependence of the emission of a near stoichiometric $EuAlO_3$ fired in ammonia. Excitation into the three excitation bands shown in Fig. 4.

Attempts were made to measure the luminescence decay curves after excitation into the three excitation bands. Because the decay was very fast, the results are not conclusive. However, the decay appears to be the same for the three excitations, namely, an initial fast decay with a time constant less than 10 μsec followed by a slightly slower component.

Discussion

The green band emission obtained by firing $EuAlO_3$ in a reducing atmosphere is due to divalent Eu(11).[3] While trivalent Eu is present, it does not emit under uv excitation and only weakly so under cathode rays. This is most likely so because of concentration quenching.[4,5] However, the Eu(III) does absorb as evidenced by the superimposed line absorptions found in the absorption, excitation, and emission spectra. The Eu(II) emission is fairly efficient partially because of its low (unknown) concentration.

It is tempting to speculate that since Eu(II) replaces Eu(III), it would also be in the same site which is lacking a center of symmetry.[6] However, because the Eu(II) ion is larger than Eu(III), it is more easily polarized, thus affecting its environment

[3] Room temperature Mössbauer measurements show that divalent Eu is present and that its concentration increases with increasing Al content (16). This trend explains the results shown in Fig. 3 and 5, *i.e.*, the brightness and the absorption increase with increasing Eu(II) concentration.

[4] The weak luminescence under cathode rays and the lack of luminescence under uv indicates two things: one is that concentrating quenching is involved in both the excitation process and emission process, and two, that the excitation mechanism is somewhat different for the two modes of excitation.

[5] Van Uitert and Johnson found that for (Y,Eu)AlO_3, the optimum Eu concentration was about 5 a/o (12). The Eu(III) concentration in $EuAlO_3$:Eu(II) is considerably higher than this.

[6] The main line in the Eu^{+3} emission is at ~614 nm ($^5D_0 \rightarrow {}^7F_2$) which is due to an electric dipole transition indicative of an activator center lacking a center of symmetry.

so that its site symmetry may be quite different from that of Eu(III).

The fact that the 310 nm excitation band is invariant relative to the 360 nm band, Fig. 4, while the 260 nm band is not would indicate that there are two divalent Eu luminescent centers present. This is supported by the fact that the slope of the brightness *vs.* Eu concentration curve for 310 and 360 nm excitation are the same, but different from that of the 260 nm curve. Since the phosphors contain both cubic and orthorhombic phases, most likely one Eu(II) center is in the former phase and the other center is in the latter. Since in both centers the emission originates from a similar 5d excited level the luminescence decay would be expected to be similar as was observed.

We can account for the 310 and 350 nm excitation bands in the following way: the absorption of divalent Eu is due to the excitation of a 4f electron to a 5d level. Assuming cubic symmetry, this level is split by the crystal field into two main levels, t_2 and e (13). We can assign the 350 and 310 nm excitation bands to these two levels in the cubic perovskite as shown in Table I. The crystal field splitting parameter 10 Dq for these two lines is 3.7 kilo Kaysers, kK, which is in good agreement with similar data reported for other Eu(II) activated phosphors (14). If we assume that the 310 and 350 nm bands are associated with Eu(II) in the cubic (major) phase, then there should be two additional weaker levels due to Eu(II) in the orthorhombic phase. In this case, the 260 nm excitation band would then be the lower energy level of another 5d splitting. The 10 Dq value in this Eu(II) center is probably in the order of 4 to 10 kK. Using these values and assuming that the Eu(II) is still in a cubic field, then there should be a higher excitation level around 42 to 46 kK corresponding to a wavelength of 240-215 nm. There is an indication of a band in this region as shown in Fig. 4. The center of gravity for this level is around 40 to 41 kK whereas it was about 31 kK for the cubic phase.

Table I. Excitation bands and crystal field splitting of $EuAlO_3$ and other phosphors containing Eu(II)

Host	Excitation bands, $\times 10^3$ kilo Kaysers		10 Dq	Center of 5d level
$EuAlO_3$	28.6	32.3	3.7	30.8
CaF_2*	27.1	45.0	17.9	37.9
NaCl*	29.4	41.5	12.1	34.2
KBr*	29.7	38.1	8.4	33.1
$BaZrO_3$*	25.2	38.2	13.0	33.0

* Data taken from ref. (14).

The only interaction between Eu ions in the two oxidation states appears to be the trivial radiative energy transfer from Eu(II) to Eu(III). This is indicated by the weak absorption lines superimposed on the Eu(II) spectra. A similar conclusion has been reached by Blasse and Bril regarding energy interactions between Eu(II) and Eu(III) in SrY_2O_4 (15).

Acknowledgment

The writer would like to thank Miss K. Wolejko and Mr. F. Escudero for their aid in phosphor preparation, Dr. G. Arai and Mr. G. Roth for the x-ray work, and Dr. H. Forest and Mr. L. Ozawa for their comments.

Manuscript submitted Dec. 22, 1969; revised manuscript received *ca.* March 30, 1970. This was Paper 71 presented at the New York Meeting of the Society, May 4-9, 1969.

Any discussion of this paper will appear in a Discussion Section to be published in the June 1971 JOURNAL.

REFERENCES

1. A. Levine and F. Palilla, *Electrochem. Tech.*, **4**, 16 (1966).
2. G. Blasse and A. Bril, *J. Chem. Phys.*, **47**, 5442 (1967).
3. H. Forest and G. Ban, *This Journal*, **116**, 473 (1969).
4. H. J. Borchardt, *J. Chem. Phys.*, **38**, 1251 (1963).
5. T. Barry, *This Journal*, **115**, 733 (1968).
6. P. M. Jaffe and J. D. Konitzer, *ibid.*, **116**, 633 (1969).
7. P. M. Jaffe, *ibid.*, **16**, 629 (1969).
8. W. A. McAllister, *ibid.*, **115**, 535 (1968).
9. R. G. Wykoff, "Crystal Structures," Vol. 2, Interscience, New York (1964).
10. A. F. Wells, "Structural Inorganic Chemistry," 3rd ed., Oxford Press (1962).
11. P. M. Jaffe and E. Banks, *This Journal*, **102**, 518 (1955).
12. L. G. Van Uitert and L. F. Johnson, *J. Chem. Phys.*, **44**, 3514 (1966).
13. L. E. Orgel, "An Introduction to Transition-Metal Chemistry," John Wiley & Sons Inc., New York (1960).
14. G. Blasse, W. Wanmaker, J. ter Vrugt, and A. Bril, *Philips Res. Repts.*, **23**, 189 (1968).
15. G. Blasse and A. Bril, *J. Inorg and Nucl. Chem.*, **31**, 1521 (1969).
16. E. Kostiner, Chemistry Dept., Cornell University, Private communication.

Distribution of Impurities in Zn,O-Doped GaP Liquid Phase Epitaxy Layers

R. H. Saul and W. H. Hackett, Jr.

Bell Telephone Laboratories, Incorporated, Murray Hill, New Jersey

ABSTRACT

A series of variously doped GaP liquid phase epitaxy (LPE) layers were analyzed to establish the distribution of Zn,O and residual impurities contributing to the net impurity gradient previously observed in the p-layer of high efficiency GaP LPE diodes. From these experiments we conclude that the net impurity gradient is primarily a consequence of a decreasing Zn concentration along the growth direction, and, to a lesser degree, an increasing residual donor concentration. The distribution of intentional and unintentional impurities was found to be independent of substrate doping level.

The effect of cooling rate on the various impurity distributions was also studied, covering the range 0.5°-18°C/min. Residual impurity levels and associated gradients were significantly reduced by decreasing the cooling rate which indicates that residual impurity incorporation is kinetically controlled, probably by slow diffusion of these impurities in front of the growing LPE layer. Similarly, the O level appears to be decreased by reduced cooling rate. In contrast, Zn doping was found to be independent of cooling rate which suggests that its incorporation was essentially under equilibrium conditions. Assuming this to be the case, we have shown that the observed Zn distribution is consistent with the temperature dependence of the Zn solid solubility. Using an equilibrium description for Zn incorporation, we have computed the near-junction Zn and O concentrations in the previously reported high efficiency diodes to be 6.7 x 10^{17} cm^{-3} and 2.7 x 10^{17} cm^{-3}, respectively. The corresponding level of residual impurities yields a net donor concentration of $\lesssim 3 \times 10^{16}$ cm^{-3}.

We previously reported (1) on the fabrication of efficient (~7%) red-light emiting GaP p-n junctions which were grown using a p-on-n liquid phase epitaxy (LPE) tipping process. In that work, the strong dependence of quantum efficiency η on Zn,O-doping in the p-type LPE layer was emphasized, and we noted that the (measured) impurity distribution was not uniform in the LPE layers. Ladany (2) observed a "spontaneous junction" or n-skin near the surface of his p-type LPE layers and suggested that impurity gradients existed in those LPE layers, although the impurity distributions were not determined. As illustrated in Fig. 1, the net impurity concentration at the surface of our p-layers is closely compensated, and thus generally leads to difficulty in providing a low-resistance ohmic contact to the p-layer since electrical contact is usually established at this surface. Consequently, the work described here was initiated to further the understanding of Zn,O and residual impurity distributions in LPE layers and how these are affected by cooling rate and substrate doping. These results have been used to determine the near-junction

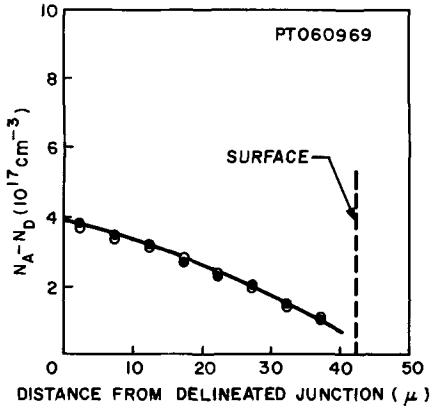

Fig. 1. Net impurity profile for a Zn,O-doped LPE layer grown at a cooling rate of 10°/min. Open and solid circles designate measurements on different rows of Schottky-barrier diodes.

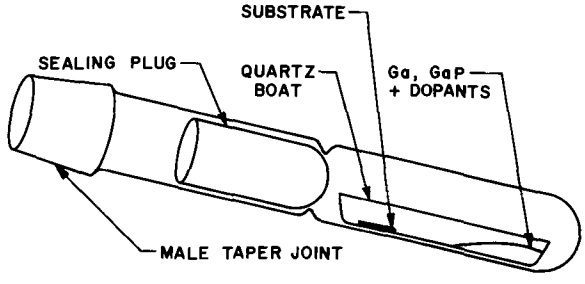

Fig. 2. Sealed capsule used for growth of LPE layers

Zn,O and residual impurity levels for high efficiency red-emitting diodes (1).

Experimental

LPE growth system.—The quartz capsule used for the sealed-tube LPE growth is illustrated in Fig. 2. The capsule, sealing plug, and boat were etched for 5 min in HF, rinsed in de-ionized water, and oven-dried just prior to loading. Polycrystalline GaP (Monsanto phosphine-synthesized material), sieved to 20-60 mesh and then etched in aqua regia, was added to Ga (99.9999+% purity obtained from Alusuisse Metals) to form the regrowth solution. Incorporation of Zn was accomplished by etching a crystalline needle (99.9999% purity obtained from United Mineral) to final weight and submerging this directly into the Ga. Powdered β-Ga_2O_3 (highest purity available from Alusuisse Metals) was added to the solution when O doping was desired. The Zn and Ga_2O_3 additions were 0.03 m/o (mole per cent) and 0.35 m/o, respectively, and correspond to the optimum doping levels found in our earlier work (1).[1] Undoped, Zn-doped, and Zn,O-

[1] In ref. (1), we noted that very large additions of Ga_2O_3 [~30 times larger than the solubility limit of Ga_2O_3 in Ga determined by Foster and Scardefield (3)] were required for efficient diodes. This was loosely attributed to kinetic effects characteristic of the LPE process. Transport of Ga_2O_3 (via Ga_2O) as a result of small thermal gradients which might exist within the capsule, together with the fact that the regrowth solution was not permitted to equilibrate at the maximum temperature, may account for the discrepancy between Foster's results and our own. In addition, the O solubility in the regrowth solution may be substantially different from that in Ga since the former is saturated with GaP.

doped LPE layers were grown on undoped solution grown (SG) crystals, Te-doped ($N_D - N_A$ = 0.3-5 $\times$ 10^{18} cm^{-3}) SG crystals or similar crystals on which Te-doped LPE layers had been previously grown.

The loaded capsules were evacuated ($<10^{-6}$ Torr), sealed by fusing the plug and capsule and loaded into a preheated (650°C) tiltable furnace which was then heated to ~1060°C at a rate of 20°/min. At the maximum temperature, LPE growth was initiated by simultaneously tipping the furnace and cooling at a programmed rate which could be varied from 0.5-18°/min. For most cases, cooling was interrupted and the crystal was annealed for 5 hr at 600°C followed by 17 hr at 500°C which for the Zn,O-doped layers, increases η by a factor of 3-4 (1). Heating, cooling, and *in situ* annealing cycle were programmed using a L&N Trend-trak control unit.

Determination of doping profiles.—A high resolution net impurity profile was obtained for each LPE layer by means of a series of surface-barrier capacitance measurements on an angle-lapped surface (4). Rectangular samples (50 x 150 mils) were lapped on a glass plate with Linde A to expose a surface lying 3° from the junction plane. Hot aqua regia was used to remove the resulting surface damage. The intersection of the junction plane and the lapped surface was delineated by etching for 1 min in a 1:1 solution of H_2O_2:HF under bright illumination (5). Schottky-barrier diodes were formed by evaporating an array of Au dots (100μ in diameter on 200μ centers) on the angle-lapped surface and alloying an ohmic contact to the top surface. Reverse bias C-V measurements on each Schottky-barrier diode yields, at the diode location, a net donor or acceptor concentration, $|N_D - N_A|$ (6, 7). This doping level was actually measured directly using an analog doping profiler (8). The resulting array of doping levels comprises a net impurity profile normal to the junction with an effective spatial resolution of 100μ · sin 3° = 5μ.[2]

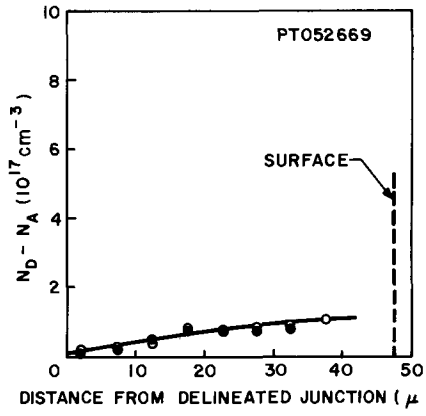

Fig. 3. Net impurity profile for an undoped LPE layer grown at a cooling rate of 10°/min. Open and solid circles designate measurements on different rows of Schottky-barrier diodes.

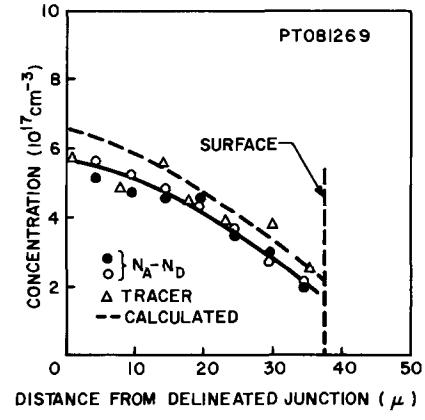

Fig. 4. Concentration profiles for a Zn-doped layer grown at 10°/min; see text.

Results and Discussion

Since the net impurity distribution in Zn,O-doped layers is the net result of various individual impurity distributions, we attempted to isolate these components by comparing impurity profiles for undoped, Zn-doped, and Zn,O-doped LPE layers. A cooling rate of 10°/min was used as in our earlier work (1). The results of these experiments are summarized in Table I.

Undoped LPE layers.—All undoped layers are n-type, the value of $N_D - N_A$ increasing with distance from the junction as in Fig. 3. This gradient is believed to result from a build-up of a slow-diffusing donor impurity, most probably Si, in front of the advancing solid-liquid interface. From the data of Table I, the residual impurity levels (and profiles) are apparently insensitive to Te concentration in the substrate; in fact, an undoped substrate (PTO61169) gave the highest net donor level at the junction. Thus, the LPE layers are not significantly autodoped by the substrate. The net impurity level at the junction is generally comparable to that observed in undoped SG crystals (~5 x 10^{16} cm^{-3}), although the latter are usually p-type. As shown later, this background impurity level is roughly an order of magnitude lower than the concentration of Zn and O. We note that, while the gradient in undoped layers is opposite from that of Zn,O-doped layers (Fig. 1), the distribution of residual impurities, by virtue of compensation, leads to a qualitatively similar net impurity profile. However, the residual impurity level is not large enough to account fully for the gradient in Fig. 1 which indicates that Zn and/or O are not uniformly distributed throughout the LPE layer.

Zn-doped LPE layers.—Figure 4 illustrates a net impurity profile (solid line) for an LPE layer doped

[2] The effective spacing between Schottky-barrier diodes was reduced to 100μ by staggering adjacent rows of Au dots.

Table I. Summary of dopant distribution in LPE layers[a]

Run	Dopant	Substrate doping level, $N_D - N_A$, cm^{-3}	LPE layer doping level, $N_A - N_D$, cm^{-3} Junction	Surface	LPE layer thickness, μ
PT052669	—	6 x 10^{17}	~−3 x 10^{16}	−1.5 x 10^{17}	48
PT061169	—	~5 x 10^{16}	−1.2 x 10^{17}	−3.0 x 10^{17}	68
PT060669	—	4 x 10^{18}	~−3 x 10^{16}	−1.5 x 10^{17}	33
PT061069	Zn	~5 x 10^{16}	5.0 x 10^{17}	2.0 x 10^{17}	30
PT052169	Zn	1.3 x 10^{18}	5.3 x 10^{17}	1.2 x 10^{17}	42
PT081269	Zn	8 x 10^{17}	5.7 x 10^{17}	1.8 x 10^{17}	37
PT051369	Zn,O	2 x 10^{18}	3.8 x 10^{17}	1.0 x 10^{17}	32
PT051569	Zn,O	7 x 10^{17}	3.8 x 10^{17}	<5 x 10^{16}	30
PT042169	Zn,O	8 x 10^{17}	4.2 x 10^{17}	1.0 x 10^{17}	62
PT060969	Zn,O	~5 x 10^{16}	4.0 x 10^{17}	7 x 10^{16}	43
PT063069	Zn,O	3 x 10^{18}	4.0 x 10^{17}	1.5 x 10^{17}	44
PT061669[b]	Zn,O	1.3 x 10^{18}	3.8 x 10^{17}	5 x 10^{16}	38

[a] Layers grown with a cooling rate of 10°/min and subsequently annealed.
[b] Unannealed.

with Zn. As shown in Table I, layers grown on variously doped substrates yielded essentially identical profiles. From the above results, it is apparent that residual impurities also contribute to the (net) gradient evident in Fig. 4. This LPE layer was doped with radioactive ^{65}Zn, so that the Zn concentration profile could also be determined. Incremental layers were successively removed from this layer by etching and the Zn activity in each layer determined from the γ photon emission peak (1.11 MeV), characteristic of ^{65}Zn decay. The method of comparative standards was employed to obtain absolute values of Zn levels, and weight loss measurements were used to determine thickness of the incremental layers. From a comparison of the $N_D - N_A$ and tracer profiles (see Fig. 4), it is clear that the gradient in the Zn-doped layers is largely due to nonuniform Zn distribution. The scatter in the data, however, precludes meaningful determination of the residual impurity distribution, although it appears to be similar to that shown in Fig. 3.

Since the epitaxial layers were annealed in Ga for 22 hr after growth, it was necessary to determine if the nonuniform Zn distribution was a consequence of out-diffusion of Zn during the annealing treatment. An unannealed Zn,O-doped layer (PTO61669) was thus profiled but found to be similar to the annealed layers. (As indicated in the next section, O acts as a compensating donor and does not appreciably affect the net impurity gradient.) Thus out-diffusion of Zn (or in-diffusion of a donor impurity) during annealing is negligible,[3] and it is concluded that all observed profiles are established during epitaxial growth.

Since the distribution coefficient of Zn decreases as the temperature is lowered (10), one expects that as the Ga solution is cooled and the epitaxial layer thickens, the level of incorporated Zn should decrease along the growth direction as in Fig. 4. Using the GaP liquidus data of Rubenstein (11) and Hall (12), and the Zn solid solubility isotherms recently computed by Jordan (13), we have calculated the resulting Zn profile assuming that (*i*) layer growth and Zn incorporation are essentially equilibrium processes, and (*ii*) partitioning of rejected GaP between substrate and other competing surfaces (*e.g.*, the 2 m/o excess GaP present) is invariant for a given run. The first assumption is consistent with the results of the cooling rate experiments, as shown later. The second assumption effectively normalizes the calculated LPE layer thickness to the observed thickness. In view of the uncertainty in the thermodynamic data, the agreement between the calculated Zn distribution (shown as a dashed line in Fig. 4) and experimental data is quite good. These results imply that the observed Zn profile is a consequence of the LPE layer having been grown over a wide temperature range.[4] This view is supported by the observation that the Zn concentration at the junction is invariant while the surface concentration is independent of layer thickness and roughly constant (see Table I).

Zn,O-doped LPE layers.—Profiles of Zn,O-doped layers are independent of substrate doping and are essentially the same as for Zn-doped layers, with the former displaced to lower (net) acceptor concentrations, *cf.*, Fig. 1 and 4. This reduction in $N_A - N_D$, being the result of compensation of Zn acceptors by O donors, provides a direct measurement of the O concentration.[5] Thus from Table I, the apparent O concentration near the junction where the red luminescence occurs (14, 15) is typically $\sim 1.3 \times 10^{17}$ cm^{-3}. However, the concentration of Zn is comparable to the intrinsic carrier concentration n_i at the growth temperature (10); hence, the simultaneous incorporation of O is expected to affect the level of incorporated Zn. As shown below this leads to an underestimate of the O concentration.

The actual O concentration is readily estimated by considering the incorporation of Zn as described by the equations (10)

$$Zn(l) + V_{Ga} = Zn_{Ga}^- + e^+; K_1 = \frac{[Zn_{Ga}^-]p}{[Zn(l)][V_{Ga}]} \quad [1]$$

$$n + [Zn_{Ga}^-] = p \quad [2]$$

and

$$np = n_i^2 \quad [3]$$

Analogous equations result for Zn,O doping except that Eq. [2] becomes

$$n_o + [Zn_{Ga}^-]_o = p_o + [O_P^+] \quad [4]$$

where the subscript o is used to represent simultaneous Zn and O incorporation. At constant $[Zn(l)]$ and $[V_{Ga}]$ (constant in dilute solutions) it follows from Eq. [1] that

$$p[Zn_{Ga}^-] = p_o[Zn_{Ga}^-]_o \quad [5]$$

Combining Eq. [2]-[5], we have the desired result

$$[O_P^+] = [Zn_{Ga}^-]_o - ([Zn_{Ga}^-]_o - [O_P^+])$$

$$= A\left[\frac{A + (A^2 + 4n_i^2)^{1/2}}{B + (B^2 + 4n_i^2)^{1/2}}\right] - B \quad [6]$$

where $A \equiv [Zn_{Ga}^-]$ and $B \equiv [Zn_{Ga}^-]_o - [O_P^+]$ are the measured quantities. Note that Eq. [6] does not depend on the details of O incorporation, but simply makes use of the measured compensation resulting from O-doping. Taking $A = 5.3 \times 10^{17}$ cm^{-3}, $B = 4 \times 10^{17}$ cm^{-3} from Table I, and a computed (16) value of $n_i = 1.6 \times 10^{17}$ cm^{-3}, we obtain for the near-junction O concentration, $[O_P^+] = 2.7 \times 10^{17}$ cm^{-3}, which is somewhat greater than our earlier estimates (1). This numerical result is relatively insensitive to the chosen value of n_i.[6]

Since the electrical measurements do not distinguish between various donor species, we considered the possible incorporation of impurities in the Ga_2O_3, most notably S which has a rather large distribution coefficient (10). (Other donor impurities could not be detected by emission spectrography.) From combustion analysis (17) of the Ga_2O_3, the S concentration was estimated to be about 1 ppm. Using the solubility data of Trumbore *et al.* (10) and the amount of Ga_2O_3 added to the Ga solutions the S concentration in the Zn,O-doped LPE layers is expected to be $\lesssim 1 \times 10^{15}$ cm^{-3} which is well below the doping levels of interest. Hence, it is concluded that O is the compensating donor in these experiments.

Effect of cooling rate on dopant distribution.—Table II summarizes the results of experiments in which the cooling rate was varied between ~20 and ~0.5°/min. The residual impurity level in undoped layers is significantly reduced by diminishing the cooling rate. This result indicates that residual impurity incorporation is a rate dependent (nonequilibrium) process in which the effective distribution coefficient k increases as the cooling rate is increased. Such behavior is characteristic of impurities with $k < 1$ which diffuse slowly in the liquid (18). These experiments also suggest that the nonuniform impurity distribution in undoped layers is primarily a consequence of rapid growth as alluded to earlier.

The Zn-doped layers, on the other hand, appear to be unaffected by cooling rate within the range studied. Thus, Zn incorporation is not kinetically controlled

[3] This result is anticipated from the diffusion data of Panish and Casey (9).

[4] From the GaP liquidus data (11, 12), approximately 90% of the epitaxial layer has grown when the Ga solution has cooled 200°C from its maximum temperature.

[5] Actually, this is the concentration of electrically active (substitutional) O and may differ from the total O concentration which includes interstitial and other inactive forms [C. K. Kim, *Radiochem. and Radioannal. Letters*, 2, 53 (1969)].

[6] This follows from Eq. [6] except when $n_i >> A/2 = 2.6 \times 10^{17}$ cm^{-3}.

Table II. Effect of cooling rate on dopant distributions in LPE layers[a]

Run	Dopant	Cooling rate, °C/min	LPE layer doping level, $N_A - N_D$, cm^{-3} Junction	Surface
PT052669	—	~10	$\sim -3 \times 10^{16}$	-1.5×10^{17}
PT091869	—	4.4	$\sim -1 \times 10^{16}$	-9×10^{16}
PT091769	—	0.7	$\sim -5 \times 10^{15}$	$\sim -5 \times 10^{15}$
PT052169	Zn	10.0	5.3×10^{17}	1.2×10^{17}
PT091269	Zn	4.8	5.0×10^{17}	1.5×10^{17}
PT091569	Zn	0.5	5.0×10^{17}	1.5×10^{17}
PT061969	Zn,O	18.6	3.5×10^{17}	7×10^{16}
PT060969	Zn,O	10.5	4.0×10^{17}	7×10^{16}
PT081969	Zn,O	4.8	4.5×10^{17}	1.0×10^{17}
PT110369	Zn,O	1.0	4.6×10^{17}	1.6×10^{17}

[a] All layers were annealed.

which is, of course, a necessary condition for equilibrium incorporation. Since the Zn-doping in the LPE layers agrees closely with the computed equilibrium values (see Fig. 4), we conclude that our earlier assumption of equilibrium Zn incorporation is valid.

As the cooling rate is decreased, the Zn,O-doped layers exhibit a systematic increase in $N_A - N_D$ at the junction which we interpret as evidence of decreased O. This result is consistent with the very low distribution coefficient of O (3). The effective reduction in the value of k for O is not readily compensated by increased Ga_2O_3 in the regrowth solution because of the very low solubility of Ga_2O_3 in Ga.

Conclusions

The net impurity distribution observed in Zn,O-doped LPE layers results primarily from a nonuniform Zn distribution and, to a lesser extent, nonuniform distribution of residual impurities. The O distribution is more difficult to ascertain but appears to be relatively constant along the growth direction even though $k << 1$. While the build-up of slow diffusing residual donor impurities in front of the growing LPE layer accounts for the nonuniform distribution of residual impurities, the grading in Zn concentration is a manifestation of the temperature dependence of the Zn distribution coefficient. Thus the impurity grading in Zn,O-doped LPE layers can be minimized by employing slow cooling rates and restricting growth to a narrow temperature range. The latter might be accomplished by mechanically separating (tipping off) the Ga solution from the substrate before the solution has cooled 25°. Layers of sufficient thickness could be grown over a narrow temperature range by appropriate increase in the ratio of regrowth solution volume to substrate area, and by eliminating the excess (source) GaP which competes with the substrate crystal for the precipitating GaP.

Decreasing the cooling rate to a rather low value of ~0.5°/min reduced the unintentional impurity level ($N_D - N_A \simeq 5 \times 10^{15}$ cm^{-3}) which is desirable for minimizing nonradiative recombination centers which may be associated with such impurities. On the other hand, the level of incorporated O appears to decrease as the cooling rate is reduced which may be detrimental owing to the probable reduction in Zn-O complexes. The Zn concentration and distribution is independent of cooling rate in the range 0.5-10°/min which is consistent with equilibrium Zn incorporation. Using an equilibrium description for Zn incorporation, the near-junction Zn and O concentrations for the previously reported high efficiency diodes (1) are computed to be 6.7 x 10^{17} cm^{-3} and 2.7 x 10^{17} cm^{-3}, respectively.

Acknowledgments

The authors are indebted to Mrs. J. Armstrong for growing the epitaxial layers, T. E. McGahan for performing the surface-barrier capacitance measurements, and Miss K. B. Wolfstirn for performing the tracer analysis. They are particularly grateful to A. S. Jordan for helpful discussions concerning oxygen incorporation and for providing them with the solubility isotherms prior to publication.

Manuscript submitted Dec. 23, 1960; revised manuscript received April 7, 1970. This was Paper 80 presented at the Los Angeles Meeting of the Society, May 10-15, 1970.

Any discussion of this paper will appear in a Discussion Section to be published in the June 1971 JOURNAL.

REFERENCES

1. R. H. Saul, J. Armstrong, and W. H. Hackett, Jr., *Appl. Phys. Letters*, **15**, 229 (1969).
2. I. Ladany, *This Journal*, **116**, 993 (1969)
3. L. M. Foster and J. Scardefield, *ibid.*, **116**, 494 (1969).
4. T. E. McGahan and W. H. Hackett, Jr., *Rev. Sci. Instr.*, To be published.
5. M. R. Lorenz and M. Pilkuhn, *J. Appl. Phys.*, **37**, 4094 (1966).
6. J. Hildebrand and R. D. Gold, *RCA Rev.*, June 1960.
7. C. O. Thomas, D. Kahng, and R. L. Manz, *This Journal*, **109**, 1055 (1962).
8. J. A. Copeland, *IEEE Trans. on Electron Devices*, **16**, 445 (1969).
9. M. B. Panish and H. C. Casey, *J. Phys. Chem. Solids*, **29**, 1719 (1968).
10. F. A. Trumbore, H. G. White, M. Kowalchik, R. A. Logan, and C. L. Luke, *This Journal*, **112**, 782 (1965).
11. M. Rubenstein, Electronics Division Abstracts of the Electrochemical Society, **11**, No. 1, p. 129 (1962).
12. R. N. Hall, *This Journal*, **110**, 385 (1963).
13. A. S. Jordan, Paper 145 presented at the Los Angeles Meeting of the Society, May 10-15, 1970.
14. M. Gershenzon, R. A. Logan, and D. F. Nelson, *Phys. Rev.*, **149**, 580 (1967).
15. W. H. Hackett, Jr., W. Rosenzweig, and J. S. Jayson, *Proc. IEEE*, **57**, 2072 (1969).
16. This value was determined using density of states effective masses of $m_e = 0.47\ m_o$ and $m_h = 1.0\ m_o$, where m_o is the electron rest mass, and an energy gap given by $E_g = 2.388\text{-}6.2\text{x}10^{-4}T^2/(T+460)$ eV (H. C. Casey, private communication). We note that the 1040°C Zn solid-solubility isotherm determined in ref. (10) indicates that $n_i < 5\times10^{17}$ cm^{-3} which is consistent with the computed value used for this work.
17. The Ga_2O_3 was analyzed by R. H. Bell of Lucius Pitkin Inc.
18. J. C. Brice, "The Growth of Crystals from the Melt," p. 80, North-Holland Publishing Co., Amsterdam (1965).

A Stagnant Layer Model for the Epitaxial Growth of Silicon from Silane in a Horizontal Reactor

F. C. Eversteyn, P. J. W. Severin, C. H. J. v.d. Brekel, and H. L. Peek

Philips Research Laboratories, N. V. Philips' Gloeilampenfabrieken, Eindhoven, Netherlands

ABSTRACT

Flow patterns have been made visible in a horizontal water-cooled epitaxial reactor by injection of TiO_2 particles into the gas flow. From these experiments, a stagnant layer model has been developed with which the epitaxial growth of silicon from silane can be described. In the case of a nontilted susceptor, the model predicts an appreciable nonuniformity in thickness along the susceptor, whereas a small angle of tilting of the susceptor should yield a much better uniformity in thickness (2% over a length of 22 cm). Experiments agree very well with the theoretical predictions of the model.

Silane as source for the epitaxial growth of silicon has several advantages over $SiCl_4$ and $SiHCl_3$: lower deposition temperature, less autodoping from substrate, less outdiffusion, and no back etching. On the other hand, silane is rather unstable and will decompose also on the hot reactor wall. This means that, as far as the construction is concerned, reactors for SiH_4 and $SiCl_4$ or $SiHCl_3$ will be different. For the time being, the most popular type is the horizontal reactor. The construction is rather simple. A large number of slices can be grown in one charge and the reactor is easy to load and unload. For SiH_4, a water-cooled reactor is preferable, because otherwise silicon would be deposited on the reactor wall, which would make measurement of the temperature of the substrates with an optical pyrometer impossible.

In the past, several authors have described the process of epitaxial growth, though mostly in vertical reactors. Bradshaw (1) developed a boundary layer model with which he was able to explain the growth experiments in a vertical reactor. Here the deposition efficiency is low, so that the decrease in concentration of the silicon compound along the susceptor can be neglected. Shepherd (2) described the epitaxial growth of silicon from $SiCl_4$ in a small horizontal reactor, assuming a parabolic gas flow in the reactor and omitting the decrease in $SiCl_4$ concentration in the length direction of the reactor. For large horizontal reactors, the deposition efficiency is found to be about 35%. This means that the decrease in concentration of the silicon compound along the reactor cannot be neglected. Taking this into account, Rundle (3) investigated the epitaxial growth of silicon from $SiCl_4$ and $SiHCl_3$, assuming that the gas flow in the reactor has a velocity component only along the axis of the reactor and that the whole system is at a constant temperature, ignoring temperature gradients.

In this paper, it is shown that these assumptions cannot be justified. From gas flow pattern experiments, it is seen that there is a thermal convection in the reactor vertically *overturning* the main gas flow and resulting in complete mixing of the gas. Directly above the heated susceptor, the temperature then drops over a thin stagnant layer which is excluded from the main gas flow. These experiments are discussed and a model derived for the epitaxial growth in a horizontal reactor is analyzed. The rate of epitaxial growth is calculated in the case of a nontilted and tilted susceptor. It is shown that there is close agreement between the predictions derived from the model and the experiments.

Investigation of the Flow Pattern

Experimental arrangement.—To make the flow pattern in the reactor visible, TiO_2 particles are injected into the gas stream by means of the equipment shown schematically in Fig. 1 (4). The horizontal reactor used for these experiments is the same as is considered later for the epitaxial deposition of silicon from silane. It consists of a water-cooled quartz tube with a rectangular cross section (5 x 4 cm) and a graphite susceptor, 30 cm long, 4 cm wide, 8 mm thick, positioned in a quartz boat which fits in the reactor. In our case, the free space between a side wall of the reactor and the quartz boat is about 0.5 mm. The quartz boat rests on the floor of the reactor. The free height above the susceptor is 2 cm. Dry hydrogen and hydrogen containing water vapor flows into the reactor where the temperature of the susceptor is 1050°C. By switching two electromagnetic valves, the dry hydrogen can be passed over $TiCl_4$. Mixing of the water vapor-loaded and the $TiCl_4$-loaded hydrogen causes the formation of TiO_2 particles, resulting in a white haze. The flow pattern in the reactor can then be observed. Photographs of the gas flow patterns have been made through the window on the right-hand end of the reactor (see Fig. 1) and are discussed below.

Experimental results.—In Fig. 2, the streamline pattern is given for the water-cooled reactor with the susceptor at room temperature. It is seen from this

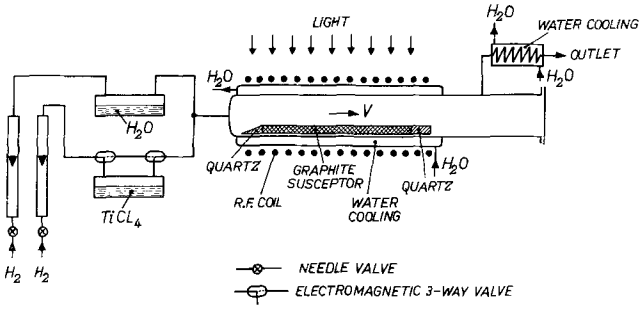

Fig. 1. Schematic view of the equipment to make gas flow patterns in the reactor visible.

Fig. 2. Streamline pattern above the nonheated susceptor ($T_S \approx 20$°C) with water-cooling around the tube (wall temperature approximately 10°C). Convective flow is visible under the influence of a small vertical temperature gradient. Rotation speed: about 1 rps.

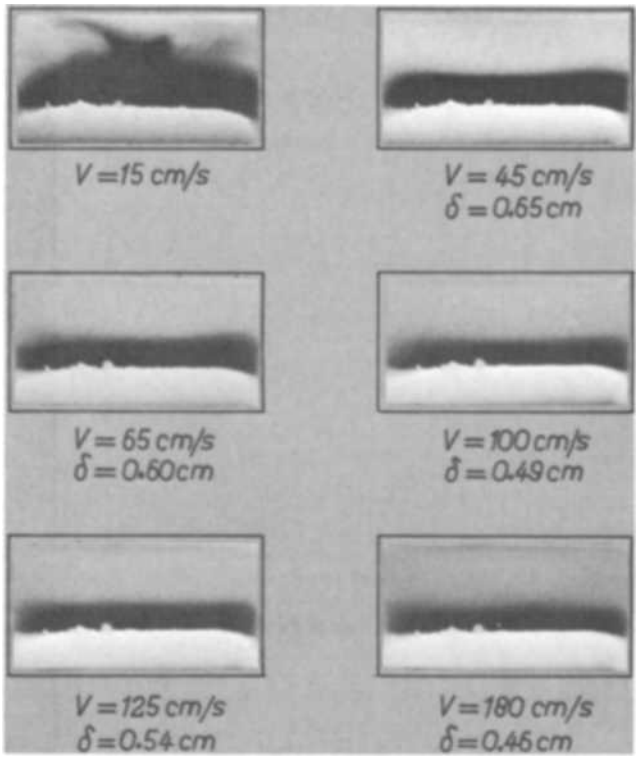

Fig. 3. Streamline patterns with TiO_2 at different gas velocities of hydrogen (corrected for heating up). Susceptor temperature 1050°C. Stagnant layer thickness decreases with increasing gas velocity.

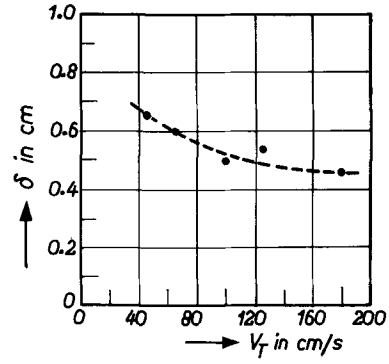

Fig. 4. Dependence of the stagnant layer thickness on the mean velocity of hydrogen in the reactor. Susceptor temperature, 1050°C.

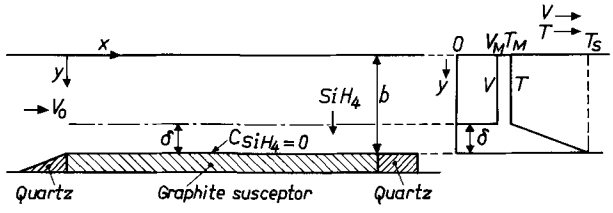

Fig. 5. Stagnant layer model for a horizontal reactor with a non-tilted susceptor.

photograph that, although the vertical temperature gradient is very small ($\Delta T \approx 10$°C over about 2 cm), a convection flow already exists which, combined with the net gas flow, results in a double screw flow pattern. When the susceptor is heated up, the vertical temperature gradient increases. Due to a buoyancy force, increased in this way, a higher rotation velocity of the spirals results and the separate streamlines mix. This is shown in Fig. 3 where hydrogen with different gas velocities flows through the reactor in which the susceptor is at 1050°C. In the case of low gas velocity the convection flow lines can be seen separately, but at higher velocity the streamline pattern is restricted to a region separated from the substrate by a dark layer. The latter is indicative of a region where the gas velocity is zero and the incoming TiO_2 particles will flow only in a region separated from the susceptor by a stagnant layer. The thickness of the stagnant layer depends on the gas velocity, as can be seen from Fig. 4. When the linear velocity in the reactor is increased, the stagnant layer thickness tends to decrease.

Epitaxial Growth with a Nontilted Susceptor

Calculations on the model.—From the experiments described above, a model has been developed with which the epitaxial growth in a horizontal reactor can be physically described and mathematically analyzed.

In Fig. 5, a schematic diagram of a horizontal reactor with a nontilted susceptor is drawn with the assumptions implied in the model for epitaxial growth. They are mainly based on the gas flow pattern experiments with TiO_2 and explicitly given below:

I. Due to vertical *overturning* caused by buoyancy forces in the gas (thermal convection), the velocity, V_m, and the temperature, T_m, are constant over the height ($b - \delta$) of the reactor tube.

II. The temperature of the gas (T_m) is taken to be constant in the length direction of the reactor. This assumption is valid for a water-cooled reactor.

III. In the stagnant layer, the gas velocity is zero and the temperature increases linearly with y from T_m to the susceptor temperature T_s: $T(y) = T_s - (T_s - T_m)(b - y)/\delta$.

IV. SiH_4 diffuses through the stagnant layer to the susceptor. At the surface of the susceptor, the SiH_4 concentration is assumed to be zero since the unstable SiH_4 reaching the susceptor decomposes immediately at the temperature considered (1050°C). Thus, the deposition rate of silicon is diffusion controlled.

With these assumptions, the rate of epitaxial growth in a horizontal reactor has been calculated and turns out to be described by the following expression (see Appendix A):

$$G(x) = 7.23 \times 10^6 \frac{D_0 T_s p_0}{R T_0^2 \delta} \exp\left(-\frac{D_0 T_s x}{T_0 V_0 b \delta}\right) \quad [1]$$

where G is the growth rate of silicon (μm/min); D_0, the diffusion coefficient at 300°K of silane in hydrogen ($D_0 = 0.2$ cm²/s); T_s, the susceptor temperature (°K); $T_0 = 300$°K; p_0, the partial pressure of silane (dynes/cm² $\approx 10^{-6}$ atm) at the inlet of the reactor; V_0, the mean velocity (cm/s) of the gas as calculated from the incoming gas flow and the free cross section of the tube; R is the gas constant (8.31 x 10^7 erg/°K). The free height above the susceptor is indicated by b (cm). The only unkown variable is δ, the thickness of the stagnant layer.

Experimental results.—Experiments were carried out on the epitaxial growth of silicon from silane in an atmosphere of hydrogen. Figure 6 shows an outline of the apparatus used for these experiments. Substrates were 0.01 ohm-cm (N- and P-type), polished slices of silicon single crystals. After etching the slices at 1200°C with HCl, the temperature of the susceptor is lowered to 1050°C, at which temperature the epitaxial growth is initiated by admitting a flow of hydrogen containing SiH_4. The temperature has been measured with an optical pyrometer and corrected for the emissivity of the silicon.

The growth rate, G, is obtained by measuring both the time of growth and the thickness of the deposited silicon layer. It has been verified that the growth rate, G, is a constant over the time of growth. The accuracy in the growth rate is affected by the accuracy with which the time of switching can be measured and by the accuracy of the thickness measurement method. The accuracy in time measurement amounts to ±0.2%.

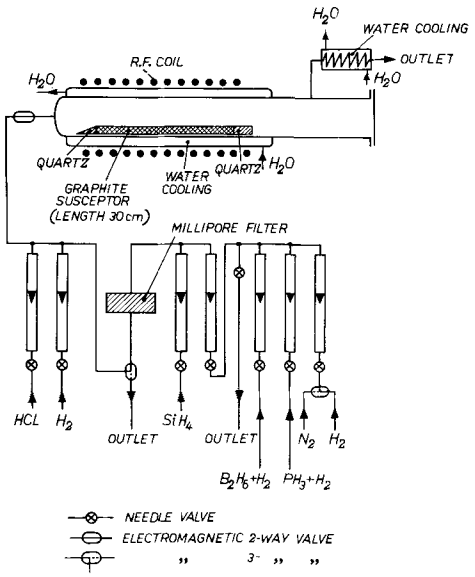

Fig. 6. Outline of the epitaxial growth equipment

The thickness has been measured by infrared multiple interference with a Hitachi EPI-G2 spectrophotometer. The data obtained allow for a final accuracy in thickness of ±0.5%. The evaluation technique used will be described by Severin (5).

According to Eq. [1], the growth rate is linearly dependent on the concentration of SiH_4 in the carrier gas. This was verified up to 10^{-1} vol % SiH_4 in a series of growth experiments. In each experiment, the slice was positioned at the same place in the reactor. The results of these experiments are given in Fig. 7. It is clear from this figure that growth rate varies linearly with the SiH_4 concentration.

Another series of experiments has been carried out to study the dependence of growth rate, G, on position x along the axis of the reactor. A typical result of these experiments is given in Fig. 8. It can be seen that, as required by Eq. [1] derived from the model, log G indeed decreases linearly with x.

Calculated and experimental values for the thickness of the stagnant layer.—From the slope of the line in Fig. 8 as well as from the value of G at $x = 0$ the thickness of the stagnant layer, δ, can be calculated. In Fig. 9, these values are given for gas flow rates (V_T) between 50 and 500 cm/s corresponding to V_o between 20 and 200 cm/s. This figure also shows the thickness of the stagnant layer as found by direct observation in gas flow pattern experiments with TiO_2 as shown in Fig. 3. Good agreement exists between these measured values of the stagnant layer thickness and the values of δ derived from $G(0)$. The values obtained from the slope turn out to be at variance. In order to proceed with the theory, a simple formal relation between δ and the velocity, V, is needed. A number of relationships have been tried but the relation:

$$\delta = \frac{A}{\sqrt{V_T}} - B \qquad [2]$$

with $A = 7$ cm$^{3/2}$ s$^{-1/2}$ and $B = 0.2$ cm appears to be the best compromise.

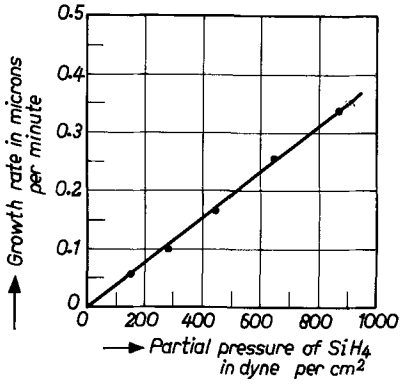

Fig. 7. Dependence of the growth rate on the partial pressure of silane (10^3 dynes/cm^2 relates to 0.1 vol % SiH_4).

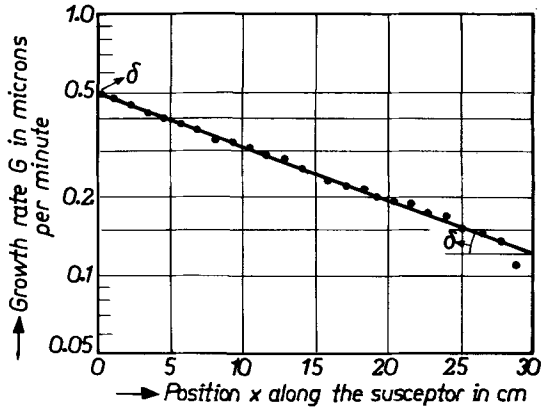

Fig. 8. Growth rate vs. position along the susceptor for V_o = 17.5 cm/s. Substrate temperature, 1050°C.

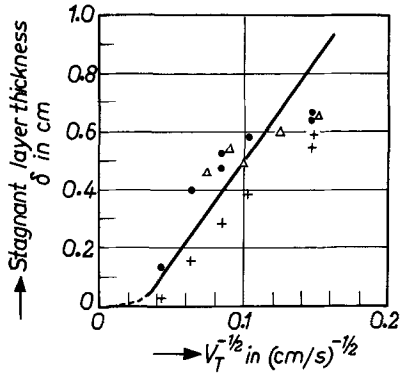

Fig. 9. Dependence of the stagnant layer thickness on the mean gas velocity in the reactor (corrected for heating up): △, from flow pattern experiments using TiO_2, + from the slope of the log $G(x)$-x curve; ●, from the growth rate at $x = 0$.

Theoretically and experimentally, the growth rate, G, decreases with increasing values of the position parameter, x. The magnitude of this effect depends on the gas flow rate. When Eq. [2] is inserted into Eq. [1], it follows that the slope of the log G *vs.* x curve as a function of V_o shows a rather flat minimum. This can be seen in Fig. 10. Some experimental data regarding this effect are also presented in this figure. It appears that the same trend is found in the experimental and in the calculated course of the slope of the log G *vs.* x curve as a function of the mean velocity, V_o. The differences in actual value of d log G/dx are due to the inaccuracies introduced by Eq. [2].

Increasing the gas flow rate from 9 to 34 cm/s results in a decrease of the slope of the log G *vs.* x curve. However, a further increase of the gas flow rate has no influence on the slope of the growth curve.

From these experiments and calculations, it is clear that it is impossible to get the same deposition rate in all positions on the susceptor. A smaller gradient in the thickness of deposited silicon should be obtainable with a stagnant layer thickness decreasing in the length direction of the reactor to compensate the effect of decreasing partial pressure of SiH_4. A gradually decreasing stagnant layer can be achieved by tilting the susceptor, as is dealt with below.

Reactor efficiency.—At this stage, it is interesting to consider the reactor efficiency, η, defined as the fraction

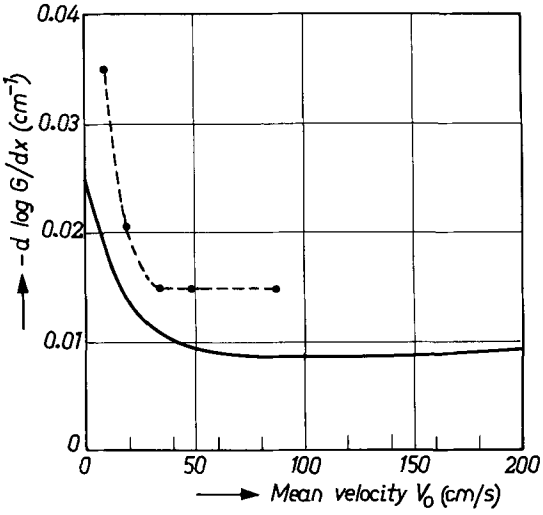

Fig. 10. Calculated values of the slope of the log $G(x)$-x curve from Eq. [1] and Eq. [2] at different values of the gas velocity (V_0). Some experimental values are also inserted into this figure (dotted line).

of the incoming SiH_4 decomposed on the hot susceptor. The reactor efficiency, η, can be expressed by

$$\eta = \frac{c\int_0^L J_y(x)\,dx}{n_0 V_0 b d} \cdot 100\% \qquad [3]$$

where L is the length of the susceptor, c the width of the susceptor, d the width of the reactor, $J_y(x)$ the molecular flux in the y-direction as a function of x, and $n_0 = p_0/kT_0$.

Integrating Eq. [3] yields

$$\eta = \frac{c}{d}\left\{1 - \exp\left(-\frac{D_0 T_s L}{b V_0 \delta T_0}\right)\right\} \cdot 100\% \qquad [4]$$

From Eq. [2] and Eq. [4], the dependence of the reactor efficiency, η, on the gas flow rate can be calculated. This is shown in Fig. 11. At low V_0, the efficiency, η, decreases with increasing V_0 and flattens up to the upper limit of the range of validity of Eq. [2]. Figure 11 also gives the experimental values of η, measured by gas chromatographic analysis of the incoming and outgoing gas. The experimental values are close to the calculated ones. As predicted, η decreases with increasing V_0 and tends to be constant at the right value of about 35%.

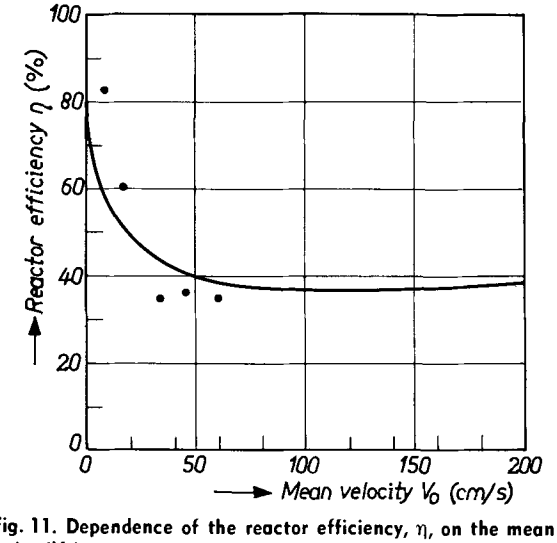

Fig. 11. Dependence of the reactor efficiency, η, on the mean gas velocity (V_0).

Epitaxial Growth of Silicon in a Horizontal Reactor with a Tilted Susceptor

Calculations on the model.—In Fig. 12, a schematic view is given of a horizontal reactor with a tilted susceptor. The assumptions for this model are the same as used for the nontilted susceptor. However, the decrease in stagnant layer thickness along the axis due to increasing gas velocity is taken into account. For this we use Eq. [2], which was found as a result of the experiments in a horizontal reactor with a nontilted susceptor. In the case of a tilted susceptor, the gas velocity is a function of x because of decreasing cross section of the free space above the susceptor

$$V_T(x) = \frac{V_0\, b\, T_m}{(b - x\tan\psi)\, T_0} \qquad [5a]$$

Of course, it has been avoided that the gas streams around and under the susceptor by filling up the space under and adjacent to the susceptor. The stagnant layer thickness, δ, and the temperature decay in the stagnant layer are supposed to be determined by the local velocity only and, hence, Eq. [2] and assumption III are modified to be a function of x

$$\delta(x) = \frac{7}{\sqrt{V_T(x)}} - 0.2 \qquad [5b]$$

and

$$T(x,y) = T_s + \frac{(T_s - T_m)\,(y - b + x\tan\psi)}{\delta(x)} \qquad [5c]$$

With these relations, the growth rate (μm/min) in a horizontal reactor with a tilted susceptor is found to be

$$G(x) = 7.23 \times 10^6 \frac{D_0 T_s p_0}{R T_0^2 \delta(x)} \exp\left\{-\frac{2 D_0 T_s T_m}{4 g T_0^2 \tan\psi}\left(\delta(0) - \delta(x) + 0.2 \ln\frac{\delta(0)}{\delta(x)}\right)\right\} \qquad [6]$$

This formula is derived in Appendix B.

Experimental results.—With Eq. [6], calculations have been carried out for a fixed angle of tilting of 2.9° and different gas velocities of 10-70 cm/s. This is shown in Fig. 13. It is seen that at low gas velocity (V_0 = 10 cm/s) the growth rate decreases in the length direction, while at a high gas velocity ($V_0 > 40$ cm/s) even an increase in growth rate is found. Between these two values, a region should exist where the growth rate is nearly independent of position x. Experiments carried out under the same conditions as those for which these curves have been calculated show a very good agreement with the calculations, as can be seen in Fig. 14. With a gas velocity V_0 = 18 cm/s a decrease in growth rate along the axis is found, while at 48.7 cm/s an increase in growth rate is obtained. With a gas velocity of 34 cm/s, the growth rate is constant within 2% over a region of 22 cm (≈80% of the susceptor length). Not only the predicted trends in the deposition rates are found experimentally, but also the experimental value of the growth rate in the case of nearly even deposition is close to the calculated value. As can be seen from Fig. 13, we obtain for p_0 = 1000 dynes/cm² and V_0 = 34 cm/s a growth rate G = 0.43 μm/min. This implies for p_0 =

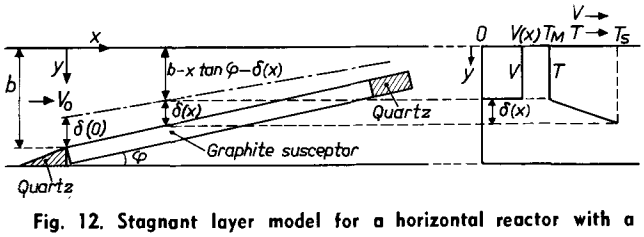

Fig. 12. Stagnant layer model for a horizontal reactor with a tilted susceptor.

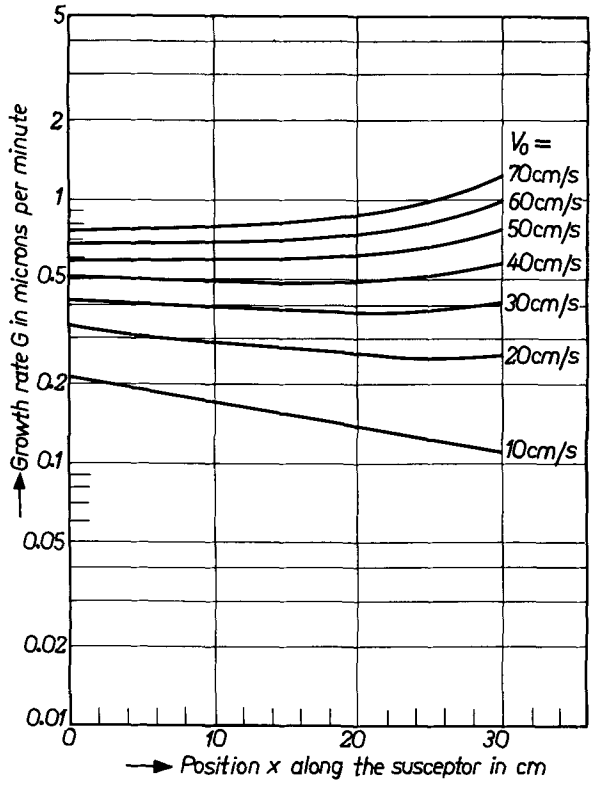

Fig. 13. Calculated values of the growth rate vs. position along the susceptor at different gas velocities for an angle of tilting of 2.9°. T_m = 700°K, T_s = 1350°K, b = 2.05 cm, p_o = 10^3 dynes/cm², D_o = 0.2 cm²/s.

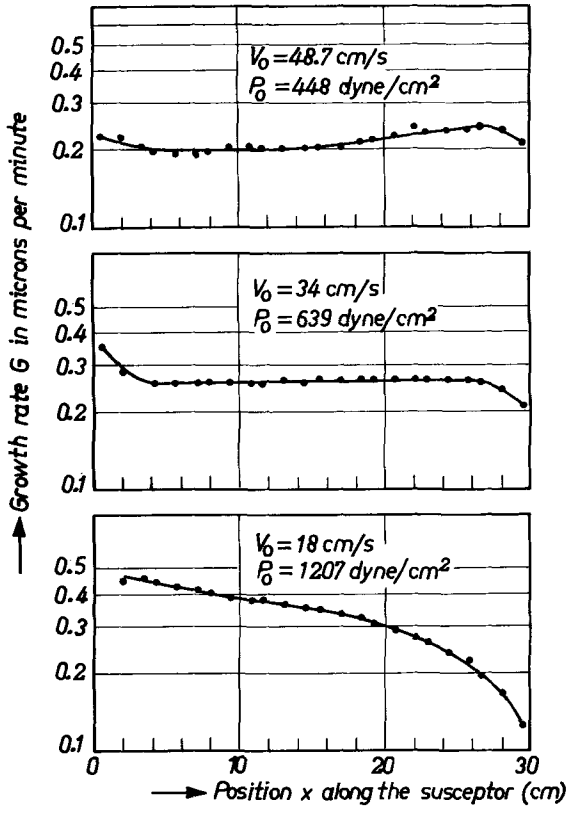

Fig. 14. Growth rate vs. position along the susceptor for an angle of tilting of 2.9° and V_o = 18, 34 and 48.7 cm/s, b = 2.05 cm, T_s = 1350°K.

639 dynes/cm² that G = 0.27 μm/min which agrees well with the experimental value G = 0.26 μm/min given in Fig. 14.

The decrease in growth rate at the end of the susceptor, as observed experimentally, is due to geometrical properties of the system where the flow and the temperature should match boundary conditions.

The uniformity in growth rate across the susceptor depends on how well the susceptor fits into the reactor. Variations in growth rate across the susceptor smaller than 5% have been found.

Discussion

From the experiments described in this paper, it is clear that the epitaxial growth of silicon from silane in a horizontal reactor can be adequately explained with a stagnant layer model. According to this model, above the heated susceptor a layer of stagnant gas is present in which the temperature gradient is very high (>100°C/mm). Above the stagnant layer the gas is vertically mixed by the high convection. When the vertical temperature gradient is small, the streamlines have been seen individually with a haze of TiO_2 and the rotation speed of the convection flow increases with the vertical temperature gradient. The experiment to which Fig. 2 refers yields for 5°C/cm a rotation speed of about 1 rps, as has also been calculated using an elementary theory in Appendix C. However, in the case of a heated susceptor, this temperature gradient is rather high resulting in so high a rotation speed that separate streamlines mix and that only a very small temperature gradient is left in the convective layer. In fact, we assume the temperature is uniform within this upper layer. This justifies the model as a whole.

The interpretation of the results presented in the sections on the experiments are based only on the equations of conservation of mass, which is expressed in the upper, convective, layer by the equation of continuity and in the lower, stagnant, layer by equating the silane diffusion flow to the growth rate of the silicon epitaxial layer, as shown in Appendixes A and B. The reactive species involved is supposed to be SiH_4.

We realize that a number of simplifying assumptions have been made in deriving the above results, particularly as regards the diffusion process. The diffusion of silane to the susceptor is rather complicated because several effects combine, which results in an effective diffusion coefficient of silane in hydrogen of 0.2 cm²/s at room temperature. In general, the temperature dependence of the diffusion coefficient is given by $D = D_o(T/T_o)^m$ with $1.75 \leq m \leq 2$. For mathematical convenience (see Appendix A), a value of m = 2 is used. However, a value of m = 1.75 would have been more reasonable because most gases diffuse in hydrogen with this m value (6). To obtain the same diffusion coefficient at high temperature (~1000°C), it is clear that the D_o value must be higher when m = 1.75 is used instead of m = 2.

Normally, thermal diffusion is neglected. In the case of a stagnant layer with a temperature gradient above 100°C/mm, this diffusion should be taken into account, as has been found by Bloem (7). Thermal diffusion results in a mass transport from the susceptor to the main gas flow and this diffusion flow is to be subtracted from the diffusion flow to the susceptor caused by a concentration gradient. The diffusion coefficient of silane in hydrogen due to a concentration gradient is not known, but on the basis of molecular weight a value of D_o = 0.6 cm²/s seems reasonable (2). The value of D_o = 0.2 cm²/s, with which the results described in this paper can be explained, should be considered as incorporating a correction for neglected thermal diffusion and the mathematically simplified temperature dependence of D.

APPENDIX A

As can be seen from Fig. 5, the space above the susceptor is divided into a convective and a stagnant layer. The derivation involves the equation of continuity in the convective layer and the diffusion equa-

tion in the stagnant layer. The solutions are coupled at the common boundary.

In an arbitrarily chosen point in the convective layer the equation of continuity should be satisfied, which reads, since only the stationary state is being considered and no decomposition of silane in the gas phase is assumed

$$\frac{\partial J_x(x)}{\partial x} + \frac{\partial J_y(x,y)}{\partial y} = 0 \qquad [A1]$$

Here, J_x is not a function of y, because due to convection all parameters concerned—temperature, T; density, n; partial pressure of silane, p; velocity, V—are uniform over the convective part of the cross section of the tube.

The second pertinent equation describes the diffusion process in the stagnant layer from the top surface to the substrate surface

$$J_y(x) = -D\frac{\partial n(x,y)}{\partial y} \qquad [A2]$$

According to elementary transport theory, $D \sim T^{1/2}/n(T)$ and a relation $D \sim T^{3/2}$ would be a reasonable assumption. Experimental evidence, however, is in favor of a $D \sim T^m$ relationship with $1.75 \leq m \leq 2$. We shall use here $m = 2$ for mathematical convenience so that $D = D_oT^2/T_o^2$.

Finally, we need the equation of state which, for the highly diluted silane, can be given by

$$p = nkT \qquad [A3]$$

where the temperature lapse rate in the stagnant layer is given by

$$T = T_s - (T_s - T_m)(b - y)/\delta \qquad [A4]$$

and $T = T_m$ in the convective part of the tube.

By straightforward calculation, it can be shown that Eq. [A2], [A3], and [A4] can be combined to give

$$J_y(x)T_o^2k\delta/D_o(T_s - T_m) = -T^2\frac{d\frac{p}{T}}{dT} \qquad [A5]$$

which can be integrated between $p = p(x,b - \delta)$, $T = T_m$ and $p(x,b) = 0$, $T = T_s$ to give

$$p(x) = J_y(x)kT_o^2\delta/D_oT_s \qquad [A6]$$

An alternative relation between $p(x)$ and $J_y(x)$ can be obtained by integrating Eq. [A1] over the cross section $0 < y < (b - \delta)$ and unit width, which yields, because J_y has a finite value only at the convective layer bottom surface and V and T are constant

$$J_y(x) = \frac{-(b - \delta)V}{kT_m}\frac{\partial}{\partial x}p(x) \qquad [A7]$$

When V, which is related to the inside parameters $(b - \delta)$ and T_m, is expressed in the corresponding outside parameters b and T_o as

$$V = V_obT_m/(b - \delta)T_o \qquad [A8]$$

Eq. [A7] can be written as

$$J_y(x) = \frac{-V_ob}{kT_o}\frac{d}{dx}p(x) \qquad [A9]$$

Eliminating $p(x)$ from the two solutions [A6] and [A9], we find

$$\frac{\partial}{\partial x}J_y(x) + \frac{D_oT_sJ_y(x)}{bV_oT_o\delta} = 0$$

which, with the boundary condition derived from [A6]

$$p(o) = \frac{J_y(o)kT_o^2\delta}{D_oT_s} \qquad [A10]$$

has the solution

$$J_y(x) = \frac{p_oD_oT_s}{kT_o^2\delta}\exp\left(-\frac{D_oT_sx}{bV_o\delta T_o}\right) \qquad [A11]$$

Using the density of silicon (2.33 g/cm^3) and the gas constant R instead of k, the growth rate of silicon in microns per minute can now easily be found to be

$$G(x) = 7.23 \cdot 10^6\frac{D_oT_sp_o}{RT_o^2\delta}\exp\left(-\frac{D_oT_sx}{bV_o\delta T_o}\right) \qquad [A12]$$

APPENDIX B

As has been made clear in the text, tilting the susceptor over a small angle, ψ, can be helpful to produce uniform thickness along the length of the reactor. As shown schematically in Fig. 12, the cross section varies both because of the tilting and because of the x-dependent stagnant layer thickness, $\delta(x)$. Equation [A8] should be written now as

$$V(x) = \frac{V_ob}{b - \delta(x) - x\tan\psi}\cdot\frac{T_m}{T_o} \qquad [B1]$$

where $V(x)$ is the velocity at high temperature in the reactor. From the experiments with a nontilted susceptor, the thickness of the stagnant layer, δ, has been found and plotted in Fig. 9 as a function of V_T where now

$$V_T(x) = \frac{V_obT_m}{(b - x\tan\psi)T_o} \qquad [B2]$$

and assuming a quasi-stationary state

$$\delta(x) = \frac{A}{\sqrt{V_T}(x)} - B \qquad [B3]$$

The temperature in the stagnant layer can be written as

$$T(x,y) = T_s + \frac{(T_s - T_m)(y - b + x\tan\psi)}{\delta(x)} \qquad [B4]$$

It can easily be verified that, apart from T being a function of x and y instead of y only, Eq. [A2], when combined with Eq. [A3] and [B4], yields the same Eq. [A5] and the same solution [A6]

$$p(x) = \frac{J_y(x)\delta(x)kT_o^2}{D_oT_s} \qquad [B5]$$

Under the actual conditions of the experiments, there is no decomposition on the wall. This means that the equation of continuity over the convective part of the cross section of the tube can be written as

$$J_y(x,b - x\tan\psi - \delta(x)) = -\frac{d}{dx}(b - \delta(x) - x\tan\psi)J_x \qquad [B6]$$

which yields for Eq. [B6] applying Eq. [A3]

$$-\frac{d}{dx}\frac{(p(x)V(x)(b - \delta(x) - x\tan\psi)}{kT_m} = J_y(x,b - x\tan\psi - \delta(x)) \qquad [B7]$$

or applying Eq. [B1]

$$J_y(x) = -\frac{V_ob}{kT_o}\frac{dp(x)}{dx} \qquad [B7a]$$

Eliminating $J_y(x)$ from Eq. [B5] and [B7a], it is found that

$$\frac{dp(x)}{dx} = -\frac{D_oT_sp(x)}{T_oV_ob\delta(x)} \qquad [B8]$$

which has the solution

$$p(x) = p(o)\exp\left[-\frac{D_oT_s}{T_oV_ob}\int_o^x\frac{dx}{\delta(x)}\right] \qquad [B9]$$

Hence, in terms of $J_y(x)$ from Eq. [B5]

$$J_y(x) = \frac{D_oT_sp(o)}{kT_o^2\delta(x)}\exp\left[-\frac{D_oT_s}{T_oV_ob}\int_o^x\frac{dx}{\delta(x)}\right] \qquad [B10]$$

It can easily be verified that for constant δ Eq. [B10] is equal to Eq. [A11], as it should be.

Integrating the exponent in Eq. [B10] with Eq. [B2] and [B3] yields the following rather cumbersome expression

$$J_y(x) = \frac{D_o T_s p_o}{kT_o^2 \delta(x)} \exp\left[-\frac{2D_o T_s T_m}{A^2 T_o^2 \tan\psi}\left(\delta(o) - \delta(x) + B \ln\frac{\delta(o)}{\delta(x)}\right)\right] \quad [B11]$$

Using the density of silicon (2.33 g/cm^3) and the gas constant R instead of k, the growth rate of silicon in microns per minute can now easily be found to be

$$G(x) = 7.23 \cdot 10^6 \frac{D_o T_s p_o}{RT_o^2 \delta(x)} \exp\left[-\frac{2D_o T_s T_m}{A^2 T_o^2 \tan\psi}\left(\delta(o) - \delta(x) + B \ln\frac{\delta(o)}{\delta(x)}\right)\right] \quad [B12]$$

APPENDIX C

In the experiments with small vertical temperature gradient (see Fig. 2), the TiO_2 particles were visibly moving upward along streamlines. This is a basic phenomenon in meteorology (8). The velocity y of the rising lump of gas can be assessed in the following way.

Denoting the vertical coordinate by y and the acceleration of gravity by g, the force experienced by a given parcel of gas, primed if not in equilibrium with the environment, increases with the deviation from hydrostatic equilibrium. This yields in a first order of approximation a force proportional to this deviation, or, since the unprimed quantities refer to equilibrium

$$\ddot{y} = -g\frac{\rho - \rho'}{\rho'} = -g\frac{\Delta T}{T} \quad [C1]$$

Integrating this equation, it is found that

$$y_o - y = \frac{g\Delta T t^2}{2T} \quad [C2]$$

which yields, when the height of the tube is b and the characteristic time to traverse this distance is τ

$$\tau = \left(\frac{2bT}{\Delta T g}\right)^{1/2} \quad [C3]$$

Numerically, this fits well: $b = 2$ cm, $\Delta T \approx 10°$K, $T = 300°$K, $g \approx 10^3$ cm/sec^2 yields $\tau \approx 1/3$ sec, which means, taking into account the lateral and downward motion, 1 rps. This has been observed experimentally.

NOMENCLATURE

x,	position on the susceptor
y,	position above the susceptor
$G(x)$,	growth rate at position x on the susceptor, μm min^{-1}
$J_x(x,y)$,	molecular flux of SiH_4 in the x-direction as a function of x and y, cm^{-2} s^{-1}
$J_y(x,y)$,	molecular flux of SiH_4 in the y-direction as a function of x and y, cm^{-2} s^{-1}
δ,	stagnant layer thickness, cm
$\delta(x)$,	stagnant layer thickness at position x on the susceptor, cm
$\delta(o)$,	stagnant layer thickness at $x = 0$, cm
c,	width of the susceptor, cm
d,	width of the reactor, cm
b,	free height of the reactor at $x = 0$, cm
L,	length of the susceptor, cm
T_m,	temperature of the gas in the convective part of the reactor, °K
T_s,	susceptor temperature, °K
$T(x,y)$,	temperature of the gas in the stagnant layer as a function of x and y
T_o,	300°K
$p(x)$,	partial pressure of silane at the position x, dynes cm^{-2}
p_o,	partial pressure of silane at the inlet of the reactor, dynes cm^{-2}
$V(x,y)$,	linear gas velocity in the reactor as a function of x and y, cm s^{-1}
V_o,	mean gas velocity in the case of a nonheated susceptor cm s^{-1}
V_m,	linear gas velocity in convective part of the reactor, cm s^{-1}
$V_T(x)$,	mean gas velocity in reactor as a function of x (corrected for heating up), cm s^{-1}
R,	gas constant (= 8.31 x 10^7 erg °K^{-1})
k,	Boltzmann constant (= 1.3 x 10^{-16} erg °K^{-1})
ρ,	gas density, g cm^{-3}
n,	number of silane molecules per unit volume, cm^{-3}
D_o,	diffusion coefficient for silane at 300°K (corrected value for thermodiffusion: 0.2 cm^2 s^{-1})
η,	deposition efficiency, %
t,	time, s
ψ,	angle of tilting of the susceptor
g,	acceleration of gravity, cm s^{-2}
τ,	characteristic time for convective flow, s

Manuscript submitted Dec. 8, 1969; revised manuscript received *ca.* April 1, 1970. This was a Recent News Paper presented at the New York Meeting, May 4-9, 1969.

Any discussion of this paper will appear in a Discussion Section to be published in the June 1971 JOURNAL.

REFERENCES

1. S. E. Bradshaw, *Int. J. Electron.*, **23**, 381 (1967).
2. W. H. Shepherd, *This Journal*, **112**, 988 (1965).
3. P. C. Rundle, *Int J. Electron.*, **24**, 405 (1968).
4. Y. Koga, Private communication. Paper to be presented at Electrochem. Soc. Meeting, Los Angeles, May 10-15, 1970.
5. P. J. Severin, To be published.
6. "American Institute of Physics Handbook," 2nd Ed., pp. 2-235, McGraw-Hill, New York.
7. J. Bloem, Private communication, To be published.
8. S. Petterssen, "Weather Analysis and Forecasting," McGraw-Hill, New York (1965).

Thermodynamic and Experimental Aspects of Gallium Arsenide Vapor Growth

A. Boucher and L. Hollan

R.T.C.—La Radiotechnique-Compelec, Laboratoire E.R.G., 92—Suresnes, France[1]

ABSTRACT

The thermodynamics of the transport of GaAs by $AsCl_3$ in an open system has been investigated theoretically and a new approach taken to determine the maximum possible amount of GaAs that can be deposited. The results of the calculations have been checked experimentally, using hydrogen and argon as a carrier gas, by measurements of the amount of Ga (or GaAs) withdrawn from the source and also of total amounts of GaAs deposited. We show that in the range of temperatures of practical interest the experimental results can be accounted for by a simple theoretical analysis assuming a single dominant equilibrium reaction. The theoretical work and the experimental measurements have led to an exact knowledge of the chemical compounds involved and have been used as a basis for a preliminary investigation of the growth mechanisms. The problem has been approached by measurements not only of the total amount of deposit but also of the rate of growth on a GaAs substrate in the presence of various temperature gradients. A kinetic limitation of the growth rate appears clearly.

The epitaxial growth of GaAs by transport in the vapor phase in the presence of $AsCl_3$ is now one of the most widely studied transport reactions. Since the early work (1) there have been many publications on the subject, but the emphasis has been on the production of a material having useful properties. More fundamental work has been rather neglected, and a detailed knowledge of transport phenomena is still lacking in many ways. With respect to thermodynamic reactions Fergusson and Gabor (2) were the first to consider the system as a whole and to calculate, on a computer and from thermodynamic data taken either from tables or from empirical formulas, the most important factors which govern the transport. The corresponding experimental results are, however, very few and incomplete. Also, their work was limited to a consideration of equilibria over the source material. The same type of analysis has been carried out by Hurle and Mullin (3). A much more experimental approach has been taken by Seki *et al.* (4); these authors also gave a simplified theory which will be discussed later.

Problems arising in this field are very numerous: for instance, the influence of factors as important as rate of growth, temperatures of the source and of the deposit, and the temperature gradient is hardly known. As for the mechanisms which really control the growth, knowledge is even scarcer. Some experimental observations have been reported (5), but it is still impossible to predict the influence of such factors as the concentrations of different chemicals at each point in the reactor (*e.g.*, the ratio Ga/As in the gas phase), the amount of supersaturation, the crystallographic orientation of the substrate, etc. All those factors, however, must be controlled in order to reasonably predict the rates of introduction of dopants and vacancies into the crystal structure, which in turn determine the electronic quality of the resulting layers.

In order to improve our understanding of the mechanisms of the reaction we have therefore undertaken on the one hand a theoretical analysis, the results of which are then compared to the experimental results, and on the other hand systematic measurements carried out in the epitaxial reactors under precise experimental conditions.

[1] This laboratory has merged effective January 1st, 1970 with the Laboratoires D'Electronique et de Physique Appliquee, 3 avenue Descartes, 94- Limeil-Brevannes, France.

Computer Calculations

We have taken into account the same reactions as Fergusson and Gabor, neglecting however the partial pressures of Cl^- and Cl, namely

$$GaCl_3 \rightleftharpoons GaCl + Cl_2 \qquad [1]$$

$$2GaCl + \tfrac{1}{2}As_4 \rightleftharpoons 2GaAs_{(S)} + Cl_2 \qquad [2]$$

$$H_2 + Cl_2 \rightleftharpoons 2HCl \qquad [3]$$

$$As_4 \rightleftharpoons 2As_2 \qquad [4]$$

together with their associated relations

$$\log k_i = \frac{\Delta G_i}{RT} \qquad [5]$$

in which the ΔG_i's are evaluated either from the data given by Fergusson (1) or from those given by Hurle (3).

In practice, in this range of temperatures, since the partial pressure of arsenic is larger than the equilibrium partial pressure over saturated gallium, a thin GaAs crust develops on the gallium. After an initial saturation period, the thickness of this layer must become stationary. Thus, this same equation [2] may be used to describe the equilibrium either over a gallium arsenide source or (again in the range of parameters considered) over an arsenic-saturated gallium source.

The three relations which are required to make the system complete can be found by expressing the conservation of the total pressure of chlorine and of arsenic. Thus, we have in all cases

$$\Sigma p_i = 1 \text{ atm} \qquad [6]$$

where the p_i's are the partial pressures, and

$$p_{GaCl} + 3p_{GaCl_3} + p_{HCl} + 2p_{Cl_2} = 3p_{AsCl_3} \equiv 3p_o \qquad [7]$$

where p_o is used to denote the (constant) $AsCl_3$ partial pressure.

Since the flow of arsenic over an arsenic-saturated gallium source is conserved, we have in this case

$$4p_{As_4} + 2p_{As_2} = p_o \qquad [8a]$$

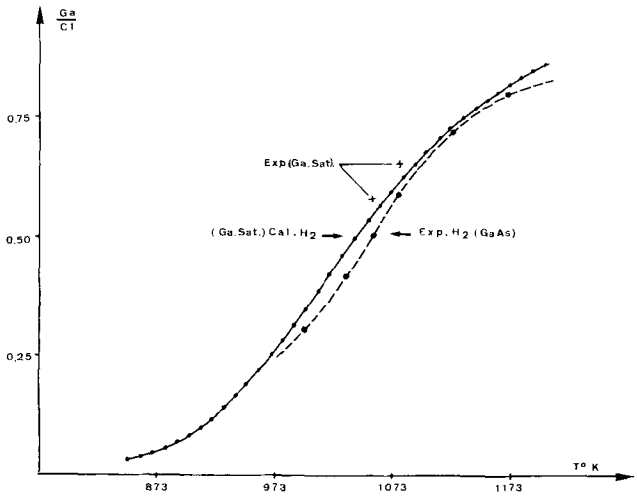

Fig. 1. Experimental and calculated curves of the Ga/Cl ratio vs. temperature at equilibrium with the source.

This equation is no longer valid[2] over the substrate (because of GaAs deposition) and must be replaced by

$$4p_{As4} + 2p_{As2} = p_o - (p^*_{GaCl} + p^*_{GaCl_3} - p_{GaCl} - p_{GaCl_3}) \quad [8b]$$

where the p^*'s denote the partial pressures over the source material, deduced from Eq. [1] through [8a].

Equation [8b] shows that equal amounts of arsenic and gallium have precipitated out of the corresponding gas phase, and the system of Eq. [1] through [7] together with Eq. [8b] characterizes the new equilibrium at any chosen temperature over a GaAs substrate farther down in the reactor, which would result if the substrate region were long enough to allow this equilibrium to be reached. This allows us to compute, by difference, the amount, ΔGaAs, of GaAs which it is thermodynamically possible to deposit, as a function of the temperature of the substrate for any given temperature of the source. The system of Eq. [1] through [8a] has been solved primarily to check our results against published ones as well as to provide the initial conditions p^*_{GaCl} and $p^*_{GaCl_3}$.

Results of Calculations

We show here only the most typical curves which were obtained from these calculations. In all cases, the $AsCl_3$ partial pressure p_o is taken to be 0.01 atm, and the ΔG_i's are those given by Fergusson and Gabor (2).

The theoretical curve of Fig. 1 (continuous line) shows the variation of the Ga/Cl ratio in equilibrium over an As-saturated Ga source in equilibrium with the incoming gas as a function of source temperature. The experimental curve on this figure will be discussed later.

The curves of Fig. 2 show the evolution of the partial pressures of the different compounds as a function of the deposition zone temperature, always assuming this zone to be infinitely long. The points on the right on each curve correspond to equilibrium over the source (which was taken to be at 1120°K). In agreement with Fergusson's results, we found the As_2 partial pressure to be quite negligible, and therefore we did not show it on Fig. 2. Other points worth noting are: (*i*) the partial pressure of $GaCl_3$ is also negligible above 1030°K. This implies that the theoretical curve of Fig. 1 can be interpreted directly in terms of the ratio p_{GaCl}/p_{HCl}; (*ii*) the decrease in p_{GaCl} is due principally to the reduction by hydrogen (formation of HCl) and not to disproportionation (p_{GaCl_3} is negligible for $T > 1030$°K; (*iii*) the limit to the reaction is due to the using up of the arsenic, as could be expected.

[2] Equation [8a] would not be valid either in the case of a true GaAs source, An approximate equation for this case will be given below, but the corresponding computer calculations have not been carried out.

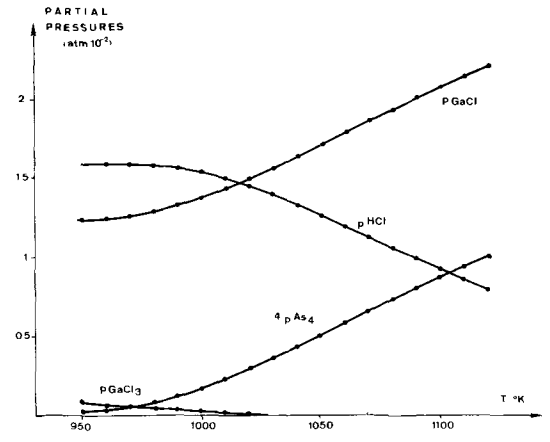

Fig. 2. Calculated equilibrium partial pressures of the chemical compounds vs. temperature.

The preceding remarks have led us to plot the curves shown in Fig. 3 in which the ratio Ga/As is shown as a function of deposition zone temperature (always assuming that equilibrium is reached) for different values of source temperature. The curves are of course limited to the right at the value of the source temperature corresponding to each curve, so that the dotted curve drawn through these points shows this same Ga/As ratio under conditions of equilibrium at the source as a function of source temperature. One can see that this ratio tends to become very large for a reasonable temperature difference between the source and the deposition zone, 100°C for instance.

Finally, the family of curves of Fig. 4 show the ratio of the amount ΔGaAs of "thermodynamically available" GaAs to the total arsenic content of the gas when it leaves the source, plotted as a function of deposition zone temperature with the source temperature as a parameter. Again, the curves are limited to the right at the value of source temperature corresponding to each curve. These curves enable us to calculate the degree of supersaturation of the gas phase over the substrate provided we measure the amount of deposit which has actually taken place on that substrate, under the condition that there has been no deposit farther up-stream.

Further discussions of the various theoretical curves will be given later.

Source Equilibrium Measurements

The purpose of this part of the work was to check the corresponding calculations, and particularly the values of the parameters ΔG_i, by carefully measuring the amounts of Ga or GaAs transported from an

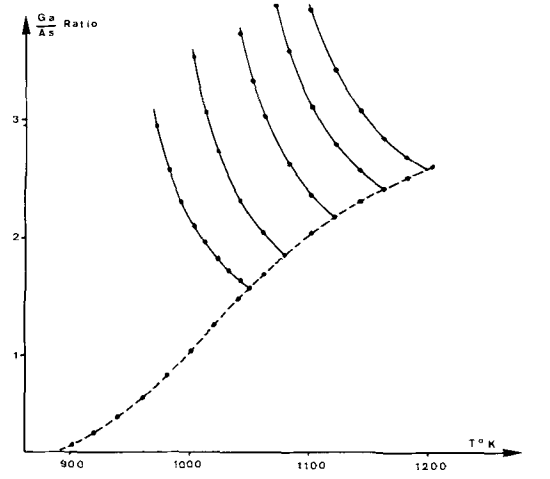

Fig. 3. Ga/As ratio at equilibrium in the reactor vs. temperature for different source temperatures.

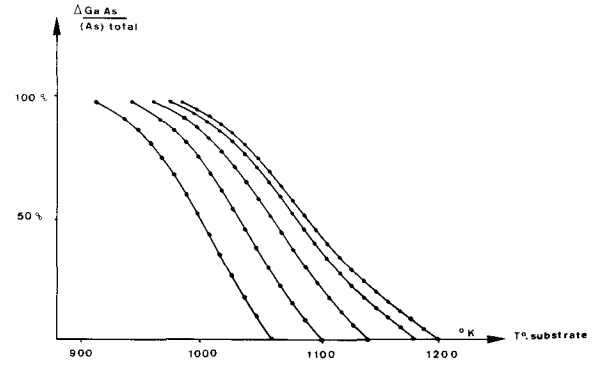

Fig. 4. Ratio of the amount of "thermodynamically available" GaAs to the total arsenic content of the gas when it leaves the source, plotted as a function of deposition zone temperature with the source temperature as parameter. Without deposit, this quantity is none other than the relative supersaturation.

arsenic-saturated source by a known amount of $AsCl_3$ as a function of source temperature. In order to know exactly the amount of $AsCl_3$ in the gas stream a determination of the saturated vapor pressure of this compound was necessary, as the data available in the literature are in disagreement with one another.

The vapor of boiling $AsCl_3$ is carried along by a hydrogen current through a thermostatically controlled distillation column. The gases then pass through washing flasks containing soda and leave the apparatus through a gas-meter. By measuring the weight of chloride formed with the soda in the washing flasks, and knowing the total gas volume, p_{AsCl_3} was determined as a function of temperature. By using different flow rates, we verified that our saturation system showed good reproducibility, and that saturated vapor tension was obtained for a wide range of flow rates. The results can be summarized by the formula

$$\log p_{AsCl_3}\ (\text{mm Hg}) = 8.7 - \frac{2300}{T}$$

which is in good agreement with Matthews' data (6).

The transport of gallium (or of GaAs) was carried out by passing the gas stream first through the saturation system described above, then over the gallium heated to the required temperature. The flow rate and also the geometrical conditions were determined so that equilibrium was reached. (This was checked as above by varying the flow rates in a reasonably wide range around the desired values.)

The transport lasted about 1 hr, the total flow integrated by the gas meter being about 10 1. The GaAs source was weighed before and after the run. In the case of a gallium source, the measurements are made more difficult by the fact mentioned above, that the gallium is not merely saturated by arsenic but is in fact covered by a thick film of gallium arsenide. Careful analyses of sources quenched after a long period of saturation have shown that the percentage of arsenic (which may be of the order of 5%) depends on the geometrical shape of the source and may vary with the temperature. It is, however, reasonable to assume that once the source is saturated the thickness of this film remains constant. The experimental procedure was then to saturate a source at a certain temperature, quench it, weigh it, and bring it back quickly to the same temperature before turning on the flow of $AsCl_3$. The source was quenched and weighed again after the run, and a first approximation of the amount of gallium transported was obtained from the weight loss. The difficulty with this procedure was of course that some evaporation of arsenic took place before equilibrium conditions could be reached over the source, and complementary experiments were necessary to determine the necessary corrective terms. Even then reproducibility was only fair, and more consistent results could be obtained with a GaAs source.

The results of these measurements are best summarized by the experimental curve of Fig. 1 (dashed line). The corresponding points represent the average of slightly scattered measurements, carried out at the same temperature, using a GaAs source. Because of the experimental difficulties described in the preceding paragraph, only two points (crosses on Fig. 1) have been obtained with a gallium saturated source; in this case also, the points represent the average of a number of measurements, but the scatter was definitely larger, so that more measurements had to be taken. The agreement between these two points and the theoretical curve calculated from Fergusson's parameters is good. The agreement when Hurle's parameters were used was definitely not as good. The discrepancy with the experimental curve corresponding to the case of a GaAs source is qualitatively explained by the decrease in arsenic partial pressure.

Interpretation of the Experimental Results

If Δm is the weight loss of Ga (or GaAs), ΔV the volume in liters under normal conditions of the carrier gas that has passed through the system, and p_o the saturated vapor pressure of $AsCl_3$, we have

$$\alpha \equiv \frac{n\ \text{Ga}}{n\ \text{Cl}} = \frac{22.4}{3M\ p_o} \cdot \frac{\Delta m}{\Delta V}$$

where M is the atomic mass of Ga (or molecular mass of GaAs), and α the ratio of the number of gallium atoms to that of Cl atoms in the gas.

Since the computer calculations show that in the presence of hydrogen the amount of $GaCl_3$ is negligible in the range of temperatures envisaged, we can assume that the predominant equilibrium is

$$2GaCl + H_2 + \tfrac{1}{2}As_4 \rightleftharpoons 2GaAs + 2HCl \qquad [9]$$

In the case of a gallium source, we have

$$3p_o = p_{HCl} + p_{GaCl} \qquad [10]$$

$$p_{As4} = \tfrac{1}{4}\, p_o \qquad [11]$$

we can then express the equilibrium constant K_1 relative to Eq. [9] as

$$K_1 = \frac{p^2(HCl)}{p^2(GaCl)\ p^{1/2}(As_4)} = \frac{2(1-\alpha)^2}{\alpha^2\, p_o^{1/2}}$$

In the case of GaAs source, Eq. [10] remains valid, but Eq. [11] is to be replaced by

$$p_{As4} = \tfrac{1}{4}(p_o + p_{GaCl}) \qquad [12]$$

whence

$$K_1 = \frac{2(1-\alpha)^2}{p_o^{1/2}\, \alpha^2 (1+3\alpha)^{1/2}}$$

where p_o is known and α is determined experimentally. If the logarithm of K_1 thus calculated is plotted against the inverse of the absolute temperature, the continuous-line curve of Fig. 5 is obtained. For temperatures higher than 1000°K, the linearity of the curve shows that the assumption is justified and that the predominant equilibrium which controls the group of reactions is indeed that expressed by Eq. [9]. Above 1000°K, a very good agreement is found between the values of K_1 determined experimentally and those calculated from Eq. [5] using Fergusson's parameters. The agreement is definitely not as good if Hurle's parameters are used (see dotted lines on Fig. 5). Below this temperature, the reaction

$$3GaCl + \tfrac{1}{2}As_4 \rightleftharpoons 2GaAs + GaCl_3 \qquad [13]$$

can no longer be neglected, and it is necessary to carry out a complete calculation in order to account for the experimental results (Fig. 1).

Another interesting verification was undertaken by using argon as carrier gas. We assume that equilibrium

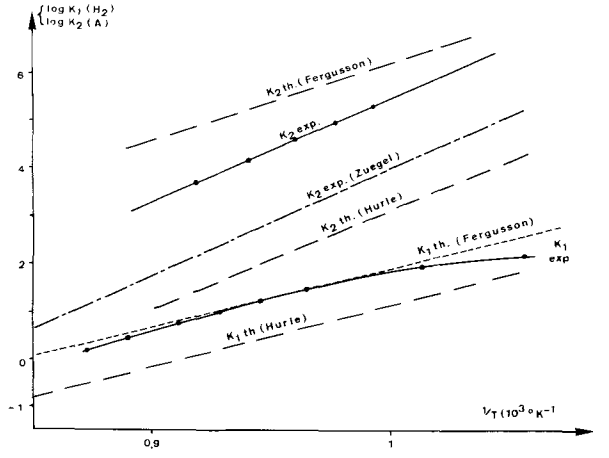

Fig. 5. Experimental and theoretical equilibrium constants vs. inverse temperature for equilibriums [9] and [13].

[13] is now the dominant one; the equilibrium constant is in this case

$$K_2 = \frac{p_{GaCl_3}}{p^3_{GaCl} p^{1/2}_{As_4}}$$

with

$$3p_o = p_{GaCl} + 3p_{GaCl_3}$$

If we set

$$p_{GaCl} = 3\,\alpha'\,p_o$$

we have, in the case of a gallium arsenide source, which was the only one used together with argon

$$p_{As_4} = \frac{p_o}{2}(1 + \alpha')$$

so that

$$K_2 = \frac{\sqrt{2}\,(1 - \alpha')}{27 p_o^{5/2}\,\alpha'^3\,(1 + \alpha')^{1/2}}$$

with α' being deduced from the experimental data by the formula

$$1 + 2\,\alpha' = \frac{22.4}{M_{P_o}} \cdot \frac{\Delta m}{\Delta V}$$

Log K_2 thus calculated is also plotted on Fig. 5 as a function of $1/T$. Here too, a good agreement with the starting assumption can be seen since a straight line is obtained. Further, the experimental curve lies between those calculated using the data of Fergusson and those of Hurle, the best fit being again obtained with the straight line corresponding to Fergusson's values. It is interesting to note the large difference between the two calculated sets of values, while the thermodynamic data are at first sight quite comparable

Fergusson: $\Delta G = -108{,}000 + 138.2T - 8.0\,T \log T - 3.2 \cdot 10^{-3}T^2$

Hurle : $\Delta G = -108{,}560 + 141.4T - 6.45T \log T - 3.2 \cdot 10^{-3}T^2$

We have also plotted on Fig. 5 the values of K_2 deduced from Zuegel's results (obtained under vacuum) (7). The agreement with our experimental results is quite acceptable.

Measurements Rate of Growth and Total Deposit

These measurements were carried out in order to investigate the extent to which a knowledge of the thermodynamics of the reactions involved would allow a prediction of these quantities.

The rate of growth was measured in a classical epitaxial system (8) with the two types of temperature gradients shown in Fig. 6. In both cases the growth was carried out under the same operating conditions, namely; flow rates, source temperature (1120°K), substrate orientation, etc. Several substrates were used in every run, the essential difference being that in the case of gradient 1 the substrates were at different temperatures; in the case of gradient 2 they were at the same temperature, but this temperature level could be varied at will without changing the source temperature nor the general shape of the curve. Typical results have been gathered on Fig. 7, which shows the growth rate as a function of the inverse of the absolute temperature.

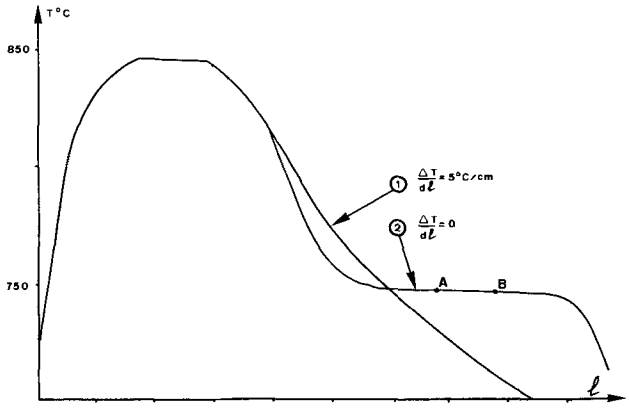

Fig. 6. Thermal gradients used in epitaxial growth

The initial results of growth rate measurements, when no special care was taken, were very widely scattered. A correlation was found however between the occurrence of low and widely scattered growth rates and the appearance of a sizable amount of deposit on the walls on the reactor. This led us to measure the total amount of GaAs deposited (on the substrate, the substrate holder, and the walls of a removable sleeve fitted inside the reactor).

It was found that reproducible growth rates would be obtained if and only if (*a*) there was no deposit except on the GaAs substrate, and (*b*) the total amount of deposited GaAs was lower than 10% of the "thermodynamically available" GaAs. If these conditions were not satisfied, low and widely scattered growth rates were obtained.

A plot of the reproducible growth rates *vs.* inverse temperature yields the solid curve of Fig. 7. The values measured are independent of the temperature gradient (type 1 or 2 of Fig. 6), of the substrate area (again provided that the total deposit remains low enough), and, in case of gradient 2, of the position of the substrate in the flat region of the curve (points A and B, Fig. 6).

These results do not agree with those obtained by Seki (4). By taking into consideration only the thermodynamic aspects of the deposition mechanism. Seki predicts that the growth rate should increase monotonically with decreasing substrate temperatures, and his results agree with this prediction. On the same

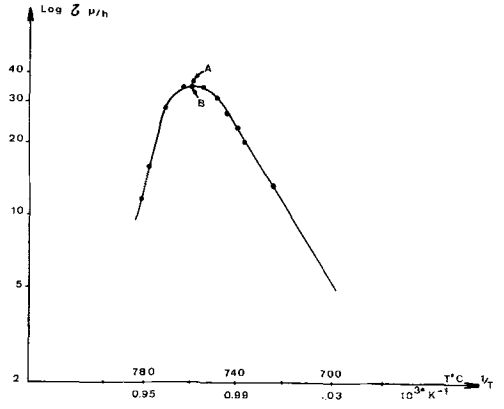

Fig. 7. Experimental growth rate vs. inverse temperature

basis, we would expect the same qualitative behavior, but our experimental data, like those of Shaw's (5), show that below 750°C the growth rate falls rapidly with decreasing temperature. The corresponding law can be characterized by a well-defined activation energy of 40 kcal/mole for a (100) substrate orientation. In view of the strong dependence of the growth rate on substrate orientation in this range of temperatures, it seems natural to assume that this activation energy corresponds to a surface reaction.

We have already noted that, when the conditions for reproducible growth rates are achieved, the total deposition rate is also low. Thus, in this case, a good approximation of the degree of the relative supersaturation and of the GaAs ratio over the substrate can be obtained from the curves of Fig. 3 and 4. These data may prove useful for an investigation of point defects, *e.g.*, vacancies, introduced in the epitaxy process.

On the other hand, when the growth rates are not very reproducible, it is impossible to obtain any correct theoretical estimate of these two parameters, or to deduce a reliable value of activation energy from the experimental data. A relative reproducibility may however be achieved, and the electrical quality of the deposits may be quite satisfactory; however, considerable experimental work is needed to find the proper operating conditions.

Summary and Conclusions

We have carried out a theoretical calculation of the amount of GaAs available for epitaxial growth in an open $AsCl_3$ system, using a more rigorous definition of this quantity than done by previous authors. We have checked the values of the relevant parameters by careful experimental measurements of transported material and have found the values given by Fergusson and Gabor (2) to give the best agreement with our measurements. These experiments were carried out under conditions very similar to those usually prevailing for actual epitaxial growth. They have shown that, in the temperature range usually involved (730°-880°C) the dominant equilibrium is

$$2GaCl + \tfrac{1}{2}As_4 + H_2 \leftrightharpoons 2GaAs + 2HCl$$

when hydrogen is used as the carrier gas. When the carrier gas is argon, the dominant equilibrium is

$$3GaCl + \tfrac{1}{2}As_4 \rightleftharpoons 2GaAs + GaCl_3$$

A comparison of calculated thermodynamic parameters with experimentally determined rates of epitaxial growth have shown that other mechanisms must be taken into account, namely a surface reaction with an activation energy of 40 kcal/mole.

The rate of epitaxial growth can be strongly affected by the occurrence of unwanted deposits on other parts of the reactor.

Acknowledgment

The authors would like to thank M. Drougard for helpful discussions, I. Bilharz and B. Bracke for programming the computer calculations, J. Chane for the chemical analyses, and J. M. Durand and C. Pataquis for their experimental assistance.

This work was carried out with the financial support of the Direction Générale de la Recherche Scientifique et Technique.

Manuscript submitted Sept. 18, 1969; revised manuscript received March 10, 1970.

Any discussion of this paper will appear in a Discussion Section to be published in the June 1971 JOURNAL.

REFERENCES

1. J. R. Knight, D. Effer, and P. R. Evans, *Solid-State Electron.*, **8**, 178 (1965)
2. R. R. Fergusson and T. Gabor, *This Journal*, **111**, 585 (1964).
3. D. T. J. Hurle and J. B. Mullin, *Proc. Internat. Conf. on Cristal Growth*, Birmingham, 1968, p. 242.
4. H. Seki, K. Moriyama, I. Asakama, and S. Horie, *Jap. J. Appl. Phys.* **7**, 1324 (1968).
5. D. W. Shaw, *This Journal*, **115**, 405 (1968).
6. J. B. Matthews, J. F. Summer, and E. A. Moelwyn-Hughes, *Trans. Faraday Soc.*, **46**, 797 (1950).
7. M. A. Zuegel, *This Journal*, **112**, 1153 (1965).
8. A. Boucher, L. Hollan, and J. M. Leduc, *J. Internat. Micro-Electronique*, Toulouse (1969).

Growth and Characterization of Lead Telluride Epitaxial Layers

John W. Wagner and Alan G. Thompson

Electronic Materials Division, Bell & Howell Company, Pasadena, California

ABSTRACT

PbTe single-crystal epitaxial layers have been grown on PbTe substrates using the tipping technique. The layers were grown on {111} and {100} oriented substrates from lead-tellurium solutions containing from 0.01 to 0.20 atomic fraction tellurium. Cooling rates of from 0.2° to 1°C/min were used. The resulting layers were characterized using x-ray, optical, etching, and electrical techniques. Diodes were fabricated from several of the resulting materials, and their characteristics were found to be substantially improved over diffused PbTe diodes.

Lead telluride crystals which are grown from stoichiometric melts have hole concentrations of approximately 8×10^{18} cm^{-3} due to deviations from stoichiometry (1). The form of the lead-tellurium phase diagram close to the stoichiometric composition has been investigated by Brebrick and Allgaier (2), who showed that by annealing PbTe in the presence of lead or tellurium-rich vapor, the carrier concentration can be made n- or p-type and varied over a wide range. Thus, by annealing at a certain temperature the hole concentration can be lowered to the desired value; by lowering the temperature and annealing for a relatively short time an n-type layer can be diffused into the surface. The resulting p-n junction is suitable for photovoltaic detector and laser fabrication.

In the case of the $Pb_{1-x}Sn_xTe$ alloy the same process is followed. However, as the tin content of the alloy is increased, the anneals and diffusions must be performed at progressively lower temperatures, resulting in extremely long material preparation times. Work

performed previously in this laboratory (3) has shown that PbTe and $Pb_{1-x}Sn_xTe$ crystals pulled from metal-rich melts have carrier concentrations substantially lower than those pulled from stoichiometric melts.

Experience with the epitaxial growth of gallium arsenide from gallium solution has shown that high-purity layers can be prepared with a planar interface. We have therefore explored the possibility of growing epitaxial layers of PbTe from lead solution with the following advantages in mind (*i*) no lengthy annealing or diffusion procedures would be necessary, (*ii*) the possibility of more planar junctions than have been obtained by diffusion, and (*iii*) the possibility of higher purity layers.

In this paper we present results for PbTe grown from lead solutions. Metallurgical data are given and various electrical measurements are reported. The characteristics of the grown p-n junctions are compared with those of diffused junctions reported in the literature.

Growth Process

The PbTe layers were precipitated from solution on to single-crystal PbTe substrates using a tipping technique similar to that of Nelson (4). The apparatus is shown schematically in Fig. 1. A quartz boat was inserted into the quartz tube. The tube was placed in a horizontal resistance furnace which could be tilted in either direction with respect to the horizontal. The source material, which consisted of Pb (Asarco, nominal 6N) and PbTe, was placed in one end of the boat. A polished and etched seed wafer of PbTe was placed in the other end of the boat. The furnace was tilted so that the seed was higher than the source material, and the temperature of the furnace was raised while a stream of hydrogen was passed through the tube. The PbTe was seen to dissolve in the lead as the temperature was increased. After the PbTe had completely dissolved, the temperature was slowly lowered to find the liquidus point of the solution. This procedure was repeated several times until the initial freezing point had been established to within approximately 1°C. The temperature was then raised to slightly above the solidifying point and the system was allowed to stabilize. The furnace was then tilted so as to transfer the solution over the seed wafer. The temperature was then slowly lowered so that the PbTe would deposit as a single-crystal growth onto the wafer. After slowly cooling over the desired temperature interval (20°-100°C), either the system was allowed to rapidly cool to room temperature or the furnace was tilted to its original position, allowing the remaining solution to flow off the layer prior to cooling to room temperature.

Layers of PbTe were grown on single-crystal {111} and {100} oriented PbTe wafers using this tipping technique. Lead-tellurium solutions containing from 0.01 to 0.20 atomic fraction tellurium were used and the cooling rate was varied from 0.2° to 1.0°C/min. The resulting layers had thicknesses of from 50 to 300μ, and the epitaxial growth rate was qualitatively observed to follow the expected dependence on the solubility *vs.* temperature curve and on the cooling rate.

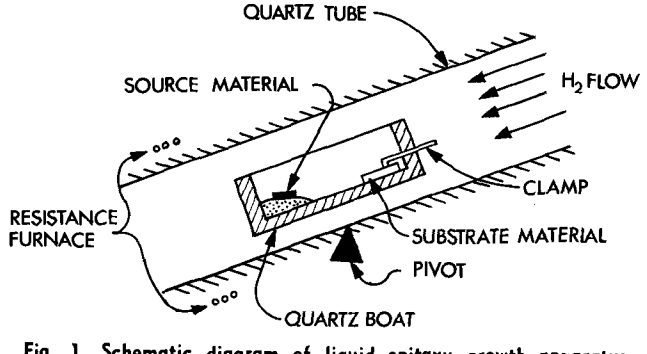

Fig. 1. Schematic diagram of liquid epitaxy growth apparatus [after Nelson (4)].

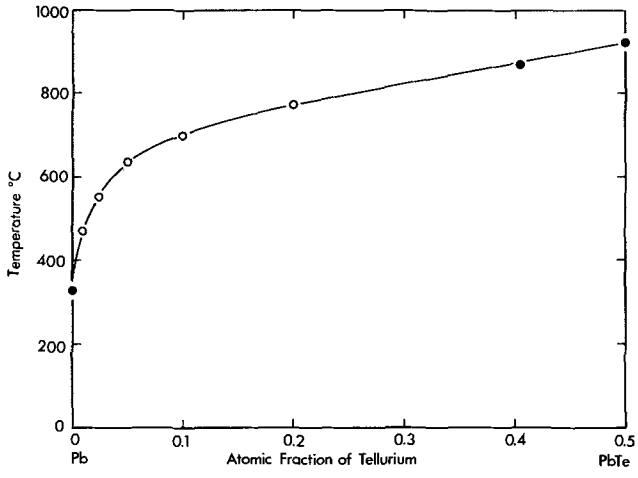

Fig. 2. Liquidus curve for the metal-rich portion of the lead-tellurium phase diagram. ●, Literature values [ref. (3, 5, 6)]; ○, present data.

The metal-rich portion of the liquidus curve of the lead-tellurium system is shown in Fig. 2. The melting points of lead, lead telluride and the p to n crossover composition were taken from the literature (3, 5, 6). The open circles are taken from the data obtained in the liquid epitaxy experiments, and are estimated to be accurate to ±5°C. Although a portion of the melt vaporizes during the stabilization period, its weight is very small in comparison with the total melt and it decreases with decreasing temperature. The accuracy of the atomic fraction of tellurium is better than ±0.005 for the higher values and probably ±0.001 for the more dilute solutions. The only other references on this portion of the liquidus are over 50 years old and are quoted in Hansen (7). These are not shown on Fig. 2 because of their large scatter and doubtful validity.

Characterization

Several techniques were used to characterize the as-grown layers: the most useful were x-ray, etching, optical, and electrical.

X-ray.—X-ray Laue photographs were taken of several of the epitaxial layers to verify their single-crystal nature and to obtain a qualitative indication of their perfection. Figure 3(a) shows a typical Laue pattern of a {100} oriented layer. The spots in these patterns were sharp and singular. Figure 3(b) is an unusual Laue photograph of a section of a {100} layer which contained a low-angle boundary. The spots are seen to be doubled with an angular separation of less than a degree; the small angle in this layer originated from a low-angle grain boundary in the PbTe substrate. It should be pointed out that these low-angle grain boundaries are very common in the lead salts,

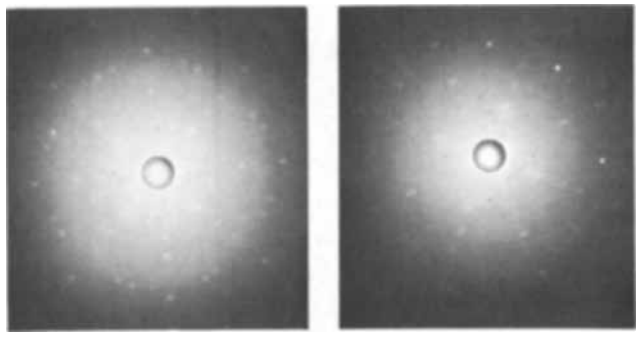

Fig. 3 (a). (left) Typical Laue pattern of {100} PbTe epitaxial layer; Fig. 3 (b). (right) Laue pattern of {100} epitaxial layer grown on a substrate containing a low-angle grain boundary.

and great care must be exercised during the preparation of bulk material to avoid them and obtain truly single-crystal ingots. Figures 3(a) and 3(b) were both taken on layers from which the solution had been tipped off prior to cooling to room temperature.

Optical.—Those layers which were cooled to room temperature with the lead-tellurium solution over the surface had to be etched in hot, concentrated HCl for several days to reveal the epitaxial layer. The HCl did not "attack" the PbTe layer, but the etching procedure did leave the layer with a dull gray appearance. Some interesting surface features were seen on {111} and {100} layers when the solution had been etched away. Figure 4(a) is a photograph of the as-grown surface of a {111} layer after removal of the Pb-Te alloy. The overlapping parallelopipeds have (100) cube faces. Figure 4(b) is a photograph of the as-grown surface of a {100} layer, again after etching away the alloy. This surface also consists of an overlapping growth structure dominated by (100) faces.

The overlapping growths shown in Fig. 4(a) and 4(b) were due to rapid growth which occurred when the solution was allowed to cool to room temperature while over the layer. Such growth was possible because the cooling process was still slow enough (a few degrees Centigrade per minute) to allow rapid precipitation from solution. Such precipitation can also occur in the epitaxial growth of other materials (such as GaAs) from solution when the solution is permitted to remain over the layer during the final cooling. The obvious answer to this problem is to remove the solution prior to the final cooling.

Those layers from which the Pb-Te solution was tipped off prior to final rapid cooling were found to be relatively flat and to have shiny, metallic surfaces. The surfaces exhibited none of the overlapping structure seen in Fig. 4, and a typical {100} layer is shown in Fig. 5. However, a few of the layers showed some interesting surface structure when viewed under an optical microscope. Figure 6(a) is a microphotograph of an as-grown surface of a {100} layer. The hillocks seen in the photograph occurred occasionally on several layers, and their height was typically a few microns. No determination was made as to the origin of these hillocks, but one can speculate that they arise around a lead precipitate or an impurity precipitate. Figure 6(b) is a photograph of a section of another {100} surface. The "waves" shown in the photograph were seen sparingly on a few of the layers and on only small portions of these layers, usually toward the edge of the substrate. These "waves" are apparently due to transient thermal gradients during the growth of the layers. It must be emphasized that the features shown in Fig. 6(a) and 6(b) were seen on only a few of the layers and then only on small portions of these layers.

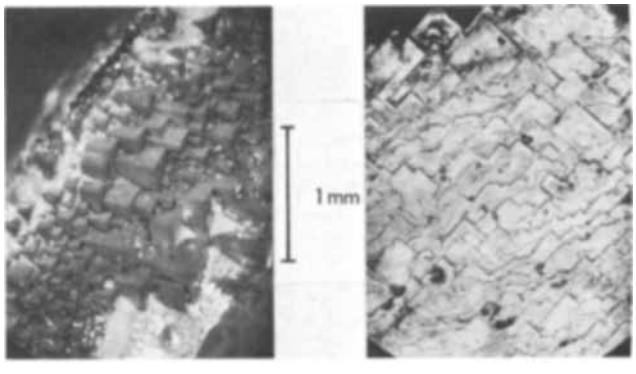

Fig. 4 (a). (left) Surface of PbTe epitaxial layer grown on a {111} oriented substrate with the melt over it during rapid cooling; Fig. 4 (b). (right) Surface of PbTe epitaxial layer grown on a {100} oriented substrate with the melt over it during rapid cooling.

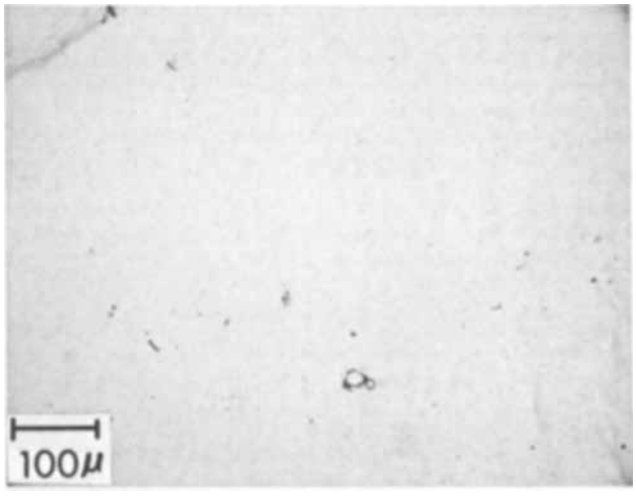

Fig. 5. Surface of a typical PbTe epitaxial layer grown on a {100} oriented substrate with the melt decanted before rapid cooling.

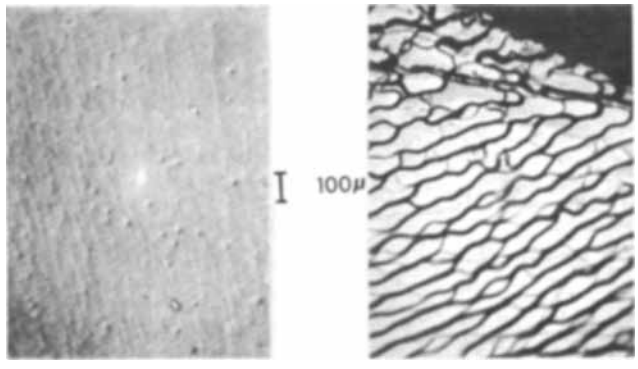

Fig. 6 (a). (left) Surface of a {100} epitaxial PbTe layer showing small hillocks; Fig. 6 (b). (right) Surface of a {100} epitaxial PbTe layer showing "waves."

Except for these features, the surfaces were quite smooth when viewed under the optical microscope, as in Fig. 5.

Etching.—Cross sections of the wafers were lapped and polished mechanically and were then polished and etched electrolytically [using an etch of Norr (8)] to reveal the growth junction. Figure 7(a) shows a typical junction; these junctions were relatively planar. Another view of the rapid growth which occurs during final cool down, if the solution remains over the layer, is shown in Fig. 7(b). The narrow straight line in this figure is the main junction formed between the substrate and the epitaxial growth. The ragged area above the epitaxial growth is the region where the rapid growth began during the final cooling phase.

Electrical.—The interface between the substrate and the layer can be appropriately termed a junction since the substrate was always p-type and the resulting layers were always n-type. This has been shown

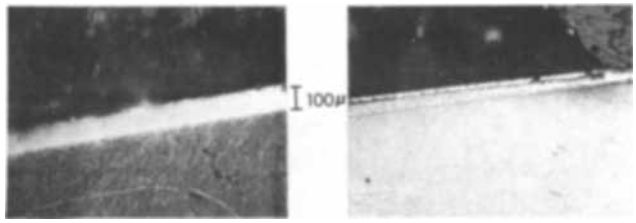

Fig. 7 (a). (left) Typical PbTe p-n junction grown by liquid epitaxy; Fig. 7 (b). "Double junction" in PbTe due to slow and rapid growths.

using a thermoelectric probe and Hall measurements. Hall measurements were performed at 77°K on the layers without attempting to remove the substrate. Such measurements assume that the layer is sufficiently isolated from the substrate so that the Hall data are characteristic of the layers. These measurements gave electron carrier concentrations ranging from 3×10^{17} to 7×10^{17} cm^{-3} for layers grown from 0.01 to 0.10 atomic fraction tellurium solutions, respectively; mobilities ranged from 30,000 to 10,000 $cm^2\ V^{-1}\ sec^{-1}$, respectively. One Hall measurement was performed on an exceptionally thick layer from which the substrate had been lapped off. The carrier concentration of this layer was measured to be 3×10^{17} cm^{-3} prior to lapping off the substrate and 4×10^{17} cm^{-3} after removal of the substrate. This reasonable agreement supports the belief that the layers are sufficiently isolated from the substrates when making Hall measurements at 77°K.

Diodes

Diodes have been fabricated from several of the epitaxial wafers. Mesas of approximately 10^{-2} cm^2 were etched into the n-type layers, and ohmic contacts were placed on the n-layer using Indalloy 5. Several different contacts were tried on the p-type substrate. Figure 8(a) shows an *I-V* curve of one of the diodes fabricated using Indalloy 2 as the contact to the p-face. The forward characteristics of this diode are rather poor and are dominated by contact resistance. The reverse characteristics are quite good. Figure 8(b) shows an *I-V* curve of a diode which had a gold contact to the p-side. The forward characteristics of this diode are vastly improved over the diode having the Indalloy contact but still exhibit substantial contact resistance. The reverse characteristics of this diode are still rather good.

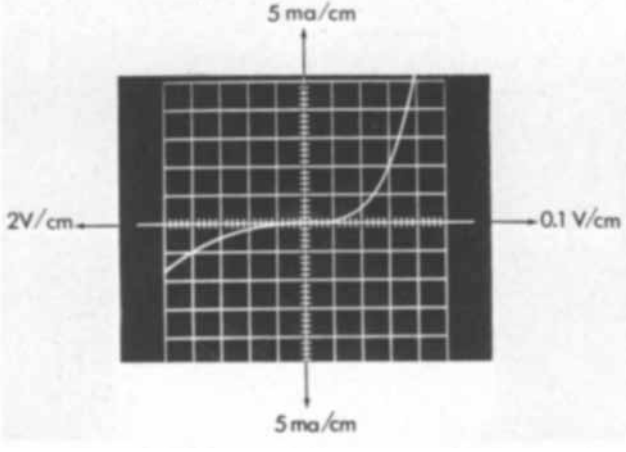

Fig. 8. (a). *I-V* curve for PbTe epitaxial diode, 2508-6A, Indalloy 2 contact to p-side; taken at 77°K.

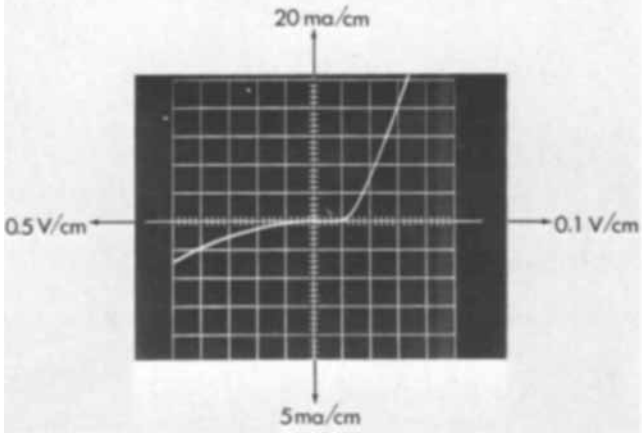

Fig. 8 (b). *I-V* curve for PbTe epitaxial diode, 2508-6A, gold contact to p-side, taken at 77°K.

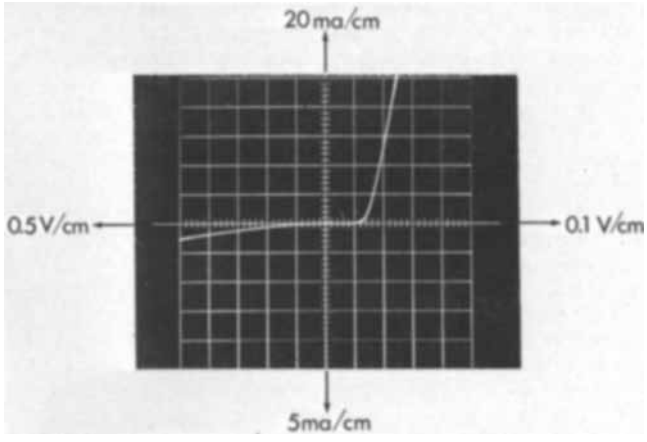

Fig. 8 (c). *I-V* curve for PbTe epitaxial diode, 2508-6B, gold-thallium contact to p-side; taken at 77°K.

We have found that a gold-thallium alloy (27:73 Au:Tl) gave the best contact to the p-side of the diodes. Figure 8(c) is a typical *I-V* curve of a diode with the Au-Tl contact. The forward characteristics of this diode are a factor of two improved over the diodes having gold contacts and are typical of those reported in the literature for diffused PbTe diodes (9, 10). The reverse characteristics are much better than those reported for diffused diodes. A few of the diodes we have fabricated using Au-Tl contacts to the p-side have had forward and reverse characteristics which were greater than a factor of two improved over the typical diode shown in Fig. 8(c).

Figure 9 is a semilogarithmic plot of the forward current-voltage characteristics of several PbTe diodes. The open squares are data from a diffused diode reported by Butler (9), while the open circles are data of Zoutendyk (10), also on a diffused diode. The solid squares are data from one of our diodes that had Indalloy 2 as the contact to the p-side. The early appearance of contact resistance is evident. The solid circles are data from one of the diodes fabricated using the Au-Tl alloy on the p-side. From the linear portion of the semilogarithmic *I-V* plots, one can calculate the *A* values for the diodes in the diode equation

$$I = I_0\, e^{qV/AkT}$$

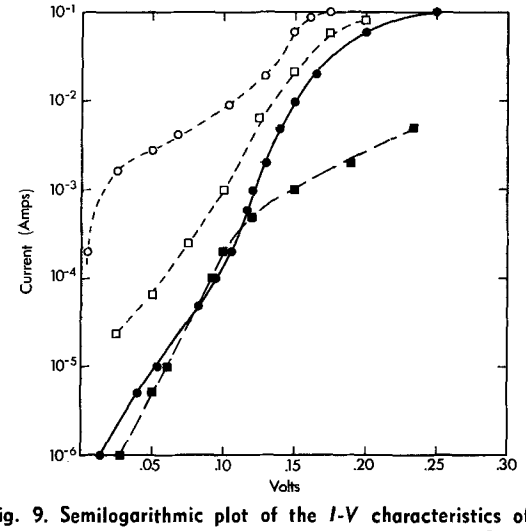

Fig. 9. Semilogarithmic plot of the *I-V* characteristics of PbTe diodes at 77°K, all having areas of the order of 10^{-2} cm^2. ○, Diffused diode [ref. (9)]; □, diffused diode [ref. (10)]; ■, liquid epitaxial diode, Indalloy 2 contact to p-side; ●, liquid epitaxial diode, gold-thallium contact to p-side.

Those diodes which we prepared using Au-Tl contacts to the p side had A values between 1.8 and 2.0.

Capacitance data were taken for several of the diodes. The capacitance was found to have a linear $1/C^2$ to $1/C^3$ dependence on the voltage, tending to follow the square law behavior for low voltage. The negative intercept of the extrapolated $1/C^2$ curves generally lay between 0.1 and 0.25V. Carrier concentrations determined from the differential capacitance measurements were in the range of 10^{16}-10^{17} cm^{-3}, corresponding to a movement of the space charge layer of 2 to 5μ. This is indicative of the region between the p substrate and n layer, where compensation would be expected because of slight melt back of the substrate and diffusion during layer growth. Any material melted and absorbed by the melt will not contribute impurities since the substrate carriers are due mainly to vacancies; this is not the case for the III-V compounds. The form of the $1/C^n$ curves substantiates this argument, since they indicate a sharp, but not discontinuous changeover from p- to n-type behavior.

Conclusion

PbTe single-crystal epitaxial layers have been grown from lead solutions on PbTe substrates using the tipping technique of Nelson; x-ray Laue patterns verified the single-crystal nature of the layers. Those layers which were cooled down to room temperature with the Pb-Te solution over the surface exhibited a region of rapid, overlapping growth due to rapid precipitation from solution. Such rapid precipitation is believed to occur in the liquid epitaxial growth of other materials when the solution is allowed to freeze over the layer. Layers from which the solution was removed prior to final cool down were relatively smooth and had shiny, metallic surfaces, with best growth on the {100} face. The growth junctions were revealed by electrolytic etching and were found to be essentially planar. The layers had majority carrier (n-type) concentrations of from 3 x 10^{17} to 7 x 10^{17} cm^{-3} and mobilities as high as 30,000 cm^2/V-sec. Diodes which were fabricated from the layers had forward characteristics which were as good as or somewhat better than those reported in the literature for diffused PbTe diodes. Their reverse characteristics were greatly improved over the reported diffused diodes. Thus, this method of p-n junction preparation shows promise for superior electrical properties because of the short time the material has to be held at a relatively high temperature and the planar interface which results.

Acknowledgments

We wish to acknowledge the assistance given by K. Schwartz in the electrical measurements, E. Masumoto for the x-ray measurements, and R. K. Willardson for helpful suggestions through the course of this work. This work was partly supported by the Naval Weapons Center, Corona, California, under Contract No. N00123-68-C-2131.

Manuscript submitted Oct. 20, 1969; revised manuscript received March 20, 1970.

Any discussion of this paper will appear in a Discussion Section to be published in the June 1971 JOURNAL.

REFERENCES

1. J. W. Wagner and R. K. Willardson, *Trans. Met. Soc. AIME*, **242**, 366 (1968).
2. R. F. Brebrick and R. S. Allgaier, *J. Chem. Phys.*, **32**, 1826 (1960).
3. J. W. Wagner and R. K. Willardson, *Trans. Met. Soc. AIME*, **245**, 461 (1969).
4. H. Nelson, *RCA Rev.*, **24**, 603 (1963).
5. D. E. Grimes, *Trans. Met. Soc. AIME*, **233**, 1442 (1965).
6. R. F. Brebrick, "Progress in Solid State Chemistry," H. Reiss, Editor, Vol. 3, pp. 217-220, Pergamon Press, New York (1966).
7. M. Hansen, "Constitution of Binary Alloys," 2nd ed., p. 1111, McGraw Hill Book Co., New York (1958).
8. M. K. Norr, NOLTR 63-156, 1967; U.S. Naval Ordnance Laboratory, White Oak, Md.
9. J. F. Butler, *This Journal*, **111**, 1150 (1964).
10. P. J. A. Zoutendyk, Ph.D. Thesis, Calif. Inst. of Tech., 1968, unpublished.

The Effect of Environment on the Fracture of Adhering Aluminum Oxide

J. C. Grosskreutz[1]

Midwest Research Institute, Kansas City, Missouri

ABSTRACT

The spacing of cracks in anodic layers grown on 1100-0 and 7075-T6 aluminum was measured as a function of the strain in the substrate and as a function of environment. The environments were distilled water, sea water, methanol, and dry air. In general, the cracks produced by a given substrate strain were densest in the materials exposed to distilled water and least dense in those exposed to dry air. An analysis is given whereby the fracture strength of the oxide, σ_f, can be derived from the minimum crack spacing observed, d_s. The result is $\sigma_f = (\tau/2t)d_s$, where τ is the interfacial shear stress between oxide and substrate, and t is the oxide thickness. Values of σ_f which are obtained in dry air approach those reported for sapphire whiskers. The effect of other environments is to reduce σ_f by 10-20% in methanol, 20-40% in sea water, and 30-40% in distilled water.

The mechanical and fracture properties of metal oxide films (Al_2O_3 in particular) have been treated in detail in a recent paper (1). It was shown that the fracture of films adhering to a strained substrate occurred as regularly spaced cracks at right angles to the tensile axis, provided that the oxide was sufficiently thick (> 1000Å for Al_2O_3). A phenomenological theory was described which accounted for the variation in crack spacing as a function of substrate strain. An interesting observation was that the crack spacing reached a minimum value, such that further straining of the substrate produced only a widening of the exist-

[1] Address until Oct. 1970: Institut für Theoretische und Angewandte Physik, Universität Stuttgart, 7 Stuttgart 1, Azenbergstrasse 12, Germany.

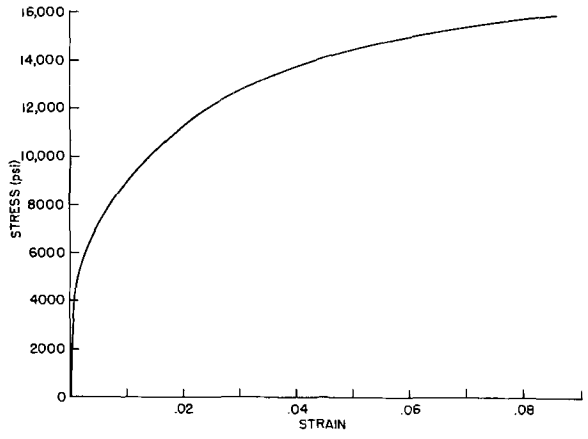

Fig. 1. Stress-strain curve for 1100-0 aluminum

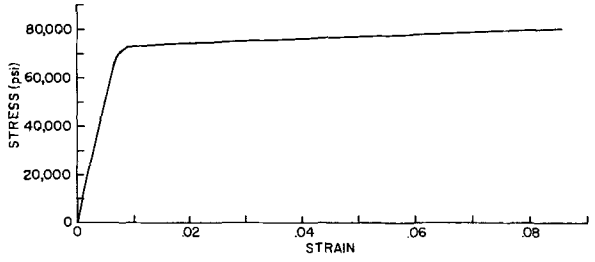

Fig. 2. Stress-strain curve for 7075-T6 aluminum

ing cracks. This minimum spacing was called the saturation spacing, d_s.

It is the purpose of the present paper to explore the effect of environment on the density of cracks in a strained Al_2O_3 oxide film and to show how the saturation spacing can be used to derive the fracture stress of the adhering oxide.

Experimental Details and Results

Anodic oxide films of a nominal thickness, 1400Å, were grown on 1100-0 and 7075-T6 aluminum substrates in a tartaric acid electrolyte (2). The substrate material was in the shape of a conventional, flat tensile specimen with a gauge length of 2 in. and a cross section of 1/32 in.^{2}. The anodized specimens were pulled to various values of strain and the density of cracks determined optically at 200X by a simple intercept method.

Control of the environment was achieved by means of a silicone rubber cup which was molded to surround a 1 in. section of the gauge length. For the case of liquid environments, the cup was simply filled and the top left open. For gaseous environments, the cup was entirely enclosed except for inlet and outlet ports. Four environments were chosen for study: distilled water, artificial sea water, methanol, and dry air (−60°C dew point).

The mechanical properties of the two substrate materials are summarized in Fig. 1 and 2 and Table I.

The results of the experiments to determine crack density as a function of substrate strain in the various environments are shown in Fig. 3 and 4. The values of the saturation (minimum) crack spacing are given in Table II.

Table I. Mechanical properties of 1100-0 and 7075-T6 aluminum

	Yield strength[a] (psi)	Tensile flow stress at strain = 0.085 (psi)	Ultimate shearing strength[a] (psi)
1100-0	5,000	15,640	9,000
7075-T6	73,000	79,775	48,000

[a] Aluminum Data Book, Reynolds Metals Co.

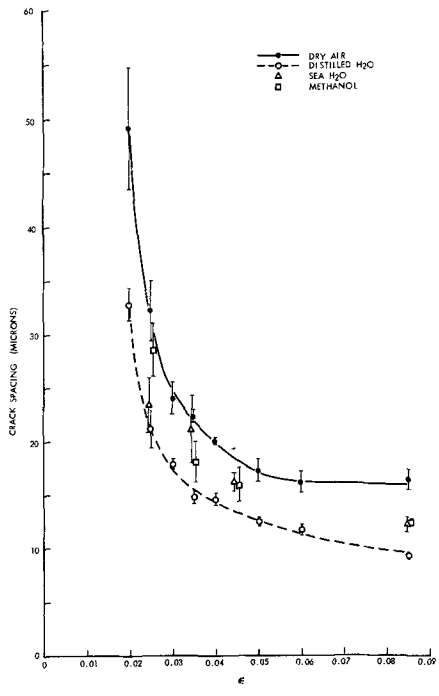

Fig. 3. Crack spacing as a function of substrate strain in various environments; Al_2O_3 on 1100-0 aluminum. Errors shown are the standard deviation.

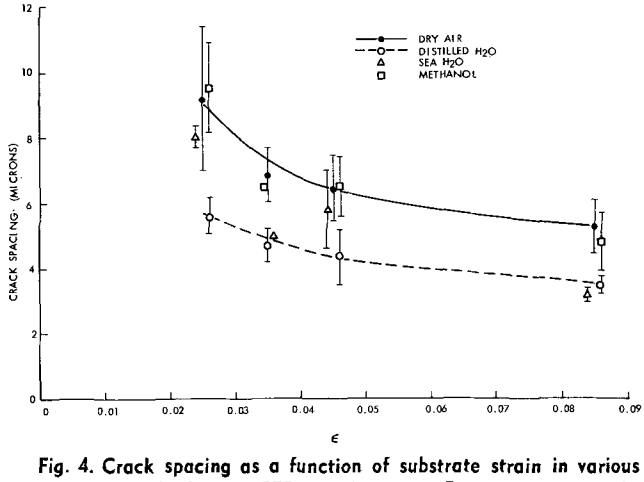

Fig. 4. Crack spacing as a function of substrate strain in various environments; Al_2O_3 on 7075-T6 aluminum. Errors shown are the standard deviation.

Discussion of Results

The discussion of these results is facilitated by a simple consideration of the stresses which produce the saturation crack spacing.

Simple theory of saturation spacing.—Begin by assuming the existence of a regularly cracked oxide film, Fig. 5(a). Once cracking has started, the strains and displacements in the oxide are not the same as those in the substrate because the moduli in the two layers are

Table II. Values of the saturation spacing, d_s, in various environments

Substrate	Environment	d_s (microns)
1100-0	Dry air	16.40 ± 0.92
	Distilled water	9.25 ± 0.19
	Sea water	12.17 ± 0.68
	Methanol	12.36 ± 0.26
7075-T6	Dry air	5.24 ± 0.83
	Distilled water	3.44 ± 0.23
	Sea water	3.15 ± 0.20
	Methanol	4.81 ± 0.89

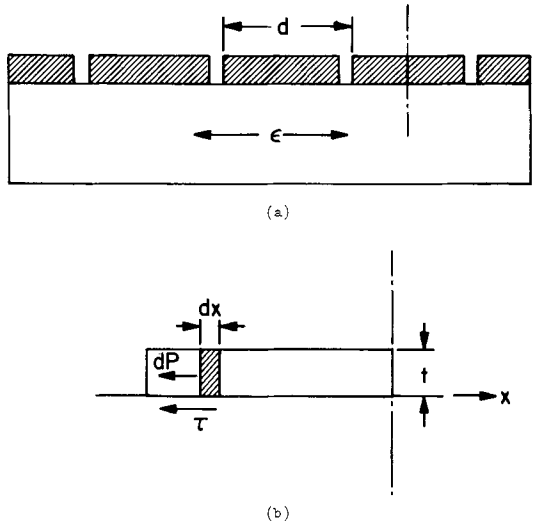

Fig. 5. (a) Schematic of regularly cracked oxide film; (b) single half-segment of oxide with relevant forces.

different (1). Hence, there are shear strains in the matrix near the interface and it is these strains which are responsible for transferring stress to the oxide coating. Figure 5(b) illustrates half of one segment of the oxide and shows the interfacial shear stress, τ, which is generally a function of x. If P is the load per unit width in the oxide (the width direction is perpendicular to the paper in the figure shown), and if the oxide is rigid with respect to shear, then the force, dP, acting on a slice of oxide, dx, is due entirely to the shear stress, τ, acting across the interfacial area of the slice. Hence

$$dP = \tau dx$$

or, in terms of the stress in the oxide segment

$$d\sigma = \frac{\tau}{t} dx$$

Thus

$$\frac{d\sigma}{dx} = \frac{\tau}{t} \qquad [1]$$

Equation [1] gives the distribution of stress in the oxide segment as a function of distance along its length.

In all cases of interest, the saturation spacing of cracks is reached after the substrate has begun to flow plasticly. Under this condition, τ never rises above the shear flow stress of the substrate. For practical purposes, we shall assume that τ is constant along the length of the segment[2] and is equal to the shear flow stress in the substrate. Equation [1] can then be integrated to give

$$\sigma = \left(\frac{\tau}{t}\right) x \qquad [2]$$

The critical spacing, d_c, will occur when the stress, σ, just rises to the fracture stress, σ_f, of the oxide at the midpoint of the section. Setting $x = d_c/2$, we have finally

$$d_c = \frac{2t\sigma_f}{\tau} \qquad [3]$$

The saturation spacing of cracks will range from about $d_c/2$ up to just less than d_c. Considering the approximations already involved in the calculation of d_c, we define the saturation spacing $d_s = d_c$.

Comparison of the results with the theory.—The difference between the spacings observed on the 1100 and 7075 substrates in a given environment can be accounted for in terms of the differences in the shear flow stress of these two materials. For a rough comparison, assume that the thicknesses and fracture strength of the oxide on the two substrates are identical; then the ratio of the saturation crack spacings should be in inverse proportion to the ratio of shear flow stresses. Substitution of the values for the dry air environment gives the result $d_s(1100)/d_s(7075) = 3.1$ and $\tau(7075)/\tau(1100) = 5.1$. While the agreement is not precise, the correctness of the interpretation does not seem to be in doubt.

Rewriting of Eq. [3] gives

$$\sigma_f = \frac{\tau}{2t} d_s \qquad [4]$$

Because t and τ are unaffected by environment, the relative values of the fracture strengths in the three aggressive environments with respect to dry air can be calculated from the d_s data, and the results are given in Table III, where σ_{fo} is taken as the fracture strength of the film in dry air.

If τ is taken as 0.577 times the tensile flow stress reported in Table I, an absolute value for σ_f can be calculated from Eq. [4]. These numbers are tabulated in the fourth column of Table III. The calculated fracture strengths of the oxide film on 1100-0 aluminum agree well with the fracture strength reported for unpolished sapphire whiskers (3), 300,000-500,000 psi. On the other hand, the calculated values for the film on the 7075 substrate are too high by at least a factor of 2. This discrepancy is further emphasized by the fact that the anodized layer on 7075-T6 aluminum contains a great many defects and voids in comparison to the layer on the 1100 aluminum (1). The difficulty here probably lies in the value assumed for τ, the interfacial shear stress at the surface of 7075 aluminum. It is well known that soft, precipitate-denuded zones exist along grain boundaries in this alloy and it is entirely possible that such a zone exists at the interface between the substrate and the anodic layer. In this case, the maximum shear stress developed in the interface would be much less than the bulk flow stress which was used in the calculation. In fact, the ultimate shear stress for 7075-0 (annealed condition) is about half that of 7075-T6, which could account for the discrepancy.

Another method for calculating σ_f makes use of the fact that the anodic layer on 1100-0 aluminum is purely elastic (1). Hence, $\sigma_f = \epsilon_f E_c$ where ϵ_f is the fracture strain in the oxide and E_c is the Young's modulus of the coating film. We take as ϵ_f that substrate strain at which significant cracks first begin to appear in the adhering oxide. In the case of the dry air environment, this strain is $\epsilon_f \sim 0.0175$. The value for E_c in dry air is 15×10^6 psi (1). These values lead to a calculated value of $\sigma_f = 262{,}500$ psi, about half that given in Table III.

These calculated fracture strengths are an order of magnitude higher than those previously reported for separated Al_2O_3 films (1) in dry air, *e.g.* ~ 43,000 psi. However, these latter fractures were dominated by the existence of defects in the oxide and the fracture, once started, grew catastrophically by a Griffith mechanism. In the case of an adhering oxide, however, this

Table III. The effect of environment on fracture strength of adhering aluminum oxide

Material	Environment	σ_f/σ_{fo}	σ_f (Calculated) (psi)
1100-0	Dry air	1.00	550,000
	Distilled water	0.56	312,000
	Sea water	0.74	410,000
	Methanol	0.76	415,000
7075-T6	Dry air	1.00	1,000,000
	Distilled water	0.65	660,000
	Sea water	0.60	605,000
	Methanol	0.92	920,000

[2] Clearly, this approximation neglects the fact that near the center of the segment the shear stress decreases, passing through zero at the center. However this fact does not seriously alter the value of σ in Eq. [2].

mechanism does not operate because of the constraint of the substrate and the effective fracture stress of the oxide apparently approaches that of sapphire whiskers.

Interpretation of the environmental effects.—In general (Fig. 3 and 4), distilled water is the most aggressive environment. The relative effect of this and the other environments on σ_f is best understood in terms of the elastic modulus of the oxide. This modulus decreases in the presence of water vapor (1) and, if the fracture strain is not appreciably affected, the decrease would account for the observed decrease of σ_f in distilled water. The slightly less harsh effect of sea water on the oxide grown on 1100 aluminum is not understood. The fact that sea water is more aggressive for the oxide grown on 7075 aluminum is likely due to localized attack at magnesium-, zinc-, and copper-rich sites which form in the oxide at undissolved second-phase particles on the surface of 7075.

The smaller effect of the methanol is attributed to the smaller amount of water available to the oxide in this environment. The fact that methanol had a smaller effect on the oxide grown on 7075 aluminum is difficult to explain. The experiments were conducted at the same time and the same source of methanol was used. So, if one assumes that the effect is real, the explanation must lie in the difference between the anodic films grown on the two substrates.

In summary, the data and the comparison with a simple theory of oxide fracture allow the following conclusions to be drawn:

1. The higher the shear strength of the substrate, the more dense the cracks in the adhering oxide.
2. Environment affects the fracture strengths of the adherent oxide films. σ_f becomes lower as the water content of the environment increases. The lowest fracture stresses occurred for distilled water environment.
3. The calculated values of the fracture stress in the various environments were of the order of 300,000-500,000 psi. Calculation of the fracture stress of the film adhering to a 7075 substrate is complicated by an apparent loss in the shear strength of the substrate near the oxide interface.

Acknowledgments

The author acknowledges with pleasure the continued support of ONR Metallurgy Branch through Contract Nonr-3908(00). I would also like to thank my colleague Dr. J. R. Hancock for calling my attention to the simple approach to calculating the oxide fracture spacing and to acknowledge the help of Mr. Sid Hamilton and Mr. Henry Moloney in determining the oxide fracture spacings.

Manuscript submitted Dec. 29, 1969; revised manuscript received Feb. 27, 1970.

Any discussion of this paper will appear in a Discussion Section to be published in the June 1971 JOURNAL.

REFERENCES

1. J. C. Grosskreutz, *This Journal*, **116**, 1232 (1969).
2. J. C. Grosskreutz and G. G. Shaw, *J. Appl. Phys.*, **35**, 2195 (1964).
3. P. D. Baver and R. E. Cooper, *J. Materials Sci.*, **4**, 15 (1969).

Technical Notes

Germanium Oxide Film Growth in $HF:H_2O_2$ Solutions

D. A. Kiewit

Hughes Research Laboratories, Malibu, California

The use of germanium oxide films to protect the semiconductor surface during processing or to electrically passivate the surface in the vicinity of p-n junctions has been suggested on several occasions (1-4). The use of SiO_2 films for these purposes in silicon planar technology is well known. Although germanium oxide films are not useful as diffusion masks because they reduce to the volatile oxide GeO at temperatures above ~600°C, it is worth considering their use in device fabrication schedules which do not involve such high temperatures, such as ion implantation, or to provide a passivating surface film that can be formed after all high-temperature stages in a process have been completed.

In the past several approaches to the problem of growing germanium oxide films on germanium surfaces have been attempted. Thermal oxidation of germanium has been used (3) to grow thin films of the hexagonal modification of GeO_2 on a bare Ge surface or beneath a pyrolytically deposited SiO_2 film (4). Anodization of germanium, especially in nonaqueous solutions, has been used by Wales (2) and others to grow GeO_2 films with resistivities as high as 10^{12} ohm-cm. Hexagonal GeO_2 films have also been formed (5) by the oxidation of germanium in nitric acid solutions more concentrated than 7*N*.

The growth of a glassy, hydrated germanium oxide film in aqueous $HF-H_2O_2$ solutions was first reported by Heidenreich (1), who recommended using the films to protect a germanium surface from contamination during processing.

Experimental

Germanium oxide films were grown on 1-40 ohm-cm n-type germanium wafers at room temperature in a variety of $HF-H_2O_2-H_2O$ solutions in which the HF concentration was varied between 100 and 300 g/liter and in which the H_2O_2 concentration was varied between 4.1 and 37.8 g/liter. B & A electronic grade HF and cp H_2O_2 and 15 Mohm deionized H_2O were used as reagents. The composition of the as-received H_2O_2 was determined with a $KMnO_4$ titration.

After the film was grown, part of it was masked with wax and the unmasked region was then stripped by a 5-10 sec immersion in aqua regia (this stripping procedure was found to remove less than 20Å from an uncovered germanium surface, and introduced a negligible error into the subsequent thickness measurement). The thickness of the germanium oxide film was measured with a Sloan M100 Fizeau-Tolansky type interferometer. The precision of the thickness measurement was about 10%.

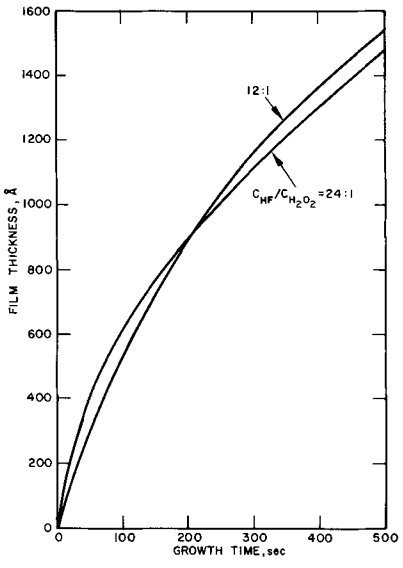

Fig. 1a. C_{HF} = 100 g/l

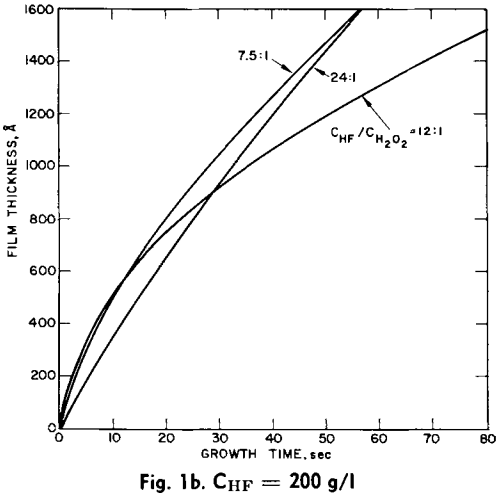

Fig. 1b. C_{HF} = 200 g/l

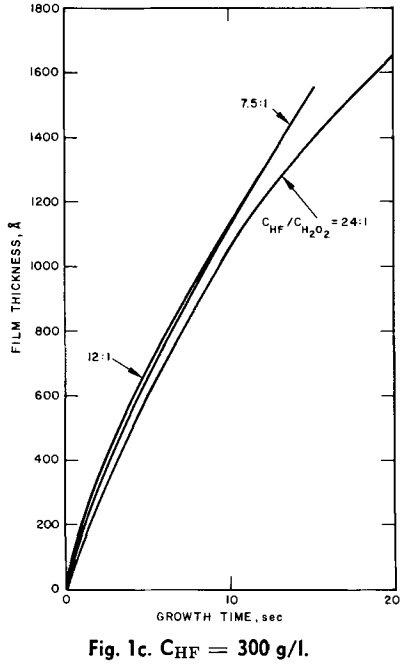

Fig. 1c. C_{HF} = 300 g/l.

Fig. 1. Growth of germanium oxide films in $HF-H_2O_2-H_2O$ solutions of various concentrations.

The thickness of germanium stripped from the wafer in the course of growing a film was measured gravimetrically using a Mettler balance accurate to 0.1 mg. The measured weight changes were generally at least 20 mg, indicating the measurement was precise to within 5%.

Neither the film growth rate nor the associated germanium etching rate depended on the sample resistivity. In the present investigation, mechanically polished surfaces were used for most of the measurements of film growth, but supplementary experiments on chemically polished germanium wafers indicated that the rate was not affected by mechanical damage introduced during polishing.

The growth of germanium oxide films in $HF-H_2O_2-H_2O$ solutions of various concentrations is described in Fig. 1. It is apparent from these data that varying the $HF:H_2O_2$ concentration ratio has little effect on the film growth rate in the investigated solutions, but that films are formed much more rapidly at higher HF concentrations.

Films less than about 400Å thick had pinholes which were clearly visible at 200X. At some other thickness, which depended on the solution, but which never exceeded 2000Å, the film began to crack. Between 400Å and the onset of cracking, the films were smooth, homogeneous, and uniform over the surface of a 2 cm wafer. After the onset of cracking, especially when a solution which grew films very rapidly was used, the film sometimes spalled off the germanium surface and a second film began to grow in its place. In addition, it was found that re-immersing a dried film in the growth solution led to a complete stripping of the film from the substrate before further film growth occurred.

The interference colors of these films agree closely with those predicted from Vasicek's (6) results for a film with a refractive index of 1.607. This value of the refractive index was reported by Kordes (7) for bulk amorphous GeO_2. The agreement between the colors observed in this work with those reported by Wales (2) for anodically grown GeO_2 is not quite as good.

Reflection electron diffraction studies indicate that the films that were grown were amorphous, and a decrease in thickness on heating to several hundred degrees centigrade indicated that they were hydrated. These observations agree with those of Heidenreich (1).

Studies of the rate of germanium etching associated with the film growth are summarized in Fig. 2. These data indicate that faster etching is associated with higher HF concentrations and a lower $HF:H_2O_2$ concentration ratio in the investigated solutions. The observation regarding the $HF:H_2O_2$ ratio must be regarded as tentative because of a lack of corroborative evidence. The lack of a saturation region in these curves indicates that the film does not effectively pro-

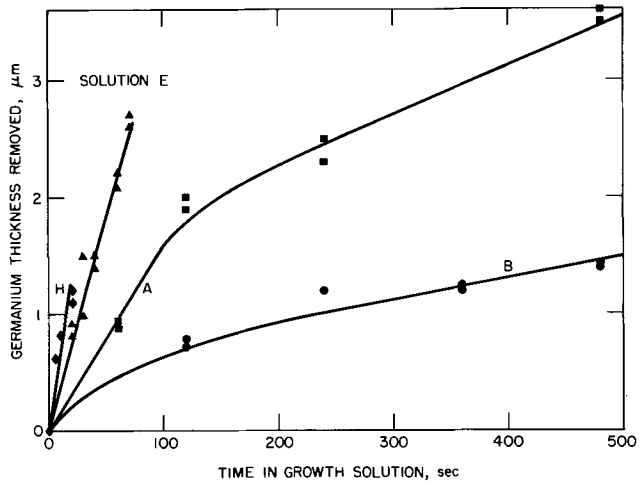

Fig. 2. Rate of germanium etching associated with film growth. A: C_{HF} = 100 g/l; $C_{HF}/C_{H_2O_2}$ = 12. B: C_{HF} = 100 g/l; $C_{HF}/C_{H_2O_2}$ = 24. E: C_{HF} = 200 g/l; $C_{HF}/C_{H_2O_2}$ = 12. H: C_{HF} = 300 g/l; $C_{HF}/C_{H_2O_2}$ = 12.

tect the surface from further etching. No inhomogeneity in etch rate was observed to be associated with the onset of cracking or spalling of the oxide films.

Summary

In view of the partial solubility of these germanium oxide films in HF, the faster growth rate in the solutions with higher HF concentrations was initially surprising. However, a comparison of the film growth rates and the germanium etching rates in the same solutions showed that the substrate is being removed 10 to 30 times more rapidly than the film is forming. Because of this disparity in the relative rates, the faster oxide growth at higher HF concentration is less surprising, as the rate of germanium removal is also higher at high HF concentrations. During growth the germanium oxide film is apparently readily permeable to the species involved in the reactions. This conclusion is supported by the high germanium etch rate both before and after the onset of oxide film cracking; the even, homogeneous etching of the germanium surface after the film has cracked or spalled; and the observed lack of agitation effects on film growth rate. This indicates that the etching and film growth reactions are not limited by mass transport through the films, and that the films do not provide a passivating layer against further chemical attack.

Since simultaneous reactions occurred at several interfaces, and since not all of the reaction products at the surfaces are known, no attempt was made to set up a quantitative model to describe the reaction kinetics. It is apparent, however, that the film growth is not diffusion limited. Hence, one of the steps in the competing processes of coalescence and dissolution of the glassy film must be rate-controlling.

Manuscript submitted Nov. 14, 1969; revised manuscript received *ca.* Feb 27, 1970.

Any discussion of this paper will appear in a Discussion Section to be published in the June 1971 JOURNAL.

REFERENCES

1. R. D. Heidenreich, U.S. Pat. No. 2,935,781.
2. R. D. Wales, *This Journal*, **110**, 914 (1963).
3. M. Lasser, C. Wysocki, and B. Bernstein, *Phys. Rev.*, **105**, 491 (1957).
4. D. S. Granberry, R. L. McCalip, and B. K. Lovelace, U.S. Pat. No. 3,431,636.
5. E. W. Valocysik, *This Journal*, **114**, 176 (1967).
6. A. Vasicek, "Optics of Thin Films," p. 137, Interscience, New York (1960).
7. E. Kordes, as cited by R. D. Wales in ref. (2).

The Estimation of Field Strengths in the Oxide during Conventional and Plasma Anodization

G. Olive, D. L. Pulfrey, and L. Young*

Electrical Engineering Department, The University of British Columbia, Vancouver, British Columbia, Canada

Most authors (1) have supposed that plasma anodization is analogous to conventional anodization in that the oxide film grows due to a process of ionic conduction at high fields, leading to an exponential dependence of ionic current density on field. To test this assumption one needs to be able to estimate the electrostatic field in the oxide from experimental data on oxide thickness and from measurements on the potential of the sample being anodized. The present work is concerned with the very real problems that arise in attempting to relate measurable quantities to the field in the oxide. These problems are only in part analogous to those that occur in the case of wet anodization, but our attempts to solve the problem in plasma anodization leads us to a reconsideration of the problem in wet anodization. As will appear, an important point is what account, if any, should be taken of the free energy of formation of the oxide. Our work is complementary to that of O'Hanlon (2) who has recently pointed out that the method used in much of the previous work on plasma anodization is inadequate and has suggested one approach to solving the problem.

As a start, it may be supposed that a probe is placed in the plasma very close to the oxide-coated electrode, which we take, for definiteness, to be tantalum. The probe could be an electrode evaporated onto a region of thicker oxide, *i.e.*, in the region in which the plasma is perturbed by the current being drawn by the tantalum electrode. Otherwise it could be a macroscopic electrode outside the sheath surrounding the tantalum. It is well known (3) that in some, but not all, plasma conditions the current-voltage characteristic of a probe (Langmuir probe) may be interpreted to give what is known as "plasma potential." Our understanding of this is that, when the probe registers plasma potential, the "macro" or "inner" potential in the plasma is constant near the probe or, at least, does not vary near the probe because of the current drawn by the probe. It would seem that, as regards points in the plasma, or, for that matter, in any phase other than absolute vacuum, potential in this sense does not mean an averaged potential but the potential corresponding through Poisson's equation with a space- and time-averaged space charge density. It is thus a property of a model not a thermodynamic quantity. The measurement of Langmuir's plasma potential corresponds to the same number of each species being removed by the probe as would cross from one side an imaginary plane replacing the probe. If the probe is very close to the tantalum, it is perhaps open to argument whether it could register plasma potential. However, if it could, or if the potential of a more distant probe could somehow be corrected for the systematic gradient of potential in the plasma due to the passage of current and for any potential drop across a perturbed sheath surrounding the tantalum, then the energy diagram of Fig. 1 would seem to apply and

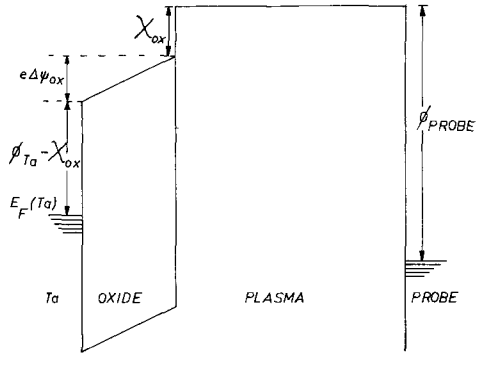

Fig. 1. Energy diagram

* Electrochemical Society Active Member.

$$\Delta\psi_{ox} = V \text{ (Ta-probe)} + \frac{1}{e}(\phi_{probe} - \phi_{Ta})$$

where $\Delta\psi_{ox}$ is the potential drop across the oxide; V(Ta-probe) is the measured (and for the more distant probe, corrected) voltage between the tantalum and the probe, *i.e.*, Fermi potential difference, and the ϕ's are work functions.

The problem may be avoided in part by taking current-voltage characteristics of the tantalum electrode at various oxide thicknesses with respect to some invariant probe which is sufficiently close that random variations in time in the potential gradient through the plasma are negligible. If the phenomena in the plasma sheath near the oxide may be assumed to be the same for a given current density independent of oxide thickness, then at least an incremental field in the oxide can be obtained associated with a given formation current. By starting with a very thin oxide the mean field $\bar{E} = \Delta\psi_{ox}/d$, where d is thickness, can be obtained to some approximation.

The question must now be considered as to whether some account should be taken of the free energy of formation of the oxide. In other words is the electrostatic field as thus estimated in fact the desired quantity for comparison with theory. We refer to standard works, such as Hauffe's (4), for discussion of how the free energy of formation corresponds to gradients of electrostatic potential and of concentrations of reactants through the film in the absence of applied fields. We suggest that if we are comparing experimental results with a model in which high field ionic conduction due to an electrostatic field is considered but in which diffusion is neglected, then we need to consider only the electrostatic field. In this case no account need be taken of the free energy of formation of the oxide. If diffusion or other effects due to concentration gradients need to be taken into account, then we are in further difficulties because the analogy with the wet system breaks down in that in plasma anodization we do not have a system at a uniform temperature; indeed the plasma species need not be even thermally distributed in energy (3). Also, it is quite possible that the reaction involves not neutral oxygen gas but some charged oxygen species in the plasma which are not in equilibrium with the neutral gas, or even at the same temperature. Hence the calculation of the free energy of reaction is to that extent uncertain.

The usual approach to the analogous problem in conventional anodization has been quite different. In this case a quantity which has been called "overfield" has been used. With the cell: Ta/oxide/solution H_2/Pt a hypothetical reversible emf may be calculated from thermal data. After elimination of ohmic potential drops in the solution, the overpotential may be defined as the excess of the cell voltage over the reversible value. The overfield was defined (5, 6) as the overpotential divided by the thickness of oxide. The close relation of the above to the method [proposed in an early paper by Vermilyea (7)] of adding in the "reaction voltage" has been discussed elsewhere (6). By "reaction voltage" is normally understood the hypothetical equilibrium voltage of the cell $Ta/Ta_2O_5/H_2O/H_2$/Pt.) At the reversible potential the overfield is zero but there is no reason why the electrostatic field in the oxide should be zero. Indeed, photovoltaic experiments have been interpreted as showing that the field in the oxide at this potential is such as to oppose the passage of ionic current in the direction causing growth (6). One advantage of the overfield is that it is at least well defined. It is also thermodynamically meaningful, *i.e.*, directly measureable. The other main reason for its acceptance as a useful way of describing experimental results is that it seems to work, in the sense that the overfield for tantalum and niobium (but not zirconium) has been found experimentally to be independent of thickness at constant ionic current density with some reservations about the significance of the data for very thin films (<200Å) (6). This may have been a delusion since one expects, not a constant field, but a transition with increasing thickness from Mott's interface control model to Verwey's model in which the ionic conductivity of the neutral bulk oxide controls the current. However, it seems to us that the argument as given above in respect to plasma anodization suggests that the overfield method works, if it works, by accident; the theoretical model involves only the electrostatic field and hence one should attempt to estimate this field (not overfield) in treating experimental data for the purpose of testing the model.

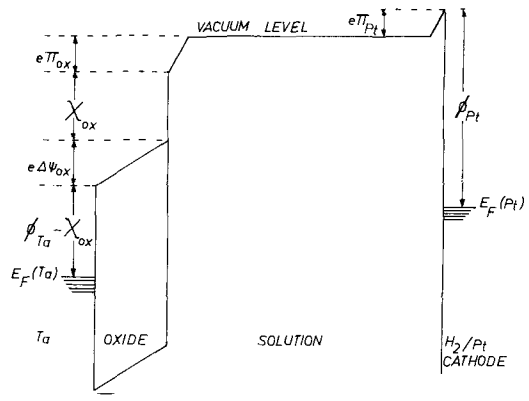

Fig. 2

Figure 2 shows one way of doing this. The difficulty of using the potential within the solution is avoided by using the vacuum level: the energy of an electron at rest just outside a hypothetical vacuum/solution interface. The electrical double layers on the platinum and oxide surfaces contribute π_{Pt} and π_{ox}, respectively. For the equilibrium situation the sum is expected to be constant, thus an equilibrium involving, say, OH^- across the oxide/solution interface would cause the interface pH-dependence of π_{ox} and π_{Pt} to cancel. Hence

$$\Delta\psi_{ox} = (1/e)(E_F(Pt) - E_F(Ta)) - (\pi_{ox} + \pi_{Pt}) + \frac{1}{e}(\phi_{Pt} - \phi_{Ta})$$

$$= V_{over} + V_{rev} - (\pi_{ox} + \pi_{Pt}) + \frac{1}{e}(\phi_{Pt} - \phi_{Ta})$$

where E_F is the Fermi energy, V_{over} is the overpotential for the production of Ta_2O_5, V_{rev} is the reversible cell emf (about 0.8V, tantalum negative). Approximating π_{Pt} by taking the zero charge point as corresponding to zero potential difference (*i.e.*, about 0.2V positive to the hydrogen potential in the same solution for pH about 0 or 1) and with recommended values (8) for the work functions ϕ_{Ta} and ϕ_{Pt} we have

$$\Delta\psi_{ox} = V_{over} - \pi_{ox} + (-0.8 - 0.2 + 5.3 - 4.1)\text{ V}$$

Perhaps the apparent success of overfield has been due to the cancellation of the terms following V_{over} on the right-hand side. The values of the work functions are, of course, uncertain, but, clearly, cancellation is likely to occur within a few tenths of a volt. A lack of cancellation would imply something about the magnitude of concentration changes of reactants across the oxide.

Acknowledgment

The authors thank the U.S. Air Force Avionics Laboratory, Wright-Patterson Air Force Base (Contract F33 615-68-C-1074) for their support for our work on plasma anodization.

Manuscript submitted Dec. 1, 1969; revised manuscript received March 26, 1970.

Any discussion of this paper will appear in a Discussion Section to be published in the June 1971 JOURNAL.

REFERENCES

1. C. J. Dell'Oca, D. L. Pulfrey, and L. Young, *Physics of Thin Films*, In press
2. J. F. O'Hanlon, *Appl. Phys. Letters*, **14**, 127 (1969).
3. L. B. Loeb, "Basic Processes of Gaseous Electronics," University of California Press (1955).
4. K. Hauffe, "Oxydation von Metallen und Metalliegeren," Springer, Berlin (1956).
5. L. Young, *Trans. Faraday Soc.*, **54**, 841 (1957).
6. L. Young, "Anodic Oxide Films," Academic Press, London and New York (1961).
7. D. A. Vermilyea, *This Journal*, **101**, 389 (1954).
8. V. S. Fomenko, "Handbook of Thermionic Properties," Plenum Press (1966).

Effects of Specimen Size and Configuration in Plasma Anodization

N. Ramasubramanian

Chalk River Nuclear Laboratories, Atomic Energy of Canada Limited, Chalk River, Ontario, Canada

In plasma anodization the potential of the specimen surface relative to the unperturbed plasma determines the charge carrier collection and hence the oxide growth (1,2). When anodizing a specimen which is large with respect to the mean free path of the plasma particles or is surrounded by a shield, the plasma in its vicinity is perturbed (3, 4). The purpose of this paper is to show that such plasma perturbations and edge effects influence the forming characteristics.

Experimental

A diagram of the Pyrex glass discharge tube and the various probes is shown in Fig. 1. A preoxidized zirconium wire and a cylindrical platinum foil formed the cathode and anode of the tube, respectively. The temperature in the vicinity of the specimens was monitored by a shielded chromel-alumel thermocouple. Oxygen pressures were in the range of 0.77 ± 0.03 Torr; accelerating voltages of 650-800V were used with a discharge current of 20 mA. With water circulating in the jacket the temperature close to the specimens was ~200°C.

The materials zirconium and Zircaloy-2 (Zr-1.5% Sn-0.1% Fe-0.1% Cr-0.05% Ni) were supplied by Wah Chang Corporation and tantalum by Fansteel Metallurgical Company. The specimens were disks of the dimensions shown in Table I. A wire of the same material was spot welded onto the disk. The combination was chemically polished using a nitric and hydrofluoric acid mixture (with or without sulfuric acid) after mechanical abrasion of the exposed face. The wire was insulated by a tight fitting ceramic capillary which in turn was housed in a Pyrex glass tube. In the case of type-B and -D unshielded samples, care was taken to expose a short piece of the wire so that the specimen was isolated from the space charge sheath on the insulation; the area of the exposed wire was a small fraction of the specimen area.

A Moseley X-Y_1-Y_2 recorder and Keithley electrometers were used to measure and plot the current and voltage. Anodization of at least two specimens could be followed simultaneously. In a typical experiment the current-voltage curve for the platinum wire probe was recorded. The floating potentials with the specimens were measured, a fixed anodizing voltage with respect to the tube anode was applied and current-time curves were followed. The platinum probe was cleaned between experiments.

Oxide thicknesses were estimated from a comparison of the capacitance data measured at 1 kHz using 1M NH_4NO_3 solution contacts with similar measurements on wet anodized films. Area/capacitance *vs.* thickness curves were constructed assuming 28 Å/V for zirconia (5) and 17 Å/V for tantalum oxide films (6). The interference colors of the plasma and wet anodized films having the same area/capacitance value were similar.

Key words: plasma perturbation, space charge sheath, diffusion sheath and edge effects.

Results

The potentials referred to are all relative to the discharge tube anode; V_p, specimen potential following anodization and V_w, floating potential of the specimen before anodization.

Specimen area.—Anodization characteristics were compared among specimens whose areas varied approximately in the ratio 1:2:20 (*c.f.* Table I). For specimens of areas 0.3 cm² or less the floating potentials, current decay and Å/V values were in close agreement. These quantities were all different for the large sized type-D specimen. Another observation with all large specimens was the obvious decrease in oxide thickness amounting to ~15% from the center to the edge. With smaller area specimens of type-A, -B, and -C the oxide film was more uniform. The oxide thick-

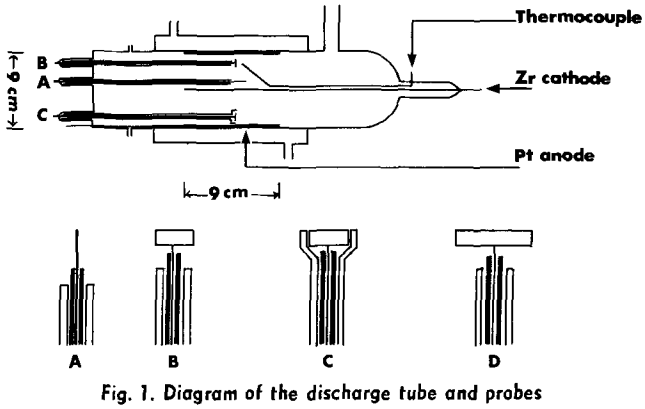

Fig. 1. Diagram of the discharge tube and probes

Table I. Dimensions of specimens in Fig. 1

Specimen	Type	Dimensions, mm Diameter	Length	Area, cm²
Pt	A	0.36	7	0.076
Zr	B	3.13	1.48	0.285
	C	3.13	—	0.073
	D	14.0	1.48	3.56
Zr-2	B	3.17	0.74	0.221
	C	3.17	—	0.075
	D	14.0	0.74	3.250
Ta	B	3.17	0.31	0.181
	C	3.17	—	0.075
	D	14.0	0.31	3.07

Type-A specimens of Zr, Zr-2 and Ta were wires 0.8 to 0.9 mm in diameter and 0.1 to 0.13 cm² in area.

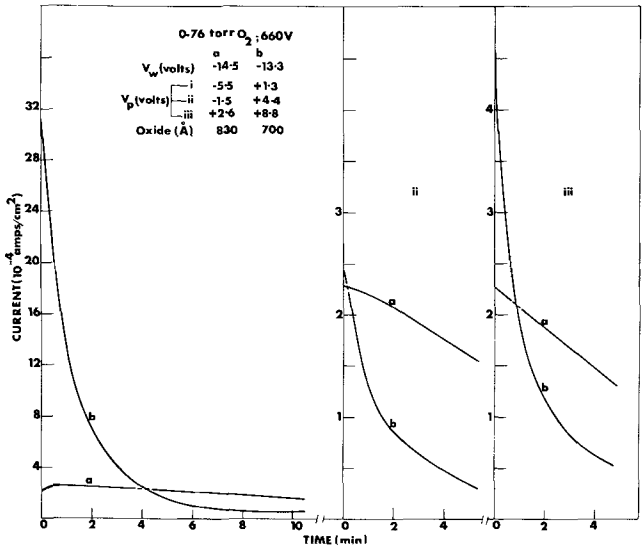

Fig. 2. Plasma perturbation effects; comparison of current-time curves obtained with zirconium samples; a, type-D, 3.56 cm² (perturbed) and b, type-B, 0.285 cm².

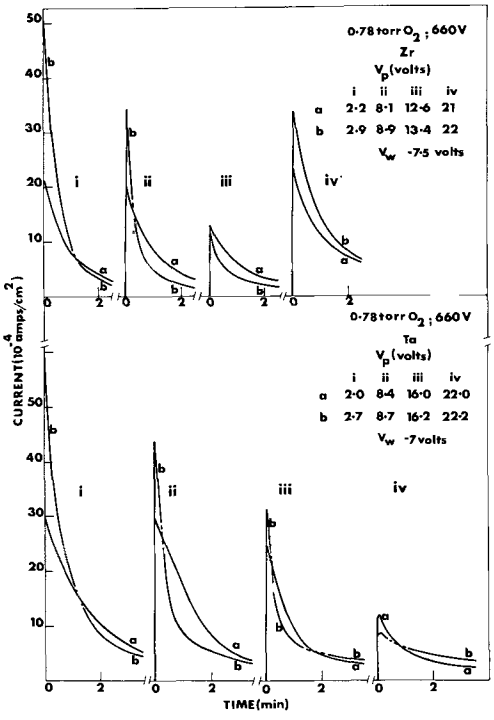

Fig. 3. Comparison of current-time curves; a, unshielded type-B and b, shielded, type-C specimens.

ness quoted here for large area samples is an average one.

Figure 2 shows a typical set of current decay curves and the experimental potentials for zirconium samples. The anodization was done in steps without interrupting the discharge; the curves a were obtained with the type-D large specimen 3.56 cm² in area and b with the type-B specimen 0.285 cm² in area. During the first step there was practically no oxide growth (judged by interference color) on the large specimen in the first few minutes. The current density was very low compared to the smaller area specimen and showed only a slight decrease with time. In the subsequent steps the current showed a considerable decrease with time, almost linear; but the rate of fall, especially in the initial stages, was very low compared to the smaller sized specimen. However, after the experiment the oxide on the large area specimen was thicker and $(V_p - V_w)$ apparently lower.

Edge effects.—The anodizing characteristics of type-C shielded specimens and the usual type-B unshielded specimens were followed simultaneously. In Fig. 3 are shown two sets of data obtained with zirconium and tantalum specimens. Similar results were obtained with Zircaloy-2 specimens. The current density in the case of the shielded specimen was higher when the anodizing voltage in the first step or the increment in it during the subsequent steps ii, iii, etc., was fairly large, about 6V or more. Under such circumstances in the initial stages the current density decreased more rapidly than for unshielded specimens. The oxide film thicknesses were zirconium B-810Å and C-775Å and tantalum B-590Å and C-560Å. In another series of experiments the oxide thicknesses were compared after the initial anodizing step. When the $V_p - V_w$ was ~9V or more the oxide thicknesses with shielded specimens were higher by about 15%. For example, voltages close to those shown in Fig. 3 gave oxide thicknesses for zirconium B-254Å and C-280Å and tantalum B-155Å and C-175Å.

Discussion

The perturbations resulting from the specimen size and presence of a surrounding shield are different in nature and are discussed under separate headings, specimen area and edge effects. There is a fundamental difficulty in applying the probe theory [a review of Langmuir and Mott-Smith's theory, assumptions involved and the technique is given by Loeb (7)] to oxygen plasmas, however, because they contain negative ions in addition to electrons and positive ions. The treatment presented here must therefore be regarded as only approximately correct.

Specimen area effects.—Waymouth (3) has given a detailed treatment of the problem and also reported experimental evidence supporting his theory (8). The conclusions can be stated in brief as follows. When probes of dimensions several times the mean free paths of electrons and ions are used the large drain of carriers leads to plasma perturbations in their vicinity. As a result (*i*) charge collection by the probe is determined by free fall space charge sheath and also a diffusion controlled presheath; (*ii*) in the perturbed region there is a large reduction in the density of carriers; and (*iii*) the plasma potential changes by ΔV at the sheath boundary; this change which is negative for probe potentials near floating potential, passes through zero, and becomes positive for probe potentials near plasma potential.

In order to compare the perturbation effects caused by the presence of various probes, it is convenient to treat them as spheres wtih the same surface areas (3). The electron mean free path in the present study is about 1.5 mm and therefore probes of area $>>0.3$ cm² introduce plasma perturbations. A schematic diagram of the changes in potential difference between the specimen surface and the plasma during constant voltage anodization for the unperturbed and perturbed cases is shown in Fig. 4. With increasing oxide thickness the specimen surface potential tends towards the floating potential V_w.

The results shown in Fig. 2 can be explained as follows. During the first anodizing step there is practically no oxide growth on the large area specimens because plasma perturbations result in a lowering of carrier density and a shift $+\Delta V$ in plasma potential which leads to only a small potential drop in the space charge sheath. In the subsequent steps with increase in the applied voltage this potential drop is larger than in the first step and anodization proceeds. The degree of perturbation decreases during anodization with the decrease in current and for comparable specimen surface potentials the potential drop in the space charge sheath is lower for the large sized specimen than that for the small area one. Therefore, in the former case

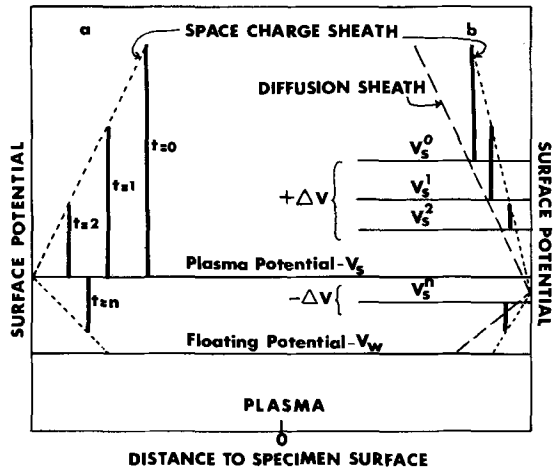

Fig. 4. Schematic diagram of changes in potential difference between the specimen surface and plasma (shown in solid vertical lines) during anodization; a, type-B specimen and b, type-D specimen (perturbed); t, time of anodization for type-B specimen; V_s^0 . . . . V_s^n, potentials of the perturbed plasma for specimen surface potentials at the respective t values

one would expect the occurrence of sputtering effects (1) to a less extent, and this might be one of the reasons for obtaining a higher Å/V ratio with the large sized specimens. In the perturbed and unperturbed plasmas the ratio of the electrons, negative ions and positive ions is also likely to be different.

Edge effects.—In plasma anodization evaporated metal specimens have been used in which the metal was surrounded by an insulating glass substrate (9,10). Such a structure is similar to the shielded specimens in the present study. The insulating shield operates at the floating potential and therefore has a negative field associated with it. One would expect a retarding influence on the negative carriers and thus a lowering of the charge collection by the shielded specimen (4). The Å/V ratio is seen to vary between the shielded and unshielded specimens depending on the size of the voltage increment for the anodizing step. However, the ratio is higher for the shielded specimens when the forming voltage in the initial step and the increment in it during the subsequent steps of anodization are large. It is suggested that ionization occurs in the space charge regions, resulting from the potential difference between the specimen surface and the insulating shield. As the anodization proceeds the specimen surface moves towards floating potential (2), the potential the shield is operating at and therefore the extent of the ionization process decreases. It should be mentioned here that the size of the Pyrex glass shield (OD 6 mm) is not large to introduce plasma perturbation effects discussed under "area effects."

Acknowledgments

The author wishes to express his thanks to Mr. T. Trottier for his assistance in performing the experiments and Dr. B. Cox for his encouragement and discussions.

Manuscript submitted Nov. 13, 1969; revised manuscript received April 13, 1970.

Any discussion of this paper will appear in a Discussion Section to be published in the June 1971 JOURNAL.

REFERENCES

1. L. D. Locker and L. P. Skolnick, *Appl. Phys. Letters*, **12**, 396 (1968); "Thin Film Dielectrics," F. Vratny, Editor, p. 432, Electrochemical Soc. Inc., New York (1969).
2. J. F. O'Hanlon, *Appl. Phys. Letters*, **14**, 127 (1969).
3. J. F. Waymouth, *Phys. Fluids*, **7**, 1843 (1964).
4. R. H. Sloane and K. G. Emeleus, *Phys. Rev.*, **44**, 333 (1933).
5. D. K. Dawson and R. H. Creamer, *Brit. J. Appl. Phys.*, **16**, 1643 (1965); N. J. M. Wilkins, AERE-R4666 (1964).
6. D. A. Vermilyea, *J. Appl. Phys.*, **36**, 3663 (1965).
7. L. B. Loeb, "Basic Processes of Gaseous Electronics," p. 329, University of California Press (1961).
8. R. G. Little and J. F. Waymouth, *Phys. Fluids*, **9**, 801 (1966).
9. J. L. Miles and P. H. Smith, *This Journal*, **110**, 1240 (1963).
10. G. J. Tibol and R. W. Hull, *ibid.*, **111**, 1368 (1964).

Forming Voltage in Plasma Anodization

N. Ramasubramanian

Chalk River Nuclear Laboratories, Atomic Energy of Canada Limited, Chalk River, Ontario, Canada

The significance of the floating potential in determining the forming voltage in plasma anodization was reported by O'Hanlon (1). In order to estimate the surface potential of the anodized specimen it was suggested that a correction could be applied based on the i x V characteristics for the specimen obtained prior to anodization. The validity of such a correction is questionable on the following grounds: (*i*) the i x V characteristics of an anodizable specimen cannot be traced out at potentials positive to the floating potential without risking oxidation; (*ii*) plasma characteristics change with time of operation of the discharge tube; and (*iii*) work functions of the materials concerned are important in determining the various potentials measured and these differ and/or change during anodization.

Results

Aging of the discharge tube.—The experimental procedure has been described elsewhere (2). At constant gas pressure the acceleration voltage needed to maintain a constant plasma current increased with operating time of the discharge tube. The plasma characteristics were evaluated from the i x V curves obtained for the platinum wire probe; these changed with the aging of the tube. The values of V_w, floating potential, and V_s, plasma potential, become more negative, and T_-, the slope of the log i_- (negative carrier current), *vs.* potential plots decreased. In plasmas of electrons and positive ions $1/T_-$ is proportional to the electron temperature. After the discharge tube had been in operation for more than about 10 hr the presence of a film deposited on the platinum anode was detected by its interference color. This film was soluble in HF-HNO_3 mixture.

i x V Characteristics of the platinum probe.—Anomalous behavior was observed during current-voltage measurements with the platinum wire probe. At potentials slightly positive to V_w, the current showed an increase with time when the voltage was kept constant, and the i-V characteristic showed the presence of a negative resistance region. The probe characteristics changed completely after 10-15 min of standing in the

plasma. No anomalies were then detected in the current-voltage sweeps. Figure 1 shows the difference between current-voltage curves for the platinum probe obtained at the beginning and at the end of an experiment. Curves obtained with a type-B Zircaloy-2 specimen before and after anodization to an oxide thickness of 700Å are also included for purposes of comparison. The V_w measured with the platinum was closer to the Zircaloy values after the experiment. The similarity between the curves b and d should be noted. At potentials slightly negative to V_w the curves are concave to the voltage axis, and they show a gradual rise at potentials slightly positive to V_w.

If, after the experiment, the platinum probe was cleaned by dipping in a HF + HNO_3 mixture, the i-V characteristic reverted almost to that in curve a (small differences were due to changes in the plasma condition). The plasma characteristics were evaluated by analyzing curves a obtained at the beginning of experiments.

Anodization of zirconium, Zircaloy-2, and tantalum.— In a plasma the V_w values obtained with tantalum, zirconium, and Zircaloy-2 probes were more negative than those obtained with platinum, by about 5-7V. In a typical experiment, the first anodizing step was to polarize the specimens to potentials slightly positive with respect to the floating potentials obtained with them, but still negative with respect to the floating potential measured with a platinum probe. The data from two such experiments using type-B specimens are shown in Fig. 2; the values of the various potentials in volts are tabulated in the insert. Oxide thicknesses following the anodization were, case a Ta-80Å and Zr-170Å and in case b Zr-190Å and Zr-2-160Å. The $V_p - V_w$ values for Ta in set a and Zr-2 in set b were less than the respective ones for Zr, but the initial current densities were higher.

Discussion

In plasma anodization a knowledge of the plasma characteristics is essential because they determine the reactions occurring at the plasma-oxide interface

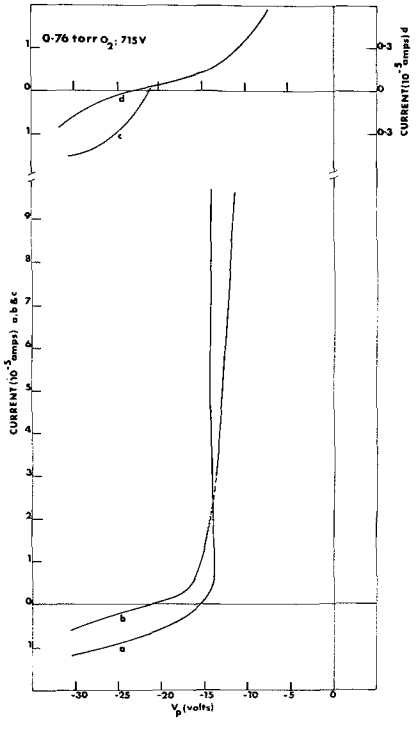

Fig. 1. Current voltage characteristics for the platinum probe (a and b) and Zircaloy-2 specimen (c and d); at the beginning of the experiment (a and c) and after anodizing Zircaloy-2 over a period of 15 min (b and d).

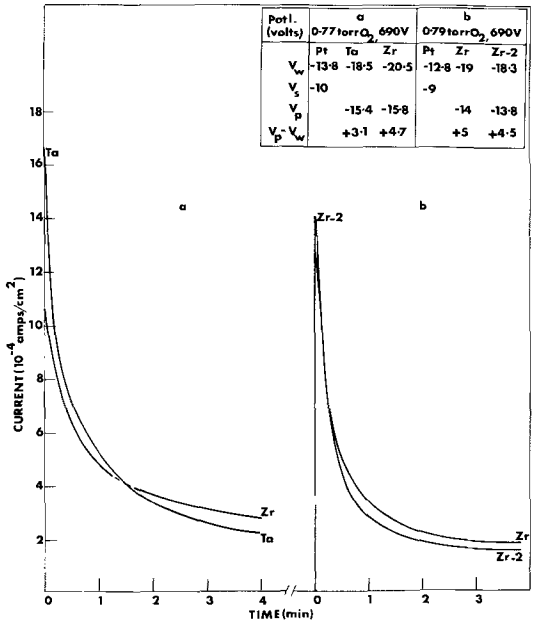

Fig. 2. Current-time curves for type-B specimens; specimen potentials negative to plasma potentials but positive to floating potential; floating potentials measured before anodization are quoted.

(1-3). The plasma characteristics can be evaluated from the i x V curves obtained for an inert probe. However, the potentials recorded during such measurements might be in error due to work function differences and/or changes in the work functions brought about by deposition of a sputtered film, ion bombardment, etc. (4). For example, in the cases of zirconium, Zircaloy-2, and tantalum the floating potentials measured were negative by 4V or more relative to that for platinum. Therefore, specimen potentials relative to a floating platinum probe do not give the true anodizing voltages as has been claimed (5), and the errors involved in such measurements are quite large.

The work function of platinum bombarded by positive oxygen ions has been shown to be higher by 1.2 eV than that of a clean surface (6). This may be responsible for the negative resistance anomaly observed in the current-voltage characteristics of the platinum probe. Then the actual difference between the plasma potential and floating potential would be higher by ~1.2V than the experimental values (*c.f.*, table inserted in Fig. 2), assuming that for a i-V sweep the V_w measured refers to positive ion bombarded and V_s determined refers to clean platinum surfaces. In the negative resistance region (cleaner platinum surface) the measured potential shifts to a more negative value. The deposition of material sputtered off the zirconium wire cathode is an additional process giving rise to changes in the platinum probe characteristics during an experiment and in the plasma characteristics with the aging of the discharge tube.

The variation of the plasma and wall potentials with the type of material used to measure them and the time of operation of the discharge tube is shown schematically in Fig. 3. It is seen that the higher the work function of the probe material the less negative are the measured potentials.

The errors in anodizing voltage measurements are due to (*i*) changes in the plasma characteristics during an experiment and (*ii*) work function differences between the anodized and unanodized specimens which is unknown. These can be eliminated to a large extent by taking the potential of the specimen relative to its floating potential (obtained from i x V measurements) at the end of the experiment. The specimen surface

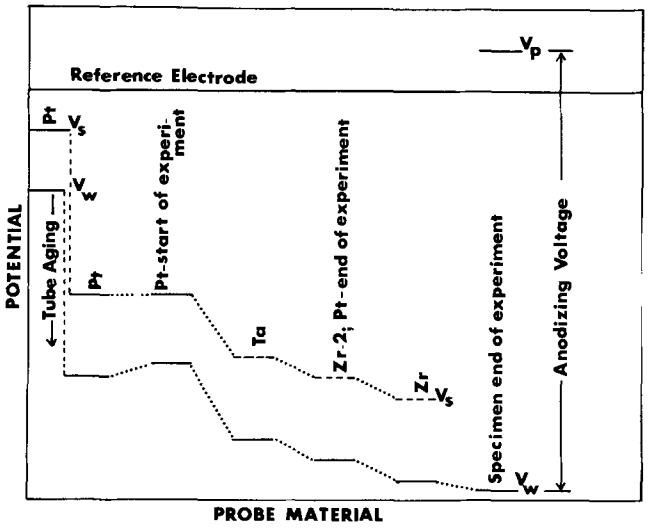

Fig. 3. Schematic diagram of the variation of plasma and floating potentials for a fixed plasma current and gas pressure with time of operation of the tube and the probe materials used.

potential would be closer to the floating potential of the plasma at the end rather than at the start of anodization.

The anodizing voltages, $(V_p - V_w)$ values given in the table in Fig. 2, are not very large compared to the corrected $(V_s - V_w)$ value for platinum. In the case of tantalum the anodizing voltage is less than the latter. It follows then that anodic oxide growth is observed at potentials negative to the plasma potential but positive to the floating potential; a conclusion which supports the model proposed by O'Hanlon (1). Therefore during i x V measurements at potentials positive to floating potential the specimen is likely to anodize; the measured potentials are thus not specimen surface potentials as assumed by O'Hanlon, but include a definite drop across the oxide grown during the measurements. The surface potentials would obviously be less than the measured potentials.

Acknowledgments

The author wishes to express his thanks to Mr. T. Trottier for his assistance in performing the experiments and Dr. B. Cox for his encouragement and discussions.

Manuscript received Nov. 13, 1969; revised manuscript received ca. March 23, 1970.

Any discussion of this paper will appear in a Discussion Section to be published in the June 1971 JOURNAL.

REFERENCES

1. J. F. O'Hanlon, *Appl. Phys. Letters*, **14**, 127 (1969).
2. N. Ramasubramanian, *This Journal*, **117**, 947 (1970).
3. L. D. Locker and L. P. Skolnick, *Appl. Phys. Letters*, **12**, 396 (1968); Electrochemical Society Extended Abstracts, Montreal Meeting, Oct. 6-11, 1968, Abstract No. 483.
4. G. Wehner and G. Medicus, *J. Appl. Phys.*, **23**, 1035 (1952).
5. N. F. Jackson, *J. Matl. Sci.*, **2**, 12 (1967).
6. C. W. Oatley, *Proc. Phys. Soc. London*, **A51**, 318 (1939).

Response of Electroluminescent ZnS:Mn,Cu,Cl Films to Rectangular Pulse Excitation

John L. Plumb[1]

Department of Electrical Engineering, University of Connecticut, Storrs, Connecticut

and Robert F. Cotellessa*[1]

Department of Electrical Engineering, Clarkson College of Technology, Potsdam, New York

Zinc sulfide doubly activated with Cu and Mn is important as an electroluminescent phosphor in that it is responsive to excitation by a d-c field. The emission spectrum of such phosphors is due to the Mn activation and peaks at approximately 5850Å. The excitation of the Mn luminescence center is generally believed to occur without ionization of the center. The role played by the Cu activation in the excitation process is not completely understood.

Electroluminescence in evaporated ZnS:Mn,Cu,Cl films was first reported by Thornton (1). A number of investigators have studied the response of such films to d-c excitation (2-6). Vecht *et al.* (7) have reported quantum efficiencies greater than unity or brightness of 1000 ft-L with d-c excitation of electroluminescent panels containing a ZnS:Mn,Cu,Cl powder set in an organic binder.

When d-c voltage is applied to an evaporated film of ZnS:Mn,Cu,Cl, a change in film characteristics takes place. Thornton (2) reported a complex response to reversal of the polarity of applied voltage, with many seconds being required to reach equilibrium. The occurrence of an electroluminescence forming process on initial application of voltage was reported by Goldberg and Nickerson (3). Soeya (8) has further investigated these slow transient effects.

Comparatively little has been published relating to the response of formed electroluminescent ZnS:Mn,Cu,Cl films to repetitive unidirectional pulse excitation. Thornton (2) has observed a dependence of emission rise time on voltage-pulse amplitude and a dependence of emission decay time on voltage-pulse repetition rate. In this paper are reported the results of varying over wide ranges the duration, repetition rate, and amplitude of the voltage pulse excitation.

Film Preparation and D-C Characteristics

Films of ZnS:Mn,Cu,Cl, approximately 5μ in thickness, were formed by a two-step evaporation-firing process similar to that described by Thornton (9). Luminescent powder, activated with 1.0% Mn, 0.3% Cu, and 1.0% Cl by weight, was evaporated and deposited onto a warmed tin-oxide-coated glass substrate. The deposited film subsequently was baked at a temperature between 650° and 675°C in contact with luminescent powder. An aluminum electrode was deposited to complete a sandwich cell configuration.

* Electrochemical Society Active Member.
[1] A major part of this work was done while the authors were with the Department of Electrical Engineering, New York University, Bronx, New York.
Key words: electroluminescence, zinc sulfide, phosphors, pulse excitation, manganese.

The cells were subjected to a thorough electrical forming process. With d-c voltage applied (the Al positive with respect to the tin oxide), the cell current decreased from its initial value with a simultaneous increase in light emission. The change was rapid at first and slowed to a very gradual change which continued over many hours. The formed cell was rectifying and light was emitted in the reverse direction of current flow (Al electrode positive).

The dependence of cell current on applied reverse voltage obeyed closely the exponential relation

$$I = a \exp b\sqrt{V}$$

where a and b are constants for a given cell. The dependence on voltage of the ratio of light emission to cell current was best described by the relation

$$L/I = A \exp (-B/\sqrt{V})$$

where A and B are constants for a given cell.

Pulse Excitation

Unidirectional rectangular voltage pulse excitation was applied to the electroluminescent cells, with the Al electrode positive with respect to the tin oxide electrode. The voltage rise time (to 90%) and fall time (to 10%) were 0.2 μsec or less. The current pulses were monitored. An initial peak occurred at the leading edge of the current pulse, due to a small cell capacitance, and this component of current decayed with a fall time of 1-2 μsec.

A 1P21 photomultiplier was used to detect light emission. To obtain a time-average of light emission, or integrated light output, the average of the photomultiplier current was measured. To observe the actual light pulse, or brightness waveform, the photomultiplier output was connected by a short cable to an oscilloscope. A variable shunt resistance permitted adjustment of the detector response time, which was reduced beyond the point where it had any effect on the shape of the light pulse.

One light pulse was emitted for every voltage pulse. At voltage-pulse durations or pulse widths of several milliseconds, emission was initiated at the leading edge of the voltage pulse and the brightness increased with a risetime of the order of 1 msec to an equilibrium value. Emission was extinguished at the trailing edge of the voltage pulse, and the brightness decayed to zero. At short pulse widths, the brightness continued to increase for a period of time following the trailing edge of the voltage pulse. The waveforms of the brightness for a pulse amplitude of 32V are shown in Fig. 1.

The decay time, to 1/3 of peak brightness, of the light pulses was 0.75 to 0.80 msec. This decay time was independent of voltage-pulse duration, repetition rate, or amplitude.

The dependence of average light emission on voltage-pulse duration, or pulse width, varied from an approximately linear relation to a dependence somewhat greater than linear (a power greater than one) from cell to cell. Log-log plots of light emission *vs.* pulse width for a typical cell are shown in Fig. 2 for several different voltage-pulse repetition rates, or frequencies. The linear character extends to pulse widths as low as 0.01 msec. It is also evident that the light emission is determined largely by the duty factor of the pulse excitation, *i.e.*, the fraction of a cycle in which nonzero voltage is applied. A semilog plot of light emission *vs.* pulse width at a constant duty factor of 0.2 is shown in Fig. 3 for two cells. The light emission passes through a broad maximum and does not change greatly as pulse width is varied from 2 to 0.02 msec. The same behavior was observed in all ZnS:Mn,Cu,Cl cells. At a pulse width of 0.01 msec, and a frequency of 2000 pps, the emission decreases with a decrease in pulse width and simultaneous increase in frequency. A pulse width of 0.01 msec is yet several times longer than the 0.001-0.002 msec fall time of the capacitive component of current.

The dependence of average light emission on frequency at constant pulse width was approximately linear. Log-log plots of emission *vs.* frequency for three different pulse widths are shown in Fig. 4 for a typical cell. Also shown in the figure is the measured emission with d-c excitation at a voltage equal to the voltage-pulse amplitude. At a frequency of approximately 1000 pps, the rate of increase of emission with frequency begins to fall off. At this frequency the ex-

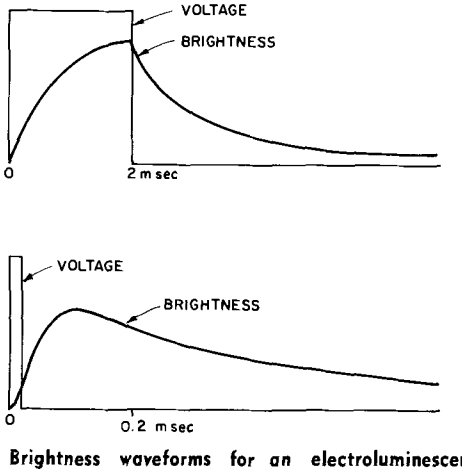

Fig. 1. Brightness waveforms for an electroluminescent cell excited by voltage pulse excitation at pulse widths of 2 msec (top) and 0.02 msec (bottom).

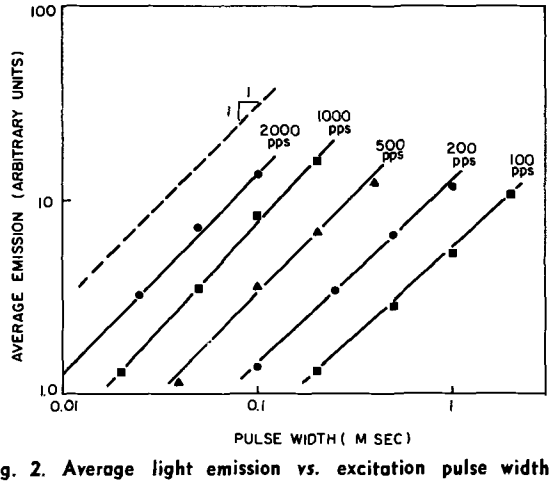

Fig. 2. Average light emission *vs.* excitation pulse width at different pulse repetition frequencies for cell 1.

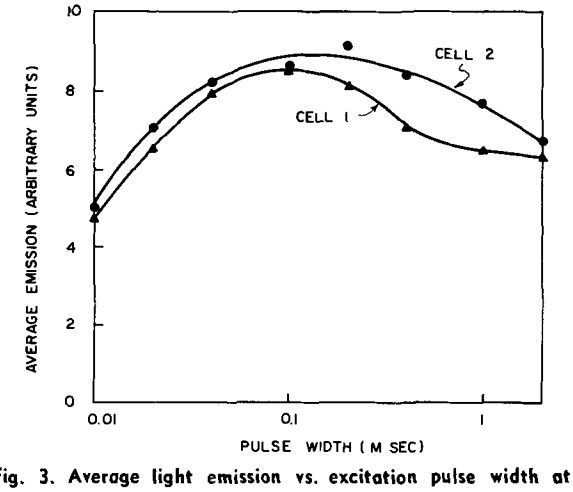

Fig. 3. Average light emission vs. excitation pulse width at a constant duty factor of 0.2 for cells 1 and 2.

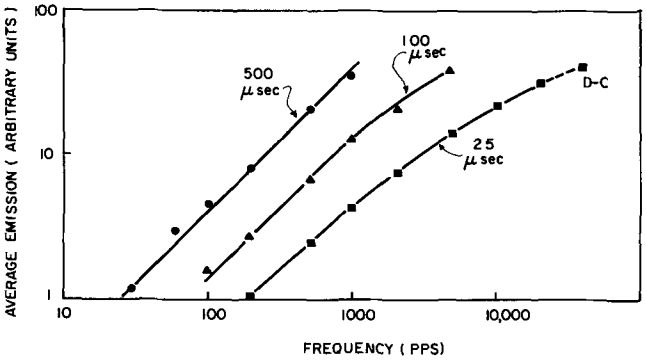

Fig. 4. Average light emission vs. excitation pulse repetition frequency at different pulse widths for cell 2.

citation period is 1.0 msec, *i.e.*, the approximate decay time of the light pulse.

The emission spectrum was recorded at room temperature for varying combinations of pulse width and frequency. No change was observed in the spectrum as pulse width or frequency were changed. The emission peak occurred at approximately 5850Å.

The dependence of average light emission on voltage-pulse amplitude appeared to be the same as the dependence on d-c voltage with d-c excitation. This relationship is shown in Fig. 5, in which the ratio of emission to cell current is plotted *vs.* the reciprocal of the square root of V_T, where V_T is the sum of pulse amplitude and d-c bias voltage. There was some enhancement of emission by this d-c bias voltage. The increase in light emission, obtained when the d-c bias voltage is increased, cannot be accounted for solely as d-c emission produced by the d-c voltage; the emission is enhanced to a significantly greater degree. The enhancement mechanism is possibly the same as that responsible for the enhanced electroluminescence resulting from the simultaneous application of a-c and d-c voltage to phosphor powder cells (10).

In some cells the Mn was omitted to obtain a ZnS:Cu,Cl film, and in others the Cu and Cl were omitted to obtain a ZnS:Mn film. The response to pulse excitation of the ZnS:Cu,Cl film, as determined by the effects of varying voltage-pulse duration, repetition rate, and amplitude, was the same as that of ZnS:

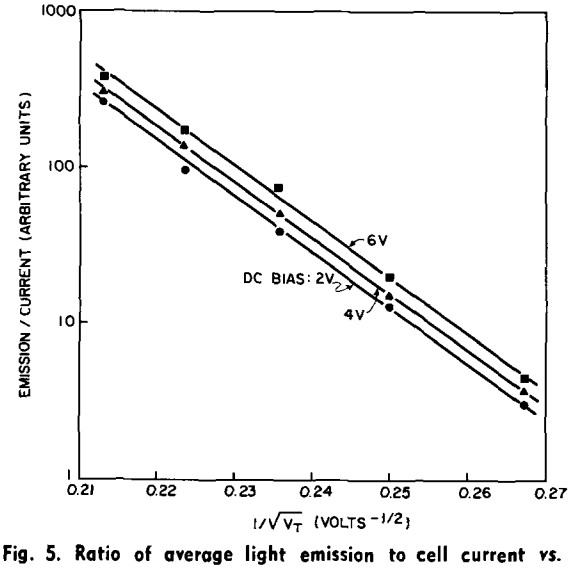

Fig. 5. Ratio of average light emission to cell current vs. the inverse square root of the sum of excitation pulse amplitude and d-c bias voltage for cell 2.

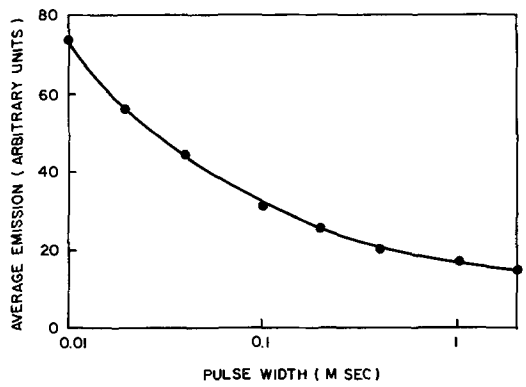

Fig. 6. Average light emission of a ZnS:Mn cell vs. excitation pulse width at a constant duty factor of 0.2.

Mn,Cu,Cl films. However, the light emission with either pulse or d-c excitation, was at least an order of magnitude less in the ZnS:Cu,Cl cells and contained shorter wavelength components.

The ZnS:Mn films did not require forming; the d-c resistance was high when voltage was first applied. Some films, of very high resistance, were not d-c electroluminescent. The emission with pulse excitation is plotted *vs.* pulse width at constant duty factor in Fig. 6. At constant duty factor, the light emission increases with increasing frequency and decreasing pulse width. This behavior is different from that of the ZnS:Mn,Cu,Cl films as demonstrated in Fig. 3. The emission apparently results partly from a-c electroluminescence that is more strongly dependent on the repetition rate of the voltage pulses than on their duration. The emission was three or more orders of magnitude less than in the ZnS:Mn,Cu,Cl cells.

Conclusion

The emission rise in ZnS:Mn,Cu,Cl phosphor films on application of a d-c field takes place in approximately 1 msec. The emission rise time and decay time are independent of duration, repetition rate, and amplitude of applied d-c pulses, as in the shape of the emission spectrum.

The excitation process does not exhibit the same slow response. The integrated light output with pulse excitation is approximately linearly dependent on pulse widths to values as low as 10 msec. It is approximately linearly dependent on frequency to values where the interpulse time approaches the emission decay time. The integrated light output is determined largely by the fraction of time voltage is applied.

Manuscript submitted Nov. 19, 1969; revised manuscript received March 13, 1970.

Any discussion of this paper will appear in a Discussion Section to be published in the June 1971 JOURNAL.

REFERENCES

1. W. A. Thornton, *J. Appl. Phys.*, **30**, 123 (1959).
2. W. A. Thornton, *ibid.*, **3**, 3045 (1962).
3. P. Goldberg and J. W. Nickerson, *ibid.*, **34**, 1601 (1963).
4. E. D. Golovkina, V. V. Pasynkov, and G. N. Khanina, *Opt. and Spec.*, **19**, 158 (1965).
5. W. Uchida, *Jap. J. Appl. Phys.*, **7**, 378 (1968).
6. K. Sasaki, S. Kurita, and Y. Omoto, *ibid.*, **7**, 1039 (1968).
7. A. Vecht, N. J. Werring, and P. J. F. Smith, *Brit. J. Appl. Phys.*, **1**, 134 (1968)
8. T. Soeya, *Jap. J. Appl. Phys.*, **6**, 205 (1967).
9. W. A. Thornton, U.S. Pat. 3,044,902 (1962).
10. W. A. Thornton, *Phys. Rev.*, **113**, 1187 (1959).

DISCUSSION SECTION

This Discussion Section includes discussion of papers appearing in the *Journal of The Electrochemical Society*, Vol. 116, No. 4 and 11 (April and November, 1969).

Some Evidence for Duplex Film Structuring Within the Anodic Alumina Barrier Layer

G. A. Dorsey, Jr. (pp. 466-471, Vol. 116, No. 4)

Robert S. Alwitt[1]: It might be of interest that the secondary phase described by Dorsey is not always obtained upon anodization of aluminum in boric acid electrolyte at 90°C. We anodized chemipolished, etched, 99.99% Al at 1.7 mA/cm^2 in aqueous 100 g/liter H_3BO_3 at 90°C. Film formation was stopped and the specimen removed when the cell voltage reached 200V. The index of refraction and thickness of the oxide film were calculated from ellipsometric measurements made at two angles of incidence. For a homogeneous film, the calculated values will be independent of the angle of incidence while a duplex film will have apparent properties that vary with the angle of incidence. The following results were obtained:

Angle of incidence	Refractive Index	Thickness (Å)
50°	1.772	2534
60°	1.787	2501

The good agreement between the two sets of data is strong evidence for the absence of a duplex film.

The major differences between this experiment and those performed by Dorsey are the current density for film formation and the absence in our experiment of any final period at constant voltage. Perhaps the second factor is the important one. From the relation between current and time for barrier film growth at constant voltage,[2] it was estimated that, at the conditions used by Dorsey, the time to reach the final current at 90°C should have been about 30% longer than the time at 60°C. This compares with a fivefold difference in the observed times. Apparently some process occurred during this period at 90°C that interfered with barrier film formation.

Dorsey refers to the primary barrier layer as an aluminum oxide trihydrate, based on his earlier interpretations of *IR* spectra.[3,4] The most convincing evidence for such a composition would be a weight loss at an elevated temperature equal to the proposed water content. Dorsey has not shown this, presumably because he thinks the iodine-methanol or bromine-methanol solutions used to isolate the oxide may alter their apparent water content.[5] We would like to point out that Bernard and Randall used this technique to measure the water content of hydrated aluminum oxide films.[6] The results were the same as those obtained by an independent method. This technique was also found to permit quantitative recovery of anhydrous aluminum oxide films.[7] Thus, there is no evidence that these methanol solutions either remove or introduce into the oxide any volatile matter.

Several years ago, we reported results on the weight loss at 900°C of isolated aluminum oxide films.[7] Films formed to 200V in aqueous H_3BO_3 solution at 90°C had a weight loss of 1.2% after 2 hr at 900°C. Clearly, these films contained no significant amount of trihydrate. Recently, the *IR* spectra of aluminum oxide films have been interpreted in a way that is consistent with these results.[8]

G. A. Dorsey, Jr.: Considering that Alwitt's anodizing conditions (sevenfold higher current density and failure to allow current-voltage equilibrium) were such as to minimize any "secondary-phase oxide" barrier layer formation, it is not surprising that none was found. However, he presents only two pieces of data and apparently disregards the dependence of ellipsometric data on (*a*) depth of penetration effects and (*b*) angle dependence effects pertaining to the proper measurements of optical constants.[9]

A recent paper by Vol'fson and Pilyankevich[10] does, however, show the same primary-secondary phase barrier layer relationship, using electron-optical data: their term for the "secondary phase" is pseudo-barrier layer. Figures 2 and 5 of their paper, plus a composite drawing in their Figure 6, are in good agreement with the photomicrographs shown in the paper that is the subject of this discussion; their further discussion follows a close parallel with that paper and another published earlier.[11] But such evidence for duplex barrier layer structure is not without precedence. Brock and Wood[12] found at least four barrier layer regions of characteristic a-c resistivity with the outer *ca.* 20% of the coating generally permeable or porous. Grosskreutz and Shaw[13] found an "ultrastructure" at the barrier layer surface, also suggestive of duplex film formation.

Further, the apparent transition sequence from primary to secondary phase barrier layer (with subsequent porous layer formation) is indirectly suggested in the data of Hunter and Fowle,[14] who found that the effective thickness of the barrier layer decreased on sealing under conditions where dissolution of alumina should be negligible. Also, Diggle, Downie, and Goulding[15] found that changes in the effective thickness of the barrier layer (decreases) are a field-assisted process rather than one attributable solely to chemical dissolution.

Regarding Alwitt's reliance on the methanol-iodine film isolation technique, there is (contrary to his statement) ample evidence to at least point with caution toward this procedure. Erdey *et al.*[16,17] point out that halogen-containing metal solvents (they used methanol-bromine) also attack $Al(OH)_3$ and are not inert toward altering the original barrier layer structure. A comparison of their XRD and DTG data show that both amorphous and crystalline aluminum trihydrates are at least partially decomposed when that reagent is used to isolate a barrier layer film.

Alwitt's own paper[18] cites this film isolation procedure in connection with weight loss measurements

[1] Research and Development Labs., Sprague Electric Co., North Adams, Mass.
[2] R. Dreiner, *This Journal*, **111**, 1350 (1964).
[3] G. A. Dorsey, Jr., *This Journal*, **113**, 169 (1966).
[4] G. A. Dorsey, Jr., *This Journal*, **113**, 284 (1966).
[5] G. A. Dorsey, Jr., *This Journal*, **115**, 1057 (1968).
[6] W. J. Bernard and J. J. Randall, Jr., *This Journal*, **107**, 483 (1960).
[7] R. S. Alwitt, *This Journal*, **114**, 843 (1967).
[8] W. Vedder and D. A. Vermilyea, *Trans. Faraday Soc.*, **65**, 561 (1969).
[9] B. Rao and R. A. Griffin, *This Journal*, **116**, 671 (1969).
[10] A. I. Vol'fson and A. N. Pilyankevich, *Zashchita Metallov*, **4**, 670 (1968).
[11] G. A. Dorsey, Jr., *This Journal*, **115**, 1053 (1968).
[12] A. J. Brock and G. C. Wood, *Electrochim. Acta*, **12**, 395 (1967).
[13] J. C. Grosskreutz and G. C. Shaw, *J. Appl. Phys.*, **35**, 2195 (1964).
[14] M. S. Hunter and P. Fowle, *This Journal*, **101**, 481 (1954).
[15] J. W. Diggle, T. C. Downie, and C. W. Goulding, *This Journal*, **116**, 737 (1969).
[16] L. Erdey, T. Kormany, and S. Gal, *Z. Anal. Chem.*, **200**, 218 (1964).
[17] L. Erdey, S. Gal, T. Kormany, and M. Mezey, *Proc. Conf. Appl. Phys. Chem. Met, Budapest*, **3**, 271 (1966).
[18] R. S. Alwitt, *This Journal*, **114**, 843 (1967).

(water content) apparently obtained by re-weighing stripped films following a 2-hr bake at 900°C. He reports *ca.* 1.2 w/o (weight per cent) water content with this technique. However, it has long been recognized that aluminas should not be cooled and re-weighed until they have come to equilibrium using at least 1200°C.[19] Otherwise, low weight loss values will be found when the alumina takes up water again on cooling or, in the case of barrier layer oxides, on immediate re-exposure to atmospheric humidity.[20]

There is no substitute for good TGA/DTG data; convincing evidence for a possible trihydrate composition, as Alwitt states. Lacking good data to report, one can only point out that various other data are suggestive of a trihydrate composition. This laboratory still does not have the necessary equipment to obtain a thermogram showing the complete weight loss/water content of barrier layer oxides, although a substitute method (for partial water content) was devised.[20] However, we now feel compelled to release data that were obtained much earlier, but not reported since they were strictly of an exploratory nature. These data were obtained for us by the Perkin-Elmer Corporation, using their TGS-1 thermobalance with a 40°C/min heating rate, and reportedly with helium purging, to 650°C.

Sample	Weight loss ($\mu g/cm^2$) at equilibrium (650°C)		Theoretical weight loss ($\mu g/cm^2$)
	Sample A	Sample B	
100V barrier layer coating intact on alloy 1199 foil	10.8	13.5	13.1 Assuming 14Å/V with a density of 2.7 g/cm^3, and assuming a uniform trihydrate composition

These data should not be viewed as anything other than a cursory examination. By now, we had hoped to have the necessary instrumentation to prepare a thorough report that might have some value toward answering Alwitt's second comment: his criticism of a much earlier paper[21] where *IR* data suggested a hydrogen-bonded cyclic trihydrate barrier layer composition, and one that appeared to consist of two structural phases.

An examination of the literature will, however, reveal that this suggested composition is still within reason. Grunwald and Fong[22] favored just such a hydrogen-bonded cyclic trihydrate dimer/polymer structure for soluble alumina in acid solution, at least near pH3 (a condensed form of this, as with the barrier layer film, does not seem unreasonable). Regarding the composition itself, Erdey *et al.*[16,17,23] report XRD, DTG, and dissolution rate data to show that the anodic alumina barrier layer film consists of at least 35 w/o $Al(OH)_3$ (at least 25% amorphous trihydrate) plus up to 14% monohydrate, with the balance consisting of γ-alumina and presumably anhydrous. Bogoyavlenskii[24] and Shreider[25] also report trihydrates in the barrier layer.

Schwabe[26] found that hydrogen ion was forced from the alumina barrier layer on reanodization (equivalent to at least 18 w/o water), while Brock and Wood's data[12] suggested at least some hydration phenomena, which increased outward to the coating surface. And, since barrier layer oxides are often reported to be γ-alumina, it might be well to point out that David and Welch[27] found that a small proportion of combined water was essential to stabilize the spinel-type γ-phase of both Fe_2O_3 and Al_2O_3. Even with an ostensively nonaqueous electrolyte, Wood and Patrick[28] found that trace amounts of water exert an influence on film growth rate and appear to be necessary for uniform film growth of thick coatings.

This still provides only indirect and inconclusive evidence for the earlier speculation[21] regarding barrier layer composition and structure. Alwitt does, however, cite an excellent and generally thorough paper by Vedder and Vermilyea[29] within which the authors present yet another interpretation of the barrier layer 960 cm^{-1} *IR* absorption band. They attribute the absorption to a translational mode (lattice vibration or "liberation" mode) of anhydrous alumina: to an absorption that has been shifted upward to an abnormally high frequency by surface polarization effects. Their discussion is based on the work of Berreman[30] who showed such an effect for thin films of lithium fluoride. This is an interesting possibility, but necessarily contains assumptions (and is lacking in data) that seem to make this equally speculative with other interpretations. One might note that Barker[31] found such liberation modes in Corundum, but these were weak absorptions at longer wavelengths and were polarization-sensitive. Gamo,[32] however, attributed the 920 cm^{-1} band of $Al_2(SO_4)_3 \cdot 18H_2O$ as due to hydrogen-bonded water coordinated to aluminum, while Pliskin and Lehman[33] found that the Si-OH bending vibration is near 930 cm^{-1}, also in a hydrogen-bonded system.

Marker Techniques for Studying the Mechanism of Scaling of Metals Based on the Use of the $O^{18}(p,n)F^{18}$ Nuclear Reaction

J. B. Holt and L. Himmel (pp. 1569-1580, Vol. 116, No. 11)

A. Brückman, S. Mrowec, and T. Werber[34]: Investigations on the contribution of individual reactants in the over-all process of the transport of matter through scales formed on metals and alloys, as well as research works on the mechanism of these processes, have been developing for years our knowledge about the mechanism of gaseous corrosion of metallic materials. These investigations also bring valuable (and sometimes not obtainable by other methods) information about the type of defects present in crystal lattices of oxides and sulfides.

In view of the importance of this problem for the physics and chemistry of the solid state, many experimental and theoretical papers discussing the methods of investigations in this field have been published in recent years. This problem is also dealt with in the paper presented by Holt and Himmel. In it, the authors present a detailed analysis of methods used today in investigating the contribution of individual reactants in the process of scale formation with the aid of neutral and radioactive markers. On the background of these considerations, the authors present their own method consisting of the use of a stable and radioactive isotope of the oxydans in the process of two-stage oxidation of metal specimens. The method involves preliminary oxidation in a medium enriched in the active isotope and then in a normal medium. After having stopped the reaction, the distribution of the active isotope in the scale is determined autoradiographically. In view

[19] C. Duval, "Inorganic Thermogravimetric Analysis," 2nd Ed., pp. 227-228, Elsevier, New York (1963).
[20] G. A. Dorsey, Jr., *This Journal*, 115, 1057 (1968).
[21] G. A. Dorsey, Jr., *This Journal*, 113, 284 (1966).
[22] E. Grunwald and D. W. Fong, *J. Phys. Chem.*, 73, 650 (1969).
[23] L. Erdey, S. Gal, and M. Mesey, *Finomechanika*, 4, 251 (1965). [*Alum. Abstr.*, 4 (10), 1337 (1966).]
[24] A. F. Bogoyavlenskii, "Anodic Protection of Metals," Paper Presented at the First Interuniversity Conference Moscow, 1964.
[25] A. V. Shreider, *J. Appl. Chem. USSR*, 39, 2533 (1966).
[26] K. Schwabe, *This Journal*, 110, 663 (1963).
[27] I. David and A. J. E. Welch, *Trans. Faraday Soc.*, 52, 1642 (1956).
[28] G. C. Wood and G. W. Patrick, *Trans. Inst. Metal Finishing*, 45, 174 (1967).
[29] W. Vedder and D. A. Vermilyea, *Trans. Faraday Soc.*, 65, 561 (1969).
[30] D. W. Berreman, *Phys. Rev.*, 130, 2193 (1963).
[31] A. S. Barker, Jr., *Phys. Rev.*, 132, 1474 (1965).
[32] I. Gamo, *Bull. Chem. Soc. Japan*, 35, 1055 (1962).
[33] W. A. Pliskin and H. S. Lehman, *This Journal*, 112, 1013 (1965).
[34] Institut of Solid State Chemistry, School of Mining and Metallurgy, Cracow, Poland.

(water content) apparently obtained by re-weighing stripped films following a 2-hr bake at 900°C. He reports *ca.* 1.2 w/o (weight per cent) water content with this technique. However, it has long been recognized that aluminas should not be cooled and re-weighed until they have come to equilibrium using at least 1200°C.[19] Otherwise, low weight loss values will be found when the alumina takes up water again on cooling or, in the case of barrier layer oxides, on immediate re-exposure to atmospheric humidity.[20]

There is no substitute for good TGA/DTG data; convincing evidence for a possible trihydrate composition, as Alwitt states. Lacking good data to report, one can only point out that various other data are suggestive of a trihydrate composition. This laboratory still does not have the necessary equipment to obtain a thermogram showing the complete weight loss/water content of barrier layer oxides, although a substitute method (for partial water content) was devised.[20] However, we now feel compelled to release data that were obtained much earlier, but not reported since they were strictly of an exploratory nature. These data were obtained for us by the Perkin-Elmer Corporation, using their TGS-1 thermobalance with a 40°C/min heating rate, and reportedly with helium purging, to 650°C.

Sample	Weight loss ($\mu g/cm^2$) at equilibrium (650°C)		Theoretical weight loss ($\mu g/cm^2$)
	Sample A	Sample B	
100V barrier layer coating intact on alloy 1199 foil	10.8	13.5	13.1 Assuming 14Å/V with a density of 2.7 g/cm^3, and assuming a uniform trihydrate composition

These data should not be viewed as anything other than a cursory examination. By now, we had hoped to have the necessary instrumentation to prepare a thorough report that might have some value toward answering Alwitt's second comment: his criticism of a much earlier paper[21] where *IR* data suggested a hydrogen-bonded cyclic trihydrate barrier layer composition, and one that appeared to consist of two structural phases.

An examination of the literature will, however, reveal that this suggested composition is still within reason. Grunwald and Fong[22] favored just such a hydrogen-bonded cyclic trihydrate dimer/polymer structure for soluble alumina in acid solution, at least near pH3 (a condensed form of this, as with the barrier layer film, does not seem unreasonable). Regarding the composition itself, Erdey *et al.*[16,17,23] report XRD, DTG, and dissolution rate data to show that the anodic alumina barrier layer film consists of at least 35 w/o $Al(OH)_3$ (at least 25% amorphous trihydrate) plus up to 14% monohydrate, with the balance consisting of γ-alumina and presumably anhydrous. Bogoyavlenskii[24] and Shreider[25] also report trihydrates in the barrier layer.

Schwabe[26] found that hydrogen ion was forced from the alumina barrier layer on reanodization (equivalent to at least 18 w/o water), while Brock and Wood's data[12] suggested at least some hydration phenomena, which increased outward to the coating surface. And, since barrier layer oxides are often reported to be γ-alumina, it might be well to point out that David and Welch[27] found that a small proportion of combined water was essential to stabilize the spinel-type γ-phase of both Fe_2O_3 and Al_2O_3. Even with an ostensively nonaqueous electrolyte, Wood and Patrick[28] found that trace amounts of water exert an influence on film growth rate and appear to be necessary for uniform film growth of thick coatings.

This still provides only indirect and inconclusive evidence for the earlier speculation[21] regarding barrier layer composition and structure. Alwitt does, however, cite an excellent and generally thorough paper by Vedder and Vermilyea[29] within which the authors present yet another interpretation of the barrier layer 960 cm^{-1} *IR* absorption band. They attribute the absorption to a translational mode (lattice vibration or "liberation" mode) of anhydrous alumina: to an absorption that has been shifted upward to an abnormally high frequency by surface polarization effects. Their discussion is based on the work of Berreman[30] who showed such an effect for thin films of lithium fluoride. This is an interesting possibility, but necessarily contains assumptions (and is lacking in data) that seem to make this equally speculative with other interpretations. One might note that Barker[31] found such liberation modes in Corundum, but these were weak absorptions at longer wavelengths and were polarization-sensitive. Gamo,[32] however, attributed the 920 cm^{-1} band of $Al_2(SO_4)_3 \cdot 18H_2O$ as due to hydrogen-bonded water coordinated to aluminum, while Pliskin and Lehman[33] found that the Si-OH bending vibration is near 930 cm^{-1}, also in a hydrogen-bonded system.

Marker Techniques for Studying the Mechanism of Scaling of Metals Based on the Use of the $O^{18}(p,n)F^{18}$ Nuclear Reaction

J. B. Holt and L. Himmel (pp. 1569-1580, Vol. 116, No. 11)

A. Brückman, S. Mrowec, and T. Werber[34]: Investigations on the contribution of individual reactants in the over-all process of the transport of matter through scales formed on metals and alloys, as well as research works on the mechanism of these processes, have been developing for years our knowledge about the mechanism of gaseous corrosion of metallic materials. These investigations also bring valuable (and sometimes not obtainable by other methods) information about the type of defects present in crystal lattices of oxides and sulfides.

In view of the importance of this problem for the physics and chemistry of the solid state, many experimental and theoretical papers discussing the methods of investigations in this field have been published in recent years. This problem is also dealt with in the paper presented by Holt and Himmel. In it, the authors present a detailed analysis of methods used today in investigating the contribution of individual reactants in the process of scale formation with the aid of neutral and radioactive markers. On the background of these considerations, the authors present their own method consisting of the use of a stable and radioactive isotope of the oxydans in the process of two-stage oxidation of metal specimens. The method involves preliminary oxidation in a medium enriched in the active isotope and then in a normal medium. After having stopped the reaction, the distribution of the active isotope in the scale is determined autoradiographically. In view

[19] C. Duval, "Inorganic Thermogravimetric Analysis," 2nd Ed., pp. 227-228, Elsevier, New York (1963).
[20] G. A. Dorsey, Jr., *This Journal*, 115, 1057 (1968).
[21] G. A. Dorsey, Jr., *This Journal*, 113, 284 (1966).
[22] E. Grunwald and D. W. Fong, *J. Phys. Chem.*, 73, 650 (1969).
[23] L. Erdey, S. Gal, and M. Mesey, *Finomechanika*, 4, 251 (1965). [*Alum. Abstr.*, 4 (10), 1337 (1966).]
[24] A. F. Bogoyavlenskii, "Anodic Protection of Metals," Paper Presented at the First Interuniversity Conference Moscow, 1964.
[25] A. V. Shreider, *J. Appl. Chem. USSR*, 39, 2533 (1966).
[26] K. Schwabe, *This Journal*, 110, 663 (1963).
[27] I. David and A. J. E. Welch, *Trans. Faraday Soc.*, 52, 1642 (1956).
[28] G. C. Wood and G. W. Patrick, *Trans. Inst. Metal Finishing*, 45, 174 (1967).
[29] W. Vedder and D. A. Vermilyea, *Trans. Faraday Soc.*, 65, 561 (1969).
[30] D. W. Berreman, *Phys. Rev.*, 130, 2193 (1963).
[31] A. S. Barker, Jr., *Phys. Rev.*, 132, 1474 (1965).
[32] I. Gamo, *Bull. Chem. Soc. Japan*, 35, 1055 (1962).
[33] W. A. Pliskin and H. S. Lehman, *This Journal*, 112, 1013 (1965).
[34] Institut of Solid State Chemistry, School of Mining and Metallurgy, Cracow, Poland.

of the lack of an appropriated radioactive isotope of oxygen, the stable isotope O^{18} is used and transformed into the radioactive isotope F^{18} according to the nuclear reaction $O^{18}/n,p/F^{18}$.

Holt and Himmel have applied their method—to check its applicability—in investigating the share of diffusion of individual reactants in the process of growth of oxide scales on Fe and Zr and on Fe-Pt alloys. On the basis of obtained results, Holt and Himmel came to several methodological conclusions and to conclusions concerning the mechanism of reactions under investigation. Several of them arouse some objections and some suggestions must be directly corrected.

According to the suggestion of Holt and Himmel, the isotope of the oxidizing element shall be used in the process of two-stage oxidation in such a way as to mark the primary formed of the reaction product, similarly as in the conventional marker method.

This method leads—as mentioned also by the authors—to unambiguous conclusions only in cases where the scale layer is compact on its whole cross section and adheres strongly to the metal surface. In cases of formation of scales which are built up of two layers with a porous inner one, the method proposed by Holt and Himmel is useless or leads to alternative conclusions only. Himmel and Holt are therefore suggesting that unambiguous results can be obtained from marker experiments (carried out by the conventional method or by the method consisting of use of radioactive isotopes) only in the case of compact monolayer scales characterized by a very good adhesion to the metal surface. This method is therefore principally useless in investigating the mechanism of heterophasic scale formation on metals and alloys. In conclusion, Himmel and Holt formulate the conditions which must be fulfilled in preparing the specimens for investigation if the formed monolayer scale is to be compact and adhere to the metal surface.

Himmel and Holt are doubtless right when they insist that the mobilities of individual reactants in the lattice of the oxidation product can be rationally determined by marker methods only in cases of monolayer scale formation. In this case, no other methods are needed, however, than those consisting of the conventional marking of the metal surface with neutral substances, as mentioned also by the cited authors in their paper.

On the other hand, the results of such investigations are interesting first of all from the point of view of solid-state physics and not of gaseous corrosion. It is well known that in the case of oxidation of metals and alloys the formation of multilayer scales prevails, the mechanism of scale growth being thereby very complex. The method proposed by Holt and Himmel gives no better possibilities to study these phenomena than the conventional marker method. The radioactive isotope of the oxidizing element can, however, be very useful in studying the mechanism of scale formation on metals and alloys under the condition it is employed in another way than that suggested by Holt and Himmel. Such a method has been used already for many years and the results of model investigations carried out by this method on metal-sulfur and alloy-sulfur systems have contributed to the development of the dissociative model of formation of multilayer scales on pure metals and on binary alloys.[35-44] Himmel and Holt do not mention these papers at all in their extensive dissertation. If they had made acquaintance with these papers, they would have avoided one-sidedness in treating this important problem.

The authors of these remarks have demonstrated that valuable information about the mechanism of mono- and multilayer scale formation on metals and alloys can be obtained by the method of two-stage oxidation but in another way than that proposed by Holt and Himmel. Namely, the radioactive isotope of the oxidizing element must be introduced into the medium in the second, and not in the first, stage of the reaction. The autoradiographs of cross sections of scales obtained in this way offer the possibility of formulating unambiguous conclusions not only in the case of monolayer scales. Figures 1 and 2 of this discussion show such autoradiographs of sulfide scale formed in the course of two-stage sulfurization on copper and on a copper-zinc alloy containing 15% zinc. Figure 1 demon-

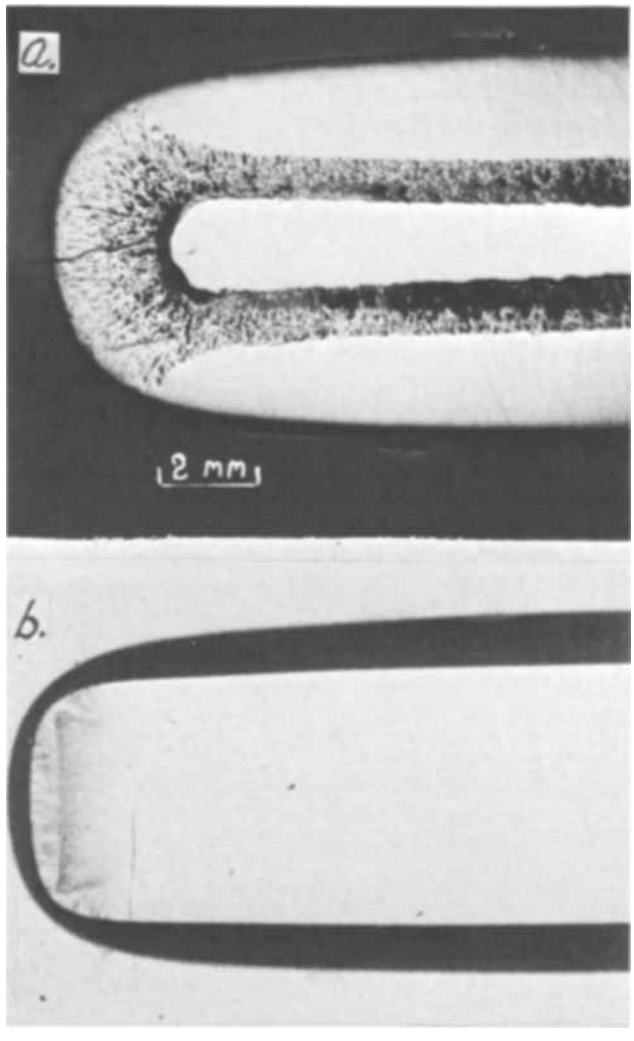

Fig. 1. Photomicrograph (a) and autoradiograph (b) of a cross section of a sulfurized sample of copper exposed for 5 min in nonradioactive, 15 min in radioactive, sulfur at 444°C.[35]

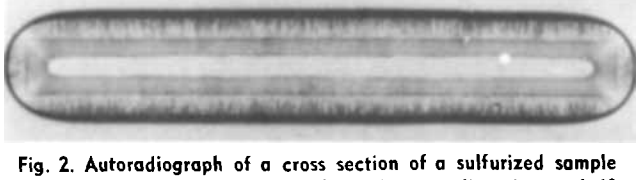

Fig. 2. Autoradiograph of a cross section of a sulfurized sample of alloy Cu-15% Zn exposed for 60 min in nonradioactive, and 60 min in radioactive, sulfur at 444°C.[40]

[35] A. Brückman, S. Mrowec, and T. Werber, *Fiz. Metal. i Metalloved.*, 15, 362 (1963).
[36] A. Brückman, S. Mrowec, and T. Werber, *Fiz. Metal. i Metallov.*, 20, 702 (1965).
[37] A. Brückman and J. Romanski, *Corro. Sci.*, 5, 185 (1965).
[38] S. Mrowec and T. Werber, *Corro. Sci.*, 5, 717 (1965).
[39] A. Brückman, J. Gilewicz-Wolter, and S. Mrowec, *Bull. Acad. Polon. Sci., Ser. Sci. Chim.*, 15, 11 (1967).
[40] A. Brückman, *Corro. Sci.*, 7, 51 (1967).
[41] S. Mrowec, *Corro. Sci.*, 7, 563 (1967).
[42] S. Mrowec and T. Werber, *Werkstoffe Korrosion*, 18, 116 (1967).
[43] S. Mrowec and T. Werber, *Werkstoffe Korrosion*, 19, 944 (1968).
[44] A. Brückman, S. Mrowec, and T. Werber, "Proceedings of the Third International Congress on Metallic Corrosion, Moscow, 1966," Vol. IV, Mir, Moscow (1969).

strates that, in spite of formation of a two-layer scale (with a porous inner one) on flat surfaces of the specimens, the inner transport of the oxidizing agent is not observed. At edges, the radioactive sulfur isotope penetrated into the interior of the scale through microfissures situated perpendicular to the metal surface. The fissures can be clearly distinguished on the autoradiograph and on the microphotograph. The mechanism of fissure formation as well as the mechanism of scale growth in these different parts of the specimens are described in detail in our cited papers. It must be emphasized that application of radioactive and not active sulfur in the way proposed by Holt and Himmel, *i.e.* in the reversed sequence, would bring to such little illustrative picture as that reproduced in their Fig. 7 [*sic*]. Also, Fig. 2 of this discussion should be compared with Fig. 9 of the Holt-Himmel paper. In Fig. 2, the inward transport of the oxidizing element through microfissures, formed as the result of secondary dissociation processes and situated perpendicular to the core, can be clearly observed. Both scale layers can also be clearly distinguished. On the basis of the autoradiograph obtained by Holt and Himmel, no precise conclusions about the mechanism of scale formation on Fe-Pt alloy can be formulated. It must be emphasized that such good results as shown in Fig. 1 and 2 can be obtained not only in cases where the preparations can be relatively easily polished. Analogous results have been obtained in many other cases, especially in investigating the mechanism of sulfurization of nickel,[36,40] iron,[37,38] Ni-Cr-alloys,[45] and other systems.[46,47]

It should also be mentioned that the radioactive isotope of sulfur was used in the case of many model reactions[39,43,44,48] investigated by Wagner's pellet method.[49]

When the contribution of the inward lattice diffusion is to be unambiguously determined, an inert marker and additionally the radioactive isotope of the oxidizing element must be used simultaneously in a way described in the papers.[36,43]

It should also be said that our investigations carried out with use of the O^{18}-isotope (according to the nuclear reaction $O^{18}/\alpha,n/Ne^{21}$) lead to identical results as in the case of sulfurization.

Concluding, we must underline that in spite of Holt-Himmel's suggestion that radioactive S^{35}-isotope was widely used in our laboratory as well as by other authors[50,51] and has contributed to a better understanding of the mechanism of scale formation on metals and alloys. Some similar conclusions appear also in Holt-Himmel's paper, suggesting thus that they have been formulated for the first time as a result of their own investigations.

J. B. Holt and L. Himmel: We must confess that, at the time our paper was submitted to this *Journal*, we were not aware of the publications cited by the discussors, nor did we know that Professor Mrowec and his colleagues had been using S^{35} as a marker in the elegant manner they have described. The convincing illustrations which they have provided demonstrate that their technique is basically sound and that it has been applied with great skill in studying the mechanism of growth of sulfide scales on metals and alloys. While we have been remiss in not making mention of this important refinement in technique, we would like to point out that the contribution made by Professor Mrowec and his co-workers to the development of the dissociative model for the growth of duplex scale was specifically acknowledged in our paper.

The primary objective of our work was to show that the $O^{18}(p,n)F^{18}$ nuclear reaction could be used successfully to study the transport of oxygen in oxide scales formed on metals and alloys. To accomplish this, we employed O^{18} as a marker and, to provide the most direct comparison with inert marker techniques, we chose to mark the original interface between the metal and the gas by oxidizing first in O^{18} and then O^{16}. In no way have we excluded the possibility or, indeed, the desirability of reversing the oxidation sequence, as Brückman, Mrowec, and Werber recommend. In fact, in connection with our experiments on the scaling of zirconium as well as in the general discussion to our paper, we have pointedly emphasized the advantages that may be gained by reversing the order of oxidation, particularly when dealing with fissured or nonadherent scales. Furthermore, in other work on the mechanism of the oxidation of magnetite, to which we have referred in our paper, we found it expedient to oxidize first in normal oxygen and then in O^{18} even though dense, adherent Fe_2O_3 layers at least 1 mm thick could easily be produced on the Fe_3O_4 substrate.

Although we agree that the choice of the marking sequence to be employed in practice is not a trivial one and should be given careful consideration, we do not exclusively favor one marking sequence in preference to the other in all circumstances. If a choice must be made, we feel that this should be dictated not only by the structural characteristics of the scale and by which of the two reacting components is the faster diffusing species in the scale lattice, but also by the type of information being sought. Our experiments on the scaling of iron in H_2/H_2O atmospheres provide a case in point. The porosity observed in thick wüstite scales grown on cylindrical iron specimens (Fig. 8c and d) is of an entirely different nature from that which originates in the sulfide scales formed on Cu or Cu-Zn alloys (Fig. 1a and 2). The internal voids which are present in the scale are not interconnected and are located relatively deep below the external surface; moreover, cracks or fissures which would permit oxygen from the gas phase to penetrate freely into the interior of the scale do not appear to be present. Thus, if we had oxidized these specimens first in H_2O^{16} and then H_2O^{18}, the chances are we would merely have confirmed what we already knew; namely, that oxygen is virtually immobile in the wüstite lattice. In all probability, the O^{18} distribution would have failed to reveal that oxygen transport actually does take place in the interior of the scale by what we have concluded must be a dissociative mechanism.

For the most part, this also applies to the scaling behavior of Fe-Pt alloys. In this case, we have deliberately tried to destroy the adherence between the scale and the metal by introducing a more noble alloying element which tends to concentrate at the metal/scale interface during growth of the scale. With rectangularly shaped specimens, relatively direct access of oxygen to the interior of the scale might be possible if the gas can enter at the corners and edges of the sample and penetrate along the metal/scale interface. To check out this possibility, it would have been instructive to oxidize in the reverse sequence. However, it is doubtful whether this would have yielded a more enlightening result concerning the relative mobilities of iron and oxygen in the scale formed on Fe-Pt alloys. The outer portion of the scale does not contain platinum and hence a marker experiment carried out in the manner recommended by the discussors would again simply confirm that iron is the mobile species in Pt-free wüstite.

[45] S. Mrowec, T. Werber, and M. Zastawnik, *Corro. Sci.*, 6, 47 (1966).
[46] S. Mrowec, T. Werber, and J. Podhorodecki, *Corro. Sci.*, 8, 815 (1968).
[47] A. Brückman, S. Mrowec, and T. Werber, *Z. Physik. Chem.*, 231, 375 (1966).
[48] A. Brückman, S. Mrowec, and J. Wolter, "Oxidation of Metals," In press.
[49] C. Wagner, *Z. Physik. Chem.*, 21, 25 (1933).
[50] W. Moore, "Radioisotopes in Scientific Research," p. 528, Pergamon, Oxford (1958).
[51] J. Pokrowskij and M. Pawljuschenko, *Dokl. Akad. Nauk SSSR*, 134, 391 (1960).

strates that, in spite of formation of a two-layer scale (with a porous inner one) on flat surfaces of the specimens, the inner transport of the oxidizing agent is not observed. At edges, the radioactive sulfur isotope penetrated into the interior of the scale through microfissures situated perpendicular to the metal surface. The fissures can be clearly distinguished on the autoradiograph and on the microphotograph. The mechanism of fissure formation as well as the mechanism of scale growth in these different parts of the specimens are described in detail in our cited papers. It must be emphasized that application of radioactive and not active sulfur in the way proposed by Holt and Himmel, *i.e.* in the reversed sequence, would bring to such little illustrative picture as that reproduced in their Fig. 7 [*sic*]. Also, Fig. 2 of this discussion should be compared with Fig. 9 of the Holt-Himmel paper. In Fig. 2, the inward transport of the oxidizing element through microfissures, formed as the result of secondary dissociation processes and situated perpendicular to the core, can be clearly observed. Both scale layers can also be clearly distinguished. On the basis of the autoradiograph obtained by Holt and Himmel, no precise conclusions about the mechanism of scale formation on Fe-Pt alloy can be formulated. It must be emphasized that such good results as shown in Fig. 1 and 2 can be obtained not only in cases where the preparations can be relatively easily polished. Analogous results have been obtained in many other cases, especially in investigating the mechanism of sulfurization of nickel,[36,40] iron,[37,38] Ni-Cr-alloys,[45] and other systems.[46,47]

It should also be mentioned that the radioactive isotope of sulfur was used in the case of many model reactions[39,43,44,48] investigated by Wagner's pellet method.[49]

When the contribution of the inward lattice diffusion is to be unambiguously determined, an inert marker and additionally the radioactive isotope of the oxidizing element must be used simultaneously in a way described in the papers.[36,43]

It should also be said that our investigations carried out with use of the O^{18}-isotope (according to the nuclear reaction $O^{18}/\alpha,n/Ne^{21}$) lead to identical results as in the case of sulfurization.

Concluding, we must underline that in spite of Holt-Himmel's suggestion that radioactive S^{35}-isotope was widely used in our laboratory as well as by other authors[50,51] and has contributed to a better understanding of the mechanism of scale formation on metals and alloys. Some similar conclusions appear also in Holt-Himmel's paper, suggesting thus that they have been formulated for the first time as a result of their own investigations.

J. B. Holt and L. Himmel: We must confess that, at the time our paper was submitted to this *Journal*, we were not aware of the publications cited by the discussors, nor did we know that Professor Mrowec and his colleagues had been using S^{35} as a marker in the elegant manner they have described. The convincing illustrations which they have provided demonstrate that their technique is basically sound and that it has been applied with great skill in studying the mechanism of growth of sulfide scales on metals and alloys. While we have been remiss in not making mention of this important refinement in technique, we would like to point out that the contribution made by Professor Mrowec and his co-workers to the development of the dissociative model for the growth of duplex scale was specifically acknowledged in our paper.

The primary objective of our work was to show that the $O^{18}(p,n)F^{18}$ nuclear reaction could be used successfully to study the transport of oxygen in oxide scales formed on metals and alloys. To accomplish this, we employed O^{18} as a marker and, to provide the most direct comparison with inert marker techniques, we chose to mark the original interface between the metal and the gas by oxidizing first in O^{18} and then O^{16}. In no way have we excluded the possibility or, indeed, the desirability of reversing the oxidation sequence, as Brückman, Mrowec, and Werber recommend. In fact, in connection with our experiments on the scaling of zirconium as well as in the general discussion to our paper, we have pointedly emphasized the advantages that may be gained by reversing the order of oxidation, particularly when dealing with fissured or nonadherent scales. Furthermore, in other work on the mechanism of the oxidation of magnetite, to which we have referred in our paper, we found it expedient to oxidize first in normal oxygen and then in O^{18} even though dense, adherent Fe_2O_3 layers at least 1 mm thick could easily be produced on the Fe_3O_4 substrate.

Although we agree that the choice of the marking sequence to be employed in practice is not a trivial one and should be given careful consideration, we do not exclusively favor one marking sequence in preference to the other in all circumstances. If a choice must be made, we feel that this should be dictated not only by the structural characteristics of the scale and by which of the two reacting components is the faster diffusing species in the scale lattice, but also by the type of information being sought. Our experiments on the scaling of iron in H_2/H_2O atmospheres provide a case in point. The porosity observed in thick wüstite scales grown on cylindrical iron specimens (Fig. 8c and d) is of an entirely different nature from that which originates in the sulfide scales formed on Cu or Cu-Zn alloys (Fig. 1a and 2). The internal voids which are present in the scale are not interconnected and are located relatively deep below the external surface; moreover, cracks or fissures which would permit oxygen from the gas phase to penetrate freely into the interior of the scale do not appear to be present. Thus, if we had oxidized these specimens first in H_2O^{16} and then H_2O^{18}, the chances are we would merely have confirmed what we already knew; namely, that oxygen is virtually immobile in the wüstite lattice. In all probability, the O^{18} distribution would have failed to reveal that oxygen transport actually does take place in the interior of the scale by what we have concluded must be a dissociative mechanism.

For the most part, this also applies to the scaling behavior of Fe-Pt alloys. In this case, we have deliberately tried to destroy the adherence between the scale and the metal by introducing a more noble alloying element which tends to concentrate at the metal/scale interface during growth of the scale. With rectangularly shaped specimens, relatively direct access of oxygen to the interior of the scale might be possible if the gas can enter at the corners and edges of the sample and penetrate along the metal/scale interface. To check out this possibility, it would have been instructive to oxidize in the reverse sequence. However, it is doubtful whether this would have yielded a more enlightening result concerning the relative mobilities of iron and oxygen in the scale formed on Fe-Pt alloys. The outer portion of the scale does not contain platinum and hence a marker experiment carried out in the manner recommended by the discussors would again simply confirm that iron is the mobile species in Pt-free wüstite.

[45] S. Mrowec, T. Werber, and M. Zastawnik, *Corro. Sci.*, 6, 47 (1966).
[46] S. Mrowec, T. Werber, and J. Podhorodecki, *Corro. Sci.*, 8, 815 (1968).
[47] A. Brückman, S. Mrowec, and T. Werber, *Z. Physik. Chem.*, 231, 375 (1966).
[48] A. Brückman, S. Mrowec, and J. Wolter, "Oxidation of Metals," In press.
[49] C. Wagner, *Z. Physik. Chem.*, 21, 25 (1933).
[50] W. Moore, "Radioisotopes in Scientific Research," p. 528, Pergamon, Oxford (1958).
[51] J. Pokrowskij and M. Pawljuschenko, *Dokl. Akad. Nauk SSSR*, 134, 391 (1960).

In the growth of wüstite on high-purity iron, a local loss of adherence occurs between the scale and the metal at the corners and edges of plate-shaped specimens and at isolated regions around the circumference of cylindrical specimens. Despite this, we had no difficulty in establishing, unequivocally, that the mobility of oxygen in wüstite is negligibly small compared to that of iron. We therefore take exception to the statement that the marking sequence we have used will yield unambiguous results only when the scale is perfectly adherent and free from porosity. The scale need not remain firmly attached to the metal substrate over the entire specimen area in order that the diffusing component be positively identified. As Brückman *et al.* have correctly pointed out, difficulties in the interpretation may arise if the scale is completely nonadherent, just as they do when inert markers are employed. This is certainly true for the growth of thick sulfide scales on Cu but not apparently for the scaling of iron in air (Fig. 10). Thus, on an iron sample oxidized in air, the O^{18} distribution was basically the same on both sides of the specimen even though the scale on one side was adherent, while that on the other side was completely nonadherent. It, therefore, appears that the real problems in interpretation are caused not by the loss of adherence *per se* but by accompanying dissociative transport of the nonmetallic component.

So far, we have considered the information obtainable using only the nonmetallic constituent as a marker. It will be recalled, however, that the generalized marker approach which we suggested in our paper involves making use of both components of the system as markers wherever possible. If this is done, we feel confident that a reliable estimate of the relative mobilities in the scale lattice can be obtained even when dissociative transport mechanisms are operative. For scaling reactions in which the nonmetallic component is the faster diffusing species, it would seem particularly desirable to employ a radioisotope of the metal as a marker, as our experiments on the scaling of zirconium have indicated.

In summary, we doubt that a single recipe for carrying out marker experiments can be formulated which is at the same time simple, completely foolproof, and ideally suited to the study of all types of scaling reactions on metals and alloys. The rich variety of phenomena encountered even in a single system such as the reaction between iron and oxygen would seem to require that a combination of techniques be used if a complete understanding of the scaling process is to be achieved. Professor Mrowec and his colleagues have concentrated on one aspect of the over-all problem which we only briefly touched upon in our article, *i.e.* the mechanism of growth of nonadherent, duplex scales. We recognize the merit of their approach to this important and practical problem but we still believe that the techniques we have developed are also useful for their intended purpose.

JOURNAL OF THE ELECTROCHEMICAL SOCIETY

ELECTROCHEMICAL TECHNOLOGY

JULY 1970

Application of Preferential Electrochemical Etching of Silicon to Semiconductor Device Technology

M. J. J. Theunissen,* J. A. Appels, and W. H. C. G. Verkuylen

Philips Research Laboratories, N. V. Philips' Gloeilampenfabrieken, Eindhoven, Netherlands

ABSTRACT

Preferential electrochemical etching of epitaxial structures has been applied to the fabrication of semiconductor devices. Preparation of thin layer devices and isolated structures is described. As an introduction to these applications, the etching of various epitaxial structures is described. Consideration is given to the manner in which the etching behavior is influenced by thermal treatment, the presence of diffusion areas, and crystal imperfections.

Anodic dissolution of silicon in hydrofluoric acid has been described by several workers (1, 2). It was found by van Dijk (3) that electrochemical etching of epitaxially grown structures can be used to make thin silicon crystals. Using silicon slices of the n^+n or the n^+p type, the low-resistivity n^+ substrate can dissolve anodically and the etching process stops near the epitaxial boundary. Thin single crystals of silicon with a thickness down to 0.5μ were prepared by van Dijk.

This paper presents some applications of this electrochemical etching process to semiconductor technology. Before this is done, the etching behavior of homogeneously doped substrates and epitaxially grown structures will be considered in more detail. One application of the electrochemical etching process is the preparation of devices in thin silicon layers of high quality. These thin silicon layers can be advantageously used to make devices having improved performance. Similar devices may be made in thin silicon layers grown on sapphire, spinel, or other insulators. However, the crystal imperfections of these layers (often made by heteroepitaxial growing techniques), still limit the applications. Two new methods of preparing thin layer devices are described. In one method, lateral devices are fabricated in a thin silicon layer which is made on top of a polycrystalline silicon substrate with a SiO_2 layer in between. In the second method of making thin layer devices, diffusions are carried out in the initial epitaxially grown structures, then the slice is etched, leaving a device with vertical junctions only.

The electrochemical etching process can also be applied successfully in the preparation of isolated structures. A technique is presented for utilization of this process in the preparation of integrated circuits with dielectric isolation and beam lead air-gap isolation.

Experimental Procedure

The samples used consisted of homogeneously doped n- and p-type silicon slices and epitaxially grown slices with a highly doped substrate ($> 3.10^{18}$ atoms/cm^3) and an epitaxial layer with a dopant concentration lower than 2.10^{16} atoms/cm^3. Both (111) and (100) oriented slices were used; slice diameters were between 32 and 40 mm.

The homogeneously doped slices were chosen in the impurity concentration range from 10^{15} to 10^{19} atoms/cm^3. Prior to the electrochemical process, the slices were etched in HF (48%)-HNO_3 (65%) (1:10) etchant to remove work damage. Contact between the anode and the silicon was made by pressing a platinum strip (15 x 3 mm^2) pressed against the silicon slice near its edge with a perspex clamp, the resistivity of the slice disregarding. The slice, including the contact, was completely immersed in the electrolyte; if the silicon anode current was to be measured, the platinum strip was covered with an apiezon wax.

The n^+ substrates of the epitaxial slices were antimony doped, the p^+ substrates boron doped. The substrates were subjected to an appropriate etching and polishing procedure and, prior to the epitaxial growing process, to an HCl(1%) and H_2 treatment for 10 min at 1220°C. Epitaxy was carried out at 1220°C in a $SiCl_4$ and H_2 mixture (growth rate 0.5 μm/min; dopants for the n-type layers were phosphorus or antimony; the dopant for p-type layers was boron). In this way, n^+n, n^+p, p^+n, and p^+p epitaxial structures were grown. The mounting and beveling of the slices and the method of making contact between the n^+ silicon and the platinum strip have been described by van Dijk (3).

During the electrochemical etching process, the anode-cathode current was recorded as a function of the time. The etching process was stopped as soon as a constant current level was reached, indicating that the low-resistivity substrate had been dissolved (except a minor part shielded by the platinum strip).

The electrochemical etching conditions of both the homogeneously doped slices and the substrate of the epitaxial ones were the same, namely: $V_{anode\text{-}cathode} = 10V$; electrolyte: 5% aqueous HF; bath temperature 18°C; complete darkness; cathode: platinum gauze (10 x 10 cm^2); cathode parallel to slice at a distance of about 5 cm.

After anodic dissolution of the low-resistivity substrate of the epitaxial slice, chemical etching of the

* Electrochemical Society Active Member.

remaining epitaxial layer was performed in a freshly prepared etchant. The composition was: 50 ml HF (48%), 50 ml acetic acid (Merck 99% minimum purity), and 200 mg $KMnO_4$ (Merck 99% minimum purity). The etch rate was approximately 0.2 μm/min at 18°C.

The Sirtl etch technique (4) and optical microscopy were used to note surface defects.

The thickness of the thin layers was measured by multiple interference microscopy (Tolansky), or indirectly derived from the known depth of diffusion layers or etched grooves, which are revealed at the rear side during chemical thinning of the slice. In the case of thin silicon layers on oxide and polycrystalline silicon, thickness measurements were done using beveling (5) or infrared interference techniques (5).

Experimental Results and Discussion

Anodic etching of silicon samples.—Homogeneously doped samples.—In order to obtain more insight into the etching behavior of nonhomogeneously doped silicon samples, such as the epitaxially grown slices used for the thin layer devices, we subjected various homogeneously doped samples to the electrochemical etching process. Experiments on anodic dissolution of n-type silicon crystals, with a donor concentration ranging from 10^{15} to 10^{19} atoms/cm^3 under the conditions specified before, indicated that there are three concentration regions, each with a different etching behavior. Above 3 x 10^{18} donors/cm^3 (<0.01 ohm-cm), we found complete dissolution of the crystals. In the range between 3 x 10^{18} and 2 x 10^{16} donors/cm^3 (0.01-0.3 ohm-cm), only partial dissolution occurred with a decreasing rate at the lower donor concentrations. As can be seen in the lower part of Fig. 1(a), a part of the silicon crystal, extending from the electrolyte-silicon interface into the bulk crystal, has been converted to a brown porous structure. Infrared transmission spectra showed that the brown layer consisted mainly of pure silicon, which is similar to the brown layers reported by Turner (1) and Beckmann (6). At donor concentrations lower than about 2 x 10^{16} atoms/cm^3 (>0.3 ohm-cm), we found no visual evidence of attack when the etching time was shorter than about ½ hr. However, when etching was continued, the silicon anode current density increased (from less than 1 to more than 5 mA/cm^2) and the crystal surface became dull. Figure 1(b) shows a cross section of a 2 x 10^{15} n-type slice after a short treatment with Sirtl etchant. As can be seen, channels locally penetrate nearly 20 μm into the crystal; their direction appeared to be crystal oriented. The cause and the nature of the channels are not fully understood; the density and the length of the channels increased with the anodizing time.

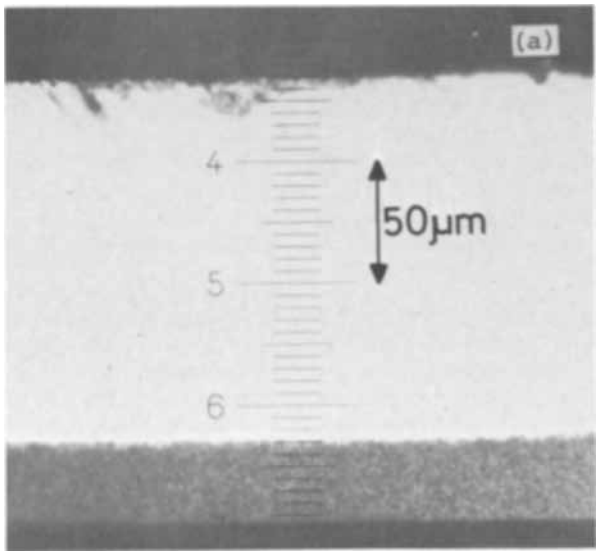

Fig. 1(a). Cross section of an n-type Si slice (N_D = 10^{17} donors/cm^3; (111) slice orientation) after an anodizing treatment of 1 hr.

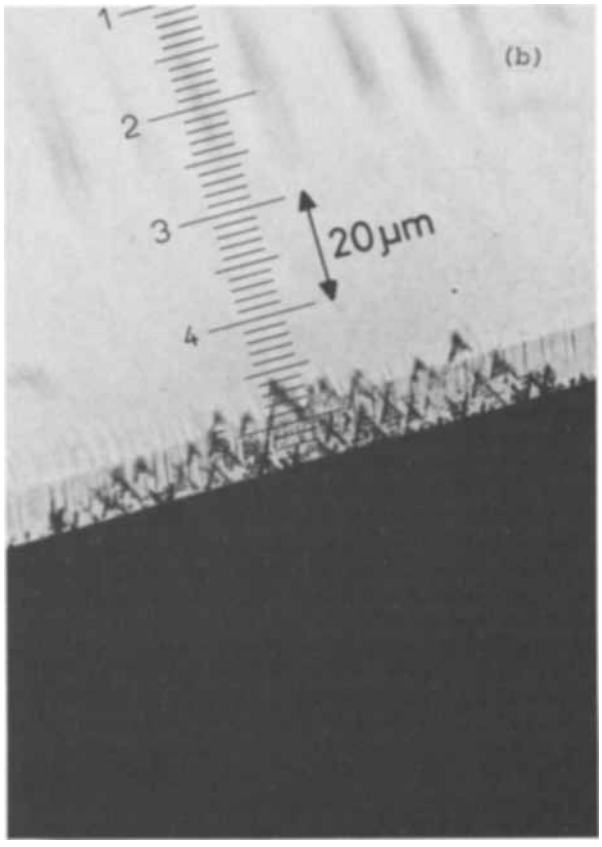

Fig. 1(b). Cross section of an n-type Si slice at a weak spot (N_D = 2.10^{15} donors/cm^3; (100) slice orientation) after an anodizing treatment of 1 hr followed by Sirtl etching.

Homogeneously doped p-type silicon samples were found to dissolve when the acceptor concentration was higher than about 5 x 10^{15} atoms/cm^3 (>3 ohm-cm). The dissolution rate of p-type silicon was found to increase with the acceptor concentration. At acceptor concentrations below 5 x 10^{15} atoms/cm^3, local attack around the platinum strips was often observed, while the other part of the slice was covered with a brownish deposit.

Epitaxially grown structures.—Figure 2 schematically shows, among other things, the profiles of the net impurity concentration as they will appear in n^+n, p^+n, n^+p, and p^+p epitaxial slices. Based on the experi-

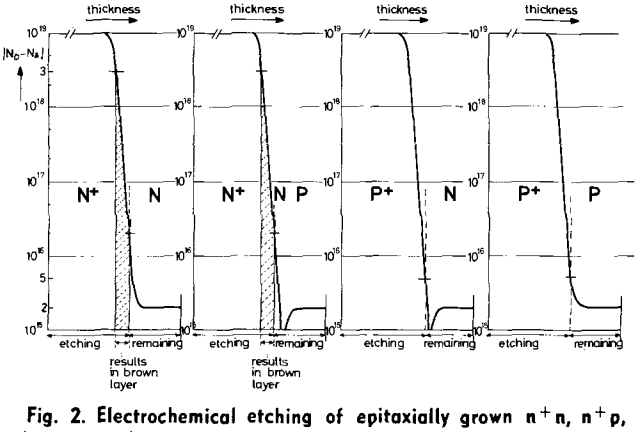

Fig. 2. Electrochemical etching of epitaxially grown n^+n, n^+p, p^+n, and p^+p structures under standard etching conditions as can be expected from the results of homogeneously doped n- and p-type crystals.

ments with homogeneously doped slices, the ranges have been indicated where etching, nonetching, and formation of a dark brown layer can be expected. More detailed considerations should probably take into account the generation and recombination of holes and electrons and their distribution at the silicon surface, combined with the nature of the electrochemical reactions. It is shown below that experiments done with epitaxial slices roughly agree with the indications as sketched in Fig. 1.

n^+n Structures.—Anodic dissolution of the n^+ substrate of an n^+n epitaxial slice resulted in a thin silicon crystal covered with a thin dark brown layer as predicted in Fig. 2. The thickness of this dark brown layer and the smoothness of the silicon under this layer appeared to depend on the slope of the net donor profile. A steep profile resulted in a smooth surface, whereas a gradual profile was characterized by an irregularly etched surface and a thicker brown layer.[1] It can be concluded that, for applications which require a smooth surface, outdiffusion of the n^+ substrate must be reduced as much as possible. Figure 2 predicts that after electrochemical etching of n^+n samples a very thin n-type layer with a higher donor concentration remains. This layer can be removed by chemical etching. This was done with the etchant indicated earlier in this paper. The etchant also appeared to be very suitable for removing the brown layer. There is another reason why chemical etching of the thin n-type layer is advisable. Sirtl etching of cross sections of the n-type crystals (thickness about 10 μm) revealed a high density of etch channels (about $10^8/cm^2$) extending a few microns (0-5 μm) from the "epitaxial" side into the n-type layer.

These channels are similar to those found for homogeneously doped n-type samples but their density was generally higher. They may originate at crystal defects at the epitaxial interface, although x-ray topography and Sirtl etching of cross sections of epitaxial n^+n slices showed no evidence of a poor interface structure. The depth of the channels appeared to increase with the distance from the platinum contact. This is due to the fact that electrochemical etching of epitaxial slices begins at the areas furthest from the platinum strip, so that these areas are longer exposed to the electrolyte.

n^+p.—Epitaxial n^+p slices showed an etching behavior similar to that of n^+n slices. The surface of the remaining thin crystal was covered with a thin dark brown layer. In addition, a thin n-type layer was found on top of the thin p-type crystal as predicted in Fig. 2. The thickness of the dark brown layer, the smoothness of the etched surface, and the thickness of the n-type layer were again found to be dependent on the amount of outdiffusion of the n^+ substrate.[2] Chemical etching was again used to reduce the thickness until a homogeneously doped p-type layer remained. No channels were observed in the p-type layer.

p^+n.—Anodic dissolution of the p^+ substrate in epitaxial p^+n slices resulted in a thin layer with a very irregularly etched surface. No brown layer was observed. Often small parts of the surface were found to be still p-type. There was a strong tendency of the n-type layer to dissolve completely around the platinum contact.

p^+p.—Electrochemical etching of p^+p epitaxial slices was found to give results similar to those of the p^+n slices, an irregularly etched surface, and a strong tendency for the p-type layer to etch completely around the platinum contact. It was not possible to smooth the thin p-type crystals by chemical etching.

The experiments with epitaxial slices show that thin n- and p-type crystals with a smooth surface can be made from epitaxial n^+n and n^+p slices with a rather steep profile. The donor concentration should preferably be higher than 3×10^{18} atoms/cm^3. The etching process stops where the donor concentration is about 2×10^{16} atoms/cm^3. When n^+n slices are used, channels are introduced in the high-resistivity n-type layer during the anodic dissolution of the low-resistivity n^+ substrate, which affects the crystallinity of the epitaxial layer. Chemical etching is necessary to remove that part of the thin epitaxial crystal in which the concentration deviates from that of the rest of the epitaxial layer or the crystal perfection is lower. High demands must be made on the quality of the epitaxial layers. These layers must be uniform in thickness and be homogeneously doped to insure that the variation thickness of the thin layer is small after chemical thinning. The crystal perfection must be high, because we observed that dislocations and stacking faults can result in etch pits and even holes in the thin layer during electrochemical etching. The substrate of the epitaxial slice must be free of striations. Electrochemical etching of substrates with striations often resulted in thin layers covered with substrate remnants arranged in the known striation circles. Most applications require a thin crystal with a smooth surface. For this reason n- and p-type layers made of p^+n and p^+p structures are less suitable for device applications.

Before the electrochemical etching process is carried out, diffusions can be done from the front side of the slice. To guarantee that the electrochemical etching process stops at the epitaxial boundary, a high-resistivity layer between the diffused layer and the substrate must always be present; *i.e.*, the diffusions are done in the top of the epitaxial layer, the rest of the epitaxial layer acts as a barrier against the anodic dissolution of the diffused areas. The quality of this barrier appeared to depend on the combination of its thickness and its free carrier concentration. It can be expected that the critical values of the thickness and the concentration are basically related to the etching mechanism. Thus, injection of holes from the diffused areas into the high-resistivity barrier (1) and avalanche breakdown (punch-through effects) of the depletion layer which is formed in the high-resistivity layer during anodic dissolution of the n^+ substrate promote the anodic attack of this barrier. The critical values of thickness and concentration of the intermediate layer appeared to be less stringent when the diffused area at the front side had been split up in local areas not interconnected by metallic leads; in practice, we used these local diffused areas. The n-type intermediate layer was between 8 and 15 μm, the resistivity ranged from 1 to 20 ohm-cm. The p-type barriers were from 5 to 10 μm, with a resistivity between 1 and 15 ohm-cm.

Applications.—Thin layer devices.—Thin monocrystalline silicon layers on insulating substrates like sapphire have gained much interest during the last few years, mainly because of the possibilities of making lateral devices, *i.e.* devices that are characterized by the presence of vertical junctions only, and which therefore have extremely low capacitances. They are made by diffusing impurities through the thin layer to the insulating substrate. Bonding pads can be made directly on the insulating substrate at places where the silicon layer is selectively removed by etching, thus lowering the metal-to-substrate capacitance. Integrated circuits can be provided with a complete isolation between the building blocks. Downing and Hagon (7) have described several lateral devices and circuits made in thin silicon layers on sapphire. Zuleeg and Knoll (8) made a lateral bipolar npn transistor

[1] This influence of the outdiffusion from the substrate was deduced from etching experiments on n^+n and n^+p slices, which had been subjected to various heat treatments; *i.e.*, $\sqrt{D_{Sb} \cdot t}$ varied from about 2×10^{-5} cm (heat treatment during epitaxy) to 10^{-4} cm. Etching experiments with n^+n type structures, made by diffusion of donors in homogeneously doped n-type samples, did not result in smooth surfaces either.

[2] Same note as footnote 1.

with promising high-frequency characteristics. The monocrystalline silicon layers on insulating substrates can also be used to make deep depletion or "junctionless" FET's in which the conduction of the thin n- or p-type layer itself is modulated by the gate potential. Heiman (9) describes an n^+nn^+ MOST, made in a silicon layer of 0.5-2.0 μm on sapphire. Excellent high-frequency behavior was shown by a Schottky gate FET made on a silicon substrate of 10-50 kohm-cm and a gate width of 1 μm as reported by Drangeid *et al.* (10). Combinations of lateral n^+pn^+ and deep depletion p^+pp^+ may be used in the fabrication of complementary MOS memory systems (11).

Despite the great amount of effort put into the fabrication of monocrystalline layers made by heteroepitaxial techniques, the fundamental electrical and physical parameters of these thin layers are in general inferior to those made by homoepitaxial techniques (Si on Si) (12, 13). The availability of the preferential electrochemical etching process makes it possible to prepare thin silicon layers of high quality of 0.5 μm and more in thickness. We now describe two methods of preparing thin layer devices. Both methods require epitaxial layers of uniform thickness and resistivity and a high crystal perfection.

In the first method, devices are made in a thin silicon layer (0.5-2.0 μm), which has been attached to a polycrystalline silicon substrate with an oxide layer in between (Fig. 3). In the experimental procedure, thermally oxidized slices of the n^+n or n^+p type, with an epitaxial layer of about 10 μm, were used. The thickness of the SiO_2 layer was usually 1 μm, but thicker oxide layers up to 5 μm, preferably made by a low-temperature process, may be used. This oxide layer serves as an insulating layer. On top of this oxide layer, polycrystalline silicon may be grown in an epitaxial reactor by hydrogen reduction of $SiCl_4$ or $SiHCl_3$ at temperatures of about 1000°-1150°C. An alternative method of making polycrystalline substrates which minimizes the total heat treatment is deposition of silicon by evaporation in accordance with the method described by Ploos van Amstel (14). In 5-10 min, layers of up to 300 μm are deposited at a substrate temperature of 900°C.

Electrochemical etching is now used to dissolve the monocrystalline n^+ substrate. The remaining thin monocrystalline layer is subjected to chemical etching to the desired thickness of, *e.g.*, 2 μm, followed by mesa etching as can be seen in Fig. 3. Devices are then made using conventional diffusion and photoetching techniques.

In the second method of making thin layer devices, diffusions are carried out first, followed by electrochemical and chemical etching of the slice to the desired thickness. In the case of junction devices, the horizontal part of the p-n junction is removed, leaving only the vertical p-n junctions with their small area. This method is illustrated in Fig. 4.

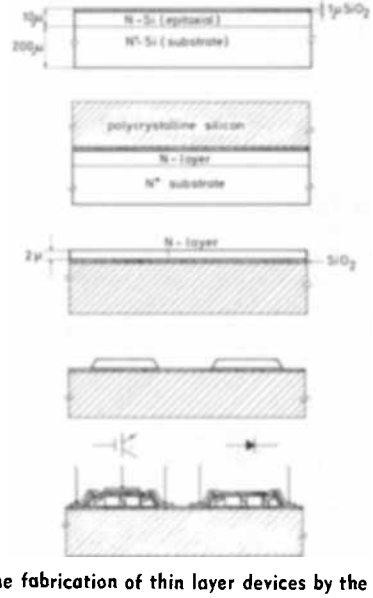

Fig. 3. The fabrication of thin layer devices by the first method

In the experimental procedure, epitaxial slices of the n^+n and n^+p type were used. In the example given in Fig. 4, discrete MOS devices of the p^+np^+ type and the n^+nn^+ type were made. A typical value of source and drain diffusion depth is 3 μm in a 12 μm thick epitaxial layer. After the metallization, grooves were etched in order to divide the thin slice into individual chips later on. The slice containing the MOS devices, each device being surrounded by a groove of 3 μm depth, was affixed "face down" on a temporary carrier (glass plate) by means of a wax. The low-resistivity n^+ silicon was then removed by electrochemical etching. The remaining epitaxial layer is thinned by chemical etching to, *e.g.*, 2 μm. During the last stage of the chemical etching process, the diffusion areas and the grooves were revealed as can be seen in Fig. 5. By the chemical etching process, the slice was divided into chips automatically. We found that the thin chips can be handled quite readily by a vacuum pipette. By means of a polymer (silicone resin), the chip can be attached to a ceramic substrate. Bonding can be performed using conventional thermocompression bonding techniques.

Comparing the two methods of preparing thin layer devices, it should be noted that in both methods the

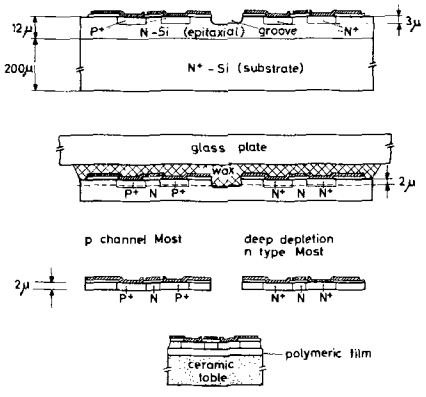

Fig. 4. The fabrication of thin layer devices by the second method.

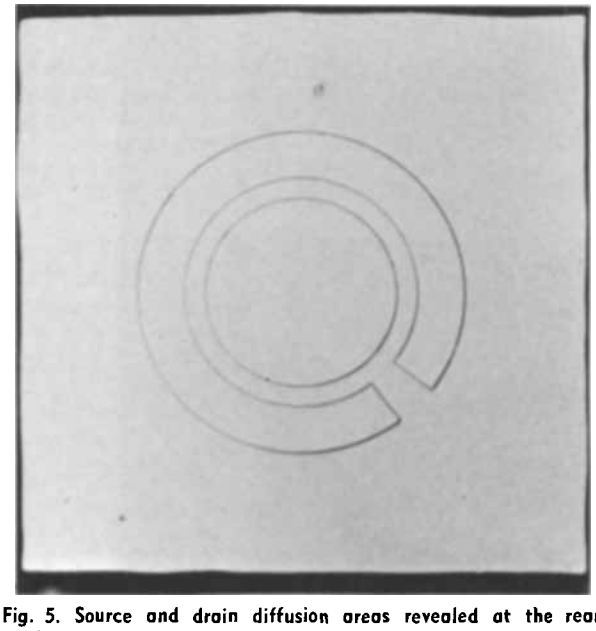

Fig. 5. Source and drain diffusion areas revealed at the rear side of a thin epitaxial crystal after chemical etching. The slice has been divided into chips.

electrochemical etching process was carried out after the epitaxial slices were subjected to high-temperature steps. As mentioned before, outdiffusion of the n^+ substrate can result in surface irregularities which seem to be the most critical in the first method because the diffusion and the photoetching steps are still to be done. Moreover, we found that the first method necessitated careful control of the deposition parameters of the oxide and of the polycrystalline silicon and of further processing; otherwise, warping of the slice (mainly due to the recrystallization of the polycrystalline silicon) would affect the accuracy in photomasking steps. An advantage of the second method is that normal processing can be used for making devices in normal epitaxial slices and, after electrochemical etching, the slice is subjected only to low-temperature steps. Furthermore, measurements of the device parameters before and after the thinning process can be done easily. Passivation of the upper and lower side surface was done by thermal SiO_2 in the first method; in the second method, passivation of the lower side was done by means of a silicone resin. In the first method, bonding pads were made upon the insulating layer (Fig. 3), whereas in the second method, these pads were made upon the thin silicon layer (Fig. 4), thus causing a metal-to-substrate capacitance. However, it is possible to provide the thin chips with beam leads which eliminates this parasitic capacitance.

Both methods were found useful for making thin layer devices. Discrete devices such as diodes, p- and n-channel MOS transistors, as well as deep depletion n^+nn^+ and p^+pp^+ MOS transistors were made.

It was found that the d-c characteristics of the devices made by the two methods were basically the same as for the thick slices. Leakage currents were found to be somewhat higher than the leakage currents of normal diodes. The capacitance reduction was considerable, as can be seen in Fig. 6. In Fig. 7, the d-c characteristics of an n^+nn^+ deep depletion MOST are shown. Deep depletion MOST's of the n^+nn^+ type with a partial gate structure showed a considerably better high-frequency power gain than a conventional n-channel MOST of the same geometry; this improvement is due to low output conductance (15).

The minority-carrier lifetime in the thin silicon layer was determined by the MOS transient response method (16), using p^+pp^+ type deep depletion MOS

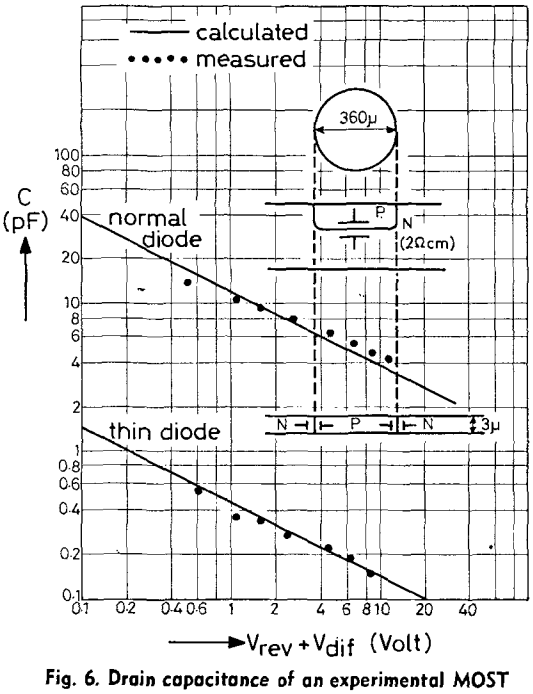

Fig. 6. Drain capacitance of an experimental MOST

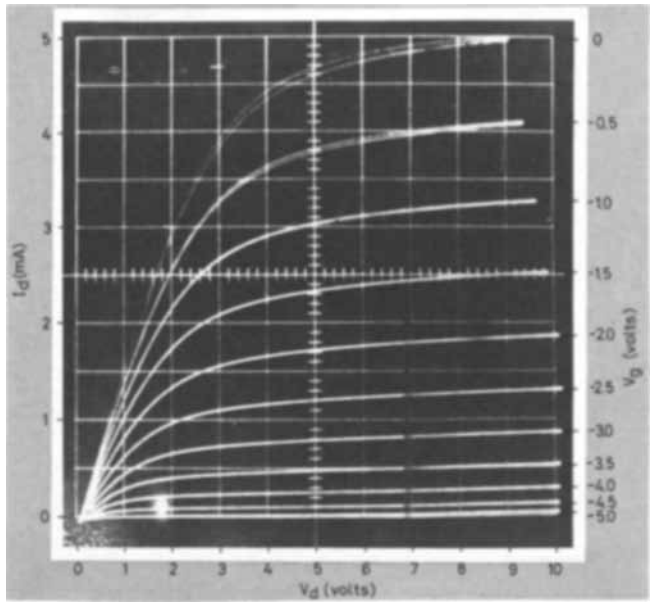

Fig. 7. Typical characteristics of an n^+nn^+ type deep depletion MOST in the depletion mode: $t_{ox} \approx 2000$Å; $t_{Si} \approx 2.5$ μm; $\rho_{Si} = 10$ ohm-cm and $W/L = 60$. (Note: In equilibrium, the maximum depletion region depth for 10 ohm-cm is about 1 μm but, due to the fact that the gate is pulsed (100 Hz), equilibrium is not reached; no inversion is built up at the oxide-silicon interface.)

transistors. The time constant, T, for a 2.5 μm thick p-type layer ($N_A = 1.6 \times 10^{15}$ acc/cm^3) was about 48 μsec, giving a lifetime τ of about 0.2 μsec. This value is quite normal for epitaxially grown silicon after processing.

Isolation techniques in integrated circuits.—The p-n isolation which is widely used does not give complete isolation. The main drawbacks are the substrate leakage and capacitance effects on the components and circuit operation. The desirability of a better isolation has resulted in several developments. The best known are the dielectric isolation process and the air gap isolation process. In the following we show that preferential electrochemical etching can advantageously be used in these processes.

Oxide isolation.—A description of this well-known technique is given in (17). A critical step in this process is lapping and etching just to the upper level of the oxide walls. Figure 8 illustrates the use made of the principle that, during preferential electrochemical etching of n^+n epitaxial slices, dissolution automatically stops at the n^+n interface. In the experimental procedure, epitaxial slices of the n^+n type with an epitaxial layer of 15 μm were used. Buried layers were made by diffusion in top of the epilayer, followed by etching of the isolation grooves which have to surround the active areas. These grooves were

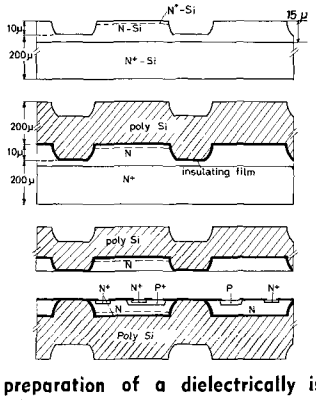

Fig. 8. The preparation of a dielectrically isolated structure starting from an n^+n slice.

etched in the n-type layer in such a way that, between the bottom of the grooves and the n^+n-interface, a high resistivity layer of about 5 μm remains. In order to accomplish this over a whole slice, epitaxial n^+n slices with well-defined and uniform layer thickness were needed. Thermal oxidation and deposition of the polycrystalline substrate have been described before.

Electrochemical dissolution of the n^+ monocrystalline substrate, followed by chemical etching of the n-type layer, reveals the top of the oxide walls of the isolation pattern. Chemical etching must be stopped at the right moment to prevent etching of the oxide and the underlying polycrystalline substrate. If chemically inert layers such as silicon nitride or aluminum oxide are used instead of silicon oxide, this problem is much less severe.

Figure 9 shows a cross section of an oxide isolated structure with diffused areas made by the preferential etching technique. Measurements done on such structures gave a resistivity of the polycrystalline silicon at 20°C of 5-10 x 10^5 ohm-cm, which is reduced to 2-4 x 10^4 ohm-cm at 100°C. Breakdown voltage of 1 μm SiO_2 > 1000V, leakage current <10 nA/cm^2 at 5V d.c., and a capacitance of 3000 pF/cm^2.

Beam lead air-gap isolation.—Beam lead air-gap isolated microcircuits were described by Lepselter *et al.* (18). Instead of diffused junctions, air gaps are used for electrical isolation of active areas. These areas are discrete silicon islands which contain the active devices. They are interconnected electrically and mechanically by metallic beams. In the fabrication of the air-gap isolated circuits, there are two important process steps in which etching can play an important role: first, the thinning of the slices from 200 to about 20 μm, usually done by chemical etching or lapping; second, the etching of the isolating air gaps. For this critical step, Rosvold *et al.* (19) used a low-temperature oxide for masking and alignment from the back of the slice of the air-gap pattern followed by anisotropic etching in KOH.

Preferential electrochemical etching can be used to reduce the slice thickness to, *e.g.*, 20 μm or even less. If buried layers are needed, multilayer structures like $n^+_{subst}nn^+n$ or n^+pn^+n can be used. Electrochemical etching may, however, be used for both etching steps. We found that the reduction of the thickness and the etching of the air gaps can be done simultaneously when a procedure is used as indicated in Fig. 10. In an epitaxial n^+n-type slice, n^+ isolation diffusions were done through the n-type layer up to the n^+ substrate. In the n-type "island" of high resistivity, devices were made and interconnected by etch-resistant metallization strips. Electrochemical etching resulted in an air-gap isolated circuit provided with beam leads. Figure

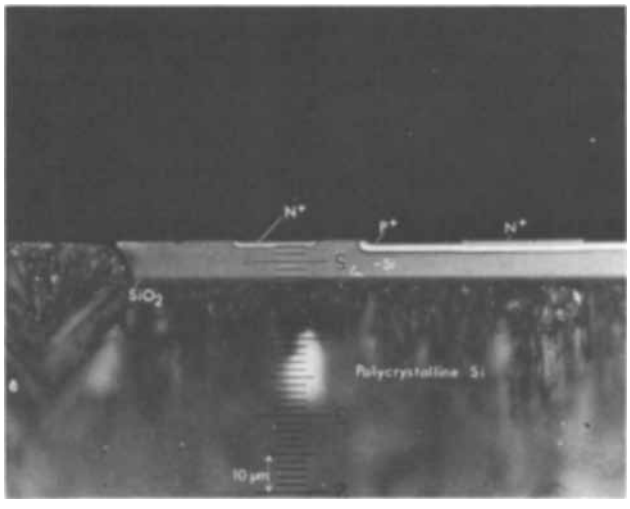

Fig. 9. A cross section of a dielectrically isolated structure

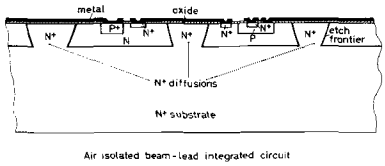

Air isolated beam-lead integrated circuit

Fig. 10. Air-gap isolated beam lead integrated circuit

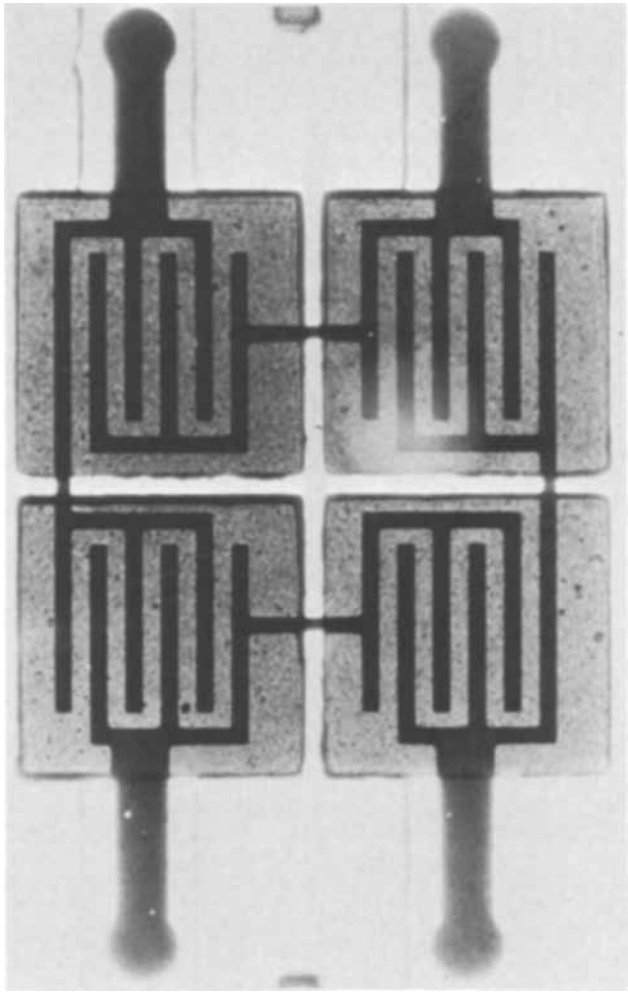

Fig. 11. A diode circuit, made using anodic dissolution of the n^+ substrate and the n^+ isolation diffusions, in transmitted light.

11 shows a simple diode circuit interconnected by thin aluminum leads. In the given example, aluminum oxide was used at those places where protection of the aluminum metal against the hydrofluoric acid was needed, *i.e.* under the air-gap interconnections and the beam leads. The width of the air gaps is defined by the width of the n^+ diffusions between the n-type "islands." It will be clear that in the case of thick epitaxial layers the lateral n^+ diffusion is considerable, thus causing the air gaps to be relatively wide. It may be added that the diodes can be made as lateral thin layer diodes by reducing the thickness of the n-type islands by chemical etching, followed by passivation of the p-n junctions.

Conclusions

Preferential electrochemical etching can be applied successfully in silicon device technology. The reduction of the thickness can be done easily and reproducibly, provided epitaxially grown slices of the n^+n and n^+p type are used as starting material for device fabrication; p^+n and p^+p are less favorable. Using standard etching conditions ($V_{anode\text{-}cathode}$ = 10V, 5% aqueous HF, bath temperature 18°C, dark), the sub-

strate concentration must be higher than 3 x 10^{18} donors/cm^3 in order to obtain completely controllable results. The etching process stops at the place where the donor concentration is about 2 x 10^{16} atoms/cm^3, but n^+n slices show channels in the high-resistivity n-type layer. The outdiffusion from the n^+ substrate must be reduced as much as possible; striations and crystal imperfections must be avoided. The electrochemical etching process has to be followed by a chemical etching process to obtain a thin homogeneously doped crystal of high perfection. The electrochemical etching process in combination with chemical etching allows the fabrication of thin layer devices with highly reduced capacitances and junctionless deep depletion devices in monocrystalline silicon of high quality. The diffusions in the epitaxial layer are not attacked during electrochemical etching if an intermediate high-resistivity layer of sufficient thickness is present; deeply diffused n^+ areas can be etched away together with the n^+ substrate. The latter has been used to prepare beam lead air-gap isolated structures.

Acknowledgments

The authors wish to thank E. Kooi and H. J. A. van Dijk for their stimulating discussions, and those persons of the Semiconductor Device Group who have contributed to this work.

Manuscript submitted Dec. 1, 1969; revised manuscript received March 13, 1970. This was Paper RN 341 presented at the New York Meeting of the Society, May 4-9, 1969.

Any discussion of this paper will appear in a Discussion Section to be published in the June 1971 JOURNAL.

REFERENCES

1. P. J. Holmes, "The Electrochemistry of Semiconductors," p. 177, Academic Press, London (1962).
2. R. Memming and G. Schwandt, *Surface Science*, **4**, 109 (1966).
3. H. van Dijk, *This Journal*, **117**, 553 (1970).
4. E. Sirtl and A. Adler, *Z. Metallk.*, **52**, 529 (1961).
5. R. M. Burger and R. P. Donovan, Editors, "Fundamentals of Silicon Integrated Device Technology," Vol. I, pp. 311 and 429, Prentice Hall, Englewood Cliffs, N. J. (1967).
6. K. H. Beckmann, *Surface Science*, **3**, 314 (1965).
7. W. Downing and P. J. Hagon, Report Autonetics X6-2044/501.
8. R. Zuleeg and P. Knoll, *Electronics Letters*, **3**, 4, 137 (1967).
9. F. P. Heiman, *IEEE Trans.*, **ED-13**, 12, 855 (1967).
10. K. E. Drangeid *et al.*, *Electronics Letters*, **4**, 17, 362 (1968).
11. J. F. Allison, *et al.*, *IEEE J. Solid State Circuits*, v. SC-2, **4**, 208 (1967).
12. H. Schlötterer, *Solid-State Electron.*, **10**, 947 (1968).
13. G. W. Cullen, G. E. Gottlieb, C. C. Wang, and K. H. Zaininger, *This Journal*, **116**, 1444 (1969).
14. J. J. A. Ploos van Amstel, *Philips Tech. Rev.*, **28**, 2, 57 (1967).
15. J. A. Appels, J. A. van Nielen, and M. J. J. Theunissen, Paper presented at IEEE "Semiconductor Device Research" Meeting, Munich, March 24-27, 1969. To be published in *Philips Tech. Rev.*
16. F. P. Heiman, *IEEE Trans.*, **ED-14**, 781 (1967).
17. "Integrated Circuit Engineering-Basic Technology" by Madland *et al.*, (ICEC) p. 64, Boston Technical Publishers Inc. (1966).
18. M. P. Lepselter, *Bell. System Tech. J.*, **45**, 23 (1966).
19. W. C. Rosvold, W. H. Legat, and R. L. Holden, *IEEE Trans.*, **ED-15**, 640 (1968).

Corrosion Problems in Decorative Chromium Plating

G. Kubach

Robert Bosch GmbH, Stuttgart, Germany

ABSTRACT

Microcracked chromium is by far more resistant to corrosion than crack-free chromium, especially if the work-piece is mechanically stressed. Corrosion with microcracked chromium penetrates bright nickel quite uniformly but it may soon reach the basis metal, provided no barricade like copper or semibright nickel is underlaid. Finally, corrosion pits increase to such a dimension that the surface is no longer decorative. Some correlations between the great loss of appearance and the nature of the underlying metal systems are described.

In an earlier series of experiments on the corrosion-preventive action of various decorative nickel-chromium coatings, we had found that microcracked chromium possessed a number of advantages over other types of chromium (*e.g.*, crack-free), but that a number of questions had still to be answered. The most important of these were the following:

Is the outstandingly good corrosion resistance of mechanically stressed nickel plated with microcracked chromium due to the lack of cracks in the nickel? Or, on the other hand, is it that cracking of the nickel is not harmful when microcracked chromium is present?

According to Völkel (1), bright nickel plated with microcracked chromium, with a crack density of 400-700 cracks/cm, is corroded to a depth of 1-3 μm in the first year of use.

However, we have observed corrosion of the basis metal, after only a few months' outdoor exposure, in steel parts coated with nickel to a thickness of 15 μm and with microcracked chromium according to specification.

Samples coated with microcracked chromium often appear very unattractive after long outdoor exposure, and we wished to establish how far this depended on the nature and thickness of the metal layer(s) under the chromium.

Mechanical stressing on nickel-chromium coatings.— To reproduce in static outdoor exposure the stress which occurs in automotive applications, we have introduced a method of treating chromium-plated samples with impacts prior to exposing them on the test stand. Test-pieces prepared in this way, with various nickel-chromium coatings, have been exposed to the very severe industrial atmosphere of Essen (Ruhr) for 19 months and then examined. Figures 1(a-d) show the damaged areas, slightly enlarged. It is readily seen that microcracked chromium performed much better than crack-free chromium. In Fig. 1(a) (crack-free chromium on bright nickel), it is clearly evident that of the many concentric cracks produced by the blow both the inner- and the outermost are more corroded than the others. This emphasizes the role of

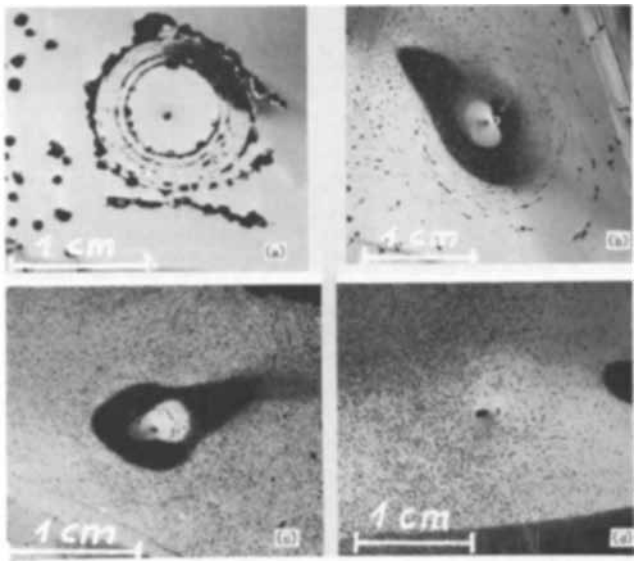

Fig. 1. Impact spots after corrosion: (a) c. 12 μm bright nickel, crack-free chromium; (b) c. 28 μm duplex nickel, crack-free chromium; (c) c. 16 μm bright nickel, microcracked chromium; (d) c. 25 μm duplex nickel, microcracked chromium.

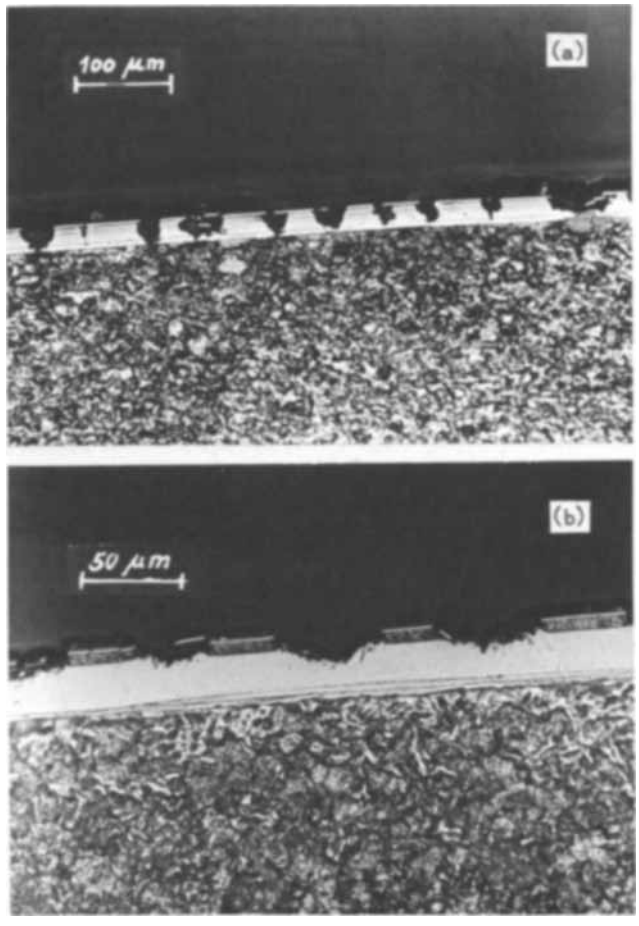

Fig. 2. Cross sections—corrosion on impact spots: (a) bright nickel, crack-free chromium; (b) duplex-nickel, crack-free chromium.

cathodic control of nickel corrosion in contact with chromium. Adjoining both these cracks there is a large unbroken area of chromium, so that these cracks have a larger cathodic area than the others.

The next two pictures [Fig. 2(a) and (b)] show sections of the samples with crack-free chromium. It is clear that in contrast to the bright nickel, which was penetrated completely by cracks, the duplex nickel system has resisted complete penetration of the cracks and has subsequently very effectively prevented penetration of the corrosion in depth. Obviously, however, the thin copper layer (about 3 μm) applied as first coating in all the test pieces with bright nickel has also considerably protected the basis metal.

These results are really only what was to be expected. It must still be asked, however, why microcracked chromium protects so well against corrosion, particularly mechanically stressed samples. Nohse (2) pointed out that damage to a microcracked chromium coating does not alter the ratio of the electrode areas, and hence also does not affect the corrosion behavior. Völkel (1), on the other hand, expected that in a microcracked chromium coating "the internal stresses should be so relaxed that no further cracks should occur in transport service, which would be propagated through the bright nickel layer beneath." Various experiments have already been made on the effect of bending of nickel-chromium coatings, and gave the fairly unanimous result that the tendency of bright nickel to crack is less under microcracked chromium than under normal chromium (3-5). We investigated the effect of individual impacts on the surface of a chromium coating. For this purpose, we plated plane panels, 10 x 5 cm, on one side with the following sequences of coatings:

1. 16 μm bright nickel, crack-free chromium.
2. 32 μm bright nickel, crack-free chromium.
3. 26 μm semibright nickel, 8 μm bright nickel, crack-free chromium.
4. 16 μm semibright nickel, 16 μm bright nickel, crack-free chromium.
5. As 3, but with fresh electrolyte for the semibright nickel.
6. 16 μm bright nickel only.
7. 16 μm bright nickel, microcracked chromium.

Masks were used in deposition, so that coatings of very uniform thickness were produced (±2 μm nickel). The plates were then laid, coated side up, in a simple holder and impact bodies of various masses, with a radius of about 3 mm at the point of impact, were dropped onto them from different heights. The support had a hole of 10 mm diameter in the middle, so that the samples could be bent by the blow.

Microscopic examination of the impact regions of the surface showed that, in all test pieces with crack-free chromium, concentric cracks had formed round the point of impact even when the blow was comparatively light. There was not a clear difference between bright nickel and duplex-nickel. The samples coated with bright nickel, but not chromium plated, remained free from cracks even after the strongest blows. The surfaces of the samples with microcracked chromium remained almost unchanged, but under the strongest blows (65g/60 cm or more), single cracks could clearly be seen widened at the areas of greatest deformation.

Sections of the impact regions then were prepared and examined under the microscope; the results are shown in Table I. It can be seen that all the chromium-plated bright nickel coatings, including those under microcracked chromium, have cracked in varying degrees. In particular, one can conclude that a somewhat heavier impact is necessary to crack through a thick bright nickel coating than through a thin one; and it is also clear that duplex-nickel tends to prevent cracking through to the basis metal, the more so the greater its portion of semibright nickel. Fresh electrolyte of the semibright nickel obviously produces better properties in this respect than old electrolyte.

Because bright nickel cracks under microcracked chromium even by impacts too weak to have produced any visible surface change (*see* above), it must be

Table I. Behavior of nickel(-chromium) coatings by impact (evaluation of sections, 1st experiment)

Impact Mass, g	Height, cm	No. of cracks[a] in test piece No.: 1	2	3	4	5	6	7
45	20	8	0	4/0	A few/0	0	0	2
45	40	21	0	25/0	16/0	0	0	0
45	60	43	24	20/0	8	0	0	20
65	60	39	27	50/0	5	20/0	0	33
85	60	115	46	8	34	30/0	0	~40
105	60	—	70	19	20	Many/3	0	~50

[a] Where two numbers are given, the first is the number of cracks which penetrated only the bright nickel, and the second is the number of cracks which penetrated through to the basis metal. A single number shows the cracks which penetrated through to the basis metal.

Table II. Behavior of nickel-chromium coatings by impact (evaluation of sections, 2nd experiment)

Kind of coating	Ni b	Ni b	Cr f	Ni b sample 1a	Cr m sample 1b	Ni b sample 2a	Cr m sample 2b
Thickness of Ni (μm)	17-19	14.3-18		17.6-22	15.8-20	20-22	15.6-18
Thickness of Cr (μm)		ca. 1		ca. 2.5	3.2	Not measured	
Chromium cracks/cm	—	—		480-640	540-600	640-820	580-800

No. of cracks through to basis metal caused by impact

Mass (g)	Height of fall (cm)						
25	20	0	0	0	0	0	0
25	40	0	0	—	—	—	—
25	60	0	8	2	0	0	2
45	40	0	34	11	3	4	1
65	40	0	96	2	3	18	31
85	20	0	20	3	—	—	—
85	50	0	—	10	10	31	41
105	60	0	—	—	10	19	30

Symbols: Ni b = brick nickel.
Cr f = crack-free chromium.
Cr m = microcracked chromium.

assumed that stress cracks are particularly easily produced at the small notches of microcracked chromium.

To check the somewhat surprising result obtained with microcracked chromium, we made further experiments of the same type. The evaluation of the sections is shown in Table II. It can be seen that the results of the first experiment are largely confirmed.

In these sections, the microcracked chromium coatings showed, besides the cracks through to the basis metal, a relatively large number of cracks which had only very slightly penetrated into the nickel, but more so in the samples marked 1 than in the samples marked 2. The network of cracks in test piece 2 was, however, not as uniform as in 1, and consisted of a large number of small cracks and fewer large cracks. It may be concluded perhaps that, with nonuniform cracks, the fine ones are hardly affected by impact, but that the large ones, on the other hand, crack almost immediately through to the basis metal under the bright nickel. With a uniform crack network, however, the impact would be better distributed over all the cracks, so that many would be propagated into the bright nickel, but only a few penetrate to the semibright nickel or substrate surface.

Both experiments agree in showing that, even with microcracked chromium, impacts produce cracks through the bright nickel but not to the same extent as with crack-free chromium. This slightly greater crack resistance is not sufficient to explain the much better corrosion resistance of microcracked chromium. This latter property is due to the ratio of the cathode and anode area and that ratio, and therefore the corrosion rate, remains unaltered when the nickel cracks. If the crack penetrates to the basis metal, however, corrosion of the latter begins at once, and proceeds, according to Flint (5), preferentially.

Hence, even with microcracked chromium, duplex-nickel is advantageous for less noble metal substrates since the ductile semibright nickel cracks to the basis metal only after very strong impact. Other samples were not deformed by single impacts before exposure to corrosion, but were treated with falling sand. Corrosion of such test pieces with microcracked chromium was practically unaffected. With crack-free chromium on duplex-nickel, however (*see* Fig. 3), well-developed corrosion is seen only in the isolated pores in the outer sand-treated zone. In the center of this zone, however, where the pores are numerous, a corrosion picture very similar to that of microcracked chromium was produced. It thus seems possible, in principle, to transform crack-free or other chromium into microcracked by treatment with falling sand. This, however, is presumably effective only if duplex-nickel (copper-nickel?) is used. With bright nickel only, there is a considerable danger that a few large cracks will penetrate through to the basis metal and cause considerable corrosion. This did actually occur in all our test pieces of this type.

Corrosion mechanism in microcracked chromium.— In some experiments, steel parts coated with 6-8 μm bright nickel and microcracked chromium were covered with a thick layer of red rust after only a few months' outdoor exposure. Samples with a thin copper underlayer showed no rusting. This led to tests to determine if the corrosion of steel could be prevented, and if so to what extent, by intermediate layers of copper (or semibright nickel).

These tests (outdoor exposure) are still in progress, but we already can say that fairly thin layers of this type do, in fact, clearly retard the corrosion of steel. Formerly this has been reported for copper underlayers by Turner (6) and by Claus and Klein (7). Intermediate observations on the test pieces in this series of experiments led us to formulate a new hypothesis on the mechanism of corrosion in microcracked chromium.

Earlier microscopic examination of the surface of samples plated with microcracked chromium had shown that after long outdoor exposure there developed, on the one hand, heavily-corroded zones, often with areas in which the chromium had completely broken away, and also other regions in which, although the crack network was clearly recognizable, the individual cracks were almost uncorroded. The same observation has already been reported by Völkel (1).

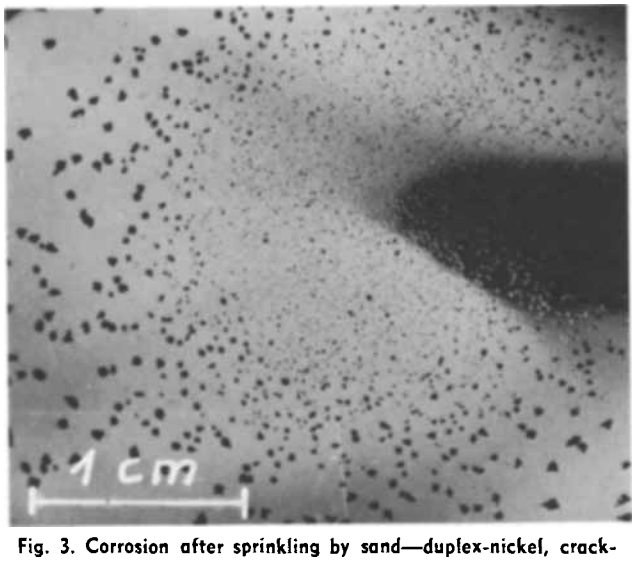

Fig. 3. Corrosion after sprinkling by sand—duplex-nickel, crack-free chromium.

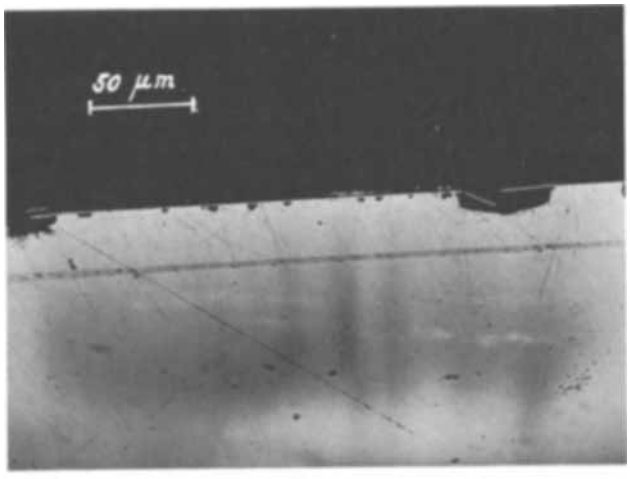

Fig. 4. Section—corrosion on microcracked chromium

Corrosion obviously does not penetrate uniformly into the nickel in these cases.

Now we prepared 5 sections of the above mentioned series, and on all samples between larger corrosion sites of various sizes we found very small ones, at which under the chromium crack only very little nickel had been corroded (Fig. 4). A quantitative evaluation of the sections for number and sizes of corrosion sites showed the following (*see* Table III). The fact that about 60% of all the corrosion sites, with good agreement among the 5 test pieces, were of the small, slightly corroded type leads us to suppose that their formation is particularly favored. It is, however, unlikely that corrosion at all these spots should have begun shortly before inspection. How are we to explain this large number of scarcely corroded cracks?

Raub (8) assumed that the fine cracks in microcracked chromium could be blocked by the corrosion products, and that the corrosion process in general was controlled by the high resistance of the electrolyte and by the resistance of the corrosion products in the narrow cracks. The other view, however, which is fairly generally accepted, is that the corrosion of nickel in contact with chromium is cathodically controlled. According to this view, the very small corrosion rate at each crack is due to the very small area of chromium available to function as cathode at each individual crack, or, in other words, because the anode surface (nickel) is large in proportion to the cathode surface (chromium) (9). We assume that this second mechanism does in fact obtain in principle, but that in microregions the corrosion can indeed be influenced by blocking the cracks, perhaps in the following way.

Corrosion begins at once at all microcracks which have penetrated to the nickel, but proceeds very slowly, because the small cathode area provided for each crack does not permit a high corrosion current. The cracks are very narrow, so that a crack easily can be blocked by the products of nickel corrosion. The electrolyte resistance rises and corrosion is retarded, or possibly completely inhibited.

The available cathodic surface for the neighboring cracks is correspondingly increased, and corrosion of these cracks will be accelerated if the resistance is small enough. At such sites, the underlying metal can be reached quickly. The small corrosion sites, however, which we found in such large numbers in the sections, are, on this basis, permanently blocked by corrosion products at an early stage. The fact that zones of strong corrosion are frequently found adjacent to almost corrosion-free areas can be explained on the assumption that, in regions where many cracks are blocked, the nickel in the few remaining cracks corrodes so strongly that larger areas of the coating are removed by the pressure of the corrosion products. This could be particularly true when the corrosion has penetrated to the basis metal. Figures 1(c) and (d) show that corrosion indeed can be completely inhibited by blocking or closing of the microcracks: The complete absence of corrosion in the center of the impact area is presumably due to pressing together the walls of microcracks at this point by the impact.

Table III. Corrosion sites after outdoor exposure

Part No.	Length of section (cm)	Total No. of corrosion sites	Small corrosion sites No.	Small corrosion sites % of total
B 90	2.25	648	391	60.5
B 92	2.05	526	296	56
B 94	2.22	604	376	62
B 96	1.82	356	188	53
B 98	1.82	534	338	63.5

The corrosion sites, which are very numerous, are statistically distributed over the surface and, if corrosion is not too far advanced, too small to be seen with the naked eye. Hence, corrosion through cracks in microcracked chromium can remain unnoticed for a long time and appear quite uniform but, in fact, it does not proceed uniformly in depth. Uniform penetration could be secured if it were possible to make corrosion proceed without hindrance in all cracks.

Turner (7), however, has established that the appearance of microcracked chromium is often considerably impaired after static outdoor exposure, but hardly after service. This can be explained in the following way.

In service, the chromium is continually subjected to impacts of sand, stones, *etc.*, causing formerly closed cracks to be reopened, and perhaps some open cracks may be closed. This should lead to a more uniform penetration in depth of corrosion of microcracked chromium in automotive service than in static corrosion testing. It is also possible that cracks which originally did not reach the nickel will completely penetrate, which would also increase the uniformity of corrosion.

Thus, the good corrosion preventive properties of microcracked chromium will be fully effective only under the mechanical stresses which occur in service.

Preservation of the decorative appearance; comparison of steel and brass substrates.—As mentioned, the decorative appearance of microcracked chromium is more or less impaired by long exposure to corrosive conditions, because the corrosion sites become visible to the naked eye. A further series of experiments showed correlations between this loss of decorative appearance and the nature and thickness of the layers under the chromium. The materials examined included bright nickel of various thicknesses, duplex-nickel, and a combination first suggested, as far as we know, by Rittner (10): a layer of bright nickel with a thin film of semibright nickel on top, which could be described as "inverted duplex-nickel." The basis metals used in our experiments were steel and brass. As usual in our laboratory, the microcracked chromium was applied as double-chromium with 400-600 cracks/cm.

After 16 months' outdoor exposure in Essen, differences between the various test pieces could be seen clearly. Results for the steel samples are shown in Table IV (not cleaned before examination). The uncleaned brass parts showed, on principle, the same appearance, except that the corrosion products naturally were much less conspicuous.

All the brass samples could easily be cleaned. Some of the steel parts gave difficulty in this respect, so that nitric acid had to be used. After cleaning, the parts could be ranked with respect to the remaining decorative effect, which was considerably different from the order of merit of the uncleaned ones. Figures 5(a-e) show the brass parts. It can be seen that the thinnest bright nickel and the "inverted duplex-nickel" still look best, while thicker bright nickel looks worse and

Table IV. Corrosion of steel parts

No.	Type of coating	Appearance
A22	7 μm Ni b	Completely covered with heavy red-brown rust
A58	18 μm Ni b	Covered with a thin yellow-brown rust layer
A94	30 μm Ni b	Nickel corrosion and thin rust film
A118	23 μm Ni d	Nickel corrosion, hardly any rusting
A143	10 μm Ni b with 6 μm Ni p on top	Nickel corrosion, extensive rusting on single sites

Symbols: Ni b = bright nickel.
Ni d = duplex nickel.
Ni p = semibright nickel.

the normal duplex-nickel is even poorer, although this had the best appearance before cleaning.

The appearance of the steel parts was about the same, but with one marked difference [Fig. 6(a-e)]: the test piece with 7 μm bright nickel had a very poor appearance. However, in the regions of this sample in which corrosion had not produced too large a corrosion site, the surface is still largely intact.

These results are in accord with the valid theories on the process of corrosion in multilayer systems, which therefore need not be repeated in detail here. The impairment of the decorative effect of a microcracked chromium coating with time, is however, obviously determined by two factors:

1. The thickness of the topmost nickel layer. This determines the size of the corrosion sites when the next metal is reached.

2. The nature of the next layer, *i.e.* whether more or less noble than the nickel. If the top layer is less noble, the corrosion of the nickel layer proceeds more rapidly, inevitably sideways, the corrosion sites become larger and in the end clearly visible, but the next metal remains effectively protected. This is known to be the case with duplex-nickel. If, however, the next layer is less noble, it is preferentially attacked and the nickel layer above with its comparatively small corrosion sites remains largely intact. The decorative effect is impaired only when the corrosion of the next

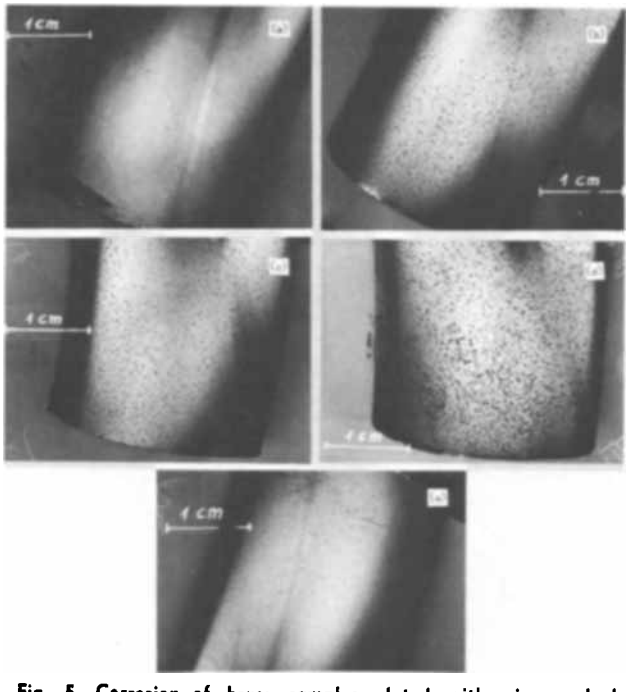

Fig. 5. Corrosion of brass samples plated with microcracked chromium over: (a) 7 μm bright nickel, (b) 18 μm bright nickel, (c) 30 μm bright nickel, (d) 23 μm duplex nickel, (e) 16 μm inverted duplex-nickel.

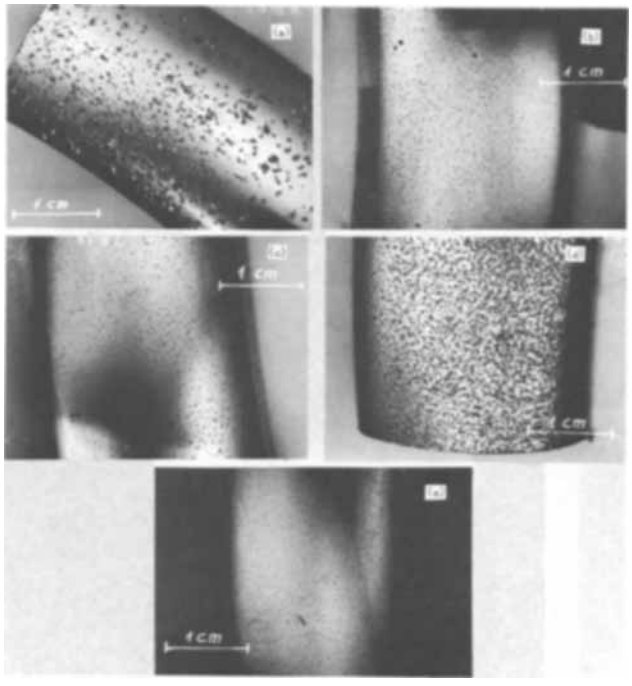

Fig. 6. Corrosion of steel samples plated with microcracked chromium over: (a) 7 μm bright nickel, (b) 18 μm bright nickel, (c) 30 μm bright nickel, (d) 23 μm duplex nickel, (e) 16 μm inverted duplex nickel.

or a subsequent layer is so strong that parts of the nickel layer are removed by the pressure of the corrosion products. This mechanical removal of the layer by the corrosion products seems hardly to occur with inverted duplex nickel as long as only the bright nickel is corroding, but to proceed rapidly when a very reactive basis metal, *e.g.* steel, is reached. Thus, a noble layer, such as semibright nickel or copper, should first be deposited on an iron substrate.

Brass as basis metal for microporous chromium plating.—The series of experiments discussed in the foregoing section confirm the finding of Seyb (11) that, with a brass substrate, even fairly thin bright nickel layers under microcracked chromium produce very good corrosion behavior. We have conducted further tests on this point.

Evaluation of polished sections.—We prepared two polished sections of each of the brass samples in the above series of tests and examined them for the number of corrosion sites, depth of penetration, and corroded surface area. The results are shown in Table V.

The fact that the number of corrosion sites penetrating to the substrate metal was smallest with duplex nickel, but very large with thin bright nickel and inverted duplex-nickel, was to be expected from

Table V. Corrosion of brass parts

Type of coating	Corrosion sites per cm Total	Corrosion sites per cm Penetrated to substrate	Corrosion sites penetrated to substrate (%)	Bright nickel corrosion per cm² section (10^{-2} mm²)
8 μm Ni b	180	56	31	3.1
6 μm Ni b	286	117	41	2.9
20 μm Ni b	175	13	7.5	3.7
18 μm Ni b	141	16	11.3	3.8
39 μm Ni b	200	1 (?)	<0.5	4.3
31 μm Ni b	168	1	0.6	4.6
31 μm Ni d	180	0	0	4.2
21 μm Ni d	150	0	0	7.0
21 μm Ni id	170	32	19	3.6
15 μm Ni id	265	84	32	3.6

Symbols: Ni b = bright nickel.
Ni d = duplex nickel.
Ni id = inverted duplex nickel.

the appearance of the test pieces. The extent of the corroded nickel in the sections (last column) shows a clear dependence on the structure of the coating; bright nickel was the most strongly corroded in the case of duplex nickel. This, again, was to be expected. The other test pieces, in which bright nickel was in direct contact with brass, showed less corrosion of the bright nickel; while more corrosion of the brass had occurred. Thus, under the conditions existing, brass behaved anodically toward bright nickel.

Contact corrosion of bright nickel and brass.—A brass plate of 42 cm^2 surface area was placed in a simple electrolytic cell, together with an electrolytically prepared bright nickel plate of the same size, and with a 1 ohm resistance in the circuit. As electrolyte, we used the solution prescribed for the acetic acid salt spray test (ASTM B 287-62): 5% aqueous NaCl, brought to a pH of 3.2 with CH_3COOH.

The quantities passing into solution in this cell in 7½ hr were:

22.5 mg Cu

13.3 mg Zn

4.3 mg Ni

It can be seen from the analysis that the brass plate was preferentially attacked, and that Cu and Zn dissolved in exactly the same ratio as that in which they were present in the brass.

In another experiment (brass and nickel in separate solutions of the above-described composition, without current), the quantities dissolved, under otherwise identical conditions, in 16 hr were:

3.25 mg Cu and 2.1 mg Zn

8.8 mg Ni

Further, the curves of current density against potential for bright nickel and brass in the neighborhood of the rest potential were plotted potentiostatically in the above solution. The size of the electrodes was 7 x 4.8 cm^2. The curves are shown in Fig. 7. The mixed potential against a saturated calomel electrode is −273 mV. Brass is the local anode; the corrosion current density is 9.2 mA/dm^2.

Analysis of the corrosion products.—The corrosion products deposited on the brass rings in the series of experiments last described were examined polarographically. For this purpose, they were dissolved from 4 cm^2 of the surface with 1N HNO_3; the time required for this was 1.5 min. This dissolution was carried out as many as 5 times on the same area, but from the 3rd dissolution onward only little nickel was removed. Table VI shows the result. The last column is particularly interesting. It can be seen that in no instance were copper and zinc found in the ratio of 63:37, corresponding to the composition of the brass; a greater proportion of zinc was always found. Further, this

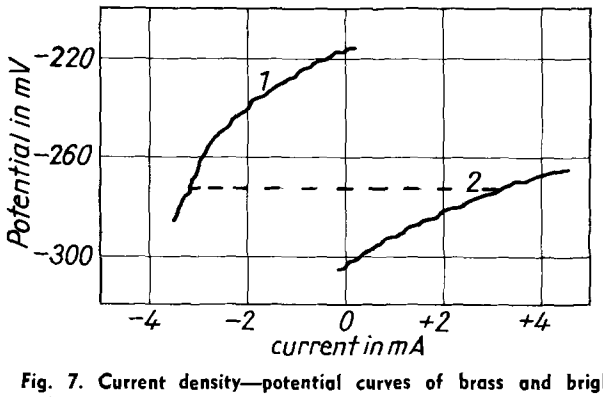

Fig. 7. Current density—potential curves of brass and bright nickel.

Table VI. Analysis of the corrosion products of chromium-plated brass rings

Type of coating		% Nickel	% Copper	% Zinc	Ratio Zn/Cu
7 μm Ni b	Cr m	48-73	0-15	19-41	c. 2.6
18 μm Ni b	Cr m	94-96	0.7-1.2	3.5-4.0	c. 4
30 μm Ni b	Cr m	95-96.5	0.8-1.1	2.4-4.1	c. 3.2
23 μm Ni d	Cr m	94.5-96.5	0.8-1.0	2.8-4.4	c. 4
16 μm Ni id	Cr m	67-83	2.6-9.2	14-24	c. 3.3
7 μm Ni b	Cr f	23	37	40	1.1

Symbols: Ni b = bright nickel.
Ni d = duplex-nickel.
Ni id = inverted duplex-nickel.
Cr m = microcracked chromium.
Cr f = crack-free chromium.

excess of zinc was more pronounced with microcracked chromium than with crack-free chromium.

Investigation with the electron microprobe.—The investigations described led to the supposition that, in the contact corrosion of brass and nickel, the brass normally corrodes as a single substance but, in the presence of narrow cracks, and particularly in corrosion under microcracked chromium, the brass is de-zinc-ed. (The possibility of the corrosion products of copper being more easily washed away than those of zinc, which could have led to the same analytical results, may be ruled out on the basis of the solubilities of the salts concerned.)

To test more closely the question of zinc removal, we investigated sections of corrosion sites by the electron microprobe in brass under microcracked chromium. Figure 8 shows the result and, in fact, a zinc deficit is clearly apparent at the bottom of the corrosion pores in the brass, but with practically no loss of copper. Since, however, a fairly large amount of copper is present in the pores, copper must also be corroded.

Thus, either the zinc is preferentially attacked in the corrosion of brass, or copper and zinc are dissolved in the ratio in which they are present in the brass, namely 63:37, and then the copper is, to a certain extent, deposited by cementation in the narrow corrosion sites. It is difficult to find a reason for the great amount of copper in the pores, if indeed the zinc has been preferentially corroded, and therefore we think that brass corrodes as a single substance and copper is deposited in the corrosion sites by cementation.

The exposure taken with SKα-radiation shows, moreover, that the corroding medium contains a large amount of sulfur. This was to be expected, as, in outdoor exposure in the severe industrial atmosphere of Essen, SO_2 would be the main corroding agent.

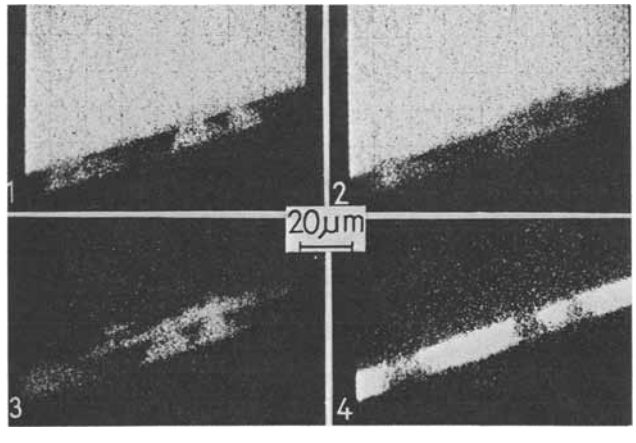

Fig. 8. Corrosion pores of bright nickel—microcracked chromium on brass—investigation of sections with the electron microprobe: 1—Cu Kα, 2—Zn Kα, 3—SKα, 4— Ni Kα.

Summary

The corrosion of nickel covered by microcracked chromium is cathodically controlled, as in the valid theories. But in static outdoor exposure, when samples plated with microcracked chromium are not mechanically stressed, many cracks are blocked, as has been shown. This results primarily from corrosion products which render such cracks ineffective for further corrosion. The result is that the neighboring, still-open cracks corrode more strongly, so that larger pores are formed at these sites and the next metal layer is reached comparatively soon. Thus, in static open-air exposure, uniform corrosion is not observed as is normally expected with microcracked chromium.

In service, however, when the part is continuously exposed to the action of sand and stones, cracks which have been blocked are repeatedly opened, and all cracks will contribute to the corrosion during its whole duration, even if periodically and to a different degree. Thus, for microcracked chromium, service conditions are not only harmless but actually beneficial. If this mechanism is right, it may be expected that microcracked chromium would behave better at exposed than at protected positions on a vehicle.

The resistance to penetration of a part plated with a microcracked chromium system also depends, of course, to a great extent on the nature and thickness of the intermediate layers. Thus, it has been shown that, with unfavorable basis metals such as steel (and probably also zinc), a ductile layer under the bright nickel is indispensable. This is primarily because bright nickel easily cracks through, even under microcracked chromium, when subjected to impact. In the absence of such a ductile layer, this will lead to immediate corrosion of the basis metal. The very ductile layer must, moreover, be more noble than the bright nickel.

Finally, it has been established that a sequence of coatings most effectively preventing corrosion of the basis metal does not necessarily also preserve the decorative effect longest. Therefore, the question of whether corrosion of the substrate metal is permissible or not should be considered in deciding the sequence of coatings. Corrosion of the substrate metal is not permissible with steel, but it is quite harmless with brass. The reason is that, in contact corrosion with nickel under microcracked chromium, brass is only slowly attacked, with preferential removal of zinc; the corrosion products are therefore inconspicuous and easily removed. Thus, for brass, a simple sequence of fairly thin bright nickel (10-15 μm) followed by microcracked chromium is adequate.

The decorative appearance could be very effectively preserved in our experiments by a thin semibright nickel layer between the bright nickel and the chromium. This sequence, namely bright nickel/semibright nickel/microcracked chromium, admittedly causes certain difficulties, particularly with the brightness and protection of the basis metal. If it is steel or zinc, therefore, a copper or semibright nickel layer must additionally be provided under the bright nickel. Such a system would, by the way, show some similarity with Tri-Nickel, which has already been used.

Acknowledgments

The author wishes to express his thanks to Robert Bosch GmbH for permission to publish this paper, and to his colleagues, particularly Mrs. Nemiroff, Mr. Binder, Dr. Fischer, Mr. Haas, Dr. Illenberger, and Mr. Pritsch, for their assistance with the experimental work, and Dr. Neumann for helpful discussions.

Manuscript submitted Sept. 26, 1969; revised manuscript received *ca.* Feb. 13, 1970. This was Paper 430 presented at the Montreal Meeting of the Society, Oct. 6-11, 1968.

Any discussion of this paper will appear in a Discussion Section to be published in the June 1971 JOURNAL.

REFERENCES

1. E. Völkel, *Galvanotechnik*, **56**, 421 (1965).
2. W. Nohse, *ibid.*, **53**, 2 (1962).
3. W. H. Safranek and H. R. Miller, *Plating* **51**, 543 (1964).
4. A. H. Du Rose, *Trans. Inst. Metal Finishing*, **41**, 59 (1964).
5. G. N. Flint, *ibid.*, **40**, Part 3, 98 (1963).
6. P. F. Turner, *Anti-Corrosion*, 20 (1967).
7. R. J. Clauss and R. W. Klein, Interfinish 1968, meeting reports.
8. E. Raub, *Werkstoffe und Korrosion*, **18**, 499 (1967).
9. R. L. Saur, *Plating*, **48**, 1310 (1961).
10. H. Rittner, D.P. 1,176,956.
11. E. I. Seyb, *Plating*, **54**, 1135 (1967).

The Measurement of Specular Defects on Semiconductor Surfaces

J. M. Adley* and E. F. Gorey

IBM Components Division, East Fishkill Laboratory, Hopewell Junction, New York

ABSTRACT

An apparatus and optical technique is described that allows the quantitative measurements of haze and other specular defects on silicon surfaces. The technique can be applied to any flat, polished specimen and yields information on the nature of the defect as well as the relative surface area covered. Data are presented for such defects as stacking faults, lapping damage, and scratches. The application of this technique to the study of epitaxial growth over steps on a silicon wafer is also described.

The most frequently used inspection in the processing of semiconductor devices is the visual inspection of silicon surfaces. Such inspection generally is made by an operator or inspector under a microscope light, on whose judgment a significant portion of the wafers inspected is often rejected. Such judgments are completely subjective and vary widely from operator to operator and day to day, even with the same operator. If such process control is to become less subjective, if valid comparisons of different wafer surfaces are to be conducted, or if any detailed study of the nature and causes of surface defects is to be made, then there exists a critical need for a more objective, quantitative technique of measuring the physical perfection of the wafer surface. Such an improved inspection technique must be at least as sensitive as the human eye, rapid,

nondestructive, and capable of observing the same features observed by the operator, but in such a way that a quantitative parameter is obtained.

Description of Technique

The basic principle of operation of this technique is that, when collimated light is normal to the surface, the light reflected at off-normal angles indicates surface defects. The light reflected to an off-normal position must be due to a surface defect face making some angle, α, with the surface: a scratch, for example, as shown in Fig. 1. A small mirror is placed next to the beam to collect the light reflected by the defects. The light incident on the mirror is focused through a telescope onto a photomultiplier tube. The wafer is then rotated using the incident beam of light as the axis of rotation. Upon rotation of the specimen such that a face of a surface defect is oriented so that it reflects light into the mirror, the photomultiplier output increases. If there are no facets oriented on the surface such that no light is reflected onto the mirror when the sample is at angle θ (Fig. 1), then only a "perfect surface" or residual signal will be seen. The photomultiplier tube output is plotted against the angle of rotation, θ, and the resulting graph contains information on the surface of the specimen under investigation. A scratch will thus produce two peaks, one corresponding to each face of the scratch. The location of the peaks reveals the angular orientation of the defect faces to each other and may give information on the type of defect; for example, a scratch or a scribe line on a silicon surface will produce two peaks 180° apart as shown in Fig. 2. The trace of the wafer before scribing, shown as the bottom line in Fig. 2, reveals a near-perfect surface free of defects as indicated by the very low minimum intensity and total absence of peaks.

The maximum-to-minimum intensity difference indicates the relative amount of a particular surface defect present, while the minimum intensity compared to a standard or reference value indicates general surface condition, in terms of surface roughness and cleanliness. The graph of a specimen having surface haze is shown in Fig. 3, where the high minimum value indicates that there is some reflection of the collected light in all directions. Correlation of the maximum-to-minimum intensity difference and the minimum intensity to surface haze "standards" reveals that increasing haze as seen by an operator is the result of increasing maximum-to-minimum intensity difference and increasing minimum intensity. Further study is under way to determine the relation of the two quantities to further processing. The two large peaks indicate that most of the defects causing the surface "haze" are oriented in the same direction, but the width of the peak indicates that not all the defects are exactly parallel. A graph of an epitaxially deposited silicon <111> wafer is shown in Fig. 4, showing the three facets of the pits at 30°, 180°, and 330°. A scribe line was placed on the wafer for the purpose of checking the orientation of the pits. The location of the peaks resulting from the scribe line reveals that the large peak at 180° is due to the long sharp edge of the pits as seen in the photograph.

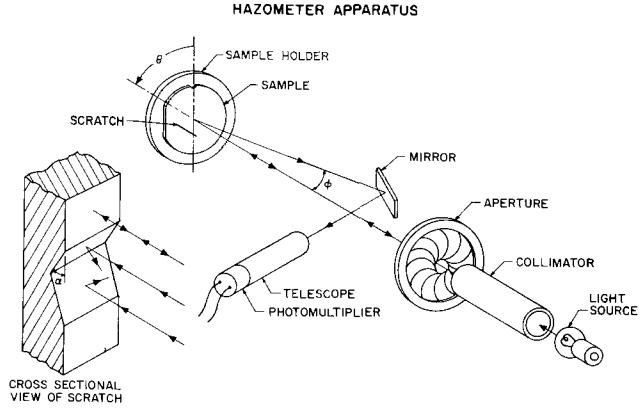

Fig. 1. Method of measuring specular defects. (The light reflected from the faces of the defect, here the scratch, is not reflected in all directions, but rather in two directions which have a component perpendicular to the surface edge of the defect face—perpendicular, that is, to the direction of the scratch here.)

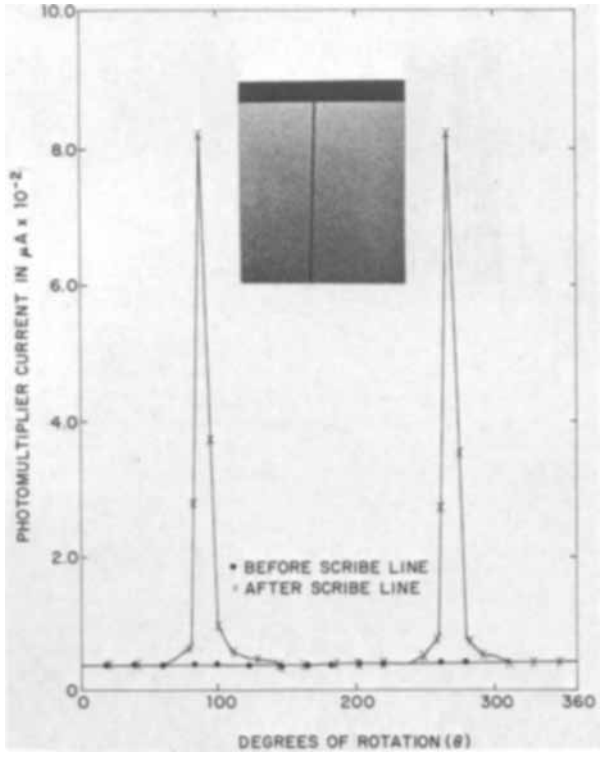

Fig. 2. Two peaks produced by single scribe line in silicon surface. (The scribe line area represented only 0.07% of the wafer area under observation and did not increase the minimum intensity value.)

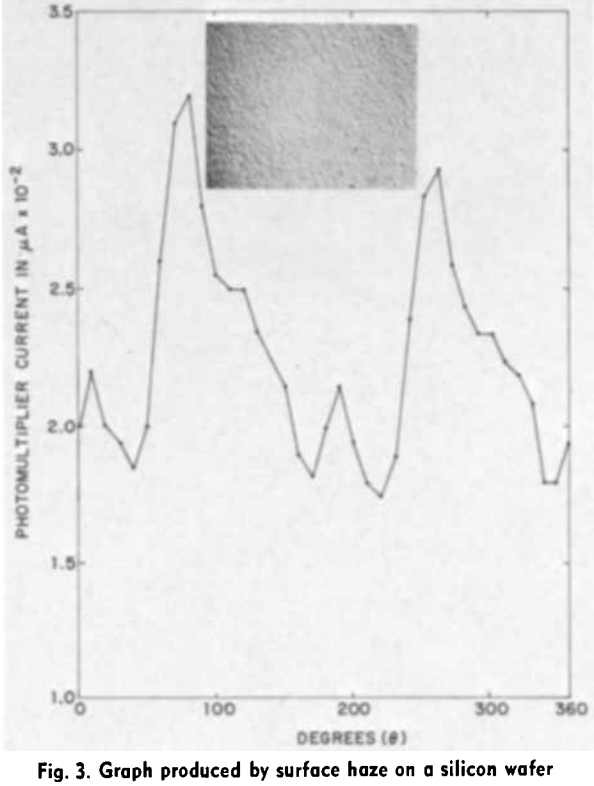

Fig. 3. Graph produced by surface haze on a silicon wafer

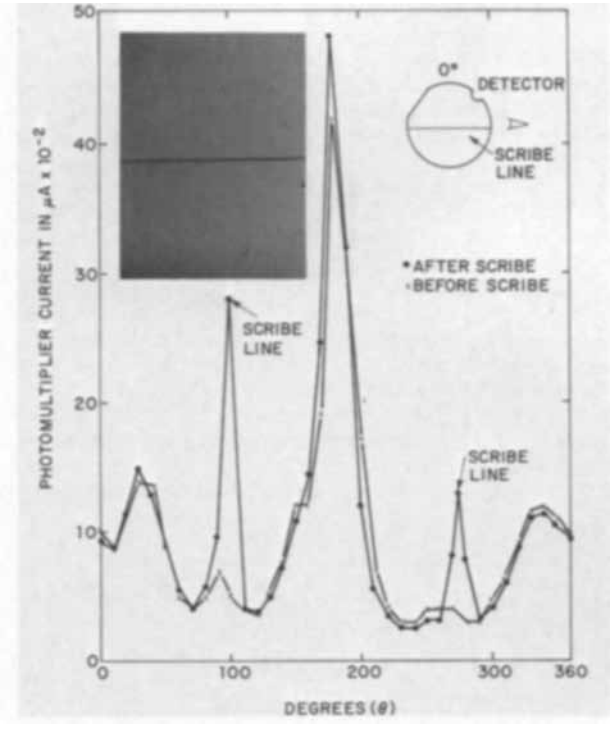

Fig. 4. Pitted, epitaxially deposited silicon <111> wafer

Dirt on the wafer has the effect of increasing the intensity value of the graph as shown in Fig. 5. Since the dirt is assumed to reflect light in all directions, the output intensity at all angles (θ) is expected to increase uniformly, thus increasing the peak and valley level by the same amount while preserving the information on the silicon surface defect given by the maximum-to-minimum intensity difference.

A mechanically polished wafer was expected to yield the same graph as the graph obtained for dirt; that is, it was assumed that the small surface scratches present from the polishing operations were completely random in orientation and would produce a constant high level output. However, as the graph in Fig. 6 reveals, the

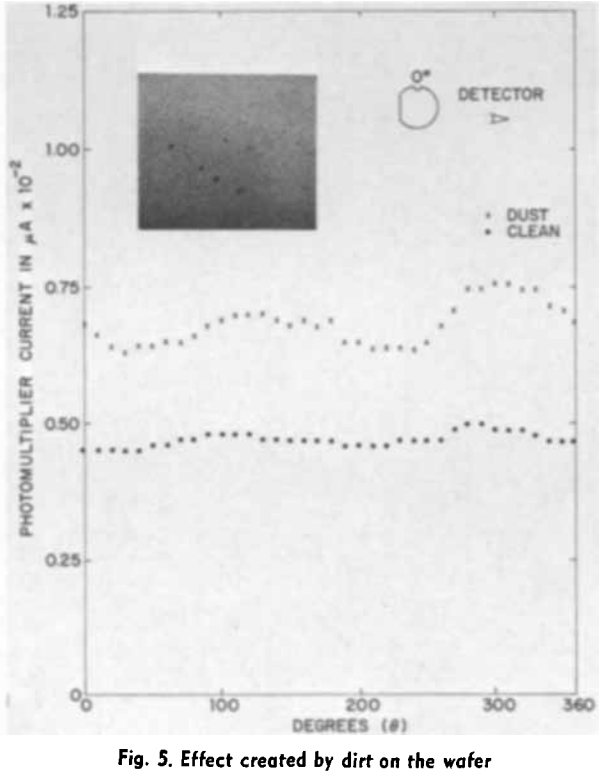

Fig. 5. Effect created by dirt on the wafer

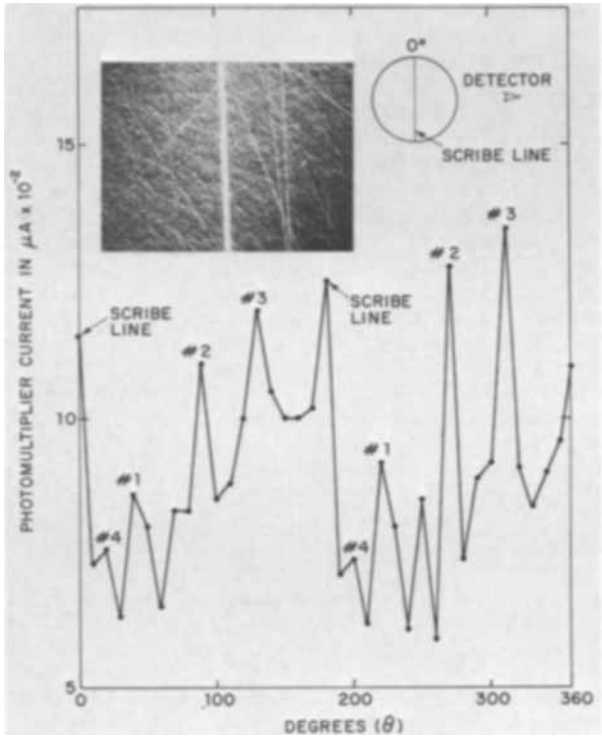

Fig. 6. Effect of scratches due to 0.25-μM grit mechanical polishing of silicon wafer.

lapping scratches show a definite structure of four preferred orientations, numbered 1-4, that are not apparent from the photograph of the surface also shown in Fig. 6. Thus, this technique is able to determine orientation dependence that is not readily apparent by any other technique.

The graph of a diffusion test square on a silicon wafer after epitaxial deposition is shown in Fig. 7. The four edges of the test square, which are of equal length, should produce equal intensity peaks; but, while three of the four peak intensities are nearly equal, one is significantly lower. The lower peak we assumed to be due to a change in the angle which that edge makes with the surface, an assumption that was verified by visual examination of similar structures

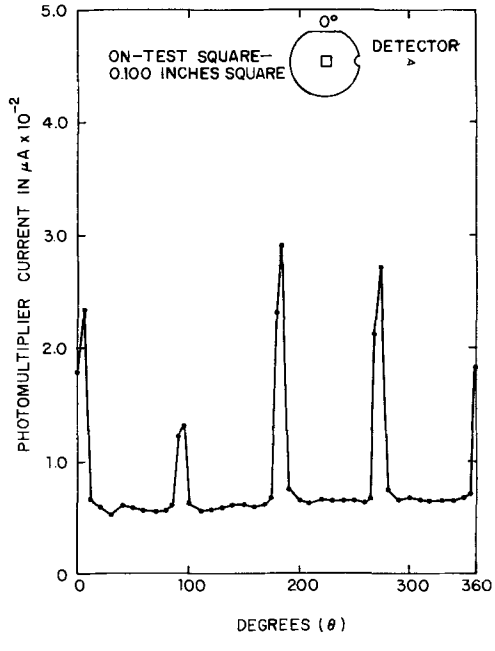

Fig. 7. The four edges of a test square on a silicon wafer after epitaxial diffusion.

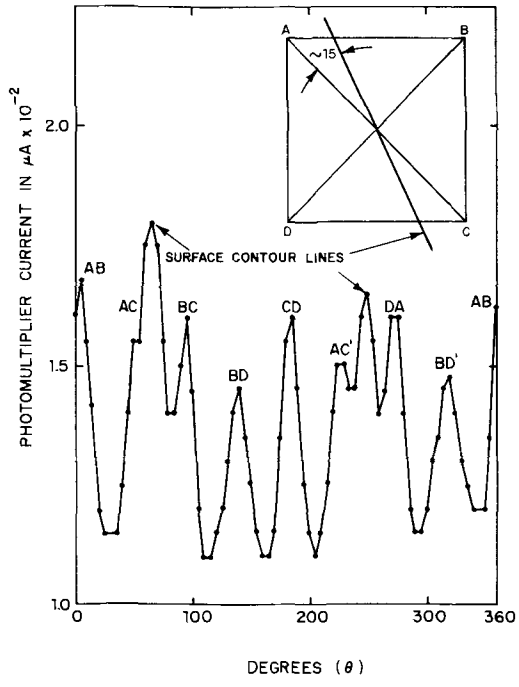

Fig. 8. Stacking fault edges, diagonals, and rolling contour lines ($\phi \approx 6°$).

under high magnification. Thus, this technique can be used to measure the angle between the defect face and the surface; in particular, the angle change of a step after epitaxial growth.

Observation of a low-temperature <100> epitaxial silicon surface produces the complex graph shown in Fig. 8. A diagram of the geometrical structure causing the peaks graphed is shown in the upper right-hand corner of the figure. The four sides of the upper right-hand figure are attributed to the four edges of the stacking fault, and the diagonals across the stacking faults appear in this specimen as four more peaks in between the four peaks due to the stacking fault edges. These edge and diagonal facets are shown in Fig. 9a, b, and c. In addition to the stacking fault structures, two additional peaks were seen on the graph that did not correspond to any possible stacking fault structure seen on the microscope photographs shown in Fig. 9a,

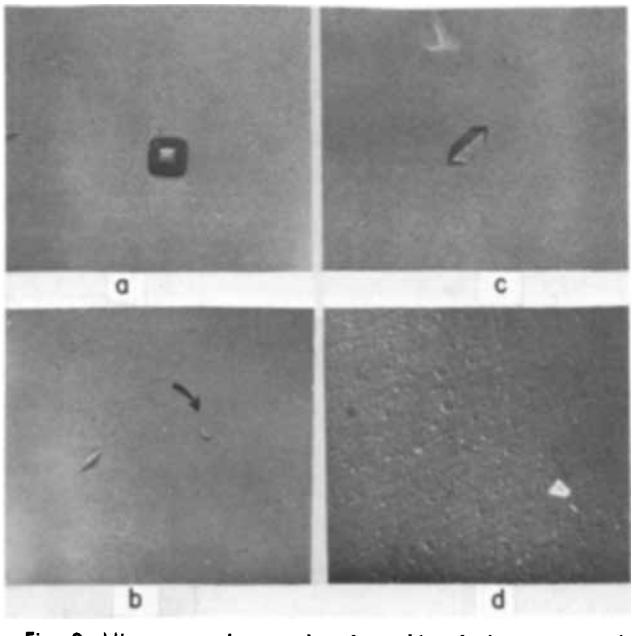

Fig. 9. Microscope photographs of stacking faults represented in Fig. 8.

b, and c. However, under Nomarski interference contrast observation, rolling contour lines were seen as shown in Fig. 9d, having the precise orientation needed to account for the two extra peaks on the graph. Thus, this technique of measuring surface defects appears to detect all geometrical features of a polished or smooth surface.

Observation of the epitaxial surface shown in Fig. 8 at larger angles of observation (ϕ in Fig. 1) will reveal the relative angle each group of facets makes with the surface. Normally the angle of observation (ϕ) is approximately 6°, but the graph in Fig. 10 was observed at approximately 11°. The intensity of the contour peaks has been greatly reduced indicating that these features are very shallow (α in Fig. 1 is small compared to the other features on the surface). The sample responsible for the graph in Fig. 11 was observed at a still larger angle (approximately 23°) and shows a further decline of the peaks due to the diagonals of the stacking faults and the contour line peaks, while the four edges of the stacking fault have in-

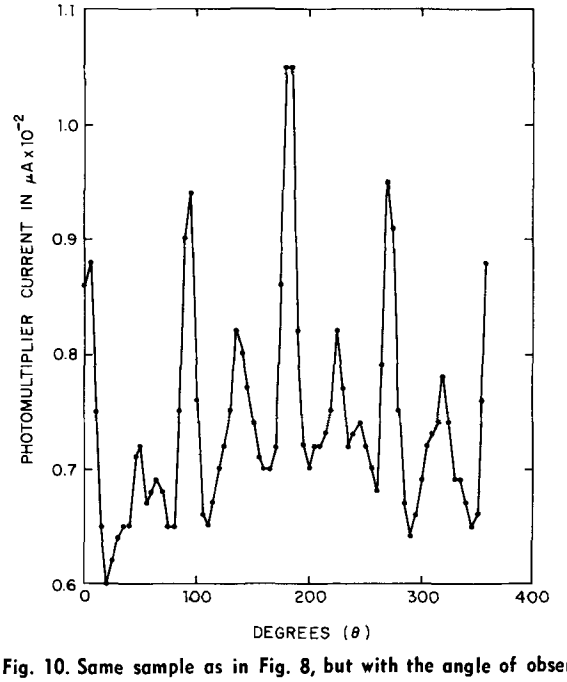

Fig. 10. Same sample as in Fig. 8, but with the angle of observation, ϕ, increased to ~11°.

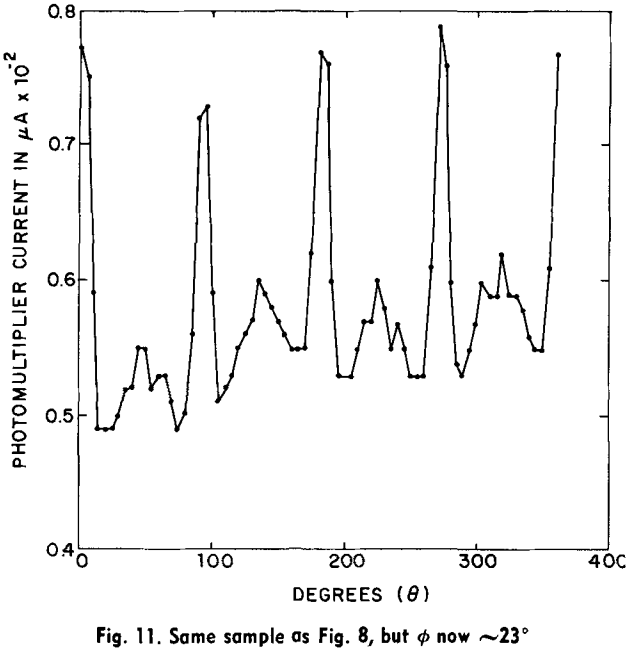

Fig. 11. Same sample as Fig. 8, but ϕ now ~23°

creased in relative intensity, thus indicating that these features make large angles with the surface.

Discussion

A technique has been developed for translating visual defects to electrical signals containing information on the nature and relative area covered by these defects. This technique allows either graphical presentation of the output as is now practiced, or allows possible future scanning of the output by computer. Because the technique can observe an entire wafer surface at once rather than by repeated scanning, this technique allows extremely rapid observation of wafers at rates possibly greater than 100 wafers per hour. But most important, this technique is operator-independent and does allow quantitative characterization of the wafer surface by using the maximum and minimum intensity difference and the minimum intensity value.

The question that must now be answered is what effect these new parameters have on subsequent processing steps. Which of the two parameters now available to characterize a surface is the more critical for further device processing and yield? Some wafers may have a very large maximum-to-minimum intensity difference but a low minimum intensity value, while others may have a small maximum-to-minimum difference and a high minimum intensity value. Studies are presently being conducted to gain some information on this question.

In summary, a quantitative measurement of surface defects has been developed and will be used to study the effects of wafer surface perfection on processing steps.

Acknowledgment

The authors would like to thank Gunar Paegle for his work in the design and building of the special sample holder. They would also like to thank all those who contributed the samples measured by this technique.

Manuscript received Jan. 30, 1970. This was a Recent News Paper presented at the Detroit Meeting of the Society, Oct. 5-9, 1969.

Any discussion of this paper will appear in a Discussion Section to be published in the June 1971 JOURNAL.

Technical Notes

Determination of the Ohmic Contribution to the Polarization of Fuel Cell Electrodes

D. Lucesoli, P. Degobert,* and E. Kochaniak

Institut Français du Pétrole, Rueil-Malmaison, France

While developing significant-size air electrodes (150 x 200 mm), having a three-layer hydrophobic structure (conductive current-collecting layer, catalytic layer, hydrophobic layer), we found high polarizations at current densities above 50 mA/cm^2. In order to determine the ohmic losses included in the polarizations, we developed a graphic method based on oscilloscope measurements. This method, when applicable, enables an optimization of the current-collecting layer properties (sintered nickel structure) in order to minimize ohmic drops.

Principle of the Method

The over-all polarization of a single electrode for a given current density is generally broken down into three distinct terms designated as:

- ohmic polarization
- concentration polarization
- activation polarization

In order to improve the performance of our electrodes, we tried to study separately the parameters influencing the total overvoltage (1) and to develop experimental procedures for studying every type of polarization.

The relaxation time, *i.e.* the time necessary to recover initial potential after a sudden interruption of the current applied to an electrode, enables the ohmic polarization to be separated from other types of polarization. The resistive component of the overvoltage disappears almost instantaneously (within about 10^{-5} sec), whereas other components decrease slowly, sometimes following exponential relationships.

Several publications have already described this method using a sudden interruption of the current to determine and eliminate ohmic polarization, both in Leclanché-type dry cells and in fuel cells (2-7).

In our case we applied this method to a half cell, measuring the actual potential compared with a reference electrode; and we tried to develop a graphical method to obtain, with sufficient accuracy, the values corresponding to the ohmic component, which are somewhat difficult to extract directly from the diagram shown on the oscilloscope screen. In order to avoid the possible limitations, which are mentioned by Niedrach and Tochner (8) (more particularly time constant of the measuring system too close to the time constant of the electrochemical system), we calculate by extrapolation the value corresponding to the interruption time zero, thus avoiding inclusion of nonlinear polarization values, in the final result. This

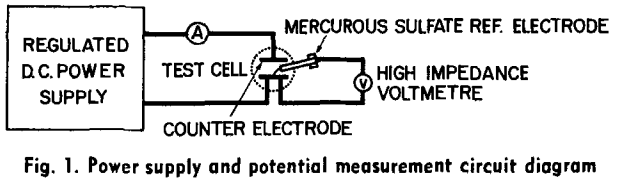

Fig. 1. Power supply and potential measurement circuit diagram

* Electrochemical Society Active Member.

graphic method allows the use of mercury-wetted switch relays which are commonly commercially available (Vynckier-France type 0612). Figure 3(a) shows the voltage drop pattern for a pure resistor, and Fig. 3(b) the same pattern for a composite overvoltage (actual fuel cell electrode).

Experimental Assembly

Measurements were made in half cells using the galvanostatic method. Potentials were measured through a Luggin capillary with mercuric sulfate reference electrodes. Figure 1 shows the experimental assembly, in which current at a constant intensity was supplied to the cell from a stabilized d-c source. Figure 2 shows the measurement circuit used to record the potential-time diagram on an oscilloscope screen immediately after the current is interrupted by an electronic switch allowing an interruption time of from 5 to 60 msec with a frequency of 1 Hz. By selecting the corresponding sweep frequency on the oscilloscope, we were able to measure the voltage drop pattern with great accuracy.

Graphic Method for Determining Ohmic Polarization

After interruption of the current, the shape of the voltage decrease on the oscilloscope screen should ideally be as shown in Fig. 3(a) (9); *i.e.*, ohmic polarization disappears before any concentration or activation polarization change can occur. In fact the actual path of the electron beam on the screen is as shown in Fig. 3(b), and accurate direct measurement of the ohmic drop is very difficult. By varying the interruption time of the electronic switch, we can have different patterns on the screen corresponding to every value of the interruption time [Fig. 4(c)]. Our graphic method consists of measuring the voltage decrease, $\Delta V_{(t)}$, for several interruption times, t, and of calculating the ohmic component from the values obtained.

Like Tvarusko (2) we can express the transient value of the voltage drop $\Delta V_{(t)}$ by relating the transient impedance, Z, to the Laplace transforms of voltage and current corresponding to the same phase angle (10)

$$\mathcal{L}\,\Delta V_{(t)} = \mathcal{L}\,I_t \cdot Z$$

By neglecting any inductive process in the measurement circuit (porous gas electrode, Luggin capillary filled with electrolyte, platinum wire) and assuming that the electrolyte conductivity remains constant throughout the Luggin capillary between the gas electrode and the platinum wire, in the equivalent electrical circuit we can take into account only a resistive component and a capacitance corresponding essentially to the double layer on the electrode. As for Leclanché type cells (2-4), the equivalent circuit consists (Fig. 5) of a pure ohmic resistance, R_o, connected in series with a polarization resistance, R_p, and in parallel with a capacitance, C. Resistance R_o is always linear, whereas under transient conditions R_p and C present nonlinear variations.

According to Tvarusko's study (2) which feeds the equivalent electrical circuit with a square-wave current (like our electronic switch), we can express the transient voltage response as

$$\Delta V_{(t)} = I\,R_o + I\,R_p\left[1 - \exp\left(-\frac{t}{RpC}\right)\right]$$

when a given intensity, I, is applied.

Transient impedance Z will be

$$Z = R_o + R_p\left[1 - \exp\left(-\frac{t}{RpC}\right)\right] \qquad [1]$$

where t is the interruption time.

For $t = 0$

$$Z_o = R_o \qquad [2]$$

We assume that the double-layer capacitance remains constant with varying potential and that the activation polarization and even concentration polarization decay exponentially with time.

The instantaneous voltage drop corresponds to the pure ohmic resistance but can be difficult to measure with accuracy from the oscilloscope pattern.

For $t = \infty$

$$Z_\infty = R_o + R_p \qquad [3]$$

If we call $L = R_o + R_p$ the asymptotic value of Z_∞, Eq. [1] may be written as

$$Z = L - R_p\left[\exp\left(-\frac{t}{RpC}\right)\right]$$

or as

$$\log_{10}(L - Z) = \log_{10} R_p - Kt \qquad [4]$$

with

$$K = \frac{\log_{10} e}{RpC}$$

Equation [4] gives a linear relationship between $\log_{10}(L - Z)$ and the interruption time, t. On a semilogarithmic diagram, as shown in Fig. 6, the intercept

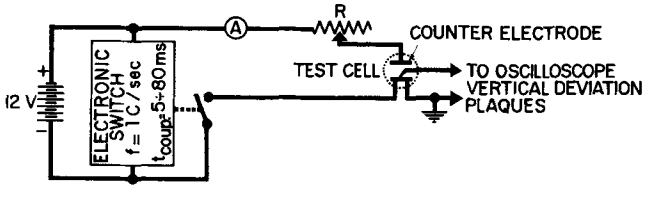

Fig. 2. Current shut-off diagram

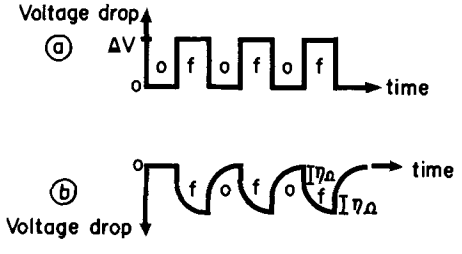

Fig. 3. (a) Pure ohmic voltage drop, (b) fuel cell electrode ohmic drop (f: closed, o: open).

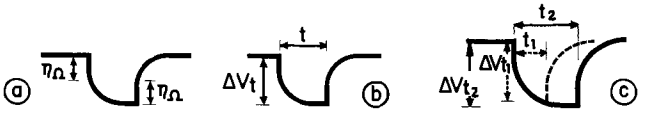

Fig. 4. Signal analysis

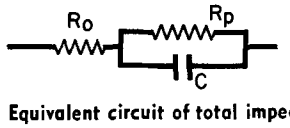

Fig. 5. Equivalent circuit of total impedance

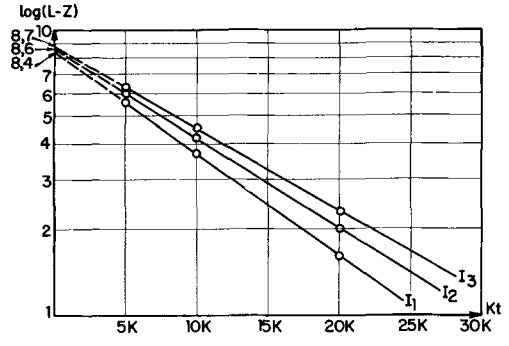

Fig. 6. Plotting equations No. 7 for different current densities

Table I

I (mA/cm²)	$I_1 = 20$				$I_2 = 40$				$I_3 = 60$			
t (msec)	5	10	20	60/80	5	10	20	60/80	5	10	20	60/80
ΔV_t (mV)	68	106	148	180	130	200	290	370	184	290	420	560
Z (ohm-cm²)	3.4	5.3	7.4	9.0	3.25	5.00	7.25	9.25	3.05	4.85	7.00	9.35
L-Z (ohm-cm²)	5.6	3.7	1.6	0	6.0	4.25	2.00	0	6.30	4.50	2.35	0
R_p (ohm-cm²)			8.4				8.6				8.7	
R_o (ohm-cm²)			0.6				0.65				0.65	

of the straight line with the $\log_{10}(L - Z)$ axis when $t = 0$ gives the value of R_p. R_o must be calculated from $R_o = L - R$, with L being determined experimentally when the over-all ohmic drop remains constant for increasing interruption times.

Table I, corresponding to Fig. 6, shows that in our case for interruption times greater than 60 msec the voltage drop reaches its asymptotic value, from which we determine that the limit for the impedance $Z = L$. Verifications were made for three different current densities.

In our case, where direct knowledge of the ohmic proportion in the over-all overvoltage is important, we can derive it by the direct plotting of

$$\log_{10}(\Delta V_\infty - \Delta V_t) = f(Kt)$$

where $\Delta V_\infty = \Delta V_{60} = \Delta V_{80}$ for $t \geq 60$ msec.

The intercept of the line when $t = 0$ gives ΔV_p (voltage drop for activation and concentration only) and

$$\eta\Omega = \Delta V_\infty - \Delta V_p$$

In the graphic method, the margin of error is less than 10%, an accuracy which is sufficient at present for development of our fuel cell electrodes. It must be mentioned that the pattern obtained for $\eta\Omega$ is valid for only one given point on the electrode surface, *i.e.* the point located at the tip of the Luggin capillary.

Application of the Graphic Method

The method was first used to study the influence of the specific properties of the current-collecting porous nickel layer on the over-all polarization, in order to choose the best suited type of porous support. Different electrodes made from several types of nickel plates were compared for their ohmic share in the over-all polarization. The same type and location of current-collecting wires was used on all the electrodes tested, and the Luggin capillary was located at the same point. Temperature was kept at 50°C.

Our porous metal support, made of sintered nickel, was drowned in the KOH electrolyte and behaved like a matrix filled with electrolyte. Its rheological properties (porosity, pore size, tortuosity) play an important part in the effective conductivity of the electrolyte inside the nickel support

$$\Psi_{eff} = \frac{\epsilon}{q}\Psi \qquad [5]$$

Ψ_{eff} = effective conductivity of electrolyte inside the porous matrix
Ψ = actual conductivity of the electrolyte (mho/cm)
ϵ = volume porosity of the porous support
q = tortuosity of the porous support

In particular, the ionic conductivity is proportional to the volume porosity of the matrix.

On the other hand, the electrical resistivity of the dry porous nickel support increases with the volume porosity (Fig. 7) for the same type of nickel plates, and when over 40% the increase in resistivity is more than linear.

Figure 8 gives the results of the apparent ohmic drop measured on electrodes of the same type, but with a nickel porous support having a different porosity although assumed to have about the same tortuosity. With a porosity of 20% to about 40% for the nickel support, the "apparent ohmic polarization" for different current densities decreases slowly, which corresponds to the increase of the effective electrolytic conductivity inside the porous matrix according to Eq. [5]. With a porosity of over 40%, the increase in electrical resistivity overcomes the decrease in ionic conductivity Ψ_{eff}. This study made on supports of the same thickness enabled the optimum porosity range (30-40%) to be chosen for the best power density in mW/cm². For 100 mA/cm², the apparent ohmic polarization, which reaches 80-85 mV for a porosity of 70%, decreases to 35-40 mV for a porosity of 40%. In terms of specific power density, this may represent 5 mW/cm² for each electrode, *i.e.* 10 mW/cm² for the cell or a 20% gain at an average power density of 50 mW/cm².

Whereas it is of great interest to decrease the volume porosity so as to improve the electrical conductivity of the support, care must be taken not to increase the weight-power ratio by using a heavier nickel support, because the specific weight of such a support increases proportionally when the porosity decreases at a con-

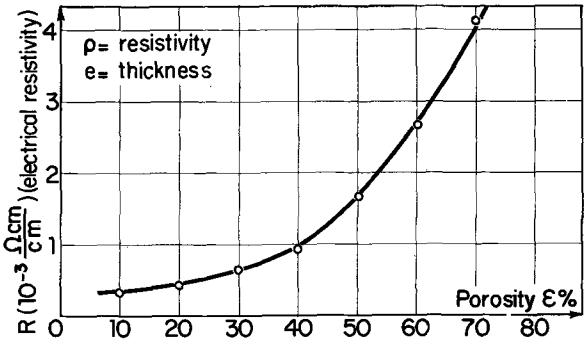

Fig. 7. Variation of electrical resistivity ($R = \rho/e$) with porosity

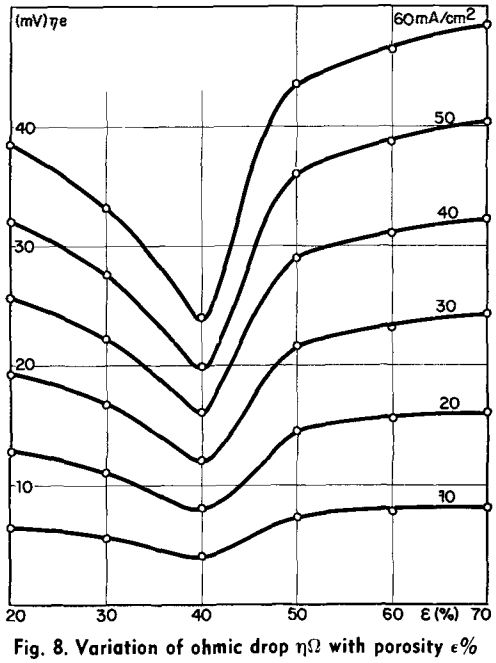

Fig. 8. Variation of ohmic drop $\eta\Omega$ with porosity ϵ%

stant thickness for the sintered plates. This conclusion leads us to replace our original 60-70% porosity plates about 0.4 mm thick by 40% porosity plates 0.25 mm thick so as to keep the same weight-power ratio, since the decrease in thickness does not significantly change the shape of the curve in Fig. 8.

Thus, the interruption technique for eliminating ohmic drop in the study of cells, combined with the graphic method described here, makes it possible to know with sufficient accuracy the value of the apparent ohmic polarization at every point of an electrode. In principle this requires four measurements at four different interruption times (with four other measurements at another current density to confirm the result). The method may be used for testing the performances of large electrodes by plotting the decay of ohmic polarization, particularly as a function of the location of the current collecting tabs. In order to improve the accuracy of our measurements, another electronic device allowing shorter interruption times (beginning at about 100 μsecs) is being developed in our laboratory. To speed up measuring, this device will be combined with electronic memories recording the values corresponding to given times after shutting off the current. Such an assembly will enable the values to be directly transferred to a digital computer which will give the values of the apparent ohmic drop directly through the corresponding program. A special test cell is now being developed to map the distribution of ohmic drop, polarization, *etc.*, on large electrodes, with the help of a digital computer. These devices and the corresponding results will be described in another paper.

Manuscript submitted March 25, 1969; revised manuscript received *ca.* Feb. 26, 1970.

Any discussion of this paper will appear in a Discussion Section to be published in the June 1971 JOURNAL.

REFERENCES

1. D. Lucesoli, Thesis, To be published.
2. A. Tvarusko, *This Journal*, **109**, 881 (1962).
3. A. Tvarusko, *Electrochem. Technol.*, **1**, 354 (1963).
4. J. Geard, G. Gerbier, and J. P. Gabano, *Proc. 4th Intern. Symp. Batteries, Brighton, Sept. 1964.*
5. K. Kordesch and A. Marko, *This Journal*, **107**, 480 (1960).
6. G. Pollnow and R. Kay, *ibid.*, **109**, 648 (1962).
7. I. Trachtenbergh, 145th Natl. Meeting Am. Chem. Soc., Div. Fuel Chem., New York, Sept. 1963.
8. L. W. Niedrach and M. Tochner, *Electrochem. Technol.*, **5**, 270 (1967).
9. M. Andrew and F. Jones, "Kinetic Effects," Part 9, "An Introduction to Fuel Cells," Williams Keith, Elsevier Publishing Co. (1966).
10. E. Weber, "Linear Transient Analysis," Vol. 1, John Wiley & Sons Inc., New York (1954).

Properties of Aluminum Nitride Derived from $AlCl_3 \cdot NH_3$

Daniel W. Lewis

Westinghouse Electric Corporation, Research and Development Center, Pittsburgh, Pennsylvania

Aluminum nitride powder has been prepared by vaporization of aluminum in a nitrogen atmosphere at temperatures of 1800°-2000°C (1) and also by striking a d-c arc between high-purity aluminum electrodes in nitrogen gas (2). These powders have been well characterized as AlN and were found to be chemically and thermally stable high-temperature dielectric materials. Renner (3) prepared aluminum nitride by thermal decomposition of the $AlCl_3 \cdot NH_3$ complex. More recently, thin layers of aluminum nitride have been applied in the fabrication of semiconductor devices for surface passivation, as diffusion masks, and as dielectric layers (4). Vapors of $AlCl_3$ and NH_3 are the usual source materials in thin film electronic applications. However, thin films of aluminum nitride have also been deposited by chemical vapor transport techniques, using NH_4Cl or HCl as the transport agent (5). Very little is known of the composition and properties of the products prepared using $AlCl_3$ and NH_3 or their addition product as starting materials.

Present Work

We were interested in examining aluminum nitride as an electrical insulation for refractory conductors operating at 800°-1000°C and at frequencies and voltages likely to be encountered in aerospace applications. Since this required continuous layers 1-10 mils thick, a vapor deposition technique was employed, using the volatile $AlCl_3 \cdot NH_3$ complex as the source material. The equation representing the formation of aluminum nitride from the complex is

$$AlCl_3 \cdot NH_3 \xrightarrow{700°\text{-}1400°C} AlN + 3HCl$$

In preparing specimens for examination, ultrapure nitrogen was used to carry vapors of the complex over the hot substrate, which was usually molybdenum rods, plates, foils, or wire coils. The substrate temperature was varied from 700° to 1400°C and the pressure in the reaction system was in the range of 5-10 Torr. A quartz U-tube reaction chamber, as sketched in Fig. 1, was

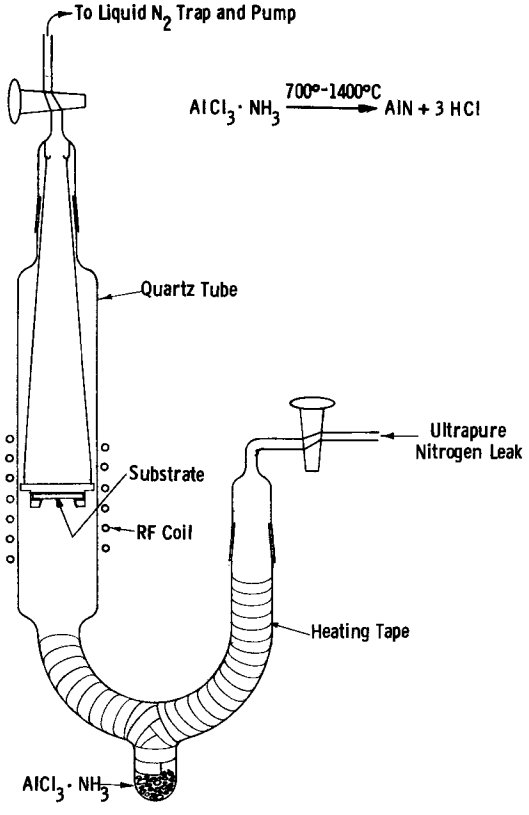

Fig. 1. Flow apparatus for vapor deposition of aluminum nitride

Key words: aluminum nitride, aluminum chloride, ammonia, pyrolytic films, dielectric properties, composition.

used and the substrate was heated by means of an external rf induction coil. Substrates were first given a heat cleaning and degassing at 1500°-1600°C and a pressure of 5-10μ. The substrate was then lowered to the desired temperature and the pressure was increased to 5-10 Torr by allowing ultrapure nitrogen to enter the system by way of a controlled leak. The cup containing the source material was heated by means of a small heating mantle. The rate of deposition was controlled mainly by the temperature to which the substrate and the source material were heated. At a substrate temperature of 1100°-1300°C, the rate of deposition was varied from 1 to 10 mils/hr by varying the source material temperature from 100° to 200°C. Films deposited in the substrate temperature range of 700°-800°C were smooth transparent electrical insulators. In the 1000°-1300°C deposition temperature range, opaque hard (8-9 on the mho scale) coatings were obtained. Using this system, it was not possible to deposit continuous films at greater than 1400°C. Either nothing deposited, or that which did was in the form of beads which made only a small area of contact with the substrate. Examples of these coatings on ½ in. diameter molybdenum rods are shown in Fig. 2.

Our aim was to determine the variation in properties of aluminum nitride films formed at various deposition temperatures. Films deposited at substrate temperatures of 800°, 1000°, and 1300°C were examined regarding their x-ray diffraction patterns, infrared spectra, hydrolytic stability, flexibility, oxidation resistance, and high-temperature electrical properties.

X-ray diffraction analysis.—Photographs of the x-ray diffraction patterns of material deposited at 800°, 1000°, and 1300°C are shown in Fig. 3. The pattern of the 800° material shows the presence of two crystalline phases. The sharp lines correspond to a crystal having the simple cubic NH_4Cl structure. Very diffuse lines of AlN are also visible. Ammonium chloride, which sublimes at about 335°C, at atmospheric pressure probably

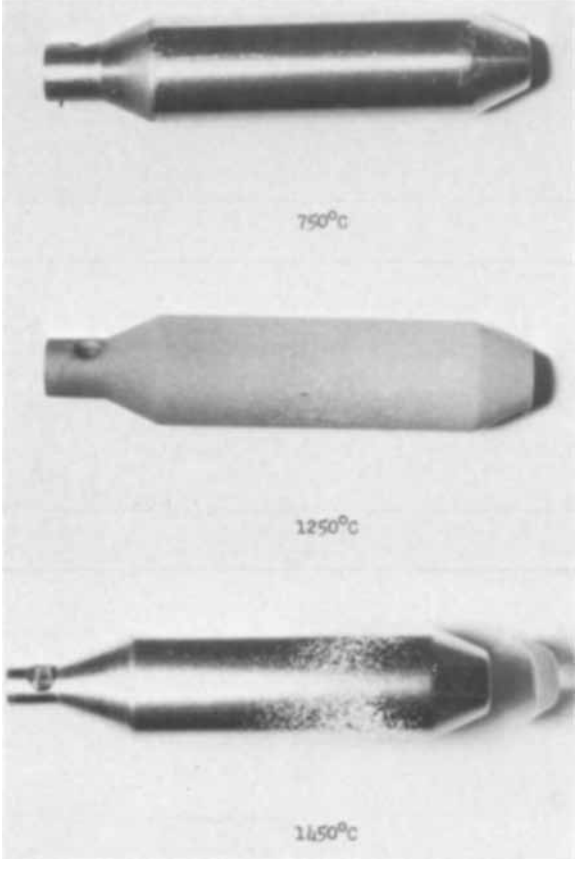

Fig. 2. Aluminum nitride deposited on molybdenum rods at 750°, 1250°, and 1450°C (1.5X).

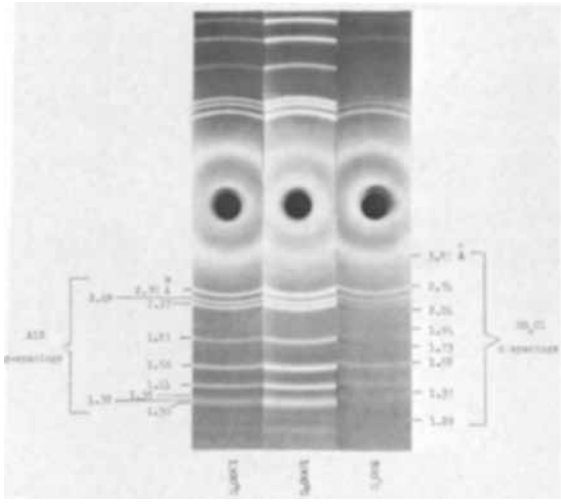

Fig. 3. X-ray diffraction patterns of aluminum nitride deposited at 800°, 1000°, and 1300°C.

was not present in the coating as deposited at 800°C, but could have been subsequently formed by hydrolysis of the powdered sample. No NH_4Cl lines are present in the patterns of the 1000° and 1300°C coatings; only the AlN structure is present. The lines in the pattern of the 1300° material are much sharper than in the 1000° deposit, indicating an increase in the crystallinity of the deposit as the deposition temperature increases.

Infrared spectra.—Infrared spectra were obtained on powdered samples of 800°, 1000°, and 1300°C aluminum nitride deposits using Nujol mulls between NaCl plates. These are shown in Fig. 4. Here, too, there is evidence of considerable amounts of ammonium chloride in the coatings deposited at 800°C. This is indicated by the sharp absorption at 7.2μ between the two Nujol peaks, and lesser NH_4Cl bands at 6.2, 5.8, 5.2μ, and several in the 3-3.5μ region. The very strong broad band centered at 14μ is characteristic of AlN. In the spectrum of the

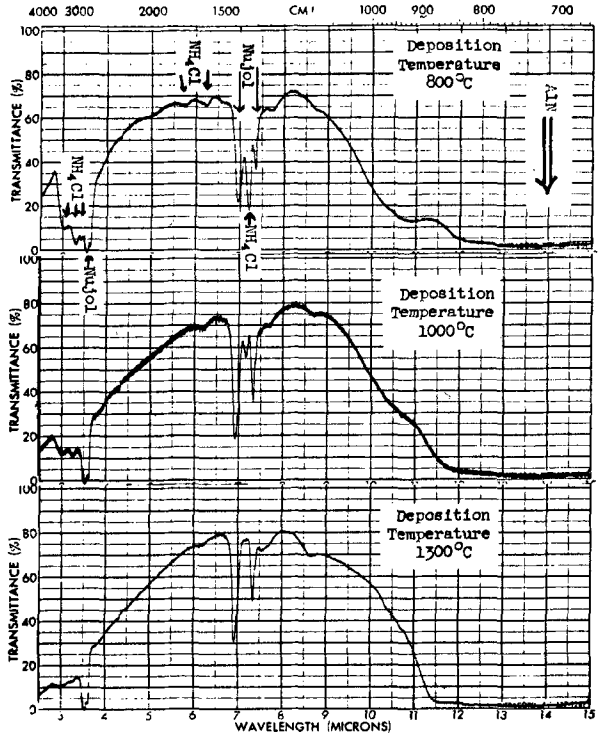

Fig. 4. Infrared spectra of aluminum nitride deposited at 800°, 1000°, and 1300°C (Nujol mull on NaCl plates).

1000° material, the 7.2μ band and all of the lesser NH_4Cl bands are much weaker than in the 800° deposit. The AlN band in the 12-15μ region is still strong. In the spectrum of the 1300° deposit the 7.2μ band, as well as the other NH_4Cl bands, has disappeared leaving only the Nujol and AlN absorption.

Once again, these spectra do not necessarily point to the presence of NH_4Cl as such in the coating as deposited. It probably results from one, or more, incompletely condensed materials still containing hydrolyzable chlorine and nitrogen.

Hydrolyzability.—To check the hydrolysis theory, some of the 800° material was soaked in water in a stoppered vial. After standing for some time the vial was opened, releasing a definite ammonia odor. No odor was detected when 1000° and 1300° deposits were similarly treated. A more quantitative measurement was made by soaking weighed amounts of finely ground samples in deionized water in stoppered flasks. After 1 hr in water with intermittent shaking, aliquots for ammonia and chloride ion determinations were removed using a pipette fitted with a filter stick. Ammonia content was determined colorimetrically by the use of Nessler's reagent. Absorbance was measured at 4000Å using a Beckman Model DU spectrophotometer. The aliquot for chloride ion determination was diluted with a mixture of methanol and acetone and then acidified with 1:1 H_2SO_4. It was titrated with 0.0025*N* $AgNO_3$ using glass and silver electrodes. After 8½ hr, aliquots were again removed for ammonia and chloride determination. Results of these determinations are shown in Table I. It can be seen that coatings deposited at 800°C are more susceptible to hydrolysis than are the 1000° and 1300°C coatings. At lower deposition temperatures, the deposit very probably contains incompletely condensed hydrolyzable materials having the general composition

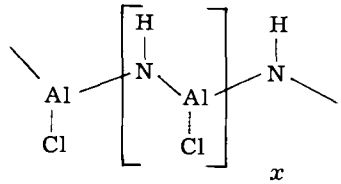

and

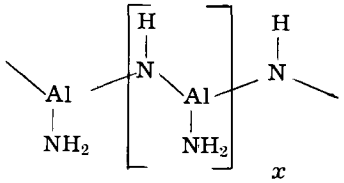

It should be noted that even though the very finely powdered samples of 1300° deposits showed some small amount of hydrolysis, 1 mil thick films of this same material could be isolated from molybdenum plates by soaking the coated plate in a mixture of HNO_3-HF. The 1/16 in. thick plate dissolved in 30-60 min with no apparent affect on the nitride film. As deposited on a molybdenum substrate, coatings appear gray, but when released from the substrate they are white or light tan.

Oxidation resistance of aluminum nitride coatings and protection offered to molybdenum.—The product of oxidation of aluminum nitride at high temperatures is alumina. Total conversion of the nitride to the oxide would result in a weight gain of 25%. To determine the extent of oxidation of a 4 mil film deposited at 1300°, it was heated in air at 1000°C for 115 hr. After 90 hr the sample stopped gaining weight. The total increase in weight during this heating was 4% which probably represents the conversion of the nitride surface to alumina.

Molybdenum rods and wire coils coated with aluminum nitride were heated in air at 700°C to determine to what extent the coating protects the metal against oxidation. Molybdenum metal begins to oxidize noticeably at 400°C and very actively at 600°C. Sublimation of the oxide layer begins at about 640°C. Judging from the oxidation resistance of the nitride film itself, a continuous nonporous film should protect molybdenum from oxidation up to 1000°C. A coil made from 40 mil molybdenum wire was coated with 0.2 mil of aluminum nitride. This coil along with an uncoated molybdenum coil of similar geometry was heated at 700°C for 16 hr. After this time, as shown in Fig. 5, there was very little left of the uncoated coil, but the coated coil was still intact. However, some attack occurred on this coil at the two points where it was found necessary to connect the coils ends to enable it to be heated inductively.

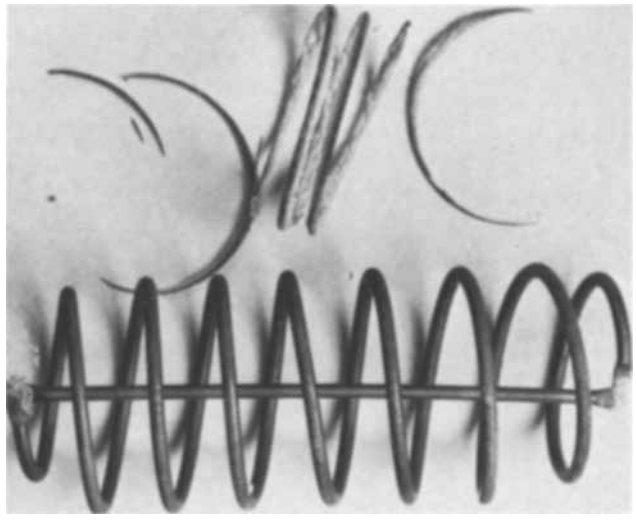

Fig. 5. Molybdenum wire coils, uncoated and coated with 0.2 mil aluminum nitride, after 16 hr at 700°C in air (2.5X).

Composition.—As noted earlier, x-ray diffraction of these deposits shows the presence of the hexagonal wurtzite structure which AlN is known to have. Infrared analysis also confirms its presence. The density of a 4.35g sample deposited at 1300° was found to be 3.13 g/cc. This compares with a value of 3.26 g/cc calculated using the cell dimensions, $a = 3.111$Å and $c = 4.980$Å. Results of elemental analysis of two separate depositions, in the 1250°-1300° range are given in Table II. It can be seen that these samples still contain about 0.3% chlorine impurity. The presence of this impurity is probably the reason why the electrical properties of the product derived from $AlCl_3 \cdot NH_3$ fall short of what is expected of high-purity AlN.

Flexibility.—Most of the aluminum nitride coatings deposited in this work, being 1 mil thick or greater, were very brittle. An attempt was made to evaluate

Table I. Products of hydrolysis of aluminum nitride deposited at 800°, 1000°, and 1300°C

Deposition temp, °C	1 hr Hydrolysis		8.5 hr Hydrolysis	
	Moles NH_3/100g sample	Moles HCl/100g sample	Moles NH_3/100g sample	Moles HCl/100g sample
800	0.120	0.102	0.160	0.113
1000	0.018	0.007	0.042	0.011
1300	0.003	0.0001	0.01	0.0001

Table II. Composition of aluminum nitride pyrolytically deposited from $AlCl_3 \cdot NH_3$ at 1250°-1300°C

	% Al	% N	% Cl
Theoretical	65.85	34.15	—
LH-103-3	66.2	33.5	0.31
LH-111-2	66.1	33.3	0.32

thinner coatings applied to 5 mil molybdenum foil. This was done by bending the coated foil over mandrels ranging from 3 to ⅞ in. in diameter. Increments between mandrels were ¼ in. A 0.2 mil film did not show evidence of cracking until bent around a 2¼ in. mandrel. No obvious cracking of 1μ films took place as the mandrel diameter was reduced to ⅞ in., but when examined under a microscope a few long cracks were evident.

Electrical properties.—High-temperature electrical properties of aluminum nitride coatings deposited at 800° and 1300°C are shown in Fig. 6, 7, and 8. At room temperature the d-c conductivity of these films is in the 10^{-15}-10^{-14} (ohm-cm)$^{-1}$ range, but as the temperature is increased this value increases rapidly. As might be expected from the foregoing properties of coatings deposited at 800°C, the conductivity and dissipation factor of this material are considerably higher than those of the 1300°C product. The d-c conductivity of the former at 300°C is 8×10^{-10} (ohm-cm)$^{-1}$. Since at this temperature the conductivity *vs.* temperature curve is becoming quite steep, measurements of this material were not made at higher temperatures. Electrical properties of the film deposited at 1300°C were measured up to 800°C. At a measuring temperature of 300°C, the d-c conductivity of the 1300°C material is lower by a factor of 10^4 than that of the coating deposited at 800°C.

These dielectric values compare very favorably with those reported (1, 6) for aluminum nitride crystals formed by a vapor phase reaction of the elements or by sublimation of an existing aluminum nitride source. Nevertheless they are somewhat inferior to similar properties of high-purity alumina or to what might be expected of high-purity aluminum nitride. It should be mentioned that, due to errors in the measurement of the thickness of some of the rougher coatings, these values may be in error by as much as 20%.

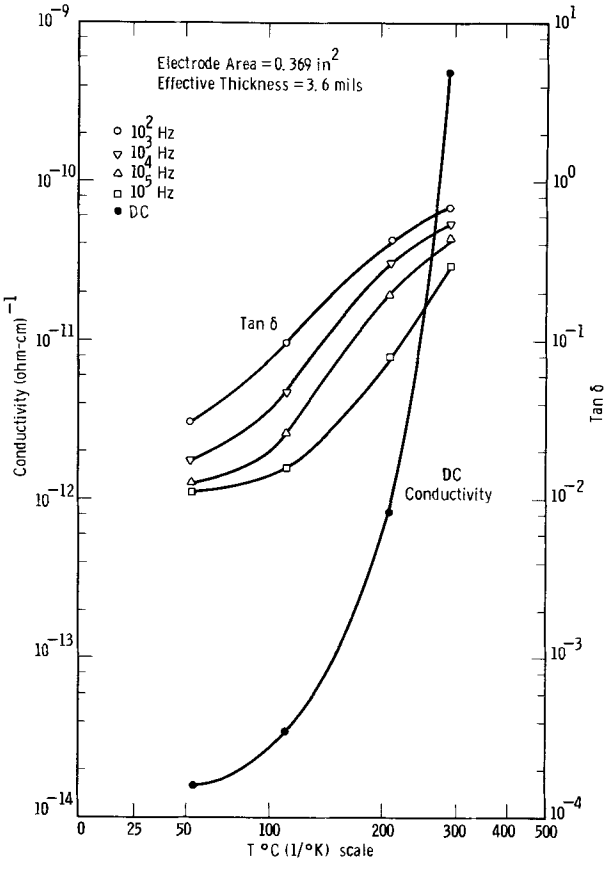

Fig. 6. Dissipation factor and conductivity of aluminum nitride deposited at 800°C.

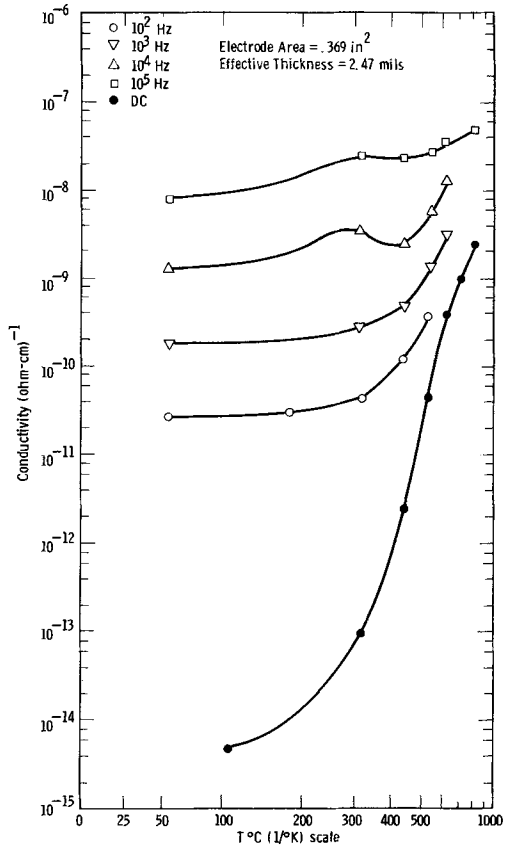

Fig. 7. Conductivity of aluminum nitride deposited at 1300°C.

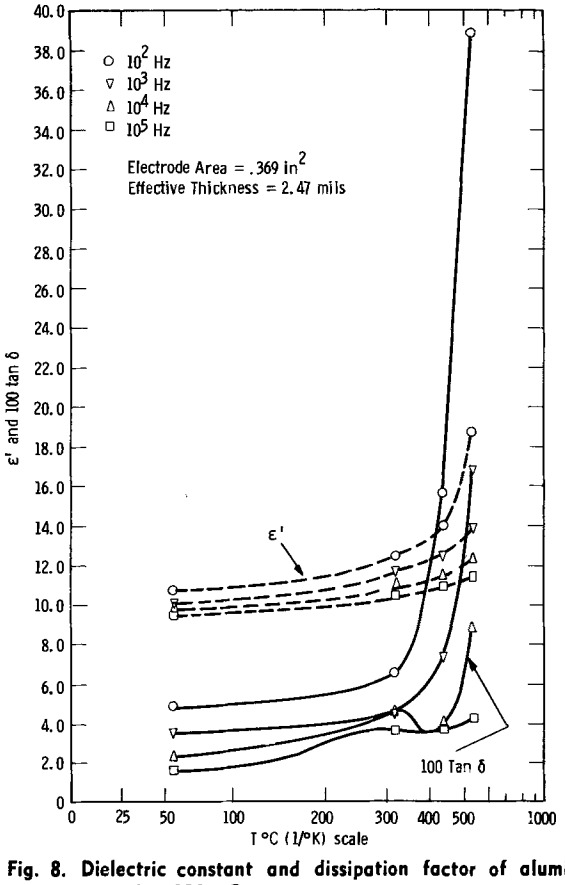

Fig. 8. Dielectric constant and dissipation factor of aluminum nitride, deposited at 1300°C.

Summary

Aluminum nitride coatings were pyrolytically deposited on refractory metal substrates using the volatile $AlCl_3 \cdot NH_3$ complex as the source material. Deposi-

tion rates depended on the temperatures of the substrates and the source material, and can be as high as 10 mils per hour. At a deposition temperature of 800°C, the transparent, amorphous films were subject to some atmospheric hydrolysis. Coatings deposited at 1300°C were stable, very hard, brittle, opaque, crystalline, and very adherent on molybdenum or tungsten. They offered considerable high-temperature oxidation protection to these refractory metals, but complete coverage of irregular surfaces was difficult. Electrical properties of these coatings are poorer than what is expected for high-purity aluminum nitride.

Acknowledgments

Support of this work by the Air Force Materials Laboratory, Wright Patterson AFB, is gratefully acknowledged. I also wish to acknowledge the assistance of Mrs. Mary L. Theodore, of the Analytical Chemistry Section, and Dr. T. W. Dakin, of Electrical Performance of Insulating Materials, of these Laboratories.

Manuscript received March 13, 1969. This paper was presented in part before the First Central Region Meeting, American Chemical Society, Akron, Ohio, May 9-10, 1968.

Any discussion of this paper will appear in a Discussion Section to be published in the June 1971 JOURNAL.

REFERENCES

1. K. M. Taylor and C. Lenie, *This Journal*, **107**, 308 (1960).
2. G. Long and L. M. Foster, *J. Am. Ceram. Soc.*, **42**, 53 (1959).
3. Von Th. Renner, *Z. Anorg. Allgem. Chem.*, **298**, 22 (1959).
4. T. L. Chu, D. W. Ing, and A. J. Noreika, *Solid-State Electron.*, **10**, 1023 (1967).
5. T. L. Chu, D. W. Ing, and A. J. Noreika, *Electrochem. Technol.*, **6**, 56 (1968).
6. G. A. Cox, D. O. Cummins, K. Kawabe, and R. H. Tredgold, *J. Phys. Chem. Solids*, **28**, 543 (1967).

Thin Tunnelable Layers of Silicon Dioxide Formed by Oxidation of Silicon

Alvin M. Goodman and James M. Breece

RCA Laboratories, Princeton, New Jersey

Although there is a considerable amount of information available about the thermal growth of relatively thick (200-90,000Å) SiO_2 films on Si as a function of time and temperature (1-8), there is comparatively little information published on the growth of thin tunnelable oxide layers at moderately elevated temperatures. The measurement of thin oxide layers by ellipsometry has been described by Archer (9), McCrackin *et al.* (10), Zaininger and Revesz (11), and Saxena (12). In addition, Archer (13) has described the growth of thin oxide films on Si in air at room temperature; these films continued to grow with time under room ambient conditions.

In the work described in this paper, a study was made of the growth of SiO_2 on freshly etched Si at 600°C in dry oxygen and in water vapor. The object of this work was to develop a technique for reproducibly fabricating thin tunnelable SiO_2 layers (on Si) and to determine the degree of thickness stability of these layers under room ambient conditions.

The layers described in this paper have been and are being used in MNOS memory capacitors and transistors of the tunneling-mode type described by Wallmark and Scott (14).

Layer Fabrication, Measurements, and Discussion

The oxidations were carried out in the center zone of a resistance heated 3-zone tube furnace. The center (flat) zone was maintained at 600° ± 1°C. For the dry oxidations, pure tank O_2 was passed through a Millipore Filter (0.2μ) and a dry ice trap into a quartz furnace tube (1.5 in. ID) at a flow rate of 80 cc/min (measured between the trap and the furnace). For the oxidations in water vapor, a quartz flask containing quadruple distilled water (maintained at 101°C) was connected to the furnace tube through quartz tubing. This quartz tubing was heated to prevent condensation on the inner walls. The vapor pressure over the water was 788 Torr (corresponding to 101°C). The vapor pressure at the sample is undoubtedly somewhat less although it is not accurately known. A region near the exit (open) end of the furnace was maintained at ~150°C; the use of this region will be discussed shortly.

The majority of the wafers used in the oxidation experiments were 6-13 ohm-cm, p-type with chemically polished 100 faces. A smaller number of "wet" oxidation experiments were carried out using wafers of different orientation and conductivity type; this is discussed later. All thickness measurements were made ellipsometrically.[1]

Our initial oxide growth results were not reproducible from day to day. A number of different wafer preparation procedures were tried before arriving at the following preoxidation wafer treatment.

Each wafer was: (i) cleaned in a solution of 4 parts distilled H_2O, 1 part H_2O_2 (30% stabilized), and 1 part NH_4OH (58%) by boiling for 5 min; (ii) triple rinsed in distilled H_2O; (iii) etched in concentrated HF for 2 min at room temperature; (iv) rinsed in distilled H_2O by diluting the HF and pouring off most of the diluted solution at least 5 times—*not allowing the wafer surface to be exposed to air until after the final dilution and rinse with H_2O*; (v) spun dry for 1 min in a clean Teflon spinner; and (vi) preheated in the 150°C region of the furnace for 2 min to drive off any remaining water (or other volatile contaminants).[2]

Each wafer was then placed in the 600°C zone of the furnace for the desired amount of time, after which the oxide thickness was measured as quickly as possible (within 2-3 min) and in some cases at various intervals thereafter.[3]

The results of the 600°C oxidations in dry oxygen are shown in Fig. 1, while the subsequent growth curves of three layers in room ambient are shown in Fig. 2.

[1] The thickness determinations were made using Saxena's correction [Fig. 2 of Ref. (12)] to the usual linear approximation (9, 11). Vedam (15) *et al.* have recently reported new values for the optical constants of silicon which are at variance with the generally accepted values (9, 11-13). If these new values had been used to obtain the film thicknesses from the ellipsometric measurements, the calculated film thicknesses would have been about 3.2% greater (16).

[2] When the furnace is connected to the water vapor source for the "wet" oxidations this step, of course, does not eliminate all water on the surface but instead brings it to a repeatable concentration before the oxidation at 600°C.

[3] The oxide thickness has also been checked at intermediate points in the preparation procedure. The oxide thickness measured (within 2-3 min) after the spin drying step has been found to be in the range 6-9Å. Similarly, the oxide thickness measured (within 2-3 min) after the preheating step has been found to be in the range 9-11Å.

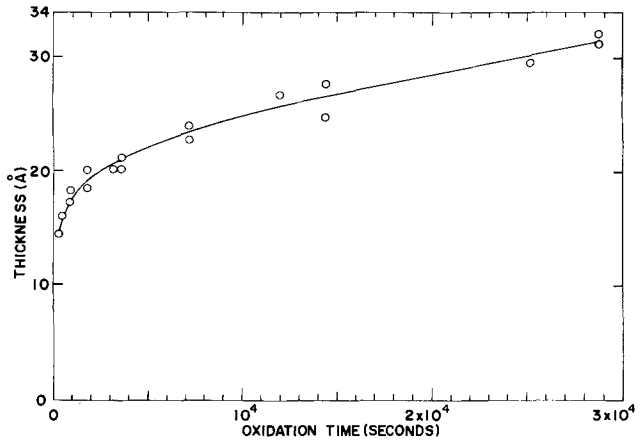

Fig. 1. Growth of silicon dioxide in dry oxygen at 600°C

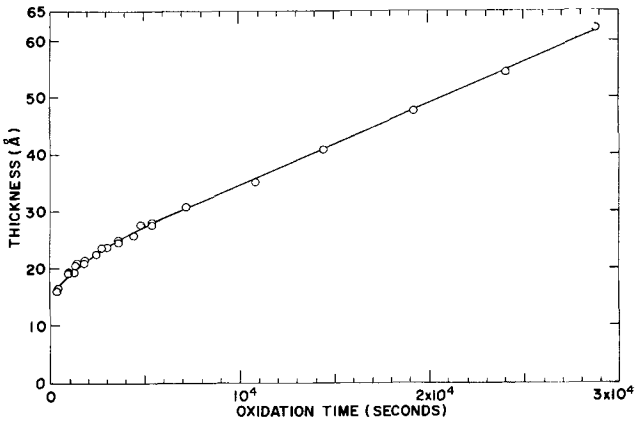

Fig. 3. Growth of silicon dioxide in water vapor at 600°C

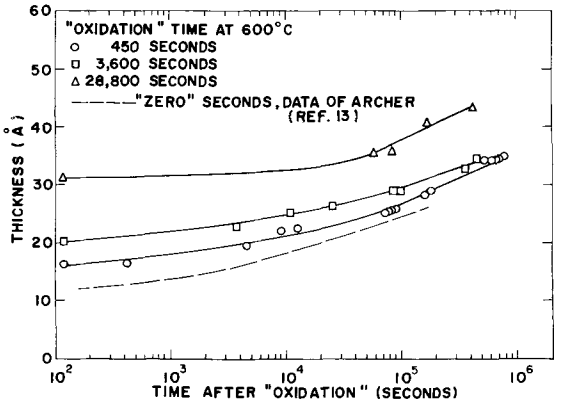

Fig. 2. Oxide growth in room ambient after "dry" oxidation at 600°C.

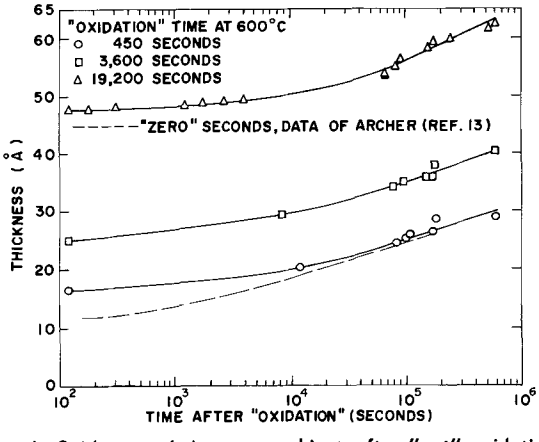

Fig. 4. Oxide growth in room ambient after "wet" oxidation at 600°C.

The room-temperature oxide growth found by Archer (13) is shown in Fig. 2 for comparison.

Only one of the experimental points in Fig. 1 lies more than 1Å off the smooth curve; it seems likely that this was due to a measurement error since a repeat oxidation for that time gave a thickness result within 1Å of the curve. It is apparent that there is a rapid initial growth region during which the growth rate diminishes with time. The growth becomes approximately linear with time for oxide thickness greater than about 25Å and the rate in this region is about 3.2×10^{-4} Å/sec. It is of interest to compare this rate with the values that can be extrapolated from the investigations of others at higher temperatures. From the dry oxidation work of Deal and Grove (3) (in the range 700°-1200°C), one would expect a growth rate of 5.5×10^{-5} Å/sec. Revesz and Evans (8) have investigated the dry oxidation of silicon both in an rf-heated system under "very clean" conditions in the range 900°-1300°C and in a resistance-heated alumina tube in the range 900°-1250°C. Their results were given in the form of values of the parameters a_o and Q_a where the rate constant a was given by $a = a_o \exp(-Q_a/kT)$. The resultant values of a at 600°C are 5.7×10^{-3} Å/sec for the rf-heated system and 2.4×10^{-4} Å/sec for the resistance-heated system.

The growth of the oxide layers after oxidation at 600°C, shown in Fig. 2, clearly indicates that the oxide thickness is not stable under room ambient conditions and that continued growth occurs at a rate similar to that for oxide growth on previously unoxidized Si wafers.

Figure 3 shows the results of the 600°C oxidations in water vapor; the subsequent growth of three "wet" oxide layers in room ambient is shown in Fig. 4. All of the data points in Fig. 3 are within ± 1Å of the smooth calibration curve. Other oxidations were carried out to check this curve and the resulting data points (not shown in Fig. 3) were also within ± 1Å of the smooth curve. Above an oxide thickness of about 25Å the growth rate is constant and equal to 1.4×10^{-3} Å/sec. This may be compared with the wet oxidation data of Deal and Grove (3) (in the range 900°-1200°C) from which one would expect a growth rate of $\sim 1.6 \times 10^{-3}$ Å/sec at 760 Torr of H_2O.

The wet oxidations of Revesz and Evans (8) were carried out in an alumina tube at a water vapor pressure of ~24 Torr; this was obtained by bubbling He through distilled water and then passing the "wet" He through the furnace tube. If one extrapolates their results (in the range 920°-1200°C) to 600°C, a linear rate constant of 7×10^{-5} Å/sec is obtained. If one assumes that the rate constant depends linearly on water vapor pressure, then this would be equivalent to a rate constant value of 2.2×10^{-3} Å/sec at 760 Torr. The agreement between these linear growth rates is better than one would expect considering the uncertainty of the water vapor pressure in each case and the fact that the growth rates for Ref. (8) and (9) are extrapolated to 600°C from experimental data at temperatures at least 300° higher.

Below an oxide thickness of about 25Å, the growth rate is higher than the linear value and not constant. A rapid initial growth phase of this type is usually observed in dry oxidations but has apparently not previously been observed in the case of oxidation in a wet ambient (17). A possible reason for this is discussed in the next section.

The growth of the "wet" oxide layers after oxidation at 600°C shown in Fig. 4 is similar to that found for the "dry" oxide layers in Fig. 2. In both cases the oxide thickness is not stable under room ambient conditions and continued growth occurs at a rate similar to that for oxide growth on previously unoxidized Si.

It is desirable for many purposes to reduce the interface state density by high-temperature annealing (18). Annealing of both "dry" and "wet" oxide layers in H_2 at 500°C for 1 hr produced no detectable growth.

Further Discussion—Oxidation Mechanisms

Deal and Grove (3) have explained the lack of observation of rapid initial growth in the wet oxidation case as follows. There is a rapid initial oxidation phase associated with the transport of an ionic species and such a phase is to be expected until the oxide thickness is large in comparison with the space-charge layer extent within the oxide. The extent of the space-charge region is characterized by the extrinsic Debye length

$$L_D = [(kT/e)(K\epsilon_0/2eC)]^{1/2}$$

where k is Boltzmann's constant, T is the absolute temperature, e is the magnitude of the electronic charge, K is the oxide relative dielectric constant (3.8 for SiO_2), ϵ_0 is the permittivity of free space, and C is the equilibrium concentration of the ionized oxidant in the oxide at the free surface. For "wet" oxidation at 1000°C, the value of C is about $3 \times 10^{19}/cm^3$ and L_D is ~6Å. Thus, the rapid initial oxidation phase would not have been observed using the multiple beam interferometric measurement technique [employed in Ref. (3)] with an accuracy of ± 25Å or any other measurement technique with a similar accuracy. On the other hand, for oxidation at 1000°C in dry O_2, they found that C is about $5 \times 10^{16}/cm^3$ and the resultant value of L_D is ~150Å. This corresponded well to their experimental observation of rapid growth of dry oxide in the region below about 200-300Å.

The temperature dependence of C in the range 900°-1200°C is very weak for both "wet" and "dry" oxidation and L_D does not vary greatly (3). If the same temperature dependence holds down to 600°C, the "wet" oxidation result observed in the present work (Fig. 3) is in accord with the explanation presented above. However, this would mean that the dry oxidation observed in the present work was still in the initial rapid growth region and a lower linear rate constant would be expected if the dry oxidation studies were extended to much greater oxidation times.

In addition to the work described in the previous section, some additional "wet" oxidation experiments were carried out using 7-11 ohm-cm p-type wafers with 111 faces and 7-13 ohm-cm n-type wafers with both 100 and 111 faces. The oxide layers grown during these experiments were all in the 16-32Å range; the resulting data were within ± 1Å of the smooth curve in Fig. 3. If the dominant rate-limiting step in the oxidation were at the $Si-SiO_2$ interface, one would expect the oxidation rate to be orientation-dependent (19). This is clearly not the case in the rather limited range studied here.

An examination of Fig. 2 and 4 shows that the growth of the oxide layers in room ambient after oxidation at 600°C is similar in character to the growth of oxide on freshly etched silicon reported by Archer (13). That is, the oxide thickness after long exposure to room ambient seems to be a logarithmic function of time. The logarithmic growth rate (Å/decade of time) varied from sample to sample but this is to be expected since the room ambient was not controlled. The variability of the room ambient is also the reason for the somewhat greater scatter of points in Fig. 2 and 4 than in Fig. 1 and 3. A variety of models exhibiting a logarithmic oxide growth law has been described by Kubaschewski and Hopkins (20); another model leading to this type of growth has been suggested more recently by Ritchie (21). We do not have sufficient information at this time to decide which (if any) of these models is applicable.

Conclusions

The results of the experiments described in this paper lead to the following conclusions:

1. It is possible to reproducibly grow thin tunnelable layers of SiO_2 on Si by both wet and dry oxidation at 600°C.
2. After the high-temperature growth period, the oxide layers continue to grow under room ambient conditions at a reduced rate.
3. The oxide layer thickness remains stable during annealing at 500°C in H_2 for 1 hr.

Acknowledgment

The authors wish to thank J. H. Scott, Jr., A. N. Saxena, and K. H. Zaininger for helpful aid and advice.

Manuscript submitted July 1, 1969; revised manuscript received Feb. 24, 1970.

Any discussion of this paper will appear in a Discussion Section to be published in the June 1971 JOURNAL.

REFERENCES

1. J. T. Law, *J. Phys. Chem.*, **61**, 1200 (1957).
2. B. E. Deal, *This Journal*, **110**, 527 (1963).
3. B. E. Deal and A. S. Grove, *J. Appl. Phys.*, **36**, 3770 (1965).
4. A. G. Revesz, K. H. Zaininger, and R. J. Evans, *Appl. Phys. Lett.*, **8**, 57 (1966).
5. P. J. Burkhardt and L. V. Gregor, *Trans. Met. Soc. AIME*, **236**, 299 (1966).
6. W. A. Pliskin, *IBM J. Res. Develop.*, **10**, 198 (1966).
7. T. Nakayama and F. C. Collins, *This Journal*, **113**, 706 (1966).
8. A. G. Revesz and R. J. Evans, *J. Phys. Chem. Solids*, **30**, 551 (1969).
9. R. J. Archer, *J. Opt. Soc. Am.*, **52**, 970 (1962).
10. F. L. McCrackin, E. Passaglia, R. Stromberg, and H. L. Steinberg, *J. Res. Nat. Bur. Stds.*, **67A**, 363 (1963).
11. K. H. Zaininger and A. G. Revesz, *RCA Rev.*, **25**, 85 (1964).
12. A. N. Saxena, *J. Opt. Soc. Am.*, **55**, 1061 (1965).
13. R. J. Archer, *This Journal*, **104**, 619 (1957).
14. J. T Wallmark and J. H. Scott, Jr., *RCA Rev.*, **30**, 335 (1969).
15. K. Vedam, W. Knausenberger, and F. Lukes, *J. Opt. Soc. Am.*, **59**, 64 (1969).
16. A. N. Saxena, Personal communication.
17. A. S. Grove, "Physics and Technology of Semiconductor Devices," p. 31, John Wiley & Sons, Inc., New York (1967).
18. W. E. Dahlke, *Appl. Phys. Lett.*, **10**, 261 (1967).
19. J. R. Ligenza, *J. Phys. Chem.*, **65**, 2011 (1961).
20. O. Kubaschewski and B. E. Hopkins, "Oxidation of Metals and Alloys," Chap. 2, Butterworth and Co., Ltd., London (1962).
21. I. M. Ritchie, *Phil. Mag.*, **19**, 421 (1969).

DISCUSSION SECTION

This Discussion Section includes discussion of papers appearing in the *Journal of The Electrochemical Society*, Vol. 116, No. 9 and 10 (September and October 1969).

A High-Voltage, Solid-State Battery System

I. Design Considerations

C. C. Liang and P. Bro (pp. 1322-1323, Vol. 116, No. 9)

II. Fabrication of Thin-Film Cells

C. C. Liang, J. Epstein, and G. H. Boyle
(pp. 1452-1454, Vol. 116, No. 10, 1969)

G. Bégin and R. Le Houillier[1]: We have read with great interest these excellent papers showing the feasibility of thin film solid electrolyte battery systems.

[1] Hydro-Québec Institute of Research, 75 Dorchester Blvd. West, Montreal 128, Que., Canada.

We would like to mention in this respect that, while working on a similar system involving bromide instead of iodide, we have obtained nearly identical results.

We, however, feel that it is worth mentioning the different conceptual approach that we used. First, we built the cell in the discharged state simply by making Ag/LiBr/Ag sandwiches. Electrolysis of the halide then insured the charging of the cell. We have then been able to observe several reproducible cycles of charges and discharges of the elementary cell.

A second difference consisted in the manufacturing of the cell. Instead of going into sophisticated vacuum deposition techniques, we simply dipped the silver electrodes into the molten halide. They were then pressed against each other after removal from the melt.

Errata

In the paper "Ultrafine Porous Polymer Membranes as Battery Separators" by J. L. Weininger and F. F. Holub which appeared on pp. 340-342 of the March 1970 issue of the JOURNAL, Vol. 117, No. 3, the last line of Table I, page 341, "Tortuosity Factor," should read "20 7.1 31" instead of "3.1 1.2 4.0."

In the paper "Study of the Behavior of Ethylene Carbonate as a Nonaqueous Battery Solvent" by Gianfranco Pistoia, Mario De Rossi, and Bruno Scrosati which appeared on pp. 500-502 of the April 1970 issue of the JOURNAL, Vol. 117, No. 4, there are several errors, corrections for which follow.

Page 500, column 1—In line 5 of paragraph 5, "Carbowax" should read "Charbowax." Column 2— In line 3, in the sentence beginning "The salts generally used . . . ," the last word should read "are" instead of "were." Table I—The last item in column 4 should read "2.0 (40°C)[c]" instead of "2.3 (40°C)[c]."

Page 501—In Table III, column 3 should read "11.84 (1.3m; 1.6*N*); 11.32 (1.0m; 1.2*N*); 7.87 (0.85m; 1.0*N*)" instead of "11.84 (11.3M; 1.6*N*); 11.32 (1.0M; 1.2*N*); 7.87 (0.85M; 0.89*N*)." In column 1, line 17 of text, "0.85M" should read "0.85m." In the third paragraph from the bottom of column 1, in lines 3 and 4, "1.3M, 1.0M, 0.85M" should read "1.3m, 1.0m, 0.85m." In the next to the last line of the next to last paragraph, "1M" should read "1m" and the comma at the end of the sentence should be replaced with a period. In the second line of the last paragraph, "(10 mA/cm^2)" should read "(5 mA/cm^2)." Column 2—In the first line of the caption for Fig. 2, "10 mA/cm^2" should read "5 mA/cm^2." In lines 6 and 18 of the text, "0.85M" should read "0.85m." In line 11, "CuF" should read "CuF_2."

Page 502—In the 1st line of the caption for Fig. 3 and the last line of Table IV, "0.85M" should read "0.85m." In Ref. (8), the correct title is "*Proc. Ann. Power Sources Conf.*"

JOURNAL OF THE ELECTROCHEMICAL SOCIETY

ELECTROCHEMICAL SCIENCE

AUGUST 1970

ES

Morphological Changes in the Lead Dioxide Electrode During Its Reduction and Reoxidation

A. C. Simon,* C. P. Wales,* and S. M. Caulder*,[1]

Naval Research Laboratory, Electrochemistry Branch, Washington, D. C.

ABSTRACT

The discharge and recharge of the PbO_2 electrode was followed by optical microscopy. During discharge the PbO_2 dissolved with simultaneous growth of relatively large $PbSO_4$ crystals. $PbSO_4$ nucleated at preferred sites on the PbO_2 and did not form a passivating film over other parts of the PbO_2 surface. The PbO_2 remaining at the end of discharge, however, had been encapsulated within $PbSO_4$ crystals grown during the discharge. During recharge these PbO_2 particles within the $PbSO_4$ crystals offered a conductive path through the highly resistive $PbSO_4$, and the formation of PbO_2 began within the encapsulating $PbSO_4$ crystals at the surface of these residual PbO_2 particles. PbO_2 thus formed grew rapidly toward the surface of the $PbSO_4$ crystals and, when reaching the surface, appeared to spread to surround the $PbSO_4$ crystals, encapsulating them in turn and leaving hollow shells as the $PbSO_4$ crystals dissolved.

The lead dioxide electrode has been, and still continues to be, the subject of considerable investigation. Despite this intensive study there still remains a number of unsolved problems concerning the behavior of this electrode, particularly when it is used as one electrode of the lead-acid storage battery.

Although numerous ingenious techniques have been developed to study the reactions taking place at this electrode during the charging and discharging of the battery, there has been surprisingly little effort made toward direct microscopic examination of the crystallogenesis in this electrode. This is remarkable since the physical condition of the electrode and its microstructure influence the degree of porosity, available reactive surface and reaction rate, and undoubtedly affect the efficiency of use of the reactive material present.

The process of charge and discharge at the electrode has been studied by Feitknecht and Gaumann (1) and also by Hisano (2), using electron microscopy. However, these studies were confined to the formation of passivating layers of $PbSO_4$ on the surface of soft lead and the subsequent further oxidation of these layers to lead dioxide. There still remained the question as to whether the PbO_2 of the active material would behave in a manner similar to that observed for the PbO_2 corrosion product of lead.

Koval and Barilenko (3) studied the charge-discharge process that occurred in the active material of actual battery plates, using optical and electron microscopy. However, their principal interest was in the effect caused by $BaSO_4$ which had been incorporated into the PbO_2 electrode. Moreover, although their photomicrographs show a definite change in the size of the $PbSO_4$ crystals formed in the presence and absence of the $BaSO_4$, there is very little additional information that can be obtained concerning the nature of the microstructure of the active material.

Further study of the actual crystallographic changes occurring in the active material during charge and discharge of the lead dioxide electrode therefore seemed to be necessary. Methods had been developed in this Laboratory (4) to study the actual microstructure of lead dioxide and other electrodes. Using these methods, numerous sections of charged positive battery plates had been examined in this Laboratory as well as a smaller number of discharged plates. In addition, a microscopic study had been made of the mechanism of electrolytic formation and the crystallographic changes that occurred in the positive electrode during the forming process (5).

Using these techniques and improvements of their own devising, Bagshaw (6) and Pierson (7) carried out further investigations of the process by which the PbO_2 electrode is electrolytically formed (oxidized) from an original mixture of PbO and basic lead sulfates. In addition, a very creditable cinematographic study of the actual electrolytic formation of the lead dioxide electrode has been prepared (8).

Despite these earlier successes, similar studies have not been made of the charge-discharge process at the PbO_2 electrode is electrolytically formed (oxidized) this process by similar techniques. Examination of completely charged or fully discharged plates gave no information of the mechanism by which the microstructural changes took place. Therefore, an experiment was set up to allow examination of sectional electrodes removed during intermediate stages of the charge-discharge process.

Procedure

The electrodes used in this investigation were commercial battery plates, received cured but unformed. The test cell consisted of two positive and three nega-

* Electrochemical Society Active Member.
[1] International Lead Zinc Research Organization Research Associate at the Naval Research Laboratory.

tive plates, and portions of the positive plate were removed at appropriate intervals during discharge and subsequent recharge. In order to insure that the test portions were of equal size and that there would be no distortion of the active material during removal of the portions, the plate was given a preliminary treatment before forming. This consisted of division of the plate into thirds by removal of the active material from between vertical grid bar rows at two locations and into sixths by the subsequent removal of active material from between horizontal grid bars midway between top and bottom of the plate. The apportioning was done in a manner to insure that the remaining pasted portions were of nearly equal area. In addition, a number of the horizontal and vertical wires were removed from the grid in the open rows, leaving just enough grid bars to give support and conductivity for the rates of charge and discharge used. This preparation of the plate made subsequent removal of portions very easy and rapid, and with minimal distortion to either the portion removed or that remaining.

The plates were formed in 1.11 sp gr acid. A current of 1.5A was used for 27 hr with the final potential reaching 2.34V. The current was then lowered to 1.0A and the cell was charged for an additional 20.3 hr to a constant potential of 2.42V. The forming acid was then replaced by 1.25 sp gr acid and the cell was on stand in this acid for 3.15 hr before the first discharge was commenced. The first discharge, which lasted for 19.3 hr, was made at the 1.0A rate but subsequent discharges were made at 3.0A. Discharge capacity declined from 18.3 A-hr at cycle 2 to 17.1 A-hr at cycle 8. All discharges were terminated at 1.80V. For identification purposes the initial forming and subsequent discharge are designated as the first cycle. All charges after the forming charge were done at 1.0A. At cycle 8, the usual charge at 1.0A was followed by a floating period at 2.25V for 72 hr.

At the beginning of the 9th cycle, after insuring that the cell was again in a fully charged state, a portion of one positive plate was removed for examination and the necessary adjustments were then made in cell current to compensate for the removal. Following this, a discharge was made at a rate equivalent to that used in the previous cycles and other portions of the plate were removed at five equal intervals based on the estimated capacity and a discharge terminating at 1.80V. With the removal of each portion the current was adjusted to compensate, so that the current density remained the same throughout the discharge.

One positive plate was thus investigated during its discharge and the other, which had been carried through the same discharge, was similarly removed in six portions during the subsequent recharge. The charge and discharge conditions and the points at which samples were removed are shown in Fig. 1.

The area of the negative plates remained greater than that of the positive throughout the experiment and there was also a large excess of electrolyte. Very little change from room temperature of 25°C occurred within the cell during the experiment.

Following removal, the various portions were immediately washed in running water, dried, and additional pellets punched out to obtain material for DTA and x-ray analysis. The remainder of each plate portion was then impregnated with a catalyzed polyester. After the hardening and curing of this resin each plate portion was sectioned and the individual sections were polished for examination by optical microscopy.

Observed Changes in Microstructure

The lead dioxide electrode in its oxidized or charged state was found by x-ray diffraction analysis to consist practically entirely of β-PbO_2, which had a microstructure that was cell-like or reticulate in nature. This was evident after cross sections had been made through the resin-impregnated electrode structure and

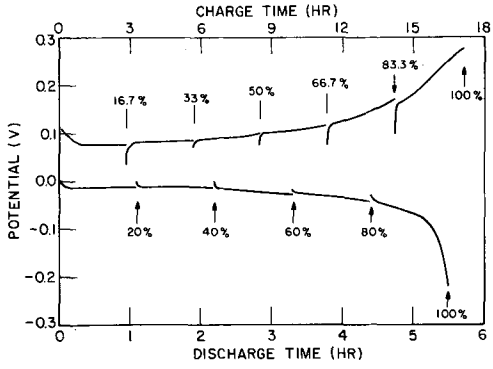

Fig. 1. Potentials of positive plate vs. $PbSO_4/PbO_2$ reference electrode, during 9th discharge (bottom) and subsequent recharge (top). At each arrow current was interrupted while a portion of the plate was removed. Numbers by the arrows indicate per cent that the plate had been discharged or charged.

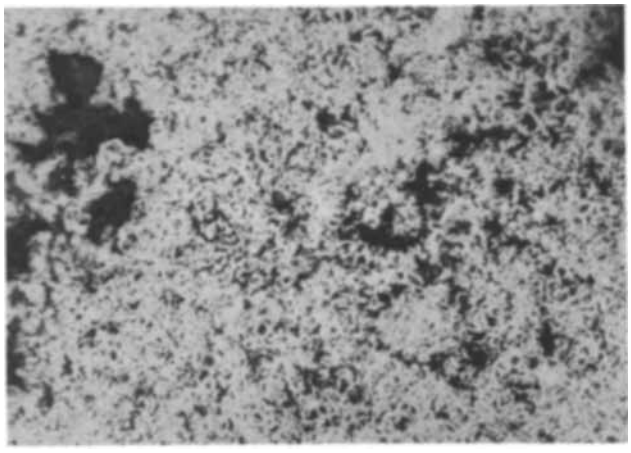

Fig. 2. Structure found in a fully charged plate. Unpolarized, vertically reflected illumination is used in this and subsequent photographs so that the reflective areas which appear bright in the photograph represent hard, dense PbO_2 particles, while the dark areas represent the voids of the plate. Note that, with the exception of a very few larger areas of porosity, the active material had a very uniform structure. The PbO_2 formed a nearly continuous cellular network, as in a sponge. Original magnification 400X.

these sections then suitably polished. An example of this type of structure is shown in Fig. 2. In this photograph the dark areas represent former voids in the plate which are now filled with the impregnating resin. The bright network represents a densely constituted PbO_2 structure which in actuality is dark brown or black. It appears white in the photograph because this and the following photographs were taken with vertical illumination of the polished surface. Under vertical illumination smooth and dense areas tend to reflect the light directly back through the eyepiece and such areas thus appear bright, or white in a photograph.

It can be noted that the lead dioxide in the network structure has an almost metallic luster, indicating a dense, hard material. If oblique lighting is used this white network is seen to be in relief upon the surface, which also indicates that the material of the network is hard, at least harder than the plastic with which the electrode material was impregnated.

Discharge process.—The initial nucleation and growth of $PbSO_4$ crystals was not observed. The first examination, when the electrode had been 20% discharged, showed that a number of crystals of normal lead sulfate, $PbSO_4$, had formed in a random fashion throughout the active material. These crystals had a reflectivity intermediate between that of the plastic and the PbO_2 so that they could be easily identified. In addition these crystals were almost invariably sur-

rounded by some void area, represented by the impregnating plastic, so that their visibility was increased. The distribution was truly random, with no greater concentration of the lead sulfate crystals in one area than another, such as at the surface or near the grid members.

The crystals were distinctly rectilinear and it was found that there was not much difference in the maximum crystal size when the 20% discharged plate was compared with that which had been 40% discharged. The total number of crystals, however, had noticeably increased in the 40% discharged electrode.

It seemed that the growth of the $PbSO_4$ crystals was slowed by some factor when the crystals reached a certain size so that growth practically stopped and new nuclei were necessary to allow the process to continue. Any of a number of factors could cause such a slowdown of crystal growth but the most probable is the depletion of one of the reacting ions at the surface of the growing crystal. The appearance of the 40% discharged plate may be estimated from Fig. 3.

At greater than 40% discharge the crystals were found to be larger. It seemed that, as sites for nucleation on the PbO_2 surface were depleted, the $PbSO_4$ crystals were crowded closer together and tended to grow upon one another so that agglomeration was increased. There was also probably continued slow growth of the earlier formed $PbSO_4$ crystals so that all of the crystals of $PbSO_4$ tended to merge together (Fig. 4). Nevertheless, their separate identity was distinguishable at high magnification.

The increase in size of the $PbSO_4$ crystals was, of course, at the expense of surrounding PbO_2, which was being dissolved at a rate proportionate to the growth of the $PbSO_4$ crystals. Comparison of Fig. 3 and 4 illustrates another characteristic of the discharge process. As the reduction of the PbO_2 to $PbSO_4$ continued, the amount of the bright shiny network of PbO_2 steadily diminished until at the end of the discharge it did not resemble a network but seemed to consist only of scattered individual particles of β-PbO_2. Although the specific volume of the $PbSO_4$ is greater than that of the PbO_2, the $PbSO_4$ forms as regular crystals that are more compact than the porous network structure of the original PbO_2. This compact form insures that the crystals of $PbSO_4$ continue to find space for growth, as can be seen in the photographs. The destruction of the PbO_2 structure during discharge is made evident by comparison of Fig. 5 and 6.

At the higher magnification of Fig. 4 it can be seen that practically all of the remaining PbO_2 particles are encapsulated within the large $PbSO_4$ crystals. It should be remembered that these photographs are of cross sections so that the white or mottled areas of PbO_2 seen surrounded by $PbSO_4$ at the surface of the section are in reality buried within the $PbSO_4$ crystals.

When polarized light was used in the examination of the sections, it was found that the $PbSO_4$ crystals did not show up well, particularly for the sections 20 or 40% discharged. At high magnification, using oil immersion it was found that as the extent of the discharge increased more of these crystals became visible, evidently because more became oriented so as to give reflections from lower surfaces. In every case, however, many more crystals were seen by vertical illumination with unpolarized light than with po-

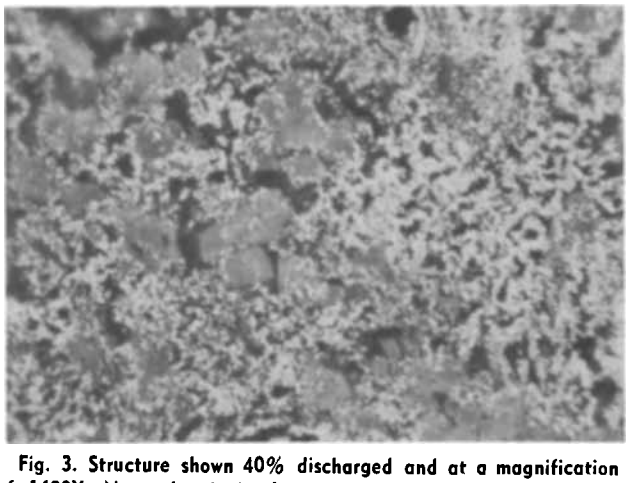

Fig. 3. Structure shown 40% discharged and at a magnification of 1600X. Note the distinctly rectilinear nature of the $PbSO_4$ crystals and that they seem to be present in small clusters.

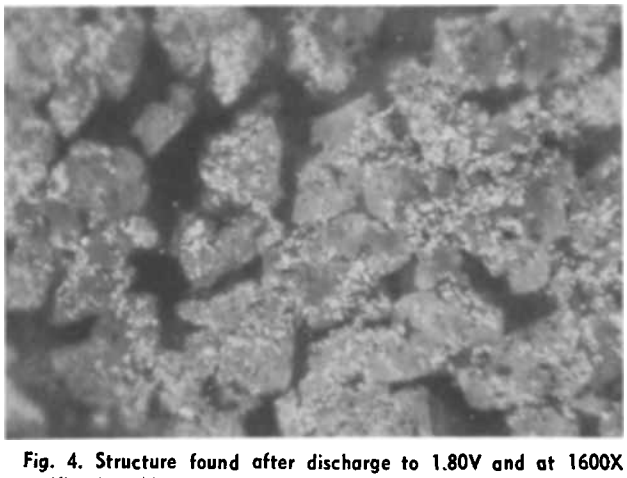

Fig. 4. Structure found after discharge to 1.80V and at 1600X magnification. Note particularly that access to remaining PbO_2 is not lost as a result of the $PbSO_4$ blocking the plate voids (still numerous), but that the PbO_2 has been rendered inaccessible by becoming encapsulated within the $PbSO_4$ crystals themselves.

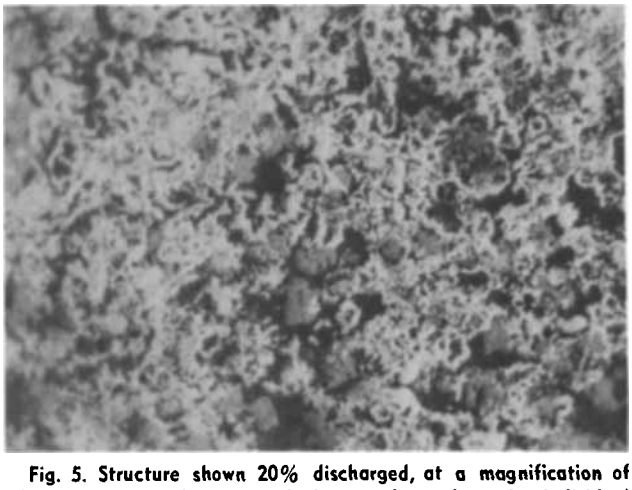

Fig. 5. Structure shown 20% discharged, at a magnification of 800X. This magnification is high enough to show the individual particles of PbO_2 and $PbSO_4$ and the field of view is sufficient to give an idea of general distribution of particles.

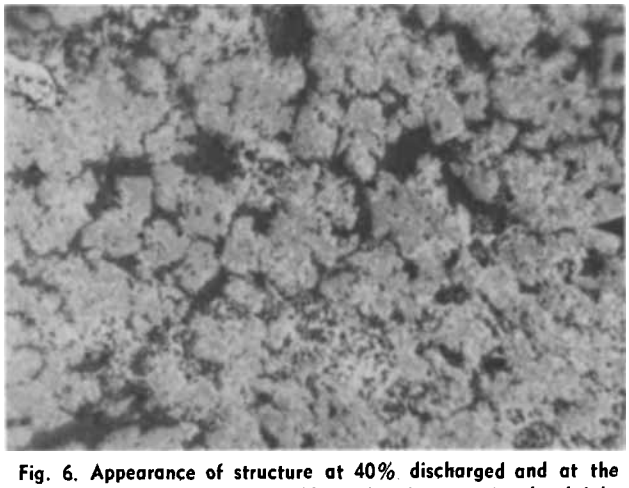

Fig. 6. Appearance of structure at 40% discharged and at the same magnification as Fig. 5. Note the decrease in the bright PbO_2 and the increase in the gray areas of lead sulfate.

larized. The crystals that could be seen by polarized light seemed to be colorless and to have a regular rectilinear form with few internal imperfections.

Another feature that was noted under polarized light was a small but distinct change of the PbO_2 to a lighter red color at the surface of the plate in those sections that had received one-half or more of the total discharge. This color change appeared only at the surface of the electrode and extended to a depth of not more than 10-20μ. It seemed that this color change took place within individual PbO_2 particles and that the color changed from a dark brown or red to a light red-orange. Examination of the surface of such electrodes after drying and before the plastic impregnation, and without the use of magnification or polarized light showed only a change from reflective black to dull brown during the course of the discharge.

Recharge process.—In many ways the oxidation or recharge of the electrode was a reverse replay of the changes that had been observed during discharge but there were some differences which at first appeared conflicting.

In examination at lower magnification it seemed that there was little change in the size or number of lead sulfate crystals as the recharge proceeded to 50%. At the same time there seemed to be a small increase in the amount of the PbO_2 network, evidenced by an increase in the bright network that had been present before discharge.

Comparing the samples at somewhat higher magnification also seemed to verify that the appearance of the $PbSO_4$ crystals was remaining practically unchanged between 17 and 50% recharged. Compare, for example, Fig. 7 and 8. The apparently unchanged $PbSO_4$ crystals and the small increase in the PbO_2 network up to the 50% recharged (Fig. 8) was puzzling, especially when compared with the considerable change that took place between 50 and 66% recharged (Fig. 9). These results made it appear that more PbO_2 was formed during the second half of the recharge than during the first half.

This inconsistency was explained, however, at the higher magnification of 1600X which revealed details that made evident what actually had occurred. In the electrode that was recharged up to 33% of the fully charged state it was found that the increase in the PbO_2 particles had occurred almost entirely within the lead sulfate crystals, with only a very few PbO_2 particles appearing at the $PbSO_4$ crystal surfaces. Thus, while a conversion of $PbSO_4$ to PbO_2 was occurring within the $PbSO_4$ crystals, their external size and form were not altered (Fig. 10). By the time that the electrode was 50% recharged the PbO_2 particles appearing at the surface of the $PbSO_4$ crystals had become quite numerous (Fig. 11) and with increasing recharge all the PbO_2 particles seemed to form at the surfaces of the remaining $PbSO_4$ crystals (Fig. 12).

Beyond 50% recharge, the $PbSO_4$ crystals definitely decreased in size while the PbO_2 now formed entirely at their surfaces and more completely encircled their dwindling masses. This caused the formation of hollow shells (Fig. 12), seen as circles in the cross section. Finally, all of the $PbSO_4$ was converted to PbO_2 and

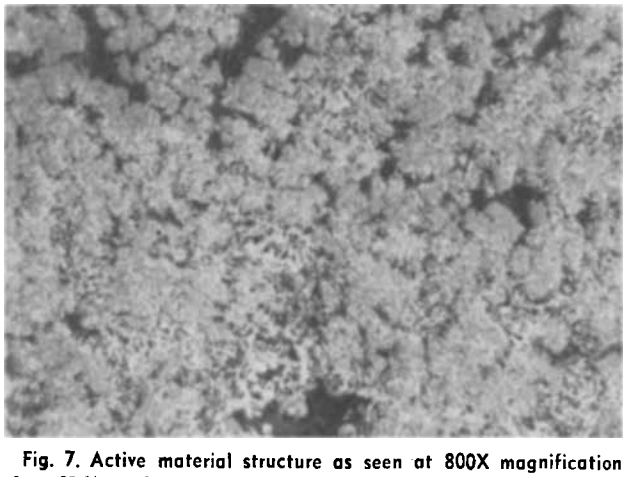

Fig. 7. Active material structure as seen at 800X magnification after 17% recharge. Notice the considerable amount of bright PbO_2.

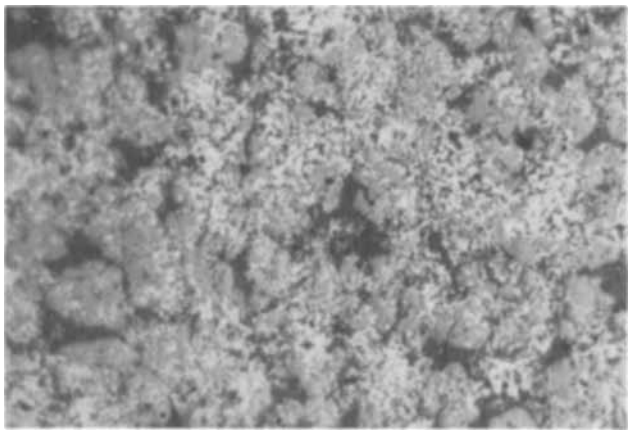

Fig. 8. Active material structure as seen at 800X magnification and after 50% recharge. Note comparatively unchanged appearance of the $PbSO_4$ areas in this photomicrograph as compared with Fig. 7. Also note that, while the amount of bright PbO_2 has increased in Fig. 8, the PbO_2 in both photographs is mainly within the $PbSO_4$ crystals and not at their surfaces.

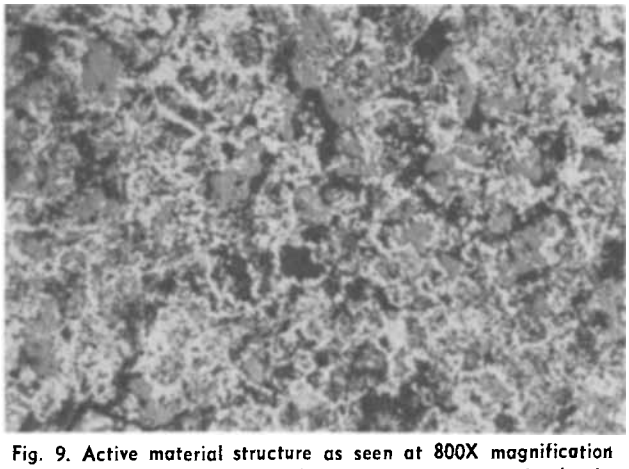

Fig. 9. Active material structure as seen at 800X magnification and after 66% recharge. Note the distinct increase in the bright PbO_2, and that this increase is now primarily at the surface of the $PbSO_4$ crystals.

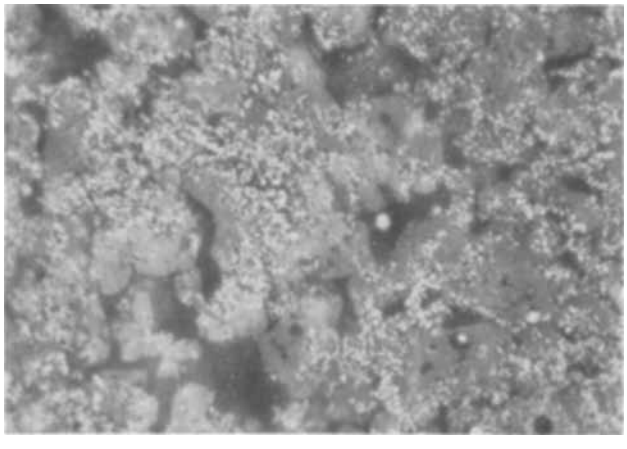

Fig. 10. Active material structure as seen at 1600X magnification and after 33% recharge.

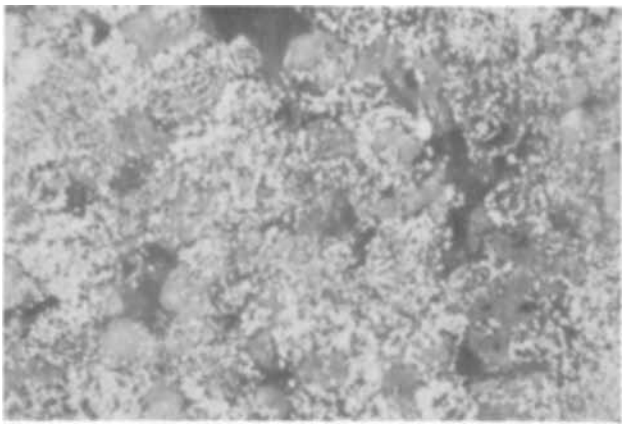

Fig. 11. Active material structure as seen at 1600X magnification and after 50% recharge.

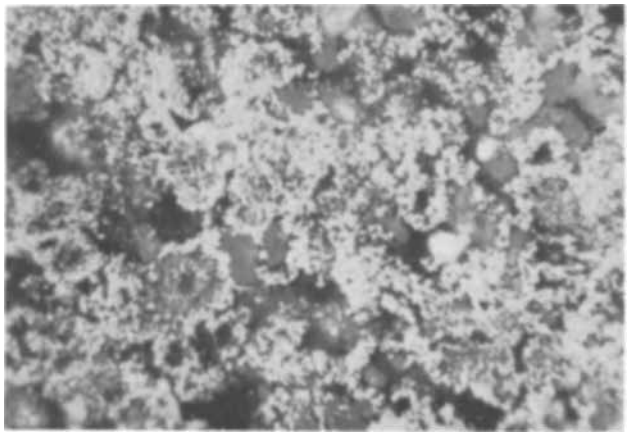

Fig. 12. Active material structure as seen at 1600X magnification and after 66% recharge.

the structure then assumed practically the same configuration as in Fig. 1. The size of the cells outlined by the PbO_2 and their configurations, do not necessarily follow that of the $PbSO_4$ crystals upon which they were formed. As previously stated, many of the $PbSO_4$ crystals contain residual PbO_2 upon which the PbO_2 of the recharge process nucleates and grows. This residual PbO_2 is itself assumed to be a connected network and the further growth of PbO_2 causes the formation of additional network within the $PbSO_4$ crystals. During its growth toward the surface this additional network subdivides the space from which the $PbSO_4$ crystal dissolves. This PbO_2 increase within, as well as at the surface of, the original $PbSO_4$ crystals causes the resultant PbO_2 structure to differ from that of the $PbSO_4$ crystals from which it was formed.

It had been observed that a thin surface layer of the active material changed from dark to light when the discharge was about half completed. This thin surface layer of lighter colored material remained during the subsequent recharge until the electrode was about one-half recharged, at which point the color became darker and indistinguishable from that of the rest of the electrode and no further change was detected throughout the remaining period of charge.

The series of samples from the discharge and subsequent recharge were also examined by x-ray and differential thermal analysis, but without uncovering any additional information. The x-ray analysis, as would be expected, showed increasing $PbSO_4$ and diminishing PbO_2 intensities as the discharge proceeded. This situation was reversed on the subsequent recharge. Plotting the relative intensities against the percentage of discharge or recharge revealed that the curve of intensities for discharge was almost exactly duplicated on recharge.

Discussion

From the above observations it would seem that the process of discharge began with the nucleation of $PbSO_4$ at various selected sites on the surface of the PbO_2, such sites always being adjacent to porous areas of the electrode. In other words the nucleation occurred at surfaces of the PbO_2 that were in contact with the electrolyte, either at the surface of the electrode or at the surfaces of the various pores and cavities within the electrode to which electrolyte had penetrated. Since PbO_2 is a relatively good conductor of electricity, differences in conductivity do not seem to be the reason for this process of nucleation occurring more frequently at one area of the electrode than at another. No noticeable difference was found in the extent of the $PbSO_4$ crystal growth near the grid or near the surface, as long as electrolyte was able to penetrate freely into the area.

Once the $PbSO_4$ crystals are nucleated further growth seems to depend on the continued dissolution of the PbO_2 crystals in the immediate vicinity, reaction between the Pb^+ and $SO_4^=$ ions, and redeposition as $PbSO_4$ upon the surface of the $PbSO_4$ crystals already present. There was no evidence that the $PbSO_4$ was forming any layer, passivating or otherwise, upon portions of the PbO_2 surface other than where nucleation had taken place.

As the discharge continued, further deposition of $PbSO_4$ was almost entirely upon already existing crystals so that these increased in size until many grew into a continuous mass containing more than one crystal. During this process of $PbSO_4$ formation, the amount of PbO_2 steadily decreased, as would be expected, until finally all PbO_2 that remained appeared to be encapsulated in the $PbSO_4$.

One assumes that initially the PbO_2 network was a continuous electrical circuit and that the electrolytic process that was making Pb^{++} ions available continued from all points of this surface except those actually covered by portions of growing sulfate crystals. Even if it is assumed that all PbO_2 particles are in contact and are part of the electric circuit of the plate at the beginning of the discharge, there is no certainty that all will remain so. Unequal solution of PbO_2 undoubtedly will remove a few PbO_2 particles from the circuit. In the path of the growing $PbSO_4$ crystals, supplied with $PbSO_4$ from other PbO_2 areas, such particles might become encapsulated and completely surrounded by $PbSO_4$. Alternatively, it is probable that at some points the continued growth of the $PbSO_4$ crystals in certain directions might cause them to grow around and encapsulate portions of the remaining PbO_2 network that yet might remain in the electrical circuit of the plate. The complexity of the PbO_2 structure insures numerous contacts between neighboring particles so that it is likely that most particles continue in the circuit even when a number of contacts have been lost. This seems to be indicated by the relatively complete conversion of the PbO_2 to $PbSO_4$. If it is assumed that the observed encapsulated PbO_2 is still in the electrical circuit of the plate several of the observed phenomena can be more easily explained, but there is, as yet, no definite evidence that such a circuit exists.

If a conductive network of PbO_2 does remain during and after the formation of the $PbSO_4$ crystals we have a ready explanation of how, in a material as nonconductive as $PbSO_4$, an electrical path is furnished both during discharge and the subsequent recharge. Because of the high electrical resistivity of $PbSO_4$ such a conductive network would be most beneficial.

The fact that in the initial stages of the recharge process PbO_2 was found to increase within the $PbSO_4$ crystals argues for a conductive network. The further observation that the recharge process changed to one where the $PbSO_4$ crystals reacted to form PbO_2 at the surface, when the internal growth of PbO_2 was extended to the surface, indicates that the process would

normally take place on the surface if it could. But the fact that it did not initially do so indicates that the process of oxidation must extend only slowly from one crystal to the next, made possible only by the conducting PbO_2 that is being formed by the process. The presence of a conducting internal network, on the other hand, makes it possible for oxidation to take place simultaneously at many crystals so that the slowness of the oxidation is not so readily apparent.

If there is a conducting network, then a $PbSO_4$ crystal can be considered as forming upon, rather than surrounding completely, the PbO_2. This means that at some point or points at the interface between $PbSO_4$ and PbO_2 the latter must extend to the surface of the $PbSO_4$ crystal. In the growth of the $PbSO_4$ crystal it is not likely that a perfect and electrolyte impervious seal was made with the PbO_2 surface that it is deposited upon and partially surrounds. It is a well known fact that corrosion processes are accelerated, or at least preferentially nucleated, at deep cracks and similar defects. Grain boundary penetration and the formation of PbO_2 has been detected in grid alloys, in sulfuric acid electrolyte and operating under similar conditions to those described here (10), which is presumably the result of microporosity and which causes greatly accelerated formation of PbO_2 deep within the metal. It seems logical to expect that the oxidation of $PbSO_4$ to PbO_2 might be similarly accelerated or stimulated at cracks. This would be particularly probable because PbO_2 is already present to nucleate the process and to form a conductive path leading into the discontinuity between the PbO_2 and $PbSO_4$ surfaces, and also because the lesser volume of the reaction product, PbO_2, would tend to enlarge the discontinuity and allow additional electrolyte to reach the area.

If, on the other hand, it is assumed that the encapsulated PbO_2 is present as separate, disconnected particles then it must also be assumed that most of these are completely surrounded by $PbSO_4$ and that the possibility of discontinuities extending to the surface is small. In this case there is no logical basis for assuming that reaction should begin in the interior. There is no access of electrolyte to the PbO_2 surface, there is a relatively very thick lead sulfate layer that probably prevents sufficient oxygen from diffusing to the reacting surfaces and there seems to be no reason to believe that a process facing these difficulties should take place within the crystal rather than at the surface.

The results of the x-ray and differential thermal analysis, as well as the optical examination, seemed to confirm that the discharge and recharge processes involved only dissolution and redeposition and that no solid state reactions were involved in going from one state of oxidation to the other. Solid state transformations would be expected to result in lattice changes detectable by x-ray analysis or by changes in thermal decomposition products, neither of which was observed. Berndt (9), among others, has also presented convincing arguments for the dissolution-reprecipitation mechanism over that of the solid state.

It is realized that the observations made in the present investigation might have been different if different current densities had been used. Berndt (9), Leibssle, Reber, Hermann, and Zehender (11), and Bode, Pasesar, and Voss (12) indicate that the reaction mechanism may be different at higher current density, while work of Metzler and Schwarz (13) indicates that the acid concentration used is also a very important consideration.

One of the puzzling features of the lead-acid storage battery has been its ability to function as efficiently as has been demonstrated when one of the reaction products is $PbSO_4$, a material of such high electrical resistivity.

The idea of a residual PbO_2 network which can provide electrical conductivity through the $PbSO_4$ of high electrical resistivity seems logical and has been supported by direct observation.

However, further investigation will be necessary to definitely confirm these observations and, if this confirmation is obtained, to determine the minimum amount of PbO_2 that must be so employed in obtaining maximum operational efficiency.

Acknowledgments

The authors wish to thank the Naval Research Laboratory for its support and for permission for publication of this work and also to thank the International Lead Zinc Research Organization, Inc., which has assisted in this and other investigations by maintaining the position of Research Associate for one of the authors at the Naval Research Laboratory.

Manuscript submitted March 9, 1970; revised manuscript received *ca.* April 23, 1970. This is Paper 51 to be presented at the Atlantic City Meeting of the Society, Oct. 5-9, 1970.

Any discussion of this paper will appear in a Discussion Section to be published in the June 1971 JOURNAL.

REFERENCES

1. W. Feitknecht and A. Gaumann, *J. Chim. Phys.*, **49**, C135 (1952).
2. S. Hisano, *Kogyo Kagaku Zasshi (J. Ind. Chem., Japan)*, **62**, 376 (1959).
3. I. I. Koval and H. I. Barilenko, *Trudy Chetvertogo Sovenshch. Elektrokhim., Moscow*, **1956**, 748 (Published 1959).
4. A. C. Simon and E. L. Jones, *This Journal*, **102**, 279 (1965).
5. A. C. Simon and E. L. Jones, *ibid.*, **109**, 760 (1962).
6. N. E. Bagshaw and K. P. Wilson, *Electrochim. Acta*, **10**, 867 (1965).
7. J. R. Pierson, *Electrochem. Technol.*, **5**, 323 (1967).
8. J. A. Orsino and E. J. Dunn, Jr., National Lead Research Laboratory Report, 253-61 (1961).
9. D. Berndt, Sixth International Power Sources Symposium, Brighton, Sussex, Sept. 23-25, 1968.
10. A. C. Simon, *This Journal*, **114**, 1 (1967).
11. H. Leibssle, H. Reber, W. Hermann, and E. Zehender, *Bosch Techn. Berichte*, **2**, (4) 159 (1968).
12. H. Bode, H. Panesar, and E. Voss, *Naturwissenschaften*, **55**, (11) 541 (1968).
13. M. Metzler and W. Schwarz, *Electrochim. Acta*, **11**, 111 (1966).

New Experiments on the Sensitization of Zinc Oxide by Means of the Electrochemical Cell Technique

K. Hauffe,* H. J. Danzmann, H. Pusch, J. Range, and H. Volz
Institut für Physikalische Chemie der Universität, Göttingen, West Germany

ABSTRACT

The "formal quantum yield" of the sensitization of the anodic photocurrent of zinc oxide by Rhodamine B has been determined by means of an electrochemical cell technique. Zinc oxide was used as a single crystal in the electrochemical cell

+ Indium | ZnO crystal | Electrolyte + Dye | Platinum −

in aqueous and methanol electrolytes. Simultaneously, the adsorption of the dye on zinc oxide powder has been measured. The influence of the solvent on the extent of the adsorption is significant. The important role of the cosensitizer on the sensitizing ability of the dye is discussed.

A decisive step in the electrophotographic process is the transfer of charge carriers through the interface, adsorbed sensitizer/zinc oxide. This transfer, however, is retarded in the dark as long as no redox systems are present with an electronic exchange level near the edge of the conduction band (1-3). Illumination with light of the optical absorption band of the sensitizer is necessary in order to supply the presupposition of an electron transfer toward zinc oxide. Electron transfer in the inverse direction occurs very easily. Furthermore, it should be mentioned that the excellent electrophotographic properties of zinc oxide are caused by the formation of electron exhaustion space-charge layers with high electrical resistance surrounding the highly conductive bulk of the zinc-oxide grains. These space-charge layers can be eliminated by illumination due to generation of charge carriers. Thus, it becomes understandable that one of the main problems is the investigation of the electronic processes and phenomena occurring between the above-mentioned interface and the space-charge layers.

Generally, for electrophotographic studies with zinc oxide, a negative charge is generated on a suitable zinc oxide-binder layer by means of a corona discharge (6). This surface charge is mainly represented by adsorbed O_2^- and O^- ions. Due to illumination with light of a wavelength $\leq$ 380 nm ($\equiv$ band gap for ZnO) electron-hole pairs are generated in the exhaustion space-charge layer near the surface of the ZnO grains. The holes recombine with the electrons trapped by the oxygen species which desorb and the freed electrons of the electron-hole pairs disappear via the grounded metal electrode. This mechanism, here only indicated, has been investigated by numerous authors (4-7). A more extensive representation and, particularly, a discussion about the participation of donors (*i.e.*, zinc ions in interstitial position) during the charging and discharging process have been given by Hauffe and Stechemesser (8).

In order to exclude the complications appearing with polycrystalline zinc oxide embedded in a resin as a binder, most of the experiments dealt with in this report have been carried out with single crystals of zinc oxide. In this paper, some results of our measurements, particularly on the charge transfer sensitized by organic dyes, are reported. As demonstrated by many authors (9-15), for the sensitization of the light-decay of electrically charged zinc oxide-resin layers, certain organic dyes with conjugated double bonds and charge resonance are especially effective. These experiments, however, have been performed mainly with polycrystalline zinc oxide. Under these experimental conditions, a quantitative evaluation of the sensitization measurements is scarcely possible because of the undefined irradiation caused, for instance, by an optical shielding of an unknown amount of ZnO crystallites in the layer. In this paper, we omit the often-discussed question as to whether or not sensitization is caused by an energy transfer or by an electron transfer, because often the two mechanisms cannot be distinguished. Markevich and Putzejko (16) found a maximum of the photovoltage with polycrystalline zinc oxide covered by various dyes at a coverage of about 50% of a monolayer.

It is our opinion, however, that optical shielding of the embedded ZnO powder, particularly at higher dye concentrations, cannot be excluded from consideration. Furthermore, since the intensity of the light responsible for the sensitization at the surface of the single grains can be only roughly estimated, we decided to perform sensitization measurements with single crystals. As discussed elsewhere (15), the single crystal was used as anode in the following electrochemical cell

+ Indium | ZnO single crystal
| Electrolyte + Dye | Platinum −

where an adsorption equilibrium with the dye in the electrolyte was established. Since in electrophotography, particularly, the behavior of dye mixtures and their mutual influence as adsorbed species is of significant interest, the interaction of two dyes and their influence on sensitization was also studied using single crystals. These experiments have been published elsewhere (17) and are continued with nonaqueous electrolytes. One of the first necessary requirements for a better understanding of the sensitization are quantum yield measurements.

Measurements of Spectral Sensitization and Adsorption

Experimental

Pretreatment of crystals and the measuring setup.— Pure single crystals of zinc oxide were supplied from the 3M Company in the form of platelets 1 mm in thickness with the (0001) face (= Zn^{++} face) and the $(000\bar{1})$ face (= $O^=$ face) perpendicular to the c-axis. These crystals were polished with diamond paste of grain sizes down to 0.25μ. In order to get a barrier-free electrical contact,[1] the $(000\bar{1})$ face was covered with

[1] The barrier-free contact of indium as electrode for zinc oxide is obviously caused by the increase of concentration of free electrons in zinc oxide near the interface In/ZnO due to the chemical exchange reaction.

$$2\ In + 3\ ZnO = In_2O_3 + 3\ Zn\ (dissolved\ in\ In) \quad [a]$$

with a subsequent dissolution of In_2O_3 into ZnO according to

$$Zn^{\cdot} + In_2O_3 = 2\ In|Zn|^{\cdot} + e' + 3\ ZnO \quad [b]$$

or by combination of Eq. [a] and [b]

$$2\ In + Zn^{\cdot} = 2\ In|Zn|^{\cdot} + e' + 3\ Zn\ (dissolved\ in\ In) \quad [c]$$

Here, $Zn^{\cdot}$ and e' denote zinc ions in interstitial positions and free electrons, respectively. Furthermore, $In|Zn|^{\cdot}$ denotes an indium ion in a zinc ion-lattice site and the dot and the prime the positive and negative excess charge, respectively. As can be seen from Eq. [c], the concentration of free electrons is increased by the incorporation of indium ions into the ZnO lattice.

* Electrochemical Society Active Member.

a translucent indium film. Then the prepared crystal was cemented with Apiezon W wax in a small window of the electrochemical cell so that usually the (0001) face was in contact with the electrolyte. If methanol electrolytes were employed, the Apiezon W wax was substituted by Teflon. The $(000\bar{1})$ face exhibited the same behavior; the sensitization, however, was only about half of the value of the other face. In Fig. 1, the experimental setup with a schematic sketch of the electrical circuit can be seen. A Wenking potentiostat served as voltage supply, and a picoammeter 417 and an electrometer 610 R from Keithley were used for current and voltage measurements, respectively. The cell was flushed with purified nitrogen. The light of a xenon high-pressure lamp was irradiated through the back side of the crystal. The employed wavelengths could be obtained by corresponding interference filters or by a monochromator. The light intensity was determined with a calibrated thermopile. Since the spectral transparency of the crystal was measured, the light intensity present at the interface ZnO/electrolyte could be determined.

The dye was dissolved in an electrolyte consisting generally of an m/10 KCl solution buffered with an m/10 acetate-acetic acid (pH = 4.6). Also a methanol electrolyte with 10^{-3} moles/liter KCl was employed. The average water content was smaller than 0.5 v/o. A noticeable change in the photocurrent was recognized only above 0.5 v/o H_2O. Experimental details can be obtained from the paper of Volz (18).

Adsorption measurements.—Since the knowledge of the amount of adsorbed dye is necessary for the determination of the effectiveness of the sensitization and since a direct measurement with single crystals is not possible, adsorption measurements have been performed with various ZnO powders. Such measurements have been carried out in our laboratory by Danzmann (19). These measurements were performed by adding an amount of 1g ZnO powder to 20 cm^3 of a dye solution of various concentration. In order to guarantee an adsorption equilibrium due to an intimate contact between the ZnO powder and the dye solution, all experiments have been carried out in a glass tube closed and assembled on a vibrating machine. The zinc-oxide powder was exposed to the solution for 2-3 hr in spite of the fact that, generally, after 1 hr no change in the dye concentration was detectable. All operations have been done under red light. The rest of the zinc oxide which remained in the dye solution was separated in a centrifuge. The change of the extinction of the solution was determined by means of a Zeiss DMR 21 spectrometer. The measuring technique corresponds to that used by Markevich and Putzejko (16). By additional adsorption experiments with a ZnO powder column, smaller amounts of adsorbed dyes also could be determined. A glass tube was filled with the corresponding ZnO powder. The dye concentrations of the various fractions of the solution passing the column have been measured until no further change in the concentration of the electrolyte was detectable. If the initial dye concentration is c and the concentrations of the fractions V_1, V_2 . . . V_n are c_1, c_2 . . . c_n, the surface concentration Γ of the adsorbed dye can be calculated according to

$$\Gamma = \Sigma(c - c_i)V_i/(\text{BET surface of the ZnO powder})$$

Results and Discussion

The sensitizing behaviors of Rhodamine B, Rose Bengale, Eosin, Fluorescein, and Methylene Blue have been studied by means of current-voltage curves in the above-mentioned electrochemical cell in the dark and under illumination (17-20). In this paper, the sensitizing ability only of Rhodamine B is dealt with in more detail. The wavelength dependence was studied in some cases, but mainly only light of the optical absorption maximum of the corresponding dye was used. While in the dark at anodic polarization of the ZnO electrode the current amounts to only 10^{-10} A/cm^2 due to the barrier action of the exhaustion space-charge layer, it can be increased by illumination to about 2-3 orders of magnitude depending on the light intensity. A typical voltage-current curve with a Rhodamine B sensitized ZnO electrode under irradiation with 545 nm light is represented in Fig. 2. Even at small voltages of about 0.5V measured *vs.* an Ag/AgCl electrode in m/10 KCl solution, a marked saturation region with a constant current is established. In this region, all electrons introduced by the sensitization step from the dye into the space-charge layer of the ZnO crystal will be exhausted by the applied electrical field to the grounded back side of the crystal. The remaining electronically unoccupied state of the adsorbed dye will be filled by an electron from the redox electrolyte or from an oxygen ion on the ZnO surface. At lower voltages, however, the current decreases. Therefore, the saturation current between 0.5 and 1V is a direct quantitative measure of the sensitizing ability of a dye.

As a suitable quantity for comparison among various measurements, particularly for the comparison of

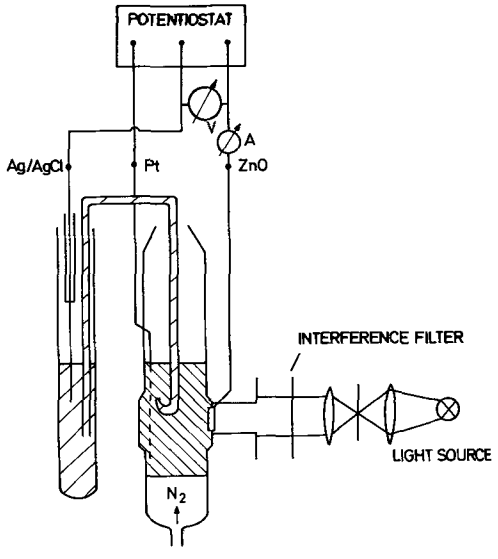

Fig. 1. Schematic representation of the electrochemical cell technique.

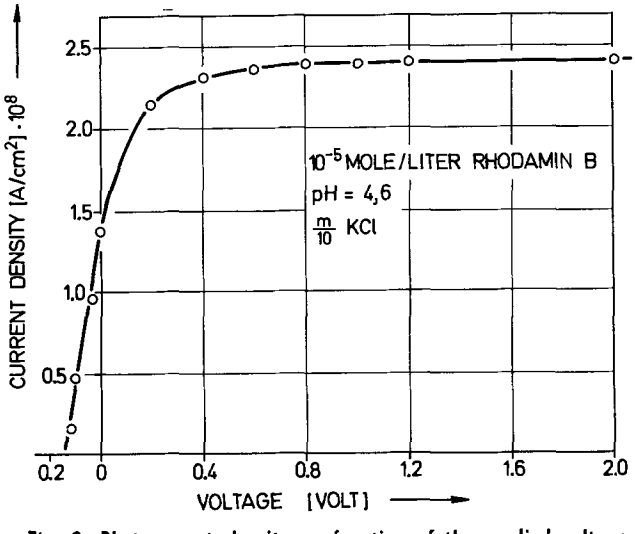

Fig. 2. Photocurrent density as function of the applied voltage under illumination with 545 nm light at room temperature. For all measurements, an m/10 acetate-acetic acid buffered aqueous m/10 KCl solution (pH = 4.6) was used. The concentration of Rhodamine B was here 10^{-5} moles/liter.

the data from electrochemical experiments with those from adsorption measurements, we introduced the "formal quantum yield" defined as the ratio of the number of flowing electrons to the number of incident photons per square centimeter and second. This quantity is readily accessible for measurement. It does not contain additional assumptions on the absorption probability of molecules as is usually the case for the determination of the direct quantum yield.

The precise proportionality of the photocurrent to the light intensity recognized in former investigations (15, 20) could be confirmed by the independence of the formal quantum yield from the light intensity, as may be seen from Fig. 3. On the basis of this result, sensitization data obtained at various light intensities can be compared. These results have been obtained not only in aqueous electrolytes but also in dye-containing methanol electrolytes. The measurements of the wavelength dependence of the photocurrents, represented in Fig. 4, 5, and 6, have been carried out by means of a monochromator with a resolution of 10 nm/mm slit width. The monochromator was used with a slit width of 0.5 mm. As can be seen, the wavelength dependence of the photocurrent for methanol (Fig. 4) and for aqueous dye solutions not too concentrated (Fig. 5) is in rather good agreement with the wavelength dependence of the extinction in Fig. 6 defined as log I_0/I. It should be noted that the curves of the spectral sensitization are shifted slightly to the longer wave range, especially for methanol solutions about 10 nm.

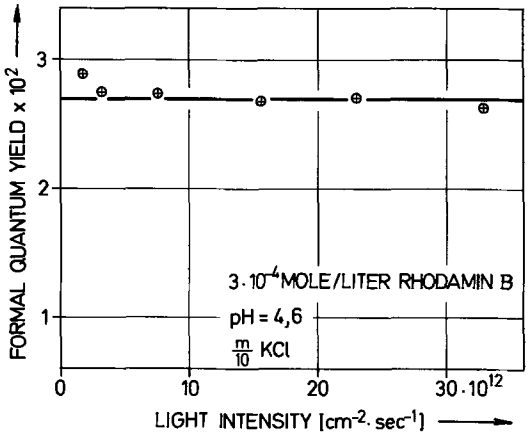

Fig. 3. The formal quantum yield as a function of the light intensity in the same electrolyte as in Fig. 2. The concentration of Rhodamine B, $c_{RhB} = 10^{-4}$ moles/liter.

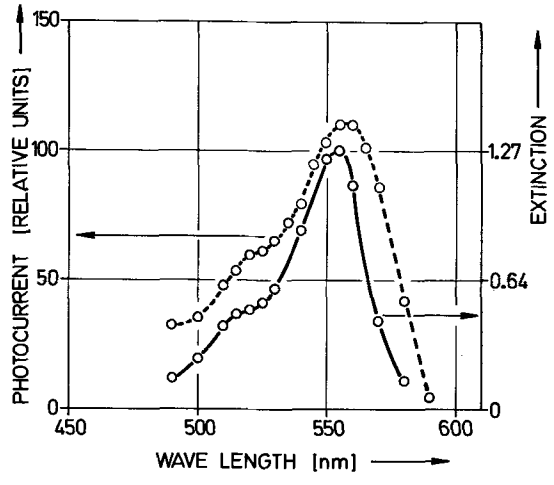

Fig. 4. Spectral sensitization of a ZnO single crystal (measured as photocurrent) and extinction of the dye-containing methanol solution as function of the irradiated wavelength in a 0.01m KCl-methanol solution with $c_{RhB} = 10^{-4}$ moles/liter.

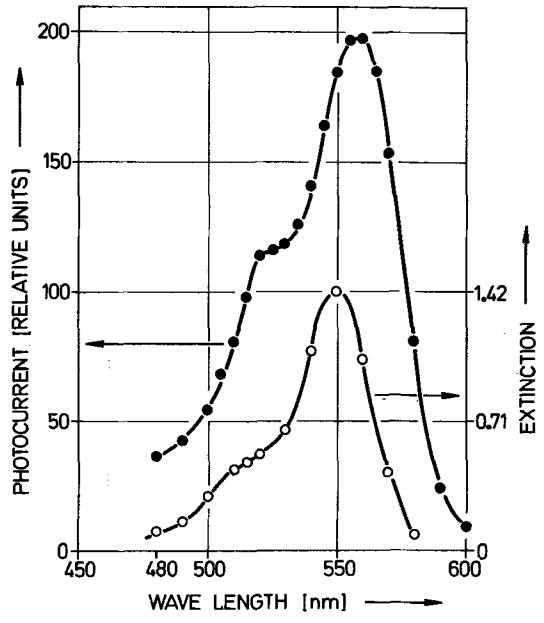

Fig. 5. Spectral sensitization of the anodic photocurrent and the extinction of Rhodamine B, aqueous electrolyte with $c_{RhB} = 10^{-5}$ moles/liter.

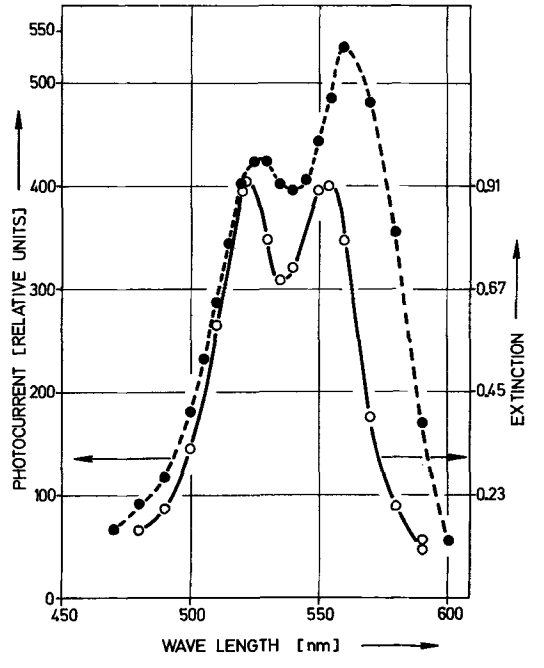

Fig. 6. Spectral sensitization of the anodic photocurrent and the extinction of Rhodamine B, aqueous electrolyte with $c_{RhB} = 2 \times 10^{-3}$ moles/liter.

Presumably, this shift is caused by the interaction between the adsorbed dye and the zinc-oxide surface resulting in a slight decrease of the excited state which is not significant if the adsorption occurs from a strong polar solvent like water. In aqueous solutions with rather large concentrations of Rhodamine B (see Fig. 6, $c_{RhB} = 2 \times 10^{-3}$ moles/liter), the extinction curve indicated the appearance of a dimer band at shorter wavelengths (21). The sensitization spectrum of the photocurrent, however, exhibits only a weak maximum in the dimer band. From this we may conclude that the sensitization by the adsorbed dimer must be poor. At present, it is unknown whether the poor sensitizing ability of the dimer is caused by a small adsorption or by a small quantum yield.

A further important result can be deduced from Fig. 7 and 8 where both the formal quantum yield and the photocurrent are plotted *vs.* the concentration of the dye in aqueous and in methanol solutions. If an aqueous electrolyte is employed, the formal quantum yield is increased continuously with increasing dye concentration. At higher concentration, however, the gradient becomes smaller. The curve corresponds roughly to an adsorption isotherm which, however, cannot be deduced, neither from a Langmuir type nor from a Freundlich type adsorption. A direct comparison with adsorption isotherms obtained on ZnO powders in a dispersion was not possible because this adsorption technique is not applicable at such high concentrations. In these cases, only adsorption measurements by means of ZnO powder columns are used. In Fig. 9, some orienting measuring points are plotted *vs.* the equilibrium concentration of the dye in the solution. The adsorption curve has a course similar to that of the curve for the formal quantum yield in Fig. 7. More precise measurements are projected. Due to the above-mentioned formation of dimers, the evaluation of the sensitization measurements becomes more difficult.

As we found, measurements with a methanol electrolyte exhibit other results. According to the course

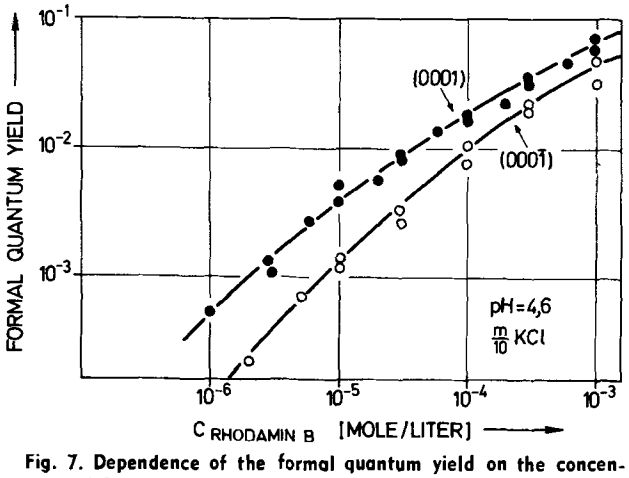

Fig. 7. Dependence of the formal quantum yield on the concentration of Rhodamine B in an aqueous electrolyte (0.1 molar KCl, pH = 4.7) at both crystallographic faces.

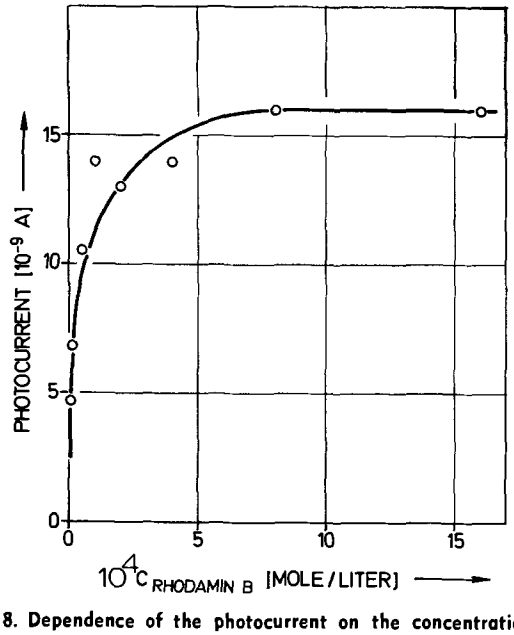

Fig. 8. Dependence of the photocurrent on the concentration of Rhodamine B in the methanol electrolyte. Here and in all other measurements, except in Fig. 7, only the (0001) face was used.

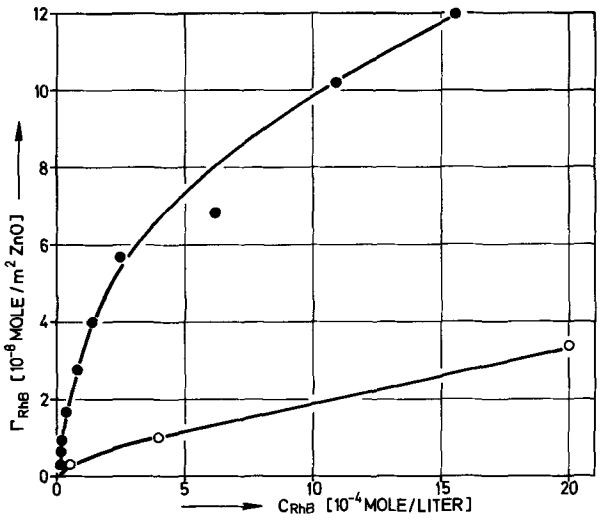

Fig. 9. Adsorption curves of Rhodamine B on zinc oxide: (a) from an aqueous solution by means of a chromatographic column technique (open circles), and (b) from a methanol solution after a classical method (solid circles) with various concentrations of Rhodamine B.

of the dependence of photocurrent on dye concentration in Fig. 8, a constant photocurrent is already established at rather low concentrations of Rhodamine B (at 2 x 10^{-4} moles/liter methanol). A maximum, as observed from photovoltage measurements with dyed polycrystalline zinc-oxide samples (16, 25), could not be detected. Furthermore, the course of the curve does not correspond to the expected one which was found by adsorption measurements represented in Fig. 9. An elucidating result is obtained if the ratio of the photocurrent obtained with a ZnO single crystal to the dye surface concentration of polycrystalline ZnO is plotted *vs.* the concentration of the dye solution. In spite of the lack of knowledge of absolute values concerning the amount of adsorbed dye on ZnO single crystals, it is allowable to apply the ratio of the relative values represented in the course of the adsorption curve for polycrystalline material to the single crystal. It results that the efficiency of sensitization becomes larger with decreasing dye concentration in the solution as can be seen from Fig. 10. This result is surprising since even at small surface concentrations the interaction of the adsorbed dye molecules in their excited state must be noticeable and, therefore, influences the efficiency of the sensitization.

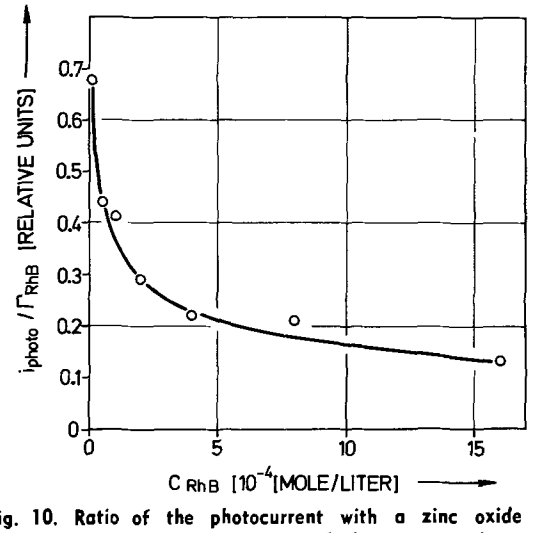

Fig. 10. Ratio of the photocurrent with a zinc oxide single crystal to the surface concentration of the dye on polycrystalline material as function of the dye concentration in the methanol electrolyte.

Further interesting information in the sensitization process is supplied by the change of the photocurrent with the time and by the bleaching rate of the dye. As can be seen from Fig. 11, at longer illumination time the photocurrent initially decreases rather sharply and later more gradually until a constant current is reached, the value of which is approximately 30% below the initial value. One has to assume that the molecules formed by the light oxidation of Rhodamine B must block the surface for the adsorption of new, undestroyed dye molecules. The decrease in the photocurrent cannot be explained by the decrease of the Rhodamine B concentration in the electrolyte since the change in the dye concentration is too small. This was demonstrated by measurements of the decrease of the dye concentration during the illumination. From simultaneous measurements of the dye concentration in the solution after various illumination periods and of the photocurrent, the very significant result was obtained that for every generated electron (*i.e.*, for every electron which has crossed the interface electrolyte/crystal) about five Rhodamine B molecules have been destroyed. If we have an open circuit, no noticeable destruction of the dye can be detected. This result leads to the conclusion that a radical mechanism must be responsible for the destruction reaction whereby the Rhodamine B molecule must give off its electron into zinc oxide. Therefore, for this reaction it is difficult to believe that an energy-transfer mechanism should govern. This result is in agreement with that of Gerischer and Tributsch (22, 23). These authors have further found that the destruction of the dye can be prevented by admission of a reducing compound into the electrolyte which can provide an electron to fill the unoccupied singlet state of the adsorbed dye. The protective compound for Rhodamine B was allylthiourea which was destroyed instead of the dye (23). By the addition of this reducing compound, the quantum yield of the sensitization process was simultaneously increased. A corresponding effect was obtained by us if the ZnO crystal was cathodically polarized before the sensitization experiments, whereby it is believed that zinc atoms have been generated on the surface of the crystal. This assumption is supported by the increase of the anodic dark current both in the absence and presence of dyes after a cathodic polarization period of the crystal. Furthermore, the difference of the sensitized anodic current and the dark current became larger. While the anodic dark current exhibited an increase of 2-3 orders of magnitude, the difference of the light and dark current became larger to a factor of 2-3.

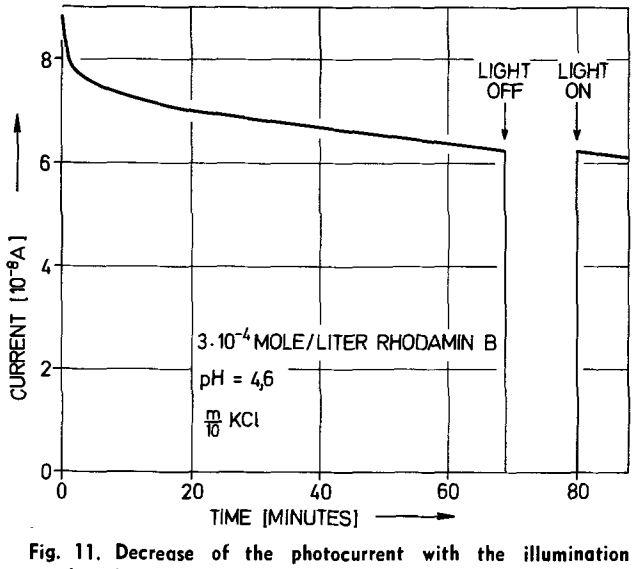

Fig. 11. Decrease of the photocurrent with the illumination time (an interruption of the illumination does not cause a recovery).

Conclusions and Final Remarks

As we discussed above, a quantitative evaluation of the sensitization experiments is possible only if simultaneous determinations are made of the quantum yield and the surface concentration of adsorbed dye molecules per unit area. With respect to further considerations, we assume that the probability of the optical absorption of a dye molecule is independent of whether the molecule is in the adsorbed or in the solved state. Under the assumption of a quantum yield of 1, 1/3, or 1/10, the number of adsorbed molecules/cm² can be calculated and compared with the data obtained from adsorption experiments. The following estimation, which is based on a correct value of absolute light intensity, was controlled by actinometric measurements of light intensity. The photocurrent generated by light of 365 nm wavelength was measured and corresponded to a quantum yield of about 0.85 which is in fair agreement with former experiments (24). As can be seen from Fig. 12, the calculated percentage of coverage of the zinc-oxide surface with the dye is much larger than the coverage obtained by adsorption experiments. For the calculation, the following formula was employed

$$1.6 \times 10^{-21} \epsilon\Gamma = \log_{10} [QY/(QY - FQY)]$$

where ϵ denotes the molar extinction coefficient and QY and FQY are the quantum yield and the formal quantum yield, respectively. Also with a quantum yield of 1, the discrepancy is still large. In the case of aqueous dye solutions, a reasonable comparison is possible only for rather small dye concentrations ($c_{RhB} = 10^{-5}$ moles/liter). Also under these experimental conditions, the surface coverage calculated from the data of the electrochemical cell experiments was larger by about a factor of 30 than that from adsorption measurements. For the evaluation of the electrochemical data, the geometrical surface area of the ZnO crystal has been used rather than the real surface area since the latter is unknown. However, the introduction of a large roughness factor is unlikely. Furthermore, the assumption of a photoadsorption (26) cannot remove this large discrepancy. Oster and Wassermann (26) have found, indeed, a photoadsorption of Fluorescein and of its halogenated derivatives on powdered zinc oxide. The speed of adsorption, however, was rather slow in contrast to our sensitization kinetic experiments. As can be seen from Fig. 13, the

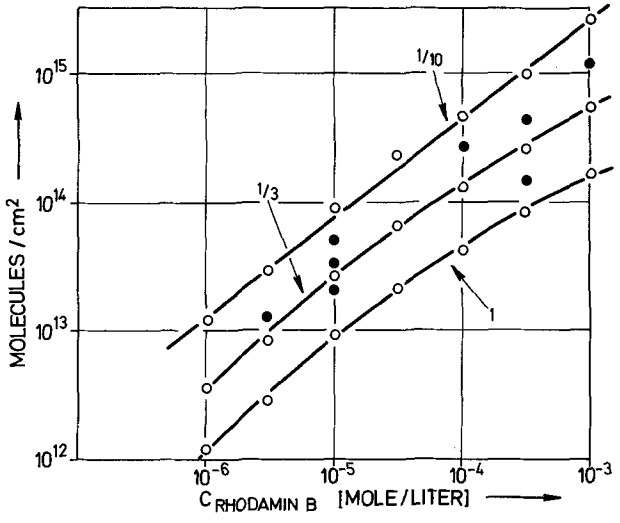

Fig. 12. Calculated coverage of the zinc-oxide surface with Rhodamine B per cm² geometrical surface in dependence on the dye concentration in an aqueous electrolyte under assumption of various formal quantum yield quantities, 1/10, 1/3, and 1 (the numbers at the curves denote the quantum yield) o—o calculated from the formal quantum yield, ●—● calculated from the current-time curves.

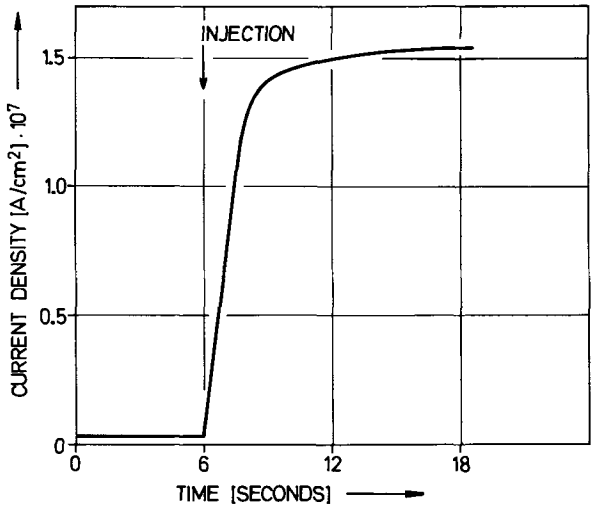

Fig. 13. Rise of the anodic photocurrent (aqueous electrolyte and 545 nm illumination) after injection of 5 cm³ of a 10^{-5} moles/liter Rhodamine B solution into 25 cm³ dye-free electrolyte.

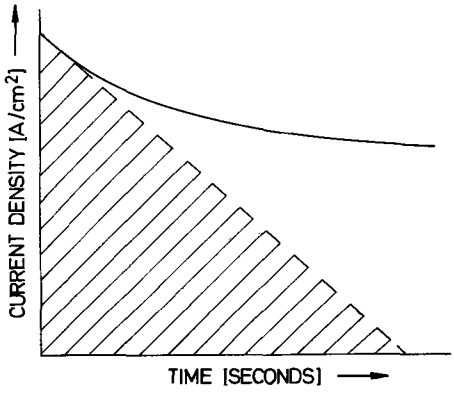

Figure 14. Evaluation of current-time curves concerning the dye coverage of a zinc-oxide surface. Schematic sketch for the calculation of the dye coverage.

photocurrent reached its final value in a few seconds after the injection of 5 cm³ of a 10^{-5} moles/liter Rhodamine B solution into 25 cm³ dye-free electrolyte. This rise time of the photocurrent caused by dye adsorption during illumination can be much shorter because the mixing in the electrolyte seems to be rate determining and depends on the stirring. Furthermore, the linear dependence of photocurrent on light intensity is not compatible with photoadsorption. Also, a significant change of the optical absorption probability of a dye molecule in the adsorbed state compared to that in the electrolyte cannot be assumed of the similarity of the sensitization spectrum to the optical absorption spectrum of the corresponding dye solution.

As can be concluded from the results in Fig. 12, the quantum yield of sensitization must be nearly 1 because a lower quantum yield would postulate a still higher coverage of the ZnO surface with dye (more than a monolayer) which should be scarcely possible. On the basis of quantum yield measurements, we may tentatively assume that preferably adsorbed dye molecules might sensitize the electron transfer since the amount of dye available from the surrounding electrolyte is too small for a noticeable contribution to the sensitization. Similar effects could be found in methanol electrolytes even if the quantities were different. At the same dye concentration of about 10^{-3} moles/liter, the anodic photocurrent through the cell with an aqueous electrolyte was twice as large as the current with methanol electrolyte. This means that the quantum yield of sensitization in an aqueous electrolyte must be significantly higher than that in a methanol solution, although the adsorbed amount of the dye from a methanol solution has been found three times larger than that of aqueous solutions. On the basis of these results, it may be concluded that the adsorption data with polycrystalline ZnO in aqueous solutions cannot be used for the evaluation of the single-crystal current experiments. Further investigations are running for the interpretation of this, at present, unknown phenomenon.

The calculations of the extent of the dye coverage in the presence of aqueous solutions will be confirmed further by an estimation by means of the current-time curves, and by measurements of the kinetics of the dye oxidation. If consideration is made of the initial gradient of the current decay extrapolated toward its intersection with the abscissa, and the destruction of five dye molecules per flowing electron, then the number of adsorbed dye molecules can be calculated from the area surrounded by the x-y axis and the tangent (see the schematic drawing in Fig. 14). The results, represented in Fig. 12, are in fair agreement with those obtained from the steady sensitization currents.[2]

The plotted measuring data are grouped near the curve estimated for a total quantum yield of 1/3. From the evaluated dye reaction, it may be concluded that the adsorbed dye molecules do inject their electron into zinc oxide during the sensitization step. By this mechanism, the increase of the quantum yield becomes understandable which was found either in the presence of partly reduced ZnO surfaces after a cathodic polarization, or in the presence of a reducing compound in the electrolyte, as for instance allylthiourea. In both cases, the regeneration of the unoccupied singlet ground state of the excited dye molecule occurs by recombination with the electron of reducing agent. This effect, called "supersensitization," is well known in the literature and the reducing compound is known as a "supersensitizer." According to this representation, however, the terminology is misleading. It is recommended that the first expression be eliminated entirely and that the second one be replaced by the term "cosensitizer," CS, which acts only as a contractor for electrons. Therefore, the general reaction scheme can be tentatively formulated as follows

$$\text{Dye(ads)} + h\nu \rightarrow \text{Dye}^*\text{(ads)} \quad [1]$$

and

$$\text{Dye}^*\text{(ads)} \rightarrow \text{Dye}^+\text{(ads)} + e'\text{(ZnO)} \quad [2]$$

or

$$\text{Dye}^*\text{(ads)} \rightarrow \text{Dye(ads)} + \text{energy} \quad [3]$$

In order to prevent the undesirable step [3] which decreases the quantum yield, the following one becomes effective in a presence of a cosensitizer, CS

$$\text{Dye}^*\text{(ads)} + \text{CS(aq)} \rightarrow \text{Dye(ads)} + \text{CS}^+\text{(ads)} + e'\text{(ZnO)} \quad [4]$$

and, also, the further oxidation of the dye, additionally

[2] The full circles in Fig. 12 are calculated under the following assumption. If Γ is the coverage of the surface and 5 molecules will be destroyed per flowing electron through the cell, it is obtained

$$d\Gamma/dt = 5 \times dn/dt$$

whereby

$$n = i/e$$

with i as the current density and e the elementary charge. If we use for small values of $d\Gamma$

$$\frac{d\Gamma}{\Gamma} = \frac{di}{i}$$

we get

$$\Gamma = \frac{d\Gamma/dt}{di/dt} i$$

and finally under consideration of Fig. 14

$$\Gamma = 5 \times \frac{F}{e}$$

where F is the area bordered by the x-y axis and the tangent.

responsible for the decrease in the quantum yield, will be significantly prevented. $e'(ZnO)$ denotes a free electron just injected into ZnO and the star denotes the electronically excited state. According to this sequence of reaction steps, the cosensitizer is oxidized and can again enter the electrolyte. If trapped electrons, for instance as O_2^- species, are available on the ZnO surface and if the electron-exchange level is not too high, then an electron-exchange reaction may occur as follows

$$CS^+(ads) + O_2^-(ads) \rightarrow CS(aq) + O_2^{\times}(ads) \quad [5]$$

Further experiments are in progress.

Acknowledgment

We appreciate the sponsorship of this research by the Deutsche Forschungsgemeinschaft, Bad Godesberg, concerning the grant for the experimental equipment and, particularly, for the salary of J. Range.

Manuscript submitted Nov. 20, 1969; revised manuscript received *ca.* March 23, 1970.

Any discussion of this paper will appear in a Discussion Section to be published in the June 1971 JOURNAL.

REFERENCES

1. S. R. Morrison and T. Freund, *J. Chem. Phys.*, **47**, 1543 (1967); *Electrochim. Acta*, **13**, 1343 (1968).
2. H. Gerischer, *This Journal*, **113**, 1174 (1966); F. Lohmann, *Ber. Bunsenges. Phys. Chem.*, **70**, 87 (1966).
3. K. Hauffe and J. Range, *Ber. Bunsenges*, **91**, 690 (1967).
4. T. H. Li and P. J Regensburger, *J. Appl. Phys.*, **34**, 730 (1963).
5. K. Hauffe, *J. Phot. Sci.*, **10**, 321 (1962).
6. K. Hauffe, *Angew. Chem.*, **72**, 730 (1960); *Naturwiss.*, **54**, 181 (1967).
7. J. A. Amick, *RCA Rev.*, **20**, 753, 770 (1962).
8. K. Hauffe and R. Stechemesser, *Phot. Sci. Engr.*, **11**, 145 (1967); *Helv. Phys. Acta*, **41**, 872 (1968).
9. G. Scheibe, *Z. Elektrochem.*, **52**, 283 (1948).
10. A. Terenin and I. A. Akimov, *J. Phys. Chem.*, **69**, 730 (1965); *J. Phys. Chem. USSR*, **217**, 307 (1961). I. A. Akimov, *J. Nautsch. Prinkl. Phot. Kine*, **4**, 64 (1959). I. A. Akimov, V. M. Bentsa, F. I. Vilesov, and A. N. Terenin, *Doklady Akad. Nauk USSR*, **172**, 371 (1967).
11. S. J. Dudkowski and L. I. Grossweiner, *J. Opt. Soc.*, **54**, 486 (1964).
12. E. Klein and R. Matejec, *Mitt. Forsch.-Lab. AGFA-Gevaert*, **4**, 16 (1964).
13. R. C. Nelson, *J. Phys. Chem.*, **71**, 2517 (1967), and further literature cited therein.
14. E. Inoue, H. Kokado, and T. Yamaguchi, *J. Phys. Chem.*, **69**, 767 (1965).
15. K. Hauffe and J. Range, *Z. Naturforsch.*, **23b**, 736 (1968).
16. N. N. Markevich and E. K. Putzejko, *Zh. Fiz. Khim. USSR*, **36**, 2393 (1962).
17. K. Hauffe, H. Pusch, and J. Range, *Z. Phys. Chem. (NF)*, **64**, 122 (1969).
18. H. Volz. Master's Thesis, Univ. of Göttingen (1969).
19. H. J. Danzmann, Master's Thesis, Univ. of Göttingen (1969).
20. K. Hauffe. V. Martinez, J. Range, and R. Schmidt, *Phot. Korr.*, **104**, 113 (1968).
21. Th. Förster and E. König, *Z. Elektrochem.*, **61**, 344 (1957).
22. H. Gerischer and H. Tributsch, *Ber. Bunsenges. Phys. Chem.*, **72**, 437 (1968); H. Tributsch, Doctor's Thesis, München (1968).
23. H. Tributsch and H. Gerischer, *Ber. Bunsenges. Phys. Chem.*, **73**, 251 (1969).
24. M. C. Markham and K. H. Laidler, *J. Phys. Chem.*, **57**, 363 (1953). V I. Vesalovskii, *Zh. Fiz. Khim.*, **22**. 1427 (1948).
25. I. Tashiro, T. Kimura, and K. Endo, *Appl. Optics, Suppl.*, **3**, 180 (1969).
26. G. Oster and M. Wassermann, *J. Phys. Chem.*, **66**, 1536 (1962).

Electrochemical Characteristics of Iron in Acidic Solutions Containing Ring-Substituted Benzoic Acids

A. Akiyama[1] and Ken Nobe*

School of Engineering and Applied Science, University of California, Los Angeles, California

ABSTRACT

The electrochemical behavior of Armco iron in 1*N* H_2SO_4 in the absence and presence of ring-substituted benzoic acids have been investigated by the measurement of the corrosion potentials, open-circuit capacitances, potential-current polarization characteristics, potential transients, and corrosion rates. Anomalous behavior was observed for iron in the presence of para-hydroxybenzoic acid. The corrosion rates of inhibited Armco iron followed a LFER with an adsorption mode of inhibition. The adsorption correlation indicated that increasing the electron density at the adsorption center increased inhibition. Corrosion inhibition of Armco iron by ring-substituted benzoic acids increased in the following order: benzoic acid < m-OH < m-NH_2 < p-OH < p-NH_2.

Recently, a series of investigations on organic corrosion inhibitors have been carried out in this laboratory. In the first paper (1), the correlation between the inductive and resonance effects of organic compounds and their inhibitive properties was quantitatively discussed and stimulated this laboratory's experimental study of the structure-inhibition relationship for organic compounds.

Initially, aniline and substituted anilines were studied as corrosion inhibitors of iron and the experimental results have been reported in a previous paper (2). A discussion of the inhibition mechanism of organic substances has been made on the basis of the experimental results of anilines (3).

This paper is a continuation of the previous work by Donahue (2, 3) and is based on a study of the electrochemical behavior of Armco iron in 1*N* H_2SO_4 containing ring-substituted benzoic acids.

Experimental

The electrochemical cell and the instrumentation have been described previously (4, 5). All electrodes

* Electrochemical Society Active Member.
[1] Permanent address: Department of Applied Electrochemistry, Tokyo Institute of Technology, Tokyo, Japan.

were prepared from the same sample of a commercial Armco iron rod (0.5 in. diameter). The analysis of the Armco iron was 0.15% Cu, 0.13% C, Mn, P, S, Si, and 99.72% Fe. The electrodes were made as follows: (*a*) the rod was cut into cylinders, (*b*) a thin part of the cylindrical surface was milled off on a lathe, (c) degreased with hot benzene in a soxhlet column for several hours, (*d*) dried under vacuum, (*e*) annealed at 900°C for 1 hr under vacuum of 10^{-5} mm Hg, (*f*) degreased with hot benzene again, (*g*) dried under vacuum, (*h*) stored in a desiccator with silica gel, and (*i*) activated in 5*N* H_2SO_4 for 10 min just before an experiment.

All organic chemicals were recrystallized from water and dried at 80°C under vacuum. The purity was checked by melting point determination.

Iron corrosion in the presence of each of the selected ring-substituted benzoic acids at a concentration of 0.02M was studied. These organic compounds were benzoic acid, para- and meta-amino and hydroxy benzoic acids. In addition, experiments with phenol were conducted. The supporting electrolyte was 1*N* H_2SO_4 which was deaerated with prepurified nitrogen. Other organic compounds which were considered but whose solubility was not sufficient for this work were para- and meta-toluic acid, para- and meta-methoxy benzoic acid, para- and meta-chloro-benzoic acid, terephthalic acid, and isophthalic acid. Para-nitrobenzoic acid was also studied to some extent, but electrochemical reduction of this compound precluded further experimentation. However, a brief discussion of these results will be given later in this paper.

Electrode potentials were measured relative to the saturated calomel electrode (SCE). The d-c pulse technique was used to determine the differential capacitances. The electrolyte was maintained at room temperature which was 24° ± 1°C.

Results

Figure 1 compares the corrosion potential-immersion time behavior of iron in the presence of all the inhibitors studied. As shown the corrosion potentials of the inhibited iron shifted toward positive potentials with respect to the uninhibited iron. Previously (6), it had been reported that the shift of the corrosion potential of iron in the presence of sodium benzoate was in the positive direction. In this study, the corrosion potential of iron in the presence of benzoic acid shifted in the positive direction only about 15 mV. The benzoate ion has been regarded as a corrosion inhibitor of metals in neutral and alkaline solutions (6-8). However, the mode of inhibition of benzoic acid in an acidic solution is different than in alkaline solutions since in a low pH solution such as 1*N* H_2SO_4, the benzoic acid is undissociated.

The cathodic overpotential of both uninhibited and inhibited iron reached steady-state within 5 sec with the exception of para-hydroxy benzoic acid which required several minutes as shown in Fig. 2. The cathodic overpotentials for 1 mA/cm² are compared in Fig. 3. In general, the cathodic overpotentials at some specified polarization changed with immersion time but

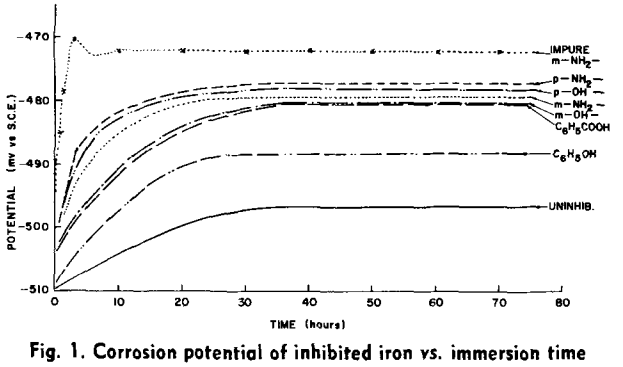

Fig. 1. Corrosion potential of inhibited iron vs. immersion time

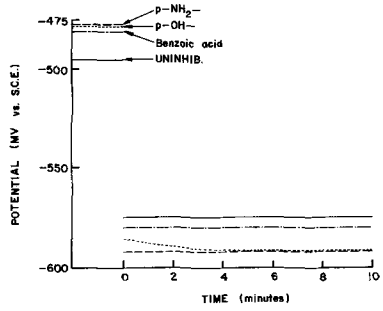

Fig. 2. Potential transient of inhibited iron during cathodic polarization of 1.0 mA/cm².

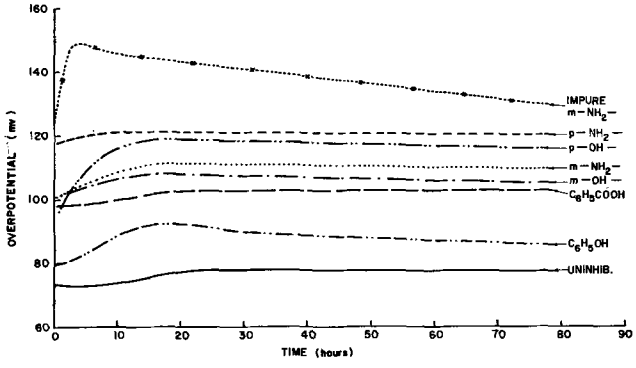

Fig. 3. Cathodic overpotential of inhibited iron at 1 mA/cm² (pulse duration = 5 sec).

were constant after about 30 hr. It is noted that iron in an acidic solution of impure meta-aminobenzoic acid was the exception. This organic compound exhibited the best inhibitor qualities.

The small positive shift in the corrosion potential and the increase in the cathodic overpotential of inhibited iron indicate that the benzoic acids studied in this investigation are mixed inhibitors (9). These results suggest that the organic compounds have a slightly greater effect on the electrodissolution of iron than on the hydrogen evolution reaction (HER).

The corrosion current was determined by extrapolation of the cathodic Tafel curves to the corrosion potential. Typical corrosion currents are plotted against immersion times in Fig. 4. The open and closed points represent different runs in order to demonstrate the reproducibility of the results. Corrosion currents (i_{corr}) and cathodic Tafel slopes (b_c), determined after an immersion time of 20 hr are given in Table I. The corrosion current reached a constant value at approximately an immersion time of 20 hr. The cathodic Tafel slopes for inhibited and uninhibited iron were essentially constant during the run.

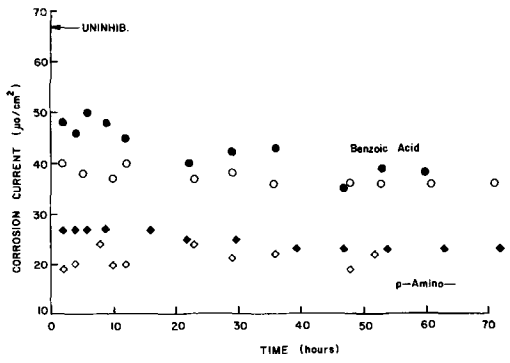

Fig. 4. Corrosion current of iron in the presence of benzoic acid and p-aminobenzoic acid.

Table I. Experimental data

(Concentration of inhibitors = 0.02M)

Inhibitor	ϕ_{corr}, mV	b_c, mV	i_{corr}, $\mu A/cm^2$	C_0, $\mu F/cm^2$	C_{50}, $\mu F/cm^2$
Uninhibited	−495	67	66	36	129
Benzoic acid	−480	71	38	35	86
m-Hydroxy-benzoic acid	−481	71	35	35	78
m-Amino-benzoic acid	−480	73	32	37	72
p-Hydroxy-benzoic acid	−478	80	33 26*	31	54
p-Amino-benzoic acid	−477	72	22	31	56
Impure m-amino-benzoic acid	−472	80	19	25	42
Phenol	−487	71	55	34	122

* Estimated using mean cathodic Tafel slope of 72 mV.

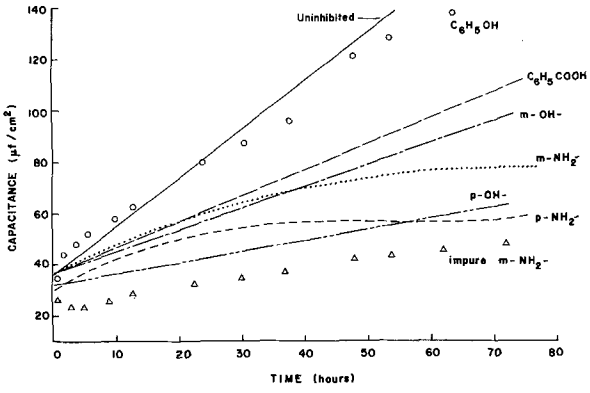

Fig. 6. Open-circuit differential capacitance of iron

Superpolarization (*i.e.*, maximum in the potential-time transient) was observed during a galvanostatic anodic pulse. The inhibited iron exhibited larger superpolarization values and attained the maximum at shorter times than the uninhibited iron. The potentials during a galvanostatic anodic polarization of 1.0 mA/cm^2 are plotted against the polarization time in Fig. 5. The steady-state polarization potentials of inhibited iron were shifted to more positive values than the uninhibited iron. As shown in Fig. 5, the positive shift of the polarization potential of iron in the presence of para-hydroxy benzoic acid was more substantial than iron in the presence of the other organic compounds.

Yamaoka and Fischer (10) studied the steady-state anodic polarization of iron in the absence and presence of inhibitors, o-phenamthroline or phenylthiourea, and observed that at high current densities, anodic polarization of inhibited iron approached that of uninhibited iron. They suggested that the superpolarization of inhibited iron during an anodic current pulse was due to the desorption of the inhibitor. Gatos (8) reported that benzoate ions did not inhibit iron corrosion when iron was coupled to gold (*i.e.*, during anodic polarization). On the other hand, he implied that inhibition of iron corrosion with benzoate ions was achieved when iron was coupled with zinc (*i.e.*, during cathodic polarization). However, further details of these results were not given.

The results of Yamaoka and Fischer (10) and Gatos (8) suggest that the larger superpolarization of iron in the presence of the benzoic acids observed in this investigation may be the manifestation of organic desorption during anodic polarization. Nevertheless, the open-circuit and cathodic polarization behavior of iron indicate that the benzoic acids inhibit anodic dissolution of iron at open circuit and small anodic currents.

The open-circuit differential capacitances (*i.e.*, at the corrosion potential) are plotted against immersion times in Fig. 6. The capacitance of uninhibited iron increased linearly with immersion time up to the end of the experiment. The capacitances of iron in the presence of benzoic acid and the hydroxybenzoic acids also increased approximately linearly with immersion, but were less than the capacitance of uninhibited iron.

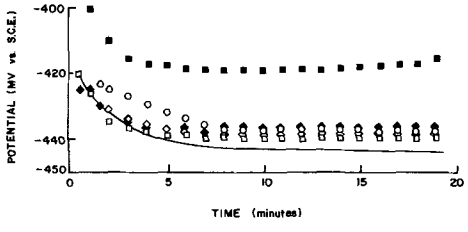

Fig. 5. Potential transient during anodic polarization of 1.0 mA/cm^2: solid line is for uninhibited iron, benzoic acid (○), m-hydroxybenzoic acid (□), p-hydroxybenzoic acid (■), m-aminobenzoic acid (◇), and p-aminobenzoic acid (◆).

On the other hand, the capacitance of iron in the presence of the aminobenzoic acids increased with immersion time, but approached a steady-state value. It should be noted that the initial open-circuit capacitances (within 2 hr immersion) were approximately 35 $\mu F/cm^2$ for inhibited and uninhibited iron. In Table I, C_0 represents the initial open-circuit capacitance. The capacitances of iron after 50 hr immersion, C_{50}, decreased in the following order as shown in Table I, phenol > benzoic acid > m-OH > m-NH_2 > p-NH_2 > p-OH.

The differential capacitance of both uninhibited and inhibited iron was not greatly affected by galvanostatic cathodic polarization indicating a low surface coverage of hydrogen atoms. On the other hand, the capacitance increased during anodic polarization as observed previously for iron in the presence of the substituted anilines (2). This increase in capacitance (adsorption pseudocapacitance) and the potential transient behavior during anodic galvanostatic polarization has been attributed to the increase in surface concentration of FeOH (11). The adsorption pseudocapacitance was approximately the same for inhibited and uninhibited iron except for para-hydroxybenzoic acid. The smaller adsorption pseudocapacitance of Armco iron in the presence of para-hydroxybenzoic acid was similar to the results obtained previously with para-toluidine (2).

In a previous investigation (2), it was shown that the electrochemical behavior of iron in 1*N* H_2SO_4 containing aniline was not significantly different than the uninhibited case. The behavior of iron in 0.02M phenol in 1*N* H_2SO_4 was examined since the effect of the hydroxy substituent on the inhibitor qualities of benzoic acid was a part of this investigation. Figures 1, 3, and 6 and Table I show that, of the inhibitors studied, phenol had the least effect on the electrochemical characteristics of iron.

Similar to results obtained previously for the impure aniline (2), impure meta-aminobenzoic acid inhibited the corrosion rate of iron more than the purified compound as shown in Table I. The impure organic compound was used "as-received," it was brownish colored. As shown in Fig. 6, the open-circuit capacitance of iron in the presence of impure meta-aminobenzoic acid was significantly lower than in the presence of the purified organic.

The impure, colored aniline and meta-aminobenzoic acid contain high molecular weight compounds which have long conjugated structures. The long conjugated structures are usually considered to enhance adsorption. From a practical point, further investigations on the identification of the impurities may be of considerable importance.

It was observed that the addition of sodium chloride (8.55 mM) to the corrosion environment containing para-aminobenzoic acid affected the electrochemical behavior of iron in the following way: the corrosion potential remained unchanged, the open-circuit capaci-

tance decreased from 56 to 42 $\mu F/cm^2$ with the addition of the sodium chloride, the corrosion current decreased from 22 to 11 $\mu A/cm^2$, and the cathodic Tafel slope remained unchanged. These results indicate that the addition of sodium chloride in modest amounts enhances the inhibition of iron with para-aminobenzoic acid. Such effects have been investigated by others as, for example, Hackerman *et al.* (12).

The reduction of para-nitrobenzoic acid on iron in 1*N* H_2SO_4 was observed for a saturated solution (~0.01M). The corrosion potential was shifted toward the positive direction by stirring the electrode, −428 mV for the stationary electrode and −417 mV for the electrode rotated with a tangential velocity of 8.5 cm/sec or with agitation of electrolyte. The capacitance at the corrosion potential was unusually large, 281, 346, and 735 $\mu F/cm^2$ for immersion times 1, 2, and 22 hr, respectively. Cathodic polarization of iron in the para-nitrobenzoic solution indicated that the reduction reaction was diffusion-controlled.

Discussion

The corrosion rates of iron in the presence of ring-substituted benzoic acids are plotted against the Hammett substituent constants in Fig. 7. For comparison, the corrosion rates of uninhibited and phenol inhibited iron are also given. It should be noted again that iron in 1*N* H_2SO_4 containing para-hydroxybenzoic acid did not achieve steady-state cathodic overpotentials as the other organics during a 5 sec pulse as shown in Fig. 2; several minutes were required. There are two data points given for the para-hydroxybenzoic acid in Fig. 7. The open point is the corrosion rate determined using the cathodic Tafel line of slope, 80 mV, obtained experimentally. The closed point is the corrosion rate estimated by the best fit of the overpotential data using a cathodic Tafel line of slope, 72 mV, which was the average value obtained with the other organic compounds.

The correlation of the corrosion rates of iron inhibited by ring-substituted benzoic acids indicate that increasing the electron density at the adsorption or reaction center by the addition of electron providing substituents on the ring increased inhibition. Furthermore, correlation was achieved by using the σ values of the free amine rather than the protonated amine for the aminobenzoic acids. In the bulk solution of the 1*N* H_2SO_4, the aminobenzoic acids should be protonated. Therefore, the correlation indicates that the adsorbed aminobenzoic acids were in the unprotonated state. This suggests that these organics were adsorbed in the flat position on the iron surface [see also p. 1013 of ref. (3)].

The anomalous anodic behavior of iron in the presence of para-hydroxybenzoic acid was manifest in the anodic transient data and the pseudocapacitance during these anodic transients. These results suggest that the para-hydroxybenzoic acid interacts with the surface intermediate formed during the electrodissolution of iron at polarization conditions of reasonably large displacement from the open circuit.

Anomalous behavior of iron in the presence of para-hydroxybenzoic acid was also observed during cathodic polarization. As shown in Fig. 2, steady-state conditions during cathodic polarization were not achieved for at least several minutes for iron in the presence of para-hydroxybenzoic acid, while less than 5 sec were required for iron in solutions containing the other organics. This cathodic behavior of iron suggests that the para-hydroxybenzoic acid interacts with the reaction intermediate during the HER.

The electrochemical polarization behavior of inhibited iron indicates that the para-hydroxybenzoic acid affects the reaction mechanism of both the electrodissolution and the HER. A mechanism was proposed previously (3) to take into account the active participation of an organic inhibitor in the electrodissolution of iron and can be used as a basis to interpret qualitatively the experimental results of this investigation including the para-hydroxybenzoic acid data. Similar mechanisms to account for the interaction between the organic compound and the reaction intermediate during the HER can also be readily devised. However, the primary purpose of this study was to investigate the possible linear free energy relationship (LFER) correlation of iron inhibition by ring-substituted benzoic acids.

To provide further information on the deviation of the para-hydroxybenzoic acid data (open point) from the correlation curve shown in Fig. 7, the cathodic overpotential of the inhibited iron was plotted *vs.* the substituent constants in Fig. 8. For all current densities, the correlation lines were drawn parallel. At low current densities, a good correlation was obtained indicating the simple adsorption mode of inhibition. However, at the higher current densities the para-hydroxybenzoic acid data substantially deviates from the correlation line and the deviation is shown to increase with increase in current density. As shown in Fig. 8, the rate of the HER on iron was less in the presence of para-hydroxybenzoic acid than in the presence of para-amino-benzoic acid at large polarization. This increase in polarization accounts for the observed larger cathodic Tafel slope of iron in the presence of para-hydroxy-benzoic acid.

It seems reasonable to assume that the closed data point for para-hydroxy-benzoic acid in Fig. 7 more closely approximates the electrodissolution rate at open circuit (*i.e.*, the corrosion rate), since it better

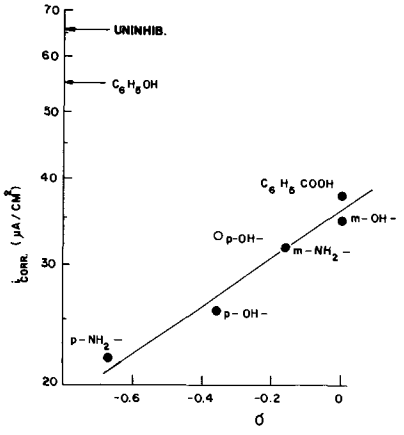

Fig. 7. Corrosion rates of inhibited iron *vs.* Hammett substituent constants.

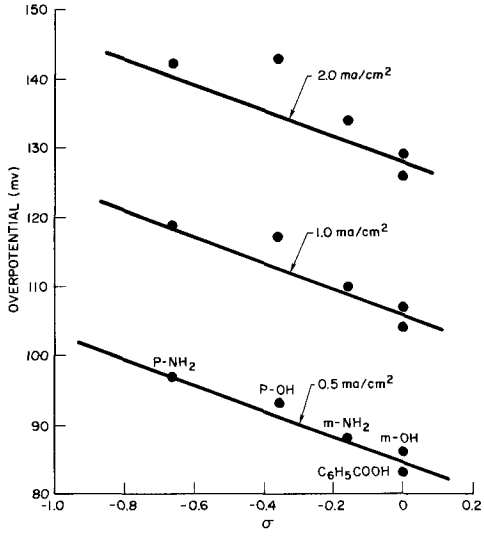

Fig. 8. Cathodic overpotentials of inhibited iron *vs.* Hammett substituent constants.

reflects the low polarization data. Therefore, it is concluded that corrosion inhibition of iron (at open circuit) by the ring-substituted benzoic acids studied is achieved by the simple adsorption mode. At larger anodic and cathodic polarization, the electrochemical behavior indicates that the para-hydroxybenzoic acid interacts with the adsorbed intermediates, FeOH and H, and thus, alters the reaction mechanisms of electrodissolution and the HER.

Acknowledgment

This work is part of a continuing University of California program in sea water desalination and was supported by funds from the Corrosion Research Council, Project 14.

Manuscript received Aug. 4, 1969.

Any discussion of this paper will appear in a Discussion Section to be published in the June 1971 JOURNAL.

REFERENCES

1. F. M. Donahue and K. Nobe, *This Journal*, **112**, 886 (1965).
2. F. M. Donahue, A. Akiyama, and K. Nobe, *ibid.*, **114**, 1006 (1967).
3. F. M. Donahue and K. Nobe, *ibid.*, **114**, 1012 (1967).
4. F. M. Donahue and K. Nobe, UCLA Engineering Report No. 65-39 (1965).
5. A. Akiyama, R. Patterson, and K. Nobe, *Corrosion* **26**, 51 (1970).
6. P. T. Gilbert and S. E Hadden, *J. Appl. Chem.*, **3**, 545 (1953).
7. F. Wormwell, *Chem. and Ind.*, 553 (1953).
8. H. G. Gatos, "Comptes Rendus du Symposium Europeen sur Les Inhibitours de Corrosion," p 257, Ferrara, Italy (1960).
9. H. Kaesche and N. Hackerman, *This Journal*, **105**, 191 (1958).
10. H. Yamaoka and H. Fischer, *Electrochim. Acta*, **10**, 679 (1965).
11. F. M. Donahue and K. Nobe, *This Journal*, **114**, 682 (1967).
12. N. Hackerman, E. S. Snavely, and J. S. Payne, *ibid.*, **113**, 677 (1966).

The Anodic Dissolution of Titanium in Sulfuric Acid

R. D. Armstrong, J. A. Harrison, H. R. Thirsk,* and R. Whitfield

Electrochemistry Research Laboratories, Department of Physical Chemistry, University of Newcastle upon Tyne, Newcastle upon Tyne, England

ABSTRACT

The mechanism of titanium dissolution in sulfuric acid has been investigated using wire, rotating disk and platinum ring-titanium disk electrodes. Titanium dissolves directly as Ti^{3+}, without any solution soluble intermediates. The reaction is H^+ catalyzed (approximately first order). A possible mechanism is suggested.

The electrochemical behavior of titanium has frequently been investigated (1-10), particularly in relation to stress corrosion cracking. The mechanism of Ti dissolution has however rarely been inferred from the results obtained, and it was for this reason that the present work was undertaken.

Experimental

Titanium electrodes (99.9%) were investigated in the form of wires (diameter 1 mm) and disks (diameter 7.5 mm). A titanium disk-platinum ring electrode system was also used (r_1 = 3.18 mm, r_2 = 3.47 mm, r_3 = 4.77 mm).[1] Before use the Ti disks were mechanically worked with emery. The solutions used were prepared from AnalaR reagents and triply distilled water. They were all deoxygenated with N_2. The reference electrodes were H_2/H^+ in 1M H_2SO_4 to which all potentials are referred, after correction for liquid junction potentials. The solutions used together with the corrosion potentials of titanium in these solutions are shown in Table I.

Repetitive triangular sweep measurements were made using a function generator and a potentiostat at sweep speeds from 3 mV/sec to 1 V/sec. Square pulse potentiostatic measurements were also used. For the ring-disk electrode two potentiostats were used so that the potentials of the ring and disk electrodes could be separately controlled. All measurements were made at 70° ± 1°C, since at lower temperatures the current levels were found to be inconveniently small.

* Electrochemical Society Active Member.
[1] A smaller spacing was not practicable for use at other than ambient temperature.

Table I. Solutions used and corrosion potentials of titanium

Solution H_2SO_4	Solution Na_2SO_4	$E_{corrosion}$, mV	pH(20°C) measured	$[H^+]$(70°C) estimated
10M	—	−580	−0.8 (estimated)	—
1M	—	−576	0.07	1.04M
0.5M	0.5M	−570	0.51	0.21M
0.1M	—	−550	0.95	0.1M
0.1M	0.9M	−470	1.51	0.02M

Results

Current-potential curves on wire electrodes.—A typical *i-E* curve obtained from a chart recorder is shown in Fig. 1. The regions corresponding to hydro-

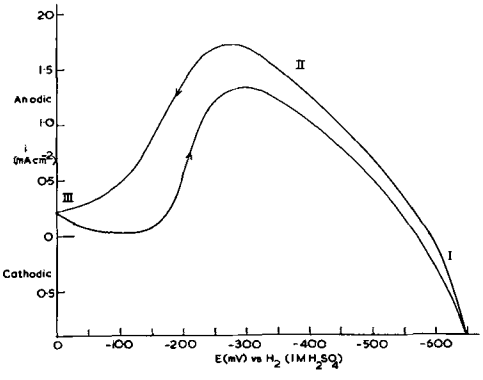

Fig. 1. *i-E* curve for a Ti wire electrode, 1M H_2SO_4

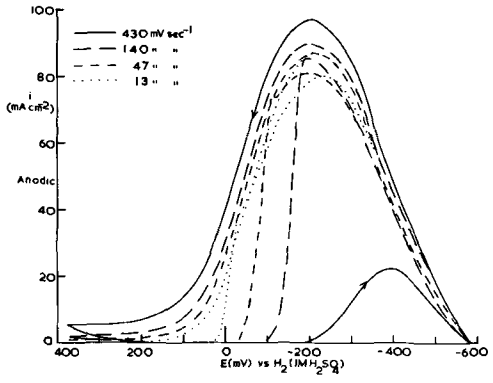

Fig. 2. Dependence of *i-E* curves on sweep rate, 10M H_2SO_4

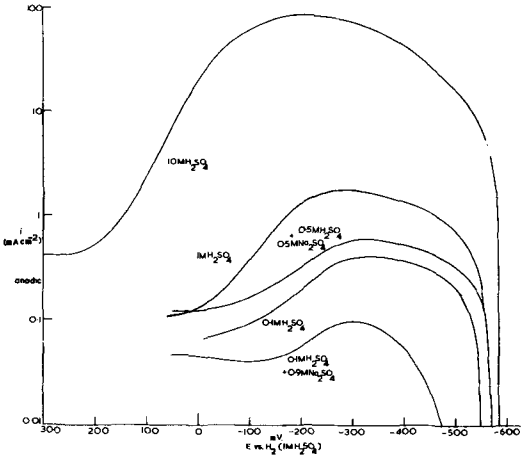

Fig. 4. Steady state *i-E* relationships for hydrogen evolution

Fig. 3. Steady state *i-E* relationships for active dissolution

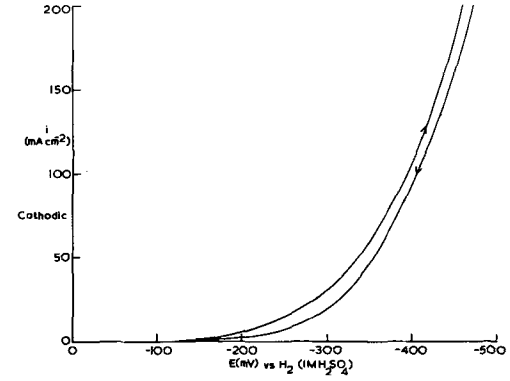

Fig. 5. Current-voltage characteristics of a hydrided electrode, 1M H_2SO_4.

gen evolution (I), active titanium dissolution (II), and passivity (III) can clearly be identified. The anodic and cathodic sweeps coincide at sufficiently slow sweep speeds. The dependence on sweep rate is shown in Fig. 2, as $dV/dt \rightarrow 0$, a convergence to a limiting *i-E* curve was found. The limiting *i-E* curves for different solutions are shown in Fig. 3 (active dissolution) and Fig. 4 (hydrogen evolution). If hydrogen evolution was maintained for some time, the electrode characteristics changed in that the rate of hydrogen evolution at fixed potential was markedly increased and the dissolution of the metal greatly suppressed (Fig. 5). We took this to be due to hydriding of the metal.

Current-potential curves on rotating disk electrodes.—Current potential curves on rotating disk electrodes showed no dependence on disk speed[2] between $\omega = 2.6$ and $\omega = 680$ rad/sec. This is shown in Fig. 6 for the active branch. The *i-E* relationships obtained coincided with those obtained from wire electrodes.

Ring-disk electrodes.—The *i-E* relationship obtained on the ring electrode while active dissolution was proceeding (Fig. 7) showed a single anodic wave before oxygen evolution. The ring current in the region of this limiting current is shown for various values of the disk potential (Fig. 8). For active dissolution

$$\frac{i_r}{i_d} = 0.13 \pm 0.01$$

Transient measurements.—Active to passive potentiostatic transient measurements showed a monotonically decreasing current with time (Fig. 9A, B), whereas passive to active transients (Fig. 10) were of a sigmoid form.

[2] In HCl there was also no dependence on rotation speed. In $HClO_4$ however there was a marked dependence which is probably associated with a homogeneous oxidation of Ti species.

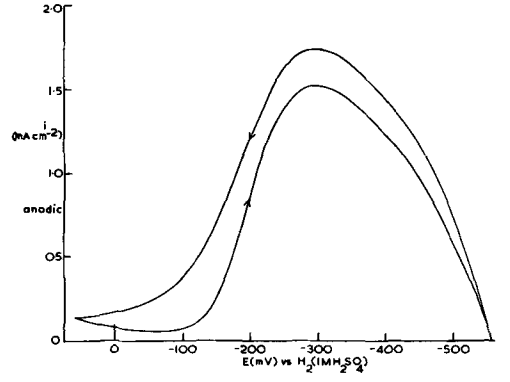

Fig. 6. Dependence of dissolution rate on disk rotation speed, 1M H_2SO_4. *i-E* curve shows results for $\omega = 2.6$, 680 rad sec^{-1}.

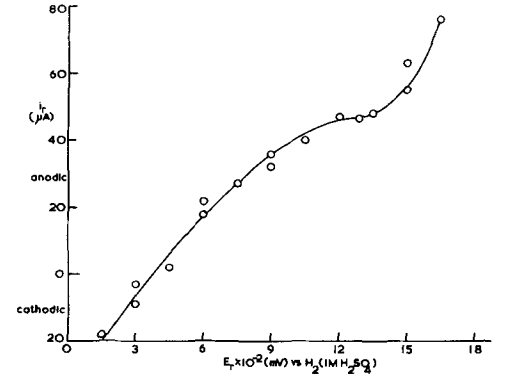

Fig. 7. Ring current as a function of ring potential. Disk at −200 mV *vs.* H_2 1M H_2SO_4, $\omega = 19$ rad sec^{-1}.

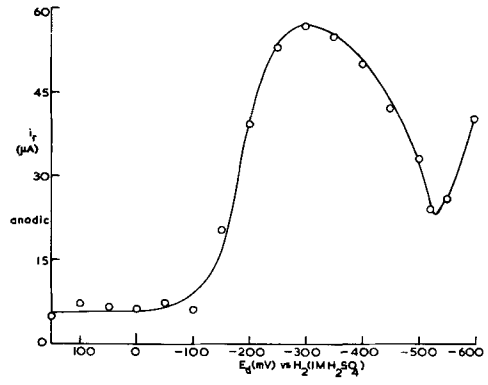

Fig. 8. Ring current as a function of disk potential. Ring potential 1.29 V, $\omega = 19$ rad sec^{-1}.

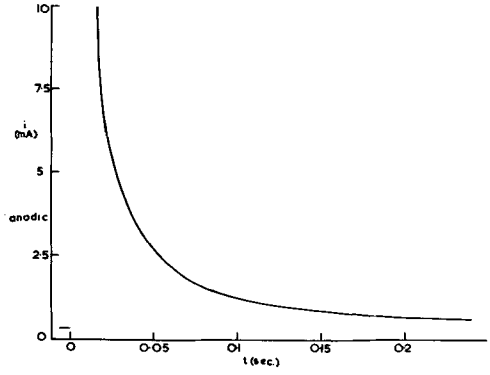

Fig. 9A. Typical active-passive transient (short time scale) —450 to 0 mV (1M H_2SO_4).

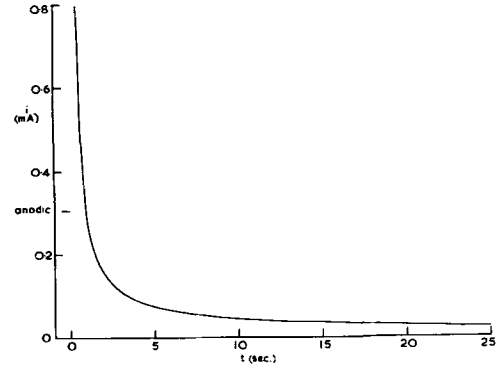

Fig. 9B. Typical active-passive transient (long time scale) —450 to 0 mV (1M H_2SO_4).

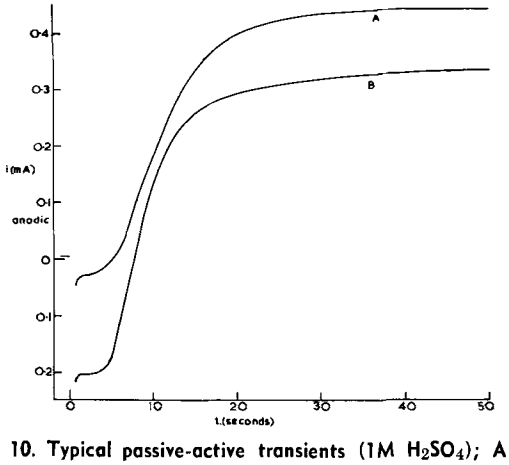

Fig. 10. Typical passive-active transients (1M H_2SO_4); A = 0 to —200 mV, B = 0 to —450 mV.

Discussion

Thermodynamic requirements.—For Ti in sulfuric acid the following potentials have been quoted (11, 12) (at 25°C)

$$Ti = Ti(H_2O)_6^{3+} + 3e \qquad E°_H = -1.21V$$

$$Ti = Ti(IV) + 4e \qquad E°_H = -0.88V$$

The Ti/Ti(II) potential is uncertain since stable solutions of Ti(II) cannot be prepared in aqueous media (13), although recent estimates (14, 15) give

$$Ti = Ti(II) + 2e \qquad E°_H = -0.6V$$

Ti(III) complexes with OH^- as (16)

$$Ti^{3+} + OH = Ti(OH)^{2+}, \log K_1 = 12.71$$

while Ti(IV) is present in sulfuric acid largely as $Ti(OH)_3HSO_4$ (17).

Thus, thermodynamically, Ti could dissolve in the potential region under investigation as Ti(II), Ti(III), or Ti(IV). However the product of the reaction must be Ti(III) or Ti(IV) since Ti(II) is oxidized by water.

Mechanism of Ti dissolution.—The independence of the dissolution current on disk rotation speed shows that (*a*) surface processes are rate determining, and (*b*) that solution soluble intermediates are absent. It is not possible to deduce a Tafel slope from the composite *i-E* curves because of the relatively small potential region between hydrogen evolution and passivation. However the reaction is approximately first order with respect to H^+ at constant potential.

This is in agreement with previous observations on the effect of hydrogen ion concentration in sulfuric and hydrochloric acids (2, 8, 10).

The product of the reaction follows from the ring disk experiments. Since it can be oxidized it must be Ti(II) or Ti(III). The collection efficiency (*N*) estimated from Alberry and Bruckenstein's (18) tables is 0.40 which fits the experimental results if

at the disk $\quad Ti \rightarrow Ti^{3+} + 3e$

at the ring $\quad Ti^{3+} \rightarrow Ti(IV) + e$

Thus the dissolution of Ti appears to be H^+ catalyzed, in contrast to Fe (19) which is OH^- catalyzed. A possible mechanism is

$$Ti \rightleftharpoons Ti_{ads}^{2+} + 2e$$

$$Ti_{ads}^{2+} + H^+ \rightarrow Ti^{3+} + H_{ads}$$

$$H_{ads} \rightleftharpoons H^+ + e$$

which would require the reaction to be first order in H^+ and have a Tafel slope of ~34 mV/decade for the case of low coverage by adsorbed species.

Another possible explanation for the H^+ dependence of the dissolution rate is that OH^- is adsorbed in the region of Ti dissolution and reduces the rate of dissolution through a surface coverage effect.

Hydrogen evolution.—Current-potential curves for hydrogen evolution showed a Tafel slope of 172 mV/decade (at 70°C) and an order of unity with respect to H^+. This indicates the slow discharge of H^+ as the rate determining step. The present work is compared with previous work (20, 21) on hydrogen evolution on Ti in Table II. Thus Ti is a high overvoltage metal while Ti-H has a low overvoltage for hydrogen evolution.

Table II. Parameters for hydrogen evolution on titanium

Solution	Temperature	log i_o, A cm^{-2}	Tafel slope, mV/decade	Reference
1M H_2SO_4	70°C	−6.37	172	This work
1M H_2SO_4	Room temp	−8.15	119	20
0.5M H_2SO_4	Room temp	−6.01	135	21
1M HCl	Room temp	−6.30	130	21

Passivation of titanium.—The i-E curve for the active-passive transition in titanium shows no dependence on rotation speed. We consider this as evidence that the passivation of Ti does not involve an intermediate dissolution reaction followed by "precipitation" in the solution as has been proposed for Ni (22). The passive-active transients which are observed (Fig. 10) can be explained by assuming that the passivating film on titanium is removed by a mechanism involving the nucleation and growth of two dimensional holes. If the holes grow a velocity v cm sec^{-1} and nuclei are formed at the rate of A nuclei cm^{-2} sec^{-1} then the fraction of active surface (S) after a time t is

$$S = 1 - \exp\left[\frac{-\pi v^2 t^3 A}{3}\right]$$

The component which will be observed is then (23) (*i*) due to the active dissolution of Ti, i_1; (*ii*) due to the passive dissolution of Ti, i_2; (*iii*) due to hydrogen evolution on the active surface, i_3; (*iv*) due to hydrogen evolution on the passive surface, i_4 and

$$i_1 = i_{01}\left[1 - \exp\left(\frac{-\pi v^2 t^3 A}{3}\right)\right]$$

$$i_2 = i_{02}\exp\left(\frac{-\pi v^2 t^3 A}{3}\right)$$

$$i_3 = i_{03}\left[1 - \exp\left(\frac{-\pi v^2 t^3 A}{3}\right)\right]$$

$$i_4 = i_{04}\exp\left(\frac{-\pi v^2 A t^3}{3}\right)$$

while the observed current is

$$i = i_1 + i_2 - i_3 - i_4$$

which qualitatively agrees with the observed transients.

Acknowledgments

We would like to thank Mr. R. D. Giles for helpful discussions during the course of this work.

Manuscript submitted Nov. 10, 1969; revised manuscript received March 12, 1970.

Any discussion of this paper will appear in a Discussion Section to be published in the June 1971 JOURNAL.

REFERENCES

1. N. Hackerman and C. D. Hall, *This Journal*, **101**, 321 (1954).
2. M. Stern and H. Wissenberg, *ibid.*, **106**, 755 (1959).
3. I. A. Menzies and A. F. Averill, *Electrochim. Acta*, **13**, 807 (1968).
4. E. G. Kuznetsova, T. I. Borisova, and V. I. Veselovskii, *Elektrokhimiya*, **4**, 167 (1968).
5. A. P. Brynza and V. P. Fedash, *Zashchita Metal.*, **4**, 252 (1968).
6. G. Sanderson and J. C. Scully, *Corrosion*, **24**, 75 (1968); *Corrosion Sci.*, **8**, 771 (1968).
7. H. L. Gegel and S. Fujishiro, *J. Less-Common Metals*, **17**, 305 (1968).
8. J. C. Griess, *Corrosion*, **24**, 96 (1968).
9. T. R. Beck, *This Journal*, **114**, 553 (1967).
10. M. Levy and G. N. Sklover, *ibid.*, **116**, 323 (1969).
11. "Stability Constants of Metal-Ion Complexes," The Chemical Society, London (1964).
12. M. Pourbaix, "Atlas d'equilibres electrochimiques," pp. 213-222, Gauthier-Villars, Paris (1963).
13. T. C. Franklin and H. V. Leklemian, *J. Inorg. Nuclear Chem.*, **12**, 181 (1959).
14. J. W. Olver and J. W. Ross, *J. Am. Chem. Soc.*, **85**, 2565 (1963).
15. P. George and D. S. McClure in "Progress in Inorganic Chemistry," F. A. Cotton, Editor, Interscience Publishers, New York (1959).
16. R. L. Pecsock and A. N. Fletcher, *Inorg. Chem.*, **1**, 155 (1962).
17. J. Beukankamp and K. D. Herrington, *J. Am. Chem. Soc.*, **82**, 3025 (1960).
18. W. J. Alberry and S. Bruckenstein, *Trans. Faraday Soc.*, **62**, 1920 (1966).
19. J. O'M. Bockris, D. Drazic, and A. R. Despic, *Electrochim. Acta*, **4**, 325 (1961).
20. A. T. Petrenko, *Zh. Fiz. Khim.*, **36**, 1527 (1962).
21. Ya. M. Kolotyrkin and P. S. Petrov, *ibid.*, **31**, 659 (1957).
22. J. O'M. Bockris, A. K. N. Reddy, and B. Rao, *This Journal*, **113**, 1133 (1966).
23. R. D. Armstrong, D. F. Porter, and H. R. Thirsk, *J. Phys. Chem.*, **72**, 2300 (1968).

Mechanism of Electrodeposition of Manganese in Alpha and Gamma Modifications

N. Dhananjayan

National Metallurgical Laboratory, Jamshedpur-7, India

ABSTRACT

A mechanism of the deposition of manganese in alpha and gamma modifications, in the presence and absence of addition agents in the electrolyte, has been proposed based on experimental results and evidence. A flash layer of amorphous manganese is deposited from pure solutions, over which gamma manganese begins to build up in the absence of reducible sulfur or selenium compounds in the electrolyte. In the presence of sulfur dioxide, the amorphous nature continues to build up to an increasing thickness over which crystalline alpha manganese is obtained. Alpha manganese is obtained in the presence of sulfur, selenium, or tellurium when the cathode polarization together with the hydrogen content of the deposit is found to be increased. Likewise, the increase in current density increases the cathode polarization together with the hydrogen content of the deposit when hard brittle amorphous manganese is obtained. The low hardness and density of electrodeposited alpha manganese, compared to its annealed state, and the increase in hardness together with ductility on heating, suggest that a part of the discharged hydrogen ions assumes positions inside the lattice or forms a complex during the deposition of alpha manganese.

According to Dean (1,2), manganese is initially deposited to a few thousandths of an inch thick in gamma modification from all electrolytes, and in the presence of SO_2 in the electrolyte, this gamma gradually transforms to the alpha form, the transition proceeding outward from the cathode plate. When the alpha form reaches the surface, manganese will plate as macroscopic crystals of alpha manganese. Dean (1,2) has

Key words: electrodeposited manganese, structure, mechanism, cathode polarization, hydrogen.

based his above inference on the "duplex structure," as he calls it, of deposited manganese and the higher hardness of the manganese surface-facing cathode.

Schlain and Prater (3) obtained good deposits of gamma manganese on copper cathodes in the absence of SO_2 with current efficiencies of 62-72% on 5-12 hr runs, but their deposits on stainless steel were poor and porous. According to them, the addition of SO_2 prevents the formation of gamma manganese. The deposited gamma manganese takes about 238 hr at 25°C for half completion of the transformation to alpha manganese (4).

Bell's work (5) does not seem to support Dean's contentions. She plated manganese on aluminum, mild steel, and copper to 0.0005-0.0015 in. thick and found only the presence of alpha manganese, although there was no reducible sulfur compound present in the electrolyte. She had used a high current density of 23-27 A/dm^2 and had used electrolytic manganese flakes in the anolyte to make up the manganese content of the bath.

According to Moiseev and Popova (6,7) and Gorbunova (8), the deposits on copper, silver, and iron from manganese ammonium sulfate baths with or without addition of glycerol to a thickness of 10-60μ, at current densities of 30 A/dm^2, and at *p*H 3.8-4 showed only x-ray patterns similar to the one from the amorphous substances. They obtained gamma manganese, in some cases, in the deposit 10μ thick, on a silver cathode, in the absence of glycerol in the bath. At room temperature, it passed over to the alpha form in about 6 hr. The deposits obtained by Moiseev and Popova (6,7) with 0.3% SO_2 in the electrolyte, at current densities of 17-25 A/dm^2 and at *p*H 2.2-3.0, showed clear crystalline structure of alpha manganese with a texture, while deposits obtained at current densities of 25-30 A/dm^2 and at *p*H 3.8-4.2 showed only a pattern of the amorphous body.

This paper proposes a new mechanism on the deposition of manganese in alpha and gamma forms, on the basis of more recent data from an extensive study (9, 10), and attempts clarification of certain anomalies in the observations of earlier investigators.

Experimental

Considerable attention was paid in the preparation and purity of the electrolyte to ensure absence of colloidal or sulfide sulfur. Unless otherwise mentioned, the conditions of deposition were as follows.

Composition of electrolyte: 23-24 g/liter of manganese as manganese sulfate and 135-140 g/liter of ammonium sulfate; initial *p*H of catholyte and feed electrolyte: 7.2; electrolyte flow to the cell: 10 ml/min; cathode current density 4.2 A/dm^2; and temperature: 28°C

Each cathode had a vertically cut slit, 4 x 1 cm, in the center (see Fig. 1). The top of the slit was 1 cm below the solution level. A 0.25 mm thick wire of the cathode material was attached in the slit. The wires were cold drawn and annealed. They were then polished with metallographic paper 2/0. A portion was cut from the middle of this wire with deposited metal and the same was used as the specimen for x-ray studies. For back-reflection x-ray studies of deposits, cathodes, with deposited manganese from a small cell, were directly used as the specimen. For microstructure studies, the metastable gamma manganese or specimens containing both alpha and gamma were cold-mounted with plastic solution and powder.

The electrode potentials were determined with a view of studying the comparative differences in the values of the various forms of manganese in identical solutions under identical conditions. They were measured directly from 1*N* $MnSO_4$ solution, prepared from transformed gamma manganese, and contained no sulfur, selenium, or any dissolved gases. The recorded potential values from the moment the metal is placed in the solution to about 30 min were extrapolated to zero time and the potential at zero time was taken for comparison. It may be mentioned that the extrapolated values to zero time of two different specimens of each of the various forms of manganese examined were in very close ranges of ±0.003V. No correction has been made for the activity coefficient and the values cannot be taken as absolute standard potential values.

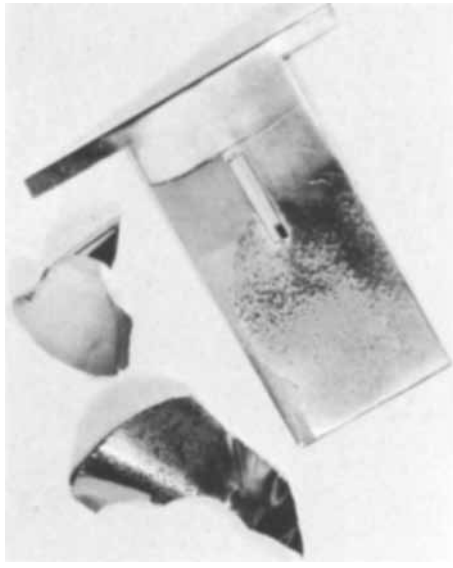

Fig. 1. Stainless steel cathode after stripping off deposited gamma manganese showing the amorphous undercoat of manganese.

The hydrogen content in deposited manganese was determined by vacuum extraction at 500°C as the solubility of hydrogen in manganese is minimum at that temperature. The order of reproducibility in the determination was about ± 5%/100g of metal.

Results and Discussion

Nature and growth of manganese deposits.—It can be seen from Table I that deposition of manganese on a stainless steel cathode in the absence of reducible sulfur or selenium compounds in the electrolyte results in a nonuniform amorphous deposit (Fig. 1) for

Table I. Structure of initial deposits of manganese from solutions in absence and presence of sulfur dioxide or selenious acid

Addition agent g/liter	Time of deposition	Structure of the deposit	
		On stainless steel cathode	On copper cathode
Nil	8 sec	Amorphous	Only diffraction pattern of copper substrate
Nil	30 sec	Gamma (diffraction line of 2.13Å only)	Only diffraction pattern of copper substrate
Nil	1 min	Gamma (diffraction line of 2.13Å only)	Only diffraction pattern of copper substrate
Nil	2 min	Gamma (diffraction line of 2.13Å only)	Amorphous (broad diffused halo at *d* value 2.08-2.15Å)
Nil	3 min	Gamma (diffraction line of 2.13Å only)	Amorphous (broad diffused halo at *d* value 2.08-2.15Å)
Nil	5 min	Gamma (all the diffraction lines of gamma)	Gamma (all the diffraction lines of gamma)
0.15 SO_2	2 min	Amorphous (broad diffused halo at low angle)	Amorphous (broad diffused halo at low angle)
0.15 SO_2	5 min	Amorphous (broad diffused halo at low angle)	Amorphous (broad diffused halo at low angle)
0.15 SO_2	10 min	Amorphous (broad diffused halo at low angle)	Amorphous (broad diffused halo at low angle)
0.15 SO_3	15 min	Alpha (all the diffraction lines of alpha)	Alpha (all the diffraction lines of alpha)
0.1 H_2SeO_3	1 min	Alpha (all the diffraction lines of alpha)	—

the first 8 sec over which gamma manganese begins to build up. Deposits on copper up to 1 min of deposition, under the same conditions, do not show any diffraction lines other than those of copper, which may perhaps be the period of alloy formation and/or diffusion, after which up to 3 min of deposition, in addition to the substrate pattern, a broad halo at a low angle indicating the amorphous nature of the growing deposit is noticed. At 5 min of deposition, all the diffraction lines of gamma manganese are noticed both on stainless steel and copper cathodes.

On the other hand, on addition of 0.15 g/liter of SO_2 to the same electrolyte under the same conditions, the deposits, both on stainless steel and copper, continue to show the initial amorphous pattern up to 10 min of deposition. At 15 min, both give a clear crystalline pattern of alpha manganese. No evidence of deposition of gamma manganese was found at any time on either cathodes in the presence of SO_2, although in its absence, gamma lines were distinguishingly clear at 5 min of deposition. The amorphous deposits show a hardness value of 652 DPN indicative of alpha manganese.

Beyond 15 min of deposition, crystalline alpha manganese is obtained on all cathodes in the presence of SO_2 or SeO_2 in the electrolyte and gamma manganese is obtained in their absence. The photomicrographs of alpha manganese, obtained in presence of S or Se, show a clear columnar structure, while those of gamma manganese, obtained in absence of these compounds, show a twinned structure as can be seen from Fig. 2a and 2b.

The surface of the alpha manganese-facing cathode, obtained in the presence of SO_2, immediately after deposition or after a period of four years of aging at room temperature, does not give any back-reflection x-ray pattern confirming that the particle size of the surface-facing cathode is below the range of diffraction by x-rays. Only after heating at 500°C for 2 hr in vacuum did this specimen give a sharp back-reflection pattern of alpha manganese.

Deposition of gamma over alpha manganese and vice versa.—Figure 3a and 3b show the photomicrographs of deposited alpha over gamma manganese and vice versa.

Back-reflection x-ray examination of the deposit obtained in 10 min, in the presence of selenium, over gamma manganese shows diffraction lines of alpha and gamma manganese, while the deposit in 10 min, in the absence of selenium, over alpha manganese shows diffraction lines of alpha manganese only. This later deposit, on x-ray powder pattern, shows a broad diffused halo at a d value of 2.10Å along with alpha manganese lines. This indicates that during deposition, from solutions containing no reducible S or Se compounds, over alpha manganese, an amorphous deposit forms initially because of which gamma deposited over alpha could be stripped off separately. On the other hand, alpha manganese deposited over gamma could not be stripped off, the entire deposit coming off together from the cathode.

Substrate influence.—Thus it can be seen that copper and manganese cathodes have some influence in the first few layers of the deposit. Beyond that, the sub-

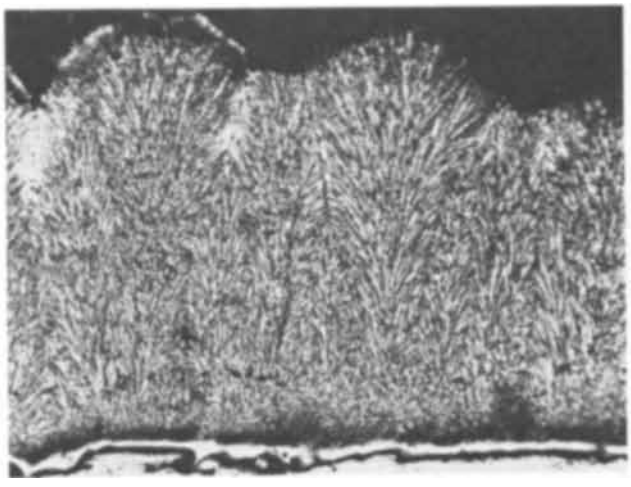

Fig. 2a. Electrodeposited alpha manganese, cross section. 270X

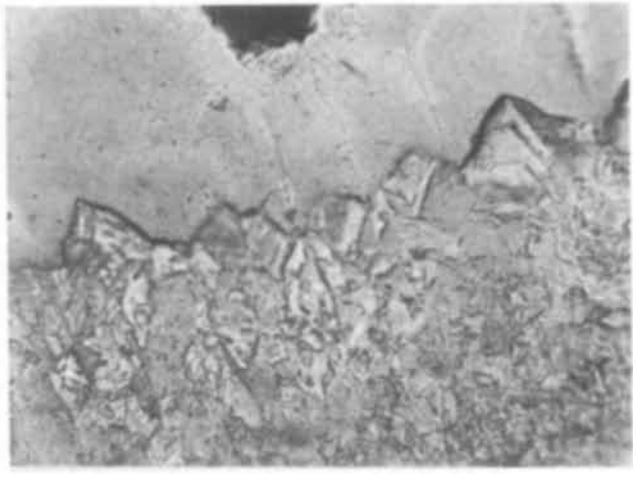

Fig. 3a. Alpha over gamma manganese. 450X

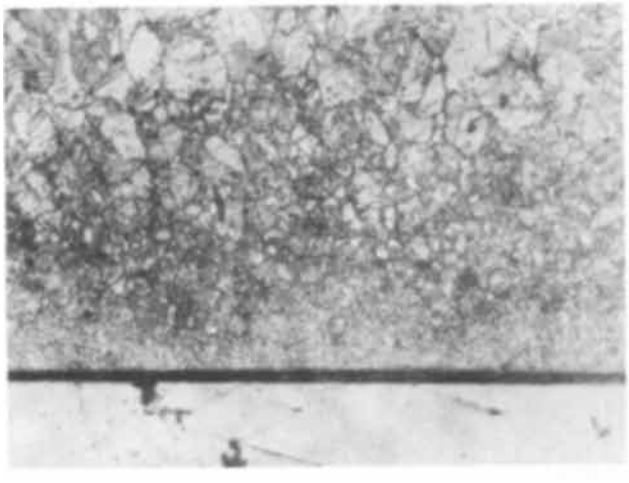

Fig. 2b. Electrodeposited gamma manganese, cross section. 270X

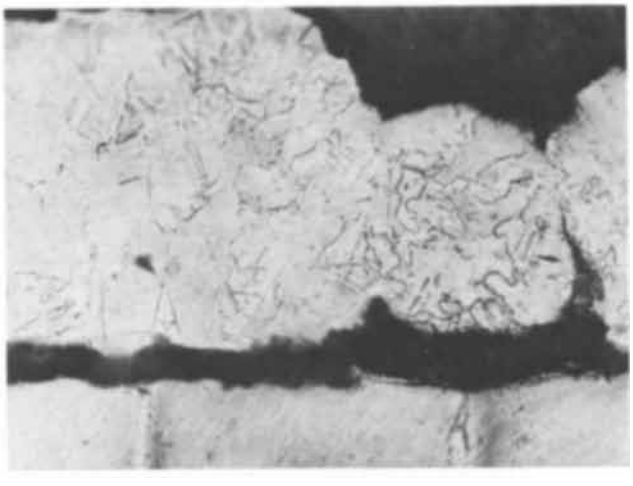

Fig. 3b. Gamma over alpha manganese. 450X

Table II. Electrode and cathode potential values

No.	Nature of manganese metal	With respect to hydrogen electrode as zero, at 27°C, V: Electrode potential in 1N $MnSO_4$ solution (extrapolated value to zero time)	With respect to hydrogen electrode as zero, at 27°C, V: Cathode potential at a current density of 4.2 A/dm²*
1.	Pure alpha manganese containing no sulfur or selenium (deposited as gamma manganese and transformed to alpha by heating at 160°C for 1 hr in vacuum)	−1.058	—
2.	Gamma manganese (electrodeposited)	−1.085	−1.392
3.	Alpha manganese containing sulfur (electrodeposited from solutions containing 0.1 g/liter of SO_2)	−1.092	−1.399
4.	Alpha manganese containing selenium (electrodeposited from solutions containing 0.1 g/liter of H_2SeO_3)	−1.125	−1.408

* No correction has been made for the ohmic drop between the Luggin capillary and electrode surface.

strates have no directing influence on the structure of the deposit. The presence of reducible S or Se compounds alone in the electrolyte determines the ultimate structure. With all other conditions of deposition such as current density, pH, temperature, composition of electrolyte, and even cathode efficiency remaining the same on any substrates, gamma or alpha manganese can be deposited depending on the absence or presence of reducible compounds of S or Se in the electrolyte.

Standard and cathode potentials.—It can be seen from Table II that the standard electrode potential of pure alpha manganese containing no sulfur or selenium should be less negative than that of gamma manganese and that the two values differ only very slightly, which is in conformity with the standard free energy of each modification (11). It is also seen that the cathode potentials under the same current densities of deposition increase in the order of (*a*) gamma manganese, (*b*) alpha manganese containing sulfur, and (*c*) alpha manganese containing selenium, which is found to be in conformity with the order of electrode potential values.

Pure alpha manganese (transformed gamma manganese) is found to have a very low hydrogen overvoltage, while gamma manganese has a comparatively higher hydrogen overvoltage.

Addition agents, polarization, and hydrogen content.—It can be seen from Table III that electrodeposited gamma manganese contains 42-70 ml/100g of hydrogen, almost the same amount soluble in gamma manganese within its temperature ranges of stability (12). On the other hand, electrodeposited alpha manganese, in presence of sulfur or selenium, contains 230-260 ml/100g of hydrogen, while the absolute solubility of hydrogen in alpha manganese is only 21.6 ml/100g at 25°C (12). It is noticed that the presence of reducible S or Se compounds in the electrolyte increases the cathode polarization with a resultant increase in the hydrogen content of the alpha deposit obtained. Both these properties can be attributed to the negative catalytic activity of sulfur and selenium on the recombination of hydrogen atoms (13, 14) to form molecules.

While the negative catalytic agents of group VIB, viz., S, Se, and Te, facilitate the deposition of alpha manganese, negative catalytic agents of group VB, viz., P, As, and Bi, do not behave similarly. With tellurium the hydrogen content increases to 598 ml/100g and the deposit shows an amorphous pattern on x-ray studies.

Organic inhibitors in the electrolyte also increase the cathode polarization, but they neither yield alpha manganese nor introduce any high amount of hydrogen in the deposit. Experiments D and E in Table III show that only cathodically reducible sulfur compounds yield alpha manganese and that the effect of SO_2 is primarily not that of a reducing agent in the deposition of manganese (1).

Effect of conditions of deposition.—Cathode current density.—With all other conditions of deposition remaining the same, increase in current density from 4-5 to 30 A/dm² prevents the formation of gamma manganese from solutions containing no reducible S or Se compounds, and an amorphous brittle manganese with the hardness of alpha and with a hydrogen content of 550 ml/100g is obtained. Heating this amorphous deposit at 125°C in a vacuum of 10^{-3} mm of Hg gives a clear crystalline pattern of alpha manganese.

Table III. Addition agents, hydrogen content, and structure of deposited manganese

(Excepting for Expt. A—1, when copper cathode was used, all the other experiments were carried out with stainless steel cathode.)
Current density: 4.6 A/dm²; time of deposition: 2 hr

No.	Addition agent, g/liter	Current efficiency, %	Structure	Hydrogen content, ml/100g	Remarks
A—1	Nil	67.35	Gamma	70	—
2	Nil	73.72	Gamma	42	No sulfide sulfur detected in the deposit
		B. Negative catalysts for hydrogen recombination			
Group VIB					
1	Sulfurous acid: 0.13	63.48	Alpha	231	0.07% sulfur in the deposit
2	Selenious acid: 0.013	64.68	Alpha	260	0.13% selenium in the deposit
3	Telluric acid: 0.1	26.02	Alpha (amorphous fine grained)	598	—
Group VB					
4	Phosphorus 0.05 as sodium hypo phosphite	65.77	Gamma	84	With bismuth oxide, only black deposit; with arsenite, deposit at edges of the cathode only were obtained
		C. Organic inhibitors			
1	Triamylamine: 0.11	68.31	Gamma	99.93	Very adherent, a very thin layer of white undercoat Mn was seen on stripping gamma manganese
2	Triethanolamine: 3 ml	54.34	Gamma	48.6	—
3	Paraformaldehyde: 0.1	73.68	Gamma	26.62	Excellent deposit, not very adherent
4	Dimethylamine benzaldehyde: 0.1	51.66	Gamma	62.8	Deposit was rather loose, not adherent. Amorphous undercoat was practically absent
5	Glycerol: 10 ml	69.28	Gamma	45.6	—
		D. Cathodically nonreducible and reducible sulfur compounds			
1	Dithionic acid: 0.4	65.55	Gamma	36.1	No sulfide sulfur detected in 6g sample
2	O-Tolythiourea: 0.26	63.43	Alpha	230.5	Very bright deposit
		E. Oxidizing agents in presence and absence of selenium			
1	Selenious acid 0.1 and ammonium persulfate 4.0	88.67	Alpha	184	—
2	Ammonium persulfate only: 10.0	50.0	Gamma	50.6	—

During deposition at high current densities, at the top solution-air interface portion, where the current is blocked due to accumulation of hydrogen bubbles and where the cathode polarization is decreased, gamma manganese is obtained. Similarly if a cathode is bent at the projected side which is drawn nearer to the anode and where the current density is high, alpha manganese (amorphous) is obtained, and on the reverse side where the current density is low, gamma manganese is obtained.

Catholyte pH.—At catholyte pH around 2, in the presence of SO_2, deposits obtained show crystalline pattern of alpha manganese, instead of the amorphous deposits obtained up to 10 min of deposition at pH around 7 as mentioned earlier. This has to be attributed to the formation of hydrogen sulfide and its direct inhibitive action on the recombination of hydrogen atoms and to direct proton inclusion in the deposit (13,14).

Hardness and evolution of hydrogen in manganese.—Unlike other electrodeposited metals like Fe, Cr, Ni, etc., electrodeposited alpha manganese does not show a high hardness value compared to its annealed state. The electrodeposited alpha manganese has a hardness of 690 DPN, which increases to 1000 DPN on heating to 500°C in vacuum, when practically all the hydrogen is removed. The electrodeposited gamma manganese has a hardness of 100 DPN.

The electrodeposited alpha manganese left at room temperature is found to be less brittle with the passage of time. Most of the hydrogen in alpha manganese can be removed on heating to 300°C in a vacuum of 10^{-4} mm of Hg without significantly affecting the broadening of diffraction rings (Table IV). On heating to 500°C, the broadening disappears, the x-ray pattern is well resolved, and the hardness is also increased. Along with hardness, the ductility of the metal also increases.

The x-ray powder patterns obtained in this investigation of gamma and alpha deposits containing various amounts of hydrogen generally confirm Potter's (15) earlier finding that the broadening of the lines was highest with transformed gamma manganese. Potter (15) explains, on the basis that all the hydrogen is in interstitial solid solution, that the highest broadening with transformed gamma manganese is because of an uneven distribution of hydrogen in the unit cell of alpha manganese so formed. On the other hand, it is felt that the highest broadening observed with transformed gamma manganese should be attributed to the volume change associated with the transformation of gamma to alpha and the resultant stress. Second, the deposits containing more than 500 ml/100g of hydrogen obtained in this investigation were generally amorphous.

General discussion.—No evidence to support Dean's theory that manganese is initially deposited in gamma which subsequently transforms to alpha in presence of SO_2 was found from x-ray studies of the deposits. The experimental results in this investigation indicate that the particle size of the initial deposit, in presence of SO_2, should be less than 0.01μ, being below the range of diffraction by x-rays. Apparently the thin crystalline deposit toward the cathode, mentioned by Dean (1), seems to be this amorphous deposit. The higher hardness and the tarnish resisting brightness of the surface-facing cathode (1) can be explained by the finer grain size and orientation of the initial deposit.

Presumably the high current density of 23-27 A/dm^2 and the sulfur present in the electrolytic manganese flakes which were used directly in the anolyte to make up to the manganese content of the bath may be responsible for the absence of the gamma modification in the deposits that Bell (5) obtained in the absence of SO_2 in the electrolyte.

The gamma manganese obtained in this investigation took about 5 days for half completion of transformation to alpha at a temperature of 32°C, corroborating Potter's data (4). In this investigation, the addition of glycerol was not found to have any effect on the structure of deposited manganese compared to those obtained from pure solutions as reported by Moiseev (6, 7). However, this investigation corroborates Moiseev's (6, 7) findings that at a lower pH, crystalline alpha manganese is obtained instead of the amorphous deposits obtained initially at higher pH values in the presence of SO_2.

Table IV. Evolution of hydrogen from electrodeposited alpha manganese (pilot plant sample) during heating to various temperatures

Temperature, °C	Evolved hydrogen in 15 min at 10^{-4} mm of Hg (ml/100g)
75	11.58
100	15.45
200	106.90
300	154.50
400	16.73
500	2.57

Proposed Mechanism

The following mechanism is suggested in the deposition of manganese in alpha and gamma modifications, at current densities of the order of 4-5 A/dm^2 and at catholyte pH values around 7.

(*i*) (*a*) Barring the exceptions of a directing influence of an active substrate in the first few atomic layers of the deposit, manganese is initially electrodeposited from pure solutions of manganese and ammonium sulfate in an amorphous nature. This amorphous deposit resembles alpha manganese.

(*b*) Pure alpha manganese containing no S or Se and especially this amorphous deposit has a very low hydrogen overvoltage, and for this reason it cannot be electrodeposited from pure solutions to any appreciable thickness.

(*c*) As soon as an initial flash layer of such extremely fine grained (alpha) manganese is formed in about 8-10 sec, it facilitates hydrogen discharge and hydrogen evolution takes place. This discharge of hydrogen ions makes the vicinity of the cathode more alkaline when the potential for evolution of hydrogen is raised.

(*d*) The standard electrode potential of gamma manganese is only slightly more negative than that of pure alpha manganese, and the increase in polarization due to the discharge of hydrogen (as mentioned under (*c*) above) enables gamma manganese to be deposited. Due to the higher hydrogen overvoltage of gamma manganese, gamma manganese begins to build up.

(*ii*) (*a*) With an addition of 0.1 g/liter of SO_2 to the electrolyte, the amorphous nature of the initial deposit continues to build up to an increasing thickness, over which crystalline alpha manganese is obtained. This bears a close resemblance to the thick amorphous brittle manganese, having hardness of alpha, obtained at high current densities, viz., 27-30 A/dm^2, from solutions containing no reducible sulfur or selenium compounds.

(*b*) Addition of reducible compounds of sulfur or selenium to the electrolyte not only increases the cathode potential values, but simultaneously increases the surface concentration of hydrogen atoms, as in the case with high current densities of deposition from pure solutions.

(c) These indicate that alpha manganese begins to build up when the cathode polarization is raised, together with a high adsorption or absorption of hydrogen as noticed from the hydrogen contents of deposited manganese in presence of sulfur or selenium in the electrolyte, and also at high current densities of deposition from solutions containing no reducible sulfur or selenium.

(*d*) The strength of the bond between manganese and sulfur or selenium may be greater with a result of the adsorption of these particles, and their effect on the discharge of metal ions may also be greater.

(*iii*) (*a*) The low hardness and density of electrodeposited alpha manganese, compared to its annealed state, and the increase in hardness together with ductility on heating suggest the possibility that a part of the discharged hydrogen ions assumes positions inside the lattice or forms complex during the formation of alpha manganese.

(*b*) On the other hand, desorption characteristics of hydrogen in alpha manganese do not favor the view that all the hydrogen in electrodeposited manganese is inside the lattice.

(*c*) After the flash layer of amorphous (alpha) manganese of the first 8-10 sec, further deposition of manganese in alpha form has to be attributed to the properties mentioned before and has to be explained presumably on the basis that a part of the hydrogen atoms goes inside the lattice and remains as protons and that the electrons are not equally shared between different kinds of atoms in alpha manganese and that the structure is more similar to that of a compound than to a true element (16).

Acknowledgment

This paper is based on a thesis submitted by the author for Ph.D. degree of the University of Madras. The author thanks the University of Madras for the kind permission to publish this paper.

Manuscript submitted Sept. 16, 1969; revised manuscript received March 20, 1970.

Any discussion of this paper will appear in a Discussion Section to be published in the June 1971 JOURNAL.

REFERENCES

1. R. S. Dean, "Electrolytic Manganese and Its Alloys," The Ronald Press Co., New York (1952).
2. R. S. Dean, C. T. Anderson, C. Moss, and P. M. Ambrose, *U.S. Bur. Mines, Rept. Invest.*, 3477 (1939).
3. D. Schlain and J. D. Prater, *Trans. Electrochem. Soc.* **94**, 58 (1948).
4. E. V. Potter, H. C. Lukens, and R. W. Huber, *Trans. Am. Inst. Min. & Met. Engrs.*, **185**, 399 (1949).
5. W. A. Bell, *Trans. Inst. Metal. Finishing*, **31**, 466 (1954).
6. V. P. Moiseev and O. S. Popova, *Phys. Metals. Metallog. (USSR) (English Transl.)*, **9**, 4, 98 (1960).
7. V. P. Moiseev and O. S. Popova, *J. Phys. Chem., Akad. Nauk (USSR)*, **33**, 10, 2183 (1959).
8. O. S. Popova and Gorbunova, *ibid.*, **32**, 9, 2020 (1958).
9. N. Dhananjayan, Ph.D. Thesis, University of Madras (India), 1966.
10. N. Dhananjayan and T. Banerjee, "Structure of Electrodeposited Manganese," National Metallurgical Laboratory (India) (1969).
11. J. W. Christian, *J. Inst. Metals*, **78**, 195 (1950-1951).
12. E. V. Potter and H. C. Lukens. *Trans. Am. Inst. Min. & Met. Engrs.*, **171**, 401 (1947).
13. H. Jarmolowicz and M. Smialowsky, *J. Catalysis*, **1**, 165 (1962).
14. Z. Szklarska-Smialowska and M. Smialowsky, *This Journal*, **110**, 444 (1963).
15. E. V. Potter and R. W. Huber, *Phy. Rev.*, **68**, 24 (1945).
16. A. J. Bradley and J. Thewlis, *J. Proc. Roy. Soc.*, **A115**, 456 (1927).

Microscopic Study of the Formation of Cathodic Films on Iron During Electrolysis of Chromium Plating Solutions at Various CrO_3:SO_4 Ratios

J. C. Saiddington and G. R. Hoey*

Corrosion Section, Extraction Metallurgy Division, Mines Branch, Department of Energy, Mines and Resources, Ottawa, Ontario, Canada

ABSTRACT

The formation of cathodic films was observed under the microscope during electrolysis of chromium plating solutions at various CrO_3:SO_4 ratios. The microscopic observations were correlated with galvanostatic and potentiostatic polarization data. It was found that an amorphous oxide film formed in chromic acid solutions. This film also formed, as a transient stage prior to chromium deposition, in solutions containing sulfate at CrO_3:SO_4 ratios ranging from 200:1 to 65:1. Chromium deposition was associated with transformations at the cathode surface that involved the breakup of the amorphous oxide film and the appearance of a viscous film. The nature and formation of these two types of cathodic films are discussed with reference to findings of other investigators.

Although the deposition of chromium from chromic acid solutions is an important industrial process little is known about its mechanism. Dubpernell (1) in a critical review of the available literature on the subject came to the conclusion that even the simplest questions about chromium plating cannot be answered with the present knowledge. A critical area of disagreement concerns the existence, role, and nature of cathodic films formed during electrolysis of chromic acid solutions in the presence and absence of sulfate.

The views regarding these films constitute two main schools of thought. One school maintains that pure chromic acid cannot be reduced to metal because a nonporous amorphous oxide film grows on the cathode surface and prevents all reduction processes other than that of hydrogen ion. The presence of sulfate alleviates the barrier-like conditions at the cathode

* Electrochemical Society Active Member.
Key words: cathodic films, chromium plating, microscopic observations.

surface by one of the following processes: (*a*) penetration by sulfate resulting in partial disruption of the amorphous oxide film suggested by Muller (2), (*b*) partial chemical dissolution of the film in the presence of sulfate suggested by Weiner (3), (*c*) modification of the film into reducible compounds that serve as an intermediate reduction stage postulated by Reinkowski and Knorr (4) and by Okada and Yamamoto (5), and (*d*) inhibition of the film growth in the presence of sulfate assumed by Kappel and Gerischer (6).

The second school of thought, represented by the views of Vagramyan and Usachev (7), Solov'eva and and Vagramyan (8), and Shluger and Kazakov (9), maintains that the deposition of chromium is brought about by formation of an entirely different type of film in the presence of sulfate. This second type of film, in distinction from the amorphous oxide type of film (film of the first type), is considered to be a colloidal complex consisting of the products of the reduction of chromic acid to the trivalent state, together with Cr^{6+} and $SO_4^{=}$ ions. This film may be observed visually on cathodes extracted from plating baths with the current on (10, 11); it dissolves easily in dilute chromic and sulfuric acids, in the electrolyte in the absence of current, and even in distilled water. Its thickness may vary in accordance with the electrolyte composition and the conditions of electrolysis, but it is always macroscopic. The colloidal film does not form in pure chromic acid, whereas the amorphous oxide film forms and grows in pure chromic acid to a considerable thickness.

The formation of an amorphous oxide film, that is, a film of the first type, has been detected in the present investigation during electrolysis of both "pure" and sulfate-containing chromic acid solutions by *in situ* microscopic observations of the cathode surface. These observations were correlated with polarization characteristics. The observations reveal that the amorphous oxide film disintegrates when chromium deposition begins in conventional plating baths and cannot therefore be considered an intermediate stage in the chromium plating process, as proposed by some investigators (4, 5). In addition, the present work points indirectly to the formation in the plating bath of the second type of film prior to the establishment of the chromium deposition process. Microscopic observations indicate that, under the conditions investigated, this second type of film is in the form of a transparent viscous layer during chromium plating and that it does not form in pure chromic acid solutions. One can assume, therefore, that such a film has a faculty of bringing about the final reduction step to metal in agreement with the results of the Russian investigators (7-9). The unconventional nature of the second type of film is not surprising in view of many phenomena associated with chromium plating that are not encountered in other electrodeposition processes.

Experimental

The experimental setup used in the investigation is represented schematically in Fig. 1. The microscopic technique used was similar to the one described by Jones and Saiddington (12) but included increased resolution of the optical system. To remove the evolving hydrogen bubbles, which would otherwise interfere with microscopic observations, a constant flow of solution at approximately 1 cm/sec was maintained between the objective and the cathode surface. For comparison, duplicate experiments were performed with solution stationary at the cathode surface.

All solutions were prepared with 250 g/l of analytical reagent quality chromium trioxide, which contained 0.02% of sulfate as an impurity. Thus, in "pure" chromic acid the ratio of chromium trioxide to sulfate was 5000:1. In addition to pure chromic acid four other concentrations of sulfate at fixed CrO_3:SO_4 ratios of 200:1, 100:1, 75:1, and 65:1 were studied. In a number of experiments the CrO_3:SO_4 ratio was varied from

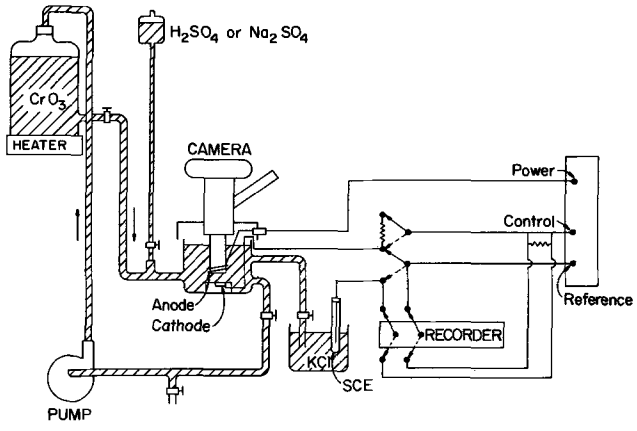

Fig. 1. Schematic diagram of the plating cell and accessories

5000:1 to 100:1 and subsequently to 400:1 or 500:1 while the electrolysis was in progress under galvanostatic or potentiostatic conditions. The variation of the CrO_3:SO_4 ratio was accomplished by increasing or decreasing the addition of H_2SO_4 or Na_2SO_4 to pure chromic acid solution passing continuously through the plating cell (see Fig 1).

An ANOTROL potential controller was used as a source of constant current and controlled potentials. Polarization curves were recorded by means of a potentiometric recorder with a ½-sec response over a full 9-in. grid and a 4-megohm input impedance off balance. Saturated calomel electrode was used throughout as a reference across a salt bridge that did not introduce significant ohmic drops at the currents employed.

Cathodes were prepared from iron rods, 3.96 mm diameter, with cross-sections polished metallographically to a fine finish. A 2-min immersion in the plating bath preceded by a thorough rinse with distilled water was the only chemical treatment employed.

All experiments were conducted at 50°C. Practically all microscopic observations were made at 100X magnification with 0.18 NA objective under conditions of dark field illumination with solutions flowing across the cathode surface. The visual observations are described in the text. Photomicrographic record is illustrated by a small number of selected photomicrographs.

Results

Electrolysis at constant current.—Voltage-time curves.—Voltage-time curves at a current density of 220 mA/cm² at CrO_3:SO_4 ratios of 5000:1, 200:1, 100:1, 75:1, and 65:1 obtained with the solution maintained stationary in the plating cell are shown in Fig. 2a. Similar curves obtained with the solution flowing across the cell at approximately 1 cm/sec are shown in Fig. 2b. The principal effect of the agitation thus introduced was a complete separation of curves 2 and 3 shown in Fig. 2b, while they coincided in the first part of their length in Fig. 2a.

The curves are considered in terms of five ranges of potential.

Potential range (*i*) is characterized by a rapid shift of potential from the value +0.85V *vs.* SCE, measured during the immersion of the electrodes in the plating cell before commencement of the electrolysis, to the potential of hydrogen evolution at −0.75V. Since the rate of the shift of the potential to this point was found more rapid than the response characteristics of the recorder, this part of the curve is shown in Fig. 2a and 2b as a straight line and can be considered, in the context of this investigation, to represent the process of charging the electrode from the potential of rest to the potential of hydrogen evolution. This range of potential was the subject of detailed studies by Okada, Nakamura, and Ishida (13).

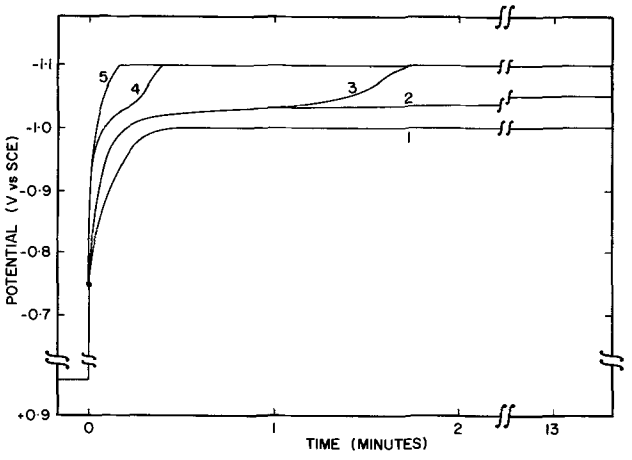

Fig. 2a. Polarization curves at a constant c.d. of 220 mA/cm^2 in stationary solutions. CrO_3, 250 g/l; temperature, 50°C. CrO_3:SO_4 ratios: curve 1, 5000:1; curve 2, 200:1; curve 3, 100:1; curve 4, 75:1; and curve 5, 65:1.

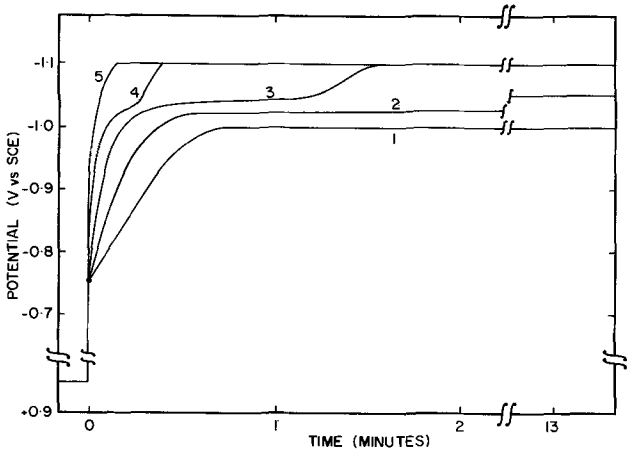

Fig. 2b. Polarization curves at a constant c.d. of 220 mA/cm^2 with a solution flowing across the cathode surface at approximately 1 cm/sec. CrO_3, 250 g/l; temperature, 50°C. CrO_3:SO_4 ratios: curve 1, 5000:1; curve 2, 200:1; curve 3, 100:1; curve 4, 75:1; and curve 5, 65:1.

Potential range (*ii*) starts with the evolution of hydrogen at −0.75V. This value is in good agreement with the potential of hydrogen evolution on iron, which, when calculated on the basis of Tafel parameters available in the literature (14-16), is −0.747 to −0.770V (*vs.* SCE) at *p*H −0.212, c.d. 0.220 A/cm^2, and temperature of 50°C. The fact that the potential of the initial hydrogen evolution was the same at all CrO_3:SO_4 ratios investigated suggests that sulfate concentration has no measurable effect on the initial discharge of the hydrogen ion. The fact that hydrogen evolution continued, from this stage onward, at potentials increasingly more negative is an evidence of the increase of the overvoltage values.

The appearance of the electrode immersed in the solution before commencement of the electrolysis is seen in Fig. 3a. Microscopic observations of the cathode surface during potential range, (*ii*) revealed always the presence of bright transparent gas bubbles against dark background as seen in Fig. 3b, taken during the experiment 3, Fig. 2b.

The end of the potential range (*ii*) was manifested by changes of the gassing pattern followed by formation of an amorphous oxide film easily observed under the microscope at about −1.00V.

Potential range (*iii*) is characterized by the formation of a visible (under the microscope) amorphous oxide film and a temporary arrest of the polarization between about −1.00 and −1.04V observed quite distinctly on the potential-time curves 1, 2, and 3 but appearing as an inflection on curve 4. In the case of 65:1 ratio no significant arrest of potential was observed, although the presence of the amorphous oxide film at the surface at about −1.00V was detected during a brief (3 sec) transition period. Since the duration of the potential arrest decreased with the decrease of the CrO_3:SO_4 ratio from 5000:1 to 75:1 one can assume that in the case of 65:1 ratio the polarization was too fast for the arrest to be resolved by the experimental technique employed.

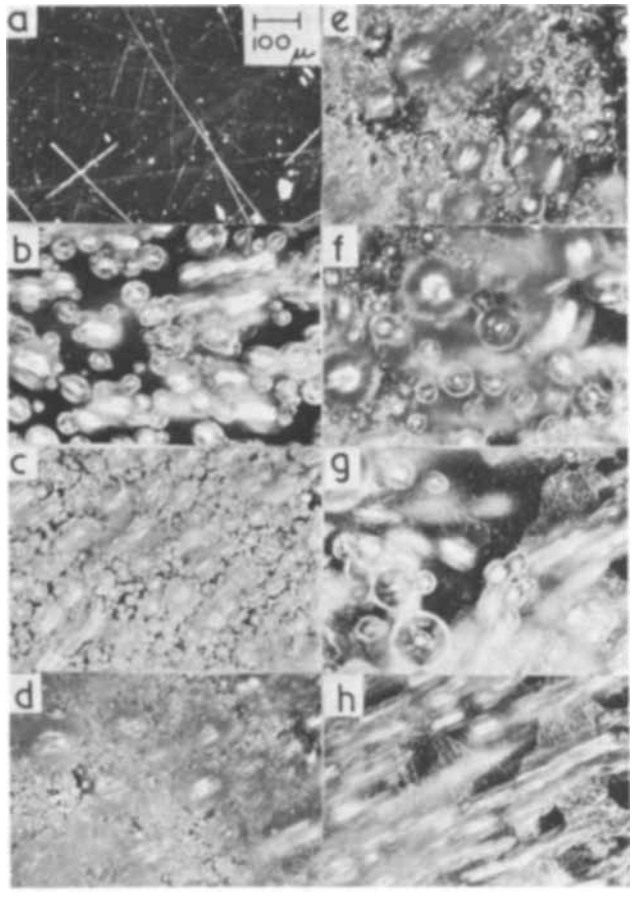

Fig. 3. Photomicrographs of the cathode surface during experiment No. 3 in Fig. 2b. Original magnification X100. Dark field illumination. Exposure 1/60 sec. a, Original surface before electrolysis; b, 10 sec; c, 55 sec; d, 70 sec; e, 75 sec; f, 85 sec; g, 90 sec; h, 100 sec.

The formation of the amorphous oxide film was always preceded by the changes of gas evolution from that seen in Fig. 3b to that seen in photomicrograph c, Fig. 3. The appearance of the cathode surface would then change gradually to that seen in photomicrograph d which shows the amorphous oxide film as a grayish background with gas bubbles moving away from the surface seen in the foreground, out of focus.

Potential range (*iv*) is characterized by further polarization from the end of potential range (*iii*) at about −1.04V to the potential of chromium deposition at steady-state conditions. The potential of chromium deposition varied with CrO_3:SO_4 ratio and is here designated, therefore, as potential range (*v*).

The shift of potential from range (*iii*) to range (*v*) is associated with certain transformations that create conditions favorable at the cathode surface for the deposition of chromium. Since chromium deposition does not take place at potential range (*iii*) the transition from range (*iii*) to range (*v*) is a step of fundamental importance.

In "pure" chromic acid the polarization would always end at about −1.00V. There was no further shift of potential, and there was no metal deposition. The

amorphous oxide film would continue to grow, flake off, then regrow, the process continuing indefinitely. In 200:1 solution, however, the potential kept on shifting gradually to more negative values until chromium deposition began at −1.05V.

In conventional baths the transition from range (*iii*) to (*v*) was observed to be rapid and quite distinct. It would always begin with an initial breakup of the amorphous oxide film followed by continuous rapid changes involving disintegration of the solid amorphous oxide film and an increase of the viscosity in the vicinity of the cathode surface, a condition that significantly reduced the mobility of the evolving hydrogen bubbles that began to become stationary and grow to larger sizes. The whole process would be completed in about 15 sec.

The beginning of the breakup of the amorphous oxide film is seen in Fig. 3e. The breakup is manifested by the appearance of dark areas representing the surface underneath. The condition at the surface 10 sec later on, when the disintegration of the amorphous oxide film is about half-way completed and the electrolyte next to (in the vicinity of) the cathode surface is more viscous, is seen in Fig. 3f. The surface is partly obscured by large gas bubbles that have just become detached from the surface and remain suspended in the viscous medium long enough to register in foreground out of focus.

Although in 75:1 and 65:1 solutions the transition from range (*iii*) to (*v*) occurred more rapidly it could still be traced through the formation and breakup of the amorphous oxide film, observed under the microscope.

The inference from these observations is that during the transition the amorphous oxide film was replaced by a viscous film which had physical and chemical characteristics distinctly different from those in the bulk of the solution. Once the film was established its existence could not be detected in the incident light unless agitation, preferably within the film itself, brought about changes in the angle of refraction across its boundary.

The ability to observe the presence of the second type of film at the cathode surface by direct observation of the electrode in the incident light was based, primarily, on the visibility of a ripple, (during hydrogen evolution) when the light was crossing media with different refractive properties near the cathode surface. Since the glass extension of the objective was immersed in the plating bath, no ripple was detectable when the evolution of gas bubbles took place in a uniform medium. If, however, gas-bubble formation occurred within or underneath a film having a composition different than that of the adjoining bulk of the solution, a ripple resulting from the stirring effect was easily recognizable as that caused by temporary intermixing of media with different consistencies. These observations, characteristic of the "schlieren effect" that indicates refractive-index changes due to composition variation, in conjunction with the evidence of the decreased mobility of the growing gas bubbles were interpreted as manifestations of increasing viscosity of the precathodic layer. The observational technique employed in the present work could not detect directly changes in viscosity. The term "viscous film" was adopted to emphasize the liquid-like properties of the second type of film in contrast with the solid "amorphous oxide film," the presence of which was associated with a different region of potential.

Potential range (*v*) is characterized by the deposition of chromium at steady-state conditions, that is, at a constant potential the value of which depended on CrO_3:SO_4 ratio. At ratios 100:1 to 65:1 it was −1.10V. In 200:1 solution the final stage of polarization reached the level of −1.05V.

The deposition of chromium from 200:1 solution is of special interest because it reveals certain details of the initial stages of deposition that could not be observed under rapidly changing conditions in other solutions. The electrolysis of 200:1 solution is discussed, therefore, under a separate heading.

The beginning of chromium deposition in the conventional plating bath is seen in Fig. 3g in the form of an epitaxial growth on the surface at the upper right hand corner of the photomicrograph. Figure 3h shows that the epitaxial growth, at various degrees of progress, has covered the whole surface area 10 sec later on. This stage of the electrolysis coincided with a new gassing pattern in the form of small mobile hydrogen bubbles.

Similar progress of initial chromium deposition was observed to occur more rapidly in 75:1 and 65:1 solutions.

Observations at CrO_3:SO_4 *ratio of 200:1.*—The observations made during electrolyses of solutions with CrO_3:SO_4 ratio of 200:1 (curve 2 Fig. 2b) merit separate discussion because they showed that the potential of chromium deposition at steady-state conditions (−1.05V *vs.* SCE) can be reached with the cathode surface completely covered by the amorphous oxide film.

The formation of the amorphous oxide film was observed to begin in 200:1 solution after about 3 min of electrolysis at potential range (*iii*). The appearance of the cathode surface covered with the amorphous oxide film about 1μ thick, is illustrated in the photomicrograph Fig. 4b. Photomicrograph a illustrates the evolution of hydrogen at potential range (*ii*) and during the initial part of potential range (*iii*), prior to the formation of the amorphous oxide film.

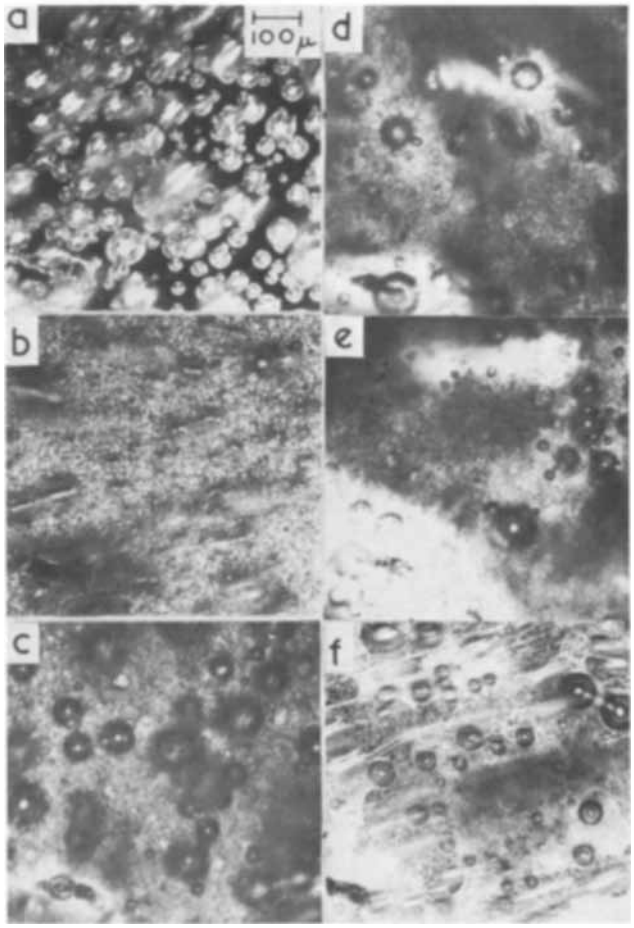

Fig. 4. Photomicrographs of the cathode surface during experiment No. 2 in Fig. 2b. Magnification and illumination as in Fig. 3. Exposure 1/125 sec. a, 1 min electrolysis; b, 6 min; c, 23 min; d, 31 min; e, 35 min; f, 38 min.

In 200:1 solution the potential kept shifting slowly to more negative values over a period of 10 min, while the amorphous oxide film remained on the surface. When the potential of −1.05V was reached in the 12th minute, permanent bright spots appeared on the cathode surface, indicating the beginning of chromium deposition at these spots, underneath the amorphous oxide film. A more advanced stage of this phenomenon is seen in Fig. 4c. The permanent bright spots could be distinguished easily from transient bright spots associated with images of gas bubbles that moved within the field of vision. The breakup of the amorphous oxide film, observed to begin around the bright nucleation spots, continued by fragmentary detachment from the surface. Partial detachment of the amorphous oxide film revealed small bright areas of chromium that can be easily seen in Fig. 4d, in contrast with the large dark areas corresponding to the overlaying oxide film. Figure 4e shows a more advanced stage of the same phenomenon when still larger portions of the chromium deposit are exposed. At this stage it was possible to observe quite distinctly the evolution of hydrogen within a viscous film in which remnants of the amorphous oxide film remained suspended for various periods of time before moving away from the cathode surface.

An example of a small portion of the amorphous oxide film suspended near the cathode surface in a viscous film is seen in Fig. 4f in the form of a small darker area in the center of the photomicrograph. Closer examination reveals that this remnant of the amorphous oxide film is slightly transparent showing small hydrogen bubbles inside or underneath. This is quite remarkable if one considers that, at this stage, the chromium deposition process has been already in progress for over 25 min.

The above observations demonstrate that the shift of potential from range (*iii*) to (*v*), at least in 200:1 solution, is not due to the breakup of the amorphous oxide film, as one could infer from interpretation of observations made in conventional plating bath, and that the breakup of the oxide film is not a process of gradual dissolution or gradual conversion into another type of cathode film, but rather a phenomenon of mechanical disruption of a redundant layer that has formed during the earlier stages of the electrolysis. Thus, the significant changes at the cathode surface that occur during the shift of potential from about −1.00 to −1.05V inhibit further growth of the amorphous oxide film and, at the same time, bring about the process of the reduction of chromic acid to metal. These fundamental changes can be attributed to the formation of a viscous film with unique characteristics that, at present, are not well understood, since they may be due to the formation of polynuclear species (17) in the form of olated polymer ions together with coordinated Werner-type complexes involving trivalent chromium (18, 19).

Effect of the addition of sulfate to "pure" chromic acid. —The transformations observed in conventional plating bath during transition from the potential range (*iii*) to (*v*) have also been observed during transitions induced by addition of sulfate to "pure" chromic acid when the cathode was kept polarized at a constant current density.

The effect of such an addition of sulfate is seen in Fig. 5 in the form of an increase of the polarization from the level of −1.00V to the level of −1.07V which, in this particular experiment, represents the potential of chromium deposition at range (*v*).

Potential range (*iii*) , as in other experiments, was characterized by the evolution of hydrogen and formation of the amorphous oxide film. The appearance of the amorphous oxide film after 20 min electrolysis of pure chromic acid is seen in photomicrograph Fig. 6a. The addition of sulfate to the solution entering the cell, marked in Fig. 5 by an arrow pointing upward, resulted in gradual changes of the CrO_3:SO_4 ratio from 5000:1 to 130:1. Simultaneously, the potential began to shift from −1.00 to −1.07V. The amorphous oxide film began to break up in a manner similar as in conventional bath. Before the breakup was completed the presence of viscous film was observed in the vicinity of the cathode surface. The transformations ended with a complete disintegration of the amorphous oxide film.

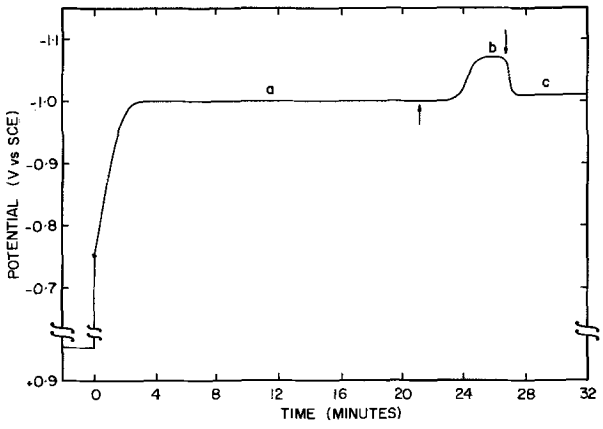

Fig. 5. Effect of increasing (arrow up) and decreasing (arrow down) the sulfate concentration at a constant c.d. of 175 mA/cm². Chromic acid solution 250 g/l of CrO_3; temperature, 50°C; solution flow across the surface 1 cm/sec (approx.). CrO_3:SO_4 ratios: a, 5000:1; b, 130:1; c, 500:1.

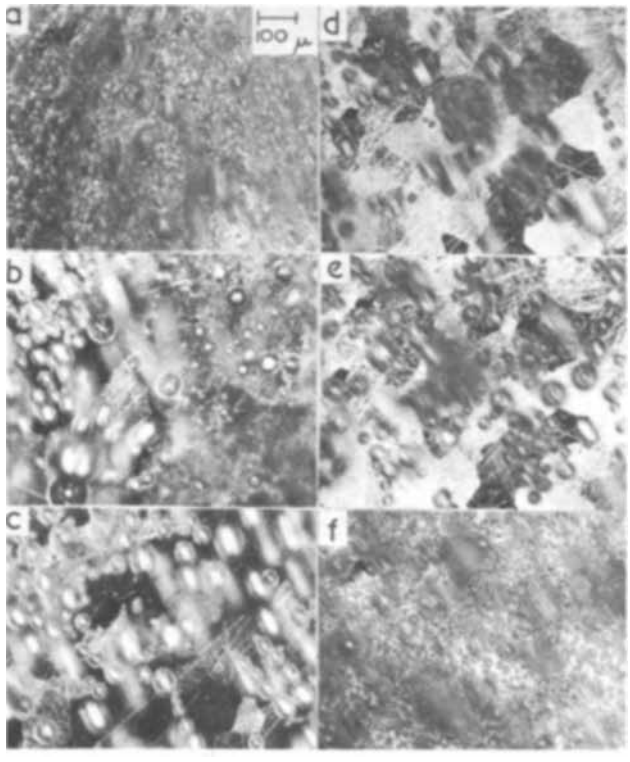

Fig. 6. Photomicrographs of the cathode surface during polarization shown in Fig. 5. Magnification X100. Dark field illumination. Exposure 1/125 sec. a, 20 min 45 sec, c.p. —1.00V; b, 25 min, c.p. —1.07V; c, 25 min 45 sec, c.p. —1.07V; d, 27 min, c.p. —1.01V; e, 28 min, c.p. —1.01V; f, 41 min. c.p. —1.01V.

The final stage of the disintegration is seen in Fig. 6b. Here, part of the surface is still covered with the amorphous oxide film. Stationary gas bubbles are observed to grow to larger sizes within a viscous film that restricts their mobility. The center and upper left hand corner of the photomicrograph shows an outline of a grain pattern indicating the presence of a coherent chromium deposit. Small mobile gas bubbles were ob-

served visually within this area. Fifteen seconds later chromium deposit, together with small bubbles overhead, was observed over the surface area as illustrated in Fig. 6c. This stage represents chromium deposition at steady-state conditions at potential range (*v*).

Effect of the withdrawal of sulfate from the plating bath.—The withdrawal of sulfate from the plating bath during electrolysis was accomplished by decreasing the addition of sulfuric acid (or sodium sulfate) to pure chromic acid entering the plating cell (see Fig. 1). This point is marked in Fig. 5 by an arrow directed downward.

As a result of the changes introduced, the CrO_3:SO_4 ratio started to increase from 130:1 to 500:1. This increase upset the steady-state process of chromium deposition shifting the potential back to the −1.00V level. As this new level of potential was being reached, amorphous oxide film began to form in certain restricted areas characterized by a very intense gassing.

The growing amorphous oxide film is seen in Fig. 6d as dark circular patches. Figure 6e shows that the formation of the amorphous oxide film extended eventually over the other parts of the surface. In the end, a uniform film covered the whole surface in a manner identical to that at the beginning of the electrolysis of pure chromic acid. This can be easily confirmed by comparison of photomicrographs a and f in Fig. 6.

The fact that the hydrogen evolution can be controlled during electrolysis of chromic acid solutions by the addition or withdrawal of sulfate, irrespective of the cathode surface, indicates that the inhibition of hydrogen ion discharge involves processes in which sulfate either interacts reversibly with the cathode surface itself or with the solution adjoining it, thus, forming an effective film barrier.

The formation of the amorphous oxide film is considered to be the result of lower hydrogen ion concentration at the cathode surface. This process is discussed in greater details under a separate heading.

Electrolysis at controlled cathode potentials.—Fixed CrO_3:SO_4 *ratios.*—Microscopic observations during electrolysis at controlled cathode potentials in solutions with fixed CrO_3:SO_4 ratios revealed the same sequence of events that was observed during electrolyses in constant current experiments, namely, initial evolution of hydrogen followed by the formation of the amorphous oxide film, its breakdown and replacement by a viscous film and a final stage consisting of the deposition of chromium at the steady-state conditions.

This preliminary study supported in all aspects the general observations on the formation and presence of cathodic films during chromium plating, made in galvanostatic investigations, and was, therefore, not pursued to completion.

Adjustable CrO_3:SO_4 *ratios.*—The results of the electrolysis at controlled cathode potentials and adjustable CrO_3:SO_4 ratios corroborate and amplify certain important features of the formation and breakup of the cathodic films observed under galvanostatic conditions and are, therefore, considered in more detail.

The effect of the addition and withdrawal of sulfate during polarization at controlled cathode potentials was investigated in a similar manner as during constant current electrolyses.

The cathodes were polarized initially in "pure" chromic acid solutions until steady-state conditions were established for a substantially long period of time (about 15 min). During this period the amorphous oxide film grew on the cathode surface to a considerable thickness. The addition of sulfate to the flowing solution was then started at a predetermined rate suitable for lowering the CrO_3:SO_4 ratio to the desirable level. When the metal deposition process was established, the addition of sulfate to the chromic acid entering the plating cell was decreased, thus increasing effectively the ratio to a new level.

Effect of the addition of sulfate to pure chromic acid.—Figure 7 shows current-time curves obtained at controlled cathode potentials of −1.10 and −1.00V *vs.* SCE. The addition of sulfate is marked by an arrow pointing downward. Prior to the addition of sulfate (region a), the cathodes were overlaid with the amorphous oxide film in a manner similar as in Fig. 5 at the potential arrest a shown in Fig. 6a.

The addition of sulfate at a predetermined rate resulted in a rapid drop of the over-all rate of electrolysis at −1.10V. The accompanying transition from the stage of hydrogen evolution and amorphous oxide film formation at a to the metal deposition at b was also very rapid and difficult to observe under the microscope in all the details.

At −1.00V, however, the transition from a to b was very protracted. The addition of sulfate was started at the 13th minute but no significant changes were observed until about the 17th minute, when the initial nucleation of chromium deposition in the form of bright spots at a number of sites became evident. The breakup of the amorphous oxide film started around such sites and continued by fragmentary detachment from the surface. The presence of a viscous film was detected at the cathode surface through a characteristic evolution of stationary hydrogen bubbles. By the time the lowest current-density value was reached (approximately 100 mA/cm^2) the cathode surface was entirely free of the amorphous oxide film and the process of chromium deposition was well established in the 24th minute.

Since all the above observations detected a sequence of events very much like the one observed during electrolysis of 200:1 solutions at constant current no photomicrographic record is included.

Effect of the withdrawal of sulfate from the plating bath.—The withdrawal of sulfate was started when it was ascertained that the process of metal deposition was established. In a number of experiments the addition of sulfate to pure chromic acid was then discontinued completely, thus allowing the CrO_3:SO_4 ratio to rise to 5000:1 level. At the 5000:1 level the chromium-plated cathode surface became completely covered with the amorphous oxide film. In the experiments represented by curves 1 and 2 in Fig. 7 the addition of sulfate was decreased sufficiently to allow the CrO_3:SO_4 ratio to increase to 500:1 and 400:1, respectively.

Curve 1 in Fig. 7 shows that such a restricted withdrawal of sulfate at the 21st minute, marked by an arrow pointing upward, resulted in a rapid increase of the over-all rate of reaction at −1.10V. The surface became partially covered with the amorphous oxide film by the time c level was reached.

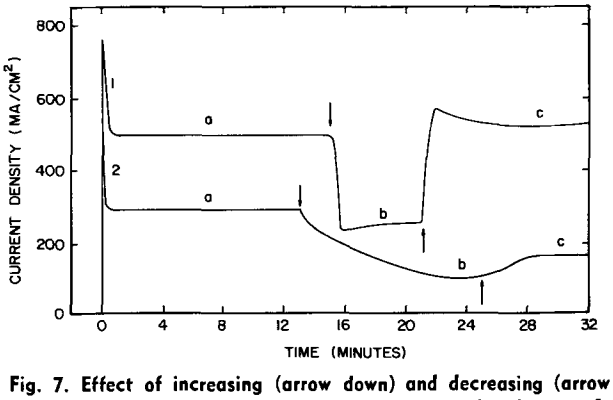

Fig. 7. Effect of increasing (arrow down) and decreasing (arrow up) the sulfate concentration at constant potentials of curve 1, −1.10V *vs.* SCE and curve 2 −1.00V *vs.* SCE. Ranges of CrO_3:SO_4 at curve 1, a = 5000:1; b = 100:1; c = 500:1; at curve 2, a = 5000:1; b = 150:1; c = 400:1.

At −1.00V (curve 2) the withdrawal of sulfate was started at the 25th minute of the experiment. Its effect was not observed immediately under the microscope. Figure 8a shows a selected area of the cathode surface 1 min-30 sec after the beginning of the withdrawal of sulfate, when the deposition of chromium was apparently still in progress in the presence of small very mobile hydrogen gas bubbles. Few seconds later on, between the time of taking photomicrographs a and b, very heavy gassing started at the site of an inclusion, seen as a dark dot in the upper part of the photomicrograph off center (marked by an arrow). The gassing and the accompanying growth of the amorphous oxide film kept spreading in a circular manner until it reached, in 2 min after withdrawal of sulfate, the size seen in Fig. 8b. The lateral growth of the amorphous oxide film (area *vs.* time) continued at a rate which was practically identical with the rate of the increase of the current density (c.d. *vs.* time). A more advanced stage of such a growth is seen in Fig. 8c, 2 min-45 sec after the withdrawal of sulfate.

Since the CrO_3:SO_4 ratio was not allowed to reach the range of pure chromic acid, the growth of the amorphous oxide film was not allowed to continue unchecked. Thus, both the increase of the current density and a further growth of the amorphous oxide film were arrested. Figure 8d shows the appearance of the film after the arrest of its growth when the gassing at the surface of the film began to decrease markedly. Figure 8e shows the same amorphous oxide film 11 min-30 sec after withdrawal of sulfate when larger stationary gas bubbles were observed to form at the surface and at the edge. Those hydrogen bubbles evolving at the edge revealed unmistakably the presence of a viscous film. The hydrogen bubbles evolving over the remaining surface area, where the deposition of chromium was observed to take place, were small and very mobile.

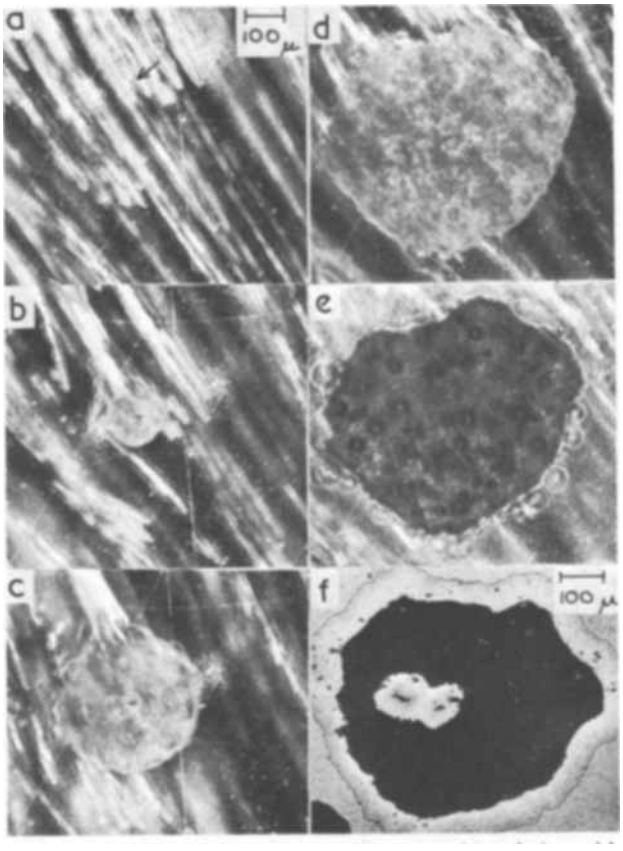

Fig. 8. Photomicrographs of the cathode surface during withdrawal of sulfate. Curve 2 in Fig. 7. a to e dark field illumination, magnification X 100. f bright field illumination, magnification X 110 (approximately). a, 26 min 30 sec, 113 mA/cm^2; b, 27 min, 121 mA/cm^2; c, 27 min 45 sec, 142 mA/cm^2; d, 29 min 30 sec, 155 mA/cm^2; e, 36 min 30 sec, 155 mA/cm^2; f, after completion of electrolysis (58 min).

The amorphous oxide film was reduced partially to metal at its edge and also around the inclusion sites. This is easily confirmed by examination of the same surface area after completion of the electrolysis shown in Fig. 8f. It is seen that during the additional 22 min of electrolysis after photomicrograph e was taken, a considerable portion of the amorphous oxide film was converted into chromium deposit. Photomicrograph f was taken under bright field illumination. The dark reddish amorphous oxide film could easily be observed then at low magnification even with the help of an ordinary magnifying glass. In the photomicrograph, the amorphous oxide film is seen as a dark area against a bright background of chromium deposit. The bright band (around the black area), corresponding to the original size of the amorphous oxide film before its reduction, appears to be superimposed over a base of coherent chromium deposit. This suggests that two reduction processes to metal proceeded simultaneously at the same surface area. In the steady-state case with the usual plating solution, this cannot occur since the amorphous oxide film begins to disintegrate below the potential at which plating occurs.

The experimental results during electrolysis at controlled cathode potentials show that the addition of sulfate to pure chromic acid brings about a drop of the over-all rate of reaction evidently due to inhibition of hydrogen evolution. Since the hydrogen evolution resumes at higher rates after withdrawal of sulfate, the inhibition is not likely due to adsorption of sulfate or its complexes at the cathode surface but rather due to the formation of a barrier in the solution adjoining the cathode surface.

The initial formation of the amorphous oxide film at inclusions, that is, at sites with low overvoltage characteristics, shows that the formation of such a film is related to higher *p*H environment. The lateral growth of the amorphous oxide film at rates parallel to the rates of current increase indicates the establishment of low hydrogen overvoltage conditions in the expanding areas.

Discussion

Interpretation of potential-time curves.—According to Dubpernell (1) there are four electrochemical reduction processes associated with cathodic polarizations in chromium plating solutions. The processes are as follows:

(I) Reduction of Cr^{6+} to Cr^{3+} involving $Cr_2O_7^=$ species.

(II) Reduction of Cr^{6+} to Cr^{3+} involving $CrO_4^=$ species.

(III) The evolution of hydrogen with a simultaneous reduction of Cr^{6+} to Cr^{3+}.

(IV) The deposition of chromium accompanied by the evolution of hydrogen and the reduction of Cr^{6+} to Cr^{3+}.

Processes (I) and (II) take place at potential ranges that vary with the type of basis metal and surface pretreatment (20), but always at values more positive than the evolution of hydrogen. Since both processes involve the formation of trivalent chromium at low current densities, their separation into distinct steps on a current-potential polarization curve is not always feasible.

The evolution of hydrogen with simultaneous reduction of chromic acid to trivalent chromium in the absence of chromium plating, that is, reduction processes (III), is sometimes not observed on metals with high hydrogen overvoltages, when the electrolysis proceeds directly from processes (I), (II) to processes (IV).

The beginning of reduction processes (I), (II), (III) on iron corresponds to about +0.50, −0.50, and −0.75V *vs.* SCE, but these potentials depend on surface prep-

aration. Chromium deposition does not start until the potential of −1.00V *vs.* SCE is reached, and this potential is not affected by the nature of the cathode surface (21).

The four reduction processes described above are used by some investigators as a basis for a division of the current-voltage curves into four branches. In the present investigation the division of potential-time curves into five ranges is more convenient and in better accord with well-defined stages of polarization observed chronologically under the microscope.

Potential range (i).—The first range of potential did not involve microscopic observations because, as mentioned before, it was too fast to be resolved by the recorder. This range of potential corresponds to processes (I), (II).

Okada, Nakamura, and Ishida (13) studied, by means of oscillographic techniques, charging curves during initial cathodic polarizations of gold and platinum electrodes at various current densities in pure and sulfate-containing chromic acid solutions. They found that in pure chromic acid the charging curves (potential *vs.* charge) from the potential of rest to the potential of hydrogen evolution were always the same irrespective of the current densities used. In the plating bath, at low current densities (50 mA/cm^2), there were current carrying reactions ($Cr^{6+} \rightarrow Cr^{3+}$) that prevented the charging of the cathode to the potential of hydrogen evolution. At higher current densities (200 mA/cm^2) the charging rates in the plating baths were the same as in pure chromic acid solutions. This means that at sufficiently high current densities the reduction of chromic acid to trivalent chromium in the presence of sulfate cannot support the over-all rate of electrolysis at potentials less negative than the evolution of hydrogen. It is justifiable, therefore, on the basis of this evidence to consider potential range (*i*), at high current densities, as predominantly a process of charging the electrode to the potential of hydrogen ion discharge.

Potential range (ii).—This range corresponds to the reduction processes designated (III). Although in the presence of sulfate the reduction of the chromic acid to trivalent chromium is assumed to account for part of the total charge transfer, the polarization rate during this range of potential is controlled by the hydrogen evolution reaction. Therefore, regardless of the presence of sulfate the shift of potential that constitutes range (*ii*) is a process sufficiently well defined to merit separate treatment. The increase of the rates of polarization with decreasing CrO_3:SO_4 ratios must be considered, therefore, in terms of increasing hydrogen overvoltages.

Potential range (iii).—This range also corresponds to the reduction processes (III). However, here the appearance of the amorphous oxide film observed clearly under the microscope together with distinct temporary arrest of the polarization at higher CrO_3:SO_4 ratios sets this range of potential apart from the previous one. The formation of the amorphous oxide film at various CrO_3:SO_4 ratios is discussed in the next section, under a separate heading.

Potential range (iv).—This is the transition range from the reduction processes (III) to (IV), that is, from the partial reduction of chromic acid ($Cr^{6+} \rightarrow Cr^{3+}$) and hydrogen evolution ($2H^+ \rightarrow H_2$) in the absence of chromium deposition, to the stage of chromium plating at steady-state conditions, in the presence of hydrogen evolution and Cr^{3+} formation.

Potential range (v).—Three reduction processes, namely, $Cr^{6+} \rightarrow Cr^{3+}$, $H^+ \rightarrow \frac{1}{2}H$, and $Cr^{6+} \rightarrow Cr^0$ occur simultaneously at steady-state conditions. Both the evolution of hydrogen and the reduction of chromate to Cr^{3+}, assuming that formation of Cr^{3+} is not due to side reactions, proceed at more negative potentials than at range (*iii*), that is, under conditions of higher voltage values. The remarkable thing is that this higher overvoltage condition exists only as long as there is adequate sulfate concentration in the plating bath. As soon as sulfate is removed the potential shifts to less negative values, the deposition of chromium ceases, and the amorphous oxide film forms rapidly on the surface.

Since the higher overvoltage during chromium plating is a phenomenon reversibly controlled by the presence of sulfate irrespective of the surface conditions, it is more likely that the overpotential is due to formation of a film which does not form a stable bond with the surface, rather, than due to a reversible adsorption of sulfate or its complexes.

There is no clear cut evidence what occurs during the transition range (*iv*).

Reinkowski and Knorr (4) postulated formation of intermediate reducible compounds containing complexes of divalent chromium. These compounds, adsorbed on the cathode surface, were considered to be involved in the final reduction step to metal.

Solov'eva and Vagramyan (8) explained the transition as a process of formation on the electrode surface of a colloidal film from the products of incomplete reduction of chromic acid, chromate and sulfate ions. According to these authors (22), a film, forming a continuous phase on the electrode surface, appears due to the accumulation of the $Cr^{6+} \rightarrow Cr^{3+}$ reaction products together with certain components of the solution. The colloidal film inhibits the reduction of chromate ions to the trivalent state and the discharge of hydrogen ion.

Okada and Yamamoto (5) assumed that the film that forms at potential range (*iii*) grows thicker gradually and, subsequently, the hydrogen overvoltage of the "filmed" electrode increases when the potential shifts to the potential range (*v*). They expressed a belief that the amorphous oxide film that forms at potential range (*iii*) in the presence of sulfate is an olated oxide compound of Cr^{3+} penetrated with sulfate anions. The rate of transition from potential range (*iii*) to (*v*) depends on the rate of the growth of the film formed at range (*iii*), according to these authors.

Present investigations show that the amorphous oxide film that forms at potential range (*iii*) begins to disintegrate when the potential shifts from range (*iii*) to (*v*) in a conventional plating bath. Thus, the increase of hydrogen overvoltage is not due to the thickening of the film formed at range (*iii*) as suggested by Okada and Yamamoto. Since potential range (*v*) can be reached with the cathode surface completely covered by the amorphous oxide film (at CrO_3:SO_4 ratio of 200:1), one cannot infer that the transition from potential range (*iii*) to (*v*) is due to the disintegration of the amorphous oxide film only.

The fact that during the transition the vicinity of the cathode surface becomes more viscous suggests formation of a viscous film, which, presumably, is the same film as the continuous phase film discussed by Vagramyan and Solov'eva. It appears that the viscous film forms independently of the amorphous oxide film, which, in turn, becomes superfluous once the potential shifts to the level of range (*v*).

Nature and the formation of cathodic films.—Amorphous oxide film.—Sysoev, Drobantseva, and Platonina (23) analyzed chemically cathodic films formed on copper and steel during electrolysis of pure chromic acid solutions. They concluded that the films consisted only of trivalent chromium apparently in the form of $Cr(OH)_3$.

Weiner and Schiele (24) examined films detached from cathodes polarized in pure and sulfate-containing chromic acid solutions. They found by electron diffraction methods that all films formed on Fe, Ni, Cr, Cu, Ag contain only Cr_2O_3. Films formed in plating baths also were found to contain traces of oxides of the cathode metal in addition to Cr_2O_3.

Since chromic oxide, presumably, at various stages of hydration, is practically the only constituent of the amorphous oxide film it is reasonable to assume that its formation will be affected by the availability of Cr^{3+} at the interface.

Trivalent chromium apparently is not produced in any measurable concentrations by direct electrochemical reduction of pure chromic acid (25). The electrolysis, in this case, consists of the evolution of hydrogen with practically 100% current efficiency. Snavely (26) has shown that chromic acid can be reduced to trivalent chromium by evolving hydrogen, but that the reaction is very slow. Thus, the low concentration of the trivalent chromium at the beginning of the electrolysis of pure or nearly pure chromic acid may account for the slow rate of the formation and growth of the amorphous oxide film observed in such solutions.

The reduction of chromic acid to trivalent chromium, that is, $Cr^{6+} \rightarrow Cr^{3+}$, is promoted by sulfate to proceed at potentials less negative than the evolution of hydrogen (27, 28). Hence, the initial stages of polarization, in the presence of sulfate, yield trivalent chromium that accumulates at the interface, before hydrogen evolution begins at potential range (*ii*). Intense hydrogen evolution lowers hydrogen ion concentration at the interface, creating conditions favorable for the formation of an oxide-type film, which, according to Pourbaix diagrams (29), can be avoided only by maintaining high degree of acidity in the catholyte.

Since the rate of $Cr^{6+} \rightarrow Cr^{3+}$ increases with sulfate concentration, the formation of the amorphous oxide film will be accelerated at lower CrO_3:SO_4 ratios. This is borne out experimentally. The formation of the amorphous oxide film was observed, for instance, to begin at 6th and 3rd minute in solution with ratios 5000:1 and 200:1, but its presence was visible already in 50th, 14th, and 3rd second in solutions with CrO_3:SO_4 ratios 100:1, 75:1, and 65:1.

Close association between hydrogen evolution and the amorphous oxide film formation is demonstrated in Fig. 8b to d. Whether the process of the film formation is entirely a chemical precipitation reaction or a reaction involving charge transfer at the interface cannot be decided on the basis of the evidence presented. The increase of the over-all rate of electrolysis during lateral growth of the amorphous oxide film indicates only an increase of the reduction rate within the expanding areas which may be entirely due to more intense hydrogen evolution.

The electron microscope examination of the amorphous oxide films by Weiner and Schiele (30) showed that there are two kinds of oxide films. One, very thin (0.02μ) and pore free, forms initially on the cathode surface. The other thicker (0.1μ) and fairly porous continues to grow over the thin one, with the line of demarcation not always distinguishable.

Presumably, the thin film forms during the initial shift of potential from -0.75 to -1.00V, that is, at potential range (*ii*), when its presence cannot be detected under the microscope and when its effect is manifested by higher rates of polarization at lower CrO_3:SO_4 ratios. The thicker film is apparently the one that is observed visually to grow at the potential range (*iii*).

The evidence of the reduction of the amorphous oxide film to metal (Fig. 8f) is in agreement with observations made by other investigators (31, 32). The process is not considered to be connected with the mechanism of chromium deposition at steady state conditions, because the amorphous oxide film is observed to break up into fragments at the onset of chromium plating.

Viscous film.—According to Kappel and Gerischer (6) the cathode is covered with mono- or bi-molecular oxide film, which serves as an intermediate stage for the final reduction step to metal. The role of sulfate is to limit the thickness of the film through a competitive dissolution reaction and, thus, to allow the release of oxygen during the reduction.

The presence of mono- or bi-molecular oxide films is difficult to detect by conventional methods. Electron diffraction examination of conventional deposits (5) did not reveal the presence of any films, although an oxide-type film has been observed together with the chromium deposit in dilute solutions (33). This is not unexpected because dilute solutions are considerably less acid and, therefore, provide an environment more favorable for the formation of the amorphous oxide film.

In conventional plating solutions the visible amorphous oxide film disintegrates when the potential of chromium deposition is reached. Whether a thin invisible amorphous oxide film remains on the surface during chromium plating cannot be resolved on the basis of the microscopic observations. The fact that the initial deposition of chromium starts underneath the amorphous oxide film during electrolysis of 200:1 solutions (Fig. 4) is an evidence pointing out to the contrary.

Shluger and Kazakov (9) investigated dissolution processes at the cathode surface after cessation of the electrolysis by observing the edge of the electrode under the microscope in transmitted light. An attempt by these investigators to observe the cathode surface in the incident light during plating was not successful because of copious hydrogen evolution. These authors concluded that there is a colloidal film present at the cathode surface during chromium plating, the dissolution of which is observed when the current is switched off.

In the present investigation microscopic observations of the cathode surface in the incident light at the termination of the electrolysis did not permit the differentiation between the dissolution of a cathodic film and the dissipation of a concentration gradient. No evidence is therefore available that the viscous film that seems to form during the transition from the potential range (*iii*) to (*v*) is still present at the cathode surface at the end of the plating process. Its existence can be detected only when the cathode surface is partially covered with the fragments of the amorphous oxide film when at least part of the evolving hydrogen originates within or underneath the viscous film, thus revealing its presence.

Whether the viscous film observed in the present investigation is the same film reported by Shluger and Kazakov is not absolutely certain. It is reasonable to assume that it is the same film since both microscopic observations were made at similar low-range magnifications which are unlikely to reveal the existence of two entirely different types of macrofilms. The viscous nature of the film does not exclude a colloidal suspension resulting from the disintegration of the amorphous oxide film.

The unconventional characteristics of the viscous film may account for a number of unusual phenomena such as: (*a*) preferential reduction of higher rather than lower oxidation states of chromium to metal (34), (*b*) inability to discharge cations during chromium plating at adequately negative potentials (35), (c) favorable environment for the reduction of anions of other metals (36, 37), and (*d*) the variation of current efficiency with current density, temperature, and electrolyte composition (38).

Conclusions

It is concluded that the amorphous oxide film itself is not involved in the mechanism of chromium deposition at steady-state conditions despite the evidence that it can be reduced electrolytically to metal. Its formation is a consequence of side-reactions facilitated by higher *p*H and higher trivalent chromium concentration.

The deposition of chromium is associated with the formation of an entirely different type of film which is

transparent and viscous in contrast with the opaque and solid nature of the amorphous oxide film.

The formation of the viscous film, which occurs only in the presence of adequate sulfate concentration, inhibits the evolution of hydrogen and the progress of other reactions that contribute to the formation of the amorphous oxide film.

Manuscript submitted Jan. 12, 1970; revised manuscript received April 2, 1970. This was Paper 263 presented at the New York Meeting of the Society, May 4-9, 1969.

Any discussion of this paper will appear in a Discussion Section to be published in the June 1971 JOURNAL.

REFERENCES

1. G. Dubpernell, Chapter on Chromium in "Modern Electroplating," p. 82, F. A. Lowenheim, Editor, John Wiley & Sons, New York (1963).
2. E. Muller, *Trans. Faraday Soc.*, **31**, 1194 (1935), *Z. Elektrochem.*, **43**, 361 (1937), *Z. Elektrochem.*, **50**, 172 (1944).
3. R. Weiner, *Metalloberflaeche*, **14**, 7 (1960).
4. D. Reinkowski and C. A. Knorr, *Z. Elektrochem.*, **58**, 709 (1954).
5. H. Okada and K. Yamamoto, *Electrochem. Technol.*, **6**, 389 (1968).
6. M. Kappel and H. Gerischer, *Z. Electrochem.*, **64**, 235 (1960).
7. A. T. Vagramyan and D. N. Usachev, *Zh. Priklad. Khim.*, **32**, 1900 (1958).
8. Z. A. Solov'eva and A. T. Vagramyan, *Zh. Fiz. Khim.*, **36**, 752 (1962).
9. M. A. Shluger and V A. Kazakov, *Zh. Priklad. Khim.*, **33**, 644 (1960), *Zh. Fiz. Khim.*, **33**, 1666 (1959).
10. Z. A. Solov'eva, Yu. S. Petrova, and A. T. Vagramyan, *Zh. Priklad. Khim.*, **34**, 2007 (1961).
11. Z. A. Solov'eva, Yu. S. Petrova, N. L. Klimasenko, and A. T. Vagramyan, *ibid.*, **35**, 1806 (1962).
12. M. H. Jones and J. C. Saiddington, *Tech. Proc. Am. Electroplaters' Soc.*, **48**, 32 (1961).
13. H. Okada, K. Nakamura, and T. Ishida, *Nature*, **185**, 377 (1960).
14. E. C. Potter, "Electrochemistry," p. 135, Cleaver-Hume Press, London (1961).
15. U. R. Evans, "The Corrosion and Oxidation of Metals," p. 1025, Edward Arnold Ltd., London (1960).
16. B. E. Conway, "Electrochemical Data," p. 335, Elsevier (1952).
17. J. Levitan, *This Journal*, **111**, 286 (1964).
18. M. Frey and C. A. Knorr, *Z. Electrochem.*, **60**, 1093 (1956).
19. Kiyokada Nishihara, Mitsuo Kurachi, Hiroshi Nishii, and Kozoo Tabata, *Suiyokaishi*, **15**, 203 (1964), *C.A.*, **63**, 3869c (1965).
20. R. Weiner, *Z. Elektrochem.*, **42**, 377 (1963), **43**, 808 (1937).
21. R. Weiner, *Metal Finishing*, **64**, 46 (1966).
22. A. T. Vagramyan and Z. A. Solov'eva, Article on The Theory of Chromium Electrodeposition. Translation of "Itogi Nauki: Khimiya" 1966, U.S. Dept. of Commerce and the National Science Foundation, Washington, D.C., p. 111.
23. A. N. Sysoev, N. T. Drobantseva, and O. A. Platonina, *Zh. Priklad. Khim.*, **33**, 372 (1960).
24. R. Weiner and C. Schiele, *Z. Physik. Chem. N.F.*, **26**, 248 (1960).
25. Z. A. Solov'eva and Yu. S. Petrova, *Zh. Priklad. Khim.*, **34**, 1752 (1961).
26. C. A. Snavely, *Trans. Electrochem. Soc.*, **92**, 537 (1947).
27. H. Feigl, L. Kandler, and J. Reinhold, *Metalloberflaeche*, **17**, 229 (1963).
28. H. Feigl, and C. A. Knorr, *Z. Elektrochem.*, **63**, 239 (1959).
29. E. Deltombe, N. deZanbov, and M. Pourbaix, Chapter on Chromium in "Atlas of Electrochemical Equilibria in Aqueous Solutions," pp. 262-264, M. Pourbaix, Editor, Pergamon Press, (1966).
30. R. Weiner and C. Schiele, *Metalloberflaeche*, **14**, 357 (1960).
31. A. V. Pamfilov and A. I. Lopushauskaya, *Ukr. Khim. Zhur.*, **26**, 461 (1960).
32. N. I. Knyazev, V. N. Matveer, and V. L. Khudyakov, *Electrokhim.*, **2**, 850 (1966).
33. E. Shuto and Y. Kondo, *Metal Finishing Abstracts*, **10**, 233 (1968).
34. C. Kasper, *J. Res. Nat. Bur. Std.*, **9**, 353 (1932).
35. C. Kasper, *ibid.*, **14**, 693 (1935).
36. D. N. Usachev and A. T. Vagramyan, *Zh. Fiz. Khim.*, **34**, 229 (1960).
37. A. T. Vagramyan. D. N. Usachev, and N. L. Klimasenko, *Z. Physik. Chem.*, **215**, 57 (1960).
38. J. L. Griffin, *Plating*, **53**, 196 (1966).

A Study of Some Primary Processes in Electropolymerization by Cyclic Voltammetry of Phenyl-Substituted Ethylenes

B. Lionel Funt and Derek G. Gray[1]

Department of Chemistry, Simon Fraser University, Vancouver, British Columbia, Canada

ABSTRACT

Tetraphenylethylene, triphenylethylene, stilbene, 1,1 diphenylethylene, and styrene were utilized as model compounds. Cyclic voltammetry in tetrahydrofuran, NBu_4ClO_4, showed that the radical anions of these compounds were protonated in this medium and are therefore stronger nucleophiles than polycyclic aromatic hydrocarbons for which similar protonation does not occur. The stability of the initial ionic species produced increased with the number of phenyl substituents in this series of substituted ethylenes. The cyclic voltammetric data was examined critically to determine the reversibility of the electron transfer steps, the number of electrons added per step, and the stability or lifetime of transient substances formed. Reaction mechanisms are proposed and the relevance of the findings to electropolymerization processes is indicated.

The passage of an electrolytic current through a nonaqueous organic solution can produce a wide variety of reduction products at the cathode. These may include radicals, radical anions, carbanions, and other related intermediates (1).

In our previous work, we had shown that in the presence of a suitable monomer, polymerization could take place (2). The rate of polymerization was, in

[1] Present address: Department of Chemistry, University of Toronto, Toronto, Ontario, Canada.

general, controlled by the magnitude of the current, and the molecular weight, in many instances, could be regulated in absolute value (3) and in distribution of molecular weight by the current programmed through the solution.

The local environment, in terms of type of solvent and supporting electrolyte, can be chosen to determine a mechanism by which the polymerization will occur. Thus it is possible to conduct free radical, anionic and cationic (4) reactions induced electrolytically.

The technique of electropolymerization has many novel and interesting possibilities. It can provide a degree of control over the rate of the reaction which is not possible in thermally conducted or chemically initiated polymerization. The reaction can also be stopped readily or caused to proceed over a program of different rates as a function of time.

The purpose of this study is to elucidate the nature of the intermediates and their roles in polymerization reactions. Our primary interest was in the polymerization mechanism rather than in the electrode mechanism, and the focus of attention was on the chemical processes and their interrelationships rather than on the theory of electrode reactions.

The phenyl-substituted ethylenes provide a particularly interesting group of model compounds. One of the members of the series, styrene, is a very important and well-characterized monomer. Another member, stilbene, will copolymerize but not homopolymerize, while others, such as tetraphenylethylene, will not undergo polymerization in conventional systems due to steric hindrance (5-7).

Cyclic voltammetry was employed as these systems are particularly sensitive to trace proton donor impurities and an upper limit of 10^{-4}M, may be placed on the impurity level if "living" polymerization is to occur. Cyclic voltammetry between stationary platinum electrodes can be adapted for work under such conditions in vacuum systems.

Experimental

The experimental conditions employed have been reported previously (8).

All solvent transfers and electrolytic measurements were conducted under high-vacuum conditions. The planar working electrode was 0.07 cm^2 platinum wire sealed in glass, and a platinum disk served as counter-electrode.

A silver wire sheathed in a glass capillary proved adequate as a reference electrode (9). Tetrahydrofuran was the solvent, and tetra-n-butyl ammonium perchlorate was the supporting electrolyte.

Cyclic voltammograms were obtained by feeding a signal from a function generator through a potentiostat to the electrolysis cell and recording the output on an x-y recorder.

The effects of uncompensated iR resistance on the values of the peak potential were corrected by extrapolating to zero current. The deviation from strict linearity will be significant in any rigorous quantitative analysis of the data but has little importance in the mechanistic interpretation and comparisons which are our prime concern. The characteristics of the species produced on the cathodic scan were investigated using a more rapid reverse anodic scan. This technique has been shown to give anodic diffusion currents proportional to the surface concentration of the cathodic products (10).

Results

Some details of the cyclic voltammetry of phenyl-substituted ethylenes are presented in Table I.

Tetraphenylethylene.—Cyclic voltammograms for tetraphenylethylene at a series of scan rates are shown in Fig. 1. The most striking feature was a large anodic peak which indicated that the reduction product was relatively stable in solution. The cathodic peak height

Table I. Cyclic voltammetric data for phenyl-substituted ethylenes

	Tetra-phenyl-ethylene	Tri-phenyl-ethylene	Stil-bene	1,1-Di-phenyl ethylene	Sty-rene
$(E_{p,c})_{i=0}$, V*	−2.47	−2.61	−2.55 −2.90	−2.56	−3.18
Millimolar peak height, μA/mM**	3.16	3.16	1.85 1.80	3.05	3.54
$\Delta E_p/\Delta i_p$, μA/mV†	18	27	22	29	20
$(E_p - E_{p^{1/2}})_{i=0}$, mV	42	36	67 —	100	100
$(E_{p,a})_{i=0}$, V*	−2.39	−0.82	−2.48 −0.65	−0.52	−0.80
Relative n_{ox}‡	2	1	1 0.05	1	0.2
$\Delta E_p/\Delta i_p$, μA/mV†	25	71	20 40	40	55

* Peak potentials at zero current *vs.* Ag wire in 0.1M $N(Bu)_4ClO_4$-THF solution.
** Scan rate, 0.15 V/sec.
† A value for $\Delta E_p/\Delta i_p$ of 20 ± 3 μA/mV is ascribed to uncompensated ohmic resistance for the solution and cell geometry used here and previously (8). Larger values are related qualitatively to irreversible charge transfers or subsequent chemical reactions.
‡ Apparent number of electrons in re-oxidation step. Determined by relative peak-height increase with scan rate.

was almost twice that obtained under identical conditions for the first reduction step of *trans*-stilbene [a known one electron reversible process (6)] and the peak height was sharper than that for *trans*-stilbene. The separation of cathodic and anodic peak potentials extrapolated to zero current was found to be 60 ± 4 mV. However, for a reversible two-electron transfer reaction, the peak height should be $2^{3/2}$ that for a single-electron transfer, and the peak separation should be 30 mV. Thus the process cannot be interpreted as a simple two-electron transfer. However, the discrepancy may be resolved by considering multi-step charge transfers. The experimental results obtained here coincide with those predicted for substances undergoing two successive reversible electron transfers at potentials separated by less than 0.1V. (11). Thus the reduction process may be written

$$(Ph)_2C=C(Ph)_2 + e = (Ph)_2C=\dot{C}(Ph)_2$$

$$(Ph)_2C=\dot{C}(Ph)_2 + e = (Ph)_2C=C(Ph)_2^{=}$$

Neither the radical anion nor the dianion appears to be protonated to any appreciable extent in the time interval between electron transfers. Thus this reaction differed from most two-electron reductions of aromatic hydrocarbons. Nevertheless, the appearance of the reverse peak on the cyclic voltammogram enables this unusual mechanism to be assigned with a high degree of confidence.

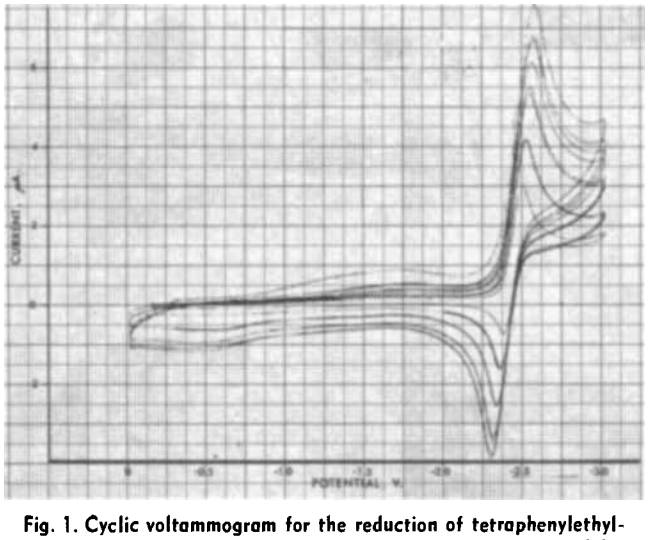

Fig. 1. Cyclic voltammogram for the reduction of tetraphenylethylene, 0.9 mM, in 0.1M $N(Bu)_4ClO_4$-THF solution. Scan rates: 0.06, 0.15, 0.30, 0.48, 0.60 V/sec.

Triphenylethylene.—The voltammetric peak height for triphenylethylene was also found to be about twice that expected for a one-electron transfer. However, no anodic peak was evident on the reverse scan and the peak was narrower and sharper than that found for reversible transfers. The results are shown in Fig. 2. The rate of potential shift with increasing current indicated an irreversible electrode process or a subsequent chemical reaction of the initial electrochemical product Two reaction paths appear plausible

$$(Ph)_2C = CHPh + e \rightarrow (Ph)_2C = CCHPh^{\cdot-} \quad [Ia]$$

$$(Ph)_2C = CCHPh^{\cdot-} + H^+ \rightarrow (Ph)_2\dot{C} - CH_2Ph \quad [Ib]$$

$$(Ph)_2\dot{C} - CH_2Ph + e \rightarrow (Ph)_2\underline{\underline{C}} - CH_2Ph \quad [Ic]$$

or

$$(Ph)_2C = CHPh + e \rightarrow (Ph)_2C = CHPh^{\cdot-} \quad [IIa]$$

$$(Ph)_2C = CHPh^{\cdot-} + e \rightarrow (Ph)_2C = CHPh^{=} \quad [IIb]$$

$$(Ph)_2C = CHPh^{=} + H^+ \rightarrow Ph_2\underline{\underline{C}} - CH_2Ph \quad [IIc]$$

The first mechanism was proposed by Hoijtink (12) for the reduction of aromatic hydrocarbon in the presence of proton donors. This author showed the molecular orbital theory predicted that the radical formed by protonation of the radical anion (reaction [Ib]) was reduced (reaction [Ic]) at lower potentials than that for initial electron transfers (Eq. [Ia]). However, this mechanism would require fast protonation of the triphenylethylene radical anion even when the only proton source in solution was the tetrabutylammonium salt. In view of the results obtained with the stilbene radical ion under identical conditions, it seemed unlikely that such reactions could occur.

The second reaction path is more likely. A second electron is transferred to the radical ion (Eq. [IIb]) at a potential close to that for the first transfer. The dianion formed is sufficiently basic to abstract a proton from a salt anion and produce a carbanion. The narrowness of the peak measured by the difference between the peak and half-peak potentials also supports a mechanism requiring two-electron reduction prior to protonation.

An attempt was made to detect the carbanion which both reaction mechanisms predicted as product. For this, the asymmetric scan technique was employed. The anodic peaks formed on varying the reverse potential scan rate was rather misshapen and indicated an irreversible reaction. However, by comparing the change of peak height with square root of scan rate for the forward and reverse reactions, the rate of peak increase for the reverse reaction was found to be about half that for the forward reaction

$$(Ph)_2\underline{\underline{C}} - CH_2Ph \xrightarrow{-e} (Ph)_2\dot{C} - CH_2Ph$$

Thus, two electrons were required for the reduction and only one for the oxidation The irreversibility of the oxidation reaction is due to the high reactivity of the free radicals formed. Unlike an anion radical, this intermediate is uncharged and therefore electrostatic repulsion does not hinder dimerization or disproportionation.

The carbanion oxidation mechanism may be assigned to the anionic peak for triphenylethylene on the basis of molecular orbital considerations (12).

Although the oxidation of carbanions derived from polycyclic aromatic hydrocarbons has been reported (13), we believe that experimental evidence for electrolytic oxidation of an ethylenic hydrocarbanion has not been found previously.

Trans-Stilbene.—This compound has been studied intensively by a number of workers who employed conventional polarography in dimethylformamide and found that *trans*-stilbene exhibited the behavior typical of polycyclic aromatic compounds (6, 14).

The cyclic voltammogram (Fig. 2) showed that the reduction occurred in two stages. If the potential scan was limited to 2.8V, the anodic and cathodic peaks were found to be of equal height and the other parameters also indicate clearly that a single reversible one electron reduction occurred. One can thus conclude that the radical ion of *trans*-stilbene is stable under these conditions

$$PhHC = CHPh + e \rightarrow PhHC = CHPh^{\cdot-}$$

The subsequent reduction at more cathodic potentials was also a single-electron transfer

$$PhHC = CHPh^{\cdot-} + e \rightarrow PhHC = CHPh^{=}$$

The absence of a corresponding anodic peak on reversing the scan indicated that the dianion had undergone further reaction. In this case, protonation by the salt cation was probable

$$PhCH = CHPh^{=} + H^+ \rightarrow PhC\underline{\underline{H}} - CH_2Ph$$

It should be noted that the product was again found to be a carbanion and an oxidation peak was formed at the potential expected.

In this case, the rate of growth of the peak height with scan rate was less than that expected for a one-electron transfer, and this may be due to further proton abstraction by the carbanion, thus reducing the amount available for oxidation on the reverse scan. Asymmetric scan data could not be employed successfully in this instance because of a small unexplained peak at −1.6V.

1,1 Diphenylethylene.—For this substance, a two-electron irreversible reduction was found. However, the peak was much broader than that found with triphenylethylene, and therefore a different mechanism is indicated. If one assumes that a radical anion is formed initially, then the absence of a phenyl substituent on one of the olefinic carbon atoms would be expected to decrease the steric hindrance toward proton abstraction from the salt cation. In this case, Hoijtink's mechanism would be expected

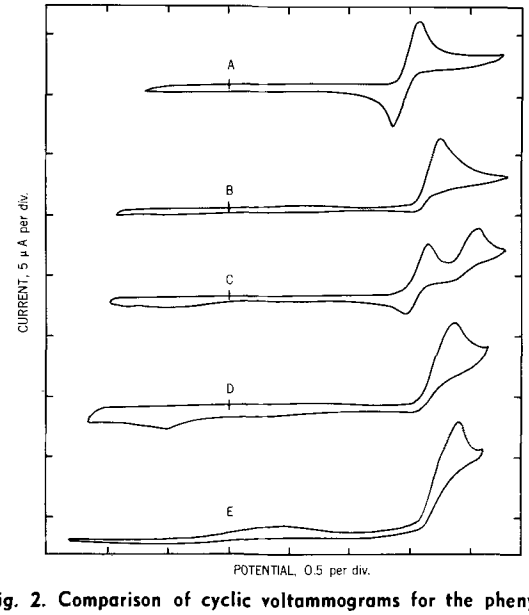

Fig. 2. Comparison of cyclic voltammograms for the phenyl-substituted ethylenes. A, Tetraphenylethylene (0.90 mM); B, triphenylethylene (0.87 mM); C, *trans*-stilbene (1.16 mM); D, 1,1 diphenylethylene (0.87 mM); E, styrene (1.44 mM). All voltammograms were obtained under similar conditions in 0.1M $N(Bu)_4ClO_4$-THF with a scan rate of 0.15 V/sec.

$$(Ph)_2C = CH_2 + e \rightarrow (Ph)_2C = \dot{C}H_2^-$$

$$(Ph)_2C = CH_2^- + H^+ \rightarrow (Ph)_2\dot{C} - CH_3$$

$$(Ph)_2\dot{C} - CH_3 + e \xrightarrow{\text{fast}} (Ph)_2\ddot{C} - CH_3^-$$

The carbanion formed was oxidized at 0.5V on the reverse scan. The asymmetric scan technique showed that the anodic peak increased at half the rate of the cathodic peak. This indicates a one-electron transfer oxidation

$$(Ph)_2\ddot{C} - CH_3^- - e \rightarrow (Ph)_2\dot{C} - CH_3$$

Unlike the corresponding stilbene carbanion, there was thus no evidence of protonation of the 1,1 diphenylethylene carbanion, presumably due to the steric effect of the two phenyl substituents at the nucleophilic site.

Styrene.—Cyclic voltammograms for styrene resemble those for 1,1 diphenylethylene except that the peak due to anodic oxidation of the carbanion was very much smaller than expected for the one-electron transfer. This behavior is consistent with the diminished steric hindrance in the styrene carbanion compared with the 1,1 diphenylethylene carbanion. Thus, the second protonation step may occur before electrolytic oxidation can take place

$$PhHC = CH_2 + e \rightleftharpoons PhHC = \dot{C}H_2^-$$

$$PhHC = CH_2^- + H^+ \rightarrow PhHC - CH_3$$

$$PhHC - CH_3 + e \rightarrow PhHC - CH_3^-$$

$$PhHC - CH_3^- + H^+ \rightarrow PhH_2C - CH_3$$

$$PhHC - CH_3 - e \rightarrow PhHC - CH_3$$

A comparison of the voltammograms of the phenyl-substituted ethylenes under similar conditions in 0.1M tetrabutylammonium perchlorate in tetrahydrofuran at a scan rate of 0.145 V/sec is shown in Fig. 2.

Discussion

A summary of the relative stabilities of the various species which we have assigned on the basis of interpretation of the numerical data and the cyclic voltammograms is shown in Table II.

The results for the phenyl-substituted ethylenes show that as expected from chemical considerations, the stability of the anionic species produced by electrolytic reduction increases with the number of phenyl substituents. This is clearly illustrated in Table I.

Cyclic voltammetry thus indicates the nature of electron transfer reactions with very little ambiguity and also permits the investigation of the carbanion electro-oxidation.

The data with 1,1 diphenylethylene are of particular interest. This compound was used as a model substance in the elegant pioneering studies on anionic polymerization conducted by Szwarc and his coworkers (15, 16). Using stop-flow techniques they found a very high rate of combination of the radical anions with a rate constant of 1-2 x 10^6 1 · $mole^{-1}$ sec^{-1}.

Table II. Summary of the relative stabilities of the anionic species derived from phenyl-substituted ethylenes under voltammetric conditions

Compound	Dianion, $R^=$	Radical anion, R^-	Carbanion, RH^-
Tetraphenylethylene	Stable	—	—
Triphenylethylene	Protonated	—	Stable
Stilbene	Protonated	Stable	Protonated
1,1-Diphenylethylene	—	Protonated	Stable
Styrene	—	Protonated	Protonated

Although the mechanism we propose involves proton abstraction rather than radical combination, this is not at variance with Szwarc's quantitative results. The concentration of the living anions in the reaction mixture is extremely low, while the concentration of tetrabutylammonium ions is relatively high. The latter are effective proton donors and cannot be used in systems in which a living anion concentration is maintained. The ratio of the concentrations of living ions to tetrabutylammonium ions must be at least a factor of 10^6, and thus protonation can be justified in competition with combination even on quantitative grounds.

The lifetime of the radical ions of 1,1 diphenylethylene has been claimed to be much longer by Evans and Evans (17), but the validity of their results have been questioned by Szwarc (16). These authors refute Szwarc's suggestion that the optical spectrum and the properties reported by them should be attributed to the benzophenone radical ion (17). Despite this, the dominant evidence in the literature favors Szwarc's quantitative results and mechanism.

The electrochemical data which we report for the diphenylethylene is based on the observation of a two-electron transfer. This observation is in keeping with a number of other investigations on phenyl-substituted ethenes. Studies by Wawzonek (6) and by Grodzka and Elving (7) indicate a single two-electron wave. However, the latter point out the difficulties in assigning an exact mechanism to the process.

A result of relevance to electropolymerization is that under the experimental conditions employed in voltammetry the ions of styrene and 1,1 diphenylethylene do not dimerize but undergo protonation and reduction. This indicates that the radical ions are more basic than those derived from polycyclic hydrocarbons, which undergo dimerization. It can be concluded that the tetrabutylammonium cations, which are the source of the protons, will be inefficient chain initiators in vinyl electropolymerization. This result also indicates clearly the importance of finding alternative electrolytes for electropolymerization studies. A number of suitable salt systems have been explored, but thus far those most suited for electropolymerization, for example sodiumtetraphenylboride, are not satisfactory for studies in cyclic voltammetry. Further exploratory work is required.

Acknowledgment

The financial assistance of the National Research Council of Canada is gratefully acknowledged.

Manuscript submitted June 9, 1969; revised manuscript received April 1, 1970. This was Paper 135 presented at the New York Meeting of the Society, May 4-9, 1969.

Any discussion of this paper will appear in a Discussion Section to be published in the June 1971 JOURNAL.

REFERENCES

1. O. R. Brown and J. A. Harrison, *J. Electroanal. Chem.*, **21**, 387 (1969).
2. B. L. Funt and F. D. Williams, *J. Polymer Sci.*, **A2**, 865 (1964).
3. B. L. Funt, D. Richardson, and S. N. Bhadani, *ibid.*, **A4**, 2871 (1966).
4. B. L. Funt, *Macromol. Rev.*, Chapter 2, **1**, 35 (1966).
5. H. A. Laitinen, and S. Wawzonek, *J. Amer. Chem. Soc.*, **64**, 1765 (1942).
6. S. Wawzonek, E. W. Blaha, R. Berkey, and M. E. Runner, *This Journal*, **102**, 235 (1955).
7. P. G. Grodzka and P. J. Elving, *ibid.*, **110**, 231 (1963).
8. B. L. Funt and D. G. Gray, *Can. J. Chem.*, **46**, 1337 (1968).
9. D. J. Fisher, W. L. Belew, and M. T. Kelley, "Polarography, 1964," G. J. Hills, Editor, Vol 2, p. 1043, Interscience, New York.
10. J. M. Saveant, *Electrochim. Acta*, **12**, 999 (1967).

11. D. S. Polcyn and I. Shain, *Anal. Chem.*, **38**, 370 (1966).
12. G. J. Hoijtink, J. van Schooten, E. de Boer, and W. V. Aalbersberg, *Rec. Trav. Chem.*, **73**, 355 (1954).
13. R. Dietz and M. E. Peover, *Trans. Faraday Soc.*, **62**, 3535 (1966).
14. A. C. Aten and G. J. Hoijtink, *Z. Physik. Chem. (Frankfurt)*, **21**, 192 (1959).
15. E. Ureta, J. Smid, and M. Szwarc, *J. Polymer Sci.*, A-1, **4**, 2219 (1966).
16. M. Szwarc, "Carbanions, Living Polymers, and Electron-Transfer Processes," John Wiley & Sons, New York (1968).
17. A. G. Evans and J. C. Evans, *Trans. Faraday Soc.*, **61**, 1202 (1965).

Thermodynamics of Liquid Copper-Silver Alloys by a Solid Electrolyte Cell

U. V. Choudary and A. Ghosh

Department of Metallurgical Engineering, Indian Institute of Technology, Kanpur, India

ABSTRACT

The reversible galvanic cell

$$\text{Cu(S), } Cu_2O\text{(S) // CaO-}ZrO_2\text{ // Cu-Ag(1), } Cu_2O\text{(S)}$$
electrolyte

was employed to determine the thermodynamic properties of liquid copper-silver alloys in the range of X_{Cu} from 0.1 to 0.8 and temperature from the liquidus to 1330°K. The activities of copper were found to be higher than the values reported by Hultgren *et al.* on the silver-rich side, whereas they agree well in the high-copper side. Values of F^E, obtained by extrapolation of the data of this study to 1400°K, agree well with those reported in literature. H^M, determined in this study, agree with the calorimetric results within the experimental uncertainty. Small values of S^E confirm the nearly regular behavior of the Cu-Ag system.

Thermodynamic properties of liquid copper-silver alloys have been determined in the past by employing three methods: calorimetry (1-3), vapor pressure measurements (4), and distribution equilibria (5). Phase diagram calculations have also been carried out (6). Hultgren *et al.* (6), in their thermodynamic compilation, have critically reviewed these studies and pointed out the need for more accurate determinations. Calorimetric measurements (2, 3) show mutual agreement. However, they do not, normally yield accurate values of activities. Direct activity measurements were done by Edwards and Downing (4) by the vapor pressure method. Their data contained large scatter and were also found to lead to some thermodynamic inconsistencies according to later analysis (6). The data of Koros and Chipman (5), obtained from measurements of distribution equilibria between liquid copper-silver and liquid iron-copper alloys were confined to a narrow range (0.01-0.12) of mole fraction of copper.

Therefore it was decided to make direct measurement of activities in this system and for this the solid electrolyte cell method was chosen. Various investigators (7-10) have demonstrated that emf measurements with the solid oxide electrolytes are capable of yielding results with good accuracy. In the present work, the cell was

$$\text{Cu(S), } Cu_2O\text{(S) // CaO-}ZrO_2\text{ // Cu-Ag alloy(1), } Cu_2O\text{(S)} \quad [I]$$
electrolyte

This type of cell has already been employed by some investigators (11-14) and is of the general type

$$\text{A, AO // Solid oxide // A-B alloy, AO} \quad [II]$$
electrolyte

Such cells yield values of activity of A in the alloy A-B directly from the cell emf's. In cell I, if $p_{O_2}{}^o$ and p_{O_2} are the partial pressures of oxygen on the left and right side of the cell respectively, then

$$E = \text{emf of the cell} = \frac{RT}{4F} \ln \frac{p_{O_2}}{p_{O_2}{}^o} \quad [1]$$

Again, 4 Cu(S or in alloy) + O_2(g) = 2 Cu_2O(S)
Therefore

$$K = \frac{a_{Cu_2O}{}^2}{a_{Cu}{}^4 \times p_{O_2}} \quad [2]$$

If Cu_2O is pure, then

$$p_{O_2} = \frac{1}{K \cdot a_{Cu}{}^4} \quad [3]$$

Taking the pure solid copper as the standard state and combining Eq. [1] and [3], we obtain

$$E = -\frac{RT}{F} \ln a_{Cu} \quad [4]$$

Other thermodynamic quantities also can be calculated, as shown later (Eq. [5]-[15]).

Accurate results can be obtained, provided the following conditions are satisfied. (*a*) The solid electrolyte is completely ionic in the range of p_{O_2} prevailing in the experiments. (*b*) The oxide of A is much more stable compared to the oxide of B. Moreover AO should be stoichiometric. (*c*) The solubilities of oxygen in A and in alloy A-B are small. (*d*) There are no side reactions, such as those between electrode and electrolyte, electrode and contact lead, and electrode and atmosphere to any significant extent.

The calcia-stabilized zirconia is a perfect ionic conductor (7-10) in the range of p_{O_2} prevailing during the experiments (greater than 10^{-10} atm). Cu_2O is much more stable compared to Ag_2O and exhibits little nonstoichiometry (15) in the range of temperature investigated. The Cu-O phase diagram (16) shows that the solubility of oxygen in solid copper in equilibrium with Cu_2O, below 1330°K, is negligibly small. Approximate calculations based on the model of Belton and Tankins (17), for the solubility of oxygen in binary alloys, reveal that liquid Cu-Ag alloys (X_{Cu} =

Key words: thermodynamics, copper, silver, solid electrolyte, emf.

0.15-0.9), when equilibrated with Cu_2O, dissolve oxygen to a maximum of 1 a/o (atom per cent) at 1300°K.

Experimental

Cell assembly.—Two types of cell, as shown schematically in Fig. 1a and b, were employed in the present work. In cell a, the electrolyte was a ⅜ in. I.D., ½ in. O.D., and 1 in. high crucible of 15 m/o (mole per cent) calcia-stabilized zirconia, obtained from the Zirconium Corporation of America. In cell b, laboratory-made crucibles from fully stabilized ZIRCOA-B powders, served as the electrolyte. The crucibles were slip-cast, presintered at 1200°C for one day, and finally sintered at 2000°C for 6 hr in a ZIRCOA pot furnace. The densities of the crucibles, after final sintering, varied between 5.5 and 5.9 g/cc. Thin copper foil was wrapped around the solid electrolyte crucible in the form of a close-fitting cup, and the annular gap was filled with Cu-Cu_2O mixture.

The furnace was globar-heated in order to avoid inductive emf's. The temperature was controlled by a Leeds & Northrup Electromax Signalling controller within ±1°C. The temperature of the cell was measured by a calibrated Pt-Pt/10% Rh thermocouple. The experiments were conducted under a flow of argon, purified by successively passing through a copper-gauze furnace, $CaCl_2$ and P_2O_5-towers, and finally through a magnesium-chip furnace. The emf's were measured by a Leeds & Northrup potentiometer with a sensitivity of 0.01 mV.

Calibration run.—Cell a was used in most of the runs. In order to make sure that there was no significant short-circuiting of the electrodes by gaseous transport via atmosphere and electronic conductivity in the electrolyte, a calibration run was taken with mixtures of Cu-Cu_2O and Ni-NiO as the two electrodes. Cu_2O and NiO powders were of Fisher Certified Reagent grade. Cu and Ni powders were obtained from Semi-Elements Inc. with a minimum purity of 99.9%.

The Cu-Cu_2O mixture was placed inside the electrolyte crucible, and contact was established by pressing a platinum disk, which was spot-welded to Pt and Pt/10% Rh wires, sheathed in a double-bore alumina tube. This served as lead as well as thermocouple. Platinum wire was wound round the electrolyte crucible and a moist paste of Ni-NiO was applied over it. The electrolyte crucible was contained in a recrystallized alumina crucible and Ni shot along with NiO powder were kept in the latter in order to provide a better environment.

The furnace chamber was first flushed with purified argon, evacuated at 150°C, and then was slowly heated to 900°C under flowing argon. Both the electrode mixtures were sintered *in situ*, establishing very good electrical contact. The duration of the run was one week and the temperature cycling was done two times in the range 1020°-1325°K. The measured emf was considered as steady, if it remained constant within ±0.2 mV for a minimum period of 6 hr. Moreover, the cell was left overnight and at times for one full day at arbitrarily selected temperatures. The emf's remained steady and the fluctuations never exceeded 0.5 mV. Reversibility of the cell emf was checked by polarization tests and by varying the gas flow rate. Table I compares or data with the most precise values available elsewhere (9, 18) and the agreement is excellent. Cell b was tested against cell a by measurements at the same compositions ($X_{Cu} = 0.5$). The emf's in these two arrangements agreed well (±1 mV).

Selection of contact lead for liquid alloy.—Dissolution of the lead by the liquid alloy is a problem in this kind of study. There are two ways to tackle it. First, one can use a lead which dissolves to a negligible extent and hence can be dipped continuously. Diaz and Richardson (19) immersed a chromium-alumina cermet continuously in liquid copper at 1100°C with success. If the lead material tends to be dissolved faster, it is immersed for a short time only, during the time of measurement of emf. Inconel, cermet, and Cu_2O were tried as leads. While the Inconel was dipped into the alloy during measurements only, the other two materials were kept immersed continuously. The cermets were hung by platinum wires, whereas Cu_2O was sintered on platinum wire for strength. Although all the above leads were found to be quite satisfactory during trials, the cermet was chosen because it gave the smallest scatter. Therefore most of the runs reported here have been taken with cermet-cermet combination, as shown in Fig. 1. The cermet was the same as that used by Diaz and Richardson (19).

Table I. Temperature dependence of emf for the calibration cell: Ni, NiO/CaO-ZrO_2/Cu, Cu_2O

	Temperature, °K	1020	1116	1150	1200	1273	1323
Emf (mV)	This work	275.9	268.3	266.3	263.6	256.7	255.0
	Rizzo, Bidwell and Frank (18)*	276.5	269.6	267.2	263.7	258.5	—
	Charette and Flengas (9)*	275.8	268.1	265.7	262.1	257.0	253.5

* Calculated values from temperature-emf relations of the investigators.

Emf measurements on copper-silver alloys.—The master alloys of Cu and Ag were prepared by melting the required amounts of copper (Semi-Elements Inc., U.S.A., purity 99.97%) and silver (American Smelting and Refining Co., U.S.A., purity 99.99%) shot either in an evacuated and sealed quartz tube or in a one-end open quartz tube under a stream of purified argon. The weight of each master alloy ranged between 7 and 10g. The alloys were taken in the recrystallized alumina crucible (cell a, Fig. 1) or in electrolyte crucible (cell b, Fig. 1) along with 1 to 2g of Cu_2O. The furnace chamber was first evacuated with the cell assembly in position, filled with purified argon, and then slowly heated to 1000°C. At this temperature, the cell attained a steady emf in less than 2 hr. Emf's were recorded at intervals of 30 min, and if the variation

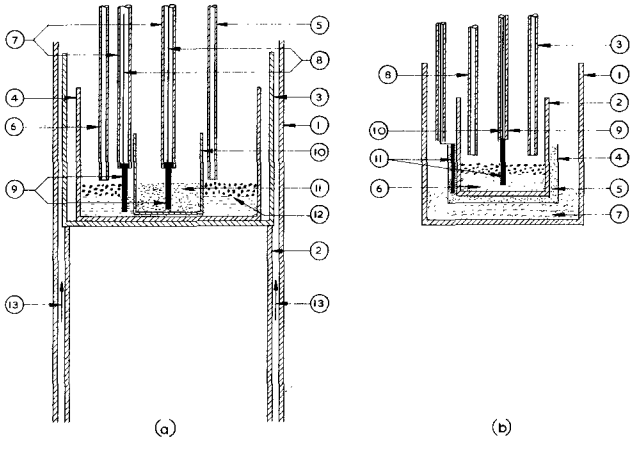

Fig. 1. Cell assembly.

a: 1, Reaction tube-mullite; 2, supporting mullite tube; 3, outer silica crucible; 4, recrystallized alumina crucible; 5, double-bore alumina sheath for Pt/Pt-Rh thermocouple; 6, addition tube-quartz; 7, alumina guide tubes for lead wires; 8, platinum lead wires; 9, Cr-Al_2O_3 cermets; 10, solid electrolyte crucible; 11, Cu-Cu_2O reference electrode; 12, Cu-Ag melt with Cu_2O; 13, purified argon from gas train.

b: 1, Recrystallized alumina crucible; 2, solid electrolyte crucible; 3, quartz tube for addition; 4, thin copper foil; 5, Cu-Cu_2O reference electrode; 6, Cu-Ag melt with Cu_2O; 7, Cu shot with Cu_2O; 8, double-bore alumina sheath; 9, alumina guide tubes for lead wires; 10, platinum lead wires; 11, Cr-Al_2O_3 cermets.

was within ±0.1 mV in a period of 2 hr the emf's were considered to be steady. A minimum of 4 hr was allowed before a temperature change was effected. Each experiment was subjected to the tests for reversibility and reproducibility just as the calibration run. Even after heavy polarization (1 mamp for 3 min), usually a maximum of 30 min were enough for re-attainment of steady emf's. Additions of Cu or Ag in the form of small shot were made at 1050°C. Immediate changes in emf's were observed and steady emf's were attained in about 2 hr.

Chemical analysis of the alloys was not made. In order to be certain of the accuracy of compositions during the experiments, a few times the same compositions were obtained either from the master alloys directly or by additions. Emf's by these two procedures differed by less than 1 mV. This observation, coupled with the facts that the temperature cycling yielded reproducible emf's and that the emf *vs.* temperature plots were straight lines with standard deviations of less than 1 mV in all the experiments, pointed out that negligible compositional changes took place during the experiments either through evaporation of Ag or in any other manner.

Results

The measurements were confined in the range of X_{Cu} from 0.1 to 0.8 and in the temperature range $T_{liquidus}$ to 1330°K. A few measurements were made below the liquidus and above 1330°K. Figure 2 shows the least-square lines for the emf *vs.* temperature relation at each composition. Table II presents the results analytically along with the standard deviations and maximum deviations. The emf's could also be extrapolated to 1400°K, after correcting for dE/dT at the melting point of copper (1356°K). The cell emf's gave partial quantities for copper directly with solid copper as the standard state. Liquid copper was employed as the standard state, by making appropriate corrections for fusion values of copper, as noted below.

$$F^{M}_{Cu} = -EF - \Delta F_{fusion} = RT \ln a_{Cu} \quad [5]$$

$$S^{M}_{Cu} = F\frac{dE}{dT} - \Delta S_{fusion} \quad [6]$$

$$H^{M}_{Cu} = F^{M}_{Cu} + T S^{M}_{Cu} \quad [7]$$

where F^{M}_{Cu}, S^{M}_{Cu}, H^{M}_{Cu} are free-energy, entropy, and

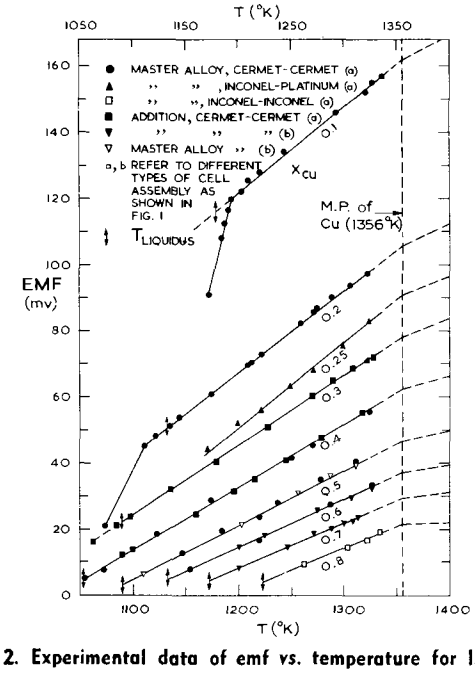

Fig. 2. Experimental data of emf *vs.* temperature for liquid Cu-Ag alloys.

Table II. Experimental data on liquid Cu-Ag alloys

X_{Cu}	Temperature range of applicability, °K	Emf (mV) $E = A + BT$ −A	B	Standard deviation, mV	Maximum deviation, mV
0.1	1181-1330	191.1	0.2606	0.7	1.6
0.2	1133-1330	229.4	0.2470	0.6	1.0
0.25	1113-1330	245.6	0.2472	0.9	2.1
0.3	1090-1330	210.6	0.2132	0.4	1.0
0.4	1052-1330	196.6	0.1909	0.4	1.1
0.5	1090-1330	177.8	0.1657	0.6	1.2
0.6	1131-1330	163.8	0.1485	0.4	0.7
0.7	1173-1330	157.6	0.1370	0.5	0.9
0.8	1220-1330	140.4	0.1190	0.8	1.0

heat of mixing of copper with liquid copper as the standard state.

The partial thermodynamic quantities for silver were determined using the following equations

$$\log a_{Ag} = \log X_{Ag} - X_{Ag}X_{Cu}\alpha_{Cu} + \int_{o}^{X_{Cu}} \alpha_{Cu} \cdot dx_{Cu} \quad [8]$$

$$F^{M}_{Ag} = 4.576\ T \log a_{Ag} \quad [9]$$

$$H^{M}_{Ag} = -X_{Ag}X_{Cu}\beta_{Cu} + \int_{o}^{X_{Cu}} \beta_{Cu} \cdot dx \quad [10]$$

$$S^{M}_{Ag} = (H^{M}_{Ag} - F^{M}_{Ag})/T \quad [11]$$

where

$$\alpha_{Cu} = \frac{\log \gamma_{Cu}}{(1 - X_{Cu})^2} \quad [12]$$

$$\beta_{Cu} = \frac{H^{M}_{Cu}}{(1 - X_{Cu})^2} \quad [13]$$

The integrals in Eq. [8] and [10] have been evaluated graphically from Fig. 3 and 4. From these partial values, integral and excess properties for Cu-Ag system were calculated. For the latter, the equations employed are noted below.

$$F^{E} = (1 - X_{Cu}) \int_{o}^{X_{Cu}} \alpha_{Cu} \cdot dx_{Cu} \quad [14]$$

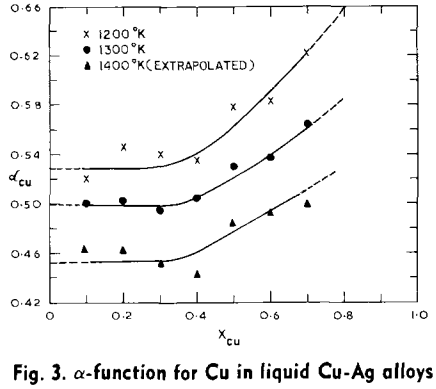

Fig. 3. α-function for Cu in liquid Cu-Ag alloys

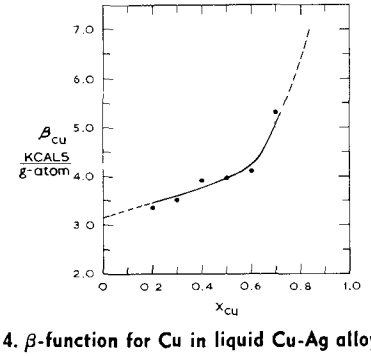

Fig. 4. β-function for Cu in liquid Cu-Ag alloys

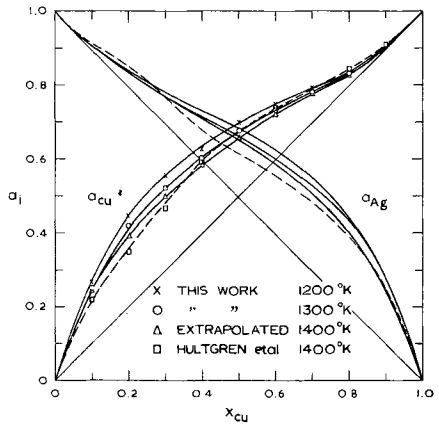

Fig. 5. Activity plots in liquid Cu-Ag alloys

$$H^E = (1 - X_{Cu}) \int_0^{X_{Cu}} \beta_{Cu} \cdot dx_{Cu} \qquad [15]$$

where the superscript E denotes excess property.

Discussion

Hultgren *et al.* (6) give a value of 0.96 ± 0.005 for the activity of copper at the eutectic temperature (1052°K). Emf data in this study at $X_{Cu} = 0.4$ and 0.7, yielded activity values of 0.953 and 0.965, respectively. This agreement is considered to be excellent. At $X_{Cu} = 0.1$, the liquidus was found to be 13°C higher than that given in the phase diagram. Repetition with another master alloy of the same composition yielded reproducible results. At $X_{Cu} = 0.2$ and 0.3, considerable supercooling (greater than 20°C) was observed. Even prolonged equilibration (12 to 18 hr) and stirring of the bath resulted in the same emf's. The dissolved oxygen could be the cause for lowering of the liquidus.

The activities of Cu and Ag at 1200°, 1300°, and 1400°K (extrapolated) are presented in Fig. 5 along with the values reported by Hultgren *et al.* (6). The standard states for both are pure liquid metals. For determination of the activity of Ag, an extrapolated value of α_{Cu} was employed only for $X_{Cu} = 0.8$, since at this composition γ_{Cu} is close to unity and a little error (0.5%) in a_{Cu} can lead to a large uncertainty in α_{Cu}. The values at 1400°K are 10 to 15% higher on silver-rich side and 3 to 5% lower on high copper side, compared to those of Hultgren *et al.* (6).

As Table IV shows, H^M_{Cu} obtained from the intercepts of emf *vs.* temperature plots, increase with decreasing X_{Cu}, except at $X_{Cu} = 0.1$, where H^M_{Cu} is unusually low. The change in solubility of oxygen with temperature could be causing this discrepancy. Quantitative explanation could not be given in the absence of oxygen solubility data in these alloys. If Cu_2O will dissolve in the liquid alloy according to the reaction

Table III. Activities in liquid Cu-Ag alloys (standard states: pure liquid metals)

X_{Cu}	1200°K γ_{Cu}*	1200°K γ_{Ag}	1300°K (±2°) γ_{Cu}*	1300°K (±2°) γ_{Ag}	1400°K (extrapolated) γ_{Cu}	1400°K (extrapolated) γ_{Ag}
0.1	2.640	1.016	2.545	1.013	2.460	1.011
0.2	2.235	1.057	2.094	1.055	1.975	1.050
0.3	1.840	1.122	1.737	1.110	1.668	1.104
0.4	1.563	1.228	1.498	1.198	1.444	1.191
0.5 (±0.005)	1.396	1.372	1.358 (±0.018)	1.316 (±0.019)	1.321	1.292
0.6	1.240	1.573	1.219	1.501	1.199	1.462
0.7	1.141	1.833	1.137	1.747	1.110	1.692
0.8	—	—	1.045	2.160	1.043	2.010

* γ_{Cu} w.r.t. solid copper as the standard state may be obtained by multiplying the values of the table by 1.170 at 1200°K and 1.050 at 1300°K.

Table IV. Heats and entropies of mixing in liquid Cu-Ag alloys (standard states: pure liquid metals) in the range: $T_{liquidus}$ to 1330°K.

X_{Cu}	H^M_{Cu}	S^M_{Cu}	H^M_{Ag}	S^M_{Ag}	H^M	S^M
0.1	2675* (1290)†	4.77*	25	0.21	295	0.67
0.2	2170	3.40	100	0.45	510	1.04
0.3	1735	2.62	255	0.70	695	1.276
0.4	1415	2.15	455	1.00	815	1.46
0.5	980 (±240)	1.52 (±0.18)	785 (±260)	1.46 (±0.2)	875 (±180)	1.50 (±0.14)
0.6	655	1.13	1130	1.90	865	1.45
0.7	480	0.86	1560	2.50	790	1.34
0.8	120	0.45	2100	3.30	640	1.11

* Extrapolated values from graph.
† Experimental values.

$$Cu_2O(S) = 2\underline{Cu} + \underline{O} \qquad [16]$$

it can lead to an increase in X_{Cu} by a fraction of few hundredths, which is enough to decrease the slope of emf *vs.* temperature plot and hence decrease measured H^M_{Cu} considerably. This process is reversible with respect to temperature and hence temperature cycling will not reveal any irreproducibility. Approximate calculations on the basis of the model proposed by Belton and Tankins (17), for the solubility of oxygen in binary alloys, confirms that oxygen solubility is at least 1 a/o at 1300°K for silver-rich alloys ($X_{Cu} = 0.1$). However, the consequent inaccuracy in the activity of Cu at $X_{Cu} = 0.1$, resulting from this departure in actual slope, is estimated to be less than 3% at 1300°K. For $X_{Cu} = 0.2$, the dissociation of Cu_2O will not cause appreciable compositional changes (less than 0.005 in X_{Cu}). Moreover, emf values for the alloys ($X_{Cu} \geq 0.2$) are much less sensitive to slight compositional changes, and the shift in H^M_{Cu} will be well within the experimental uncertainty. Even if an approximate correction for oxygen solubility is made in a_{Cu}, the present values are higher than those reported by Hultgren *et al.* (6). The molar free energies of mixing (F^E) of this work are compared with those of Hultgren *et al.* (6) in Fig. 6 and the agreement is quite good.

In Fig. 4, the curve of β_{Cu} *vs.* X_{Cu} has been extrapolated from the middle ranges of composition toward the terminal regions. For the low-copper side the reason for this extrapolation will be obvious from the preceding discussion. On the high-copper side, the values of $(1 - X_{Cu})^2$ becomes small, making β_{Cu} very sensitive to any error in H^M_{Cu}. Therefore extrapola-

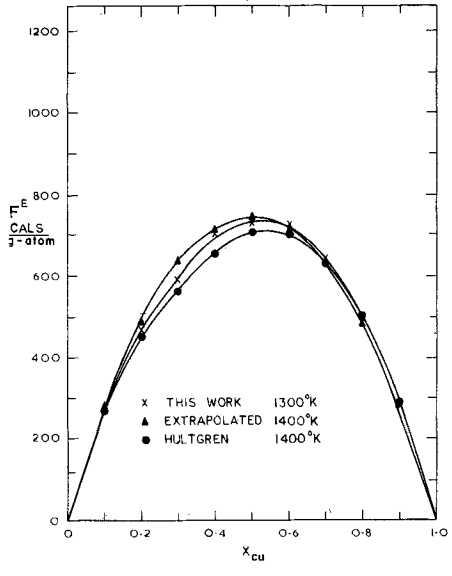

Fig. 6. Excess molar free energies of mixing in liquid Cu-Ag alloys.

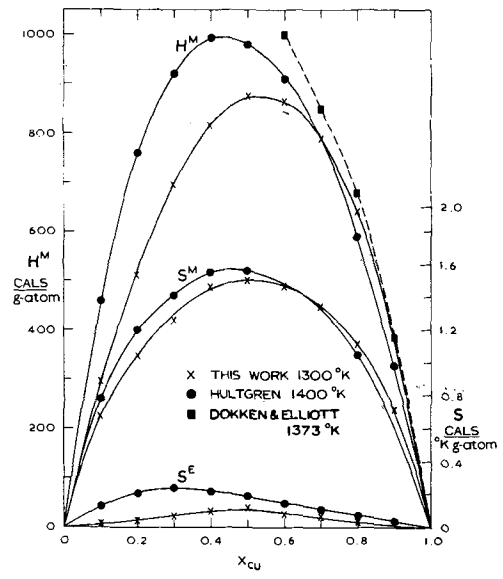

Fig. 7. Integral molar heats and entropies of mixing in liquid Cu-Ag alloys.

tion from the middle composition ranges was preferred. As Fig. 7 shows, the values for integral molar heats of mixing, H^M, agree well with the calorimetric determinations (2, 3) in the high-Cu range, whereas on the lower copper side, the values are somewhat lower. Considering the uncertainty of nearly 200 cal in H^M values of present work, the agreement is good.

Acknowledgments

The authors wish to thank Mr. P. J. Ray Chowdhury for his active help in the construction of apparatus and during experimentation; Mr. K. P. Jagannathan for his timely assistance in some of the runs. The authors are indebted to Mr. K. Thomas Jacob of Imperial College, London, for helpful discussions.

Manuscript submitted June 19, 1969; revised manuscript received April 2, 1970.

Any discussion of this paper will appear in a Discussion Section to be published in the June 1971 JOURNAL.

REFERENCES

1. N. Kawakami, *Sci. Rept. Imp. Tohoku Univ., Japan*, **19**, 52 (1930).
2. R. A. Oriani and W. K. Murphy, *J. Phys. Chem.*, **62**, 199 (1958).
3. R. N. Dokken and J. F. Elliott, *Trans. AIME*, **233**, 1351 (1965).
4. R. K. Edwards and J. H. Downing, *J. Phys. Chem.*, **60**, 108 (1956).
5. P. J. Koros and J. Chipman, *J. Metals*, **8**, 1102 (1956).
6. R. Hultgren, R. L. Orr, P. D. Anderson, and K. K Kelley, "Selected Values of Thermodynamic Properties of Metals and Alloys," John Wiley & Sons, London (1963).
7. K. Kiukkola and C. Wagner, *This Journal*, **104**, 379 (1957).
8. B. C. H. Steele and C. B. Alcock, *Trans. AIME*, **233**, 1359 (1965).
9. G. G. Charette and S. N. Flengas, *This Journal*, **115**, 796 (1968).
10. Y. Matsushita and K. Goto, *J. Fac. Eng., Univ. Tokyo*, **27**, 217 (1964).
11. C. R. Cavanaugh and J. F. Elliott, *Trans. AIME*, **230**, 633 (1964).
12. K. Goto and G. R. St. Pierre, *Tetsu To Hagane*, **49**, 1873 (1963).
13. R. J. Freuhan, *Trans. AIME*, **242**, 2007 (1968).
14. A. Kubik and C. B. Alcock, *Metal Science J.*, **1**, 19 (1967).
15. M. O'Keefe and W. J. Moore, *J. Chem. Phys.*, **36**, 3009 (1962).
16. R. Vogel and W. Pocher, *Z. Metallk.*, **21**, 333 (1929).
17. G. R. Belton and E. S. Tankins, *Trans. AIME*, **233**, 1892 (1965).
18. F. E. Rizzo, L. R. Bidwell, and D. F. Frank, *ibid.*, **239**, 593 (1967).
19. C. Diaz and F. D. Richardson, *Trans. IMM*, **76**, C 196 (1967).

Supporting Electrolyte Effects in Electrochemistry: Copper and Mercury Acetylacetonates in Acetonitrile Solvent

J. N. Burnett,[1] L. K. Hiller, Jr.,[2,3] and Royce W. Murray*,[4]

Department of Chemistry, University of North Carolina, Chapel Hill, North Carolina

ABSTRACT

The anodic mercury wave of acetylacetonate and the reduction of $Cu(acac)_2$ have been investigated in acetonitrile solvent. The electrochemistry of both species is substantially modified by the presence of lithium perchlorate in the tetraethylammonium perchlorate supporting electrolyte. The anodic mercury wave of acetylacetonate yields a stable mercury(II) acetylacetonate product in lithium-containing medium; the product complex undergoes rapid decomposition in the absence of lithium. A coordinative interaction of lithium ion with $Hg(acac)_2$ is postulated. The reduction of $Cu(acac)_2$ proceeds in a single two electron wave in Et_4NClO_4 electrolyte and in two single electron steps in $LiClO_4$-Et_4NClO_4 electrolyte. An interpretation resting on the instability of $Cu(acac)_2^-$ and the coordination of acetylacetonate by lithium ion, to give $Li_2(acac)^+$, is given to account for this behavior.

In acetonitrile solvent, the tetraalkylammonium enolate salt of 1,3-pentanedione (acetylacetonate, R_4N^+ $acac^-$) is, at most, weakly associated as an ion pair. When lithium or tetraalkylammonium acetylacetonate is dissolved in acetonitrile containing $LiClO_4$ electrolyte, the β-diketonate becomes coordinated in a stable dilithium complex, $Li_2(acac)^+$ (1). The cathodic electrochemistry of various metal acetylacetonates is sensitive to the presence of $LiClO_4$ electrolyte because of this lithium coordination. For instance, the one-electron reduction of *tris*(acetylacetonato)iron(III), $Fe(acac)_3$, in tetraethylammonium perchlorate electrolyte yields a stable $Fe(acac)_3^-$ complex. In lithium

* Electrochemical Society Active Member.
[1] Present address: Department of Chemistry, Davidson College, Davidson, North Carolina.
[2] Present address: Procter and Gamble Company, Winton Hill Technical Center, Cincinnati, Ohio.
[3] NSF Cooperative Fellow, 1962-1963; Ethyl Corporation Fellow, 1965-1966.
[4] Alfred P. Sloan Research Fellow, 1968-1970.
Key words: copper, mercury, acetylacetonate, acetonitrile, polarography, cyclic voltammetry, supporting electrolyte, lithium.

perchlorate-tetraethylammonium perchlorate electrolyte, charge transfer is immediately followed by a poorly reversible abstraction of an acetylacetonate ligand by lithium ion to give $Fe(acac)_2$ and the dilithium complex (2). Investigation into the details of lithium electrolyte effects in acetonitrile has continued. Reported here are some further results on two electrochemical reactions: the anodic reaction at a mercury electrode in the presence of acetylacetonate and the reduction of *bis*(acetylacetonato)copper(II), $Cu(acac)_2$, at mercury.

Experimental

Acetonitrile solutions contained 0.1*M* tetraethylammonium perchlorate (Et_4NClO_4) as supporting electrolyte; various concentrations of lithium perchlorate were added to this. Acetylacetonate was added to lithium-containing solutions as Li(acac), forming $Li_2(acac)^+$, and to 0.1*M* Et_4NClO_4 solutions as the tetrabutylammonium salt, $Bu_4N^+acac^-$. The latter compound was prepared by a procedure provided by Posner *et al.* (3), in which acetylacetone is mixed with a solution of tetrabutylammonium hydroxide (Eastman) in methanol, the reaction mixture cooled, and ethyl acetate added to precipitate the white salt. This was recrystallized from methylene chloride, again using ethyl acetate to induce precipitation. All acetylacetonate solutions were used within a few hours of their preparation; solutions of $Li_2(acac)^+$ are quite stable, while those of Bu_4N^+ $acac^-$ give ultraviolet spectral indication of decomposition after about 10-12 hr. Standard $Cu(acac)_2$ solutions were prepared from J. T. Baker material recrystallized from benzene.

Working electrodes were either a DME or a hanging mercury drop electrode of the design of Shain *et al.* (4). Potentials reported are *vs.* an aqueous NaCl-SCE reference electrode isolated from the working electrode compartment with a Et_4NClO_4-acetonitrile salt bridge. Coulometry experiments on the anodic mercury wave of acetylacetonate were carried out with a micrometer thin layer cell (5) equipped with a mercury-coated platinum working electrode. The cell was calibrated by potential step coulometry of $Fe(acac)_3$ ($n = 1$) in 0.1*M* Et_4NClO_4-acetonitrile. A range of solution thicknesses were employed in both the calibration and thin layer determination of acetylacetonate n values. Instrumentation and other details are as cited earlier (2).

Results and Discussion

Anodic mercury wave of acetylacetonate.— Solutions of Bu_4N^+ $acac^-$ in Et_4NClO_4 electrolyte exhibit an anodic polarographic wave with $E_{1/2} = -0.242$V *vs.* SCE; those containing Li(acac) dissolved in $LiClO_4$-Et_4NClO_4 supporting electrolyte exhibit this wave at more positive, $[LiClO_4]$-dependent potentials (Table I). On Pt and Au electrodes, these solutions yield anodic waves at +0.3 and +0.9V, respectively. The anodic reactions on the solid electrodes are of demonstrably different properties and origin (6), however. The anodic reaction of acetylacetonate at mercury is assigned to an oxidation of mercury to yield a mercury acetylacetonate complex.

The anodic mercury wave of $Li_2(acac)^+$ [Li(acac) dissolved in $LiClO_4$-containing media] is considered first; various data are summarized in Table I. Polarographic ($i/h^{1/2}$), chronopotentiometric ($i\tau^{1/2}$), and potential sweep ($i_{p(a)}/v^{1/2}$) criteria establish diffusion control of the anodic reaction by $Li_2(acac)^+$. Stability of the mercury-containing anodic product, and its nonadsorption, is demonstrated by accord of cyclic voltammetric $i_{p(a)}/i_{p(c)}$, chronopotentiometric τ_f/τ_b, and thin layer coulometric Q_{anod}/Q_{cath} ratios with diffusion-only expectations.

The anodic mercury acetylacetonate product is anticipated to represent a mercury(II) species; mercury(I) acetylacetonates are unknown. The following results bear on the stoichiometry of the mercury(II)

Table I. Characteristics of the anodic mercury wave of Li(acac) dissolved in $LiClO_4$-0.1*M* Et_4NClO_4-acetonitrile solvent (dilithium acetylacetonate)

Results independent of $[LiClO_4]$ unless otherwise noted

Polarography:		
I_d ($i_{max}/m^{2/3}t^{1/6}C^\circ$)		2.69[a,b]
D (cm^2/sec)		2.24×10^{-5}
$E_{1/2}$ (V); $[LiClO_4]$ =	0 m*M*	+0.091
	9.5 m*M*[c]	+0.210
	21.4 m*M*	+0.232
	26.7 m*M*	+0.238
	40.0 m*M*	+0.250
	49.4 m*M*	+0.252
	79.6 m*M*	+0.262
Chronopotentiometry:		
$i\tau^{1/2}/AC^\circ$ (amp cm $sec^{1/2}$/mole)		268 ± 3[a,d]
D (cm^2/sec)		2.44×10^{-5}
τ_f/τ_b		2.97 ± 0.10[e]
Cyclic voltammetry:		
$i_{p(a)}/AC^\circ v^{1/2}$ (amp cm $sec^{1/2}$/mole)		1001 ± 45[f]
ΔE_{peak} (mV)		38[g]
$i_{p(a)}/i_{p(c)}$		1.03 ± 0.04[e]
Thin layer electrochemistry:		
n_{acac}		0.83 ± 0.03
Q_{anod}/Q_{cath}		1.04

[a] From ref. (1).
[b] Independent of mercury column height and [acac].
[c] [acac] < 0.1 $[LiClO_4]$ in all cases; dissociated $[Li^+]$, calculated as in ref. (1), is 1.84, 4.04, 5.00, 7.33, 8.90, 13.8 m*M*.
[d] Independent of applied current and [acac].
[e] $[LiClO_4] > 10$ m*M*.
[f] Independent of potential sweep rate.
[g] At $v = 0.1$ V/sec.

complex: Potential step thin layer coulometry gives a result of 0.83 electrons/acac. This result, n near unity, indicates a $Hg(acac)_2$ product, with perhaps some higher coordination, such as $Hg(acac)_3^-$, occurring as well. Proximity of the polarographic I_d constant, 2.69, with those of known one-electron metal acetylacetonate reactions in acetonitrile [I_d = 3.18, $Fe(acac)_3$; I_d = 3.06, $Co(acac)_3$ (2); I_d = 3.2, first wave of $Cu(acac)_2$, see below] is consistent with this observation. Verification of the 1:2 stoichiometry is provided by an amperometric (polarographic) titration of 0.5 m*M* $Hg(ClO_4)_2$ with a $Li_2(acac)^+$ solution [Li(acac) dissolved in 0.1*M* $LiClO_4$]. The initial mercury(II) wave is linearly attenuated (to zero current) and replaced with the more cathodic reduction wave of coordinated mercury(II) (rising to a maximum current), with an end point corresponding to a 1(Hg)/2(acac) mole ratio. An excess of acetylacetonate initiates precipitation of the fairly insoluble mercury complex and appearance of the anodic $Li_2(acac)^+$ wave. A polarogram of the "end point" solution (which contains 16 m*M* $LiClO_4$) shows that the cathodic $Hg(acac)_2$ wave has $E_{1/2} = +0.22$V, the same potential as that of the anodic $Li_2(acac)^+$ mercury wave at this $[LiClO_4]$ (Table I). The cathodic-anodic couple in a cyclic voltammogram of the $Hg(acac)_2$ solution exhibits a similar correspondence to one observed for a solution of $Li_2(acac)^+$.

The most interesting feature of the anodic $Li_2(acac)^+$ mercury wave is revealed by examination of the dependency of its $E_{1/2}$ on the concentration of dissociated lithium ion (to which $[LiClO_4]$ is nearly proportional, Table I). This examination, strictly speaking, can be semiquantitative only, owing to the imperfect reversibility of the reaction: $\Delta E_{peak} > 30$ mV. In solutions containing sufficient excess lithium ion that $[LiClO_4]_{x=0} \approx$ constant and that most of the acetylacetonate exists as the dilithium complex [>80% as $Li_2(acac)^+$ for $[LiClO_4] > 10$ mM, (1)], a plot of $E_{1/2}$ *vs.* log $[Li^+]_{free}$ should be linear with slope 0.059 m/n, where $n = 2$ and m is the number of lithium ions released by the anodic process. If two $Li_2(acac)^+$ reactants combine with mercury to give as product simply $Hg(acac)_2$, a slope of 118 mV is anticipated. The actual 58 mV slope of the linear plot of experimental results (of which those in Table I are a sampling of about one-third of those available) is

quite divergent from this simple expectation, and indicates retention of two lithium ions in the mercury(II) acetylacetonate product complex

$$2Li_2(acac)^+ + Hg \rightarrow Li_2Hg(acac)_2^{2+} + 2Li^+ + 2e \quad [1]$$

Accepting the result of the $E_{1/2}$ — $\log[Li^+]_{free}$ analysis as proof of mixed coordination of acetylacetonate to mercury(II) and lithium ion admittedly, owing to the reversibility factor, requires some caution. Two additional factors serve to add plausibility to a process such as reaction [1]. The first centers on previous chemical evidence. Among the metal β-diketonates, mercury(II) complexes apear to be unique in that the diketonate ligand bonds to the metal as an enolate (unidentate) ligand (as opposed to the usual cyclic geometry). Hammond and Nonhebel (7, 8) have shown this from arguments based on infrared and ultraviolet spectra and solubility and chemical reactivity (benzoylation) data. One oxygen site on an acetylacetonate ligand bound to mercury(II) is thus free for association with another metal ion. The acetylacetonate ligand is known, through demonstration (1) of the existence of $Li_2(acac)^+$, to be capable of bonding in an open chain form each of its oxygens to a metal ion. Postulation of a lithium ion $Hg(acac)_2$ association is, against this background of previous evidence, chemically reasonable.

The second argument centers on the behavior of the anodic reaction of $Bu_4N^+acac^-$ in 0.1*M* Et_4NClO_4 (lithium absent). The anodic acetylacetonate mercury wave in this medium has a polarographic $I_d = 4.00$, $E_{1/2} = -0.242$V, and is diffusion controlled in the polarographic experiment. The product of this anodic reaction, in contrast to that found in the presence of lithium ion, is quite unstable; cyclic voltammetric $i_{p(a)}/i_{p(c)} > 1$ and chronopotentiometric $\tau_f/\tau_b > 3$ ratios (poorly reproducible) both indicate extensive decomposition. Anodic thin layer charge-time curves exhibit only a poor inflection at an $n_{acac} = 1$ charge, and substantial further charge accumulation (exceeding edge diffusion and background values) occurs on prolonged electrolysis ($n = 14$ after ~15 min). Evidently the decomposition slowly leads to further oxidizable materials. Surface effects of the anodic product(s) are indicated by polarographic electrocapillary observations. The details of the decomposition reaction(s) of the mercury(II) acetylacetonate anodic product are unknown. It is quite clear, however, that the absence of such decomposition in solutions containing lithium ion provides additional circumstantial evidence for a coordinative interaction of lithium ion with $Hg(acac)_2$ such as that of reaction [1].

Reduction of $Cu(acac)_2$ *in acetonitrile.*—Several polarographic studies of $Cu(acac)_2$ in aqueous solvent and in aqueous mixtures with ethanol, methoxymethanol, dioxane, and methyl cellosolve (9, 12) have described a single, two-electron reduction wave. In a 50% aqueous-50% pyridine solvent mixture, on the other hand, Calvin and Bailes (13) report that $Cu(acac)_2$, and other copper(II) β-diketonates, are reduced in two one-electron waves, the second polarographic wave exhibiting the same reduction potential found for Cu(I) in this medium in the absence of acetylacetonate. The reduction pattern in Calvin and Bailes' solvent is interpretable as resulting from a combination of the greatly lessened stability of copper(I) β-diketonate in the presence of pyridine [its post-electron transfer decomposition shifting the potential of the Cu(II)/Cu(I) couple to more positive values], with the stabilization of the "free" copper(I) state by pyridine solvation (shifting the $E_{1/2}$ of the Cu(I)/Cu(0) reaction to more negative values), the combination removing the overlap between the potentials of the two couples.

The polarographic reduction of $Cu(acac)_2$ in acetonitrile solvent can proceed by either the one two-electron or the two one-electron wave pattern, depending on the supporting electrolyte employed. Independently, Hiller (2, 14) and Leddy (15) showed that the former pattern results when using Et_4NClO_4 electrolyte and the latter occurs with a $LiClO_4$ or a $LiClO_4$-Et_4NClO_4 electrolyte, and ascribed this effect to the coordination of acetylacetonate by lithium ion. To clarify the mechanistic details of this effect, the $Cu(acac)_2$ reduction has been examined further by polarographic, cyclic voltammetric, and chronopotentiometric experiments in these media.

Figure 1 shows polarograms of $Cu(acac)_2$ in acetonitrile containing Et_4NClO_4 and $LiClO_4$-Et_4NClO_4 supporting electrolytes. The single, diffusion-controlled ($i_d/h^{1/2}$ constant) wave in Et_4NClO_4 electrolyte is of two electron height ($I_d = 7.10$) and has the asymmetrical shape and $[Cu(acac)_2]$-dependent reduction potential [$E_{1/2} = -0.58$, -0.62V for 0.10, 0.50 m*M* $Cu(acac)_2$, respectively] expected for an electrode reaction involving three diffusing products [two $acac^-$ and one Cu^o (Hg)]. The polarographic wave is irreversible; an E *vs.* log $[(i_d - i)/i^3]$ plot is curved and of average slope ~130 mV. Addition of $LiClO_4$ to the Et_4NClO_4 supporting electrolyte splits this wave and causes a pronounced positive potential shift until, at >1:1 ratio of $[LiClO_4]/[Cu(acac)_2]$, two clearly defined reduction waves are evident. Both waves are diffusion-controlled and are approximately equal in height ($I_d = 3.2$, 3.5). In this medium the reduction clearly is resolved into its Cu(II)/Cu(I) and Cu(I)/Cu(0) steps. Increasing $[LiClO_4]$ shifts the $E_{1/2}$ of the first wave to continually more positive values, but the $E_{1/2}$ of the second wave is independent of lithium concentration for $[LiClO_4]/[Cu(acac)_2] > \simeq 4$. The $E_{1/2}$ of the second, nearly reversible, wave, -0.34V *vs.* SCE, is coincident with that reported for the reduction of "free" copper(I) in acetonitrile solvent (16).

These polarographic results can be interpreted in terms of the following reactions

$$Cu(acac)_2 + e^- \rightarrow Cu(acac)_2^- \quad [2]$$

$$Cu(acac)_2^- \rightleftarrows Cu^+ + 2(acac^-) \quad [3]$$

$$2(acac^-) + 4Li^+ \rightleftarrows 2Li_2(acac)^+ \quad [4]$$

$$Cu^+ + e^- \xrightarrow{-0.34} Cu^o(Hg) \quad [5]$$

Pertinent to this interpretation, which is analogous to that for Calvin and Bailes' experiment (13), is the literature observation (17) that the *mono*-acetylacetonate of copper(I) is quite unstable. The copper(I) *bis*-acetylacetonate resulting from the first charge transfer step (reaction [2]) is presumed to be also unstable and to undergo dissociation (reaction [3]) to the stable, "free" (acetonitrile-solvated) copper(I) ion.

In the Et_4NClO_4 electrolyte, the potential for the reduction reaction [2] remains, in spite of the following chemical process [3], more cathodic than that for the second charge transfer step reaction [5]. In this medium, then, the reaction sequence [2, 3, 5] occurs in a single, two-electron polarographic wave.

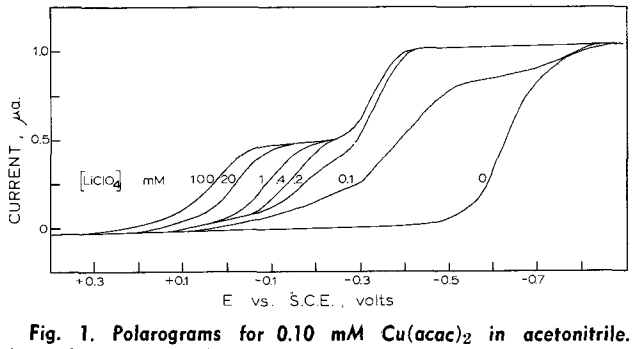

Fig. 1. Polarograms for 0.10 mM $Cu(acac)_2$ in acetonitrile. $[Et_4NClO_4] = 0.10M$, $[LiClO_4]$ indicated on figure.

In the presence of lithium ion (*i.e.*, in the $LiClO_4$-Et_4NClO_4 electrolyte), the dissociation reaction [3] is followed by lithium coordination to acetylacetonate (reaction [4]). This event can influence the potential at which the reaction sequence [2, 3] occurs only if the dissociation reaction [3], while lying far to the right, is nevertheless not chemically irreversible, or alternatively, if the lithium ion participates as a reactant in the dissociation process. Apparently one of these circumstances (it is thought to be the former) is the case, since the potential for reaction [2] is strongly dependent on the lithium ion concentration and can be shifted to a value less cathodic than that for the reduction of Cu^+ ion. Two one-electron polarographic waves result: reactions [2, 3, 4] and reaction [5].

The result of a cyclic voltammetric experiment in the $LiClO_4$-Et_4NClO_4 electrolyte is shown in Fig. 2. The two cathodic waves observed on the first potential sweep correspond to the polarographic steps observed at the same [$LiClO_4$]. The second of these, at −0.34V, exhibits an anodic partner, is nearly reversible electrochemically (ΔE_{peak} = 70 mV), and is completely reversible chemically ($i_{p(a)}/i_{p(c)}$ = 1.00), which is consistent with expectations (16) for reaction [5]. The first cathodic wave shows no reverse peak at any sweep rate examined (0.05-5.0 V/sec), which is consistent with the decidedly drawn-out polarographic shape of this wave. The reverse rate of reaction [3] and/or [4] must be quite slow. The residual $Li_2(acac)^+$ in the diffusion layer thus generates, on continuing positive potential sweeping, an anodic mercury wave with potential (E_{peak} = +0.28V) and reverse cathodic wave ($i_{p(c)}/i_{p(a)}$ = 1.0) precisely corresponding to that expected for reaction [1].

Chronopotentiometric experiments, shown in composite form in Fig. 3, produce the same pattern of waves observed by cyclic voltammetry. The chronopotentiometric constants for the two cathodic waves, $i\tau_1^{1/2}/AC^o$ = 263 ± 13 and $i\tau_2^{1/2}/AC^o$ = 650 ± 23 amp $sec^{1/2}$ cm/mole, are current-independent. Current reversal at time t_1 gives an anodic wave at the potential of reaction [1]. The experimental time ratio t_1/τ_3 = 1.33 is in accord with the theoretical prediction (18) of 1.25 for a one-electron-forward, two-electron-reverse chronopotentiometric reaction sequence. Current reversal at t_2 yields an anodic wave (τ_4) for the one-electron production of Cu^+ followed by the anodic mercury acetylacetonate wave. The theoretical $t_2/[\tau_4 + \tau_5]$ = 1.79 for a two-electron-forward, three-electron-reverse reaction sequence agrees quite well with the experimental 1.76 result.

At sweep rates >0.6 V/sec, cyclic voltammetry of $Cu(acac)_2$ in Et_4NClO_4 electrolyte yields, like the polarography, a single cathodic wave. This is followed on sweep reversal by a corresponding anodic wave (Fig. 4A). The couple is electrochemically irreversible (ΔE_{peak} = 0.21V) but, at these sweep rates, chemically reversible ($i_{p(a)}/i_{p(c)}$ = 1.0). (An analogous anodic-cathodic couple is observable at a copper amalgam electrode in a solution of $Bu_4N^+acac^-$ in the Et_4NClO_4 electrolyte.) Thus, in the absence of lithium ion, a sufficient population of the unstable $Cu(acac)_2^-$ species exists for the cathodic reaction sequence [2, 3, 5] to be quantitatively reversed.

Cyclic voltammetry of $Cu(acac)_2$ in Et_4NClO_4 at lower potential sweep rates produced an unexpected result, Fig. 4B. The anodic reversal wave at −0.52V becomes kinetically controlled; $i_{p(a)}/i_{p(c)}$ decreases with decreasing potential sweep rate. A result of the kinetic diminution of the extent of Cu^o(Hg) reoxidation at −0.52V is the appearance of a subsequent anodic wave at −0.25V. The oxidation of Cu^o(Hg) to Cu^+ (reverse of reaction [5]) and the oxidation of mercury in the presence of $acac^-$ both occur at this potential. A cathodic partner to this wave is visible (at −0.34V) only on prolonged cycling of potential (dashed curve). In the absence of a completely satisfactory explanation for the kinetic limitation of the anodic wave at −0.52V, attempt at further interpretation of the second anodic wave (−0.25V) does not seem worthwhile.

In summary, in both the anodic mercury wave of acetylacetonate and the cathodic electrochemistry of $Cu(acac)_2$, a more definitive understanding proved possible in the $LiClO_4$-containing medium. It is also clear that the mechanistic results for the reduction of $Cu(acac)_2$ in the $LiClO_4$-Et_4NClO_4 electrolyte were of utility in understanding some features of the reaction in the absence of lithium. A previous comment (2) that supporting electrolyte effects such as that of the lithium ion can allow interpretively useful perturbations can be reiterated here.

Acknowledgment

This research was supported by the UNC Materials Research Center under Contract SD-100 with the Advanced Research Projects Agency.

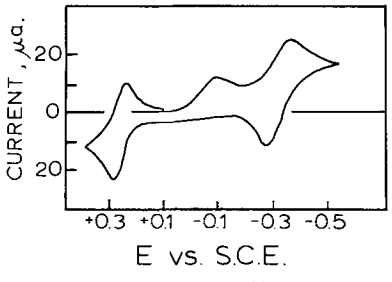

Fig. 2. Cyclic voltammogram of 2.0 mM $Cu(acac)_2$ in acetonitrile containing 0.10M Et_4NClO_4 and 0.10M $LiClO_4$; v = 0.10 V/sec.

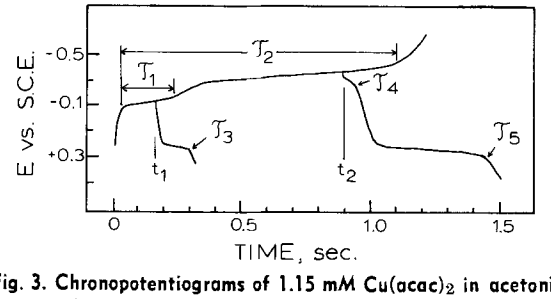

Fig. 3. Chronopotentiograms of 1.15 mM $Cu(acac)_2$ in acetonitrile containing 0.10M Et_4NClO_4 and 0.10M $LiClO_4$.

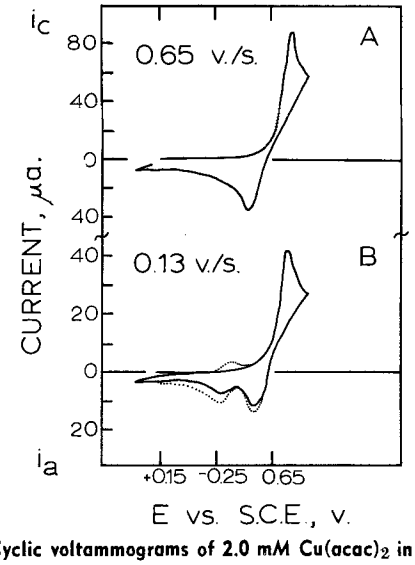

Fig. 4. Cyclic voltammograms of 2.0 mM $Cu(acac)_2$ in acetonitrile containing 0.10M Et_4NClO_4. Curves —— are first cycle, ... are after several cycles.

Manuscript submitted Feb. 26, 1970; revised manuscript received ca. April 6, 1970. This work was presented in part as Paper 153 at the New York Meeting of the Society, May 4-9, 1969.

Any discussion of this paper will appear in a Discussion Section to be published in the June 1971 JOURNAL.

REFERENCES

1. L. K. Hiller, Jr., J. R. Cockrell, and R. W. Murray, *J. Inorg. Nucl. Chem.*, **31**, 765 (1969).
2. R. W. Murray and L. K. Hiller, Jr., *Anal. Chem.*, **39**, 1221 (1967).
3. J. C. Posner, D. E. Smith, and D. F. Shriver, Northwestern University, Evanston, Ill., Private communication, 1966.
4. J. W. Ross, R. D. DeMars, and I. Shain, *Anal. Chem.*, **28**, 1768 (1956).
5. D. M. Oglesby, S. H. Omang, and C. N. Reilley, *ibid.*, **37**, 1312 (1965).
6. T. E. Neal and R. W. Murray, Electro-Organic Division, New York Meeting of the Society, May 4-9, 1969.
7. G. S. Hammond, D. C. Nonhebel, and C. S. Wu, *Inorg. Chem.*, **2**, 73 (1963).
8. D. C. Nonhebel, *J. Chem. Soc.*, **1963**, 738.
9. H. F. Holtzclaw, K. W. R. Johnson, and F. W. Hengeveld, *J. Am. Chem. Soc.*, **74**, 3776 (1952).
10. H. F. Holtzclaw, A. H. Carlson, and J. P. Collman, *ibid.*, **78**, 1838 (1956).
11. E. R. Nightingale and H. F. Holtzclaw, *ibid.*, **81**, 3523 (1959).
12. M. Petek, J. Kuta, and M. Branica, *Collect. Czech. Chem. Communs.*, **32**, 3510 (1967).
13. M. Calvin and R. H. Bailes, *J. Am. Chem. Soc.*, **68**, 949 (1946).
14. L. K. Hiller, Jr., Ph.D. Thesis, University of North Carolina, Chapel Hill, 1966.
15. D. G. Leddy, Ph.D. Thesis, University of Kansas, Lawrence, 1966.
16. I. M. Kolthoff and J. F. Coetzee, *J. Am. Chem. Soc.*, **79**, 1852 (1957).
17. R. Nast, R. Mohr, and C. Schultze, *Chem. Ber.*, **96**, 2127 (1963).
18. R. W. Murray and C. N. Reilley, *J. Electroanal. Chem.*, **3**, 182 (1962).

Hydrodynamic Potentiometry and Amperometry at Ring-Disk Electrodes

Barry Miller* and Stanley Bruckenstein*,[1]

Bell Telephone Laboratories, Incorporated, Murray Hill, New Jersey

ABSTRACT

An electronically regulated speed control unit has been programmed to produce an $\omega^{1/2} = kt$ relation for disk and ring-disk electrodes. Besides automatic hydrodynamic amperometry (Levich plots), one can perform two new techniques of hydrodynamic potentiometry: (*a*) recording of disk potential (E_D) *vs.* $\omega^{1/2}$ at constant disk current (i_D); and (*b*) recording of E_D *vs.* i_D at constant surface concentrations of all species, obtained by holding $i_D/\omega^{1/2}$ constant while scanning i_D. The equations governing (*a*) are derived and the implications of (*b*) for measuring rate constants and/or uncompensated solution resistance are discussed.

The rotating ring-disk electrode geometry is particularly favorable for electrochemical studies in that it is possible to control the rate of mass transfer in addition to either potential or current. Advantages inherent in programmed control of the electrode rotation speed (ω) have not been exploited in the past. Ordinarily, (ring-) disk electrode experiments are carried out at constant ω, controlling either potential or current. Additional information contained in the ω-dependence can be obtained only by repeating the particular experiment at a series of different, constant ω's.

The purpose of this work is to develop the theory required to interpret data obtained when $\omega^{1/2}$ is varied continuously and to describe a method for programming ω while effectively retaining a hydrodynamic steady state (Levich equation conditions).

The functional form of the Levich equation

$$i = 0.62\, n\, A\, D_i^{2/3}\, \omega^{1/2}\, \nu^{-1/6}\, (C_i - C_i^s)$$
$$= nK_i\, \omega^{1/2}\, (C_i - C_i^s) \qquad [1]$$

indicates that it is of particular value to obtain a recordable voltage which is proportional to $\omega^{1/2}$. In Eq. [1], C_i and C_i^s are the bulk and surface concentrations of the i^{th} species and the other symbols have their conventional significance.

Creason and Nelson (1) have recently reported briefly on a method in which the square root of a voltage produced by a tachometer generator (geared to the rotator drive motor) is recorded *vs.* current. We have used an operational amplifier circuit containing a squaring module to program an exisitng electronically regulated motor speed controller (2) to produce, rather than compute, the desired $\omega^{1/2}$ dependence. This apparatus has been used to perform automatically

1. Hydrodynamic amperometry—plots of i *vs.* $\omega^{1/2}$ at constant E_D (disk potential) and constant bulk concentration C_i—Eq. [1].
2. Hydrodynamic potentiometry
   (*a*) plots of E_D *vs.* $\omega^{1/2}$ at constant i and C_i (Method HP1).
   (*b*) plots of E_D *vs.* i at constant C_i where the ratio $i/\omega^{1/2}$ is held constant (Method HP2).

The latter two techniques are new, to the knowledge of the authors. Method HP1 may be thought of as a translation of the chronopotentiometric experiment at stationary electrodes to the steady-state convective diffusion control regime where rotation speed replaces time as the third variable. Method HP2 has application to the measurement of exchange currents and the direct determination of solution resistance between reference capillary tip and disk.

Theoretical

Hydrodynamic Amperometry

The theoretical aspects of (ring-) disk experiments of this type are well developed and require no elaboration here [for a complete bibliography, see Ref. (3)].

* Electrochemical Society Active Member.
[1] Present address: Department of Chemistry, State University of New York at Buffalo, Buffalo, New York.

However, it is worth pointing out that the direct recording of i *vs.* $\omega^{1/2}$ at constant E_D, (*a*) generally produces greater reproducibility, (*b*) shortens the time of an experiment to a few minutes, and (c) makes obvious any deviations from the expected $\omega^{1/2}$ behavior such as those arising from kinetic or film-forming complications.

Hydrodynamic Potentiometry

E_D vs. $\omega^{1/2}$ at constant i and C_i, Method HP1.—The general shape of an E_D *vs.* $\omega^{1/2}$ curve can be deduced graphically from the conventional current-potential curve of a particular system. Consider a solution containing two species, A and C, which are reduced according to

$$A + n_1e \rightarrow B \qquad [2]$$

$$C + n_2e \rightarrow D \qquad [3]$$

with half-wave potentials of $E_1^{1/2}$ and $E_2^{1/2}$, respectively, where $E_2^{1/2} < E_1^{1/2}$.

Suppose that Eq. [2] and [3] represent reversible systems involving soluble species. Then a plot of $i/\omega^{1/2}$ *vs.* E_D, as shown in Fig. 1*A*, is constant for given C_A and C_C when uncompensated ohmic potential drops are ignored. The sigmoid curve in Fig. 1*A* is independent of the manner in which the ratio $i/\omega^{1/2}$ is established. In conventional practice, a series of $i - E_D$ curves would be obtained at different constant $\omega^{1/2}$ values. In hydrodynamic potentiometry, Method 1, i is held constant at a value I, ω is varied, and E_D is recorded *vs.* $\omega^{1/2}$. In Fig. 1*B* we have plotted $\omega^{1/2}/i$ *vs.* E_D simply by taking the reciprocal of the ordinate of Fig. 1*A* at all values of E_D.

Since it is not possible to have $\omega^{1/2}$ approach zero and maintain rotating disk transport assumptions, only part of the $\omega^{1/2}/i$ *vs.* E_D curve can be observed experimentally.

Sharp potential changes in the $E_D - \omega^{1/2}$ plot occur at potentials in the vicinity of the limiting current regions (4). If ω_1 represents the angular velocity when I corresponds to the limiting current for reaction [2] and ω_2 the angular velocity when I corresponds to the sum of the limiting currents for reactions [2] and [3], one can relate $\Delta\omega^{1/2}$ $(= \omega_1^{1/2} - \omega_2^{1/2})$ to the concentration of A and C in solution. The curves for these two angular velocities and an intermediate one are shown in Fig. 2.

We shall refer to ω_1 and ω_2 as transition velocities. In practice, transition velocities at a disk electrode are determined graphically from $E_D - \omega^{1/2}$ plots in a manner analogous to that used for transition times in chronopotentiometry. Alternatively, plots of ring currents *vs.* $\omega^{1/2}$ obtained at ring-disk electrodes may be more precise in defining the transition velocity for the $E_D - \omega^{1/2}$ data, particularly for irreversible systems, wherever such ring reactions are feasible.

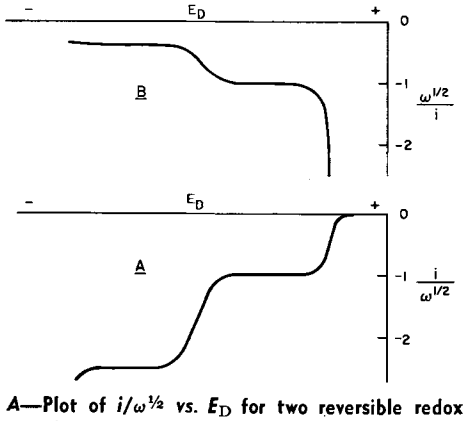

Fig. 1. *A*—Plot of $i/\omega^{1/2}$ *vs.* E_D for two reversible redox systems at a rotating disk electrode. Anodic currents are treated as positive and positive potentials increase from left to right. *B*—Plot of the reciprocal of the ordinate of *A* *vs.* E_D.

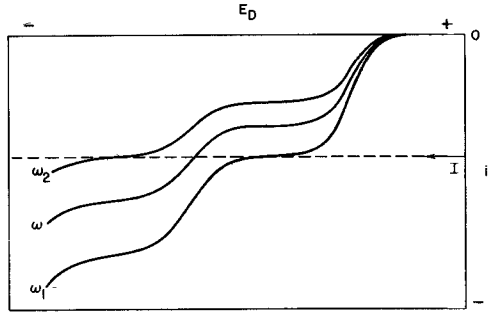

Fig. 2. Plot of the i-E_D curves for two reversible redox systems at three rotation speeds, $\omega_1 > \omega > \omega_2$; reaction [2] yields the first wave, the sum of reactions [2] and [3] contributes toward the second wave. At ω_1, I equals the limiting current of the first wave and, at ω_2, I equals the sum of the limiting currents of the first and second waves.

$\omega^{1/2}$-Concentration relations.—If a constant cathodic current, I, of appropriate magnitude is passed through a cell containing A and C which have the i-E curves in Fig. 2, the following limiting current relations may be written for ω_1 and ω_2, respectively (giving cathodic current a negative sign).

$$-I\omega_1^{-1/2} = K_An_1C_A \qquad (C_A^s = 0) \qquad [4]$$

$$-I\omega_2^{-1/2} = K_An_1C_A + K_Cn_2C_C \qquad (C_A^s = C_C^s = 0) \qquad [5]$$

At rotation speeds $\omega \geqq \omega_1$ the current efficiency for reaction [2] is essentially 100%, whereas at $\omega_2 < \omega < \omega_1$ both reactions [2] and [3] proceed. In the general case, at ω_2 both B and D are produced at limiting currents. For the special case of consecutive oxidation or reduction reactions of a single substance, $C_A = C_C$, $B \equiv C$, and the electrode reaction at ω_2 produces D exclusively (the $n_1 + n_2$ electron product of the starting substance, A).

From Eq. [4] and [5]

$$-I(\omega_2^{-1/2} - \omega_1^{-1/2}) = K_Cn_2C_C \qquad [6]$$

or

$$\frac{\omega_2^{1/2}\,\omega_1^{1/2}}{\Delta(\omega^{1/2})} = \frac{-I}{K_Cn_2C_C} \qquad [7]$$

If C_C is held fixed, and ω_1 and ω_2 determined from the $E_D - \omega^{1/2}$ plot for a series of constant currents, Eq. [7] predicts that the function $\omega_1^{1/2}\,\omega_2^{1/2}/\Delta(\omega^{1/2})$ is proportional to I with a slope from which the diffusion coefficient of C can be obtained.

On dividing Eq. [5] by Eq. [4], we have

$$\frac{\omega_1^{1/2}}{\omega_2^{1/2}} = \frac{K_Cn_2C_C + K_An_1C_A}{K_An_1C_A} \qquad [8]$$

which may be rewritten as

$$\omega_1^{1/2} - \omega_2^{1/2} = \Delta(\omega^{1/2}) = \omega_1^{1/2}\left(\frac{K_Cn_2C_C}{K_An_1C_A + K_Cn_2C_C}\right) \qquad [9]$$

or, on substitution of Eq. [4]

$$\Delta(\omega^{1/2}) = -I\left(\frac{K_Cn_2C_C}{K_An_1C_A}\right)\left(\frac{1}{K_An_1C_A + K_Cn_2C_C}\right) \qquad [10]$$

In the general case, both C_A and C_C are obtained from two equations, [4] and [5] or [7] and [10], in the manner of transition time-concentration relations in chronopotentiometry where τ_2 is dependent on τ_1 as $\omega_2^{1/2}$ is on $\omega_1^{1/2}$. If $C \equiv B$, as is the case in the step-wise reduction of A to D, we may set $C_A \equiv C_C$ and $K_A \equiv K_C$, yielding

$$\frac{\omega_1^{1/2}}{\omega_2^{1/2}} = \frac{n_1 + n_2}{n_1} \text{ and}$$

$$\Delta(\omega^{1/2}) = \left(\frac{-I}{K_AC_A}\right)\left(\frac{n_2}{n_1}\right)\left(\frac{1}{n_1 + n_2}\right) \qquad [11]$$

In the special case that $n_1 = n_2 = 1$ (Cu(II) → Cu(I) → Cu in 0.5M KCl), $\omega_1^{1/2}/\omega_2^{1/2} = 2$ and $\Delta(\omega^{1/2}) = -I/2\,K_A C_A$.

Potential-$\omega^{1/2}$ Curves

Two consecutive electrochemical reactions involving different substances.—If reactions [2] and [3] are assumed to occur at sufficiently separated potentials, they will yield a distinct $E_D - \omega^{1/2}$ step for [3].

$\omega > \omega_1$.—The $E_D - \omega^{1/2}$ curve for $\omega > \omega_1$ corresponds to the situation in which only B is produced at the electrode surface and, assuming Nernstian behavior, is obtained by substitution into

$$E_{A-B} = E^f_{A-B} + \frac{0.059}{n_1} \log \frac{C_A^s}{C_B^s} \quad [12]$$

from the appropriate expressions. E^f_{A-B} is the formal potential for the A-B couple in the medium being studied. Eliminating C_A from Eq. [1] when $i = -I$, using Eq. [4] yields

$$C_A^s = \frac{I}{n_1 K_A} (\omega_1^{-1/2} - \omega^{-1/2}) \quad [13]$$

The flux of A and that of B are of equal absolute magnitude, hence

$$I\omega^{-1/2} = n_1 K_B C_B^s \quad [14]$$

Eliminating C_A^s and C_B^s from [12] using [13] and [14] gives

$$E_{A-B} = E^f_{A-B} + \frac{0.059}{n_1} \log \left(\frac{D_B}{D_A}\right)^{2/3} + \frac{0.059}{n_1} \log \frac{(\omega_1^{-1/2} - \omega^{-1/2})}{\omega^{-1/2}} \quad [15]$$

since $K_B/K_A = (D_B/D_A)^{2/3}$. The half-wave potential, $E_{A-B}^{1/2}$, occurs at $\omega = 4\omega_1$ (unity value of the log argument) and would be observable only if starting the scan at $\omega \geq 4\omega_1$ were feasible for a given current level, I. The dimensions of $\omega^{-1/2}$ are time$^{1/2}$; the close parallel of both Eq. [15] and the $4\omega_1$ condition to the corresponding equation of chronopotentiometry and the $\tau_1/4$ point are obvious.

$\omega_1 > \omega > \omega_2$.—In this range of speed, both reactions [2] and [3] proceed. The current, I, may be written in terms of the fluxes of A and C and the Levich equation as

$$-I\omega^{-1/2} = n_1 K_A C_A + n_2 K_C [C_C - C_C^s] \quad [16]$$

The second term on the right-hand side of [16] may be expressed in terms of the flux of D, namely

$$-I\omega^{-1/2} = n_1 K_A C_A + n_2 K_D C_D^s \quad [17]$$

Since $C_C^s = 0$ at $\omega = \omega_2$ and $n_1 K_A C_A$ is given by Eq. [4], Eq. [16] may be written as

$$-I\omega_2^{-1/2} = -I\omega_1^{-1/2} + n_2 K_C C_C \quad [18]$$

and Eq. [17] as

$$-I\omega^{-1/2} = -I\omega_1^{-1/2} + n_2 K_D C_D^s \quad [19]$$

On substituting Eq. [18] and [4] into Eq. [16] to obtain C_C^s and solving Eq. [19] for C_D^s, one obtains

$$C_C^s = \frac{-I}{n_2 K_C} (\omega_2^{-1/2} - \omega^{-1/2}) \quad [20]$$

and

$$C_D^s = \frac{-I}{n_2 K_D} (\omega^{-1/2} - \omega_1^{-1/2}). \quad [21]$$

$$E_{C-D} = E^f_{C-D} + \frac{0.059}{n_2} \log \frac{C_C^s}{C_D^s} \quad [22]$$

whereupon substitution of Eq. [20] and [21] gives

$$E_{C-D} = E^f_{C-D} + \frac{0.059}{n_2} \log \left(\frac{D_D}{D_C}\right)^{2/3} + \frac{0.059}{n_2} \log \frac{(\omega_2^{-1/2} - \omega^{-1/2})}{(\omega^{-1/2} - \omega_1^{-1/2})} \quad [23]$$

The half-wave potential, $E_{C-D}^{1/2}$, occurs at $\omega^{-1/2} = \frac{\omega_2^{-1/2} + \omega_1^{-1/2}}{2}$.

In the case of a step-wise reduction where the second reaction is

$$B + n_2 e \rightarrow D \quad [24]$$

rather than [3], Eq. [17] remains valid. However, Eq. [16] must be replaced. We equate the flux of A to the sum of the fluxes of B and D, namely

$$n_1 K_A C_A = n_1 K_B C_B^s + n_2 K_D C_D^s \quad [25]$$

On substitution of Eq. [4] and [19] and rearrangement

$$n_1 K_B C_B^s = -I(2\omega_1^{-1/2} - \omega^{-1/2}) \quad [26]$$

The limiting current at ω_2 corresponds to that of the reaction $A + (n_1 + n_2)e \rightarrow D$ which is given by

$$-I\omega_2^{-1/2} = (n_1 + n_2) K_A C_A \quad [27]$$

Combining Eq. [27] and [4] yields

$$\omega_1^{-1/2} = \left(\frac{n_1}{n_1 + n_2}\right) \omega_2^{-1/2} \quad [28]$$

permitting the introduction of $\omega_2^{-1/2}$ into Eq. [26],

$$n_1 K_B C_B^s = -I \left(\frac{2n_1}{n_1 + n_2} \omega_2^{-1/2} - \omega^{-1/2}\right) \quad [29]$$

The $E_D - \omega^{1/2}$ curve for reaction [24], on combining Eq. [21] and [29] and assuming Nernstian behavior, is

$$E_{B-D} = E^f_{B-D} + \frac{0.059}{n_2} \log \left(\frac{D_D}{D_B}\right)^{2/3} \left(\frac{n_2}{n_1}\right) + \frac{0.059}{n_2} \log \left[\frac{\left(\frac{2n_1}{n_1 + n_2}\right) \omega_2^{-1/2} - \omega^{-1/2}}{\omega^{-1/2} - \omega_1^{-1/2}}\right] \quad [30]$$

$E_{B-D}^{1/2}$ is obtained for

$$\omega^{-1/2} = \frac{1}{2} \left[\left(\frac{2n_1}{n_1 + n_2}\right) \omega_2^{-1/2} + \omega_1^{-1/2}\right]$$

In the special case $n_1 = n_2$, the right-hand log terms of Eq. [23] and [30] are identical. When the n_2 electron transfer step produces a constant activity state (*e.g.*, metal deposition as in $CuCl_2$ reduction in 0.5M KCl), C_D^s is taken as 1 and Eq. [30] becomes

$$E_{B-D} = E^f_{B-D} + \frac{0.059}{n_2} \log (D_B)^{-2/3} + \frac{0.059}{n_2} \log \left[\frac{-I}{n_1 K_B} \left(\frac{2n_1}{n_1 + n_2} \omega_2^{-1/2} - \omega^{-1/2}\right)\right] \quad [31]$$

For the $CuCl_2$ case, $n_1 = n_2 = 1$, and Eq. [31] reduces to

$$E_{B-D} = E^f_{B-D} + 0.059 \log (D_B)^{-2/3} + 0.059 \log \left[\frac{-I}{K_B} (\omega_2^{-1/2} - \omega^{-1/2})\right] \quad [32]$$

As in the conventional i-E representation, the half-wave potential at $\omega^{1/2} = 4/3\ \omega_2^{1/2} = 2/3\ \omega_1^{1/2}$ for such a system depends on the current level, I.

Ring Current-$\omega^{1/2}$ Relation

The transition velocities may be determined by using a ring electrode for amperometric detection of one or more of the species A, B, C, or D in the general case, or of A, B, or D in the step-wise reduction. To illustrate calculating the ring current, i_r, in any specific case, consider detecting B in the step-wise re-

duction $A \rightarrow B \rightarrow D$ in the region $\omega_1 > \omega > \omega_2$ where both B and D are being formed. The surface concentration of B at the disk is given by Eq. [26] or [29]. The disk current, i_d, that may be assumed to be producing B with 100% current efficiency is related to C_B^s by $i_d = -n_1 K_B \omega^{1/2} C_B^s$, hence

$$i_d = I(2\omega_1^{-1/2} - \omega^{-1/2})\omega^{1/2}$$

$$= I\left[\left(\frac{2n_1}{n_1 + n_2}\right)\omega_2^{-1/2} - \omega^{-1/2}\right]\omega^{1/2} \quad [33]$$

The ring current is

$$i_r = \pm N \frac{n_r}{n_d} i_d \quad [34]$$

where $n_d = n_1$, the number of electrons in the B-producing disk reaction, n_r is the number of electrons in the ring reaction detecting B, N is the geometric collection efficiency, and $\pm$ refers to the sign appropriate to the direction of the ring reaction. Then ($\omega_1 < \omega < \omega_2$)

$$i_r = \pm N\left(\frac{n_r}{n_d}\right) I\left(\frac{2\omega^{1/2}}{\omega_1^{1/2}} - 1\right)$$

$$= N\left(\frac{n_r}{n_d}\right) I\left[\frac{2n_1\omega^{1/2}}{(n_1 + n_2)\omega_2^{1/2}} - 1\right] \quad [35]$$

At $\omega > \omega_1$, the ring current is constant at (n_r/n_d) N I since the entire cathodic current, I, is going to form B. At $\omega < \omega_2$, the ring current is zero as the reaction proceeds entirely to D. In the region $\omega_1 > \omega > \omega_2$, the ring current varies linearly with $\omega^{1/2}$.

Collecting the quantities in Eq. [35] that are constant in a particular experiment, and assuming $n_d = n_1 = n_2 = 1$ [$CuCl_2$ in 0.5M KCl, Cu(I) → Cu(II), oxidation at the ring requiring a minus sign] yields

$$i_r = \left(\frac{-N I}{\omega_2^{1/2}}\right)(\omega^{1/2} - \omega_2^{1/2}) \text{ for } \omega_1 \geqq \omega \geqq \omega_2 \quad [36]$$

E_D vs. i at constant C for $i/\omega^{1/2}$ ratio held constant. Method HP2.—If the ratio $i/\omega^{1/2}$ is held constant by suitable instrumentation while i is scanned at a rotating disk electrode, the surface concentration, C^s, corresponding to the ratio, $i/\omega^{1/2}$, remains constant under the conditions of Eq. [1]. Thus, for the anodization of a metal, the surface concentration of the dissolving species is fixed. For a soluble redox couple, the ratio of the surface concentrations of Ox and Red will be held constant. During the experiment, E_D is determined while i is scanned. If the solution resistance is negligible, the derivative $(\partial E_D/\partial i)_{Cs}$ can be obtained over a range of C^s and i values. The extrapolation of this partial derivative to zero current yields the polarization resistance and, thus, the exchange current at that particular surface concentration. Since the polarization resistance may be determined as a function of surface concentration, the method is of general application to electrode kinetic problems. A detailed discussion of this procedure for determining the d-c polarization resistance kinetic parameters will be forthcoming. The present paper is devoted to the experimental basis of this method, and only one particular theoretical aspect is developed here. The measurement of the solution resistance between rotating disk and reference electrode capillary, neglected in the above discussion, is considered below.

All determinations of the derivative $(\partial E_D/\partial i)_{Cs}$ contain the uncompensated part of the series resistance that always exists between the disk electrode and the Luggin capillary tip. For fast reactions and/or sufficient surface concentration of electroactive species, kinetic contributions to the polarization may become negligibly small compared to the IR drop, reversing the situation previously considered. This condition of negligible reaction polarization may be tested experimentally by determining $(\partial E_D/\partial i)_{Cs}$ at $i \rightarrow 0$ for several values of C^s, and observing whether or not a constant value of $(\partial E_D/\partial i)_{Cs}$ is found. In kinetic studies, the derivative will normally not be constant and the IR term must be corrected for, possibly using the approach to be outlined.

For any given value of $i/\omega^{1/2}$, the extrapolated value of E_D at $i = 0$ is the Nernst potential of the system for the particular fixed value of C^s, independent of kinetic parameters and IR drop. Any deviation of the actual value of $i/\omega^{1/2}$ from the programmed ratio will distort the i-E_D curve and introduce an error in the extrapolated Nernst potential. Such experimental problems are not serious. In the case of a reaction with a very high exchange current, for which $(\partial E_D/\partial C)_{Cs}$ at $i \rightarrow 0$ equals R, even a 5% variation in $i/\omega^{1/2}$ is equivalent to only a $0.6/n$ mV shift in the (reversible) disk potential, where n electrons are transferred in the potential determining reaction. In practice, the ratio of $i/\omega^{1/2}$ can be controlled to better than 1%, and this introduces no significant experimental errors.

Experimental

Figure 3 shows the $\omega^{1/2}$-scanning scheme. An operational amplifier integrator fed with a constant current produces a linear voltage ramp, $E_S = at$. Squaring this output produces a voltage, $E_o = a^2b^2t^2$, where b^2 is a constant introduced in the squaring operation. (A second integration instead of direct squaring would produce an equivalent result.) A tachometer generator attached directly to the disk electrode produces a d-c voltage, E_T, that is proportional to rotational speed, $E_T = \omega/c^2$. A fraction, R_s/R_g, of E_T is compared to the output of the squaring module and made equal to it by a control amplifier supplying the armature of the driving motor (2), causing the motor speed to vary according to $\omega = (a^2b^2c^2\ R_g/R_s)\ t^2$. The constants b and c are not adjustable and are characteristic of the squaring module and tachometer generator, respectively. Hence, it is necessary to divide the tachometer output with the divider network R_s/R_g (Fig. 3) to produce the desired relation between $\omega^{1/2}$ and E_S.

$$E_S = \left(\frac{R_s}{R_g}\right)^{1/2} \frac{\omega^{1/2}}{bc} \text{ and } \omega^{1/2} = abc\left(\frac{R_g}{R_s}\right)^{1/2} t$$

Driving the X axis of an X-Y recorder with E_S yields a calibrated, linear $\omega^{1/2}$ scale. In practice, a set of R_s values has been used to provide $\omega^{1/2}$ scans from 0-1000, 2500, 5000, and 10,000 rpm. In the apparatus used in this study, the manual speed adjustment within the original speed controller is still operative, so that the $\omega^{1/2}$ scans may be started at any arbitrary initial value of $\omega^{1/2}$ as well as zero.

Since the motor speed is actually being controlled to give $\omega^{1/2} = kt$, rather than being linearly scanned

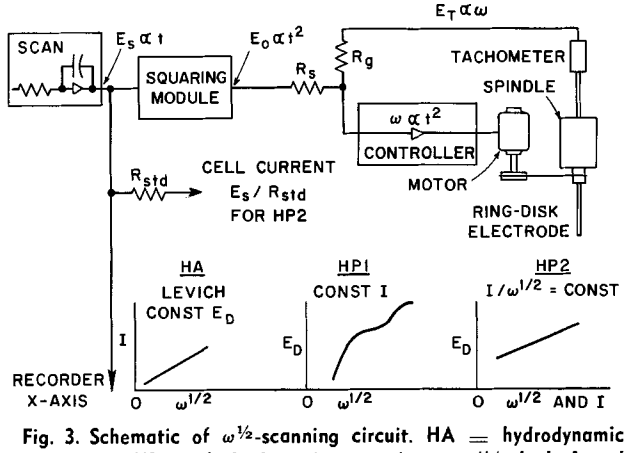

Fig. 3. Schematic of $\omega^{1/2}$-scanning circuit. HA = hydrodynamic amperometry, HP = hydrodynamic potentiometry (Methods 1 and 2). See text.

vs. time and the tachometer generator output voltage square rooted (1), the time derivative, $d\omega^{1/2}/dt$, is being held constant rather than $d\omega/dt$ (1). This allows one to scan wide ω ranges with increasing angular acceleration at the higher speeds, where it can be more readily tolerated. The transit time from disk to ring, for example, is inversely related to ω (5), as is the time required to reach a specified fraction of the steady-state limiting current at the disk in a potential jump experiment (6).

For the experiments in which $I/\omega^{1/2}$ is held constant, the output E_S is also used to provide, with the aid of an intermediary buffer amplifier equipped with a 0.5A booster, a cell current equal to E_S/R_{std}. R_{std} is a precision six-decade, 10-megohm resistance box (General Resistance Model DS166B). The X axis of the recorder is thus simultaneously calibrated in both $\omega^{1/2}$ and I units. The ratio, $I/\omega^{1/2}$, is fixed and given by $(R_s/R_g)^{1/2}$ $(1/R_{std}bc)$.

The linearity and calibration of the $\omega^{1/2}$-E_S relations depend on the squaring module accuracy (Burr Brown 9874/19, 0.1% full scale), the linearity of the tachometer-reference system in the controller, the R_g/R_s ratio for tachometer output division, and the amplifier bias at the summing point (the R_s-R_g junction in Fig. 3). With proper adjustment of the latter two factors, the $\omega^{1/2}$ scale was found to be linear with E_S (X axis) from 10-100 rpm$^{1/2}$ (high range, ω_{max} = 10,000 rpm) to within ±1%. The accuracy increases with speed where the bias adjustment is less critical. Calibration can be achieved by setting E_S = 1V, adjusting the amplifier bias until $\omega^{1/2}$ = 10 rpm$^{1/2}$ and then, at E_S = 10V, trimming the tachometer divider until $\omega^{1/2}$ = 100 rpm$^{1/2}$. This cycle is repeated until the accuracy is within the desired limit.

Rotation speeds were measured with a General Radio 1536A photoelectric pickoff and a Hewlett-Packard 5216A counter. All curves were recorded on a Honeywell 580 X Y Y' plotter.

The cell, electrode construction, and electronics have been previously described (7). A gold split ring-disk operated with shorted half-rings was employed for reduction experiments in 2 mM $CuCl_2$-0.5M KCl; the disk of the same electrode was used for experiments in 1M H_2SO_4 containing millinormal level Fe(III) and MnO_4^-. The Fe(III)-MnO_4^- solution was not analyzed, since the same solution was used to obtain both hydrodynamic potentiograms and conventional i-E curves. The comparison of these does not require knowledge of $C_{MnO_4^-}$ or $C_{Fe(III)}$. Solutions were prepared with triply distilled water. The geometrically calculated collection efficiency for the gold electrode was 0.349. The disk of a silver disk-graphite split ring electrode was used for anodic experiments in 1N $HClO_4$. The disk areas of both electrodes were 0.178 cm^2.

Mating of the motor scan electronics to the cell operational amplifier circuitry (7) requires further comment since Fig. 3 suggests that the motor controller employs a ground-referenced, operationally programmable power supply. The motor controller (2) actually used required a floating reference source in a bridge circuit, and therefore both controller and scan circuitry had to be isolated from ground by suitable transformers. Capacitive grounding of the low point in the controller circuit reduced the a-c level of the common return in the $\omega^{1/2}$-scan circuitry, with respect to power line ground, to about 2V. A unity gain difference amplifier referenced to power line ground was then used to convert E_S, measured between the integrator output and the isolated common, to a single-ended signal compatible with the existing ground referenced cell control electronics and recorder. Careful measurements with a 0.1% digital voltmeter (Hewlett-Packard Model 3430A) proved that no detectable errors were introduced into E_S by these manipulations. The constant speed regulation of this configuration, better than 1 ppt at 2000 rpm, is actually superior to that originally claimed (2) (0.5%).

Results and Discussion

Hydrodynamic Amperometry—Disk and Ring

The current-voltage curve for the gold disk electrode in a solution of 2 mM $CuCl_2$ in 0.5M KCl is shown in Fig. 4*A*. The ring current-voltage curve for a constant current producing Cu(I) at the disk is shown in Fig. 4*B*. The $\omega^{1/2}$-scanning device was tested by controlling the disk potential to give the limiting current of the Cu(II) → Cu(I) wave while controlling the ring potential to give the limiting current value for the oxidation of Cu(I) → Cu(II). The $\omega^{1/2}$-scan was made from zero to >8100 rpm. Because of inertia and the motor low speed limit of 15-20 rpm, the electrode does not begin to rotate until the X-axis deflection corresponds to ~30-40 rpm (the spindle gear ratio was 2:1). Once the motor begins to rotate, it rapidly reaches the *nominal* speed required by E_S. The rotation speed of the electrode is within 1% of the indicated X-axis value at 100 rpm when $d\omega^{1/2}/dt$ = 0.33 rpm$^{1/2}$-sec^{-1}. The entire Levich plot, obtained automatically under these conditions, along with the simultaneously recorded ring current, is shown in Fig. 5. It is satisfactorily linear (±1%) for ω > 300 rpm. If $d\omega^{1/2}/dt$ > 0.33 rpm$^{1/2}$-sec^{-1}, the speed at which i_d or i_r linearity with $\omega^{1/2}$ is reached becomes greater. The ring current plot is within ±2% of the best straight line in the region 300-8000 rpm and yields a collection efficiency (the negative of the ratio of the i_r- and i_d-

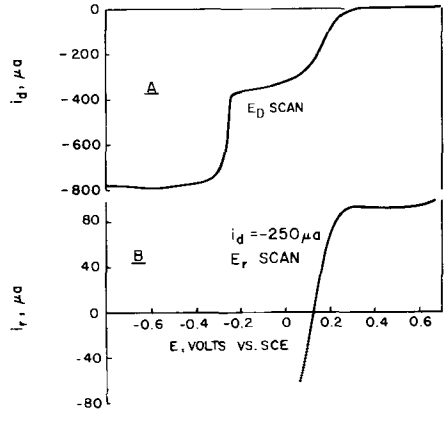

Fig. 4. *A*—Current-potential curve for the reduction of 2 mM $CuCl_2$ in 0.5M KCl at a gold disk; rotation speed 5000 rpm, potential scan 20 mV/sec. *B*—Ring current-potential curve for 0 < E_r < 0.7V for the above system when a cathodic disk current of 250 μA is applied.

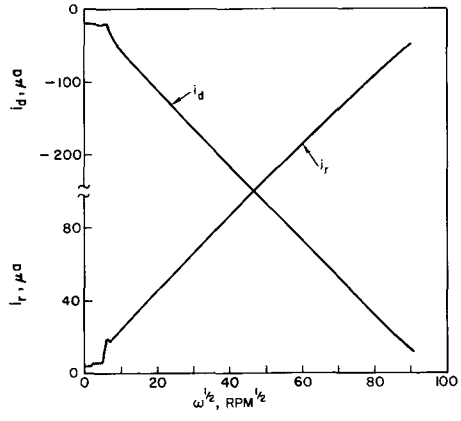

Fig. 5. Automatically recorded disk current and ring current as a function of $\omega^{1/2}$ for the 2 mM $CuCl_2$-0.5M KCl solution and the conditions E_D = −0.170V, E_r = +0.650V, and $\omega^{1/2}$ scan rate of 0.33 rpm$^{1/2}$ sec^{-1}. Scan started from ω = 0.

$\omega^{1/2}$ slopes) of 0.375. This experimental value of N is 7% larger than the calculated value of 0.349 for the gold ring-disk electrode, presumably because of Cu(I) produced during many previous $\omega^{1/2}$-scans in the same solution. The i-E curve of Fig. 4A also indicates a small second-wave enhancement of the same origin.

The ring current reaches a linear slope as rapidly as does the disk current when $d\omega^{1/2}/dt = 0.33$ rpm$^{1/2}$ sec^{-1}, indicating that no additional problems are introduced in collection studies with ordinary electrode geometries by $\omega^{1/2}$ scanning. For $d\omega^{1/2}/dt = 0.33$ rpm$^{1/2}$-sec^{-1}, a scan from 0-10,000 rpm takes 5 min. Starting at 1000 rpm, no deviation from linearity was observed when the speed was scanned to 8000 rpm in less than 90 sec. The value of D for Cu(II) calculated from the slope of the disk trace in Fig. 5 is 6.3 x 10^{-6} cm^2/sec.

Hydrodynamic potentiometry—Method HP1.—Cu(II)-Cu(I)-Cu system.—The hydrodynamic potentiogram for the $CuCl_2$-0.5M KCl system is shown in Fig. 6, along with the limiting Cu(I) → Cu(II) ring current. The E_D-$\omega^{1/2}$ curve can be related to Fig. 4A, the conventional i-E curve, by the transformation indicated in Fig. 1. However, it is to be noted that a nucleation overpotential peak for Cu deposition is visible in the E_D-$\omega^{1/2}$ curve. Such a peak cannot occur during a conventional controlled potential scan. The experiments were performed by adjusting $\omega^{1/2}$ to about 90 rpm$^{1/2}$, applying the desired constant current, and then scanning toward lower rotation speeds. Experiments were ended when the disk electrode potential reached the hydrogen evolution region, *i.e.* when the impressed current became greater than the limiting current for the complete reduction of Cu(II).

Fifteen runs similar to those shown in Fig. 6 were made using applied currents from 230 to 470 μA. Below 230 μA, the ω_2 transition [Cu(II) → Cu(0)] occurs at motor speeds too low for Levich conditions to apply and, above 470 μA, the limiting current of the Cu(II) → Cu(I) step is exceeded at the starting (high) motor speed. For the $\omega^{1/2}$ scans with currents between 230 and 470 μA, the $\omega_1^{1/2}$ and $\omega_2^{1/2}$ transitions were clearly defined. In order to determine these transition velocities, an arbitrary graphical procedure was adopted in which the linear regions on either side of ω_1 and ω_2 were extrapolated and the intersections used to define the value of $\omega_1^{1/2}$ and $\omega_2^{1/2}$.

The theoretical prediction of Eq. [7] is tested in Fig. 7, where the function $\omega_2^{1/2}\,\omega_1^{1/2}/\Delta(\omega^{1/2})$ is plotted *vs.* the impressed current. The plot is linear over the accessible current range and, within the experimental error, extrapolates to zero. A value for the diffusion coefficient of Cu(II) of 6.8 x 10^{-6} cm^2-sec^{-1} was obtained from the slope, compared to the 6.3 x 10^{-6} cm^2-sec^{-1} from the one electron Levich plot in Fig. 5, and 6.8 x 10^{-6} cm^2-sec^{-1} from a previous rotating disk determination (8) on the same system.

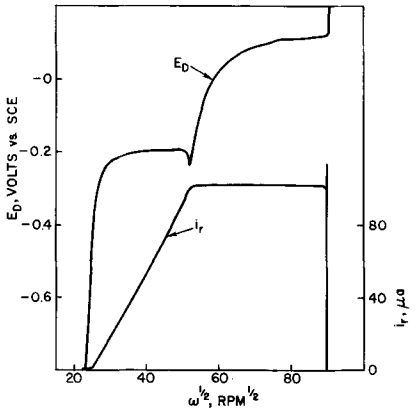

Fig. 6. (Upper trace) E_D as a function of $\omega^{1/2}$ for 2 mM $CuCl_2$-0.5M KCl at a constant cathodic current of 273 μA which was turned on at the upper right point. $\omega^{1/2}$ scan rate 0.33 rpm$^{1/2}$ sec^{-1}. (Lower trace) Ring current at +0.65V measured concurrently.

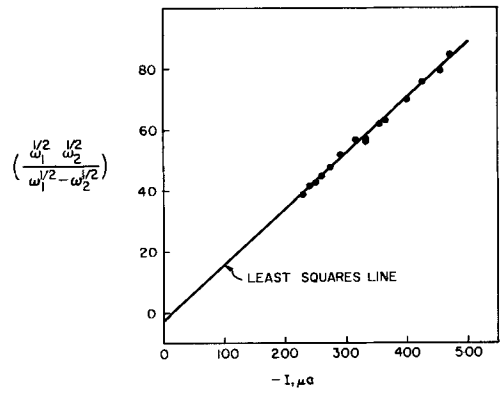

Fig. 7. Plot of the function $\frac{\omega_1^{1/2}\,\omega_2^{1/2}}{\Delta(\omega^{1/2})}$ *vs.* I from data of 15 hydrodynamic potentiograms as in Fig. 6 for the $CuCl_2$-KCl system.

According to Eq. [11], the theoretical value of $\omega_1^{1/2}/\omega_2^{1/2}$ is 2. The 15 curves from which Fig. 7 was constructed yielded an average value of 2.09 with a standard deviation of 0.04. The very slight positive bias is in the direction predicted if, as previously discussed, a small fraction of Cu(II) is assumed to have been converted to Cu(I) in the course of the experiment. Considering this factor, the experimental $\omega_1^{1/2}/\omega_2^{1/2}$ is in agreement with the predicted value.

In Fig. 6, the ring current $-\omega^{1/2}$ traces for the oxidation of Cu(I) to Cu(II) show constant collection efficiency until the rotation speed drops below ω_1, whereupon the disk current efficiency for Cu(II) → Cu(I) reduction becomes less than 100%. After copper metal nucleation occurs at the disk electrode, the ring current decreases linearly with $\omega^{1/2}$ to zero at the ω_2-transition velocity. The i_r-$\omega^{1/2}$ behavior is exactly that predicted in Eq. [36], and the intersections of the straight lines of the i_r-$\omega^{1/2}$ trace can be used to define the values of $\omega_1^{1/2}$ and $\omega_2^{1/2}$. This gives results in excellent agreement with the previously described method using the E_D-$\omega^{1/2}$ plots, which was feasible because the $dE_D/d\omega^{1/2}$ slopes were quite linear in our experiments. However, many disk electrode reactions can be extremely irreversible; *e.g.*, a drawn-out E_D-$\omega^{1/2}$ curve between the transition velocities would have been seen if the Cu(I) → Cu(0) reaction were very slow. Even in such an instance, the i_r-$\omega^{1/2}$ plots would still give well-defined $\omega_1^{1/2}$ and $\omega_2^{1/2}$ values since such plots depend only on current efficiency. As long as the steps in the i-E_D plot are separated by a limiting current region (as here for Cu(II) → Cu(I) → Cu at the disk), the i_r-$\omega^{1/2}$ plot ought not to be affected because of irreversibility at the disk electrode, provided an adequate limiting current region for the ring reaction exists. When two disk reactions slightly overlap in potential, instead of being separated by a clear limiting current region, the corresponding E_D-$\omega^{1/2}$ transition will be ill defined and i_r-$\omega^{1/2}$ intersections for suitable ring reactions will be rounded. However, the latter traces will be linear in the regions away from the theoretical intersection points and thus can readily be extrapolated to the transition velocity intersection. This is comparable to the general advantage of amperometric titrations, which have basically two linear regions, over potentiometric ones in end point definition.

An experimental equivalent of a ring electrode is of course absent in constant current stationary electrode techniques, *viz.* chronopotentiometry. In hydrodynamic voltammetry, the combination of constant IR drop at the disk electrode, and ring electrode-defined $E^{1/2}$-values may be of special value as compared to single-electrode techniques in situations complicated by irreversibility, potential overlap, and/or high re-

sistance, provided a suitable ring electrode reaction or sequence of reactions is available.

Fe(III)-Fe(II) and MnO_4^--Mn(II) Systems

The E_D-$\omega^{1/2}$ behavior predicted by Eq. [23] for a mixture of two different electroactive components was tested with a Fe(III)-MnO_4^- mixture in 1M H_2SO_4. In this experiment, the Fe(III)-Fe(II) potential is represented by $E_{C\text{-}D}$ in the region $\omega_1 > \omega > \omega_2$. In a conventional i-E curve of this system, a plot of E_D *vs.* log $(i_d - i)/i$ for the Fe(III) step is linear with a slope close to that characteristic of a reversible one-electron transfer, 59 mV/decade. From Eq. [23], the equivalent reversibility test using hydrodynamic potentiometry is a plot of E_D *vs.* log $[(\omega_2^{-1/2} - \omega^{-1/2})/(\omega^{-1/2} - \omega_1^{-1/2})]$. Such a plot should be linear and have a slope of $59/n$ mV/decade for an n electron reversible reaction.

The E_D-$\omega^{1/2}$ and i-E_D behavior of a gold disk for the Fe(III)-Fe(II) step in 1M H_2SO_4 solution containing both Fe(III) and MnO_4^- was found to be quite dependent on electrode pretreatment and direction of potential scan. In this work, we sought only to compare the log plot relationships for i-E_D and E_D-$\omega^{1/2}$ curves under electrode surface conditions as equivalent as possible. Brief anodization of the disk electrode at a constant current equal in magnitude to the cathodic current used in the E_D-$\omega^{1/2}$ experiment proved adequate, as did holding the disk electrode equally briefly at about 1.3V *vs.* SCE prior to the i-E_D experiments. Immediately after pretreatment, E_D was made to vary from − to + potentials, *i.e.* from H_2 evolution to more positive potentials by increasing $\omega^{1/2}$ during the E_D-$\omega^{1/2}$ experiment and by scanning E_D positively in the i-E_D experiment.

Two controlled potential i-E curves and one hydrodynamic potentiogram are shown in Fig. 8, as actually recorded on the same chart. The x-axis of the recorder was successively calibrated for current, and then for $\omega^{1/2}$.

The rotation speeds for the i-E_D plots were selected to give limiting currents for the sum of the two steps not very different from the constant 167 μA cathodic current used in the hydrodynamic potentiogram. The appropriate log analyses of the three curves are shown in Fig. 9. The two i-E_D plots yield slopes (60 and 62 mV) that are in experimental agreement with reversible behavior. The log function of Eq. [23] is also linear with potential and gives a slope in accord with the others (56 mV). If the electrode surface is not treated as described, the log functions have varying irreversible slopes (>59 mV). Each such plot, however, appears to be reasonably linear, as would be expected from the form of Eq. [23] after it had been properly modified by incorporating the effects of irreversibility into the pre-logarithmic factor.

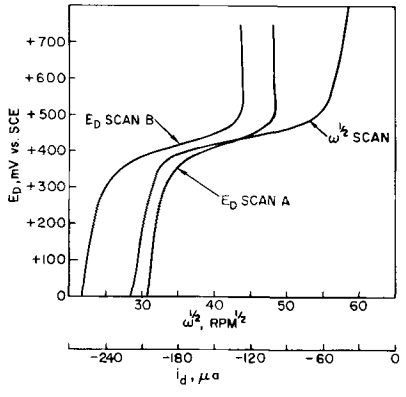

Fig. 8. E_D scans *A* and *B* are conventional 20 mV/sec potential scans vs. disk current at 835 and 1330 rpm, respectively. $\omega^{1/2}$ scan is E_D vs. $\omega^{1/2}$ hydrodynamic potentiogram at a constant 167 μA cathodic disk current. Solution is approximately millinormal Fe(III) and MnO_4^- in 1M H_2SO_4. $\omega^{1/2}$ scan rate 0.33 rpm$^{1/2}$ sec^{-1}.

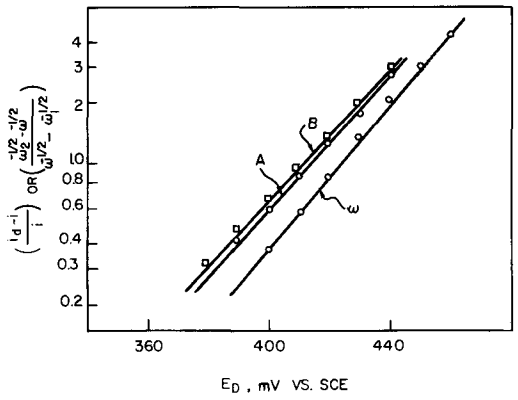

Fig. 9. Fe(III) → Fe(II) waves of Fig. 8 analyzed logarithmically. For E_D scans *A* and *B*, log $[(i_d - i)/i]$ is plotted vs. E_D and for the hydrodynamic potentiogram log $\left(\frac{\omega_2^{-1/2} - \omega^{-1/2}}{\omega^{-1/2} - \omega_1^{-1/2}}\right)$ is plotted vs. E_D.

The log function of ω in Fig. 9 is unity at +423 mV or, from the curve in Fig. 8, for $\omega^{-1/2} = 0.0246$ rpm$^{-1/2}$. The theoretical value of $\omega^{-1/2}$ at this point is, from Eq. [23], $(\omega_2^{-1/2} + \omega_1^{-1/2})/2$. Values of $\omega_2^{1/2}$ and $\omega_1^{1/2}$ were obtained from the intersections of linear extrapolations of the steepest and flattest parts of the E_D-$\omega^{1/2}$ curve, giving for the theoretical value, $(0.0176 + 0.0314)/2 = 0.0245$ rpm$^{-1/2}$, in excellent agreement with the result from the logarithmic plot. Furthermore, the experimental ratio of $\omega_1^{1/2}/\omega_2^{1/2}$ is 1.78, which, from Eq. [8], should be equal to the ratio of the total limiting current for Fe(III) + MnO_4^- divided by the MnO_4^- limiting current alone, when ω is constant. This ratio was found to be 1.82 by continuing i-E_D scans of the type shown in Fig. 8 anodically to the residual current level at the base of the MnO_4^- wave, again showing satisfactory internal consistency.

Hydrodynamic Potentiometry—Method HP2

Determination of uncompensated ohmic resistances.— As described in the Experimental section, recording i *vs.* E_D while scanning the current, i, through the disk electrode and holding the ratio, $i/\omega^{1/2}$, constant may yield information about the kinetics of the redox couple being studied. In the limiting case of a high exchange current when the polarization resistance is much less than the solution resistance between reference capillary and the disk, the slope of the i-E_D curve gives the solution resistance. This case was tested with a silver disk in 1*N* $HClO_4$. The plot of E_D *vs.* i obtained using a controlled, constant value of $i/\omega^{1/2} = 0.25$ mA-rpm$^{-1/2}$ is shown in Fig. 10. The slope of Fig. 10 yields a resistance of 3.2 ohms. This $i/\omega^{1/2}$ ratio corresponds to a Ag^+ surface concentration of

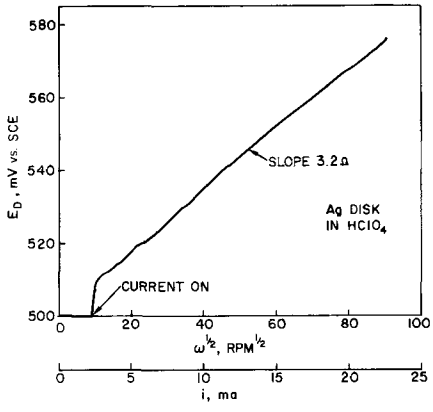

Fig. 10. Controlled $i/\omega^{1/2} = 0.25$ mA-rpm$^{-1/2}$ current and $\omega^{1/2}$ scan of a silver disk in 1*N* $HClO_4$. Disk potential plotted simultaneously against $\omega^{1/2}$ and anodic current, *i*.

0.054M, for which the exchange current is > 1 A/cm^2, according to Gerischer and Tischer (9). The corresponding polarization resistance is calculated to be less than 0.2 ohm for the electrode used. Hence, the value of 3.2 ohms should correspond to the solution resistance between the Luggin capillary tip and the disk electrode (about 1 cm).

Without altering the position of any of the components in the electrode cell, a potentiostatic interrupter method (10) was used to measure independently the uncompensated ohmic potential drop. The average of several measurements was 3.5 ± 0.5 ohms.

Further evidence that the i-E_D method was yielding solution resistance was obtained by lowering the reference capillary away from the disk electrode, which gave a slope of 3.5 ohms. Then a 10 ohm $\pm$ 0.05% resistor was inserted in series with the disk electrode, and the slope was found to be 14.0 ohms. The difference in the latter two values yielded 10.5 ohms for the resistance inserted in series with the disk, and is indicatve of the accuracy limits of this method for determining uncompensated ohmic resistance at that level, about 5%. The reproducibility of the i-E_D traces was considerably better than that obtained by the interrupter method using an oscilloscope.

Summary and Conclusions

The theoretical consequences of programming the rotation speed of (ring-) disk electrodes according to $\omega^{1/2} = kt$ have been successfully verified under three schemes of current, potential, and surface concentration control. The linearity of ring and disk currents with $\omega^{1/2}$ at constant E_D and E_r under Levich conditions confirms the expected features of considerably shortened experiment time, satisfactory reproducibility, and ready observation of deviations from i *vs.* $\omega^{1/2}$ behavior occurring at the electrode. Other particular benefits of a continuous $\omega^{1/2}$ scan and the consequent minimal ring and disk perturbation (shortened time and fewer coulombs passed) will depend on the experiment being done and need not be elaborated here.

Using hydrodynamic potentiometry, method HP1, satisfactory values of diffusion coefficients and agreement with theoretical behavior were obtained for the predicted

$$\omega^{1/2},\ \omega_1^{1/2}/\omega_2^{1/2},\ \frac{\omega_1^{1/2}\,\omega_2^{1/2}}{\Delta(\omega^{1/2})},\ \text{and}\ \frac{(\omega_2^{-1/2} - \omega^{-1/2})}{(\omega^{-1/2} - \omega_1^{-1/2})}$$

functions of ring and disk i-E parameters. Using method HP2, reliable solution resistance measurements have also been obtained. While these techniques might be carried out manually, such plotting in method HP1 would be tedious and as omissive of possible important detail as the equivalent procedure in conventional current-potential methodology. Similarly, our experience with method HP2 has shown that the precision of i-E_D data is significantly improved with the scanning technique as opposed to manual adjustment of both i and $\omega^{1/2}$ values with measurement of E_D point-by-point. This is of considerable importance when the total E_D excursion is only a few millivolts since the precise measurement of E_D is a limiting factor in determining the magnitude of the rate constants that can be handled in applications of the method to kinetic analysis (11).

Method HP1 with concurrent ring measurements can offer a substantial improvement in the experimental determination of transition velocities and in wave analysis. The precise location of apparent $E^{1/2}$ values in relatively resistive solutions, as in most organic solvents, and for irreversible reactions might make this technique the method of choice in those cases. The constant IR drop also simplifies analysis.

The motor speed scanning circuitry employs a squaring module to generate the $\omega^{1/2} = kt$ relation. For any other kind of rotation speed dependence, as might be required for kinetic studies, a log operator, a succeeding variable gain stage, and then an antilog conversion could be used to generate any required ω-power. The transformation of E-$\omega^{1/2}$ curves into i-E plots as outlined in Fig. 1 could be accomplished automatically using analog division of a constant voltage proportional to I by the E_S output proportional to $\omega^{1/2}$ and recording the quotient. The transformed plot is likely to have certain features different from the i-E plots done by either current or potential scanning. For example, in the $CuCl_2$ experiment, conventional potential scanning would miss the metal nucleation overpotential. Current scanning would show this feature but, along with the potential sweep, would suffer from a variable IR correction not present in the transformed HP1 data.

Acknowledgment

Stanley Bruckenstein is grateful to the Bell Telephone Laboratories for their hospitality during the summer of 1969 when work on this paper and the two following papers was done.

Manuscript submitted Feb. 13, 1970; revised manuscript received *ca.* April 23, 1970. This was Paper 305 presented at the Los Angeles Meeting, May 10-15, 1970.

Any discussion of this paper will appear in a Discussion Section to be published in the June 1971 JOURNAL.

REFERENCES

1. S. C. Creason and R. F. Nelson, *J. Electroanal. Chem.*, **21**, 49 (1969).
2. R. H. Sonner, B. Miller, and R. E. Visco, *Anal. Chem.*, **41**, 1498 (1969).
3. R. N. Adams, "Electrochemistry at Solid Electrodes," Marcel Dekker, Inc., New York (1969).
4. L. Hsueh and J. Newman, *Electrochim. Acta.*, **12**, 429 (1967).
5. S. Bruckenstein and G. A. Feldman, *J. Electroanal. Chem.*, **9**, 395 (1965).
6. S. Bruckenstein and S. Prager, *Anal. Chem.*, **39**, 1161 (1967).
7. B. Miller, *This Journal*, **116**, 1117 (1969).
8. D. T. Napp, D. C. Johnson, and S. Bruckenstein, *Anal. Chem.*, **39**, 481 (1967).
9. H. Gerischer and R. P. Tischer, *Z. Elektrochem.*, **61**, 1159 (1957).
10. S. Bruckenstein and B. Miller, *This Journal*, **117**, 1040 (1970).
11. B. Miller and S. Bruckenstein, To be published.

Circuit for Transient-Free Current-Potential Control Conversion

Stanley Bruckenstein*[1] and Barry Miller*

Bell Telephone Laboratories, Incorporated, Murray Hill, New Jersey

ABSTRACT

A general technique for switching a closed loop control circuit from one function to another is described. A closed loop exists at all times, even during the switching operation. A potentiostat that can be switched to a galvanostat and *vice versa* in less than 10 μsec was built. No spurious potential or current transients were observed on test or real cells. This potentio-galvanostat has been tested with a conventional three electrode cell, with a ring-disk electrode, and as a potentiostatic interrupter.

The use of active circuit elements, *e.g.*, operational amplifiers, in closed loop configurations to control the potential of or the current through an electrode is commonplace today. In general, these circuits are far superior to ones involving only passive elements. However, the closed loop configurations that we are familiar with do not permit changing from one control situation to another and back again, without opening the loop and causing the controlling element to limit. Such limiting is sometimes fatal to the experiment. For example, in order to go from galvanostatic to potentiostatic control and back again, the various active and passive elements are rearranged by switching. In currently used configurations this requires opening the loop in one or both switching directions. A particularly ingenious method of this type described by Warner and Schuldiner (1) involves using a back-biased diode to open the loop. The same pulse that limits the potentiostat is used in the current mode as the voltage source to supply the current to the cell through a series resistance. This circuit functions well in transferring controlled potential control to a simple resistive current source, but potential overshoots occur on re-establishing potentiostatic control.

Any attempt to change the control function of a single closed loop operational amplifier circuit that opens the loop produces an unstable condition that is accompanied by undesirable electrical transients in the supposedly controlled system. In general, if a circuit is designed with two closed loop paths involving the same control amplifier, it is possible to make changes in control function, unaccompanied by conditions of instability. To our knowledge, this concept has not been previously applied to electrochemical studies. In such circuits, one control function exists when one loop is closed, while the second control function is imposed when the second loop is closed. This second loop simultaneously performs two functions. First, it negates the control function of the first loop and second, it establishes the desired control situation.

Negation of the control situation established by the first loop is accomplished by appropriate use of an inverting amplifier whose output is made the negative sum of every signal fed to the input of the control amplifier. The input of the inverter is taken from the same signal sources as those going to the negative input of the control amplifier and through identical impedances. The output voltage of the inverter is fed through an appropriate resistance to a single pole, single throw switch connected to the negative input of the control amplifier. If the various resistors associated with the inverting amplifier are properly chosen, closing the switch produces a zero output voltage and current at the control amplifier. In effect, the first closed loop has been opened since the output current of the control amplifier drops to zero.

Closing the switch can also establish the control function desired in the second situation. Any other signals fed to the same side of the switch as the inverter, or alternatively to the summing point of the inverter, will not be cancelled and can establish the second control situation. This situation will correspond to the required one if proper choice of the controlling parameters is made. Since only one control amplifier is used for both control loops and at least one closed loop always exists regardless of the switch position, control is maintained at all times.

The phase shifts of the two closed loop situations are slightly different. It is necessary to choose the passive components associated with the various active circuit elements to satisfy the less stable of the two configurations.

In this paper we describe one of the many possible circuits fulfilling the design principles outlined above which will function either as a potential or current controlling device. This circuit contains two closed loops with one common control amplifier, and no spurious potential or current transients are observed on switching from one configuration to the other.

Experimental

Chemicals and apparatus.—All chemicals were of reagent grade, and ordinary distilled water was doubly distilled from quartz.

The rotator for the ring-disk electrode was manufactured by the Pine Instrument Company of Grove City, Pennsylvania.

The ring-disk electrode had a platinum disk and a platinum ring and was insulated with Teflon. The disk radius was 0.2410 cm, the ring electrode outer radius was 0.4858 cm, and the ring width varied from 0.0053 to 0.0131 cm. The geometry of this particular electrode is such that the variation in ring width introduces a large uncertainty in the calculated value of the collection efficiency, *i.e.*, a change in inner diameter of the ring by 0.0010 cm changes N by $\sim$ 6%. For this reason N was determined experimentally using the oxidation of Br^- to Br_2 at the disk electrode and the reverse reaction at the ring electrode. The solution used in all experiments contained $3.6 \times 10^{-3} M$ NaBr and $0.2 M$ $HClO_4$. The value of N found was 0.078 ± 0.001. This mean N corresponds to a ring electrode inner radius of 0.4733 cm, which lies within the experimental measurements of this dimension.

The disk of this ring-disk electrode was also used for all experiments not involving a ring electrode.

* Electrochemical Society Active Member.
[1] Permanent address: Department of Chemistry, State University of New York at Buffalo, Buffalo, New York.

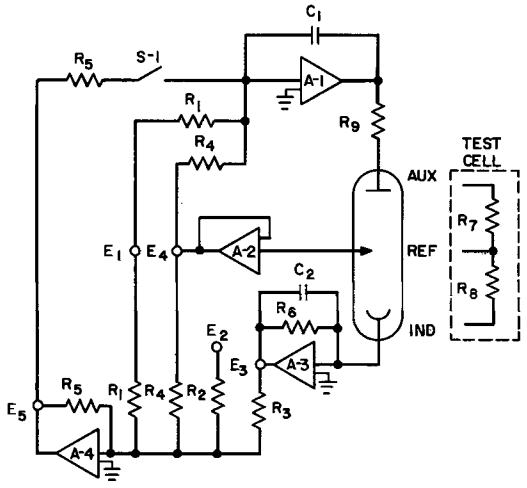

Fig. 1. Schematic circuit of potentio-galvanostat for transient-free switching from potential (S-1 open) to current (S-1 closed) control.

In the ring-disk experiment, two previously described instruments were used. Instrument 1 independently controls the potential of both ring and disk electrodes (2). Instrument 2 controls the current through the disk electrode while independently controlling the potential of the ring electrode and can also be switched to perform the function of circuit 1 (3). Potentiostatic control of the disk electrode is maintained in instruments 1 and 2 using the configuration of amplifiers A-1, A-2, and A-3 shown in Fig. 1. The disk potentiostats for both these instruments were modified according to Fig. 1 to provide disk current control on closing S-1.

Steady-state experiments were performed using the disk electrode potentiostats of instruments 1 and 2 modified according to Fig. 1, and with the original version of instrument 2 in which current control through the disk electrode was maintained using a more conventional single loop controlled current source. Nonsteady-state experiments were performed using the modified form of instrument 2. The amplifiers employed in obtaining the results displayed in Fig. 2-7 were all Burr-Brown amplifiers: Models 3072/15 (A-1 and A-3), 3013/15 (A-2) and 3003/15 (A-4)[2] (see Fig. 1.)

The ring electrode control circuits of instruments 1 and 2 do not interfere with experiments involving only the disk electrode.

All potentials are reported *vs.* the Ag/AgBr electrode in contact with the test solution, whose potential was −14 mV *vs.* SCE.

Switching.—Conventional mechanical switches bounce on closing, and these switching interruptions are visible in experiments analogous to those shown in Fig. 2 to 7 below. The use of a mercury wetted relay obviates this problem. We have used a Western Electric Model 276B relay with an 0.01 μF capacitor across the relay coil. However, energizing this relay coil can still induce a spurious pulse into the potentio-galvanostat circuitry unless care is taken in shielding and physically locating the relay. This problem is far more serious when a real electrochemical cell is used in place of the test cell.

Even more rapid bounce-free transfer was obtained using an electronic switch (Burr Brown 9859/15) as S-1. In this case the switching of the test cell (C_1, C_2, and R_9 all zero) between potentiostat and galvanostat was complete in less than 10 μsec in either direction with no trace of overshoot. The specified operating time of the switch itself is 3 μsec on, 5 μsec off. The logic pulse (+5V on, 0V off) operating the switch was obtained from an operational amplifier zero crossing detector caused to flip between its limits, with a blocking diode in one direction providing the zero volt condition. Any voltage step source would serve. Application of the pulse through a mechanical switch may be satisfactory (no bounces), depending on the quality of the switch, since the Burr-Brown FET device has a 0.5V noise immunity.

[2] Later experience of the authors indicates the lower offset of the chopper stabilized Model 3072/15 is preferable for the A-4 function.

Circuitry

Figure 1 is a schematic diagram of a circuit which permits switching from a controlled electrode potential to a controlled electrode current and *vice versa* without introducing spurious transients. When switch S-1 is open, the potential of the indicator electrode is controlled by amplifiers making up the closed loop, A-1 and A-2. A-3, the current follower, maintains the indicator electrode potential at virtual ground. In the commonly used version of this circuit, $R_1 = R_4$, and E_1 may be any function of time produced by a suitable signal generator. The current through the indicator electrode, i_D, is obtained from E_3 and R_6 using Eq. [1]

$$i_D = -E_3/R_6 \qquad [1]$$

For simplicity in the derivation given below, we assume ideal operational amplifiers of infinite open loop gain, zero input current, and zero error voltage between the positive and negative inputs.

The summing point restraint at the input of the inverting amplifier, A_4, requires that

$$\frac{E_1}{R_1} + \frac{E_2}{R_2} + \frac{E_3}{R_3} + \frac{E_4}{R_4} + \frac{E_5}{R_5} = 0 \qquad [2]$$

When the switch S-1 is closed, the summing point restraint condition at the negative input of the control amplifier A-1 yields

$$\frac{E_1}{R_1} + \frac{E_4}{R_4} + \frac{E_5}{R_5} = 0 \qquad [3]$$

Solving Eq. [1], [2], and [3] for the controlled cell current gives

$$i_D = \frac{E_2 R_3}{R_6 R_2} \qquad [4]$$

E_2 may also be any function of time supplied by an appropriate signal generator.

The transient and steady state behavior of the circuit shown in Fig. 1 is reported below. A purely resistive and a resistive-capacitive analog of an electrochemical cell were used in addition to an electrochemical cell in which a rotating platinum disk electrode served as the indicator electrode. The test (resistive) cell was required to study the circuit's transient response in the absence of electrode-solution processes. Under certain circumstances the electrochemical behavior of a real system prevents the circuit response from being studied. Such a situation occurs in two cases in an electrochemical cell:

(*i*) On switching from constant current control to constant potential control, the current follower potential limits; and (*ii*) on switching in the opposite direction the potential of the reference electrode follower A-2 relaxes in a relatively slow fashion after the initial uncompensated ohmic potential drop.

The circuit configuration shown in Fig. 1 will be referred to as a potentio-galvanostat since this combination of existing terminology implies the control functions of the circuit. The effect of the second control loop on the ring control circuits of instruments 1 and 2 was also studied.

Results and Discussion

Steady-state behavior. Controlled current mode.—Test cell.—The same signal source was used to supply

E_1 and E_2 with switch S-1 closed. The outputs of the current follower and of the voltage follower were recorded *vs.* E_2 on an X-Y-Y' recorder. Within the control limits of the operational amplifier, the slopes of these lines corresponded within ~ 0.2% (recorder limitation) to those which would be predicted from the resistance values listed in the legend to Fig. 2. The currents controlled varied from 10^{-7} to 10^{-2}A. Scanning E_1 along with E_2 had no effect on the controlled current, nor did stepping E_1 by ± 1V about any preset value of E_2.

The independence of the circuit performance on E_1 clearly demonstrates the negation of potentiostatic control in the loop A-1, A-2, and A-3 by the inverting amplifier, A-4, and transfer to current control on closing the second loop through S-1.

Ring-disk electrode.—Circuit 2 in the current-controlling (conventional single loop) configuration was used to determine N_{exp}, the experimental collection efficiency, in a solution containing 3.6 x $10^{-3}M$ NaBr and 0.2M $HClO_4$, scanning the anodic disk current from 0 to 0.500 mA. Next, the modified versions of circuits 1 and 2 in the current controlling mode were used to determine N_{exp} for disk currents of 0 to 0.500 mA. Again E_1 was set equal to E_2 in order to test the potentiostatic rejection property of the double loop configuration.

Values of N_{exp} obtained in all three experiments agreed within 1% with each other and were, within experimental error, indistinguishable from the theoretical value of N.

Transient behavior.—Test cell.—Resistors R_7 and R_8 (Fig. 1) simulated the simplest transient control situation required of the potentio-galvanostat. The response of amplifier A-2, the reference electrode follower, on opening and closing switch S-1 (mercury relay, see above) is shown in Fig. 2. For convenience, in this section, we shall refer to the negative of the reference electrode follower voltage, $-E_4$, as the indicator or disk electrode potential, (E_D). The indicator electrode potential changes between the required limits in about 2 x 10^{-4} sec, without overshooting either potential limit. The output potential of the current follower, E_3, changes between the values required by the constant current and constant potential situations on closing and opening switch S-1 in an equally satisfactory fashion, as shown in Fig. 3.

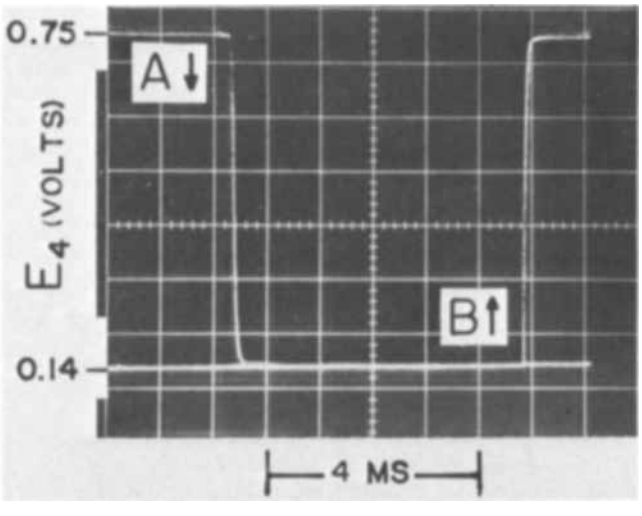

Fig. 2. Response of test cell reference potential E_4 between current and potential control. R_7 = 2K, R_8 = 1K in Fig. 1. Horizontal time scale 1 msec/major division. C_2 and R_9 = 0, C_1 = 100 pf. Trace A, start upper left with —0.75 mA constant current switching to —0.14V constant potential; trace B, start lower horizontal line (constant potential) switching to constant current, same values as trace A. Note: $E_4 = -E_D$, R_6 = 10K.

Electrochemical cell.—The transient behavior of the potentio-galvanostat was studied using a platinum rotating disk electrode. The auxiliary (counter) electrode was a large area platinum gauze electrode that was not separated from the disk electrode by a porous diaphragm. The reference electrode was a silver wire coated with silver bromide in a Luggin capillary filled with the solution in the cell. The resistance between the disk and auxiliary electrode was 14 ohms at 1 kHz.

The circuit in Fig. 1 tended to break into oscillation, whether S-1 was open or closed, unless the series resistance, R_9, was introduced between the output of the control amplifier, A-1, and the auxiliary electrode. In the work reported below R_9 = 1470 ohms. If the auxiliary electrode is separated from the disk electrode compartment, the total cell resistance becomes sufficiently large to make R_9 unnecessary under most conditions. The mercury relay was used for S-1.

Figures 4 and 5 illustrate the transient response of the disk electrode current follower (E_3) and that of the reference electrode follower (E_2) on closing

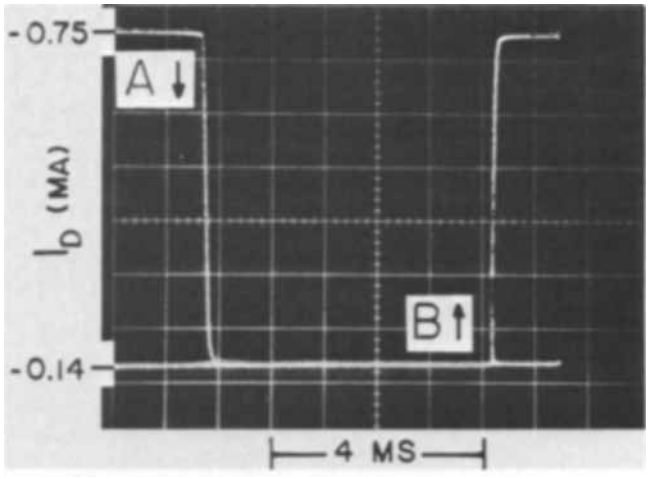

Fig. 3. Response of current follower A-3 for conditions of Fig. 2. Trace A, start upper left (constant current), switching to constant potential; trace B, start lower horizontal line (constant potential), switching to constant current.

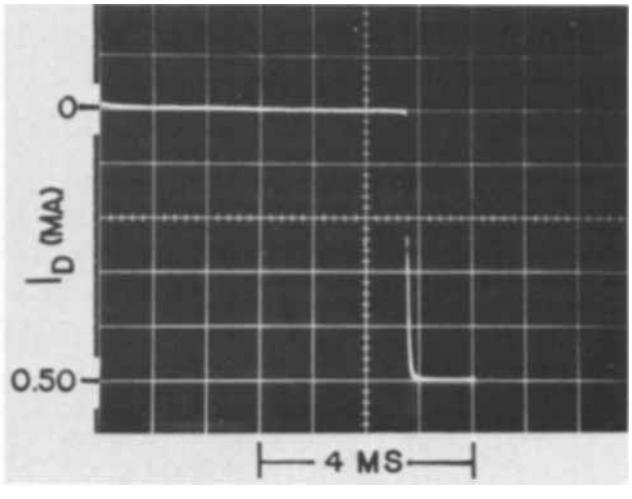

Fig. 4. Current follower (E_3) response during potential to current control switching on 2500 rpm disk electrode in 3.6 x 10^{-3}M NaBr, 0.2M $HClO_4$. Constant —0.10V E_D (upper left) switched to + 0.50 mA constant I_D (lower right). 1 msec/major div. horizontal axis. R_6 = 10K.

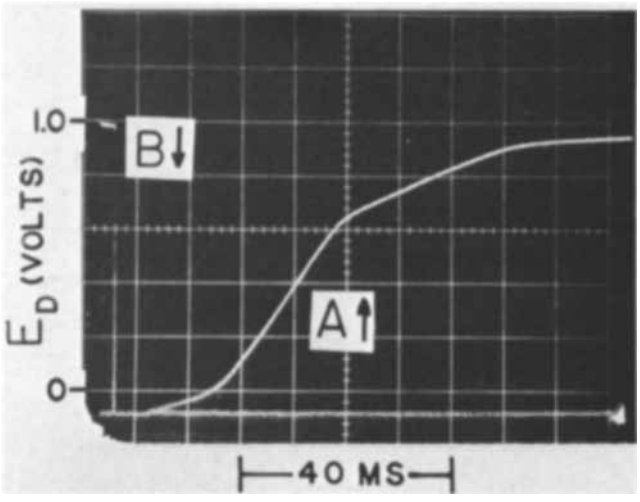

Fig. 5. Reference electrode (E_D) response during potential to current control switching under solution and rotation conditions of Fig. 4. 10 msec/major div. horizontal axis. Curve A, potential (−0.10V) to current (+0.50 mA); curve B, current (+0.50 mA) to potential (−0.10V).

S-1. The initial potentiostatic condition corresponded to $E_D = -0.10$V, while the final galvanostatic condition corresponded to $i_D = 0.500$ mA (anodic disk current). The limiting convective diffusion current for the oxidation of bromide to bromine at the disk electrode was 0.88 mA at 2500 rpm.

As can be seen in Fig. 4, the disk electrode current changes rapidly ($\sim 10^{-4}$ sec) and smoothly between practically zero current and 0.500 mA without any overshoot. The behavior of E_D (curve A, Fig. 5) is governed by surface and convective diffusion processes in solution. The relatively slow, sigmoid variation in E_D with time reflects the charge necessary to oxidize any hydrogen adsorbed at −0.10V, oxidation of the disk electrode, and the time required to establish steady-state surface concentrations of Br_2 and Br^- at the disk electrode. The potential variation is smooth and of the expected shape (4).

Curve B, Fig. 5 and Fig. 6 show the response of the disk electrode when S-1 is opened. Before opening S-1, $i_D = 0.500$ mA, and $E_D = 0.935$V. On opening S-1, E_D changes rapidly ($\sim 10^{-4}$ sec) to the preselected potential, −0.10V without overshooting. The disk-electrode current-follower potential, Fig. 6, shows a

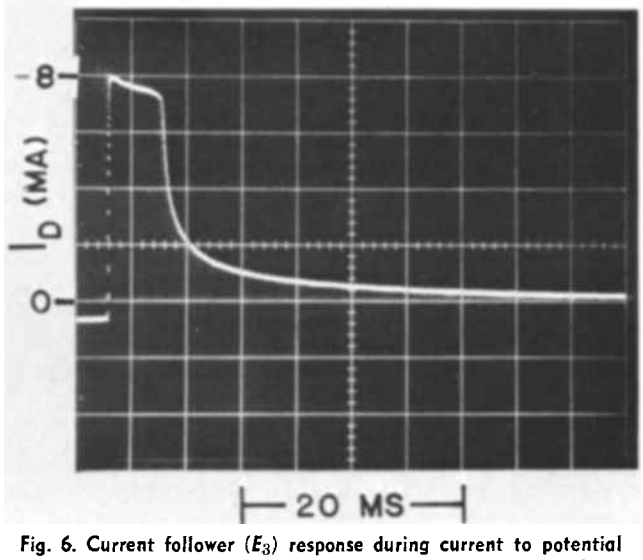

Fig. 6. Current follower (E_3) response during current to potential control switching under Fig. 4 conditions. 5 msec/major div. horizontal axis. From left, constant current (+ 0.50 mA) switched to constant potential (−0.10V).

relatively flat region for about 5×10^{-3} sec, followed by the expected current variation for a disk electrode potential step (5). The initial flat current region is caused by voltage limiting of the control amplifier, as was verified in three different ways. First, oscilloscopic observation of the output potential of amplifier A-1 demonstrated voltage limiting for about 5×10^{-3} sec. Second, halving the initial anodic current decreased the length of the initial flat region by ~30%. Third, the output of the control amplifier was biased 9V using a Kepco Precision Voltage Source in the sense required to overcome the external ohmic potential drop, and the experiment shown in Fig. 6 repeated. The length of the flat current region was reduced to $\sim 2 \times 10^{-3}$ sec.

Ring-disk electrode.—The potentio-galvanostatic circuitry in Fig. 1 was incorporated into circuit 2, which independently controls disk and ring electrode potentials. Ring electrode potentials and currents were observed on opening and closing S-1. The ring electrode potential was unaffected, and ring electrode currents had the expected nonsteady-state shapes (6).

Changing E_1 by a potential step of ± 1.1V produced no detectable changes in the potentials or currents at the ring or disk electrodes while S-1 was closed.

Interrupter application.—Switching the potentio-galvanostat from a controlled potential to a zero controlled current state produces the equivalent of a potentiostatic interrupter experiment. Hence it is possible to measure the true potential of the indicator electrode and calculate the uncompensated ohmic drop between the reference and indicator electrodes. The frequency and time of the interruption period are readily controlled by applying a suitable signal to the logic gate of the Burr-Brown FET switch. Such signals are readily obtained from a number of pulse generators and, in the interrupter experiment reported below, we have used a General Radio Model 1340 Pulse Generator.

The test-circuit of McIntyre and Peck (7) was employed to examine the interrupter performance of the potentio-galvanostat. This circuit differs from the test cell shown in Fig. 1, in that $R_7 = 420$ ohms and R_8 was replaced by a 50-ohm resistor, the uncompensated cell resistance, in series with a parallel *RC* network ($R = 100$ ohms, $C = 8.6$ μf), to simulate the equivalent circuit of a disk electrode. An additional 20 Kohm resistor was inserted in the lead to A-2 (Fig. 1) to represent the resistance of the Luggin capillary and reference electrode.

Approximately 80 μsec pulses, at a repetition rate of about 2270 Hz were used to gate the FET switch, thereby imposing a controlled potential of 1.50V or a zero current state at the indicator electrode. These conditions correspond to an uncompensated ohmic potential drop of 0.50V. The results of two pulses are shown in Fig. 7. The uncompensated ohmic drop was obtained from the intersection at 1.0V of the two stages of potential decay. The rapid potential change immediately after interruption is 5 divisions or 0.50V, in excellent agreement with the actual uncompensated ohmic potential drop in the test circuit. The slower potential change visible at longer times after interruption corresponds to the voltage decay within the *RC* circuit. Removal of the gate pulse switches the circuit back to potentiostatic control, with barely detectable potential overshoot. Depending on the application envisioned, pulse width and repetition frequency can be adjusted over very wide limits. The pulse width may, in many situations, be made narrow enough to make unimportant any relaxation of the electrode potential during the interrupt time interval. Thus, the circuit in Fig. 1 is well adapted to use as a repetitive interrupter for applications which require monitoring (or recording) of the true potential of an electrode.

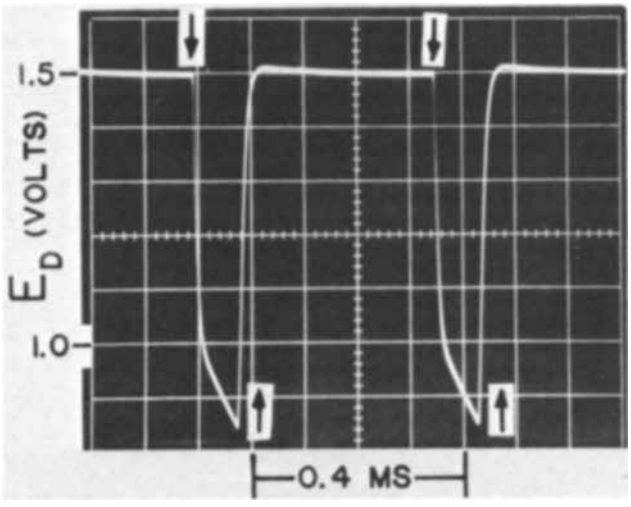

Fig. 7. Potentiostatic interrupter mode. 80 μsec gate pulse width, repetition rate 2270 Hz. Two interruptions shown; ↓ S-1 closed (switch to zero current), ↑ S-1 opened. Horizontal axis 100 μsec/major div. Vertical axis 0.10 V/major div. Cell description, see text.

It is to be kept in mind that test cell switching time is a property of the particular combination of logic pulse rise time, switch operating time, and amplifier slew rates. There is no reason to believe that, where required, the circuit principle cannot be extended to over-all switching times considerably better than those cited here (~ 10 μsec) by choice of faster operating components, either currently or soon to be available from a rapidly developing technology.

Conclusion

The potentio-galvanostat circuit described in this paper permits switching from a controlled electrode potential to a controlled electrode current situation and *vice versa* without introducing spurious potentials or currents in an electrochemical cell. The performance of the circuit in one state is identical to that of an individual potentiostat and in the other is comparable to that of a more conventional galvanostat. The general principle described may be used to switch other potentiostat configurations to galvanostats. Alternatively, a potentiostat may be added to an existing galvanostat using the second loop principle without loss of control during switching.

The potentio-galvanostat may also be used as a transient free interrupter by rapidly switching to a zero controlled current, if S-1 is a FET switch whose gate is driven by an appropriate signal.

Acknowledgment

Stanley Bruckenstein is grateful to the Bell Telephone Laboratories for their hospitality during the summer of 1969 when this work was done.

Manuscript submitted Feb. 13, 1970; revised manuscript received *ca.* March 27, 1970.

Any discussion of this paper will appear in a Discussion Section to be published in the June 1971 JOURNAL.

REFERENCES

1. T. B. Warner and S. Schuldiner, *This Journal*, **114**, 359 (1967).
2. G. W. Tindall and S. Bruckenstein, *Anal. Chem.*, **40**, 1937 (1968).
3. B. Miller, *This Journal*, **116**, 1117 (1969).
4. R. P. Buck and H. E. Keller, *Anal. Chem.*, **35**, 400 (1963).
5. S. Bruckenstein and S. Prager, *ibid.*, **39**, 1161 (1967).
6. S. Bruckenstein and D. T. Napp, *J. Am. Chem. Soc.*, **90**, 6303 (1968).
7. J. D. E. McIntyre and W. F. Peck, Jr., *This Journal*, **117**, 747 (1970).

An Experimental Study of Nonuniform Current Distribution at Rotating Disk Electrodes

Stanley Bruckenstein*,[1] and Barry Miller*

Bell Telephone Laboratories, Incorporated, Murray Hill, New Jersey

ABSTRACT

The theoretical predictions of Newman (1, 2) concerning the existence of a nonuniform current distribution at rotating disk electrodes have been verified in media containing insufficient supporting electrolyte. Measurements of the thickness of copper films deposited on a platinum disk yield results qualitatively of the form predicted by Newman. The primary current distribution is approached at currents corresponding to a small fraction of the limiting convective diffusion current in the absence of appreciable supporting electrolyte, while a uniform current distribution is found in the limiting current region. Nonuniform current distribution at a disk electrode has been found to have significant effects on the collection efficiency of a ring-disk electrode. These effects depend markedly on the geometry of the electrode. Similar behavior has been noted in the currents observed at "shielded" rings of ring-disk electrodes. Under conventional polarographic conditions in solutions containing fifty- to a hundred-fold excess of supporting electrolyte, no significant deviations from a uniform disk current distribution could be detected.

The theory of ring-disk electrodes has been developed assuming Levich's concept of uniform accessibility of the disk electrode. Recently (1,2), Newman has calculated the effect of the ohmic potential drop outside the diffusion layer of a disk electrode using Laplace's equation, considering the cases of (*a*) a single salt, and (*b*) a diffusing species present in excess electrolyte. In the absence of a large excess of supporting electrolyte, he concluded that there will not be a radially independent current density at a disk

* Electrochemical Society Active Member.
[1] Permanent address: Department of Chemistry, State University of New York at Buffalo, Buffalo, New York.

electrode except for the limiting current region and discussed several generalized situations.

In the case where the current passed through the disk electrode is much less than the limiting current and the exchange current, we combine his (2) Eq. [30] and [36] to obtain

$$J = \frac{r_0}{k_0} \frac{di}{d\eta_s}\Big|_0$$

where k_0 is the specific conductance of the particular solution, r_0 is the radius of the disk electrode, $di/d\eta_s|_0$ is the slope of the disk current-overpotential curve at zero current, and J is a parameter used in Fig. 2 of Newman's paper (2). This figure shows that a uniform current density is approached only when $di/d\eta_s|_0$ is small. The initial slope is small only for irreversible reactions and will be higher for more reversible couples. In the limit, for a reversible couple, the current density at the center of the electrode is one half of the average current density, as is the case for the primary current distribution. Note that these conclusions hold only when concentration polarization may be ignored.

Newman has compared his theoretical calculations to an experiment involving copper deposition from 0.1*M* $CuSO_4$ at a rotating disk electrode, obtaining fair agreement between theory and experiment (2). Further experimental studies of the magnitude of this effect in the presence of varying amounts of supporting electrolyte seem to us to be quite important since it would be incorrect to use existing ring-disk theory in solutions which yield significantly nonuniform disk electrode currents. We have used three approaches.

First, thin copper deposits have been plated on a rotating disk electrode, and their thickness measured with the aid of a Talysurf surface roughness instrument (4). We find that the deposit thickness increases with the radial coordinate under Newman-type conditions and that it is independent of radius under Levich-type (uniformly accessible) conditions.

Second, we have used the novel approach of Albery and Ulstrup (5). They showed, theoretically, that the collection efficiency of a thin ring-thin gap ring-disk electrode reflects the concentration profile at the outer edge of the disk. Under Newman-type conditions the disk electrode current densities are higher at the edge than under Levich-type conditions; hence higher values of N should be observed when significant nonuniform disk electrode currents exist. Qualitatively, the same conclusions should hold for all geometries of ring-disk electrodes. However, Albery and Ulstrup's experimental study of NaBr-$HClO_4$ solutions yielded N-values in agreement with, or lower than those calculated using the assumptions of a uniform disk current (5). We have repeated some of their experiments with three different ring-disk electrodes of widely different geometries in NaBr-$HClO_4$ solutions, and, contrary to them, always find N-values equal to or greater than the geometrical N-value, as their theory for Newman-type conditions predicts. The Albery-Ulstrup approach has been used by us in two other experiments, involving electrochemical oxidation of a Cu disk in NH_3-$(NH_4)_2SO_4$ solutions and a Ag disk in $HClO_4$ solutions and collection of the metal ion at a ring electrode. Again we find N-values that are equal to or greater than the theoretical value.

Third, we have used ring-disk electrodes with insulating gaps of radically different thicknesses to determine the ring current for the oxidation of Br^- to Br_2 in solutions containing different concentrations of $HClO_4$. During this experiment the potential of the ring electrode was held at the instantaneous potential of the disk electrode. If a uniform current density exists at the disk electrode, the ratio $i_r/i_d = \beta^{2/3} - N$ (7), where $\beta = (R_3^3 - R_2^3)/R_1^3$, and R_3, R_2, and R_1 are the outer and inner radii of the ring and the disk radius, respectively. As $R_2 - R_1 \rightarrow 0$ and $R_3 - R_2 >>$ $R_2 - R_1$ (thin gap, thick ring electrode) $i_r/i_d \rightarrow (R_3^2 - R_2^2)/R_1^2$. This result is the equivalent of considering a thick ring-thin gap ring-disk electrode to be a disk electrode of radius R_3 for which it is possible to measure the current in the regions $0 \leq r \leq R_1$ and $R_1 \leq r \leq R_3$ separately.

Under Newman-type conditions, the current density increases across a disk as the radial distance grows larger. Hence the average current density in the region $R_2 \leq r \leq R_3$ (ring electrode) will be higher than that in the region $0 \leq r \leq R_1$ (disk electrode). Thus, for all ring-disk electrode geometries i_r/i_d should be greater than $\beta^{2/3} - N$ or greater than $(R_3^2 - R_2^2)/R_1^2$ at a ring-disk electrode with a thin gap and thick ring. As reported below, we have found this to be the case for the oxidation of Br^- in the presence of insufficient supporting electrolyte.

The use of a thick ring-thin gap ring-disk electrode to test for nonuniformity of current distribution has recently been suggested by Marathe and Newman (3), who propose comparing the ring and disk current densities when both electrodes are held at the same potential. As shown above, this is merely the limiting case in comparing values of $\beta^{2/3} - N$.

Experimental

Reagents.—All chemicals were of reagent grade. House distilled water was doubly distilled from quartz and collected in quartz.

Ring-disk electrodes and control circuitry.—Experiments involving the determination of the collection efficiency of copper in NH_3—$(NH_4)_2SO_4$ mixtures and of silver in perchloric acid solutions used epoxy-type electrodes and the circuit reported by Miller (6), while all other experiments used Teflon-type platinum ring, platinum disk electrodes (Pine Instrument Company, Grove City, Pennsylvania) and the circuit reported by Bruckenstein and co-workers (7). A Honeywell Model 580 X-Y recorder was used.

All electrodes were ground and polished using standard techniques. The final finish was produced using 0.3μ alumina.

All experiments were performed at room temperature (23°C).

Measurement of copper film thickness on disk electrodes.—The thickness of deposited copper films was measured using a Taylor-Hobson Ltd. Talysurf Model 4 stylus-type surface roughness instrument. The accuracy obtainable is of the order of 5% (4) and in our experiments seems to be determined primarily by the smoothness of the copper deposit. The Talysurf device conveniently measures step heights and its 0.3μ full-scale and 1.0μ full-scale ranges were used. These steps were produced in our copper experiments by covering exactly half the copper-plated platinum disk electrode with Scotch Brand electroplaters' tape and dissolving the unprotected copper with a few drops of concentrated nitric acid. The electrode surface was then immediately washed with water, the electroplaters' tape removed, and the entire electrode surface rinsed with acetone. The disk electrode was mounted on a micrometer stage positioned on the bed of the Talysurf instrument, and the stage adjusted so that the step between the copper-plated surface and the platinum surface was at right angles to the direction of travel of the diamond stylus. A 2 in. diameter aluminum rod of length equal to the disk electrode was also fastened to the micrometer stage. This rod was necessary to support the shoe affixed to the arm holding the diamond stylus of the Talysurf instrument. The center of the disk electrode was located using the micrometer stage to measure the diameter and setting the stage at the calculated position. Repetitive measurements indicate that the disk electrode center can be located to within 0.003 cm. Step heights

were determined at intervals of about 0.06 cm along the step.

Results and Discussion

Copper film thickness measurements.—The radial flux dependence across a disk electrode was determined by plating approximately 2.7 coulombs/cm^2 of copper metal at 900 rpm on a platinum disk electrode at specified fractions of the limiting current and measuring the film thickness using the Talysurf instrument. This charge corresponds to an average thickness of $\sim 10^{-4}$ cm.

Marathe and Newman (3) have discussed the importance of keeping the deposit thickness considerably less than the momentum boundary layer, and our deposit thickness corresponds to a smaller fraction of the momentum boundary layer than in their experiments. Copper was plated from a solution 3.0 m*M* in $CuSO_4$ and 0.2 m*M* in $HClO_4$ before and after adding known amounts of $NaClO_4$. The results obtained are shown in Fig. 1 in which L/L^0 is plotted *vs.* r/R_1. L^0 represents the thickness of the deposit at the center of the electrode while L represents the deposit thickness at a distance of r from the center of a disk electrode of radius R_1.

Within the experimental error, the thickness of the copper plate is independent of r if copper is plated on the convective-diffusion limiting current region in the solution containing no added $NaClO_4$. This result is in agreement with the predictions made by Newman (2). Marathe and Newman (3) were unable to perform an equivalent experiment because their deposit became powdery.

In this same solution, if the copper is plated at 20% of the limiting current, marked deviations from the uniform flux condition exist. The results of this experiment are indistinguishable from the theoretical curve derived assuming the primary current distribution first calculated at a disk electrode by Newman (1). Newman's result for the primary current distribution can be rewritten in the form

$$\frac{L}{L^0} = \frac{1}{(1 - (r/R_1)^2)^{1/2}}$$

and is the dashed line shown in Fig. 1.

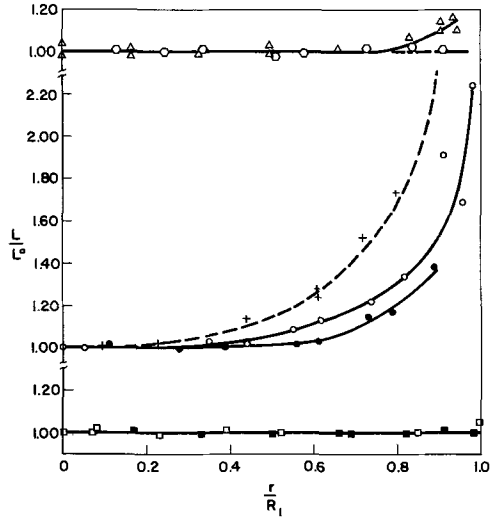

Fig. 1. Effect of supporting electrolyte on the radial dependence of the thickness of a deposited Cu film. 2 x 10^{-3}M $CuSO_4$ + 2 x 10^{-4}M $HClO_4$, platinum disk electrodes of $R_1 \simeq 0.394$ cm used. Rotation speed = 900 rpm (15.00 Hz). Average film thickness = 1.0μ. Key: □, on limiting current; +, 20% of limiting current; ○, 4.2 x 10^{-3}M $NaClO_4$ added, 20% of limiting current; ●, 4.2 x 10^{-2}M $NaClO_4$ added, 20% limiting current; △, 0.10M $NaClO_4$ (total) added, 20% of limiting current; ⬡, 50% of limiting current; ■, 0.40M $NaClO_4$ (total) added, 20% of limiting current.

As $NaClO_4$ is added to the original solution, the film thickness becomes more uniform, but it is only when as much as 0.4*M* $NaClO_4$ is present that a uniformly thick film of copper deposits at 20% of the limiting current. No significant deviations from a radially uniform deposit can be detected in 0.1*M* $NaClO_4$ solution at 50% of the limiting current.

If we neglect individual differences in ionic equivalent conductivities, the above results suggest that no appreciable deviation from Levich's assumption of uniform accessibility will occur provided at least a fifty-fold excess (on a normality basis) of supporting electrolyte is present and currents measured are in excess of 20% of the limiting current.

Collection efficiency measurements.—Oxidation of NaBr.—The collection efficiency at a platinum ring electrode for the reduction of Br_2 (produced by oxidation of Br^- at a platinum disk electrode) was studied in a 3.0 m*M* NaBr solution as a function of $HClO_4$ concentration using three different ring-disk electrodes. The collection efficiency was determined by scanning an anodic current, i_d, through the disk electrode linearly with time and measuring the ring electrode current, i_r, at 0 volt *vs.* SCE. i_d was plotted *vs.* i_r on an X-Y recorder. In all cases, this plot was a straight line and independent of scan direction provided, (*i*) the disk electrode potential did not become so positive that electrode oxidation occurred, and (*ii*) the electrode was briefly cathodized in the solution being studied to reduce thoroughly the platinum disk surface. If these precautions are not observed, $i_d - i_r$ plots become nonlinear at positive potentials, and the apparent collection efficiency becomes smaller than the theoretical value.

The results of the experiments are shown in Fig. 2 in which N_c/N is plotted *vs.* log C_{HClO_4}/C_{NaBr}. N_c is the observed value of N at c molar $HClO_4$, while N is the value observed when $C_{HClO_4}/C_{NaBr} > 100$. The latter value always agreed within a per cent or so of the theoretical value, N_{theor}, in our experiments and did not change detectably on adding excess perchloric acid.

With all three electrodes, $N_c/N \geqq 1$, as was predicted by Albery and Ulstrup but not observed by them when they performed this identical experiment. The reasons for the experimental discrepancy between our

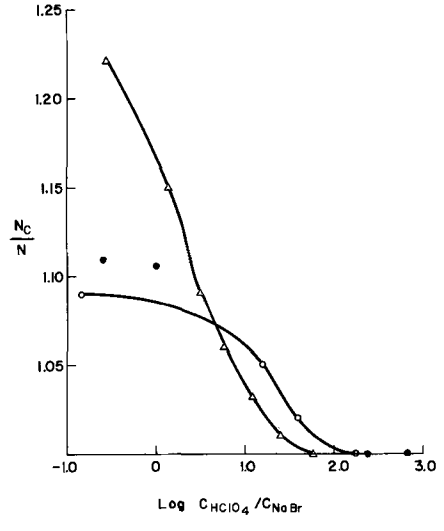

Fig. 2. Effect of C_{HClO_4} on the collection efficiency of ring-disk electrodes. Disk electrode reaction $2Br^- \rightarrow Br_2 + 2e$, ring electrode reaction, $Br_2 + 2e \rightarrow 2Br^-$. Key: △, $C_{NaBr} = 3.6 \times 10^{-3}$M, $N = 0.173$, and $\beta^{2/3} = 0.335$ (thin gap, thin ring electrode); ●, $C_{NaBr} = 3.6 \times 10^{-3}$M, $N = 0.399$, and $\beta^{2/3} = 1.16$ (thin gap, wide ring electrode); ○, $C_{NaBr} = 1.73 \times 10^{-2}$M, $N = 0.399$, and $\beta^{2/3} = 1.16$ (thin gap, wide ring electrode). Rotation speed = 2500 rpm (41.67 Hz).

results and those of Albery and Ulstrup is not clear; however, Albery and Hitchman (8) have confirmed that $N_c/N \geq 1$ on repeating one of our experiments.

The extent of deviation of N_c from N is a function both of the geometry of the ring-disk electrode and the amount of supporting electrolyte present. The largest deviation in 1 m*M* $HClO_4$ is observed with a thin gap, thin ring electrode, $N_c/N = 1.22$ (Δ in Fig. 2). The deviation is smaller for an electrode with a wider gap (○ and ● in Fig. 2). For an electrode with an extremely wide gap (N = 0.079 and $\beta^{2/3} = 0.73$) the value of $N_c/N = 1.02$ in a solution for which $C_{NaBr} = 3.6 \times 10^{-3}M$ NaBr and $C_{HClO_4} = 1.00 \times 10^{-3}M$. N_c/N *vs.* log C_{HClO_4}-data for the latter electrode are so close to 1.00 they are not plotted in Fig. 2. Thus, it appears that, for a given disk electrode radius, the wider the gap between the ring and disk electrodes, the more the concentration profile at the inside edge of the ring approaches the Levich situation. This result is seen by the simple analogy of fluid flowing in a tube into which a solute is injected upstream. The further downstream an observer is positioned, the less able he is to detect whether or not the solute was injected uniformly throughout a given upstream volume element.

On the basis of Fig. 2, it seems valid to conclude for ring-disk electrodes of the usual geometries that a fifty-fold excess of perchloric acid is sufficient to eliminate the possibility of detecting, through N, the effect of any nonuniform current distribution during the oxidation of Br^- at the disk electrode. Since the collection efficiency of a wide gap electrode is extremely insensitive to any nonuniform disk current distribution, such an electrode should prove quite valuable in situations where only the average flux leaving the disk need be determined.

Oxidation of metals.—A copper-disk, gold-ring electrode was used to study the collection efficiency of Cu(I) produced by oxidizing the copper disk in ammoniacal media. The current scanning technique used for the bromide studies was employed. The ring process was Cu (I) → Cu(II) + e and the ring current was proportional to the anodic disk current. As seen in Table I, $N_c/N_{theor} = 1.09$ in 0.1*M* NH_3 and is within a per cent of unity when $C_{NH_4^+} \geq 0.02M$.

A silver disk, graphite ring electrode was used to study the effect of C_{HClO_4} on N_c/N_{theor}. In these experiments silver dendrites grew very rapidly at the ring electrode, and the ring current for the reduction of silver increased with time at a constant anodic disk current. Therefore, N_c was obtained from the ring current extrapolated back to zero time. The results of these experiments are also shown in Table I. In 0.1*M* $HClO_4$, $N_c/N_{theor} = 1.00$ and does not change for $C_{HClO_4} = 1.0M$.

In both of these experiments, the electrode geometry is one that has been used fairly extensively in other studies. These electrodes are not overly sensitive to a nonuniform current distribution at the disk. The maximum disk current levels used in the above experiments correspond to disk electrode surface concentrations of 0.5 m*M* Cu (I) and 1.0 m*M* Ag (I). The appreciable positive effect in 0.5 m*M* $HClO_4$ for silver corresponds to the case in which the supporting electrolyte is not in excess of the surface concentration of the electrogenerated species. Supporting electrolyte concentrations approximately 50-100 fold larger than the surface concentrations were required to approach N_{theor} within 1%.

Table I. Variation of *N* with electrolyte concentration during the oxidation of metal disks

Cu disk in 0.1*M* NH_3[a]		Ag disk[b]	
$C_{(NH_4)_2SO_4}$, m*M*	N_c/N_{theor}	C_{HClO_4}, m*M*	N_c/N_{theor}
0	1.09	0.500	1.24
5.00	1.05	2.00	1.15
20.0	1.00	10.0	1.13
50.0	0.99	100.0	1.00
		1000.0	1.00

[a] $N_{theor} = 0.344$, copper disk, gold split ring, split corrected for in calculating N_{theor}, $i_d = 100$ μA. Rotation speed = 2000 rpm (33.3 Hz). $R_1 = 0.239$ cm, $R_2 = 0.263$ cm, and $R_3 = 0.323$ cm.
[b] $N_{theor} = 0.348$, silver disk, graphite split ring, split corrected for in calculating N_{theor}, $i_d = 100$ μA and 200 μA at each C_{HClO_4}. Average N_c/N_{theor} reported. Rotation speed = 2000 rpm (33.3 Hz). $R_1 = 0.227$ cm, $R_2 = 0.259$ cm, and $R_3 = 0.324$ cm.

Effect of supporting electrolyte on the ratio of ring and disk currents.—A plot of anodic ring electrode current *vs.* anodic disk electrode current was obtained for two ring-disk electrodes in 3.6×10^{-3} *M* NaBr solution containing 1.00 m*M* $HClO_4$. The ring potential was maintained equal to the disk electrode potential while the current through the disk electrode was scanned linearly with time. Next, sufficient concentrated $HClO_4$ was added to make the solution 0.2*M* in acid, and the previous experiment repeated. Both experiments yielded straight line plots, provided the electrode potential did not become so positive that platinum surface oxidation occurred. The slopes of these plots correspond to $\beta^{2/3}-N$ and are given in Table II, along with the theoretical values for $\beta^{2/3}-N$ calculated from the electrode geometry.

The higher current density at the ring electrode as compared to that at the disk electrode in the absence of excess supporting electrolyte is confirmed by the data in Table II.

The principal difference between the geometries of electrodes 1 and 2 (Table II) is in the width of the ring electrode. In such a situation, it is expected that the electrode with the narrower ring (electrode 1) should have the higher average current density arising from the nonuniform current density distribution caused by the absence of excess supporting electrolyte. This is the case, since the ratio of $\beta^{2/3}-N$ in the presence and absence of excess $HClO_4$ is greater for electrode 1, whose ring is about half the width of that of electrode 2.

Visual evidence for nonuniform current distribution.—A simple experiment can be performed which dramatically demonstrates the effects of a nonuniform current distribution at a disk electrode. First, copper is deposited on a rotating platinum disk electrode from a solution containing 3.0 m*M* $CuSO_4$ and 0.2 m*M* $HClO_4$ under conditions which yield a uniform deposit, *i.e.*, at a potential in the limiting current region. The amount of copper is not critical, and for demonstration purposes 5-10 min of deposition at 900 rpm produces a clearly visible deposit. Next, an anodic current equal in magnitude to the convective diffusion limiting current is passed through the electrode. As shown above by the collection efficiency studies involving the oxidation of copper and silver disks, the copper disk will be oxidized nonuniformly because of the lack of excess supporting electrolyte. Rather larger current densities are to be expected at the edge of the disk as compared to the center of the disk. Visual examination of the disk during the oxidation step produces the following observations which can only be explained by the more rapid oxidation of copper at the edge of the disk. First, immediately after starting the oxidation cycle, no visible change of the electrode

Table II. Effect of supporting electrolyte concentration on $\beta^{2/3}$-*N*

Solution	$\beta^{2/3}$-*N* for electrode 1[a]	$\beta^{2/3}$-*N* for electrode 2[a]
$3.6 \times 10^{-3}M$ NaBr + 1.0 m*M* $HClO_4$	0.45	1.25
$3.6 \times 10^{-3}M$ NaBr + 0.200*M* $HClO_4$	0.19	0.78
Theoretical value	0.17	0.76

[a] Rotation speed = 2500 rpm (41.67 Hz).

surface occurs. Then, a perfectly concentric band of platinum becomes visible at the edge of the disk, and the width of this band increases with time as the central area of the disk covered with copper shrinks. Ultimately the area covered by copper becomes zero. If the oxidation of the copper is interrupted some time after the outer platinum band becomes visible and the electrode is examined under 10X magnification, the border between the copper and platinum is seen to be very sharply defined. This result clearly demonstrates that the current density at the edge of the copper deposit is very much higher than the average current density.

Conclusions

Nonuniform current distribution effects at a rotating disk electrode, as predicted by Newman (2) and experimentally verified in a 0.1*M* $CuSO_4$-0.1*M* H_2SO_4 solution by Marathe and Newman (3), have been studied as a function of supporting electrolyte concentrations using a number of redox systems. A fifty-fold excess of supporting electrolyte is sufficient to produce a uniformly accessible disk surface during the deposition of Cu(II) from $NaClO_4$ media, provided the applied current exceeds 20% of the limiting current. The effects of nonuniform accessibility on the collection efficiency of a ring-disk electrode predicted by Albery and Ulstrup (5) have been observed and depend on the electrode geometry. Thin ring-thin gap electrodes are most sensitive to nonuniform current distribution effects, while extremely wide gap electrodes show barely detectable effects. The magnitude of the quantity $\beta^{2/3}$-N of a ring-disk electrode is also sensitive to nonuniform current densities at a disk electrode.

For practical purposes, results obtained with a ring-disk electrode in the presence of a 50 to 100-fold excess of supporting electrolyte may be assumed to be free of problems arising from nonuniform current density effects.

Manuscript submitted Feb. 27, 1970; revised manuscript received *ca.* April 7, 1970.

Any discussion of this paper will appear in a Discussion Section to be published in the June 1971 JOURNAL.

REFERENCES

1. John Newman, *This Journal*, **113**, 501 (1966).
2. John Newman, *ibid.*, **113**, 1235 (1966).
3. Vinay Marathe and John Newman, *ibid.*, **116**, 1704 (1969).
4. N. Schwartz and R. Brown, "1961 Transactions of the Eighth Vacuum Symposium and Second International Congress," pp. 1-10, Pergamon Press, Oxford (1961).
5. W. J. Albery and J. Ulstrup, *Electrochim. Acta*, **13**, 281 (1968).
6. B. Miller, *This Journal*, **116**, 1117 (1969).
7. D. T. Napp, D. C. Johnson, and S. Bruckenstein, *Anal. Chem.*, **39**, 481 (1967).
8. W. J. Albery and M. L. Hitchman, Private communication.

The Transient Regime of the Anodic Dissolution of a Three-Valent Metal Proceeding in Two Steps under Galvanostatic Conditions

I. H. Plonski*

Institute for Atomic Physics, Bucharest, Romania

ABSTRACT

The transient regime of the anodic dissolution of a three-valent metal, proceeding in two steps under galvanostatic conditions, is studied for the particular case when $z_1 = 1$, $z_2 = 2$ and $i_{01} > i_{02}$. It has been found in going from low to high current densities that the $\eta - t$ curve changes its shape, namely: for $i < i_{cr1}$, monotone increasing η toward the steady state; for $i_{cr1} < i < i_{cr2}$, peaked-shaped $\eta - t$ curves; for $i > i_{cr2}$, monotone increasing η toward the steady state again. Under particular conditions of $[M^+]_0$ values, the overvoltage peak may disappear for $i_{cr1} < i < i_{cr2}$. At the same time the $[M^+]_0 - t$ curves have shapes depending on the i and $[M^+]_0$ values. The steady-state value of the intermediate ion concentration increases with increasing current density, passes through a maximum, and then, for very high values of i, decreases toward zero. The decay curves do not display a peak. An apparent remanent overvoltage is noticed, especially for high values of $[M^+]_0$, when the decrease of $[M^+]$ toward $[M^+]_0$ is slow in comparison with the decrease of η toward zero.

In the present paper, the third of a series (1, 2) on the subject of the transient regime of two stepwise-proceeding electrode reactions, the case of the anodic dissolution of a three-valent metal is considered. The complete system of equations, describing the stepwise metal dissolution

$$M \rightleftharpoons M^{z_1+} + z_1 e^- \qquad [I]$$

$$M^{z_1+} \rightleftharpoons M^{(z_1+z_2)+} + z_2 e^- \qquad [II]$$

when the electron transfer and the mass transfer of the intermediate and final ion are taken into account (2), is

$$\frac{d\eta}{dt} = \frac{1}{C}\left[i + i_{02}\frac{[M^{(z_1+z_2)+}]}{[M^{(z_1+z_2)+}]_0} e^{-\alpha_{c2}\eta} - i_{01}e^{\alpha_{a1}\eta} - \frac{[M^{z_1+}]}{[M^{z_1+}]_0}\left(i_{02}e^{\alpha_{a2}\eta} - i_{01}e^{-\alpha_{c1}\eta}\right)\right] \qquad [1]$$

$$\frac{d[M^{z_1+}]}{dt} = \frac{i_{01}}{z_1\mathbf{F}} e^{\alpha_{a1}\eta} + \frac{i_{02}}{z_2\mathbf{F}}\frac{[M^{(z_1+z_2)+}]}{[M^{(z_1+z_2)+}]_0} e^{-\alpha_{c2}\eta} - \frac{[M^{z_1+}]}{[M^{z_1+}]_0}\left(\frac{i_{01}}{z_1\mathbf{F}} e^{-\alpha_{c1}\eta} + \frac{i_{02}}{z_2\mathbf{F}} e^{\alpha_{a2}\eta}\right) + D_1\left(\frac{\partial M_1}{\partial x}\right)_{x=0} \qquad [2]$$

* Electrochemical Society Active Member.

and

$$\frac{d[M^{(z_1+z_2)+}]}{dt} = \frac{i_{02}}{z_2\mathbf{F}}\left(\frac{[M^{z_1+}]}{[M^{z_1+}]_0}\,e^{\alpha_{a2}\eta} - \frac{[M^{(z_1+z_2)+}]}{[M^{(z_1+z_2)+}]_0}\,e^{-\alpha_{c2}\eta}\right) + D_2\left(\frac{\partial M_2}{\partial x}\right)_{x=0} \quad [3]$$

Here, η is the overvoltage, t the time, C the double layer capacity, i the current density, i_{01} and i_{02} the exchange current densities for the first and second step, respectively, $\mathbf{F}$ the Faraday number, $[M^{z_1+}]$ and $[M^{z_1+}]_0$ the intermediate ion concentration, $[M^{(z_1+z_2)+}]$ and $[M^{(z_1+z_2)+}]_0$ the final ion concentration at the electrode surface at the time t and at equilibrium; z_1 and z_2 are the number of electrons involved in the first and second step, respectively, and α_{a1}, α_{c1}, α_{a2}, and α_{c2} are given by the expressions: $\alpha_{a1} = \beta_1 z_1\mathbf{F}/RT$; $\alpha_{c1} = (1-\beta_1)z_1\mathbf{F}/RT$; $\alpha_{a2} = \beta_2 z_2\mathbf{F}/RT$; $\alpha_{c2} = (1-\beta_2)z_2\mathbf{F}/RT$ with β_1 and β_2 the symmetry factors for the first and second step, respectively, R the gas constant, and T the absolute temperature; the M_1 and M_2 are the concentrations of the intermediate and final ion, respectively, in the bulk of the solution; the terms $D_1\left(\frac{\partial M_1}{\partial x}\right)_{x=0}$ and $D_2\left(\frac{\partial M_2}{\partial x}\right)_{x=0}$ represent the rate of the appearance (or disappearance) of the respective ion at the electrode surface due to mass transfer.

In order to investigate the behavior of the electron transfer in a first approximation, the final ion concentration is assumed constant and the mass transfer processes are neglected. Therefore, the system of equations reduces to Eq. [1] and [2] with $D_1\left(\frac{\partial M_1}{\partial x}\right)_{x=0} = 0$.

Also, the treatment of the two mechanisms, $z_1 = 1$, $z_2 = 2$ and $z_1 = 2$, $z_2 = 1$, each of them for $\frac{i_{01}}{z_1} > \frac{i_{02}}{z_2}$, $\frac{i_{01}}{z_1} = \frac{i_{02}}{z_2}$ and $\frac{i_{01}}{z_1} < \frac{i_{02}}{z_2}$ in both anodic and cathodic directions, would be interesting, but the computations are very laborious so we studied only the case of $z_1 = 1$, $z_2 = 2$, and $\frac{i_{01}}{z_1} > \frac{i_{02}}{z_2}$. We also take $\beta_1 = \beta_2 = 0.5$, i.e., $\alpha_{a1} = \alpha_{c1} = \alpha$; $\alpha_{a2} = \alpha_{c2} = 2\alpha$.

Steady State, the Moment of Switching on the Current, and Their Critical Values

Under steady-state conditions the values of $[M^{z_1+}]$ and η, marked by the index ∞, are given by (1)

$$\frac{[M^{z_1+}]_\infty}{[M^{z_1+}]_0} = \frac{\frac{z_2}{z_1}\frac{i_{01}}{i_{02}}\,e^{\alpha_{a1}\eta_\infty} + e^{-\alpha_{c2}\eta_\infty}}{\frac{z_2}{z_1}\frac{i_{01}}{i_{02}}\,e^{-\alpha_{c1}\eta_\infty} + e^{\alpha_{a2}\eta_\infty}} = \frac{2\frac{i_{01}}{i_{02}}\,e^{\alpha\eta_\infty} + e^{-2\alpha\eta_\infty}}{2\frac{i_{01}}{i_{02}}\,e^{-\alpha\eta_\infty} + e^{2\alpha\eta_\infty}} \quad [4]$$

and

$$i = \frac{z_1+z_2}{z_2}\,i_{02}\,\frac{e^{(\alpha_{a1}+\alpha_{a2}+\alpha_{c1})\eta_\infty} - e^{-\alpha_{c2}\eta_\infty}}{1+\frac{z_1}{z_2}\frac{i_{02}}{i_{01}}\,e^{(\alpha_{a2}+\alpha_{c1})\eta_\infty}} = \frac{3}{2}\,i_{02}\,\frac{e^{4\alpha\eta_\infty} - e^{-2\alpha\eta_\infty}}{1+\frac{i_{02}}{2i_{01}}\,e^{3\alpha\eta_\infty}} \quad [5]$$

Equation [4] is evaluated for different values of η_∞ and $\frac{i_{01}}{i_{02}}$. The results are given in Fig. 1, from which we can note the following:

1. The intermediate ion concentration increases with increasing η_∞, passes through a maximum value, and decreases then toward zero.
2. The maximum value of $[M^+]_\infty$ and the overvoltage or the current density at which it is attained increase with increasing of the ratio $\frac{i_{01}}{i_{02}}$.

By forming the derivative of Eq. [4] and equating it to zero we obtain the expression of $\eta_{\infty[M^+]_{\infty\,\max}}$

$$\eta_{\infty[M^+]_{\infty\,\max}} = \frac{1}{3\alpha}\ln\frac{\left(1-\frac{i_{02}^2}{2i_{01}^2}\right)+\sqrt{\left(1-\frac{i_{02}^2}{2i_{01}^2}\right)-\frac{i_{02}^2}{4i_{01}^2}}}{\frac{i_{02}}{2i_{01}}} \quad [6]$$

from which in conjunction with Eq. [4], we obtain the maximum value of $[M^+]_\infty$ attainable for a given system.

The value of η_∞ for which the steady-state value of $[M^+]$ equals its equilibrium value results from Eq. [4]

$$\eta_{\infty[M^+]_\infty} = [M^+]_0 = \frac{1}{\alpha}\ln\frac{i_{01}+\sqrt{i_{01}^2-i_{02}^2}}{i_{02}} \quad [7]$$

Transient Regime

Because the system is too intricate to be used in the discussion of the critical values of i and η_∞ from which the $\eta - t$ curves can change their shapes we consider for a moment, as in the previous paper (1), that the capacitive current density is negligible, that is

$$i_{\mathbf{F}} = i_{01}\left(e^{\alpha_{a1}\eta} - \frac{[M^{z_1+}]}{[M^{z_1+}]_0}\,e^{-\alpha_{c1}\eta}\right) + i_{02}\left(\frac{[M^{z_1+}]}{[M^{z_1+}]_0}\,e^{\alpha_{a2}\eta} - e^{-\alpha_{c2}\eta}\right) = i \quad [8]$$

and

$$\frac{d\eta}{dt} = \frac{(i_{02}\,e^{\alpha_{a2}\eta} - i_{01}\,e^{-\alpha_{c1}\eta})\,[(z_1+z_2)\,i_{01}i_{02}(e^{(\alpha_{a1}+\alpha_{a2})\eta} - e^{-(\alpha_{c1}+\alpha_{c2})\eta}) - i\,(z_2\,i_{01}\,e^{-\alpha_{c1}\eta} + z_1\,i_{02}\,e^{\alpha_{a2}\eta})]}{N} \quad [9]$$

where

$$N = z_1z_2\,\mathbf{F}[M^{z_1+}]_0\,\{(\alpha_{c1}+\alpha_{a1})i_{01}^2\,e^{(\alpha_{a1}-\alpha_{c1})\eta} + (\alpha_{c2}+\alpha_{a2})\,i_{02}\,e^{(\alpha_{a2}-\alpha_{c2})\eta} + i_{01}i_{02}[(\alpha_{c2}-\alpha_{c1})\,e^{-(\alpha_{c1}+\alpha_{c2})\eta} + (\alpha_{a2}-\alpha_{a1})\,e^{(\alpha_{a1}+\alpha_{a2})\eta}] - i(\alpha_{a2}\,i_{02}\,e^{\alpha_{a2}\eta} + \alpha_{c1}\,i_{01}\,e^{-\alpha_{c1}\eta})\}$$

It can be seen from Eq. [9] that $\left.\frac{d\eta}{dt}\right|_{t=0} = 0$ in two particular cases:

1. When the first round bracket is zero, that is for

$$\eta_{(0+\epsilon)} = \frac{1}{\alpha_{a2}+\alpha_{a1}}\ln\frac{i_{01}}{i_{02}} \quad [10]$$

where $\eta_{(0+\epsilon)}$ is the value of η which the electrode potential assumes when the current is switched on. Because the $\eta - t$ curve, determined by Eq. [9], has no maxima, minima, or inflection points, $\left.\frac{d\eta}{dt}\right|_{t=0} = 0$ implies that $\eta_{(0+\epsilon)} = \eta_\infty$, in other words the overvoltage, attains its steady-state value from the beginning. From this critical value of η_∞, denoted by $\eta_{\infty cr1}$ (which

corresponds, in accordance with Eq. [8], to a critical value of i, denoted by i_{cr1}), the $\eta - t$ curve will change its curvature.

2. When the second bracket is zero, which is satisfied for the steady state (1), *i.e.*, for $[M^{z_1+}] = [M^{z_1+}]_\infty$. It can be seen from Eq. [4] or from Fig. 1 that $[M^{z_1+}]_0 = [M^{z_1+}]_\infty$ in two particular cases, namely; for $\eta_\infty = 0$) (*i.e.*, $i = 0$) which is an uninteresting case, and for η_∞ given by Eq. [7]. For this reason we denoted η_∞ given by Eq. [7] by $\eta_{\infty cr2}$ and its corresponding i by i_{cr2}.

In conclusion, if $C = 0$, the $\eta - t$ curve can change its curvature twice.

The fact that the double-layer capacity is in parallel with the equivalent impedance of the electrode reaction implies $\eta_{(0+\epsilon)} = 0$, *i.e.*, any real $\eta - t$ curve begins from zero, even for $i \neq 0$, with $\left.\frac{d\eta}{dt}\right|_{t=0} > 0$.

On the basis of expressions [1] and [2], theoretical curves of $\eta - t$ (Fig. 2) and $[M^+] - t$ (Fig. 3) were computed for the special case of $C = 3 \times 10^{-5}$ (**F**), $[M^+]_0 = 5 \times 10^{-11}$ ($M/1$), $i_{01} = 1 \times 10^{-4}$(A), $i_{02} = 1 \times 10^{-5}$(A) and different values of i pointed out on the figures.

From Fig. 2 the following observations are made:

1. As expected from the discussion of the case of $C = 0$, as a consequence of the competition between the charging of the double layer and the transitory electron transfer process, the $\eta - t$ curves are peak-shaped between i_{cr1} and i_{cr2}.

2. The difference $\eta_{peak} - \eta_\infty$ increases at first, passes through a maximum value, then, for $i \to i_{cr2}$, decreases toward zero. The maximum value of this difference and the corresponding i may be computed.

3. It is generally valid that the time necessary to reach the steady state decreases with increasing of i, except for i_{cr2} when the steady state of η is attained sooner. If $[M^+]_0$ is great enough, no noticeable change in the intermediate ion concentration takes place. Consequently, for i_{cr2} the $\eta - t$ curve reflects the charging of the double layer, only.

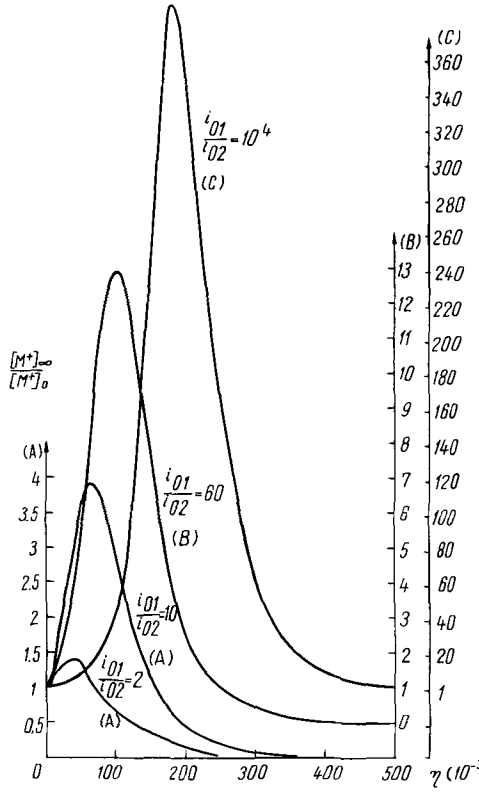

Fig. 1. Ratio between the intermediate ion concentration in the steady state and at equilibrium, $[M^+]_\infty/[M^+]_0$, as a function of steady-state overvoltage, η_∞, for different values of the ratio i_0/i_{02} written on the curves. (The capital letter on the curves indicates the ordinate.)

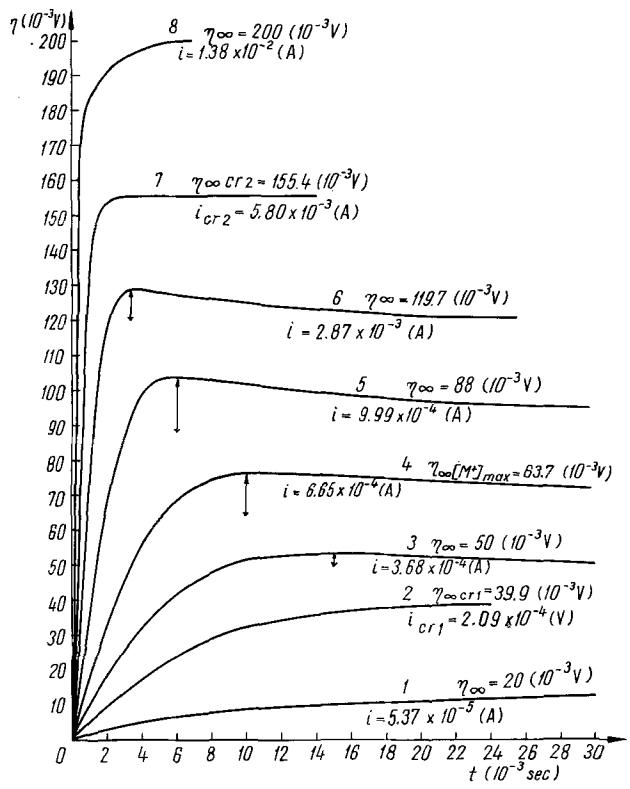

Fig. 2. Overvoltage, η, as a function of time, t, for different values of current density written on the curves. The arrows indicate the difference $\eta_{peak} - \eta_\infty$.

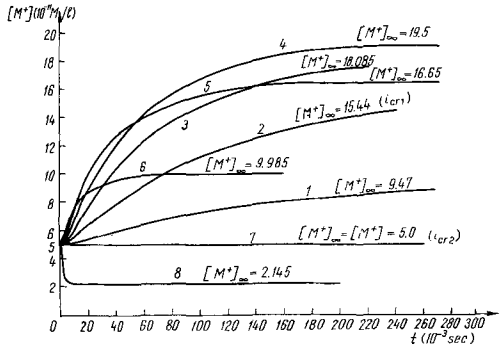

Fig. 3. Intermediate ion concentration, $[M^+]$, as a function of time, t, for the current densities corresponding to the same numbers as the curves in Fig. 2.

From Fig. 3A it may be noticed that for $i < i_{[M^+]_\infty max}$, the $[M^+] - t$ curves are S-shaped; for $i > i_{[M^+]_\infty max}$, these curves may be S-shaped or may have maxima, depending on the $[M^+]_0$ value. This is discussed later. Furthermore, the influence of the change of intermediate ion concentration at equilibrium is studied.

Due to the complexity of the expression for the production rate of the intermediate ion, $\frac{d[M^+]}{dt}$, it is difficult to discuss quantitatively the influence of the change of $[M^{z_1+}]_0$ on it, but it is known that this rate can vary between $\frac{2i_{01} - i_{02}}{2\mathbf{F}(i_{01} + i_{02})} i$ (the maximum value attainable at $t = 0 + \epsilon$ if $C = 0$) and zero (the rate at the steady state) (1).

On the other hand, it follows from Eq. [4] that the steady-state intermediate ion concentration is proportional to its equilibrium concentration.

The fact that $\frac{d[M^+]}{dt}$ cannot surpass the maximum value given before, but that $[M^+]_0$ can theoretically be as high as we desire means that the period of time necessary to attain $[M^+]_\infty$ and η_∞ increases with increasing $[M^+]_0$. This can be seen from Fig. 4A and 5A.

For large values of $[M^+]_0$ (curves c) there appears a disproportion between the period of time necessary to attain, say, 90% of η_∞ for η and the same proportion of $[M^+]_\infty$ for $[M^+]$, *i.e.*, the overvoltage increases rapidly to a value near η_∞ as $[M^+]$ changes very little.

For very low values of $[M^+]_0$ (curves a) $[M^+]$ also will have very low values; consequently, the change of the intermediate ion concentration does not affect the $\eta - t$ curves noticeably. In contrast, little changes of η lead to large changes in the $[M^+] - t$ curves, for example, the maxima presented by curves 5a and 8a.

It is interesting to notice the influence of the change of the intermediate ion concentration at equilibrium on the $\eta - t$ curves for $i_{cr1} < i < i_{cr2}$, *i.e.*, for the domain of possible peak-shaped $\eta - t$ curves. For very low values of $[M^+]_0$ (curve 4a, Fig. 4A), when the overvoltage attains for the first time the value of η_x, the intermediate ion concentration attains the $[M^+]_\infty$ value too, so that the steady state is established. In this case the peak disappears and the overvoltage at the plateau corresponds to η_x. For moderate values of $[M^+]_0$ (curves 4b, Fig. 4A) because at the very moment when η attains the value of η_∞ first, $[M^+]$ is far from its steady-state value, η increases continuously and then decreases to η_∞. The peak appears. The difference $\eta_\infty - \eta_{peak}$ increases with increasing $[M^+]_0$ approaching its maximum value given by the difference $\eta_\infty - \eta_{(0+\epsilon)}$. For very high values of $[M^+]_0$ (curve 4c, Fig. 4A), we have an apparent disappearance of the peak. The slope of the decrease of η from η_{peak} to η_∞ being very little, a pseudoplateau is established so that η_{peak} and η_∞ cannot be distinguished experimentally.

The effect of $[M^+]_0$ on the shape of $\eta - t$ curves will be explained clearly by means of an equivalent scheme which will be given elsewhere.

In addition to this, the following observations are made from Fig. 5A:

1. The $[M^+] - t$ curves have shapes depending on the value of $[M^+]_0$ besides the value of i.
2. For large values of $[M^+]_0$, the $[M^+] - t$ curves are only S-shaped (curves c).
3. For an intermediate value of $[M^+]_0$ (curves b) and $i > i_{[M^+]_\infty max}$, the $[M^+] - t$ curves may be S-shaped for lower values of i and may display maxima for larger currents.
4. For low values of $[M^+]_0$ and $i > i_{[M^+]_\infty max}$ all $[M^+] - t$ curves display maxima even for the case of $[M^+]_\infty = [M^+]_0$ (not given on the figure) or of $[M^+]_\infty < [M^+]_0$ (curve 8a). The maximum transition value of $[M^+]$, attainable in this case, is the greater the lower is the value of i, but can never surpass the maximal value of $[M^+]$ given by Eq. [4] in conjunction with Eq. [6].

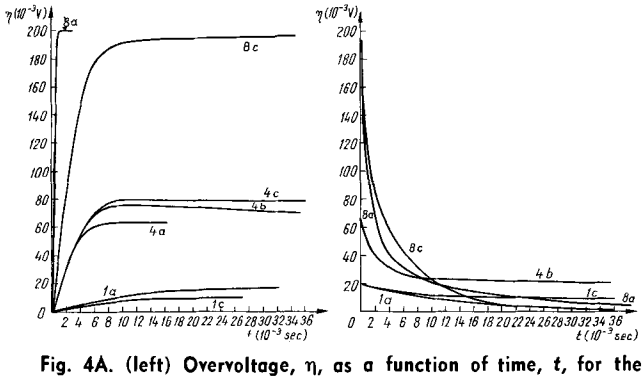

Fig. 4A. (left) Overvoltage, η, as a function of time, t, for the current densities corresponding to the same numbers as the curves in Fig. 2 and to the following values of initial intermediate ion concentration, $[M^+]_0$: curves a, $[M^+]_0 = 5 \times 10^{-13}$ M/l; curves b, $[M^+]_0 = 5 \times 10^{-11}$ M/l; curves c, $[M^+]_0 = 5 \times 10^{-10}$ M/l.

Fig. 4B. (right) Decay curves corresponding to the curves in Fig. 4A.

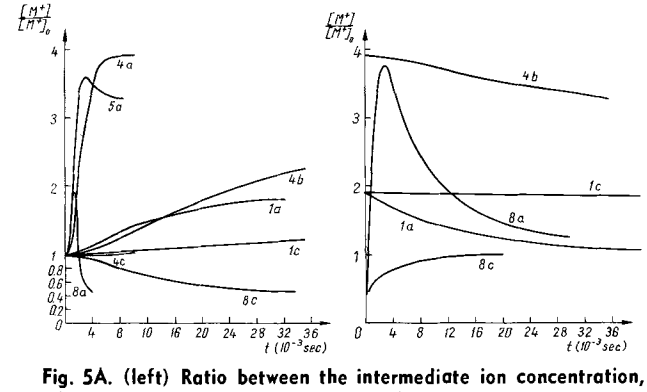

Fig. 5A. (left) Ratio between the intermediate ion concentration, $[M^+]$, and its value at equilibrium, $[M^+]_0$, as a function of time, t, corresponding to the curves in Fig. 4A. The upper abscissa is valid only for curve 8a.

Fig. 5B. (right) Ratio between the intermediate ion concentration and its value at equilibrium, $[M^+]/[M^+]_0$ as a function of time, t, corresponding to the curves in Fig. 5A.

Decay Curves

The decay curves were computed on the basis of Eq. [1] and [2] with η_∞ and $[M^+]_\infty$ as initial values of η, $[M^+]$, and $i = 0$, in other words we consider that the current is switched off after the reaching of the steady state. Some specific curves corresponding to the curves of Fig. 4A and 5A are given in Fig. 4B and 5B.

From Fig. 4B two observations are made:

1. The decay curves are monotone, η decreasing toward zero. No peak, which would imply transitory negative values of η, is noticed.
2. From a certain time, the decrease toward the steady state is slow so that an apparent remanent overvoltage may be noticed experimentally (curves 1c and 4b).

From Fig. 5B characteristic shapes of $[M^+] - t$ curves as functions of i and $[M^+]_0$ values result.

1. For $i < i_{cr1}$, curves 1, $[M^+]_0$ is monotonously decreasing. For high values of $[M^+]_0$, curve 1c, the decrease of the intermediate ion concentration is very slow, so that when the electrode potential approaches a pseudoplateau of η, $[M^+]$ is diminished very little.
2. For $i_{cr1} < i < i_{cr2}$, curve 4b, $[M^+]$ decreases following an S-shaped $[M^+] - t$ curve.
3. For $i > i_{cr2}$, $[M^+]$ increases to the equilibrium value following a simple monotonously increasing curve for high values of $[M^+]_0$, curve 8c, or following a peak-shaped curve for very low values of $[M^+]_0$.

Conclusions

1. The appearance of $\eta - t$ curves with peaks in a certain domain of i in the anodic dissolution of a trivalent metal may prove a stepwise mechanism in which $z = 1$, $z = 2$, and $i_{01} > i_{02}$.
2. The absence of $\eta - t$ curves with peaks does not prove that the dissolution is not proceeding stepwise. In this case attention must be given not to confuse η_∞ with η_{peak}.
3. The decay curves do not have peaks. Due to an apparent remanent overvoltage and $[M^+]$, attention must be paid not to apply a second current pulse too soon, because this second pulse would start with com-

pletely different initial values than the equilibrium values corresponding to the former pulse.

4. By anodic dissolution of a three-valent metal, proceeding in two steps which were dealt with above, intermediate ion concentrations higher than a critical value cannot be obtained.

Manuscript received Feb. 17, 1970.

Any discussion of this paper will appear in a Discussion Section to be published in the June 1971 JOURNAL.

REFERENCES

1. I. H. Plonski, *This Journal*, **116**, 944 (1969).
2. I. H. Plonski, *ibid.*, **116**, 1688 (1969).

Faradaic Impedances: Diffusion Impedance and Reaction Impedance

Israel Epelboin* and Michel Keddam

Groupe de Recherche du C.N.R.S., "Physique des Liquides et Electrochimie," associé à la Faculté des Sciences, 9, quai Saint-Bernard, Paris 5°, France

ABSTRACT

Relative contributions of double-layer and faradaic impedances have been studied for two typical cases involving important electrochemical processes. The faradaic impedance has been interpreted quantitatively in terms of models which describe either the mass transport or the reaction mechanism at the electrode. The first case is the electrochemical reduction of the I_3^- ion at a rotating platinum disk in the presence of a supporting electrolyte (KI 0.1*N*). The mass transport impedance has been computed by means of a Laplacian transformation of the impulsional response of the system. It is shown that this impedance accurately follows an expression based on Nernst's hypothesis. The diffusion layer thickness, determined by means of impedance measurements, is in agreement with that deduced from hydrodynamic data. The second case is the anodic dissolution of iron in aqueous sulfuric acid at different pH's. The steady-state current-potential curves and the complex impedance in the whole frequency range, between 30 kHz and 10^{-5} kHz, have been interpreted in terms of a dissolution mechanism in two steps involving an adsorbed FeOH intermediate.

Despite the capacitive behavior of the over-all impedance of an electrode in the high-frequency range, separating the double-layer impedance from the faradaic impedance is very difficult, and often impossible, when rapid electrode reactions occur. For slow electrochemical processes, the theoretical justification of an *a priori* distinction between double-layer charging and charge transfer is still controversial (1), even in the presence of a supporting electrolyte (2) and in the absence of specific adsorption.

In this article, the problem has been approached from an experimental point of view, turning to account the complete analysis of variations of the impedance of the electrode up to its limit at zero frequency. For this purpose, we chose two markedly different electrochemical systems, the first having a diffusion impedance, the second a reaction impedance. The two examples are the polarographic discharge of the I_3^- ion at a platinum electrode, and the anodic dissolution of iron in an acidic medium, respectively. In both cases, exact determination of faradaic impedance is an effective method for testing the validity of models that describe mass transport or the succession of heterogeneous reaction steps at an electrode surface. In the first system, the presence of a supporting electrolyte and the limiting of the reaction rate by a slow process, *i.e.*, convective diffusion, are favorable conditions for distinguishing between double-layer capacity and faradaic impedance. On the other hand, neither of these conditions is satisfied in the second example, and separation seems more delicate.

Experimental

Compounds.—Water for electrolyte solutions was distilled and then treated on an ion exchange resin. Reagents such as I, KI, H_2SO_4, and Na_2SO_4 were analytically pure (Merck).

Electrodes and cell.—Platinum was provided by the Lyon-Allemand Laboratories (Paris) and iron, spectroscopically pure, by Johnson-Matthey Chemicals Ltd. (London). The disk electrode is made up of a cylindrical cross section whose surface is isolated by a polyolefinic thermoretractable sheath. The surface in contact with the electrolyte is treated with emery paper (600 grade), then polished with alumina or diamond paste (7 μm).

The rotation speed of the disk, driven by an asynchronous motor, is checked by a stroboscope and is stable to better than 1%. A double compartment saturated calomel reference electrode (SCE) is directly immersed in the cylindrical glass cell, maintained at 25° ± 0.1°C by water circulation. The counterelectrode is a coaxial platinum mesh having a large surface area.

Electronic set-up.—A detailed description of the potentiostatic apparatus, essentially a wide-band potentiostat (PZ1 Electronique Appliquée, Paris), has been given elsewhere (3, 4). Impedances have been determined by two methods: the one using a sinusoidal potential, the other an impulsion technique. For frequencies f greater than 0.01 kHz, measurements have always been carried out under sinusoidal conditions with an impedance meter giving the phase and modulus of the impedance (3). For frequencies below 0.01 kHz, different methods have been used in the two cases considered: (*i*) for I_3^- discharge, impedance is deduced from the response of the system to a small amplitude step by means of a Laplacian transformation in real terms. Impedances were electronically computed; (*ii*) for iron dissolution, impedance is determined by means of Lissajous' oscillographic method

* Electrochemical Society Active Member.

(Tektronix oscilloscope, Type 536, two W plug-in units).

Results and Discussion

Diffusion impedance: polarographic discharge of an ion.—The over-all electrochemical reaction in aqueous solutions is

$$I_3^- + 2e^- \rightarrow 3I^-$$

The presence of the supporting electrolyte KI (0.1*N*) allows us to neglect all coupling between layer charging and charge transfer. For the same reason, electrical migration does not contribute to transport of the I_3^- ion, which is solely due to convective diffusion. Use of a rotating disk electrode ensures that the diffusion layer is of uniform thickness at the electrode surface (uniformly accessible surface). Figure 1 shows a group of current-potential curves $I = f(V)$ obtained, for solutions 2.44 x 10^{-3} M in I_3^-, at different rotation speeds Ω (in rpm). We have checked that the limit currents are proportional to $\Omega^{1/2}$ under conditions of laminar flow, in conformity with hydrodynamic theory. Impedance diagrams in the complex plane $Z = R - jG$ have been recorded under the same conditions as for Fig. 1. An example is given in Fig. 2 for a potential of 0.25 V/SCE and a rotation speed Ω = 900 rpm. Diffusion impedance Z_d and transfer resistance R_t then have comparable values. The double-layer capacity C_d, in parallel with R_t, gives rise to the circular part of the

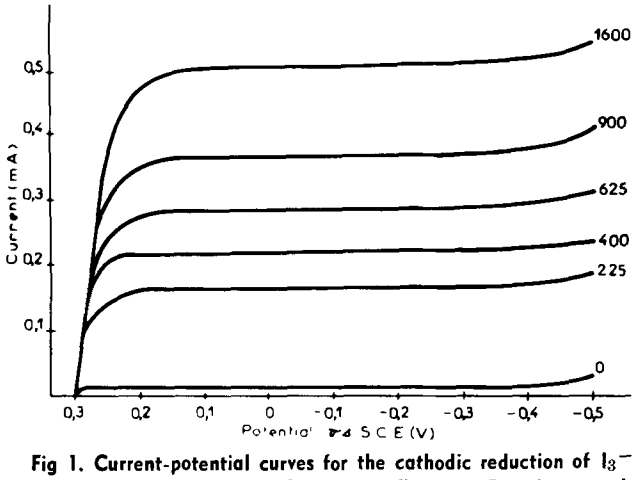

Fig 1. Current-potential curves for the cathodic reduction of I_3^- at a rotating platinum disk 0.4 cm in diameter. Rotation speeds Ω in rpm; $[I_3^-]$ = 2.44 x 10^{-3}M; [KI] = 0.1M; temperature, 25° ± 0.1°C.

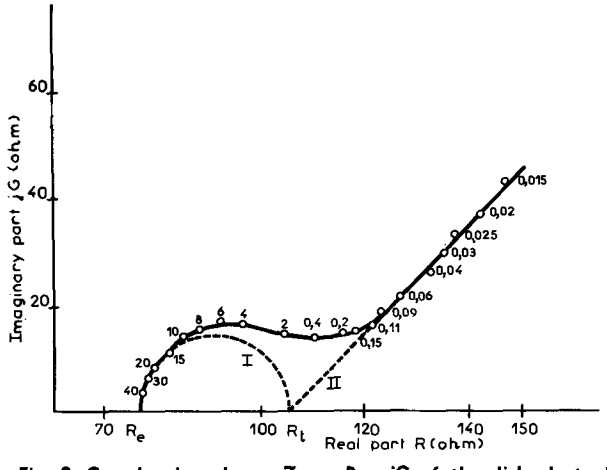

Fig. 2. Complex impedance $Z = R - jG$ of the disk electrode measured under the same conditions as for Fig. 1 (Ω = 900 rpm; V = 0.25 V/SCE). Experimental points correspond to frequencies in kHz. Dotted lines: I = C_d shunted by Z_f; II = Warburg's impedance (see Eq. [1]).

diagram between 40 and 0.2 kHz (line I, in Fig. 2). For this frequency range, C_d can be calculated as 8 μF · cm^{-2}. As well as the resistance of the electrolyte R_e, the capacity C_d is independent of the rotation speed of the disk, and hence of the concentration of I_3^- in the interface. After correcting the total impedance for the effect of C_d by assuming it to be of constant value (8 μF · cm^{-2}) in parallel with the faradaic impedance, we verify that this result is in agreement with the role of KI as supporting electrolyte. It is to be noted that the pretreatment of the electrode surface is of great importance: a diamond-polished disk gives a double-layer capacity almost three times as large as that for an alumina-polished disk.

After eliminating C_d, presumed to be in parallel with the faradaic impedance $Z_f = R_t + Z_d$, we verify that, for frequencies greater than about 10 Hz, the frequency dependence of the diffusion impedance can be expressed by Warburg's formula

$$Z_d = \frac{A}{\sqrt{j\omega}} \qquad [1]$$

where A = constant and $\omega = 2\pi f$. A straight line of slope unity (line II, in Fig. 2) corresponds to this equation.

Analysis of the variation of the diffusion impedance for frequencies below 0.01 kHz, measured by the method given in the experimental section, shows that Z_d no longer obeys Eq. [1], but can be accounted for satisfactorily by the analytical expression [2]

$$Z_d = \frac{R_d \operatorname{th} \sqrt{j\omega\, \delta^2/D}}{\sqrt{j\omega\, \delta^2/D}} \qquad [2]$$

based on the assumption (4, 5, 6) that transport is due exclusively to diffusion through an electrolyte layer of thickness δ and with a diffusion coefficient D (Nernst's hypothesis). It can be easily ascertained that for sufficiently high frequencies (th $\sqrt{j\omega\, \delta^2/D} \sim 1$), Eq. [2] becomes Eq. [1].

To illustrate the good agreement between theory and experiment, we list in Table I the values of δ_1 and δ_2 calculated from Eq. [2] at different rotation speeds, for two different frequency ranges; Table I also gives the thickness of the Nernst layer calculated from the hydrodynamic equation for a rotating disk, Eq. [3]

$$\delta_N = 1.61 \left(\frac{D}{\nu}\right)^{1/3} \left(\frac{\nu}{\Omega}\right)^{1/2} \qquad [3]$$

where ν denotes the kinematic viscosity of the solution. Table I shows that δ_1 and δ_2 values, obtained from diffusion impedance measurements, are indeed independent of frequency, which is in agreement with Eq. [2]. Furthermore, it can be seen from the last column of Table I that the thickness thus determined is accurately proportional to $\Omega^{-1/2}$.

Table I. Determination of the Nernst layer thickness, δ, by diffusion impedance measurements (diffusion coefficient D = 1.13 x 10^{-5} cm^2 sec^{-1}; kinematic viscosity ν = 0.00874 cm^2 sec^{-1})

Rotation speed of the disk Ω (rpm)	Nernst layer thickness (10^{-3} cm) δ_1*	δ_2**	δ_N***	$\Omega^{1/2}\left(\frac{\delta_1 + \delta_2}{2}\right)$
1600	1.7	1.7	1.32	68
900	2.3	2.3	1.75	69
625	3.1	3.0	2.20	78
400	3.6	3.6	2.64	72
225	4.3	4.4	3.62	65

* Calculated from Eq. [2] for 10^{-4} kHz $\leq f \leq 10^{-2}$ kHz.
** Calculated from Eq. [2] for 10^{-5} kHz $\leq f \leq 10^{-4}$ kHz.
*** Calculated from Eq. [3].

Reaction impedance: anodic dissolution of iron.—The over-all anodic reaction in aqueous sulfuric acid is

$$Fe \rightarrow Fe^{2+} + 2e^-$$

The rate of this reaction increases with increasing electrolyte pH, as shown by the current-potential curves (Fig. 3). Curves 1 to 4 correspond to pH values of 0.03, 1.61, 2.68, and 3.50, respectively. The electrode rotation speed (2000 rpm) is sufficiently high to make all effects of mass transport on dissolution rate negligible, even for the highest anodic currents reached here. These curves have been corrected for ohmic drop, previously determined either by an interruptor method (7) or from the high frequency limit of the impedance. The current-potential curves tend, for high anodic potentials, to a common line, independent of pH. For lower anodic potentials, these curves become almost parallel; the reaction is then nearly first order in OH^-, as can be calculated from the following equation

$$\left(\frac{\partial \log I}{\partial pH}\right)_V = -\left(\frac{\partial \log I}{\partial V}\right)_{pH}\left(\frac{\partial V}{\partial pH}\right)_I$$

This result strongly supports one of the mechanisms proposed by Bockris, Drazič, and Despič (8) which implies the formation of an adsorbed FeOH intermediate. On the other hand, the hypothesis that FeOH acts as a catalyst, suggested by Heusler (9), which predicts a reaction order of 2 tending to 1 for high anodic polarizations (7), must be rejected. The mechanism proposed in ref. (8) involves the following steps

$$Fe + (OH^-)_{ads} \underset{K_1'}{\overset{K_1}{\rightleftharpoons}} (FeOH)_{ads} + e^- \qquad [I]$$

$$(FeOH)_{ads} \xrightarrow{K_2} (FeOH)^+ + e^- \qquad [II]$$

$$(FeOH)^+ + H^+ \rightleftharpoons Fe^{2+} + H_2O \qquad [III]$$

In step [I], the adsorbed hydroxyl gives an adsorbed $(FeOH)_{ads}$ intermediate. In step [II], iron would leave the lattice as a cation $(FeOH)^+$; then, in step [III], would pass into the solution as a Fe^{2+} ion. This reaction mechanism can be accounted for, if step [III] is neglected, by calculations similar to those already used in the case of hydrogen evolution (10) and iron dissolution (11). Steps [I] and [II] being simultaneous, we shall consider they occur on fractional electrode areas of $(1 - \theta)$ and θ, respectively; according to the Langmuir isotherm, the fraction θ is covered by a monolayer of FeOH. The relationship between current and potential can then be expressed (7) as

$$I = \frac{2FK_1K_2\beta\,[OH^-]}{K_1[OH^-] + (K_1' + K_2)\,\beta} \qquad [4]$$

where β denotes the maximum superficial density of $(FeOH)_{ads}$. The electrochemical rate constants K_1, K_1', and K_2 of steps [I] and [II] are supposed to follow Tafel's law

$$K_i = k_i \exp b_i V$$

where k_i is the pre-exponential rate constant and b_i the Tafel exponent.

If the anodic potential is sufficiently high, the rate constant K_1' of the reverse reaction in step [I] can be neglected in the denominator of Eq. [4]. If we define the partial currents I_1 and I_2, determined by the rates of reactions [I] and [II], as

$$I_1 = 2F\,K_1[OH^-] \qquad [5]$$

and

$$I_2 = 2F\,K_2\,\beta \qquad [6]$$

expression [4] then simplifies to

$$I = \frac{I_1 I_2}{I_1 + I_2} \qquad [7]$$

and the coverage coefficient can be expressed as

$$\theta = \frac{I_1}{I_1 + I_2} \qquad [8]$$

According to Eq. [7], when the potential increases steps [I] and [II] become successively rate determining, in an order which depends on the relative values of b_1 and b_2. These two coefficients can be determined by means of the curves in Fig. 3.

1. In a range from 4 to 100 mA, the form of the $I = f(V)$ characteristics is in agreement with Eq. [7] (4, 7).
2. When the anodic polarization is low, the curves tend toward the straight lines I_{1A}, I_{1B}, I_{1C}, and I_{1D} (Fig. 3, in dotted lines) which represent the variations of the current I_1, following Eq. [5], their common slope being $b_1 = 36V^{-1}$.
3. When the anodic polarization is very high, the curves approach a common asymptote I_2 (dotted line), which is in agreement with Eq. [6], its slope being $b_2 = 10.5V^{-1}$.
4. Below 4 mA, the experimental plot deviates from the I_1 lines, because of the influence of cathodic reactions (reverse reaction in step [I], reduction of dissolved oxygen, discharge of the solvated proton). Moreover, partial coverage by adsorbed hydrogen diminishes the effective area of the electrode (7).

Taking into account the sign of $(b_1 - b_2)$, it is found, from Eq. [8], that the degree of coverage by $(FeOH)_{ads}$ increases with increasing anodic potential, reaches 0.5 for $I_1 = I_2$ (points N_1, N_2, N_3, or N_4, in Fig. 3), then tends toward 1.

By studying the relaxation of θ, by analysis of the faradaic impedance Z_f, we should be able to confirm these first results. In fact, by assuming that the potential V undergoes sinusoidal oscillations of very small amplitude and of frequency f, we have deduced from Eq. [4] an expression for Z_f; this expression, already proposed elsewhere (4), can be simplified under conditions where K_1' is negligible (this is the case for $I >$ 4 mA), and becomes

$$\frac{1}{Z_f} = \frac{FK_1\,[OH^-]\,K_2\beta}{K_1\,[OH^-] + K_2\beta}\left[\, b_1 + b_2 + \frac{(K_2\beta - K_1\,[OH^-])\,(b_1 - b_2)}{j\,\omega\,\beta + K_1\,[OH^-] + K_2\beta}\,\right] \qquad [9]$$

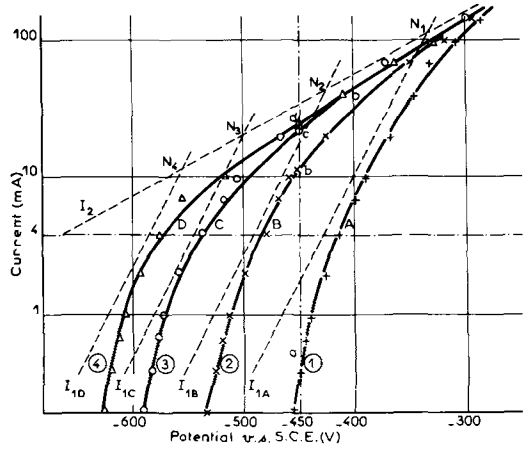

Fig. 3. Steady-state current-potential curves for the anodic dissolution of a rotating disk of Johnson-Matthey iron 0.5 cm in diameter. (Ω = 2000 rpm; temperature, 25° ± 0.1°C.) + Curve 1: H_2SO_4 1M, pH = 0.03; × curve 2: H_2SO_4 0.1M, Na_2SO_4 0.9M, pH = 1.61; ● curve 3: H_2SO_4 0.01M, Na_2SO_4 0.99M, pH = 2.68; △ curve 4: H_2SO_4 0.0012M, Na_2SO_4 1M, pH = 3.50. Continuous line = experimental curves; dotted line = partial currents deduced from Eq. [15] and [6].

In terms of Eq. [5], [6], and [7], Eq. [9] becomes

$$\frac{1}{Z_f} = \frac{I}{2}\left[b_1 + b_2 + \frac{(b_1 - b_2)(I_2 - I_1)}{2\mathbf{F}j\omega\beta + (I_1 - I_2)} \right] \qquad [10]$$

This expression, a rational fraction in $j\omega$, corresponds to an equivalent scheme whose elements are independent of frequency and depend on potential only through currents I, I_1, and I_2 defined above. Since $b_1 > b_2$, the reactive element of the scheme will be a capacity for $I_1 > I_2$ (*i.e.*, for potentials more anodic than those corresponding to points N_1, N_2, N_3, or N_4, in Fig. 3) and a self-inductance in the contrary case.

The four diagrams of Fig. 4, 5, 6, and 7 which correspond to this last case, have been recorded under the same conditions (of pH and polarization) as points A, B, C, and D in Fig. 3. We verified in all cases that the extrapolated impedance at zero frequency is equal to dV/dI.

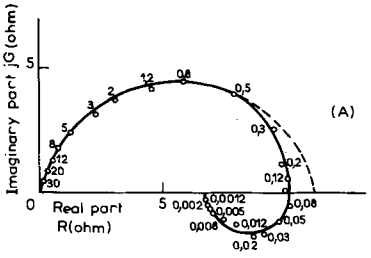

Fig. 4. Complex impedance $Z = R - jG$ for an iron anode under the same conditions as for Fig. 3. (A) represents the polarization point.

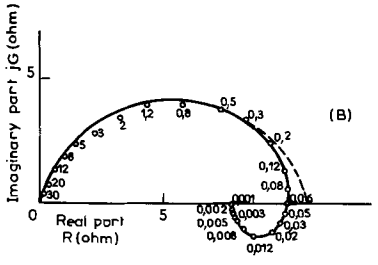

Fig. 5. Complex impedance $Z = R - jG$ for an iron anode under the same conditions as for Fig. 3. (B) represents the polarization point.

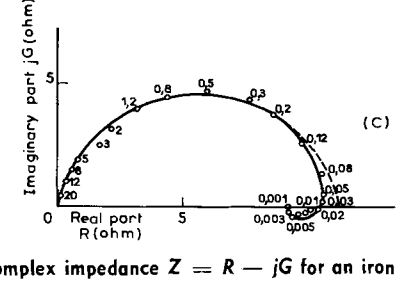

Fig. 6. Complex impedance $Z = R - jG$ for an iron anode under the same conditions as for Fig. 3. (C) represents the polarization point.

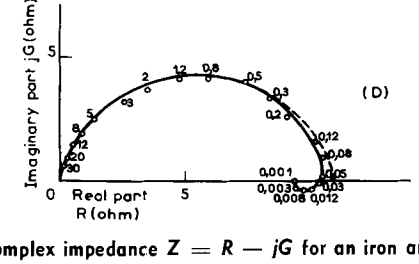

Fig. 7. Complex impedance $Z = R - jG$ for an iron anode under the same conditions as for Fig. 3. (D) represents the polarization point.

The variations of the experimental impedance with frequency are in agreement with the theoretical expression of Z_f (Eq. [10]), if the electrochemical double layer is taken into account. This layer introduces a capacitive contribution on the over-all impedance Z in the high-frequency range.

The inductive behavior of Z_f is shown in the $Z = R - jG$ diagrams by (*a*) a maximum of the real component R, and (*b*) a negative value of the imaginary component G.

Using these results, we tried to determine the equivalent circuit elements in order to compare them with values calculated by means of Eq. [10] which can also be expressed as

$$\frac{1}{Z_f} = \frac{1}{R_t} + \frac{1}{jL\omega + \rho} = \frac{1}{R_t} + \frac{1}{\rho(1 + j\omega\tau)}$$

where

the transfer resistance

$$R_t = \frac{2}{I(b_1 + b_2)} \qquad [11]$$

the faradaic resistance

$$\rho = \frac{2(I_1 + I_2)}{I(b_1 - b_2)(I_2 - I_1)} \qquad [12]$$

the faradaic time-constant

$$\tau = \frac{L}{\rho} = \frac{2\mathbf{F}\beta}{I_1 + I_2} \qquad [13]$$

A numerical analysis (carried out in collaboration with J. C. Lestrade) of the diagrams in Fig. 4 to 7 reveals that it is impossible to describe adequately the experimental results by assuming that the equivalent scheme of Eq. [10] is shunted by a constant capacity. We have therefore represented the observed systematic deviation by a distribution of the capacitive time-constant in the high frequency range, about a characteristic value τ_{HF}. For this purpose, two empirical relations, frequently adopted in dielectric relaxation studies, have been used. The first one, of a symmetrical type (12), leads to an expression of the over-all impedance of the electrolyte, including the resistance of the electrolyte

$$Z = R_e + \left\{ \frac{1}{R_t}\left[1 + (j\omega\,\tau_{HF})^{\gamma}\right] + \frac{1}{\rho(1 + j\omega\tau)} \right\}^{-1} \qquad [14]$$

The second one is of an asymmetrical type (13)

$$Z = R_e + \left\{ \frac{1}{R_t}(1 + j\omega\,\tau_{HF})^{\gamma} + \frac{1}{\rho(1 + j\omega\tau)} \right\}^{-1} \qquad [15]$$

where γ is a nondimensional number between 0 and 1.

Parameters R_e, R_t, τ_{HF}, γ, ρ, and τ have been determined by means of the least-squares method applied to nonlinear complex functions, in the same manner as for certain relaxation problems already studied in our laboratory (14). The calculations have been carried out on a IBM 360/75 computer. These results are presented in Table II, with their confidence interval calculated on the 10% level of significance (15). They indicate that the two resistances R_e and R_t are scarcely affected by the adopted distribution law, whereas the characteristic elements of low frequency behavior of the system, *i.e.*, ρ and τ, depend markedly on this law. The data in the third column are deduced from steady-state measurements, corresponding to Fig. 3, by means of Eq. [11], [12], and [13]. The value of β adopted in Eq. [13], *i.e.*, 3×10^{-9} cm^{-2}, corresponds to a FeOH layer on the plane (110) of the α-Fe crystal lattice. Agreement between measured (columns 1 and 2) and calculated (column 3) values is quite good except for τ. The differences observed in the case of the time-constant might be explained by the fact that the theory

Table II. Comparison between measured (columns 1 and 2) and calculated (column 3) parameters for the electrode impedance

Polarization points*	Parameters	Deduced from Z and Eq. [14]	Deduced from Z and Eq. [15]	Calculated from $I = f(V)$ and Eq. [11], [12], and [13]
A	R_o (ohm)	2.23 ± 0.09	1.99 ± 0.13	**
	R_t (ohm)	10.75 ± 0.33	10.40 ± 0.25	10.5
	τ_{HF} (millisec)	0.153 ± 0.096	0.23 ± 0.02	**
	γ	0.831 ± 0.024	0.679 ± 0.039	**
	ρ (ohm)	19.7 ± 1.3	22.7 ± 1.7	25.5
	τ (millisec)	10.4 ± 1.6	12.2 ± 2	0.96
B	R_o (ohm)	7.50 ± 0.11	7.03 ± 0.20	**
	R_t (ohm)	11 ± 0.28	10.74 ± 0.23	10.5
	τ_{HF} (millisec)	0.173 ± 0.009	0.324 ± 0.031	**
	γ	0.775 ± 0.023	0.559 ± 0.038	**
	ρ (ohm)	29.35 ± 1.55	38.60 ± 3.10	31.4
	τ (millisec)	11.5 ± 1.5	14.3 ± 2.5	1.75
C	R_o (ohm)	8.55 ± 0.16	8.06 ± 0.25	**
	R_t (ohm)	11.28 ± 0.5	11.25 ± 0.25	10.5
	τ_{HF} (millisec)	0.268 ± 0.018	0.48 ± 0.06	**
	γ	0.802 ± 0.030	0.584 ± 0.047	**
	ρ (ohm)	49 ± 6.2	62.5 ± 10	40
	τ (millisec)	23 ± 7	37.4 ± 14	3
D	R_o (ohm)	8.21 ± 0.11	7.72 ± 0.26	**
	R_t (ohm)	11.15 ± 0.25	10.95 ± 0.30	10.5
	τ_{HF} (millisec)	0.163 ± 0.007	0.308 ± 0.035	**
	γ	0.781 ± 0.021	0.561 ± 0.046	**
	ρ (ohm)	74 ± 8	125 ± 27	78.5
	τ (millisec)	12.2 ± 3.3	25 ± 15	3.5

* Corresponding to points A, B, C, and D in Fig. 3 to 7.
** Not calculated.

based on the Langmuir isotherm assumes that all sites on the electrode surface are equivalent, a situation that cannot be realized because, among other reasons, of the polycrystalline structure of the electrode used.

Conclusions

Separation of the double-layer capacity and faradaic impedance, for the polarographic discharge of I_3^-, leads to the conclusion that the diffusion impedance at the surface of a rotating disk can be satisfactorily calculated in terms of the model of the Nernst layer and shows that the Warburg impedance is a limiting case.

The analysis of an iron anode impedance, in H_2SO_4 aqueous solutions, reveals that the double-layer impedance cannot be described as a constant capacity in parallel with the faradaic impedance. However, a partial separation of respective contributions of these two impedances, by means of empirical relationships, made it possible to compare the experimental data with a mechanism implying that dissolution occurs in two steps (8). Inductive impedances, quite comparable to that of an iron anode, are well-known in the case of certain biological systems involving membranes (16). As for the metal-electrolyte interface, evidence for such an impedance was obtained in our laboratory in 1952 (17). However, in the present article, an interpretation of inductance in terms of a faradaic process is given for the first time.

Manuscript submitted July 28, 1969; revised manuscript received May 7, 1970.

Any discussion of this paper will appear in a Discussion Section to be published in the June 1971 JOURNAL.

REFERENCES

1. P. Delahay and G. Susbielles, *J. Phys. Chem.*, **70**, 3150 (1966).
2. K. Holub, G. Tessari, and P. Delahay, *ibid.*, **71**, 2612 (1967).
3. M. L. Boyer, I. Epelboin, and M. Keddam, *Electrochim. Acta.*, **11**, 667 (1966).
4. M. Keddam, Thèse de Doctorat d'Etat, Paris (1968), No. d'enregistrement C.N.R.S.: AO 2192; *idem., Traitements de Surface*, No. 95, 39 and No. 96, 3 (1970).
5. D. Schuhmann, *C. R. Acad. Sci., Paris*, **262**, 1125 (1966).
6. I. Epelboin, M. Keddam, and J. C. Lestrade, *ibid.*, **263**, 1110 (1966).
7. Ph. Morel, Thèse de Doctorat d'Etat, Paris (1968), No. d'enregistrement C.N.R.S.: AO 2346; *idem., Traitements de Surface*, No. 89, 9 (1969) and No. 91, 37 (1970).
8. J. O'M. Bockris, D. Drazić, and A. R. Despić, *Electrochim. Acta*, **4**, 315 (1961).
9. K. E. Heusler, *Z. Elektrochem.*, **62**, 582 (1958).
10. H. Gerischer and W. Mehl, *ibid.*, **59**, 1049 (1955).
11. E. J. Kelly, *This Journal*, **112**, 124 (1965).
12. R. H. Cole and K. S. Cole, *J. Chem. Phys.*, **9**, 341 (1941).
13. D. W. Davidson and R. H. Cole, *ibid.*, **19**, 1484 (1951).
14. J. P. Badiali, H. Cachet, and J. C. Lestrade, To be published.
15. J. Mandel, "The Statistical Analysis of Experimental Data," Interscience Publishers, New York (1964).
16. K. S. Cole and R. E. Baker, *J. Gen. Physiol.*, **24**, 771 (1941).
17. I. Epelboin, *C. R. Acad. Sci.*, **234**, 950 (1952).

Technical Notes

Potential Oscillations of the H_2-CO System at Low CO Content

S. Szpak

Naval Weapons Center, Corona Annex, Corona, California

This communication considers the development of potential oscillations in a gas-diffusion electrode operating under galvanostatic conditions. Qualitatively, results seem to agree with those reported recently by Deibert and Williams (1). The essential difference appears in the frequency and the potential range in which they occur.

Present address: Chemical Laboratory, Mare Island Naval Shipyard, Vallejo, California 94542.

Experimental

The experimental arrangement was patterned after Will (2), except for details in the construction of the working electrode. Will's "inverted pore" was replaced by a "slit-electrode," assembled as follows: two platinized platinum foils, of equal areas by charging curve measurements, mounted in plastic frame were assembled to form a narrow slit (0.236 cm) configura-

tion. The extent of immersion of the electrode assembly, *i.e.*, the film length h, was determined by the use of a cathetometer. The electrode was operated at constant gas composition (99.7% H_2 + 0.3% CO) and pressure slightly higher than atmospheric and controlled by a needle valve in the exit stream.

To assure the reproducibility of results, the following procedure was adapted: totally immersed electrode was subjected to an anodic potential of +1.8V (*vs.* H_2 electrode in the same solution) followed by cathodic potential of −0.5V for 30 sec, each. Entrapped gaseous reaction products (O_2, H_2 respectively) were removed from the space between platinum foils by withdrawal of the electrode assembly from the solution. After exposure to the reactant for 10 min, the working electrode was immersed again, adjusted to the desired depth and equilibrated for at least 20 min. It is noteworthy that for pure hydrogen this procedure yielded results identical to those of an inverted pore.

Development of Potential Oscillations

The necessary condition for the development of potential oscillations are the existence of film of critical length, the presence of two component reactive gas mixture, and constant current from an external source within a rather narrow range of current. No potential oscillations were observed when the film length exceeded 0.3 cm, or when pure hydrogen, or hydrogen diluted with an inert gas, was used. The range of current necessary to initiate and sustain periodic behavior is proportional to the film length. For example, for h = 0.07 cm, $1.0 < i_{cr} < 2.0$ mA, while for h = 0.113 cm, $1.0 < i_{cr} < 3.0$ mA.

The V/t curves, shown in Fig. 1, exhibit two distinct branches prior to the initiation of periodic behavior. The initial portion, AB, is characterized by rapid growth in potential with time, and it is usually completed within seconds after closure of the switch. The second branch, terminating at C, requires substantially longer times; in some cases, more than 20 min. This induction time for the development of periodic behavior appears to be a complex function of impressed current and depth of immersion.

Discussion

Equivalent circuit.—The stability conditions for the electrode processes can be investigated, using the concept of an equivalent circuit (3). Such a circuit, shown in Fig. 2, consists of a combination of resistance R_1 and capacitance C in series, short-circuited by resistances $R_{2,1}$,$R_{2,2}$ . . . . Resistances R_1, $R_{2,1}$,$R_{2,2}$ are the faradaic discharge resistances, *i.e.*, essentially non-ohmic in character, and C is the adsorption pseudocapacitance arising from the potential dependent surface coverages (4). The film resistance, R_f, is assumed to operate in series with R_1. Taking$R_f >> R_1$, $R_{2,n}$, and $C_{dl} << C$, we have (by Kirchhoff's law)

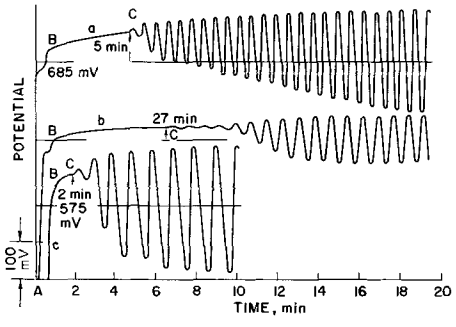

Fig. 1. Potential oscillations in gas-diffusion electrode. Electrolyte: 6 NH_2SO_4; gas composition: 99.7% H_2, 0.3% CO; pressure: 1 atm; temperature: room. Curve a: i_p = 2.0 mA, h = 0.113 cm; curve b: i_p = 1.5 mA, h = 0.113; curve c: i_p = 1.5 mA, h = 0.07 cm.

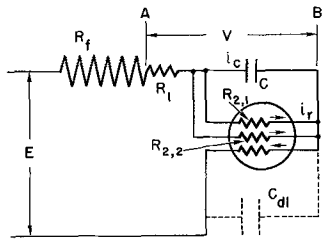

Fig. 2. Equivalent electric circuit. R_f = film resistance (ohmic); C = pseudocapacitance; C_{dl} = double layer capacitance.

$$E = R_f (i_c + i_r) + V \qquad [1]$$

where E is the time-independent potential operating across the cell and V is the experimentally measured potential. Replacing i_c and i_r by appropriate expressions containing V (*i.e.*, $i_c = C\,dV/dt$, $i_r = f(V)$) and solving for dV/dt, we get

$$\frac{dV}{dt} = \frac{1}{R_f C}[E - V - R_f f(V)] \qquad [2]$$

The conditions for potential oscillations are determined by the nature of $f(V)$ (5); this function must not be single-valued, and its derivatives at the points of stationary states (equilibrium) (6) must be positive.

Nature of $f(V)$ for H_2 + CO system.—The $i_r = f(V)$ curve is the usual steady-state potential/current relationship. For the gas-diffusion electrode, the steady-state $f(V)$ is identical with the potentiodynamic curve of $dV/dt < 100$ mV/min, and $V \leq +800$ mV, irrespective of the direction of potential sweep, as indicated by the dashed line in Fig. 3a. Considerably different behavior is observed when small amounts of CO were introduced into the hydrogen stream. Typical behavior for the latter case is shown by the solid line.

Evidently, the introduction of CO into H_2 stream resulted in non-single-valued $i_r = f(V)$ curve (ABCDA-curve in Fig. 3a). The details of this curve, for h = 0.113 cm, are shown in Fig. 3b. The characteristic points are: (*i*) if the potential sweep was reversed at $V \leq +700$ mV, the forward and reverse traces coincided; (*ii*) if the reversal of potential sweep was executed at $V > +700$ mV, a "hysteresis" was

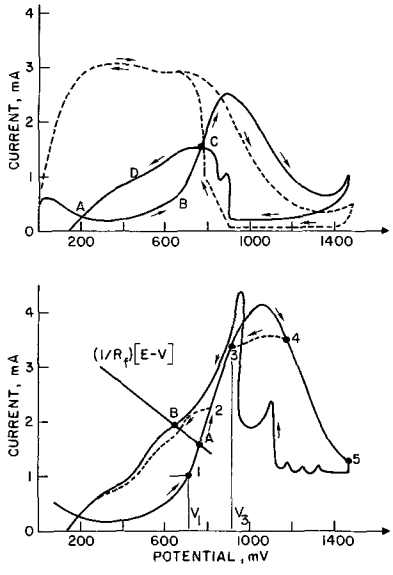

Fig. 3. Potentiodynamic i/V curves for gas diffusion electrode. (a, upper figure): dashed-pure hydrogen; solid-hydrogen containing carbon monoxide, with h = 0.07 cm, dV/dt = 75 mV/min. (b, lower figure): for hydrogen containing carbon monoxide with h = 0.113 cm, dV/dt = 75 mV/min.

observed. It is seen that the extent of hysteresis depends on the potential at which the reverse sweep took place, being essentially unaffected for $V > +900$ mV (points 3, 4, and 5 in Fig. 3b).

Assuming that the curve ABCDA (Fig. 3b) represents the required function, one seeks points of equilibrium; or, what is equivalent, the solution of [2] for $dV/dt = 0$, and determine the sign of $f'(V)$, at V_1, V_2, representing the roots of

$$\frac{1}{R_f}(E - V) = f(V) \qquad [3]$$

The simplest procedure is the graphical solution, since $f(V)$ is obtained in that form. The roots V_A, V_B are given by the intersection of a straight line $i = 1/R_f\ (E - V)$ with $i = f(V)$, as shown in Fig. 3b. It is seen that $f'(V)$ at V_1 and V_3 is positive, thus fulfilling the condition for oscillatory behavior.

Qualitatively, the above analysis is consistent with the observations, particularly with regard to the narrow range of impressed c.d., the effect of film length, and the potential range which is lower than reported by Deibert and Williams for higher CO content and different electrode geometry.

Mechanism of periodic behavior at low CO concentration.—Total constant current, i_p, can be split into the capacitance current i_c and reaction current i_r. The presence of two-component gas mixture suggests that i_r can be further split to represent the contribution due to oxidation of hydrogen and carbon monoxide. The contribution of each reaction is governed by the composition of gas mixture, the applied potential, the kinetics of individual reaction, and the effect of one reaction on the other.

The kinetics of hydrogen oxidation in a gas-diffusion electrode is limited by the transport of hydrogen across the electrolyte film (2). The kinetics of carbon monoxide oxidation is more complex. Its essential feature, as far as the development of potential oscillation is concerned, is that the oxidation rate is inversely proportional to the surface coverage, θ_{co}, and occurs at substantial rates at potential higher than +800 mV, but less than those where the formation of surface oxide exerts an inhibitive effect (7).

Assuming, as a first approximation, that the oxidation of hydrogen and carbon monoxide occurs independently, and taking into account the composition of the reacting gas (99.7% H_2, 0.3% CO), one can conclude that the reaction current is essentially due to hydrogen oxidation.

Evidently, two critical potentials exist along the ABC-curve, Fig. 3a. Below the lower critical potential, V_1, Fig. 3b, $f(V)$ is single-valued only if this potential is not exceeded on forward potential sweep. This implies that the electrode retains a steady-state surface concentration of CO, which depends on its concentration in the gas phase. As the potential is increased, the oxidation of adsorbed CO takes place, thus making additional electrode surface available for hydrogen oxidation. At sufficiently high potentials, where the oxidation of CO is controlled by diffusional transport (the upper critical potential V_3, Fig. 3b), the electrode operates essentially as a hydrogen electrode, and free from CO interference.

At intermediate points, *i.e.*, points located between the critical potentials, where the rate of CO oxidation is greater than CO adsorption, that is, where the number of "free sites" for hydrogen adsorption increases, lower potential is required to support the impressed constant current, i_p. As the potential is decreased, however, conditions favorable for CO adsorption reappear, thereby resulting in increase in potential to maintain the impressed constant current, until oxidation of CO can occur again. Thus, the cyclic process is realized.

Manuscript submitted Feb. 16, 1970; revised manuscript received *ca.* April 24, 1970.

Any discussion of this paper will appear in a Discussion Section to be published in the June 1971 JOURNAL.

REFERENCES

1. M. C. Deibert and D. L. Williams, *This Journal*, **116**, 1290 (1969).
2. F. Will. *ibid.*, **110**. 145 (1963); **110**, 152 (1963).
3. W. Schwenk, *Electrochim. Acta.*, **5**, 301 (1961).
4. B. E. Conway, "Theory and Principle of Electrode Processes," The Ronald Press Co., New York (1965).
5. U. F. Franck, *Z. Phys. Chem. N.F.*, **3**, 183 (1955).
6. A. A. Andronow and C. E. Chaikin, "Theory of Oscillations," Princeton University Press (1949).
7. S. Gilman, *J. Phys. Chem.*, **68**, 70 (1964).

Electrochemistry of Silver in Condensed Phosphoric Acid

David P. Lake*,[1] and John H. Kennedy

The University of California, Santa Barbara, California

Work in this laboratory (1) has demonstrated that condensed phosphoric acid [78 w/o (weight per cent) P_2O_5] is an excellent solvent for transition metal ions, and that solutions of these ions can be analyzed *in situ* by volumetric titrations with potentiometric end points. Condensed phosphoric acid offers several advantages as an electrochemical solvent, especially its wide range of operating voltage. The only electrochemical reactions taking place in the pure acid are the reduction of H^+ and the oxidation of water. The potential of H^+ reduction is slightly dependent on P_2O_5 concentration, but is at most 0.2V less than in water. However, the oxidation potential of H_2O is very dependent on P_2O_5 concentration, and the decomposition potential of 85% P_2O_5 is about 5V.

According to McMillan (2), Ag(II) is stable in strong acids for a few hours at 0°C. Davis and Lingane (3) successfully used Ag(II) as an electrolytically generated coulometric titrant in 5M HNO_3 at 0°C, but they found the other acids less successful. In light of the high stability toward oxidation exhibited by condensed phosphoric acid, a study of silver(I) oxidation was made in this electrolyte medium.

Experimental

The 78 w/o acid was prepared by adding analytical grade P_2O_5 to 85% H_3PO_4 (68 w/o P_2O_5) with heating and stirring. A liter of the acid was treated with a few drops of concentrated H_2O_2 and then heated to 300°C to decompose excess H_2O_2. The resulting water-clear solution was cooled and analyzed for P_2O_5 content. This solvent had a viscosity of 5000 centipoises at the ambient temperature of this study.

* Electrochemical Society Active Member.
[1] Present address: Research Laboratories, General Motors Corporation, Warren, Michigan.
Key words: silver (I), silver (II), chronopotentiometry, voltammetry, condensed phosphoric acid.

Table I. Transition times for reverse chronopotentiograms. 0.0995M Ag(I)

i (μA)	$\tau_{forward}$ (sec)	$\tau_{reverse}$ (sec)	$E_{0.222\tau_r}$ (volt)	$E_{.025\tau_f}$ (volt)	τ_f/τ_r	$i\tau_r^{1/2}$ (μA · sec$^{1/2}$)
35	99.2	31.0	1.43	1.46	3.22	195
70	24.9	8.0	1.42	1.47	3.11	198
140	5.94	1.97	1.27	1.49	3.05	197

A known volume of the solvent was placed in an H-cell constructed from two 100-ml beakers connected with a tube containing a glass frit. Mounted on one side were the reference electrode, the working electrode, a silver sheet for generating Ag(I), and a magnetic spin bar. A platinum auxiliary electrode was in the other compartment. The working electrode consisted of a platinum sheet 0.226 cm^2 in area. The reference electrode was contained in an 8-mm diameter x 10 cm long glass tube with a wire sealed into the bottom end. Mercury was placed in the tube and condensed phosphoric acid poured over it. Some of the mercury was electrochemically oxidized until the acid became filled with white, solid mercury phosphate. One end of a 2 mm diameter Teflon tube filled with condensed phosphoric acid was placed inside the top of the glass tube, with the other end held with Teflon cord in the H-cell next to the working electrode. The Teflon tube was plugged with glass wool at both ends to prevent diffusion of electrochemically active ions into or out of the H-cell.

Ag(I) was generated in the stirred solution by electrochemically oxidizing the silver sheet with respect to the counterelectrode. The desired concentration was obtained by using a constant current for a predetermined time. The silver electrode was then disconnected, the platinum working electrode connected in its place, and the stirrer turned off. A Beckman Electroscan was used for constant current coulometry, chronopotentiometry and voltage sweeps.

Results and Discussion

Chronopotentiometry.—A chronopotentiometric wave, attributed to oxidation of Ag(I), was observed in solutions which were > 0.01M. For solutions containing 0.0995M Ag(I), $i\tau^{1/2}$ was 374 μA-sec$^{1/2}$ with a standard deviation of ± 2 μA-sec$^{1/2}$. The product $i\tau^{1/2}$ was reasonably constant in spite of the long transition time (385 sec) for the lowest current. Condensed phosphoric acid is sufficiently viscous that the usual problem of convective stirring was not encountered. $E_{\tau/4}$ increased from 1.45 to 1.53V with increasing current which may have been caused by the placement of the reference electrode probe, $E_{\tau/4}$ dependence on current for silver(I) oxidation cannot be ruled out. By plotting Ag(I) concentration *vs.* $\tau^{1/2}$, the diffusion coefficient was calculated to be 2.7 x 10^{-8} cm^2/sec from the slope.

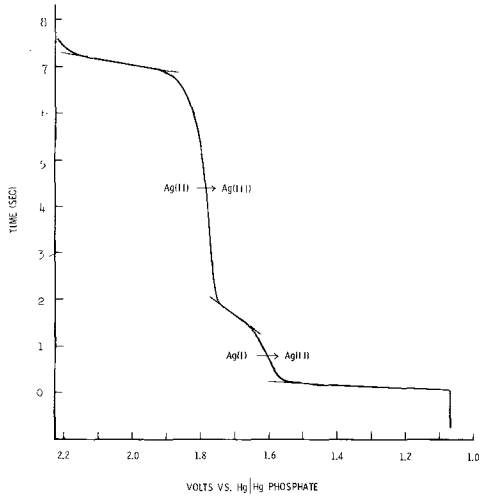

Fig. 1. Chronopotentiogram of 0.174M Ag(I) in condensed phosphoric acid. Current, 500 μA.

Reverse chronopotentiometric curves were taken, and the results are shown in Table I. The ratio τ_f/τ_r was close to three indicating a soluble product with a diffusion rate about equal to the reactant. The E° values from the forward and reverse waves compare very well, showing the reaction to be virtually reversible.

In solutions of 0.0995M Ag(I) a second wave appeared around 1.8V *vs.* Hg/Hg phosphate reference (Fig. 1). Assuming that the first wave corresponds to Ag(I) → Ag(II), the second wave could be attributed to further oxidation to Ag(III) or that either the reactant Ag(I), or the product Ag(II), exists in two forms. For example, one species may be adsorbed on the electrode. The chronopotentiometric data do not distinguish between these alternatives. Table II shows that τ_2/τ_1 for the two waves is 5-7, in poor agreement with the theoretical value of 3 for the simple process: Ag(I) → Ag(II) → Ag(III). However, the discrepancy may lie in an irreversible second reaction.

The E° values of the two electrode reactions were estimated to be $+1.47 \pm 0.02$V and $+1.70$V *vs.* Hg/Hg phosphate reference electrode from the $E_{\tau/4}$ values. However, reversibility of the second wave was not established, and thus, is only an estimate.

One other comment might be made regarding the chronopotentiometric data for the first wave. Since the ratio of τ_f/τ_r is nearly three (slightly greater), there is no fast decomposition of Ag(II). If a fast decomposition did occur, the ratio would be smaller because Ag(II) would be removed from the electrode by decomposition as well as by diffusion. Since no decomposition was indicated, Ag(II) should be reasonably stable in condensed phosphoric acid.

Scanning voltammetry.—Further information concerning silver(I) oxidation was sought from scanning voltammetry, and in particular, to identify the nature of the second oxidation step. Two anodic peaks were easily identified when solutions of Ag(I) were scanned from 1.2 to 2.1V. A typical scan is shown in Fig. 2, with data for various scan rates at two concentrations given in Table III. The value of $i_P/v^{1/2}$ was reasonably constant, even with the low scan rates because of the high viscosity of the solvent.

The separation of Ag(I) oxidation and Ag(II) reduction peaks was greater than the 58 mV theoretical value for a reversible case. However, the chronopotentiometric data for Ag(I) oxidation indicated a reversible process and for this reason it was of interest

Table II. Transition times for first and second waves in 0.0995M Ag(I)

i (μA)	τ_1 (sec)	τ_2 (sec)	$E_{\tau_2/4}$ (volt)	τ_2/τ_1	$i\tau_2^{1/2}$ (μA · sec$^{1/2}$)
50	56.0	384	1.69	6.86	980
70	29.0	196	1.70	6.76	980
100	13.75	92.5	1.71	6.73	962
170	4.70	26.9	1.74	5.72	882
250	2.15	11.6	1.75	5.39	852

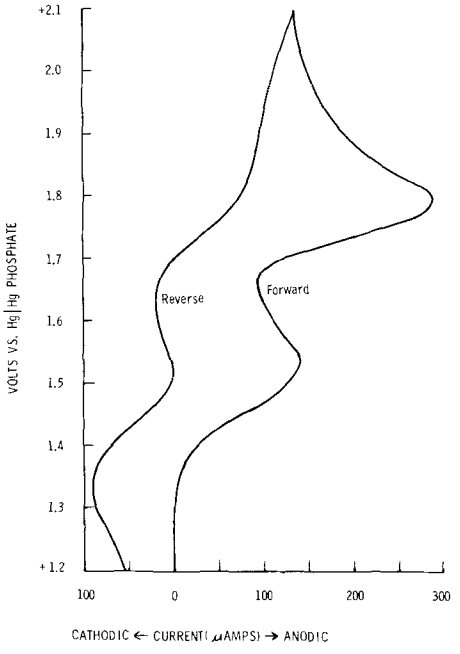

Fig. 2. Triangular voltage sweep of 0.0995M Ag(I). Rate, 20 mV/sec.

to calculate D from the Ag(I) voltammogram peak. Values for the diffusion coefficient ranged from 2.7-2.9 x 10^{-8} cm²/sec, in excellent agreement with the value calculated from the chronopotentiometric data.

As mentioned in the section on the chronopotentiometry of Ag(I), one of the possibilities for explaining the second peak is adsorption of one of the silver species on the electrode. Wopschall and Shain, in a detailed treatment (4) showed that when the reactant was strongly adsorbed, a second peak appeared after the normal diffusion peak; and when the product was strongly adsorbed, a second peak appeared before the diffusion peak. In both cases the adsorption peak is symmetrical both in voltage and current when a triangular voltage sweep is applied.

The fact that the first peak obtained during oxidation of Ag(I) fits the theory for a diffusion-controlled process, rules out adsorption for that peak. The second peak, however, could be caused by adsorption of the reactant Ag(I). Figure 2 shows a triangular sweep with an unsymmetrical peak, indicating that it is not an adsorption peak. Wopschall and Shain also point out that a given concentration, the ratio of the adsorption peak to the diffusion peak increases with the scan rate. The data in Table III show the opposite. Thus, both tests show that the second peak is not an

Table III. Cyclic voltammetry of Silver (I)

Peak current and peak voltage as a function of scan rate for (a) 0.0746M and (b) 0.00545M Ag(I) at 25° on a platinum electrode. Scanned from +1.20 to +2.10V, *vs.* the Hg/Hg phosphate reference electrode.

v (mV/sec)	E_{p_1} (volt)	E_{p_2} (volt)	i_{p_1} (μA)	$i_{p_1}/\sqrt{v}$	i_{p_2} (μA)	i_{p_2}/i_{p_1}
(a) 0.0746M Ag(I)						
100	1.55	1.84	237	23.7	245	1.03
50	1.51	1.81	189	26.7	219	1.16
20	1.51	1.79	113	25.3	174	1.54
10	1.51	1.78	79	25.0	142	1.80
5	1.50	1.76	56	25.0	106	1.89
(b) 0.00545M Ag(I)						
100	1.55		11.0	1.10		
50	1.53		7.1	1.00		
20	1.52		4.6	1.03		
10	1.50		3.4	1.07		
5	1.50		2.55	1.14		
2	1.48		1.67	1.18		
1	1.48		1.20	1.20		

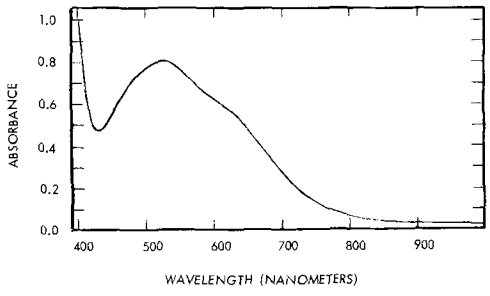

Fig. 3. Absorption spectrum of 0.019M Ag(II) in condensed phosphoric acid.

adsorption peak. Since the second wave was not an adsorption peak, it is reasonable to conclude that the second oxidation step was the formation of Ag(III).

The $E°$ values of the two electrode reactions can be estimated from the peaks although strict reversibility was not established. For the first peak, this may result from some kinetic complications for the reduction of the stable Ag(II) species, since the oxidation of Ag(I) was shown to be reversible from chronopotentiometry. In any case, the estimated $E°$ values of +1.48 and +1.75V *vs.* Hg/Hg phosphate reference agree quite well with the values obtained from the chronopotentiograms.

Preparation of Ag(*II*).—In view of the indication that Ag(II) should be stable, an electrochemical preparation was carried out. A platinum electrode of about 10 cm² was placed in a 1.5 cm diameter tube. The bottom end, which was made of fritted glass, was placed along with the counterelectrode in a beaker of acid. Three cubic centimeters of 0.05M Ag(I) were placed in the tube, and oxidized with a 10V power supply. The whole apparatus was provided with a dry N_2 cover. After 1 hr there was a slight pink color near the electrode; after one week the entire solution was dark purple. The current efficiency was low because the high voltage applied also produced oxygen as a by-product.

A known volume of this solution was diluted with condensed phosphoric acid and placed in the H-cell. The voltage of the platinum working electrode was set at +0.8V, the stirrer was turned on, and the current resulting from the reduction of the purple solution was recorded. When the current had fallen to 2% of its original value, the total number of coulombs was calculated. Comparing this number with the number of moles of silver used for this coulometric titration showed that 0.94 electrons/mole participated in the reduction, thus indicating the presence of Ag(II). This solution of Ag(II) was stable at room temperature for at least several months.

The absorption spectrum (Fig. 3) showed a single band as expected for the d^9 configuration, and the molar extinction coefficient was 80 at 525 nm.

Conclusion

This study demonstrates that condensed phosphoric acid is a suitable solvent for electrochemical studies, and furthermore, the stability of Ag(II) showed the ability of this solvent to support species having a high oxidation potential. Electrochemical preparation of Ag(II) for spectral studies was accomplished, and this technique may be applied to other strong oxidants.

Earlier work (1) showed that the $E°$ of the Hg/Hg phosphate reference was +0.54V *vs.* SHE. The $E°$ values of Ag(II) and Ag(III) found in this work were +1.47 and +1.70V *vs.* Hg/Hg phosphate. When converted to the SHE scale, the Ag(I-II) and Ag(II-III) couples were +2.01 and +2.24V, respectively. Latimer (5) reports the aqueous value for Ag(II) as −1.98V

and estimates Ag(III) as about −2.1V (Latimer sign convention).

Manuscript submitted July 25, 1969; revised manuscript received April 3, 1970.

Any discussion of this paper will appear in a Discussion Section to be published in the June 1971 JOURNAL.

REFERENCES

1. D. P. Lake, The Nature of Transition Metal Ions In Condensed Phosphoric Acid, Ph.D. Thesis, Department of Chemistry, University of California, Santa Barbara, California.
2. J. A. McMillian, *Chem. Rev.*, **62**, 65 (1962).
3. D. G. Davis and J. J. Lingane, *Anal. Chim. Acta.*, **18**, 245 (1953).
4. R. H. Wopschall and I. Shain, *Anal. Chem.*, **39**, 1514, 1535 (1967).
5. W. M. Latimer, "Oxidation Potentials," p. 11, Prentice-Hall, Englewood Cliffs, New Jersey (1952).

JOURNAL OF THE ELECTROCHEMICAL SOCIETY

SOLID STATE SCIENCE

AUGUST 1970

The Distribution Coefficient of Boron in Germanium

W. D. Edwards

Communications Research Centre, Ottawa, Ontario, Canada

ABSTRACT

The equilibrium distribution coefficient of boron in germanium was found to be 12.2. The variation with growth rate was interpreted in terms of a theory by Burton, Prim, and Slichter. As the growth rate was increased the width of the diffusion dominated layer initially increased followed by a later decrease. This was due to a change from a thermally produced melt flow pattern to a hydrodynamically produced pattern. The results show that a slow growth rate and a high rotation rate should be used to obtain equilibrium distribution coefficients.

The effective distribution coefficient of boron in germanium as a function of crystal growth rate has been measured by Bridgers and Kolb (1). The results were obtained for a particular crystal rotation rate of 60 rpm and an unspecified crystal growth direction. They were interpreted in terms of a theory proposed by Burton, Prim, and Slichter (2).

Boron in germanium is unusual in that the distribution coefficient is greater than one. A recent theoretical paper by Hurle and Jakeman (3) predicted anomalous results for systems with $k > 1$. Additional values of the effective distribution coefficient *vs.* growth rate for a 30 rpm rotation rate and specifically for the <111> growth direction are presented here. The departure of these results from those predicted by the theory is ascribed to the approximate equality of the thermal convection flow and hydrodynamic flow patterns at this rotation rate.

Experimental

The germanium crystals were produced by the Czochralski technique. The germanium melt was contained in a 48 mm diameter carbon crucible which was heated by a slotted carbon heater. Resistive heating gives a more massive system than is usual with induction heating. This reduces temperature gradients and gives better short term temperature stability. The furnace was evacuated and crystal growth took place in a vacuum of between 2 x 10^{-6} and 10^{-5} Torr. The seed was oriented in the <111> direction and the crystals were grown at a number of growth rates between 0.1 and 3 mm/min. A rotation rate of 30 rpm was used. Boron dissolves slowly in germanium and hence all melts were made from previously grown, boron-doped crystals. The seed to crystal joints were 2-3 mm in diameter and the growing crystals were expanded slowly so that the full diameter of ~2 cm was not reached until approximately 3 cm of crystal had been grown. The furnace gradients were such that the solid-liquid interface was slightly convex to the melt. On completion of growth the crystals were cooled to room temperature over a period of 2 hr.

Key words: germanium, boron in germanium, distribution coefficient of boron in germanium.

The completed crystals were removed from the furnace and a volume *vs.* length-grown measurement was made by liquid displacement. The crystals were then sectioned longitudinally to give parallelepiped samples suitable for two-probe resistivity measurements. Other, transverse, samples were cut so that Hall measurements could be made.

Results and Discussion

The incorporation of impurity atoms into single crystals during growth has been discussed by a number of authors (2, 4). For a liquid-solid system in equilibrium the ratio of the concentration of impurity in the solid, C_s, to that in the liquid at the interface, C_o, is defined as the equilibrium distribution coefficient, k_o. For the particular case of boron in germanium, k_o is greater than unity. Under the conditions of Czochralski crystal growth discussed here, there is a departure from equilibrium. As crystal growth proceeds boron is preferentially incorporated into the solid and, because of the limited stirring and the finite boron diffusion rate in the liquid, a boron concentration gradient is established in the liquid germanium adjacent to the liquid-solid interface. The result is less boron in the solid than expected. This departure from equilibrium may be expressed in terms of an effective distribution coefficient, k_{eff}, defined as C_s/C_l where C_l is the boron concentration in the bulk of the liquid. Burton *et al.* (1) have derived an expression relating k_{eff} to k_o in terms of the crystal growth parameters

$$k_{eff} = \frac{1}{1 + [1/k_o - 1] \exp - (\delta f/D)} \qquad [1]$$

where D is the solute diffusion coefficient in the liquid, diffusion in the solid is neglected, f is the crystal growth rate, and δ is the thickness of the diffusion dominated region in the liquid. δ itself is somewhat arbitrary and may be expressed as

$$\delta = bD^{1/3} \nu^{1/6} \omega^{-1/2} \qquad [2]$$

where ω is the crystal rotation rate, b is a constant, and ν the liquid viscosity. For the small solute concentrations considered here k_o is assumed independent of concentration.

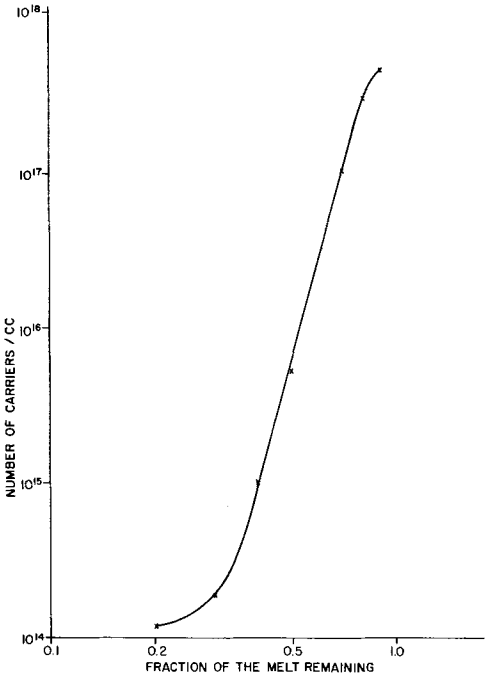

Fig. 1. Log-log plot of the carrier concentration in the crystal, C_s, as a function of (1 — x) the fraction of the melt remaining.

As a result of the preferential incorporation of the boron into the germanium the melt is steadily depleted of boron as crystal growth proceeds. The relationship (4) between the solute concentration in the solid and the fraction of the melt that is crystallized, x, is

$$C_s = k_{eff}\, C_l^o\, (1 - x)^{k_{eff}-1} \qquad [3]$$

If the crystal growth and rotation rates are kept constant then k_{eff} may be determined (1) from the slope of the curve obtained by plotting log C_s *vs.* log $(1 - x)$. A plot of this type was made for each crystal grown.

A set of experimental results for a growth rate of 0.33 mm/min are shown in Fig. 1 plotted as log C_s *vs.* log $(1-x)$. These points were obtained from the crystal volume *vs.* length and resistivity *vs.* crystal length plots. The concentration values were obtained from the resistivity values by using the curves published by Sze and Irvin (6). Concentration values calculated from Hall measurements made were used as checks only. The plot of Fig. 1 is seen to be linear with deviations at both high and low carrier concentrations. At high concentrations the crystal was still expanding and at the low concentration end of the plot the residual impurities, *i.e.*, other than boron, were becoming significant. Hence, only the linear portion of the plot was considered.

An effective distribution coefficient of 9.3 for a growth rate of 0.33 mm/min was determined from Fig. 1. In Table I are shown the effective distribution coefficients calculated in this manner for a number of growth rates. Equation [1] may be rearranged to give

$$1 - (1/k_{eff}) = [1 - (1/k_o)] \exp(-\delta f/D) \qquad [4]$$

A plot of ln $[1 - (1/k_{eff})]$ *vs.* f, the growth rate, should give a straight line with slope $-\delta/D$. The results of Table I are shown plotted in this form in Fig. 2. The results that Bridgers and Kolb obtained for a rotation rate of 60 rpm are also shown in Fig 2. From the probable intercept on the ordinate a value of

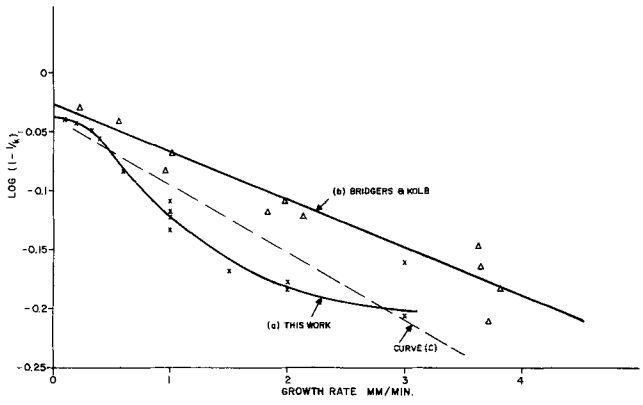

Fig. 2. Results of this work and those of Bridgers and Kolb plotted as a function of growth rate according to Eq. [4]. The slope, δ/D, for curve b is 56 sec/cm and for curve c is 79.2 sec/cm.

k_o of 12.2 is obtained, a figure which is definitely lower than the value of 17.4 ± 20% calculated by Bridgers and Kolb. The difference is most likely due to an orientation effect. The specific reference by these authors to the repeatability of their crystal growth without loss of boron and their use of a carbon crucible would appear to eliminate an explanation for the difference, based on an assumption of less boron oxidation, in the case of the present work. It has been shown that the oxidation of boron effectively removes the boron (7) as an electrically active dopant and consequently an oxygen leak into the crystal grower could give an apparent increase in k_{eff} as measured from a plot such as Fig. 1. The apparent disappearance of boron observed by Swiggard and Shenker (8) also raises the possibility that an equilibrium with a nonelectrically active boron (9) dope could be affecting such measurements.

Recently Hurle and Jakeman calculated the effect of temperature perturbations on the effective distribution coefficient. Where $k_o > 1$ they predict that the distribution coefficient measured, which is an average value when perturbations are present, will be less than the effective value expected from the Burton, Prim, and Slichter theory. In the particular case of crystal melt-back just failing to occur with the peak of each temperature fluctuation (the so-called marginal case) the measured k_{eff}^m will equal $k_{eff}/2$. Their calculated results are subject to several boundary conditions or restraints. The Hurle and Jakeman relationships for the marginal case and $k > 1$ have been evaluated for the experimental conditions used here. At the lowest growth rate used of 0.1 mm/min the maximum depression of k_{eff} due to fluctuations is 7% even for the marginal case. Growth took place in the < 111 > direction and the possible existence of facets would lead to delays between any driving perturbation present and the interface response. The concentration variations as a result of the temperature fluctuations would thus be reduced (10). Very little faceting is thought to have occurred because transverse resistivity plots did not reveal any evidence of resistivity coring. The Hurle and Jakeman calculations are not really applicable when facets are present.

It is also relevant that for part of the growth of the 0.1 mm/min crystal a small island due to a scum particle existed at the edge of the melt. Such islands accentuate temperature asymmetries leading to more definite striations (11). In this instance no irregularity

Table I. Values of k_{eff} for several crystal growth rates

Growth rate, mm/min	0.1	0.2	0.33	0.4	0.6	1.0	1.0	1.0	1.0	1.5	2.0	2.0	3.0	3.0
Effective K	11.6	10.7	9.3	8.2	5.7	4.5	3.77	4.2	4.08	3.1	2.89	2.97	2.64	3.24

in the log C_s *vs.* log $(1 - x)$ curve was found. This point together with the observations of the last paragraph are taken as an indication that any temperature fluctuations present and particularly those due to the crystal rotation are not sufficient to cause a significant lowering of k_{eff} due to the mechanism discussed by Hurle and Jakeman. Closer comparison with the results of Bridgers and Kolb is not possible as they did not give some key growth information, *e.g.*, the doping levels used and the crystal growth direction.

From Eq. [4] it is seen that the slope of the plot of Fig. 2 gives a value for δ/D. The results obtained here give a nonlinear plot which has a greater average slope than a similar plot of Bridgers and Kolb's results. The increased slope is expected because of the reduced rotation rate. The relationship calculated from Eq. [2] and the Bridgers and Kolb δ/D value for 60 rpm is plotted as curve *C* in Fig. 2. It is necessary to consider the possible reasons for the nonlinearity.

The diffusion coefficient, *D*, is temperature dependent and the temperature gradient will vary with growth rate. However, the region over which *D* is considered is very small and the consequent variation in temperature across δ is very small compared with the actual temperature at the interface. The liquid-solid interface temperature is essentially fixed at the freezing point; hence *D* is practically constant and the cause of the nonlinearity is δ, the width of the diffusion dominated layer.

At the rotation rate used the amount of stirring that is induced is particularly sensitive to the relative magnitude of the thermally produced convection current and the crystal-rotation induced flow pattern (12,13). With the particular resistive heating arrangement used the melt rises at the sides of the crucible and falls at the center due to the effect of the cooled seed (Fig. 3). This picture is reinforced by the experimental observation that scum particles, once dislodged from the crucible, will travel inward toward the seed as would be expected from the flow diagram of Fig. 3.

The flow pattern due to the crystal rotation is the opposite of the thermally induced pattern, *i.e.*, the liquid rises at the center beneath the crystal and falls at the crucible sides (12-14). It has been shown that at crystal rotation rates of ~30 rpm the predominant stirring mechanism is changing from the thermally induced flow to the crystal-rotation induced flow. The diffusion layer thickness, δ, which depends on this flow pattern will be especially sensitive to the growth conditions at the crystal rotation rate of 30 rpm.

As the pull rate is increased for a given rotation rate the latent heat of solidification rejected by the growing crystals increases. If we ignore the radiation loss at the interface the heat balance equation is

$$f \rho L = K_s \frac{\delta T}{\delta z} - K_L \frac{\delta T}{\delta \gamma} \qquad [5]$$

where f is the growth rate, ρ is the density, L the latent heat of fusion, K_s and K_L the thermal conductivities in the solid and liquid, respectively, and $\delta T/\delta z$ and $\delta T/\delta \gamma$ the temperature gradients in the solid and liquid, respectively.

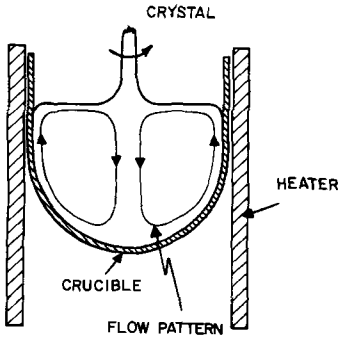

Fig. 3. Thermal flow pattern established in the melt for zero or low rotation rates.

An upper limit to the growth rate is reached when the heat flowing along the solid arises entirely from the latent heat of fusion. At quite modest growth rates the heat rejected is a significant fraction of that being conducted along the crystal. For example, if for germanium $K_s = 0.058$ cal cm^{-1} C^{-1} sec^{-1}, $\delta T/\delta z = 110°/cm$, $\rho = 5.32$ g/cc, and L = 114 cal/g, then for a growth rate of 3 mm/min the latent heat of fusion is contributing some 47% of the heat being conducted along the crystal. As may be seen from Eq. [5] this will reduce the temperature gradient in the liquid, *i.e.*, the cooling effect of the seed on the liquid is reduced and the over-all effect is a reduction in the effectiveness of the thermal convection flow pattern (Fig. 3).

The results shown in Fig. 2 support this premise. As the growth rate increases and the effectiveness of the thermal flow pattern is reduced the diffusion layer thickness, δ, initially increases, as was observed. An effect of this type was predicted by Robertson (13). At the higher growth rates the rejection of significant amounts of latent heat of solidification facilitates the establishment of the hydrodynamic flow pattern at the given rotation rate. Once again a definite flow pattern is established in the melt with a consequent reduction in the diffusion layer thickness, δ, as observed. There is a suggestion of this behavior, *i.e.*, an initial increase in δ and a later decrease, in the experimental results of Bridgers and Kolb, reproduced in Fig. 2. These workers used a higher crystal rotation rate of 60 rpm and the effect would therefore not be as great as for the 30 rpm of the present work. To eliminate effects due to a thermally induced flow pattern it is thus necessary to use even higher rotation rates, *e.g.*, >100 rpm. The growth system described here is limited to a maximum rotation rate of ~45 rpm because of mechanical stability problems.

Conclusion

The value of the distribution coefficient of boron in germanium was found to be 12.2. This is significantly lower than the value of 17.4±20% found by Bridgers and Kolb. It is not clear whether this difference arises because of an effect due to the crystal orientation, the ready oxidation of the boron, or the presence of boron in a nonelectrically active form.

The relationship between the effective distribution coefficient and growth rate agrees with that calculated by Burton *et al.* and the results of Bridgers and Kolb, if allowance is made for the particular growth conditions. An effect predicted by Robertson and due to a reduction in the degree of stirring in the melt with increase in growth rate has been observed.

A rotation velocity of at least 100 rpm and a small growth rate should be used to obtain values of k_0. A high rotation rate establishes a hydrodynamic flow pattern. A small growth rate minimizes thermal effects due to the latent heat of fusion and also reduces the amount of extrapolation necessary to obtain the value of k_0.

Acknowledgment

The author wishes to thank Mr. K. Gustafson for his help with the growth of the germanium crystals.

Manuscript received March 30, 1970.

Any discussion of this paper will appear in a Discussion Section to be published in the June 1971 JOURNAL.

REFERENCES

1. H. E. Bridgers and E. D. Kolb, *J. Chem. Phys.*, **25**, 648 (1956).
2. J. A. Burton, R. C. Prim, and W. P. Slichter, *ibid.*, **21**, 1987 (1953).
3. D. T. J. Hurle and E. Jakeman, *J. Crystal Growth*, **5**, 227 (1969).

4. W. G. Pfann, *J. Metals*, **4**, 861 (1952).
5. R. N. Hall, *Phys. Rev.*, **57**, 836 (1953).
6. S. M. Sze and J. C. Irvin, *Solid-State Electron.*, **11**, 599 (1968).
7. W. D. Edwards, *J. Appl. Phys.*, **39**, 1784 (1968).
8. E. M. Swiggard and H. Shenker, *This Journal*, **92**, 113 (1966).
9. M. Berkenblit, A. Reisman, and T. B. Light, Recent News Paper presented at the Montreal Meeting of the Society, Oct. 6-11, 1968.
10. A. F. Witt and H. C. Gatos, *This Journal*, **115**, 70 (1968).
11. W. D. Edwards, *Can. J. Phys.*, **38**, 439 (1960).
12. B. M. Turovski and M. G. Mil'Vidski, *Soviet Phys. Cryst. (Engl. Transl.)*, **6**, 606 (1962).
13. D. S. Robertson, *Brit. J. Appl. Phys.*, **17**, 1047 (1966).
14. A. J. Goss and R. E. Adlington, *Solid State Phys. Electron. Telecommun.*, **1**, 28 (1960).

The S-Shift Curve Characteristics of Si-O Stretching Band of Amorphous Silica

Kenzo Sato

Musashi Works, Hitachi, Ltd., Kodaira-shi, Tokyo, Japan

ABSTRACT

The absorption profile of the Si-O stretching band of a silica layer was studied as a function of layer thickness. Behavior of the S-shift curve which relates the wave number of the reflection/absorption peak and the layer thickness was found to vary with the conditions of layer growth and thermal treatment. Tentatively, these effects were explained as related to the presence of two types of loosely bound lattice oscillators derived from the expression $(Si_xO_y)_n$, and they were considered to be present both on the surface and inside the silicon-silica interface layer.

The properties of a thin amorphous silica layer grown above a silicon wafer have been studied by many researchers for interest regarding its electrical characteristics as an insulator and for crystallographic interests (1-4) as well as the study of crystalline quartz (5-8). Also, much interest is concerned with the structural evaluation of the thin silica layer which was formed by the compound shown as $(Si_xO_y)_n$ by means of x-ray diffraction analysis and infrared absorption spectroscopy. Various network models based on x-ray diffraction data have been proposed (9,10) which suggest that the amorphous silica layer consists of an extended three-dimensional network lacking periodicity, the construction of which may be inhomogeneous and which would undergo modifications according to its growth and impurity inclusion. Especially, precise measurements of the lattice vibrational spectra by the infrared spectroscopical method in the 1-30μ region suggest many interesting optical properties which are seen as peculiar to thin films (11-14). For example, the O-H stretching band formed by wet oxygen gas visible in the 2.5-3.5μ region is apt to become modified by thermal treatment (11). Profile of the Si-O stretching band seen in the 9-10μ region and the bending band seen in the 21-23μ regions is sensitively modified by the conditions for layer growth and impurity inclusion (13).

Furthermore, wavelength of the peak of the Si-O stretching band and bending band is not always seen at definite points, and it is noticeable that the peak fluctuates according to the conditions of layer growth and that the conditions shift toward the longer wavelength side with layer thickness (12). This effect can be called a surface shift (S-shift), considered as caused by certain essential optical properties of very thin films, presumably due to the presence of loose bonds formed by unsaturated lattice oscillators.

In this paper, the main interest was concerned in studying the profile of Si-O stretching band characteristics because the band is considered as the most basic spectrum representing the properties of $(Si_xO_y)_n$ compounds in a silica layer. Especially the effect of the S-shift was studied experimentally, and the origins of this effect are considered related to the inhomogeneous structure of the silica layer.

Experiments

Considering the peculiar properties of the sample, its thickness is less than 1μ and characteristics of the thin layer are not always uniform, not only at the silicon-silica interface but also on the surface of the silica layer. Both the reflection and transmission methods were used to measure the step etched samples. The etchant used is shown as (NH_4F:HF = 6:1), and the layer thickness was measured by observing the surface color formed by interference. Accuracy is considered as within an error of ±200Å.

The infrared spectrophotometer used was a Hitachi EPI-2, double-beam type with NaCl optics whose resolving power is 2.5 cm^{-1}/mm in the 9μ region. The area of samples for the measurements was about 10 mm in diameter with an incident angle of 10 degrees for the reflection measurements.

The results of these measurements are summarized as follows:

Thermally grown and chemical vapor deposited silica (C.V.D.).—Shown in Fig. 1a, b, and c are some examples of measuring the silica layer which was grown thermally at 1100°C with a flow of wet oxygen gas (A sample) and chemically deposited silica at 800°C by decomposition reaction of tetra-etoxysilane by oxygen gas (B sample). In reflection measurements, sample A shows that the wave number of the reflection maximum of the Si-O stretching band is shifting continuously from 1100 to 1045 cm^{-1} with a variation of layer thickness from 7000Å down to 1200Å. Also, the transmission minimum shifts from 1080 cm^{-1} (at 7000Å) down to 1069 cm^{-1} (at 3300Å) and returns to 1075 cm^{-1} (at 1250Å).

These phenomena were commonly seen in the thermally grown silica layer, although the wave number somewhat fluctuates in the samples. On the other hand, concerning sample B which was deposited from tetra-etoxysilane, as shown in Fig. 1c, the S-shift curve of transmission measurements did not return to the shorter wavelength side even when the layer thickness became smaller than 3000Å.

Fig. 1a. Infrared reflection and transmission spectrum of silica layer.
The three parts of Fig. 1a show reflection and transmission spectra of silica layers.

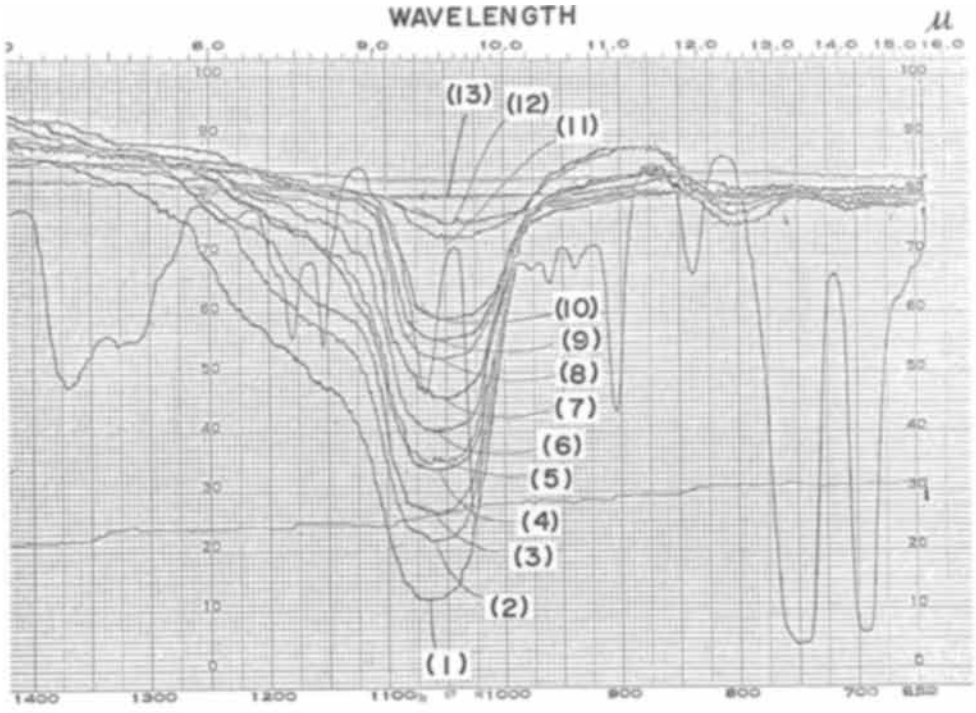

Fig. 1a(i). One example of absorption measurements of silica layer which was deposited by decomposition reaction of tetraethoxysilane using oxygen gas at 800°C. The thickness of step-etched sample corresponding to the running number is shown in the note. The absorption minima of Si-O stretching band is shifting continuously from 1065 to 1040 cm^{-1}, but Si-Si stretching band at 800 cm^{-1} is not shifting.

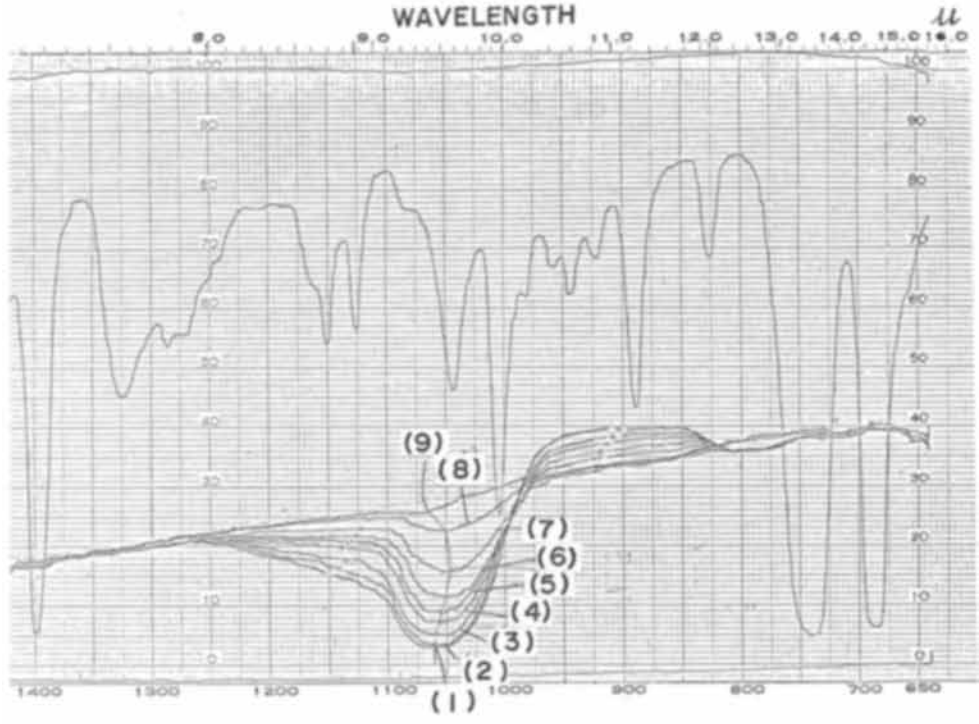

Fig. 1a(ii). One example of absorption measurements of silica layer which was grown thermally at 1100°C using wet oxygen gas. The thickness of step-etched sample corresponding to the running number is shown in the note. The absorption minima of Si-O stretching band is shifting from 1060 cm^{-1} (at 7200Å) to 1045 cm^{-1} (at 2750Å) and return to 1065 cm^{-1} (at 100Å).

As-grown layers.—In this case, also, properties of the S-shift curve were measured to the silica layers, their thickness in an as-grown state differing from each other. The two groups of samples which were grown thermally changed the duration time of the layer growth in wet oxygen gas, and the layer thickness in an as-grown state is 8000Å (C sample) and 3700Å (D sample), respectively. Also, deposited silica layers whose thickness in an as-grown state was 6000Å (E sample) and 3000Å (F sample) were used as samples and their S-shift curves were measured. The results are shown in Fig. 2, where the C sample reveals that the reflection maximum is shifting from 1103 cm^{-1} (at 8000Å) to 1055 cm^{-1} (at 1250Å; and in the D sample, from 1090 cm^{-1} (at 3800Å) to 1060 cm^{-1} (at 750Å). In these two curves, the wave number of the D sample is shifting toward the shorter wavelength side approximately 10 cm^{-1} from that of sample C. This effect can be termed as the P-shift (phase shift) of the as-grown layer.

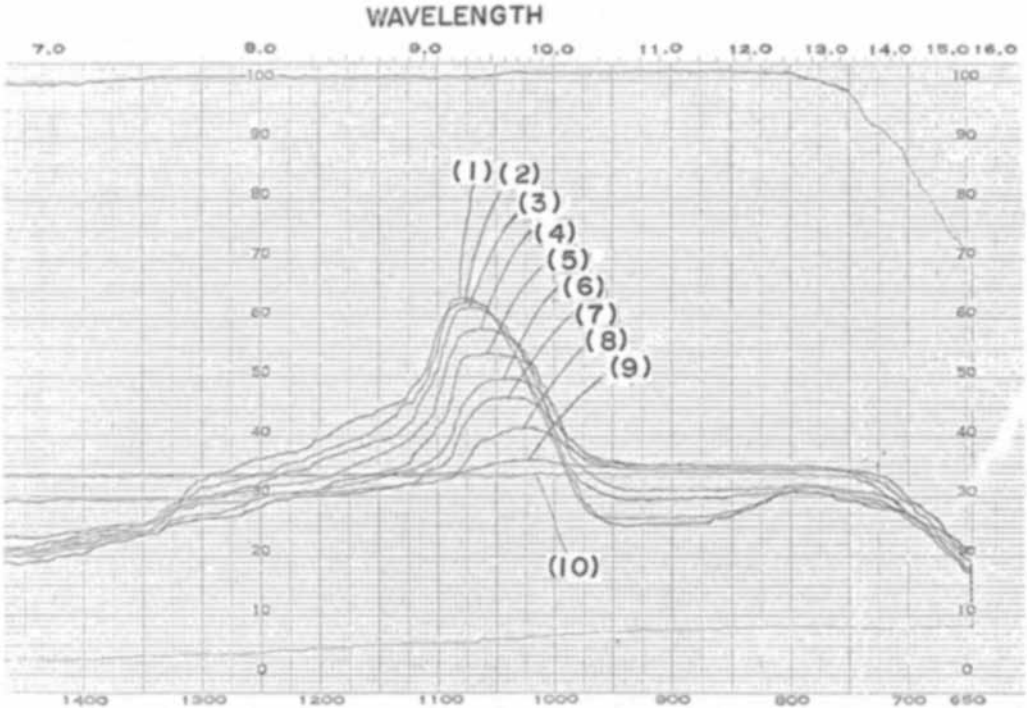

Fig. 1a(iii). One example of reflection measurements of silica layer which was grown thermally at 1100°C using wet oxygen gas. The thickness of the silica layer corresponding to the running number is shown in the note. The reflection maxima of Si-O stretching band is shifting continuously from 1075-1030 cm^{-1} but Si-Si stretching band at 775 cm^{-1} is not shifting.

Note: The thickness of step-etched samples corresponding to the running number in Fig. 1a (i), (ii), and (iii).

Sample No.	(i) Absorption, Å	(ii) Absorption, Å	(iii) Reflection, Å
1	6300	7200	6000
2	5200	6200	5500
3	4450	5400	4900
4	3650	4260	4200
5	3250	3650	3650
6	2750	2750	3050
7	2500	1600	2250
8	2000	600	1500
9	1500	100	850
10	1250	—	0
11	750	—	—
12	500	—	—
13	0	—	—

On the other hand, in the E sample, the wave number is shifting from 1070 cm^{-1} (at 6000Å) to 1036 cm^{-1} (at 1500Å); and in the F sample, it is shifting from 1050 cm^{-1} (at 3000Å) to 1030 cm^{-1} (at 1000Å). It is clear that the effect of the P-shift is not visible in the sample of the C.V.D. silica layer.

Thermal treatment.—In the third measurements, the effect of the S-shift was also studied on two kinds of samples. The G sample is thermally grown and the H sample is the C.V.D. silica layer.

Here, a sample wafer was divided into four pieces and these were heated at 700°C at duration times of 0, 3, and 6 hr, and their S-shift curves were measured. They are as shown in Fig. 3a and b.

In this figure, no special effect requiring consideration was observed in the G sample; but in the H sample, the S-curves shifted toward the shorter wavelength side with the duration of thermal treatments.

Discussion

To explain the above-described experimental results, especially the effects of the S-shift, the P-shift, and their modifications, it seems necessary to assume the ununiform statistical distribution of the concentration of lattice oscillators which were formed by Si-O bondings in the frequency region from 4.61 x 10^{13} Hz (7.0μ) down to 3.0 x 10^{13} Hz (10μ). And it is necessary to admit the presence of different types of lattice oscillators, their force constant and reduced mass differing from each other.

It is reasonable to consider that the main part of the silica layer consists of silicon dioxide shown as $(SiO_2)_n$ and that they form polyhederon networks. But near the silicon-silica interface, the ratio of concentration of oxygen and silicon atoms is considered to vary because the supply of oxygen atoms to the interface during layer growth is not sufficient to form a saturated silicon dioxide layer. In another type of

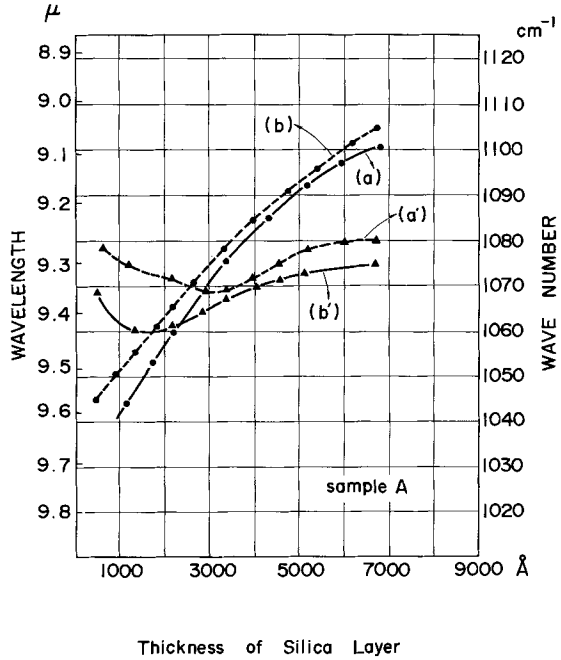

Fig. 1b. S-shift curve of thermally grown silica layer; (a), (b) are reflection measurements, and (a'), (b') are transmission measurements of (a) and (b).

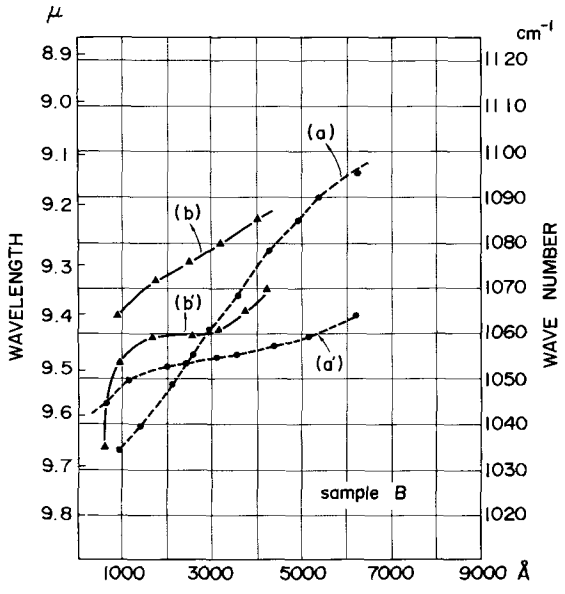

Thickness of Silica Layer

Fig. 1c. S-shift curve of the C.V.D. silica layer; (a) and (b) are reflection measurements, and (a') and (b') are transmission measurements of (a) and (b).

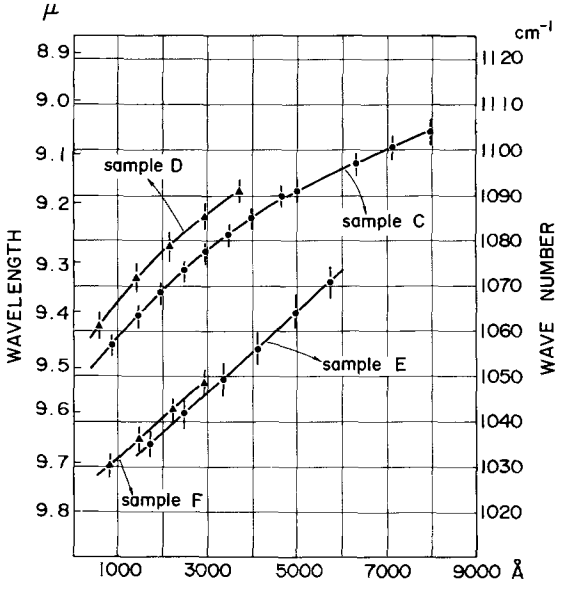

Thickness of Silica Layer

Fig. 2. S-shift curves of silica layer in as-grown state

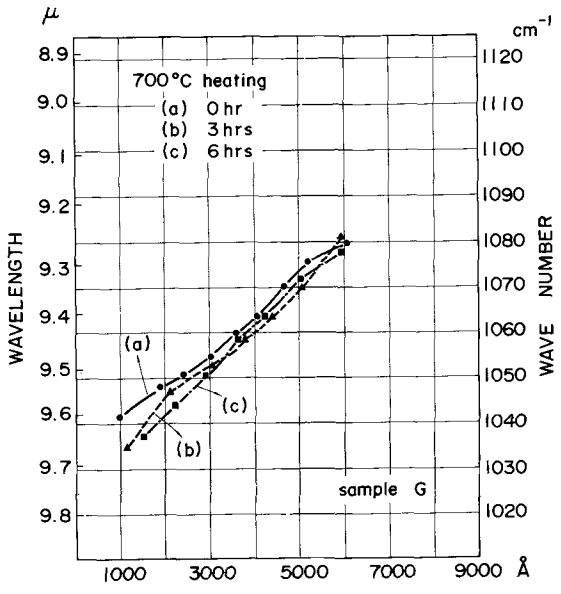

Thickness of Silica Layer

a. Thermally grown wafer

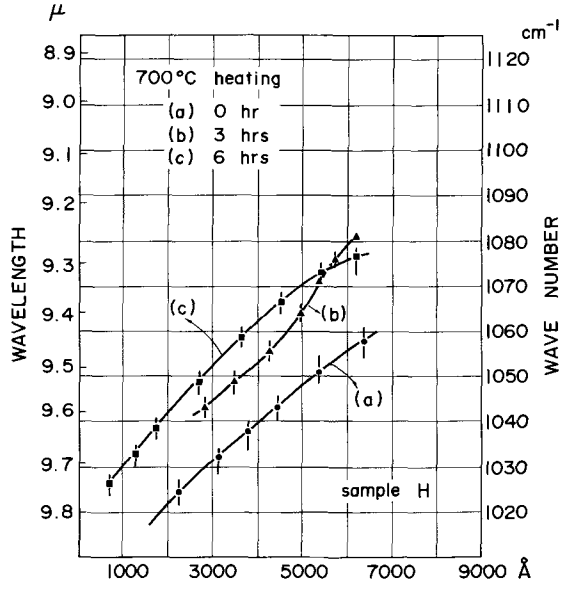

Thickness of Silica Layer

b. C.V.D. silica layer

Fig. 3. Variation of S-shift curves due to thermal treatments at 700°C with duration times of 0, 3, and 6 hr.

situation it is necessary also to assume the surface of the silica layer, because presence of the dangling bond is considerable below the surface. Considering these situations, the variety of Si_xO_y compounds and their configurations which are related to the Si-O oscillator can be summarized as presented in Table I.

The four kinds of lattice oscillators which were formed by the replacement of silicon atoms with oxygen atoms were summarized as type 1 oscillators, and they are classified into four types. Also, six types of dangling bonds which were formed by stripping one, two, and three oxygen atoms from type 1 oscillators were summarized as type 2 oscillators. The configurations of each oscillator mode are shown in Table I. It is reasonable to assume that frequencies of the lattice oscillators of each mode differ from each other as experimentally indicated by Ritter (20) (see Fig. 4).

Considering these situations, the concentration profile of each lattice oscillator inside the silica layer is shown schematically in Fig. 5, where (a) represents the concentration profile of each oscillator. In this figure, type 1 oscillators are visible mainly at the silicon-silica interface and type 2 are seen at the surface of the silica. Furthermore, this figure indicates the structural difference of the surface of the silica which is in an as-grown state and in an as-etched state. From this figure, it is clear that there is a larger concentration of type 2 oscillators on the as-etched surface than on the as-grown. Figure 5b shows the

Table I. Variety of Si-O stretching bondings

In the expression of $(Si_xO_y)_n$, we see with the variation of y/x the frequency of Si-O stretching band changes (15-18). Here, it is reasonable to assume the relation shown as $f_4 > f_3 > f_2 > f_1$ and $f_4 > f'_4 > f''_4 > f'''_4$.

Type 1 oscillator			Type 2 oscillator								
Concentration, cm^{-3}	Frequency	Configuration	Concentration, cm^{-3}	Frequency	Configuration	Concentration, cm^{-3}	Frequency	Configuration	Concentration, cm^{-3}	Frequency	Configuration
N_0	f_0	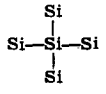									
N_1	f_1	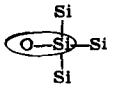									
N_2	f_2	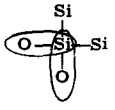	N'_2	f'_2	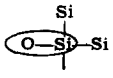						
N_3	f_3	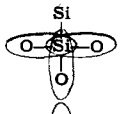	N'_3	f'_3	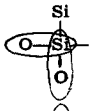	N''_3	f''_3				
N_4	f_4	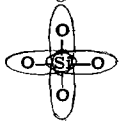	N'_4	f'_4	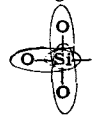	N''_4	f''_4		N'''_4	f'''_4	

atomic concentration profile inside the silica and silicon-silica interface relating to the concentration profile of Si-O oscillators.

Assuming the lattice oscillators concentration profile as shown in Fig. 5, the effects which were observed concerning the S-shift can be explained qualitatively as follows;

1. Effect of the S-shift was commonly observed in all samples, which may be due to the presence of type 1 oscillators at the silicon-silica interface and type 2 oscillators on the surface. With the progress of step etching, the contribution of surface oscillators (type 2 oscillators), sensitively related to the occurrence of reflection, increases because the type 1 oscillators are apt to become type 2 oscillators. Thus, the contribution due to more loosely bound oscillators becomes stronger.

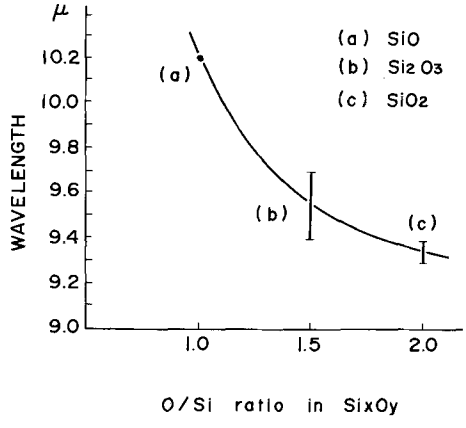

Fig. 4. Relation between wavelength of absorption maximum and O/Si ratio in Si_xO_y (20).

2. As shown in sample A, the wave number of the transmission measurements initially shifts toward the longer wavelength side than that of the reflection measurements. This effect may suggest that reflection intensity is mainly influenced by type 2 oscillators present on the surface, and that transmission intensity is influenced rather strongly by type 1 oscillators. Also, type 1 oscillators are more loosely bound than are type 2 oscillators.

3. When thickness of the silica layer becomes smaller than 3000Å, the S-shift curve of the thermally grown layer returns to the shorter wavelength side by about 10 cm^{-1}, while that of the C.V.D. layer shifts to the longer wavelength side. This effect may be due to a difference in construction of the silica-silicon interface of the two layers.

4. The S-shift curve of sample D shifts toward the shorter wavelength side by about 10 cm^{-1} compared with that of sample C. This effect also suggests that the thin silica layer in an as-grown state is rich in tight bondings, which implies that the concentration of type 1 oscillators is smaller than that of the thick silica layer. This effect can be derived from the fact that the supply of oxygen atoms to form the silica layer at the silicon-silica interface is better as long as the silica layer is thinner.

5. S-shift curves of the C.V.D. silicon layer, samples E and F, shift toward the longer wavelength side by about 30 cm^{-1} from that of the thermally grown silica layer, sample C. This effect may suggest that the C.V.D. layer is rich in loosely bound oscillators throughout the layer thickness. And the S-shift curve of sample F is present at almost the same wave number region as that of sample E, suggesting that there is no special difference in construction between the thin layer and the thick layer regarding the C.V.D. silica layer.

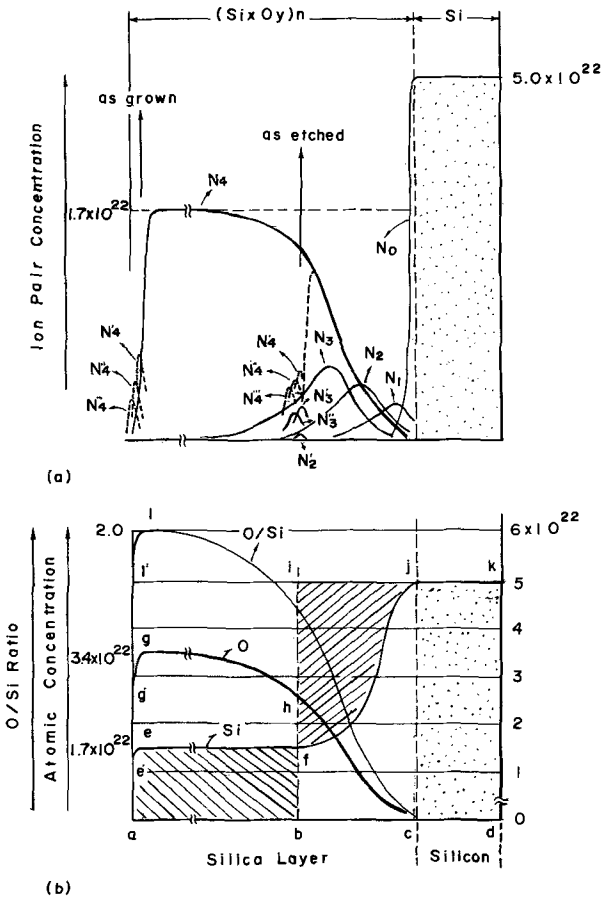

Fig. 5. Distribution profiles of lattice oscillators and atoms inside the silica layer.

a. Lattice oscillator concentration profile. Inside the silica layer, many kinds of lattice oscillator are considered to be present. The type 1 oscillator is rich at the Si-silica interface and the type 2 oscillator is at the surface of the silica layer. With the step etching, the type 1 oscillator is apt to become type 2 oscillators. Type 2 oscillators are sensitively related to the reflection and type 1 and 2 oscillators are to the absorption. It is clear that the concentration profile of the oscillators, N_1, N_2, N_3 and N_4, depends on the ratio N_o/N_{si}.

b. Atomic concentration distribution profile. The number of silicon atoms represented as a area of (ijf) is equal to (feab) and they form the silica layer in the range of (bc) and (ab). The concentration of silicon atom, $1.7 \times 10^{22}/cm^3$ was derived by assuming that the $(SiO_2)_n$ is piled up with pentagonal dodecahedral polyhedrons, whose atomic distance of Si-Si bonding is 3.23Å and that of Si-O is 1.62Å (19). The profile of the curves (gc) and (jf) can be assumed as error functions as

$$N_o(x,t) = \frac{N_o}{2}\left\{1 - erf\frac{x}{2\sqrt{D_1 t}}\right\} \quad [1]$$

$$N_{si}(x,t) = \frac{N'_o}{2}\left\{1 - erf\frac{x}{2\sqrt{D_2 t}}\right\} \quad [2]$$

here, the constants D_1 and D_2 are considered to vary with the conditions for the layer growth. And the ratio N_o/N_{si} varies in the range of 2-0.

6. By thermal treatment at 700°C, the S-curve of the thermally grown silica did not reveal any special changes. On the other hand, the C.V.D. silica displayed shifting toward the shorter wavelength side by about 20 cm^{-1}, suggesting that the loose bondings inside the deposited layer are apt to become tight due to thermal treatments.

Acknowledgments

I express my thanks to Dr. S. Tauchi for his discussions concerning the experimental data and to Messrs. H. Inoue and T. Kiya for preparing the samples and measurements.

Manuscript submitted Dec. 1, 1969; revised manuscript received *ca.* March 30, 1970.

Any discussion of this paper will appear in a Discussion Section to be published in the June 1971 JOURNAL.

REFERENCES

1. F. Matossi and C. L. Schaefer, "Das Ultrarote Spectrum," p. 318, Verlag von Julius Springer, Berlin (1930).
2. Howard A. Robinson, *J. Phys. Chem. Solids*, **26**, 202 (1965).
3. B. E. Deal and M. Sklar, *This Journal*, **112**, 430 (1965).
4. H. C. Evite, H. W. Cooper, and S. S. Flaschen, *ibid.*, **111**, 688 (1964).
5. I. Simon, *J. Opt. Soc. Am.*, **41**, 336 (1951).
6. W. G. Spitzer and D. A. Kleinman, *Phys. Rev.*, **121**, 1324 (1961).
7. D. K. Kleinman and W. G. Spitzer, *ibid.*, **125**, 16 (1962).
8. K. Sato, *J. Phys. Soc. Japan*, **20**, No. 5, 795 (1965).
9. W. H. Zachrisen, *J. Am. Chem. Soc.*, **54**, 3841 (1941).
10. W. H. Zachrisen, *ibid.*, **3**, 162 (1935).
11. W. A. Pliskin and H. S. Lehman, *This Journal*, **112**, 1013 (1966).
12. K. Sato and M. Shibata, *J. Phys. Soc. Japan*, **21**, No. 6, 1088 (1966).
13. W. A. Pliskin, *Thin Solid Films*, **2**, 1 (1968).
14. J. R. Ligenza and W. G. Spitzer, *J. Phys. Chem. Solid*, **14**, 131 (1960).
15. G. Herzberg, "Spectra of Diatomic Molecules," p. 75, D. Van Nostrand Co., Inc., Toronto (1953).
16. G. Herzberg, "Infrared and Raman Spectra of Poli-atomic Molecules," p. 61 D. Van Nostrand Co., Inc. Toronto (1953).
17. G. Herzberg, "Electronic Spectra of Poliatomic Molecules," p. 419. D. Van Nostrand Co., Inc., Toronto (1967).
18. F. Matossi, *J. Chem. Phys.*, **17**, 679 (1949).
19. H. A. Robinson, *J. Phys. Chem. Solids*, **26**, 214 (1965).
20. E. Ritter, *Opt. Acta*, **9**, 197 (1962).

Electron Microscopy of Phosphor Raw Materials

P. J. Walitsky and F. M. Vodoklys*

Lamp Division, Westinghouse Electric Corporation, Bloomfield, New Jersey

ABSTRACT

The reaction of $CaHPO_4$ with the individual activators and modifiers used to produce cool white phosphor was studied using electron microscopy and x-ray diffraction. Electron micrographs were obtained of $CaHPO_4$, $CaCO_3$, CaF_2, Sb_2O_3, $MnCO_3$, $CdCO_3$, and NH_4Cl. Micrographs were also obtained of the material produced by adding one additive at a time to $CaHPO_4$ and firing at ~1200°C in N_2. The conversion of $CaHPO_4$ to β-$Ca_2P_2O_7$ was accompanied by considerable grain growth. Combining with either $CaCO_3$ or CaF_2 enhanced this grain growth. X-ray diffraction was used to identify the products. Particle size data obtained with the Coulter Counter indicated that the size of the final phosphor is determined primarily by the $CaHPO_4$, $CaCO_3$, and CaF_2 components.

The use of electron microscopy to study lamp phosphors has been reported previously by Walitsky (1). The development of a technique for single stage replication was described and examples of calcium halophosphate phosphor shown. A logical extension of this work was the study of the raw materials from which the phosphor is made.

The preparation of calcium halophosphate phosphors is well known and goes back to the nineteen thirties. The starting materials are usually $CaHPO_4$, $CaCO_3$, Sb_2O_3, $CdCO_3$, $MnCO_3$, CaF_2, and NH_4Cl. Wanmaker, Hoekstra, and Tak (2), in 1955, studied the reactions of the various components individually and in various combinations using differential thermal analysis. Many similar studies have been done since. However, as far as can be determined in the published literature, there has been no electron microscopic study of the raw materials or of the various reactions occurring in the calcium halophosphate system. Bodi and Tufts (3) have studied the recrystallization of ZnS phosphor which is primarily a cathode-ray phosphor. Recently Brown has also studied ZnS (6).

While the intent of the work was primarily to obtain electron micrographs, x-ray diffraction data were also obtained. The x-ray diffraction data were especially valuable in pinpointing and explaining structural changes observed in the microscope. They also provided the information necessary to establish correlation with past work.

The electron micrographic study of phosphors mentioned above (1) raised several questions which were unanswered at the time of presentation. Many of the phosphors observed exhibited a surface topography resembling metallurgical structures. It appeared that grain structure covered much of the surface. There was no firm explanation as to its origin. Second, small particles or surface debris were seen on the surface of the large phosphor particles. These were also not fully explained.

Results and Discussion

Samples of each of the raw materials were first studied separately. Following this, samples of $CaHPO_4$ were mixed with each of the separate materials. Samples of $CaHPO_4$ + $CaCO_3$, $CaHPO_4$ + Sb_2O_3, $CaHPO_4$ + CaF_2, etc., were thus obtained. These mixed samples plus a separate sample of $CaHPO_4$ were then fired at ~ 1200°C in a N_2 atmosphere for several hours. The $CaHPO_4$ was studied separately as it is considered the basic structure from which this phosphor forms. The same amounts of material were added as would normally be done when preparing phosphor. The $CaCO_3/CaHPO_4$ mole ratio was approximately 0.5:1, the $CaF_2/CaHPO_4$ mole ratio was approximately 0.13:1, $Sb_2O_3/CaHPO_4$ and $CdCO_3/CaHPO_4$ mole ratios were both approximately 0.01:1, $NH_4Cl/CaHPO_4$ was approximately 0.02:1, and finally the mole ratio for $MnCO_3/CaHPO_4$ was approximately 0.1:1.

$CaHPO_4$.—Figure 1 shows a section of a typical $CaHPO_4$ particle at 10,000X. (All micrographs were at 10,000X.) Figure 2 is a section of a particle from the same lot as Fig. 1 given the heat-treatment described above. Transformation has occurred and grain boundaries are evident. Wanmaker *et al.* (2) state that the transformation of $CaHPO_4$ to β-$Ca_2P_2O_7$ starts at 380°C. The x-ray diffraction data obtained as a part of this investigation indicated that the samples represented by Fig. 2 were indeed β-$Ca_2P_2O_7$.

Comparison of micrographs not shown with Fig. 4 indicates that considerable grain growth has occurred subsequent to the transformation. The development of the grains and their growth is part of a separate investigation which will be discussed in the future. The particle shown in Fig. 4 represents the final result of the grain growth which has occurred.

$CaHPO_4$ + $CaCO_3$.—The next micrograph (Fig. 3) shows a $CaCO_3$ crystal. Some of these particles were observed as almost perfect cubes, while others were

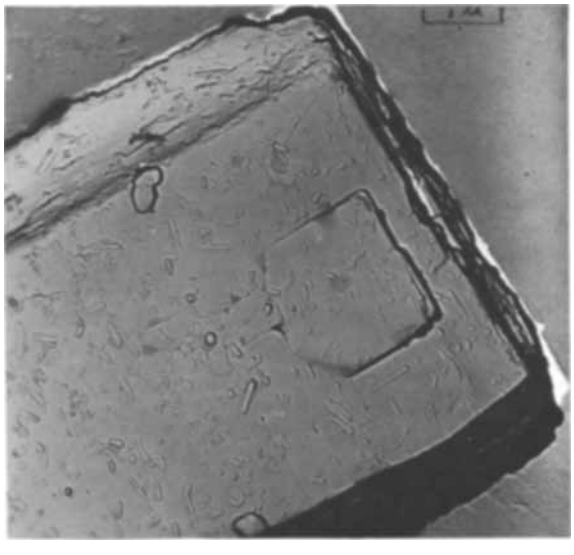

Fig. 1. $CaHPO_4$

* Electrochemical Society Active Member.
Key words: phosphor, electron microscopy, reactions.

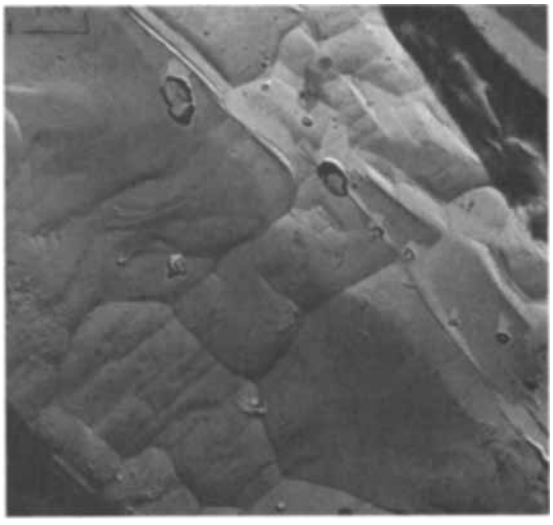

Fig. 2. β-$Ca_2P_2O_7$

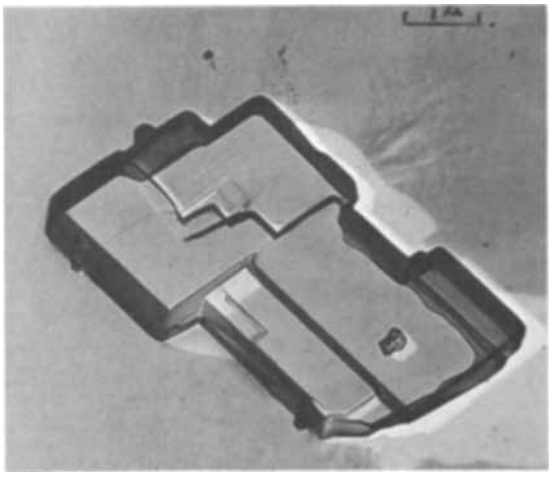

Fig. 3. $CaCO_3$

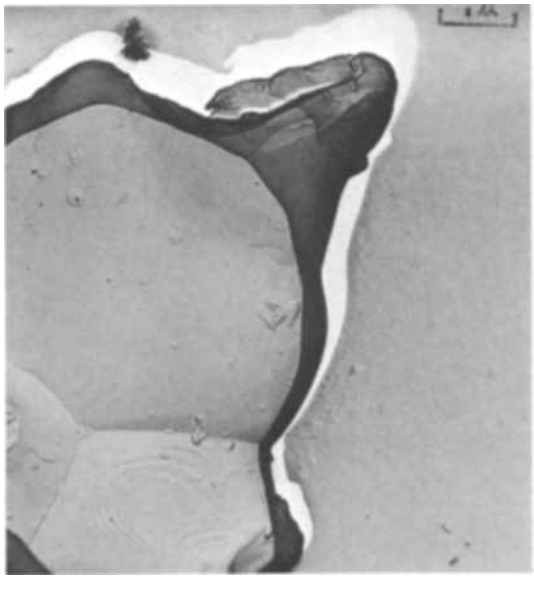

Fig. 4. α-$Ca_3(PO_4)_2$, prepared by heating $CaHPO_4$ + $CaCO_3$

less regular in shape. Combining $CaHPO_4$ and $CaCO_3$ produces a new structure, α-$Ca_3(PO_4)_2$ (Fig. 4). As with the previous reaction, correlation between our x-ray diffraction data and Wanmaker's work was obtained, plus some additional information.

The α-$Ca_3(PO_4)_2$ was indeed the major product found by x-ray diffraction analysis. However a detailed examination of the diffraction pattern revealed the presence of β-$Ca_3(PO_4)_2$ and β-$Ca_2P_2O_7$. Examination of the phase diagram P_2O_5/CaO (7) indicates that these phases will exist if one has a composition slightly richer in CaO than the ratio of 2CaO to $1P_2O_5$. Our starting composition was slightly richer. The temperature to which the sample was heated would suggest that we should also have the phase α-$Ca_2P_2O_7$. This phase was not detected. It may well be that this phase transformed on cooling to β-$Ca_2P_2O_7$.

The grain structure seen in Fig. 4 is somewhat larger than that observed in the transformed $CaHPO_4$. The reaction with $CaCO_3$ apparently changes the final grain size of the α-$Ca_3(PO_4)_2$ from that of the β-$Ca_2P_2O_7$. According to Wanmaker the $CaCO_3$ breaks down to CaO at 900°C, at 1000°C the reaction β-$Ca_2P_2O_7$ + CaO→α-$Ca_3(PO_4)_2$ takes place. (The β-$Ca_2P_2O_7$ had been formed at ~ 380°C.) The reaction is exothermic and perhaps provides a part of the energy necessary for grain growth.

$CaHPO_4$ + Sb_2O_3.—Particles of Sb_2O_3 are seen in Fig. 5. The particle size of this activator apparently covers a fairly wide size range. Combining $CaHPO_4$ and Sb_2O_3 results in formation of β-$Ca_2P_2O_7$ and is seen in Fig. 6. While there is no change in structure as compared to the transformed phosphate there did

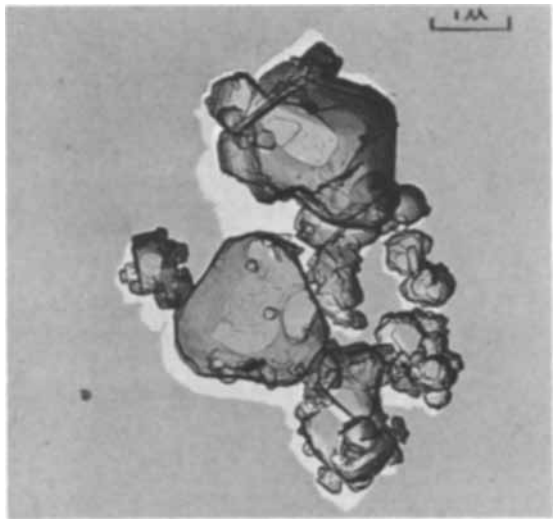

Fig. 5. Sb_2O_3

Fig. 6. β-$Ca_2P_2O_7$, prepared by heating $CaHPO_4$ + Sb_2O_3

appear to be a change in grain structure. The grain size is between that shown in Fig. 2 and 4. There was also evidence of material in the grain boundaries. Stereo electron microscopy indicated that the boundaries were quite deep. From the metallurgical viewpoint two other interesting features were seen: structures resembling twin planes and others strikingly similar to slip lines.

$CaHPO_4$ + $CdCO_3$.—The next material considered was $CdCO_3$. This was revealed as fine material with some agglomeration (Fig. 7). β-$Ca_2P_2O_7$ is again the reaction product and appeared almost identical to the particle in Fig. 6. The only difference was that material was not observed in the grain boundaries. In the preparation of the electron microscope samples $CdCO_3$ was the least soluble in HNO_3 of any of the additions. This necessitated longer dissolution times when preparing the replicas or a change in acid.

$CaHPO_4$ + $MnCO_3$.—$MnCO_3$ is seen in Fig. 8. Platelet growth is the prominent feature of this activator. A few of the particles observed were, however, smooth and did not exhibit this type of structure. As with the preceding two materials, combining it with $CaHPO_4$ does not disturb the transformation to β-$Ca_2P_2O_7$. Its appearance was similar to the $CdCO_3$ and $CaHPO_4$ material and the Sb_2O_3 combination (Fig. 6)

$CaHPO_4$ + CaF_2.—CaF_2 does produce a change in transformation. The material itself is shown in Fig. 9. Its appearance is somewhat similar to the $CdCO_3$, but the CaF_2 is present as much larger particles. Firing produces a mixture of β-$Ca_2P_2O_7$ and Ca apatite [$Ca_5(PO_4)_3F$] as revealed by x-ray diffraction. This

Fig. 7. $CdCO_3$

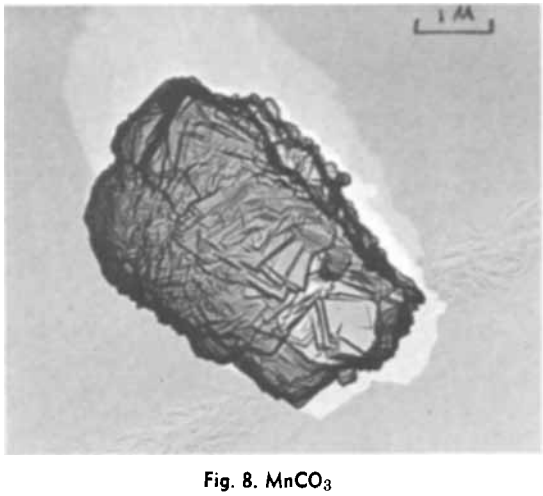

Fig. 8. $MnCO_3$

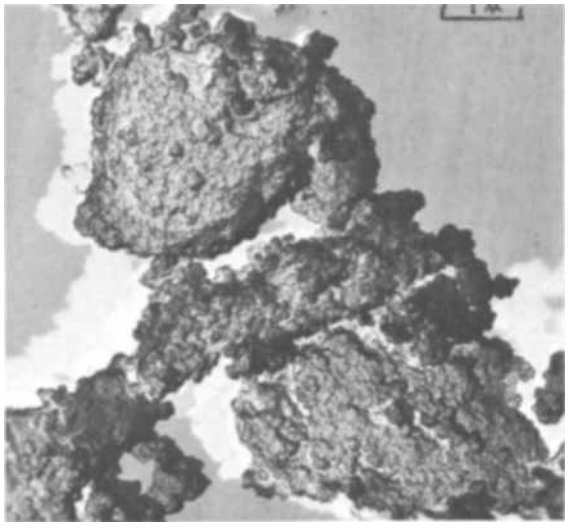

Fig. 9. CaF_2

correlates with Montel (4) who states that $18Ca_2P_2O_7$ + $14CaF_2$ → 5 apatite + $6POF_3(g)$. Rabatin and Gillooly (5) confirmed the reaction using reaction rate studies. They stated that when excess β-$Ca_2P_2O_7$ is present it will appear in the product.

During the microscopic examination it was very difficult to distinguish between β-$Ca_2P_2O_7$ and apatite. Most of the material observed was similar in topography to the β-$Ca_2P_2O_7$. However, examination of the micrographs indicate that some of the particles resembled the final phosphor more than the β-$Ca_2P_2O_7$. As the final phosphor does have the apatite structure it may be that these are apatite particles. An example of this is seen in Fig. 10.

$CaHPO_4$ + NH_4Cl.—The last material examined was NH_4Cl. This material is soluble in water which simplified the replication procedure. A complicating factor was the large size of the particle. It was impossible to obtain micrographs of an entire particle due to folding of the replica film. Fragments were obtained, however, and one is shown in Fig. 11. The material was covered with a very fine step structure. Particles which did not display this structure were generally smaller in size. Combination of NH_4Cl and the $CaHPO_4$ did not disturb the transformation to β-$Ca_2P_2O_7$. Its apearance was similar to Fig. 6 and the $CdCO_3$ combinations.

Phosphor.—A section of a phosphor particle is seen in the last micrograph (Fig. 12). Its topography is

Fig. 10. $Ca_5(PO_4)_3F$, prepared by heating $CaHPO_4$ + CaF_2

Fig. 11. NH_4Cl

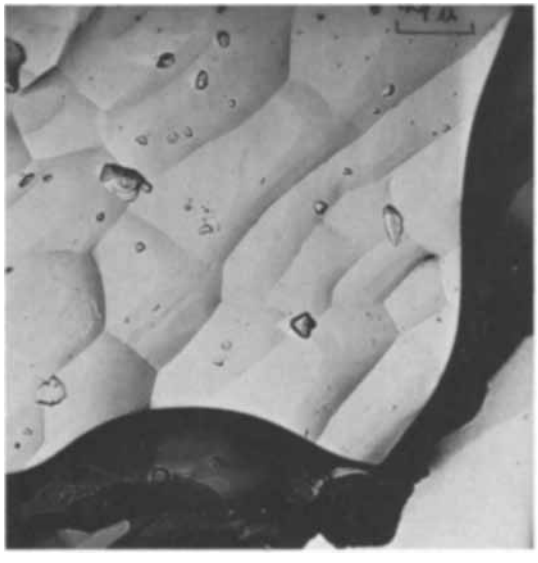

Fig. 12. $(Ca, Cd)_5(PO_4)_3(Cl, F)$:Sb, Mn finished phosphor (cool white).

similar to that seen in many of the earlier micrographs. Quite a few small particles appear on the phosphor surface. These were also observed on the combinations. Examination of the individual components lead us to the conclusion that this material is mostly small bits of activators and modifiers not fully incorporated into the phosphor crystal.

Particle size.—The effects of the different raw materials on the particle size of the finished phosphors were also studied. Calcium dibasic phosphate ($CaHPO_4$) is considered to be the basic "building block" for a calcium halophosphate phosphor, as stated in the introduction. Particle size measurements made with the Coulter Counter indicated that this compound experienced a reduction in particle size when fired to form the β-$Ca_2P_2O_7$ (Fig. 13). The increase in particle size when going from β-$Ca_2P_2O_7$ to the finished phosphor was due mostly to the $CaCO_3$ (Fig. 14).

Also evident was the growth of the β-$Ca_2P_2O_7$ resulting from the reaction with the CaF_2 (Fig. 15). This increase was of lesser magnitude than that caused by the $CaCO_3$. The effects of the other constituents on particle size were insignificant. Thus only those materials which produce a phase change in the β-$Ca_2P_2O_7$ have a significant effect on the final phosphor size.

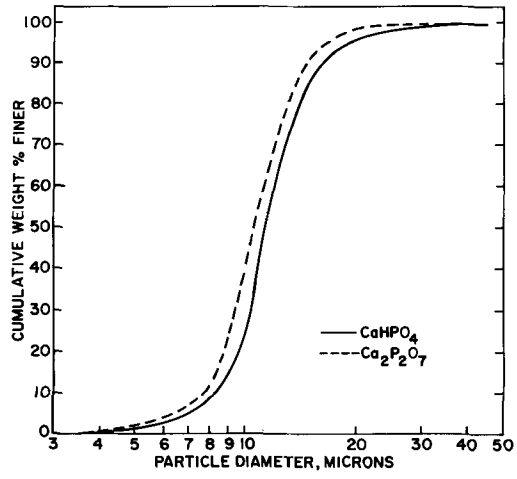

Fig. 13. Particle size distributions $Ca_2P_2O_7$, $CaHPO_4$

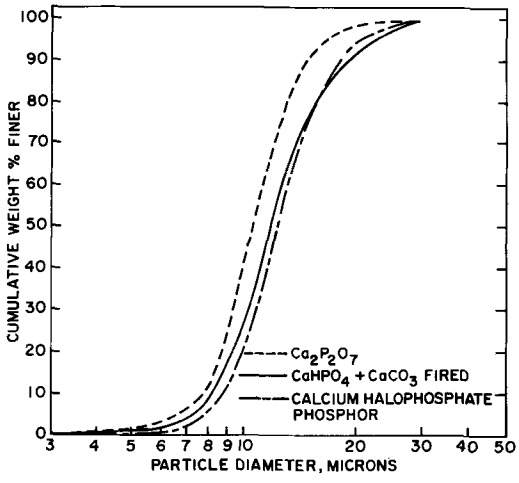

Fig. 14. Particle size distributions, $Ca_2P_2O_7$, $CaHPO_4$ + $CaCO_3$ fired and $(Ca, Cd)_5(PO_4)_3(Cl, F)$:Sb, Mn.

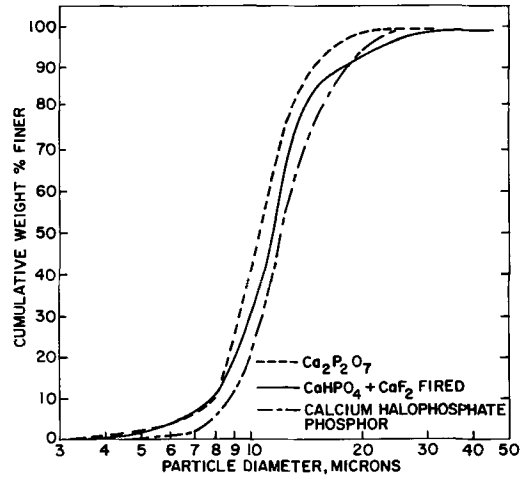

Fig. 15. Particle size distributions, $Ca_2P_2O_7$, $CaHPO_4$ + CaF_2, and $(Ca, Cd)_5(PO_4)_3(Cl,F)$:Sb, Mn.

Conclusion

The question of grain structure on the final phosphor, raised in the introduction, has been explained. It is primarily due to the transformation of $CaHPO_4$ to β-$Ca_2P_2O_7$. Correlation of the micrographs with x-ray diffraction data has provided evidence for supporting several experimental studies done with differential thermal analysis. It is evident that the electron micro-

scope can also provide some new insight into exactly what is occurring during the solid-state reactions involved in the production of lamp phosphors.

Acknowledgment

The authors wish to express their thanks to Miss S. Hamalian who took most of the electron micrographs; appreciation is due also to Dr. C. K. Lui Wei for the x-ray diffraction data, and to Mr. C. E. Oberst for the phosphate-mixture preparations.

Manuscript submitted Aug. 15, 1969; revised manuscript received *ca.* April 27, 1970.

Any discussion of this paper will appear in a Discussion Section to be published in the June 1971 JOURNAL.

REFERENCES

1. P. J. Walitsky, "Electron Microscopic Techniques for Fluorescent Lamp Phosphor Studies by Single Stage Replication," Proc. 1967 Electron Microscopy Society of America, p. 370.
2. W. L. Wanmaker, A. H. Hoekstra, and M. G. Tak, *Philips Res. Repts.*, **10**, 11 (1955).
3. L. J. Bodi and C. F. Tufts, *Science*, **153**, 872 (1966).
4. G. Montel, Silicium, Schwefel, Phosphate, Colloq. Sek, Munster, 1954, pp. 178-183 (1955).
5. J. G. Rabatin and G. R. Gillooly, *This Journal*, **112**, 489 (1965).
6. R. A. Brown, *ibid.*, **116**, 298 (1969).
7. E. R. Kreidler and F. A. Hummel, *Inorg. Chem.*, **6**, 891 (1967); as shown in Fig. 2304, Phase Diagrams for Ceramists, M. K. Reser, Editor, American Ceramic Society, p. 85 (1969).

A Quasi-Chemical Equilibrium Calculation of the Ge-Si-Sn and Ge-Si-Pb Ternary Phase Diagrams

G. B. Stringfellow and P. E. Greene

Hewlett-Packard Company, Palo Alto, California

ABSTRACT

The ternary phase diagrams Ge-Si-Sn and Ge-Si-Pb have been calculated based on the quasi-chemical equilibrium treatment of the lattice model for both the liquid and solid solutions. The calculation, using temperature independent interaction parameters obtained by fitting the calculated binary liquidus curves to experimental data, agrees to within experimental error with liquidus and tie line data obtained from the steady-state epitaxial growth of Si-Ge alloys from Sn and Pb solutions.

Alloy semiconductors have recently become important because their properties can be tailored for specific applications (1-5). A convenient method for the growth of these alloys is from solutions rich in a metal solvent. One difficulty with this method of crystal growth is the lack of reliable temperature composition ternary phase diagrams. The purpose of this paper is to demonstrate the feasibility of calculating accurate ternary phase diagrams for Ge-Si-M, where M is the metal solvent, using thermodynamic properties of the elements and interaction parameters obtained from the three binary phase diagrams Ge-M, Si-M, and Ge-Si.

The Model

The ternary phase diagram is calculated for the quasi-chemical equilibrium (QCE) model solution which was chosen as the simplest one which is capable of fitting the experimental data for the three associated binary systems. The QCE model has the following properties:

1. Each atom has Z nearest neighbors.
2. Nearest neighbors interact pairwise with the temperature and composition independent interaction parameter, Ω, defined as

$$\Omega_{AB} = H_{AB} - \tfrac{1}{2}(H_{AA} + H_{BB})$$

3. Only the configurational free energy of mixing is considered, *i.e.*, the vibrational free energy of mixing is neglected.
4. The distribution of constituent atoms is calculated using a mass action-like expression

$$N_{AA}N_{BB}/(N_{AB})^2 = \tfrac{1}{4}\exp(2\Omega_{AB}/ZRT) \qquad [1]$$

To test the QCE model, calculated liquidus curves for the binary Ge-M and Si-M systems are compared with the data of Thurmond *et al.* (10) in Fig. 1 and 2. The equations describing the binary liquidus curve for a QCE solution in the case of no solid solubility of B in A are as follows (7)

$$\ln\left[\frac{1}{X_A(1-X_A)\gamma_A\gamma_B}\right] = \frac{\Delta S_A^F}{R}\left(\frac{T_A^F}{T} - 1\right) \qquad [2]$$

$$\gamma_A = \left\{\frac{\beta - 1 + 2X_A}{X_A(\beta+1)}\right\}^{Z/2} \qquad [3a]$$

$$\gamma_B = \left\{\frac{\beta - 1 + 2X_A}{(1-X_A)(\beta+1)}\right\}^{Z/2} \qquad [3b]$$

where

$$\beta = [1 + 4X_A(1-X_A)(\eta^2 - 1)]^{1/2}$$

and

$$\eta = \exp(\Omega_{AB}/ZRT)$$

In these equations A represents Ge or Si and B the metal solvent. ΔS_A^F and T_A^F are the entropy and temperature of fusion of pure A. The interaction parameters were determined by making a best fit to the experimental data. In all cases the calculated liquidus curves are seen to fit the experimental data well.

The Ge-Si binary, both solidus and liquidus, were also calculated treating the solid and liquid as QCE solutions. The method of calculation is the same as that described in the next section with $X_{Sn} = 0$. The calculated liquidus and solidus fit well with the experimental data of Thurmond (16) as shown in Fig. 3.

Calculation of the Ge-Si-Sn Phase Diagram

The first step in the calculation of the ternary phase diagram Ge-Si-Sn is to equate chemical potentials of Ge and Si in the two phases

$$\mu_{Si}^c(T) = \mu_{Si}^l(T) \qquad [4a]$$

$$\mu_{Ge}^c(T) = \mu_{Ge}^l(T) \qquad [4b]$$

Key words: system Ge-Si-Sn, system Ge-Si-Pb, calculated phase diagrams, calculated ternary phase diagrams, system Ge-M, system Si-M.

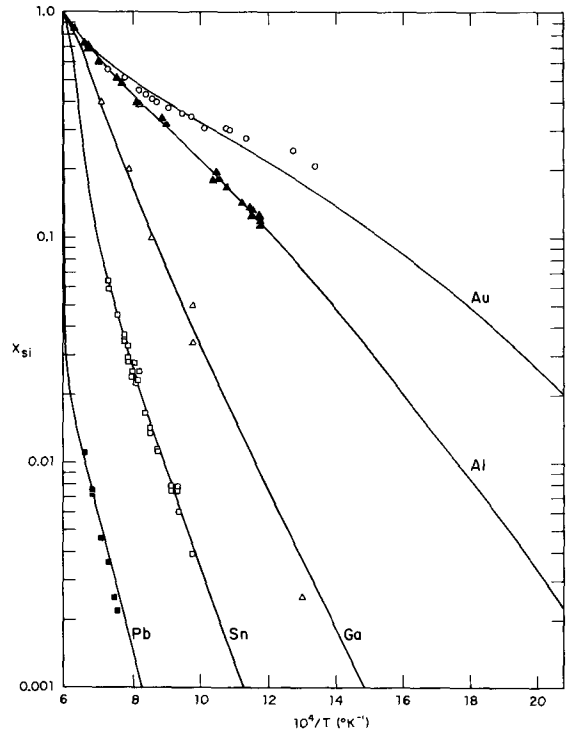

Fig. 1. Liquidus curves for Si-M systems calculated using the QCE model with constant interaction parameters compared to experimental data of Thurmond et al. (10). Values of interaction parameter used were $\Omega_{Si\text{-}Au} = -5020$, $\Omega_{Si\text{-}Al} = -2860$, $\Omega_{Si\text{-}Ga} = 1960$, $\Omega_{Si\text{-}Sn} = 6410$, $\Omega_{Si\text{-}Pb} = 13{,}220$ cal/mole.

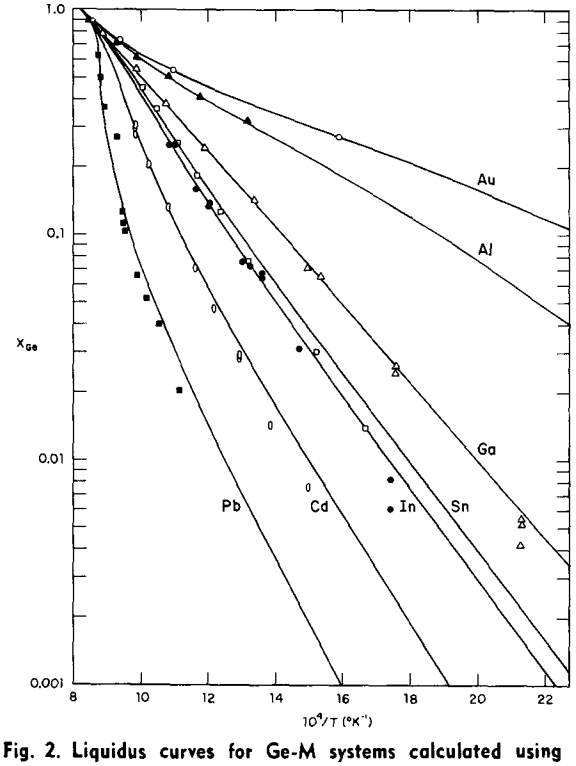

Fig. 2. Liquidus curves for Ge-M systems calculated using the QCE model with constant interaction parameters compared to experimental data of Thurmond et al. (10). Values of interaction parameter used were $\Omega_{Ge\text{-}Au} = -3655$, $\Omega_{Ge\text{-}Al} = -2470$, $\Omega_{Ge\text{-}Ga} = -210$, $\Omega_{Ge\text{-}Sn} = 735$, $\Omega_{Ge\text{-}In} = 1015$, $\Omega_{Ge\text{-}Cd} = 2520$, $\Omega_{Ge\text{-}Pb} = 4675$ cal/mole.

where

$$\mu_i^p(T) = \mu_i^{op} + RT \ln \gamma_i^p X_i^p \quad [5]$$

The superscript p represents the phase and the subscript i represents the component. The chemical potentials of the two phases in the standard state at $T \neq T^F$ are related as follows (14)

$$\mu_i^{oc} = \mu_i^{ol} - \Delta S_i^F (T_i^F - T) + \Delta C_p [T_i^F - T - T \ln (T_i^F/T)] \quad [6]$$

Combining Eq. [4]-[6], neglecting the ΔC_p term in Eq. [6], yields

$$\ln \left[\frac{\gamma_{Si}^c X_{Si}^c}{\gamma_{Si}^l X_{Si}^l} \right] = \frac{\Delta S_{Si}^F}{R} \left(\frac{T_{Si}^F}{T} - 1 \right) \quad [7a]$$

$$\ln \left[\frac{\gamma_{Ge}^c (1 - X_{Si}^c)}{\gamma_{Ge}^l X_{Ge}^l} \right] = \frac{\Delta S_{Ge}^F}{R} \left(\frac{T_{Ge}^F}{T} - 1 \right) \quad [7b]$$

$$X_{Ge}^l + X_{Si}^l + X_{Sn}^l = 1 \quad [7c]$$

These equations assume no solubility of Sn in the Ge-Si solid alloy.

The activity coefficients in the liquid solution may be calculated as a function of temperature and composition using the QCE model. The following six equations specify the thermodynamic properties of the liquid solution.

$$N_{AA}N_{BB}/(N_{AB})^2 = \tfrac{1}{4} \exp (2\Omega_{AB}/ZRT) \quad [8a]$$

$$N_{BB}N_{CC}/(N_{BC})^2 = \tfrac{1}{4} \exp (2\Omega_{BC}/ZRT) \quad [8b]$$

$$N_{AA}N_{CC}/(N_{AC})^2 = \tfrac{1}{4} \exp (2\Omega_{AC}/ZRT) \quad [8c]$$

$$2N_{AA} + N_{AB} + N_{AC} = ZN_A \quad [9a]$$

$$2N_{BB} + N_{AB} + N_{BC} = ZN_B \quad [9b]$$

$$2N_{CC} + N_{AC} + N_{BC} = ZN_C \quad [9c]$$

The equations can be solved to obtain N_{AB}, N_{AC}, and N_{BC}, *i.e.*, the distribution of A, B, and C atoms over the available sites. The total free energy of the system can be calculated and hence the activity coefficients. The details of the numerical calculation can be found in ref. (13).

The activity coefficients in the solid solution assumed to have only two components, are given by Eq. [3a, b]. Z is taken to be 4 for the solid since it has a diamond structure.

Equations [7a]-[7c] can then be solved numerically for a given X_{Si}^l and X_{Ge}^l to yield X_{Sn}^l, the liquidus temperature and the solidus composition in terms of the thermodynamic properties of the elements T_{Si}^F, T_{Ge}^F, ΔS_{Si}^F, ΔS_{Ge}^F, and the four temperature and composition independent interaction parameters $\Omega_{Si\text{-}Sn}$, $\Omega_{Ge\text{-}Sn}$, $\Omega_{Si\text{-}Ge}^l$, and $\Omega_{Si\text{-}Ge}^c$. The first two interaction parameters are obtained by fitting the Si-Sn and Ge-Sn

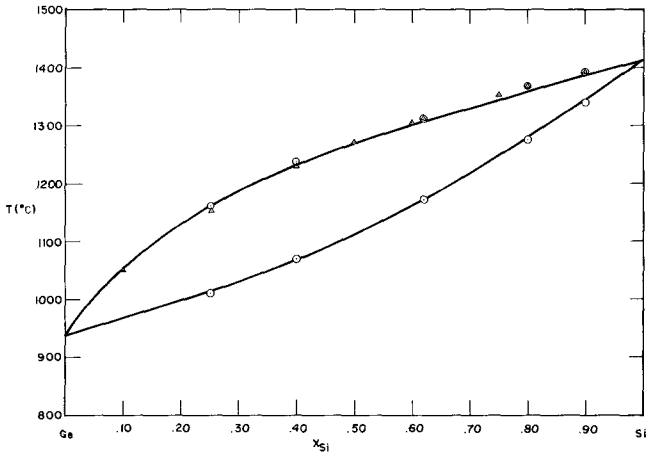

Fig. 3. Comparison of calculated to experimental (16) T-X phase diagram for the Ge-Si system. The QCE calculation used the following interaction parameters $\Omega_{Ge\text{-}Si}^l = 1615$ and $\Omega_{Ge\text{-}Si}^c = 1210$ cal/mole.

Table I. Parameters used for the QCE calculation of the Ge-Si-Sn and Ge-Si-Pb phase diagrams

Parameter	Value used in ternary calculation
T_{Si}^F	1683°K (10)
T_{Ge}^F	1210°K (10)
ΔS_{Si}^F	7.2 eu (10)
ΔS_{Ge}^F	6.7 eu (10)
Ω_{Ge-Sn}	735 cal/mole
Ω_{Ge-Pb}	4675
Ω_{Si-Sn}	6410
Ω_{Si-Pb}	13,220
Ω_{Si-Ge}^l	1615
Ω_{Si-Ge}^s	1210

phase diagrams, Fig. 1 and 2, and Ω_{Si-Ge} for the solid and liquid solutions are obtained by fitting the Ge-Si binary liquidus and solidus data. Fig. 3. The values of the parameters used are tabulated in Table I.

Computed isothermal liquidus lines for the Ge-Si-Sn system are presented in Fig. 4. Iso-(solid composition) lines are presented in Fig. 5. In this figure, each curve represents the liquid compositions in equilibrium with a solid Ge-Si alloy of a given composition. To clarify this somewhat unconventional representation tie lines for the 1200°K liquidus isotherm are included in Fig. 4. By comparing Fig. 4 and 5 it can be seen that tie lines extend from the intersection of the iso-(solid concentration) lines with the 1200°K liquidus to the solid Ge-Si concentration with which the iso-(solid concentration) line is labeled.

Calculation of the Ge-Si-Pb Phase Diagram

The Ge-Si-Pb phase diagram was calculated as described for the Ge-Si-Sn system except for the complication of the liquid immiscibility. The isothermal liquidus curves for the liquid-liquid equilibrium were calculated by equating chemical potentials of Ge, Si, and Pb in the two liquid phases in the same way as for the solid-liquid equilibrium. The two liquidus surfaces were superimposed with the higher temperature liquidus being the equilibrium liquidus surface. This allowed the determination of the monotectic line in the Ge-Si-Pb ternary. The thermodynamic parameters used in the calculation are listed in Table I. The calculated liquidus isotherms are plotted in Fig. 6. In Fig. 7 the iso-(solidus concentration) lines are plotted.

Experimental

Several liquidus isotherms of the ternary phase diagrams were determined by solubility measurement of Si in Ge-M solutions. A schematic of the apparatus used is shown in Fig. 8. The temperature is measured using a Pt/Pt-13% Rh thermocouple enclosed in a fused quartz tube inside the crucible, above the melt. The actual temperature of the melt was determined at several temperatures by inserting a test thermocouple, enclosed in a fused quartz tube, into the melt. It was determined that a correction of +2° is necessary to make the thermocouple located above the melt give the actual melt temperature. The maximum error in measured temperature is estimated to be ±2°. The apparatus is designed so that the Si wafer can be inserted into or removed from the melt at the experimental temperature by tilting the crucible. During the entire experiment the high-purity graphite crucible is in an atmosphere of flowing H_2 purified by diffusion through a palladium membrane.

The experimental procedure is as follows. Appropriate amounts of 6-9's Sn or Pb, Ge, and Si were

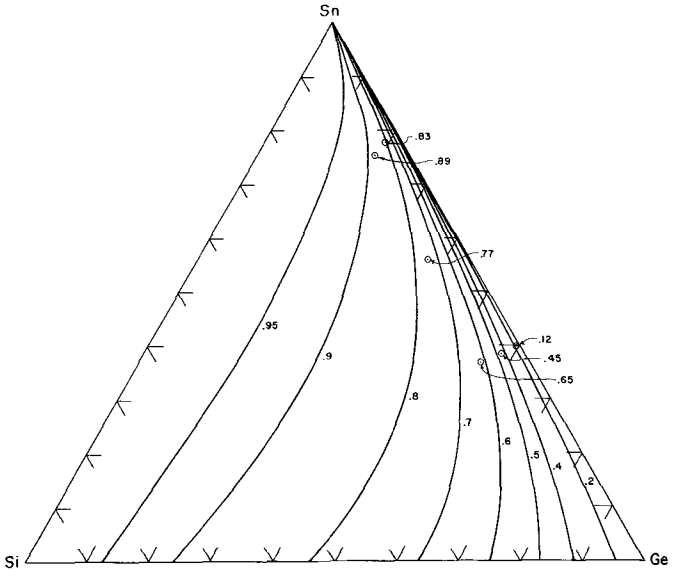

Fig. 5. Calculated iso-(solid concentration) lines for the system Ge-Si-Sn compared with experimental results. Each line represents the liquid compositions in equilibrium with a solid Ge-Si alloy of the given composition.

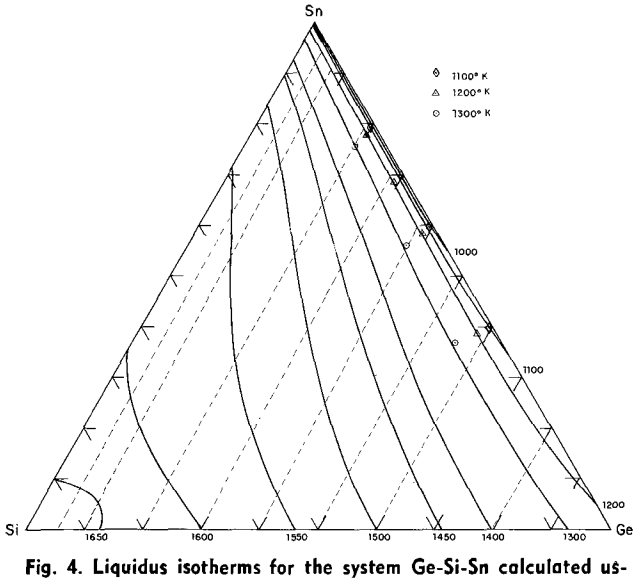

Fig. 4. Liquidus isotherms for the system Ge-Si-Sn calculated using the QCE model compared with experimental liquidus data at 1100°, 1200°, and 1300°K. The dashed lines are tie lines at 1200°K.

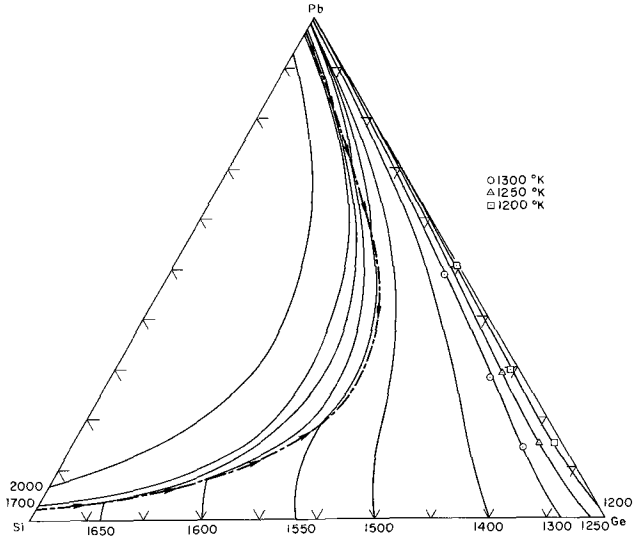

Fig. 6. Ge-Si-Pb isotherms calculated using the QCE model compared with experimental liquidus data at 1200°, 1250°, and 1300°K. The heavy dashed line is the ternary monotectic line.

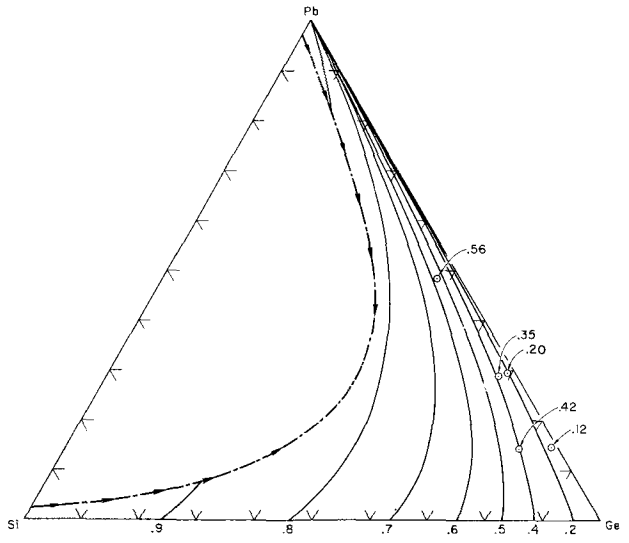

Fig. 7. Comparison of calculated iso-(solid concentration) lines with experimental data for the Ge-Si-Pb system. The heavy dashed line is the ternary monotectic line.

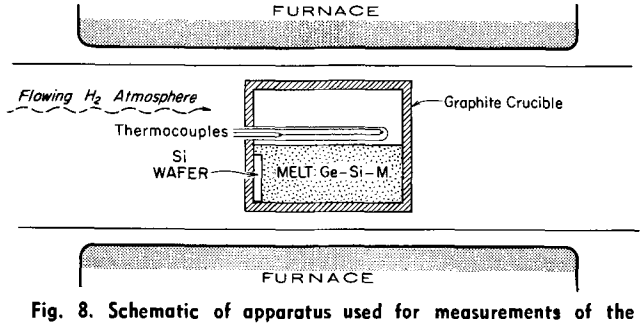

Fig. 8. Schematic of apparatus used for measurements of the solubility of Si in Ge-Sn and Ge-Pb solutions and the growth of Ge-Si alloys from the equilibrium liquidus solutions.

placed in the crucible. A Si wafer was polished mechanically and chemically, weighed, and attached to the holder in the crucible. The crucible was placed in the apparatus. After thorough purging, the crucible was moved into the furnace. The melt was allowed to equilibrate for approximately 1 hr before the Si wafer was inserted into the melt. During the experiment the crucible was slowly rocked to facilitate attainment of equilibrium. After no less than 6 hr, the substrate was removed from the melt and the crucible withdrawn to the cold zone of the apparatus. After allowing the crucible to cool, the Si wafer was removed to determine the weight of Si dissolved.

Due to a slight lateral temperature gradient across the sample, after equilibrium was established, Si would dissolve from one half of the wafer and a Ge-Si alloy crystal would grow epitaxially on the other half. This allowed the composition of the Ge-Si alloy in equilibrium with a given liquid to be determined. In reality crystal growth never occurs under equilibrium conditions but since the crystal growth was very slow, at a constant temperature, and the crystals obtained were homogeneous, as described below, they would be expected to have very nearly the equilibrium solid composition. After each experiment the alloy was removed from the Si substrate and was used to make a Debye-Scherrer x-ray diffraction pattern. This powder pattern was used to obtain the lattice parameter and to determine the homogeneity of the alloy. The half width of the alloy diffraction lines was found to be the same as for pure Si, indicating that the alloys are homogeneous. The composition was determined from the lattice parameter using the a_o *vs.* x data of Dismukes *et al.* (15). The accuracy of the determination of composition is ±1 a/o Si.

The solubility of Si in the Ge-M melt was determined as follows. After the alloy was removed and its weight and lattice parameter determined, the remaining Si was weighed and its dimensions measured. The Si weight was taken as the product of volume and density. This was done to minimize errors due to melt or alloy remaining on the Si surface since Sn, Pb, and Ge all have much higher densities than Si. The amount of Si dissolved in the melt was determined as (original weight of Si added to melt + weight of Si wafer)—(weight of Si wafer after run)—(alloy weight x weight fraction Si in alloy). Since the weight of the Si added to the melt was normally larger than the weight of the Si wafer, errors in determining the final weight of dissolved Si produced only small errors in liquidus composition. The estimated maximum errors resulting from thus determining the weight of Si dissolved are represented by the size of the experimental points on the phase diagrams.

The experimental results are presented on the calculated phase diagram Ge-Si-Sn and Ge-Si-Pb in Fig. 4-5 and 6-7, respectively.

Discussion

The ternary phase diagram is calculated for a model solution which is chosen as the simplest one which fits the experimental data for the three binary systems. Some model solutions which might describe the thermodynamic properties of Ge-Si-M solutions are discussed in terms of a binary solution A-B. All models discussed are based on the lattice model where the constituent atoms are located on a fixed lattice with Z nearest neighbors. The configurational free energy of mixing is determined by pairwise interactions.

The simplest model is the ideal solution where the constituent atoms do not interact so $\Omega_{AB} = 0$.

A second commonly used model is the regular solution (6). In this model Ω_{AB} is nonzero and the A and B atoms are distributed randomly, giving

$$N_{AA}N_{BB}/(N_{AB})^2 = \tfrac{1}{4}$$

The regular solution model is internally inconsistent since, in a system of interacting atoms, certain configurations have lower energy than others, thus the distribution is nonrandom and temperature dependent.

The subregular solution model (8) is similar to the regular solution except Ω_{AB} is taken to be linear in mole fraction A. This model is a specific case of a nonphysical approach where the chemical potential is expressed as a power series in temperature and composition (9). These approaches are useful for extrapolating or interpolating available ternary phase diagram data, but cannot be used to calculate a ternary phase diagram from data on the binary systems.

An internally consistent and more reasonable model is the QCE model described in the second section of this paper. The nonrandom distribution of constituent atoms is calculated using a mass actionlike expression, Eq. [1].

A comparison of calculated *vs.* experimental phase diagram data is necessary to select the appropriate model for the Ge-Si-M systems. Thurmond *et al.* (10) made a systematic study of binary liquidus curves for 14 different elements with Si and Ge. They found that most of the data could be fit using a regular solution model only if Ω were temperature dependent contrary to a basic assumption of the model, *i.e.*

$$\Omega_{AB} = a - bT$$

with a direct relationship between a and b.

Binary liquidus curves calculated using the QCE model with temperature independent interaction parameters, Fig. 1-3, were found to fit the experimental data well. These results suggest that the temperature

dependence of Ω in the regular solution calculation is an artifice to compensate for a failure of the model, in that it does not take into account the temperature dependence of the distribution function. The interaction parameter is forced to include not only $H_{AB} - \frac{1}{2}(H_{AA} + H_{BB})$, but also the changing pair distribution with temperature. This explains the functional relationship between a and b, since the temperature dependence of the distribution function is determined by Ω.

These results in the Ge-M and Si-M systems are similar to those in the Ga-As system which Thurmond (11) and Arthur (12) fitted using the regular solution model with

$$\Omega = a - bT$$

The authors (13) demonstrated that the data could be fit using the QCE model with a temperature independent Ω.

Summary

The Ge-Si-Sn and Ge-Si-Pb ternary phase diagrams, both liquidus isotherms and tie lines, were calculated based on the QCE model for both the liquid and solid solutions. The parameters needed for the calculations were T_{Si}^F, T_{Ge}^F, ΔS_{Si}^F, and ΔS_{Ge}^F, which were extracted from the literature, and the interaction parameters $\Omega_{Ge\text{-}M}$, $\Omega_{Si\text{-}M}$, $\Omega_{Si\text{-}Ge}^c$, and $\Omega_{Si\text{-}Ge}^l$, which were determined by fitting respectively the Ge-M, Si-M, and Ge-Si experimental binary diagram data.

Experimental liquidus data were obtained for the Ge-Si-Sn and Ge-Si-Pb systems by solubility measurements of Si in Ge-M, and tie lines were obtained by growth of Ge-Si alloys from liquid solutions of known composition.

The calculated phase diagrams were found to agree within the experimental data to within the experimental error. This illustrates the accuracy of the QCE calculation of ternary phase diagrams in these particular systems. The results suggest that the calculation would apply to other systems for which the binary liquidus can be fit using the QCE calculation.

Manuscript submitted Sept. 30, 1969; revised manuscript received April 2, 1970.

Any discussion of this paper will appear in a Discussion Section to be published in the June 1971 JOURNAL.

REFERENCES

1. N. Kh. Abrikosov, V. S. Zemskov, E. K. Iordanishvili, A. V. Petrov, and V. V. Rozhdestvenskaya, *Soviet Physics-Semiconductors*, **2** [12], 1468 (1969).
2. M. R. Lorenz, N. Renter, W. P. Dumke, R. J. Chicotka, G. D. Pettit, and J. M. Woodall, *Appl. Phys. Letters*, **13** [12], 421 (1968).
3. J. J. Tietjen and J. A. Amick, *This Journal*, **113** [7], 724 (1966).
4. J. C. Woolley and J. Warner, *Can. J. Phys.*, **42**, 1879 (1964).
5. F. B. Alexander, V. R. Bird, D. R. Carpenter, G. W. Manley, P. S. McCermott, J. R. Peloke, H. F. Quinn, R. J. Riley, and L. R. Yetter, *Appl. Phys. Letters*, **4**, [1], 13 (1964).
6. J. H. Hildebrand, *J. Am. Chem. Soc.*, **51**, 66 (1929).
7. E. A. Guggenheim, "Mixtures," Oxford University Press, London (1952).
8. H. K. Hardy, *Acta Met.*, **1**, 202 (1953).
9. R. Hiskes and W. A. Tiller, *Mat. Sci. & Eng.*, **II**, 320 (1967-68).
10. C. D. Thurmond and M. Kowalchik, *Bell Syst. Tech. J.*, **169** (January, 1960).
11. C. D. Thurmond, *J. Phys. Chem. Solids*, **27**, 785 (1965).
12. J. R. Arthur, *J. Phys. Chem. Solids*, **28**, 2257 (1967).
13. G. B. Stringfellow and P. E. Greene, *J. Phys. Chem. Solids*, **30**, 1779 (1969).
14. L. J. Vieland, *Acta. Met.*, **11**, 137 (1963).
15. J. P. Dismukes, L. Ekstrom, and R. J. Paff, *J. Phys. Chem.*, **68** [10] 3021 (1964).
16. C. D. Thurmond, *J. Phys. Chem.*, **57**, 827 (1953).

Technical Notes

Standing Wave Interference Patterns in Photoresists Observed with a Scanning Electron Microscope

L. J. Fried, R. Flachbart, D. F. Itlen, J. W. Raniseski,* F. W. Anderson, and K. V. Patel

IBM Components Division, East Fishkill Facility, Hopewell Junction, New York

The existence of standing light waves was first demonstrated experimentally by Weiner (1) in 1890, and was used as a basis of a method of color photography by Lippmann (2) in 1891. More recently, the existence of standing wave interference during exposure of photoresists was postulated by Altman and Schmitt (3) to explain the splitting of KTFR[1] films on chromium after development and has been used by Sheridan to produce holograms(4). The objective of this paper is to demonstrate, by use of the scanning electron microscope (SEM), the existence of standing wave interference during photoresist exposure.

Samples were prepared by spinning AZ-1350H[2] photoresist on Si wafers with 5000Å of thermally grown silicon dioxide. The resist was approximately 1.2-1.6μ thick. Patterns were formed in the resist by exposing with an unfiltered 200W Hg arc source with major u.v. lines at 3650, 4050, and 4360Å. Exposure was performed through a silver halide mask for 10-20 sec. The exposed resist was then removed in AZ developer. No post-baking was performed after development. Finally, approximately 500Å of Au was evaporated on the wafers to minimize charging during observation under the scanning electron microscope.

Figure 1 is a SEM micrograph illustrating an edge of one of the resist lands. Of interest are the fringes seen along the thickness of the resist, a higher magnification of which is shown in Fig. 2. These fringes are due to standing wave interference during exposure of the resist.

* Electrochemical Society Active Member.
[1] Eastman Kodak Company, Rochester, New York 14650.
[2] Shipley Company, Inc., 2300 Washington St., Newton, Massachusetts 02162.

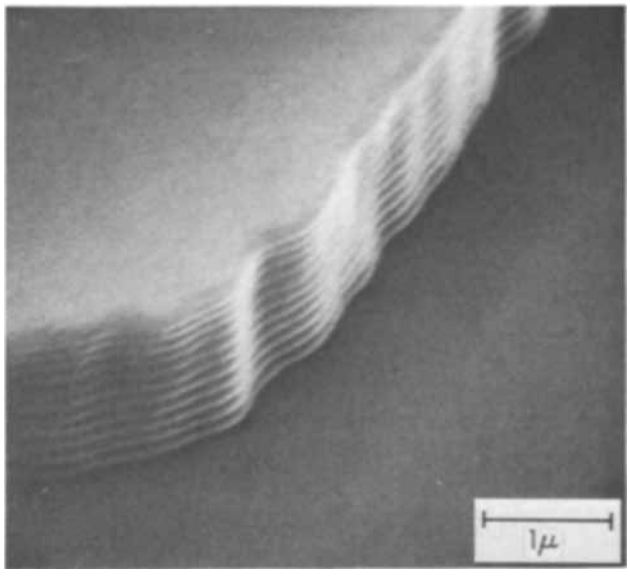

Fig. 1. Edge of AZ-1350H

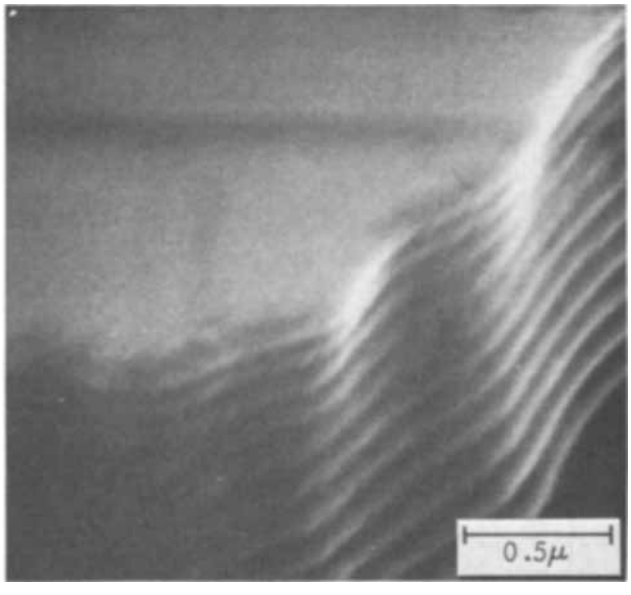

Fig. 2. Detail of Fig. 1

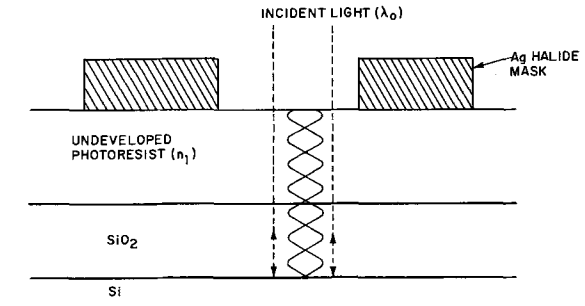

Fig. 3a. Schematic showing formation of standing wave from SiO_2-Si interface. (Change in wavelength between resist and oxide is not shown.)

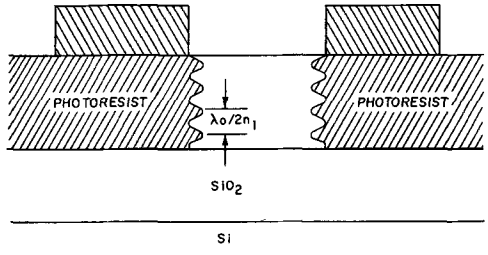

Fig. 3b. Schematic showing resist edge after development

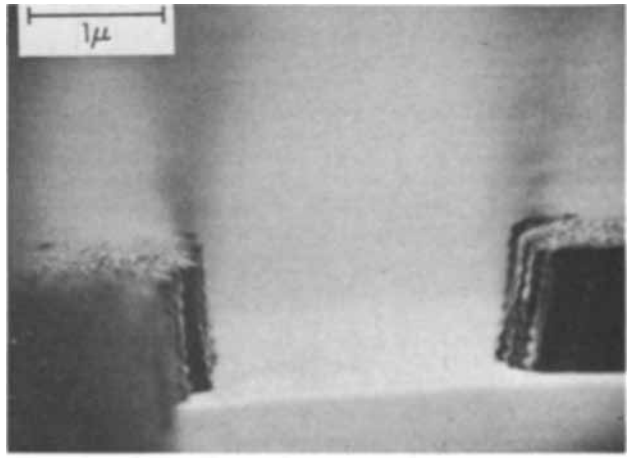

Fig. 4. Edge profile of AZ-1350H

Figure 3a schematically illustrates the formation of the standing wave from the SiO_2-Si interface, and Fig. 3b shows the resulting resist edge after development. Areas where maxima in the resist occur represent nodes in the standing wave where the resist is not adequately exposed and is not removed in the developer. Likewise, areas where minima in the resist occur represent antinodes in the standing wave where the resist is adequately exposed and removed in the developer. The distance between adjacent nodes or antinodes for monochromatic radiation is given by $\lambda_0/2n_1$, where λ_0 is the wavelength of the incident radiation in air, and n_1 the index of refraction of the resist. Figure 4 illustrates the sinusoidal profile of the resist edge.

To determine what contribution was due to a standing wave generated at the photoresist-SiO_2 interface, AZ-1350H was spun onto a glass slide and exposed, with black paper beneath the slide to eliminate a high reflectance substrate. The fringes which were produced were less pronounced than those produced from an SiO_2-Si or photoresist-Si interface; it was therefore concluded that the standing wave was primarily from the Si interface.

To eliminate the possibility that the fringes might have been an inherent structure in the photoresist enhanced by the developer, a resist edge was cleaved, left unexposed, and then immersed in the developer. No fringes were produced.

To determine the effect of the wavelength of the incident radiation on fringe spacing, wafers with AZ-1305H were exposed through band-pass filters, isolating the 3650, 4050, and the 4360Å Hg lines. Table I shows a comparison between the fringe spacing as calculated from the micrographs and that given by

Table I. Comparison between theoretical and measured fringe spacing

Wavelength of incident light, Å λ	n_1*	Fringe spacing, Å Theoretical	Measured
3650	1.70	1070	1100
4050	1.67	1210	1200
4360	1.66	1310	1285

* Index of refraction of photoresist: the indices of refraction were measured (5) on an AZ-1350 polymer (Phenol Formaldehyde Resin), using the laser-VAMFO technique (6).

$\lambda_0/2n_1$. The excellent results are undoubtedly somewhat fortuitous, as the error in the measurements is probably about 10%. However, the change in fringe spacing with wavelength is demonstrated.

It should be emphasized that all of the samples were not baked after development. If postbaking is performed at a temperature such that the resist flows, the fringes wash out.

The existence of fringes due to standing wave interference has been seen in such other positive resists as AZ-1350 and AZ-111 and, to a lesser extent, in negative resists such as KTFR. This difference in extent between positive and negative resists may possibly be due to a swelling of the KTFR during development washing out some of the structure.

To conclude, a scanning electron microscope enabled us to observe fringes along the thickness of the exposed photoresist. These fringes were found to be due to preferential exposure caused by a standing wave originating at the SiO_2-Si interface.

Acknowledgments

The authors would like to thank Drs. H. Levine and W. Pliskin for several helpful discussions; C. Bremmer, G. James, and D. Van Oppens for technical assistance; and A. J. Warnecke for supplying the data on the indices of refraction of AZ-1350H.

Manuscript submitted Jan. 30, 1970; revised manuscript received May 4, 1970. This was a Recent News Paper presented at the Detroit Meeting of the Society, Oct. 5-9, 1969.

Any discussion of this paper will appear in a Discussion Section to be published in the June 1971 JOURNAL.

REFERENCES

1. O. Weiner, *Ann. Physik*, **40**, 203 (1890).
2. G. Lippmann, *C. R. Acad. Sci. Paris*, **112**, 274 (1891).
3. J. H. Altman and H. C. Schmitt, Jr., "Kodak Photoresist Seminar Proceedings," (1968 Edition), Vol. II, May 20-21, 1968; Los Angeles, California.
4. N. K. Sheridan, *Appl. Phys. Letters*, **12**, 316 (1968).
5. A. J. Warnecke, To be published.
6. A. J. Warnecke, Presented at Kodak Seminar on Photoresist, Philadelphia, May 1969.

Deposition of Epitaxial $InAs_xP_{(1-x)}$ on GaAs and GaP Substrates

H. A. Allen* and E. W. Mehal*,[1]

Texas Instruments Incorporated, Dallas, Texas

There is considerable interest in semiconductors which have band gaps in the near-infrared region of the spectrum (1.4-0.33 eV) for solid-state light-emitting and laser diode, detector, and photoemitter applications. The specific areas of photoemitters and related photocathodes have generated specific interest because of the very high photoemissive yields which have been obtained from Cs_2O activated III-V surfaces (1,2) which show promise of giving a sensitive, high-efficiency photocathode for electromagnetic radiation beyond 0.9 μm, where the quantum efficiency of the classical alkalai-metal photocathodes is less than 1%. However, in order to make photocathodes practical for image-intensifier purposes, the active III-V material must be deposited on a substrate transparent to radiation of wavelengths longer than 0.9 μm.

$InAs_xP_{(1-x)}$ is a III-V alloy system which has band gaps that span this spectral region. GaAs could serve as a substrate window for radiation of 0.9 μm and longer, and GaP could serve as a broader-band window, transmitting light of wavelengths longer than 0.56 μm. The chemical-vapor deposition of $InAs_xP_{(1-x)}$ on InAs substrates, using AsH_3 and PH_3 as the source of As and P, was recently reported (3). A similar process has been used to deposit epitaxial layers of this alloy on chromium-doped and tellurium-doped GaAs and undoped GaP substrates.

Experimental

Materials preparation.—The open-tube deposition system (Fig. 1) used in these studies is constructed of fused quartz. A mixture of anhydrous HCl and purified hydrogen passes over a heated indium reservoir and transports the volatile InCl thus formed to the deposition zone. Purified hydrogen and high-purity AsH_3 and PH_3 (each in hydrogen gas) are mixed in a chamber prior to introduction to the reactor. The composition of the deposited alloys was controlled by the relative flow rates of the AsH_3-H_2 and PH_3-H_2 gases, each of which could be varied continuously from 0 to about 250 cc/min. For these experiments, mixtures containing 4% AsH_3 and 4% PH_3 (each in hydrogen) were obtained from the Matheson Company. Elemental indium (six-nines pure) was purchased from Cominco American, Incorporated.

A two-zone resistance furnace provided independent temperature control (± 2°C) of the indium reservoir and the GaAs or GaP substrate. There was a gradual temperature gradient between the indium zone (maintained between 750° and 850°C) and the substrate (maintained between 630° and 750°C). The seed and indium reservoir were located 3-4 in. apart. In most runs, the seed was held normal to the direction of gas flow by a quartz pin through a hole in the slice.

The GaAs substrates were (100), (111)A, (111)B, and (110) oriented slices (20 mils thick) cut from chromium- or tellurium-doped pulled crystals and chemically polished with 8:1:1 (H_2SO_4:H_2O_2:H_2O) immediately before use. The GaP substrates were grown by chemical-vapor deposition on (111)A GaAs substrates. The substrates were removed by lapping. The as-grown surfaces were used for alloy deposition.

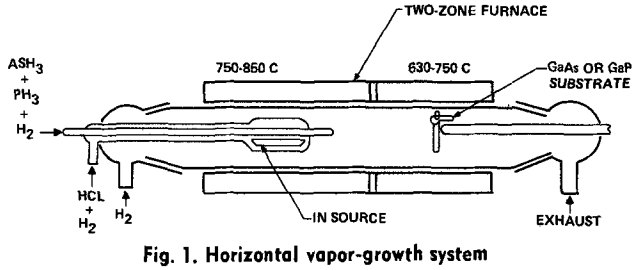

Fig. 1. Horizontal vapor-growth system

* Electrochemical Society Active Member.
[1] Present address: Spectronics Incorporated, Richardson, Texas.

Materials evaluation.—Epitaxial layer thicknesses were determined by either cleave or bevel-lap, and stain. Staining with a 1.5% NaOCl solution in H_2O gave a sharp contrast between the GaAs substrate and the layer; no stain was required for the GaP substrates. Alloy compositions were determined by electron microprobe analysis and/or x-ray diffraction. The sharpness of the diffraction peaks and the reproducibility of microprobe readings (taken in at least four positions on the surface) were used to determine the homogeneity of the layers. Infrared absorption measurements were made routinely to determine the absorption edge and to provide a semiquantitative measure of composition. However, accurate band gap values are difficult to obtain using this procedure because the sharpness of the absorption-edge measurement appears to depend strongly on the method of surface preparation.

Carrier concentrations and mobilities were determined by a-c or d-c Hall and resistivity measurements at room temperature on ultrasonically cut, six-armed samples with indium contacts.

Results and Discussion

Physical properties.—The alloy composition of the epitaxial layers was varied by changing the relative flow rates of the AsH_3 and PH_3 mixtures. The alloy composition (expressed in mole per cent InAs) is plotted in Fig. 2. Against the gas-phase composition calculated from the flow rates (expressed in mole per cent As, taking into account the Group V components only), it is seen that the alloys are systematically higher in arsenic content than the corresponding vapor phase. These results are in close agreement with those of Tietjen *et al.*(3).

Alloy samples grown in a given run were similar in composition. The surface composition did not vary by as much as 1 m/o (mole per cent) for most of the layers grown on (111)A and (110) substrates. The (111)B and (100) layers were less homogeneous for alloys containing more than 50 m/o InAs and were as homogeneous as any other orientation for those having more than 75 m/o InAs. The composition and crystallinity of various samples were checked by x-ray diffraction with compositions being determined by the method described by Howard and Dobrott (4) and the crystalline perfection of the layers was determined by a Laue topographical method developed by Swink(5).

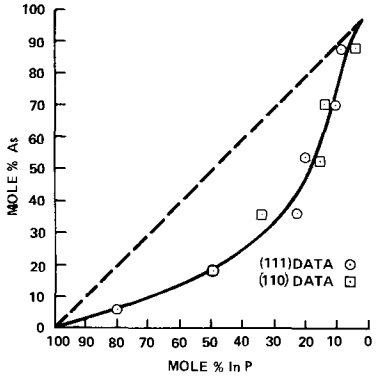

Fig. 2. Per cent InAs in $(InAs)_x(InP)_{1-x}$ deposited *vs.* per cent of As as total V component in the gas phase.

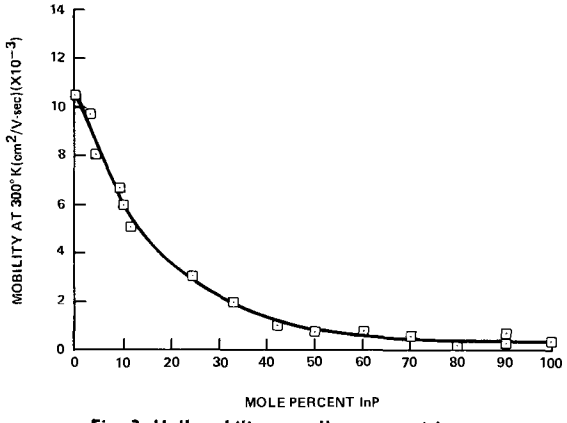

Fig. 3. Hall mobility *vs.* alloy composition

The optimum orientation appears to depend on alloy composition. For InP and alloys with <0.50, the (111)A orientation produced the highest-quality layers. The (100) orientation appeared to become more favorable for alloys having InAs contents of 75 m/o or greater. High-quality layers were grown on (110) substrates up to the middle of the composition range; erratic results were obtained using (111)B substrates. A more complete study of this orientation dependence is under way and will be reported at a later time. The optimum growth temperature appears to increase with InAs composition of the layers from around 640° to 650°C for InP to near 700°C for the InAs layers. Typical deposition rates were 50 ± 10.0 μm/hr.

The deposits on GaP substrates were generally of lower perfection than those of GaAs substrates as evidenced by broader x-ray diffraction peaks. However, some relatively shiny surfaces with a smooth alloy-GaP interface were grown throughout the composition range, but with more difficulty and less reproducibility than on the GaAs substrates. The larger lattice mismatch undoubtedly contributes to the imperfection of the deposits on GaP compared with those on GaAs. However, this might be alleviated by finding a set of growth parameters more favorable to deposition on GaP.

Electrical properties.—The electrical properties of $InAs_xP_{(1-x)}$ layers deposited on chromium-doped semi-insulating GaAs substrates were measured throughout the composition range. The deposits were all N-type having carrier concentrations in the (1-5) X $10^{16}cm^{-3}$ range. The Hall mobilities measured here increase monotonically from about 400 cm^2/V-sec for InP to 10,000 to 11,000 cm^2/V-sec for InAs. It is to be expected that the mobilities for these deposits on GaAs would be considerably lower than those for the deposits on InAs obtained by using the same reactant system (3), due to the large lattice mismatch between the alloy layers and the GaAs substrates. The lower mobilities for the InAs deposits as compared to those of Cronin *et al.* who used $AsCl_3$ and system-generated HCl to prepare InAs layers on GaAs substrates (6,7) are probably due to the incorporation of more compensating impurities originating from the commercial AsH_3 and HCl starting materials. No electrical measurements were made on the $InAs_xP_{(1-x)}$ depositions on GaP.

Manuscript submitted June 25, 1969; revised manuscript received *ca.* April 5, 1970. This was Recent News Paper 353 presented at the New York Meeting, May 4-9, 1969.

Any discussion of this paper will appear in a Discussion Section to be published in the June 1971 JOURNAL.

REFERENCES

1. J. J. Scheer and J. VanLarr, *Solid State Commun.*, **3**, 189 (1965).
2. R. L. Bell and J. J. Uebbing, *Appl. Phys. Letters*, **12**, 76 (1968).
3. J. J. Tietjen, H. P. Maruska, and R. B. Clough, *This Journal*, **116**, 492 (1969).
4. J. K. Howard and R. P. Dobrott, *ibid.*, **113**, 567 (1966).
5. L. Swink, *Trans. AIME*, (data incomplete).
6. G. R. Cronin, R. W. Conrad, and S. R. Borrello, *This Journal*, **113**, 1336 (1966).
7. G. R. Cronin and S. R. Borrello, *ibid.*, **114**, 1078 (1967).

JOURNAL OF THE ELECTROCHEMICAL SOCIETY

ELECTROCHEMICAL TECHNOLOGY

AUGUST 1970

A Pseudo-Resistance Method for Collating Battery Discharge Data

Olle Lindström*

Department of Chemical Technology, The Royal Institute of Technology, Stockholm, Sweden

ABSTRACT

A pseudo-resistance method is described for transformation of discharge curves obtained with a storage battery into one characteristic curve, which is called the *Ri*-curve. This graphical procedure yields useful figures of merit for storage batteries and is particularly valuable for estimates of battery data at high current and energy drains and for studies of variations and variability in battery performance. Two versions are presented. "Version I," which is sufficient for most purposes, uses three characteristic constants: *a* (the resistance parameter), *b* (the capacity parameter), and *Vr*, where *Vr* is a reference voltage and *a* and *b* are obtained from the regression line $Ri = a + b\ (Ri \cdot D)$, with $Ri = (Vr - V)/I$ and $D = \int I\,dt$ (*V* is the operating voltage, *I* discharge current, and *t* discharge time). The regression line represents the linear part of the *Ri*-curve $Ri = \phi\ (D \cdot Ri)$ which is plotted in the so-called *Ri*-diagram. "Version II," the R&D version, yields four figures of merit: *Vr*, *Dr*, *Rc*, and *Rk*, where *Dr* is a limit capacity, *Rc* a minimum internal resistance, and *Rk* a resistance factor for estimating the fraction of *Ri*, which depends on *D*.

The electric car is expected to become a very demanding application for storage batteries in the future. In contrast to the general level of technology, in this and other novel applications for storage batteries, *e.g.*, on the motor side, the methods for describing the electrical characteristics of the battery itself are unsatisfactory and incomplete. There are very good reasons for this situation. The storage battery is a much more complicated technical system than its electromechanical partner. The motor constitutes an invariant system, whereas the properties of the storage battery change during charge and discharge.

Methods for detailed presentation of the electrical qualities of the storage battery are desired both by the manufacturer and by the user. The manufacturer needs figures of merit in his R&D and for his quality-control functions. The user, *e.g.*, a submarine captain or an "electro-motorist"—a driver of an electric car—needs relevant data presented in an understandable and usable form. This kind of information is needed particularly at high current drains and/or large energy drains, *i.e.*, in the domain of the performance limits of the battery. The user depends less on detailed information of this kind when the battery is in its fully charged condition.

Figures of merit or characteristic parameters for batteries should be derived entirely from the inherent qualities of the battery. The basic relation should, with a minimum of terms, be capable of describing the whole array of discharge curves and associated voltage/current curves with particularly high precision in the domain of the performance limits of the battery. The constants involved should preferably have a physical meaning to help understanding and analysis. The most important goal would, however, be to achieve an efficient reduction of experimental data. This is in line with the purpose of the comprehensive work by Shepherd (1) who derived an equation describing battery discharge. The present approach has much in common with Shepherd's studies. The present work should, however, not be considered an extension of Shepherd's work; rather, the purpose has been to bring to focus the most interesting area from the user's point of view, *i.e.*, the domain of the performance limits of the battery, and to find a more practical procedure for deriving figures of merit for the battery in this domain.

Shortcomings of Present Methods

The performance of storage batteries is today almost universally reported by means of discharge curves. The battery voltage is plotted against the discharge time or the amount of electricity delivered at constant current. The discharge is interrupted at an end voltage, *Vs*, and the obtained capacity figure, *Ds* A-hr, reported as a figure of merit. The choice of *Vs* depends on the application in question and the discharge current.

The familiar Peukert relation is frequently used in lead acid battery studies for estimates of *Ds* at various *I*. Unfortunately, the constants of the Peukert regression line are much influenced by the choices of *Vs* as illustrated by Fig. 1. Figure 1 also includes a Peukert curve for a hypothetical battery with a constant capacity independent of the discharge current. This curve does not deviate too much from the others in the graph.

* Electrochemical Society Active Member.

Key words: battery characterization, *Ri*-curves, *Ri*-diagrams, discharge curves, end voltages, battery parameters, Peukert relation, Shepherd equation, battery variability, voltage-current curves, internal resistance of batteries, electrode structure, overcharging lead acid batteries, sintered iron electrodes.

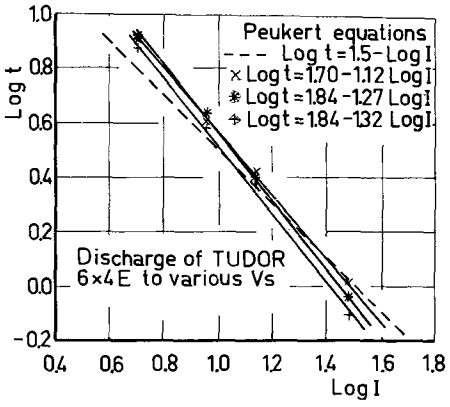

Fig. 1. Peukert curves, $^{10}\log t = a + b\ ^{10}\log I$, derived from discharge curves obtained with a lead acid battery, Tudor 6 x 4E (I, discharge current; t, discharge time; and Vs, end voltage. End voltages, Vs, were chosen according to (a) practice in the laboratory for general evaluation, x; (b) practice for tractionary batteries, ✲; and (c) practice for stationary batteries, +. The dashed line represents a hypothetical battery with constant capacity independent of discharge current.

The concept of end voltage is apparently of little value as a basis for putting up equations describing battery performance because of its arbitrary character. The situation would of course be different if Vs could be related to the electrical properties of the battery and not be decided by the actual application. The following route might, however, be used for defining Vs in a manner which would be satisfactory from this point of view. End voltages plotted against the corresponding discharge currents frequently follow a kind of linear voltage/current curve. The $D = Ds$ curve in Fig. 2 shows end voltages, Vs, against discharge currents. Such V/I curves are also obtained when voltages at constant ratios, D/Ds, are plotted against the current, Fig. 2 (D denotes the number of amperehours that have been delivered at the time of the voltage reading, whereas Ds represents the capacity at the discharge current used). These special V/I curves frequently have the same slopes at different D/Ds ratios. One could then adopt the policy that: (a) end voltages should be chosen so that the Vs/I curve becomes parallel to other V/I curves, valid for various constant D/Ds ratios, and (b) that the constant voltage difference between the Vs/I curve and the V/I curve for $D = 0$ should be related in a simple numerical way to the difference between the V/I curve for $D = 0$ and, *e.g.*, the curve for $D/Ds = 0.5$. This route is fairly complicated, requires that the discussed V/I curves are reasonably parallel, and involves an iteration procedure. The curves in Fig. 2 which are based on present practice to define Vs for tractionary batteries are almost, though not exactly, parallel. The voltage difference between the $D = 0$ and the $D = Ds$ curve is 0.29V. Shepherd considered discharges to be ended at voltages equal to those of the $D = 0$ curve, minus 0.25V.

Shepherd's equation (1) is capable of describing complete sets of discharge curves very efficiently. In spite of this highly desirable feature most laboratories, however, do not seem to use this tool because of (a) the somewhat complex procedures involved in determining the numerical values of the constants of the equation, (b) the diffuse physical meaning of some of the constants, (c) the fact that consistent and good curve fits can be obtained with different sets of constants, and (d) the variability in battery performance which makes any attempt to fit experimental data to any equation over the entire range of discharge curves dubious to the mind of the experimentalist.

The fourth point is particularly relevant when $D < 0.5\ Ds$, as illustrated by the V/I curves in Fig. 3. These V/I curves were obtained with a 260 A-hr stationary lead acid battery. The battery was discharged at various constant discharge currents in the normal way (I = 26, 45, 64 and 111A). The constant current discharge was, however, interrupted for a short time three times during the discharge, at D = 40, 64, and 107 A-hr. On these occasions the load was varied so as to obtain a V/I curve valid for the battery under the prevailing conditions. The battery voltage and the variable load current were recorded after 90 sec of operation at the new current load.

The 12 V/I curves in Fig. 3 obtained in this way (one for each combination of D and I) exhibit three features: (a) linearity, (b) some variability, and (c) fairly small differences—from a practical point of view—between the various runs. The range of the intercepts on the voltage axis for $I = 0$ represents only ± 1.2% of the battery voltage. This domain of battery operation evidently does not provide a good starting point for putting up relations describing battery performance. A better route would be to start at the other end of the discharge profile where more dramatic things happen that are important to the user.

Pseudo-Resistance Method (*Ri*-Method) "Version I"

Obviously, a minimum of three parameters would be required to define the performance of a battery: (a) a capacity parameter, (b) an internal resistance parameter, and (c) a reference voltage. Since the

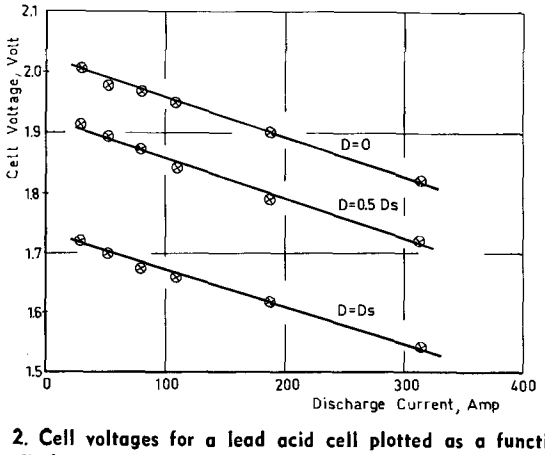

Fig. 2. Cell voltages for a lead acid cell plotted as a function of the discharge current at states of discharges characterized by $D = 0$, $D = 0.5\ Ds$ and $D = Ds$, respectively. Data taken from discharge curves in a battery catalog at the 10, 5, 3, 2, 1, and ½ hr rates (2).

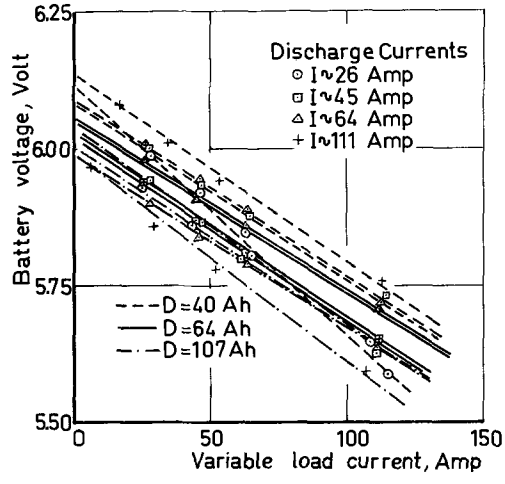

Fig. 3. V/I curves for a 260 A-hr lead acid battery Tudor 3 Spg obtained at D = 40, 64, and 107 A-hr, respectively. The discharge was performed with 26, 45, 64, and 111A, except when readings for the V/I curves were taken.

slope of the V/I curve depends on the state of charge, and the capacities, which can be obtained under various conditions, depend on the shape of the V/I curves, the sought relation should at least include a relationship between these two parameters. The capacity parameter should preferably be related to the capacity found at very small discharge currents, whereas the internal resistance parameter should be related to the properties of the battery in its nearly fully discharged state.

The so called *Ri*-diagrams, introduced in this paper, are in their most simplified version, completely in harmony with the above requirements, and give a good fit of experimental data. This version, here called "Version I," makes use of an apparent resistance term, *Ri*, calculated as

$$Ri = (Vr - V)/I \qquad [1]$$

where Vr is a reference voltage which is estimated as the averaged intercept of the relevant V/I curves extrapolated to $I = 0$, and V is the voltage of operation. *Ri* obtained in this way is plotted against the product $(Ri \cdot D)$ where D is the quantity of electricity, here in A-hr, that has been delivered by the battery at the time of the measurement.

A linear *Ri*-curve indicates that the potential drop, $Vr - V$, increases with discharge time, t, in an accelerated way, being proportional both to $(Vr - V)$ and t. As a matter of fact, the *Ri*-curves, $Ri = \Phi\ (Ri \cdot D)$, most frequently turn out to be linear, except at low energy drains (*i.e.*, early in the discharge). This regression line is here expressed by

$$Ri = a + b\ (Ri \cdot D) \qquad [2]$$

The slope b has the dimension of inverted capacity, $(\text{A-hr})^{-1}$, whereas the intercept on the *Ri*-axis, a, is a characteristic resistance term. Equation [2] is thus based on the three parameters Vr, a, and b. At the moment we consider the *Ri*-diagram, "Version I," to be an empirical relation. We, however, introduce a "Version II" below in which case some remarks of a deductive nature will help in understanding the meaning of the constants a and b.

The *Ri*-diagram in Fig. 4, covering different charge states and discharge currents, shows that this simple route is a fairly efficient procedure for reduction of experimental data into one single curve. Points from different discharges with different currents fall on the same *Ri*-curve. A regression line valid for large energy drains which satisfies [2] is obtained by extrapolating the linear part of the curve toward the *Ri*-axis. In this particular case, $1/b$ corresponds to 45.9 A-hr to be compared with the 15 hr capacity of Ds = 43.5 A-hr.

It is thus realized from Fig. 4 that the *Ri*-diagram could also be useful for a presentation of the electrical properties of the battery for small energy drains even if the linear relation [2] no longer holds in this region.

The *Ri*-diagram is, however, of course no remedy against variability in battery performance. The variability may frequently manifest itself as a variation in the regression constants, a, whereas the slopes, b, of the regression lines in most cases come out fairly constant. This is illustrated in Fig. 5 with four consecutive cycles with a large battery. Clearly the *Ri*-diagram is an excellent tool to study and define this kind of variability, since the variability can often be attributed to one single parameter. It seems quite natural that the well-known variability in battery performance from one cycle to another under seemingly rigorously controlled experimental conditions should be connected with some kind of resistance factor, small in itself but with a large influence on performance. (Variations may occur in the contact between the current-collecting grid and the active

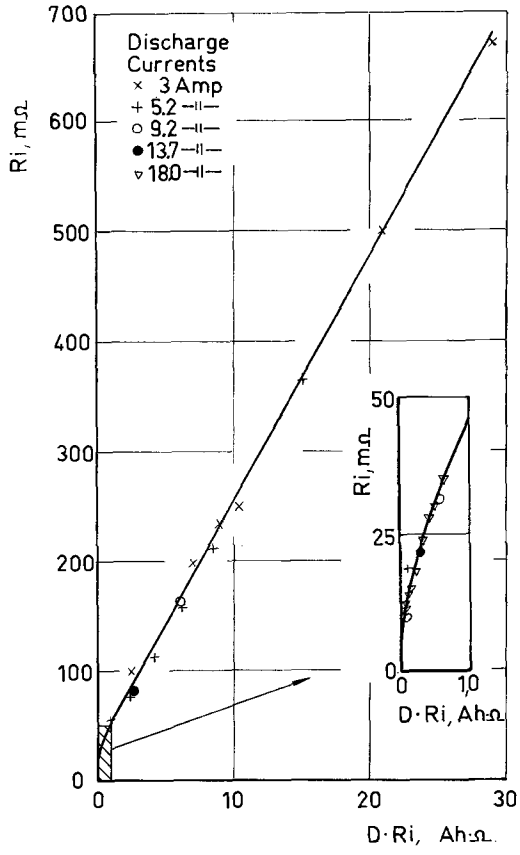

Fig. 4. *Ri*-diagram, "Version I," for a lead acid battery, Tudor 6 x 4E. Constants of the linear regression line are a = 30 mohm b = 0.0223 $(\text{A-hr})^{-1}$. Vr = 2.02V. The section of the diagram near the origin is magnified to demonstrate the typical bend of the *Ri*-curve.

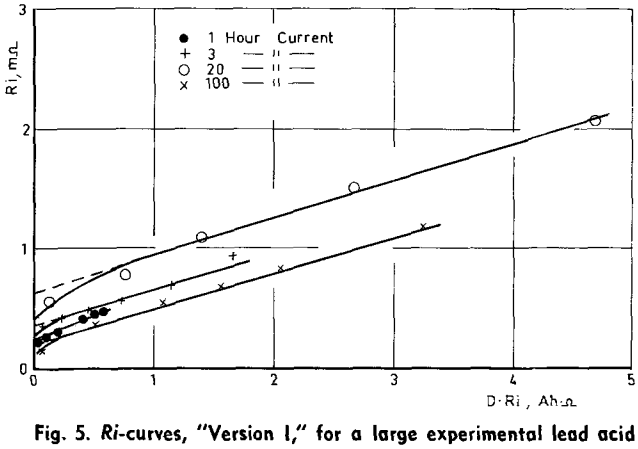

Fig. 5. *Ri*-curves, "Version I," for a large experimental lead acid cell demonstrating variability of the regression constant, a, frequently met with in development work. Vr = 2.02V.

materials due to thin corrosion layers. Minute gas bubbles may remain from the foregoing charging period in the porous structure, etc.)

The different characters of the two regression constants a and b are also evident from the experiments reported in Fig. 6. This lead acid battery was heavily overcharged during many days. The *Ri*-diagram indicates that the slopes in the *Ri*-diagram are quite constant, whereas the regression constant, a, increases with the amount of overcharge. Figure 7 gives a plot of the two regression constants. There is an approximately linear increase of the resistance parameter, a, whereas the capacity parameter, $1/b$, is influenced but slightly by overcharging.

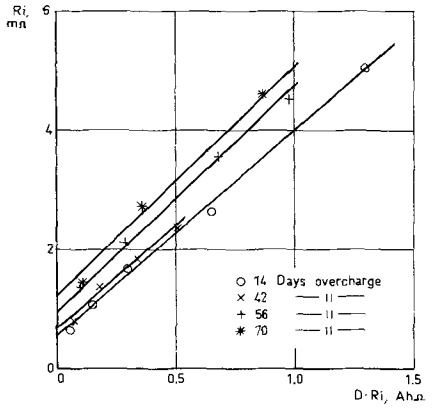

Fig. 6. *Ri*-curves, "Version I," for overcharge experiments with a lead acid battery (Tudor 3 Pg 410). $Vr = 2.02V$.

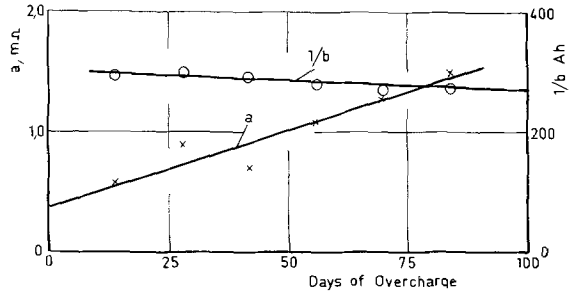

Fig. 7. Parameters *a* and *1/b* from regression lines for *Ri*-curves in Fig. 6.

Figure 8 displays discharge curves taken from a battery catalog (2) in the condensed form of the *Ri*-diagram. The simple method for estimating D at any voltage and discharge current within practical limits is exemplified on the graph. Since one *Ri*-curve is sufficient for one battery, the performance of several batteries can be presented on the same graph for easy comparison. The two constants of the linear part of the *Ri*-curve can be obtained in one single discharge run with two voltage readings at two D (discharge time at constant current to two predetermined voltages recorded). A logarithmic scale makes it possible to accommodate batteries with widely varying properties on the same graph.

By means of values for Ri, taken from the *Ri*-diagram, and the figure for Vr, the V/I curve for the state of charge in question is easily put up according to [1]. Because of the time required to establish steady state in the battery system, V/I curves derived from discharge data at constant current may differ from those obtained with rapid variation of the load.

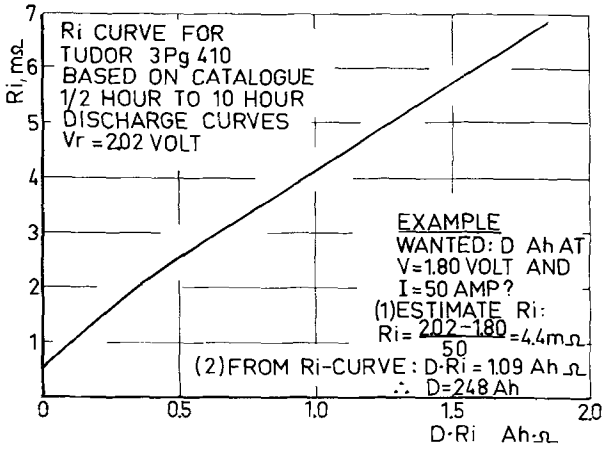

Fig. 8. Use of the *Ri*-diagram, "Version I," for estimates of discharge data.

The *Ri*-Method, "Version II"

So far the *Ri*-method in its "Version I" has been presented as an empirical finding; it is in this respect much like the Peukert relation. The procedure is thus considered to be justified by its practical merits, and can be recommended for any battery system which yields data that give consistent *Ri*-curves.

There must of course be a consistent theoretical background to a consistent *Ri*-curve. Consistent means here that plots taken from discharge runs with different discharge currents fall on the same *Ri*-curve—in the (rare) cases with no variability. This theoretical background may differ in its details from one battery system to another but probably some important elements in the theoretical framework will be common for most batteries. An attempt is therefore made to organize those elements into a formal relationship to get some understanding of some of the features behind the *Ri*-diagram. The result of this treatment is an equation which contains the important elements of the Shepherd equation. The derivation, however, follows a slightly different course and the interpretation of the physical meaning of the constants also differs somewhat. It is shown how the feature of the present paper, the *Ri*-diagram, is related to the type of numerical relationship that was first derived by Shepherd (1).

This treatment suggests a correction which can be applied to "Version I" of the *Ri*-method described above. The somewhat more elaborated "Version II" is useful in R&D work, whereas "Version I" is quite satisfactory from the user's point of view.

Clearly, the concept of a linear voltage/current curve is a logical starting point for the analysis. These curves are characterized by slope and intercept.

From, *e.g.*, Fig. 3, it is realized that two types of voltage drops have to be taken into account: (*a*) $Vo - Vr$, which is a function of the state of charge; (*b*) $Vr - V$, which is the voltage drop due to the passage of current under the prevailing conditions.

The open-circuit voltage of a fully charged battery, Vo, can be defined as the intercept for $I = 0$ from the linear part of the V/I curve for $D = 0$. The actually observed open-circuit voltage could also be used. It is of course important to make clear in numerical work which route is followed.

One might first expect an approximately linear relation between Vr and the state of charge. Shepherd used an equation with log $(Vo - Vr)$ proportional to D. Data in Fig. 2 in Shepherd's paper are, however, fairly consistent with a linear relation; the system was here lead dioxide, zinc, and sulfuric acid. The open-circuit voltage of lead acid batteries at various acid concentrations is, *e.g.*, frequently estimated by means of simple linear relations like voltage equal to (0.84 + density in grams/cm^3), *etc.* Since the density of the acid is approximately linearly related to the state of charge, one might therefore expect a similar linear relation also between Vr and the state of charge even if Vr is not a true open-circuit voltage. Figure 9(a), which is based on data presented in Fig. 3, however indicates that things may not always be that simple. Figure 9 (b) shows furthermore that it is not possible to observe any influence of the discharge current on Vr in this case. Figure 10, which contains data calculated from a battery catalog (2), also indicates a fairly complicated pattern. Vr drops at first with increasing D, but then increases again. There is also a fairly small difference between the maximum and the minimum values for Vr in this graph. The average Vr comes out as 2.02V in this case, which seems to be a good reference value for most lead acid batteries of conventional design.

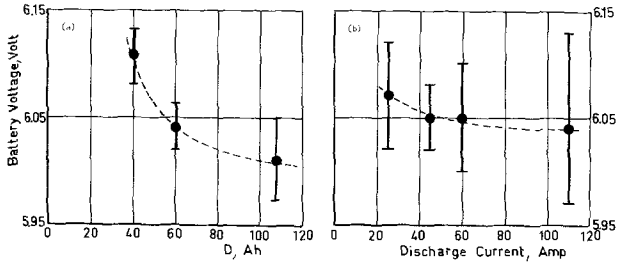

Fig. 9. Averages of *Vr* estimated from *V/I* curves in Fig. 3. Max deviations also shown in the graph. (a) *Vr* as a function of the state of charge (*D* constant in each group, *I* varies); (b) *Vr* as a function of the discharge current (*I* constant in each group, *D* varies).

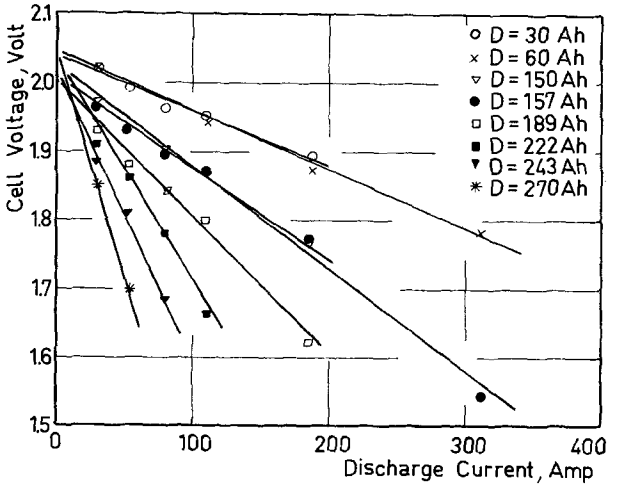

Fig. 10. *V/I*-curves calculated for a tractionary lead acid cell on the basis of catalog data (2).

It is clear that any equation describing the electrical characteristics of a storage battery at low currents and small D is very much influenced by the components of the equation which take care of $Vo - Vr$ since the contribution of $Vr - V$ associated with the current drain as such compared to the total drop $Vo - V$ may be quite small in this region.

The slope of the V/I curve represents an apparent internal resistance of the battery. This resistance should constitute a sum of resistance terms connected with the different process steps in the battery. For comparison it can be mentioned that in fuel cell studies the fairly constant total resistance which in general is observed for an electrode system may be split up in three terms: (*a*) a term associated with the diffusion of gas through the electrolyte film, (*b*) a term associated with the charge transfer step, and (c) a resistance term associated with the migration of ions along the electrolyte film (3).

The empirically found constancy of Ri at a certain state of charge could be due to two causes: (*a*) contributing terms of *any importance* are constant, and (*b*) variations are internally compensated. The fact that practically linear V/I curves are obtained for many different batteries and electrode structures indicates that explanation (*a*) is probably valid.

The apparent internal resistance, Ri, will then be split up in two sums of terms, one representing resistances which are not influenced by the state of charge, *e.g.*, resistance terms associated with the conduction of electrons in the electrode current-collecting structure, and one sum of terms which depend on the state of charge only. These two sums are denoted Rc and Rv, respectively, and thus

$$Ri = Rc + Rv \qquad [3]$$

The state of charge is here defined as $L = (Dr - D)/Dr$, where Dr is the capacity at infinitely low currents, assuming no self-discharge. The resistance term, Rv, can thus be written

$$Rv = \phi(L) = \phi(Dr - D)/Dr \qquad [4]$$

Rc must evidently be smaller than or equal to the minimum value of Ri which can be observed in any measurement. It is realized that it must be possible to find expressions for [4] for any assumed Rc-value satisfying this condition and [3].

Figure 10 illustrated how the apparent internal resistance may depend on the state of charge. We now seek a formal description of this relationship.

The current used in the discharge in general has less influence than generally believed on the structure and conditions of the electrodes of the battery. A general experience with, *e.g.*, lead acid batteries is also that the number of ampere-hours which can be extracted out of the battery when the discharge current is varied during the discharge is fairly constant, within say ± 3%, and approximately equal to Ds for the lowest discharge current in the discharge profile, provided that the final discharge is done at this discharge current. The variation in Ds with the discharge current thus does not reflect differences between the quantities of available active electrode materials due to current-induced effects. The view that the physical state of the electrode is governed mainly by D and not so much by the discharge profile, the course taken to D, is supported by scanning electron micrographs of lead acid battery positive plates which have been discharged at high and low current drains to about the same D. The structure of the plates looks nearly the same, independent of the current used in the discharge, Fig. 11. The appearance of the sintered iron electrodes in Fig. 12 is also in harmony with this view.

It is well known that the active materials in most types of storage batteries with porous electrode structures are not used up entirely in the discharge reaction even if the discharge current is kept very low. Positive and negative materials in the lead acid batteries are thus frequently utilized only to 30-35% (thin electrodes may exceed 50%, however). There are exceptions to this, *e.g.*, the silver oxide electrode which is used to near 100%. The end point of the discharge with, *e.g.*, a lead acid battery at very low current is thus not determined by the amount of active materials present but by the internal resistance which increases to very high values near the end point. A mathematical expression should thus give infinite internal resistance at the end point at very low current drains. The end point, characterized by infinite Ri, could thus represent the maximum available capacity at infinitely low current drains, Dr, assuming no self-discharge. The simplest relation satisfying this requirement is apparently

$$Ri = Rc + Rv = Rc + Rk \cdot Dr/(Dr - D)$$
$$= Rc + Rk/L \qquad [5]$$

The resistance terms which are influenced by the state of charge, and summed as Rv, are thus here assumed to be inversely proportional to the state of charge, which makes $Ri \to \infty$ when $D \to Dr$.

The inverted value of the resistance term Rv, $1/Rv = L/Rk$, is apparently a conductivity term, which thus should be proportional to L, if [5] is valid. It seems quite reasonable that this conductivity term should be proportional to L, at least in a crude way. The active parts of most electrode structures contain well-conducting charged material (in an amount proportional to $Dr - D$) and poorly conducting discharged material (in an amount proportional to D). The resulting conductivity of these active parts of the electrode is then expected to be approximately proportional to $Dr - D$,

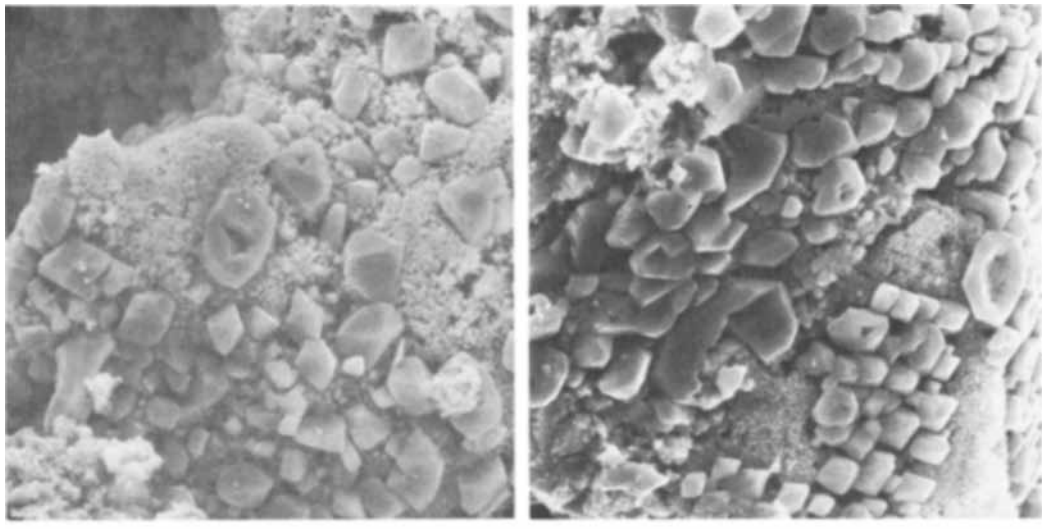

Fig. 11. Micrographs of out layer of tubular positive lead electrodes discharged to ~ 0.6 *Dr* at ½ hr current *(left)* and 20 hr current *(right)*. Lead sulfate crystals in *unreacted* lead dioxide mass.

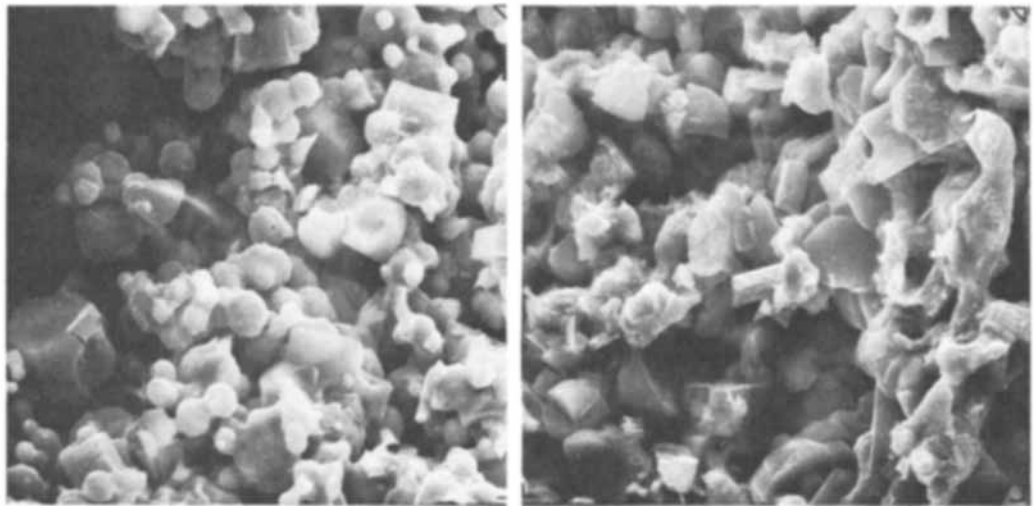

Fig. 12. Micrographs of middle of experimental sintered iron electrode discharged to 0.18 A-hr/g at 12.5 mA/cm^2 *(left)* and 50 mA/cm^2 *(right)*.

i.e., to L. Several other processes in the battery should follow the same pattern. If, *e.g.*, the electrolyte is used up in the discharge, one may expect a linear relation between the conductivity of the electrolyte and L. Actually, most mass transfer processes at play should respond to the change in the state of charge in a related way.

Relation [5] thus seems to exhibit the characteristic features we want to formalize. Shepherd arrived at the same relationship assuming a linear relation between the overpotential and the "active material current density," with the active material current density being inversely proportional to the amount of unused active material in the electrode structure. Shepherd, however, concluded that the successful use of his equations did not necessarily imply that his theoretical deduction did apply. This remark is certainly valid also for the present considerations. The above discussion may thus be summarized

$$\begin{cases} Vo - Vr = \phi\,(L) = \phi\,(Dr - D)/Dr & [6] \\ Vr - V = I\,(Rv + Rc) = I \cdot Rk \cdot Dr/(Dr - D) \\ \qquad\qquad + I \cdot Rc = I(Rk/L + Rc) & [7] \end{cases}$$

In "Version I," Ri was defined as $Ri = (Vr - V)I$. We here start with a more general definition of the apparent internal resistance and refer it to the open voltage of the battery at $D = 0$

$$Ri = (Vo - V)/I \qquad [8]$$

In this case, Ri will vary with the current when $Vo \neq Vr$. Summation of [6] and [7] gives

$$Ri = \phi\,(L)/I + Rk/L + Rc \qquad [9]$$

or

$$Ri = \phi(L)/I + Rk \cdot Dr/(Dr - D) + Rc \qquad [10]$$

Multiplication with $L = (Dr - D)/Dr$ and rearrangement gives

$$Ri = Rk + Rc + 1/Dr\,\{D(Ri - Rc)\} + L/I \cdot \phi(L) \qquad [11]$$

Relation [11] approximates to [2] when $L \to 0$ ($Ri >> Rc$) and at large currents in cases where the expression $L/I \cdot \phi(L)$ in [11] has some significance.

As was mentioned above, it is evidently necessary to know the function $L/I \cdot \phi(L)$ when dealing with nearly fully charged batteries and small currents. The voltage drop, $Vo - Vr$, associated with the state of charge, though in itself small, may be large compared to the drop due to the passage of current under these circumstances. There are no difficulties of a principal nature involved here. One may, *e.g.*, try the relation used by Shepherd; see [13] below. As was mentioned in the introduction, this domain of battery operation is of little significance in this context, however, and we shall therefore drop the term $L/I \cdot \phi(L)$ in [11] and thus put $Vr = Vo$ as was done in the "Version I" treatment. This reduces relation [11] to

$$Ri = Rk + Rc + 1/Dr \cdot D(Ri - Rc) \qquad [12]$$

which may be referred to as the "Version II" equation.

The "Version II" procedure evidently gives a possibility of obtaining two resistance parameters, Rk and Rc, *e.g.*, by solving equation systems of [12] with sets of data for Ri and D. However, this is complicated by

the fact that Rk is not a true constant but frequently varies in the region $D < 0.5\ Dr$. Unfortunately, it is not possible to measure Rc directly since there are also ohmic components in Rk/L. Figure 13 illustrates, however, how differences in Rc show up in the Ri-diagram. In this case the Ri-difference between the two curves, 0.04 mohm, corresponds very well with the calculated differences between ohmic resistances of the two types of grids used in the two batteries.

Most batteries, however, exhibit a fairly flat discharge curve (neglecting the initial drop from the true open-circuit voltage) down to at least $L \sim 0.5$. Thus Ri does not change much during this part of the discharge. This implies that in these cases $Rc >> Rk/L$ in this region. Since Rc is to be considered a correction term in the term $1/Dr \cdot D\ (Ri - Rc)$ of [12], the value for Ri determined from the slope of the V/I curve at $D \sim 0$ could be used as an upper estimate of Rc in [12]. This is the preferred method of calculation in the "Version II" procedure. This is exemplified in Fig. 14, which reports Ri-curves obtained in this way for an experimental sintered iron electrode under development for electric car batteries.

These sintered iron electrodes, 50 mm diameter, were run in half cells in 5N KOH at 50°C. The potential *vs.* a standard Hg/HgO reference electrode was recorded. The discharge current was kept constant at 25 mA/cm². This particular experimental electrode was chosen for this presentation because of the feature exhibited by the Ri-curves in Fig. 14. The first cycle with the new electrode gives peak performance with $Dr = 0.110$ A-hr/cm². Cycle 2 gives $Dr = 0.092$ A-hr/cm² and cycle 3 $Dr = 0.079$ A-hr/cm², whereafter Dr stabilizes at 0.065 A-hr/cm². There is, however, but little variation in the intercepts of the Ri-curves on the Ri-axis. The decrease in performance is thus here attributed mainly to a decrease in the term Dr. This effect may be compared with the overcharge experiments with lead acid batteries reported in Fig. 6 and 7 where decrease in battery performance could be attributed to a change in the resistance parameter, whereas the capacity parameter $1/b$ remained fairly constant. These observations illustrate how the Ri-method can give valuable hints about causes for changes in battery performance.

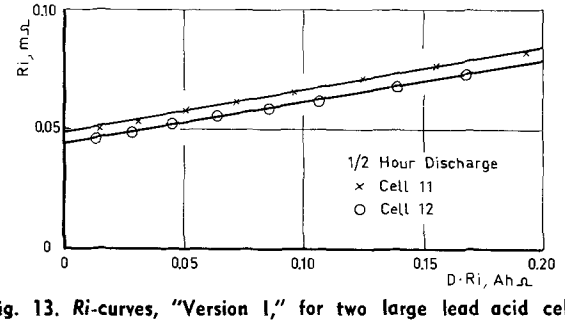

Fig. 13. Ri-curves, "Version I," for two large lead acid cells. Cells identical except for different grid resistance in the positive plates: for cell 11 estimated as 0.002 mohm and for cell 12 as 0.008 mohm.

The calculations involved in the "Version II" procedure are demonstrated for cycle 1 in Fig. 14. A plot of the V/I curves for $D = 0$ showed a fairly small variation of the intercepts, Vr, with the average $Vr = 0.939$V within the limits 0.924-0.954 (± 1.6%). Consequently, use of a constant $Vr = 0.939$V for all Ri-estimates was considered justified. (For comparison, it can be mentioned that the average true open-circuit voltage was $Vo = 0.975$V within the limits 0.960-0.980V). The slope of the V/I curve for $D = 0$ and the discussed cycle 1 corresponds to $Ri = 0.72 \pm 0.10$ ohm-cm², estimated 95% confidence limits. [In this research study, battery parameters are referred to unit area (1 cm²) of the cell section which is carrying the current.] From the discharge curve with voltage plotted as a function of the discharge time at 25 mA/cm², figures for Ri were obtained at various D estimated as $Ri = (0.939 - V)/0.025$ ohm-cm². The figure $Ri = 0.72$ ohm-cm² at $D = 0$ was used as an estimate of Rc to get $(Ri - Rc)$. The Ri-curve was then obtained by plotting Ri against $D(Ri - Rc)$ as shown in Fig. 15. The intercept of the extrapolated linear part of the curve is equal to $Rc + Rk$, which here comes out as 0.93 ohm-cm². The factor Rk is estimated as $Rk = 0.21$ ohm-cm² at $D > 0.5\ Dr$, since Rc was assumed = 0.72 ohm · cm². The factor Rk thus increases from $Rk \equiv 0$ at $D = 0$ to a value which is fairly constant when $D > 0.5\ Dr$ as indicated by the linear course of the Ri-curves in this region. The slope of the regression line corresponds to $Dr = 0.110$ A-hr/cm² to be compared with $Ds = 0.101$ A-hr/cm² for $Vs = 0.700$V.

This method of calculation thus implies a very precise meaning of Rc and Rk. The increase in Ri for increasing D is wholly attributed to the term $Rk \cdot D/(Dr - D)$ of Eq. [10] due to increase both of Rk from zero to a constant value and the increase of $D/(Dr - D)$.

Comparison with the Shepherd Approach

Our Eq. [10] and the evaluation of its constants is compared with Shepherd's Eq. [9] which, with Shepherd's glossary and after minor rearrangement, reads

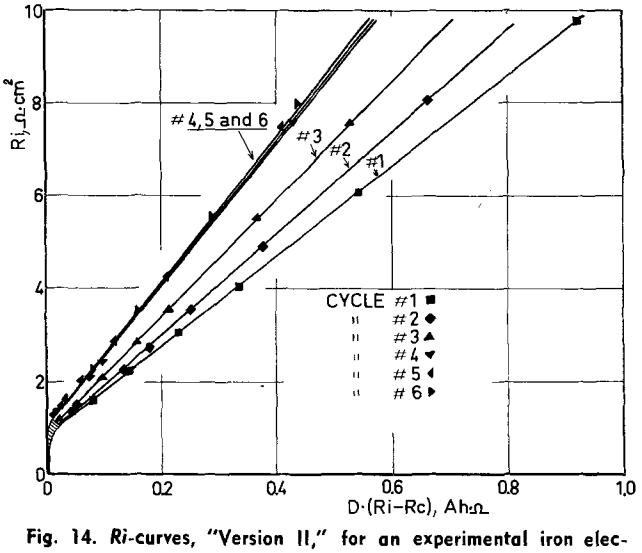

Fig. 14. Ri-curves, "Version II," for an experimental iron electrode.

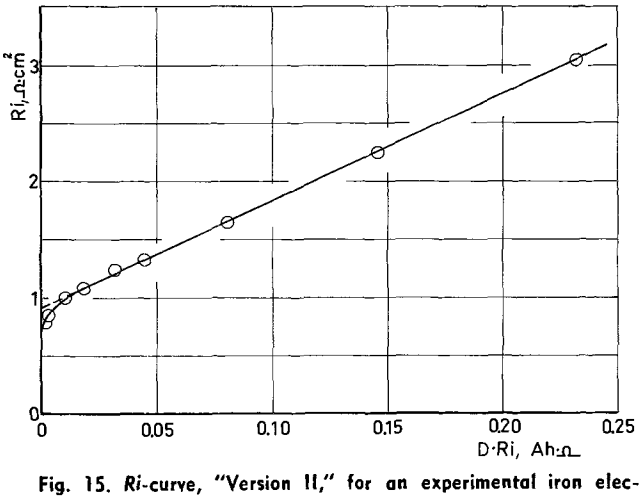

Fig. 15. Ri-curve, "Version II," for an experimental iron electrode (cycle 1 in Fig. 14).

$$(Es - E)/i\ (= Ri) = K \cdot Q/(Q - it) + N - A/i \exp(-BQ^{-1}\, it) \quad [13]$$

This relation is apparently formally identical with the present relation [10], provided $Es = Vr$; $Q = 1/G \cdot Dr$; $N = 1/G \cdot Rc$; $K = 1/G \cdot Rk$ and $-A/i \cdot \exp(-BQ^{-1}\, it) = 1/G \cdot \phi(L)/I$, where G is the area of the cross section through which current is flowing between the electrodes in the battery. However, the above formal identities are not valid from a physical point of view: Shepherd's Q is determined by the amount of available active material on the controlling electrode, whereas our Dr is the capacity at infinite Ri. Shepherd's K is referred to the activation overpotential and N is the internal resistance. Both Rk and Rc as defined above contain ohmic terms; the sole condition is that Rc is independent of the state of charge and Rk is zero at $D = 0$. Shepherd determines his constants by means of an equation system using four points taken from each of two discharge curves, one obtained at a moderately high current density and the other one obtained at a moderately low current density. This procedure uses only a fraction of available experimental data. Physical interpretation is furthermore made difficult by the fact that the internal resistance term frequently comes out as a negative term.

The transformation of [10] into [11], however, seems to give a simple and useful method for graphical reduction of the discharge data. This is the main advantage of the present method. This feature is also demonstrated by means of data taken from lead acid battery curves in Shepherd's paper. The result of the treatment is shown in Fig. 16. Data for this Ri-diagram were taken from discharge curves for a lead acid battery reported in Fig. 9 and 10 in Shepherd's paper.

Shepherd's Fig. 10 is a V/I curve for a fully charged battery, $D = 0$, from which the apparent internal resistance under this condition is obtained as $Ri = 3.8$ mohm. The curves in Shepherd's Fig. 9 give the cell potential as a function of $Q/(Q - D)$ where Q is the amount of active material on the controlling electrode in Ah (Shepherd's glossary) for different current densities. Ri-values were calculated from data from these curves for $Q/(Q - D)$ equal to 6, 4, 3, 2, 1.5, and 1.25. Averaged Ri-values for each D were corrected by subtracting $Rc = 3.8$ mohm and the terms $D(Ri - Rc)$ calculated for the Ri-diagram. The slope of the resulting diagram corresponds to $Dr = 0.9\ Q$, whereas $Rk + Rc$ for large D comes out as 9 mohm. Consequently, it can be concluded that $Rc \sim 4$ mohm, whereas Rk increases from $Rk = 0$ at $D = 0$ to $Rk \sim 5$ mohm at $D > 0.5\ Dr$. These figures plus the estimate of Dr, in this case reported as $Dr = 0.9\ Q$, give a satisfactory description for this particular lead acid battery. (Observe that $Dr \neq Q$!)

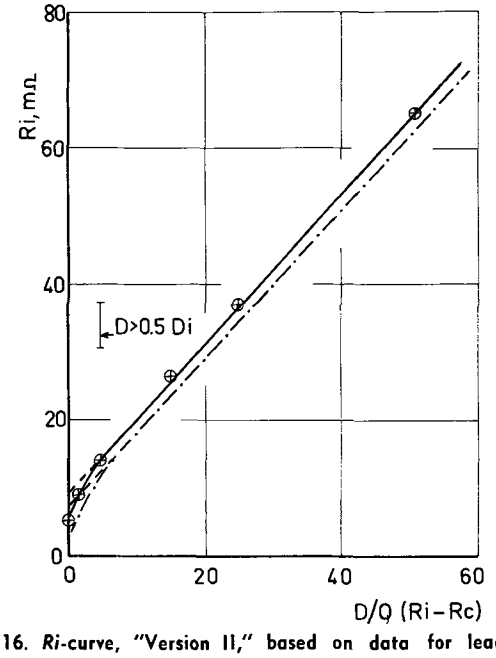

Fig. 16. Ri-curve, "Version II," based on data for lead acid battery reported by Shepherd (1). (Dashed line represents "Version I" procedure.)

Figure 16 also contains for comparison an Ri-curve based on the same data but calculated according to the simplified procedure, "Version I," with no Rc-term. The two curves run in parallel and apparently the "Version I" procedure is as good as "Version II" for the purpose of general battery characterization in this case.

One may also visualize a more refined treatment than the "Version II" procedure described above. The purpose of this procedure, "Version III," should obviously be to establish a relation between Rk and D so as to describe how Rk varies with D. The only, but very serious, limitation is here the difficulty of obtaining sufficiently precise and reproducible experimental data. At present, "Version II" seems to be on the borderline of what is practically feasible.

Acknowledgments

This study was made in conjunction with the Swedish electric car project "El-Tjorven" sponsored by the Swedish National Development Company, the Swedish Board for Technical Development, Kalmar Verkstads AB, and the Battery (Tudor) Division and the Innovation Division of AGA.

NOMENCLATURE

V,	voltage
Vo,	open-circuit voltage
Vr,	reference voltage
Vs,	voltage at end of discharge
I,	discharge current
D,	delivered ampere-hours
Ds,	capacity at Vs
Dr,	limit capacity
L,	state of charge
Ri,	apparent internal resistance
Rc,	part of Ri not depending on L
Rv,	part of Ri depending on L
Rk,	resistance factor in Eq. [5]
a and b,	regression constants of Ri-curve

For symbols in Shepherd's Eq. [13], see Ref. (1).

Manuscript submitted Jan. 5, 1970; revised manuscript received *ca.* May 15, 1970.

Any discussion of this paper will appear in a Discussion Section to be published in the June 1971 JOURNAL.

REFERENCES

1. C. M. Shepherd, *This Journal*, **112**, 657 (1965).
2. Tudor Catalog, "Tractionary Batteries," Stockholm (1964).
3. O. Lindström, *Energy Conversion*, **8**, 33 (1968).

The Stress of Electroless Nickel Deposits on Beryllium

K. Parker* and H. Shah

General American Research Division, General American Transportation Corporation, Niles, Illinois

ABSTRACT

The residual stress of electroless nickel coatings on one side of 0.01 in. beryllium strips was determined by bow deformation measurements. Different plating conditions can produce either a tensile or compressive stress. The parameters controlling stress are those which determine the phosphorus content of the deposit, of which *p*H is the most important. The stress increases in the negative direction with increase in phosphorus content of the deposit. "As-plated" 4 mil coatings containing more than 8.5% phosphorus are compressively stressed, while those with lower phosphorus content are in tensile stress. Contraction during annealing decreases the compressive and increases the tensile stress of the plate. With close control of the plating parameters, reproducible, essentially "stress-free" electroless nickel coatings can be plated on critical optical beryllium surfaces such as aerospace mirrors.

This investigation was prompted by a recent article (1), which concluded that Kanigen®[1] deposits on beryllium induce significant tensile stresses in the composite: "For diffraction-limited precision optical surfaces, these stresses may produce unacceptable distortions." Precision beryllium mirrors require electroless nickel coating to provide a hard surface for final optical polishing and low scattering reflectivity. The primary purpose of the work was to find the plating conditions inducing the least tensile stress in the plate.

Internal stresses developed in plated deposits are either tensile due to contraction or compressive due to expansion. A tensile stress in the coating will decrease its adhesion, corrosion resistance, and sometimes the fatigue strength of the substrate. It is therefore desirable to minimize tensile stress or produce a slightly compressive plating. Generally the degree of stress decreases with increase in thickness of the deposit.

The stress in plated coatings is most readily measured by plating only one side of thin metal strips. Any residual stress in the coating is released by bending of the strip. The bow at the center is a measure of the internal stress. On thick, rigid substrates no bending can occur and the stress is "locked-in" the deposit. Large stresses exceeding the tensile strength of the deposit will induce cracks, while small stresses may create surface or interphase disturbances such as ripples.

The deformation of metal strips nickel plated on one side only is due in part to the bimetallic effect, *e.g.* the difference in thermal expansion coefficients of electroless nickel (13×10^{-6}/°C) and beryllium (11.6×10^{-6}/°C). If this were the only factor, then an electroless nickel deposit on beryllium would always be in slight tensile stress of about 4000 psi due to its larger contraction, when the composite cools from 95°C plating to room temperature. Other factors such as the plating conditions and bath formulation also produce residual stresses, since they affect the composition and crystal structure of the deposit. Our work was primarily concerned with the effect on stress of two critical plating process variables: *p*H and temperature.

Nickel, which is chemically reduced by sodium hypophosphite, is deposited as a nickel-phosphorus alloy in a metastable state. The phosphorus content in electroless nickel deposits can vary from 3 to 13% depending on the plating conditions and solution employed. Heat treatment above 250°C gradually stabilizes the system by precipitation of nickel phosphide (Ni_3P). This increases the hardness from 50 Rockwell C to a maximum of 70.

Experimental Procedure

To investigate the stresses in electroless nickel deposits, a 10 liter Kanigen® plating system and bath[2] were employed. This process incorporates continuous circulation and filtration, as well as external steam heating of the plating solution. The operating temperature was varied in the range of 82°-97°C and the *p*H of the bath from 3.9 to 5.1. During plating the concentration of all chemicals and the *pH* were maintained by frequent additions to the regeneration tank as indicated by analysis.

The main components of the plating solution were: 0.08M $NiSO_4$ $6H_2O$, 0.23M $NaH_2PO_2 \cdot H_2O$, and 0.36M lactic acid as the nickel chelating agent. Minor amounts of stabilizer, wetting agent, and organic acid promoters were also present. The pH was adjusted with 10% NaOH solution and measured to 0.01 units every 30 min with a Beckman *p*H meter. In the last experiments the hypophosphite concentration was increased to 0.4M.

Beryllium strips, 3 in. long, 0.30 in. wide, 0.01 in. thick, milled and then stress relieved by chemical etching, were used for all plating experiments. Length and width of each strip were determined to 0.01 in.; its thickness to 0.0001 in. Most of the beryllium strips were straight before plating; however, any initial deflection was measured with an optical comparator and recorded. After pretreatment in alkaline cleaner and dilute hydrofluoric acid etch, the strips were plated on both sides under various plating conditions with 0.5-4 mils of electroless nickel. In the first series of experiments, the strips were plated with 3.9-4.3 mils to compare the deformation at similar thicknesses. In most experiments, triplicate or duplicate strips were plated under the same conditions.

In previous stress investigations, the thin metal strips were first masked on one side. After plating, the masking was peeled off. Unless great care is taken, the strips are easily bent when handled during masking or when the masking is removed. A new method to determine the coating stress was therefore employed in which both sides of the strips are plated to minimize handling.

One side of the plated strip was covered with tape before the other side was coated with molten stop-off wax. After removal of the tape the strip was immersed in concentrated nitric acid, which does not attack beryllium. As the nickel alloy is gradually dissolved from the unmasked side, the thin strip assumes a bow shape. After the nickel was completely stripped, the wax was removed by soaking in perchloroethylene. The bow-out at the center (sagitta of the arc) was then accurately measured to 0.0001 in. A concave

* Electrochemical Society Active Member.

[1] Registered trade-mark of General American Transportation Corporation and its licensees.

[2] The composition and process are covered by U.S. Pat. 2,658,839; 2,658,841; 2,762,723; 2,822,293; 2,822,294; and others assigned to GATX.

nickel surface indicates a tensile (+) stress, while a convex surface shows a compressive (−) stress in the deposit. Any deflection prior to stripping was subtracted to obtain the net change in bow-out (L_1) of the strip due to internal stress in the nickel plating.

After the deflection measurements in the "as-plated" condition, the strips were annealed in an oven for 4 hr at 190°C and the bow-out (L_2) redetermined at room temperature. In some instances the plated strips were annealed a second time to determine any additional change (L_3), which may occur during final stress relief annealing after polishing.

The nitric acid containing the stripped alloy was analyzed for nickel content by EDTA titration, and for phosphorus by the vanadate-molybdate photometric method (ASTM E 156).

Results

The bow measurements of the beryllium strips plated with 4 mils electroless nickel under varying plating conditions are shown in Table I. They are arranged in order of increasing phosphorus content of the deposits. The bow data vary from +0.17 in. (concave) to −0.075 in. (convex). Annealing increases the concave, but decreases the convex curvature.

The internal stresses in the deposits were calculated according to the method of Soderberg and Graham (2), who derived an equation based on a strip rigidly held during plating, and no bending occurs until after deposition is complete. The over-all stress, S, in a compound beam is calculated from the equation

$$S = \frac{E_b I}{r\left(c - \frac{d}{2}\right) dw}$$

E_b = Elastic modulus of basis metal = 44×10^6 psi for Be

I = Moment of inertia of effective section weighted to the base modulus, in psi

$$I = \frac{w}{3}\left[a(d+t)^3 - (a-1)t^3 - 3(t+ad)(d+t-c)^2\right]$$

$$a = \frac{\text{Elastic modulus of coating}}{\text{Elastic modulus of basis metal}} = \frac{20 \times 10^6 \text{ psi}}{44 \times 10^6 \text{ psi}}$$ [3]

c = Distance of neutral axis to outside surface of deposit, in.

$$= \frac{a\,d^2 + 2dt + t^2}{2(a\,d + t)}$$

[3] The modulus of elasticity of electroless nickel "as-plated" is 17×10^6 psi. It increases with heat treatment.

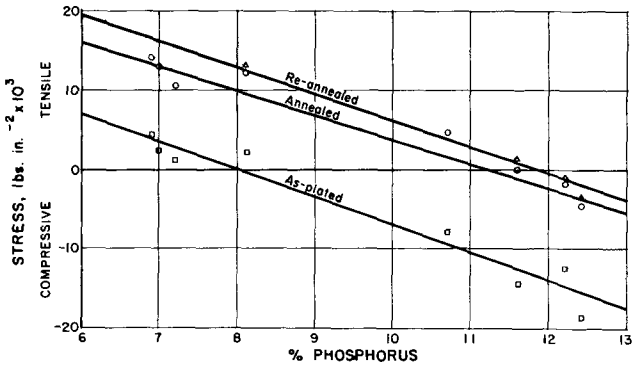

Fig. 1. Stress of electroless nickel on beryllium as a function of phosphorus content of the deposit.

d = Thickness of coating, in.

t = Thickness of the strip, in.

w = Width of the strip = 0.30 in.

r = Radius of curvature, in.

$$= \frac{l^2 + 4L^2}{8L} \simeq \frac{l^2}{8L}$$ (since L is much smaller than l)

l = Length of strip, in.

L = Net change in bow-out, in.

The development assumes that bending of the strip is caused by two kinds of stress, one by the structure of the deposit, the other by the difference in thermal contraction of base metal and the plate, when the plated strip is removed from the hot plating bath. Another assumption is that the net force in the nickel acts in the center plane parallel to the neutral surface of the deposit. The total force or stress in the coating at equilibrium (in bent condition) can be calculated from the measured deformation of the strip. The original force or stress, S, in the unflexed coating is then the sum of this calculated equilibrium force and the additional force necessary to return the coating alone to its unbent condition.

The average stress values vary from +7.9 Ksi [4] tensile for low phosphorus to −18.5 Ksi compressive for high phosphorus deposits in the as-plated condition. After annealing at 190°C, either an increase in the tensile stress or a decrease in the compressive stress is found. Reannealing produced slight additional changes in stress. These results are plotted in Fig. 1.

[4] Ksi = lb in.$^{-2}$ x 10^3.

Table I. Electroless nickel on beryllium; variation of plating pH and temperature

No.	Length l, in.	Thickness t, Be, in.	Thickness d, Ni, in.	Plating conditions pH	Plating conditions Temp, °C	Plating conditions Rate, mil/hr	Deposit % P	As-plated L_1, in.	As-plated S_1, Ksi	Annealed 4 hr/190°C L_2, in.	Annealed 4 hr/190°C S_2, Ksi	Reannealed 4 hr/190°C L_3, in.	Reannealed 4 hr/190°C S_3, Ksi
8	2.97	0.0099	0.0042	5.0	82	0.35	6.9	0.0175	4.6	0.0545	14.3		
9	2.98	0.0101	0.0042	5.0	82	0.35	6.9	0.0172	4.6	0.0480	12.9		
11	3.01	0.0107	0.0041	5.0	82	0.35	6.9	0.0173	5.0	0.0495	14.3		
23	2.99	0.0102	0.0042	5.0	88	0.50	7.0	0.0135	3.6	0.0505	13.6		
24	2.94	0.0102	0.0039	5.0	88	0.50	7.0	0.0080	2.3	0.0515	14.8		
25	3.00	0.0109	0.0040	5.0	88	0.50	7.0	0.0085	2.6	0.0355	10.7		
27	3.04	0.0100	0.0042	4.9	95	0.75	7.2	0.0045	1.1	0.0380	9.6		
28	3.04	0.0096	0.0041	4.9	95	0.75	7.2	0.0050	1.2	0.0450	11.1		
31	3.03	0.0098	0.0042	4.9	95	0.75	7.2	0.0050	1.2	0.0432	10.7		
4	2.93	0.0102	0.0040	4.5	93	0.50	8.1	0.0070	2.0	0.0445	12.8	0.0505	14.5
5	2.97	0.0104	0.0041	4.5	93	0.50	8.1	0.0075	2.1	0.0415	11.8	0.0425	12.1
6	3.04	0.0103	0.0042	4.5	93	0.50	8.1	0.0100	2.6	0.0450	11.9	0.0485	12.8
12[a]	2.98	0.0093	0.0041	4.5	93	0.50	8.4	0.0275	6.7	0.0915	22.3	—	—
15[a]	3.01	0.0108	0.0042	4.5	93	0.50	8.4	0.0272	7.9	0.0860	25.1	—	—
26	3.01	0.0100	0.0042	4.0	97	0.33	10.7	−0.0365	−7.1	0.0150	3.9	—	—
32	3.03	0.0097	0.0040	4.0	97	0.33	10.7	−0.0450	−10.1	0.0180	4.5	—	—
35	3.04	0.0098	0.0042	4.0	97	0.33	10.7	−0.0350	−9.5	0.0260	6.4	—	—
19	2.99	0.0108	0.0039	4.0	94	0.21	11.6	−0.0480	−14.5	0	0	0.0045	1.4
22	2.98	0.0103	0.0043	3.95	93	0.17	12.2	−0.0470	−12.8	−0.0050	−1.4	−0.0030	−0.8
34	3.02	0.0097	0.0043	3.95	93	0.17	12.2	−0.0495	−12.1	−0.0065	−1.6	−0.0040	−1.0
29	3.01	0.0096	0.0042	3.95	91	0.12	12.4	−0.0755	−18.5	−0.0190	−4.7	−0.0145	−3.5

[a] Masked before plating.

Table II. Electroless nickel (12.3% P) on beryllium; effect of deposit thickness

No.	Beryllium Length, l, in.	Beryllium Thickness, t, in.	Nickel Thickness, d, in.	As-plated L_1, in.	As-plated S_1, Ksi	Annealed 4 hr/190°C L_2, in.	Annealed 4 hr/190°C S_2, Ksi	Reannealed 4 hr/190°C L_3, in.	Reannealed 4 hr/190°C S_3, Ksi
3	3.03	0.0103	0.0005	0	0	0.0010	1.4	0.0020	2.8
13	2.96	0.0100	0.0005	0	0	0	0	0	0
14	3.01	0.0101	0.0011	−0.0130	−8.7	0.0050	3.3	0.0055	3.7
36	3.01	0.0096	0.0011	−0.0170	−10.3	0.0020	1.2	0.0025	1.5
16	2.95	0.0099	0.0020	−0.0305	−12.5	0.0050	2.1	0.0065	2.7
37	3.03	0.0098	0.0020	−0.0237	−9.1	0.0045	1.7	0.0055	2.1
18	2.96	0.0098	0.0031	−0.0485	−14.6	0.0130	3.9	0.0160	4.8
30	3.00	0.0095	0.0031	−0.0445	−12.4	0.0160	4.5	0.0175	4.9
22	2.98	0.0107	0.0042	−0.0550	−16.0	−0.0010	−0.3	0.0	0
34	3.02	0.0102	0.0042	−0.0495	−13.1	−0.0040	−1.1	−0.0020	−0.5
7	2.99	0.0100	0.0050	−0.0620	−15.4	−0.0185	−4.6	−0.0050	−1.2
10	3.00	0.0108	0.0050	−0.0640	−17.4	−0.0140	−3.8	−0.0040	−1.1

A decrease of plating pH and/or temperature increases the phosphorus content of the alloy. Thus, at a plating temperature of 88°C the phosphorus increases from 7% at pH 5 to over 12% at pH 4. At a pH of 4 the phosphorus increases linearly from 10.7 to 12.4% with decrease in plating temperature from 97° to 91°C.

The effect of varying the thickness of coatings containing 12.3 ± 0.1% phosphorus is shown in Table II and Fig. 2. In the "as-plated" deposits there is a linear increase in bow-out with increase in thickness and a gradual increase in compressive stress between 1-5 mils thickness. The reannealed stress values varied from +4.9 to −1.2 Ksi. Since thinner coatings became slightly tensile stressed during annealing, a 4 mil thickness is desirable for annealed low stress coatings.

The plating conditions which produce the least stressed coating after annealing slow the plating rate to less than 0.2 mil/hr. The rate can be increased by raising the plating temperature to 93°C; however, it is then necessary to increase the hypophosphite concentration of the bath to 0.4 mole/liter in order to attain the desired 11.5+% phosphorus level in the deposit (4).

As a result of this investigation the plating conditions for the electroless nickel coating of four 13 in. diameter beryllium mirrors (Fig. 3) were adjusted to produce a low stress deposit for precision aerospace experiments. These mirrors were plated at pH 3.95-4.05 and 93°C in a 25 gal Kanigen® system. About 20 hr were required to obtain 4 mils + thickness. Beryllium strips plated at the same time were measured for bow-out and showed a compressive stress in the range of −6 to −16 Ksi as-plated and +1 to −1 Ksi after reannealing.

Discussion

Comparison of the bow data obtained by the old "masking" *vs.* the new "stripping" method shows substantially lower tensile deformation for the latter. Bow measurements of strips plated under the same conditions are generally in good agreement.

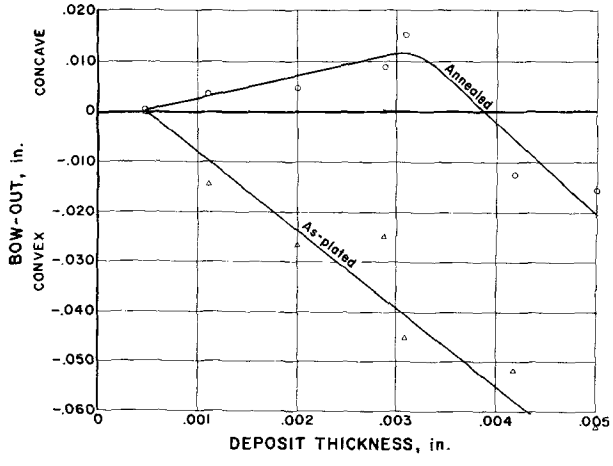

Fig. 2. Effect of deposit thickness on bow-out of electroless nickel (12.3% P) plated beryllium strips.

As shown in Fig. 1 the stress of the electroless nickel deposits is inversely related to the phosphorus content of the deposit. Thus, the tensile stress decreases linearly with increase in phosphorus. At a phosphorus content of about 8.5+%, the "as-plated" coatings are compressively stressed. All coatings with lower phosphorus content show tensile stress. Under "normal" Kanigen® plating conditions of pH 4.5, the phosphorus content of the deposit is 8.5 ± 0.5%.

In electroless nickel plating the phosphorus content of the deposit depends primarily on the pH of the bath. The reaction equilibrium (5)

$$H + H_2PO_2^- \rightleftharpoons P + H_2O + OH^-$$

shifts to the right with decrease in pH—*i.e.*, increase in hydrogen ion concentration. Conversely, raising the pH to 5 lowers the phosphorus content of the alloy. The plating temperature has a smaller effect on phosphorus; however, at pH 4 the temperature should not exceed 93°C to obtain an 11.5% + P deposit.

The higher phosphorus nickel alloys have been found to give more diffuse x-ray diffraction patterns (4, 6) attributed to an "amorphous-like" structure: If in the as-plated alloy the phosphorus is present not only in a supersaturated nickel solution but also at the microcrystallite boundaries, this would move the crystals apart and induce internal compressive stresses.

During annealing the deposits apparently contract, increasing the stress in the positive or tensile direction. Therefore in order to obtain a low-stress annealed coating, a deposit containing 11.5-12% phosphorus is required with a compressive stress of −12 Ksi in

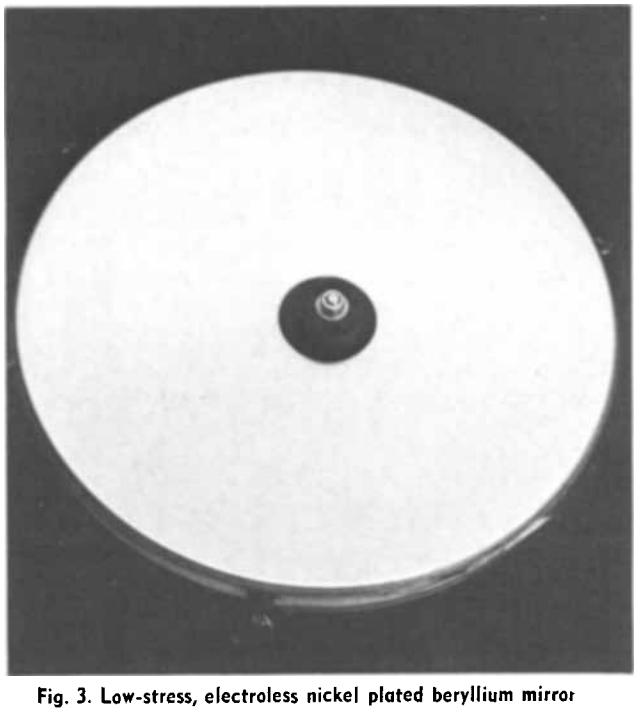

Fig. 3. Low-stress, electroless nickel plated beryllium mirror

the as-plated condition. This apparent shrinkage may be due to the elimination of structural defects and hydrogen from the coating. In any case, during annealing the electroless nickel approaches equilibrium condition and a more orderly lattice arrangement.

These results are in fair agreement with previous findings of Shemenski *et al.* (1). Apparently, all of their coatings contained about 7-8% phosphorus and were therefore in comparatively strong tensile stress after annealing. They also agree with Baldwin and Such (7), who measured at plating temperature a linear increase in mean internal stress from −8 to +16 Ksi with increase in pH of the plating bath from 4.0 to 6.0. Comparison of these results indicates that the bimetallic effect makes only a minor contribution to the internal stress of electroless nickel on beryllium.

The results obtained by Bartlett *et al.* (8) on brass strips plated in a pH 10.5-11.0 pyrophosphate electroless nickel bath should be mentioned. Their nickel deposits contained only 3.2-4.2% phosphorus and showed as much as 50 Ksi tensile stress.

Further plating experiments with metal strips of steel, nickel, aluminum, and titanium are in progress to determine the effect of phosphorus content on the residual stress of the deposit on these substrates.

Summary

On the basis of the results, the following conclusions can be drawn:

1. The difference in thermal expansion coefficients between electroless nickel and beryllium produces a relatively small tensile stress in the composite.
2. The deformation and stress induced by the electroless nickel plating on beryllium varies from compressive to tensile, depending on plating conditions.
3. The plating parameters controlling the residual stress are primarily those which determine the phosphorus content of the electroless nickel deposit.
4. A phosphorus content of 8.5% or higher produces a compressive stress in the as-plated deposit.
5. During annealing at 190°C, the electroless nickel deposits contract with either increase in the tensile stress or decrease in compressive stress.
6. To obtain a "stress-free" annealed electroless nickel coating on beryllium requires an 11.5%+ phosphorus deposit, which is compressively stressed in the as-plated condition.
7. A relatively "stress-free" 4 mil electroless nickel deposit on beryllium mirrors is obtained by close control of plating conditions in a Kanigen® system using a bath adjusted to pH 4.0, containing 0.4 mole/liter hypophosphite and operating at 93°C.
8. A new method for determining the stress of plated coatings by plating both sides of thin strips is shown to give reproducible results.

Acknowledgment

This investigation was partially funded by the Hughes Aircraft Company; their cooperation is gratefully acknowledged.

Manuscript submitted Dec. 17, 1969; revised manuscript received March 26, 1970.

Any discussion of this paper will appear in a Discussion Section to be published in the June 1971 JOURNAL.

REFERENCES

1. R. M. Shemenski, J. G. Beach, and R. E. Maringer, *This Journal*, **116**, 402 (1969).
2. R. G. Soderberg and A. K. Graham, *Proc. Am. Electroplaters' Soc.*, **34**, 74 (1947).
3. H. Wiegand and K. Schwitzgebel, *Metalloberfläche*, **22**, 304 (1968).
4. J. P. Randin and H. E. Hintermann, *Plating*, **54**, 423 (1967).
5. G. Gutzeit, *ibid.*, **46**, 1158, 1275, 1377 (1959); **47**, 63 (1960).
6. A. W. Goldenstein, W. Rostoker, F. Schossberger, and G. Gutzeit, *This Journal*, **104**, 104 (1957).
7. C. Baldwin and T. E. Such, *Trans. Inst. Metal Finishing*, **46**, 74 (1968).
8. B. C. Bartlett, L. Cann, and J. L. Hayward, *Plating*, **56**, 168 (1969).

Electrolytic Removal of P-Type GaAs Substrates from Thin, N-Type Semiconductor Layers

C. J. Nuese and J. J. Gannon

RCA Laboratories, Princeton, New Jersey

ABSTRACT

An electrolytic etching technique has been developed which can remove p-type GaAs substrates from thin (2-10μ) n-type layers of GaAs or $GaAs_{1-x}P_x$, $0 \leq x \leq 1$. Sodium hydroxide is used as the electrolyte, and is sprayed continually over the etching surface to prevent the build-up of "flakes" on the p-type surface as by-products of the etching process. Such flakes serve as an effective mask to the etching process and, unless removed, result in irregular or matte surfaces on the n-type layer after removal of the p-type material. The removal of these flakes by the spray of NaOH leads to shiny, unblemished n-type surfaces over large-area wafers (2-5 cm^2). The extension of this electrolytic etching technique to thin, vapor-grown layers has applications in electron microscopy, luminescence and optical measurements, and in semiconductor device fabrication.

The anodic etching of p-type semiconductors in an appropriate electrolytic solution has been used routinely for polishing and shaping surfaces of germanium (1-5) and silicon (3-6), and for removing damaged material or reducing the active junction area (7) in III-V compounds. However, when an attempt is made to similarly etch n-type samples, a blocking potential barrier is established at the semiconductor surface (3,6), which restricts the passage of electrolytic current, and significantly reduces the etching rate.

This difficulty in electrolytically etching n-type semiconductors, particularly those with a relatively large energy gap (6), and hence a more effective surface barrier, can be used to good advantage for the selective removal of an adjoining p-type layer without significant penetration into the n-type layer. In the present paper, we report a simple electrolytic etching

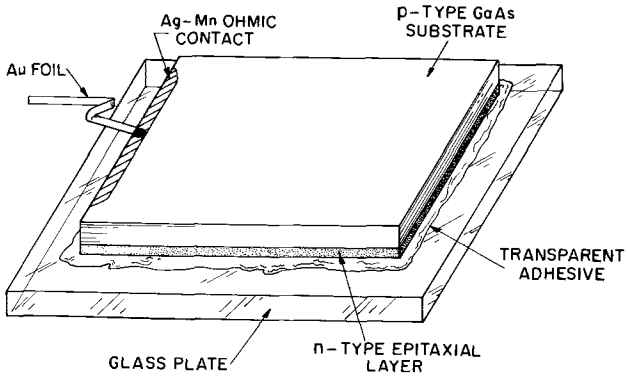

Fig. 1. Geometry of sample used for electrolytic etching. In this case, the sample is mounted permanently on a glass plate for optical transmission measurements.

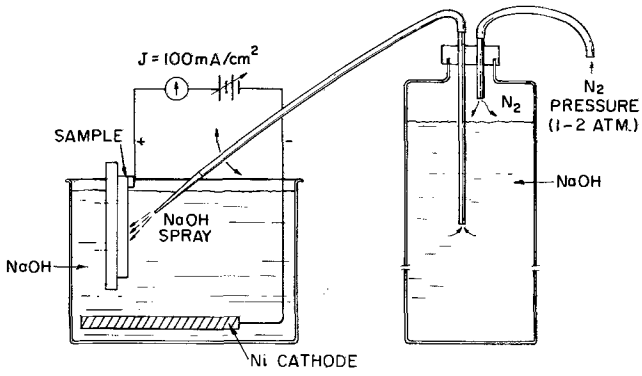

Fig. 2. Electrolytic etching system employing sprayed NaOH electrolyte. Pressurized reservoir of NaOH can be replaced by electric pump for convenience.

technique which has been used successfully for this purpose on large-area p-n junctions in several III-V compounds. This technique has been found to be especially useful for isolating thin (2-10μ) epitaxial layers from thick (250-500μ) p-type substrates, and has been used frequently for this purpose throughout the $GaAs_{1-x}P_x$ alloy system. For such structures, conventional lapping or chemical etching procedures usually cannot be controlled with sufficient accuracy to remove all of the p-type region without penetrating significantly, and often irregularly, into the thin n-type layer.

The thin n-type specimens which can be isolated by this technique have found a variety of applications in electron microscopy, luminescence and optical measurements, and in multilayer device fabrication. Several of these applications are discussed briefly below. It is not our intention in this paper to consider the basic physical or chemical properties of the electrolytic reactions, except where these properties directly affect the extension of our electrolytic etching technique to the large-area layers considered here.

Experimental

Most of the samples used for the etching studies reported here consisted of an epitaxial n-type layer of GaAs or $GaAs_{1-x}P_x$ which had been deposited directly on a <100>-oriented p-type GaAs substrate via a vapor-phase growth technique (8). For such samples the p-n junction was therefore at the substrate-epitaxy interface. In some samples, however, a p-type GaAs or $GaAs_{1-x}P_x$ layer was first deposited on the p-type substrate, followed by the thin n-type layer, in which case the p-n junction was then located within the epitaxial layer. For both cases, the electrolytic technique described below was found to be capable of selectively removing all of the p-type material, leaving only the n-type layer bordering the p-n junction.

The n-type epitaxial layers were typically between 2 and 10μ thick, whereas the substrates were about 500μ thick initially, but were mechanically lapped to a thickness on the order of 200μ to reduce the etching time needed for their removal.

For general sample preparation, an ohmic contact strip of Ag-Mn(9) is evaporated and sintered to the lapped p-type surface (Fig. 1) although, for samples with a heavily-doped p-type substrate, a simple conducting-epoxy contact is often adequate. The wafer for etching is then mounted n-side down on a glass microscope slide by (*a*) tacking a spot beneath the contact area with Apiezon wax,[1] for applications where the n-type layer is to be removed from the slide after etching, or by (*b*) bonding the entire n-type surface to the slide with a clear epoxy (BiPax Tra-Bond)[2] for permanent mounting. Finally, for a current lead, a gold or platinum foil is connected to the p-type contact with silver paste or conducting epoxy.

For the electrolytic etching process, a 3 molar aqueous solution of NaOH has been most commonly used in the system shown in Fig. 2, although the exact degree of dilution does not appear to be critical. Alternately, a simple electrical pump[3] can be used to drive the NaOH spray, in which case the cumbersome pressurized cylinder in Fig. 2 would not be required. In either case, the sample is immersed in the electrolyte to a depth such that the metal contact is just out of solution.

Three conditions were found to be essential for obtaining a smooth, shiny surface on the n-type layer upon the total removal of the p-type layer.

1. Most important, the region being etched must be continually agitated or rinsed during the entire etching process. The electrolytic reactions of GaAs and $GaAs_{1-x}P_x$, unlike those of Ge, produce compounds which are only very slowly soluble in the NaOH solution, and which therefore remain loosely attached to the crystal surface in the form of gray-brown "flakes" (10-12), tentatively identified here as arsenolite, As_2O_3.[4] These flakes have been found to effectively mask the etching process, so that when a sample is etched vertically in the electrolyte, and not intentionally agitated, portions of the flakes drop randomly from the surface under their own weight, causing the etching to proceed irregularly, and resulting in a dull, matte n-type surface upon removal of the p-type material. When a sample is placed horizontally in solution, so that the flakes do not readily fall from the surface, and etched *without agitation*, masking occurs to such an extent that the measured etching current drops by about a factor of four within several minutes. We have found that by continually rinsing away the flakes with a rapidly flowing (0.15 liters/min) stream of NaOH under a pressure head of 3-4 ft of solution, a flat, unblemished n-type surface is usually obtained.

2. A steady d-c current density should be maintained throughout the etching process. Whenever the current density is changed discontinuously (*e.g.*, by dipping the wafer in and out of solution) a distinct etching line appears on the epitaxial surface, probably due to an abrupt change in the etching rate. Best results are obtained by gradually decreasing the etching current as the area of the p-type layer is reduced, so that a current density of approximately 100 mA/cm² is maintained throughout the etching process. A constant *voltage* supply is convenient for this purpose, since the supply current is then automatically determined by the resistance of the layer during etching.

[1] Arthur H. Thomas Co., Philadelphia, Pa.
[2] Tra-Con Inc., 55 North St., Medford, Mass.
[3] CRC Vibrostaltic Pulsation Pump, Cat. No. 65/1705; Chemical Rubber Co., Cleveland, Ohio.
[4] This identification results from x-ray powder patterns, which reveal a cubic structure with a lattice constant, a_o of 11.075Å. The x-ray measurements did *not* indicate the presence of GaAs (a_o = 5.653Å) in the flakes, contrary to previous results (11, 12).

3. The cathode should be placed directly *below* the sample. Because of the low-resistance path through the p-type layer (0.1-1 ohm) as compared to that through the electrolyte (~50 ohms), the etching then proceeds most rapidly near its bottom edge, closest to the cathode, and soon becomes noticeably beveled away from the contact. The unetched portion of the p-type material then progresses upward from the bottom, until reaching the surface of the electrolyte near the ohmic contact. Only rarely has the etching been cut off by more rapid etching inward from the sides than upward from the bottom. However, should this be a problem, the wafer can be readily lapped to a bevel, away from the contact, to ensure an upward "travel" of the unetched p-type material.

Results and Discussion

The technique described above has been used frequently to remove thick p-type GaAs substrates from thin n-type epitaxial layers of $GaAs_{1-x}P_x$ over the entire alloy composition range, $0 \leq x \leq 1$. The surfaces of the n-type layers after etching are usually shiny and highly reflecting, as illustrated in Fig. 3 for a 5μ thick $GaAs_{0.5}P_{0.5}$ sample prepared from vapor-phase growth. The surface of this specimen was found to be free of microscopic imperfections at magnifications up to approximately 1000 (see Fig. 4), and was estimated to be flat to within about a micron over most of its surface. A typical etch rate for the electrolytic process here is about 4μ/min.

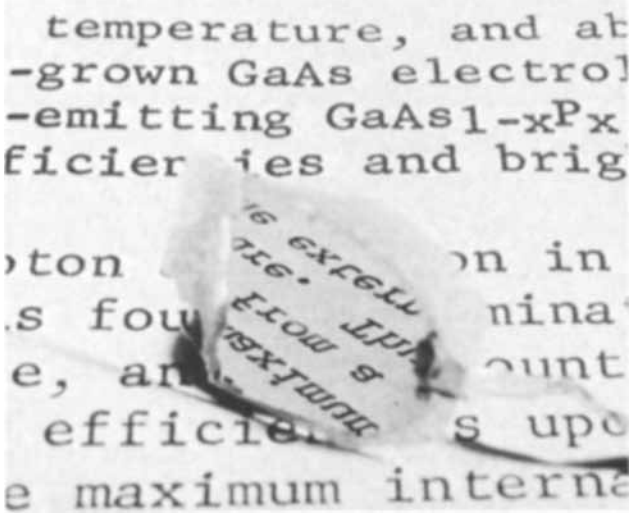

Fig. 3. Reflection from exposed surface of $GaAs_{0.5}P_{0.5}$ n-type layer, 5μ thick, after electrolytic removal of thick p-type GaAs substrate.

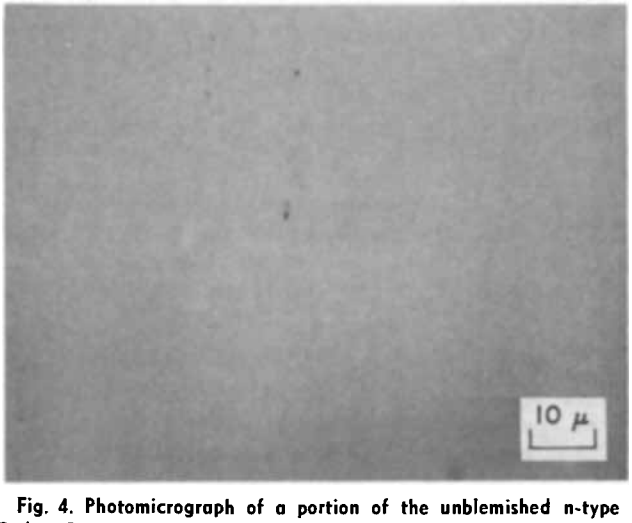

Fig. 4. Photomicrograph of a portion of the unblemished n-type $GaAs_{0.5}P_{0.5}$ surface after electrolytic removal of the adjoining p-type GaAs substrate. Magnification is 1000X. Surface is the same as that shown in Fig. 3.

Whereas n-type layers of $GaAs_{1-x}P_x$ have generally yielded unblemished surfaces, like that shown in Fig. 3 and 4, similar layers of n-type GaAs have occasionally appeared slightly less shiny after etching of the bordering p-type layer. This is thought to be due to a very slight penetration of the etching into the n-type GaAs layer. Since the potential barrier at the interface between the n-type semiconductor and the electrolyte blocks majority carrier electrons, the penetration of the etching into the n-type layer can occur only from the diffusion of minority holes to the semiconductor-electrolyte interface from within the n-type material, or from the generation of electron-hole pairs in the space-charge layer of the interface barrier (13). In either case, the magnitude of the small reverse (etching) current will depend directly on the intrinsic carrier concentration, which in turn varies exponentially with the semiconductor energy gap. Since the energy gap of $GaAs_{1-x}P_x$ can be appreciably larger than that of GaAs, the intrinsic carrier concentration, and hence the magnitude of the etching current, should be much less for n-type $GaAs_{1-x}P_x$ than for GaAs. Furthermore, the diffusion coefficient for holes is somewhat smaller in $GaAs_{1-x}P_x$ than in GaAs, which can further reduce the magnitude of any hole diffusion current responsible for penetration into the n-side of a p-n junction.

The surface perfection of the n-type layer after etching also depends somewhat on the metallurgical perfection of the p-n junction itself, and on the impurity concentrations on the n- and p-sides of the junction. For example, lightly doped n-type ($n \approx 10^{15} - 10^{16}$ cm^{-3}) layers of GaAs and $GaAs_{1-x}P_x$ have consistently been free of surface imperfections, whereas more heavily doped n-type layers have shown slight pitting or matteness, probably due to a breakdown of the potential barrier, which occurs at relatively low voltages for such layers (13).

To the contrary, moderate or heavy doping in the *p-type* substrate or epitaxial layer is desirable to spread the current uniformly across a large area of the wafer. For our applications, p-type layers with acceptor concentrations greater than about 10^{18} cm^{-3} have provided adequate current spreading as well as smooth etching behavior.

Although most of the p-type vapor-grown layers removed by this electrolytic technique have been of $GaAs_{1-x}P_x$, $0 \leq x \leq 1$, the etching process has also been occasionally applied, with success, to p-type layers of InP, $In_xGa_{1-x}P$, and $Al_xGa_{1-x}As$.

Applications.—The thin n-type specimens which can be isolated by the electrolytic technique described below have found a variety of applications. For example, in transmission electron microscopy studies, the region bordering a p-n junction has been consistently located and isolated by selectively etching away all of the bordering p-type layer (14). Such layers are similarly useful for photoluminescent or cathodoluminescent studies, where the n-type region which was originally adjacent to the p-n junction is of interest. In fact, with a photon or electron beam of sufficient intensity, such layers in a suitable material (*e.g.*, GaAs) might well support laser emission within the large-area cavity formed by the two closely spaced surfaces of the n-type layer.

Furthermore, the electrolytic removal of p-type GaAs substrates from thin n-type epitaxial layers of $GaAs_{1-x}P_x$ has been instrumental in measuring the extent of warpage in the epitaxial layers due to the mismatch in the lattice coefficients between the two regions (14). Optical absorption measurements, particularly at photon energies near or above band gap, have also been enhanced by the thin large-area specimens.

A large absorption coefficient (10^4 to 10^6 cm^{-1}) and an ordinarily thick sample usually reduce the transmitted light intensity below normal detection levels.

Finally, a thin n-type base layer sandwiched between two p-type layers of a p-n-p transistor structure has been selectively exposed (for contacting) by masking portions of the uppermost p-type layer from the electrolytic process. Such masking is provided by either a thin film of SiO_2, or by an evaporated array of Ag- or Au-based alloys, which also serve as the ohmic contacts to the emitter. The large array of p-type "mesas" provided over an entire wafer by this masking and etching procedure has also found applications in electroluminescent diodes and in avalanche microwave oscillators(15).

Conclusions

An electrolytic etching techinque has been developed which can remove thick p-types substrates from thin n-type layers of $GaAs_{1-x}P_x$, $0 \leq x \leq 1$. This technique utilizes a spray of NaOH to rinse away "flakes" of arsenolite which form on the p-type surface and which effectively mask the etching process; a constant current density of 100 mA/cm^2; and a cathode located below the bottom edge of the sample, in order to ensure continuous upward etching of the p-type layer. N-type layers of $Ga_{1-x}P_x$ as thin as 2μ and as large in area as 5 cm^2 can be isolated from p-type substrates in this fashion, with exposed surfaces which are shiny and free of surface blemishes under magnifications of $\approx$1000. Light doping in the n-type layer and moderately heavy doping in the p-type material most often yield unblemished surfaces. Such layers of $GaAs_{1-x}P_x$, $x > 0$, have consistently yielded shiny surfaces, whereas similar layers of GaAs have occasionally appeared less perfect. The extension of this technique to thin, vapor-grown layers has applications in electron microscopy, luminescence and optical measurements, and in semiconductor device fabrication.

Acknowledgments

The authors wish to acknowledge the assistance of R. L. Rodgers for preliminary etching experiments, R. J. Paff for x-ray identification of the As_2O_3 "flakes," and H. F. Gossenberger for preparation of the vapor-grown layers used in this investigation. C. J. Buiocchi first simplified the etching system described in this paper by substituting an electric pump for the pressured reservoir of NaOH shown in Fig. 2.

Manuscript received Feb. 9, 1970.

Any discussion of this paper will appear in a Discussion Section to be published in the June 1971 JOURNAL.

REFERENCES

1. M. V. Sullivan and J. H. Eigler, *This Journal*, **103**, 132 (1956).
2. T. M. Donovan and B. O. Seraphim, Paper 91 presented at Electrochem. Soc. Meeting, Los Angeles, Calif., May 6-10, 1962.
3. A. Uhlir, Jr., *Bell System Tech. J.*, **35**, 333 (1956).
4. M. V. Sullivan *et al.*, *This Journal*, **110**, 412 (1963).
5. G. R. Booker and R. Stickler, Paper 72 presented at Electrochem. Soc. Meeting, Los Angeles, Calif., May 6-10, 1962.
6. D. R. Turner, *This Journal*, **105**, 402 (1958).
7. J. J. Tietjen, G. Kupsky, and H. F. Gossenberger, *Solid-State Electron.*, **9**, 1049 (1966).
8. J. J. Tietjen and J. A. Amick, *This Journal*, **113**, 724 (1966).
9. C. J. Nuese and J. J. Gannon, *ibid.*, **115**, 327 (1968).
10. S. A. Greenburg and R. N. Sanders, "Extended Abstracts of Electronics Division," ECS Fall Meeting, New York (1963), Abstract No. 157, p. 117.
11. H. Gerischer, *Ber. Bunsengellschaft Physik. Chem.*, **69**, 578 (1965).
12. W. W. Harvey, *This Journal*, **114**, 472 (1967).
13. Yu. V. Pleskov, *Doklady Akad. Nauk SSSR*, **143**, 1399 (1962).
14. M. S. Abrahams, L. R. Weisberg, and J. J. Tietjen, *J. Appl. Phys.*, **40**, 3754 (1969).
15. P. A. Levine and C. J. Nuese, To be published.

Technical Notes

Reaction of Aluminum with Sodium Hydroxide Solution as a Source of Hydrogen

David Belitskus

Aluminum Company of America, Alcoa Research Laboratories, New Kensington, Pennsylvania

Generation of hydrogen for fuel cells by reaction of hydrides with water or aqueous solutions reduces storage weight or volume over high pressure or cryogenic storage (1-3) but is expensive. Reaction of aluminum in aqueous solutions provides an inexpensive, compact source of hydrogen. While 100°-500°F is required for useful rates with mercuric chloride solution (4), room temperature is satisfactory with sodium hydroxide solution.

Experimental Results and Discussion

A shallow Teflon cup holding the aluminum sample was lowered into a sodium hydroxide solution in a flask and the gas evolution-time curve recorded from a gas burette.

Key words: hydrogen, fuel cell, aluminum, atomized powder.

Particular attention was paid to the rate of gas generation from a specific aluminum surface area, since immersion of pellets into a solution provides a convenient form of activation. A prototype portable fuel cell (3) operates under full load with a hydrogen generation rate of 7 ft^3/hr. Assuming that a pellet having a geometric surface area of about 0.5-1 ft^2 is convenient for this purpose, a specific generation rate of 7-14 cubic feet of gas per hour per square foot of surface area (3.5-7 ml of gas per minute per square centimeter of surface area) is required.

Figure 1 shows the reaction rates of 10 cm^2 area cylinders of several aluminum alloys in 200 ml of 10M NaOH at 25°C. The gas volumes reported are for 25°C and 740 Torr. The most rapid reaction (with

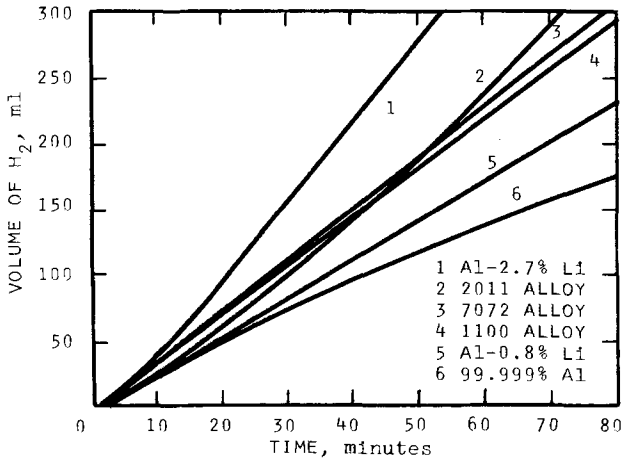

Fig. 1. Hydrogen evolution rate of aluminum cylinders (10 cm^2 geometric surface area) machined from ingots or plates, and immersed in 200 ml of 10M NaOH at 25°C: 99.999% Al, 1100 alloy, 2011 alloy, 7072 alloy, Al-0.8% Li, and Al-2.7% Li.

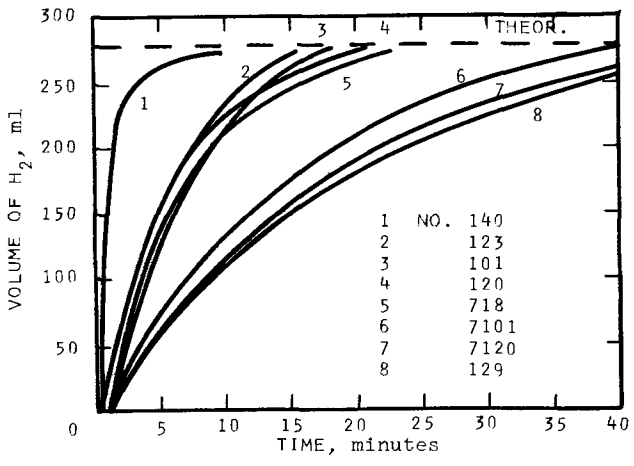

Fig. 2. Hydrogen evolution rate of 0.2g samples of various atomized aluminum powders in 200 ml of 1M NaOH at 25°C.

Al-2.7% Li) had a specific hydrogen generation rate of 0.6 ml/min/cm^2, much lower than desired.

Hence, a more reactive form of aluminum, atomized powder, was tried. Compositions, particle sizes, and surface areas for the powders are given in Table I. Reaction of 0.2g of the highest surface area powder, No. 140, in 1M NaOH proceeded nearly to completion (275 ml of gas) in 10 min. For comparison, reaction in saturated mercuric chloride solution began after a delay of several minutes, but the hydrogen production rate was only 0.06 ml/min. After 40 min of no detectable gas generation in 1M HCl, reaction proceeded at a rate of 0.6 ml/min. Only sodium hydroxide solution seemed suitable for rapid hydrogen generation at room temperature.

Figure 2 shows the gas evolution rates for 0.2g of each powder in 200 ml of 1M NaOH. Relative rates for the powders made from 99.8% Al are as expected from surface area data. High-purity (99.99% Al) powders No. 7101 and 7120 reacted nearly as slowly as No. 129, though having surface areas approximately the same as several 99.8% Al powders which reacted at intermediate rates. This purity effect agrees with the results for ingot samples in 10M NaOH (Fig. 1), but is different from that found by Bobb (4) in comparing alloys of lower purity, 98.8% Al and 99.4% Al in mercuric chloride solution. All unalloyed powders eventually reacted to completion; No. 718 (the Al-12% Si alloy powder) yielded less hydrogen than the unalloyed powders.

The maximum rates of hydrogen generation from 0.2g of No. 140 powder in 10M NaOH, 1M NaOH, and 0.1M NaOH, were, respectively, >500, 130, and 13 ml/min. Rate was directly dependent on sample size for 0.1-0.4g samples of No. 140 powder in 200 ml of 1M NaOH. A delay of about 0.25 min preceded rapid gas generation using No. 140 powder. Delay increased with powders having lower surface areas. When aluminum and solid sodium hydroxide were added to water without mixing, generation of hydrogen was as rapid as, or more rapid than, reaction in predissolved sodium hydroxide solutions.

The gas evolution rates shown in Fig. 3 for compacted 0.75g pellets of No. 140 atomized powder in 200 ml of 1M NaOH decreased with increasing density as might be expected. Even the densest pellet (85% of crystal density) evolved hydrogen rapidly, at 25 ml/min initially or 7 ml/min/cm^2, 17.5 times faster than 1100 alloy ingot cylinder in more concentrated (10M) NaOH. Both higher density pellets remained in one piece during reaction. The lower density pellet broke up and evolved gas at a rate of 500 ml/min or 125 ml/min/cm^2.

Pellet density was more important than surface area of the uncompacted powder in determining the reaction rates of pellets. Three-fourths-gram pellets were compacted at various pressures from samples of powders No. 140, 101, and 129, whose surface areas decrease in this order. Pellets with densities of 2.1 g/cm^3 reacted at similar rates in 200 ml of 1M NaOH. Pellets with densities of 2.3 g/cm^3 also reacted at similar, slower rates. This contrasts with a 12-fold difference in rates found for No. 140 and No. 129 powders in tests with 0.2g samples of uncompacted powder (Fig. 2).

One difference in behavior of the three powders was retained in the pellets. Delay times before rapid

Table I. Micromeretic data

Powder[1] designation	Alloy	Nominal average particle diameter, μ	Surface area[3] per unit weight, m^2/g
101	99.8% Al[2]	17-24	0.235
120	99.8% Al[2]	25-30	0.253
123	99.8% Al[2]	15-19	0.227
129	99.8% Al[2]	—	0.126
140	99.8% Al[2]	3-6	0.853
718	Al-12% Si	17-20	0.335
7101	99.99% Al	17-24	0.339
7120	99.99% Al	25-30	0.290

[1] Aluminum Co. of America, Atomized Aluminum Powders.
[2] Purity of aluminum before atomization. Typical analysis of powder: Al, 98.7-99.7% (decreasing with increasing surface area of powder); Al_2O_3, 0.1-1.1 (increasing with increasing surface area of powder); Fe, 0.15; Si, 0.07.
[3] Determined by radiochemical method (5) on particular lots of powder used.

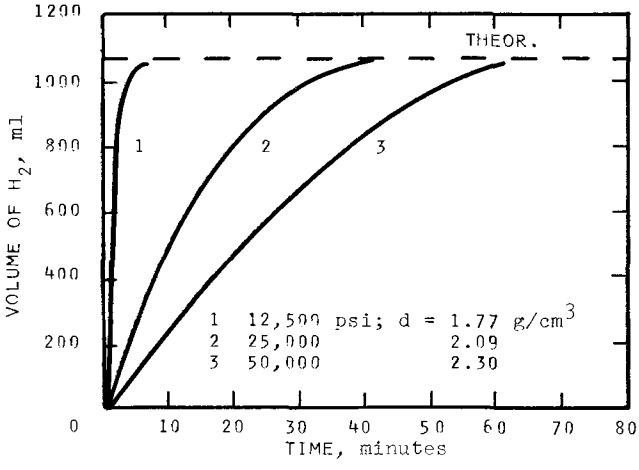

Fig. 3. Hydrogen evolution rate of 0.75g samples of atomized aluminum powder No. 140 compacted at room temperature and the stated pressures into 1.25 cm diameter cylinders and allowed to react in 200 ml of 1M NaOH at 25°C.

reaction were independent of density and were less than 1 min for pellets of No. 140 powder, about 2 min for pellets of No. 101 powder, and 3 min for pellets of No. 129 powder.

Experiments with less than 200 ml solution volume (133 times the stoichiometric amount of water for 0.75g of aluminum) were conducted to observe the effect of reaction heat (14.6 Btu/g Al) on rates and the effect of reduced sodium hydroxide. Reaction of a 0.75g pellet of No. 140 powder (2.1 g/cm^3 density) in 25 ml of 1M NaOH (17 times stoichiometrically required water) proceeded rapidly with 400 ml of gas evolved in 5 min, then gradually slowed to a rate of only 2 ml/min in 35 min. Similar pellets in 25 ml of 2M and 3M NaOH yielded about 300 ml of gas per minute with localized boiling of water. The bulk water temperature rose slowly to a maximum of 70°C when 800 ml of gas had been generated. Delay time decreased noticeably with increased concentration.

The reactions of aluminum in sodium hydroxide solutions are

$$2Al + 6H_2O + 2NaOH \rightarrow 2NaAl(OH)_4 + 3H_2\uparrow \quad [1]$$

$$NaAl(OH)_4 \rightarrow Al(OH)_3\downarrow + NaOH \quad [2]$$

Sodium hydroxide consumed (1.48g NaOH/g Al) in the hydrogen-generating reaction can be regenerated in reaction [2]. The relative rates of reactions [1] and [2] will affect both the rate and the extent of hydrogen evolution if a stoichiometric amount of sodium hydroxide is not present. Reaction [2] is important in both the Bayer process and Al-air batteries (6)

Twenty-five milliliters of 1M NaOH contain 1g of sodium hydroxide, or 90% of the amount required by reaction [1] for 0.75g of aluminum. The rapid decline in rate before the theoretical hydrogen volume (based on weight of aluminum) had been generated in this solution indicates that reaction [2] is not sufficiently rapid to sustain initial gas generation rates.

A final experiment was performed with a 0.75g cylinder (density of 2.1 g/cm^3) of No. 140 powder placed in 2.5 ml of 2M NaOH (or 18% of the stoichiometric amount of sodium hydroxide and 150% the stoichiometric amount of water, according to reaction [1]). The initial rate was very rapid, with boiling of the solution. Within a minute, the volume of gas reached 190 ml; then the rate dropped off sharply, but continued for 20 hr at 0.05 ml/min, the rate at which sodium hydroxide was being regenerated by reaction [2].

After about 20 hr, the hydrogen evolution rate increased to 0.15 ml/min. With time, the aluminum hydroxide precipitate may become a more effective seed surface for regeneration of sodium hydroxide by reaction [2]. Nonetheless, stoichiometric quantities of sodium hydroxide are required for rapid reaction rates. The possibility of rapid gas generation from uncompacted aluminum powder and sodium aluminate solutions has not been tested.

Summary

Hydrogen generation rates from massive aluminum in sodium hydroxide solutions are inconveniently slow for fuel cell use, even in 10M NaOH. Compacts of atomized aluminum powder in sodium hydroxide solutions yield hydrogen at suitable rates without external heating and with a start-up time in the range of 1 min. Rapid hydrogen generation to complete consumption of aluminum requires at least 1.5g NaOH/g Al, but slow generation can continue even with a lower sodium hydroxide to aluminum ratio.

Acknowledgment

The author wishes to thank Mr. Walter W. Hill for his technical assistance.

Manuscript submitted Jan. 5, 1970; revised manuscript received *ca.* May 13, 1970.

Any discussion of this paper will appear in a Discussion Section to be published in the June 1971 JOURNAL.

REFERENCES

1. L. G. Austin, "Fuel Cells— A Review of Government-Sponsored Research, 1950-1964," N.A.S.A. SP-120 (1967).
2. K. V. Kordesch, in "Fuel Cells," Will Mitchell, Jr., Editor, p. 349, Academic Press (1963).
3. E. A. Oster and L. E. Chapman, in "Fuel Cells," G. J. Young, Editor, Vol. 2, p. 168, Reinhold (1963).
4. F. H. Bobb, *J. Eng. Ind.*, Paper No. 67-WA/UnT-3, **89** (1967).
5. J. E. Lewis and R. C. Plumb, *Intern. J. Appl. Radiation Isotopes*, **1**, 33 (1956).
6. S. Zaromb and R. A. Foust, Jr., *This Journal*, **109**, 1191 (1962).

The Electropolishing of Zinc Specimens

R. W. Powers* and E. C. Jerabek

General Electric Research and Development Center, Schenectady, New York

Very smooth, bright surfaces of zinc have been of considerable utility in electrochemical studies. For example, such surfaces were not only helpful in delineating the various anodic films that form on zinc but also were useful in observing the early stages of dendrite formation during the deposition of zinc from alkaline zincate solutions (1-3). The process of electropolishing is often used for producing smooth, bright surfaces in the unworked state. In this note, a new procedure for electropolishing zinc specimens based on a sulfuric acid bath is described. In our experience, it gives rise to a better surface on zinc than that produced by any electropolishing method described previously. A number of such procedures have been summarized by Tegart and by Fedotev and Grilikhes (4). The conditions for optimum polishing given in this note differ significantly from those of Maitak (5). The work of Ovari seems more concerned with brightening zinc rather than with electropolishing (6).

The zinc specimen, usually a disk 0.5-1 in. in diameter, is held in a horizontal plane about 1½ in. off the bottom of a liter beaker that serves as the bath container. The jig on which the specimen is mounted has been described elsewhere (7). The electrolyte consists of about 650 ml of an aqueous solution of sulfuric acid, 20% by weight. The cathode is a 3 in. by 12 in. strip of nickel foil (or, better, platinum foil) with attached tab to serve as the current lead. The cathode foil is arranged along the inside wall of the beaker. For this work, a filtered d-c power supply, Electro Products Laboratories Model NFB, has been used. To prevent hydrogen bubbles, generated at the cathode, from reaching the specimen, a thin porous sheet of material such as Fiberglas, nonwoven nylon, or polypropylene is used as a diaphragm. It is wrapped

* Electrochemical Society Active Member.

about a perforated polyethylene cylinder, 3 in. in diameter by 4 in. high, cut from a polyethylene bottle.

The jig with specimen attached is placed in the electrolyte at room temperature with 2.5V applied between the specimen and the cathode. Because the anodic overpotential comprises most of the cell voltage, the former is controlled adequately by maintaining the cell voltage constant. A value of 2.5V corresponds to a position on the current plateau of the current-potential curve. Smoothing takes place in the presence of a light gray anodic film that covers the specimen surface. Following the initial current surge, the current density is approximately 0.3 A/cm^2. After 1-2 hr of electrolytic smoothing and just prior to removal of the specimen from the bath, the cell voltage is increased to 7-9V. The gray film is removed in 20-60 sec and the specimen surface becomes very lustrous. The specimen is then quickly removed from the bath with voltage applied and immediately plunged into distilled water. It is dried rapidly with a stream of dry gas.

The surface produced according to this procedure is mirrorlike, very lustrous, and smooth as indicated by the Nomarski interferogram shown in Fig. 1. Since the reference plane in the Nomarski technique is formed optically and can be tilted arbitrarily with respect to the specimen surface, only the waviness of the fringes, not the distance between them, is significant in indicating surface smoothness. The photomicrograph shown in Fig. 1 was taken midway between the center and edge of a ¾ in. disk of 99.9999% zinc with yellow light. Grain boundaries are faintly discernible. Slight differences in the heights of individual grains appear to be the cause of the slightly jagged character of the interference fringes.

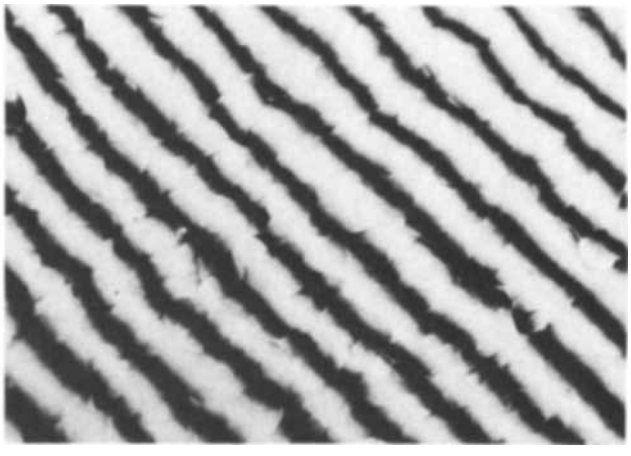

Fig. 1. Nomarski interferogram of zinc specimen after 2 hr of electropolishing. 60X.

The polishing procedure described in this note is not satisfactory for most zinc alloys. Alloying additions evidently increase the conductivity of the gray anodic film. During removal of this film by application of 7-9V, oxygen is evolved on the alloys. This leads to the formation of fine pits.

Acknowledgment

The senior author is grateful to the International Lead Zinc Research Organization, 292 Madison Avenue, New York, New York, for partial financial support of this work.

Manuscript received Jan. 7, 1970.

Any discussion of this paper will appear in a Discussion Section to be published in the June 1971 JOURNAL.

REFERENCES

1. R. W. Powers, *This Journal*, **116**, 1652 (1969).
2. R. W. Powers, To be submitted to *This Journal*.
3. R. W. Powers, *Electrochem. Technol.*, **5**, 429 (1967).
4. W. J. Tegart, "The Electrolytic and Chemical Polishing of Metals," Pergamon Press, London (1959). N. P. Fedotev and S. Y. Grilikhes, "Electropolishing, Anodizing and Electrolytic Pickling of Metals," Robert Draper, Ltd., Teddington, England (1959).
5. G. P. Maitak, *J. Applied Chem. USSR*, **31**, 1488 (1958); **31**, 1741 (1958).
6. F. Ovari, *Veszpremi Vegyip. Egyet Kozlemen*, **8**, 151 (1964), as abstracted in *Chem. Abstracts*, **63**, 242d (1965).
7. R. W. Powers, *Electrochem. Technol.*, **2**, 274 (1964).

A Method for the Synthesis of BI_3 for Use as a Dopant Source

M. Berkenblit* and A. Reisman*

IBM Thomas J. Watson Research Center, Yorktown Heights, New York

Although B_2H_6 is generally used as a p-type dopant source for Ge layers grown by the $GeCl_4$ or GeH_4 processes, it was found to have limited applications when used with the GeI_2 disproportionation reaction. Under low growth rate conditions using B_2H_6 as a dopant source in the iodide process (1), Ge epitaxial layers were obtained with resistivities as low as 0.005 ohm-cm. However, under the high growth rate conditions necessary to obtain smooth and shiny epitaxial layers on (110) oriented substrates (2, 3), B addition *via* B_2H_6 presented a problem. The maximum usable p-type doping obtained was 0.02 ohm-cm. With further increase of B_2H_6 concentrations, the surface quality of the epitaxial layer degraded.

At the low temperatures (350°-400°C) used in the disproportionation epitaxial reaction, the incorporation of B into the growing layer was assumed to occur *via* an intermediate formation of BI_3 by the reaction of B_2H_6 with HI in the gas stream. (HI was present as one of the gas species during the deposition process.) The BI_3 yield was limited by the available HI and the efficiency of this reaction at the temperature of the epitaxial reactor. Thus, in order to establish a high BI_3 concentration, a large excess of B_2H_6 was needed, which in turn perturbed the epitaxial reaction.

Substitution of a solid BI_3 source (vendor supplied material) proved to be unsatisfactory because of large variations in purity from lot to lot, and difficulties encountered in transferring the material into the reaction system. It is the purpose here to describe a method for an *in situ* synthesis of BI_3 which yields a reproducible source of boron and enables deposition of low-resistivity Ge single-crystal layers.

The synthesis of BI_3 involved the reaction of B_2H_6 (obtained from the Matheson Company in a H_2-He

* Electrochemical Society Active Member.

Key words: semiconductor materials, doping of semiconductors, p-type dopant source.

carrier gas at 100-1000 ppm level), and HI (delivered from a generator similar to that used for the Ge epitaxy) (4) in appropriate quantities to satisfy the stoichiometry shown in Eq. [1] (5).

$$6B_2H_6 + 6HI \rightleftarrows 2BI_3 + 5B_2H_6 + 6H_2 \qquad [1]$$

Both the B_2H_6 and HI were carried into a furnace by a H_2-He gas mixture and reacted at 250°C. Figure 1 is a schematic representation of the system used. At the output of the reaction chamber, BI_3 was condensed in an ice trap, while other effluent vapors (including B_2H_6) were swept out of the system. Once a sufficient quantity of BI_3 was collected, the synthesis was terminated. Then, using a suitable valving arrangement, the BI_3 was introduced into the epitaxial reactor. During the epitaxial reaction, the BI_3 was maintained at 24°C, and the concentration in the reactor varied by the carrier gas flow rate.

According to calculations made using the JANAF thermochemical data tables, the equilibrium constant for the reaction as written in Eq. [1] varies from 10^{10} to 10^5 in the range 25°-800°C, respectively. The synthesis was attempted at 250°, 450° and 800°C, and only at 250°C was any measurable amount of BI_3 observed. At the higher temperatures, there was no measurable trace of BI_3, indicating that K is much smaller ($\rightarrow 0$)

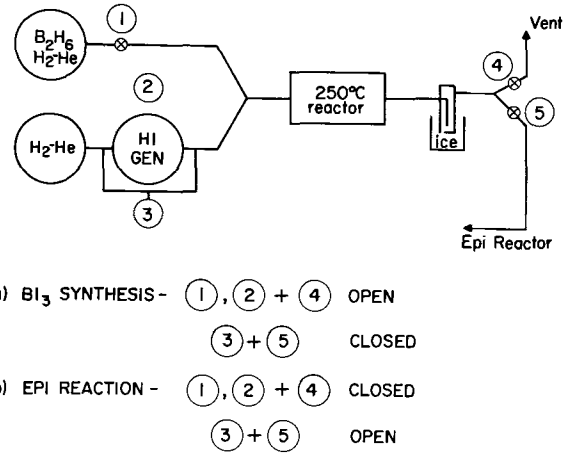

Fig. 1. Schematic representation of the BI_3 synthesis-epitaxial reactor train.

than the calculated value. Since the kinetics of the reaction would increase with increasing temperature, these results do not appear to be due to kinetic limitations, and would indicate that the thermochemical data are in considerable error.

An indication of the applicability of Eq. [1] in describing the over-all reaction and a measure of the reaction efficiency at 250°C were obtained *via* chemical analysis of the reaction products. Thus, if one obtains the ratio of BI_3 to B_2H_6 in the effluent, starting with equimolar mixtures of B_2H_6 and HI, the BI_3/B_2H_6 ratio would be expected to vary between zero when no reaction occurs to 2:5 if the reaction goes essentially to completion. A series of 3 H_2O bubblers were attached to the output of the reaction train (BI_3 and B_2H_6 decompose in water to form B_2O_3 in solution). With the ice trap in place, unreacted B_2H_6 in the exit gas was trapped and decomposed in H_2O while the BI_3 was entrained in the ice trap. After the reaction was terminated, this trapped BI_3 was flushed into a new set of water bubblers and decomposed. The boron content in both solutions was then determined colorimetrically by the methylene blue method (6). Within the precision of the method of analysis (*ca.* 5%), the mole ratio of BI_3 to B_2H_6 was found to be 2:5 indicating that at 250°C the reaction goes essentially to completion.

Acknowledgments

The authors wish to thank M. Sampogna for his assistance with the synthesis and B. L. Gilbert and B. L. Olson for the boron analysis.

Manuscript received March 30, 1970.

Any discussion of this paper will appear in a Discussion Section to be published in the June 1971 JOURNAL.

REFERENCES

1. A. Reisman and M. Berkenblit, *This Journal*, **112**, 315 (1965).
2. M. Berkenblit, A. Reisman, and T. B. Light, *ibid.*, **115**, 66 (1968).
3. M. Berkenblit, T. B. Light, and A. Reisman, *ibid.*, To be published.
4. A. Reisman and M. Berkenblit, *ibid.*, **113**, 146 (1966).
5. "Boron, Metallo-Boron Compounds and Boranes," R. M. Adams, Editor, p. 604, John Wiley & Sons, Inc. (1964).
6. L. Pasztor and J. D. Bode, *Anal. Chem.*, **32**, 277 (1960).

JOURNAL OF THE ELECTROCHEMICAL SOCIETY

REVIEWS AND NEWS

MAY 1970

Chemical Approaches to the Approximate Prediction of Band Gaps of Binary Semiconductors and Insulators

Ashok K. Vijh*

Hydro-Quebec Institute of Research, Varennes, Quebec, Canada

ABSTRACT

The chemical approaches to the approximate prediction of band gaps of binary inorganic semiconductors and insulators have been briefly reviewed with special emphasis on relatively recent work. These approaches involve establishment of correlations between band gaps and various other quantities, *e.g.* heats of formation, bond energies and electronegativities, *etc.* It has been shown that some of these correlations provide semiquantitative means for the estimation of band gaps of several materials for which it is either too difficult or impossible to compute accurate band gaps on the basis of methods of theoretical physics. The possible theoretical foundations of some of these correlations, as examined previously, have also been presented. Some of the recently proposed correlations, *e.g.* between band gaps and heats of formation per equivalent, even though rough, have universal validity in that they are applicable to all types of binary inorganic compounds covering a wide range of ionicity, crystal type, and band gaps.

It is generally recognized that the methods of theoretical physics are either inadequate or cumbersome for computing the width of forbidden gaps of all but the simplest semiconductors, *e.g.* Ge. The width of the forbidden gap is, of course, an extremely important parameter for the case of semiconducting compounds since it constitutes the basis for the calculation of band structure and the computation of the number of intrinsic carriers, and other properties. This situation has prompted a number of investigators to predict, albeit approximately, the band gaps of semiconductors by chemical approaches involving a variety of correlations (1-8). For example, band gaps have been related to heats of formation per mole (1), heats of formation per equivalent (7), electronegativities (3), atomic numbers (6), heats of atomization per atom (5), single bond energies (4), and average bond energies (8). Many of these correlations are purely empirical in nature. In some cases, however, attempts have been made to present some theoretical justifications (1, 5, 8-10).

In the present article, an attempt is made to present an outline of the more significant of these approaches with special emphasis on relatively recent work. It is assumed that the reader is familiar with the qualitative description of the band theory of solids as presented, *e.g.* in a recent lucid article (11). Other excellent articles on the band theory of solids, at a relatively elementary level, are also available in the literature (2, 3, 12-16).

It may be added that the fundamental contributions of Mooser and Pearson (17), Goodman (18), Suchet (19), and Welker (20) to the subject of prediction of semiconductivity in materials are not included in this article since their work has already been reviewed previously in some detail (10).

* Electrochemical Society Active Member.

Correlation of Band Gaps to Various Quantities

It was demonstrated by Ruppel, Rose, and Gerritsen (1) that band gaps, E_g, of several semiconductors and insulators lie between one and two times the heats of formation per *mole* of the corresponding compounds (Fig. 1). It was pointed out (7), however, following Sanderson (21), that in correlations of the type shown in Fig. 1 the thermodynamic data must be "normalized," *i.e.* the heats of formation should be plotted as per equivalent (*i.e.* neither as per mole nor as per atom but as per atom equivalent). This correlation (Fig. 1) was extended to several more compounds by including this concept of normalization (7), and the results are shown in Fig. 2. It is clear from Fig. 2 that, *roughly*, a very large variety of semiconductors and insulators obey the relation:

$$E_g = 2\,\Delta H_e \qquad [1]$$

where ΔH_e is the heat of formation per equivalent. For the case of polyatomic compounds formed between polyvalent ions, it is particularly glaring that (Table I) the proposal of Ruppel *et al.* (1) is not sustained, whereas Vijh's relation (Fig. 2) gives rather satisfactory predictions of approximate values of the band gaps (Table I).

In a correlation proposed by Hooge (Fig. 3), band gaps of several binary compounds may be satisfactorily estimated from electronegativities by means of an empirical equation. This correlation (3) does not, however, include polyatomic compounds.

In a very interesting paper, Manca related the single bond energies of several compounds, calculated by Pauling's empirical equation (22), to their band gaps,

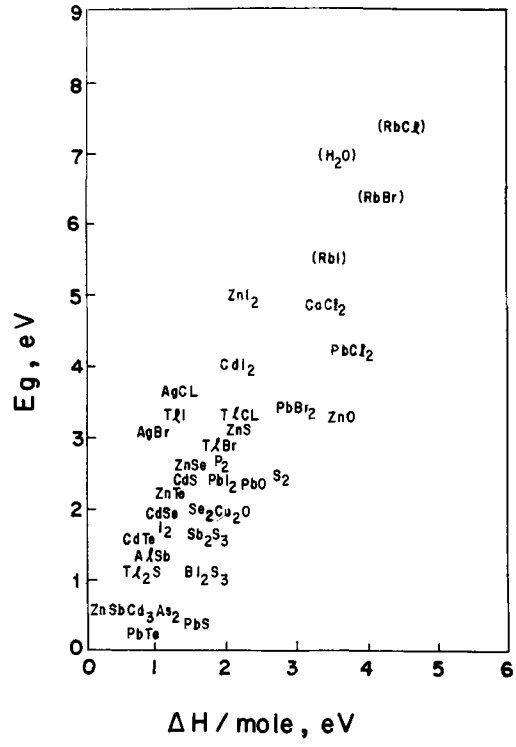

Fig. 1. Correlation between band gaps and heats of formation (standard state) per *mole* for several compounds, after Ruppel, Rose, and Gerritsen (1).

Table I

Compound	E_g (Ruppel *et al.*), eV	E_g (Vijh), eV	E_g (experimental), eV
Al_2O_3	17-34	5.67	7
Ta_2O_5	21.75-43.5	4.35	4.6
TiO_2	9.46-19.92	4.73	3.0
Ga_2O_3	11.19-22.38	3.73	4.4
In_2O_3	9.63-19.26	3.21	2.8

through an empirical relation of the type:

$$E_g = a\,(E_s - b) = 2\,(E_s - b) \qquad [2]$$

where E_g is the band gap value; E_s is the single bond energy; a and b are constants characteristic of a given class (*e.g.* $A^{IV}\,B^{IV}$, $A^{III}\,B^{V}$, *etc.*) of semiconductors. For the compounds examined by Manca, the value of a is roughly equal to 2. Manca's results showing the validity of Eq. [2] for several compounds have been presented in Fig. 4. In another paper, Bailly and Manca (5) have shown that for several compounds the following relation is obeyed:

$$E_g = \overline{A}\,(\Delta G^s - \overline{B}) \qquad [3]$$

Here ΔG^s is the free energy of sublimation per atom of the semiconducting compounds and $\overline{A}$ and $\overline{B}$ are parameters characteristic of each series of semiconducting material. It may be seen from Fig. 5 that Eq. [3] holds for a typical series of compounds. Bailly and Manca have also analyzed the factors that determine the magnitude of parameters $\overline{A}$ and $\overline{B}$ for several series of inorganic compounds (5).

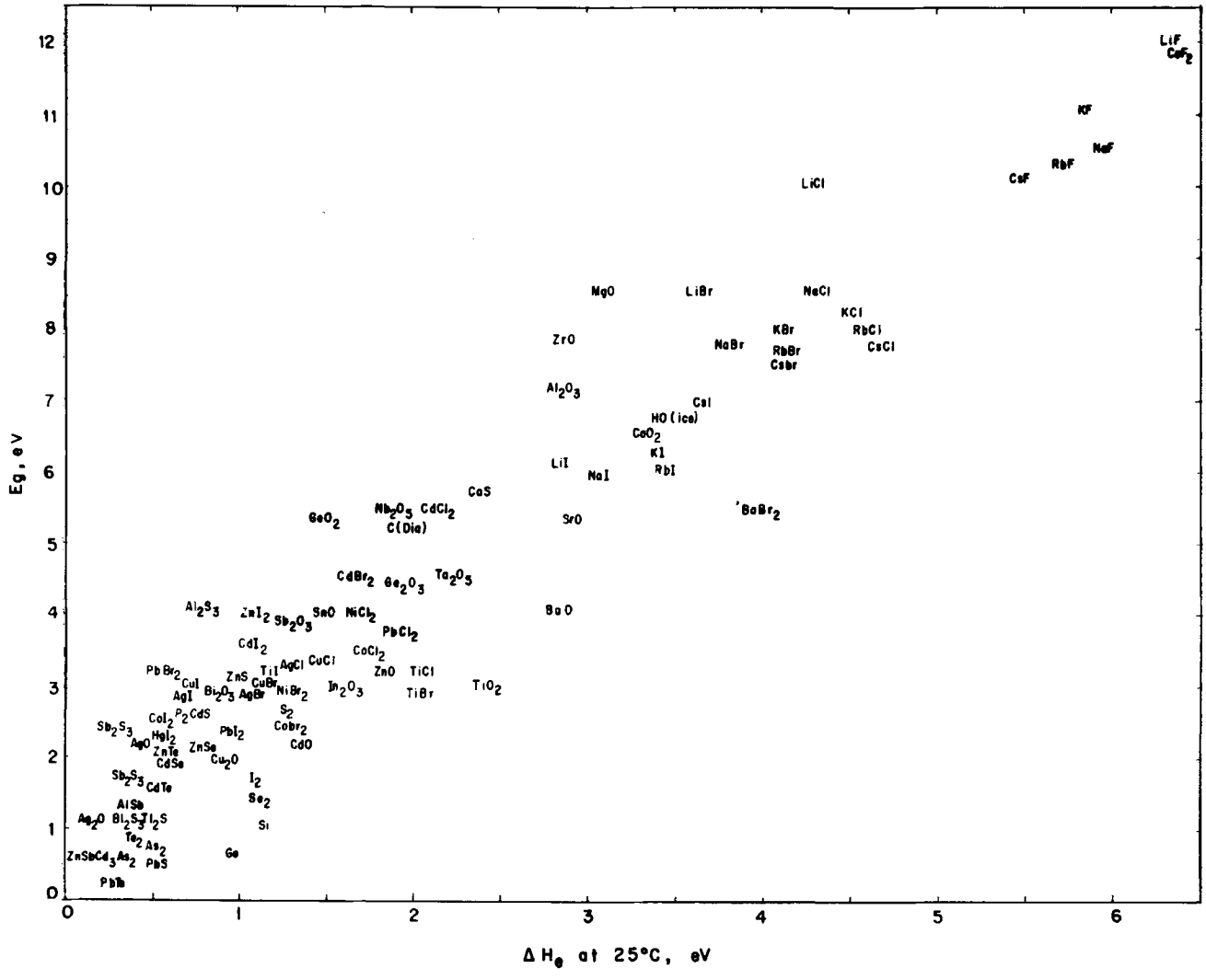

Fig. 2. A plot of band gaps *vs.* heats of formation (standard state) per equivalent for a large number of inorganic binary compounds (7)

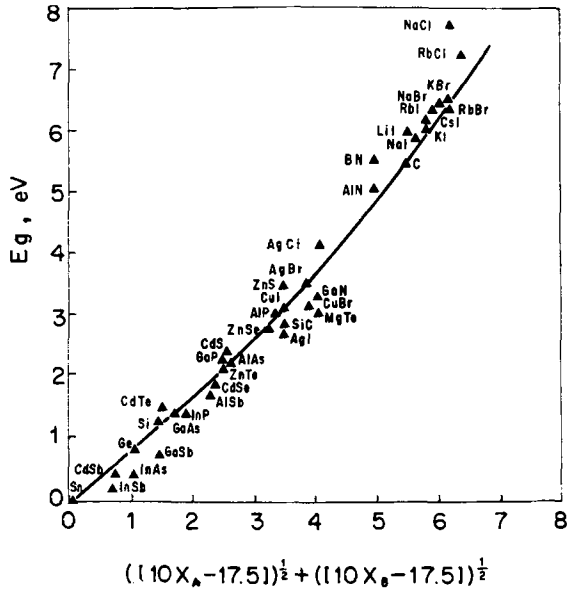

Fig. 3. Hooge's (3) relationship between band gaps and a function of electronegativities, X, for some semiconductors and insulators.

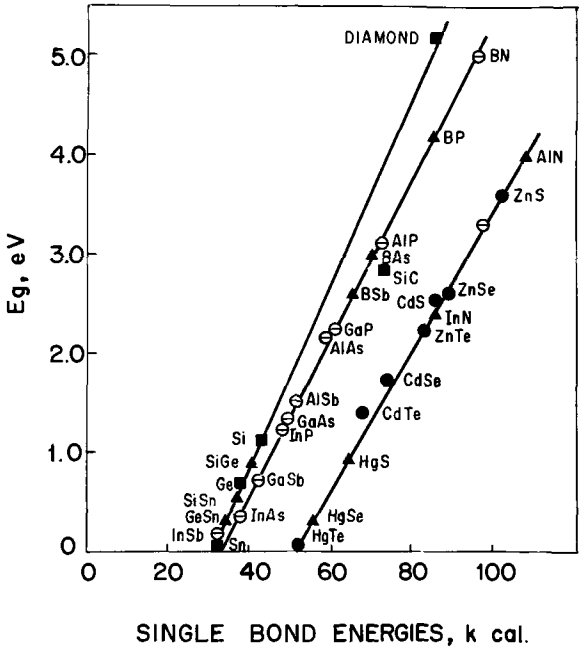

Fig. 4. Manca's correlation between single bond energies, as estimated by Pauling's method, and band gaps for several series of inorganic substances (4).

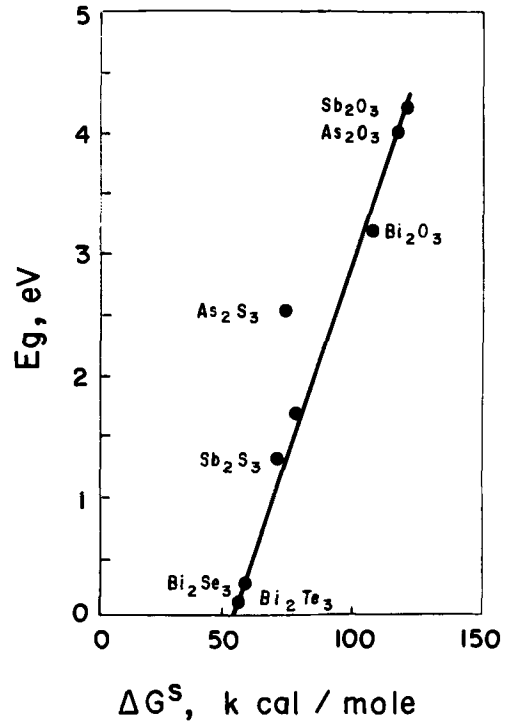

Fig. 5. A typical plot of free energy of sublimation per atom against band gaps for a given series of semiconductors, as presented by Bailly and Manca (5).

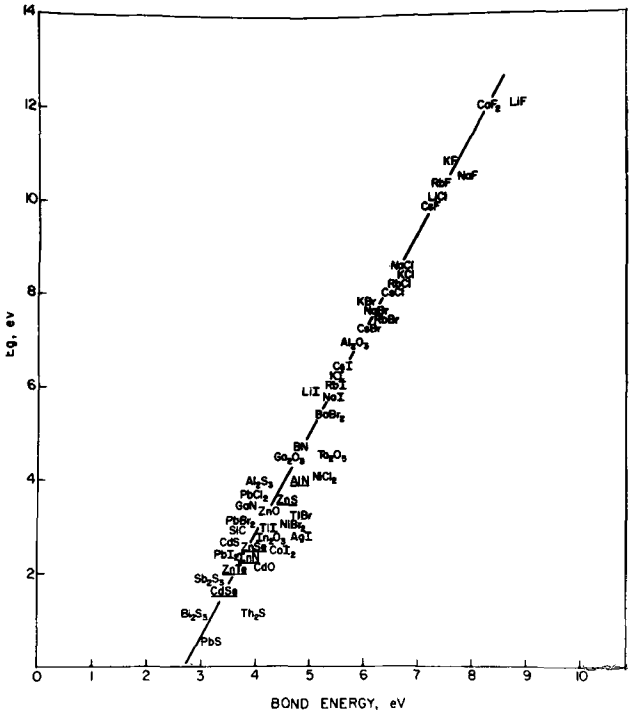

Fig. 6. A plot depicting correlation of average bond energies with band gaps for a wide range of inorganic binary compounds. Bond energies for CdSe, ZnTe, InN, ZnSe, ZnS, and AlN are single bond energies estimated by Pauling's empirical equation since reliable thermodynamic data are not available for calculation of average bond energies (8).

All the foregoing correlations (Fig. 1-5) have a serious limitation in that they are empirical in nature. Further, most of them (Fig. 1, 3-5) are restricted to certain special classes of compounds and lack universal applicability. However, the relationship presented in Fig. 2 is an exception in this particular respect; *i.e.* it has general applicability. A point that may be emphasized here is that most of these correlations are rather approximate in nature.

Recently, Vijh (8) has presented a correlation (Fig. 6) between average bond energies and band gaps, E_g, of several inorganic binary compounds. In fact it has been shown that Manca's Eq. [2] is applicable to a large variety of compounds (Fig. 6) if E_s in Eq. [2] is assumed to denote an average bond energy as calculated by a thermochemical procedure, instead of representing a single bond energy value. It is important to note that this correlation (Fig. 6) is *not* restricted to some particular class of semiconductors and is in fact a general one and includes compounds which cover the following spectrum of behavior:

(i) Inorganic compounds which range from highly covalent (Sb_2S_3) to those which are highly ionic (NaF).

(ii) Semiconductors and insulators representing a rather large range of band gap values, *e.g.* 0.5 to 12 eV.

(iii) There are several substances in Fig. 6 (and Table I) which are polyatomic binary compounds formed between *polyvalent* ions, *e.g.* Sb_2S_3, Bi_2S_3, Al_2O_3, Ta_2O_5, *etc.*

(iv) A wide range of crystal structures as represented in Fig. 6, *e.g.* Wurzite, zinc blende, Corundum, cuprite, fluorite, NaCl, and CsCl.

The relationship presented in Fig. 6 is not only a rather general one but it can also be derived theoretically (8) for the case of ionic compounds, *e.g.* alkali halides. The theoretical basis of Fig. 6 and Fig. 2 has been outlined in the following section.

Some Theoretical Considerations

In this section, an attempt is made to indicate the theoretical basis of Eq. [2] and [1] for the case of alkali halides, assuming that E_s in Eq. [2] represents an average bond energy value. It is important, however, to precede this analysis by a discussion of some matters related to the question of proper definition of bond energies and band gaps.

Bond energies.—There are two procedures frequently used for the calculation of bond energies:

1. *Pauling's method—single bond energies*

The bond energy of an isolated diatomic molecule formed between two univalent atoms, *e.g.* NaCl, may be estimated by Pauling's empirical equation:

$$D(\text{Na-Cl}) = \tfrac{1}{2}\{D(\text{Na-Na}) + D(\text{Cl-Cl})\} + 23(X_{\text{Na}}-X_{\text{Cl}})^2 \quad [4]$$

Here, D(Na-Cl) is the bond energy between Na and Cl in NaCl; D(Na-Na) is the bond energy between Na atoms; D(Cl-Cl) is the bond energy between two chlorine atoms; X_{Na} and X_{Cl} are the electronegativities of Na and Cl, respectively, on the Pauling Scale (22). This method gives fairly accurate estimates of bond energy between two univalent atoms held together by a single bond, *e.g.* NaCl. However, when more than one bond is involved, *e.g.* in CH_4, Pauling's procedure does not give a good estimate of the average C-H bond energy, but only yields a value for the last dissociation energy, *i.e.* C-H bond, when only one H is present on C. When applied to cases involving either divalent or multivalent atoms, *e.g.* Ta_2O_5, Sb_2S_3, GaN, this method gives an estimate of the energy of the last bond in the molecule after all other bonds have been removed. It is believed that such a quantity is not a very good measure of the *general* magnitude of binding in a complex molecule, which must be represented by an average bond energy. The average bond energy thus obtained, it is believed, is more pertinent to the discussion of relation between binding and band gaps in inorganic compounds. This bond energy is calculated from the appropriate thermochemical data, as follows.

2. *Thermochemical procedure—average bond energies*

The bond energy of a compound, *e.g.* NaCl, may be obtained from the equation:

$$D(\text{Na-Cl}) = \Delta H_S + \tfrac{1}{2}\,\Delta H^\circ_{\text{diss}} + H^\circ_f \quad [5]$$

Here, D(Na-Cl) is the required bond energy; ΔH_S is the heat of sublimation of Na metal per *mole*; ΔH_{diss} is the heat of dissociation of Cl_2 molecule into Cl atoms, again, per mole; ΔH°_f is the heat of formation of NaCl in its standard state, again per mole. The quantity given by Eq. [5] (*i.e.* bond energy) is, of course, the heat of atomization of NaCl. In the case of NaCl, only one shared electron pair is involved in the bonding. For complex compounds, *e.g.* Al_2O_3, several bonds (*i.e.* shared electron pairs) are involved and hence an appropriate normalizing factor must be used to obtain from Eq. [5] the bond energy per *bond* and not the total energy for all the bonds in Al_2O_3. This is done by computing, first from Eq. [5], the heat of atomization per mole which is then normalized with respect to the participating valences in order to obtain heat of atomization per equivalent, which is, of course, the bond energy. For example, the heat of atomization per equivalent (*i.e.* the bond energy) for Al_2O_3 is 1/6 of the heat of atomization per mole as calculated from Eq. [5]. Further details on these and related matters are available elsewhere (7, 8, 21-23).

The heat of atomization per equivalent thus obtained, after some second-order corrections (*e.g.* spin correlation stabilization energies, coordinate valence) as discussed by Howald (23), are the actual values of the average bond energies as obtained from the experimental thermochemical data.

These average bond energy values have been used in constructing Fig. 6 (see, however, caption to Fig. 6). The accuracy of these bond energies is limited only by the accuracy of the thermodynamic data which were used in their calculation. These data have been obtained from reliable compilations (23-25). In obtaining these average bond energies, corrections to the heats of atomization per equivalent were applied only for spin correlation stabilization energies (23). The possible presence of coordinate valence has been ignored because unambiguous estimates of the extent of participation of coordinate valence in compounds are not always easily obtained as discussed by Howald (23). Since the theoretical derivation of Eq. [2] and [3] (see below) is claimed to be strictly valid for alkali halides only, this neglect of coordinate valence in the calculation of bond energies is not serious, because alkali halides do not involve any coordinate bonds.

Band gaps.—These band gaps (Fig. 6) refer to k space at $k = 0$. It may be mentioned that precise definition and determination of band gaps involves some real difficulties. For example, in large band gap semiconductors like alkali halides, experimental values quoted are strongly influenced by coulomb effects, even though there is no significant difference between the direct and indirect gap since the bands are very narrow. This is because of the reason that the optical absorption is determined rather by the exciton structure in front of the energy gap than by the energy gap itself (8). In small band gap semiconductors, on the other hand, there are appreciable differences between direct and indirect gaps since the bands are rather wide (8). The significance of values of band gaps used in Fig. 6 must be accepted only in relation to these difficulties. It is believed, however, that the aforementioned difficulties in the precise definition and determination of band gaps are not serious enough to render values of band gaps in Fig. 6 so uncertain as to make the relationship presented invalid.

Derivation of Eq. [2] and [3] for ionic compounds.—As shown previously by Mark (26), the forbidden gap E_g of an ionic compound like NaCl is given by:

$$E_g = 2M - (I_m - A_x) \quad [6]$$

where M is the Madelung energy, I_m is the ionization potential of Na; A_x is the electron affinity of Cl. From Eq. [6],

$$E_g = 2(U - R) - I_m + A_x \quad [7]$$

where U is the experimental (thermochemical) lattice energy and R is an energy term which includes repulsive, London, and other components (*e.g.*, crystal field stabilization energy) of theoretical lattice energy (12) so that

$$M = (U - R) \quad [8]$$

is quite valid.

It may be readily shown, by means of a Born-Haber thermochemical cycle, that (12):

$$\Delta H^\circ_f = \Delta H_s + I_m + \tfrac{1}{2}\,\Delta H_D + A_x + U \quad [9]$$

where,

ΔH°_f is the heat of formation, *e.g.* of NaCl
ΔH_s is the heat of sublimation of Na
I_m is the ionization potential of Na

ΔH_D is the energy of dissociation of Cl_2 (g) into atoms
A_x is the electron affinity of Cl
U is the lattice energy of NaCl

The quantities defined above are all as per *mole* of the corresponding substance.

On obvious rearrangement, Eq. [9] gives:

$$-U = \Delta H_s + I_m + \tfrac{1}{2}\Delta H_D + A_x - \Delta H^\circ_f \quad [10]$$

Now we note that U, A_x, and ΔH°_f are exothermic quantities (hence with $-$ sign) and ΔH_s, I_m, and ΔH_D are endothermic quantities (hence with $+$ sign) for alkali halides. On making these substitutions for exothermicity and endothermicity in Eq. [10], we obtain:

$$U = \Delta H_s + I_m + \tfrac{1}{2}\Delta H_D + \Delta H^\circ_f - A_x \quad [11]$$

Substituting Eq. [11] in Eq. [7],

$$E_g = 2\Delta H_s + 2I_m + \Delta H_D + 2\Delta H^\circ_f - 2A_x - 2R - I_m + A_x \quad [12]$$

or

$$E_g = 2\Delta H_s + I_m + \Delta H_D + 2\Delta H^\circ_f - A_x - 2R \quad [13]$$

On making an approximation that I_m is roughly equivalent to A_x in magnitude, one obtains:

$$E_g = 2\Delta H_s + 2\Delta H^\circ_f + \Delta H_D - 2R \quad [14]$$

or

$$E_g = 2(\Delta H_a - R) \quad [15]$$

where ΔH_a is the heat of atomization per *mole*, and for a diatomic molecule formed between two univalent ions (*e.g.* NaCl) is identical with the heat of atomization per equivalent, which is, of course, the average bond energy (8, 21-23).

When considering a polyatomic compound formed between either univalent or polyvalent ions, Eq. [15] has to be suitably modified. This is owing to the fact that Eq. [6] and [7] refer to the transfer of *one* valence electron only, *i.e.* from Na to Cl; in order to maintain the validitiy of Eq. [12], U in Eq. [11] must also be taken as per valence electron, *i.e.* as per equivalent. As a result, the ΔH_a term in Eq. [15] must be changed from ΔH_a/mole to ΔH_a/eq. for a polyatomic compound. As mentioned earlier, ΔH_a/eq. is, of course, the bond energy E_s. Hence,

$$E_g = 2(E_s - R) \quad [16]$$

For a closely related series of compounds, *e.g.* alkali halides, R may roughly be treated as a constant. Hence, Eq. [15] may be written as:

$$E_g = 2(E_s - b) \quad [17]$$

where "b" is a constant. This Eq. [17] is identical with Manca's equation, *i.e.* Eq. 2 in this paper.

The approximation made in the derivation of Eq. [17] may now be considered. If I_m is not roughly equivalent to A_x, then R in Eq. [16] may be transformed into R' where,

$$R' = R + \tfrac{1}{2}I_m - \tfrac{1}{2}A_x \quad [18]$$

For structurally related compounds, R' may again be assumed as, *roughly*, a constant. For example, for several alkali halides, values of R' lie close to 2.5 ± 0.5 eV. It is obvious, of course, that Eq. [18] must be appropriately modified for compounds involving positive electron affinities.

On the basis of the foregoing analysis, the possible theoretical basis of Fig. 2 may now be explored. Rewriting Eq. [14], by substituting Eq. [18] into it, one obtains:

$$E_g = (2\Delta H_s + \Delta H_D - 2R') + 2\Delta H^\circ_f \quad [19]$$

For several compounds, it turns out, fortuitously, that quantities in the parentheses of Eq. [19] either roughly cancel each other out or assume rather small net value (8). Hence, Eq. [19] may be approximated as:

$$E_g \simeq 2\Delta H^\circ_f \quad [20]$$

As mentioned in the foregoing discussion, in all such discussions the quantities must be properly normalized (7, 8, 21-23), *i.e.* taken as per equivalent which for a diatomic substance formed between uni-univalent ions is, of course, the same thing as per mole. Hence, Eq. [20] may be written as:

$$E_g \simeq 2\Delta H_e \quad [21]$$

Equation [21] is identical with Eq. [1], and it constitutes the possible theoretical basis of Fig. 2.

Limitations of the foregoing theoretical analysis.— It is clear that the foregoing analysis is invalid for elementary semiconductors since lattice energy for these substances has no significance. Also, molecular semiconductors like anthracene are not covered by the foregoing discussions. Further, theoretical foundations of Fig. 2 and 6 for the case of predominantly covalent binary compounds like Sb_2S_3 are not completely clear.

For the case of some covalent compounds, however, *e.g.* those included in Fig. 6, it is possible that the increase in cohesive energy due to homopolar binding approximately cancels out the decrease in lattice energy that may result from partial ionicity of the compound (8, 26). In these cases, experimental lattice energy values, U, will be nearly equivalent to the $(M + R)$ values that would have been obtained, had the compound been predominantly ionic. In some fortuitous cases of this type, the entire analysis presented here would still be valid, despite significant covalent bonding.

In some other cases of covalent compounds, the present analysis may be extended by modifying Eq. [17] to give:

$$E_g = 2(E_s - b) \pm \Delta U \quad [22]$$

where ΔU is the difference between the thermochemical and theoretical lattice energies (12) again taken as per equivalent.

It is important to emphasize that it is rather fortuitous that several covalent compounds obey the relationship shown in Fig. 6, despite the fact that no correction for homopolar bonding has been applied to them.

Concluding Remarks

It has been shown in the foregoing discussion that it is possible to obtain by chemical approaches some significant, semiquantitative correlations between band gaps and other properties, *e.g.* heats of formation and bond energies. The important points that have been brought out in this article are as follows:

(A) These correlations (Fig. 2 and 6) need not necessarily be limited to certain restricted classes of compounds.

(B) They yield semiquantitative results and not just qualitative trends.

(C) These correlations also lend themselves to some theoretical analysis.

It is obvious, of course, that these correlations are not very exact yet and would need considerable improvements and more sophisticated theoretical analysis before yielding procedures for accurate prediction of band gaps of materials.

Manuscript submitted Nov. 3, 1969; revised manuscript received Jan. 19, 1970.

Any discussion of this paper will appear in a Discussion Section to be published in the December 1970 JOURNAL.

REFERENCES

1. W. Ruppel, A. Rose, and H. J. Gerritsen, *Helv. Phys. Acta*, **30**, 238 (1957); see also, A. Rose, "Concepts in Photoconductivity and Allied Problems," last chapter, Interscience (1963).
2. H. Gatos and A. Rosenberg, "The Physics and Chemistry of Ceramics," C. Klingsberg, Editor, Gordon and Breach, New York (1963).
3. F. N. Hooge, *Z. Physik. Chem. Neve Folge*, **24**, 275 (1960).

4. P. Manca, *J. Phys. Chem. Solids*, **20**, 268 (1961).
5. F. Bailly and P. Manca, *ibid.*, **27**, 783 (1966).
6. R. H. Bube, "Photoconductivity of Solids," John Wiley & Sons (1966).
7. A. K. Vijh, *J. Phys. Chem. Solids*, **29**, 2233 (1968).
8. A. K. Vijh, *ibid.*, **30**, 1999 (1969); *idem*, *Solid State Commun.*, **7** (9), Vi (1969).
9. S. A. Semenkovich in "Chemical Bonds in Semiconductors and Solids," N. N. Sirota, Editor, Consultants Bureau, New York (1967).
10. J. P. Suchet, "Chemical Physics of Semiconductors," London (1964); see also, J. P. Suchet and F. Bailly, *Ann. Chim. (Paris)*, **10**, 517 (1965).
11. E. F. Gurnee, *J. Chem. Ed.*, **46**, 81 (1969).
12. W. J. Moore, "Seven Solid State," W. A. Benjamin, Inc., New York (1967).
13. Sir Nevill Mott, "The Solid State" in "Materials," W. H. Freeman and Co., San Francisco (1967).
14. L. V. Azaroff, "Introduction to Solids," McGraw-Hill Book Co., New York (1960).
15. L. H. Van Vlack, "Elements of Materials Science," Addison-Wesley Publishing Co., Inc. (1966).
16. A. J. Dekker, "Solid State Physics," Prentice Hall, Inc., Englewood Cliffs, N. J. (1957).
17. E. Mooser and W. B. Pearson, *J. Electron.*, **1**, 629 (1956).
18. C. H. L. Goodman, *J. Phys. Chem. Solids*, **6**, 305 (1958).
19. J. P. Suchet, *ibid.*, **12**, 74 (1959).
20. H. Welker, *Z. Naturforsch.*, **7a**, 744 (1952); **8a**, 248 (1953).
21. R. T. Sanderson, "Chemical Periodicity," Reinhold Publishing Co., New York (1960).
22. L. Pauling, "The Nature of the Chemical Bond," Cornell Press, Ithaca, N. Y. (1960).
23. R. Howald, *J. Chem. Ed.*, **45**, 163 (1968).
24. R. Rossini *et al.*, "Selected Thermodynamic Properties," N.B.S. 500, U.S. Govt. Printing Office, Washington, D.C. (1952).
25. "Handbook of Chemistry and Physics," 47th Ed., The Chemical Rubber Co. (1966).
26. P. Mark, *J. Phys. Chem. Solids*, **29**, 689 (1968).

SECTION NEWS

Columbus Section

A symposium on battery separators was held in Columbus, Ohio, on February 18-19, 1970 under the sponsorship of the Columbus Section of The Electrochemical Society. 19 papers covered separator materials and performance in lead-acid, nickel-cadmium, silver-zinc, and silver-cadmium batteries and rechargeable fuel cells. Approximately 100 scientists and engineers from the United States, Canada, England, and Sweden were in attendance.

The proceedings of the symposium will be published in a softbound book in approximately two months. A limited number of copies are still available at $7.00 each. Orders for copies of the proceedings should be sent to Dr. H. L. Goering, Battelle Memorial Institute, 505 King Avenue, Columbus, Ohio 43201. Checks should be made payable to Columbus Section of The Electrochemical Society.

The program consisted of the following papers:

"General Requirements and Characterization of Secondary Battery Separators,"—J. J. Lander, Air Force Aero Propulsion Laboratory, and E. J. Casey, Defense Research Establishment;

"A New Type of Microporous Polymeric Separator,"—Erik Sundberg, Tudor Sweden, and J. Q. Selsor, Ameraace, Esna Corporation;

"Characterization of Anisotropic Films for Battery Separators,"—Michael J. Lysaght, Amincon Corporation;

"The Selection of Textile Fibers and Fabricating Techniques in Separator Design,"—Phoenix N. Dangel, Kendall, Fiber Products Division;

"Characterization and Performance of Separators for Ni-Cd Aircraft Batteries,"—Louis Belove and Paul Scardaville, Sonotone Corporation;

"QC Procedures and Measurements —Polypropylene Separators for Sealed Ni-Cd Batteries,"—T. E. King, Defense Research Establishment;

"Separators for Heat Sterilizable Ni-Cd Batteries," —R. Lutwack, Jet Propulsion Laboratory;

"Ultrafine Porous Polymer Membranes as Battery Separators,"—J. L. Weininger, General Electric Company;

"Cellulosic Separators for Alkaline Batteries—A Review,"—G. A. Dalin, Yardney Electric Corporation;

"Silver-Zinc Battery Separator Material Development,"—E. V. Kirkland, Monsanto Research Corporation;

"Improved Separator Materials for Alkaline Batteries,"—H. E. Hoyt, Borden, Inc., Chemical Division;

"Preparation and Properties of Separators for Silver-Zinc Cells,"—A. Langer and L. C. Scala, Westinghouse Electric Corporation;

"Preparation and Properties of Grafted Membrane Separators for Silver-Zinc Cells,"—V. D'Agostino, RAI Research Corporation;

"Performance of Organic Membranes and Inorganic Coatings as Separators in Silver-Zinc Cells,"—T. J. Hennigan, Goddard Space Flight Center;

"Charged Stand and Cycle Life Test Results on Separator Systems for Alkaline Cells,"—R. S. Bogner, Jet Propulsion Laboratory;

"QC for Heat Sterilizable Silver-Zinc Separator Materials,"—W. von Hartmann, Jet Propulsion Laboratory;

"Chemical and Physical Analysis of Grafted Membranes for Silver-Zinc Batteries,"—E. F. Cuddihy and J. Moacanin, Jet Propulsion Laboratory;

"Separator Developments for Rechargeable H_2O_2 Fuel Cells,"—M. G. Klein, Electro-Optical Systems, Inc.;

"Recent Advances in Ion Exchange Membranes for Use in Rechargeable Fuel Cells,"—A. P. Fickett, General Electric Company.

Concluding the program was a panel discussion chaired by Arthur Fleischer, with panelists T. J. Hennigan, R. Lutwack, T. E. King, and J. J. Lander.

Detroit Section

The Detroit Section held a meeting on March 19, 1970, at the McGregor Memorial Conference Center, Wayne State University. The guest speaker was Dr. C. V. King, Vice-President of the Society, and also President of American Gas & Chemicals, Inc. Dr. King gave a very interesting and lucid account of methods for determining gas leaks. Most of the methods described were chemical tests, involving the use of color-change tapes or papers, which could be used for rocket and missile fuels and oxidizers, for carbon monoxide, ammonia, hydrazine, unsymmetrical dimethyl hydrazine, hydrogen sulfide, for engine fuels, oils, and hydraulic fluids. A simple bubble test for butane lighters was described which involved immersion in water containing a suitable detergent. Dr. King also described a few electrochemical methods for determining leaks. The presentation was illustrated with several demonstrations.

Prior to the technical part of the meeting Dr. King spent fifteen minutes or so discussing Society affairs. The main topics covered were the transfer of the National Office to Princeton, N. J., the running of National Meetings by the National Office, and the Society's membership and financial standing.

Raymond Thacker
2nd Vice Chairman

naces in the 2000-3000°C range; the use of electric arcs for material synthesis, purification, and crystal growth; and new methods for vapor growth of single crystals of ZnTe, using a "transparent furnace" especially suited for vapor growth of crystals. After a lively period of questions and answers, Dr. Reed demonstrated a model of the transparent furnace. Dr. Carr presented the speaker with a telescoping pocket pointer as a token of the appreciation of the Section for the fine lecture and the meeting was closed with a rising vote of thanks for Dr. Thomas B. Reed.

Dodd S. Carr
Vice-Chairman

North Texas Section

The winter meeting of the North Texas Section was held on January 26, 1970 in the Meadows Building Cafeteria in Dallas.

The speaker was Dr. Charles Tobias of the University of California. Dr. Tobias conducted an informal discussion of several aspects of Electrochemical Society activities such as the new location of the national headquarters. Following this discussion he made a technical presentation on "Electrolysis at High Rates."

Active and transpassive anodic dissolution modes of copper are characterized by different overpotentials and different resulting surface textures. Voltage transients observed during these dissolution processes are related to current densities and electrolyte flow rates. Passivation phenomena and the formation and removal of solid anodic reaction products are likely controlled by mass transport.

David F. Cole
Chairman

Pacific Northwest Section

The Pacific Northwest Section held its third meeting at Andy's Diner, Seattle, Wash., on March 16, 1970. After a social hour and dinner, Robert Glockling, Chairman, introduced David Roe, the guest speaker. Dr. Roe is on the faculty of the Oregon Graduate Center, Portland, Oreg. His illustrated talk was entitled "An Electrochemical and Mass Spectrometric Investigation of Platinum Electrodes."

In spite of their extensive use in electrochemistry, platinum electrodes show some unusual characteristics which eluded thorough explanations. The literature of the past ten years, in particular, is replete with electrochemical investigations of the surface oxidation of platinum and studies of oxidation of organic compounds on "activated" platinum. Deductive development of rigorous, or even consistent molecular models from such information is hampered by incomplete knowledge of, for example, true surface area, "active" surface area, adsorption sites, surface contamination, and the chemical nature of surface oxides.

Further insight in some of these problems has been obtained from combining mass spectrometry with electrochemical measurements. From these results it can be shown how to obtain a clean platinum surface, free of organic adsorbants. Also, anodic oxidation of platinum does not produce an oxide with any of the properties of PtO_2, as noted by decomposition behavior in vacuum. However, exposure of platinum to oxygen and water vapor at 210°C does result in detectable surface oxidation. This oxide can be reduced electrochemically and compared with anodically-formed oxide. Rate and equilibrium measurements of the vapor phase oxidation at 210°C leads to identification of the reaction as requiring one water molecule per atom of oxygen, i.e. $Pt + \frac{1}{2}O_2 + H_2O \rightarrow Pt(OH)_2$.

Sidney Gross
Secretary

1971 Palladium Medal Award, ECS

The tenth Palladium Medal of The Electrochemical Society will be awarded at the Fall Meeting of the Society to be held in Cleveland, Ohio, October 3-8, 1971. The medal was established in 1951 by the Corrosion Division.

The candidate shall be distinguished for his original contributions to theoretical electrochemistry or to fundamental scientific knowledge of corrosion processes. He need not be a member of the Society. There shall be no restrictions or reservations made regarding his citizenship, age, or sex.

To be eligible, the candidate shall agree to receive the award in person at the designated national meeting of the Society. He shall also agree to present a general lecture before the Society, at the above designated national meeting, to be called the Palladium Medal Address. This address will in general describe some area of the candidate's researches, and will be presented at a time and place during the meeting to be specified in each instance by the Board of Directors.

Previous medalists have been: Carl Wagner, Max Planck Institut fur Physikalische Chemie; N. H. Furman, Princeton University; U. R. Evans, Cambridge University; K. F. Bonhoeffer, Max Planck Institut fur Physikalische Chemie (posthumous award); A. N. Frumkin, Electrochemical Institute of the USSR; H. H. Uhlig, Massachusetts Institute of Technology; Norman Hackerman, University of Texas; Paul Delahay, New York University; and Thomas P. Hoar, Cambridge University.

Sections, Divisions, and members of the Society are invited to send suggestions for candidates, accompanied by supporting information, to Mr. Ernest G. Enck, Executive Secretary, The Electrochemical Society, 30 East 42nd St., New York, N. Y. 10017, for forwarding to the Committee Chairman. Deadline for submission of suggestions is August 31, 1971.

BOOK REVIEWS

"Thin Film Technology," by R. W. Berry, P. M. Hall, and M. T. Harris. Published by D. Van Nostrand Co. Inc., Princeton, N. J., 1969. 206 pages; $15.00.

"Thin Film Phenomena," by K. L. Chopra. Published by McGraw-Hill, New York, 1969. 793 pages; $24.50.

Both of the above books are introductions in a way to thin film activities. The former, prepared by the staff of Bell Telephone Laboratories, is perfect for the novice who wishes to engineer a thin film operation. Bare on fundamentals but heavily loaded with specific equations for various topics, it covers the entire gamut, in a surface manner, from the vacuum system itself to generation of the film assembly line. As such it is excellent, but it only covers the thin film capacitors and resistors with its main emphasis on tantalum components. It is, in essence, an engineering manual.

The latter book, by Chopra, could be considered a manual also—but of a different type. Dr. Chopra collects all the phenomena that could occur in thin films, their properties and their experimental aspects, briefly and sparsely covers them and then presents a fantastic amount of references (over 2000). The book is really an encyclopedia of phenomena, techniques and properties. As such it is a surface coverage for someone wishing to enter into thin film research.

Both books serve useful functions. However, I prefer the series on "Physics of Thin Film" published by Academic Press as a more comprehensive starting point.

Julius Klerer
The Cooper Union, New York

Section News 178C
ECS Palladium Award 180C
Book Review 180C
New Members 181C
People 181C
News Items 182C
New Products 183C
Positions Available 184C
Positions Wanted 184C

JOURNAL OF THE ELECTROCHEMICAL SOCIETY

ELECTROCHEMICAL SCIENCE

SEPTEMBER 1970

ES

Growth Processes of the Anodic Crystalline Layer on Potentiostatic Oxidation of Lead in Sulfuric Acid

D. Pavlov and N. Iordanov

Institute of Physical Chemistry, Division of Electrochemical Power Sources, Bulgarian Academy of Sciences, Sofia-13, Bulgaria

ABSTRACT

The dependence of the composition of the anodic layer, the electric capacity, and the current on the quantity of electricity passed on potentiostatic oxidation of lead in sulfuric acid are investigated. Oxidation runs were performed in the lead sulfate, the lead oxide, and the lead dioxide potential regions. It was established that at all oxidation potentials the electrode is passivated by the formation of a dense crystalline layer after passing a given quantity of electricity. Subsequently this layer grows. If the oxidation takes place in the lead oxide region, tetragonal PbO and basic lead sulfate form during the growth of the anodic layer. On oxidation in the lead dioxide region, tetragonal PbO and α-PbO_2 form in the deposit (at -950 mV with respect to the Hg/Hg_2SO_4 electrode). At $+1000$ and $+1100$ mV after the formation of α-PbO_2, $PbSO_4$ is oxidized to β-PbO_2. The change in the composition on oxidation is due to change in ionic conductivity between the $PbSO_4$ crystals. When the current through the anodic layer begins to be transported by O^{2-} at the lead/anodic layer interface, tetragonal PbO is formed. If the oxidation potential exceeds $+950$ mV, α-PbO_2 forms in addition to the tetragonal monoxide. At potentials more positive than $+1000$ mV, the solute Pb^{2+} ions are oxidized to β-PbO_2 at the α-PbO_2/solution interface.

During anodic oxidation of lead in sulfuric acid an insoluble layer is formed whose composition depends both on the potential and the quantity of electricity. In the region lying between the equilibrium potentials of the $Pb/PbSO_4$ and $PbSO_4/PbO_2$ electrodes Lander (1) found tetragonal PbO and explained the formation of this compound in terms of a solid-state reaction between PbO_2 and Pb. Burbank (2) suggested a model of the structure of the anodic layer depending on the oxidation potential. At high oxidation potential Ruetschi and Cahan (3) established the alpha polymorph of PbO_2 and found that $PbSO_4$ is oxidized to β-PbO_2. Ruetschi and Angstadt (4) introduced layers of lead basic sulfates in the model of the anodic deposit. In a previous work (5) we determined the dependence of the composition of the anodic layer on the oxidation potential of the electrode. According to the phases present the potential interval lying between the equilibrium potential of the $Pb/PbSO_4$ electrode -956 mV and $+1400$ mV (with respect to the Hg/Hg_2SO_4 electrode) can be divided into three regions: (*a*) lead sulfate region between -950 and -300 mV. The anodic deposit is constituted by $PbSO_4$ crystals; (*b*) lead oxide region from about -300 to about $+900$ mV. The deposit contains tetragonal PbO and $PbSO_4$ in commensurable amounts as well as minor amounts of basic sulfates of lead; and (*c*) lead dioxide region above approximately $+950$ mV. The anodic layer is built up mainly by the two polymorphs of PbO_2.

Key words: lead sulfate electrochemical formation, lead oxide electrochemical formation, lead dioxide electrochemical formation, lead oxide/lead sulfate layers ionic conductivity, lead oxide/lead sulfate layers x-ray analysis.

In order to elucidate the processes which take place on anodic polarization of the lead electrode in sulfuric acid, it is also necessary to establish the dependence of the composition of the anodic layer on the quantity of electricity passed at constant oxidation potential. This dependence is controlled by the processes which take place on growth of the crystalline anodic layer. This is the purpose of the present paper.

Methods

The following parameters were measured during the potentiostatic oxidation of the lead electrode in sulfuric acid: composition of the anodic layer, current and electric capacity of the electrode. The change in the electrode potential was followed during the first 2 min after interrupting the polarization. The anodic layer was observed by electron microscopy at the end of the measurement.

High-purity 99.9999% lead electrodes with dimensions 16 x 11 x 1 mm were subjected to oxidation in analytical grade electrochemically purified 1*N* H_2SO_4 at 25°C. The oxidation was performed by means of an electronic potentiostat IP-410B Elektroimpex. The electrode potential was measured with respect to a Hg/Hg_2SO_4 electrode by means of a CP-2 voltmeter, Elektroimpex. All values of the electrode potential will be thereafter given with respect to this particular reference electrode. The current and the quantity of electricity were continuously recorded by means of a combined potentiometer-coulometer Goerz R-512.

The determination of the electrode capacity during the potentiostatic oxidation was effected by the method suggested by Pangarov, Christova, Atanasov,

and Kertov (6). To this effect potentiostatic pulses from an IG-3 generator constructed in this Institute were fed to the input of the potentiostat. By means of a C-1-15 oscillograph the quantity of electricity passed either during the potentiostatic pulse or on interrupting the pulse was recorded. The measurement of capacity of the electrode prior to oxidation was performed by applying single rectangular galvanostatic pulses of a duration of 20 μsec. The capacity was determined from the slope of the pulse transient (7). The block diagram of the electric circuit is given in Fig. 1.

The phases present were identified by x-ray diffraction. A Müller Mikro 111 diffraction unit was used. The diffraction patterns were recorded with filtered copper radiation and with the following goniometer settings: goniometer speed 2° 2θ/min, and slits 1°/1°/0.1 mm. The diffractometer traces were measured down to d = 1.60Å. The intensities were measured by the area under the peaks. The x-ray identification of the composition of the anodic layer was performed after 1, 10, and 30 min and 1, 3, 6, 20, 40, and 72 hr potentiostatic oxidation runs. To this effect the electrode was removed from the electrolytic cell, washed, x-rayed, after which the oxidation was continued. This way of determining the composition was adopted after several trial runs which showed that no changes occurred in the phases present during washing and recording of the x-ray diffraction pattern.

After completion of the oxidation at a given potential and after recording the x-ray pattern the electrode was shaded by the platinum-carbon replica technique. The replicas were stripped using a 40% solution of ammonium acetate and observed under the electron microscope Zeiss EF-4.

Experimental Results

Lead sulfate region.—Oxidation runs were performed at −900 and −500 mV. All diffraction lines of the powder pattern of lead sulfate appeared in an interval up to the thirtieth minute. From Fig. 2, it is seen that the intensity increase of the lead sulfate lines is accompanied by a decrease of the lead lines due to the increase in the thickness of the lead sulfate layer.

The capacity and current changes as a function of the quantity of electricity at −500 mV are represented in Fig. 3. Two characteristic stages are observed on the capacity curve. In the first initial stage (ab) the capacity rapidly falls down to 4-5 μF/cm^2. During this stage the electrode is passivated by the anodic layer formed. During the second stage (bc) a slow decrease in capacity and current occurs down to comparatively constant values. At the same time the thickness of the anodic layer increases.

After interrupting the polarization the electrode potential immediately falls down to the Pb/$PbSO_4$ equilibrium potential.

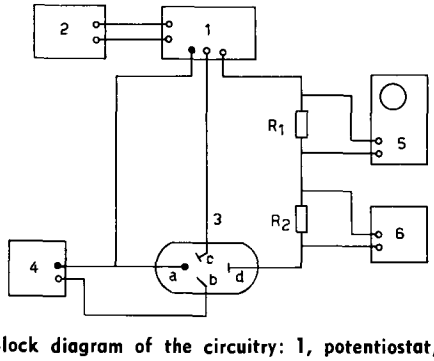

Fig. 1. Block diagram of the circuitry: 1, potentiostat; 2, pulse generator; 3, electrolytic cell (a) working lead electrode, (b) reference Hg/Hg_2SO_4 electrode, (c) reference Pb/$PbSO_4$ electrode, (d) Pt counterelectrode; 4, valve voltmeter; 5, oscillograph; 6, potentiometer-coulometer.

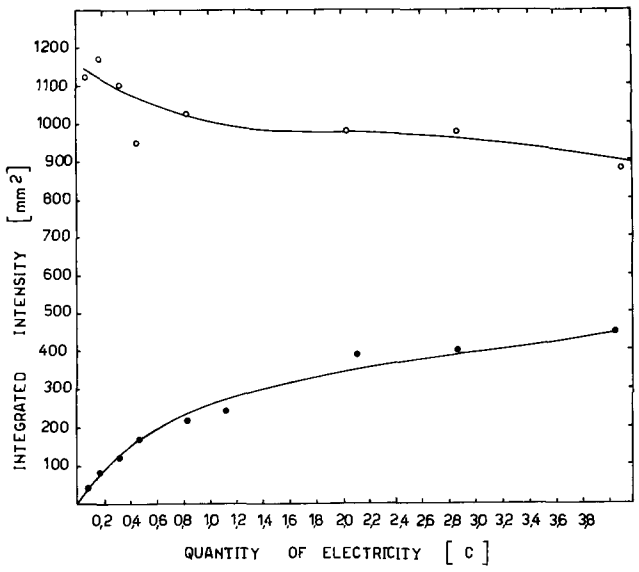

Fig. 2. Change in intensity of diffraction lines of $PbSO_4$ with d = 3.00Å (●) and of Pb with d = 2.85Å (○) as a function of the quantity of electricity after oxidation at −500 mV.

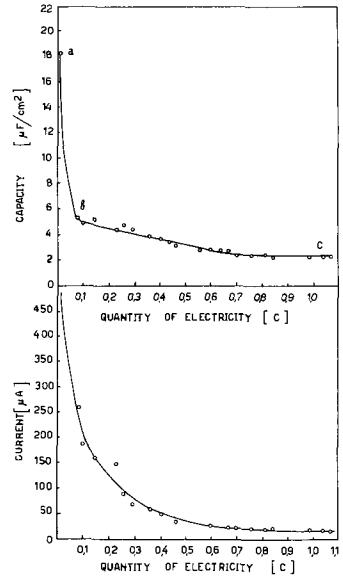

Fig. 3. Change in electrode capacity and current during oxidation at −500 mV.

An electron micrograph of the anodic layer is given in Fig. 4. The deposit is built up by well-defined crystals of different sizes.

Lead oxide region.—Oxidation runs were performed at −200, 0, +300, +700, and +900 mV. The change in the amounts of the phases present in the anodic layer was determined from the changes in the intensities of their diagnostic diffraction lines: for $PbSO_4$, d = 3.00 and 3.33Å (10); for Pb, d = 2.85 and 2.45Å; for tetragonal PbO, d = 3.12Å, 2.80[1] and 1.68Å (5, 11); for PbO·$PbSO_4$, d = 2.95Å (10, 5); for 5PbO·2H_2O, d = 3.08Å (12, 11, 5). The majority of these diagnostic diffraction lines occur in a relatively restricted interval of d-spacings between 2.70 and 3.20Å. Portions of diffraction patterns taken in this interval at different potentials and as a function of the oxidation time (up to 20 hr) are represented in Fig. 5. Only the lower portions of the diffraction peaks are represented since our interest was directed mainly toward the time at which the various compounds ap-

[1] As shown in ref. (5) the intensity of this particular diffraction is enhanced and dominates in the pattern owing to preferred orientation.

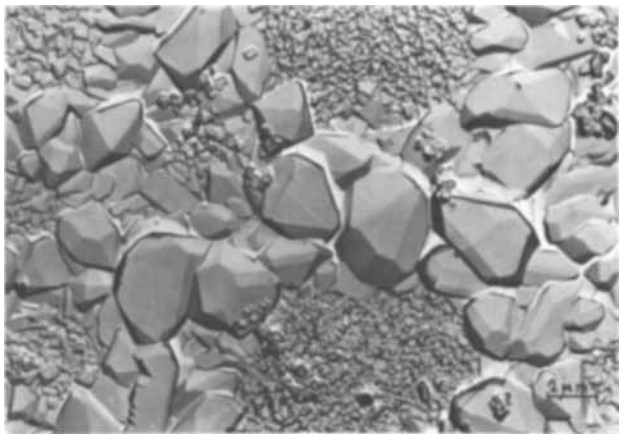

Fig. 4. Electron micrograph of the anodic layer after oxidation at −900 mV. 6500X.

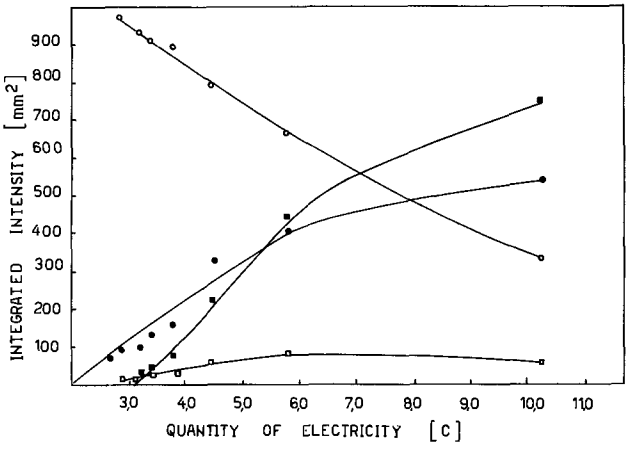

Fig. 6. Change in intensity of diffraction lines of $PbSO_4$ with d = 3.00Å (●), of Pb with d = 2.85Å (○), of tetragonal PbO with d = 2.80Å (■), and of $PbO \cdot PbSO_4$ with d = 2.95Å (□) as a function of the quantity of electricity after oxidation at +300 mV.

pear. Lead sulfate crystals appear during the first minute of the oxidation process. The amount of this compound increases with time. Concomitantly at −200 mV monobasic lead sulfate and tetragonal PbO appear at the sixth hour. The amounts of these compounds in the anodic deposit remain small as compared to that of $PbSO_4$ even after the seventieth hour. Monobasic lead sulfate begins to form at 0 mV after 1-hr oxidation, while after 3 hr tetragonal PbO appears and increases predominantly. At +300 mV monobasic lead sulfate, $5PbO \cdot 2H_2O$ and tetragonal PbO appear at the tenth minute. After a 1-hr polarization the amount of tetragonal PbO rapidly increases. After passing 5-6 coulombs the amounts of $PbSO_4$ and tetragonal PbO become commensurable (Fig. 6). The change in the composition of the anodic layer at +700 and +900 mV (Fig. 5) is similar to that observed at +300 mV, but $PbO \cdot PbSO_4$ appears at the first minute as well as two diffraction lines with interplanar spacings 3.16 and 2.73Å belonging to an unidentified compound. The remaining lines of this compound probably coincide with those of $PbSO_4$. These lines disappear after a 1-hr oxidation. At these potentials the formation of tetragonal PbO becomes the main process after 1 hr. The results obtained show that with the increase of the potential toward the more positive values the time elapsed before the formation of tetragonal PbO

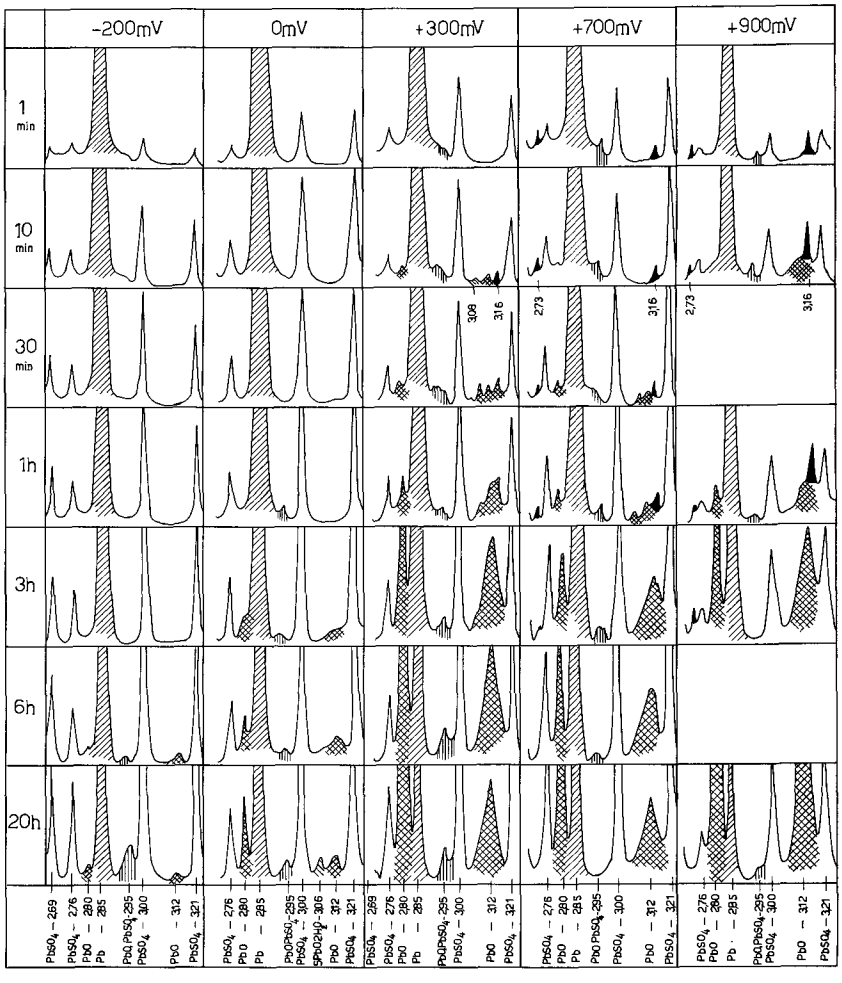

Fig. 5. Portions of diffraction patterns at various potentials after different oxidation times in the lead oxide region.

decreases. The formation of this compound is accompanied or preceded by that of monobasic lead sulfate. Whereas tetragonal PbO begins to predominate the monobasic sulfate remains constant.

From −200 to +900 mV the dependence of the capacity and current on the quantity of electricity passed is similar to that observed at −500 mV but the values are lower. After passing 4-5 coulombs the capacity reaches 0.1-0.3 μF/cm^2.

After interrupting the polarization the electrode potential falls down to the region of the equilibrium potentials of the basic sulfates in 1N H_2SO_4.

Fig. 7 represents an electron micrograph of the anodic layer after oxidation at a potential of +300 mV.

Lead dioxide region.—The change in composition and in capacity was studied at the following potentials: +950, +1000, +1100, +1200, +1300, and +1400 mV. In this potential interval the time for which the electrode acquired the given potential was 3-4 sec.

During the first minutes of oxidation at +950 mV the composition is similar to that found at +700 and +900 mV (Fig. 5). A lead sulfate layer is formed which contains monobasic lead sulfate as well as the unidentified lead compound with diffraction lines d = 3.16 and 2.73Å. After about an hour tetragonal PbO and α-PbO_2 d = 3.12 and 1.84 (13) also appear. The formation of PbO_2 at +950 mV was confirmed by the chemical analysis of the layer. From Fig. 8 it is seen that after passing 2 coulombs three processes occur simultaneously at the electrode. As a result the deposit contains $PbSO_4$, α-PbO_2, and tetragonal PbO. Figure 9 depicts the change in capacity and current changes during the oxidation. After switching on the polarization the electrode capacity falls immediately down to 2.0 μF/cm^2 and remains constant up to 0.25 coulombs of electricity. Subsequently the capacity rapidly increases. The x-ray data indicate that after 2 coulombs a new phase, α-PbO_2, appears. Taking into account the electronic conductivity of α-PbO_2 and the higher sensitivity of the capacity method as compared to x-ray diffraction, it is clear that the increase in capacity is due to the formation of α-PbO_2.

The appearance of the anodic layer obtained on oxidation at +950 mV is shown on Fig. 10. Since lead dioxide is insoluble in ammonium acetate it remains on the replica and is seen on the micrograph as a black deposit.

During the first minutes of the oxidation at 1000-1100 mV the composition is analogous to that found at +950 mV. After 1 coulomb α-PbO_2 and tetragonal PbO form in the anodic layer (Fig. 11). After 18 coulombs β-PbO_2 is detected by diffraction lines d =

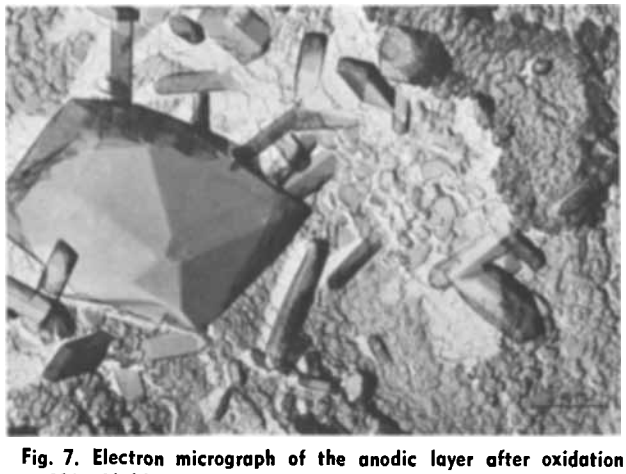

Fig. 7. Electron micrograph of the anodic layer after oxidation at +300 mV. 1000X.

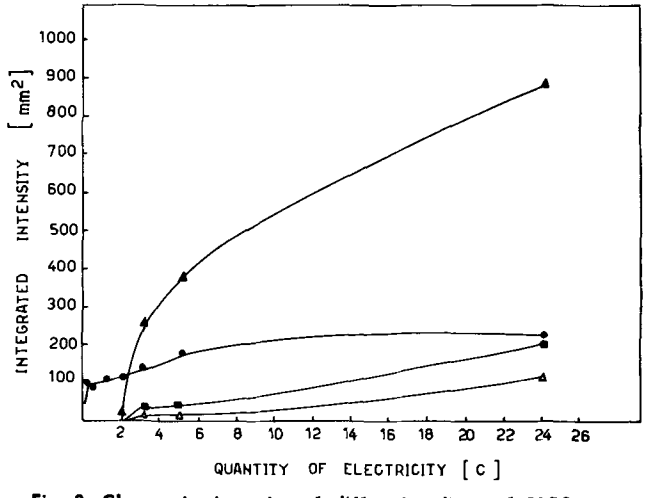

Fig. 8. Change in intensity of diffraction lines of $PbSO_4$ with d = 3.00Å (●); of tetragonal PbO with d = 2.80Å (■); of α-PbO_2 with d = 1.84Å (△), and d = 3.12Å (▲) overlapping with tetragonal lead monoxide as a function of the quantity of electricity after oxidation at +950 mV.

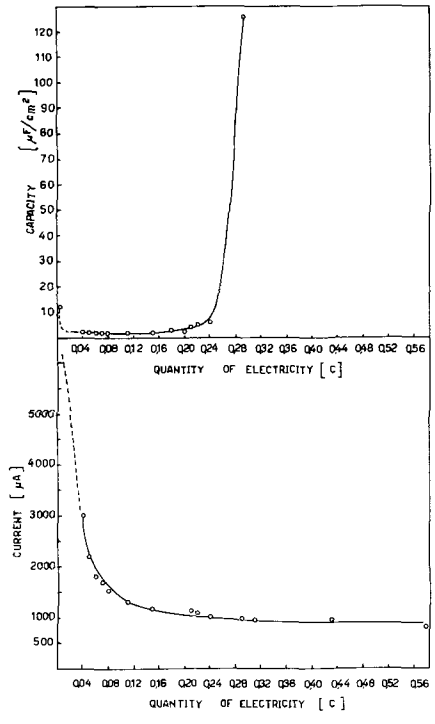

Fig. 9. Change in electrode capacity and current during oxidation at +950 mV.

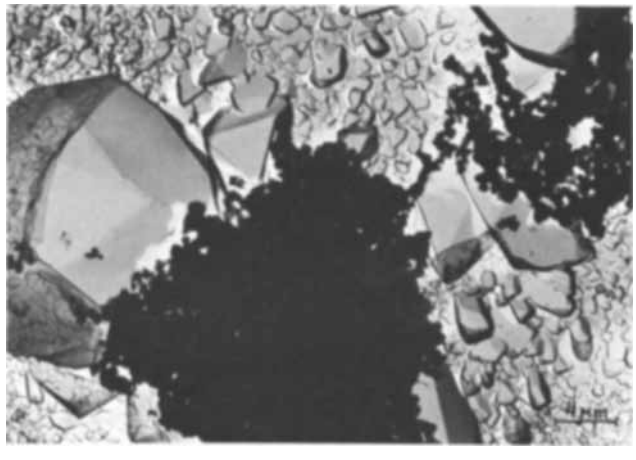

Fig. 10. Electron micrograph of the anodic layer after oxidation at +950 mV. 4000X.

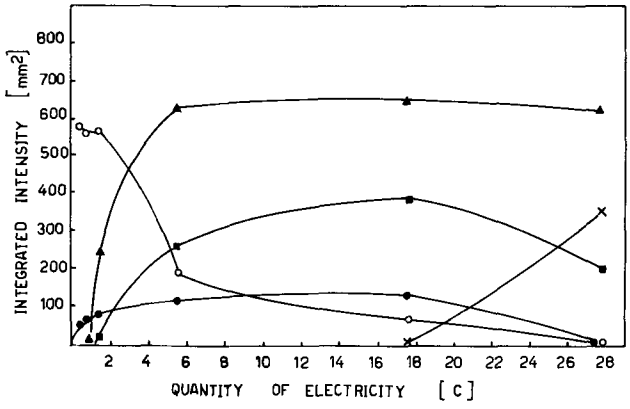

Fig. 11. Change in intensity of diffraction lines of $PbSO_4$ with d = 3.00Å (●); tetragonal PbO with d = 2.80Å (■); of Pb with d = 2.85Å (○); β-PbO_2 with d = 3.50Å (X) and α-PbO_2 and tetragonal PbO with d = 3.12Å (▲) as a function of the quantity of electricity after oxidation at +1000 mV.

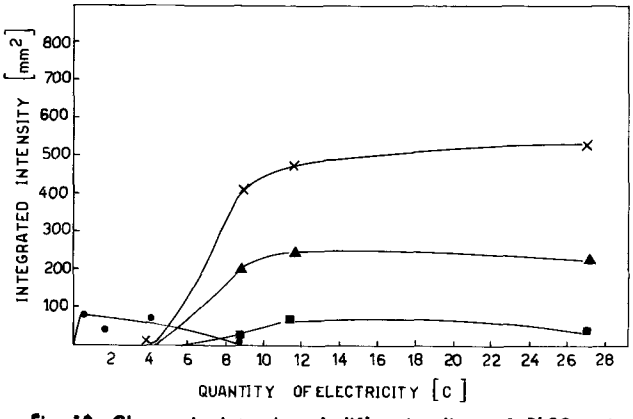

Fig. 12. Change in intensity of diffraction lines of $PbSO_4$ with d = 3.00Å (●); tetragonal PbO with d = 1.68Å (■); β-PbO_2 with d = 3.50Å (X); α-PbO_2 and tetragonal PbO with d = 3.12Å (▲) as a function of the quantity of electricity after oxidation at +1200 mV.

3.50 and 2.78Å, while the line with d = 1.84Å (13) increases. With the progress of the oxidation the amount of β-PbO_2 increases while those of $PbSO_4$ and tetragonal PbO decrease. After 28 coulombs the anodic layer contains α-PbO_2, β-PbO_2, and tetragonal PbO.

Between +1200 and +1400 mV the composition in the first minute of the oxidation is similar to that at +950 mV. After about 4 coulombs α-PbO_2, β-PbO_2, and tetragonal PbO form almost simultaneously (Fig. 12). The sulfate formed at the beginning is oxidized to β-PbO_2 much more rapidly than at +1000 mV. The amount of lead sulfate oxidized is substantially smaller than the β-PbO_2 formed. This means that β-PbO_2 does not form at the expense of $PbSO_4$ only. Tetragonal PbO does not form at +1300 and +1400 mV. At +1300 mV intensive oxygen evolution occurs after 1.6 coulombs when the anodic layer is constituted only by α- and β-PbO_2.

Figure 13 illustrates the capacity and current changes as a function of the quantity of electricity. At higher potentials the time interval elapsed before the increase in capacity becomes shorter. During its increase the capacity reaches values which cannot be accurately determined by the method used. A well-defined maximum is observed on the i/t curve at oxidations above +1200 mV,[2] after the formation of α-PbO_2.

The electron micrograph on Fig. 14 shows the appearance of the lead dioxide at oxidation potential

[2] On repeated oxidation and reduction a maximum in the i/t curves is observed at potentials higher than +1000 mV (17).

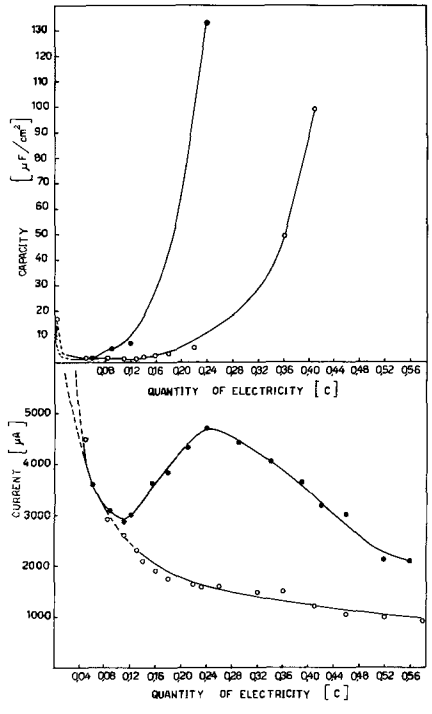

Fig. 13. Change in electrode current and capacity during oxidation at +1000 mV (○) and +1200 mV (●).

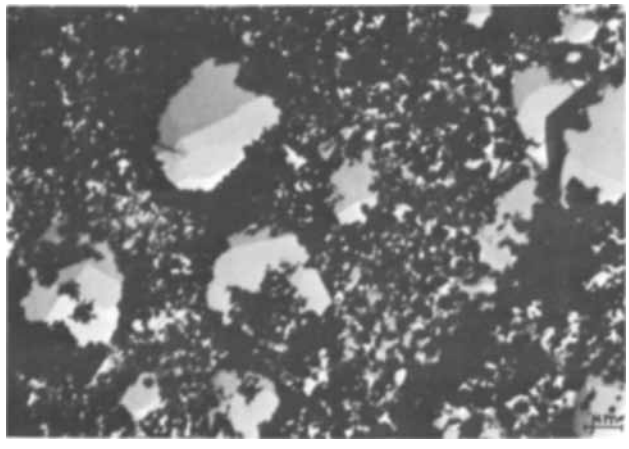

Fig. 14. Electron micrograph of the anodic layer at +1300 mV. 1000X.

+1300 mV. Since the oxidation was interrupted at the beginning of the formation of PbO_2 it is obvious that this compound forms in the intercrystalline spaces left between the $PbSO_4$ crystals.

Discussion of Results

Passivation of the electrode.—On anodic polarization of the electrode at small overvoltages lead is oxidized to Pb^{2+} ions which give, together with the sulfate ions in the solution, $PbSO_4$ crystals. The growth of the lead sulfate crystals hinders the motion of the SO_4^{2-} flow toward the lead surface. The flow of lead ions generated at the lead surface remain uncompensated in the intercrystalline spaces. To remain electroneutral the solution between the crystals is alkalinized and basic sulfates form as a consequence. Thus a continuous dense layer constituted by lead sulfate crystals connected by basic sulfate is formed. This layer passivates the electrode. The time of formation of a dense layer constitutes the passivation stage of the potentiostatic oxidation. These processes were studied in some detail in a previous work (7).

At a given moment of the passivation stage the capacity, C_t, per unit area represents the sum of three

terms: the capacity of the portion of the area, θ_1, occupied by $PbSO_4$ crystals, the capacity of the intercrystalline spaces occupied by basic sulfates, and the capacity of the intercrystalline spaces where the solution is in contact with lead. Therefore the total capacity is given by the equation

$$C_t = \theta_1 \frac{\epsilon_1}{4\pi d_1} + \theta_2 \frac{\epsilon_2}{4\pi d_2} + (1 - \theta_1 - \theta_2) Cd$$

where θ_2 is the portion of the surface occupied by intercrystalline basic sulfates, ϵ_1 and ϵ_2 are the dielectric constants of $PbSO_4$ and the basic sulfates, respectively, and d_1 and d_2 are their effective thicknesses. Cd is the capacity of the double layer at the lead/solution interface. On switching on the polarization the last term in this equation is largest. During oxidation this value rapidly decreases (Fig. 3 ab). It becomes zero when the electrode is covered by a continuous anodic layer. After passivation of the electrode the capacity slowly decreases (Fig. 3 bc). This is brought about by the increase in the effective thickness of the $PbSO_4$ crystals and of the basic sulfate connections between them.

The passivation stage of lead oxidation in sulfuric acid is determined by the quantity of electricity required for building the dense anodic layer. During this period the initial current depends on the overvoltage of the electrode, that is, on the difference between the oxidation potential and the equilibrium potential of the $Pb/PbSO_4$ electrode. The increase in overvoltage gives rise to an increase in the initial current and to a decrease of the duration of the passivation stage. Passivation times and current reach values which exceed the upper limit of the possibilities afforded by modern potentiostats:[3] response time 1-2 μsec at current 10-50 mA.

At overvoltages higher than 1.5V at the first moment the current reaches several hundreds of milliamperes which cannot be accepted by the potentiostat. Thus the passivation stage proceeds at potentials more negative than that fed to the potentiostat. Therefore, x-ray data show that on oxidation above +700 mV (Fig. 8, 11, 12) in the first minute of the run the anodic deposit is constituted by $PbSO_4$ even when the electrode is polarized at potentials lying in the lead dioxide region. After passivation the current decreases and the oxidation takes place at the potential fed to the potentiostat. This potential determines the growth processes of the dense anodic layer.

Growth of the anodic layer.—The object of the present investigation is the study of the changes in the phase composition during the growth of the anodic layer. The growth of the dense anodic layer is determined by its ionic conductivity. It is complicated by the processes of transition through the lead/anodic layer and anodic layer/sulfuric acid interfaces. Owing to the crystallinity of the deposit the ionic conductivity may be achieved in two ways: through the lattice of the lead sulfate crystals and through the basic sulfates connecting them. The lead sulfate crystals are of various sizes. This means that the intensity of the electric field at every point of the anodic layer will be different. The distance between the lead surface and the solution is the smallest in the intercrystalline spaces where the intensity of the electric field is therefore largest. Owing to the very complex conditions of formation of the basic sulfates the latter have probably imperfect structures. These features of the anodic layer require that the motion of the ions take place only through the intercrystalline spaces. This is confirmed by the electron micrograph taken by Grauer, Wehr, and Engel (15) of a lead surface after oxidation in concentrated sulfuric acid and at high temperature. It is seen there that the dissolution of lead occurs at the boundary of the lead sulfate crystals.

[3] This type of potentiostats was used in (14, 4) as well as in the present work.

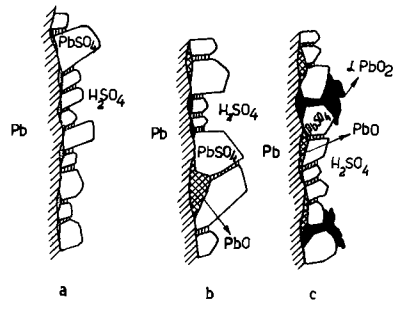

Fig. 15. Model of the anodic layer *(a)* in the lead sulfate region, *(b)* in the lead monoxide region, *(c)* in the lead dioxide region (+950 mV).

The ions which can move upon oxidation up to +900 mV are Pb^{2+} and Pb^{2-}.[4] These ions have equal charges and the same Goldschmidt radii of 1.32Å. The SO_4^{2-} ions have a radius of 2.30Å, *i.e.*, they are very large and do not participate in the current transport through the layer.

Pb^{2+} ions are formed at the lead/anodic layer interface. Under the action of the electric field they reach the second interface and return to the solution. Since the solution is saturated with respect to $PbSO_4$ the Pb^{2+} ions diffuse to the growth front of some of the lead sulfate crystals and are incorporated in it. The ionic current is very small. Therefore the supersaturation of the solution at the surface of the lead crystals is small and the latter have very well-defined faces (Fig. 4 and 7). Owing to these processes of transport of Pb^{2+} through the anodic layer, microvoids are formed between the lead sulfate crystals and the lead surface (Fig. 15a). This gives rise to mechanical stresses in the anodic layer. Under their action some of the lead sulfate crystals are displaced. Sulfuric acid permeates through them and thus reaches the lead surface. Intensive dissolution begins and lead sulfate forms. During growth the lead sulfate crystals come once more closer to one another and the access of the acid to the metal is interrupted. Short abrupt rises in current were observed in the lead sulfate potential region.

The direction of the motion of the O^{2-} ions in the anodic layer is inverse to that of Pb^{2+}. The oxygen ions pass from the solution into intercrystalline spaces. Under the action of the field the O^{2-} ions reach the lead surface. The last stage is related either with the transition of Pb^{2+} which form PbO with the O^{2-} ions or with the inclusion of O^{2-} in the lattice of lead where PbO is also formed. Bode and Voss (16) stressed the close similarities in the structures of lead, tetragonal PbO, and α-PbO_2. The O^{2-} may travel the way indicated in the presence of a corresponding potential drop at the two interfaces and in the layer. Such a drop is created if the electrode has a potential more positive than the given value. This determines the limit between the lead oxide and lead sulfate potential regions. The x-ray diffraction patterns of the anodic layer showed that finely crystalline tetragonal PbO forms above −200 mV.

From Fig. 5 it is seen that the formation of tetragonal PbO becomes the main process after passing a certain quantity of electricity. The detection limit by x-ray diffraction is about a few per cent. Therefore this method is unable to reveal the actual processes taking place at the beginning of the oxidation. Between −200 and +900 mV there is probably at the beginning of the oxidation an ionic current due to the oxygen ions. Therefore the transference number of the Pb^{2+} ions is smaller than unity. During a given time interval this oxygen component of the ionic current brings changes in the structure and composition of the

[4] The solute OH^- ions at the anodic layer/solution interface evolve H^+.

basic sulfates between the $PbSO_4$ crystals. In addition, lead oxide compounds are formed at the metal/anodic layer interface. This change in the nature of the interface and in the structure of the basic sulfates leads to changes in the ionic conductivity. As a result the transference number of O^{2-} increases and that of Pb^{2+} decreases. The formation of tetragonal lead monoxide becomes the main process (Fig. 5 and 6). The appearance and growth of tetragonal PbO underneath the $PbSO_4$ crystals creates internal stresses in the crystalline anodic layer. Under their effect some of the lead sulfate crystals are displaced with respect to one another. The distance between them increases. This makes it possible for the sulfuric acid to intrude between these crystals. The pH decreases. Monobasic lead sulfate and tetragonal PbO are dissolved. The solution becomes supersaturated with respect to Pb^{2+} and SO_4^{2-}. This leads to the further growth of the $PbSO_4$ crystals. The distance between them once again decreases down to sizes which block the flow of sulfuric acid between the crystals. The dissolution of tetragonal PbO stops. Thus the $PbSO_4$ crystalline layer protects the lead monoxide layer from the acid. A two-layer anodic deposit is formed (Fig. 15 b).

As already mentioned, on oxidation at potentials lying in the lead dioxide region first a layer made up of normal and basic lead sulfates is formed owing to the limitations of the potentiostat. Subsequently these compounds as well as the lead are oxidized to lead dioxide (Fig. 11 and 12). In addition another electrochemical reaction takes place, namely oxidation of the OH^- ions of the solution to O_2. This substantially complicates the mechanism of the processes occurring at the electrode and hampers their study.

There are two polymorphs of PbO_2: orthorhombic (α) which is formed on electrolysis from neutral and alkaline solutions and tetragonal (β) obtained in acid solutions. Both polymorphs are electronic conductors.

Tetragonal PbO and α-PbO_2 are simultaneously formed in the anodic layer at +950 mV after a given oxidation time (Fig. 8). This process takes place at given locations of the lead/anodic layer interface (Fig. 10). Since this interface is isolated from the acid the α-polymorph of lead dioxide is formed. The new phases create internal stresses in the anodic deposit which disturb the overlying lead sulfate crystals. Since α-PbO_2 is insoluble in sulfuric acid a new durable interface occurs (Fig. 15c, 10). The total capacity C_t in this case is determined from the expression

$$C_t = C_1 + C_2 + S_t C_{d^1}$$

where C_1 is the capacity of the $PbSO_4$ crystals, C_2 is the capacity of the intercrystalline spaces occupied lead monoxide and basic sulfates, and S_t is the area of the α-PbO_2/H_2SO_4 interface which is in electronic contact with Pb. C_{d^1} is the capacity of the electrical double layer of this surface.

When α-PbO_2 comes into contact with the sulfuric acid the third term of the equation acquires its largest value and becomes capacity-determining. With the proceeding of the oxidation S_t and the total capacity increase (Fig. 9). From the same figure it is easily seen that the current is small and does not change as a result of the formation of alpha lead dioxide. This means that only ionic current passes through the anodic layer as is the case in the lead oxide region.

At potentials more positive than 1000 mV oxidation of Pb^{2+} to Pb^{4+} takes place at the α-PbO_2/electrolyte interface. Since the oxidation is performed in acid medium the β-polymorph of PbO_2 appears (Fig. 11). This process introduces an electronic component of the current which passes through the α-PbO_2 of the anodic layer. With the increase in potential the formation of β-PbO_2 is accelerated (Fig. 12).

Figure 12 shows that the amount of β-PbO_2 is substantially larger than that of the oxidized $PbSO_4$ and tetragonal PbO. This leads to the assumption that prior to the beginning of the oxygen evolution process an ionic current of Pb^{4+} passes through the anodic layer which gives rise to β-PbO_2 at the solution interface. Pb^{2+} ions do not form at these strong high positive potentials. At more positive potentials the ionic Pb^{4+} component of the current is larger while the O^{2-} current, the amount of α-PbO_2, is smaller (Fig 11, 12). An intensive oxygen evolution process begins at potentials more positive than +1200 mV after the formation of the lead dioxide layer. The potential gradient in the layer strongly decreases and tends to zero. Ionic current flows only by diffusion through the layer. The oxygen evolution processes as well as the oxidation of lead through a PbO_2 layer (steady-state corrosion of lead) will be dealt with in future work.

Acknowledgments

Thanks are due to M. Lekova. C. N. Poulieff, I. Tomov, V. Kertov, G. Taleva, and M. Marinov for their active assistance in the preparation of this work.

Manuscript submitted Feb. 17, 1970; revised manuscript received *ca.* May 6, 1970.

Any discussion of this paper will appear in a Discussion Section to be published in the June 1971 JOURNAL.

REFERENCES

1. J. J. Lander, *This Journal*, **98**, 213 (1951); **103**, 1 (1956).
2. J. Burbank, *ibid.*, **106**, 369 (1959).
3. P. Rüetschi and B. Cahan, *ibid.*, **104**, 406 (1957).
4. P. Rüetschi and R. Angstadt, *ibid.*, **111**, 1323 (1964).
5. D. Pavlov, C. N. Poulieff, E. Klaja, and N. Iordanov, *ibid.*, **116**, 316 (1969).
6. N. Pangarov. I. Christova, M. Atanasov, and V. Kertov, *Electrochim. Acta*, **12**, 717 (1967).
7. D. Pavlov and R. Popova, *ibid.*, In press.
8. B. Kabanov and D. Leikis, *Z. Elektrochem.*, **62**, 660 (1958).
9. D. Pavlov, *Electrochim. Acta*, **13**, 2051 (1968).
10. J. D. Esdaile, Ph.D. Thesis, University of Adelaide (1963).
11. ASTM X-Ray Powder Data File, 5-0561, 5-0570.
12. G. Todd and E. Parry, *Nature*, **202**, 386 (1964).
13. N. E. Bagshaw, R. L. Clarke, and B. Halliwell, *J. Appl. Chem.*, **16**, 180 (1966).
14. M. Fleischmann and H. R. Thirsk, *Trans. Faraday Soc.*, **51**, 71 (1955).
15. R. Grauer, P. Wehr, and H. J. Engell, *Werkstoffe Korrosion*, **20**, 94 (1969).
16. H. Bode and E. Voss, *Ber. Bunsengesellschaft*, **60**, 1053 (1956).
17. D. Pavlov, *ibid.*, **71**, 398 (1967).

Anionic Inhibition in Electroless Plating

N. Feldstein,* and P. R. Amodio

RCA Laboratories, Princeton, New Jersey 08540

ABSTRACT

The incorporation of a specific class of oxy-anions in electroless plating baths reveals that above a certain critical concentration limit, a drop in the plating rate takes place. The critical concentration for a specific anion is primarily proportional to those parameters which affect the bath's reactivity. Adsorption of the anions at the electrode-solution interface along with a chemical interaction between the adsorbed layer and the reducing agent is proposed to account for the inhibition effect.

The phenomenon of electroless plating of metals may be best defined as an autocatalytic chemical reduction taking place at heterogenous interfaces. Due to its catalytic and heterogenous character, it is well documented that trace additives may alter the plating process, either to accelerate or decrease the plating rate. Typically, it has been reported (1) that heavy metal ions, such as Pb^{++}, Cd^{++}, and others, as well as sulfur-containing compounds, tend to poison this autocatalytic process. With respect to anionic poisoning, it has been reported that thiocyanate (CNS^-) and cyanide (CN^-) in trace quantity exhibit an inhibiting effect. It has been observed in our laboratory that the presence of nitrate and other oxy-anions may also inhibit electroless plating. The effect was reversible; *i.e.*, samples which did not plate in a nitrate-containing bath would begin plating immediately when immersed in a bath from which nitrate was absent.

This investigation was undertaken to develop a model to account for the inhibition effect and also to test the proposed model against currently accepted theories of electroless plating.

Experimental Procedures

Chemicals.—All chemicals used in preparing the plating solutions with or without the additives were reagent grade. The water used was deionized and then distilled.

Rate.—For comparison of the relative effect(s) of the various anions, standard 2 x 2 in. alumina substrates (American Lava Corporation No. 614 plain) having a geometrical surface area of 52 cm^2 were used. These substrates had a 40 μin. surface roughness. Volume of solutions was held at 200 cc unless otherwise stated. Electroless plating on these substrates was carried out following a tin-palladium sensitization and activation sequence and the weight gain during plating was recorded. No agitation was provided during the plating.

The plating time in all cases was chosen as 10.0 min unless otherwise stated and the temperature was maintained at 25.0° ± 0.1°C. Due to the visible nonuniformities of plating (especially under inhibited conditions) as well as slight variations in induction time, the results are presented as the weight gain per standard area (52 cm^2) for a constant plating time of 10 min. For most of our work, a room temperature electroless Ni-P (2) bath having the following composition was employed: $NiSO_4$, 0.095M; NaH_2PO_2, 0.24M; $Na_4P_2O_7$, 0.11M; and NH_4OH (2.64M), 70 cc/liter. Some of the unique characteristics of this plating bath include: (*I*) The plating rate is strongly dependent on the ammonia content, rising rapidly at first and then falling slowly as the ammonia content increases further. (*II*) Over the *p*H range 9.0-11.5, the plating rate is independent of *p*H, provided the ammonia content is constant. (*III*) For the composition given above, the plating rate is dependent on the hypophosphite ion concentration but independent of the nickel ion concentration.

The inhibition effect for the bath was first checked as a function of the bath composition: *i.e.*, hypophosphite concentration, ammonia content, and *p*H. The *p*H was varied by either changing the ammonia content or maintaining the ammonia content fixed and adding alkali hydroxides.

In monitoring the hydrogen evolved, hydrogen was collected via a simple displacement apparatus. Prior to each run, the plating solution (approximately 500 cc) was saturated with hydrogen. The 2 x 2 in. ceramic substrates mentioned above were used for this work.

Potential measurements.—Potential measurements were carried out using a recording potentiometer. All steady-state potentials (mixed potentials) were obtained using freshly deposited nickel electrodes against SCE at 25°C. Potential measurements were obtained as the concentration of a specific anion varied.

The nitrate activity for different initial concentration levels (10^{-2}-10^{-1}M) was monitored as function of time using a nitrate specific ion electrode (product of Orion Research Model 92-107).

Results and Discussion

Figure 1 shows the over-all inhibition effect associated with each of the oxy-anions. From the results, it can be seen that these anions show inhibition at different concentration levels, leading to the following sequence

Group I: AsO_2^{-1}, IO_3^{-1}, NO_2^{-1}, BrO_3^{-1}, and NO_3^{-1}

The order assigned in group I corresponds to the increasing bulk concentrations required to give inhibition. With the oxy-anions of group II, no inhibiting effects were noted employing concentrations up to 1M.

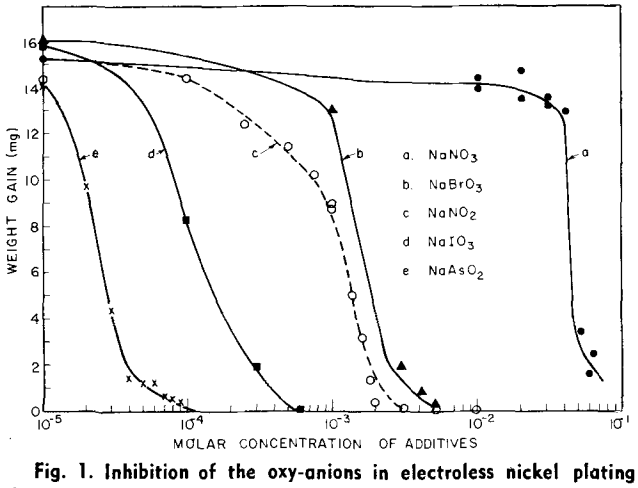

Fig. 1. Inhibition of the oxy-anions in electroless nickel plating bath.

* Electrochemical Society Active Member.

Group II: SO_4^{-2}, HPO_3^{-2}, CHO^{-1}, ClO_3^{-1}, ClO_4^{-1}, AsO_4^{-3}, PO_4^{-3}, CO_3^{-2}, and others

All of the oxy-anions of group I with the exception of the nitrate may be classified as "soft" bases (3), while members of group II are all "hard" bases. Soft bases have donor atoms which are generally easily polarized and oxidized, and are of low electronegativity. Nitrate, the exception, must be present in high concentration in order to yield the inhibiting effect. According to Pearson metal atoms and bulk metals may be classified as soft acids. From the general rule (3) of acid-base interaction, soft pairs have the greatest tendency to interact. On this basis it might be anticipated that soft bases interact with the metallic substrate in an adsorption-type reaction and as a consequence would affect the catalytic nature of the surface. It is interesting to note that the order of effectiveness among the oxy-anions (group I) follows their order of basicity (or degree of softness).

Since the nitrate anion causes the inhibiting effect at a fairly high concentration (10^{-2}-10^{-1}M), its activity for various initial concentrations was monitored as function of time employing a suitable specific ion electrode. This examination was carried out over an interval of several hours with suitable substrates in the plating bath. No change in the nitrate activity was observed. Hence a competing chemical or electrochemical reduction that consumes the nitrate, hindering the main electroless plating process, can be ruled out. Thus the nitrate anion must cause the inhibition through an interfacial adsorption mechanism, even though the interaction is not strong.

With inhibited solutions, if I^-, Br^-, or AsO_4^-, are added, the inhibiting effect can be reversed with I^- addition, but only where NO_3^- or IO_3^- are the inhibitors, provided a thin nickel layer is present on the surface. In other words, the plating rate of a solution inhibited with either nitrate or iodate can be raised greatly if I^- is added to the bath. Typically, it was found that solutions having 8 x 10^{-4}M IO_3^- (Fig. 1d) required at least 6.5 x 10^{-4}M I^- in order to completely nullify the inhibition effect. For inhibited solutions containing the nitrate anion (Fig. 1a), qualitatively it was demonstrated that addition of I^- in a 1:1 molar ratio to the nitrate, caused a reversal of the inhibition effect. Neither Br^- nor AsO_4^- have such an influence on the inhibition.

The dependency of the inhibiting effect on the bath reactivity revealed that the critical concentration required to yield the abrupt inhibition, with the nitrate or the iodate anion, is displaced toward higher concentrations as the bath reactivity is increased. The bath reactivity can be increased by increasing the temperature, the hypophosphite concentration, or the ratio of ammonia to pyrophosphate concentration. To be specific, plating compositions having a hypophosphite content of 0.095, 0.24, and 0.28M required a nitrate concentration of about 2.2 x 10^{-2}, 4.3 x 10^{-2}, and 4.7 x 10^{-2}M, respectively, to yield the onset of inhibition. Similarly, by altering the temperature from 25°, 30°, and 35°C, the nitrate concentration required to yield the inhibition was about 4.3 x 10^{-2}, 5.0 x 10^{-2}, and 7.5 x 10^{-2}M, respectively. No dependency on pH was noted; this is consistent with the kinetic characteristic of the bath, further ruling out any possible competing redox reaction in which the oxy-anions participate, since these reactions are known to be pH sensitive.

Examination of the steady-state potential (mixed potential) as the concentration of the inhibiting ions is increased shows that an abrupt drop occurs at a characteristic concentration. Typical potential variations for different initial nitrate concentrations are shown in Fig. 2. From this figure the potential for the inhibited region is about −570 mV *vs.* SCE. Furthermore, a plating bath without hypophosphite yielded a steady-state potential of about −580 mV *vs.* SCE.

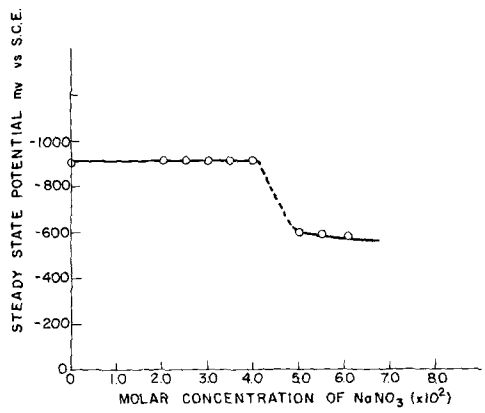

Fig. 2. Steady-state potential vs. nitrate concentration

Examination of the other anions, AsO_2^-, IO_3^-, NO_2^-, and BrO_3^- in their respective inhibition regions (Fig. 1), showed that the steady-state potential at 25°C was in the range of −550 to −600 mV *vs.* SCE. Hence, it can be stated that the addition of nitrate and other inhibiting anions tends to mask the presence of hypophosphite at the electrode solution interface.

In an attempt to characterize the observed phenomena, the data of Fig. 1 was defined as follows

$$\theta = \frac{w_o - w}{w_o}$$

where w_o = weight gain without inhibitor, w = weight gain with added inhibitor, and θ = fraction of inhibition. Figure 3 shows the manner in which θ varies with the concentration of typical additives. Analysis of thiourea inhibition is provided in Fig. 3 for comparison. Since it is reasonable to anticipate that the degree of inhibition is proportional to the fraction of surface sites occupied, Fig. 3 may be classified as an adsorption isotherm. Specifically, the manner in which θ varies with concentration of inhibitors seems to follow the behavior associated with the Frumkin type isotherm (4). Apparently there is an associative enhancement mechanism which accounts for the sudden rapid increase in inhibition taking place over a small concentration change.

The data of Fig. 1 and 3 demonstrate the manner in which the over-all weight gain varies with concentration of inhibiting anions in the bath. Figure 4 shows how each of the main products of the deposition reaction (Ni and H_2) depends on inhibitor concentration. The relative ratio of Ni/H_2 is fairly constant and, in fact, follows closely a 1:1.1 molar ratio (neglecting the hydrogen trapped in the deposit). In contrast to the nickel-hydrogen ratio, the nickel-phosphorus ratio is a variable. The per cent phosphorus in the deposit increases as the inhibitor concentration is increased, typically from 3% without any additives to about 10% with a nitrate concentra-

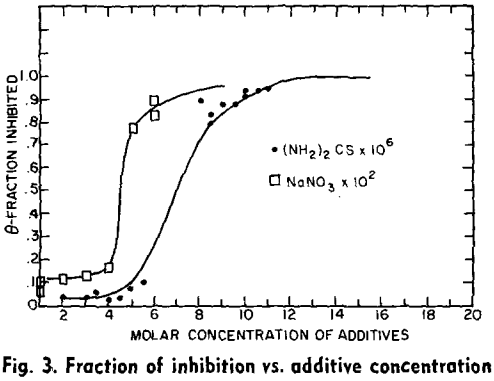

Fig. 3. Fraction of inhibition vs. additive concentration

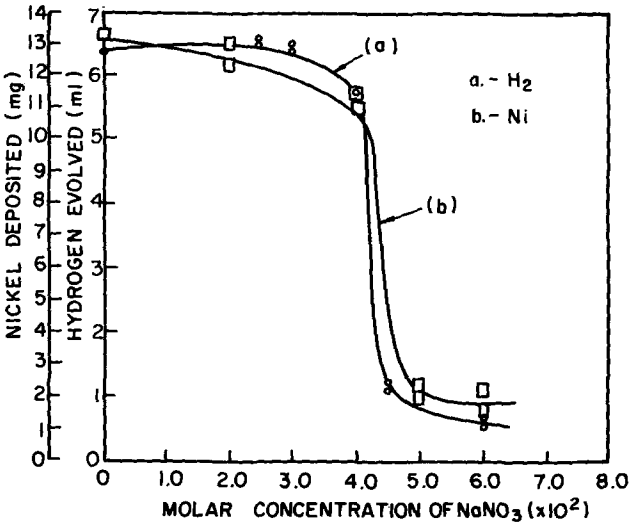

Fig. 4. Nickel and hydrogen deposition vs. nitrate concentration

tion of 5 x 10^{-2}M. Similar behavior was noted when AsO_2^- was employed as the inhibiting anion. For all points along the inhibition curve, the extent of *p*H drop during plating is proportional to the rate of deposition. Since the hydrogen ions come from the anodic reaction of hypophosphite with surface, it can be postulated that the inhibition of the process is related to the anodic reaction(s) leading to the hydride formation rather than to subsequent reactions in which nickel is reduced at the surface. In a recent investigation (5) of Ni/Fe electrodeposition, it was reported that the addition of $NaAsO_2$ up to 0.5 g/l resulted in no effect on the rate of deposition or alloy composition. This result reinforces the belief that the AsO_2^- anion does not interfere with the cathodic process (Fig. 5, reactions 2 through 5) and hence the inhibiting effect must be attributed to interference in the anodic reaction(s).

These observations, while at first sight are puzzling, seem to be consistent with the hydride theory (6) which best accounts for the mechanism of electroless plating of nickel. The hydride theory suggests that the hydrogen evolved is primarily due to the nickel reduction rather than a distinct electrochemical-type reaction. However, the formation of phosphorus in the deposit is best accounted for by separate electrochemical reduction. Since there are two apparent electrochemical redox reactions, *i.e.*, the nickel and phosphorus formation, it is not surprising that each can be altered, but not in the same manner, due to changes in the electrochemical parameters (α, ϕ_2, and η) which affect their reduction kinetics. It is commonly noted in corrosion systems that additives will alter various redox reactions and electroless-plating processes do fall within the general domain of corrosion systems.

In a study of the structure of adsorbed species on metal surfaces (7), application of infrared spectral absorption revealed that nitric oxide when adsorbed

		REACTION TYPE
1.	$H_2PO_2^- + 2OH^- + X^{a} \xrightarrow{k_1} [X\cdots H]^- + HPO_3^= + H_2O$	ELECTROCHEMICAL[b]
2.	$2[X\cdots H]^- + N_i^{++} \xrightarrow{k_2} N_i + 2X\cdots H$	ELECTROCHEMICAL
3.	$2X\cdots H \xrightarrow{k_3} 2X + H_2$	CHEMICAL
4.	$[X\cdots H]^- + H_2O \xrightarrow{k_4} H_2 + OH^- + X$	ELECTROCHEMICAL[b]
5.	$[X\cdots H]^- + H_2PO_2^- \xrightarrow{k_5} 2OH^- + X\cdots H + P$	ELECTROCHEMICAL[b]

a. X DENOTES A CATALYTIC SITE.
b. REACTION APPLIES TO ALKALINE MEDIA.

Fig. 5. Hydride transfer mechanism

on nickel surfaces yields a preferred configuration whereby the bonding to the surface takes place via the nitrogen part of the oxide. Similar observations on the configuration of adsorption were made with respect to carbon monoxide. These two examples, although they constitute a gas-solid interaction, may also be classified as soft-base soft-acid interactions. They suggest that the preferred configuration for adsorption of the oxy-anions is via the atom which is the most polarizable, easiest to oxidize, and of lowest electronegativity.

In view of the results of this investigation and the fundamentals of hard and soft acids and bases, it is proposed that the inhibition effect associated with the oxy-anions of group I is primarily by a surface adsorption mechanism. For all inhibiting anions, the atom bonded to the surface is As, I, N, and Br rather than oxygen. Due to the adsorption of these anions, the number of vacant catalytic sites decreases, reducing the probability for interaction of hypophosphite with the catalytic sites. Furthermore, due to the preferred orientation associated with the adsorbed anions and, specifically, with the oxygens away from the surface, it is anticipated that the hypophosphite in the proximity of the absorbed layer would also have a preferred orientation. A simple coulombic attraction suggests the models shown in Fig. 6. It is suggested that the formation of hydrogen bonding between the adsorbed layer and the hypophosphite probably accounts for the rapid inhibition taking place within a small concentration range of additives. Whether the chemical interaction between the adsorbed layer and hypophosphite is in a molar ratio of 2:1 or 1:1 is not certain and cannot be resolved with the results of this investigation. Although Fig. 6 utilizes the commonly accepted isomer for hypophosphite, the model proposed is believed to be consistent when employing the other isomer (8) of hypophosphite commonly referred to as the "active form."

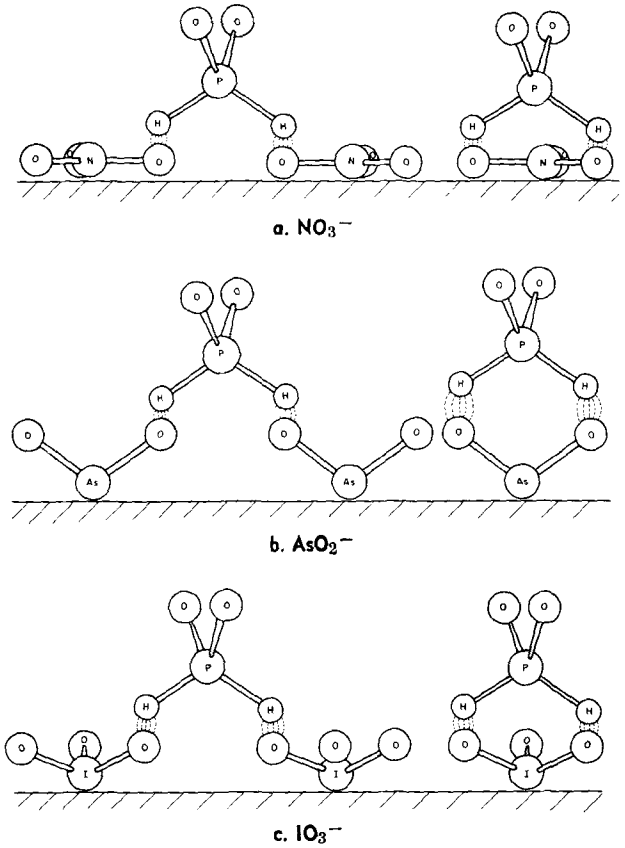

Fig. 6. Proposed model for the interaction of adsorbed oxy-anions with hypophosphite.

Conclusions

The inhibition of the electroless plating of nickel with the incorporation of a specific group of oxy-anions may be best accounted for by an interfacial adsorption mechanism, which reduces the number of catalytic sites for anodic oxidation of hypophosphite. It is further apparent that the abrupt increase of inhibition as the inhibitor concentration increases can be accounted for by any of the following, operating singly or in combination.

I. A chemical interaction between the adsorbed layer and the hypophosphite leading to a strengthening of the P-H bond in hypophosphite.

II. The adsorbed anions alter the structure of the double layer, modifying (or increasing) the degree of surface adsorption and affecting the kinetics of the redox reactions.

III. The number of adjacent pair catalytic sites available for the catalytic dehydrogenation of hypophosphite decreases rapidly once a critical concentration of adsorbed inhibitor is reached.

Although the inhibition effect was examined in detail employing an alkaline room temperature Ni-P bath, additional experiments have shown that the effect also holds for other electroless baths, typically an acidic (9) nickel bath. However, the extent of interaction is not the same. Further study is in progress to determine the applicability of this effect to other electroless plating compositions.

Due to the strong adsorption tendency exhibited by some of the anions, it is anticipated that these anions can be used effectively in the stabilization (10) of electroless plating baths, thereby overcoming major pitfalls associated with some stabilizers (*i.e.*, sulfur-containing compounds), such as their tendency to hydrolyze and the incorporation of sulfur in the deposit.

From the variation of potential as inhibitor concentration increases, and the observed relationship between the onset of inhibition for a given oxy-anion concentration and the hypophosphite concentration, a potentiometric method of analyzing hypophosphite in plating baths is proposed (9). Such a technique would be a rapid and direct method for analyzing the hypophosphite anion concentration in plating baths without interference by the phosphite byproduct, and would closely resemble potentiometric titration methods.

A better understanding of the effects of additives on labile hydrogen (11) in common reducing agents (boraneamine, hypophosphite, formaldehyde, etc.) should lead to a means for accelerating the plating rates of electroless baths.

Acknowledgments

The authors wish to acknowledge the valuable discussions with J. A. Amick and G. Lozier of RCA Laboratories.

Manuscript submitted Dec. 12, 1969; revised manuscript received March 10, 1970. This was Paper 147 presented at the Detroit Meeting of the Society, Oct. 5-9, 1969.

Any discussion of this paper will appear in a Discussion Section to be published in the June 1971 JOURNAL.

REFERENCES

1. A. Brenner and G. Riddell, *J. Res. Nat. Bur. Std.*, **37**, 31 (1946); **39**, 385 (1947).
2. N. Feldstein, *RCA Rev.* **31** [2] (1970).
3. R. G. Pearson, *J. Chem. Education*, **45**, 581 (1968).
4. E. Gileadi, "Electrosorption," p. 12, E. Gileadi, Editor, Plenum Press, New York (1967).
5. W. O. Freitag, G. DiGuillio, and J. S. Mathias, Paper 81, The Electrochem. Soc., Extended Abstract Fall Meeting 1965.
6. R. M. Lukes, *Plating*, **51**, 969 (1964).
7. G. Blyholder and M. C. Allen, *J. Phys. Chem.*, **69**, 3998 (1965).
8. W. A. Jenkins and D. M. Yost, *J. Inorg. Nucl. Chem.*, 297 (1959).
9. N. Feldstein, T. S. Lacsek, and J. A. Amick, *J. Anal. Chem.*, **42**, 945 (1970).
10. E. R. Ramirez, U.S. Pat. 2,884,344.
11. K. A. Holbrook and P. J. Twist, *Plating*, **56**, 523 (1969).

Electrochemical Oxidation of 2,6-Dithiopurine at the Pyrolytic Graphite Electrode

Reaction Products and Mechanism

Glenn Dryhurst

Department of Chemistry, University of Oklahoma, Norman, Oklahoma 73069

ABSTRACT

At the pyrolytic graphite electrode (PGE) 2,6-dithiopurine is oxidized electrochemically by way of three voltammetric processes. The first pH dependent peak observed is due to oxidation of 2,6-dithiopurine partially in an adsorbed state to give a layer of strongly adsorbed product, bis(6-purinyl)-disulfide-2,2′-dithiol. The second pH dependent peak appears to be further oxidation of the adsorbed product of peak I to a further strongly adsorbed product bis(6-purinyl)disulfide-2,2′-disulfide. The third pH dependent peak is very much larger than the other two and is a $12e/12H^+$ oxidation of 2,6-dithiopurine to purine-2,6-disulfonic acid. In ammonia containing supporting electrolyte systems the evidence suggests that the product of the third peak is purine-2,6-disulfonamide.

There have been several recent reports of the electrochemical oxidation of biologically important purines (1-5) at the pyrolytic graphite electrode (PGE). It is of particular significance that there is an apparent similarity between the modes of electrochemical oxidation and various biological (*e.g.*, enzymic) oxidative processes especially in the case of nonsulfur-containing purines. Purines such as 6-thiopurine (3) which contain exocyclic sulfur groups appear to be oxidized electrochemically by mechanisms which involve the

sulfur grouping, while biological oxidation of this compound consists in oxidation within the purine ring system. However, in view of the very incomplete knowledge of the metabolism and enzymic oxidations of the thiopurines it is probable that the electrochemical mechanisms might aid in understanding the complete and detailed electron transfer reactions of such compounds. In view of the fact that of the thiopurines only 6-thiopurine has been investigated in detail (3) several other important purine systems containing one or more exocyclic thiol groups are being investigated in order to ascertain the generality of the previously observed processes. In addition, electrochemical oxidation of 6-thiopurine results in formation of some interesting products which can otherwise be obtained only by quite complex chemical routes, *e.g.*, purine-6-sulfonamide. Because of our interest in developing electrochemical synthetic routes for such potentially biologically active compounds which are chemically prepared with difficulty or which have never otherwise been prepared it is of interest to further investigate these sulfur-containing systems.

Reported here is the electrochemical behavior of 2,6-dithiopurine.[1]

Only a very limited number of chemical and biochemical studies of 2,6-dithiopurine has been reported. Bergmann and co-worker (6) reported oxidation with the purine oxidizing system *Pseudomonas aeroginosa* which actually had a high xanthine oxidase activity. Oxidation proceeded very slowly at C-8 to give 2,6-dithio-8-oxypurine.

The work reported here indicates that 2,6-dithiopurine is oxidized in three steps. The first peak is due to oxidation probably of weakly adsorbed 2,6-dithiopurine to a product that is very strongly adsorbed. The current density and voltammetric properties of this adsorbed product suggest that it is formed by a 1*e* oxidation of 2,6-dithiopurine to give bis(6-purinyl)disulfide-2,2'-dithiol. The second peak is only observed indistinctly but again the voltammetric behavior suggests that the product is again very strongly adsorbed. In view of the observed voltammetry of this adsorbed product it is likely that it is due to further oxidation of the peak I product to bis(6-purinyl)disulfide-2,2'-disulfide. The third peak which is very much larger than the other two results in formation of a third new compound, purine-2,6-disulfonic acid in a $12e/12H^+$ process. In ammonia containing backgrounds the primary product from the third peak appears to be purine-2,6-disulfonamide.

Experimental

Chemicals.—2,6-Dithiopurine (2,6-dimercaptopurine) was obtained from K & K Laboratories. Buffer solutions were prepared from analytical reagent grade chemicals. Argon (Linde) used for deoxygenating purposes was equilibrated with water; no other purification was necessary.

Chemical synthesis of purine-2,6-disulfonic acid.—Half a gram of 2,6-dithiopurine was dissolved in 8.7 ml of 0.5*M* potassium hydroxide solution. Then a warm solution of approximately 1*M* potassium permanganate was added in a dropwise fashion with vigorous stirring until a permanent slight excess was present (approximately 14 ml $KMnO_4$ required). The excess of permanganate was removed by dropwise addition of dilute sodium bisulfite solution.

The precipitated MnO_2 was filtered at a fine sintered glass funnel. The colorless filtrate was adjusted to *p*H 9 with glacial acetic acid. The resulting solution was evaporated to about 15 ml and, after cooling, was adjusted to *p*H 7.9 with 2*M* acetic acid, when very pale yellow crystals appeared. The solution was chilled for 30 min at −5°C after which the precipitate was filtered and washed sequentially with 85% ethanol, ethanol and ether. Recrystallization was accomplished by reprecipitation from *N* potassium hydroxide with 2*M* acetic acid.

Elemental analysis of the product agreed closely with that expected for the dipotassium salt of purine-2,6-disulfonic acid dihydrate. A yield of about 80% was obtained mp > 300°C.

Ultraviolet absorption data: at *p*H 2.3 λ_{max} = 278.5 mμ; at *p*H 6 λ_{max} = 279.5 mμ; at *p*H 12.6 λ_{max} = 286 mμ.

Electrochemical synthesis of purine-2,6-disulfonic acid.—Approximately 0.2g of 2,6-dithiopurine was suspended in about 190 ml of 1*M* HOAc in a conventional electrolysis cell (2) and with vigorous stirring a potential of 1.4V was applied at the large PGE. Complete electrochemical oxidation usually required 3-4 days and was confirmed by the absence of the characteristic u.v. peaks of 2,6-dithiopurine. At the end of the electrolysis some white precipitate was normally present in the solution and is due to 2,6-dihydroxypurine formed by hydrolysis of the 2,6-disulfonic acid. The water and acetic acid were removed by lyophilization. The resulting solid was dissolved in approximately 15 ml of water and 0.5*M* KOH added until the solution was *p*H 9. The resulting solution was evaporated to very low volume when further white precipitate was produced; this 2,6-dihydroxypurine was removed in a fine sintered glass filter and washed with cold water. The resulting pale yellow filtrate was again evaporated to low volume and the *p*H adjusted to 7.9 with dilute acetic acid. On cooling to 5° a pale yellow precipitate appeared which was filtered and washed sequentially with 85% ethanol, ethanol and ether.

Recrystallization was accomplished in the same way as for the chemically synthesized product. A yield of about 20% was obtained.

The spectra and polarography of this compound were identical to the purine-2,6-disulfonic acid synthesized chemically.

Apparatus.—Apparatus for polarography, voltammetry, cyclic voltammetry, coulometry, macroscale electrolysis, spectral data acquisition, and lyophilization have been described in detail elsewhere (2-5).

Results and Discussion

Voltammetry.—At the stationary PGE 2,6-dithiopurine shows three anodic peaks (Fig. 1). The least positive peak (peak I) is observed between *p*H 1-8; a second peak (peak II) appears at more positive potential between about *p*H 4.7-9, although it is always very poorly formed and is at best merely an inflection on the lower rising portion of the largest and most positive peak (peak III) which itself is observed between *p*H 4.7-12.5. The peak potentials (E_p) for all three peaks shift linearly more negative with increasing *p*H (Fig. 2); $E_p = 0.61\text{-}0.057$ *p*H for peak I, $E_p = 1.26\text{-}0.062$ *p*H for peak II, and $E_p = 1.86\text{-}0.10$ *p*H for peak III.

The current density observed for peak I on average was about 1.0 μa mm^{-2} mM^{-1}; peak II was much too indistinct to allow accurate computation of its current. Wave III showed an average current density at *p*H 4.7 where it was studied most closely of about 10-12 μa mm^{-2} mM^{-1}. By comparison to earlier data (1-3) this would tend to support the view that peak I involved about 1-2*e* and peak III > 10*e* per mole of 2,6-dithiopurine.

Cyclic voltammetry.—Cyclic voltammetry of peak I of 2,6-dithiopurine at a stationary PGE showed that having once scanned peak I on the initial anodic sweep at least one well-formed cathodic peak was observed on the reverse scan (Fig. 3). The peak potentials for these two peaks were separated by *ca.* 0.8V. At low

[1] The *Chemical Abstracts* numbering system is employed throughout this paper.

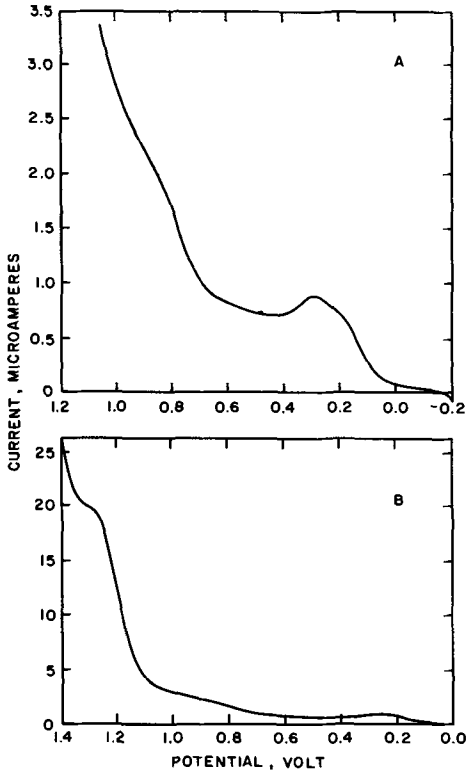

Fig. 1. Voltammograms of *ca.* 0.1 mM 2,6-dithiopurine in acetate buffer *p*H 5.4 at stationary PGE. A, Peaks I and II; B, peaks I, II, and III; scan rate 5 mV sec^{-1}.

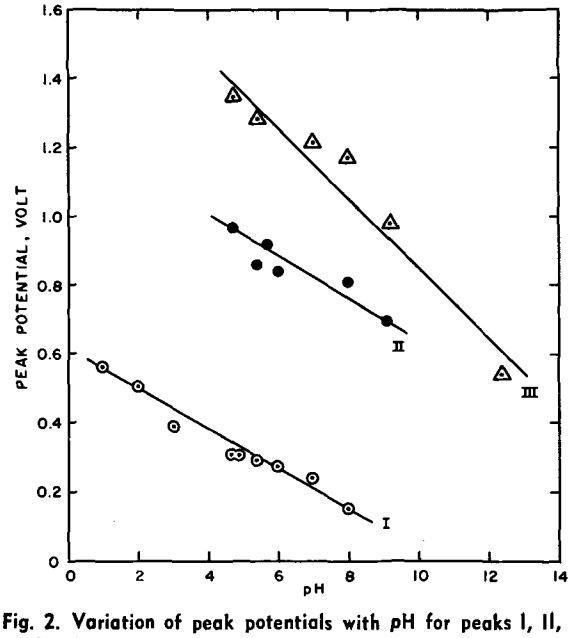

Fig. 2. Variation of peak potentials with *p*H for peaks I, II, and III of 2,6-dithiopurine at stationary PGE.

scan rates and at the higher end of the concentration limit (e.g., at 0.05 m*M*) a small post peak was often observed after the principal cathodic peak. This post peak was clearly observed in acetate buffer *p*H 4.7 (Fig. 3). It was not observed at very low concentrations (*ca.* 0.016 m*M*) or at fast scan rates (*i.e.*, hardly noticeable at scan rates of 50 mV sec^{-1} or above). It was particularly noticeable that the peak current for the main cathodic peak was usually greater than that for the initial anodic peak I and that the cathodic peak was the more symmetrical. Anodic peak I in many

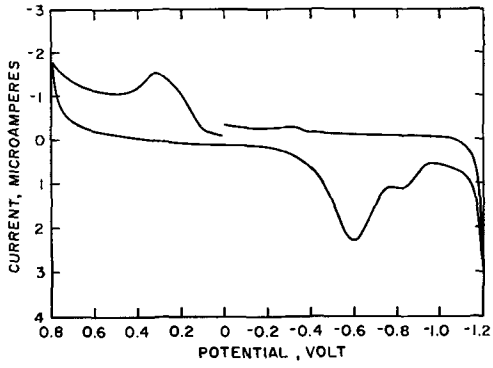

Fig. 3. Cyclic voltammogram of *ca.* 0.1 mM 2,6-dithiopurine in acetate buffer *p*H 4.7. Scan pattern: 0.0V → 0.8V → —1.2V → 0. Scan rate: 5 mV sec^{-1}.

slow scan voltammograms had the appearance of two very close overlapping peaks (*e.g.*, Fig. 1, 3). Such phenomena suggests the involvement of adsorption processes in the current and potential determining reactions.

As the sweep rate increases the value of the experimental equivalent of the peak current function ($i_p/ACV^{1/2}$) (7) increases (Fig. 4). Because of the very limited solubility of 2,6-dithiopurine concentration studies could only be performed over limited concentration ranges. Nevertheless over the range 0.016-0.062 m*M* at scan rates of 20, 50, 100, and 200 mV sec^{-1} in acetate buffer *p*H 4.7 linear i_p-*C* plots were obtained although the graphical plot did not pass through the origin.

With increasing scan rate the peak potential for peak I (anodic) shifted more positive, $E_p = 0.31V$ at 5 mV sec^{-1} and $E_p = 0.48V$ at 500 mV sec^{-1}. The value of E_p for the principal reverse cathodic peak was essentially constant at $E_p = -0.61 \pm 4$ mV over the same scan rate range.

Consideration of the above data in the light of the theoretical data presented by Wopschall and Shain (7) tends in part to support the view that both 2,6-dithiopurine and the oxidation product of peak I are adsorbed. Thus, the symmetry of peak I suggests the presence of two very close overlapping waves, which considered in the light of the increase of the peak current function with scan rate suggests adsorption of the 2,6-dithiopurine. The symmetry, relative peak height, and occasional post-peak formation associated with the reverse cathodic process is indicative of adsorption of the product of oxidation of 2,6-dithiopurine as does the increase of the peak current function with scan rate. At this time the theories of adsorption in

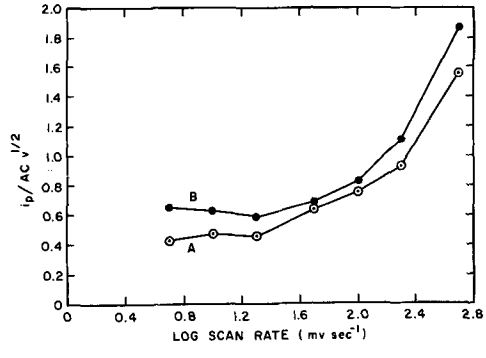

Fig. 4. Variation of experimental peak current function, $i_p/ACV^{1/2}$ in units of $\mu A\ mm^{-2}\ mM^{-1}\ (mV/sec)^{-1/2}$ with scan rate for 0.109 mM 2,6-dithiopurine in acetate buffer *p*H 4.7 at stationary PGE. A, Anodic peak I; B, cathodic peak.

irreversible systems of this type are insufficiently developed to allow calculation of the relative strengths of product and reactant adsorption. The shift of the peak potential for peak I to more positive potential with increasing scan rate is quite the opposite to that expected for a reversible system (7). The disappearance of the occasionally observed cathodic post peak at low concentration or fast scan rate is anomalous, at least as predicted for a reversible system, and accordingly this peak may be a result of secondary chemical processes rather than being specifically associated with adsorption processes.

Cyclic voltammetry embracing anodic peaks II and III did not reveal any significant cathodic peaks.

Coulometry and Macroscale Electrolysis

Peaks I and II.—Attempted coulometric, measurement of faradaic n values at potentials corresponding to peaks I or II of 2,6-dithiopurine were never successful; the current always quite rapidly decayed to a level equal to or less than that observed for background solutions alone. On removal the massive PGE presented a very dull surface unlike that after background electrolysis, which suggested a surface film formation.

In order further to study these processes a clean 4 mm PGE was maintained at a potential corresponding to either peak I or peak II in an acetate buffer *p*H 5.65 saturated with respect to 2,6-dithiopurine. (This buffer system was selected because in it a saturated solution of 2,6-dithiopurine gave a reasonably distinct plateau for peak II.) After 5 min electrolysis the PGE was removed from the electrolysis cell, the controlled potential then turned off, and the PGE thoroughly washed with water for at least 30 sec. Excess water from the glass walls of the PGE was removed with a paper tissue. The electrode was then inserted into a fresh deaerated solution of acetate buffer *p*H 5.65 and various voltammetric scans were run. The voltammetric data can be understood by reference to Fig. 5.

If the PGE was maintained at 0.35V ($\approx$ peak I), after washing and immersion in a fresh buffer solution then on sweeping initially toward negative potential, from a starting potential of 0.0V, two large cathodic peaks were observed at $E_p = -1.05$ and -1.42V (Fig. 5A), the more negative peak being about twice as high as the less negative peak. After scanning the first or both of these peaks then on the subsequent sweep toward positive potential a single anodic peak at 0.35V was observed which corresponds to peak I for 2,6-dithiopurine. Once having scanned this peak then on the next sweep toward negative potential two new cathodic peaks appeared at $E_p = -0.70$ and -1.10V; the peak originally at $E_p = -1.05$V had disappeared and that at $E_p = -1.42$V had decreased to about one third of its original height. If the initial sweep from 0.0V was toward positive potential then no peak corresponding to peak I of 2,6-dithiopurine could be observed, but a peak at 0.85V is observed which corresponds to peak II of 2,6-dithiopurine (Fig. 5B). On the reverse sweep to negative potential two cathodic peaks are observed at the same potentials as outlined for Fig. 5A and the subsequent sweeps to first positive and then negative potentials were also identical to the previously described voltammograms.

If the PGE was maintained at 0.95V for 5 min before washing and scanning, then if the initial scan was toward negative potential, two large cathodic peaks were observed at $E_p = -1.16$ and -1.43V, both peaks being of about the same height (Fig. 5C). Having scanned the first or both of these peaks then on the positive-going sweep a single anodic peak at

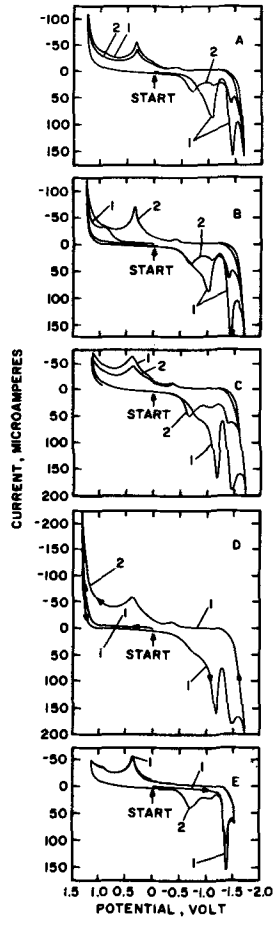

Fig. 5A. Cyclic voltammogram of PGE after electrolysis of 2,6-dithiopurine (saturated) at 0.35V for 5 min in acetate buffer *p*H 5.65. Electrode washed and scanned in fresh, deaerated acetate buffer *p*H 5.65. Scan pattern: 0.0V → −1.65V → 1.25V → −1.65V → 1.25V.

Fig. 5B. Repeat of A but initial scan toward positive potential. Scan pattern: 0.0V → 1.25V → −1.65V → 1.25V → −1.65V.

Fig. 5C. Cyclic voltammogram of PGE after electrolysis of 2,6-dithiopurine (saturated) at 0.95V for 5 min in acetate buffer *p*H 5.65. Electrode washed and scanned in fresh, deaerated acetate buffer *p*H 5.65. Scan pattern: 0.0V → −1.65V → 1.15V → −1.65V → 1.15V.

Fig. 5D. Repeat of C but initial scan toward positive potential. Scan pattern: 0.0V → 1.30V → −1.65V → 1.30V.

Fig. 5E. Cyclic voltammogram of a saturated solution of 2,6-dithiopurine in acetate buffer *p*H 5.65 at clean PGE. Scan pattern: 0.0V → −1.50V → 1.15V → −1.50V → 1.15V. Scan rate: 200 mV sec^{-1}.

$E_p = 0.36$V is observed which corresponds to peak I of 2,6-dithiopurine. On the subsequent second negative-going sweep two new peaks at $E_p = -0.70$ and -1.10V are observed along with the most negative of the initial cathodic peaks at $E_p = -1.40$V which was less than one third of its original height (Fig. 5C). If the initial sweep 0.0V was toward positive potential no anodic peaks were noted and the subsequent cathodic and anodic sweeps gave identical traces to those observed if the initial sweep was to negative potentials (Fig. 5D).

Under identical conditions 2,6-dithiopurine at a clean PGE showed only a single cathodic peak on the initial negative-going sweep at $E_p = -1.37$V but having scanned the anodic peak I, $E_p = 0.36$V then two cathodic peaks at $E_p = -0.70$ and -1.08V ap-

peared; the original cathodic peak at $E_p = -1.37V$ had decreased in height (Fig. 5E).

This observed voltammetric behavior can be rationalized as follows: Oxidation of 2,6-dithiopurine at peak I gives rise to a strongly adsorbed and probably highly insoluble product. This latter product can be reduced (stripped) at −1.05V to reform 2,6-dithiopurine. That 2,6-dithiopurine is the result of the latter cathodic process is evidenced by the appearance of a more negative peak at about −1.40V [which is due to partial reduction of 2,6-dithiopurine and partially to catalytic hydrogen discharge (8), the latter process accounting for the major portion of the current] and to the formation of anodic peak I and the normal cathodic peaks at −0.70 and −1.10V on the subsequent cathodic scan, all of which agree with the peaks observed with authentic 2,6-dithiopurine. The adsorbed product from peak I can be further oxidized, this process corresponding to peak II. The product from peak II is also strongly adsorbed; the adsorbed product can be reduced (or stripped) at −1.16V in a process that involves about double the current observed for reduction of the product of peak I (at −1.05V). Again the cyclic voltammetry of the reduction product of the adsorbed peak II product is identical to that of 2,6-dithiopurine.

Peak III.—Coulometry at potentials corresponding to the crest of peak III in acetate buffers pH 2, 3, 4.7, and 5.7 where the peak was most clearly observed gave an average faradaic n value of 10.6. The product of the electrolysis in all of these buffers had a single u.v. absorption peak at $\lambda_{max} = 278$-279 mμ. Polarography of the product solutions showed some very characteristic waves. In 1*M* acetic acid the product showed three waves at $E_{1/2} = -0.85$, −1.05, and −1.23V; in acetate buffer pH 4.7 two waves at $E_{1/2} = -1.14$ and −1.29V were observed. Authentic purine-2,6-disulfonic acid (see Experimental) gave identical spectral and polarographic data. A small scale electrochemical synthesis of purine-2,6-disulfonic acid was successfully carried out (see Experimental) and, although low yields were obtained under the rather crude conditions employed, the product obtained was identical to the chemically synthesized product in terms of melting point, spectra, and polarography in a variety of media. The mechanism of electrochemical reduction of purine-2,6-disulfonic acid is presently under investigation and will be reported in due course (9). It was clear from the polarographic data in particular that purine-2,6-disulfonic acid was the major product; however, several minor polarographic waves also were often observed indicating the presence of less important electrochemical products. No doubt these are sulfinic acids or other sulfur-containing products where the sulfur is in a lower state of oxidation than in the disulfonic acid.

When electrochemical oxidation of 2,6-dithiopurine in ammonia containing background electrolytes was performed extremely erratic faradaic n values were obtained. The major product that was obtained differed spectrally and polarographically from purine-2,6-disulfonic acid. In 1*M* ammonia background the product of oxidation of 2,6-dithiopurine at potentials corresponding to peak III showed two u.v. absorption peaks ($\lambda_{max} = 305$, 225 mμ), while purine-2,6-disulfonic acid showed only a single peak ($\lambda_{max} = 285$ mμ). Macroscale electrolysis of 2,6-dithiopurine in 5*M* ammonia, followed by lyophilization gave a pale yellow product which was extremely insoluble in water (unlike the disulfonic acid) although soluble in strongly alkaline solution and which melted above 300°C. Electrochemical oxidation of a few tenths of a gram of 2,6-dithiopurine in ammonia medium always took excessively long times under the experimental conditions employed, and in fact a product free of 2,6-dithiopurine was never obtained. The product was quite stable to boiling water. The infrared spectrum revealed the characteristic sulfonamide peaks at 1330 and 1153 cm^{-1}. Because of the difficulty of maintaining a sufficiently high ammonia concentration over extended periods of time and the variable coulometric data the exact nature of the products and the mechanism will be reported after more extensive study. Tentatively, however, the evidence suggests that the major product is purine-2,6-disulfonamide, which would be a new and potentially biologically active species.

Mechanism

Peaks I and II.—The voltammetric data supports the view that 2,6-dithiopurine is adsorbed at the PGE and that the products of peak I and peak II are also adsorbed. Cyclic voltammetry of the adsorbed products of peak I and peak II indicates that the products of the two processes are different but that they are reduced directly to 2,6-dithiopurine. The product of peak II is more difficultly reduced than the product of peak I and involves about twice as much current. It is well known that thiols are relatively easily oxidized to disulfides both chemically (10) and electrochemically (3). Electrochemical evidence also suggests that bis(6-purinyl) disulfide, the first oxidation product of 6-thiopurine, is adsorbed at the PGE (3). In view of the magnitude of the anodic current for peak I, the mechanism for peak I is probably formation of bis(6-purinyl) disulfide-2,2′-dithiol (II, Fig. 6) which is strongly adsorbed at the PGE (Fig. 6); the reactant 2,6-dithiopurine being only weakly adsorbed.

The close proximity of the two remaining thiol groups in (II, Fig. 6) suggests that further electrochemical oxidation at peak II would result in further oxidation to the double disulfide, bis(6-purinyl)disulfide-2,2′-disulfide (III, Fig. 6) which is also strongly adsorbed at the PGE. There is only scant evidence for the formation of such complex polysulfides as III (Fig. 6) although 1,4-dithiobenzene is thought to form an analogous species (11), which is also extraordinarily insoluble. Because of the nature of the electrode reaction neither of the above disulfide species has been chemically characterized, their identity being inferred from the observed electrochemical behavior, and by analogy with known chemical and electrochemical properties of thiols.

In view of the insolubility of 2,6-dithiopurine and of the great insolubility of the product of oxidation of 1,4-dithiobenzene (11), it is not unlikely that at least part of the surface coverage of the products of peaks I and II might result from simple precipitation of product.

The third peak in the absence of ammonia is clearly due to oxidation of 2,6-dithiopurine or compounds II and III (Fig. 6) to purine-2,6-disulfonic acid in a 12e/12 H^+ process. The fact that a little less than 12e on average were observed coulometrically is no doubt due to partial formation of derivatives with the sulfur in a lower oxidation state.

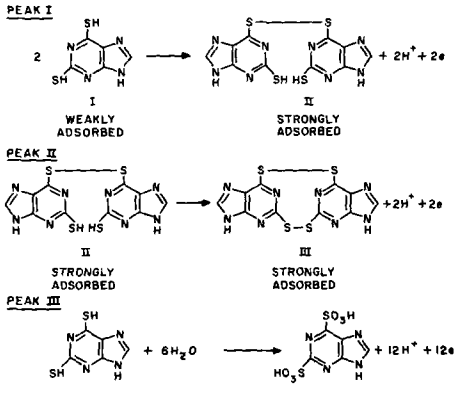

Fig. 6. Interpretation of the observed electrochemical oxidation of 2,6-dithiopurine at peaks I, II, and III.

Manuscript submitted Jan. 12, 1970; revised manuscript received ca. April 28, 1970.

Any discussion of this paper will appear in a Discussion Section to be published in the June 1971 JOURNAL.

REFERENCES

1. W. A. Struck and P. J. Elving, *Biochemistry*, **4**, 1343 (1965).
2. G. Dryhurst and P. J. Elving, *This Journal*, **115**, 1014 (1968).
3. G. Dryhurst, *ibid.*, **116**, 1097 (1969).
4. G. Dryhurst, *ibid.*, **116**, 1411 (1969).
5. G. Dryhurst and G. F. Pace, To be published.
6. F. Bergmann, H. U. Waron, H. K. Govrin, H. Goldberg, and S. Leon, *Biochim. Biophys. Acta*, **55**, 512 (1962).
7. R. H. Wopschall and I. Shain *Anal. Chem.*, **39**, 1514 (1967).
8. G. Dryhurst, *This Journal*, **117**, 1118 (1970).
9. G. Dryhurst and D. A. McAllister, Work in progress.
10. E. E. Reid, "Organic Chemistry of Bivalent Sulfur," Vol. III, Chap 7, Chemical Publishing Co., New York (1960).
11. V. C. Parekh and P. C. Guha, *J. Indian. Chem. Soc.*, **11**, 95 (1934).

Electrochemical Reduction of 2,6-Dithiopurine at the Dropping Mercury Electrode and the Pyrolytic Graphite Electrode

Glenn Dryhurst

Department of Chemistry, University of Oklahoma, Norman, Oklahoma 73069

ABSTRACT

The electrochemical reduction of 2,6-dithiopurine has been investigated polarographically at the dropping mercury electrode (DME) and the stationary pyrolytic graphite electrode (PGE). At the DME two reduction waves are observed; the first wave occurs between pH 1-5.7 and is due partly to electrochemical reduction of 2,6-dithiopurine and partly to catalytic hydrogen discharge. The second wave appears between pH 4-8 and is a typical catalytic hydrogen discharge wave catalyzed by adsorbed monoanionic 2,6-dithiopurine. Only a single peak is observed at the PGE between pH 1-7 and again is due to two simultaneous processes, the major process is catalytic hydrogen discharge catalyzed by adsorbed neutral 2,6-dithiopurine accompanied by a minor process which is reduction of 2,6-dithiopurine to a product which is also obtained on reduction of 2-thiopurine under the same conditions; this product is 1,6-dihydro-6-thiopurine.

Recent reports from this group have been concerned with the electrochemical electron transfer reactions of biologically important purines and the relation of these reactions to biological electron transfer processes (1-6), as well as the analytical utility of the electrochemical phenomena (2, 7). Purines containing exocyclic sulfur such as 6-thiopurine are electrochemically oxidized by quite different mechanisms from those observed for the naturally occurring purines; their reduction mechanisms, although complex, were similar to those observed for the non-sulfur-containing compounds. In view of the potential of developing some extremely sophisticated electrochemical syntheses of purines containing sulfur in oxidation states higher than the thiols, such as bis(purinyl) disulfides, sulfinic and sulfonic acids and sulfonamides as a result of oxidation at the pyrolytic graphite electrode, and the very incomplete knowledge of metabolic degradation of the thiopurines, which are often anticarcinogens, as well as a dearth of selective and sensitive analytical procedures, we have continued to examine in detail the electrochemistry of several other thiopurine systems.

Reported here is the electrochemical reduction of 2,6-dithiopurine[1] at both the dropping mercury electrode (DME) and the pyrolytic graphite electrode (PGE).

Horn and Zuman (8) have reported the formation of anodic waves at the DME for 2,6-dithiopurine, while Zuman and Kuik (9) briefly indicate that in ammoniacal cobalt solutions 2,6-dithiopurine gives a catalytic wave for hydrogen evolution.

[1] The *Chemical Abstracts* numbering system is employed throughout this paper.

The work reported here indicates that 2,6-dithiopurine is reduced at the DME and the PGE between about pH 1-6 in a process which partially involves catalytic hydrogen discharge and partial faradaic reduction of the 2,6-dithiopurine. Above about pH 6 at the DME a further large reduction wave appears which is a true catalytic hydrogen wave.

Because of the earlier data (8) no attention was given to the anodic waves reported and expected at positive potential at the DME.

Experimental

Chemicals.—2,6-Dithiopurine and 2-thiopurine were obtained from K&K Laboratories.

Buffer solutions were prepared from analytic reagent grade chemicals. Argon (Linde) used for deoxygenating purposes was equilibrated with water; no other purification was necessary.

Triple distilled mercury was employed throughout the work.

Apparatus.—Apparatus for polarography, voltammetry, cyclic voltammetry, coulometry, macroscale electrolysis, and spectral data acquisition are described elsewhere (3-7).

Results and Discussion

Polarography at DME.—2,6-Dithiopurine exhibits two polarographic reduction waves; the first wave (wave I) occurs between pH 1 and 5.65, the second wave (wave II) occurs between pH 4 and 8. The half-wave potentials for both waves shift linearly more negative with increasing pH (Fig. 1B); $E_{1/2} = -0.79 - 0.076$ pH for wave I and $E_{1/2} = -0.97 - 0.102$ pH for wave II.

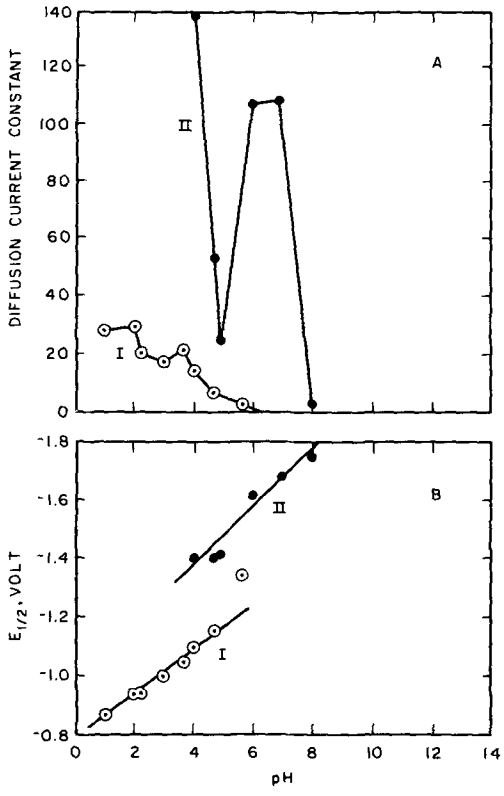

Fig. 1A. Variation of diffusion current constant for waves I and II of 2,6-dithiopurine with pH at the DME.

Fig. 1B. Variation of $E_{1/2}$ for waves I and II of 2,6-dithiopurine with pH at the DME.

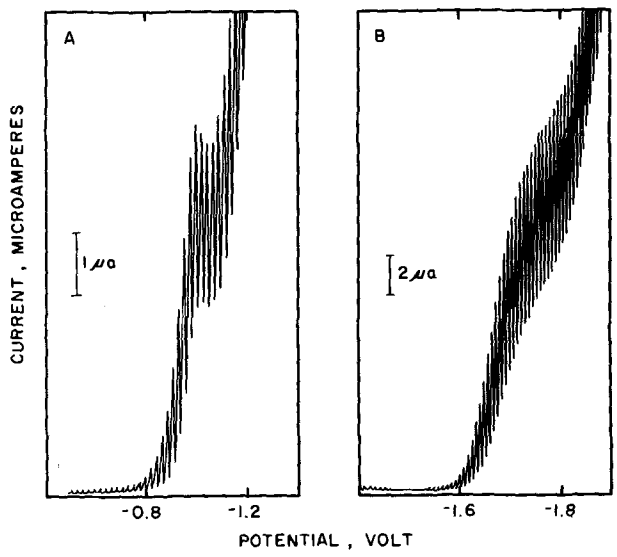

Fig. 2. Polarograms of 0.069 mM 2,6-dithiopurine at the DME in (A) chloride background pH 1.0, and (B) McIlvaine buffer pH 7.

The diffusion current constant for wave I is 28 at pH 1 and decays at pH values above 2 in a more or less regular fashion to zero at about pH 6 (Fig. 1A).

The droptime dependence of wave I in chloride background pH 1.0 is not in accord with a process entirely under diffusion control; for a 0.057 m*M* solution of 2,6-dithiopurine the ratio of $i_l/h^{1/2}$ decreased from 0.526 to 0.36 as h was varied from 32.5 to 92.5 cm, respectively. This decrease coupled with the magnitude of the diffusion current constant indicated that the process was at least partly under catalytic control. In agreement with this conclusion the temperature coefficient of the wave in chloride background pH 1.0 was 3.2%/°C which is larger than expected for a diffusion controlled process, but somewhat smaller for a process solely under catalytic control. The solubility of 2,6-dithiopurine is very low so that although a 0.1 m*M* supersaturated solution can be prepared in water, it slowly precipitates over the course of a few days. Nevertheless, it was found that the current observed for wave I in chloride background pH 1.0 was linearly proportional to concentration over the concentration range 0.02 to 0.10 m*M* with an i_l/C ratio of 57.1 ± 2.4 μA mM^{-1}.

Wave II for 2,6-dithiopurine is first observed at pH 4 as an extraordinarily large wave which occurs close to background discharge. Between pH 4 and 4.9 the diffusion current constant decays steadily from 138 to 25.4 and then increases again to 107 at pH 6 and 108 at pH 7 (Fig. 1A). At pH 8 wave II is extremely small.

In McIlvaine buffer pH 7 (Fig. 2B) the limiting current for wave II appears to increase with decreasing height of the mercury column, but owing to the shift of background discharge to more positive potential in the presence of 2,6-dithiopurine it was very difficult to correct the wave for background current, particularly at low column heights. Nevertheless, the large magnitude of the diffusion current constant and the virtual independence of the limiting current with mercury column height indicated that the wave was effectively under catalytic control.

In McIlvaine buffer pH 7 the temperature coefficient of wave II was —0.98%/°C, *i.e.*, the wave height decreased slightly with temperature. Over the concentration range 6.6 x 10^{-6} to 6.6 x 10^{-5} *M* of 2,6-dithiopurine in the same background the limiting current for wave II increased linearly with concentration although the ratio i_l/C increased from 88 to 162 μA mM^{-1}, respectively.

Voltammetry at PGE.—At the stationary PGE (4 mm diameter) 2,6-dithiopurine gives only a single voltammetric reduction peak, which occurs between pH 1 and 7, the peak potential for which shifts linearly more negative with increasing pH according to the equation $E_p = -0.96 - 0.068$ pH (Fig. 3B). The peak itself is extremely sharp (Fig. 4), more so than expected for a simple diffusion controlled process. The current density decreases in a more or less regular fashion as the pH is increased, ranging from 8.0 μA mm^{-2} mM^{-1} at pH 1.0 to almost zero at pH 7 (Fig. 3A). By comparison with earlier data (1) a current density of 8.0 would indicate an apparent faradaic n value of 13-14 electrons.

In chloride background pH 1.0 the peak current did not increase linearly with concentration (Fig. 5) but over the range 0.02 to 0.10 m*M* at 5 mV sec^{-1} scan rate $i_p - C$ plots are essentially exponential with i_p apparently tending to a limiting value at somewhat above the 0.1 m*M* concentration level. The limited solubility of 2,6-dithiopurine prevented extending the concentration study to higher levels. The ratio i_p/C decreased from 224 μA mM^{-1} at the 0.02 m*M* concentration level to 142 μA mM^{-1} at 0.1 m*M*.

Coulometry at mercury electrodes.—Attempts to determine faradaic n values by macroscale electrolysis of 2,6-dithiopurine at a massive mercury pool electrode in chloride pH 1.0, acetate pH 4.7, and McIlvaine pH 7 backgrounds could not be meaningfully performed because of a quite rapid reaction between 2,6-dithiopurine and mercury to give a gray-black suspension in solution and a gray-black discoloration to the mercury pool surface. This reaction was so rapid, as evidenced by u.v. spectral studies, that within 15 min about 50% of the 2,6-dithiopurine of concentration 0.05 m*M* in acetate pH 4.7 had disappeared. The resultant product was not electrochemically reducible. Accordingly all further information regarding the electrolysis product and electrode mechanism was gained by electrolysis of 2,6-dithiopurine solutions at a large PGE.

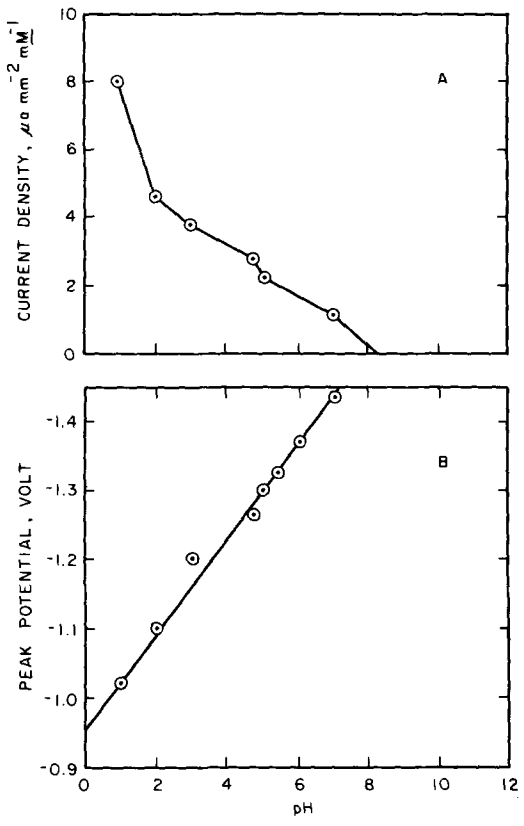

Fig. 3A. Variation of current density for voltammetric reduction peak of 2,6-dithiopurine at PGE with pH.

Fig. 3B. Variation of peak potential for voltammetric reduction peak of 2,6-dithiopurine at PGE with pH. Area PGE: 12.5 mm^2; concentration: 2,6-dithiopurine 0.10 mM; scan rate: 5 mV sec^{-1}.

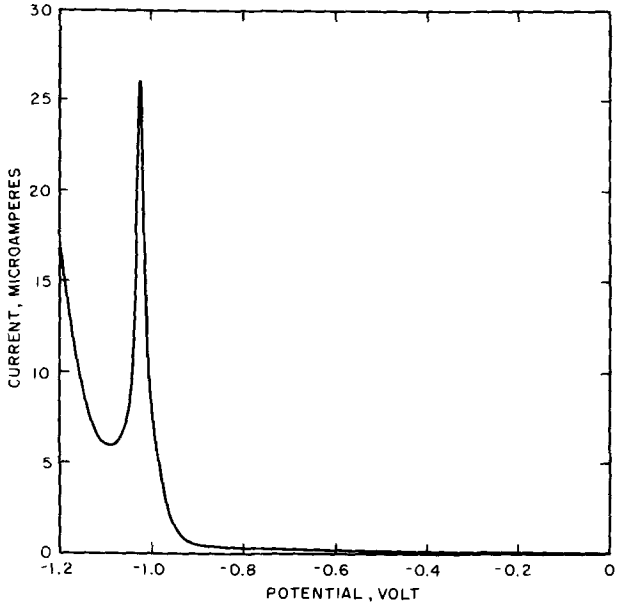

Fig. 4. Voltammogram of 0.10 mM 2,6-dithiopurine in chloride background pH 1.0 at a 4 mm diameter PGE. Scan rate: 5 mV sec^{-1}.

Coulometry at PGE.—Electrolysis of a 0.066 m*M* solution of 2,6-dithiopurine solution in chloride background pH 1.0 on the rising portion of the single voltammetric peak (−0.98V) resulted in the immediate liberation of H_2S (lead acetate paper). The current observed initially was very high (> 50 mA) and did not decay appreciably but remained at an extremely high level. By monitoring the u.v. absorption spectra and

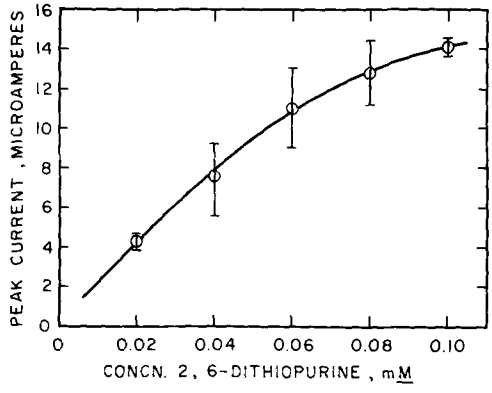

Fig. 5. Variation of peak current with concentration on voltammetric reduction of 2,6-dithiopurine in chloride background pH 1.0 at stationary PGE. Scan rate: 5 mV sec^{-1}.

by employing cyclic voltammetry at PGE it was clear however that the 2,6-dithiopurine was electrochemically reduced. The data accumulated, particularly the cyclic voltammetry, suggested that the product was identical to that obtained upon reduction of 2-thiopurine. Since more extensive data were available on the electrochemical reduction of 2-thiopurine in acetate buffer pH 4.7 (10) where more definitive u.v. spectra and cyclic voltammograms are obtained, a more detailed examination of the reduction of 2,6-dithiopurine in this buffer was carried out.

Attempts to reduce 2,6-dithiopurine in acetate buffer pH 4.7 on the rising portion of the peak (−1.26V) again resulted in formation of H_2S and disappearance of the characteristic spectrum of this compound (λ_{max} = 350, 292.5, 250 mμ) and formation of a species with a quite different absorption spectrum at pH 4.7 (λ_{max} = 282, 246 mμ). Although the observed current was only about one fifth of that observed at pH 1.0 it did not decrease appreciably over the course of several hours, although it was quite obvious from spectral data that all 2,6-dithiopurine had been reduced.

Cyclic voltammetry at PGE of the product revealed that there were no reduction waves remaining (apart from slight traces of 2,6-dithiopurine itself), but a well-formed oxidation peak at E_p = 0.38 → 0.40V was present. Once having scanned this single anodic peak, four cathodic peaks were observed on the subsequent sweep in the negative direction at E_p = −0.77 → −0.78V; −1.02 → 1.03V; −1.27 → −1.29V and −1.52 → −1.54V (Fig. 6C, D). None of these cathodic peaks are observed on cyclic voltammetry of 2,6-dithiopurine itself (Fig. 6A), although at pH 4.7, 2,6-dithiopurine is oxidized at E_p = 0.41V (Fig. 6A, B); the mechanism of this process will be discussed elsewhere. Electrolysis of 2-thiopurine at approximately the same concentration and under otherwise identical conditions did not give rise to H_2S evolution. The characteristic u.v. spectrum of 2-thiopurine at pH 4.7 (λ_{max} 285, 243 mμ) disappeared and a product having an identical spectrum (λ_{max} 282, 246 mμ) to that produced from 2,6-dithiopurine under the same conditions was observed. Cyclic voltammetry of the electrolysis product of 2-thiopurine was essentially identical to that produced from 2,6-dithiopurine (Fig. 6E, F). Complete interpretation of the various peaks observed for these solutions will be reported elsewhere (10).

It was thus quite clear that reduction of 2-thiopurine and 2,6-dithiopurine at potentials corresponding to the single reduction peak of the latter compound gave rise to the identical product; this product appears to be extremely effective in facilitating catalytic hydrogen reduction.

Electrochemical Mechanism

Polarography at DME.—As evidenced by the magnitude of the diffusion current constant, the droptime and temperature dependence, and controlled potential

electrolysis data, wave I is due to two simultaneous processes. At low pH the most important of these processes is catalytic hydrogen discharge accompanied by some electrochemical reduction of 2,6-dithiopurine. As the pH increases the decrease in wave height must be related primarily to a decrease in the catalytic process. The decrease in current can be related to the state of ionization of the 2,6-dithiopurine. Viout and Rumpf (11) determined the pK_a values of 2,6-dithiopurine as 5.02 and 10.06 using a potentiometric titration method. Employing a spectrophotometric method based on the three u.v. absorption peaks of 2,6-dithiopurine we have found $pK_{a1} = 4.9$ and $pK_{a2} \simeq 8.8$; the latter figure is of somewhat doubtful accuracy because the peak which was employed for its determination occurred very close to end absorption in most buffer systems employed.

Accordingly, the reaction apparently giving rise to the catalytic contribution is typical of such waves given by many thiols (12) (Eq. [1]).

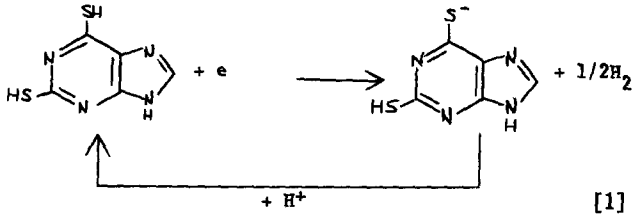

[1]

As the solution pH increases the concentration of neutral 2,6-dithiopurine decreases as does the proton concentration resulting in a decrease in the current for wave I. Above pH 5 most of the 2,6-dithiopurine will be in the monoanionic form and accordingly the catalytic current would be expected, as observed, to decay to zero. By analogy with the polarographic behavior of 6-thiopurine (4) it might be expected that any true faradaic reduction of 2,6-dithiopurine might decay to zero at pH values much above pK_{a1}, *i.e.*, it is the uncharged species that is reduced. As a result of the reaction (or adsorption) of 2,6-dithiopurine with mercury, coupled with the catalytic processes it is not possible to decide on the nature of the true faradaic process. The very limited solubility of 2,6-dithiopurine does not allow a detailed comparison of the catalytic process proposed for wave I with other systems (12). At the 0.05 m*M* concentration level solutions of 2,6-dithiopurine in acetate and MacIlvaine buffers did not result in any appreciable depression or shifts of electrocapillary curves; at such low concentration levels this was not unexpected.

Wave II shows the typical behavior expected of a normal catalytic wave except for its anomalous temperature dependence. Since wave II is not observed until pH 4 it is likely that it is associated with the monoanionic form of 2,6-dithiopurine which has reached significant concentrations at this pH. Accordingly it is possible to designate the probable catalytic reaction as follows (Eq. [2]).

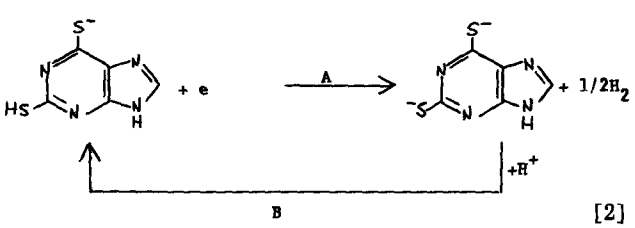

[2]

The observed shifts in the magnitude of the diffusion current constant (I_d) between pH 4 and 8 may be explained by the fact that at pH 4 (assuming a value of $pK_{a1} = 5.0$) about 10% of the 2,6-dithiopurine exists in the monoanionic form; however, as a result of the high proton concentration and buffer capacity of the buffer employed (MacIlvaine, ionic strength 0.5*M*) a large catalytic current is observed, the current for which is likely limited by reaction [2B], reaction [2A] being a fast electron transfer process. As the pH increases up to pH 4.9 the concentration of the monoanionic 2,6-dithiopurine still accounts for considerably less than 50% of the compound, whereas the proton concentration has decreased an order of magnitude and the buffer capacity has decreased. As a result the systematic current decrease up to pH 4.9 is observed. At pH 6, in excess of 90% of the 2,6-dithiopurine is in the monoanionic form which, as a result of increased catalyst concentration, more than compensates for the decrease in proton concentration and between pH 6 and 7 the catalytic current is again high. At pH 8 the combination of decreased proton concentration and further ionization of the monoanionic 2,6-dithiopurine results in a drastic decay of the observed catalytic current. The anomalous negative temperature coefficient of wave II can only be rationalized by invoking the generally accepted theory that thiols giving rise to catalytic waves do so in an adsorbed state of the catalyst. However, in the case of wave II the catalyst is a negatively charged species and, at potentials of the catalytic wave, the electrode carries a large negative charge. It is not unlikely, therefore, that the thiol adsorption is

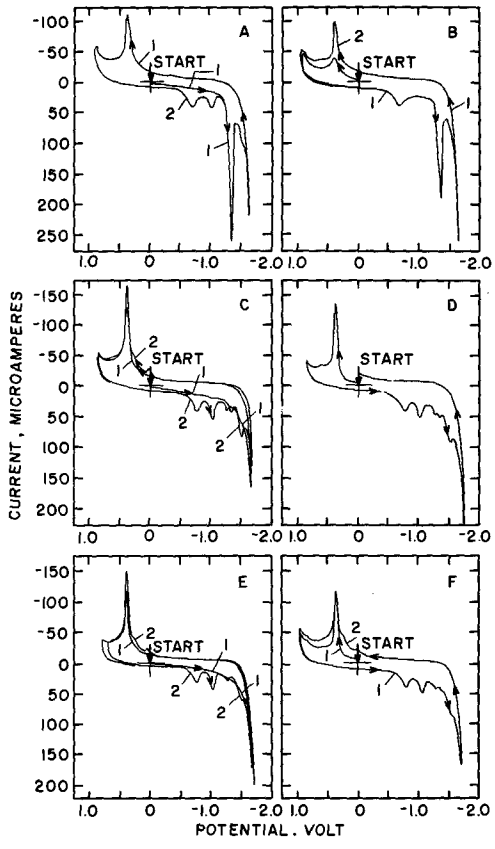

Fig. 6A,B. Cyclic voltammograms of a saturated solution of 2,6-dithiopurine in acetate buffer pH 4.7 at stationary PGE. Scan pattern: A, 0.00V → −1.65V → 0.90V → −1.25V; B, 0.00V → 0.98V → −1.65V → 0.98V → 0.00V.

Fig. 6C,D. Cyclic voltammograms of product of electrochemical reduction of 2,6-dithiopurine at −1.26V at PGE in acetate buffer pH 4.7 at stationary PGE. Scan pattern: C, 0.00V → −1.70V → 0.90V → −1.70V → 0.90V → 0.00V; D, 0.00V → 0.90V → −1.75V → 0.00V.

Fig. 6E,F. Cyclic voltammograms of product of electrochemical reduction of 2-thiopurine at −1.26V at PGE in acetate buffer pH 4.7 at stationary PGE. Scan pattern: E, 0.00V → −1.75V → 0.80V → −1.75V → 0.80V → 0.00V; F, 0.00V → 1.00V → −1.70V → 1.00V → 0.00V. Scan rate: 200 mV sec^{-1}; PGE: area 12.5 mm^2.

weak and would have a high temperature coefficient of desorption. The net result being therefore that the usually large positive temperature coefficient of the catalytic process is more than offset by a decrease in catalyst adsorption at elevated temperature. Electrocapillary curves of 0.05 m*M* 2,6-dithiopurine at *p*H 7 showed little difference from the background solution alone.

Voltammetry at PGE.—2,6-dithiopurine is reduced at PGE in a process where apparently the reactant (and possibly product) facilitates catalytic hydrogen discharge. The known pK_{a1} of 2,6-dithiopurine, the variation of E_p and the current density with *p*H, and controlled potential electrolysis data support this view. The product of faradaic reduction of 2,6-dithiopurine appears to be spectrally and voltammetrically identical to that obtained by reduction of 2-thiopurine under the same conditions. The product of this latter reduction of 2-thiopurine appears to be 1,2-dihydro-2-thiopurine (10). Since reduction of 2,6-dithiopurine appears to involve loss of H_2S this must occur by reduction of the 1,6-N=C- double bond in much the same way postulated for 6-thiopurine (4), purine and adenine (13). Accordingly a mechanism for faradaic reduction of 2,6-dithiopurine is proposed (Eq. [3]).

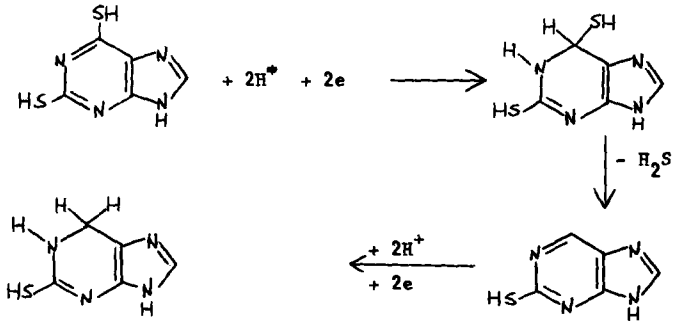

[3]

The process responsible for catalytic hydrogen discharge is no doubt identical to that observed for wave I at DME.

Acknowledgment

The author would like to thank the National Science Foundation which supported the work described through Grant No. GP 8151.

Manuscript submitted Jan. 12, 1970; revised manuscript received *ca.* April 28, 1970.

Any discussion of this paper will appear in a Discussion Section to be published in the June 1971 JOURNAL.

REFERENCES

1. G. Dryhurst and P. J. Elving, *This Journal*, **115**, 1014 (1968).
2. G. Dryhurst and P. J. Elving, *Talanta*, **16**, 855 (1969).
3. G. Dryhurst, *This Journal*, **116**, 1097 (1969).
4. G. Dryhurst, *ibid.*, **116**, 1357 (1969).
5. G. Dryhurst, *ibid.*, **116**, 1411 (1969).
6. G. Dryhurst and G. F. Pace, *ibid.*, To be published.
7. G. Dryhurst, *Anal. Chim. Acta*, **47**, 275 (1969).
8. G. Horn and P. Zuman, *Coll. Czech. Chem. Communs.*, **25**, 3401 (1960).
9. P. Zuman and M. Kuik, *ibid.*, **24**, 3861 (1959).
10. G. Dryhurst, *J. Electroanal. Chem.*, In press.
11. A. Viout and P. Rumpf, *Bull. soc. chim. France*, 1123 (1959).
12. S. G. Mairanovskii, "Catalytic and Kinetic Waves in Polarography," Chap. IX, p. 269, Plenum Press, New York (1968).
13. D. L. Smith and P. J. Elving, *J. Am. Chem. Soc.*, **84**, 1412 (1962).

Polarography of Uranyl-Diethylenetriaminepentaacetate Complexes and Adsorption Kinetics at the Dropping Mercury Electrode

Tsai-Teh Lai and Chaur-Shyong Wen

Department of Chemical Engineering, Cheng Kung University, Tainan, Taiwan, China

ABSTRACT

The chelation of uranium(VI) with diethylenetriaminepentaacetate was investigated polarographically over the *p*H range 3.7-8.4 and ligand concentration range 0.005-0.1M. The predominant chelate species was found to be $UO_2(OH)H_2A^{2-}$ with the logarithmic formation constant of 2.96 at *p*H 6.4-7.5 and ionic strength 0.25. In the presence of Triton X-100 <0.003%, a single irreversible and diffusion-controlled wave was obtained. The kinetic parameters were determined (k_s is the order of 10^{-3} cm/sec and $\alpha = 0.42 \pm 0.02$). When the concentration of Triton X-100 is greater than 0.003%, the single wave splits into two irreversible waves, due to the adsorption of surface active substance.

Diethylenetriaminepentaacetic acid (DTPA) is well known to form stable complexes with many metals. Polarographic determinations of copper(II), bismuth(III), and antimony(III) using DTPA as supporting electrolyte have been studied (1). Kalland and Jacobsen have studied the effect of surface-active substances on the polarographic waves of iron-DTPA complexes (2) and also the polarography of copper-DTPA complexes (3,4). The polarographic behavior of europium (5) and thallium(I) (6) in DTPA solution has been reported. The metal ligand ratio of uranyl-DTPA complex has been shown to be 1:1 by spectrophotometry (7).

Since the diethylenetriaminepentaacetic acid is a versatile chelating agent, the polarographic data and the constants of the chelates of uranium(VI) with

Key words: cathodic action, formation constant, kinetic parameters, uranium (VI), DTPA.

DTPA provide an indispensable clue for the extraction, separation, and determination of uranium.

In an attempt to offer this important information, in this paper the polarographic characteristics, the formation constants, and the kinetic parameters due to the adsorption effect of the electrode process for the uranium-DTPA system are reported.

Experimental

Apparatus.—Polarograms were recorded with a Yanagimoto Pen-Recording Polarograph Model p8 at 30° ± 0.1°C. The characteristics of the DME were: m = 1.864 mg/sec and t = 4.53 sec at 74.9 cm mercury height in a 0.15M $NaClO_4$ solution at an applied potential of −0.40V *vs.* SCE.

The pH values of the solutions were adjusted with perchloric acid or sodium hydroxide and determined by a Toa Denpa HM-5A glass electrode pH meter.

Chemicals.—The stock solution of 0.1M uranyl perchlorate was prepared and analyzed as described in the earlier paper (8).

A 0.2M stock solution of DTPA was prepared by dissolving the acid (Aldrich Company) 19.668g and NaOH 6.0g in distilled water and diluting to 250 ml.

Triton X-100 was used as a surface-active substance and 0.15M sodium perchlorate as a supporting electrolyte.

Results and Discussion

Wave characteristics in the absence of surface-active substance.—A well-defined reversible wave was obtained when [DTPA] > 0.02M and 4.35 < pH < 8.40 in the absence of surface-active substance, Triton X-100 (Table I). However, a maximum appeared when pH < 4.35. As shown in Table II, the value of $i_d/h^{1/2}$ is 0.324 ± 0.004 at pH 5.2. This indicates that the limiting current is proportional to the square root of the height of the mercury column and proves that the reductions are entirely diffusion-controlled.

The temperature coefficient of half-wave potential is −0.2 mV/°C and the mean slope of the conventional log plots is 0.059 ± 0.004. These data indicate that the electrode reductions are a one-electron reversible process for the polarographic solutions of [DTPA] > 0.02M at 4.4 < pH < 8.4 in the absence of surface-active substance, Triton X-100.

As shown in curve A of Fig. 1, at pH < 6.4 and pH > 7.5, the slope of $\Delta E_{1/2}/\Delta pH$ is −0.060V showing that one hydrogen ion takes part in the reduction. At 6.4 < pH < 7.5, the half-wave potential is independent of pH. Curve A also shows that the half-wave potential is independent of ligand concentration for a given pH value. It reveals that the reduced complex species, uranium(V)-DTPA, has the same metal-ligand ratio of 1:1 as that of uranium(VI)-DTPA complex. Curve B shows that, in the absence of DTPA, the hydroxylation of uranyl ion occurs at pH > 4.0.

Since the successive pK values of DTPA are 1.75, 2.45, 4.23, 8.50 and 10.02 (9), respectively, the probable chelate species at 4.5 < pH < 8.4 can be deduced to be $UO_2(OH)H_2A^{2-}$ from the half-wave potential relation as had been reported in our earlier paper (10).

It is obvious from Fig. 2 that an anodic wave precedes the normal cathodic wave at pH > 6.0 and the half-wave potential shifts slightly to negative side as the ligand concentration and pH value increase. These phenomena were attributed to the depolarization of mercury by formation of a stable chelate with DTPA.

Formation constants of uranyl-hydroxo and uranyl-DTPA complexes.—It is obvious from curve B of Fig. 1 that in the absence of chelating agent and at pH < 4.0, the half-wave potential remains constant at −0.18V *vs.* SCE; the electrode reduction is

$$UO_2^{2+} + e \rightleftharpoons UO_2^{+} \qquad [1]$$

However, at pH > 4.0, the half-wave potential shifts to more negative side; the slope of $\Delta E_{1/2}/\Delta pH$ is −0.060V indicating that one hydroxyl ion is involved in the electrode reduction. Therefore, it was concluded that the uranyl-hydroxo complex undergoes the following electrode reduction without prior dissociation

$$UO_2(OH)^{+} + e \rightleftharpoons UO_2^{+} + OH^{-} \qquad [2]$$

The half-wave potential can be given as

$$(E_{1/2})_{UO_2(OH)^+} = (E_{1/2})_{UO_2^{2+}} - 0.060 \log K - 0.060 \log [OH^-] \qquad [3]$$

Where K is the formation constant of $UO_2(OH)^+$, which was calculated to be log K = 9.95 (Table III).

Table I. Polarographic characteristics and reversibility of uranyl-DTPA complex

(1.0 mM $UO_2(ClO_4)_2$, 0.15M $NaClO_4$, 0% Triton X-100)

C_{DTPA}, M	pH	$-E_{1/2}$, V *vs.* SCE	$-\Delta E_{d.e.}$ / $\Delta \log \frac{i}{i_d - i}$	i_d, μA
0.1	4.36	0.305	0.063	4.08
	5.30	0.360	0.056	2.75
	6.40	0.425	0.064	2.14
	7.25	0.440	0.061	2.14
	7.50	0.450	0.063	2.14
	8.40	0.520	0.062	1.50
0.02	5.45	0.360	0.064	2.70
	6.50	0.425	0.071[a]	2.13
	7.45	0.450	0.062	1.90
	8.05	0.490	0.061	1.70
0.005	5.15	0.340	0.076[a]	3.10
	5.95	0.395	0.071[a]	2.25
	6.75	0.430	0.063	2.12
	7.30	0.430	0.062	2.09
	7.60	0.460	0.061	1.90

[a] Irreversible wave.

Table II. Variation of limiting current with height of mercury column

(1.0 mM $UO_2(ClO_4)_2$, 0.1M DTPA, 0.15M $NaClO_4$)

pH	Height, h cm, corr.	i_d, μA	$i_d/h^{1/2}$
5.2	84.9	2.94	0.321
	74.9	2.80	0.323
	64.8	2.64	0.328
			Avg. 0.324 ± 0.04

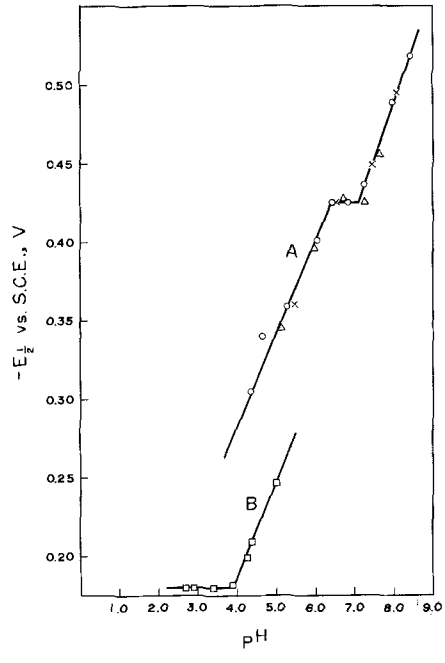

Fig. 1. Effect of pH on the half-wave potential of uranyl-DTPA complex. 1.0 mM $UO_2(ClO_4)_2$, 0.15M $NaClO_4$, 0% Triton X-100, and various ligand concentrations: ○ 0.1M; x 0.02M; △ 0.005M; □ 0.000M.

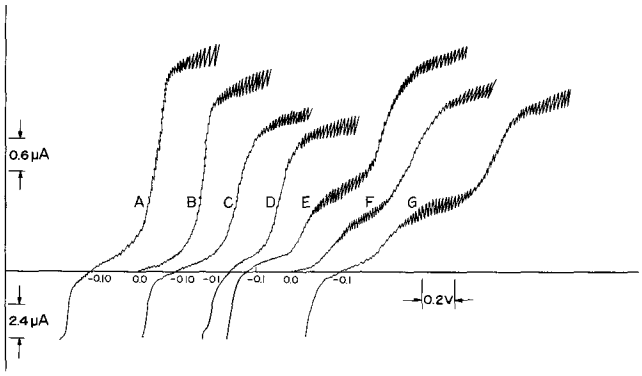

Fig. 2. Polarographic waves of uranyl-DTPA complex. 1.0 mM $UO_2(ClO_4)_2$, 0.15M $NaClO_4$, and varying concentration of DTPA and Triton X-100 at various pH:

	A	B	C	D	E	F	G
pH	5.0	5.0	6.0	6.5	5.0	5.0	6.0
C_{DTPA}, M	0.1	0.02	0.02	0.1	0.1	0.02	0.02
Triton X-100, %	0.002	0.002	0.002	0.002	0.004	0.004	0.004

At $6.4 < pH < 7.5$, the half-wave potential of the complex $UO_2(OH)(H_2A)^{2-}$ is independent of both pH value and ligand concentration (Fig. 1, curve A). Therefore, the half-wave potential of the complex $UO_2(OH)(H_2A)^{2-}$ can be written simply as

$$(E_{1/2})_c = (E_{1/2})_s - 0.060 \log \frac{K_{OC}}{K_{RC}} \qquad [4]$$

where K_{OC} and K_{RC} are the formation constants of the oxidized and reduced forms of the uranyl-DTPA complexes, respectively, and the K_{OC} was determined by the following method which had been reported previously (11).

In the modified Ilkovic equation (12)

$$i_d = 607\, nD^{1/2}m^{2/3}t^{1/6}\left(1 + \frac{AD^{1/2}t^{1/6}}{m^{1/3}}\right)C \qquad [5]$$

the concentration C of the reducible substance can be expressed as the complex species concentration of

$$[UO_2(OH)H_2A^{2-}] = \frac{C_{UO_2(OH)^+} \cdot \alpha_3}{\frac{1}{K_{OC}} + \alpha_3} \qquad [6]$$

where

$$\alpha_3 = \frac{C_{DTPA}}{\frac{[H^+]^3}{k_1k_2k_3} + \frac{[H^+]^2}{k_2k_3} + \frac{[H^+]}{k_3} + 1 + \frac{k_4}{[H^+]} + \frac{k_4k_5}{[H^+]^2}}$$

Substitute the corresponding experimental data for two pH values in the range of pH 6.4-7.5, into Eq. [5] and [6] and by solving the simultaneous equations

$$\begin{cases} (i_d)_1 = f_1(D, K_{OC}) \\ (i_d)_2 = f_2(D, K_{OC}) \end{cases} \qquad [7]$$

the formation constant and the diffusion coefficient of the complex $UO_2(OH)H_2A^{2-}$ can be obtained (Table IV).

Table III. Formation constants of $UO_2(OH)^+$

(1.0 mM $UO_2(ClO_4)_2$, 0.15M $NaClO_4$)

pH	$(E_{1/2})_{UO_2(OH)^+}$, V vs. SCE	log K
4.2	−0.200	10.02
4.5	−0.210	9.94
4.7	−0.226	9.90
		Avg. 9.95 ± 0.07

$(E_{1/2})_{UO_2^{2+}} = -0.18V$ vs. SCE.

Table IV. Formation constant of $UO_2(OH)H_2A^{2-}$

(1.0 mM $UO_2(ClO_4)_2$, 0.1M DTPA, 0.15M $NaClO_4$)

pH	i_d, μA	D, $cm^2\ sec^{-1}$	log K_{OC}
6.40	2.140		
7.25	2.139	3.31×10^{-6}	2.96 ± 0.01
7.50	2.138		

Current sensitivity = 30 n A/mm.

Effects of Triton X-100 on the polarograms.—The polarograms were influenced greatly by the addition of Triton X-100. The reversible waves which were observed at $4.4 < pH < 8.4$ and DTPA concentration range of 0.02 to 0.1M were distorted into irreversible waves by the addition of Triton X-100 < 0.003%. Furthermore, when the concentration of Triton X-100 is increased above 0.003%, the wave splits into two more irreversible waves at a more negative potential due to the adsorption of surface active substances (13); the first wave is smaller than the second wave (Fig. 2). The polarographic characteristics of the two waves are shown in Table V.

The electrocapillary curve of mercury, which is illustrated in Fig. 3, shows that the addition of Triton X-100 to the solution causes a large decrease in the drop time of the capillary; the electrocapillary maximum shifts to the positive side with increasing concentration of Triton X-100.

These facts show that an adsorption of Triton X-100 occurs on the mercury electrode; the film formation of surface-active substance can be regarded as a rapid process (14). The inhibiting effect of the adsorbed film of Triton X-100 on the electron transfer renders the current-potential curve more irreversible.

The limiting current of the total wave is independent of the concentration of DTPA but decreases with increasing pH value (Fig. 4). It is interesting to note that the limiting current of the total wave increases with increasing concentration of Triton X-100 and reaches a plateau at 0.008% Triton X-100 (Fig. 4).

Electrode kinetics influenced by the adsorption of surface active substance.—As mentioned above, a single irreversible wave was obtained by the presence

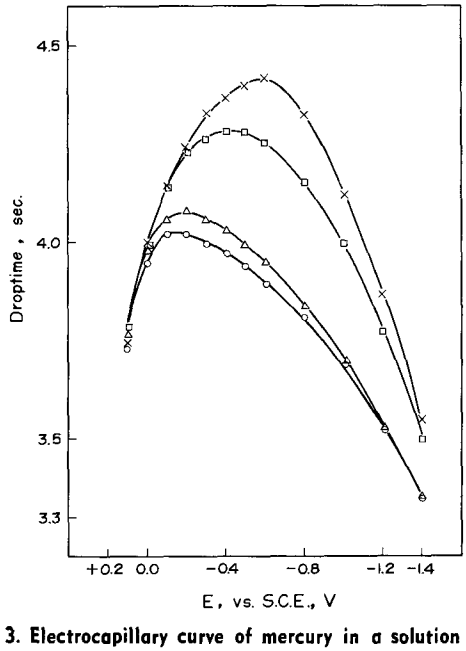

Fig. 3. Electrocapillary curve of mercury in a solution containing 1 mM $UO_2(ClO_4)_2$, 0.1M DTPA at pH 5.0, and various concentration of Triton X-100: x 0%; □ 0.002%; △ 0.004%; ○ 0.01%.

Table V. Polarographic characteristics of the two waves of the uranyl-DTPA complex

(1.0 mM $UO_2(ClO_4)_2$, 0.15M $NaClO_4$ and 0.004% Triton X-100)

C_{DTPA}, M	pH	$(-E_{1/2})_1$, V vs. SCE	$\left[\frac{-\Delta E_{d.e.}}{\Delta \log \frac{i}{i_d - i}}\right]_1$	i_{l_1}, μA	$(-E_{1/2})_2$, V vs. SCE	$\left[\frac{-\Delta E_{d.e.}}{\Delta \log \frac{i}{i_d - i}}\right]_2$	i_{l_2}, μA	i_{l_t}, μA
0.1	3.75	0.34	0.104	1.77	0.75	0.120	1.50	3.27
	4.40	0.35	0.102	1.59	0.84	0.114	1.44	3.03
	5.15	0.38	0.084	1.05	0.85	0.114	1.37	2.42
	6.15	0.40	0.080	0.57	0.90	0.130	0.99	1.56
	6.65	0.44	0.078	0.45	0.95	0.150	0.78	1.23
	7.60	0.47	0.068	0.50	1.02	0.142	0.70	1.20
0.02	3.75	0.31	0.098	1.50	0.72	0.130	1.89	3.39
	4.40	0.31	0.099	1.41	0.78	0.120	1.62	3.03
	5.05	0.35	0.094	1.02	0.78	0.122	1.49	2.51
	5.60	0.38	0.080	0.62	0.84	0.122	1.20	1.82
	6.10	0.37	0.088	0.55	0.89	0.123	1.10	1.65
	7.30	0.43	0.080	0.45	0.97	0.132	1.02	1.47
0.005	3.48	0.28	0.101	2.21	0.57	0.120	2.40	4.61
	4.02	0.28	0.099	1.72	0.71	0.124	2.14	3.86
	4.45	0.29	0.121	1.26	0.71	0.126	1.78	3.04
	4.68	0.31	0.095	1.10	0.72	0.134	1.60	2.70
	3.53	0.31	0.110	1.05	0.82	0.140	1.20	2.25
	5.80	0.36	0.095	0.98	0.86	0.138	1.10	2.08

of Triton X-100 < 0.003%. This phenomenon can be attributed to the slower electron transfer in the electrode reduction in the presence of surface-active substance. Therefore the determination of the kinetic parameters of electrode reduction was carried out.

The plots of $E_{d.e.}$ *vs.* log $i/(i_d - i)$ were found to be good straight lines, but the mean slope for the series is 75 ± 5 mV (Table VI). The temperature coefficient of the diffusion current is 0.82%/°C and the value of $i_d/h^{1/2}$ is 0.299 ± 0.020 at pH 5.0. These data show that although the electrode reactions are diffusion-controlled, the process is not reversible.

The corrected reversible half-wave potential $E_{1/2}^r$ for a quasi-reversible system can be expressed by the following relation (15)

$$E_{1/2}^r = \lim_{i \to 0} \left[E_{d.e.} - \frac{RT}{n\mathbf{F}} \ln \frac{i_d - i}{i} \right] \qquad [8]$$

Thus, by plotting $[E_{d.e.} - RT/n\mathbf{F} \ln i_d - i/i]$ against i and by extrapolating it to $i = 0$, the $E_{1/2}^r$ can be obtained (Fig. 5).

The degree of irreversibility of the electrode reduction is expressed by Eq. [9] (15)

$$Z = \text{anti} \log_{10} \left[\frac{n\mathbf{F}}{2.303\,RT} (E_{1/2}^r - E_{d.e.}) - \log \left(\frac{i}{i_d - i} \right) \right] \qquad [9]$$

The standard rate constant k_s and transfer coefficient α can be determined by the following equation

$$\log (Z - 1) = \log \frac{1.13\, D_o^{1/2}}{k_s \sqrt{t_d}} + \frac{(1 - \alpha) n\mathbf{F}}{2.303\,RT} (E_{1/2}^r - E_{d.e.}) \qquad [10]$$

Table VI. Polarographic characteristics and kinetic parameters of uranyl-DTPA chelate

(1.0 mM ($UO_2(ClO_4)_2$, 0.1M DTPA, 0.15M $NaClO_4$ and 0.002% Triton X-100)

pH	$-E_{1/2}$, V vs. SCE	$-E_{1/2}^r$, V vs. SCE	i_d, μA	$-\frac{\Delta E_{d.e.}}{\Delta \log \frac{i}{i_d - i}}$	α	$k_s \times 10^3$, cm/sec
4.45	0.325	0.305	3.42	0.081	0.40	3.68
5.25	0.360	0.344	2.80	0.081	0.40	3.60
5.50	0.362	0.354	2.64	0.075	0.43	3.13
6.20	0.400	0.397	1.50	0.072	0.44	3.08
6.50	0.400	0.415	1.48	0.075	0.42	3.33
6.60	0.428	0.416	1.44	0.075	0.41	3.09
7.35	0.440	0.418	1.38	0.074	0.40	2.72
8.40	0.500	0.495	0.96	0.071	0.43	2.29

where t_d is the drop time, D_o is the diffusion coefficient of oxidized form.

Equation [10] shows that the plot of log $(Z - 1)$ *vs.* $(E_{1/2}^r - E_{d.e.})$ should give a straight line and the value of k_s and α can be obtained from the intercept and the slope of the plot (Fig. 6). The data obtained at various pH values are listed in Table VI.

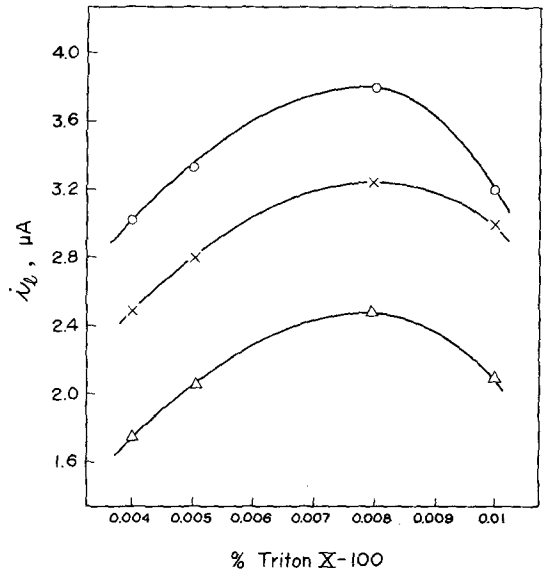

Fig. 4. Effect of Triton X-100 on the total limiting current of uranyl-DTPA complex. 1.0 mM $UO_2(ClO_4)_2$, 0.02M DTPA, 0.15M $NaClO_4$; ○ pH 4.4; x pH 5.0; △ pH 6.0.

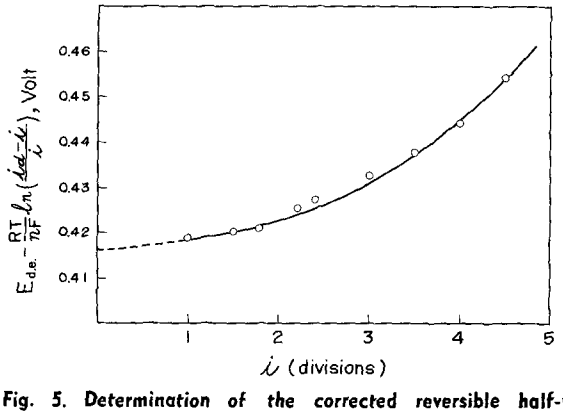

Fig. 5. Determination of the corrected reversible half-wave potential. 1.0 mM $UO_2(ClO_4)_2$, 0.1M DTPA, 0.15M $NaClO_4$, and 0.002% Triton X-100 at pH 6.6.

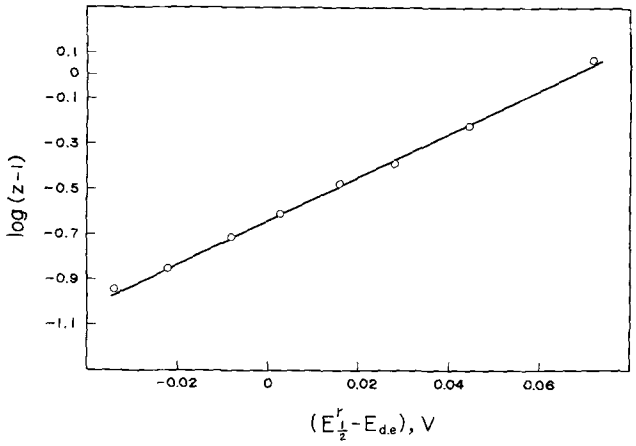

Fig. 6. Plot of log (Z — 1) against ($E_{1/2}{}^r$ — $E_{d.e.}$). 1.0 mM $UO_2(ClO_4)_2$, 0.1M DTPA, 0.15M $NaClO_4$, and 0.002% Triton X-100 at pH 6.6.

The k_s values were found to be of the order of 10^{-3} cm/sec, which indicates that the electrode reduction is quasi-reversible (16). As the pH increases, k_s was found to decrease, showing that the irreversibility increases with increasing pH value. The adsorption of surface-active substance on the dropping mercury electrode inhibited the reaction rate and resulted in the increase of irreversibility. The transfer coefficient α was found to be 0.42 ± 0.02 (Table VI).

Acknowledgment

The authors thank the National Science Council for financial support of this work.

Manuscript submitted Feb. 9, 1970; revised manuscript received *ca.* May 4, 1970.

Any discussion of this paper will appear in a Discussion Section to be published in the June 1971 JOURNAL.

REFERENCES

1. T. Dono, G. Nakagawa, and T. Nomura, *J. Chem. Soc., Japan*, **83**, 1249 (1962).
2. G. Kalland and E. Jacobsen, *Acta Chem. Scand.*, **17**, 2385 (1963).
3. G. Kalland and E. Jacobsen, *ibid.*, **18**, 1412 (1964).
4. E. Jacobsen and G. Kalland, *Talanta*, **11**, 139 (1964).
5. S. Misumi and A. Iwase, *Rev. Polarog. Japan*, **11**, 147 (1963).
6. M. Kodama, T. Noda, and M. Murata, *Bull. Chem. Soc., Japan*, **41**, 354 (1968).
7. L. M. Razbitnaya and I. A. Korovina, *Radiokhimiya*, **3**, 593 (1961).
8. T. T. Lai and B. C. Wang, *Anal. Chem*, **36**, 26 (1964).
9. M. Kodama and A. Kimura, *Bull. Chem. Soc., Japan*, **40**, 1639 (1967).
10. T. T. Lai and S. J. Wey, *This Journal*, **111**, 1283 (1964).
11. T. T. Lai and S. T. Lee, *Anal. Chem.*, **41**, 1316 (1969).
12. I. M. Kolthoff and J. J. Lingane, "Polarography," Vol. 1, p. 63, Interscience Publishers, New York (1952).
13. J. Heyrovsky and J. Kuta, "Principles of Polarography," p. 299, Academic Press, New York (1966).
14. P. Zuman and I. M. Kolthoff, "Progress in Polarography," Vol. 1, p. 96, Interscience Publishers, New York (1962).
15. J. N. Gaur and D. S. Jain, *Rev. Polarog. Japan*, **14**, 206 (1967).
16. J. Heyrovsky and J. Kuta, "Principles of Polarography," p. 214, Academic Press, New York (1966).

Cation Transport Numbers in Molten $AgNO_3$-AgCl Mixtures by Pressure-EMF Measurements

H. E. Townsend*[1] and Paul Duby*[2]

Department of Metallurgy and Laboratory for Research on the Structure of Matter, University of Pennsylvania, Philadelphia, Pennsylvania 19104

ABSTRACT

The pressure-emf, or difference in electrode potential which results from a hydrostatic pressure difference, was measured in molten salt cells represented schematically as

$$Ag(s)/AgNO_3, AgCl(l)\ [P_1]//AgNO_3, AgCl(l)\ [P_2]/Ag(s)$$

containing 0-42.8 m/o AgCl, from 200° to 260°C. Measurements of this effect, which depends on the difference between anion and cation mobilities, indicate that the cation transport number increases with increasing AgCl content or with decreasing temperature. Because of the small differences between anion mobilities, the pressure-emf alone is shown to provide a good approximation to all three ion constituent transport numbers in this system.

It has been reported previously (1) that a pressure-emf can be measured in fused salts by applying a pressure difference between two electrode compartments separated by a porous diaphragm and by recording the changes in potential difference between two identical metallic electrodes in equilibrium with the same electrolyte. Equations have been derived (2) which show that this pressure-emf is a linear function of the mass transport numbers of the various components relative to an external reference frame such as the cell or the diaphragm. Although the theory in general applies to any electrolyte, the experiments have so far been limited to single fused salts, and only the results on silver nitrate have been reported in detail (3). The present paper describes a similar investigation which has been carried out with molten mixtures of silver nitrate and silver chloride.

In the general case of a cell, at uniform temperature and composition, containing a mixture of c elemental components (ion constituents), one of which (denoted

* Electrochemical Society Active Member.
[1] Present address: Homer Research Laboratories, Bethlehem Steel Corporation, Bethlehem, Pa.
[2] Present address: Henry Krumb School of Mines, Columbia University, New York, N. Y.
Key words: cation transport numbers, molten salt mixtures, pressure-emf, silver nitrate melts, silver chloride melt, transport number.

by subscript 1) is oxidized or reduced at either of the two identical electrodes, it can be easily shown (2) that as a consequence of Saxen's relation,[3] the pressure-emf is given by the following equation

$$\frac{\Delta E}{\Delta P} = -\frac{1}{\mathbf{F}}\left[\frac{\overline{V}_1^{\circ}}{z_1} + \sum_{k=2}^{c} \tau_k \left(\frac{\overline{V}_k}{|z_k|} - \frac{z_k}{|z_k|}\frac{\overline{V}_1}{z_1}\right)\right] \quad [1]$$

where: ΔE is the electrical potential difference which is caused by the hydrostatic pressure difference ΔP; $\mathbf{F}$ is the Faraday constant (96,487 coulombs); $\overline{V}_1$ and z_1 are the partial molar volume and the oxidation number of the constituent of the electrolyte which reacts at the electrodes; $\overline{V}_1^{\circ}$ is the partial molar volume of the same constituent in the electrode phase; $\overline{V}_k$ and z_k are the partial molar volume and the oxidation number of the remaining elemental components which constitute the electrolyte and which can be determined by chemical analysis.

τ_k is the equivalent mass transport number of the component k relative to an external reference frame, and it is defined as the number of equivalents of the elemental component which would be transported across the diaphragm per faraday of electricity during an electrodiffusion experiment. The transport numbers are algebraic numbers, positive for a transport toward the cathode, and the sum of their arithmetic values equals one.

As discussed previously (2), these definitions, which lead to the above equation by a straightforward thermodynamic calculation, do not require any knowledge or any assumption concerning the ionic species actually present in the melt. The transport numbers are macroscopic quantities that describe the total fluxes resulting from all possible transport mechanisms.

The pressure-emf equation has been derived by the application of theories of thermodynamics of irreversible processes and Onsager's reciprocal relation. It requires only the assumption that the transport numbers and partial molar volumes remain constant within the range of electric field and hydrostatic pressure gradient across the fritted disk, and these conditions are easily verified experimentally. It is also assumed for the purpose of deriving the equation that the chemical composition and temperature remain uniform throughout the system. These conditions are actually fulfilled, even with a mixture as the electrolyte, because the pressure-emf can be measured very fast and because, with a suitable measuring device, no appreciable current is drawn from the cell so that no transport of matter occurs and no concentration gradient builds up.

Equation [1] is readily applied to a mixture of silver nitrate and silver chloride with two metallic silver electrodes. Silver, chlorine, and the nitrate group are the obvious choices as the elemental components, and the oxidation numbers are +1 for the silver and −1 for the chlorine and nitrate. Thus, for the cell which can be schematically represented as

$$\mathrm{Ag(s)/AgNO_3,\ AgCl(1)\ [}P_1\mathrm{]//AgNO_3,\ AgCl(1)\ [}P_2\mathrm{]/Ag(s)}$$

the pressure-emf for uniform temperature and composition is given by

$$-\mathbf{F}\frac{\Delta E}{\Delta P} = V_{Ag} + \tau_{NO_3}\overline{V}_{AgNO_3} + \tau_{Cl}\overline{V}_{AgCl} \quad [2]$$

Experimental

The pressure-emf, or difference in cell potential resulting from a pressure difference between the electrodes, has been measured by continuously recording the voltage of the cell described above and noting the changes that occur as the difference in hydrostatic pressure, $\Delta P = P_2 - P_1$, is alternately applied and released. A glass frit separates the two electrode compartments and allows the pressure difference to be maintained for finite times; 10-15 sec is usually allowed to apply, measure, and release a given pressure difference. Voltage changes were recorded with a Keithley 150 microvoltmeter (10^7 ohms input resistance on the 10 μV range) and a Bausch and Lomb VOM-5 recorder which were calibrated after a series of measurements at a particular temperature by use of a Keithley 260 (better than ± 0.05 μV for a 10 μV output) nanovolt source. The technique employed was with some minor changes identical to that previously described in detail in connection with the measurement of pressure-emf in pure molten salts (3). The modifications which were made as a matter of experimental convenience and do not appear to change the results include the use of silver wire electrodes secured by Teflon seals, instead of silver-plated tungsten wire electrodes sealed in glass, and fine (4-5μ) rather than medium (10-15μ) porosity fritted glass disks.

The pressure-emf has been studied in $AgNO_3$-AgCl mixtures of five compositions (0.057, 0.117, 0.232, 0.345, 0.428 equivalent fraction AgCl) at temperatures extending from the liquidus (indicated by the left-hand termini of the lines on Fig. 1) to the useful limit of the Teflon seals, about 260°C. For each composition, measurements were taken in a random sequence of temperatures. At each temperature which was held constant within ± 1°C by immersion of the cell in a molten Pb-Sn bath, we performed 20-30 individual measurements of the potential changes attending the applied pressure differences which ranged from 5 to 70 cm Hg. The direction of flow was reversed on alternate measurements. Plots of the potential changes, ΔE, against the corresponding pressure differences, ΔP, typically result in straight lines, the slopes of which are the pressure-emf, $\Delta E/\Delta P$. Standard deviations of these slopes were generally within the range 0.05-0.15 μV/atm. This scatter is related to changes in the slope of the background drift (total background generally less than 200 μV) which accompany the flow of salt under the applied pressure difference. Typical recordings of the changes in cell potential as the pressure is applied and released as well as additional experimental details are given elsewhere (3, 11).

The minus sign on the $\Delta E/\Delta P$ values measured in this investigation indicates that in all cases the electrode at the higher pressure became more anodic on application of the pressure difference.

The salt mixtures were prepared from Baker reagent-grade salts, which were fused, mixed, and filtered prior to placing within the cell.

Results and Discussion

The measurements of pressure-emf for mixtures of $AgNO_3$-AgCl are summarized in Fig. 1. At each com-

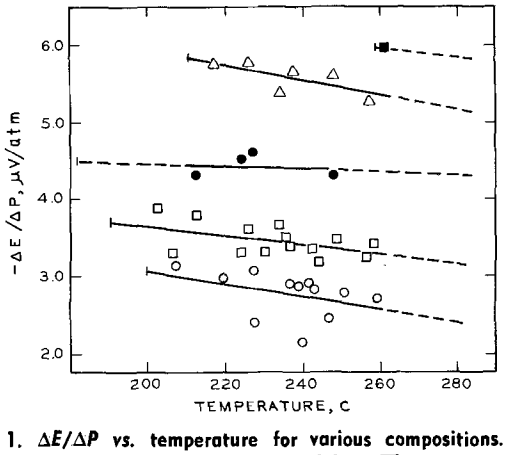

Fig. 1. $\Delta E/\Delta P$ vs. temperature for various compositions. Mole fractions of AgCl are respectively: ○ 0.057, □ 0.117, ● 0.232, △ 0.345, ■ 0.428.

[3] See, for example, G. N. Lewis, M. Randall, K. S. Pitzer, and L. Brewer, "Thermodynamics," 2nd ed., p. 458, McGraw-Hill Book Co., New York, N. Y. (1961).

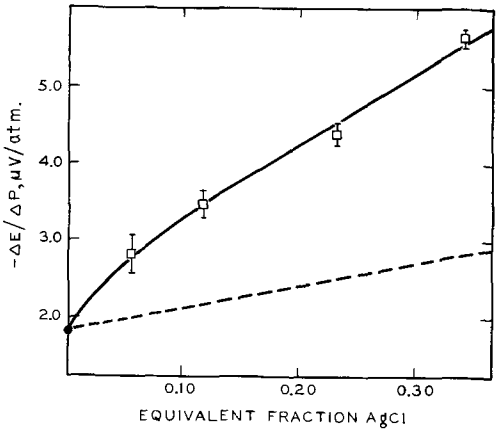

Fig. 2. $\Delta E/\Delta P$ vs. composition, $t = 230°C$. ● pure salt value (ref. 3), □ this work, – – – calculated assuming τ^*_- remains constant with composition.

position (except at $N_{AgCl} = 0.428$, where only one temperature was studied) there appears to be a slight decrease in the absolute value of $\Delta E/\Delta P$ with increasing temperature. The lines drawn through the points at each composition were constructed by a least squares fit.

At those compositions for which measurements were performed at the greatest number of temperatures, it was observed that measurements (those which deviate most from the least squares lines of Fig. 1) at the first few temperatures differed by several standard deviations from the least squares lines. After the initial measurements, however, the results which followed seemed to fit more closely to the downward sloping line. Accordingly, one might be justified in rejecting the initial data on the basis of a possible systematic error.[4] We have chosen not to do this because (*a*) only a few measurements were performed for two of the compositions and (*b*) the salient results of this study, namely, the composition dependence at constant temperature of the pressure-emf and of the transport numbers, are largely unaffected.

At a given temperature, the value of pressure-emf increases markedly with increasing concentration of AgCl. Figure 2 clearly shows the increase of $\Delta E/\Delta P$ relative to the pure salt value (3) as AgCl concentration is increased at 230°C. The error limits associated with each point are based on the standard deviation calculated from the distribution of the data about the least squares lines of Fig. 1.

The composition dependence of $\Delta E/\Delta P$ can now be considered in relation to mass transport in this system. An average anion mass transport number, τ^*_-, can be defined as

$$\tau^*_- = \frac{1}{V_m}\left(\tau_{NO_3}\,\overline{V}_{AgNO_3} + \tau_{Cl}\,\overline{V}_{AgCl}\right) \qquad [3]$$

where $V_m = N_{AgNO_3}\,\overline{V}_{AgNO_3} + N_{AgCl}\,\overline{V}_{AgCl}$ is the equivalent volume of the mixture and N_{AgCl} and N_{AgNO_3} are the equivalent fractions of those components. This allows Eq. [2] to be written as

$$-\mathbf{F}\frac{\Delta E}{\Delta P} = V_{Ag} + \tau^*_- V_m \qquad [4]$$

The broken line shown in Fig. 2 is a plot of Eq. [4] where the assumption has been made that τ^*_- remains unchanged as AgCl is added to pure $AgNO_3$. The slight upward slope reflects the decrease in V_m (4) with increasing N_{AgCl}. The measured values occur significantly above this line, thus indicating that the average anion mass transport number decreases with increasing concentration of AgCl.

[4] Since similar behavior was not observed in experiments with pure $AgNO_3$ (3), we suspect that incomplete mixing in the case of the initial measurements with mixtures may be a possible source of error.

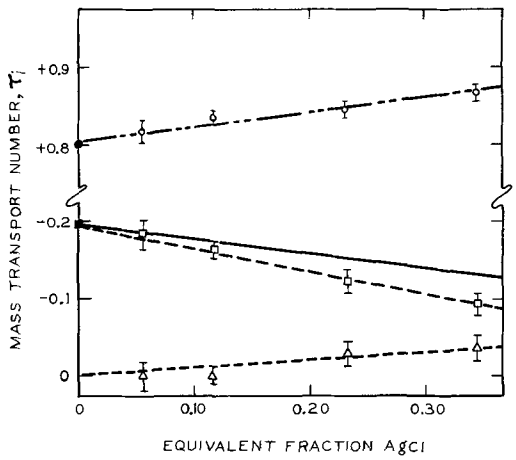

Fig. 3. Mass transport numbers vs. composition, $t = 230°C$. $-\tau^*_-$ calculated from Eq. [4]; ———— $(1 - \tau^*_-)$. ●, ■ pure salt values of mass transport number (ref. 3) of Ag^+ and NO_3^-, respectively; ○ τ_{Ag}; □ τ_{NO_3}; △ τ_{Cl}; – – – $\tau^*_-\,N_{AgNO_3}$ (negative slope) and $\tau^*_-\,N_{AgCl}$ (positive slope).

The decrease in τ^*_- with increasing AgCl is shown explicitly in Fig. 3, where the solid line has been drawn through values computed from Eq. [4]. Correspondingly, there is an increase in the average cation mass transport number, τ^*_+, defined by

$$\tau^*_+ = 1 + \tau^*_- \qquad [5]$$

shown at the top of Fig. 3.

The average anion mass transport number can be related to those of the elemental components by

$$\tau_{NO_3} = \tau^*_-\,N_{AgNO_3} - \phi\frac{V_{AgCl}}{V_m}$$

$$\tau_{Cl} = \tau^*_-\,N_{AgCl} + \phi\frac{V_{AgNO_3}}{V_m} \qquad [6]$$

where

$$\phi = \tau_{Cl}\,N_{AgNO_3} - \tau_{NO_3}\,N_{AgCl} \qquad [7]$$

The function ϕ is a measure of the difference between the mobilities of the two unlike elemental components with the same oxidation number in a binary common-ion mixture. It is often used to summarize results such as those of a Hittorf experiment (5, 6), a measurement of liquid junction potential (7, 8), or a measurement of the potential of a gravity cell (4), which all depend on that difference and are related to the function ϕ. For the system $AgNO_3$-AgCl, it has been previously shown that ϕ is quite small (4) (less than 0.03), which indicates that the values of the mobilities of the two anionic elemental components are nearly equal in these ranges of composition and temperature. Thus, the last term in Eq. [6] may be neglected as a first approximation, allowing computation, within a reasonable degree of precision, of τ_{NO_3} and τ_{Cl}, as well as τ_{Ag} from

$$\tau_{Ag} - \tau_{NO_3} - \tau_{Cl} = 1 \qquad [8]$$

Values of τ_{NO_3} and τ_{Cl} that result from neglecting the last terms in Eq. [6] are plotted as the two lowermost dashed lines in Fig. 3. Exact values of elemental component mass transport numbers, τ_{Ag}, τ_{NO_3}, and τ_{Cl}, which have been computed without approximation using Eq. [4] and [6], with the experimental values of ϕ (4), are also shown on Fig. 3 with the associated uncertainties. Within the cumulative uncertainty, the exact values are coincident with the approximate quantities which have been inferred from the pressure-emf measurements alone, assuming equal anion mobilities. Thus, the approximations

$$\begin{aligned}\tau_{Ag} &= 1 + \tau^*_-\\ \tau_{NO_3} &= \tau^*_-\,N_{AgNO_3}\\ \tau_{Cl} &= \tau^*_-\,N_{AgCl}\end{aligned} \qquad [9]$$

are quite satisfactory; and this system as well as others (8, 9), for which ϕ has been determined to be small relative to the precision with which it can be measured, are amenable to description in terms of a single mass transport number, τ^*_-, determined by the relatively simple experimental technique of pressure-emf.

Without necessarily invoking any microscopic model one can define electrical mobilities which correspond to the quantities τ^*_- and τ^*_+ as

$$U^*_- = \tau^*_- \frac{\Lambda}{\mathbf{F}} \qquad [10]$$

$$U^*_+ = \tau^*_+ \frac{\Lambda}{\mathbf{F}}$$

where Λ is the equivalent conductance. These mobilities have been calculated at 10-degree intervals by use of available conductivity data (10) and are shown in Fig. 4 for each of the compositions studied. Although the slope dU^*_+/dT is greater than dU^*_-/dT, the fractional rate of increase is greater for U^*_-, a fact which is significant for two reasons. First, it indicates that the average cation mass transport number

$$\tau^*_+ = \frac{U^*_+}{U^*_+ - U^*_-} \qquad [11]$$

is decreasing with temperature. Second, it indicates that the activation energies for electrical transport, which can be deduced from an Arrhenius plot of these mobilities, are larger for anion transport. A trend of decreasing anion mobility and hence increasing activation energy with increasing concentration of AgCl is also evident in Fig. 4.

At all temperatures the values calculated for U^*_+ are identical up to 0.232 AgCl as shown on Fig. 4. However, within experimental uncertainty (about 5%, cf. Fig. 3), it would be possible to assume that, with increasing concentration of AgCl. a linear increase in U^*_+ occurs simultaneously with the decrease in U^*_-.

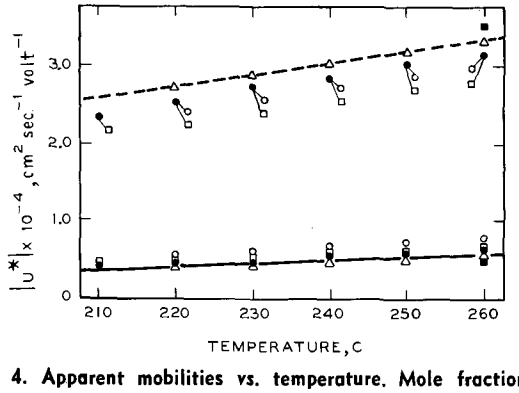

Fig. 4. Apparent mobilities vs. temperature. Mole fractions of AgCl are respectively: ○ 0.057; □ 0.117; ● 0.232, △ 0.345; ■ 0.428. The continuous and the interrupted lines represent U^*_- ———, and U^*_+, – – –, for $N_{AgCl} = 0.345$. Values of U^*_+ for 0.057 and 0.117 are coincident with that at 0.232.

On the basis of the relative anion mobilities as well as the concentration dependence of conductivity and the thermodynamic properties of these mixtures, it has been previously suggested (4) that the process of mixing molten $AgNO_3$ and AgCl could be described in terms of the formation of relatively low-mobility mixed anionic complexes, the simplest example of which is $ClAgNO_3^-$. The results of this investigation, notably (*a*) the decrease in combined anion mobility (as shown in Fig. 3 and 4), and (*b*) the larger (absolute) value of activation energy for anion mobilities, may be consistent with that point of view.

The relationship of item (*a*) above to a model of mixed anionic complexes is obvious enough, particularly when one notes that the values of τ_{NO_3} and τ_{Cl} seem to approach the same value at $N_{AgCl} = N_{AgNO_3}$. Item (*b*) could be related to the same phenomenon in that an additional activation energy is required for thermal dissociation of the complex species as they are formed to an increasing extent with increasing N_{AgCl}. However, any models of complex ion formation based solely on macroscopic transport and thermodynamic information will admittedly remain quite speculative until further information such as self-diffusion, x-ray, and spectroscopic data become available.

One might also inquire as to the generality of the phenomenon of decreased average mobility for the noncommon elemental components in common-ion binary mixtures exhibiting negative heats of mixing. Additional transport measurements in other systems would be useful in this regard.

Acknowledgment

This work was performed at the Laboratory for Research on the Structure of Matter, Department of Metallurgy, University of Pennsylvania and was supported by the Advanced Research Projects Agency, Office of the Secretary of Defense.

Manuscript submitted Dec. 3, 1969; revised manuscript received April 28, 1970. This was Paper 342 presented at the Los Angeles Meeting of the Society, May 10-15, 1970.

Any discussion of this paper will appear in a Discussion Section to be published in the June 1971 JOURNAL.

REFERENCES

1. P. Duby and H. H. Kellogg, *This Journal*, **110**, 349 (1963).
2. P. Duby, Thesis, Columbia University (1962); Dissertation Abstr., **23**, 2711 (1963).
3. P. Duby, submitted to J. Electrochem. Soc.
4. H. E. Townsend and P. Duby, submitted to Electrochimica Acta; presented at the 20th meeting of CITCE, Strasbourg, France, September, 1969.
5. S. Hill and F. E. W. Wetmore, *Can. J. Chem.*, **32**, 864 (1954).
6. P. Aziz and F. E. W. Wetmore *ibid.*, **30**, 779 (1952).
7. K. H. Stern, *This Journal*, **112**, 1049 (1965).
8. R. W. Laity, *J. Am. Chem. Soc.*, **79**, 1849 (1957).
9. R. W. Laity and C. T. Moynihan, *J. Phys. Chem.*, **67**, 723 (1963).
10. R. C. Spooner and F. E. W. Wetmore, *Can. J. Chem.*, **29**, 277 (1951).
11. H. E. Townsend, Ph.D. Dissertation, University of Pennsylvania (1967).

Thermodynamics of Molten Silver Chloride-Alkali Chloride Solutions by Electromotive Force Measurements

A. D. Pelton and S. N. Flengas*

Department of Metallurgy and Materials Science, University of Toronto, Toronto 5, Ontario, Canada

ABSTRACT

Electromotive force measurements have been made using the reversible formation cell

$$Ag \mid \begin{matrix}\text{AgCl-alkali chloride} \\ \text{(liquid)}\end{matrix} \mid \text{graphite, } Cl_2$$

Various aspects of the cell design are discussed. Measurements were of sufficient precision to give the concentration dependence and the magnitude of the excess free energies, enthalpies, and excess entropies of mixing in the AgCl-ACl (where A = Na, K, Rb, or Cs) systems. The results are discussed in terms of covalent bonding in molten silver chloride. A simple semiquantitative "dual bonding" model is developed in which "ionic" and "covalent" silver coexist.

A knowledge of the thermodynamic properties of molten AgCl-alkali chloride mixtures is of importance in the understanding of the fundamental properties of simple fused salt systems. Accurate enthalpies of mixing in these systems are available from the calorimetric measurements of Hersh and Kleppa (1). Several authors have studied the AgCl-LiCl (2, 3), AgCl-NaCl (4-7), and AgCl-KCl (7-9) systems using electrochemical formation cells. This work is reviewed by Dijkhuis *et al.* (10). Recently, Guion *et al.* (7) have made some measurements in the AgCl-CsCl system. Such measurements in the AgCl-RbCl system have not been reported. From these results, the magnitude of the free energies of mixing are known with reasonable accuracy in these systems. However, asymmetry terms in the concentration dependences of the free energies of mixing are at best poorly defined. The temperature dependences of the measured emf's are of sufficient precision to give only a very approximate estimate of the excess entropies of mixing. A knowledge of the excess entropies of mixing is of prime importance in understanding the solution properties of these mixtures. In the present investigation, measurements of the emf's of formation cells of the following type were made

$$Ag \mid AgCl\text{-}ACl \mid \text{graphite, } Cl_2$$

(where A = Na, K, Rb, or Cs). The measurements were of sufficient precision to permit the calculation of not only the magnitudes but also the asymmetries in the concentration dependences of the excess free energies, enthalpies, and excess entropies of mixing in these systems.

Experimental

A quartz cell was used. A diagram of this cell is shown in Fig. 1. The inner quartz crucible was filled to a depth of about 1½ in. with the melt. The cell was surrounded by a grounded Inconel metal sheath and placed in a tube furnace. Temperatures were read with a calibrated chromel-alumel thermocouple placed as shown in Fig. 1. In a preliminary experiment in which another identical thermocouple was placed in the melt, it was found that the thermocouple in the thermocouple well read the melt temperature correct to within about 0.5°K and also that the temperature gradients over the 1½ in. depth of the melt were of the order of 0.5°K. The total error in temperatures reported is probably about ±1°K. The cell emf and the thermocouple output were tested for induced pickup from the a-c field of the furnace windings by taking readings as the furnace was switched off and on. With the Inconel sheath grounded, no detectable pickup was observed.

A silver electrode of 99.9+% purity and of ⅛ in. diameter welded to a 0.040 gauge silver lead was used. The cell emf was independent of depth of immersion provided that the electrode was immersed deeper than about ¼ in. Only a very small amount of dendrite formation was observed on the silver after operating the cell for a period of two to three days. However, if a finer gauge silver electrode were used, more dendrites formed, and cell voltages were slightly less stable. Possibly, the larger silver wires, having higher thermal conductance, tend to have smaller temperature gradients along their lengths.

The graphite used in the chlorine electrode was ⅛ in. diameter special spectroscopic "SPK" graphite from National Carbon Company. The graphite rods were pretreated by being held at 900°C alternately for 12 hr under vacuum and under an atmosphere of chlorine for a total of 48 hr. A small amount of tar-like im-

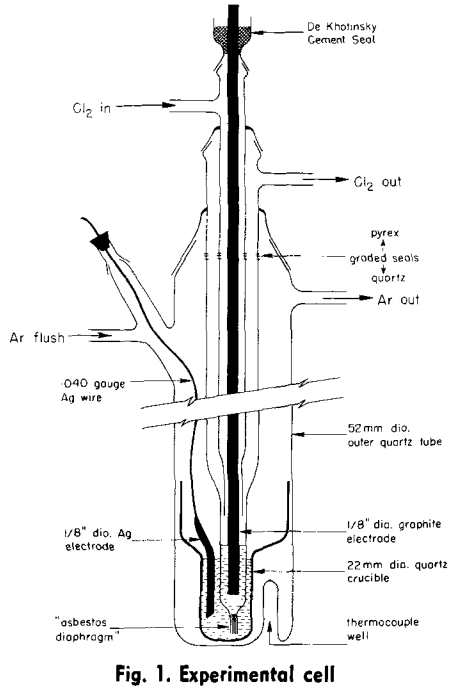

Fig. 1. Experimental cell

* Electrochemical Society Active Member.

Key words: silver chloride, alkali chlorides (sodium chloride, potassium chloride, rubidium chloride, cesium chloride), molten salts (fused salts), formation cells, chlorine electrode, silver electrode, thermodynamics.

purity was removed in this manner. The chlorine used was Matheson "high purity" grade. The chlorine was passed over magnesium perchlorate before being admitted to the cell. It was found that saturation of the melt with chlorine could be achieved without the necessity of bubbling the chlorine through the melt. An arrangement as in Fig. 1 with the Cl_2 inlet tube ending 1 cm above the melt was used.

Of major importance in the present cell design is the "asbestos diaphragm" which separates the two electrode compartments and prevents the diffusion of chlorine to the silver electrode (11). Briefly, these diaphragms are made by tightly rolling a small strand of asbestos string, firing it to a white ash, and then collapsing 6 mm quartz tubing around it with tweezers. Very fine capillary channels result. Cell resistances of 1000 to 20,000 ohms were obtained with these diaphragms. No noticeable attack of the silver electrode after several days of operation was noticed. Most other investigators have used quartz frits or capillary tubes as diaphragms, with cell resistances of about 50 ohms. It is believed that the very stable cell voltages in the present study are, to a large degree, a result of these high resistance asbestos diaphragms.

Reagent grade AgCl, NaCl, and KCl were used. The CsCl (Fisher) was of 99.9% purity, and the RbCl (Matheson) was of 99+% purity. All salts were dried under vacuum and with dry HCl gas at 400°C in the case of AgCl and at 550°C for the alkali chlorides. All salts were stored in a vacuum dessicator.

In a typical experiment, the quartz crucible was filled with the salts and, with the silver electrode in place, the outer cell was capped with a rubber stopper and the salts were melted under vacuum. If melting was not done under vacuum, cell voltages would be slightly less stable for the first 24 hr, possibly because of the effect of dissolved oxygen on the silver electrode. After fusion had occurred, dried purified argon was admitted to the outer cell, and the inner cell, containing the proper amount of salts, was quickly lowered into place. After 2 min, when the salts in the inner cell had melted, the graphite electrode assembly was lowered into place and the inner cell was quickly flushed with dried argon. Cell voltages were found to be slightly more stable if about 12 hr were allowed to elapse before readings were taken.

The chlorine electrode compartment was flushed with chlorine at a high flow rate. After about 1 hr the cell voltage would be stable. Thereafter, readings were taken with the Cl_2 flowing at about 25 ml/min. Voltages were independent of flow rate. The cell emf was measured with a Leeds and Northrup K3 potentiometer. All voltages reported in this work are in absolute volts. No appreciable condensation of salt in the upper part of the apparatus was observed, and so volatility of the salts is not a problem at the temperatures employed in these experiments.

The Cl_2 pressure in the cell was measured with a manometer filled with H_2SO_4. The pressure was about 3 mm Hg above barometric because of the exit bubbler heads. All readings reported were corrected to a Cl_2 pressure of 1 standard atmosphere (1.01325×10^5 newton-m^{-2}). Voltages measured would remain stable to ±0.2 mV for several hours. Response to temperature changes was immediate. Voltages were reproducible on repeated heating and cooling cycles as shown later. All cells were subjected to a polarization test in which about 1 mA was passed through the cell for about 1 min in each direction using an external dry cell. Cell voltages would return to within 0.1 mV of their previous values within 15 sec after the external dry cell was disconnected.

Pressure dependence.—The response of the cell to changes in chlorine pressure was studied. This was done previously, but only over the limited pressure range of 760 to 1050 mm Hg, by Wachter and Hildebrand (12) who observed the expected Nernst behavior.

The chlorine pressure was controlled by mixing the Cl_2 with dry purified argon. Chlorine and argon flow rates were measured using Gilmont "RGI" spherical float flowmeters which were calibrated for the specific gases with a soap-bubble column. Chlorine pressures from 1.0 to 10^{-1} atm could be determined with an accuracy of about ±5%, and from 10^{-1} to 10^{-2} atm with about ±15% accuracy. Calculations show, then, that an accuracy of about ±2 mV at higher Cl_2 pressures and about ±6 mV at the lowest Cl_2 pressures should be obtained at the temperatures of the experiments. At the lowest Cl_2 pressure, when the Ar flow rate was very high, some of the gas mixture was bled off before reaching the cell so that the total flow rate through the cell was about 50 ml/min. Flow rates were kept steady to about ±2% for the duration of a measurement using needle valves.

Five pressure-dependence studies were made, three with pure AgCl electrolyte at different temperatures, and two with fairly dilute solutions of AgCl in NaCl. No hysteresis was observed on increasing and decreasing pressure cycles. The cell voltage responded very quickly to the presure changes. Steady voltages were obtained within about 15 min of a flow rate change, which is about the time one would expect to be required for the gas phase to reach equilibrium. Results are shown in Fig. 2. Theoretical lines calculated from the Nernst equation are also shown. Results are within the error limits expected from the accuracies of the pressure measurements.

Several authors (4, 8, 13-15) have noted that pretreatment of the graphite electrode (usually with Cl_2 at high temperature as in the present study) is necessary for the attainment of stable voltages. It has been suggested that the pretreatment is necessary to saturate the graphite with chlorine. However, the rapid response of the cell emf to changes in Cl_2 pressure as observed in the present study would indicate that saturation is no problem. Perhaps the main effect of the pretreatment is to oxidize impurities (such as ungraphitized binder) in the graphite. Several of these authors have also stated that a pre-electrolysis step was sometimes required to achieve stability. This was not required in the present study.

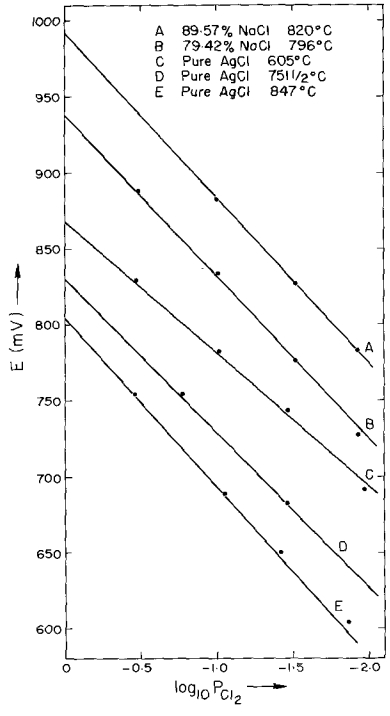

Fig. 2. Results of pressure-dependence studies. Lines shown are calculated from the Nernst equation.

Thermoelectric correction.—The correction for the voltage of the Ag-C couple was determined by measuring the voltage of a cell in which the contact between the silver and the graphite was made with a silver wire instead of the molten electrolyte. Results are shown in Fig. 3. Voltages were quite reproducible on continued heating and cooling. Carbon is negative to silver at the cold junction, and so the thermoelectric potential opposes the emf of the cell. The voltages are very nonlinear with temperature. Voltages as measured by Hamby (16) are also shown in Fig. 3. Panish *et al.* (4) do not give their correction, but state that it was "from 1-9 mV" over the temperature range of interest, which is close to the values obtained in the present study. Literature values (17) give the voltage of the Ag-C couple as varying from 1.2 to 2.6 mV from 500° to 900°C. It would appear that these values are questionable.

The equation of the curve shown in Fig. 3, as obtained by a least squares analysis is

$$V\ (\text{mV}) = 4.36 - 0.08802T + 0.01288T \ln T \quad [1]$$

where T is in Kelvins. This thermoelectric correction only affects the absolute values of E° for the formation of pure AgCl, and does not, of course, affect the differential solution properties.

Results

Formation potential, E°, of pure AgCl.—The formation potential, E°, of pure AgCl was determined in three separate experiments. Results as shown in Fig. 4 are not corrected for the thermoelectric potential. These results were obtained on several heating and cooling cycles.

Recent measurements in this laboratory (18) indicate that the heat capacity, C_p, of liquid AgCl is 13.7 cal/K-mole. Using this value along with literature (19) values of C_p for Ag and Cl_2, ΔC_p for the reaction

$$Ag + \tfrac{1}{2}Cl_2 \rightarrow AgCl_{(liq)} \quad [2]$$

was calculated as

$$\Delta C_p = 4.2 - 2.07(10^{-3})T \text{ cal/K-mole} \quad [3]$$

where T is in Kelvins. (In the present work, 1 calorie is defined as 4.1840J.) Therefore, from the relationship

$$\Delta C_p = nFT\left(\frac{\partial^2 E^\circ}{\partial T^2}\right) \quad [4]$$

(where $n = 1$ for reaction [2] and **F** is the Faraday constant) it may be shown that the expected functional form of E° is

$$E^\circ(\text{mV}) = A + BT + 0.182T \ln T - 4.48(10^{-5})T^2 \quad [5]$$

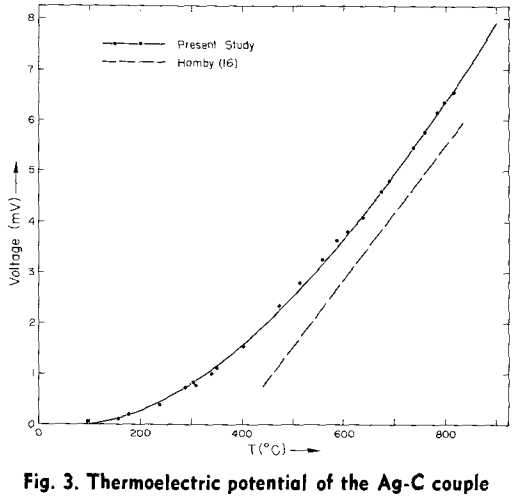

Fig. 3. Thermoelectric potential of the Ag-C couple

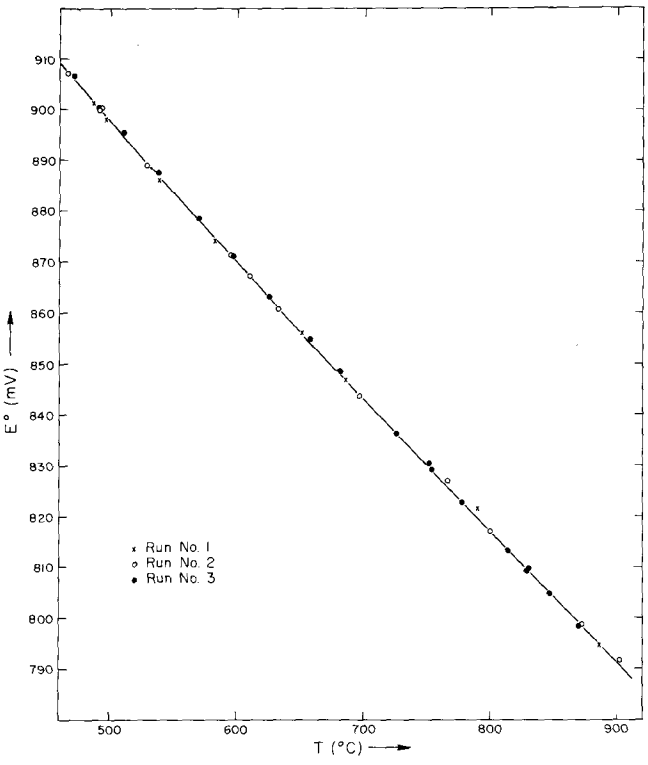

Fig. 4. Formation potential of pure AgCl (uncorrected for thermoelectric potential).

The 39 data points from the three experiments were fitted by a least squares method to an equation of the form of Eq. [5], giving

$$E^\circ(\text{mV}) = 1227.0 - 1.5973T + 0.182T \ln T - 4.48(10^{-5})T^2 \quad [6]$$

The standard deviation was 0.57 mV, and only one point deviated by more than 1.0 mV from the line. The curvature of the experimental curve is thus in very good agreement with that predicted on the basis of heat capacity measurements. In Fig. 4 are shown the experimental points and the fitted curve. Values shown in Fig. 4 are uncorrected for the thermoelectric effect, and the curve shown is Eq. [6] with Eq. [1] subtracted from it.

Hamer *et al.* (20) calculated E° from thermochemical data. If Hamer's calculations are corrected by taking C_p for liquid AgCl as 13.7 (instead of 16.0 as used by Hamer), then the thermochemical curve of E° *vs.* T is very close to the curve measured in the present study and is nearly parallel to it. This is shown in Table I. Agreement between the present results and E° values measured electrochemically by other authors (4, 7, 11, 13, 14, 21) is also reasonable. Values taken from Senderoff and Mellors' (13) curve are listed in Table I. Much of the discrepancy between the present results and those of Senderoff and Mellors probably results from their use of the literature (17) values for the thermoelectric correction. Values measured by Flengas and Ingraham (11) by extrapolating emf's measured in concentration cells are also shown in Table I and are in good agreement with the present values and also with the thermochemical data.

Table I. Formation potentials, E°, of pure AgCl (mV)

	500°C	600°C	700°C	800°C	900°C
Present study	900.4	873.6	848.0	823.3	799.4
Thermochemical	896	869	844	819	794
Senderoff and Mellors (13)	—	868.4	842.1	815.8	789.5
Flengas and Ingraham (11)	—	—	845	820	795

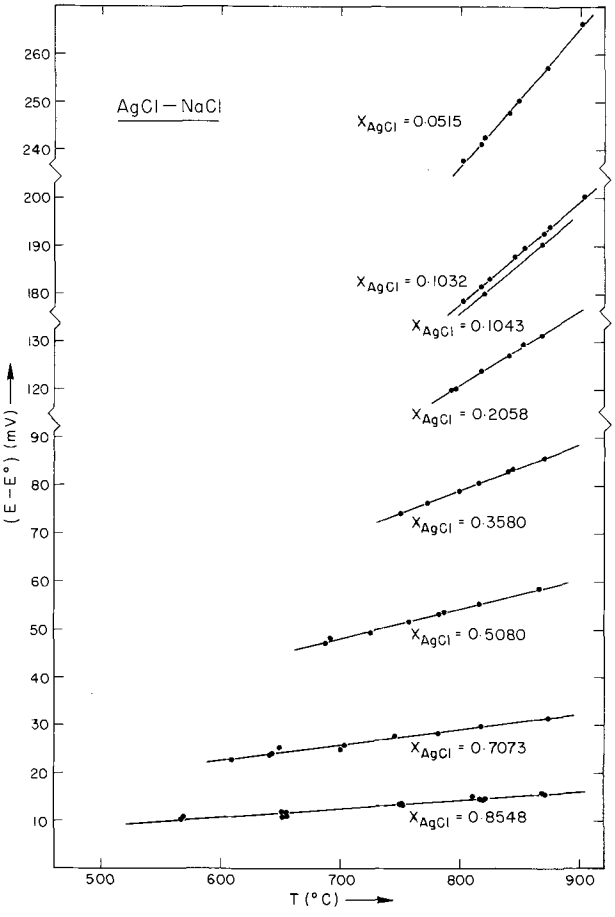

Fig. 5a. (E — E^o) vs. temperature in the AgCl-NaCl system

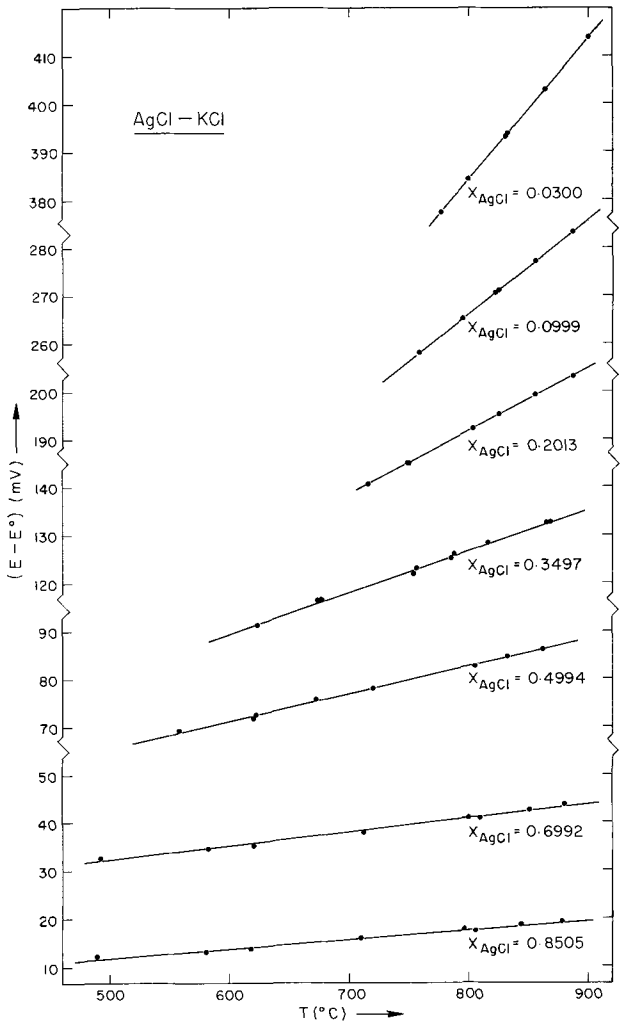

Fig. 5b. (E — E^o) vs. temperature in the AgCl-KCl system

AgCl-alkali chloride solutions.—Cell potentials, E, were measured with electrolytes at several compositions in the AgCl-ACl systems (where A = Na, K, Rb, and Cs). Values of (E — E^o) were calculated for each experimental point using Eq. [6] for E^o. The results are shown in Fig. 5(a-d). The points shown for any one experiment were obtained during at least one, and usually two, heating and cooling cycles. In all cases, the points were well-fitted by straight lines. Least square lines are shown in Fig. 5 (a-d), and the equations of the lines are given in Table II along with the mean and maximum deviations for each line. The mean deviation is never greater than 0.5 mV, and the average maximum deviation is about 0.6 mV.

For a few compositions in the "eutectic wells" of the systems, it was possible to measure values of E at temperatures below the melting point (455°C) of pure

Table II. Linear least squares fits for (E — E^o) vs. temperature at compositions in AgCl-alkali chloride systems (1 cal = 4.1840J)

System	X_{AgCl}, mole fraction	E — E°, mV (T = °K)	Mean dev, mV	Max dev, mV	$\Delta\bar{S}^E_{AgCl}$, cal/K-mole	$\Delta\bar{H}_{AgCl}$, cal/mole	$\Delta\bar{G}^E_{AgCl}$ at 800°C, cal/mole
AgCl-NaCl	0.0515	−72.0 + 0.2875T	0.4	0.6	0.74	1661	870
	0.1032	−54.2 + 0.2163T	0.2	0.5	0.47	1251	741
	0.1043	−49.5 + 0.2101T					765
	0.2058	−45.5 + 0.1553T	0.2	0.4	0.44	1050	579
	0.3580	−24.9 + 0.0968T	0.1	0.1	0.19	574	368
	0.5080	−12.8 + 0.0625T	0.2	0.5	0.10	294	191
	0.7073	−6.4 + 0.0331T	0.3	1.0	0.07	147	67
	0.8548	−5.2 + 0.0182T	0.3	0.9	0.11	119	4
AgCl-KCl	0.0300	67.3 + 0.2952T	0.1	0.1	−0.16	−1553	−1382
	0.0999	53.5 + 0.1981T	0.1	0.1	−0.01	−1233	−1224
	0.2013	49.6 + 0.1324T	0.1	0.2	−0.13	−1143	−1001
	0.3497	34.2 + 0.0862T	0.3	1.0	−0.10	−788	−681
	0.4994	21.2 + 0.0572T	0.3	0.6	−0.06	−489	−425
	0.6992	9.7 + 0.0290T	0.3	0.6	−0.04	−225	−180
	0.8505	−2.7 + 0.0188T	0.3	0.5	0.11	61	−58
AgCl-RbCl	0.0297	120.2 + 0.2796T	0.2	0.4	−0.54	−2771	−2191
	0.0997	111.2 + 0.1750T	0.3	0.6	−0.55	−2564	−1978
	0.1999	90.6 + 0.1198T	0.1	0.3	−0.44	−2089	−1622
	0.3509	63.6 + 0.0766T	0.3	0.6	−0.31	−1467	−1129
	0.5007	33.5 + 0.0536T	0.3	0.5	−0.14	−772	−623
	0.5995	20.0 + 0.0407T	0.1	0.1	−0.08	−462	−377
	0.7007	10.7 + 0.0299T	0.1	0.4	−0.02	−247	−229
AgCl-CsCl	0.0292	171.4 + 0.2703T	0.2	0.3	−0.79	−3953	−3107
	0.0861	156.0 + 0.1826T	0.4	0.6	−0.66	−3596	−2886
	0.1989	127.0 + 0.1154T	0.3	0.7	−0.55	−2929	−2341
	0.3575	95.6 + 0.0632T	0.5	1.4	−0.59	−2205	−1575
	0.5132	54.3 + 0.0407T	0.5	0.9	−0.39	−1252	−837
	0.7082	25.9 + 0.0142T	0.5	1.0	−0.36	−598	−212
	0.8497	2.5 + 0.0142T	0.4	1.1	0.00	−58	−62
	0.8501	3.6 + 0.0122T	0.3	0.5	−0.04	−83	−38

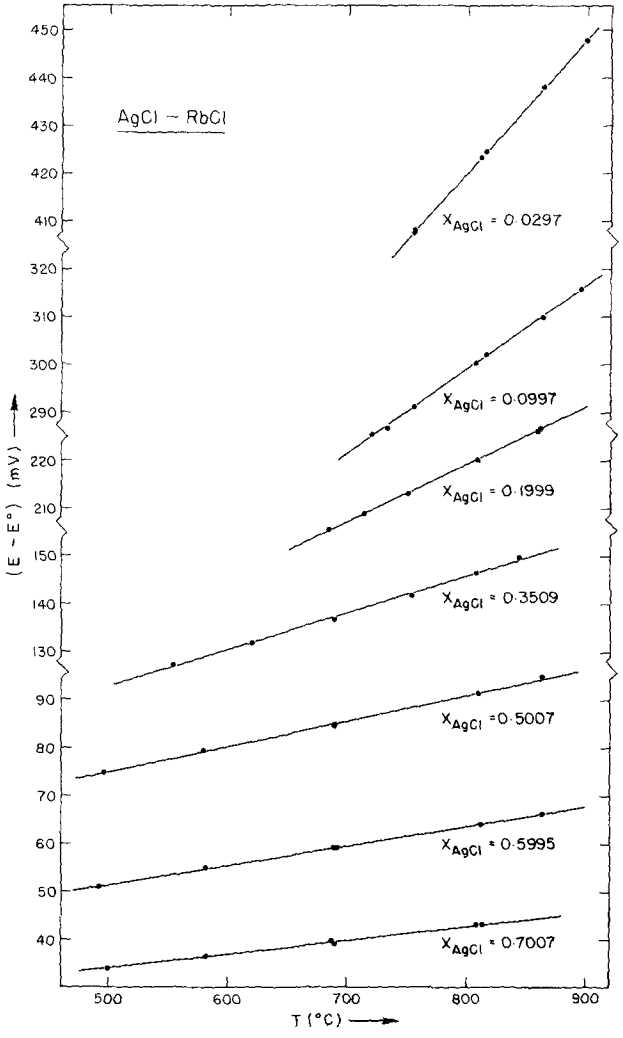

Fig. 5c. ($E - E^o$) vs. temperature in the AgCl-RbCl system

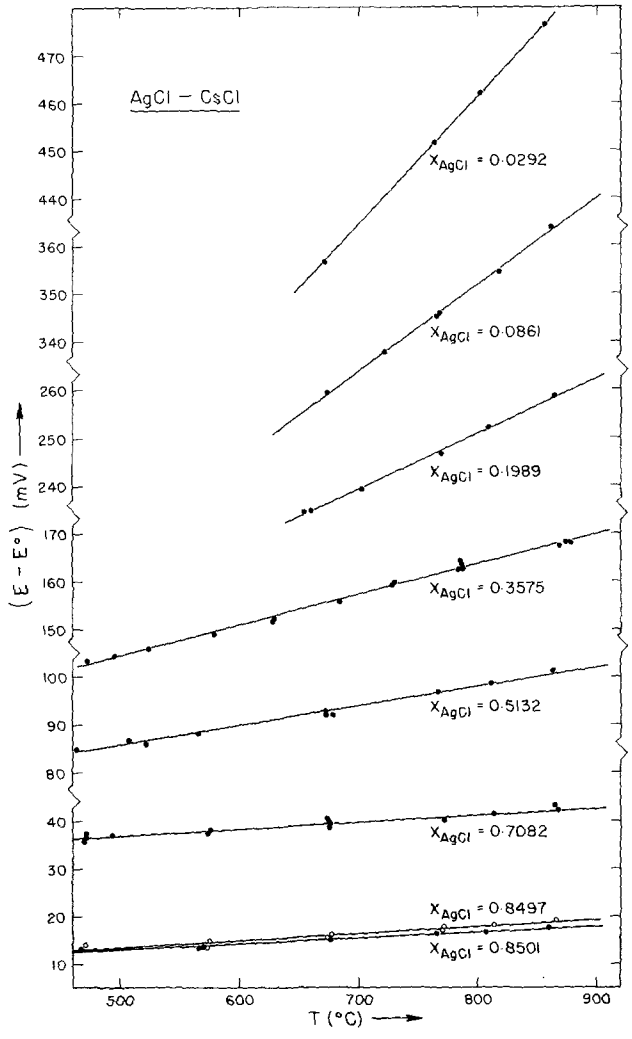

Fig. 5d. ($E - E^o$) vs. temperature in the AgCl-CsCl system

AgCl. From these values of E, and values of $(E - E^o)$ extrapolated using the linear equations in Table II, it was possible to calculate E^o values for pure supercooled liquid AgCl at temperatures down to about 275°C. Calculated values of E^o lay close to the curve obtained by extrapolating Eq. [6]. The disagreement was about 3 mV at 275°C, with the extrapolated curve lying below the calculated points.

In Table II, the partial molar excess free energy of mixing of AgCl, $\Delta\bar{G}^E_{AgCl}$, as calculated from the fitted line, is listed for each composition studied at 800°C. Also listed are the partial molar enthalpy and excess entropy of mixing of AgCl, $\Delta\bar{H}_{AgCl}$ and $\Delta\bar{S}^E_{AgCl}$, calculated from the temperature dependence of $(E - E^o)$. These two properties are temperature independent within experimental accuracy since the $(E - E^o)$ curves are linear within experimental accuracy. (For the composition at $X_{AgCl} = 0.1043$ in the AgCl-NaCl system, there are only two data points, and it was felt that the slope of this line is not sufficiently well defined for partial enthalpies and excess entropies to be calculated.)

For each system, the three partial properties listed in Table II were fitted, using a least squares technique, to power series of the form

$$\Delta\bar{F}_{AgCl} = aX^2_{ACl} + bX^3_{ACl} + cX^4_{ACl} + \ldots \quad [7]$$

where $\Delta\bar{F}_{AgCl}$ is the partial property in question, and X_{ACl} is the mole fraction of alkali chloride. The fitted equations and mean and maximum deviation for each fit are given in Table III. These fits are discussed in detail below. Also in Table III are the fitted equations for $\Delta\bar{G}^E_{AgCl}$ at 700°C for each system.

Excess free energies of mixing.—Values of $\Delta\bar{G}^E_{AgCl}$ at 800°C and of the quantity, $\Delta\bar{G}^E_{AgCl}/X^2_{ACl}$, for the four systems are plotted in Fig. 6(a-d) along with the fitted curves.

It must be remembered when examining the plots of $\Delta\bar{G}^E_{AgCl}/X^2_{ACl}$, that dividing $\Delta\bar{G}^E_{AgCl}$ by X^2_{ACl} greatly magnifies the discrepancy between the fitted curve and the experimental points when X_{ACl} is small. When $X_{ACl} = 0.3$, for instance, errors are magnified about eleven times more than when $X_{ACl} = 1$. The least squares fit is done on the values of $\Delta\bar{G}^E_{AgCl}$, not on the values of $\Delta\bar{G}^E_{AgCl}/X^2_{ACl}$.

In the AgCl-NaCl system, $\Delta\bar{G}^E_{AgCl}$ is positive, and in the AgCl-KCl, AgCl-RbCl, and AgCl-CsCl systems, $\Delta\bar{G}^E_{AgCl}$ is negative. From the plots of $\Delta\bar{G}^E_{AgCl}/X^2_{ACl}$ for the present study, it is seen that 2-coefficient power series fits are justified in the NaCl and KCl systems, and 3-coefficient fits are justified in the RbCl and CsCl systems. Values measured by other authors (4, 7, 8) are also shown in Fig. 6(a, b, d). [Points shown in Fig. 6b from the work of Murgulescu and Sternberg (8) were corrected from lower temperatures to 800°C using partial molar enthalpy data as measured in the present study.] The present study is the first work in which it has been possible to define the second and third coefficients in the power series expansion [7] for $\Delta\bar{G}^E_{AgCl}$.

In order to show clearly the magnitude of the deviations from ideality in these systems, the activities of

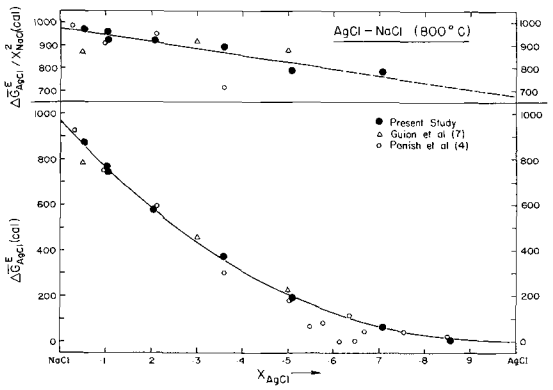

Fig. 6a. Partial molar excess free energy of mixing of AgCl at 800°C *vs.* composition in the AgCl-NaCl system. (Line shown is least squares fit.)

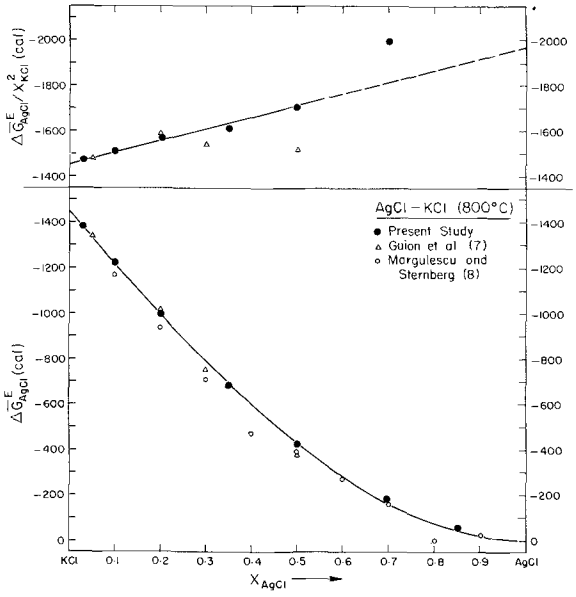

Fig. 6b. Partial molar excess free energy of mixing of AgCl at 800°C *vs.* composition in the AgCl-KCl system. (Line shown is least squares fit.)

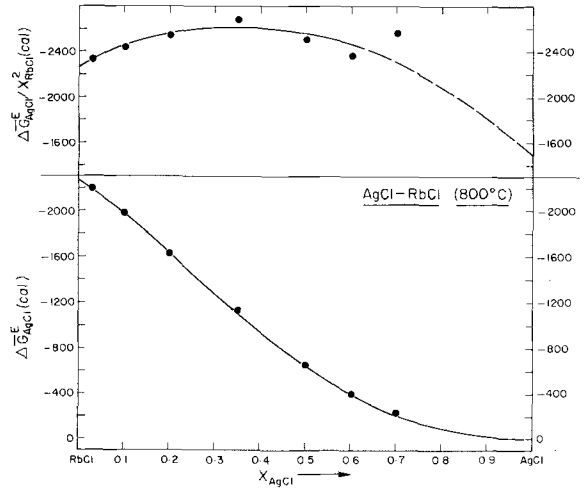

Fig. 6c. Partial molar excess free energy of mixing of AgCl at 800°C *vs.* composition in the AgCl-RbCl system. (Line shown is least squares fit.)

AgCl, calculated from the fitted free energy curves in Table III, and the activities of alkali chloride, calculated analytically from the Gibbs-Duhem equation

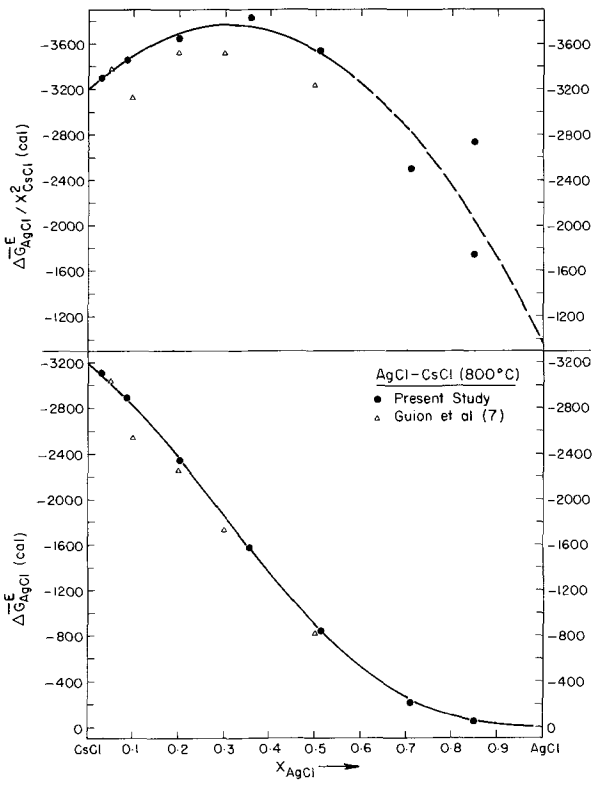

Fig. 6d. Partial molar excess free energy of mixing of AgCl at 800°C *vs.* composition in the AgCl-CsCl system. (Line shown is least squares fit.)

using the method of Margules (22) in the form proposed by the present authors (23), are plotted in Fig. 7 for all four systems at 800°C.

Enthalpies of mixing.—The values of $\Delta\overline{H}_{AgCl}$ and of the quantity, $\Delta\overline{H}_{AgCl}/X^2_{ACl}$, are plotted in Fig. 8(a-d) along with the fitted curves. Values measured electrochemically by Guion *et al.* (7) are also shown. Values calculated from the data of Panish *et al.* (4) or of Murgulescu and Sternberg (8) are too scattered to be meaningful.

Enthalpies of mixing are positive in the AgCl-NaCl system, and negative in the other systems studied. From the plots of $\Delta\overline{H}_{AgCl}/X^2_{ACl}$, it is seen that in all systems a 2-coefficient power series fit is justified. (Remember that errors in $\Delta\overline{H}_{AgCl}/X^2_{ACl}$ are greatly magnified at lower values of X_{ACl}.)

Table III. Least squares fits for partial molar properties of mixing of AgCl *vs.* composition in AgCl-alkali chloride systems (1 cal = 4.1840J)

	System	a	b	c	Mean deviation	Maximum deviation
$\Delta\overline{G}^E_{AgCl}$ at 800°C, cal/mole	AgCl-NaCl	677	298		8	19
	AgCl-KCl	−1973	518		8	16
	AgCl-RbCl	−1479	−3549	2759	14	25
	AgCl-CsCl	−955	−8144	5913	15	28
$\Delta\overline{G}^E_{AgCl}$ at 700°C, cal/mole	AgCl-NaCl	690	361		8	19
	AgCl-KCl	−2027	567		8	16
	AgCl-RbCl	−1422	−3908	3006	15	27
	AgCl-CsCl	−1523	−7095	5347	15	35
$\Delta\overline{H}_{AgCl}$, cal/mole	AgCl-NaCl	768	1043		60	120
	AgCl-KCl	−2345	776		50	110
	AgCl-RbCl	−3773	758		80	90
	AgCl-CsCl	−6957	2876		60	100
$\Delta\overline{S}^E_{AgCl}$, cal/K-mole	AgCl-NaCl	0.080	0.701		0.06	0.11
	AgCl-KCl	−0.340	0.233		0.05	0.12
	AgCl-RbCl	−0.744	0.127		0.04	0.05
	AgCl-CsCl	−2.508	1.819		0.07	0.19

a, b, c are coefficients of the power series expansions as in Eq. [7].

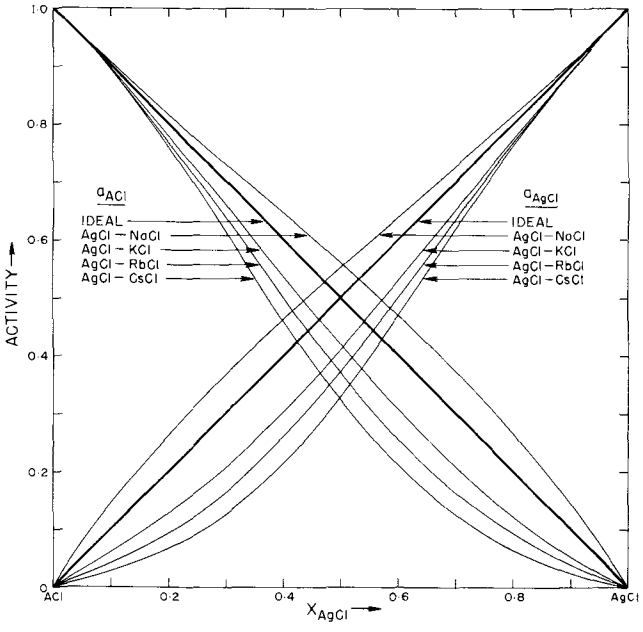

Fig. 7. Activities of AgCl and of alkali chloride (ACl) at 800°C vs. composition in AgCl-alkali chloride systems.

Curves calculated from the calorimetric data of Hersh and Kleppa (1) at 660°C are also shown in Fig. 8 (a-d). Hersh and Kleppa used a 3-coefficient fit to their data in the CsCl system and 2-coefficient fits in the other systems. Agreement between the present results and the calorimetric data is very good. In Fig. 9, the integral molar enthalpies of mixing, ΔH, as measured by Hersh and Kleppa (1) and as calculated analytically from the present data using the Gibbs-Duhem equation are compared. Values of $\Delta H_{0.5}$ (at $X_{AgCl} = X_{ACl} = 0.5$) are in agreement within 100 cal.

Calorimetric measurements made in this laboratory (24) are in good agreement in magnitude with the curves in Fig. 9 for the AgCl-KCl and AgCl-RbCl systems. However, the reported asymmetries, while of the same sign, were much greater than those measured in the present work or in the work of Hersh and Kleppa. In the AgCl-CsCl system, a value of $\Delta H_{0.5}$ of −1600 cal was reported, and this is not in agreement with the curves in Fig. 9. In view of the good agreement between the present work and that of Hersh and Kleppa (1), it would seem that these values are more trustworthy.

Excess entropies of mixing.—Values of $\Delta\bar{S}^E_{AgCl}$ are plotted in Fig. 10 (a, b) along with the fitted curves. Excess entropies of mixing are positive in the AgCl-NaCl system, and negative in the other systems studied. The points were fitted by 2-coefficient power series. Points as measured by Guion *et al.* (7) are also shown.

In Fig. 11a are plotted integral excess entropies of mixing. ΔS^E, calculated analytically from the present

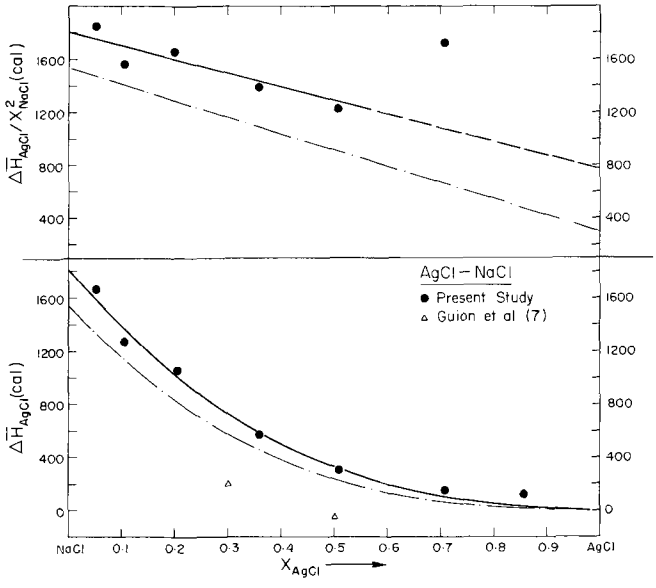

Fig. 8b. Partial molar enthalpy of mixing of AgCl vs. composition in the AgCl-KCl system. ——— Least squares fit to present data; — — — calculated from calorimetric data (1).

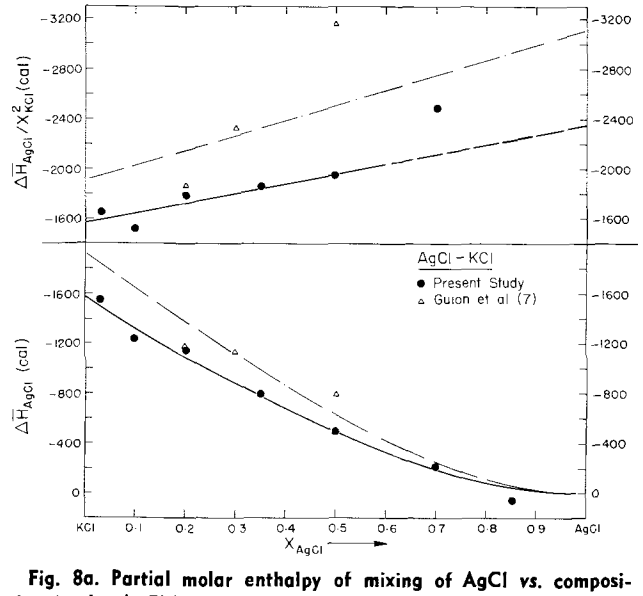

Fig. 8a. Partial molar enthalpy of mixing of AgCl vs. composition in the AgCl-NaCl system. ——— Least squares fit to present data; — — — calculated from calorimetric data (1).

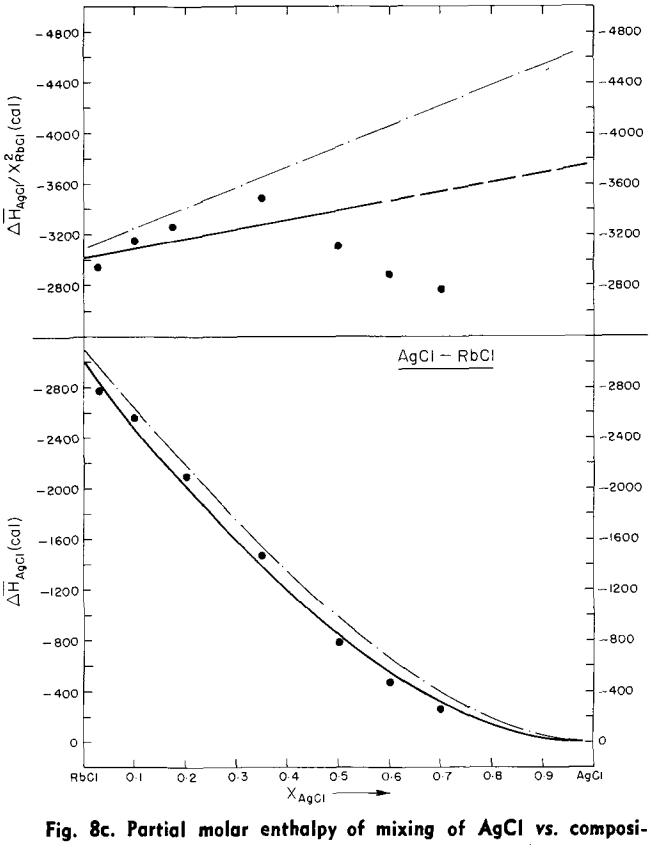

Fig. 8c. Partial molar enthalpy of mixing of AgCl vs. composition in the AgCl-RbCl system. ——— Least squares fit to present data; — — — calculated from calorimetric data (1).

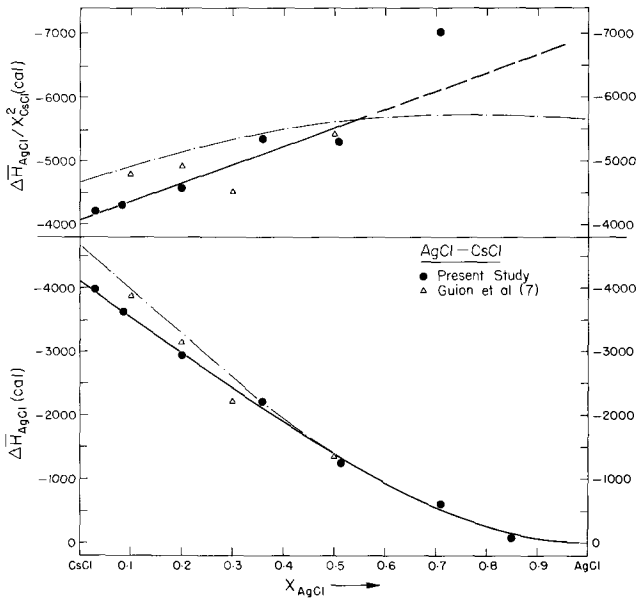

Fig. 8d. Partial molar enthalpy of mixing of AgCl vs. composition in the AgCl-CsCl system. ——— Least squares fit to present data; — — — calculated from calorimetric data (1).

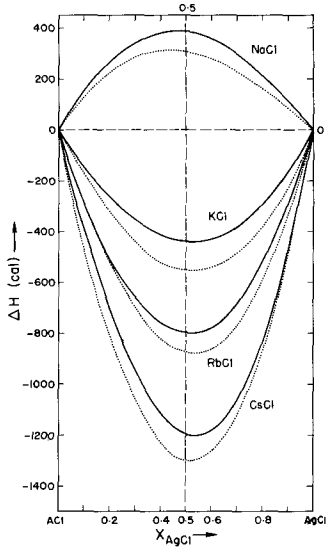

Fig. 9. Integral molar enthalpies of mixing vs. composition in AgCl-alkali chloride systems. ——— Calculated from data of present study; - - - - - calorimetric measurements (1).

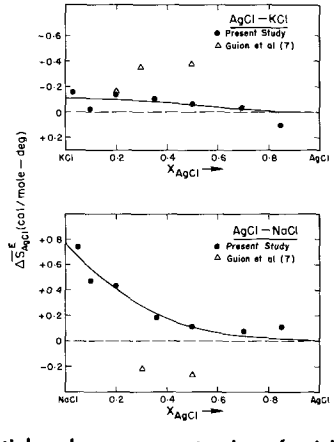

Fig. 10a. Partial molar excess entropies of mixing of AgCl vs. composition in the AgCl-NaCl and AgCl-KCl systems. (Lines shown are least squares fits.)

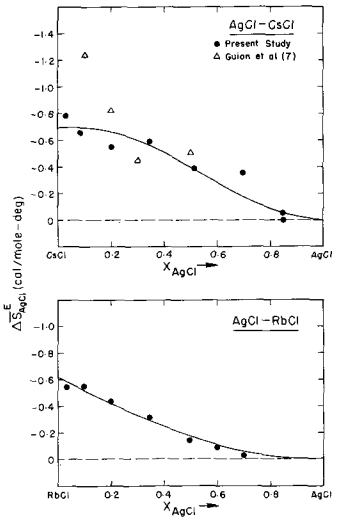

Fig. 10b. Partial molar excess entropies of mixing of AgCl vs. composition in the AgCl-RbCl and AgCl-CsCl systems. (Lines shown are least squares fits.)

results using the Gibbs-Duhem equation. In Fig. 11b are plots of ΔS^E calculated by using the integral ΔH values at 660°C of Hersh and Kleppa (1) along with integral excess free energies of mixing, ΔG^E, calculated analytically from the present results using the equations for $\Delta\overline{G}^E_{AgCl}$ at 700°C in Table III. Values of $\Delta S^E_{0.5}$ (at $X_{AgCl} = X_{ACl} = 0.5$) in Fig. 11a and Fig. 11b are in agreement to within 0.1 cal/K-mole. The sign of the asymmetry is in agreement for each system. All the systems in which ΔS^E is negative have asymmetries of the same sign, and the asymmetries of ΔG^E, ΔH, and ΔS^E are of the same sign within any one system of the four.

Discussion

From Fig. 12 it can be seen that there is an approximate linear relationship between $\Delta H_{0.5}$ and $\Delta S^E_{0.5}$ for the four systems studied. Furthermore, the line passes approximately through the origin. Hersh and Kleppa (1) measured $\Delta H_{0.5}$ for the AgCl-LiCl system at 660°C as being +490 cal, and this is in the expected direction. By combining the emf measurements of Panish *et al.* (3) at 700°C with the calorimetric data, $\Delta S^E_{0.5}$ was calculated as being almost exactly 0.00 for the LiCl system, whereas in Fig. 12 a value of $\Delta S^E_{0.5} = +0.13$ is predicted. The difference is probably within experimental error limits, but also it may be that, as in many other comparisons of properties involving the alkali

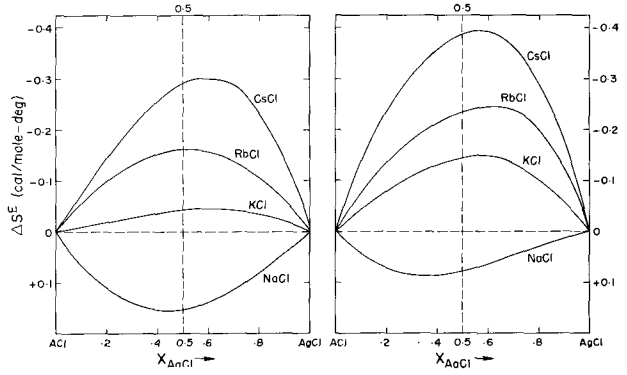

Fig. 11a (left). Integral molar excess entropies of mixing vs. composition in AgCl-alkali chloride systems as calculated from temperature dependences of cell potentials in the present study.

Fig. 11b (right). Integral molar excess entropies of mixing vs. composition in AgCl-alkali chloride systems as calculated using free energies measured in the present study and calorimetric (1) enthalpies of mixing.

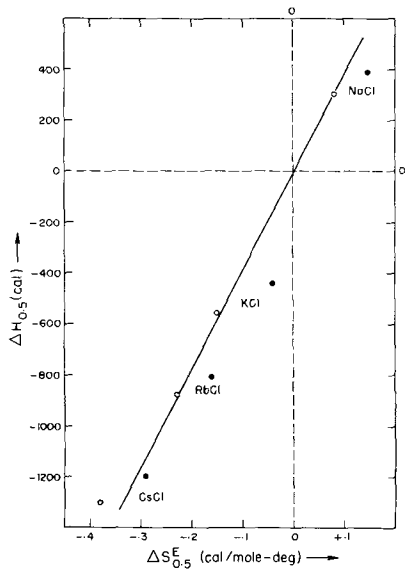

Fig. 12. Integral enthalpy of mixing vs. integral excess entropy of mixing values at $X_{AgCl} = 0.5$ in AgCl-alkali chloride systems. ● Both $\Delta H_{0.5}$ and $\Delta S^E_{0.5}$ from temperature dependences of cell potentials in present study; ○ $\Delta H_{0.5}$ from calorimetric (1) data. $\Delta S^E_{0.5}$ by combining electrochemical free energies and calorimetric enthalpies (as in Fig. 11b).

halide series, the very small size of the Li^+ ion causes anomalous behavior.

Reiss, Katz, and Kleppa (25) have developed a conformal solution theory for molten salts having a coulombic-type interionic pair potential. Essentially, the theory is concerned with a dimensional analysis of the partition function and predicts the functional relationship between the enthalpies of mixing and the ionic radii. The theory has been shown (1) to explain the observed trends in various nitrate systems, and also, with an additional term to account for van der Waals-London energy between next-nearest neighbors, the theory has been shown (1) to account for the enthalpies of mixing in solutions of alkali halides. Large discrepancies between theory and experiment resulted, however, when Hersh and Kleppa (1) attempted to explain their values of ΔH in the AgCl-alkali chloride systems. This is evidence, then, that the bonding in AgCl systems has a large covalent character.

The concept of covalent bonding in such solutions was discussed earlier by Thurmond (26) as an explanation of the enthalpies of mixing in the AgBr-alkali bromide mixtures observed by Hildebrand and Salstrom (27). ΔH is positive in the AgBr-LiBr and AgBr-NaBr systems and is negative in the AgBr-KBr and AgBr-RbBr systems, and in all cases the magnitude of $\Delta H_{0.5}$ is very close to the value in the corresponding chloride system. Thurmond suggested that there is a resonance between covalent and ionic Ag-Br bonds. If there is a small cation with a high field strength such as Li^+ or Na^+ on the other side of the bromine, then the resonance is disturbed, resulting in a higher energy for the solution. If however, there is a large weak cation such as K^+, Rb^+, or Cs^+ next to the bromine, the silver can more easily form strong covalent bonds with the bromine, resulting in a negative enthalpy of mixing.

Using the quasichemical method in the manner discussed by Førland (28), it may be shown easily that the negative excess entropies of mixing observed in the present study in three systems are much too negative to be explained by simple ordering on the cation lattice. And such ordering will not, of course, explain the positive values of ΔS^E in the AgCl-NaCl system. However, in view of Thurmond's (26) explanation for the ΔH values, it seems reasonable that the positive and negative ΔS^E values might also be explained as resulting from a decrease or increase in covalency on mixing.

Simple "dual bonding" model.—In order to make these ideas at least semiquantitative, a simple structural model for these systems will be developed.

A very similar model has recently been proposed (29), with much success, to explain the thermodynamic properties of molten $MgCl_2$-alkali chloride mixtures. The essentials of the model for these systems are that there are two bonding configurations for magnesium in solution and in pure $MgCl_2$, with some of the magnesium existing as free Mg^{2+} cations, and some existing in $MgCl_4^{2-}$ complexes. Also, the energy of formation of a complex was shown to depend on the type of cation in its first coordination sphere.

In the AgCl-ACl systems, then, it is proposed that some of the silver exists as "ionic" silver, and some exists as "covalent" silver. Let α be the fraction of silver which is "covalent." It is assumed that the two types of silver can exchange positions with each other and with alkali cations on cation sites. (In this sense the present model differs from the model used for the $MgCl_2$ systems in which the $MgCl_4^{2-}$ complexes exchanged positions with Cl^- anions.)

Possibly, in view of the atomic orbital structure of silver, and from experimental evidence in aqueous and in dilute molten salt solutions (30), the "covalent" silver could be considered to form covalent bonds to two chlorine neighbors through sp digonal hybrid orbitals. However, it is not necessary to know the precise nature of the "ionic" and "covalent" bonding. This is why these terms are placed in quotation marks. It is only necessary that there be two types of bonding configurations available to a silver on a cation site, so that two silver ions, one in each type of configuration, become distinguishable statistical entities.

In one mole of solution, X_{ACl} moles of A^+ ions, αX_{AgCl} moles of "covalent" silver, and $(1 - \alpha)X_{AgCl}$ moles of "ionic" silver ions are randomly distributed over the cation sites. The multiplicity, Ω, of one mole of solution is thus given by

$$\Omega = \frac{N^o!}{(X_{ACl}N^o)!\ (\alpha X_{AgCl}N^o)!\ ((1-\alpha)\ X_{AgCl}N^o)!} \quad [8]$$

where N^o is Avogadro's number. The configurational entropy, S, of one mole of solution is then given by

$$S = k \ln \Omega = -R\,[X_{ACl} \ln X_{ACl} + \alpha X_{AgCl} \ln (\alpha X_{AgCl}) + (1-\alpha)X_{AgCl} \ln (1-\alpha)X_{AgCl}] \quad [9]$$

where k is Boltzmann's constant, and Stirling's approximation has been used. R is the ideal gas constant.

If α^o is the value of α in pure AgCl, then the molar configurational entropy, S^o_{AgCl}, of pure AgCl is given by setting $X_{AgCl} = 1$ in Eq. [11] such that

$$S^o_{AgCl} = -R[\alpha^o \ln \alpha^o + (1-\alpha^o) \ln (1-\alpha^o)] \quad [10]$$

For pure ACl, the configurational entropy, S^o_{ACl}, is zero. Assuming that vibrational contributions to the entropy of mixing may be neglected, the entropy of mixing, ΔS, is given by

$$\Delta S = S - X_{AgCl}S^o_{AgCl} \quad [11]$$

The leading term in the expression for the enthalpy of mixing is assumed to arise from the changes in bond character on mixing and, as in the model for the $MgCl_2$ systems, terms resulting from residual coulombic and polarization interactions not accounted for in the first term are neglected.

Let Δe_1 be the molar energy change for the following process occurring in pure AgCl

$$Ag_{(\text{"ionic"})} \rightarrow Ag_{(\text{"covalent"})} \quad [12]$$

Let Δe_2 be the molar energy change for the same process occurring at infinite dilution in alkali chloride solvent. As discussed earlier, the energy change of this process will depend on the type of cation in the second

coordination shell of the central silver. Thus, if A^+ is a cation with a high field strength such as Li^+ or Na^+, it would be expected that $\Delta e_2 > \Delta e_1$, and if A^+ is K^+, Rb^+, or Cs^+, then the weak alkali cation favors covalency and $\Delta e_2 < \Delta e_1$. In general, the molar energy change, Δe, of process [12] should vary between Δe_1 and Δe_2 depending on the mole fractions of AgCl and ACl. As a first approximation, a linear variation was assumed. That is

$$\Delta e = X_{AgCl}\,\Delta e_1 + X_{ACl}\,\Delta e_2 \qquad [13]$$

Since the pressure-volume work of mixing is negligible, ΔH of mixing may be equated to the change in internal energy on mixing. Since there are αX_{AgCl} moles of "covalent" silver in one mole of solution and α^o moles in one mole of pure AgCl

$$\Delta H = \alpha X_{AgCl}\,(X_{AgCl}\,\Delta e_1 + X_{ACl}\,\Delta e_2) - \alpha^o X_{AgCl}\,\Delta e_1 \qquad [14]$$

Let us define

$$b_1 = \Delta e_1$$
$$b_2 = \Delta e_2 - \Delta e_1 \qquad [15]$$

where b_1 and b_2 are the adjustable parameters in the model and are taken to be independent of temperature and concentration. The parameter b_1 is independent of the type of alkali cation, A^+. The parameter b_2 will have a different value for each binary system. Equation [14] may be rearranged as follows

$$\Delta H = X_{AgCl}\,(\alpha - \alpha^o)\,b_1 + \alpha X_{AgCl} X_{ACl}\,b_2 \qquad [16]$$

The values of α and of α^o which actually occur may be calculated as those which minimize the free energy of mixing. That is, α and α^o may be calculated from the equations

$$\frac{\partial(\Delta G)}{\partial\alpha} = \frac{\partial(\Delta H)}{\partial\alpha} - T\frac{\partial(\Delta S)}{\partial\alpha} = 0 \qquad [17]$$

$$\frac{\partial(\Delta G)}{\partial\alpha^o} = \frac{\partial(\Delta H)}{\partial\alpha^o} - T\frac{\partial(\Delta S)}{\partial\alpha^o} = 0 \qquad [18]$$

Substituting Eq. [12] and [16] into Eq. [17] and [18], performing the differentiations, and rearranging terms yields the following expressions for α and α^o

$$\alpha^o = C_1/(1 + C_1) \qquad [19]$$

$$\alpha = C_1C_2/(1 + C_1C_2) \qquad [20]$$

where

$$C_1 = \exp(-b_1/RT) \qquad [21]$$

$$C_2 = \exp(-X_{ACl}b_2/RT) \qquad [22]$$

If values of b_1 and b_2 are chosen, Eq. [19] and [20] may be used to give values of α and α^o. These values may then be substituted back into Eq. [11] and [16] to give numerical solutions for ΔH and ΔS at any composition.

Numerical solutions were obtained in this manner. Good fits to the experimental data in the four systems studied were obtained with $b_1 = -3.5$ kcal and b_2 values of -4.5, -3.0, -2.0, and $+1.5$ kcal in the CsCl, RbCl, KCl, and NaCl systems, respectively. These values of b_1 and b_2 are reasonable in view of the physical significance attached to them by the model. When $b_1 = -3.5$ kcal, $\alpha^o = 0.836$. Values of α at various compositions in the four systems are listed in Table IV.

Table IV. Values of α calculated from the "dual-bonding" model

b_2, kcal \ X_{AgCl}	0.1	0.3	0.5	0.7	0.9	1.0
				($b_1 = -3.5$ kcal)		
−4.5 (AgCl-CsCl)	0.97	0.96	0.94	0.91	0.86	0.836
−3.0 (AgCl-RbCl)	0.95	0.93	0.91	0.89	0.86	0.836
−2.0 (AgCl-KCl)	0.92	0.91	0.89	0.87	0.85	0.836
+1.5 (AgCl-NaCl)	0.73	0.76	0.78	0.81	0.83	0.836

Calculated curves are shown in Fig. 13 and 14. By comparison with Fig. 9 and 11 it may be seen that the ΔH and ΔS^E curves are simultaneously fitted in magnitude within the limits of experimental accuracy (although ΔS^E calculated for the CsCl system is probably not negative enough). The calculated ΔH curves are almost perfectly symmetric (i.e., parabolic) about $X_{AgCl} = 0.5$. The calculated ΔS^E curves for the KCl, RbCl, and CsCl systems show some asymmetry in the same direction as the experimental curves. For the NaCl system, ΔS^E is calculated as nearly perfectly symmetric.

A good fit to ΔH, as measured by Hersh and Kleppa (1), for the AgCl-LiCl system is obtained with $b_2 = +2.0$ kcal. In this case, $\Delta S^E_{0.5}$ is calculated to be $+0.10$ cal/K-mole. This is as predicted from Fig. 12, but, as discussed earlier, there is evidence that ΔS^E in this system may show anomalous behavior.

Summary

A reversible silver-chlorine formation cell for use in molten salt electrolytes has been built. Voltages are highly stable and reproducible. It is believed that the use of a very high resistance (>1000 ohms) asbestos diaphragm between the two electrode compartments is important in achieving the observed stability. The dependence of the cell potential on chlorine pressure from 10^{-2} to 1.0 atm has been measured. The very fast response of the voltage to changes in chlorine pressure indicates that there is no difficulty in saturating the graphite electrode as was previously thought.

The curvature of the measured E^o *vs.* T curve is in very good agreement with the thermochemical values

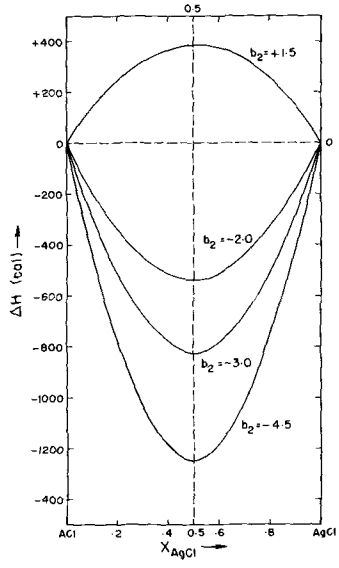

Fig. 13. Integral molar enthalpies of mixing calculated from the "dual bonding" model with $b_1 = -3.5$ kcal and for values of b_2 (kcal) shown.

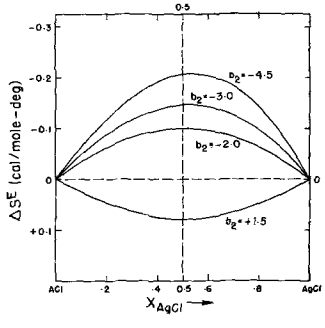

Fig. 14. Integral molar excess entropies of mixing calculated from the "dual bonding" model with $b_1 = -3.5$ kcal and for values of b_2 (kcal) shown.

of ΔC_p for the formation of AgCl, and the curve itself is in very good agreement with the curve calculated from the thermochemical data. Previously noted discrepancies between the thermochemical and electrochemical E° values were the result of the use of an incorrect C_p value for liquid AgCl.

Measurements were made over the total composition ranges in four AgCl-alkali chloride systems. Excess free energies of mixing were in reasonable agreement with values measured by other authors where measurements were available. The precision of the results is such as to give the second and third coefficients in the expansions for the excess free energies as power series in the mole fractions. Enthalpies of mixing, calculated from the temperature dependences of the cell potential, were of sufficient precision to permit 2-coefficient fits as power series in the mole fractions. In all systems, values of $\Delta H_{0.5}$ (at $X_{AgCl} = 0.5$) agreed with calorimetric (1) values within 100 cal, and in all systems the asymmetry of ΔH was also in agreement both in sign and magnitude. Excess entropies of mixing, calculated from the temperature dependences of the cell potential, were of sufficient precision to permit the sign of the asymmetry to be determined. Values of ΔS^E were also calculated using free energies measured in the present work, and calorimetric ΔH values (1). The two sets of curves agreed within 0.1 cal/K-mole at $X_{AgCl} = 0.5$, and in all cases the signs of the asymmetries were in agreement.

Values of ΔG^E, ΔH, and ΔS^E were positive in the AgCl-NaCl system and were negative in the AgCl-KCl, AgCl-RbCl, and AgCl-CsCl systems. Within each system, the asymmetries of ΔG^E, ΔH, and ΔS^E were of the same sign.

It has been shown that the results provide evidence for the occurrence of covalency in molten solutions containing AgCl. A simple "dual bonding" model for these melts was developed in which "ionic" and "covalent" silver coexists. With the use of only one composition-independent adjustable parameter for each system, and one other adjustable parameter for all the systems taken together, it was possible to simultaneously explain the signs and magnitudes of the enthalpies and excess entropies of mixing in all four systems and to explain some of the observed asymmetries.

Acknowledgments

The authors wish to thank Dr. W. T. Thompson for many valuable discussions. Financial assistance from the National Research Council of Canada and a maintenance fellowship from Shell Canada are also gratefully acknowledged.

Manuscript submitted Feb. 24, 1970; revised manuscript received May 21, 1970.

Any discussion of this paper will appear in a Discussion Section to be published in the June 1971 JOURNAL.

List of Symbols

A	any alkali metal
T	temperature in Kelvins
ln	natural logarithm
V	thermoelectric potential (mV)
E	reversible cell potential (mV)
E°	reversible cell potential with pure AgCl electrolyte (mV)
C_p	heat capacity (cal/K-mole)
ΔC_p	change in heat capacity for a chemical reaction (cal/K-mole)
n	number of equivalents per mole
$\mathbf{F}$	Faraday constant (23.0610 cal/mV-equiv)
ΔG^E	integral molar free energy of mixing (cal/mole)
ΔH	integral molar enthalpy of mixing (cal/mole)
ΔS^E	integral molar excess entropy of mixing (cal/K-mole)
$\Delta \bar{G}^E_i$	partial molar excess free energy of mixing of component i (cal/mole)
$\Delta \bar{H}_i$	partial molar enthalpy of mixing of component i (cal/mole)
$\Delta \bar{S}^E_i$	partial molar excess entropy of mixing of component i (cal/K-mole)
$\Delta \bar{F}_{AgCl}$	any of the three partial molar properties of mixing of AgCl (excess free energy, enthalpy, or excess entropy)
X_i	mole fraction of component i
a_i	activity of component i
$\Delta H_{0.5}$	integral molar enthalpy of mixing when $X_{AgCl} = X_{ACl} = 0.5$ (cal/mole)
$\Delta S^E_{0.5}$	integral molar excess entropy of mixing when $X_{AgCl} = X_{ACl} = 0.5$ (cal/K-mole)
α	fraction of silver which is "covalent" in the dual bonding model
α°	value of α in pure AgCl
Ω	configurational multiplicity of the solution
N°	Avogadro's number
R	ideal gas constant
k	Boltzmann's constant
S	molar configurational entropy of solution (cal/K-mole)
S°_i	molar configurational entropy of pure component i (cal/K-mole)
Δe	molar energy change for reaction [12], (cal/mole)
Δe_1	value of Δe in pure AgCl (cal/mole)
Δe_2	value of Δe in pure ACl (cal/mole)
b_1	Δe_1 (cal/mole)
b_2	$\Delta e_2 - \Delta e_1$ (cal/mole)

REFERENCES

1. L. S. Hersh and O. J. Kleppa, *J. Chem. Phys.*, **42**, 1309 (1965).
2. E. J. Salstrom, T. J. Kew, and T. M. Powell, *J. Am. Chem. Soc.*, **58**, 1848 (1936).
3. M. B. Panish, R. F. Newton, W. R. Grimes, and F. F. Blankenship, *J. Phys. Chem.*, **63**, 668 (1959).
4. M. B. Panish, F. F. Blankenship, W. R. Grimes, and R. F. Newton, *ibid.*, **62**, 1325 (1958).
5. K. H. Stern, *ibid.*, **62**, 385 (1958).
6. S. Sternberg and S. Gheorghiu, *Studii Cercet. Chim. Acad. Rep. Populaire Roumaine*, **7**, 107 (1959).
7. J. Guion, M. Blander, D. Hengstenberg, and K. Hagemark, *J. Phys. Chem.*, **72**, 2086 (1968).
8. I. G. Murgulescu and S. Sternberg, *Rev. Chim. Acad. Rep. Populaire Roumaine*, **2**, 251 (1957).
9. K. Stern, *J. Phys. Chem.*, **60**, 679 (1956).
10. C. Dijkhuis, R. Dijkhuis, and G. J. Janz, *Chem. Rev.*, **68**, 253 (1968).
11. S. N. Flengas and T. R. Ingraham, *This Journal*, **106**, 714 (1959).
12. A. Wachter and J. H. Hildebrand, *J. Am. Chem. Soc.*, **52**, 4655 (1930).
13. S. Senderoff and G. W. Mellors, *Rev. Sci. Instr.*, **29**, 151 (1958).
14. J. Leonardi and J. Brenet, *Compt. Rend.*, **261**, 116 (1965).
15. M. F. Lantratov and A. F. Alabyshev, *J. Appl. Chem. USSR.*, **26**, 321 (1953).
16. D. C. Hamby, Private communication.
17. American Institute of Physics Handbook, pp. 4-7 (1963).
18. W. T. Thompson, Ph.D. thesis, University of Toronto (1969).
19. C. E. Wicks and F. E. Block, *U.S. Bur. Mines Bull.*, 605 (1963).
20. W. J. Hamer, M. S. Malmberg, and B. Rubin, *This Journal*, **103**, 8 (1956).
21. E. J. Salstrom, *J. Am. Chem. Soc.* **56**, 1272 (1934).
22. M. Margules, *Sitz-ber. Math.-Naturw. Kl. Bayer. Akad. Wiss. München*, IIa, **104**, 1243 (1895).
23. A. D. Pelton and S. N. Flengas, *Can. J. Chem.*, **47**, 2283 (1969).
24. R. Baboian and S. N. Flengas, *ibid.*, **45**, 813 (1967).
25. H. Reiss, J. L. Katz, and O. J. Kleppa, *J. Chem. Phys.*, **36**, 144 (1962).
26. C. D. Thurmond, *J. Am. Chem. Soc.*, **75**, 3928 (1953).
27. J. H. Hildebrand and E. J. Salstrom, *ibid.*, **54**, 4257 (1932).
28. T. Førland, "Fused Salts," B. Sundheim, Editor, Chap. 2, pp. 86-88, McGraw Hill Book Co., New York (1964).
29. A. D. Pelton and W. T. Thompson, *Can. J. Chem.*, **48**, 1585 (1970).
30. F. R. Duke and H. M. Garfinkel, *J. Phys. Chem.*, **65**, 461 (1961).

Electrochemical Behavior of 2-(1-Naphthyl)-5-Phenyl- and 2,5-Diphenyloxazole

W. N. Greig and J. W. Rogers

Department of Chemistry, Midwestern University, Wichita Falls, Texas 76308

ABSTRACT

The electrochemical reduction of 2-(1-naphthyl)-5-phenyl- and 2,5-diphenyloxazole in N,N-dimethylformamide has been studied at platinum and mercury electrodes in the presence and absence of proton donors. Polarographic, potentiostatic, voltammetric, and spectrophotometric techniques were employed in the study. Both compounds are reduced via two polarographic steps. The first is a reversible one-electron transfer producing a stable anion radical. The second is a reversible one-electron transfer followed by rapid protonation of the dianion (EC process). The resulting protonated species undergoes a slow irreversible reaction. Addition of hydroquinone as a source of protons enhances the formation of the long term electrolysis product.

The value of electrochemical measurements in the elucidation of the oxidation-reduction behavior of organic compounds is well documented (1-4). Adams has recently organized and presented a lucid description of mechanisms for the electrochemical oxidation of aromatic hydrocarbons and amines (5). Bard has contributed a great amount of information to the study of electrolytic reduction mechanisms of organic compounds (6-9). Peover has discussed much of the work in this area in a review (10).

However, polarographic data for five-membered, aromatic heterocyclics in aprotic media is very sketchy. There have been no electrochemical investigations of the oxazole nucleus, substituted oxazoles or related compounds in aprotic solvents.

We have undertaken a study of 2-(1-naphthyl)-5-phenyl- and 2,5-diphenyloxazole in N,N-dimethylformamide (DMF) solvent in an attempt to establish a mechanism for their electrochemical reduction. The stability of reduction intermediates and the nature of homogeneous reactions of the intermediates are considered. Polarographic, cyclic voltammetric, potentiostatic, mass electrolytic, and spectrophotometric techniques were employed in the study. The voltammetric behavior of these compounds at mercury and platinum electrodes in the absence and presence of proton donors is described. A reduction mechanism consistent with the electrochemical results is postulated.

Results

Voltammetric methods.—Both 2,5-diphenyl-(I) and 2-(1-naphthyl)-5-phenyloxazole (II) exhibit two well-defined polarographic waves in DMF with 0.1M tetra-N-propylammonium perchlorate (TPAP) as supporting electrolyte. The polarographic half-wave potentials, $E_{1/2}$'s, are −2.13V and −2.47V *vs.* saturated calomel electrode (SCE) for compound I and −1.88V and −2.24 *vs.* SCE for II. The diffusion current (i_d) of both waves of I and II varied as the square root of the height of the mercury head ($h^{1/2}$) above the dropping mercury electrode (DME), indicating that material transfer to the electrode is diffusion controlled. The slope of a plot of potential (E) *vs.* log $i/(i_d-i)$ for the first wave is 60 mV for I and II.

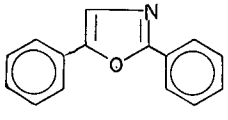

I

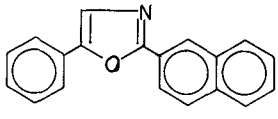

II

Key words: Electrochemical reduction oxazole.

The cyclic voltammetric behavior of compound I at a hanging mercury drop electrode (HMDE) is shown in Fig. 1. Voltage excursion and reversal past the first polarographic wave at HMDE yields a voltammogram with a substantial anodic current. The ratio of the cathodic peak current to the anodic peak current $[(i_p)c/(i_p)a]$ is approximately 1.0 at all sweep rates (v), Table I. The cathodic peak potential to half-peak potential separation $[(E_p)c - (E_p)c/2)]$ is 60 mV at all v and the current function $((i_p)c/v^{1/2})$ is invariant to changes in v, Table I. The 60 mV separation is not strictly in accord with the theory for a reversible one-electron transfer. However, the over-all behavior is indicative of such a process producing a radical

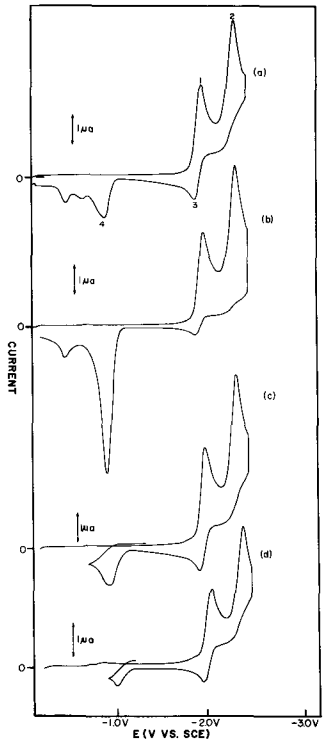

Fig. 1. Cyclic voltammograms of 2,5-diphenyloxazole at HMDE in DMF containing 0.1M TPAP showing sweep range from 0.0V. All solutions were 1 mM in oxazole. Sweep rate was 250 mV/sec in all experiments. (a) Excursion and reversal past second wave, (b) forward excursion held at potential above second peak for 5 sec before reversal, (c) multicyclic voltammogram showing no current peak corresponding to follow-up oxidation current, (d) same as "c" with solution 1 mM in HQ.

Table I. Cyclic voltammetric data for the reduction of compound I and II in DMF at HMDE[a]

	2,5-Diphenyloxazole (I)					
	First wave				Second wave	
Scan rate (V/min)	$[(E_p)_c - (E_p)_{c/2}]$ (mV)	$-(E_p)_c$[b] (V)	$(i_p)_c/(i_p)_a$[c]	$(i_p)_c/v^{1/2}$ (μA sec$^{-1/2}$)[d]	$-(E_p)_c$ (V)	$(i_p)_c/v^{1/2}$ (μA sec$^{-1/2}$)[d]
12.0	60	2.17	1.02	0.17	2.53	0.153
6.0	60	2.17	1.00	0.18	2.52	0.154
2.4	60	2.16	1.02	0.17	2.50	0.154
1.2	60	2.16	0.98	0.18	2.48	0.176
	2(1-Naphthyl)-5-Phenyloxazole (II)					
	First wave				Second wave	
Scan rate (V/min)	$[(E_p)_c - (E_p)_{c/2}]$ (mV)	$-(E_p)_c$[b] (V)	$(i_p)_c/(i_p)_a$[e]	$(i_p)_c/v^{1/2}$ (μA sec$^{-1/2}$)	$-(E_p)_c$ (V)	$(i_p)_c/v^{1/2}$ (μA sec$^{-1/2}$)[d]
12.0	60	1.96	—	0.27	2.37	0.32
6.0	60	1.94	—	0.27	2.35	0.40
2.4	60	1.94	—	0.29	2.34	0.42
1.2	60	1.94	—	0.29	2.34	0.46

[a] The solution was 0.1M in TPAP.
[b] Small $(E_p)_c$ shift probably due to uncompensated iR drop.
[c] Scan reversal 100 mV past $(E_p)_c$. i_p measured by employing the potential hold method (14).
[d] i_p measured by extrapolating current from first peak.
[e] Anodic stirring prevented measurement.

species stable during the course of the experiment (11). Similar behavior is observed for the first wave of I at a planar platinum disk electrode (PPDE), Table II.

Voltage sweep and reversal at potentials above the second polarographic plateau yields a second cathodic peak with no corresponding anodic current at sweep rates up to 500 mV/sec., Fig. 1. The $(E_p)_c$ of the second wave shifts approximately 30 mV in a cathodic direction and the current function decreases approximately 20% with a tenfold increase in v, Table I. This behavior suggests a reversible electron transfer followed by a rapid homogeneous reaction of the radical species (EC process) (11).

A second anodic peak current appears at potentials less cathodic than that representing the oxidation of the monoanion radical if sweep excursion is reversed at potentials past the second wave, Fig. 1a, peak 4. This oxidation peak is not present if the voltage excursion is reversed at potentials past only the first cathodic current peak. Multisweep voltammograms exhibit no cathodic current corresponding to peak 4, Fig. 1c. The intensity of the anion radical oxidation current (peak 3, Fig. 1a) is markedly decreased and that of peak 4 is correspondingly increased by pausing at potentials above the second polarographic plateau before sweep reversal, Fig. 1b. These observations suggest that follow-up anodic wave represents the oxidation of a product produced by the EC process occurring at the potential of the second wave. The absence of a cathodic current or any subsequent oxidation-reduction couple is consistent with the regeneration of starting material at the follow-up wave.

Table II. Cyclic voltammetric data for the reduction of compound I and II in DMF at PPDE[a]

	2,5-Diphenyloxazole (I)			
	First wave			
Scan rate (V/min)	$[(E_p)_c - (E_p)_{c/2}]$ (mV)	$-(E_p)_c$[b] (V)	$(i_o)_c/(i_p)_a$[c]	$(i_p)_c/v^{1/2}$ (μA sec$^{-1/2}$)
12.0	60	2.19	1.00	3.2
6.0	60	2.19	1.00	3.3
2.4	60	2.18	1.00	3.7
1.2	60	2.18	1.00	3.7
	2-(1-Naphthyl)-5-Phenyloxazole (II)			
	First wave			
Scan rate (V/min)	$[(E_p)_c - (E_p)_{c/2}]$ (mV)	$-(E_p)_c$[b] (V)	$(i_p)_c/(i_p)_a$[c]	$(i_p)_c/v^{1/2}$ (μA sec$^{-1/2}$)
12.0	65	1.96	1.00	10.1
6.0	65	1.94	1.00	10.7
2.4	65	1.94	1.00	10.5
1.2	65	1.94	1.00	10.7

[a] The solution was 0.1M in TPAP.
[b] Small $(E_p)_c$ shift due to uncompensation iR drop.
[c] Scan reversal 100 mV past $(E_p)_c$. i_p measured by employing the potential hold method (14).

Compound II exhibits similar behavior under the same conditions. Cyclic voltammetric data at a PPDE and a HMDE for compound II are given in Tables I and II. The differences in the current peak potentials and the diffusion $E_{1/2}$ values seem large considering the nature of the substituents and suggest differing reduction mechanisms. However, analysis of all the experimental information strongly indicates similar reduction paths.

Potentiostatic method.—The available electrochemical data show that the first polarographic plateau is representative of a diffusion-controlled one-electron transfer. The number of electrons (n) transferred at potentials above the second polarographic reduction step can be estimated as 2.0 with reference to the ratio of diffusion currents for the first and second polarographic waves. Comparison of slopes of i *vs.* $t^{-1/2}$ plots corresponding to potentials at the first and second polarographic plateaus in experiments carried out on a HMDE yields an n value of 1.0 for the second wave for compounds I and II. The over-all reduction process carried to potentials above the second wave requires two electrons.

The voltammetric and potentiostatic results suggest the following reduction mechanism for I and II

First wave

$$R + e^- \rightleftarrows R^{\cdot -}$$

Second wave

$$R^{\cdot -} + e^- \rightleftarrows R^{=}$$

$$R^{=} + SH \rightarrow RH^- + S^-$$

Regeneration wave

$$RH^- \rightarrow R + H^+ + 2e^-$$

Where R is the substituted oxazole and SH is a proton source. This mechanism has been suggested by Bard (7) for the electrochemical reduction of aromatic azo compounds and is analogous to the behavior exhibited by aromatic hydrocarbons (10).

Effect of proton donors.—To test the postulate of proton addition to the dianion, the polarographic and voltammetric behavior of I and II in the presence of varying amounts of hydroquinone (HQ) was studied (8). The intensity of the first polarographic wave grows at the expense of the second and the second shifts toward more positive potentials with increasing concentration of HQ. At very high concentrations of HQ (0.1M) only one polarographic wave is observed. The pronounced effect of the HQ is consistent with the postulated mechanism and entirely analogous to the behavior of polycyclic aromatic hydrocarbons in the presence of proton donors (10). Hoijtink (12) has shown that this behavior can be explained by the fact that the RH· radical of an alternant aromatic hydrocarbon formed by protonation of the R^{-} ion has a higher electron affinity than the parent compound, R. At potentials above the first polarographic wave the over-all process becomes

$$R + e^- \rightleftarrows R^{\cdot -}$$

$$R^{\cdot -} + HQ \rightarrow RH\cdot$$

$$RH\cdot + e^- \rightarrow RH^-$$

The anodic shift of the second wave with increasing HQ is also suggestive of an increasing rate of the follow-up reaction after the second electron transfer. Addition of HQ has a pronounced effect on the intensity of the product regeneration wave observed in the cyclic voltammetric experiments, Fig. 1d. The anodic current decreases on addition of HQ, and at concentrations as low as 1 mM the regeneration wave is not observed. The behavior suggests a further irreversible reaction of the protonated dianion, RH^-, possibly of the type

$$RH^- + HQ \rightarrow RH_2 + Q^-$$

Mass electrolysis.—Mass electrolysis experiments at a stirred mercury pool working electrode were undertaken to further study the stability of the proposed intermediates and to investigate possible long term reactions. The course of each mass electrolysis experiment was monitored with a PPDE in a three electrode configuration *in-situ* in the electrolysis vessel. Aliquots of the electrolyzed solution were removed and u.v. spectra were recorded at various time intervals.

Electrolysis of 200 ml of a 1 mM solution of I in DMF at potentials above the first polarographic plateau produced a yellow solution containing a paramagnetic species.[1] Electrolysis at this potential for 6 hr produced no detectable change in the anodic current of peak voltammograms corresponding to the oxidation of the 2,5-diphenyloxazole anion radical, Fig. 2a. No decrease in the intensity of the u.v. absorption of the parent compound (λ_{max} = 309 mμ in DMF) was noted after 6 hr of electrolysis, Fig. 3b. Introduction of trace amounts of oxygen destroyed the yellow color.

Increasing the electrolysis voltage to potentials above the second polarographic wave resulted in a purple solution unstable to oxygen. A peak voltammogram of this solution initiated at potentials above the first wave with voltage sweep in the anodic direction exhibited a small current peak corresponding to the oxidation of the anion radical and an intense anodic current at the potential corresponding to the anodic regeneration process, Fig. 2b. Purging the solution with a small amount of oxygen and then degassing with nitrogen destroyed the regeneration anodic current of a peak voltammogram with the potential sweep initiated at potentials above the first polarographic plateau, Fig. 2c. This behavior is consistent with the postulated radical nature of the EC process product.

[1] Analysis of ESR spectrum will be reported later.

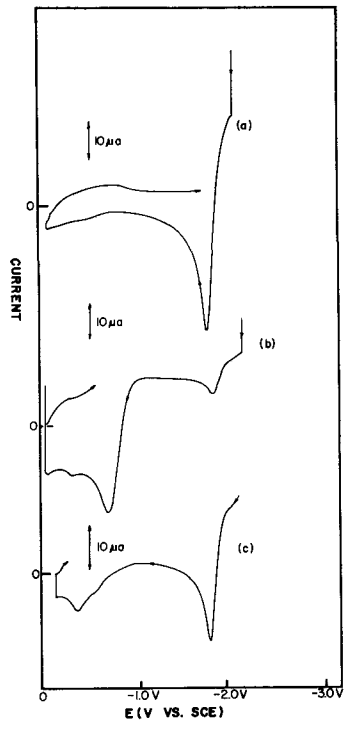

Fig. 2. Single sweep voltammograms at 250 mV/sec at a PPDE of a 1 mM solution of 2,5-diphenyloxazole in DMF undergoing electrochemical mass reduction at various potentials. (a) Single sweep voltammogram initiated at —2.0V; mass electrolysis potential —2.0V for 4 hr, (b) single sweep voltammogram initiated at —2.0V; mass electrolysis potential —2.5V for 30 min. (c) single sweep voltammogram initiated at —2.0V; solution from "b" after introduction of trace O_2 and then degassing with N_2.

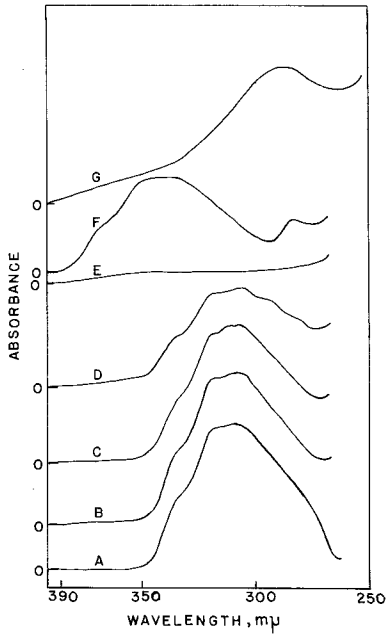

Fig. 3. (a) U.V. spectrum of 2,5-diphenyloxazole in DMF before reduction at a mercury pool electrode, (b) u.v. of solution from "a" after mass electrolysis at potential above first wave for 6 hr, (c) u.v. of solution from "b" after mass electrolysis at potential above second wave for 3 hr, (d) u.v. of solution from "c" after mass electrolysis at potential above second wave for 8 hr, (e) u.v. of solution from "d" after 24 hr of mass electrolysis at potential above the second wave. (f) u.v. of 2-(1-naphthyl)-5-phenyloxazole (II) in DMF, (g) u.v. of mass electrolysis product of II in ether solvent.

Continued electrolysis at potentials above the second wave for 3 hr produced a slight decrease in the intensity of the u.v. absorption of the parent com-

pound, Fig. 3c. No u.v. absorption could be detected after 36 hr of electrolysis at potentials above the second plateau, Fig. 3e. These observations suggest that the radical product of the EC process undergoes a slow, irreversible reaction yielding a product not electroactive at potentials less cathodic than the first polarographic plateau. Mass electrolysis experiments at a mercury pool electrode indicate that compound II behaves in a similar manner with the EC radical product undergoing a slow chemical reaction.

The long term electrolysis products of compounds I and II were extracted from the electrolysis solutions with small portions of benzene until the benzene layers were clear. The benzene solvent was evaporated under vacuum and the brown residue was dissolved in ethanol. The solutions were concentrated by evaporation and then treated with cold anhydrous ether.

The product of II melts at 169°C and exhibits a u.v. spectrum with a λ_{max} of 287 mμ in ether, Fig. 3g. Compound II exhibits a λ_{max} at 333 mμ in ether. The long term electrolysis product of I exhibits a λ_{max} at 276 mμ in ether while the parent substance absorbs at 305 mμ. The u.v. cutoff of DMF does not allow the observation of product production from I during electrolysis.

Discussion

Electrochemical data have been presented that indicate 2,5-diphenyloxazole and 2-(1-naphthyl)-5-phenyloxazole are reduced in two polarographic steps in DMF solvent. The first is a reversible one-electron transfer process producing a stable anion radical. Mass electrolysis experiments indicate that the anion radical does not undergo significant reactions over long periods of time. The second reduction step is a reversible one-electron transfer process producing a dianion which undergoes rapid protonation. The protonated dianion product is oxidizable to the parent compound at potentials more anodic than that corresponding to the oxidation of the anion radical.

The electrochemical reduction mechanism is analogous to that found for polycyclic hydrocarbons in aprotic solvents (10). The analogy is interesting in view of the difference in structure of the oxazole nucleus and an aromatic hydrocarbon.

Addition of small quantities of HQ decreases the intensity of the anodic current corresponding to the process

$$RH^- \rightarrow R + H^+ + 2e$$

This suggests that the product of the EC process, RH^-, undergoes further rapid protonation and reduction in the presence of a proton source.

The protonated dianion is found to undergo a slow chemical reaction even in the absence of HQ. Spectroscopic studies show that the λ_{max} of the long term electrolysis product of each compound is at a wavelength less than that of the parent substance. This wavelength shift between the parent substance and the electrolysis product is consistent with decreased conjugation in the product brought about by saturation of the oxazole ring.

Bezuglyi, Shimanskaya, and Peresleni (13) have studied the electrochemical reduction of oxazoles in methanol-water solvent. Their infrared data indicate that 2-(1-naphthyl)-5-phenyloxazole is reduced in the following manner

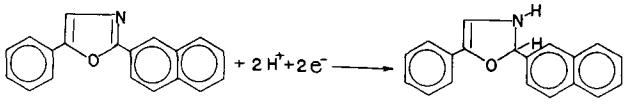

All other oxazoles were reported to be reduced under similar conditions to a ring-opened product via a 6-electron process. The lack of further reduction of (II) in methanol-water solvent suggests that the reduction should proceed no further in an aprotic medium. The great similarity in electrochemical behavior of (I) and (II) in DMF solvent indicates that the reduction of both proceeds primarily by the above mechanism.

Experimental

Apparatus.—The voltammetric experiments were carried out using a multipurpose instrument with three electrode cell configurations produced by Beckman Instruments, Inc. The instrument consists of a high-speed, high-impedance potentiometric recorder, and an electrolysis module that incorporates a high-gain operational amplifier with circuits for either voltage or current control. All u.v. spectra were recorded with a Perkin Elmer 202 u.v.-visible spectrophotometer.

The platinum working electrode (PPDE) consisted of a platinum disk sealed in a soft glass tube. The PPDE was cleaned in hot nitric acid, washed in distilled water, and hydrogen flamed before each experiment. The area of the electrode was 80 mm^2. The HMDE was a mercury drop suspended on a mercury-coated platinum wire sealed in soft glass. The auxiliary electrode was a coiled platinum wire. The reference electrode in all experiments was an aqueous SCE connected to the test solution by means of an Agar plug and sintered-glass disk. All solutions were deoxygenated with nitrogen gas which was purified by passage over hot copper gauze and then saturated with DMF.

The mass electrolysis experiments were carried out in a 300 ml vessel at a mercury pool cathode having an area of 28 cm^2. The platinum foil anode was oriented 1 cm from the cathode pool and was housed in a fritted glass chamber. The solution was stirred during electrolysis with a stream of purified nitrogen. A Dressen-Barnes regulated power supply was employed as a source of constant potential.

Chemicals.—Compounds (I) and (II) were obtained commercially from Picker Nuclear. They were both recrystallized from pure methanol before use. Compound (I) melts in the range 70°-72°C, compound (II) melts in the range 104°-106°C. Hydroquinone (HQ) was obtained from J. T. Baker Chemical Company and was recrystallized from a 50% water ethylether solution.

Spectroquality N,N-dimethylformamide containing approximately 0.03% water was obtained from Eastman Organic Chemicals. The solvent was vacuum distilled twice from anhydrous $CuSO_4$ before use.

Tetra-N-propylammonium perchlorate was produced by mixing equal molar mixtures of tetra-N-propylammonium hydroxide and perchloric acid. The product was washed with cold distilled water, recrystallized from a 20% acetonitrile-water mixture and dried under vacuum. The hydroxide was obtained from Eastman Organic Chemicals.

Acknowledgment

The financial support of The Robert A. Welch Foundation (Grant No. AO-337) is gratefully acknowledged.

Manuscript submitted April 20, 1970; revised manuscript received *ca.* May 13, 1970.

Any discussion of this paper will appear in a Discussion Section to be published in the June 1970 JOURNAL.

REFERENCES

1. P. H. Given, M. E. Peover, and J. M. Schoen, *J. Chem. Soc.*, **1958**, 2674.
2. A. H. Maki and D. H. Geske, *J. Chem. Phys.*, **33**, 825 (1960).
3. P. H. Reiger, I. Bernal, W. H. Reinmuth, and G. K. Fraenkel, *J. Am. Chem. Soc.*, **85**, 683 (1963).
4. S. Wawzonek and A. Gunderson, *This Journal*, **111**, 324 (1964).
5. Ralph N. Adams, *Acc. of Chem. Res.*, **2**, 175 (1969).

6. K. S. V. Santhanam and A. J. Bard, *J. Am. Chem. Soc.*, **88**, 2669 (1966).
7. J. L. Sadler and A. J. Bard, *ibid.*, **90**, 1979 (1968).
8. K. S. V. Santhanam and A. J. Bard, *ibid.*, **90**, 118 (1968).
9. J. L. Sadler and A. J. Bard, *This Journal*, **113**, 343 (1968).
10. M. E. Peover in "Electroanalytical Chemistry," A. J. Bard, Editor, Marcel Dekker, New York (1967).
11. R. S. Nicholson and I. Shain, *Anal. Chem.*, **36**, 706 (1964).
12. C. J. Hoijtink, J. Van Schooten, E. de Boer, and W. Y. Aalbersberg, *Rec. Trav. Chim.*, **73**, 355 (1954).
13. V. D. Bezuglyi, N. P. Shimanskaya, and E. M. Peresleni, *Zh. Obshch. Khim.*, **34**, 3540 (1964).
14. R. Nelson, E. T. Seo, D. Leedy, and R. N. Adams, *Z. Anal. Chem.*, **224**, 184 (1967).

Study of the Fluoride Complexes of Antimony(III) in Acidic Media by Rapid A-C Polarography

Evaluation of Complex Ion Systems by A-C Polarography for the Quasi-Reversible Electrode Process

A. M. Bond

Department of Inorganic Chemistry, University of Melbourne, Parkville, 3052, Victoria, Australia

ABSTRACT

The antimony(III)-fluoride complex ion system has been evaluated from data obtained from rapid a-c polarographic measurements. Four complexes are indicated to exist with stability constants of

$$\beta'_1 = 10^3\ (SbF^{++}),\ \beta'_2 = 5 \times 10^5\ (SbF_2^{+})$$

$$\beta'_3 = 2 \times 10^8\ (SbF_3),\ \text{and}\ \beta'_4 = 9 \times 10^{10}\ (SbF_4^{-})$$

where β'_n values refer to equilibria of the type $Sb^{3+} + nF^- \overset{\beta'_n}{\rightleftharpoons} SbF_n^{(3-n)+}$. Before evaluating this system, a detailed study into the nature of the electrode reaction occurring was undertaken and the conditions necessary for convenient polarographic study were ascertained. These conditions, the theory and other aspects of using a-c polarography to examine the system, in which an a-c quasi-reversible electrode reaction was observed, are considered in detail.

Recently (1), the author has shown that rapid polarographic techniques can be applied to the determination of stability constants of metal ion complexes. In this work it was pointed out that the rapid method should be applicable to certain systems which could not be studied by conventional d-c polarography. In other cases, where either conventional or rapid polarography could be used, the rapid method, with its short controlled drop time and fast scan rate of potential, offers the advantages of convenience and considerable time saving.

To verify the usefulness of the rapid polarographic method in the study of complex ion systems, a study of the bismuth(III)-fluoride system was undertaken (2). This particular system necessarily had to be studied in acidic media to prevent hydrolysis of bismuth. In acid media, and under the conditions for polarographic study of complex ions, any fluoride present must be in the form of hydrofluoric acid (HF). HF is especially corrosive toward glass, and conventional polarographic methods with long drop times and fairly slow scan rates of potential cannot be used because the contact time of the glass dropping mercury electrode (DME) with the HF is sufficient for considerable corrosion of the glass DME to occur. The rapid polarographic method, however, because of the fast scan rate of potential which can be used, enables measurements to be made in such a short time that no significant attack on the glass DME occurs. In fact HF concentrations of up to 25% can be tolerated by this method (3).

Key words: fluoride complexes, antimony(III), quasi-reversible a-c polarography.

Antimony, like bismuth, is a lower member of group (V) in the periodic table, and consequently both these elements normally exhibit somewhat similar chemical behavior. Very little, however, is known about the aqueous fluoride chemistry of these two species and information available on the stability or nature of the fluoride complexes formed in solution by Sb(III) or Bi(III) is very limited (4).

If in fact the electrode reaction of Sb(III) at the DME is similar to Bi(III), then use of the rapid polarographic technique and the equation and conditions suggested previously for study of the bismuth(III)-fluoride system (2) should enable the antimony(III)-fluoride system to be studied and thus allow a useful comparison of the two fluoride complexing systems.

As it in fact turned out, the Sb(III) electrode reaction at the DME was not found to be quite identical with that for Bi(III). However, as is discussed later, the use of rapid a-c polarography should still permit a simple calculation procedure being used to evaluate the number and magnitude of the consecutive stability constants of the fluoride complexes of Sb(III) formed in acidic media. This a-c method, the Sb(III) electrode reaction, and the results are discussed in detail in the remainder of this paper.

Experimental

All chemicals used were of reagent-grade purity.

The concentrations of stock solutions from which appropriate aliquots were taken to give the desired concentrations were determined as follows: (*i*) sodium perchlorate by precipitation of potassium perchlorate,

(*ii*) sodium iodide by potentiometric titration against silver nitrate, and (*iii*) perchloric acid by titration against sodium hydroxide.

Fluoride was added as sodium fluoride. Antimony(III) solutions were prepared by dissolving antimony(III) trioxide (Sb_2O_3) in 6*M* perchloric acid.

All measurements were made at 30° ± 0.1°C and at an ionic strength of 2.0 maintained by sodium perchlorate. Oxygen-free nitrogen was used to deaerate the solutions.

The concentrations of Sb(III), sodium iodide, and perchloric acid were 4 x $10^{-4}M$, 3 x $10^{-4}M$, and 1.2*M*, respectively in all solutions measured, unless otherwise stated. The concentrations of fluoride added to each solution are shown in the tables.

Polarograms were obtained using the Metrohm Polarecord E 261. A-C polarography was carried out using the Metrohm A-C Modulator E 393 with an applied a-c voltage of 10 mV, rms at 50 Hz. Rapid polarographic techniques with drop times of 0.16 sec and scan rate of potential of 0.5V/min were used with both d-c and a-c work using Metrohm Polarographie Stand E 354.

To minimize cell impedance, the a-c polarography was carried out with a three-electrode arrangement, with Ag/AgCl as the reference electrode and tungsten as the third or auxiliary electrode.

The DME used in all measurements had a value of $m^{2/3}\,t^{1/6}$ of 1.93 $mg^{2/3}\,sec^{1/6}$ in distilled water at zero applied potential *vs.* the Ag/AgCl electrode.

The method for recording rapid polarograms in aqueous HF was the same as that described previously (2).

All potentials measured in this work refer to a silver/silver chloride reference electrode (Ag/AgCl, 5*M* NaCl) connected to the polarographic solution via a 5*M* $NaClO_4$ salt bridge. No correction was made to the applied potential of the cell for either junction potentials or cell resistance (IR drop).

Antimony(III) electrode reaction at the DME.—Polarographic data for complex formation can most easily be understood and interpreted when reduction or oxidation of species under consideration is reversible.

The nature of the polarographic reduction of antimony(III) at the DME has been observed to vary markedly with change in supporting electrolyte. In hydrochloric acid and acidic chloride media, reversible reduction of the type

$$Sb(III) + 3e \rightleftharpoons Sb \text{ (amalgam)}$$

has been observed by many workers [*e.g.*, ref. (5-10)] using conventional d-c methods.

In noncomplexing perchloric acid-sodium perchlorate media, however, reduction of antimony(III) has been found to be irreversible (7, 11). Addition of fairly low concentrations of the halide ions, chloride, bromide, or iodide to these perchlorate solutions leads to the observation of a reversible three-electron reduction wave.

The above features were also observed in this work, by conventional a-c, d-c, and rapid polarographic techniques. Figure 1a shows a conventional d-c polarogram of antimony(III) in 1.2*M* perchloric acid/0.8*M* sodium perchloric media. Two waves close together are observed. The first wave is very small in height and is dominated by the second wave which makes the major contribution to the polarogram. The first wave has a half wave potential, $E_{1/2}$, of −0.07V and the second wave an $E_{1/2}$ value of −0.17V. The complete a-c polarogram also consists of two waves (Fig. 1b) with a very small peak with a summit potential, E_s, of −0.05V and a large, fairly symmetrical peak with E_s of −0.21V being observed.

The half-width of the second wave is about 110 mV, which is significantly larger than the value expected for a reversible three-electron reduction of approximately 90/*n*. The half-width of the first wave cannot be estimated because it overlaps to a large extent with the second wave.

Fig. 1a. Conventional d-c polarogram of antimony(III) in $NaClO_4/HClO_4$.

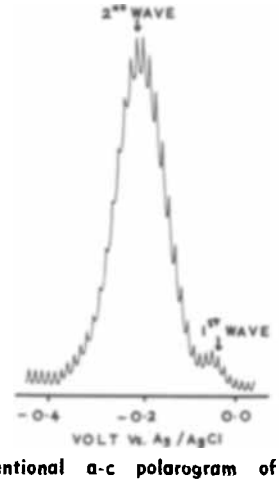

Fig. 1b. Conventional a-c polarogram of antimony(III) in $NaClO_4/HClO_4$.

The rapid d-c and a-c polarograms (Fig. 1c and d) are very similar to the conventional d-c and a-c polarograms. Again the first wave is very small relative to the second and is just discernible. E_s values of −0.05 and −0.22 and $E_{1/2}$ of −0.05 and −0.21 are obtained, respectively, for the first and second waves under rapid polarographic conditions. It can be seen by comparison of Fig. 1a and b with 1c and d that

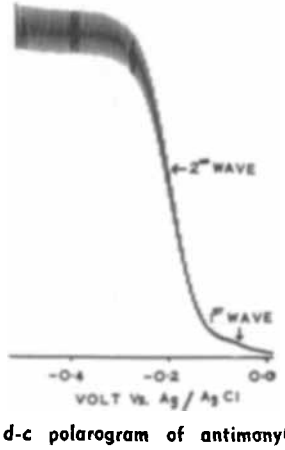

Fig. 1c. Rapid d-c polarogram of antimony(III) in $NaClO_4/HClO_4$.

Fig. 1d. Rapid a-c polarogram of antimony(III) in $NaClO_4$/$HClO_4$.

the very short drop time of the rapid polarographic method does not alter the shape or nature of the polarographic waves significantly.

The addition of a trace of iodide to the $NaClO_4$/$HClO_4$ solutions (Fig. 2a and b) gives reversible polarograms. Plots of $E_{d.e.}$ *vs.* log $(i/id - i)$ are linear with slope 22 ± 2 mV; half-widths of a-c polarograms are 40 ± 2 mV (uncompensated for IR drop); the a-c polarograms are highly symmetrical and $E_{1/2}$ and E_s values are in excellent agreement.

In aqueous solutions, the Sb^{3+} ion has a great tendency to hydrolyze to SbO^+ and even in acidic media the hydrolysis would not be expected to be completely suppressed. In fact, except in concentrated perchloric acid, only a very small concentration of Sb^{3+} could

Fig. 2a. Rapid d-c polarogram of antimony(III) in $NaClO_4$/$HClO_4$/NaI.

Fig. 2b. Rapid a-c polarogram of antimony(III) in $NaClO_4$/$HClO_4$/NaI.

be expected. The two waves in perchloric acid may therefore arise from equilibria of the type $Sb^{3+} + H_2O \rightleftharpoons SbO^+ + 2H^+$. One wave would thus be due to the electrode reaction $Sb^{3+} + 3e \rightleftharpoons Sb$ (amalgam) and the other to an electrode process of the type $SbO^+ + 2H^+ + 3e \rightleftharpoons Sb$ (amalgam) + H_2O. This second process would be expected to be a slow, nonreversible, electrode process as it requires the breakage of a metal-oxygen bond.

When a trace of chloride, bromide, or iodide is added several phenomena could occur leading to the observation of a reversible wave and mechanisms involving adsorption and complex formation have been postulated (8). These halides are readily deformable, and thus adsorbable at the DME on the positive side of the electrocapillary maximum at which the antimony(III) wave occurs. In the absence of a halide the equilibrium concentration of triply charged positive Sb^{3+} ion to be reduced has to move toward a positively charged DME, the kinetics of the electrode reaction are slow, and an irreversible wave due to Sb^{3+} is observed. In the presence of adsorbed halide, the positive charge on the DME is partially neutralized and it could be considered that the rate of the electrode reactions can increase to reversible because it is now easier for the Sb^{3+} to reach the DME. This mechanism implies that at least one of the waves observed in perchloric acid is due to Sb^{3+} and it is this wave which becomes reversible on the addition of halide. Alternatively, complex formation of Sb(III) could occur and give rise to the observed reversible wave.

Formation of $SbX_n^{(3-n)+}$ type complexes in solution could lead to a reversible wave provided that association and dissociation of the complexes is rapid. The electrode reaction could then be considered as a two-stage process with the charge transfer step being reversible and rate determining

$$SbX_n^{(3-n)+} \rightleftharpoons Sb^{3+} + nX^-$$
$$Sb^{3+} + 3e \rightleftharpoons Sb \text{ (amalgam)}$$

As the Sb(III) electrode reaction is similar to that of Bi(III) with regards to the effect of chloride, bromide, and iodide ions, a discussion of the Bi(III) electrode reaction (2, 8, 11) should be consulted for further details as to the possibility of either adsorption or complex formation being the cause of the observed reversible wave. However, it does not appear possible to distinguish between the two possibilities from this or other work.

Addition of fluoride to the 1.2*M* $HClO_4$/0.8*M* $NaClO_4$ solutions leads to rapid a-c and d-c polarograms as given in Fig. 3a, b, c, and d. The $E_{1/2}$ and E_s values become more negative on addition of fluoride and the very small first wave is not observable. The d-c shape of this wave virtually remains unaltered by the addition of fluoride and the a-c wave becomes just slightly broader. (Compare appropriate polarograms from Fig. 1, 2, and 3.)

Fluoride ion, like perchlorate ion, is nondeformable and nonadsorbable at the DME. Furthermore, in acid media most of the fluoride would exist as undissociated HF rather than as free fluoride ion because hydrofluoric acid is a fairly weak acid. Thus neither of the possible adsorption or complex formation mechanisms leading to a reversible wave as observed with chloride, bromide, or iodide could be expected to occur on addition of fluoride.

West and co-workers (12) in 0.5*M* sodium fluoride (*p*H 3.0-4.4) observed a well-defined wave for antimony(III) which had an $E_{1/2}$ value of −0.683V *vs.* SCE. They also observed a prewave. This system would appear to be very similar to that in perchloric acid, where two waves were observed. In the fluoride media the two waves could be attributed to $SbOF_n^{(1-n)+}$ and $SbF^{(3-n)+}$ type complexes, respectively. Comparison with perchloric acid solutions would suggest that

Fig. 3a and b. Effect of added fluoride on the d-c antimony(III)-$NaClO_4/HClO_4$/NaF polarogram. Figure 3b has a higher concentration of fluoride than Fig. 3a and the negative shift in $E_{1/2}$ due to fluoride complexing can be seen.

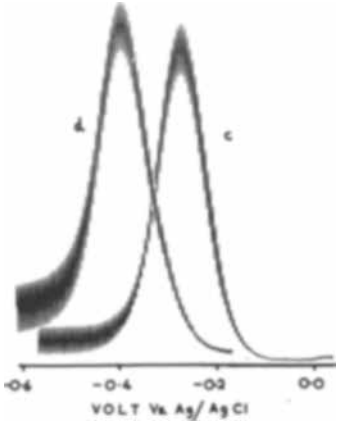

Fig. 3c and d. Effect of added fluoride on the antimony(III)-$NaClO_4/HClO_4$/NaF polarogram. Figure 3d has a higher concentration of fluoride than Fig. 3c and the negative shift in E_s due to fluoride complexing can be seen.

both the SbO^+ and Sb^{3+} waves have shifted to considerably more negative potentials due to fluoride complexing. Pavlov and Lazarov (13, 14) have confirmed the shift in $E_{1/2}$ due to fluoride complex formation. However, their work was carried out using 0.5*M* KCl to maintain constant ionic strength, so somewhat different electrode reactions could be occurring as the chloride would not be an inert electrolyte. In the more acidic medium of 0.1*M* HF-0.1*M* NH_4F, and with a Teflon DME (15) only one irreversible d-c wave was reported with $E_{1/2}$ of −0.65V *vs.* SCE ($E_{1/4}$-$E_{3/4}$) = 90 mV.

Addition of fluoride to the reversible wave found in 1.2*M* $HClO_4$-0.8*M* $NaClO_4$-3 x 10^{-4}*M* NaI causes a negative shift in E_s and $E_{1/2}$ values. Figures 4a and b show that the shape of the d-c and a-c waves also changes slightly with addition of fluoride. In actual fact, the reversible waves are now both a-c and d-c quasi reversible as is shown by the nonlinear d-c plots of $E_{d.e.}$ *vs.* log ($i/id - i$), and the slight broadening of the a-c wave accompanied by the appearance of the shoulder at high fluoride concentrations (16).

The large negative shift in $E_{1/2}$ and E_s could not be, however, completely attributed to change in reversibility and must be partially due to fluoride complexing. The nature and magnitude of the fluoride complexing are discussed in the following sections.

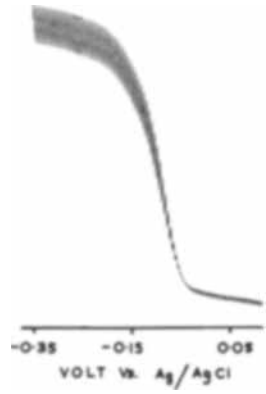

Fig. 4a. D-C polarogram of the antimony(III)-$NaClO_4/HClO_4$/NaI/NaF system at high fluoride concentrations.

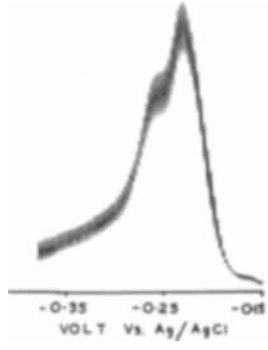

Fig. 4b. A-C polarogram of the antimony(III)-$NaClO_4/HClO_4$/NaI/NaF system at high fluoride concentrations.

Theory

De Ford and Hume (17) have derived an equation for evaluation of consecutive stability constants from polarographic data.

This equation can be written as follows

$$F_o(X) = \text{antilog}\left\{0.4343\frac{n\mathbf{F}}{RT}[(E_{1/2})_F - (E_{1/2})_C] + \log I_F/I_C\right\} = \sum_n \beta_n C^n \quad [1]$$

where the symbol $F_o(X)$ is introduced for convenience to represent the experimentally measurable quantity on the left hand side of the equation. β_n is the formation or stability constant of the n^{th} complex and refers to equilibria of the type

$$M^{x+} + nX^- \overset{\beta_n}{\rightleftharpoons} MX_n^{(x-n)+}$$

The subscripts F and C in Eq. [1] refer to the free ion and complexed ion, respectively. Other symbols are those conventionally used in polarographic terminology.

If fluoride complexing of Sb^{3+} occurs to give rise to $SbF_n^{(3-n)+}$ type complexes, then the electrode reaction occurring can be represented simply as a two-stage process

$$SbF_n^{(3-n)+} \rightleftharpoons Sb^{3+} + nF^- \quad [2]$$

and

$$Sb^{3+} + 3e \rightleftharpoons Sb \text{ (amalgam)} \quad [3]$$

For the De Ford-Hume expression above to be valid the following two conditions must hold: (*A*) The complexed and uncomplexed species are in rapid equilibrium as represented by Eq. [2]. (*B*) Nernstian conditions prevail, *i.e.*, the electrode reaction in Eq. [3] is polarographically reversible. Under these conditions

the half-wave potential measured directly from the polarogram is the reversible half-wave potential, $E_{1/2}{}^r$. Thus Eq. [1] should more correctly be expressed as

$$F_o(X) = \text{antilog}\left\{0.4343\frac{n\mathbf{F}}{RT}[(E_{1/2}{}^r)_F - (E_{1/2})_C{}^r] + \log I_F/I_C\right\} = \sum_n \beta_n C_x{}^n$$

If the electrode reaction is reversible then the a-c summit potential E_s is equal to $E_{1/2}{}^r$ and the De Ford-Hume equation can be solved as

$$F_o(X) = \text{antilog}\left\{0.4343\frac{n\mathbf{F}}{RT}[(E_s)_F - (E_s)_C] + \log I_F/I_C\right\} = \sum_n \beta_n C_x{}^n \quad [4]$$

The first parameter which must be obtained for a successful solution to the De Ford-Hume equation is the $(E_{1/2}{}^r)_F$ value for the free, uncomplexed ion. In this case, this would be for Sb^{3+}.

As previously mentioned, in the presence of a trace of iodide, the d-c electrode reaction was observed to be polarographically reversible by conventional plots of $E_{d.e.}$ *vs.* log $(i/id - i)$.

Reversibility of the a-c polarography was confirmed as follows. With 3 x 10^{-4} NaI the a-c half width was (40 ± 3) mV. Theoretically, at 25°C and for an applied a-c voltage of $\leq 8/n$ mV, (16) the half-width should be approximately $(90/n)$ mV. This work was done at 30°C with an applied a-c voltage of 10 mV, rms at 50 Hz. Under these conditions, with temperature greater than 25°C, and the applied a-c voltage considerably greater than $(8/n = 2.67)$ mV, the theoretical half-width would be expected to be somewhat greater than $(90/n)$ mV, so that the half-width value observed of 40 ± 3 mV, uncompensated for IR drop, indicates a high degree of a-c reversibility. The excellent agreement of $E_{1/2}$ and E_s and the highly symmetrical nature of the a-c wave provides further evidence for the electrode reaction being reversible.

Thus $E_s = E_{1/2}{}^r$, in the presence of a trace of iodide, but whether the value of E_s is $(E_s)_F$ needs to be considered.

If the sole function of the small concentration of the iodide is to provide a reversible electrode reaction by an adsorption mechanism then the necessary equivalence

$$E_s = E_{1/2}{}^r = (E_{1/2}{}^r)_F = (E_s)_F$$

will be satisfied exactly.

If complex formation of iodide is involved then the $E_{1/2}{}^r$ value observed, $(E_{1/2}{}^r)_0$, will be related to $(E_{1/2}{}^r)_F$, by an equation

$$\text{antilog}\left\{0.4343\frac{n\mathbf{F}}{RT}[(E_{1/2}{}^r)_F - (E_{1/2}{}^r)_0] + \log I_F/I_0\right\} = 1 + \beta_1[I^-] + \beta_2[I^-]^2 + \ldots\ldots \beta_j[I^-]^J$$

where β_j is the stability constant of the j^{th} complex derived from equilibria of the type

$$Sb^{3+} + jI^- \overset{\beta_j}{\rightleftharpoons} SbI_j{}^{(3-j)+}$$

Thus, as long as the concentration of iodide is low and β_j complexes are not too strong it can be seen that to a good approximation $(E_{1/2}{}^r)_0 = (E_{1/2}{}^r)_F$. If iodide complex formation is involved in providing the reversible wave, $(E_{1/2}{}^r)_F$ could in fact be calculated provided the β_j values are known. Unfortunately no values for β_j are available (4) and the procedure of neglecting iodide complex formation had to be used. As the concentration of iodide is small, and in fact less than that of antimony, it was hoped that this procedure would not involve a very large source of error. A third possibility, that the reversibility results from a combination of adsorption and complex formation could also be considered. That is, iodide complexation with Sb(III) may occur via a surface reaction or in the immediate vicinity of the electrode surface where the iodide concentration, because of adsorption, would be significantly higher than in the bulk of the solution.

In view of the reversible wave provided by low concentrations of iodide, and the simplifying effect this has on calculations, all the $E_{1/2}$ and E_s values quoted are measured in the presence of 3 x $10^{-4}M$ sodium iodide and the $F_o(X)$ values are assumed to be close to correct whatever the mechanistic effect of iodide on the electrode reaction is, and no correction for iodide complexation was made.

Close examination of the electrode process in fluoride media and in the presence of sodium iodide, showed it to be classified as nonreversible by both a-c and d-c polarography for fluoride concentrations greater than $0.02M$. For concentrations of fluoride greater than this, the nonlinear plots of $E_{d.e.}$ *vs.* log $(i/id - i)$ from d-c polarograms, and the broadening and appearance of shoulders in a-c polarograms, suggested that the electrode process has become quasi reversible.

For fluoride concentrations less than $0.02M$ the electrode reaction was found to be d-c reversible but a-c quasi reversible. Table I verifies the d-c process possesses a high degree of reversibility up to $0.02M$ in fluoride as $(E_{1/4}\text{-}E_{3/4})$ values are within the range 23 ± 1 mV. The a-c half-width, however, increases with added fluoride, indicating a change in rate of electrode reaction is occurring, a fact not observed by the d-c method.

Table I shows the effect of fluoride concentration on (i_d) and $(i_d\sim)$ values. The d-c (i_d) is virtually unaltered by added fluoride but the a-c $(i_d\sim)$ decreases significantly with increasing fluoride concentration. Thus the fluoride complexation reaction is sufficiently rapid so that it does not contribute to rate control in the d-c electrode process. The decrease in $(i_d\sim)$ with increasing fluoride concentration indicates that the a-c electrode process is no longer solely diffusion controlled. If the fluoride complexation reaction is sufficiently rapid so that it does not contribute to rate control in either the d-c or a-c electrode processes, then the experimental observations may be explained entirely in terms of charge transfer effects as follows.

In the absence of fluoride, but in the presence of a trace of other halide ion, the electrode process is diffusion controlled and shows a high degree of reversibility in both the d-c and a-c sense. As the concentration of fluoride is increased, the charge transfer rate is decreased and becomes sufficiently slow so that the a-c electrode process is no longer reversible. For fluoride concentrations less than $0.02M$, the d-c electrode

Table I. Variation of $E_{1/2}$; E_s, i_d, $i_d\sim$, $(E_{1/2}\text{-}E_{3/4})$, and a-c half width for the Sb(III) ⇌ Sb(O) (amalgam) electrode reaction with increasing fluoride concentration. [Sb(III)] = 4 x 10^{-4} M, [NaI] = 3 x 10^{-4} M, [$HClO_4$] = 1.2M. Ionic strength = 2.0 ($HClO_4$/$NaClO_4$)

[F⁻], M	$-E_{1/2}$, V *vs.* Ag/AgCl	$-E_s$, V *vs.* Ag/AgCl	i_d, μA	$i_d\sim$, μA	$(E_{1/4} - E_{3/4})$, mV	A-C half width, mV
0.000	0.0312	0.0293	3.88	1.95	22	40
0.002	0.0416	0.0440	3.92	1.70	22	44
0.003	0.0520	0.0515	3.90	1.52	22	46
0.004	0.0599	0.0593	3.92	1.48	24	49
0.006	0.0721	0.0701	3.88	1.30	23	56
0.008	0.0794	0.0786	3.96	1.13	24	58
0.012	0.0926	0.0905	3.94	1.06	24	60
0.016	0.1027	0.1025	3.88	0.95	23	66
0.020	0.1089	0.1086	3.92	0.90	24	76

process is still sufficiently rapid so that it is reversible, as evidenced by the linear plots of $E_{d.e.}$ vs. log $(i/i_d - i)$ with slopes close to the theoretical value. When the fluoride concentration becomes greater than 0.02*M* the charge transfer reaction has become sufficiently slow so that it is no longer reversible in either the d-c or the a-c sense. Under these conditions the quasi-reversible a-c wave becomes significantly broader and may exhibit shoulders (16) (*cf.*, Fig. 4b).

To evaluate the stability constants of the antimony(III)-fluoride system, by the De Ford-Hume method, only d-c results obtained for fluoride concentrations less than 0.02*M* could be used. For this concentration range the d-c electrode reaction is reversible and $E_{1/2} = E_{1/2}^r$. Over this concentration range it was also found that $E_s = E_{1/2} = E_{1/2}^r$ for the quasi-reversible a-c process as shown in Table I, which suggests that a-c polarography can be used despite the fact that an a-c quasi-reversible electrode process is observed.

The theory for a-c polarography involving quasi-reversible electrode processes is rather difficult to solve exactly.

However at low frequency and for $ke^0 \geq 10^{-2}$ cm sec^{-1} it can be shown that E_s approaches $E_{1/2}^r$ (16). Thus, using low frequency a-c polarography, $E_{1/2}^r$ can be calculated directly and simply from the E_s value. A frequency of 50 Hz was used in this work and $(E_{1/2}^r)_C$ values used, were those taken directly from the a-c polarogram as the $(E_s)_C$ value. The previous use of a-c polarography for study of complex ion systems for reversible electrode reactions [1], [2] can thus be extended satisfactorily to the quasi-reversible electrode process. However, care in using the quasi-reversible a-c procedure should be exercised, as only results for which $ke^0 \geq 10^{-2}$ cm sec^{-1} are valid. In this work, solutions of high fluoride concentration which gave shoulders on the a-c polarogram, were not used because ke^0 probably is $< 10^{-2}$ cm sec^{-1}.

The complete $F_0(X)$ function also involves the term log I_F/I_C. For reversible a-c electrode reactions the wave height $(i_d\sim)$ could be used to solve the expression as log $(i_d\sim)_F/(i_d\sim)_C$. However, because of the a-c quasi-reversible reaction this a-c treatment cannot be applied. The d-c treatment, log $(i_d)_F/(i_d)_C$, however, is still valid and can be used for any diffusion controlled reaction. In actual fact, the term log $(i_d)_F/(i_d)_C$ was found to be very small and can conveniently be neglected in calculations of $F_0(X)$.

Thus the equation used to solve the Sb(III)-fluoride complex system was the a-c expression

$$F_0(X) = \text{antilog } 0.4343 \frac{n\mathbf{F}}{RT}[(E_s)_F - (E_s)_C] = 1 + \beta_1[F^-] + \beta_2[F^-]^2 + \ldots \beta_n[F^-]^2 \quad [5]$$

Inclusion of the equilibrium constant K_a, for hydrofluoric acid modifies this equation to give

$$F_0(X) = \text{antilog } 0.4343\,[(E_s)_F - (E_s)_C] = 1 + \beta_1 K_a \frac{[HF]}{[H^+]} + \beta_2 K_a^2 \frac{[HF]^2}{[H^+]^2} \ldots \beta_n K_a^n \frac{[HF]^n}{[H^+]^n} \quad [6]$$

or

$$F_0(X) = 1 + \beta'_1\left(\frac{a}{b-a}\right) + \beta'_2\left(\frac{a}{b-a}\right)^2 + \ldots \beta'_n\left(\frac{a}{b-a}\right)^n \quad [7]$$

where β'_n is the stability constant for the equilibria

$$Sb^{3+} + HF \overset{\beta'_n}{\rightleftharpoons} SbF_n^{(3-n)+} + nH^+$$

and a is the concentration of sodium fluoride added to the solution, initially b *M* in perchloric acid. In the presence of excess acid over added fluoride, and because HF is a weak acid, virtually all fluoride will be present as undissociated HF and the ratio $[HF]/[H^+]$ is given by $(a/b - a)$ as described in a previous paper (2).

If the symbol y is used in place of $(a/b - a)$, the equation has the form

$$F_0(X) = 1 + \beta'_1 y + \beta'_2 y^2 + \ldots \beta'_n y^n$$

If the function $F_1(X) = (F_0(X) - 1)/y$ is now introduced and a graphical plot of $F_1(X)$ *vs.* y is made, then the value of $F_1(X)$ at the intercept equals β'_1. Likewise the value of β'_2 is given by the value of $F_2(X)$ at the intercept when the function $F_2(X) = (F_1(X) - \beta'_1)/y$ is plotted against y and is extrapolated to $y = 0$. The formation constants of higher complexes (if present) may be determined in a similar manner.

As a consequence of the nature of the $F_n(X)$ functions, a plot of $F_n(X)$ *vs.* y for the last complex will be a straight line parallel to the y axis, and this allows the determination of the number of complexes.

In obtaining values of β'_n for the Sb(III)-fluoride system, the extent of error involved in making two approximations must be kept in mind.

First, the β'_n values are to be calculated neglecting any complex formation from iodide. If any occurs, then the electrode reaction should more explicitly be written as

$$\left.\begin{aligned} &SbI_j^{(3-j)+} \overset{\beta_j}{\rightleftharpoons} Sb^{3+} + jI^- \\ &SbF_n^{(3-n)+} + nH^+ \overset{\beta'_n}{\rightleftharpoons} Sb^{3+} + nHF \end{aligned}\right\} \quad [A]$$

$$Sb^{3+} + 3e \rightleftharpoons Sb \text{ (amalgam)} \quad [B]$$

It can be readily shown that β'_n values calculated for fluoride complexes in the manner indicated, by neglect of iodide complexes, will be too low by a factor $(1 + \beta_1[I^-] + \ldots . \beta_j[I^-]^j)$. Thus providing β_1 is not too large for iodide, then at the concentration of iodide used in this work, the approximation of neglecting iodide complexation should be satisfactory. Alternatively, if β_j values were known then the β'_n values could be corrected.

Second, it has been assumed that the fluoride complexes of Sb(III) are of the type $SbF_n^{(3-n)+}$ rather than $SbOF_n^{(1-n)+}$. Both of these can be related by an equilibrium

$$SbF_n^{(3-n)+} + H_2O \rightleftharpoons SbOF_n^{(1-n)+} + 2H^+$$

In this work solutions measured all contained a very high concentration of H^+ which strongly favors formation of $SbF_n^{(3-n)+}$. Furthermore, in this highly acidic media only one wave is observed compared with the two waves at *p*H (3.0-4.4) (12). In the work at higher *p*H (3.0-4.4) the two waves probably result from the equilibrium concentrations of fluoride and oxy-fluoride complexes. In the considerably more acidic media used in this work it is postulated that only the wave from $SbF_n^{(3-n)+}$ is observed because the equilibrium concentration of $SbOF_n^{(1-n)+}$ is now too low to be detected. Analogy of the fluoride system with the corresponding antimony(III)-chloride and the chemically similar bismuth(III)-chloride systems is somewhat hazardous, but for these systems neglecting the $SbOCl_n^{(1-n)+}$ or $BiOCl_n^{(1-n)+}$ complexes at high acidity is satisfactory (4) and they need only be considered at fairly high *p*H. These chloride systems have in fact been successfully investigated polarographically in acid media by assuming formation of simple chloride complexes only (7, 9).

Results and Discussion

Table II and Fig. 5 summarize the results obtained, using the calculation method described previously. Four complexes were observed with values of $\beta'_1 = 10^3$ (SbF^{2+}), $\beta'_2 = 5 \times 10^5$ (SbF_2^+), $\beta'_3 = 2 \times 10^8$ (SbF_3) and $\beta'_4 = 9 \times 10^{10}$ (SbF_4^-). The large errors involved

Table II. Analysis of $F_n(X)$ functions for the antimony(III)-fluoride system

aM	$\left(\frac{a}{b-a}\right)$ × 10³*	$-E_s$ V vs. Ag/AgCl	$F_0(X)$	F_1X × 10⁻³	F_2X × 10⁻⁶	$F_3(X)$ × 10⁻⁸	$F_4(X)$ ×10⁻¹⁰
0.000	0.000	0.0293	1.000	—	—	—	—
0.002	1.669	0.0440	5.433	2.656	0.992	2.95	—
0.003	2.506	0.0515	12.88	4.741	1.49	3.95	7.8
0.004	3.344	0.0593	31.62	9.157	2.44	5.80	11.4
0.006	5.025	0.0701	109.6	21.61	4.10	7.16	10.3
0.008	6.711	0.0786	291.7	43.32	6.31	8.66	9.9
0.012	10.10	0.0905	1148	113.6	11.1	10.5	8.4
0.016	13.51	0.1025	4571	338.3	25.0	18.1	12.0
0.020	16.95	0.1086	9226	544.2	32.0	18.6	9.8

* a = concentration of sodium fluoride added to solutions initially b M in perchloric acid.

in calculations, by the time $F_4(X)$ values are obtained, could possibly conceal higher but fairly weak complexes. However, at least four can be detected.

Comparison of these results with the bismuth(III)-fluoride system studied previously, for which $\beta'_1 = 26(BiF^{2+})$, $\beta'_2 = 2(BiF_2^+)$ and $\beta'_3 = 500(BiF_3)$ indicate two marked differences in these systems.

First, the stability of Sb(III)-fluoride complexes is considerably greater than for Bi(III)-fluoride species. The very high stability for the Sb(III) complexes is in agreement with the work of Pavlov and Lazarov (13, 14).

Second, an anionic form of Sb(III)-fluoride was detected as SbF_4^-. Such a species was not observed with Bi(III). This difference observed, is in agreement with anion exchange studies made by Faris (17) and Nelson *et al.* (18) in hydrofluoric acid media. In the solid state, SbF_3 is also known to be capable of acting as a Lewis base to form SbF_4^- with the fluoride ion (19), so that detection of an anionic complex in solution containing excess HF could be anticipated.

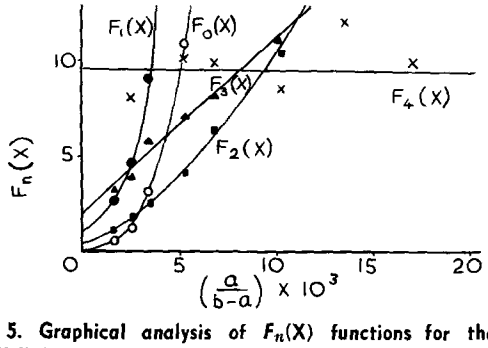

Fig. 5. Graphical analysis of $F_n(X)$ functions for the antimony (III)-fluoride system. ○, $F_0(X) \times 10^{-1}$; ●, $F_1(X) \times 10^{-3}$; ■, $F_2(X) \times 10^{-6}$; ▲, $F_3(X) \times 10^{-8}$; x, $F_4(X) \times 10^{-10}$.

Thus the fluoride complex systems of Sb(III) and Bi(III) exhibit marked differences in aqueous media, both as to the stability and number of complexes formed, according to polarographic data. This idea is also consistent with the rather limited data available from other sources, and this fact at least provides some indication that the theories and ideas used in this work, as well as the assumptions made, are valid.

Manuscript submitted Dec. 10, 1969; revised manuscript received March 18, 1970.

Any discussion of this paper will appear in a Discussion Section to be published in the June 1971 JOURNAL.

REFERENCES

1. A. M. Bond, *J. Electroanal. Chem.*, **23**, 277 (1969).
2. A. M. Bond, *ibid.*, **23**, 269 (1969).
3. A. M. Bond and T. A. O'Donnell, *Anal. Chem.*, **41**, 1801 (1969).
4. "Stability Constants of Metal-Ion Complexes," *Chem. Soc. (London)*, Special Pubication Number 17 (1964).
5. J. Heyrovsky and D. Ilkovic, *Coll. Trav. Chim. Tchecosl.*, **7**, 198 (1935).
6. B. Breyer, F. Gutman, and S. Hacobian, *Australian J. Sci. Res.*, **A3**, 567 (1950).
7. F. Pantani and P. G. Desideri, *Gazetta*, **89**, 1360 (1959).
8. B. Breyer and H. H. Bauer, "Alternating Current Polarography and Tensammetry, Chemical Analysis," Vol. 13, pp 135-137, Interscience, New York/London (1963).
9. A. M. Bond and A. B. Waugh, *Electrochim. Acta*, In press.
10. I. M. Kolthoff and J. J. Lingane, "Polarography," Vol. II, pp. 545-550, 2nd edition, Interscience, New York/London (1952).
11. B. Breyer, F. Gutman, and S. Hacobian, *Australian J. Sci. Res.*, **A4**, 595 (1951).
12. P. W. West, J. Dean, and E. J. Breda, *Coll. Czech. Chem. Comm.*, **13**, 1, (1948).
13. D. Pavlov and D. Lazarov, *Proc. Acad. Sci. USSR* (Chemistry Section) **118**, 19 (1958) (*English Transl.*) *Doklady Akad Nauk SSSR*, **118**, 103 (1958) (Russian).
14. D. Pavlov and D. Lazarov, *J. Inorg. Chem., USSR*, **3**, 142 (1958) (*English Transl.*). *Zhur. Neorgan. Khim.*, **3**, 2099 (1958) (Russian).
15. J. B. Headridge, A. G. Hamza, D. P. Hubbard, and M. S. Taylor, "Polarography 1964," Proceedings of the Third International Conference, Southampton, p. 625, G. J. Hills, Editor, Macmillan, London/Melbourne, (1966).
16. D. E. Smith, "Electroanalytical Chemistry," Vol. 1, pp. 1-148. A. J. Bard, Editor, Marcel Dekker Inc., New York (1966).
17. J. P. Faris, *Anal. Chem.*, **32**, 520 (1960).
18. F. Nelson, R. M. Rush, and K. A. Kraus, *J. Am. Chem. Soc.*, **82**, 339 (1960).
19. F. A. Cotton and G. Wilkinson, "Advanced Inorganic Chemistry," p. 380, Interscience, New York/London (1962).

Technical Notes

A Contribution to the Applicability of Critical Pitting Potentials

H. P. Leckie

Inland Steel Research Laboratories, Coated Products Division, East Chicago, Indiana 46312

Many metals may exhibit passivity or undergo intense localized corrosion in aqueous chloride media depending on the relative position of their open circuit corrosion potential with respect to a "critical pitting potential," V_c. Included in this category are titanium, aluminum, zirconium, nickel, and some of their alloys together with many of the austenitic and ferritic stainless steels. Pitting of these passive metals and alloys is inhibited if the potential, controlled either by local cell action or some outside impressed source, is maintained more active than V_c. Should the metal/solution potential become more noble than V_c localized attack may occur often resulting in environment concentration changes which shift V_c to more active values. Such concentration changes caused by the pitting process itself probably explain the hysteresis effects described by Pourbaix *et al.* (1) who noted both a pitting potential and a "repassivation potential" (occurring at some more active value) for stainless steels in chloride media.

The concept of a critical potential is not new, being first reported in terms of a "breakthrough" potential by Brennert (2) as far back as 1937. Very little follow up to this work took place, save for the work of Mahla and Neilson (3) in 1947, until the last five or six years during which a considerable amount has appeared in the literature (4-9).

From the work of Leckie and Uhlig (8) and Horvath and Uhlig (9) as well as others a considerable amount of information has been obtained relating to the effect of environmental factors on the value of the critical pitting potential for 18-8 stainless steel and aluminum. Other passive materials have been studied to a more limited extent. It is somewhat surprising, therefore, that full utilization of critical potential measurements has not been employed as a more widespread means for rapidly predicting the tendency for localized attack on materials of construction in naturally occurring environments A criticism is often put forth of critical potential measurements as a criterion for predicting localized pitting corrosion under naturally corroding conditions in that such measurements are obtained under short-term dynamic conditions and as such bear no relation to long-term immersion behavior.

It is the purpose of this note to show that critical pitting potentials do indeed provide a valuable criterion in determining passive film stability and may serve as a useful tool in one aspect of materials evaluation for design in much the same way as isothermal transformation curves and pH-potential (Pourbaix) (10) diagrams (although both of these represent "unreal" conditions) serve to provide information regarding the behavior of metals and alloys with respect to thermal and environmental effects, respectively.

Key words: critical pitting potential, pitting potential in chlorides.

Table I. Composition of AISI type stainless steel

Composition, per cent							
C	Mn	P	S	Si	Cr	Ni	Mo
0.05	0.75	0.018	0.015	0.56	18.7	8.8	0.15

Experimental

All experiments were conducted on AISI Type 304 stainless steel and have the composition shown in Table I. Cylindrical specimens cut from rods were abraded to 3/0 emery paper followed by pickling in a solution containing 15% HNO_3, 2% HF, 5% HCl by volume at 60°C for 5 min. Specimens were mounted in a manner previously described (8) such that only the stainless steel was exposed to the environment. The all-glass cell incorporated a platinized platinum counterelectrode, Luggin capillary connected to a saturated calomel reference electrode, and an inlet for gas agitation and deaeration. Electrolytes were deaerated for four or more hours using prepurified nitrogen. All electrolytes were made from double distilled water and Reagent grade chemicals.

Polarization measurements were obtained using a Wenking potentiostat in conjunction with a Wenking potential programmer. The latter permitted sweeps to be conducted over a very wide range of scan rates. An X-Y recorder permitted simultaneous measurement of potential and current. In all cases the stainless steel specimens were activated by holding at a potential of −1.5V SCE for a period of 5 min. The

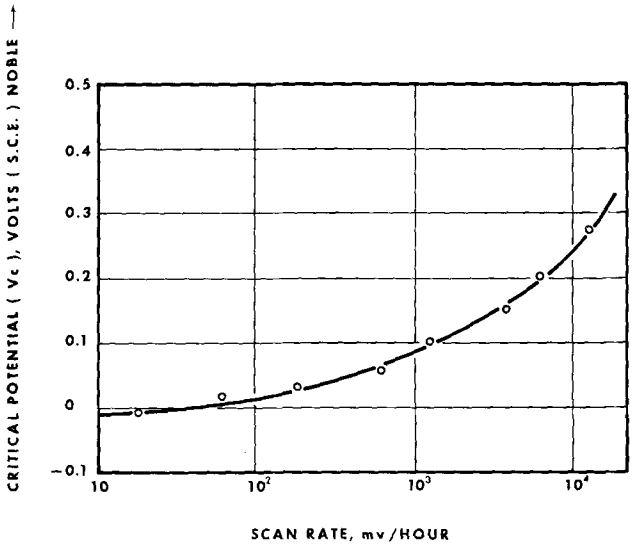

Fig. 1. Effect of potential scan rate on the value of V_c for Type 304 stainless steel in 0.1M NaCl.

potential was then shifted in the noble direction at a scan rate of 10 V/hr and on reaching −0.3V SCE, was held for a further 15 min. Holding at this potential in the passive region allowed the formation of a uniform film. Critical potentials were then measured by again sweeping the potential in the noble direction at various controlled, constant rates.

Results and Discussion

The effect of potential scan rate on the critical potential for pitting for Type 304 stainless steel in 0.1*M* NaCl is shown in Fig. 1. Over a three order of magnitude variation in scan rate, the as-measured critical potential varied by 280 mV. Increasing scan rates resulted in a shift in the critical potential in the noble direction. At lower scan speeds V_c approaches some limiting value. Although no "absolute" value of V_c may be measured on this basis without waiting for an infinite period of time, no breakdown was observed on Type 304 stainless steel held in 0.1*M* NaCl at −0.1V SCE for a period of 14 weeks (2352 hr). This data would indicate that a realistic value for the true critical pitting potential for this material under the described environmental conditions would lie between −0.1 and −0.01V SCE. The latter breakdown potential corresponds to the value measured at the slowest scan rate (18 mV/hr). It would not appear realistic to consider the existence of incubation periods longer than 14 weeks in the confined experimental cell conditions with ready availability of chloride ions.

Under practical conditions the propensity for pitting in a given environment may be determined by measuring the value of the corrosion potential with respect to the critical pitting potential. If the open circuit corrosion potential lies at some value more active than the critical pitting potential (allow a "safety factor" of say 50 mV), it may be reasonably assumed that the passive material under investigation will be immune to pitting corrosion. In this manner the pitting characteristics of passive materials in naturally occurring chloride containing environments may be determined. Any means which will shift V_c in the noble direction (either by alloying or the use of inhibitors) results in a decreased tendency for pitting. Should no pitting occur up to a potential corresponding to the equilibrium oxygen reduction potential, pitting will be inhibited since the corrosion potential arising from local cell action can never be more noble than this value. For this reason titanium having a critical pitting potential ~ + 12V (11), at room temperature can never undergo spontaneous pitting corrosion in chloride solutions in the absence of an externally imposed potential. Therefore, the value of V_c provides a parameter which rates alloys as to their resistance to pitting. In conjunction with a sound experimental design and incorporating multiple regression analysis techniques for data analysis, V_c measurements may be successfully used as a tool in the development of alloys having resistance or immunity to pitting corrosion.

Figure 2 shows the effect of pH on the critical pitting potential as a function of three different chloride ion concentrations. This data was obtained in the manner previously outlined using a scan rate of 500 mV/hr. The data is shown in terms of a nomograph which clearly delineates potential-pH zones corresponding to pitting, general corrosion, inhibition, and immunity. At this scan rate V_c is shifted in the noble direction by 70 mV for each tenfold decrease in chloride ion concentration. Using a potential-step technique Leckie and Uhlig (8) reported a shift of 90 mV for the same change in chloride ion concentration. In all three chloride solutions the critical pitting potential for 18-8 stainless steel was independent of pH in the acid region. At some fairly critical pH in

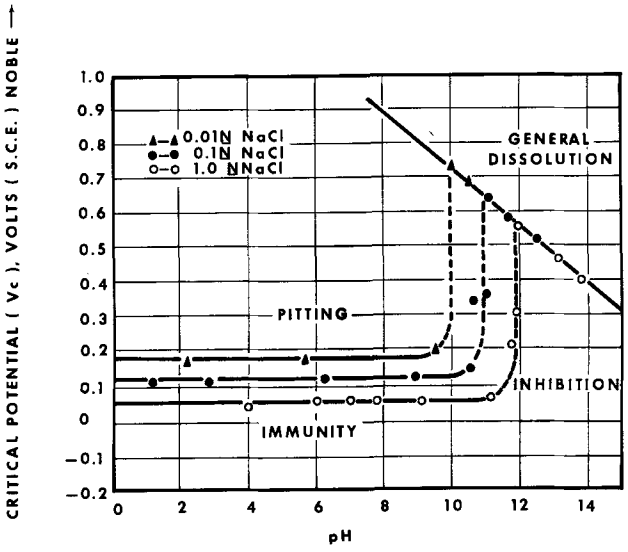

Fig. 2. Effect of pH on V_c for Type 304 stainless steel in 0.01M, 0.1M, and 1.0M NaCl.

the alkaline region V_c shifts in the noble direction. The lines are shown dashed since erratic pitting or general dissolution occurs over a very small pH range and although actual critical pitting potentials may be measured in this transition region these tend to be nonreproducible. The addition of hydroxyl ions thus changes the dissolution behavior from one of pitting corrosion at active potentials to general corrosion and the formation of chromates by the reaction

$$Cr + 4H_2O \rightarrow CrO_4^{--} + 8H^+ + 4e \qquad [1]$$

at noble potentials. Figure 2 shows that the slope of the potential *vs.* pH for this reaction is independent of chloride ion concentration and has a value of −0.082 V/pH unit. The calculated value of slope according to Eq. [1] is −0.079 V/pH. Other inhibitor ions have also been shown to shift V_c in the noble direction at some critical concentration value, dependent on the effectiveness of the inhibitor. Thus, Leckie and Uhlig (8) showed that the efficiency of four ions in inhibiting pitting of 18-8 stainless steel by chlorides decreased in the order $OH^- > NO_3^- > SO_4^{--} > ClO_4^-$.

Nomographs similar in form to that shown in Fig. 2 may be constructed to show the corrosion behavior of other passive metals as a function of chloride and inhibitor ion concentrations.

Conclusion

It is the author's opinion that the critical pitting potential, V_c, has a firm foundation in theory and wide applicability in practice. Measurements of V_c provide a rapid method for predicting the tendency for localized attack in chloride containing environments and serve as a parameter for pitting tendency which may be quantitatively used in the development of pit resistant alloys.

Manuscript submitted Jan. 5, 1970.

Any discussion of this paper will appear in a Discussion Section to be published in the June 1971 JOURNAL.

REFERENCES

1. M. Pourbaix, L. Klimzack-Mathieu, Ch. Mertens, J. Meunier, Cl. Vanleugenhaghe, L. De Munch, J. Laureys, L. Neelemans, and M. Warzu, *Corrosion Sci.*, **3**, 75 (1963).
2. S. Brennert, *J. Iron and Steel Inst.*, **135**, 101 (1937).
3. E. M. Mahla and N. A. Neilson, *Trans. Electrochemical Soc.*, **89**, 167 (1946).
4. E. Brauns and W. Schwenk, *Archiv. Eisenhüttenw.*, **32**, 387 (1961).
5. G. Herbsleb, *Werkstoffe Korrosion*, **16**, 929 (1965).

6. N. Tomashov, G. Chernova, and O. Marcova, *Corrosion*, **20**, 166t (1964).
7. Ya. Kolotyrkin, *ibid.*, **19**, 261t (1963).
8. H. P. Leckie and H. H. Uhlig, *This Journal*, **113**, 1262 (1966).
9. J. Horvath and H. H. Uhlig, *ibid.*, **115**, 791 (1968).
10. M. Pourbaix, "Atlas of Electrochemical Equilibria Aqueous Solutions," Pergamon Press, Cebelcor.
11. A. Piggott, H. P. Leckie, and L. L. Shreir, *Corrosion Sci.*, **5**, 165 (1965).

The Effect of Tin and Tetraethylammonium Ions on the Characteristics of Zinc Deposition on a Zinc Single Crystal in Aqueous KOH

F. Mansfeld*[1] and S. Gilman*

NASA/Electronics Research Center, Cambridge, Massachusetts 02139

In a recent paper (1), the authors reported the effect of lead ions added to the electrolyte, on the dissolution and deposition characteristics of a zinc single crystal. The deposit obtained at −200 mV polarization (all potentials refer to the rest potential of pure zinc in the same solution) is converted by the addition of Pb ions from classical dendrites with side branches to compact cylinders with rounded tops consisting of many small crystallites. It was shown that lead blocks most of the sites active for dissolution and deposition of zinc. Growth is nucleated preferentially at sites of macroscopic defects in the crystal, where impurity segregation is also expected. In the present communication, the effect of tin and tetraethylammonium ions on the morphology of zinc deposits at −200 mV is discussed. As a dendrite-inhibiting additive for secondary zinc battery applications, Sn offers the advantage over Pb in that the oxidation potential of Sn is not much higher than that of Zn, as shown by thermodynamic data (2) and potentiostatic polarization curves in 6*N* KOH. On discharge both Zn and Sn may therefore ionize simultaneously making Sn ions available for the recharge process.

In the experiment of Fig. 1, tin was plated out on a polycrystalline zinc rod in 6*N* KOH at −100 mV for 3 min, followed by a linear voltage sweep in the noble direction. The second peak, noble by about +0.19V to the zinc oxidation peak, is not observed in the absence of tin and corresponds to oxidation of that metal

For reference, Fig. 2 obtained using a scanning electron microscope (SEM), illustrates the type of dendritic growth obtained when Zn is electrodeposited on the basal plane of a zinc single crystal from a zincate solution containing no additives [for details of the experimental procedure, see ref. (1)]. Comparison of Fig. 3 and 2 reveals the effect of additions of 10^{-4}M of $SnCl_2$ on the morphology of the Zn deposit. The effect of tin is similar to that of lead (1). The morphology is changed from dendritic (Fig. 2) to a structure consisting of many small crystallites arranged in a spongy array. While the electrodeposit obtained in the presence of Pb (1) was

* Electrochemical Society Active Member.
[1] Present address: Science Center, North American Rockwell Corporation, Thousand Oaks, California 91360.
Key words: electrodeposition, dendrites, zinc batteries, battery additives, microscopy.

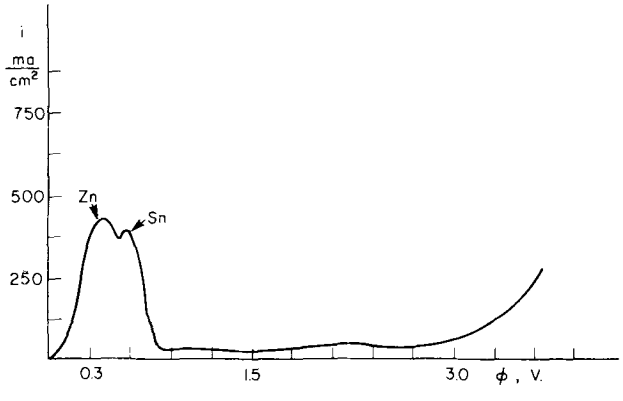

Fig. 1. Polarization curve on polycrystalline zinc in 6*N* KOH + 10^{-3}M $SnCl_2$, 25°C, after 3 min at ϕ = −100 mV. Sweep rate = 390 mV/sec.

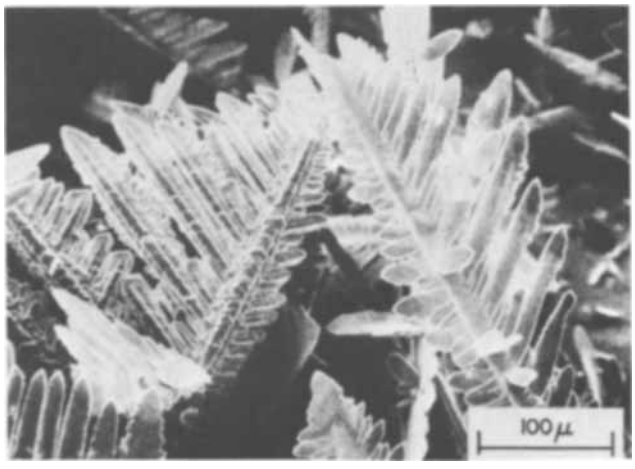

Fig. 2a. Deposit at −200 mV from 6*N* KOH + 20 g/l ZnO after 900 sec, SEM, 34°. 190X.

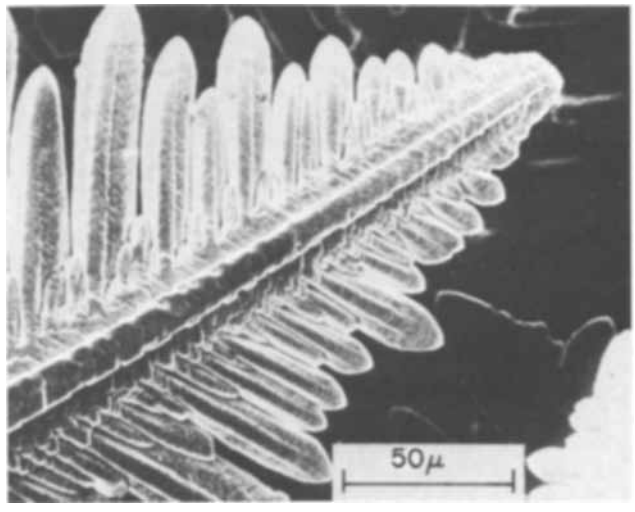

Fig. 2b. 480X

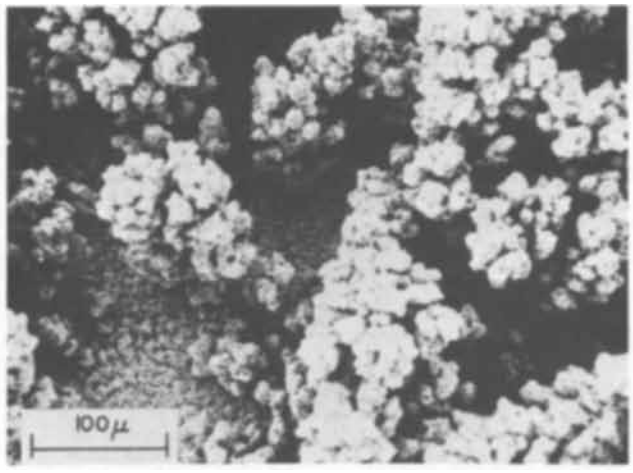

Fig. 3a. Deposit at —200 mV from 6*N* KOH + 20 g/l ZnO + 10^{-4} M/l $SnCl_2$ after 2050 sec, SEM, 34°. 190X.

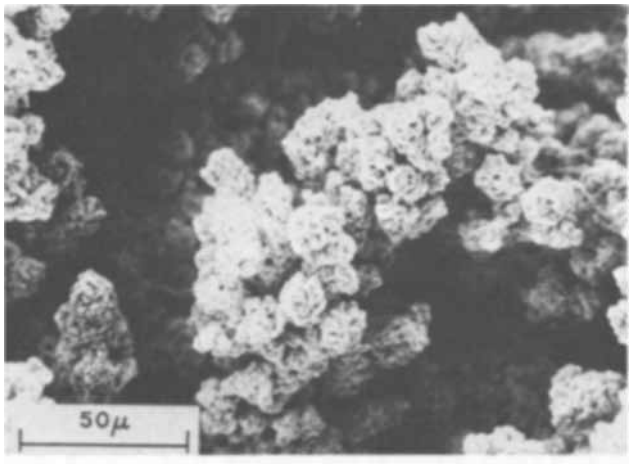

Fig. 3b. 480X.

similarly microcrystalline, the over-all structure was more compact than in the present case.

The effect of tetraethylammonium ion (TEA) was also studied, since a beneficial effect of such ions has been mentioned in (3-5) but no microscopic studies reported. Figure 4 reveals the effect of addition of 10^{-4}M of TEA-ion under the same conditions as in Fig. 2. A dendritic structure is still observed, but dendrites in the presence of TEA ions have become finer with the stem and the side branches shorter and the number of dendrites probably greater. It cannot be shown with these preliminary data whether dendrites are completely suppressed as the concentration of TEA ions is increased or higher members of these compounds added as reported in (4, 5), but the effect of TEA-ions is certainly smaller than that of lead or tin ions at a given potential, concentration, and equal time for deposition.

While it is possible that the slight effect of TEA-ions on the electrodeposit may be due to specific adsorption of the large cations, as suggested by Diggle *et al.* (4, 5) (or of TEA decomposition products which might be present in alkaline solutions), the effect of lead and tin ion additions must more logically be attributed to the codeposition of the corresponding metals with zinc. The foreign metal can be expected to deposit on preferred growth sites blocking further zinc deposition on the particular crystallite and leading to nucleation of new grains.

The effect of lead, tin, and TEA-ions on the corrosion behavior of polycrystalline zinc (99.999%) has been reported recently by the authors (6) for 200-hr tests in 6*N* KOH at 25°C.

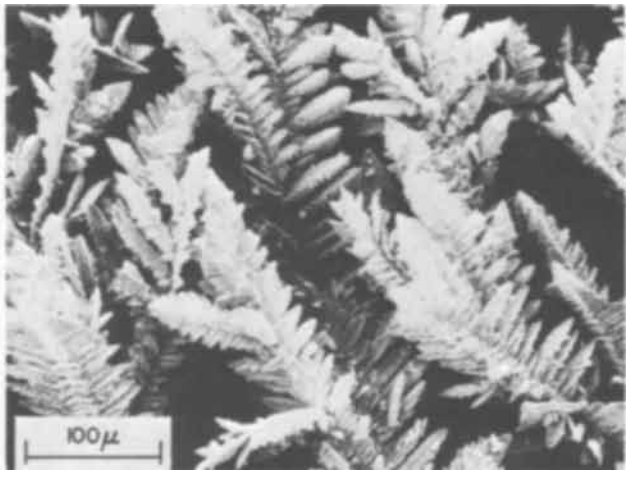

Fig. 4. Deposit at —200 mV from 6*N* KOH + 20 g/l ZnO + 10^{-4} M/l tetraethylammonium perchlorate after 2000 sec, SEM, 34°. 190X.

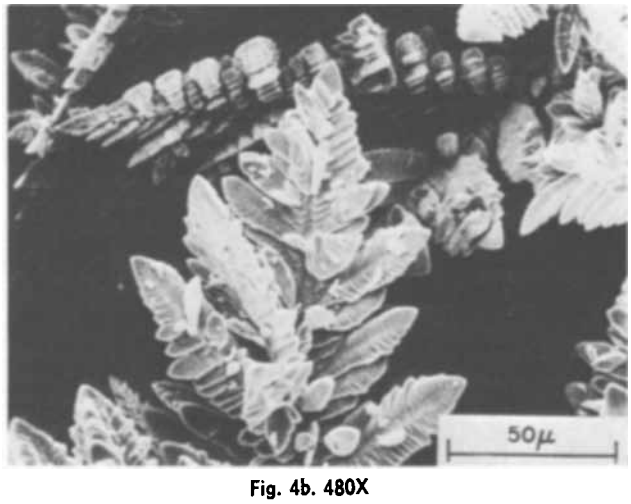

Fig. 4b. 480X

Acknowledgment

One of the authors (F.M.) wishes to acknowledge support under a National Academy of Sciences Research Associateship. Scanning electron micrographs were taken with the help of Mr. J. Herman of Professor Ogilvie's laboratory, Massachusetts Institute of Technology.

Manuscript submitted Feb. 19, 1970; revised manuscript received *ca.* May 14, 1970.

Any discussion of this paper will appear in a Discussion Section to be published in the June 1971 JOURNAL.

REFERENCES

1. F. Mansfeld and S. Gilman, *This Journal*, **117**, 588 (1970).
2. M. Pourbaix, "Atlas of Electrochemical Equilibria in Aqueous Solutions," Pergamon Press, New York (1966).
3. P. Bauer, "Batteries for Space Power Systems", NASA report NASA SP-172, U.S. Government Printing Office, Washington, D. C., 1968.
4. J. W. Diggle, A. Damjanovic, and J. O'M. Bockris, 2nd Quarterly Report to NASA, 4/1/69 to 6/30/69, NGR 39-010-002.
5. J. W. Diggle, A. Damjanovic, and J. O'M. Bockris, Paper 18 presented at the Detroit Meeting of the Society, Oct. 5-9, 1969.
6. F. Mansfeld and S. Gilman, *This Journal*, In press.

Chemical Deposition of Single Crystal Gold Films

Richard Sard*

Bell Telephone Laboratories, Inc., Murray Hill, New Jersey 07974

An electron microscopic investigation has disclosed that epitaxial single crystal gold films can be chemically deposited on copper substrates from aqueous solutions. This unexpected result was observed in the course of an investigation of the growth and structure of gold deposits obtained from the electroless solutions formulated by Okinaka (1).

Initially, annealed copper sheet was used as substrates and the large grained structure, characteristic of recrystallized copper, was copied by gold deposits 0.1-0.2μ in thickness. A series of experiments carried out with single crystal copper substrates that were cut (Servo Met Spark Cutter) and polished parallel to {100}, {110}, or {111} confirmed that the gold deposits were, in fact, epitaxial, *i.e.* they were in parallel orientation with the substrate and exhibited bulk values of the interplanar spacings.

Gold deposits were obtained on at least four single crystal substrates in each orientation as part of the over-all investigation (2) of the structures obtained from electroless solutions. The solutions used for these experiments contained various amounts of the reducing agent, KBH_4, in addition to the other constituents: $KAu(CN)_2$, KOH, and KCN.[1] These solutions will produce gold deposits approximately 1000-1500Å thick in from 2 to 20 min at 80°C, depending on the specific bath composition (1). However, the exact formulations used are not of primary relevance to this note as we are concerned here only with the general features of the initial stages of epitaxial gold deposition on copper substrates. Thus, the fact that autocatalytic solutions were used is not too important because the growth process in this case is due to a displacement mechanism as discussed below. A much more detailed study of the growth, structure and properties of electroless gold deposits has been conducted (2) and will be submitted for publication in the near future.

The gold films were stripped from their copper substrates in a chromic-sulfuric acid solution (3). Stop-off lacquer (Michigan Chrome and Chemical Company) was used to protect the crystals and permit dissolution only at windows on the appropriate surfaces where grid-size regions (2-3 mm) were scribed with tweezers. When the deposits floated free from the substrates they were picked up on grids, carefully washed and dried, then placed in a vacuum dessicator until examination in a Siemens electron microscope operated at 100 kV.

Examples of the single crystal electron diffraction patterns of gold films deposited on {100} and {111} surfaces are shown in Fig. 1 and 2, respectively. These patterns are similar to those observed for epitaxial deposits of face-centered cubic metals prepared by vacuum evaporation (4) and electrodeposition (5, 6). The "satellite" spots in Fig. 1 are due to microtwin faults on the four inclined {111} planes and double diffraction at their boundaries as discussed by previous authors (4, 7, 8). In Fig. 2 the six interior spots in hexagonal array are of the type 1/3 <422> and are due to diffraction at double positioning boundaries (8). Bright-and dark-field observations of the microstructure indicate that the defect densities of these films are quite high; typically $> 10^{10}$ cm^{-2}.

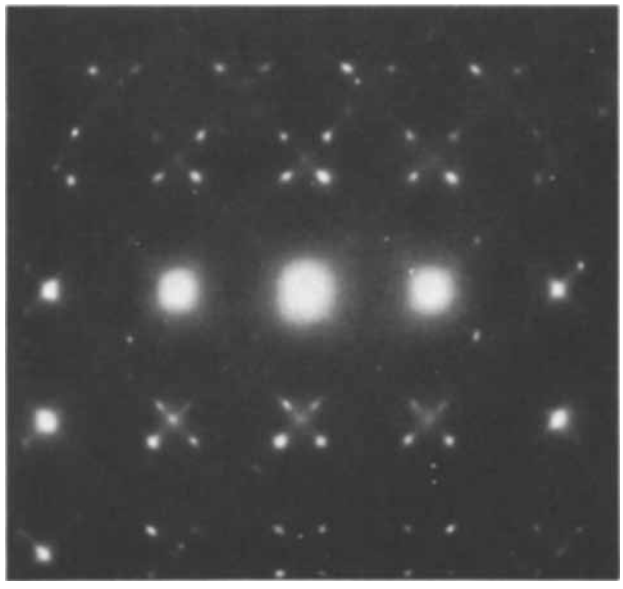

Fig. 1. Transmission electron diffraction pattern of gold deposit on {100} copper single crystal.

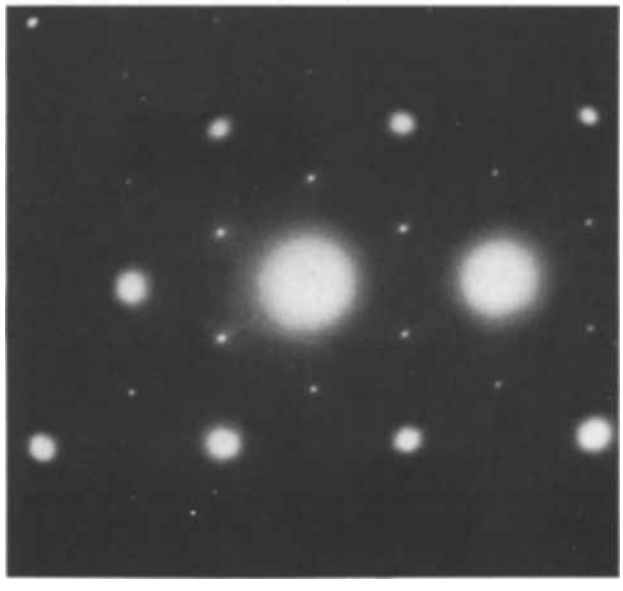

Fig. 2. Transmission electron diffraction pattern of gold deposit on {111} copper single crystal.

As indicated above, a displacement mechanism is responsible for the initial stages of gold deposition on copper substrates. Analytical evidence obtained by atomic absorption spectroscopy indicates that copper dissolves from the surface and goes into solution, presumably to form a more stable cyanide complex. Converting from mass units to equivalent thickness (assuming uniform dissolution over the geometrical area) one obtains values of approximately 100Å for the magnitude of the initial displacement process under favorable conditions, *i.e.*, when pores are sealed by catalytic deposition.

Aqueous solutions that yield deposits of particular metals (*e.g.*, Ag, Cu, Ni, Pd, Pt, Sn) on specific sub-

* Electrochemical Society Active Member.

Key words: chemical deposition, single crystal films, gold, transmission electron microscopy.

[1] A typical composition used was: 0.4M KBH_4, 0.02M $KAu(CN)_2$, 0.2M KOH, and 0.2M KCN.

strates have been available for some time (9-11). These deposits are usually termed "immersion" coatings, and they apparently result from galvanic displacement. Unlike electroless solutions, these baths produce relatively thin deposits as the reaction will cease when the solution and original substrate are no longer in contact. Moreover, such deposits are usually quite porous which is why their thickness increases over extended periods of time.

However, it is important to note that the structures of gold deposits obtained from an immersion gold solution (11) and two proprietary (12, 13) solutions were found to be qualitatively similar to those obtained with the electroless solutions. These deposits were obtained at the recommended operating conditions with annealed, polycrystalline copper substrates and the diffraction patterns exhibited single crystal spots corresponding to the various substrate grains.

Thus, it is concluded that the displacement process responsible for the initial deposition of gold films on copper substrates occurs by an epitaxial growth mechanism. There is additional evidence which indicates that such a mechanism may be quite general for the initial stages of displacement processes. This question will be treated in greater detail in a future publication.

Acknowledgment

The atomic absorption data were provided by T. Y. Kometani, and Laue patterns were taken by M. J. Tomsky.

Note added in proof: The work of Professor Y. Tanabe of Tokyo Metropolitan University, who has also observed epitaxial deposition in chemical displacement systems (Cu/Fe and Au/Fe), has been brought to the authors' attention by Y. Okinaka.

Manuscript submitted March 11, 1970; revised manuscript received June 8, 1970.

Any discussion of this paper will appear in a Discussion Section to be published in the June 1971 JOURNAL.

REFERENCES

1. Y. Okinaka, Paper 36 presented at American Electroplaters Society Montreal Meeting, June 1970. Submitted for publication in *Plating*.
2. R. Sard, Unpublished results.
3. R. Weil and R. Paquin, *This Journal*, **107**, 87 (1960).
4. D. W. Pashley, *Advanc. Phys.*, **14**, 327 (1965).
5. R. Sard and R. Weil. To be published in *Electrochim. Acta*.
6. E. R. Thompson and K. R. Lawless, *Electrochim. Acta*, **14**, 269 (1969).
7. R. D. Burbank and R. D. Heidenreich, *Phil. Mag.*, **8**, 651 (1963).
8. D. W. Pashley and M. J. Stowell, *ibid.*, **8**, 1605 (1963).
9. M. E. Straumanis and C. C. Fang, *This Journal*, **98**, 9 (1951).
10. R. Glicksman, H. Mouquin, and C. V. King, *ibid.*, **100**, 580 (1953).
11. Metal Finishing Guidebook, p. 489, Metals and Plastics Publications, Inc., Westwood, N. J., (1968).
12. Sel Rex Corp., "Lectroless Au" Solution.
13. American Chemical and Refining Co., "24K Neutral Immersion" Solution.

Oxygen Reduction on Bright Osmium Electrodes in 85% Orthophosphoric Acid

A. J. Appleby*

Institute of Gas Technology, Chicago, Illinois 60616

Work on the oxygen electrode behavior of osmium has been infrequently reported in the literature. In 1940, Bain[1] reported rest potentials of osmium black films in oxygen-saturated 1*N* H_2SO_4 solution of 0.87V *vs.* hydrogen. Charging curves for —O adsorption on osmium electrodes were studied by Khomchenko *et al.* (2), who noted a general resemblance in properties to those of ruthenium (3), although osmium was observed to go into the solution at lower potentials. Llopis and Vazquez (4) obtained cyclic voltammetric scans in acid solutions on osmium black electrodes. Gnanamuthu and Petrocelli (5) reported steady-state oxygen reduction Tafel slopes of approximately $2RT/\mathbf{F}$ in oxygen-saturated 1*N* H_2SO_4 solution. Electrodes were of comparatively low activity, with overpotentials much greater than those on platinum.

In the present work, oxygen reduction on phase-oxide-free osmium surfaces in 85% orthophosphoric acid was studied as a function of temperature.

Experimental

Osmium electrodes were prepared by electrolytic deposition on 1 cm^2 gold foils from molten cyanides by a previously published method (6). The electrolytic deposits were bright, though somewhat granular. Roughness factors were measured by using a charging-curve technique (2) (see below). Electrodes were suspended on gold wires in the all-silica cell used in previous work (7). A bubbling hydrogen reference electrode was used, to which all potentials are referred. The electrolytic cell contained a gold counterelectrode, so that any contamination of the electrolyte would be confined to traces of nonelectrocatalytic metal. For the same reason, traces of oxidizable material were removed from the electrolyte by hydrogen peroxide treatment rather than by pre-electrolysis.

Apart from the charging curves, all data were obtained by a steady-state galvanostatic technique, allowing sufficient time for less than 0.2 mV/min change in potential at each applied current density. This condition requires 5-15 min at higher current densities; up to 2 hr was required in the 10^{-8}-10^{-9} A/cm^2 range.

Results

Electrode area determinations.—After preparation the electrodes were washed in conductivity water to remove cyanides and were then rinsed in concentrated HCl, conductivity water, and the purified electrolyte.

Electrodes were potentiostated over night at 21.0°C in nitrogen-saturated 85% orthophosphoric acid at 50 mV HRE to ensure reduction of any residual phase oxide, after which chronocoulometric scans were carried out.

Figure 1 shows a typical complete anodic-cathodic charging curve in N_2-saturated 85% orthophosphoric acid at 21°C, at a current density of 200 mA/cm^2 (geometric).

This charging curve is the final one of a series of six, all of which were identical. The curves were terminated at a potential of 0.84V to prevent any

* Electrochemical Society Active Member.
Key words: oxygen reduction, osmium electrodes, electrocatalysis.

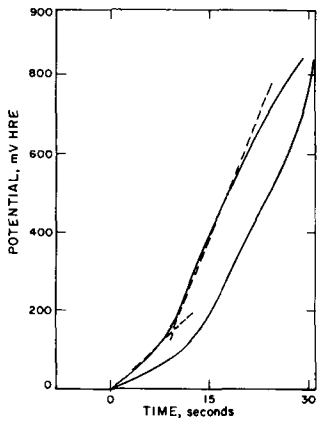

Fig. 1. Charging curve on osmium at 200 mA/cm² in N_2 saturated 85% orthophosphoric acid (21°C).

extensive oxidation of osmium to OsO_2 or OsO_4, or any electrode dissolution.

The electrode shows well-defined hydrogen and oxygen regions, with Q_H about $2Q_O$, where Q_O is the number of coulombs for oxygen. The hydrogen deposition region finishes at about 200 mV; the region of monolayer oxygen deposition starts at about 250 mV and continues through 800 mV.

There is some hysteresis between anodic and cathodic portions, as indicated in Fig. 1, but much less than is shown by platinum (8). The general behavior is close to that of ruthenium (3). The greater hysteresis between anodic and cathodic potential scans on platinum compared with osmium is particularly well shown by Llopis and Vazquez (3).

Preliminary experiments established that the concentration of the acid used has little effect on the charging curves. In addition, results obtained in 1*N* H_2SO_4 and 85% orthophosphoric acid were virtually identical.

Khomchenko *et al.* (2) have shown that electrode areas measured from the hydrogen-charging region agree with BET data on osmium black electrodes. Using 22.48 g/cm³ as the density of osmium and assuming one adsorbed H radical per metal atom, osmium will adsorb 1.73×10^{15} H atoms/cm². If one assumes about 30 μF/cm² for the double-layer capacity in H_3PO_4, then the total charge in going from 0 to about 150 mV (the end of the hydrogen-charging region) is $270 + 30 \times 0.15$ μC/real cm²: *i.e.*, 275 μC/cm².

In Fig. 1 the H-charging region is about 1800 coulombs, indicating a roughness factor of 6.5.

Open-circuit potentials.—Open-circuit potentials were about 850-880 mV HRE 2 hr after immersion of the electrode in oxygen-saturated 85% H_3PO_4 or after cathodic polarization. A complete list is given in Table I.

At 21.0°C the initial value refers to 30 min after polarization: The final value was attained after 12 hr in the solution. Open-circuit potentials rose slowly over several days. This is illustrated by the value at 35.0°C (941 mV) attained after 2 days in the solution.

Tafel plots.—Figure 2 shows a series of steady-state galvanostatic Tafel plots for the osmium electrode at 21.0°, 35.0°, 52.1°, 76.0°, 104.0°, and 136.0°C. In each

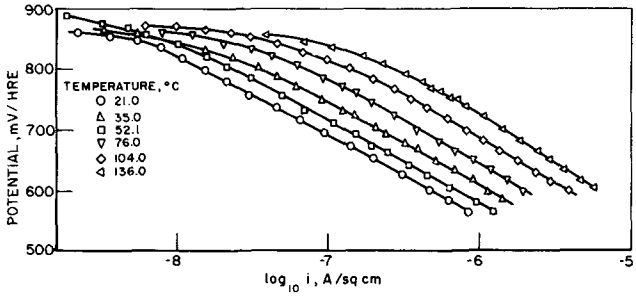

Fig. 2. Tafel plots for oxygen reduction on osmium in O_2 saturated 85% orthophosphoric acid as a function of temperature.

case, the slope is about $2RT/F$. Current densities are corrected for the roughness factor of the electrodeposit.

The Tafel plot at 35.0°C was obtained from the high open-circuit value reported in Table I and is characterized by a more gentle curve into the Tafel region at the high-potential portion of the plot than is observed when results are obtained on electrodes at initially lower open-circuit values. The Tafel region, however, is not affected by the initial open-circuit value.

The above charging curve and polarization results refer to the same electrode. Data obtained on other electrodeposited osmium surfaces were consistently within ±25 mV of the plots shown in Fig. 2, and the discrepancy in each case was not significantly temperature-dependent.

Unlike phase-oxide-free platinum oxygen electrodes, osmium electrodes appear not to be substantially affected by adsorbed impurities, as potentials showed no tendency to decay with time and results are unaffected by preliminary pulsing between 0.9V and 50 mV (9), which should serve to remove any adsorbed impurities (9, 10) that diffuse to the electrode surface from the solution. However, as already indicated, electrodes took a considerable time to come to steady state at any applied current density, indicating that development of equilibrium —O and —OH coverage from water oxidation is slow. However, there was no hysteresis between ascending and descending Tafel plots, provided sufficient time was allowed at each applied current density.

Kinetic data.—Values of i_0 corrected for oxygen partial pressure (assuming a first-order process), roughness factor, $1/\alpha$ values, and Tafel slopes are given in Table II.

An Arrhenius plot of $\log_{10} i_0$ against $1/T$ is given in Fig. 3. Activation energy at the reversible potential on this basis is 13.5 ± kcal/mole.

Discussion

In the potential range 600-850 mV, equilibrium —O and —OH coverage from water oxidation on osmium electrodes may be expected to be high: The charging curve illustrated in Fig. 1 indicates that about one monolayer of —O is adsorbed at 800 mV HRE after 20 sec. On this basis, adsorption of reaction intermediates will take place under Langmuir rather than Temkin conditions.

The Tafel slope of $2RT/F$ is indicative of a primary charge transfer as the rate-determining step, under

Table I. Open-circuit potentials of osmium oxygen electrodes

Temp, °C	Potential, mV
21.0	854-875
35.0	868
52.1	870
76.0	869
104.0	873
136.0	857

Table II. Kinetic data for oxygen reduction on osmium

Temp, °C	Tafel slope, mV/decade	$1/\alpha$	i_0, A/cm²
21.0	128	2.19	3.5×10^{-12}
37.0	130	2.18	8.3×10^{-12}
52.1	136	2.11	2.6×10^{-11}
76.0	141	2.07	9.2×10^{-11}
104.0	146	1.95	3.8×10^{-10}
136.0	158	1.95	2.5×10^{-9}

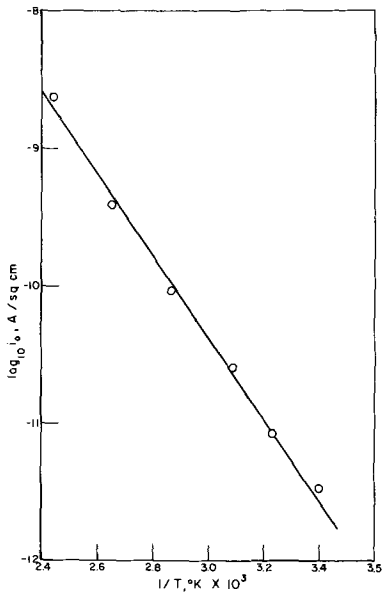

Fig. 3. Arrhenius plot of $\log_{10} i_0$ for oxygen reduction on osmium in 85% orthophosphoric acid.

Langmuir conditions of adsorption (9). On ruthenium electrodes it has been shown that the primary charge-transfer reaction

$$O_2 + H_3O^+ + e^- \rightarrow (O_2H)_{ads}$$

is rate determining in acid solution (11). In view of the chemical resemblance between ruthenium and osmium and the general similarity of their —O adsorption behavior (2, 3, 4, 11), it is tempting to suggest that the same step is rate determining on osmium electrodes, although precise identification of the process requires reaction-order measurements.

Osmium and ruthenium have similar d-orbital characters (2.2 vacancies) (12) and would be expected to show strong adsorption of oxygenated species compared with gold, on which the same reaction has been shown to be rate determining (13). This is reflected in their measured activation energies at the reversible potential (13.5 kcal on osmium, 11.7 kcal (11) on ruthenium, 23.6 kcal (13) on gold). This demonstrates the effect of heat of adsorption of reaction intermediates on activation energies, first discussed by Horiuti and Polanyi (14) with reference to the hydrogen evolution reaction.

Acknowledgment

The author wishes to thank the sponsors of the TARGET fuel cell program and Pratt & Whitney Aircraft Division of United Aircraft Corp. for permission to publish this work. The help of members of IGT in the preparation of this publication is also greatly appreciated.

Manuscript received April 13, 1970.

Any discussion of this paper will appear in a Discussion Section to be published in the June 1971 JOURNAL.

REFERENCES

1. H. G. Bain, *Trans. Electrochem. Soc.*, **78**, 173 (1940).
2. G. P. Khomchenko, N. G. Ul'ko, and G. D. Vovchenko, *Elektrokhim.*, **1**, 659 (1965).
3. T. N. Stoyanovskaya, G. P. Khomchenko, and G. D. Vovchenko, *Vestn. Mosk Univ. Ser. II, Khim.*, **17**, [5], 30 (1962).
4. J. Llopis and M. Vazquez, *Anales Real Soc. Espan. Fis. Quim. (Madrid)*, **B63**, 273 (1967).
5. D. S. Gnanamuthu, and J. V. Petrocelli, *This Journal*, **114**, 1036 (1967).
6. A. J. Appleby, *ibid.*, **117**, 1059 (1970).
7. A. J. Appleby, *J. Electroanal. Chem.*, **24**, 97 (1970).
8. Ts. Zalkind and B. V. Ershler, *Zh. Fiz. Khim.*, **25**, 565 (1951).
9. A. J. Appleby, *This Journal*, **117**, 328 (1970).
10. S.D. James, *ibid.*, **114**, 1113 (1967).
11. A. J. Appleby, to be published in *J. Electroanal. Chem.*
12. M. L. B. Rao, A. Damjanovic, and J. O'M. Bockris, *J. Phys. Chem.*, **67**, 2508 (1963).
13. A. J. Appleby, to be published in *J. Electroanal. Chem.*
14. J. Horiuti and M. Polanyi, *Acta Physicochim. U.R.S.S.*, **2**, 505 (1935).

Brief Communication

Oxygen Reduction on Phase-Oxide-Free Platinum-Ruthenium Alloys in 85% Orthophosphoric Acid at High Temperature

A. J. Appleby*

Institute of Gas Technology, Chicago, Illinois 60616

A series of studies conducted by Hoar and Brooman (1, 2) on oxygen reduction in dilute acid solution using Pt-Ru, Pt-Rh, and Pt-Ir alloy electrodes containing low atomic percentages of the alloying metal indicated that such alloys are more active electrocatalysts than pure platinum. Rate enhancement for similar alloys over pure platinum in gas-phase catalysis processes has also been noted. In particular, Bond and Webster (3, 4) showed that Pt-Ru alloys were more reactive than either pure metal for hydrogenation reactions. Other examples of synergistic effects have been noted, both in the gas phase (5) and in electrocatalysis (6).

A recent study by Hoare on Pt-Rh alloys (7) as oxygen reduction catalysts in purified dilute acid

* Electrochemical Society Active Member.
Key words: oxygen reduction, platinum-ruthenium alloys, electrocatalysis.

solution does not confirm Hoar and Brooman's findings: No synergistic effects were noted, and the log exchange current was proportional to the platinum content of the alloy.

In view of the above observations, a study of oxygen reduction on smooth Pt-Ru alloys was carried out in purified 85% orthophosphoric acid at elevated temperature (104°C, approximating to energy conversion device conditions) in a fused-silica electrochemical cell to determine the activity of the alloys under different surface conditions.

Experimental

Polished electrodes of Pt-8 a/o (atom per cent) Ru and Pt-18 a/o Ru were cut from a stock Engelhard alloy sheet of 99.9% purity using a diamond saw. Electrode areas varied between 0.8 and 1.40 cm.^{2} In addition, a 2.0 cm^2 pure platinum electrode of 99.999% purity and a pure ruthenium electrode were studied.

All electrodes were carefully welded to gold wires and after mechanical polishing using alumina powders were degreased with organic solvents and washed with concentrated HCl, conductivity water, and finally the electrolyte (purified 85% orthophosphoric acid).

The electrolyte was purified by treatment with hydrogen peroxide, as described in previous work (8, 9). A thermostatic oil bath maintained the fused silica electrolytic cell (8) at a temperature of 104.0° ± 0.2°C. A stream of high-purity oxygen was passed continuously through the electrolyte at a rate of about 10 ml/min. The reference electrode was an isothermal bubbling hydrogen 85% orthophosphoric acid electrode, to which all potentials throughout this paper are referred (HRE potentials). A gold counter-electrode was used to avoid contaminating the pure ruthenium electrode surface with traces of platinum. Separate batches of electrolyte were used for each alloy.

Results

Rest potentials.—After the preparative procedure described above, each electrode was potentiostated for 2 hr at 50 mV HRE to reduce any superficial oxide that might have been present. Following this treatment, the electrode was allowed to reach its open-circuit potential. Typical values have been plotted as a function of alloy composition in Fig. 1.

In each case, the lower result is the value attained a few minutes after the release of the potentiostatic circuit. The higher values were attained after 2-3 hr. On being left overnight, the value for Pt tended to fall to 980-990 mV; those for Pt-8 a/o Ru and Pt-18 a/o Ru fell to about 990-1000 mV. This may be attributed to the slow adsorption of capillary-active impurities that are not removed by oxidative purification treatment, for example, polyphosphates and traces of organic polymers. Little change in potential was noted for the above electrodes on longer exposures to the electrolyte. On the Pt-40 and 60 a/o Ru alloys, potentials remained essentially constant after 2-3 hr, whereas the value on Ru tended to rise very slowly (5-10 mV/day).

The open-circuit potentials appear to go through a maximum at about Pt-8 a/o Ru (Fig. 1).

Tafel plots.—After equilibration for 8 hr at open circuit in the oxygen-saturated electrolyte, a descending galvanostatic Tafel plot was made for each metal and alloy. In each case, the plot was taken down to the point where diffusion control became apparent; the plotting direction was then reversed. A hysteresis due to desorption of capillary-active material on the electrode surface was observed in each case. The pattern of the hysteresis is changed according to the alloy composition. Plots for each material are shown in Fig. 2 and 3. Plot A for each electrode is the downward plot; plot B is taken in the upward direction. Sufficient time was allowed at each applied current density for the potential to change by less

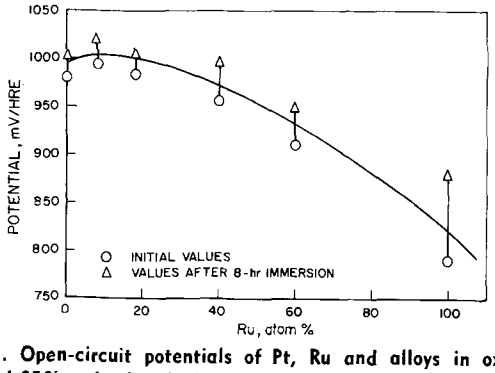

Fig. 1. Open-circuit potentials of Pt, Ru and alloys in oxygen-saturated 85% orthophosphoric acid (104°C).

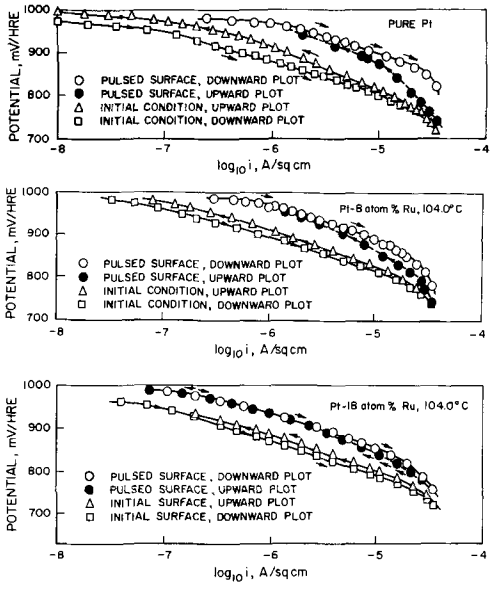

Fig. 2. Tafel plots on Pt and low atom per cent Pt-Ru alloys showing desorption hysteresis in oxygen-saturated 85% orthophosphoric acid (104.0°C).

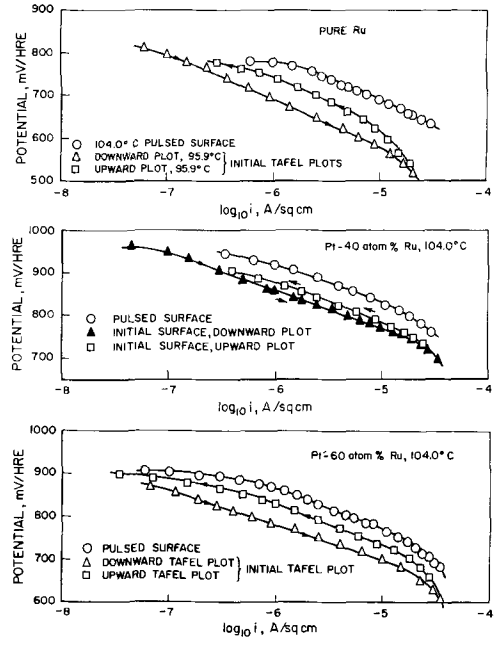

Fig. 3. Tafel plots on Ru and high atom per cent Pt-Ru alloys showing desorption hysteresis in oxygen-saturated 85% orthophosphoric acid (104.0°C).

than 0.5 mV/min. This normally was so within 2-10 min, the time decreasing with increasing current density.

In the case of pure platinum, desorption hysteresis is most marked at about 930-950 mV HRE; the initial plot indicates less activity than for the Pt-8 a/o Ru alloy (Fig. 2). The desorption potential range is broad in the case of the 8 a/o Ru alloy, but desorption becomes marked only below 930 mV HRE on the Pt-18 a/o Ru alloy. For Pt-40 a/o Ru, Pt-60 a/o Ru, and pure[1] Ru, desorption is marked only below 920, 900, and 800 mV, respectively. The enhancement factor of Pt-8 a/o Ru over pure Pt is about 1.5 at 900 mV under these surface conditions. Activities of Pt, Pt-18 a/o Ru, and Pt-40 a/o Ru are similar at 900 mV in plot A.

Tafel plots were also obtained after a standard activation procedure, intended to desorb impurities. Electrodes were pulsed galvanostatically three times between open circuit and 50 mV HRE. The last pulse was always cathodic, and after it a continuous upward plot, starting at about 35 $\mu A/cm^2$, was made. This is represented by plot C in each case in Fig. 2 and 3. Plot D for each electrode in Fig. 2 and 3 is a downward galvanostatic Tafel plot taken from open circuit immediately after completion of plot C. For both plots C and D points were taken after each current density had been applied for 2 min.

For Pt-40 a/o Ru, Pt-60 a/o Ru, and pure Ru, plots C and D were essentially identical. Further pulsing before each point to +1000 and +50 mV led to no further improvement. For pure Ru and the Pt-60 a/o Ru alloy, these plots show deactivation effects (*i.e.*, deviation from linearity) at higher potentials in the ranges above 750 and 850 mV HRE, respectively. Similarly, deactivation effects occur for Pt-40 a/o Ru above about 900 mV HRE. For the platinum-rich compositions, a hysteresis effect is noted between the activated curve plotted in the upward direction and the downward curve (Fig. 3).

It appears that certain adsorbed impurities are not removed from these electrodes by pulsing to +50 mV, but are desorbed at the higher potential end of the plot above about 950 mV. This effect is most marked in the case of pure platinum. On this electrode metal points in the high current density region of curve D are unstable and decayed within a few minutes to values corresponding to those in curve C. Separate pulsing was necessary between each point in curve D to obtain a consistent curve. It was however, established that pulsing to higher anodic potentials (to about 1.4V) led to no further improvement in curve D for pure platinum. This can be considered to be a plot for a clean (*i.e.*, impurity-free) surface. It was established earlier that pulsing of platinum beyond 1.4V leads to surface area changes. Alloys were not pulsed anodically beyond 1000 mV because of the danger of composition changes.

For the Pt-8 a/o Ru alloy, much more stable plot D points were obtained than on pure platinum, and it was possible to trace the whole plot without separate activation for each point. No improvement was noted in individual points by separate activation between points. It therefore appears that pure platinum is much more rapidly deactivated by adsorption of impurities than the Pt-8 a/o Ru alloy (Fig. 2.) The plots for all the impurity-free electrode surfaces (*i.e.*, plot D in each case) are shown in Fig. 4.

[1] The plot for pure Ru is from data at 95.9°C, but may be taken as representative.

Table I. Tafel slopes of Pt-Ru alloy electrodes

	Slope, mV/decade	$1/\alpha$
Pure Pt	77	1.03
Pt-8 a/o Ru	83	1.11
Pt-18 a/o Ru	90	1.20
Pt-40 a/o Ru	95	1.27
Pt-60 a/o Ru	103	1.38
Pure Ru	115	1.54

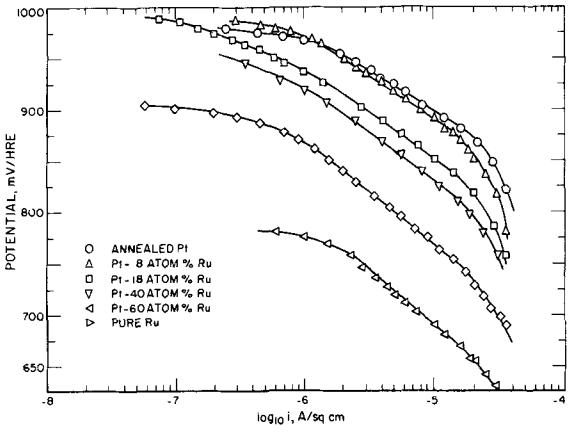

Fig. 4. Tafel plots on pulsed surfaces of Pt, Ru, and alloys in 85% orthophosphoric acid (104.0°C).

Tafel slopes for clean surfaces.—Tafel slopes and $1/\alpha$ values are given in Table I.

There is a definite tendency for the slope to increase as the ruthenium content of the alloy increases.

Discussion

Hoar and Brooman (1, 2) have published work carried out in dilute sulfuric acid to show that Pt-Ru alloys with Ru content up to 9.3 a/o are more active than pure platinum at 25°C. However, the oxide-free platinum electrode data they report indicate that their electrode is considerably less active than the corresponding surface in 85% orthophosphoric acid at 25°C (9) (by about 200 mV at the same current density) and that [from Damjanovic and Brusic's (10) data] it is about 10,000 times less active than the same surface in perchloric acid at the same temperature. According to Hoar and Brooman (1), the inflections in their plots were caused by adsorption of an intermediate. It is more likely, however, that they are due to adsorbed impurities, as only cathodic pre-electrolysis was used for purification. The poor performance of their platinum electrode implies that oxidizable impurities were present in their experiments.

The results of the present experiments show that platinum is more susceptible to poisoning by impurities than alloys containing small amounts of ruthenium, as shown by the initial Tafel plots (Fig. 2 and 3). This is also reflected in the open-circuit potentials and the relative performance of pure Pt and Pt-8 a/o Ru at current densities below 1 $\mu A/cm^2$. The adsorptive properties of Pt-Ru alloys are thus different from those of pure Pt. Their activity in direct hydrocarbon oxidation (6) and their tolerance to poisoning are probably related phenomena.

Results obtained on clean platinum surfaces also decay much more rapidly than on Pt-8 a/o Ru alloy. Hence, in not extensively purified solution, Pt-Ru alloys containing small amounts of ruthenium may be more active than platinum alone, but for clean surfaces at moderate overpotentials activity increases with increasing platinum content.

As may be seen in Fig. 4, the increase in activity is a combination of two factors: improvement in i_o and in Tafel slope. Figure 5 shows the log current at 850 mV HRE plotted against atom per cent Ru. A straight-line relationship is obtained. Similar results have been obtained on the Pt-Rh alloy oxygen electrode system by Hoare (7).

As d-orbital vacancies in solid solutions are proportional to atomic composition, it appears that the energy of activation for the rate-determining step of

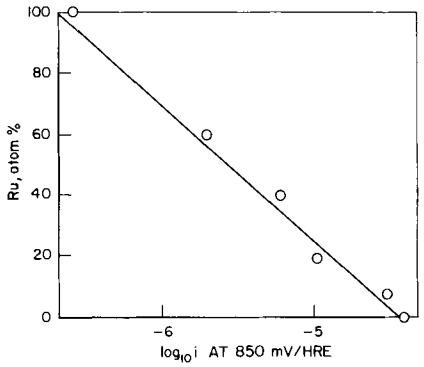

Fig. 5. Correlation between current density at 850 mV/HRE and alloy composition for Pt-Ru solid solutions: oxygen reduction in 85% orthophosphoric acid (104.0°C).

the reaction depends directly on the electronic structure of the alloy.

Acknowledgment

The author wishes to thank the sponsors of the TARGET fuel cell program and Pratt & Whitney Aircraft Division of United Aircraft Corp. for permission to publish this work. The help of members of IGT in the preparation of this publication is also greatly appreciated.

Manuscript received April 13, 1970.

Any discussion of this paper will appear in a Discussion Section to be published in the June 1971 JOURNAL.

REFERENCES

1. T. P. Hoar and E. W. Brooman, *Electrochim. Acta*, **11**, 545 (1966).
2. E. W. Brooman and T. P. Hoar, *Platinum Metals Rev.*, **9**, 122 (1966).
3. G. C. Bond and D. E. Webster, *Proc. Chem. Soc.*, 398 December 1964.
4. G. C. Bond and D. E. Webster, *Platinum Metals Rev.*, **9**, 12 (1965).
5. D. W. McKee and F. J. Norton, *J. Phys. Chem.*, **68**, 481 (1964).
6. J. O'M. Bockris and H. Wroblowa, *J. Electroanal. Chem.*, **7**, 428 (1964).
7. J. P. Hoare, *Electrochim. Acta*, **14**, 797 (1969).
8. A. J. Appleby, *J. Electroanal. Chem.*, **24**, 97 (1970).
9. A. J. Appleby, *This Journal*, **117**, 382 (1970).
10. A. Damjanovic and V. Brusic, *Electrochim. Acta*, **12**, 615 (1967).

JOURNAL OF THE ELECTROCHEMICAL SOCIETY

SOLID STATE SCIENCE

SEPTEMBER 1970

The Transient Oxidation of Fe-Cr and Ni-Cr Alloys

B. Chattopadhyay and G. C. Wood

Corrosion Science Division, Department of Chemical Engineering, University of Manchester Institute of Science and Technology, Manchester, England

ABSTRACT

The early stages of oxidation of Fe-Cr and Ni-Cr alloys, containing respectively nominally 5, 10, 15, and 30 a/o Cr, in 1 atm oxygen at 600°C have been studied by transmission electron microscopy of stripped films and by electron diffraction. Substantial amounts of iron and nickel oxides, respectively, are produced on all alloys before steady-state, healing, chromium-containing oxide layers are developed. This occurs more rapidly and more completely as the alloy chromium content is increased. For dilute Fe-Cr and very dilute Ni-Cr alloys, grain and subgrain boundaries and other substructural defects of the alloy are covered by thicker oxide. This is due either to their efficiency as cation vacancy sinks or to more local diffusional paths in the oxide above them. Conversely, for alloys richer in chromium (up to 30%), healing is most rapid in these locations due to rapid chromium diffusion to the alloy/oxide interface, leading to thin oxide above the defects. The tendency of rapidly growing iron oxides to overgrow the chromium-containing oxides, and also to undermine them by encroaching on the alloy, is countered by the rapid development of a general healing layer of $FeFe_{(2-x)}Cr_xO_4$ ($O \leq x \leq 2$) for the dilute Fe-Cr alloys and Cr_2O_3 for the concentrated alloys. $NiCr_2O_4$ probably does not form a healing layer for dilute Ni-Cr alloys and the completion of a healing Cr_2O_3 layer is slower than for Fe-Cr alloys. This is largely due to the lower alloy interdiffusion coefficient. However, the slow growth of NiO limits overgrowth and scale encroachment. Cr_2O_3 healing is eventually approached by dense internal oxide formation, resulting partly from the relatively high solubility of oxygen in Ni-Cr alloys.

Relatively little is known about the transient films formed in the initial, nonsteady-state stages of oxidation. Particularly with alloys whose oxidation behavior is borderline between protective and nonprotective, the spatial distribution, amount, composition, and structure of the initial phases determine the oxidation rate and the subsequent approach to steady-state oxidation. A considerable total oxide thickness is often developed before steady-state conditions are established. Wagner (1) has considered presteady-state conditions briefly, and relatively detailed studies of Cu-Ni and Cu-Zn alloys have been made by Whittle and Wood (2, 3). Other papers relevant to the subject have been published on Fe-Cr alloys (4-6, 14) and copper-base materials (7-9).

The present paper is one of a series in which transient oxidation of a wide range of practically important alloys has been studied by transmission electron microscopy and by transmission and reflection electron diffraction of stripped films. By using standard heating and cooling conditions for oxidation in a single oxygen pressure at one temperature, for single-phase Fe-Cr and Ni-Cr alloys of various fixed compositions, the main variables emerge as (*a*) the bulk alloy composition, (*b*) the alloy interdiffusion coefficient, (*c*) the solubility and diffusivity of oxygen in the alloy, and (*d*) the relative growth rates of the doped and complex oxides. The standard free energies of formation for oxides of the relatively noble metals, nickel, cobalt, and iron are so similar, compared with the value for the much less noble metal, chromium, that differences in this factor are insignificant in this series. Complex oxide formation is, however, different in the different systems. Particularly under relatively mild conditions, epitaxy effects and the influence of the substrate substructure must be expected to be significant. Plastic flow of the oxide and substrate may also influence the scale morphology.

A subsidiary object of the paper was to investigate the interrelationship between the substructure of the oxide and the subjacent alloy. This subject is still in its infancy but has been studied for pure metals, for example in ref. (10-21).

Key words: oxidation, Fe-Cr alloy, Ni-Cr alloy.

Experimental Procedure

The alloys were prepared from vacuum-melted materials as cold-rolled strip 0.05 cm thick. The analyses were pure iron, Fe-4.35 w/o Cr (4.7 a/o), Fe-9.4 w/o Cr (10.0 a/o), Fe-15.5 w/o Cr (16.4 a/o), Fe-28.5 w/o Cr (30.1 a/o), pure nickel, Ni-5 w/o Cr (5.6 a/o), Ni-10 w/o Cr (11.1 a/o), Ni-15 w/o Cr (16.6 a/o), and Ni-27 w/o Cr (29.5 a/o). The nominal compositions of 5, 10, 15, and 30 a/o are used throughout the remainder of the paper.

After annealing for 4 hr at 800°C at 10^{-5} Torr, most specimens, 2 x 0.5 x 0.05 cm, were individually electropolished for 5 min in 30 sec pulses at 0.5 A cm^{-2} (25V) in 90% glacial acetic acid, 8% perchloric acid (sp gr 1.61), 2% water (all v/v). This was sufficient to remove about 15 mg cm^{-2} from each side of the specimens. It ensured the complete removal of any

chromium-depleted surface layer developed during fabrication and not removed by annealing. Pure nickel was electropolished under identical conditions in 50% v/v sulfuric acid. All the polished samples were rinsed in water and methanol and dried prior to oxidation.

Oxidation was restricted to 1, 2.5, 5, 10, and 15 min at 600°C. Since the oxidation times were short, the specimens had to be brought to temperature as quickly as possible and then after oxidation cooled very rapidly. The following technique, a refinement of that of Whittle and Wood (2, 3), ensured identical although arbitrary heating and cooling for each specimen. A glass tube, 80 cm long and 3.75 cm in diameter, was suspended by a vacuum-tight joint above a vertical furnace containing flowing oxygen at 1 atm pressure. The furnace inner tube was 66 cm long and 2.85 cm in diameter and the outer tube was 37.5 cm long and 4.5 cm in diameter. The specimen was hung inside the glass tube using a Kanthal hook, 6.25 cm long and 0.05 cm in diameter, passing through a 0.1 cm hole in the specimen. The hook itself was attached to an 18% Cr, 8% Ni stainless steel rod, 60 cm long and 1 cm in diameter, resting freely on an upper suspension rod. Upon release of this suspension rod, the stainless steel rod and attached sample fell 57.5 cm to a second suspension rod, permitting the specimen to reside exactly in the center of the hot zone of the furnace. At the end of the run, the second suspension rod was released, dropping the stainless steel rod and attached specimen directly into a quenching water bath beneath. The oxidation time was designated as the time elapsing between the two releases. The specimens were immediately dried and placed in a desiccator.

Any effects of "overheating" of the sample and the time taken for it to reach 600°C were investigated. A Pt/Pt-Rh thermocouple was spot-welded to the specimen in its usual assembly. Identical temperature/time curves were obtained for iron and Fe-30% Cr. It took about 80 sec to reach the vicinity of 600°C, as shown by automatic recording (Fig. 1). A similar curve was obtained when the thermocouple was attached to the Kanthal hook in the absence of the specimen. If any overheating due to the heat of formation of the oxide occurred, it was masked by the rapid rise to temperature. The other alloys would be expected to give similar curves because iron and Fe-30% Cr were, respectively, the fastest and slowest oxidizing alloys.

After evaporation of carbon onto the surfaces for supporting purposes in some cases, most oxide films were stripped chemically. A saturated solution of iodine in 10% w/v potassium iodide, or sometimes a 12% w/v solution of iodine in absolute methanol, proved successful for Fe-Cr alloys, and a solution of HCl/water/ethanol (10 ml : 30 ml : 40 ml), to which a few milliliters of hydrogen peroxide had been added, proved successful for Ni-Cr alloys. The stripped films

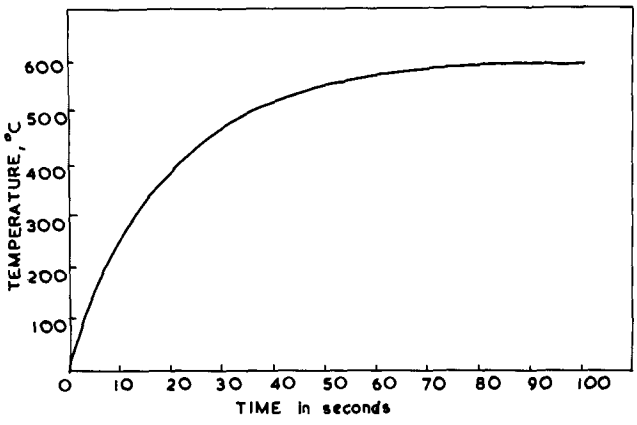

Fig. 1. Temperature of iron or Fe-30% Cr specimen as a function of time during the heating-up period.

were washed in methanol and water prior to examination in an A.E.I-E M6G electron microscope with diffraction attachment at 80 kV.

The top surfaces of films were examined by reflection electron diffraction at grazing incidence, interpretation of the pattern being subject to the usual severe restrictions of this technique. Transmission electron diffraction was applied with greater confidence. Selected area electron diffraction, limited in resolution by the minimum aperture of 1.25 μm, was inadequate to resolve the finely divided phases. Electron probe microanalysis in plan (2, 3) was so near its limits of usefulness, films generally being <1000Å in thickness, that it could not be employed significantly.

Results and Interpretation

Electron diffraction.—The oxides displayed interference colors, often blue to blue-brown, and electron opacity experiments with stripped films indicated them to be in the range 400-2000Å thick. Relative thicknesses between films on 30% Cr alloys could not be judged. It appeared that although for a given oxidation time films were thicker on iron than on nickel, they were thinner on Fe-5 to 15% Cr than on Ni-5 to 15% Cr.

Generally 2 or 3 diffraction photographs were taken from different regions over the surface of every specimen, using large and small apertures as appropriate. The experimental d_{hkl} values were compared with the values obtained from standard x-ray data and the pattern was identified. Some reflection lines were missing in the Fe-Cr patterns which were very diffuse. The diffraction data are summarized in Tables I and II, referring to the phases from the x-ray patterns used in identification. Where an expected oxide (on the basis of general theory and steady-state data) was

Table I. Electron diffraction results for oxidation of Fe-Cr alloys at 600°C

	1 min		2.5 min.		5 min		10 min		15 min	
	T	R	T	R	T	R	T	R	T	R
Fe-5 Cr			Fe_3O_4 (s)				Fe_3O_4 (s)		Fe_3O_4 (s) RhC (w)	
Fe-10 Cr	Fe_3O_4 (s) Rh (tr)	Rh (m)	Fe_3O_4 (s) Rh (w)	Fe_3O_4 (s) Rh (m)	Fe_3O_4 (s) RhC (w) $FeCr_2O_4$ (w)		Fe_3O_4 (s) Rh (s)	Rh (s) Fe_3O_4 (tr)	Fe_3O_4 (s) Rh (s)	Fe_3O_4 (s) Rh (s)
Fe-15 Cr	Fe_3O_4 (s) Rh (tr)	Rh (m) Fe_3O_4 (m)	Fe_3O_4 (s) Rh (m) RhC (m)		Fe_3O_4 (s) RhC (s) Rh (tr)	Rh (m) RhC (tr)	Fe_3O_4 (s) Rh (m) RhC (tr)	Rh (m) Fe_3O_4 (w)	Fe_3O_4 (s) Rh (s) RhC (w)	Rh (s) Fe_3O_4 (s)
Fe-30 Cr			RhC (s) $FeCr_2O_4$ (w) Rh (tr) Fe_3O_4 (tr)		RhC (s) Fe_3O_4 (w) Rh (tr)		RhC (s) Fe_3O_4 (m) Rh (tr)		RhC (s) Fe_3O_4 (m) Rh (w)	

T = transmission diffraction.
R = reflection diffraction.
s = strong, m = medium, w = weak, tr = trace.
Rh = rhombohedral phase (α-Fe_2O_3 or Fe_2O_3-Cr_2O_3 relatively rich in Fe_2O_3).
RhC = Cr_2O_3-Fe_2O_3 rich in Cr_2O_3.

Table II. Transmission electron diffraction results for oxidation of Ni-Cr alloys at 600°C

	1 min	2.5 min	5 min	10 min	15 min
Ni-5 Cr	NiO (s)	NiO (s) $NiCr_2O_4$ (tr)	NiO (s) $NiCr_2O_4$ (m)	NiO (s) $NiCr_2O_4$ (s) Also NiO (s) in reflection pattern	
Ni-10 Cr	NiO (s)	NiO (s) $NiCr_2O_4$ (s)	$NiCr_2O_4$ (s) NiO (m)	$NiCr_2O_4$ (s) RhC (s) NiO (tr)	
Ni-15 Cr	NiO (s)	NiO (s)	NiO (s) $NiCr_2O_4$ (w) RhC (tr)	$NiCr_2O_4$ (s) RhC (s) NiO (tr)	
Ni-30 Cr	NiO (s)	NiO (s) RhC (w)	NiO (s) $NiCr_2O_4$ (w)	NiO (s) $NiCr_2O_4$ (w)	NiO (s) RhC (m) $NiCr_2O_4$ (m)

Nomenclature as in Table I.

missing, this is indicated in the text. Relative amounts of phases indicated by electron diffraction data must not always be accepted literally. This is because the oxides may be buried in certain cases, missed in random sampling, or present in too small an amount to be detected, particularly if the major lines are in close coincidence with those of another predominating phase. Although it was possible in the Fe-Cr system to differentiate spinel oxides, that is, Fe_3O_4 and $FeCr_2O_4$ from the rhombohedral phases, that is, α-Fe_2O_3 and Cr_2O_3, only with great difficulty could members within each phase group be identified. Thus, identification as $FeCr_2O_4$ or Fe_3O_4 could mean $FeFe_{(2-x)}Cr_xO_4$ ($0 \leq x \leq 2$) rich and lean in chromium, respectively, and Cr_2O_3 and Fe_2O_3 would indicate Cr_2O_3-Fe_2O_3 rich and lean in chromium, respectively. Some evidence of single as well as polycrystalline patterns was observed, but in the absence of alloy attached to the oxide, epitaxy relationships were not identified.

Oxidation of Fe-5% Cr revealed Fe_3O_4 as the only major phase for up to 10 min, with some Cr_2O_3 appearing at 15 min. No $FeFe_{(2-x)}Cr_xO_4$ rich in chromium (usually indexed as $FeCr_2O_4$) was found. However, it is likely that a thin healing layer of the spinel relatively dilute in chromium existed at the scale base, as found for thicker scales produced at high temperatures. The Cr_2O_3 was possibly a healing layer which can develop at the base of the spinel, or internal oxide. A little rhombohedral oxide (probably α-Fe_2O_3) would be expected at the outer surface if the oxidation rate had slowed sufficiently, but this was not detected. For comparison, Phelps, Gulbransen, and Hickman (14) found Fe_3O_4 and perhaps, surprisingly, Cr_2O_3 for Fe-5% Cr after 5 min at 400°C, using reflection diffraction, but only Fe_3O_4 and $FeCr_2O_4$, after cooling by transmission diffraction.

As expected, reflection diffraction revealed Fe_3O_4 with a presumably overlying, rhombohedral layer on Fe-10% Cr at all times. In transmission, the existence of Fe_3O_4 as the major phase was naturally emphasized because the entire film was now being traversed by the electron beam. $FeCr_2O_4$ was occasionally indexed, but again some of the material indexed as Fe_3O_4 could have been spinel dilute in chromium. The weak Cr_2O_3 lines observed in transmission after 5 min could have been a healing layer or possibly a local area where Cr_2O_3 developed from the outset. The latter explanation was supported by the occasional finding of weak Cr_2O_3 lines in reflection patterns. Alternatively this could be a case where an initial Cr_2O_3 layer lifted off the surface, became perforated, and allowed iron-containing oxides to grow beneath it.

For Fe-15% Cr, again, Fe_3O_4 and rhombohedral oxide (probably α-Fe_2O_3 but the presence of Cr_2O_3 after 5 min indicated that some of it could have been α-Fe_2O_3-Cr_2O_3) were detected as the outer phases by reflection electron diffraction. Transmission diffraction revealed additionally Cr_2O_3, which would be expected at the scale base. It is curious that the apparent amount decreased with time. Phelps, Gulbransen, and Hickman (14) also detected Fe_3O_4 and Cr_2O_3 as predominant phases in the stripped film for Fe-13% Cr after 15 min at 600°C.

The presence of Cr_2O_3 as the major phase at all times on Fe-30% Cr was expected, but it is reasonable that minor amounts of Fe_3O_4 (or spinel rich in iron), rhombohedral oxide, and spinel rich in chromium should have been identified. These almost certainly lay at the outside of the films, being the result of the nucleation stages. Further outward diffusion of iron ions, trapped originally in the inner Cr_2O_3-rich layer, toward the location of higher oxygen potential could also occur.

The patterns were much simpler to interpret for Ni-Cr alloys because only three oxides had to be considered. Virtually all the diffraction data were obtained by transmission.

For Ni-5% Cr and Ni-10% Cr, NiO was the major phase, with increasing amounts of $NiCr_2O_4$ as oxidation proceeded. If behavior at higher temperatures was followed here, the spinel did not exist as a complete layer but as particles produced by interaction between the main NiO layer and the Cr_2O_3 internal oxide. It would appear that a healing Cr_2O_3 layer initiated after 10 min for Ni-10% Cr. The low amount of NiO found on this specimen could have been due to very rapid healing or to substantial interaction between the initial NiO layer and the healing Cr_2O_3 layer. The same phenomenon was found after 10 min with Ni-15% Cr, so possibly the second explanation is favored. The extent of NiO formation was still high even with Ni-30% Cr, but the amount of Cr_2O_3 detected, although small, did increase with the alloy chromium content and also became detectable earlier. Apart from the fact that such layers could have been quite thin, these scales tend to crack between the Cr_2O_3 and the outer oxide on cooling. Adhesion between the Cr_2O_3 and the substrate is much better in the Ni-Cr than the Fe-Cr system, due to interlocking. Although most of the oxide would have been stripped from the substrate, some of the Cr_2O_3 may have floated away from the outer layer rich in NiO and containing $NiCr_2O_4$ and not have been detected. There is, however, no direct evidence that a more complete spinel layer did not form at this lower temperature and play a more important role than at higher temperature.

Electron microscopy.—General comments.—Pt/C replicas revealed that electropolished surfaces were smooth and virtually uniform. Etched surfaces of annealed samples showed large grains, of typical diameter 10-50 μm, with relatively uniform surfaces apart from a few minor dimples and some fine columnar grains occasionally grown on grain boundaries. Several areas of each stripped oxide film were studied to ensure representative micrographs.

For pure metals and dilute alloys (very dilute in the Ni-Cr case), the alloy grain boundaries, subgrain

boundaries, and certain other substructural features, which could be dislocation loops and forests, produced thicker oxide. This could have been partly due to impurity segregation in this location but was more likely due to their acting as excellent vacancy sinks. This permitted a high vacancy concentration gradient across the scale and prevented void formation at the scale base, so permitting rapid oxidation (12). Alternatively, the thicker oxide was due to more local paths of easy diffusion, due to lattice disregistry between coalescing epitaxial nuclei in the oxide, the introduction of misfit dislocations, incoherent twin boundaries, mosaic structures, *etc.* (10, 11, 13, 16). The latter explanation also shows why certain grains oxidized faster than others. It appears quite common to make reference to subgrains in the oxide (10, 11), but it is not always easy to differentiate between genuine features and replication effects. Some artifacts may have been introduced on quenching or stripping, but there is no direct evidence of this and most features are considered genuine.

As the alloy chromium content increased, it became progressively more possible for preferential healing of the scale by chromium-rich oxides at the substrate defects. This was due to the more rapid diffusion of chromium to the alloy/oxide interface through such defective regions, permitting the transition from internal to external Cr_2O_3 formation there. There is some evidence that the effect was relatively greater for Ni-Cr alloys, but the situation was complex as discussed later. The term "healing" is used in this paper to mean the development of a compact, slowly growing, oxide layer at the scale base and does not imply closure of cracks and so forth.

Fe-Cr alloys.—Characteristic thickening of the oxide at grain boundaries (up to 1 μm) and other vacancy sinks occurred for pure iron after times of about 2.5 min. Figure 2b-d shows similar features for Fe-5% Cr. Clearly oxidation was most rapid at the main grain boundaries which thickened to different extents due to orientation differences, illustrating that the zone of influence extended beyond the boundaries themselves. Lesser thickening at alloy subgrain boundaries was then followed by the gradual "filling-in" of the areas between the subboundaries. The filling-in was again faster on some grains than others, the process being virtually complete after 15 min. Assuming the subgrains visible in the oxide were not independent features but did replicate the alloy, the subgrains of the alloy appeared equi-axed and about 1-3 μm in size, the small thicker oxide regions usually being 0.5-3 μm. The oxide grain size was, therefore, very much smaller than the alloy grain size even by the time the crystallites formed at the defective regions had thickened, grown, and coalesced to give an opaque oxide.

Figure 2a, typical of several such features, shows an area of thin oxide, probably over a minute healed region of scale (which would be too small to detect by electron diffraction). The features leading radially into the thin oxide could have been dislocations in the oxide, or produced in the replication of dislocation structures in the substrate, or merely have been compositional or contrast effects in the films. The features were still visible on tilting but did not move in the electron beam, probably supporting the replication concept. If they were dislocation arrangements, differential stresses in the oxide or the substrate produced during growth could have been responsible for the distribution. However, the remarkable similarity to the micrographs of Howes (5) and Taylor, Holmes, and Boden (21) suggests they may have been diffraction contrast fringes. Such fringes may have been due to severe strains in the oxide or at the alloy/oxide interface, as a result of epitaxial growth or of stress developed in the oxide at a later stage (5), or electron optical extinction phenomena as a result of rust rosettes (21).

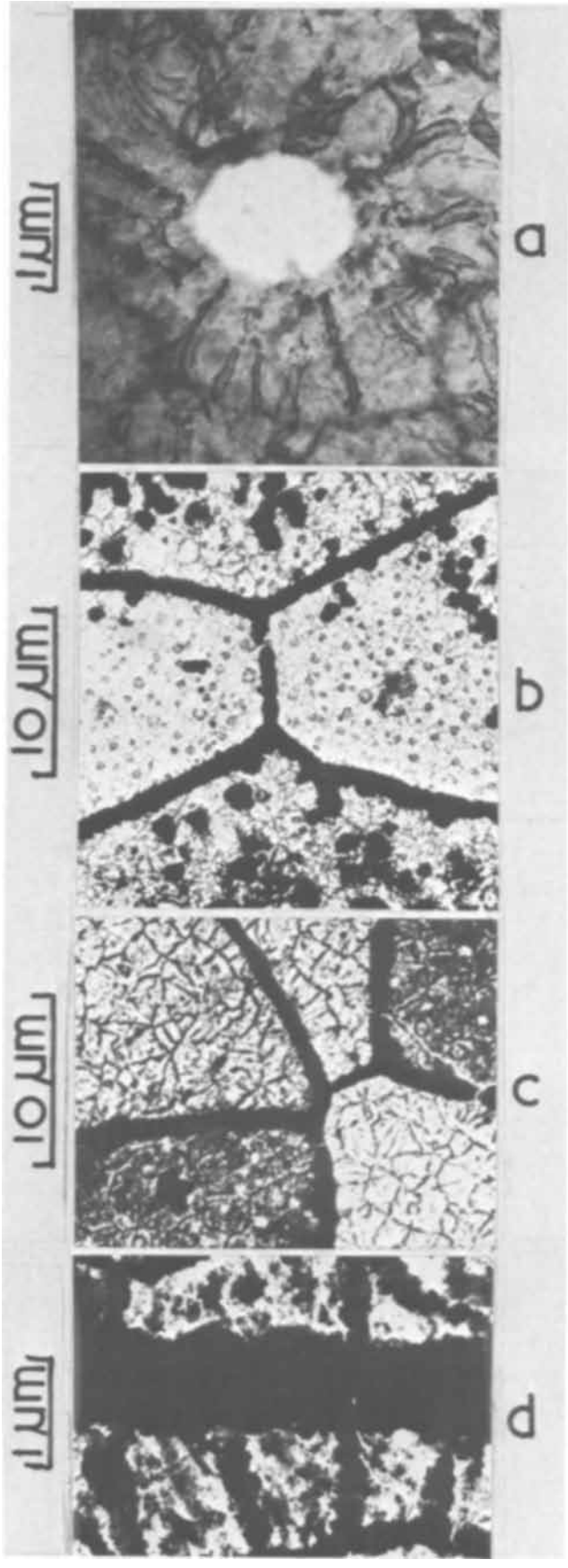

Fig. 2. Transmission electron micrographs of oxide films formed on Fe-5% Cr for (a) 1 min, (b) 2.5 min, (c) 5 min, and (d) 5 min at 600°C; (a) shows radial structural or contrast features leading into a thin oxide disk, (b)-(d) show initial oxide thickening at alloy grain boundaries and other sites and the gradual filling in of the subgrain regions.

Nevertheless, in the present work they were never observed on pure iron.

A similar pattern of boundary growth and the filling in of subgrains was observed on Fe-10% Cr (Fig. 3), the rate appearing to be somewhat similar to that for Fe-5% Cr. The borderline nature of the alloy was illustrated by the fact that in some regions the oxide above the main grain boundaries had thickened everywhere more rapidly than above the grains themselves, whereas, in others (Fig. 4d) oxidation had been slower there due to preferential healing. The intermediate situation is given in Fig. 4a where breaks in the grain boundary darkening indicate localized healing. Remarkable differences in oxide thickness from place to place on this sample may also have been evidence of some localized healing within certain metal grains.

Close scrutiny of certain grains in Fig. 4a reveals a myriad of small disks with dark peripheries, generally separate but occasionally impinging on one another.

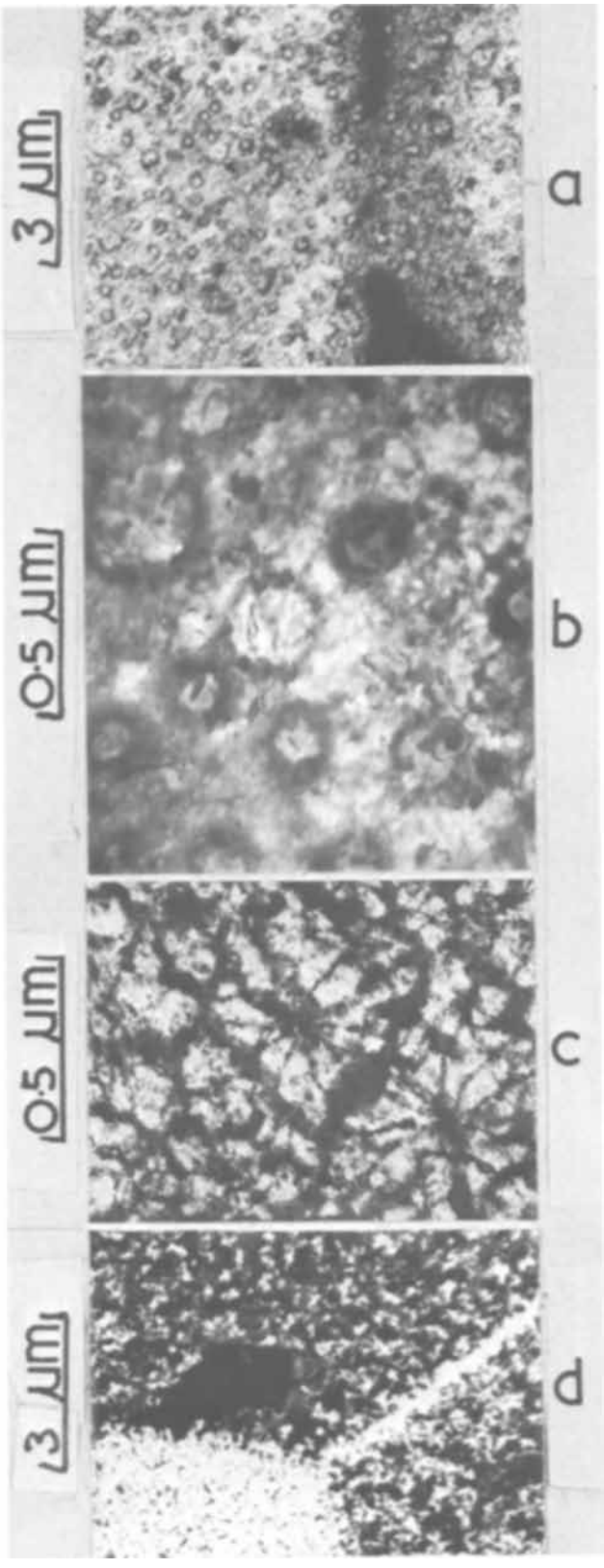

Fig. 3. Transmission electron micrographs of oxide films formed on Fe-10% Cr for (a) 2.5 min, (b) 2.5 min, (c) 5 min, and (d) 10 min at 600°C; (a) and (d) show preferential grain boundary healing in certain locations, with thickening still present elsewhere; (a) also gives the general distribution and (b) the detail of loop structures; (c) shows rosette structures.

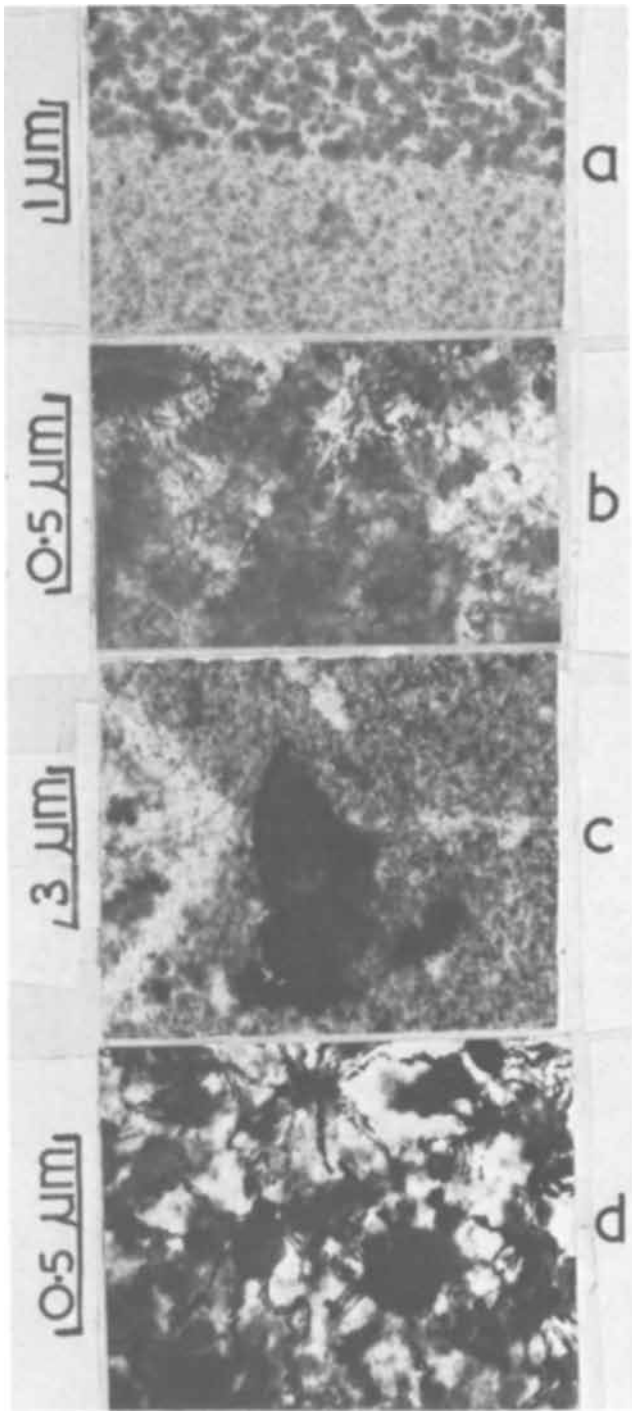

Fig. 4. Transmission micrographs of oxide films formed on Fe-15% Cr for (a) 1 min, (b) 2.5 min, (c) 5 min, and (d) 15 min at 600°C; (c) demonstrates complete preferential healing along grain boundaries; (a)-(c), various local healing features within the grains, and (d), a rosette structure with the "hub" containing thick oxide.

Although they may have been due to minor undulations in the film or local healing within the circles, it appears much more likely that they were genuine features. Figure 4b gives the detail of the disks, the typical diameter being 0.1-0.4 μm and the population 10^9 cm^{-2}. A likely explanation is that the film replicated dislocation loops which were produced in the substrate by rapid cation vacancy injection. Such vacancies, produced by the oxidation process, aggregated and eventually collapsed during the initial stages of oxidation. The peripheries of the loops acted as good cation vacancy sinks, so the oxide thickened above them. Alternatively, the lattice mismatch argument is applicable. Certain loops appear to have been connected with other dislocations. The loops were stable in the beam, which favors the concept that they replicated loops produced in the alloy surface and remained present on tilting. They were also seen in specimens oxidized for 1 min. Similar loops or replicated loops have been observed previously by Howes (5) on Fe-28% Cr, although they were smaller than here, and by Ali and Wood on nickel (22). They have been studied in detail by transmission of thin metal foils covered by thin oxide in the case of magnesium, zinc, and cadmium (17-20).

"Rosette" structures, somewhat similar to those in Fig. 2a except that the central region contained thick rather than thin oxide, were also observed on this alloy (Fig. 3c). The interbranch spacings of the rosettes were thin and bright.

The results for Fe-15% Cr (Fig. 4) revealed complete preferential healing along grain boundaries (Fig. 4c) due to the higher alloy chromium content, with the zones of influence of the boundaries extending more into the grain with certain boundaries than others. Although the oxidation rate still varied from grain to grain, this was somewhat less pronounced than with dilute alloys, with less local scale thickening above substrate defects. The considerable local healing seen in some grains (Fig. 4a-c) could have been due to thin oxide above metal subgrain boundaries or other substrate defects, or due to reduced thickening above chromium-rich oxide which commenced as internal oxide. Features which could have been dislocation forests are visible in Fig. 4b. The rosette structures observed on previous alloys (Fig. 2a and 3c) were again clearly visible, particularly over large areas of the 10 and 15 min specimens (*e.g.* Fig. 4d).

With Fe-30% Cr there was less oxidation at grain boundaries and their peripheries and at certain sites within the grains than over the general surface (Fig. 5a). However, the influence of the grain orientation on the oxidation rate generally appeared less than for the other alloys. As healing by a Cr_2O_3 layer is expected fairly rapidly with this alloy, the mottled oxide was probably mainly the Fe_3O_4 and rhombohedral oxide other than Cr_2O_3 detected by electron diffraction and produced in the initial scale establishment stages. The fine dark particles were almost certainly rhombohedral oxide rich in α-Fe_2O_3, standing proud (Fig. 5a). Perhaps these subsequently acted as centers of rosettes which appeared in ruptured forms. With increasing time, preferential growth at the grain boundaries again began to predominate (Fig. 5b). This is reasonable because once Cr_2O_3 was the major phase over the entire surface and it became thick compared with the outer, residual iron-containing oxides the boundaries could again act as vacancy sinks or enhanced mismatch centers with respect to Cr_2O_3 formation, and local thickening could occur there. The matrix now consisted of fine oxide crystallites up to about 0.2 μm in size (Fig. 5c). Other areas of oxide showed fringes and possible dislocation structures.

Ni-Cr alloys.—Grain boundary thickening of oxide and the variation in oxidation rate from grain to grain also held for pure nickel. The general features were similar to these already described (10-12), with apparent oxide crystallites growing with time and dislocation forests, mosaic structures, *etc.*, visible in the oxide. Many of the oxide films on nickel and the dilute Ni-Cr alloys curled up into rolls on stripping, presumably due to residual stresses within the films.

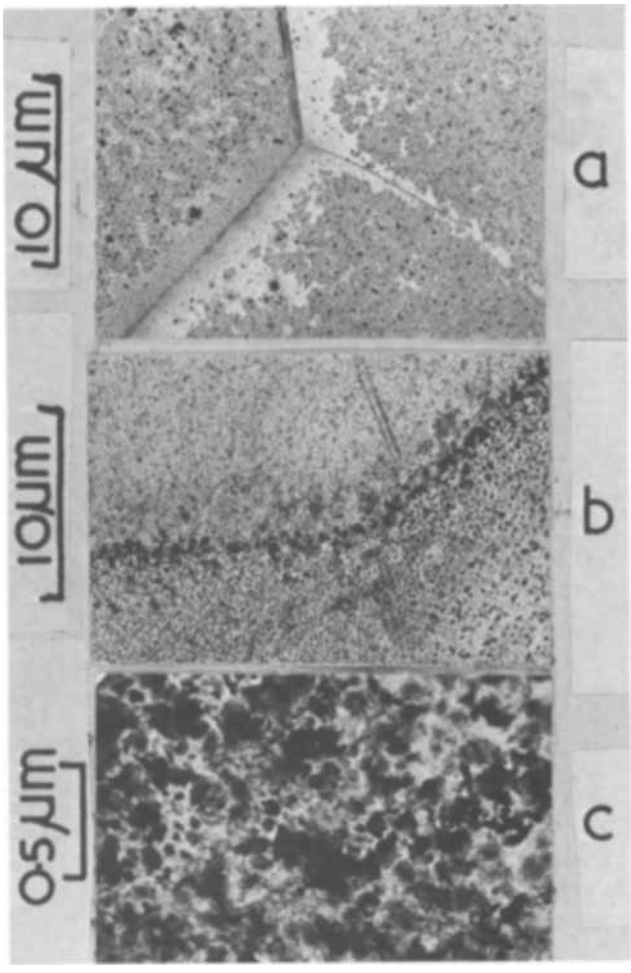

Fig. 5. Transmission electron micrographs of oxide films formed on Fe-30% Cr for (a) 2.5 min, (b) 15 min, and (c) 15 min at 600°C; (a) displays rapid healing at grain boundaries and limited healing within the grains, with a few minor oxide protrusions; (b), local oxide thickening above alloy grain boundaries at a later stage; and (c), the detail of the oxide within the grains.

Oxidation of Ni-5% Cr for 1 min showed a uniform distribution of small, bright, disk-like structures (0.05-0.2 μm in diameter) throughout the matrix, with some evidence of agglomeration of these structures along the grain boundaries (Fig. 6a and b). After 2.5 min and longer times the disks disappeared and larger light regions within the grains and broader grain boundary regions were apparent. The width of the grain boundary bands varied from boundary to boundary and tended to increase with time (Fig. 6c and d). The orientation dependence of the grain boundary zone of influence is presumably related more to the angle at which the boundary has been cut by the surface than to any anisotropy of the alloy interdiffusion coefficient. The extent of thick and thin regions of oxide from grain to grain varied enormously and there were occasional hints of filled-in subgrains and boundary thickening in isolated regions. The general effect of crystallites filling in became more pronounced with time but the evidence of locally healed areas had not always been completely eradicated over the time scale used. Grain boundary healing occurred with much lower alloy chromium contents on Ni-Cr alloys than

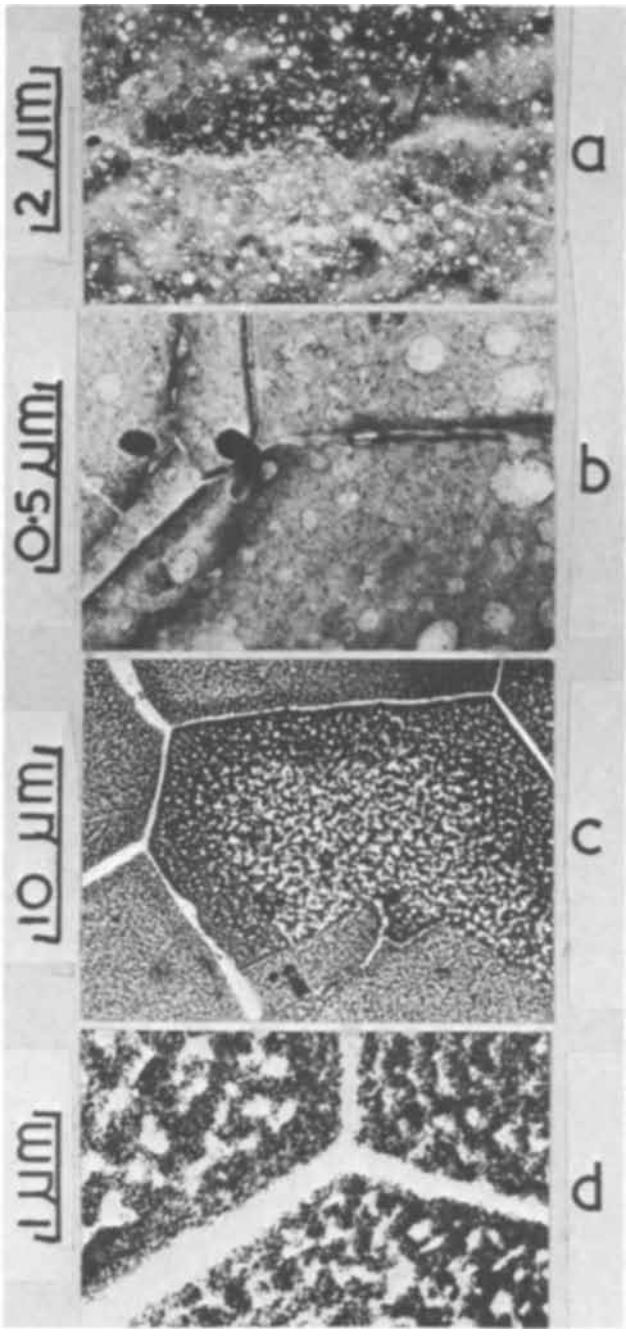

Fig. 6. Transmission electron micrographs of oxide films formed on Ni-5% Cr for (a) 1 min, (b) 1 min, (c) 2.5 min, and (d) 2.5 min at 600°C; (a) and (b) show slow oxidation above disks, probably internal oxide particles or initial nuclei; and (c) and (d), the zones of influence of grain boundaries in producing local healing, as well as local healing within the alloy grains themselves.

on Fe-Cr alloys. Grain boundary thickening, although occurring with dilute alloys, was rare with Ni-5% Cr.

Although possessing a superficial similarity to the disks seen during Fe-Cr oxidation, the present disks were in fact different, showing little peripheral darkening, and were much thinner than the matrix oxide, suggesting local healing. Indeed the explanation is that the NiO could not grow rapidly above internal oxide particles of Cr_2O_3 developed in the alloy for Ni-Cr alloys or above the $NiCr_2O_4$ particles produced on incorporation of the internal oxide into the scale. Such phases could, of course, also have existed as initial nuclei on the surface after only 1 min. Although the disks were not replicated dislocation loops in the present case, it is possible that the first internal oxide nucleated at such sites during the initial stages of oxidation. The disks disappeared after longer oxidation times, partly due to their lateral overgrowth by the rapidly developing NiO and partly due to the development of larger regions of healed oxide (Fig. 6c and d). Despite the evidence of extensive $NiCr_2O_4$ from electron diffraction data, previous work would indicate that healing in this system is usually by Cr_2O_3. Subgrain filling in was much less evident than with Fe-Cr alloys. The nucleation pattern for nickel oxide seemed less related to specific sites than did that of iron oxides on Fe-Cr alloys.

Ni-10% Cr behaved similarly to Ni-5% Cr, healing at grain boundaries being readily apparent, except where they were obscured by lateral overgrowth by NiO. Twin boundaries did not show local thickening or healing, perhaps because such boundaries are coherent (10-11).

Oxidation of Ni-15% Cr showed much more rapid and general healing in the early stages (Fig. 7a), but there was substantial variation from area to area and grain to grain. The areas of the bright regions in Fig. 7b are typically 1-1.5 μm^2. The very fine light areas in Fig. 7b must have been minor grain boundaries, twin boundaries, or, just possibly, slip bands. It is not possible to say categorically whether the light areas were virtually Cr_2O_3 alone or whether they were regions where outer NiO and $NiCr_2O_4$ had become separated from the alloy by healing Cr_2O_3 layers or particles.

The situation was similar for Ni-30% Cr, with even slower oxidation and more pronounced healing at grain boundaries and within the grains (Fig. 8a-c). The width of the healed grain boundary regions visible in the microscope increased with time (Fig. 8b). Certain substructural features where local healing occurred were also revealed within the grains (Fig. 8b). As happened with other alloys, although less clearly (*e.g.*,

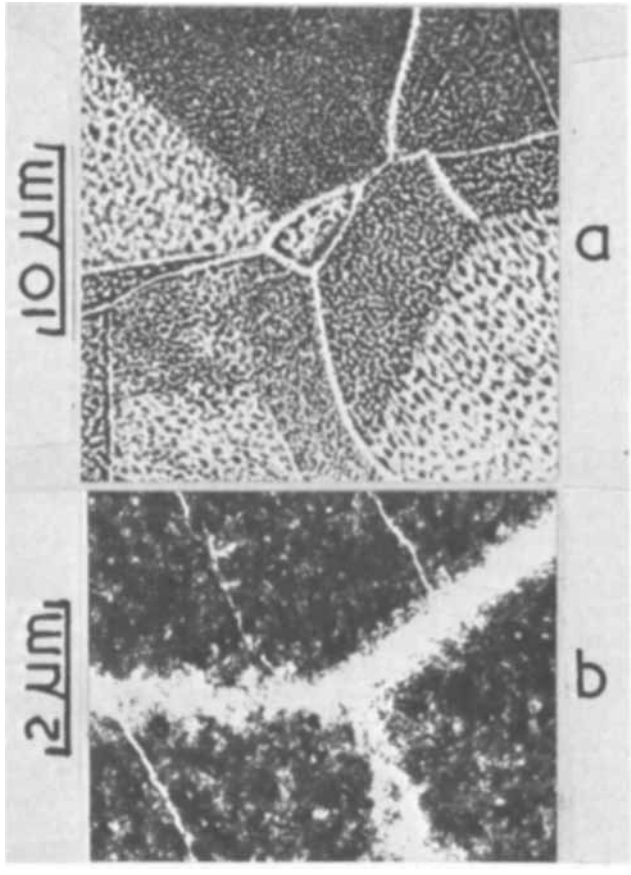

Fig. 7. Transmission electron micrographs of oxide films formed on Ni-15% Cr for (a) 2.5 min and (b) 10 min at 600°C. Preferential healing is most rapid at grain boundaries but is also prevalent within the grains.

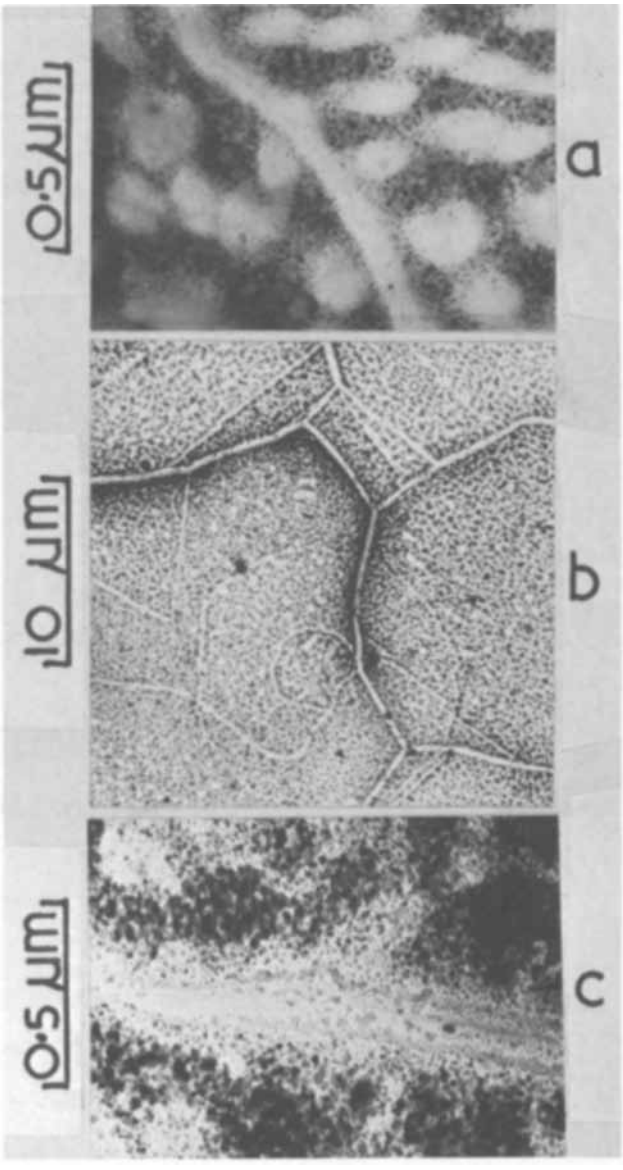

Fig. 8. Transmission electron micrographs of oxide films formed on Ni-30% Cr for (a) 1 min, (b) 15 min, and (c) 15 min at 600°C. Preferential healing sites are clearly visible, as is the grain structure within and adjacent to the healed areas.

Fig. 6b), thickening of the oxide along certain but not all grain margins occurred (*e.g.*, Fig. 8b). This was due to preferential oxidation above a chromium-depleted zone on either side of the grain boundary, lateral diffusion of chromium to the grain boundary occurring to promote continued growth of the chromium-rich oxide there. The width of this zone increased with time due to the inability of the bulk grains to replenish chromium to the margins. A fine oxide grain structure existed within the region over the alloy grain boundaries (Fig. 8c).

General Discussion

The heating and cooling procedure for the specimens was rather arbitrary but is considered to give a good guide to behavior. The slower the heating-up process, generally the greater is the likelihood of establishing the steady state and often the thermodynamically predicted scale at an early stage. The standard free energies of formation of the oxides only predict the thermodynamically stable oxides, not necessarily the steady-state scale, which may be determined by the spatial distribution of phases in the initial film. It is now possible to discuss the influence of the bulk alloy chromium content, the alloy interdiffusion coefficient, the solubility and diffusivity of atomic oxygen in the alloy, and the relative growth rates of the doped sample and complex initial oxide nuclei on the film establishment stages, as far as the limited data on these parameters permit. The data are scattered, often do not refer to 600°C, sometimes depend on material purity, and will be detailed elsewhere (23). Here, for brevity, only order of magnitude values are indicated and the original references are omitted.

The same general pattern of behavior occurs initially for each alloy. The first nuclei of oxide, which rapidly coalesce to give a complete oxide layer, contain particles of the simple and complex oxides of all the alloy components, according to the schematic diagram of Wagner (1) and the observations and theories of Whittle and Wood (2, 3). In principle it should be possible to get scale enriched in the faster growing noble metal oxide. Subsequently a steady-state scaling situation is established, in which the thermodynamically favored oxide (in this case usually Cr_2O_3) attempts to provide a healing layer as the scale base and diffusional factors come more into play. As this occurs the oxidation rate declines, little further noble metal enters the scale and that which is within it redistributes itself in a way determined by the oxygen potential gradient.

It is reasonable to assume that the initial nuclei, rapidly forming from an initial amorphous skin (9), an air-formed film, or a prenucleated surface oxide (15), could be very small indeed and even little above atomic dimensions. However, they rapidly grow into larger crystallites, as observed in the present study, to decrease the interfacial energy. They also tend to interdiffuse to give solid solutions and complex oxides, and noble metal oxides may even be reduced back to metal by the displacement reaction. Particularly at the lower temperature used here, epitaxy effects may be more important than suggested by Whittle and Wood (2, 3) in determining the size, structure, and composition of the initial nuclei. This contribution of epitaxy has been emphasized by various workers (4-6). For example, all the nuclei on Fe-Cr alloys may tend to be cubic (4).

Considering first the 30% Cr alloys in which a healing Cr_2O_3 layer is established relatively quickly, several factors are operative in deciding the thickness of the outer layers containing the simple oxides of iron and nickel and the spinels. For Fe-Cr alloys, the tendency of the very rapidly growing iron-rich oxide nuclei is to overgrow the chromium-rich nuclei and encroach on the alloy, undermining and incorporating any initiating internal oxide particles or layers into the main scale. This is countered by the ease of formation of a healing layer of Cr_2O_3 near the alloy/oxide interface, rather than as internal oxide. As a result of the high alloy interdiffusion coefficient (3-8 x 10^{-10} cm^2 sec^{-1} at 1000°C), and relatively low oxygen solubility (6-80 x 10^{-4} w/o in iron at 700°-800°C) and possibly diffusivity (1 x 10^{-10} cm^2 sec^{-1} at 1000°C), sufficient Cr_2O_3 is precipitated near the surface to prevent further internal oxidation. A further point is that a layer of $FeFe_{(2-x)}Cr_xO_4$ ($O \leq x \leq 2$) may be developed in the initial nuclei and between the outer iron oxides and the developing inner Cr_2O_3 particles or layer. Thus the fast oxidation rate of iron (kp 7.6 to 13 x 10^{-11} g^2 cm^{-4} sec^{-1} at 600°C) would have a chance to show up only in very early stages indeed (kp for Cr is 8 x 10^{-15} at 700°C). Some reaction between residual Fe_3O_4 and α-Fe_2O_3 outside the Cr_2O_3 with the Cr_2O_3 would produce the spinel and rhombohedral oxide detected by electron diffraction.

A similar general picture applies to the oxidation of Ni-Cr alloys where nickel has a higher oxidation rate than chromium. The lower alloy interdiffusion coefficient (1-4 x 10^{-11} cm^2 sec^{-1} at 1000°C) and higher oxygen solubility (200 x 10^{-4} w/o at 600°C) and probably diffusivity (24 x 10^{-10} cm^2 sec^{-1} at 1000°C) com-

pared with the Fe-Cr system mean that the Cr_2O_3 tends to be formed as an internal oxide, although with a very dense population.[1] This possibly coalesces to give a healing layer and is assisted in doing so by the relatively slow overgrowth and encroachment rate of the NiO, (kp for Ni is 3.9×10^{-14} at 600°C) which is much more protective than the iron oxides. The longer time required to "shut off" the growth of the noble metal oxide in the Ni-Cr case means that the initial oxides are of comparable thickness to those on Fe-Cr alloys. It has not been established definitively that $NiCr_2O_4$ does not give a complete layer, but the electron micrographs and higher temperature data possibly tend to favor its presence as particles in the scale. Its relatively fixed composition reduces its amount likely to be found in a scale. No reliable data are available for the formation rates of $NiCr_2O_4$, or indeed for $FeFe_{(2-x)}Cr_xO_4$ ($O \leq x \leq 2$). Really preparabolic oxidation rates of doped oxides should have been used in the above comparisons, but the very limited data suggest similar trends to the kp values (23).

As the alloy chromium content is decreased, the extent of healing becomes more localized in the Ni-Cr system, and within the grains thin oxide often occurs only above Cr_2O_3 internal oxide or recently incorporated $NiCr_2O_4$ particles. Oxidation, determined largely by the rate of thickening of doped NiO, partially blocked by the spinel particles, is still relatively low. It is not as catastrophic as would be expected with dilute Fe-Cr alloys because a healing layer of $FeFe_{(2-x)}Cr_xO_4$, more protective than iron oxides but less protective than Cr_2O_3, is soon developed at the scale base and this determines the oxidation rate. This actually means that the oxidation rate up to 15 min is slower for dilute Fe-Cr alloys than Ni-Cr alloys. Even with the dilute alloys it may become possible to develop a healing Cr_2O_3 layer in the later stages, beneath the $FeFe_{(2-x)}Cr_xO_4$.

The intrinsic diffusion coefficients in the respective Fe-Cr and Ni-Cr system are probably sufficiently similar to avoid any Kirkendall voids in the depleted alloy zone under the oxide as a result of alloy interdiffusion. This is not to say that voids are not eventually produced at the alloy/oxide interface by cation vacancies diffusing in through the scale.

One final point is that it is clear from this study how difficult it is going to be to understand the mechanical properties of oxidizing samples on terms of substructural factors, many of which produce highly localized effects.

Acknowledgments

The authors thank Prof. T. K. Ross for provision of facilities and for encouragement of this study, Mr. B. Vaszko for his collaboration with the electron microscopy and the Science Research Council for a postdoctoral award to one of them (B. C.). They are indebted to International Nickel Ltd. and the British Iron and Steel Research Association for the provision of alloys.

Manuscript submitted Dec. 11, 1969; revised manuscript received *ca.* May 26, 1970.

Any discussion of this paper will appear in a Discussion Section to be published in the June 1971 JOURNAL.

[1] If the alloy interdiffusion coefficient is substantially lower at 600° than at 800°C, such densely populated internally oxidized regions may constitute the "healing layer" entirely in some cases. The relative ease of extensive spinel formation at 600°C would thereby be explained by incorporation of such Cr_2O_3 particles into the NiO as oxidation continues.

REFERENCES

1. C. Wagner, *This Journal*, **99**, 369 (1952); **103**, 627 (1956).
2. D. P. Whittle and G. C. Wood, *J. Inst. Metals*, **96**, 115 (1968).
3. D. P. Whittle and G. C. Wood, *Brit. Corrosion J.*, **3**, 244 (1968).
4. H. J. Yearian, W. D. Derbyshire, and J. F. Radavich, *Corrosion*, **13**, 597t (1957).
5. V. R. Howes, *Corrosion Sci.*, **7**, 735 (1967).
6. A. Fursey, B. Kent, and G. O. Lloyd, Extended Abstracts of 4th Intern. Congress on Corrosion, Amsterdam, September 1969.
7. F. Bouillon and J. Stevens, *Belg. Chem. Ind.*, **24**, 1335 (1959).
8. J. V. Cathcart, G. F. Petersen, and C. J. Sparks, "Surfaces and Interfaces I. Chemical and Physical Characteristics," p. 333, Burke, Reed, Weiss, Editors, Syracuse University Press, New York (1968).
9. M. D. Sanderson and J. C. Scully, *Corrosion*, **25**, 291 (1969).
10. J. M. Perrow, W. W. Smeltzer, and R. K. Ham, *Acta Met.*, **15**, 577 (1967).
11. J. M. Perrow, W. W. Smeltzer, and J. D. Embury, *ibid.*, **16**, 1209 (1968).
12. S. I. Ali and G. C. Wood, *J. Inst. Metals*, **97**, 6 (1969).
13. J. F. Cathcart and G. F. Petersen, *This Journal*, **115**, 595 (1968).
14. R. T. Phelps, E. A. Gulbransen, and J. W. Hickman, *Ind. Eng. Chem. Anal. Ed.*, **18**, 391, 640 (1946).
15. A. Ronnquist and K. Thomas, *Brit. Corrosion J.*, **1**, 47 (1965).
16. K. R. Lawless and A. T. Gwathmey, *Acta Met.*, **4**, 153 (1956).
17. J. E. Harris and B. C. Masters, *Proc. Roy. Soc. (London)*, **292A**, 240 (1966).
18. P. S. Dobson and R. E. Smallman, *ibid.*, **293A**, 423 (1967).
19. R. Hales, P. S. Dobson, and R. E. Smallman, *Metal Sci. J.*, **2**, 224 (1968).
20. D. Michell and G. J. Ogilvie, *Phys. Stat. Sol.*, **15**, 83 (1966).
21. M. F. Taylor, E. Holmes, and P. J. Boden, *Corrosion Sci.*, **9**, 683 (1969).
22. S. I. Ali and G. C. Wood, Unpublished work.
23. B. Chattopadhyay and G. C. Wood, *Oxidation of Metals*, **2**, 373 (1970).

Ionic Current as a Function of Field in the Oxide during Plasma Anodization of Tantalum and Niobium

W. L. Lee,[1] G. Olive, D. L. Pulfrey, and L. Young*

Electrical Engineering Department, The University of British Columbia, Vancouver 8, British Columbia, Canada

ABSTRACT

The plasma anodization of tantalum and niobium in an oxygen d-c glow discharge was confirmed to be analogous to anodization in aqueous solutions in that evidence was obtained that the ion current J in the oxide was a function of field E in the oxide. Experimental data on $J(E,T)$ were obtained using *in situ* ellipsometry to determine the thickness of oxide D, and hence E (using probe measurements to obtain the potential difference across the oxide) and J from dD/dt. The ellipsometry data are consistent with a two-layer oxide, and this may indicate that both metal and oxygen ion motion is involved in the growth process.

Plasma anodization differs from ordinary anodization in that the electrolyte solution is replaced by an oxygen plasma. As a method of producing dielectric films, it is of particular interest in the fabrication of electronic devices since it is compatible with other vacuum processing steps. In wet anodization the high field ionic conduction in the oxide is believed to be the principal growth mechanism, and little is known to indicate that the electrolyte acts as more than a conducting medium and source of oxygen and contaminant species for the construction of the oxide film. Most authors have assumed that plasma anodization is analogous (1). One exception is Ligenza (2) who has considered, in the case of silicon, a growth mechanism in which implantation in the oxide of energetic ion species from the plasma sets up a concentration gradient leading to diffusion-controlled growth. The analogy may fail for other reasons also. For example, with tantalum and some other metals it is known that in plasma anodization the ion current density is normally a small fraction of the total current density in the oxide, in contrast to ordinary anodization. Under ultraviolet irradiation, however, the ion current in the ordinary wet system may also become a small fraction of the total current due to electronic photoconductivity. In this case the oxide tends to have anomalous properties with regard to homogeneity and refractive index, and the oxide grows faster at a given field strength, *i.e.*, the ionic current at the given field strength is enhanced (3). This might suggest that the photoelectronic current stimulates the ionic current A specific mechanism for electronic current-induced growth was suggested by Fritzsche (4) in connection with yet another case where the ion current is a small fraction of the total current, namely the ordinary anodic growth of oxide films on silicon.[2] Fritzsche's model is that the electronic current involves hot electrons which generate electron-hole pairs by impact ionization. The formation of positive holes, which anodic dissolution experiments on silicon show to have some of the physical attributes of broken bonds, implies the loosening of atoms in the SiO_2 glass which then become mobile. In plasma anodization the large electronic current may be due merely to the presence in the gas of many electrons which are energetic enough to be able to enter the oxide. However, the plasma is itself a source of u.v. radiation so that any effects due directly to u.v. absorption (as opposed to the consequences of electronic photoconduction) may appear in this case also.

Another possible effect of the electron current might be the formation of a net space charge, which would modify the field in the oxide and thus alter the ion current at a fixed mean field. Negative or positive space charge is possible, *e.g.*, electron bombardment of SiO_2 produces positive space charge due to trapped holes (5). Positive space charge would increase the field at the outside of the oxide at the expense of the field near the metal, with obvious consequences according to the kinetics of the process at these interfaces. Finally, if the plasma and wet processes are indeed analogous, then the drastic difference in the conditions at the outer interface must have some observable consequences which may be of help in discovering what part this interface plays. Possibly some limiting growth rate might be expected corresponding to the diffusion limited supply of some participating species in the plasma. There is in fact some evidence that faster growth rates and higher current efficiencies may be obtained in denser plasmas (2, 6) and plasmas of different composition (7), respectively. There is, however, the alternate possibility that the rate of entry into the oxide of electrons from the plasma limits the field which may be set up in the oxide and hence limits the rate of growth, *i.e.*, the different rates in different plasmas may be a function of the relative electron and ion densities.

The aim of the work to be described below was to see whether the ion current density J in the oxide could in fact be identified as a function of the field strength E in the oxide and its temperature T, and in addition, to seek effects on the rates of growth due to a variation of the concentration of plasma species. The growth of the oxide was followed by *in situ* ellipsometry. This indicated that the films were two-layered. J was determined from the rate of growth and E calculated from the thickness and from estimates of the potential difference across the oxide obtained from probe measurements. The calculation involves some difficult points regarding interface p.d.'s and the relation to the free energy of formation of the oxide. These have been discussed elsewhere (8).

Experimental Procedures

The apparatus is shown in Fig. 1. A d-c glow discharge was struck between aluminum disk electrodes of 99.999% specified purity. The cathode (K) was of the "inverse-brush" type, *i.e.*, it had many small holes drilled into the front surface. Musal (9) showed that this gives larger currents and increased plasma stability. The specimen position was fixed by the need for alignment with the windows (O): the light beam of

* Electrochemical Society Active Member.
[1] Present address: Physics Department, National University of Taiwan, Taipei, Taiwan.
Key words: gaseous oxidation, thin dielectric films, Tafel plots.
[2] Silicon differs from tantalum in that the fields for observable ion currents are larger ($1\text{-}2 \times 10^7$ V cm^{-1}) but Fritzche's statement that log J is not dependent on E at low or medium J does not agree with the ellipsometric evidence on wet anodization of Si [ref. (11)].

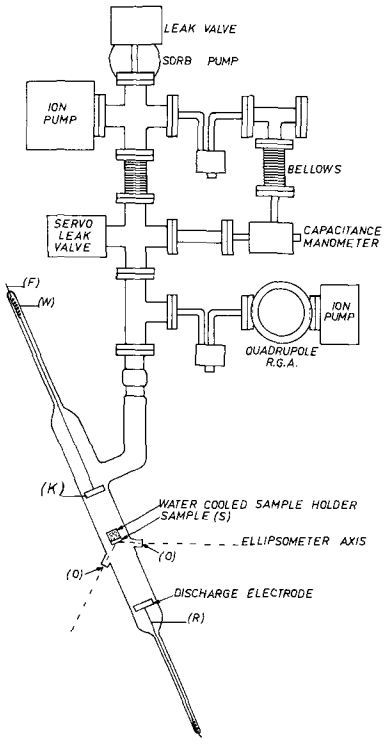

Fig. 1. Schematic diagram of the discharge cell and pumping station.

the ellipsometer should enter and leave the windows at as close as possible to normal incidence in order to minimize polarization errors. The glow discharge could be moved relative to the specimen by adjusting the position of the electrodes with external magnets acting on pieces of iron (not shown) sealed in glass and positioned between the Al rods (R) and coiled Ta wire (W). Connection to a d-c regulated power supply and series resistor was made via the tungsten feedthroughs (F). The discharge cell was a borosilicate glass tube 5 cm in diameter and 30 cm long with tails to allow the motion of the electrodes. It was connected via a metal bellows to a stainless steel pumping system built from standard components with copper gaskets. The whole system was bakeable in a demountable furnace with the sorption pump external. After bakeout at only 110°C the ion pump gave pressures of 10^{-9} Torr as indicated by the ion gauge: organic contamination was shown by the quadrupole residual gas analyzer to be negligible. Matheson 99.999% oxygen was admitted through a leak valve, and the system was normally operated with the sorption pump on.[3] The leak valve could be servo-controlled using a Granville Phillips capacitance manometer and pressure controller. Manual control was also used and, rather than maintain a constant indicated pressure, it was found desirable to control gas inflow to keep constant the potential, with respect to the anode, of a floating probe close to the sample. This procedure was used for the Nb sample and pressure variations of about ±5% around the mean value (60m Torr) were needed.

The specimens were single crystal or polycrystalline sheets about 1 x 1 cm with a tab. These were electropolished in a Teflon cell with circulated solution. Typically current densities of about 150 mA cm^{-2} were used for several minutes with periodic inspection of the surface. The electrolyte was 9 parts by volume of 98 w/o (weight per cent) H_2SO_4 and 10 parts 48 w/o HF for tantalum and 4 parts of 98 w/o H_2SO_4, 2 parts 48 w/o HF, and 5 parts 85 w/o lactic acid for niobium (10). Both were used warm. Single crystal material was preferred because it is easier to obtain a good electropolish, there being no development of ridges or grooves at grain boundaries or of steps due to unequal dissolution rates on different faces.

The samples were fixed to the hollow stainless steel support using a minimum of Ultek high vacuum epoxy with a thin mica sheet for electrical insulation. Water from a thermostatted bath was circulated through the substrate holder and the temperature of the assembly was monitored with a glass-enclosed thermistor embedded in that face of the substrate holder to which the specimen was fixed. The sample holder was supported by a stainless steel crosspiece which was connected to a side-arm of the cell through a metal flange and bellows. During specimen alignment the crosspiece could be adjusted with screws with respect to a metal post which extended from the plate supporting the cell. The water feedthrough tubes were sufficiently flexible to allow the specimen to be rotated for alignment using a bellows-type rotary feedthrough plus bevel gears.

Electrical connections to the thermistor, probes, and specimen entered though an octal header flange on the crosspiece. The probes were tungsten wire with glass sheathing except at the melted spherical tip. Connection to the specimen was via a spot-welded anodized tantalum wire sheathed in small diameter glass tubing.

The ellipsometer was the same as described previously (11), and an angle of incidence of 65° was used. Even with an extra interference-type filter before the photomultiplier the light from the plasma at the wavelength used (5461Å) made balance difficult with the plasma present. A lock-in amplifier as opposed to a tuned amplifier has in later work been used to overcome this.

Normally a constant total current derived from an electronic constant current supply was applied to the specimen and returned via the discharge anode which was grounded. It was found best not to exceed 20% of the total discharge current of 10 mA if unacceptable nonuniformity of oxide thickness was to be avoided.

The potential of the specimen relative to a nearby probe (at zero current, *i.e.*, floating or wall potential) was recorded continuously during growth on a strip-chart recorder using a Keithley-type 602 electrometer with back-off voltage supply as shown in Fig. 2. The potential difference between either the above probe, or one about 1 cm nearer the anode, and the discharge anode was also recorded in similar fashion.

The results to be reported refer to specimens in the negative glow region of the discharge. It was found necessary to have the specimen face away from the cathode to avoid pick-up of aluminum sputtered from the cathode.

Results and Discussion

Ellipsometric evidence for two-layered films.—In wet anodization, see, *e.g.* ref, (1), tracer studies in-

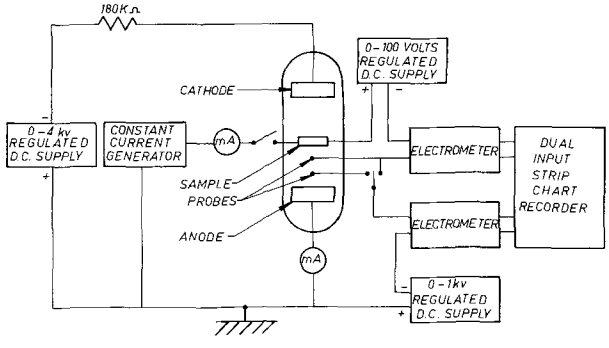

Fig. 2. Schematic diagram of the electrical circuits

[3] In later work (since this paper was submitted) fresh oxygen was flowed through the discharge tube (rather than merely added elsewhere to maintain pressure): there is evidence that this gives increased J at given E.

dicate that metal and oxygen ions move to comparable extents. The film consists of an outer part corresponding to metal ion motion and an inner part due to oxygen motion. With films formed in H_3PO_4, the outer part has a lower refractive index, permittivity, and ionic conductivity. If only slight electrolyte incorporation occurs (*e.g.*, in the case of dilute H_2SO_4 or citric acid), the films are optically homogeneous and nonabsorbing with the possible exception of a very thin outer layer.

The ellipsometric measurements (as illustrated by those in Fig. 3 and 4) on the present films were inconsistent with a homogeneous film with refractive index independent of thickness, but were well accounted for by a two-layer film (12). The inner part had a refractive index close to that of films formed on Ta and Nb in dilute sulfuric acid (11). The outer part in each case had a lower index. This is what might be expected if plasma anodization is analogous in mechanism to ordinary anodization, *i.e.*, if both metal and oxygen ions are mobile. The growth process at the metal/oxide interface would then be the same, and the ellipsometric data were fitted on this basis with, *e.g.*, in Fig. 4, a root mean square error of 0.4° in Δ and 0.12° in Ψ. The different refractive index of the outer film suggests that the reaction at the plasma/oxide interface is affected by the plasma, *e.g.*, bombardment by high energy particles or even u.v. irradiation could lead to a more porous film developing from this interface.

After removal from the cell, the oxide thickness of some samples was mapped out over the surface using ellipsometry. Typically it was 10% greater at the top, presumably due to the nonuniformity of the plasma caused by the substrate holder.[4]

Current efficiency and the growth rate.—Current efficiencies were consistently low, *i.e.*, the amount of oxide produced at 30°C normally corresponded on Faraday's law to about 0.5% of the charge passed, although slightly higher efficiencies (1%) were recorded with Ta substrates at 77°C. Growth rates at the temperatures and current densities used did not usually exceed 3 Å/min.

An obvious factor distinguishing plasma from solution anodization is the absence of water in the former technique and, as it appears that the presence of water can have a catalytic effect in some oxidation processes (13), the plasma anodization of a niobium sample was carried out in a discharge struck in a mixture of O_2 and H_2O. Results are given in Table I, from which it can be seen that the growth rate actually decreases on the addition of water vapor to the system at the same total pressure. A similar result for the anodization of Si in a h.f. discharge has been reported (14), but no explanations were given. However from residual gas analysis results in the present experiment it appears that on striking the discharge the water vapor dissociates into OH, H, and O. The process of dissociative electron attachment in H_2O has a relatively large capture cross section (5×10^{-18} cm^2 as compared with 1.3×10^{-18} cm^2 for attachment in O_2) (15), and H^- ions are probably produced rather than OH^- ions, *i.e.*

$$e^- + H_2O \rightarrow (H_2O^-) \rightarrow H^- + OH$$

Further dissociation of OH according to

$$e^- + OH \rightarrow O + H^-$$

probably occurs and would hence account for the residual gas analysis data. It appears then that, on the addition of water vapor, although a measure of growth control is achieved, some of the electrons usually available for producing the pertinent species for the anodization process are used up in the formation of H^-. In this case, then, the growth rate is reduced, but this does not preclude the possibility of other gas mixtures being effective in increasing growth rates.

[4] More uniform films were obtained in a RF plasma system in which the substrate holder was coaxial with the discharge tube.

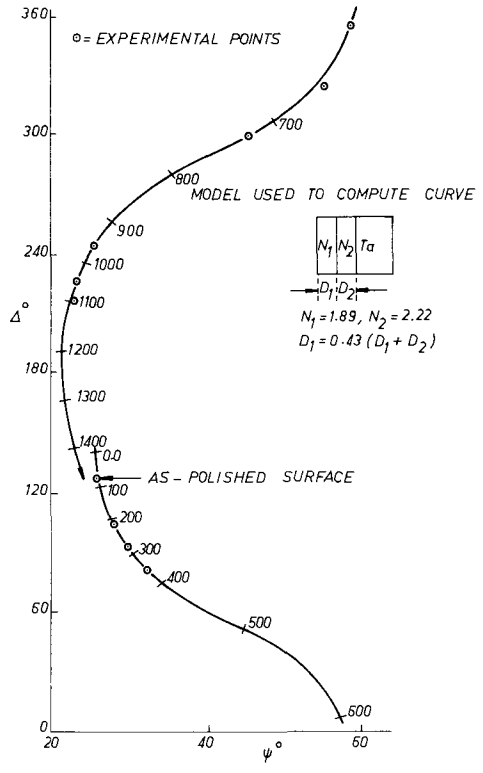

Fig. 3. Ellipsometry results for the plasma anodization of Ta. Experimental conditions: oxygen pressure 80 mTorr, sample temperature 30°C. Values marked on curve are computed total film thicknesses in angstroms.

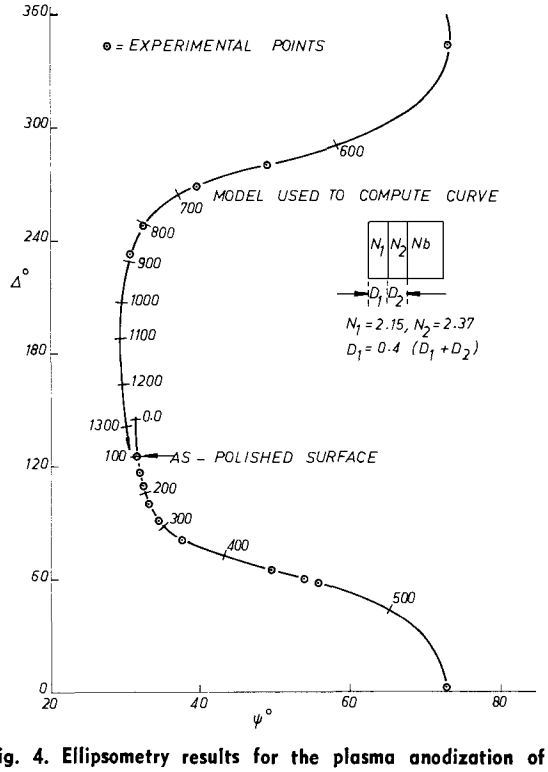

Fig. 4. Ellipsometry results for the plasma anodization of Nb. Experimental conditions: oxygen pressure 60 mTorr; sample temperature 30°C. Values marked on curve are computed total film thicknesses in angstroms.

Table I. Current, field and gas content data for the plasma anodization of Nb in a water/oxygen plasma at 30°C

Formation order	Total sample current, mA	Percentage partial pressure of water vapor, %	Mean growth rate, Å min^{-1}	Estimated field Integral 10^6 V cm^{-1}	Estimated field Differential, 10^6 V cm^{-1}	Ionic current density, 10^{-6} A cm^{-2}	Current efficiency, %
1	0.5	—	0.93	4.0	4.2	2.7	0.53
2	1.0	—	3.6	4.5	4.3	10	1.0
3	1.0	2.2	2.7	4.4	4.4	7.7	0.77
4	1.0	~100	1.7	4.6	4.6	4.9	0.49
5	1.0	~70	(1.4)	4.6	(5.9)	(4.0)	(0.40)*
6	1.0	<70	1.4	4.7	4.7	4.0	0.40

* The sample temperature was greater than 30°C for the first half of formation 5.

Permittivity.—Bridge measurements on plasma-anodized samples after evaporation of gold counter-electrodes gave distinctly lower values of the relative permittivity, *e.g.*, 17 and 34 for Ta and Nb, as compared to 27.6 and 41, respectively, (3) for films anodized in 0.2*N* H_2SO_4 at about 25°C and 10 mA cm^{-2}. It is probable that the permittivity varies with formation conditions, as it does in wet anodization.

The losses of the best specimens were not significantly different from those existing in conventional films, but films with higher losses were met more frequently than is the case for wet-anodized specimens.

Variation of voltage with time at constant total current.—Figure 5 shows a plot of the potential V_{sp} of a niobium specimen relative to a probe during anodization at constant current. The plot is fairly typical of both tantalum and niobium specimens in that the potential rises rapidly when the current is first applied and then settles to a slower, more or less constant rate of rise. The explanation of the fast initial rise is probably as follows. Since the current is mostly electronic the effect is clearly an increase of resistance to electronic current. Electron injection from the plasma appears to occur at comparatively low fields. With little or no space charge in the oxide, the field throughout the oxide is also low. However, electronic space charge develops due to capture of electrons by the heavy concentration of traps present in the amorphous oxide. This would cause the field at the plasma interface to be reduced so that a higher mean field would be required to maintain the given electronic current. Finally, a steady state would be reached in which the slow rise of voltage would be due more or less entirely to the slow rate of growth of the oxide. An alternative explanation is possible in terms of patching of leaky spots in the oxide, but this seems unlikely in view of the fact that the same behavior was exhibited by films prepared by wet anodization and then tested in the plasma.

The type of behavior in Fig. 5 has several implications. First, the ionic current density should be calculated on the basis of total thickness increase during the formation period divided by the total time less the time for the initial transient. This ionic current is then an estimate during the final steady-state period of the formation. Second, the differential field and the integral field may be estimated during this period. Finally, it is evident that, if the space charge explanation is correct, the field distribution in the oxide is modified by space charge so that the situation is expected to differ from wet anodization.

Voltage vs. thickness for steady-state conditions.—Figure 6 (which is for niobium) shows voltages with respect to a nearby probe recorded at the end of each of a series of formations at the same total current, plotted against the corresponding thickness of oxide. The corresponding ionic current density, as deduced from the change of thickness during the anodization period, is recorded beside each point. Clearly the linear dependence of voltage on thickness indicates a constant mean field strength in the film. This constant field gave a more or less constant ionic current. This is analogous with wet anodization, but does not mean necessarily that the field was constant through the thickness of the film. The intercept H_I at zero thickness gives information on the net work function corrections but with an unknown error due to any changes in the drop in plasma potential between the probe surface and the oxide surface.

Relation between log J, E, and T.—Figure 7 is for niobium and shows values of log *J* for various estimated fields. We included here all "integral" fields for one final specimen, in which it was believed that the control of pressure had been very precise, plus data at low anodizing currents for films greater than 450Å thick from two earlier specimens. (With thicker films the zero error in voltage has less effect on the estimate of field.) Differential fields ($\Delta V/\Delta D$) have been omitted since they were prone to scatter, as is

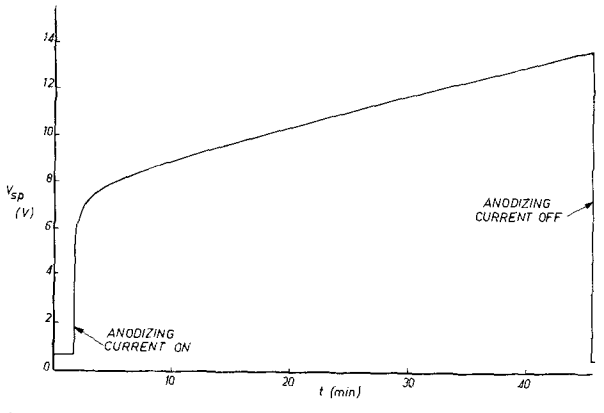

Fig. 5. Typical variation of the potential of a Nb sample (with respect to a floating probe) during plasma anodization at constant current.

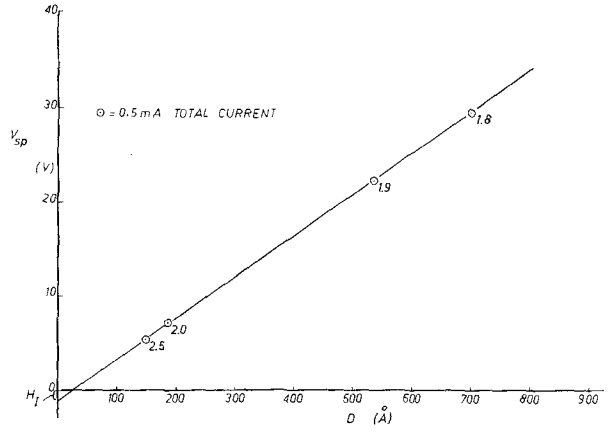

Fig. 6. Variation of the potential of a Nb sample (with respect to a floating probe) with oxide thickness for a series of formations at 0.5 mA total current.

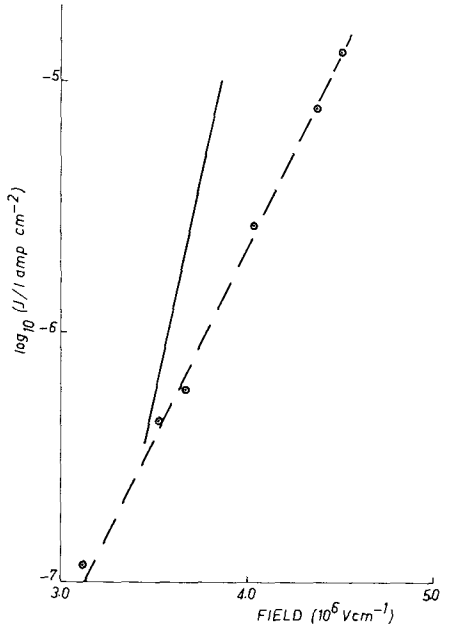

Fig. 7. Variation of ionic current with field in the oxide for the anodization of Nb. ⊙, plasma anodization—oxygen pressure 60 mTorr, sample temperature 30°C; continuous line, solution anodization, Young and Zobel (11), sample temperature 25°C.

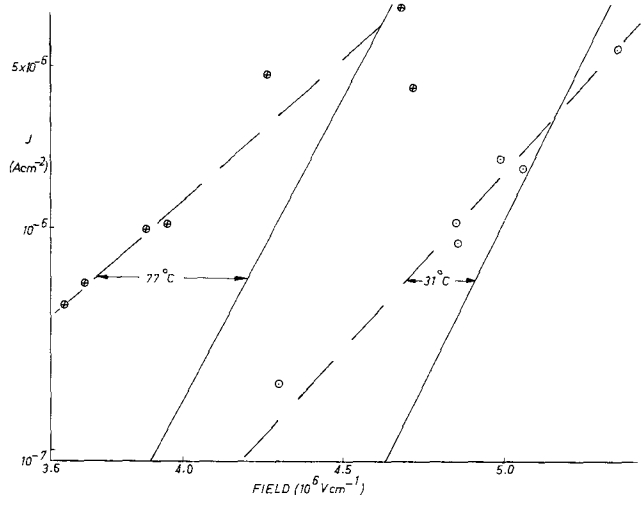

Fig. 8. Variation of ionic current with field in the oxide for the anodization of Ta. ◯ ⊕, plasma anodization—oxygen pressure 80 mTorr, sample temperature as indicated; continuous line, Young and Zobel (11).

to be expected from the discussion above. Also included is a line referring to the anodization of Nb in 0.2N H_2SO_4 (11). Figure 8 shows log J *vs.* E at two temperatures for Ta, plus equivalent data for growth in 0.2N H_2SO_4 (11).

The data in Fig. 7 and 8 appear to show that ionic current is indeed determined by the field in the oxide. The same type of change from wet anodization is shown for both Ta and Nb, *i.e.*, for plasma anodization the value of $d \log J/dE$ is less and $J_0 \exp -W/kT$ in $J = J_0 \exp(-W/kT) \exp(+\beta E)$ is greater than for the wet case.

These two changes are what might have been predicted from the lower refractive index and permittivity of the plasma oxide, or at least of the outer layer. The lower refractive index probably indicates a less dense film so that the zero field activation energy W should be less, thus giving the higher intercept on the log J axis at zero field. Also, as has been noted in conventional anodization for some time, there appears to be a correlation between permittivity and ionic conductivity. The most acceptable model is that ionic conduction is controlled by an effective field, *e.g.*, the Lorentz field $1/3\ (\epsilon_r + 2)E$. This would predict the change of slope. However, the latter could also be explained by the previously mentioned effect of a negative space charge in reducing the oxide field near the oxide/plasma interface below the mean (estimated) field.

It is perhaps worth noting by way of caution that, if the ionic current was in fact controlled by the electronic current, which was itself controlled by the field, then once again log J would show some dependence on E. This possibility could perhaps be evaluated by varying the plasma conditions so that different electronic currents were obtained at the same field.

Acknowledgments

Grateful acknowledgment for financial support is given to the Defence Research Board of Canada (ECRDC project C91) and the United States Air Force, Avionics Laboratory, Wright-Patterson Air Force Base (contracts F33615-68-C-1704 and F33615-70-C-1225). The authors are also grateful for the assistance received from Dr. C. J. Dell'Oca in developing the computer programs for the two layer model.

Manuscript submitted Feb. 16, 1970; revised manuscript received May 25, 1970. This was Paper 22 presented at the New York Meeting, May 4-9, 1969. The work on niobium is based on a M.A.Sc. thesis by one of the authors (G.O.).

Any discussion of this paper will appear in a Discussion Section to be published in the June 1971 JOURNAL.

REFERENCES

1. C. J. Dell'Oca, D. L. Pulfrey, and L. Young, Review in "Physics of Thin Films," in press.
2. J. R. Ligenza, *J. Appl. Phys.*, **36**, 2703 (1965).
3. L. Young, "Anodic Oxide Films," Academic Press, New York (1961).
4. C. R. Fritzsche, *Solid State Comm.* **6**, 341 (1968); *J. Phys. Chem. Sol.*, **30**, 1885 (1969).
5. M. Simons, L. K. Monteith, and J. R. Hauser, 1968, NASA CR-1088 (available from Clearinghouse for Federal Scientific and Technical Information, Springfield, Virginia); K. H. Zaininger and A. G. Holmes-Siedle, *RCA Rev.*, XXVIII, 209 (1967); J. P. Mitchell, *IEEE Trans. Electron Dev.*, **ED14**, 764 (1967).
6. J. Kraitchman, *J. Appl. Phys.*, **38**, 4323 (1967).
7. T. A. Jennings, W. McNeill, and R. E. Salomon, *This Journal*, **114**, 1134 (1967).
8. G. Olive, D. L. Pulfrey, and L. Young, *ibid.*, **117**, 945 (1970).
9. H. M. Musal, *J. Appl. Phys.*, **37**, 1935 (1966).
10. J. Pelleg, *J. Less Common Metals*, **12**, 421 (1967).
11. L. Young and F. G. R. Zobel, *This Journal*, **113**, 278 (1966).
12. C. J. Dell'Oca and L. Young, *Surf. Sci.*, **16**, 331 (1969).
13. E. Kooi, "The Surface Properties of Oxidized Silicon," p. 35, Springer-Verlag, New York (1966).
14. E. R. Skelt and G. M. Howells, *Surf. Sci.*, **7**, 490 (1967).
15. R. I. Reed, "Ion Production by Electron Impact," p. 87, Academic Press, New York (1962).

Sealing Effects near the Barrier-Porous Layer Interface of Anodic Aluminas

G. A. Dorsey, Jr.

Kaiser Aluminum and Chemical Corporation, Center for Technology, Pleasanton, California 94566

ABSTRACT

Effluent gas detection, infrared analysis, impedance measurements, and gross weight changes were used to study the effects of boiling water exposures on anodic oxide films: the "sealing" reaction. Certain changes in film structure and composition were found to be significant with regards to the effectiveness of the sealing treatment. Particularly important were transitions leading to an effect localized at the interfacial region between the barrier and porous layers. In retrospect, hydration and structural changes at the outer surface of the porous layer (generally regarded as the only effect of sealing) may contribute little to at least the initial impedance increase, on sealing. Alloy 1199 foil was anodized in 0.3M sulfuric acid at 1.08 A/dm^2 (10 A/ft^2) and 30°C. Anodizing times varied from 1 to 18 min, and a detailed study was made of coatings prepared in the 3.0-to-4.6μ thickness range. Unsealed, as well as sealed, foils were examined.

The term "sealing" probably originated with the observation that dyes were permanently retained within an anodic coating if, following the dye operation, the anodized workpiece was subjected to a brief immersion in boiling water. Then too, it was found that the same immersion treatment rendered the anodic coating more durable than unsealed films and subsequently more protective to the substrate metal. Sealing was first considered to be a pore-closure mechanism that was limited to the outer surface of the film and caused by oxide swelling due to the formation of the monohydrate boehmite. And while this basic view can still be substantiated, later work has shown the sealing process to be relatively complex. The electron microprobe work of Wood *et al.* (1) shows that at least some bulk effects, in addition to surface hydration, are involved, while Spooner (2) found hydration and structural changes taking place for at least the first 50 hr of sealing. More recently (3) an anion exchange mechanism (hydroxide replacing incorporated sulfate, within the oxide structure) was proposed, while the streaming potential measurements of Yokota (4) and others (5) seem to indicate that trihydrates, rather than monohydrates, are formed on sealing. Further background may be found in a detailed review by Diggle, Downie, and Goulding (6).

Earlier (7) we found that sealing appeared to produce a decrease in the amount of barrier layer oxide, in keeping with the earlier observation of Hunter and Fowle (8). At the same time, however, the amount of porous layer cross-linking was found to increase. This led to the speculation that at least one important effect of sealing involved a structural transition at the interface between the barrier and porous layers. The barrier layer was proposed to consist of two layers [confirmed by electronoptical data (9), also by the recent work of Vol'fson and Pilyankevich (10)], and it was the more permeable open-structured secondary phase barrier layer that appeared involved in this transition. Schematically, this might be represented as shown in Fig. 1.

Conventionally, the effects of sealing are measured by observations regarding the changed nature of the porous layer surface, for example, by dye rejection tests (11, 12). Certainly, the outer surface of the porous layer is changed, structurally hydrated, by the sealing process. However, it may be that an equally important change is that which takes place at the barrier layer-porous layer interface.

Key words: anodic aluminas, sealing.

Experimental

Sample preparation. —Cleaned alloy 1199 aluminum foils (99.99% Al) were chemically brightened, then anodized in 0.3M H_2SO_4 at 30°C and 1.08 A/dm^2 (10 A/ft^2) with an anode-cathode potential of 20V. These conditions were employed to slow down structural transitions that normally (1.7M H_2SO_4 at 1.3 A/dm^2) take place too quickly to allow a detailed study. Anodizing times varied from 1 to 18 min. Afterward, the foil coupons were cut in half, and one-half of each was sealed in pH 6.0 boiling distilled water for either 10-, 15-, or 20-min periods. These coupons were then tested, along with the unsealed halves, after air drying but without any further delay.

Nonanodic aluminas were also prepared to illustrate a comparison between the structure of acid gel aluminas and the anodic barrier layer. These were formed by adding $AlCl_3$ to dilute HCl solutions, adjusted to various pH levels with NaOH. Each solution was centrifuged before the *IR* examination of (*a*) the clear and water-white supernatant liquid, in Irtran cells *vs.* a water blank and (*b*) the precipitate (formed above pH 4) after air drying this, then preparing a KBr pellet for use *vs.* a KBr blank.

Test methods.—The samples were examined within the 4000-600 cm^{-1} range of the Beckman *IR*-7, as before (13) using, for the anodized foils, a reflectance attachment set at 45° angle of incidence. The amount of barrier layer present was taken from the absorbance of the 900-to-1000 cm^{-1} band. The amount of porous layer was based on the absorbance of the 1325 cm^{-1} Al=O band (13); actually, this is probably an Al=O←S band associated with structurally incorporated sulfate. We did not use far infrared here since,

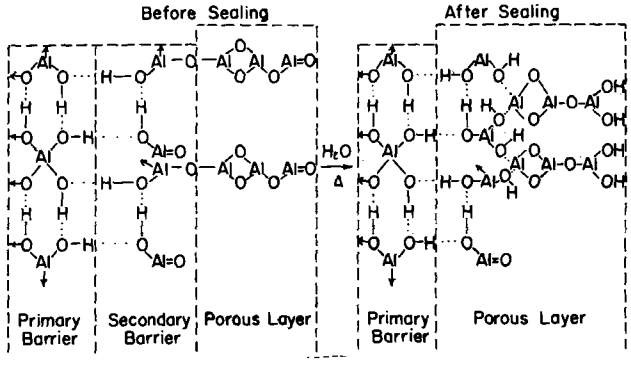

Fig. 1. Proposed sealing effect caused by barrier layer transition

for thin films, this 1325 cm^{-1} band provides as reliable a measure of porous layer quantity as does the far infrared Al-O-Al stretch. This may be seen by comparing these data with those given in ref. (7).

The effluent gas detection (EGD) data were taken in the usual manner, described earlier (14). Impedance measurements were made immediately after anodizing and air drying the same films from which sections were taken for examination by the other techniques. The data reported are average values from multiple readings obtained with a Twin City Testing Corporation Z-Scope (1 kHz impedance bridge), using a 3.5 w/o NaCl media (15).

Coating weight and weight gain on sealing measurements were made in the standard manner, using the chromic-phosphoric acid stripping technique (15) for the coating weight determinations. Film thicknesses were obtained by metallographic cross sectioning.

Results and Discussion

Earlier (17) we suggested a two-phase oxide structure for the anodic barrier layer. This was proposed to consist of a primary barrier layer phase (seemingly, a cyclic trihydrate) and a secondary phase with a lower polymer weight than the primary, apparently less dense and comprised of μ-hydroxy linkages (as opposed to the apparent hydrogen bonding of the primary phase). There was some limited precedence for this already in the literature, but a recent article (18) by Vedder and Vermilyea puts forth an excellent alternative to this earlier *IR* interpretation.

They propose that the substrate metal produces a polarization effect on a translational mode Al-O-Al lattice vibration, thereby leading to a 950 cm^{-1} absorption band that would otherwise occur at longer wavelengths. While their interpretation also contains elements of speculation, it offers many interesting possibilities. We would like to point out, however, that elemental aluminum need not be present to sustain this ~950 cm^{-1} absorption. If the earlier interpretation (17) has some basis, and apart from other data then presented, then acid gel aluminas should also have this same structural feature. Grunwald and Fong (19) recently did in fact suggest a similar structure for acid gel aluminas.

In connection with this it should again be noted that the ~950 cm^{-1} absorption band is found both in soluble aluminic acids and in the solid gels corresponding. Figure 2 shows the *IR* spectra of aqueous solutions prepared by dissolving $AlCl_3$ in dilute HCl. Figure 3 shows *IR* spectra of the gels precipitated from these solutions at higher pH values, along with representative spectra of the primary and secondary phases of the anodic barrier layer. One principal difference between these two alumina types is that the nonanodic alumina undergoes complete dehydration at or below 250°C, whereas the anodic aluminas

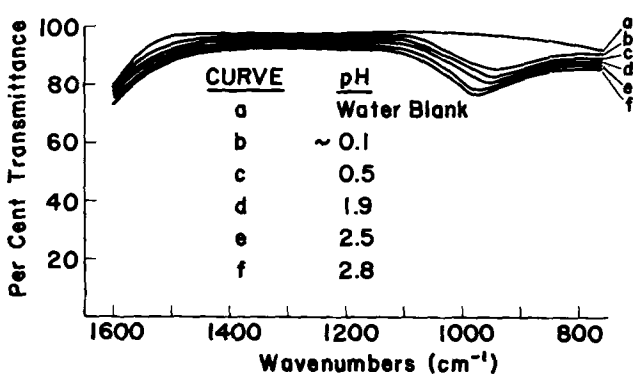

Fig. 2. Infrared spectra of aqueous solutions prepared from $AlCl_3$ and HCl: in Irtran cells *vs.* matching water blank.

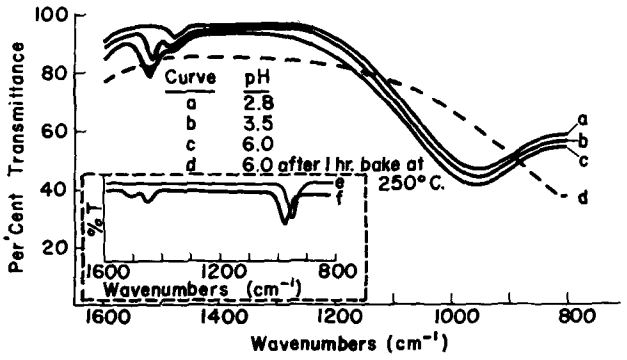

Fig. 3. Infrared spectra of hydrous and dehydrated (curve d) alumina gels precipitated from $AlCl_3$ solutions: in KBr *vs.* KBr blank. Spectra for primary phase (curve e) and secondary phase (curve f) anodic barrier layer oxides are included.

apparently require far higher temperatures (14), possibly owing to a higher degree of polymerization.

Returning to the subject now at hand. Figure 4 shows the linear relationship that was obtained between the anodic coating thicknesses and the anodizing times, in the 0.3M H_2SO_4 electrolyte at 1.08 A/dm^2 and 30°C. However, as has been noted earlier (7), the composition of the coating did not remain constant but changed as anodizing progressed. Figure 5 shows *IR* data for changes in the amounts of barrier and porous layers with respect to anodizing time. These again illustrate the transitions within the barrier layer, and from barrier layer to porous layer,

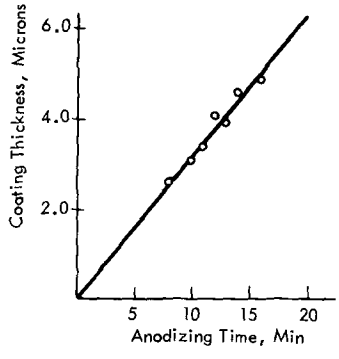

Fig. 4. Coating thicknesses for increasing anodizing time in 0.3M H_2SO_4 at 1.03 A/ft^2 and 30°C.

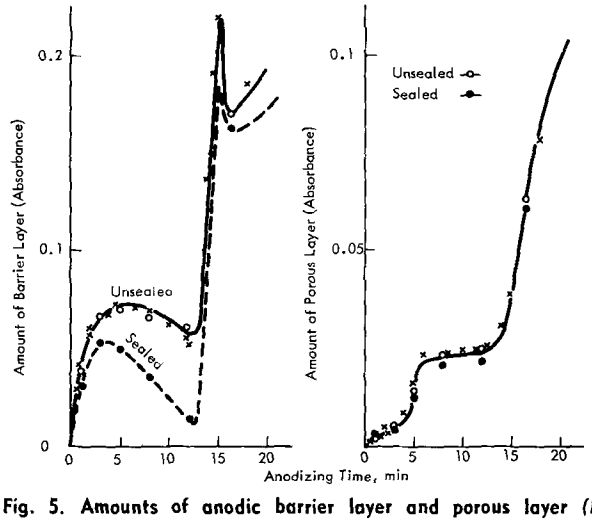

Fig. 5. Amounts of anodic barrier layer and porous layer (*IR* data) for sealed and unsealed films. Open and filled circles are data points obtained for this report. The X points were obtained earlier (14) for unsealed films also prepared by these same anodizing conditions.

that were discussed earlier (7,9,14). Most pertinent is the transition from primary to secondary barrier layer phase that begins at the end of 4 min of anodizing, under these conditions. This transition is rapid in the 10-15 min region, being complete after 15 min. Figure 6 also illustrates this transition, using the characteristic band position shift from 930 to 980 cm^{-1}. We would, therefore, expect the film prepared in this transition region (films anodized between 10 and 15 min, 3.0-4.6 μm) to be structurally unstable. There was no structurally established barrier phase here, no established equilibrium between primary and secondary barrier layer phases. The sealing effect, which alters both the amount and nature of the barrier layer, might therefore be most pronounced in this region.

As before, sealing decreased the amount of barrier layer (Fig. 5), the decreased amount of barrier layer being caused by the sealing-affected transition (an "inner seal" effect) consisting of a structural change from barrier layer to porous layer oxide. As anticipated, the magnitude of this effect was greatest for films within the ~10-15 min range, and was less elsewhere. The *IR* spectra themselves serve better to illustrate such effects in the film transition region. The differences between an unsealed and sealed film spectrum, for a 12-min film (center of transition zone) is shown in Fig. 7.

Note the nearly complete transition from secondary barrier phase (unsealed) to porous layer trihydrate (sealed). For films prepared outside this transition zone (with less than 10 min or more than 15 min of anodizing time) such a change was far less pronounced (Fig. 8).

Data from another technique, to illustrate the same structural sensitivity to sealing, are shown in Fig. 9. These are effluent gas detection (EGD data) obtained for the transition zone films, and with the ratio of partial water contents for sealed and unsealed films (water removable to 350°C, with helium purge) plotted *vs.* anodizing time. Note that this ratio

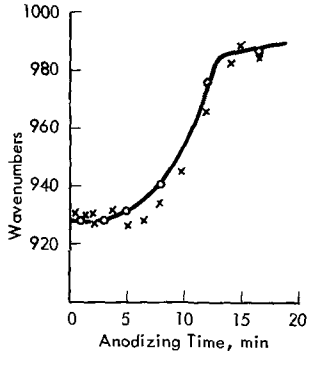

Fig. 6. Placement of barrier layer band center showing transition from primary barrier phase (930 cm^{-1}) to secondary barrier phase 980 cm^{-1}). Open circles are data points obtained for this report (there was no detectable change in wavenumber between sealed and unsealed films of the same thickness). The X points were obtained earlier (14), with these same anodizing conditions.

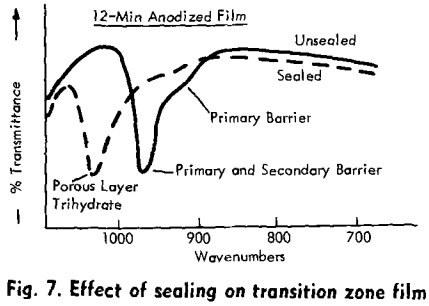

Fig. 7. Effect of sealing on transition zone film

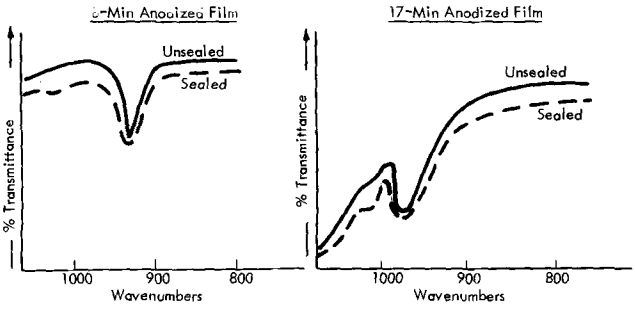

Fig. 8. Effect of sealing on films outside of transition zone

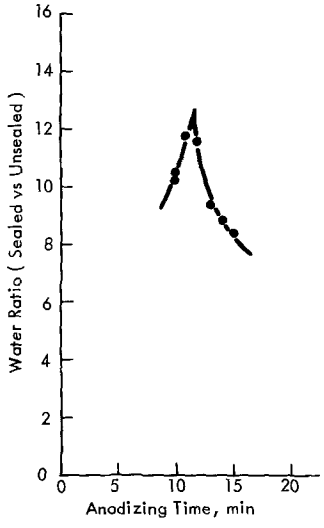

Fig. 9. Ratio of water contents between sealed and unsealed films (EGD data) when baked to 350°C.

(degree of change, on sealing) reached a peak near 12 min of anodizing time. Beyond 15 min of anodizing time, the ratio decreased. A correlation between the *IR* data and the EGD data themselves may be seen by a comparison of Fig. 10 and 5.

The porous layer Al=O←S bond data do not reflect any such change as a result of sealing however, since the increase in porous layer cross-linking [as a result of sealing (7)] did not materially alter the Al=O←S band absorbance. We would expect,

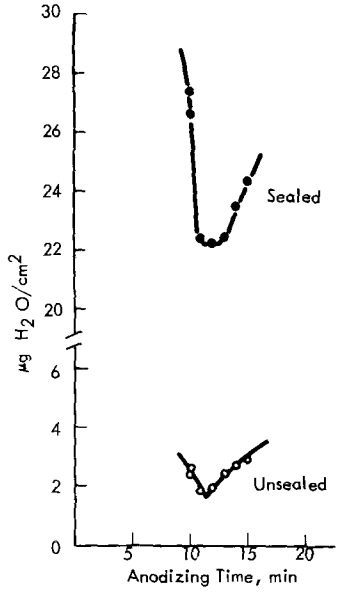

Fig. 10. Micrograms per square centimeter water released from sealed and unsealed films (EGD data) when baked to 350°C.

however, to find a large amount of physically sorbed water in the porous layer after sealing, due to surface hydration and to effects other than those occurring near the interface between barrier and porous layers.

The weight gain on sealing data (Fig. 11) shows such an increase. Note, first, that the total quantity of water in the sealed film was far more than that indicated by the EGD technique. Earlier (14), it was suggested that at least some of the water removed by the EGD technique (below 350°C) corresponded to barrier layer hydroxide. The comparison between total weight gain, on sealing, and the EGD-measured hydrate would seem to lend some further support toward this speculation. That portion of the porous layer hydrate which is not related to the barrier layer, or to its transition product, must then be removable only by baking above 350°C, under the conditions of the EGD technique (10°C/min heating rate, with helium purge).

Figure 11 also shows that the total weight gain on sealing, plotted *vs.* anodizing time, does not extrapolate back to 0 min. Instead, an extrapolated 0 weight gain falls on the plot at approximately 7 min anodizing time. However, but perhaps only by coincidence, this correlates nicely with the *IR* data for the porous layer. Note (Fig. 5) that the porous layer only begins to form, in any appreciable quantity, after 4 min of anodizing time, and its growth rate reaches an equilibrium (plateau) after 6-7 min. If the porous layer is responsible for the bulk of the water taken up during sealing, and if only a trivial amount of porous layer was formed before the 6-7 min anodizing time, we would not expect to find a gross weight gain, on sealing, that was linear with respect to film thickness (or to anodizing time).

Thus, these *IR*, EGD, and gross weight change data have demonstrated the apparent transition zone that exists during anodizing, and within which zone the anodic oxide structure is highly vulnerable to changes caused by sealing. On either side of this zone, sealing effects appear lessened. Some physical significance to this can be given, now, by an examination of impedance data.

The 1 kHz impedance values (kilohm/cm²) are usually at least two to fivefold higher with sealed films than with unsealed films. Explanations of this are usually given in terms of changes relating to film porosity (a physical plugging of the outer pore surface, a leaching of electrolyte from the pore volume, etc.) which may be hard to reconcile with the over-all linear increase of impedance with increasing sealed-film thickness. When equal sealing conditions are employed, any surface effects should be approximately equal in magnitude and relatively independent of minor changes in film thickness. Current reasoning now seems to fall along the lines of Wood *et al.* (20, 21): that sealing effects are not limited to pore blockage at the coating surface, but are also due to structural rearrangement and agglomeration processes that take place within the bulk of the coating as well.

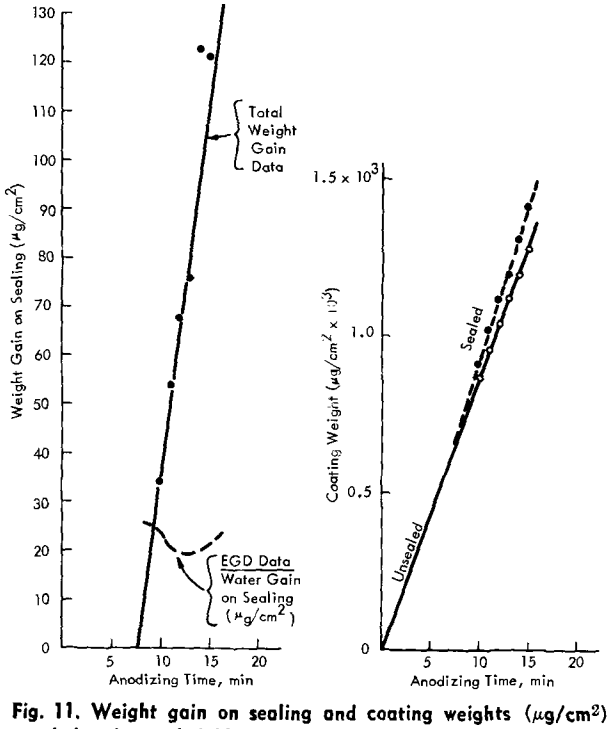

Fig. 11. Weight gain on sealing and coating weights (μg/cm²) for sealed and unsealed films.

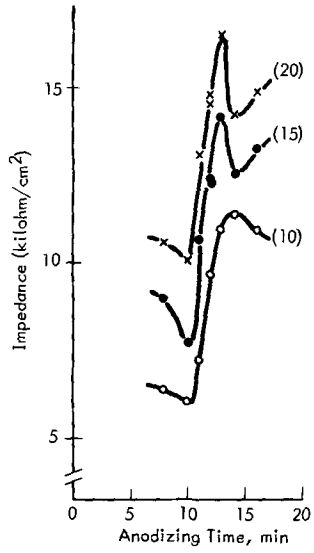

Fig. 12. Coating impedance data for sealed films, plotted as a function of anodizing time. Curves are for 10, 15, and 20 min sealing times, respectively.

Figure 12 shows impedance data for these same anodic coatings, and again in the transition region of from 10 to 15 min anodizing time. Note the peak at 12 min where the preceding data have shown the inner seal effect to be at its maximum. If the only factors altering impedance values were a combination of surface effects and a linear increase in bulk film thickness, then a more nearly linear relationship should have been obtained. This would be especially so if the effective barrier layer thickness were constant, with only bulk and surface porous layer effects to influence impedance values. This is not meant to imply that only inner seal effects are important in the mechanism of sealing, but that they are a potentially equal contributor to whatever effects sealing may produce.

Acknowledgment

The author wishes to thank the Kaiser Aluminum and Chemical Corporation for its support of this work and for its permission to publish these results.

Manuscript submitted March 11, 1970; revised manuscript received *ca.* June 2, 1970.

Any discussion of this paper will appear in a Discussion Section to be published in the June 1971 JOURNAL.

REFERENCES

1. G. C. Wood, V. J. J. Marron, and B. W. Lambert, *Nature*, **199**, 239 (1963).
2. R. C. Spooner and W. J. Forsyth, *ibid.*, **200**, 1002 (1963).
3. J. F. Murphy, *Plating*, **54**, 1241 (1967).
4. H. Yokota, *Denki-Kagaku*, **35**, 14 (1967).
5. K. Kuroda and K. Uja, *Kinzoku Hyomen Gijutsu*, **18**, 169 (1967).

6. J. W. Diggle, T. C. Downie, and C. W. Goulding, *Chem. Rev.*, **69**, 365 (1969).
7. G. A. Dorsey, Jr., *This Journal*, **115**, 1053 (1968).
8. M. S. Hunter and P. Fowle, *ibid.*, **101**, 481 (1954).
9. G. A. Dorsey, Jr., *ibid.*, **116**, 466 (1969).
10. A. I. Vol'fson and A. N. Pilyankevich, *Zashchita Metallov*, **4**, 670 (1968).
11. J. Elze, *Aluminium*, **38**, 161 (1962).
12. B. A. Scott, *Electroplating Metal Finishing*, **18**, 47 (1965).
13. G. A. Dorsey, Jr., *This Journal*, **113**, 169 (1966).
14. G. A. Dorsey, Jr., *ibid.*, **115**, 1057 (1968).
15. ASTM Test Method B457-67.
16. ASTM Test Method B137.
17. G. A. Dorsey, Jr., *This Journal*, **113**, 284 (1966).
18. W. Vedder and D. A. Vermilyea, *Trans. Faraday Soc.*, **65**, 561 (1969).
19. E. Grunwald and D. W. Fong, *J. Phys. Chem.*, **73** 650 (1969).
20. J. P. O'Sullivan, J. A. Hockey, and G. C. Wood, *Trans. Faraday Soc.*, **65**, 535 (1969).
21. G. C. Wood and J. P. O'Sullivan, *This Journal*, **116**, 1351 (1969).

Structural Features of Anodic Aluminas Adjusted to Influence the "Degree-of-Seal"

G. A. Dorsey, Jr.

Kaiser Aluminum & Chemical Corporation, Center for Technology, Pleasanton, California 94566

ABSTRACT

Different two-step current density programs were used to prepare 7.4 μm anodic oxides in an attempt to determine a set of anodizing conditions best suited to properly sensitize the oxide structure for maximum sealing effect. Effluent gas detection, infrared analysis, and impedance measurements were used to study these films. The desired structure was achieved, in a 1.7M H_2SO_4 electrolyte, by anodizing to a 4.84 x 10^2 coulomb/dm^2 current quantity using a current density of 1.3 A/dm^2, then rapidly increasing the current density to 3.5 A/dm^2 for a total current quantity of 13.9 x 10^2 coulomb/dm^2 (yielding 7.4 μm films). Sealed and unsealed coatings were examined.

In the preceding paper (1) a structural transition was described that takes place, as a result of sealing, near the interfacial region between the secondary phase barrier layer and the porous layer of anodic coatings on aluminum. However this sealing effect was limited to films of ~4 μm thickness, using the anodizing conditions then employed: 0.3M H_2SO_4 at 1.08 A/dm^2 and 30°C. A proposed requirement for this sealing transition, or "inner seal effect," was that the structure of the anodic barrier layer should be in a transition form that represents approximately 50% conversion of primary into secondary phase oxide. With the more commonly used porous layer anodizing conditions of 1.7M H_2SO_4 at 1.3 A/dm^2 and 25°C, such a transition zone would be expected to be limited to films of only ~2 μm thickness. This is supported by data presented earlier (2) and shown again here for purposes of comparison, in Fig. 1. The apparently required structure occurred at 12 min anodizing time (~4 μm film thickness) with the 0.3M H_2SO_4 electrolyte, using 1.08 A/dm^2 and 30°C, and at 5.7 min (~2 μm film) with 1.7M H_2SO_4, using 1.3 A/dm^2 and 25°C

We now seek to bring about this same structural feature in the anodic coating, in order to maximize the inner seal effect, but with thicker, 7.4 μm films prepared in 1.7M H_2SO_4 at 25°C. A two-step current density sequence seemed to be a feasible approach, in order to first develop the necessary oxide structure, then to "freeze" this structure by using a high current density, which nevertheless allows the film to thicken to the desired value. This would amount to a reversal of the normal transitions of the anodizing process, so as to produce a 7.4 μm thick film with the same structural proportions of a threefold thinner coating.

Experimental

Sample preparation.—Alloy AS32 (alloy 1100 clad with 1100:99.2% Al) sheet coupons were cleaned and chemically brightened, then anodized in 1.7M H_2SO_4 at 25°C for a total current quantity of 13.9 x 10^2 coulombs/dm^2. One group was anodized at a current density of 1.3 A/dm^2. The remainder were anodized at 1.3 A/dm^2 for the first 4.84 x 10^2 coulomb/dm^2 (6.25 min), then the current density was immediately increased to a higher value, which was maintained for the balance of the anodizing program. In the latter case, final current density values ranged from 2.16 to 4.32 A/dm^2. One coupon from each set of anodizing conditions was left in the unsealed condition, while the other was sealed for 10 min in boiling pH 6.0 distilled water, buffered with acetic acid and sodium hydroxide. Coupons intended for impedance measurement were also sealed for 20 and 30 min, respectively. Table I lists these various anodizing conditions, together with the final voltage values and the coating thicknesses that resulted.

Test methods.—The samples were examined within the 4000 - 35 cm^{-1} ranges of the Beckman *IR*-7 and *IR*-11 spectrophotometers, according to procedures

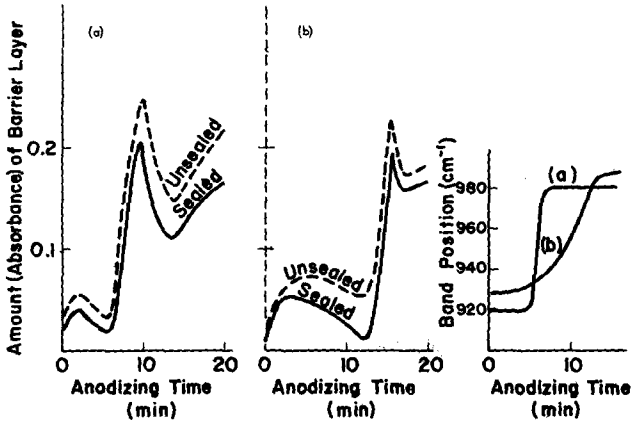

Fig. 1. Amount of barrier layer vs. anodizing time, produced in (a) 1.7M and (b) 0.3M H_2SO_4 electrolytes, also showing *IR* band position. Anodizing conditions were: (a) 1.7M H_2SO_4-1.3 A/dm^2, 25°C and (b) 0.3M H_2SO_4-1.08 A/dm^2, 30°C.

Key words: anodic aluminas, sealing.

Table I. Anodizing conditions and metallographic coating thicknesses

Initial period Current quantity, coulombs/ dm^2	Current density, A/dm^2	Final period Current quantity, coulombs/ dm^2	Current density, A/dm^2	Final voltage, V	Coating thickness, μm Unsealed	Sealed
13.9 ($\times 10^2$)	1.3	—	—	14.5	7.4	7.1
4.84	1.3	9.04 ($\times 10^2$)	2.16	15.0	7.1	6.9
4.84	1.3	9.04	2.70	15.0	7.4	7.6
4.84	1.3	9.04	3.24	19.0	7.4	7.4
4.84	1.3	9.04	3.78	20.0	7.4	7.6
4.84	1.3	9.04	4.32	20.0	7.6	7.6

already described (2). Infrared absorbance values and band positions were then determined, to measure (*a*) the amount and type of barrier layer, (*b*) the amount of porous layer cross-linking, and (*c*) the amount of structurally incorporated porous layer sulfate (1325 cm^{-1} infrared band).

Effluent gas detection (EGD) data were obtained as before (3), and impedance values were measured with a 1 kHz. impedance bridge (1). Coating thicknesses were obtained by metallographic cross sectioning. With the exception of these thickness measurements, all sample analyses were made immediately after air drying the sample, without any storage period.

Results and Discussion

As shown in Table I, all coatings were of the same thickness: 7.4 ± 0.2 μm. The data that follow should therefore show no effects that might be caused by gross differences in coating thickness.

As discussed earlier, we sought to achieve a certain steady-state coating structure, the nature of which, and modes of transition, are described in more detail elsewhere (1, 2). Briefly, we sought to find the two-step current density program that would produce an anodic coating which was highly receptive to sealing effects near the barrier-porous layer interface. There should be a current density range within which the coating is in this desired state. Current densities on either side of this range might then produce coatings of lower sealing sensitivity.

Figure 2 shows the kilohm per square centimeter impedance values that were obtained with these 7.4 μm films; plotting kilohm/cm^2 impedance values *vs.* final current density, with each film having been prepared with 1.3 A/dm^2 for at least the first portion (4.84 x 10^2 coulomb/dm^2) of the anodizing program. A nearly 80% improvement in coating impedance (film impermeability) was realized with a final current density near 3.46 A/dm^2, *vs.* 1.3 A/dm^2, with films sealed for 10 min. More prolonged sealing times decreased this factor to about 40%. Effluent gas detection (EGD) and infrared data confirm this by showing the same correlatable trends that were reported earlier (1) for nearly threefold thinner films.

Figure 3 presents the EGD partial water contents (water removable to 350°C, with helium purge), again for both sealed (10 min) and unsealed films. These data indicate, however, that the optimum second current density value lies closer to 3.24 A/dm^2. The minimum inflection in the curve at this point is an indication of inner seal effect (1). It can be seen more clearly in Fig. 4: the water ratio (μg H_2O/cm^2, sealed *vs.* unsealed) plotted against second current density values. With reasonable justification, we can make the assumption that these EGD data apply directly to the inner seal effect, and not to hydrate structures that occur elsewhere in the porous layer or at its surface (1).

The infrared data, Fig. 5 through 8, are equally definitive, but require interpretation. We seek a coating structure whose barrier layer is undergoing a transition, and where neither the primary nor the secondary phase barrier layer is the established

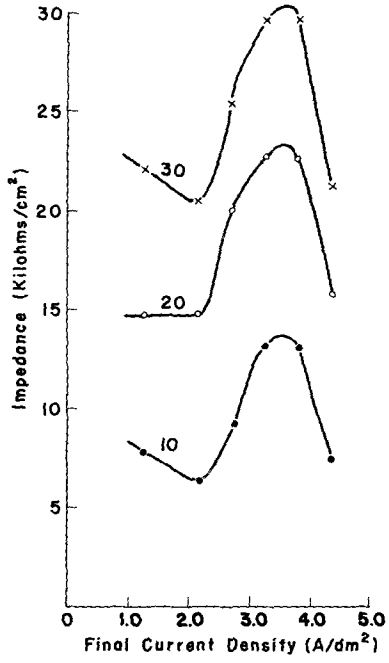

Fig. 2. Coating impedance for sealed films as a function of final current density. Curves are for 10, 20, and 30 min sealing time, respectively.

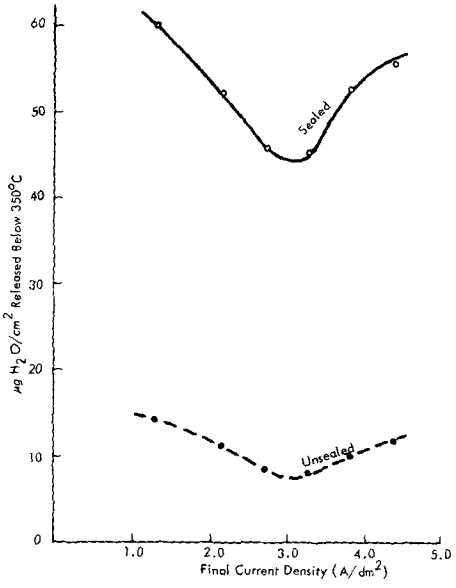

Fig. 3. Micrograms per square centimeter of water released from sealed and unsealed films (EGD data) when baked to 350°C.

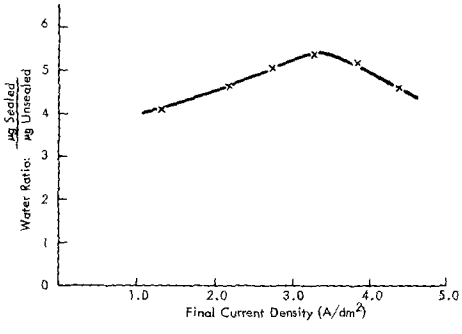

Fig. 4. Ratio of water released (EGD) from sealed *vs* unsealed films, plotted against final current density.

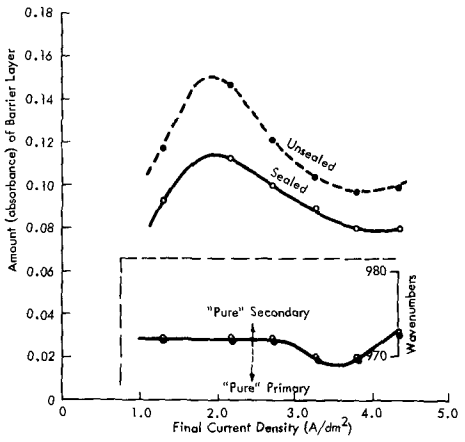

Fig. 5. Amount of barrier layer in sealed and unsealed films, also showing placement of *IR* band.

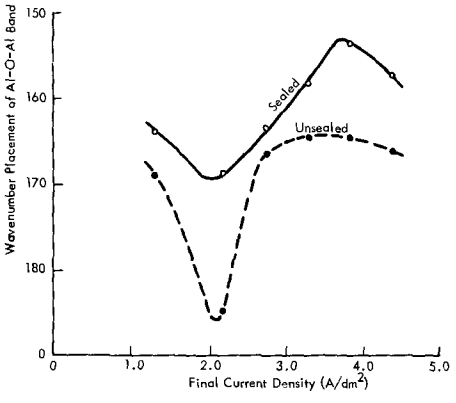

Fig. 6. Placement of porous layer Al-O-Al far *IR* band center, showing effect of sealing transition.

structure. As noted earlier (1, 2), this would require that the wavenumber peak position of the barrier layer be somewhere within the region near 965 cm^{-1}, and the amount (absorbance) of the barrier layer should be at a minimum. Figure 5 shows that these conditions are best met with a second, or final, current density whose value is between 3.24 and 3.78 A/dm^2.

Far infrared data are equally well suited, but indirectly, to measure the extent of this transition-state property of the barrier layer. Although the far *IR* data are strictly a measure only of the porous layer, the barrier layer sealing transition produces a direct result in the porous layer. Sealing transforms a portion of the secondary-phase barrier layer into porous layer hydroxide. This transformation increases the amount of porous layer cross-linking, thereby shifting, to lower wavenumbers, the peak placement of the porous layer Al-O-Al stretching vibration. Figure 6 illustrates such a shift in band position, which is at its minimum (most favorable) value with a final current density in the region 3.24-3.78 A/dm^2.

Figure 7 is a plot of amount (absorbance) of porous layer cross-linking, for sealed and unsealed films, and again (2) shows that, for unsealed films, the amount of porous layer cross-linking follows an inverse relationship with the amount of barrier layer The minimum inflection near 3.24 A/dm^2, in Fig. 7, is an indication that the barrier layer structure has undergone a change that puts it back into the inner seal transition zone. The inflection shows that, in this region, the

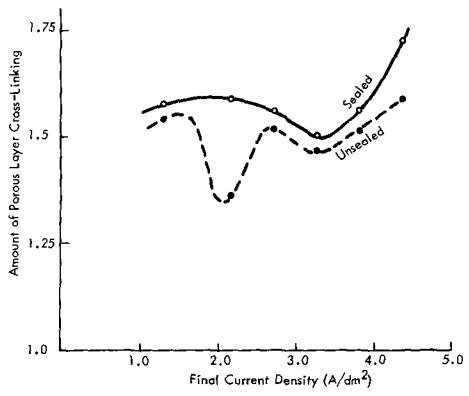

Fig. 7. Amount of porous layer cross-linking (far *IR* data) for sealed and unsealed films.

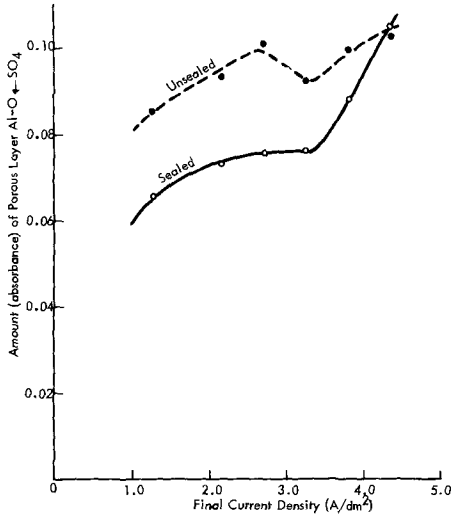

Fig. 8. Amount of porous layer incorporated sulfate (Al=O—S band at 1325 cm^{-1}) for sealed and unsealed films.

barrier layer has reverted from predominantly secondary phase (which gives rise to the porous layer) to a primary-secondary transition zone, within which the growth of the porous layer subsides slightly.

Figure 8 shows a plot of structurally incorporated porous layer sulfate (Al-O-S linkage) plotted *vs.* final current density. Sealing removes some of the incorporated electrolyte anion and probably replaces it with an hydroxyl group (4). Less directly, since the Al-O-S bond is insensitive to changes in porous layer cross-linking, these data also show some of the effects that were discussed earlier in connection with Fig. 5.

Acknowledgment

The author wishes to thank the Kaiser Aluminum & Chemical Corporation for its support of this work and for its permission to publish these results.

Manuscript submitted March 11, 1970; revised manuscript received ca. June 2, 1970.

Any discussion of this paper will appear in a Discussion Section to be published in the June 1971 JOURNAL.

REFERENCES

1. G. A. Dorsey, Jr., *This Journal*, **117**, 1177 (1970).
2. G. A. Dorsey, Jr., *ibid.*, **115**, 1053 (1968).
3. G. A. Dorsey, Jr., *ibid.*, **115**, 1057 (1968).
4. J. F. Murphy, *Plating*, **54**, 1241 (1967).

Electronic States of Mn^{2+}-Activated Phosphors.

I. Green-Emitting Phosphors

D. T. Palumbo*

Sylvania Electric Products Inc., Chemical and Metallurgical Division, Towanda, Pennsylvania 18848

and J. J. Brown, Jr.*

Virginia Polytechnic Institute, Department of Metals and Ceramic Engineering, Blacksburg, Virginia 24601

ABSTRACT

The electronic states of Mn^{2+} are derived from excitation spectra for five green-emitting phosphors: (*i*) $MgGa_2O_4$:Mn, (*ii*) Zn_2SiO_4:Mn, (*iii*) $ZnAl_2O_4$:Mn, (*iv*) Zn_2GeO_4:Mn, and (*v*) $Li_2ZnGe_3O_8$:Mn. Only $MgGa_2O_4$:Mn is found to give a spectrum consistent with octahedral (or tetrahedral) symmetry of Mn^{2+}; the other four phosphors show spectra typical of Mn^{2+} in symmetry lower than octahedral. Solution of the Tanabe-Sugano energy matrices using the $MgGa_2O_4$:Mn levels as input gave Racah parameters of $B = 624$ cm^{-1} and $C = 3468$ cm^{-1}.

Most studies of the optical spectra of Mn^{2+} compounds have been concerned with aqueous solutions of Mn salts, hydrated crystals, and Mn^{2+} halides. Where studies of Mn^{2+}-activated phosphors have been made, the principal concern was to account for observed differences in emission color, the phosphors falling in two classes, those with green emission and those with orange-to-red emission. In similar fashion, we catalog the spectra of Mn^{2+} phosphors in two parts. In this paper we give spectra for five phosphors with green emission and reserve for a later paper presentation of spectra for the orange-to-red emitters. Aside from the obvious division based on color difference, the division follows naturally from the observed position of the ^4A-^4E level for the two classes. For the green emitters the level is found at about 23,500 cm^{-1}, while for the orange-to-red emitters, the level is found at about 24,700 cm^{-1}.

We give below, then, excitation and emission spectra for $MgGa_2O_4$:Mn, Zn_2SiO_4:Mn, $ZnAl_2O_4$:Mn, Zn_2GeO_4:Mn; and $Li_2ZnGe_3O_8$:Mn, give assignments for the observed levels, compare our observations, where possible, with previously reported results, and, finally, fit the observed levels of $MgGa_2O_4$:Mn for given values of the Racah parameters and crystal field strength.

The energy levels of the $3d^5$ Mn^{2+} ion in an octahedral crystal field have been given by Orgel (1), Tanabe and Sugano (2), and Druzhinin (3). Moore (4) gives the free-ion levels. In brief, the free-ion levels, in order of increasing energy are ^6S, ^4G, ^4P, ^4D, and ^4F. In the octahedral field the designations are $^6A_{1g}(^6S)$, $^4T_{1g}(^4G)$, $^4T_{2g}(^4G)$, ^4E_g-$^4A_{1g}(^4G)$, etc., where the free-ion level origins are given in parentheses. The labels A, E, and T refer to single, double, and triple orbital degeneracies, respectively. For completeness, Orgel's crystal field diagram is reproduced in Fig. 1.

The theory has been applied by Pappalardo (5) to $MnCl_2$ and $MnBr_2$, by Goode (6) to $MnCl_2$ complexes, by Ford *et al.* (7) to MnS, by Medlin (8) to naturally occurring minerals, by Heidt *et al.* (9) to $Mn(ClO_4)_2$, by Cotton *et al.* (10) to tetrahalo anions, by Lawson (11) to Mn^{2+}-halo hydrates, by Bingham and Parke (12) to glasses, and by Curie (13), McClure (14), Ryskin *et al.* (15), and Langer (16) to ZnS. In the above systems, the position of the ^4E-$^4A(^4G)$ level varied from 21,237 cm^{-1} (ZnS:Mn) to 25,550 cm^{-1} (MnF_2). In general, no splitting of the two lowest-lying ^4T levels was observed.

With particular reference to the phosphors we report on below, Klick and Schulman (17) give the excitation spectrum of Zn_2SiO_4:Mn. They note three broad bands in the visible. Kostantinova-Schlezinger (18), and Konstantinova-Schlezinger and Kabakova (19) give excitation spectra for green and red emitters; in particular, for green-emitting Zn_2SiO_4:Mn and Zn_2GeO_4:Mn they show three bands in the visible for each. For $ZnAl_2O_4$:Mn, Kroger (20) indicates one band in the visible. Schrader (21) and Vlam (22) report fine structure on the emission band of Zn_2SiO_4:Mn at low temperature. Butler (23), Nagy (24), and Makai (25) fit the silicate emission spectrum with Gaussian bands. Brown (26) discusses the luminescence of $MgGa_2O_4$:Mn and Grisafe (27), the luminescence of $Li_2ZnGe_3O_8$:Mn. Klick (28) gives a brief summary of the Mn^{2+} luminescent center.

A knowledge of expected site symmetry of Mn^{2+} in each of the lattices considered here serves as basis for comparison of observed spectra with group theoretical predictions. In all five phosphors the site symmetry is expected to be either octahedral or tetrahedral. $ZnAl_2O_4$ (20), $MgGa_2O_4$ (29), and $Li_2ZnGe_3O_8$ (27) are spinels with both octahedral and tetrahedral sites. Zn_2SiO_4 (30, 31) and Zn_2GeO_4 (32) have tetrahedral sites. For the $3d^5$ configuration Orgel's diagram applies for both octahedral and tetrahedral symmetry (33).

Experimental Procedures

Excitation and emission spectra were measured at room and liquid-N_2 temperature using a Hitachi-Perkin Elmer MPF-2A spectrofluorimeter. Liquid-He spectra were taken on the same instrument using an Air Products "Cryo-Tip" dewar. The excitation source was a 150-W xenon-arc lamp for measurements below 380 nm and a 1000-W quartz-iodine (tungsten) lamp for measurements above 380 nm. The line structure of

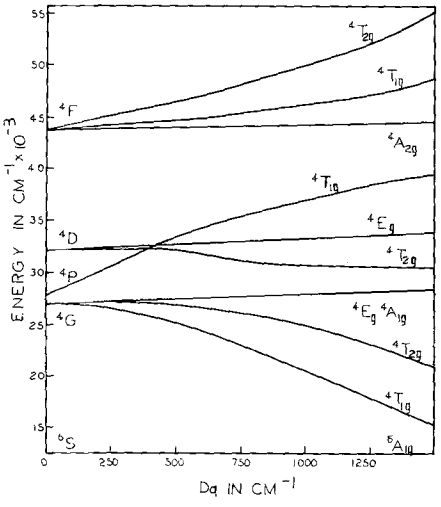

Fig. 1. Orgel's diagram for Mn^{2+} ion in octahedral symmetry

* Electrochemical Society Active Member.

Key words: manganese, phosphors, luminescence, crystal field.

Table I. Mn^{2+} excitation bands (in Å and cm^{-1})

Free-ion levels	Levels in octahedral symmetry	$MgGa_2O_4$		Zn_2SiO_4		$ZnAl_2O_4$		Zn_2GeO_4		$Li_2ZnGe_3O_8$	
				4973	20,109			5060	19,763		
	$^4T_{1g}$	4787	20,890	4884	20,475	Not observed		4860	20,578	Not observed	
				4754	21,035			4740	21,097		
				4430	22,573	4575	21,858	4500	22,222	4640	21,552
^4G	$^4T_{2g}$	4468	22,381	4330	23,095	4520	22,124	4450	22,472	4585	21,810
						4445	22,497	4360	22,936	4460	22,422
				4230	23,640			4258	23,485	4290	23,310
	^4Eg-$^4A_{1g}$	4241	23,578	4208	23,764	4265	23,447	4249	23,535		
				4204	23,787			4230	23,640	4260	23,474
				3851	25,967	3890	25,707	3990	25,063	3870	25,840
	$^4T_{2g}$	3800	26,316	3792	26,371	3860	25,907	3740	26,738	3810	26,247
^4D				3713	26,932	3760	26,596				
	^4Eg	3578	27,948	3578	27,949	3620	27,624	Not observed		3640	27,472
				3450	28,985	3590	27,855			3450	28,986

the xenon arc in the region of 430 to 500 nm interferes with accurate determination of band positions. The spectra obtained were uncorrected for energy.

The compounds measured were formulated with Mn^{2+} concentrations designed to give maximum quantum efficiency as determined by extensive empirical testing, except as noted below, where Mn^{2+} concentration variations revealed additional band structure. Preparative techniques were typical of usual solid state phosphor synthesis and are given in the literature (20, 21, 26, 27, 32).

In deriving band locations, no attempt was made to resolve overlapping bands into Gaussians to obtain a more precise value of wavelength. Values quoted for these bands are therefore only estimates.

Results and Discussion

A few comments are in order before detailing the results, summarized in Table I for ready reference: (*i*) only $MgGa_2O_4$:Mn gives the expected spectrum for octahedral (or tetrahedral) symmetry, *i.e.*, no splitting of degenerate E and T levels, (*ii*) the position of the ^4A-$^4E(^4G)$ level is relatively constant in all five samples at about 23,500 cm^{-1}, (*iii*) where splittings of the degenerate E and T levels occur, some of the expected levels are not observed, and (*iv*) Orgel's criterion that the levels with minimum slope (A and E levels) show the narrowest bandwidth is used as the starting point for assignments.

The spectrum for $MgGa_2O_4$:0.02 Mn is given in Fig. 2. Not shown is the weak lowest-lying $^4T_1$ level at 478.7 nm. The sharp level at 424.7 nm is the ^4E-$^4A(^4G)$. The remaining assignments are given in Table I. Levels above the $^4E(^4D)$ are not observed; they are masked by the charge transfer band. The structure observed at about 415.0 nm is not uniquely assigned. A possible assignment would be a $^2T_2(^2I)$ level, not shown in Orgel's diagram, but which Tanabe and Sugano indicate crosses the lower-lying levels (2). An alternative assignment, as a splitting of the ^4E-^4A level, is not consistent with the observed band intensities for Zn_2GeO_4:Mn and Zn_2SiO_4:Mn, noted below.

In contrast, Zn_2GeO_4:0.03 Mn shows complete splitting of the $^4T_1(^4G)$, $^4T_2(^4G)$, and ^4E-$^4A(^4G)$ levels. The spectrum is given in Fig. 3. Not obvious in the figure is the third band of the ^4E-^4A level, but shown in greater detail and higher resolution in Fig. 4. The $^4T_2(^4D)$ level lying above the ^4E-$^4A(^4G)$ level is not a distinct triplet as might be expected. Only two of the expected three bands are well-resolved. Higher lying levels, again, are masked by the main broad excitation band.

Zn_2SiO_4:0.06 Mn gives splittings paralleling those of Zn_2GeO_4:Mn. Here, the third band of the $^4T_2(^4G)$ level is not observed. The triplet character of the ^4E-$^4A(^4G)$ level is shown in Fig. 4; the complete spectrum is shown in Fig. 5. Attempts to resolve the third band of the $^4T_2(^4G)$ level at lower (down to 0.5 m/o [mole per cent] and higher Mn (up to 12.0 m/o) contents were fruitless. The possibility that one of the three assigned ^4E-$^4A(^4G)$ levels belongs to the $^4T_2(^4G)$ triplet was considered, but rejected as inconsistent with assignments for the Zn_2GeO_4:Mn spectrum.

The spectrum of $Li_2ZnGe_3O_8$:0.035 Mn is given in Fig. 6. Here, the lowest-lying $^4T_1$ level was not observed. The $^4T_2(^4G)$ level splits into a triplet. Only doublet character appears in the ^4E-$^4A(^4G)$ and the $^4T_2(^4D)$ levels, where we might expect triplets in analogy with the complete splitting of the $^4T_2(^4G)$ level. The $^4E(^4D)$ level shows the expected doublet. At lower Mn content (0.5 m/o) no splitting of the

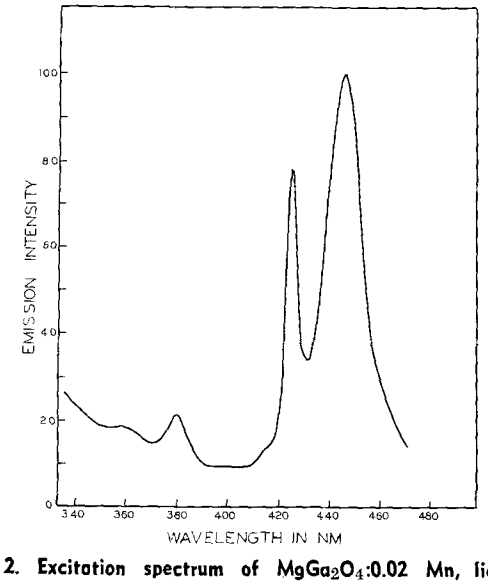

Fig. 2. Excitation spectrum of $MgGa_2O_4$:0.02 Mn, liquid-N_2 temperature.

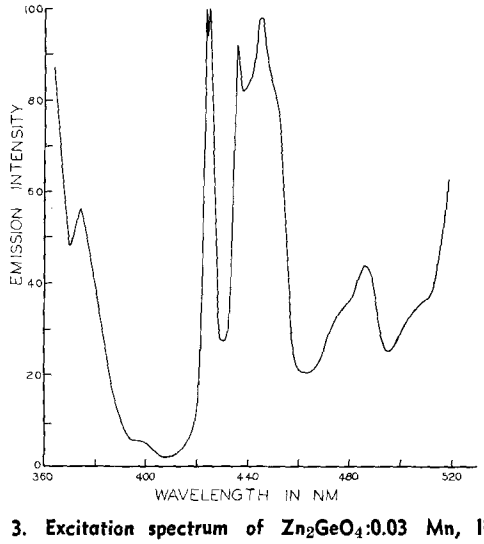

Fig. 3. Excitation spectrum of Zn_2GeO_4:0.03 Mn, liquid-N_2 temperature.

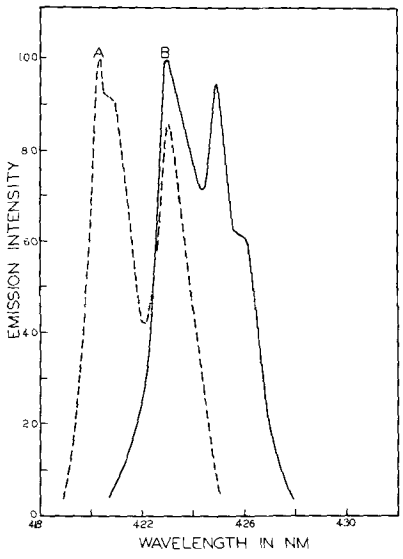

Fig. 4. Splitting of the ^4E-$^4A(^4G)$ level in: (A) Zn_2SiO_4:0.06 Mn and (B) Zn_2GeO_4:0.03 Mn at liquid-N_2 temperature.

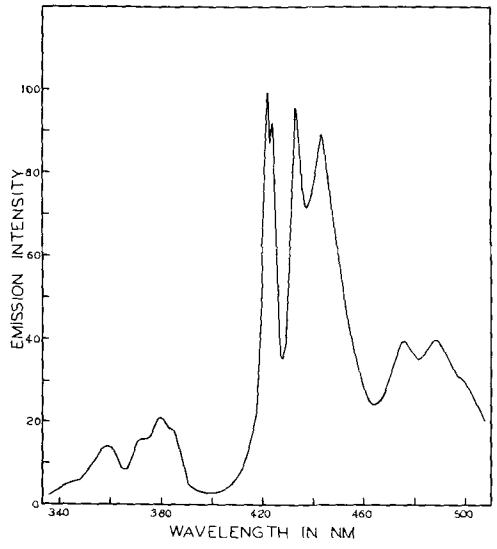

Fig. 5. Excitation spectrum of Zn_2SiO_4:0.06 Mn at liquid-N_2 temperature.

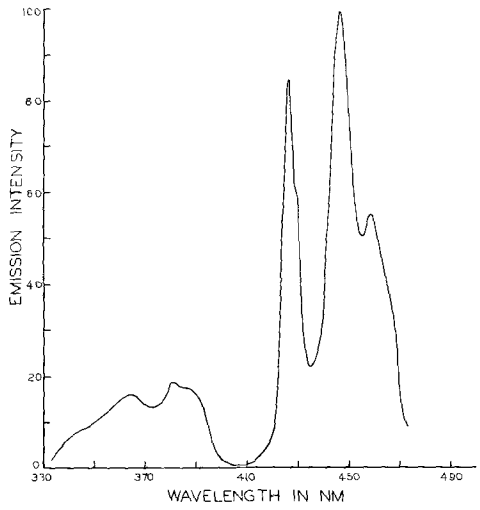

Fig. 6. Excitation spectrum of $Li_2ZnGe_3O_8$:0.035 Mn at liquid-N_2 temperature.

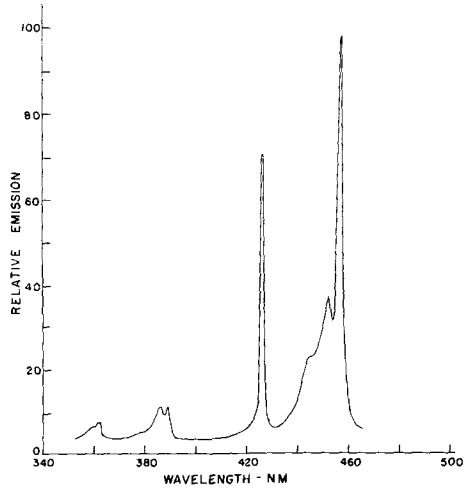

Fig. 7. Excitation spectrum of $ZnAl_2O_4$:0.02 Mn at liquid-N_2 temperature.

^4E-$^4A(^4G)$ level is noted, although the rest of the levels split as given in Fig. 6.

For $ZnAl_2O_4$: 0.02 Mn, no structure is resolved in the ^4E-$^4A(^4G)$ level although the $^4T_2(^4G)$ level is a distinct triplet. The spectrum is given in Fig. 7. The $^4T_1(^4G)$ level was not observed; the $^4T_2(^4D)$ and the $^4E(^4D)$ levels split into the expected triplet and doublet, respectively. We attribute the apparent structureless nature of the ^4E-$^4A(^4G)$ level to instrumental limitations; our maximum resolution for excitation spectra is about 0.6 nm. We note fine structure appearing in the $^4T_2(^4D)$ level (not shown in Fig. 7) at 384.3, 385.6, 386.3, and 387.2 nm. Goode (6) attributes similar structure in $MnCl_2 \cdot 2H_2O$ to spin-orbit splittings. The splittings here ($\sim$65 cm^{-1}) are consistent with his calculated values.

We noted above failure to observe the $^4T_1(^4G)$ level in $ZnAl_2O_4$:Mn and $Li_2ZnGe_3O_8$:Mn. Either the levels are too weak to observe or they lie so near the emission band (small Stokes shift) they cannot be measured in the excitation mode. We favor the latter explanation based on the observed magnitude of splitting of the $^4T_2(^4G)$ level from the ^4E-$^4A(^4G)$ level. Larger splittings are observed for $ZnAl_2O_4$:Mn and $Li_2ZnGe_3O_8$:Mn than are observed for the remaining three phosphors. We expect then the $^4T_1(^4G)$ level in these two compounds to be found at lower energy than the $^4T_1(^4G)$ level of the silicate, gallate, and orthogermanate, hence closer to the emission band and possibly overlapping it. The predicted position of these $^4T_1$ levels, derived from calculations indicated below and plotted in Fig. 11, supports the interpretation.

The spectral characteristics of the emission bands of the five phosphors vary from simple to complex. $MgGa_2O_4$:Mn and Zn_2GeO_4:Mn show no fine structure. At liquid-N_2 temperature the gallate peaks at 508 nm and has a 27 nm bandwidth at half-maximum intensity (spectrum not shown). Zn_2GeO_4:Mn peaks at 524 nm and has a 30 nm bandwidth; the spectrum is given in Fig. 8. Also shown in Fig. 8 is the $ZnAl_2O_4$:Mn spectrum; it is almost a mirror image of the $^4T_2(^4G)$ excitation band (Fig. 7). However, one extra band is observed in emission. Since the emission transition is presumably $^4T_1(^4G) \rightarrow {}^6A_1(^6S)$, complete splitting of the triplet can account for only three of the observed bands. Alternatives are that the structure results from superposition of vibrational modes or that spin-orbit coupling produces the additional splitting. Goode (6), in his calculations including spin-orbit coupling, gives splittings of the $^4T_1(^4G)$ level of about 62 cm^{-1}, smaller than we observe in emission ($\sim$150 cm^{-1}). At present we can make no definitive assignment for the origin of the fine structure.

Similar considerations apply to the Zn_2SiO_4: 0.005 Mn spectrum shown in Fig. 9. We observe more structure than reported by Schrader (21), but less structure

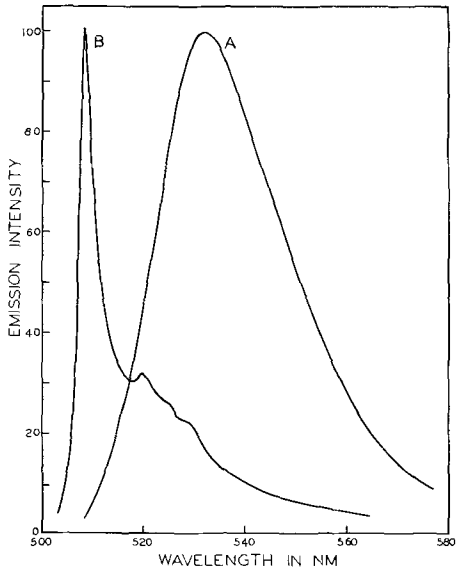

Fig. 8. Emission spectra of: (A) Zn_2GeO_4:0.03 Mn and (B) $ZnAl_2O_4$:0.02 Mn at liquid-N_2 temperature.

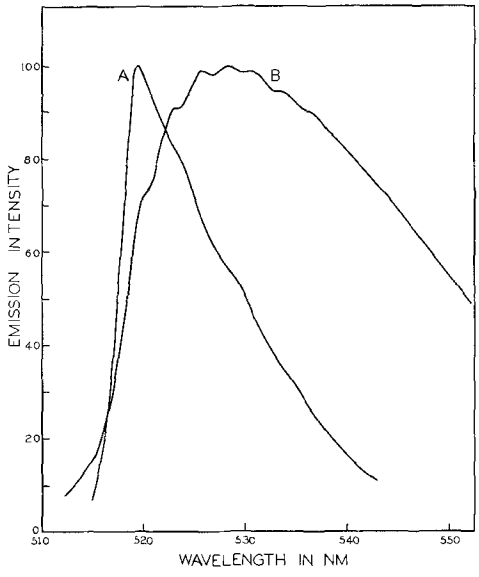

Fig. 10. Emission spectra of: (A) $Li_2ZnGe_3O_8$:0.005 Mn and (B) $Li_2ZnGe_3O_8$:0.035 Mn at liquid-N_2 temperature.

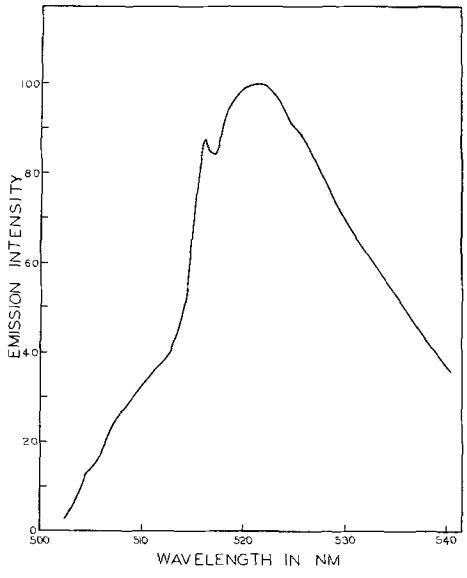

Fig. 9. Emission spectrum of Zn_2SiO_4:0.005 Mn at liquid-He temperature.

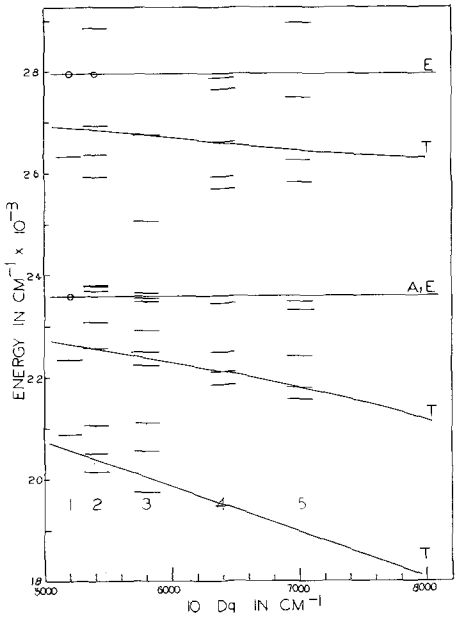

Fig. 11. Calculated energy level diagram for Mn^{2+} based on position of the ^4E levels in $MgGa_2O_4$, for B = 624 cm^{-1} and C = 3468 cm^{-1}. Lines and circles show level positions for: 1. $MgGa_2O_4$, 2. Zn_2SiO_4, 3. Zn_2GeO_4, 4. Zn_2AlO_4, and 5. $Li_2ZnGe_3O_8$.

than reported by Vlam (22). The marked asymmetry and fine structure observed suggest that more than one mechanism is operative here.

For $Li_2ZnGe_3O_3$:Mn, Fig. 10, the spectrum broadens with increased Mn content and at 3.5 m/o Mn shows a series of seven fine-structure components superimposed on a broad asymmetric band; the fine-structure levels occur at 520.1, 522.8, 525.8, 528.0, 530.6, 533.7, and 536.6 nm. The regularity of the fine-structure separations about the 528.0 nm level suggest vibrational structure as their origin; the average separation in levels is about 100 cm^{-1}.

As a final exercise, we use the Tanabe-Sugano matrices to fit the $MgGa_2O_4$:Mn levels. We use the ^4E observed levels (23,578 and 27,948 cm^{-1}) to derive values of the Racah parameters, using the $^4\Gamma_3$ matrix, which is independent of the crystal field strength. The values of B (624 cm^{-1}) and C (3468 cm^{-1}) obtained are then used in the crystal-field-dependent matrices to determine the remaining levels. The results are shown in Fig. 11, where we include the observed levels of the other four compounds for qualitative comparison. A value of 10 Dq of 5200 cm^{-1} gives a reasonable fit for the gallate levels. A more accurate fit can be obtained by a least squares procedure, using B and C as adjustable parameters. However, in the absence of experimental values for the higher-lying levels, the refinement seems unwarranted. Table II gives a comparison of our derived values for B, C, and 10 Dq with those reported in the literature. Our values are in fair agreement with those reported for Mn^{2+} complexes (9-11).

We noted above that Mn^{2+} is expected to be in an octahedral or tetrahedral site in all five compounds

Table II. Value of B, C, and 10 Dq in cm^{-1} for Mn^{2+} systems

System	B	C	10 Dq	Reference
$MgGa_2O_4$:Mn	624	3468	5200	This work
$[Mn(H_2O)_6]^{2+}$	671	3710	8480	9
$[MnBr_4]^{2+}$	536	3530	3100	10
$MnCl_2 \cdot 2H_2O$	630	3600	8000	11

studied (1). If so, no splitting of degenerate E and T levels is expected (2). However, only $MgGa_2O_4$:Mn gives the expected spectrum, *i.e.*, no splitting of degenerate levels. Two mechanisms may account for observed splittings; either the symmetry is lower than is expected, or Mn^{2+} occupies both octahedral and tetrahedral sites in the $Li_2ZnGe_3O_8$:Mn and $ZnAl_2O_4$:Mn spinels, and both (unequivalent) tetrahedral sites in Zn_2SiO_4:Mn (31). The latter mechanism would, at most, account for doubling the number of expected levels, but would not account for the observed triplets (Fig. 11). We assume, therefore, that the splittings result from a lowering of the site symmetry. The point group symmetries consistent with complete lifting of the degeneracies are C_2v, C_2h, D_2, or D_2h (33).

The apparent dependence of the ^4E-$^4A(^4G)$ level-splitting in $Li_2ZnGe_3O_8$:Mn on Mn^{2+} concentration is unexpected and deserves further study. (The observation is not an artifact attributable to spectra measured at different instrumental resolutions.) Group theoretical arguments require that complete splitting of the $^4T_1(^4G)$ level be reflected in complete splitting of the remaining levels. Until additional data are available, we forgo explanations that must be couched in speculation.

On emission spectra we have said little and can say little more. Where structure is observed in a phosphor emission spectrum, it usually follows that structure is also observed in the excitation spectrum. The converse statement may or may not be true. In particular, the Zn_2GeO_4:Mn emission spectrum shows no fine structure, while the excitation spectrum does (Fig. 3 and 8).

Summary

Of the five compounds examined, only $MgGa_2O_4$:Mn shows the expected behavior for Mn^{2+} in octahedral (or tetrahedral) symmetry. The complete splitting of at least one of the ^4T levels in all the remaining compounds requires distortion of the expected octahedral (or tetrahedral) symmetry down to C_2v, C_2h, C_2, or D_2h symmetries (33). The question of the effects of spin-orbit coupling and vibrational modes on splittings and fine structure we leave unresolved, requiring additional experimental data taken at higher resolution and embracing a wider range of Mn concentrations for more definitive conclusions.

Acknowledgments

The authors wish to thank D. A. Grisafe for preparing the $Li_2ZnGe_3O_8$:Mn and $ZnAl_2O_4$:Mn phosphors, J. D. Deysher for preparing the Zn_2GeO_4:Mn phosphor, and J. P. Frazier, III for programming the matrix solutions.

Manuscript submitted Dec. 29, 1969; revised manuscript received May 13, 1970. This paper was presented in part at the Cleveland Meeting of the Society, May 1-6, 1966.

Any discussion of this paper will appear in a Discussion Section to be published in the June 1971 JOURNAL.

REFERENCES

1. L. E. Orgel, *J. Chem. Phys.*, **23**, 1004 (1955).
2. Y. Tanabe and S. Sugano, *J. Phys. Soc. Japan*, **9**, 753 (1954).
3. V. V. Druzhinin, *Opt. Spectry. (USSR) (Engl. Transl.)*, **22**, 446 (1967).
4. C. E. Moore, "Atomic Energy Levels," Vol. II, NBS Circular 467 (1952).
5. R. Pappalardo, *J. Chem. Phys.*, **31**, 1050 (1959).
6. D. H. Goode, *ibid.*, **43**, 2830 (1965).
7. R. A. Ford, E. Kauer, A. Rabenau, and D. A. Brown, *Ber. Bunsenges Physik. Chem.*, **67**, 460 (1963).
8. W. L. Medlin, *J. Opt. Soc. Am.*, **53**, 1276 (1963).
9. L. J. Heidt, G. F. Koster, and A. M. Johnson, *J. Am. Chem. Soc.*, **80**, 6471 (1959).
10. F. A. Cotton, D. M. L. Goodgame, and M. Goodgame, *ibid.*, **84**, 167 (1962).
11. K. E. Lawson, *J. Chem. Phys.*, **44**, 4159 (1966).
12. K. Bingham and S. Parke, *Phys. Chem. Glasses*, **6**, 224 (1965).
13. D. Curie, *Compt. Rend.*, **258**, 3269 (1964).
14. D. S. McClure, *J. Chem. Phys.*, **39**, 2850 (1963).
15. A. I. Ryskin, G. I. Khilco, B. I. Maksakov, and K. K. Dubenskii, *Opt. Spectry. (USSR) (Engl. Transl.)*, **16**, 149 (1965).
16. D. Langer and S. Ibuki, *Phys. Rev.*, **138**, A809 (1965).
17. C. C. Klick and J. H. Schulman, *J. Opt. Soc. Am.*, **42**, 910 (1952).
18. M. A. Konstantinova-Schlezinger, *Bull. Acad. Sci. USSR*, **30**, 707 (1966).
19. M. A. Konstantinova-Schlezinger and A. I. Kabakova, *Zh. Prikl. Spectros.*, **6**, 632 (1967).
20. F. A. Kroger, "Some Aspects of the Luminescence of Solids," p. 100, Elsevier Publishing Co., New York (1948).
21. R. E. Schrader, *J. Opt. Soc. Am.*, **39**, 699 (1949).
22. C. C. Vlam, *ibid.*, **41**, 558 (1951).
23. K. H. Butler, *This Journal*, **95**, 267 (1949).
24. E. Nagy, *J. Opt. Soc. Am.*, **39**, 42 (1949).
25. E. Makai, *This Journal*, **95**, 107 (1949).
26. J. J. Brown, Jr., *ibid.*, **114**, 245 (1967).
27. D. A. Grisafe, *ibid.*, To be published.
28. C. C. Klick, *Brit. J. Appl. Phys.*, Sup. 4, S74 (1955).
29. C. W. V. Hoffman and J. J. Brown, Jr., *J. Inorg. Nucl. Chem.*, **30**, 63 (1968).
30. W. L. Bragg and W. H. Zachariasen, *Z. Krist.*, **72**, 518 (1930).
31. H. K. Perkins and M. J. Sienko, *J. Chem. Phys.*, **46**, 2398 (1967).
32. H. W. Leverenz, "An Introduction to the Luminescence of Solids," p. 221, John Wiley & Sons, New York (1950).
33. F. A. Cotton, "Chemical Applications of Group Theory," Interscience Publishers, New York (1963).

Luminescence of Divalent Europium in Ba-Ca, Ba-Sr, and Ca-Sr Orthophosphate and Pyrophosphate Compositions

Costas C. Lagos*

Phosphor Research Laboratory, Sylvania Lighting Center, Danvers, Massachusetts 01923

ABSTRACT

Divalent europium was used as an activator in Ba-Ca, Ba-Sr, and Ca-Sr orthophosphate and pyrophosphate compositions. Luminescence was observed in most of the compositions and spectral energy distribution measurements were made on all samples. Changes in the mixed cation ratios produced variations in emission band intensities, shifting of emission peak positions, and changes in emission band widths A new compound with the formula $Ba_2Ca(PO_4)_2$ was found.

Compositions along the binary joins between the orthophosphates and pyrophosphates of Ca-Sr, Ba-Sr, and Ca-Ba were doped with divalent europium and examined for luminescence under 2537Å excitation. Many of the compositions fluoresced quite strongly and emission band peak positions varied from 407 to 550 nm. During the course of the investigation, a previously unreported orthophosphate compound with the composition of $Ba_2Ca(PO_4)_2$ was found.

Other papers (1-6) have previously reported on the divalent europium activation of alkaline earth orthophosphates and pyrophosphates, but in most cases the authors either presented data primarily on the substitution of Mg for Ba, Ca, or Sr, or they did not report extensively on their results. In this paper we shall endeavor to present a more comprehensive picture on the divalent europium activation of the mixed alkaline earth orthophosphates and pyrophosphates with the major emphasis being placed on empirical results.

Experimental

The samples were prepared using luminescent grade Ba, Ca, and Sr carbonates, $BaHPO_4$, $CaHPO_4$, and $SrHPO_4$, and 99.99% pure Eu_2O_3. After dry mixing, the blends were fired in air and then mixed again prior to a final reduction firing in a 1% H_2-99% N_2 atmosphere. The firing temperatures used were varied and were determined by the particular composition join being studied. A concentration of 0.02 gram atom of Eu were added per gram atom of alkaline earth cation and a slight excess of phosphate (0.02 gram atom) was also used.

X-ray diffraction data were obtained on all samples. Spectral energy distribution data (SED curves) using 2537Å radiation were also obtained on all luminescent samples, and emission peak height intensities were compared as described previously (3).

Results and Discussion

Orthophosphates

Ca-Sr *compositions.*—The only noteworthy luminescence observed in these compositions was that of the pure end members, $Ca_3(PO_4)_2$ and $Sr_3(PO_4)_2$. Each end member has two polymorphic forms, α and β (7, 8). $Ca_3(PO_4)_2$ has a β to α transition temperature of 1180°, while the β-form of $Sr_3(PO_4)_2$ is not stable at room temperature unless it is stabilized by the addition of a number of various foreign cations of which Ca is one (8).

Calcium was substituted for strontium in $Sr_3(PO_4)_2$:Eu^{+2} in 0.5 mole increments and samples were fired at 1100° and 1250°C. X-ray diffraction data of the mixed Ca-Sr compositions from both firing temperatures showed only the presence of either β-$Sr_3(PO_4)_2$, β-$Ca_3(PO_4)_2$, or some solid solution between them. The end members were found to be β-$Ca_3(PO_4)_2$ at 1100°C, α-$Ca_3(PO_4)_2$ at 1250°C, and α-$Sr_3(PO_4)_2$ at both temperatures.

Figure 1 shows the emission curves for α and β-$Ca_3(PO_4)_2$:Eu^{+2} and α-$Sr_3(PO_4)_2$:Eu^{+2}. The latter had an intense narrow emission band peaking at 415 nm, while β-$Ca_3(PO_4)_2$:Eu^{+2} had a similarly narrow emission band peaking at 408 nm. An extremely wide emission curve peaking at 488 nm was obtained with α-$Ca_3(PO_4)_2$:Eu^{+2}. This phosphor, because of its wide emission curve, appeared to be a moderately bright whitish green when visually observed under 2537Å excitation, but its peak intensity was only about 6% of the 1200°C fired α-$Sr_3(PO_4)_2$:Eu^{+2} phosphor, the brightest of this particular orthophosphate group. Table I lists the emission properties of these end-member phosphors which were the only significant phosphors found in the Ca-Sr orthophosphate compositions. Data on some standard phosphors are also included for reference.

As Ca was substituted for Sr in α-$Sr_3(PO_4)_2$, the β-form of $Sr_3(PO_4)_2$ was formed. The only luminescence observed here was an extremely weak reddish-orange emission. On examination by the spectral energy distribution radiometer, the red portion of the luminescence was found to be weak trivalent europium emission. Apparently, the trivalent europium in the β-$Sr_3(PO_4)_2$ compound could not be reduced to divalent europium.

In addition to the weak red Eu^{+3} emission, there was also observed an extremely weak orange emission

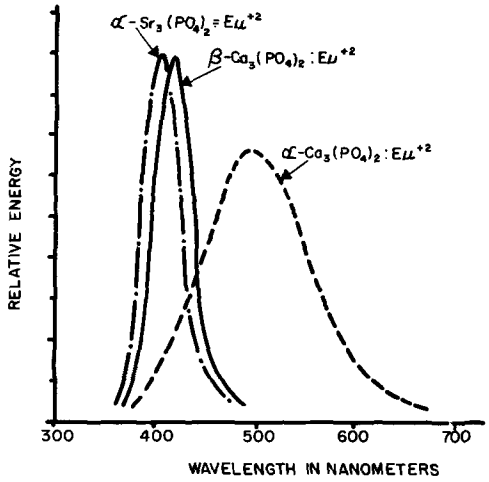

Fig. 1. Spectral energy distribution of the emission of α-$Ca_3(PO_4)_2$:Eu^{+2}, β-$Ca_3(PO_4)_2$:Eu^{+2}, and α-$Sr_3(PO_4)_2$:Eu^{+2}. 2537Å excitation.

* Electrochemical Society Active Member.

Key words: luminescence, phosphors, 2537Å excitation, divalent europium activation, spectral energy distribution, barium-calcium pyrophosphates, barium-strontium pyrophosphates, calcium-strontium pyrophosphates, barium-calcium orthophosphates, barium-strontium orthophosphates, calcium-strontium orthophosphates.

Table I. Emission properties of significant orthophosphate compositions

Composition	Position, nm	Width at half-height, nm	Peak height intensity as % of Zn_2SiO_4:Mn
α-$Sr_3(PO_4)_2$:Eu^{+2}	415	38	104
α-$Ca_3(PO_4)_2$:Eu^{+2}	488	122	7
β-$Ca_3(PO_4)_2$:Eu^{+2}	408	46	9
$Ba_3(PO_4)_2$:Eu^{+2}	415	34	84
$Ba_2Ca(PO_4)_2$:Eu^{+2}	463	48*	11
	520*	160*	10
$CaWO_4$:Pb	446	124	39
$MgWO_4$	488	142	45

* These figures are close approximations because of the partial merging of the two emission bands.

Table II. X-ray diffraction data for $Ba_2Ca(PO_4)_2$ (Copper Kα radiation)

2θ	I/I_o	d	2θ	I/I_o	d
15.25	4	5.805	38.02	3	2.365
18.89	39	4.694	38.32	3	2.347
19.41	19	4.569	38.72	13	2.324
21.35	3	4.157	39.36	11	2.287
22.69	24	3.916	40.32	23	2.235
22.97	4	3.868	42.18	16	2.141
25.95	72	3.431	43.42	24	2.082
27.82	100	3.204	45.50	5	1.992
29.51	3	3.024	45.81	13	1.979
30.75	3	2.905	46.29	13	1.960
31.83	33	2.809	46.89	5	1.936
32.70	89	2.736	47.90	3	1.897
36.26	4	2.475	48.32	13	1.882

Plus other lines.

in the vicinity of 510-660 nm which had also been reported previously by Gorbacheva (5).

Ba-Ca *orthophosphates.*—Calcium was substituted for barium in $Ba_3(PO_4)_2$:Eu^{+2} in 0.5 mole increments and samples were fired at 1000° and 1200°C. As in the case of Ca-Sr orthophosphate compositions, the brightest phosphors obtained in this binary system were the pure end members, α- and β-$Ca_3(PO_4)_2$:Eu^{+2}, which were mentioned previously in the discussion of the Ca-Sr orthophosphate compositions, and $Ba_3(PO_4)_2$:Eu^{+2} which had an intense emission band at 415 nm.

Figure 2 shows the emission curve for the $Ba_3(PO_4)_2$:Eu^{+2} phosphor and Table I lists its emission properties.

Also included in Fig. 2 is the emission curve for the new compound that was discovered during this investigation. This compound had the formula $Ba_2Ca(PO_4)_2$, with an emission peak intensity about 10% of the $Ba_3(PO_4)_2$:Eu^{+2} end member, but it appeared a moderately bright pale yellow-white under 2537Å excitation because of its extremely wide emission band. The emission properties of this phosphor are also given in Table I.

The presence of the two emission peaks in the SED curve of this $Ba_2Ca(PO_4)_2$:Eu^{+2} phosphor appeared to indicate that a mixture of two phases was present. X-ray diffraction data, however, showed extremely sharp and well-defined lines of a single compound whose x-ray pattern did not correspond to any single pattern or combinations of patterns of any other known compounds in either the BaO-P_2O_5 or CaO-P_2O_5 binary systems. Table II gives the x-ray diffraction data for the new $Ba_2Ca(PO_4)_2$ compound.

The $Ba_2Ca(PO_4)_2$:Eu^{+2} phosphor was also inspected under 2537Å excitation with a microscope. The emission color of all particles was identical. SED curves of some individual luminescent particles were obtained using a modified fiber optic single particle microspectroradiometer which was previously described by Bouchard (9). The single particle SED curves were identical to the SED curve shown in Fig. 2 which was obtained from a powder sample. The two peaks in the emission curve are probably the result of the activator being in two different crystallographic sites.

Figure 3 shows the variation of emission peak intensity with composition for the 1200°C firing. As Ca was substituted for Ba, there was a drastic decrease in emission intensity until the composition of $Ba_2Ca(PO_4)_2$ was reached. Further Ca substitution resulted only in a small gradual increase in intensity until the wide band pale green-white emitting α-$Ca_3(PO_4)_2Eu^{+2}$ end member was reached.

It also can be seen from Fig. 3 that there was a substantial increase in the width of the emission band as Ca was substituted for Ba. The emission band width began to increase at $Ba_{2.5}Ca_{0.5}$ and continued to increase quite rapidly until the $Ba_{1.5}Ca_{1.5}$ composition was reached. X-ray diffraction of compositions in this region ($Ba_{3.0}$ to $Ba_{1.5}Ca_{1.5}$) showed the presence of (*a*) $Ba_3(PO_4)_2$, (*b*) a mixture of $Ba_3(PO_4)_2$ and $Ba_2Ca(PO_4)_2$, (c) $Ba_2Ca(PO_4)_2$, and (*d*) lower *d*-spacing values of $Ba_2Ca(PO_4)_2$, respectively.

At concentrations of Ca greater than $Ca_{1.5}$ larger *d*-spacing values and line intensities of α-$Ca_3(PO_4)_2$ began to appear in increasing amounts in the x-ray diffraction data, the rate of increase of the emission band width began to level off, and the peak of the weak emission curve began to shift from 500 nm for $Ba_{1.5}Ca_{1.5}$ to 554 nm, 560 nm, and 530 nm for the next three Ba-Ca compositions until finally the emission peak position of 488 nm for α-$Ca_3(PO_4)_2$:Eu^{+2} was obtained.

Emission results of samples fired at 1000°C were similar to those obtained at 1200°C except for slightly reduced emission intensities which were due to decreased reactivity. This was confirmed by the x-ray data which showed x-ray diffraction lines of reduced intensity and sharpness. Here again as was the case in the 1200°C firing, α-$Ca_3(PO_4)_2$ was found to be the only phase present in the compositions from $Ba_{0.25}Ca_{2.75}$ to $Ba_{1.0}Ca_{2.0}$. This was quite surprising since the 1000°C firing temperature was considerably lower than the normal β to α transition temperature of 1180°C, as determined by differential thermal analysis in our lab-

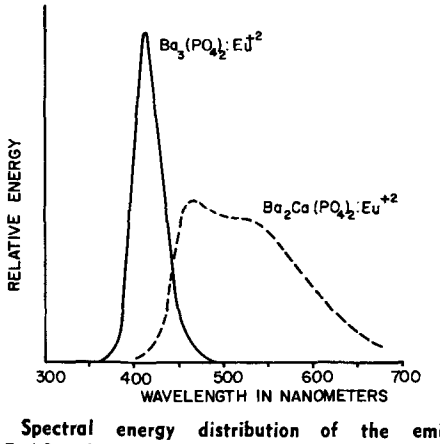

Fig. 2. Spectral energy distribution of the emission of $Ba_3(PO_4)_2$:Eu^{+2} and $Ba_2Ca(PO_4)_2$:Eu^{+2}. 2537Å excitation.

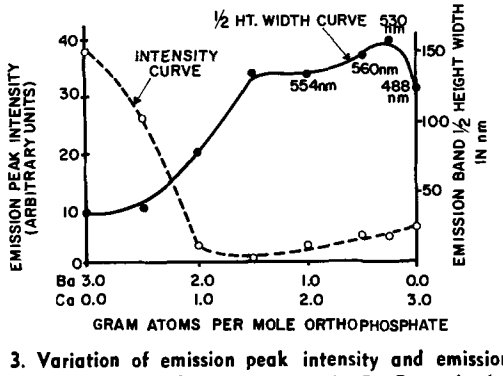

Fig. 3. Variation of emission peak intensity and emission band half-height width with changing cation in Ba-Ca orthophosphate compositions.

oratory. Apparently, the substitution of the larger Ba ion for Ca up to the compositions of Ba_1Ca_2 tended to stabilize the α rather than the β-form of $Ca_3(PO_4)_2$ even at as low a temperature as 1000°C.

Ba-Sr *orthophosphates.*—Ba-Sr orthophosphate compositions were fired at 1000° and 1200°C, and substitutions of Ba for Sr were made in 0.5 mole increments. X-ray diffraction data indicated that there was a complete solid solution formed between $Ba_3(PO_4)_2$:Eu^{+2} and α-$Sr_3(PO_4)_2$:Eu^{+2}. Because of this complete solid solution and the intense brightness of the end-member phosphors, the intermediate Ba-Sr compositions were also quite bright. The emission curve of $Ba_3(PO_4)_2$:Eu^{+2} was shown in Fig. 2 and that of α-$Sr_3(PO_4)_2$:Eu^{+2} in Fig. 1. Table I gives the emission properties of α-$Sr_3(PO_4)_2$:Eu^{+2} and $Ba_3(PO_4)_2$:Eu^{+2}.

Figure 4 shows the variation of emission peak intensity and the shifting of the emission peak with changing composition for the 1000°C firing. The change in intensity for compositions between the two end members was almost a straight line which was as expected because of the complete solid solution between the Sr and Ba orthophosphates. As Sr was substituted for Ba, there was a slight shifting of the emission band toward the longer wavelengths before it began to shift toward the 407 nm peak of the α-$Sr_3(PO_4)_2$:Eu^{+2} phosphor.

Because Ba was not one of the cations which stabilized the β-form of $Sr_3(PO_4)_2$, there were no results to be reported on β-$Sr_3(PO_4)_2$-$Ba_3(PO_4)_2$ compositions.

Pyrophosphates

Ca-Sr *pyrophosphates.*—There are three polymorphic forms of $Ca_2P_2O_7$, α, β, and γ (7), and two polymorphic forms of $Sr_2P_2O_7$, α and β (10). The γ-form of $Ca_2P_2O_7$ was not studied, because it was only stable at low temperatures (320°-340°C). The transition temperature from β-$Ca_2P_2O_7$ to α-$Ca_2P_2O_7$ was at 1140°C, and Ca-Sr compositions were fired at two different temperatures of 1050°C and 1250°C in order to study the effect of β-$Ca_2P_2O_7$:Eu^{+2}-α-$Sr_2P_2O_7$:Eu^{+2}, and α-$Ca_2P_2O_7$:Eu^{+2}-α-$Sr_2P_2O_7$:Eu^{+2} compositions.

A weak blue emission at 424 nm was obtained with β-$Ca_2P_2O_7$:Eu^{+2}, while strong emission peaks at 419 and 422 nm were obtained with α-$Ca_2P_2O_7$:Eu^{+2} and α-$Sr_2P_2O_7$:Eu^{+2}, respectively. β-$Sr_2P_2O_7$:Eu^{+2} was dead to 2537Å excitation. Table III lists the emission properties of these phosphors along with those of the various Ca-Sr compositions fired at 1050° and 1250°C. The emission properties of a standard $CaWO_4$:Pb phosphor were also included for reference.

Sr was substituted for Ca in $Ca_2P_2O_7$:Eu^{+2} in 0.25 mole increments and samples were fired at 1050° and 1250°C, as mentioned previously. Longer firing times of 8-12 hr were needed for these particular compositions since the normal firing times of 2-4 hr produced nonequilibrium conditions and erroneous results in emission intensities and emission peak positions.

For the 1050°C firing, x-ray diffraction data showed only the presence of either β-$Ca_2P_2O_7$, and/or α-$Sr_2P_2O_7$ in all compositions. The $Ca_2P_2O_7$ and

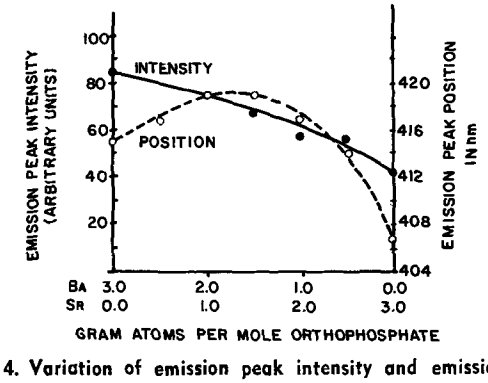

Fig. 4. Variation of emission peak intensity and emission peak position with changing cation in Ba-Sr orthophosphate compositions.

Table III. Emission properties of Ca-Sr pyrophosphate compositions

Composition	Peak position, nm	Band width at ½ height, nm	Peak height intensity as % of Zn_2SiO_4:Mn
	1050°C Firing		
β-$Ca_2P_2O_7$:Eu^{+2}	424	39	7
$Ca_{1.75}Sr_{0.25}P_2O_7$:Eu^{+2}	420	43	44
$Ca_{1.50}Sr_{0.50}P_2O_7$:Eu^{+2}	420	46	57
$Ca_{1.25}Sr_{0.75}P_2O_7$:Eu^{+2}	430	45	60
$Ca_{1.0}Sr_{1.0}P_2O_7$:Eu^{+2}	430	43	70
$Ca_{0.75}Sr_{1.25}P_2O_7$:Eu^{+2}	431	40	72
$Ca_{0.50}Sr_{1.50}P_2O_7$:Eu^{+2}	429	38	82
$Ca_{0.25}Sr_{1.75}P_2O_7$:Eu^{+2}	426	35	119
α-$Sr_2P_2O_7$:Eu^{+2}	422	32	149
	1250°C Firing		
β-$Ca_2P_2O_7$:Eu^{+2}	419	30	86
$Ca_{1.75}Sr_{0.25}P_2O_7$:Eu^{+2}	423	40	70
$Ca_{1.50}Sr_{0.50}P_2O_7$:Eu^{+2}	431	48	79
$Ca_{1.25}Sr_{0.75}P_2O_7$:Eu^{+2}	439	43	94
$Ca_{1.0}Sr_{1.0}P_2O_7$:Eu^{+2}	440	39	110
$Ca_{0.75}Sr_{1.25}P_2O_7$:Eu^{+2}	438	37	123
$Ca_{0.50}Sr_{1.50}P_2O_7$:Eu^{+2}	434	35	145
$Ca_{0.25}Sr_{1.75}P_2O_7$:Eu^{+2}	430	35	162
α-$Sr_2P_2O_7$:Eu^{+2}	422	30	156
$CaWO_4$:Pb (Reference)	446	124	39

$Ca_{1.75}Sr_{0.5}P_2O_7$ compositions were β-$Ca_2P_2O_7$ with the intensity and sharpness of the β-$Ca_2P_2O_7$ diffraction lines being drastically reduced in the latter composition. In the $Ca_{1.5}Sr_{0.5}$, $Ca_{1.25}Sr_{0.75}$, and the $Ca_{1.0}Sr_{1.0}$ compositions, α-$Sr_2P_2O_7$ was present, but with diffraction lines of greatly reduced intensity and sharpness. The remaining compositions, $Ca_{0.75}Sr_{1.25}$ through $Sr_2P_2O_7$ were also α-$Sr_2P_2O_7$ but with moderately strong diffraction lines of increasing sharpness as the concentration of Sr was increased.

Table III lists the emission properties of the 1050°C fired compositions. The most intense phosphor of the group was the unsubstituted α-$Sr_2P_2O_7$:Eu^{+2} phosphor, and it appeared that with increasing Ca substitution the good phosphor was simply being diluted with the poor β-$Ca_2P_2O_7$:Eu^{+2} phosphor resulting in steadily decreasing emission intensities. No important changes occurred in the emission peak positions and widths at half height as the Ca-Sr compositions were varied.

At the 1250°C firing temperature x-ray diffraction data showed that α-$Ca_2P_2O_7$ was formed and that it was present in the compositions from $Ca_2P_2O_7$ to $Ca_1Sr_1P_2O_7$. In the $Ca_{1.75}Sr_{0.25}$ and the $Ca_{1.5}Sr_{1.5}Sr_{0.5}$ compositions, the α-$Ca_2P_2O_7$ had higher d-spacing values. In the $Ca_{1.25}Sr_{0.75}$ and the $Ca_{1.0}Sr_{1.0}$ compositions mixtures of decreasing amounts of α-$Ca_2P_2O_7$ and increasing amounts of α-$Sr_2P_2O_7$ were found, while in the $Ca_{0.75}Sr_{1.25}$ through the $Sr_2P_2O_7$ compositions only α-$Sr_2P_2O_7$ was found with lower d-spacing values in the former composition.

The emission properties of the 1250°C fired Ca-Sr compositions are also given in Table III. All of these phosphors were moderately intense, but again as in the 1050°C firing the brightest phosphors were in the Sr-rich compositions. There was, however, a slightly larger change in the emission peak positions from about 420 for the end members to 440 nm for the Ca_1Sr_1 composition, as compared to the 1050°C firing temperature where the peak position change was from about 422 nm for the end members to 431 nm for the $Ca_{0.75}Sr_{1.25}$ composition. The widths at half-height for the 1250°C temperature were about the same as those obtained at the 1050°C firing temperature.

Ba-Sr *pyrophosphates.*—There are two polymorphic forms of $Ba_2P_2O_7$, α and δ (11), and two forms of $Sr_2P_2O_7$, α and β (10). The α and δ-$Ba_2P_2O_7$:Eu^{+2} and β-$Sr_2P_2O_7$:Eu^{+2} compositions resulted in virtually dead phosphors. As reported previously, α-$Sr_2P_2O_7$:Eu^{+2} was a very bright phosphor whose emission properties were given in Table III.

Sr was substituted for Ba in $Ba_2P_2O_7$:Eu^{+2} in 0.25 mole increments and samples were fired at 1000° and 1200°C. X-ray diffraction data of the 1000°C fired samples showed: (a) δ-$Ba_2P_2O_7$ and α-$Sr_2P_2O_7$ for the end members; (b) solid solution of α-$Sr_2P_2O_7$ in δ-$Ba_2P_2O_7$

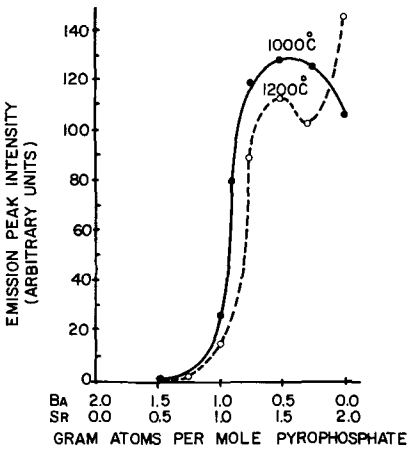

Fig. 5. Variation of emission peak intensity with changing cation in Ba-Sr pyrophosphate compositions fired at 1000° and 1200°C.

in the $Ba_{1.75}Sr_{0.25}$ and $Ba_{1.5}Sr_{0.5}$ compositions; (c) solid solution of δ-$Ba_2P_2O_7$ in α-$Sr_2P_2O_7$ in the $Ba_{0.75}Sr_{1.25}$, $Ba_{0.5}Sr_{1.5}$, and $Ba_{0.25}Sr_{1.75}$ compositions; and (d) mixtures of δ-$Ba_2P_2O_7$ and α-$Sr_2P_2O_7$ in the $Ba_{1.25}Sr_{0.75}$ and Ba_1Sr_1 compositions.

Figure 5 shows the variation of emission peak intensity of the Ba-Sr pyrophosphate compositions at the two firing temperatures of 1000° and 1200°C. At 1000°C there was no substantial luminescence until the area of the Ba_1Sr_1 composition was reached. At this point further substitution of Sr for Ba led to a rapid increase in emission intensity which reached a maximum at $Ba_{0.5}Sr_{1.5}$ before decreasing slightly at the $Ba_{0.25}Sr_{1.75}$, and the α-$Sr_2P_2O_7$:Eu^{+2} phosphor compositions.

The shape of the emission intensity curve for the 1200°C fired samples was quite similar to the 1000°C fired samples except at the pure α-$Sr_2P_2O_7$:Eu^{+2} composition. Here the intensity of the 1200°C sample was increased substantially over that of the 1000°C fired sample and this increased intensity was considerably out of line with the intensities from the remaining 1200°C fired compositions. A repeat test with new samples gave the same results.

A possible explanation for this irregularity is that the emission intensity of the unsubstituted α-$Sr_2P_2O_7$:Eu^{+2} phosphor is instrinsically higher at 1200°C, but when Ba is substituted for Sr, a substantial decrease occurs in the general level of emission intensity of the Ba-containing samples causing a discontinuity in the intensity curve between these samples and the α-$Sr_2P_2O_7$:Eu^{+2} composition.

This effect did not occur at 1000°C probably because of the decreased reactivity between the Ba and Sr ions at this lower firing temperature. Indeed, x-ray diffraction data of the 1200°C samples did show sharper lines and better crystallinity, although the compounds present in the various compositions were identical to the compounds present in the same compositions at the 1000°C firing temperature.

No shifts in emission band positions or changes in band widths were observed at either firing temperature. The luminescence observed for all samples was due entirely to the emission of the bright α-$Sr_2P_2O_7$:Eu^{+2} phosphor, which was simply being diluted by the nonluminescent δ-$Ba_2P_2O_7$:Eu^{+2} phase.

Ba-Ca *pyrophosphates.*—The end-member phosphors of the Ba-Ca pyrophosphate composition series, α and δ-$Ba_2P_2O_7$:Eu^{+2} and α and β-$Ca_2P_2O_7$:Eu^{+2} were discussed previously, and the emission properties of the latter two phosphors were given in Table III.

Increasing amounts of Ba in 0.25 mole increments were substituted for Ca in $Ca_2P_2O_7$:Eu^{+2} and the compositions fired at two different temperatures, 1000° and 1120°C. Bright phosphors with emission peaks in the 430-450 nm spectral region were found in the Ca-rich half of the composition join. In these high emission intensity compositions α-$Ca_2P_2O_7$ with higher d-spacing values was found by x-ray diffraction to be either the predominant or only phase present at both firing temperatures.

For the 1000°C firing α-$Ca_2P_2O_7$ with higher d-values was found in the range of compositions from $Ba_{0.25}Ca_{1.75}$ to $Ba_{0.75}Ca_{1.25}$ while mixtures of α-$Ca_2P_2O_7$ and predominantly δ-$Ba_2P_2O_7$ were found in composition range from $Ba_{1.0}Ca_{1.0}$ to $Ba_{1.5}Ca_{0.5}$. δ-$Ba_2P_2O_7$ was found for the pure Ba end member and the $Ba_{1.75}Ca_{0.25}$ composition, while β-$Ca_2P_2O_7$ was found for the pure Ca end member.

For the 1120°C firing temperature α-$Ca_2P_2O_7$ with higher d-values was found in the composition range from $Ba_{0.25}Ca_{1.75}$ to $Ba_{1.0}Ca_{1.0}$ and was also the predominant phase in the $Ba_{1.25}Ca_{0.75}$ composition. β-$Ca_2P_2O_7$ and δ-$Ba_2P_2O_7$ were found for the end members, and mixtures of α-$Ca_2P_2O_7$ and predominantly δ-$Ba_2P_2O_7$ in the remaining compositions, $Ba_{1.75}Ca_{0.25}$ and $Ba_{1.5}Ca_{0.5}$.

It appears that the partial substitution of Ba for Ca in $Ca_2P_2O_7$ leads to the stabilization of α-$Ca_2P_2O_7$ at temperatures where one would normally expect β-$Ca_2P_2O_7$ (β to α transition temperature approximately 1140°C) (7).

Table IV lists the emission properties of the Ba-Ca pyrophosphate compositions fired at the two different temperatures. Also included for comparison are the emission properties of unsubstituted α-$Ca_2P_2O_7$:Eu^{+2} prepared by firing at 1200°C and a reference phosphor, $CaWO_4$:Pb. The last column in this table lists the intensities of the Ba-stabilized α-$Ca_2P_2O_7$:Eu^{+2} phosphors, which even though fairly intense, are only about two-thirds of the intensity of the unstabilized α-$Ca_2P_2O_7$:Eu^{+2} phosphor obtained from a 1200°C firing.

Also in Table IV are the data for changes of emission peak positions and changes in band widths at half-height for varying compositions at the two firing temperatures. For the compositions fired at 1000°C, there was a shifting of the emission peak from 424 nm for β-$Ca_2P_2O_7$:Eu^{+2} to 460 nm for the $Ba_{1.25}Ca_{0.75}$ composition as Ba was substituted for Ca. There was also a substantial increase in the band width at half-height changing from 40 nm for β-$Ca_2P_2O_7$:Eu^{+2} to 97 nm for the $Ba_{1.25}Ca_{0.75}$ composition. Peak positions and widths at half-height of compositions with a greater Ba concentration of 1.25 could not be measured because of low emission intensity.

The changes that occurred in the emission peak positions and the emission band widths at half-height for the 1120°C fired compositions were considerably less than those that were fired at 1000°C. Emission peaks shifted only over a range from 428 nm for β-$Ca_2P_2O_7$:Eu^{+2} to 447 nm for both the $Ba_{0.5}Ca_{1.5}$ and $Ba_{0.75}Ca_{1.25}$ compositions, and the band widths at half-height ranged from 40 nm for β-$Ca_2P_2O_7$:Eu^{+2} to 61 nm for

Table IV. Emission properties of Ba-Ca pyrophosphate compositions

Composition	Peak position, nm	Band width ½ height, nm	Peak height intensity as % of Zn_2SiO_4:Mn
	1000°C Firing		
β-$Ca_2P_2O_7$:Eu^{+2}	424	40	8
$Ba_{0.25}Ca_{1.75}P_2O_7$:Eu^{+2}	429	51	63
$Ba_{0.5}Ca_{1.5}P_2O_7$:Eu^{+2}	443	54	64
$Ba_{0.75}Ca_{1.25}P_2O_7$:Eu^{+2}	445	55	46
$Ba_{1.0}Ca_{1.0}P_2O_7$:Eu^{+2}	456	94	16
$Ba_{1.25}Ca_{0.75}P_2O_7$:Eu^{+2}	460	97	5
	1120°C Firing		
β-$Ca_2P_2O_7$:Eu^{+2}	424	40	13
$Ba_{0.25}Ca_{1.75}P_2O_7$:Eu^{+2}	440	56	47
$Ba_{0.5}Ca_{1.5}P_2O_7$:Eu^{+2}	447	52	63
$Ba_{0.75}Ca_{1.25}P_2O_7$:Eu^{+2}	447	52	58
$Ba_{1.0}Ca_{1.0}P_2O_7$:Eu^{+2}	440	52	38
$Ba_{1.25}Ca_{0.75}P_2O_7$:Eu^{+2}	439	54	22
$Ba_{1.5}Ca_{0.5}P_2O_7$.Eu^{+2}	438	61	5
α-$Ca_2P_2O_7$:Eu^{+2} (1200°C)	419	30	97
$CaWO_4$Pb (Reference)	446	124	39

$Ba_{1.5}Ca_{0.5}$ with the majority of the compositions having a width at half-height between 52 and 56 nm.

Summary

Bright Eu^{+2} activated phosphors exist in the Ba-Ca, Ba-Sr, and Ca-Sr orthophosphate and pyrophosphate compositions. In the orthophosphate compositions the brightest phosphors were $Ba_3(PO_4)_2:Eu^{+2}$ and α-$Sr_3(PO_4)_2:Eu^{+2}$, and various composition mixtures of the two. α- and β-$Ca_3(PO_4)_2:Eu^{+2}$, and β-$Sr_3(PO_4)_2:Eu^{+2}$ resulted in either low intensity or dead phosphors, as did the majority of the phosphors that were obtained from composition mixtures of these poor phosphors with the two bright phosphors.

The substitution of small amounts of Ba in $Ca_3(PO_4)_2$ had a tendency to stabilize α-$Ca_3(PO_4)_2$ rather than β-$Ca_3(PO_4)_2$ even at temperatures considerably below the normal β to α transition temperature of 1180°C. A new compound with the formula $Ba_2Ca(PO_4)_2$ was also discovered in the $Ba_3(PO_4)_2$-$Ca_3(PO_4)_2$ system.

In the pyrophosphate compositions the brightest phosphors were α-$Ca_2P_2O_7:Eu^{+2}$ and α-$Sr_2P_2O_7:Eu^{+2}$. Weak or dead phosphors were obtained with α and δ-$Ba_2P_2O_7:Eu^{+2}$, β-$Ca_2P_2O_7:Eu^{+2}$, and β-$Sr_2P_2O_7:Eu^{+2}$. Mixtures of α-$Ca_2P_2O_7:Eu^{+2}$ and α-$Sr_2P_2O_7:Eu^{+2}$ resulted in bright phosphors, while composition mixtures of either of these two bright phosphors with any of the weak or dead pyrophosphate phosphors resulted in phosphor compositions with reduced intensities caused by the dilution of the good phosphors by the poor phosphors.

The brightest phosphors found in the present study, α-$Sr_3(PO_4)_2:Eu^{+2}$, $Ba_3(PO_4)_2:Eu^{+2}$, α-$Sr_2P_2O_7:Eu^{+2}$, and α-$Ca_2P_2O_7:Eu^{+2}$ were all from 200 to 400% more intense than the $CaWO_4$:Pb reference phosphor. Many of the partially substituted phosphors were also considerably more intense than $CaWO_4$:Pb, but, in almost every case, less intense than the unsubstituted materials.

Acknowledgments

The author wishes to thank Mr. Allen Rudis and Miss Marion Skeadas for the spectral energy distribution and x-ray diffraction measurements and Dr. K. H. Butler and Dr. M. J. B. Thomas for helpful discussions and suggestions.

Manuscript submitted Sept. 5, 1969; revised manuscript received *ca.* May 12, 1970. This was Paper 58 presented at the New York Meeting of the Society, May 4-9, 1969.

Any discussion of this paper will appear in a Discussion Section to be published in the June 1971 JOURNAL.

REFERENCES

1. W. L. Wanmaker and J. W. ter Vrugt, *Philips Res. Rept.* **23,** 363 (1968).
2. W. L. Wanmaker and J. W. ter Vrugt, *ibid.*, **22,** 355 (1967).
3. C. C. Lagos, *This Journal,* **115,** 1271 (1968).
4. M. V. Hoffman, *ibid.*, **115,** 560 (1968).
5. N. A. Gorbacheva, *Bull. Acad. Sci., USSR,* **30,** 1586 (1966).
6. V. P. Nazarova, *ibid.*, **25,** 322 (1961).
7. A. O. McIntosh and W. J. Jablonski, *J. Anal. Chem.*, **28,** 1424 (1956).
8. J. F. Sarver, F. A. Hummel, and M. V. Hoffman, *This Journal,* **108,** 1103 (1961).
9. A. C. Bouchard, *ibid.*, **115,** 1279 (1968).
10. R. C. Ropp, M. A. Aia, C. W. W. Hoffman, J. J. Veleker, and R. W. Mooney, *J. Anal. Chem.*, **31,** 1163 (July 1959).
11. P. W. Ranby, D. H. Mash, and S. T. Henderson, *Brit. J. Appl. Phys.*, Supplement No. 4S-18.

Preparation and Properties of Bulk $In_{1-x}Ga_xAs$ Alloys

John W. Wagner

Electronic Materials Division, Bell & Howell Company, Pasadena, California 91109

ABSTRACT

Single crystals of $In_{1-x}Ga_xAs$ have been grown by Czochralski techniques for $0.0 \leq x \leq 0.2$ and $0.8 \leq x \leq 1.0$. Polycrystalline single-phase $In_{1-x}Ga_xAs$ material has also been pulled for $0.2 < x < 0.8$. Two Czochralski techniques were employed: (*i*) the sealed system or Gremmelmaier technique, and (*ii*) the liquid encapsulation technique. Mass spectrographic data have been correlated with alloy lattice parameter determinations on the as-grown material to yield information on the solidus curve of the InAs-GaAs system. Hall measurements were made and impurity analyses were performed using the spark source mass spectrometer.

Since Woolley and Smith (1) initially demonstrated that continuous solid solution occurs in the InAs-GaAs system, a number of investigators have prepared homogeneous, single-phase $In_{1-x}Ga_xAs$ alloys throughout the entire range of composition using directional freezing techniques (2-4), zone-leveling techniques (5, 6), and vapor-growth techniques (7-10). These material investigations have been generated by the attractive thermoelectric properties of the InAs-GaAs alloys and by their light-emitting capabilities. Of the above studies, only the vapor epitaxial experiments have produced single-crystal alloys throughout the entire composition range. Diodes fabricated from these epitaxial layers have exhibited coherent light emission from 0.84μ for GaAs to 3.1μ for InAs.

Bulk single crystals of $In_{1-x}Ga_xAs$ are desirable for many applications. The work reported herein involves the growth of such single crystals by Czochralski pulling from the melt. When growing volatile materials from the melt at high temperatures, the Czochralski technique has several advantages (and disadvantages) when compared with directional freezing and zone leveling. The most important advantage is the direct three-dimensional observation of the growth process. One can therefore observe if the growing material is a single crystal or is polycrystalline, and can then determine whether to continue growth or to reseed and begin again. Visual observation is extremely difficult to achieve in directional freezing and zone-leveling processes when volatile materials at high temperatures are involved.

Key words: semiconductor, alloys, indium-gallium arsenide, crystal growth, Czochralski method, phase diagram, electrical properties.

Crystal Growth

The growth of $In_{1-x}Ga_xAs$ crystals from the melt required the use of special growth techniques in order to contain the volatile arsenic in the melts. Two tech-

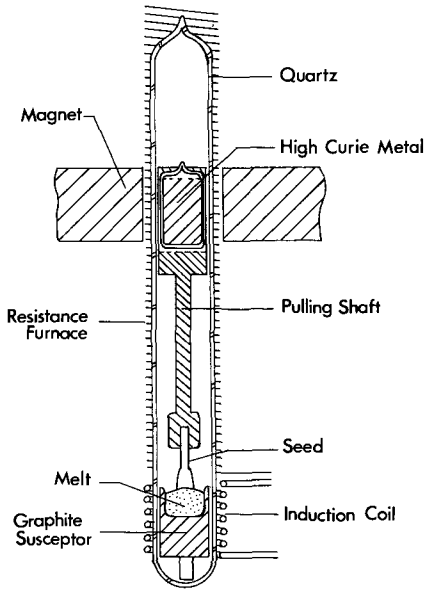

Fig. 1. Diagram of apparatus used for pulling crystals by the Czochralski technique [after Gremmelmaier (11)].

niques were used in this study: (*i*) Czochralski growth by maintaining a partial pressure of arsenic throughout the growing chamber (Gremmelmaier technique), and (*ii*) Czochralski growth by covering the melt with a transparent liquid (liquid encapsulation).

Sealed system.—In order to maintain a partial pressure of arsenic throughout the growing chamber, adaptations were made on the sealed all-quartz pulling apparatus used by Gremmelmaier (11). Figure 1 is a diagram of this system. Quartz was used as the growing chamber due to the reaction of the volatile arsenic with most other materials. Since the growing chamber is completely sealed, rotation and pulling were accomplished by magnetic coupling through the quartz tube. The entire growing chamber was enclosed in a resistance-heated furnace in order to hold an excess amount of arsenic in the vapor state and thus establish the required partial pressure. In order to grow from a stoichiometric melt, the partial pressure of arsenic had to be varied when growing different compositions of the alloy by changing the amount of the excess arsenic in the system. The partial pressures of arsenic over the InAs and GaAs melts were 0.2 and 1.0 atm, respectively. The partial pressures were calculated by using a two-to-one ratio for the As_4 to As_2 molecules. It was assumed that the partial pressures of arsenic necessary to maintain approximately stoichiometric melts for the alloys would vary linearly over this 0.2-1.0 atm range, *i.e.*, a melt containing 50 m/o (mole per cent) InAs and 50 m/o GaAs would need a pressure of 0.6 atm.

The indium-gallium alloy was melted by rf coupling (450 kc) and then was allowed to react with the arsenic at high temperature. Invariably, quartz crucibles were used. During the initial experiments, the rf was allowed to couple directly to the melts. However, direct coupling was found to yield unwanted thermal fluctuations in the melt (as evidenced by polycrystalline boules containing very small grains, less than 100μ in the largest dimension). Therefore, a graphite susceptor was placed around the quartz crucible. By allowing the rf to couple to the graphite susceptor, improved thermal stability was attained in the melt. All boules reported herein which were grown using the Gremmelmaier technique were pulled from melts heated indirectly via a graphite susceptor. In order to minimize contamination problems from the graphite (Grade UT-6, Ultra Carbon Corporation), the susceptor was baked out for several hours under vacuum at high temperatures, typically 1000°C and sealed in quartz. The temperature sensing device was a sapphire rod which transmitted the radiant energy from the base of the crucible to a thermopile. The growth temperatures ranged from 938°C for InAs to 1238°C for GaAs.

Liquid encapsulation.—The alternative to establishing a partial pressure of arsenic over the melt to maintain stoichiometry is to contain the arsenic using the liquid encapsulation technique (12-14). By covering the melt with liquid boric oxide (B_2O_3) and maintaining on the outer surface of the liquid an inert gas pressure, which was greater than the vapor pressure of the arsenic at the melt surface, volatilization was suppressed. Boric oxide was chosen in this study because it was less dense than the melts, was optically transparent, and was virtually nonreactive with the melt constituents. The hygroscopic nature of the boric oxide necessitated vacuum heat treating (10^{-4} Torr) at approximately 1000°C for 24 hr. If the heat treatment was not performed, numerous gas bubbles existed on the melt surface while trying to pull.

A schematic diagram of the liquid encapsulation growth apparatus is shown in Fig. 2. The quartz tube is sealed at both ends by O-ring flanges so that a vacuum or a positive pressure may be maintained in the growth chamber. The pull rod and the crucible may both be rotated. Heating was by resistance furnace (rf coupling is also possible with this technique), and the temperature was sensed by a thermocouple. The thermocouple was placed near the heater element so as to obtain as high a sensitivity as possible. The temperature near the element was controlled to within $\pm\frac{1}{4}$°C. The seed was lowered through the boric oxide to the melt surface and the crystal was pulled slowly through the B_2O_3. Often the boric oxide was so viscous that a thin layer remained on the crystal as it was pulled out of the B_2O_3. This was actually desirable, since if the boric oxide were permitted to flow off the crystal too rapidly, the crystal would still be in a relatively hot zone and would lose a substantial amount of arsenic from the crystal surface by vaporization. This arsenic would then cause a problem with visibility as it deposited on the cooler sections of the quartz tube. The thin layer of B_2O_3 remaining on the crystal was not a problem, since it was easily removed by dissolution in hot water.

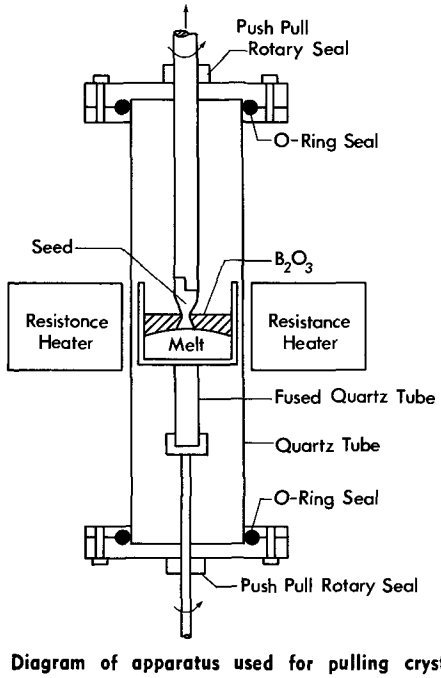

Fig. 2. Diagram of apparatus used for pulling crystals under B_2O_3 glass.

The liquid encapsulation technique offers several advantages over the Gremmelmaier technique. First, the boric oxide glass provides thermal insulation at the surface, minimizing gaseous convection currents, and yielding greater thermal stability at the melt surface. Second, the liquid encapsulation allows pulling and rotating by direct mechanical means, thereby ensuring less vibration in the system. Third, the boric oxide layer tends to allow the establishment of better thermal gradients across the melt surface (as judged by the relative ease of obtaining a nearly flat growth interface).

General.—Single crystals of $In_{1-x}Ga_xAs$ were prepared for $0.0 \leq x \leq 0.2$ and $0.8 \leq x \leq 1.0$ using both the Gremmelmaier and liquid encapsulation techniques. All of the single crystals were grown in the {111} direction. The crystals were typically 10-30g in weight and were 5-10 mm in diameter. The melts used ranged in size from 100 to 300g. Polycrystalline, single-phase material was also produced for $0.2 < x < 0.8$. For crystals grown using the Gremmelmaier technique pulling rates were varied from 1 cm/hr to as low as 1 mm/hr. Crystals grown using the liquid encapsulation technique were pulled at rates of 1-3 mm/hr. In both techniques, seeding required undercutting of the seed diameter to 1-2 mm for a length of up to 3 cm in order to reduce crystal strains. This is especially important in growing the alloys, since strains due to initial lattice mismatch between the seed and the first portion of the alloy to be grown are quite important.

Phase Diagram

The phase diagram of the InAs-GaAs system has been reported by several investigators (6, 15, 16). Agreement is lacking between the investigators and, therefore, in order to have control of the composition of each crystal grown, the InAs-GaAs phase diagram was investigated in this study.

The compositions of the first-to-freeze portions of several $In_{1-x}Ga_xAs$ ingots grown in this study were determined using spark-source mass spectrographic analyses. The estimated accuracy of these compositions is ±10% of the values given. The lattice parameters, a_o, from these first-to-freeze sections were determined from x-ray powder photographs using the $\sin^2\theta$ extrapolation technique. The accuracy of these parameters is estimated to be ±0.001Å. The resulting data are listed in Table I. Correlation of the mass spectrographic data with the lattice parameters indicates that Vegard's law is followed in this system, a fact which has been previously shown by several investigators (1, 6, 7). Therefore, the final composition of each first-to-freeze portion was determined under the assumption that Vegard's law holds in the InAs-GaAs system throughout the entire range of composition.

Once the composition of the first-to-freeze portion of each crystal had been determined, the solidus points of this system were then plotted using the liquidus curve given by Van Hook and Lenker (16). The resulting phase diagram is shown in Fig. 3. Also shown are the solidus data of Van Hook and Lenker (16), Woolley and Smith (15), and Hockings *et al.* (6). Our solidus data are seen to be in good agreement with those of Woolley and Smith (15) and Hockings *et al.* (6) who also used Vegard's law for composition determinations. Since we have used the liquidus curve of Van Hook and Lenker (16) in plotting the solidus, the good agreement between our solidus and that of Woolley and Smith (15) (who used an anneal-quench-x-ray technique to obtain these solidus values) and Hockings *et al.* (6) suggests that this liquidus is essentially correct. However, the solidus curve of Van Hook and Lenker (16) is believed to be incorrect for temperatures of less than 1025°C due to nonequilibration of their alloy samples at the relatively low temperatures. Stringfellow and Greene (17) have calculated the pseudobinary phase diagram of the InAs-GaAs system and their calculated solidus curve is in reasonable agreement with that shown here of Woolley and Smith (15), Hockings *et al.* (6), and the present paper.

Table I. Composition and lattice parameters of first-to-freeze portion of $In_{1-x}Ga_xAs$ boules

Sample No.	Mole fraction of GaAs in melt	x in First-to-freeze section, mole fraction (from mass spectrometer)	Lattice parameter (Å) of first-to-freeze section	x in First-to-freeze section, mole fraction (from Vegard line)
119	InAs	—	6.057	—
6	0.003	0.0040 ± 0.0004	6.056	0.004
17	0.004	0.0074 ± 0.0008	6.055	0.0075
8	0.005	0.0090 ± 0.0009	6.054	0.010
110	0.012	0.037 ± 0.004	6.045	0.034
133	—	0.042 ± 0.004	6.043	0.040
129	0.016	0.049 ± 0.005	6.037	0.050
126	0.018	0.062 ± 0.006	6.035	0.058
124	0.036	0.11 ± 0.01	6.012	0.110
132	0.094	0.31 ± 0.03	5.926	0.320
131	0.105	0.35 ± 0.04	5.900	0.385
139	0.350	—	5.710	0.850
138	0.490	—	5.688	0.905
19	0.773	—	5.665	0.960

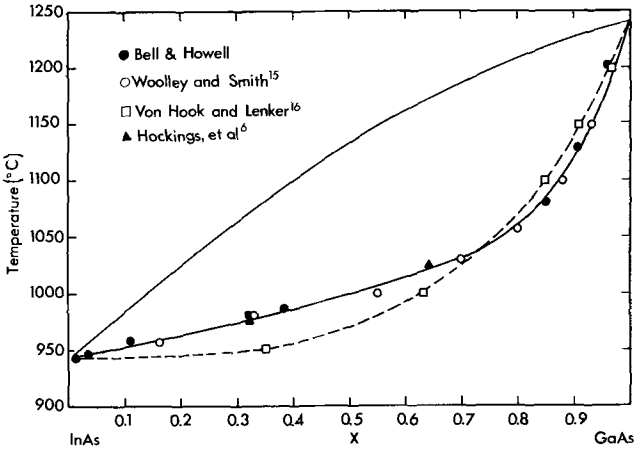

Fig. 3. Phase diagram of the $In_{1-x}Ga_xAs$ system

Characterization

As previously mentioned, x-ray powder patterns were used to determine the lattice parameter of each $In_{1-x}Ga_xAs$ ingot grown, and these parameters were compared with the Vegard line to determine the compositions of these ingots. X-ray Laue patterns were made to yield a qualitative indication of crystal perfection and to verify the single-crystal nature of several of the ingots. Most of the powder photographs and Laue photographs had sharp lines and spots, respectively, which indicate that the materials are relatively free of strains and compositional inhomogeneities.

Electrical measurements were made using conventional d-c potentiometric techniques to determine Hall coefficients and resistivities. The Hall mobilities and carrier concentrations were then calculated using the equations $\mu = R\sigma$ and $n = 1/Re$. The standard Hall sample was a bridge-type rectangular parallelopiped with dimensions of ~1 mm thickness, ~1 mm width, and ~1 cm length. These samples were always taken from the area of the boule just below the "crown" and were all representative of the "first-to-grow" section of the ingot. The sample was ultrasonically cut so as to have several arms to which the electrical contacts were attached. The resulting data are shown in Table II, and the electron mobilities at 300° and 77°K of our best $In_{1-x}Ga_xAs$ samples are plotted *vs.* composition in Fig. 4. Also plotted in Fig. 4 are electron mobility data at 300°K taken from Conrad *et al.* (9) which were measured on vapor-epitaxially deposited InAs-GaAs alloys on GaAs substrates. The data of Conrad *et al.* (9) indicate a minimum in electron mobility near the midrange of composition, which was suspected to be due to alloy scattering. However,

Table II. Electrical properties of InAs-GaAs boules

Boule No.	x, Mole fraction GaAs (from Vegard's law)	300°K $n \times 10^{16}$, cm^{-3}	300°K μ, cm^2/V-sec	77°K $n \times 10^{16}$, cm^{-3}	77°K μ, cm^2/V-sec
119	InAs	2.3	25,700	2.1	48,300
8**	0.010	1.2	17,400	0.95	19,000
110	0.034	1.6	16,900	1.6	24,600
133**	0.040	2.5	20,000	2.4	35,000
124	0.110	3.7	17,800	3.6	29,400
132	0.320	6.2	12,300	6.2	17,500
131	0.385	3.2	14,900	—	—
115**	~0.015	12	18,500	12	25,500
19*	0.960	120	3,100	120	3,200

* Sample doped with tellurium.
** Pulled under B_2O_3. The B_2O_3 in boule No. 115 was not as well-purified as that used for boules 8 and 133.

our room temperature (and also 77°K) data do not indicate a minimum in the mobility curve. Also, the electron mobilities of our InAs-GaAs samples increase from 300° to 77°K in contrast to the results reported by Conrad *et al.* (9) This implies that scattering from an unknown charged center (which was apparently seen in the vapor epitaxial material) is not present in melt-grown material.

Several of the $In_{1-x}Ga_xAs$ crystals were analyzed for impurities using the spark-source mass spectrometer. An impurity analysis which is typical for crystals containing 0.05-0.10 mole fraction GaAs is given in Table III. Silicon and sulfur are the most important of the major electrically active impurities. Analyses of the elemental arsenic show both of these impurities in quantities of such a magnitude as to account for their concentration in the $In_{1-x}Ga_xAs$ after consideration of the appropriate distribution coefficients. Both the silicon and sulfur can be removed from the arsenic by several purification steps, and in our laboratory such purification has yielded GaAs crystals having Si and S levels of an order of magnitude lower than those given in Table III for the alloys. In fact, GaAs crystals have been grown from quartz crucibles with carrier concentrations as low as 2×10^{15} cm^{-3} and room temperature mobilities of 8600 cm^2 V^{-1} sec^{-1}. These results indicate the quartz crucible and chamber do not significantly add silicon to the melt. However, care must be taken not to allow the melt temperature to exceed 1260°C. At 1300°C silicon pickup from the crucible can exceed 1 ppm. No difference was seen in the levels of electrically active impurities in crystals grown by the two techniques, *i.e.*, they typically contained approximately 1 ppm of such impurities.

Conclusion

Single crystal $In_{1-x}Ga_xAs$ alloys have been pulled from the melt using both the Gremmelmaier and liquid encapsulation techniques. Although only polycrystalline materials were prepared for $0.2 < x < 0.8$, it is believed that single crystals can be pulled from the melt throughout the entire composition range if greater mechanical and thermal stability is provided, slower growth rates are employed, and higher quality seeds are generated, *i.e.*, single-crystal seeds with compositions matching that of the crystals to be grown. The solidus for the InAs-GaAs system was determined and our results are in agreement with Woolley and Smith (15) and Hockings *et al.* (6). The electron mobilities of the InAs-GaAs crystals did not show a minimum with respect to composition and increased on cooling from 300° to 77°K.

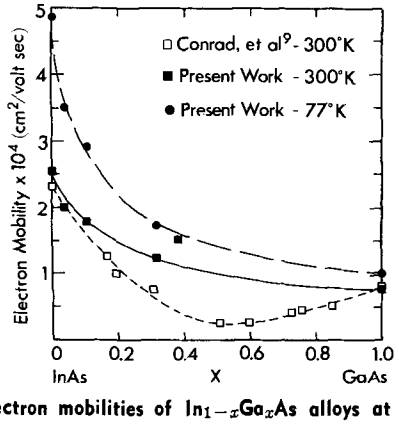

Fig. 4. Electron mobilities of $In_{1-x}Ga_xAs$ alloys at 300°K and 77°K.

Table III. Typical impurity analysis of InAs-GaAs (parts per million atomic)

Element*	Detection limit**	Concentration in crystal
Li	0.03	5.0
C	0.3	5.0
N	0.3	1.0
O	0.3	5.0
F	0.3	0.4
Al	0.1	0.2
Si	0.3	0.5
S	0.3	2.0
Cl	0.3	2.0
K	0.05	2.0
Ca	0.3	0.5

* Elements not listed were not detected and had concentrations of less than 0.5 ppma.
** The detection limit is not the ultimate limit of the apparatus, but rather is peculiar to the specific exposure time used for this sample.

Acknowledgments

The author wishes to thank Harold Olsen for growth of the crystals via the Gremmelmaier technique. He also thanks R. K. Willardson, M. C. Arst, and A. G. Thompson for useful discussions. This research was supported in part by the U. S. Naval Weapons Center, Corona, California, under Contract Number N123-(62738)55582A.

Manuscript submitted Oct. 17, 1969; revised manuscript received *ca.* May 20, 1970. This paper was presented in part at the Dallas Meeting of The Society, May 7-12, 1967.

Any discussion of this paper will appear in a Discussion Section to be published in the June 1971 JOURNAL.

REFERENCES

1. J. C. Woolley and B. A. Smith, *Proc. Phys. Soc.*, **70**, 153 (1957).
2. J. C. Woolley, C. M. Gillett, and J. A. Evans, *ibid.*, **77**, 700 (1961).
3. A. G. Thompson and J. C. Woolley, *Can. J. Phys.*, **45**, 2597 (1967).
4. I. Melngailis, A. J. Strauss, and R. H. Rediker, *Proc. IEEE*, **51**, 1154 (1963).
5. M. S. Abrahams, R. Braunstein, and F. D. Rosi, *J. Phys. Chem. Solids*, **10**, 204 (1959).
6. E. F. Hockings, I. Kudman, T. E. Seidel, C. M. Schmeltz, and E. F. Steigmeier, *J. Appl. Phys.*, **37**, 2879 (1966).
7. E. K. Muller and J. L. Richards, *ibid.*, **35**, 1233 (1964).
8. H. T. Minden, *This Journal*, **112**, 300 (1965).
9. R. W. Conrad, P. L. Hoyt, and D. C. Martin, *ibid.*, **114**, 164 (1967).
10. R. J. Sirrine, *ibid.*, **111**, 750 (1964).
11. R. Gremmelmaier, *Z. Naturforsch.*, **11a**, 511 (1956).
12. E. P. A. Metz, R. C. Miller, and R. Mazelsky, *J. Appl. Phys.*, **33**, 2016 (1962).
13. J. B. Mullin, B. W. Straugham, and W. S. Bricksell, *J. Phys. Chem. Solids*, **26**, 782 (1965).
14. J. W. Wagner and R. K. Willardson, *Trans. Met. Soc. AIME*, **242**, 366 (1968).
15. J. C. Woolley and B. A. Smith, *Proc. Phys. Soc.*, **72B**, 214 (1958).
16. H. J. Van Hook and E. S. Lenker, *Trans. Met. Soc. AIME*, **227**, 220 (1963).
17. G. B. Stringfellow and P. E. Greene, *J. Phys. Chem. Solids*, **30**, 1779 (1969).

Technical Notes

Argon Content in (111) Silicon for Sputtering Energies below 200 eV

J. Comas and E. A. Wolicki

Naval Research Laboratory, Washington, D. C. 20390

A technique for detecting implanted argon in silicon by the neutron activation of argon has been described and data have been given in the 200 to 2200 eV bombarding range (1). These data showed that the argon content rises very sharply from around 225 eV and appears to approach a plateau around 2200 eV. We have been able to extend the low energy implantation data well below 200 eV by improving the shielding and the counting system for the radioactive argon. In addition absolute calibration of the counting system has been obtained from standard Ar-Si samples. In this communication we present data on argon implanted in (111) Si below 200 eV for bombarding currents of 1 and 2 mA and from 50 to 2200 eV at 1 mA. The low energy, high beam intensity, range is of special interest in sputtering experiments and the argon trapping presented go much lower in energy than most studies. The bombarding argon energies as stated do not include corrections due to the plasma potential; this would increase the argon bombarding energies by about 5.0 eV.

The targets used were thin (111) Si wafers about 25 mm in diameter. The bombarded surface area, defined by a graphite guard ring, was 3.14 cm^2. Prior to being bombarded, the wafers were chemically etched in a modified CP_4 solution and rinsed with ethyl alcohol. The etching produced a shiny smooth surface and reduced the sample thickness to about 0.060 in. Thin Si samples were used in order to minimize the interference from the Si^{31} beta activity produced by the neutron irradiation, which introduces counting errors, as well as being a considerable health hazard.

The bombarding apparatus for the bombardment at 200 eV and above is similar to that previously described (1). An argon ion beam is drawn through a screen placed at the edge of a thermionically sustained, magnetically confined, arc discharge. Argon ions that pass through the screen are further accelerated between the screen and the target by applying a negative potential on the target with respect to the screen. For bombardments below 200 eV the screen is removed and the target is placed in its position mounted on a graphite holder (2). The target is biased negatively with respect to the arc discharge and bombarded normally with argon ions drawn from the arc. In this position the target acts like a large Langmuir probe placed in a plasma, and low energy, high intensity, bombarding beams can be readily obtained. The bombarding times of 10 min were long enough to produce an equilibrium condition between the incident argon beam and the trapped argon being released as the Si surface is sputtered away. The accuracy of the bombarding current measurement is 3.5%.

After argon bombardment the targets were removed from the sputtering apparatus and placed in NRL's nuclear reactor for activation. A lithium-drifted germanium detector was used to obtain the gamma ray spectrum of the radioactive Ar^{41} and Si^{31} produced (1.293 and 1.265 MeV, respectively). A small Ar background, due to the activation of natural argon in the air by the reactor, was eliminated by shielding of the detection system. A graded shield made of ⅛ in. plates of lucite, lead, and aluminum [aluminum plate against the Ge(Li) detector] greatly reduced the "cooling" time. The procedure more than doubled the number of events from Ar^{40} recorded in the gamma ray spectrum.

Absolute calibration of the counting efficiency was accomplished by using Si samples which were bombarded at 3.0 MeV with a known number of argon ions, and which were otherwise similar to the samples used for the sputtering runs. It is reasonable to assume that all the Ar ions at this energy are trapped, since the sticking probability approaches unity for energies above 20 KeV (3). Less than 10^{-5} % of the implanted argon in a Si wafer undergoes transmutation for each 1 hr exposure in the reactor. The prepared Si-Ar calibration standard was then activated and counted under the same conditions as the low energy argon sputtered targets; in this way a calibration for the system was obtained which required no further corrections.

The NRL Van de Graaff accelerator was used to produce the 3.0 MeV beam of Ar^{40} ions. The beam was magnetically analyzed before striking the target and, to insure uniform irradiation over the bombarded area, the beam spot was scanned electrostatically. Tests were made for the presence of a neutral beam component which would contribute to the implanted Ar content, but not be measured as part of the integrated beam charge. The neutral component was obtained by comparing the coloration produced in LiF by a given dose of 3.0 MeV Ar^{40} ions (4), to the coloration produced when the charged beam was removed from the target by a deflecting voltage. Three permanent magnets were also placed along the beam transport tube between the deflecting plates and the target in order to remove any particles which were ionized after passing through the deflecting plates. The neutral beam component obtained from the coloration measurements was found to be less than 3% of the total charge delivered to the target.

The number of incident 3.0 MeV Ar ions was obtained from the total electrical charge which was collected in a Faraday cup arrangement and integrated during bombardment. A negatively biased guard ring was placed at the entrance of the chamber to suppress secondary electrons. The beam size (as measured on a quartz plate) was about 1.6 cm^2 and the bombarding beam current was 1.5 μA. For each of three samples, 9.59×10^{15} argon ions were implanted; a fourth sample was bombarded with 3.84×10^{16} argon ions as a test for saturation and none was observed. The (111), (110), and (100) orientations were used in different bombardments to test for any orientation dependence which might occur; as would be expected in the MeV range, no orientation dependence was observed in the argon content. The argon content in a 3.0 MeV Ar implanted Si sample was also examined as a function

Key words: ion implantation, activation analysis, ion-atom collisions, surface interactions, ion trapping.

of temperature. The sample was heated in vacuum for 15 min in 100°C steps. No significant change in the argon content was observed until near melting temperatures were reached. This is consistent with the observations of Kelly and Brown (5) on the release of 40 KeV Xe^+ ions injected into Al, Ta_2O_3, and Al_2O_3.

The argon content in each Si target was obtained by considering the initial argon activity, integrating the argon signal, and using the counter efficiency as measured from the 3.0 MeV Ar-Si standards. Results of a series of bombardments from 12 to 200 eV for a bombarding beam of 2 mA and from 50 to 200 eV for a 1 mA beam are shown in Fig. 1. The argon content rises very sharply from approximately 7.6 x 10^{13} Ar/cm^2 at 12 eV to approximately 1.1 x 10^{16} Ar/cm^2 at 85 eV for the 2 mA curve. The same sharp initial increase is seen in the 1 mA case. Above 85 eV the rise is not as drastic and at 200 eV the amount retained is approximately 2.15 x 10^{16} Ar/cm^2. In Fig. 2 the argon content for a 1 mA beam is shown for a series of bombardments from 50 to 2200 eV; data in the 50-200 eV range was taken from Fig. 1. Above 800 eV there is a gradual increase in the argon content to about 7.0 x 10^{16} Ar cm^2. It appears from the above results that the threshold for the trapping of argon in Si is in the same range as the threshold for sputtering, around 20 eV, as estimated by extrapolation of Ar-Si yield curve of Wolsky and Zdaunk (6).

The above curves resemble the rapid rise in the W(100) sticking probability *vs.* ion energy curves of Ne, Ar, Kr, and Xe of Kornelsen and Sinha (7). The

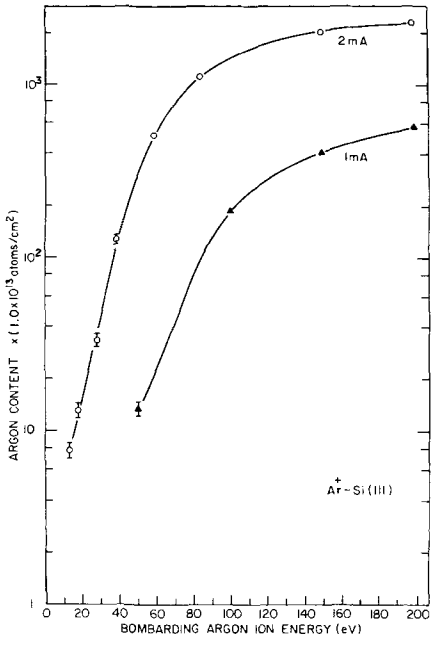

Fig. 1. Argon content in (111) Si *vs.* argon ion energy from 12 to 200 eV for a 2 mA beam and from 50 to 200 eV for a 1 mA beam. Absolute calibration was obtained by using an Ar-Si standard with a known number of trapped argon atoms.

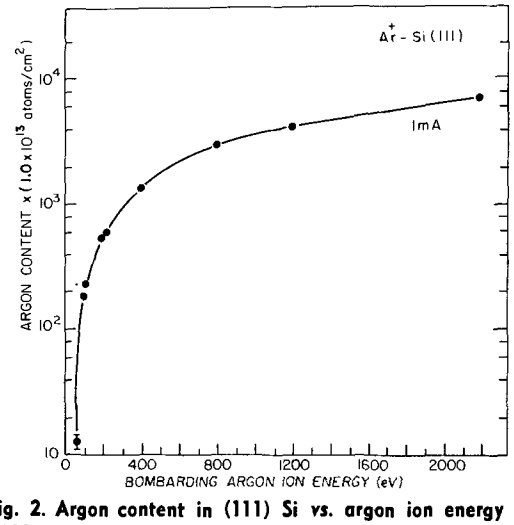

Fig. 2. Argon content in (111) Si *vs.* argon ion energy from 50 to 2200 eV for a 1 mA beam.

sticking probability of Ar goes from about 1.5 x 10^{-3} at 100 eV to about 0.41 at 1 KeV. They obtained desorption spectra from W(100) bombarded with Ne, Ar, Kr, and Xe from 40 eV to 5 KeV. The desorption spectra at low energies shows the influence that the surface has in the trapping process. The Ne desorption spectrum at 40 eV for a dose of 1.5 x 10^{13} ions/cm^2 showed no detectable desorption. Ne was the lowest energy spectrum presented and had a Ne detection limit of ~3 x 10^{10} atoms/cm^2. Distinct Ne desorption peaks were observed, however, from the 60 eV bombardment.

Our results cannot be compared directly since the doses in our bombardments are considerably higher (1.9 x 10^{19} ions/cm^2 for the 2 mA case), and the argon is detected *in situ*. We, however, observe significant trapping for the 2 mA bombardment below 60 eV. The difference in the argon content between the 1 and 2 mA curves is believed due to the trapping of argon at sites on or near the surface which are created during the bombardment, as well as bombarding argon-trapped argon collisions on the surface.

Manuscript submitted Feb. 9, 1970; revised manuscript received May 1, 1970.

Any discussion of this paper will appear in a Discussion Section to be published in the June 1971 JOURNAL.

REFERENCES

1. J. Comas and C. A. Carosella, *This Journal*, **115**, 975 (1968).
2. J. Comas and C. B. Cooper, *J. Appl. Phys.*, **37**, 2820 (1966).
3. F. Brown and J. A. Davies, *Can. J. Phys.*, **41**, 844 (1963).
4. K. L. Vander Lugt, J. Comas, and E. A. Wolicki, *J. Phys. Chem. Solids*, **30**, 2486 (1969).
5. R. Kelly and F. Brown, *Acta. Met.*, **13**, 169 (1965).
6. S. P. Wolsky and E. J. Zdanuk, *Phys. Rev.*, **121**, 374 (1961).
7. E. V. Kornelsen and M. K. Sinha, *J. Appl. Phys.*, **39**, 4546 (1968).

Negative Surface Charge in Ge MOS Structures

T. O. Sedgwick* and S. Krongelb

IBM Thomas J. Watson Research Center, Yorktown Heights, New York 10598

It has been reported (1, 2) previously that Ge surfaces covered with deposited SiO_2 films and subjected to hydrogen annealing exhibit a midgap surface acceptor state, and either a second acceptor state near the valence band or fixed negative charge in the oxide. This second negative charge center was observed to appear prominently only after hydrogen annealing at 800°C, although it could be removed simply by inert gas annealing. Such formation and removal conditions are somewhat different from those for the hydrogen-induced midgap acceptor state. We have recently found that negative oxide charge also appeared in Al-SiO_2-Ge MOS devices, but not in Au-SiO_2-Ge MOS structures, when they were annealed with the metal in place. This note presents this data and indicates that the negative charge is due to exposure of the surface to atomic hydrogen. It also shows that the negative charge appears in high density on Ge <110> surfaces and only in moderate density on Ge <111> surfaces. Si samples do not show any negative surface charge formation when subjected to equivalent processing.

Experimental

Samples were prepared by coating 1 to 10 ohm-cm p-type Ge or Si wafers with 300-2000Å pyrolytic SiO_2 (3).

Final premetallization annealing.—All samples were then annealed in 10% H_2-90% N_2 at 800°C for 17 min, henceforth referred to simply as H_2 annealing. Some of these samples had a final anneal in air at 230°C for about 17 hr or for shorter times in dry O_2 at 420°C, henceforth referred to as O_2 annealing. A few Ge <110> samples received a final anneal in dry N_2 at 650°C for 5-60 min. Finally, approximately 5000Å Al or Au field plate dots about 30 mil in diameter were evaporated (metallization) onto the oxide (the samples were not intentionally heated during evaporation and their temperature probably did not exceed 75°C for more than a few minutes). The fixed charge density, Q_{fc}, of these MOS devices was determined by capacitance-voltage measurements and the results are shown in Fig. 1.

Post metallization annealing.—After the above-mentioned annealing steps and initial measurements, some of the same samples were then annealed with the Al or Au dots in place for about 17 hr in air at 230°C. The fixed charge density Q_{fc} was remeasured and the results are shown in Fig. 2.

It was necessary to use a variation (1, 2) of the usual MOS measurements technique to measure Q_{fc} in the Ge samples. In this method, capacitance voltage curves are determined at 150 kHz and at 77°K. The advantage of this technique is that the midgap surface acceptor states introduced by hydrogen annealing cannot follow the a-c measuring signal, and do not therefore introduce excess capacitance[1] which would cause an error in the Q_{fc} determination. Q_{fc} is determined simply by measuring the voltage shift at the flat band point. The inability of this technique to distinguish between surface states lying very close to the valence band and fixed oxide charges has been discussed previously (1). The silicon samples were measured at 150

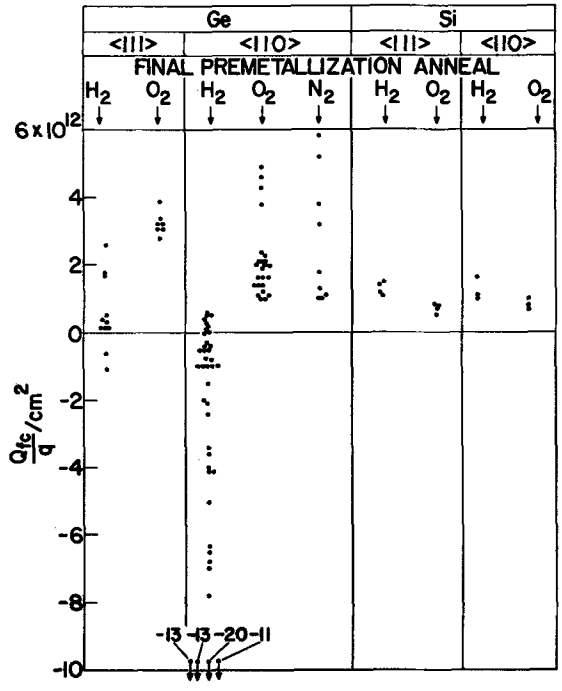

Fig. 1. Effect of final premetallization annealing ambient on fixed charge density showing dependence on semiconductor material and orientation. Each point represents one device.

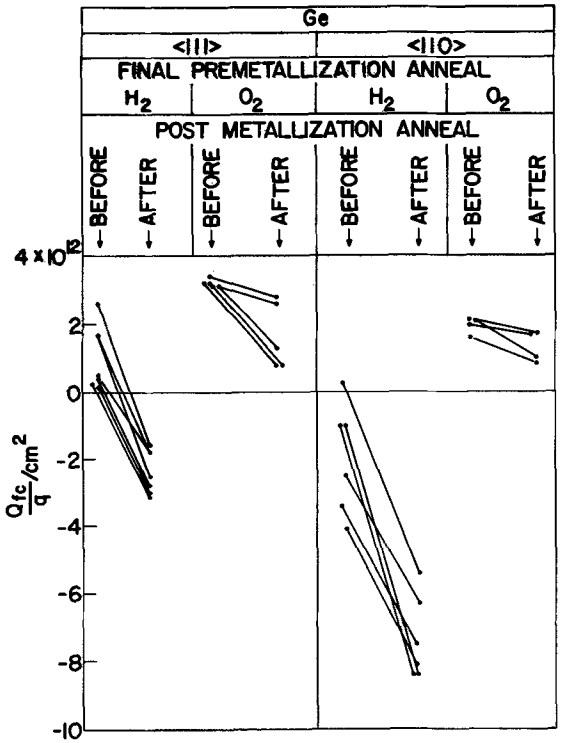

Fig. 2. Changes in fixed charge density caused by post-metallization annealing as a function of Ge crystal orientation and premetallization annealing ambient. Lines (———) connect data points for the same device.

* Electrochemical Society Active Member.

Key words: annealing MOS structures, electrode effects annealing MOS structures, semiconductor orientation MOS structures, Si *vs.* Ge MOS structures.

[1] This excess capacitance in the case of some Ge samples is so large that at room temperature the normal MOS capacitance "dip" is not seen at all.

kHz and room temperature[2] and exhibited the normal MOS capacitance "dip."

Results

Figure 1 shows the effect of the final premetallization annealing ambient on Q_{fc} for <110> and <111> oriented Ge and Si surfaces. Large negative Q_{fc} values only occur on Ge <110> surfaces exposed to H_2. Ge <111> surfaces subject to H_2 annealing show a small tendency toward negative Q_{fc} values. Note that Ge <110> samples subjected to the usual hydrogen anneal, but then finally annealed in dry N_2 show the usual positive Q_{fc} found for O_2 annealed samples. Si samples show a shift of opposite sign in Q_{fc} after hydrogen annealing.

Figure 2 shows the effect of post-metallization annealing, and the dependence of this effect on the last premetallization annealing ambient for the two Ge orientations. The lines connect before and after results on the same device. All samples show some negative shift of Q_{fc} on annealing with Al dots. The largest shifts are observed on samples which have received H_2 treatment as their final premetallization annealing with Ge <110> surfaces showing shifts of 5×10^{12} and Ge <111> surfaces exhibiting the slightly smaller change of 3×10^{12}. O_2 annealed samples show the smallest negative Q_{fc} shift (approximately 1×10^{12}), and this shift has saturated and does not increase on further post-metallization annealing. The increase in negative Q_{fc} for the H_2 annealed samples, on the other hand, was found not to be saturated after the 17 hr post-metallization anneal. Thus on further post-metallization annealing there is further significant increase in the negative fixed charge. For example, an additional 11-day anneal (not shown in Fig. 2) at 230°C increased the negative Q_{fc} of two samples by an additional $3.5\text{-}4.5 \times 10^{12}/cm^2$.

In neither Fig. 1 nor 2 was there a correlation between measured Q_{fc} and oxide thickness in the range 300-2000Å, although an attempt was made to find such a correlation.

Samples provided with Au dots and subjected to the same annealing cycles as indicated in Fig. 2 showed very small shifts in Q_{fc}. In one case, samples provided with Au dots showed no increase in negative charge, and in a second case Au dot samples showed a factor of ten smaller increase in negative charge than the control sample which was an identically treated Al-SiO_2-Ge MOS device.

Discussion

The appearance in Fig. 1 of a large but variable negative Q_{fc} on Ge <110> and to a lesser extent on Ge <111> surfaces correlates clearly with hydrogen exposure. Since we observe the same pattern of occurrence in Fig. 2 for samples annealed with Al (but not Au!) dots in place, we hypothesize that this effect is also due to hydrogen which has presumably been produced by the reaction of Al with residual water or hydroxyl groups in the SiO_2 layer. There are two additional pieces of evidence which lend support to this same hypothesis. First, it has been shown that SiO_2 films on Ge which contain water have an abnormally high dielectric constant. Annealing such films with Al dots reduces the dieletric constant, an effect which is attributed to the removal of water by reaction with Al (4). Second, in the Si planar transistor technology, a similar annealing is believed to produce atomic hydrogen which diffuses through the oxide and eliminates fast surface states at the Si interface (5).

A p-type electrical effect due to hydrogen exposure was noted by Heiland and Handler (6) who observed a strong increase in the p-type surface conductivity on clean <111> Ge after exposure to atomic hydrogen which could be removed readily by vacuum annealing at 550°C for ½ hr. Molecular hydrogen seems to have no effect electrically on clean surfaces at room temperature (7), and it is essentially completely desorbed above 280°C (7, 8). Therefore, it is suggested that atomic hydrogen is the active species which is physically trapped at the interface by the oxide layer. The trace of atomic hydrogen present at equilibrium in hydrogen gas at 800°C (9) could account for the results of Fig. 1, and the reduction of hydroxyl or water at 230°C by Al to yield atomic hydrogen could account for the results of Fig. 2. The fact that the negative Q_{fc} is very rapidly removed by an inert gas anneal at 650°C suggests that the hydrogen is loosely bound near the Ge surface and readily out-diffuses through the SiO_2 layer, although much more slowly than would occur from a Ge surface not covered with a deposited oxide layer.

It does not seem possible to postulate a convincing structural model for the interaction of atomic hydrogen with Ge surfaces. We note, however, that a similar p-type shift in Ge surface potential has been observed by Gerischer *et al.* (10) and Memming and Neumann (11). They observe a p-type surface potential shift from capacitance voltage measurements after the surface has been reduced by cathodic polarization in aqueous solution. They postulate that the reduced surface is covered with →GeH groups.

We have also not been able to satisfactorily explain why only Ge <110> surfaces show a marked negative surface charge effect, while Ge <111> surfaces show a smaller effect. Neither can we offer the reason why Si <111> and <110> surfaces exposed to the same reducing treatments show no effect whatsoever.

Manuscript submitted Feb. 26, 1970; revised manuscript received May 20, 1970.

Any discussion of this paper will appear in a Discussion Section to be published in the June 1971 JOURNAL.

REFERENCES

1. T. O. Sedgwick, *J. Appl. Phys.*, **39**, 5066 (1968).
2. T. O. Sedgwick and J. A. Aboaf, *IEEE Trans. on Electron Devices*, **ED-15**, 1015 (1968).
3. E. L. Jordan, *This Journal*, **108**, 487 (1961).
4. T. O. Sedgwick and S. Krongelb, To be published.
5. P. Balk, Paper No. 111 presented at the Buffalo Meeting of the Society, Oct. 10, 1965; B. E. Deal, E. L. MacKanna, and T. L. Castro, *This Journal*, **116**, 997 (1969).
6. G. Heiland and P. Handler, *J. Appl. Phys.*, **30**, 446 (1959).
7. A. H. Boonstra, "Some Investigations on Germanium and Silicon Surfaces," thesis presented at Technische Hogeschool, Eindhoven, Netherlands, June 27, 1967, p. 48.
8. K. Tamura and Boudart, *Advan. Catalysis*, **9**, 699 (1957).
9. T. Moeller, "Inorganic Chemistry," p. 399, John Wiley & Sons, Inc., New York (1952).
10. H. Gerischer, M. Hoffman-Perez, and W. Mindt, *Ber. Bunsenges. Physik. Chem.*, **69**, 130 (1965); H. Gerischer, A. Mauerer, and W. Mindt, *Surface Sci.*, **4**, 431 (1966).
11. R. Memming and G. Neumann, *Phys. Letters*, **24A**, 19 (1967); R. Memming and G. Neumann, *Surface Sci.*, **10**, 1 (1968).

[2] Since the p-type Si samples were measured at room temperature, the charge density results may be in error by indicating a too large negative (or too small positive) oxide charge. This does not influence our conclusions, however.

On the Origin of Diamagnetism in MgO and CdO

T. Mookherji

Physical Sciences Research Laboratories, Teledyne Brown Engineering, Huntsville, Alabama 35807

The solid state properties of semiconductors have been the subject of many studies from both experimental and theoretical points of view. Group II-Group VI semiconductors have been studied by many workers because of their interesting properties and some, for example ZnO, have space applications as thermal control coating pigment. The magnetic susceptibility of some of these has recently been measured (1, 2).

The present investigation includes the accurate measurement of the diamagnetic susceptibility of MgO and CdO and a description of the type of bonding in these substances by a theoretical calculation of the susceptibility. This is part of a program to find other materials suitable for space application which will supplement ZnO.

The susceptibility at room temperature is measured with a quartz-microbalance (3) by the method of Mookherji (4), the sensitivity and accuracy of which are already established. The chemicals used were Matheson Coleman & Bell's Reagent grade which meets the ACS specifications. The substances, in the form of powder, were packed in small glass ampoules for measurement. The susceptibility of the ampoules was predetermined and taken into account in the calculation. This was necessary since diamagnetic susceptibility of CdO and MgO is very small. Two types of calibration standards were used: freshly prepared triclinic single crystal of $CuSO_4 \cdot 5H_2O$, whose susceptibility, χ_1, along the c-axis is accurately known (3), is used where the total susceptibility of the system is paramagnetic; and very pure carbon tetrachloride (4), where the total susceptibility is diamagnetic. The measured susceptibility values are shown in Table II.

There is some difference between our measured values and that reported in the literature (5, 6) where the measurements were made using Gouy method. The microbalance technique employed for the present measurements is free from the sources of errors encountered with Gouy method and has much higher sensitivity and accuracy. Moreover, ref. (5, 6) used KCl as standard substance. The measured values given in (5, 6) are always less than that measured by the author and given in (2). This difference is probably due to the increased sensitivity and accuracy of the present method.

In a semiconductor, the total magnetic susceptibility is the net effect of the susceptibility due to the lattice, χ_L, the free charge carrier susceptibility, χ_c, and the susceptibility of the impurity atoms χ_i and is expressed as

$$\chi = \chi_L + \chi_c + \chi_i$$

The lattice susceptibility can be expressed as

$$\chi = \chi_1 + \chi_2$$

Key words: diamagnetism, metal oxide, covalent bond, partial ionic character.

Table I. Values of the ionic susceptibilities calculated

Ion	Inner electron contribution to χ_1	Valence electron contribution to χ_2	$\chi_1 \times 10^6$	$\chi_2 \times 10^6$	$\chi_L \times 10^6$
Mg	$1s^2$, $2s^2$, $2p^6$	$3s^{1.73}$	−2.88	−9.58	−12.46
O	$1s^2$, $2s^2$	$2p^{4.27}$	−1.45	−5.25	−6.70
Cd	$1s^2$, $2s^2$, $2p^6$, $3s^2$, $3p^6$, $3d^{10}$, $4s^2$, $4p^6$, $4d^{10}$	$5s^{1.55}$	−33.46	−9.50	−43.06
O	$1s^2$, $2s^2$	$2p^{4.45}$	−1.45	−5.48	−6.93

where χ_1 is the susceptibility of the inner electrons of the lattice atoms and χ_2, the susceptibility due to the valence electrons of the lattice atoms.

There are different methods to calculate each of these susceptibilities separately. At present, we only consider χ_L as it contributes most to the diamagnetic susceptibility.

Calculations were first made by assuming that both inner and valence electrons obey the Langevin equation

$$\chi = -\frac{Ne^2}{6mc^2}\sum \overline{r_i^2}$$

where the symbols have their usual meaning. The values of $\overline{r_i^2}$ were calculated by the method of Slater (7), as modified by Angus (8). This calculation was carried out for the electronic structures $A^{++}B^{--}$ and $A^{--}B^{++}$, where A is the metal atom and B is the nonmetal atom. The susceptibility values thus obtained are found to be very different from the experimental values.

Since the experimental susceptibilities could not be accounted for by the above method, the method of covalent bonding with partial ionic character was tried, with the inner electron susceptibility, χ_1, calculated as before, since this method gives fairly good results for some II-VI compounds.

Following Pauling (9), the amount of ionic character, I, can be found from the electronegativities of the metal and the nonmetal atoms, x_A and x_B, respectively, using the equation

$$I = 1 - \exp\left[-\tfrac{1}{4}(x_A - x_B)\right]$$

This gives an ionic character of 73% for MgO and 55% for CdO corresponding to an effective charge of ±0.27 and ±0.45, respectively. As a result, the effective number of valence electrons on Mg, O, Cd, and O will be 1.73, 4.27, 1.55, and 4.45, respectively

The valence electron susceptibility, χ_2, is calculated using the Langevin equation, but tetrahedral radii of Pauling (9) are used instead of calculating by the Angus method (8), as the calculation of $\overline{r_i^2}$ by the Angus method gives a high value for the calculated susceptibility. Table II shows the comparison between experimental and calculated susceptibilities, and Table I gives the values of the ionic susceptibilities calculated. The susceptibilities are in cgs emu.

From the agreement between experimental and calculated susceptibility for the covalent model with partial ionic character, it is felt that this method can well be applied in the case of MgO and CdO.

Acknowledgments

The author wishes to express his thanks to W. C. Snoddy and G. M. Arnett of the Space Thermodynamics Branch for allowing the use of their magnetic susceptibility balance and to Dr. H. J. Watson for continued interest during the progress of the work.

Table II. Comparison between experimental and calculated susceptibilities

Substance	$X_M \times 10^6$ experimental	$X_M \times 10^6$ calculated		
		$A^{++}B^{--}$	$A^{--}B^{++}$	Intermediate
MgO	−18.23	−37.58	−20.85	−19.16
CdO	−48.74	−68.16	−52.23	−49.93

Manuscript received March 9, 1970.

Any discussion of this paper will appear in a Discussion Section to be published in the June 1971 JOURNAL.

REFERENCES

1. H. Mikhail and F. K. Agami, *J. Phys. Chem. Solids*, **27**, 909 (1966).
2. R. B. Lal, *Solid State Communications*, **4**, 529 (1966).
3. D. Neogy and R. B. Lal, *J. Sci. Ind. Res.*, **21B**, 103 (1962).
4. T. Mookherji, *Indian J. Phys.*, **36**, 215 (1962).
5. M. Prasad, S. S. Dharmatti, and H. V. Amin, *Proc. Indian Acad. Sci.*, **A26**, 312 (1967).
6. M. Prasad, S. S. Dharmatti, C. R. Kanekar, and R. A. Bhobe, *Proc. Indian Acad. Sci.*, **A31**, 289 (1950).
7. J. C. Slater, *Phys. Rev.*, **36**, 57 (1930).
8. W. R. Angus, *Proc. Roy. Soc. (London)*, **A136**, 569 (1932).
9. L. Pauling, "The Nature of Chemical Bonds," Cornell University Press, Ithaca, N.Y. (1960).

Liquidus Isotherms in the Ga-In-As System

M. B. Panish

Bell Telephone Laboratories, Incorporated, Murray Hill, New Jersey 07974

Recently several temperature-composition points on the liquidus surface of the $Ga_xIn_{1-x}As$ primary phase field of the Ga-In-As system were determined in this laboratory. They were obtained by a simple technique in which dissolution of crystals of the solid phase was observed visually and which has been described elsewhere for studies of the II-VI-Bi systems (1), the In-P system (2) and the Ga-In-P system (3). The experimental data for two cuts along constant Ga concentration lines [25 and 55 a/o (atom per cent) Ga] in the ternary system are presented in Table I and Fig. 1 and 2.

Somewhat more difficulty is encountered in using the observational technique for this system than was encountered with any of the other systems mentioned, primarily because the precipitated solid appears to remain under the surface of the liquid. This accounts for the greater scatter in these data than in those obtained for the other systems. The experimental data could only be checked against one other experimental determination of the liquidus temperature in this ternary, that is the GaAs-InAs pseudobinary data of Van Hook and Lenker (4). The intersection of their data for that pseudobinary and the data obtained here at the highest experimental temperature is shown in Fig. 2. The agreement of the two experimental points is within 2°K, although the precision of the data obtained here appears to be closer to ±10°K.

Recently Stringfellow and Greene (5) have used a quasichemical model for the liquid and for the solid solutions, along with phase and thermodynamic data for the Ga-As, In-As, GaAs-InAs (pseudobinary), and Ga-In systems to calculate a ternary phase diagram for the Ga-In-As system. In Fig. 1 and 2 curves for the liquidus temperatures which were obtained by picking points from isotherms in their ternary phase diagram are shown.

The experimental curves of Fig. 1 and 2, have been used with the liquidus curve plotted by Thurmond (6) for Ga-As, the data of Hall (7) and Koster and Thomas (8) for In-As, and the data of Van Hook and Lenker (4) for the GaAs-InAs pseudobinary to plot experimental liquidus isotherms in the Ga-In-As ternary phase diagram of Fig. 3. Since experimental data were obtained only along two cuts in this ternary, the experimental isotherms thus obtained are shown partially as dashed curves. Also plotted is the 1200°K quasichemical curve of Stringfellow and Greene. The shapes of these isotherms are similar to those which have previously been described for other III-V systems such as Ga-Al-As (9), Ga-Al-P (10) and Ga-In-P (3). Such isotherms are characteristic of ternary sytems in which there is only one high melting III-V binary compound for each III-V binary with a

Key words: Ga-In-As system; phase diagram Ga-In-As.

Table I. Liquidus temperatures in the Ga-In-As system

Atom per cent Ga	Atom per cent In	Atom per cent As	$T_{Liquidus}$ °K
25.0	73.0	2.0	972
25.0	70.0	5.0	1048
25.0	62.5	12.5	1128
25.0	59.0	16.0	1181
25.0	55.0	20.0	1220
25.0	45.0	30.0	1320
25.0	35.0	40.0	1372
25.0	25.0	50.0	1407
55.0	43.5	1.5	975
55.0	41.8	3.2	1059
55.0	40.0	5.0	1091
55.0	35.0	10.0	1173
55.0	25.0	20.0	1296
55.0	10.0	35.0	1442

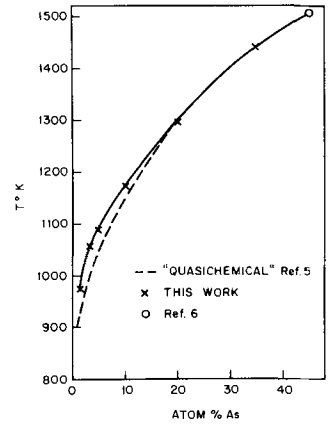

Fig. 1. Liquidus temperatures along the 55 a/o gallium cut of the Ga-In-As system.

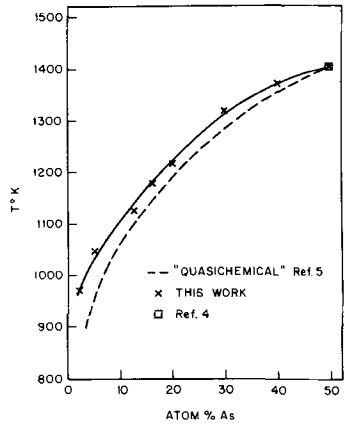

Fig. 2. Liquidus temperatures along the 25 a/o gallium cut of the Ga-In-As system.

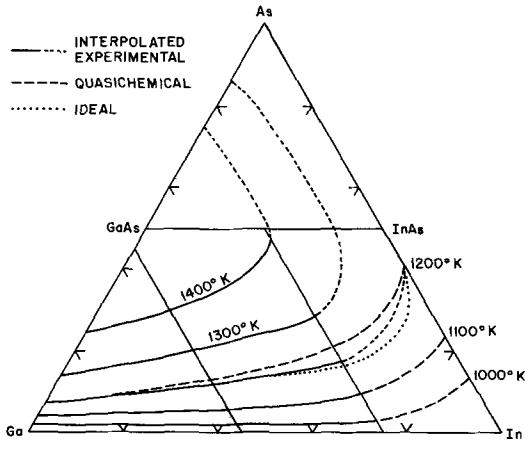

Fig. 3. Liquidus isotherms in the Ga-In-As ternary system

complete or extensive series of solid solutions between the two binary compounds.

It is interesting and instructive to compare the isotherms obtained experimentally with those computed with the quasichemical model and simply on the basis that the entire system is ideal. This latter assumption leads to the relation (9)

$$K_{InAs}(X_{Ga} - X_{Ga}^2 - X_{Ga}X_{In}) + K_{GaAs}(X_{In} - X_{In}^2 - X_{Ga}X_{In}) - K_{InAs}K_{GaAs} = 0 \quad [1]$$

where the X's are the atom fractions of Ga and In in the liquid at the liquidus composition and the K's are the ideal equilibrium constants

$$K_{III\,V} = X_{III}X_V \quad [2]$$

for the liquidus of the binary. An "ideal" 1200°K isotherm has been calculated with K(1200°K, GaAs) = 0.067 from Thurmond's liquidus for Ga-As (6) and K(1200°K, InAs) = 0.242 from a smooth curve drawn through the liquidus data of Hall (7) and Koster and Thoma (8) for In-As. This isotherm is plotted in Fig. 3 and can be seen to approximate the experimental data at least as well as the quasichemical isotherm.

Conclusion

The liquidus temperatures along two cuts in the Ga-In-As ternary system have been used with phase data for the boundary binary systems to plot the positions of the liquidus isotherms in that system. Isotherms of 1200° which were estimated on the basis of a quasichemical model and on the assumption of total ideality are shown to be in fair agreement with the experimental curve. This degree of agreement between the positions of isotherms calculated on the basis of these two different assumptions about the thermodynamic properties of the liquid and the solid emphasizes that in the III-V systems the shapes of the isotherms are primarily determined by the differences in the free energies of formation of the binary compounds (3, 9, 10). Any model which includes this difference as a major contributor to the behavior of the system will yield isotherms in fair agreement with the true isotherms. This does not, however, imply that the model selected is a true description of the system, but merely that the shapes of the liquidus isotherms are insensitive to the model.

Manuscript submitted Dec. 19, 1969.

Any discussion of this paper will appear in a Discussion Section to be published in the June 1971 JOURNAL.

REFERENCES

1. S. Kimura and M. B. Panish, *J. Chem. Thermo.*, **2**, 77 (1970).
2. M. B. Panish and J. R. Arthur, *ibid.*, **2**, 299 (1970).
3. M. B. Panish, *ibid.*, **2**, 319 (1970).
4. H. J. Van Hook and E. S. Lenker, *Trans. Met. Soc.*, **227**, 220 (1963).
5. G. Stringfellow and P. Greene, *J. Phys. Chem. Solids*, **30**, 1779 (1969).
6. C. D. Thurmond, *ibid.*, **26**, 785 (1965).
7. R. N. Hall, *This Journal*, **110**, 385 (1963).
8. W. Koster and B. Thoma, *Z. Metall.*, **46**, 241 (1955).
9. M. B. Panish and S. Sumski, *J. Phys. Chem. Solids*, **30**, 1083 (1969).
10. M. B. Panish, R. T. Lynch, and S. Sumski, *Trans. Met. Soc.-AIME*, **245**, 559 (1969).

JOURNAL OF THE ELECTROCHEMICAL SOCIETY

ELECTROCHEMICAL TECHNOLOGY

SEPTEMBER 1970

Testing Batteries for Vehicular Applications

I. Test Facility

B. Agruss*

Electrochemistry Department, Research Laboratories, General Motors Corporation, Warren, Michigan 48090

ABSTRACT

A versatile facility was required to test a variety of batteries applicable to vehicular propulsion. Such a facility was designed and built to characterize all types of batteries in the 1-10 kW range. It was built around a motor-generator set and load bank. The unique features of this test facility are that it can be operated either manually or automatically at constant *power*, *current*, or *voltage* whether charging or discharging a test battery.

Battery capacity is determined today almost exclusively by varying constant current discharges. Vehicle loads, however, are expressed as constant power requirements. The ability of batteries to fulfill these requirements cannot be determined directly from the usual battery tests at constant current or voltage. What has been required is a versatile test facility to test a variety of batteries applicable to vehicular propulsion. It had to supply, directly, battery characteristics at constant power as well as at constant current and voltage.

Early power plants may be hybrid battery systems consisting of an energy battery and a power battery connected together through some type of charging device whereby the power battery is charged at idle or cruise speeds by the energy battery. Each battery operates under different conditions and needs different characteristics. The energy battery provides energy and power for range at cruise speeds and for charging the power battery. It must have a good energy density but not necessarily a good power density. The power battery must provide the bursts of power required for acceleration and other short-duration, high-power requirements. So it must have a good power density but not necessarily a good energy density. Constant power and constant current tests will characterize the energy battery. However, for the power battery these tests must be augmented by a test which will show the ability of this battery to give repeated acceleration power pulses. The test facility, too, must reveal how the two batteries interact when operated in a hybrid mode.

For both types of batteries, it is important to know the charge acceptance at varying depths of discharge. These data will show the power and energy requirements for recharging both types of batteries.

A versatile battery test facility was built from available items to perform all of the enumerated special tests plus the usual battery tests. Data are provided to characterize all types of batteries in the 1-10 kW range. The facility was built around a motor-generator set and a load bank. The unique feature is that the motor-generator set can be operated manually or automatically at constant power, current, or voltage whether charging or discharging a test battery. Repeated acceleration power pulses can be obtained also, manually or automatically.

* Electrochemical Society Active Member.

Key words: battery tests, lead-acid batteries, storage batteries, vehicular application tests.

Description of Facility

An over-all view of the test facility is shown in Fig. 1. All areas are self-explained. The relationship among the several parts of the facility is shown in the block diagram of Fig. 1(a) which also lists the figure numbers where detailed schematics for each part may be found.

Load bank.—The load bank shown in Fig. 2 consisted of ¼ in. stainless steel tubes clamped at varying lengths to give varying resistances. The tubes were water-cooled internally to remove heat. Currents of 100-500A could be carried by these pipes by using one or more in parallel. This was done by means of contactors actuated by pushbuttons, as shown in Fig. 3. Fine adjustment was made by having the motor-generator set buck or aid the battery current.

Fig. 1. Battery test facility

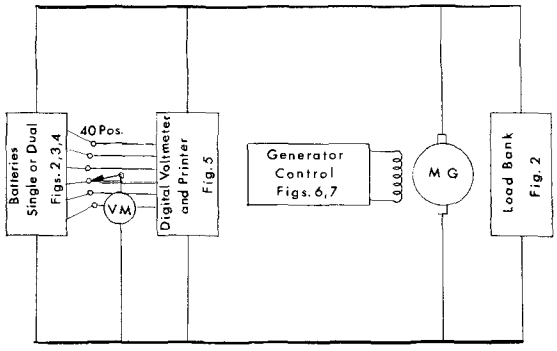

Fig. 1(a). Facility block diagram

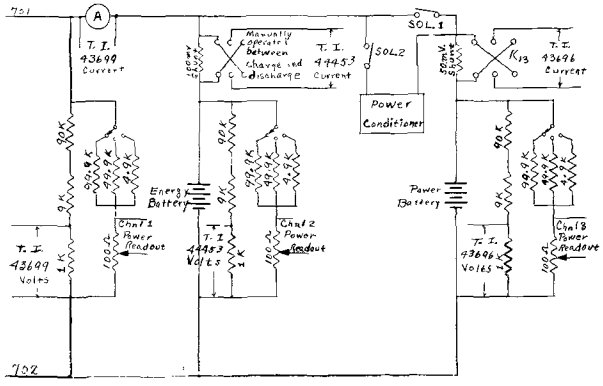

Fig. 4. Dual battery instrumentation schematic

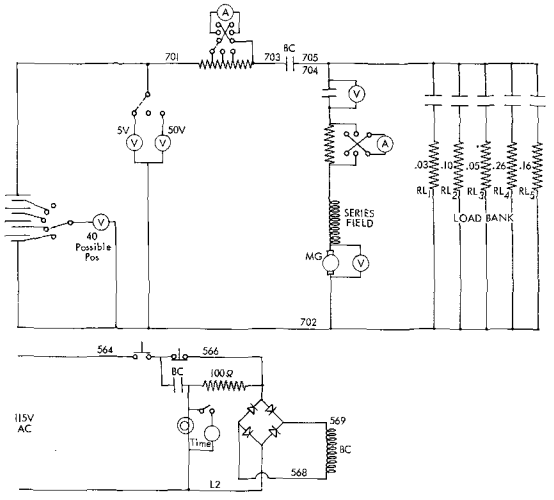

Fig. 2. Load bank schematic

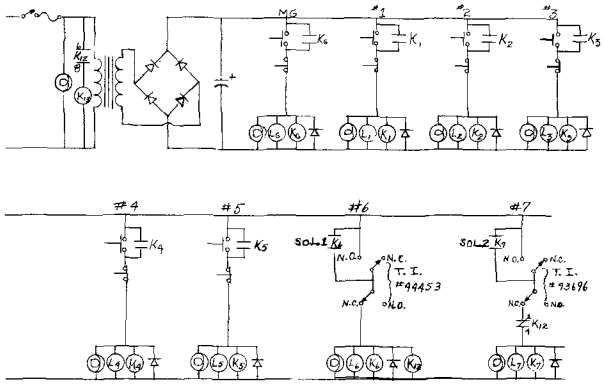

Fig. 3. Relay and switch schematic

Dual battery operation.—Early experimental electric power plants may be dual battery systems consisting of an energy battery and power battery. The energy battery charges the power battery during low-power periods when no power is required from the power battery. The energy battery, at exhaustion, is charged with the motor-generator set. Voltage limits, depending on battery type and characteristics, govern the charge-discharge operation.

Figure 4 shows the means by which this operation is accomplished. Adjustable cams on the servomotor shaft of two Texas Instrument Servo-riters actuate microswitches which open and close solenoids No. 1 and 2 at the proper voltage levels. Stations No. 6 and 7 in Fig. 3 show how the microswitches are connected to actuate the solenoids.

Normally, solenoid No. 2 is closed since the upper cam on T.I. 43696 is set to make contact on N.O. at battery open circuit and lower voltages. This causes the power battery to be charged at a rate determined by the conditioner. The lower cam on 43696 is set to open N.C. and close N.O. when the battery reaches maximum charge voltage. This opens solenoid No. 2 and charging stops.

When power is called for at the load, the voltage of the energy battery falls. At the set voltage, the upper cam on T.I. 44453 closes N.O. and opens N.C. This causes solenoid No. 1 to close and also energizes K_{12} whose normally closed contacts open, opening solenoid No. 2. Now both batteries are supplying power to the load. When the load demand drops, the energy battery voltage will rise. Now the lower cam on T.I. 44453 will open at N.C., de-energize solenoid No. 1, and allow T.I. 43696 to take over. The power battery voltage will be low, so solenoid No. 2 will close. Now the power battery is being charged by the energy battery. The power conditioner limits the high charge current to a discharged battery and by a voltage sensor reduces the charge current to the end of charge rate at the end of charge voltage.

Voltage dividers are used, as shown, to limit the signals to the Servo-riters. The reversing relay (K_{13}) attached to the 50 mV shunt shown in Fig. 4 is actuated in unison with solenoids No. 1 and 2 through relay K_{12} in Fig. 3.

Power measurement and recording.—A novel means was used to measure and record power without resorting to expensive electronic multipliers or d-c wattmeters. A 100 ohm retransmitting slide wire was attached to the shaft of the servomotor being actuated by the current shunt signal in each of the Servo-riters. This slide wire formed one leg of a voltage divider system which was placed across the battery as shown in Fig. 4. A three-position switch changed resistors so that battery voltages from 0-5, 5-50, and 50-100V would yield reasonable signals, yet limit the drain on the battery to 1 mA.

The position of the wiper on the slide wire is directly proportional to the current. The drop across the slide wire is directly proportional to the battery voltage. Hence, the voltage signal from wiper to one end of the slide wire is directly proportional to the product of current and voltage or power. This signal can be read with a high impedance millivoltmeter or recorded as shown. The channel numbers in Fig. 4 refer to channels in the four-channel recorder shown in Fig. 1 labeled "Power Readout." Any one signal can be used to control the motor-generator set at constant power as is described later.

Non Linear Systems monitor.—A Non Linear Systems 20-point scanner, digital voltmeter and printer was used to monitor individual cell voltages. The period between print-outs could be varied from 5 to 30 min. The event marker on the Servo-riters would show just when the readings were being taken. Each timer was wired to start the other when its time ran out and thereby actuate the scanner advance and start relays. Print-out would continue indefinitely at the

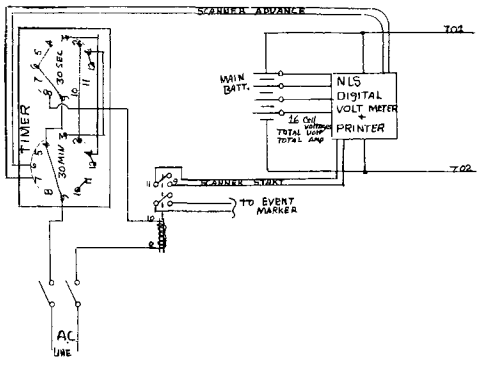

Fig. 5. Print frequency timer for NLS system electrical schematic

desired intervals until the a-c line switch was opened (Fig. 5).

Generator output control.—Figure 6 is a schematic of the d-c generator output control panel. The upper half of the figure relates to manual control only. The coupled exciter furnishes field current, the magnitude of which is controlled by the field rheostat and the series resistor. This mode is used for gross testing or where pulses are desired.

The bottom half of Fig. 6 relates to automatic control at constant voltage, current, or power. In this mode, the field current is supplied by a Sorenson 150V, 5A power supply with remote control tabs. The electronic control presents a controlled varying resistance to the remote control tabs of the power supply, thus controlling the field current. The electronic control can sense either three levels (5, 50, 100V) of battery voltage from the voltage dividers, current from the shunt signal, or power from the retransmitting slide-wire signal described previously. Each mode of operation is selected by the six-position selector switch and the two-position sensor switch. To reverse the generator output, the field current is reversed. The four-pole double-throw switch shown reverses both the field current and the shunt signal to the sensor so it can operate properly. The battery voltage does not reverse on charge or discharge; hence, no reversing switch is necessary.

Electronic motor-generator control.—The heart of the generator control system is the electronic controller diagrammed in Fig. 7. This is a simple feedback loop which compares an input voltage to an internally generated one, and applies the difference to make a transistor more or less conducting. In parallel with the base and emitter of the transistor is a resistor which is the remote control for the field power supply. A millivolt signal proportional to voltage, current, or power is applied at terminals 1 and 2 of the shunt

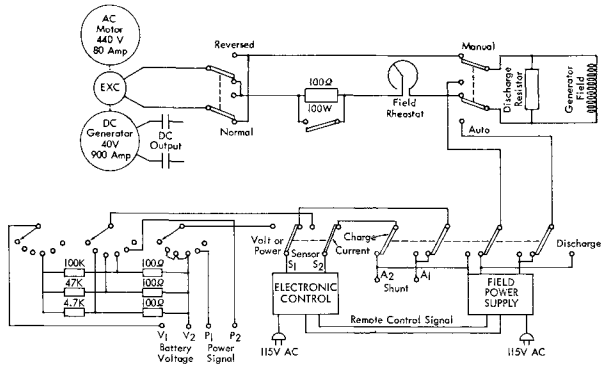

Fig. 6. D-C generator output control

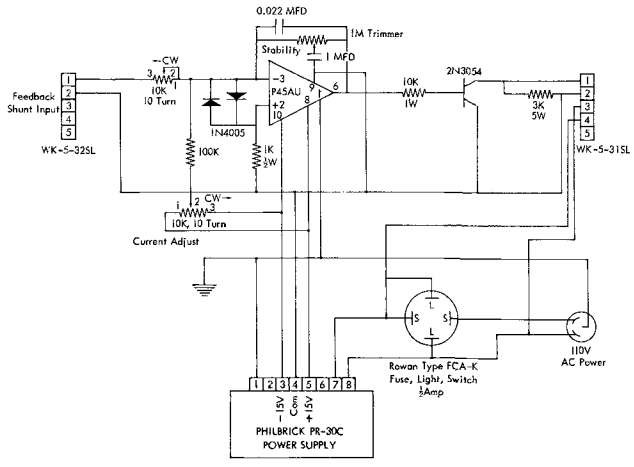

Fig. 7. Current control-motor generator

input. This signal voltage is bucked by an interval voltage whose magnitude is varied by the current-adjust potentiometer. The error signal is applied to operational amplifier P45AU, which controls the conductance of transistor 2N3054.

Across terminals 1 and 2 of WK-5-31SL is a 3K resistor. The same terminals are connected to the remote control tabs of the power supply. The specifications for remote control are 20 ohms/V; hence, 3000 ohms will bring the power supply to 150V, and 300 ohms to 15V. Thus, by varying the resistance, the voltage of the power supply can be varied. By varying the conductance of the transistor in parallel with the 3K resistor, the resistance, seen by the power supply, is varied.

To accomplish constant generator output, the current-adjust potentiometer is adjusted until the desired voltage, current, or power is obtained. If the input signal decreases, the error signal decreases, reducing the conductance of the transistor, which then increases the field current; this, in turn, increases the generator output, so that the error signal is brought up to its original level. The opposite occurs if the input signal increases—the generator output decreases to bring the signal back to its former level. Hence, constant generator output is achieved for either voltage, current, or power.

A big advantage of this control is that it can be programmed for an infinite variety of charge-discharge profiles. By having a number of current-adjust potentiometers connected to appropriately programmed switches, the output of the generator can be programmed to a variety of profiles. Each potentiometer can be infinitely adjusted to any charge or discharge level desired. This allows excellent versatility.

Conclusions

1. A versatile battery test facility was constructed from a motor-generator set and load bank.
2. The facility has the capability to provide hitherto unavailable battery data for vehicular applications.
3. Besides the standard constant current battery tests, constant power and acceleration pulse tests can be performed also.
4. By appropriate programming, an infinite variety of charge and discharge profiles are available.

Manuscript submitted Dec. 22, 1969; revised manuscript received ca. May 11, 1970. This was presented in part as Paper 42 at the Detroit Meeting, Oct. 5-9, 1969.

Any discussion of this paper will appear in a Discussion Section to be published in the June 1971 JOURNAL.

Testing Batteries for Vehicular Applications

II. Tests on Some Commercially Available Energy Batteries

B. Agruss*

Electrochemistry Department, Research Laboratories, General Motors Corporation, Warren, Michigan 48090

ABSTRACT

Using a versatile test facility previously described (1), a number of commercially available Pb-acid batteries were tested. Typical test results are presented, especially those most meaningful to vehicular applications. It is shown that at varying power discharges the energy capabilities are additive. By this means, performance, range, and capability of batteries under varying duty cycles can be ascertained. Power density *vs.* energy density curves are obtained almost by inspection from constant power discharges. Voltage-current characteristics, both for charge and discharge, at varying capacity levels are presented. It is shown that Pb-acid batteries can be charged rapidly to 80-85% of their capacity before battery voltage rises rapidly.

The ability of batteries to fulfill vehicular requirements cannot be determined directly from the usual battery tests at constant current or voltage. Vehicle loads are expressed as constant power requirements; hence battery characteristics at constant power as well as constant current and voltage are needed.

Early power plants may be hybrid systems consisting of an energy battery and a power battery connected together through some type of charging device whereby the power battery is charged at idle or cruise speeds by the energy battery. The energy battery provides power for range at cruise speeds and for charging the power battery. It must have good energy density but not necessarily a good power density. The power battery must provide the bursts of power required for acceleration and other short-duration, high-power requirements. So it must have a good power density but not necessarily a good energy density.

This paper concerns itself with energy batteries. Constant power and constant current tests characterize the energy battery. Also, it is important to know the charge acceptance at varying depths of discharge. These data show the power and energy requirements for recharging the batteries.

Battery data are shown which were obtained on several commercially available Pb-acid batteries which may be generalized as energy batteries. Power battery data will be reported at a later date in another paper.

Battery Tests

Two diesel batteries were connected in series for check-out tests on the previously described test facility (1). These batteries had 205 A-hr, 20 hr capacity, and could deliver up to 5 kW so that sufficient power and capacity were available. After the check-out tests, several commercially available S.L.I. batteries were characterized as energy batteries. Between each capacity test, the batteries were fully charged to constant voltage and specific gravity at the finishing rate. All battery tests were carried out at ambient temperature.

In the following discussion, each kind of test is listed separately. The data obtained for each respective test are shown. Useful information derived from these data are described.

Constant current tests.—Figure 1 shows the results of the usual constant current discharges obtained during check-out on the diesel batteries. These discharges give the capacity of the battery at different current drains. These data may be replotted to give capacity *vs.* current as shown in Fig. 2 for the S.L.I. batteries. The first capacity on each curve at the lowest current was taken at the nominal 5 hr rate. In some S.L.I. applications, a voltage *vs.* current curve with time as a parameter might be helpful. These curves do not readily yield power output results except by an iterative process. For S.L.I. use these capacities are sufficient, but for vehicular applications they do not suffice.

Constant power tests.—Of much more practical value are the constant power discharges. Battery voltage is the limiting factor in vehicle operation. A minimum cut-off voltage is normally specified. Hence, voltage *vs.* ampere-hours or time is plotted as shown in Fig. 3 and 4 for the diesel batteries. It has been found (as shown later) that voltage *vs.* time curves are more useful; hence the S.L.I. battery data have all been plotted that way in Fig. 5-7 inclusive. All of these curves have somewhat the same shape as the constant current curves, but the slopes are much steeper since both voltage and current are changing.

The usefulness comes in directly obtaining range at any road load (power level). For instance, in Fig. 5, if

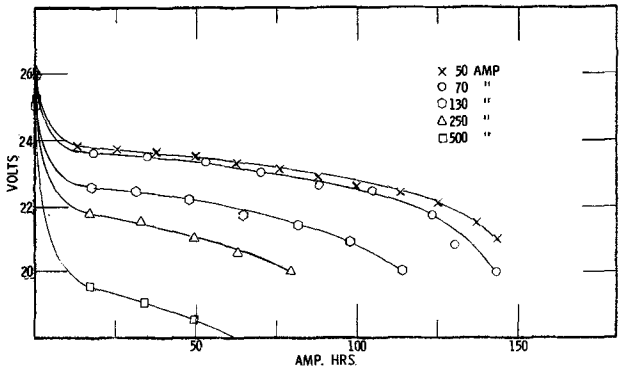

Fig. 1. 200 Ampere-hour diesel battery, constant current discharge.

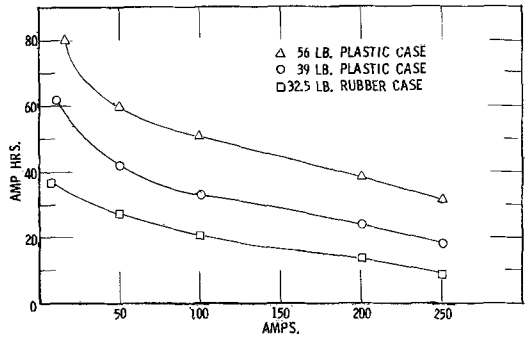

Fig. 2. S.L.I. batteries, ampere-hour capacity *vs.* current drain.

* Electrochemical Society Active Member.

Key words: battery tests, lead-acid batteries, storage batteries, vehicular application tests, constant power capacity, battery capacity additivity principle, V-I plots S.L.I. batteries, S.L.I. batteries, energy density-power density.

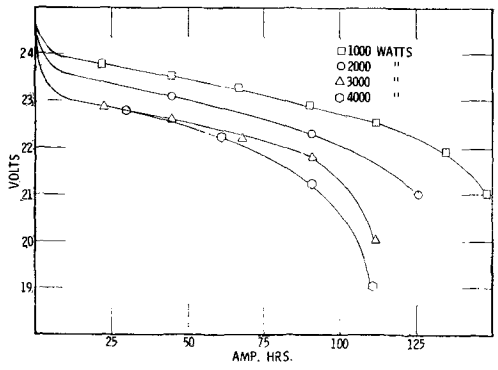

Fig. 3. 200 Ampere-hour diesel battery, constant power discharge *vs.* ampere-hours.

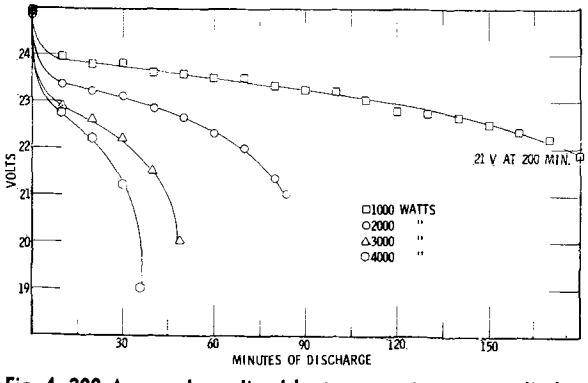

Fig. 4. 200 Ampere-hour diesel battery, constant power discharge *vs.* time.

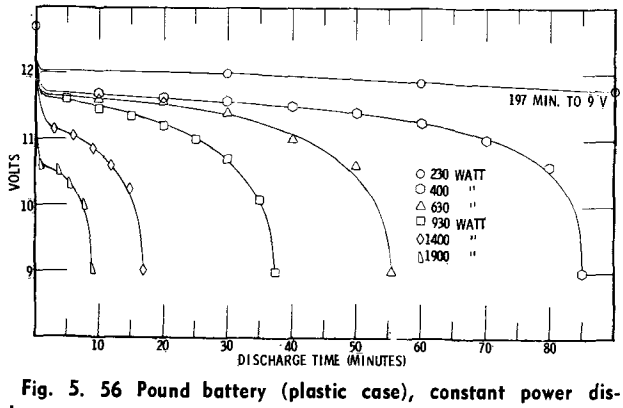

Fig. 5. 56 Pound battery (plastic case), constant power discharge.

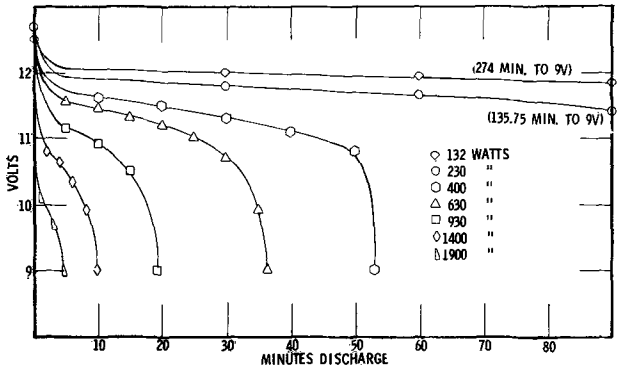

Fig. 6. 39 Pound battery (plastic case), constant power discharge.

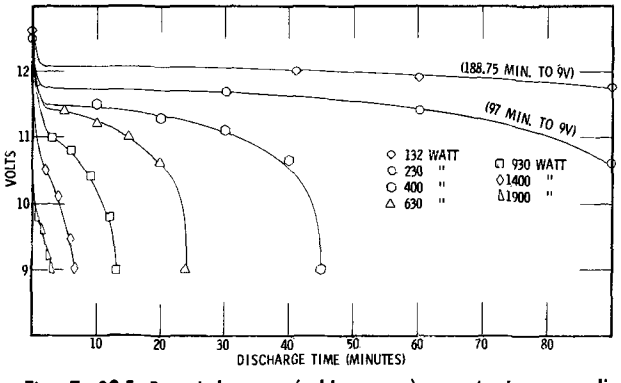

Fig. 7. 32.5 Pound battery (rubber case), constant power discharge.

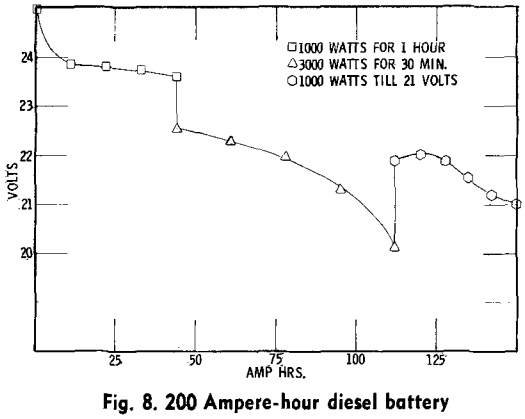

Fig. 8. 200 Ampere-hour diesel battery

the 400W level meant 30 mph, then the vehicle could travel 42.5 miles before recharge. This is a simple calculation by inspection rather than a time-consuming iterative process.

A description of several duty cycles further shows this usefulness. Also, the principle of additivity of ampere-hours or time is described, and how this principle can be used to construct duty cycles. In Fig. 8 is shown a duty cycle of 1000W for 1 hr, followed by 3000W for 30 min, then 1000W again to the 21V cutoff. The versatility of this facility allows a rapid change from one power level to another. Thus, any duty cycle can be applied to the battery. The additivity principle can be illustrated now. Comparing Fig. 3 and 8, it is seen that, within experimental error, the two 1000W portions of Fig. 8 coincide with the 1000W curve of Fig. 3, both at the low and high ampere-hour ends; *i.e.*, from 0 to 45 A-hr and from 100 to 150 A-hr. The 3000W portion of Fig. 8 between 45 and 100 A-hr coincides with the same portion of Fig. 3. The same coincidence was noted for voltage *vs.* time constant power discharge curves.

The coincidence of all of these profiles illustrates the principle of additivity. The capacity removed at any power level in ampere-hours or time may be added to that removed at a different power level to determine total amount consumed and amount remaining before the battery cutoff voltage is reached.

Plots of projected duty cycles show at what portion of the cycle the battery reaches cutoff voltage and limits performance. Incidentally, Fig. 8 shows also the ability of a Pb-acid battery to supply useful energy at decreasing power levels.

To use the principle of additivity more effectively, the data of Fig. 5, 6, and 7 were replotted as capacity *vs.* time in Fig. 9, 10, and 11, respectively. Now it is possible to determine battery capability, performance, and range. First, all of the limiting points were connected, as shown, with a dotted line. Capacities beyond this line are not attainable because cutoff voltage is reached at this line. Assume that the constant power curves represent road loads at specified vehicle speeds. Now assume a duty cycle specifying time at various vehicle speeds. It is very easy to ascertain the ability of

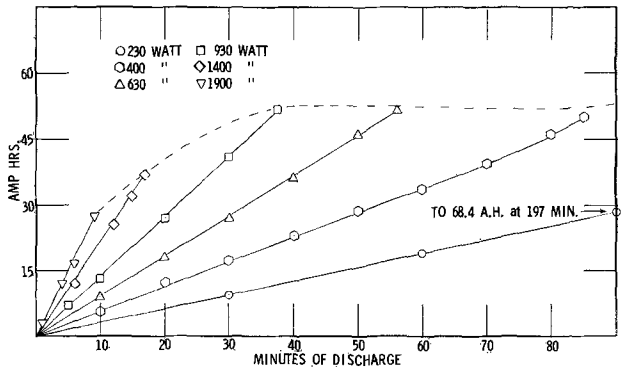

Fig. 9. 56 Pound battery (plastic case), constant power discharge capacity *vs.* discharge time.

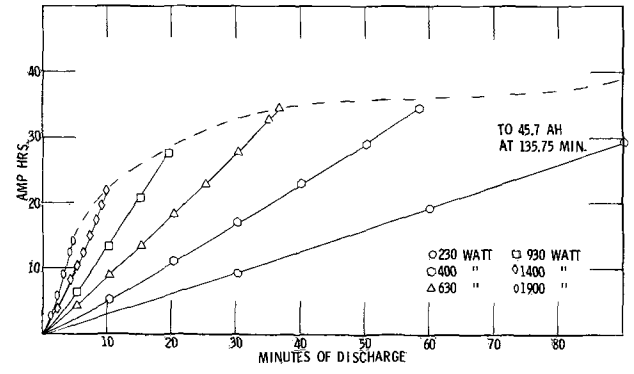

Fig. 10. 39 Pound battery (plastic case), constant power discharge capacity *vs.* discharge time.

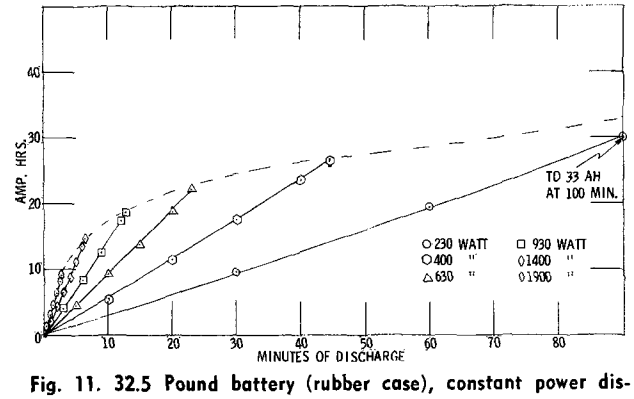

Fig. 11. 32.5 Pound battery (rubber case), constant power discharge capacity *vs.* discharge time.

any battery to perform that cycle. For instance, suppose a duty cycle of 30 min at 230W, 10 min at 1400W, 10 min at 630W, and finally 15 min at 400W were imposed upon the battery in Fig. 9. After 30 min at 230W, 9 A-hr were consumed. This is equivalent to 5 min at 1400W. An additional 10 min brings the time of discharge to 15 min where a total of 32 A-hr have been consumed. This is equal to 35 min discharge at 630W. An additional 10 min at 630W (45 min) brings the ampere-hours consumed to 42. Now this is equivalent to 73 min discharge at 400W. The limit at 400W is 85 min. This means the battery can deliver only 12 min at 400W instead of the 15 min assumed. Battery voltage at each point, if desired, can be obtained from Fig. 5 at the appropriate power and time of discharge intersections. It is also seen that only a maximum of 12 min can be obtained at 1400W after 30 min at 230W. Thus, performance limits are obtained. A summation of the products of vehicle speed and time at that speed gives the vehicle range. Performance at power levels other than those portrayed may be interpolated between the appropriate power curves.

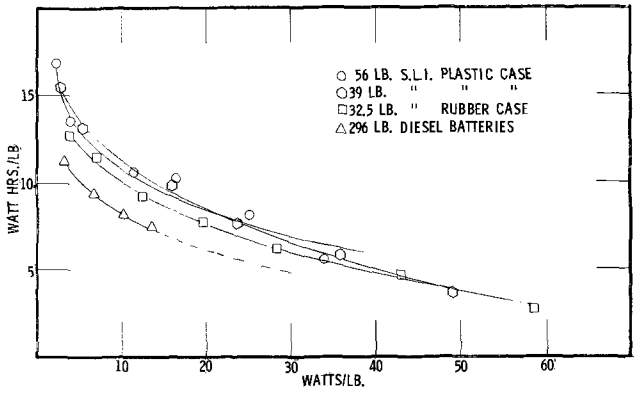

Fig. 12. Energy density vs. power density, various Pb-acid batteries.

The curves in Fig. 9, 10, and 11 are very close to straight lines. The 10-20% change in voltage and current is not seen on this small scale. An expanded scale would emphasize the curvature. It just so happens that, for these batteries, these curves can be approximated by straight lines. However, for other types of batteries, the curvature is pronounced enough so that the data cannot be approximated easily by straight lines.

Energy density-power density.—A very useful application of Fig. 4-7 inclusive is in the construction of energy density *vs.* power density curves. The time to cutoff voltage for any constant power discharge multiplied by the power gives the watt-hour capacity at that power level. This value divided by the battery weight gives the energy density. The power divided by the weight gives the power density. Thus, each constant power discharge yields one point for the energy density *vs.* power density curve. The curves in Fig. 12 were made this way. This is a fast, easy method to construct these much valued curves. Constant current discharges do not yield such data readily.

The two plastic-case batteries show almost identical energy and power densities in spite of their large difference in ampere-hour capacity. This shows that the gain in capacity was due to the gain in weight which was largely active material and lead supporting structure. A larger plastic container contributes very little extra weight.

The plastic case batteries show a 10-20% gain in energy density over the rubber-case battery at the low power levels. At the high power levels, there was very little difference in energy density between the differently contained batteries.

The rugged construction of the diesel batteries shows up in their low energy and power densities.

Voltage-current characteristics.—The test facility lends itself to fast, easy determinations of voltage-current characteristics. The electronic generator control makes it easy to pass smoothly from charge to discharge, or *vice versa*, through open circuit (V at zero I). The current adjustment control can be manipulated so that the generator voltage exceeds, equals, or is less than the battery voltage. Thus, the battery is charged, at open circuit, or discharged, respectively.

Voltage-current curves obtained in this manner are shown in Fig. 13 through 16, inclusive, for varying states of charge. Note the smooth passage through open circuit. At high current drains, the voltage readings had to be taken instantly since the reading would change rapidly with time. At low drains, the voltage would remain stable for ½ to 1 min.

All the S.L.I. batteries had about the same discharge characteristics. At the 25% capacity level, the slope with increasing current was somewhat greater for the lower capacity batteries.

It is interesting to note that, except for a fully charged battery, the battery will accept a charge easily; that is, the voltage does not rise abruptly with an

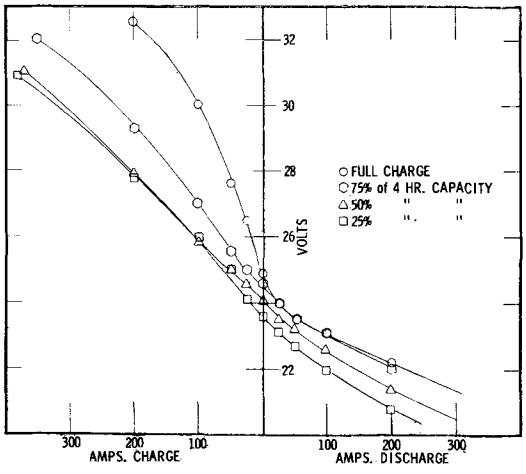

Fig. 13. 200 Ampere-hour diesel batteries, charge discharge, voltage *vs.* current.

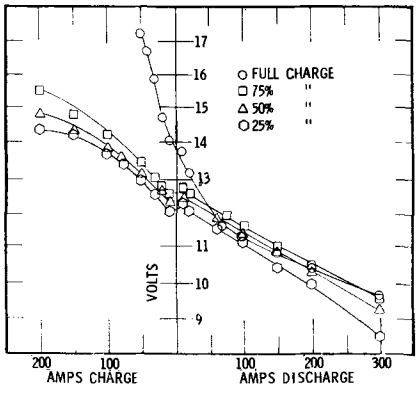

Fig. 14. 56 Pound battery (plastic case), charge discharge, voltage *vs.* current.

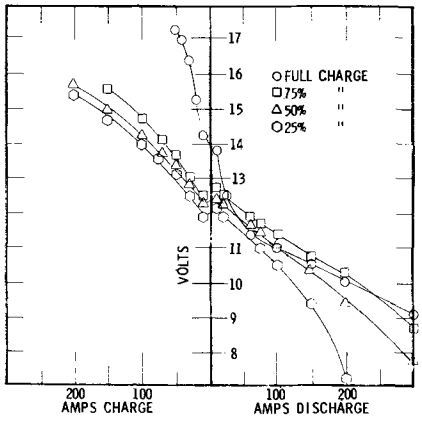

Fig. 15. 39 Pound battery (plastic case), charge discharge, voltage *vs.* current.

increase in current. The rapid rise in charge voltage for a fully charged battery shows poor charge acceptance, as expected, and the onslaught of gas evolution. There is no rapid rise in charge voltage even at 75% capacity. Further data, which will be reported at a later date, seem to indicate that the rapid rise begins about 80-85 capacity.

Except for the fully charged battery, the charge and discharge curves are nearly projections of one another. The slight rise in slope for the charge portion may be due to the higher specific gravity acid within the pores of the plates. There is a greater slope for the rubber-

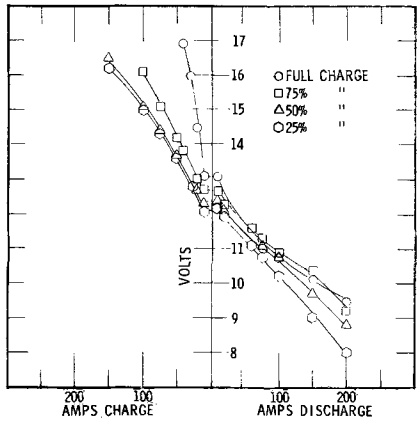

Fig. 16. 32.5 Pound battery (rubber case), charge discharge, voltage *vs.* current.

cased battery. This can be caused by differences in call design and active material make-up, especially negative plate expander.

Comments.—The data contained herein cover a good range of S.L.I. batteries. Although curves for only one battery would be sufficient to explain all the tests and describe the principles involved, much more confidence is obtained if more than one size battery follows the same trend, especially with lead-acid batteries. There is an added advantage in including all the data. The performance of any other battery as an energy battery may be ascertained by judicious interpolation or extrapolation of the data herein.

Future work.—It is planned to repeat these tests at −18°C (0°F) and 71°C (160°F) and find the effect of temperature on duty cycle capacities.

In forthcoming reports, other types of batteries will be characterized; acceleration power pulses will be included.

Conclusions

1. It was found that a few power profiles, a voltage-current test, the usual constant current tests, plus charging data with state-of-charge as a parameter, provided our data needs for vehicular applications.
2. During any varying power discharge, the principle of additivity was followed; *i.e.*, the capacity removed at any power level expressed in ampere-hours or time may be added to that removed at a different power level to determine total amount consumed and amount remaining before the battery cutoff voltage is reached.
3. By applying the additivity principle, the ability of batteries to perform varying duty cycles can be obtained rapidly, and the range is easily calculated.
4. Constant power capacity discharges readily yield energy density-power density relationships.

Acknowledgments

The author wishes to express his indebtedness to Mr. Walter Wright for his invaluable suggestions in the design and construction of the facility. He was responsible also for carrying out most of the battery tests. Thanks are due to the Management of General Motors Corporation for permission to publish these data.

Manuscript submitted Dec. 22, 1969; revised manuscript received *ca.* May 11, 1970. This was presented in part as Paper 42 at the Detroit Meeting, Oct. 5-9, 1969.

Any discussion of this paper will appear in a Discussion Section to be published in the June 1971 JOURNAL.

REFERENCE

1. B. Agruss, *This Journal*, **117**, 1204 (1970).

Surface Chromium on Chromate Treated Tin Plate

Joseph J. Becker*[1]

Jones & Laughlin Steel Corporation, Graham Research Laboratory, Pittsburgh, Pennsylvania 15230

ABSTRACT

The surface chromium composition of tin plate treated cathodically in sodium dichromate solution was analyzed by three methods: (*a*) alkali stripping, (*b*) acid stripping, and (*c*) treatment with bromine methanol solution. It is suggested that the surface chromium insoluble in alkali is anhydrous chromic oxide, while that soluble in alkali is hydrated chromic oxide. The potential time curves from galvanostatic anodic treatment of tin plate cannot be interpreted in the simplistic manner commonly accepted for tin-free steels with a chromium-chromium oxide coating.

By far the largest percentage of commercial tin plate is given a cathodic treatment in dichromate solution with current densities in the region of 25-35 A/ft^2 and treatment times of the order of 1 sec. The concentration of the solution is about 3% sodium dichromate. Traditionally, acid stripping or alkali plus acid stripping (1, 2) has been used to remove and estimate the quantity of surface chromium[2] deposited on the tin plate during the chromate treatment. Such procedures give total surface chromium concentration.

A coulometric method for the estimation of surface chromium on passivated tin plate was proposed by Britton (3). The sample is made the anode of a cell with sodium phosphate solution as the electrolyte. The potential difference between the sample and a reference electrode is monitored as a function of time for a galvanostatic treatment. According to Britton, during the potential arrest shown on the potential time curves, Cr^{3+} is oxidized to Cr^{6+} with about 56% current efficiency.

A coulometric method basically the same as that suggested by Britton for tin plate is generally employed for the determination of metallic chromium on TFS (tin-free steels with a chromium-chromium oxide coating) (4, 5). Although Britton recommended a neutral phosphate solution for tin plate, sodium hydroxide solutions are generally used for TFS. However, curves may be obtained for passivated tin plate using either solution with no very significant difference in results. The question, therefore, arises as to whether or not such curves from tin plate samples can be used to demonstrate and estimate surface metallic chromium concentrations.

This question is central to a disagreement which has recently arisen concerning the detailed chemical nature of the surface chromium on commercial CDC (cathodic dichromate) tin plate. Much of the work involved is unpublished; however, the suggestion has been made (6, 7) that metallic chromium is present on the surface of commercial CDC tin plate, and that this concentration can be estimated from potential time curves.

From Britton's work it was already evident that the quantity of charge passed during the potential arrest from "as-received" tin plate was too large for the potential arrest to be interpreted in terms of 100% current efficiency for the reaction $Cr^{3+} \rightarrow Cr^{6+}$. Since not all the surface chromium could be metallic chromium this is also true for the reaction $Cr^0 \rightarrow Cr^{6+}$. Britton cited the work of Shah and Davies (8) indicating oxidation of tin at these potentials. However, it has been suggested that the smaller quantity of charge passed during the potential arrest obtained during galvanostatic, anodic treatment of CDC tin plate which had been previously treated in hot KOH (8.5M KOH at 180°F for 2 min) is entirely used for the oxidation of metallic chromium. This suggestion was associated with the contention that the surface chromium which is insoluble in hot alkali is metallic chromium (6). According to Rocquet and Aubrun (7), the potential arrest from plate previously treated in hot 1*N* NaOH cannot be interpreted in terms of 100% current efficiency for the reaction $Cr^0 \rightarrow Cr^{6+}$. However, these workers claim that the potential arrest from plate previously treated in a NaOH-H_2O_2 solution can be so interpreted.

The present work was undertaken to further the knowledge of the chemical composition of the surface chromium on commercial CDC tin plate. We sought first a chemical method which would inform us as to whether or not metallic chromium was one of the constituents on the surface of CDC tin plate. The method adopted was to treat samples with bromine methanol solutions. Chromic oxides are insoluble in these solutions, whereas chromium trioxide and metallic chromium are soluble. By analyzing the insoluble residue from attack by bromine methanol on samples previously subjected to one of the stripping methods, as well as samples in the as-received condition, it was possible to determine whether or not the surface chromium is soluble in bromine methanol.

Methods

Details of each of the methods used are given below. Most of the results were obtained using disks of 8 in.^{2} surface area.

Alkali stripping.—The sample was placed in 20 cc of 8.5M (48%) KOH at 180°F for 2 min. The sample was removed and rinsed into the solution. Twenty cubic centimeters of 10% sulfuric acid and 10 cc of 85.5% phosphoric acid were added. One to two drops of saturated potassium permanganate were added and the solution boiled for 5 min. Ten cubic centimeters of 38% HCl were then added to reduce the excess permanganate and obtain again a colorless solution. Diphenylcarbazide reagent (9) was added, the solution was brought to 100 cc, and the chromium content determined colorimetrically. The solutions have a *p*H lower than the preferred range for use with this reagent. Nevertheless, meaningful and consistent results were obtained. In later work, the method has been modified to give solution of higher *p*H with no difference in results.

Acid + alkali stripping.—The method used was a modification of that described by Hill (1). The sample was placed in 25 cc of sodium hydroxide-sodium phosphate solution (40g NaOH + 50g Na_3PO_4/liter). The solution was heated and allowed to boil for 2 min. The sample was removed and rinsed into the solution. This procedure was repeated in 25 cc of 1:3 sulfuric acid, the solution being allowed to boil for 1½ min.

* Electrochemical Society Active Member.

Key words: surface chemistry, surface passivation, chromium analysis, tin plate surface chemistry.

[1] Present address: 44 West 63 St., New York, N. Y. 10023.

[2] In this paper, chromium is used as the name of an element without prejudice to its valence state, *e.g.* as the pure metal or in a compound. When metallic chromium is specifically meant, the paper so states.

The alkali and acid solutions were mixed. Potassium permanganate was added and the procedure given above for colorimetric determination of chromium was followed.

Bromine methanol attack.—The sample was placed in a solution of 12 cc of bromine and 25 cc of methanol. After all reaction had ceased, the solution was filtered using a Millipore suction filtering apparatus and a Gelman Metricel filter of pore size 0.45μ supported by a Whatman No. 42 filter paper. The residue was rinsed free of all bromine, then ignited and fused with borate and carbonate in a platinum crucible. The fusion was dissolved in 30 cc of 13% H_2SO_4. The solution was brought to 50 cc and the chromium content determined by atomic absorption. An alternative procedure sometimes used was to add 30 cc of the alkali-phosphate solution to the sulfuric acid solution of the fusion, followed by 10 cc of phosphoric acid. This was followed by oxidation with permanganate and colorimetric determination of chromium.[3]

Coulometry.—The procedure used closely followed Britton's work. Samples were subjected to anodic galvanostatic treatment at a current density of 25 μA/cm^2 in a solution of 7.5 g/liter disodium phosphate buffered to a *p*H of 7.4 with phosphoric acid. A saturated calomel electrode was used as the reference electrode and the variation of sample potential with time was recorded.

Results

In one set of experiments, samples were first stripped according to the acid plus alkali method and then subjected to bromine methanol attack. In other cases the samples were subjected to attack by bromine methanol in the "as-received" condition. Tables I-III show the results of these experiments.

Figure 1 shows the results of two experiments in which different sized samples (the sample weight being proportional to surface area) were subjected to complete attack by bromine methanol. The results are used in Table II. It is apparent that for three different lots of commercial CDC tin plate the sum of the surface chromium removed by the alkali plus acid stripping plus the remaining chromium insoluble in bromine methanol was equal to the total chromium insoluble in bromine methanol for the "as-received" samples. This means that all, or very nearly all, the surface chromium removed by the alkali plus acid stripping was insoluble in bromine methanol. The chromium, insoluble in bromine methanol, that was found for samples that had previously been treated by the alkali plus acid stripping is contributed by the base steel.

[3] Extra special precautions to minimize hydrolysis reactions due to the presence of water during the bromine methanol attack on samples were not necessary since we were interested only in the chromium content of the residue. However, samples which were stripped in acid or alkali and then were subjected to bromine methanol attack were rinsed free of water with methanol prior to the latter treatment.

Table I. Bromine methanol analysis of tin plate samples—plate lot 1

All samples had a surface area of 8 in.^{2}
The results are given in μg/sample

Surface Cr removed by alkali + acid stripping	Cr in residue from subsequent Br_2-MeOH treatment	Total	Cr in residue from Br_2-MeOH treatment of samples As received	Baked
23.5	10.5	34.0	40.0	31.5
19.5	13.0	32.5	38.5	42.5
23.5	13.0	36.5	38.5	42.5
22.0	10.0	32.0	37.0	36.5
20.0	9.0	29.0	30.0	40.5
22.5	10.5	33.0	28.5	36.5
20.0	10.0	30.0	30.0	34.5
18.5	13.0	31.5	38.5	34.5
Avg = 21.2	11.1	32.3	35.1	37.3

Table II. Bromine methanol analysis of tin plate samples—plate lot 2

All samples had a surface area of 8 in.^{2}
Results are given in μg/sample

Surface Cr removed by alkali + acid stripping	Cr in residue from subsequent Br_2MeOH treatment	Total	Cr in residue from Br_2MeOH treatment of "as-received" samples
24.5	32.0	56.5	56 from graphs in Fig. 1, 15 samples
36.0	27.5	63.5	
30.5	30.0	60.5	
30.0	27.5	57.5	
31.5	25.0	56.0	
27.5	21.5	49.0	
Avg = 30.0	27.3	57.2	

Table III. Bromine methanol analysis of tin plate samples—plate lot 3

All samples had a surface area of 8 in.^{2}
Results are given in μg/sample

Surface Cr removed by alkali + acid stripping	Cr in residue from subsequent Br_2MeOH treatment	Total	Cr in residue from Br_2MeOH treatment of "as-received" samples
34.0	82.5	116.5	110.0
30.5	82.0	112.5	113.0
31.5	80.5	112.0	117.0
36.5	83.0	119.5	111.5
29.0	82.0	111.0	110.0
34.0	83.0	117.0	119.5
31.0	86.0	117.0	119.0
33.0	78.0	111.0	118.0
Avg = 32.4	82.1	114.6	114.8

Tables IV and V show the results of similar experiments in which the samples were first stripped in hot concentrated KOH and then subjected to bromine methanol attack. The consistency of the data in Tables IV and V with those in Tables I and II should be noted.

The total is the same whether the sample is first treated by the KOH method or by the alkali plus acid method. The surface chromium removed by each method is insoluble in bromine methanol, but more is removed by the alkali plus acid stripping method than by the KOH method.

Figure 2 shows the results of a series of experiments in which sample disks of 8 in.^{2} area of lot 2 plate were subjected to bromine methanol attack to different weight losses, the reaction not being allowed to go to completion. The weight loss was plotted against the quantity of chromium found in the insoluble residue from that weight loss. The results confirm by extrapolation to zero weight loss that about 32 μg/8

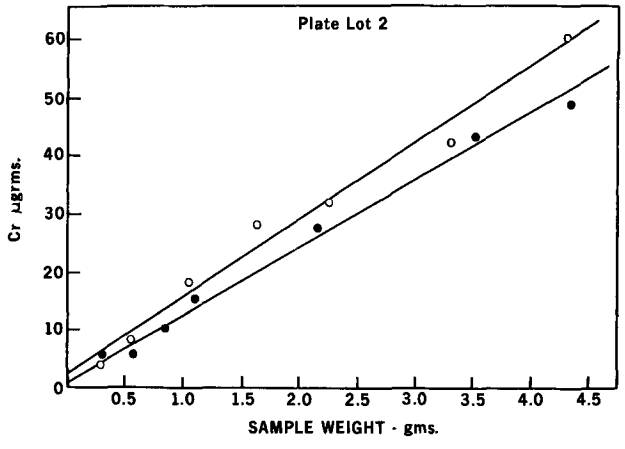

Fig. 1. Cr in residue from bromine methanol attack in tin plate samples as a function of sample weight (includes Cr_2O_3 in steel base).

Table IV. Bromine methanol analysis of tin plate samples—plate lot 1

All samples had a surface area of 8 in.^{2}
The results are given in μg/sample

Surface Cr removed by KOH	Cr in residue from subsequent Br_2-MeOH treatment	Total
5.5	30.0	35.5
9.5	32.0	41.5
11.0	27.0	38.0
4.0	32.0	36.0
8.5	27.5	36.0
7.0	28.0	35.0
2.5	32.5	35.0
8.0	25.0	33.0
Avg = 7.0	29.3	36.3

Table V. Bromine methanol analysis of tin plate samples—plate lot 2

All samples had a surface area of 8 in.^{2}
The results are given in μg/sample

Surface Cr removed by KOH	Cr in residue from subsequent Br_2MeOH treatment	Total
15.0	44.0	59.0
16.0	45.0	61.0
8.5	44.0	53.5
13.5	41.0	54.5
14.0	46.5	60.5
13.5	45.5	59.0
Avg = 13.6	44.3	57.9

in.^{2} of chromium insoluble in bromine methanol are on the surface of this plate. Also shown in Fig. 2 are the results of similar experiments for a sample size of 18 in.^{2} surface area. The low chromium values associated with the lower weight loss arise from the fact that, since the surface chromium measured is insoluble in the medium, it must be released by undercutting. The base steel has a lower concentration of chromium insoluble in bromine methanol than the surface, so preferential attack of the base produces results below the linear relationship. The latter represents complete release of the surface chromium plus an amount proportional to the extent of attack on the base steel.

The results in Table VI show that about half the surface chromium remains on the surface of the CDC tin plate after the anodic treatment in phosphate solutions. This is in agreement with Britton's (3) observation. Table VII shows that this surface chromium is insoluble in bromine methanol solutions after the anodic treatment.

Figure 3 shows a typical potential time curve for a sample that had been previously treated in hot concentrated KOH (curve b). For comparison, a curve from "as-received" plate is also shown (curve a). The numerical results obtained by interpreting the potential arrests, as measured by AB, AC, and DC, from KOH-treated samples in terms of the oxidation of Cr^0 to Cr^{6+} are shown in Table VIII. The sample area used

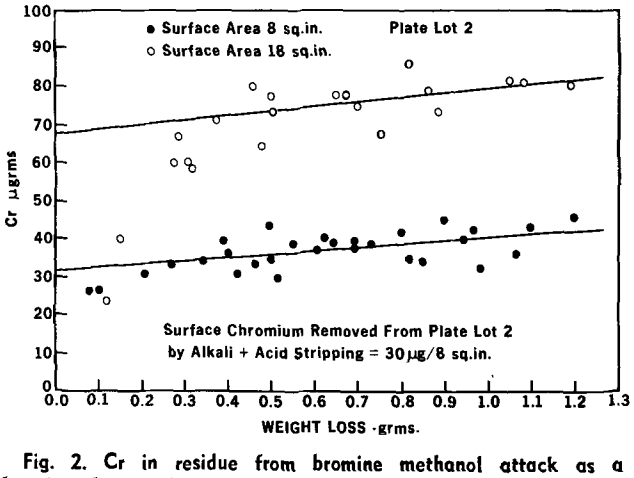

Fig. 2. Cr in residue from bromine methanol attack as a function of weight loss.

Table VI. Surface chromium remaining after anodic treatment—plate lot 1

Alkali + acid stripping method
All samples had a surface area of 8 in.^{2}
Results are given in μg/samples

As-received samples	Samples previously given anodic treatment Set 1	Set 2
21.5	11.5	10.0
20.5	12.0	10.0
24.0	8.5	7.0
19.5	12.0	12.0
21.5		
20.5	Avg = 11.0	9.8
23.0		
21.5		
Avg = 21.5		

Table VII. Surface chromium remaining after anodic treatment—plate lot 1

Cr in residue from Br_2MeOH treatment
All samples had a surface area of 8 in.^{2}
Results are given in μg/sample

As-received samples	Samples previously given anodic treatment	Samples previously treated by alkali + acid stripping
40.0	20.0	10.5
38.5	28.0	13.0
38.5	20.5	13.0
37.0	21.0	10.0
30.0	31.5	9.0
28.5	20.0	10.5
30.0	22.5	10.0
38.5	28.0	13.0
Avg = 35.1	23.9	11.1

Table VIII. Potential arrest interpreted in terms of $Cr^0 \rightarrow Cr^{6+}$

Results are calculated to a Cr^0 concentration in terms of μg Cr^0/8 in.^{2}

Pretreatment	Definition of potential arrest*	As-received samples	Baked samples
8.5M KOH at 180°F for 2 min	AB	4.8	12.3
8.5M KOH at 180°F for 2 min	AC	6.8	16.3
8.5M KOH at 180°F for 2 min	DC	12.0	20.2
1N NaOH with 0.3% H_2O_2 at 141°F for 1 min	AB	16.7	—
1N NaOH with 5% H_2O_2 at 141°F for 1 min	AB	14.0	—

* As designated on curve in Fig. 3.

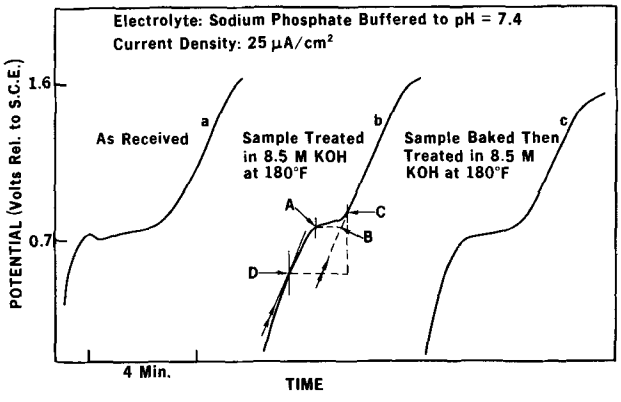

Fig. 3. Anodic treatment of CDC tin plate (potential-time curves)

to obtain the curve was 2.2 cm^2, and each side of the plate was run separately. The results given in Table VIII have been calculated for 4 $in.^2$ of both sides and thus are comparable with the results of the chemical analyses. Also shown in Fig. 3 is a typical potential time curve (curve c) for plate which had been baked (15 min at 350°F) and then treated in KOH prior to anodic polarization. Numerical results obtained from such curves are also shown in Table VIII. Following the suggestion of Rocquet and Aubrun (7), potential time curves were also obtained from plate which had been treated in $NaOH-H_2O_2$ solutions, and results from such experiments are also included in Table VIII.

Discussion

Chemical analysis.—Despite the limitations on accuracy that are apparent, for example in Fig. 1, the results clearly indicate that all, or very nearly all, the surface chromium removed by the alkali plus acid strip is insoluble in bromine methanol. Thus, it had been demonstrated that the surface chromium on these commercial CDC samples that is alkali insoluble and acid soluble is insoluble in bromine methanol, and, therefore, is not metallic chromium.[4] Since metallic chromium is soluble in hot sulfuric acid, it is evident that there is no appreciable quantity of surface metallic chromium on these plates. The literature (10) indicates that the solubility in acid of anhydrous chromic oxide is dependent on the thermal history of the chromic oxide. It is possible for anhydrous chromic oxide to have a slight solubility in acid. Thus, we have found that after treatment of samples of commericial anhydrous chromic oxide in sulfuric acid, chromium could be detected in the solution in concentrations considerably greater than the concentrations occurring in our analyses. After treatment of the anhydrous chromic oxide with 25 cc of hot 8.5M KOH, not even microquantities of chromium could be found in the solution. This suggests that the alkali insoluble surface chromium on commercial CDC tin plate may be anhydrous chromic oxide, which is, of course, insoluble in bromine methanol solutions.

The alkali soluble portion of the surface chromium is indicated by our results also to be insoluble in bromine methanol and is, therefore, not a simple hexavalent chromium compound. The suggestion here is that the alkali soluble surface chromium is a hydrated chromic oxide. Concentrated solutions of caustic are used to remove and estimate the hydrated chromic oxide on the surface of TFS materials (4, 5).

It is, of course, possible that, rather than anhydrous and hydrated chromic oxide, there may be two forms of hydrated oxide with different degrees of hydration, one soluble the other insoluble in alkali.

It will be noted that there is a large percentage of variation in the quantity of chromium found in the alkali stripping solutions from different samples of the same plate. This has been generally found to be true in our work. This may represent the limit of reproducibility in these experiments, and it may be due to a certain amount of undercutting through etching of the tin. However, it may reflect genuine variations in the surface concentration of alkali soluble chromium oxide.

Although we have concluded that there is no metallic chromium on the commercial CDC plates we have examined, we cannot say that metallic chromium is not deposited during the CDC process. It may be that the CDC process does deposit metallic chromium but that the chromium is subsequently oxidized, resulting in a product which has no surface metallic chromium.

[4] Experiments using metallic chromium have shown that under the experimental conditions about 200 mg of chromium dissolve in the bromine methanol solution in 20 min, the shortest time employed. For the plate with the highest content of metallic chromium in the base, the quantity of metallic chromium per 8-sq.-in. sample was about 1.6 mg. Thus, surface metallic chromium in concentrations equivalent to the total surface chromium concentration on CDC tin plate would still leave the quantity of metallic chromium well within the practical solubility limit.

Potential-time curves.—It is realized that, if treatment in hot concentrated KOH removed surface chromic oxide leaving behind metallic chromium, some, if not all, of this metallic chromium would oxidize when the samples were re-exposed to the atmosphere. Thus, when subsequently subjected to anodic treatment as in the work to which reference has been made, the sample would have some surface chromium oxide. However, this oxide is not necessarily involved in any electrolytic reaction during the galvanostatic anodic treatment. For example, in the case of TFS materials it is claimed (4) that the same charge is passed during the potential arrest whether or not the chromic oxide is first removed by treatment in hot KOH. A less ambiguous consideration is that we have already shown that the alkali insoluble and acid soluble surface chromium is not metallic chromium. Nevertheless, in view of the various interpretations that have been applied to the potential time curves from anodic treatment of tin plate, we felt it of interest to examine these curves briefly.

It may be noted that the original suggestion that the curves from KOH-treated samples could be used to estimate surface metallic chromium on CDC tin plate defined the potential arrest as portion DC of the curve (Fig. 3). The results so obtained, Table VIII, are inconsistent with the results of the chemical analyses discussed above. The accuracy of the results reported in Table II is not sufficient to rule out with certainty the possibility of 5 μg of metallic chromium per 8 $in.^2$ indicated in the first line of Table VIII. However, our results show this possibility as unlikely, and the larger numbers obtained from baked plate show that the potential arrest is not correctly interpreted in terms of 100% current efficiency for the reaction $Cr^0 \rightarrow Cr^{6+}$. An increase in surface metallic chromium on baking is hardly a reasonable interpretation and, in any case, the data in Table I show that there is no loss of chromic oxide on baking. Quite clearly, it cannot be assumed *a priori* that the potential arrest, however measured, from samples previously treated in KOH is due only to the oxidation of metallic chromium. A possible explanation of the larger potential arrest from the baked plate is an increase in the amount of chromic oxide not removed by the KOH treatment. However, we have not been able to confirm this experimentally.

The large concentrations of surface metallic chromium calculated from the curves from samples treated in $NaOH-H_2O_2$ solution are, of course, inconsistent with the results of the chemical analyses discussed above. Thus, also in this case, we conclude that the potential arrest cannot be interpreted only in terms of the oxidation of metallic chromium.

Conclusions

1. The surface chromium on the commercial CDC tin plate was insoluble in bromine methanol. It was retained on the surface not as metallic chromium but as a chromic oxide, probably a mixture of hydrated and anhydrous chromic oxide or possibly a mixture of two different hydrated forms.

2. The potential time curves from anodic treatment of CDC tin plate cannot be interpreted in the simple manner employed in the case of TFS materials, even if the plate be first treated in hot concentrated KOH.

3. Anodic polarization of samples previously treated in $NaOH-H_2O_2$ solution does not yield potential arrests that may be interpreted entirely in terms of the oxidation of Cr^0 to Cr^{6+}.

Acknowledgments

The author gratefully acknowledges the analytical work of P. Kelly and R. Kerr, and the Chemistry Section of the Graham Research Laboratory. A special acknowledgment is made to F. Johnson for his assistance with this project.

Manuscript submitted Sept. 15, 1969; revised manuscript received *ca.* May 14, 1970.

Any discussion of this paper will appear in a Discussion Section to be published in the June 1971 JOURNAL.

REFERENCES

1. W. E. Hoare, E. S. Hedges, B. T. K. Barry, "The Technology of Tinplate," pp. 368-369, St. Martins Press (1965).
2. U. T. Hill, Oral presentation, Pittsburgh Conf. on Analytical Chemistry and Spectroscopy, 1953.
3. S. C. Britton, *Brit. Corr. J.*, **1**, 91 (1965).
4. H. Uchida, O. Yanabu, and T. Hada, *Iron Steel Engr.*, **46**, 75 (1960).
5. E. J. Schneider, R. L. Martin, V. Kupsis, and S. M. Purdy, "Structure and Properties of Thin, Chemically Treated Chromium Electrodeposits," Presented at 27th AIME Annual Meeting, Feb. 1968.
6. Annual Report of the International Tin Research Council, Greenford, Middlesex, England, 1968.
7. P. Rocquet and P. Aubrun, *Corrosion, Traitment, Protection Finition*, **16**, 229 (1968).
8. S. N. Shah and E. D. Davies, *Electrochim. Acta*, **8**, 703 (1963).
9. E. B. Sandell, "Colorimetric Determination of Traces of Metals," Vol. III, p. 260, Interscience Publishers (1950).
10. J. W. Mellor, "A Comprehensive Treatise on Inorganic & Theoretical Chemistry," Vol. XI, p. 181, Longman, Green & Co. (1931), and references therein.

Improvements in the Etching of Hard Aluminum Electrolytic Capacitor Foil

M. S. Hunter*

Alcoa Research Laboratories, Aluminum Company of America, New Kensington, Pennsylvania 15068

ABSTRACT

Improved procedures are described for etching hard electrolytic capacitor foil for low and intermediate voltage applications. For low voltage formation (0-100V), high capacitance was obtained by etching at high current density in a solution containing a high NaCl concentration and 10 g/liter Na_2SO_4. For intermediate voltage formation (100-250V), optimum etching conditions consisted of a lower current density and NaCl concentration, along with the sulfate addition. In both applications, the combination of hard foil and the sulfate addition in the etch bath were particularly advantageous.

The continuing demand for aluminum electrolytic capacitors has been for units of greater capacity and smaller size. This demand can be met by improving etching techniques, with special aluminum foils, and through the selection of optimum combinations of foil and etch process for specific applications.

The ability of hard-rolled aluminum foil to produce capacitor anodes of greater capacitance was discovered over 30 years ago (1), but no use was made of this discovery for almost 25 years. In 1962, it was stated that, since dislocations act as preferred sites for etch attack, the large number of dislocations in a work-hardened foil should lead to a finer etch (2). Such an etch would be expected to have a greater surface area and, hence, higher capacitance. Shortly thereafter, it was shown that this actually was the case, although this fact did not appear in the literature for several years (3).

Two of the most significant advancements in electrolytic etching technology have been: (*a*) the discovery that etching current density has a profound effect on capacitance with both high and low formation voltages (2-3), and (*b*) the discovery that the addition of sodium sulfate to the electrolytic etching bath increases greatly the capacitance of annealed foil at low formation voltages (4-6). Present work describes additional improvements in electrolytic etching technology in sodium chloride solutions, which can be used to obtain considerably higher capacitance at both low and intermediate formation voltages.

Low Voltage Formation

In experiments involving low voltage formation (0-100V), 0.003-0.0035 in. thick foils of 99.99, 99.93, and 99.88% aluminum in both the annealed (0) and hard (H19) tempers were used. In evaluating the effect of NaCl concentration, a current density of 0.99A/cm^2 (6.4 A/in.^{2})[1] was employed because high current density has proven to be advantageous in etching foil for low voltage applications. NaCl concentrations from 80 to 310 g/liter were evaluated since this is the range over which relatively high current densities can be obtained conveniently. Formation was in an aqueous solution containing 30 g/liter tartaric acid and adjusted to *p*H 5.5 with NH_4OH. Measurement was at 60 Hz in a solution having a resistance of 30 ohms, using 3 in. x 1½ in. samples centered between stainless steel cathodes 1 in. apart.

NaCl concentration affected capacitance with all purities and both tempers of foil, as shown by the data for 30V formation in Table I. Capacitance increased progressively with NaCl concentration throughout the range. The effect was more pronounced with hard foil than with annealed foil. With annealed foil, the improvement over the concentration range was greatest with highest purity foil. With hard foil, however, the improvement was greatest with lowest purity foil.

[1] All areas are projected area; *e.g.*, 2 in. × 2 in. sample has 4 in.^{2} area.

Table I. Effect of temper and NaCl concentration[1] on 30V capacitance[2]

Purity	Temper	NaCl concentration, g/liter 80	120	200	310
99.99	Annealed	40.0	43.1	44.0	49.9
99.99	Hard	59.3	62.0	68.0	72.8
99.93	Annealed	40.1	41.8	41.3	45.4
99.93	Hard	52.1	56.9	64.7	68.8
99.88	Annealed	40.7	41.3	42.7	44.4
99.88	Hard	43.2	50.0	53.1	65.0

[1] 6.4 A/in.^{2}; 7.2 A-min/in.^{2}; solution at 90°C.
[2] mfd/in.^{2} after room-temperature formation in 3% ammonium tartrate solution at *p*H 5.5.

* Electrochemical Society Active Member.
Key words: aluminum foil (hard), electrolytic capacitors, electrolytic etching, capacitance.

Table II. Effect of temper and sulfate[1] on 30V capacitance[2]

Purity	Temper	Without sulfate	10 g/liter Na_2SO_4	Per cent improvement from sulfate
99.99	Annealed	44.0	52.0	+18
99.99	Hard	68.0	102.2	+50
99.93	Annealed	41.3	51.8	+25
99.93	Hard	64.7	96.6	+49
99.88	Annealed	42.7	51.4	+20
99.88	Hard	53.1	84.6	+59

Purity	Per cent difference—hard *vs.* annealed: Without sulfate	10 g/liter Na_2SO_4
99.99	+54	+97
99.93	+57	+86
99.88	+24	+65

[1] 200 g/liter C.P. NaCl at 90°C; 6.4 A/in.² for 7.2 A-min/in.².
[2] mfd/in.² after room-temperature formation in 3% ammonium tartrate solution at pH 5.5.

In evaluating the effect of sulfate, the same etching current density was used, along with various combinations of NaCl and sodium sulfate concentrations. It was found that the maximum benefit from the sulfate addition was achieved at a concentration of about 10 g/liter. With this sulfate content, best consistency of etch and highest capacitance were obtained with NaCl concentrations in the range of 200-230 g/liter. Data for the 200 g/liter solution are listed in Table II.

The data in this table show the beneficial effect of sulfate with annealed foil that has been described previously in patents (4-6). They also show that the beneficial effect of sulfate is considerably greater with hard foil, which increased 4.8-5.3 mfd/cm² (31-34 mfd/in.²), than with annealed foil, which gained 1.24-1.55 mfd/cm² (8-10 mfd/in.²). In addition, the combined effect of temper and sulfate is decidedly synergistic. For example, with 99.99 foil, the improvement in capacitance of annealed foil from the sulfate addition is 1.24 mfd/cm² (8.0 mfd/in.²). The improvement from annealed to hard foil, without sulfate in the etch, is 3.7 mfd/cm² (24 mfd/in.²). On the simple assumption that effects would be additive, it might be expected that the combination would increase capacitance by about 5 mfd/cm² (32 mfd/in.²). The actual improvement, however, was 9 mfd/cm² (58.2 mfd/in.²), 80% greater than expected. This improvement is particularly impressive because the increase in capacitance with the hard foil-sulfate combination is over 130% with the two higher purities of foil and almost 100% with the lowest purity foil.

Electron microscope examinations revealed the changes in etch configuration associated with changes in NaCl concentration and the addition of sulfate to the etch bath. These observations supported the principles stated previously (2) that capacitance is determined not only by the surface area developed during etching, but also by the degree of smoothing during formation which results from the consumption of aluminum to form the oxide dielectric film. For this reason, relatively coarse etches are best for high voltage formation because the surface area is retained better during formation. On the other hand, in low voltage applications, advantage can be taken of finer etches, which develop greater surface area, because so little metal is consumed during formation.

Electron microscope examinations were made using plastic-carbon replicas. These showed that hard foil developed a much finer etch configuration under all etching conditions. Increasing NaCl concentration and adding sulfate to the etch bath also produced a finer etch. Thus, the optimum combination for low voltage formation was hard foil, high current density, high NaCl concentration, and sulfate addition in the etch bath.

The effects of temper and sulfate addition on the etch configurations of 1199 foil are shown in Fig. 1 and 2. In these micrographs, the etch facets are the (100)

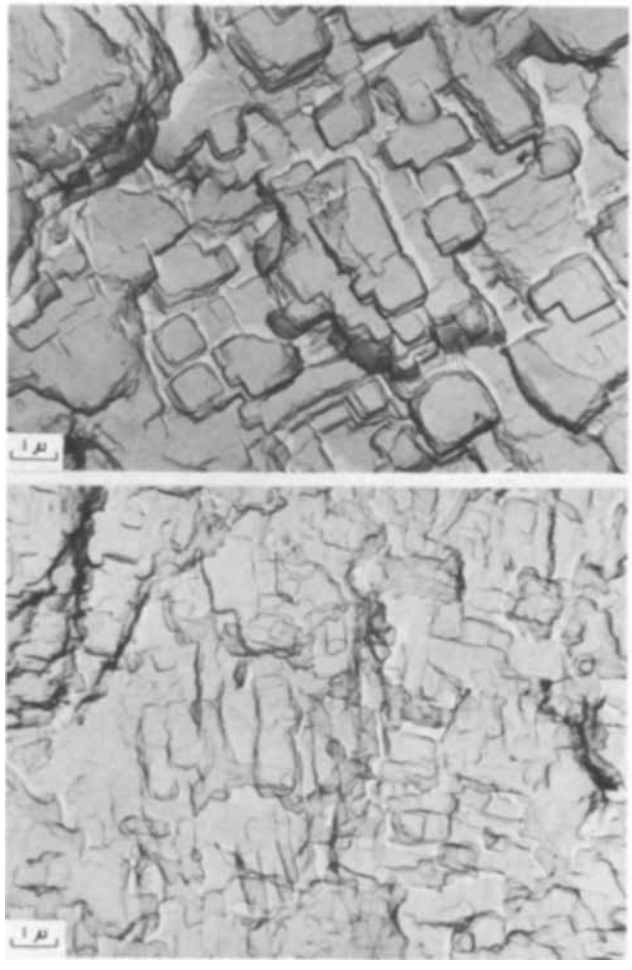

Fig. 1. Etch configurations developed by etching 1199 foil at 4.8 A/in.² in 200 g/liter NaCl solution (X6000). *Top*—annealed foil, 45.8 mfd/in.² at 30V formation. *Bottom*—hard foil, 82.4 mfd/in.² at 30V formation.

planes of the aluminum lattice. In annealed samples, these form a regular array because the fields shown are within single grains. With hard-rolled foil, the etch facets are arrayed more irregularly because of the highly fragmented structure of the foil. Sulfate addition (Fig. 2) brought about further refinement of the general etch configuration and, in addition, developed additional smaller steps and facets superimposed on the larger facets.

In the lower micrograph of Fig. 2, a very fine speckling of the metal surface is apparent. This configuration has been noted with sulfate-bearing etches and has tended to be more prevalent with hard foil and with high NaCl concentrations.

Intermediate Voltage Formation

The investigation of the potentialities of hard foil for use in the intermediate forming voltage range (100-250V) was concerned primarily with defining optimum etching conditions. Foils of 99.99, 99.93, and 99.88% minimum purity, in the 0 and H19 tempers, were used. Basing the choice of etch parameters on the principles defined previously, and the known effect of the possible etch variables, samples were etched at current densities from 0.25 to 0.75 A/cm² (1.6-4.8 A/in.²), in solutions containing from 40 to 240 g/liter NaCl, both with and without an addition of 10 g/liter Na_2SO_4. Formation was in an aqueous solution containing 1 g/liter $NH_4H_2PO_4$ operated at 90°C. Measurement was the same as for low voltage formation except that a measuring solution having a resistance of 1440 ohms was used.

It was found, as had been expected, that optimum conditions for intermediate voltage formation were

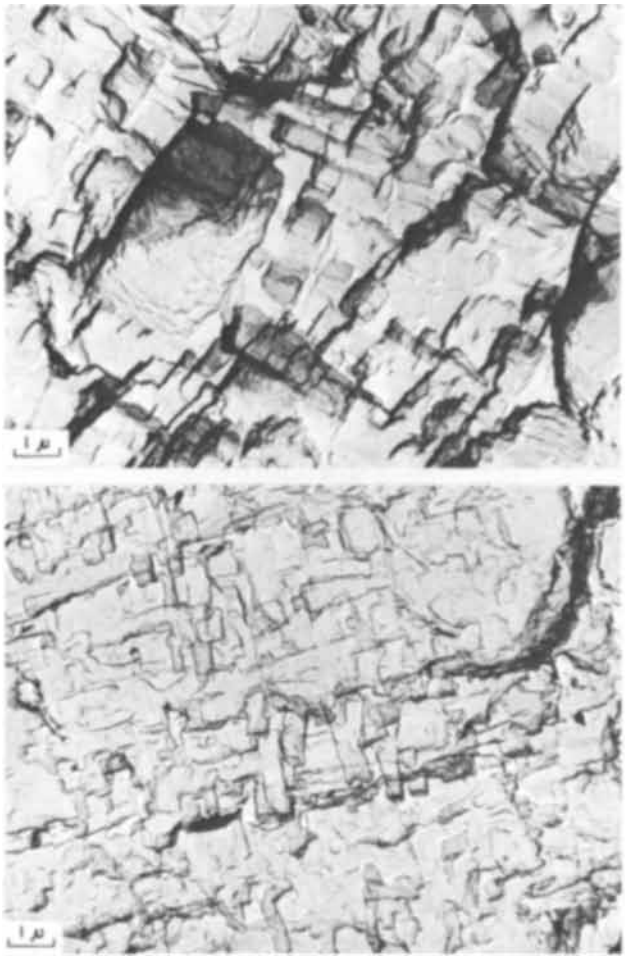

Fig. 2. Etch configurations developed by etching 1199 foil at 4.8 A/in.^{2} in solution of 200 g/liter NaCl + 10 g/liter Na_2SO_4 (X6000). *Top*—annealed foil, 56.7 mfd/in.^{2} at 30V formation. *Bottom*—hard foil, 114.2 mfd/in.^{2} at 30V formation.

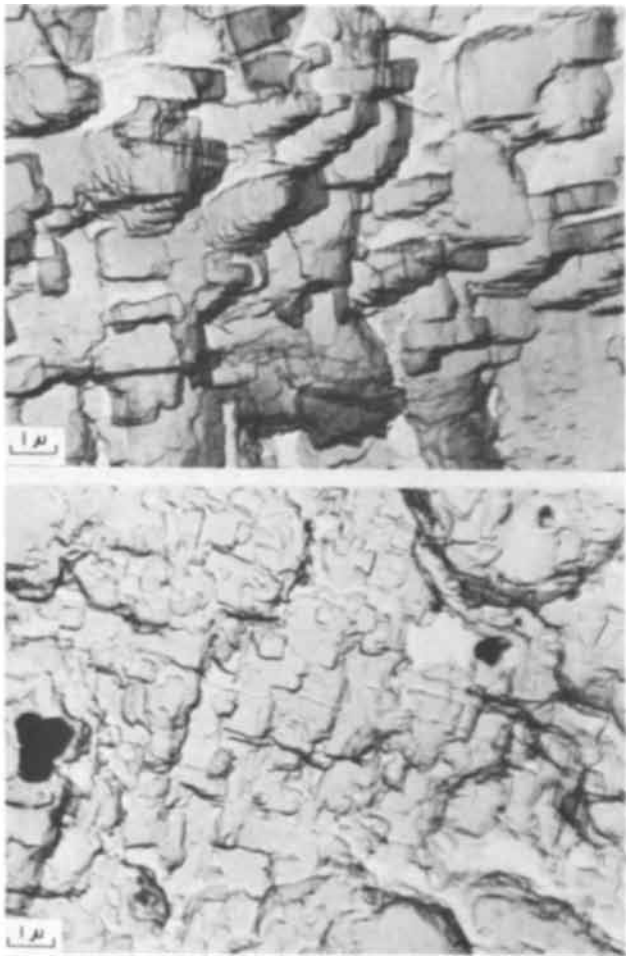

Fig. 3. Etch configurations developed by etching 1199 foil under conditions optimum for intermediate voltage formation (X6000). *Top*—annealed foil, 4.71 mfd/in.^{2} at 165V formation. *Bottom*—hard foil, 7.89 mfd/in.^{2} at 165V formation.

different from those for either high-voltage or low-voltage applications. Without sulfate addition, moderately high NaCl concentrations (160-240 g/liter) and current density (~3.2 A/in.^{2}) were optimum. Under these conditions, hard foil of all purities showed some advantage over annealed foil at 125V formation (Table III). As formation voltage was increased, however, this advantage decreased rapidly, particularly with lowest purity foil.

With sulfate addition to the etch solution, the etch-refining effect of the sulfate had to be offset somewhat for maximum capacitance. This was done by reducing NaCl concentration to about 80 g/liter. With this modification, the combination of hard foil and sulfate addition produced greatly increased capacitance as shown by the values in Table III. At these capacitance levels, hard foil showed an advantage over annealed foil with all purities and at all forming voltages.

A further increase in wet-cell capacitance was obtained by hydrating the etched samples prior to formation as shown by the data in Table IV. These higher values could be utilized only if the alpha-alumina-monohydrate formed during hydration had no adverse effect on other capacitor characteristics.

Table III. Effect of temper and sulfate on capacitance at intermediate formation voltages[1]

Purity	Temper	No sulfate in etch[2]—mfd/in.^{2}				Sulfate in etch[3]—mfd/in.^{2}			
		125V	165V	200V	250V	125V	165V	200V	250V
99.99	Annealed	6.13	4.13	3.00	2.03	6.71	4.58	3.42	2.34
99.99	Hard	7.64	4.71	3.27	2.09	13.20	8.09	5.47	3.56
99.93	Annealed	5.76	3.87	2.67	1.80	6.60	4.44	3.27	2.22
99.93	Hard	6.89	4.02	2.73	1.64	11.60	6.98	4.69	2.98
99.88	Annealed	5.67	3.76	2.67	1.78	6.31	4.42	3.16	2.20
99.88	Hard	6.69	3.73	2.47	1.46	11.29	6.67	4.56	2.84
		Per cent difference—hard *vs.* annealed							
		No sulfate in etch[2]				Sulfate in etch[3]			
Purity		125V	165V	200V	250V	125V	165V	200V	250V
99.99		+25	+14	+9	+3	+97	+73	+60	+52
99.93		+20	+4	+2	−9	+76	+57	+43	+34
99.88		+18	−1	−7	−18	+79	+51	+44	+29

[1] Formed without hydration. Formation in 1 g/liter $NH_4H_2PO_4$ solution at 90°C.
[2] Etched at 3.2 A/in.^{2} for 7.2 A-min/in.^{2} in 90°C solutions; 99.99 in 160 g/liter, others in 240 g/liter.
[3] Etched as above but in solution of 80 g/liter NaCl + 10 g/liter Na_2SO_4.

Table IV. Effect of hydration[1] on capacitance of hard foil etched in sulfate-bearing solution[2] and formed at intermediate voltages

Purity	Temper	Without hydration—mfd/in.[2] 125V	165V	200V	250V	With hydration—mfd/in.[2] 125V	165V	200V	250V
99.99	Annealed	6.71	4.58	3.42	2.34	8.56	6.20	5.16	3.56
99.99	Hard	14.27	8.50	5.53	3.56	16.48	10.18	7.58	5.24
99.93	Annealed	6.60	4.44	3.27	2.22	8.22	6.00	4.58	3.44
99.93	Hard	12.91	7.60	5.00	3.07	15.62	9.35	6.84	4.47
99.88	Annealed	6.31	4.42	3.16	2.20	7.87	5.89	4.73	3.40
99.88	Hard	12.47	7.20	4.73	2.89	16.27	8.82	6.31	4.42

Purity	Temper	Per cent improvement with hydration 125V	165V	200V	250V
99.99	Annealed	+28	+35	+51	+52
99.99	Hard	+15	+20	+37	+47
99.93	Annealed	+25	+35	+40	+55
99.93	Hard	+21	+23	+37	+45
99.88	Annealed	+25	+33	+50	+54
99.88	Hard	+30	+22	+33	+53

[1] Ten minutes in boiling distilled water.
[2] Etched at 3.2 A/in.[2] for 7.2 A-min/in.[2] in 80 g/liter NaCl + 10 g/liter Na_2SO_4 at 90°C.
[3] Formation in 1 g/liter $NH_4H_2PO_4$ solution at 90°C.

Electron microscope examinations were made to show the character of the roughness found optimum for intermediate voltage formation. The roughness of annealed and hard foil samples etched under conditions optimum for hard foil are shown in Fig. 3. The difference in general roughening between the two tempers is apparent, although the basic facet size is somewhat larger than that found optimum for low voltage formation. The larger facet size results from lower NaCl concentration used. Superimposed on general roughness is the finer faceted pattern, apparently generated by sulfate addition.

Summary and Conclusion

For low voltage formation, hard foil develops maximum capacitance with high NaCl concentration, high etching current density, and a sulfate addition to the etch. For intermediate forming voltages, optimum conditions involve lower current density and somewhat lower NaCl concentration. With proper etch parameters, hard foil is superior to annealed foil up to 250V formation.

Manuscript submitted March 30, 1970; revised manuscript received *ca.* May 26, 1970.

Any discussion of this paper will appear in a Discussion Section to be published in the June 1971 JOURNAL.

REFERENCES

1. F. Pavelka, U.S. Pat. 2,168,135 (1939).
2. M. S. Hunter, *Electrochem. Technol.*, **1**, 151 (1963).
3. R. Bakish, R. J. Kornhaas, and E. Z. Borders, *ibid.*, **5**, 192 (1968).
4. H. A. Martin, U.S. Pat. 3,284,326 (1966).
5. C. E. Welch, Jr., U.S. Pat. 3,316,164 (1967).
6. D. J. Anderson, U.S. Pat. 3,321,389 (1967).

Mechanism of Operation of a Voltage-Sensitive Switch

John J. Randall, Jr., Ernest N. Urfer, Henry F. Puppolo, and William S. Goruk*

Research and Development Laboratories, Sprague Electric Company, North Adams, Massachusetts 01247

ABSTRACT

Electron microscopy and electron microprobe analysis have shown that discrete iron-rich impurity sites in aluminum foil cause the formation of voids 2-40μ in diameter in the porous part of a duplex porous-barrier anodic film used as the insulating element in a voltage-sensitive switch. It is postulated that the existence of these voids allows the counterelectrode material to penetrate the porous layer and contact the underlying barrier layer. Since the cross-sectional area penetrated is very small, the probability of direct contact to imperfections in the barrier layer is much lower than would be the case with a simple metal-barrier oxide-metal system. As a result, breakdown strength of a device made with the duplex oxide is more uniformly reproducible than that of the latter and is also more nearly characteristic of bulk aluminum oxide.

A single-shot, voltage-sensitive switch with extremely reproducible breakdown characteristics can be prepared on an aluminum substrate by anodizing the aluminum sequentially in a porous film forming electrolyte and in a barrier film forming solution and then applying an appropriate counterelectrode. This device is designed to short-circuit when a pulse voltage of a predetermined magnitude is applied across the electrodes. Prior to closure the characteristics of the device are those of a low-leakage, low-capacitance capacitor, while after breakdown it behaves as a low-resistance conductor. The devices used for this study were designed to close at low voltages (5-15V), but higher closure voltages can be achieved by increasing the thickness of the barrier portion of the porous film formed by the duplex anodization. Closure time for the device is dependent on the height of the voltage pulse applied, but can easily be controlled to within a few microseconds.

Although it has been recognized that films containing porous aluminum oxide of the type which is

* Electrochemical Society Active Member.
Key words: voltage sensitive switch, aluminum oxide, breakdown strength.

formed in chromic acid anodizing electrolytes give more reproducible results for this switching application than do films of the pure, compact barrier type oxide which is used in electrolytic capacitors (1, 2), the reasons for the different behavior have not been elucidated. In this communication we describe our attempts to establish the mechanism of operation of switches utilizing porous oxide by means of optical and electron microscopical examination of the system before and after breakdown had occurred.

Experimental

Aluminum foil for the base electrode was either 99.88, 99.99, 99.999, or 99.9999% pure and was electropolished in a perchloric acid-acetic anhydride solution prior to anodization. Specimens were carefully washed in distilled water after polishing. In the few experiments where evaporated substrates were used, the source material was 99.999% aluminum.

Anodization in aqueous 1.5% chromic acid was carried out at constant current at 38°C for a predetermined length of time. Under the experimental conditions used, anodization in chromic acid solution is known to produce a porous type of aluminum oxide with a layer of compact barrier oxide at the base of the pores. At the current densities used here ($\sim$ 0.5 mA/cm^2), the barrier layer reaches a limiting thickness in less than 10 min, as evidenced by the constancy of the cell voltage beyond that time. The porous layer, however, continues to grow.

Following the anodization in chromic acid, all specimens were anodized at a constant voltage which was slightly higher than the terminal voltage in the CrO_3 solution in 0.1% aqueous ammonium dihydrogen phosphate solution (ADP) at 85°C. This second anodization has been shown to improve the uniformity of closure voltage (2), presumably by healing imperfections in the compact portion of the original film formed in CrO_3. Some increase in the thickness of the compact layer also occurs during this step, but the amount of oxide formed is very small compared to that formed during the first anodization.

The usual counterelectrode material was a relatively heavy coating of silver paste which was dried at 125°C after application, but, for purposes of revealing the appearance of the film after breakdown, in some cases a thin silver paste was applied to the oxide to form a relatively transparent counterelectrode.

Observations

Figure 1 shows low magnification appearances of aluminum foil of three different purities after electropolishing and anodization in chromic acid solution. Anodization in ADP did not noticeably change the appearance of the foil. The spots which appear on all specimens, which will hereafter be referred to as defects, are most obviously prominent on the lowest purity foil; 99.9999% foil showed no evidence of the presence of defects. In no case was it possible to see defects of this type when samples had been electropolished but had not been anodized in chromic acid. It was further observed that variations in the density of sites occurred from one manufacturer's product to the next even with metal foil specimens which had the same over-all purity.

Electron microprobe examination of the defect sites showed that a concentration of metallic impurities occurs at these locations. The roughly circular sites, which are about 2-40μ in diameter, have, as may be seen in Fig. 2, a central core which is 1-2μ across which appears to contain the bulk of the impurity. In the case of 99.88 and 99.99% metal, the impurity was primarily iron in amounts of 0.5 and 0.1%, respectively, in the volume of material analyzed by the microprobe; a small amount of nickel was also present. In the 99.999% foil about 0.05% chromium was found. At high magnification in the optical microscope, it was easily determined that the central region was lower by several microns than the surrounding site area and

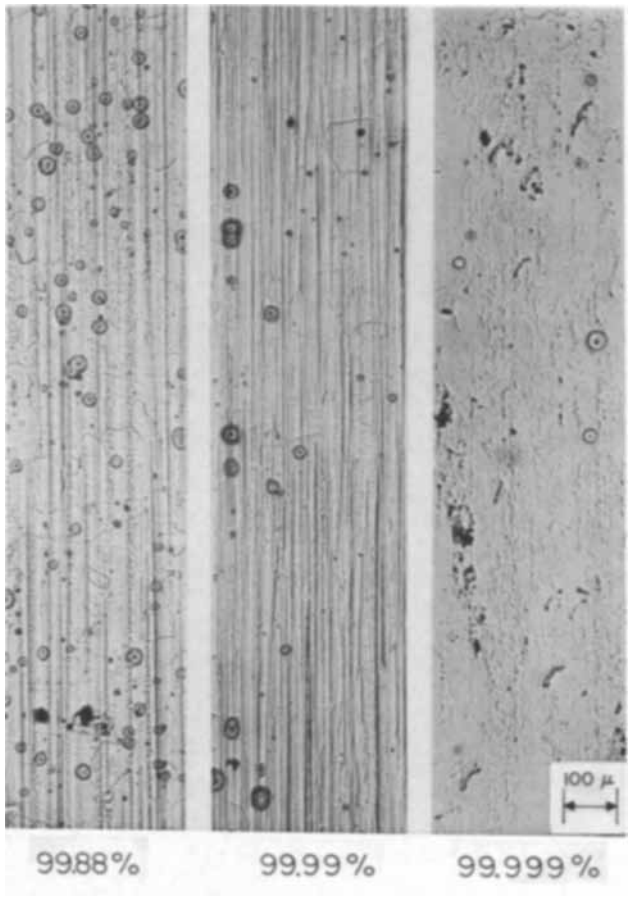

Fig. 1. Appearance of aluminum foil of three different purities after electropolishing and anodizing in chromic acid solution.

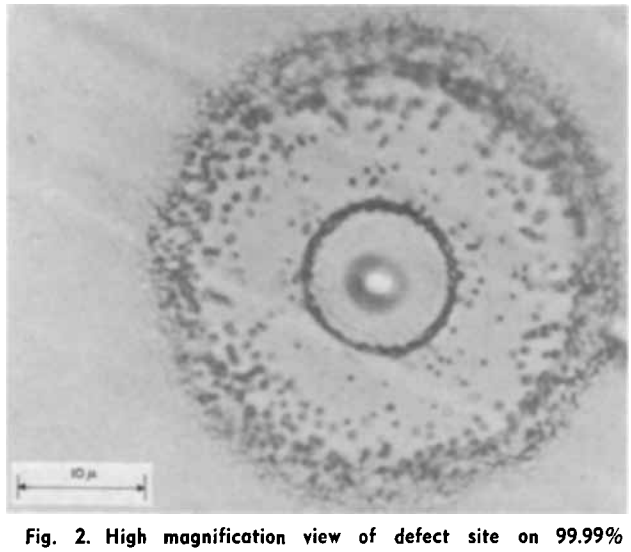

Fig. 2. High magnification view of defect site on 99.99% aluminum.

that the whole site was somewhat lower than the rest of the foil surface.

Switches made using thin silver electrodes were closed by applying the appropriate pulse voltage in order to observe the appearance of specific breakdown locations; Fig. 3 shows one such specimen. From the similarity of appearance of the specimen which had been broken down to that seen in Fig. 2, it seems obvious that breakdown is localized at the impurity sites.

Oxide films were then isolated from anodized foil by the use of an aqueous mercuric chloride solution which amalgamates with the aluminum and allows the film to float free. Pieces of film were rinsed and then

Fig. 3. Defect sites where breakdown has occurred. Black material is thin silver counterelectrode.

picked up on copper screens for examination in the electron microscope. Figure 4 contains a selection of transmission micrographs of areas of oxide which (presumably) were located above defect sites in the metal. The darker areas are thicker than the lighter and indicate the presence of porous Al_2O_3, while the lighter areas, as can be seen particularly in Fig. 4(b), have a structure more typical of barrier-type oxide. In several cases, the thin-film area has apparently separated from the thicker film and left a hole in the specimen.

When the anodization time in chromic acid is greatly increased, the sites have a slightly different appearance as is shown in Fig. 5. It appears that the porous oxide on both sides of the annular void has begun to grow across the barrier oxide region. It seems possible that these growths might ultimately form a bridge across the thin-film area when the film is grown to still greater thickness, but this was not verified directly due to the fact that the electron beam could not penetrate a film much thicker than that of Fig. 5.

Correlation of Physical Structure with Electrical Characteristics

Typical ramp-type closure data (applied voltage was increased at 0.1 V/sec until breakdown occurred) for films formed on two different purity substrates are plotted in Fig. 6 as a function of anodization time in chromic acid (which is roughly proportional to the total film thickness). For both purities, a plateau is observed for short anodization times and a sharply increasing slope thereafter. On the plateau region of the curves closure voltage is very reproducible, while beyond that region breakdown is erratic.

Since the breakdown voltage in the plateau region is roughly the same as the ADP anodization voltage, and since it can be demonstrated that the porous layer continues to grow throughout the plateau regions of these curves, it is apparent that the porous portion of the film does not contribute to the breakdown voltage until it has grown beyond a critical thickness, which thickness is larger for lower purity aluminum. Effectively, anything less than the critical thickness of porous oxide is shorted-out by the defect sites so that it makes no contribution to the closure voltage. The more sites that are present, or perhaps the larger or deeper they are, as is probably the case with 99.88% metal, the thicker the layer of oxide which can be affected, and the longer the plateau region of the curve.

From the appearance of the film over the impurity sites and the known structure of porous oxide films on aluminum, we deduce the cross-sectional structure of the sites shown in Fig. 7 and the following explanation for device performance. The nonhomogeneity of the

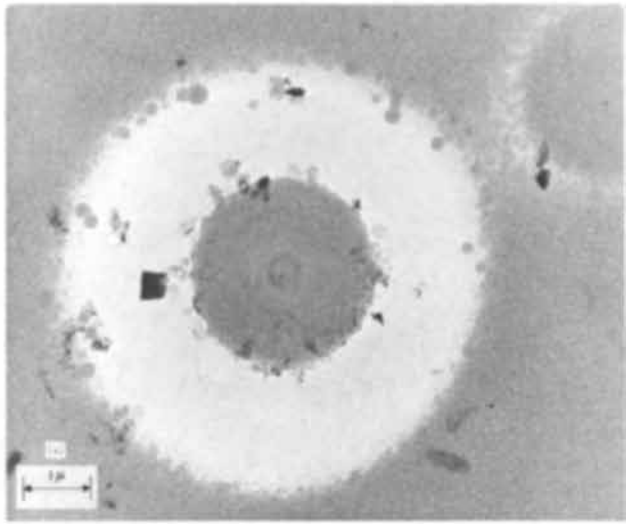

Fig. 4a

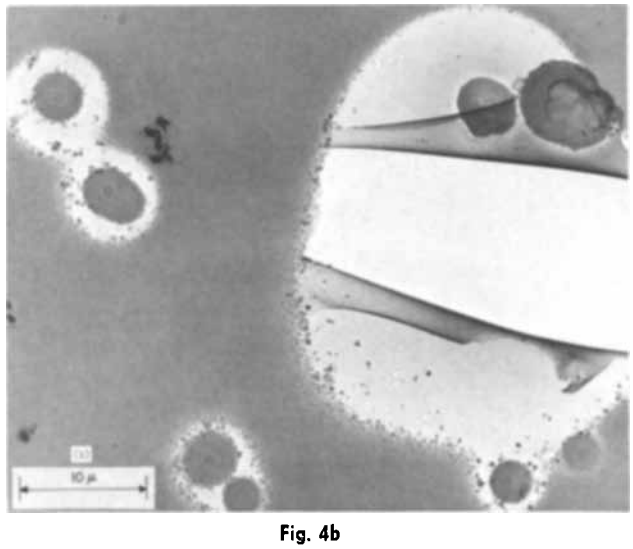

Fig. 4b

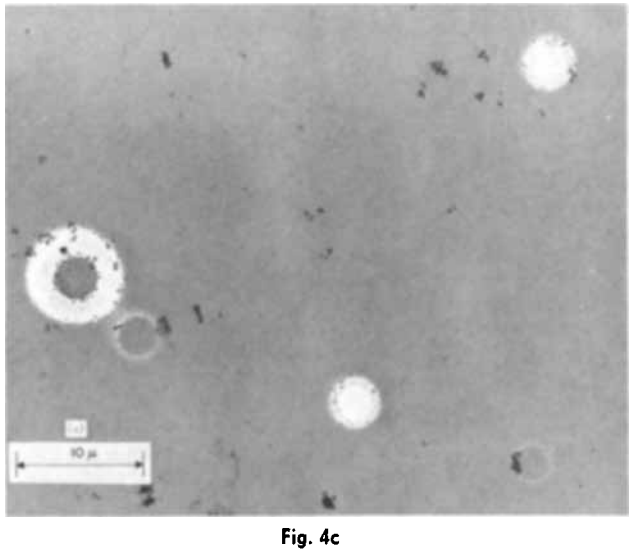

Fig. 4c

Fig. 4 (a), (b), (c). Transmission electron micrographs of oxide films formed by anodization of electropolished 99.99% aluminum foil for 5 min in chromic acid solution.

iron impurities appears to be due to the low solubility of iron in aluminum, which causes segregation of an iron-rich phase at specific sites. From the transmission photographs it appears that porous oxide does not

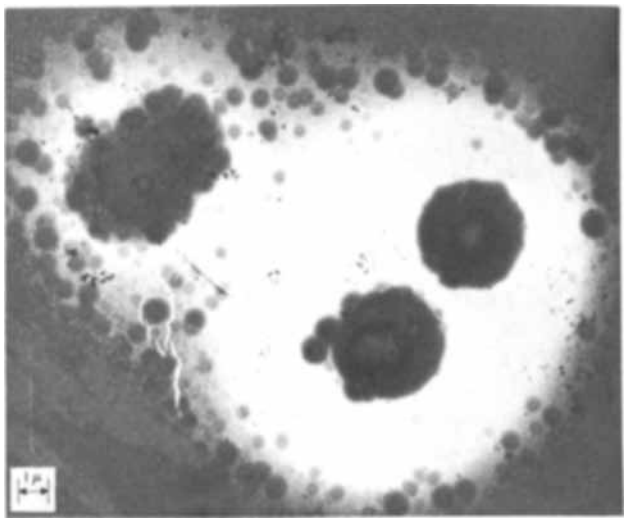

Fig. 5. Transmission electron micrograph of oxide film formed by anodization of electropolished 99.99% aluminum for 15 min in chromic acid solution.

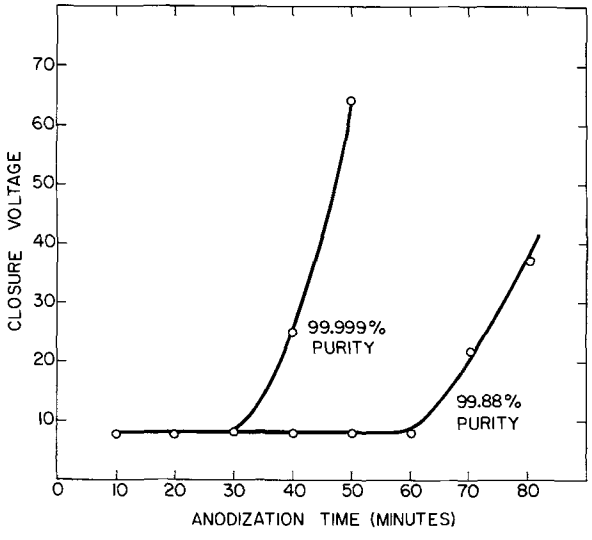

Fig. 6. Closure voltage as a function of anodization time in chromic acid solution.

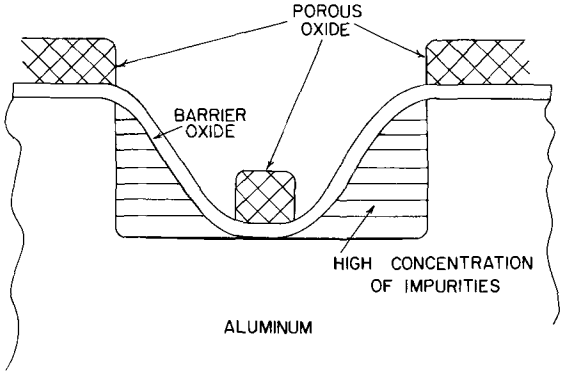

Fig. 7. Proposed cross-sectional structure of defect site

form over an annularly shaped region on top of these discrete iron locations in the original foil. However, barrier oxide apparently does form in the annular region, as can be seen in Fig. 4(b), where the thinner barrier oxide has broken and rolled back on itself. The barrier layer has the typical "orange peel" appearance which has often been observed on electropolished aluminum and on thin dielectric Al_2O_3 films (3, 4). The reasons for the formation of porous oxide over the very center of the site but not around its periphery are not known, but may indicate that iron is absent from the most central region. Unfortunately, the diameter of the electron beam in the microprobe was too large to tell precisely whether the impurity was located in the exact center of the site or in the annular ring, so that a complete correlation was not possible.

Because of the presence of these annularly shaped voids in the porous layer it is possible for the counterelectrode material to penetrate through to the barrier film at a considerable number of locations, particularly when a liquid or semiliquid vehicle is used for application of the counterelectrode. Since the total insulator thickness is then less at these points than at the surrounding locations, the switch is most likely to break down at the defect sites. In fact, electron microprobe analysis of devices made from 99.99% aluminum showed that iron was present at every shorted area in a closed switch. This explains why the closure voltage on the plateau sections in Fig. 6 is characteristic of the barrier layer alone rather than of the barrier-porous combination. The fact that closure voltage rises sharply as anodization time is further increased is taken as evidence that counterelectrode penetration of the voids becomes less likely either because of "bridging" mentioned above or to the increased vertical height of the void. The former could perhaps come about as a result of the complete consumption of the iron impurity by the anodic oxidation.

The total area of contact to the barrier layer is rather small; in 99.99% aluminum, the approximately 600 sites/cm^2 occupy only an estimated 0.05% of the geometric surface area of the specimen. Hence, most of the barrier layer is covered by porous oxide, and other types of defects, such as those caused by surface contamination or roughness (5, 6), which are present in much larger numbers and which are known to give rise to low-voltage breakdown of dielectric films (7) are, for the most part, insulated from the counterelectrode. (Conceiving of the porous layer and the barrier layer as two distinct entities, the result is not unlike the improved insulation resistance achieved when two layers of paper are utilized in a paper capacitor, for the probability of a defect in one layer being exactly aligned with one in the second layer is extremely small.) It is this insulation of defects having low breakdown strengths which is thought to account for the more uniform breakdown behavior of the duplex film, as compared to that of a barrier oxide film of the type used in capacitors.

As might be predicted, switches prepared on evaporated aluminum substrates had considerably higher breakdown voltages than foil-based devices. This is presumably due either to the fact that the evaporation nearly totally separates the iron and other high melting point impurities from the aluminum, or to the homogenization of impurities which would be expected to occur during the process of deposition. Since the evaporated substrates have no discrete impurity sites, the porous part of the duplex insulator makes a positive contribution to the breakdown strength regardless of its thickness, and plots of closure voltage *vs.* anodization time (or total film thickness) do not exhibit the plateau region of Fig. 6.

Acknowledgments

The authors are grateful for a number of very helpful discussions with Dr. Walter J. Bernard and Mr. Richard J. Millard and are indebted to the Analytical Department of the Sprague Electric Company for the electron microprobe and electron microscope work.

This work was supported by a contract with the Conductron Corporation of St. Charles, Missouri.

Manuscript submitted Jan. 21, 1970; revised manuscript received *ca.* May 22, 1970.

Any discussion of this paper will appear in a Discussion Section to be published in the June 1971 JOURNAL.

REFERENCES

1. K. O. Otley, R. F. Shoemaker, and P. J. Franklin, *Proc. IRE*, **46**, 1723 (1958).
2. H. F. Puppolo and A. E. Scherr, U.S. Pat. 3,412,220, "Voltage Sensitive Switch and Method of Making," Nov. 19, 1968.
3. G. L. Bucknell, G. A. Geach, and N. C. Welch, *Research (London)*, **5**, 289 (1952).
4. J. J. Randall, Jr., and W. J. Bernard, *J. Appl. Phys.*, **35**, 1317 (1964).
5. D. A. Vermilyea, *This Journal*, **110**, 250 (1963).
6. G. P. Klein, *ibid.*, **113**, 348 (1966).
7. N. W. Silcox and L. I. Maissel, *ibid.*, **109**, 1151 (1962).

Technical Notes

Mounting Specimens in Teflon for Electrochemical Studies

Z. Nagy* and J. McHardy*

The Electrochemistry Laboratory, University of Pennsylvania, Philadelphia, Pennsylvania 19104

Electrochemical studies frequently involve the use of strong acids or alkalies which attack most mounting materials (epoxy resins, waxes, *etc.*) (1) to some extent and result in contamination of the test solution. In our experience, only Teflon has proved fully satisfactory as a mounting material. Three techniques have been described for mounting specimens with Teflon (2-4), but each one has certain shortcomings. The method described here has proved sufficiently versatile for mounting both brittle, irregular crystals of so-called "sodium tungsten bronze" (5) and wires of pure zinc.

1. Sodium tungsten bronze.—Crystals of the nonstoichiometric compound Na_xWO_3 (where $0.4 < x < 1$) are prepared by electrolytic deposition from a $Na_2WO_4 + WO_3$ melt onto a gold wire. A short length of the wire is left projecting from the crystal for making electrical contact. The crystal is placed in a clean metallographic mounting mold (the use of Teflon eliminates the need for mold lubricants) as shown in Fig. 1. The mold is partially filled with a pre-established amount of molding powder (Teflon 8 granular TFE resin) and pressed at about 5000 psi (compression ratio 3:1) to form a ½ in. diameter, ¾ in. long pellet. At this point, the compact has sufficient mechanical strength to be handled easily. The tip of the gold wire is exposed by cutting away a few millimeters of Teflon, then the compact is sintered in a stream of pure nitrogen for 2 hr at 380°C. Between 280° and 380°C, the warm-up and cool-down rates are controlled at 50°C/hr. TFE Teflon undergoes large dimensional changes in this range and rapid heating or cooling can result in cracking. Slow cooling also produces a high degree of crystallinity in the finished piece, a characteristic needed for good creep resistance and low gas permeability (6). Below 280°C, the rates are not critical.

A wire is soldered to the gold contact, and the specimen is mounted in the Teflon and glass assembly illustrated in Fig. 2. The Teflon part of the assembly is a "Straight Union Reducer" (Fluorocarbon Incorporated).

2. Zinc wire electrode.—A somewhat different approach is used in this case. A pellet of Teflon is pressed as before, then a hole, about 3% under size, is drilled in the center, and the zinc wire (1/32 in. diam) is forced into the hole. The compacted pellet has the re-

* Electrochemical Society Student Member.

Key words: Teflon, specimen mounting.

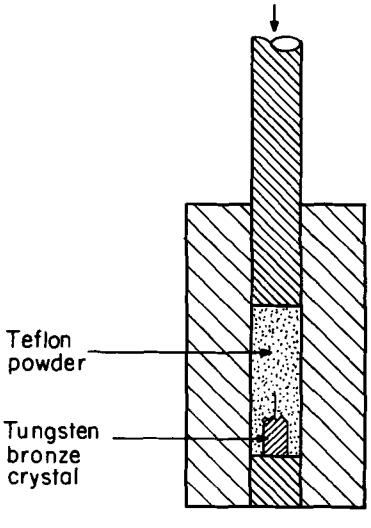

Fig. 1. Assembly for pressing Teflon

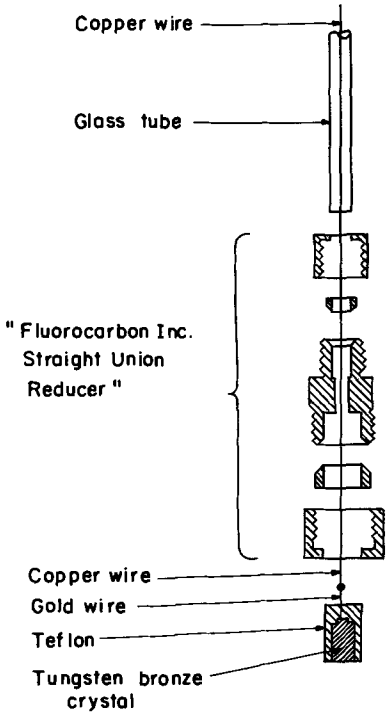

Fig. 2. Electrode assembly for tungsten bronze specimens

Table I. Comparison of four Teflon specimen mounts

Mount	Compression gasket	Hot-pressed FEP	Shrink-fit tubing	Sintered TFE
Source	Stern & Makrides (2)	Mannan (3)	Alwitt & Vijh (4)	Present work
Specimen requirements	Drilled and tapped rod	No limitation	Simple shape	No limitation
Versatility	Limited to machinable materials	Unsuitable for reactive materials	Good but not well suited for repeated polishing	Good
Convenience	Good	Poor, requiring simultaneous application of heat and pressure	Good	Good, but requires care during sintering

quired mechanical strength to allow these operations with only occasional failure. The pellet is sintered under the same conditions as described in case 1 and then machined to fit the glass part of a "Lab-Crest Solv-Seal Joint" (Fischer & Porter Company). The electrical contact to the zinc wire is made by spot welding a platinum foil to it, which in turn is spot welded to copper wire. (Spot welding the zinc to copper was found to be difficult.) The full assembly is shown in Fig. 3. The working face of the assembly is mechanically polished before each test.

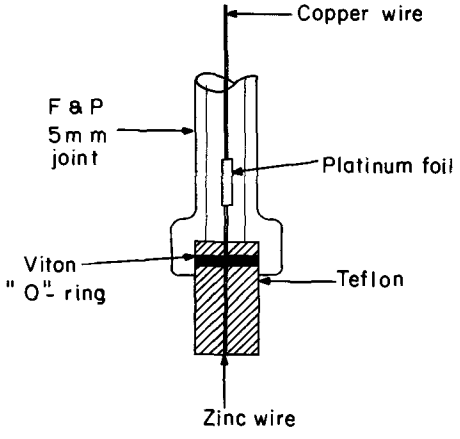

Fig. 3. Electrode assembly for zinc wire specimens

Each of the four types of Teflon mount fulfills the primary requirement of a clean, leakproof electrode. The differences among them lie in such considerations as convenience and versatility (*cf.* Table I). The present technique was developed for applications requiring greater versatility than the three earlier methods could provide.

Acknowledgments

Our thanks are due to E. I. du Pont de Nemours and Company, Incorporated, for the Teflon samples. Financial support for this work was provided by the National Science Foundation under grant number GK-1724, and the U.S. Army Mobility Equipment Command, Fort Belvoir, Virginia, under contract number DA 44 009 AMC 469(T).

Manuscript submitted March 2, 1970; revised manuscript received *ca.* May 29, 1970.

Any discussion of this paper will appear in a Discussion Section to be published in the June 1971 JOURNAL.

REFERENCES

1. N. D. Greene, W. D. France, Jr., and B. E. Wilde, *Corrosion*, **21**, 275 (1965).
2. M. Stern and A. C. Makrides, *This Journal*, **107**, 782 (1960).
3. R. J. Mannan, Ph.D. Thesis, Univ. of Pennsylvania, Philadelphia, Pa. (1967).
4. R. S. Alwitt and A. K. Vijh, *This Journal*, **117**, 413 (1970).
5. See *e.g.*, P. G. Dickens and M. S. Whittingham, *Quart. Rev.*, **22**(1), 30 (1968).
6. Information Bulletin No. X-7d, E. I. du Pont de Nemours and Co., Inc., Wilmington, Del.

JOURNAL OF THE ELECTROCHEMICAL SOCIETY

ELECTROCHEMICAL SCIENCE

OCTOBER 1970

The Sulfur Cathode in Liquid Ammonia

M. H. Miles*

Department of Chemistry, Middle Tennessee State University, Murfreesboro, Tennessee 37130

and W. S. Harris*,[1]

Naval Weapons Center, Corona Laboratories, Corona, California 91720

ABSTRACT

Electrochemical studies of sulfur-H_2S solutions in acid liquid ammonia electrolytes on silver and platinum surfaces over the temperature range of +20° to −50°C show that sulfur is a useful cathode for low-temperature fuel cells and batteries. The maximum theoretical coulombic efficiency of two electrons per sulfur atom can be obtained. The potentiostatic reduction of the sulfur species in stirred solutions shows that even at subzero temperatures the reactions achieve rates limited only by mass transport. The reaction on platinum apparently involves physical adsorption of the reacting sulfur species, while the reaction on silver involves chemical bonding of the sulfur species and formation of Ag_2S. Insoluble, electronically conducting Ag_2S should prove useful as a rechargeable cathode in batteries and fuel cells.

Solutions of elemental sulfur in liquid ammonia have been proposed for use as cathodes in low-temperature batteries (1-3). The actual species present when sulfur is dissolved in ammonia is still in question, especially since recent work has refuted the existence of S_4N_4 to any appreciable extent (4-8). The high solubility of sulfur in ammonia (5, 7) makes this inexpensive element attractive for use as the oxidant in low-temperature fuel cells and batteries using liquid ammonia electrolytes. A fuel cell consisting of liquid lithium ammoniate as the fuel and sulfur as the oxidant gives a theoretical energy density comparable to that of the H_2/O_2 fuel cell and, furthermore, shows promise of operation at subzero temperatures. Studies on the liquid lithium anode are in progress; results presented here are restricted to electrochemical investigations of sulfur solutions in liquid ammonia.

Experimental

The chemicals used include Matheson N.F. sublimed powder sulfur, Baker reagent NH_4NO_3 and $LiNO_3$, and Matheson anhydrous ammonia (99.99%), each used without further purification.

Potentiostatic measurements were made in liquid ammonia solutions stirred by a stream of ammonia gas. The current between the working and counterelectrodes was recorded *vs.* time and usually appeared to be fairly constant after several minutes. Measurements were made in the direction of both increasing and decreasing potentials, and the average value is reported.

Solution preparation, electrochemical cells, reference electrodes, temperature control, and electronic equipment is described elsewhere (9-10).

* Electrochemical Society Active Member.

[1] Present address: Mare Island Naval Shipyard, Vallejo, California.

Key words: ammonia, cathode, electrocatalysts, platinum, polysulfides, silver, silver sulfide, reduction, sulfur.

Results

Rate of solution.—Although sulfur is soluble in ammonia solutions in excess of 30% by weight (10M), the rate of solution is often slow; for example, in attempting to prepare a 0.1M sulfur solution in concentrated NH_3-$LiNO_3$ a dichroic blue-red solution formed which changed gradually to a yellow solution, but some of the sulfur remained undissolved even after ten days. During potentiostatic reduction, the color of this solution changed to a deep brownish red, and the excess sulfur dissolved. When H_2S is present even in low concentrations, however, the rate of solution of sulfur in ammonia is very rapid.

Electrocatalysts.—The electrochemical oxidation or reduction reactions of the sulfur-H_2S solution in acid liquid ammonia depend markedly on the nature of the metal electrode used. The platinum metals tested (Pt, Pd, Ir, Rh) along with Re, Au, W, Mo, and V show a large (over 0.3V) difference in the potentials at which significant electrode oxidation and reduction of the sulfur solution occur. For Ag, Hg, Cu, Pb, and Sn the oxidation reactions of the sulfur-H_2S solution are observed at potentials considerably more negative than for the Pt metals, and the reduction occurs at potentials close to those of oxidation. Results for Co and Ni are intermediate to those for Ag and Pt. For Fe, a large oxidation peak is observed, but no subsequent reduction peak could be detected.

The metals Ti, Zr, Hf, Th, Nb, Ta, Al, Ga, and In are completely inert toward any electrochemical reaction of the sulfur solution.

The results for the various metals are summarized in Table I by listing the metal at the potential (to the nearest 0.1V) where the oxidation and reduction currents due to sulfur or H_2S attain a value of 2 mA/cm^2 when the sweep rate is 125 mV/sec. Oxidation is repre-

Table I. Sulfur reactivity on various metals in NH_3-NH_4NO_3 at 20°C from cyclic voltammetric experiments

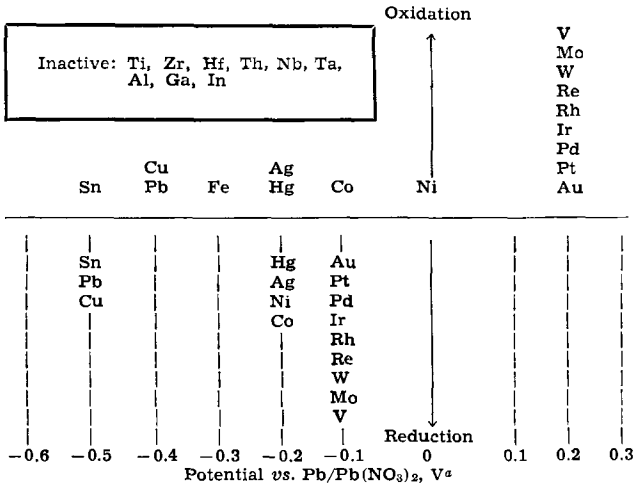

[a] The potential where the current density for the sulfur reaction is 2 mA/cm² at a sweep rate of 125 mV/sec (0.02M S + H_2S).

sented above and reduction below the center horizontal line.

Cyclic voltammetric experiments.—Figures 1-3 show cyclic voltammograms of sulfur-H_2S solutions in acid liquid ammonia. Figure 1 shows a typical cyclic voltammetric trace for sulfur on a platinum electrode with the dashed line indicating the background current of the NH_3-NH_4NO_3 solution alone.

Figure 2 shows the effect of the potential sweep rate on the oxidation and reduction peaks when a silver electrode is used. Making repeated sweeps with no wait time between successive sweeps gave very reproducible results. The anodic and cathodic peak currents are proportional to the square root of the sweep rate. The displacement of the peak potentials with increasing scan rates suggests uncompensated iR effects (11, 12) due to the large currents obtained. From Fig. 2, this effect is about 1.5 V/A, suggesting that the uncompensated resistance between the reference and working electrodes is a reasonable value of about 1.5 ohms. Figure 3 shows the sulfur reactions on the silver

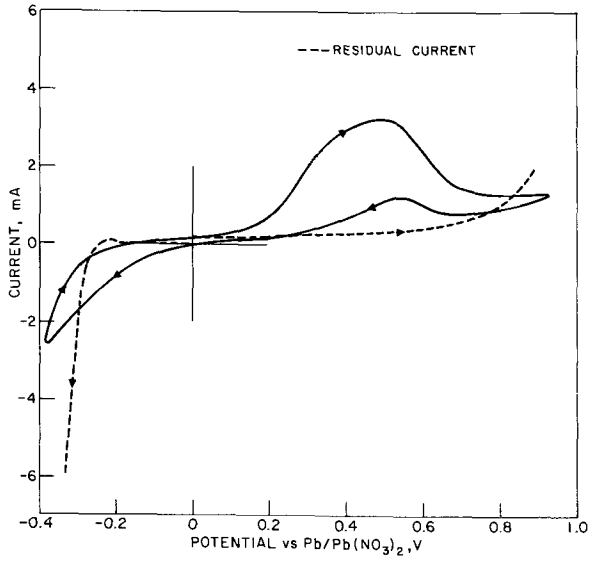

Fig. 1. Cyclic voltammogram for 0.1M sulfur, H_2S solution in NH_3-NH_4NO_3 at 15°C using platinum wire electrode with geometrical area = 0.3 cm². Potential sweep began at 0.0V and swept first in the anodic direction. Sweep rate = 100 mV/sec.

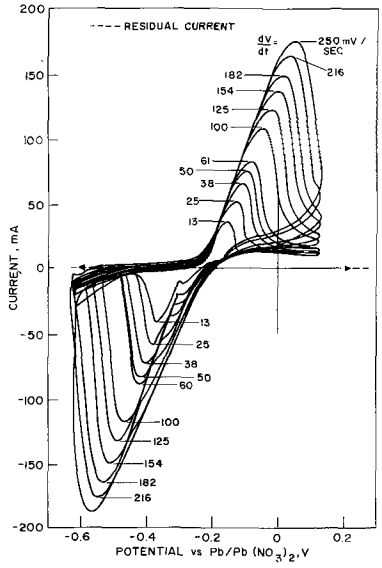

Fig. 2. Effect of potential sweep rate on cyclic voltammograms for 0.1M sulfur, H_2S solution in NH_3-NH_4NO_3 at 15°C using silver wire electrode with geometrical area = 0.3 cm².

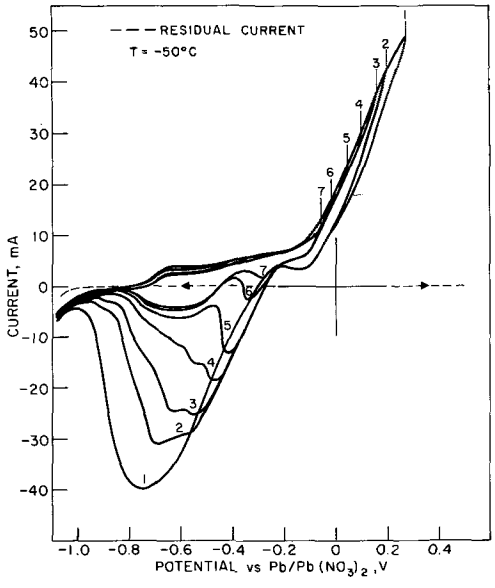

Fig. 3. Cyclic voltammograms for 0.1M sulfur, H_2S solution in NH_3-1M NH_4NO_3 at −50°C on the silver wire electrode as a function of the anodic potential sweep limit.

electrode at −50°C as a function of the anodic sweep range limit during continuous potential sweeps.

Constant current experiments.—Typical curves for the constant current reduction of sulfur in stirred acid ammonia solutions at 15°C on silver and platinum electrodes are shown in Fig. 4. A sharp inflection in potential is observed when 2 electrons are consumed in the reaction per atom of sulfur initially present. A similar study at −10°C on silver also gave nearly 2 electrons per sulfur atom. Constant current studies on nickel show evidence for sulfur reduction but gave no clear inflection, while tantalum showed complete inactivity toward any sulfur reduction.

Potentiostatic experiments.—Potentiostatic studies of the electrochemical reduction of sulfur solutions on silver and platinum surfaces in stirred acid liquid ammonia solutions at 15° and −35°C are presented in Fig. 5-6. The residual current shown is the current obtained before sulfur and H_2S were added and results mainly from the reduction of NH_4^+ to hydrogen gas. The rest potential in the 0.1M sulfur, H_2S solution was −0.15V with the silver electrode and 0.0V for the

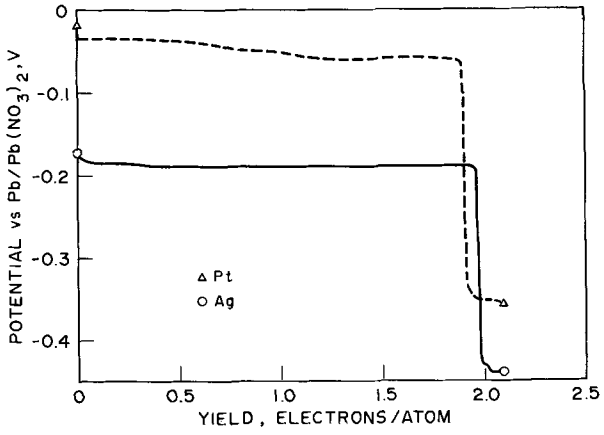

Fig. 4. Constant current reduction of sulfur, H_2S solutions in stirred NH_3-NH_4NO_3 on platinum and silver electrodes of about 50 cm^2 geometrical area. I = 1.00 mA; T = 15°C.

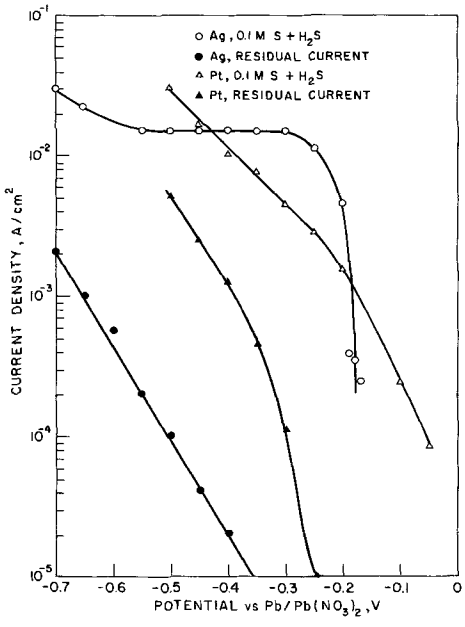

Fig. 5. Potentiostatic reduction of 0.1M sulfur, H_2S solutions in NH_3-NH_4NO_3 on silver and platinum electrodes. T = 15°C.

platinum electrode, both potentials measured at 15°C against a Pb/saturated $Pb(NO_3)_2$ reference electrode. The reaction rate for the reduction of sulfur appears to be faster on silver than on platinum since with the silver electrode there is a sharper increase in reduction current density with overvoltage (Fig. 5). The reduction of sulfur on silver achieves mass transport limitation since a limiting current is reached which is markedly dependent on the rate of stirring. Stopping the stirring action causes the current to fall suddenly; recovery is quick when stirring is resumed. The reduction current for the sulfur reaction on platinum at high overvoltage is also affected by the rate of stirring. Note that the limiting current attained on silver is higher at −35°C (Fig. 6) than at +15°C, probably resulting from the lower viscosity of the less concentrated 1M NH_4NO_3 solution.

Neutral solutions.—Thus far the results have all been for acid (NH_4NO_3) ammonia solutions to which H_2S was added to accelerate the rate of solution of the sulfur. The results are quite different for sulfur dissolved in neutral ($LiNO_3$) ammonia solutions where no H_2S is used. Cyclic voltammetric experiments on the sulfur dissolved in neutral liquid ammonia showed no evidence for any electrochemical oxidation or reduction of sulfur on silver or platinum electrodes. Con-

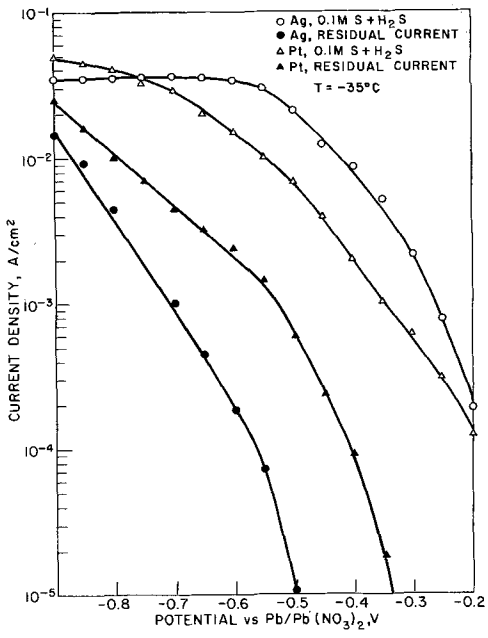

Fig. 6. Potentiostatic reduction of 0.1M sulfur, H_2S solutions in NH_3-1M NH_4NO_3 at −35°C on silver and platinum electrodes.

stant current experiments in stirred neutral ammonia solutions on silver and platinum electrodes showed similar negative results. Unlike the behavior shown in Fig. 4, when reduction begins, the potential quickly drops to about −2.3V, indicating that the sulfur remains unreacted, and lithium ions are being reduced. Addition of Li_2S produced no change in these experiments, but the addition of H_2S quickly rendered the sulfur reducible. Similarly, potentiostatic measurements showed very little reduction of sulfur until H_2S is added to the solution.

These very different effects of Li_2S and H_2S on the sulfur solution in neutral ammonia supports the findings of Nelson and Lagowski (8) that H_2S in ammonia forms a hydrogen-bonded species, $[SHNH_3]^-$, but produces no free sulfide ions, while sulfide ions added to ammonia do not undergo ammonolysis to HS^-. Apparently, the species $[SHNH_3]^-$ is necessary to render the dissolved sulfur electrochemically active. The reactive forms of sulfur probably are polysulfides since solutions of sulfur and H_2S in liquid ammonia have been shown to produce polysulfides, and the compound $(NH_4)_2S_5$ has been isolated (5, 13).

Discussion

In evaluating the sulfur cathode for fuel cell or battery use in liquid ammonia electrolytes, the constant current studies are a measure of the coulombic efficiency. The constant current studies of sulfur reduction on platinum and silver (Fig. 4) show that, within experimental error, the maximum theoretical coulombic efficiency of two electrons per sulfur atom can be obtained on these two metals. This indicates that there are no detrimental side reactions or decomposition of the reactant during the 40-hr time span of the experiments. Similar studies on silver at −10°C gave approximately the same results as obtained at +15°C, showing that this high coulombic efficiency does not decrease appreciably with decreasing temperature.

The potentiostatic investigations in the stirred solutions are a measure of the dynamic performance of the sulfur cathode in a flowing electrolyte feed fuel cell. Figures 5 and 6 indicate that the dynamic performance of the sulfur cathode is at least as good on silver as on platinum. The rest potential of the sulfur cathode is more negative on silver than on platinum, but a limiting current is reached at considerably lower overvoltages on the silver electrode. The dynamic performance of the sulfur cathode at −35°C (Fig. 6) indicates

satisfactory low-temperature operations, especially considering that the reactions achieve rates limited only by mass transport, and that much higher sulfur concentrations are feasible. Using the expression (14)

$$i_L = nFD\delta^{-1}C \qquad [1]$$

for the limiting current dsnsity, i_L, where D is the diffusion coefficient, δ is the thickness of the diffusion layer, C is the bulk concentration of reactant, and n and $\mathbf{F}$ are the usual electrochemical quantities, we calculate from the results on silver (Fig. 5 and 6) that $D\delta^{-1} = 10^{-3}$ cm sec^{-1}. Since δ is usually about 10^{-3} cm in stirred systems, the diffusion coefficient of the reacting sulfur species is roughly 10^{-6} cm^2 sec^{-1}, a reasonable value (10), indicating that the reaction is indeed limited by mass transport.

A probable general reaction mechanism for the sulfur reactions in ammonia is

$$xM + yS \rightleftharpoons M_x \ldots S_y \underset{-2ye^-}{\overset{+2ye^-}{\rightleftharpoons}} xM + yS^= \qquad [2]$$

where M represents the electrode metal and S and $S^=$ are likely part of a polysulfide ion, $S_x^=$. The $M_x \ldots S_y$ bond may range from simple electrode absorption to an actual metallic sulfide compound. Both Ag_2S and PtS, like most sulfides of the electrode metals tested, are black compounds which are insoluble in liquid ammonia, and therefore readily detectable if formed in significant amounts. During the electrochemical studies on platinum of the sulfur-H_2S solutions in liquid ammonia, the platinum electrodes maintain a bright, metallic luster indicating very little build-up of any metallic sulfide compounds. However, when a silver electrode remains at open circuit in the sulfur-H_2S solution, or during electrochemical oxidation of the solution on silver, the silver electrode becomes black, indicating formation of Ag_2S from the chemical reaction

$$2Ag + S \rightleftharpoons Ag_2S \qquad [3]$$

or from the electrochemical reaction

$$2Ag + S^= \rightleftharpoons Ag_2S + 2e^- \qquad [4]$$

Constant current coulometry experiments show that the electrochemical oxidation of ammonia-H_2S solutions on silver produces insoluble products which can be quantitatively reduced. An acid ammonia solution saturated with H_2S was oxidized on silver for 1800 sec at 0.500 mA, turning the electrode black. The solution was then stirred for 30 min to allow any soluble sulfur products to dissolve, then the electrode was transferred to a separate compartment with fresh electrolyte. Reduction at the same current, 0.500 mA, produced a gradual fading of the black color with a sharp inflection in potential after 1815 sec, indicating that the silver had been oxidized to insoluble Ag_2S and then was quantitatively reduced. Figure 7 shows the results of this test and results for a silver control electrode in a similar solution showing that the reduction is not observed without first forming silver sulfide. Similar tests on platinum showed oxidation of the ammonia-H_2S solution at about 0.0V with the electrode remaining bright. Reduction in a separate compartment showed only hydrogen evolution, indicating that no insoluble platinum sulfide compounds were formed on the platinum electrode during oxidation of the ammonia-H_2S solution. These experiments suggest that in reaction [2], $M_x \ldots S_y$ represents chemical bonding with formation of a metallic sulfide compound on silver while the bonding on platinum is of a different nature.

The very different peak potentials and peak currents observed in the cyclic voltammetric experiments on platinum and silver (Fig. 1 and 2) reflect the different nature of the sulfur reactions on these two surfaces. On the silver electrode, formation of the electronically conducting Ag_2S greatly increases the

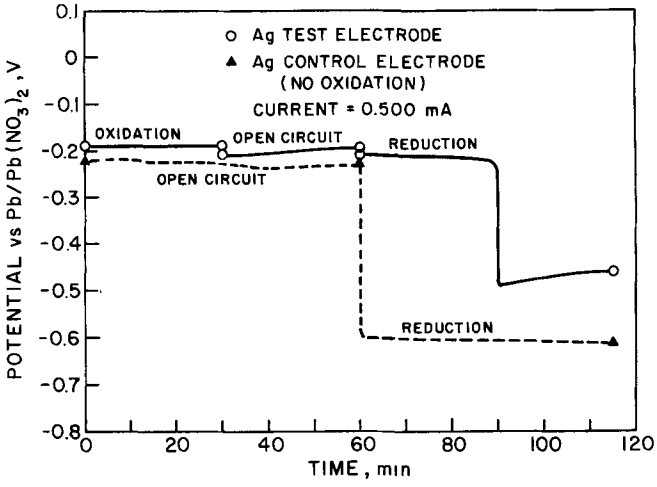

Fig. 7. Constant current coulometry experiments on silver in NH_3-NH_4NO_3 solutions containing H_2S using constant currents of 0.500 mA. Electrode area = 2 cm^2, T = 15°C.

effective electrode area, resulting in higher currents. The peak currents on the silver electrode in sulfur-H_2S solutions are quite insensitive to the bulk sulfur concentration; also the number of coulombs involved in the reaction peaks (Fig. 2) are independent of the potential sweep rate, indicating that we are essentially observing reaction [4] involving insoluble Ag_2S. The reversibility of this reaction suggests use of Ag_2S as a rechargeable cathode in liquid ammonia batteries or fuel cells. Figure 3 indicates that reaction [4] occurs readily even at −50°C, indicating good performance of the Ag_2S cathode at subzero temperatures.

Table II gives the free energy of formation, ΔG_f°, for several metallic sulfides along with the calculated standard electrode potential for the reaction $M_xS_y + 2ye^- \rightleftharpoons xM + yS^=$ in aqueous solutions. The variation in the standard potentials from that for silver, E°-$E^\circ_{Ag_2S}$, reflects solely the differences in ΔG_f° for the metallic sulfide, hence the variation should be the same in liquid ammonia solutions for the above reaction. The difference in the potentials in Table I at which electrochemical oxidation of the sulfur-H_2S solution in ammonia is observed may reflect such thermodynamic effects when the $M_x \ldots S_y$ bond involves chemical bonding. Comparing Tables I and II indicates that the sulfur reactions on Hg, Fe, Cu, Pb, and Sn probably involve chemical bonding as found for silver since, as thermodynamically expected, the reactions are observed at potentials negative to the reaction on silver. The sulfur oxidation reactions on Pt, Ir, Mo, Ni, and Co are observed at potentials considerably more positive than thermodynamically expected,

Table II. Thermodynamic data[a]

Compound	ΔG_f°, kcal/mole[b]	E°, V[c]	$E^\circ - E^\circ_{Ag_2S}$, V
Ag_2S	−9.72, α	−0.66	0.00
HgS	−11.4, black	−0.69	−0.03
PtS_2	−23.8	−0.70	−0.04
CuS	−12.8	−0.72	−0.06
IrS_2	−33.0*	−0.80	−0.14
PtS	−18.2	−0.84	−0.18
NiS	−19.0	−0.86	−0.20
CoS	−19.8*	−0.87	−0.21
FeS_2	−39.9	−0.88	−0.22
Cu_2S	−20.6, α	−0.89	−0.23
SnS	−23.5	−0.95	−0.29
PbS	−23.6	−0.96	−0.30
FeS	−24.0	−0.97	−0.31
MoS_2	−54.0	−1.03	−0.37

[a] See USNBS Tech. Notes 270-3 (Jan., 1968) and 270-4 (May, 1969).
[b] Gibbs free energy of formation for the metallic sulfide compound.
[c] Standard electrode potential at 25°C for the reaction $M_xS_y + 2ye^- \rightarrow xM + yS^=$ in aqueous solution. For $S^=$(aq), ΔG_f° = 20.5 kcal/mole from the above reference.
* ΔH_f° (ΔG_f° is not given).

indicating that metallic compounds are not involved in these reactions. Much weaker $M_x \ldots S_y$ bonds are apparently formed on these metals. From the difference in rest potentials for the Ag and Pt electrodes in sulfur-ammonia solutions (0.15V), it is estimated that $\Delta G_f^\circ = -3$ kcal/mole for the Pt . . . S bond formed in the electrochemical reaction. This small value suggests that weak, adsorption bonding of the sulfur species to the platinum surface is involved.

Other metals which form weak, adsorption bonds with the sulfur species would be expected to show electrochemical behavior similar to platinum. The metals inactive toward the sulfur-ammonia solution apparently do not form either chemisorption or physical adsorption bonds with the sulfur species. This inactivity may be due to oxide or nitride films on the metal which persist during the electrochemical experiments.

Summary

1. The reduction of sulfur in platinum and silver electrodes in acid ammonia solutions yields the maximum theoretical coulombic efficiency of two electrons per sulfur atom.

2. Potentiostatic measurements in stirred solutions show that even at subzero temperatures the reactions achieve rates limited only by mass transport.

3. The electrochemical reactions of sulfur on platinum and silver are different in nature. Apparently, physical adsorption is involved on platinum, while chemisorption and Ag_2S formation occurs on silver.

4. Electronically conducting Ag_2S may be useful as a rechargeable cathode in liquid ammonia batteries and fuel cells. The oxidation and reduction reactions involving this compound occur readily even at −50°C.

5. Cyclic voltammetric screening of various metals indicates their activity toward the sulfur reactions. Interpretations of these results are given in terms of the thermodynamics of the metal-sulfur bond.

Manuscript submitted Nov. 17, 1969; revised manuscript received *ca.* April 15, 1970. This is Paper 59 which was presented at the Atlantic City Meeting of the Society, Oct. 4-8, 1970.

Any discussion of this paper will appear in a Discussion Section to be published in the June 1971 JOURNAL.

REFERENCES

1. W. F. Meyers, U.S. Pat. 2,996,562 (*C.A.*, **56**, 1294, 1962).
2. A. L. Almerini and H. R. Knapp, U.S. Pat. 3,309,230 (*C.A.*, **67**, 17317, 1967).
3. K. Posey and J. K. Truitt, U.S. Pat. 3,408,299 (*C.A.*, **69**, 112904, 1968).
4. A. P. Zipp, Ph.D. Dissertation, University of Pennsylvania, 1964.
5. A. P. Zipp and S. G. Zipp, *Sulphur Inst. J.*, **2** (Spring, 1968).
6. A. P. Zipp and E. C. Evers, *Inorg. Chem.*, **8**, 1746 (1969).
7. J. T. Nelson and J. J. Lagowski, *ibid.*, **6**, 1292 (1967).
8. J. T. Nelson and J. J. Lagowski, *ibid.*, **6**, 862 (1967).
9. M. H. Miles and P. M. Kellett, *This Journal*, **115**, 1225 (1968).
10. M. H. Miles and P. M. Kellett, *ibid.*, **117**, 60 (1970).
11. R. S. Nicholson, *Anal. Chem.*, **37**, 667 (1965).
12. B. L. Funt and D. G. Gray, *Can. J. Chem.*, **46**, 1337 (1968).
13. P. J. Durrant and B. Durrant, "Introduction to Advanced Inorganic Chemistry," p. 829, John Wiley & Sons, Inc., New York (1962).
14. K. R. Williams, Editor, "An Introduction to Fuel Cells," pp. 36-40 Elsevier Publishing Co., New York (1966).

Anodic Polarization of Passive Electrodes

D. A. Vermilyea*

Surfaces and Reactions Branch, Physical Chemistry Laboratory, General Electric Company, Schenectady, New York 12301

ABSTRACT

Anodic current flow at a passive electrode lowers the surface *p*H and increases the corrosion and film dissolution rates. Analytical expressions are obtained to permit the calculation of the rates of formation of new film and soluble species. It is shown that when equilibrium is achieved between the film and the solution, as with magnesium, polarization of only a few tens of millivolts can result in current densities of the order of 1 A/cm². For metals forming films which dissolve more sluggishly it is often necessary to exceed the oxygen evolution potential before large currents can be achieved. Thick anodic films can be formed when the film blocks oxygen evolution and when the film dissolution rate constant is small. Buffers suppress the *p*H change at the surface and may prevent rapid dissolution and corrosion.

The purpose of this paper is to discuss the effects on the current and corrosion rate of the application of anodic currents to passive metals. Passivity is difficult to define adequately, and for this discussion a passive metal is one covered with an oxide or hydroxide film which substantially impedes corrosion. Such a film will often comprise a dense barrier layer of a poorly crystallized material next to the metal and a porous layer of a better crystallized product next to the solution. Application of an anodic current will usually lower the *p*H at the electrode surface, and that in turn will effect the rate of dissolution of the protective film. It is this effect of *p*H on film dissolution which is to be considered. Localized attack is outside the scope of this paper.

* Electrochemical Society Active Member.
Key words: corrosion, films, dissolution.

The Initial Condition

Consider a film covered specimen in a nearly steady state, with a barrier layer of constant thickness and a porous layer whose thickness is changing slowly. Corrosion at this specimen produces more film (which could be oxide or hydroxide) at a rate r_{fo} according to a reaction like

$$M + zH_2O \rightarrow M(OH)_z + z/2\ H_2 \qquad [1]$$

where z is the metal valence, and soluble species at a rate r_{so} according to

$$M + zH_2O \rightarrow M^{+z} + zOH^- + z/2\ H_2 \qquad [2]$$

the total rate being r_o.

Application of Current

Upon application of an external current, additional hydroxide will be formed at a rate r_f according to

$$M + zH_2O \rightarrow M(OH)_z + zH^+ + ze \quad [3]$$

and additional metal ions at a rate r_s according to

$$M \rightarrow M^{+z} + ze \quad [4]$$

It may be noted that, as far as soluble species are concerned, metal ions are generated by r_s and r_{so}, hydroxyl ions are generated by r_{so}, and protons are generated by r_f.

For simplicity it will be assumed that the solution is sufficiently concentrated that electrical transport can be neglected and the Nernst approximation will be used to describe diffusion near the specimen. Equations for mass balances are then the following

$$\dot{n}_M + z = \frac{10^{-3} D_{M+z} \Delta C_{M+z}}{\delta} = r_{so} + r_s \quad [5]$$

$$\dot{n}_{H+} = \frac{10^{-3} D_{H+} \Delta C_{H+}}{\delta} = zr_f - zr_{so} \quad [6]$$

if there is a net production of protons in an acid solution

$$\dot{n}_{H+} = \frac{10^{-3}[D_{H+}(C_{H+})_i + D_{OH-}C_{OH-}]}{\delta} = zr_f - zr_{so} \quad [7]$$

if there is a net production of protons in a solution containing C_{OH-} hydroxyl ions per liter

$$\dot{n}_{OH-} = \frac{10^{-3} D_{OH-} \Delta C_{OH-}}{\delta} = zr_{so} - zr_f \quad [8]$$

if there is a net production of hydroxyl ions in a basic solution; and

$$\dot{n}_{OH-} = \frac{10^{-3}[D_{OH-}(C_{OH-})_i + D_{H+}C_{H+}]}{\delta} = zr_{so} - zr_f \quad [9]$$

if there is a net hydroxyl ion production in an acid solution with a proton concentration C_{H+}. In Eq. [5]-[9] the $\dot{n}$'s represent rates of generation or removal of the various species, the D's represent diffusion coefficients, δ (assumed the same for all ions) is the thickness of the Nernst layer, the ΔC's represent the concentration difference in moles per liter between the surface and the bulk solution, and the subscript i indicates an interface concentration.

The total external current density, i, is given by

$$i = \sum_j m_j \mathbf{F} \dot{n}_j \quad [10]$$

in which the summation is over all species, and where m_j is the charge on each particle. It can readily be verified that $i = z\mathbf{F}(r_f + r_s)$. Equations [5]-[10] can now be used to find out how an external current will influence the corrosion of the metal. There are two situations of interest, depending on whether or not equilibrium is achieved at the film-solution interface.

Case I. Equilibrium at Film-Solution Interface

For this case the equilibrium conditions are given by

$$K_s = (M^{+z})(OH^-)^z \quad [11]$$

and

$$K_w = (H^+)(OH^-) \quad [12]$$

where the quantities in brackets represent activities. From Eq. [11] and [12], approximating activities with concentrations

$$(C_{M+z})_i = \frac{K_s (C^z_{H+})_i}{K_w{}^z} \quad [13]$$

Equation [10] can now be used with Eq. [13] to find the current density in situations of interest.

Two examples of the use of the equations will illustrate their utility. Consider first magnesium with a film of $Mg(OH)_2$,[1] with $z = 2$, $\delta = 10^{-2}$ cm, $D_{Mg+2} = 10^{-5}$ cm^2/sec, $D_{OH-} = 3 \cdot 10^{-5}$ cm^2/sec, $D_{H+} = 10^{-4}$ cm^2/sec, $\mathbf{F} = 10^5$ coul/eq., $K_s = 10^{-11}$, $K_w = 10^{-14}$, and in the bulk solution $C_{OH-} = 10^{-4}$ moles/liter. In this example there is a net production of protons in an alkaline solution, assumed to contain an excess of supporting electrolyte. Equations [5], [7], [10], and [13] give for the current density

$$i = \frac{10^{-3}\mathbf{F}[D_{H+}(C_{H+})_i + D_{OH-}C_{OH-}]}{\delta} + \frac{10^{-3} z\mathbf{F}}{\delta} D_{M+z} \frac{K_s}{K_w{}^z} (C^z_{H+})_i \quad [14]$$

For a current density of 10^{-1} A/cm^2 the surface concentrations of magnesium ions and protons are found to be 0.5M and 2.24 x 10^{-9}M (pH 8.65), respectively, and nearly all the current is carried by Mg^{+2}. Previous studies of corrosion of magnesium and of dissolution of $Mg(OH)_2$ (2) have shown that a dissolution or corrosion rate of 10^{-10} moles/cm^2 sec can be expected at about pH 9. Using that rate for r_{so} in Eq. [7] we find $zr_f = 2.14 \times 10^{-10}$ moles/cm^2 sec, or $i_f = 2.14 \times 10^{-5}$ A/cm^2. Thus a very small fraction of the applied current produces more film.

Magnesium does actually behave in solutions with pH > 5 as predicted by these equations. The hydroxide layer covering the surface is porous and its growth slows the reaction only moderately (1). Presumably this porous film can readily accept the additional small amount of reaction product corresponding to r_f without blocking the reaction. As a result of this film formation, however, the pH is reduced and the magnesium ion concentration becomes large enough to carry a high current. The end result of anodic corrosion of thin magnesium specimens is a very porous, fragile, but coherent hydroxide replica of the original specimen, which shows that hydroxide is indeed formed by the passage of current.

As a second example consider beryllium, with a film of $Be(OH)_2$ having $K_s = 10^{-26}$ in a pH 5 solution containing excess supporting electrolyte. Taking $D_{Be+2} = 10^{-5}$, Eq. [5], [6], [10], and [13] show that for $i = 10^{-1}$ A/cm^2 $C_{H+} = 0.05$ moles/liter, $C_{Be+2} = 0.25$ moles/liter. If r_{so} is assumed to be 10^{-14} moles/cm^2 sec, a value calculated from the solubility product of $Be(OH)_2$ assuming that the spontaneous reaction is diffusion controlled in the pH 5 solution, then Eq. [6] gives $zr_f = 5 \times 10^{-7}$ moles/cm^2 sec so that $i_f = 0.05$ A/cm^2 and $i_s = 0.05$ A/cm^2. In this example a very large change in pH is required to produce a high current density, so that a large amount of new film must be produced, and both protons and metal ions carry a significant fraction of the current. The experimental situation is not so well known for beryllium as for magnesium, and in particular it is not known whether equilibrium is achieved at the solution-film interface.

Discussion of Case I.—Constancy of r_{so} was assumed and in the examples given the values of r_{so} were so low compared to other rates that the approximation is reasonable. Usually anodic polarization would decrease the spontaneous cathodic reaction and hence decrease r_{so}, and for some situations a good approximation may be to ignore r_{so} in Eq. [5]-[9]. On the other hand, strong anodic polarization and a large decrease in pH may decrease the barrier film thickness significantly and result in an enhanced cathodic reaction and increased r_{so}.

It is possible that the specimen may become film free as a result of anodic polarization. For example, for a metal which is relatively unreactive in a thermodynamic sense the hydrolysis of metal ions may produce a pH low enough to make the film unstable at

[1] There may be a MgO layer between this film and the metal, but at long times the $Mg(OH)_2$ layer controls the corrosion behavior.

the applied potential. The present analysis does not apply to such a situation.

Finally, the current-potential behavior is of interest. If equilibrium is achieved at the interface, and if the solution is very concentrated so that no changes in the total ion concentration take place in the Nernst layer, then only a resistive polarization occurs. In a less concentrated solution concentration polarization occurs in the Nernst layer and some additional polarization will be present. Such concentration polarization can be calculated from the equation (3)

$$E = \frac{RT}{z\mathbf{F}} \ln\left(1 + \frac{i\delta}{z\mathbf{F}D \cdot 10^{-3}C_o}\right) \qquad [15]$$

in which E is the potential difference and C_o is the bulk anion concentration. If $C_o = 1$ mole/liter, for a current density of 1 A/cm^2 $E = 0.023$V for a divalent anion. It can be seen that the electrode polarization (exclusive of iR drop) for such anodic corrosion can be very small.

Case II. Equilibrium Not Achieved at Film-Solution Interface

If equilibrium is not achieved it is convenient to use the relationship

$$i = z\mathbf{F}(r_f + r_s) \qquad [16]$$

It has been predicted theoretically (4) and observed experimentally (2, 5) that the relationship between dissolution rate and hydrogen ion concentration for oxides and hydroxides has the form

$$r_s = k\,C^n{}_{H+} \qquad [17]$$

in which k is the dissolution rate constant and n has values which differ markedly for various systems and range from 0 to 4/3. For the situation in which Eq. [6] is valid, Eq. [6], [16], and [17] give

$$i = z\mathbf{F}\left[r_f + k\left\{\frac{\delta}{10^{-3}D_{H+}}(zr_f - zr_{so})\right\}^n\right] \qquad [18]$$

A slight rearrangement, the substitution of values for δ, D_{H+} and $\mathbf{F}$, and of i_f for $z\mathbf{F}r_f$ and i_{so} for $z\mathbf{F}r_{so}$ gives

$$i = i_f + z\mathbf{F}k(i_f + i_{so})^n \qquad [19]$$

Three ranges of values of n are of interest:

(a) $n = 0$.

It has been observed (5) that the rate of dissolution of anodic Al_2O_3 films in aqueous solutions at 100°C is nearly independent of pH between pH 1 and pH 10, so that $n = 0$.[2] Then

$$i = i_f + z\mathbf{F}k \qquad [20]$$

In such a situation, if k is small, most of the current produces more oxide and the film simply thickens. The case $n = 0$ is of great practical importance in anodic oxidation, for if $n = 0$ and k is small then large currents and low pH can be tolerated without the disruption of film formation.

(b) $0 < n < 1$.

Magnesium hydroxide dissolves with $n \sim \frac{1}{2}$ at pH < 5 (2), and it is expected theoretically (4) that many oxides and hydroxides would have n between 0 and 1. Note that equilibrium is not achieved for $Mg(OH)_2$ at pH < 5, where a surface reaction controls the rate. Figure 1 shows the behavior of various currents as functions of i_f for a hypothetical material with $n = \frac{1}{2}$ and $k = 10^{-7}$ (the value of k for $Mg(OH)_2$ is 10^{-7}), and for which $r_{so} = 0$. The dissolution current, i_s, increases less rapidly than does i_f, and the total current may produce mostly ions at low current density and mostly film at high current density. Having most of the applied current produce ions as in this example at low currents does not necessarily mean that

[2] The rates in ref. (5) are initial rates and decrease with time at pH 4-10 due to the formation of a porous AlOOH layer. This example is thus only valid for pH < 4. For other systems this restriction may not be present.

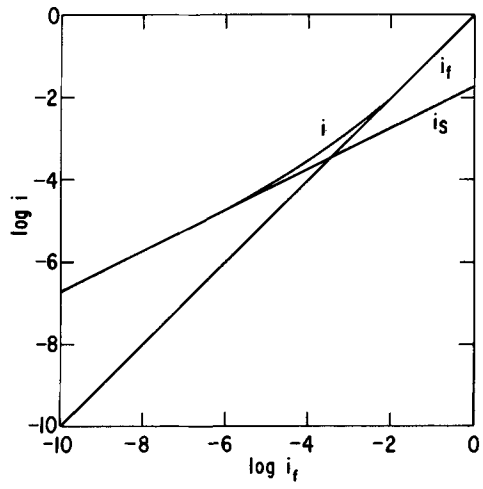

Fig. 1. Relationship between total current density i, the current density of formation of metal ions i_s, and the current density of film formation i_f, for a hypothetical metal covered with an oxide whose rate of dissolution is given by Eq. [17] with $k = 10^{-7}$ and $n = \frac{1}{2}$.

there is a net film dissolution and eventual cleaning of the specimen in a real situation, for the spontaneous corrosion rate may be high enough to keep the specimen covered with a film.

(c) $n > 1$.

For $n > 1$ the dissolution rate increases faster with total current than does the film formation rate. Depending on the value of k, therefore, it is possible that film formation could predominate at low currents with mostly dissolution at high currents. A practical example is not known.

Discussion of Case II.—Absence of surface equilibrium is probably the situation existing with many metals forming dense barrier films having low values of spontaneous corrosion (r_o). Such dense barrier films grow by high field ion conduction, and as the film thickness increases a considerable potential drop occurs in the film. In order to reach the large currents needed to lower the pH sufficiently to increase the film dissolution rate it is necessary to raise the potential to a point where some proton producing electrode reaction other than film formation occurs. A common situation is that large currents are not found until oxygen evolution occurs in the transpassive region. Rapid corrosion of the metal usually accompanies such oxygen evolution, possibly because of the enhanced proton concentration. When the film is a good insulator or blocks current for any reason so that no oxygen evolution occurs then application of very large potentials and growth of thick anodic films may be possible, as with Al, Ta, Zr, Nb, etc.

General Discussion

Two major problems in predicting results of anodic polarization are that it is not now possible to predict (except from experience) what will happen to any new film which is produced, and it is not possible to predict when surface equilibrium may be achieved or what values of k and n will be encountered when equilibrium is not achieved. If the new film is added to the dense barrier, then application of an additional anodic potential may simply thicken the barrier and the current may remain low. It seems generally true that metals yielding films with low values of k (the dissolution rate constant, Eq. [17]) are also the ones which give dense barrier films, but evidence is fragmentary. Future progress requires studies of the character of reaction products and of their reactivity.

The role of anions in these phenomena is important. Buffers, for instance, may prevent any large pH change until a critical film forming current is reached. If the hydroxyl ion or a buffer ion is the only anion present,

then current flow may concentrate the ion in the solution near the specimen so that little pH change can occur despite large polarization. For example, when magnesium is polarized to +1.2V on the standard hydrogen electrode scale in a 10^{-2}M solution of KOH the current is only a few microamperes per square centimeter, while in 10^{-2}M Na_2SO_4 a current of 0.1 A/cm^2 is reached at a potential of −1.26V (open-circuit potential −1.39V). The explanation for this fact is the following. Most of the large potential difference in the KOH solution is doubtless applied across the film. Should any break occur in the film so that a large local anodic current starts to flow the concentration of hydroxyl ions near the break would be increased by the current so that further precipitation of $Mg(OH)_2$ would occur and the break would be healed. In the Na_2SO_4 solution, on the other hand, any rupture of the film and accompanying current flow concentrates sulfate ions which are not effective buffers. The pH is then free to fall, and the dissolution rate can become very large.

Acknowledgment

The author is grateful to M. Indig and C. S. Tedmon, Jr., for comments regarding the manuscript. He is also indebted to two very able reviewers whose pertinent comments have resulted in a considerable clarification and simplification of the paper.

Manuscript submitted Feb. 24, 1970; revised manuscript received *ca.* May 14, 1970. This was Paper 224 presented at the Atlantic City Meeting of the Society Oct. 4-8, 1970.

Any discussion of this paper will appear in a Discussion Section to be published in the June 1971 JOURNAL.

REFERENCES

1. D. A. Vermilyea and C. F. Kirk, *This Journal*, **116**, 1487 (1969).
2. D. A. Vermilyea, *ibid.*, **116**, 1179 (1969).
3. D. A. Vermilyea and C. S. Tedmon, Jr., *ibid.*, **117**, 437 (1970).
4. D. A. Vermilyea, *ibid.*, **113**, 1067 (1966).
5. W. Vedder and D. A. Vermilyea, *Trans. Faraday Soc.*, **65**, 561 (1969).

The Anodic Behavior of Zn-Cd Binary Alloys in 1M Sulfamic Acid-Formamide Solutions

I. A. Menzies, R. A. Brodie, D. Gearey, and G. W. Marshall

Corrosion Laboratories, Department of Chemical Engineering, University of Manchester Institute of Science and Technology, Manchester 1, England

ABSTRACT

The anodic behavior of zinc, cadmium, and Cd-Zn binary alloys has been studied in 1M sulfamic acid-formamide solution. The anodic polarization curves for the single metals and alloys containing 90, 81.9, and 40% Cd are typical of electropolishing systems. In all cases a-c impedance measurements indicate the formation of solid anodic films at the onset of polishing. Under steady-state conditions of dissolution (300 coulombs) of the alloys the ratios of metal dissolved anodically are similar to those in the original alloys. All current efficiencies were 100 ± 2.5%. All of the alloys are deeply etched under appropriate conditions and considerable phase contrast is found during polishing conditions. Here there is a small amount of preferential dissolution of Cd-rich phases which give rise to phase contrast while film formation suppresses crystallographic etching. The effects of anode shape and method of polarization on polarization data in sulfamic acid-formamide solutions are also discussed.

The present work is a continuation of previous studies (1-4) of the anodic dissolution and polishing of metals in organic electrolyte solutions. Among the organic systems which have been investigated, a solution of sulfamic acid in formamide has proved to be a highly versatile polishing medium producing good results on Cu, Sn, Pb, Zn, Cd, and Ag. It has also been shown that Mo, W, and Ti can also be polished at high overpotentials. Zinc and cadmium have both been found to polish well in sulfamic acid-formamide solutions, dissolving at current efficiencies close to 100%. Most recently (4) evidence has been obtained from viscosity and a-c impedance measurements which indicate that anodic dissolution of Zn is under diffusion control and that polishing occurs by random dissolution through an anodic film with suppression of crystallographic etching. The present study is concerned with a number of aspects of the behavior of Zn-Cd alloys. In choosing an alloy system for this initial work on dissolution in organic electrolytes the Zn-Cd system was selected since both of the single metals were known to electropolish and the associated limiting current densities were similar. Furthermore the alloy system is a simple eutectic system.

Key words: anodic dissolution, zinc-cadmium alloys, organic electrolytes, electropolishing, electro-etching, formamide.

The objectives of the work were: (*a*) to obtain preliminary data concerning the polarization characteristics of a range of Zn-Cd alloys; (*b*) to confirm and extend previous investigations (4) concerning the presence of films using a-c impedance techniques; (*c*) to determine metal dissolution ratios and current efficiencies and to relate the nature of the surfaces produced to conditions of polarization. Since previous investigations (3-4) had shown that in this particular system potentiostatic and galvanostatic polarization curves were similar, the galvanostatic technique used previously (4) was used again.

Experimental

Preparation and purification of materials.—Alloys.— The alloys were prepared from 99.9999% purity zinc and cadmium by melting in Pyrex glass tubes under an argon atmosphere. After the alloys had melted, the tubes were vigorously agitated and the contents maintained in the molten state for some time to ensure homogeneity of the liquid. After cooling the alloys were placed in 'Pyrex' casting tubes with a little 'Analar' $ZnCl_2$ to act as a flux. This improved the quality of the cast rods by reducing porosity and oxide inclusions. During heating the casting tube was evacuated and flushed with purified argon twice, and after

melting of the alloys the tubes were evacuated to remove residual gas. Finally, the alloy was allowed to solidify slowly under dry argon. Samples of the castings were removed for metallographic examination. Two diameters of rod (1 and 0.75 cm) were prepared and the larger rods were rolled to sheet while the smaller ones were used as electrodes in galvanostatic polarization studies.

Solute and solvent.—Microanalytical reagent grade sulfamic acid was supplied by British Drug Houses Ltd., to the following specification: acidimetric assay >99.9% moisture <0.1%; sulfate <0.05%; nonvolatile matter <0.05%. This material was stored in a vacuum desiccator before use. Formamide was purified as described elsewhere (1, 3).

Apparatus and experimental methods.—Electrolyte preparation and metering systems.—The electrolyte preparation and metering systems used were as described previously (1, 5, 6). A weighed quantity of sulfamic acid was placed in the electrolyte vessel, and the required volume of purified formamide to give a 1N sulfamic acid solution was metered from the burette. These operations were carried out under dry nitrogen flow, and on completion the electrolyte vessel was sealed, removed, and shaken at intervals. After complete dissolution had taken place the solution was ready for transfer to the electrolysis cell.

Constant current measurements.—Cells of the pattern previously described (1) were used for these measurements. The alloy anode Fig. 1A was 1.5 x 1.0 cm and approximately 0.1 cm thick, and the surrounding cathode was a Ta cylinder of ~84 cm^2 surface area. For the measurement of anodic current efficiencies at constant current density a Wareham Measuring Systems Ltd. galvanostat type C223 capable of delivering 1A at 80V was used with a copper coulometer in series. In all experiments a total of 300 coulombs was passed. The anodes were gently abraded to 600 grade SiC paper, pickled lightly in 10 v/o (volume per cent) HNO_3 to remove surface films, washed with distilled water and acetone and finally dried in a stream of warm air, weighed and placed in the cell. All measurements were carried out at 25° ± 0.1°C in an atmosphere of purified and dried nitrogen.

A.C. impedance measurements.—These measurements were made using the same type of cell but with a central anode of the type shown in Fig. 1B, all details of the method of measurement and bridge circuit being as previously described (4). Various current densities in the range 1-100 mA/cm^2 were applied using a 120V dry battery and the corresponding readings of resistance and capacitance recorded.

Galvanostatic measurement of polarization curves.—The cell used for these measurements was similar to that described previously (3) and used for potentiostatic measurements. The technique used in the present work was similar to that in previous work (4) all potentials being measured with respect to the Cd/$CdCl_2$, KCl (satd)-formamide reference electrode. In the polishing region it was found that potential fluctuations tended to occur irregularly, and potential readings were taken at fixed time intervals. The current was raised in increments of 5 mA by means of the calibrated control, and the potential reading was noted 15 sec later and the current again increased. A fresh solution was used for each experiment.

Analytical procedures.—The metal dissolution ratios were determined by atomic absorption spectrophotometry (7) and over-all current efficiencies from weight loss measurements. There was some random scatter in the results of atomic absorption measurements, and total metal dissolution was found to be more accurately represented by weight loss measurements. However, the metal dissolution ratios were considered to be sufficiently accurate for the results to be meaningful.

Results

Anodic polarization curves measured galvanostatically with respect to the reference electrode.—Excellent reproducibility was obtained except in the very high current density regions where considerable oscillations of potential tended to occur. For each metal or alloy all of the points obtained during four separate measurements were plotted on a large scale, the best line drawn through the experimental points, and the resulting smoothed lines are shown in Fig. 2. At all current densities in the etching range zinc and cadmium had lower overpotentials for normal dissolution than any of the alloys. The transition from etching to polishing was sharp in all cases. The limiting current density for zinc was ~54 mA/cm^2 while that for cadmium and the alloys was 65-70 mA/cm^2. Although the transitions and limiting current densities were well defined the upper parts of the polishing regions were much less well defined. However, the anodic overpotential ranges

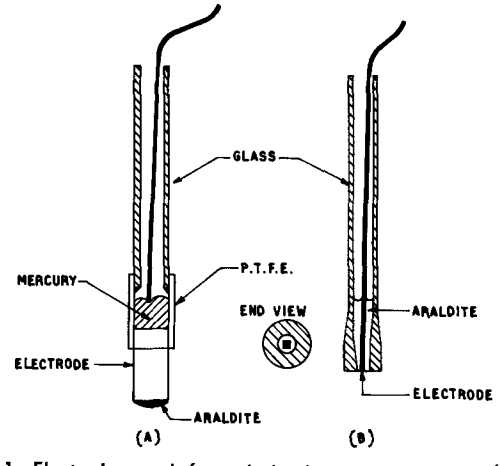

Fig. 1. Electrodes used for polarization measurements: (a) galvanostatic, (b) a-c impedance.

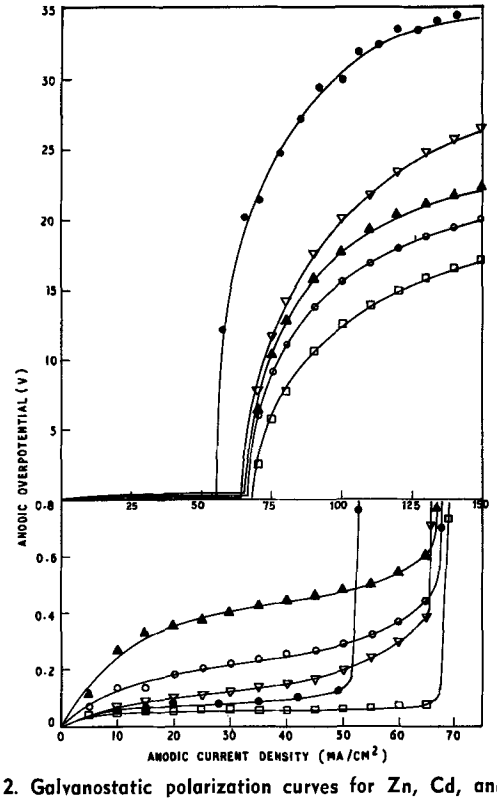

Fig. 2. Galvanostatic polarization curves for Zn, Cd, and three alloys at 25°C. (a) upper part polishing range (b) lower part etching range. ● Zn, ▽ alloy 1 (60% Zn), ▲ alloy 2 (18.1% Zn), ○ alloy 3 (10% Zn), □ Cd.

Table I. Polishing voltage ranges for Zn, Cd, and binary alloys of these elements in sulfamic acid-formamide solutions at 25°C

Material	Galvanostatic anodic overpotential, V
Zinc	11.0
Alloy 1 (60% Zn)	8.0
Alloy 2 (18.1% Zn)	6.0
Alloy 3 (10% Zn)	5.5
Cadmium	3.0

at the limiting current density decreased with increasing cadmium content of the alloy (Table I).

A-C impedance measurements.—The curves for resistance as a function of current density are shown in Fig. 3, the main feature in all cases being the sudden extremely large increase in resistance (5-150 ohm-cm^2) coinciding with the onset of polishing conditions. When no net current was flowing through the electrode the resistances, with the exception of cadmium, were ~4 ohm-cm^2. On applying a net current the initial resistances all fell to slightly lower values which rose again with increasing current density until the limiting current density was reached when the very large increase in resistance was observed. After the limiting current density, the resistances for zinc and alloy 1 (60% Zn 40% Cd) increased slowly with current density whereas materials with a cadmium content of >40% the resistance became completely unstable and violent oscillations of the null detector made it impossible to obtain more than one reading for each specimen. The limiting current densities from these measurements were 50-60 mA/cm^2 for Zn, alloy 1, and alloy 3, 65 mA/cm^2 for alloy 2 (18.1% Zn, 81.9% Cd) and 80 mA/cm^2 for cadmium.

The initial capacitance for all specimens was ~10 μF/cm^2 Fig. (4), and initially there was a rapid rise to ~100 μF/cm^2 with increasing applied current density. Following this there was a slight increase in capacitance with increasing current density until the limiting current density was attained when the capacitance fell sharply to values ~0.5 μF/cm^2. Since the bridge could not be balanced at current densities high in the polishing region for specimens containing >40% cadmium, curves for such specimens have only one point in this region.

Over-all it is clear from these measurements that the anode resistance is extremely high in the polishing region and that under these conditions the capacitance is correspondingly low.

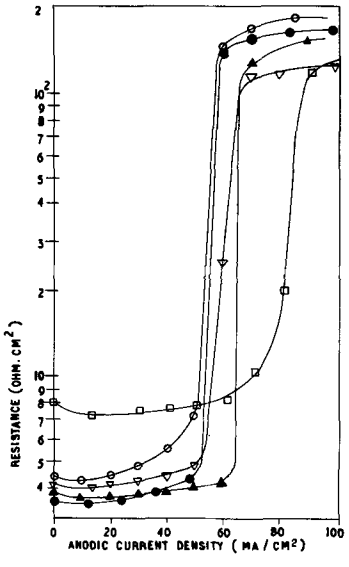

Fig. 3. Series resistances of Zn, Cd, and three alloys as a function of current density at 25°C. (10 kHz) ● Zn, ▽ alloy 1 (60% Zn), ▲ alloy 2 (18.1% Zn), ○ alloy 3 (10% Zn), □ Cd.

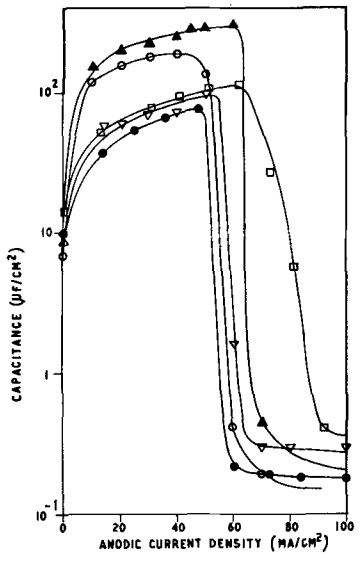

Fig. 4. Series capacitances of Zn, Cd, and three alloys as a function of current density at 25°C. (10 kHz) ● Zn, ▽ alloy 1 (60% Zn), ▲ alloy 2 (18.1% Zn), ○ alloy 3 (10% Zn), □ Cd.

Anodic dissolution ratios and dissolution efficiencies at constant current density.—After each anodic dissolution experiment the electrolyte was analyzed for zinc and cadmium and the proportions of each metal dissolved was calculated for comparison with the proportions present in the alloy (Table II). For alloy 1 (60% Zn 40% Cd) there is some evidence that at the lowest current density (8 mA/cm^2) the Zn:Cd ratio in solution was slightly greater than that in the alloy whereas at current densities >70 mA/cm^2 the ratio was lower. For alloy 2 (18.1% Zn 18.9% Cd) the dissolution ratio was 17 Zn : 83 Cd, *i.e.*, slightly lower than that in the alloy. In the case of alloy 3 the ratio in solution was 11 Zn : 89 Cd and hence a slightly higher proportion of Zn appears in solution than that nominally present in the alloy (10% Zn 90% Cd). Overall, however, it is clear that the metal dissolution ratios are similar in all cases to the ratios initially present in the alloys. The total metal dissolution efficiencies did not vary significantly with anodic current density or alloy composition since all were within the range 100 ± 2.5%. There was some indication that the current efficiencies increased slightly (~1%) with increasing cadmium content of the alloy.

Observations of surface features after treatment at constant current density.—The surface features of all three alloys were recorded as a function of current density.

Alloy 1. (60% Zn 40% Cd).—This alloy has a composition midway between the eutectic composition and pure zinc and in the as-cast condition (Fig. 5a) is composed of primary dendrites of Zn-rich solid solu-

Table II. Proportions of zinc and cadmium in solution after anodic dissolution of binary alloys of these metals in sulfamic acid-formamide solutions at 25°C

Anodic current density, mA/cm^2	Alloy 1 60% Zn 40% Cd		Alloy 2 18.1% Zn 81.9% Cd		Alloy 3 10% Zn 90% Cd	
	Proportion of each element in solution after dissolution, w/o					
	Zn	Cd	Zn	Cd	Zn	Cd
8	65.6	34.4	18.5	81.5	12.4	87.6
16	57.0	43.0	16.9	83.1	10.1	89.9
24	60.1	39.9	17.7	82.3	10.8	89.2
32	56.1	43.9	18.2	84.8	9.5	90.5
40	54.5	45.5	16.2	83.8	9.8	90.2
48	59.5	40.5	18.8	81.2	11.9	88.1
56	60.1	39.9	18.9	81.1	11.1	88.9
64	55.7	44.3	15.2	84.8	9.9	90.1
72	58.7	41.3	18.1	81.9	11.0	89.0
80	55.3	44.7	15.6	84.4	11.5	88.5
96	54.2	45.8	15.8	84.2	10.7	89.3

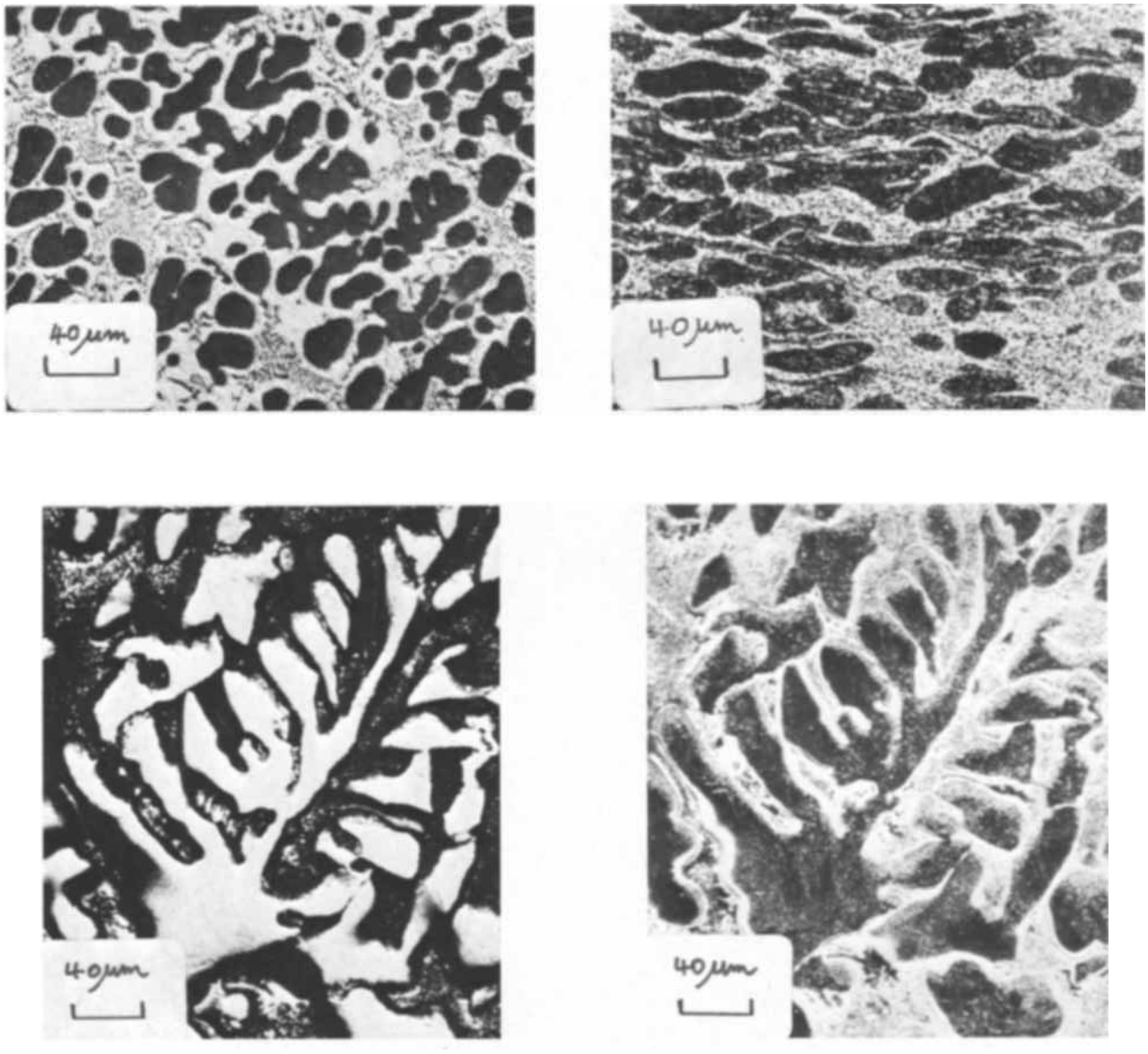

Fig. 5. Photomicrographs of specimens of alloy 1 (60% Zn) (a) as-cast structure; (b) as-rolled structure; (c) polished zinc dendrites (72 mA/cm²); (d) polished zinc dendrites (72 mA/cm²) dark ground illumination.

tion (dark phase) in a matrix of eutectic composed of the cadmium-rich solid solution (light phase) and the zinc-rich phase. After rolling into strips the dendritic pattern was distorted but still recognizable (Fig. 5b).

Anodic treatment of sheet specimens of the alloy at constant current density resulted in two distinct types of surface. At current densities <32 mA/cm² the specimen surfaces were dull matt gray and etched. However, pits were also present and these were found to correspond in shape, size, and depth (12-20 μm) to areas of zinc-rich phase present in the alloy. At intermediate current densities (32-56 mA/cm²) polishing specimens where the local current density was highest was evident on the lower corners and edges of the specimens where the local current density was highest due to rather poor current distribution. Completely bright and reflective surfaces were obtained at current densities >56 mA/cm². A fine relief pattern was apparent even to the naked eye. Examination of the specimen surface under oblique illumination (Fig. 5c) indicated by the shadows produced that either the height of the eutectic phase was lower than that of the zinc-rich phase or that a groove was present at the boundary between the two phases. By changing to dark ground illumination (Fig. 5d) all light directly reflected from the specimen surface was eliminated, and at the same time scattered light was brought into focus producing an image of all surfaces which were not plane and perpendicular to the optical axis. The light areas in Fig. 5d thus represent the hollows or grooves at the edges of the zinc-rich phase. Most of the central areas of the dendrites were polished to a smooth highly reflective surface.

Alloy 2. (18.1% Zn *81.9%* Cd).—This alloy was close to the eutectic composition (17.4% Zn) and the as-cast structure was almost completely eutectic (Fig. 6a), the presence of a few small particles of zinc-rich phase confirming that the zinc content was slightly in excess of the true eutectic composition. Rolling of the alloy did not change the structure significantly. Overall, the general relationship between structure and current density observed with alloy 1 was also observed with this alloy. At current densities ≤ 32 mA/cm² there was poor definition of grain boundaries and in this case no etch pits were observed. The first signs of polishing were observed on the lower corners and edges of specimens exposed at 32 mA/cm² and increasing the current density from 32 to 56 mA/cm² progressively increased the area of the specimen which was polished. At current densities >56 mA/cm² the whole specimen surface became bright and polished although relief

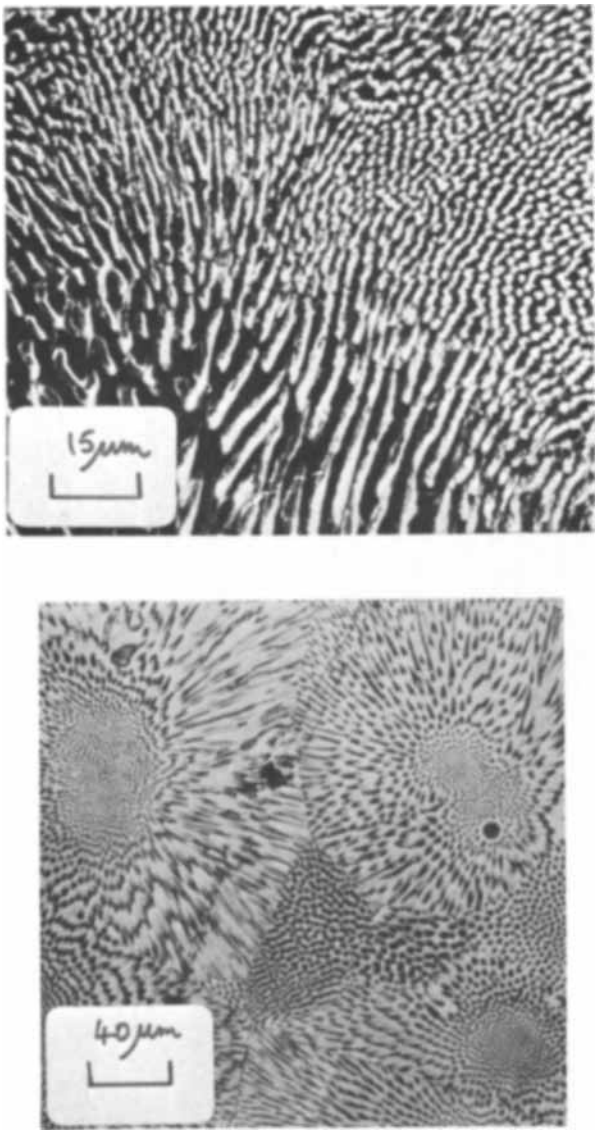

Fig. 6. Photomicrographs of specimens of alloy 2 (18.1% Zn-eutectic) (a) (top) as-cast structure (b) (bottom) polished surface (72 mA/cm^2) showing selective removal of one component during polishing.

effects were observed (Fig. 6b), the Zn-rich phase being proud of the eutectic. This was, however, best observed under dark ground illumination at relatively high magnifications, and under normal direct illumination at moderate current densities only a low degree of relief was observed due to the relatively fine structure and uniformity in the alloy.

Alloy 3. (10% Zn 90% Cd).—The composition of this alloy was intermediate between that of the eutectic and pure cadmium and in the as-cast condition (Fig. 7a) it consisted of primary dendrites of cadmium-rich phase set in a fine eutectic mixture. The lens-shaped markings on some of the dendrites are probably deformation twins induced during metallographic preparation. After rolling the cadmium-rich phase was irregularly shaped.

Again the over-all anodic behavior of this alloy was similar to that of alloys 1 and 2. Deep etching occurred at current densities up to ~32 mA/cm^2, and the individual phases could not be readily distinguished. Again the first signs of polishing appear round the bottom edges and corners of the specimen at 32 mA/cm^2, and the area of polished surface increased with increasing current density up to 56 mA/cm^2. The surfaces resulting from anodic treatments at 56-96 mA/cm^2 were completely polished although slight relief effects were observed. The cadmium-rich phase was generally

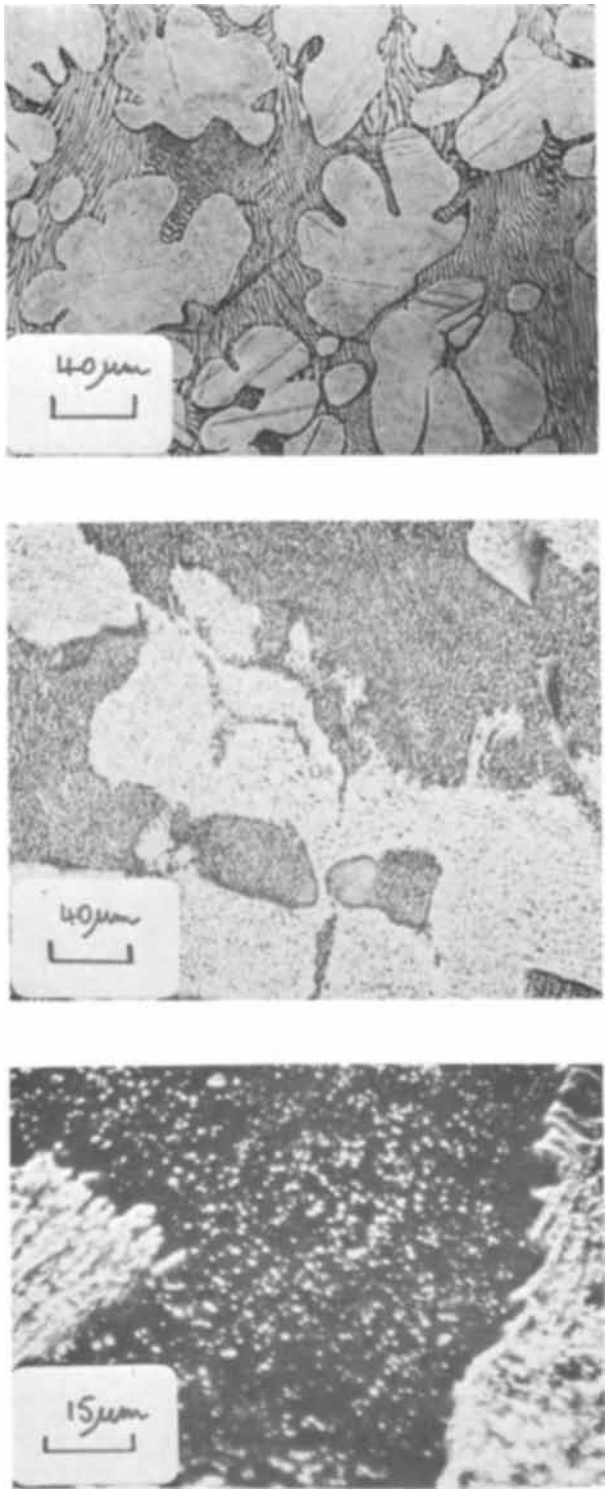

Fig. 7. Photomicrographs of specimens of alloy 3 (10% Zn): (a) (top) as-cast structure; (b) (center) polished surface (72 mA/cm^2) showing depression of Cd-rich phase; (c) (bottom) as (b) dark ground illumination, showing rounded pits in cadmium phase as light spots.

1-2 μm below the general level of the eutectic as can be seen by the shadows in this phase in Fig. 7b. The surfaces of the cadmium-rich dendrites, although highly reflective, were covered with minute pits (0.25-1.50 μm diameter), and this could best be seen at higher magnification under dark ground illumination where the pits are seen as light spots on a dark background. (Fig. 7c)

Additional general observations.—Polished specimens after removal from the solution very rapidly formed a dull gray film on the surface if they were not washed

immediately after breaking the electrical circuit. These films were studied using electron microscopy. Black particles with angular shapes (cf. Fig. 8a) were found associated with the fine two-phase material of the eutectic, the single phase zinc-rich areas being free of such particles. This close association of the particles with the intimate mixture of phases in the eutectic is seen in more detail in Fig. 8b where it is clear that they appear to propagate from the rods of the dispersed phase. An extensive study of the particles was made using transmission electron diffraction, but diffractograms of sufficient quality to permit measurement and calculation of lattice parameters could not be obtained. The material was certainly crystalline, often opaque to electrons, and probably metallic. A particularly interesting dendritic formation is shown in Fig. 8c, and despite the lack of direct evidence it seems almost certain that crystals of cadmium were deposited on the surface by an exchange reaction between zinc in the eutectic phase and cadmium ions in solution.

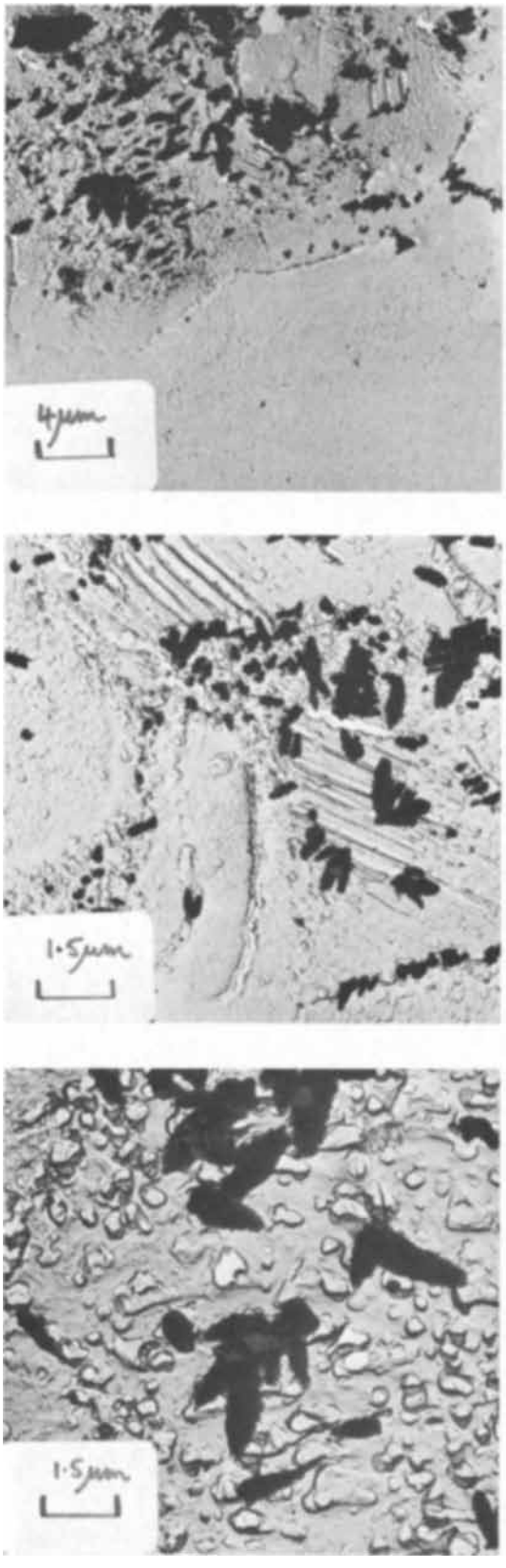

Fig. 8. Electron micrographs of precipitates on polished specimen: (a) (top) presence of particles only on eutectic areas; (b) (center) association of particles with rods of dispersed phase; (c) (bottom) metallic dendrites.

During anodic dissolution of the alloys qualitatively similar viscous layers were observed streaming from the electrode surfaces and these were observed during both etching and polishing. Since there was evidence of film formation during polishing some of the polished specimens were subjected to electron probe microanalysis for sulfur in plan, but the presence of this element could not be confirmed.

Discussion

The present work represents one of the first investigations of the anodic behavior of alloys in organic electrolyte solutions and as such must be regarded as exploratory and rather general in nature. It must however be pointed out at the outset that the anodic dissolution ratios and the metallographic features represent long-term steady-state conditions and not the early stages of dissolution. Caution is therefore necessary in discussing these features in relation to the galvanostatic polarization curves.

Dissolution of alloy 1 (60%) Zn at 16 mA/cm^2 within the etching range resulted in deep pitting and metallographic examinations suggested that this was associated with preferential dissolution of Zn-rich dendrites. Clearly although preferential dissolution of zinc may occur in the early stages cadmium dissolution also occurs, and only at the lowest current density (8 mA/cm^2) was there significant evidence of preferential dissolution of zinc under steady-state conditions. At 72 mA/cm^2 there was evidence that the Zn-rich dendrites were raised above the matrix of Cd-rich eutectic. There was also some indication (Table II) that the solution contained a slightly higher proportion of cadmium than the alloy. This is no doubt associated with the higher limiting current density for cadmium dissolution (Fig. 2 and 3).

In the case of alloy 2 it was not possible because of the fine eutectic structure to determine which phase was preferentially dissolved during etching and polishing. Again under steady-state conditions there was little preferential dissolution of either metal (Table II). With alloy 3 the metallographic evidence suggested some slight preferential dissolution of cadmium.

Under the etching conditions used in the present work good metallographic contrast apparently was not obtained. This was most probably due to excessive surface roughening during steady-state dissolution. A much higher degree of contrast was obtained during polishing, the difference in height between the phases being 4-8 x 10^{-5} in. In the polishing region the differentiation ratio for cadmium (D_{Cd}) as defined by Greene, Rudlaw, and Lee (8), is given by $(i_{\lim Cd}/i_{\lim Zn})_E$ at any potential (E) where $i_{\lim M}$ are the observed limiting current densities for dissolution of Zn and Cd. At almost all potentials in the polishing region D has values of ~1.2. Thus under steady-state conditions during polishing there appears to be a difference in height ~10^{-4} in. and phase contrast with a dissolution ratio somewhat lower than that specified as necessary by Greene, Rudlaw, and Lee. This is not surprising as their criteria were derived for short-time etching conditions. It must however be made clear that in the present work crystallographic etching was sup-

pressed in the polishing region. It is noteworthy that long-term dissolution (300c) results in a Zn/Cd dissolution ratio the same as the Zn/Cd weight ratio in the alloy over a range of current densities in both polishing and etching regions. Generally accepted theory (9-11) indicates that in the initial stages of dissolution the two constituents in the alloy dissolve independently of each other at the current density appropriate to the potential or overpotential setting (heterogeneous or homogeneous alloys) as derived from the polarization data for the single constituents. Then, taking the fraction of the alloy surface occupied by each component to be proportional to its volume fraction in the alloy and assuming two constituents 1 and 2 with molecular weights M_1, M_2, dissolution valencies Z_1, Z_2, and current densities of dissolution i_1, i_2 under set conditions we have

$$\frac{\text{Weight of 1 dissolved}}{\text{Weight of 2 dissolved}} = \frac{i_1 M_1 x_1 \rho_2 z_2}{i_2 M_2 x_2 \rho_1 x_1} \qquad [1]$$

where x_1, x_2 are weight fractions of 1 and 2 in the alloy and ρ_1, ρ_2 are respective specific gravities.

In the polishing range in the present results the rates in Eq. [1] becomes approximately

$$\frac{\text{Weight of Cd dissolved}}{\text{Weight of Zn dissolved}} \approx 3\,\frac{x_{Cd}}{x_{Zn}}$$

since $i_{Cd} \sim 7/5\ i_{Zn}$ (Fig. 2), $Z_{Cd} = Z_{Zn}$, $\rho_{Cd} \approx \rho_{Zn}$, and $M_{Cd} \approx 2M_{Zn}$. Thus the ratios of metal dissolved according to Eq. [1] are a factor of ~3 different from that actually observed.

Several modifications of the above behavior have been suggested usually in connection with the protective properties of components in strongly passivating systems. Thus it has been suggested that modification results from the accumulation of the less active component on the surface by re-orientation of the latter after dissolution of the more active atoms, or alternatively by re-precipitation of less active atoms after primary dissolution (11). In the present results the remarkable consistency of the dissolution ratios in etching and polishing regions despite a variety of alloy structures seems to indicate a more general explanation. In any case, on a geometrical basis it can easily be appreciated that there must be a tendency for less active atoms to accumulate on the surface. Thus if the dissolution rates of the two components are at all comparable long-term dissolution will not result in over-all preferential dissolution of one component, although at any time a certain amount of preferential dissolution, of the order of the grain or particle size, of the more active component would be expected. Hence in the polishing region a rather fine etch of the eutectic is noticed, Fig. 6b, although it must be stressed again that crystallographic etching is suppressed. This is indeed an attractive demonstration of the primary importance of the suppression of crystallographic etching in polishing phenomena. The larger scale component etching (which, of course, would not be suppressed by the polishing film) does not prevent the appearance of a visually polished surface.

The results of the a-c impedance measurements on the alloys and cadmium were generally similar to those previously obtained (4) for zinc. The magnitude of the increase in resistance corresponding to the onset of the limiting current and the associated decrease in capacitance are again best interpreted in terms of formation of anodic films. Over-all anodic dissolution is controlled by diffusion processes in solution at higher potentials, and this may well be true at potentials in the etching range. Most theoretical treatments of alloy dissolution processes (9-12) are based on short-term activation controlled processes, and it is not possible to discuss the present system in detail until further studies of dissolution as a function of time have been completed.

The solutions produced by the anodic dissolution of alloys 2 and 3 (Cd-rich) frequently contained a cloudy yellow precipitate which was shown to be cadmium sulfide. The cathodic reaction in 1M sulfamic acid-formamide must therefore include the reduction of sulfamic acid to sulfide ion either directly or by means of cathodic hydrogen. Redeposition, presumably of Cd, the more noble metal, was also a problem with polished specimens unless these were removed from the electrolyte while they were still connected to the power supply and washed immediately in pure formamide. Similar difficulties have been reported by Moulen (13) during the electropolishing of Pb-Sn alloys in aqueous fluoboric acid.

Acknowledgments

The authors wish to thank Professor T. K. Ross for the provision of laboratory facilities and the Science Research Council for their support. Two of us (D.G. and G.W.M.) wish to thank the Council for the award of postdoctoral research assistantships whilst one of us (R.A.B.) wishes to thank the Council for the award of an Advanced Course Studentship.

Manuscript submitted Feb. 20, 1970; revised manuscript received May 14, 1970.

Any discussion of this paper will appear in a Discussion Section to be published in the June 1971 JOURNAL.

REFERENCES

1. I. A. Menzies, D. N. Bulgin, and G. W. Marshall, *Trans. Inst. Metal Finishing*, **45**, 122 (1967).
2. I. A. Menzies and A. F. Averill, *Electrochim. Acta*, **13**, 807 (1968).
3. I. A. Menzies, G. W. Marshall, and G. B. Griffin, *Corrosion Sci.*, **9**, 287 (1968).
4. I. A. Menzies, G. W. Marshall, D. Gearey, and G. B. Griffin, In press.
5. I. A. Menzies, T. Broughton, and V. O. Nwoko, *Trans. Inst. Metal Finishing*, **43**, 9 (1965).
6. I. A. Menzies, P. J. Moreland, and S. R. Oulsnam, *ibid.*, **45**, 181 (1967).
7. "Atomic Absorption Analytical Methods," Vol. 1, Evans Electroselenium Ltd., Halstead, Essex.
8. N. D. Greene, P. S. Rudlaw, and L. Lee, *Corrosion Sci.*, **6**, 371 (1966).
9. R. F. Steigerwald and N. D. Greene, *This Journal*, **109**, 1026 (1962).
10. M. Stern, *Corrosion*, **14**, 329t (1958).
11. W. A. Mueller, *ibid.*, **18**, 73t (1962).
12. H. W. Pickering and C. Wagner, *This Journal*, **114**, 698 (1967).
13. A. W. Moulen, *ibid.*, **99**, 133c (1952).
14. R. A. Brodie, M.Sc. Dissertation, Manchester, England, 1968.

A Rapid Anodic Porosity Test for Ni-Fe Electrodeposits on Copper Wire

W. O. Freitag*

UNIVAC, Division of Sperry Rand Corporation, Blue Bell, Pennsylvania 19422

ABSTRACT

A 10-min semiquantitative polarographic test is described which measures the area of copper substrate left exposed by pinholes or defects in electrodeposited memory wire. The wire sample is made the anode in an electrolytic cell, the Ni-Fe outer film is rendered passive with a controlled potential sequence, and the anodic current due to oxidation of exposed copper is recorded as a function of potential. The height of a copper passivation peak is measured, and this height is shown to be proportional to exposed Cu area. The method is useful in quality control and in following the course of corrosion in environments when the attack at local defects is the major mechanism.

The occurrence of pinholes or other plating defects which leave some of the substrate exposed is a familiar problem with decorative or protective electrodeposits. As a part of the development of plated wires for computer memories, it became necessary to measure the porosity of thin magnetic alloy films on copper. The test developed for this purpose is described, and we believe that the same general approach might be applicable to other situations.

The plated wire memory elements consist of a substrate of beryllium-copper wire 0.005 in. in diameter coated with an electrodeposited film of permalloy. Wires of this type were prepared first by Long (1) and the process was described more recently by Sagal (2). The alloy films have an average composition near 80% Ni and are generally about 8000Å in thickness. Usually, a layer of pure copper is interposed between the substrate and the magnetic alloy. Pinholes or other defects which leave part of the copper substrate exposed affect the magnetic performance of the wires. Furthermore, pinholes could provide sites for corrosion and so affect the long-term stability and reliability of the elements.

Tests for porosity in electrodeposits usually consist in rendering the pores visible by means of some chemical reaction which is specific to the substrate material and leaves the deposit unchanged. Evaluation is then carried out by visual or microscopic examination. In electrography, the test panel is made anodic in a cell and is held in contact with filter paper which is saturated with an appropriate electrolyte so that ions from the exposed substrate areas produce a colored precipitate. These methods are not easily applied to cylinders of small diameter, such as plated memory wire.

The literature describes methods wherein anodic currents are measured which represent metal dissolution from the basis metal at pores in the deposit under conditions at which the deposit is passive. Ehrhardt (3) applied this approach to gold on copper by measuring the diffusion limited anodic current of copper dissolution in 5% H_2SO_4 at a potential at which no other electrode reaction was occurring. Khan recently reviewed this method (4) and found that the gold layers were not sufficiently passive during this treatment and gave background currents which rendered the tests inaccurate. Shome and Evans (5) reported on the use of a corrosion cell for determining porosity of nickel deposits on iron. They used a large auxiliary cathode of copper and measured either the corrosion current or the amount of iron accumulating in the electrolyte after a period of time. Clarke and Britton (6), dealing with tin, nickel, or copper on steel, related the slope of E *vs.* i curves to the resistance of electrolyte within the pores. Their approach, however, depends on certain conditions being valid which are difficult to achieve experimentally, and is not applicable to very thin deposits in any event.

In the present work, pores in nickel-iron alloy films on copper are detected by measuring the anodic passivation current peaks from exposed copper areas after a prescribed polarization sequence which leaves the Ni-Fe areas passive.

Pinhole Test Sequence

The wire sample is made the working electrode in a polarographic cell using dilute sodium pyrophosphate as electrolyte. Figure 1 summarizes the polarization sequence and diagrams the currents observed.

First, a negative potential, −1.8V *vs.* SCE, is applied to reduce surface oxides and effect a certain degree of cathodic cleaning. Then the sample is brought to +800 mV whereupon passivating films grow on both the permalloy and the copper areas. After the observed current falls to a very low level, usually 0.6 to 0.8 μA/cm of sample length (in about 4 min) the cell is placed on open circuit.

The anodic film which formed on copper is soluble and dissolves within 2 min after removing the potential (the "reactivation" time), while the anodic film on the magnetic alloy remains intact. After this reactivation step, the potential scan is begun at −200 mV and run to about +300 mV at a rate of 200 mV/min. An anodic current peak is observed as the copper

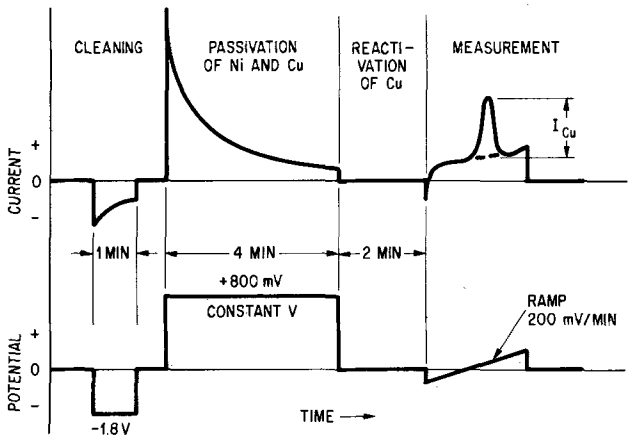

Fig. 1. Potential sequence applied to test wire (lower line) and typical current response (upper line). Ordinate units are arbitrary and not to scale.

* Electrochemical Society Active Member.

Key words: polarograph, pyrophosphates, corrosion, passivity, magnetic alloys for computer memories.

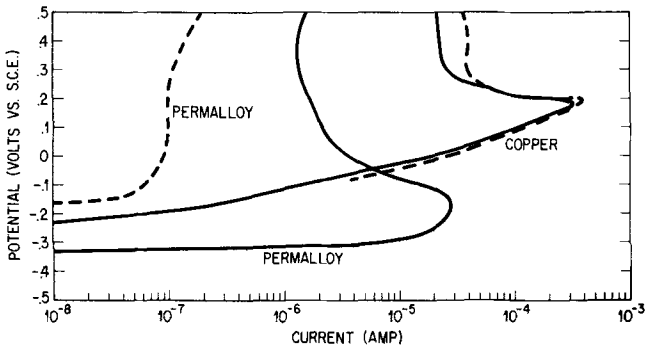

Fig. 2. Anodic traces of unplated copper and solid permalloy wires in the active condition (solid lines) and after polarization as in Fig. 1 (dashed lines). The electrolyte is 0.085M $Na_4P_2O_7$ at pH = 5.2.

areas repassivate, and the height of this peak is measured.

Apparatus and Procedure

Two kinds of electrolytic cells were used in this work. One was a simple "H-cell"[1] one leg of which was a saturated calomel electrode with a mercury surface about 1 in. in diameter. The calomel cell was used as the counterelectrode under the assumption that up to 400 μA of current (the upper limit of the polarograph) would not polarize it, and that any polarization which might occur would not alter test results. Potentials are not measured more accurately than $\pm$10 mV. The H-cell could accommodate sample lengths up to 5 cm. When longer lengths of wire were tested, a three-electrode cell was used which consisted of a platinum foil counterelectrode and a standard calomel reference electrode.[2] The relative location of the three electrodes was not controlled since, again, critical voltage control was not necessary. A Fisher Elecdropode with recorder was used with both cells, but an operational amplifier circuit was added to drive the three-electrode cell.

Wire samples were masked top and bottom with Scotch Electroplater's Tape (3M Company) making sure that the immersed end was completely insulated. There was no evidence that impurities from the tape interfered in any way with the test.

The electrolyte was 0.085M $Na_4P_2O_7$ adjusted to a pH of 5.2 with H_3PO_4. The tests were carried out at room temperature. A very few test runs were done with the electrolyte saturated with O_2 or swept with N_2, but no significant differences were immediately apparent, and virtually all of the work was done under ambient conditions.

Identification of Passivation Current Peaks

The passivation behavior of copper and permalloy in this electrolyte are shown in Fig. 2. The solid lines are taken from current voltage traces while scanning 0.005 in. diameter solid permalloy wire[3] (1 cm) and copper plated beryllium-copper wire (0.2 cm). Voltage scanning was started at -500 mV (*vs.* SCE) at $+200$ mV/min. The cathodic currents are not shown.

The dashed lines in Fig. 2 are traces of scans of the same samples run according to the procedure in Fig. 1; the permalloy is passive but the copper was virtually unchanged.

The passivation behavior for the alloy is similar to that described for Fe-Ni alloys by Economy *et al.* (7) in sulfuric acid solutions. The passivation current density for permalloy in Fig. 2 is on the order of 1 mA/cm^2, compared to a value less than 25 mA/cm^2 extrapolated from Economy's results, which covered a pH range only up to 3.7. The location of the current peak is about -0.18V (SCE) in pyrophosphate at pH = 5.2 compared to -0.15V (SCE) in H_2SO_4 at pH 2.7, *i.e.*, in fair agreement and not much affected by pH.

Figure 3 shows a trace made on a plated wire before and after the alloy deposit was deliberately nicked with a razor blade. The resulting scratch was sufficient to render that point on the wire useless for memory application. The occurrence of the copper passivation peak is clearly evident at $+100$ mV. In practice, the copper peak occurs at $+20$ to $+120$ mV (SCE), with larger copper areas usually peaking at the higher potentials. This shift is expected to be related to the voltage scanning rate. The method used to measure the peak height is also illustrated in Fig. 3.

The scan is started at a potential such that little or no cathodic current flows. Cathodic current will, of course, reduce some of the nickel passivation and a current peak due to the repassivation of nickel will appear. However, some nickel passivation current can be tolerated since the Ni peak usually does not interfere with observations of the Cu peak.

The electrode reaction mechanisms are doubtlessly complex. In broad terms, the rate of formation of the passivating copper pyrophosphate film is determined by competition between a precipitation reaction

$$Cu^{++} + P_4O_7^{----} \rightarrow \text{insoluble salt}$$

and a dissolution reaction:

$$\text{insoluble salt} + P_4O_7^{----} \rightarrow \text{soluble complex}$$

The existence of insoluble salts and complex ions in the copper pyrophosphate system at pH 5.2 is well known (8-11), but no attempt is made here to identify the species involved. Above a pH of about 6, where no copper-pyrophosphate precipitate is found, the present method fails. On the other hand, below pH 4 passivity is difficult to obtain, direct attack on the nickel is excessive, and samples are rapidly destroyed.

Area Calibration of the Copper Peak Current

In order to validate the test sequence, it is necessary to prove that a direct correlation exists between the height of the copper passivation peak and the area of exposed copper. Electrodes of known area were prepared by potting 1-mil diameter copper wires so that only polished cross sections were exposed to the electrolyte. The peak heights of assemblies containing from 1 to 25 wires were measured. The results are shown in line A, Fig. 4, which has the expected slope of 1. Similarly potted electrodes containing single wires of larger diameter yielded curve B, which has a slope of about 0.8.

Neither of these lines can properly be extrapolated to lower currents to provide a quantitative calibration curve. The peak current is at least partially controlled by diffusional processes whose rate is maximized by multiple small-sized copper electrodes which permit essentially three-dimensional supply of reactants to the electrode. Large cross-section electrodes undergo a transition from three- to one-dimensional diffusion behavior with an expected reduced over-all rate or

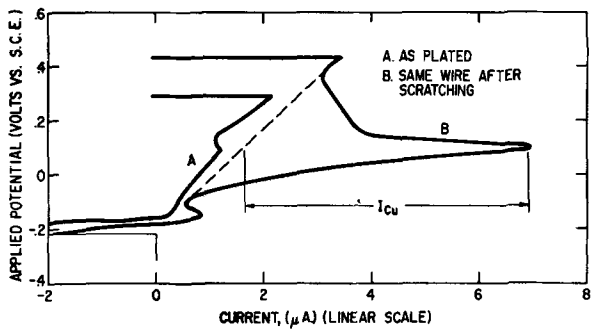

Fig. 3. Anodic traces of a plated wire before (curve A) and after (curve B) scratching the permalloy deposit with a razor blade.

[1] Sargent, H-Form Electrolysis Vessel, S-29401.
[2] A. H. Thomas, 4851-K30.
[3] 18.94% Fe, Hamilton Precision Metals, Lancaster, Pennsylvania.

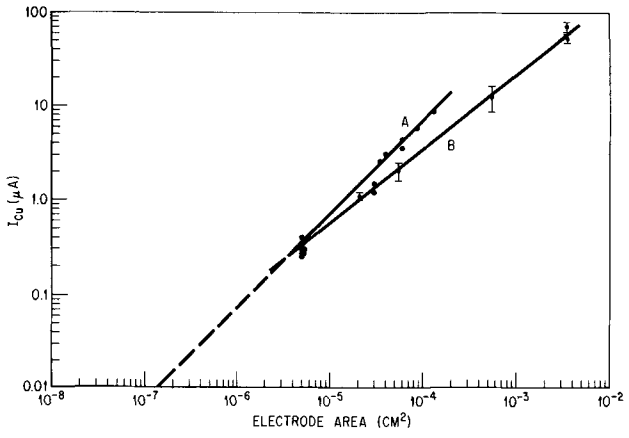

Fig. 4. Copper peak current vs. electrode area correlation curves for multiple electrodes comprised of 1 mil diameter sections (curve A) and single electrodes of larger diameters (curve B).

current. Pinhole arrays in actual plated wires will behave as isolated multiple electrodes of various diameters. The smaller pinholes will contribute disproportionately large partial currents to the total current until other effects predominate, such as high electrolyte resistance in very small pinholes, failure of the previously formed anodic film on copper to dissolve in the allowed two minutes, or failure of the electrolyte to penetrate very small pinholes. A true calibration curve would lie to the left of the extrapolation of line A, Fig. 4, and would be parallel to line A only if the pinholes have approximately the same diameter.

The repeatability of the measurement on sanded electrodes consisting of a single 1-mil diameter copper wire was slightly better than ±20%. Eleven measurements taken from four different electrodes gave an average I_{Cu} value of 0.30 μA, with a standard deviation of 0.05 μA. Standard derivations of measurements using the larger diameter single-wire electrodes are indicated by the error flags in Fig. 4. Most of this error arises from real surface area variations due to roughness of the copper cross sections. The peak heights found for a 25-mil diameter copper section were consistently lower when the surface was prepared by electropolishing than when it was sanded.

The advantage of this method over Ehrhardt's (3) is that the effects of solution convection, which must be dealt with when measuring a diffusion limited anodic current, are minimal. Copper wire calibration samples gave essentially the same distribution of peak heights when the copper electrode faced downward in the electrolyte, or was inverted to face upward. The peak of the copper current is reached in 15-30 sec, a time apparently too short for the buildup of density gradients which are sufficient to cause local convection. Furthermore, any Ni-Fe passivity that is lost between the initial passivation and the measuring sweep, is quickly re-established during the sweep before the copper dissolution potential is reached. Thus the passivation peak for copper stands out unambiguously.

The repeatability of measurements on plated wire samples could not be determined because of the cumulative destructive effects described below. It is believed that except for the occurrence of gross defects, most acceptable wire deposits are characterized by microfissures which are relatively uniformly distributed. All-in-all the method yields useful data over a range of five orders of magnitude. Acceptable plated wires display copper peaks of 0.03-0.005 μA or less per centimeter of wire length, while poorly plated wires ranged from 0.1 to 1 μA. Variation of the thickness of the permalloy deposit from 3000 to 10,000Å, plated under "acceptable" conditions, had little or no effect on the observed defect area. Badly corroded wires have been observed with currents up to 400 μA, or about 50% exposed substrate area.

Effect of Repeated Scanning

Some of the charge passed during the initial passivation step represents active dissolution of nickel and iron. Thus, there exists the possibility that high results would be obtained if the passivation stage removes some of the magnetic alloy. Existing pinholes could be enlarged or thinly plated areas could be stripped and a pinhole generated.

To estimate the magnitude of this source of error, the cumulative effect of repeated pinhole test cycles was examined. Figure 5, line A, shows that when passivation is carried out as in Fig. 1, there is indeed a slow increase in the measured copper peak height, but that this levels off after about 8–10 test cycles. The increase in copper peak height from the first to the second scan of a given sample was usually found to be about 20 to 30%. It is estimated, therefore, that the true copper height would lie about 20-30% below that measured by the first scan. The test is clearly partially destructive, but the error is no greater than other uncertainties.

Line B in Fig. 5 shows the effect of using a passivation technique which permitted much greater anodic currents to flow. Instead of polarizing at a constant +800 mV, passivation was done by scanning from −200 to +800 mV at 200 mV/min. This provided greater opportunity for active dissolution of nickel, and the more rapid sample destruction is evident in curve B. The passivation of a normal wire requires passage of about 6 x 10^{-4} to 30 x 10^{-4} coulombs/cm length. If all of this charge represents dissolution, distributed uniformly, a layer of magnetic alloy 50-250Å is lost. As a check, a portion of electrolyte that has been used to test a total of 90 cm of wires was analyzed by atomic absorption and found to contain Ni in an amount equivalent to the dissolution of 20 ± 20 Å/cm of wire. The dissolution is almost surely not uniform, and pinhole enlargement has not been preventable.

Dissolution is even more serious when impurities are present which prevent the passivation of the Ni-Fe. Such impurities are provided, for example, by tarnish layers which form under certain conditions during corrosion tests in sulfur-containing atmospheres. A dip in 1:1 HCl was found adequate for removing the tarnish layers, but this operation also removes up to 300Å of alloy.

Selection of Sample Length

Production wire batches consisting of 20 to several hundred 20-in. long wires, are characterized by apply-

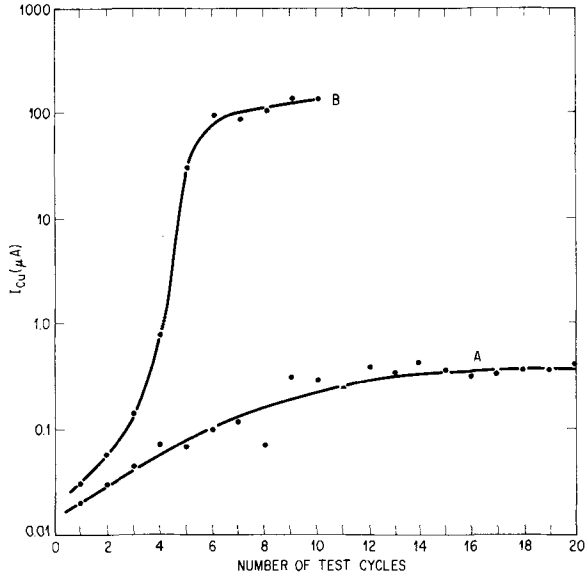

Fig. 5. Effect of repeated test cycles on the observed copper peak height, I_{Cu}. Curve A, procedure as in Fig. 1; curve B, first passivation done by slow scan to +800 mV.

ing the test to a 10-cm length from each of several wires, and copper peak currents range from <0.005 to 0.03 μA/cm. When plating defects other than microfissures occur, they are scattered at random along the length of the wire. A short sample could obviously lead to erroneous interpretations if it happens to fall between defects. Too long a sample, on the other hand, could cause an infrequent defect to be averaged over too long a length with an equally erroneous underestimation. For example, when one 38-cm length was tested 1 cm at a time, all sections fell in the range of 0.01-0.1 μA except one with the abnormally high reading of 0.7 μA. The same wire taken as a whole showed an average current of 0.04 μA/cm which would have been considered only slightly outside the "normal" range. While the statistically ideal sample length was not determined, a length of 10 cm was selected as a good working compromise and in general two such lengths were cut from each production wire tested.

Conclusions

A porosity test has been worked out which gives a measure of the substrate area left exposed by plating defects or pinholes in Ni-Fe alloy films plated on copper. Even with the errors discussed above, the test is useful in quality control of the plating process and in following the course of corrosion reactions. The accuracy has proved more than adequate for measurements of exposed substrate area ranging from less than 0.0004 to 50% and can undoubtedly be improved by optimizing the test conditions.

The method makes use of the current peak associated with a metal being anodically passivated during a potential scan. The technique might be adaptable to other metal pairs if an electrolyte can be found in which the two passivating layers have widely different rates of dissolution.

Acknowledgments

The writer wishes to express his appreciation to Dr. Leonard Nanis for much helpful discussion and to Mr. Andrew Sloss who spent many tedious hours before the polarograph.

Manuscript submitted Nov. 12, 1969; revised manuscript received June 8, 1970.

Any discussion of this paper will appear in a Discussion Section to be published in the June 1971 JOURNAL.

REFERENCES

1. T. R. Long, *J. Appl. Phys.*, **31**, 123S (1960).
2. S. W. Sagal, *This Journal*, **112**, 174 (1965).
3. R. A. Ehrhardt, *Proc. Am. Electroplaters' Soc.*, **47**, 78 (1960).
4. A. A. Khan, *Plating*, **57**, 1374 (1969).
5. S. C. Shome and V. R. Evans, *J. Electrodepositors' Tech. Soc.*, **27**, 45 (1951).
6. M. Clarke and S. C. Britton, *Trans. Inst. Met. Finishing*, **36**, 58 (1959).
7. G. Economy, R. Speisor, F. H. Beck, and M. G. Fontana, *This Journal*, **108**, 337 (1961).
8. O. E. Schupp, P. B. Sturrock, and J. I. Watters, *Inorg. Chem.*, **2**, 106 (1963).
9. C. Heitner-Wirguin and J. Kendy, *J. Inorg. Nucl. Chem.*, **22**, 253 (1961).
10. J. I. Watters and A. Aaron, *This Journal*, **75**, 611 (1953).
11. L. B. Rogers and C. A. Reynolds, *J. Am. Chem. Soc.*, **71**, 2081 (1949).

The Approach to Limiting Current in a Stagnant Diffusion Cell

Limin Hsueh and John Newman*

Inorganic Materials Research Division, Lawrence Radiation Laboratory, and Department of Chemical Engineering, University of California, Berkeley, California 94720

ABSTRACT

The transient behavior of surface concentration and current density in a stagnant diffusion cell has been worked out with consideration of surface and concentration overpotentials and the ohmic resistance of the solution. Both theoretically and experimentally, the current density is found to overshoot the limiting current density during part of the transient.

A stagnant diffusion cell is a capillary cell with an electrode at one end of a capillary filled with solution and open at the other end into a container with solution and containing the counterelectrode. Such a cell is commonly used for diffusivity measurements (1, 2) because of its simple experimental setup and the easy measurement of current and time.

Early analyses (3, 4) showed that, for a constant concentration at the electrode surface, the current decreases in inverse proportion to the square root of time in an unsteady, one-dimensional diffusion, or $i\sqrt{t}$ is a constant for a given concentration of solution. Accordingly, the current would be infinite at zero time. Actually, for a constant applied potential, the current is finite and remains more or less constant until the reactant concentration at the electrode surface approaches a value of zero. The time required for this depends on the potential difference applied across the two electrodes and the properties of the solution itself. It may range from less than 100 sec in a well-supported solution to several tens of thousands of seconds in a solution of a single electrolyte.

Davis, Horvath, and Tobias (2) have included the surface overpotential for linear electrochemical kinetics in their treatment. In the present work, the analyses is extended to include the ohmic resistance of the solution, as well as nonlinear electrochemical kinetics.

This work was motivated not so much by the ohmic and kinetic limitation at short times but more by the shape of the logarithmic current-time curves obtained in the measurement of integral diffusion coefficients (5), the study of the effect of ionic migration on limiting currents (6), and attempts to obtain limiting currents in cupric sulfate solutions in the absence of sulfuric acid (7). Under certain conditions, the current overshoots the limiting current. A similar phenomenon was predicted in the analysis of the current distribution on a rotating disk electrode (8-10) and on

* Electrochemical Society Active Member.
Key words. mass transfer, current distribution, copper sulfate-sulfuric acid system, polarization.

plane electrodes in the walls of a flow channel (11, 12). Experimental confirmation obtained in the present work may thus lend support to those analyses. The similarity to polarography in a binary salt solution (13) should also be noted. No overshoot was predicted in that work, but a recalculation for that system shows that there can be an overshoot for large applied potentials.

Analysis

With the assumption of constant physical properties, the equation for unsteady diffusion in a stagnant diffusion cell for a solution without supporting electrolyte or with an excess of supporting electrolyte reduces to

$$\frac{\partial c}{\partial t} = D\frac{\partial^2 c}{\partial y^2} \qquad [1]$$

where $c = c_+/\nu_+ = c_-/\nu_-$ and

$$D = \frac{z_+u_+D_- - z_-u_-D_+}{z_+u_+ - z_-u_-}$$

for a solution of a single electrolyte, and where c and D represent the concentration and effective diffusion coefficient of the reactant for a solution with an excess of supporting electrolyte.

Equation [1] should be solved with the initial condition that the concentration is uniform, $c = c_\infty$, throughout the capillary at $t = 0$. The concentration at the electrode surface can be taken, for the moment, to be an unknown function of time, $c = c_0(t)$ at $y = 0$. By taking the Laplace transform of Eq. [1] with respect to time and solving the resulting ordinary differential equation, one obtains for the transform of the concentration

$$\bar{c} = \frac{c_\infty}{s} + \left[\bar{c}_0(s) - \frac{c_\infty}{s}\right] e^{-y\sqrt{s/D}} \qquad [2]$$

where s is the Laplace transform variable. The length of the capillary has been taken to be much greater than the thickness of the diffusion layer. Differentiation of Eq. [2] with respect to y, setting y equal to zero, and inversion by means of the convolution integral produce an equation relating the concentration gradient at the surface to the variation of the surface concentration

$$\left.\frac{\partial c}{\partial y}\right|_{y=0} = \frac{-1}{\sqrt{\pi D}}\int_0^t \frac{dc_0(t')}{dt'}\frac{1}{\sqrt{t-t'}}\,dt' \qquad [3]$$

This equation is useful because the current density is also related to the concentration gradient at the surface

$$i = \frac{n\mathbf{F}D}{1-t_R}\left.\frac{\partial c}{\partial y}\right|_{y=0} \qquad [4]$$

where t_R is the transference number of the reactant ($t_R = 0$ with an excess of supporting electrolyte). The current density is further related to the surface overpotential η_s by

$$i = i_o\left(\frac{c_0}{c_\infty}\right)^\gamma\left[\exp\left\{\frac{\alpha Z\mathbf{F}}{RT}\eta_s\right\} - \exp\left\{-\frac{\beta Z\mathbf{F}}{RT}\eta_s\right\}\right] \qquad [5]$$

where i_o is the exchange current density, αZ and βZ are the transfer coefficients, and γ expresses the concentration dependence of the exchange current density.

The ohmic drop in a capillary of length L is

$$\Delta\Phi_{ohm} = iL/\kappa_\infty \qquad [6]$$

and the concentration overpotential is (14)

$$\eta_c = \frac{RT}{Z\mathbf{F}}\left[\ln\left(\frac{c_0}{c_\infty}\right) + t_R\left(1 - \frac{c_0}{c_\infty}\right)\right] \qquad [7]$$

where $Z = -z_+z_-/(z_+ - z_-)$ for reaction of a cation from a solution of a single electrolyte, and $Z = -n$ for a solution with an excess of supporting electrolyte. For the case of metal deposition from a solution of a single electrolyte, the concentration overpotential expressed by Eq. [7] includes an ohmic contribution due to the variation of the conductivity in the diffusion layer (14). Hence, it is appropriate to use the conductivity of the bulk solution in Eq. [6]. The total potential difference V^* applied between the electrode and the solution outside the capillary (as measured by a reference electrode of the same kind as the working electrode) is the sum of the concentration overpotential, the surface overpotential and the ohmic potential drop

$$V^* = \eta_c + \eta_s + \Delta\Phi_{ohm} \qquad [8]$$

It seems appropriate to define a dimensionless current density I and a dimensionless exchange current density J as

$$I = \frac{Z\mathbf{F}L}{RT\kappa_\infty}i, \quad J = \frac{Z\mathbf{F}L}{RT\kappa_\infty}i_o \qquad [9]$$

to define a dimensionless applied potential V and total overpotential η as

$$V = \frac{Z\mathbf{F}}{RT}V^*, \quad \psi = \frac{Z\mathbf{F}}{RT}(\eta_c + \eta_s) \qquad [10]$$

and a dimensionless surface concentration θ as

$$\theta = c_0/c_\infty \qquad [11]$$

Then Eq. [5] through [8] can be rewritten as

$$I = V - \psi = J[\theta^\gamma e^{-\alpha E} - \theta^\gamma e^{+\beta E}] \qquad [12]$$

where

$$E = \psi - t_R(1-\theta) \qquad [13]$$

and Eq. [3] and [4] can be combined to read

$$I = \frac{NL}{\sqrt{\pi D}}\int_0^t \frac{d\theta(t')}{dt'}\frac{1}{\sqrt{t-t'}}\,dt' \qquad [14]$$

where

$$N = -\frac{nZ\mathbf{F}^2Dc_\infty}{(1-t_R)RT\kappa_\infty} \qquad [15]$$

If we now define a dimensionless time τ by

$$\tau = t/t_c \qquad [16]$$

where

$$t_c = N^2L^2/\pi D \qquad [17]$$

then Eq. [14] can be written as

$$I = \int_0^\tau \frac{d\theta(\tau')}{d\tau'}\frac{1}{\sqrt{\tau-\tau'}}\,d\tau' \qquad [18]$$

Equations [12], [13], and [18] constitute four equations for the determination of the time dependence of I, θ, and ψ, as well as E. They can be solved numerically when the six parameters, α, β, γ, J, V, and t_R are known for a given system. One more parameter, V, could be eliminated, but this might obscure the physical significance of the results.

Numerical Calculation Method

The integral in Eq. [18] was approximated by a sum by an adaptation of the method of Acrivos and Chambré (15). Since Eq. [18] involves an indefinite integral, it is only necessary to solve a nonlinear set of equations at each time step. By the nature of the problem, $\theta = 1$ at $\tau = 0$. For the details of the calculation method, one may refer to ref. (16).

Theoretical Results

The dimensionless current density I is plotted against the dimensionless time τ in Fig. 1 with V as a parameter. The values of α, β, γ, J, and t_R are all taken to be equal to 0.5. The higher the total applied potential V, the shorter the flat part of the curve. For high values of V, the current density overshoots the limiting cur-

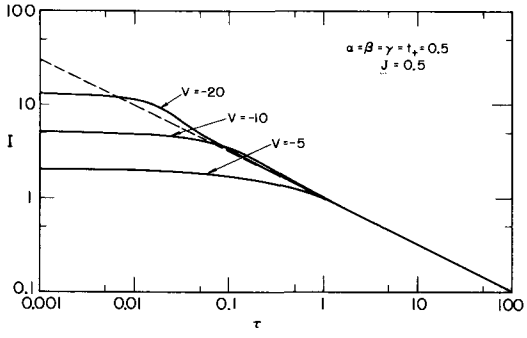

Fig. 1. Decrease of current density in a stagnant diffusion cell

rent, a phenomenon that has been observed experimentally in many of our curves of log current *vs.* log time. For a given value of V, the flat part of the curve persists longer for larger values of the characteristic time t_c. A high value of t_c results from a high transference number of the reactant and a low conductivity of the solution.

For a capillary tube of $L = 10$ cm, some estimated values of t_c for copper sulfate and sulfuric acid at 25°C are

$[CuSO_4]$ M	$[H_2SO_4]$ M	t_c sec
0.05	0	3.0×10^6
0.5	0	6.7×10^6
0.05	1.0	5.6×10^2

In the calculations, $Z = 1$, $t_R = t_+ = 0.4$ for copper sulfate only. $Z = 2$, $t_R = 0$ for the solution with sulfuric acid as supporting electrolyte.

The decrease of surface concentration θ with time is plotted in Fig. 2 with identical parameters. The higher the applied potential, the faster the surface concentration drops to zero. The time required for the surface concentration to drop to 10 and 1% of the bulk value is plotted in Fig. 3.

Experimental Results

Figure 4 shows the transient behavior of the current density with various amounts of supporting electrolyte. These curves have qualitatively the same shape as the theoretical curves in Fig. 1, particularly with regard to the transient overshooting of the limiting current.

The surface concentration was also measured optically for an unsupported, 0.0385M cupric sulfate solution at 25°C; the results are shown in Fig. 5 for two values of the applied potential, 0.80 and 0.60V. The measured variations of the surface concentration are compared with the theoretical predictions in Fig. 5. The following data were used for the calculations:

		ref.
Conductivity κ_x	4.13×10^{-3} mho/cm	(17)
Diffusivity D	6.07×10^{-6} cm²/sec	(18)
Transference number t_R	0.383	(19)
Kinetic parameters, α, β, γ	0.5	
Z	1	

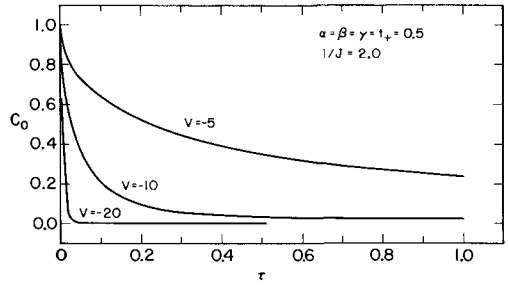

Fig. 2. Decrease of surface concentration in a stagnant diffusion cell.

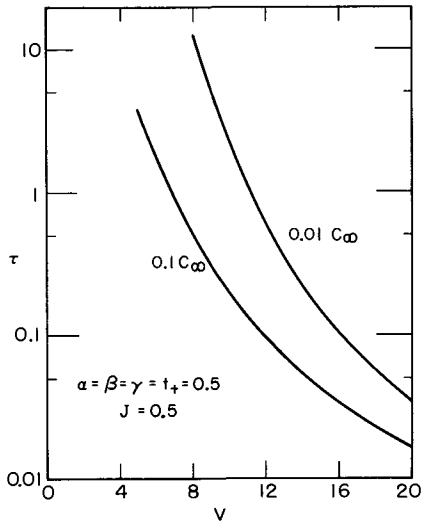

Fig. 3. Transient time in a stagnant diffusion cell, showing the dimensionless time required for the surface concentration to drop to 10 and 1% of the bulk value.

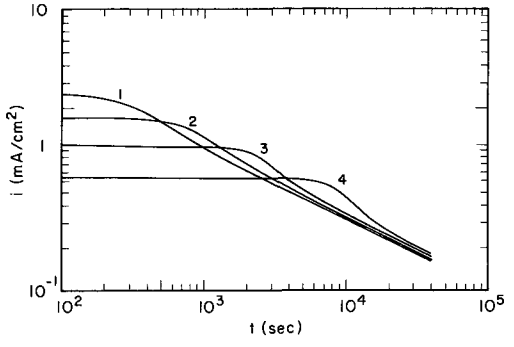

Fig. 4. Observed transient behavior in a stagnant diffusion cell (5 cm long), showing the effect of concentration of supporting electrolyte.

	$CuSO_4$ M	H_2SO_4 M	Applied potential V	t_c/V^2 sec
1	0.1003	0.175	0.355	28.5
2	0.0998	0.100	0.355	71.2
3	0.0999	0.050	0.355	198
4	0.1001	0.020	0.350	553

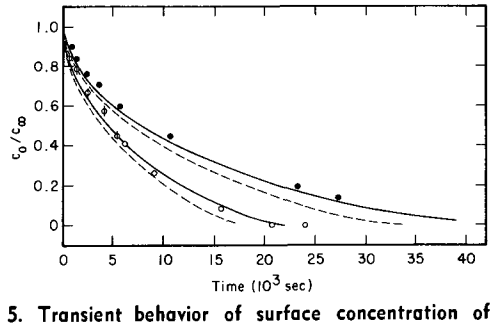

Fig. 5. Transient behavior of surface concentration of copper sulfate (0.0385M) in a stagnant diffusion cell: ● 0.60V; ○ 0.80V; dashed lines, $i_o = 1.0$ mA/cm², solid lines, $i_o = 0.1$ mA/cm²).

The length of the cell L was 15 cm, the area of the electrode was 0.178 cm², and the calculated characteristic time t_c was 5.60 x 10^6 sec. There are no exchange current density data available in the literature for an unsupported $CuSO_4$ solution, a reasonable estimate being that it lies between 0.1 and 1.0 mA/cm². The solid lines are theoretical calculations at an exchange current density of 0.1 mA/cm², and the dashed lines

are calculated at 1.0 mA/cm². The solid lines represent a satisfactory fit to the experimental results.

An unexplained observation should be recorded here. For a solution 0.1*M* in $CuSO_4$ and 1.375*M* in H_2SO_4, the current time curves in Fig. 6 were obtained. The current drops suddenly at about 0.3 sec. This phenomenon was fairly reproducible in a well-supported electrolyte. No such step change was observed for solutions with little or no supporting electrolyte.

Before the runs, the electrode was predeposited with copper at 0.1V for 1 to 3 min. Values of the parameters for the theoretical calculations are $\alpha = 0.75$, $\beta = 0.25$, $\gamma = 0.5$, $t_R = 0$, $\kappa_z = 0.4925$ mho/cm, $Z = 2$, $L = 7.0$ cm, $D = 5.09 \times 10^{-6}$ cm²/sec, $t_c = 740$ sec, $V^* = 0.225$V, and the exchange current density is estimated to lie between 1 and 10 mA/cm² for a cathode surface prepared by electrodeposition (20).

Before the step change of current density, the horizontal part of the curve was found to fall between the curves for theoretical predictions of exchange current of 1 and 10 mA/cm². The charging of the electrode double layer should be complete in a time of about 0.5 msec.

A reviewer suggests the following possible explanations for the step change of current density: (*a*) cuprous ions are initially present in the solution in equilibrium with cupric ions and will tend to react before the cupric ions due to kinetic factors (20); (*b*) crystallographic defects in the deposit may be different from those in the substrate metal and thus lead to a change of kinetic parameters with time; and (*c*) adsorption of inhibitors or impurities may lead to changes of kinetic parameters although the effect would not be expected to be reproducible. However, calculations based on the equilibrium concentration of cuprous ions suggest that the transition time for their concentration to drop to zero at the electrode surface would be much smaller than the time at which the step change in current density occurs.

Conclusion

In this work, the transient behavior has been worked out for a stagnant diffusion cell. The resulting time dependence of the surface concentration for an unsupported electrolyte agrees with the theoretical predictions within the uncertainty of the available electrochemical kinetic parameters. The current density is found, experimentally and theoretically, to overshoot the limiting current, in harmony with predictions for the current distribution on plane and disk electrodes.

Acknowledgment

This work was supported by the United States Atomic Energy Commission and by the Petroleum Research Fund, administered by the American Chemical Society.

Manuscript submitted Dec. 10, 1969; revised manuscript received *ca.* May 26, 1970.

Any discussion of this paper will appear in a Discussion Section to be published in the June 1971 JOURNAL.

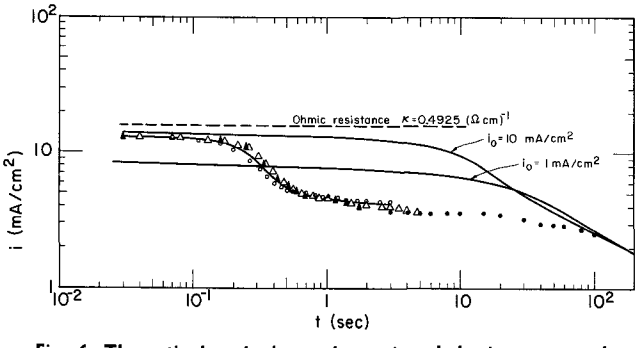

Fig. 6. Theoretical and observed transient behavior at very short time. Total applied voltage 0.225V; ● run 82; ○ run 83; ▲ run 84; △ run 85.

LIST OF SYMBOLS

c_i	concentration of species i, mole/cm³
c_o	surface concentration of reactant, mole/cm³
D	diffusion coefficient, cm²/sec
$\mathbf{F}$	Faraday's constant, 96,500 coul/equiv
i	current density, A/cm²
i_o	exchange current density, A/cm²
I	dimensionless current density
J	dimensionless exchange current density
L	length of diffusion cell, cm
n	number of electrons produced when one reactant ion or molecule reacts
N	dimensionless parameter
R	universal gas constant, joule/mole-deg
s	Laplace transform variable, sec⁻¹
t	time, sec
t_c	characteristic time, sec
t_R	transference number of reactant
T	temperature, °K
u_i	mobility of species i, cm²-mole/joule-sec
V	dimensionless applied potential
V^*	applied potential, V
y	distance from electrode, cm
z_i	charge number of species i
Z	$-z_+z_-/(z_+ - z_-)$ for unsupported electrolyte $-n$ with excess supporting electrolyte
α, β, γ	electrochemical kinetic parameters
ψ	dimensionless total overpotential
η_c	concentration overpotential, V
η_s	surface overpotential, V
θ	dimensionless surface concentration
κ_z	conductivity of the bulk solution, mho/cm
ν_+, ν_-	numbers of cations and anions produced by dissociation of one molecule of electrolyte
τ	dimensionless time
$\Delta\Phi_{ohm}$	ohmic potential drop, V

REFERENCES

1. M. v. Stackelberg, M. Pilgram, and V. Toome, *Z. Electrochem.*, **57**, 342 (1953).
2. R. E. Davis, G. L. Horvath, and C. W. Tobias, *Electrochim. Acta*, **12**, 287 (1967).
3. F. G. Cottrell, *Z. physik. Chem.*, **42**, 385 (1903).
4. N. Ibl and G. Trümpler, *Helv. Chim. Acta*, **34**, 1217 (1951).
5. Limin Hsueh and John Newman, UCRL-19101, In preparation.
6. Limin Hsueh and John Newman, UCRL-19102. July 1970.
7. Limin Hsueh and John Newman, UCRL-19099, October 1969.
8. John Newman, *This Journal*, **113**, 1235 (1966).
9. John Newman, *ibid.*, **114**, 239 (1967).
10. Vinay Marathe and John Newman, *ibid.*, **116**, 1704 (1969).
11. W. R. Parrish and John Newman, *ibid.*, **116**, 169 (1969).
12. W. R. Parrish and John Newman, *ibid.*, **117**, 43 (1970).
13. Thomas W. Chapman and John Newman, *J. Phys. Chem.*, **71**, 241 (1967).
14. John Newman, *Intern. J. Heat Mass Transfer*, **10** 983 (1967).
15. Andreas Acrivos and P. L. Chambré, *Ind. Eng. Chem.*, **49**, 1025 (1967).
16. Limin Hsueh, Dissertation, University of California, Berkeley, December, 1968. (UCRL-18597).
17. B. B. Owen and R. W. Gurry, *J. Am. Chem. Soc.*, **60**, 3074 (1938).
18. W. G. Eversole, H. M. Kindsvater, and J. D. Peterson, *J. Phys. Chem.*, **46**, 370 (1942).
19. J. J. Fritz and C. R. Fuget, *ibid.*, **62**, 303 (1958).
20. E. Mattsson and J. O'M. Bockris, *Trans. Faraday Soc.*, **55**, 1586 (1959).

Stoichiometry of Anodic Copper Dissolution at High Current Densities

K. Kinoshita,*[1] D. Landolt,*[2] R. H. Muller,* and C. W. Tobias*

Inorganic Materials Research Division, Lawrence Radiation Laboratory and Department of Chemical Engineering, University of California, Berkeley, California 94720

ABSTRACT

The influence of current density, flow rate, and electrolyte composition on the stoichiometry of anodic copper dissolution was investigated under conditions comparable to those of electrochemical machining. Weight loss measurements, x-ray diffraction, and chemical analysis were used for the characterization of the dissolution reaction. A sharp change in dissolution mechanism coincided with the transition from active to transpassive dissolution. For active dissolution, an apparent valence of the dissolution process of two was found in sulfate and nitrate electrolytes, and of one in chloride electrolytes. For transpassive dissolution, mixed valences lying between 1 and 2 were found in all electrolytes. The mixed valences are interpreted to result from the simultaneous production of monovalent and divalent reaction products, some of which are in solid form.

Anodic dissolution of metals at current densities of up to several hundred amperes per square centimeter and with electrolyte flow velocities of many meters per second is being carried out on a technical scale in the process of electrochemical machining (ECM). In an attempt to provide quantitative information on the electrochemical processes under high current densities, the anodic dissolution of copper is being investigated (1-3). Copper was chosen because its electrochemical properties are reasonably well understood (4-8). In a previous paper (1), the role of mass transfer in determining the occurrence of passivation phenomena during copper dissolution in K_2SO_4 and KNO_3 solutions has been reported. It was found that apparent anode potentials and surface textures resulting from dissolution changed drastically while going from a low voltage (active) to a high voltage (transpassive) mode of dissolution.[3]

In the present study, the valence of the electrode reaction and the composition of reaction products of copper have been investigated in nitrate, sulfate, and chloride electrolytes. Weight loss measurements of the anode, x-ray diffraction analysis of solids, and chemical analysis of the solution were used for the characterization of the dissolution reaction. Current densities employed ranged from 0.1 to 80 A/cm^2. Experiments were performed under forced convection conditions in a flow channel at flow rates from 30-700 cm/sec, as well as in unstirred solutions under free convection conditions.

Experimental

Most experiments were carried out under forced convection conditions in an experimental flow system similar to that described in a previous study (1) and schematically shown in Fig. 1. The electrolyte was pumped by a positive displacement pump,[4] and the flow rate was measured with a rotameter.[5] One half inch stainless steel pipes were used throughout the system.

A 30 cm long rectangular flow channel of 1 x 3 mm cross section, constructed of laminated polyvinyl chloride, was positioned upstream of the experimental cell to establish fully developed velocity profiles at

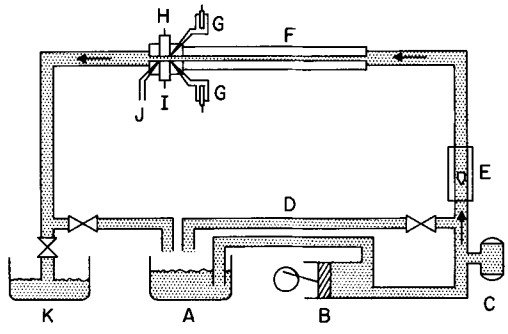

Fig. 1. Schematic of flow system: A, supply tank; B, dual piston pump; C, accumulator; D, bypass line; E, rotameter; F, entrance length of flow channel; G, reference electrodes; H, cathode; I, anode; J, capillary for precipitate collection; K, drain tank.

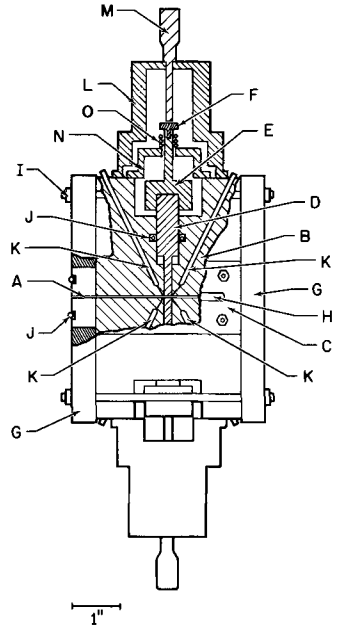

Fig. 2. Side view of experimental cell with partial cross sectioning: A, rectangular flow channel; B, epoxy cell body; C, stainless steel side plate; D, copper electrode; E, aluminum cap; F, nylon screw; G, stainless steel end flange; H, glass side window; I, bolt and nut assembly; J, O-ring seal; K, liquid junction connection to backside capillaries; L, aluminum micrometer holder; M, micrometer head; N, aluminum base plate; O, coil spring.

* Electrochemical Society Active Member.

[1] Present address: Pratt & Whitney Aircraft Corporation, Middletown, Connecticut 06457.

[2] Present address: University of California, School of Engineering & Applied Science, Los Angeles, California 90024.

Key words: anodic metal dissolution, copper anode, passivity.

[3] Different definitions for the phenomenon of passivation can be found in the literature. The term is used here to describe an abrupt increase in measured anode potential with time for certain combinations of flow rate and current density (see e.g., Fig. 3).

[4] Constametric Pumps, Milton Roy Company, Philadelphia, Pennsylvania. Varidrive Motor, U. S. Electrical Motors, Inc., Los Angeles, California.

[5] Type 18410, Schutte and Koerting Company, Cornwall Heights, Pennsylvania.

the electrodes (1). The electrolysis cell is shown schematically in Fig. 2. The cell body (B) was made of epoxy resin with the two glass side walls (H) held together by plates (C). The cell was connected to the inlet and outlet channel by end flanges (G). Optical observation of the interelectrode gap could be performed through the glass walls. Back-side capillaries (K) which enter the channel walls next to the electrodes were used for electrode potential measurements and, in some experiments, for the sampling of solution on the downstream side of the electrodes. The copper electrodes (D) (purity ≧99.9%) had a geometrical surface area of 3 x 3 mm. The electrodes could be advanced manually by turning micrometer head (M). The electrode assembly was pushed back against insert (F) by sprint (O). Silicone rubber gaskets[6] cast between glass wall and epoxy cell body were used for sealing the cell.

Measurements of cell voltage, electrode potentials, and current were made simultaneously on a multi channel light beam oscillograph.[7] Electrical power connections to the cell were made by threaded connections screwed into aluminum cap (E). The current was recorded by measuring the voltage drop across a shunt. Anode and cathode potentials were measured with respect to saturated calomel reference electrodes, which were placed in small glass containers connected to the capillaries by Tygon tubing. The electrolysis current was provided by an electronically controlled constant current supply.[8]

Prior to each run, the electrodes were ground on 600 grit emery paper and washed with aqueous detergent. Following a dip in concentrated HCl, they were rinsed with distilled water and reagent grade acetone and stored in vacuum until use. The electrodes were aligned with the channel wall by using a microscope with 20X magnification. During electrolysis, the 1 mm electrode gap was approximately maintained by manual adjustment of the micrometer.

During a typical experiment, 25 mg of copper were dissolved, which corresponded to an average depth of dissolution of about 0.3 mm. After each run, the anode was removed from the cell, rinsed with water, dried with acetone, and weighed on an analytical balance. The accuracy of the weight loss determination is estimated at ±1-2%. The amount of charge passed during the experiment was determined from the oscillographically recorded current trace. The accuracy of the charge measurement is estimated at ±2-3%.

From the measurement of charge and weight loss, an apparent valence n of the dissolution process was calculated according to Eq. [1]

$$n = \frac{ItM}{\Delta W \mathbf{F}} \qquad [1]$$

where I is the current passed during time t, M is the atomic weight of copper, ΔW is the anode weight-loss, and $\mathbf{F}$ is the Faraday constant.

Solid reaction products formed during the anodic dissolution of copper were analyzed by x-ray diffraction. Initial analyses were made using a 11.46 mm Debye-Scherrer powder camera mounted on an x-ray diffraction unit.[9] Ni filtered Cu radiation (40 kV, 20 mA) was used.

A sample of the anodic reaction product from the flow cell was collected by rubbing a glass fiber through the precipitate adhering to the wet surface. Diffraction patterns obtained were, however, difficult to analyze because of the faintness of the diffraction lines. Also, because of the small samples, exposure times to the x-ray beam from 6-12 hr were necessary.

[6] Encapsulant 502 RTV, Dow Corning Corporation, Midland, Michigan.
[7] Series 2300, Brush Instrument Division, Cleveland, Ohio.
[8] Type C618, Electronic Measurements Company, Eatontown, N. J. or Model KS 120-10M, Kepco Inc., Flushing, New York.
[9] Norelco X-Ray Diffraction Unit, Type 12045 with Debye-Scherrer Camera Type 52056-O, North American Philips Company, Inc., New York, N. Y.

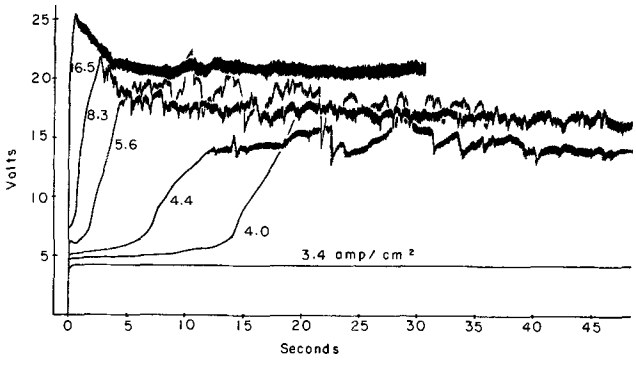

Fig. 3. Cell voltage transients measured in 2N KNO_3 at different current densities, flow rate 30 cm/sec.

To provide a larger specimen, a continuous sampling technique was developed. An x-ray diffractometer[10] using a Ni filtered Cu radiation (40 kV, 14 mA) could then be used. Solution escaping through the (0.014 in. diameter) capillary on the downstream side of the anode was collected on a Whatman No. 41 paper by continuous vacuum filtration. Without washing, the filter paper with adhering precipitate was dried under vacuum, mounted on a Lucite sample holder using double-sided adhesive tape, and placed in the diffractometer. A preliminary x-ray pattern of the blank showed strong diffraction peaks at low θ values which did, however, not interfere with the diffraction peaks of possible compounds present in the precipitate.

In order to substantiate the apparent valence determination carried out under forced convection conditions, some experiments were performed in a stagnant electrolyte which allowed quantitative determination of dissolved Cu^+ and Cu^{2+} ions. Since Cu^+ is unstable in aqueous solution unless complexing agents are present, only chloride electrolytes were analyzed this way. The electrolysis was carried out in an H cell with a glass frit separating anode and cathode compartments (2). In contrast to the highly diluted dissolution products obtained in the flow channel, concentrations which can be determined by simple analytical techniques could be obtained in this system. The analytical determination of Cu^{2+} and Cu^+ was based on that given by Vogel (9). Cuprous ion was oxidized with ferric ammonium sulfate, and the resulting ferrous ion was titrated with ceric sulfate. The cupric ion concentration was obtained as the difference between total copper concentration and cuprous ion concentration. The total copper concentration was determined iodometrically after oxidation of cuprous ion to cupric ion by sodium peroxide.

Results

Current-voltage behavior.—Figure 3 illustrates the transient cell voltage behavior during galvanostatic copper dissolution in 2N KNO_3 under a given flow rate (30 cm/sec). At low current density (3.4 A/cm²), the dissolution proceeds indefinitely in a low voltage (active) mode. Above a critical current density, which is shifted to higher values by increased flow rates, the dissolution process switches to a high voltage (transpassive) mode, after a transition time with active dissolution. The length of the transition period decreases with increasing current density and decreasing flow rate (not shown). Figures 4 and 5 are examples of transient cell voltage behavior with K_2SO_4 and KCl solutions. In all cases, dissolution in the transpassive mode occurs at a cell voltage which is 10-20V higher than in the active mode. Voltage fluctuations are observed in the transpassive region and, at the higher current densities, a voltage maximum occurs before steady state is reached.

Apparent valence.—Average steady-state values of the cell voltage and apparent valence values are

[10] Picker X-Ray Corporation, Waite Manufacturing Division, Inc., Cleveland, Ohio.

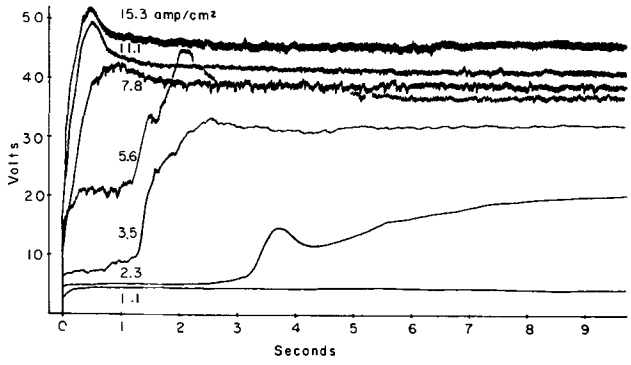

Fig. 4. Cell voltage transients measured in 1*N* K_2SO_4 at different current densities, flow rate 50 cm/sec.

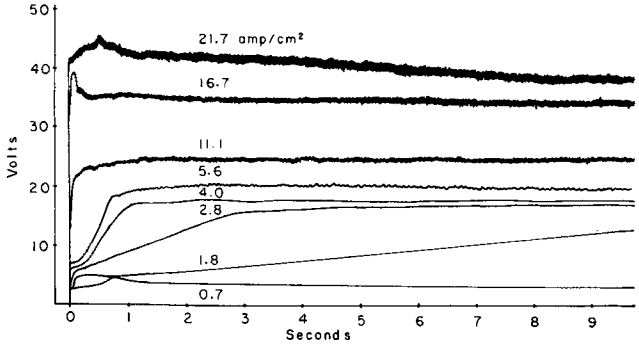

Fig. 5. Cell voltage transients measured in 2*N* KCl at different current densities, flow rate 50 cm/sec.

plotted *vs.* current density in Fig. 6 to 8. The behavior in 2*N* KNO_3 and 1*N* K_2SO_4 solutions is very similar. With the transition from active to transpassive dissolution, a sharp drop in apparent valence occurs. The apparent valence value of $n = 2$ observed in the active region indicates that copper is dissolved almost exclusively to divalent cupric ions. This is consistent with expectations based on thermodynamic considerations of the reversible potential of a copper electrode in contact with dissolved mono and divalent copper ions (8). In the transpassive region, on the other hand, the apparent valence depends on the value of the applied current density with respect to the current density at which passivation occurs. A limiting value of $n \simeq 1.5$-1.6 is reached at high current densities. In order to account for this value of n, it has to be assumed either that part of the copper is dissolved to a monovalent form, or that part of the metal disintegrates during the dissolution process. Since *p*H might have an influence in determining the reaction path (8), additional experiments were performed in a 2*N* KNO_3 solution adjusted to *p*H 1 by the addition of concentrated nitric acid, and also in a 1*N* H_2SO_4 solution. Voltage readings and apparent valences obtained in both of these electrolytes corresponded within experimental accuracy to those of the nitrate and sulfate solutions, respectively. This indicates that, within the range studied, *p*H has a negligible influence on apparent valence of the dissolution process. As illustrated by Fig. 8, the behavior in KCl solutions was quite different from that in KNO_3 and K_2SO_4 solutions. A sharp transition between active and transpassive dissolution was absent. Instead, periodic fluctuations occurred (indicated by dotted lines in Fig. 8) in the transition region. Such oscillations in the copper/chloride system have also been reported in the literature for low current density conditions (6, 10). Periodic oscillations have also been observed during high rate copper dissolution in sulfate and chlorate electrolytes under certain conditions (1-3). The apparent valence, in the case of chloride solution, is $n = 1$ at low current densities. A maximum of $n = 1.4$ is observed at intermediate current densities, and the apparent valence drops to $n \simeq 1.2$ in the range of high current densities. While it appears that the observed changes in apparent valence are related to the occurrence of passivation, the relationships are not as clear cut as in

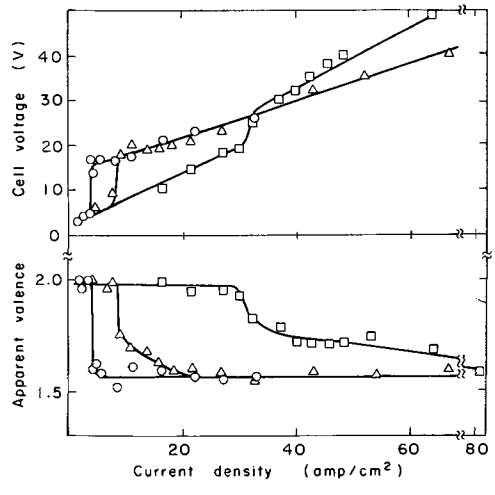

Fig. 6. Variation of apparent valence and cell voltage with current density in 2*N* KNO_3 for different flow rates: ○, 30 cm/sec; △, 200 cm/sec; □, 627 cm/sec.

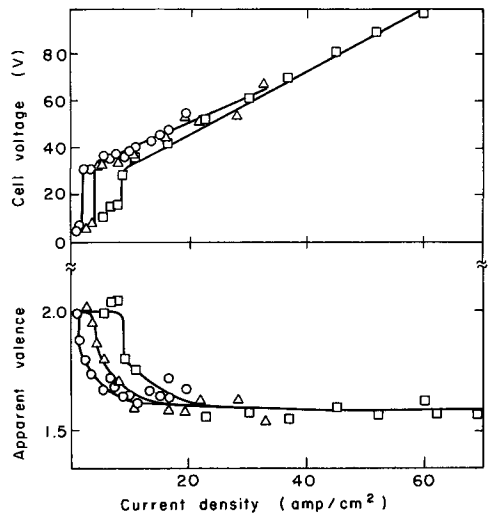

Fig. 7. Variation of apparent valence and cell voltage with current density in 1*N* K_2SO_4 for different flow rates: ○, 50 cm/sec; △, 200 cm/sec; □, 686 cm/sec.

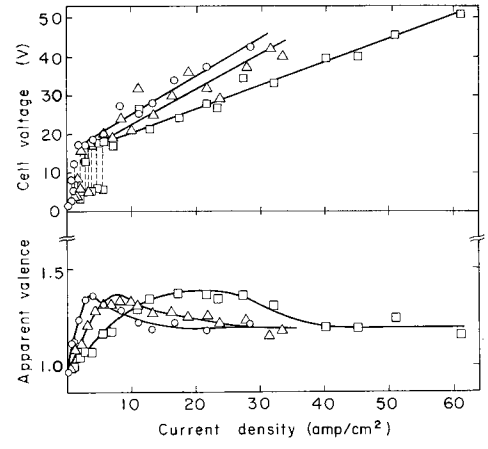

Fig. 8. Variation of apparent valence and cell voltage with current density in 2*N* KCl for different flow rates: ○, 50 cm/sec; △, 200 cm/sec; □, 606 cm/sec.

Table I. X-ray analysis of anode solid reaction products

Electrolyte	Compounds identified
2N KNO_3	Cu_2O, Cu
2N KNO_3 + HNO_3 (pH 1)	Cu
1N K_2SO_4	Cu_2O, Cu
1N H_2SO_4	Cu

nitrate and sulfate solutions. For example, at the highest flow rate (606 cm/sec), the maximum value of n was attained at much higher current density than that corresponding to the active-passive transition derived from cell voltage measurements.

Analysis of solid reaction products.—Anode precipitates were found during transpassive dissolution only. X-ray analysis of precipitates collected from experiments performed in KNO_3 and K_2SO_4 solutions showed Cu_2O to be the principal copper compound. Diffraction peaks for metallic copper were also present in some experiments. The metallic copper contents of precipitates from acidified solutions was increased at the expense of the cuprous oxide contents (Table I). No analysis of anodic precipitates in chloride solution was possible because precipitates could not be collected in sufficient amounts. A typical diffraction pattern of anode precipitate is given in Fig. 9 together with patterns of known samples of Cu_2O and Cu. Precipitates collected in the drain tank showed a different composition from those collected close to the anode. They contained basic oxides of complex composition, owing to contact with the alkaline solution produced at the cathode.

Analysis of dissolved reaction products.— Apparent valence determinations in chloride solution were also carried out in a separate cell under absence of forced convection. In these experiments, values of apparent valence obtained from weight loss measurements could be compared with those obtained by chemical analysis of dissolved reaction products. Calculation of the chemically determined apparent valence n^* was based on Eq. [2]

$$Cu \rightarrow xCu^+ + yCu^{2+} + n^*e \qquad [2]$$

where x and y are the fractional amounts of Cu^+ or Cu^{2+}, respectively. Since, from the mass balance $x + y = 1$ and from the charge balance $x + 2y = n^*$, one gets Eq. [3]

$$n^* = 2 - x = 1 + y \qquad [3]$$

The results given in Table II illustrate the good agreement between the valence determined by chemical analysis with that derived from weight loss measurements for a wide range of current densities. In all cases a mass balance could be established within 1-2%. Changes in apparent valence with current density in chloride solutions are therefore indeed due to different ratios of Cu^+ and Cu^{2+} produced. No oxygen evolution was observed during the experiments. The experiments also confirmed that the anodic behavior, *i.e.*, the occurrence of active and transpassive dissolution, was essentially the same in stagnant as in flowing solutions,

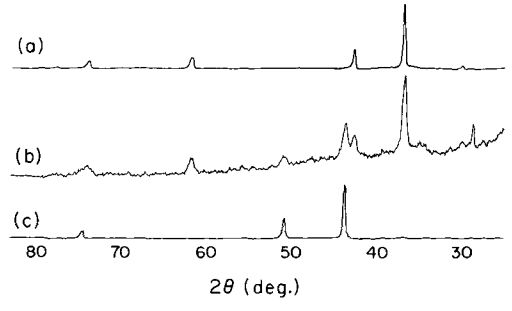

Fig. 9. X-ray diffractometer trace of anode precipitate (b) compared to known samples of Cu_2O (a) and Cu (c). Anode precipitate obtained at 11.1 A/cm² and 50 cm/sec in 1N K_2SO_4.

Table II. Chemical analysis of dissolved reaction products in 3N KCl solution after passage of 60 coul, anode area 1 cm²

Current density, A/cm²	Valence from dissolved Cu^+ and Cu^{++}	Valence from weight loss
0.05	1.00	1.00
0.10	1.19	1.15
0.13	1.21	1.28
0.16	1.27	1.31
0.21	1.28	1.30
0.26	1.26	1.28
0.51	1.22	1.20
0.82	1.19	1.20
1.00	1.13	1.10
1.31	1.14	1.16
1.58	1.10	1.08
1.87	1.08	1.06
1.98	1.07	1.07

with the exception that passivation sets in at much lower current densities in the absence of external convection.

Discussion

Nitrate and sulfate solutions.—Two dissolution modes, active and transpassive, were found differing in overvoltage and apparent valence of dissolution. The transition between active and transpassive dissolution depends on mass transfer conditions. Using the mass transfer correlations for channel flow discussed earlier (1), the interfacial concentration of ionic dissolution product at the onset of transpassive dissolution was estimated from the passivation current density for different flow rates and electrolytes. (A diffusion coefficient of 5×10^{-6} cm²/sec was assumed for this calculation.) A comparison of the results shown in Table III with solubility data given in Table IV indicates that the onset of transpassive dissolution coincides, at least qualitatively, with the limiting transport of dissolved reaction products by convective diffusion. This substantiates the validity of previous results (1) which were obtained in a different flow system, mostly at higher current densities and flow rates. In addition, it was found here that passivation current densities in 1N H_2SO_4 were essentially the same as in 1N K_2SO_4. This suggests that limitations in the transport of cupric salt, rather than the formation of oxide or hydroxide, initiates the change to transpassive dissolution.

The present study also demonstrates that the transition between active and transpassive dissolution is associated with a drastic change in current efficiency for the metal removal process, with more copper being

Table III. Calculated interfacial concentration of copper salts at onset of transpassive dissolution

Electrolyte	Flow velocity, cm/sec	Reynolds number	Passivation current density, A/cm²	Interfac. conc., moles/l
2N KNO_3	30	510	3.8	4.5
	200	3390	8.5	4.6
	627	10600	31.0	8.5
1N K_2SO_4	50	730	1.5	1.4
	200	2920	4.1	2.2
	686	10000	8.5	2.2
1N H_2SO_4	50	770	3.6	3.4
	200	3090	4.7	2.5
	686	10600	11.8	3.0
2N KCl	50	820	0.4	0.8
	200	3270	1.2	1.2
	606	10000	2.5	1.2

Table IV. Solubilities of copper salts at room temperature

Salt	Solvent	Solubility, moles/l	Reference
Cupric nitrate	H_2O	7.0	(24)
Cupric sulfate	H_2O	1.4	(24)
	1N H_2SO_4	1.1	(25)
Cuprous chloride	2N KCl	1.0	(17), (18)
	3N KCl	1.9	(17), (18)

dissolved for a given amount of charge in the transpassive region. A mechanism involving the formation of monovalent copper species at the anode, especially cuprous oxide, rather than anodic disintegration by grain boundary attack (11, 12), seems to be the cause for the apparent increase in current efficiency. The above conclusion, although it cannot be rigidly proven on the grounds of our results, is supported by the following experimental observations: (*A*) Cuprous oxide has been found to be the main constituent of anodic films. (*B*) Substantial amounts of metallic copper were observed in the x-ray patterns in acidic solutions only, consistent with the fact that Cu_2O disproportionates in these solutions into Cu^{2+} and Cu. (*C*) No grain boundary attack was observed microscopically in the transpassive region. Instead, the surfaces after transpassive dissolution had a shiny appearance and were almost randomly pitted (1, 2). (*D*) At least in the case of chloride solutions, the presence of cuprous ion could be verified quantitatively. All these factors indicate that a distintegration mechanism, which has been proposed primarily for more reactive metals (beryllium, magnesium, cadmium, zinc) at low current densities (13-16), is not likely to be of importance in the present anodic dissolution process.

Measured apparent valences tended to reach a constant limiting value at high current densities. No satisfactory explanation for this phenomenon can be given at the present time. From a purely kinetic point of view we would expect a continuous variation of n with current density. A possible explanation of the observed constancy of n may, perhaps, be sought in a model viewing the surface as an ensemble of small surface area elements randomly fluctuating between active and passive states. Such active-passive fluctuations, which are most pronounced in chlorate electrolytes (2, 3), are now being studied in this laboratory.

Chloride solutions.—The dissolution behavior in chloride electrolytes is different because the monovalent ionic state becomes thermodynamically more favorable than the divalent state due to the formation of cuprous ion complexes (17, 18). Thus, disproportionation of Cu^+, which usually occurs in aqueous solutions is avoided. Since a variety of different complexes may be formed, depending on the local chloride concentration, the dissolution process in chloride solutions is expected to be much more complicated than in nitrate and sulfate solutions. For example, due to the effect of chloride concentration on the solubility of cuprous ion, the formation of precipitate layers depends not only on the rate of departure of cations from the interface, but also on the rate of arrival of anions. In addition to the mass transport of the dissolution product, the mass transport of chloride ion may therefore become a limiting factor, since chloride ions are consumed at the anode by complex formation. Such a mechanism has, for example, been reported by Landsberg *et al.* (19) for the dissolution of gold in HCl. During the course of stoichiometric determinations in stagnant solution, a number of transient measurements were performed in 3*N* KCl solutions at constant current density. Table V summarizes the transition times determined for the onset of transpassive behavior. In spite of that the geometrical arrangement was not ideal to exclude free convection completely, the application of Sand's equation is justified because of the short times involved. From the average measured quantity $i\sqrt{\tau}$, a value for ΔC, the rate-limiting concentration difference, was calculated according to Eq. [4]

$$\Delta C = \frac{2i\sqrt{\tau}}{n\mathbf{F}\sqrt{\pi D}} \qquad [4]$$

assuming $D = 5 \times 10^{-6}$ cm²/sec and $n = 1$. The resulting value of $\Delta C = 3.6$ mole/liter is similar in magnitude to the solubility of CuCl in 3*N* KCl [1.9 mole/liter (17)]. This indicates that, under the conditions of these experiments, passivation may have been caused by a similar precipitation mechanism as in nitrate and sulfate solutions.

Table V. Transition times τ for copper dissolution at different current densities i in 3*N* KCl without external convection

i, A/cm²	τ, sec	$i\sqrt{\tau}$
0.10	38.90	0.62
0.16	11.60	0.56
0.21	9.20	0.69
0.26	5.63	0.62
0.51	1.85	0.70
0.82	0.65	0.68
1.00	0.48	0.69
1.31	0.28	0.69
1.58	0.20	0.70
1.87	0.16	0.75
1.98	0.15	0.77

The increase in apparent valence n on passivation (Fig. 8) is consistent with the fact that at higher anode potentials, the reaction $Cu \rightarrow Cu^{2+}$ becomes thermodynamically possible. No true anode potential measurements were possible under the conditions of this study; therefore, a discussion has to remain qualitative. The subsequent decrease in n at still higher current densities may then be explained by assuming formation of Cu_2O, as observed in the case of nitrate and sulfate solutions. The oozing of a reddish brown, finely dispersed dissolution product from localized anode areas which changed their positions during electrolysis was observed visually in stagnant KCl solutions in the transpassive region (2). This solid might have been Cu_2O, but it was not possible to collect the precipitate due to its chemical instability in the chloride electrolyte. The formation of cuprous oxide during copper dissolution in chloride media has also been reported in the literature (20-23). The formation of a thin cuprous chloride film during transpassive dissolution in chloride solution was indicated by the white appearance of the surface.

Summary and Conclusions

1. The present study has confirmed earlier findings (1) obtained under different experimental conditions that in nitrate and sulfate electrolytes the transition from active to transpassive dissolution of copper is controlled by the mass transfer of dissolved dissolution products.

2. Although the details of copper dissolution in chloride solution are probably different from those in nitrate and sulfate, the gross current-voltage behavior is similar. Ionic mass transfer limitations seem, therefore, to be the dominating factor determining the onset of passivation in chloride solutions, too.

3. The apparent valence of the dissolution process undergoes a noticeable change with the transition from active to transpassive dissolution. In nitrate and sulfate solutions, active dissolution proceeds with an apparent valence of 2. Transpassive dissolution leads to a lower apparent valence, which reaches a limiting value of 1.6 at high current densities. This drop in apparent valence is interpreted to be caused by the anodic production of monovalent copper species, rather than by anodic disintegration.

4. Active dissolution in chloride solution occurs with an apparent valence of one. This is due to the stabilization of cuprous ion by complex formation. Upon passivation the apparent valence increases, going through a maximum of 1.4 with increasing current density before reaching a limiting value of 1.2. This increase in apparent valence on passivation is due to part of the copper being dissolved in divalent form.

5. No significant oxygen evolution occurred during copper dissolution under all the experimental conditions employed.

6. The formation of solid anodic dissolution products during transpassive dissolution has been demonstrated in agreement with earlier optical observations. Anal-

ysis of the precipitates by x-ray diffraction has shown Cu_2O to be the main constituent produced in potassium nitrate and sulfate solutions. Metallic copper, resulting from disproportionation of Cu_2O, is found in acidified solutions. In chloride solutions optical observation indicated the formation of cuprous chloride films.

Acknowledgment

This work was done under the auspices of the U. S. Atomic Energy Commission.

Manuscript received May 13, 1970.

Any discussion of this paper will appear in a Discussion Section to be published in the June 1971 JOURNAL.

REFERENCES

1. D. Landolt, R. H. Muller, and C. W. Tobias, *This Journal*, **116**, 1384 (1969).
2. K. Kinoshita, Ph.D. Thesis, University of California, Berkeley, UCRL-19051, Sept. 1969.
3. D. Landolt, R. Acosta, R. H. Muller, and C. W. Tobias, *This Journal*, **117**, 839 (1970).
4. E. Mattson and J. O'M. Bockris, *Trans. Faraday Soc.*, **55**, 1586 (1959).
5. A. Hickling and D. Taylor, *ibid.*, **44**, 262 (1948).
6. R. S. Cooper and J. H. Bartlett, *This Journal*, **105**, 109 (1958).
7. F. H. Giles and J. H. Bartlett, *ibid.*, **108**, 266 (1961).
8. M. Pourbaix, "Atlas of Electrochemical Equilibria in Aqueous Solutions," p. 384, Pergamon Press, New York (1966).
9. A. I. Vogel, "A Textbook of Quantitative Inorganic Analysis Including Elementary Instrumental Analysis," 3rd ed., John Wiley & Sons, Inc., New York (1961).
10. H. Lal and H. R. Thirsk, *J. Chem. Soc.*, **1953**, 2638.
11. U. R. Evans, "Corrosion and Oxidation of Metals," Arnold, London (1960).
12. I. A. Menzies and A. F. Averill, *Electrochim. Acta*, **13**, 807 (1968).
13. M. E. Straumanis and Y. Wang, *Corrosion*, **22**, 132 (1966).
14. M. E. Straumanis, J. L. Reed, and W. J. James, *This Journal*, **114**, 885 (1967).
15. M. E. Straumanis and B. K. Bhatia, *ibid.*, **110**, 357 (1963).
16. W. J. James, M. E. Straumanis, and J. W. Johnson, *Corrosion*, **23**, 15 (1967).
17. W. U. Malik, S. M. F. Rahman, and S. A. Ali, *Z. anorg. u. allgem. Chem.*, **299**, 322 (1959).
18. W. U. Malik, S. M. F. Rahman, and S. A. Ali, *ibid.*, **301**, 220 (1959).
19. G. Just and R. Landsberg, *Electrochim. Acta*, **9**, 817 (1964).
20. R. S. Cooper, *This Journal*, **103**, 307 (1956).
21. D. Miller, *J. Phys. Chem.*, **13**, 256 (1909).
22. H. W. Gillett, *ibid.*, **13**, 332 (1909).
23. A. G. Arend, *Paint Tech.*, **13**, 265 (1948).
24. Int. Crit. Tables 4, 222, McGraw-Hill (1928).
25. W. J. Muller and L. Holleck, *Monatsh. Chem.*, **52**, 409 (1929).

Comparative Activity of (111), (100), (110), and Polycrystalline Platinum Electrodes in H_2-Saturated 1M H_2SO_4 under Potentiostatic Control

Sigmund Schuldiner,* Murray Rosen,*[1] and David R. Flinn*[1]

Electrochemistry Branch, Naval Research Laboratory, Washington, D. C. 20390

ABSTRACT

Potentiostatic measurements of the three principle faces of oriented single Pt crystals and polycrystalline Pt showed some interesting comparisons. True areas are based on Pt atom densities, and under the electrochemical treatment used, no changes in these areas were found once the initial surface cleaning was completed. The hydrogen overvoltage was independent of crystal orientation or other metallurgical factors; however, the passivation of the hydrogen oxidation reaction and the oxygen generation reactions were different for each single crystal orientation with a large difference between these faces and a polycrystalline bead electrode. Steady-state relations between potential and amounts of associated H atoms and number of sites available for coverage with O atoms were determined also. These steady-state values are generally less than the comparative amounts found under transient conditions. Oxygen evolution on the Pt faces was not observed below a potential of 1.8V. It appears that grain boundaries, stress, and impurity inclusions may have more effect in determining the catalytic activity for some reactions than does the actual atomic density or geometry of Pt atoms.

Although there have been numerous investigations of the hydrogen reaction on polycrystalline Pt electrodes and of the potentiostatic behavior of Pt in H_2-saturated solutions, our knowledge of the effects of the geometry of Pt atoms on such behavior is very limited. Using the voltage sweep method, Will (1) studied the relationship between hydrogen adsorption and potential on single Pt crystals of (111), (100), and (110) orientations.

Our approach was to conduct a comparative investigation of polycrystalline Pt with Pt single crystal orientations with respect to reactivity for steady-state hydrogen generation, hydrogen oxidation, and oxygen generation reactions. In addition, steady-state relations between surface coverage with potential were determined, both in the presence and absence of dermasorbed oxygen.

Experimental

The high-purity, gas-tight electrochemical system, the experimental conditions, and the method of measurement were the same as used in ref. (2). Three single crystal Pt electrodes with orientations (111), (100), and (110) were in the cell. A fourth Pt electrode, polycrystalline bead, similar to previous ones (2), was substituted for one of the single crystal electrodes to confirm that the experimental conditions

* Electrochemical Society Active Member.
[1] National Academy of Sciences-National Research Council Postdoctoral Research Associates at NRL.
Key words: overvoltage, adsorption, catalysis, atom geometry, dermasorption.

used for the single crystal electrodes duplicated the previous work.

The single crystal Pt electrodes were prepared and mounted in the following way. Three high-purity (99.999%, 3 pass electron beam zone refined) single crystals were welded to Pt wires and then were spark cut to the three principle faces (111), (100), and (110).[2] The faces were then electropolished in a melt consisting of equal weights of KCl and NaCl at 700°C in accordance with the procedure reported by Brouillet and Epelboin (3). After rechecking the orientation by x-ray diffraction, each crystal was mounted by placing a thin cylinder of virgin polyethylene (this polyethylene gave a water-clear melt) snugly against the sides of each crystal. A tightly fitting heat-shrinkable TFE Teflon tube was then placed over the polyethylene sleeve. Upon heating with an electric heat gun the polyethylene melted and the Teflon tube shrunk. Upon cooling the single crystal is tightly enclosed in a Teflon-polyethylene envelope. During heating some molten polyethylene covered part of the oriented Pt face. This polyethylene was largely removed by carefully cutting with a razor around the edge of the squeezed out polyethylene and carefully stripping the excess polyethylene from the Pt surface. Photomicrographs[3] showed that tiny particles of polyethylene remained on the surface; however, these were removed during the initial electrolysis as was shown by photomicrographs taken after such treatment. (A polyethylene particle is shown in the encircled area on Fig. 1a as a dark gray fragment. Similar fragments are apparent).

The Pt wire connected to the single crystal, which is covered by the Teflon tube, is sealed through a glass cap. Upon insertion of the electrode into the cell, the glass cap, which has a ¼ in. standard glass pipe connector, is connected to the cell via a Viton-A ring and screw clamp which gives a gas-tight seal.

The initial set of three oriented faces was carefully wiped with a fine soft paper and then cleaned with concentrated nitric acid and rinsed with triply distilled water. Upon close examination scratches were noted on these electrodes, and after the electrochemical measurements were made, photomicrographs showed many fine scratches on each crystal face. These crystal faces were re-electropolished, and after mounting great care was taken not to contact the exposed faces with anything but nitric acid, triply distilled water, and electrolyte. This careful treatment avoided scratches on the soft exposed Pt face. Potentiostatic measurements on each face were repeated after another polishing, and for the scratch-free surfaces, the results were essentially the same. However, the scratched surfaces showed some important variations which will be discussed.

The first measurements on the Pt bead (mounted in glass) were taken after the forming of the bead by melting the end of a Pt wire in a H_2/O_2 flame, cleaning in nitric acid, rinsing, and pre-electrolysis. To assure that the electropolishing procedure itself did not cause changes or leave a residue on the single crystal surfaces which could affect their electrochemical properties, a second set of potentiostatic measurements was made on the bead after electropolishing it under the same conditions used for the single crystals. The electropolished Pt bead, after the usual cleaning treatment, gave essentially the same results as were initially obtained before electropolishing.

All of the Pt electrodes had mirror bright surfaces, but as Fig. 1 shows they were by no means flat surfaces. Mechanical means of flattening the surface were avoided since it was felt that scratching or the inclusion of polishing agents could have strong effects. It seems obvious that atomically smooth surfaces are not feasible at the present time, and it is felt that the predominant orientation of surface atoms is influenced by the underlying Pt atoms of the given orientation.

True area (4) was calculated on the basis of a one-to-one correspondence between each Pt atom and O_{ad}. Since different crystal orientations were used, it was necessary to determine the number of Pt at./cm^2 for each face and bead. Atom densities for perfectly smooth electrodes of the (111), (100), and (110) orientations were calculated to be 1.5×10^{15}, 1.31×10^{15}, and 0.92×10^{15}, respectively, using 3.9231Å (5) as the lattice parameter. The atom density for the bead was assumed to be 1.31×10^{15} (2). On this basis and correcting for double layer charging (36 μC/cm^2), the number of μC/cm^2 for a 1 cm^2 true area electrode for each face and bead was calculated. The experimental true area of each electrode was then determined, and Table I shows areas of unscratched electrodes. All areas given in this paper are so-defined true areas.

Two types of electrochemical measurements were performed. The first was the type of potentiostatic measurement previously reported (2) for a bead electrode and gave the steady-state current density *vs.* potential relation for each electrode in H_2-saturated 1M H_2SO_4 under conditions of very rapid stirring with H_2 gas (> 1000 ml H_2/min).

The second type of measurement gave anodic charging curves taken by applying galvanostatic pulses (1.2-2 A/cm^2) after potentiostating the electrodes until steady state was reached. In this case steady state refers to no change in the number of coulombs of charge

[2] The orientation, spark cutting, and x-ray diffraction confirmation of the orientation was done by C. L. Vold, Metallurgy Division, Naval Research Laboratory.

[3] Photomicrographs of the Pt electrodes were made by A. C. Simon, Electrochemistry Branch, Naval Research Laboratory.

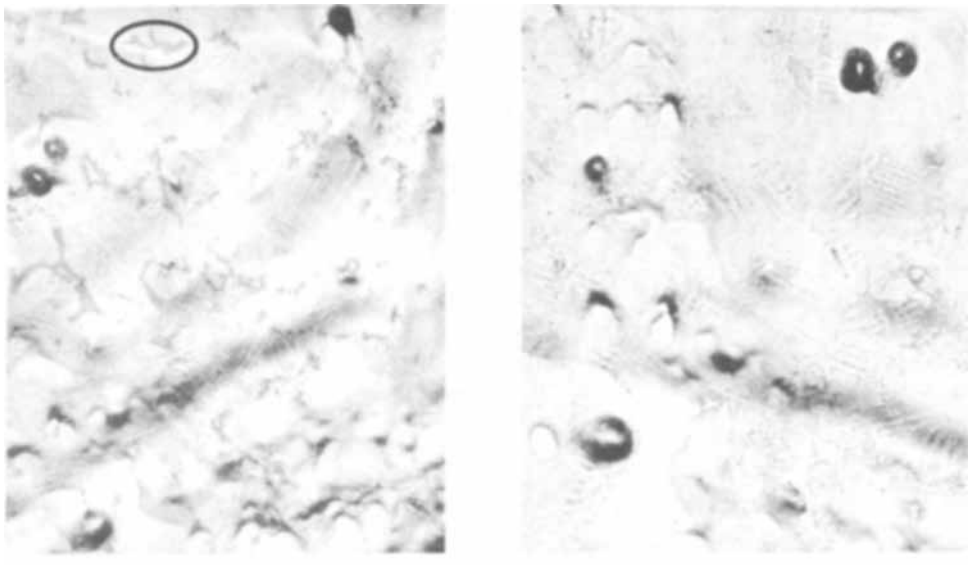

Fig. 1. Comparative photomicrographs of Pt (111) before (a, left, 100X) and after (b, right, 135X) electrolysis.

Table I. Pt electrode true areas

Electrode	$\mu C/cm^2$	Area,* cm^2
Bead	420	0.54 ± 0.01
Bead, electropolished	420	0.60 ± 0.01
(111), first electropolish	484	0.15 ± 0.01
(111), second electropolish	484	0.125 ± 0.01
(100), first electropolish	420	0.20 ± 0.01
(100), second electropolish	420	0.15 ± 0.01
(110), first electropolish	294	0.048 ± 0.001
(110), second electropolish	294	0.043 ± 0.006

$$* \text{ Area} = \frac{\text{current } (A) \times \mu\text{sec to form one monolayer of } O_{ad}}{(\mu C + 36)/cm^2}$$

required to oxidize sorbed H atoms and/or to saturate the surface with O_{ad}. The steady state obtained in the first type of measurements meant no change in current density with time. The times required in most cases to reach coulombic steady state was shorter than the time required to reach steady-state current densities. However, under conditions of initially high dermasorbed O content followed by a lowering of potential to a value that resulted in a large loss of dermasorbed O, overnight potentiostating was necessary. After steady state was reached, the high-speed switching arrangement previously reported (6) was used to switch from potentiostatic control to a galvanostatic anodic charging pulse. These measurements were carried out under initial electrode conditions of either no dermasorbed O (by first taking the potential to 0V for at least 5 min) or fully charged with dermasorbed O (by first taking the potential to 1.8V for at least 30 min). After the initial treatment, the electrode was potentiostated to a set value.

The determination of the amounts of sorbed H atoms oxidized and O atoms formed during galvanostatic anodic charging was done in the following way. Anodic charging curves applied at the H^+/H_2 equilibrium potential for each electrode were determined at the beginning and end of each set of measurements. The end of the hydrogen region and the length of the linear atomic oxygen adsorption, O_{ad}, region were determined in the standard way (4) by drawing a straight line through the linear O_{ad} region and finding the intercepts with straight lines drawn from the slope of the so-called double layer region (from about 0.5 to 0.9V) and from the linear extrapolation of the O_2 generation region starting at about 1.75V. Dropping a perpendicular line from the intercepts at the beginning and end of the O_{ad} linear region to the anodic charging curve gave potentials that were considered to be the end of the H oxidation region and the end of the O_{ad} formation region, respectively. The voltages determined in this way varied from 0.8 to 0.95V for the end of the H oxidation region and varied from 1.65 to 1.85V for the end of the O_{ad} formation region. The specific voltages for a given run were very reproducible, and the actual values were directly dependent on the actual current densities used in the anodic charging pulse. The voltages determined in this way were used to calculate the number of coulombs, q_H and q_O [after correcting for double layer charging (4)], of sorbed H and O_{ad} formation for each anodic charging curve for each electrode at the various potential settings. This method of determining the H and O regions differs from the procedure used in earlier work (7) where these regions were always determined by intercepts from the linearly extended O_{ad} region. Although the linear extrapolation method is basic in determining the area of the Pt electrodes (4) and is a reliable technique, under anodic potentiostatic control the H associated with the Pt is low at potentials above 0.3V and the linearity of the O_{ad} region decreases. Therefore, the difficulty of determining the length of the O_{ad} regions increases. Although a determination of coverage of O_{ad} is possible by the method used in ref. (7), we feel that the present technique is less subjective and better defines the method of determining surface coverage. Later in the paper data will be given which can be compared with the data given in Fig. 2 of ref. (7). Such a comparison will show fairly good correspondence for the two methods. Although our measurements do not assure an absolute relation of amounts of H and O_{ad} and potential, the values obtained do give a valid comparison of the four different Pt electrodes. The temperature was 25° ± 1°C, and all measurements were made in H_2-saturated (1 atm) 1M H_2SO_4.

Results and Discussion

Area determinations.—Will (1) concluded from his experimental results that the areas (roughness factors) of his Pt single crystal faces increased with increased number of potential sweeps. Recently, Biegler (8) reviewed the problem of area increases on polycrystalline Pt and also concluded from his own work that there are significant increases in electrode area under repetitive, cyclic treatment that involved fast reduction of surface oxide and that smoothening can occur under slow reduction of oxide. Our own experience with Pt electrodes over a period of many years showed that under our experimental conditions no significant changes in electrode areas were found either in the pre-electrolysis treatment or in use of polycrystalline electrodes over long periods of time. Taking into consideration the findings of Will and Biegler, we decided to investigate carefully the problem of surface roughening and to determine if recrystallization or significant changes in surface atom arrangement occurred.

We point out that our electrodes were not subjected to rapid repetitive, cyclic treatment and that the only rapid potential changes experienced by the electrodes were during anodic charging and switching. Figure 1a is a photomicrograph (100X) of the (111) Pt face electrode. This picture was taken immediately after electropolishing and placing the electrode in the Teflon-polyethylene mount. The encircled area shows a typical remnant of the polyethylene film stripped from the surface during electrode mounting. Many other similarly shaded and appearing particles of polyethylene can be observed on the surface. After cleaning the electrodes and placing them in the cell, the equilibrium hydrogen potential was obtained on each electrode before any electrolysis was applied. Upon applying an anodic charging pulse to each electrode, it was observed that the hydrogen regions were very short and indistinct and that the oxygen regions were somewhat rounded. After applying about 10 pulses, the hydrogen region lengthened and the oxygen region became less rounded. Each electrode was then potentiostated to 1.5V for a period of at least 16 hr. After this time the anodic charging curves for each face showed a normally clean linear oxygen region. Significant increases in area were observed over a period of several days. The largest change was experienced in one run with the (110) electrode which underwent a change from 0.0264 to 0.047 cm^2 over a period of one week. After these inital area changes frequent area determinations showed that each electrode experienced no further significant change.

Figure 1b is a photomicrograph (135X) of the same electrode shown in Fig. 1a after that electrode (111) was in the cell for a period of two months. During that time the electrode underwent potentiostatic polarization ranging from −0.04 to 2.1V for eight days and was subjected to potentiostatic control and anodic charging during a period of four more days. Figure 1b shows the complete removal of the bits of polyethylene and further shows no significant change in the Pt surface. The same dendritic areas, pits, terraces, and structure are apparent in both photos.

Our interpretation of the initial area changes and shape of the anodic charging curves is that the polyethylene residue in contact with the electrodes is being

removed primarily by being scrubbed off by the formation of oxygen. Some oxidation of the polyethylene in close contact with the surface may occur. It may take quite a bit of time (possibly as long as a week) to remove the last trace of polyethylene. Once this initial cleaning of the surface occurs, photomicrographic evidence and electrochemical area determinations show that actual roughening or structure changes on the electrode surface do not occur under the conditions of our experiments. Our findings do not mean that roughening could not occur under Biegler's (8) or Will's (1) experimental conditions. However, there is a possibility that Will's polishing of the single crystal faces with alumina powder did result in an incorporation of some alumina in the surface layer. The two hundred or more sweeps required to get a reproducible surface may be related to the removal of some, if not all, of the alumina by a scrubbing action by hydrogen and oxygen.

Hydrogen overvoltage.—Hydrogen overvoltage data are shown in Fig. 2 and 3. The interesting feature of these curves is that there is no significant difference between the bead and (111), (100), and (110) faces. The Tafel b slope is -0.025, and the i_o for the equilibrium hydrogen/hydrogen ion exchange is 1.9 mA/cm^2. The assumed atomic densities of the four electrodes in terms of atoms per square centimeter are: 1.5 x 10^{15} for (111), 1.31 x 10^{15} for (100), 0.92 x 10^{15} for (110), and 1.31 x 10^{15} for the polycrystalline bead. Hence, since the calculated true areas are based on these numbers of Pt atoms per square centimeter, one can conclude that Pt atom density and spacing do not determine the kinetics. It may be argued that diffusion is the rate-controlling process; however the true areas include a roughness factor, and since the geometric area is the important consideration in diffusion, it would be necessary to show that the roughness factor for all the electrodes are essentially the same. The method we used to mount the single crystals left an uneven rim of polyethylene around the edge of the electrode so that accurate determination of the geometric area was difficult. However, several determinations of geometric area by use of a Bausch and Lomb Measuring Magnifier showed differences in roughness factor. For example, for the (110) face the roughness factor after the first electropolishing was 2.1, whereas after the second electropolishing it was 1.4. However, the hydrogen overvoltage results, based on true area, were essentially the same.

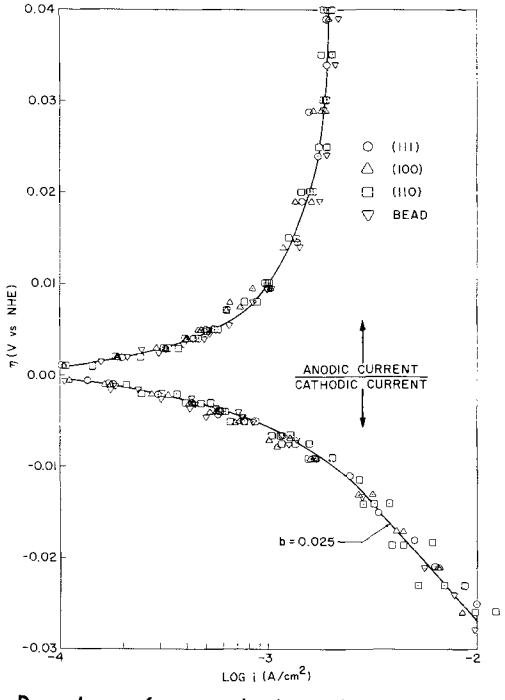

Fig. 2. Dependence of current density on hydrogen overvoltage

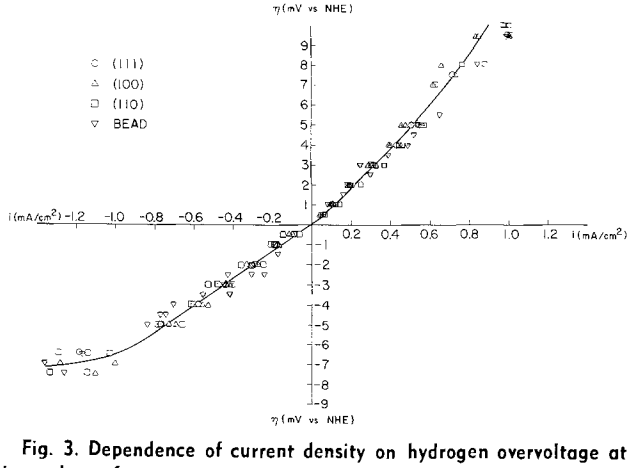

Fig. 3. Dependence of current density on hydrogen overvoltage at low values of η.

The data in Fig. 3 satisfactorily compares with data previously obtained [(9) Fig. 4], however, the Fig. 3 data are on a more expanded potential scale. This expansion clearly illustrates that for $\eta > 0.5$ mV the experimental data points do not fit on an extrapolated linear curve from -6 mV through zero. This deviation shows that the amount of adsorbed H which is in rapid equilibrium with H^+ and H_2 dissolved in solution is very small.

Potentiostatic anodic current density vs. voltage relations.—Figures 4-6 show the potentiostatic anodic current density *vs.* voltage relations for the (111), (100), and (110) faces. Figures 7 and 8 compare the three crystal faces with previous results (2) for a polycrystalline bead electrode for the increasing and decreasing potential sequences, respectively. The former bead electrode results were checked with a new bead electrode, both before and after the same electropolishing used on the single crystal faces. The present results confirmed the previously reported values and further demonstrated that effects due to electropolishing and differences in solution composition were negligible. In addition, Fig. 9 and 10 compare three lightly scratched (by rubbing with soft tissue paper) principle faces and a Pt bead electrode.

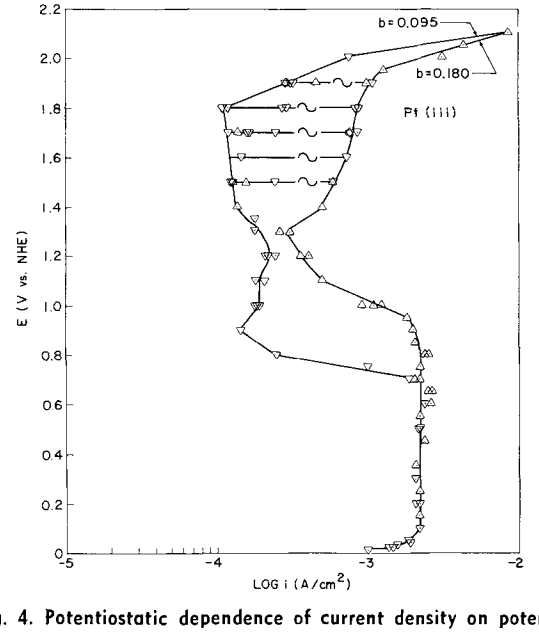

Fig. 4. Potentiostatic dependence of current density on potential for Pt (111): △ increasing potential sequence; ▽ decreasing potential sequence; ~ cyclic behavior, frequency about 20 min.

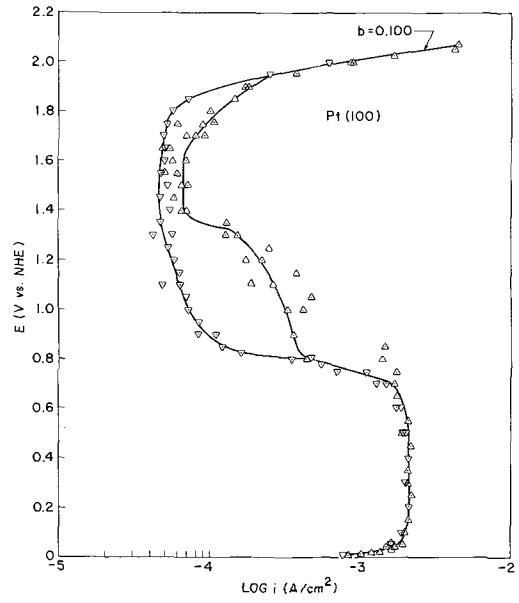

Fig. 5. Potentiostatic dependence of current density on potential for Pt (100): △ increasing potential sequence; ▽ decreasing potential sequence.

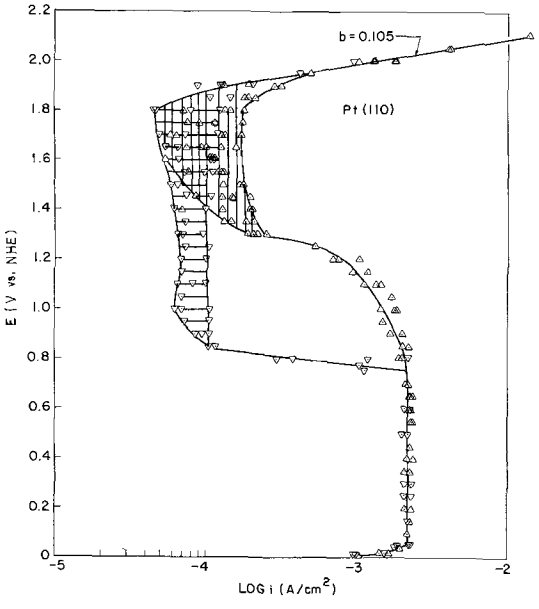

Fig. 6. Potentiostatic dependence of current density on potential for Pt (110): △ increasing potential sequence; ▽ decreasing potential sequence.

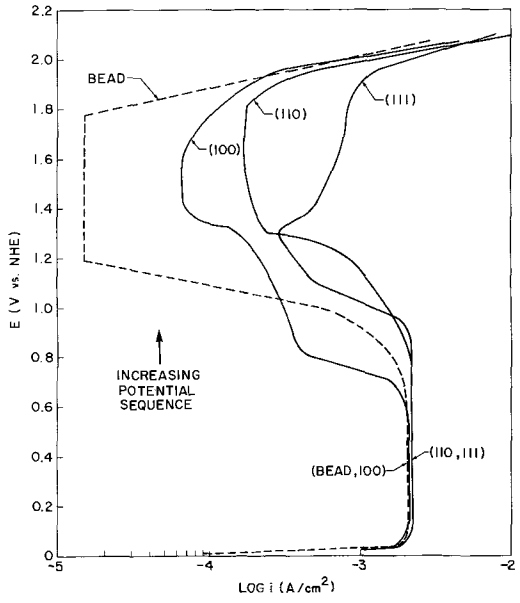

Fig. 7. Comparative potentiostatic relations for increasing potential sequence. Curves are lines shown in Fig. 4-6.

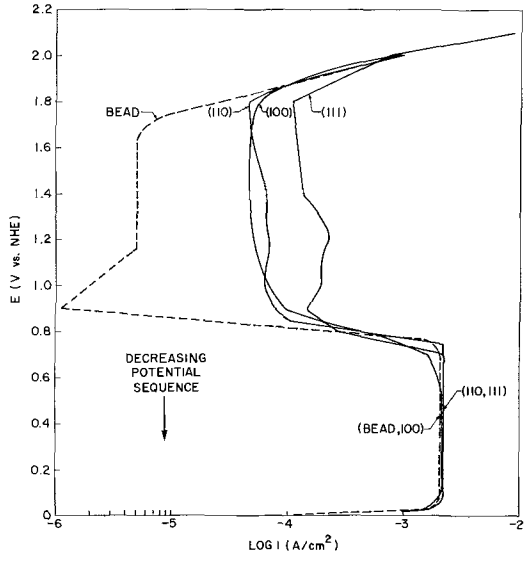

Fig. 8. Comparative potentiostatic relations for decreasing potential sequence. Curves are lines shown in Fig. 4-6.

The data in Fig. 4-10 show that the limiting H_2 oxidation reaction is esssentially independent of crystal orientation. Small differences are noticeable for the bead and the (100) face which had about 10% lower limiting current densities than the (111) and (110) faces (see Fig. 7 and 8). Small differences can also be seen for the lightly scratched faces (Fig. 9 and 10). These differences are just about within the limits of the experimental error (about 10%), and even though these differences were consistent after two electropolishings, they are too uncertain to be considered significant. The fact that the scratched electrodes which would, of course, have higher roughness factors than the smooth electrodes gave virtually the same limiting current densities further demonstrates that the limiting current density is not primarily diffusion-controlled. This conclusion holds because the data in Fig. 4-10 are plotted on the basis of true area (4) which means that if the data were plotted on the basis of geometric area, there would be significant differences between the scratched and unscratched Pt faces.

The really significant differences in the three principle faces and the bead are in the passive (decreased rate of H_2 oxidation) region and the transpassive (oxygen evolution) region. Figure 7 shows that the onset of passivity and the shape of the passive region is very much dependent on the orientation. For example, the potential at which passivity commences increases in the order (100), bead, (110) and (111), whereas for the decreasing potential sequence, Fig. 8, the activation (increased rate of H_2 oxidation) of each electrode has little dependence on orientation. The differences for the scratched electrodes (Fig. 9 and 10) are significantly less.

The differences in behavior shown in the shapes of the passive regions and the Tafel slopes of the oxygen generation region are at the same time remarkable and unexplicable on the basis of Pt atom geometry. Figure 4 shows that for the (111) face at potentials between 1.4 and 1.9V the current density, for both the increasing and decreasing potential sequences, is cyclic (at about 20-min intervals) over one order of magnitude. At and below 1.4V, dermasorbed oxygen

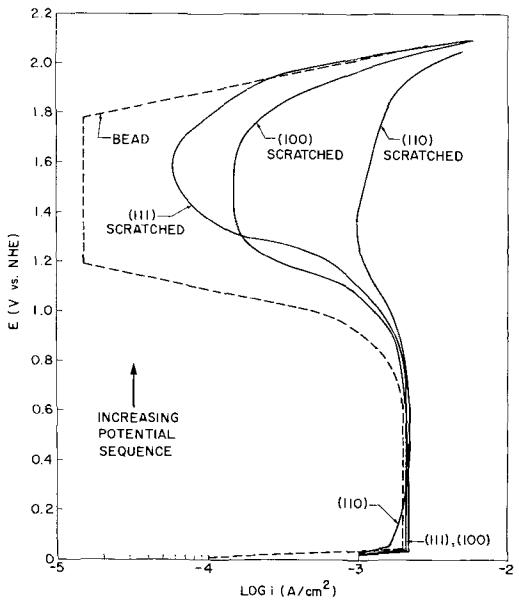

Fig. 9. Comparative potentiostatic relations for scratched single crystals. Increasing potential sequence. Curves represent maximum current densities. Bead electrode is unscratched.

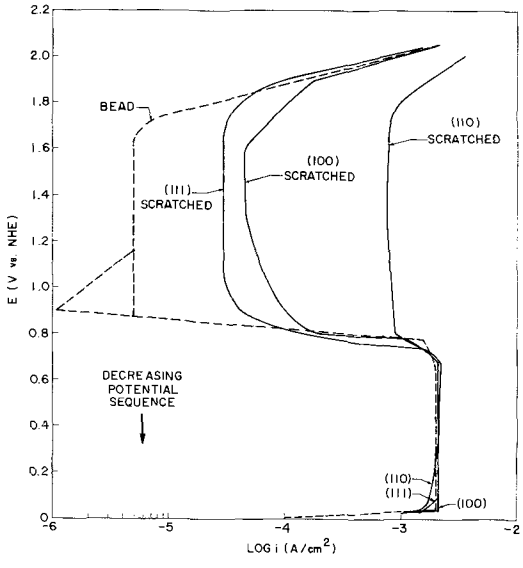

Fig. 10. Comparative potentiostatic relations for scratched single crystals. Decreasing potential sequence. Curves represent minimum current densities. Bead electrode is unscratched.

(decreasing potential sequence data) reduces the rate of hydrogen oxidation until 0.7V where the dermasorbed oxygen is removed. The Tafel slope of the oxygen evolution reaction is 0.180 for the increasing potential sequence and 0.095V for decreasing potentials. The Tafel slope for both the increasing and decreasing potential sequence for the bead was 0.13 (2).

The (100) face, Fig. 5, shows no cyclic behavior at potentials above 1.4V, but the differences in the rates of oxidation between 1.4 to about 1.7V is small. Dermasorbed oxygen appears to only have a significant effect from 1.4 to 0.8V. For this electrode, the O_2 evolution Tafel b value is 0.100 for both the increasing and decreasing potential sequence.

For the (110) face, Fig. 6, there is a great deal of overlap and scatter of points from 1.4 to 1.9V for the increasing and decreasing potential sequence. Below 1.4V the separation due to dermasorbed oxygen is apparent down to 0.75V. The O_2 evolution Tafel b value for both the increasing and decreasing potential sequence is 0.105.

Figures 7 and 8 show that the passivation of the oriented single crystals are all significantly less than that of the bead, but there is no order as far as Pt atom densities are concerned. All that one can say is that the presence of grain boundaries or stress in the beads or differences in impurities in the bead and the single crystals greatly enhance passivation. Figures 9 and 10 for the scratched oriented crystals also show enhanced activity over the bead. In this case the (110) scratched face is the least passivated of all the electrodes investigated. For this electrode the change in activity above 0.7V was small for both the increasing and decreasing potential sequences. In fact, the presence of dermasorbed oxygen (Fig. 10) has only a minor effect on the activity of this electrode.

Another interesting observation that was made during the course of the potentiostatic measurements on the unscratched faces was the potential at which visible oxygen evolution occurred. Each of the faces was mirror bright so that under bright illumination, if gas evolution occurred, the formation of extremely small bubbles would be obvious. On the three oriented faces it was noticed that bubbles of oxygen were not observed unless the electrodes were potentiostated at 1.8V or above. Figures 4 to 8 showed that at potentials from 1.4 to 1.8V, the current densities for each crystal face did not vary greatly, and at potentials down to 0.7V the current densities generally increased. In addition, Fig. 7 shows that at the three faces the current densities varied considerably at, and immediately below, 1.8V. If the net reaction were an electrochemical generation of O_2, the potential at which this reaction occurs should be detected easily, especially since measurements at potentials above 0.7V took anywhere from an hour to hours to reach steady state. The fact that no oxygen bubbles were evident below 1.8V shows that the net reaction below this value was not the formation of O_2.

This conclusion means that there must have been some interaction of molecular hydrogen with whatever current-consuming reaction occurred. The following possibilities are apparent:

$$H_2 \rightarrow 2H^+ + 2e \quad [I]$$

$$2H_2O + Pt \rightarrow 4H^+ + Pt - O_2 + 4e \quad [IIa]$$

$$Pt - O_2 + 2H_2 \rightarrow Pt + 2H_2O \quad [IIb]$$

$$H_2O + Pt \rightarrow 2H^+ + Pt - O + 2e \quad [IIIa]$$

$$Pt - O + H_2 \rightarrow Pt + H_2O \quad [IIIb]$$

$$H_2O + Pt \rightarrow H^+ + Pt - OH + e \quad [IVa]$$

$$2Pt - OH + H_2 \rightarrow 2H_2O + 2Pt \quad [IVb]$$

Other oxygenated species can be visualized also.

The important conclusion that one can derive from the observation that O_2 bubbles are not formed until a potential of 1.8V is reached is that for the oriented single crystals, and as was previously concluded for a heterogenous Pt electrode (2, 7, 10), H_2 in solution reacts with oxygen or oxygenated products of water in the passive region. Only when the rate of oxygen generation (1.8V) exceeds the rate of the interaction of H_2 with the oxygenated species is the net reaction the formation of O_2. This conclusion does not, of course, mean that oxygenated products of water may not exist on the surface of Pt (or O be dermasorbed in Pt) in the passive region below 1.8V, but it does imply that below 1.8V saturation of the surface with oxygenated species of water is infeasible. In addition, support is given to the previously reported conclusion from this laboratory (2, 7, 10) that the cause of the initiation of passivation at 0.7V on a Pt bead is not due to surface coverage with oxygen or an oxygenated product of water, but rather by anion adsorption. As the potential is increased above the value where passivation is initiated, the amount of oxygen or oxygenated products of water is increased, but sulfate ions also play an important role. In summary, the fact that a high voltage of 1.8 is required before visible O_2 evolution occurs is strong evidence that under steady-state conditions, the net accumulation of water oxida-

tion products on the Pt surface is strongly restricted both by the interaction with H_2 and by the presence of sulfate ions.

Relation between potential and amount of associated H atoms.—Figure 11 shows the relationships obtained for the dependence between the amount of hydrogen, q_H, oxidized by a high current density anodic pulse and the potentiostated steady-state potential for all electrodes. Figure 12 compares the four electrodes on a normalized scale, $q_H/q_{H,E=0}$. Since on the normalized scale, the q_H of each electrode is compared to its q_H at the H^+/H_2 equilibrium, the amount of coulombs is related to the number of Pt atoms per square centimeter for each electrode since the ratio q_H/q_O was about the same for all three faces. Thus the atom densities for the three faces and for the bead are normalized, and the curves in Fig. 12 show the fraction of the number of the equilibrium associated H atoms at each potential. On the normalized scale, the differences between the four electrodes are small. Only at potentials of 0.1V and below does there appear to be a significant difference between the (111) and (100) compared to the (110) and bead. However, Fig. 11 shows that on the defined (4) true area scale, there are considerable differences in the amounts of H associated with each electrode. It is interesting that Fig. 11 shows that under steady-state conditions small amounts of hydrogen are associated wtih Pt at potentials above 0.35V.

The dashed line for the bead data in Fig. 11 is the q_H *vs.* E relation for a single anodic charging curve from the H^+/H_2 equilibrium. This dashed curve shows that transient and potentiostatic H content do not have the same dependence on potential. The steady-state amount of H associated with Pt at any potential above 0V is always less than the high current density transient values.

Will (1), using a cyclic voltametric technique, obtained a normalized $q_H/q_{H,E=0}$ separation between the three faces in the order (100) > (111) > (110). Our comparative data (Fig. 12) gives (100) = (111) > (110) = bead.

Relation between potential and amount of O atoms formed by anodic charging.—A series of anodic charging curves typical for any of the electrodes is represented in Fig. 13 by a (100) electrode. Figure 14 gives the q_O *vs.* potential data for all electrodes and Fig. 15 gives the normalized $q_O/q_{O,E=0}$ data for all electrodes. As brought out in the experimental section of this paper, q_O is the number of coulombs per square centimeter of oxygen atoms formed on the electrode surface with a high current density galvanostatic pulse under the given potentiostatic conditions.

All of the open symbols signify that the electrode was taken to open circuit (zero volt) for at least 5 min before the given potential was applied. The closed symbols signify that the electrode was taken to 1.8V for at least 30 min. Thus, for the open symbols, the initial electrode condition was the equilibrium hydrogen electrode free of dermasorbed oxygen, whereas

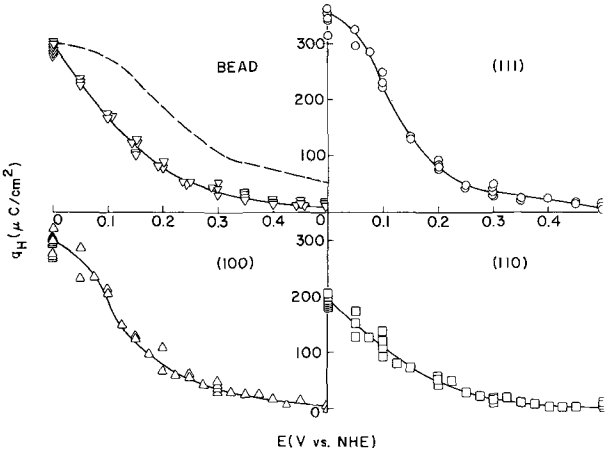

Fig. 11. Steady-state amounts of H atoms, q_H, associated with each Pt electrode at given potentials. See text for meaning of dashed line.

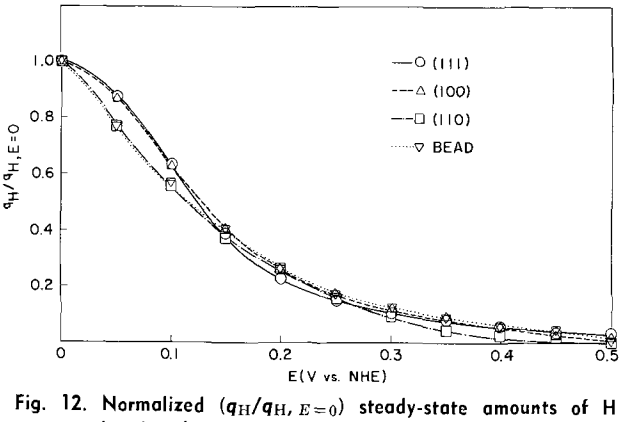

Fig. 12. Normalized ($q_H/q_{H,E=0}$) steady-state amounts of H atoms associated with each Pt electrode at given potentials.

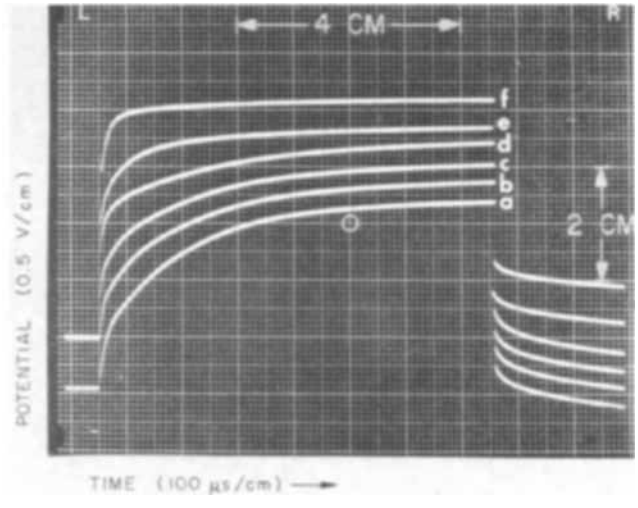

Fig. 13. Anodic charging curves for Pt (100) from set potentiostated values. i = 1.824 A/cm^2

a, 0.3V } potentiostated for
b, 0.5V } 5 min at each
c, 0.7V } potential

d, 0.9V } Starting at H^+/H_2
e, 1.1V } equilibrium followed
f, 1.3V } by potentiostating for 15 min at each potential

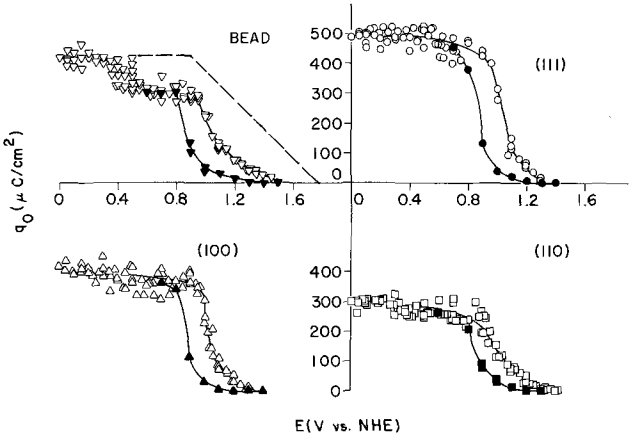

Fig. 14. Amounts of O atoms, q_O, formed on each Pt electrode when an anodic galvanostatic pulse is applied at given steady-state potentials. Open symbols are values for initial potentiostating at 0V. Closed symbols are values for initial potentiostating at 1.8V. See text for meaning of dashed line.

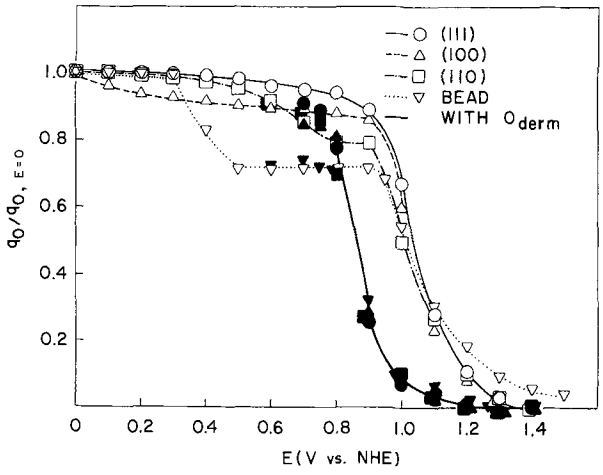

Fig. 15. Normalized ($q_O/q_{O,E=0}$) amounts of O atoms formed on each Pt electrode when an anodic galvanostatic pulse is applied at given steady-state potentials. Open symbols are values for initial potentiostating at 0V. Closed symbols are values for initial potentiostating at 1.8V.

for the closed symbols the initial electrode condition was saturation with dermasorbed oxygen.

The data in Fig. 14 and 15 show that for all of the oriented faces, there is a relatively small decrease in the amount of O atoms required to form a monolayer with the anodic charging pulse from zero to 0.9V. On the other hand, the data for the bead is similar to previously reported data (7) and shows a significant decrease in the required amount of O to form a monolayer at 0.4V, followed by a plateau to 0.9V and then a sharp drop similar to the oriented faces. The hysteresis (closed symbols) is believed to be caused by dermasorbed oxygen. The data in Fig. 14 and 15 show that dermasorbed oxygen is virtually completely removed at a potential of 0.8V. About 16 hr of potentiostating at 0.8V (after saturating the electrode at 1.8V with O) was required before the steady-state q_O was found for all electrodes. This q_O at 0.8V, as were closed symbol values at lower potentials, corresponded to the open symbol, initially dermasorbed O-free cases.

The dashed line for the bead in Fig. 14 shows the linear q_O *vs.* E relation for a single anodic charging curve beginning at the H^+/H_2 equilibrium. The amount of O_{ad} which can be formed by an anodic pulse starting at a given E above 0.5V is always less than the O_{ad} formed under high current density transient conditions starting at zero. The rapid decrease in the deposited quantity of O_{ad} at E above 0.9V supports the conclusion that sulfate ion adsorption does decrease the number of sites available for O_{ad}.

Because under steady-state potentiostatic conditions H_2 will react with oxygen and/or oxygenated water species, the large decreases in the amounts of O required to form a monolayer under galvanostatic charging are believed to be due to anion (sulfate ion) adsorption (2, 7). Further, from kinetic considerations (2), it is felt that anion adsorption not only initiates passivation, but is the major cause of the rapid decrease in the rate of H_2 oxidation up to at least 1.2V. The data in Fig. 7 and 8 correspond sufficiently well with the sharp drop at 0.9V to show a real relation between increased surface coverage and decreased rate of H_2 oxidation. The most pronounced difference in the four electrodes is the comparison of the bead to the three oriented faces. Both the drop in q_O at 0.4V and the much lower minimum current densities shown in Fig. 7 and 8 indicate that such differences as grain boundaries, stress, or differences in impurities in the Pt play an important role both in anion adsorption and passivation. The differences in the three faces are too small to be highly significant, but several trends are apparent. There is a sharper decrease in q_O at potentials in excess of 0.4V for the (110) face (Fig. 15), and at potentials from 0.7 to 0.9V, its behavior is intermediate to the (111), (100), and the bead. The q_O for the (100) face drops significantly at 0.1V but then changes very little until 0.9V.

In summary, differences in behavior of the various orientations are apparent, but they are small and follow no logical sequence, such as atom density or spacing. The really significant differences are those between the oriented single crystal faces and the polycrystalline bead. This difference indicates that factors such as grain boundaries, stress, and possible variations in impurities in the Pt can play an important role in some adsorption phenomena and may influence the catalytic activity of some reactions. Another possible variation may be differences in the potential of zero charge between the bead and single crystal faces.

The open-circuit rate of reaction of a rapidly generated monolayer of Pt-O formed by an anodic galvanostatic charging pulse with H_2 in solution (11) was determined in the hope that single crystals, which would be in an essentially ideally annealed state, would differ significantly from a bead electrode which would contain strains. The rates of the $Pt - O_{ad} + H_2$ reaction for all four electrodes varied from about 1 to 5 mA/cm^2. These differences were random and were independent of orientation or polycrystallinity. Actually, previous work (11) with bead electrodes gave rates which ranged both lower or higher than these values, so that no particular relation between the metallurgical state or single crystal orientation of Pt and the rate of the reaction of $Pt - O + H_2$ was obtained.

Conclusions

Figure 16 shows photomicrographs at magnification of 325X of (111), (100), and (110) faces after prolonged electrochemical measurements. These photomicrographs show no particular metallurgical changes on the electrode surface as compared to those taken before electrochemical treatment (see Fig. 1 also). The present study has shown that there are areas of marked differences in electrochemical behavior of single crystal orientation as compared with a polycrystalline electrode, and that for some reactions (*i.e.*, hydrogen overvoltages below 0.7V) the effects of metallurgical fac-

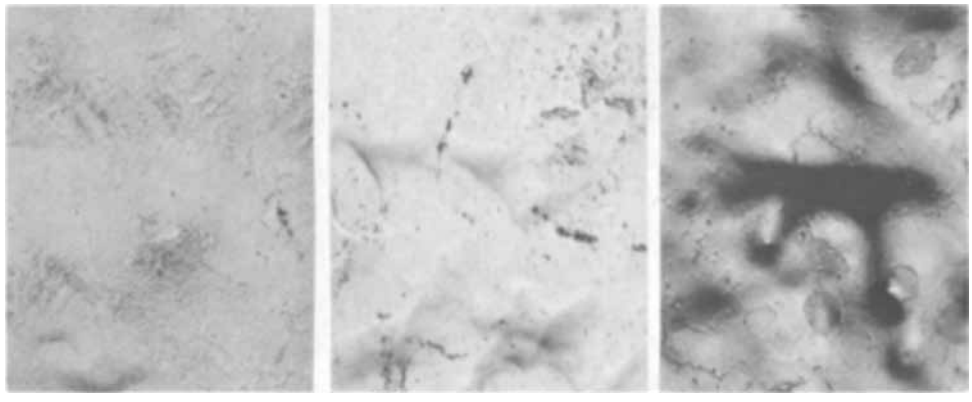

Fig. 16. Photomicrographs of (a) (left) Pt (111), (b) (center) Pt (100), and (c) (right) Pt (110) after electrolysis (325X).

tors are minor. Changes in electrode area or in character of the electrode surfaces were not found. Undoubtedly an improved technique for polishing the electrode to give orientations that approach atomic smoothness would be desirable as would observations of surface atomic arrangement by such techniques as LEED. It is apparent that grain boundaries, stress, and impurity inclusions in the electrode may be of much more importance in determining catalytic activity for some reactions than is the actual atomic density or geometry of platinum.

Surface defects on oriented single crystals caused by scratching had marked effects on the passivation of Pt electrodes for hydrogen oxidation starting at about 0.7V. Comparisons with a polycrystalline bead showed large differences which were most likely caused by grain boundaries, stress, and possibly metallic impurities. It is believed that the passivity behavior is due to anion (sulfate ion) adsorption and that the various defects somehow influence this factor.

The primary conclusion that this investigation has led to is that there is no simple correlation between atomic geometry and electrode behavior. Investigations of other more complex electrochemical reactions and better definition and control of metallurgical factors are required before generalizations concerning atomic geometry should be made.

Manuscript submitted Nov. 25, 1969; revised manuscript received May 20, 1970.

Any discussion of this paper will appear in a Discussion Section to be published in the June 1971 JOURNAL.

REFERENCES

1. F. G. Will, *This Journal*, **112**, 451 (1965).
2. S. Schuldiner, *ibid.*, **115**, 362 (1968).
3. P. Brouillet and I. Epelboin, *Rev. Met.*, **51**, 693 (1954).
4. S. Schuldiner and R. M. Roe, *This Journal*, **110**, 332 (1963); M. Rosen and S. Schuldiner, *ibid.*, **117**, 35 (1970).
5. R. W. G. Wyckoff, "Crystal Structures," 2nd ed., Vol. I, p. 10, Interscience Publishers, New York (1963).
6. T. B. Warner and S. Schuldiner, *This Journal*, **114**, 359 (1967).
7. S. Schuldiner, *ibid.*, **115**, 897 (1968).
8. T. Biegler, *ibid.*, **116**, 1131 (1969).
9. S. Schuldiner, *ibid.*, **106**, 891 (1959).
10. S. Schuldiner, *ibid.*, **116**, 767 (1969).
11. S. Schuldiner and T. B. Warner, *ibid.*, **112**, 212 (1965); T. B. Warner, S. Schuldiner, and B. J. Piersma, *ibid.*, **114**, 1120 (1967).

Electrochemical Oxidation of Guanine at the Pyrolytic Graphite Electrode

Glenn Dryhurst and Gerald F. Pace[1]

Department of Chemistry, The University of Oklahoma, Norman, Oklahoma 73069

ABSTRACT

The electrochemical oxidation of guanine at the pyrolytic graphite electrode was investigated by linear and cyclic scan voltammetry between pH 0-12.5 and by controlled electrode potential electrolysis in aqueous 1M acetic acid solution. Guanine is oxidized by an initial $2e/2H^+$ potential determining attack at the —N(7) = C(8)— double bond followed by a further $2e/2H^+$ oxidation of the —C(4) = C(5)— double bond to give 2-amino-6,8-dioxypurine-4,5-diol which, being unstable, undergoes further reaction by two routes: (*a*) further electrochemical oxidation to parabanic acid, guanidine, and carbon dioxide; and (*b*) hydrolysis to oxalyl guanidine and carbon dioxide. The exact nature of intermediate species in the electro-oxidation of guanine and uric acid were more thoroughly established by extensive use of fast sweep cyclic voltammetry. In particular it appears that in ammonia buffers at moderately high pH, the intermediate is a 4,5-diamine rather than a 4,5-diol.

Guanine (2-amino-6-oxypurine) is one of the two principal purines found in nucleic acids and as such is involved in many biological processes. Previous work has indicated a similarity between the heterogeneous electrochemical and enzymatic oxidation of naturally occurring purines such as adenine or uric acid (1, 2), although this parallelism does not appear to extend to purines with exocyclic sulfur atoms (3, 4). Nevertheless, the observed electrochemistry of these latter compounds might aid in interpreting the very incompletely understood biological oxidation. Fast scan cyclic voltammetry of several nonsulfur-containing purines has indicated that a general mechanism might be operative involving formation of a common ultimate primary electrochemical product which has been postulated to be a dicarbonium ion or a 4,5-diol (5). However, recent results on some methylated xanthines (6) which will be published shortly indicates that if the N-7 position is methylated, then no intermediate comparable to those observed for other purines can be detected or is much smaller than for other compounds. Faradaic n values also support this idea. In view of these latter findings and the importance of guanine in biological systems, it was felt that the electrochemical oxidation mechanism for this compound should be elucidated in detail rather than arbitrarily assuming that its oxidation proceeded by a route essentially identical to uric acid. A further reason for studying guanine was that if parabanic acid was an electrochemical product, then as a result of the effective labeling of the pyrimidine ring by the 2-amino group, it should be possible to assign correctly the ring origin of this acid which was not possible with adenine and uric acid.

Many of the biological and chemical reactions of purines are presented in the reviews of Lister (7) and Robins (8). Little, however, appears to be known of the mechanism of biological oxidation of guanine. Generally, biological oxidation processes are characterized only in terms of the major or most easily detected products. In many animals guanine is converted

[1] Present address: Continental Oil Company, Ponca City, Oklahoma.

Key words: guanine, electro-oxidation, 2-amino-6-oxypurine, bioelectrochemistry, pyrolytic graphite.

to uric acid and allantoin (9) although in xanthinuric man, guanine ingested as yeast RNA or as 3′-guanylic acid appears to be converted primarily to xanthine (10). Guanine is oxidized only slowly in the presence of very large excesses of xanthine oxidase to uric acid. Wyngaarden (11) has suggested that this process might be brought about by traces of guanase present in the xanthine oxidase. In rat liver, guanine is converted to hypoxanthine (12). Photodynamic inactivation of DNA on irradiation with visible light in the presence of the dye lumichrome is due to breakdown of guanine (13). Using tracer techniques, the photodynamic degradation of guanine involved formation primarily of guanidine and parabanic acid. Urea has also been detected as a photo-oxidation product (14). Chemical oxidation of guanine by MnO_2 in aqueous suspension at 100° gave guanidine and urea (15).

The study reported here of the electrochemical oxidation of guanine at controlled electrode potential at the pyrolytic graphite electrode (PGE) indicates a mechanism whereby guanine is oxidized in a primary 4e process to give an unstable compound which has been characterized as 2-amino-6, 8-dioxypurine-4, 5-diol or -4, 5-diamine in ammonia containing backgrounds [equivalent to the dicarbonium ion intermediate postulated for uric acid and adenine (1)]. The subsequent chemical or electrochemical reactions of this primary product decides the final nature of the over-all reaction. Again, it appears as if the initial sites of electrochemical and biological oxidation are similar, but the normal biological deamination reaction at C-2 does not occur under electrochemical conditions.

Experimental

Chemicals.—Chemicals were obtained from the sources listed; guanine (Nutritional Biochemicals); parabanic acid, guanidine sulfate, 4-chloro-meta cresol (Eastman); guanidine hydrochloride (Matheson); 2, 3-butanedione monoxime (Fisher). Buffer solutions were prepared from reagent grade chemicals.

Argon (Linde) used for deoxygenating purposes was equilibrated with water; no other purification was necessary.

Apparatus.—Polarograms and voltammograms were recorded on a Sargent Model XVI Polarograph using a water-jacketed three-compartment cell maintained at 25° ± 0.1°C and containing a saturated calomel reference electrode (SCE) and a platinum gauze counterelectrode in saturated potassium chloride solution. All potentials are referred to the SCE at 25°C. The dropping mercury electrode had normal m and t values. The preparation of the various pyrolytic graphite electrodes was described earlier (1). Apparatus for cyclic voltammetry, controlled potential electrolysis, coulometry, and lyophylization are described elsewhere (3, 5). Ultraviolet absorption spectra were recorded on a Perkin Elmer-Hitachi Model 124 Spectrophotometer; infrared spectra were recorded on a Beckman IR8 spectrophotometer.

Voltammetric procedure.—Because of the low solubility of guanine, saturated solutions in appropriate buffers were prepared, the excess of guanine removed by filtration, and the concentration computed by measurement of the u.v. absorbance. A portion of these solutions was then placed in the polarographic cell and deaerated with argon for about 10 min. Once in position, the 4 mm diameter PGE was allowed to stand for about 30 sec without applied potential; the starting potential was then applied for 5 sec (usually 0.00V) and the voltammetric scan commenced.

The PGE was resurfaced before every run by polishing on a 600 grade silicon carbide paper disk mounted on a motor driven rotating disk. The electrode was washed thoroughly with a jet of distilled water; the surface was then very gently touched onto a clean paper tissue to remove excess of water.

Coulometry.—A measured volume of background solution was electrolyzed at the appropriate potential in the working electrode compartment until the titration coulometer (16) gave a small constant titration rate. Then, between 0.1 to 0.2 mmole of guanine was introduced. The electrolysis was then continued until all of the suspended guanine had disappeared and the current had decayed to the background level. Completion of the electrolysis was always confirmed by the disappearance of the characteristic guanine u.v. absorption peak.

Macroscale electrolysis.—The same apparatus was used for macroscale electrolysis as for coulometry except that between 1 and 2 mmoles of guanine was suspended in 200 ml of 1*M* HOAc. Electrolysis was continued until no suspended guanine remained and the characteristic u.v. absorption of guanine had disappeared. At completion of the electrolysis, the solution in the working electrode compartment was shell frozen onto the walls of a 1 liter flask and lyophilized which resulted in a white fluffy powder.

Thin layer chromatography.—With the exception of urea, which was spotted as a solution (1 mg/ml), all reference compounds and the lyophilized electrolysis product were applied to thin layer sheets as very small crystals and were dissolved by repeated addition of water. Two different solvent systems were employed, n-butanol, acetic acid, water (120-30-50) and n-propanol, water (70-30). Two thin layer supports were employed, silica gel with fluorescent indicator (Eastman Chromogram 6060) and alumina (Eastman Chromogram 6062).

Parabanic acid was identified as a major product as a spot on the fluorescing silica gel plate having an r_f value in butanol, acetic acid, water solvent of 0.83, and 0.70 in propanol, water both being identical with authentic parabanic acid.

Urea was detected as a very minor product using butanol, acetic acid, water as solvent, and the silica gel adsorbent with Ehrlich's reagent ($r_f = 0.68$). Allantoin was not detected under the same conditions.

Ammonia was tested for on silica gel in the same solvent with Nessler's reagent but was not detected.

Guanidine was identified in the product on an alumina plate using propanol, water as solvent with sodium nitroprusside reagent (17) (r_f of 0.43), and on silica gel in butanol, acetic acid, water with the same reagent ($r_f = 0.63$).

Ion exchange isolation and identification of guanidine.—Thin layer chromatography indicated that guanidine was a product of electro-oxidation. Since all other products or potential products except urea, which was only a very minor product, were acidic or could be hydrolyzed to salts in strong base, isolation of guanidine was attempted.

One hundred milligrams of lyophylized electrolysis product was dissolved in 30 ml water and passed through a Dowex X-8 ion exchange column (hydroxide form) and washed with 150 ml water. The effluent was neutralized with hydrochloric acid and lyophylized. The infrared spectrum of the product was essentially identical to authentic guanidine hydrochloride.

Ion exchange isolation and identification of parabanic acid.—One hundred milligrams of lyophylized electrolysis product was dissolved in 30 ml water and passed through a column of Dowex 50W-X8 ion exchange resin (strongly acid form) and washed with 150 ml of water. The product was lyophylized. The infrared spectrum of the product was essentially identical to that of authentic parabanic acid.

Parabanic acid was further confirmed by the polarographic behavior of the product in 1M acetic acid ($E_{1/2} = -0.68$V) and ammonia buffer pH 9 ($E_{1/2} = -1.06$V) and from the fact that in the latter solution it rapidly decomposed to oxaluric acid ($E_{1/2} = -1.60$V) (18).

Determination of parabanic acid.—At completion of the electrolysis, parabanic acid was determined by transferring about 20 ml of the electrolysis solution to

a polarographic cell, and after deaeration a polarogram was run between 0 and −1.4V. The height of the wave at *ca.* −0.7V was compared with a calibration curve prepared from authentic parabanic acid.

Determination of guanidine and guanidyl residues.—Guinidine or guanidyl residue was determined by modification of the procedure described by Staron *et al.* (19). In our hands the sensitivity of this procedure was about five to ten times lower than claimed. In order to overcome this low sensitivity, the solution produced on electrolysis of 0.1-0.2 mmole guanine was lyophylized and the resulting solid product dissolved in 10.0 ml water. To 2.0 ml of this latter solution was added 2.0 ml of a 10% solution of 4-chloro-meta cresol in 95% ethanol. After agitating, 2.0 ml of *N* sodium hydroxide was added followed by 1.0 ml of freshly prepared sodium hypobromite solution (1 ml Br_2 in 99 ml *N* NaOH). The absorbance of the yellow color which developed was measured at 440 mμ in a 1.0 cm stoppered quartz cell. Calibration curves were prepared with guanidine sulfate solutions which contained between 0.2 and 2 mg guanidine in the initial 2.0 ml aliquot of solution.

Determination of oxalyl guanidine.—Oxalyl guanidine, allantoin, or any other similar species capable of being quantitatively hydrolyzed to glyoxylic acid by sequential base then acid hydrolysis responds quantitatively to the method of Young and Conway (20). The experimental procedure is described elsewhere (1) except that under the present conditions, a 3.0 ml aliquot of the electrolysis solution diluted to 5.0 ml with 1*M* HOAc was employed.

Results and Discussion

Voltammetry.—Guanine shows a single well-formed anodic voltammetric peak at the stationary PGE between *p*H 0 and 12.5. Above *p*H 11 there was some indication of a small second wave close to background discharge. Because these latter waves appeared only occasionally at very high *p*H, they were not examined further. The peak potential, E_p, for the main guanine wave shifts linearly more negative with increasing *p*H

$$E_p = 1.115 - 0.065\ pH$$

at 3.33 mV sec^{-1} scan rate. The shift of peak potential of 65 mV per *p*H unit is in fairly close agreement with that expected for a process where the rate-controlling step involves an identical number of protons and electrons. Considering the guanine peak observed over the whole *p*H range study, an average current density of 3.72 μA · $mmole^{-1}$ mm^{-1} was obtained. However, between *p*H 2.3-10 guanine is rather insoluble so that the data in these regions corresponds to that observed for essentially saturated solutions, and in these regions the current density was much more variable, no doubt reflecting contributions of adsorbed guanine to the total current. Below *p*H 2 where guanine is somewhat more soluble and solutions well below the saturation limit were employed, the mean current density was 2.72 μA · $mmole^{-1}$ mm^{-2}. This latter figure is in good agreement with that expected for involvement of 4e per guanine molecule. In 2*M* H_2SO_4 guanine shows linear ip-C curves between 0.005-1.0 m*M* which indicates that the electrochemical reactions are probably diffusion controlled.

Coulometry.—At *p*H 2.3, coulometry at a potential corresponding to the crest of the guanine oxidation peak gave faradaic *n* values ranging from 4.2 to 4.7e. At completion of the electrolysis, the characteristic u.v. absorption spectra of guanine (λ max = 275 mμ) had disappeared.

Preparative electrolysis.—Exhaustive electrolysis of guanine at fixed anodic potential allowed the preparation of sufficiently large amounts of products to permit their isolation, identification, characterization, and quantitative determination. Several isolation and detection approaches were employed including lyophylization (freeze drying), ion exchange, thin layer chromatography, polarography, u.v. and *IR* spectrophotometry, and other physical measurements. These revealed the presence of guanidine and parabanic acid as major products along with a slight trace of urea. Neither allantoin nor ammonia was detected. A species was detected, however, which when subjected to a sequential base then acid hydrolysis gave rise to glyoxylic acid; the latter compound is readily detected and quantitatively determined by formation of its condensation product with phenylhydrazine which is oxidized by ferricyanide to the characteristic red chromophore (20).

Quantitative analysis (typical) of a solution after complete electrolysis of 0.22 mmole of guanine in 200 ml of 1M HoAc revealed that 1 mole of guanine yielded 0.35 mole parabanic acid (polarography), 0.90 mole of guanidyl residue [procedure of Staron *et al.* (19)] and 0.55 mole of a species which could be hydrolyzed to glyoxylic acid [Young and Conway procedure (20)]. It was noted that the value of the measured *n* value in excess of 4.0 was numerically twice the moles of parabanic acid produced per mole of guanine.

Cyclic voltammetry.—The involvement of about 4e per molecule of guanine in the oxidation suggested a mechanism similar to that observed for adenine (1), *i.e.*, initial oxidation at C-8 followed by further oxidation of the C(4)-C(5) double bond. In order to gain more detail into these processes, cyclic voltammetry, at fast scan rates, was employed.

Scanning from 0.0V at a clean electrode toward positive potential only a single anodic peak (peak I_a) is observed for guanine. Once having scanned this peak and then sweeping toward negative potential, however, at least two cathodic peaks are observed. The first (peak I_c) always occurs at potentials more positive than zero, the second (peak II_c) occurs at much more negative potential. On the second sweep toward positive potential a new anodic peak (peak II_a) appears before the peak I_a and forms an almost reversible couple with peak I_c.

Figure 1A shows a voltammogram for these first and second cycles. In order to detect peaks I_c and II_a, it is necessary to employ high sweep rates, *i.e.*, > 300 mV sec^{-1} (5), indicating that the product of the main oxidation peak I_a is very unstable. Earlier reports of the electro-oxidation of uric acid (2) and adenine (1) postulated that the primary electrochemi-

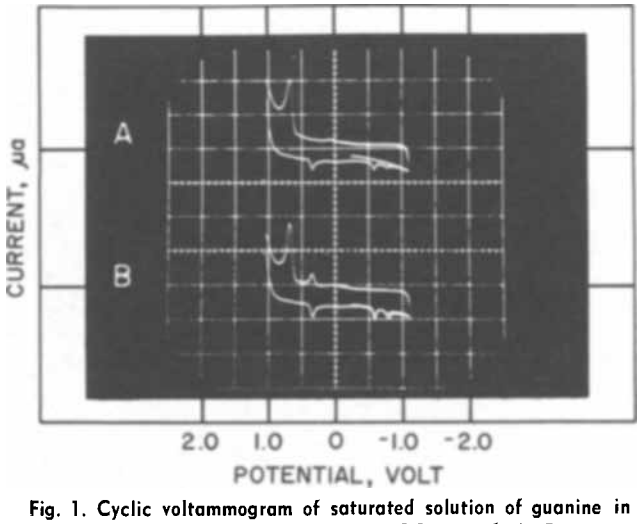

Fig. 1. Cyclic voltammogram of saturated solution of guanine in MacIlvaine buffer *p*H 6 at PGE. Scan rate 8.8 $Vsec^{-1}$. A, First scan at a clean electrode, sweep started at 0.0V and run toward negative potential; scan pattern, 0.0V → −1.1V → +1.05 → −1.1V. B, Second scan. Scan pattern: 0.0V → −1.1V → +1.05V → 0.0V. Calibration marks on current axis indicate zero current for the appropriate voltammogram. Current above the calibration mark is anodic (—). Current sensitivity 200 μA per div.

cal product was a dicarbonium ion formed by removal of two π electrons from the —C(4) = C(5)—double bond. However, since the peak potential for uric acid oxidation was shown to be *p*H dependent, although only two *p*H values were examined (2), and involved direct attack at the 4,5 position unlike adenine and guanine which must involve attack elsewhere in the molecule before the 4,5 bond is oxidized (*vide infra*), then protons must be involved in the energy (*i.e.*, potential) controlling process. This led to the suggestion that the intermediate in uric acid oxidation was in fact 2,6,8-trioxypurine-4,5-diol (5). We have confirmed that uric acid is oxidized in a *p*H dependent process and that the cathodic peak due to reduction of the unstable 4,5-diol is also *p*H dependent. At a scan rate of 8.8 $Vsec^{-1}$ the primary uric acid oxidation peak followed the relation

$$(E_p) = 0.83 - 0.071\ pH$$

between *p*H 1 and 12.5. The reversible cathodic peak followed the relation

$$(E_p)_{red} = 0.68 - 0.061\ pH$$

although it was only observed distinctly between *p*H 1 and 8.

All of the peaks observed for guanine are *p*H dependent at 8.8 $Vsec^{-1}$ being described by the relations: $E_p = 1.20\text{-}0.077\ pH$ for peak I_a; $E_p = 0.72\text{-}0.059\ pH$ for peak I_c; $E_p = -0.54\text{-}0.026\ pH$ for peak II_c, and $E_p = 0.9\text{-}0.077\ pH$ for peak II_a. A peak of similar appearance and *p*H dependence to peak II_a was also observed for uric acid. Actually one or occasionally two additional cathodic peaks were also observed at many *p*H values. These usually occurred at more positive potential than peak II_c except occasionally at high *p*H. An example is shown in Fig. 1B where a clear peak at −0.6V is observed before peak II_c at −0.75V. These additional peaks were most clearly observed at *p*H 2.3 (acetate), 3.0 (MacIlvaine), 4.0 (MacIlvaine), 4.9 (MacIlvaine), and 6.0 (MacIlvaine).

In ammonia background *p*H 9.1 the cyclic voltammetry of guanine was considerably different to that observed at all lower and higher *p*H values (Fig. 2). Thus, after scanning peak I_a the primary oxidation peak, a peak corresponding to peak I_c at positive potential did not appear (from the *p*H dependence of peak I_c it should have occurred at +0.19V). Instead, a new peak at −0.55V appeared followed by three more negative peaks one of which corresponded to peak II_c. Then on the second anodic sweep a new anodic peak at −0.52V appeared forming a reversible couple with the cathodic peak at −0.55V. In addition, however, a peak corresponding to peak II_a also appeared (E_p = 0.13V)

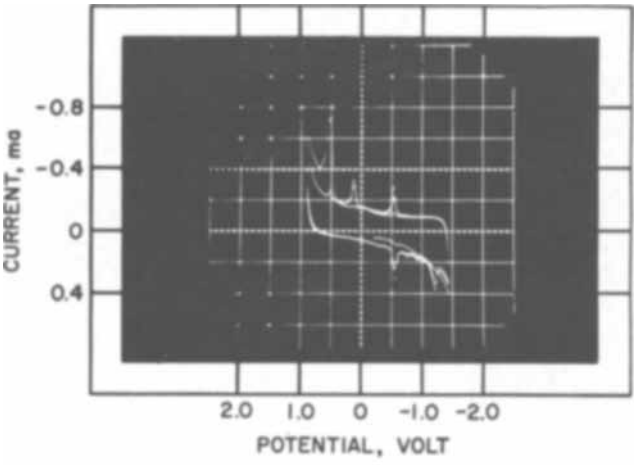

Fig. 2. Cyclic voltammogram of a saturated solution of guanine in ammonia-ammonium chloride buffer *p*H 9.1 at PGE. Scan rate 10 $Vsec^{-1}$. First scan started at 0.0V and swept toward negative potential.

although under no conditions did the reversible $II_a - I_c$ couple appear. Uric acid showed similar behavior, namely after scanning the primary oxidation peak; no reversible cathodic peak was observed but a new reversible couple at $(E_p)_{cathodic} = -0.55V$ and $(E_p)_{anodic} = -0.52V$ appeared.

Mechanism

The characteristic uv absorption spectrum of guanine (λ_{max} = 275 mμ in 1M HOAc) is due to the —C(4) = C(5) — C(6) = 0 chromophore (21, 22). In view of the disappearance of this spectrum and consideration of the adenine and uric acid mechanisms it is likely that the —C(4) = C(5)—double bond is oxidized.

Removal of 4e from guanine along with the observed *p*H dependence of the anodic peak suggests that the process proceeds by two sequential two-electron, two-proton oxidations. Enzymes such as xanthine oxidase, always preferentially attack an —N=CH— double bond. In guanine only the —N(7)=C(8)H— bond of this type is available. Theoretical calculation of the nucleophilic localization energy of this same bond predicts that it will be preferentially oxidized (23). Accordingly it appears that the —N(7)=C(8)— bond is that which would be initially attacked electrochemically. It is observed experimentally (1-5, 24) and predicted theoretically, from the energies of the highest occupied molecular orbitals (23), that the ease of electron removal from purines increases with the number of ring substituted oxygen groups in the molecule. Accordingly, once the initial potential controlling oxidation at —N(7)=C(8)— has occurred, further oxidation should take place; since the u.v. spectrum of guanine is lost, it must take place at the —C(4)=C(5)— double bond.

Fast sweep cyclic voltammetry clearly allows observation of the reduction of the unstable product (peak I_c) of the primary electrochemical reaction (peak I_a) and re-oxidation in turn of the product (peak II_a) of this secondary reduction at a less positive potential than required for the initial oxidation of guanine. These latter redox processes are essentially reversible and are *p*H dependent to an extent indicative of the involvement of an identical number of protons and electrons. The reversible couple occurs at potentials very similar to those observed for the uric acid oxidation-reduction couple. Accordingly, the electrochemistry of the cyclic voltammetry of guanine (I, Fig. 3) can be interpreted as an initial two-electron, two-proton rate-determining oxidation to 2-amino-6,8-dioxypurine (II, Fig. 3) followed by a further rapid two-electron, two-proton oxidation to 2-amino-6,8-dioxypurine-4,5-diol (some of which is even further electrochemically oxidized to parabanic acid and guanidine III) (Fig. 3) which corresponds to peak I_a. Provided a fast enough sweep rate is employed, reduction of III to II can be observed and corresponds to peak I_c, and on the next anodic sweep, peak II_a is observed which corresponds to oxidation of II back to III.

The cathodic peak (peak II_c) observed for both guanine and uric acid is probably due to reduction of a product of partial further oxidation of III, namely, parabanic acid (V, Fig. 3) (25). Authentic parabanic acid shows a similar *p*H dependence to peak II_c although the peak potential for its reduction generally occurred at somewhat more negative potential. A possible explanation of this effect is that the parabanic acid produced by breakdown of intermediate III (Fig. 3) is situated very close to the electrode surface and is reduced under *p*H conditions which are quite appreciably lower than those extant in the bulk solution owing to the liberation of protons as a result of reaction I → II, the result being therefore a shift in the peak to more positive potential. The peak observed at more negative potential than II_c at high *p*H is no doubt due to oxaluric acid which is known to the hydrolysis product of parabanic acid at high *p*H and

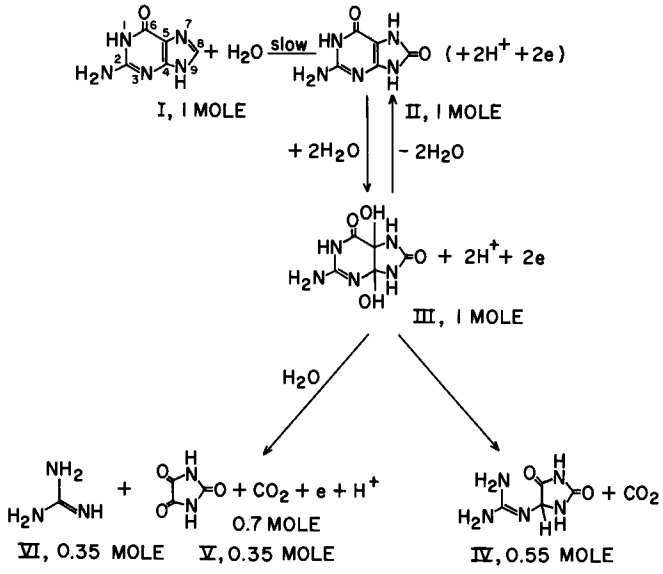

Fig. 3. Proposed pathways for electrochemical oxidation of guanine in moderately acidic solution. The molar quantities refer to the amount involved per mole of guanine. Compounds listed are as follows: I, guanine; II, 2-amino-6,8-dioxypurine; III, 2-amino-6,8-dioxypurine-4,5-diol; IV, oxalyl guanidine; V, parabanic acid; VI, guanidine.

which is electrochemically reducible at more negative potential (26).

The nature of the processes giving rise to other cathodic peaks at various *p*H values is difficult to assign. It is possible that intermediates such as the so called "Behrend Compound" postulated for uric acid oxidation (2) might exist at certain *p*H values and be electroactive. However, saturated solutions of guanine were employed at most *p*H values for cyclic voltammetry; the presence of adsorption or capacitive peaks is also likely. The reversible redox couple observed for guanine and uric acid in ammonia buffer at *p*H 9 is not observed at any other *p*H in the absence of ammonia and hence must be specifically associated with this latter species. The likely explanation of the effect is shown in Fig. 4, namely, that the primary potential controlling step is identical to that at other *p*H values, *i.e.*, two-electron, two-proton oxidation of the —N(7)=C(8)—bond to give 2-amino-6,8-dioxypurine (II, Fig. 4). However, in the presence of ammonia two-electron, two-proton oxidation results in formation of 2-amino-6,8-dioxypurine-4,5-diamine (III, Fig. 4). It would then seem that it is this latter species

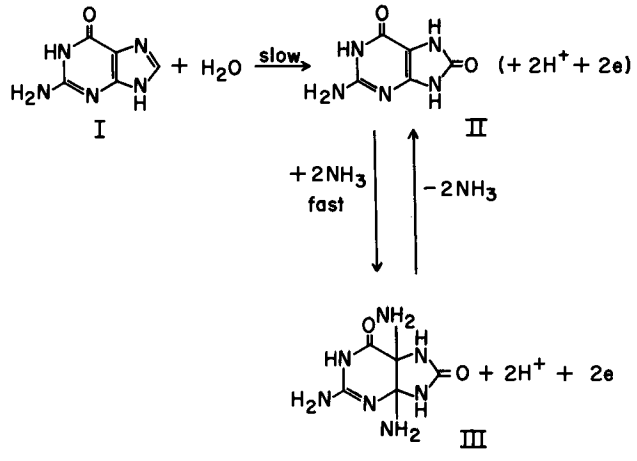

Fig. 4. Proposed primary electrochemical pathways for electrochemical oxidation of guanine in ammonia buffer *p*H 9.1. Compounds listed are as follows: I, guanine; II, 2-amino-6,8-dioxypurine; III, 2-amino-6,8-dioxypurine-4,5-diamine.

which forms the reversible redox couple at *ca.* —0.5V. The explanation of the anodic peak at 0.15V, which is the potential expected for the normal peak II_a is difficult to decide. A possible cause is decomposition of the 4,5-diamine (III, Fig. 4) to an electroactive species capable of being oxidized in this potential region. The most negative cathodic peak ($E_p = -1.4$V) most probably is due to oxaluric acid. In moderately acid solution, it is clear that the primary 4,5-diol product (the most usual product) is unstable and under conditions of constant potential oxidation decomposes by two routes, the first by further electro-oxidation to parabanic acid, guanidine, and carbon dioxide. Solution analysis supports this view since the faradaic n value and parabanic acid produced are in agreement with theory, *i.e.*, 0.35 mole parabanic acid per mole of guanine with an n value of 4.7e. In addition, the total guanidyl residue found per mole of initial guanine accounts for 0.9 mole, while oxalyl guanidine (IV, Fig. 3) determined by hydrolysis to glyoxylic acid accounts for only 0.55 mole, which therefore by difference indicates that 0.35 mole of free guanidine (VI, Fig. 3) is produced. This latter figure is in accord with the 0.35 mole of parabanic acid detected. These data further support the view that the parabanic acid is derived exclusively from the imidazole ring of guanine.

The material balance achieved accounts for only 90% of the initial guanine. No doubt additional hydrolysis of the above products accounts for the remaining 10%.

Conclusions

Guanine is electrochemically oxidized by a mechanism very similar to that observed for other naturally occurring purines such as uric acid and adenine. The evidence put forward supports the view that the locus of initial electron removal is the same for enzymic and electrochemical processes and is in accord with theoretical molecular orbital predictions. Unlike most enzyme reactions where the 2-amino group of guanine is removed, this group remains intact under electrochemical conditions, and further electrochemical reaction is centered at the —C(4)=C(5)—bond.

It is particularly striking that the photodynamic degradation of guanine and indeed DNA appears to be identical to the electrochemical degradation.

Acknowledgment

The authors would like to thank the National Science Foundation which supported the work described through Grant No. GP 8151.

Manuscript submitted Dec. 4, 1969; revised manuscript received May 25, 1970.

Any discussion of this paper will appear in a Discussion Section to be published in the June 1971 JOURNAL.

REFERENCES

1. G. Dryhurst and P. J. Elving, *This Journal*, **115**, 1014 (1968).
2. W. A. Struck and P. J. Elving, *Biochem.*, **4**, 1343 (1965).
3. G. Dryhurst, *This Journal*, **116**, 1097 (1969).
4. G. Dryhurst, Work in progress (1969).
5. G. Dryhurst, *This Journal*, **116**, 1411 (1969).
6. G. Dryhurst and B. J. Hansen, Work in progress (1969).
7. J. H. Lister, "Advances in Heterocyclic Chemistry," Vol. 6, p. 1, A. R. Katritsky and A. J. Boulton Editors, Academic Press, New York (1966).
8. R. K. Robins, "Heterocyclic Compounds," Vol. 8, p. 162, R. C. Elderfield, Editor, John Wiley & Sons, Inc., New York (1967).
9. G. P. Wheeler and J. A. Alexander, *Cancer Research*, **21**, 390 (1961).
10. J. H. Ayvazian and S. Skupp, *J. Clin. Invest.*, **45**, 1859 (1966).
11. J. B. Wyngaarden, *J. Biol. Chem.*, **224**, 453 (1957).
12. A. J. Guarino and G. Yuregir, *Biochem. Biophys. Acta*, **36**, 157 (1959).
13. J. S. Sussenbach and W. Berends, *ibid.*, **95**, 185 (1965).

14. L. A. Waskell, K. S. Sastry, and M. P. Gordon, *Biochem. Biophys. Acta Previews*, **6**, [3] xx (1966).
15. A. S. Jones, R. T. Walker, and A. R. Williamson, *J. Chem. Soc.*, **1963**, 6033.
16. J. J. Lingane, "Electroanalytical Chemistry," Chap. XIX, pp. 457-458, Interscience Publishers, New York (1966).
17. J. J. Pfiffner and V. C. Myers, *J. Biol. Chem.*, **87**, 345 (1930).
18. G. Dryhurst and P. J. Elving, *Anal. Chem.*, **40**, 492 (1968).
19. T. Staron, C. Allard, M. M. Chambre, and D. W. Xuong, *Compt. rend.*, **257**, 2552 (1963).
20. E. G. Young and C. F. Conway, *J. Biol. Chem.*, **142**, 839 (1942).
21. F. Bergmann and S. Dikstein, *Biochem. J.*, **77**, 691 (1955).
22. L. F. Cavalieri, A. Bendich, J. F. Tinker, and G. B. Brown, *J. Am. Chem. Soc.*, **70**, 3875 (1948).
23. B. Pullman and A. Pullman, "Quantum Biochemistry," Chap. V, Interscience Publishers, New York (1963).
24. P. J. Elving, W. A. Struck, and D. L. Smith, *Mises au Point Chim. Anal. Org. Pharm. Bromatol.*, **14**, 141 (1965).
25. W. A. Struck and P. J. Elving, *Anal. Chem.*, **36**, 1374 (1964).
26. G. Dryhurst and P. J. Elving, *ibid.*, **40**, 492 (1968).

Technical Notes

Effect of Sb_2O_3 on the Microstructure of the PbO_2 Electrode

A. C. Simon* and S. M. Caulder*[1]

Naval Research Laboratory, Washington, D. C. 20390

and E. J. Ritchie*

Eagle-Picher Industries, Incorporated, Joplin, Missouri 64801

Unusual properties have been attributed to battery plates which contain lead-antimony grids. The supposition is that antimony dissolves from the grid and then reacts in some manner with the active material.

In a comparison of lead-calcium *vs.* lead-antimony grids (1), it was reported that the presence of antimony increased the amount of α-PbO_2 during formation, helped to retain the active material and capacity during cycle tests, and modified the crystal structure of the PbO_2. Electron micrographs indicated that, in plates containing antimony in the grid metal, the PbO_2 material was in the form of complex clusters of prismatic crystals. In plates containing lead-calcium grids, however, the PbO_2 particles were nondescript globules. It was suggested that the prismatic morphology was required to maintain a firm texture in the active material of the $PbO_2/PbSO_4$ electrode. It has also been suggested (2) that antimony may act as an inhibitor of PbO_2 crystal growth, the assumption here being that increasing growth size decreased surface area and structural strength of the active material.

In the present investigation another phenomenon has been noted which is directly attributable to the antimony oxide and which offers a clue for attaining greater strength in the active material without the necessity of using lead-antimony grid alloys. A number of cells were prepared in which various oxides or oxide blends had been used in the preparation of the plates. Duplicate cells were prepared from each of these paste compositions, one with plates containing grids of lead and the other containing grids of lead-antimony. Optical microscopy was used to determine the microstructure of the cured plates, formed plates, and plates that had received a number of cycles.

* Electrochemical Society Active Member.
[1] International Lead-Zinc Research Organization Research Associate at the Naval Research Laboratory.
Key words: antimony trioxide, Sb_2O_3, microscopy, lead dioxide electrode.

In the preparation of the plates for microscopic examination, use was made of a polyester resin for impregnation. After this hardened, the plates were cut and the cross section was polished.

Usually, such polished sections, particularly of cured plates, are quite stable. It was noticed, however, that in samples taken from two of the cured plates, the polished surface had been etched by the atmosphere, after a considerable time on the shelf. The remainder of the cured plate sections were then reexamined and none was found with a similar etch pattern.

The etch pattern was quite distinct and suggested that long, needlelike crystals had been present in the polished surface that were completely invisible until the etching took place (Fig. 1). When polarized light was used to examine the specimen at the same location, it was found that crystals were present at the areas where an etch pattern was seen. These crystals were colorless, transparent, and indistinct and blended into the surrounding material, so that their outline was blurred (Fig. 2). Nevertheless, they could be seen sufficiently well to determine that they usually coincided with the etched portions of the surface and that they were actually acicular rather than cross sections through tabular crystals.

Because they had given no indication of their presence in the polished surface when examined by vertical illumination (unpolarized light) before the etching had occurred, these crystals had been completely overlooked in the original examination. This invisibility in the polished section also indicated that the crystals consisted of material different from the usual constituents found in the uncured plate which indicate their presence by differences either in reflectivity or in the amount of relief polishing.

The acicular crystals, showing atmospheric etching, were found only in cured plates to which 0.10% of

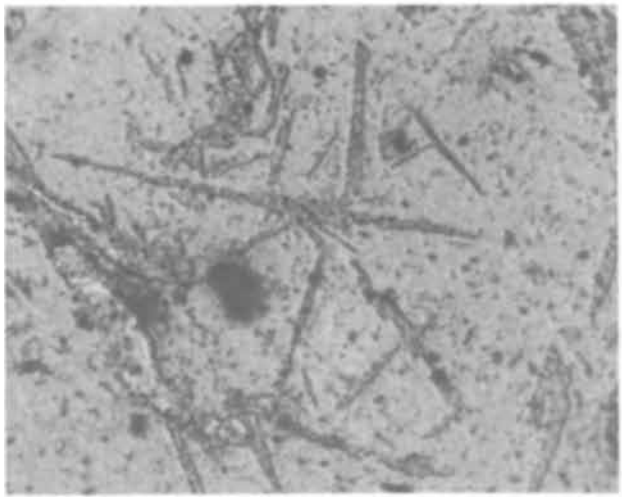

Fig. 1. Distinct etch pattern suggesting the presence of long, needlelike crystals.

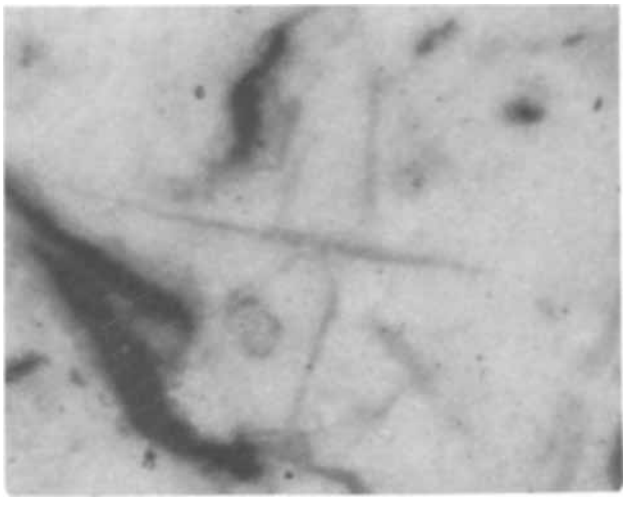

Fig. 2. Colorless, transparent, indistinct crystals found at areas where an etch pattern was seen.

Sb_2O_3 had been intentionally added to the paste during mixing. Two batches had contained this added Sb_2O_3 and both were otherwise identical except for a difference in the paste density. In the one case this was 64 g/in.^{3} and in the other, 69 g/in.^{3}. Both of these formulations had been pasted on lead grids, and both showed similar crystals and surface etching.

The same paste formulation, without the added Sb_2O_3, did not show any indication of such crystals as have been described, even when pasted on lead-antimony alloy grids. All indications were that this crystal type appeared only when Sb_2O_3 was a constituent of the paste mix.

The most interesting point, however, was that needles with very similar acicular shapes were also found in the formed plate (Fig. 3). These were composed of PbO_2 and were easily seen in the polished

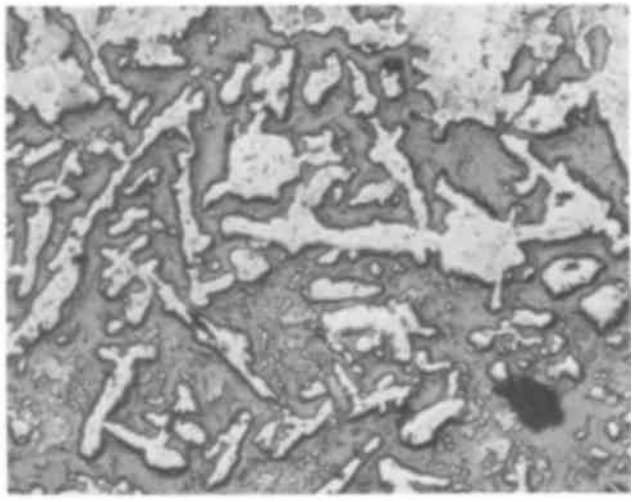

Fig. 3. Acicularly shaped needles found in the formed plate

sections and in size and shape suggested a relationship with those in the cured but unformed plate. These areas of PbO_2 with acicular external form were found only in the formed plates to which Sb_2O_3 had been added in the original mixing.

The lack of these needlelike crystals of PbO_2 in the formed plates with lead-antimony grids indicates that the amount of antimony that can be obtained from the grid is insufficient for the formation of such crystals. This is particularly true because the type of crystal responsible for the acicular PbO_2 crystals in the formed plate was first formed in the cured plate. Under curing conditions the electrolytic action necessary for solution and transport of the antimony is missing.

In the samples examined which contained 0.10% Sb_2O_3, the number of needlelike PbO_2 groups formed seemed insufficient to bind the plate active material together, either by intergrowth at contacts (such as seems to have occurred at several points in Fig. 3) or by the formation of an interlocking structure.

It would seem advisable to investigate this phenomenon further by using various amounts of Sb_2O_3 in the paste and combining this with capacity and life-cycle tests to see if this type of structure can be improved and whether it proves to be beneficial.

Acknowledgment

The International Lead Zinc Research Organization is gratefully acknowledged for maintaining the position of Postdoctoral Research Associate at NRL and for supporting that portion of the work done at Eagle-Picher through an ILZRO research contract.

Manuscript submitted April 18, 1970; revised manuscript received *ca.* June 22, 1970.

Any discussion of this paper will appear in a Discussion Section to be published in the June 1971 JOURNAL.

REFERENCES

1. J. Burbank, *This Journal*, **111**, 1112 (1964).
2. E. J. Ritchie and J. Burbank, *ibid.*, **117**, 229 (1970).

Mass Transport Limitations in Lithium-Cupric Fluoride Cells

R. Keller*

Research Division, Rocketdyne,
A Division of North American Rockwell Corporation, Canoga Park, California 91304

The lithium-cupric fluoride battery system which has an excellent theoretical energy density has been studied by various investigators (1). Severe performance limitations were encountered in regard to discharge rates. Such limitations appeared to depend on the electrolyte, *e.g.*, they were significantly greater in propylene carbonate electrolytes than in those based on methyl formate.

It appears that the performance of the cathode generally is the factor limiting the performance of lithium-cupric fluoride batteries under study. Factors possibly limiting cathode performance include (*a*) internal conductance of the cathode material, if reduction occurs *in situ;* (*b*) dissolution rate of the electroactive material, if reduction of dissolved copper species occurs; (*c*) formation of complexed copper species causing changes in discharge potentials and/or loss by diffusion and migration; (*d*) blocking of discharge sites by reaction products, particularly insoluble lithium fluoride; and (*e*) mass transport in the electrolyte. Mass transport limitations are being scrutinized in this note. It is shown below that, in certain cases, mass transport in the electrolyte alone may account for the observed performance limitations. It should not be implied, however, that the factors limiting the performance of prototype cells in actual discharge tests have been identified.

The lithium-cupric fluoride cell, *e.g.*, with a $LiClO_4$ electrolyte, is somewhat unique inasmuch as the cation of the electrolyte is being precipitated at the cathode during cell discharge, according to

$$CuF_2 + 2Li^+ + 2e = \underline{Cu} + \underline{2LiF} \qquad [1][1]$$

Lithium fluoride has generally a very low solubility in aprotic solvents and solutions; some solubility values obtained in our laboratory are given in Table I. Because of this very low solubility of LiF, and since lithium is the only cation present (disregarding copper), practically all fluoride ions potentially formed at the cathode are readily precipitated. This causes a depletion of the electrolyte at the cathode. Under limiting conditions, this depletion will be complete, and mass transport cannot be increased by higher electric fields (higher *IR*-drops). A similar effect, incidentally, can occur also in aqueous systems, *e.g.*, when insoluble hydroxide forms at the anode; in such "conventional" cases, this effect is, however, much less critical because of higher diffusion coefficients and because a higher amount of electrolyte solute (as reservoir) can be tolerated without severely jeopardizing the energy density of the cell.

In the following, a lithium-cupric fluoride cell with a 1M $LiClO_4$ in propylene carbonate (PC) electrolyte shall be considered as an example. At a discharge under mass transport limitations, an electrolyte concentration profile, shown schematically in Fig. 1, will eventually result. The electrolyte concentration at the anode will correspond to a saturated $LiClO_4$ solution and will be practically zero at the cathode.

Table I. Solubility of LIF

Solvent/solution	Temp, °C	Solubility of LiF, moles/liter
Propylene carbonate	25; 60	$<5 \times 10^{-6}$
1M $LiClO_4$/PC	25	1×10^{-4}
Dimethyl formamide	25	3×10^{-5}
Dimethyl formamide	60	5×10^{-5}
Acetonitrile	25	2×10^{-6}
Methyl formate	25	3×10^{-5}

Table II. Calculation of limiting current

Li precipitated as LiF at cathode:	$j_{Li,c} = -\frac{i}{F}$
Li^+ transported by migration:	$j_{Li,m} = \frac{i \cdot t_+}{F}$
Li^+ transported by (linear) diffusion:	$j_{Li,d} = -D\frac{dC_{Li}}{dy}$
Li^+ transported by convection:	Zero

$$j_{Li,c} + j_{Li,m} + j_{Li,d} = 0 = -\frac{i_l}{F} + \frac{i_l \cdot t_+}{F} - D\frac{\Delta C_{Li}}{\Delta y}$$

$$i_l = -D\frac{F\,\Delta C_{Li}}{t_- \cdot d}$$

The diffusion limiting current for such a case is calculated for a simplified, linear model where: (*a*) no separator is present; (*b*) the distance between anode and cathode is $d = 1$ mm; (*c*) convection is negligible; (*e*) the diffusion coefficient, D, is constant throughout the cell; and (*f*) the solubility of $LiClO_4$ at the anode is 2.1 moles/liter, the solubility of LiF at the cathode is negligible, and a linear concentration profile for $LiClO_4$ forms between anode and cathode. The concentration gradient for the lithium ion can then be represented by

$$\frac{dC_{Li}}{dy} = \frac{\Delta C}{d} = \frac{-2.1 \times 10^{-3}}{0.1} \text{ moles cm}^{-4} \qquad [2]$$

Lithium ions are transported by migration and diffusion (convection neglected). At steady-state limiting conditions, the amount of lithium ions reaching the cathode equals the amount of lithium ions precipitated at the cathode. The limiting current, i_l, can be calculated as shown in Table II.

$$i_l = -D\frac{F \cdot \Delta C_{Li}}{t_- \cdot d} \qquad [3]$$

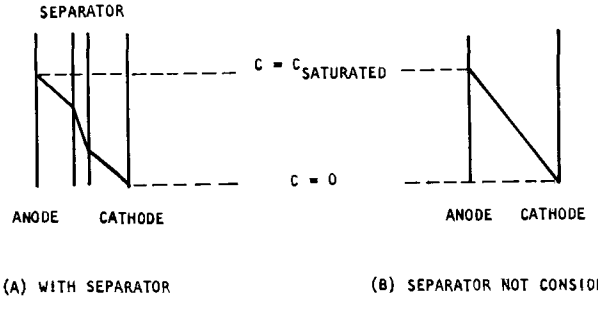

Fig. 1. Schematic electrolyte concentration profile

* Electrochemical Society Active Member.

Key words: lithium cells, copper fluoride cathode, mass transport, nonaqueous battery.

[1] According to solubility studies, the reaction $2LiClO_4 + CuF_2 = \underline{2LiF} + Cu(ClO_4)_2$ may occur on open circuit, although such studies have indicated that it may progress very slowly. It is not certain how far such a reaction would extend, i.e., if $Cu(ClO_4)_2$ would form in significant amounts beyond the solubility of this compound in an actual electrode. Such a process would cause a depletion of the electrolyte, but, overall, an excess of CuF_2 would have to remain because in a practical system a stoichiometric amount of ClO_4^- could not be permitted without jeopardizing the high-energy density feature of the cell. After an initial discharge of $Cu(ClO_4)_2$, the limiting conditions would therefore occur as discussed.

Selecting the value of $D = 2.6 \times 10^{-6}$ cm^2 sec^{-1} determined as the integral diffusion coefficient for a 1M $LiClO_4$/PC solution at 25°C in this laboratory (2), and a value of $t_- = 0.75$ based on transference and conductance measurements (3), a value of

$$i_l = 7 \times 10^{-3}\ \text{Acm}^{-2}$$

results for $d = 0.1$ cm and $\Delta C = -2.1$ moles/liter.

By assuming a simple cell model, some factors have not been considered:

1. Convection has been neglected. It was found experimentally by Boehm and Ibl (4) for an aqueous system that convection was negligible at electrode distances smaller than about 0.4 to 0.6 mm. Because the distances between walls in the presence of a separator should be assumed to be smaller than 0.5 mm, and, in addition, the viscosity of the propylene carbonate electrolyte is higher than the viscosity of aqueous solutions, disregard of convection effects is indeed appropriate.
2. The diffusion coefficient in the separator material is lower than in the electrolyte, and somewhat lower values for limiting currents should result if the presence of separators is considered.
3. Increases in cell temperatures during discharge cause higher diffusion rates and hence higher limiting currents; a temperature increase from 25° to 70°C might be expected to approximately quadruple the limiting current in analogy to aqueous solutions (5).
4. A reservoir of electrolyte may be contained in the cathode. However, such excessive amounts of electrolyte solution or solute depress the total cell energy density.
5. A layer of saturated $LiClO_4$ solution may build up at the anode if sufficient $LiClO_4$ is available and hence increase the concentration gradient by reducing the distance between saturated solution and cathode.
6. Higher currents will be obtained in the transition period before diffusion limitation will be reached.

Conclusions

Limitations to low or moderate discharge rates can be predicted for certain lithium cells because of transport limitations in the electrolytes. It appears essential to consider such factors.

Limitations by mass transport as discussed may be reduced by:

1. Use of electrolytes with higher diffusion coefficients;
2. Use of an electrolyte or a cathode material which does not form insoluble cathode discharge products;
3. Use of excess electrolyte solute as ion reservoir at the cathode;
4. Proper choice of separator to minimize separator action as diffusion barrier;
5. Reduction of the electrode spacing.

Acknowledgment

This paper was stimulated by the work performed under Contract NAS3-8521 which was supported by the NASA Lewis Research Center. The author wishes to thank Professor N. Ibl and Mr. R. B. King for their valuable comments.

Manuscript submitted June 16, 1969; revised manuscript received June 22, 1970. This was Paper 52 presented at the Detroit Meeting of the Society, Oct. 5-9, 1969.

Any discussion of this paper will appear in a Discussion Section to be published in the June 1971 JOURNAL.

REFERENCES

1. R. Jasinski, *Electrochem. Technol.*, **6**, 28 (1968).
2. J. M. Sullivan, D. C. Hanson, and R. Keller, *This Journal*, **117**, 779 (1970).
3. R. Keller, J. N. Foster, D. C. Hanson, J. F. Hon, and J. S. Muirhead, Contract NAS3-8521, Report No. NASA CR-1425 (August 1969).
4. U. Boehm and N. Ibl, *Electrochim. Acta*, **13**, 891 (1968).
5. S. Glasstone, "Introduction to Electrochemistry," 5th ed., p. 452 (1951).

Rapid Determination of Electronic Conductivity Limits of Solid Electrolytes

D. A. J. Swinkels*

Central Research Laboratories, The Broken Hill Proprietary Company Limited, Shortland, N. S. W. 2307, Australia

Solid oxide-ion conductive electrolytes have found many applications for the determination of oxygen activities at elevated temperatures. However, at low oxygen activities and high temperatures, such as for example in the determination of dissolved oxygen in liquid steel (1), the onset of electronic conductivity causes a reduction in cell emf from that calculated from the simple Nernst equation.

Schmalzried (2, 3) has treated the emf relationships for solid electrolyte cells in which the electrolyte shows mixed ionic and electronic conductivity. Free electrons may be generated by the reaction

$$O_o = O_2(g) + 2V_o^{\cdot\cdot} + 4e^- \qquad [1]$$

where O_o is an oxygen atom in a regular oxygen site, $V_o^{\cdot\cdot}$ is a doubly ionized oxygen vacancy, and e^- is an excess electron. For heavily doped materials such as $(ZrO_2)_{0.9}(Y_2O_3)_{0.1}$ or $(ZrO_2)_{0.88}(CaO)_{0.12}$, O_o and $V_o^{\cdot\cdot}$ are approximately constant, and hence the electronic conductivity at a given temperature will vary with oxygen pressure according to

$$\sigma_e = \sigma_e^{\circ} P_{O_2}^{-1/4} \qquad [2]$$

The resulting cell emf for a cell with oxygen pressures P_1 and P_2 is then given by

$$E = \frac{RT}{\mathbf{F}} \ln \frac{P_\ominus{}^{1/4} + P_2{}^{1/4}}{P_\ominus{}^{1/4} + P_1{}^{1/4}} \qquad [3]$$

where P_θ is the oxygen pressure at which the electronic conductivity becomes equal to the ionic conductivity, *i.e.*, the ionic transport number $t_i = 0.5$. Equations similar to [2] and [3] are available for materials showing hole conductivity and for materials showing both electron and hole conductivity. The current analysis is limited to materials showing only ionic and electron conductivity. Values of $P_\ominus$ have been determined from resistance measurements as a function of P_{O_2} (4), from emf measurements on cells with known oxygen activities (5, 6), from polarization measurements between a reversible and a nonreversible electrode (4), and by

* Electrochemical Society Active Member.

Key words: oxide ion conductor, oxygen pump, coulometric titration.

coulometric titration procedures (7). Resistance measurements result in limited precision values of $P_\ominus$ since extreme experimental difficulty exists in fixing the very low P_{O_2} values which are required. At high temperatures, errors due to changes in surface and gas conduction and to contact resistances can readily occur. Methods involving emf measurements all require quite impervious electrolyte specimens and mountings since otherwise the resulting lower emf values are due to gas permeability, but may be interpreted as being due to electronic conductivity.

A new technique similar to the coulometric titration method (7) or the oxygen pumping approach of Yuan and Kröger (8) is proposed. Such a method can be used with both porous and dense samples, and $P_\ominus$ values, over a wide range of temperatures are determined in a single run. An emf cell is made up, from the sample of the electrolyte to be tested, with a Pt-air electrode on one side and a liquid metal electrode on the other side (see Fig. 1 for typical geometries). Fine silver (99.95%+ Ag) was used in our measurements since the temperature range of interest was 1000°-1650°C, but other metals can be used at lower temperatures. Contact to the liquid silver was made *via* an iridium wire.

Oxygen is pumped from the metal side of the cell by passing a d-c current in the appropriate direction, and the cell becomes polarized to an extent determined by the rate of oxygen removal with the current and by the leak rate of oxygen back into the system through the sample or its mounting or from the argon cover gas. The current is increased until it exceeds the total leak rate. The oxygen level in the metal is then reduced to an extremely low level. Further increases in current rapidly increase the proportion of the electronic current through the sample. Under these conditions $P_2 >> P_\ominus >> P_1$ and hence Eq. [3] may be simplified to

$$E_m = \frac{RT}{4F} \ln \frac{P_2}{P_\theta} \qquad [4]$$

where $P_2 = 0.21$ atm. E_m is obtained by momentarily interrupting the current and measuring the cell emf without *IR* drop and correcting for the Ir-Pt thermal emf. The open-circuit emf decays at a rate determined by the total leak rate of oxygen back into the silver.

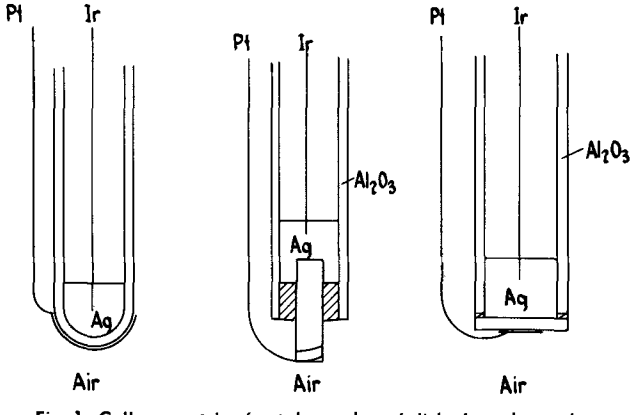

Fig. 1. Cell geometries for tube, rod, and disk shaped samples

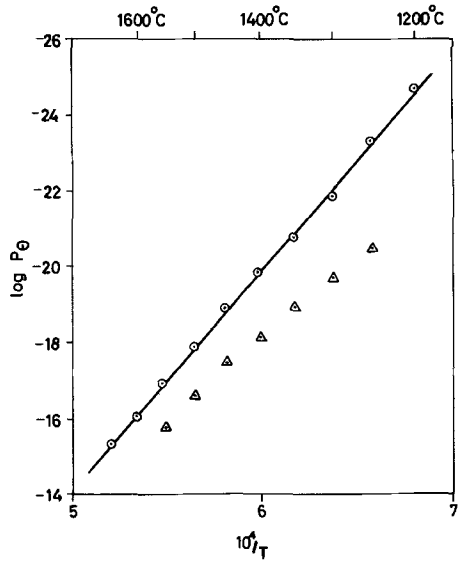

Fig. 2. Values of log $P_\ominus$ determined from resistance measurements (△) and by the present polarization technique (○).

i.e., the sum of molecular oxygen flow (through pores) and O^{--} flow (balanced by electronic flow).

Results obtained for a high-purity 7 m/o Y_2O_3 stabilized zirconia material prepared by coprecipitation, calcining, pressing, and sintering (9) are shown in Fig. 2. The sample consisted of a ⅛ in. diameter 1 in. long cylinder mounted in an alumina tube using Ceramabond 503 alumina cement. The polarizing current was interrupted for 0.5 msec at 50 msec intervals and the emf was measured by a track-store circuit synchronized with the interruptions and displayed on a DVM. $P_\ominus$ values calculated from 2 terminal resistance measurements in air and in H_2/H_2O atmospheres at 1592 Hz are shown for comparison. The resistance measurements were reproducible to ±1 in the value of log $P_\ominus$ calculated while the polarization measurements were generally reproducible to ±0.2 in log P_θ.

Manuscript submitted April 13, 1970; revised manuscript received June 25, 1970.

Any discussion of this paper will appear in a Discussion Section to be published in the June 1971 JOURNAL.

REFERENCES

1. C. Gatellier, K. Torssell, M. Olette, N. Meysson, M. Chastant, A. Rist, and P. Vicens, *Rev. Met.*, **14**, 673 (1969).
2. H. Schmalzried, *Z. Phys. Chem. N.F.*, **38**, 87 (1963).
3. B. C. H. Steele and C. B. Alcock, *Trans. Met. Soc. AIME*, **233**, 1359 (1965).
4. J. W. Patterson, E. C. Bogren, and R. A. Rapp, *This Journal*, **114**, 752 (1967).
5. R. Baker and J. M. West, *J. Iron & Steel Inst.*, **204**, 212 (1966).
6. W. A. Fischer and D. Janke, *Arch. Eisenhuettenw.*, **39**, 89 (1968).
7. Yu. D. Tretyakov and A. Muan, *This Journal*, **116**, 331 (1969).
8. D. Yuan and F. A. Kröger, *ibid.*, **116**, 594 (1969).
9. W. G. Garrett and N. A. McKinnon, Private communication.

Evidence for a Complex Chloromolybdate Ion in a Molten Salt Medium from Transference Experiments

Vernon A. Lamb

National Bureau of Standards, Washington, D. C. 20234

Considerable indirect evidence exists for the presence of anionic chloro complexes of molybdenum in molten alkali chloride media, based mainly on emf measurements (1-4). It was thought that experiments that would provide direct evidence for the existence or absence of such complexes would be worthwhile. A transference technique was chosen for this purpose. The molten system was a solution of K_3MoCl_6 in KCl-LiCl eutectic.

If, at a particular temperature, the equilibria between Mo(III) ions and chloride ions lie predominantly in the direction of negative Mo-containing species, Mo should be electrically transported from the cathode compartment to the anode compartment of a transference cell. A blank experiment (no current) run under similar conditions should give the amount of transport by diffusion. A positive difference between Mo in the anode compartment resulting from electrolysis and from diffusion would indicate the presence in the molten system of a preponderance of negatively charged complex ions. On the other hand, if no electrical transport to the anode compartment were found, it would indicate that either the transference number of the complex is zero, or that it is dissociated to such a degree that neutral $MoCl_3$ or positive chlorocomplexes of Mo(III) predominate. In the latter case, electrical transport of molybdenum into the cathode compartment could be detected by electrolysis of a cell in which the molybdenum salt was initially present only in the anode compartment.

Experimental

Preliminary experiments showed that it was necessary to pass a large number of coulombs through a cell to produce transport of sufficient molybdenum to permit its measurement with reasonable accuracy. The cell shown in Fig. 1 was, therefore, designed to permit a large coulomb flow. Silver chloride is used in cathode compartment D. This arrangement prevents deposition of molybdenum from cathode compartment E that would occur if compartment D were absent and the cathode were placed directly in compartment E. The diaphram, C, between the two sections of the anode compartment prevented large amounts of nickel from entering compartment B-C. The number of coulombs that could be passed was limited by the amount of silver ion in the cathode compartment and the mass of nickel anode in contact with the eutectic melt in the anode compartment. These had capacities of about 7000 coulombs, whereas 2600 was the largest amount passed (Table I).

Key words: hexachloromolybdate complex ion, molten salt, transference numbers.

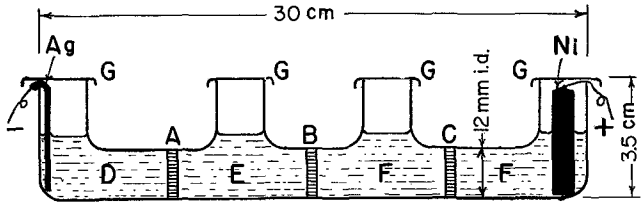

Fig. 1. Design of Vycor transference cell. A, B, C, porous quartz diaphrams; D, LiCl-KCl eutectic + AgCl, 25% by wt; E, K_3MoCl_6 + LiCl-KCl eutectic; F, LiCl-KCl eutectic; G, caps to reduce evaporation of salt.

The quartz disks shown in Fig. 1 were 1.5 mm thick and had a nominal pore diameter of <15 μm. As obtained from the manufacturer they had pore volumes ranging from 33 to 45%. Under a pressure differential of approximately 1 atm, the flow of water through these disks was 10-15 ml/min. To reduce the porosity of the disks and, hence, the interdiffusion rate between the contents of the cell compartments, the disks were partially plugged with silica by treating successively with ethyl silicate and hydrochloric acid, followed by baking at 800°C (5). Disks so treated to give a water flow under suction of about 0.5 ml/hr were used by Lunden (6), who estimated their effective total pore cross section to be about 0.3 to 0.4%. In our experience, disks this tightly plugged were extremely difficult to impregnate with molten salt, passed only a very small current at several hundred volts, and showed evidence of conductance by arcing. Most of the runs were therefore made with cells containing disks plugged to a flow under 1 atm pressure of 3-10 ml/hr. Such disks were estimated to have a pore cross section of about 3%. They permitted passage of currents of the order of 100 mA at cell potentials in the range of 5-10V, and interdiffusion was adequately reduced, as shown by the data in Table I.

Preparation of salts.—Potassium and lithium chlorides were purified by the method of Maricle and Hume (7). Potassium chloromolybdate was prepared by the method of Senderoff and Brenner (8) and purified by heating in vacuum at 150°C for ¾ hr, followed by successive washes in water, HCl-methyl alcohol, methyl alcohol, and ethyl ether, followed by vacuum removal of the ether. Analysis gave Mo, 19.95%; Cl, 49.6%. Theoretical: Mo, 23.1%; Cl, 51.2%.

Table I. Summary of experiments on transport of molybdenum

Exp. No.	Temp, °C	Current, mA	Time, hr	Coulombs	Disk flow at 1 atm, ml/hr	Initial location of K_3MoCl_6	Mo found in opposite compartment, mg	$t_{MoCl_6^{3-}}$
				Part A. Control experiment				
16B	720	None	53	None	12	—	0.55	
				Part B. Transport experiments				
5	800	80	1.8	520	42	Cathode	2.1	0.012
14	800	23	5	410	2.2	Cathode	1.5	0.011
8	800	140	4	2,000	3.5	Cathode	4.9	0.0074
15	800	180	4	2,600	10	Cathode	5.3	0.0062
12	800	100	2.8	1,000	4.0	Anode	0.9	—
							Arithmetic mean	0.009
							Standard deviation	0.0028

The found analysis is approximately accounted for if the preparation contained 12% of excess KCl. A eutectic mixture of LiCl and KCl plus potassium chloromolybdate was prepared that contained LiCl, 40%; KCl, 47%; K_3MoCl_6, 13% by weight (57, 41, and 2 m/o, respectively) of the constituent salts. On melting the molybdenum salt-eutectic mixture, a small amount of black precipitate formed, which was probably a molybdenum oxide or a higher valent chloride. It was separated by settling, freezing, and mechanical removal. Transfer and mixing operations were done in a dry-box.

Procedure.—The cells described above were filled in a dry-box and stoppered during transfer to the furnace tube. They were exposed to air only briefly while inserting the electrodes, capping the openings, and placing in the furnace tube. The Vycor furnace tube, 6 cm OD, was then sealed, evacuated, filled with argon, and heated in a horizontal tube furnace. When the salt had melted, several successive evacuations and pressurizations were usually required to cause filling of the disk pores, indicated by good electrical conductivity. Coulombs passed were measured by integrating the current-time curve recorded on a strip-chart.

After electrolysis was completed, the cell was allowed to cool in the furnace and was then removed. To recover the salt from the segment B-C (Fig. 1), the cell was broken at the respective disks and the salt dissolved in water in a beaker. Molybdenum in the portion of salt from segment B-C was determined spectrophotometrically by the thiocyanate method. Separate experiments with known mixtures showed that nickel from the anode compartment did not interfere. The accuracy of the molybdenum determinations is judged to be within ± 3%.

Results.—The results are summarized in Table I. The control experiment, 16B, shows that the amount of molybdenum transferred by diffusion to the adjacent section of the cell that initially contained no molybdenum salt is negligible (0.01 mg/hr). The amounts of molybdenum found in the anode compartments, B-C, in experiments 5, 8, 14, and 15 definitely indicate transport of molybdenum by a negative molybdenum-containing complex ion.

The data in the last line of Table I, experiment 12, show that there was no significant transport of a molybdenum-containing ion from the anode to the cathode compartment. This result reinforces the evidence of experiment No. 5, 8, 14, and 15 and indicates that any positive chloro complexes of Mo(III), if present, are in rapid equilibrium with the predominant negative complexes. (The small amount of molybdenum found in the cathode compartment in this experiment is ascribed to diffusion and to trace contamination from the adjacent Mo-containing compartment, which is difficult to avoid completely when the frozen salt is salvaged for analysis.)

The values for the transference number in the last column of Table I were calculated from

$$t_- = \frac{(96500)\,(\text{mass of Mo transferred})}{(\text{coulombs})\,(\text{Equivalent wt. of Mo})} \quad [1]$$

The undissociated hexachloro complex ion is assumed for calculating the tabulated transference numbers; hence, the equivalent weight of molybdenum is 1/3 of its molecular weight.

Conclusions

With the apparatus and procedure described, direct evidence for the existence of an anionic chloromolybdenum complex at 800°C has been obtained. Its transference number of approximately 1% in the KCl-LiCl solvent has been determined with an accuracy of about ±30%. This value of the transference number of the complex shows that alkali and free chloride ions carry most of the current, and its magnitude is reasonable in view of the mol fraction of molybdenum in the melt (2%).

Acknowledgments

Acknowledgment is made to the U.S. Atomic Energy Commission, Division of Research, Chemistry Branch, for support of this work, to Dr. Abner Brenner for helpful discussions, and to V. D. Pennington and J. F. Berkeley for determinations of molybdenum.

Manuscript submitted Dec. 4, 1969; revised manuscript received June 29, 1970.

Any discussion of this paper will appear in a Discussion Section to be published in the June 1971 JOURNAL.

REFERENCES

1. S. Senderoff and A. Brenner, *This Journal*, **101**, 16, 31 (1954).
2. M. V. Smirnov and O. A. Ryzhik, Transactions (Trudy) No. 6 of the Institute of Electrochemistry, Urals Academy of Sciences, Electrochemistry of Molten and Solid Electrolytes, Vol. 3, A. N. Baraboshkin, Editor, Sverdlovsk, USSR, pp. 9, 25 (1965). Translation by Consultants Bureau, New York, 1966.
3. S. M. Selis, *This Journal*, **113**, 37 (1966).
4. S. Senderoff and G. W. Mellors, *ibid.*, **114**, 556 (1967).
5. F. R. Duke and A. L. Bowman, *ibid.*, **106**, 626 (1959).
6. A. Lundén, *ibid.*, **109**, 260 (1962).
7. D. L. Maricle and D. N. Hume, *ibid.*, **107**, 354 (1960).
8. S. Senderoff and A. Brenner, *ibid.*, **101**, 28 (1954).

The Electrodeposition of Nickel from Heavy Water

F. E. Ammermann, S. Ghosh, J. A. Larson, and C. R. Lewis

Research Office, Product Planning and Development, Chrysler Corporation, Detroit, Michigan 48231

Since no information was available concerning the effect of substituting deuterium for hydrogen in electroplating solutions, a short experiment was undertaken to determine the effects of this substitution. Nickel was deposited from baths identical except for the presence of hydrogen in one and deuterium in the other, and the resulting deposits were subjected to metallographic and x-ray diffraction examination.

Procedure

For the electrodeposition experiment, two solutions were made, each containing 2.4g of nickel chloride ($NiCl_2$) and 13.9g of nickel sulfate ($NiSO_4$) as dessicated salts. One was dissolved in 100 ml normal water and the other in a like amount of heavy water. One drop of hydrochloric acid was added to each solution to suppress hydrolysis and each was allowed to stand for 24 hr. Anodes were prepared from rolled electrolytic nickel. Cathodes, 1 in.^{2} were cut from polished brass sheet. The anodes were bagged in filter paper.

Electrolysis was performed in glass jars at room temperature. The electrodes were spaced 1 in. apart. The systems were connected in series and current supplied from a rectifier at the equivalent density of 30 A/ft^2 at the cathode. Each jar contained one cathode

Key words: deuterium, electroplating, stresses, nickel.

and anode arranged so that the opposed surfaces carried the principal amount of current and the backs were shielded. It was recognized that the conditions of high pH, low temperature, and lack of buffer (usually boric acid) would yield a burned and brittle plate, but it was felt that the unfavorable circumstances were more likely to emphasize any significant differences in deposition.

At the onset of deposition it was noted that hydrogen evolution was much reduced in the deuterium oxide solution. The cathodes were periodically examined in order to note significant alterations in appearance. As expected, the deposits were cracked and burned but that from the deuterium oxide much less so. Deposition was stopped when a sufficient thickness of nickel had been deposited to permit further examination. The total plating time was 2.5 hr during which the current was kept constant by periodic adjustment. Visual inspection showed the deuterium plate to be relatively smooth and metallic, whereas the normal system had produced the expected scaled and discolored surface. Somewhat unexpected was the appearance of the anodes. The anode from normal water appeared uniformly pitted but the heavy water anode was distinguished by large widely spaced holes in the surface.

Metallurgical Results

Both anodes and cathodes were given a detailed metallurgical examination. Because the deposits, especially from the normal water, were curled and fragmented, superficial hardness measurements were not taken. Figures 1 and 2 show the microscopic aspects of the anode dissolution. Since both the anodes and plating conditions were the same, any differences must be attributed to the presence of the heavy water in the electrolyte. The internal cavity structure and the nature of localized, uniform, tri-axial dissolution, irrespective of grain orientation, appears to be the same in both cases. Therefore, the difference lies in the behavior of the anode surface layer in the presence of the two electrolytes. In the heavy water solution, the surface characteristics of the anode appear to present no problem for dissolution (Fig. 4), whereas in the normal water solution, the surface layer appears to be passivated (Fig. 3) to a high degree. The improved anode utilization in the heavy water cell is apparent.

Figures 5 and 6 show cross sections of the deposits from heavy and normal water, respectively. The following observations can be made:

1. Both systems produced a deposit almost similar in appearance except for depth, uniformity, and tenacity with the substrate.
2. Both deposits are difficult to etch, basically columnar in nature and similar in microstructure except for the grain size difference.
3. The deposit from the heavy water system shows more ductility and better metallurgical bond with the substrate than the deposit from normal water.
4. In both systems, the structural continuity is broken by intermittent plating, indicating perhaps the effect of oxidation. Electron microscopic investiga-

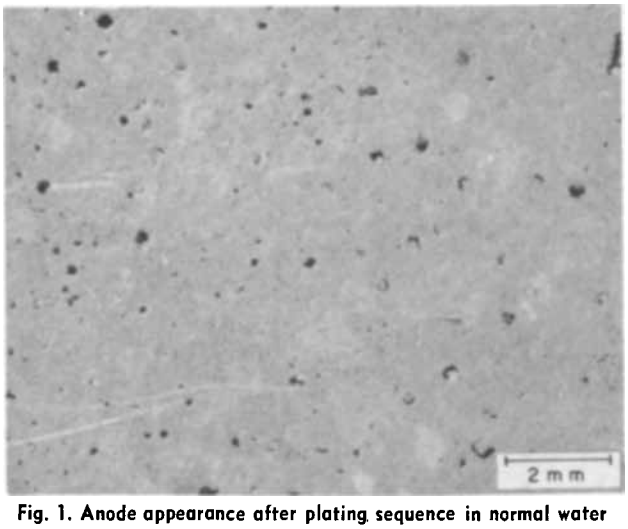

Fig. 1. Anode appearance after plating sequence in normal water

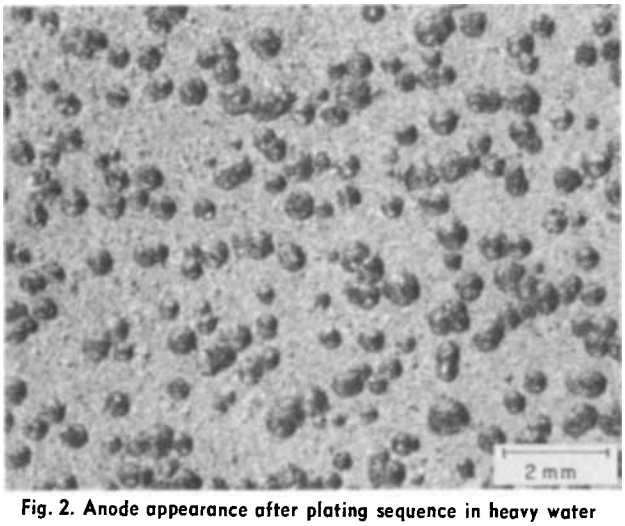

Fig. 2. Anode appearance after plating sequence in heavy water

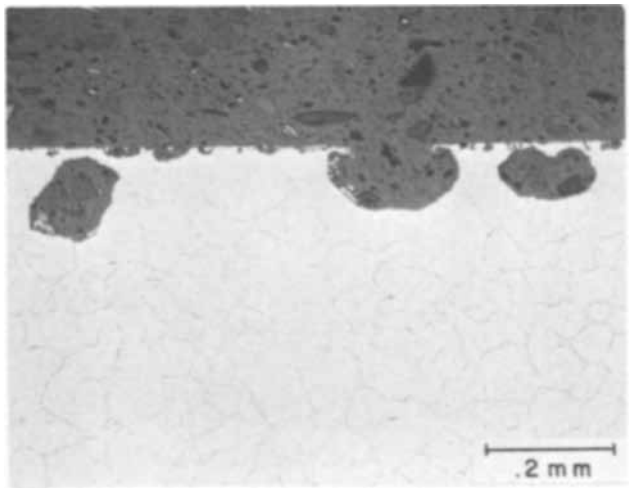

Fig. 3. Microstructure of anode surface dissolution pattern (normal H_2O) (100X).

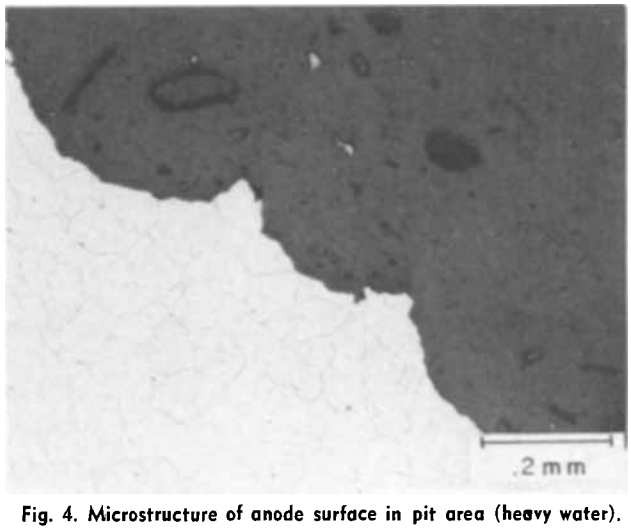

Fig. 4. Microstructure of anode surface in pit area (heavy water). (100X).

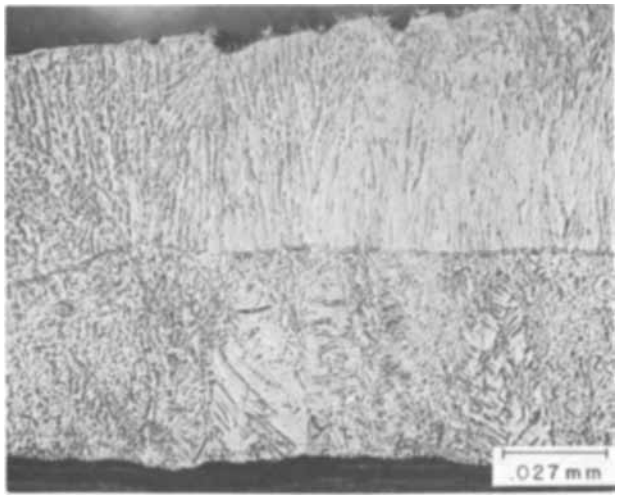

Fig. 5. Microstructure of plate from heavy water

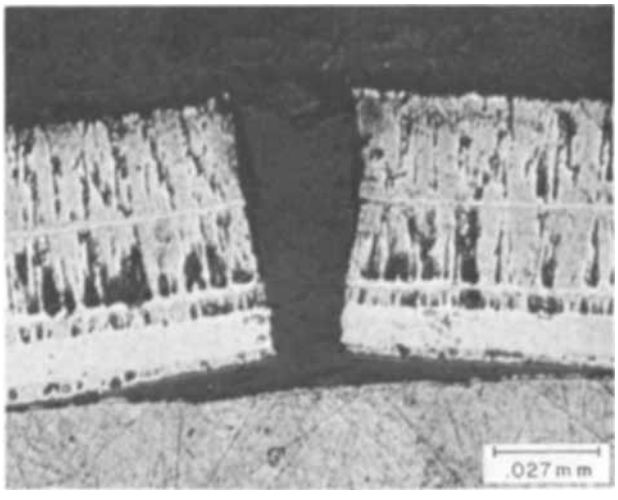

Fig. 6. Microstructure of plate from normal water

tion of the structure of both the anode and the plating is being pursued and may reveal further information.

X-Ray Results

Since distinct differences in grain size and stress levels were apparent in the two deposits, Fourier analysis of the x-ray diffraction peak shapes was undertaken to make these differences more quantitative. The analysis was performed on the (200) and (400) lines using copper radiation. Since the Rachinger (1) technique for doublet separation depends heavily on the tails of the diffraction lines, an interfering line from the brass substrate (which was evident in the tail of one diffraction line), made doublet separation difficult. Therefore, a computer program based on the unresolved doublet was used (2). The correction for instrumental broadening was made with the method devised by Stokes (3), using annealed nickel powder as the instrumental standard. The separation of the broadening into microstrain and particle size terms was accomplished utilizing the Warren and Averbach technique (4). The results of this analysis are shown in Table I.

The values of De and microstrain shown in Table I are in order-of-magnitude agreement with those given

Table I. X-ray results

Plating solution	Effective particle size De_{200}, A	Microstrain $\langle E^2_{50A} \rangle^{1/2}_{200}$	Microstrain $\langle E^2_{100A} \rangle^{1/2}_{200}$
H_2O	190	14.3×10^{-4}	3.5×10^{-4}
D_2O	140	Very small	Very small

by Hinton (5) for electrodeposited silver. The general conclusion from the results shown is that the observed physical difference between the two plates can be attributed primarily to microstrains. In interpreting these microstrain differences, one must keep in mind that, since the Fourier analysis was carried out centered on the mid-point of the annealed peak, the microstrain values obtained must be corrected for any macrostrain which may be present. *i.e.*, the observed values are actually equal to $[\langle E_L^2 \rangle - \langle E_L \rangle^2]^{1/2}$. However, due to the poor adherence of the plates, it can probably be assumed, in this case, that any macrostrains have been relieved. It should also be noted that it is apparently possible for hardness (or ductility) differences to be accounted for by twin faults (5), and these were not evaluated in this case. However, it is felt that the large differences in microstrains are the primary cause of the ductility variation between the two plates, and twin fault variations are probably small.

It is apparent that visual, structural, and physical differences do exist in nickel deposited from normal and heavy water under the conditions described. The major effects are a lower stress level and smaller grain size in the nickel deposits and a more uniform removal of the anode surface from the heavy water solution. It is likely that these differences would diminish under conditions conducive to a more normal deposit such as higher temperatures, although the effects on anode dissolution should not depend strongly on this particular plating condition. The anode effect may represent a combination of D_2O as a solvent and the changes relative to H_2O during a plating cycle.

There are certain difficulties inherent in plating experiments using deuterium oxide that arise from the necessity of excluding normal hydrogen and the fairly high cost of deuterium oxide. However, the interesting results achieved in a simple experiment suggest that further investigation of deuterium oxide in both the deposition and etching of metals would be fruitful.

Acknowledgment

The authors would like to thank Mr. D. H. Mott for the photographs and Mr. T. C. Scott for help with the x-ray computer program.

Manuscript submitted May 7, 1970; revised manuscript received *ca.* June 20, 1970.

Any discussion of this paper will appear in a Discussion Section to be published in the June 1971 JOURNAL.

REFERENCES

1. W. H. Rachinger, *J. Sci. Instr.*, **25**, 254 (1948).
2. R. J. DeAngelis, "Local Atomic Arrangements Studied by X-ray Diffraction," Met. Soc. Conf., Vol. 36, p. 271, Gordon-Breach, N. Y. (1966).
3. A. R. Stokes, *Proc. Phys. Soc., London,* **61,** 302 (1948).
4. B. E. Warren and B. L. Averbach, *J. Appl. Phys.*, **21,** 595 (1950).
5. R. W. Hinton, L. H. Schwartz, and J. B. Cohen, *This Journal,* **110,** 103 (1963).

JOURNAL OF THE ELECTROCHEMICAL SOCIETY

SOLID STATE SCIENCE

OCTOBER 1970

A Kinetic Study of the Fluorination of Silver

Patricia M. O'Donnell*

Lewis Research Center, National Aeronautics and Space Administration, Cleveland, Ohio 44135

ABSTRACT

The effect of the variables, temperature, and pressure, on the kinetics of the reaction of fluorine with silver were studied. The temperature range of the investigation was from 25° to 300°C, and the reaction was measured at fluorine pressures of 50-600 Torr. The reaction was found to be pressure dependent. Three reaction products are identified: silver subfluoride, silver monofluoride, and silver difluoride. No simple rate law could describe the data over the entire time interval of the reaction.

The majority of the kinetic studies on heterogenous systems that have appeared in the literature in general discuss metal-oxygen systems. There have been some kinetic studies reported on metal-fluorine systems (1-15); however, the majority of the research on metal-fluorine systems has been compatability studies. In the present investigation the fluorination of silver was studied by exposing silver coupons to fluorine gas and following the reaction by the pressure drop method. The effect of both temperature and pressure on the rate of reaction are presented.

Experimental

The system used to study the fluorination of silver is shown in Fig. 1. Fluorine is brought from the tank through copper tubing into the system which is Pyrex throughout except for the reaction furnace which is made of quartz. A cold trap using a methylcyclohexane slush (−116°C) was used to remove any hydrogen fluoride impurity from the fluorine. The fluorine is analyzed by reaction with mercury in the still (1). Analysis of the fluorine indicated 99.83% fluorine plus 0.17% HF before purification and 100% fluorine after purification. Enough purified fluorine for one run is stored in the storage bulb. The mercury manometers in the system indicate the pressures in the storage and reaction sections of the apparatus. A layer of fluorocarbon oil is floated on top of the mercury to prevent it from reacting with the fluorine. All readings are corrected for density differences between the oil and the mercury. The metal samples are silver plates 1.27 x 15.24 x 0.012 cm. Spectrographic analysis gave a purity of 99.999%.

A plate is inserted into the cold reaction furnace under flowing argon and is positioned upright in the center of the furnace. The end plug is put in place and the argon pumped out. The furnace is turned on and the reaction section brought up to the appropriate temperature. Temperature profiles have been run with an instrumented metal sample, and the results show that the temperature variation across the sample is not more than 1°C. Meanwhile the storage section is filled with fluorine. The general experimental method used to determine the rate of fluorine consumption by silver was to measure the pressure decrease in a vessel of known volume containing the silver sample. In order to maintain approximately constant fluorine pressure, the pressure was allowed to drop only about 2 Torr and then more fluorine is introduced to return the pressure to its initial value. Pressures are recorded automatically by the pressure transducer and recording system. The perfect gas law was used to calculate the amount of fluorine consumed from the incremental pressure drop, the vessel volume, and the temperature. From the calibrated volume of the system, pressure changes on the time trace can be converted to milliliters of fluorine consumed at STP. After approximately a 4-hr exposure time the heaters were turned off, the system was allowed to cool to 25°C, and then the fluorine was pumped out of the system through the two soda lime scrubbers. The system is then brought up to atmospheric pressure with argon. A dry box is connected to the end of the furnace and the sample is pulled into it under flowing argon to prepare it for chemical and instrumental analysis.

Results and Discussion

The fluorine consumption by the silver samples was measured at several temperatures and pressures. The reaction was followed as a function of time and is reported as milliliters of fluorine consumed at STP per square centimeter of silver surface based on the geometrical area of the silver surface.

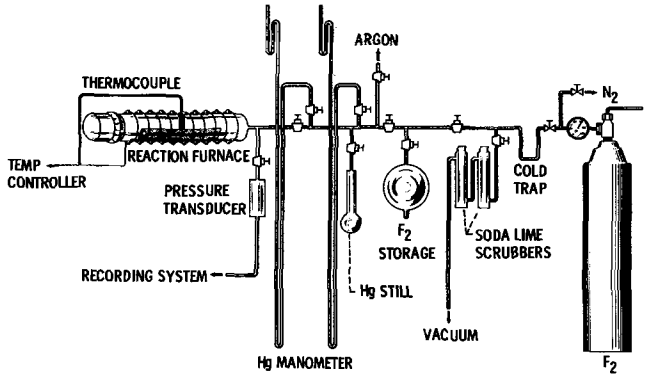

Fig. 1. Fluorination apparatus

* Electrochemical Society Active Member.

Key words: kinetics of fluorination of silver, fluorination of silver.

The effect of temperature on the reaction at a constant fluorine pressure of 50 and 200 Torr is shown in Fig. 2 and 3, respectively. The effect of pressure on the reaction at a constant temperature of 100° and 200°C is shown on Fig. 4 and 5. Note that at both temperatures there is a pressure reversal. This observed reversal in pressure dependency is not unique to this system but has been observed in other fluorination studies where multiple products are formed (16).

Data were not obtained at $t = 0$, the initial contact time of fluorine with the silver, because it takes a finite period of time to pressurize the apparatus with fluorine.

No simple rate law will describe the silver-fluorine reaction over the entire time interval studied. A linear rate law is applicable at short times, but as the time interval increases the data points deviate from a straight line as illustrated in Fig. 6. The data at the longer time intervals can best be described by a parabolic rate law as shown in Fig. 7.

Several products are formed when silver is reacted with fluorine at the temperatures and pressures studied. The products were identified by x-ray diffraction and by chemical and physical analysis as the subfluoride Ag_2F, the monofluoride AgF, and the difluoride AgF_2. Where more than one fluoride appeared the films were layered with the fluoride richest in silver adjacent to the metal and the one richest in fluorine at the gas-fluoride surface. The monofluoride was found as the middle layer. The relative amounts of

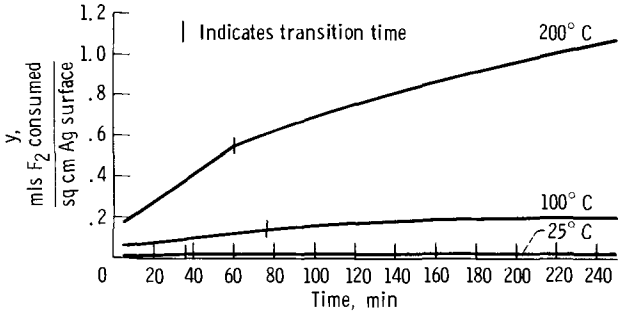

Fig. 2. Temperature effect at 50 Torr F_2 pressure

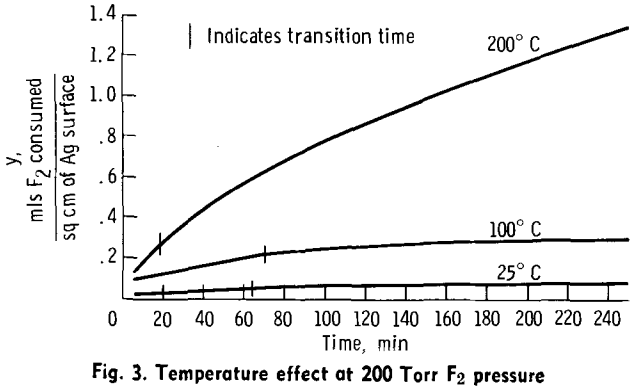

Fig. 3. Temperature effect at 200 Torr F_2 pressure

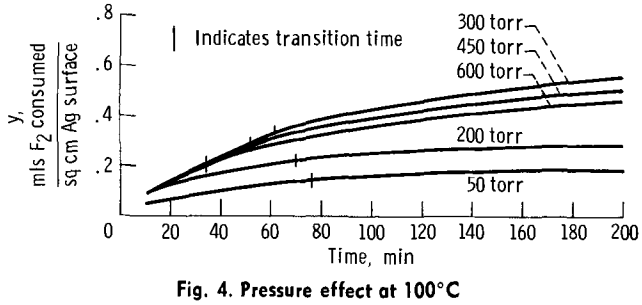

Fig. 4. Pressure effect at 100°C

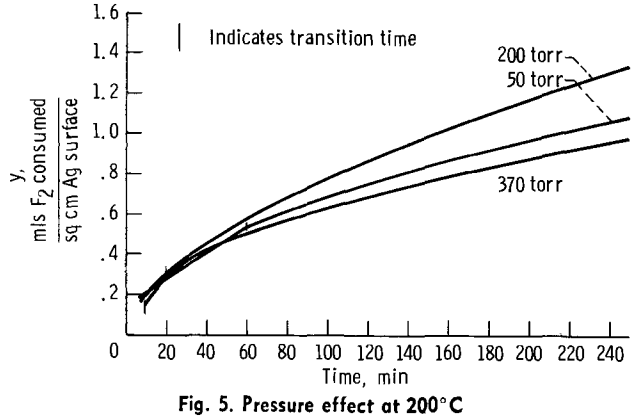

Fig. 5. Pressure effect at 200°C

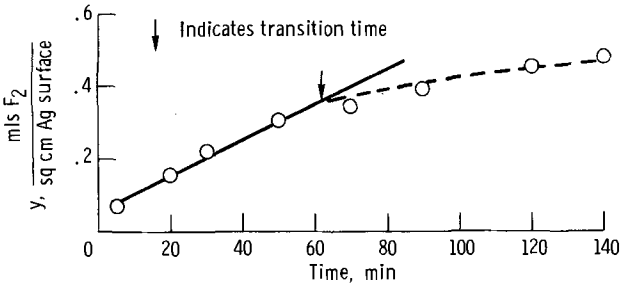

Fig. 6. Linear plot of fluorine consumption (100°C, 300 Torr)

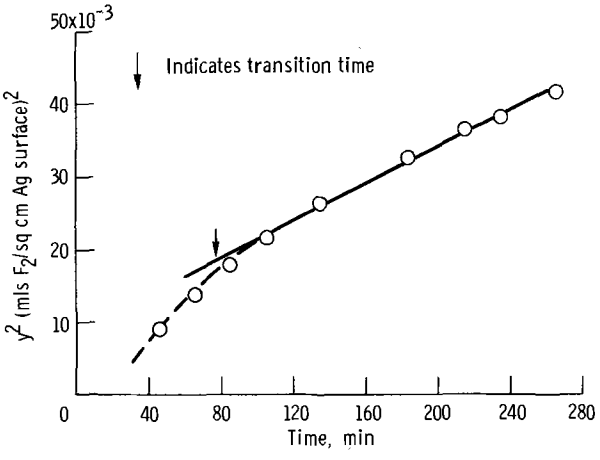

Fig. 7. Parabolic plot of fluorine consumption (50 Torr, 100°C)

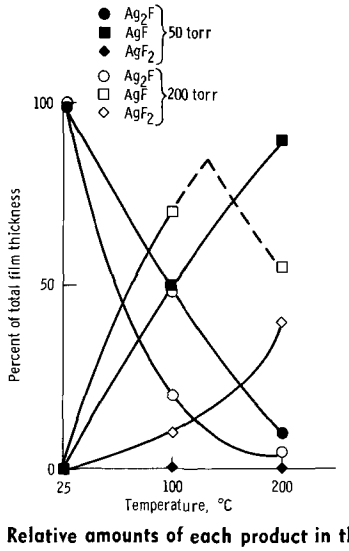

Fig. 8. Relative amounts of each product in the film

each product in the film, obtained from cross-section microscopy are shown in Fig. 8 for two pressures as a function of temperature. The amount of Ag_2F is shown by the circular symbols. As the temperature increases the amount of Ag_2F decreases. At 25°C only Ag_2F is formed at both pressures. The amount of AgF, shown by the square symbols, seems to increase to a maximum amount and then decrease as the temperature increases. The amount of AgF_2 is shown by the diamond symbols. No AgF_2 is formed at 50 Torr regardless of the temperature while at 200 Torr the amount increases as the temperature is increased. Not only temperature but pressure also affects the products formed. At 25°C and all pressures studied the only product formed was the subfluoride Ag_2F. As the temperature is increased, one or more reactions are possible including the decomposition of the subfluoride.

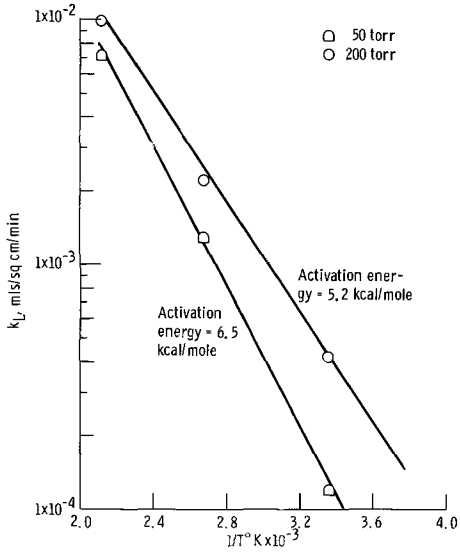

Fig. 9. Effect of temperature on rate constant in the boundary controlled region.

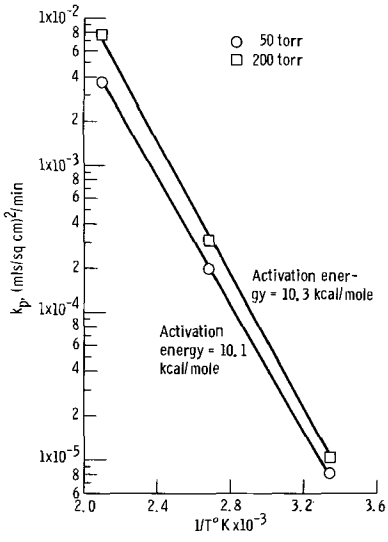

Fig. 10. Effect of temperature on rate constant in the diffusion controlled region.

At 300°C the product melted even though the temperature was well below the reported melting points of the monofluoride (435°C) and the difluoride (690°C) This could be due to the formation of a known low melting eutectic $AgF \cdot AgF_2$ (17).

Reaction rate constants are plotted against $1/T$ on Fig. 9 and 10. The data on Fig. 9 show a pressure effect. Brown and Crabtree (1) observed a pressure effect on the activation energy, but could offer no explanation.

The reaction of silver and fluorine is a complex reaction and the applicability of different rate laws is difficult to explain in the absence of definitive solid-state data.

Summary

The experimental results presented in this paper point to the fact that the reaction between fluorine and silver is a complex reaction, and the kinetics are not simple. In a study of this type it is the over-all rate that is determined, and no attempt was made to determine individual specific rates.

Manuscript submitted Feb. 9, 1970; revised manuscript received *ca.* June 15, 1970. This was Paper 408 presented at the Montreal Meeting of the Society, Oct. 6-11, 1968.

Any discussion of this paper will appear in a Discussion Section to be published in the June 1971 JOURNAL.

REFERENCES

1. P. E. Brown, J. M. Crabtree, and J. F. Duncan, *J. Inorg. Nucl. Chem.*, **1**, 202 (1955).
2. P. M. O'Donnell and A. Spakowski, *This Journal*, **111**, 633 (1964).
3. P. M. O'Donnell and A. Spakowski, NASA TN D-768, 1961.
4. R. K. Steunenberg, L. Seiden, and H. E. Griffin, Chemical Engineering Div. Summary Report for July, August, September 1958, Rep. ANL 5924 Argonne National Lab., pp. 42-43.
5. M. J. Steindler and D. V. Steidl, Chemical Engineering Div. Summary Report, January, February, March 1959, Rep. ANL 5996, Argonne National Lab., June 1959, pp. 135-139.
6. P. M. O'Donnell, *This Journal*, **114**, 218 (1967).
7. Iwasaki *et al.*, *Kogyo Kagakw Zassi.*, **65**, 1165 (1962).
8. A. K. Kuriakose and J. L. Margrave, *J. Phys. Chem.*, **68**, 2671 (1964).
9. A. K. Kuriakose and J. L. Margrave, *ibid.*, **68**, 2671 (1964).
10. P. M. O'Donnell, *This Journal*, **114**, 1206 (1967).
11. M. J. Steindler, D. V. Steidl, and R. K. Steunenberg, Chemical Engineering Div. Report, June 1958, Rep. ANL 5875 Argonne National Lab., June 1958.
12. R. K. Steunenberg and J. Fisher, Chemical Engineering Div. Summary Report, January, February, and March 1959, Rep. ANL 5996 Argonne National Lab., June 1959, pp. 134-135.
13. A. K. Kuriakose and J. L. Margrave, *J. Phys. Chem.*, **68**, 290 (1964).
14. A. K. Kuriakose and J. L. Margrave, *J. Phys.* Chem., **68**, 2343 (1964).
15. R. L. Ritter and H. A. Smith, *ibid.*, **71**, 2036 (1967).
16. Gerard Vandenbussche, Rep. CEA-R-2859 Centre d'Etudes Nucleaires, Dec. 17, 1964.
17. Von Otto Ruff and Manfred Giese, *Z. fur anorg. u. allgem. chem.*, **219**, 143 (1934).

Effect of Sealing Variables on the Degree-of-Seal

G. A. Dorsey, Jr.

Kaiser Aluminum & Chemical Corporation, Center for Technology, Pleasanton, California 94566

ABSTRACT

At least three separate effects occur during sealing (*a*) gross water adsorption by the bulk and surface of the porous layer, probably also accompanied by anion loss (as in the case of H_2SO_4-anodized films), (*b*) an oxide transition near the barrier-porous layer interface, which results in a net decrease in the amount of barrier layer and a net increase in the amount of porous layer cross-linking, and (*c*) a seemingly thin-layer effect that takes place with aging and may be localized in the pore base region of the porous layer. A two-step current density program was used to prepare 7.4-7.6 μm (0.3 mil) anodic films on alloy 1100, using a 1.7M H_2SO_4 electrolyte at 25°C. These coatings were then sealed for from 10 to 65 min, at temperatures from 65° to 95°C, in weakly buffered sealing baths whose *p*H was adjusted within the region of 5.0 to 6.5. Corresponding films were also left in the unsealed condition. Data for these films were obtained using 1 kHz impedance measurement of coating permeability, effluent gas detection (EGD technique) of partial water contents, and infrared determinations of coating structures. For these 7.4-7.6 μm (0.3 mil) coatings, the greatest benefit was derived with the following sealing conditions: sealing *p*H range, 6.15 ± 0.15; seal time, 30 min, but not more than 40; sealing temperature, 95°C-to-boiling, or higher, as might be achieved by pressurized steam sealing.

References (1) and (2) describe the "inner seal" effect and point out its potential importance in the over-all mechanism of sealing. This involves a structural transition that appears to take place, as a result of sealing, near the interfacial region between the secondary phase barrier layer and the anodic oxide porous layer. It seemingly is an hydration effect that has the nature of a structural hydrate rearrangement, the net result being a forming together (or agglomeration) of oxide at the base of the individual alumina fibrils that comprise the porous layer. This is apart from surface hydration changes and anion loss that occur elsewhere in the porous layer oxide.

Earlier work dealt with the "effect" itself, and not with factors introduced by changes in sealing variables. Only one set of sealing conditions was employed for this: *p*H 6.0 boiling water, with a seal time of 10 min. Now we seek to determine the varying results that are brought about by employing different sealing temperatures, seal times, and *p*H values.

This sealing effect was limited to only thin films (~2 μm) when conventional anodizing conditions were employed (2): 1.3 A/dm², 1.7M H_2SO_4 and 25°C. However, the same effect could be achieved with three-fold thicker films (7.4 μm) when the proper oxide transition structure was obtained with a two-step anodizing current density program (2) in this same electrolyte. An initial current density of 1.3 A/dm² was used to develop a near-optimum oxide structure. This structure was then "frozen" by a higher current density (3.5 A/dm²) that allowed the film to thicken normally while nevertheless maintaining the oxide structure characteristic of the thinner ~2 μm film. In this manner, at least for ~7 μm (0.3 mil) films, the inner seal effect could be realized independent of actual film thickness.

However, this sealing transition, or inner seal effect, is undoubtedly sensitive to changes in sealing variables, although in this regard it should be no different from films prepared by more common practice. High-temperature sealing conditions may rapidly create surface blockage that could close off otherwise reactive sites, or the effect that we describe could be a slow reaction and relatively independent of surface effects: dependent only on temperature, in a nondehydrating environment. Additional boiling water seal times might be required, beyond the 15-min time period normally employed with ~7 μm films, in order to realize the completion of a slow reaction. There is, too, the potential effect of sealing *p*H, which may also be a factor if the mechanism of this transition involves hydrogen or hydroxyl ion from the sealing medium.

Key words: anodic aluminas, sealing.

Experimental

Sample preparation.—Alloy AS32 (alloy 1100 clad with 1100: 99.2% Al) sheet coupons were cleaned and chemically brightened, then anodized in 1.7M H_2SO_4 at 25°C. The initial current density of 1.3 A/dm² was maintained for the first 4.84 x 10^2 coulombs/dm² of current quantity (6.25 min at 1.3 A/dm²), then the current density was immediately raised to 3.46 A/dm² and maintained at that level for the balance of the anodizing period. The total current quantity expended was 13.9 x 10^2 coulombs/dm², equivalent to a 7.4 μm film thickness.

The various seals were prepared from distilled water containing 5 x 10^{-6}M acetic acid as a buffering additive and were adjusted to the desired *p*H with sodium hydroxide. The *p*H value was measured at the temperature selected for operation of the seal. Four *p*H values were employed: 5.0, 5.5, 6.0, and 6.5. Sealing temperatures were 65°, 75°, 85°, and 95°C. Sealing times ranged from (*a*) unsealed, to (*b*) 10, 20, 30, 50, and 65 min. Impedance and EGD values were determined immediately, and the same coupons were then re-examined periodically over storage periods of up to 100 days, stored in a clean environment, at ambient room humidity. Infrared data were obtained after an approximate 30-day storage period following sample preparation.

Test methods.—Effluent gas detection (EGD) data were obtained as before (3). The anodized sample was placed in a leak-tight chamber within the oven of a gas chromatograph, then continuously purged with helium which passed on to a thermal conductivity detector. The chamber was heated from ambient temperature to 350°C, at a rate slightly less than 10°C/min (3). As volatile materials, in this case, water, are evolved from the sample, the water-bearing helium effluent is carried on to the detector which then provides a continuous plot of evolved water *vs.* temperature. The result is exactly the same as a thermobalance operated in differential mode, but provides far more sensitivity.

Impedance values were measured with a 1 kHz impedance bridge (Twin City Testing Corporation's Z-Scope), using a 3.5 w/o NaCl media. The data re-

ported are average values taken from multiple readings with each anodized coupon. Infrared spectra were obtained within the 4000-35 cm^{-1} ranges of the Beckman IR-7 and IR-11 spectrophotometers, according to procedures already described (4).

Results and Discussion

Effluent gas detection (EGD).—A limitation of this technique is its failure to allow for baking temperatures above 350°C, which is usually insufficient to allow complete dehydration of most types of anodic coatings. Nevertheless, it has been shown (1-3) that the partial water content, measured by the lower-temperature EGD method, has value. This fraction of the films' total water content apparently corresponds directly with that portion of the oxide that is altered by the barrier layer sealing transition; EGD data are seemingly a reliable indicator for the degree of completion of the inner seal effect. The partial water measured by the EGD technique is independent of total porous layer oxide thickness and is independent of total water content, with neither of these two factors directly influencing the inner seal effect. The EGD data provide isolated data pertaining only to the inner seal effect itself and, when coupled with data sensitive to other changes within the coating structure, should provide a clearer picture of over-all sealing mechanisms.

The EGD technique proved not to be sensitive to effects related to the aging of sealed coatings (Fig. 1), and these sealed films were therefore stored, for convenience, prior to EGD measurement. Unsealed films are, however, affected by aging (Fig. 1), and subsequent coatings were tested immediately after air drying. Figures 2 through 5 show these EGD data plotted *vs.* sealing time, and including the effects of different sealing *p*H and temperatures. These curves

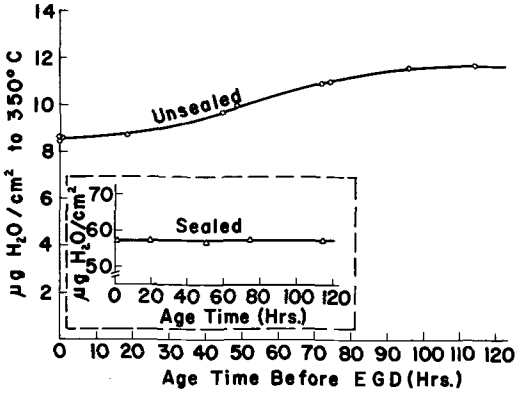

Fig. 1. Effect of aging on partial water content (EGD) of sealed and unsealed coatings.

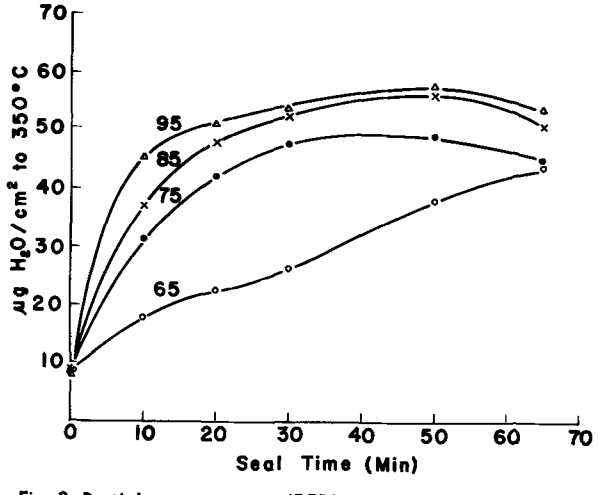

Fig. 2. Partial water content (EGD) of coatings sealed at *p*H 5.0; tie line notation gives seal temperature: °C.

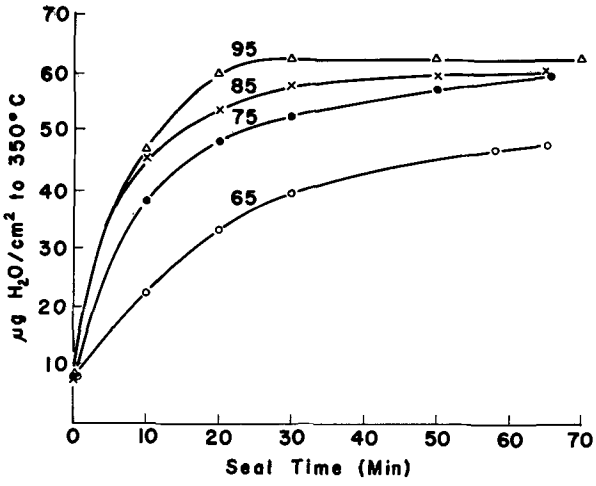

Fig. 3. Partial water content (EGD) of coatings sealed at *p*H 5.5; tie line notation gives seal temperature: °C.

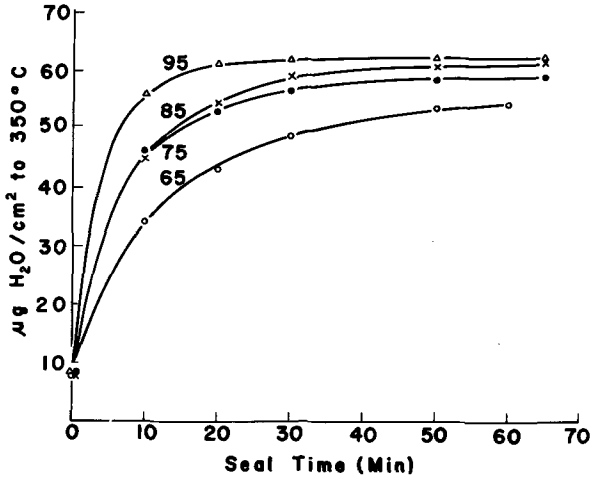

Fig. 4. Partial water content (EGD) of coatings sealed at *p*H 6.0; tie line notation gives seal temperature: °C.

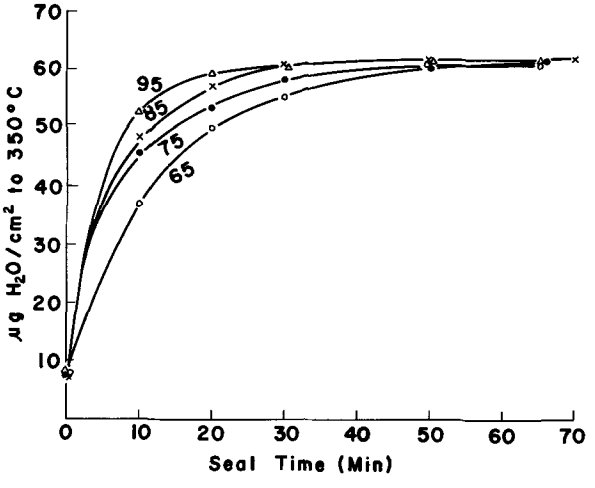

Fig. 5. Partial water content (EGD) of coatings sealed at *p*H 6.5; tie line notation gives sealed temperature: °C.

are symmetrical except for the low-*p*H seal data (Fig. 2, *p*H 5.0) which show what might be regarded as a solubility effect, with prolonged seal times, that becomes more pronounced as sealing temperature is increased toward boiling. This would indicate that, except for *p*H 5.0 seals, the apparent solubility effects did not penetrate down to that portion of the oxide that is responsible for the EGD data, the barrier-porous layer interface.

Figures 3-5 show (with seals at pH 5.5 or higher) a plateau or maximum endpoint in the sealing reaction. Beyond this point, further sealing times had no effect. This maximum value (63 μg H_2O/cm^2) represents the apparent completion of the sealing reaction, at least so far as the inner seal is concerned.

Earlier (4) the inner seal effect was proposed to be a structural conversion of pre-existing aluminum hydroxide. It was proposed that the secondary phase barrier layer hydroxide converted into a lower polymer form of hydroxide that was incorporated into the porous layer at the base of its individual alumina fibrils. If such was the case here, there should be a plateau or maximum endpoint in the sealing reaction, since all oxide (secondary phase barrier layer) available for this transition would have been converted. If the EGD technique is sensitive only to the quantity of this transformed oxide and not to other sealing reactions such as gross water content, then these data should show (as is seen in the data, Fig. 3-5) a maximum value that remains unchanged by further sealing.

With freshly anodized unsealed films, the 1 kHz a-c impedance correlates with the primary phase barrier layer thickness, giving the following relationship: 14.2 Å/kohm/cm^2 impedance. This places the average primary phase barrier layer thickness for these coatings at 180Å. Similarly, using earlier *IR* data (2, 5), and the current *IR* data to be discussed later, the average unsealed (initial) secondary phase barrier layer thickness may be calculated as 1.12 x 10^4Å. Using densities of 2.7 and 2.4 g/cm^3 for these oxides, respectively, complete dehydration to the monohydrate should release, at most, a quantity of water corresponding to 23% of the initial oxide weight. This would be 63 μg H_2O/cm^2, exactly the value of the plateau (endpoint) region shown in Fig. 3-5. Assuming, still speculatively, an initial trihydrate composition for the unsealed secondary phase barrier layer, and assuming that the plateau maximum value corresponds to an endpoint in the depolymerization reaction for this oxide, as one result of sealing, then the following interpretation can be made:

(*A*) Initially and before sealing, the EGD technique detects only a small fraction of the trihydrate water that is actually present in this oxide sublayer: about 10%.

(*B*) After a short but inadequate seal time, some of this trihydrate has undergone the depolymerization transformation. While its composition remains unchanged, the partial transformation increases the percentage of water driven off from this oxide by the temperature-limited EGD technique.

(*C*) Correspondingly more water is detectable *via* EGD as more of the oxide is converted by further sealing. Eventually, sealing consumes all of the oxide that is available for transformation. Beyond this point, the EGD data show no further increase in apparent water content as a result of further sealing. A maximum-value plateau has been reached.

(*D*) While the initial EGD data show only about 10% of theoretical water content for unsealed samples, this percentage increases as the degree of sealing becomes complete. Samples that have reached the maximum value plateau region should release (via EGD) an amount of water corresponding to 2 moles of water for each mole of sublayer oxide.

This does not mean that this particular water has been gained as a result of sealing. It may already have been present but needed the impetus of sealing to transform the oxide structure into one that dehydrates more readily: into an oxide that dehydrates under the low-temperature conditions (to 350°C) of the EGD technique.

Similar plots (unpublished) of water released *vs.* sealing *p*H for varying seal times at 95°C show a maximum value that appears to lie near *p*H 6.0. The 10-min seal data show this more clearly, since data in the plateau region mask out the effect of *p*H. The transformation, once complete, is unaltered by changes in seal *p*H (except for what might be solubility effects near *p*H 5.0). While sealing is ordinarily carried out in the *p*H range of 5.5 to 6.5 (6), there may be more advantage to sealing near *p*H 6.0. This is consistent with Bogoyavlenskii and Belov (7) and may also be seen with impedance data to be discussed shortly.

An attempt at kinetic data, using Van't Hoff's differential method, provides another tool for the interpretation of these data. Ordinarily, such data are obtained by measuring the decrease in reactant concentration as a function of time, with varying initial reactant concentrations. Where c_1 and c_2 denote two different initial concentrations and where n denotes the apparent order of the reaction with k being the rate constant, or specific reaction rate, then

$$-dc_1/dt = kc_1^n$$

and

$$-dc_2/dt = kc_2^n$$

and

$$n = \frac{\log(-dc_1/dt) - \log(-dc_2/dt)}{\log c_1 - \log c_2}$$

A plot of log $(-dc_1/dt)$ *vs.* log c, will be linear and the slope will be the apparent order of reaction, n, if the reaction proceeds without complication. Extraneous features in the reaction will, on the other hand, yield a curved plot to indicate that the reaction proceeds without a simple order.

Sealing eventually produced the same maximum-value plateau (end point) in the EGD data: 63.4 μg H_2O/cm^2, a value which remained unchanged with further seal times. Unsealed samples, prepared in an identical fashion, also gave a constant EGD value of 8.54 μg H_2O/cm^2. Therefore we assumed that the amount of alumina being transformed, on sealing, was equivalent to the difference between these two values, or 54.9 μg H_2O/cm^2. This value serves as "initial reactant" for the Van't Hoff concentration term "c". After, for example, a 10-min seal at *p*H 5.5, the EGD technique detected 22.8 μg H_2O/cm^2 indicating a "reactant" concentration equivalent to 40.6 μg H_2O/cm^2 remaining. Then one point on the plot would be represented by log $(-dc_1/dt)$ = log (54.9-40.6/10), with log c_1 = log (54.9). Similar calculations led to the values that are plotted in Fig. 6 through 8; calculations were prevented for the *p*H 5.0 data, because of what appear as solubility effects (Fig. 2) in this low *p*H seal.

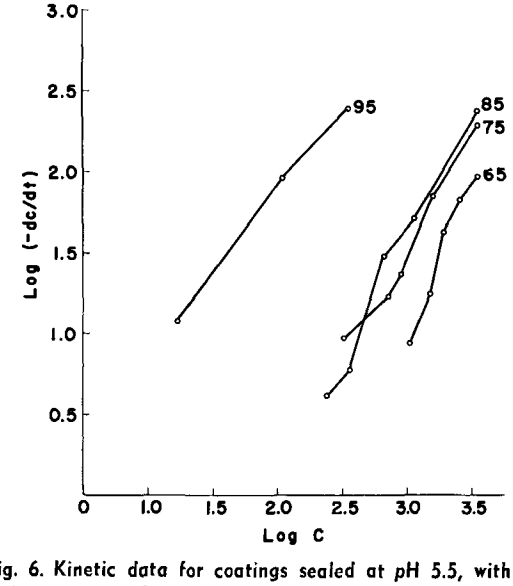

Fig. 6. Kinetic data for coatings sealed at *p*H 5.5, with tie line notation giving seal temperature: °C. The apparent reaction order was, at 65°C, 1.7; at 75°C, 1.4; at 85°C, 1.5 and, at 95°C, 1.0.

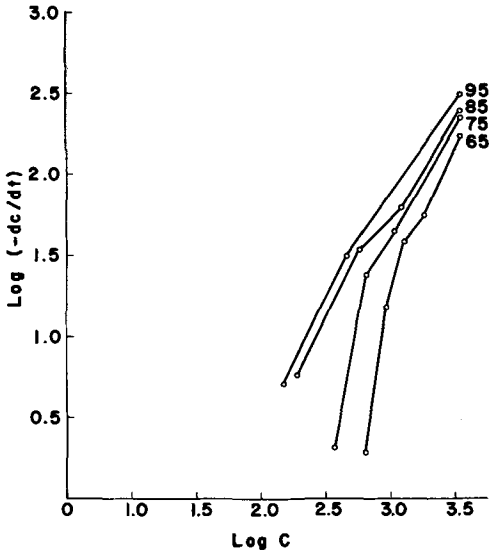

Fig. 7. Kinetic data for coatings sealed at pH 6.0, with tie line notation giving seal temperature: °C. The apparent reaction order was, at 65°C, 2.0; at 75°C, 1.8; at 85°C, 1.2 and, at 95°C, 1.2.

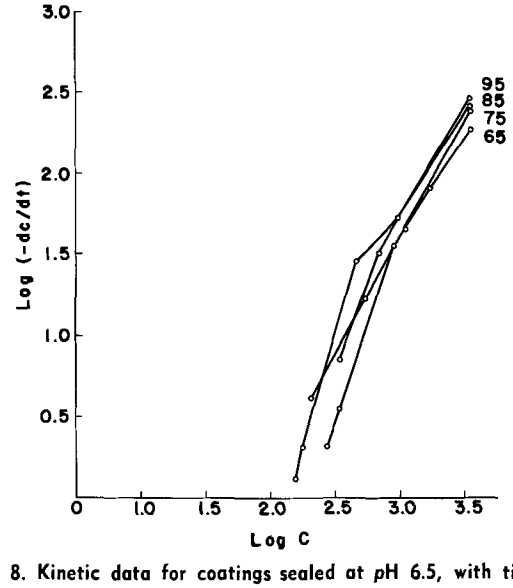

Fig. 8. Kinetic data for coatings sealed at pH 6.5, with tie line notation giving seal temperature: °C. The apparent reaction order was, at 65°C, 1.3; at 75°C, 1.7; at 85°C, 1.5 and, at 95°C, 1.5.

The apparent order of the sealing reaction was generally greatest (as high as $n = 2$) for the low temperature (65°C) seals. The reaction order approached unity as the seal temperature increased. This could be interpreted in at least two different manners

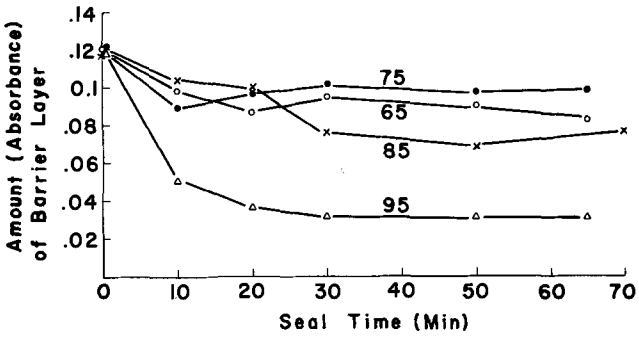

Fig. 9. Infrared absorbance (amount) of barrier layer for coatings sealed at pH 6.5; tie line notation gives seal temperature: °C.

hydration reaction (*via* EGD technique) has some complicating feature. This would tend to favor sealing reaction' (a), which employs a depolymerization reaction on sealing rather than simple water sorption. That portion of the hydrated alumina which is detected by the low-temperature EGD technique then appears to be hydrated before sealing, and releases progressively more water (on baking via EGD) as its structural cross-linking is progressively lowered by sealing. Eventually, sealing lowers this cross-linking to a minimum value that (with the EGD technique) releases a stoichiometric amount of water, as did the mineralogical trihydrates gibbsite and bayerite (8). Further, the data show that after this point sealing produces no further change in the amount of water released (with EGD baking) by the coating. Such behavior is consistent with earlier *IR* data (1, 2, 4) which served as the basis for describing this same sealing effect. When this, the inner seal effect, is complete, the apparent order of the reaction is near unity.

Intermediate and far infrared analyses.—Ordinarily, *IR* data show much better precision than was obtained here. Since this poor interrelationship shows only for sealed coatings, and not for unsealed samples, it seems likely that these samples should have been analyzed immediately after preparation. As it was, they were stored at random for approximately 30 days prior to analysis. In any event, the observable trends are still valid, but what might be poor structural reproducibility (for sealed samples) makes quantitative interpretation difficult.

Figure 9 shows the amount of barrier layer plotted *vs.* sealing time. These data include each of the various sealing temperatures at pH 6.5 and are representative of the entire group. Initially, each coating (unsealed) had the same amount of barrier layer: total amount of barrier layer being comprised of both primary and secondary barrier layer phases. After sealing, the amount of barrier layer decreased due to the secondary barrier-to-porous layer conversion. At pH

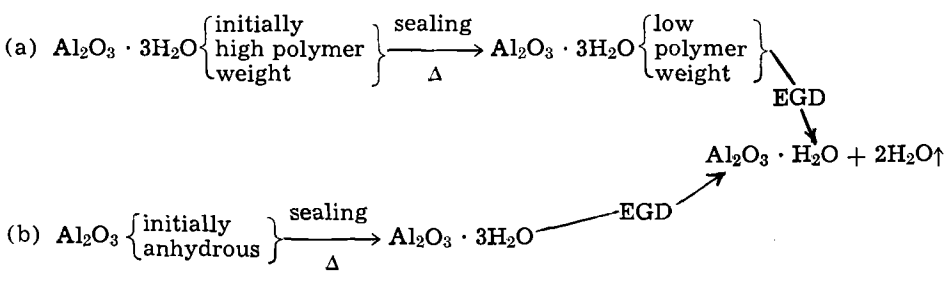

However, as seen in Fig. 6-8, the plots of log $(-dc/dt)$ *vs.* log c are more nearly linear only for the 95°C sealing conditions. This implies the possibility that, at least at lower sealing temperatures, the EGD dehydration reaction proceeds with complexity: that the de-

5.0 the extent of this conversion was less at 65°C than at 75°C; the 85°C and 95°C data show approximately equal conversion and at about the same rates. Similar data obtained at pH 6.5 (Fig. 9) show a better differentiation between 85°C and 95°C data: the 95°C seal

causing the greater degree of transformation. At a given temperature, the pH 6.5 seal gave a greater degree of barrier-to-porous transformation than did the pH 5.0 seal.

Figure 10 shows the amount of porous layer cross-linking plotted *vs.* sealing time for each sealing temperature and at pH 6.5. Before being sealed, each coating had about the same amount of porous layer cross-linking. After sealing, this amount varied greatly depending on seal time, pH, and temperature. However, just as the amount of barrier layer always decreased on sealing, due to the secondary barrier-to-porous layer transformation, the amount of porous layer cross-linking always increased on sealing.

Figure 10 also shows the generally adverse effects of too prolonged a sealing time, although this decrease in cross-linking was usually more pronounced for the 95°C seals. These data show that maximum sealing benefit is obtained near a sealing time of 30 min. Sealing at a lower temperature tended to retard the apparently detrimental effect due to oversealing, but lower temperatures also gave lesser amounts of porous layer cross-linking. These porous layer data are, of course, not specific for changes that occur near the barrier-porous interface, but would include cross-linking changes in the bulk of the porous layer as well. While these data show the advantages of 95°C and 30-min sealing conditions (as did the EGD data) there is still reason to suggest that still higher seal temperatures would further accelerate the sealing process, perhaps a pressurized steam seal at 150°C, with condensate pH controlled.

Impedance.—Figure 11 shows the initial impedance values plotted *vs.* sealing time and temperature at a sealing pH of 5.5. These values were obtained immediately after air-drying the coatings and before any storage period. At 95°C (and regardless of seal pH) the impedance increased almost linearly with seal times of up to 30 min. After 35 min, the rate of impedance change lessened to form a plateau beyond which the impedance change (with further seal time) was comparatively slight. This point (~38 kohms/cm^2 impedance) would correspond to the total impermeability of this oxide and would reflect changes taking place both in the barrier layer region of the film and elsewhere in the porous layer, and also at the oxide surface (9, 10).

At progressively lower sealing temperatures, there appeared to be an initial period during which minimal impedance change took place. Afterward, the impedance increased quickly. The time span of this initial period was greatest at low temperatures but showed no obvious dependence on pH. This is seemingly indicative of a temperature-dependent reaction rate, consistent with the "inner seal effect" mechanism described earlier. A plot of log impedance *vs.* sealing temperature is essentially linear for most of these data.

Figure 12 shows the effect of sealing pH on impedance levels. For each sealing time period, the impedance increased as the seal pH increased toward pH 6.0, then decreased beyond that. Extrapolation would seem to indicate that optimum results (highest impedance) were obtained at pH 6.15 ± 0.15.

Aging also alters (increases) the 1 kHz a-c impedance of sealed films but, as seen in Fig. 13, aging produces little change in unsealed films. The same figure also shows data for marginally sealed films: films sealed at pH 5.0 and 65°C, also showing only a minor increase in impedance with aging. In contrast, films sealed at the same pH (pH 5.0) but at 95°C and for 30 min, showed a pronounced change in impedance value on aging. Figure 14 shows other such data for these sealing temperatures at pH 6.0 with 30-min sealing time.

Generally and exclusive of unsealed and marginally sealed films, impedance values increased most rapidly during the first 5 days of aging. The impedance increase, with aging, then lessened but continued until the film had aged ~30 days. Afterward, comparatively little or no further change in impedance took place. There are also the following additional observations that may be made for the generalized effect of aging on sealed films.

1. Aging prior to exposure has no recognized, or at least reproducible, effect on the results of outdoor service testing of sealed films.

2. Similarly, aging does not alter the results of aggressive laboratory-accelerated corrosion tests: pitting corrosion tests such as CASS, or acid solubility tests such as Kape (sulfurous acid solubility).

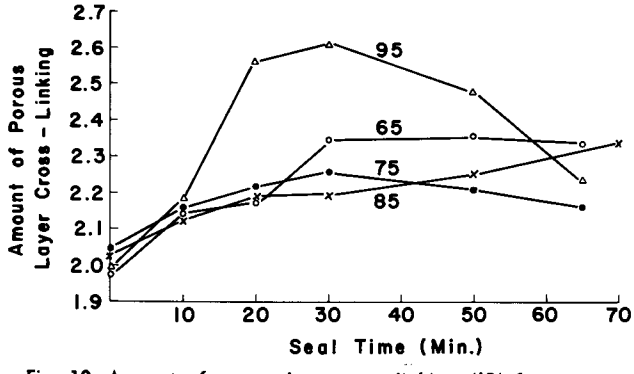

Fig. 10. Amount of porous layer cross-linking *(IR)* for coatings sealed at pH 6.5; tie line notation gives seal temperature: °C.

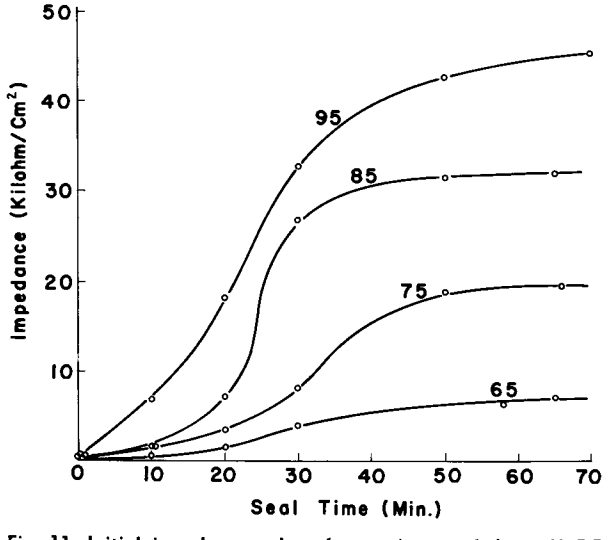

Fig. 11. Initial impedance values for coatings sealed at pH 5.5, with the tie line notation giving seal temperature: °C.

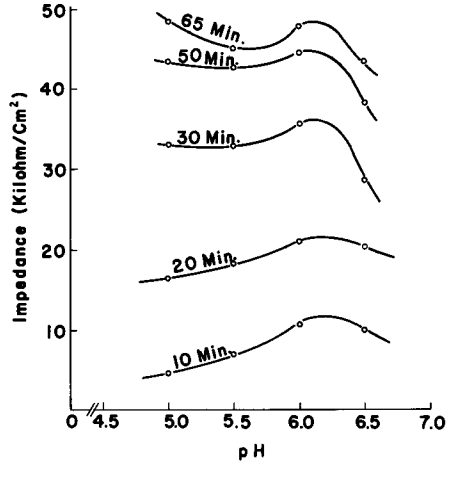

Fig. 12. Initial impedance values for coatings sealed at 95°C, with the tie line notation giving sealing times: minutes.

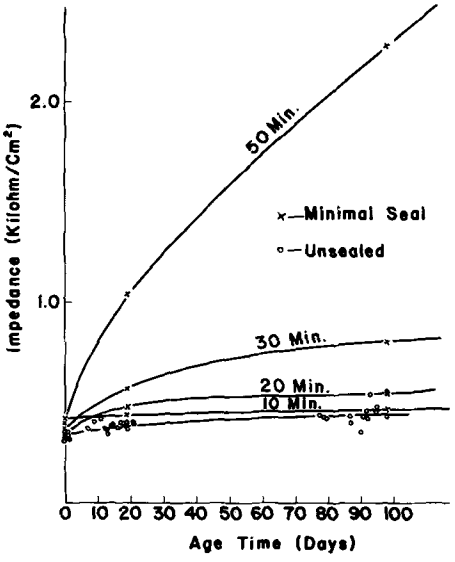

Fig. 13. Effect of aging on impedance values for (a) unsealed coatings and for coatings marginally sealed, at pH 5.0 and 65°C, by immersion for: (b) 10 min, (c) 20 min, (d) 30 min, and (e) 50 min.

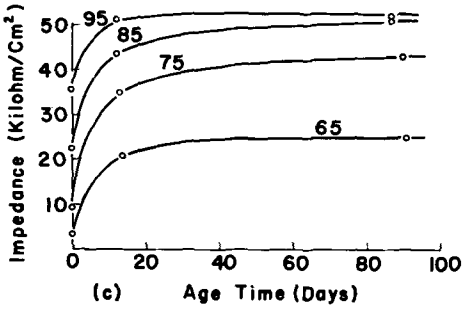

Fig. 14. Effect of aging on impedance values for coatings sealed at pH 6.0 for 30 min.

3. Aging (with sealed films only, not the case with unsealed films) does not alter the EGD test results, which would detect changes related to the barrier layer sealing transition, or inner seal effect.

4. Aging does alter (increase) the results of tests that are surface sensitive. The FACT test (dielectric breakdown in an acidic copper-containing electrolyte) is one such example (9).

5. While aging doubles the impedance value of sealed films, this effect may be virtually eliminated (and the impedance restored to approximately the initial value) by a brief exposure to a mildly aggressive environment (10). A few seconds in boiling distilled water, or immersion in room temperature dilute acid, will suffice.

It seems reasonable, therefore, to suggest that aging is a short-ordered effect that is of little consequence, when the anodic film is placed in a mildly aggressive environment where it is rapidly degraded. The effect of aging might be speculated to be equivalent to the formation of a thin film, from agglomerate particles. If such a filmlike thin layer were at the outer surface

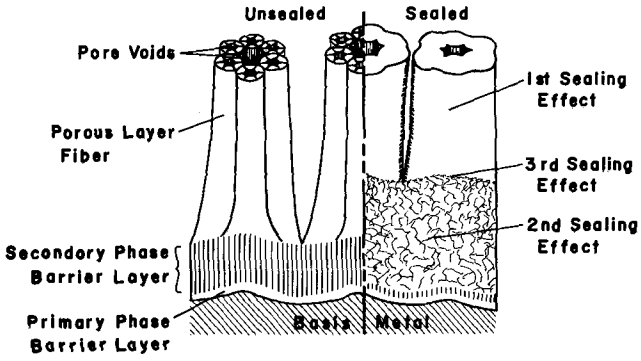

Fig. 15. Illustration of proposed sealing effects: 1st sealing effect [according to Wood et al. (11, 12)]: A pore closure mechanism that probably does not alter gross pore (large central pore) diameter to point of closure. Pores that are affected are micropore channels or permeable sites that lie within the fiber itself. 2nd sealing effect: An oxide transition, from barrier into porous layer oxide that results in a relatively impermeable gel formation at the base of the porous layer. 3rd sealing effect: A short-ordered thin film effect of glazing at the surface of the porous coating gel layer.

of the anodic coating, however, impedance values would likely have been increased far more than was observed; no more than a twofold increase was found on aging. By contrast, a thin oil layer at the outer coating suface raises impedance beyond the range of our instrument. Thus, instead of a surface condition, it seems reasonable to suggest that the aging effect might represent a coalescence of fibrils at the base of the porous layer, equivalent to a film at the surface of any agglomerate particles created by the inner seal effect.

A summary illustration of these sealing effects is shown in Fig. 15.

Acknowledgment

The author wishes to thank the Kaiser Aluminum & Chemical Corporation for its support of this work and for its permission to publish these results.

Manuscript submitted March 11, 1970; revised manuscript received June 2, 1970.

Any discussion of this paper will appear in a Discussion Section to be published in the June 1971 JOURNAL.

REFERENCES

1. G. A. Dorsey, Jr., *This Journal*, **117**, 1276 (1970).
2. G. A. Dorsey, Jr., *ibid.*, **117**, 1181 (1970).
3. G. A. Dorsey, Jr., *ibid.*, **115**, 1057 (1968).
4. G. A. Dorsey, Jr., *ibid.*, **115**, 1053 (1968).
5. G. A. Dorsey, Jr., *ibid.*, **116**, 466 (1969).
6. C. J. Amore and J. F. Murphy, *Metal Finishing*, **63**, 50 (1965).
7. A. F. Boguyavlenskii and V. T. Belov, *J. Appl. Chem. USSR*, **39**, 2221 (1966); UDC 620.197: 541. 183.24:539.163.
8. G. A. Dorsey, Jr., *Anal. Chem.*, **41**, 350 (1969).
9. R. C. Spooner, *Metal Finishing*, **67**, 80 (1969).
10. E. G. Englehart and D. J. George, *Materials Protection*, **3**, 24 (1964).
11. J. P. O'Sullivan, J. A. Hockey, and G. C. Wood, *Trans. Faraday Soc.*, **65**, 535 (1969).
12. G. C. Wood and J. P. O'Sullivan, *This Journal*, **116**, 1351 (1969).

Side Reactions during the Anodization of Aluminum in a Glycol Borate Electrolyte

Robert W. Santway and Robert S. Alwitt*

Sprague Electric Company, Research and Development Laboratories, North Adams, Massachusetts 01247

ABSTRACT

A study of the anodization of aluminum in a glycol borate electrolyte at voltages sufficiently high for side reactions to occur, but below the sparking voltage, showed that the formation of barrier oxide was accompanied by solvent oxidation, aluminum dissolution, and production of a thick oxide that grew in cracks of the barrier film. Surprisingly, the presence of the crack network has little effect on electrical properties. It is believed that side reactions initiate at flaws in the barrier oxide.

In suitable electrolytes, anodic oxide films can be grown on metals such as aluminum or tantalum at 100% current efficiency. For an anodization at constant current a film thickness is finally reached, characteristic of each system, above which current is consumed in other anodic reactions and the rate of film growth decreases. Continued passage of current may ultimately result in sparking (scintillation) over the anode surface.

Some observations on the sparking process have been presented recently (1), but it is still not a well understood phenomenon. Little information appears to have been published on the processes preceding sparking (2). This region is of practical importance to the operation of electrolytic capacitors since the onset of side reactions limits the maximum voltage of these devices. In this paper we report our observations of the secondary reactions that occur at an aluminum anode in a glycol borate electrolyte. The nature of the reactions and their effect on surface morphology and electrical characteristics are considered.

This type of electrolyte was chosen for several reasons. It is typical of systems used in electrolytic capacitors. Oxide can be formed at 100% current efficiency and contains little incorporated matter from the electrolyte (3). For some electrolyte compositions there is a wide voltage range in which side reactions can be studied prior to the onset of sparking. A disadvantage of using this electrolyte is that the chemical species in solution are not well defined. Borates react with glycol to produce coordination compounds, esters, and water (4).

Experimental

Anodizations were performed in an electrolyte of 17.2 w/o (weight per cent) ammonium pentaborate ($NH_4B_5O_8 \cdot 4H_2O$) in ethylene glycol (17% APB-EG). High-purity (99.97%) aluminum foil and wire were used as anodes. These were prepared by chemical polishing in a HNO_3-H_3PO_4 mixture (15 ml of 70% HNO_3, 85 ml of 85% H_3PO_4) for 2 min at 85°C, followed by a 10-min etch in 1M NaOH at room temperature. Anodization was at room temperature at constant current densities in the range 0.1-1.2 mA/cm^2.

Series capacitance and RC of anodized foils were measured at several frequencies using a conventional resistance ratio arm bridge with an a-c signal less than 100 mV. Measurements were against platinized electrodes in either aqueous 0.8M H_3BO_3 with sufficient NH_4OH added to give a resistivity of about 225 ohm-cm, or aqueous ammonium formate with a resistivity of 10 ohm-cm (*ca.* 2*N*).

In some experiments gas generated at the anode was collected and analyzed in a dual column, programmed temperature gas chromatograph, using a molecular sieve column. Aluminum in solution was measured using a previously established photometric procedure (5).

Results and Discussion

Description of side reactions.—A typical voltage-time recorder trace is shown in Fig. 1. The voltage at which dV/dt started to decrease was little affected by current density. For example, in one experiment it was about 247V at 1.0 mA/cm^2 and increased to 260V when the current density was dropped to 0.10 mA/cm^2. Weight measurements showed that during the initial voltage rise all the charge can be accounted for by production of an anodic Al_2O_3 film. In the region of reduced dV/dt the following events were observed:

1. Sharp decreases in voltage accompanied by equally rapid return. The frequency and intensity of these excursions increased as the voltage increased.
2. Gas bubbles were evolved at points on the anode surface.
3. Weight measurements showed that anodic oxide was produced at less than 100% efficiency.
4. The anode surface appeared blemished. At low magnification it was seen that the oxide had cracked,

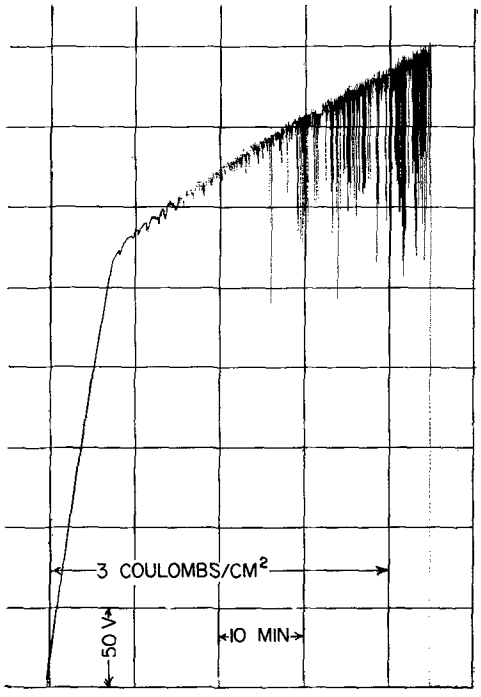

Fig. 1. Typical voltage-time trace for anodization in 17% APB-EG at 1.24 mA/cm^2.

* Electrochemical Society Active Member.

Key words: anodic oxides, aluminum, breakdown, electrolytic capacitors.

and in the cracks had grown a new solid many times thicker than the barrier film.

5. Analysis of the electrolyte showed the presence of dissolved aluminum.

6. The solution turned yellow and eventually sparking took place at about 450V.

These observations will now be described in more detail.

Gas evolution.—In a typical experiment, a current density of 0.33 mA/cm^2 applied overnight resulted in the production of a volume of gas equivalent to 0.013 ml/coulomb. Gas collection was halted prior to the onset of sparking. Analysis of the gaseous products from two experiments gave an average composition of 40% CO, 10% CO_2, and 50% H_2. The carbon monoxide and carbon dioxide must have been the products of glycol oxidation. The hydrogen did not come from the cathode compartment but was a true anode product. Since it could not be produced electrochemically at the anode, the hydrogen most likely was the result of some subsequent chemical reactions at the anode.

Cracks and new oxide growth.—Cracks in the oxide started at apparently random points on the surface and then spread in a network pattern. In Fig. 2a and 2b an early and a later state of crack development are illustrated. Examination of a number of specimens showed that in general crack initiation is not associated with grain boundaries of the substrate metal (6). Even after prolonged anodization the cracks never covered more than a few per cent of the surface.

The cracks were filled with a white solid many times thicker than the surrounding barrier oxide film. In the metal substrate was found a pattern of deep grooves identical to that of the cracks, suggesting that the new phase extended below, as well as above, the level of the original barrier film. The cracks were bounded by what appeared to be small tight cylinders of curled barrier film. The light outline of the empty cracks in Fig. 2c is believed to be an optical effect of this curled film.

No positive identification of the new solid material could be made. It was white, translucent, and gave no x-ray diffraction pattern. It was not soluble in some common organic solvents and heating for 2 hr at 900°C produced no change in appearance. We believe it to be an aluminum oxide. Perhaps it is similar to the material observed on aluminum after prolonged exposure to this 17% APB-EG electrolyte at high temperature (5).

An important observation was that during anodization gas bubbles were produced only at the tips of cracks. This indicates that the new oxide material was not a good electronic conductor, and that it maintained intimate contact with barrier film along the length of the cracks. It suggests that the secondary reactions took place only at the growing tip of a crack, a potentially complex region in which four phases could be in contact, viz., metal, barrier film, new oxide, and electrolyte.

Some of these observations are similar to those made by Vermilyea on the field crystallization of amorphous anodic Ta_2O_5 films (7). In that case, under the influence of a strong electric field, crystalline Ta_2O_5 nucleated at the metal/film interface, broke through the barrier film, and spread over the surface as irregular polygons until the amorphous film was completely replaced.

Dissolved aluminum.—During anodization up to about 250V no significant amount of aluminum was detected in solution. Coincident with a decreased dV/dt and the onset of gas evolution, the aluminum concentration began to increase uniformly with time. For a specimen that was anodized at 1.24 mA/cm^2, dissolved aluminum accounted for 10% of the charge passed following the onset of secondary reactions.

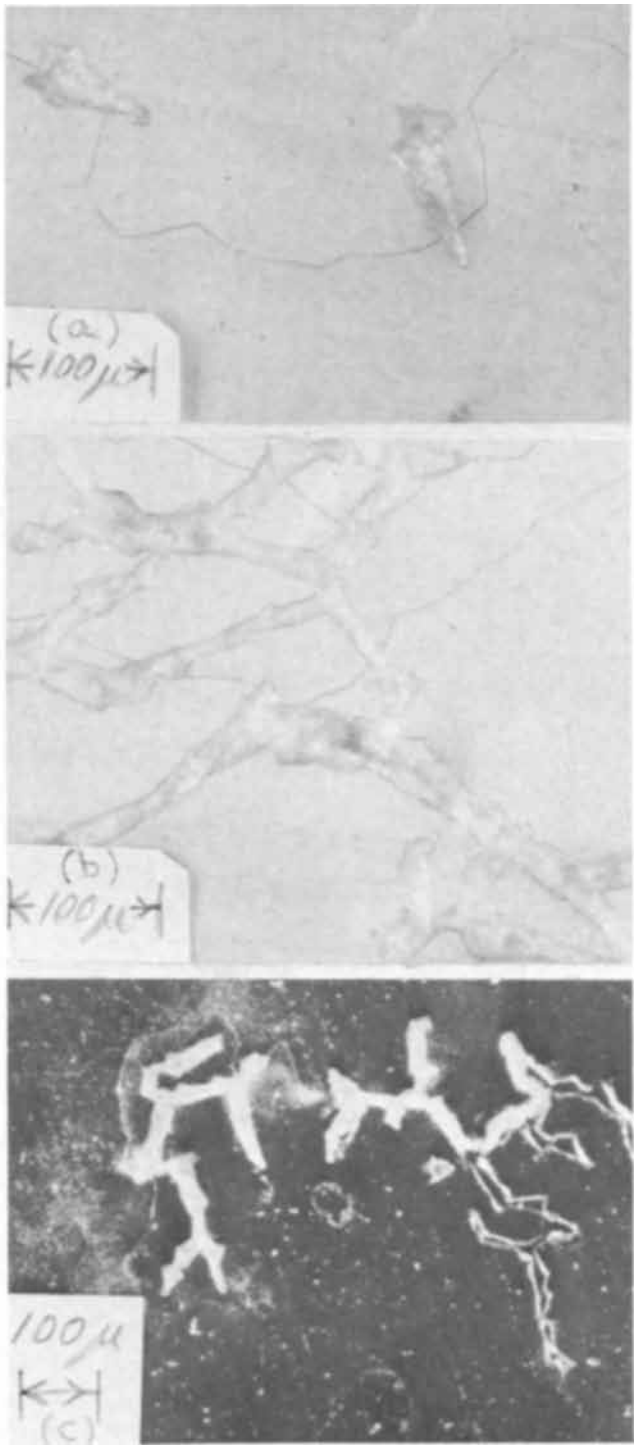

Fig. 2. Micrographs of Al foil anodized in 17% APB-EG at 0.27 mA/cm^2 to 320V. (a) Early state of crack development; (b) later state; (c) transmitted light through isolated oxide. Dark background is barrier film, white network is new oxide. Outlined pattern on right resulted from loss of new oxide during handling.

Distribution of aluminum oxidation reactions.—The amount of charge consumed in each of the aluminum oxidation processes (barrier film formation, new oxide growth, and metal dissolution) was estimated from measurements made on specimens anodized at 1.24 mA/cm^2. A typical voltage-time curve is shown in Fig. 1. The charge passed during the initial period of 100% barrier film production and the sample weight at the end of this period were measured. After further anodization the specimens were again weighed

and finally the weight was obtained after stripping oxide in H_3PO_4-CrO_3 solution. Oxide stripping was done in two stages, an initial room temperature immersion followed by one at 85°C. The new oxide was removed much more rapidly than the barrier film and the two materials could be easily distinguished at room temperature during a series of successive stripping measurements. The remaining barrier film was removed at 85°C. The weight of aluminum consumed in all oxidation reactions was determined as the difference between the specimen weight after stripping and the weight of base metal at the onset of side reactions. This latter figure was obtained by subtracting from the specimen weight at that point the calculated weight of anodic oxide produced at 100% efficiency.

The results are listed in Table I. The charge consumed in aluminum dissolution was taken as the difference between that calculated for metal consumption and that used in oxide formation. For the purpose of calculating charge consumption the thick oxide was assumed to be Al_2O_3.

It appears that these measurements were made in a region where the barrier film continued to thicken at a steady though reduced rate. This is indicated by the constant fraction of charge used for film formation. The weight of the new oxide was only about 4% of the total barrier film weight. The fraction of the surface covered by this material would be even smaller.

Other reactions.—The details of the glycol oxidation reactions resulting in CO and CO_2 production are not known, but the maximum charge consumed in these reactions was estimated by assuming that no more than three electrons were transferred per mole of CO and five electrons per mole of CO_2. From the volume and composition of gas collected it was calculated that these reactions could account for up to 9% of the charge passed in the region of low dV/dt. Since total metal oxidation accounted for less than 30% of the charge, clearly other anodic reactions took place.

In a recent study in our laboratory (8), Vijh found that in acidic aqueous solution the major products of glycol oxidation at a smooth Pt electrode were glyoxal and oxalic acid. The gaseous product accounted for only 1-2% of the total charge passed and was composed of roughly equal volumes of CO and H_2 with a slight amount of CO_2. The similarity in the compositions of the gas phases produced at the smooth Pt and the oxidized aluminum electrodes and the fact that in both cases the gaseous products accounted for only a small part of the total charge, suggested that at the aluminum electrode the remainder of the charge might be accounted for by production of glyoxal and oxalic acid. However, any glyoxal produced in the glycol borate electrolyte would be complexed by borate (9) and hence escape detection, and no test for carboxylates was found that was sufficiently sensitive in this solution. Thus, we were unable to verify the reactions that consumed more than half the charge passed during side reactions.

Effect of side reactions on electrical properties.—It was expected that the heterogeneous nature of the cracked oxide film would have a significant effect on dielectric properties. Young has suggested that the presence of fissures can be demonstrated by a dependence of impedance on measuring electrolyte resistivity (10). To investigate this, foil specimens were anodized in the 17% APB-EG electrolyte at 1.0 mA/cm² to several voltages up to 400V. At the higher voltages cracks had developed to a considerable extent. The series capacitance and resistance were measured at several frequencies in electrolytes with resistivities of 230 and 10 ohm-cm.

The frequency dependence of reciprocal capacitance and series resistance for a 400V specimen are shown in Fig. 3 and 4. The frequency dependence of $1/C$ was unaffected by electrolyte resistivity. Although a higher resistance was obtained in the low resistivity solution at low frequencies, the increase was small and no greater than was encountered with normal barrier films. Thus, at these ambient conditions there appeared to be no significant electrolyte penetration through the cracked areas.

Table I. Aluminum oxidation reactions during period of side reactions

Charge,* coul/cm²	Weights,* μg/cm² Barrier oxide	New oxide	Total Al consumed	Per cent of charge Barrier oxide	New oxide	Al diss.†	Total
1.59	45.7	4.2	37.3	16.3	1.5	7.4	25.2
2.02	56.1	5.8	51.8	15.7	1.6	10.1	27.4
2.51	73.2	6.2	69.6	16.6	1.4	11.7	29.7

* Measured from onset of side reactions.
† By difference.

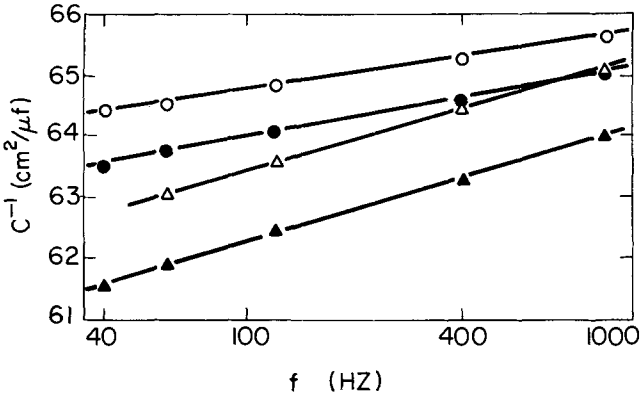

Fig. 3. Frequency dependence of series capacitance of 400V films formed in two electrolytes and measured in two solutions. Triangles = 17% APB-EG anodization; circles = 39% APB-EG anodization. Open symbols = 230 ohm-cm measuring solution; filled symbols = 10 ohm-cm measuring solution.

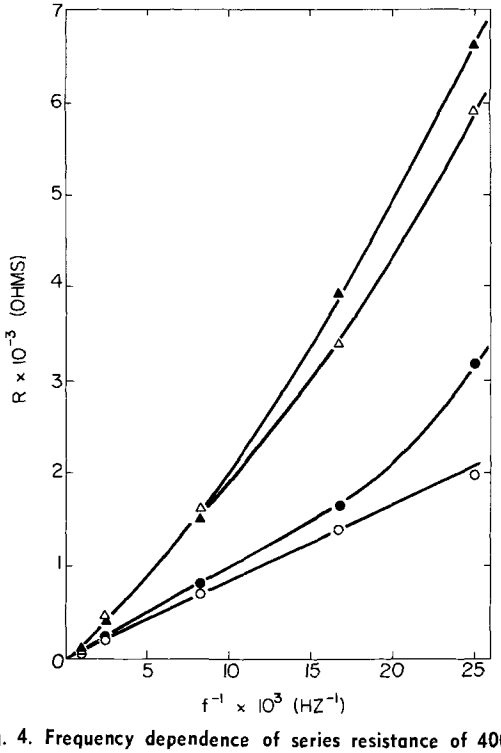

Fig. 4. Frequency dependence of series resistance of 400V films formed in two electrolytes and measured in two solutions. Same symbols as Fig. 3.

The presence of the new thick oxide within the cracks could make the film behave like a two-phase dielectric which might have different properties than a normal barrier film. To examine this, use was made of another glycol borate electrolyte. A solution of 39% APB in ethylene glycol will support anodization at 100% current efficiency up to 450V. Specimens were anodized in this electrolyte at 1.0 mA/cm^2 to 400V, forming barrier films free of cracks. The frequency dependence of these samples is also shown in Fig. 3 and 4.

A comparison of the results obtained with the cracked and crack-free oxides shows that the capacitance level of the films is about the same but the cracked film exhibits a slightly greater frequency dependence of capacitance and a much greater frequency dependence of series resistance. At the lowest measuring frequency the resistance of the film formed in 17% solution was more than twice that of the film formed in 39% electrolyte.

The effect of the crack network on leakage current was examined by comparing results obtained with films formed in the two electrolytes. Foils were anodized to 400V at 0.28 mA/cm^2 in both of the APB-EG electrolytes. The samples anodized in the 17% solution have well-developed cracks whereas those processed in the 39% solution were free of cracks. Leakage currents were measured in the 39% electrolyte at several voltages up to 350V. At all voltages, the leakage current decreased slightly with time for both sets of samples, and the current was somewhat lower for the cracked oxide. For example, after 3 hr at 350V the leakage current was 1.8 μA/cm^2 for the uniform film and 0.7 μA/cm^2 for the cracked oxide.

From the a-c and d-c properties it can be inferred that the oxide in the cracks is in sufficiently intimate contact with the barrier film to prevent electrolyte paths through the film. Also, the new oxide is an inferior dielectric, though a relatively good insulator.

Some details of anodization with side reactions.—An important observation was that when foils with uniform, thick (*e.g.*, 400V) films formed in the 39% APB-EG electrolyte were anodically polarized in the 17% solution, side reactions took place at voltages as low as 250V. After such treatment the appearance of thick films was the same as that of films grown in the 17% electrolyte (compare Fig. 5 with Fig. 2). Thus, side reactions in a particular electrolyte started at a voltage that was independent of film thickness. This is not an unusual observation, since many workers in this field have observed that anodization electrolytes appear to have a limiting voltage, as measured by leakage current, gassing, etc., that is not very dependent on barrier oxide thickness.

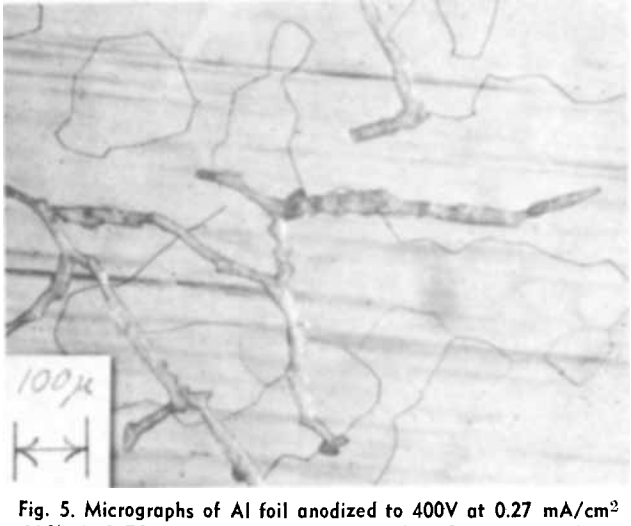

Fig. 5. Micrographs of Al foil anodized to 400V at 0.27 mA/cm^2 in 39% APG-EG and then held at 0.27 mA/cm^2 in 17% APB-EG for 140 min. Final voltage was about 300V.

The rate of the side reactions seemed to depend on film thickness and current density of formation. Foils were anodized in the 39% APB-EG electrolyte to three film thicknesses at each of three current densities. Reciprocal capacitance was the measure of film thickness. These specimens then were polarized anodically in the 17% electrolyte for 3 min at 350V. This was sufficient for new oxide growth to start at a number of points on the surface. The density of growth spots seen at 150X was taken as a measure of the extent of side reactions. The results are listed in Table II. Samples with the smallest initial film thickness had the greatest spot density. Moreover, the current density of film formation affected the extent of side reactions, with films formed at the lowest current density exhibiting the smallest amount of growth of new oxide. It should be noted that the initial films were all formed at 100% current efficiency, and bridge measurements showed no differences in dielectric properties among these samples other than those expected on the basis of film thickness.

The films formed in 39% APB-EG could be uniformly thinned in H_3PO_4-CrO_3 stripping solution at 85°C, as determined from the correlation between capacitance increase and weight loss. The films on some 400V specimens were thinned to approximate the thickness (weight basis) of 350 and 300V films. When these were immersed in 17% APB-EG electrolyte for 3 min at 350V the spot density was an order of magnitude greater than for comparable unthinned samples. The results are shown in Table III. It appears that chemical thinning exposed many points for subsequent side reactions.

Behavior of cracked oxides.—Some experiments were done using foil that was first anodized to produce a uniform film and then the oxide was cracked by bending the specimen. On re-anodizing such samples, three observations were made. First, any thick oxide growth was seen only within these cracks or in cracks that had obviously initiated at these induced cracks. Second, when re-anodization was done at constant current, thick oxide was observed only when the current density was relatively high. At low current densities the cracks appeared to be healed with normal barrier film, although voltage fluctuations accompanying this process indicated the possibility of other side reactions. For example, a 200V cracked film re-anodized to 200V in 17% APB-EG had thick oxide growth in the cracks when the C.D. was 280 μA/cm^2 (based on total area) but exhibited no signs of the new oxide when the C.D. was 28 μA/cm^2. This example also illustrates the third important observation. There was evidence of side reactions on these flexed specimens at voltages much lower than encountered during normal anodizations. In the above case, voltage fluctuations were observed at 75V when

Table II. Growth spot density as related to anodization current density and film thickness

Current density, μA/cm^2	Thickness		Spots/cm^2
	Volts	μFd^{-1}	
2.8	400	3.769	35
2.8	350	3.296	91 (1000)*
2.8	300	2.793	245 (5000)*
28	420	3.790	45
28	365	3.269	281
28	310	2.785	332
280	440	3.869	96
280	385	3.300	327
280	325	2.838	838

* Thinned in H_3PO_4-CrO_3 solution.

the C.D. was 280 μA/cm^2 and at 120V when the C.D. was 28 μA/cm^2.

From these observations we infer that the growth of the thick oxide occurs preferentially in cracks and is promoted by high current density. Furthermore, under normal anodizing conditions cracks must not develop until high voltages are reached, for example, 250V in 17% APB-EG and 450V in 39% APB-EG.[1]

Conclusions

It is likely that the sites for the initiation of side reactions are flaws in the barrier oxide film similar to those found in anodic Ta_2O_5 films (11). Although direct evidence for this is lacking, it does seem significant that slight chemical thinning of the oxide resulted in an order of magnitude increase in subsequent growth centers (Table II). This corresponds to Vermilyea's observation that flaws in Ta_2O_5 films were preferential sites for chemical dissolution (11).

It would be expected that reactions at a cracked flaw would be like those at a crack produced by flexing in that the resulting high local current density would result in production of thick oxide rather than barrier film. This more voluminous oxide would cause a strain in the surrounding barrier film sufficient to crack the film and side reactions would then occur in this region. The cycle would continue until the crack reached a point where the growth of new oxide sealed off the tip of the crack before the strain in the surrounding barrier film produced further extension. It is believed that the immediate cause of the formation of thick oxide rather than barrier film is the occurrence of the glycol oxidation reaction. This parallel reaction might change the local electrolyte composition so that normal barrier film could not be produced.

The high degree of reproducibility of the voltage at which side reactions start is apparently a characteristic of the initial film fracture process. From the experiments with flexed specimens it is evident that side reactions can occur over a wide range of lower voltages if cracks are present. It is surprising that the critical voltage for side reactions was independent of average film thickness in these experiments. It is reported that flaw thickness increases less rapidly with formation voltage than does the average thickness (11). Perhaps some flaws reach a limiting thickness which is maintained as the formation voltage increases.

[1] Further support for this came from an anodization in the 39% solution which was followed with an oscilloscope set at a sweep rate of 50 μsec/cm and a sensitivity of 20 V/cm. No discontinuities in the voltage trace were observed up to 350V, at which point the anodization was stopped.

Reactions at flaws may play a role in all aluminum anodizations when the eventual decrease in current efficiency occurs. Other features of the present case, such as the development of a crack network, are probably specific to the particular system. For example, one can picture a side reaction in which no product is formed that affects the composition of the growing oxide. In that case barrier film formation and side reaction would proceed in parallel at the cracked flaw until film growth stifled the side reaction. The net effect would be growth of barrier oxide at reduced current efficiency.

Apparently the presence of the thick oxide network might not be objectionable in an electrolytic capacitor since it only affects the series resistance. It is the growth process which is undesirable in a device since it would give rise to high leakage currents and inability to support a steady voltage. Moreover, the gas generated at both anode and cathode during side reactions would contribute to other failure modes (12).

Acknowledgments

The authors are grateful to Mr. J. Barry for performing the gas analyses and to Mrs. E. Vigna for obtaining many of the laboratory results reported here.

Manuscript submitted Dec. 22, 1969; revised manuscript received June 8, 1970. This was Paper 32 presented at the New York Meeting of the Society, May 4-9, 1969.

Any discussion of this paper will appear in a Discussion Section to be published in the June 1971 JOURNAL.

REFERENCES

1. R. S. Alwitt and A. K. Vijh, *This Journal*, **116**, 388 (1969); G. C. Wood and C. Pearson, *Corrosion Sci.*, **7**, 119 (1967).
2. S. Tajima, S. Itoh, T. Fukushima, *J. Electrochem. Soc. Japan*, **23**, 296, 342, 395 (1955).
3. W. J. Bernard and J. W. Cook, *This Journal*, **106**, 643 (1959).
4. H. Steinberg, "Organoboron Chemistry," Vol. 1, Interscience Publishers, New York (1964).
5. R. S. Alwitt and R. G. Hills, *This Journal*, **112**, 974 (1965).
6. R. M. Goldstein and J. E. O'Neal, *Thin Solid Films*, **4**, R21 (1969).
7. D. A. Vermilyea, *This Journal*, **102**, 207 (1955).
8. A. K. Vijh, Submitted for publication.
9. B. Pesetsky and N. R. Eldred, *Tetrahedron*, **25**, 4137 (1969).
10. L. Young, *Trans. Faraday Soc.*, **55**, 842 (1959).
11. D. A. Vermilyea, *This Journal*, **110**, 250 (1963).
12. R. S. Alwitt and R. G. Hills, *IEEE Trans.*, **PMP-1**, 28 (1965).

Effects of Material and Processing Parameters on the Dielectric Strength of Thermally Grown SiO_2 Films

N. J. Chou and J. M. Eldridge

IBM Thomas J. Watson Research Center, Yorktown Heights, New York 10598

ABSTRACT

The influence of several material and processing parameters on the dielectric strength of thermally grown SiO_2 films on silicon has been assessed. This was accomplished by statistically analyzing the breakdown characteristics of a large number of MOS capacitor structures, which had been fabricated in various ways. Although the results of this investigation are only qualitative, they clearly demonstrate that the effective breakdown strength of these films is strongly dependent on: SiO_2 purity, structural perfection and thickness; the presence of a passivating phosphosilicate glass layer; the presence and reactivity of the metal electrode; and, the duration of the post-metallization heat treatment. The morphology of certain micron-size defects which develop in the MOS structure during annealing is described in some detail, since these faults are apparently responsible for oxide shorting in some instances.

Since the oxide layer under the gate electrode in MOSFET's is subjected to very large electric fields (up to 2 MV-cm^{-1}), its dielectric strength has an important bearing on the reliability of these devices. Although interest in electrical breakdown phenomena in such films has increased in recent years, along with the rapid development of MOSFET technology, the effect of various process and material variables on the effective dielectric strength of thermally grown SiO_2 films has not yet been well characterized. This is due to the extreme sensitivity of this property to changes in oxide composition and structure, which are, in turn, quite dependent on device fabrication procedures. An additional uncertainty is introduced by the dependence of the breakdown characteristics on the particular testing technique employed.

The dielectric strength of thermally grown SiO_2 has been reported by Deal (1) to increase with the density of the insulating film, going from 4.8 to 5.5 MV-cm^{-1} as the density was raised from 2.04 to 2.22 g-cm^{-3}. Breakdown strength values of 4 to 6 MV-cm^{-1} for 2000Å thick SiO_2 films on silicon were found by Ainger (2), who also observed that lower values were encountered on oxide films grown on more heavily doped, p-type silicon. A more thorough investigation of breakdown phenomena in Al-SiO_2-Si structures has been made by Klein (3,4), who found that a succession of breakdown events could be initiated at low fields (< 2 MV-cm^{-1}) when the applied voltage was slowly increased. These events produced visible spark discharges which created individual macroscopic holes in the capacitor, due to localized evaporation of oxide and metal. Such events were labeled "single-hole" or "self-healing" because the test capacitor was still operational after they occurred. When the applied field reached the 5 to 9 MV-cm^{-1} range, the dielectric failure was accompanied by arcing or by propagation of single-hole events to adjacent sites. This resulted in permanent destruction of the capacitor. Consequently, Klein's data indicate that the effective breakdown strength of SiO_2 films does not have a well-defined value but increases as the weak spots in the oxide are eliminated by continued testing, until the ultimate value (in the range, 5 to 10 MV-cm^{-1}) is reached. It should be noted that this range of ultimate strength values is appreciably higher than those observed in earlier studies where unspecified measurement and testing techniques were employed (1, 2).

Key words: dielectrics, dielectric strength, MOSFET devices, morphology of SiO_2.

In a different approach, Fritzsche (5) examined the statistical distribution of breakdown strength values of a large number of Al-SiO_2-Si capacitors. Here, the breakdown field was taken as the value at which the first breakdown event occurred in a capacitor, self-healing or otherwise. His results are typically shown in Fig. 1, where the fraction ($\Delta N/N$) of capacitors tested, which break down in a small interval of field, is shown as a function of the corresponding field. Maxima were observed which consistently fell into three ranges: 0-0.6, 1-3, and 7-9 MV-cm^{-1}. According to Fritzsche: the peak labeled "primary" represents the intrinsic (or electronic) breakdown strength of the oxide; the "secondary" one is attributable to the presence of small, randomly distributed, crystallized regions (structurally similar to quartz, too minute to be detected by conventional techniques but large enough to cause breakdown by serving as flaws in the otherwise amorphous dielectric); and the "tertiary" to the effect of gross structural defects such as pinholes. Note that the primary strength corresponds to the ultimate dielectric strength values reported by Klein and his co-workers (3, 4). Fritzsche's interpretation was supported by the following observations: (*i*) the temperature dependences of the primary and secondary peak positions are similar to those of amorphous silica and crystalline quartz, respectively; (*ii*) as-grown anodic SiO_2 is amorphous and fails to exhibit a secondary-type peak until it has been subjected to heat treatment probably capable of inducing recrystallization; (*iii*) the tertiary failure mode is promoted by mechanically damaging the oxide; and (*iv*) the expected random nature of oxide defects can be inferred by the increase in secondary and tertiary breakdown with the electrode area (5).

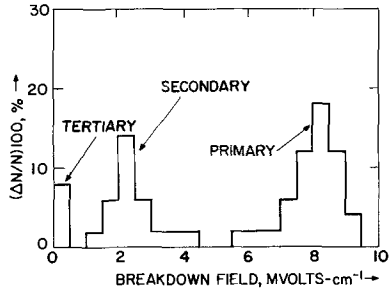

Fig. 1. Typical breakdown strength distribution curve for Al-SiO_2-Si (after Fritzsche).

Fritzsche found that the primary mode of breakdown in SiO_2 was electronic in nature, thus exhibiting no dependence on the duration of the applied field. In contrast, Worthing (6) found that when a constant, positive voltage was applied to the metal for the time required to cause breakdown, the breakdown field of SiO_2 films on n-type, degenerate Si was proportional to $(\text{time})^{-1/4}$. This particular time dependence has been frequently observed for bulk insulators where it is known as Peek's law (7). This has the effect of lowering the dielectric strength of the SiO_2 film from 6.7 MV-cm^{-1} for fast stressing rates to approximately 3 MV-cm^{-1} for a testing voltage applied at an infinitely slow rate. However, no time dependence was observed by Worthing when the metal was negatively biased.

The present investigation was undertaken to ascertain the influences of various processing and material parameters on the dielectric strength of oxide films and to resolve the apparent differences in the findings of some of the above investigations. An attempt was made to separate the effects of these variables, in view of the fact that they were found to interact frequently to alter the breakdown characteristics. Since the breakdown behavior is also affected by measurement technique, this separation was facilitated by employing a standardized testing procedure. The statistical approach (5) was then utilized to evaluate the dependence of the dielectric strength of the thermally grown oxide on SiO_2 purity and thickness, phosphosilicate glassing, electrode metal reactivity, and post-metallization heat treatment. Although most of the results of this investigation are of a semiquantitative nature, many of these will be seen to be quite relevant both to the development of MOSFET technology and to the understanding of the mechanism of oxide breakdown.

Experimental Procedure and Results

Specimen preparation.—Various types of oxide films were prepared in the following ways on Monsanto chemically-mechanically polished, <100>- and <111>-oriented silicon substrates of 2 to 10 ohm-cm resistivity.

"Regular" SiO_2 preparation.—The as-received substrates were cleaned in transistor grade reagents according to the following sequence: boiling trichloroethylene, boiling isopropyl alcohol, de-ionized (DI) water, boiling nitric acid, DI water, dilute hydrofluoric acid, DI water, and blown dry in N_2. Thermally grown SiO_2 films of so-called "regular" quality were formed with the desired thicknesses (in the 200-2000Å range) at 1100°C in a single-walled, high-purity silica tube in a resistance-heated furnace. As will be seen later, SiO_2 films prepared in this manner under normally clean laboratory conditions have quite reproducible dielectric breakdown characteristics and, as such, provided a convenient reference material for this investigation; hence, they have been designated to be of "regular" quality. The mobile cation (presumably Na^+ ions) concentration of such films, as established by measuring the flat-band voltage shift upon bias-temperature stressing (8), was typically $\sim 2 \times 10^{11}$ Na^+ ions-cm^{-2}. It should be emphasized that this concentration (assuming the mobile species is Na^+ ions) represents only a fraction of the total sodium content of the oxide (9).

"Ultraclean" SiO_2 preparation.—Ultra-pure SiO_2 films were prepared also by using extremely clean conditions. The silicon substrates were vapor-etched first in a very pure and dry HCl-H_2 ambient, followed by an *in situ* oxidation at 1100°C in dry O_2. Heating was accomplished using a silicon carbide-coated graphite susceptor placed inside a water-cooled, fused silica jacket. The mobile cation concentrations of these films was established to be $\lesssim 2 \times 10^{10}$ cm^{-2}; *i.e.*, about an order of magnitude less than that of "regular" SiO_2.

Phosphosilicate glass preparation.—Other specimens were prepared by alloying the surface of "regular" SiO_2 with P_2O_5 to form phosphosilicate glass (PSG)-SiO_2 layered structures. These glass films were typically thin and relatively low in phosphorus content [*e.g.*, 125Å thick with 4 m/o (mole per cent) P_2O_5] (10). Since these thin PSG-SiO_2 composite layers are particularly effective for preventing threshold drifts in MOSFET devices (11-13), such structures are termed "stabilized" in this paper.

Metallization and annealing.—Sixty-four metal electrodes of a given area (in the range 0.05-1.3 mm^2) were deposited through metal masks onto each wafer. The high purity metals (99.999+% aluminum, for example) were evaporated, using an electron gun heat source. Finally, the completed structures were heated for 5 min at 500°C in a nitrogen ambient in order to anneal out the E-gun induced radiation damage at the oxide-semiconductor interface. Any departures from the above preparation procedures will be detailed when necessary.

General testing procedure.—In order to select appropriate breakdown testing conditions, the following series of measurements were carried out on Al-SiO_2 (1000Å, regular)-Si structures. Large numbers of capacitors (typically 100 to 200 samples) were tested by applying a voltage, which was made to increase linearly with time, to each electrode until breakdown (self-healing or otherwise) occurred. In this technique, the development of breakdown causes the appearance of an abrupt departure from linearity in an otherwise smooth voltage *vs.* time trace. The breakdown field is evaluated at this point which corresponds to a current density on the order of approximately 10^{-6} A-cm^{-2}. The resultant breakdown distributions were then displayed as bar graphs, wherein those fractions ($\Delta N/N$) of capacitors failing in a small interval (0.5 MV-cm^{-1}) of field are plotted against the corresponding breakdown fields.

Electrode area.—Typical breakdown distributions for regular SiO_2 films are shown in Fig. 2, where it may be seen that the secondary failure mode increases with electrode area (F). As shown in the Appendix, the oxide defect concentration can be estimated from this areal dependence. When this is done, a value of ~10 defects-cm^{-2} is obtained, which is significantly lower than the estimated value (~80 cm^{-2}) (5) for the SiO_2 film shown in Fig. 1. In view of their better perfection, it is not surprising that the films in Fig. 2 do not show a tertiary peak. In general, the 0.5 mm^2 electrode seems to provide a useful reference distribution for further work because the secondary failure mode is significant with this area although most of the breakdown is still intrinsic.

Field application rate.—Both the intrinsic strength and the mode of breakdown of 1000Å, regular SiO_2 films are unaffected by decreasing the rate of field application over the range from 1 to 0.01 MV-cm^{-1}-sec^{-1}. Only for films with much higher defect con-

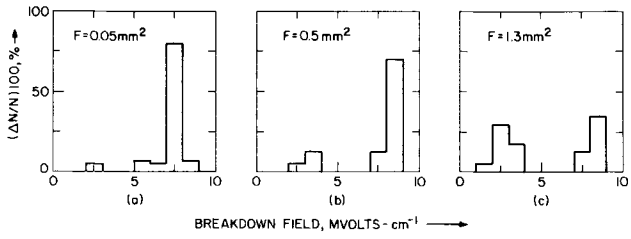

Fig. 2. Area dependence of the breakdown strength distribution for regular oxide in Al-1000Å SiO_2-Si structures.

centrations (>90 defects-cm^2) was a significant shift of the primary peak toward lower field values observed to occur with decreasing ramp speed. We believe that this effect of defect concentration on the rate dependence of breakdown strength may account for the discrepancy between the findings of Fritzsche (5) and Worthing (6). However, the relationship between the extent of this shift and the ramp speed (or biasing time) was not established in the present investigation because this would have required the preparation of oxide films with reproducibly high defect densities. Since the specimens to be tested were of a lower defect density, it was feasible to use the highest ramp speed tested (*i.e.*, 1 MV-cm^{-1}-sec^{-1}) in order to minimize the measuring time.

Temperature.—A limited amount of testing indicated that the statistical distributions of breakdown strengths were relatively insensitive to changes in the testing temperature, in the 25°-150°C range, for regular oxide and for phosphosilicate glass-SiO_2 composite layers. Hence, all subsequent measurements were done at room temperature.

Polarity.—In order to avoid loss of field across a depletion region in the semiconductor, breakdown measurements in this investigation were carried out with a field polarity such that an accumulated silicon surface was always maintained.[1] This was accomplished by biasing the metal positively for n-type and negatively for p-type substrates. When breakdown data were taken under this polarity restriction, the distribution curves for the Al-SiO_2 (1000Å, regular)-Si structures showed no significant dependence on the duration of the applied field.

Effects of material and processing parameters on oxide breakdown.—Type of oxide film.—In contrast with that observed for regular oxide films, the breakdown distribution curves for ultraclean SiO_2 exhibited no measurable areal dependence (*cf.* Fig. 2 and 3a). Although the intrinsic strengths of both grades of SiO_2 are the same (*i.e.*, 6 to 9 MV-cm^{-1}), the higher purity films exhibited no noticeable defect-related breakdowns. It is important to note that when HCl vapor-etched Si substrates are thermally oxidized in a resistance-heated, fused silica tube, the resultant breakdown properties are generally quite similar to those of regular oxide. These results suggest that the lower impurity (most likely sodium) concentrations that are typically attained in the oxidation step of the ultraclean processing procedure lead to superior SiO_2 breakdown characteristics. To understand this impurity effect, it may be instructive to note that the structure of thermally grown SiO_2 is apparently quite similar to that of fused silica. That is, it is comprised of SiO_4 tetrahedra (with Si^{+4} ions in their centers) which are linked together at the corners or oxygen sites to form a three-dimensional network essentially devoid of long-range order. Although phase transformations are very sluggish in this oxide, they are greatly accelerated by the addition of small quantities of network modifiers, such as sodium (14). For example, sodium contamination has been reported (15) to result in the formation of locally crystallized regions in thermally grown SiO_2 films, thereby causing defect-related breakdown. Depending on the magnitude of this phase transformation, it should first appear as an increase in secondary breakdown [in accord with Fritzsche's model (5)] and eventually as a rise in the incidence of tertiary oxide failures. It will also be seen that shorting can develop as a result of a solid state reaction between the metal electrode and the oxide during post-metallization annealing.

In the case of PSG-stabilized specimens, the glass addition was found to virtually eliminate defect-type breakdown in regular SiO_2, and to raise its primary strength to 9-12 MV-cm^{-1} (*cf.* Fig. 2 and 3b). The first improvement may be accounted for by the fact that the phosphosilicate layer is liquid at its temperature of formation (10, 16), and therefore would form a continuous film over the underlying SiO_2. The second beneficial effect can be largely attributed to the higher dielectric strength of the PSG itself (17).

Oxide thickness.—For regular and stabilized films prepared with various total oxide thicknesses (in the 200-880Å range), the likelihood of defect-related breakdown was found to increase appreciably with decreasing insulator thickness (see Fig. 4). The addition of a PSG layer is again seen to substantially reduce the frequency of defect-related breakdowns.

A quantitative determination of the oxide defect density (ρ, cm^{-2}) was carried out for the data in Fig. 4. The predicted proportionality between ln P (P being the fraction of primary breakdowns) and F was obtained for several thicknesses (Fig. 5). The apparent departure from linearity for the 200Å, regular SiO_2 at the largest electrode area may be due to the use of too small a sampling. Defect densities of the films were estimated from the slopes and are listed in Table I. It may be seen that the density of defects of regular SiO_2 increases by a factor of approximately sixty as the thickness is reduced from 630 to 200Å.

The enhancement of the intrinsic strength by PSG is again evident in Fig. 6. The rise in dielectric strength, on going from 880 to 410Å, can be attributed to the relative increase in the PSG-to-SiO_2 thickness ratio. However, the primary breakdown strength for both oxides decreases significantly for thinner (< 400Å) films and shows a marked dependence on area, in contrast to the thicker oxides. Thus, the

[1] Numerous comparative tests have shown that inflated values of dielectric strength are obtained when Si surfaces are depleted during breakdown measurement since part of the potential drop occurs in the semiconductor.

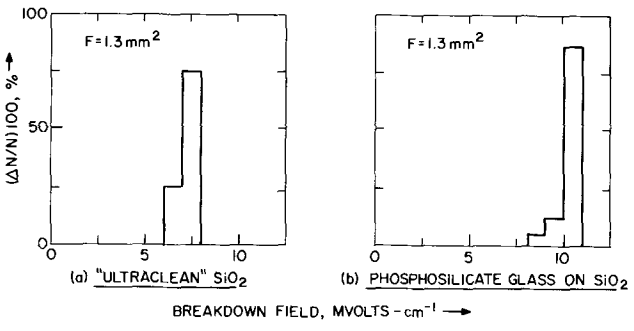

Fig. 3. Dielectric strength distributions for: *(a)* Al-SiO_2 (1000Å, ultra-clean)-Si; and *(b)* Al-PSG (125Å, 4% P_2O_5)-SiO_2 (900Å, regular)-Si structures. Note absence of defect-related breakdown in both oxides.

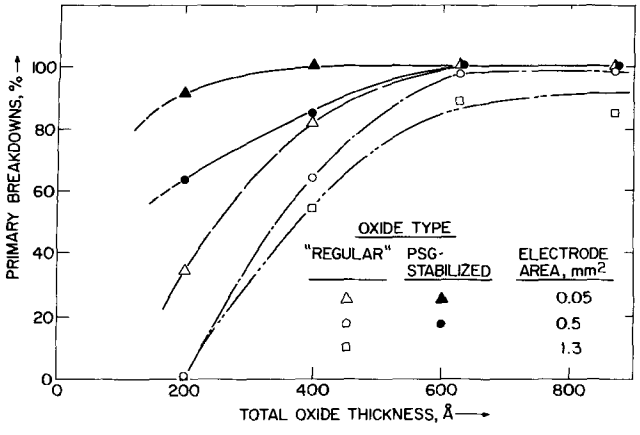

Fig. 4. Dependence of breakdown mode for regular and phosphosilicate glassed oxides on thickness. Note that the PSG addition is relatively most beneficial for the thinnest films.

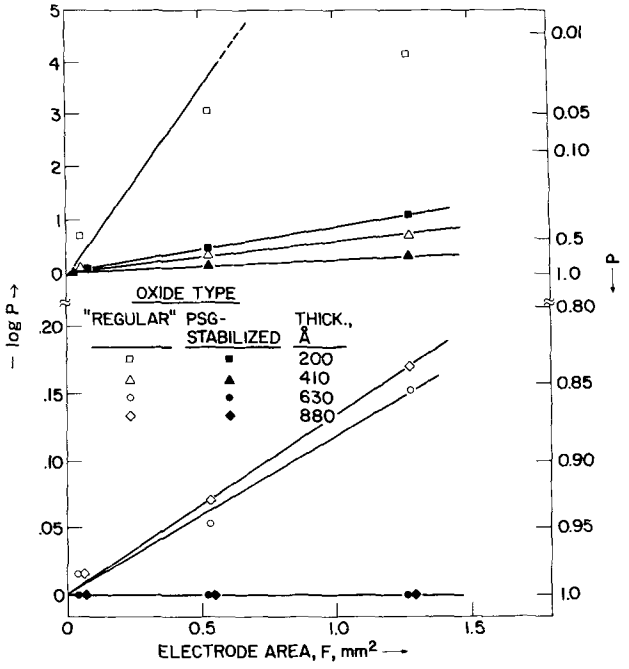

Fig. 5. Dependence of the fraction (*P*) of the total film area exhibiting primary breakdown on insulator thickness and electrode area for regular and phosphosilicate glassed oxide.

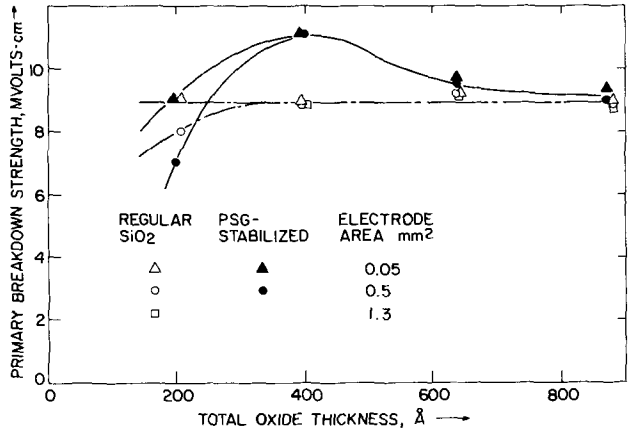

Fig. 6. Dependence of primary breakdown strength on total thickness of regular and phosphosilicate glassed SiO_2 films, where the thickness of the PSG layer is held constant at 125Å. Note that this strength is independent of electrode area, except for films thinner than 400Å.

mechanism responsible for primary-type breakdown is apparently no longer electronic in nature for these highly defected, very thin films. This change is consistent with the development of field-induced thermal instabilities at weak spots (3,4) and may well give rise to a time-dependence of the strength (6).

Impurities introduced after formation of SiO_2.—Protracted, post-metallization annealing treatments (viz., on the order of 30 min at 500°C) can promote extensive, tertiary-type breakdown (18) (see Fig. 7). The catalytic effect of certain cationic impurities in accelerating the devitrification of SiO_2 (14, 15), prob-

Table I. Dependence of defect density on oxide thickness

Oxide \ d, Å / ρ, cm⁻²	200	410	630	880
"Regular" SiO_2	750	65	12	12
PSG-stabilized	120	30	<1	<1

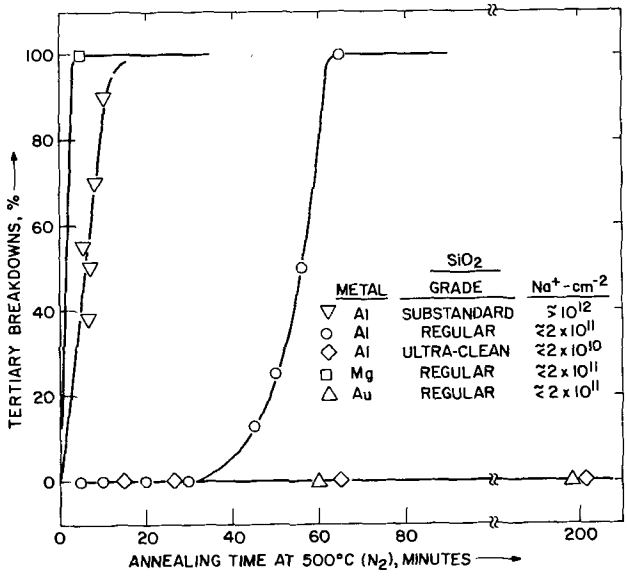

Fig. 7. Combined effects of electrode metal reactivity and post-metallization annealing on the development of electrode shorts in metal-1000Å SiO_2-Si structures, where the purity of the oxide is varied.

ably accounts for most of this behavior since it is most severe for films grown with a high sodium content and when highly reactive metal electrodes are used. In fact, electrical shorts (*i.e.*, tertiary breakdown) were rarely observed in oxide areas that were not covered by metals, or when noble metal electrodes such as gold were used, even after many hours of heating at 500°C. Mechanical stresses, arising from steps in the oxide thickness or from differences in the thermal expansion coefficients of the components on the MOS structure, may also contribute to oxide deterioration. Protracted annealing at 500°C also results in the growth of gross structural defects, under the edge of the metal electrode (18), which are probably responsible for the shorting. This particular type of tertiary failure mode will be described later.

The role of the metal electrode on the development of tertiary breakdown in stabilized film was evaluated by depositing 0.5 mm² dots of several metals on PSG (125Å, 4 m/o P_2O_5)-SiO_2(900Å, regular)-Si substrates, followed by determinations of the statistical breakdown distributions in both the unannealed and annealed (100 min at 500°C in N_2) conditions. From the results in Fig. 8, it is apparent that Mg, Ti, and Ni markedly promote oxide failure, while Al and Au have essentially no effect for PSG-stabilized struc-

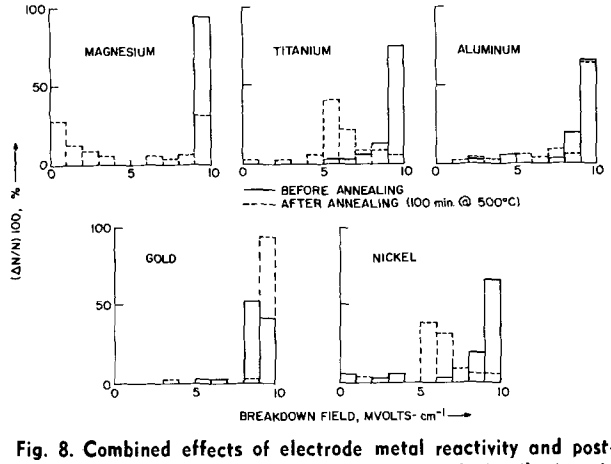

Fig. 8. Combined effects of electrode metal reactivity and post-metallization annealing on the breakdown strength distributions in PSG-stabilized, 1000Å oxide films.

tures. A comparison of the results for aluminum electrodes on regular and PSG-stabilized SiO_2 indicates that the PSG layer has the effect of retarding the development of electrical shorts due to extended annealing treatments. This retardation effect of the glass is more pronounced for structures with magnesium electrodes (*cf.* Fig. 7 and 8).

It is well-known that impurity ions can be introduced into the oxide in ways other than by electrode-oxide interactions. Thus, it is important to evaluate the possible effects of this type of contamination on breakdown. It was found in this investigation, for example, that when sodium (in concentrations of approximately 5 x 10^{12} cm^{-2}) was added after oxide formation (by boiling the oxidized wafers in NaCl-H_2O solutions prior to aluminization), relatively little additional deterioration was observed relative to the untreated, regular SiO_2 control material, for heating times up to approximately 50 min at 500°C. Therefore, it would appear that Na^+ ions which are introduced after SiO_2 formation, do not have much of an effect on crystallizing the oxide during subsequent post-metallization annealing at these temperatures.

In order to investigate the effect of localized damage in the insulator and at the insulator-semiconductor interface on tertiary breakdown, ultraclean SiO_2 films were irradiated with various O^+ dosages (using a constant beam energy of 75 keV). After deposition of 0.5 mm^2 Al dots, the capacitors were annealed for various times at 300°C in N_2 and tested in the usual way. Although the unannealed specimens exhibited the usual primary strength and essentially no indication of oxide deterioration, extensive shorting appeared after a very modest anneal of 20 min at temperatures as low as 300°C (see Fig. 9). Oxide failure was markedly increased by a small rise in the O^+ dosage and by a reduction in the oxide thickness. As in the earlier cases, oxide deterioration is intimately related to the presence and reactivity of the metal electrode. That is, electrical shorts were not observed in areas not covered by metal during heating [as subsequently established by using a removable mercury probe (19)] or when deposited gold electrodes are used. The network damage, due to implantation, apparently accelerates the metal-oxide reaction, thereby promoting shorting (18).

Glassing of Na^+-contaminated SiO_2.—Since sodium can be introduced inadvertently into SiO_2 during MOSFET processing before the PSG protective layer is added, it is very important to know what such contamination can do to the dielectric strength of the resulting layered oxide. This is of particular concern

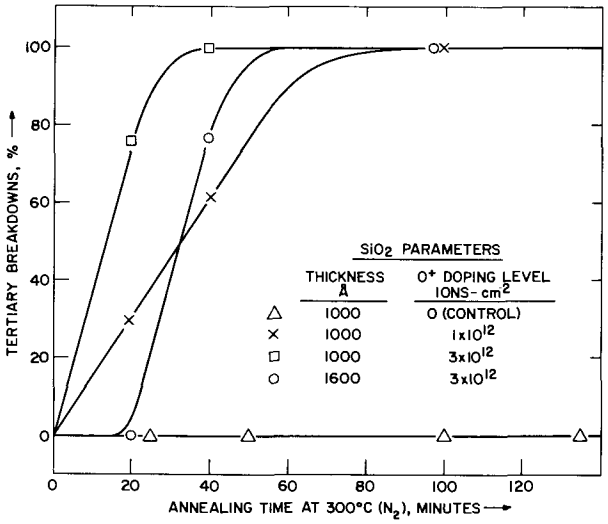

Fig. 9. Development of electrical shorts on annealing at 300°C in ultra-clean SiO_2 films, implanted with various O^+ ion dosages.

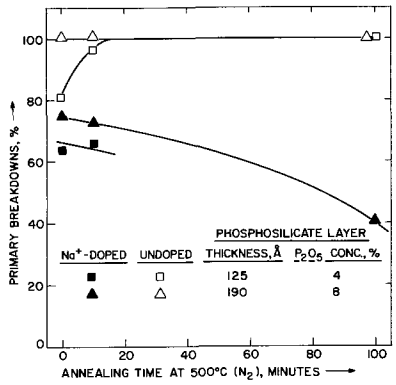

Fig. 10. Effect of post-metallization annealing on the breakdown characteristics of 1000Å SiO_2 films, deliberately contaminated with sodium, prior to phosphosilicate glassing. Characteristics of uncontaminated films are included for comparison.

because the glassing is carried out at temperatures, (800°-1100°C) where the promotion of crystallization by sodium is at a maximum (14). Therefore, the breakdown distributions were determined for oxide films prepared by: (*i*) growing 1000Å SiO_2 films of regular quality, (*ii*) immersing these oxidized substrates for 15 min in boiling NaCl-H_2O solutions to incorporate Na^+ ions in the oxide (8), (*iii*) diffusing P_2O_5 into the outer SiO_2 surfaces (at 800°-1000°C) to form phosphosilicate films, (*iv*) depositing 0.5 mm^2 aluminum dots, (*v*) annealing at 500°C (N_2) for various times, and (*vi*) breakdown testing. The severe deterioration of oxide quality due to Na^+ contamination is quite apparent in the results shown in Fig. 10. Experiments on regular SiO_2 films, subjected to the salt-water and subsequent high-temperature treatment (30 min at 1000°C in O_2) before aluminization, indicated that this oxide exhibited much more deterioration than the glassed ones. It may be concluded that even the addition of a PSG layer cannot prevent the formation of oxide faults at high temperatures when appreciable sodium concentrations are present in the SiO_2.

Morphology of annealing-induced defects.—The gross structural features of large defects, produced by extended annealing of Al-SiO_2-Si structures (see section on Impurities introduced after formation of SiO_2), are described below. It may be seen that these defects are quite massive, relative to the thickness of the insulating film. As such, they are probably mainly responsible for most of the tertiary breakdowns, even for the case where the capacitors have been subjected to a normal post-metallization heat treatment (*e.g.*, 5 min at 500°C).

Metallographic examination of shorted capacitors reveals the presence of well-defined, oriented defects on the periphery of the aluminum. Although partially covered by metal, their shapes are clearly rectangular and triangular for <100>- and <111>-oriented silicon, respectively, while their sides coincide with the (110) family of directions in the substrate. Evidently, the heating required to produce such defects decreases with a lowering of oxide perfection. Thus, they are readily visible at 500X magnification after an hour of annealing 1000Å, regular SiO_2 capacitors at 500°C, and ion-implanted oxide at 300°C. While becoming larger and more numerous with annealing time, they only develop under or in close proximity to reactive metal electrodes. The defects do not appear in regions away from the aluminum, for example, or in gold-deposited capacitors.

Conventional collodion replicas were made of the oxide surface for examination by electron microscopy, after removing the aluminum in a dilute HCl etchant. For specimens previously subjected to severe annealing treatments for aluminized structures (*e.g.*, ~ 2

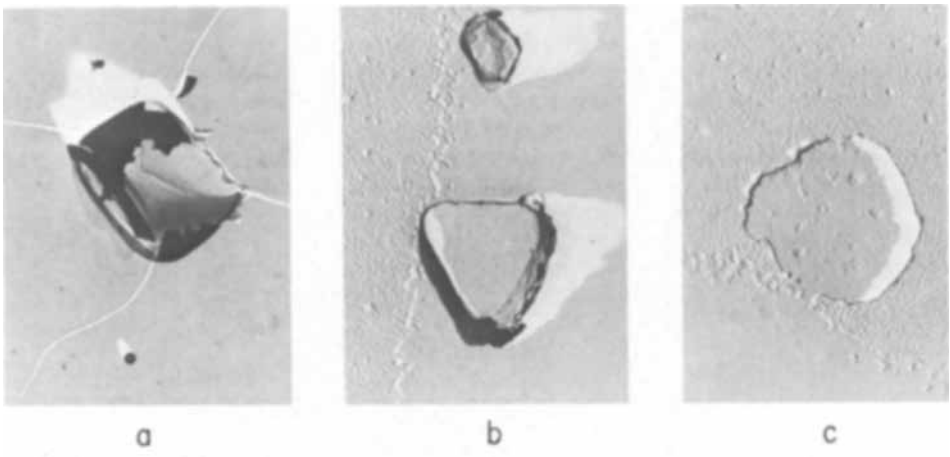

Fig. 11. Electron microscope replicas (at 9000X) of gross defects, developed in Al-SiO_2-Si structures during protracted annealing, as they appear after the aluminum is etched off. (a) and (b) show the faceted pits developed in <100>- and <111>-oriented Si, respectively, where pit sizes can be compared with that of ½μ latexsphere visible in (a). A typical, irregularly shaped raised area in the substrate is shown in (c).

hr at 500°C), the metallized oxide region was readily discernible, since considerable surface roughening had occurred as a result of a solid state reaction between the SiO_2 and Al. Electron micrographs of the replicas show that these defects are faceted pits, 1-10μ on a side and extending 1-2μ into the silicon (see Fig. 11a and b). With the aluminum removed, it was apparent that the pits are preferentially located along the perimeter of the metallized region, rather than in the center. Based on crystallographic considerations, it is evident that the facet faces are (111) planes.

Black films line the (111) faces of the pits. Since this material adheres to the collodion, it was possible to identify it as γ-Al_2O_3, using electron diffraction and microprobe analyses. Electron microprobe measurements, on specimens still covered with aluminum (*i.e.*, unetched), indicated that the faceted pits are filled with metallic aluminum, while the adjacent electrode region is depleted of metal. Finally, large irregularly shaped plateaus (approximately half a micron high) were frequently observed to occur in the substrate, adjacent to the pits (see Fig. 11c). Thus, the growth of pits and plateaus in close proximity and the presence of γ-Al_2O_3 in the pits suggests that a rapid transfer of mass occurs during annealing. It appears that silicon atoms can diffuse away from the receding faceted planes to form raised areas in the substrate covered by aluminum, while aluminum can penetrate the relatively thin oxide barrier to fill the γ-Al_2O_3 lined pits in the silicon. It is expected that large flaws in the oxide layer would also result from the development of the plateau regions. One effect of this mass rearrangement is the appearance of extensive shorting in MOS structures subjected to severe post-metallization heat treatments. As such, it constitutes another mode of tertiary failure, in addition to the presence of pinholes which develop during oxide growth.

Summary

Electrical breakdown characteristics of SiO_2 films thermally grown on silicon have been found to depend strongly on oxide preparation and various subsequent treatments:

1. While a lowering of the concentration of mobile impurities reduces the occurrence of defect-related breakdowns, it does not change the magnitude of the intrinsic breakdown strength of SiO_2. Appropriate phosphosilicate glassing, on the other hand, not only effectively obliterates oxide defects but also raises the intrinsic strength of the composite films.

2. Under identical SiO_2 growth conditions, reduction of film thickness is accompanied by an increase in the density of oxide faults. Excessively high defect density in the oxide gives rise to a time dependence of the breakdown characteristics and can therefore lower the magnitude of the primary breakdown strength under certain testing conditions. The addition of a PSG layer removes this dependence by eliminating the effect of oxide weak spots on breakdown. The amount of glassing required for this purpose is greater for SiO_2 films which have initially a higher defect density.

3. Sodium contamination can result in severe oxide deterioration, especially during film growth at temperatures in the 1000°-1200°C range. In contrast to this, sodium contamination after SiO_2 growth has much less of an adverse effect on the dielectric properties.

4. Protracted annealing of MOS structures (*e.g.*, 30 min at 500°C) can cause oxide deterioration by promoting a solid state reaction between certain electrode metals and SiO_2. This effect is more pronounced for oxides having a higher defect concentration. When aluminum is used, micron-size structural defects develop, concurrently with increased defect-related breakdown. These results suggest that another mechanism for oxide shorting can be operative, in addition to the breakdown which can be attributed to pinholes produced during oxide growth. This newer mode involves a rapid redistribution of massive quantities (relative to the dielectric thickness) of aluminum and silicon during the annealing process.

5. Lattice defects created by ion implantation have virtually no effect on the breakdown strength prior to annealing. Deterioration of implanted oxide during annealing at 300°C may be attributed to either an accelerated injection of electrode metal ions into the film, or by local crystallization facilitated by the presence of lattice defects.

The above observations are consistent with Fritzsche's breakdown model (5) which implies that processing steps promoting local crystallization of the oxide will result in an increase in defect-related breakdown, while glassing has an opposite and beneficial effect. Furthermore, the structural mismatch between the crystallites and the oxide matrix, which provides rapid diffusion paths, may also account for the observed annealing failure mode in Al-SiO_2-Si structures.

APPENDIX

The defects are assumed to be randomly distributed and have a size roughly comparable to the film thickness (therefore, much smaller than the electrode area, F). The total area (A) of the film may be subdivided into N cells of an area a, which is just large enough to accommodate a defect if it happens to be there. It follows that the probability (p) of randomly selecting an occupied cell is equal to $n/N = \rho \cdot a$, where n is the total number of occupied cells. Conversely, the probability (q) of picking an unoccupied cell is equal to $(1-p)$.

When an electrode is deposited, the number of cells covered by metal is $n' = F/a$. Consequently, the probability (P) for the electrode to not cover a defect is

$$P = q^{n'} = (1 - p)^{F/a} \quad [1]$$

Since $n << N$, it can be shown that

$$\ln P = -F \cdot \rho \quad [2]$$

A fraction P, of the total film area, will consequently exhibit primary-type breakdown. Equation [2], which was also used by Fritzsche, was derived here to give the reader a better appreciation of the significance of the results that can be determined by its application.

Acknowledgments

The authors are indebted to Dr. F. X. Montillo for providing the ultraclean SiO_2 specimens, to Dr. B. L. Crowder for ion implantation of SiO_2 films, to Dr. P. Balk and Dr. T. O. Sedgwick for their comments on this manuscript, and to Messrs. R. J. Dendall, W. Gordon, Jr., R. Hammer, and D. Johnson for their invaluable assistance with the breakdown measurements, and C. F. Aliotta for the electron microscope work.

Manuscript submitted March 2, 1970; revised manuscript received May 19, 1970.

Any discussion of this paper will appear in a Discussion Section to be published in the June 1971 JOURNAL.

REFERENCES

1. B. E. Deal, *This Journal*, **110**, 527 (1963).
2. F. W. Ainger, *J. Materials Sci.*, **1**, 1 (1966).
3. N. Klein, *IEEE Trans. on Electron Devices*, **ED-13**, 788 (1966).
4. N. Klein and H. Gafni, *ibid.*, **ED-13**, 281 (1966).
5. C. Fritzsche, *Z. angew-Phys.*, **24**, 48 (1967).
6. F. L. Worthing, *This Journal*, **115**, 88 (1968).
7. D. F. Miner, "Insulation of Electrical Apparatus," p. 40, McGraw-Hill Book Co., New York (1941).
8. E. H. Snow, A. S. Grove, B. E. Deal, and C. T. Sah, *J. Appl. Phys.*, **36**, 1664 (1965).
9. E. Yon, W. H. Ko, and A. B. Kuper, *IEEE Trans. on Electron Devices*, **ED-13**, 276 (1966).
10. J. M. Eldridge and P. Balk, *Trans. Met. Soc. AIME*, **242**, 539 (1968).
11. J. M. Eldridge, R. B. Laibowitz, and P. Balk, *J. Appl. Phys.*, **40**, 1922 (1968).
12. J. M. Eldridge and D. R. Kerr, *Abs. Electronics Div., Electrochem. Soc.*, **13**, 530 (1968).
13. P. Balk and J. M. Eldridge, *Proc. IEEE*, **57**, 1558 (1969).
14. H. Rawson, "Inorganic Glass Forming Systems," pp. 51-61, Academic Press, New York (1967).
15. R. Schmidt, Silicon Interface Specialists Conference, Las Vegas, Nevada, March 1968.
16. P. Balk, C. F. Aliotta, and L. V. Gregor, *Trans. Met. Soc. AIME*, **233**, 563 (1965).
17. E. H. Snow and B. E. Deal, *This Journal*, **113**, 263 (1966).
18. N. J. Chou, J. M. Eldridge, and W. Gordon, Jr., *Abs. Electronics Div., Electrochem. Soc.*, **13**, 534 (1968).
19. R. Hammer, *Rev. Sci. Instr.*, **41**, 292 (1970).

Preparation, Forming, and Aging of Electroluminescent ZnS:Mn,Cu,Cl Films

W. Riemer*[1] and R. E. W. Lake

Department of Electrical Engineering, University of Toronto, Toronto, Ontario, Canada, and Canadian Westinghouse Company, Hamilton, Ontario, Canada, respectively

ABSTRACT

The d-c characteristics (luminance-voltage-current) of electroluminescent films of ZnS:Mn,Cu,Cl prepared by two different methods were investigated during the operating life of the films. For the devices investigated a shift in the characteristics and an increase in the efficiency with operation time was observed. It is suggested that the terms forming and aging do not describe the time-dependent changes in the characteristics, but rather reflect practical aspects of the properties of the films.

Electroluminescence (radiative emission on application of an electric field) in activated ZnS has been recently reviewed in general (1, 2) and for the case of thin film devices (3). The usual configuration for investigating the electroluminescence of thin films of ZnS resembles a capacitor in that it consists of a film of ZnS sandwiched between two parallel electrodes, of which one is transparent to permit the observation of the emitted light.

Under operation ZnS:Mn,Cu,Cl films undergo time-dependent changes in the observed characteristics which are commonly referred to as forming and aging. Forming (4, 5) describes the observation that, on first applying a voltage to a film of this composition, a large current flows but no emission occurs. With the subsequent gradual decrease in current electroluminescence commences and increases in luminance. The duration of this process depends on the fabricating method and is typically a few seconds to as much as an hour (6, 7). One of the reasons that electroluminescent devices have not been more successfully applied is the aging effect or deterioration of emission on operation (8). The longest half-life (time to half initial luminance) for a ZnS thin film was reported to be just over a thousand hours (9) under a-c excitation. The d-c half-life of thin films is considerably shorter than that obtained under a-c conditions, and in some instances the devices are unstable (10).

In common terminology forming and aging are used to designate apparently distinct periods in the operating life of ZnS:Mn,Cu,Cl films. This paper describes the results of an investigation to determine whether a significant change in the d-c device characteristics can be associated with forming and aging, and whether these two phenomena are affected by the method of preparing the devices.

Experimental

The devices investigated consisted of a layer of phosphor sandwiched between two electrodes in a capacitor arrangement, and supported by a glass substrate. The phosphor used as source material for these experiments was ZnS:Mn,Cu,Cl with the following impurity concentrations determined by activation

* Electrochemical Society Active Member.
[1] Present address: Institut für Angewandte Physik, Universität Basel, Basel, Switzerland.
Key words: aging, electroluminescence, forming, thin films, vacuum deposition, zinc sulfide.

analysis: Cu 1.6%, Mn 0.2%, and Cl less than 0.1%. It was not possible to establish the corresponding concentrations in the films. A tin oxide layer on the substrate constituted the transparent electrode, and a matrix of 1 mm square aluminum electrodes on the phosphor film completed the array of devices. All evaporations of materials other than metals were performed in an Edwards High Vacuum Ltd. Model 12EX coating unit. The equipment had been modified to accommodate the special requirements for the production of uniform thin films. In pre-evaporation pumpdown the pressure observed on the dry air calibrated ionization gauge was approximately 1×10^{-5} Torr. A range of phosphor film thicknesses between 0.2 and 2.0μ was investigated. Interferometric measurements were used to determine the thickness of the films and also to calibrate the crystal monitor used for rate control.

Two methods were employed for the preparation of phosphor films. A procedure that gives good control over the impurity incorporation and satisfactory recrystallization is based on diffusing the impurities from a relatively large bulk of powder of desired impurity content into the film, previously deposited, contiguous to the powder under equilibrium conditions (11). The substrate with the evaporated ZnS film is embedded in the activated powder and the combination is heated in a double crucible (12) to approximately 750°C for a brief period. Using diffusion-activation relatively good films can be made, although only certain types of glass substrate and tin oxide layer survive this treatment.

The alternate method, deposition-activation, is based on the crystallization and activator incorporation during the deposition of the film (13). The source material, sintered pressed pellets of phosphor, was deposited onto a heated substrate. A very efficient method of substrate heating consisted of using the tin oxide layer on the substrate (subsequently used as transparent electrode) as a resistive heater (14). In preliminary experiments it was found that the characteristics of devices prepared by deposition-activation were primarily sensitive to the substrate temperature and the deposition rate. With increasing substrate temperature, the condensation rate decreased as in Fig. 1. A series of films were deposited under similar conditions, but the deposition rate was varied over a range from 5 to 45 Å/sec by varying the source temperature. For deposition rates in excess of 10 Å/sec the breakdown field of the film decreased and reduced the attainable luminance of the device (Fig. 2). For deposition rates less than 5 Å/sec, presumably as a consequence of the residual gas at the vacuum prevailing during evaporation, the maximum attainable luminance also decreased. The properties of the deposited film depend on the constitution of the vapor from which it condenses. For the given vacuum environment and boat design an optimum substrate temperature of approximately 240°C and deposition rate of 5 Å/sec were used in the preparation of films on which change in characteristics measurements were made.

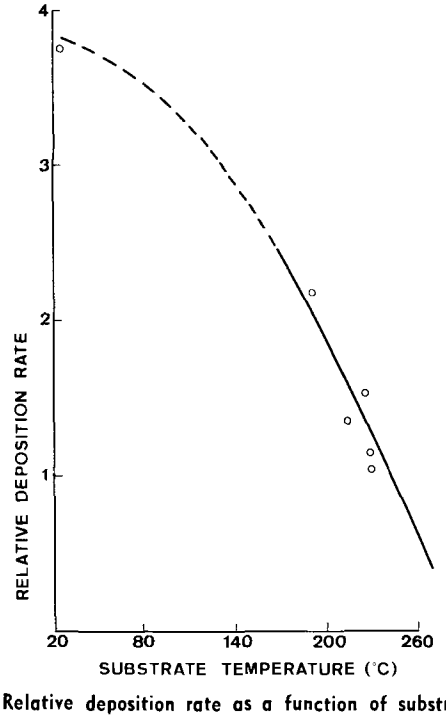

Fig. 1. Relative deposition rate as a function of substrate temperature.

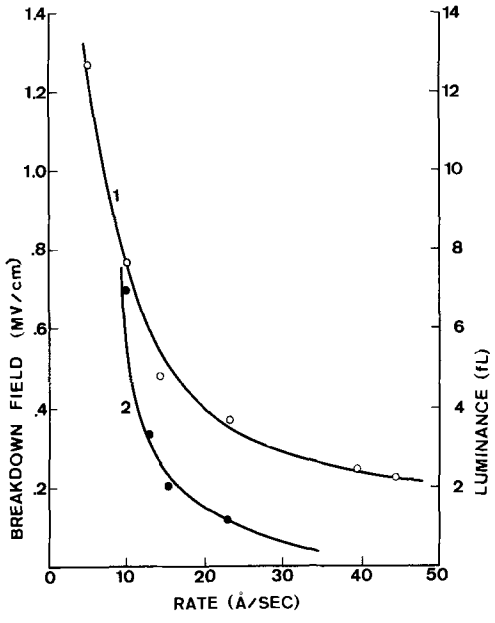

Fig. 2. Effect of film deposition rate on: 1, break-down field; 2, luminance.

The three variables that describe the operation of an electroluminescent film are the voltage (V) applied to the tin oxide and aluminum terminals, the current (I) through the device, and the luminance (L). The electrodes were connected in series with a large resistor to a stabilized voltage supply. The voltage across the film was monitored with a Keithley 601 electrometer. A small series resistor was used to record the current. Reproducible luminance results were obtained with a Spectra Pritchard photometer. The characteristic curves, L-V-I, were recorded with a Honeywell 550 recorder.

Observations

Both deposition-activated (80 films) and diffusion-activated (44 films) films were investigated. Although, under d-c operating conditions, diffusion-activated films generally showed a higher luminance (maximum observed 240 fL) than deposition-activated films (maximum observed 50 fL) the change in characteristics on operating was qualitatively similar, and consequently only representative results for deposition-activated films are presented.

In preliminary experiments it was observed that, for the devices investigated, emission was most effective when the aluminum electrode was made positive. In order to investigate the change on operation in d-c characteristics this polarity (aluminum positive) was therefore used. From first turn-on to the final breakdown of the device the current was maintained constant at 1 mA.

The voltage across the device and the luminance were continually monitored as a function of time. The voltage and luminance history for film 5-31 is described in Fig. 3. For constant current the voltage increases continuously. The actual trace, from which this graph is constructed, shows that as the break-

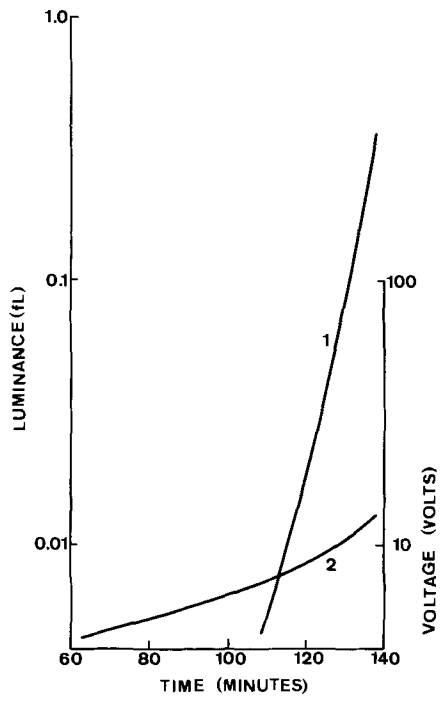

Fig. 3. Time-dependence of voltage and luminance for constant current for film 5-31. 1, Luminance; 2, voltage.

down voltage is approached the device becomes very noisy and final destructive break-down is preceded by numerous voltage spikes to low resistance values. Near break-down the luminance reaches a maximum value and decreases again. This decrease can be explained by the observation that near break-down individual portions of the device extinguished. Consequently the photometer, integrating over a large portion of the device, records a decreasing luminance.

In order to determine the change of the device characteristics as a result of operation, the V-L-I characteristics were plotted periodically. In earlier experiments it had been established that interrupting the current through a device did not result in a relaxation to a lower voltage on turning the current back on. It could be assumed, therefore, that the characteristics at any point in time described the degree of change in the device. To ensure that the measurements of the V-L-I curves did not affect the device significantly the current was limited to a range less than 1 mA.

The variation of voltage with current is shown in Fig. 4. It appears that the device was initially linear, but with operation became increasingly nonlinear and asymmetrical. Measurable emission started as the device became nonlinear and was macroscopically uniform over the entire electrode area.

Electroluminescent devices are often described by their L-V curve. The interpretation of the electroluminescence mechanism is also often based on this relationship. For the film already described the L-V graph at various points during its operating life is given in Fig. 5. It is noticed that the curves are parallel and progressively displaced to higher voltage values.

The L-I characteristics are shown in Fig. 6. It is observed that emission efficiency (in fL/mA) increases both with time of operation and, for small values of current, with current. For large currents near break-down, as for example curve 4, the efficiency decreases presumably as active areas of the device are eliminated.

In order to determine to what extent the change that had occurred during operation was irreversible, several films were operated under conditions where the voltage polarity was regularly reversed. At no point could the previous characteristics be regained. Although a minor degree of recovery occurred, a permanent change had been established that modified the device characteristics.

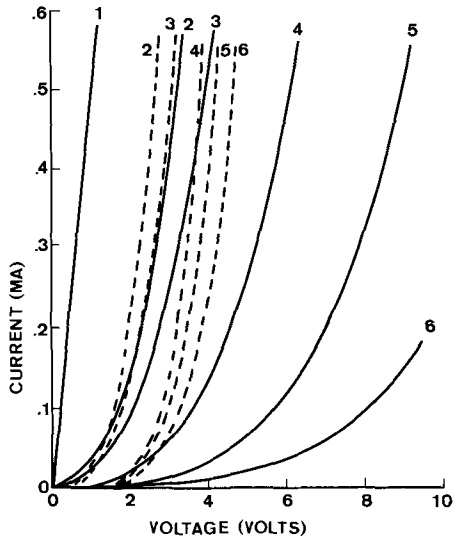

Fig. 4. For film 5-31, voltage variation with current after operating device for the following period: 1, start; 2, 72 min; 3, 117 min; 4, 133 min; 5, 141 min; 6, 157 min. Solid line: aluminum electrode positive; dashed line: aluminum electrode negative.

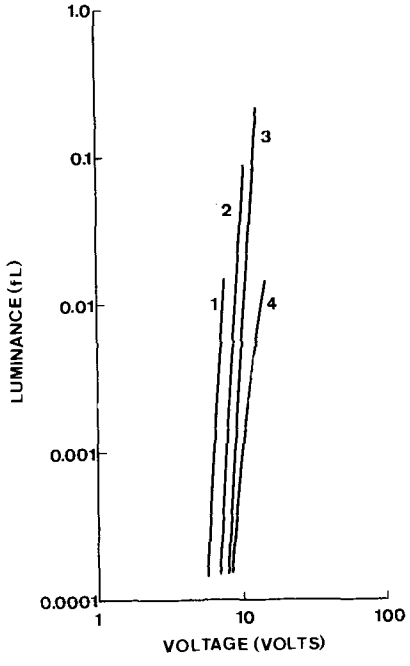

Fig. 5. For film 5-31, luminance variation with voltage after operating device for following period: 1, 117 min; 2, 133 min; 3, 141 min; 4, 157 min.

To establish whether the time-dependent effects observed could be associated with the formation of an oxide between the film and the aluminum electrode (15) the measurements were repeated on a matrix of devices which included a SiO layer between the film and the opaque electrodes, for which a number of different metals were used. For this case it was observed that emission commenced on first applying a voltage to the device, but that the same shift in characteristics occurred as with devices that did not have an oxide layer, and that in the presence of the oxide layer metals other than aluminum also led to electroluminescence.

Discussion

The terms forming and aging, as applied to thin films of ZnS:Mn,Cu,Cl, are commonly used to refer to apparently identifiable distinct processes. Thus, the virgin device on first application of a voltage under-

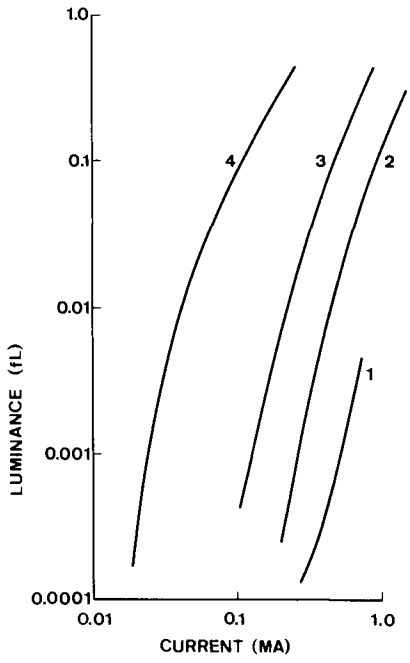

Fig. 6. For film 5-31, luminance variation with current after operating device for following period: 1, 117 min; 2, 133 min; 3, 141 min; 4, 157 min.

goes forming, whereupon electroluminescence is possible. Once emission has been achieved, the film is subject to aging, or decrease in luminance on constant voltage operation. The observations reported in this paper suggest that forming and aging are two labels that are convenient but arbitrary in the description of the time-dependent behavior of the devices under operation, since they reflect practical aspects of the devices rather than any distinct phase of device change.

For every device investigated electroluminescence was associated with nonlinear I-V characteristics. The initial linear I-V curve, not observed in the experiments with an additional oxide layer, is probably caused by parasitic conductive paths which must be eliminated for electroluminescence to occur.

Two possible explanations for the shift in device characteristics suggest themselves: the growth of an oxide layer at the aluminum electrode, and a change in the bulk of the film. The observation that, in the presence of a SiO layer, the shift in device characteristics occurred with metals other than aluminum would indicate that the formation of an aluminum oxide layer probably serves to eliminate parasitic conductive paths, but that changes in the film bulk cause the observed shift.

The nature of the change in the ZnS:Mn,Cu,Cl films has not been conclusively demonstrated. In the fabrication of certain types of rectifiers and transistors an electronically active region is created by a "forming" process that involves substantial ionic current (16). It is proposed that, in view of the concentration of copper in the films greatly in excess of the solubility (17), copper ions diffuse to capturing boundaries creating electronically active phases of Cu_xS (18, 19) and leading to an electroluminescence mechanism described by Vlasenko and Gergell (20). The constancy of slope of the shifted I-V curves and the increasing efficiency with operation of the devices support this interpretation.

Acknowledgments

This investigation was made possible by the support received from the Canadian Westinghouse Company, and by the encouragement and advice given by Professor G. Dick of the University of Toronto.

Manuscript submitted May 26, 1969; revised manuscript received June 15, 1970.

Any discussion of this paper will appear in a Discussion Section to be published in the June 1971 JOURNAL.

REFERENCES

1. A. G. Fischer, in "Luminescence of Inorganic Solids," p. 541, P. Goldberg, Editor, Academic Press, New York (1966).
2. F. F. Morehead, in "Physics and Chemistry of II-VI Compounds," p. 613, M. Aven and J. S. Prener, Editors, North-Holland Publishing Co., Amsterdam (1967).
3. P. Goldberg, in "Luminescence of Inorganic Solids," p. 385, P. Goldberg, Editor, Academic Press, New York (1966).
4. D. A. Cusano, Ph.D. thesis, Troy, 1959.
5. P. Goldberg and J. W. Nickerson, *J. Appl. Phys.*, **34**, 1601 (1963).
6. G. A. Antcliffe, Ph.D. thesis, Adelaide, 1964.
7. W. A. Thornton, N. T. D. C. Research Report BL-R-6-2329-JE3-11 (1962).
8. S. Roberts, *J. Appl. Phys.*, **28**, 2 (1957).
9. E. J. Soxman, JANAIR Report EL-1 (1965).
10. W. Riemer, Ph.D. thesis, Toronto, 1968.
11. W. A. Thornton, U.S. Pat. 3,044,902 (1962).
12. R. E. W. Lake, DIR Semi-annual Report No. 1 (1963).
13. L. R. Koller and H. D. Coghill, *This Journal*, **107**, 973 (1960).
14. J. F. O'Hanlon and R. R. Haering, *Rev. Sci. Instr.*, **38**, 1542 (1967).
15. J. L. Plumb and R. F. Cotellessa, Paper 46 presented at the Boston Meeting of the Society, May 5-9, 1968.
16. M. J. O. Strutt, in "Semiconductor Devices," Vol. 1, Academic Press, New York (1966).
17. A. A. Bundel *et al.*, *Bull. Acad. Sci. USSR, Phys. Series*, **30**, 656 (1966).
18. S. G. Ellis, *J. Appl. Phys.*, **38**, 2906 (1967).
19. S. Ruben, *Trans. Electrochem. Soc.*, **87**, 275 (1945).
20. N. A. Vlasenko and A. N. Gergell, *Phys. Stat. Sol.*, **26**, K77 (1968).

Luminescence of Pr^{+3} Activated Y_2O_2S

Lyuji Ozawa* and Philip M. Jaffe*

Zenith Radio Corporation, Chicago, Illinois 60639

ABSTRACT

The luminescent properties of the green emitting $Y_2O_2S:Pr^{+3}$ have been studied. The emission lines in the visible region are assigned to the transitions from $^3P_0$ to ^3H_J and to $^3F_2$ of Pr^{+3}; the main green emission lines around 514 nm are attributed to the transition $^3P_0 \rightarrow {}^3H_4$. There was a small shift, about 160 cm^{-1}, of the emission lines to higher energy with an increase in host cation radius (Y to Gd to La). The two broad excitation bands in $Y_2O_2S:Pr^{+3}$, centered at 255 and 290 nm, are due, respectively, to host excitation and to excitation associated with an interaction of activator and host. The optimum activator concentration of $Y_2O_2S:Pr^{+3}$ phosphor is at about 1×10^{-2} mole Pr_2O_2S per mole of phosphor. Quadrupole-quadrupole interaction is involved in the concentration quenching of the green emission.

Y(Gd and La)$_2O_2S:Pr^{+3}$ phospors[1] emit a green emission under cathode-ray or ultraviolet excitation (1, 2). The energy levels of Pr^{+3} in $PrCl_3$ (3, 4), in $LaBr_3$ (5, 6), in YCl_3 (7), in other crystals (8, 9), and in the vapor state (10) have been studied in detail from their absorption and fluorescent spectra. However, it is somewhat difficult to assign the electronic transitions within the Pr^{+3} ($4f^2$) configuration which are responsible for the emission and excitation lines in Y(Gd and La)$_2O_2S$ because there is some discrepancy, about 400 to 1800 cm^{-1}, between the positions of the observed emission and excitation lines of Y(Gd and La)$_2O_2S:Pr$ phosphors and the positions of the lines reported in ref. (3)-(10).

In this paper, the assignment of the emission and excitation lines of $Y_2O_2S:Pr$ phosphor is made by comparison with the energy levels of Pr^{+3} in YCl_3. The small shift of the Pr^{+3} emission lines with a change in host cation radius, the origin of the two broad excitation bands, the optimum activator concentration, and the concentration quenching mechanism of the Pr^{+3} emission in Y_2O_2S are also reported.

Experimental

The rare earths used[2] were yttrium oxide 6*N*, gadolinium oxide and lanthanum oxide 5*N*, and praseodymium oxide 3*N*. The rare earth oxide as host component and praseodymium oxide were dissolved in hot nitric acid and precipitated with oxalic acid. The precipitate was dried, then heated in air at 900°C for 2 hr to convert to the oxide, using alumina crucibles. This mixed oxide (1 mole) plus sulfur (3 moles) and sodium carbonate as flux (1 mole) were mixed in a mortar and then fired at 1100°C for 2 hr in air. After firing, the samples were washed with hot deionized water several times. By this treatment, residual sulfur and sodium compounds were removed from the phosphors. The samples obtained were confirmed as the oxysulfide by x-ray diffraction analysis.

The emission, excitation, diffuse reflectance spectra, and cathodoluminescence data were obtained with the equipment described elsewhere (11). No correction of the emission spectra was made for the spectral response of the monochromator and photomultiplier. The concentration dependence of the intensity of selected lines was determined from the recorded emission spectra by measuring their amplitudes.

* Electrochemical Society Active Member.

Key words: multipolar interaction, concentration dependence, excitation spectra, transition, emission line shift.

[1] The Pr^{+3} was substituted for a portion of the rare earth host cation in all preparations as for example $(Y_{1-x}Pr_x)_2O_2S$. However, the conventional phosphor notation will generally be used, *i.e.*, $Y_2O_2S:Pr$. Unless indicated otherwise, Pr is always trivalent.

[2] Obtained from Lindsey Division, American Potash and Chemical Corporation.

Results and Discussion

Assignment of lines of Pr^{+3}.—The emission and excitation spectra of $Y_2O_2S:Pr$ phosphor were similar to the spectra of $Gd_2O_2S:Pr$ and of $La_2O_2S:Pr$ phosphors. For this reason, the spectrum of the $Y_2O_2S:Pr$ phosphor is primarily discussed in this paper. The small differences between the emission spectra of the Y(Gd and La)$_2O_2S:Pr$ phosphors will be discussed in the section on Effect of host cation radius on the emission line wavelength.

The emission spectrum of $Y_2O_2S:Pr$ phosphor under 254 nm radiation from a low-pressure mercury lamp is shown in Fig. 1. No change of the emission spectrum was observed under excitation by other wavelengths or by cathode rays. In Fig. 1, the weak emission lines at wavelengths longer than 540 nm are also shown with higher magnification (about 10 times). The emission spectrum consists of lines ranging from about 470 to 700 nm. The main group, which consisted of many lines, peaks at about 514 nm, so that the emission color of the phosphor appears green. The $Y_2O_2S:Pr$ emission spectrum is due to the transitions between the energy levels of the $4f^2$ configuration of Pr^{+3}.

The position of the lines and bands in the excitation spectrum of the 514 nm emission was coincident with the position of the lines and bands in the excitation spectrum of the 670 nm emission. Since the direct excitation spectrum of the 670 nm emission clarified to a greater extent the distinctions between the excitation lines, a study of the excitation spectrum of the 670 nm emission was made.

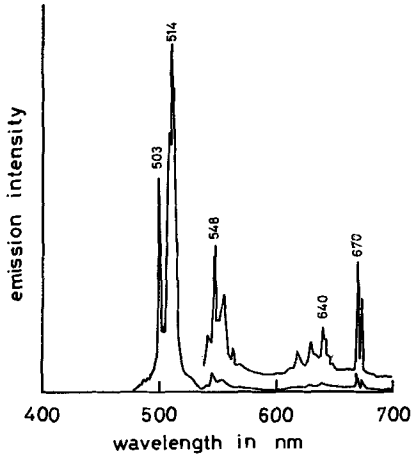

Fig. 1. Emission spectrum of $Y_2O_2S:Pr^{+3}$ phosphor. Above 540 nm the highly magnified spectrum is also shown.

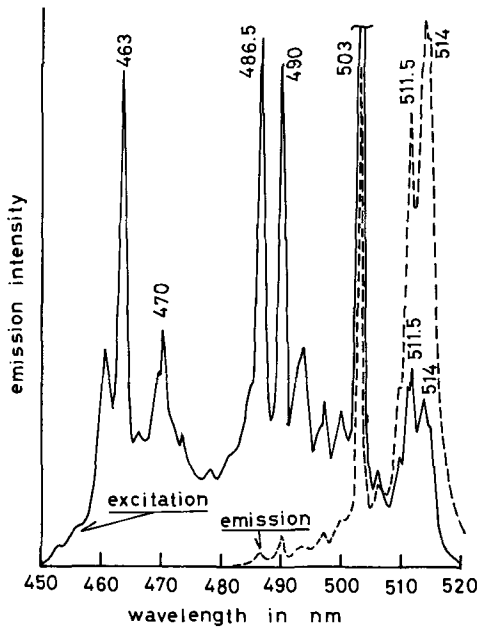

Fig. 2. Detail excitation and emission spectra of $Y_2O_2S:Pr^{+3}$ phosphor. The lines are assigned as the transition between ground level $^3H_4$ and excited levels.

The excitation spectrum of the 670 nm emission consisted of two broad and strong bands centered at about 255 and 290 nm, respectively, and of several weak lines at wavelength longer than 450 nm. The broad excitation bands are described in more detail below. The direct (line) excitation spectrum is shown in Fig. 2. Figure 2 also gives the green emission spectrum of $Y_2O_2S:Pr$ obtained with 290 nm excitation. The emission lines coincided in position with the excitation lines for the 670 nm emission. The direct excitation spectrum of $Y_2O_2S:Pr$ was classified into three groups: 463, 486.5, and 503 nm. These excitation lines may be attributable to direct transitions from the $^3H_4$ ground level to the excited levels of the Pr^{+3} ion. However, as shown in Table I the positions of the lines were about 1800 cm^{-1} lower in energy from those for the free ion (12). The large differences of the energy level positions between free Pr^{+3} and Pr^{+3} in Y_2O_2S is due to the fact that the position of the J levels of Pr^{+3} in crystals depends on bonding character of Pr^{+3} with the nearest neighbor anions and that the separation decreases in energy with an increase in covalent bonding (5, 9). Ionic character of bonding increases with an increase in electronegativity of the elements.

The Pr^{+3} energy levels which participate in the direct excitation and emission lines of $Y_2O_2S:Pr$ phosphor are comparable to the energy levels of Pr^{+3} in YCl_3 which may have a little more ionic bonding than Y_2O_2S. By assuming that the position of the energy levels of ^3P_J Pr^{+3} in Y_2O_2S is about 400 cm^{-1} lower than the corresponding position of the energy levels of Pr^{+3} in YCl_3 (7) because of more covalent bonding than in the chloride, the groups of the direct excitation lines of $Y_2O_2S:Pr$, 463, 486.5, and 503 nm, can be attributable to the transitions from the Pr^{+3} ground level $^3H_4$ to the excited levels $^3P_2$, $^3P_1$, and $^3P_0$, respectively. The strong excitation lines at 486.5 and 490 nm in Fig. 2 may be due to transitions to the sublevels of $^3P_1$ which is split by the crystal field. There may be a line around 480 nm which corresponds to the transition $^3H_4 \rightarrow {}^1I_6$ but it is too weak to verify. The weak excitation lines at wavelengths longer than 503 nm in Fig. 2 are attributable to the transitions from the $^3H_4$ ground level, which is split into many levels by the Stark effect, to the $^3P_0$ which is not split.

Table I. ^3P_J and $^1I_6$ excited energy levels of free Pr^{+3} and Pr^{+3} in yttrium compounds

Energy levels	Free ion* cm⁻¹	nm	YCl_3* cm⁻¹	nm	Y_2O_2S cm⁻¹	nm
$^3P_0$	21,390	466	20,214	495	19,460†	514
					19,880	503
$^3P_1$	22,007	455	20,831	480	20,400	490
					20,580	486
$^1I_6$	22,211	450	21,076	474		
$^3P_2$	23,161	431	21,867	457	21,320	469

* From ref. (7).
† Fluorescent main line.

In the emission spectrum of $Y_2O_2S:Pr$ shown in Fig. 1, there are no emission lines originating from the levels above $^3P_0$ because there is no change of the emission spectrum of $Y_2O_2S:Pr$ under direct excitation of the $^3P_0$, $^3P_1$, or $^3P_2$ levels, *i.e.*, with 503, 486.5, and 463 nm radiation, respectively. The emission lines of the $Y_2O_2S:Pr$ spectrum consisted of four main lines, 514, 548, 640, and 670 nm. These were attributable to the transitions from $^3P_0$ to $^3H_4$, $^3H_5$, $^3H_6$, and $^3F_2$, respectively.

The transition between $^3P_0$ and $^3H_4$ is an electric dipole transition (3, 13) and this transition is allowed when a Pr^{+3} ion occupies a lattice site lacking a center of symmetry. The crystal structure of Y(Gd and La)$_2O_2S$ crystals belongs to the D_{3d} space group and the rare earth cation site symmetry is C_{3v}(3m) (14). The rare earth ion is coordinated with seven anions; four oxygens and three sulfurs, having different bonding lengths; 2.23 and 2.90Å. The Pr^{+3} ions are expected to occupy the cation sites in Y(Gd and La)$_2O_2S$ crystals, so that electric dipole transition which give rise strong emission is allowed.

Effect of host cation radius on the emission line wavelength.—It was observed that the positions of the emission lines of Pr^{+3} in Y, Gd, and La oxysulfide phosphors did change with wavelength with a change in host cation. Since these oxysulfides all have the La_2O_3 structure, the change in line position must be due to a change in the crystal field caused by the change in host cation. Figure 3 gives the relationship between the wavelength (in cm^{-1}) of several emis-

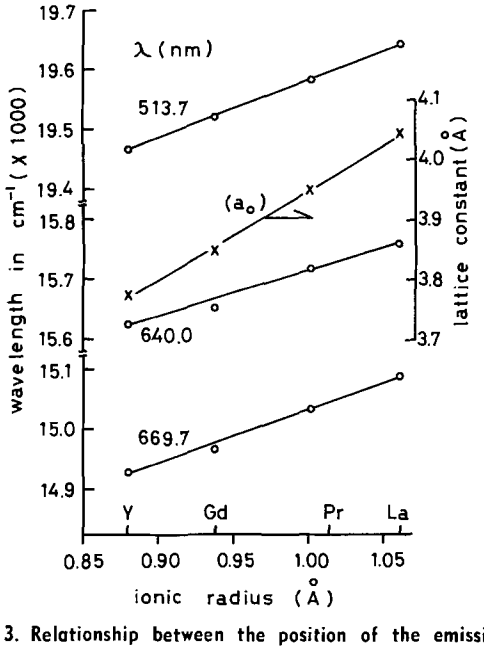

Fig. 3. Relationship between the position of the emission lines and ionic radius of rare earth cation in Y(Gd and La)$_2O_2S$. Lattice constant a_0 also indicated in the figure.

sion lines and the lattice constants as determined by x-ray analysis *vs.* the cation radius (15) of the host crystal. The wavelengths of the emission lines of Pr^{+3} in $(La_{0.5}Gd_{0.5})_2O_2S$ and its lattice constant are also plotted in Fig. 3.

All of the emission lines in the visible region shifted linearly to higher energies when the ionic radius of the rare earth cation increased, Fig. 3. The slope of the curves for 513.7 and 669.7 nm emission lines coincided with each other because the emitting level of all of these lines was the Pr^{+3} $^3P_0$ level. Because of their weak intensity, it was difficult to study the emission lines due to other emitting levels. From the slope of Fig. 3, the emission line shifted about 90 cm^{-1} when the cation radius changed by 0.1Å. The linear shift in spectral lines of Pr^{+3} in rare earth (Gd to La) trichlorides with cation radius have been reported by McLaughlin and Conway (16) and by Dieke (7). However, the shift in the rare earth trichlorides, about 50 cm^{-1} per 0.1Å change in radius is smaller than the shift observed in the rare earth oxysulfides.

The shift of emission with a change in host cation can be explained in the following way: Since the ionic radius of Pr^{+3} is 1.01Å and of La^{+3} is 1.06Å, Pr^{+3} ions substitute for La^{+3} in La_2O_2S crystal with little lattice distortion. On the other hand, in Gd_2O_2S and Y_2O_2S crystals, the Pr^{+3} ions would be incorporated with a perturbation because of the smaller radius of Gd^{+3} (0.99Å) and of Y^{+3} (0.88Å). The distortion of the Pr^{+3} center increases with a decrease in lattice constant. This distortion results in the lowering of the excited level $^3P_0$ of the Pr^{+3} ions.

The shift of the wavelength position of the emission lines of Eu^{+3} in Y(Gd and La)$_2O_2S$ with cation radius was also observed. However, the shift was half of that of Pr^{+3}. The small shift may be caused by the small difference in ionic radius between Eu^{+3} (0.95Å) and Y^{+3} and Gd^{+3}.

Excitation spectrum.—As already described in the section Assignment of lines of Pr^{+3}, the excitation spectrum of Pr^{+3} in Y_2O_2S crystals consisted of two strong broad bands centered at about 255 and 290 nm, respectively, and of many weak lines which were due to the direct excitation of the Pr^{+3} excited levels. These direct excitation lines were already described in the above mentioned section. This section discusses the origin of the broad excitation bands.

For this study, samples of $(Y_{1-x}Pr_x)_2O_2S$ were prepared in which x varied from 10^{-5} to 10^{-1}.

The broad excitation spectra obtained with representative samples are shown in Fig. 4. The relative number of quanta of each curve are comparable to each other. The 290 nm band increased with increasing praseodymium concentration, whereas the 255 nm band stayed relatively constant. The above results are more easily seen in the concentration

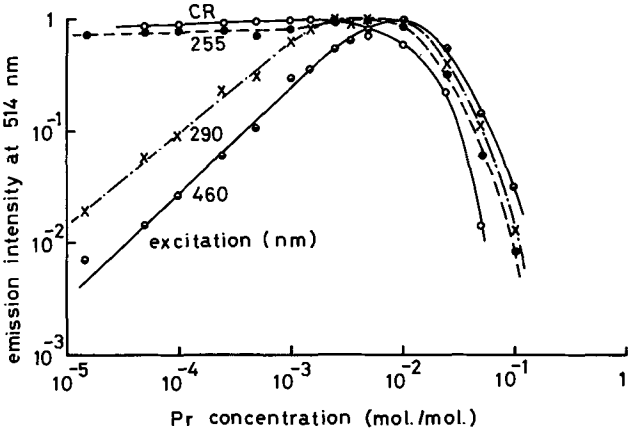

Fig. 5. Concentration dependence curves of $Y_2O_2S:Pr^{+3}$ phosphor under cathode-ray (CR), 255, 290, and 460 nm excitation.

dependence curves of the emission intensity of Y_2O_2S:Pr phosphors under various excitation modes, as shown in Fig. 5.

Since the emission intensity under 255 nm excitation was maintained at about constant level, the indication is that the amount of the energy absorbed by this excitation was independent of the activator concentration and that a constant portion of the absorbed energy was transferred to the Pr^{+3} activator ions. Therefore, it could be inferred that the 255 nm excitation band was due to the host excitation.

The emission intensity under 290 and 460 nm excitation increased linearly and with the same slope with an increase in praseodymium concentration when the praseodymium concentration was below about 1×10^{-3} mole Pr_2O_2S per mole of phosphor, Fig. 5. The 460 nm excitation is the direct Pr^{+3} ($4f^2$) excitation. Reflectance spectra of Y_2O_2S:Pr with various praseodymium concentration are shown in Fig. 6. When the praseodymium concentration increased, the reflectance at 290 nm decreased. From the above results, it was inferred that the 290 nm broad excitation band was due to the excitation associated with the Pr^{+3}.

Several lines superimposed on the broad excitation bands of Gd_2O_2S:Pr phosphors were observed at room temperature. The recorded uncorrected excitation spectrum of Gd_2O_2S:Pr (1×10^{-3} mole Pr_2O_2S) phosphor to give the 514 nm emission is given in Fig. 7. There are lines at 314, 307, 303, 282, 278, and 275 nm. These lines could be identified as the direct transitions from the ground level $^8S_{7/2}$ to the excited levels ^6P_J and ^6I_J of Gd^{+3} (17). The quantitative data on the energy transfer efficiency in mixed $(Y,Gd)_2O_2S$:Pr phosphors as a function of gadolinium concentrations were not obtained because of strong broad excitation

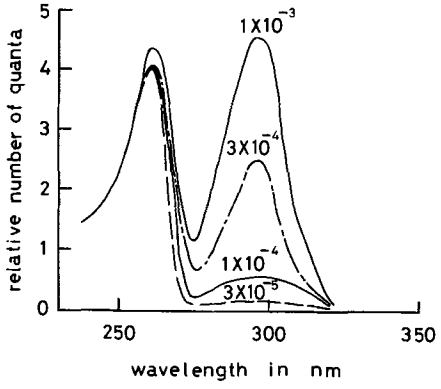

Fig. 4. Broad excitation spectra of $Y_2O_2S:Pr^{+3}$ phosphors having various activator concentrations.

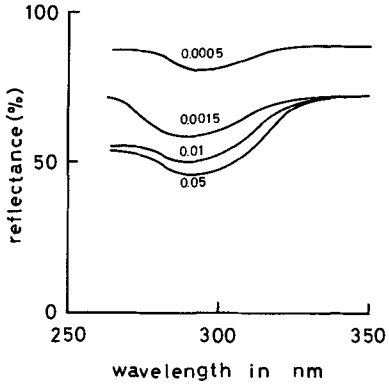

Fig. 6. Reflectance spectra in u.v. region of $Y_2O_2S:Pr^{+3}$ phosphor having various activator concentrations.

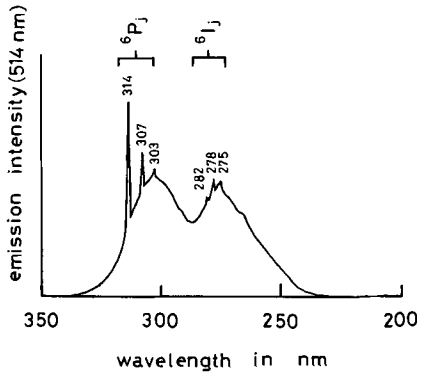

Fig. 7. Recorded excitation spectrum (uncorrected) of the green emission of $Gd_2O_2S:Pr^{+3}$ phosphor. Lines superimposed on the broad bands are believed due to absorption by paired gadolinium ions.

bands. However, there was evidence of the energy transfer from trivalent gadolinium to Pr^{+3} resulting in Pr^{+3} emission for the samples containing above 0.01 mole gadolinium, but there was no evidence of energy transfer below 0.005 mole gadolinium. This result is similar to that obtained with mixed $(Y,Gd)_2O_3$ phosphors activated with the rare earths where the energy transfer involved pairs of trivalent gadolinium ions (17). Therefore, it is deduced that the energy transfer from gadolinium to Pr^{+3} emission in $Gd_2O_2S:Pr$ may occur in a similar way.

Concentration dependence.—As already shown in Fig. 5, the optimum praseodymium concentration markedly changed with a change in the exciting modes: 0.25 m/o (mole per cent) under cathode rays, 0.3 m/o under 255 nm, 0.5 m/o under 290 nm, and 1.0 m/o under 460 nm.

Since the weighted number of nearest neighbor cation sites of Y_2O_2S crystal is twelve, the optimum activator concentration should be at 0.08 mole, if the concentration quenching is due to a decrease in the concentration of the isolated single activator ions (18). If so, an electrostatic multipolar interaction is involved in the concentration quenching (19).

When electrostatic multipolar interactions are involved in concentration quenching, the observed emission intensity I_{ob} as a function of the activator concentration is given by the following expression (20)

$$I_{ob} = KI_o\,[1 - \exp(-\alpha C)]\,[1 + \beta\,(C)^{\theta/3}]^{-1} \quad [1]$$

where I_o is intensity of the exciting light, α effective absorption coefficient for the exciting light, C activator concentration, β a constant for each interaction in a given structure, θ is 6, 8, or 10 for dipole-dipole, dipole-quadrupole, quadrupole-quadrupole interaction, respectively, and K is a constant. This expression indicates that the optimum activator concentration is not only a function of the luminescent centers but also of the absorption coefficient for exciting radiation. The experimental results agree qualitatively with the results predicted by expression [1]. Since it is difficult to determine the α value of powder phosphors, no quantitative analysis could be done. For the exciting radiation used here, Fig. 5, the absorption coefficient decreased with exciting wavelengths. For a weak absorbing exciting radiation, Eq. [1] becomes

$$I_{ob}/C = A\,[1 + \beta\,(C)^{\theta/3}]^{-1} \quad [2]$$

The value of θ for the green emission of Pr^{+3} (514 nm) in Y_2O_2S was 10.5 as indicated in Fig. 8. Therefore, quadrupole-quadrupole interaction ($\theta = 10$) was involved in the concentration quenching of the green emission of $Y_2O_2S:Pr$ phosphor. This result agrees closely with the result which quadrupole-quadrupole interaction predominantly involved in the concentration quenching of Pr^{+3} emission in LaF_3 (21). When the interaction of Pr^{+3} ions with each other increases as the praseodymium concentration increases, the excited electrons in the $^3P_0$ level of one Pr^{+3} ion relax to $^1D_2$. This relaxation energy $^3P_0 \rightarrow {}^1D_2$, 3800 cm^{-1}, is simultaneously transferred to other Pr^{+3} ions by the transition $^3H_4 \rightarrow {}^3H_6$, 4100 cm^{-1}. Because the ground level $^3H_4$ of Pr^{+3} in Y_2O_2S crystal is split into many levels (maximum of $2J + 1$) with energy difference of 450 cm^{-1}, the energy difference of 300 cm^{-1} is inconsequential and the energy transfer from $^3P_0 \rightarrow {}^1D_2$ to $^3H_4 \rightarrow {}^3H_6$ occurs readily.

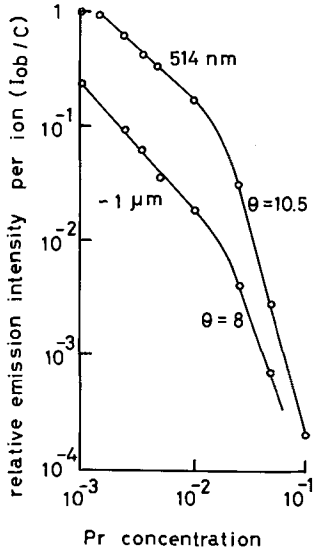

Fig. 8. Relative emission intensity from $^3P_0$ (514 nm) and from $^1D_2$ (~1 μm) per one Pr^{+3} ion (I_{ob}/C) of $Y_2O_2S:Pr^{+3}$ phosphor. θ values for 514 nm emission is 10.5 and for the 1 μm emission is 8. Concentration is mole Pr_2O_2S per mole phosphor.

When a multipolar interaction is involved in emission quenching, the decay time of the emission should vary according to the intensity of the multipolar interaction. Since the decay time of the green emission of $Y_2O_2S:Pr$ was very fast, several microseconds, the change of the lifetime due to multipolar interaction could not be detected in this study.

The optimum activator concentration of the emission from the lowest emitting levels of Eu^{+3} and of Tb^{+3} in Y_2O_2S is 0.08 mole fraction (20). However, the optimum activator concentration for the emission line from the lowest emitting level of Pr^{+3}, $^1D_2$, λ about 1 μm, was about 1×10^{-2} mole fraction. The slope of the (I_{ob}/C) curve was 8/3 as shown in Fig. 8. Thus dipole-quadrupole interaction was involved in the concentration quenching of the Pr^{+3} $^1D_2$ emission line. The transition responsible for this interaction is

$$^1D_2 \rightarrow {}^1G_4\ (6700\ cm^{-1});\ {}^3H_4 \rightarrow {}^3F_4\ (6600\ cm^{-1})$$

Under cathode-ray excitation, all of the excitation modes are involved in the excitation process. However, the host excitation may be dominant among these excitation modes. If so, then the concentration dependence curve for cathode-ray excitation of the phosphors which have a host excitation band should be similar to the concentration dependence curve under host excitation. As shown in Fig. 5, the concentration dependence curves obtained by cathode-ray excitation are indeed very similar to the concentration dependence curve obtained by 255 nm host excitation.

The green emission of $Y_2O_2S:Pr$ phosphor under cathode-ray excitation had good response to high current, *i.e.*, did not saturate at relatively low current densities like sulfide phosphors. Since the lifetime of the electrons remaining in the excited level $^3P_0$ is

very short, the saturation of the excited electrons in $^3P_0$ does not occur until very high beam current excitation. Therefore, the green emission of Y_2O_2S:Pr may be used as the green component in projection-type color TV picture tubes.

Conclusion

Y_2O_2S:Pr phosphors emit a green fluorescence under excitation by short u.v. and by cathode rays. The energy level assignment of the Pr^{+3} lines was made by the reference to the transitions within Pr^{+3} in YCl_3. In Y_2O_2S:Pr, all of the emission lines in the visible region are attributed to the transitions from $^3P_0$. The green emission lines around 514 nm are due to the transitions from $^3P_0$ to the ground level $^3H_4$ which is split into many levels with energy difference of about 450 cm^{-1}.

All of the emission lines of Pr^{+3} in Y(Gd and La)$_2O_2S$ shifted linearly to higher energy when the ionic radius of the rare earth host cation increased. This change was related to the distortion of the lattice caused by the change in size of the host cation.

The excitation spectrum consisted of two broad bands centered at 255 and 290 nm and of weak lines located around 480 nm. The latter is due to the direct excitation of Pr^{+3}. It is inferred that the 255 nm excitation band is due to host excitation and that the 290 nm excitation band is due to the excitation associated with an interaction of activator and host. The energy transfer from a pair of gadolinium ions to Pr^{+3} was observed. The optimum Pr^{+3} concentration in Y_2O_2S:Pr is around 1 x 10^{-2} mole Pr_2O_2S per mole of phosphor. Quadrupole-quadrupole interaction is involved in the concentration quenching of the green emission. The concentration dependence curve under cathode-ray excitation is almost identical to that obtained by host excitation indicating that the two process are similar.

Acknowledgment

The authors wish to thank Mrs. H. Stanczyk for her assistance in preparation of samples, Mr. L. Flemming for cathodoluminescent data, and Dr. G. Arai for x-ray data.

Manuscript submitted Feb. 20, 1970; revised manuscript received June 10, 1970. This was Late News Paper 329 presented at the New York Meeting of the Society, May 4-9, 1969.

Any discussion of this paper will appear in a Discussion Section to be published in the June 1971 JOURNAL.

REFERENCES

1. L. Ozawa, *Oyo Butsuri* (Applied Physics), **37**, 80 (1968) in Japanese.
2. M. R. Royce and A. L. Smith, Extended Abstract 34, Boston Meeting, Electrochemical Society, May 5-9, 1968.
3. G. H. Dieke and R. Sarup, *J. Chem. Phys.*, **29**, 741 (1958).
4. J. S. Morgolis, *ibid.*, **35**, 1367 (1961).
5. E. Y. Wong and I. Richman, *ibid.*, **36**, 1889 (1962).
6. N. H. Kiess and G. H. Dieke, *ibid.*, **45**, 2729 (1966).
7. G. H. Dieke, "Spectra and Energy Levels of Rare Earth Ions in Crystals," p. 200, Interscience Publishers, New York (1968).
8. J. B. Gruber, *J. Chem. Phys.*, **38**, 946 (1963).
9. E. Y. Wong, O. M. Stafsudd, and D. R. Johnston, *ibid.*, **39**, 1037 (1963).
10. J. Sugar, *Phys. Rev. Letters*, **14**, 731 (1965).
11. P. M. Jaffe and J. D. Konitzer, *This Journal*, **116**, 633 (1969).
12. H. M. Crosswhite, G. H. Dieke, and Wm. J. Carter, *J. Chem. Phys.*, **43**, 2047 (1965).
13. E. V. Sayre, K. M. Sancier, and S. Freed, *ibid.*, **23**, 2060 (1955).
14. O. J. Sovers and T. Yoshioka, *ibid.*, **49**, 4945 (1968).
15. J. A. Gibson and G. S. Harvey, Air Force Materials Laboratory, Wright-Patterson AFB, Technical Report AFML-TR-65-430, (1966).
16. R. D. McLanghlin and J. G. Conway, *J. Chem. Phys.*, **38**, 1037 (1963).
17. L. Ozawa and S. Nishikawa, *Japan. J. Appl. Phys.*, **7**, 1354 (1968).
18. L. G. Van Uitert and L. F. Johnson, *J. Chem. Phys.*, **44**, 3514 (1966).
19. D. L. Dexter and J. H. Schulman, *ibid.*, **22**, 1063 (1954).
20. L. Ozawa, H. Forest, P. M. Jaffe, and G. Ban, Extended Abstract 45, Los Angeles Meeting, Electrochemical Society, May 10-15, 1970.
21. M. R. Brown and J. S. S. Whiting, *J. Chem. Phys.*, **43**, 1 (1965).

Calculation of the Ga-In-P Ternary Phase Diagram Using the Quasi-Chemical Equilibrium Model

G. B. Stringfellow

Hewlett-Packard Company, Palo Alto, California 94304

ABSTRACT

The Ga-In-P solid-liquid-vapor equilibrium phase diagram has been calculated based on the quasi-chemical equilibrium solution model. The calculated phase diagram, both isothermal liquidus and iso-(solid concentration) lines, and P_2 and P_4 vapor pressure curves, is found to be in agreement with recently published experimental data.

The thermodynamic properties of the III-V binary system In-As, Ga-As, and In-Sb have been calculated using the quasi-chemical equilibrium (QCE) treatment of the lattice solution model (1-2). A method of calculating a general III-V ternary phase diagram was also presented in ref. (2) and applied to the calculation of the In-As-Sb and Ga-In-As systems. Because of the lack of experimental data, the accuracy of the calculated ternary phase diagrams could not be adequately tested. The Ge-Si-Sn and Ge-Si-Pb phase diagrams, calculated using the QCE treatment, were found to be in excellent agreement with experimental phase diagram data (3).

Recently, experimental phase diagram data has been obtained for the system Ga-In-P (4-5). It is the purpose of this paper to compare the calculated phase diagram with the experimental data for the system Ga-In-P and thus test the accuracy of the QCE cal-

Key words: gallium-indium-phosphorus system, calculated phase diagram.

culation and present the entire Ga-In-P solid-liquid-vapor equilibrium phase diagram.

Calculation of Ga-In-P Phase Diagram

The calculation is based on the quasi-chemical equilibrium (QCE) model. The major assumptions on which this model is based are:

1. Each atom has Z nearest neighbors.
2. Nearest neighbors interact pairwise with the temperature and composition independent interaction parameter, Ω, defined as

$$\Omega_{AB} = Z[H_{AB} - \tfrac{1}{2}(H_{AA} + H_{BB})]$$

where H_{ij} is the energy of an i-j nearest neighbor pair.

3. Only the configurational free energy of mixing is considered, *i.e.*, the vibrational free energy of mixing is neglected.
4. The distribution of constituent atoms is calculated using a mass action-like expression

$$N_{ii}N_{jj}/(N_{ij})^2 = \tfrac{1}{4}\exp(2\Omega_{ij}/ZRT)$$

where i and j each represent either A, B, or C.

The equilibrium equations for the (ternary liquid)-(binary solid) equilibrium may be written

$$\ln(\gamma_{AC}X) = \ln\left(\frac{4\gamma_A\gamma_C N_A N_C}{\gamma^{s.l.}{}_A\gamma^{s.l.}{}_C}\right) + \Delta S^F{}_{AC}(T^F{}_{AC} - T)/RT \quad [1a]$$

$$\ln\gamma_{BC}(1-X) = \ln\left(\frac{4\gamma_B\gamma_C N_B N_C}{\gamma^{s.l.}{}_B\gamma^{s.l.}{}_C}\right) + \Delta S^F{}_{BC}(T^F{}_{BC} - T)/RT \quad [1b]$$

$$N_A + N_B + N_C = 1 \quad [1c]$$

The activity coefficients, γ_{ij}, in the ternary liquid phase cannot be expressed analytically but are computed numerically in terms of temperature and composition using the QCE model. The activity coefficients in the solid phase may be written

$$\gamma_{AC} = \left(\frac{\beta - 1 + 2X}{X(\beta+1)}\right)^{Z/2}$$

$$\gamma_{BC} = \left(\frac{\beta + 1 - 2X}{(1-X)(\beta+1)}\right)^{Z/2}$$

where

$$\beta = [1 + 4X(1-X)(\eta^2 - 1)]^{1/2}$$

$$X = N_{AC}/(N_{AC} + N_{BC}) \text{ and } \eta = \exp(\Omega_{AC-BC}/ZRT)$$

For the zinc blende lattice, where AC-BC interactions are considered, the appropriate value of Z is 12.

Using the activity coefficients calculated from the QCE model, Eq. [1a-c] can be solved numerically with N_A and N_C given to yield N_B, X, and T. A detailed description of the calculation is given in ref. (2).

The equilibrium P_2 and P_4 pressures over the liquidus surface were calculated from the following equilibrium equations

$$P_{P_4} = P^\circ{}_{P_4}(N_A\gamma_A)^4$$
$$P_{P_4}{}^2/P_{P_4} = K_P(T)$$

where $P^\circ{}_{P_4}$, the P_4 pressure over pure liquid phosphorus, and $K_P(T)$ may be calculated from data available in the JANAF Tables (6).

The parameters used in the calculation are listed in Table I. The In-Ga interaction parameter was determined by Macur, Edwards, and Wahlbeck (7). The In-P and Ga-P interaction parameters were obtained by making a least squares fit of the calculated binary phase diagrams to the experimental data (8-10) (see Fig. 1). The entropy (11) and temperature (11-14) of fusion for InP and GaP were extracted from the literature. The only parameter not available from binary data is the $InP_{(s)}$-$GaP_{(s)}$ interaction parameter. It was obtained by constraining the solid in equilibrium with a liquid composed of 35% Ga, 50% In, 15% P, to be 97.2% GaP, as per Panish's data (4). It was found that the liquid composition in equilibrium with a given solid near pure GaP is the variable most sensitive to the InP-GaP interaction parameter.

Table I. Parameters used in the QCE calculation of the Ga-In-P phase diagram

Parameter	Value used in the calculation
$T^F{}_{GaP}$	1740°K (11-13)
$T^F{}_{InP}$	1333°K (10)
$\Delta S^F{}_{GaP}$	16.25 eu* (10)
$\Delta S^F{}_{InP}$	14.7 eu* (10)
Ω_{Ga-P}	−3500 cal/mole
Ω_{In-P}	0 cal/mole
Ω_{In-Ga}	1066 cal/mole (6)
$\Omega_{InP-GaP}$	4000 cal/mole

* ΔS^F was calculated from the value of ΔH^F given by Sirota (10) and the values of T^F used in the calculation; $\Delta S^F = \Delta H^F/T^F$.

The calculated results are presented in Fig. 2-5. In Fig. 2, the calculated isothermal liquidus lines are presented for comparison with points obtained from interpolating between Panish's data points. No points from the extrapolation of his data are included since they are subject to large errors. The agreement between calculated and experimental liquidus compositions is within 2 a/o (atomic per cent). Low temperature liquidus isotherms in the In-rich corner of the phase diagram are the most useful for crystal growth information. This area of the phase diagram is expanded in Fig. 3. In Fig. 4, calculated iso-(solid composition) lines are plotted along with the experimental data. Each line represents the locus of liquid compositions in equilibrium with a given solid composition. Each data point is labeled with the mole fraction GaP in the solid in equilibrium with that particular liquid composition.

The agreement between calculated and experimental liquid composition in equilibrium with a particular

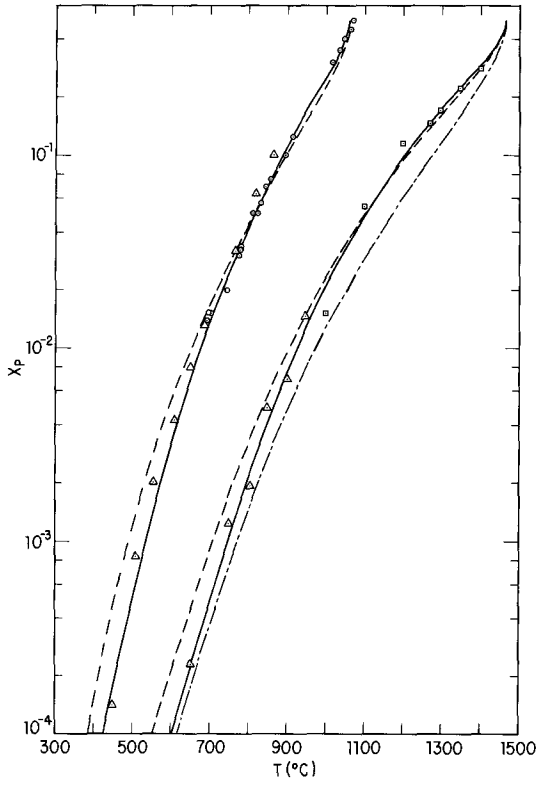

Fig. 1. Ga-P and In-P temperature-composition phase diagrams. — — — — Ideal solution calculation —GaP; — — — — — QCE calculation, $\Omega_{Ga-P} = -3500$, $\Omega_{In-P} = 0$; ——— QCE calculation with temperature dependent interaction parameters $\Omega_{Ga-P} = 4650 - 5.85T$, $\Omega_{In-P} = 8220 - 7.57T$; ○ Panish (8) InP; △ Hall (9) InP, GaP; □ Rubenstein (10) GaP.

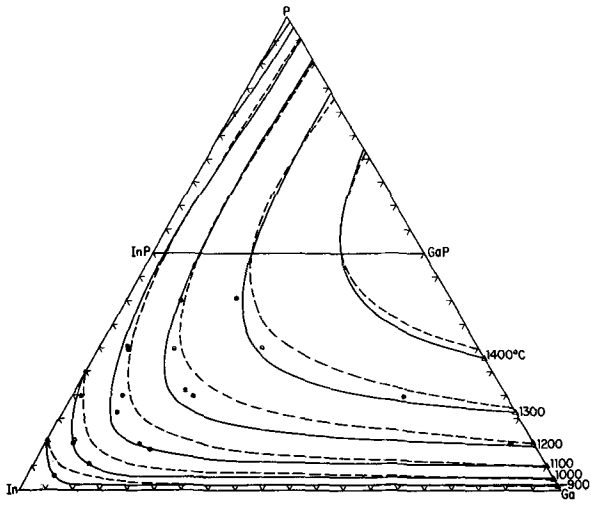

Fig. 2. Ga-In-P liquidus isotherms. ——— QCE calculation with $\Omega_{In-P} = 0$, $\Omega_{Ga-P} = -3500$; - - - - - - - - QCE calculation with temperature dependent interaction parameters $\Omega_{In-P} = 8220 - 7.57T$ and $\Omega_{Ga-P} = 4650 - 5.85T$; ○ Panish (4); △ Rubenstein (10).

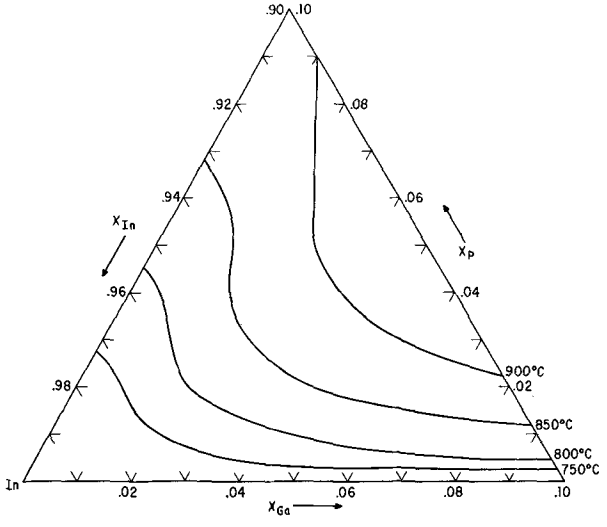

Fig. 3. Liquidus isotherms in the expanded In-rich corner of the ternary Ga-In-P phase diagram.

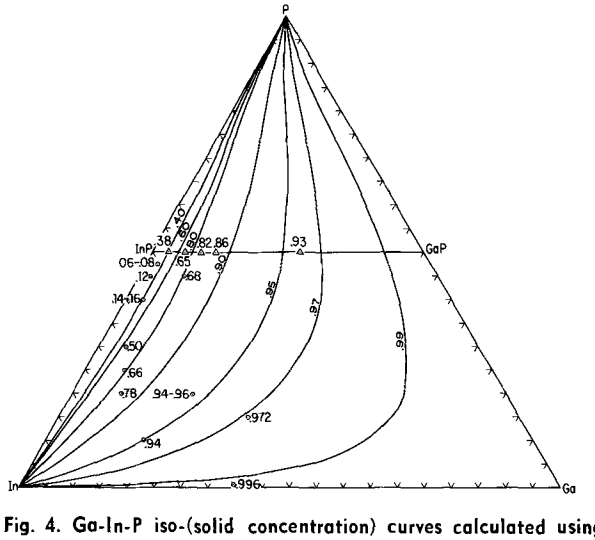

Fig. 4. Ga-In-P iso-(solid concentration) curves calculated using QCE model, $\Omega_{In-P} = 0$, $\Omega_{Ga-P} = -3500$. Each curve and point is labeled with X_{GaP}. ○ Panish (4); △ Foster (5).

solid composition is generally good. There is a systematic deviation from Panish's data at the low GaP concentrations, even though the agreement with Foster's data is excellent. It should be pointed out that Panish's method of determining the solid composition in equilibrium with a given liquid by slowly cooling to 20° below the liquidus temperature leads to errors, especially when the mole fraction of GaP in the solid is low; because the equilibrium solid composition changes on cooling. For example, cooling from 1100°C by 20°C changes the equilibrium solid composition on the pseudobinary from 30 to 14% GaP. If error bars were extended from each of Panish's data points to the liquidus 20° below the original liquidus, Panish's data would be in agreement with the calculated results.

Calculated P_2 and P_4 pressures in equilibrium with the liquid composition on the liquidus surface are plotted in Fig. 5. The calculated curves are compared with data from the interpolation of Panish's data (4), and the data of Johnson (15) for pure GaP. The agreement is excellent for pure InP and GaP; and even though the agreement is good within the Ga-In-P ternary system, the calculated curves are systematically higher than the experimental data. The curves for 750°, 800°, and 850°C where there is no experimental pressure data are included because this information is useful for crystal growth experiments in this temperature range.

Discussion

To determine the usefulness of the QCE calculation, it is necessary to compare the calculated results with experimental results and with the results calculated using other model solutions. Panish compared his experimental results with liquidus curves calculated for an ideal solution and for a solution with $\gamma_{Ga} = \gamma_{In} = 1$ and γ_P determined from experimental results. Neither method gives satisfactory results. To further compare the QCE and ideal solution calculations, the ideal Ga-P liquidus curve is included in Fig. 1. The iso-(solid concentration) curves calculated for ideal solid and liquid solutions are compared with experimental data

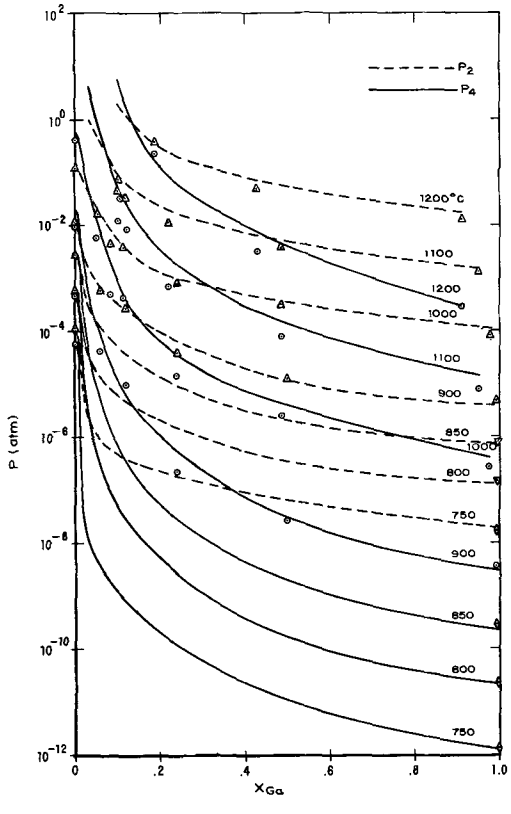

Fig. 5. P_2 and P_4 vapor pressures in equilibrium with the Ga-In-P liquidus surface. - - - - - - - - P_2; ——— P_4; △ Panish (4) P_2; ○ Panish (4) P_4; ◇ Johnson (15) P_4; ▽ Johnson (15) P_2.

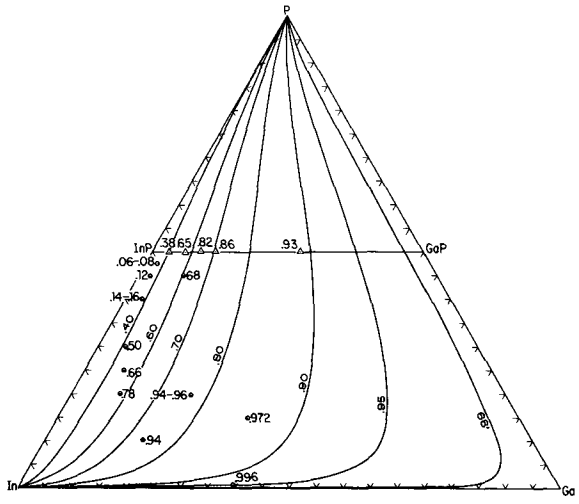

Fig. 6. Ga-In-P iso-(solid concentration) curves calculated using ideal solution model. Each curve and point is labeled with X_{GaP}. ○ Panish (4); △ Foster (5).

in Fig. 6. These comparisons clearly show the QCE calculation to be a dramatic improvement over the ideal calculation, but there is a systematic deviation from the experimental results for liquidus, iso-(solid concentration) and vapor pressure curves. This deviation can be seen in the In-P, Ga-P, In-As, Ga-As, and In-Sb binary liquidus curves (2), so it is not entirely due to the inadequacy of the QCE model in describing the solid solution, where one would expect the largest deviations from any simple model.

There are two approaches which might be taken in attempting to improve the phase diagram calculation: (*i*) use the same model and allow the interaction parameters to be an arbitrary function of T and/or X; (*ii*) use a more sophisticated model which contains the elements necessary to better describe the real solution. The first approach is simply bending the model to fit the binary data, since Ω is constant for the simple QCE model. The second approach involves trying to determine the physical processes which might make the interatomic interactions change with temperature or composition and building them into the model solution.

Guggenheim (1) suggested that Ω could be taken as a linear function of T, $L(T)$, to improve the agreement between calculated properties of the QCE solution and experimental data. An attempt was made to improve the calculation of the Ga-In-P phase diagram using this procedure. By calculating Ω for each experimental point on the liquidus and determining the $L(T)$ which best fit the data, the In-P and Ga-P interaction parameters were determined to be

$$\Omega_{\text{In-P}} = 8220 - 7.57T \text{ and } \Omega_{\text{Ga-P}} = 4650 - 5.85T$$

The respective binary phas diagrams calculated using these interaction parameters are plotted in Fig. 1. As expected, allowing $\Omega = L(T)$ improves the fit to the experimental data.

The Ga-In-P phase diagram was calculated using these new temperature dependent interaction parameters, all other parameters remaining the same as for the regular QCE calculation. The isothermal liquidus curves are compared with the regular QCE results and the experimental results in Fig. 2. The iso-(solid concentration) curves are the same as those presented in Fig. 4. The phase diagram calculated using temperature dependent, interaction parameters is in substantially worse agreement with the experimental data. This result illustrates the danger of bending the model to fit the binary results. The ternary calculation is more than an extrapolation of binary data. It is based on finding a self-consistent solution model which contains the elements necessary to describe the binary systems and then calculating the ternary using the same conceptual basis. The appropriate method of improving the calculation is to use a more sophisticated model which includes the physical processes which make the interatomic interactions temperature and composition dependent.

Kleppa (16) classfied many binary metal systems according to whether they had symmetric ΔH_M *vs.* X curves, characteristics of ideal, regular, and QCE solutions. He found that only systems from the same group of the periodic table had symmetrical ΔH_M *vs.* X curves. This is consistent with the results of Stringfellow and Greene (3) where the Ge-Si, Ge-Sn, Ge-Pb, Si-Sn, and Si-Pb systems were found to behave as QCE solutions. It would be expected that III-V systems could be better described using a more sophisticated model giving the more general asymmetrical ΔH_M *vs.* X curves.

One approach to improving the model would be to retain the lattice model but improve the QCE assumptions: (*i*) nearest neighbors interact pairwise, (*ii*) only configurational free energy of mixing is important, *i.e.*, vibrational free energy of mixing is neglected. The surrounded atom model (17) is similar to the QCE model except the basic entity is an atom with all its nearest neighbors, rather than atom pairs. This is an example of building into the model the physical processes which make the interatomic interactions change with composition. It improves the QCE approximations above and gives the more general asymmetric ΔH_M *vs.* X, but involves 12 interaction parameters for the binary system and 84 for the ternary system. Approximations can be made to reduce the number of parameters, but a calculation of the ternary phase diagram based on the surrounded atom approach is still not practical.

Other, more sophisticated models such as cell models, hard sphere models, and conformal solution theory have been developed for nonpolar spherical molecules and sophisticated models have been developed for ionic solutions. Work is needed in the construction of more sophisticated models applicable to metallic solutions. One problem is that the basic interactions in metallic systems are not well understood. Only recently has progress been made in understanding the intermolecular potentials in liquid metals (18-20). Cell models using intermolecular potentials may be useful in better describing the thermodynamic properties of liquid metals, in particular in III-V systems.

Thus, the QCE model appears to be the best, presently available, practical basis for the calculation of III-V ternary phase diagrams.

Acknowledgments

The author gratefully acknowledges the kindness of M. Panish and M. Foster for allowing him to use their results prior to publication. The author also wishes to thank R. A. Burmeister for many helpful discussions.

Manuscript submitted Feb. 13, 1970; revised manuscript received May 20, 1970.

Any discussion of this paper will appear in a Discussion Section to be published in the June 1971 JOURNAL.

REFERENCES

1. E. A. Guggenheim, "Mixtures," Oxford University Press, Oxford (1952).
2. G. B. Stringfellow and P. E. Greene, *J. Phys. Chem. Solids*, **30**, 1779 (1969).
3. G. B. Stringfellow and P. E. Greene, *This Journal*, **117**, 1075 (1970).
4. M. B. Panish, *J. Chem. Thermo.*, **2**, 319 (1970).
5. L. M. Foster and J. E. Scardefield, *This Journal*, **117**, 534 (1970).
6. JANAF, Interim Thermochemical Tables, Thermal Laboratories, Dow Chemical Co.
7. G. J. Macur, R. K. Edwards, and P. G. Wahlbeck, *J. Phys. Chem.*, **72**, 1047 (1968).
8. M. B. Panish and J. R. Arthur, *J. Chem. Thermo.*, **2**, 299 (1970).
9. R. N. Hall, *This Journal*, **110**, 385 (1963).

10. M. Rubenstein, *Electrochem Soc., Electronics Division Abstracts*, **11**, 129 (1962).
11. N. N. Sirota, in "Semiconductors and Semimetals," Vol. 4, p. 35, R. K. Willardson and A. C. Beer, Editors, Academic Press, New York (1968).
12. D. Richman, *J. Phys. Chem. Solids*, **24**, 1131 (1963).
13. K. Weiser, in "Compound Semiconductors," Vol. 1, p. 471, R. K. Willardson and H. L. Goering, Editors, Reinhold, New York (1962).
14. M. Rubenstein, *This Journal*, **109**, 69C (1962).
15. W. D. Johnson, *ibid.*, **110**, 117 (1963).
16. O. J. Kleppa, *Acta. Met.*, **6**, 225 (1958).
17. P. Hicter, J. C. Mathieu, F. Durand, and E. Bonnier, *Adv. in Physics*, **16** (62), 523 (1967).
18. M. D. Johnson and N. H. March, *Phys. Letters*, **3**, 313 (1963).
19. J. E. Enderby and N. H. March, *Adv. Phys.*, **16**, 691 (1967).
20. M. Shimoji, *ibid.*, **16**, 705 (1967).

Phase Diagram of the Zn-Cd-Te Ternary System

Jacques Steininger, Alan J. Strauss,* and Robert F. Brebrick*

Lincoln Laboratory, Massachusetts Institute of Technology, Lexington, Massachusetts 02173

ABSTRACT

The ternary Zn-Cd-Te liquidus surface and the pseudobinary CdTe-ZnTe solidus curve have been determined by thermal analysis of cooling and heating curves, respectively, of homogenized liquid and solid alloy samples. The binary Cd-Te and Zn-Te liquidus arrest temperatures are in good agreement with most of the previously published data and confirm the presence of well-defined inflections on the metal-rich and Te-rich sides of both liquidus curves. The binary interchange energy parameters calculated along each liquidus curve for the regular and quasi-chemical approximation solution models give essentially similar values for dilute solutions. Near equiatomic composition however, they show values respectively in excess of 200 kcal/mole and less than 40 kcal/mole. The pseudobinary CdTe-ZnTe liquidus and solidus curves exhibit monotonic and sublinear increases in temperature with increasing ZnTe content. The gap between the two curves remains less than 0.16 mole fraction and shows excellent agreement with the values calculated from the ideal liquidus-solidus thermodynamic relationship. The ternary liquidus temperatures form a smooth surface with a narrow ridge near the pseudobinary CdTe-ZnTe composition line and practically degenerate ternary eutectic and boundary lines.

The II-VI compounds CdTe and ZnTe form a complete series of solid solutions with cubic zincblende structure and with band gaps varying from 1.5 to 2.3 eV at room temperature. The alloys containing up to 85 m/o (mole per cent) ZnTe can be made both n- and p-type, and efficient visible electroluminescence at 77°K has been obtained with $Zn_xCd_{1-x}Te$ diodes prepared by diffusion of Zn and P into Al-doped CdTe single crystals (1). The samples prepared by this method however showed evidence of strain which became more severe with increasing x. Recently, alloy crystals have been grown directly from the liquid phase by the Bridgman and slow cooling techniques (2), but details on their crystallographic and optical quality were not reported.

Because of interest in the growth of alloy crystals from the melt and from Te-rich solutions (3), we have investigated the phase diagram of the ternary Zn-Cd-Te system by thermal analysis of homogenized liquid and solid alloy samples. Particular attention was paid to the CdTe-ZnTe subsystem, which was assumed to be pseudobinary, and to the Te-rich region of the ternary liquidus surface. The binary Cd-Te and Zn-Te liquidus curves were also re-investigated because of discrepancies in the published data. Finally, the metal-rich region of the ternary liquidus surface was selectively surveyed in order to present the first comprehensive set of data for thermodynamic analysis of ternary mixed II-VI systems.

Experimental

Thermal analyses were conducted in a vertical platinum-wound resistance furnace by slow cooling of homogenized liquid samples and slow heating of homogenized solid samples at temperatures up to 1265°C. A 10-15g charge of an accurately weighed mixture of 6-9's purity elements was placed in a 1 by 10 cm silica ampoule with a 2.5 cm re-entrant thermocouple well. The free space inside the ampoule was less than 5 cm^3, and the loss by evaporation of the most volatile component was estimated to be less than 0.1% by weight over the experimental range of temperatures. A similar ampoule containing about 8g of silicon was used as a reference. The ampoules were sealed under forepump vacuum (10^{-3} Torr) and placed in two symmetrical cavities drilled in a 5 by 12.5 cm nickel cylinder fitted with a nickel lid. A Pt-Pt 13% Rh thermocouple was inserted in each ampoule, and the two were connected for simultaneous recording of the sample temperature and of the temperature difference between sample and reference as a function of time. To increase the sensitivity of the temperature readings, the emf from the sample thermocouple was partially balanced out with a millivolt potentiometer. The outputs from the two channels were then amplified by d-c microvolt amplifiers and recorded on a two-pen recorder with 1 and 0.1 mV full scale deflection, respectively. Calibration with a gold sample (melting point 1063.0°C) gave melting and freezing arrests of 1063.0° ± 0.1°C and showed that no correction of the sample temperature readings was necessary.

The samples were slowly heated to reaction temperature, melted, and then equilibrated for at least 16 hr at 50°C above the estimated liquidus temperature. Because of apparently slow kinetics of dissolution of CdTe and ZnTe in liquid Te, shorter equilibration times produced erratic results which may explain some of the discrepancies observed in previously published data. Particular care was taken to approximate equilibrium conditions at the onset of freezing.

* Electrochemical Society Active Member.

Key words: ternary phase diagram, thermal analysis, zinc, cadmium, tellurium, alloy crystal growth, quasi-chemical interchange energy, liquidus-solidus thermodynamics.

This was achieved by cooling melts that were only slightly superheated (20°-25°C above the liquidus temperature) at sufficiently low rates (1°-2° C/min) to avoid appreciable supercooling. Under these conditions, there was usually no evidence of supercooling and the cooling curve showed a break that could be reproduced to within ± 1°C (Table I). When supercooling could not be prevented, the liquidus arrest temperature was taken to be the maximum in the recalescence curve. No attempts were made to obtain liquidus data from heating curves because the end of melting for noncongruently melting compositions is poorly defined and can be erroneously interpreted.

Solidus arrests for the pseudobinary CdTe-ZnTe system were obtained from slow heating curves (1°-2° C/min) of samples that had been melted as indicated above, resolidified and homogenized by annealing for at least 16 hr at about 20°C below the solidus temperature. X-ray powder analysis of samples annealed in this way showed no evidence of inhomogeneity and gave lattice parameters in agreement with published values. The temperature of each thermal arrest was obtained from the intersection of the nearly straight lines below and above the solidus break on the sample temperature recording. More prolonged annealing (up to 10 days) resulted in sharper breaks but did not cause any substantial displacement of the intersections. The reproducibility of the solidus arrests was about ± 3°C (Table I).

Because of the large thermal effects in this system, differential thermal recording was used only to confirm the arrests observed on the sample temperature recording. The over-all accuracy of both liquidus and solidus temperatures is estimated to vary from within ± 1°C near the compounds to within a few degrees at higher dilution in excess elements or in the middle of the pseudobinary composition range.

Table I. Experimental thermal analysis data

System	Composition Zn	Cd	Te	Supercooling, °C	Arrest temperature, °C	Reproducibility, °C
Liquidus (cooling curves)						
CdTe-ZnTe	0.10	0.40	0.50	0	1121.6	±0.6
	0.175	0.325	0.50	0	1144.5	—
	0.20	0.30	0.50	2.4	1156.6	—
	0.25	0.25	0.50	0	1176.1	±0.1
	0.30	0.20	0.50	0	1198.1	—
	0.40	0.10	0.50	0	1244.9	±0.2
Zn-Te	0.70	0	0.30	4.5	1215.5	—
	0.60	0	0.40	0	1226.2	—
	0.40	0	0.60	0	1164.7	±0.3
	0.30	0	0.70	0	1060.5	—
	0.20	0	0.80	0	967.7	±0.3
	0.10	0	0.90	0	869.5	—
Cut A: $(Zn_{0.80}Cd_{0.20})_{1-x}Te_x$	0.32	0.08	0.60	0	1124.8	±0.3
	0.24	0.06	0.70	0	1027.7	—
	0.16	0.04	0.80	0.5	927.4	—
Cut B: $(Zn_{0.50}Cd_{0.50})_{1-x}Te_x$	0.45	0.45	0.10	0	1043.5	±0.3
	0.35	0.35	0.30	0	1111.7	±0.1
	0.20	0.20	0.60	0	1052.5	±0.7
	0.15	0.15	0.70	0	959.2	±0.1
	0.10	0.10	0.80	0	870.5	—
	0.05	0.05	0.90	2.7	770.7	—
Cut C: $(Zn_{0.20}Cd_{0.80})_{10x}Te_x$	0.18	0.72	0.10	0	969.8	±0.1
	0.14	0.56	0.30	0	1045.5	±0.7
	0.08	0.32	0.60	0	992.8	±0.8
	0.06	0.24	0.70	2.7	902.0	—
	0.04	0.16	0.80	0	819.4	—
Cd-Te	0	0.90	0.10	0	888.7	±0.8
	0	0.70	0.30	0	983.0	±0.5
	0	0.50	0.50	0	1092.0	±0.2
	0	0.45	0.55	0	1027.3	±0.6
	0	0.40	0.60	0	967.4	—
	0	0.30	0.70	0	879.2	—
	0	0.20	0.80	0.7	798.4	±0.2
	0	0.10	0.90	0.1	683.6	±2.0
Solidus (heating curves)						
CdTe-ZnTe	0.10	0.40	0.50	—	1112.0	—
	0.20	0.30	0.50	—	1130.0	—
	0.25	0.25	0.50	—	1153.5	±3.5
	0.30	0.20	0.50	—	1164.7	±2.3
	0.40	0.10	0.50	—	1218.0	—

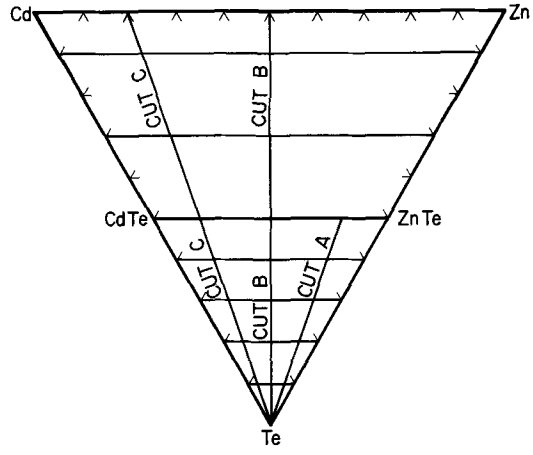

Fig. 1. Zn-Cd-Te ternary system

Results

The liquidus and solidus arrest temperatures, the amount of supercooling observed on the cooling curves, and the reproducibility of repeat runs are listed in Table I for the following subsystems (Fig. 1): Cd-Te binary liquidus; Zn-Te binary liquidus; CdTe-ZnTe pseudobinary liquidus and solidus; liquidus isopleths at constant Zn/Cd ratios of 4.0, 1.0, and 0.25 (Cuts A, B, C); and liquidus isopleths at constant Te concentrations of 0.10, 0.30, 0.60, 0.70, 0.80, and 0.90.

Binary Cd-Te *system (Fig. 2).*—The Cd-Te binary liquidus curve has been previously investigated by de Nobel (4) by visual observation of initial freezing, and by Lorenz (5) and Kulwicki (6) by DTA in sealed quartz ampoules. Their data show generally good agreement on the Cd-rich side, with the exception of the high-temperature data of de Nobel which is significantly lower, probably because of supercooling. On the Te-rich side, they also show good agreement except for the values of Kulwicki which are significantly higher in the 50 to 80 a/o (atomic per cent) Te region. Our arrest temperatures are listed in Table I and shown in Fig. 2 together with the values of Lorenz and Kulwicki. Melting and freezing arrests of 1092.0° ± 0.2°C were observed for CdTe in good agreement with the previously reported values of 1090° ± 2°C (de Nobel), 1092° ± 3°C (Lorenz), and 1091° ± 2°C (Kulwicki). Our liquidus arrests are in best agreement with the data of Lorenz, on both sides of the liquidus curve. Substantial supercooling, which might have explained the differences between the results of Lorenz and of Kulwicki on the Te-rich side, was not in evidence on our cooling curves (Table I). It is therefore suspected that the high temperatures observed by Kulwicki in both binary systems (see below) may have been caused by in-

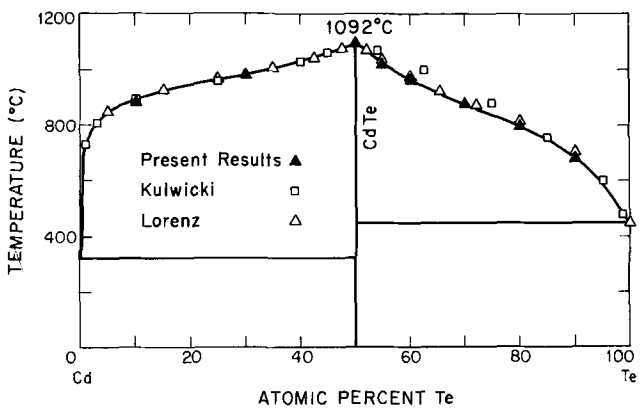

Fig. 2. Cd-Te binary liquidus curve

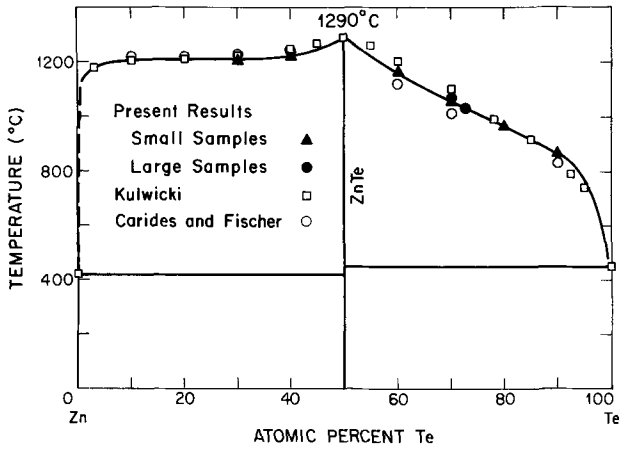

Fig. 3. Zn-Te binary liquidus curve

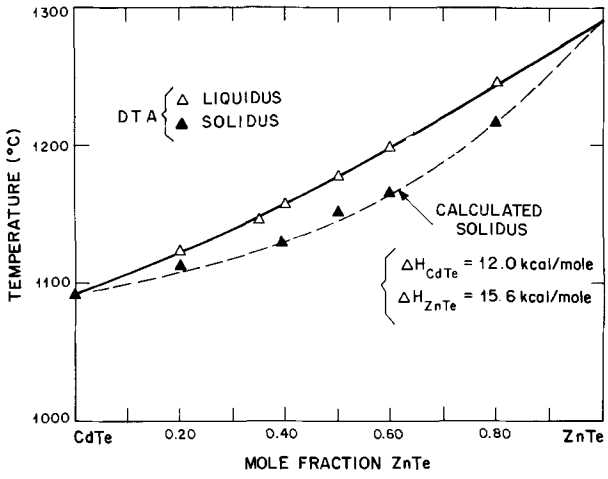

Fig. 4. CdTe-ZnTe pseudobinary liquidus and solidus curves

complete homogenization of the Te-rich liquid samples.

Binary Zn-Te *system (Fig. 3).*—The Zn-Te liquidus curve was investigated almost 60 years ago by Kobayashi (7) in an open system and more recently by Carides and Fischer (8) by thermal analysis in a high pressure autoclave and by Kulwicki (6) by DTA in sealed quartz ampoules. The data of the two more recent investigations are in generally good agreement except in the region between 50 and 80 a/o Te where the values of Kulwicki are almost 100°C above those of Carides and Fischer. Our arrest temperatures are listed in Table I and shown in Fig. 3 together with the data of Carides and Fischer and of Kulwicki. No attempt was made to redetermine the melting point of ZnTe because of its relatively high temperature, and we adopted the value of Kulwicki (1290° ± 2°C), which is in agreement with that of Carides and Fischer (1295° ± 20°C). On the Zn-rich side, our liquidus temperatures are in good agreement with the previously reported experimental curves, showing an almost horizontal inflection near 1210°C. From theoretical calculations of the activities in a regular associated solution model (see Discussion), Jordan (9) has recently suggested a miscibility gap in the liquid phase between 9 and 35 a/o Te. However, careful analysis of several of our cooling curves at 30 and 40 a/o Te did not reveal the monotectic arrest which he predicted near 1213°C. On the Te-rich side, our liquidus temperatures are intermediate between the low values of Carides and Fischer (probably due to supercooling) and the higher values of Kulwicki. Contrary to Kulwicki's diagram, our liquidus curve shows a well-defined inflection (near 1025°C and 70 a/o Te) which is comparable to that observed in the Cd-Te system in the same composition range.

Because of the discrepancies observed on the Te-rich side in both binary systems, two additional points were determined on the ZnTe-Te liquidus curve by slow cooling of large liquid samples (about 150g) in another, previously described (10), DTA apparatus. The arrest temperatures of 1070° and 1030°C for compositions of 70 and 72.5 a/o Te are in good agreement with the rest of our data (Fig. 3) and confirm the inflection on the liquidus curve.

Pseudobinary CdTe-ZnTe *system (Fig. 4).*—No previous investigation of the pseudobinary liquidus and solidus curves has been reported. X-ray diffraction data (11) show that the $Zn_x\ Cd_{1-x}Te$ alloys form a complete series of solid solutions and that the lattice parameter varies linearly with composition in agreement with Vegard's law.

Our liquidus and solidus arrest temperatures are listed in Table I and shown in Fig. 4. Both temperatures show a monotonic and sublinear variation with composition from the melting point of CdTe (1092°C) to that of ZnTe (1290°C). This type of variation suggests small and nearly comparable positive deviations from ideality in the liquid and solid phases (see Discussion) and is similarly observed in several other II-VI pseudobinary systems, such as HgTe-HgSe (12), ZnTe-ZnSe (13), and CdTe-CdSe (14). Of particular interest are the slow increase in liquidus temperatures and the relatively narrow gap between liquidus and solidus curves (less than 0.16 mole fraction). These are both favorable for the growth of alloy crystals from the melt in standard quartz ampoules up to relatively high values of Zn content.

Ternary liquidus surface (Fig. 5-8).—No previous study of the ternary liquidus surface has been reported.

The Te-rich ternary liquidus isopleths for constant Zn/Cd ratios (Fig. 5) show the same type of variation as the limiting CdTe-Te and ZnTe-Te binary liquidus curves, with an inflection near 70 a/o Te and a marked increase in temperature near the equiatomic composition. On the metal-rich side, there is a gradual transition from the smooth Cd-CdTe liquidus curve to the initially steep and then almost flat Zn-ZnTe curve. The inflections on both sides of the isopleths suggest a tendency for separation into different liquid phases. Such separations actually occur on the Se-rich side of other II-VI systems such as Hg-Se (10), Cd-Se (15), and probably Zn-Se (16). However, no monotectic arrests have been observed in the Zn-Cd-Te system.

Like the pseudobinary CdTe-ZnTe liquidus curve, the constant-Te isopleths exhibit slow, monotonic increases in temperature from the Cd-Te liquidus to

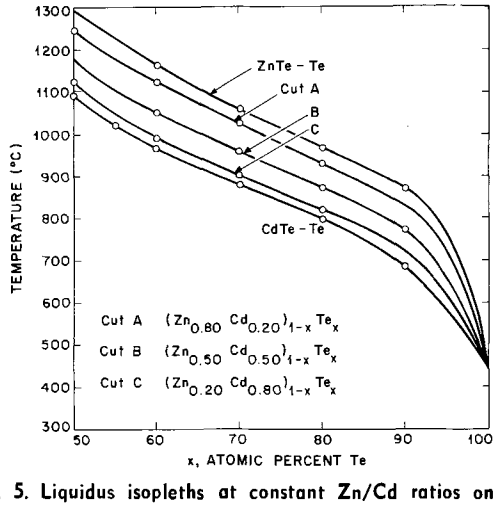

Fig. 5. Liquidus isopleths at constant Zn/Cd ratios on Te-rich side.

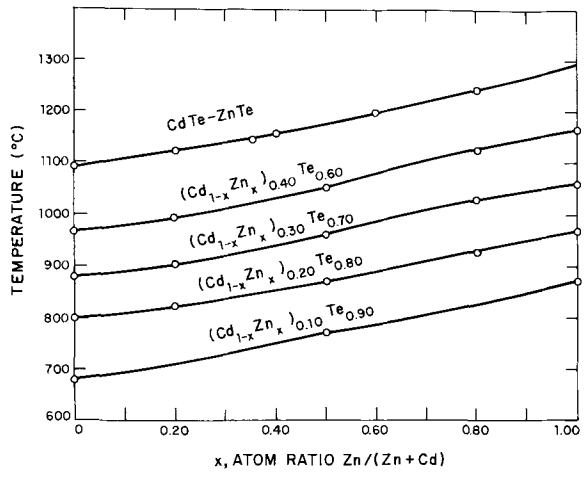

Fig. 6. Liquidus isopleths at constant Te concentrations on Te-rich side.

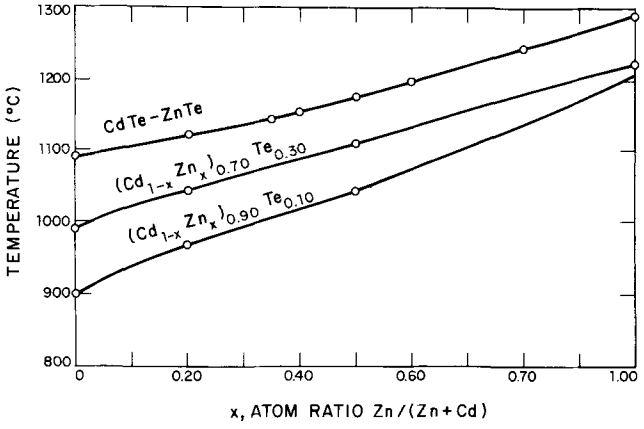

Fig. 7. Liquidus isopleths at constant Te concentrations on metal-rich side.

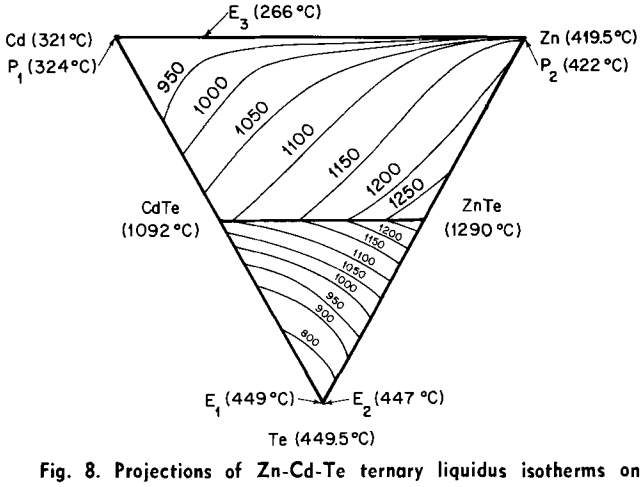

Fig. 8. Projections of Zn-Cd-Te ternary liquidus isotherms on composition plane.

the Zn-Te liquidus, both on the Te-rich side (Fig. 6) and on the metal-rich side (Fig. 7).

The projections of the ternary liquidus isotherms on the composition plane (Fig. 8) have been constructed by interpolation along the various liquidus curves. They vary smoothly between the binary Cd-Te and Zn-Te liquidus curves but show sharp peaks along the pseudobinary CdTe-ZnTe composition line which correspond to the marked increase in temperature as the composition approaches 50 a/o Te. The binary Cd-Zn system (17) shows a eutectic at 26.5 a/o Zn and 266°C. The binary Cd-Te and Zn-Te systems however show almost completely degenerate eutectics or peritectics, the thermal arrests being very close to the melting points of the pure elements (6). As a consequence, the ternary eutectic and boundary lines are also expected to be degenerate (Fig. 8).

Discussion

Liquidus surface.—Solution models of increasing complexity have been called upon to interpret the thermodynamic properties of III-V and II-VI binary and ternary systems. The relatively moderate deviations from ideality in the III-V systems led early investigators (18-20) to use expressions derived by Wagner (21) and Vieland (22) for a regular solution model with an interchange energy parameter varying linearly with temperature. Recently however, Stringfellow and Greene (23) have shown that the first-order quasi-chemical approximation of Guggenheim (24) with a temperature independent interchange energy parameter leads to satisfactory representation of the liquidus temperatures and of the activities in the III-V systems In-Sb, Ga-As, In-As, and the corresponding mixed ternary systems.

In the II-VI systems, the larger differences in electronegativity between metal and chalcogen atoms produce more ionic and stronger interactions between unlike atoms, as evidenced by the marked increase in temperature in the Zn-Cd-Te liquidus surface near the pseudobinary CdTe-ZnTe composition line (Fig. 8). As a result, the interchange energy parameter calculated along the liquidus curve from Vieland's regular solution expression exhibits a steep minimum (in excess of 200 kcal/mole) near the equiatomic composition (Fig. 9) instead of the approximately linear temperature dependence found in the III-V systems. This led Jordan (9) to propose the Regular Associated Solution model which postulates the existence of stable CdTe or ZnTe complexes in the liquid phase and effectively shows an interchange energy parameter that becomes very large at equiatomic composition.

This effect apparently stems from the failure of the regular solution model to account for the nonrandom distribution of atoms in the liquid phase. The quasi-chemical approximation, on the contrary, postulates a nonrandom distribution of pairs of atoms weighted exponentially in terms of the energy of interchange between pairs of unlike atoms and the corresponding pairs of like atoms (24).

Values of the quasi-chemical interchange energy parameter have been calculated in this study for experimental points along the Cd-Te and Zn-Te liquidus curves. A computer half-interval search method (25) was used to solve the liquidus equation derived by

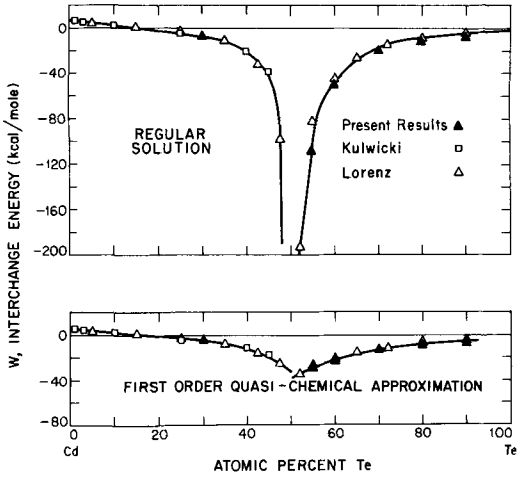

Fig. 9. Interchange energy parameter for regular and quasi-chemical approximations (Cd-Te binary system).

Stringfellow and Greene (23) from the general liquidus equation of Vieland (22) and the quasi-chemical activity coefficients of Guggenheim (24). (The values of Kulwicki (6) were used for the entropies of fusion of CdTe and ZnTe.) The variation of the interchange energy parameter for the Cd-Te system is shown in Fig. 9 for a coordination number of 4. Unlike the III-V systems investigated by Stringfellow and Greene, the II-VI systems show significant variations of the quasi-chemical parameter along the liquidus curve. The minimum near equiatomic composition however is much shallower than in the regular solution model and remains less than 30 and 35 kcal/mole on the Cd-rich and the Te-rich sides, respectively.

Both the regular and the quasi-chemical models are based on the assumption that the energy of the solution is a function solely of the number of pairs of unlike atoms and they fail to differentiate between metal-rich and chalcogen-rich solutions. The phase diagrams of the II-VI systems are highly unsymmetrical, because of the difference in energy of metal-metal and chalcogen-chalcogen bonds, and they cannot be adequately represented by either of these two models, unless they are arbitrarily separated into metal-rich and chalcogen-rich subsystems (6, 9). The more recent Non-Random Two-Liquid solution model of Renon (26) takes account of the differences in bond energy of the solvent atoms and offers the possibility of representing unsymmetrical phase diagrams with a single consistent set of parameters. Preliminary results indicate that it gives a better representation of the Ga-As liquidus curve and thermodynamic functions than the quasi-chemical model. Good fits to the Cd-Te and Zn-Te liquidus curves are also obtained, but some questions remain concerning the values of the temperature dependent bond energy parameters in these two systems.

Pseudobinary liquidus-solidus gap.— A general expression for the thermodynamic relationship between liquidus and solidus equilibrium compositions has recently been derived (27) for non-ideal but homogeneous and monotonic alloy systems (*i.e.*, systems showing complete liquid and solid mutual miscibility and monotonic variations of the liquidus and solidus curves). For a system of two components A and B with melting temperatures $T_A < T_B$, the molar fractions of A and B in the liquid and solid phases, X^l_A, X^l_B and X^s_A, X^s_B, in equilibrium at the intermediate temperature T such that $T_A < T < T_B$, are related by

$$RT\left(\ln\frac{X^s_A}{X^s_B}-\ln\frac{X^l_A}{X^l_B}\right)=\Delta H_A\left(1-\frac{T}{T_A}\right)-\Delta H_B\left(1-\frac{T}{T_B}\right)-D \quad [1]$$

where R is the ideal gas constant, ΔH_A and ΔH_B are the enthalpies of fusion of A and B, and D represents the difference between the partial excess free energies of mixing in the solid and liquid phases

$$D=\frac{\partial\Delta G^s_{e,m}}{\partial X^s_A}-\frac{\partial\Delta G^l_{e,m}}{\partial X^l_A} \quad [2]$$

If the liquid and solid solutions are ideal, the excess free energies of mixing are zero and $D = 0$. The ideal form cf Eq. [1] with $D = 0$ has also been found to fit the experimental data for a large number of binary and pseudobinary alloy systems (metallic, semiconducting, and ionic) in which the liquidus and solidus curves vary monotonically with composition (27). Although the liquid and solid phases in these systems are generally not ideal solutions, the ideal liquidus-solidus expression is applicable because the difference between the partial excess free energies of mixing is small enough to be neglected. The ideal expression can therefore be used to calculate one of the boundaries of the two-phase field when the other one and the enthalpies of fusion of the pure components are known. The solidus curve for the pseudobinary CdTe-ZnTe system in Fig. 4 has been calculated from our experimental liquidus data and from the enthalpies of fusion determined by Kulwicki (6). It shows excellent agreement with the solidus data (the root mean square of the difference between calculated and experimental temperatures for five points is 3.8°C), therefore confirming that the deviations from ideality in the two pseudobinary phases are small and nearly equal.

Acknowledgment

The authors wish to acknowledge the capable assistance of R. E. England and D. Apelian in the thermal analyses, of Mary C. Finn and Mrs. M. J. Button in the x-ray analyses, and of Mrs. B. Palm in computer programming. This work was sponsored by the Department of the Air Force.

Manuscript submitted Nov. 24, 1969; revised manuscript received June 15, 1970. This was Paper 118 presented at the New York Meeting of the Society, May 4-9, 1969.

Any discussion of this paper will appear in a Discussion Section to be published in the June 1971 JOURNAL.

REFERENCES

1. F. F. Morehead and G. Mandel, *Appl. Phys. Letters*, **5**, 53 (1964).
2. M. S. Brodin, M. V. Kurik, V. M. Marlak, and B. S. Oktyabr'skii, *Sov. Phys.-Semicond.*, **2**, 603 (1968).
3. J. Steininger and R. E. England, *Trans. Met. Soc. AIME*, **242**, 444 (1968).
4. D. de Nobel, *Philips Res. Rept.*, **14**, 361 (1959).
5. M. R. Lorenz, *J. Phys. Chem. Solids*, **23**, 939 (1962).
6. B. M. Kulwicki, Ph.D. Dissertation, Univ. of Michigan (1963).
7. M. Kobayashi, *Z. Anorg. Chem.*, **69**, 1 (1911).
8. J. Carides and A. G. Fischer, *Solid State Comm.*, **2**, 217 (1964).
9. A. S. Jordan, *Met. Trans.*, **1**, 239 (1970).
10. A. J. Strauss and L. B. Farrell, *J. Inorg. Nucl. Chem.*, **24**, 1211 (1962).
11. B. T. Kolomiets and A. A. Mal'kova, *Zh. Tekh. Fiz.*, **28**, 1662 (1958) [*Sov. Phys.-Tech. Phys.*, **3**, 1532 (1958)].
12. T. C. Harman, "Physics and Chemistry of II-VI Compounds," p. 786, M. Aven and J. S. Prener, Editors, John Wiley and Sons, Inc., New York (1967).
13. A. G. Fischer and W. H. Fonger, Report No. 3 (1965), Contract No. AF 19(628)-3866, U.S. Air Force, Cambridge Research Laboratories, Bedford, Mass.
14. A. J. Strauss and J. Steininger, *This Journal*, To be published.
15. A. Reisman, M. Berkenblit, and M. Witzen, *J. Phys. Chem.*, **66**, 2210 (1962).
16. M. R. Lorenz, "Physics and Chemistry of II-VI Compounds," p. 85, M. Aven and J. S. Prener, Editors, John Wiley and Sons, Inc., New York (1967).
17. M. Hansen, "Constitution of Binary Alloys," p. 446, McGraw-Hill Co., New York (1958).
18. W. F. Schottky and M. B. Bever, *Acta Met.*, **6**, 320 (1958).
19. C. D. Thurmond, *J. Phys. Chem. Solids*, **27**, 785 (1965).
20. J. R. Arthur, *ibid.*, **28**, 2257 (1967).
21. C. Wagner, *Acta. Met.*, **6**, 309 (1958).
22. L. J. Vieland, *ibid.*, **11**, 137 (1963).
23. G. B. Stringfellow and P. E. Greene, *J. Phys. Chem. Solids*, **30**, 1779 (1969).
24. E. A. Guggenheim, "Mixtures," p. 39, Clarendon Press, Oxford (1952).
25. S. S. Kuo, "Numerical Methods and Computers," p. 83, Addison-Wesley, Reading, Mass. (1965).
26. H. Renon and J. M. Prausnitz, *Chem. Eng. Sci.*, **18**, 244 (1968).
27. J. Steininger, *J. Appl. Phys.*, **41**, 2713 (1970).

Growth Characteristics of Rutile Film by Chemical Vapor Deposition

R. N. Ghoshtagore and A. J. Noreika

Westinghouse Research Laboratories, Pittsburgh, Pennsylvania 15235

ABSTRACT

Thin film rutile has been grown by the chemical vapor deposition reaction of $TiCl_4$ and O_2 on silicon and a variety of oxide substrates over a range of temperatures (673°-1320°K) and reactant partial pressures ($p_{TiCl_4} = 2.9 \times 10^{-2}$ to 9.28×10^{-1} Torr, $p_{O_2} = 2.5 \times 10^{-1}$ to 760 Torr). At high oxygen partial pressures between 990° to 1100°K, the films have been found to contain the rutile modification of TiO_2 almost exclusively. Polycrystalline deposits on silicon, fused quartz, and amorphous silica (thermally grown or chemically vapor deposited) substrates displayed some preferred growth orientation (fiber texture). Epitaxial films were obtained on (001)-, (110)- and (111)-rutile, (100)-MgO, and (0001)-sapphire substrates at elevated temperatures.

The process of chemical vapor deposition (CVD) has recently attracted considerable attention as a method of depositing thin films of refractory materials on a variety of substrates (1). However, very few data are available on the nucleation and growth behavior in CVD systems. One such CVD process of potential importance is the growth of thin film ceramic oxides on semiconductors for use as insulators or dielectrics.

Among the simple oxides, titanium dioxide in rutile modification is known to have one of the highest dielectric constants (90 $\perp$ and 180 $\parallel$ c-axis) (2). Both physical and chemical deposition techniques have been reported for the preparation of titanium dioxide films. The former include the evaporation of titanium followed by oxidation, reactive sputtering of titanium in oxygen, and rf sputtering of titanium dioxide (3). The pyrolysis of titanium alcoholates (*e.g.*, tetraisopropyl titanate) (4), hydrolysis of titanium tetrachloride (5), and anodization of titanium films (6) are examples of chemical deposition of titanium dioxide. In this study, a new chemical vapor deposition process to form TiO_2 has been explored on a variety of substrates. Where practical, the growth characteristics, *i.e.*, crystal size and orientation, have been observed. Some relevant kinetic data regarding the formation of TiO_2 films on silicon have been reported elsewhere (7).

Experimental Technique

The experiments utilize the chemical reaction between titanium tetrachloride and oxygen on a heated substrate in a conventional horizontal quartz tube "silicon epitaxial" reactor at atmospheric pressure (8). Purified titanium tetrachloride (prepared by multiple distillation of 99.995% pure material) in thermostat-held quartz bottles is used as a titanium source bubbler through which a carrier gas of ultrapure argon or ultrapure oxygen (Matheson) is passed at a controlled rate. This gas (saturated with $TiCl_4$ vapor) is then mixed with additional ultrapure oxygen and/or argon through a set of calibrated flowmeters, liquid traps, and filters and the mixture reacted on a quartz encapsulated high purity graphite susceptor heated by rf induction. The over-all reaction can be described by

$$TiCl_4(g) + O_2(g) \rightleftarrows TiO_2(\text{rutile})\ (s) + 2Cl_2(g) \quad [1]$$

Free energy changes (ΔF) for this reaction, calculated from known thermochemical data (9), are −33.0, −30.3, −27.7, and −25.2 kcal/mole at 700°, 900°, 1100°, and 1300°K, respectively.

Single crystal silicon wafers (15-20 mils thick) of (111), (100), and (110) orientations, obtained from Texas Instruments, were lapped, polished in Linde B, and then chemically etched in 15:5:3 HNO_3:HAc:HF to a mirror finish by the supplier. Substrates for TiO_2 deposition were prepared by scribing 5 mm squares out of these wafers. The substrates were then degreased by boiling in trichloroethylene and acetone and chemically polished in 15:5:3 HNO_3:HAc:HF to remove about 5-10μ of surface layer. The substrates were then blown dry in dry nitrogen, mounted on the susceptor and baked for 20-30 min in ultrapure hydrogen at 1175°-1275°K to remove any residual oxide film (10).

The reactor atmosphere is then flushed with ultrapure argon and the substrate temperature is adjusted, the temperature being monitored with an optical pyrometer [corrected for absorption by the quartz tube wall, reactor atmosphere, and substrate emissivity (11)] and/or an infrared radiation pyrometer. Titanium tetrachloride vapor in the carrier gas is then passed into the reactor (after prolonged purging to vent), argon flow is discontinued, and mainline ultrapure oxygen is introduced at a predetermined flow rate. The deposits and substrates are then pushed off the susceptor at regular time intervals with a quartz push rod, and the deposition rate is determined from an average of 16 to 18 samples run for 8 to 9 different time periods. Film thicknesses were determined by reference to an ellipsometrically calibrated color chart (12). The temperature of titanium tetrachloride was maintained at 298° ± 0.5°K and that of the substrates to ± 5°K.

Similar experiments were performed using fused quartz and single crystal MgO, Al_2O_3, and TiO_2 (rutile) substrates, an exception to the previously described experimental procedure when using these substrates being the omission of the hydrogen anneal. The reported data on the fused quartz, MgO, and Al_2O_3 substrates were determined from the change in weight (to microgram accuracy) of several substrates of known surface area before and after depositing a 4000-6000Å thick rutile film. The theoretical density of 4.26 g/cm^3 (for bulk rutile) was used for thickness computation of the rutile film. Determinations of crystallite size and film orientation were made from transmission electron microscopy (TEM) and reflective electron diffraction (RED) studies, respectively. The Si substrates were particularly well suited for the TEM study since they lend themselves to a well-established chemical jet-etching technique (13). In this technique, selected areas of the substrates are dissolved in a chemical jet-etch solution, the remainder being retained as support for the TiO_2 membranes which span the etched areas.

Key words: rutile, film, epitaxy, nucleation, deposition, orientation, growth, dielectric.

Results and Discussion

Nucleation density and deposition rate.—Figure 1 shows Arrhenius plots relating the deposition rate of TiO_2 to substrate temperature at three constant partial pressures of titanium tetrachloride. Within the range of experimental error the rates are seen to be independent of both substrate composition and substrate orientation. Consequently, it can be inferred that the mechanism of TiO_2 film formation is identical on all the substrates studied and is that which has been elucidated by kinetic studies in the case of single crystal silicon substrates (7). Nucleation in the vapor phase by gas phase reaction becomes predominant around 1125°K in all cases, above which temperature the rates decline. The effects of vapor phase reaction and consequent reduction of the effective vapor pressure of the rate-limiting reactant $TiCl_4$ are also evident in Fig. 2, a plot of the number of embryo crystallites, *i.e.*, those formed during the first minute of deposition, as a function of temperature. At temperatures less than 1125°K, the count increases with temperature; above 1125°K, the crystallite density decreases.

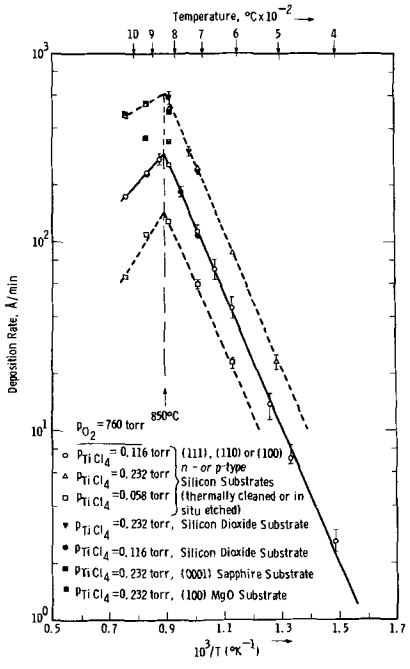

Fig. 1. Arrhenius plot of rutile thin film deposition rate

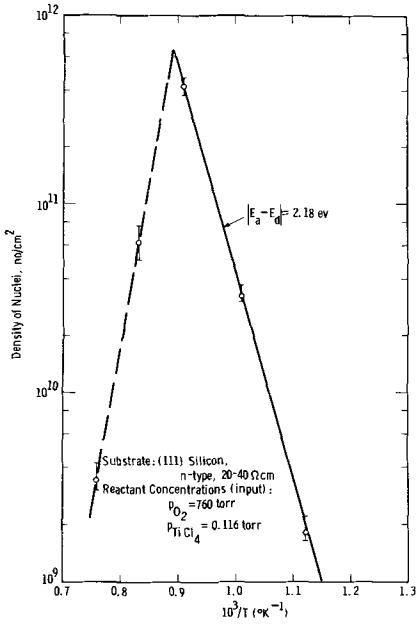

Fig. 2. Arrhenius plot of the density of TiO_2 nuclei on (111) silicon.

The trend of the data, *i.e.*, the exponential rise as a function of increasing substrate temperature, in both sets of curves (Fig. 1 and 2) below 1125°K is presumably due to two complementary effects, (*i*) an increase of the rate of reaction of component gases as the thermal energy supplied to the substrate is increased, *i.e.*, the exponential dependence of the surface reaction rate constant with temperature (7), and (*ii*) an almost negligible vapor pressure of the solid reaction product (TiO_2) in the temperature range of interest (9). The latter effect is equivalent to an "ideal" complete condensation of impinging product atoms or molecules as envisioned in physical vapor deposition systems. Coupling of the above two effects produces an effective supersaturation which also increases with temperature exponentially. Deposition rate and nucleation density, both strongly related to supersaturation, assume a similar temperature dependence. However, the activation energies of deposition and nucleation are quite different in magnitude because of the difference in the physicochemical processes involved in each phenomenon.

It is well known that when a solid surface catalyzes a hetereogeneous gas reaction, the energy of the reaction is decreased by the adsorption of one or more of the reactants. If E_H and E_s are the energies for uncatalyzed and catalyzed reactions, respectively, and E_i^A is that for the adsorption and/or desorption of the ith reaction species on the catalyst, then

$$E_H - \sum_1^n E_i^A = E_s \qquad [2]$$

where n is the number of species involved in the reaction.

E_H can be calculated from the available thermodynamic data (9) and is $\sim$ 1.25 eV whereas E_s can be obtained from Fig. 1 and is $\sim$ 0.8 eV. Since only the adsorption of atomic oxygen is involved in our CVD mechanism (7), $\sum_i^n E^{A}_{\text{atomic oxygen}} = E_o^A \cong 1.25 - 0.80$ eV $= 0.45$ eV.

Now, if ΔE_o is the enthalpy of activation for the reaction

$$\frac{1}{2} O_2 \rightleftarrows O \qquad [3]$$

and K is the equilibrium constant, then

$$K = \frac{p_O}{p_{O_2}^{1/2}} = \text{Exp} \frac{-\Delta E_o}{kT} \qquad [4]$$

or

$$p_O = p_{O_2}^{1/2} \text{Exp} \frac{-\Delta E_o}{kT} \qquad [5]$$

where p_O and p_{O_2} are the partial pressures of atomic and molecular oxygen, respectively.

Since TiO_2 is formed by the adsorption of atomic oxygen (charged or uncharged) (7) on the substrate, the saturation nucleation density of TiO_2 (N_s) is proportional to the density of adsorbed oxygen which, in turn is, proportional to the gas phase concentration of atomic oxygen produced by the reaction represented by Eq. [3]. Using Eq. [5], we obtain

$$N_s = C_1 p_O^{\text{adsorbed}} = C_1 C_2 p_O \text{Exp} \frac{E_o^A}{kT}$$

$$= C_1 C_2 p_{O_2}^{1/2} \text{Exp} \frac{-\Delta E_o + E_o^A}{kT} = C \exp \frac{-\Delta E_o + E_o^A}{kT}$$

$$= C \text{ Exp} - 2.14 \text{ eV}/kT \qquad [6]$$

where C_1, C_2, and C are constants, and $E_o^A \cong 0.45$ eV and $\Delta E_o = 2.58$ eV (14). The excellent agreement of the calculated activation energy of saturation nucleation density (Eq. [6]) with the experimental data (Fig. 2) also seems to validate earlier conclusions on the mechanism of the surface nucleation. Furthermore, the other possible mechanism of surface nucleation by the collection of the nuclei formed in the vapor phase seems to be ruled out by the experimental facts that (*i*) the nuclei do not have spherical morphology (see later), and (*ii*) the saturation nucleation density does not remain constant above 1125°K, when the gas phase reaction has overtaken the surface reaction.

When vapor phase reaction becomes predominant (above 1125°K, Fig. 1 and 2), the model described still applies although the curve appears to assume a positive slope. As the gas phase temperature is raised along with that of the substrates, nucleation in the vapor phase is enhanced, and the effective pressure of the rate-limiting reactant gas ($TiCl_4$) seen by the substrate diminishes. Since the rate of surface reaction and the supersaturation are also functions of this pressure, both deposition rate and nucleation density decrease. The data above 1125°K, in both Fig. 1 and 2, represent a sum of two competing physicochemical processes. Thus, above 1125°K, the nucleation density (N_s) can be described by Eq. [6] modified by an additional factor for the amount of unreacted $TiCl_4$ present. A similar adjustment can be made to describe the deposition rate above 1125°K.

Orientation behavior.—Some variations were observed in the crystallographic orientations adopted by TiO_2 films, on the several types of substrates used. On oriented Si wafers, for example, crystal orientation within the films was found to be independent of substrate orientation. These data obtained from RED observations are presented as functions of the substrate temperature (630°-1320°K) and orientation in Fig. 3. All Si substrates were of the low-index type, *i.e.*, (100), (110), and (111). Figure 3 indicates that with a change of substrate temperature, different crystal orientations are produced in the films. At temperatures below 630°K, the crystallites are oriented at random. A strong {110}-orientation occurs between 630° and 730°K. This is succeeded by a {101}-orientation between 730° and 990K, then by a {301}-orientation between 990° and 1125°K; and finally, by a strong {100} orientation at higher temperatures, at least to 1320°K. Deposition of TiO_2 on fused quartz substrates over a temperature range of 990°-1100°K produced films having orientations similar to those for TiO_2 on Si.

This similarity prompted additional experiments in which oxides of Si were deliberately formed on oriented Si surfaces. The oxide layers were either

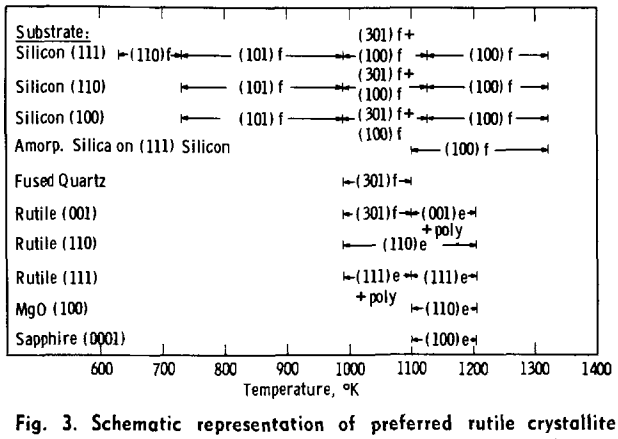

Fig. 3. Schematic representation of preferred rutile crystallite orientation in thin films (as a function of substrate material, temperature, and orientation) grown at $p_{O_2} \simeq 760$ Torr and $p_{TiCl_4} = 0.058$ to 0.232. Symbols f and e stand for fiber and epitaxial habits, respectively.

thermally grown or chemically vapor deposited (by the reaction of SiH_4 and O_2). When TiO_2 films were subsequently deposited, orientations were the same as those deposited on both the hydrogen annealed Si and the silica surfaces. In another experiment, *in situ* gaseous etching of Si substrates with HCl was performed prior to TiO_2 deposition. After 1-2 μm of the substrate surface had been removed, the reaction components were introduced, and films were deposited. Orientations altered slightly in this case, the onset of {100}-orientation occurred at a temperature of 1000°K, and the {301}-orientation was eliminated.

The evidence suggests that the observed TiO_2 orientations represent equilibrium orientations on both neutral and neutralized surfaces; the single crystal Si substrates being neutralized by exposure to oxygen. Moreover, the presence of neutralized surfaces is virtually inevitable since the adsorption of oxygen at the surface is a prime requirement in the reaction sequence. The cause of slight modification in the results for films etched *in situ* by HCl is, as yet, not well established. Since the etch was intended to remove the natural surface oxide, as was the hydrogen anneal, one assumes that the predeposition treatments of the substrate did not produce equivalent results and that the {301}-orientation, where it occurs, may be artificially stabilized.

Efforts to detect the presence of SiO_2 between substrate and film included infrared absorption measurements. Known thicknesses of SiO_2 in especially prepared Si-SiO_2-TiO_2 structures served as standards. Since infrared absorption was not observed for either the experimental films or for the standards in which SiO_2 thickness was less than 200Å, oxide films, if present, had not exceeded the absorption thickness limit.

Since oxygen neutralized surfaces may well be the rule on metallic and semiconductor single crystal substrates, single crystal oxide substrates appear to offer the most likely surfaces for the epitaxial growth of rutile. Deposits on cleaved and polished surfaces of rutile, MgO, and sapphire, in fact, showed varying degrees of epitaxy, Fig. 3, at temperatures between 990° and 1205°K.

Figure 3 also indicates that the best orientation match between the film and substrate occurs for (110)-oriented rutile substrates. Good epitaxial alignment is also evident on the (111)-oriented substrates at temperatures greater than 1100°K. Films deposited on (001)-oriented substrates showed a moderate degree of epitaxy at temperatures near 1200°K; orientations of deposits prepared at lower temperatures ranged from a {301}-fiber texture at 990°K to a badly twinned (001)-epitaxial layer near 1100°K. The degree of twinning was greatly reduced and often completely eliminated in all homoepitaxial growth experiments, *i.e.*, on (110), (100), and (111)-oriented rutile substrates, by *in situ* etching of the substrates in gaseous chlorine at 1320°K; 1000-1500Å of a substrate was so removed.

Films prepared on (100)-oriented MgO and (0001)-oriented sapphire substrates in a temperature range of 1100°-1205°K also exhibited strong epitaxial behavior. Some of their representative RED patterns are shown in Fig. 4. The orientation relationships between rutile films and substrates (where TiO_2 represents the rutile film and Al_2O_3 represents the sapphire substrate) were $(110)_{TiO_2} \parallel (100)_{MgO}$, $[001]_{TiO_2} \parallel [011]_{MgO}$ and $(100)_{TiO_2} \parallel (0001)_{Al_2O_3}$, $[010]_{TiO_2} \parallel [110]_{Al_2O_3}$, $[011]^*_{TiO_2} \parallel [110]_{Al_2O_3}$. ([ ]* = R.L. vector). Inspection of the orientation relationship observed for rutile films on (100)-oriented MgO substrates indicates that a continuous oxygen sublattice exists across the substrate-film interface with titanium atoms occupying unoccupied octahedral sites of MgO lattice. Since the respective oxygen ion densities for observed crystallographic planes are MgO(100) $= 1.13 \times 10^{15}/cm^2$ and rutile (110) $= 1.04 \times 10^{15}/cm^2$, some interfacial dis-

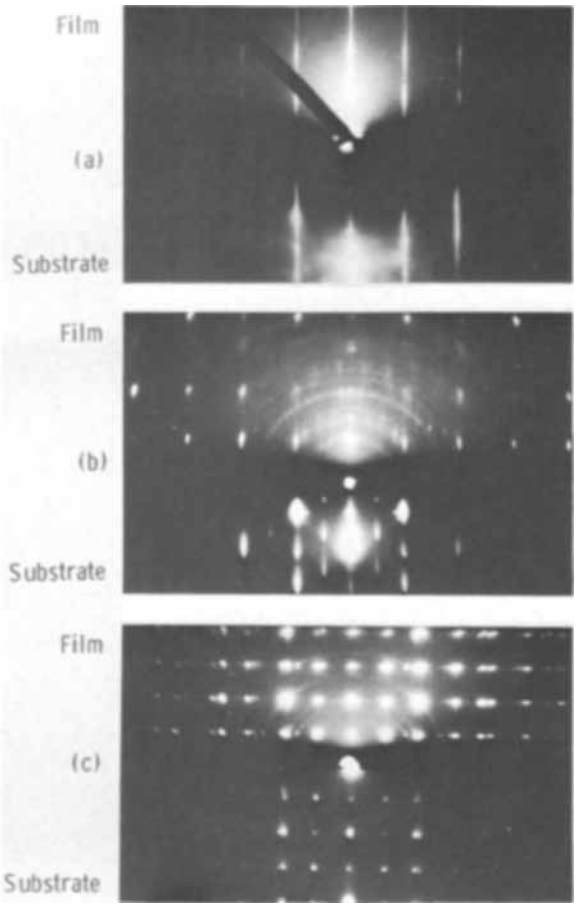

Fig. 4. Reflection electron diffraction (RED) patterns of epitaxial rutile films on (a) (110) rutile, (b) (100) MgO, and (c) (0001) sapphire. Corresponding RED patterns of substrates are shown on the bottom half of each photograph. Substrate temperature = 1100°K, $p_{O_2} \simeq 760$ Torr, $p_{TiCl_4} = 0.232$ Torr.

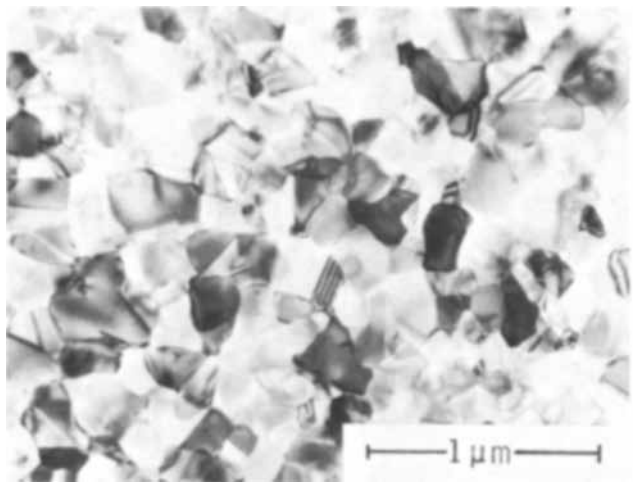

Fig. 5. Typical transmission electron micrograph of rutile film grown on silicon. $p_{O_2} \simeq 760$ Torr, $p_{TiCl_4} = 0.116$ Torr, $T = 1100°K$, $t \simeq 1500Å$.

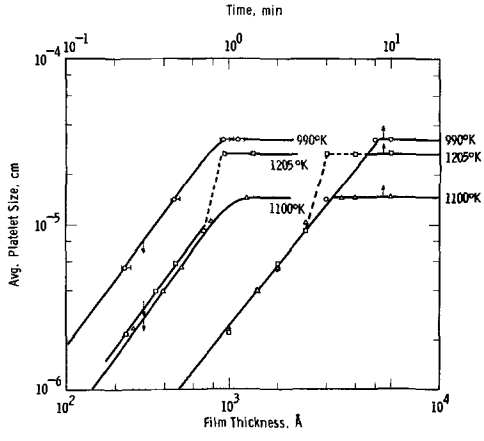

Fig. 6. Average lateral size of rutile crystallites in the thin films grown on (111) silicon single crystal substrates as functions of film thicknesses and growth times at 990°, 1100°, and 1205°K. $p_{TiCl_4} = 0.116$ Torr, $p_{O_2} \simeq 760$ Torr.

tortion is expected. A somewhat similar alignment occurs on (0001)-oriented sapphire crystals where the oxygen-filled substrate surface becomes common to both substrate and film. In this case, the respective oxygen ion densities are sapphire (0001) = 5.12 x 10^{14}/cm^2 and rutile (100) = 7.37 x 10^{14}/cm^2. In deposits on to single crystal rutile surfaces (homoepitaxy), the oxygen-titanium stacking becomes that of the substrate.

Growth behavior.—The growth behavior of TiO_2 films was most conveniently observed by transmission electron microscopy (TEM) of films deposited on Si substrates. The majority of films so investigated had mean thicknesses between 230 and 1500Å, were deposited in a fixed set of reactant partial pressures ($p_{TiCl_4} = 0.116$ Torr, $p_{O_2} \simeq 760$ Torr), and at one of three predetermined temperatures, 990°, 1100°, or 1205°K. All films on silicon showed a platelet morphology as shown in Fig. 5. The data obtained from such micrographs are given in Fig. 6 where the average platelet dimension is plotted both as functions of film thickness and equivalent growth time. The average platelet size was observed from the electron micrographs by linear analysis (error $\cong \pm 10\%$). Since average values did not change with annealing at the growth temperatures in oxygen ($p_{O_2} = 760$ Torr) (the annealing period was at least ten times the period of the deposition), they were considered to represent equilibrium dimensions. From the data in Fig. 6, deposits prepared between 990° and 1205°K show lateral extension of individual grains at almost a constant rate until a film thickness between 700 and 1000Å are reached. At these thicknesses, further lateral growth ceases. The ultimate lateral dimensions reflect the differences in nucleation densities observed earlier, i.e., deposits where nucleation density was greatest show crystallites of smallest lateral dimension and vice versa. Approximate dimensions (maximum) are 1470Å (1100°K), 2700Å (1205°K), and 3300Å (990°K). The data from films deposited at 1205°K indicate that at this temperature the rate of lateral extension is irregular in the thickness range 700-900Å. These growth results are regarded as uncertain at present and are indicated by a dashed line in Fig. 6. The size irregularities are likely related to the appearance of another TiO_2 phase during deposition [electron diffraction reveals the presence of TiO_2 (anatase) in deposits prepared above 1125°K]. The observed two-component multilayered film is likely to produce crystallites of various dimensions, the averaging of which could cause the observed discrepancy. The mechanism for formation of the second phase may well occur via a homogeneous reaction between $TiCl_4$ and O_2; such a reaction has been reported in a similar CVD reaction (4) although no structural data of the reaction product is available.

Effects of partial pressure ratio.—The effects of the variation of partial pressure ratio p_{O_2}/p_{TiCl_4} on the deposition rate of TiO_2 film is shown in Fig. 7 at two substrate temperatures. The slope of 1/2 is due to the fact that atomic oxygen is a reactant species at both these temperatures; this has been discussed in detail elsewhere (7). The pressure ratio at which TiO_2

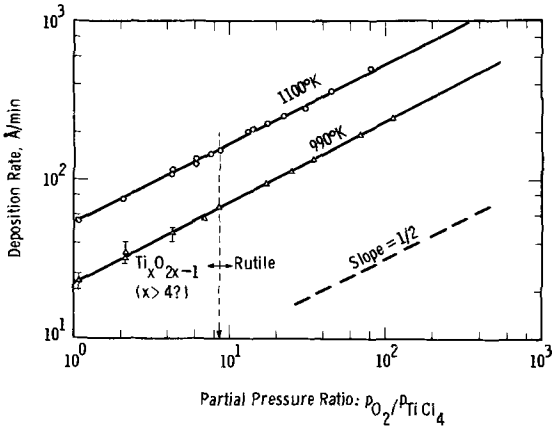

Fig. 7. TiO_2 thin film deposition rate as a function of the reactant partial pressure ratio (p_{TiCl_4} = 0.058 to 0.232 Torr, p_{O_2} = 0.25 to 25 Torr) at two substrate temperatures.

(rutile) formation is prominent is 8.62; below this ratio an unidentified reaction product is formed which is stable to the extent of complete resistance to further oxidation in pure oxygen (760 Torr) at temperatures up to 1320°K and at annealing durations of up to 8 hr. Thermodynamic calculations, using free energy change values from the JANAF thermochemical tables (9) and assuming equilibrium, *i.e.*

$$2p_{Cl_2} = p_{TiCl_4} \text{ and } p_{O_2}/p_{TiCl_4} = \tfrac{1}{4} Kp \qquad [7]$$

predict that the minimum p_{O_2}/p_{TiCl_4} ratio for rutile formation is 7.7 x 10^{-7} at 1100°K. This is orders of magnitude lower than the experimental value of 8.62 and is in the right direction for a reaction sequence controlled by the surface adsorption kinetics of atomic oxygen produced in the gas phase.

Refractive index data.—The refractive indices (n_D) and thicknesses of TiO_2 films on silicon were determined by ellipsometric methods (12). For films in the thickness range of 200-1500Å the average value of n_D was 2.83 ± 0.03. A few films thinner than ~ 500Å had a refractive index 5-8% lower than this average value. Such data are not uncommon in thin films, viz., indices of refraction of the oxides (Al_2O_3, Ta_2O_5, Nb_2O_5) are less in thin film form than in the bulk (15). The average refractve index of TiO_2 films (2.83 ± 0.03) produced for the present studies is greater than that obtained by a similar CVD process (n_D = 2.0) using tetrabutyl titanate and tetraisopropyl titanate (16) and compares favorably with the single crystal n_D values (17) (2.909 for the extraordinary ray and 2.613 for the ordinary ray). No reproducible behavior of change in n_D as a function of film thickness and/or deposition temperature could be detected.

Summary and Conclusions

The present study on the structure of chemically vapor deposited TiO_2 thin films on a variety of substrates has shown that (*a*) the crystallographic modification of TiO_2 produced by the reaction of $TiCl_4$ (g) and O_2(g) on all substrates studied is predominately rutile at and above a $p_{O_2}:p_{TiCl_4}$ ratio of 8.62; (*b*) the film is always polycrystalline on single crystal silicon between 0.001 to 30 ohm-cm, p- or n-type and low-index orientations and silica (amorphous or fused quartz) substrates and exhibits a particular fiber texture which is a function of only the temperature of deposition; (c) at temperatures below 1100°K, growth on (001) and (111) rutile substrates generates polycrystalline films and at relatively high deposition temperatures (> 1100°K) epitaxial films were produced on single crystal rutile, MgO and sapphire substrates; (*d*) *in situ* HCl etching of single crystal substrates produces preferred crystalline orientation at lower temperatures (in the case of silicon) and better quality epitaxial films (little or no twinning) on rutile substrates; (*e*) under a fixed set of experimental conditions comparable growth rates were obtained on all substrates; (*f*) between 990° and 1205°K the rutile crystallites grew laterally (on silicon) at about the same rate up to a film thickness of about 700Å; and (*g*) the density of TiO_2 nuclei (on silicon) increased exponentially with increasing temperature up to about 1125°K with an activation energy of 2.18 eV.

The energetics of the rutile crystallite formation process (on silicon) has been analyzed to support an earlier conclusion that the kinetics of the reaction $TiCl_4(g) + O_2(g) \rightarrow TiO_2$ (rutile) + $Cl_2(g)$ (on the silicon surface) involve adsorbed atomic oxygen and $TiCl_4$ molecular species (in the gas phase). Also, the epitaxial rutile thin film grown on low-index MgO, rutile, and sapphire substrates have easily understandable film-substrate structural relationships.

Acknowledgment

The authors wish to thank R. F. Yut and J. H. Rieger for experimental assistance and Dr. J. R. Szedon for arranging to have ellipsometric measurements done by his laboratory.

Manuscript submitted Feb. 2, 1970; revised manuscript received May 1, 1970.

Any discussion of this paper will appear in a Discussion Section to be published in the June 1971 JOURNAL.

REFERENCES

1. Proc. Conf. Chem. Vap. Deposition of Refractory Metals, Alloys and Compounds, Gatlinburg, Tenn., Sept. 12-14, 1967, Am. Nucl. Soc. (1967).
2. S. Zerfoss, R. G. Stokes, and C. H. Moore, *J. Chem. Phys.*, **16**, 1166 (1948).
3. L. Holland, "Vacuum Deposition of Thin Films," p. 466, J. Wiley & Sons, Inc., New York (1956).
4. M. Yokozawa, H. Iwasa, and I. Teramoto, *Japan. J. Appl. Phys.*, **7**, 96 (1968).
5. A. E. Fuersanger, *Proc. IEEE*, **52**, 1463 (1964).
6. F. Huber, *This Journal*, **115**, 203 (1968).
7. R. N. Ghoshtagore, *ibid.*, **117**, 529 (1970).
8. E. F. Cave and B. R. Czorny, *RCA Rev.*, **24**, 523 (1963); T. L. Chu, J. R. Szedon, and G. A. Gruber, *Trans. Met. Soc. AIME*, **242**, 532 (1968).
9. JANAF Interim Thermochemical Tables, Dow Chemical Co., Midland, Mich., Dec. 13, 1960.
10. H. D. Hagstrum, *J. Appl. Phys.*, **32**, 1020 (1961); J. J. Lander and J. Morrison, *ibid.*, **33**, 2089 (1962); F. Jona, *Appl. Phys. Letters*, **6**, 205 (1965).
11. F. G. Allen, *J. Appl. Phys.*, **28**, 1510 (1957).
12. B. Schwartz and N. Schwartz, Editors, "Measurement Techniques for Thin Films," The Electrochemical Society, New York (1967).
13. G. R. Booker, and R. Stickler, *Brit. J. Appl. Phys.*, **13**, 446 (1962).
14. F. D. Rossini, D. D. Wagman, W. H. Evans, S. Levine, and I. Jaffee, Nat. Bur. Standards, 1952, Selected values of chemical thermodynamic properties.
15. J. A. Aboaf, *This Journal*, **114**, 948 (1967); M. Duffy, K. H. Zaininger, and C. C. Wang, *ibid.*, **115**, 61C (1968).
16. D. R. Harbison and H. L. Taylor in "Thin Film Dielectrics," pp. 254-278, F. Vratny, Editor, The Electrochemical Society, New York, (1969).
17. J. R. DeVore, *J. Opt. Soc. Am.*, **41**, 416 (1951).

Technical Notes

Deposition of Silicon and Silicon Carbide by Film-Boiling

Raymond W. Conrad*

Physical Sciences Laboratory, U. S. Army Missile Command, Redstone Arsenal, Alabama 35809

When a substrate is immersed in a liquid and heated to a temperature much higher than the boiling point of the liquid, a sheath of vapor forms, separating the liquid from the substrate. This process is generally called "film boiling." If the liquid thermally decomposes or otherwise reacts to produce a substance which is nonvolatile at the temperature of the substrate, plating of this substance onto the substrate may occur. Basically, such a process is simply vapor deposition, at the high vapor concentration limit.

Recently Nieberlein (1) has used the film-boiling method to deposit polycrystalline silicon carbide onto tungsten filaments from mixtures of trimethylchlorosilane and cyclohexane at temperatures of ~900°C. Deposition rates of up to 100 μm/min were obtained. X-ray investigations (2) have not yet unraveled the crystal structure of the deposits. However, an extensive transition layer of tungsten carbide was identified.

This report presents the initial results of our attempts to adapt the film-boiling technique to the production of materials for electronics applications, particularly silicon carbide. Graphite and single-crystal silicon substrates were used in an attempt to eliminate transition layers. Several liquid systems were investigated.

Experiments and Results

The deposition system (Fig. 1) consisted of a pair of copper electrodes, with adjustable spacing, immersed in the liquid under study. The deposition cell was cooled with chilled acetone (~0°C) to minimize evaporation. The substrates were clamped between the electrodes by tightening the Teflon spacers and heated with a variable autotransformer. A current-limiting resistor was required when using silicon substrates. This consisted of a coil of resistance wire wound on a spiral-grooved ceramic core (total resistance, 15 ohm). Several intermediate taps were provided for lower resistances.

Temperature was monitored with an optical pyrometer. Sight-path effects introduced an uncertainty of ±50°C. The boiling, liquid sheath did not interfere with the temperature measurements during the early stages of deposition. However, the solutions eventually became turbid, making temperature measurements unreliable toward the end of deposition.

Graphite substrates, nominally 2 × 0.3 × 0.1 cm, were cut from disks of spectroscopic grade graphite (National Carbon, Grade CCH), lightly sanded with fine emery paper, rinsed with acetone and wiped dry. Silicon substrates, nominally 2 × 0.3 × 0.05 cm, were obtained by scribing and fracturing from 0.2 to 0.5 ohm-cm, (111), p-type silicon wafers. These were degreased in trichloroethylene and etched in $HF-HNO_3$ before use. Solutions for deposition were prepared from reagent grade materials without further purification. They were used only once because of the turbidity produced during deposition.

Graphite substrates.—Deposition from pure trimethylchlorosilane at ~1100°C produced thick, adherent layers of polycrystalline material which were identified by x-ray diffraction as the 6H polytype of α-silicon carbide. Deposition rates were ~350 μm/min for runs of up to 1½ min duration. Knoop microhardness values averaged 2200. No electrical evaluations have yet been made on these deposits, other than to note that they appeared to be n-type by thermal probe and to have relatively high resistivity.

Dilution of the trimethylchlorosilane with cyclohexane decreased the rate of deposition, but otherwise had no apparent effects on the gross characteristics of the deposits. Dilution with methanol, however, produced a rather dramatic effect. For mixtures with less than ~65 v/o (volume per cent) methanol, the deposits resembled those from pure trimethylchlorosilane. For mixtures with higher methanol concentrations, a black, lustrous deposit was obtained. Fracture surfaces of this material appeared glassy (see Fig. 2). Pro-

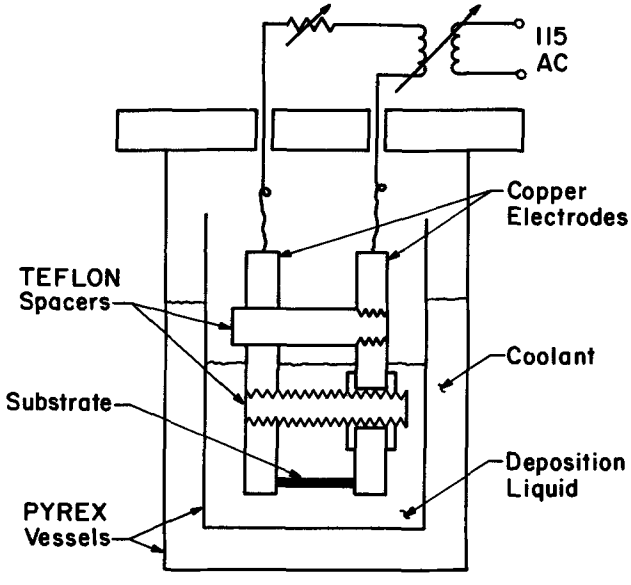

Fig. 1. Film-boiling cell

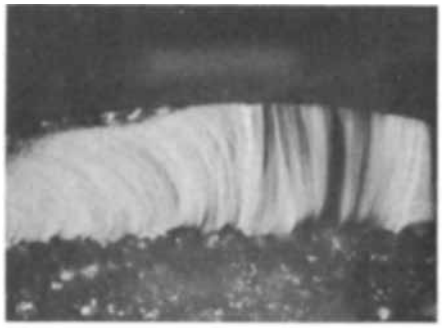

Fig. 2. Fracture surface showing a 230 μm-thick layer of glassy material deposited from a solution of 10 v/o trimethylchlorosilane in methanol, onto a graphite substrate.

* Electrochemical Society Active Member.
Key words: silicon, silicon carbide, vapor deposition, film-boiling.

longed etching in $HF-HNO_3$ (4 days in a 50-50 mixture) revealed that some areas of the deposits were not single-phase. X-ray diffraction indicated the material was indeed noncrystalline. Knoop microhardness values averaged 1800. The chemical composition has not yet been determined. However, the material was observed to form a liquid phase when heated in an inert atmosphere to 1700°C. Microscopic examination of the surface after this treatment revealed that portions of the layer had been transformed into a colorless glassy material which we suspect is silica.

The preparation of a similar, black, glassy substance by the decomposition of methyltrimethoxysilane vapor on a hot tungsten filament was reported by Hough and Early (3). They reported the composition to be $\sim Si_{33}C_6O_{40}$.

Silicon substrates.—Deposition from pure trimethylchlorosilane at ~950°C produced thick, polycrystalline layers shown by x-ray diffraction to be silicon. Deposition rates were 200 μm/min for runs of up to 1½ min duration. The deposits appeared to have relatively high resistivity. Thermal probing indicated n-type conduction.

Dilution with cyclohexane not only decreased the deposition rate but materially improved the physical quality of the deposit. Figure 3 shows a 94 μm thick layer deposited in 4½ min from a mixture containing 20 v/o trimethylchlorosilane. Back reflection x-ray diffraction indicates that some areas of the deposit are (111) single crystal. Thermal probing showed the deposit to be n-type. The electrical characteristics of the p-n junction have not yet been investigated. No deposits could be obtained using trimethylchlorosilane and methanol mixtures because the conductivity of such solutions was higher than that of the substrate.

Discussion

The deposition of silicon onto silicon substrates from trimethylchlorosilane, both with and without cyclohexane, was an unexpected result in view of the results obtained using tungsten and graphite substrates. The influence of deposition temperature on the composition of the deposit, however, has yet to be determined. The results reported here were for a relatively low deposition temperature, and the formation of silicon carbide at higher temperatures cannot be ruled out. Different results might also be obtained by using a different silane or an organic diluent or both. Nevertheless, the effect of the substrate on the course of the reactions occurring is vividly illustrated.

The suitability of material prepared by film-boiling for device fabrication has yet to be demonstrated. The rather unsophisticated technique used here can certainly be improved upon. By using highly purified liquids and inert electrodes (*e.g.*, graphite), the purity of the deposits should be substantially improved. Actually, this technique should be inherently cleaner than solution epitaxy, since the container for the liquids is not heated. Should it prove to be detrimental, the turbidity of the liquids, produced during deposition, might be eliminated by using a liquid flow system in which the liquids are continuously pumped from the deposition chamber through a filter, thence back to the chamber. Dopants might also be thus introduced.

There are several characteristics of the film-boiling technique that may limit its usefulness for epitaxial deposition. For example, there is a very large temperature gradient along the substrate major axis. This might be reduced, however, by using very long, thin substrates. High resistivity substrates obviously could not be used. The inability to vapor etch might also be a disadvantage. However, some degree of etching might be obtained by heating the substrate to a relatively low temperature if the liquid easily decomposes to produce vapors of an etchant, *e.g.*, HCl. The tendency to deposit thick polycrystalline layers from concentrated solutions, although undesirable for epitaxy, may have applications to the technology of integrated circuit fabrication using dielectric isolation.

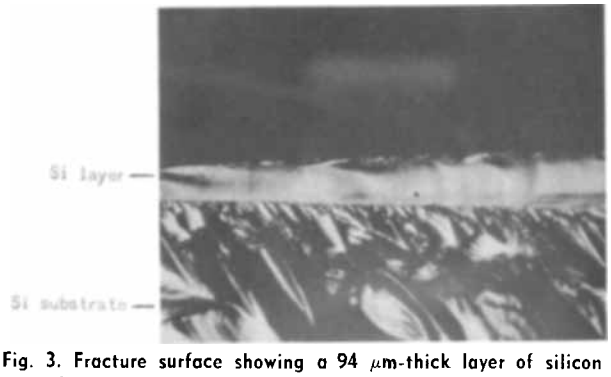

Fig. 3. Fracture surface showing a 94 μm-thick layer of silicon deposited from a solution of 20 v/o trimethylchlorosilane in cyclohexane, onto a single crystal silicon substrate.

Acknowledgments

The author thanks J. F. Bebbs, Jr. for his assistance in the laboratory, V. A. Nieberlein for his valuable discussions, and C. W. Austin for the x-ray diffraction work.

Manuscript submitted March 17, 1970; revised manuscript received *ca.* June 9, 1970.

Any discussion of this paper will appear in a Discussion Section to be published in the June 1971 JOURNAL.

REFERENCES

1. V. A. Nieberlein, *SAMPE Journal*, **4**, 72 (1968).
2. V. A. Nieberlein, PhD Thesis, University of Alabama, University, Ala. (1970).
3. R. L. Hough and D. E. Early, Technical Report AFML-TR-66-174, July 1966.

Gallium Diethyl Chloride: A New Substance in the Preparation of Epitaxial Gallium Arsenide

K.Lindeke, W. Sack, and J. J. Nickl

Forschungslaboratorium für Festkörperchemie am Institut für Anorganische Chemie der Universität München, München, Germany

Manasevit *et al.* (1, 2) and Rai-Choudhury (3) have reported on the use of alkyl-gallium compounds and arsine in the preparation of gallium arsenide epitaxial layers. However, these compounds are distinguished by a high reactivity (4) [$Ga(CH_3)_3$ ignites with O_2 even at −76°C, and a mixture of its vapor with air explodes at room temperature; $Ga(C_2H_5)_3$ ignites in air and explodes in O_2.] The use of trialkyl-gallium together with highly toxic arsine (threshold limit value 0.05 ppm) is extremely hazardous in case of any leakage.

Key words: materials, preparation, gas epitaxy, organic Ga source, arsine.

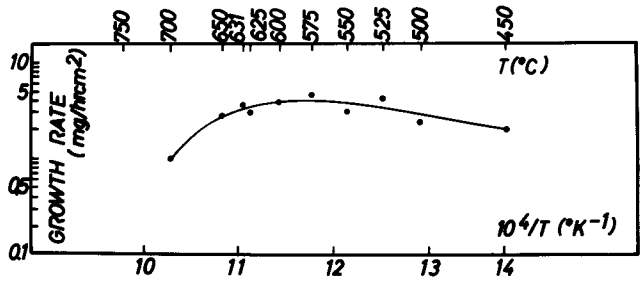

Fig. 1. Growth rate of (100) GaAs layers vs. $10^4/T$

The reaction between $Ga(CH_3)_3$ and Pyrex has also been reported (2). This causes difficulties during distillation for purification purposes. In a technical application it would be important to have a Ga-compound which is safer to handle even in large quantities.

Therefore, the comparable low reactive gallium diethyl chloride (GDC) has been used as the Ga source. This substance hydrolyzes slowly even in 0.1*N* NaOH. Although 1 mole of HCl is generated per mole GaAs, this should not have a negative influence on the layer quality because, in the Cl-transport system, layers of highest purity can also be produced (5, 6). In addition, gas-phase etching occurs in the reaction mixture just before growing the crystal by increasing the temperature to 750°C, which may be very helpful in preparing an absolutely clean surface.

GDC was obtained commercially and is used without further purification. The arsine (purity 99.5%) concentration was 5.5% in high-purity H_2. Semi-insulating Cr doped GaAs wafers of $(\bar{1}\bar{1}\bar{1})$ ("B" face), (110) and (100) orientation were etched in 10% Br_2/CH_3OH and washed in methyl alcohol just before use.

The experiments were performed in a vertical rf heated flow-type reactor designed to permit evacuation. Quartz, Pyrex, Teflon, and stainless steel have been used in constructing the system. This kind of CVD apparatus has also been used successfully in the preparation of elemental semiconductors such as Si and Ge (7, 9) and has many advantages. A thermocouple NiCr/Ni, calibrated at the freezing point of Al, was embedded in the graphite susceptor in close proximity to the GaAs wafer.[1] The susceptor was coated with pyrolytic carbon. A bubble-type vaporizer inserted into an oil bath at about 60°C contained the liquid gallium source. Three special bubblers containing H_2O, Br/H_2O, and 30% NaOH, are used downstream to destroy the waste products, especially AsH_3.

Before deposition takes place the wafers are heated to 900°C for 1 min to remove surface contaminations. In the early stage of the investigation the grown layers often showed holes; this could be prevented by this annealing step. Then the temperature is lowered to the growth temperature and the AsH_3-stream (0.7 l/hr) is started. After As deposits at the reactor walls the H_2 (3.5 l/hr) is bubbled through the GDC, and GaAs is formed on the substrate. The GaAs wafers were heated to growth temperature (450°-700°C) and after deposition cooled to room temperature in Pd-diffused H_2. It is recommended that the wafers not be cooled in the reaction mixture, since GaAs is formed down to 450°C (Fig. 1). Below growth temperature of 500°C the layers are of high resistivity and have rough surfaces. Single crystallinity as determined by reflection x-ray Laue pattern was obtained as low as 450°C. At 750°C gas-phase etching takes place, as observed by weight changes of the wafers before and after the process. The nature of this reaction is not known so far. We believe that 1 Cl from the GDC transports 1 Ga as GaCl from the surface and the other part of the GDC is evaporated as a alkyl subcompound Ga $(alkyl)_{1\text{ or }2}$ from the surface. However, no visible amount of metallic Ga could

[1] The influence of the rf was prevented by a capacitor shunted to the thermocouple.

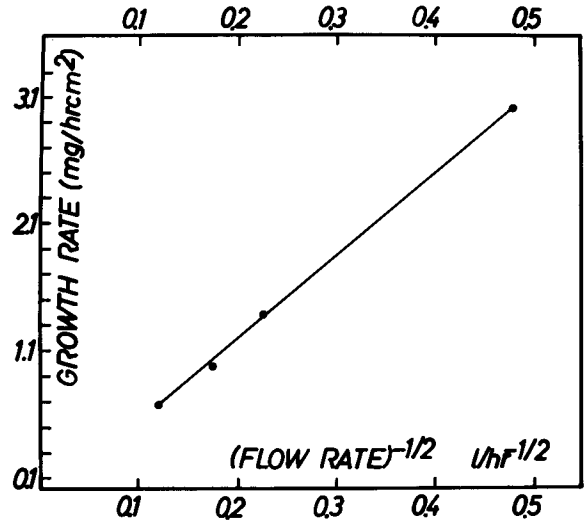

Fig. 2. Growth rate of (100) GaAs layers vs. (total flow rate)$^{-1/2}$ at constant GDC and AsH_3 flux.

be detected at the substrate or anywhere in the reaction chamber (by reaction 3 $GaR_1 \rightarrow GaR_3 + 2$ Ga).

Mirror smooth layers of epitaxial GaAs on (100), (110), $(\bar{1}\bar{1}\bar{1})$-surfaces were obtained, but the reported data are measured on layers with (100)-orientation. Layer thickness was determined by two methods: first by etching (10); second by the weight gain of the wafers. Growth rate was evaluated as function of substrate temperature (Fig. 1) and gas stream velocity at constant GDC and AsH_3 input values. Since the reaction is nearly independent of the temperature, we assume a mass transport phenomenon to be the rate-controlling step. This is supported by Fig. 2 which shows the growth rate increasing with the reciprocal square root of the gas stream velocity.

The electrical properties of the layers were assessed using the van der Pauw method (11). For this purpose contacts of Sn/In (48/52) were alloyed at about 250°C in a H_2, Ar, HCl (80/15/5) atmosphere. The ratio of the two van der Pauw resistivities $R_1:R_2$ was constant within 3% from 70° to 300°K. The Hall coefficient R_H and the resistivity ρ were measured in this temperature range. The mobility was calculated from the ratio R_H/ρ. The magnetic field was 4 kG. Plots of carrier concentrations as a function of reciprocal temperature are shown in Fig. 3. The mobility plots *vs.* temperature are shown in Fig. 4. The correlation between deposition temperature, layer thickness, the measured carrier concentration, and mobility are shown in Table I. The

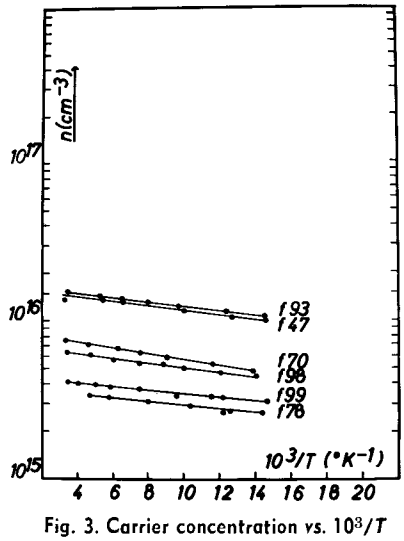

Fig. 3. Carrier concentration vs. $10^3/T$

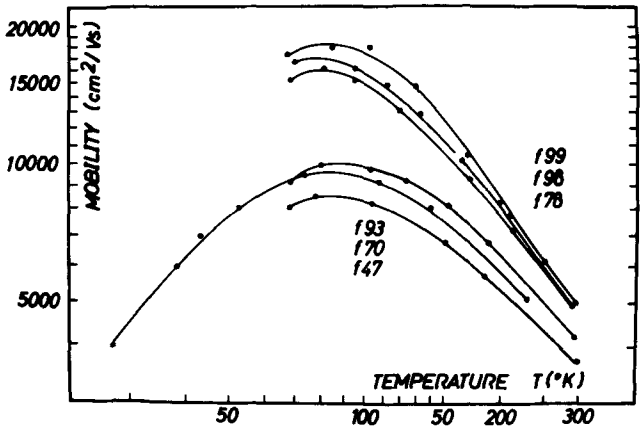

Fig. 4. Mobility vs. temperature

samples seem to have an impurity with an ionization energy of about 8 meV, calculated under the assumption of one single donor term, partly compensated by acceptor terms. The impurity has not yet been identified. No carbon could be detected in the reaction chamber or on the layers either by microanalytical methods or by x-ray investigations.

The results, listed in Table I, show that GDC is a suitable substance for the preparation of epitaxial GaAs layers. However, better results should be obtained when purer starting materials are used.

Acknowledgment

The authors are greatly indebted to Dr. Doetzer, Siemens AG. Erlangen, Germany, for supplying GDC. Thanks are given to Mrs. M. Betz for technical assistance.

Table I. Characteristics of typical GaAs layers grown by the GDC/AsH_3 CVD process

Sample No.	Thickness, μm	Depos. temp, °C	Mobility, cm^2/vs. $\mu_{300°K}$	$\mu_{70°K}$	Carrier conc. $n_{300°K}$, cm^{-3}	Resistivity $\sigma_{300°K}$, ohm-cm
f 47	5-6	635	3750	8500	$1.5 \cdot 10^{16}$	0.12
f 70	5-8	631	3850	9500	$7.5 \cdot 10^{15}$	0.18
f 78	5.5	550	4800	16000	$3.5 \cdot 10^{15}$	0.33
f 93	2-3	631	4200	9800	$1.5 \cdot 10^{16}$	0.10
f 98	7.5	575	4850	16500	$6.4 \cdot 10^{15}$	0.20
f 99	11.6	575	5050	18000	$4.2 \cdot 10^{15}$	0.30

Manuscript submitted March 31, 1970; revised manuscript received *ca.* June 25, 1970.

Any discussion of this paper will appear in a Discussion Section to be published in the June 1971 JOURNAL.

REFERENCES

1. H. M. Manasevit and W. I. Simpson, Paper 63 presented at the Boston Meeting of the Society, May 5-9, 1968; Extended Abstract, Vol. 5, p. 154.
2. H. M. Manasevit and W. I. Simpson, *This Journal*, **116**, 1725 (1969).
3. P. Rai-Choudhury, *ibid.*, **116**, 1745 (1969).
4. J. A. Sheka, J. S. Chaus, and T. T. Mityureva, "The Chemistry of Gallium," Elsevier Publishing Co., Amsterdam (1966).
5. D. Effer, *This Journal*, **112**, 1020 (1965).
6. M. Maruyama, S. Kikuchi, and O. Mizuno, *ibid.*, **116**, 413 (1969).
7. H. C. Theuerer, *ibid.*, **108**, 649 (1961).
8. V. J. Silvestri, *ibid.*, **116**, 81 (1969).
9. S. A. Papazian and A. Reisman, *ibid.*, **115**, 961 (1968).
10. M. S. Abrahams and J. Buiocchi, *J. Appl. Phys.*, **36**, 2855 (1965).
11. van der Pauw, *Philips Res. Repts.*, **13**, 1 (1958).

JOURNAL OF THE ELECTROCHEMICAL SOCIETY

ELECTROCHEMICAL TECHNOLOGY

OCTOBER 1970

Development of a Controlled Porosity Silver Electrode

G. W. Mao, D. S. Polcyn,* and R. E. Tieder

Gould Incorporated, Gould Laboratories, Energy Technology, Minneapolis, Minnesota 55414

ABSTRACT

Silver electrodes which require no supporting grid and have a porosity graded structure were fabricated by combining silver powder of uniform mesh size with a plasticizer and pore forming additives. The proportions of these materials are selected to give a uniform doughlike mixture which is rolled and then sintered. Porosity control is achieved by controlled decomposition of the plasticizer and pore forming additives. Multilayered graded porosity electrodes are assembled by a combination of sintering and compaction. Performance data based on cycling tests and coulombic efficiencies demonstrated that these electrodes are comparable to conventional silver electrodes and the absence of the grid is not a limiting factor.

Silver electrodes for electrochemical cells can be produced by various methods either from silver or silver oxide powders. Junger (1), Morrison (2), and Jirsa (3) have produced silver electrodes by various methods of pasting a silver grid. Moulton and Enters (4) describe producing a sintered porous silver mass by thermally decomposing a dried silver(I) oxide pasted grid. More recently, electrodes have been prepared by application of silver(II) oxide paste to a silver grid using methylcellulose or sodium carboxymethylcellulose as binders (5). Wilburn (6) and Wilburn *et al.* (7, 8) have described methods for producing electrodes by dry compaction of silver(II) oxide to silver grids. Additional methods for producing porous silver electrodes primarily for use in fuel cells have been described by Schroeder *et al.* (9) and Niedrach and Alford (10).

Even though several methods are available for producing silver electrodes, they are normally prepared from silver powder which has been compacted on a silver grid, sintered, and electroformed (6). In these processes little regard is given to available electrode porosity, a known control factor of battery electrode performance, other than pressing sintered silver powder to various densities. Experience has shown that this practice is used to increase the A-hr/g capacity rather than controlling porosity.

Since these electrodes may be rather dense, they must be kept relatively thin; otherwise the interior active material becomes electrolyte-starved during cycling because of restricted electrolyte flow. Production of an electrode with controlled porosity would make all portions of the electrode equally accessible to electrolyte and enables the use of relatively thick electrodes for high efficiency, primarily at low discharge rates. At high discharge rates, the zinc electrode is the limiting electrode rather than the silver electrode, so the silver electrode can be made thin. However, porosity control provides an additional advantage in controlling the over-all performance of the cell. Since a controlled porosity sintered silver electrode would oxidize uniformly during charge, a silver grid would not be required since a continuous network of silver during discharge should remain throughout the electrode, and act as a more efficient conductor than the conventional silver grid. Presumably the process of hot rolling a mixture of polyethylene and silver powder followed by heating to burn out the polyethylene (11) may well be used to control porosity. No data to this effect have been published.

This paper describes the fabrication and electrochemical behavior of sintered silver electrodes of uniform pore size, produced by sintering a rolled sheet of uniformly mixed wet silver and binder powders. High efficiency thick electrodes were produced by sintering electrode material of 60% and 78% accessible porosities into a porosity-graded layered structure. It is expected that the electrochemical behavior of these porosity layered electrodes may possess good performance in comparison to conventional pressed and sintered grid-containing silver electrodes.

The work of Bogenschutz *et al.* (12) interrelating porosity and sintering temperature showed that, over the porosity range 57-65%, the capacity varied 20%. These results were used in determining our optimum sintering temperature for gridless silver electrodes.

Electrode Processing Procedure

The first processing step for producing porosity controlled silver electrodes consists of rolling a doughy silver powder-methyl cellulose mixture into a continuous sheet. The mixture is composed of 93 parts −325 mesh silver powder (44μ diam) blended with 7 parts methyl cellulose. The components are mechanically shear mixed with 10 ml of 10% aerosol and approximately 35 ml of alcohol per 100g until "dough" consistency is achieved. After suitable mixing, the material is rolled to the desired thickness and allowed to air dry. Any scrap, prior to sintering, can be reprocessed with the appropriate liquid addition. The dry material is sintered in air by placing it into a 788°C furnace for 15 min. Sintering produces a porous structure by burning out the plasticizer and creates sufficient strength by joining adjacent silver particles.

The sintered sheet (0.05 cm thick) was cut into 3.8 cm squares, and a 0.32 cm wide silver strip current collector was attached to one edge. Several methods

* Electrochemical Society Active Member.

Key words. silver electrodes, porous electrodes, sintered electrodes, gridless, porosity graded.

for attaching the current collector were tried, but the most successful method was to first position the silver strip with a single spot weld along the edge of the square electrode. Then the electrode assembly was placed in a furnace at 780°C for 3 min. While in the furnace, the current collector section of the electrode was rolled at a pressure of about 0.07 g/m^2. This rolling process assured contact of the strip to the silver electrode over the entire collector-electrode contact area.

In comparing the structure of gridless electrodes with conventional pressed and sintered electrodes, it was apparent that the experimental process produces an evenly distributed, uniform pore size. Many of the silver particles of conventional electrodes are massively sintered together in the press and sinter technique resulting in poor contact between portions of the supporting grid and adjoining silver. This lack of contact indicates that the sintered silver structure may be the primary current conductor instead of the grid. In the case of the gridless electrode, the interconnected silver network which remains after oxidation of the silver should provide efficient current conduction because of its uniform distribution.

Porosity Control

Available porosity can be increased by blending pore-forming agents with the silver powder and methocel. Ground charcoal and wood flour were chosen as porosity controllers, since burn-out during sintering forms gases which produce interconnecting pores upon leaving the silver mass and minimizes residual contaminants. These additives were used to increase the accessible porosity from nominal 68-80% as seen in Fig. 1. Porosity was determined by comparison of the bulk density with the true density where:

$$\text{Total porosity} = 1 - \frac{\rho\text{Bulk}}{\rho\text{True}}$$

The relationship between the amount of pore agent and per cent void volume is not linear since, as porosity increases, the silver structure partially collapses during sintering. Therefore, 80% was determined to be the practical upper porosity limit. Chemical analysis shows that -100 $+140$ mesh ground charcoal was completely removed during sintering. With the other porosity controllers, a trace of carbonaceous material remained. Photomicrographs showed that the wood particles contain a greater volume per mesh size, because they are fibrous, while the charcoal is particulate. Therefore, it seems reasonable to assume that wood flour would result in less surface area per unit volume in comparison to an equal volume of charcoal because of the difference in particle shape and over-all size.

Available porosity can be decreased from the nominal 68% by adding additional silver to the basic batch mix. For example, an extra 50 parts silver decrease porosity to 60%. Larger additions were not evaluated, since producing a dense electrode with little interconnection between pores was not desirable.

Porosity Layered Electrode Fabrication

In preparing porosity gradient electrodes, the sintered material of 0.05 cm thickness and of 60% and 78% accessible porosity was cut into 3.8 cm squares and three-layered assemblies of 60-60-60%, 60-78-60%, 78-60-78%, and 78-78-78% porosity were made. These layered structures are designated as *DDD, DPD, PDP,* and *PPP,* respectively, where D=60% porosity and P=78% porosity.

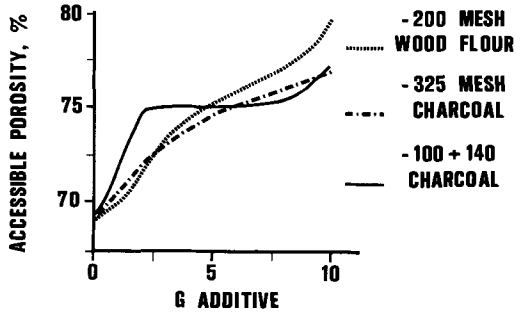

Fig. 1. Porosity effect of additives per 100g Ag-methocel

Material using -100 $+140$ mesh charcoal pore agent was used to produce these porosities, since it was completely removed during sintering. Furthermore, preliminary testing indicated higher capacity than with -100 $+140$ mesh wood flour or -325 mesh charcoal as pore-forming agents.

A 0.33 x 0.02 cm silver lead was positioned along the edge of an outside layer. Spot welding at a single point maintained alignment of the silver layers and lead. Each assembly was placed in a 788°C furnace for 3 min and hand rolled with a ceramic roller at a pressure not exceeding 0.07 g/m^2. The electrodes were immediately removed from the furnace to prevent densification. It was found that the rolling operation is necessary and sufficient to create sintered bonding between the layers.

Testing Procedure

Charge-discharge testing was done in open-top 5 x 6.2 x 1.8 cm cells so cycling characteristics of the electrodes could be observed. The silver electrode under test was placed between two nickel counterelectrodes (3.8 x 3.8 cm) in approximately 40 cc of 40% KOH. An Hg/HgO reference electrode which had a Luggin capillary probe was placed between the nickel and silver electrodes. During discharge, Ag/AgO, AgO_2//Hg/HgO potential was monitored to determine electrode discharge stability and capacity. This potential varied with distance between reference and silver electrode due to IR drop and nonuniform current distribution, but an attempt was made to minimize the variation by maintaining this distance constant. The use of nickel counterelectrodes prevented problems of zinc dendrites and corrosion that are associated with silver-zinc cells. Furthermore, the silver electrode performance here is much more favorable than would be expected in cells with separators and zinc anodes.

Experimental single-layer electrodes with 70% porous structure and a conventional silver electrode which was also 70% porous were charged and discharged at currents based on the silver weight. Porosity layered electrodes were cycled in two groups, one at charge and discharge currents determined by 70% conversion of silver weight to silver oxides, and another at a charge of 0.021 A/cm^2 for 8 hr, followed by alternate discharges at 2.21 A/cm^2 and 0.038 A/cm^2 to the hydrogen evolution potential. An example of the calculations based on the 70% conversion are included in the section titled Calculations.

Experimental Results

Charge/discharge of grid and gridless electrode.— Discharge curves for 0.05 cm sheet silver electrodes (3.50g, 70% accessible porosity) were measured in 40% KOH at the 5 hr, 1 hr, and ½ hr rate for a conventional grid structure and for a gridless structure. The discharge curves are shown in Fig. 2. Comparing the discharge curves at the 5 hr rate for the grid and gridless silver electrodes, the discharge times agree within 2.5%. At the 1 hr rate a difference of 1.3 min was observed, while at the ½ hr rate the conventional grid electrode discharged about 10% longer than the gridless electrode, but at a lower voltage level. Voltage decay of the conventional grid electrode is more rapid at each of the rates.

Considering voltage levels of the discharge curves, the voltage (*vs.* Hg/HgO) is lower for the grid electrode at the ½ hr and 1 hr rate, but is nearly identical at the 5 hr rate. This voltage difference may be due to lower resistivity of the gridless electrode, but there are not sufficient data to determine the variation exactly. Analysis of the two electrodes showed that

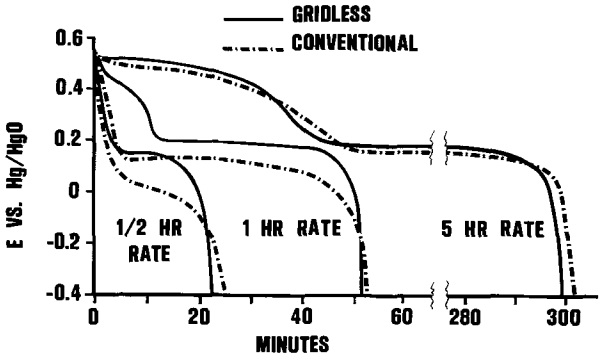

Fig. 2. Silver electrode discharge

the grid electrode contained 17.4% free silver, whereas the gridless electrode contained 14.1% silver. This slight difference in silver content is not sufficient to produce the observed voltage variations.

A characteristic of silver electrode discharge curves is the two-step voltage pattern. This two-step pattern results from the discharge of the divalent oxide to the monovalent oxide and then the monovalent oxide to the metal. Generally this two-step phenomenon is undesirable, either in battery charging or in its application as a power source. The presence or absence of this two-step discharge has been found to be dependent on the physical and electrochemical properties of silver electrodes.

Comparing discharge curves for the conventional and gridless electrodes, it is noted that at all discharge rates a two-step discharge occurred. At the ½ hr and 1 hr rate, the discharge time at the divalent oxide potential was less for the conventional electrode structure and nearly identical at the 5 hr rate.

Further evidence of the improved electrochemical behavior of these electrodes is that, after extended cycling, the cells maintained their performance at a high level. The cells were cycled over 100 times in an open-cell configuration without any significant decrease in performance. It is expected that cell life could be increased considerably by using a closed cell in which the electrodes maintain their physical shape due to tight packing.

During the test period no evidence of unusual charge acceptance, discharge behavior, or physical deterioration was noticed on visual examination of the electrodes. After cycling, both electrode structures, conventional and gridless, are quite brittle. With severe deformation, the gridless electrode fractures quite easily, breaking up into several small parts. The grid electrode is also brittle after cycling, but on deformation the electrode is held together by the grid. This should not be a problem in application since, in the cell assembly, the electrodes are tightly packed and breakage will be minimal.

On the basis of the experimental observations, the gridless electrode performs as well or better than the conventional electrode, indicating that the silver electrode is not limited by the absence of a supporting internal grid. Furthermore, comparing the voltage levels, discharge times, and capacities for the two structures, the gridless electrode is superior to the conventional electrode.

Electrochemical behavior of layered silver electrodes with constant current charge/discharge.—Four electrodes of graded porosity construction were tested. The 60% porous material is designated by *D* and the 78% by *P*. Four combinations of these abbreviations are used to refer to the different electrode structures. The data on physical properties are summarized in Table I.

These electrodes were charged for 8 hr at 0.21 A/cm² and then discharged at two different currents, alternately at 0.021 A/cm² and 0.038 A/cm². At this low rate of charge, the four different structures showed essentially the same charge rate on the basis of the amount of silver present. It is expected that at high-rate charging the more porous electrodes would have improved charge acceptance when compared with the dense structures.

Table I. Physical dimensions of graded porosity electrodes

Porosity layer, %	Electrode	Weight, g	Thickness, cm
60-60-60	*DDD*	7.87	0.152
60-78-60	*DPD*	6.48	0.147
78-60-78	*PDP*	5.27	0.142
78-78-78	*PPP*	4.14	0.142

The average A-hr/g capacity of four discharges was used as the basis for determining the average discharge curves of Fig. 3 and 4. Since the discharge time is proportional to the electrode weight and the weights of the various assemblies were different, a nondimensional time scale was chosen to allow direct comparison of the discharges. The time scale is $t/t_{\text{theoretical}}$, where $t_{\text{theoretical}}$ is the time for discharge assuming 100% utilization of the silver. In addition, the coulombic efficiency was found to be independent of the discharge rate.

From Fig. 3, at a discharge current of 100 mA/cm², the voltage levels and discharge times are similar for the mixed porous structures with *PDP* having the longest discharge time and *DPD* discharging at a higher voltage. The monoporous structures, *DDD* and *PPP*, have nearly identical discharge curves, indicating that the porosity or layered structure is not a controlling factor at this discharge current.

Figure 4 shows the discharges of these graded electrode structures at a current density of 20 mA/cm². The discharge times and voltage levels are similar for

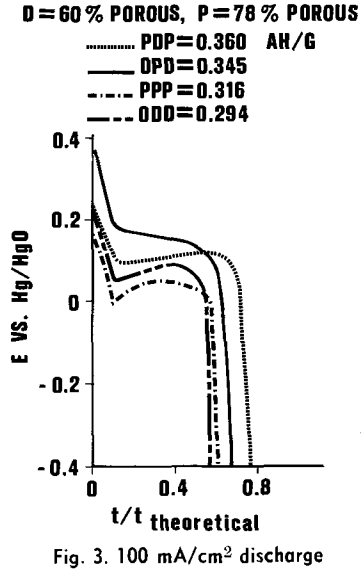

Fig. 3. 100 mA/cm² discharge

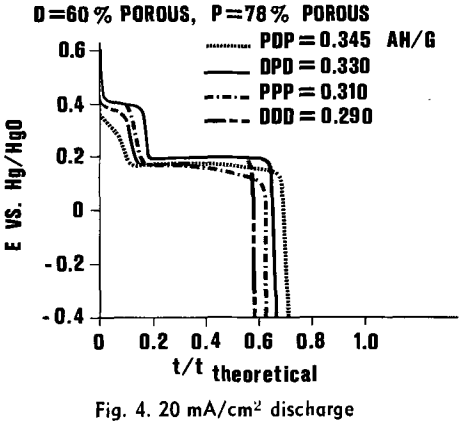

Fig. 4. 20 mA/cm² discharge

Table II. Charge-discharge rate based on electrode weight

Porosity layer, %	Electrode	Weight, g	Thickness, cm	Charge, A 5 hr	Charge, A 25 hr	Discharge, A ½ hr	Discharge, A 5 hr
60-60-60	*DDD*	8.32	0.154	0.582	0.116	5.82	0.582
60-78-60	*DPD*	6.92	0.149	0.484	0.097	4.84	0.484
78-60-78	*PDP*	5.39	0.142	0.377	0.075	3.77	0.377
78-78-78	*PPP*	4.15	0.142	0.290	0.058	2.90	0.290

the multiporous layered electrodes, *PDP* and *DPD*, and, as at the high rate, the DDD and PPP show nearly identical behavior. Discharge time at the divalent oxide potential is longest for the *DPD* structure and decreases in the order *PPP*, *DDD*, and *PDP*. However, no significant differences in the discharge curves are noted at this low rate which could be attributed to variations in the layered structure.

Electrochemical behavior of layered silver electrodes with charge discharge rate determined by electrode weight.—These electrodes were discharged alternately at the ½ hr and 5 hr rates for eight cycles, with the charging done in two steps: charge at a 5 hr rate until oxygen evolution occurs, followed by charging at a 25 hr rate until oxygen evolution again occurs. The experimental data for these electrodes are given in Table II.

The average ampere-hour/gram capacity of four discharges was used for determining the average ½ hr and 5 hr rate discharge curves of Fig. 5 and 6. The coulombic efficiency was found to depend directly on the electrode weight.

From Fig. 5, at the ½ hr discharge rate, the porous outside layers appear to control the discharge, since *PPP* and *PDP* both show higher discharge efficiency than electrodes with dense outer layers. Furthermore, the *PPP* electrode appears most efficient. This was expected, since a more porous electrode outperforms a dense electrode structure at relatively high rates because of the lower effective current density on the porous structure and accessibility of the active material for reaction. It appears that highly porous gridless electrodes have an optimal pore size for the ½ hr rate discharge, as evidenced by the similarity of the discharge voltage-time relationship and the efficiency data. However, the *DDD* structure shows a significant voltage drop at this discharge rate, indicating that only the surface layer is discharged and the discharge process is probably mass transport limited.

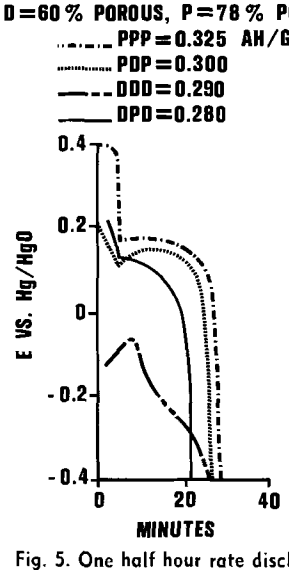

Fig. 5. One half hour rate discharge

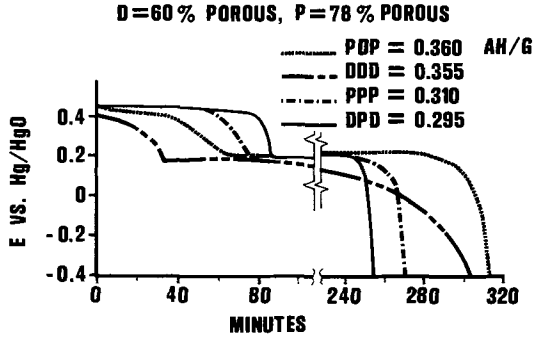

Fig. 6. Five hour rate discharge

Discharge curves at the 5 hr rate are shown in Fig. 6. Here the discharge is at a low enough current density so that the dense inside layer is also discharging and becomes the control layer. This is evidenced by *PDP* and *DDD* electrodes outperforming the electrodes with porous centers. However, the electrodes with porous outside layers outperform the electrodes with dense outside layers, regardless of center layer porosity. Even at low rates the porous layers control the discharge, especially at the divalent oxide potential.

The divalent oxide potential is markedly evident at the 5 hr rate, especially for the *DPD* structure where about one third the discharge time is at the higher potential. The other structures also discharge at this higher potential, but for much shorter times. Probably, explanations for the presence of the divalent oxide potential are weak metal contact between the layered structures, decreased conductivity, nonuniform current distribution due to the porous structure, and poor contact between the silver-to-silver bonds due to the semiconductor AgO in the electrode.

Since discharge time at the divalent oxide potential is greatest for the *DPD* structure and decreases in the order *PPP*, *PDP*, and *DDD*, it appears that the center porous layer may be a controlling factor. However, the manner in which the porous layers control the divalent potential for these electrodes has not been thoroughly investigated in this work, and will be considered in future studies.

Conclusions

The gridless electrode has been shown to have physical and electrochemical properties exceeding, or as good as, those of the conventional grid structured silver electrode. The manufacturing process is simple and economical. Considerable savings will be realized on the total amount of silver used by elimination of the grid. Furthermore, the process permits controlling the porosity of the silver electrode which is not realizable with the conventional silver electrode.

Comparing the electrochemical performance of the (0.05 cm thick) gridless and grid electrodes, the gridless electrode's performance was not limited by the absence of a conducting grid, as evidenced by the discharge data.

On extending the controlled porosity layer concept, to a multiporosity structure, the mixed porosity combinations performed significantly better than the monoporosity combinations. In fact the *PDP* structure was superior in three of the four tests, with the *DPD* closely approximating it. It also appears that, in the conventional Ag-Zn battery, several thin electrodes could be replaced by a single thick graded structure, if the separator and anode space requirements, as well as the discharge rate, are considered.

Although it has been demonstrated that the layered structure is feasible, no attempt has been made to determine the optimum pore size of the layered structure. This will be considered in further investigations of gridless electrodes. Further testing of these electrodes at higher rates is also under investigation, since the high discharge rate performance was not thoroughly studied.

CALCULATIONS

70% Conversion

As an example of charge/discharge cycling with currents determined by silver weight, consider the following example for a silver electrode weighing 2.8g.

From Faraday's law it can be shown that 1.0g of silver will theoretically require 0.5 A-hr to be produced from AgO. Therefore:

$$2.8g\ Ag = 1.4\ A\text{-}hr\ theoretical$$

Actual conversion based on AgO is 70% since some Ag^+ and Ag^o remain during charging to Ag^{++}. Therefore

$$1.4 \times 70\% = 0.98\ A\text{-}hr$$

is actually expected to force discharge 1.0g of fully charged silver. Testing commences by charging at a 5 hr rate until oxygen evolution. The charging current is decreased to 25 hr rate until oxygen evolution once again occurs.

Currents would be

$$\frac{0.98\ A\text{-}hr}{5\ hr} = 0.196A\text{—}5\ hr\ rate\ charge$$

$$\frac{0.98\ A\text{-}hr}{25\ hr} = 0.039A\text{—}25\ hr\ rate\ charge$$

Testing continues by discharging at a 1 hr rate until hydrogen evolution

$$\frac{0.98\ A\text{-}hr}{1\ hr} = 0.98A\ discharge$$

Note that the discharge time is such that, in 1 hr, 70% efficiency based on Ag^{++} would be achieved. Theoretically, the longest discharge would be

$$\frac{1.4\ A\text{-}hr}{0.98A} \times 60 = 85.8\ min\ at\ the\ 1\ hr\ rate$$

Manuscript submitted Nov. 3, 1969; revised manuscript received *ca.* May 1, 1970. This was Paper 26 presented at the Detroit Meeting of the Society, Oct. 5-9, 1969.

Any discussion of this paper will appear in a Discussion Section to be published in the June 1971 JOURNAL.

REFERENCES

1. E. W. Junger, U.S. Pat. 692,298 (1902).
2. W. Morrison, U.S. Pat. 975,980 (1910).
3. F. Jirsa, *Z. Elektrochem.*, **88**, 129 (1927).
4. J. D. Moulton and R. F. Enters, U.S. Pat. 2,615,930 (1952).
5. J. R. Coleman and T. E. King, "Power Sources 1966," p. 193, D. H. Collins, Editor, Symposium Publications Division, Pergamon Press, New York (1967).
6. N. T. Wilburn, Abstract No. 303, *Electrochem. Soc. Extended Abstracts*, p. 57, Montreal, Oct. 6-11, 1968.
7. N. T. Wilburn, K. E. Meade, and C. J. Bradley, "Dry Process Divalent Silver Oxide Electrodes," Tech. Report ECOM-2628 USAECOM, Fort Monmouth, N. J. (1965).
8. N. T. Wilburn, K. E. Meade, and C. J. Bradley, "Dry Process Divalent Silver Oxide Electrodes," Tech. Report ECOM-2749 USAECOM, Fort Monmouth, N. J. (1966).
9. J. E. Schroeder, D. Pouli, and H. J. Seim, Abstracts, 154th National Meeting of the American Chemical Society, September 1967, Chicago, Ill.
10. L. W. Niedrach and H. B. Alford, *This Journal*, **112**, 117 (1965).
11. ESB Incorporated, Union of South Africa Pat. 59/2001 (1959).
12. A. F. Bogenschütz, P. Krahl, and V. Schulz, *Electrochem. Technol.*, **5**, 405 (1967).

Study of Lithium-Lead Alloys as Grid Material for Lead-Acid Batteries

G. W. Mao, T. L. Wilson,* and J. G. Larson

Gould Incorporated, Research Division, Minneapolis, Minnesota 55414

ABSTRACT

Lithium-lead alloys with low contents of lithium were investigated for lead-acid battery grids. The metallographical alloy structures, mechanical properties, anodic corrosion resistance, cell performance, and castability were determined. Experimental data are interpreted and compared with the well-known antimony-lead and calcium-lead battery grid alloys. A useful lithium-lead alloy range is presented. The potential electrochemical superiority and economical feasibility are discussed.

Although the positive grid does not participate directly in primary discharge/charge processes, it is this member that often limits battery life and utility. A suitable positive grid must: (*a*) have sufficient mechanical strength to support its own weight and that of the active material, (*b*) conduct electrical current evenly and efficiently, (*c*) provide a low impedance electrical contact between grid and active material, (*d*) be relatively resistant to anodic corrosion, and (*e*) be easily formed.

Antimony-lead alloys in the range of 4.5-12 w/o (weight per cent) Sb are generally used as battery grids in lead-acid batteries; the presence of antimony, however, enhances self-discharge (1). In addition, stibine gas evolution excludes use of these alloys in confined areas.

Over 30 years ago, the advantages of using alloying elements electronegative to lead were outlined, and the properties of a 0.1 w/o Ca alloy were discussed (2, 3). Although similar compositions still serve as alloys for storage battery grids, poor cycling characteristics have limited their use in many applications. In addition, corrosive attack under anodic conditions can be selective, causing problems in dimensional stability (4).

Chemically, lithium resembles calcium in the free state, whereas it resembles antimony metallurgically (5). Lithium-lead binaries were thus selected for study as possible grid alloys with the expectation that they would possess some of the better properties of both the calcium- and antimony-lead alloys. The possibility of using alloys containing lithium as grid alloy has not gone without previous investigation (6). Earlier investigators, however, were probably concerned with alloys too rich in lithium.

This paper presents experimental results that are believed to have a bearing on the applicability of lithium-lead as a positive grid alloy. The mechanical strength, resistance to anodic corrosion, cell performance, and castability are compared with similar data for calcium- and antimony-lead alloys. A usable alloy

* Electrochemical Society Active Member.

Key words: battery grid, lithium-lead, lead-acid battery.

range is outlined and the characteristics of the lithium alloys are compared with grid alloys used at present.

Procedure

The alloys referred to in this paper were prepared from Tadanac lead of 99.998% purity (principal impurities were copper, silver, antimony, and bismuth) and 99.9+% lithium (Na 0.007-0.01%, Ca 0.02-0.05%, Fe 0.001-0.01%, Si 0.006-0.01%). Alloys were prepared either by adding lithium directly to a melt held at 650°F, or by adding a concentrated master alloy to lead in iron crucibles. The combination of reactivity of lithium in the melt, stirring, and a nominal holding time after the melt had stabilized appeared adequate to insure homogeneity of the alloy. Flame spectroscopy of nitric acid solutions of samples systematically selected during casting gave no indication that segregation had occurred.

All melting and casting was done under an inert atmosphere of argon. Except where noted, the melt temperature prior to pouring was maintained at 700°F and the mold temperature 350°F. The molds were coated with a layer of a silicate-cork dust slurry as standard practice. The alloy compositions referred to later represent the chemical analyses of gates taken from the castings and are generally the average of several such samples. Cast ¼ in. by 5 in. rods were used as the anodes for corrosion studies. Tensile specimens were cast to the shape prescribed for sheet lead samples, *i.e.* providing a gauge area of 2 x ½ x ⅛ in. The castability data were obtained using the method described in the literature (7).

Briefly, castability was determined by pouring the lead alloy into an inverted tree-type mold cavity at controlled melt and mold temperatures, and cast samples were compared. Casting was scored by assigning points to each portion of the inverted tree mold. The more difficult areas to fill were given higher values than the easier to fill areas. The highest possible index score was arbitrarily set at 100.

The metallographic techniques of sample preparation have been presented in detail in an earlier paper (8). Briefly, these comprised mounting the sample in a low-temperature setting plastic, polishing through successively finer lubricated abrasives to a final 0.1μ alumina slurry, and etching in a dilute citric acid-ammonium molybdate solution.

Alloy rods were corroded separately at constant potential (the potential being higher than the solvent decomposition voltage) or at constant current in 1.115 sp gr sulfuric acid at room temperature. Pure lead sheet cathodes with a surface area of 170 cm^2 were concentrically arranged at a distance of 3 cm from the anode (surface area of 17 cm^2). Current and voltage were recorded throughout the experiments, and weight losses due to corrosion were determined by stripping the corrosion product from the surface of the corroded rods in a hot alkaline mannitol solution. Duplicate alloy rods were corroded so one experiment could be interrupted to metallographically observe the progress and the morphology of the anodic corrosion.

Battery grids were cast under inert atmosphere using optimum mold and melt temperatures. Grids were hand pasted in a manner simulating commercial practice and formed accordingly. Cells constructed from these grids were discharged in deep cycle tests. Historically, cycle life tests have been proven indicative of a grid alloy's capability. Although pure, calcium-, and dispersion-strengthened-lead satisfy many of the requirements of grid alloys, they are characterized by an inability to maintain cyclic capacity (9-12). Lithium-lead alloys were therefore submitted to a comparison with commercial alloys in cycle life tests.

Five-plate, miniature cells were constructed with paste:grid weights resembling industrial conditions. Theoretical capacities were approximately 3 A-hr so that at 35% efficiency a reasonable charge:discharge cycle could be maintained daily with a 16 hr overcharge. Cells were discharged at a theoretical 4 hr rate (thus taking 1 hr at 25% efficiency) and charged back at a theoretical 20 hr rate (normally taking 6 hr). A particularly deep cycle (1.1V cutoff) was used to accelerate failure—as much paste as possible was used in each cycle without deliberate sulfation. It was commonly observed that nonantimony cells fell to one third their capacity under this test regime.

A 16 hr, 2.2V float cycle (64 hr on weekends) was incorporated into the test procedure. Earlier results had indicated that grain boundary corrosion was severe in two-phase, lithium-lead alloys. Despite the fact that cells normally spent 520 hr on overcharge compared to 20 on discharge, tests were invariably terminated because of paste, not grid, failures.

Experimental Results

Anodic corrosion.—Under conditions of exceeding the $PbO_2/PbSO_4$ potential, the net effect of making dilute additions of lithium to lead is to reduce the anodic corrosion rate, as shown in Fig. 1. Corrosion was carried out at 82 mA/cm^2 constant current density for a period of 4 weeks in 1.115 sp gr sulfuric acid.

Two composition-dependent types of corrosion morphology were found, and these areas are noted in Fig. 1. For dilute alloys (lithium content less than 0.02 w/o) attack was generally uniform, maintaining much the same characteristics as pure lead. For lithium contents between 0.02-0.03 w/o lithium, penetration was concentrated at grain boundaries. Examples of these morphologies are illustrated in Fig. 2.

The critical composition distinguishing these classes of alloys, based on anodic corrosion, essentially defines and restricts the maximum alloying addition that may be made to obtain a usable binary. Grids containing greater amounts of lithium would be expected to "grow" during service, and this penetration type of attack may lead to premature grid fracture.

In the accelerated corrosion tests of this study, the kinetics of corrosion appeared to be chemically controlled since the depth of grain boundary penetration exceeded the grain size in alloys containing more than

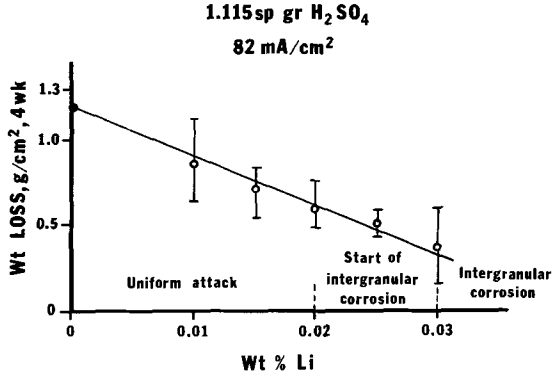

Fig. 1. Anodic corrosion of Li-Pb

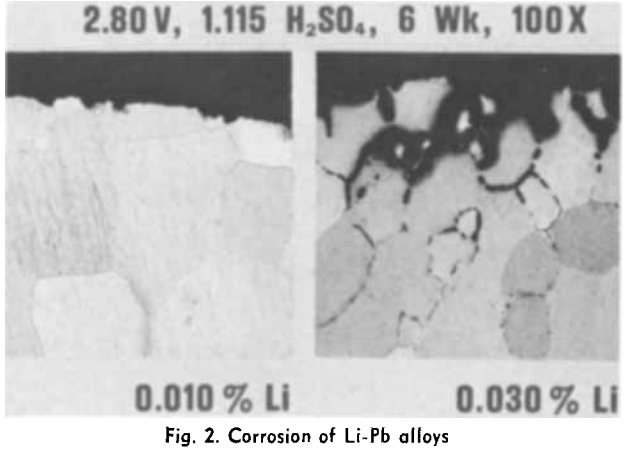

Fig. 2. Corrosion of Li-Pb alloys

0.03 w/o Li. This undoubtedly is a consequence of the dissolution of the LiPb intermetallic compound. Such chemical attack leads both to increasing the area exposed to corrosion and to locally increasing the alloy temperature. The latter factor could lead to catastrophic failure because it accelerates the rate of anodic attack and favors the kinetics of precipitation resulting in increased rate of precipitation.

On anodic corrosion, the deceptiveness of weight loss data cannot be overemphasized in interpreting corroded microstructures. The corrosion of lithium-lead alloys is a classic example of the necessity of microscopically studying the morphology of corrosion attack. The tendency for grain boundary attack increases with increasing lithium content, but catastrophic dissolution does not occur until alloy compositions in excess of 0.03 w/o Li are reached. Apparently, once started, the process of grain boundary consumption is one that propagates itself on a localized basis.

X-ray diffraction analyses of the oxide films stripped or brushed from the surface of the anodically corroded rods indicated that the corrosion products resulting from the conditions referred to above were largely αPbO_2. Both free lead and βPbO_2 patterns were observed but only in minor quantities. In a 0.03 w/o Li-Pb alloy, these phases were observed to constitute 5% free lead and 3% βPbO_2 of the total oxide film. The elemental lead is thought to result from complete grain boundary dissolution, thus mechanically freeing individual grains. The beta lead dioxide is also tentatively associated with the corrosion of the alloy-rich boundary layer. This latter conclusion was reached largely on the basis of a 3% shift in lattice parameter of the beta phase. The lattice parameter, a_o, for beta lead dioxide formed on lithium-lead differs from the value for beta lead dioxide formed from pure lead. It would appear from this latter observation that selective partitioning of lithium occurs between the oxides.

Chemical analysis of corroded rods proved that there was a slight decrease in lithium content. However, no lithium was found either in the cell electrolyte or the cell sludge. The other possible place where lithium could concentrate is in the adherent oxide layer. As the lithium contents were extremely low, x-ray diffraction did not detect its definite presence.

Comparisons of type of anodic attack were made with pure lead and representative calcium and antimony alloys. Corrosion was carried out at constant potential (2.8V) to get an indication of the alloy performance during overcharge conditions. Lithium-lead appeared to be very similar to pure lead both in degree of attack and corrosion morphology. Typical results of observed weight losses are reproduced in Table I and the general features of corrosion morphology are shown in Fig. 3.

Alloys corroded anodically above the decomposition potential of the electrolyte illustrate decisively the tendency for preferential grain boundary attack of the alloys. Even the cast 99.998% pure lead demonstrated a tendency toward preferential grain boundary penetration, presumably due to the segregation of elements to the boundary area. Westbrook and Aust have documented the propensity of solutes to segregate to grain boundaries in dilute lead alloys (13).

Mechanical strength and metallography.—Photomicrographs of cast structures of compositions ranging from 0.01 to 0.10 w/o Li are reproduced in Fig. 4. These figures reflect directly on the corrosion performance noted previously and the mechanical strength results presented in this section. As might be expected from the broad two-phase liquid plus solid field, the effects of coring in the lithium-lead system are quite evident. The first interdendritic type intermetallic compound is observed in alloys containing less than 0.04 w/o Li. In the 0.10 w/o alloy, the intermetallic is continuous and defines the grain size.

Table I. Anodic corrosion of lead alloys at constant voltage

Alloy composition (w/o)	2.8 V, 1.115 H_2SO_4, 4 weeks total time: Corrosion weight loss (mg/cm^2)
4.5 Sb-Pb	135.4
0.07 Ca-Pb	49.5
0.01 Li-Pb	46.8
0.02 Li-Pb	48.0
0.03 Li-Pb	63.1
Pure Pb	61.1

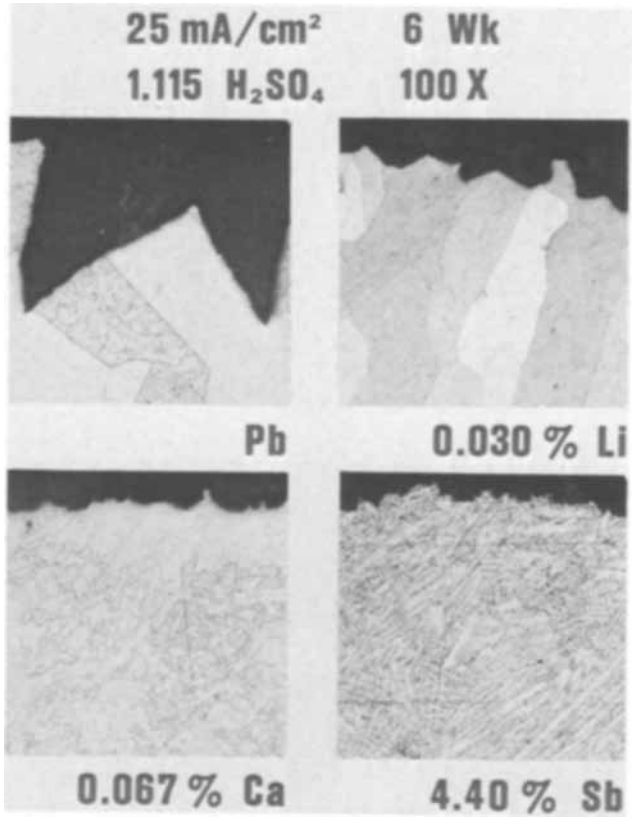

Fig. 3. Anodic corrosion of grid alloys

The kinetics of precipitation are reasonably rapid. At room temperature, the alpha solid solution grain boundaries of alloys containing 0.02 w/o Li are decorated with the intermetallic precipitates. Complete coverage ostensibly occurs in 0.04 w/o Li alloys. This heterogeneous precipitate morphology strongly affects the chemical reactivity of alloys in this system, as mentioned previously in corrosion studies.

The other effect that lithium has on the as-cast structure is a marked reduction in primary grain size. The 0.01 w/o Li alloy has a grain size approximately one fourth that of pure lead cast under identical conditions, and increasing the lithium content from 0.01 to 0.05 w/o reduces the grain size further by a factor of two. This observation of a decrease in grain size within the solid solution is in agreement with that reported by Greenwood (14). Although this grain size reduction has only a secondary effect on the chemical behavior of the alloys, it does contribute to its strength characteristics.

Tensile results are in general accord with an age-hardening system in which precipitation occurs from a supersaturated solution. Figure 5 shows a rapid increase in strength for alloys of less than 0.02 w/o Li and then a more gradual, linear increase for richer alloys. The rapid increase is primarily associated with solid solution strengthening, with the remaining 25% contribution from grain refinement. The linear portion of the strength increase is a consequence of the dispersion hardening influence of the intermetallic.

Tensile strength, yield strength, and per cent elongation varied only slightly with aging time for compositions up to 0.015 w/o Li. For compositions up to 0.025

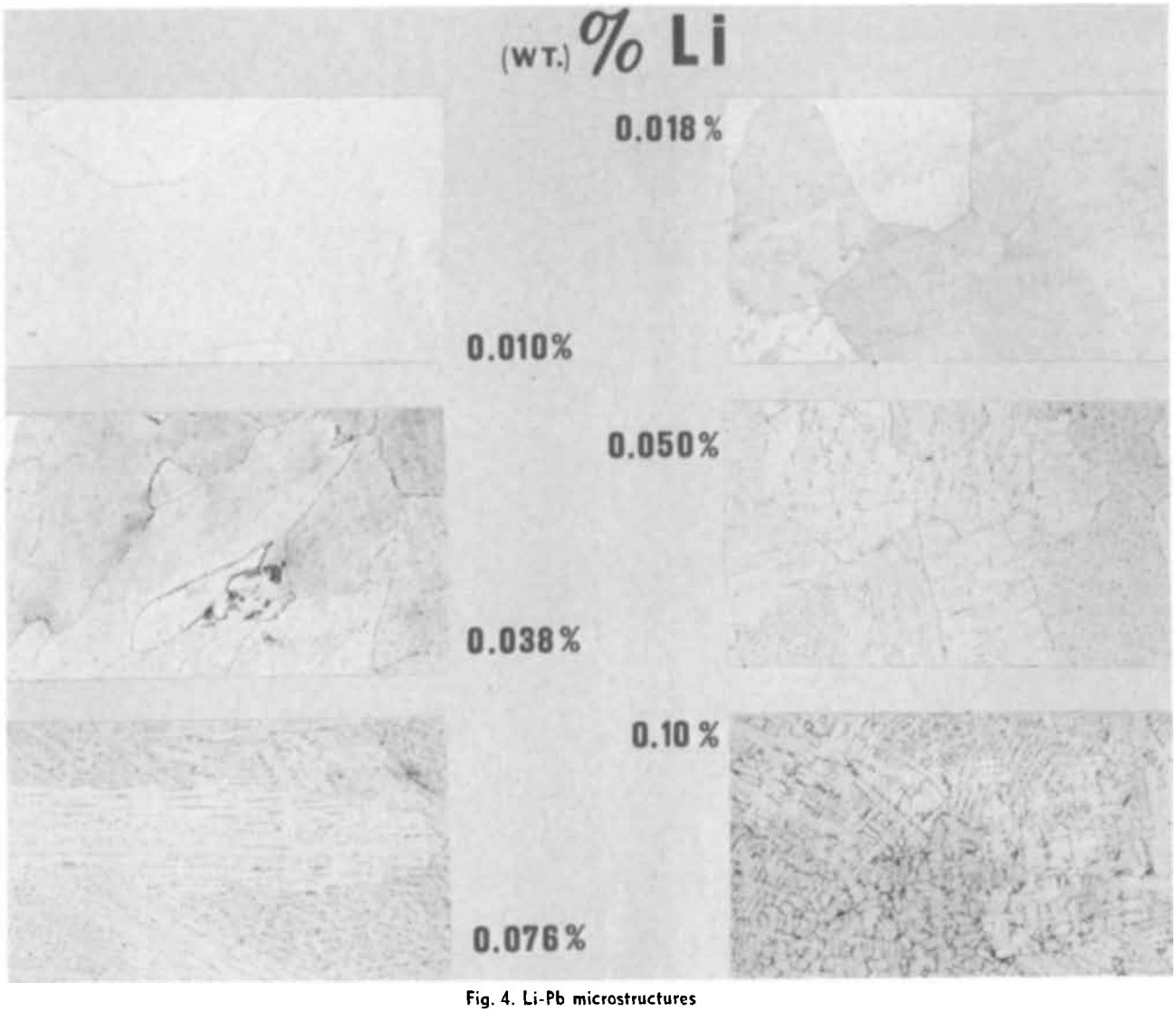

Fig. 4. Li-Pb microstructures

w/o, changes were noted largely in yield strength, whereas ultimate strength and elongation were relatively stable. An embrittlement associated with precipitation from the supersaturated solid solution existed above 0.025 w/o Li, however. The instability was the type where both the ultimate strength and elongation decreased, while the yield strength increased. In other age-hardening systems where this occurs, embrittlement is associated with overaging at grain boundaries, frequently with solute depleted regions (15).

Aging at room temperature apparently imparts a ripening process to the precipitate. Samples tested after a period of 4 weeks lost the dispersion hardening contribution to their tensile strength, whereas the ultimate tensile strength levels out to a value of about 5000 psi. The instability that exists in the richer alloys correlates qualitatively with the corrosion results. The corrosion as well as strength results indicate that

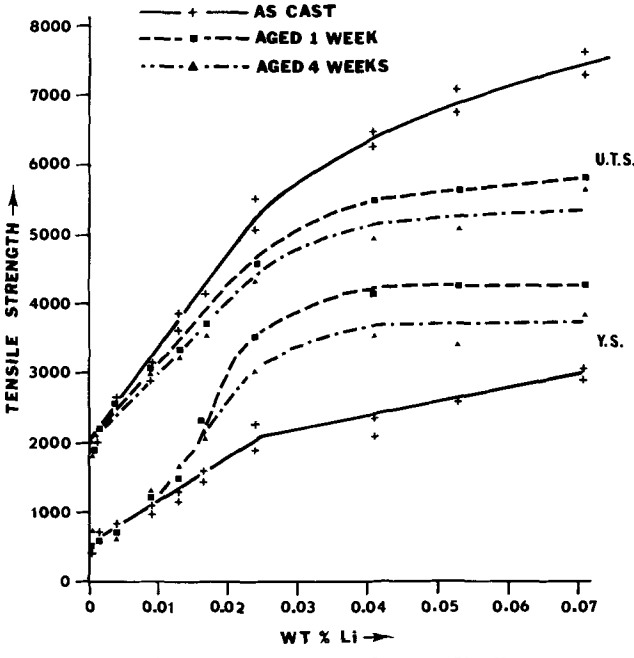

Fig. 5(a). Tensile properties of cast Li-Pb alloys

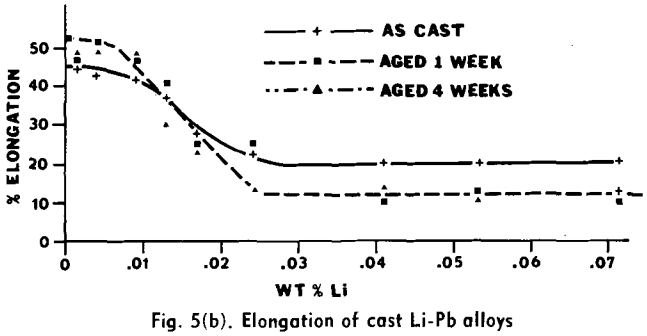

Fig. 5(b). Elongation of cast Li-Pb alloys

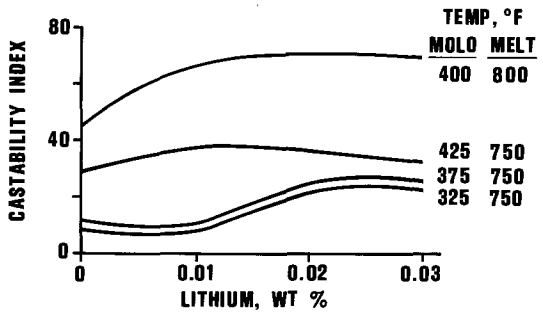

Fig. 6. Castability of dilute Li-Pb

ripening must proceed to a greater extent at grain boundaries. The aging data are included in Fig. 5.

For comparison, tensile strengths of calcium and antimony alloys are reproduced in Table II for two aging conditions that simulate conditions met during stripping, pasting, and use. Relatively dilute lithium alloys are comparable with the other two alloys.

Casting behavior of lithium-lead.—Inasmuch as the general grid fabrication process is one of casting, the casting behavior of any grid alloy is of primary concern. Both castability and the shrink associated with solidification were determined for standard casting practice for the alloys of concern. Castability data are illustrated in Fig. 6 and Table III. The internal shrink of alloy rods was determined by rolling samples into sheets and determining the change in density before and after rolling. The porosities (*i.e.*, per cent change in density values) for pure lead, 0.03 w/o Li-Pb, 0.07 w/o Ca-Pb, and 4.5 w/o Sb-Pb rods were 0.20, 0.08, 1.16, and 0.00%, respectively.

These casting parameters show antimony-lead is superior to the other alloys with which it was compared, since it solidifies with an eutectic phase present in the lead-rich matrix. Lithium-lead is a reasonably castable alloy in the useful grid composition range. Since the castability test essentially describes the ability to fill 1/16 in. diameter capillaries under various conditions (7), it is apparent that this may be done with little internal porosity with lithium alloys in the solid solution range. Grids of various shapes, and as thin as 0.06 in., are cast freely with lithium-lead.

Cell Performance.—Under the test regime used in this study, it was observed that nonantimony cells lost capacity from cycle to cycle. Antimony cells, on the other hand, regained and maintained their capacity after an initial loss. Both observations are in substantial agreement with earlier studies. The data gathered for the standards (7.0 antimony-, 0.07 calcium-, and unalloyed-lead) are reproduced in Fig. 7.

For comparison, the data for the lithium alloys are shown in Fig. 8. It appears that the performance of lithium-lead is composition-independent in the range studied and most similar to pure lead.

Table II. Ultimate tensile strength of lead alloys

Alloy composition (w/o)	As-cast, psi	Aged 1 week (room temp) psi
4.5 Sb-Pb	5100	5400
0.07 Ca-Pb	4200	5300
0.01 Li-Pb	3300	3100
0.02 Li-Pb	4700	4250
0.03 Li-Pb	5700	5000

Table III. Castability index of lead alloys

Melt temp, °F	Mold temp, °F	4.5% Sb-Pb	0.07% Ca-Pb	0.01% Li-Pb	0.02% Li-Pb	0.03% Li-Pb
700	325	56	8	7	28	23
700	425	80	27	39	31	33
800	400	84	48	74	67	71

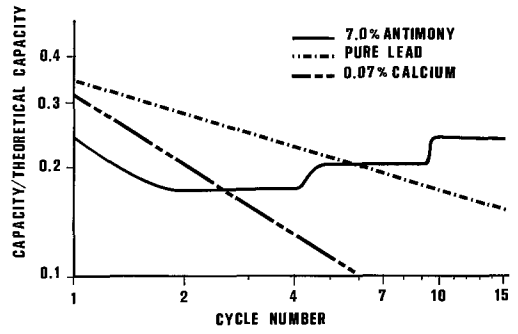

Fig. 7. Cyclic characteristics of grid alloys

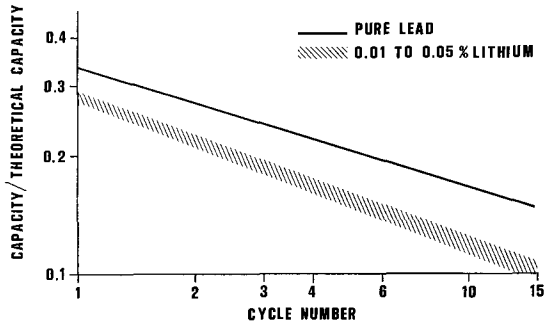

Fig. 8. Cyclic characteristics of Li-Pb alloys

Discussion

The useful composition range for lithium-lead binary alloys as battery grids is limited by anodic corrosion to lithium contents of less than 0.03 w/o. Lithium-lead binary alloys with lithium content higher than 0.03 w/o do not withstand high rate anodic corrosion. Below 0.03 w/o, the grid strength will be 4000-4500 psi and castability is midway between commercial antimony-lead and calcium-lead alloys. Total casting porosity should, however, be less than that generally obtained in the latter type grids. Under deep cycling, performance is similar to that obtained in pure lead grids.

If a general comparison is made with present alloys, it becomes immediately evident that lithium-lead alloys present the possibility for construction of low self-discharge grids at low material cost, due to the low alloy content. Balancing these merits are problems like the difficulty in maintaining lithium within the melt at high temperatures.

Positive grid elements of the three main classes of lead-acid batteries are constructed of particular alloys because of performance requirements. A review of these three classes is useful to place lithium-lead in perspective and to assess the merits of lithium-lead grids.

Automotive grids require frequent high-rate discharges, in which only a portion of the capacity is used, and reasonable life on overcharge. Strength and ease of casting are important because it is desirable to have the grids made as thin as possible (usually of 0.060 in. thickness). Lithium-lead, even with its pure lead type cycle behavior, might satisfy these requirements, but the castability of a hypoeutectic definitely surpasses that of a single-phase alloy. Competition with 4.5% antimony alloys would be enhanced if a different method of casting lithium-lead grids other than gravity casting is developed. On the other hand, if the industry is considering a maintenance-free, quasi-sealed, storage battery, then an alloy of the lithium-lead type would be a necessity.

Grids of industrial batteries where a long cycle (8 hr discharge rate) is desired are made of even richer antimony alloys (7.5-12 w/o). The chief requirement in the class is the cycle life and this parameter for Li-Pb appears to be an area open for improvement. In this respect, additives to the grid, paste, or electrolyte might be considered to obtain a flatter capacity: cycle

number curve. This general problem is something the whole lead-acid industry is considering due to the mounting price of antimony.

Finally, industrial standby cells utilize calcium-lead or pure lead grids because of low self-discharge requirements. Li-Pb alloys should perform adequately in this respect because they possess many of the properties necessary for this use. In addition, good welding and casting properties of lithium-lead should be a definite advantage.

Manuscript submitted Nov. 3, 1969; revised manuscript received *ca.* June 19, 1970. This was Paper 38 presented at the Detroit Meeting of the Society, Oct. 5-9, 1969.

Any discussion of this paper will appear in a Discussion Section to be published in the June 1971 JOURNAL.

REFERENCES

1. J. J. Lander, *This Journal*, **99**, 339 (1952).
2. H. E. Haring and U. B. Thomas, *Trans. Electrochem. Soc.*, **68**, 293 (1935).
3. E. E. Schumacher and G. S. Phipps, *ibid.*, **68**, 309 (1935).
4. J. B. Burbank, *This Journal*, **104**, 693 (1957).
5. M. Hansen and K. Anderko, "Constitution of Binary Alloy," p. 200, McGraw-Hill, New York (1958).
6. (*a*) German Pat. 476,259; (*b*) Brit. Pat. 494,069; (*c*) U.S. Pat. 1,360,269; (*d*) U.S. Pat. 1,791,148; (*e*) U.S. Pat. 1,926,545; (*f*) U.S. Pat. 2,140,544.
7. J. O. Johnstone, Metals Refining Publication (1935).
8. G. W. Mao, J. G. Larson, and P. Rao, *Metallography*, **1**, 399 (1969).
9. E. J. Ritchie and J. Burbank, *This Journal*, **117**, 299 (1970).
10. J. Burbank, *ibid.*, **111**, 1112 (1964).
11. S. Tudor, A. Weisstrech, and S. V. Davary, *Electrochem. Technol.*, **4**, 406 (1966).
12. N. E. Bagshaw and T. A. Hughes, "Batteries 2," p. 1, D. H. Collins, Editor, Pergamon Press (1964).
13. J. H. Westbrook and K. T. Aust, *Acta Met.*, **11**, 1151 (1963).
14. J. N. Greenwood, *Met. Rev.*, **6**, 279 (1961).
15. A. Kelly and R. B. Nicholson, *Prog. Mater. Sci.*, **10**, 151 (1963).

The Effect of Several Electrode and Electrolyte Additives on the Corrosion and Polarization Behavior of the Alkaline Zinc Electrode

F. Mansfeld*,[1] and S. Gilman*

NASA/Electronics Research Center, Cambridge, Massachusetts 02139

ABSTRACT

The corrosion behavior of zinc in 6*N* KOH at 25°C was investigated through measurement of the rate of hydrogen evolution (r_{H_2}) at the corrosion potential. Anodic and cathodic potentiostatic polarization curves as a function of alloying and additions to the electrolyte were obtained. It was found that the corrosion and polarization behavior of 99.999% zinc can be explained by mixed-potential theory assuming that the reactions were $Zn + 4\,OH^- \rightleftharpoons Zn(OH)_4^{2-} + 2e^-$ and $H_2O + e^- \rightleftharpoons \frac{1}{2}H_2 + OH^-$. Good agreement between theoretical curves obtained by computer solution of the kinetic equations corresponding to the above reactions and actual polarization measurements was obtained in the absence and presence of zincate. Theoretical and experimental corrosion rates also agreed well. Binary Zn-Pb alloys [0.2-1.0 w/o (weight per cent)] and Zn-Al alloys (0.2-0.8 w/o) made up from high-purity metals had r_{H_2}-values which were lower than those for zinc, while r_{H_2}-values of commercial zinc alloys were much higher than those of zinc, most likely due to the presence of low overvoltage impurities such as Cu, Ni, or Fe. Addition of 10^{-3}M copper, tin, or lead ions to the electrolyte also influenced r_{H_2}, which in the presence of metal ions noble to zinc is no longer equivalent to the corrosion rate. The strong increase of r_{H_2} in the presence of Cu ions is explained by the low hydrogen overvoltage of Cu, while the decrease of r_{H_2} in the presence of Pb ions is explained by the high hydrogen overvoltage of Pb. Anions such as Cl^- or Br^- do not affect r_{H_2}. In the presence of thiourea, r_{H_2} increases steadily, while S^{2-} leads to severe corrosion.

The rate of hydrogen evolution on zinc in slightly acid and in concentrated alkaline solutions has been measured on zinc sheets, rods, powders, and on battery electrodes. Correlation of the few data obtained until now is very difficult. Dirkse and Timmer (1) found a decrease of the rate of hydrogen evolution (r_{H_2}) on zinc wire (99.999%) in 20-45% KOH with increasing concentration of KOH, saturation of the electrolyte with ZnO, or amalgamation of the wire. Oxley and Humphrey (2) observed that As, Co, and Cu ions increased r_{H_2} on zinc ribbon (99.99%) in 30% KOH at 60°C in measurements which extended over several days, while Sn, Cd, and Pb ions decreased r_{H_2}, Pb having the most pronounced effect. The effect of Pb was also observed at a practical zinc electrode, although to a somewhat smaller extent. Additions of zincate also lowered r_{H_2} as observed in (1). The effect of additions of metal ions to the electrolyte has been also studied by Era *et al.* (3) on zinc sheets (99.99%) in a solution of 25% NH_4Cl + 10% $ZnCl_2$ + HCl at pH = 5, 50°C. Additions of Pb decreased r_{H_2}, while Fe, Cu, Ni, As, and Sb increased r_{H_2} in tests which were conducted for 14 days. Krug and Borchers (4) found that alloying with Fe (up to 310 ppm) increased r_{H_2} in a solution of 1% NH_4Cl + 0.12% HCl (pH = 2) at 45°C; alloying with Pb up to 1% reduced this increase. Zinc alloys with small additions were studied earlier by Vondracek and Izak-Krizko (5) who found that, in 0.5*N* H_2SO_4, additions of Cd, As, Sn, Sb, Fe, and Cu increase r_{H_2}, while additions of Al, Pb, and Hg decrease r_{H_2}.

* Electrochemical Society Active Member.
[1] Present address: Science Center, North American Rockwell Corporation, Thousand Oaks, California 91360.
Key words: hydrogen evolution, electrode kinetics, zinc and zinc alloys, alkaline batteries.

It is difficult to arrive at mechanistic interpretations or even to derive general trends, based on the experiments cited above, since the data are scanty for the considerable number of experimental parameters being varied. The present study of the effect of Pb and other metal ions on corrosion and hydrogen evolution on zinc was made as a logical sequel to the authors' (6) previous studies of the effect of Pb ions on Zn dissolution and deposition. The topic is of additional interest from a theoretical standpoint since it was reported in (2) that current-voltage curves in 30% KOH at room temperature exhibited a higher hydrogen overvoltage on zinc than on all other metals studied in (2). The authors point out that the overvoltage characteristics of the metal added to the electrolyte alone cannot explain the observed behavior.

The corrosion potential of zinc in a solution of KOH is a mixed potential, the partial oxidation reaction being

$$Zn + 4\,OH^- = Zn(OH)_4^{2-} + 2e^- \qquad [1]$$

while the partial reduction mechanism is

$$H_2O + e^- = \tfrac{1}{2}H_2 + OH^- \qquad [2]$$

The relationship between current and potential for reaction [1] can be expressed as (7)

$$i_{Zn} = i_{Zn}^{o}\,\frac{\exp\left\{\frac{n\alpha_{Zn}\mathbf{F}}{RT}\Delta\phi_{Zn}\right\} - \exp\left\{-\frac{n(1-\alpha_{Zn})\mathbf{F}}{RT}\Delta\phi_{Zn}\right\}}{1 + \frac{i_{Zn}^{o}}{i_{Zn}^{L}}\exp\left\{\frac{-n(1-\alpha_{Zn})\mathbf{F}}{RT}\Delta\phi_{Zn}\right\}} \qquad [3]$$

where i_{Zn}^{o} is the exchange C.D. for reaction [1], $\Delta\phi_{Zn}$ the deviation from the reversible potential ϕ_{rev} of reaction [1] and i_{Zn}^{L} is the limiting C.D. for zinc deposition. The other symbols have their usual meaning. The form of Eq. [3] results from the fact that there is a limiting diffusion C.D. for metal deposition, but not for metal dissolution under ordinary corrosion conditions (7). If it is assumed that the concentration of zincate in the electrolyte is small (corroding zinc specimen in pure KOH) with a value of $C_{Zn(OH)_4^{2-}} = 10^{-5}$M, one obtains

$$i_{Zn}^{L} = 2\mathbf{F}DC/\delta = 1.4 \times 10^{-6}\ A/cm^2 \qquad [4]$$

by assuming a value for the diffusion coefficient D of 7×10^{-6} cm^2/sec (7) and a value of $\delta = 10^{-2}$ cm (unstirred solutions).

Theoretical polarization curves according to Eq. [3] have been calculated using an IBM 7094 computer for values of i_{Zn}^{o} from 10^{-1} to 10^{-6} A/cm^2 using $n = 2$, $\alpha = 0.5$, and $T = 298$°K (Fig. 1). ϕ_{Zn}^{rev} was calculated (8) as -532 mV with respect to a hydrogen electrode in the same solution,[2] pH = 14 and $C_{Zn(OH)_4^{2-}} = 10^{-5}$M.

The hydrogen-evolution reaction [2] can be expressed by the simple relationship

$$i_H = i_H^{o}\left[\exp\left\{\frac{(1-\beta_H)\mathbf{F}}{RT}\phi\right\} - \exp\left\{\frac{-\beta_H\mathbf{F}}{RT}\phi\right\}\right] \qquad [5]$$

Plots of ϕ *vs.* log i_H, assuming values of i_H^{o} from 10^{-10} to 10^{-8} A/cm^2 and $\beta_H = 0.5$ are also given in Fig. 1. Their intersection with the anodic part of the zinc curves gives the corrosion potentials and currents. It is evident that for the range of i_H^{o} values under consideration here, the value of i_{Zn}^{o} would have to be decreased drastically by additives to the electrode or electrolyte (to $<\sim 10^{-5}$ A/cm^2) from the literature value of 0.1 A/cm^2 (9) before there is an effect on the corrosion potential and corrosion current density. Significant effects on both these quantities will, however, always be produced by variations in i_H^{o}.

[2] All potentials cited in this paper are based on this electrode.

If the ion of a metal which is more noble than zinc (*e.g.*, Cu, Pb, Sn) is added to the electrolyte, an additional reduction process will occur and the corrosion current will increase, if the hydrogen overvoltage stays constant

$$i_{corr} = i_{Zn}^{ox} = i_H(\phi_{corr}) + i_{Me}^{red}(\phi_{corr}) \qquad [6]$$

where $i_H(\phi_{corr})$ and $i_{Me}^{red}(\phi_{corr})$ are the respective hydrogen and metal reduction currents at ϕ_{corr}. In this case a measurement of the rate of hydrogen evolution cannot give the exact value of the corrosion C.D., a fact which has been overlooked in previous work (2-5). Figure 2 shows this relationship for the same conditions as in Fig. 1 with the current-voltage curve for metal ions other than zinc added. It is assumed that ϕ_{rev}^{Me} of these metal ions is sufficiently noble to ϕ_{rev} of zinc; the reduction process is therefore completely under diffusion control. For the values of i_H assumed, $i_{Me}^{red}(\phi_{corr})$ is larger than $i_H(\phi_{corr})$ and

$$i_{corr} \approx i_{Me}^{red}(\phi_{corr}) \qquad [7]$$

For this case, corrosion potential and current are almost independent of the parameters of hydrogen evolution. Polarization curves in the anodic region are independent of i_H^{o} and i_{Zn}^{o} as long as $i_{Zn}^{o} > 10^{-3}$ A/cm^2.

In the present work the effect of addition of ions, neutral molecules, or metal cations to the electrolyte and alloying of small amounts of metals to zinc has been investigated and an attempt has been made to explain the results obtained by the mechanism outlined below.

Experimental

Zinc rod used for studies of hydrogen evolution was of 99.999% purity.[3] Alloys of Zn-Pb and Zn-Al were made by Ventron Electronics Corporation from Zn(99.999%), Pb(99.99%), and Al(99.98%). The content of Pb or Al was increased step-wise from 0.2 to 1.0 w/o. The commercial alloys Zamak 3, 5, and 7, and zinc alloy "955" were donated by Belmont Smelting and Refining Works, Incorporated, Brooklyn, New York. A typical analysis is given in Table I.

Solutions of 6*N* KOH were prepared using AR grade KOH pellets and triple-distilled water (quartz still).

[3] The effect of purity and temperature is reported in (18).

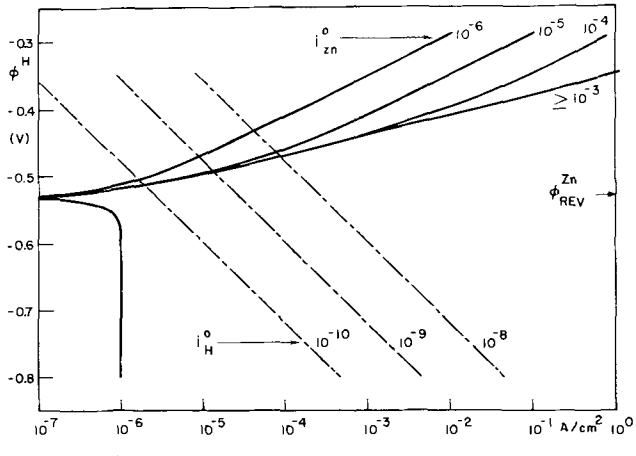

Fig. 1. Theoretical Tafel plots for the zinc dissolution-deposition and hydrogen evolution processes as a function of the exchange current density: ——— Eq. [3], — — — Eq. [6] (assuming $\alpha_{Zn} = \beta_H = 0.5$, $n = 2$, $\phi^{Zn}_{rev} = -0.532$V, $i_{Zn}^{L} = 10^{-6}$ A/cm^2, $T = 298$°K).

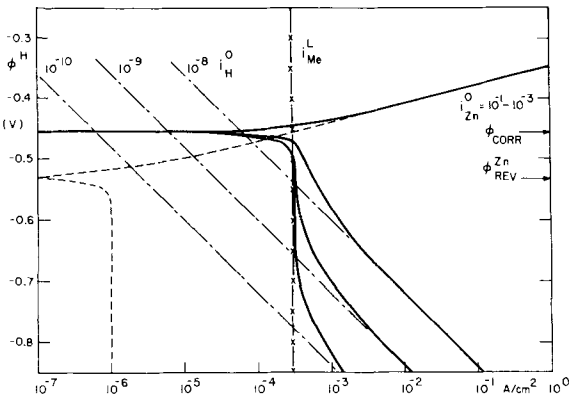

Fig. 2. Theoretical Tafel plots for reactions at a zinc electrode in the presence of added reducible metal ions: ——— Zn dissolution-deposition (Eq. [3], assuming $i_{Zn}^0 \geq 10^{-3}$ A/cm²); — — — — hydrogen evolution (Eq. [6]); x – x – deposition current, i_{Me}^L, for added metal ions; ——— Over-all reaction.

The rate of hydrogen evolution (r_{H_2}) was measured in cells as proposed in (3) or (10) in a water-thermostat at 25°C. Lead was added to the electrolyte as the acetate, tin and copper as chlorides. These, and all other additives, were of AR grade purity.

Zinc electrodes (zone refined) were degreased in benzene for 5 min at 80°C and then etched for 2 min in 10% $HClO_4$. Samples of Pb and Sn were etched in 5% HNO_3. The electrodes were then washed with distilled H_2O and immediately immersed in the electrolyte. Polishing with emery paper was avoided, since this led to irregular behavior in some cases.

Polarization curves were carried out in deaerated 6*N* KOH at room temperature (24° ± 1°C) using zinc rod counterelectrodes and a hydrogen electrode in the same solution as reference electrode. When polarization curves on Pb or Sn were measured, Pt counterelectrodes were used, since it was observed that small amounts of zincate produced while the working electrode was cathode diffused from the counterelectrodes to the Pb or Sn electrode and were reduced or oxidized during potential sweeps from the rest potential of Pb or Sn to H_2 evolution and back.

Potentiostatic polarization curves were obtained using a Tacussel potentiostat and function generator. Values of current were recorded on a Moseley strip chart or X-Y recorder and the potential was monitored on a Keithley electrometer. Runs were usually started at a potential of −900 mV. The potential was then increased step-wise in the noble direction and the current recorded after 1 min at each potential. To obtain a quick survey of the polarization behavior of zinc or the zinc alloys, cyclic voltammetry was carried out between −1.5 and +3.0V at sweep speeds of 4.5-45 mV/sec. When the effect of such additives to the electrolyte as Sn, Pb, Sn, and Cu ions was studied, runs were started at the corrosion potential and the potential was increased step-wise to more cathodic values.

Results

Corrosion tests.—The effect of metal ions in the electrolyte on r_{H_2} is shown in Fig. 3. While additions of

Table I. Typical analyses of Asarco die casting alloys

	Zamak 3	Zamak 5	Zamak 7	"955"*
Mg	0.03-0.04%	0.03-0.04%	0.010-0.020%	
Pb	0.002	0.002	0.002	
Cd	<0.001	<0.001	<0.001	
Sn	n.d.	n.d.	n.d.	
Fe	0.001	0.001	0.001	
Al	4.0	4.0	4.0	5.5
Cu	<0.01	1.0	<0.01	
Ni	—	—	0.007	
Zn	Balance	Balance	Balance	

* No exact analysis for the alloy "955" was obtained.

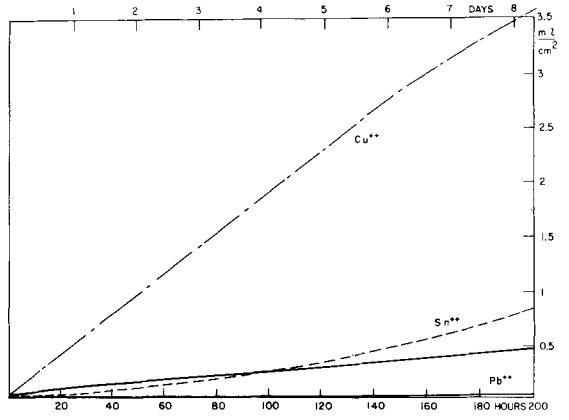

Fig. 3. Effect of 10^{-3}M of $CuCl_2$, $SnCl_2$, or PbAC on hydrogen evolution from zinc; 6*N* KOH, 25°C.

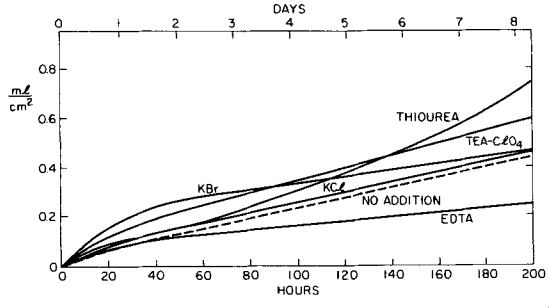

Fig. 4. Effect of 10^{-3}M of KCl, KBr, tetraethylammonium-ClO_4, thiourea and EDTA on hydrogen evolution from zinc; 6*N* KOH, 25°C.

10^{-3}M Cu markedly increase r_{H_2}, additions of 10^{-3}M Pb decrease r_{H_2}. The effect of 10^{-3}M Sn is the same as observed in 0.5*N* H_2SO_4 (5) for a Zn-1% Sn alloy. The curves of hydrogen evolution *vs.* time for pure Zn-Pb and Zn-Al alloys were similar in appearance to those of zinc. The r_{H_2} values are summarized in Table II, which also contains the values for the commercial die casting alloys. The rate of hydrogen evolution was lower for the Zn-Pb alloys than for zinc; it was also lower for the Zn-Al alloys except for the alloy with the highest Al content. The commercial zinc alloys have much higher r_{H_2} values, especially the alloy containing 1% Cu. Additions[4] of KCl apparently do not change r_{H_2} (Fig. 4), while the Br^- ions increase r_{H_2} in the initial stage of the experiments. Tetraethylammonium-perchlorate increases and EDTA lowers r_{H_2},

[4] The concentration of additions was 10^{-3}M.

Table II. Corrosion rates r_{H_2} $\left[\frac{\text{ml } H_2}{\text{cm}^2 \text{ day}}\right]$ of zinc and zinc alloys

Specimen	r_{H_2} (5 hr)	r_{H_2} (29 hr)	r_{H_2} (53 hr)	r_{H_2} (200 hr)
Zinc 99.999%	f(t)	0.065	0.050	0.050
Zn-Pb-alloys				
0.2 w/o	f(t)	0.011	0.011	0.011
0.4 w/o	f(t)	0.009	0.009	0.009
0.6 w/o	f(t)	0.067	0.023	0.023
0.8 w/o	f(t)	0.026	0.013	0.013
1.0 w/o	f(t)	0.010	0.010	0.010
Zn-Al-alloys				
0.2 w/o	f(t)	0.026	0.026	0.026
0.4 w/o	f(t)	0.009	0.009	0.012
0.6 w/o	f(t)	0.009	0.009	0.012
0.8 w/o	f(t)	0.042	0.042	0.042
1.0 w/o	f(t)	0.29	0.29	0.29
"955"	6.5	3.4	3.4	—
Zamak 3	8.9	5.0	7.0	—
Zamak 5	17.6	11.0	11.0	—
Zamak 7	7.2	3.4	2.3	—

while r_{H_2} increases steadily in the presence of thiourea. The S^{--} ion had a catastrophic effect on the zinc: after several hours r_{H_2} increased greatly, the specimen was full of holes and deep pits, while a white deposit (probably ZnS) covered the bottom of the test cell.

Polarization curves.—In order to obtain a better understanding of the effect of additives on the rate of hydrogen evolution and corrosion of zinc, polarization curves have been recorded for pure zinc (with or without additions to the electrolyte) and for zinc alloys. Figure 5 shows a polarization curve for zinc in 6*N* KOH, 25°C in the region of hydrogen evolution and active dissolution. Included for comparison is a theoretical curve using Eq. [3] and [5] for $i_H{}^o = 10^{-9}$ A/cm² and $i_{Zn}{}^o = 10^{-1}$ A/cm², $i_{Zn}{}^L = 10^{-6}$ A/cm², $\phi^{Zn}{}_{rev} = -532$ mV, $\alpha = \beta = 0.5$. The agreement is very good considering that only approximate values were chosen for these parameters. The corrosion potential obtained in this measurement was −505 mV, which agrees well with corrosion potentials extrapolated from measurements of Bartelt and Landsberg (11). The corrosion C.D. obtained by extrapolation from the anodic Tafel line to the corrosion potential was found to be 7 μA/cm² corresponding to a corrosion rate of 20 mdd, compared to a theoretical value of 13 μA/cm² obtained by the same extrapolation, *i.e.* 38 mdd. The initial rate of H_2 evolution in corrosion tests at 25°C was 0.065 ml/cm² day which corresponds to 10 mdd. The satisfactory agreement of two independent measurements (10 and 20 mdd) with theoretical value (38 mdd) shows that the corrosion behavior of zinc in 6*N* KOH in the absence of additives can be very well explained by the mechanisms in Eq. [3] and [5].

Polarization curves in the active and passive region for zinc and the commercial die-casting alloys were rather similar except for a lowering of oxygen overvoltage produced by the alloyed impurities. Curves for the pure Zn-Pb and Zn-Al alloys were very similar to those of pure zinc.

Figure 6 shows the effect of addition of ZnO to the electrolyte on the shape of the polarization curves. A plot of the limiting C.D. for zinc deposition in the concentration range of 10^{-3}M to 0.25M ZnO *vs.* concentration gave a value of $D/\delta = 2.9 \times 10^{-4}$ cm/sec. This value justifies the value for $i_{Zn}{}^L$ of 10^{-6} A/cm² used for the theoretical curves in Fig. 1, where it was assumed that a "pure" solution of KOH contains about 10^{-5}M of zincate (based on polarization curves measured in KOH equilibrated with Zn) due to the corrosion of zinc. Higher amounts of ZnO decrease the critical C.D. for passivation of zinc and lead to passivation at a more active potential. Theoretical corrosion rates as a function of ZnO concentration, have been calculated using values of $i_{Zn}{}^L$ based on the experimental value of $D/\delta = 2.9 \times 10^{-4}$ cm/sec, values of $\phi^{Zn}{}_{rev}$ from Ref. (8) and assuming no effect of zincate additions on $i_H{}^o$ which was again taken as 10^{-9} A/cm². Table III shows theoretical and experimental values for the corrosion potential and corrosion rates. Agreement is fair except at high ZnO concentration.

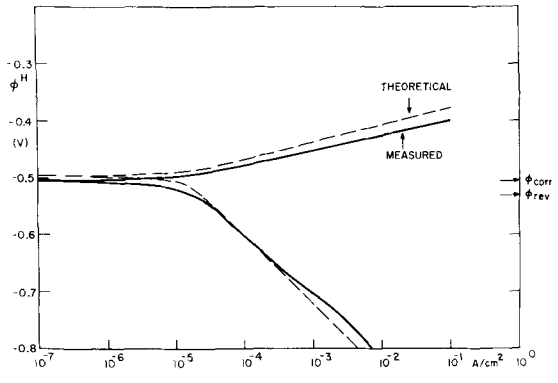

Fig. 5. Theoretical and measured polarization curves on zinc in 6*N* KOH, 25°C.

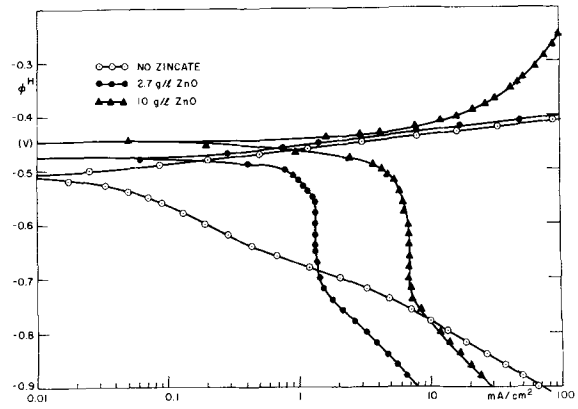

Fig. 6. Polarization curves for zinc with and without additions of ZnO, 6*N* KOH, 25°C.

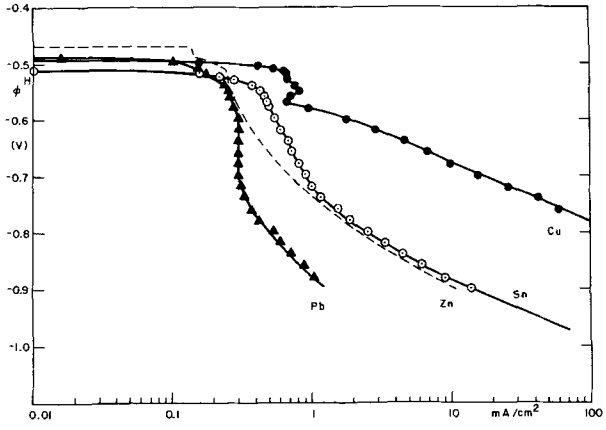

Fig. 7. Polarization curves for zinc in the presence of 10^{-3}M of ZnO, $CuCl_2$, $SnCl_2$, or PbAC; 6*N* KOH, 25°C.

The effect of additions of 10^{-3}M Cu, Sn, Pb, or Zn to the electrolyte on the polarization behavior of zinc in 6*N* KOH is shown in Fig. 7. Copper decreases hydrogen overvoltage markedly, Sn seems to have no effect compared to a solution containing equal amounts of zincate, while Pb increases overvoltage for hydrogen evolution markedly. The limiting C.D. for deposition of all these metals on zinc is near the value for Pb of 3×10^{-4} A/cm² which was used in Fig. 2. A comparison of Fig. 7 and Fig. 2 shows good agreement of theoretical and measured polarization curves in the regions of the limiting C.D. and hydrogen evolution. According to these curves, the exchange C.D. for the hydrogen evolution reaction on zinc in the presence of 10^{-3}M Cu would be between 10^{-8} and 10^{-7} A/cm², and between 10^{-11} and 10^{-10} A/cm² in the presence of 10^{-3}M Pb. Measurements of polarization curves on pure Sn or Pb in deaerated 6*N* KOH (Fig. 8) are not easy to interpret since Tafel behavior was not found, which is partly due to hydride formation observed at more negative potentials for both metals. In general it seems that the overvoltage for hydrogen evolution is somewhat higher for Pb than for Sn and that both metals have a higher hydrogen overvoltage than zinc, contrary to what was observed by Oxley and Humphrey (2).

Table III. Corrosion potentials and rates of hydrogen evolution as a function of ZnO additions to 6*N* KOH, 25°C

[ZnO] (mole/liter)	$\phi^{exptl}{}_{corr}$ (mV)	$\phi^{th.}{}_{corr}$ (mV)	$r_{H_2}{}^{exptl}$ (mdd)	$r_{H_2}{}^{th.}$ (mdd)
0	−497	−497	8	38
0.0625	−445	−419	—	9
0.125	−446	−410	1.8	7
0.25	−436	−401	0.8	6

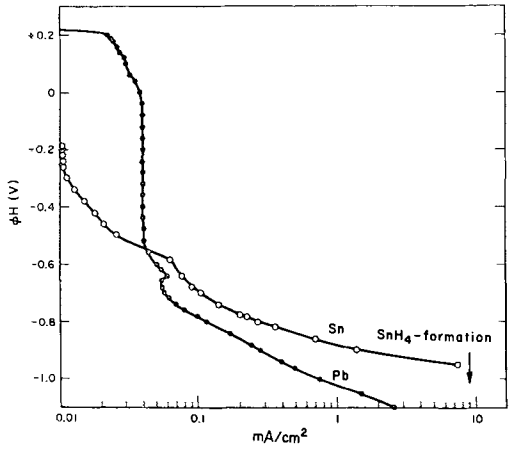

Fig. 8. Polarization curves for tin (AR) and lead (99.999%) in 6*N* KOH, 25°C.

Discussion

The good agreement between experimental and theoretical corrosion rates (Table III) and polarization curves (Fig. 5) confirms our assumption that the corrosion behavior of zinc in KOH can be readily explained by mixed potential theory; zinc metal is oxidized to the zincate ion, while water is reduced to hydrogen gas. It is not necessary to consider the rate of dissolution of interfacial ZnO or $Zn(OH)_2$ as rate controlling as done by Rüetschi (10) and partly by Dirkse and Timmer (1). The formation of ZnO or $Zn(OH)_2$ in 6*N* KOH at the rest potential seems unlikely, since the reversible potential for these reactions is more noble than the observed corrosion potential of zinc. An over-all reaction similar to the one assumed by Dirkse and Timmer (1)

$$Zn + 2H_2O \rightleftharpoons H_2 + Zn(OH)_2 \qquad [8]$$

with a reversible potential of $\phi_{rev} = -439$ mV (12) is not consistent with a corrosion potential of $\phi_{corr} = -497$ mV in 6*N* KOH, 25°C.

The effect of addition of the metal cations Cu, Sn, or Pb on hydrogen evolution rates and polarization behavior can be explained only on a qualitative basis since a third process (reduction of the metal ions) is added to the process of zincate formation and water reduction. In this case a measurement of r_{H_2} no longer gives the exact value of corrosion rates (Eq. [6]). It seems, however, still possible to explain the changes of r_{H_2} (Fig. 3) by assuming that the large increase of r_{H_2} upon additions of Cu results from a lowering of hydrogen overvoltage on the surface of the test specimen, while the decrease of r_{H_2} upon additions of Pb results mainly from an increase of hydrogen overvoltage. The high rate of hydrogen evolution of the commercial alloys (Table II) must result from low overvoltage impurities[5] and, characteristically, the alloy containing 1% Cu (Zamak 5) has the highest corrosion rate.

The effect of zincate (Table III) can be explained by mixed potential theory by considering the decrease in r_{H_2} and the shift of the polarization curve of zinc in the noble direction as zincate is added to the electrolyte (ϕ^{Zn}_{rev} becomes more noble). The fact that experimental corrosion rates are lower and experimental corrosion potentials more active than the theoretical values based on constant hydrogen overvoltage could be explained using the suggestion by Dirkse and Timmer (1) that dissolved zincate lowers the activity of water according to

$$ZnO + H_2O + 2\,OH^- \rightleftharpoons Zn(OH)_4^{2-} \qquad [9]$$

which thereby increases the hydrogen overvoltage slightly. Evidence for this can be found in Fig. 6 where increasing amounts of zincate increase hydrogen overvoltage at the most negative potentials.

From Eq. [3] it follows that for $i^o_{Zn} \geq 10^{-3}$ A/cm^2, variations in the value of i^o_{Zn} caused by additions to the electrolyte or the electrode would not influence the polarization curve for zinc oxidation. It is for these reasons not expected that anions which, through adsorption, affect the dissolution of other metals, as for example of Fe in H_2SO_4 (14), would have a similar effect for zinc in KOH. An effect of anions is unlikely also in view of the fact that the point of zero charge for zinc is approximately at +0.16V *vs.* hydrogen electrode at *p*H = 14 (15) and therefore noble to the corrosion potential of zinc by about 0.7V. In fact, as can be seen from Fig. 4, addition of KCl had no effect of r_{H_2}, while the effect of KBr is small. The small increase in r_{H_2} in the presence of tetraethylammonium ions is presumably due to the effect of specific adsorption on the kinetics of hydrogen evolution (16). The tremendous effect of the S^{2-} ion also observed by Merkulov and Flerov (17) might result from formation of ZnS, while the effect of thiourea (Fig. 4) which produced a constantly increasing corrosion rate might result from complex formation between the sulfur group and the zinc.

Conclusions

1. The polarization and corrosion behavior of zinc with and without additions of zincate is accounted for by mixed potential theory. In the presence of metal cations which are more noble than zinc and which therefore plate out on zinc at the rest potential, the rate of hydrogen evolution can increase or decrease, depending on the relative values of hydrogen overvoltage of zinc and the metal deposit on zinc.

2. The low corrosion rates of Zn-Pb alloys suggest that the rate of hydrogen evolution of zinc can be lowered if the impurity level of the electrode is carefully controlled. This and the beneficial effect of lead additions to the electrolyte on growth morphology reported by the authors (6) explain the beneficial action of lead in zinc batteries.

3. The expected absence of an effect of inorganic anions on gassing rates has been confirmed experimentally.

4. Compounds containing sulfur and especially the $S^=$ ion must be avoided since they increase hydrogen evolution rates to very high values.

Acknowledgments

One of the authors (F.M.) acknowledges support under a National Academy of Sciences Postdoctoral Research Associationship. The authors are indebted to Dr. M. Salomon for the writing of the computer program and many helpful discussions, and to Dr. A. Glatz and Mr. A. Pinella for help and advice in metallurgical questions.

Manuscript submitted Jan. 30, 1970; revised manuscript received *ca.* June 1, 1970.

Any discussion of this paper will appear in a Discussion Section to be published in the June 1971 JOURNAL.

REFERENCES

1. T. P. Dirkse and R. Timmer, *This Journal,* **116,** 162 (1969).
2. J. E. Oxley and J. R. Humphrey, Final Report for NASA, Contract NAS 7-671, July 22-Oct. 22, 1968.
3. A. Era, Z. Takehara, and S. Yoshizawa, *Electrochim. Acta,* **13,** 383 (1968).
4. H. Krug and H. Borchers, *ibid.,* **13,** 2203 (1968).
5. R. Vondracek and I. I. Izak-Kriszko, *Rec. Trav. Chim.,* **44,** 376 (1925).
6. F. Mansfeld and S. Gilman, *This Journal,* **117,** 588 (1970).
7. H. Kaesche, "Die Korrosion der Metalle," Springer-Verlag, Berlin, Heidelberg, New York (1966).
8. F. Jolas, *Electrochim. Acta,* **13,** 2207 (1968).
9. J. P. G. Farr and N. A. Hampson, *J. Electroanal. Chem.* **13,** 433 (1967).

[5] Although the typical analysis (Table I) shows a Fe content of only 0.001%, it is possible that the alloys contain more Fe if prepared in Fe containers, a possibility discussed by Drotschmann (13).

10. P. Rüetschi, *This Journal*, **114**, 301 (1967).
11. H. Bartelt and R. Landsberg, *J. Phys. Chem.* **222**, 217 (1963).
12. M. Pourbaix, "Atlas of Electrochemical Equilibria in Aqueous Solutions," Pergamon Press (1966).
13. C. Drotschmann, *Korrosion*, **19**, 156 (1965).
14. G. M. Florianovitch, L. A. Sokolova, and Ya. M. Kolotyrkin, *Electrochim. Acta*, **12**, 879 (1967).
15. L. I. Antropov, "Kinetics of Electrode Processes and Null Points of Metals," Council of Scientific and Industrial Research, New Dehli (1960).
16. K. J. Vetter, "Electrochemical Kinetics," p. 567 Academic Press, New York London (1967).
17. A. V. Merkulov and V. N. Flerov, *Elektrokhimiya*, **4**, 587 (1968); *Soviet Electrochemistry*, **4**, 527 (1968).
18. F. Mansfeld, Submitted for publication in *Electrochim. Acta*.

Anodic Discharge of Chloride Ions on Pt-Ir Alloy Electrodes

G. Faita and G. Fiori

Laboratory of Electrochemistry and Metallurgy, University of Milan, Milan, Italy

and A. Nidola

Oronzio De Nora-Impianti Elettrochimici, Milan, Italy

ABSTRACT

The behavior of Ti-supported Pt-Ir alloys in the electrolysis of NaCl has been examined as a function of Ir content, NaCl concentration, and electrolysis time. Short-time experiments show that an iridium content as low as 0.5% is sufficient to eliminate almost completely the passivation effects (in 1M and saturated NaCl solution). Long-run experiments make clear that the minimum percentage of 5/10% Ir is necessary in order to have low potentials after thousands of hours; in such a case, however, complicating factors such as mechanical stability and chemical corrosion should be taken into account.

It is known that Pt electrodes undergo strong passivation (1) when used as anodes in brine electrolysis. A previous work (1) showed that Pt-Ir electrodes (30% Ir) do not passivate under similar experimental conditions. The aim of the present paper is to deal with the behavior of Pt-Ir electrodes as function of Ir content, NaCl concentration, and electrolysis time.

Experimental Methods

The measurements were carried out by means of a rotating disk electrode (2); this equipment allows the Cl_2 bubbles to be quickly removed from the surface. Consequently, currents and potentials are highly stable and their value can be read with sufficient precision and accuracy.

Pt, Pt-Ir alloys, and Ir coatings were obtained by a new thermal method (3): the titanium matrices were turned into a cylindrical shape (10 mm diameter) and were degreased, ground, and painted with a mixture containing $(NH_4)_2PtCl_6$ and $(NH_4)_2IrCl_6$ in the suitable ratio (see below). The painting was followed by decomposition at 500°C in air; the sequence, painting and decomposition, was repeated five times. Annealing at 550°C (2 hr) and air quenching completed the thermal treatment.

In the case of 30% Ir alloy, the following amount of mixture was applied to each square centimeter:

$(NH_4)_2PtCl_6$	6.4 mg
$(NH_4)_2IrCl_6$	2.8 mg
NH_4Cl	1-4 mg
$HCONH_2$	0.2-0.5 ml
Polyrad 1110/A (Hercules)	0.1-0.3 ml

The same amount of mixture was used in the preparation of the other alloys, the only difference being in the ratio of Pt and Ir salts.

Key words: chlorine electrochemistry, chlorine Pt/Ir electrodes, anode chlorine evolution.

Electrochemical measurements were carried out both in potentiostatic and galvanostatic conditions; electrode potentials were read by means of a 610B Keithley electrometer and were freed from ohmic drop contributions. These were determined by the usual current interruption technique, using a Tektronix mod. 531A oscilloscope and a transistor-driven mercury relay. Typical rise times were in the 1.5-2μs range. Before each experiment, the electrodes were brought to a reproducible state of activity by polarizing for 10 sec alternatively at 1.7V (NHE) and at −0.4V (NHE) for ten times. In addition, before each measurement the electrodes were held at −0.4V (NHE) for 3 sec: this treatment appeared to remove all oxides from the electrode surface. During each experiment, nitrogen containing 1% chlorine was bubbled through the NaCl solutions whose *pH* was held to a value of 3.

Results

Potentiostatic measurements.—In 0.1M NaCl (Fig. 1), all electrodes follow the Tafel law (slope: 0.03V/decade of current) up to 40 mA/cm^2; at higher current densities, Pt and Pt-Ir 0.5% show a kind of limiting current which can be attributed to a passivation process (see discussion below).

Ir, Pt-Ir 4%, Pt-Ir 2% show quite smaller deviations from the Tafel straight line at current densities above 90 mA/cm^2.

In 1M and saturated NaCl solution, the electrode behavior is qualitatively similar to that in 0.1M NaCl: again, the electrodes follow Tafel law with a slope of 0.03V/decade of current. Pt shows clearly a beginning of passivation (see discussion below) at 140 mA/cm^2 in 1M NaCl and 300 mA/cm^2 in saturated NaCl solution.

It must be mentioned that the potentiostatic measurement current values were always read after 15 sec.

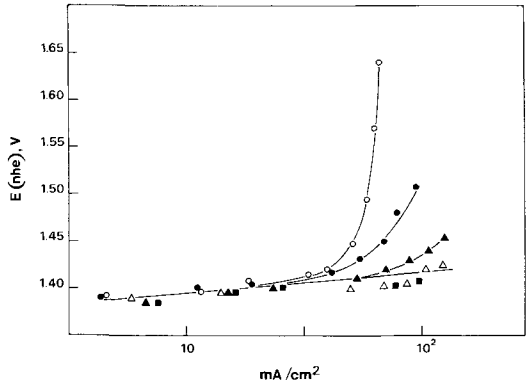

Fig. 1. Polarization curves in 0.1M NaCl, pH = 3, Cl_2 1%, T = 30°C, rotation speed = 2800 rpm. ○, Ti/Pt; ●, Ti/Pt-Ir (0.5%); △, Ti/Pt-Ir (2%); ▲, Ti/Pt-Ir (4%); ■, Ti/Ir.

Galvanostatic measurements.—Figure 4 shows the behavior in galvanostatic conditions (current density: 8 mA/cm²) in 0.1M NaCl: the increase in potential difference with respect to the value after 15 sec ($\Delta\eta$) has been plotted against time. This difference is time dependent and increases as Ir content decreases.

The Pt-Ir alloys (5, 10, 20, and 30%) were also tested under more drastic conditions: 1 A/cm² (constant current density), 70°C, 310 g/l NaCl. In this case, the coatings were deposited on the Ti network by the previously described procedure and the electrodes were used as anodes in pilot brine cells.

From Fig. 5 it can be seen that Pt-Ir 20% and 30% display a potential as low as 1.6V (NHE) after 8000 hr of electrolysis, whereas the potential of the Pt-Ir 5% and 10% is higher than 2V (NHE) after 1000 and 7000 hr, respectively.

Pt electrodes show a sufficiently low potential, about 1.5V (NHE), during the first few hours of electrolysis. After this time, quick passivation takes place; *i.e.*, the electrode potential jumps to values of about 2.5-3.0V (NHE) in the space of a few minutes.

Discussion

The different behavior between Pt and Ir electrodes can be explained by the different properties of chemisorbed oxygen.

The chemisorbed oxygen on Pt is characterized by some degree of irreversibility: capacitance measurements (4), for instance, show that the "oxide" amount is nearly constant when the electrode potential is decreased from 1.4V (NHE) to 0.9V (NHE). A similar conclusion can be drawn from the analysis of the current/potential curves obtained when a periodic triangular voltage is applied potentiostatically to the electrode (4).

In addition, it has been found (5) that the building up of the "oxide" layer on Pt starts at more anodic potentials in solutions containing halide ions; moreover, the amount of chemisorbed oxygen decreases when halide ion concentration increases. In the short-time experiments (5), the oxygen chemisorption disappears almost completely when chloride ion concentration is higher than 0.01M.

More likely, under these conditions oxygen adsorption has been considerably slowed down rather than completely prevented. Now from Fig. 1 to 3 it can be concluded that Cl^- ions are discharged at a Pt electrode at low potentials only when the surface is free from chemisorbed oxygen, whose formation rate is inversely proportional to Cl^- concentration and electrode potential. Clearly, the amount of chemisorbed oxygen is proportional to the electrolysis time; this means that under potentiostatic conditions the current values decrease with time, whereas under galvanostatic conditions the electrode potentials increase with electrolysis time (see Fig. 4).

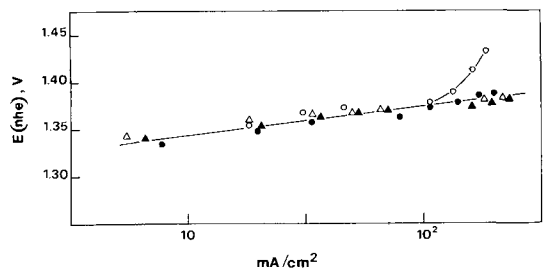

Fig. 2. Polarization curves in 1M NaCl, pH = 3, Cl_2 1%, T = 30°C, rotation speed = 2800 rpm. ○, Ti/Pt; ●, Ti/Pt-Ir (0.5%); △, Ti/Pt-Ir (2%); ▲, Ti/Pt-Ir (4%).

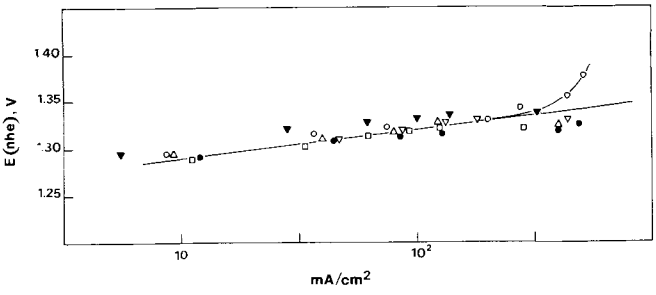

Fig. 3. Polarization curves in saturated NaCl, pH = 3, Cl_2 1%, T = 30°C, rotation speed = 2800 rpm. ○, Ti/Pt; ●; Ti/Pt-Ir (0.5%); △, Ti/Pt-Ir (2%); □, Ti/Pt-Ir (10%); ▽, Ti/Pt-Ir (20%); ▼, Ti/Pt-Ir (30%).

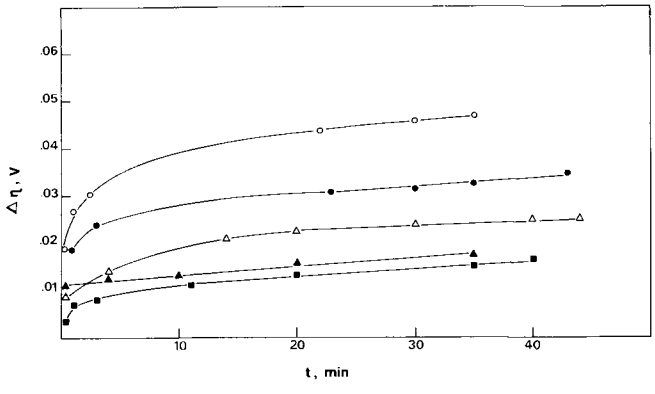

Fig. 4. Potential difference (with respect to the value after 15 sec) against time. Constant current density = 8 mA/cm². 0.1M NaCl, pH = 3, Cl_2 = 1%; T = 30°C, rotation speed = 2800 rpm. ○, Ti/Pt; ●, Ti/Pt-Ir (0.5%); △, Ti/Pt-Ir (2%); ▲, Ti/Pt-Ir (4%); ■, Ti/Ir.

Ir, on the contrary, shows a nearly reversible behavior with respect to the formation and removal of the chemisorbed oxygen (4). The breaking of the Ir-O bond is characterized by an absence of significant energy barrier; an irreversible passivation of the surface due to an "oxide" layer cannot take place (see Fig. 4).

As regards Pt-Ir alloys, the potentiostatic measurements (short-time experiments) in 1M and saturated NaCl solutions show that very low percentages (0.5%) of Ir are quite effective in decreasing the passivation effect (see Fig. 2 and 3). Long-run experiments (Fig. 5) show clearly that a minimum content of 5-10% in Ir is necessary in order to assure a lifetime of thousands of hours. In such a case, however, a number of phenomena must be taken into account, especially:

(*i*) mechanical stability related to gas evolution in the pores of the coating

(*ii*) chemical corrosion which can be brought about in the pores by the acidity due to some oxygen evolution.

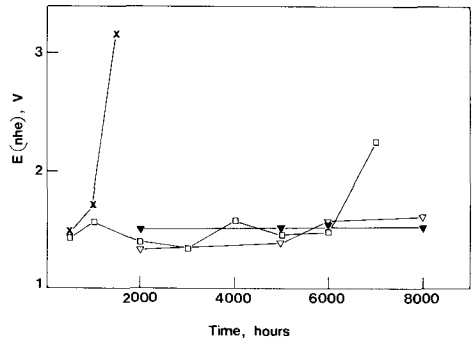

Fig. 5. Electrode potential as a function of electrolysis time. Constant current density = 1 A/cm^2. NaCl = 310 g/l, pH = 3, T = 70°C. ×, Ti/Pt-Ir (5%); □, Ti/Pt-Ir (10%); ▽, Ti/Pt-Ir (20%). ▼, Ti/Pt-Ir (30%).

It should be remembered that the lowest pH value where Pt is stable in the presence of the chlorine and chlorides is about 2. However, it is apparent that mechanical stability and chemical corrosion are negligible in short-time experiments where the catalytic properties of the electrode surface are predominant.

As regards the kinetics, it must be pointed out that all the electrodes show a Tafel b-coefficient equal to 0.03 V/decade of current; according to this low value, the electrode mechanism could be the following one

$$Cl^- \rightleftarrows Cl_{ads} + e$$
$$2Cl_{ads} \rightarrow Cl_2$$

The second step being rate determining.

Manuscript submitted March 9, 1970; revised manuscript received June 3, 1970.

Any discussion of this paper will appear in a Discussion Section to be published in the June 1971 JOURNAL.

REFERENCES

1. G. Faita, G. Fiori, and J. W. Augustynski, *This Journal*, **116**, 928 (1969).
2. G. Faita, G. Fiori, and J. W. Augustynski, *Electrochim. Metall.*, **2**, 437 (1967).
3. G. Bianchi and A. Nidola, I, 795, 565 (1.12.67).
4. M. W. Breiter, *Electrochim. Acta*, **8**, 973 (1963).
5. M. W. Breiter, *ibid.*, **8**, 925 (1963).

Technical Note

Polarization Cell for Potentiostatic Crevice Corrosion Testing

E. A. Lizlovs*

Climax Molybdenum Company of Michigan, Research Laboratory, Ann Arbor, Michigan 48106

Several electrochemical methods, including potentiostatic techniques, have been proposed in recent years for the investigation of crevice corrosion (1-6). In general, two major problems are involved in designing a suitable electrode for crevice corrosion studies: elimination of unwanted crevices while maintaining a well-defined exposed electrode area, and introduction of a reproducible crevice. Considering that fissures involved in crevice corrosion of stainless steels are of the order of 10^{-3} in. or less, both of these problems are quite formidable. The present investigation was prompted by the observations of crevice attack during potentiodynamic polarization experiments with stainless steels in hydrochloric acid (7). It was envisioned at that time that, if an appropriate working electrode could be designed, the potentiostatic polarization current in the passive state could be utilized to measure the progress of crevice corrosion. In addition, if reproducible crevices could be introduced in electrode design, the relative resistance to crevice corrosion of a series of alloys could be determined by comparing the polarization current at some selected potential.

Experimental

Crevice corrosion cell.—The polarization cell for the crevice corrosion studies consisted of a 5 in. long, 3½ in. diameter glass tubing mounted between two rectangular polycarbonate blocks. The essential parts of the cell are shown in Fig. 1. The cell was equipped with two 10/30 and two 24/40 standard taper ground glass necks to accommodate the electrolytic bridge from the reference electrode, inlet and outlet tubes for purging gas, and auxiliary platinum electrode, which was separated from the bulk of the solution by a fritted glass disk. The glass tube was mounted to polycarbonate blocks by placing the tube on the blocks in a proper position and applying silicone rubber (G.E. RTV-12 adhesive) around it and allowing the adhesive

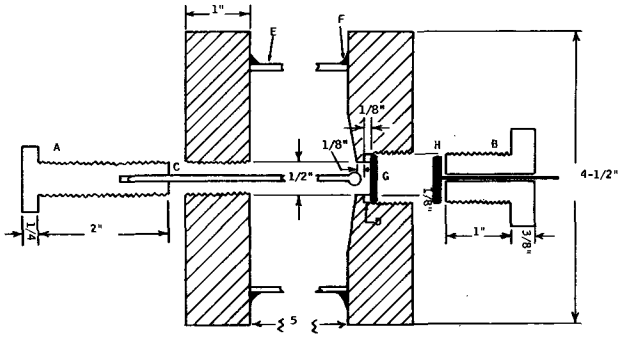

Fig. 1. Cross section through polycarbonate end-blocks and plastic bolts of crevice corrosion cell: A—Teflon bolt ½-20 thd; B—PVC bolt with hexagonal head, ⅞-14 thd; C—⅛ in. diameter glass rod with 4 mm diameter glass bead at the end; D—Teflon gasket, ⅛ in. thick by 0.810 in. OD; E—3 ½ in. OD glass tubing; F—silicone rubber mount; G—stainless steel working electrode; H—copper disk with copper lead wire.

* Electrochemical Society Active Member.

Key words: crevice corrosion, potentiostatic, testing, stainless steel, molybdenum, chloride.

Table I. Compositions of alloys studied

Alloy	Composition, %								
	C	Cr	Ni	Mo	Mn	Si	P	S	N
Type 304	0.063	18.55	10.48	—	1.72	0.43	0.026	0.013	—
Type 316	0.059	17.20	13.27	2.83	1.20	0.32	0.019	0.011	—
17% Cr	0.003	17.08	—	0.03	—	0.05	0.009	—	0.0065
17% Cr-3% Mo	0.003	16.68	—	2.99	—	0.06	0.007	—	0.0048
25% Cr	0.002	25.66	0.13	0.002	—	~0.02[a]	~0.01[a]	~0.002	~0.01[a]
25% Cr-3.5% Mo	0.002	25.58	0.13	3.49	—	~0.02[a]	~0.01[a]	~0.001	~0.01[a]

[a] Not analyzed but assumed to be approximately at indicated levels. See Ref. (9).

to solidify for a day. One of the end-blocks served as a working electrode holder. The design of the electrode holder was a modified version of the electrode holder described by France (8). The working electrode, which was a disk approximately ¾ in. in diameter, was pressed against a Teflon washer by a PVC[1] bolt. Electrical contact to the sample was established by a copper back-up disk and copper wire extending through the PVC bolt. The opposite end-block contained a threaded ½ in. diameter hole, concentric with the working electrode opening. This opening was fitted with a Teflon bolt with inserted glass rod with a smooth, approximately 4 mm diameter, glass bead at the end. A variable crevice was produced by advancing the bolt through the threaded hole until the bead was pressed against the surface of the working electrode. If the same glass bead is employed for all experiments, it can be assumed that crevices of equal geometries are produced. The crevice can be applied or removed as desired at any stage of the experiment by simply manipulating the Teflon bolt.

Materials.—Commercial stainless steels, Types 304 and 316, and high-purity laboratory alloys, 17% Cr, 17% Cr-3% Mo, 25% Cr and 25% Cr-3.5% Mo, were selected for the evaluation of the performance of the crevice corrosion cell and feasibility of the potentiostatic method for crevice corrosion tests. Chemical compositions of the steels are given in Table I.

Procedures.—All experiments were performed in N_2-saturated 1*N* NaCl at room temperature (24° ± 1°C). The working electrode was first polarized for 10 min at −1.00V (SCE), then the potentiostat was switched off for 10 min, and then switched on again. The potential of the working electrode was then carefully changed from −1.00 to −0.20V, and the electrode was passivated at this potential for 2 hr. Timing was started from the moment the polarization current fell down to 5 μA. After a 2 hr passivation, the potential was scanned from −0.20 to 0.00V at the rate of 0.15 mV/sec, and then the glass bead was pressed to the surface. The electrode with the "crevice applied" was kept at 0.00V for 1-3 hr, and then the crevice was removed. Polarization current and potential were recorded continuously throughout the above operations by a two-pen strip chart recorder.

After the experiment, the electrode was removed from the assembly and inspected for corrosion damage. Only those experiments were considered acceptable in which corrosion occurred under the glass bead and no place else.

Results and Discussion

A noticeable polarization current rise, indicating the onset of crevice corrosion, usually started almost immediately after the glass bead was pressed against the electrode surface. No critical potential for crevice corrosion was found and the attack could be initiated at potentials as low as −0.20V. Polarization current as a function of time for various stainless steel electrodes is shown in Fig. 2. Since the electrode area for samples was the same (1.26 cm^2) and the same glass bead was applied to the surface, the polarization current itself rather than current density may be used to compare the relative rates of crevice corrosion. Polarization current-time curves at 0.00V in the presence of a crevice were for the most part quite irregular and indicated a complex corrosion process. Comparison of the behavior of various grades of stainless steels and evaluation of the relative resistance to crevice corrosion, however, were possible. Type 304 and high-purity 25% Cr stainless steels showed about the same relative resistance to crevice corrosion and both materials repassivated immediately upon removal of the crevice. The high-purity 17% Cr alloy showed the highest polarization current of all materials over a 1 hr period and it did not repassivate immediately after removal of the crevice. Instead, the 17% Cr alloy continued to corrode at almost the same rate for at least 1 min after removal of the crevice, after which time the experiment was interrupted. Examination of the electrode showed that corrosion was localized under the glass bead. Apparently, for the 17% Cr alloy, a stable pit could be formed at 0 volt at the site of the crevice damage. Both Type 316 stainless steel and 17% Cr-3% Mo steel repassivated while the bead was still applied to the surface. The 17% Cr-3% Mo alloy repassivated within 30 min of the initiation of crevice corrosion, while Type 316 repassivated 90 min after crevice was applied. Apparently the potential of 0.00V was not sufficiently oxidizing to sustain corrosion under the bead for these alloys. Type 316 steel also showed higher polarization current than the 17% Cr-3% Mo alloy. No crevice corrosion could be initiated for the 25% Cr-3.5% Mo alloy either at 0 volt or at +0.80V. This alloy was also tested for crevice corrosion in 1*N* hydrochloric acid at room temperature. In this experiment, the electrode was first activated, then allowed to corrode for about 7 min, then the potentiostat with potential set at +0.80V was switched on. Immediately after the potential was applied to the electrode, the glass bead was brought against the electrode surface. The polarization behavior under these drastic conditions is shown in Fig. 3. The electrode completely passivated and no effect of the presence of a crevice on the electrode surface was discernible on the polarization current-time curve.

The results of the two successive applications of the crevice to two different points of the same 17% Cr-3% Mo alloy are shown in Fig. 4, which illustrates the kind of reproducibility expected in the operation of the crevice corrosion cell. Both curves were quite

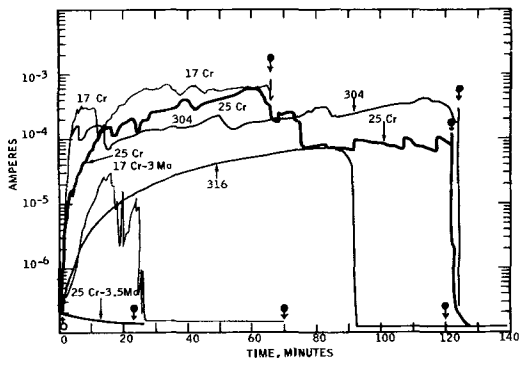

Fig. 2. Variations in polarization currents with time at 0.00V (SCE) in 1*N* NaCl at 24° ± 1°C: ⏚, crevice applied to the electrode surface; ↕, crevice removed from electrode surface.

[1] Polyvinyl chloride.

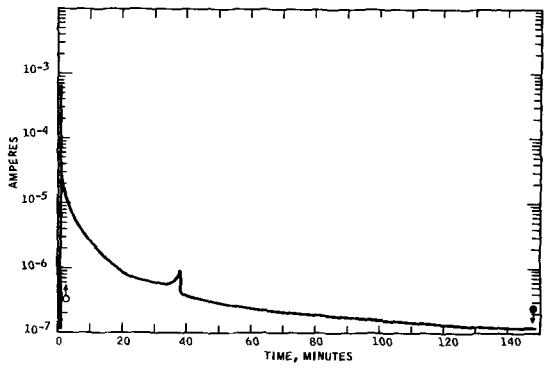

Fig. 3. Variation in polarization current with time at 0.80V for 25% Cr-3.5% Mo in 1N HCl (24° ± 1°C): ⇩, crevice applied to the electrode surface; ⇧, crevice removed from electrode surface.

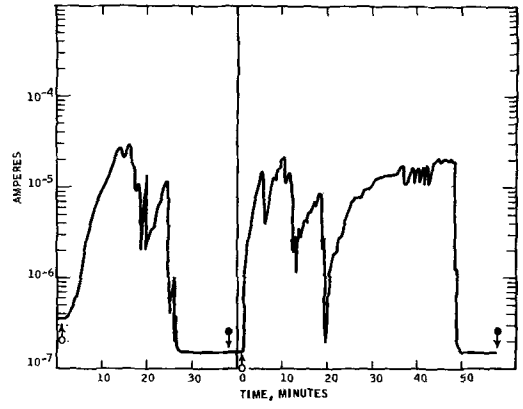

Fig. 4. Two successive polarization current-time curves at 0.00V (SCE) for 17% Cr-3% Mo alloy in 1N NaCl (24° ± 1°C): ⇩, crevice applied to the electrode surface; ⇧, crevice removed from electrode surface.

irregular and, in both, repassivation occurred before the removal of the crevice. In the first curve, repassivation occurred in about 25 min and in the second in about 50 min. Maximum current reached for both was about the same.

On the basis of the above observations, it can be concluded that the relative order of the resistance to crevice corrosion is 17% Cr (least resistant) <T304 = 25% Cr <T316 <17% Cr-3% Mo<<25% Cr-3.5% Mo (immune to crevice corrosion at room temperature in 1N Cl^-). In previous qualitative work, with 25% Cr alloys in acidified 10% Fe Cl_3 solution with crevice applied by means of a rubber band and Teflon disk, it was found that 25% Cr alloy did suffer crevice attack, while the 25% Cr-3.5% Mo alloy was immune to crevice as well as pitting corrosion. Earlier potentiostatic experiments in 1N HCl also indicated that 25% Cr-3.5% Mo alloy should be immune to crevice corrosion, while 25% Cr alloy would suffer crevice corrosion under the same conditions (9). Thus, these previous results with 25% Cr alloys are in agreement with the results from this investigation. Furthermore, all other stainless steels investigated here are known to suffer crevice corrosion in chloride media.

Conclusion

The crevice corrosion cell described in this paper makes it possible to obtain potentiostatic measurements with simple and easily prepared electrodes. Since the same crevice geometry is employed in every experiment, a relative resistance to crevice corrosion for a series of alloys can be deduced from comparison of polarization current-time curves at a given potential. Furthermore, the initiation and progress of the crevice attack can also be conveniently observed. Since the crevice can be applied or removed at will, many experiments which would not be possible with a fixed crevice can be performed.

Manuscript submitted April 1, 1970; revised manuscript received ca. June 15, 1970.

Any discussion of this paper will appear in a Discussion Section to be published in the June 1971 JOURNAL.

REFERENCES

1. I. L. Rozenfel'd and I. K. Marshakov, *Zavodskaya Lab.*, **21**, 1346 (1955).
2. R. R. Salem, *Zavodskaya Lab.*, **26**, 291 (1960); Transl. *Industrial Lab.*, **26**, 306 (1960).
3. I. B. Ulanovskii, *Zhur. Prikl. Khim.*, **39**, 814 (1966); Transl. *J. Appl. Chem. U.S.S.R.*, **39**, 768 (1966).
4. G. Bombara, D. Sinigaglia, and G. Taccani, *Electrochim. Metal.*, **3**, 81 (1968).
5. W. D. France and N. D. Greene, *Corrosion*, **24**, 247 (1968).
6. D. A. Jones and N. D. Greene, *ibid.*, **25**, 367 (1968).
7. E. A. Lizlovs and A. P. Bond, *This Journal*, **116**, 574 (1969).
8. W. D. France, *ibid.*, **114**, 818 (1967).
9. E. A. Lizlovs and A. P. Bond, "Anodic Polarization Behavior of 25% Chromium Ferritic Stainless Steels," *This Journal*, submitted for publication.

JOURNAL OF THE ELECTROCHEMICAL SOCIETY

ELECTROCHEMICAL SCIENCE

NOVEMBER 1970

Electron Microscope Study of Positive Lead-Acid Electrodes during Formation

W. O. Butler,* C. J. Venuto,* and D. V. Wisler

ESB Incorporated, Research Center, Yardley, Pennsylvania 19067

ABSTRACT

The formation process of positive lead-acid electrodes was studied using electron microscopy, and these results were correlated with those of x-ray diffraction and chemical analysis. Both the surface and the interior reactions taking place during active material formation were examined. The study showed the conversion of $PbSO_4$ crystals to β-PbO_2 and the subsequent growth of β-PbO_2 crystals to fully formed crystals. In addition, the crystal habits of $3PbO \cdot PbSO_4 \cdot H_2O$, $PbSO_4$, and β-PbO_2 in lead-acid electrodes were characterized.

Even though a number of years have elapsed since Planté presented his first storage battery to the French Academy of Sciences in 1860, the physical and chemical reactions taking place during electrode processing are still not fully understood. The literature abounds with publications on electrical and chemical studies of the system, and in recent years the more sophisticated techniques have been used to investigate these processes. X-ray diffraction, optical and electron microscopy, and electron microprobe analysis are now being used to study not only the physiochemical reactions taking place during electrode processing but also the reactions taking place during electrode cycling.

However, the work reported here is limited to a study of the formation process, that is, the anodization of fully cured electrodes to convert the electrode's active material from a mixture of $3PbO \cdot PbSO_4 \cdot H_2O$, PbO, and Pb to PbO_2.

Simon and Jones (1) used optical microscopy to great advantage in studying the formation process. Pierson (2) combined optical microscopy with x-ray diffraction and chemical analysis in his formation studies. An electron probe was used by Chiku and Nakajima (3) to study the formation process. Fully formed active material was studied using electron microscopy by Burbank and Ritchie (4, 5). To our knowledge, only Buskirk, Boyd, and Smith (6) used electron microscopy to study the active material during the different stages of formation. However, no correlation was made between the electron microscopy data and x-ray diffraction, optical microscopy, and chemical analysis.

This paper describes a study of both the surface and interior active material, examined *in situ* on Pb grids at various stages of formation. The electron microscopy data is closely correlated with x-ray diffraction data and with previous formation studies in our laboratory using optical microscopy and chemical analysis.

* Electrochemical Society Active Member.

Key words: electrode microstructure, electron microscopy, lead acid electron microscopy, and lead acid formation.

Experimental

Fully cured electrodes using Pb-5.75% Sb grids were formed at the rate of 160 A-hr/lb of active material for 1, 3, 7, 9, 11, 15, and 20 hr. The formation current was selected so that at 20 hr the electrodes received a full 160 A-hr/lb and were thus considered fully formed. The forming electrolyte was 1.060 sp gr H_2SO_4. After the desired formation time the electrodes were washed for 15 hr in distilled H_2O and then dried at 60°C in a mechanically pumped vacuum oven. Both the surface and the interior of the electrodes were examined. Single stage carbon replicas preshadowed with platinum-carbon pellets (7) were made of the surfaces of the different samples. The replicas were released using 25-50% HCl. The surface was also examined by x-ray diffraction.

The interiors of the sample electrodes were examined after scraping the surface parallel to the face of the electrode. A 1½ in. square was cut from the sample electrode. The surface was scraped with a clean razor blade until approximately one-half of the active material was removed. Prior to replication, the scraped surface was analyzed by x-ray diffraction. The carbon replicas of the surface and interior (scraped surface) were then examined in an RCA EMU-3G electron microscope. In addition, the active material, after it was removed from the Pb grid, of all seven formed samples was examined by x-ray diffraction. To characterize fully the crystal habits of the different compounds in lead-acid electrodes, plates consisting of only $PbSO_4$, $3PbO \cdot PbSO_4 \cdot H_2O$, tetragonal and orthorhombic phases of PbO, and the α and β phases of PbO_2 (confirmed by x-ray diffraction) were examined by electron microscopy. The crystal habits of $PbSO_4$, $3PbO \cdot PbSO_4 \cdot H_2O$, and β-PbO_2 were definitely characterized. Both β-PbO_2 and $PbSO_4$ have an equant crystal habit. Beta-PbO_2 usually exhibits a dipyramidal crystal form while $PbSO_4$ exhibits a combination of crystal forms with the prismatic and domal forms being more prevalent. $3PbO \cdot PbSO_4 \cdot H_2O$, as it appears in cured electrodes, is columnar in crystal habit.

Orthorhombic-PbO appeared as equidimensional grains and was difficult to distinguish from free Pb particles. Tetragonal-PbO has several crystal habits, one similar to orthorhombic-PbO and another tabular. Alpha-PbO_2 was particularly hard to characterize in that it is difficult to produce a pure standard and it seems to crystallize in a variety of crystal habits.

Observations

Surface examination.—A typical electron micrograph of the surface of a fully cured, unformed, positive electrode used in this study is shown in Fig. 1. The long columnar crystals are $3PbO \cdot PbSO_4 \cdot H_2O$, and the irregular grains are tetragonal or orthorhombic-PbO. X-ray diffraction indicates $3PbO \cdot PbSO_4 \cdot H_2O$ and orthorhombic and tetragonal-PbO to be present on the surface. No free Pb was detected by x-ray diffraction on the surface of the cured electrode.

The surface of an electrode formed for 1 hr is shown in Fig. 2. Both the large well-developed crystals and the smaller crystals are $PbSO_4$. No effect of the anodization process was noted at this time. X-ray diffraction did detect a little tetragonal and orthorhombic-PbO. No $3PbO \cdot PbSO_4 \cdot H_2O$ or PbO_2 was detected by x-ray diffraction.

Active material areas near grid members were converted to β-PbO_2 after 5 hr of formation. The β-PbO_2 crystals are initially rounded agglomerate crystal growths as shown in areas A of Fig. 3b. Beta-PbO_2 crystals next to the grid members, see Fig. 3a, are better formed since the formation reaction is initiated at the grid active material interface and then progresses toward the center of the active material pellets. The central portion of the active material pellets are still composed of unaltered $PbSO_4$ crystals as shown in Fig. 2.

After 9 hr of formation the β-PbO_2 crystals which make up the formed aggregates have become larger and their dipyramidal crystal form can be observed (Fig. 4). In addition, much more β-PbO_2 is present on the electrode surface.

At the end of 11 hr of formation the β-PbO_2 crystals have continued their development. At this state of formation the central portions of the pellet surface

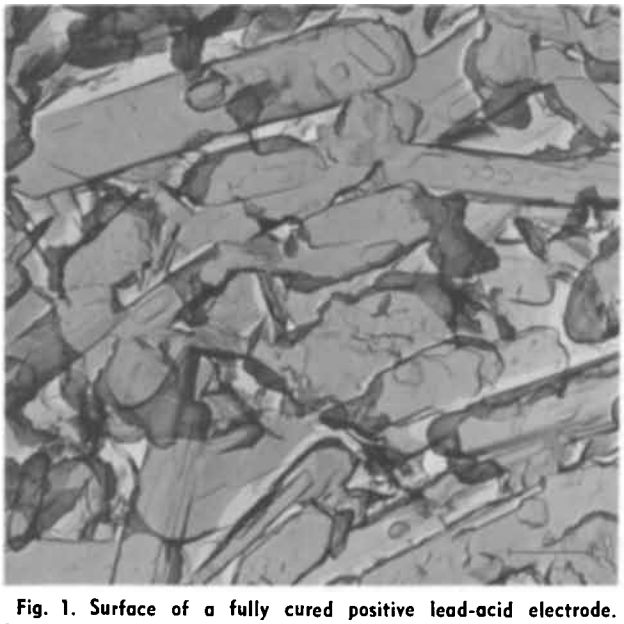

Fig. 1. Surface of a fully cured positive lead-acid electrode. Shows elongated $3PbO \cdot PbSO_4 \cdot H_2O$ crystals and irregular grains of PbO.

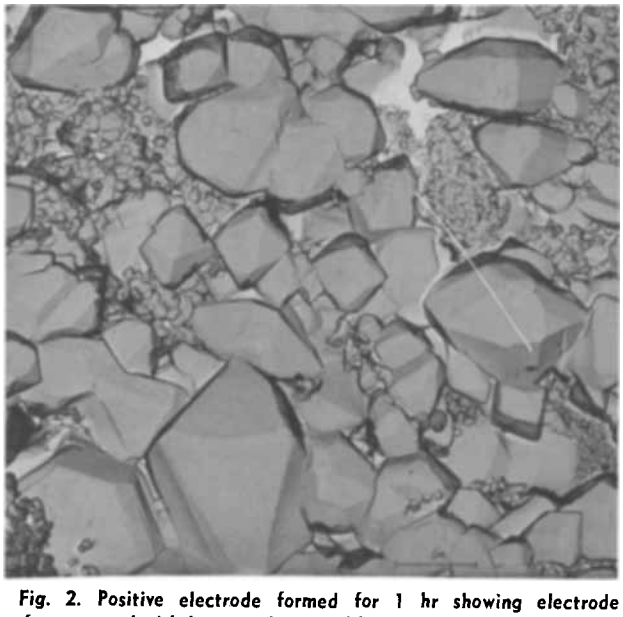

Fig. 2. Positive electrode formed for 1 hr showing electrode surface covered with large and small $PbSO_4$ crystals.

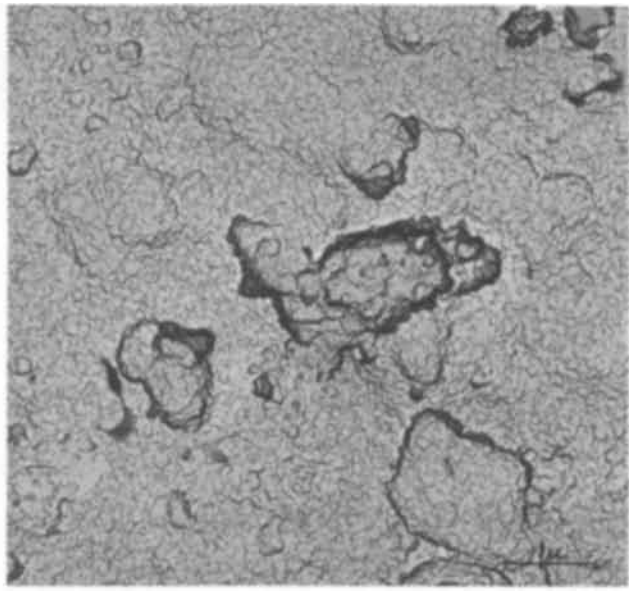

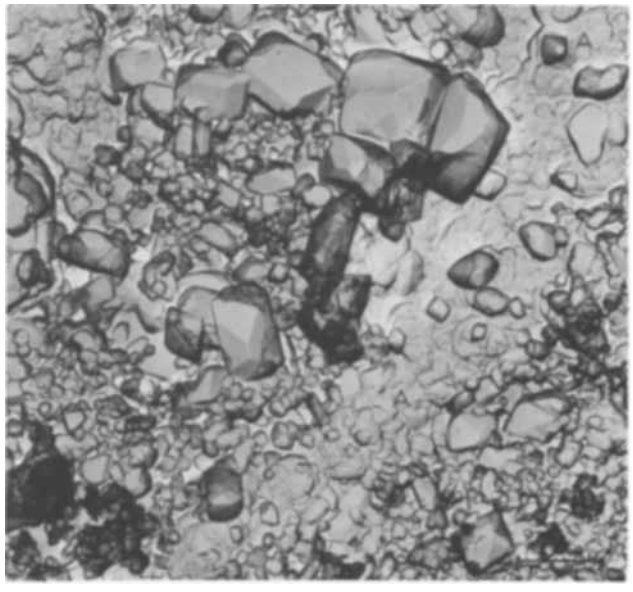

Fig. 3. Electrode surface after 5 hr of formation: (a, *top*) active material next to a grid member; small crystals are β-PbO_2; (b, *bottom*) active material further away from a grid member. Well developed crystals are $PbSO_4$. The initial appearance of β-PbO_2 occurs as rounded crystal agglomerates and appear in areas A of the electron micrograph.

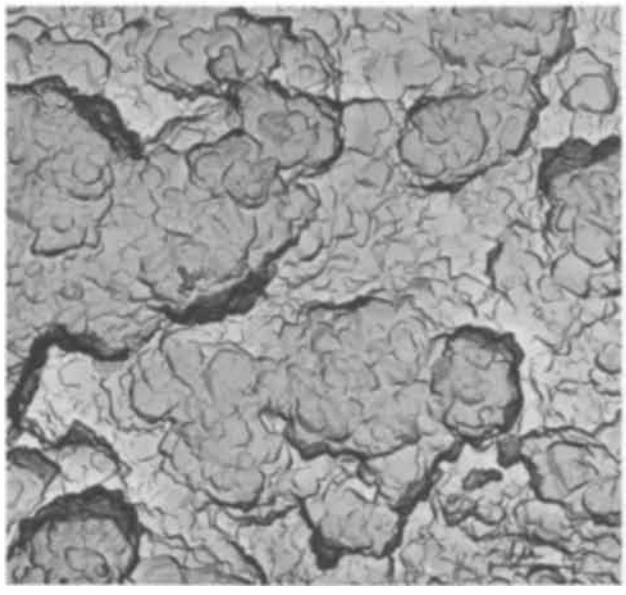

Fig. 4. Electrode surface after 9 hr of formation showing the development of the initial rounded crystal agglomerates of β-PbO_2 into larger well-defined crystal groups.

begin to form and appear similar to the areas shown in Fig. 3. These reactions continue throughout the remainder of the electrochemical formation. An electron micrograph of a fully formed surface observed in the central pellet area is shown in Fig. 5. The well-developed dipyramidal β-PbO_2 crystals are typical for a fully formed electrode. X-ray diffraction showed that the surface of the fully formed electrode consists of β-PbO_2 with trace amounts of the tetragonal and orthorhombic-PbO.

Interior examination.—The interior of the above electrodes were examined as above in order to determine if the same general sequence of formation reactions occurred in the interior as on the surface. X-ray diffraction examination of the fully cured active material indicated it is composed of mainly $3PbO \cdot PbSO_4 \cdot H_2O$ plus minor amounts of Pb and orthorhombic and tetragonal PbO.

The interior active material after 1 hr of formation (Fig. 6) is still essentially the same as for a fully cured electrode (unformed). It consists of $3PbO \cdot PbSO_4 \cdot H_2O$, tetragonal and orthorhombic-PbO, $PbSO_4$, and Pb.

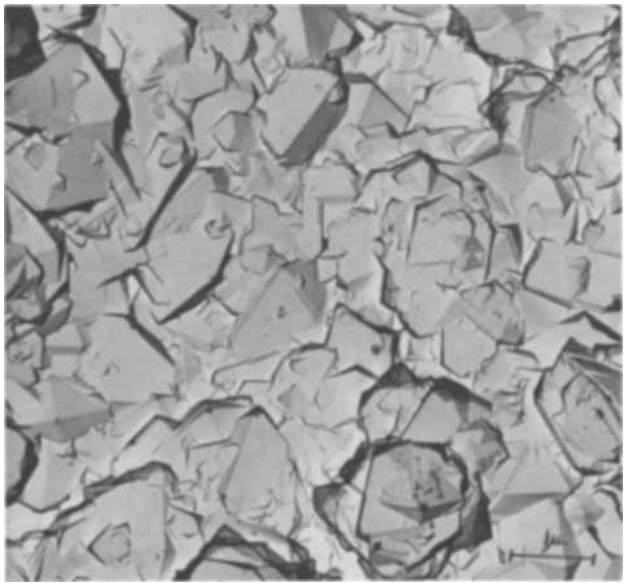

Fig. 5. Surface of a fully formed (20 hr) positive electrode. Shows well developed β-PbO_2 dipyramidal crystals.

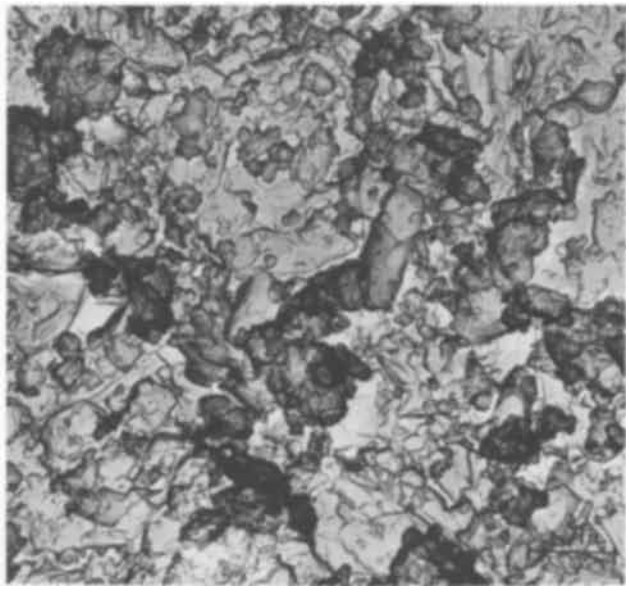

Fig. 6. Interior active material of a 1-hr formed electrode. Compounds present are $3PbO \cdot PbSO_4 \cdot H_2O$, $PbSO_4$, orthorhombic and tetragonal-PbO, and free Pb.

After 5 hr of formation, only a small amount of $3PbO \cdot PbSO_4 \cdot H_2O$ remains (Fig. 7). The interior is primarily composed of $PbSO_4$, β-PbO_2,, and tetragonal-PbO. A small amount of α-PbO_2 was also detected by x-ray diffraction.

The interior of an 11 hr formed electrode no longer contains any $3PbO \cdot PbSO_4 \cdot H_2O$ (Fig. 8). It is primarily composed of β-PbO_2, tetragonal-PbO, α-PbO_2, and $PbSO_4$. Figure 8 shows agglomerates of β-PbO_2 forming at the expense of large $PbSO_4$ crystals.

The reaction sequences are very similar to those observed on the electrode surfaces for the remainder of the formation time. X-ray diffraction shows that the fully formed interior active material is composed of α- and β-PbO_2 plus some tetragonal-PbO. Chemical analysis indicates the total (surface and interior) fully formed active material contains 81% PbO_2, 17% PbO, with the remaining 2% being Pb and $PbSO_4$.

An electron micrograph of a typical fully formed interior is shown in Fig. 9. The overgrowths on the

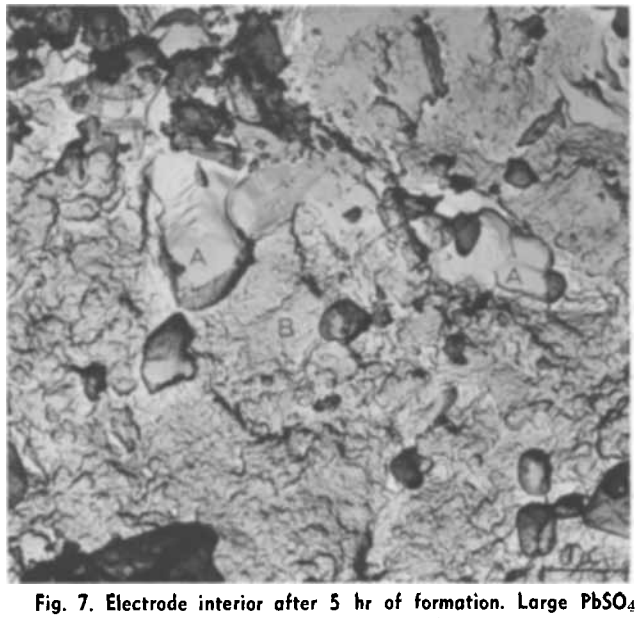

Fig. 7. Electrode interior after 5 hr of formation. Large $PbSO_4$ crystals (A), agglomerate crystalline mass of β-PbO_2 (B), and a small amount of tetragonal-PbO which is indistinguishable are shown.

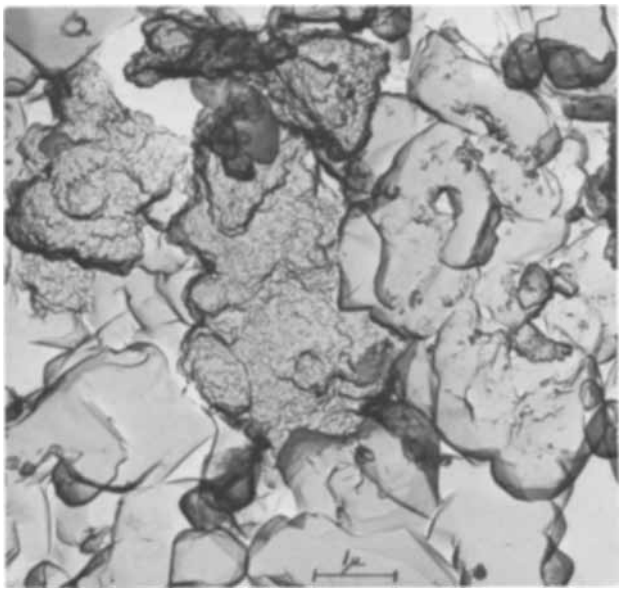

Fig. 8. Interior of positive electrode after 11 hr of formation showing large $PbSO_4$ crystals being converted to crystalline aggregates of β-PbO_2.

faces of the β-PbO_2 crystals in Fig. 9 were observed on crystals both on the surface and in the interior of the fully formed electrode. Once the β-PbO_2 crystals reach a definite size, growth of an individual crystal slows considerably or even ceases, and any further formation occurs as new crystals developing on the faces (presumably where imperfections are present) of the fully matured crystals. This phenomenon was naturally more prevalent in active material nearer grid members.

The sequence of reactions observed in the interior of the electrodes is very similar to those observed on the electrode surfaces. The main differences are (*i*) the presence of more $PbSO_4$ on the surface, especially during the initial formation period, and (*ii*) no α-PbO_2 was detected on the surfaces of the different formed electrodes. Crystals believed to be α-PbO_2 were observed in the active material interior near the grid members as shown in Fig. 10. However, these

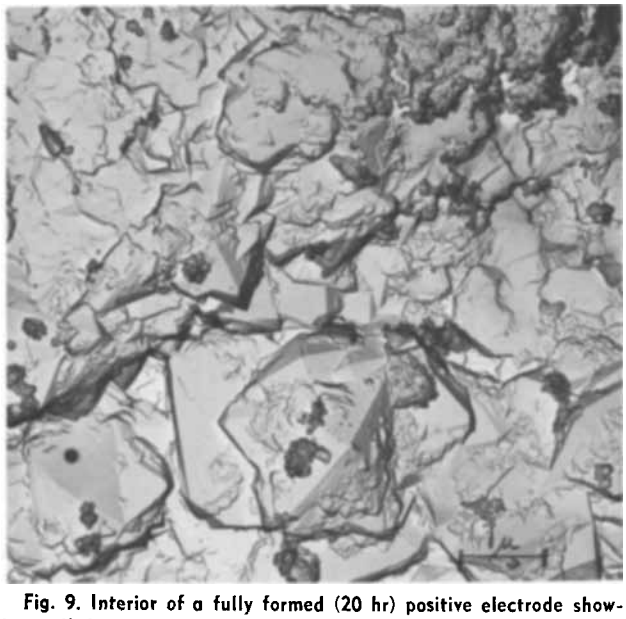

Fig. 9. Interior of a fully formed (20 hr) positive electrode showing well-developed β-PbO_2 dipyramidal crystals.

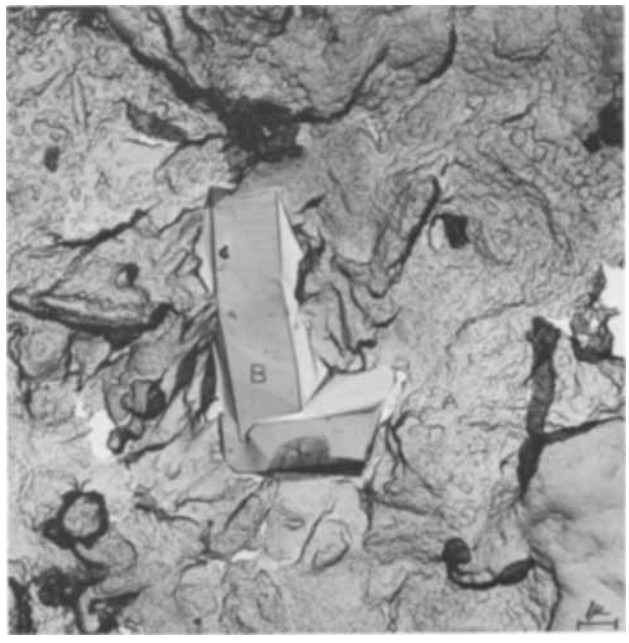

Fig. 10. Interior of active material after 15 hr of formation showing undeveloped crystalline masses (A) and large well-developed crystals believed to be α-PbO_2 (B). Active material area is very near a grid member. These and similar areas were observed in both 15- and 20-hr formed electrodes.

crystals could not be definitely characterized as α-PbO_2 with a standard as was done with the other lead compounds.

Concluding Remarks

This study established that the initial reactions taking place during formation are essentially chemical. These chemical reactions consist mainly of converting $3PbO \cdot PbSO_4 \cdot H_2O$ and orthorhombic-PbO to $PbSO_4$. Tetragonal-PbO is not as easily converted to $PbSO_4$. Second, the resulting $PbSO_4$ and PbO are then electrochemically converted to PbO_2. The interior and surface reactions are essentially the same. The one major difference is the absence of α-PbO_2 forming on the electrode's surface. Also, α-PbO_2 preferentially forms in the interior near the grid members and assumes a variety of crystal habits.

The crystal habits of $3PbO \cdot PbSO_4 \cdot H_2O$, $PbSO_4$, and β-PbO_2 in positive lead-acid electrodes were definitely established, and electron micrographs were obtained showing the conversion of $PbSO_4$ crystals to PbO_2 crystals and the subsequential growth of β-PbO_2 crystals to their full size as found in a fully formed electrode.

Manuscript submitted May 19, 1970; revised manuscript received *ca.* July 22, 1970.

Any discussion of this paper will appear in a Discussion Section to be published in the June 1971 JOURNAL.

REFERENCES

1. A. C. Simon and E. L. Jones, *This Journal*, **109**, 760 (1962).
2. J. R. Pierson, *Electrochem. Technol.*, **5**, 323 (1967).
3. T. Chiku and K. Nakajima, *This Journal*, **116**, 1407 (1969).
4. J. Burbank, *ibid.*, **113**, 10 (1966).
5. J. Burbank and E. J. Ritchie, *ibid.*, **116**, 125 (1969).
6. J. E. Buskirk, P. D. Boyd, and V. V. Smith, Paper 19 presented at the Houston Meeting of the Society, Oct. 9-13, 1960.
7. D. E. Bradley, "Techniques for Electron Microscopy," H. Kay, Editor, p. 109, F. A. Davis Co., Philadelphia (1965).

Electrochemical Properties of Polycrystalline Tin Oxide

D. Elliott, D. L. Zellmer,[1] and H. A. Laitinen*

Department of Chemistry, University of Illinois, Urbana, Illinois 61801

ABSTRACT

Some electrochemical properties of polycrystalline tin oxide in the form of thin films have been examined. For a variety of antimony-doped specimens the carrier concentration has been determined from the space charge capacity and compared with donor concentrations. Disparities between the two values have been found, and explanations have been sought in terms of structural defects as well as chloride impurity and nonstoichiometry. Analyses for the last two have been made. The kinetics of several reactions at highly doped specimens (5.9 x 10^{20} carriers/cc) indicate that the space charge region is completely transparent to electrons due to tunneling. With a series of samples of diminishing carrier concentration the increasing limitation of the tunneling process is demonstrated until it becomes the principal current controlling factor at about 3 x 10^{19} carriers/cc.

Polycrystalline tin dioxide, deposited as a thin conducting layer on glass or quartz, has recently come into some use as an electrode material with unique properties. Among these are transparency, resistance to oxidation, and the absence of adsorption by organic surfactants.[2] Extensive use of the first property, for example, has been made by Kuwana and co-workers (1), and also by others (2). The present investigation is part of a series aimed at characterizing the electrode surface (3, 4). The latter reference contains a fairly comprehensive list of references dealing with the electronic properties of tin oxide. A recent paper by others on the electrode properties has also appeared (5).

Tin oxide is a semiconducting material of large band-gap (3.7 eV). Its intrinsic resistivity is very high but may be decreased enormously by the introduction of appropriate doping agents. Minimum values down to about 2.5 x 10^{-4} ohm cm are reached with a few per cent antimony. Further increase in the antimony concentration causes the resistance to get larger again, probably caused by increasing lattice disorder (6, 7).

Experimental

Two types of electrode have been used in the study. The first was a commercially available tin oxide coated glass (here designated IRR).[3] This was analyzed[4] to contain 2.5 m/o (mole per cent) Sb. Also included under this heading are some special samples made by the same manufacturer to the author's specifications and containing varying percentages of antimony (Table I). The second type was prepared in the laboratory by hydrolysis of an atomized solution of acidified $SnCl_4$ containing various percentages of $SbCl_3$ on a hot substrate which was variously Pyrex, quartz, or polished platinum. In both cases the thickness ranged up to about 1 μm. The mounting technique has been described (3). Electrical contact was made via a flat silver ring of about ½-in. diameter which pressed against the surface concentric with the exposed working area of 5/32-in. diameter (0.1236 cm^2). This ensured that for tin oxide layers on nonconducting bases the series resistance was as low as possible to facilitate capacitance measurements up to 20 kHz. Such a contact also minimizes capacitance dispersion due to the distributed resistance of the thin film (Appendix). Capacitance measurements were made with base electrolyte only under conditions of cyclic linear potential scan at a rate of 0.5 V/min. Using a phase sensitive detector, Fig. 1, and with a Pt counterelectrode of about 24 cm^2 area, the reciprocal capacitance was recorded directly. No change in capacitance or background current was produced by deaeration of the electrolyte or shielding from daylight. With electroactive species present linear sweep voltammograms at the stationary electrode were recorded using a conventional three-electrode system. Thickness of the conducting layer was determined from the variation of the interference maxima and minima as a function of wavelength for a reflected light beam at 45° inci-

Table I. Carrier concentrations

Spray	Sb content, m/o Analysis*	Carrier conc./cm^3	Donor conc. equiv. to carriers, m/o	Resistivity, ohm cm
8**	13	$2.9_7 \times 10^{21}$†	10.7	1.32×10^{-2}
3**	5.4	$1.3_9 \times 10^{21}$	5.0	1.62×10^{-3}
0.8**	1.7	$4.8_3 \times 10^{20}$	1.74	1.23×10^{-3}
0.3**	0.6	$3.4_9 \times 10^{20}$	1.26	9.7×10^{-4}
0.1**	0.2	$2.6_3 \times 10^{20}$	0.95	2.09×10^{-3}
Sample IRR	2.5	$5.9_3 \times 10^{20}$	2.13	9.2×10^{-4}

* By emission spectroscopy.
** Special samples made by Corning.
† At 10 kHz corrected for "transmission sheet" dispersion.

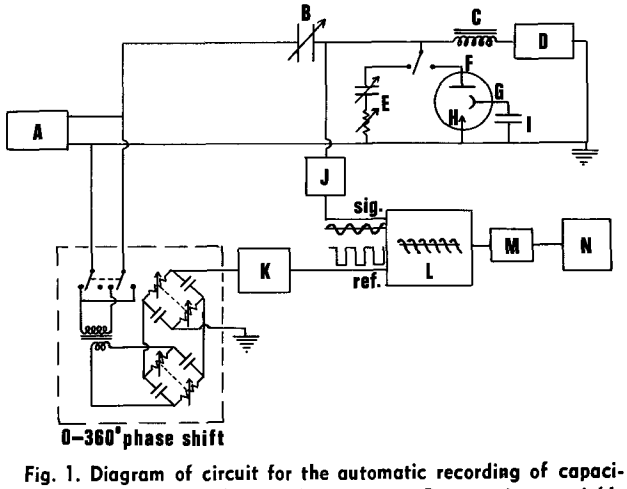

Fig. 1. Diagram of circuit for the automatic recording of capacitance and resistance: A, signal generator; B, capacitor, variable 50-1000 pf; C, choke, 300H; D, linear sweep voltage source; E, standard resistance and capacitance decade boxes; F, tin oxide electrode; G, counterelectrode; H, saturated calomel electrode (SCE); I, 250 μf capacitor; J, amplifier; K, square wave generator; L, phase sensitive detector; M, filter; N, recorder.

* Electrochemical Society Active Member.
[1] Present address: Fresno State College, Department of Chemistry, Fresno, California 93721.
[2] The measured capacity is unaffected for example by the addition of 0.01% Triton X-100.
[3] "Infra-Red Reflecting" from Corning Glass Works, Corning, New York.
[4] By emission spectroscopy.
Key words: semiconductor, thin film electrode, transparent electrode, differential capacitance measurement.

dence. Conductivity was determined by a four-point probe method. Reproducible results for the capacity and linear sweep base current were found only after specimens had been polished. Polishing was effected with 0.3 and 0.05 μm alumina abrasives and also with a polishing compound made of powdered tin oxide.[5] The electrodes were then boiled in water or cleaned in steam before use, and allowed to dry in air or heated in an air oven.

Results

Variation of capacity with various parameters.—Measurements made in the first minutes after contact with the electrolyte are about 5% lower than the values finally reached after several hours when equilibrium is attained. This may be associated with the slow adsorption of ions causing a shift in the flat band potential. A positive shift is indicated suggesting that a slow chemisorption of H^+ ions to the oxide ions of the lattice is the dominant factor. This is in accordance with the observation that the surface after contact with acid electrolyte is completely wetted whereas the initially prepared surface after polishing and boiling in water is strongly hydrophobic. Measurements of the contact angle in fact show large changes during the first hour of contact. This phenomenon together with an account of the adsorption of halide ions is discussed in ref. (4). The measurements of capacitance were made after several hours contact, and data were taken from the recorded graph after two or three cycles of the scanning voltage. Only a small difference ($\sim$1%) is noted in the capacitance values for the cathodic and anodic sweeps; likewise the difference between the first and successive cycles is less than 1% suggesting that the value recorded was at equilibrium. The background current varies between specimens but is generally between 0.1 and 0.05 μA for the area used (0.124 cm^2) in 1M acid. Such values are observed within the cathodic and anodic limits set by the decomposition of the electrolyte. The potential of H^+ reduction is near the reversible value especially after prolonged contact with the electrolyte. Oxidation, however, occurs with a large overvoltage which depends on the doping level; *e.g.*, for IRR this takes place at about +2V *vs.* SCE in 1M H_2SO_4.

In the absence of surface states the capacity of a semiconductor-electrolyte system may be subdivided into three series capacitances due to the semiconductor space charge, the compact double layer, and the diffuse double layer. The last two would be expected to be large in 1M electrolyte especially at the positive potentials used (up to +2.0V *vs.* SCE) so that the measured capacitance should closely approximate to the space charge value. The experimental justification for this is based on the application of the Mott-Schottky relationship (8, 9) valid for high carrier concentrations.

$$\frac{1}{C^2} = \frac{2}{qK\epsilon C_D}\left(V - \frac{RT}{F}\right)$$

where C = space charge capacitance
q = electronic charge
K = dielectric constant (mean value 12.7) (10)
ϵ = permittivity of vacuum
C_D = carrier concentration
V = potential with respect to the flat band potential V_B (zero charge potential)

It is implicit in the use of this relationship that the surface potential should remain constant while the potential of the bulk of the semiconductor is varied, thus approximating to the one sided step junction concept (9). Because of the adsorption of ions the surface potential differs from the bulk value even in concentrated electrolytes. For this difference to remain constant the net adsorbed charge must increase negatively as the electrode is positively changed. If these charges are not matched, the $1/C^2$ graph can be curved or have a slope other than that determined solely by the carrier concentration. Electrode roughness can also cause curvature of the characteristic since the effective area decreases as the depletion layer extends into the bulk of the electrode with increasing applied voltage. These considerations are particularly relevant for highly doped specimens where the depletion layer (9) is only a few tens of angstroms thick, *e.g.*, for IRR containing 5.9 x 10^{20} carriers/cm^3 the thickness is 16.9Å at 1.0V *vs.* SCE).

Effect of donor concentration and frequency.—Satisfactory linear graphs of $1/C^2$ *vs.* applied potential have been obtained for samples containing up to 13% antimony; an example is shown in Fig. 2.

Table I shows a comparison of computed carrier concentrations based on capacitance measurements (at 20 kHz except where noted) with the antimony concentrations of a series of samples coated on glass.

At low concentrations the carrier values are higher than those due to the antimony alone probably because of other carrier mechanisms, *e.g.*, oxygen deficiency and residual chloride. The two values agree at about 1.7% Sb which is not far from the value where the conductivity is a maximum. Samples containing more than this percentage are noticeably blue colored (the 13% sample is almost opaque). This behavior, together with the sharp increase in resistance, has been interpreted as being due to increasing lattice disorder (6, 7) causing scattering of the carriers. Such disorder could also involve appreciable segregation of the antimony in its stable oxidized form (Sb_2O_5) which would not then donate carriers. This accounts for the fall off in apparent carrier concentration with percentage of antimony. In addition, the finite value of the solution-side capacitance would cause the measured value to be lower than the true space charge capacitance causing the carrier concentration to appear lower.

These results are for polished samples in 2N H_2SO_4. Other strong acids give similar results. The effect of polishing is to reduce the measured capacity, possibly by reducing the surface area, and to eliminate surface states of the type described previously (3). Such surface states show up in the impedance characteristic as peaks in the capacity and resistance, particularly at

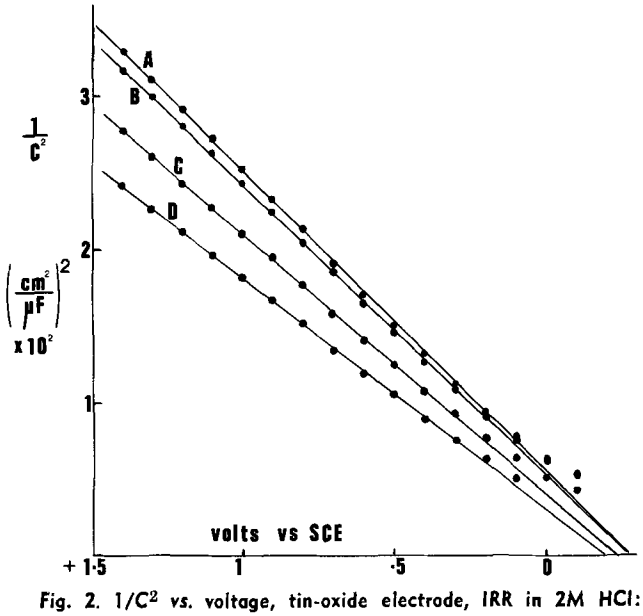

Fig. 2. $1/C^2$ *vs.* voltage, tin-oxide electrode, IRR in 2M HCl: A, 20 kHz; B, 10 kHz; C, 1 kHz; D, 50 Hz.

[5] All products of Beuhler, Ltd., Evanston, Illinois.

low frequencies. Surface states can also be produced by adsorbed impurities from the electrolyte. For example, some samples of KCl electrolyte at *p*H 2 gave a particularly marked enhancement in capacitance at −0.4V which persisted up to 20 kHz indicating very fast states. Peaks in the linear sweep voltammograms were also present. The behavior was finally traced by spectroscopic analysis of the KCl as being due to molybdenum impurity. In a separate experiment with "pure" NaCl at *p*H 2 as little as $2 \times 10^{-6}M$ molybdate produced a fourfold increase in capacitance. This surface property could not be removed even with boiling HCl. Surface states of some sort are probably responsible for the frequency dispersion observed even for polished specimens. Under the most favorable conditions, high doping and strong acid electrolytes, the capacity tends to a constant value with frequency at about 20 kHz whereas the value at 50 Hz is about 15% higher. The series resistance also tends to a constant value at 10-20 kHz being much higher at lower frequencies. Such dispersion is not predicted for a purely space-charge capacitance under depletion conditions although it would occur under so-called "inversion" conditions (8) where the minority carriers (holes) become predominant in the space charge region. This might occur if the applied potential with respect to the flat band value approaches the band gap (3.7V); however, it is not relevant in the present instance.

Frequency dispersion increases as the doping level diminishes. In such cases, as the potential increases positively, marked frequency dispersion is still present at 20 kHz and the $1/C^2$ values are not linear with voltage. The slope increases as the potential increases positively. This is not to be explained by the ionization of deep donors with increasing voltage which would cause a decrease in slope (8). For such samples the slope of the first part of the graph is used where the dispersion is small. Extrapolation of this part of the graph also provides an intercept, (V_B), in the region of those for the highly doped samples, and this would not be expected to change much with doping level. The less highly doped specimens have a higher resistance tending to cause "transmission sheet dispersion" (Appendix). Some samples were made by putting the test layer on top of a more highly doped layer, but because of the possibility of contamination a series of samples was made by deposition on a polished platinum disk at approximately 700°-800°C. The layer does not adhere so tenaciously as it does to glass or quartz and may be scratched off. However, it is quite coherent enough to withstand polishing and can be examined electrochemically provided the potential excursion on the cathodic side stops short of the hydrogen evolution region (~0V). Extension into this range causes the layer to be lifted off in patches possibly due to the evolution of gas underneath.

Table II shows the variation of carrier concentration with the spray concentration of donor. These results are for $1N$ H_2SO_4 at 20 kHz. The variation of apparent donor concentration with spray concentration bears a similar relationship to the variation of the analyzed antimony concentration in the case of the glass samples (Table I). Thus for the glass samples, the ratio Sb (analyzed)/Sb (spray) is about 2 over the range while the ratio Donor equiv./Sb (spray) for the platinum varies between 3 and 5. Direct determination of antimony has not yet been accomplished due to difficulty in removing the film in a form suitable for emission spectrographic analysis. Because of the above it is believed that the actual values approach the donor equivalents much more closely than in the case of the samples on glass. The much higher temperatures operative during the preparation on platinum (800°) compared with that for glass (~600°) should favor lower chloride retention, less oxygen deficiency, and less lattice disorder. Further studies are under way to test these conclusions. The greater concentration in the layer compared to the spray is qualitatively the same as indicated in one of the patents dealing with the material (7). With no doping, the carrier concentration drops to about 3×10^{19} which, being far above the intrinsic level, may be due to residual chloride or to oxide vacancies. Possible oxide deficiency (nonstoichiometry) was looked for in samples of IRR. The technique, which has been described (4), was to dissolve[6] the layer in a molten bead of LiClKCl eutectic at 450° in a stream of dry HCl causing the Sn(IV) component to volatilize and leaving the Sn(II) behind. The latter was determined by anodic stripping from a stationary mercury drop. The Sn(II) was found to vary between 0.02 and 0.3 m/o SnO for a series of samples of IRR. Analysis for chloride was conducted on specimens prepared by hydrolysis on an electrically heated gold wire and was determined by spark source mass spectrometry to be in the region of 0.1 to 0.2%.

Table II. Variation of carrier concentration

Spray Sb, m/o	Carrier conc./cm³	Donor conc. equiv. to carriers, m/o
2.5	$3.4_7 \times 10^{21}$	12.5
1.0	$1.1_9 \times 10^{21}$	4.3
0.25	$2.5_2 \times 10^{20}$	0.91
0.08	$7.0_2 \times 10^{19}$	0.25
0	3.2×10^{19}	0.11

Table III. Variation of properties of IRR

*p*H	−0.2	1.95	4.2	6.9	9	12
Carrier conc (10 kHz)	5.84	5.81	5.21	5.24	5.09	5.09×10^{20}
V_B (*vs.* SCE)	−0.25	−0.45	−0.61	−0.95	−1.42	−1.52

Effect of *p*H.—The variation of the properties of IRR in $2M$ Cl^- with *p*H is shown in Table III.

Frequency dispersion increases with increase in *p*H, and the apparent carrier concentration at 10 kHz decreases. Surface states due to adsorbed impurities could be responsible; slight peaks in the capacity curves are observed. Displacement of adsorbed chloride with hydroxyl could also affect the variation of net adsorbed anions with applied potential thus causing changes in the $1/C^2$ slope as discussed above. These factors make the extrapolation of high *p*H values very uncertain. At low *p*H values the trend is not far from 60 Mv/*p*H unit which is the value observed for ZnO (11) and generally expected for oxide electrodes (12, 13).

Reaction kinetics at the tin oxide electrode.—Reaction at highly doped specimens (IRR).—The techniques of chronopotentiometry and linear sweep voltammetry were used to examine the kinetics of a number of reactions.

Studies of the bromine-bromide couple showed highly irreversible behavior at the IRR electrodes, whereas this couple is reversible on platinum electrodes. Chronopotentiometric and linear sweep tests for adsorption or other complications indicated simple diffusion controlled irreversible charge transfer kinetics (4).

The kinetics of several other couples were studied to determine if the slow charge transfer rates could be attributed to depletion effects taking place at potentials far removed from the flat-band potential of tin oxide. Rate constants were measured using chronopotentiometry (14) or linear sweep voltammetry (15, 16); the results are given in Table IV.

Comparing these seven systems, there seems to be no correlation between the equilibrium potentials of

[6] The material is impervious to most normal reagents such as strong acids or oxidizing agents. It can, however, be brought into solution by electrolytic reduction or with acid chromous chloride solution.

Table IV. Comparison of charge transfer rate constants for tin oxide and platinum electrodes

Substance	Medium		E_{formal} vs. SCE	E_p	$E_{p/2}$	$E_{p,return}$	αn_a	Estimated k_{sh}, cm/sec
*10 m*M* Ce^{4+}	1*M* H_2SO_4	/Pt	1.20	0.905	1.805	1.330	0.26	1.4×10^{-4}
		/SnO_2	1.20	0.460	0.756	—	0.16	2.2×10^{-5}
*12.5 m*M* Cu^{2+} ($\rightarrow Cu^{+}$)	1*M* HCl	/Pt	0.205	0.174	0.255	0.291	—	1.4×10^{-3}
		/SnO_2	0.205	0.008	0.141	0.410	0.36	1.8×10^{-4}
*10 m*M* HBr	1*M* $HClO_4$	/Pt	0.92	0.946	0.903	0.887		reversible
		/SnO_2	0.92	2.276	2.084	0.319	1-0.25	1.2×10^{-3}
*9.56 m*M* Fe^{3+}	1*M* H_2SO_4	/Pt	0.435	0.363	0.460	0.600	—	4×10^{-4}
		/SnO_2	0.435	0.063	0.174	1.290	0.43	6.3×10^{-6}
*10.7 m*M* $Fe(o\text{-phen})_3^{2+}$	1*M* H_2SO_4	/Pt	0.870	0.900	0.840	0.840		reversible
		/SnO_2	0.870	0.917	0.825	0.825		reversible
**$K_3Fe(CN)_6$	1*M* KCl in pH 4.5 buf.	/Pt	0.289					reversible
		/SnO_2	0.289					reversible
**1.24 m*M* bromine	2*M* HBr	/Pt	0.689					reversible
		/SnO_2	0.689				0.44	6.6×10^{-6}

* Linear sweep voltammetry.
** Chronopotentiometry.

the couples and their reversibility on tin oxide. Iron (II) o-phenanthroline is very nearly reversible at +0.87V *vs.* SCE, whereas HBr at 0.92V is highly irreversible on tin oxide. The reversibility of ferricyanide at 0.289V has been demonstrated at concentrations as high as 0.2*M* and current densities up to 6.61 mA/cm² (4). On the other hand, Fe(III) at 0.435V and chlorocomplexes of Cu(II)/Cu(I) at 0.205V show 10 to 100 times faster rates on platinum than on tin oxide.

Since semiconductor depletion effects do not account for the irreversibility of some couples on the highly doped IRR tin oxide, the explanation for the slow charge transfer kinetics observed may lie in interferences caused by the oxide nature of the surface. It may be significant that the couples which are reversible on tin oxide have bulky ligands which may prevent a surface interference effect.

Variation of reaction rate with doping level.—The specimens prepared on platinum and described in Table II were used with two redox couples, the $Fe(CN)_6^{4-}/Fe(CN)_6^{3-}$ and the $Fe(o\text{-phen})_3^{3+}/Fe(o\text{-phen})_3^{2+}$ systems where o-phen represents 1, 10, o-phenanthroline. Both were chosen for their substantial reversibility on highly doped specimens. Linear sweep voltammograms are shown in Fig. 3 and 4. In the case of $Fe(CN)_6^{3-}/Fe(CN)_6^{4-}$ a transition to apparently irreversible behavior is observed as the donor concentration is lowered. The effect is more marked for the second redox system which has a reversible potential of 0.87V. The initially symmetric drop in rate constant is due to the diminishing density of states of the semiconductor according to the theory of Dogonadze and Chizmadzev (17, 18). At lower carrier concentrations asymmetry in the current characteristic is introduced because of limitation of the tunneling process through the depletion layer. For the lowest carrier concentration the anodic peak is suppressed completely and dependence on sweep rate is eliminated though there is a small difference in the current as the potential scan is reversed. This represents the condition when tunneling becomes current limiting. The corresponding potential diagram is shown in Fig. 5 where for simplification the variation of potential in the double layer is left out. E_o is the reversible potential of the couple which is considered to be a sufficiently large source of electrons that concentration polarization does not occur. The tunneling probability into the bulk of the semiconductor is governed by the shape of the energy barrier which in principle should follow the quadratic relationship (9).

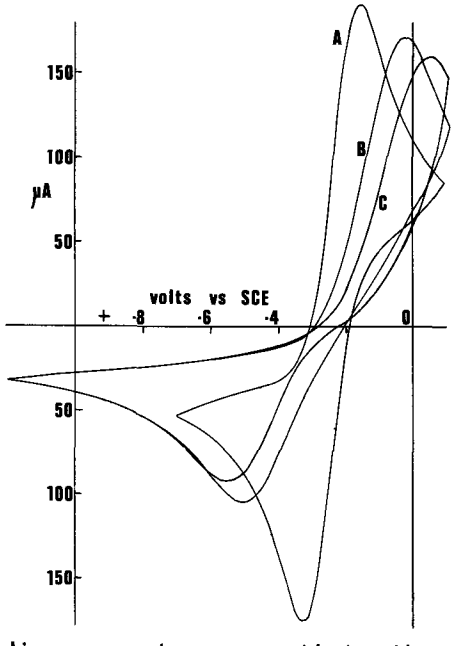

Fig. 3. Linear sweep voltammograms with tin oxide on platinum 1*N* Na_2SO_4, 0.1*N* H_2SO_4, 10 mM $K_3Fe(CN)_6$, 10 mM $K_4Fe(CN)_6$. Area = 0.124 cm²; sweep rate = 2 V/min. A, $2.5_2 \times 10^{20}$ carriers/cm³; B, $7.0_2 \times 10^{19}$ carriers/cm³; C, 3.2×10^{19} carriers/cm³.

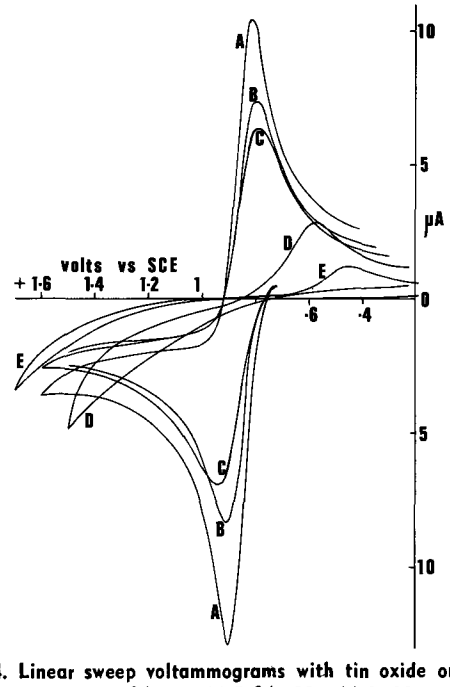

Fig. 4. Linear sweep voltammograms with tin oxide on platinum 1*N* Na_2SO_4, 1 mM Fe^{3+}, 1 mM Fe^{2+}, 33 mM 1, 10 o-phenanthroline; pH 2.5; area = 0.124 cm² sweep rate = 2 V/min. A, $3.4_7 \times 10^{21}$ carriers/cm³; B, $1.1_9 \times 10^{21}$ carriers/cm³; C, $2.5_2 \times 10^{20}$ carriers/cm³; D, $7.0_2 \times 10^{19}$ carriers/cm³, E, 3.2×10^{19} carriers/cm³.

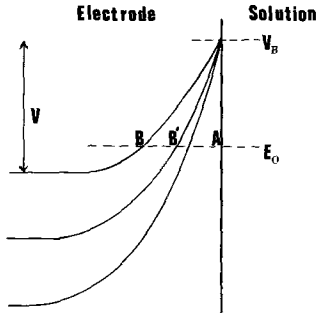

Fig. 5. Potential energy diagram at tin-oxide solution interface

$$\phi = x\sqrt{\frac{2qC_DV}{K\epsilon}} - \frac{qC_Dx^2}{2K\epsilon} \qquad [1]$$

where ϕ = potential in the space charge region and x = distance from the surface. The validity of the band model at such high fields as are necessary to promote tunneling is, however, suspect so that it is reasonable for ease of treatment to consider a linear barrier. As V becomes increasingly greater than $E_0 - V_B$ the linear approximation becomes more satisfactory because tunneling occurs across the gap AB or AB' (Fig. 5). In this region also, only the current in the direction $A \rightarrow B$, B' need be considered. Under these conditions the anodic current is given by (19, 20)

$$i = I \exp -\left[\frac{4\pi(8m^*)^{1/2}}{3h} \cdot (q[E_0 - V_B])^{1/2} l\right] \qquad [2]$$

where m^* is the effective mass, h = Planck's constant, $(E_0 - V_B)$ is the value (in volts) by which the potential barrier height exceeds the total energy of electrons incident on the barrier, l is the gap AB, and I is a factor depending on the rate and energy of electron collision at the barrier. Assuming I to be constant for a given reagent concentration, and expanding l (from Eq. [1]) in the form

$$l = \sqrt{\frac{K\epsilon}{2qC_DV}}(E_0 - V_B)\left[1 + 1/4\frac{E_0 - V_B}{V}\ldots\right]$$

one obtains

$$\text{Log } i = \text{Log } I - \frac{1}{2.303}\frac{4\pi}{3h}\left(\frac{8m^*K\epsilon}{2C_D}\right)^{1/2} (E_0 - V_B)^{3/2}\frac{1}{\sqrt{V}}\left[1 + 1/4\frac{E_0 - V_B}{V}\ldots\right]$$

The second order term is to some extent compensated for by the fact that the actual barrier slope is curved rather than flat causing the current to be larger than indicated in Eq. [2]. Consequently, by eliminating the second order term and putting $C_D = 3.2 \times 10^{19}$ carriers/cm^3 and $V_B = -0.1$V (for 1N $SO_4^=$) one obtains

$$\text{Log } i = \text{Log } I - 9.23\left(\frac{m^*}{m}\right)^{1/2} \cdot \frac{1}{\sqrt{V}}$$

Figure 6 shows a graph of Log i *vs.* $1/\sqrt{V}$ which gives a mean slope of 6.73 thus indicating a mass ratio of approximately 0.54. A range of values for this ratio for the bulk semiconductor has been given varying between 0.15 (6, 21) to 0.3 (10). It is not clear whether such bulk values are relevant to the present situation so that considering the drastic approximations applied, the experimental results can be considered reasonable.

For undoped specimens with approximately 3 x 10^{19} carrier/cm^3 it is concluded that tunneling probability is the principal current limiting factor. The carrier concentration and conductivity can be further reduced by prolonged heating, *e.g.*, at 800° for 12 hr and also by

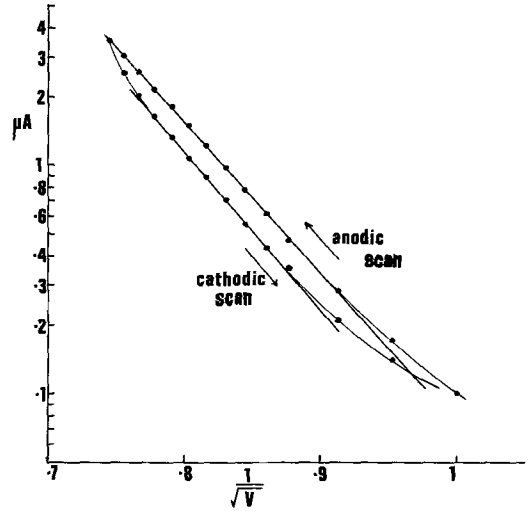

Fig. 6. Log$_{10}i$ vs. $1/\sqrt{V}$. Area = 0.124 cm^2; sweep rate = 2V/min; 3.2 x 10^{19} carrier/cm^3.

the addition of indium (5). Under these conditions it is expected that two other current generating mechanisms would become dominant. These are the space charge generation current which is proportional to the depletion layer thickness and the diffusion current which is independent of this thickness (9, 22). These currents depend on the characteristics of the semiconductor material, *e.g.*, number of defects, electron-hole pair generation, diffusion lifetime of carriers, etc., and are strongly influenced by temperature and illumination. These currents can become significant only when tunneling becomes negligible which happens as the carrier density drops still further below the lowest value encountered in the present study. It is suggested that the more highly resistive specimens investigated in reference (5) are operating in the nontunneling region since the currents reach limiting values as the voltage increases.

Acknowledgment

This research was supported by the National Science Foundation under grants GP 7773 and GP 12831. Mass spectrometric analysis by Mr. W. C. Philips of the University of Illinois and by Dr. A. E. Cameron of Oak Ridge National Laboratory, and neutron activation analysis by Dr. W. D. Shults and Mr. J. F. Emery of Oak Ridge National Laboratory are gratefully acknowledged.

Manuscript submitted May 4, 1970; revised manuscript received July 10, 1970.

Any discussion of this paper will appear in a Discussion Section to be published in the June 1971 JOURNAL.

APPENDIX

The finite resistance of the thin layer causes the potential to vary over the area that is exposed to the electrolyte. The equivalent circuit for the electrode only is a finite, two-dimensional, transmission line or transmission "sheet" with distributed resistance and capacitance. If the exposed area is circular and contact is made via a concentric ring, the distribution of potential follows a solution of the equation

$$\frac{\partial^2 v}{\partial r^2} + \frac{1}{r}\frac{\partial v}{\partial r} - \rho C\frac{\partial v}{\partial t} = 0$$

where v = voltage at distance r from the center
ρ = resistivity per square
C = capacitance per unit area

The solution of an equivalent problem (in heat conduction) with periodic boundary conditions, has been given (23). The result here is to cause frequency dis-

persion in the measured impedance. The measured capacity, C*, can be expressed in the form

$$\frac{1}{C^*} = \frac{1}{C}\left[1 + \frac{\rho^2\omega^2C^2a^4}{2^6\cdot3} - \frac{\rho^4\omega^4C^4a^8}{2^{10}\cdot3^2\cdot5} + \cdots\right]$$

where ω is the angular frequency and a is the radius of the area exposed to the solution. The correction is negligible at 20 kHz for samples of optimum conductivity (~10 ohms per square) but increases rapidly with decreasing conductivity.

REFERENCES

1. J. W. Strojek and T. Kuwana, *J. Electroanal. Chem.*, **16**, 471 (1968).
2. W. Cooper, *Nature*, **194**, 569 (1962).
3. H. A. Laitinen, C. A. Vincent, and T. M. Bednarski, *This Journal*, **115**, 1024 (1968).
4. D. L. Zellmer, Ph.D. Thesis, University of Illinois, 1969.
5. O. G. Deryagina and E. N. Paleolog, *Elektrokhim.*, **5**, 315 (1969).
6. T. Arai, *J. Phys. Soc. Japan*, **15**, 916 (1960).
7. J. M. Mochel, U.S. Pat. 2,564,707, Aug. 21, 1951.
8. V. A. Myamlin and Yu V. Pleskov, "Electrochemistry of Semiconductors," (translated from Russian) Plenum Press, New York (1967).
9. A. S. Grove, "Physics and Technology of Semiconductor Devices," John Wiley & Sons, Inc., New York (1967).
10. H. J. Van Daal, *Solid State Comm.*, **6**, 5 (1968).
11. F. Lohmann, *Ber. Bunsengesell. Berlin*, **70**, 87 (1966).
12. S. M. Ahmed and D. Maksimov, *J. Coll. Interface Sci.*, **29**, 97 (1969).
13. D. J. G. Ives and G. J. Janz, "Reference Electrodes, Theory and Practice," Academic Press, New York (1961).
14. M. Passnovic, *J. Electroanal. Chem.*, **14**, 447 (1967).
15. R. S. Nicholson and I. Shain, *Anal. Chem.*, **36**, 706 (1964).
16. R. S. Nicholson, *ibid.*, **37**, 1351 (1965).
17. R. R. Dogonadze and Yu A. Chizmadzev, *Dokl. Akad. Nauk. USSR*, **145**, 849 (1962).
18. M. V. Vojnovic and D. B. Sepa, *J. Chem. Phys.*, **51**, 5344 (1969).
19. N. H. Frank and L. A. Young, *Phys. Rev.*, **38**, 80 (1931).
20. A. G. Chynoweth, W. L. Feldman, C. A. Lee, R. A. Logan, G. L. Pearson, and P. Aigrain, *ibid.*, **118**, 425 (1960).
21. K. Ishiguro, T. Sasaki, T. Arai, and I. Imai, *J. Phys. Soc. Japan*, **13**, 296 (1958); I. Imai, *ibid.*, **15**, 937 (1960).
22. M. Green, in "Modern Aspects of Electrochemistry," No. 2, p. 343. J. O'M Bockris, Editor, Academic Press Inc., New York (1959).
23. H. S. Carslaw and J. C. Jaeger, "Conduction of Heat in Solids," O. U. P., 1959.

Electrochemical Measurements on Austenitic Stainless Steels in Boiling Magnesium Chloride

J. A. Davis and B. E. Wilde*

Applied Research Laboratory, U. S. Steel Corporation, Monroeville, Pennsylvania 15146

ABSTRACT

Electrochemical polarization measurements have been made on AISI Type 304 and USS 18-18-2 stainless steels in magnesium chloride boiling at 150°C. Little difference in the cathodic Tafel constant was noted; the observed values being equal to that expected from a charge transfer rate-determining step. Steady-state corrosion currents increased in the order Type 304 > USS 18-18-2 for the unstressed and the stressed condition. Analysis of corrosion potential *vs.* time and cyclic polarization data indicates the presence of a film on the corroding surface, which affects the corrosion kinetics. The presence of two mixed potentials during cyclic polarization does not support the noble metal enrichment concept of crack propagation, but rather, the film rupture model.

The mechanism of stress corrosion cracking (SCC) in austenitic stainless steels exposed to chloride-containing media has been the subject of many publications (1-6) and has recently received an excellent review (7). It appears that two major theories have been proposed for crack propagation, both involving plastic deformation at the crack tip and the subsequent influence on the anodic dissolution kinetics.

The mechanochemical model proposed by Hoar and Hines (8) outlines the concept of stress- (or strain-) assisted anodic dissolution of the film-free metal at the tip of the crack.

The film rupture model suggested by Champion (9) and Logan (10) invokes the repetitive rupture of a passive film at the crack tip due to plastic deformation, allowing localized anodic dissolution to take place. This latter model has been criticized because it is not considered likely for passive films to form on austenitic stainless steels in magnesium chloride solutions (8, 11). To overcome this criticism, the concept of noble metal enrichment has been proposed by Latanision and Staehle (12), who suggest the formation of a nickel-rich film at the crack tip which is subsequently ruptured periodically by dislocation movement resulting from plastic flow.

The present work was conducted on both a resistant and a susceptible austenitic stainless steel to see if the different cracking behavior could be explained in terms of electrochemical parameters, and also to see if information could be gained to support either of the above mechanistic theories.

Materials and Experimental Work

The composition of the alloys studied are shown in Table I, and some pertinent mechanical properties determined at 150°C appear in Table II. Tests were conducted on wires having a diameter of 0.102 cm. The

Table I. Chemical composition of test materials

Material	Weight per cent C	Mn	P	S	Si	Cu	Ni	Cr	Mo
Type 304 stainless steel	0.042	1.23	0.028	0.013	0.39	0.21	9.07	18.4	0.16
USS 18-18-2 stainless steel	0.061	1.5	0.007	0.009	1.90	0.03	18.0	18.4	0.01

* Electrochemical Society Active Member.

Key words: electrochemical polarization, stress corrosion, scanning microscopy, anodic dissolution kinetics, film rupture.

Table II. Mechanical properties of the test materials at 150°C

	0.2% Offset yield strength ksi	Ultimate tensile strength ksi
Type 304 stainless steel	33	67
USS 18-18-2 stainless steel	33	73

wires were heat-treated at 1000°C in argon for 15 min and water-quenched. The annealed wires were abraded through 600-grit silicon carbide paper, degreased in a detergent in an ultrasonic cleaner, washed and dried in hot air. The corrodent was aqueous magnesium chloride boiling at 150°C prepared from reagent grade chemical and distilled water (6.3 megohm cm, at 25°C).

Potentiostatic and potentiodynamic polarization measurements were conducted by using the apparatus and procedure described elsewhere (13, 14). All potentials were measured against a saturated calomel electrode at 25°C, connected to the corrodent through a ground-glass stopper filled with solid $MgCl_2$. No attempt was made to correct for junction, thermal diffusion, or IR potentials.

The wires were mounted in a glass cell similar to that described elsewhere (11), such that stress was applied by uniaxial dead weight loading. The steady-state corrosion current, I_{corr}, was determined by extrapolating the linear activation controlled region of the polarization curve to steady-state corrosion potential, E_{corr}.

Reaction films formed on the alloys after 200 hr (3μ Al_2O_3 polished unstressed coupons 2.54 cm by 2.54 cm by 0.127 cm) in boiling $MgCl_2$ were stripped by treating the specimens with 10% iodine/methanol solution similar to that described previously (15).

Results and Discussion

A summary of the electrochemical parameters of the alloys determined potentiostatically in boiling $MgCl_2$ is given in Table III. All unstressed polarization measurements were made after the specimens had reached a steady-state E_{corr}. In the case of the stressed experiments, the stress was applied to the wire at steady-state E_{corr}, and the runs were commenced after 5 min of application of stress on Type 304 stainless steel and 1 hr on 18-18-2 stainless steel. The polarization parameters for the test alloys were very similar in the unstressed state. No reliable anodic data could be obtained due to the interference of pronounced pitting at potentials only 25 mV noble to E_{corr}.

With the application of stress (90% of the 150°C yield strength), a marked increase in I_{corr} was observed on Type 304 stainless steel while I_{corr} increased only slightly on 18-18-2 stainless steel. The application of stress also shifted E_{corr} of both steels in the active direction. While E_{corr} on 18-18-2 stainless steel returned to the unstressed E_{corr} in 30 to 40 min, the E_{corr} on Type 304 stainless steel only shifted to slightly more noble values with time.

Potentiostatic anodic polarization on stressed Type 304 specimens produced early cracking or failure due to pitting through the wire in approximately 5 to 15 min. On the basis of the data shown in Table III, it is not apparent why the silicon steel is superior to Type 304 stainless steel. It is possible, however, that the effect of stress on the E_{corr} reflects the tendency of surface films to rupture (in a manner similar to the scratching experiment), and in this light the films formed on USS 18-18-2 stainless steel may be more resistant to fracture.

The unstressed potential *vs.* time behavior of the two steels was recorded and is shown in Fig. 1. The character of the transient was similar to that reported by Hoar and Hines (16) for Type 304 stainless steel. They suggest that the shift in the noble direction was due to the formation of a protective film. Other workers (12), however, have described this type of transient to be the result of noble component enrichment on the corroding surface. When an unstressed specimen of Type 304 stainless steel was equilibrated to steady-state E_{corr} and scratched with a diamond stylus, the E_{corr} immediately decreased from —0.360 V_{SCE} to —0.415 V_{SCE}. This behavior was taken as confirmation that the establishment of the noble E_{corr} was the result of a surface reaction between the metal and the corrodent. Unfortunately, both of the above hypotheses for the shape of the transient could be invoked to explain the scratching experiment.

The time required for the potential to reach steady state (less than 5 mV shift in 15 min), was markedly different for the two test materials. Type 304 stainless steel achieved steady state after 2 to 10 min, compared with 50 to 100 min for USS 18-18-2. The shape of the potential-time transient observed in these experiments was reminiscent of that observed by other workers when studying the active to passive transition of stainless steels in aerated acidic media (17, 18). The similarity in these transients suggested that an analogous passivation process was occurring in boiling $MgCl_2$ but not necessarily by the same species as with steels in dilute acid.

The polarization behavior of the two materials under potentiodynamic conditions is of interest. Typical cyclic polarization curves are shown in Fig. 2, where an unstressed specimen of USS 18-18-2 stainless steel was polarized from the steady-state corrosion potential to —0.800V at a rate of 15 volts per hour in boiling $MgCl_2$. At —0.800V the sweep was reversed and continued to —0.200V, after which it was reversed again to —0.800V. It is clear from Fig. 2 that two steady-state mixed potentials exist at points *A* and *B*, similar to those reported on other materials in dilute acid (19, 20). The results for Type 304 stainless steel (Fig. 3) were practically the same.

Table III. Summary of potentiostatic electrochemical parameters in boiling $MgCl_2$

Material	Condition	β_c, V	β_a, V	E_{corr}, V_{SCE}	I_{corr}, $\mu A/cm^2$
Type 304 stainless steel	Unstressed	—0.162	0.069	—0.360**	260
USS 18-18-2	Unstressed	—0.170	0.062	—0.312**	210
Type 304 stainless steel	Stressed to 90% of yield	—0.100	N.D.*	—0.420†	900
USS 18-18-2	Stressed to 90% of yield	—0.175	N.D.	—0.312†	310

* N.D. = not determined.
** Steady-state value (see Fig. 1).
† Value attained within 5 min after applying the load to Type 304 stainless steel specimen. In the case of USS 18-18-2 stainless steel, the load was applied after 1 hr at the unstressed steady-state E_{corr}.

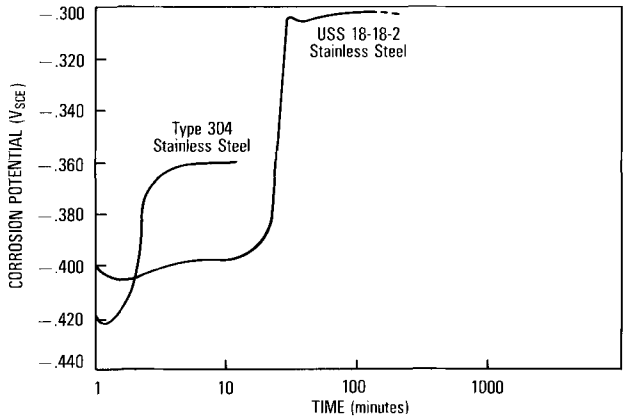

Fig. 1. Potential-time transients in boiling magnesium chloride

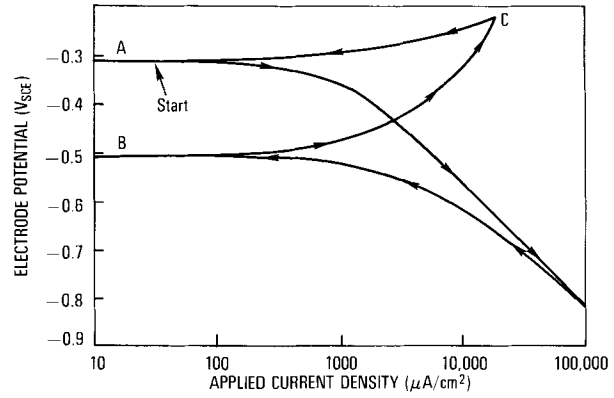

Fig. 2. Cyclic polarization curve for unstressed USS 18-18-2 stainless steel in boiling $MgCl_2$. (Sweep speed 15 V/hr.)

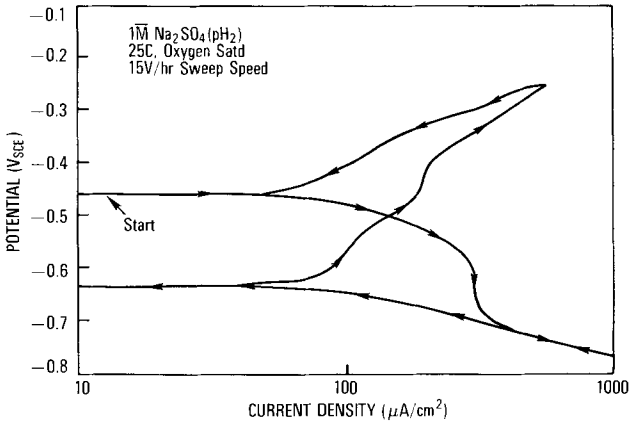

Fig. 3. Cyclic polarization curve for unstressed AISI Type 304 stainless steel in acidified Na_2SO_4. (Sweep speed 15 V/hr.)

To explain this behavior we suggest that E_{corr} at point *A* in Fig. 2 is the result of a reaction film covered surface after the specimen has come to steady state (see Fig. 1). When polarized in the active direction, hydrogen-ion reduction occurs and normal Tafel behavior is obtained down to −0.800V, during which process the film on the surface is reduced. Reversal of the sweep results initially in hydrogen-ion reduction at the same rate as with the active-going sweep. However, since the surface is now film-free, a new mixed potential is developed at *B*. Electrochemical oxidation of this surface results in anodic dissolution along *BC* and is not significantly affected by pitting because of the rather rapid sweep rate. Polarization in the cathodic direction from *C* results in the dissolution curve *AC*, which is similar to that obtained by anodic polarization of a steady-state surface from *A*.

If the above interpretation is correct, it should be possible to duplicate the cyclic response (Fig. 2) with a steel in an unambiguous state of stable passivity. In an attempt to demonstrate this behavior, a Type 304 stainless steel electrode was exposed to an oxygen-saturated solution of 1M Na_2SO_4, (where the *pH* was adjusted to 2.0 with H_2SO_4). Cyclic polarization of this electrode produced a similar type of curve to that in Fig. 2, as shown in Fig. 3. An active mixed potential was observed because the kinetics for the re-passivation of the surface following cathodic reduction are slower than the speed of the sweep. These data lend strong support to the theory of film formation and passivation-type electrode kinetic behavior of austenitic alloys in boiling $MgCl_2$.

Although the theory of noble metal enrichment could account for the phenomenon observed in both the unstressed potential-time behavior and the scratch experiment, it cannot in our opinion be reconciled with the presence of a new mixed potential following cathodic reduction.

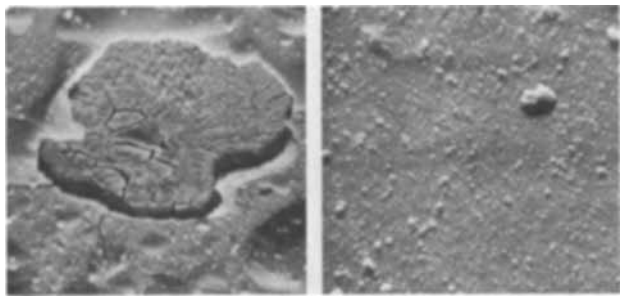

Fig. 4. Scanning electron micrographs of austenitic stainless steels exposed for 200 hr unstressed to boiling magnesium chloride (150°C) X 1000. (Left) AISI Type 304 stainless steel. (Right) USS 18-18-2 stainless steel.

Attempts to strip films off corroded surfaces were successful. Films of variable thickness were lifted from both steels after 200 hr exposure to boiling $MgCl_2$. Bulk electron diffraction studies produced an unidentified pattern, with diffuse Debye rings. It is worthy of note, however, that the patterns from both Type 304 and USS-18-18-2 stainless steel appeared to be identical. Small inclusions were observed in the films which gave diffraction patterns of a chromium nitride structure, which is isomorphous with NiO.

Emission spectrographic analysis of film residues indicated that the composition was the same for both steels, with magnesium as a major component. Scanning electron micrographs were obtained on corroded surfaces (after 3 hr at steady-state E_{corr}, as in Fig. 1) of two alloys and are shown in Fig. 4. A wide variation in surface structure was observed at 2000X. The Type 304 stainless steel sample evidenced pronounced spalling of the surface film while USS 18-18-2 stainless steel showed a rather featureless nonporous film.

Conclusions

The following conclusions can be drawn from the data presented:

1. The values of the cathodic Tafel constant for Types 304 and USS 18-18-2 stainless steel in boiling $MgCl_2$ are equal to that which would be expected for a charge transfer controlled discharge process.
2. No systematic relationship between electrochemical polarization parameters (stressed or unstressed) and the stress corrosion cracking behavior of the above two materials was observed.
3. Analysis of potential-time data and cyclic polarization curves has indicated the presence of a stable film on the metal surface, which can be reduced by cathodic hydrogen evolution.
4. The presence of two mixed potentials on a cyclic polarization plot cannot be rationalized on the basis of noble metal enrichment, but it can be explained by a passive type of behavior entirely analogous to that observed on Type 304 stainless steel in sodium sulfate solutions at room temperature.

Manuscript submitted Jan. 12, 1970; revised manuscript received *ca.* June 25, 1970. This was Paper 63A presented at the Detroit Meeting, October 5-9, 1969.

Any discussion of this paper will appear in a Discussion Section to be published in the June 1971 JOURNAL.

REFERENCES

1. H. L. Logan, *J. Res. Nat. Bur. Std.*, **48**, 99 (1952).
2. T. P. Hoar and J. G. Hines, *J. Iron Steel Inst.*, (London) **177**, 248 (1954).
3. C. Edeleanu, *ibid.*, **173**, 140 (1953).
4. R. B. Mears, R. H. Brown, and E. H. Dix, "Symposium on Stress Corrosion Cracking of Metals," p. 323, ASTM-AIME (1945).
5. J. C. Hodge and J. L. Miller, *Trans. Am. Soc., Metals*, **28**, 25 (1940).

6. W. D. Robertson, in "Stress Corrosion Cracking and Embrittlement," W. D. Robertson, Editor, p. 32, Wiley, New York (1956).
7. E. N. Pugh, J. A. S. Green, and A. J. Sedriks, RIAS Technical Report 69-3, (March 1969).
8. T. P. Hoar and J. G. Hines, in "Stress Corrosion Cracking and Embrittlement," W. D. Robertson, Editor, p. 107, Wiley, New York (1956).
9. F. A. Champion, "International Symposium on Stresses in Metals and Alloys," p. 468, Institute of Metals, London (1948).
10. H. L. Logan, *J. Res. Nat. Bur. Std.*, **48**, 99 (1952).
11. S. Barnartt and D. Van Rooyen, *This Journal*, **108**, 222 (1961).
12. R. M. Latanision and R. W. Staehle, "Stress Corrosion Cracking of Iron-Nickel-Chromium Alloys," in "Proceedings of Conference on Fundamental Aspects of Stress Corrosion Cracking," R. W. Staehle, A. J. Forty, and D. Van Rooyen, Editors, NACE, Houston, Texas (1969).
13. B. E. Wilde and J. S. Armijo, *Corrosion*, **23**, 208 (1967).
14. W. D. Henry and B. E. Wilde, *ibid.*, **25**, 515 (1969).
15. J. S. Armijo and B. E. Wilde, *Corrosion Sci.*, **8**, 649 (1968).
16. T. P. Hoar and J. G. Hines, *J. Iron Steel Inst.*, (London), **182**, 124 (1956).
17. C. Edeleanu, *Metallurgia*, **50**, 113 (1954).
18. B. E. Wilde and N. D. Green, *Corrosion*, **25**, 300 (1969).
19. B. E. Wilde and F. G. Hodge, *Electrochim. Acta.*, **14**, 619 (1969).
20. C. Wagner and W. Traud, *Z. Elektrochem.*, **44**, 391 (1938).

Preparation of 2,3,4,5-Tetraphenyl-1,6-Hexanedioic Acid

S. Wawzonek,* A. R. Zigman, and G. R. Hansen

Department of Chemistry, University of Iowa, Iowa City, Iowa 52240

ABSTRACT

2,3,4,5-Tetraphenyl-1,6-hexanedioic acid has been prepared electrochemically by the reductive dimerization of α-phenylcinnamic acid and α-phenylcinnamonitrile. The latter gave a mixture of 1-amino-2,3,4,5-tetraphenyl-5-cyano-1-cyclopentene and 2,3,4,5-tetraphenyl-1,6-hexanedinitrile. Both the cyclopentene derivative and the dinitrile were converted chemically to the desired acid. Chemical methods based on condensation reactions of benzil were not successful for the preparation of this acid.

2,3,4,5-Tetraphenyl-1,6-hexanedioic acid (V) was required as a starting material for the preparation of 5,11-diphenyl-6,12-diketochrysene. This paper describes electrochemical and chemical studies of the preparation of this acid.

Experimental[1]

2,3,4,5-Tetraphenyl-1,6-hexanedioic acid (V).—The electrochemical reductive dimerization of α-phenylcinnamic acid (22.4g) in dimethylformamide (190 ml) containing 28% sulfuric acid (72 ml) was carried out at a mercury cathode using the directions given for cinnamic acid (1). The resulting solution was poured into water, and the oily layer was separated and taken up in benzene. Extraction with sodium hydroxide followed by acidification of the alkaline solution gave an oil which solidified. Treatment with benzene and chloroform gave 5.2g of a white solid melting at 275°-290°C. Two crystallizations from ethanol gave the desired acid (0.7g); mp 306°-308°C. The IR spectrum showed absorptions at 3.5-3.8 (OH) and 5.84, 6.04μ (COOH).

Anal. Calcd. for $C_{30}H_{26}O_4$: C, 79.91; H, 5.81; Found: 79.67; H, 5.81.

Electrolytic reduction of α-phenylcinnamonitrile.—A solution of α-phenylcinnamonitrile (20.5g) in dimethylformamide (300 ml) containing 150 ml of a 57% solution of tetraethylammonium *p*-toluenesulfonate in water was reduced at a mercury cathode (68 cm^2). The platinum anode was placed in a porous cup in a similar solution without the nitrile. The solution during the electrolysis was kept neutral by the addition of acetic acid. After the passage of a current of 1A for 3 hr the white solid (13.8g) formed was filtered and could be separated into two compounds with hot benzene. The soluble fraction (75%) was the cyanoamine (I) and the insoluble part was 2,3,4,5-diphenyl-1,6-hexanedinitrile (25%). Addition of water to the filtrate gave an additional 2.2g of the cyanoamine (I). This compound, 2,3,4,5-tetraphenyl-5-cyano-1-amino-1-cyclopentene (I), melted at 219°-225°C after one recrystallization from a mixture of benzene and ethanol; IR: 3.03 (NH_2), 4.54 (CN) and 6.15μ (C = C); NMR (CD_3CN) δ7.5 (s C_6H_5); 7-7.48 (m $3C_6H_5$), 5.04 (d 1 H J = 10 Hz), 4.02 (s 2 H) and 3.54 (d 1 H J = 10 Hz). In the presence of D_2O the broad singlet at 4.02 disappeared.

Anal. Calcd. for $C_{30}H_{24}N_2$: C, 87.37; H, 5.86; N, 6.79. Found: C, 87.70; H, 5.83; N, 6.57.

2,3,4,5-Tetraphenyl-1,6-hexanedinitrile after recrystallization from a large volume of benzene melted with sublimation at 348°-355°C. TGA indicated that the sublimation started at 240°C; IR 4.53μ (CN); mass spectral analysis gave a peak at 412.

Anal. Calcd. for $C_{30}H_{24}N_2$: C, 87.37; H, 5.86; N, 6.79. Found: C, 87.75; H, 5.85; N, 6.66.

2,3,4,5-Tetraphenyl-2-cyanocyclopentanone (II).—A solution of the cyanoamine (I) (1.2g) in dioxane (50 ml) was refluxed with 6*N* hydrochloric acid (15 ml) for 1 hr and poured into water. The cyanoketone (1.1g) melted at 178°-180°C after two crystallizations from ethanol. On solidification this compound would occasionally remelt at 190°-192°C. The IR and NMR spectra, however, were the same as those for the 178°-181°C compound; IR: 4.45 (CN) and 5.74μ(CO); NMR ($CDCl_3$): δ7.04-7.25 (m $4C_6H_5$); 3.92-4.21 (m 3 H).

Anal. Calcd. for $C_{30}H_{23}NO$: C, 87.14; H, 5.61; N, 3.39. Found: C, 87.30; H, 5.73; N, 3.28.

2,3,4,5-Tetraphenyl-5-cyanopentanoic acid (III).—The cyanoketone (II) (1g) was refluxed with potassium hydroxide (1g) in methanol (40 ml) for 15 hr. The resulting solution when poured into water and acidified gave a solid (1.0g) which was recrystallized

* Electrochemical Society Active Member.

Key words: hydrodimerization; 1-amino-2,3,4,5-tetraphenyl-5-cyano-1-cyclopentene; 2,3,4,5-tetraphenyl-1,6-hexanedinitrile.

[1] Melting points are not corrected. Infrared spectra were determined as nujol mulls on a Perkin-Elmer Infracord. NMR spectra were determined on a Varian A60 Spectrometer.

from benzene; yield, 0.35g; mp 235°-237°C. A second recrystallization from benzene gave a sample melting at 236°-237°C; IR: 3.5-3.9 (OH), 4.43 (CN) and 5.8μ (COOH). The more soluble fraction obtained in this reaction was not investigated further.

Anal. Calcd. for $C_{30}H_{25}O_2N$: C, 83.53; H, 5.80; N, 3.25. Found: C, 83.34; H, 5.94; N, 3.31.

2,3,4,5-Tetraphenyladipamic acid (IV).—The nitrile acid (III) (0.4g) was refluxed with 10 ml of 50% sulfuric acid in acetic acid (28 ml) for 28 hr and the resulting solution was poured into water. The solid (0.32g) obtained, when recrystallized from a large volume of benzene, melted at 292°-293°C; IR: 2.8-3.0 (NH_2), 3.5-9 (OH); 5.83 (COOH) and 6.01μ ($CONH_2$).

Anal. Calcd. for $C_{30}H_{27}O_3N$: C, 80.18; H, 6.01; N, 3.12. Found: C, 79.97; H, 6.14; N, 3.19.

2,3,4,5-Tetraphenyl-1,6-hexanedioic acid (V).—The amide acid (0.5g) in 10 ml of acetic acid containing 1 ml of concentrated hydrochloric acid was treated at 100°C with excess 20% sodium nitrite solution. The white solid (0.4g) on recrystallization from ethanol and water melted at 304°-307°C and gave an identical ir spectrum to that of the acid obtained by the dimerization of α-phenylcinnamic acid.

Hydrolysis of 2,3,4,5-tetraphenyl-1,6-hexanedinitrile.—The dinitrile (2.75g) was refluxed with 25 ml of 50% sulfuric acid in acetic acid (250 ml) until all the solid material had dissolved. This process required 11 days. The resulting solution was poured into water, and the white solid (3.0g) was filtered. Extractions with alkali gave a mixture of acids containing nitrogen. Deamination of a portion (0.8g) in acetic acid (10 ml) containing concentrated hydrochloric acid (1 ml) at 100° with 2 ml of 20% sodium nitrite gave 0.42g of an isomeric 2,3,4,5-tetraphenylhexanedioic acid. Recrystallization from benzene gave a sample melting at 291°-295°C. A mixture with the acid prepared from the cyanoketone method melted at 265°-280°C. IR: 3.5-4 (OH) and 5.88μ (COOH).

Anal. Calcd. for $C_{30}H_{26}O_4$: C, 79.91; H, 5.81. Found: C, 79.70; H, 5.94.

Cyclization of 2,3,4,5-tetraphenyl-1,6-hexanedinitrile.—The dinitrile (0.65g) was refluxed in benzene (150 ml) and absolute ethanol (50 ml) with sodium methoxide (0.3g) for 22 hr. Removal of the solvent gave a solid which was treated with water, filtered, and dried. The resulting solid was treated with cold benzene, and the insoluble starting material was separated; yield, 0.38g. The filtrate was treated with ethanol and on concentration gave a white crystalline solid (0.21g) melting at 239°-242°C; IR: 2.9 (NH_2), 4.45 (CN) and 6.10μ (C = C); NMR ($CDCl_3$) δ6.6-7.6 (m $4C_6H_5$), 4.63 (d 1H J = 8 Hz), 3.95 (d 1H J = 8 Hz) and 3.8 (broad s 2H). In the presence of D_2O the broad singlet at 3.8 disappeared. The NMR spectrum in CD_3CN in which the compound is much less soluble gave a similar coupling constant for the two doublets. A mixture with isomer I melted at 199°-220°C.

Anal. Calcd. for $C_{30}H_{24}N_2$: C, 87.37; H, 5.86; N, 6.79. Found: C, 86.99; H, 5.59; N, 6.45.

Reaction of benzil with benzyl cyanide.—A solution of benzil (15.7g) and benzyl cyanide (17.5g) in ethanol (250 ml) was treated at reflux with a solution of potassium hydroxide (3g) in ethanol (15 ml). The solution became purple and was refluxed for 30 min. Removal of the solvent was followed by acidification and extraction with ether. The ether layer after treatment with dilute alkali and acid gave an orange oil (28g). Addition of alcohol gave crystals of α-phenylcinnamonitrile (4.0g); mp 85°-88°C. Identification was made by comparison with an authentic sample (2).

Reaction of benzil with ethyl alpha-bromophenylacetate.—A stirred refluxing mixture of zinc dust (6.8g) in dry benzene (100 ml) was treated with a solution of benzil (11.56g) and ethyl α-bromophenylacetate (25.0g) in benzene (100 ml). After approximately 40 ml of this solution was added, reaction occurred, and the addition was completed dropwise with further heating. The resulting solution was refluxed an additional 12 hr, cooled, and treated with ice-cold 10% sulfuric acid. The benzene layer gave 16g of the monoadduct. Recrystallization from ethanol gave a sample melting at 121°-124°C; IR: 2.87 (OH), 5.80 ($COOC_2H_5$) and 5.91μ(CO).

Anal. Calcd. for $C_{24}H_{22}O_4$: C, 77.00; H, 5.92. Found: C, 76.51; H, 5.78.

Results

2,3,4,5-Tetraphenyl-1,6-hexanedioic acid (V) was prepared directly by the electrochemical reductive dimerization of α-phenylcinnamic acid using the procedure for dimerizing cinnamic acid (1). The amount of benzene soluble by-products formed was larger than that obtained with cinnamic acid. In view of the complexity reported for these products (1), the by-products were not studied further.

The low yield of acid obtained suggested a study of the electrochemical hydrodimerization of α-phenylcinnamonitrile as a source of this acid. This reduction actually behaved differently than expected and gave a mixture of 1-amino-2,3,4,5-tetraphenyl-5-cyano-1-cyclopentene(I) and 2,3,4,5-tetraphenyl-1,6-hexanedinitrile. The structure of the former was based on IR and NMR spectra and its chemical behavior.

The NMR spectrum showed two doublets centered at δ3.54 and 5.04 ppm for the 3- and 4-hydrogens and a broad singlet at δ4.02 integrating for two hydrogens which disappeared in the presence of deuterium oxide. This spectrum favors the designation of I exclusively as the enamine form. The presence of the imine isomer would be expected to shift the hydrogen absorptions to the same region shown by the ketone II.

The large splitting constant of 10 Hz indicates that the 3- and 4-hydrogens are cis and that the configuration is *meso* for this portion of the compound.

Hydrolysis with acid gave the ketonitrile(II) which could be cleaved with alkali to the cyano acid (III). This acid (III) when hydrolyzed with sulfuric acid gave the amide acid (IV) which was resistant to further hydrolysis with acid or alkali. Deamination with nitrous acid gave the same acid (V) as is obtained by the dimerization of α-phenylcinnamic acid.

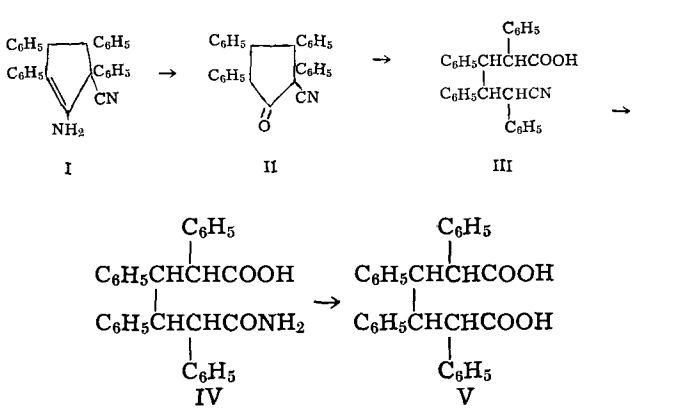

A similar cyclization has been observed in the electrochemical reductive dimerization of benzalacetophenone in dimethylformamide in the presence of carbon dioxide (3) and ethyl cinnamate in aqueous dimethylformamide (4).

The structure of 2,3,4,5-tetraphenyl-1,6-hexanedinitrile was based on its ir spectrum, mass spectral data, and chemical conversion to an isomeric 2,3,4,5-tetraphenylhexandioic acid (V) and an isomeric 1-amino-2,3,4,5-tetraphenyl-5-cyano-1-cyclopentene(I). The last compound gave an nmr spectrum which showed two

doublets centered at δ4.63 and 3.95 ppm for the 3 and 4-hydrogens and a broad singlet at δ3.8 for the two hydrogens of the amino group. A coupling constant of 8 Hz indicates that the 3- and 4-hydrogens are *trans* and that the configuration is *dl* for this portion of the molecule. Such an assignment is based on the Karplus rule (5).

The cyclopentene derivative I no doubt is formed from the anion of the expected hydrodimer (VI) by a Ziegler condensation even though the electrolyte was kept at the neutral point with acetic acid during the electrolysis.

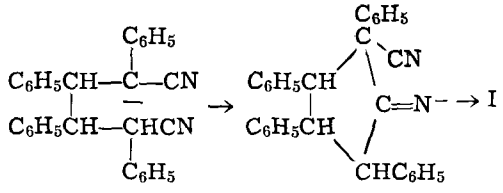

This anomaly may be caused by the tetraethylammonium ions adsorbed on the electrode surface. Such an environment would be more anhydrous than that of the bulk of the solution and less susceptible to the addition of acid.

The higher ratio of *meso/dl* suggests that in the dimerization of the anion radical directly at the surface of the electrode, steric factors and repulsion of the negative charges would favor form A and would lead to the formation of the *meso* isomer which cyclizes to the cyclopentane derivative I.

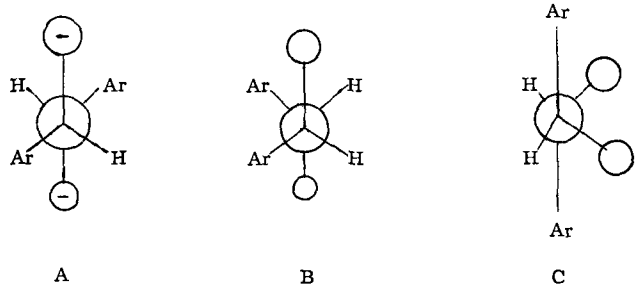

A B C

The second method of forming the dimer is by dimerization of the radical formed by protonation of the anion radical. Such a dimerization would be governed only by the steric effects of the groups involved and could give forms B and C. This type of addition would be expected to predominate in the bulk of the solution and to give the *dl*-isomer of the dinitrile.

Similar factors may be involved in the high ratio of *meso/dl* pinacols observed in the reduction of benzaldehyde in the presence of tetraalkylammonium and iodide ions (6).

Chemical methods leading to the synthesis of 2,3,4,5-tetraphenyl-1,6-hexanedioic acid (V) based on the condensation reactions of benzil were not successful. The Reformatsky reaction with ethyl α-bromophenylacetate gave only the monoadduct, ethyl 2,3-diphenyl-3-benzoyl-3-hydroxypropionate.

The alkaline condensation of phenylacetonitrile with benzil gave α-phenylcinnamonitrile.

Manuscript submitted Feb. 26, 1970; revised manuscript received *ca.* July 13, 1970. This was Paper 136 presented at the New York Meeting of the Society, May 4-9, 1969.

Any discussion of this paper will appear in a Discussion Section to be published in the June 1971 JOURNAL.

REFERENCES

1. C. L. Wilson and K. B. Wilson, *Trans. Electrochem. Soc.*, **84**, 153 (1943).
2. S. Wawzonek and E. M. Smolin, *Org. Syntheses, Coll.*, **3**, 715 (1955).
3. S. Wawzonek and A. Gundersen, *This Journal*, **111**, 324 (1964).
4. J. P. Petrovich, M. M. Baizer, and M. R. Ort, *ibid.*, **116**, 749 (1969).
5. M. Karplus, *J. Am. Chem. Soc.*, **85**, 2870 (1963).
6. V. J. Puglici, G. L. Clapper, and D. H. Evans, *Anal. Chem.*, **41**, 279 (1969).

The Electrochemical Oxidation of N,N-Dimethylaniline

Rodney Hand and R. F. Nelson*

Department of Chemistry, Sacramento State College, Sacramento, California 95819

ABSTRACT

The electrochemical oxidation of N,N-dimethylaniline (DMA) has been investigated in nonaqueous media in some detail. The products formed were found to depend on DMA concentration and the time of electrolysis. At low concentrations (10^{-3}M), the main product formed is N,N,N′,N′-tetramethylbenzidine. At intermediate concentrations (10^{-2}M) the major product is 4,4′-methylenebis (N,N-dimethylaniline), and at higher concentrations, especially at longer electrolysis times, the dye crystal violet and its leuco form were produced in large amounts. The mechanism to form these products depends on the lability of the methyl groups on the amine nitrogen; when other N,N-dialkylanilines were electrolyzed under similar conditions, only the corresponding tetraalkylbenzidines could be isolated.

The oxidation of N,N-dimethylaniline (DMA), by both chemical and electrochemical means, has commanded a good deal of attention for a number of years. The amine exhibits a multitude of reactions, as evidenced by the large number of products generated under varying conditions. The products formed seems to depend upon a bewildering series of variables: the solvent medium, the oxidizing agent, temperature, and concentration of reactants, for example, (1-9) and references therein. In addition, electrochemical oxidation under proper conditions can lead to substitution in either the aromatic ring (10-12) or on the N-methyl groups (13, 14). Thus, upon oxidation one can expect the cation radical to decompose by one or more of several pathways.

* Electrochemical Society Active Member.

Key words: organic electrochemistry, mechanism, coulometry, cyclic voltammetry.

As part of a study involving the anodic oxidation pathways of aromatic amines, the electrochemistry of DMA was investigated in some detail. Previous work in both aqueous and nonaqueous media had shown N,N,N',N'-tetramethylbenzidine (TMB) to be the primary electrolysis product. However, upon inspection of cyclic voltammograms in acetonitrile, it was apparent that indeed TMB was being formed by oxidation of DMA at platinum, but the amount formed was not at all equivalent to the quantity of DMA present, *i.e.*, it appeared that other unidentified products were forming. Various electrochemical and spectroscopic techniques were employed and it was found that other products were formed, the identities and amounts of which depended markedly upon solution conditions. In addition, several other N,N-dialkylanilines were studied electrochemically and their behavior correlated with that of DMA.

Experimental Procedures

The electrochemical and spectroscopic instrumentation and techniques were as previously described (15). The NMR spectra were recorded in $CDCl_3$ using a Perkin-Elmer R-20 spectrometer.

The N,N-dimethylaniline was obtained commercially and purified according to a standard procedure (16). N,N-Diethylaniline, N,N-di-n-butylaniline, N,N-di-sec-butylaniline, and N,N-di-n-decylaniline were all obtained commercially and were not further purified. The tetramethylbenzidine and tetraethylbenzidine were prepared by methylation and ethylation, respectively, of benzidine using trialkyl phosphates and were purified by column chromatography and recrystallization. N,N,N',N'-Tetramethyl-2,2'-diaminobiphenyl (o-oTMB) and N,N,N'N'-tetramethyl-2,4'-diaminobiphenyl (o-pTMB) were prepared by catalytic hydrogenation of the dinitro compounds (17). The diamino compounds were then methylated and purified by chromatography and recrystallization. 4,4'-Methylenebis (N,N-dimethylaniline) (MBDMA) and 4,4',4"-methylidynetris (N,N-dimethylaniline) (LCV) were obtained commercially and purified by recrystallization. N-p-Dimethylaminobenzyl-N-methylaniline was prepared by a benzoyl peroxide oxidation of DMA (1).

The purification of acetonitrile and the preparation and purification of tetraethylammonium perchlorate (TEAP) have also been previously described (15). Benzonitrile was obtained commercially and used with no further purification.

Constant potential mass electrolyses were carried out using a Wenking 61RH potentiostat. A two-compartment cell with a fine frit was used for electrolyses. A platinum gauze electrode was used as the working electrode, and an SCE was used as the reference electrode. All oxidation potentials were set about 100 mV anodic of the primary oxidation waves of the dialkylanilines as determined from cyclic voltammograms. The electrolyses were carried to virtual completion, *i.e.*, to a point where the current was less than 1% of the value at initiation of the electrolysis. In addition, after exhaustive oxidation the solutions were electrolyzed at −0.6V in order to convert any species in the oxidized state to the neutral form and to reduce protons generated by the various coupling reactions involved. It was found that if these protons were not electrolyzed before product isolation appreciable amounts of starting material and electrolysis products were lost during work-up.

Constant current mass electrolyses were carried out using the Wenking potentiostat modified according to procedures set forth in the operation manual (18). The constant current electrolyses were stopped after proceeding for calculated time intervals corresponding to one-half, one, one and one-half, and two electron n-values for DMA.

Products were isolated by evaporation of the solvent from the electrolysis mixture and extraction with dichloromethane. The TEAP taken up was precipitated out by the addition of ether. The supernatant was taken to dryness and chromatographed on Woelm neutral alumina with benzene, then dichloromethane and, if necessary, ethanol; the products were then recrystallized from benzene-ethanol. Thin layer chromatography experiments were carried out on "Baker-flex" aluminum oxide grade 1B T.L.C. paper using mixtures of benzene and petroleum ether as solvents (the per cent composition was not critical). The chromatograms were developed with iodine.

Results and Discussion

When the possible products that could form by oxidation of DMA were considered, the most likely prospects seemed to be the isomeric benzidines, TMB, o-pTMB, and o-oTMB. This was based on intuition as well as tritium tracer experiments run on DMA suggesting some sort of *ortho*-coupling (6) taking place. Consequently, the electrochemical properties of the previously mentioned benzidines were studied, and their cyclic voltammograms matched up with the DMA system, as shown in Fig. 1. One can see that a fertile imagination could find any of the benzidines in the DMA cyclic upon careful inspection. Consequently, recourse was taken to other means of identification of products. Attempts were made to detect the benzidines using *in situ* electrolysis in a Cary 14 uv-visible spectrometer, but the TMB band was so broad and intense that it swamped out any o-pTMB or o-oTMB (both of which had weak bands in this region) that might be present. Results with thin-layer chromatography were somewhat more successful. Using benzene-petroleum ether as a solvent medium, solutions from electrolysis of 10^{-3}M DMA were spotted along with authentic samples of the three isomeric benzidines.

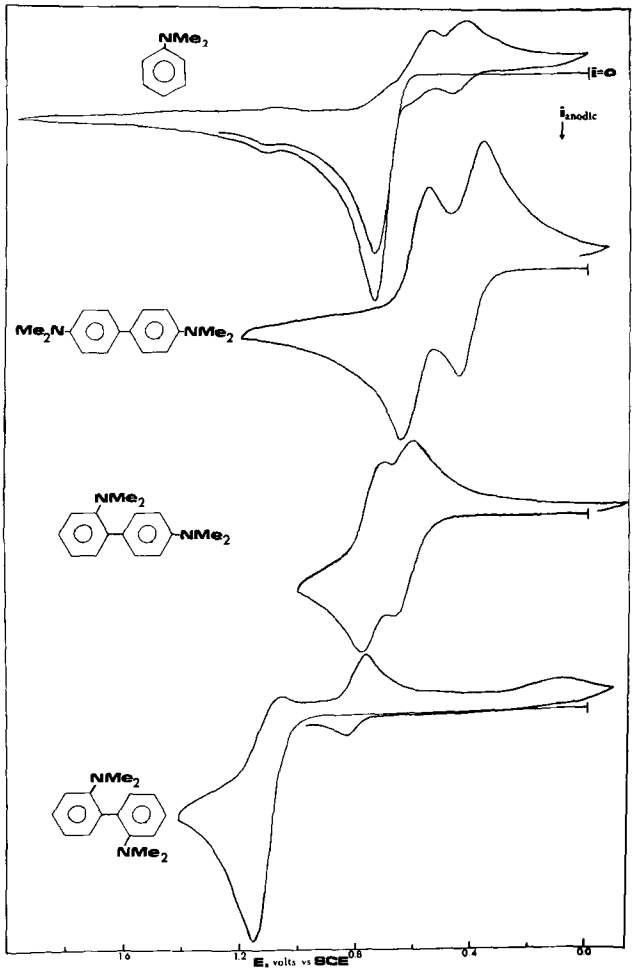

Fig. 1. Cyclic voltammograms of DMA and the isomeric benzidines in acetonitrile/0.1M TEAP.

TMB was definitely identified and another spot from the electrolysis solution matched up with either the o-pTMB or the o-oTMB. Since there is considerably less steric hindrance to *ortho-para*-coupling, it is believed that the other product formed in dilute solution is o-pTMB, in minor amounts.

Thus, in the region of milliformal concentration, the reaction mechanism seems to be relatively uncomplicated; DMA is oxidized to the cation radical; these then couple in one or more of several ring coupling fashions. As would be anticipated, the least sterically hindered pathway, *para-para*-coupling, predominates. One problem was finally solved after considerable consternation: on cyclic voltammograms it seemed that much less than quantitative amounts of TMB were forming from the oxidation of DMA. In addition, the electrochemical data gave an n-value of about one as opposed to the two electrons that would be expected for this classical ECE system (TMB is more easily oxidized than DMA). This is due to the fact that appreciable amounts of the DMA are protonated by protons released in the coupling reaction to form TMB. Since DMA is a moderately strong base, the degree of protonation, estimated at 40-50% when compared with aliphatic amines (19), is appreciable. This factor must be considered when one is working on the electrochemistry of organic bases in nonaqueous media.

As the concentration of DMA is increased from 10^{-3} to 10^{-1}M, the composition of the electrolysis products obtained changes markedly. At intermediate concentrations (10^{-3} to 10^{-2}M), relatively little TMB is obtained, and instead, another product resulted in fairly high yields (30-40%). This product eluded identification for some time until heed was paid to work that cited the formation of MBDMA from DMA via various chemical oxidation pathways (1, 2); small amounts had also been isolated from electrochemical oxidations in aqueous media (4). Once the product was acknowledged, identification was straightforward. Normally, cyclic voltammograms are not a reliable matching-up tool for suspected electrolysis products, but in this case the cyclic of the electrolysis product was found to be very similar to that of an authentic sample of MBDMA, as shown in Fig. 2. The electrolysis product was verified by melting point, its IR spectrum and its NMR spectrum, in each case compared with an authentic sample of MBDMA.

Since the MBDMA contains a methylene group inserted between two DMA segments, the question of the origin of the methylene group seemed pertinent. In the normal electrolysis situations, a methylene group could conceivably be abstracted from either the solvent (CH_3CN) or the ethyl groups of the supporting electrolyte, TEAP. Accordingly, a mass electrolysis of a 10^{-2}M solution of DMA in benzonitrile using 0.1M sodium perchlorate as supporting electrolyte was conducted. In this system, the only source of methyl groups would be from the DMA. Similar results were obtained compared to the acetonitrile/TEAP experiments (however, product yields were much lower due to problems in work-up from benzonitrile), so it seems safe to conclude that the electrochemical oxidation pathway involves abstraction of a methyl group from the dimethylamino portion of DMA to form the MBDMA. In addition, chemical oxidations of DMA to MBDMA have been carried out in solvents such as benzene and carbon tetrachloride using benzoyl peroxide as oxidant (1, 20).

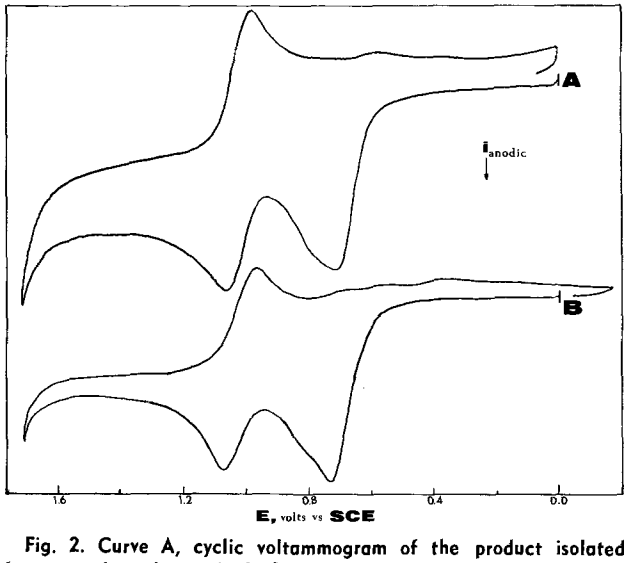

Fig. 2. Curve A, cyclic voltammogram of the product isolated from an electrolysis of 10^{-2}M DMA in acetonitrile/0.1M TEAP; curve B, cyclic voltammogram of an authentic sample of MBDMA in acetonitrile/0.1M TEAP.

The most plausible mechanism for formation of MBDMA from DMA has been proposed as the reaction pathway followed in the benzoyl peroxide oxidation and gamma radiolysis of DMA (21, 22). This involves initial formation of a DMA cation radical, not an unreasonable assumption. It should be pointed out that no direct evidence for the existence of DMA cation radical was found in the present work or in any previous studies. However, based on other studies on aromatic amines in general and substituted DMA's in particular, it seems safe to assume that the DMA cation radical is the first intermediate formed (I). This radical can then attack a parent DMA molecule, the *para*-ring position of the cation attacking one of the methyl groups of the parent to form a substituted benzyl amine, N-p-dimethylaminobenzyl-N-methylaniline (II). This species is then protonated to form (III). This then breaks up to give (IV) and N-methylaniline. A molecule of DMA then reacts with (IV) to form MBDMA. Attack of (I) on MBDMA could then lead to a molecule of leuco crystal violet, LCV. Since LCV is more easily oxidized than DMA, formation of crystal violet dye from LCV ensues. In addition to all this, there is a parallel reaction pathway, the one classically cited, whereby TMB is formed by coupling of two DMA radicals. The over-all reaction pathway is shown in Fig. 3. Due to the coupling reactions occurring in these systems, protons are generated in substantial amounts; protonation of DMA and the various products certainly occurs, but this has not been shown for the sake of clarity.

Several alternative paths to this general mechanism are possible and should be mentioned, although they are difficult or impossible to verify. Reaction [3] in Fig. 3 may go by the pathway shown below[1] rather than by attack of (I) on the methyl group of a parent DMA molecule. The over-all result is identical in both cases, *i.e.*, formation of (II), but this alternative mechanism is certainly a possibility.

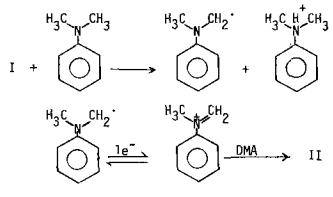

These mechanistic steps are consistent with the fact that MBDMA and crystal violet are formed only at intermediate and high DMA concentrations, where parent DMA molecules are available to act as bases toward DMA cation radicals. Deprotonation of the cation radical (I) has also been suggested from the results of chemical oxidation studies (23). This work is particularly pertinent since the oxidizing agents employed, chloranil and copper(II), are one-electron types and hence might furnish data more applicable to reactions of the DMA cation radical. In fact, the product distribution obtained in this study was markedly similar to that from the present electrochemical work.

[1] This alternative mechanism was suggested by a referee.

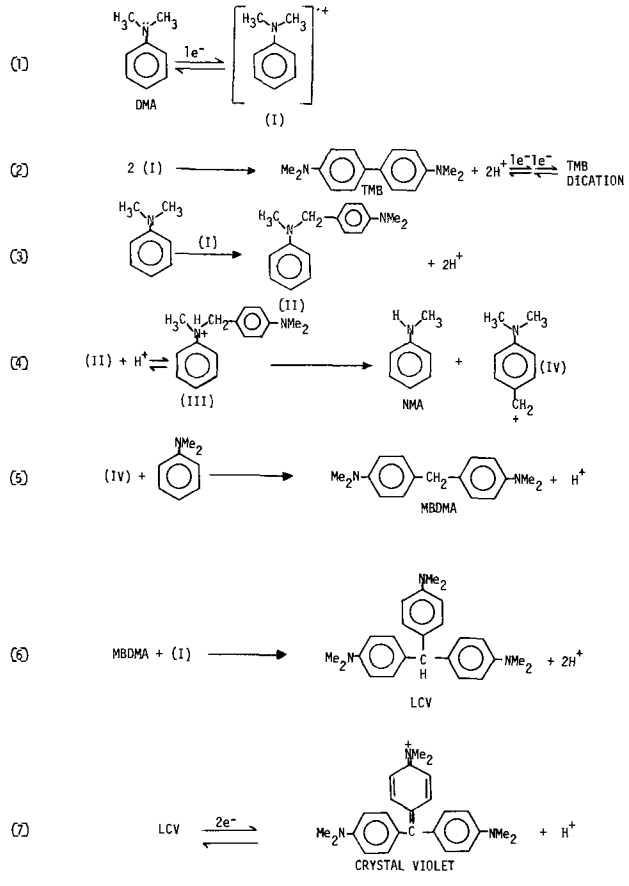

Fig. 3. Proposed reaction pathways for the anodic oxidation of N,N-dimethylaniline in acetonitrile.

Reaction [6] in Fig. 3 is also somewhat less than certain. It would seem just as likely that the formation of leuco crystal violet might occur via reaction between oxidized MBDMA and parent DMA, rather than by the opposite radical-parent route; this is so because the oxidation potentials of DMA and MBDMA are almost identical. Thus, it was not possible to carry out studies where one would be electrolyzed in the presence of the other to induce formation of leuco crystal violet. Again, the pathways are different, but the end product is identical; verification of the correct pathway must await more sensitive studies in order to differentiate.

Repeated attempts were made to isolate the substituted benzyl amine intermediate by terminating electrolyses well short of the calculated end point and attempting recovery by chemical means. These attempts were singularly unsuccessful probably due to the fact that this intermediate is quite unstable; the application of even moderate heat induces its conversion to MBDMA in the presence of any excess DMA.

It was felt that detection of N-methylaniline (NMA) in the electrolysis mixtures was essential to verifying the proposed mechanism, but this task was hampered by the fact that NMA is oxidized at about the same potentials as DMA, leading to unknown products. However, visible absorption spectra of electrolysis solutions of DMA and NMA show a common peak at about 550 mμ that cannot be ascribed to any of the DMA oxidation products previously mentioned. Likewise, a common spot is obtained on thin-layer chromatograms of the two solutions. Further work now under way on the oxidation of NMA may clarify this aspect of the work.

At higher DMA concentrations (10^{-1}M and higher), less MBDMA is found; as shown in the reaction scheme the next highest analog, leuco crystal violet, is formed in small amounts and a goodly portion of the yield is in the form of the dye crystal violet. This is an intensely colored dye and its presence was confirmed by comparison of the visible absorption spectra of a DMA electrolysis solution and an authentic sample of the dye; the match-up is striking. The gradual formation of the dye can be seen in the visible absorption spectra shown in Fig. 4. These spectra were recorded after various times of electrolysis of a 0.2M solution of DMA in acetonitrile. Note that even at this concentration it appears that TMB is formed initially. However, as the electrolysis proceeds the concentration of crystal violet increases and the TMB fades away in comparison. At the end of the electrolysis the only species giving rise to an absorption band in the visible region of the spectrum is the crystal violet dye. It is felt that parallel reaction pathways are operative to produce TMB and the other electrolysis products; fairly extensive studies on the electrochemical oxidation of TMB alone and in the presence of DMA, though complicated, have not shown evidence for formation of MBDMA or crystal violet (24). At first, the concept of crystal violet being formed from the oxidation of DMA is implausible at best, but again recourse to the literature shows that it is not unheard of. In fact, chemical oxidation of DMA by chloranil and copper(II) leads to appreciable yields of crystal violet (23, 25) (see above).

In order to verify that all the products cited are formed concurrently, a constant current electrolysis of a 1M DMA solution in MeCN was run and terminated well before completion ($n = 0.5$). The major products formed were MBDMA and LCV; small amounts of TMB and crystal violet were also detected. It would seem, then, that the formation of the various products depends markedly on DMA concentration. This is certainly true, but another variable was also found to be important, namely current density (or electrolysis duration). At low current densities (or long electrolysis times), more of the crystal violet and its leuco form were produced from DMA. This was confirmed with a series of constant current electrolyses at varying current densities, and it was found that solutions containing intermediate concentrations of DMA (10^{-2} to 10^{-1}M) yielded progressively larger amounts of the

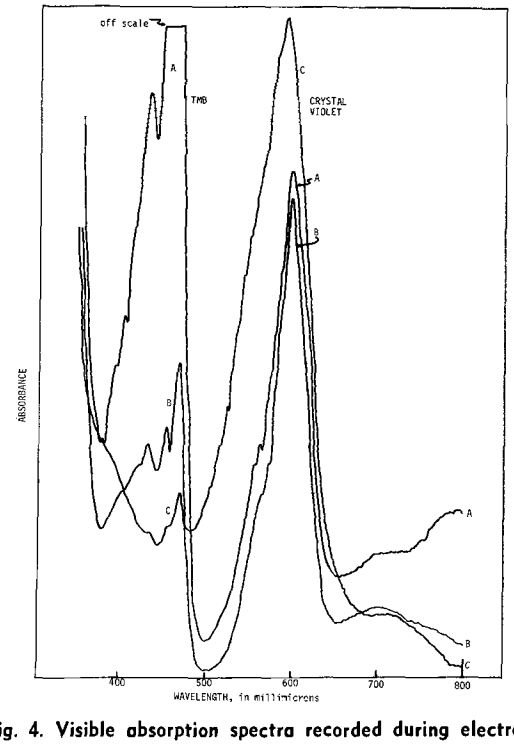

Fig. 4. Visible absorption spectra recorded during electrolysis of a DMA solution (0.2M) in acetonitrile/0.1M TEAP. Concentrations are not comparable (samples were diluted to various extents) from one curve to the next. Curve A, early in the electrolysis; curve B, middle electrolysis; curve C, late in the electrolysis.

dye with decreasing current density. This is reasonable in view of the deprotonation mechanism mentioned above. At low current densities, the ratio of parent DMA to cation radical is greater and deprotonation is more likely to occur.

Several other N,N-dialkylanilines were briefly investigated to determine whether the bulk and abstractability of the alkyl group would have an effect on the course of the electrochemical oxidation pathway. The electrochemical properties of DMA and these other N,N-dialkylanilines are shown in Table I. Over-all, the properties do not vary a great deal with the nature of the alkyl group; most of the variation can be ascribed to differences in diffusion coefficients. Electrochemical data for N,N-dimethyl-p-anisidine, a model one-electron, reversible system, are included for purposes of comparison. The *n*-value data obtained at varying concentrations confirm the relatively uncomplicated behavior at low concentrations, *i.e.*, formation of benzidines, and the complex nature of the electrode process at higher concentrations, especially for DMA. At low concentrations, one would anticipate a ratio of reverse to forward current of 0.5 if only benzidine formation were taking place, analogous to the triphenylaminetetraphenylbenzidine system (26). This is generally observed for all the dialkylanilines at low concentrations and for all but DMA at intermediate and higher concentrations. The very low value for DMA at 10^{-1}M is due to the fact that the major product formed by multiple electrochemical and chemical steps, crystal violet, is not re-reduced after the initial oxidation.

When exhaustive electrolyses were carried out on 10^{-1}M solutions of the ethyl and n-butyl derivatives, only the *para-para*-benzidines corresponding to the dialkylanilines were isolated, with some difficulty and in only moderate yields of 40-50%. The fact that the ethyl and n-butyl analogs of MBDMA and crystal violet were not detected is further evidence to confirm the origin of the central carbon of MBDMA and crystal violet as coming from DMA itself and not the solvent or supporting electrolyte. No other products could be isolated and identified in these systems, although the rather low yield of benzidines indicates further complications. This may be due, in fact, to follow-up reactions involving the benzidine dications. These systems, previously thought to consist only of reversible electron transfer steps, have been found to contain chemical complications as yet undefined (24).

From the foregoing data, it would seem that the products formed in the anodic oxidations of N,N-dialkylanilines depend on a number of factors, namely, concentration, length of electrolysis (or current density), and the nature of the alkyl groups attached to the amine nitrogen. The concentration dependence most likely stems from the relative concentrations of parent amine and radical cation near the electrode surface, the area in which the homogeneous chemical reactions take place. At low bulk concentrations of parent amine, the ratio of radical to parent near the electrode surface is high, hence radical-radical coupling occurs to form the benzidines. At higher bulk concentrations there is more parent amine near the electrode surface, and so the rather complicated series of homogeneous chemical reactions leading ultimately to crystal violet dye ensues. However, even at high DMA concentrations benzidine formation still occurs as a parallel reaction pathway.

It was not unexpected that the anodic oxidation pathways of the other N,N-dialkylanilines, as opposed to DMA, would be less complicated. In the former species, the alpha-carbon of the dialkylamino groups is much less susceptible to attack by incoming radicals; therefore, it is not surprising that benzidine formation predominates even at higher concentrations.

Table I. Electrochemical properties of N,N-dialkylanilines

	$E_{p/2}$[a]	$ip/v^{1/2}C$[b]	$it^{1/2}/C$[c]	n-values[d]	$i_{rev}/i_{for.}$[f]
R=CH_3	0.72	35.0	57.0	1.1, 1.0, 1.2	0.50, 0.34, 0.05
C_2H_5	0.70	34.0	54.0	1.1, 1.1, 1.4	0.50, 0.47, 0.37
n-C_4H_9	0.69	32.5	49.6	1.2, 1.2, 1.4	0.48, 0.40, 0.35
sec-C_4H_9	0.70	33.5	51.0	1.1, 1.2	0.54, 0.48
n-$C_{10}H_{21}$	0.69	29.0	43.0	1.0, 1.1	0.47, 0.42
	0.52	36.0	56.0	1.0, 1.0	1.0, 0.98

[a] Half-peak potentials measured at a scan rate of 21.0 V/min; in volts *vs.* SCE. There is a marked anodic shift with increasing scan rate.
[b] Peak current data; values stated are averages from several different scan rates ranging from 3.0 to 60.0 V/min.
[c] Chronoamperometry data; values stated are average values taken from current-time curves from 0.5 to 8.0 sec.
[d] Values stated are for concentrations of 10^{-5}, 10^{-3} and 10^{-1}M, respectively.
[e] One-electron model compound; data are presented for purposes of comparison.
[f] Ratio of reverse to forward integrated currents taken from coulometric n-value determinations shown. The oxidation potential was set at +0.90V; re-reduction was effected at 0.00V; thus proton reduction is not included in $i_{rev.}$.

Acknowledgments

Grateful acknowledgment is made to NSF Grants GP-8941 and GY-4189 for financial support of this work. Special thanks are also due to Dr. R. N. Adams and Dr. D. E. Smith for their support and encouragement.

Manuscript submitted March 30, 1970; revised manuscript received *ca.* June 19, 1970.

Any discussion of this paper will appear in a Discussion Section to be published in the June 1971 JOURNAL.

REFERENCES

1. J. M. Fayadh, D. W. Jessop, and G. A. Swan, *Proc. Chem. Soc.*, 236 (1964).
2. D. M. Graham and R. B. Mesrobian, *Can. J. Chem.*, **41**, 2938 (1963).
3. Fr. Fichter and E. Rothenberger, *Helv. Chim. Acta*, **5**, 166 (1922).
4. W. Lob, *Z. Elektrochem.*, **7**, 579 (1901).
5. Z. Galus and R. N. Adams, *J. Am. Chem. Soc.*, **84**, 2061 (1962).
6. Z. Galus, R. M. White, F. S. Rowland, and R. N. Adams, *idem.*, 2065.
7. T. Mizoguchi and R. N. Adams, *idem.*, 2058.
8. J. E. Dubois, P. C. Lacaze, and A. Aranada, *Compt. rend.*, **260**, 3383 (1965).
9. V. Dvorak, I. Nemec, and J. Zyka, *Microchem. J.*, **12**, 99 (1967).
10. Fr. Fichter and P. Schonmann, *Helv. Chim. Acta.*, **19**, 1411 (1936).
11. E. L. Helwig, U.S. Pat. 1,816,848 (1931); *Chem. Abstr.*, **25**, 5355 (1931).
12. N. N. Mel'nikov and E. M. Cherkasova, *J. Gen. Chem. USSR Eng. Transl.*, **16**, 1025 (1946).
13. N. L. Weinberg and E. A. Brown, *J. Org. Chem.*, **31**, 4058 (1966).
14. N. L. Weinberg and T. B. Reddy, *J. Am. Chem. Soc.*, **90**, 91 (1968).
15. J. F. Ambrose and R. F. Nelson, *This Journal*, **115**, 1159 (1968).
16. A. I. Vogel, "A Textbook of Practical Organic Chemistry," 3rd Ed., p. 573, Wiley & Sons, New York (1956).
17. S. D. Ross, G. J. Kahan, and W. A. Leach, *J. Am. Chem. Soc.*, **74**, 4122 (1952).
18. "Wenking Potentiostat 61RH Operating Instructions," 1966.
19. P. J. Smith and C. K. Mann, *J. Org. Chem.*, **34**, 1821 (1969).
20. R. B. Roy and G. A. Swan, *Chem. Commun.*, 427 (1966).
21. J. M. Fayadh and G. A. Swan, *J. Chem. Soc.* (C), 1775 (1969).
22. G. A. Swan, *idem.*, 2015.
23. J. R. L. Smith, R. O. C. Norman, and W. M. Walker, *J. Chem. Soc.* (B), **1968**, 269.
24. R. Hand, Unpublished data.
25. J. W. Eastman, G. Engelsma, and M. Calvin, *J. Am. Chem. Soc.*, **84**, 1339 (1962).
26. E. T. Seo, R. F. Nelson, J. M. Fritsch, L. S. Marcoux, D. W. Leedy, and R. N. Adams, *ibid.*, **88**, 3498 (1966).

Preparation of N-Alkylacetamides by the Anodic Oxidation of Carboxylic Acid Salts

D. L. Muck* and E. R. Wilson

The Procter & Gamble Company, Miami Valley Laboratories, Cincinnati, Ohio 45239

ABSTRACT

The possibility of preparing N-alkylacetamides by the electrolytic oxidation of carboxylate ions at a carbon anode in the presence of acetonitrile has been investigated. A yield of substituted acetamide of about 50% was obtained with potassium valerate, but it gradually dropped to zero in favor of the Kolbe coupled product in going from potassium octanoate to potassium laurate. An explanation of this effect involving specific orientation of the adsorbed long chain carboxylates on the electrode surface is included. Products derived from intermediate carbonium ions were found, and a mechanism for their formation is proposed.

After a period of time when little work was done on the Kolbe electrosynthesis, the last few years have seen a definite surge of interest in the reaction. Most of this recent work has been directed toward the elucidation of the mode of electron transfer taking place at the electrode surface, but one very important feature which may have definite synthetic implications is the relatively recent discovery that carbonium ions are sometimes formed in the reaction (1-14). The important variables affecting carbonium ion formation are apparently the nature of the anode material and the structure of the carboxylate salt employed. In the case of an oxidation run under normal Kolbe conditions where platinum anodes are employed, carbonium ions are apparently formed only when the radical initially generated in the reaction has an electron impact ionization potential (I.P.) of less than 8 eV (3). However, Koehl (6) has shown that the use of a carbon anode promotes carbonium ion formation even with carboxylates derived from simple straight chain fatty acids, where the I.P. may be 8-10 eV. We have been very interested in this development, since it ideally presents a way to functionalize the alkyl chains derived from fatty acids.

In addition to the more common nucleophiles known to react with carbonium ions, acetonitrile has been shown to give nitrilium salts (7, 15) which can then react with water to give N-substituted acetamides. A precedent for

$$R^+ \xrightarrow{CH_3CN} R{-}N{=}\overset{+}{C}{-}CH_3 \xrightarrow{H_2O} RNHC(=O)CH_3 \quad [1]$$

the trapping of anodically generated carbonium ions with acetonitrile had previously been set by Eberson (7), so we also used acetonitrile and employed carbon anodes to promote carbonium ion formation. During the period of our work, the results of a similar study were published by Kornprobst and co-workers (12). In this case, however, the oxidations were carried out at platinum anodes, so that products derived from carbonium ions were isolated in yields of more than 20% only when branched chain carboxylates were employed (where the I.P. of the alkyl radical was less than 8 eV). In our work we have found that butyl cations react with acetonitrile and water to give two unexpected products, an N-acylvalerylamide and an N-butylvalerylamide in addition to the desired acetamide and other by-products. This work confirms and complements the results of Kornprobst and co-workers. We have also uncovered an intriguing phenomenon involving a gross variation in reaction products: longer chain fatty acid carboxylates give decreasing amounts of carbonium ions as the chain length increases, thereby yielding larger quantities of normal Kolbe coupled products. Explanations for this variation are discussed.

* Electrochemical Society Active Member.

Key words: Kolbe electrosynthesis, n-alkylacetamides, carbon anodes, carbonium ions.

Experimental

Materials.—The acetonitrile employed was Matheson, Coleman, and Bell spectral grade. The carboxylic acids, the isomeric heptyl alcohols, and docosane used were all obtained commercially and were used without further purification.

Apparatus.—A d-c power supply capable of producing 5A current and potentials of up to 220V was employed. The electrolysis cell consisted of a resin pot with 3 ground glass joints in the lid through which the electrode leads and a cooling coil were sealed. The system was flushed with He before each reaction. The gases evolved during the reaction were passed through the tube of Drierite, a tared tube of Ascarite, and finally through a trap cooled in liq N_2. The electrodes were carbon rods 1 in. in diam and 2 in. long (A = 7.0 in.^{2}; 45.7 cm^2). Infrared spectra were obtained with a Perkin-Elmer Infracord spectrophotometer, while the NMR spectra were obtained on Varian T-60 and HA-100 spectrometers. Gas chromatographic separations were made on an F&M Model 700 equipped with a 6 ft x 0.25 in. column packed with 10% Apiezon L on 60-80 mesh Chromosorb W, acid washed and dimethyldichlorosilane treated. Mass spectra were obtained with an Atlas CH-4 instrument.

General electrolysis procedure.—A description of the oxidation of potassium valerate is given as being typical. Potassium valerate (140.0g, 0.10 mole) was dissolved in 22 cc of water and diluted with 200 cc of acetonitrile. A d-c voltage of about 20V was applied until a current of 2.0A flowed. The applied voltage was then held constant and the electrolysis was continued for a period equal to three times the half-life of the reaction (the half-life of each reaction was taken as the time required for the current to drop to 50% of its original value). The reaction solution was then removed from the cell, the cell was rinsed with a little water, and the rinse was combined with the bulk solution. The resulting solution was analyzed for octane and butyl alcohol by GLC, and then refluxed under a condenser connected to a liq N_2 trap to collect any remaining volatile hydrocarbons. The solvents were then removed from the reaction solution on a rotary evaporator, about 75 cc of water were added, and this solution was extracted with ether. The ether extracts were combined, dried over $MgSO_4$, and concentrated on a rotary evaporator to give about 5g of organic products. The aqueous layer was acidified with 6*N*

HCl, extracted continuously overnight with ether, and the resulting ether layer was dried over $MgSO_4$ before evaporation on a rotary evaporator to give 0.5-3g of unreacted valeric acid. The volatile hydrocarbons collected in both liq N_2 traps were warmed to dry ice-acetone temperature before being weighed, and were then analyzed by NMR and mass spectrometry. They were found to be essentially the same mixture of butenes and methyl cyclopropane as previously reported. The liquid organic products were isolated and purified by preparative scale GLC. The identities of the products were established by comparison of GLC retention times, *IR* spectra and NMR spectra with those obtained on samples prepared by independent methods.

Preparation of N-alkylacetamides.—Samples of the various N-alkylacetamides needed for comparison purposes were prepared by adding an ether solution of acetyl chloride drop-wise to an equimolar quantity of the appropriate amine in ether at room temperature. The resulting ether solution was filtered and the solvent removed from the filtrate on a rotary evaporator. The crude acetamides were then purified by preparative scale GLC.

N-(sec-butyl)-N-acetylvalerylamide.—To 4.8g (0.03 mole) of N-(sec-butyl)valerylamide which was prepared by reacting valeryl chloride with sec-butyl amine were added 100 ml of ether and 4.8g (0.06 mole) of pyridine. A solution of 2.4g (0.03 mole) of acetyl chloride in 20 ml of ether was added drop-wise, and the resulting solution was refluxed for 2 hr. More acetyl chloride (1.2g; 0.015 mole) was then added and the mixture was refluxed for 2 hr more. About 5 ml of ethanol were added, and the resulting solution was washed twice with dil HCl, 3 times with satd. $NaHCO_3$, and finally once with water before drying over anhyd $MgSO_4$. The solvents were removed with a rotary evaporator to give 1.0g (17%) of a clear oil with no N-H infrared absorption. Purification by preparative scale GLC gave a colorless liquid.

Anal Calc for $C_{11}H_{21}NO_2$: C, 66.33; H, 10.55; N, 7.04. Found: C, 66.50; H, 10.85; N, 7.32.

Stability of N-(sec-butyl)-N-acetylvalerylamide to reaction conditions.—The conditions for the electrolysis of potassium valerate as described above were repeated, except that 15% water in acetonitrile was used as the solvent, and 2.0g of N-(sec-butyl)-N-acetylvalerylamide were added. The electrolytic oxidation of the valerate was then carried out as before, and the products were isolated. Octane (0.1g; 0.0009 mole) and N-sec-butyl acetamide (1.8g; 0.016 mole) were obtained along with 4.8g of the above substituted valeryl amide. Subtracting out the amount of this latter material that was added to the initial reaction solution (2.0g), a yield of 2.8g (0.014 mole) was obtained, which is very close to the average of 2.4g obtained in three normal reactions.

Electrolysis of potassium octanoate in water.—Octanoic acid (14.4g; 0.10 mole) and 5.6g (0.10 mole) of potassium hydroxide were dissolved in 200 ml of water and electrolyzed according to the general procedure described before. The aqueous solution obtained was then extracted three times with ether, and the combined extracts were dried over anhydrous magnesium sulfate. The solvent was then removed on a rotary evaporator to give 0.8g of heptyl alcohols. This mixture was analyzed on capillary column GLC using known samples of the various isomeric heptyl alcohols as standards. The following amounts of each were found: 1-heptanol, 18.5%; 2-heptanol, 43.8%; 3-heptanol, 37.7%.

Results

Since long-chain compounds are often difficult to work with, potassium valerate was employed initially as the starting material. In every case, contrary to normal Kolbe reaction conditions, the valeric acid was completely neutralized, since it has previously been shown that high carboxylate concentrations favor carbonium ion formation (14). For anodes, we initially attempted to use the types of carbon used before by Koehl (6), but the acetonitrile dissolved the organic binders they contained and eroded the electrodes badly. A shift was then made to regular amorphous hard carbon rods, the apparent density of which varied in the range of 1.42-1.53 g/ml, and these anodes seemed to serve very well. A cylindrical perforated copper cathode was used, and the initial reactions were run in a 10% water in acetonitrile solvent mixture. We did obtain the desired acetamide **2** in a 26% yield, but we also isolated the unexpected products **3** and **4** as well as isomeric butenes and methyl cyclopropane arising from loss of a proton from the intermediate butyl cation.

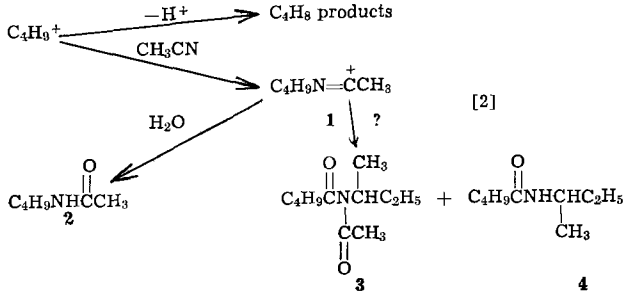

In an effort to maximize the yield of the desired acetamide **2**, a study of the variation of products with an increase in the amount of water employed was made. Concentrations of water below 10% were not used because the starting material was not completely soluble. At least four runs were made for each set of conditions, and the average values of these are shown in Table I. The yields for each run were generally within 5% of the average value, but they sometimes varied as much as 15% from the average.

Since it was conceivable that products **2** or **4** could have resulted from a degradation of **3**, a sample of **3** prepared by an independent synthesis was added to a normal electrolytic reaction to check its stability to reaction conditions. The amount of **3** obtained from this reaction was greater than normal by essentially the amount added to the reaction, and the quantities of other products isolated were within their normal ranges. Therefore, **3** is stable to the reaction conditions and could not be a source of **2** or **4**.

In order to investigate the possible variations in the product distribution with changes in the type of carbon used for the anode, normal graphite as well as pyrolytic graphite anodes were also used. The characteristics of

Table I. Product distribution as a function of the water concentration

Yields are based on mole per cent of the organic products.

Per cent water	10	15	20	25	30	35	40
$CH_3CNHCHC_2H_5$ (O, CH_3)	26	50	50	40	26	31	26
$CH_3(CH_2)_3CNCHC_2H_5$ (O, CH_3, CCH_3, O)	35	23	15	12	2	0	0
$CH_3(CH_2)_3CNHCHC_2H_5$ (O, CH_3)	8	8	11	8	6	3	0
C_4H_8 Products	21	13	23	39	23	44	26
C_8H_{18}	10	6	1	1	0	0	0
C_4H_9OH	0	0	0	0	43	22	48

these materials are shown in Table II, and the data on the product trends observed in a 15% water in acetonitrile solvent mixture are listed in Table III. The yields obtained on a platinum anode are included in Table III for the sake of comparison.

From Table I, one can see that the best yields of N-sec-butyl acetamide were obtained in 15-20% water in acetonitrile solvent mixtures. Therefore, the potassium salts of octanoic and lauric acids were electrolyzed under these conditions to verify that similar results could be obtained with longer chain fatty acids. Surprisingly however, the results differed with these salts. As the length of the carbon chain attached to the carboxy group increased, the amount of normal Kolbe coupled product increased markedly to the point at which only docosane, $C_{22}H_{46}$, was formed in the oxidation of potassium laurate. A summary of the data obtained from the oxidation of these salts is shown in Table IV.

Kornprobst and co-workers (12) observed a number of alkyl group rearrangements in their work. With potassium valerate we found the same isomerization of the C_4H_9 chain to give sec-butyl derivatives. In order to study the alkyl rearrangements in longer chain salts, we analyzed the alcohols obtained from the oxidation of potassium octanoate in a 50% water in acetonitrile solvent mixture by capillary column gas chromatographic comparison with known samples of the isomeric heptyl alcohols. The results showed 18.5% 1-heptanol, 43.8% 2-heptanol, and 37.7% 3-heptanol with no 4-heptanol found.

Discussion

Oxidation of valeric acid.—The products obtained from the oxidation of potassium valerate were generally those expected. It has previously been established that side reactions of the butyl cation give isomeric butenes as well as some methylcyclopropane (6). The fact that butyl alcohol was observed in these reactions is not unusual because its formation from a carbonium ion generated in the presence of water would certainly be predicted, but it does seem unreasonable that the amount of water would have to be greater than 25% for this reaction to take place. One can justify the result by assuming that adsorption of carboxylate ions and/or acetonitrile on the anode surface prevents the water from reaching the reactive carbonium ion generated on that surface.[1]

While the above products were generally expected, the formation of the N-acyl amide **3** and the valeryl amide **4** was somewhat unusual. In order to explain the formation of these products, the following is presented as a reasonable mechanism which is consistent with the observed results. The basic concept was substantiated by the report of Kornprobst and co-workers (12), who also explained the formation of the N-acyl amide **3** by rearrangement of **5**. The rearrangement of **5** to the products **3** and **4** is postulated in our mechanisms as proceeding *via* a 4-membered ring transition state which may or may not be a concerted process. The hypothetical intermediate **6** is shown to illustrate the rearrangement more clearly. A similar rearrangement involving a 1,3-acyl migration from carbon to nitrogen has been reported by Curtin and Richman (16).

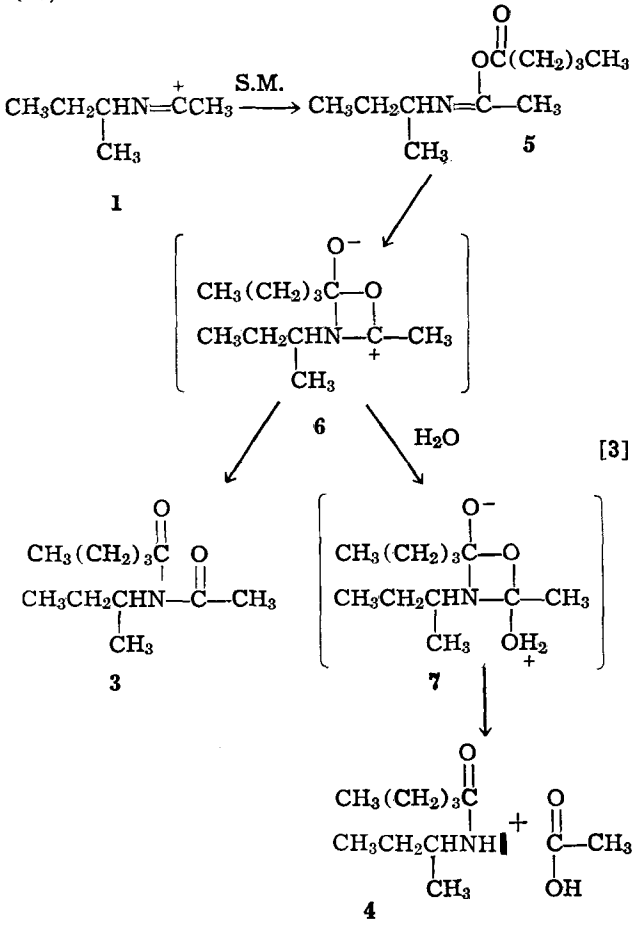

The trends in the variation of these products as the concentration of water changes are generally consist-

Table II. Carbon used for anodes

Form of carbon	Manufacturer	Type	Apparent density (g/ml)
Unmachined amorphous carbon	Great Lakes Carbon	BC	1.42-1.53
Graphite	Poco Graphite	AXZ	1.50-1.60
Graphite	Poco Graphite	AXZ-5Q	1.80-1.88
Pyrolytic graphite	General Electric	EC	2.20-2.23

Table III. Product distribution as a function of the anode

Yields are based on mole per cent of the organic products.

	Amorphous carbon	Pyrolytic graphite	AXZ graphite	AXF-5Q graphite	Platinum
$CH_3CNHCHC_2H_5$ (O, CH_3)	50	29	49	46	19
$CH_3(CH_2)_3CNCHC_2H_5$ (O, CH_3)	23	3	10	18	0
$CH_3(CH_2)_3CNHCHC_2H_5$ (O, CH_3)	8	12	10	8	6
C_4H_8 Products	13	56	31	28	42
C_8H_{18}	6	0	0	0	33
C_4H_9OH	0	0	0	0	0

Table IV. Kolbe product distribution as a function of chain length

Yields are based on amount of starting acid used up.

Acid	Product	Yield
$C_4H_9CO_2H$	C_8H_{18}	10
$C_7H_{15}CO_2H$	$C_{14}H_{30}$	58
$C_{11}H_{23}CO_2H$	$C_{22}H_{46}$	69

[1] A referee has suggested that the anode potential in these reactions may be high enough that water is being oxidized, thereby depleting its concentration at the electrode surface. This could explain the high concentration of water required to form alcohol from the butyl cation. We cannot rule out this possibility but tend to discount it for the following reasons. Numerous electrochemical studies in the past have demonstrated that the electrolysis of water ceases in the Kolbe electrosynthesis when the potential becomes anodic enough to oxidize carboxylate ions. In addition, one would not expect the current to decrease in value with time as it does in these reactions if water were being electrolyzed because the amount of water is so great that its concentration would remain essentially constant during the time span involved.

ent with the scheme above. The yield of N-(sec-butyl)acetamide, **2**, increases sharply as the per cent of water changes from 10 to 15%, indicating that the concentration of water is such that it can effectively compete with the starting material for reaction with the nitrilium cation. The large molar excess of water required for this to happen may be the result of the carboxylate anion adsorbing on the positively polarized anode. The yield of substituted acetamide then begins to decrease with increasing water concentration due to increased side reactions of the butyl cation, initially to form olefins and later to react directly with the water to form alcohol. The drop in the amount of the N-acyl amide **3** formed with an increase in the amount of water present would be predicted. The over-all yield of N-(sec-butyl) valeryl amide formed was never high and, therefore, the small changes observed are not significant. The Kolbe product in this case is octane, and while about 10% was formed in the 10% water in acetonitrile solvent system, generally negligible quantities were observed in the solutions with greater amounts of water present.

Although the data obtained in the above studies involving varying water concentrations were reproducible only to about ± 15%, there seems to be no obvious explanation. Each experiment was conducted with a new carbon anode, and while a third electrode for maintaining a controlled potential at the electrode surface was not employed, each reaction was initiated at a potential necessary to generate an initial current of 2A. The applied potential was then held constant throughout the reaction and the current allowed to decrease as the starting material was depleted. An attempt was made to use a third electrode for monitoring the potential near the surface of a rotating carbon rod, but the potentials observed were so high (3.5-5V *vs* SCE) that it was apparent that uncompensated *IR* drop was making the measurement meaningless. A factor which might have caused the inconsistency in the yields of products would be variation in the extent of reaction of the starting material. Most of the reactions were continued for a period of time equivalent to three half-lives of the reaction (as measured by the current drop). However, varying amounts of unreacted valeric acid were recovered from these reactions. When a series of oxidations was run to a degree of completeness where essentially equal amounts of valeric acid remained, a similar trend in product distribution was obtained. Since an accurate measure of the net potential at the electrode surface was not attainable, the nonreproducibility in yields observed may simply be due to a variation in the potential obtained at the surface of the anode. It has been suggested (13) that the potentials required for the oxidation of carboxylate ions and for the oxidation of alkyl radicals are significantly different to allow two distinct waves. Assuming that the oxidation of an alkyl radical to a carbonium ion takes place at a more anodic potential than the oxidation of a carboxylate ion, it is possible that some of the reactions described herein might have been carried out at potentials slightly more cathodic than that required for efficient oxidation of the alkyl radicals to carbonium ions. This would lead to differing rates of formation of carbonium ions, and thereby varying yields of products from these ions.

The results obtained from the electrolysis of potassium valerate at a number of different anodes (Table III) indicate that similar processes are taking place at amorphous carbon and normal graphite anodes. This agrees with the work of Koehl reported earlier (6). However, of the other carbons studied, pyrolytic graphite behaved atypically. This is not unreasonable since the surface structure of pyrolytic graphite is essentially voidless due to the layered platelet structure it possesses.

When platinum anodes were employed, much larger quantities of the normal Kolbe dimer were obtained, as would be expected. However, the amount of products derived from the butyl cation are higher than would be predicted. The N-(sec-butyl)acetamide formed in a 19% yield represents carbonium ion which has reacted with acetonitrile, while the 42% yield of C_4H_8 products indicates the amount of carbonium ion which lost a proton. Since the electron impact ionization potential of the n-butyl radical is higher (8.64 eV) than the 8 eV limit suggested as being the maximum value for promoting carbonium ion formation, this combined yield of 61% of ion is unreasonably high.

Oxidation of octanoic and lauric acids.—The observation that the yield of Kolbe coupled products increased with increasing chain length in the fatty acids studied was not anticipated. The yield of dimer obtained under normal Kolbe reaction conditions is generally constant as the chain length increases, except for propionic and butyric acids which give unusually low yields (17).

In considering an explanation of the phenomenon observed in this work, the most logical proposal to make is that attractive forces between the long chain alkyl radicals are keeping them from reaching the electrode surface where they would undergo further oxidation. A reasonable scheme based on this premise can be proposed if two assumptions are made. First, assume that as the carboxylate anions approach the electrode surface they will assume an orientation dependent on the chain length of the molecule involved. Short chain carboxylates (possibly up through C_6) will be adsorbed on the surface in a more or less random fashion. However, as the alkyl chains become longer, they will tend to adsorb in an orientation perpendicular to the electrode surface, with a subsequent stacking or layering effect becoming pronounced as more and more ions are adsorbed. This stacking effect

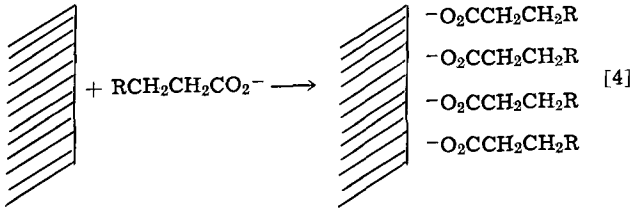

[4]

would be predicted to be enhanced by the Van der Waals attraction of the hydrophobic alkyl chains for each other, since they would constantly be searching for a more organic environment than the polar solvent surrounding them. Now also assume that the radicals generated in this reaction are separated from the electrode surface at the instant of formation by the width of the leaving CO_2 molecule (about 6Å), as has been previously postulated by Eberson (3, 10). The over-all net effect predicted then would be that the radicals would be generated in layers perpendicular to the electrode surface, and about 6Å away from the surface. Whether or not the intermolecular attractions these radicals experience would be enough noticeably to slow their migration through such a short distance is debatable, but it is certain that the stacked orientation described would be predicted to increase significantly the probability of radial coupling.

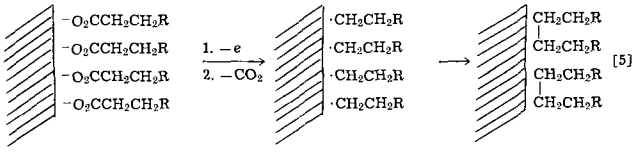

[5]

Since both the processes of radical-radical coupling and migration through a few angstroms of solution would be expected to be very fast, it would not take much of an effect to noticeably favor one or the other

of these processes. The simple slowing of the rate of migration of long chain alkyl radicals due to the increase in molecular weight might even be enough of a factor to cause the observed change in reaction.

The assumption made above that the radicals formed in the Kolbe reaction are separated from the electrode surface by the width of a molecule of carbon dioxide deserves further discussion. Eberson made this proposal after obtaining evidence that the radicals generated under similar conditions did not react stereospecifically as one would predict for reaction of an adsorbed radical. It now appears that the "long chain effect" observed in this work supports Eberson's postulation. If the radicals were generated in an adsorbed state and were never really "free," the only obvious way one could explain the observed increase in coupling with increasing chain length would be by assuming that there existed enough difference in the ionization potentials of the alkyl radicals to cause preferential oxidation of those with shorter chain lengths. However, this argument is unreasonable since the ionization potentials that have been measured for alkyl radicals decrease with increasing chain length, which would indicate that the long chain radicals would be more easily oxidized to carbonium ions.

Acknowledgments

The authors are deeply grateful to Drs. D. W. Leedy, J. P. Haberman, W. F. Erman, and L. Benjamin for helpful discussions, to Mr. L. H. Sickman, Jr., for his technical assistance, and to Mrs. R. Schlensker and Mrs. L. Walsh for secretarial help in preparing the manuscript.

Manuscript submitted April 10, 1970; revised manuscript received *ca.* July 14, 1970. This was Paper 129 presented at the New York Meeting of the Society, May 4-9, 1969.

Any discussion of this paper will appear in a Discussion Section to be published in the June 1971 JOURNAL.

REFERENCES

1. H. J. Dauben and M. A. Muhs, Private communication in C. Walling, "Free Radicals in Solution," p. 581, John Wiley & Sons, New York (1957).
2. E. J. Corey, N. L. Bauld, R. T. LaLonde, J. Casanova, Jr., and E. T. Kaiser, *J. Am. Chem. Soc.*, **82**, 2645 (1960).
3. L. Eberson, *Acta. Chem. Scand.*, **17**, 1196 (1963).
4. J. A. Waters, *J. Org. Chem.*, **29**, 428 (1964).
5. W. A. Bonner and F. D. Mango, *ibid.*, **29**, 430 (1964).
6. W. J Koehl, Jr., *J. Am. Chem. Soc.*, **86**, 4686 (1964).
7. L. Eberson and K. Nyberg, *Acta. Chem. Scand.*, **18**, 1567 (1964).
8. J. S. Dehn, "Anodic Oxidations of Medium Ring Cycloalkanecarboxylic Acids," Thesis, Louisiana State Univ., 1966.
9. B. E. Conway and A. K. Uijh, *Electrochim. Acta*, **12**, 102 (1967).
10. L. Eberson, *ibid.*, **12**, 1473 (1967).
11. L. Rand and C. S. Rao, *J. Org. Chem.*, **33**, 2704 (1968).
12. J. M. Kornprobst, A. Laurent, and E. Laurent-Dieuzeide, *Bull. Soc. Chim. France*, **1968**, 3657.
13. P. H. Reichenbacher, M. D. Morris, and P. S. Skell, *J. Am. Chem. Soc.*, **90**, 3432 (1968).
14. L. Eberson, in "Chemistry of Carboxylic Acids and Esters," S. Patai, Editor, Chap. 6, John Wiley & Sons, London (1969).
15. (a) J. J. Ritter and P. P. Minieri, *J. Am. Chem. Soc.*, **70**, 4045 (1948).
    (b) H. Meerwin, P. Laasch, R. Mersch, and J. Spille, *Ber.*, **89**, 209 (1956).
    (c) L. L. Miller and A. K. Hoffmann, *J. Am. Chem. Soc.*, **89**, 593 (1967).
16. D. Y. Curtin and J. E. Richman, *Tetrahedron Letters*, 3081 (1969).
17. B. C. L. Weedon, in "Advances in Organic Chemistry," R. A. Raphael, E. C. Taylor, and H. Wynberg, Editors, Vol. 1, p. 5, Interscience, New York (1960).

Polarography in Acetone of Tris(Dithioacetylacetonato)-Complexes of Iron(III), Ruthenium(III), Osmium(III), and Rhodium(III)

A. M. Bond, G. A. Heath, and R. L. Martin

Department of Inorganic Chemistry, University of Melbourne, Parkville, 3052, Australia

ABSTRACT

Polarographic studies have been carried out in acetone on the dithio(acetylacetonato)-complexes $[M(SacSac)_3]$ ($SacSac^- = CH_3{\cdot}CS{\cdot}CH{\cdot}CS{\cdot}CH_3^-$) where M = Fe(III), Ru(III), Os(III), (all d^5, low-spin) and Rh(III) (d^6, low-spin). The iron and osmium complexes are reversibly reduced at the DME, whereas the ruthenium complex undergoes a quasi-reversible reduction. For the d^5 systems the electrode reaction is believed to be $[M^{III}(SacSac)_3] + e^- \rightleftharpoons [M^{II}(SacSac)_3]^-$. However reduction of $[Rh(SacSac)_3]$ is highly irreversible and may involve adsorption or compound formation at the mercury surface. Millicoulometric studies indicate the electrode reaction is Rh(III) + $2e^- \rightarrow$ Rh(I). The half-wave potentials (Fe, −0.21; Ru, +0.04; Os, −0.05; Rh, 1.05V *vs.* Ag/AgCl) accord with the known chemistry and spectroscopic properties of the complexes. The development of polarographic techniques for use in acetone is described in detail.

Recently, considerable attention has been directed to transition metal derivatives of the sulfur-containing ligand dithioacetylacetone (1-17). Complexes of all the group VIII transition metals have been characterized although the parent ligand has not yet been isolated in the monomeric state. X-ray structural investigations confirm that the coordinated dithioacetylacetonato anion is planar and attached to the metal by both sulfur atoms as in (I). Table I summarizes the compounds $[M(SacSac)_x]$ (I) presently known.

Key words: polarography, tris(dithioacetylacetonato)-complexes, acetone.

(I)

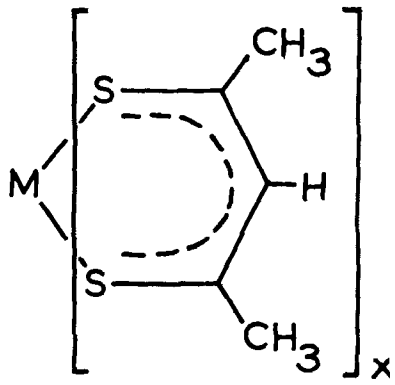

Studies by various workers have employed the techniques of infrared, electronic, e.s.r., p.m.r., and mass spectroscopy. Magnetic susceptibility and magnetic anisotropy measurements have also been performed. However, until recently no electrochemical studies had been reported.

The polarographic method is capable of furnishing considerable thermodynamic and structural information on such compounds. It is also an effective means of identifying new species which are related to the known compounds by oxidation or reduction. In this way further synthetic and chemical investigations may be suggested.

Examination of Table I reveals that the complexes [Co(SacSac)$_3$] and [Co(SacSac)$_2$] provide the only instance where dithioacetylacetone derivatives have been characterized for two oxidation states of the one transition metal.

The reduction of [Fe(SacSac)$_3$] with sodium dithionite was reported to yield "auto-oxidizable" [Fe(SacSac)$_2$], but no further characterization was described (3). Attempts to repeat this work have been unsuccessful (18). A more recent report of [Fe(SacSac)$_2$] (12), based on a sulfur analysis only, has been questioned (14) and, in our hands, the published method reliably yields [Fe(SacSac)$_3$] with the expected analytical and physical properties (15). In these circumstances, we thought it worthwhile to make a detailed polarographic investigation of the redox behavior of [Fe(SacSac)$_3$].

The compounds [Fe(SacSac)$_3$], [Ru(SacSac)$_3$], and [Os(SacSac)$_3$] were thus chosen as a representative group for the initial polarographic studies of dithioacetylacetone complexes. Each of these low-spin $d\epsilon^5$ chelates was found to undergo a ready one-electron reduction which might be regarded as completing the metal $d\epsilon$ subshell. A convenient comparison was provided by the polarographic behavior of the low-spin $d\epsilon^6$ complex [Rh(SacSac)$_3$], in which the metal $d\epsilon$ subshell is fully occupied. These results, which have been briefly reported elsewhere (15), are now discussed in detail.

Recently, polarographic data for the analogous cobalt(II) and nickel(II) complexes were described in a note by Ouchi *et al.* (19). However, neither the compounds, the solvent system, nor the reference electrode are common to the studies described herein.

The dithioacetylacetone complexes are insoluble in water. Acetone was chosen as a suitable solvent since preliminary investigations showed that a stable Ag/AgCl reference electrode could be maintained in this solvent. Furthermore, acetone was known not to interact chemically with the compounds and was commercially available in sufficient purity. Polarographic techniques, suitable for use in acetone, have been developed and are described here. These techniques include conventional and rapid polarography with a dropping mercury electrode (DME), inverse polarography with a hanging drop mercury electrode (HDME), and the millicoulometric determination of n values with a DME.

Table I. Dithioacetylacetone complexes

[M(SacSac)$_x$]	Spin state, S	Structure (by x-ray)	References
[Ni(SacSac)$_2$]	0	Planar[2,17]	(1), (2), (4), (9), (12), (19)
[Pd(SacSac)$_2$]	0	—	(1), (12)
[Pt(SacSac)$_2$]	0	—	(1), (12)
[Co(SacSac)$_2$]	½	Planar[2,9]	(1), (2), (9), (12), (13), (16), (19)
[Co(SacSac)$_3$]	0	—	(10), (11)
[Rh(SacSac)$_3$]	0	Octahedral[17]	(10), (11)
[Ir(SacSac)$_3$]	0	—	(10), (11)
[Fe(SacSac)$_3$]	½	Octahedral[14]	(3), (14), (15)
[Ru(SacSac)$_3$]	½	—	(15)
[Os(SacSac)$_3$]	½	—	(15)

So far as the present authors are aware, acetone has been used only occasionally as an electrolytic solvent (20), and rarely for polarography (21). One of the problems confronting its use is the need for a suitable reference electrode system. Aqueous calomel electrodes have been used (20), but are undesirable in otherwise nonaqueous media, particularly if junction potentials are to be minimized. A satisfactory Hg/Hg_2Cl_2, LiCl (acetone) system has been reported (22), but the Ag/AgCl/LiCl(acetone) electrodes described here commend themselves for stability and ease of construction.

Acetone is a versatile solvent for both organic and complex inorganic compounds; the development of this simple reference system may encourage its much wider use as a polarographic medium.

Experimental

Polarography.—Conventional d-c polarographic studies were carried out in B.D.H. Analar grade acetone with tetraethyl-ammonium perchlorate (0.1 mole/liter) as the supporting electrolyte. A Metrohm Polarecord, E 261, was used in conjunction with a Metrohm IR compensator, E 446, and a three-electrode system. The two reference electrodes were identical Metrohm Ag/AgCl EA 425 electrodes filled with a solution of LiCl in acetone (0.1 mole/liter). The glass capillary dropping mercury electrode (DME) had the following characteristics in acetone/0.1M Et_4NClO_4 (at open circuit and a mercury column height of 40 cm): flow rate of mercury, $m = 3.25$ mg sec^{-1}; drop time, $t = 2.70$ sec; $m^{2/3}t^{1/6} = 2.58$. In the rapid polarographic method, the short controlled drop times were achieved with a Metrohm Polarographie Stand, E 354. Hanging mercury drops used in this work were 0.52 mm in diameter with a surface area of 1.38 ± 0.04 mm^2 and were produced by a Metrohm BM 5-03 hanging drop mercury electrode (HDME).

Preliminary experiments showed that acetone/0.1M $LiClO_4$ gave a polarographically useful potential range of +0.8 to −1.6V at the DME *vs.* Ag/AgCl, whereas for acetone/0.1M Et_4NClO_4 the useful range was +0.8 to at least −2.0V. The latter supporting electrolyte was preferred because of the wider potential range. The reference electrodes were fitted with geometrically identical salt bridges containing acetone/0.1M Et_4NClO_4 to minimize LiCl leakage into the test solution. Potentials measured relative to a Ag/AgCl(acetone) reference electrode are qualitatively similar to those measured relative to Ag/AgCl(water). In acetone, $LiClO_4$ and $Co(ClO_4)_2$ reduction and Hg oxidation all occur at potentials about 0.4V more positive than the corresponding processes in water.

The very high resistance of acetone, even with a carrier electrolyte, makes compensation of the large ohmic potential (IR drop) essential. The three-electrode system provides a convenient means for achieving this. For optimum compensation, the measuring reference electrode should be positioned in the field shadow of the mercury electrode and the working reference electrode, *i.e.*, the three electrodes must be in one plane. Identical Ag/AgCl electrodes were thus employed and were symmetrically disposed in the test solution in relation to the mercury electrode. With only one reference electrode in circuit (*i.e.*, no IR com-

pensation), the ohmic potential drop rendered any polarographic wave unobservable (c.f. Fig. 4).

The reliability of the three-electrode system and the stability of the nonaqueous reference electrodes were checked throughout this work by frequent recording of the polarogram of [Rh(SacSac)$_3$] in acetone solution (among other tests). As reported below, this system has a well-defined wave with $E_{1/2} = -1.05$V *vs.* Ag/AgCl. Over three months duration, the reproducibility of this value was better than ±10 mV. Transposition of the functions of the two Ag/AgCl electrodes was regularly confirmed not to alter the polarogram in any respect.

Test solutions were degassed with argon which was previously passed through two acetone-filled wash bottles and a spray-trap. Twenty minutes was sufficient for effective deoxygenation. All solutions were thermostated in a water-jacketed cell at 20.0° ± 0.1°C, unless otherwise stated.

Millicoulometry.—The number of electrons involved in the reduction of [Rh(SacSac)$_3$] was determined by coulometric studies involving controlled-potential reduction at the DME. The decrease in concentration due to reduction was conveniently measured by the change in the polarographic diffusion current. The coulometric determination of n values with the DME employed a considerably smaller volume of solution than that used in conventional polarography. The small volume limits the time necessary for the reduction of the compound at controlled potential to cause a significant decrease in concentration. The polarographic cell was modified as in Fig. 1 and enabled volumes between 0.5 and 3 ml to be used. For [Rh(SacSac)$_3$], electrolysis times were between 30 min and 1 hr.

Each test solution was prepared by dissolving the compound in degassed acetone/0.1M Et_4NClO_4 in a 5-ml standard flask fitted with a rubber seal. By means of a micrometer syringe an accurately known volume was transferred directly to the inner coulometry cell, the whole apparatus having been previously flushed with argon. Throughout the electrolysis, the whole vessel was thermostated at 0°C to minimize evaporation, and acetone-saturated argon was gently bubbled through the acetone in the outer "moat". Blank runs, where no electrolysis occurred, showed that the concentration of the test solution did not alter measurably over 90 min.

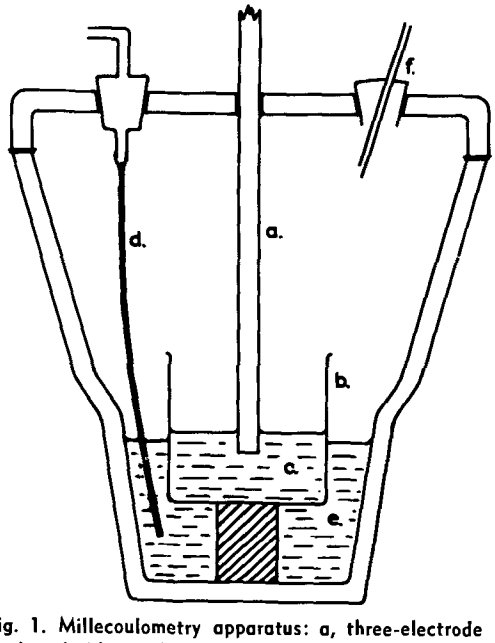

Fig. 1. Millecoulometry apparatus: a, three-electrode planar array, viewed side-on; b, inner cell; c, test solution; d, argon inlet; e, acetone moat; f, rubber seal, with argon outlet.

Materials.—Tetraethyl-ammonium perchlorate was prepared by admixture of aqueous solutions of Et_4NI and $NaClO_4$. The precipitated product was recrystallized three times from 95% alcohol and dried under vacuum. The pure compound was stored over silica gel until use. Solutions in dilute nitric acid gave no precipitate with silver nitrate.

The dithioacetylacetonato chelates [Fe(SacSac)$_3$] (14, 15), [Ru(SacSac)$_3$] (15), [Os(SacSac)$_3$] (15), and [Rh(SacSac)$_3$] (10) were prepared and purified as described elsewhere. The concentration of each compound in solution was checked spectrophotometrically by reference to the known optical spectrum (15).

Results and Discussion

[Fe(SacSac)$_3$], [Ru(SacSac)$_3$], [Os(SacSac)$_3$].—These complexes form a useful group for comparison since the first, second, and third row transition metals are all represented, and in each case the central metal atom formally has oxidation state III and d electron configuration d^5. The complexes each exhibit one extremely well-defined polarographic reduction wave at a potential near zero volt *vs.* Ag/AgCl. Figure 2 shows a typical [Os(SacSac)$_3$] polarogram. Polarograms of the other complexes have a similar appearance.

For each complex, graphical plots of diffusion current, i_d, *vs.* concentration are linear, and pass through the origin. Plots of i_d *vs.* the square root of the mercury column height, h, are linear. The waves are therefore diffusion controlled.

Plots of $E_{d.e.}$ *vs.* log $i/(i_d - i)$ are linear for [Fe(SacSac)$_3$] and [Os(SacSac)$_3$]. In each case the slope of this plot is 60 ± 2 mV, indicating that the electrode reaction is a reversible one-electron step. For [Ru(SacSac)$_3$], the log plot (Fig. 3) is slightly curved and the electrode reaction is quasi-reversible. The limiting slope, determined from potentials at the foot of the wave, is 62 mV in accord with a quasi-reversible one-electron reduction (23).

For the iron and osmium systems, the $(E_{1/4} - E_{3/4})$ values are independent of DME drop-time and equal to 58 ± 2 mV, providing further evidence for the reversible nature of the electrode reactions. In the case of [Ru(SacSac)$_3$], $(E_{1/4} - E_{3/4})$ values increase slightly with decreasing drop-time (Table II). The latter feature is consistent with the electrode possessing a high but not complete degree of reversibility, and confirms the quasi-reversible assignment.

The $E_{1/2}$ values for each complex (Fe, −0.21; Ru, +0.04; Os, −0.05V *vs.* Ag/AgCl/0.1M LiCl) are independent of drop-time; typical results for [Ru(SacSac)$_3$] are included in Table II.

In general, reversible half-wave potentials $E_{1/2}^r$, rather than measured $E_{1/2}$ values, have real thermodynamic significance as they are closely related to E° values. For the reversible iron and osmium electrode reactions, $E_{1/2}^r = E_{1/2}$. For the quasi-reversible [Ru(SacSac)$_3$] electrode process, $E_{1/2}^r$ may be calcu-

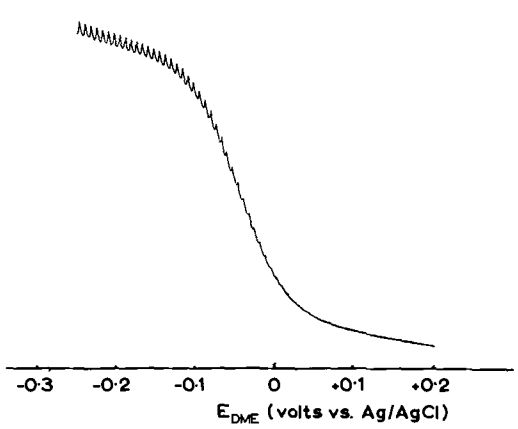

Fig. 2. [Os(SacSac)$_3$] polarogram (in acetone/0.1M Et_4NClO_4)

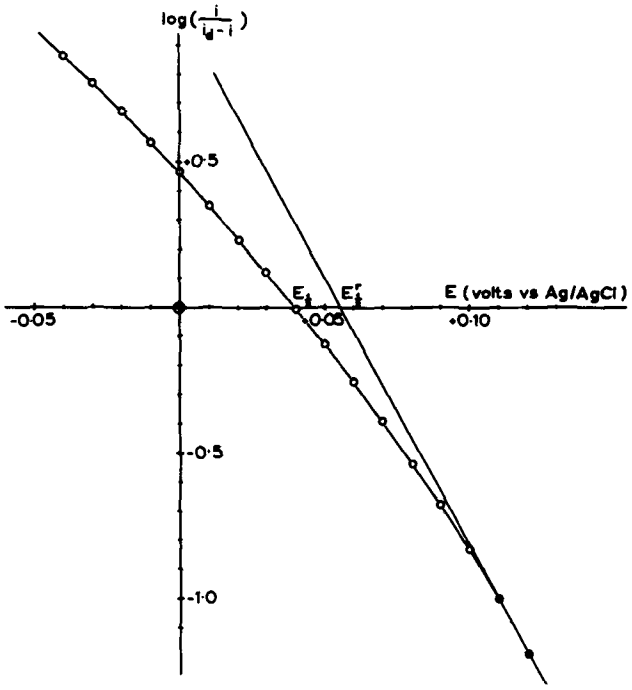

Fig. 3. Logarithmic analysis of [Ru(SacSac)3] polarogram

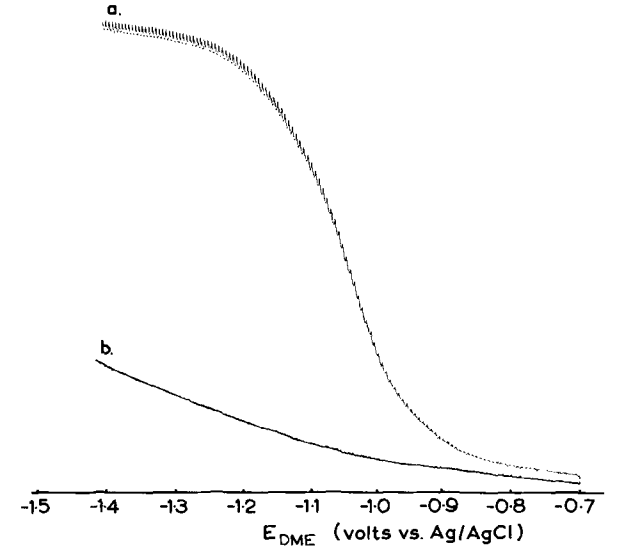

Fig. 4. [Rh(SacSac)3] polarogram (in acetone/0.1M Et_4NClO_4): a, IR compensated, 3-electrode system; b, uncompensated, 2-electrode system.

lated (23) from the limiting slope of the logarithmic analysis shown in Fig. 4 and is found to be +0.055V *vs.* Ag/AgCl. Comparison of the $E_{1/2}^r$ values shows that the standard free energy required for reduction of the complexes decreases in the order Fe > Os > Ru.

When a reversible electrode process is observed, it is implied that the charge transfer kinetics are rapid compared to the time scale of the polarographic experiment. It generally follows that the oxidized and reduced forms have the same molecular structure and differ only in their electronic populations. Therefore, in the present systems, the suggested electrode reaction is

$$[M(SacSac)_3] + e^- \rightleftharpoons [M^{II}(SacSac)_3]^-$$

The reduced form, $[M^{II}(SacSac)_3]^-$ should have essentially the same six-coordinate structure as the original $[M(SacSac)_3]$ species. If the reduction did involve gross structural change, such as the loss of a bidentate ligand, then this step would be unlikely to occur rapidly in terms of the polarographic time scale and a nonreversible electrode process should result. The kinetic inertness of low spin d^5 and d^6 systems is well known. That rapid, reversible, and complete ligand dissociation does not occur is indeed clear from the absence of subsequent polarographic steps which would be anticipated for the free divalent metal ions. The slight departure of the $Ru^{III} \rightarrow Ru^{II}$ wave from reversibility might result from a minor structural modification during the reduction; however, it is not clear why [Ru(SacSac)3] should behave differently from its congeners.

Several interesting features of the polarography of these complexes are apparent. First, all three compounds are reduced around 0V *vs.* Ag/AgCl, *i.e.*, reduction of the complexed metal ion to the divalent oxidation state is relatively easy. However no further reduction occurs in the useful potential range. The ready one-electron reduction corresponds to completion of the stabilized metal $d\epsilon$ subshell so that the reduced species $[M^{II}(SacSac)_3]^-$ would be isoelectronic with the neutral Co(III), Rh(III), and Ir(III) complexes. Further reduction would require electrons to be placed in the much higher energy $d\gamma$ level.

Second, these compounds are typified by rather low-frequency ligand-to-metal electronic charge transfer transitions as well as ready one-electron reduction waves (15). Both these properties are no doubt associated with the vacancy in the metal $d\epsilon$ subshell. The readier reduction of [Ru(SacSac)3] than either its first or third row congener, while unexpected in itself, correlates nicely with the observation that [Ru(SacSac)3] has the lowest frequency ligand-to-metal charge transfer absorption.

Finally, crystalline derivatives of the postulated $[M^{II}(SacSac)_3]^-$ complex anions are now being sought. The polarography suggests that the trivalent complexes should react readily with moderately strong reducing agents. Sodium dithionite has been reported to reduce [Fe(SacSac)3] to a species having no e.s.r. signal (3), however the suggested product, neutral $[Fe^{II}(SacSac)_2]$, is now questioned. It is, of course, possible that chemical reduction takes a different route from the polarographic electrode process, or that the complex anions are only stable during the life-time of the polarographic experiment.

[Rh(SacSac)3].—This complex shows one well-defined reduction wave at the DME with $E_{1/2} = -1.05$V *vs.* Ag/AgCl (Fig. 4).

The graph of i_d *vs.* concentration is linear, and the dependence of i_d on h is almost linear (Fig. 5). The electrode process therefore possesses a high degree of diffusion control. Table III shows that, as the drop-time increases, $E_{1/2}$ remains constant but $(E_{1/4} - E_{3/4})$ values increase markedly. Plots of $E_{d.e.}$ *vs.* log $i/i_d - i$ also vary greatly with drop-time. Such behavior indicates that the electrode reaction is highly irreversible.

In this case the number of electrons involved in the reduction, n, cannot be evaluated by the logarithmic analysis of the polarographic wave.

The current-voltage curve obtained with an HDME in unstirred solution (Fig. 6) was almost identical to the conventional d-c polarogram. A potential at half-wave height, $E_{p/2}$, of −1.00V *vs.* Ag/AgCl and a $(E_{p/4} - E_{3p/4})$ value of 80 mV were observed using a potential scan rate of 1 V/min. Such current-voltage curves were only obtained as the first scan on a new

Table II. Variation of $E_{1/2}$ and $(E_{1/4} - E_{3/4})$ with drop-time for [Ru(SacSac)3]

Drop-time, t, sec	$E_{1/2}$, V *vs.* Ag/AgCl	$(E_{1/4} - E_{3/4})$, mV
4.21	+0.040	72
3.67	+0.044	74
3.10	+0.042	76
2.70	+0.040	78
2.15	+0.038	80
1.62	+0.042	80

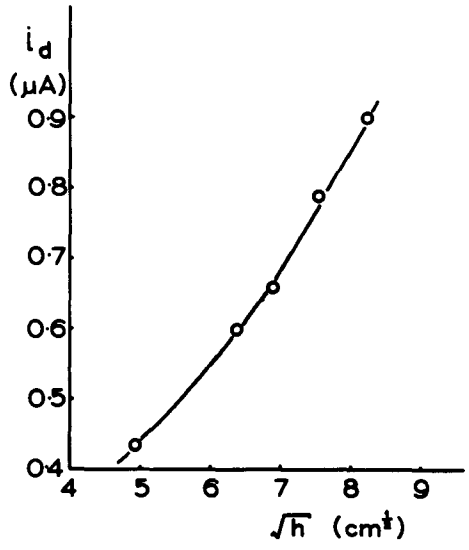

Fig. 5. Dependence of i_d on $\sqrt{h}$ for [Rh(SacSac)$_3$] (concentration = 6.5 x 10^{-5}M).

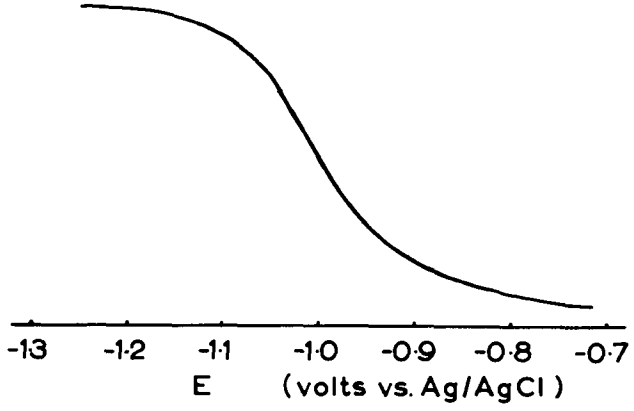

Fig. 6. [Rh(SacSac)$_3$] current-voltage curve at the HDME (in acetone/0.1M Et_4NClO_4).

mercury drop. Repeated scans using the same drop produced diminishing currents until no reduction was observable. When a fixed potential more negative than that required for reduction was maintained, the cathodic current decayed to zero within a few minutes. After such electrolysis at −1.45V *vs.* Ag/AgCl, inverse scanning in the positive direction revealed no anodic wave. The mercury drop was not affected by mere immersion, but became obviously tarnished during electrolysis.

Apparently, at sufficiently negative potentials, a reduced species or decomposition product becomes adsorbed on the HDME. The adsorbed substance eventually covers the entire surface of the drop preventing further reduction. Since inverse scans do not strip this species from the drop it must be tightly bound. Possibly mercury compound formation rather than adsorption occurs at the drop surface.

Table III. Variation of $E_{1/2}$ and $(E_{1/4} - E_{3/4})$ with drop-time for [Rh(SacSac)$_3$]

Drop-time, t, sec	$E_{1/2}$, V *vs.* Ag/AgCl	$(E_{1/4} - E_{3/4})$, mV
3.41	−1.048	72
2.03	−1.050	84
1.68	−1.052	88
1.38	−1.056	96
1.13	−1.052	104
0.32[a]	−1.050	120

[a] Drop-time of 0.32 sec by rapid polarographic method.

The interaction of [Rh(SacSac)$_3$] with the HDME indicated that coulometric evaluation of n would require a continually renewing mercury surface. A millecoulometric method at the DME was resorted to in the apparatus described above. A controlled potential of −1.45V *vs.* Ag/AgCl was employed, and the charge consumed by the electrode process was calculated by graphical integration of the current-time curves. Four independent determinations gave n values of 2.27, 2.09, 2.18, and 2.05.

The suggested electrode process is therefore Rh(III) + $2e^-$ → Rh(I). The electrode reaction is undoubtedly more complicated for [Rh(SacSac)$_3$] than for the previous complexes. It shows substantial diffusion control, irreversibility, and evidence for compound formation or adsorption at the mercury surface. A feasible product of the two-electron reduction of [Rh(SacSac)$_3$] would be [Rh(SacSac)$_2$]$^-$, isoelectronic with the well-characterized planar d^8 complex, [Pd(SacSac)$_2$]. However, the reduction product is not identified by these electrochemical studies.

It seems that, for [Rh(SacSac)$_3$], the completely filled metal d_ϵ subshell is associated with two properties; the highly negative $E_{1/2}$ value and the absence of low energy ligand-to-metal charge transfer. In comparison, one-electron reduction of the d^5 systems, [Fe(SacSac)$_3$], etc., occurs relatively easily to give complex anions isoelectronic with [Rh(SacSac)$_3$]; not surprisingly, no further reduction is observed.

Reduction of [Rh(SacSac)$_3$] has been attempted using zinc amalgam, sodium borohydride, and other strong chemical reductants without success. This is understandable in view of the polarographic data.

In conclusion, it appears that the polarographic results for the present complexes are consistent with their known chemical and spectroscopic properties. The existence of new stable entities has been indicated. Polarographic studies on other dithioacetylacetonato derivatives have been equally informative, and will be reported shortly.

Manuscript submitted May 25, 1970; revised manuscript received July 8, 1970.

Any discussion of this paper will appear in a Discussion Section to be published in the June 1971 JOURNAL.

REFERENCES

1. R. L. Martin and I. M. Stewart, *Nature*, **210**, 522 (1966).
2. R. Beckett and B. F. Hoskins, *Chem. Commun.*, 909, **1967.**
3. K. Knauer, P. Hemmerich, and J. D. W. van Voorst, *Angew. Chem. Int. Edn.*, **6**, 262 (1967).
4. A. Ouchi, M. Hyodo, and Y. Takahashi, *Bull. Chem. Soc. Japan*, **40**, 2819 (1967).
5. G. A. Heath, R. L. Martin, and I. M. Stewart, *Chem. Commun.*, **1969**, 55.
6. G. A. Heath, R. L. Martin, and I. M. Stewart, *Aust. J. Chem.*, **22**, 83 (1969).
7. G. A. Heath, R. L. Martin, and I. M. Stewart, *Inorg Nucl. Chem. Letters*, **5**, 169 (1969).
8. M. Nakatani, Y. Takahashi, and A. Ouchi, *J. Inorg. Nucl. Chem.*, **31**, 3330 (1969) and references cited therein.
9. C. G. Barraclough, R. L. Martin, and I. M. Stewart, *Aust. J. Chem.*, **22**, 891 (1969).
10. G. A. Heath and R. L. Martin, *Chem. Commun.*, **1969**, 951.
11. G. A. Heath and R. L. Martin, *Proc. XIIth I.C.C.C.*, pp. 116, 117, 1969.
12. O. Siiman and J. Fresco, *Inorg. Chem.*, **8**, 1846 (1969).
13. R. J. Fitzgerald and G. R. Brubaker, *ibid.*, **8**, 2265 (1969).
14. R. Beckett, G. A. Heath, B. F. Hoskins, B. P. Kelly, R. L. Martin, I. A. G. Roos, and P. L. Weickhardt, *Inorg. Nucl. Chem. Lett.*, **6**, 257 (1970).
15. G. A. Heath and R. L. Martin, *Aust. J. Chem.*, **23**, 1721 (1970).

16. A. K. Gregson, R. L. Martin and S. Mitra, *Chem. Phys. Letters*, **5**, 310 (1970).
17. R. Beckett and B. F. Hoskins, To be published.
18. D. H. Gerlach and R. H. Holm, *Inorg. Chem.*, **8**, 2292 (1969).
19. A. Furuhashi, S. Kawai, Y. Hayakawa, and A. Ouchi, *Bull. Chem., Soc. Japan*, **43**, 553 (1970).
20. C. K. Mann, "Electroanalytical Chemistry," A. J. Bard, Editor, Vol. 3, pp. 124, 125, Marcel Dekker, New York (1969).
21. J. F. Coetzee and W. S. Siao, *Inorg. Chem.*, **2**, 14 (1963).
22. P. Arthur and H. Lyons, *Anal. Chem.*, **24**, 1424 (1952).
23. J. Heyrovsky and J. Kuta, "Principles of Polarography," Academic Press, New York (1966).

Oxygen Adsorption on Gold and the Ce(III)/Ce(IV) Reaction

R. A. Bonewitz*[1] and G. M. Schmid*

Department of Chemistry, University of Florida, Gainesville, Florida 32601

ABSTRACT

In 1*N* $HClO_4$ and in 2*N* H_2SO_4, "oxygen" uptake on Au electrodes begins at 1.25V *vs.* NHE. Using a roughness factor of 1.4, monolayer coverage (600 μcoul/cm^2) is reached at 1.45V; a second monolayer is completed at 1.75V. Oxygen, once adsorbed, is removed at approximately 1.3V. Thus, the kinetic parameters of the Ce(III)/Ce(IV) reaction in 1*N* $HClO_4$ and in 2*N* H_2SO_4 can be obtained at oxygen coverages $\theta = 1.5$-2.0 and $\theta = 0.7$-2.0, respectively. Apparent exchange current densities, i_o^a, were obtained from low overvoltage data ($\leq$10 mV). The charge transfer coefficient, $\alpha = 0.65 \pm 0.06$, was determined from the slope of plots of log i_o^a *vs.* equilibrium potential. It is independent of oxygen coverage in the range indicated. The apparent rate constant, k_o^a, was calculated from i_o^a and α to be $k_o^a \approx 3 \times 10^{-4}$ cm/sec in the range $1 \leq \theta \leq 2$ ($1.5 \leq \theta \leq 2.0$ in $HClO_4$). Extrapolation of the data to $\theta = 0$ yields $k_o^a \approx 12 \times 10^{-4}$ cm/sec. This change in k_o^a can be interpreted as a change in the potential across the inner double layer which appears as a change in ϕ_2, $\Delta\phi_2 = 7.9$ mV. It appears that up to $\theta = 1$, oxygen adsorbs uniformly and is an excellent electronic conductor which simply serves as an extension of the electrode surface. The constancy of k_o^a at $1 \leq \theta = 2$ indicates no changes in the over-all structure of the interface in this region.

The influence of noble metal surface "oxides" on redox reactions has been known for some time. Davis (1) noted an increase in the standard rate constant of the vanadium(IV)-vanadium(V) reaction on platinum electrodes in the presence of surface oxides followed by a decrease in the rate constant as the oxygen coverage increased. A similar effect was shown for the oxidation of oxalic acid and the reduction of iron(III). Baker and MacNevin (2) found that heavy platinum oxides decreased the electrolysis currents for iron(II) and arsenic(III) by approximately an order of magnitude. Greef and Aulich (3) have shown that the reduction of cerium(IV) is inhibited more by platinum oxides in perchloric than in sulfuric acid.

Anson (4, 5) has explained the increased reversibility of the iron(II)-iron(III) reaction and the iodate and vanadium(V) reduction by an increase in electrode surface area due to platinization upon oxide reduction. Müller, on the other hand, pointed out that the platinum oxides themselves can have a twofold effect. At low oxide coverage they exhibit a catalytic effect on the reduction of such molecules as hydrogen peroxide (6, 7), thiosulfate (8, 9), iodate (8), hypochlorate (10), nitrous acid and hydroxylamine (8). Here the oxide effects a catalytic heterogeneous dissociative adsorption breaking or weakening the X-O or X-OH bond (X represents the main portion of the molecule) allowing reduction to proceed more readily at more anodic potentials than might ordinarily be found. As the oxide coverage increases, however, the electrochemical charge transfer is inhibited and the reduction current decreases. On the other hand, reduction of such species as cobalt(III) (8, 11) and oxygen (6, 7) is inhibited only. Thus the presence of surface oxides may have a variety of effects on the reaction of an electroactive species.

Except for the work of Davis (1) no attempts have been made to determine quantitatively the influence of oxides on the standard rate constant of an electrochemical reaction. The present work was undertaken in view of the theoretical interest attached to the effect of adsorbed layers on reaction kinetics. The system cerium(III)-cerium(IV)-gold was chosen because the cerium(III)-cerium(IV) reaction is a relatively simple one and because gold is inert in acidic solution. In addition, oxygen shows considerable hysteresis in its adsorption on gold (12, 13) and the kinetics of a redox reaction can be studied for a variety of oxygen coverages for any given equilibrium potential of the particular electrochemical reaction.

Experimental Procedure

The all-Pyrex cell was of standard design with the reference electrode compartment separated from the main cell by two ground glass stopcocks to prevent chloride contamination of the test solution. It initially contained a cylindrical platinum gauze polarizing electrode (Engelhard Industries) of approximately 100 cm^2 apparent area. Use of this electrode apparently caused platinum plating at the test electrode. The gauze was therefore plated with gold from a cyanide bath prepared according to Rosebury (14). In measurements where rapid stirring was important the gauze was removed and replaced by a gold foil electrode. The reference electrode was a saturated calomel electrode. All potentials are reported with respect to the normal hydrogen electrode.

The test electrode was a gold disk 0.071 cm^2 in apparent (geometric) area. It was made by pressure sealing a gold rod (Engelhard Industries, Fine Gold) into a Teflon mount according to Breiter (15). The

* Electrochemical Society Active Member.
[1] Present address: Alcoa Research Laboratories, New Kensington, Pennsylvania.
Key words: oxygen coverage, gold, kinetics of redox reaction.

test electrode was prepared by grinding with No. 1 to No. 4/0 emery paper and then polishing the surface with 600 grit alumina (Buehler). Excess alumina was removed by polishing the electrode on a clean cloth using copious amounts of water. The electrode was cleaned with warm chromosulfuric cleaning solution and rinsed thoroughly with triply distilled water before being placed in the cell. Before use all test electrodes were electrochemically "aged" by holding the potential alternately at 1.65 and −0.25V for 10 min each. The cycle was repeated three times to bring the electrode to a reproducible state.

All solutions were prepared from water first distilled from alkaline permanganate and then twice more in a Heraeus quartz still. The supporting electrolyte was 1*N* perchloric or 2*N* sulfuric acid prepared from Baker reagent grade 70% perchloric or concentrated sulfuric acid. Ultrahigh-purity perchloric acid (E. Merck Suprapur), acid-washed charcoal, and acid treated with H_2O_2 according to Visscher and Devanathan (16) did not affect the results and were therefore not used.

Cerium sulfate solutions were prepared from G. F. Smith reagent grade cerous and ceric sulfate without further purification. The 0.1*N* stock solutions were standardized with ferrous ammonium sulfate using Ferroin as an indicator (17). Cerous solutions were first oxidized with ammonium persulfate. When ceric sulfate solutions were first oxidized and then standardized, their normality was increased by 7.5%, indicating the presence of cerous ions. Test solutions were prepared volumetrically from the standardized stock solutions taking the amount of cerous ion in the ceric sulfate into account. Solutions were made with either the cerous or ceric concentration constant at 0.01*N*, varying the other between 0.01 and 0.0008*N*.

Solutions were prepared, also, using cerous sulfate which had previously been recrystallized three times from triply distilled water. These solutions were electrolyzed between gold electrodes to obtain the correct ceric concentrations for the desired equilibrium potential. In all cases the cerous concentration was 0.01*N*. The concentrations were checked by the Brucine method (18).

Cerium perchlorate solutions were prepared using G. F. Smith reagent grade cerous perchlorate salt and ceric perchlorate solution. Because perchlorates interfere with the oxidation of cerous to ceric ion with ammonium persulfate (17), silver(II) oxide was used as the oxidant (19). When the ceric perchlorate solutions were first oxidized and then standardized, the normality increased by 3.5%, again indicating the presence of cerous ion. Because of the high equilibrium potentials, E_e, in perchlorate solutions (see below) and the danger of irreversible oxidation of the gold at potentials above 1.75V, only test solutions containing 0.01*N* cerous and from 0.001 to 0.0001*N* ceric ion were used.

The solutions were purged of oxygen with a constant stream of helium (99.99% pure). This gas was purified by passing it through a 12 cm column of Linde 5A molecular sieve pellets held at −78°C. All gas lines were made of Pyrex glass and 5/16-in. Teflon tubing connected with Teflon Swageloks.

The charge necessary to remove adsorbed oxygen was determined by constant current cathodic stripping. The potential from which stripping was initiated was set with a Wenking 61TRS potentiostat allowing the potentiostat to buck the current from a Hewlett Packard 881A power supply. After waiting 10 min for the oxygen coverage to come to steady state, the potentiostat was removed from the circuit with a Western Electric mercury wetted relay (total switching time 1 msec), and the potential time curve was observed on a Tektronix 549 storage oscilloscope. The constant current from the power supply was measured with a Keithley 602 electrometer. The current density was usually 1.27 mA/cm^2 referred to the geometric area. Going in the anodic direction the electrode was first held at potentials less than 0.5V where the surface was free of adsorbed oxygen. The potential was then set to a value in the range of 1.25 to 1.75V. After 10 min at this potential, the constant cathodic current was applied and the charge due to adsorbed oxygen was obtained from the potential-time curve. Going in the cathodic direction the potential was raised from a value less than 0.5V to between 1.40 and 1.75V. The potential was held there for 10 min and was then lowered to the desired value $\geq$1.25V for another 10 min. The electrode was then stripped, and the charge obtained as before.

In order to determine the influence of cerium in solution on the charge due to the adsorbed oxygen on gold, a linear cathodic potential sweep of 50 mV/sec was applied, and the current was recorded as a function of time with a Beckman Electroscan 30. The area under the reduction peak represents the charge necessary for removal of the adsorbed oxygen.

The apparent exchange current, i_o^a, for the cerium(III)-cerium(IV) reaction was obtained at various equilibrium potentials between 1.35 and 1.50V and electrode coverages with adsorbed oxygen between $\theta = 0.7$ and 2. First, the electrode was set for 10 min at the anodic potential giving the desired electrode coverage with a Wenking 61TRS potentiostat. The potential was then lowered to about 15 mV above E_e as estimated from the Nernst equation, and the current was measured at 5 mV intervals over a range of 30 mV through E_e. These potentials could be set to within 0.1 mV using a Keithley 660 guarded differential voltmeter. The current was determined by placing a standard resistor (±0.1%) across the recorder output of the potentiostat and measuring the potential drop across it with a Keithley 602 electrometer. The apparent exchange current was then calculated from the slope of the potential-current curve taking into account the proper correction for mass transfer.

Results and Discussion

Cathodic stripping.—In preliminary work in 1*N* perchloric acid on etched disk electrodes, two types of stripping curves were found, one with arrests at 1.25V and at 0.75V, and one with only one arrest at 1.25V (20). Several aspects of the electrodes with an arrest of 0.75V were observed: (A) the total charge on the electrode surface was the same whether one or two arrests were present; (B) the length of the second arrest was not dependent on the stirring rate, indicating that it was not due to bulk solution impurity; and (C) electrodes with an arrest at 0.75V showed higher H_2 evolution currents (order of magnitude) at −0.25V than did freshly prepared electrodes. The arrest at 0.75V appeared only on electrodes that were not repolished over a period of several weeks; then if they were polished, the arrest disappeared.

Because the tendency of platinum to dissolve under mild anodic conditions has been recently recognized (21-24), contamination of the test electrode with platinum from the auxiliary electrode seemed possible. Therefore, an electrode with only one potential arrest (at 1.25V) was cathodized in a 2% solution of platinum chloride in 2*N* HCl for 10 sec at 10^{-5} A/cm^2. After potentiostating for 10 min at 1.65V and at −0.25V each several times, the arrest at 0.75V became apparent. Simultaneously, the H_2 evolution current increased from 10 to 200 mA/cm^2 at −0.25V. This is in agreement with Breiter (25), who demonstrated that as gold is made richer in platinum the activity of the electrode towards the Volmer reaction increases. Thus it appears that the arrest at 0.75V found in this laboratory (13, 20) and by other workers (26) is due to platinum deposition on the test electrode. After the auxiliary electrode was goldplated, the arrest at 0.75V was never detected and H_2 evolution currents always stayed below 10 mA/cm^2 at −0.25V. The adsorbed

oxygen is removed during cathodic stripping with 1.27 mA/cm² during a single arrest at 1.25V.

Charge-potential curves for a freshly mounted and polished gold electrode (never used in the presence of platinum) are shown in Fig. 1. The charge due to oxygen adsorption differed from electrode to electrode by ±20%. Any one electrode could be reproduced to ±5%. Each point shown was done in triplicate in 1*N* perchloric and in 2*N* sulfuric acid. There were no differences in the two media, and the results were computed together.

The charge values found here agree well with the results of other work. For example, at 1.65V they are within 10% of the data shown by Laitinen and Chao (12), Vetter and Berndt (27), and Schmid and O'Brien (13), and within 25% of those of Brummer and Makrides (26). The values of Will and Knorr (28) are some 35% higher. The hysteresis between the charge found on electrodes cathodically pretreated and those which were anodically pretreated has previously been noted by Schmid (13) and by Laitinen and Chao (12). A break at 1.45V in the curve coming from cathodic potentials is apparent in Fig. 1 at 600 μcoulombs/cm². Hickling (29) has calculated the charge equivalent of a monolayer of divalent oxygen adsorbed on gold and found it to be about 450 μcoulombs/cm². Brummer and Makrides (26) considered the break at 1.45V to be the point at which a monolayer of divalent oxygen atoms are adsorbed on the surface. Adopting this interpretation leads to the conclusion that the electrodes used here had a roughness factor of about 1.4, a reasonable value for mechanically polished electrodes. Brummer and Makrides (26) found only 400 μcoulombs/cm² for monolayer coverage. However, they were using electropolished electrodes which might be expected to have a roughness factor very close to 1.0.

Various values have been given for the potential at which oxygen adsorption on gold goes to zero. The cathodic stripping data presented here show that this potential is 1.25V, *i.e.*, adsorption at this point is less than about 25 μcoulombs/cm², the smallest charge that could be clearly measured in the present work. Brummer and Makrides (26) concluded that the surface was essentially free of oxygen below 1.3V and Huq (30) found it free below 1.2V. Laitinen and Chao (12) find oxygen adsorption at potentials as low as 0.65V. However, if one linearly extrapolates the major portion of their charge curves to zero charge, one finds a value of 1.25V. This is also the actual potential of the arrest

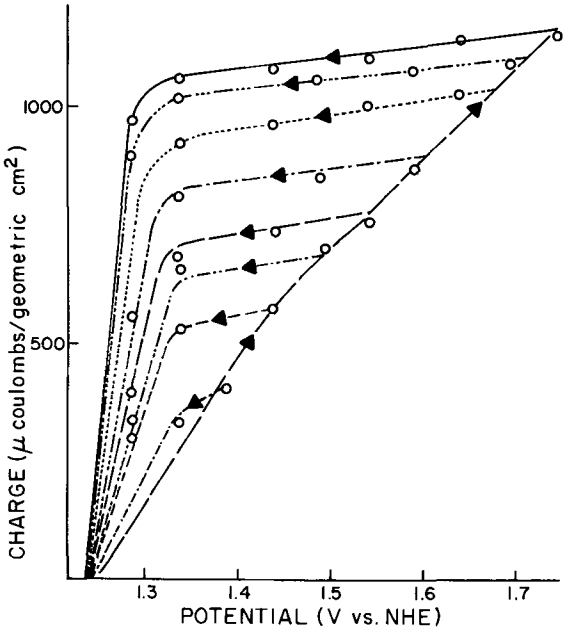

Fig. 1. Charge *vs.* potential for oxygen adsorption, Au in 1*N* $HClO_4$ and in 2*N* H_2SO_4.

in their stripping curves. The electrodes used by Laitinen and Chao were heated to 300°C. It has been noted by Clark, Dickenson, and Mair (31) that the potential arrest on annealed electrodes is followed by a region of slope much less steep than one usually associates with double layer charging. They suggest that this is due to impurities in the gold accumulated on the surface during heating. Apparently, Laitinen and Chao mistook this for oxygen adsorption. Thus, it appears that significant oxygen adsorption is absent at potentials below 1.20 to 1.30V.

The cerium(III)-cerium(IV) reaction.—The cerium redox couple shows different apparent standard potentials in solutions containing various electrolytes. Thus, in 2*N* sulfuric acid a formal potential of 1.44V is found (32). Here, cerium(IV) is complexed to $Ce(SO_4)^{++}$, $Ce(SO_4)_2$, and $Ce(SO_4)_3^{=}$, with stability constants of 3500, 200, and 20, respectively (32, 33). Therefore, virtually all the cerium(IV) is in the form of $Ce(SO_4)_3^{=}$ and the activity of the free cerium(IV) ion is considerably less than its formal concentration. Also, about half of the total cerium(III) in solution undergoes complexation to $Ce(SO_4)^{+}$ (32, 34). On the other hand, in 1*N* perchloric acid the formal potential is about 1.70V (32). This higher value is due to the fact that neither cerium(IV) nor cerium(III) forms complexes with the perchlorate ion. Instead cerium(IV) hydrolyzes to $Ce(OH)^{+3}$ which dimerizes to $CeOCe^{+6}$, the stability constant being 5.2 and 6.5, respectively (32, 35). Cerium(III) apparently does not undergo any reaction in perchloric acid (32). This difference in the formal potentials between a sulfuric acid and a perchloric acid solution makes reaction kinetic studies possible in various regions of oxygen coverage and was used to advantage in this study.

Effect of cerium ion on electrode coverage.—Results from potential sweep measurements showed an 11% reduction in the charge associated with the oxygen reduction peak in cerium-containing solutions as compared to blank acid solutions. This is within the error limits of the experimental procedure used in view of a 5% reproducibility in the charge on the electrode (stripping curve measurements), a 5% reproducibility in peak area measurements, and a 5% reproducibility of the Electroscan. It appears, then, that the oxygen coverage of the gold electrode is determined only by the potential pretreatment of the electrode and is independent of the cerium concentration in solution. Greef and Aulich (3) obtained an identical result on platinum. They concluded also that cerium had essentially no effect on oxygen adsorbed on their electrodes.

The apparent exchange current.—The polarization resistance, R_p, was obtained as the slope of the potential-current curves at zero overvoltage. It is thought to be composed of a charge transfer resistance, R_t, and a diffusion resistance, R_d, according to

$$R_p = R_t + R_d$$

$$= \frac{RT}{n\mathbf{F}}\left(\frac{1}{i_o{}^a}\right) + \frac{RT}{n\mathbf{F}}\sum^{j}\left|\frac{\nu_j}{i_{d,j}}\right|$$

where ν_j and $i_{d,j}$ are the stoichiometric factor and diffusion limiting current of species j. From this the apparent exchange current, $i_o{}^a$, was found as a function of oxygen coverage of the electrode by appropriate selection of the initial anodic potential of the electrode. As can be seen in Fig. 1, the coverage initially set at potentials >1.30V is retained down to 1.30V and, therefore, for a given E_e in the range from 1.75 to 1.40V various initial coverages could be chosen. All values for $i_o{}^a$ were averaged from three separate determinations.

The results of these experiments are shown in Fig. 2-4. All values are given in terms of the true area by using the roughness factor of 1.4 previously obtained. The reproducibility of $i_o{}^a$ in all sulfate solutions was

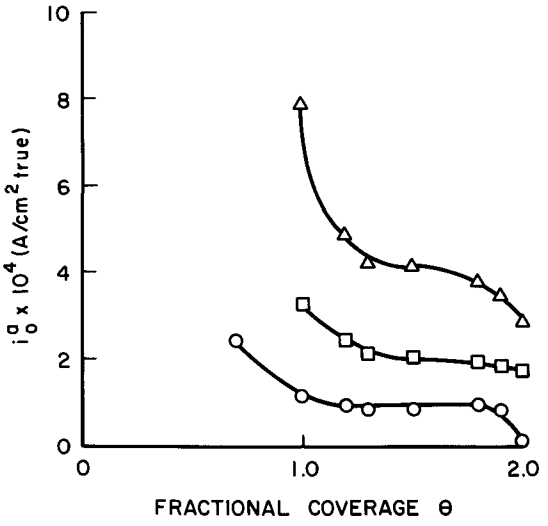

Fig. 2. Apparent exchange current, i_o^a, vs. coverage, Au in 2*N* H_2SO_4 with 0.01*N* Ce(III) and △: 1 x 10^{-2}, □: 5 x 10^{-3}, and ○: 1 x 10^{-3} *N* Ce(IV) sulfate (recrystallized).

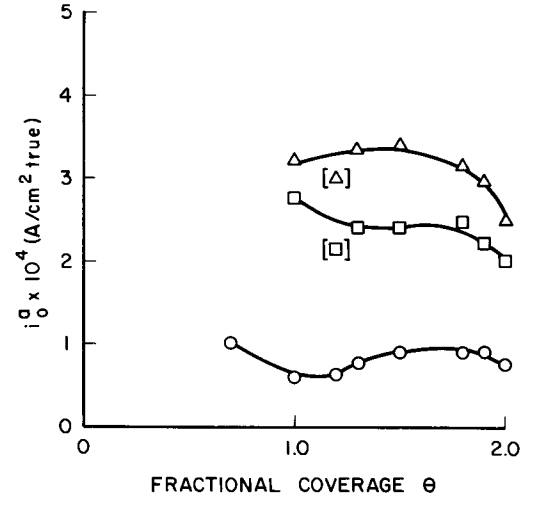

Fig. 3. Apparent exchange current, i_o^a, vs. coverage, Au in 2*N* H_2SO_4 with 0.01*N* Ce(III) and △: 1 x 10^{-2}, □: 5 x 10^{-3}, and ○: 1 x 10^{-3}*N* Ce (IV) sulfate.

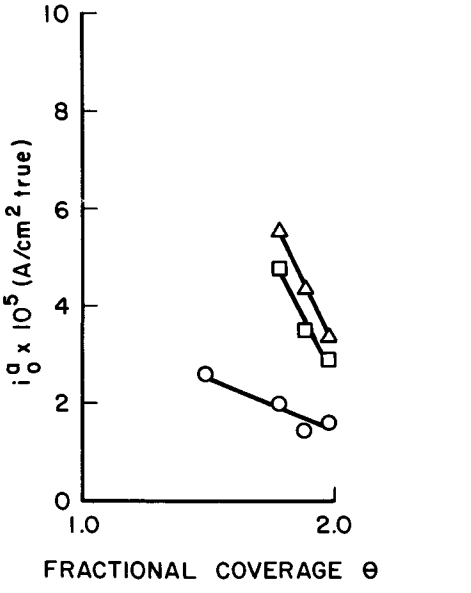

Fig. 4. Apparent exchange current, i_o^a, vs. coverage, Au in 1*N* $HClO_4$ with 0.01*N* Ce(III) and △: 1 x 10^{-3}, □: 3 x 10^{-4}, and ○: 1 x 10^{-4} *N* Ce(IV) perchlorate.

better than ±6%. Agreement between recrystallized and unrecrystallized salts was good. A slight depression which appears in the i_o^a for unrecrystallized salts (Fig. 3) at $\theta = 1.2$ is not significant and is probably due to the adsorption of impurities. The i_o^a with cerium(IV) = 0.01*N* is smaller by a factor of 0.8 in unrecrystallized salts as compared with the recrystallized ones. This is possibly due to the greater amounts of impurities introduced in unrecrystallized solutions. In perchlorate solutions, due to the large E_e potentials, the i_o^a could be obtained only for coverages of $\theta = 1.5$ to 2.0. The relative standard deviation there was less than ±5%

The charge transfer coefficient.—The anodic charge transfer coefficient, α, was obtained using the expressions (36)

$$(\partial \log i_o^a/\partial E_e)_{c_r} = \alpha \mathbf{F}/2.3RT$$

and

$$(\partial \log i_o^a/\partial E_e)_{c_o} = -(1-\alpha)\mathbf{F}/2.3RT$$

where c_o and c_r are the concentrations of the oxidized and the reduced species, respectively. Thus, α is obtained from the slope of plots of log (i_o^a) *vs.* E_e, keeping either c_r or c_o and the coverage with adsorbed oxygen constant. One such plot is shown in Fig. 5 for θ — 1.3, the coverage set at 1.55V. The slope was determined by a least squares analysis (37), assuming E_e to be known precisely. At a 70% confidence level $\alpha = 0.65 \pm 0.06$ for all values of θ between 0.7 and 2 in both sulfuric and perchloric acid.

Values of α for the cerium(III)-cerium(IV) reaction have been reported by other authors. Galus and Adams (38) determined α to be 0.79 and 0.72 on platinum and carbon paste electrodes, respectively. Vetter (39) determined α to be 0.75 on platinum. The charge transfer coefficient found here is somewhat less but not significantly so. This indicates that the mechanism of the cerium reaction is essentially independent of the electrode material.

The constancy of α with oxygen coverage found here is in agreement with the results obtained on other systems. Davis (1) found no change in α with the extent of oxygen coverage of a platinum electrode for either the vanadium(IV)-vanadium(V) or arsenic(III)-arsenic(V) couples. This same phenomenon has also been found with adsorption of organic species. Aramata and Delahay (40) found that α for the zinc(II) discharge on a zinc amalgam electrode was not affected by coverage with n-amyl alcohol. Biegler

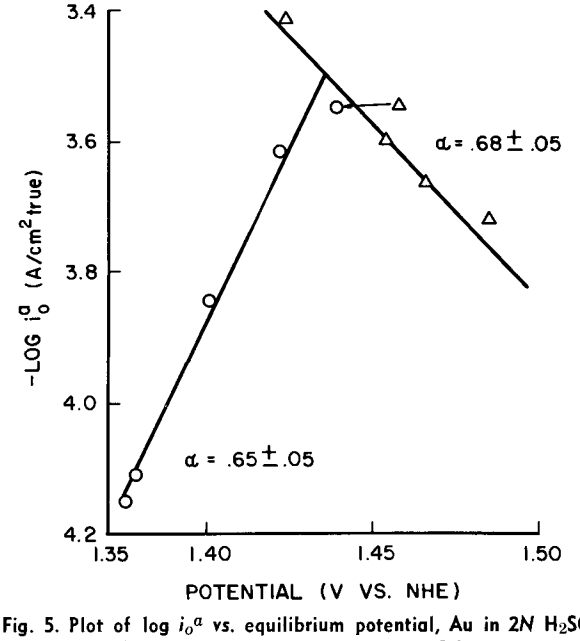

Fig. 5. Plot of log i_o^a vs. equilibrium potential, Au in 2*N* H_2SO_4 with Ce(III)/Ce(IV) sulfate, oxygen coverage $\theta = 1.3$.

and Laitinen (41) concluded that for the discharge of cadmium(II), α possibly decreased slightly on mercury, but this conclusion is not at all certain. On the other hand, Müller (10) found that for hypochlorate reduction on platinum α decreases with coverage.

The standard rate constant.—From the data for i_o^a and α, the standard rate constant, k_o^a, was calculated using the equation (36)

$$i_o^a = n\mathbf{F}k_o^a c_r^{(1-\alpha)} c_o^{\alpha}$$

with $\alpha = 0.65$. The concentrations c_r and c_o were taken as their bulk values since the diffusion-limiting currents (not shown) are the same in both sulfuric and perchloric acid and approximately of the magnitude expected from the analytical concentration of cerium(III) and cerium(IV) in solution. Thus, even though the equilibrium potential is dependent on the activity of free cerium, all the cerium is available when needed for reaction. This means that there is no limiting chemical reaction step and kinetic parameters may be calculated on the basis of bulk concentrations.

Values of k_o^a *vs.* oxygen coverage are given in Fig. 6. Each point on this curve was averaged from five values in sulfates and four values in recrystallized sulfates and perchlorates corresponding to the different cerium(III)-cerium(IV) ratios obtained for each coverage. The relative standard deviation was ±7% in unrecrystallized sulfates and ±17% in recrystallized sulfates and perchlorates.

It is seen that in sulfates k_o^a is approximately constant at 4 x 10^{-4} cm/sec above $\theta = 1.0$, *i.e.*, above monolayer coverage with oxygen. This can be compared to $k_o^a = 3.7 \times 10^{-4}$ cm/sec (38) and 4.8 x 10^{-4} cm/sec (39) found on platinum and $k_o^a = 3.8 \times 10^{-4}$ cm/sec (38) on carbon paste electrodes. The similarity between k_o^a found on different electrode surfaces indicates that the energy of activation is essentially independent of the electrode surface for the cerium(III)-cerium(IV) reaction. In perchlorates k_o^a appears to decrease from $\theta = 1.5$ to 2.0. However, this is still within experimental error and may not be significant. Further, the point at 1.5 is based on limited data so that speculation seems tentative.

The presence of adsorbed oxygen can have several effects on an electrochemical reaction. (*i*) It can cause a change in $\Delta\phi_c$, the potential drop across the compact double layer, and since the electrode potential is kept constant, this will result in a change in ϕ_2, the potential drop across the diffuse double layer. This changes the electric field and would directly affect k_o^a but not α. (*ii*) Alternatively, the presence of adsorbed oxygen could result in a change in the position of the effective plane at which the reaction occurs, leaving the electric field unchanged. This would lead to a change in the fraction of $\Delta\phi_c$ effective on the activation energy and would thus change α. (*iii*) It could cause a change in both $\Delta\phi_c$ and the effective plane of the reaction. This would cause a change in both α and k_o^a. Finally, (*iv*) a change in the reaction mechanism may lead to a change in α and k_o^a.

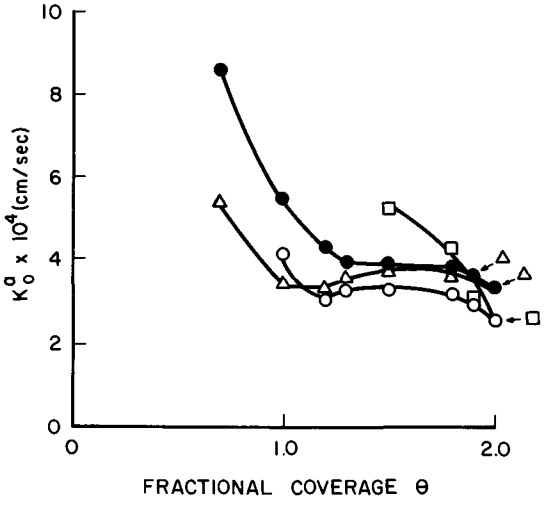

Fig. 6. Standard rate constant for the Ce(III)/Ce(IV) reaction on Au as a function of coverage with oxygen. ●: Recrystallized sulfates, Ce(III) = 0.01*N*, ○: sulfates, Ce(III) = 0.01*N*, △: sulfates, Ce(IV) = 0.01*N*, □: perchlorates, Ce(III) = 0.01*N*.

The results presented here indicate that α is independent of coverage, and possibilities *ii*, *iii*, and *iv* can therefore be discarded. This means, as a first order approximation, that there is no change in the reaction mechanism and that the plane of the reaction is not affected by the adsorbed oxygen, at least not with respect to the potential across the compact double layer. Because k_o^a does decrease, however, there must be a change in $\Delta\phi_c$ with a concomitant change in ϕ_2.

This change in ϕ_2 can be estimated from the following consideration. Assuming that there is an apparent standard rate constant for oxygen covered surfaces, k_o^a, and one for bare surfaces, $k_o^{a'}$, then the latter can be obtained to a first order approximation by linear extrapolation to $\theta = 0$ of the plot in Fig. 6. Thus, $k_o^{a'} \approx 12 \times 10^{-4}$ cm/sec. Then, writing

$$k_o^a = k_o^t \exp\left[-(z_r + \alpha)\mathbf{F}/RT\ \phi_2\right] \qquad (36)$$

and

$$k_o^{a'} = k_o^t \exp\left[-(z_r + \alpha)\ \mathbf{F}/RT\ \phi_2'\right]$$

where k_o^t is the true standard rate constant and z_r is the charge of the reduced species, one obtains $\Delta\phi_2 = \phi_2 - \phi_2' = 7.9$ mV as the difference in $\Delta\phi_c$ between a bare surface and an oxygen-covered surface at any given potential E.

This small change in $\Delta\phi_c$ indicates that the adsorbed oxygen is a good electronic conductor which contributes only little to the potential drop in the compact double layer. The adsorbed oxygen then acts simply as an extension of the electrode surface, and the double layer forms outside the adsorbed oxygen atoms as usual. Thus, the over-all potential drop effective on the electrochemical reaction is the same as before, less a small potential drop of a few millivolts in the adsorbed oxygen layers.

The gradual decrease in k_o^a up to $\theta = 1.1$ indicates a uniform adsorption of oxygen over the gold surface. This occurs possibly by a continuous transition with increasing potential from adsorbed water to adsorbed oxygen, with little difference in the electron

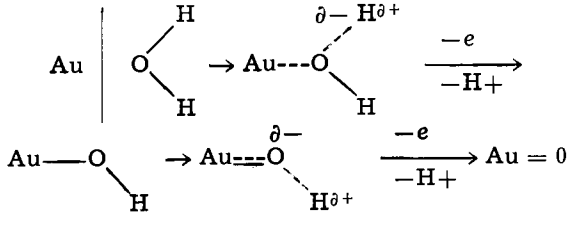

exchange through adsorbed water, adsorbed hydroxyl radical and/or adsorbed oxygen.

The constancy of k_o^a at higher coverages where $\theta > 1$ indicates that once a monolayer is formed further adsorption has little effect on the reaction rate. This argues that there is little change in the over-all structure of the interface in this range.

Conclusion

The adsorption of oxygen on gold electrodes in 1*N* perchloric acid and in 2*N* sulfuric acid was measured as a function of potential and potential-prehistory using constant current cathodic stripping. Coming from potentials <1.20V, oxygen uptake begins at 1.25V. A slight inflection in the charge-potential curve at 600 μcoulombs/cm^2 (1.45V) is thought to indicate monolayer coverage and corresponds to an electrode roughness factor of 1.4. A coverage of $\theta = 2$ is reached at 1.75V. Coming from potentials ≧1.35V the cover-

age with adsorbed oxygen is essentially independent of potential down to 1.35V. The electrode is free of adsorbed oxygen at $\leq$ 1.20V. Potential arrests found in cathodic stripping curves below 1.20V are probably due to platinum deposition on the gold electrode, either from solution or from the interior of the electrode.

The kinetic parameters of the Ce(III)/Ce(IV) reaction on gold in 1*N* perchloric acid and in 2*N* sulfuric acid were obtained at coverages $\theta = 1.5$-2.0 and $\theta = 0.7$-2.0, respectively. Apparent exchange current densities, i_o^a, were calculated from potentiostatic low overvoltage data. The anodic charge transfer coefficient, α, was determined, at constant coverage, from the slope of plots of log i_o^a *vs.* the equilibrium potential at constant Ce(III) or Ce(IV) concentration. At the 70% confidence level $\alpha = 0.65 \pm 0.06$. Apparent standard rate constants, k_o^a, were calculated from i_o^a and α to $k_o^a \approx 4 \times 10^{-4}$ cm/sec, independent of coverage $1 \leq \theta \leq 2$. Extrapolation of the data to $\theta = 0$ yields $k_o^{a'} \approx 12 \times 10^{-4}$ cm/sec.

The slight change in k_o^a in going from $\theta = 0$ to $\theta = 1$ (at constant potential) is considered to be due to a change in the potential drop across the inner double layer caused by the adsorbed oxygen accompanied by a corresponding change in the potential across the diffuse double layer, ϕ_2. The latter can be calculated to 7.9 mV. Once monolayer coverage has been reached, further adsorption to $\theta = 2$ does not change the potential drop across the double layer.

It seems that the adsorbed oxygen on gold in acidic solution, as far as the Ce(III)/Ce(IV) reaction is concerned, is an excellent electronic conductor, contributes only little to the potential drop across the inner double layer, and simply serves as an extension of the electrode surface. There is little discernible change at $1 \leq \theta \leq 2$ and this suggests no change in the over-all structure of the interface in this region.

Acknowledgment

The authors would like to take this opportunity to thank the National Science Foundation for financial support of this work under Grant No. NSF-GP-7742. One of the authors is indebted to The Electrochemical Society for the Colin Garfield Fink Fellowship, 1968.

Manuscript submitted Feb. 18, 1970; revised manuscript received July 15, 1970.

Any discussion of this paper will appear in a Discussion Section to be published in the June 1971 JOURNAL.

REFERENCES

1. D. G. Davis, Jr., *Talanta*, **3**. 335 (1960).
2. B. B. Baker and W. M. MacNevin, *J. Am. Chem. Soc.*, **75**, 1476 (1953).
3. R. Greef and H. Aulich, *J. Electroanal. Chem.*, **18**, 295 (1968).
4. F. C. Anson, *Anal. Chem.*, **33**, 934 (1961).
5. F. C. Anson and D. M. King, *ibid.*, **34**, 362 (1962).
6. L. Müller and L. N. Nekrassow, *J. Electroanal. Chem.*, **9**, 282 (1965).
7. L. Müller and L. N. Nekrassow, *Dokl. Akad. Nauk. SSSR*, **157**, 416 (1964).
8. L. Müller, *J. Electroanal. Chem.*, **16**, 531 (1968).
9. L. Müller, *ibid.*, **13**, 275 (1966).
10. L. Müller, *Elektrokhimija*, **4**, 199 (1968).
11. L. Müller, *Electrochim. Acta*, **12**, 557 (1967).
12. H. A. Laitinen and M. S. Chao, *This Journal*, **108**, 726 (1961).
13. G. M. Schmid and R. N. O'Brien, *ibid.*, **111**, 832 (1964).
14. R. Rosebury, "Handbook of Electron Tube and Vacuum Technique," Addison-Wesley, Reading, Mass. (1965).
15. M. W. Breiter and K. H. Hoffmann, *Z. Elektrochem.*, **64**, 462 (1960).
16. W. W. Visscher and M. A. V. Devanathan, *J. Electroanal. Chem.*, **8**, 127 (1964).
17. I. M. Kolthoff, P. J. Elving, and E. B. Sandell, "Treatise on Analytical Chemistry," Part II, Vol. 8, pp. 71-77, Interscience, New York (1963).
18. E. B. Sandell, "Colorimetric Determination of Traces of Metals," pp. 357-562, Interscience, New York (1944).
19. J. J. Lingane and D. G. Davis, *Anal. Chim. Acta*, **15**, 201 (1956).
20. R. A. Bonewitz, *This Journal*, **116**, 78C (1969).
21. S. B. Brummer, *ibid.*, **112**, 633 (1965).
22. A. N. Chemodanov, Ya. M. Kolotyrkin, M. A. Demrovske. and T. V. Krudryavina, *Dokl. Akad. Nauk. SSSR*, **171**, 1384 (1966).
23. S. D. James, *This Journal*, **114**, 1113 (1967). **114**, 1104 (1967).
24. P. Malachesky, R. Jasinski, and B. Burrows, *ibid.*,
25. M. W. Breiter, *J. Electroanal. Chem.*, **11**, 157 (1966).
26. S. B. Brummer and A. C. Makrides, *This Journal*, **111**, 1122 (1964).
27. K. J. Vetter and D. Berndt, *Z. Elektrochem.*, **58**, 378 (1958).
28. F. G. Will and C. A. Knorr, *ibid.*, **64**, 270 (1960).
29. A. Hickling, *Trans. Faraday Soc.*, **42**, 518 (1946).
30. A. K. M. Shamsul Huq, *Sci. Tech. Aerospace Rept.*, **3**, 1036 (1965), N.A.S.A. Accession No. N 65-16949, rept. no. AD414800 (1963).
31. D. Clark, T. Dickenson, and W. N. Mair, *Trans. Faraday Soc.*, **55**, 1937 (1959).
32. E. Wadsworth, F. R. Duke, and C. A. Goetz, *Anal. Chem.*, **29**, 1824 (1957).
33. T. J. Hardwick and E. Robertson, *Can. J. Chem.*, **29**, 828 (1951).
34. T. W. Newton and G. M. Arcand, *J. Am. Chem. Soc.*, **75**, 2449 (1953).
35. T. J. Hardwick and E. Robertson, *Can. J. Chem.*, **29**, 818 (1951).
36. P. Delahay, "Double Layer and Electrode Kinetics," Interscience, New York (1965).
37. H. A. Laitinen, "Chemical Analysis," pp. 537-594, McGraw-Hill Book Co., Inc., New York (1960).
38. Z. Galus and R. N. Adams, *J. Phys. Chem.*, **67**, 866 (1963).
39. K. J. Vetter, *Z. Physik. Chem. (Leipzig)*, **196**, 360 (1951).
40. A. Aramata and P. Delahay, *J. Phys. Chem.*, **68**, 880 (1964).
41. T. Biegler and H. A. Laitinen, *This Journal*, **113**, 852 (1966).

Correction

In the paper "Oxygen Reduction on Oxide-Free Platinum in 85% Orthophosphoric Acid: Temperature and Impurity Dependence" by A. J. Appleby which appeared on pp. 328-335 in the March 1970 JOURNAL, Vol. 117, No. 3, on p. 333, Eq. [1] should read

$$i_{\text{forward}} = \mathbf{F}\frac{kT}{h}(\theta^{\bullet})[\mathrm{H}^+]\left(\exp -\frac{[\Delta G^{\neq} + (1-\beta)(\Delta G_p - \Delta G_r)]}{RT}\right)\cdot\exp -\left(\frac{(1-\beta)\mathbf{F}V}{RT}\right) \quad [1]$$

Oxygen Reduction and Corrosion Kinetics on Phase-Oxide-Free Palladium and Silver Electrodes as a Function of Temperature in 85% Orthophosphoric Acid

A. J. Appleby*

Institute of Gas Technology, Chicago, Illinois 60616

ABSTRACT

Oxygen reduction on oxide-free palladium and silver surfaces has been studied as a function of temperature in purified 85% orthophosphoric acid. In each case, oxygen reduction is first order, and available evidence suggests that on both metals the reaction

$$O_2 + H_3O^+ + e^- \rightarrow (O_2H)$$

is the rate-determining step. Experimental activation energies, extrapolated to the reversible oxygen electrode potential, are 22.4 ± 2.0 kcal on palladium and about 26 kcal on silver. Activity of the palladium electrode is only slightly (< one decade) less than on platinum under the same conditions, whereas silver is even less active than gold. On palladium, as with platinum, the extrapolated activation energy includes a heat of adsorption term corresponding to the effect of Temkin-type equilibrium adsorption of —O species derived from water oxidation, which are present on the electrode under the experimental conditions. This term may be eliminated by considering activation energies extrapolated to potentials at which —O adsorption is small, where an activation energy difference between silver and palladium on the order of 9.8 kcal occurs. This suggests that the intermediate (O_2H) is relatively strongly adsorbed on palladium and only weakly on silver, and accounts for the rate difference on the two metals.

Rest potentials of the metals are corrosion mixed potentials and the metal dissolution reaction is fast in both cases so anodic processes are under Nernstian control. Palladium passivates at potentials greater than 900 mV HRE. No passivation of silver was observed.

Studies on oxygen reduction on silver and palladium electrodes in acid solution have been reported relatively infrequently in the literature.

On silver, Krasil'shchikov (1, 2) reported a *p*H-independent mechanism in neutral and acid solutions down to *p*H 2, and suggested that under these conditions the reaction

$$O_2 + e^- \rightarrow O_2^-$$

is rate-determining. Akopyan (3) reported the effect of temperature on the electrode reaction and Nikulin (4) showed the specific effect of single crystal faces on oxygen reduction. Bianchi *et al.* (5, 6) have shown that silver electrodes give Tafel slopes for oxygen reduction of 2 $RT/\mathbf{F}$ in 0.5M H_2SO_4 at overvoltages even higher than those for gold (7) under similar conditions. Again, *p*H-dependence was shown to be small (5) at least in the neutral *p*H range thus confirming Krasil'shchikov's mechanism (1, 2).

Palous and Buvet (8) also examined oxygen reduction on silver over a wide *p*H range. Their results show an H^+ dependence for the reaction in the *p*H range 0-2, with no *p*H dependence at higher *p*H. Hydrogen peroxide has been detected as a reaction product (1-3, 5).

In contrast with acid solution the amount of work reported on silver oxygen electrodes in alkaline solution is considerable and has been reviewed (9, 10).

Oxygen reduction on palladium electrodes was reported by Sawyer *et al.* (11, 12) to resemble that on platinum in acid solution. In oxygen-saturated 2*N* H_2SO_4 solution Hoare (13, 14) reported rest potentials of palladium electrodes of about 870 mV HRE and potentiostatic Tafel plots of slope 102 mV/decade (14) for oxygen reduction on electrodes that had been anodized, then reduced. Damjanovic *et al.* (15-17) indicated that Tafel behavior of oxide-free palladium and platinum in dilute $HClO_4$ was almost identical, although palladium electrodes were about 50 mV less active than corresponding platinum electrodes. This and other considerations, for instance, —O adsorption character (18), suggest similarity of rate-determining step, which is supported by ring-disk electrode experiments using the two metals (19).

In this paper, oxygen reduction on and corrosion behavior of phase-oxide-free palladium and silver electrodes are studied in 85% orthophosphoric acid as a function of temperature.

Experimental Techniques

The present series of experiments was conducted in an all-silica cell (20) using the same galvanostatic technique as in previous work (21). Temperatures were maintained to ± 0.2°C by means of an oil bath or a refrigerated bath, as appropriate.

The electrodes used were palladium and silver foils of 99.99% purity, with areas of approximately 1 cm^2. The palladium foils were welded to gold wires and were hung in the cell in Teflon sliding seals as described in previous experiments (20). The silver foils were similarly suspended in a separate series of experiments, although in this instance silver wires were used.

A gold counterelectrode was used in all experiments to avoid the possibility of contamination of working electrodes with electroactive deposits (as is the case if platinum is used). For the same reason, the electrolyte (85% orthophosphoric acid) was not given pre-electrolytic purification treatment before being used in the cell. Cleaning of the solution was done by refluxing several times with 5% hydrogen peroxide, followed by distillation of the excess water.

* Electrochemical Society Active Member.

Key words: oxygen reduction, corrosion, palladium, silver.

Oxygen or oxygen-nitrogen mixtures were supplied to the cell via presaturators from a capillary flowmeter gas mixing system and a purification train.

A dual isothermal bubbling hydrogen-85% phosphoric acid reference electrode was used, to which all potentials throughout this paper are referred (HRE potentials).

Results

Palladium electrodes.—Oxygen reduction data.—The palladium foil electrodes were degreased with organic solvents and washed with concentrated HCl, conductivity water, and the electrolyte itself before use. They were then potentiostated for a short time in oxygen-saturated electrolyte at 22.0°C at 350 mV HRE to reduce any residual oxide. After this preparation, electrodes took up rest potentials in the range 895-898 mV; these rest potentials fell by about 10 mV after 1-2 hr, thereafter remaining constant. A descending cathodic galvanostatic steady-state Tafel plot was then made on each electrode, allowing sufficient time (5-15 min) between points for a final potential to be set up at each applied current density that varied by less than 1 mV/min. This polarization study was followed by a similar ascending plot. These have been shown in Fig. 1 as "initial" Tafel plots. Results were very reproducible, and Tafel lines could be accurately retraced forward and backward.

Cathodic Tafel plots were also obtained by means of the pulsing technique used in previous work (21). Before each point was taken, the electrode was given a series of anodic and cathodic galvanostatic pulses to ensure that a surface in a reproducibly clean condition was present. Potentials were read after 2 min at each current density.

Pulses for palladium were restricted to +850-+200 mV HRE. At the high potential, some dissolution starts to occur. Below about +200 mV palladium starts to occlude large quantities of hydrogen. The plot for the palladium surface in this clean condition is shown in Fig. 1. The electrode is only slightly less active than platinum under the same conditions and has a similar Tafel slope ($\sim RT/\mathbf{F}$).

Corrosion behavior.—Corrosion behavior was tested by means of a steady-state anodic plot (Fig. 1). A Tafel plot was obtained with the low slope of $RT/2\mathbf{F}$ in the anodic direction. The slope led into what was apparently a diffusion current at about $i = 3.5 \times 10^{-6}$ A/cm². Corrosion currents were estimated by extrapolation of anodic and cathodic Tafel plots to their point of intersection (represented by dashed lines in Fig. 1).

The electrolyte in the cell was replaced after each series of anodic polarization studies on the electrode.

Temperature dependence.—Results were repeated at 52.0°, 76.0°, and −3.0°C. Although the freezing point of 85% orthophosphoric acid is normally quoted as being 21.1°C, it may be supercooled to a very viscous liquid at well below 0°C (22). Results obtained are shown in Fig. 2-4. In the anodic polarization experiments, no passivation was observed at 76.0°C, whereas at the other temperatures studied the onset of passivation occurred at a potential of about 900-930 mV. At −3.0°C no definite corrosion behavior was seen in the anodic plot, and anodic currents above 4.0×10^{-8} A/cm² resulted in passivation. Under these conditions, palladium exhibits a behavior like that of platinum.

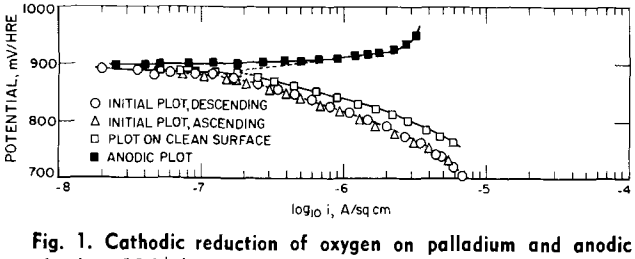

Fig. 1. Cathodic reduction of oxygen on palladium and anodic production of Pd^{++} at 22.0°C.

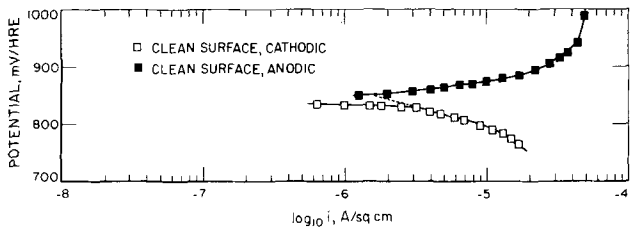

Fig. 2. Cathodic reduction of oxygen on palladium and anodic production of Pd^{++} at 52.1°C.

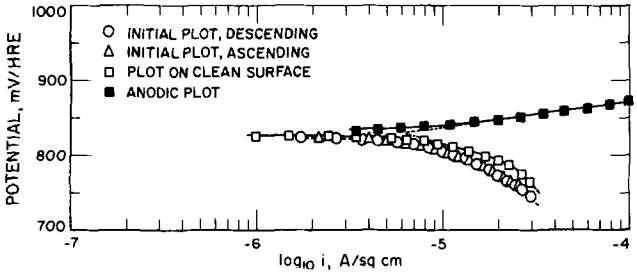

Fig. 3. Cathodic reduction of oxygen on palladium and anodic production of Pd^{++} at 76°C.

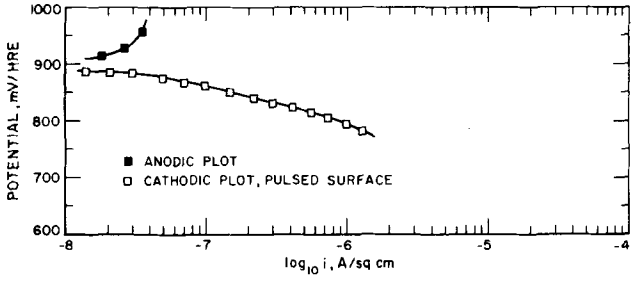

Fig. 4. Cathodic reduction of oxygen on palladium at −3.0°C

Tafel slopes and $1/\alpha$ values for the oxygen reduction reaction together with values of the exchange current obtained by extrapolation of the Tafel line to the reversible potential at each temperature are given in Table I. Similarly, data for the anodic dissolution reaction are given in Table II. The corrosion current and the corrosion potential are in each case obtained from the intersection of the extrapolated anodic and cathodic Tafel plots.

Order of reaction in oxygen reduction.—A series of experiments was carried out on the same palladium foil electrode using oxygen partial pressures of 1.0, 0.26, 0.080, and 0.025 atm at 22.0°C.

The pulsing procedure mentioned previously was used before each point to ensure that a reproducible

Table I. Oxygen reduction on palladium

Temp, °C	Slope, mV/decade	$1/\alpha$	i_o, A/cm²
−3.0	58	1.08	3.0×10^{-15}
22.0	63	1.08	1.9×10^{-13}
52.1	68	1.06	3.5×10^{-12}
76.0	71	1.04	2.2×10^{-11}

Table II. Palladium corrosion data

Temp, °C	Anodic slope, mV/decade	$1/\alpha$	i_{corr}, A/cm²	E_{corr}, mV/HRE
−3.0	—	—	1.7×10^{-8}	905
22.0	31	0.53	1.7×10^{-7}	888
52.1	32	0.50	1.6×10^{-6}	849
76.0	35	0.51	6.3×10^{-6}	830

surface was present. Results obtained are shown in Fig. 5, which also includes an anodic plot obtained at 0.025 atm oxygen partial pressure.

Inspection of the data indicates that oxygen reduction approximates to first order at constant potential (Fig. 9).

Activation energy for oxygen reduction on palladium.—Figure 6 shows an Arrhenius plot of extrapolated i_0 values on oxide-free palladium, corrected to 1 atm oxygen partial pressure. Activation energy at the reversible potential is 22.4 ± 2.0 kcal, close to the values previously reported on oxide-free rhodium (22.0 kcal) and platinum (22.9 kcal).

Silver electrodes.—Silver foil electrodes were degreased, welded to silver wires, and mechanically polished using graded alumina powders. They were then washed in dilute nitric acid and lightly etched in a dilute hydrogen peroxide-ammonium hydroxide solution. Preliminary experiments established that electrodes prepared in this way gave high results when cathodically polarized, with nonstirring-dependent reduction currents that were in excess of the limiting current for the oxygen reduction in the electrolyte. These high currents were apparently due to the reduction of passivating silver oxides and oxygen dissolved in the silver foil; such electrodes exhibited rest potentials 100-200 mV higher than the eventual corrosion potentials. The electrodes showed a limiting behavior after cathodic polarization for 5-8 hr at 2.0 μA/cm^2, after which consistent cathodic oxygen reduction Tafel plots could be obtained. Under these conditions the rest potential (corrosion potential) of the silver electrode was 360-365 mV HRE at 22°C. An alternative preparation procedure, involving heating the etched electrode in a stream of hydrogen at 330°-400°C for 5-10 min followed by cooling under hydrogen, gave electrodes with the same properties as those that have been electrochemically reduced. The oxygen electrode and corrosion behavior reported here refer to electrodes that have been prepared by final treatment in hydrogen.

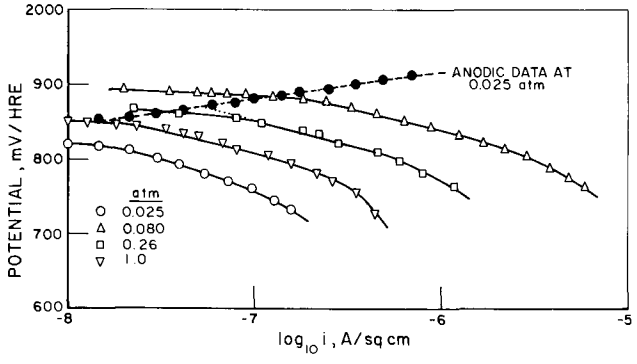

Fig. 5. Oxygen electrode on palladium at 22°C in 85% orthophosphoric acid; effect of oxygen partial pressure.

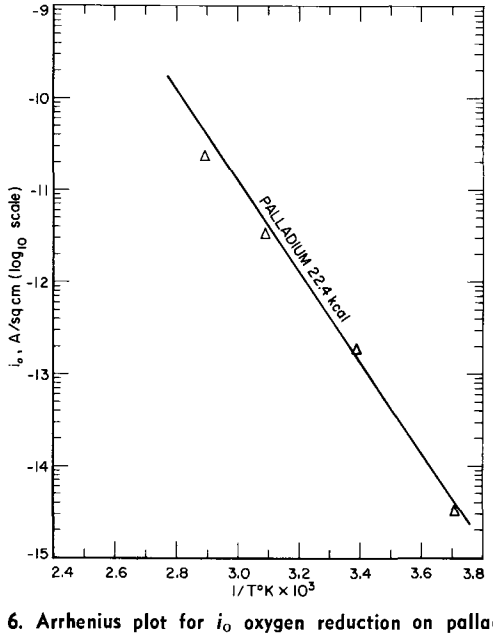

Fig. 6. Arrhenius plot for i_0 oxygen reduction on palladium in 85% orthophosphoric acid.

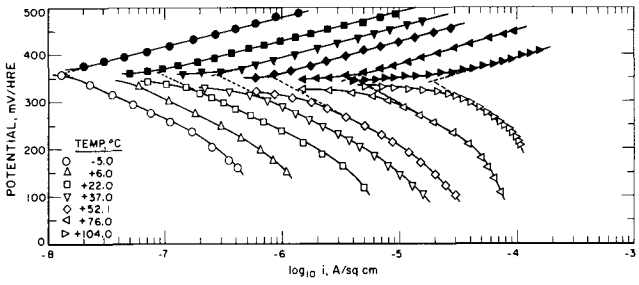

Fig. 7. Temperature dependence of cathodic reduction of oxygen and anodic production of Ag^+ on silver in 85% orthophosphoric acid.

Oxygen reduction data.—Hydrogen-reduced electrodes took up rest potentials of 340-345 mV HRE at 104.0°C to 362-365 mV HRE at −5.0°C in the oxygen-saturated electrolyte. A galvanostatic descending Tafel plot was started immediately on immersion. As in the case of the experiments on palladium electrodes, the silver electrodes were left for sufficient time (2-5 min at each applied current density) for stabilization of the potential to within 1 mV change in 1 min. These plots could be traced forward and backward several times with little hysteresis. Potentials, once established at any given current density, were very stable and showed no tendency to decay. Preliminary pulsing of the electrode galvanostatically between 50 mV HRE and open circuit caused no changes in the Tafel plot. Silver is thus insensitive to impurity deactivation when acting as an oxygen reduction surface in acid solution. Previous work has demonstrated that gold is also essentially unaffected by impurity adsorption (23).

Tafel plots on different silver electrodes were generally within 10 mV at the same current density, the differences between individual electrodes being temperature independent. A series of Tafel plots for a typical hydrogen-reduced electrode is shown in Fig. 7; kinetic data as a function of temperature are given in Table III.

Corrosion behavior of silver electrodes.—After completion of the oxygen reduction tests on the above electrode a series of plots was carried out to show the anodic behavior of the electrode as a function of temperature. Ascending galvanostatic Tafel plots were made at each temperature, starting from the open-circuit potentials of the electrode, using a freshly prepared electrolyte for each plot. At each applied current density a stable potential was very rapidly attained (within 30 sec. at the lowest current densities

Table III. Oxygen reduction on silver

Temp, °C	Slope, mV/decade	1/α	i_0,* A/cm^2
−5.0	110	2.07	4.5×10^{-17}
6.0	118	2.13	5.2×10^{-16}
22.0	119	2.03	2.4×10^{-15}
37.0	131	2.13	4.6×10^{-14}
52.1	133	2.07	1.9×10^{-13}
76.0	139	2.04	2.5×10^{-12}
104.0	150	2.01	4.8×10^{-11}

* i_0 values are approximate.

Table IV. Silver corrosion data

Temp, °C	Anodic slope, mV/decade	$1/\alpha$	i_{corr}, A/cm²	E_{corr}, mV/HRE
−5.0	62	1.17	1.35×10^{-8}	364
22.0	62	1.06	8.5×10^{-8}	363
37.0	65	1.06	2.8×10^{-7}	358
52.1	66	1.02	8.1×10^{-7}	353
76.0	71	1.04	4.2×10^{-6}	352
104.0	72	0.96	2.0×10^{-5}	344

studied, within a few seconds at 10^{-5} A/cm²), and no sign of passivation was observed. Normally the electrolyte was gently stirred with oxygen at the rate of 20 ml/min, and it was noted that the potentials achieved at each current density were somewhat dependent on the rate of stirring, as was the case with palladium. Table IV gives data on the corrosion potential and corrosion current obtained by extrapolation of anodic and cathodic Tafel lines, together with anodic Tafel slopes and $1/\alpha$ values as a function of temperature.

Order of reaction for oxygen reduction.—Tafel plots were obtained on a silver electrode at oxygen partial pressures of 1.0, 0.26, 0.080, and 0.025 atm at 22.0°C. The plots obtained are shown in Fig. 8, which includes an anodic plot at the lowest oxygen partial pressure studied. The limiting current region of the plot at 0.025 atm merges with the plot for the hydrogen evolution reaction.

A log pO_2-log i plot at constant potential is given for the Tafel region of both palladium and silver electrodes in Fig. 9. In both cases the oxygen reaction order is close to unity.

Activation energy for oxygen reduction on silver.—Because of the difficulty of extrapolation over many decades of current density back to the theoretical reversible oxygen potential, activation energy for oxygen reduction has been estimated by plotting the current densities at an overpotential within the measurement range, at $\eta = 960$ mV (300 mV HRE at 22°C). Current densities have been corrected to 1 atm oxygen partial pressure.

An Arrhenius plot on this basis is shown in Fig. 10. Activation energy is 15.5 ± 0.8 kcal under these potential conditions. Tafel slopes for the oxygen electrode on silver have close to theoretical temperature dependence; the mean slope is 2.07 $RT/\mathbf{F}$. Consequently, assuming the same reaction is still rate determining at the reversible potential, we may expect that the activation energy at $\eta = 0$ to be $15.5 + \alpha\eta\mathbf{F}$ kcal.

For $\alpha = 1/2.07$ and $\eta = 0.96$V, $\alpha\eta\mathbf{F} \sim 10.7$. Thus the activation energy at the reversible potential should be about 26.7 kcal on silver for the primary charge transfer step. This is somewhat greater than the value previously determined (23) on gold electrodes (23.6 kcal).

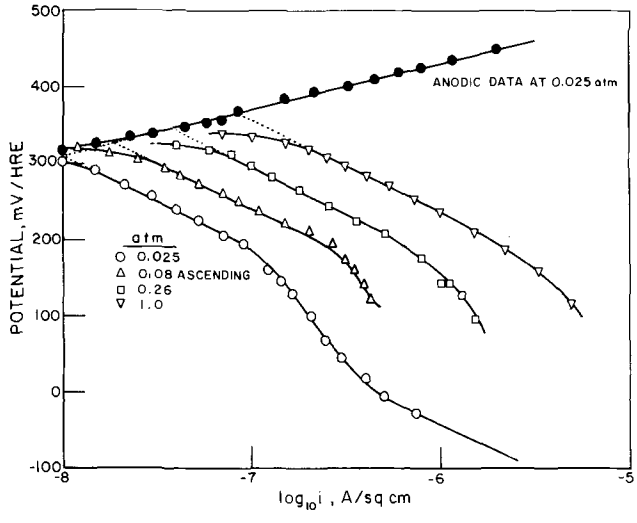

Fig. 8. Oxygen electrode on silver at 22°C in 85% orthophosphoric acid; effect of oxygen partial pressure.

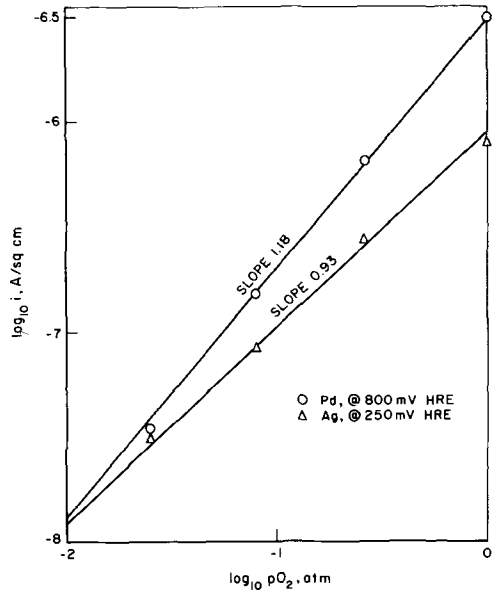

Fig. 9. Oxygen reduction reaction order at constant potential (Tafel Region) on palladium and silver electrodes.

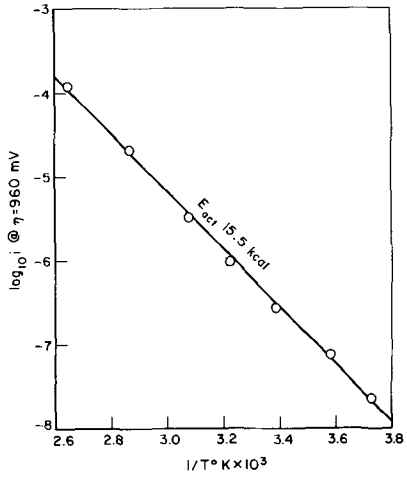

Fig. 10. Arrhenius plot of i at $\eta = 960$ mV, corrected for oxygen partial pressure, for oxygen reduction on silver in 85% orthophosphoric acid.

Discussion

Corrosion of palladium and silver.—Tables II and IV indicate that the anodic log current-potential plots on palladium and silver have slopes of $RT/2\mathbf{F}$ and $RT/\mathbf{F}$, respectively.

Because of the stirring dependence of the plots and the fact that the dissolution reaction in silver has been shown by Gerischer and Tischer (24) to have an exchange current considerably in excess of the current range explored here, it is reasonable to suppose that the reactions on both metals are diffusion controlled.

In such a case we can write for the anodic process

$$E = E_0 + \frac{RT}{z\mathbf{F}} \ln [X^{z+}]$$

where E_0 is the standard potential of the electrode, and X^{z+} is the concentration of the ion of valence z produced in the double layer by anodic dissolution.

If the reaction is under diffusion control

$$X^{z+} = \frac{\delta}{DzF}(i_a + i'_c) = k\,(i_a + i'_c)$$

where i_a is the imposed anodic current at potential E, and i'_c is the current due to the cathodic process (oxygen reduction) under the same conditions. In this expression D is the diffusion coefficient of X^{z+} and δ is the thickness of the Nernst diffusion layer. The other symbols have their usual meanings. Thus

$$E - E_o = \frac{RT}{zF} \ln [k(i_a + i'_c)]$$

As

$$i'_c = i_c \exp - \frac{\alpha F}{RT}(E - E_o)$$

where α is the transfer coefficient for the oxygen reduction reaction, and i_c is the rate of the oxygen reduction reaction at potential E_o, we obtain

$$i_a = \frac{1}{k} \exp \frac{zF}{RT}(E - E_o) - i_c \exp - \frac{\alpha F}{RT}(E - E_o)$$

This expression has a similar form to the Butler-Volmer equation, and the right-hand term may be discarded at comparatively small values of $E - E_o$, when

$$\partial E/\partial \ln i_a = RT/zF$$

The experimental Tafel slopes are close to RT/F for silver and $RT/2F$ for palladium, indicating dissolution as Ag^+ and Pd^{++} ions or complexes with the same oxidation number. The passivation of Pd at about 900 mV appears to be due to the formation of a film of $Pd(OH)_2$ (25) or PdO. Corrosion of palladium under these conditions is a result of its lower lattice energy compared with that of platinum.

Oxygen reduction reaction.—Palladium.—Palladium has a low Tafel slope for oxygen reduction ($\sim RT/F$) and in this respect resembles platinum (21, 26) and rhodium (27). On all three oxide-free metals oxygen reduction has been determined to be first order at constant potential (21, 26, 27), implying that the stoichiometric number (υ) of the rate-determining step is unity. It has been shown previously that an RT/F Tafel slope with $\upsilon = 1$ is not explicable if Langmuirian adsorption of reaction intermediates is assumed. In the case of rhodium and platinum electrodes in the phase-oxide-free state, a mechanism has been proposed in which the heat of adsorption of the product of the rate-determining step (—O_2H) falls as the total coverage of —O and —OH radicals derived from water oxidation rises (26). The coverage of —O and —OH rises linearly with potential (26) and the experimental coverage potential data are explained in terms of an isotherm in which adsorbed molecules are considered immobile and in which interaction effects are accounted for in the second virial coefficient (Frumkin isotherm or in the coverage range $0.1 < \theta < 0.9$, the Temkin isotherm). When such an isotherm operates, it effects the heat of adsorption of all adsorbed species on the electrode (28). A similar explanation of the effect of adsorbed anions on the hydrogen evolution reaction, which assumes that the chemical potential of the activated complex in the charge-transfer reaction depends on the second virial coefficient for the adsorption of the adsorbed anion, was recently provided by Parsons (29).

On this basis it can be shown that the observed Tafel slope and oxygen reaction order, together with the pH dependence at constant ionic strength, are consistent with theory (21, 26, 27). In view of the resemblance of linear potential-scan oxygen pseudocapacitance data on platinum (30, 31) and rhodium (32) to that on palladium (32) in acid solution, all of which may be accounted for by Temkin behavior (31), it is reasonable to suppose that the reaction

$$O_2 + H_3O^+ + e^- \rightarrow (O_2H)_{ads}$$

is also rate-determining on palladium. This view is supported by the similar experimental activation energies at the reversible potential on palladium, 22.4 kcal (27), and platinum, 22.9 kcal (21), for the oxygen reduction reaction.

Silver.—On silver, —O and —OH equilibrium coverage (from water oxidation) in the potential range where experimental measurements were made may be expected to be low because the electrode potential under these conditions was ~850 mV lower than the reversible potential for oxide formation (33). In alkaline solution, silver and gold electrodes show almost indistinguishable cyclic voltammetric scans (34), so on this basis a generally similar —O adsorption behavior would be expected, with low coverage (Langmuir conditions) on both metals.

Experimental Tafel slopes on silver are approximately $2RT/F$, and again oxygen reduction is first order. As has been shown for gold and iridium (23), these data are consistent with a primary charge transfer under Langmuir adsorption conditions. Thus the two possible rate-determining steps on this metal are

Reaction A: $O_2 + H_3O^+ + e^- \rightarrow (O_2H)$

Reaction B: $O_2 + e^- \rightarrow O_2^-$

Reaction A, involving a superoxide ion, is improbable in strongly acid solution, although it has been postulated by Krasil'shchikov (1, 2) to explain his pH-independent results for oxygen reduction on silver at pH 2. However, rotating electrode results of Palous and Buvet (8) show $(\partial\eta/\partial pH)_i > RT/F$ at pH values between 0 and 2 [see also ref. (5)]. On this basis Reaction B, shown already to be the rate-determining step on gold electrodes, appears to be the most likely rate-determining step on silver. Both metals have similar Tafel slopes ($2RT/F$) and similar activation energies at the reversible oxygen potential (23.6 kcal on gold, 26.2 kcal on silver).

The cyclic voltammetric data (34) imply similar heats of adsorption for oxygenated species on gold and silver. As this quantity, to a first approximation, is the only factor that determines activation energy differences between electrode materials, the similar experimental heats of activation on gold and silver are thus accounted for.

Conclusions

The rate-determining step in oxygen reduction on palladium and silver in strongly acid solution is a primary charge transfer, in all probability involving a proton

$$O_2 + H_3O^+ + e^- \rightarrow —O_2H$$

Although both metals have similar activation energies at the reversible potential (22.4 kcal on palladium, 26.2 kcal on silver), the figure on palladium includes a heat of adsorption term that depends on the equilibrium coverage of —O and —OH derived from water oxidation adsorbed on the electrode (21, 26). This coverage is linearly potential dependent—that is, adsorption follows the Temkin isotherm. For this reason it is more legitimate to compare activation energies on the two metals at potentials where —O coverage is low. Under such conditions there is a marked difference in activation energy between palladium and silver. At a potential of 750 mV HRE, where both metals can be expected to show low oxygen coverage (Langmuir conditions of intermediate adsorption), the activation energy will be approximately

$$E_1 - E_2 + (\alpha_1 - \alpha_2)\,\eta F$$

where E and α are the respective reversible potential activation energies and transfer coefficients and η is the overpotential. Taking η to be −500 mV (+760 mV HRE at 25°C), with $\alpha_2 = 1.0$ (Pd), $\alpha_1 = 1/2.07$ (Ag), E silver-E palladium ~ 9.8 kcal.

Thus, the intrinsic heat of activation for oxygen reduction on phase-oxide-free palladium (in the absence of poisoning effects due to equilibrium —O and —OH coverage) is appreciably lower than on silver, which accounts for the much greater rate of the reaction on palladium electrodes. Palladium and platinum, both with d-band vacancy values of about 0.6 (18), show similar oxygen reduction rates (15), whereas gold and silver electrodes, both with filled d-bands, give rates some orders of magnitude lower. The difference in rates in acid and alkaline solution for the latter two metals is particularly striking.

Acknowledgment

The author wishes to thank the sponsors of the TARGET fuel cell program and Pratt & Whitney Aircraft Division of United Aircraft Corporation for permission to publish this work. The help of members of IGT in the preparation of this publication is also greatly appreciated.

Manuscript submitted May 25, 1970; revised manuscript received June 27, 1970.

Any discussion of this paper will appear in a Discussion Section to be published in the June 1971 JOURNAL.

REFERENCES

1. A. I. Krasil'shchikov, *Z. Fiz. Khim.*, **23**, 332 (1949).
2. A. I. Krasil'shchikov, *ibid.*, **26**, 216 (1952).
3. A. U. Akopyan, *Izv. Akad. Nauk. Arm. S.S.R., Khim. Nauki*, **11**, 141 (1958).
4. V. N. Nikulin, *Z. Fiz. Khim.*, **35**, 84 (1961).
5. G. Bianchi, *Corrosion Anti-Corrosion*, **5**, 146 (1957).
6. G. Bianchi, G. Caprioglio, F. Mazza, and T. Mussini, *Electrochim. Acta*, **4**, 232 (1961).
7. G. Bianchi, F. Mazza, and T. Mussini, *ibid.*, **11**, 1509 (1966).
8. S. Palous and R. Buvet, *Bull. Soc. Chim. France*, 1606 (1962).
9. V. S. Bagotskii, L. N. Nekrasov, and N. A. Shumilova, *Usp. Khim.*, **34**, 1697 (1965).
10. J. P. Hoare, "The Electrochemistry of Oxygen," pp. 211-238 Wiley-Interscience, New York (1968).
11. D. T. Sawyer and L. V. Interrante, *J. Electroanal. Chem.*, **2**, 310 (1961).
12. D. T. Sawyer and R. J. Day, *Electrochim. Acta*, **8**, 589 (1963).
13. J. P. Hoare, *This Journal*, **111**, 610 (1964).
14. J. P. Hoare, *ibid.*, **112**, 1129 (1965).
15. A. Damjanovic and V. Brusic, *Electrochim. Acta*, **12**, 1171 (1967).
16. A. Damjanovic and V. Brusic, *J. Electroanal. Chem.*, **15**, 29 (1967).
17. A. Damjanovic, V. Brusic, and J. O'M. Bockris, *J. Phys. Chem.*, **71**, 2741 (1967).
18. M. L. B. Rao, A. Damjanovic, and J. O'M. Bockris, *ibid.*, **67**, 2508 (1963).
19. V. V. Sobol', E. I. Khrushcheva, and V. A. Dagaeva, *Elektrokhimiya*, **1**, 1332 (1965).
20. A. J. Appleby, *J. Electroanal. Chem.*, **24**, 97 (1970).
21. A. J. Appleby, *This Journal*, **117**, 328 (1970).
22. J. R. VanWazer, "Phosphorus and Its Compounds," Vol. 1, pp. 482-483, Interscience Publishers, New York (1958).
23. A. J. Appleby, To be published.
24. H. Gerischer and R. P. Tischer, *Z. Elektrochem.*, **61**, 1159 (1957).
25. M. Pourbaix, "Atlas d'Équilibres Electrochimiques à 25°C," p. 360, Gautier-Villars, Paris (1963).
26. A. Damjanovic and V. Brusic, *Electrochim. Acta*, **12**, 615 (1967).
27. A. J. Appleby, To be published.
28. B. E. Conway and E. Gileadi, *Trans. Faraday Soc. London*, **58**, 2493 (1962).
29. R. Parsons, *J. Electroanal. Chem.*, **21**, 35 (1969).
30. F. G Will and C. A. Knorr, *Z. Elektrochem.*, **64**, 258 (1960).
31. W. Böld and M. Breiter, *Electrochim. Acta*, **5**, 145 (1961).
32. F. G. Will and C. A. Knorr, *Z. Elektrochem.*, **64**, 270 (1960).
33. Ref. (25), p. 396.
34. J. Giner, J. M. Parry, and L. Swette, "Fuel Cell Systems II," p. 102. Advances in Chemistry Series, **90**, B. Baker, Editor, American Chemical Society, Washington, D. C. (1969).

The Ultraviolet Photovoltaic Effect in Evaporated Silver Bromide Conduction Cells

Joseph I. Masters

Technical Operations, Incorporated, Burlington, Massachusetts 01803

ABSTRACT

Ag/AgBr/Ag cells fabricated by a suitable masking of three overlapping evaporations exhibit a photovoltage when one semitransparent silver electrode is illuminated with 3650Å light and the AgBr electrolyte layer is much thicker than an absorption length for this radiation. Below a saturating illumination of approximately 1 mW/cm^2, a photocurrent proportional to the intensity of illumination flows in an external circuit. In this linear range the quantum yield is typically 40%; however, the energy conversion efficiency is only about 0.01%. In general, discoloration and gradual cell deterioration were observed as a result of photovoltaic operation. Conclusions are drawn from a comparison, using the same cell, of photoconduction and of dark conduction produced by an applied voltage. The former is characterized by a lower internal resistance.

We are concerned with the specific cell Ag/AgBr/Ag in which a current may be passed from one silver electrode to the other through an evaporated AgBr electrolyte film. The electrochemistry of solid electrolyte cells employing various types of electrodes was treated by Wagner (1, 2), and several authors (3-9) have studied mixed conduction in cells using electrolytes of compressed AgBr pellets or bulk AgBr crystals. Recently, reproducible miniature rechargeable batteries in the form of evaporated Ag/AgBr/Pt and Ag/AgI/Pt concentration cells were fabricated and studied (10).

On the other hand, photovoltaic activity from an AgBr electrolyte in contact with Ag is less well known.

Key words: Dember effect, photolysis, solid electrolyte, thin films, silver/silver bromide.

In 1929, Vanselow *et al.* (11) reported voltages in the millivolt range from the illumination of one electrode of an (Ag, AgBr)/liquid electrolyte/(AgBr, Ag) cell. Within the last decade, Eggert (12) investigated and described a photovoltaic effect caused by the illumination of an Ag/AgBr/Ag sandwich cell in which the AgBr layer was grown by brominating the surface of a bulk silver substrate rather than by the evaporation method employed here. The bromination method gave poor sample reproducibility. It was, nevertheless, possible to make observations of linearity in response, a high quantum yield, and a strong dependence on the wavelength of the illumination. By employing the evaporation method of deposition, reproducible cell samples can be fabricated more readily, allowing a convenient configuration for confirmation of earlier findings as well as a more detailed view and further study of the photovoltaic effect. The latter includes a comparison of the transient and steady photocurrent, believed characterized by both electronic and ionic diffusion, with the predominantly ionic dark current produced by application of a d-c voltage step.

Interest in the AgBr uv photovoltaic effect stems from a general interest in quantum detection, as well as from a parallel interest in evaporated AgBr as a photographic recording surface. The charge separation process associated with the effect almost certainly involves the diffusion and trapping of photolytic species, the basis of photographic sensitivity in AgBr systems. Generally speaking, successful deposition of reproducible silver halide layers by evaporation is a recent technology, and measurements of the type performed in the past using relatively thick AgBr materials have yet to be made on samples of thin evaporated AgBr films and cell structures.

Cell Fabrication

Pinhole-free Ag/AgBr/Ag overlapping sandwich cells were made by the successful evaporation procedure reported previously (10). Even in AgBr films of submicron thicknesses, continuous coatings of a contiguous domain structure are readily obtained, as shown in the Fig. 1 electron micrograph of a 0.5μ film. The sequence of evaporations for cell fabrication is shown in Fig. 2. The Ag and AgBr evaporations are best performed in separate vacuum systems to avoid bromination of the Ag electrodes by free bromine present when AgBr is evaporated. In the purification of AgBr used in this work, the prevalent impurities are silicon, iron, lead, and copper. Normally, the concentration of silicon is held to less than 25 ppm, and the remaining impurities to less than 5 ppm. Further purification results from deposition of the AgBr by evaporation.

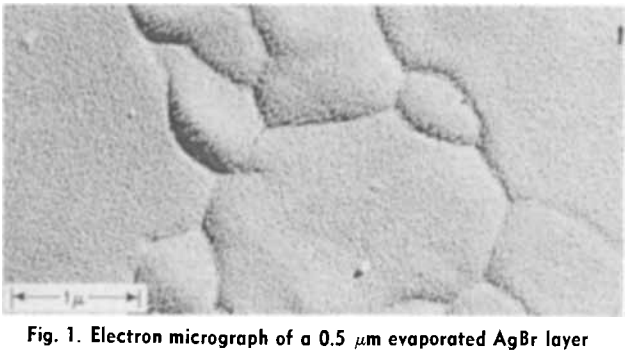

Fig. 1. Electron micrograph of a 0.5 μm evaporated AgBr layer

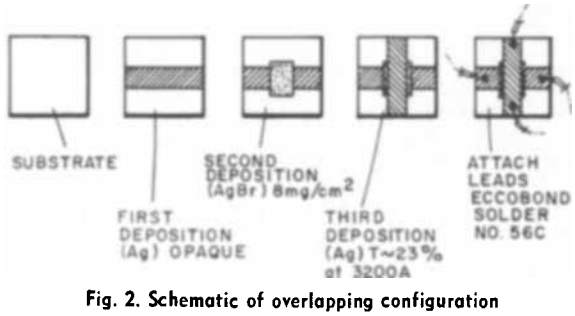

Fig. 2. Schematic of overlapping configuration

Ag/AgBr/Ag cells were made with an AgBr coverage of 8 mg/cm^2, and as a check on thickness dependence, two cells were covered with 3 mg/cm^2 of AgBr. Films in this thickness range approach a density equal to the bulk density of 6.5, yielding thicknesses estimated, respectively, of 13 and 5 μm. The bottom Ag electrodes were deposited to an arbitrarily opaque thickness on a glass substrate. The top electrodes were deposited to give about 20% transparency at 3200Å, the approximate peak of the uv window in silver.

After fabrication, the cells' electrolyte resistance was measured with a 1000 Hz a-c bridge and their open-circuit voltage with a high-impedance vacuum-tube voltmeter. The cells with a 3 mg/cm^2 layer of AgBr had an a-c resistance in the 21-25 ohm range, and the a-c resistance of cells with an 8 mg/cm^2 layer of AgBr was in the 42-46 ohm range.[1] The nonlinearity in the dependence of the measured values of electrolyte resistance with electrolyte thickness is an expected consequence of boundary effects (see following section). In general, measured values of AgBr thin film resistivity at room temperature are about 3 to 4 order of magnitude lower than bulk crystal values because the films are structure-sensitive and conduction along low resistance domain boundaries predominates.

Because of the chemical symmetry of the cells, they would be expected to have no open-circuit voltage. However, this was not the case. Cells produced by the method indicated in Fig. 2 had what appeared to be a random distribution of open-circuit voltage in the 0.0001 to 0.0005V range, with the top electrode always positive. The effect is believed to result from a difference in electrode potentials caused by a difference in the stress at the two electrodes, in turn caused by the shrinkage of the AgBr deposit in cooling to its substrate temperature. This suggests that the bottom Ag electrode remains under compression with respect to the top electrode. Support of this hypothesis is given by some related work on the deformation potential in solid-state cells (13).

In the measurements reported here, corrections for the deformation potential are made as required. However, measurements are normally under closed-circuit conditions, causing a relaxation of the open-circuit deformation potential to a much lower value.

Total Dark Conductivity

In an ionic semiconductor such as AgBr, conduction at room temperature is predominately by interstitial Ag^+ ions and silver ion vacancies, V^-. In addition, there is a small electronic contribution to the conductivity. The magnitude and type of the electronic portion of the total conduction (electrons or holes) depends on the AgBr sample's metal/nonmetal ratio. A silver excess, established by equilibration of AgBr with an Ag electrode, results in an electronic current predominately by conduction band electrons, and to detect it, the much greater ionic current must be suppressed by the use of a blocking or inert material such as carbon as the positive electrode (3). However, when a d-c voltage below the decomposition voltage is applied to an ideal Ag/AgBr/Ag cell, Ag^+ ion transport between the Ag electrodes is unblocked and ohmic, and the electronic contribution to the total conductivity is negligible. Nevertheless, in practice, the reactions that take place at the positive and negative silver electrodes are not reversible, and a significant amount of electrode resistance to Ag^+ ionic flow is encountered, generally much larger than the resistance within the thin electrolyte. This is especially noticeable if no attempt is made to fabricate graded or porous electrodes.

[1] Stated values of cell resistance, current, capacitance, etc., are for an effective cell area of 1 cm^2.

It is significant that R, the resistance to the ionic current at the electrodes, is caused by a capacitive pileup of ionic carriers unable to exchange charge with the electrodes freely. As a first order approximation, the polarization lends itself to a parallel R, C representation of the electrode interface impedance shown in the circuit analogue insert of Fig. 3. The build-up of cell voltage V to the steady state for this circuit is given by the exponential function

$$\frac{V}{V_0} = \frac{R}{R_L + R}\{1 - \exp[-(R_L + R)/R_L RC]t\} \quad [1]$$

in which V_0 is the applied voltage, R and C are constants, and where we have safely neglected the small contribution of the electrolyte resistance term $R_e << R$.

We may note here that the standard method of determining R_e is suggested by the circuit analogue, namely the substitution of d-c by an a-c voltage of frequency high enough (>0.1 kHz) to reduce the electrode impedance to a relatively low value of capacitive reactance. The a-c method, in which an impedance bridge is usually employed (10), yields upper bound values of R_e that may include a contribution from electrode resistance that is in effect not capacitively shunted.

From Eq. [1] the time constant of the equivalent circuit may be broken down as follows
when

$$R_L >> R, \ \tau \cong RC \quad [2a]$$

when

$$R >> R_L, \ \tau \cong R_L C \quad [2b]$$

and for the matching condition

$$R_L \cong R, \ \tau = RC/2 \quad [2c]$$

In an actual cell a dependence of R and C on cell voltage, as well as differences in conduction at the two electrodes, is expected. These factors are neglected in this simple model. Nevertheless, it is a guide in the evaluation of a typical cell's dark current response to a d-c voltage step.

By using an external circuit as shown inserted in Fig. 3, typical rise and decay curves of cell voltage were recorded for applied voltage steps from 0.003 to 0.03V. The electrode capacitance C derives from a very thin double layer and for cell voltages <0.015V, is in the order of 1000 μF/cm^2. Therefore, the use of load resistances smaller than a matching load was done in accord with Eq. [2b] at a sacrifice in accuracy to avoid a sluggish transient. Note that even in this low voltage range, the curves do not asymptotically approach a true steady state. Rather the room temperature mass transfer of silver from the positive to the negative electrode appears to cause a continuous increase in the value of R, which may be accompanied by some irreversible cell deterioration. Accordingly, cell parameters cannot generally be considered constant but depend on cell history.

To compare the dark current's slowly increasing R values with the smaller internal resistance encountered when the cell is operated as a photovoltaic element, it was necessary to assume the attainment of a quasi-steady dark current after an arbitrary 5 min time lapse, roughly the time allowed in the measurement of quasi-steady photocurrents. Thus, R is calculated from Eq. [1] for $t = \infty$, but using values of cell voltage obtained from the curves of Fig. 3, at time $t = 5$ min. The uncertainty of calculated effective internal resistance values (Fig. 4) includes variations caused by hysteresis observed as a result of reversing both the order of the measurements and the polarity of the applied voltage. We note, however, an indication of an increase in internal resistance with decreasing values of the cell voltage.

The Photovoltaic Effect

Theory.—The photovoltaic effect produces a potential difference between the electrodes of a symmetric Ag/AgBr/Ag cell. The phenomenon is observed if an asymmetry existis in the density of photolytic species as a result of the absorption of light close to a partially transparent electrode. If, for example, a 10^{-3} cm thick Ag/AgBr/Ag sandwich cell is illuminated with 4600Å light, for which the absorption coefficient is relatively low ($\alpha \cong 10^2$ cm^{-1}), then asymmetry in the distribution of photoelectrons and photoholes would be negligible, with no possibility of a detectable electrode potential difference. In such a thin cell, asymmetry is, however, assured by illuminating with light of wavelength below 4000Å, where the absorption coefficient in AgBr rises sharply with decreasing wavelength. At the wavelength of the convenient mercury 3650Å line, α is approximately 10^4 cm^{-1}, corresponding to an absorption depth of 1μ in the AgBr electrolyte.

Clearly, the effect must depend on certain properties well established in AgBr crystals at room temperature, namely, a sufficiently small recombination rate for photoelectrons and photoholes allowing their migration to trapping sites. The trapped photoelectrons

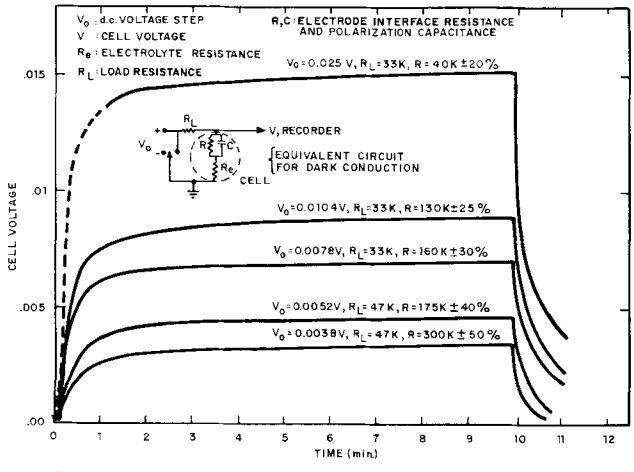

Fig. 3. Transient cell voltage, Ag/AgBr/Ag conduction cell

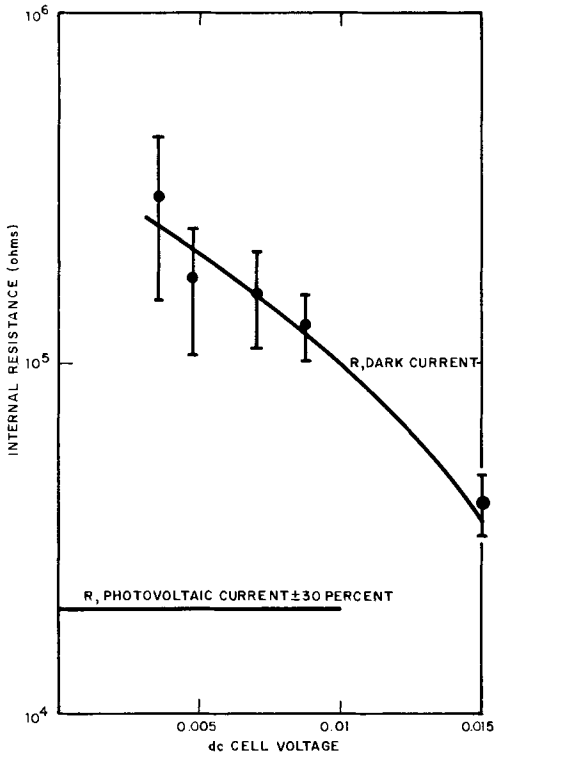

Fig. 4. Internal resistance. Ag/AgBr/Ag conduction cell dark current, photovoltaic current.

attract available interstitial Ag^+ ions, forming neutral silver atoms. A photohole can be trapped and neutralized by an existing negative silver ion vacancy V^-, or alternatively, by forcing a lattice Ag^+ ion into an interstitial site. A bound neutral bromine atom is thus formed.

Because of their much greater drift mobility (approximately 2 orders greater than the photohole mobility and with a diffusion length roughly half the thickness of a 13 μm cell), an appreciable fraction of the photoelectrons are trapped at depth in the AgBr layer, a small fraction possibly reaching the unlighted electrode. This leaves a net positive space charge near the lighted electrode due to the concentration of two relatively immobile species; the photoholes and the excess of interstitial Ag^+ ions resulting from the neutralization of trapped photoholes. In the absence of appreciable electrode charge transfer leading to an external photocurrent, this electrolyte polarization is expected to produce an induced or Dember effect photovoltage (14), measurable at the electrodes and with the lighted electrode positive. Of interest here, however, is the more complex photovoltaic effect that supports an external photocurrent of electrons from unlighted to lighted electrode and depends upon a charge transfer at both electrolyte-electrode interfaces.

The mechanism of negative charging of the unlighted electrode is postulated as follows: We assume that the aforementioned positive space charge prevents the lighted electrode from supplying Ag^+ ions to the electrolyte to make up for those that are neutralized by photoelectrons at trapping sites. Instead these ions are supplied primarily by the unlighted electrode giving this electrode a negative charge. The unlighted electrode is thus consumed by the flux of injected Ag^+ ions which numerically approaches the external photocurrent flux. A mechanism providing for the numerically equal charge transfer required at the lighted electrode is, however, less certain, as indicated by the variety of competitive reactions listed in Table I.

As a result of the photocurrent, the lighted electrode's silver mass is increased or decreased to the extent of plating or bromination as described in reactions of the type 3a or 3b (Table I). The photocurrent's quantum yield is less than unity to the extent of direct electron-hole recombination and noncontributory reactions of the type 3b. Departure from this optimum conversion would result from the arrival of some of the photoelectrons at the lighted electrode, the very unlikely arrival of the much shorter range photoholes at the unlighted electrode, or the lighted electrode acting as a donor of Ag^+ ions to replenish the electrolyte. These activities, assumed suppressed for cell thicknesses large compared to the illumination's absorption depth, cancel photovoltaic collected charges. In terms of quantum yield they are, therefore, twice as costly as recombination alone.

We must also account for a possible bromination (discoloration) of the lighted electrode. Bromination would require diffusion of normally bound neutral bromine atoms through the lattice toward a boundary. Although unlikely in a pure crystal, the outer layer of a thin AgBr film is a dislocation region which can support the diffusion of halogen atoms (15). This relates to experiments (16, 17) in the vacuum photolysis of thin silver halide films indicating that light absorbed close to the surface causes appreciable Br_2 evolution from the surface. The positive vacancy left by a diffusing neutral Br atom may be neutralized by a neighboring Ag^+ lattice ion jumping to an interstitial site (leading to reactions 3a or 3b, Table I), or by an electron (reaction 2b). Alternatively, a V^- vacancy may trap and thus neutralize a photohole, this neutral center then diffusing to the Ag/AgBr boundary (18). Note, the diffusion of bromine atoms toward the nearby lighted electrode, followed by electrode bromination (reaction 3b), is in itself a neutral process in the sense that it fails to charge the lighted electrode positively. However, to the extent that interstitial Ag^+ ions, generated in the aforementioned production of neutral Br atoms, are in turn neutralized at photoelectron trapping sites or serve to replenish those previously so neutralized, bromination represents a loss in the collection of photolytic charges and, from a quantum yield viewpoint, is equivalent to recombination.

Table I. Lighted electrode reactions

1. Charge transfer by photohole migration: $h + e \rightarrow Br^-$
2. Charge transfer by electrons from external photocurrent that neutralize h and Ag^+ in electrolyte:
   (a) $e + h \rightarrow Br^-$ (recombination)
   (b) $e + Ag^+ \rightarrow Ag^o$ (print out)
3. Results of Ag^+ and Br^o generated by trapped photoholes:
   (a) $Ag^+ + e \rightarrow Ag^o$ (charge transfer, with plating)
   (b) $Br^o + Ag^o \rightarrow AgBr$ (bromination, no charge transfer)

Response of photovoltaic cells.—The photovoltaic effect exists as an open-circuit cell voltage and does not require an external circuit. For a continuous uv illumination of the lighted electrode, the open-circuit voltage increases, but various loss phenomena cause the cell voltage to reach a quasi-steady value. Under closed-circuit conditions continuous uv illumination of the lighted electrode is partially converted, as discussed above, into a quasi-steady d-c photocurrent with the lighted electrode as the positive electrode.

The photovoltaic effect in the Ag/AgBr/Ag cell is a conversion process that alters, essentially irreversibly, the original structure. At best, the unlighted electrode is consumed and reappears as printout silver at trapping sites. This case might be approached with low current levels (low light intensity) and with small values of load resistance. On the other hand, the use of large light levels or a large load resistance appears to saturate the mechanism and to intensify the competitive processes of electrode bromination. In view of the dynamic nature of the irreversibility, defining a saturating radiant power level is difficult. For the cells tested, however, it was found that illumination exceeding $P = 1$ mW/cm^2 of 3650Å light caused indications of saturation, and therefore measurements were made at lower levels of illumination. Here we do not make the distinction between saturation in terms of nonlinear response, or intensification of cell deterioration, hysteresis effects, electrode discoloration, etc.

A study of the transient and steady behavior of the photocurrent generated by photovoltaic cells was carried out by illuminating the covering electrode of each cell with a spatially uniform light beam from a calibrated 3650Å source; *i.e.*, radiation in the 3650Å line from a stable mercury arc was isolated with suitable filters, and its radiant power measured with a thermopile. The intensity was varied using attenuators that were also calibrated at 3650Å. The photocurrent generated by a cell was recorded as the voltage common to both the cell and its parallel load resistor, which was varied in the $10^2 \rightarrow 10^5$ ohm range. Variation of the load provided data for calculating the effective internal resistance and for studying the dependence of response time on load resistance. The illumination of the cells was in the range from $P = 0.03$ mW/cm$^2 \rightarrow 1.0$ mW/cm^2, which allowed an observation of linearity and quantum yield.

Typical response curves for 13 μm thick cells under various loads are shown in Fig. 5 for cells illuminated with light at an intensity level of about 0.3 mW/cm^2. When $R_L << R$, the cell behaves as a current source and the quasi-steady current is nearly independent of the load. The transient is roughly exponential, and the rise time, which is the order of 1 sec for $R_L \sim 10^2$ ohms, increases with R_L.

The specific origin of the transient portion of the photocurrent is uncertain, because of the variation in the character of conduction throughout the electrolyte. However, some insight may be gained by satisfying charge conservation conditions. At the onset of illumi-

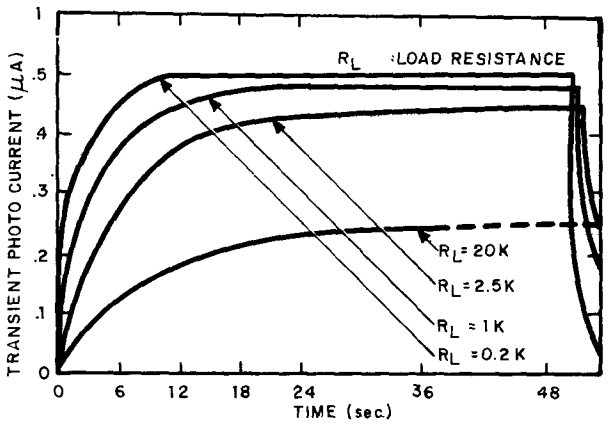

Fig. 5. Photovoltaic response of a 13 μm Ag/AgBr/Ag cell to 3650Å, 0.3 mW/cm² illumination.

nation, if the proximity of photolytic charge generation causes charge transfer to one electrode[2] charge neutrality of the cell is satisfied, not entirely by an equal and opposite charge on the other electrode, but partially by an excess of charges of opposite sign in the electrolyte. For example, if nearby photoholes first charge the lighted electrode positively (reaction 1, Table I), cell neutrality may result from a V^- excess created by a loss of Ag^+ interstitials to electron trapping sites, and from some yet unneutralized sites, rather than by a negatively charged unlighted electrode. The transient phase of the photocurrent then appears to be due to a sluggishness in the actual negative charging of the unlighted electrode by the suggested electrode reaction $Ag^o \rightarrow Ag^+ + e$. This reaction describes Ag^+ injection into the AgBr lattice that would be enhanced by the arrival at this electrode of the diffusing V^- species. The combination of low ion mobility and electrode impedance, the latter as described previously under dark conduction, are believed responsible for the sluggishness.

As in the case of dark ionic conduction (Fig. 3), a true steady photocurrent is not observed because the cells deteriorate slowly. Once the cell is illuminated, the transient response (as shown in Fig. 5) is followed by a plateau in photocurrent of several minutes duration, and then a gradual decay. For example, when a 13 μm thick evaporated cell connected to a 1 kohm load was illuminated for a prolonged period by a 3650Å beam for which $P = 1$ mW/cm², the photocurrent fell by 30% in 1 hr.

Plateau values of the photocurrent $i_1, i_2, \ldots$, obtained by using various load resistances $R_{L1}, R_{L2}, \ldots$, are in approximate agreement with the ratio

$$\frac{i_1}{i_2} = \frac{(R_{L2} + R)}{(R_{L1} + R)}$$

This formula applies in the case of an emf in series with an internal resistance R that is independent of the load, as in a battery. From this formula, R is defined as the effective internal resistance of an Ag/AgBr/Ag photovoltaic cell. Not only was the photovoltaic internal resistance found to be approximately independent of the load, but it was also nearly independent of P. The estimated over-all accuracy in determining the photovoltaic internal resistance is ±30%.

When a dark cell's internal resistance is compared to the same cell's internal resistance to a photocurrent the latter is, therefore, constant over the applicable photovoltaic cell voltage range (see Fig. 4). It is also much less than the voltage-dependent internal resistance of the dark current. For either type of cell operation we recall that $R >> R_e$, so that the origin of the difference in R lies in a comparison of electrode reactions. The unlighted electrode of an Ag/AgBr/Ag photovoltaic cell and the positive electrode of the same cell supporting dark conduction are assumed doner electrodes with similar roles, in the sense that they both supply Ag^+ ions to the electrolyte. The photovoltaic cell's lower resistance may be due in part to a larger V^- concentration at its doner electrode due to photolysis, or to dissimilarities at the acceptor electrodes of the two cell types. At the dark conduction cell's acceptor electrode plating occurs, reaction 3a, Table I; whereas the reflecting surface of the photovoltaic cell's lighted electrode, after prolonged uv exposure (cited above), shows discoloration attributed to bromination on an area strictly confined to the exposure region with no evidence of silver plating. These observations indicate that the electronic transport reactions 1 and/or 2, Table I, support the steady photocurrent whereas reaction 3b dominates over 3a and causes bromination. A technique to show the relative frequency of occurrence of reactions 1 and 2, which would give evidence of photohole diffusion length, does not seem possible in this type of experiment.

Quantum yield.—Determination of the quantum yield of the photovoltaic effect involves the use of the formula

$$Q = 3.2 \times 10^3 \, i/\beta P \quad \text{electrons/photon}$$

where i is the photocurrent in amperes for a 1 cm² cell, P is the intensity of the incident 3650Å illumination in mW/cm², and β is the fraction of these uv photons transmitted by the silver covering electrode (lighted) to the AgBr electrolyte. Values of the quasi-steady current i were obtained by measuring the voltage across the cell's load resistance with a precision digital voltmeter. The radiation intensity was measured with a calibrated thermopile. Unfortunately, because of the large uv absorption coefficient in AgBr, β was not measured directly. Instead the 3650Å transmission of the partially transparent electrode film was measured at a region off the cell where it was not backed by the AgBr layer. However, as a result of equilibration with evaporated AgBr or cell aging caused by photovoltaic operation, this technique leaves some doubt as to the transmission of the part of the silver film covering the cell surface. Since such factors would tend to reduce the effective silver thickness of the covering electrode film, and hence increase β, the calculated values of Q are taken to represent, at best, an upper bound approximation of the actual quantum yield. For $P < 1$ mW/cm², 13 μm thick cells, for which the measured value of $\beta = 0.017$ ±20%, produced calculated values of $Q = 0.4$ ±20%. This is in rough agreement with a similar determination by Eggert (12) for cells containing a 10 μm thick layer of AgBr fabricated by bromination of an Ag base. The photocurrent measurements reported here were performed on fresh cells and therefore represent a minimum of cell usage. The calculated value of Q decreases with prolonged use in proportion to the decrease in photocurrent. In the case of the thinner 5 μm cells the quantum yield was considerably less, namely, $Q = 0.1$ to 0.15, presumably a result of the aforementioned competitive phenomena arising from the proximity of the unlighted electrode.

The efficiency of converting radiant power into useful electrical power is

$$\eta = i^2 R_L 10^3/P \cong Q^2 \beta F R_L/10^4$$

where $F = \beta P$ is the radiant power in mW/cm² delivered to the electrolyte, and the condition $R_L = R$ is implied for optimizing η. For the configuration of the cells tested, in which β is the order of 0.01 and hence the saturation value of $F \cong 10^{-2}$ mW/cm², the conver-

[2] For a short duration after illumination (<0.1 sec) nearby photoelectrons may charge the lighted electrode negatively prior to dominant positive charging. This effect, which was not observed using the slow recording techniques of this experiment, has been reported (11, 12) in cases where positive hole migration was chemically suppressed using a halogen acceptor between electrode and electrolyte. The cell voltage resulting from such charging should endure for a time $\tau \sim R_L C_i$ where C_i is the relatively small interelectrode capacitance of the cell.

sion efficiency is very small, namley, $\eta \cong 0.0001$. It would appear that η should increase if β and P are increased. For instance, the efficiency of solar cells does not become large ($\eta = 0.1$) until the power input approaches the solar constant ($P = 100$ mW/cm^2). However, more than likely any increase in the value of F above the aforementioned estimated saturation limit will bring down the value of Q, and no increase in η will be realized. Relevant to this argument are some measurements by Eggert (12). Although his data are widely scattered, there is evidence of a decrease in Q as β is increased above the value of $\beta \cong 0.01$ employed in this investigation.

Manuscript submitted Dec. 3, 1969; revised manuscript received July 17, 1970.

Any discussion of this paper will appear in a Discussion Section to be published in the June 1971 JOURNAL.

REFERENCES

1. C. Wagner, Proceedings of 7th Meeting of *International Committee of Electrochemical Thermodynamics and Kinetics*, Butterworth Publications, Ltd., London (1957).
2. J. Wagner and C. Wagner, *J. Chem. Phys.*, **26**, 1597 (1956).
3. B. Ilschner, *ibid.*, **28**, 1109 (1958).
4. R. J. Friauf, *J. Phys. Chem.*, **66**, 2380 (1962).
5. R. J. Friauf, *J. Chem. Phys.*, **22**, 1329 (1954).
6. J. N. Mrgudich, "Solid Electrolyte Batteries," in "Encyclopedia of Electrochemistry," p. 84, C. A. Hampel, Editor, Reinhold Publishing Co., New York (1964).
7. D. O. Raleigh, "Progress in Solid State Chemistry," Vol. 3, pp. 102-107, Pergamon Press, New York (1966).
8. G. Luckey and W. West, *J. Chem. Phys.*, **24**, 879 (1956).
9. R. C. Hanson and F. C. Brown, *J. Appl. Phys.*, **31**, 210 (1960).
10. P. Vouros and J. Masters, *This Journal*, **6**, 880 (1969).
11. W. Vanselow, S. E. Sheppard, and V. C. Hall, *J. Phys. Chem.*, **33**, 331, 1403 (1929).
12. J. Eggert, *Angew. Chem.*, **73**, 417 (1961).
13. Unpublished memorandum: J. H. Mrgudich, U.S. Army Electronics Command, Fort Monmouth, New Jersey.
14. Y. T. Tan and F. Trautweiler, *J. Appl. Phys.*, **40**, 66 (1969).
15. J. I. Masters, *Nature*, **223**, 611 (1969).
16. G. Luckey, *J. Phys. Chem.*, **57**, 791 (1953).
17. F. A. Kroger, "The Chemistry of Imperfect Crystals," pp. 951-952, John Wiley & Sons, Inc., New York (1964).
18. N. Mott and R. Gurney, "Electronic Processes in Ionic Crystals," 2nd ed., p. 231, Oxford Press, London (1950).

Correction

In the paper "Theory of the Separation in Displacement Electrophoresis" by G. Brouwer and G. A. Postema which appeared on pp. 874-878 in the July 1970 JOURNAL, Vol. 117, No. 7, on p. 876, Eq. [17]-[19] should read

$$\beta_{lk} = E_l/E_k \qquad [17]$$

it results in

$$\sum_{K=G}^{Q} \frac{\alpha_K C_{Kk}}{\mu_G/\mu_K - \beta_{lk}} = 0 \qquad [18]$$

for

$$1 < \beta_{lk} < \mu_G/\mu_H \qquad [19]$$

JOURNAL OF THE ELECTROCHEMICAL SOCIETY

SOLID STATE SCIENCE

NOVEMBER 1970

SSS

Steady-State Chemical Potential Profiles in Solid Electrolytes

N. S. Choudhury and J. W. Patterson

Department of Metallurgy and Engineering Research Institute, Iowa State University, Ames, Iowa 50010

ABSTRACT

Steady-state chemical potential profiles in a solid electrolyte under open-circuit and ion-blocking conditions, may be obtained by balancing the steady-state flux at points inside the electrolyte. Steady-state oxygen chemical potential profiles inside a scaling layer of thoria and inside yttria-doped thoria specimens under open-circuit and ion-blocking (d-c polarization) conditions are illustrated in special cases.

Wagner (1) has shown that the oxidation of metals may be treated quantitatively in cases where the tarnishing is rate limited by steady-state transport through the tarnishing layer. Many other problems may be considered which also conform to this type of irreversible thermodynamic steady-state treatment. A partial listing might include specific diffusion problems and thermal conduction problems as well as problems involving charge conduction through mixed conductors with various blocking electrodes. The important feature common to all such problems is that quantitative expressions for local internal transport fluxes may be integrated over the length of the transport medium. By this integration device, the steady-state flux may be written in terms of the boundary values of the driving force potential, *i.e.*, the limits of integration. To arrive at explicit relationships, however, one must know how the transport parameter (thermal conductivity, for example) depends on the magnitude of the potential (temperature or thermal energy, for example). Here we are concerned with the problem of deducing steady-state profiles for certain of these potentials inside transport media for which the required conductivity dependences are known functions.

In particular we are concerned with deducing the steady-state chemical potential profiles (μ_{X_2} or equivalently log P_{X_2} *vs.* x) inside M_aX_b mixed conductors subjected to selected boundary conditions and/or boundary values for log P_{X_2}. Applying the analysis to solid electrolytes allows interesting prediction regarding the emf generated by double electrolyte tablets placed in series in galvanic cell measurements (2-4). The same analysis may also be used to calculate the steady-state log P_{X_2} *vs.* x profile that prevails in a homogeneous solid electrolyte being employed in a typical solid electrolyte galvanic cell experiment. Actually the profile determination in solid electrolytes is a special case of the profile determination problem for general mixed conductors. This more general problem is solved below and then used to discuss the log P_{X_2} profile types that may occur in ionic and electronic conducting scaling layers. In addition to these open-circuit type problems, the method may be used to calculate the steady-state log P_{X_2} profiles induced in mixed conductor specimens subjected to applied emf's under selected ion-blocking conditions. In particular, log P_{X_2} *vs.* distance profiles corresponding to the Hebb-Wagner (5-7) d-c polarization technique are calculated and discussed below.

Key words: chemical potential, solid electrolytes, mixed conductors, d-c polarization, scaling, electronic conductivity, hole conductivity, ionic conductivity, ionic transference number, open circuit emf.

General Determination of Steady-State Profiles

Before proceeding to specific cases, we outline the general features of the method by considering a somewhat generalized transport medium. We consider the medium to be capable of supporting a flux transport I_η (where η may be mass, charge, heat, etc.). This flux results locally from a gradient in some variable V (where V may be a chemical potential, electrostatic potential, temperature, etc.). The local flux equation may be written as

$$I_\eta/A = J_\eta(x) = -\sigma_\eta(x)\nabla V \qquad [1]$$

where $J_\eta = I_\eta/A$ is the η flux or the amount of η transported per unit time and cross sectional area due to the local gradient ∇V of the potential V. Equation [1] is typical of conductive-type transport processes such as Fick's law of diffusion, Fourier's law of heat conduction, or Ohm's law of charge conduction. In such processes ∇V acts as the driving force for the transport process and the proportionality parameter σ_η is called the conductivity parameter for η and very often is found to be a function of V. Although more general geometries may be readily considered, we limit consideration to the case of linear conduction geometry for simplicity. In this case ∇V in Eq. [1] may be replaced by dV/dx so that the equation may be rearranged and integrated to give

$$\int_o^L \frac{I}{A}\eta\, dx = \int_{V(O)=V'}^{V(L)=V''} \sigma_\eta(V)\, dV \qquad [2]$$

Because we are considering the steady-state case, I_η is independent of x and because of the linear geometry, A is independent of x. Equation [2] may be recast as

$$J_\eta L = \Delta \qquad [3]$$

where I_η/A has been replaced by J_η

$$\Delta = \int_{V(O)=V'}^{V(L)=V''} \sigma_\eta(V)\,dV \qquad [4]$$

and L is the total specimen thickness measured in the direction of transport. Note that Δ may be evaluated explicitly in terms of the end point values $V(L) = V''$ and $V(O) = V'$ if the functional dependence of $\sigma_\eta(V)$ on V is known.

Applying these elementary results to the series composite medium depicted in Fig. 1 yields for medium L

$$x^I J_\eta' = \Delta' \qquad [5]$$

where

$$\Delta' = \int_{V(O)=V'}^{V(x^I)=V^I} \sigma_\eta'(V)\,dV \qquad [6]$$

and yields for medium R

$$(L - x^I) J_\eta'' = \Delta'' \qquad [7]$$

where

$$\Delta'' = \int_{V(x^I)=V^I}^{V(L)=V''} \sigma_\eta''(V)\,dV \qquad [8]$$

The primes and double primes denote quantities in the left and right hand medium, respectively. To be consistent with these steady-state expressions, however, we must also invoke the additional steady-state relation

$$I_\eta' = I_\eta'' \qquad [9]$$

For the linear transport geometry being considered, this result is equivalent to

$$J_\eta' = J_\eta'' \qquad [10]$$

which, together with expressions [5] and [7], yields

$$\frac{x^I}{L} = \frac{\Delta'}{\Delta' + \Delta''} \qquad [11]$$

where Δ' and Δ'' may be evaluated from the integrals in Eq. [6] and [8], respectively. Wagner used an alternative, equivalent approach to calculate the silver chemical potential at the interface between contacting Ag_2S and AgI specimens (8).

In cases where the left and right side portions of the transport medium are the same material, Eq. [11] gives a formula for deducing the V *vs.* x profile. This is done by merely picking values of V intermediate between V' and V'', evaluating the Δ' and Δ'' integrals from Eq. [6] and [8], and then calculating the x/L values to which these selected V values correspond. For example, in the analysis of oxide solid electrolyte galvanic cell applications or of oxidation processes, V' and V'' may be taken to be the end point log P_{O_2} values log P_{O_2}' and log P_{O_2}'', respectively. The Δ' and Δ'' expressions are then generated by the appropriate integration of Wagner's general expression (1) for the net flux of mobile ions through any compact M_aX_b scaling layer as discussed in more detail below.

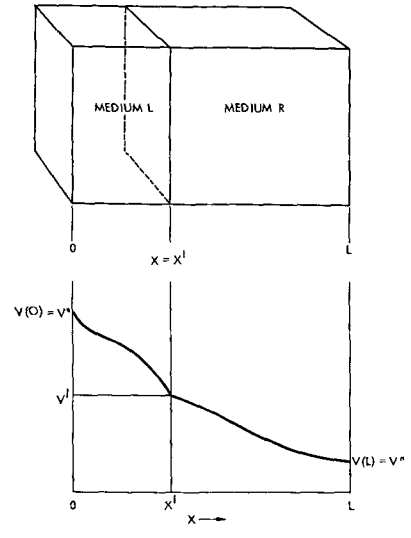

Fig. 1. Schematic steady-state potential distance profile inside two transport media in series contact.

In the cases where the composite medium is actually two different materials, the log P_{X_2} profiles inside each medium may be calculated individually according to the procedure outlined above with both contacting surfaces sharing the same μ_{X_2} value, *i.e.*, the interfacial value, log $P_{X_2}{}^I$. It is apparent from Eq. [6], [8], and [11] that when the conductivity parameters of both media are V independent, the V *vs.* x profiles reduce to two straight line segments connected at the point V^I, x^I. Much more interesting and less obvious profiles result when the conductivities exhibit a more or less complicated functional dependence on the driving force variable V.

Application to Mixed Conductors under Open-Circuit Conditions

Consider the case of a general mixed conductor specimen pressed between two reversible electrodes that establish the nonmetal chemical potential μ_{X_2} at the left and right hand faces of the specimen. According to Wagner's scaling rate theory (1), J_η for this case may be taken to be the electronic current J_e and the driving force variable is the electrochemical potential for electrons η_e. Under various assumptions involving local equilibria among various electronic, ionic, and atomic components and assumptions involving virtual stoichiometry constraints on the M_aX_b compound, Wagner's theory allows $\nabla\eta_e$ to be written in terms of $\nabla\mu_{X_2}$ so that the location-independent steady-state electronic current density $J_e = I_e/A$ may be written in terms of the alternative driving force variable μ_{X_2} as follows

$$J_e = [1/(2z_X\mathbf{F})]\, t_{ion} t_e \sigma\, d\mu_{X_2}/dx \qquad [12]$$

where z_X is the anion's valence, $\mathbf{F}$ is Faraday's constant, σ is the total electrical conductivity, and t_{ion} and t_e are the ionic and electronic transference numbers, respectively. Rearranging Eq. [12] and integrating from $x = 0$ to x^I and from x^I to L (*i.e.*, over two mixed conductors in series contact at x^I) yields

$$\Delta' = [1/(2z_X\mathbf{F})] \int_{\mu_{X_2}'}^{\mu_{X_2}{}^I} t_{ion}' t_e' \sigma'\, d\mu_{X_2} \qquad [13]$$

$$\Delta'' = [1/(2z_X\mathbf{F})] \int_{\mu_{X_2}{}^I}^{\mu_{X_2}''} t_{ion}'' t_e'' \sigma''\, d\mu_{X_2} \qquad [14]$$

These may be used in Eq. [11] to generate μ_{X_2} *vs.* x profiles in cases where the functional dependences of t_{ion}', t_e', σ' and t_{ion}'', t_e'', and σ'' on μ_{X_2} are known. For example, one may use Eq. [11], [13], and [14] to calculate the μ_{X_2} profile prevailing inside a scaling layer growing on an oxidizing metal. This is done by letting x^I be any arbitrary location inside the scale. In such cases, however, it is more conventional to use log P_{X_2} instead of μ_{X_2} as the variable V. Then, for the scaling layer example, P_{X_2}' is the P_{X_2} value established by equilibrium coexistence between the metal and the M_aX_b scale material and may be calculated from tabulated data for the standard free energy of formation ΔG° of the M_aX_b compound. P_{X_2}'', the ambient P_{X_2} of the "X-idizing" atmosphere, must be determined from the specified ambient conditions. In this example the interface at x^I separates two regions of the same material, hence the functional forms of t_{ion}, t_e, and σ are the same whether double or single primed. Figure 2 shows the results of such a log P_{O_2} *vs.* x/L profile inside a scaling layer of ThO_2 forming on thorium metal in O_2 gas at 1 atm pressure and at 1000°C. The necessary transport parameters ($P_\oplus$, $P_\ominus$, n and σ as discussed in detail below) were deduced from reported conductivity measurements on ThO_2 (9, 10) and also

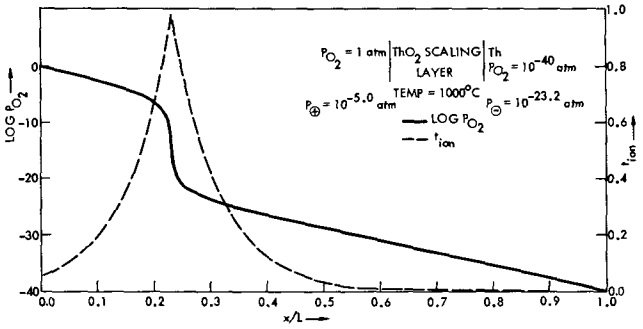

Fig. 2. Log P_{O_2} vs. x/L profile inside a ThO_2 scaling layer forming on Th metal at 1000°C in 1 atm P_{O_2}.

from as yet unpublished measurements on ThO_2 made in our laboratory.

To further illustrate the application of these ideas, let us specialize considerations to the class of mixed conductors known as solid electrolytes. For these materials, $t_{ion}\sigma \equiv \sigma_{ion}$ is known to be invariant over wide ranges of log P_{X_2} and may therefore be moved outside the integrals of Δ' and Δ'' in these ranges. Considering the entire medium between $x = 0$ and L to be comprised of the same solid electrolyte material, Eq. [11] reduces to

$$\frac{x^I}{L} = \frac{\log \left| \frac{P_{X_2}{}^I}{P_{X_2}{}'} \right| - \int_{\log P_{X_2}'}^{\log P_{X_2}{}^I} t_{ion}\, d \log P_{X_2}}{\log \left| \frac{P_{X_2}{}''}{P_{X_2}{}'} \right| - \int_{\log P_{X_2}'}^{\log P_{X_2}{}''} t_{ion}\, d \log P_{X_2}} \quad [15]$$

where we have changed the variable of integration from μ_{X_2} to log P_{X_2} through the relationship

$$\mu_{X_2} = \mu_{X_2}{}^{\circ} + 2.303RT \log P_{X_2} \quad [16]$$

According to an analysis by Schmalzried (11, 12) the integrals appearing in Eq. [15] may be evaluated by employing the formula

$$\int_{\log P_{X_2}(a)}^{\log P_{X_2}(b)} t_{ion}\, d \log P_{X_2} = [2.303n/\sqrt{w}] \log \left| \frac{2(P_{X_2}/P_{\oplus})^{1/n} + 1 - \sqrt{w}}{2(P_{X_2}/P_{\oplus})^{1/n} + 1 + \sqrt{w}} \right|_{P_{X_2}(a)}^{P_{X_2}(b)} \quad [17]$$

where

$$w = 1 - 4\left(\frac{P_{\ominus}}{P_{\oplus}}\right)^{1/n} \quad [18]$$

In Eq. [17] and [18], $P_{\ominus}$ is the P_{X_2} where $\sigma_{\ominus} = \sigma_{ion}$. $P_{\oplus}$ is the P_{X_2} where $\sigma_{\oplus} = \sigma_{ion}$, and $\ominus$ and $\oplus$ denote excess electron and positive hole carriers, respectively. The empirical parameter n characterizes Schmalzried's presumed dependence of the electronic conductivities $\sigma_{\ominus}$ and $\sigma_{\oplus}$ on $P_{X_2}{}^{-1/n}$ and $P_{X_2}{}^{+1/n}$, respectively. Thus the parameters $P_{\ominus}$, $P_{\oplus}$, and n must be known from independent experiments if quantitative results are to be obtained. A computer program with these parameters and P_{X_2}' and P_{X_2}'' as input is used to generate x^I/L values according to Eq. [15], [17], and [18] for an array of $P_{X_2}{}^I$ values between P_{X_2}' and P_{X_2}''. The resulting tabulation of x^I/L vs. $P_{X_2}{}^I$ values is then plotted to provide the desired profiles. All the profiles for open-circuit conditions, *i.e.*, Fig. 2-5 were generated in this fashion.

Figures 3-5 show the results of such an application for the oxide solid electrolyte YDT ($Th_{0.85}$ $Y_{0.15}$ $O_{1.925}$)

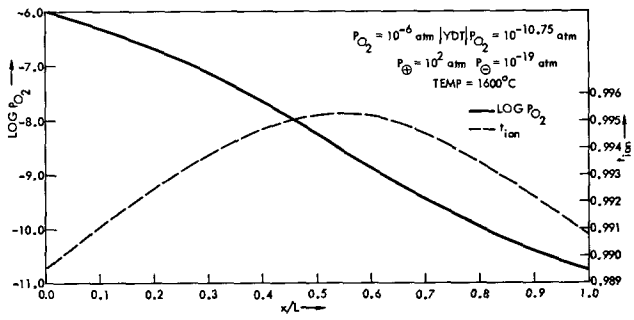

Fig. 3. Log P_{O_2} vs. x/L profile inside a yttria-doped thoria electrolyte for reversible electrode P_{O_2} values within the electrolytic domain at 1600°C.

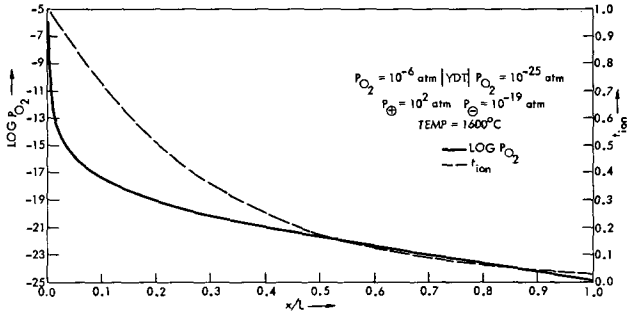

Fig. 4. Log P_{O_2} vs. x/L profile inside a yttria-doped thoria electrolyte for reversible electrode P_{O_2} values spanning the mixed conduction region between the electrolytic and excess electron conduction domains at 1600°C.

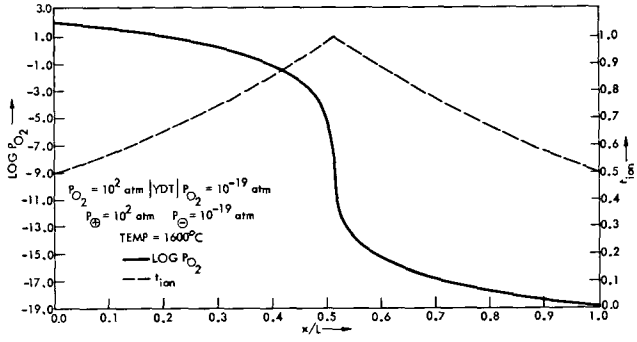

Fig. 5. Log P_{O_2} vs. x/L profile inside a yttria-doped thoria electrolyte for reversible electrode P_{O_2} values located at $P_{\ominus}$ and $P_{\oplus}$, respectively, at 1600°C.

at 1600°C. The values of $P_{\ominus}$, $P_{\oplus}$, and n at 1600°C were determined from an assessment of conductivity and galvanic cell data involving the electrolyte YDT. The values of P_{O_2}' and P_{O_2}'' were chosen so that three interesting cases could be demonstrated. Figure 3 shows the log P_{O_2} vs. x/L profile for the case where P_{O_2}' and P_{O_2}'' both lie within the electrolytic conduction domain[1] for YDT. The P_{O_2}' and P_{O_2}'' values for Fig. 4 span a mixed conduction region from the electrolytic domain down into the domain where excess electron conduction becomes predominant. Similarly the P_{O_2}' and P_{O_2}'' values for Fig. 5 were chosen well outside the domain where ionic conduction predominates. Thus in this case $P_{O_2}' = P_{\ominus}$ and $P_{O_2}'' = P_{\oplus}$ so that the entire electrolytic domain is spanned. In addition to giving the log P_{O_2} vs. x/L profile, each figure also shows the t_{ion} vs. x/L profile. The t_{ion} values were determined

[1] That is, the log P_{O_2}, $1/T$ domain where $t_{ion} > 0.99$ according to a recent paper (13) which also elucidates the details of electron hole and excess electron conduction domain on log P_{X_2}, $1/T$ diagrams.

for these log P_{O_2} profiles by evaluating

$$t_{ion} = [1 + P_{\oplus}^{-1/n} P_{O_2}^{1/n} + P_{\ominus}^{+1/n} P_{O_2}^{-1/n}]^{-1} \quad [19]$$

Note that the log P_{X_2} profiles show a steep gradient at the region where t_{ion} is a maximum, the region having predominantly ionic conduction. Wagner long ago (1) alluded to this feature of such chemical potential profiles inside mixed conductors but reported no quantitative calculations.

This procedure may be readily adapted to the determination of log $P_{X_2}{}^I$ values that prevail at the contacting interface between two different X (or M) ion conductors in series. In cases where two different oxide solid electrolytes are used in series for galvanic cell emf measurements, it is important that the log $P_{O_2}{}^I$ value prevailing at their contacting interface lie within the electrolytic domain for both electrolytes at all times. Otherwise the measured emf's will depart from the thermodynamic values by unknown amounts. However, by applying the above methods one may readily calculate the log $P_{O_2}{}^I$ values to be sure they do fall within the electrolytic domains. No example profiles for this type problem are offered in the present context, however, because others (4, 8) have already solved this class of problems by an alternate method.

Application to Mixed Conductors Subjected to Applied EMF's and Ion Blocking Conditions

Now let us consider the case of a mixed conductor between a reversible electrode and an ion-blocking electrode which are both capable of transporting electrons with negligible impedance. Let an emf E be applied across the mixed conductor, as in d-c polarization experiments (14-17). The situation is schematically illustrated in Fig. 6.

For ion-blocking conditions, Wagner (6, 7) has derived a general expression for the steady-state current due to electrons and holes in ionic crystals. Wagner's result is related to the quantity of Eq. 3 by the relation

$$\Delta = J_e L = -[1/(2z_X \mathbf{F})] \int_{\mu_{X_2}(O)}^{\mu_{X_2}(L)} \sigma_e \, d\mu_{X_2} \quad [20]$$

where

$$\mu_{X_2}(L) = \mu_{X_2}(O) - 2z_X \mathbf{F} E(L)$$
$$= \mu_{X_2}(O) + RT \ln [P_{X_2}(L)/P_{X_2}(O)] \quad [21]$$

and where $\sigma_e = \sigma_{\oplus} + \sigma_{\ominus}$ is the sum of the electron hole $\oplus$ and excess electron $\ominus$ conductivities inside the specimen.

For most ionic compounds capable of predominant ionic conduction we may assume the following transport parameter dependences

$$\sigma_{\oplus} = \sigma_{ion} P_{\oplus}^{-1/n} P_{X_2}^{1/n} \quad [22]$$

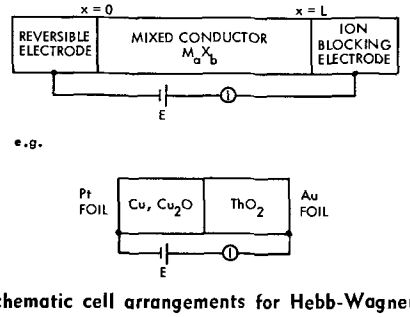

Fig. 6. Schematic cell arrangements for Hebb-Wagner d-c polarization experiments.

$$\sigma_{\ominus} = \sigma_{ion} P_{\ominus}^{1/n} P_{X_2}^{-1/n} \quad [23]$$

σ_{ion} is P_{X_2} independent where as before $\sigma_{\oplus} = \sigma_{ion}$ at $P_{X_2} = P_{\oplus}$ and $\sigma_{\ominus} = \sigma_{ion}$ at $P_{X_2} = P_{\ominus}$. Equations [11], [20], [21], [22], and [23] may be combined to yield

$$\frac{x}{L} = \frac{[P_{\oplus}^{-1/n} P_{X_2}^{1/n}(O) \{\exp(-2z_X \mathbf{F} E(x/L)/nRT) - 1\} + P_{\ominus}^{1/n} P_{X_2}^{-1/n} \{1 - \exp(2z_X \mathbf{F} E(x/L)/nRT\}]}{[P_{\oplus}^{-1/n} P_{X_2}^{1/n}(O) \{\exp(-2z_X \mathbf{F} E(L)/nRT) - 1\} + P_{\ominus}^{1/n} P_{X_2}^{-1/n} \{1 - \exp(2z_X \mathbf{F} E(L)/nRT\}]} \quad [24]$$

Equation [24] combined with Eq. [21] gives the log P_{X_2} profile within the mixed conductor under ion-blocking conditions.

Figures 7 and 8 show log P_{O_2} profiles induced in YDT under ion-blocking conditions at 1600°C. Figure 7 shows such a profile for both electrodes having P_{O_2} values inside the electrolytic domain. The P_{O_2} value at the reversible electrode is established by the presence of oxygen gas at 10^{-6} atm, whereas the effective P_{O_2} at the blocking electrode is established at $10^{-10.75}$ atm as a result of the imposed emf $E = -0.442$V. Figure 8 shows the effect of increasing the magnitude of the applied voltage. In this case the reversible electrode is presumed to be established at $P_{\oplus}$ so that the applied emf of $E = -1.951$V renders the effective P_{O_2} at the blocking electrode to be $P_{\ominus} = 10^{-19}$ atm at 1600°C.

Interestingly, an emf *vs.* x/L profile for Ag_2S has been obtained by Hebb (5). Unfortunately, his data cannot be correlated with Eq. [24] because no effort was made to establish the silver chemical potential with a reversible electrode in Hebb's experiment.

A comparison of Fig. 7 and 8 shows that, under blocking conditions at least, a significant region of an oxide conductor can be made substantially n-type by merely controlling the magnitude of the applied voltage. Theoretically reversing the voltage (under

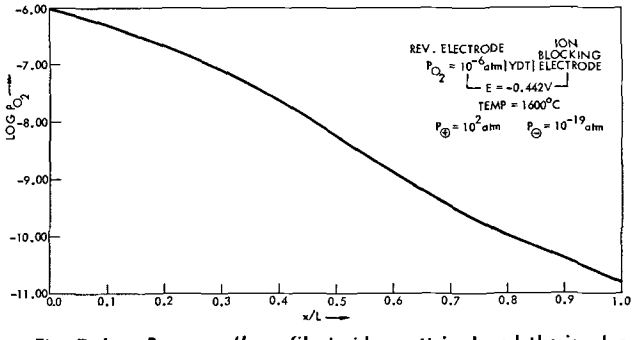

Fig. 7. Log P_{O_2} *vs.* x/L profile inside a yttria-doped thoria electrolyte with the reversible electrode P_{O_2} at 10^{-6} atm and the ion-blocking electrode at 0.442V negative polarity, $T = 1600$°C.

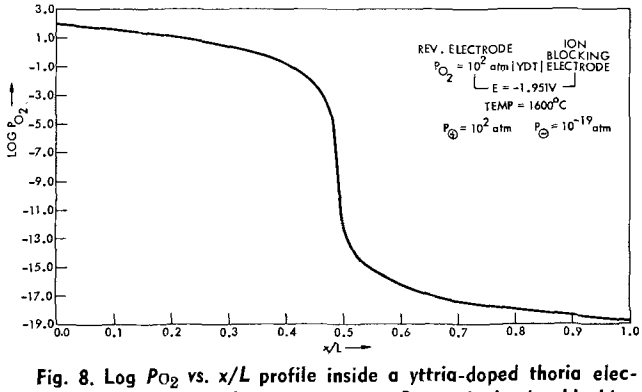

Fig. 8. Log P_{O_2} *vs.* x/L profile inside a yttria-doped thoria electrolyte with the reversible electrode at $P_{\oplus}$ and the ion-blocking electrode at a sufficient negative emf to induce an effective P_{O_2} equal to $P_{\ominus}$ at 1600°C.

blocking conditions) should induce a p-type region. This property could be important in catalysis engineering where the electronic nature of the catalyzing substrate is often vital, although the above calculations assume that there is no source of oxygen (the mobile species) other than at the reversible electrode. These calculations do suggest that some degree of control over the n- or p-type nature of an oxide lateral surfaces may be possible even if a limited amount of oxygen exchange between the oxide and the ambient is permitted.

APPENDIX

The Conductance of a Solid Electrolyte When Subjected to a Difference in the Nonmetal Chemical Potential at the Ends under Open-Circuit Condition

With reference to Fig. A-1, let us assume the mixed conductor of length L and uniform cross section A, subjected to nonmetal chemical potential $\mu_{X_2}(1)$ and μ_{X_2} (2) at its two ends.

The conductance is then given by

$$1/G = [1/A] \int_0^L [1/\sigma(l)]dl \qquad [25]$$

where G = total conductance and $\sigma(l)$ = the total conductivity at location l.

We can write Eq. [25] as

$$1/G = [1/A] \int_0^L [t_{ion}/\sigma_{ion}(l)]dl \qquad [26]$$

In the case of solid electrolyte σ_{ion} is a constant and is independent of l. Therefore

$$1/G = 1/(A\sigma_{ion}) \int_0^L t_{ion}(l)\,dl \qquad [27]$$

Since a plot of t_{ion} *vs.* x/L can be obtained, as discussed earlier, graphical integration of Eq. [27] is possible, yielding the value of G.

Experimental determination of the quantity G under open-circuit condition becomes difficult if an a-c bridge or any other instrument is connected across the ends of the specimen, because the open-circuit condition is violated. However, the cell assembly illustrated in Fig. A-2 allows determination of the conductance.

The total conductance G' of the double cell can be determined with an a-c bridge without violating the open-circuit conduction, because the nonmetal chemical potentials at the two ends are identical. The total conductance G' is then given by

$$1/G' = [1/(A\sigma_{ion})]\left\{\int_0^{L_1} t_{ion}(l)\,dl + \int_0^{L_2} t_{ion}(l)\,dl\right\} \qquad [28]$$

The quantities on the right can be determined as explained earlier and thus an experimental check may be obtained.

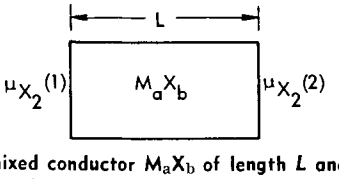

Fig. A-1. A mixed conductor M_aX_b of length L and uniform cross section A, subjected to nonmetal chemical potential μ_{X_2} (1) and μ_{X_2} (2) at its two ends.

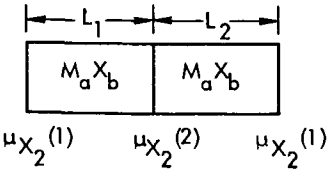

Fig. A-2. A symmetric double cell with solid electrolyte M_aX_b to determine the conductance when the solid electrolyte is subjected to a difference in the nonmetal chemical potential at its two ends.

LIST OF SYMBOLS

A	cross-sectional area
E	electrical potential difference
$E(L)$	electrical potential difference from O to L
$E(x/L)$	electrical potential difference from O to x
$\mathbf{F}$	Faraday's constant
G	total electrical conductance
I_η	current of species η
J_e	electronic current density
J_η	flux of species η
l	distance coordinate inside the specimen
L	total length of the specimen
n	empirical parameter characterizing presumed dependence of electronic conductivity
P_{X_2}	partial pressure of nonmetal gaseous dimer (X_2 gas)
$P_\oplus$	P_{X_2} at which $\sigma_\oplus = \sigma_{ion}$
$P_\ominus$	P_{X_2} at which $\sigma_\ominus = \sigma_{ion}$
R	gas constant
t_e	electronic transference number
t_{ion}	ionic transference number
T	temperature, °K
V	generalized potential
V'	potential at location O
V''	potential at location L
V^I	potential at location x^I
x	distance coordinate inside the specimen
z_X	valence of anion
η_e	electrochemical potential for electrons
μ_{X_2}	chemical potential/mole of nonmetal gaseous dimer (X_2 gas)
$\mu_{X_2}^o$	chemical potential for one mole of X_2 gas in the standard state
σ	total electrical conductivity
σ_e	total electronic conductivity
σ_{ion}	ionic conductivity
σ_η	conductivity parameter for species η
$\sigma_\oplus$	hole conductivity
$\sigma_\ominus$	excess electronic conductivity

Acknowledgment

Research was sponsored by the Aerospace Research Laboratories, Office of Aerospace Research, United States Air Force, Contract F33615-68-C-1034.

Manuscript received May 4, 1970.

Any discussion of this paper will appear in the Discussion Section to be published in the June 1971 JOURNAL.

REFERENCES

1. C. Wagner, *Z. Phys. Chem.*, **21**, 25 (1933).
2. C. B. Alcock and B. C. H. Steele, in "Science of Ceramics," Vol. 2, p. 397, G. H. Stewart Editor, Academic Press, London (1965).
3. T. L. Markin and M. H. Rand, in "Thermodynamics I," p. 145, International Atomic Energy Agency Symposium (1966).
4. D. A. Shores and R. A. Rapp, Private communication.
5. M. Hebb, *J. Chem. Phys.*, **20**, 185 (1952).
6. C. Wagner, *Z. Elektrochem.*, **60**, 4 (1956); **63**, 1027 (1959).
7. C. Wagner, in "International Committee of Electrochem. Thermodynamics and Kinetics Proc. 7th Meeting London 1955," Butterworth Scientific Publications, London (1957).
8. C. Wagner, *Z. Elektrochem.*, **40**, 365 (1934).
9. M. F. Lasker and R. A. Rapp, *Z. Physik. Chem. N.F.*, **49**, 198 (1968).
10. J. E. Bauerle, *J. Chem. Phys.*, **45**, 4162 (1966).
11. H. Schmalzried, *Z. Elektrochem.*, **66**, 572 (1962).
12. H. Schmalzried, *Z. Physik Chem. N.F.*, **38**, 87 (1963).
13. J. W. Patterson, in "The Physics of Electronic Ceramics," L. L. Hench and D. B. Dove, Editors, Marcel Dekker Inc., New York (1970).
14. J. B. Wagner and C. Wagner, *J. Chem. Phys.*, **26**, 1597 (1957).
15. B. Ilschner, *ibid.*, **28**, 1109 (1958).
16. D. O. Raleigh, *J. Phys. Chem. Solids*, **26**, 329 (1965).
17. J. W. Patterson, E. C. Bogren, and R. A. Rapp, *This Journal*, **114**, 752 (1967).

Alkaline Earth Sulfide Phosphors Activated by Copper, Silver, and Gold

Willi Lehmann*

Westinghouse Research Laboratories, Pittsburgh, Pennsylvania 15235

ABSTRACT

Emission spectra of cathodoluminescence of Cu, Ag, and Au in MgS, CaS, SrS, and BaS, at room temperature and near 80°K, are presented. The spectra depend very much on the coactivators used including the alkalies and the halides. The observations indicate the luminescence to be caused by centers containing both activator and coactivator.

Copper, silver, and gold are well known to be most effective activators in ZnS-type phosphors. They are probably incorporated as acceptors and, for charge compensation, require the simultaneous incorporation of a donor impurity, *e.g.*, a halide (except F) or a trivalent metal (*e.g.*, Al) as coactivator. Earlier workers have noted already, that the situation is quite different in alkaline earth sulfides where not Cl, Br, or I but F is the preferred halide and where even alkalies are effective coactivators (1, 2).

Investigations on alkaline earth sulfide phosphors activated by copper, silver, or gold are surprisingly rare, and the few publications are not always in agreement with each other. Lenard (1) reported three different emission bands, at 420, 512, and 600 nm, respectively, in CaS:Cu, but in view of the uncertain compositions of the materials of his days, the results may be questioned. More recently, and apparently working with better materials, Sorge (2) reports a single emission band in CaS:Cu,F, at 430 nm with 0.1% Cu and at 480 nm with 1% Cu. Gradual replacement of CaS by SrS and BaS shifts the copper emission to lower energies. Other reports on CaS:Cu include those by Avinor *et al.* (3) (one emission band at 460 nm) and by Wachtel (4) (two bands, at 435 and 500 nm). Reports on silver or gold activated alkaline earth sulfides do not seem to exist. Our investigations were made to clarify the reported contradictions on CaS:Cu and, more generally, to improve our knowledge of the entire alkaline earth sulfide phosphor system.

The compounds MgS, CaS, SrS, and BaS all crystallize in the cubic NaCl lattice. Some properties of interest are summarized in Table I. The optical absorption "edge" actually is the spectral position where, in a compound as pure as we could make, the optical absorption coefficient goes through the value of about 100 cm^{-1}. These points were determined by simple powder reflection measurement at room temperature; they are not necessarily identical to the true band gaps of the compounds which may be (and apparently are) obscured by various native defects, exciton absorptions, *etc*, and which may be slightly higher than the "edges" mentioned in Table I. The cationic radii are those reported by Pauling (5), and the next-neighbor distances are simply the sums of cationic and anionic radii (with 1.84Å for S^{--}). The interstitial radius is the maximum radius of a solid sphere which could be placed interstitially in the lattice without deformation of the latter.

* Electrochemical Society Active Member.

Key words: magnesium sulfide, calcium sulfide, strontium sulfide, barium sulfide, alkaline earths, phosphors, luminescence, spectra, copper, silver, gold.

Table I. Some properties of alkaline earth sulfides

		MgS	CaS	SrS	BaS
Optical abs. edge	(eV)	~5.4	4.8	4.4	3.8
Cation radius	(Å)	0.65	0.99	1.13	1.35
Next-neighbor distance	(Å)	2.49	2.83	2.97	3.19
Interstitial radius	(Å)	0.32	0.61	0.73	0.93

Preparation

Alkaline earth sulfides of luminescence grade purity do not seem to be commercially available. We prepared CaS, SrS, and BaS by a method described by Sorge (2) and Wachtel (4). The purest available nitrates are dissolved in water and, for several hours, kept boiling in the presence of magnesium metal ribbon. Heavy metal impurities either deposit on the magnesium or are trapped in small amounts of hydroxide which, afterwards, is filtered out. The sulfates are then precipitated with H_2SO_4, briefly washed in water to remove excess acid, dried, and converted to the sulfides by firing in an atmosphere of H_2 and H_2S (4). The results are white, nonluminescent powders containing no spectroscopically detectable traces of Fe, Mn, Cu, etc. The major remaining impurity is silicon (usually about 100 ppm), probably from the quartz containers. Oxygen, due to unavoidable contact with atmospheric air, probably is also present but cannot be detected spectroscopically. We believe silicon to have no effect on the luminescence properties of the sulfides, and a possible effect of oxygen is minimized by the strongly sulfurizing atmosphere of the final firing step and by protection of the phosphors from air by an inert atmosphere (*e.g.*, argon) during storage. Only MgS cannot be prepared in this way ($MgSO_4$ is soluble in water). It was made by firing $MgCO_3$ (luminescence grade purity) in argon loaded with CS_2 (6). The conversion is quantitative but the resulting MgS has, at best, only the purity of the used $MgCO_3$.

Desired impurities were added to the prefired pure sulfides before the final firing step. It is considered to be an important point in these investigations that, whenever possible, only one activator element (here Cu, Ag, or Au) and one co-activator element were tested in any one of the samples, and that all other impurities were kept out as well as possible. Copper and silver were added as sulfides, gold as fine metal powder. Alkali metals, whose sulfides are too inconvenient to handle, were added as sulfates or carbonates. Halides were added as alkaline earth halides (*e.g.*, CaF_2 in case of CaS phosphors) or as ammonium halides, the latter react quickly with the host sulfides with liberation of small amounts of NH_3 and H_2S. The presence of traces of ammonium in this case, or of carbon in case of added carbonates, are not harmful since it was especially ascertained that both have no visible effect on the luminescence of the final phosphor. The presence of oxygen from decomposing sulfate or carbonate is somewhat more serious, but we believe to have reduced the influence to a negligibly low level by means of the sulfurizing atmo-

sphere during firing. All samples were fired in small amounts (a few grams) either in open quartz boats in flowing H_2S, or in capped quartz tubes containing, besides the phosphor, some free sulfur, and surrounded by argon[1] for one to two hours, MgS and CaS at 1200°C, SrS at 1000°C, and BaS at 800°C. Strontium sulfide and especially barium sulfide tend to form polysulfides if prepared in sulfurizing atmosphere. They were converted back to single sulfides by a brief refiring, at 700°C, in pure H_2.

Measurements

The emission spectra of luminescence were measured on thin powder layers excited in a demountable cathode-ray tube by 10 kV electrons at approximately 1 $\mu A/cm^2$ current density, either at room temperature or cooled to near 80°K. The luminescence was observed through a quartz window, with a quartz prism monochromator (Beckman DU) and a photomultiplier (1P28) in quartz glass. Spot tests showed the mode of excitation (electron beam or short wave ultraviolet) to have little or no effect on the spectra. All spectra presented here are corrected for monochromator transmission and photomultiplier response by means of a standard incandescence lamp supplied by the National Bureau of Standards, and given in terms of quantum intensity per unit energy interval as function of the quantum energy. The limit of spectral resolution is about 0.02 eV, or better, fairly independent of the spectral position. All spectra are normalized to equal peak height (= 100 units) irrespective of the emission intensities actually observed.

Experimental Results

The influence of the added copper concentration on the emission spectra of a series of CaS:Cu,Na (3%) phosphors is demonstrated in Fig. 1. The emission intensity increases with the copper concentration up to about 0.1% Cu and then decreases again. At low copper concentrations, the spectrum consists of two structureless bands about 0.28 to 0.30 eV apart. These two bands disappear at high copper concentrations (about 0.5% and more) and, instead, a very broad and irregularly shaped band with the peak at about 2.3 to 2.4 appears. We observe similar dependence on the activator concentration also within other alkaline earth sulfides activated by copper, silver, or gold. The spectra observed at low concentrations apparently are due to isolated luminescence centers and the broad bands, observed at high concentration, to interaction between adjacent centers. The following results are limited to materials with low activator concentrations, *i.e.*, about 0.1 mole % or less.

Various co-activators have an influence (reproducible) on the peak positions and the widths of the two emission bands of CaS:Cu and (less quantitatively reproducible) on their intensity ratio. Some representative spectra are shown in Fig. 2. The following observations may especially be mentioned:

(*a*) Even CaS:Cu containing only copper (no intentionally added coactivator) is well luminescent in two separate emission bands.

(*b*) The observed peak positions, as function of the added coactivator, scatter over a range clearly exceeding the unavoidable uncertainties in phosphor reproducibility (about ± 0.02 eV) and accuracy of measurements.

(*c*) The two emission bands resemble, in width and separation, very much the two emission bands observed in ZnS:Cu phosphors.

(*d*) The emission of CaS:Cu with Cl (similar also Br) as coactivator is weak. Its emission spectrum resembles the broad band observed, with other coactivators, only at high copper concentrations.

The influence of the coactivator on the emission spectrum is not limited to CaS:Cu but almost universally observable within all alkaline earth sulfides activated by Cu, Ag, or Au. It is very pronounced in some cases (*e.g.*, in SrS:Au, Fig. 3), weaker but still clearly visible in others (*e.g.*, in BaS:Cu, Fig. 4) but nearly always present. This is demonstrated also in Fig. 5 and 6 showing the peak positions of the

[1] The latter method is described by Wachtel (4).

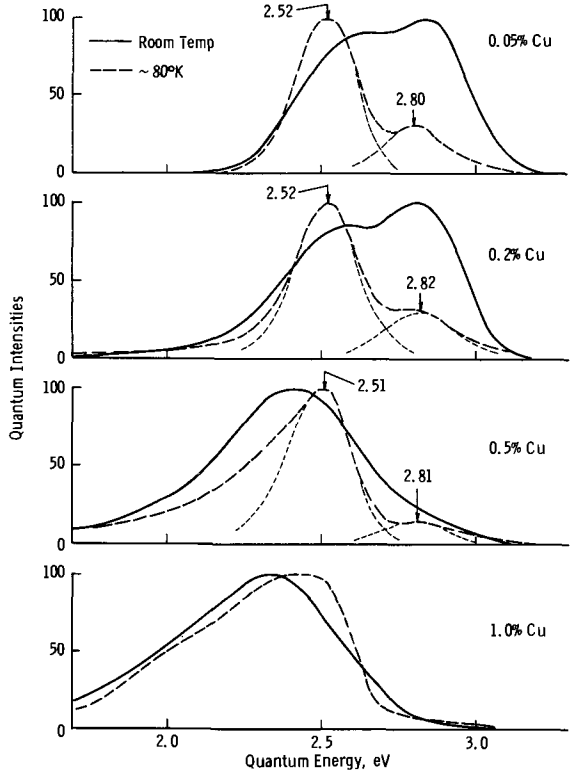

Fig. 1. Emission spectra of CaS:Cu,Na(3% added) phosphors of varied copper concentrations.

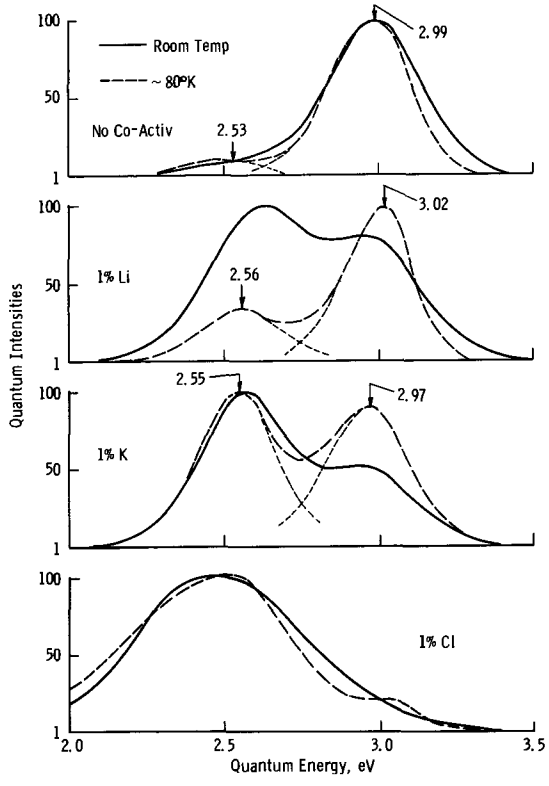

Fig. 2. Emission spectra of CaS:Cu(0.1%) with different coactivators (1% added).

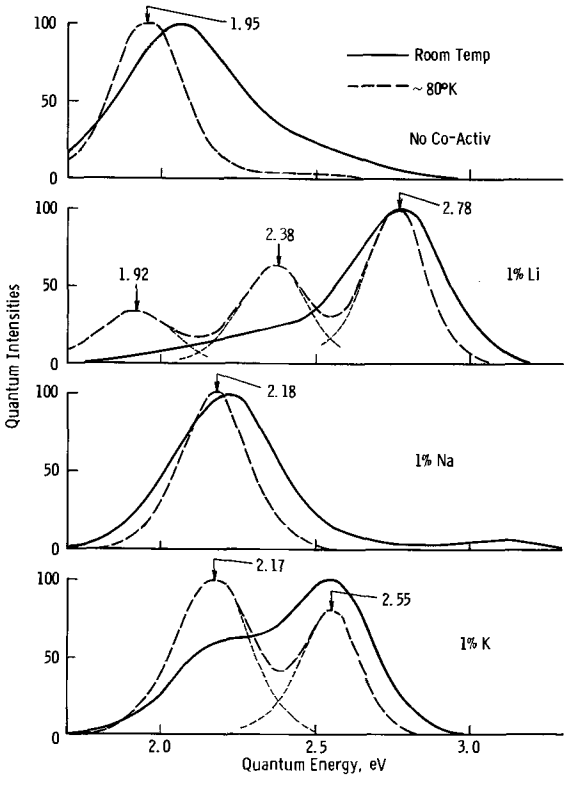

Fig. 3. Emission spectra of SrS:Au(0.1%) with different coactivators (1% added).

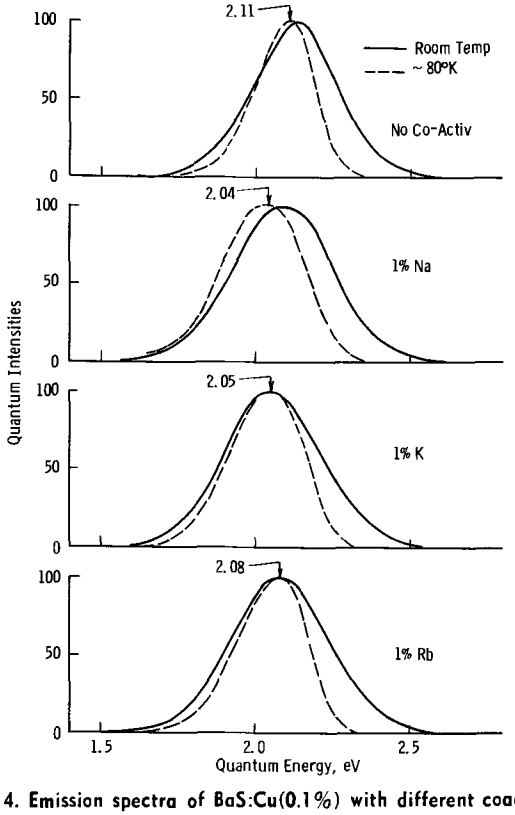

Fig. 4. Emission spectra of BaS:Cu(0.1%) with different coactivators (1% added).

emission bands of alkaline earth sulfides activated by Cu and by Au as function of the used co-activator. The length of each horizontal bar indicates approximately the accuracy of the determination of the peak positions. It is clear that the scatter due to variation of the coactivator by far exceeds the limit of accuracy in many cases. It may especially be stressed here that these variations are not accidental due to poor reproducibility of the materials; they are well reproducible.

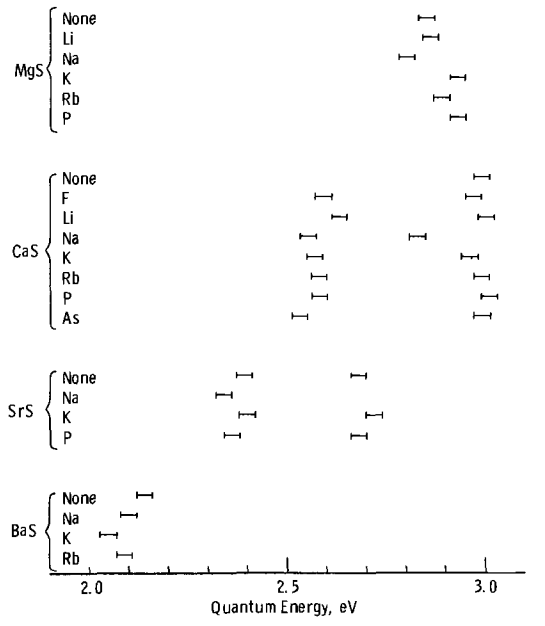

Fig. 5. Peak positions of alkaline earth sulfide phosphors all made with 0.1% of copper and 1% of various coactivators, measured at room temperature.

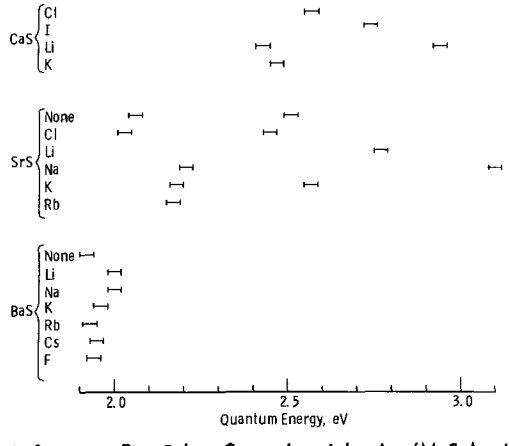

Fig. 6. Same as Fig. 5 but Cu replaced by Au (MgS:Au is nonluminescent).

In view of these complications it is not surprising that no simple "shift" of an emission spectrum to lower energies is observed if, with any activator-coactivator pair, the host crystal is varied from MgS to CaS to SrS to BaS. Some spectra demonstrating this are shown in Fig. 7-9. The closest resemblance to a simple spectral shift exists for copper (Fig. 7), but deviations appear here also. Any regular behavior is missing in cases of silver (Fig. 8) and gold (Fig. 9).

The following general remarks may be made to the efficiencies of copper, silver, and gold in alkaline earth sulfide phosphors:

Copper-activated alkaline earth sulfides normally are efficient phosphors, quantum efficiencies of photoluminescence of about 50% or more, and energy efficiencies of cathodoluminescence of 10 to 15%, can routinely be obtained. Exceptions are only materials containing Cl, Br, or I which perform very poorly.

Silver is an inefficient activator in any one of the alkaline earth sulfides and with any coactivator, efficiencies of photo- and of cathodo-luminescence rarely come to about 10% and 1%, respectively. Silver does enter the lattices, however, and produces emission spectra clearly different from those caused by copper or gold.

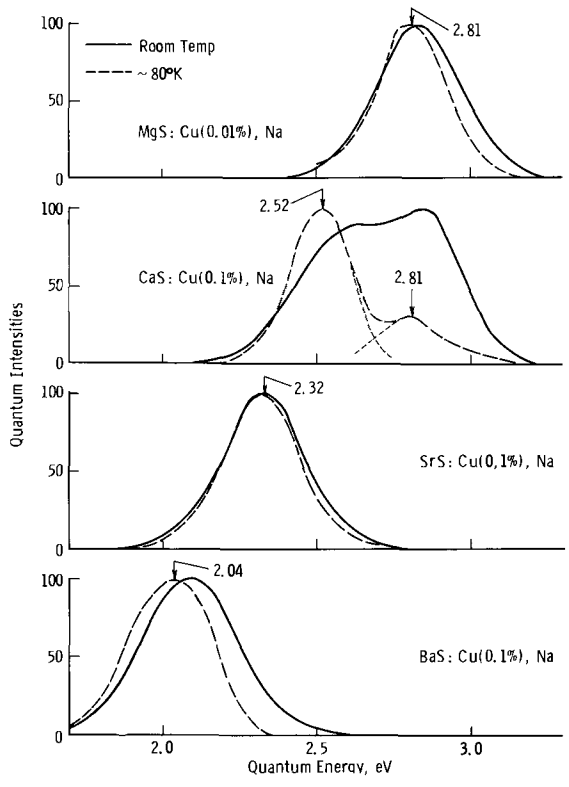

Fig. 7. Emission spectra of MgS, CaS, SrS, and BaS activated by copper and sodium (1% added).

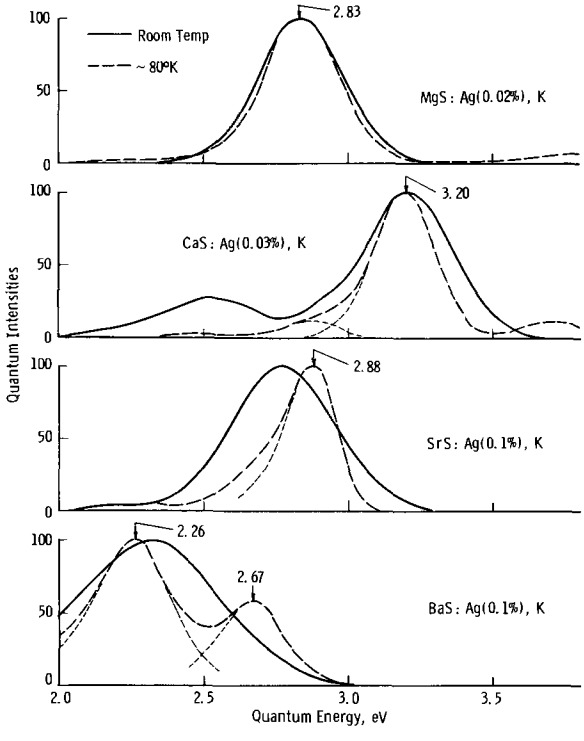

Fig. 8. Emission spectra of MgS, CaS, SrS, and BaS activated by silver and potassium (1% added).

Gold-activated alkaline earth sulfides containing Cl, Br, or I as coactivator are about as efficient in photo- and in cathodo-luminescence as Cu-activated materials containing halides. The alkalies perform somewhat poorer in combination with gold. Gold is completely ineffective in MgS, however. All attempts to make luminescent MgS:Au phosphors, without or with added coactivators (tested: F,Cl,Br,I,Li,Na,K, Rb,P) failed; the materials invariably were dead. It

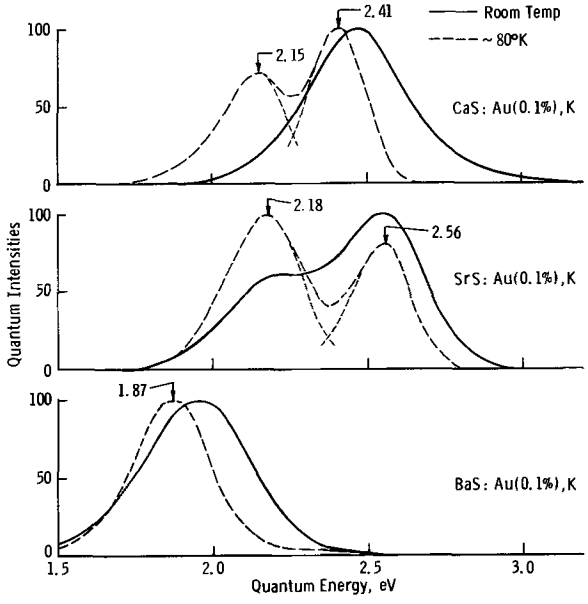

Fig. 9. Emission spectra of CaS, SrS, and BaS activated by gold and potassium (1% added). MgS:Au is nonluminescent.

may be that gold is too big (ionic radius = 1.37Å) to replace the small Mg^{2+} ion (0.65Å) in the lattice of MgS.

Discussion

The Schön-Klasens model of luminescence in ZnS-type phosphors assumes the emission to be due to an electron transition from the lower edge of the conduction band, or from a level very close to that edge, into a previously emptied level (caused by Cu^{+}, etc.) not too far above the valence band edge. This model certainly does not apply to alkaline earth sulfide phosphors because:

(*a*) It would require independence of the emission spectra on the used coactivator.

(*b*) It would require the emission spectra simply to shift to lower energies, parallel to the change of the width of the band gap, as the host crystal is varied from MgS to CaS to SrS to BaS.

Both predictions are in strong disagreement with the observations. The emission spectra do very definitely depend on the coactivator, and there is no spectral shift over a range corresponding to the change in band gap (compare Fig. 5-7 with data in Table I). The observations can only be understood on the basis of a Prener-Williams type of recombination (7, 8) in which both, activator and coactivator, are directly involved. Shionoya *et al.* (9) recently presented strong evidence that this type of recombination is responsible for all the main emission bands of copper and silver in ZnS-type phosphors.

No attempt shall be made here to present a model to explain quantitatively the observed variations in alkaline earth sulfide phosphors activated by copper, silver, or gold.

Acknowledgment

The writer is indebted to H.F. Dorman for much careful preparation work.

Manuscript submitted March 2, 1970; revised manuscript received June 3, 1970.

Any discussion of this paper will appear in a Discussion Section to be published in the June 1971 JOURNAL.

REFERENCES

1. P. Lenard, F. Schmidt, and R. Tomaschek, "Handb. d. Exp. Phys.," Vol. 23 (1928).
2. O. Sorge, "Untersuchungen über die Erdalkalisulfidphosphore," Thesis, Techn. Univ. Berlin (1959).

3. M. Avinor, A. Carmi, and Z. Weinberger, *J. Chem. Phys.*, **35**, 1978 (1961).
4. A. Wachtel, *This Journal*, **107**, 199 (1960).
5. C. H. Ballhausen, "Introduction to Ligand Field Theory," McGraw-Hill (1962).
6. E. Tiede and F. Richter, *Ber. Deutsch. Chem. Ges.*, **55**, 69 (1922).
7. J. S. Prener and F. E. Williams, *This Journal*, **103**, 342 (1956).
8. E. F. Apple and F. E. Williams, *ibid.*, **106**, 224 (1959).
9. S. Shionoya *et al.*, *Proc. Intern. Conf. Lumin., Budapest*, pp. 962 and 1164 (1966), and *J. Phys. Chem. Solids*, **29**, 1827, 1843 (1968).

Liquid-Phase Epitaxy of $In_xGa_{1-x}As$

G. A. Antypas*

Central Research Laboratories, Varian Associates, Palo Alto, California 94303

ABSTRACT

$In_xGa_{1-x}As$ layers grown by liquid-phase epitaxy were obtained in the range of $0.0 < x < 0.23$, when grown on the (111 Ga) plane of GaAs. Attempts to grow alloys on the (110), (111 As), (100), and (112 As) planes resulted in polycrystalline layers. The alloy composition was determined by x-ray fluorescence and the band gap by infrared transmission. The ternary-phase diagram was calculated using Darken's quadratic formalism to describe the ternary liquid and assuming the solid solution in equilibrium with the liquid to be regular. It was found that the experimental results were in good agreement with the calculated phase diagrams. A number of liquidus isotherms were calculated in the temperature range of 700°-1200°C. Gallium arsenide isoconcentration curves are shown for 0.95, 0.90, 0.80, 0.50, and 0.30 GaAs mole fraction.

Early experimental investigation of the solid solutions of III-V compounds indicated that systems having a column V common element do not form continuous solid solutions, while systems having a common III element do. This observation was based on the report by Koster and Thoma (1) on GaSb-InSb, AlSb-InSb, and GaSb-AlSb, and the work of Folberth (2) on the InAs-InP and GaAs-GaP systems. Goryunova and Fedorova (3), however, reported that complete solid solutions were obtained in the InSb-GaSb system, and an almost complete solid solution was obtained for the InAs-GaAs system when the alloys were annealed at relatively high temperatures for extended periods of time. Since then, the InAs-GaAs system has received wide attention primarily due to its wide direct band gap range. Woolley and Smith (4) have obtained a series of alloy compositions by annealing compressed powders at 900°C. X-ray diffraction studies on these samples indicate that Vegard's law was obeyed. Abrahams *et al.* (5) studied the electrical, thermal, and optical properties of InGaAs alloys prepared either by gradient freezing or zone leveling techniques. Van Hook and Lenker (6), using the techniques described by Shafer and Weiser (7), obtained InGaAs alloys across the whole composition range. All of the mentioned techniques yielded polycrystalline material; furthermore, the mixed crystals were annealed or grown at temperatures close to the melting point of InAs (942°C).

Liquid-phase epitaxy as reported by Nelson (8) has been used previously in growing high-quality epitaxial layers with low native defect density (9). This technique was used by Antypas and James (10) in growing $GaAs_xSb_{1-x}$ epitaxial layers on GaAs substrates in the range $1.00 > x > 0.75$. Olsen *et al.* (11) reported the growth of InGaAs epitaxial layers on GaAs substrates in the temperature range of 750°-600°C. The author, however, was unable to obtain any more information on the growth characteristics and/or properties of the grown layers. Recently, Stringfellow and Greene (12) reported that Ewing grew InGaAs epitaxial layers across the alloy series on (111 As) InAs substrates by liquid-phase epitaxy. Their results were in excellent agreement with their calculated ternary-phase diagram based on the quasi-chemical theory.

* Electrochemical Society Active Member.

Key words: III-V alloy semiconductors, InGaAs ternary phase diagram.

The present investigation was oriented toward developing InGaAs epitaxial layers, preferably on GaAs substrates, to be used as high-efficiency, long-wavelength threshold semitransparent photoemitters. Similar investigations in our laboratory have led to the development of high-efficiency 1.06μ photoemitters based on $GaAs_xSb_{1-x}$ epitaxial layers.

Experimental Procedure

The epitaxial layers were grown using the horizontal technique initially described by Nelson (8). The In-Ga melts are prepared in a carbon boat, over which palladium-purified hydrogen is flowing, inside a quartz tube. A preweighed InAs crystal which is the source of As is also placed in the boat. The melts are heated to the starting growth temperature (sgt) for approximately 3 hr. After the equilibrium amount of InAs is dissolved, any further dissolution will result in the growth of a ternary layer of InGaAs on the seed, which will be in equilibrium with the melt. This would prevent any further dissolution of the substrate.[1]

Following saturation, the undissolved InAs is removed and reweighed, thus determining the composition of the melt. The saturation experiments are repeated for longer periods of time, and at 750°C (which is the temperature of interest in our investigation) weight losses between experiments of less than 1% were observed. This could be accounted for by both temperature fluctuations of the furnace and As evaporation. In any event, the loss of As as a source of error in determining the liquidus composition can be neglected at low temperatures.

Prior to growth, the substrate was placed at one end of the boat and a dendrite of GaAs was introduced in the melt so that it would prevent any etch-back from the substrate due to temperature fluctuations in the furnace or due to the loss of As from the melt. The furnace was then tilted about 10° from the horizontal position so that the melt would roll over the substrate, at which point a programmed cooling cycle was initiated. At the end of the growth cycle, the furnace was

[1] We attempted to identify this thin epitaxial layer on experiments performed on the GaAsSb system by monitoring the photoluminescence spectra of GaAs seeds that were used in saturating Ga-Sb melts. In all cases, only GaAs band gap radiation was observed. Apparently the layers present cannot be detected by this technique.

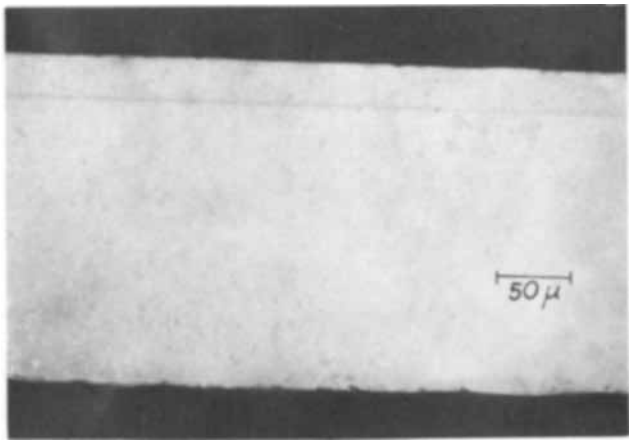

Fig. 1. Cross section on cleaved (110) plane showing an $In_{0.03}Ga_{0.97}As$ epitaxial layer grown on (100) oriented GaAs substrate.

tipped back to the horizontal position and the melt was removed from the substrate with the aid of a quartz hoe.

Experimental Results

During early experiments, it was observed that the distribution coefficient of GaAs when grown from In-Ga-As solutions is greater than unity. Similar behavior has been observed for GaAlAs when grown from Ga-Al-As melts (13). Thus, epitaxial layers of InGaAs will have to be grown from In-rich melts. Figure 1 shows an epitaxial layer (sample No. 4-5-B) of InGaAs grown on (100) Cr-doped GaAs substrates. The sample was cleaved and etched in a $H_2O:H_2O_2:HF$ (10:1:1) delineation etch for 10 sec. Details of melt composition, solid composition, and growth temperatures are given in Table I.

A representative epitaxial layer grown on (100) GaAs substrates from melts having higher In concentration than those from which sample No. 4-5-B was prepared is shown in Fig. 2. The layers were polycrystalline in nature, with a very rough surface which is the result of a great number of In-Ga inclusions. Further experimentation showed that it was impossible to grow high-quality InGaAs epitaxial layers having InAs concentrations greater than 5% on (100) GaAs substrates.

Growth of InGaAs layers on (110), (111 As), and (112 As) GaAs faces exhibited similar characteristics to those grown on (100) faces. However, when growing on the (111 Ga) plane, the layers have mirror-smooth surfaces and planar interfaces. Figure 3 represents an epitaxial layer of InGaAs (1.17 eV band gap) grown from In-rich melts, the details of which are shown in Table I. The (111 Ga) GaAs substrates were chemically polished in dilute NaOCl solutions. Epitaxial layers grown on the (112 Ga) plane of GaAs were of lower quality and did not have the mirror-smooth surface exhibited by the layers grown on the (111 Ga) plane.

The band gap of the epitaxial layers grown on GaAs substrates was determined by infrared transmission corrected for sample thickness. The absorption edge

Table I. Results and summary of the growth conditions of the InGaAs epitaxial layers

Sample No.	Melt composition in a/o In	Ga	As	Growth temp (°C)	Band gap (eV)	x_{GaAs}	Substrate orientation
4-5-B	55.5	40.5	4.0	740-690	1.35	0.97	(100)
9-15-A	61.5	33.5	5.0	740-700	1.30	0.94	(111 Ga)
9-16-A	67.0	27.5	5.5	740-700	1.26	0.93	(111 Ga)
9-17-A	71.0	21.5	7.5	750-720	1.22	0.91	(111 Ga)
8-28-A	74.0	18.0	8.0	730-700	1.17	0.89	(111 Ga)
9-29-C	81.0	8.5	10.5	740-690	0.98	0.77	(111 Ga)

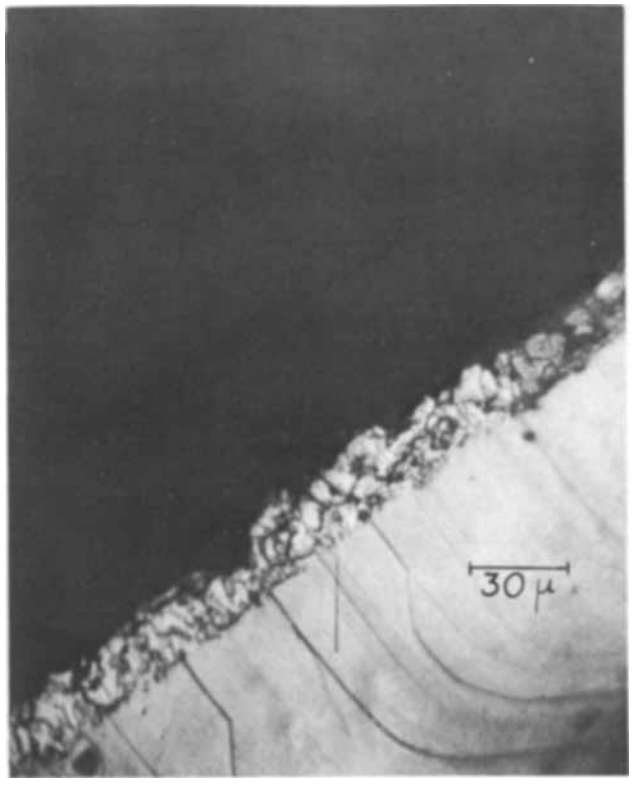

Fig. 2. Cross section of polycrystalline InGaAs epitaxial layer grown on the (100) plane of GaAs substrates. Similar layers have been obtained when InGaAs epitaxial layers are grown on the (110), (111 As), and (112 As) planes of GaAs from melts resulting in $x_{InAs} > 0.05$.

Fig. 3. Cross section of representative InGaAs epitaxial layers grown on the (111 Ga) plane of GaAs. Similar layers were obtained in the composition range of $0.77 < x_{GaAs} < 1.0$.

was very sharp, and the band gap was taken as the 10% transmission point. Figure 4 shows the band gap variation as a function of alloy composition. The band gap of InGaAs alloys reported by a number of investigators is also shown.

Epitaxial layers of InGaAs grown on (111 As) InAs substrates had mirror-smooth surfaces only when grown at temperatures around 650°C. At higher temperatures (~750°C), it was observed that on a number of occasions the layer substrate interface was completely obliterated and, in general, the layers appeared rougher than those grown at lower temperatures.

Phase Diagram Calculation

Phase diagram calculations for ternary III-V compounds have been reported by Stringfellow and Greene

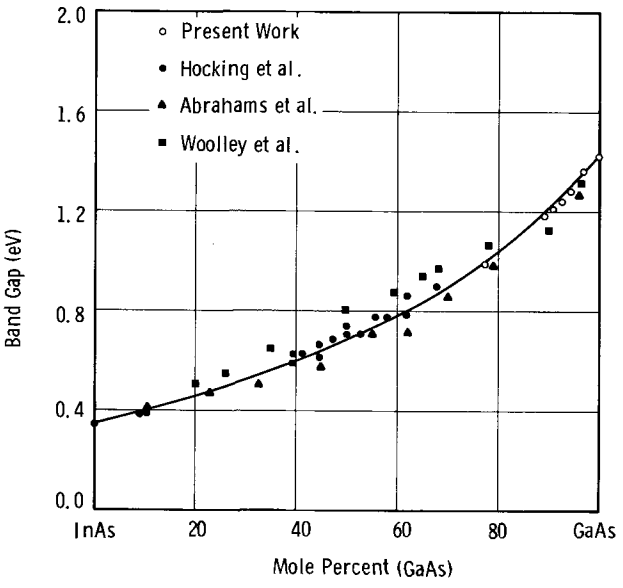

Fig. 4. Dependence of the band gap on the composition of InGaAs alloys prepared by a variety of techniques.

(12) who used the quasi-chemical approach to describe both the solid and liquid solutions, and by Ilegems and Pearson (13) who calculated the ternary-phase diagrams of $Ga_xAl_{1-x}As$ using the regular solution theory to describe the ternary liquid and ideal solution for the pseudobinary solid. Antypas and James (10) recently calculated the ternary-phase diagrams of $GaAs_xSb_{1-x}$, using Darken's (14) quadratic formalism to describe the liquid and assuming the pseudobinary solid to be described by a regular solution. They found it to be in good agreement with experiment. Antypas (15) has also calculated the ternary-phase diagram of GaAsP based on the same theory and found it to be in excellent agreement with available experimental data.

In computing the conditions for equilibrium between a ternary liquid solution A, B, C, (In,Ga,As) and a pseudobinary solid solution AC-BC (InAs-GaAs), Stringfellow and Greene (12) derived the following equations:

$$\ln \gamma_{AC}x = \ln 4N_AN_C + \ln (\gamma_A\gamma_C/\gamma_A^{STC}\gamma_C^{STC}) + \Delta S^F_{AC}(T^F_{AC} - T)/RT$$

$$\ln \gamma_{BC}(1-x) = \ln 4N_BN_C + \ln (\gamma_B\gamma_C/\gamma_B^{STC}\gamma_C^{STC}) + \Delta S^F_{BC}(T^F_{BC} - T)/RT \quad [1]$$

where γ_{AC} and γ_{BC} are the activity coefficients of AC and BC in the solid solution, x is the mole fraction of AC, N_i and γ_i ($i = A,B,C$) are the atom fraction and activity coefficient of i in the liquid solution, respectively, γ_i^{STC} is the activity coefficient of N_i at the stoichiometric composition, ΔS^F_{AC} is the entropy of fusion of AC, T^F_{AC} is the temperature of fusion of AC, R is the universal gas constant, and T is the temperature in °K.

Under the restriction

$$N_A + N_B + N_C = 1 \quad [2]$$

Eq. [1] can be solved numerically on a computer to yield two sets of curves, one describing the liquidus isotherms and the other describing the solidus isoconcentration curves of the system.

In previous investigations, the activity coefficients were determined by the quasi-chemical equilibrium (12) approach and by considering the ternary liquid as a strictly regular solution (13). In the present communication, however, the determination of the activity coefficient in the liquid phase is based on Darken's (16) quadratic representation, which for a binary liquid is

$$\ln \gamma_A = \alpha_{AC}N_C^2$$

$$\ln (\gamma_C/\gamma_C^0) = \alpha_{AC}(-2N_C + N_C^2) \quad [3]$$

where A is the solvent and C is the solute, γ_C^0 is the activity coefficient of C at infinite dilution, and α_{AC} is the interaction parameter of the system. Equation [2] reduces to that describing a regular solution if $\ln \gamma_C^0 = \alpha_{AC}$. This formalism has been satisfactorily applied by Darken (16) and Turkdogan and Darken (17) to a number of liquid metallic solutions for concentration of up to 60%. This formalism is consistent with the Gibbs-Duhem equation and satisfies Raoult's and Henry's laws as the limiting cases. The activity coefficients for a ternary liquid based on Darken's quadratic formalism are given by

$$\ln \gamma_A = \alpha_{AB}N_B^2 + \alpha_{AC}N_C^2 + (\alpha_{AB} + \alpha_{AC} - \alpha_{BC})N_BN_C$$

$$\ln (\gamma_B/\gamma_B^0) = -2\alpha_{AB}N_B + (\alpha_{BC} - \alpha_{AB} - \alpha_{AC})N_C + \alpha_{AB}N_B^2 + \alpha_{AC}N_C^2 + (\alpha_{AB} + \alpha_{AC} - \alpha_{BC})N_BN_C$$

$$\ln (\gamma_C/\gamma_C^0) = -2\alpha_{AC}N_C + (\alpha_{BC} - \alpha_{AB} - \alpha_{AC})N_B + \alpha_{AB}N_B^2 + \alpha_{AC}N_C^2 + (\alpha_{AB} + \alpha_{AC} - \alpha_{BC})N_BN_C \quad [4]$$

where component A is the solvent and components B and C are the solutes, γ_B^0 is the activity coefficient of component B at infinite dilution, and α_{i-j} are the interaction energies of the various binary systems. The above formalism is also consistent with the Gibbs-Duhem equation, and furthermore it reduced to the binary quadratic formalism as one of the solutes in the ternary approaches infinite dilution.

The solid solution in equilibrium with the ternary liquid was assumed to be regular, *i.e.* $\Delta F^{xs} = \alpha_{AC-BC}x(1-x)$, where α_{AC-BC} is the interaction energy and x is the mole fraction of one of the components in the solid. The activity coefficients are thus given by

$$\ln \gamma_{AC} = \alpha_{AC-BC}(1-x)^2$$

$$\ln \gamma_{BC} = \alpha_{AC-BC}x^2 \quad [5]$$

Substituting Eq. [4] and [5] in Eq. [1], the ternary-phase diagram can be calculated numerically to yield the liquidus and solid distribution curves.

The parameters necessary in calculating the ternary-phase diagram are the temperatures T^F and entropies ΔS^F of fusion of the III-V compounds and the interaction parameters α_{AB}, α_{AC}, α_{BC}, and α_{AC-BC}. T^F and ΔS^F for InAs and GaAs can be obtained directly from the literature and are shown in Table II. Vieland (18) has used regular solution theory to calculate the liquidus of III-V compounds. The interaction parameter obtained from such a treatment is

$$\alpha = \frac{\Delta S^F(T - T^F)[1 + R/\Delta S^F]\ln 1/4x(1-x)}{2(x-0.5)^2} \quad [6]$$

where x is the column V element in solution. For a regular solution, α should be independent of temperature and composition. Thurmond (19), however, demonstrated that for GaAs α is a linear function of temperature given by

$$\alpha_{GaAs} = 9960 - 11.15T \quad [7]$$

(When the interaction parameter, α, is divided by RT so that it will be thermodynamically consistent with Darken's formulation, it takes the form of

$$\omega = \frac{\mathcal{L}}{RT} - \frac{\delta}{R} \quad [8]$$

Table II. Parameters used in calculating the ternary-phase diagram

	InAs	GaAs	In-Ge	InAs-GaAs
α (cal/mole)	$-9.160\,T + 4300$	$-3.7\,T$	1000	2000
ΔS^F (eu)	14.52 [Ref. (24)]	16.64 [Ref. (24)]	—	—
T^F (°C)	942	1238	—	—

which is of the form derived by Turkdogan and Darken (17), where $\mathcal{L}$ and δ have the units of enthalpy and entropy, respectively.)

In calculating α_{GaAs}, Thurmond assumed a ΔS^F_{GaAs} value of 14.0 eu. Arthur (20) pointed out that, when a recently measured value for ΔS^F_{GaAs} of 16.64 eu is used, then

$$\alpha_{GaAs} = 5160 - 9.16T$$

Arthur has also calculated the activity coefficient of As from As vapor pressure measurements, and using a regular solution treatment found that the interaction parameter is accurately given by

$$\alpha_{GaAs} = -3.7T$$

A similar analysis performed on the InAs system based on the solubility data of Hall (21) and Liu and Peretti (22) resulted in an interaction parameter given by

$$\alpha_{InAs} = -9.160T + 4300$$

The interaction parameter for the In-Ga system was calculated to be 1000 cal/mole by fitting the liquidus curve to a regular solution model and comparing it to available experimental data (23). Similarly, the interaction parameter of the InAs-GaAs system was determined by fitting the solidus curve to published data of the InAs-GaAs pseudobinary. Calculations performed are in good agreement with experiment when $\alpha_{InAs\text{-}GaAs} = 2000$ cal/mole. In the ternary phase diagram calculations, the activity coefficient of Ga at infinite dilution, $\ln \gamma_{Ga}^{o}$, was varied between 0 and -1.8. The best fit to the experimental liquidus, and solidus, data for the 750° and 700°C isotherms were obtained when $\ln \gamma_{Ga}^{o} = -0.8$.

Figure 5 shows the calculated phase diagram where the solid lines represent the liquidus isotherms, while the dotted lines are the GaAs isoconcentration curves. A number of experimental points are also shown. The composition of the pseudobinary solid was determined by x-ray fluorescence. The pseudobinary diagram obtained from Fig. 5 is shown in Fig. 6. It is seen that the calculated phase diagram is in good agreement with available experimental data. For Fig. 7, we replotted a portion of the ternary-phase diagram in cartesian coordinates. It shows the calculated solidus isotherms for 700° and 800°C along with experimental results.

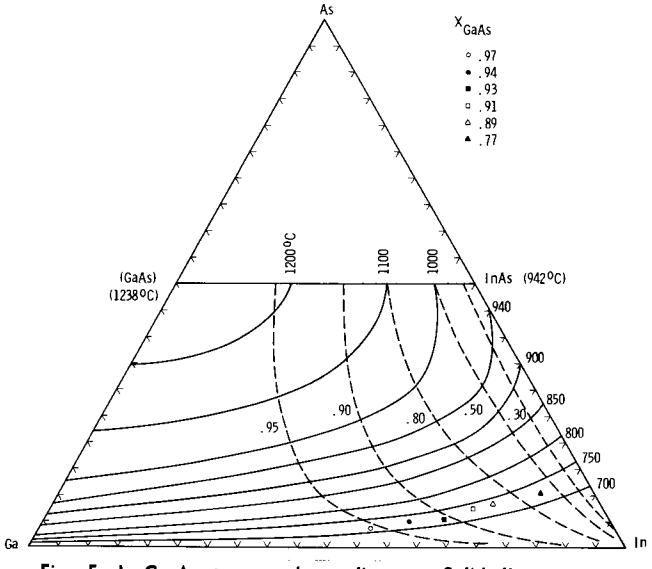

Fig. 5. In-Ga-As ternary-phase diagram. Solid lines represent the liquidus isotherms, while dotted lines represent GaAs isoconcentration curves. Details of the experimental points shown are given in Table I.

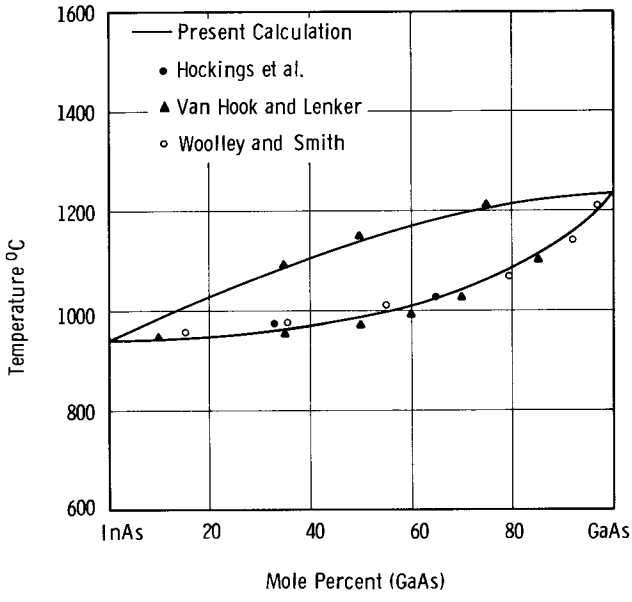

Fig. 6. InAs-GaAs pseudobinary phase diagram

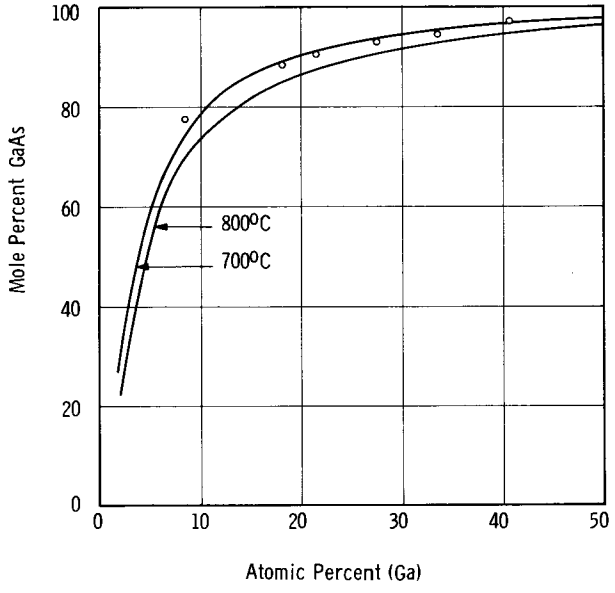

Fig. 7. The 700° and 800°C calculated GaAs solidus isotherms. Details of experimental points are given in Table I.

Conclusions

InGaAs layers have been grown on GaAs substrates. It has been observed that, when growing from In-rich melts, epitaxy of $In_xGa_{1-x}As$ layers on GaAs with $x > 0.05$ can be obtained only when growing on the (111 Ga) face. The In-Ga-As ternary-phase diagram was calculated using Darken's quadratic formalism to describe the ternary liquid while treating the solid as a regular solution; it was found to be in good agreement with experiment. The calculated pseudobinary phase diagram was in excellent agreement with available experimental data. The composition of the mixed crystals was determined by x-ray fluorescence techniques, and the band gap by infrared transmission, corrected for sample thickness. The variation of the band gap was plotted as a function of composition along with the data obtained by a number of investigations for InGaAs alloys prepared by a variety of techniques. Stringfellow and Greene (12) reported that Ewing obtained alloys of InGaAs grown on InAs substrates across the alloy series, from a starting growth temperature of as high as 780°C. Our experi-

ence is that high-quality epitaxial layers on InAs substrates could be grown only at lower temperatures.

Acknowledgments

The author wishes to thank L. Garbini who performed the x-ray fluorescence analysis of the samples, and S. Reita for his technical assistance.

Manuscript submitted Jan. 20, 1970; revised manuscript received ca. July 2, 1970.

Any discussion of this paper will appear in a Discussion Section to be published in the June 1971 JOURNAL.

REFERENCES

1. W. Koster and B. Thoma, *Z. Metallk.*, **46**, 291 (1955).
2. O. G. Folberth, *Z. Naturforsch.*, **10a**, 502 (1955).
3. N. A. Goryunova and N. N. Fedorova, *Zh. Teckn. Fiz.*, **25**, 1339 (1955).
4. J. C. Woolley and B. A. Smith, *Proc. Phys. Soc.*, **72**, 214 (1958).
5. M. S. Abrahams, R. Braunstein, and F. D. Rosi, *J. Phys. Chem. Solids*, **10**, 204 (1959).
6. H. J. Van Hook and E. S. Lenker, *Trans. Met. Soc. AIME*, **227**, 220 (1963).
7. M. Shafer and K. Weiser, *J. Phys. Chem.*, **61**, 1424 (1957).
8. H. Nelson, *RCA Rev.*, **24**, 603 (1963).
9. E. W. Williams and D. M. Blacknall, *Trans. Met. Soc. AIME*, **239**, 387 (1967).
10. G. A. Antypas and L. W. James, *J. Appl. Phys.*, **41**, 2165 (1970).
11. H. Olsen, H. Robbins, and R. K. Willardson, Abs. No. 103, Extended Abstract, Electrochem. Soc. Meeting, Dallas, May 7-12, 1967.
12. G. B. Stringfellow and P. E. Greene, *J. Phys. Chem. Solids*, **30**, 1779 (1969).
13. M. Ilegems and G. L. Pearson, "Proceedings 1968 Symposium on GaAs," p. 3, Institute of Physics and Physical Society, London (1969).
14. L. S. Darken, *Trans. Met. Soc. AIME*, **239**, 90 (1967).
15. G. A. Antypas, *This Journal*, **117**, 700 (1970).
16. L. S. Darken, *Trans. Met. Soc. AIME*, **239**, 80 (1967).
17. E. T. Turkdogan and L. S. Darken, *ibid.*, **242**, 1997 (1968).
18. L. J. Vieland, *Acta Met.*, **11**, 137 (1963).
19. C. D. Thurmond, *J. Phys. Chem. Solids*, **26**, 798 (1965).
20. J. R. Arthur, *ibid.*, **28**, 2257 (1967).
21. R. N. Hall, *This Journal*, **110**, 385 (1963).
22. T. S. Liu and E. A. Peretti, *Trans. ASME*, **45**, 677 (1953).
23. G. J. Macur, R. K. Edwards, and P. G. Wahlbeck, *J. Phys. Chem.*, **72**, 1047 (1968).
24. B. D. Lichter and P. Sommelet, *Trans. Met. Soc. AIME*, **245**, 1021 (1969).

Silicon Epitaxy from Mixtures of SiH_4 and HCl

J. Bloem*

Semiconductor Development Laboratory, N. V. Philips Gloeilampenfabrieken, Nijmegen, Holland

ABSTRACT

An investigation of the epitaxial growth of silicon from $SiCl_4$ in H_2 and from mixtures of SiH_4 and HCl in H_2 indicates that the gas phase reactions are slow and that equilibrium between solid and gas occurs at the interface. Kinetic data point to a diffusion controlled reaction rate, and it is shown that thermodiffusion in the stagnant gas layer on the silicon surface retards the growth rate of silicon and enhances the etching reaction.

In the epitaxial growth of silicon several studies of the thermodynamics and kinetics of the system have been published. Surveys are given in ref. (1) and (2).

At temperatures over 1100°C the reaction is considered to be diffusion controlled, with chemical equilibrium occurring at the solid-gas interface.

Recently Eversteyn *et al.* (2) introduced the concept of a stagnant gas layer of constant thickness over the substrates in a horizontal reactor. In the stagnant layer a steep temperature gradient (~1000°/cm) is present (2), and it is interesting to examine whether gas phase reactions occur in this boundary layer and whether the diffusion of species from and to the growing interface will be influenced by the presence of the temperature gradient.

In this investigation epitaxy from $SiCl_4$ in H_2 and from mixtures of SiH_4 and HCl in H_2 is studied because, if chemical equilibrium is attained in the gas phase, $SiCl_4$ in H_2 would be expected to give the same growth rate and the same temperature dependence of growth rate, as a mixture of $SiH_4 + 4HCl$ in H_2.

The calculations of Eversteyn *et al.* (2) on the growth rate have been extended to include the effect of thermodiffusion (3). The results of the extended calculation are applied here to the growth rate of Si from SiH_4 and to the etch rate of Si by HCl. The former reaction is governed by the diffusion of SiH_4 toward the reacting surface, the latter by the diffusion of the reaction products of the etching reaction, mainly $SiCl_2$ (1, 4) away from the interface.

* Electrochemical Society Active Member.
Key words: silicon, epitaxy, vapor growth.

Growth and Etch Rates

In a diffusion controlled reaction involving a stagnant layer of constant thickness, δ cm, the growth rate of silicon can be calculated from the material balance at the interface.

The flux of material toward the interface in moles/cm² sec, for a given position on the susceptor, is given by (5)

$$J_x = -D_i n \left[\frac{d \frac{n_i}{n}}{dy} \right] \qquad [1]$$

where D_i is the diffusion coefficient of the rate-determining species in cm²/sec, n is the total gas density (moles/cm³), n_i is the concentration of the diffusing species (moles/cm³), and y is the direction perpendicular to the growing interface.

In the Appendix the growth rate of silicon is calculated for the case where the diffusion of SiH_4 toward the surface is the rate-controlling step.

At temperatures around 1150°C HCl etching of silicon proceeds via the reaction.

$$Si + 2HCl \leftrightharpoons SiCl_2 + H_2 \qquad [2]$$

For $p_{H_2} = 1$

$$K_{SiCl_2} = \frac{p_{SiCl_2}}{(p_{HCl})^2} \qquad [3]$$

The value of K_{SiCl_2} at 1500°K is nearly unity (1, 4), which implies that with $p_{HCl} = 10^{-2}$ the maximum value of p_{SiCl_2} will be about 10^{-4} atm. For a diffusion

limited reaction the silicon etch rate will be slow, because the diffusion of $SiCl_2$ away from the surface constitutes the rate-controlling step in the steady-state condition, assuming that the diffusion coefficients of HCl and $SiCl_2$ in hydrogen do not differ markedly. The HCl partial pressure at the silicon interface will be nearly equal to the HCl partial pressure in the main gas ($\sim 10^{-2}$ atm).

Because the growth rate depends on diffusion toward the interface and the etch rate depends on diffusion away from the interface, the ratio of growth and etch rates may give information regarding second order effects in the transport processes, *i.e.*, thermodiffusion.

For a binary gas mixture in a temperature gradient a concentration gradient is produced, given by (3, 5, 6)

$$\frac{d\frac{n_1}{n}}{dy} = K_T \frac{d \ln T}{dy} \qquad [4]$$

where n_1 is the concentration of the heavier molecule in the gas (moles/cm^3), K_T is the thermodiffusion ratio, and T is the temperature with a gradient in the y-direction (°K).

The thermodiffusion ratio can also be expressed as

$$K_T = \alpha \frac{n_1}{n} \cdot \frac{n_2}{n} \qquad [5]$$

where α is the thermodiffusion factor, and n_2 is the concentration of the second component in the binary gas mixture.

Equations [4], [5], and [1] can be combined to give the expected growth and etch rates including the thermodiffusion effect. In the Appendix it is shown that the ratio of growth rate (G) and etch rate (E), neglecting thermodiffusion, is given by (13)

$$\frac{G}{E} = \frac{D_{SiH_4} \cdot p_{SiH_4}}{D_{SiCl_2} \cdot p_{SiCl_2}} = \frac{D_{SiH_4} \cdot p_{SiH_4}}{D_{SiCl_2} \cdot K_{SiCl_2} \cdot (p_{HCl})^2}$$

Including thermodiffusion for the simplified case that α_1 and α_2 are equal the expression [20] in the Appendix becomes

$$\frac{G}{E} = \frac{D_{SiH_4} \cdot p_{SiH_4}}{D_{SiCl_2} \cdot K_{SiCl_2} (p_{HCl})^2} \cdot \frac{T_g^{\alpha_1}}{T_s^{\alpha_2}}$$

where D_{SiH_4} and D_{SiCl_2} are the diffusion coefficients in H_2 of SiH_4 and $SiCl_2$, respectively (cm^2/sec), p_{SiH_4} is the partial pressure of SiH_4 in the main gas (atm), p_{SiCl_2} is the equilibrium pressure of $SiCl_2$ at the silicon surface (atm). T_g and T_s are the temperatures of the main gas and the substrate in °K, and α_1 and α_2 are the thermodiffusion factors of SiH_4 and $SiCl_2$, respectively.

The greater the values of α and the smaller the ratio T_g/T_s the greater will be the difference between growth and etch rates arising from the diffusion of SiH_4 toward the interface being hampered and the diffusion of $SiCl_2$ away from the interface being promoted. The value of α depends on the relative molecular diameters and relative masses of solute and solvent. For heavy molecules in a light gas, relatively high values of α can be expected, up to a value of about 3 for an extreme case (6, 7).

Taking reasonable values for the molecular diameters gives the following results

$$\alpha_{SiH_4-H_2} = 1.0; \quad \alpha_{SiCl_2-H_2} = 1.5; \quad \alpha_{SiCl_4-H_2} = 1.7$$

Not much is known about the temperature dependence of α, but a slight increase with temperature is to be expected (5).

Apart from thermodiffusion there are other factors that can cause growth and etch rates to differ from the values calculated. Two important ones are the temperature dependence of the diffusion coefficients and the value of the chemical equilibrium constant, K_{SiCl_2}. For the diffusion coefficients, the value of the exponent, m, in the expression for the temperature dependence $D = D_0(T/T_0)^m$, theoretically may vary from 1.5 to 2.0 (8); a smaller value of m being expected for SiH_4 than for $SiCl_2$. Analysis of the literature (9, 10) indicates a value of 1.0 ± 2.5 for the equilibrium constant K_{SiCl_2} at 1500°K. Moreover SiH_2Cl_2 and possibly $SiHCl_3$ also occur in concentrations that increase the etch rate, and an effective value of K_{SiCl_2} of 2.5 therefore is not unreasonable.

The experimental approach involves: (*a*) estimating the magnitude of the thermodiffusion effect for SiH_4, (*b*) selecting the temperature dependence of D_{SiH_4} to fit the experimental growth rate of silicon, (*c*) using the data of (*a*) and (*b*) to estimate reasonable values of α and m for $SiCl_2$, (*d*) obtaining an estimate of the magnitude of K_{SiCl_2} from the closeness of the fit between experimental and calculated rates, and from the ratio of growth and etch rates.

Experimental

The conventional horizontal RF heated epitaxial reactor employed an 80 cm long quartz tube with rectangular cross section (10 x 2.5 cm^2), in which a SiC coated graphite susceptor was placed (10 x 24 x 1.25 cm^3). The total hydrogen gas stream was kept at 75 l/min giving a stagnant layer thickness over the heated susceptor of about 0.30 cm at a mean gas temperature of 750°K (2).

The exhaust gas left the system via a water-cooled heat exchanger; the gas pressure in the system being 1 atm. Flow rates of SiH_4, $SiCl_4$, and HCl were controlled by calibrated flow meters. Ten silicon substrate slices of 38 mm diameter were placed on the susceptor in two rows. The slices were n-type, Sb-doped (0.007 ohm cm) with an orientation 3° from the (111) orientation in the direction of the nearest (110) (11). After slicing, the silicon substrates were lapped, etched and polished to a surface finish good enough to allow epitaxial growth, free of stacking faults without HCl etching prior to growth. By giving the susceptor a tilt of 1°30′ against the direction of gas flow the growth and etch rates over the length of the susceptor were kept constant to within ±5% excluding the first 4 cm of the susceptor. Prior to epitaxial growth the silicon slices were heated in H_2 at 1250°C for 15 min. Growth rates were obtained from measurements of epitaxial layer thickness by the infrared interference technique. A linear plot of layer thickness *vs.* growth time was found. In the thickness determination the ASTM correction for the phase shift at the interface between epitaxial layer and substrate was used (12). The temperature of the substrates were measured with an optical pyrometer, and the values were corrected for the emissivity of silicon and absorption of the quartz wall (13).

Results and Discussion

In Fig. 1 the growth rates from SiH_4 + 4HCl in H_2, $SiCl_4$ in H_2, and $SiHCl_3$ in H_2 are given as a function of temperature. In the literature conflicting data are presented on the temperature dependence of the growth rate, but the results given here agree with those of Shepherd (1), Charig (14), and Oldham *et al.* (15). It will be noted that, in order to reach a growth rate of 1 μ/min, concentrations of about 0.1% for SiH_4 (10^{-3} mole SiH_4/mole H_2), 0.2% for $SiHCl_3$, and 0.5% for $SiCl_4$ were required. In the high-temperature region the temperature dependence of the growth rates was small and the influence of concentration was great, as expected for a diffusion controlled reaction rate (Fig. 1, curves for $SiCl_4$ 0.1% and 0.5%). At lower temperatures the temperature dependence was much greater, with surface reactions controlling the rate and the concentration dependence being much smaller.

The difference between the behavior of SiH_4 + 4HCl and $SiCl_4$ indicates that equilibrium in the gas phase is not established, the differences in growth rate at the higher temperatures being of the order to be expected from the differences in diffusion coefficients of the re-

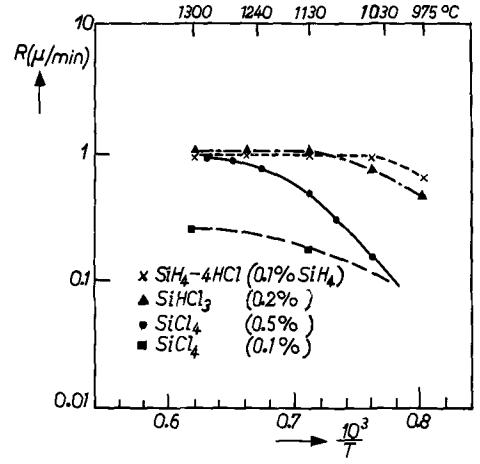

Fig. 1. Temperature dependence of the growth rate of epitaxial silicon layers from $SiCl_4$, $SiHCl_3$, and a mixture of SiH_4 + 4HCl in H_2. The concentrations indicated refer to mole percentages of the silicon compound in the gas phase.

acting silicon compounds. Gas phase reactions are expected to be nearly absent. This, however, does not exclude the possibility of equilibrium being reached at the solid-gas interface at the higher temperatures.

The temperature dependences of the reaction rates in the low-temperature region indicate that here the reaction rate was controlled by the rate at which surface reactions proceed, and not by mass transfer over the stagnant gas layer. The higher the chlorine content of the species the higher the temperature at which mass transfer became the dominant factor. For silicon growth from SiH_4 and for etching of silicon by HCl the temperature dependence of the reaction rates was small at temperatures from 1100° to 1300°C (16). This indicates that for both processes surface reactions are fast, and it can be assumed that in this range of temperatures equilibrium between solid and gas was reached. This means that for SiH_4 the surface concentration was practically zero and that for $SiCl_2$, the main reaction product in etching, a concentration as given by [3] was reached.

Figure 2 shows the growth rate of silicon at 1150°C from mixtures of SiH_4 and HCl, the HCl concentration varies up to an HCl/SiH_4 ratio greater than 15 where etching of the substrates occurs. Growth rates from mixtures with an HCl/SiH_4 ratio of 3 and 4, corresponding to the stoichiometry of $SiHCl_3$ and $SiCl_4$, respectively, are only 5-10% smaller than those for SiH_4. The growth rate decreases proportionally to $(p_{HCl})^2$ and can be described by[1]

$$G = 0.95 \times 10^3 p_{SiH_4} - 4.27 \times 10^3 (p_{HCl})^2 \ \mu/\text{min} \quad [6]$$

If gas phase reactions are absent, then SiH_4 and HCl are diffusing independently through the stagnant layer, transport of SiH_4 giving silicon growth, transport of HCl leading to the etching of silicon. The net result is the growth rate given in Eq. [6] and shown in Fig. 2. The etch rate of silicon deduced from [6] should have the same value as etching with HCl in H_2 without the presence of SiH_4. In Fig. 3 the etch rate given by [6] is plotted as a function of the partial pressure of HCl, together with the etch rates for pure HCl in H_2 found by Spakovskis (17) in a comparable reactor.[1]

The fit between the two curves is good; for low HCl concentrations the etch rate is proportional to $(p_{HCl})^2$, and for HCl partial pressures greater than 0.1 the etch

[1] Another set of experiments in a comparable reactor gave

$$G = 0.7 \times 10^3 p_{SiH_4} - 3 \times 10^3 (p_{HCl})^2 \ \mu/\text{min}$$

From these results it can be seen that small differences in reactor geometry, temperature distribution, gas flow pattern, and boundary layer thickness cause differences in the absolute values of the growth and etch rates; the ratio between the values remaining about the same.

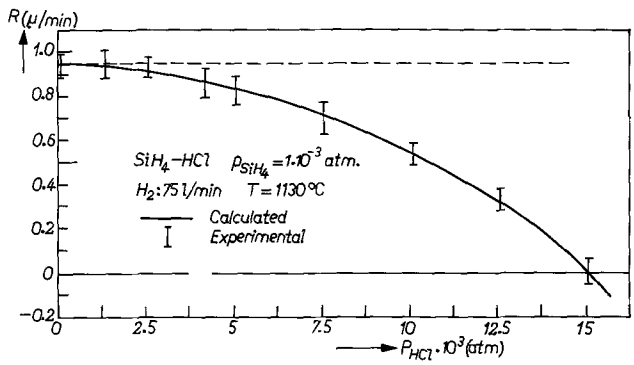

Fig. 2. Growth rate of silicon from mixtures of SiH_4 and HCl, the partial pressure of SiH_4 is kept constant at 1.10^{-3} (atm).

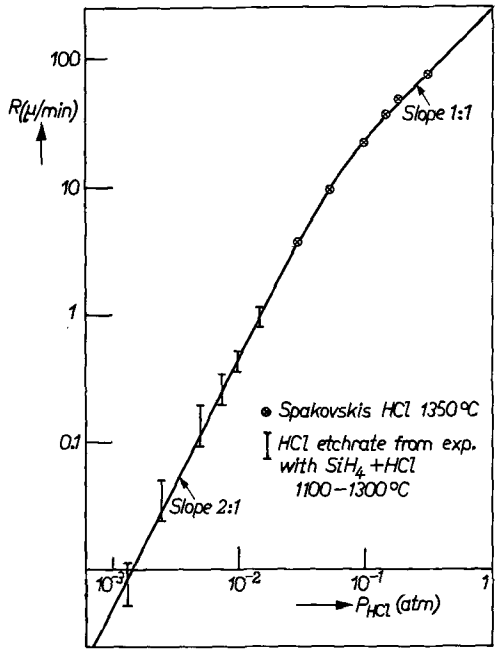

Fig. 3. Etch rate of silicon in HCl + H_2 as a function of the partial pressure of HCl. The low concentration values are from the present work, the high concentration values from Spakovskis (17). The curve gives a best fit of the experimental data to lines of slope 2:1 or 1:1 (see text).

rate is proportional to p_{HCl}. Here the assumption $p_{H_2} = 1$ in [3] is no longer valid, and the transport of HCl toward the interface is beginning to be rate controlling.

With Eq. [6], [11], and [12] it is possible to compare the experimental and the calculated results.

Introducing room temperature diffusion coefficients of SiH_4 and $SiCl_2$ of 0.60 cm^2/sec and 0.26 cm^2/sec, respectively (1), together with $\delta = 0.3$ cm, $T_s = 1500°K$; $T_g = 750°K$, $T_o = 273°K$, $R = 82$ cal/atm degree, and $K_{SiCl_2} = 1$ the calculated values of growth and etch rates are found to be

$$G = 2.57 \times 10^3 p_{SiH_4}$$

(experimental value $G = 0.95 \times 10^3 p_{SiH_4}$) [7]

$$E = 1.10 \times 10^3 (p_{HCl})^2$$

(experimental value $E = 4.2 \times 10^3 p_{SiH_4}$) [8]

The calculated growth rate is nearly a factor of three higher than the experimental one, and the calculated etch rate is more than a factor of 3 lower than that found experimentally.

The silicon growth rate including thermodiffusion effects corresponding to the estimated value $\alpha_{SiH_4} = 1$ gives, according to the calculation in the Appendix [18].

$$J = \frac{D_{SiH_4} \cdot p_{SiH_4}}{\delta R T_0^2} \cdot T_g \qquad [9]$$

This gives a decrease in growth rate by a factor 1.43 compared with [11]. In the expression for D_{SiH_4} the temperature dependence is taken to be $D = D_0(T/T_0)^2$. Experimental and calculated results are brought into agreement if the exponent is taken to be 1.6 instead of 2.0. For SiH_4, $\alpha_{SiH_4} = 1.0$ and $m = 1.6$ are selected, and for $SiCl_2$ $\alpha = 1.5$ and $m = 2$ are thought to be realistic values.

Introducing these quantities in the etch rate formula [17] gives an increase in etch rate by a factor of 1.64. To bring the experimental and calculated results into agreement an effective value of $K_{SiCl_2} = 2.4$ has to be taken, which is well within the possible limits.

In view of the accuracies involved it can be said that a reasonable fit is obtained and that the model used has been shown to yield a qualitative and semi-quantitative description of the epitaxial process.

Conclusion

Silicon growth rates from mixtures of SiH_4 and HCl can be interpreted in terms of a mutually independent growth of silicon from SiH_4 and an etching of silicon by HCl. Comparison of growth rates from mixtures of $SiCl_4$ in H_2 and SiH_4 + 4HCl in H_2 indicates that gas phase reactions are slow, and that equilibrium between solid silicon and the gas phase is established.

Growth and etch rates calculated on the basis of a diffusion controlled model differ somewhat from the experimental results, the growth rates being lower and the etch rates being higher than those calculated from the model. Three possibilities to explain the differences are discussed: (*i*) thermodiffusion in the steep temperature gradient over the silicon substrates; (*ii*) uncertainty in the temperature dependence of the diffusion coefficients giving rise to differences in the calculated growth rate by up to a factor of two; and (*iii*) uncertainty in the chemical equilibrium constant K_{SiCl_2} which gives the $SiCl_2$ concentration during HCl etching of silicon; K_{SiCl_2} at 1500°K = 1.0 ± 2.5.

It is shown that the growth and etch rates may be explained by taking account of these three factors.

APPENDIX

The mass transfer of silicon in the diffusion controlled model is given by

$$J = \frac{G \cdot \rho}{6.10^5 M} = -D_i n \left[\frac{d\frac{n_i}{n}}{dy} \right] \qquad [10]$$

G is the growth rate in μ/min, ρ is the density of Si in g/cm^3, and M is the molecular weight of Si. It will be assumed that the temperature dependence of the diffusion coefficients is given by $D = D_0(T/T_0)^2$, $T_0 = 273$°K. For an ideal gas the total gas density $n = p/RT$ moles/cm^3, and in the open tube reactor $p = 1$ atm, and thus $n = (RT)^{-1}$ and $n_i/n = p_i$ (atm).

Furthermore, in the stagnant layer over the susceptor a linear temperature gradient gives

$$T = T_s - \frac{\Delta T}{\delta} \cdot y$$

where T_s is the surface temperature of silicon, T_g is the temperature of the main gas, $\Delta T = T_s - T_g$, δ is the thickness of the stagnant layer (cm), and y is the distance from the surface (cm). For $p_{SiH_4} = 0$ at the solid-gas interface the growth rate is found to be

$$G = \frac{7.2 \times 10^6 D_{SiH_4} \cdot p_{SiH_4}}{\delta R T_0^2} \cdot \frac{\Delta T}{\ln (T_g/T_s)} \qquad [11]$$

The etch rate of Si by HCl, assumed to depend on the transport of $SiCl_2$ away from the substrate, gives

$$E = \frac{7.2 \times 10^6 \cdot D_{SiCl_2} \cdot p_{SiCl_2}}{\delta R T_0^2} \cdot \frac{\Delta T}{\ln (T_s/T_g)} \qquad [12]$$

From [11] and [12] the ratio of growth and etch rates is found to be

$$\frac{G}{E} = \frac{D_{SiH_4} \cdot p_{SiH_4}}{D_{SiCl_2} \cdot p_{SiCl_2}} \qquad [13]$$

Thermodiffusion gives an additional concentration gradient in the temperature gradient over the substrates

$$\frac{d\frac{n_1}{n}}{dy} = K_T \frac{d\ln T}{dy}$$

With $K_T = \alpha\, n_1/n \cdot n_2/n$, $n_2 \approx n$ and 1 atm total pressure, $n_1/n = p_1$ (atm), this gives for the extra concentration gradient

$$K_T \frac{d\ln T}{dy} = \frac{\alpha p_1}{T} \frac{dT}{dy} \qquad [14]$$

Equation [14] can be combined with [10] to include the effect of thermodiffusion in the calculation of growth and etch rates.

$$J = -Dn \left(\frac{d p_1}{dy} + \frac{\alpha p_1}{T} \frac{dT}{dy} \right) \qquad [15]$$

with

$$D = D_0 (T/T_0)^2 \text{ and } n = (RT)^{-1}$$

$$J = -\frac{D_0}{RT_0^2} (T dp_1 + \alpha p_1 dT)/dy$$

in the model

$$T = T_s - \frac{\Delta T}{\delta} \cdot y$$

then

$$J = -\frac{D_0}{RT_0^2} \left\{ \left(T_s - \frac{\Delta T}{\delta} \cdot y \right)^{\frac{dp}{dy}} - \alpha p_1 \frac{\Delta T}{\delta} \right\}$$

$$-\frac{JRT_0^2}{D_0} + \alpha p_1 \frac{\Delta T}{\delta} = \left(T_s - \frac{\Delta T}{\delta} \cdot y \right)^{\frac{dp}{dy}}$$

integration gives

$$\int \frac{dt_1}{-\frac{JRT_0^2}{D_0} + \alpha p_1 \frac{\Delta T}{\delta}} = \int \frac{dy}{T_s - \frac{\Delta T}{\delta} \cdot y}$$

and

$$\ln \left(-\frac{JRT_0^2}{D_0} + \alpha \frac{\Delta T}{\delta} \cdot p_1 \right) = \ln \left(T_s - \frac{\Delta T}{\delta} \cdot y \right)^{\alpha} + c$$

for Si growth: at $y = 0$, $p_1 = 0$, $T = T_s$

at $y = \delta$, $p_1 = p_{SiH_4}$, $T = T_g$

$$J = \frac{D_{SiH_4} p_{SiH_4} \cdot \Delta T}{\delta R T_0^2} \cdot \frac{\alpha_1 T_g^{\alpha_1}}{T_s^{\alpha_1} - T_g^{\alpha_1}} \qquad [16]$$

for Si etching: at $y = 0$, $p_1 = p_{SiCl_2}$, $T = T_s$

at $y = \delta$, $p_1 = 0$, $T = T_g$

$$J = \frac{D_{SiCl_2} \cdot p_{SiCl_2} \cdot \Delta T}{\delta R T_0^2} \cdot \frac{\alpha T_s^{\alpha_2}}{T_s^{\alpha_2} - T_g^{\alpha_2}} \qquad [17]$$

For $\alpha > 0$ the growth rate decreases and the etch rate increases. For SiH_4 the value of α is expected to be $\alpha_{SiH_4} = 1.0$ giving

$$J = \frac{D_{SiH_4} \cdot p_{SiH_4}}{\delta R T_0^2} \cdot T_g \qquad [18]$$

For etching $\alpha = 1$ gives

$$J = \frac{D_{SiCl_2} \cdot p_{SiCl_2}}{\delta R T_0^2} \cdot T_s \qquad [19]$$

For α values greater than 1 and $T_s >> T_g$, Eq. [19] approximates to

$$J = \frac{D_{SiCl_2} \cdot p_{SiCl_2}}{\delta R T_0^2} \cdot \Delta T \cdot \alpha_2$$

directly proportional to the values of α and the temperature gradient over the slices.

The ratio of growth and etch rates, including thermodiffusion, from [16] and [17] is found to be

$$\frac{G}{E} = \frac{D_{SiH_4} \cdot p_{SiH_4}}{D_{SiCl_2} \cdot p_{SiCl_2}} \cdot \frac{\alpha_1}{\alpha_2} \cdot \frac{T_g^{\alpha_1}}{T_s^{\alpha_2}} \left(\frac{T_s^{\alpha_2} - T_g^{\alpha_2}}{T_s^{\alpha_1} - T_g^{\alpha_1}} \right) \quad [20]$$

Manuscript submitted Jan. 5, 1970; revised manuscript received May 5, 1970.

Any discussion of this paper will appear in a Discussion Section to be published in the June 1971 JOURNAL.

REFERENCES

1. W. H. Shepherd, *This Journal*, **112**, 988 (1965).
2. F. C. Eversteyn, P. J. W. Severin, C. H. J. v.d. Brekel, and H. I. Peek, *ibid.*, **117**, 925 (1970).
3. S. Chapman and T. G. Cowling, "The Mathematical Theory of Nonuniform Gases," Cambridge University Press, London (1952).
4. R. F. Lever, *IBM J.*, **1964**, 460.
5. J. O. Hirschfelder, C. F. Curtiss, and R. B. Bird, "Molecular Theory of Gases and Liquids, J. Wiley & Sons, Inc., New York (1954).
6. K. E. Grew and T. L. Ibbs, "Thermodiffusion in Gases," Cambridge University Press, London (1952).
7. S. Chapman, *Proc. Roy. Soc.*, **A177**, 38 (1940).
8. Ref. (5) section 14.4.
9. H. Schäfer and J. Nickl, *Z. anorg. u. allgem. Chem.*, **274**, 250 (1953).
10. E. Wolf, *ibid.*, **313**, 228 (1961).
11. K. E. Bean and P. S. Gleim, *Proc. IEEE*, **57**, 1469 (1969); S. K. Tung, *This Journal*, **112**, 437 (1965).
12. ASTM F 95-68T.
13. F. G. Allen, *J. Appl. Phys.*, **28**, 1510 (1957).
14. J. M. Charig and B. A. Joyce, *This Journal*, **109**, 957 (1962).
15. W. G. Oldham and R. Holmstrom, *ibid.*, **114**, 381 (1967).
16. G. A. Lang and T. Stavish, *RCA Rev.*, **24**, 488 (1963).
17. V. Spakovskis, Private communication.

Anisotropy of Macrostep Motion and Pattern Edge-Displacements during Growth of Epitaxial Silicon on Silicon Near {100}

C. M. Drum and C. A. Clark

Bell Telephone Laboratories, Incorporated, Allentown, Pennsylvania 18103

ABSTRACT

For growth of epitaxial silicon by the $SiCl_4/H_2$ process onto silicon surfaces oriented from 0° to 9° off {100}, data are reported on the lateral motion of fabricated macrosteps (~500Å high) and on the resultant displacement of shallow surface depressions bounded by the steps. The displacements ranged from less than a tenth of the layer thickness to greater than twice the layer thickness, depending on the surface orientation. The depressions mark the sites of localized n^+ diffused regions which become buried layers after epitaxy in the fabrication of integrated circuits. Step-broadening was found to be anomalously large for exact {100} surfaces for growth at 1215°C, whereas all orientations from 0° to 9° off {100} had similar step-broadening at 1240°C. At 1240°C, the displacement of the center of the depression relative to the center of the buried layer was a minimum for exact {100} surfaces. Both advancing and receding step-motion was found, and the symmetry of the step-motion was consistent with the crystal symmetry as previously reported for surfaces near {111}. A design graph is developed relating the necessary tolerance of substrate orientation near {100} to the desired epitaxial thickness and allowable alignment errors of masks during the fabrication of integrated circuits. For example, with an allowable 1 μm displacement and with $\leq$15 μm epitaxial thickness, the surface should be {100} within 10 min of arc, whereas up to 30 min off {100} is adequate for $\leq$2 μm displacement with a 7 μm epitaxial layer.

During the fabrication of p-n junction isolated integrated circuits with buried layers of n^+ material, epitaxial silicon is grown onto substrates whose surfaces contain an array of steps about 500Å high. These macrosteps mark the positions of the buried layers, whose function is to reduce the collector series resistance (1, 2). During epitaxy, the steps may be displaced laterally, which can lead to errors in the alignment of subsequent masking operations. The reason for this is that growth at steps can be anisotropic whereas volume diffusion (the buried layer) is isotropic. It was previously reported that the exact substrate orientation near {111} has a considerable influence on the displacement of the steps (3, 4). Here we present new data on this effect for substrates oriented up to 9° off {100}. One purpose of this work was to establish tolerances on the substrate orientation for the control of the displacement.

Key words: epitaxial silicon, buried layers, step motion, integrated circuits.

The motion of steps during crystal growth has previously been studied for a variety of systems, with the usual point of view being that lateral motion of steps can be a basic part of the growth mechanism. Theoretical treatment is given by Burton *et al.* (5) and by Schwoebel and Shipsey (6). The present case is somewhat different in that we are dealing with fabricated steps of height equal to several hundred monolayers. There is evidence that spreading of monolayer steps does occur during the growth of epitaxial silicon near {111}, both for the cases of epitaxy by sublimation-condensation (7) and by chemical reaction (8, 9). For {100} epitaxial silicon, similar observations have not been reported. It is generally believed that the ideal {100} surface is rather rough structurally, hence should be expected to grow without the necessity of step-motion. However, the present work shows that the macrosteps can move considerably, and the relationship between the motions of macrosteps and the monolayer steps is yet to be established.

Experimental

The fabrication of the steps during integrated circuit processing was described previously (4). Briefly, windows are opened in an oxide on a p-type substrate using standard photolithographic techniques. Then n^+ regions are formed by diffusion, and a subsequent thermal oxidation causes growth of about 1000Å of SiO_2 at the site of the diffusion. Removal of all the SiO_2 with HF leaves the silicon surface with an array of depressions bounded by steps which mark the sites of the n^+ regions. Then an epitaxial layer is grown, with thickness usually greater than a micron. The array of steps on the epitaxial surface will correctly identify the buried n^+ regions if the displacements of the steps during growth are taken into account. Epitaxial growth was by the $SiCl_4 + H_2$ process, with 1 m/o (mole per cent) of $SiCl_4$. Temperatures were near 1200°C (after correcting for emissivity) as indicated in the data. Surface orientations were measured with Laue x-ray photographs and with x-ray goniometry (10).

Definitions

Characterization of the step-motion involves many geometrical variables such as surface orientation, step-orientation, sense of the step, and also growth temperature. Cross-sectional drawings for the case of n-type and p-type epitaxial layers are shown in Fig. 1, along with a drawing of the steps and buried layers as observed by interference contrast of angle-lapped-stained sections. The coordinate system is chosen to be symmetrical, with origin at the center of the buried layer and with positive directions outward from the center. The displacements of the steps relative to the border of the stain are denoted X_R and X_L for the right- and left-hand steps, respectively; the detailed crystallographic meaning of these designations for the purposes of this paper is given by Fig. 2. For a deep (9 μm) diffused layer, X_R and X_L will each measure -9 μm prior to epitaxial growth. The most important quantity is the magnitude of the displacement of the center of the depression relative to the buried layer, given by

$$X_C = |(X_R - X_L)/2| \qquad [1]$$

For a rectangular depression X_C can be measured for two independent directions in the plane of the surface. Perfectly symmetrical pattern-edge motion would give $X_C = 0$ in each case. For good results on registry of the next mask, X_C should be smaller than 2.5 μm. The over-all measurement error can be nearly 1 μm, however, since X_C for a slice prior to epitaxy was measured to be 0.7 μm. This is due to the fact that there is a finite width to the surface step and some uncertainty about the exact position of the edge of the stain. So a value of $X_C \leq 1$ μm after epitaxy is about as low as one can expect to measure. The sensitivity of the measurement (200X photograph, comparator) is about 0.5 μm.

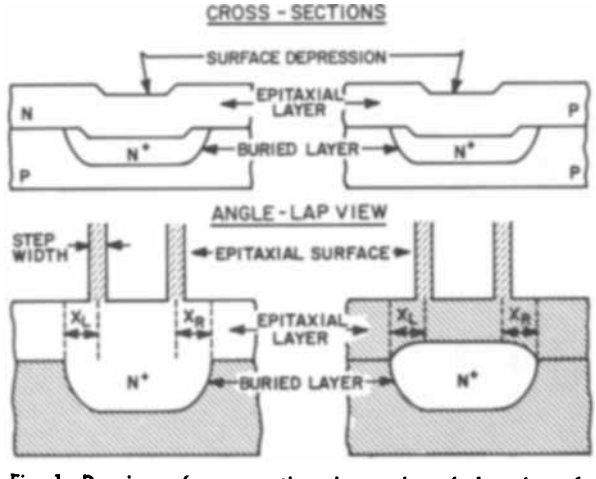

Fig. 1. Drawings of cross-section view and angle-lap view of n-type and p-type epitaxial layers with n^+ buried layers. The sense of X_R and of X_L is negative as shown.

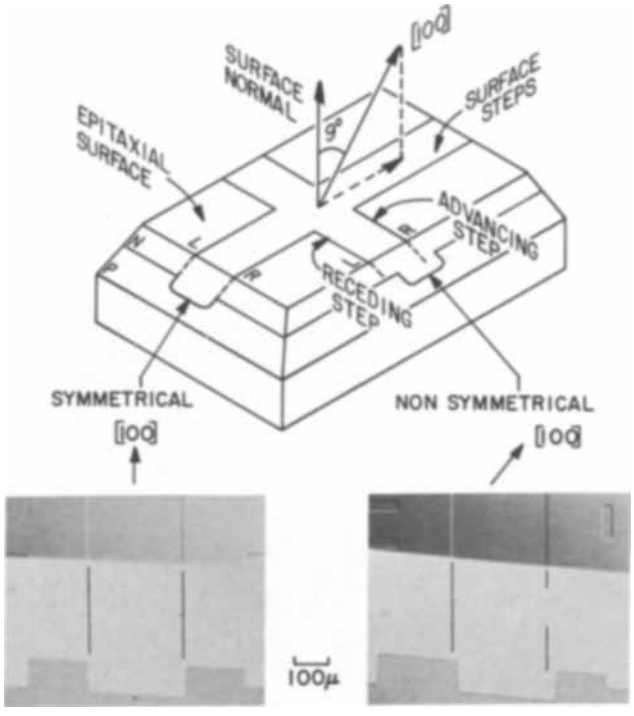

Fig. 2. Drawing of double-angle-lapped epitaxial layer, to illustrate orientation relationships used in this study.

The relationship of the steps to the crystal symmetry is important. We define the symmetrical case as that in which a mirror plane of symmetry in the lattice is normal to the surface and is also parallel to the macrosteps. This is illustrated by Fig. 3. Whatever crystal face is exposed by the left step, the same face will be exposed by the right step by symmetry. This is not true for the nonsymmetrical case illustrated in Fig. 3.

Results

One set of data on X_R, X_L, and X_C is plotted *vs.* substrate orientations from 0° to 9° off (100) toward

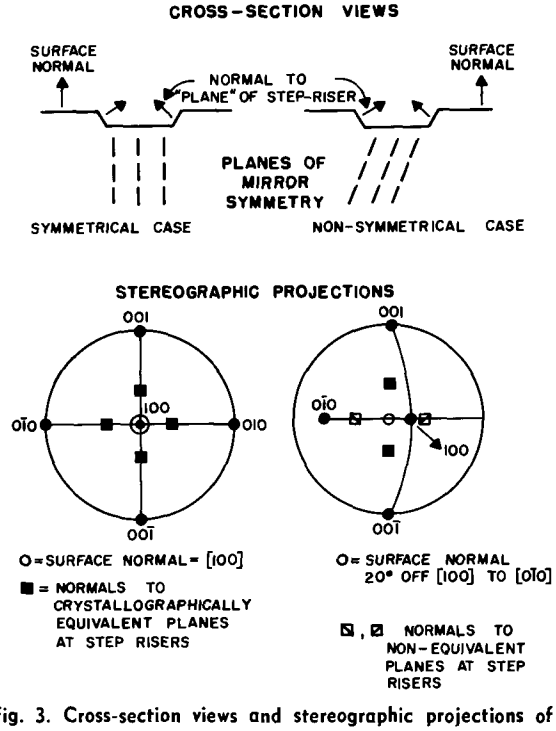

Fig. 3. Cross-section views and stereographic projections of the symmetrical case and the nonsymmetrical case.

a nearest {110}, in Fig. 4. For each surface with a pattern of rectangular depressions, data on the displacement were recorded for four edges of the depressions. We have deliberately oriented the surface and pattern so that one pair of these edges would always be the "symmetrical case" as in Fig. 3. For exact (100) surfaces, the other pair of edges would then also be the symmetrical case; the geometry is illustrated in Fig. 3 by a stereographic projection for surfaces 1° → 9° off (100), and the other pair of edges would be the nonsymmetrical case. The distinctions of symmetrical and nonsymmetrical are indicated in the data of Fig. 4. Four situations were studied, growth at 1215° and 1240°C, with and without HCl etching (1% HCl in H_2, 2 min at 1250°C). Complete data from one set are given in Fig. 4. Data from the other sets show essentially the same features. In each case there was a marked effect of crystal symmetry. Even at 9° of {100}, X_C is very small for the symmetrical part but large for the nonsymmetrical part as illustrated in Fig. 2. Both portions of the patterns were symmetrical on the exact {100} and exhibited very small X_C. It should be noted that the positive displacements of Fig. 4 correspond to receding step-motion, illustrated in Fig. 2.

Further data were recorded for slices 0°, 0.5°, and 1° off {100}, as shown in Fig. 5. Each point is the average of several measurements. In spite of the scatter, the trend of larger X_C with larger misorientation is evident.

Data on the observed step widths are given in Fig. 6. The lower temperature (1215°C) leads to a broadening of steps only on the 0° to 0.5° off {100} surfaces, whereas all orientations had similar step-widths after growth at 1240°C. Larger step-broadening is undesirable since it is associated with imprecise definition of the boundary of the surface depression. This effect is illustrated in Fig. 7.

Further information of interest is obtained by plotting X_C *vs.* epitaxial thickness; this is shown in Fig. 8. Taking X_C to be ideally zero at zero epitaxial thickness, the data show that the displacement of the center is greater with increasing film thickness, but it is still less than 2 μm at 15 μm thickness for exact (100) surfaces.

A design graph (Fig. 9) can be constructed, to select orientation tolerances when desired values of X_C and epitaxial thickness are known. This information can be

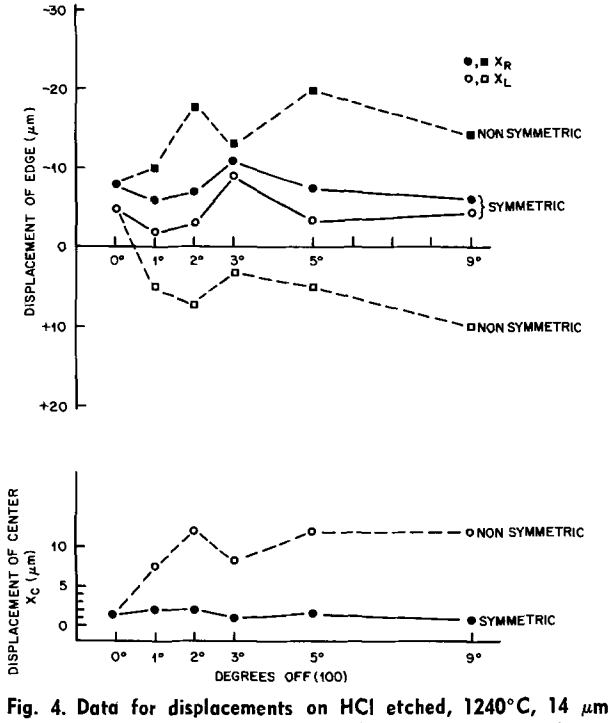

Fig. 4. Data for displacements on HCl etched, 1240°C, 14 μm n-type epitaxial layer. The direction of the misorientation is indicated in Fig. 2.

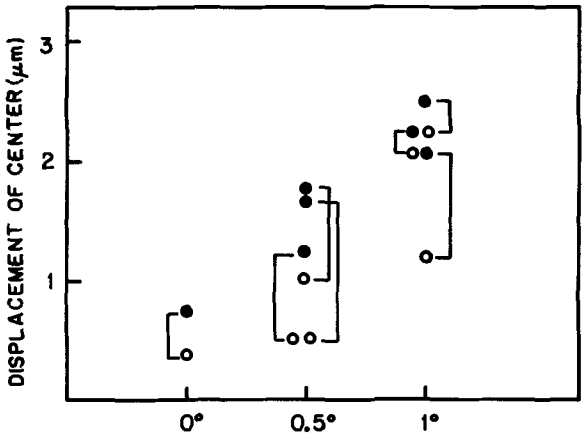

Fig. 5. Displacement data for surfaces 0°, 0.5°, 1° off {100}. Brackets indicate data from the same slice.

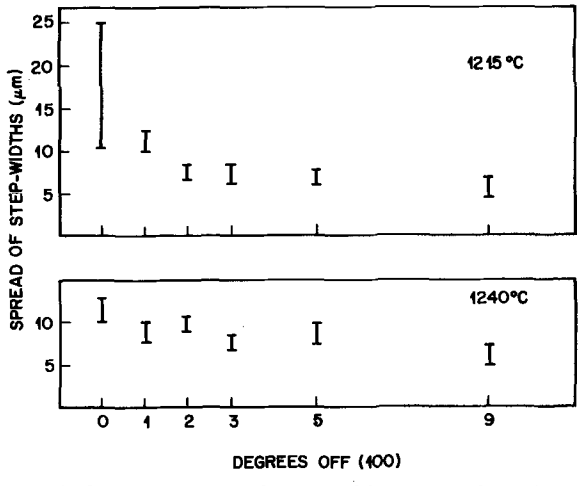

Fig. 6. Data on spread of step widths vs. angular orientation from (100), in direction indicated in Fig. 2.

important when large quantities of material are being considered. Data with the greatest displacement have been used to construct Fig. 9, to give the greatest design safety.

To use the graph, one chooses the epitaxial thickness t and center displacement X_C. Let t = 15 μm, X_C = 2.5 μm. Find the point on the t = 15 μm line with X_C = 2.5 μm, and note that the corresponding angle is 10 min off (100). This means that surfaces (100) ± 10 min would be required. For another example, let t = 7 μm. For X_C = 2.5 μm, then the maximum allowed angular misorientation is 35 min. So (100) ± 35 min would be adequate. To make this graph reasonably complete, interpolated lines for 9, 11, 13 μm thickness are drawn. Actual data are used for 7 and 15 μm thicknesses. It may be argued that a limitation of these design data is that only one type of misorientation from {100} was studied. However, the region of interest is clearly from 0° to 1° off {100}, and in this region the distinction between the various ways of misorienting a surface off {100} is difficult to determine in practice.

From the previous data, it is predicted that pattern displacement would be very small for thin epitaxial layers. This has been confirmed by the data in Table I for p-type epitaxial layers on p-type substrate with n+ buried layers.

Discussion

The data show that lateral motion of macrosteps can range from a negligibly small value up to several times the epitaxial layer thickness, depending on the orientations of the surface and of the steps. Also, the

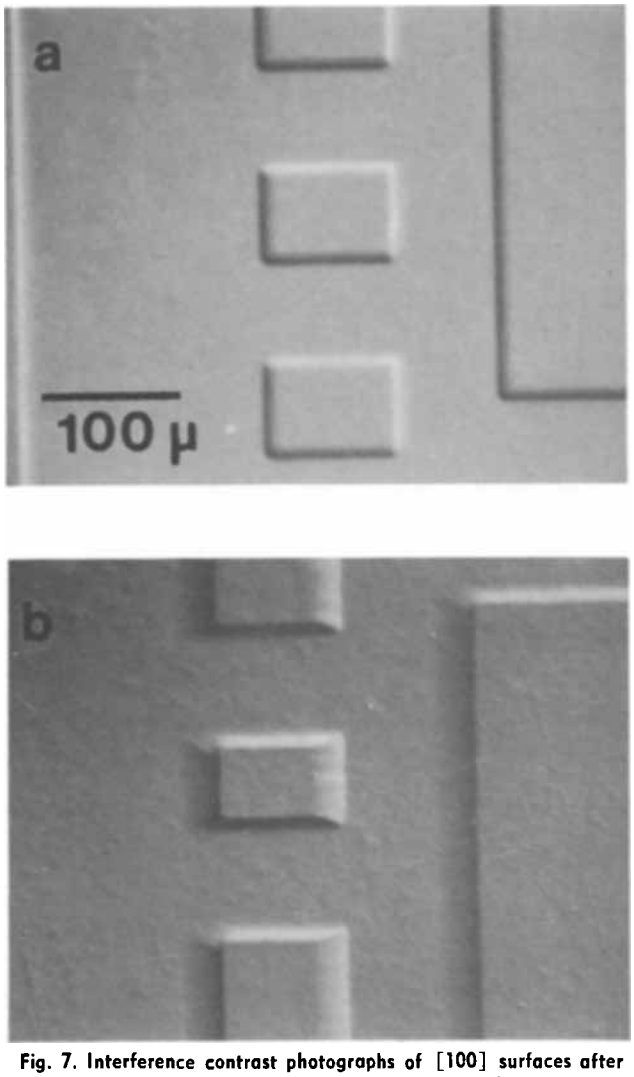

Fig. 7. Interference contrast photographs of [100] surfaces after epitaxy showing: *a*, sharp steps, growth at 1240°C; *b*, wide steps, growth at 1215°C.

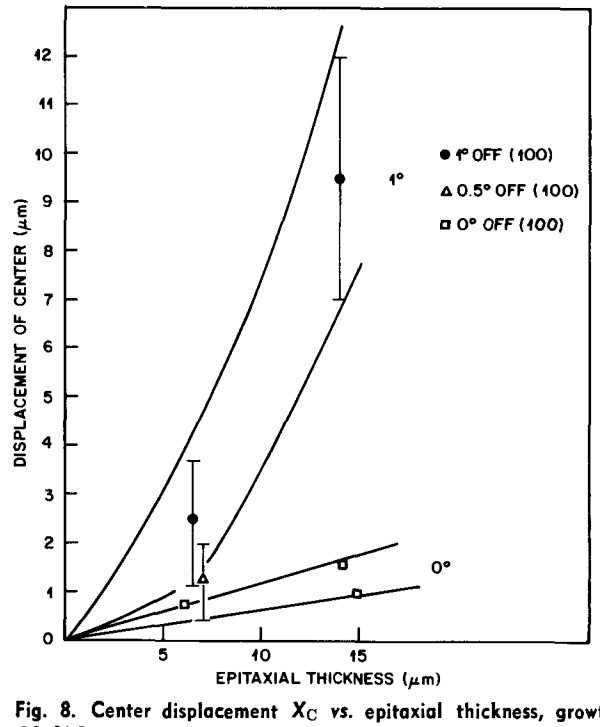

Fig. 8. Center displacement X_C *vs.* epitaxial thickness, growth at 1240°C.

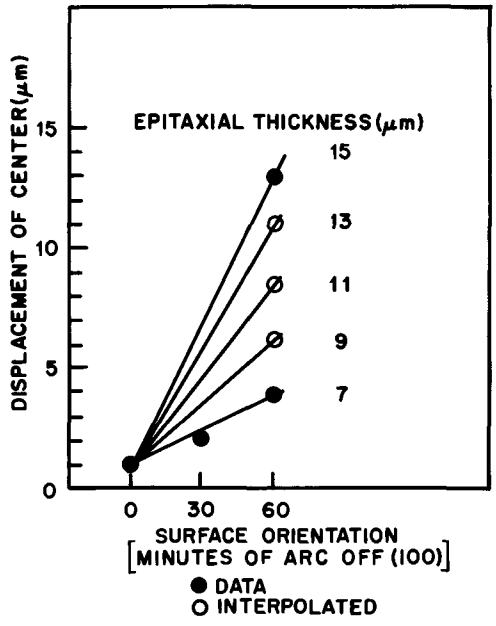

Fig. 9. Design graph for tolerance on surface orientation near {100}.

symmetry of the step-motion follows the symmetry of the lattice. In addition to the advance of steps across a surface, receding step-motion was also observed while at the same time vertical growth occurred on either side of the receding step. Each of the above results for {100} was also found previously for substrates near {111}, but with the opposite effect that greater displacements occurred nearer {111} whereas greater displacements occur farther from {100} according to the present data.

The results provide information on the orientation tolerances, as given in Fig. 9. Furthermore, the results raise some more fundamental questions about the growth mechanism. One can ask how these steps would move as a function of step-height. Very small steps should approach the behavior of monolayer steps which may be fundamental to growth. Very large steps (25 μm) have been studied by Runyan *et al.* (11), and the relationships between behavior of these various steps should be clarified. Very small steps can be fabricated by the present technique by reducing the oxide thickness, and 30Å steps can be observed optically with interference contrast (12), so it should be possible to obtain data on the behavior of steps covering a wide range of heights.

Information on the behavior of the steps during epitaxy by other techniques such as molecular beam (13), evaporation, and silane decomposition should be useful. The receding motion of steps is apparently an unexpected etching effect which may be associated with the inevitable HCl by-product in the $SiCl_4/H_2$ system. Other growth systems should be helpful in clarifying this phenomenon.

To interpret the macrostep motion, it is tempting to start with a macroscopic model which assumed that an appreciable facet exists at the step-riser as drawn in Fig. 3, and that the end result depends primarily on the growth rates of the various exposed crystallo-

Table I

Epitaxial thickness (μm)	Orientation	X_0 (for two directions) (μm)
4.1	181′ off {111}*	<1, <1
5.0	23′ off {100}	<1, <1
3.2	19′ off {100}	<1, <1
5.6	158′ off {111}*	1, 1.5
2.9	180′ off {111}*	<1, <1

* Toward a nearest {110}.

graphic planes. This model is unsatisfactory, since it does not explain (*a*) why the displacement is generally greater for larger misorientation from {100}, (*b*) why the lower temperatures cause step-broadening at {100}, or (*c*) why some receding step-motion occurs. This model might be more plausible if the data on growth rate *vs.* orientation showed a definite minimum at {100}, but this was not the case with the present study. Bean and Gleim (14) on the other hand do report a lower growth rate for {100} as opposed to 1.5° off {100}; as pointed out by Runyan (15) data from various experimenters seldom seem to agree on the numerical values of the growth rate.

An alternate model of greater complexity would involve a consideration of the atomic structure at the steps; the rate at which atoms could be attached to the various structures would then determine the resultant displacement. Edge effects, *e.g.*, at the bottom of a step, would probably be important in this model, whereas the simpler macroscopic model would ignore what happens at such an edge. Either model is sufficient to explain the symmetry effect, since in each model the growth rate depends on the crystal structure. This implies that atoms are readily supplied to all possible growth centers by transport mechanisms, which may include surface diffusion as suggested by the work of Runyan *et al.* (11).

Manuscript submitted Feb. 2, 1970; revised manuscript received *ca.* July 9, 1970.

Any discussion of this paper will appear in a Discussion Section to be published in the June 1971 JOURNAL.

REFERENCES

1. K. E. Bean and W. R. Runyan, U.S. Pat. 3,379,584 (1968).
2. B. T. Murphy, V. J. Glinski, P. A. Gary, and R. A. Pedersen, *Proc. IEEE*, **57**, 1523 (1969).
3. D. W. Boss and V. Y. Doo, Ex. Abs. 186, Electronics Div., Vol. 15, No. 2, p. 59, Electrochem. Soc. Meeting, Philadelphia, Oct. 9-14, 1966.
4. C. M. Drum and C. A. Clark, *This Journal*, **115**, 664 (1968).
5. W. K. Burton, N. Cabrera, and F. C. Frank, *Phil. Trans. Roy. Soc. (London)*, **A243**, 299 (1950).
6. R. L. Schwoebel and F. J. Shipsey, *J. Appl. Phys.*, **37**, 3682 (1966).
7. H. C. Abbink, R. M. Broudy, and G. P. McCarthy, *ibid.*, **39**, 4673 (1968).
8. A. G. Revesz and R. J. Evans, *Trans. Met. Soc. AIME*, **230**, 581 (1964).
9. B. A. Joyce, J. H. Neave, and B. E. Watts, *Surface Science*, **15**, 1 (1969).
10. E. A. Wood, "Crystal Orientation Manual," Columbia Univ. Press, New York (1963).
11. W. R. Runyan, E. G. Alexander, and S. E. Craig, Jr., *This Journal*, **114**, 1155 (1967).
12. R. H. Dudley, *J. Appl. Phys.*, **35**, 1360 (1964).
13. B. A. Joyce and R. R. Bradley, *Phil. Mag.*, **14**, 289 (1966).
14. K. E. Bean and P. S. Gleim, *Proc. IEEE*, **57**, 1469 (1969).
15. W. R. Runyan in "Semiconductor Silicon," p. 169, R. R. Haberecht and E. L. Kern, Editors, Electrochem. Soc., New York (1969).

Doped Oxides as Diffusion Sources

II. Phosphorus into Silicon

M. L. Barry*

Research and Development Laboratory,
Fairchild Camera and Instrument Corporation, Palo Alto, California 94304

ABSTRACT

The diffusion of phosphorus from a deposited doped oxide into silicon has been found to be consistent with a previously derived model describing doped oxides as diffusion sources. Diffusion coefficients of phosphorus in both silicon and silicon dioxide have been measured in terms of this model over surface concentrations varying from 6×10^{17} to 2×10^{20} atoms/cm^3 at diffusion temperatures of 1000°, 1100°, and 1200°C.

The use of doped oxides which have been deposited at low temperatures as diffusion sources adds considerable flexibility to the processing of semiconductor devices. Perhaps the greatest advantage over standard gas-phase doping techniques is independent control of the surface concentration over several orders of magnitude. Other advantages include better process control, adaptability to low defect processing, and the ability to control the final oxide thickness independently of the diffusion conditions. In addition, it is possible to make certain device configurations, such as self-aligned-gate metal-oxide-semiconductor transistors, or complementary MOS integrated circuits, which are very difficult with standard technology.

In an earlier paper (1), a model describing the diffusion of a dopant into a semiconductor from a doped oxide was presented and shown to describe reasonably well the case of boron diffusing into silicon. The purpose of this paper is to extend this model to the case of phosphorus diffusing into silicon and to report measured values of the constants of the diffusion. Interpreting these constants in terms of atomistic descriptions of the diffusion mechanism is not within the scope of the present paper.

Diffusion from deposited doped oxides has been reported fairly extensively (2-13), including several descriptions of the diffusion of phosphorus into silicon. However, values of the appropriate diffusion coefficients have not been reported in these papers over the range of temperature and concentration covered in the present work. The literature treating the diffusion process itself of phosphorus into silicon is very extensive and cannot be reviewed here.

Theory

The general one-dimensional case for diffusion of a dopant from a uniformly doped oxide of thickness $x_o - x_B$ and initial concentration C_o into a silicon substrate is shown in Fig. 1. Inclusion of an undoped oxide of thickness x_B, which acts as a barrier to diffusion, allows the measurement of the diffusion parameters of the dopant in the oxide; in actual device

* Electrochemical Society Active Member.
Key words: solid-state diffusion, semiconductor processing.

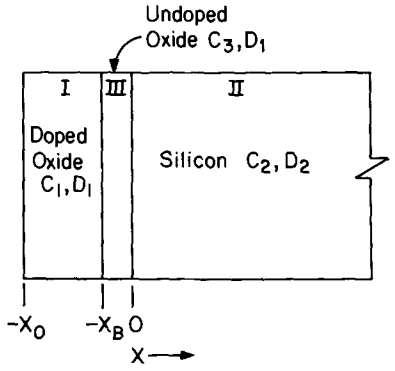

Fig. 1. Diffusion from a deposited doped oxide through a barrier oxide into a semiconductor substrate.

fabrication, this barrier oxide is normally reduced to a minimum. The diffusion equations in each region can be written

$$\frac{\partial C_i(x,t)}{\partial t} = D_i \frac{\partial^2 C_i(x,t)}{\partial x^2} \quad [1]$$

where the subscript i takes the value 1, 2, or 3 depending on the region. This formulation implicitly assumes that no field-aided diffusion terms are operating on ionized dopants and that ion-vacancy interactions can be ignored. The conditions under which these assumptions appear valid and the corrections to be made when they are not are discussed in a later section. The solution of Eq. [1] with the appropriate boundary conditions has been described in some detail in earlier work (1); suffice to say that when the thickness of the doped oxide is much greater than the diffusion length of the dopant in the oxide, the solution for the concentration in the silicon reduces to a simple form

$$C_2(x,t) = \frac{C_o\sqrt{D_1/D_2}}{(1+k)} \operatorname{erfc}\left[\frac{x_B + mkx}{2\sqrt{D_1 t}}\right] \quad [2]$$

where t is the diffusion time; m is the segregation coefficient, or the ratio of the concentration of dopant in the silicon to the concentration in the oxide at the silicon-oxide interface; and

$$k = \frac{1}{m}\sqrt{D_1/D_2} \quad [3]$$

Determination of D_2.—For the case of no undoped barrier oxide ($x_B = 0$), Eq. [2] reduces to the simple case of diffusion from a semi-infinite source into a semi-infinite sink, or a complementary-error-function diffusion with an equivalent surface concentration C_s

$$C_s = \frac{C_o\sqrt{D_1/D_2}}{(1+k)} \quad [4]$$

Thus, the surface concentration for this simple case is independent of time and depends on the initial concentration of dopant in the oxide, the square root of the ratio of the diffusion coefficients, and the segregation coefficient. Integration of Eq. [2] also leads to a simple expression for the sheet conductivity when $x_B = 0$ and the substrate resistivity is reasonably high (greater than 1 ohm-cm for this work)

$$I/V = 8.15 \times 10^{-23}\,\bar{\mu} C_s \sqrt{D_2 t} \quad [5]$$

where I/V is the inverse of the V/I commonly measured with a 4-point probe, $\bar{\mu}$ is the effective mean mobility of carriers, and the constant includes the electron charge, the spreading-current factor for the 4-point probe, and $2/\sqrt{\pi}$, a constant of the integration. It can also be shown for the case of no barrier oxide that the junction depth can be written

$$x_j = 2\sqrt{D_2 t}\ \text{argerfc}\left[\frac{C_b}{C_s}\right] \quad [6]$$

where C_b is the bulk concentration of the substrate.

From Eq. [5] and [6], the junction depth and sheet conductivity should be linear functions of the square root of the diffusion time, and the slopes of the corresponding straight lines are measures of the diffusivity of the dopant in silicon

$$\sqrt{D_2} = \frac{1.23 \times 10^{22}}{\bar{\mu} C_s} \frac{d(I/V)}{d(\sqrt{t})} \quad [7]$$

$$\sqrt{D_2} = \frac{\dfrac{d(x_j)}{d(\sqrt{t})}}{2\text{argerfc}\left[\dfrac{C_b}{C_s}\right]} \quad [8]$$

If the surface concentration is greater than about 1×10^{19} atoms/cm^3, it is possible to measure C_s by a plasma-frequency method; it is then possible to determine two independent values of D_2 from sheet conductivity and junction depth data. For low values of C_s, Eq. [7] and [8] can be combined, and self-consistent values of D_2 and C_s can be calculated.

Determination of D_1.—Inclusion of an undoped barrier oxide as shown in Fig. 1 allows the measurement of D_1, the diffusivity of the dopant in the oxide. If the subscript B refers to a wafer with a thin, undoped oxide of thickness x_B, and the subscript N refers to a wafer with no such barrier oxide, then Eq. [2] can be manipulated to show for a given C_o

$$\sqrt{D_1} = \frac{x_B}{2\sqrt{t}\ \text{argierfc}\left[\dfrac{\bar{\mu}_N (I/V)_B}{\bar{\mu}_B (I/V)_N \sqrt{\pi}}\right]} \quad [9]$$

$$\sqrt{D_1} = \frac{x_B}{2\sqrt{t}\ \text{argerfc}\left[\dfrac{(C_s)_B}{(C_s)_N}\right]} \quad [10]$$

$$\sqrt{D_1} = \frac{x_B\sqrt{D_2}}{(x_j)_N - (x_j)_B} \quad [11]$$

Thus, by measuring the differences in sheet conductivities, junction depths, and surface concentrations between wafers diffused with and without a barrier oxide, it is possible to determine D_1 by three independent measurements.

Determination of m.—In theory, the segregation coefficient can be determined from different variants of Eq. [2] once D_1 and D_2 are known and C_o, the concentration of the dopant in the oxide, is measured (1). Numerically, however, m is calculated as the reciprocal of a small difference between two large experimentally determined numbers, and for the case of phosphorus the resulting uncertainties are large enough to render its calculation meaningless. This will be enlarged upon in a later section.

Experimental

The substrates used in this study were (111) silicon wafers, sliced from Czochralski-grown crystals, lapped on both sides, and mechanically and chemically polished on one side. The phosphorus doped oxides were deposited by oxidation of silane and phosphine at a substrate temperature of 400°C, and the diffusions were performed in dry nitrogen ambients at within ±2°C of the nominal diffusion temperature. The thickness of the doped oxide normally was 0.6μ. The

phosphorus concentration in the films was determined by a spectrophotometric analysis using films deposited simultaneously with those used for diffusion (14). The sheet conductivity was measured with a 4-point probe, and junction depths were measured using the Nomarsky interference technique after grooving and staining. The mean mobilities were calculated as a function of surface concentration by numerical integration of Irvin's conductivity mobility data (15) assuming complete ionization. The junctions were delineated by staining with a nitric-hydrofluoric acid solution (0.1:50:50 by volume of 70% HNO_3:49% HF:H_2O). The surface concentration was determined from the minimum in the infrared reflection spectrum (plasma-frequency), using the curves of Gardner *et al.* (16) and corrected for shallow junctions by the method of Abe and Nishi (17). Ellipsometric methods were used to measure the thickness of the barrier oxides.

Results

Values of the diffusivity of phosphorus in silicon as determined by this technique are shown in Fig. 2 for surface concentrations ranging from 6×10^{17} to 2×10^{20} atoms/cm^3 and temperatures from 1000° to 1200°C. For surface concentrations of 1×10^{19} atoms/cm^3 and above, where C_s generally could be measured independently, the values of $\sqrt{D_2}$ measured by the sheet conductivity method are shown as closed points, while the values measured from the junction depth method are open points. For lower values of C_s, the calculated self-consistent values of $\sqrt{D_2}$ and C_s are shown as partially closed points. These data indicate that the diffusivity of phosphorus in silicon is relatively independent of C_s up to values of about 1×10^{19} atoms/cm^3 and that it then increases with increasing concentration.

The reliability of these values of $\sqrt{D_2}$ has been estimated by geometrically combining the standard deviations or uncertainties of each of the factors entering into the calculations. The estimated accuracy of $\sqrt{D_2}$ as measured by the sheet conductivity method includes a 20% uncertainty in the measurement of C_s, a 10% uncertainty in the mean mobility, and a 1% relative standard deviation in the slope of the $I/V - \sqrt{t}$ curve (from a least-squares fit assuming no uncertainty in the diffusion time). These combine to yield a total uncertainty of about 25%; however, at high surface concentrations (over 1×10^{20}) the uncertainty in C_s reduced to about 10%, and the total uncertainty drops to about 15%. In a similar fashion, the $\sqrt{D_2}$ as measured by the junction depth method has an estimated uncertainty of less than 10%, primarily because it is relatively insensitive to values of C_s. As Fig. 2 shows, there is generally excellent agreement between values determined by the two techniques, and agreement between duplicate measurements also is good.

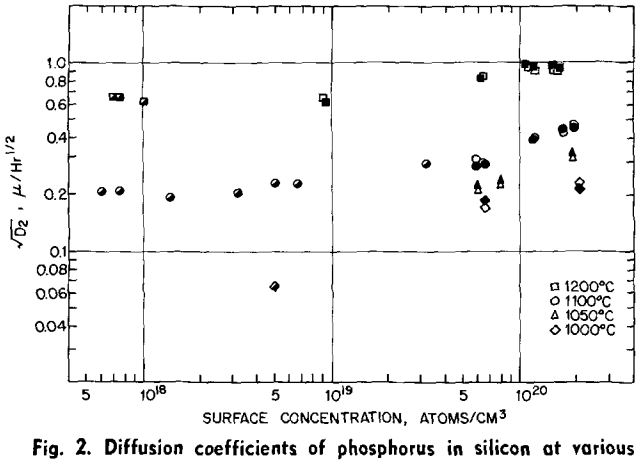

Fig. 2. Diffusion coefficients of phosphorus in silicon at various temperatures and surface concentrations.

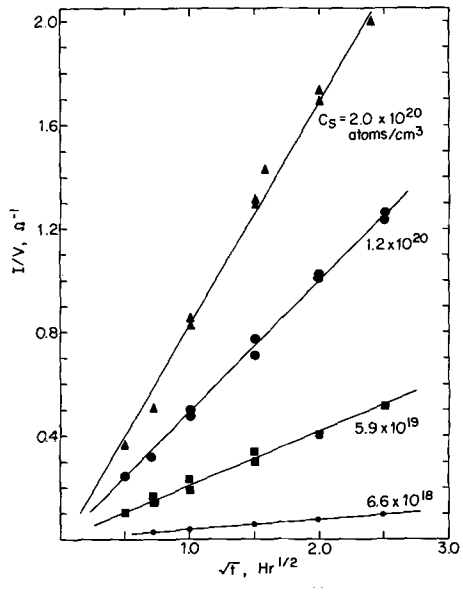

Fig. 3. Sheet conductivities resulting from diffusion of phosphorus into silicon at 1100°C from deposited oxides with different initial phosphorus concentrations.

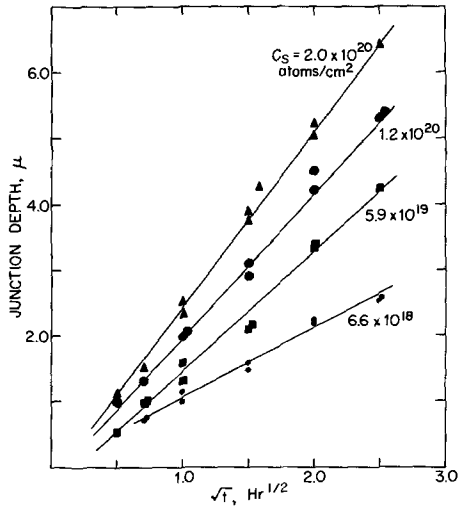

Fig. 4. Junction depths resulting from diffusion of phosphorus into silicon at 1100°C from deposited oxides with different initial phosphorus concentrations.

In the case of boron diffusing from a doped oxide at high surface concentrations ($C_s > 1 \times 10^{20}$ atoms/cm^3), the sheet conductivity was found to be anomalously high at short diffusion times (1). This behavior appears to be absent in the case of phosphorus, as indicated by Fig. 3 and 4. The sheet conductivity, as shown in Fig. 3, is a linear function of $\sqrt{t}$ at surface concentrations as high as 2×10^{20},[1] and it extrapolates properly back through the origin or to a very small intercept on the positive time axis. The junction depth is also linear in $\sqrt{t}$ over all concentration ranges utilized. In addition, the surface concentration remains independent of the diffusion time in all these studies, as predicted by Eq. [4]. The surface concentrations of phosphorus in the silicon for various initial concentrations of phosphorus in the oxide are shown in Fig. 5.

[1] The upper limit of C_s in these experiments is controlled by a phase change of the doped oxide. At high phosphorus concentrations, the oxide appears to liquefy at the diffusion temperature, increasing $\sqrt{D_1}$ to a high value and thereby increasing C_s, as indicated by Eq. [4]. This phase change corresponds quite well to the phase diagram for SiO_2-P_2O_5 proposed by Tien and Hummel (18).

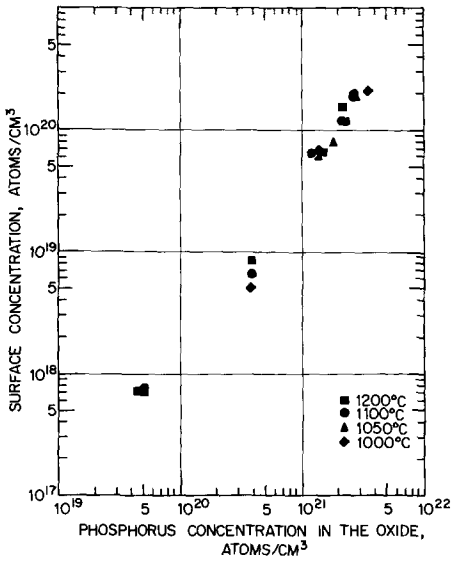

Fig. 5. Surface concentrations of phosphorus in silicon resulting from various concentrations of phosphorus in the deposited oxide.

Concentration profiles for diffusions from two different concentrations of doped oxide are shown in Fig. 6. These profiles were determined by measuring the sheet conductivity gradient normal to the wafer surface using the anodic oxidation technique of Tannenbaum (19). The deviation of the high surface concentration profile from the expected erfc relation is discussed in a later section.

The measurement of D_1, the diffusivity of phosphorus in the oxide, is slightly more complicated than in the case of boron. Glasses containing more than about 2×10^{21} phosphorus atoms/cm^3 dissolve the undoped barrier oxide at a finite rate at the diffusion temperatures, and this tends to obscure the diffusion process in the oxide. This case can be treated as diffusion from a moving boundary (20), but the experimental results do not justify the effort. This dissolution does not affect the measurement of $\sqrt{D_2}$, of course, wherein no barrier oxide is used. As a matter of fact, the dissolution of the very thin naturally occurring oxide on the silicon surface insures that the sheet conductivity and junction depth curves for high surface concentrations will pass through the origin rather than be shifted along the positive time axis, as may be the case for boron.

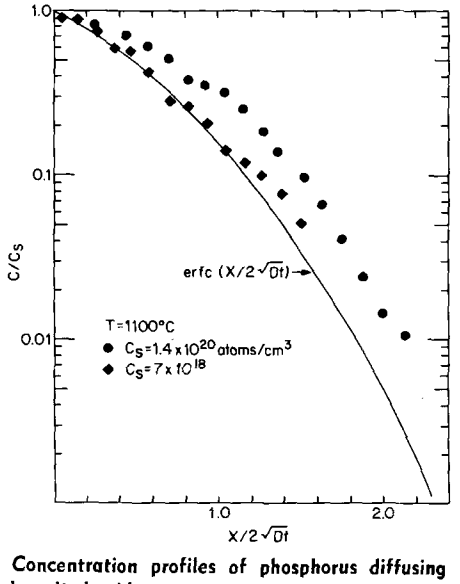

Fig. 6. Concentration profiles of phosphorus diffusing into silicon from deposited oxides.

For phosphorus concentrations below about 2×10^{21} atoms/cm^3 in the oxide, the dissolution of the barrier oxide is negligible, and the diffusion coefficient can be measured. Figure 7 shows values of $\sqrt{D_1}$ at temperatures from 1050° to 1200°C. Because of the required low concentrations, determination of D_1 by differences in C_s (Eq. [10]) is not possible, but there is good agreement between the other two techniques. Of these, the method using differences in junction depths (Eq. [11]) appears most reliable. The sheet conductivity technique (Eq. [9]) involves estimating the effective mean mobility, and electron mobilities change quite rapidly with surface concentration in the region where these measurements are made. In addition, for much of the data the surface concentrations are too low to be measured directly; in these cases calculation of C_s, $\bar{\mu}$, and D_1 must be done by a reiterative procedure. On the other hand, measurement of D_1 by the junction depth method can involve taking small differences between two large numbers. Estimated uncertainties in these measurements vary from 10% at 1100°C to about 25% at 1200°C, and must be combined with the uncertainties in $\sqrt{D_2}$, since this quantity enters directly into the calculation of D_1. As a result, values of $\sqrt{D_1}$ may be good only within ±30%. Typical data for this technique are shown in Fig. 8.

As mentioned earlier, values of the segregation coefficient, m, are not reported here. The equations for

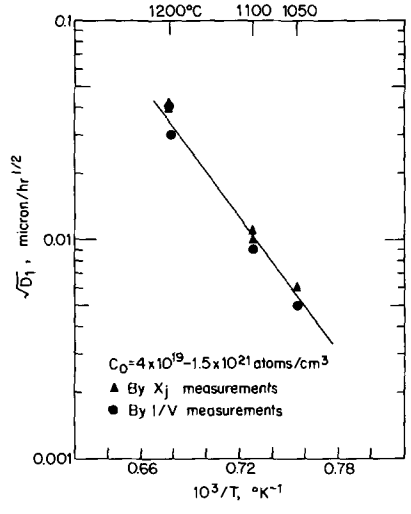

Fig. 7. Diffusion coefficients of phosphorus in SiO_2

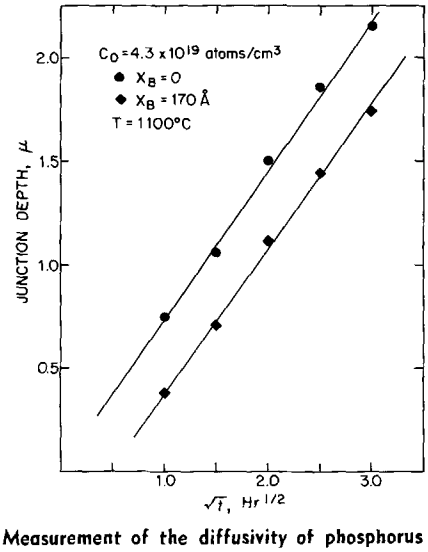

Fig. 8. Measurement of the diffusivity of phosphorus in oxide by the difference in junction depths after diffusion through a barrier oxide.

calculating m all have the form

$$m = \frac{1}{\frac{C_0}{C_s} - \sqrt{D_2/D_1}} \quad [12]$$

Since values of m are expected to be greater than unity (21), the denominator of Eq. [12] will be less than one. Since the ratios of C_0 to C_s and $\sqrt{D_2}$ to $\sqrt{D_1}$ are typically in the range twenty to fifty, with sizable uncertainties, small differences between these ratios cannot be considered significant.

Discussion of Results

At high surface concentrations the diffusivity of phosphorus in silicon is not strictly independent of concentration, as has been assumed in this simple model. As can be seen from Fig. 2, there is a one-and-a-half- to threefold increase in $\sqrt{D_2}$ as the surface concentration varies from below 1×10^{19} to 2×10^{20} atoms/cm^3, depending on the diffusion temperature. Effects that have been advanced to account for such an increase are the action of the self-induced field on the ionized impurities (22, 23) and an increase in the equilibrium lattice vacancy concentration (24-26). The first effect should result in a factor of 2 increase in D_2 as the dopant concentration becomes large compared to the intrinsic carrier concentration at the diffusion temperature. The vacancy mechanism should result in D_2 being nearly proportional to the dopant concentration at values well above the intrinsic carrier concentration.

Profiles for the low surface concentration diffusions agree within the accuracy of the profiling technique with the predicted complementary error function, as shown in Fig. 6. However, a higher surface concentration diffusion shows some deviation from the expected profile (the kinks in either curve are not significant experimentally). The non-normalized data for this second diffusion are plotted in Fig. 9 together with curves representing the expected behavior mentioned above, as interpolated from the curves of Hu and Schmidt (25). Curve A is the concentration profile predicted for this surface concentration if only field-aided diffusion terms are taken into account, while curve B shows the additional effect of the equilibrium vacancy terms. In both cases, the value of the intrinsic $\sqrt{D_2}$ has been taken as 0.20 $\mu/hr^{1/2}$, the apparent value of the low-C_s asymptote at 1100°C as shown in Fig. 2. As can be seen from Fig. 9, agreement of the data with either of these curves is worse than with the simple error function curve of Fig. 6. The curve that seems to fit the data best is that for field-aided diffusion using 0.40 $\mu/hr^{1/2}$, the value of $\sqrt{D_2}$ which was actually measured for this diffusion assuming a simple erfc relation.

The proper interpretation of the high surface concentration data is not obvious, and as mentioned in the introduction, it is beyond the scope of this paper to discuss mechanisms of diffusion in silicon. The deviations of the concentration profiles from the expected values are not large, but are significant. On the other hand, there is excellent agreement between the values of $\sqrt{D_2}$ measured independently from both sheet conductivity and junction depth data, and this should not be the case for large deviations from the erfc relation. The conclusion drawn is that the low surface concentration values of D_2 are valid intrinsic diffusivities of phosphorus in silicon, while the values at high surface concentrations are effective diffusivities (averaged over some range of concentration) which adequately describe the diffusion characteristics.

A comparison is made in Fig. 10 of some of these data with that reported by other investigators. The values of the diffusivity presented here for high surface concentrations are lower in general than those reported by Mackintosh (27), but higher than those of Fuller and Ditzenberger (28). The apparent activation energy is lower for the high surface concentration diffusion than for the low surface concentration (2.6 eV compared to 3.7 eV), as predicted by the vacancy mechanism, but the difference is larger than that suggested by Hu and Schmidt (25).

Conclusions

Diffusion of phosphorus from a deposited doped oxide source is an attractive technique for fabricating both emitter and base junctions in silicon transistors because of the independent control of surface concentration over a wide range. The diffusion appears describable by a simple model, although there are small discrepancies in the concentration profiles at surface concentrations near 1×10^{20} atoms/cm^3. Measurement of diffusivities of phosphorus in heavily doped oxides is complicated by the dissolution of the undoped barrier oxide used in this technique. However, values of the diffusivity of phosphorus in lightly doped oxides are measurable.

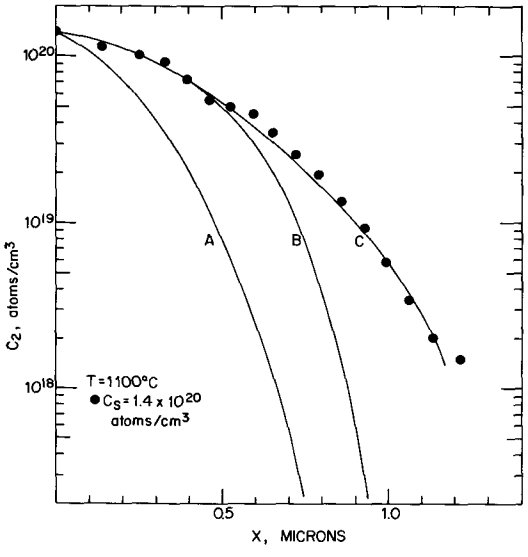

Fig. 9. Comparison of the concentration profile of phosphorus from a high surface concentration diffusion with profiles predicted for: curve A, field-aided diffusion only; curve B, field-aided plus equilibrium-vacancy diffusion; curve C, best fit by field-aided diffusion with $\sqrt{D_2} = 0.40$ $\mu/hr^{1/2}$.

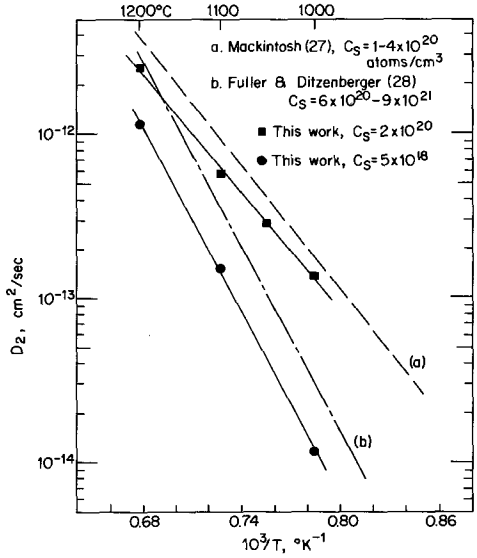

Fig. 10. Effect of temperature on the diffusion coefficient of phosphorus in silicon.

Acknowledgment

The author is indebted to Mrs. J. Bien for her assistance in the experimental part of this work, to R. Ceynowa for development of suitable techniques of chemical analysis, and to W. H. Shepherd for many technical discussions and much administrative support.

Manuscript received April 2, 1970.

Any discussion of this paper will appear in a Discussion Section to be published in the June 1971 JOURNAL.

REFERENCES

1. M. L. Barry and P. Olofsen, *This Journal*, **116**, 854 (1969).
2. P. F. Schmidt and A. E. Owen, *ibid.*, **111**, 682 (1964).
3. J. Scott and J. Omstead, *RCA Rev.*, **26**, 357 (1965).
4. P. F. Schmidt, T. W. O'Keefe, J. Oroshnik, and A. E. Owen, *This Journal*, **112**, 800 (1965).
5. W. von Meunch, *Solid-State Electron.*, **9**, 619 (1966).
6. D. L. Tolliver and D. L. Elgon, Paper 183 presented at the Philadelphia Meeting of the Society, Oct. 9-14, 1966.
7. T. L. Chu and G. A. Gruber, *Electrochem. Technol.*, **5**, 44 (1967).
8. D. B. Lee, *Solid-State Electron.*, **10**, 623 (1967).
9. A. E. Owen and P. F. Schmidt, *This Journal*, **115**, 548 (1968).
10. B. M. Mecs, Paper 93 presented at the Boston Meeting of the Society, May 5-9, 1968.
11. K. Nagano, S. Iwauchi, and T. Tanaka, *Japan. J. Appl. Phys.*, **7**, 1361 (1968).
12. T. Abe, K. Sato, M. Konaka, and A. Miyazaki, Paper 184 presented at the Detroit Meeting of the Society, Oct. 5-9, 1969.
13. F. L. Gittler, Paper 182 presented at the Detroit Meeting of the Society, Oct. 5-9, 1969.
14. AASGP Committee Rept., *J. Am. Water Works Assoc.*, **50**, 1563 (1958), as modified by B. Yurash and R. Ceynowa, Fairchild Research and Development Laboratory.
15. J. C. Irvin, *Bell System Tech. J.*, **41**, 387 (1962).
16. E. E. Gardner, W. Kappallo, and C. R. Gordon, *Appl. Phys. Letters*, **9**, 432 (1966).
17. T. Abe and Y. Nishi, *Japan. J. Appl. Phys.*, **7**, 397 (1968).
18. T.-Y. Tien and F. A. Hummel, *J. Am. Ceram. Soc.*, **45**, 422 (1962).
19. E. Tannenbaum, *Solid-State Electron.*, **2**, 123 (1961).
20. C. T. Sah, H. Sello, and D. A. Tremere, *J. Phys. Chem. Solids*, **11**, 288 (1959).
21. A. S. Grove, O. Leistiko, and C. T. Sah, *J. Appl. Phys.*, **35**, 2695, (1964).
22. F. M. Smits, *Proc. IRE*, **46**, 1049 (1958).
23. S. Zaromb, *IBM J. Res. Develop.*, **1**, 57 (1957).
24. M. F. Millea, *J. Phys. Chem. Solids*, **27**, 315 (1966).
25. S. M. Hu and S. Schmidt, *J. Appl. Phys.*, **39**, 4272 (1968).
26. S. M. Hu, *Phys. Rev.*, **180**, 773 (1969).
27. I. M. Mackintosh, *This Journal*, **109**, 392 (1962).
28. C. S. Fuller and J. A. Ditzenberger, *J. Appl. Phys.*, **27**, 544 (1956).

Electrical Characteristics of the Silicon Nitride-Gallium Arsenide Interface

J. E. Foster and J. M. Swartz

The National Cash Register Company, Dayton, Ohio 45409
and The Ohio State University, Columbus, Ohio 43210, respectively

ABSTRACT

The results of an investigation of the electrical characteristics of the silicon nitride-gallium arsenide interface as determined by capacitance-voltage (C-V) curves is presented and discussed. The Si_3N_4 was pyrolytically deposited from SiH_4 and NH_3 in the range 650°-750°C on n- and p-type, <111>, GaAs. A hysteresis of the C-V curve is noted; the amount of curve shift is shown to be heavily process dependent. Times involved in curve shift both with and without applied bias are given. Surface state density for the best p sample is in the 10^{12} range.

In the rapid advance of the semiconductor industry over the last two decades, silicon has emerged as the most important material. Silicon can be purified to a very high degree by relatively simple methods so that high-purity material is readily available at low cost. In the 1960's, the III-V compounds have attracted increased attention. Of these materials, gallium-arsenide (GaAs) is the most serious competitor to silicon. The major advantages of GaAs over silicon as a transistor material are: (*a*) greater energy gap allowing operation at higher temperatures, (*b*) high electron mobility giving theoretically higher frequency response, and (c) a direct band gap providing much shorter recombination time. The materials technology of GaAs is, however, much more difficult than silicon. Because of the volatility of arsenic from the compound, refinement is much more difficult than for the elemental semiconductors. Only recently have such new technologies as liquid encapsulation (1) been developed. It is to be expected that, as research and development continue on this important material, high-purity, economical substrates will be achieved.

Key words: MOS, semiconductor, amorphous, pyrolysis.

In order to maximize drain current, transconductance, and operating frequency of an insulated gate field effect transistor (IGFET), it is desirable to have the largest possible value of effective channel conductance ($\bar{\mu}$) and also to use a gate insulator having a high dielectric constant (2). The value of $\bar{\mu}$ depends on the mobility, μ, of the substrate—$\bar{\mu}$ being typically one half that of μ. It has been widely recognized, therefore, that GaAs with its high electron mobility is potentially a better substrate material for FET's than silicon.

There has recently been a great deal of attention (3-35) focused on amorphous silicon nitride (Si_3N_4) as a passivating and masking film partly or fully replacing silicon dioxide. Silicon nitride is much more impervious to diffusants of all kinds than silicon dioxide. In addition, the use of silicon nitride as an insulator in a metal-nitride-semiconductor (MNS) FET increases the

transconductance and drain current compared to SiO_2 by 50% because of its higher dielectric constant.

A GaAs FET utilizing silicon nitride as the gate insulator would have considerable advantage over the silicon MOS-FET. Before such a GaAs metal-nitride-semiconductor (MNS) FET can be realized, however, a great deal of investigation into the Si_3N_4-GaAs interface must be made. This paper gives the results of an investigation of the Si_3N_4-GaAs interface with particular attention to those properties which would affect the achievability of a GaAs MNS-FET. The Si_3N_4 films were pyrolytically deposited from SiH_4 (silane) and NH_3. Major emphasis was placed on p-material since an n-channel enhancement-mode device would be desired to utilize the high electron mobliity of GaAs.

A hysteresis effect in the Si_3N_4-Si system has been reported (18). This effect is also present in the Si_3N_4-GaAs system as is shown.

The metal-insulator-semiconductor (MIS) capacitor was used as the principal device for this investigation. The theory of MIS capacitors has been presented by many authors (36-37) and hundreds of articles have been written on the metal-insulator-semiconductor system. An extensive bibliography has been given by Schlegel (38, 39).

Deposition and Measurement Techniques

Si_3N_4 deposition.—The vapor deposition of Si_3N_4 has been accomplished by the ammonolysis of both silicon tetrachloride and silane (7). The reaction between silane (SiH_4) and ammonia (NH_3) has been favored recently. Films deposited using SiH_4 and NH_3 are reported to be amorphous at deposition temperatures below 900°C (9) with deposition possible down to 650°C (11). The vapor pressure of As over GaAs is given for four-atom and two-atom molecules of arsenic vapor in the range 950°-1200°K by Drowart and Goldfinger (40). Using their results as a guide, it was anticipated that amorphous films of Si_3N_4 could be deposited at the low end of the SiH_4-NH_3 temperature range (*e.g.*, 650°-750°C) without appreciable loss of arsenic from the GaAs surface.

Semiconductor-grade nitrogen used as a carrier gas was purchased from the Mineweld Company. The SiH_4 diluted with nitrogen (96% N_2, 4% SiH_4) and the ultrahigh-purity (99.999%) NH_3 was purchased from Matheson.

A schematic of the deposition apparatus used is shown in Fig. 1. All tubing was Teflon; flow meters were stainless steel. A two-way valve allowed the NH_3 and SiH_4 to be turned from exhaust to the quartz reaction tube to start deposition. N_2 was allowed to flow to exhaust as well as through the quartz tube at all times when depositions were not being made. In this manner, the system did not have to be pumped down or otherwise purged.

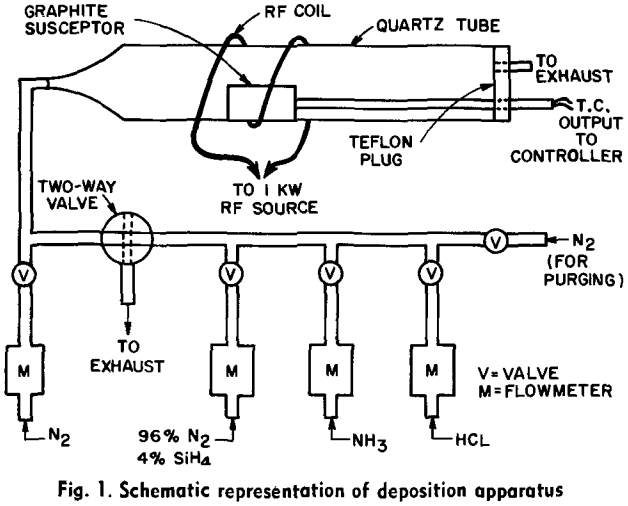

Fig. 1. Schematic representation of deposition apparatus

The quartz reaction tube was 30 mm ID. The susceptor was formed from a graphite cylinder 1 in. in diameter and ⅝ in. long. The cylinder was cut in half (lengthwise) to form a 1 in. x ⅝ in. horizontal surface upon which the sample was laid. A hollow quartz tube served as a handle for the graphite susceptor.

A thermocouple rod passed down the hollow quartz handle into the graphite susceptor. The leads from the thermocouple connected to a Research Inc., Thermac 6000 Temperature Controller. The controller output, by means of an interfacing circuit, controlled the d-c plate voltage of 1 kW, 475 kHz Ther-Monic induction heating unit.

Sample preparation.—The GaAs wafers used in this investigation were purchased from Bell and Howell Research Laboratories. Both n- and p-type wafers were 0.020 in. thick and <111> oriented. The n-type material was tellurium doped and showed an electron mobility of 6600 $cm^2/V\text{-}sec$ and a carrier concentration of $3.84 \cdot 10^{16}$ cm^{-3} as determined by Hall measurements. Carrier concentration of the zinc-doped p-material was 1.4×10^{17} cm^{-3}.

The wafers were hand lapped on an iron plate using 9μ aluminum oxide in an oil slurry to obtain a dull, smooth surface, then mounted on a polishing block and polished on a wheel covered with a polishing cloth (Buehler Ltd., No. 40-7618). A ½% solution of bromine in methanol was dripped onto the cloth to effect the chemical polishing. This method of polishing GaAs was first reported by Sullivan and Kolb (41). The wafers were polished to a mirror finish, scribed by a diamond scribe, and broken into chips approximately ¼ in. square.

Final preparation included ultrasonic cleaning in trichloroethylene and acetone, rinsing in methanol, then rinsing in deionized water having a resistivity greater than 15 meg and etching for 20 sec in an etch consisting of HCl, H_2O_2, and H_2O in volume ratio 3:1:1. The chips were again rinsed in the deionized water, blown dry with high-purity N_2, and put on the graphite susceptor in the quartz tube of the rf furnace. N_2 flowed through the tube until the deposition temperature was reached, at which time the SiH_4 and NH_3 gases were switched to the tube to begin the deposition. The color changes were clearly visible as the Si_3N_4 deposited. Nearly all samples tested had film thickness in the 850-1050Å range (dark blue to blue).

After deposition of the Si_3N_4, aluminum dots were evaporated onto the chip through a metal mask. The dots were nominally 10 and 20 mils in diameter. The aluminum was approximately 10,000Å thick.

Since C-V measurements were to be made on the MNS (metal-nitride-semiconductor) capacitors, a contact resistance at the substrate (*i.e.*, the back contact) of less than 100 ohms was adequate. Indium was applied to the back of n-type chips with a soldering iron. This gave a contact resistance of less than 10^{-3} $ohm\text{-}cm^2$. An alloy of 30% Ag-70% Ga was used on the back surface of p-type chips. This alloy could be applied to the chips with a soldering iron, and gave a contact resistance of 20-50 ohms.

C-V measuring techniques.—The chips were placed on the stage of a micromanipulator for making the C-V tests. The stage was gold plated and provided the electrical contact to the substrate. A 0.010 in. beryllium-copper wire probe made contact to the aluminum dot field plate.

Leads from the probe station were connected to the appropriate test instrument. Most measurements were made with a Boonton Electronics Model 75C Capacitance Bridge which has a frequency range of 5-500 kHz. Measurements at higher frequencies were made on a modified Boonton Type 250A RX Meter which has a frequency range from 0.5 to 250 MHz.

Experimental Results

An overview.—Table I gives the results of a preliminary test on several n-type samples at different

Table I. Etch rate, dielectric constant, and maximum field strength of Si_3N_4

Flow rate of NH_3 (cc/min)	Vol ratio NH_3 to SiH_4	Etch rate (Å/min)	ϵ_r	Max field strength (V/cm)
18	5:1	300-350	7.9	5×10^6
30	25:1	800-1000	6.3	9×10^6
60	62.5:1	800-1000	6.2	1.1×10^7
290	80:1	800-1000	6.1	2.9×10^7
290	121:1	800-1000	6.15	2.8×10^7

NH_3 to SiH_4 ratios. Deposition temperature was 725°C with an N_2 carrier flow of 5 ft^3/hr. The etch test was made in 49% HF acid at room temperature. The relative dielectric constant given in the table is the average of 3 to 5 samples.

Thickness was measured by interference fringes and by means of a Bausch and Lomb Spectrophotometer (Model 505). Only a slight difference is seen in the etch rate, dielectric constant, and maximum field strength for films deposited with NH_3 to SiH_4 ratios of 25 to 1 or greater. The relative dielectric constant appears to decrease somewhat and the field strength increases as the NH_3:SiH_4 ratio increases—both effects saturating at high ratios. The film deposited at 5:1, however, shows a distinct difference in all three parameters. Other workers (6, 7, 10, 31) have reported Si_3N_4 films deposited at 900°-1100°C on silicon to have etch rates of 150-300 Å/min in 49% HF. Their results also show higher etch rates for lower deposition temperatures. The etch rates of 800-1000 Å/min given here for a deposition temperature of 725°C are in good agreement with their findings. The relatively low etch rate of 300-350 Å/min for the 5:1 film suggests that this film contains excess silicon. This agrees also with the conclusion of Bean *et al.* (9) that a 5:1 ratio is silicon rich. It is interesting to note that Saxena and Thal (26) reported etch rates of 350 Å/min with films deposited at 400°C from NH_3 and SiH_4 in a glow discharge. The ratio of NH_3 to SiH_4 was not reported, however. The higher dielectric constant and lower field strength for the 5:1 film here also would seem to support the conclusion that the film is silicon rich.

The C-V curves obtained on p-substrates showed two prominent characteristics, presence of fast surface states and a field-induced hysteresis. The presence of fast surface states is indicated by the curves of Fig. 2. For this sample, a test frequency of 1.5 MHz was required to "freeze out" the fast states, frequencies above 1.5 meg yielding the same curve. Zaininger (42) has outlined a method of determining the effective density of surface states which can respond to frequencies up to that of the test signal. The intent here is to point out that the energy distribution and frequency response of these fast states is affected by the NH_3:SiH_4 ratio. The NH_3 to SiH_4 ratio for the sample of Fig. 2 was 25:1; at higher NH_3 to SiH_4 ratios, the frequency response of the fastest states decreased until at a ratio of 55:1 the surface states for good samples could not follow a 500 kHz signal (Fig. 3). A comparison of Fig. 2 and 3 shows, moreover, a difference in the energy position of those states which could respond to 100 kHz but not 500 kHz. In Fig. 2, the greatest difference between the 100 and 500 kHz curves is in the inversion region. In Fig. 3, however, the greatest difference between the 100 and 500 kHz curves lies in the accumulation and depletion regions. This indicates that, whereas the fastest states lie near or above midgap (the inversion position of the Fermi level) for the sample of Fig. 2, they lie in the lower half of the band gap (the depletion and accumulation position of the Fermi level) for the sample of Fig. 3. A frequency of 500 kHz was sufficiently high to freeze out all fast states for nearly all films deposited at NH_3 to SiH_4 ratios of 55:1 or greater. The curves of Fig. 3 are shifted toward more negative voltages than the curves of Fig. 2. This shift was found to be generally true as the NH_3 to SiH_4 ratio was increased.

Depositions on n-type substrates were made only at 700°C with NH_3:SiH_4 ratios ranging from 25 to 121 to 1. These samples also show a very large effect of fast surface states. Figure 4 shows a sample for which a frequency of 1.5 meg was required to "freeze out" the fast states. The flat band voltage is +20V. As in the case of p-type samples, depositions made at high NH_3 to SiH_4 ratios (62.5 and above) gave surface states that could not respond at 500 kHz. Figure 5 shows C-V curves for six representative samples taken at 1.5 MHz. There is considerable difference in samples deposited at the same NH_3 to SiH_4 ratio as for examples N30 and N33. N-type samples showed much poorer repeatability than p-type samples. Flat band voltages for most samples were greater than 22V—cor-

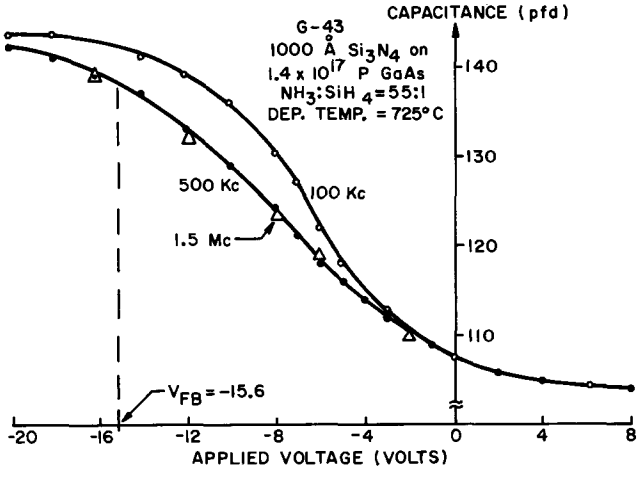

Fig. 3. C-V curves showing fast states in depletion region.

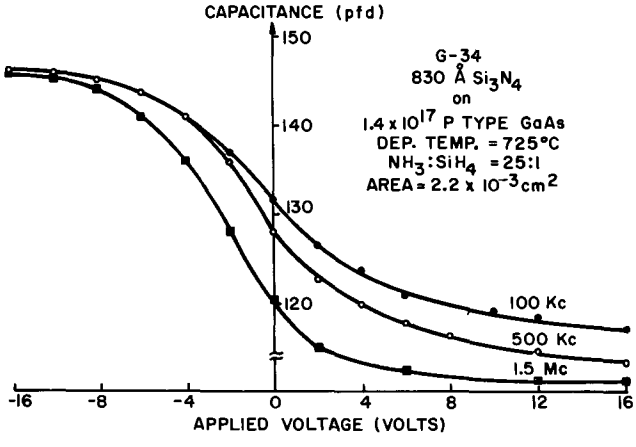

Fig. 2. C-V plot showing fast states

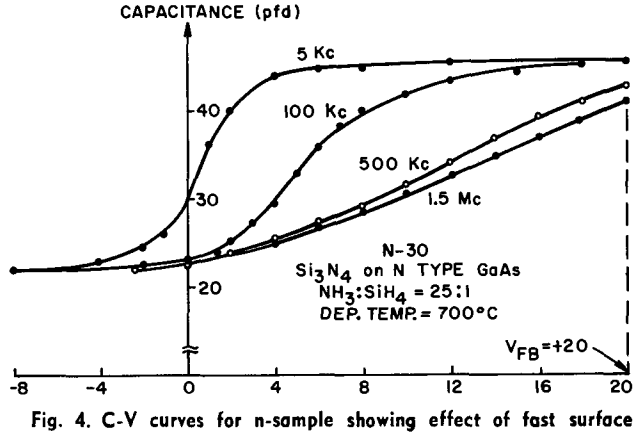

Fig. 4. C-V curves for n-sample showing effect of fast surface states.

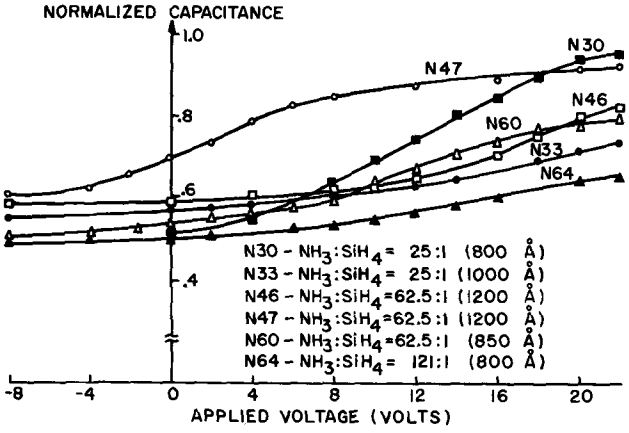

Fig. 5. Normalized C-V curves for samples on n-substrates

responding to field strengths greater than 2-3 x 10^6 V/cm.

The Fermi level for the p-substrates lies very close to the valence band (within 0.1 eV) so that at flat band most of the energy gap lies above the Fermi level. For the n-substrates, the Fermi level is about 0.125 eV below the conduction band, so that most of the energy gap is below the Fermi level at flat band. For n- and p-type samples processed in the same manner, the ionic contamination should be similar. Any significant difference in flat band voltage beyond that due to ϕ_{MS} (difference in metal, semiconductor work functions) should, therefore, reflect the nature of the surface states. The C-V curves for n-substrates are shifted to the right giving positive flat band voltages in contrast to negative flat band voltages for p-type samples. This strongly suggests that the surface states are negative when below the Fermi level, thus accounting for the difference between the curves on p- and n-substrates. The positive charge causing the shift of C-V curves on p-substrates must, then, be accounted for by traps that are positive when empty.

The hysteresis effect.—Figure 6 shows a C-V plot made on an x-y plotter. The voltage sweep was 5 V/sec so that both curves were swept out in about 15 sec. The curve swept from left to right lies some 8V to the left of the return sweep. This field-induced hysteresis has been reported in the case of Si_3N_4 deposited on Si (17, 18) and is also present for the Si_3N_4-GaAs system.

The displacement of the two curves indicates either a transfer of charge across the Si_3N_4-GaAs interface, or a movement of charge within the Si_3N_4. The direction of the curve shifting is, however, in the wrong direction to be explained by movement of charge within the Si_3N_4. It must be concluded that charge moves across the semiconductor-insulator interface and is trapped. The direction of the curve shifting as well as the recovery times involved can be explained, at least in a qualitative way, by such a trapping model. Herman and Warfield (43) have treated the effects of traps in the MOS structure. Ross and Wallmark (44) have dealt with trapping in the metal-Si_3N_4, SiO_2-silicon

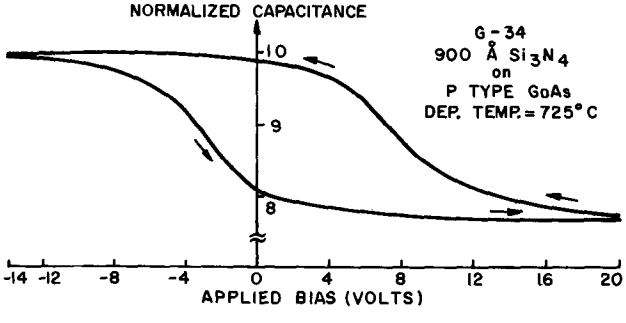

Fig. 6. C-V curves showing hysteresis

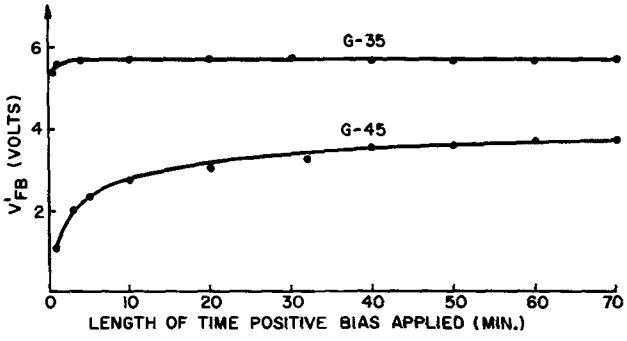

Fig. 7. Shift of flat band voltage by positive bias

system. The difficulty in obtaining a quantitative model lies in the fact that no method has yet been devised to determine both the spatial and energy distribution of the traps.

Figure 7 shows the "trap filling" response for two p-type samples having Si_3N_4 thicknesses of 850Å. A 20V bias was applied and the capacitance at flat band, which had previously been determined, was used as an indication of curve shift. The application of the bias was interrupted at each test point for about 10 sec in order to determine how much the flat band voltage (*i.e.*, the voltage required to yield flat band capacitance) had shifted. Whereas sample G-35 reached equilibrium in about 2 min with a shift of 5.7V, G-45 reached a shift of only 3.7V after an hour. G-35 was deposited at a NH_3:SiH_4 ratio of 49:1 at 725°C, whereas G-45 was deposited at a 62:1 ratio at 700°C. It can be concluded that, whereas G-35 has a relatively high density of traps near the interface (*i.e.*, within the tunneling distance) and/or the traps have a large electron capture cross section so that equilibrium is soon reached, G-45 has a lower density of states near the interface so that when equilibrium is finally reached the shift in flat band voltage is less.

The filling of traps involves electrons crossing the semiconductor-nitride interface and being captured by traps, which accounts for the right-most curve of Fig. 6. As the bias voltage sweeps out to +20V traps fill, so that the return path is displaced to the right indicating a net increase of negative charge at the interface.

The complementary part of the cycle is completed as the bias swings negative. The bias is then in a direction to raise the energy levels of the traps causing trapped electrons to tunnel back to the semiconductors. As the bias is swept negative to −20V, traps empty as electrons tunnel back to the semiconductor. The subsequent sweep from left to right is displaced to the left, indicating a net gain of positive charge.

In addition to the emptying of those traps which at flat band lie above the Fermi level, it is possible that some traps which are below the flat band Fermi level also empty as they are raised in energy by the negative bias. When the negative bias is released, these latter traps must fill before equilibrium is again achieved.

Establishing an equilibrium condition.—The discussion above has pointed out the nature of the hysteresis cycle—filling of traps with positive bias, emptying of traps with negative bias. Before quantitative measurements could be made on the samples, however, it was necessary to establish an equilibrium or reference condition. In particular, the "zero bias, equilibrium capacitance" (ZBEC) would be the value of capacitance at zero bias when the sample is in complete thermal equilibrium. Any procedure outlined for returning the sample to the ZBEC[1] should be repeatable. Such a procedure can be drawn up only after examination of the relaxation times involved in returning the sample to equilibrium.

[1] The term ZBEC will be used interchangeably to denote "zero bias equilibrium capacitance" and "zero bias equilibrium condition." The meaning should be clear from context.

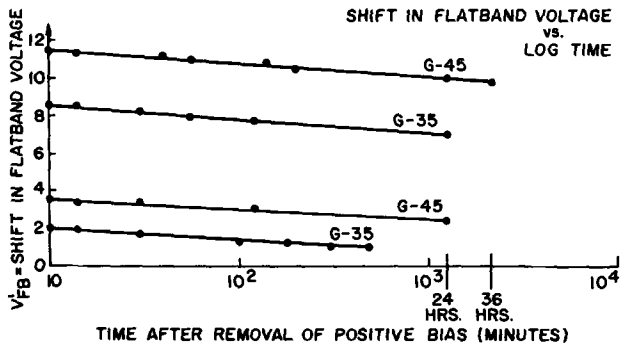

Fig. 8. Relaxation after filling of traps by positive bias

Figure 8 shows relaxation curves for two p-samples after removal of positive bias. The two curves for each sample result from a difference in the initial shift before relaxation. V'_{FB} represents the change in flat band voltage from its value prior to application of the positive bias.

It is apparent from the straight line plots of Fig. 8 that

$$\Delta V'_{FB} = -A \log t$$

with A in the range 0.5-0.7 for t in minutes. All samples tested showed similar relaxation curves. There was no apparent correlation between the NH_3:SiH_4 ratio and the value of A. The relaxation of filled traps is very slow. For an initial shift of 6V in flat band voltage, and using a value of 0.6 for A, 10^{10} min would be required for relaxation back to equilibrium. This is nearly 20,000 years.

In contrast to the extremely long time required for the traps to empty with no applied bias, they could be emptied in a short time by the application of a negative bias. A typical plot of this resetting of V'_{FB} as a function of time is shown in Fig. 9. Notice that V'_{FB} does not return to zero but goes to negative values. In terms of the C-V plot of Fig. 10, the following sequence has occurred:

1. Starting at "equilibrium" curve A, a positive bias is applied which shifts the curve to the position marked B as traps fill.

2. A negative bias is applied which moves the curve from B to C, overshooting the equilibrium position A.

In going from position B to C, not only have the traps that were filled by application of the positive bias been emptied, but also some traps which are filled in the equilibrium condition have been emptied. It is to be expected that these latter traps would fill exponentially, the dominant process being described by

$$\frac{dn_t}{dt} = A\, n(N_t - n_t)$$

where n_t is the density of filled traps, N_t is the total density of filled traps at equilibrium, n is the density of conduction band electrons, and A is a capture con-

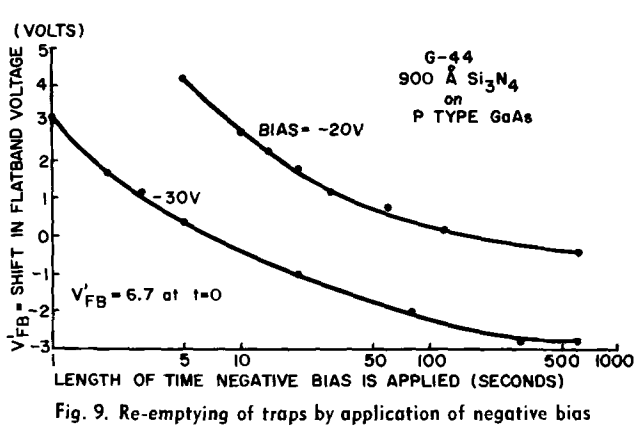

Fig. 9. Re-emptying of traps by application of negative bias

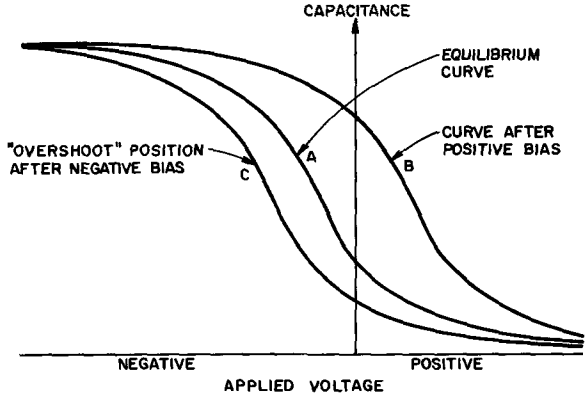

Fig. 10. Shift of C-V curve shift with positive and negative bias.

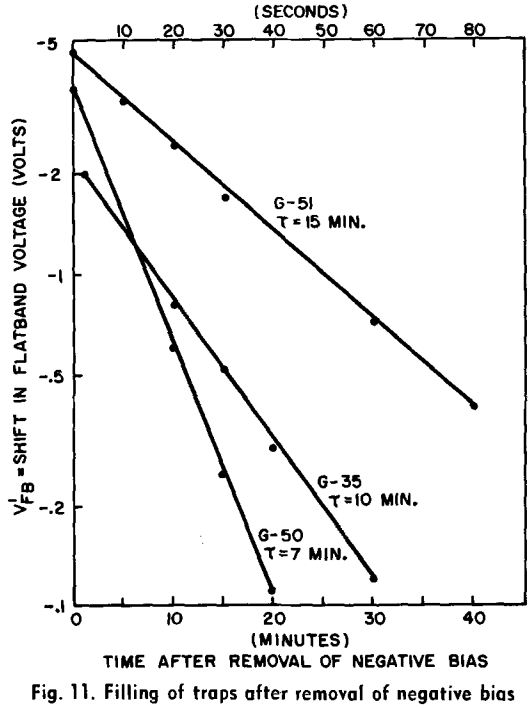

Fig. 11. Filling of traps after removal of negative bias

stant. Figure 11 shows this recovery for three samples. The shift in flat band voltage is given by

$$V'_{FB} = V_0\, e^{-t/\tau}$$

Typical values for τ are 5-15 min for the samples in the dark.

At this point a procedure for establishing a ZBEC can be given:

1. Apply a negative bias for 5 min. A bias of −30V for Si_3N_4 films in the 850-1000Å range is adequate. All traps above the flat band Fermi level will empty, as will some traps below the flat band Fermi level.

2. Remove all bias for 45 min to allow traps below the Fermi level to fill.

Effects of NH_3:SiH_4 *ratio on hysteresis.*—A detailed investigation was made to determine how the hysteresis varies as the NH_3:SiH_4 ratio is changed. Over a hundred samples were investigated. The zero bias equilibrium capacitance (ZBEC) was carefully established for each sample as outlined above. Using this capacitance as a reference, a positive bias was first applied to the sample and the voltage (V_0') required to again achieve the reference capacitance was noted. This cycle was repeated for a given positive bias until no further voltage shift was obtained. In this manner, the amount of shift in the C-V curve for a given bias was found. The flat band capacitance could have been

used as the reference point, but the ZBEC was more convenient since it could be found directly by measurement.

Figure 12 shows the shift in C-V plot, as determined by monitoring the voltage (V_o') required to obtain the ZBEC, as a function of bias for seven representative p-type samples. Film thickness for all samples was 900Å ± 10%. The samples can be divided into two groups, those deposited at NH_3:SiH_4 ratios above or below about 50:1. Samples deposited at ratios below 50:1 show a relatively large amount of shift at low bias with the rate of shift reducing at higher bias. Samples deposited at ratios above 60:1 show the reverse effect, *i.e.*, lower shift at low bias and a great deal of shift as the bias voltage was increased. A ratio of about 55:1 gave a nearly linear plot—intermediate to the two groups.

The above grouping was independent of deposition temperature over the temperature range 700°-725°C. It was found, however, that depositions at 725°C at ratios above 60:1 did not give good C-V plots. Little or no change in capacitance *vs.* bias was found, although the films had good physical appearance and good field strength (> 10^7 V/cm). Judging from the thickness of the films, the capacitances were always low. This indicated that the samples were so heavily inverted that it was impossible to achieve accumulation. Reducing the temperature to 700°C gave good curves at high ratios.

Looking at Fig. 12 in greater detail, it is clear that processing has a very pronounced affect on the density of traps as a function of distance from the insulator-semiconductor interface. Samples G-25, G-26, G-34, and G-35 exhibit 2-3 times as much shift as the other samples at a bias of 10V. Since the bias at each value was repeatedly applied until no more shift was obtained, it must be concluded that G-25, G-26, G-34, and G-35 have a much greater density of traps within the tunneling distance than do the other samples. This is also in agreement with the discussion relating to Fig. 7 above where it was concluded that G-35 had a much higher density of traps near the interface than G-45. At higher bias (> 25V), samples G-26, G-34, and G-35 show a decreasing amount of shift—indicating a decreasing density of traps.

Samples G-45, G-49, and G-50 show an increasing amount of shift with increasing bias. At high bias, the slopes of these curves approach unity. These samples appear to have a high density of traps at greater distance from the interface.

Depositions were made on p-substrates from 650° to 725°C at NH_3:SiH_4 ratios ranging from 25:1 to 300:1. Best results were obtained at a NH_3:SiH_4 ratio of about 60:1 at 700°C. These samples show low hysteresis at fields below 2-3 x 10^6 V/cm. Higher NH_3:SiH_4 ratios (up to at least 121:1) give about the same amount of hysteresis at low fields, but the C-V curves for these samples are increasingly shifted toward negative voltages. Figure 13 shows the improvement in hysteresis at low fields (< 3 x 10^6) for one of the best p-type samples (G-45) processed at 700°C at a NH_3:SiH_4 ratio 62:1 over the best sample (G-35) obtained at 725°C. Both curves were made at 100 kHz on an x-y plotter.

Although the C-V curves for n-type samples are quite different from those for p-type samples, the hysteresis effect is very similar. As for p-samples, the C-V curves for n-samples show the effect of trap filling and emptying. Application of positive bias results in a shift of the C-V curve toward more positive voltages. The relaxation (trap emptying) with no bias applied was again found to be logarithmic with time. A relaxation rate of 0.5-0.6 V/decade in excellent agreement with that of p-type samples was found. Again the traps could be emptied by the application of negative bias—a field of 2-3 x 10^6 V/cm for 2-5 min being sufficient.

Figure 14 shows the shift in ZBEC for several n-samples. As in the case of p-type samples, the shapes of the curves are quite dependent on the NH_3 to SiH_4 ratio. Samples deposited at low ratio show greatest shift at low fields, while samples having higher NH_3 to SiH_4 ratios (62.5:1 or greater) show the opposite effect. These results are in good agreement with those for p-type samples.

Density of surface states.—Because of the hysteresis effect in these samples, the concept of surface state density does not have its usual meaning. In the normal situation (*e.g.*, grown silicon dioxide on silicon) surface state density is a function of surface potential but is not dependent on the past history of the sample. The situation here is different, however, since the shape of the C-V curve is a function of the direction in which the voltage is varied. Figure 15 shows two curves for the p-type sample (G-45) exhibiting the least amount of hysteresis at low fields. Curve *A* was taken by varying the voltage in the negative and positive direction starting each time from zero volts in the equilibrium condition. This was the standard procedure used in taking C-V curves as discussed above. Curve *B* was taken by first adjusting the bias to +25V and then taking data as the voltage was decreased back through zero to negative voltages. The dotted curve in Fig. 15 is Curve *B* shifted next to Curve *A*. Curve *B* is somewhat steeper than Curve *A*.

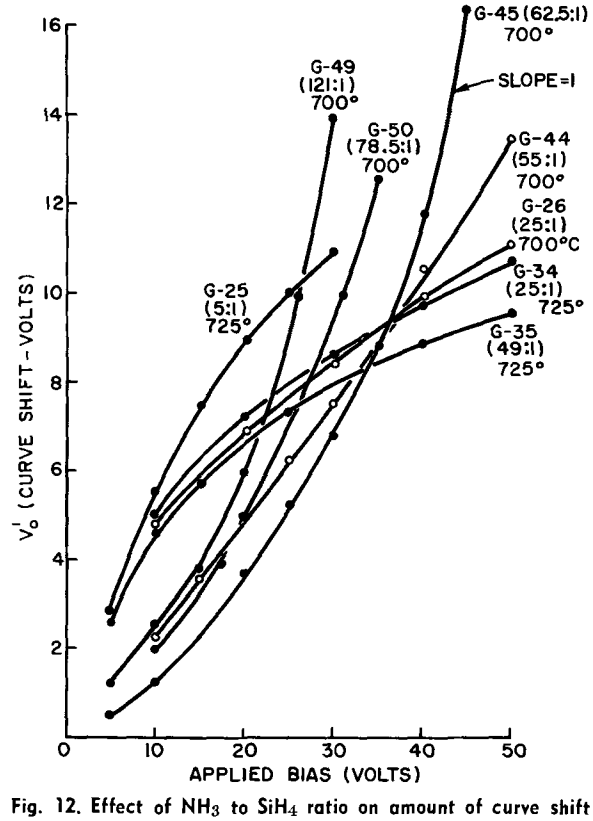

Fig. 12. Effect of NH_3 to SiH_4 ratio on amount of curve shift

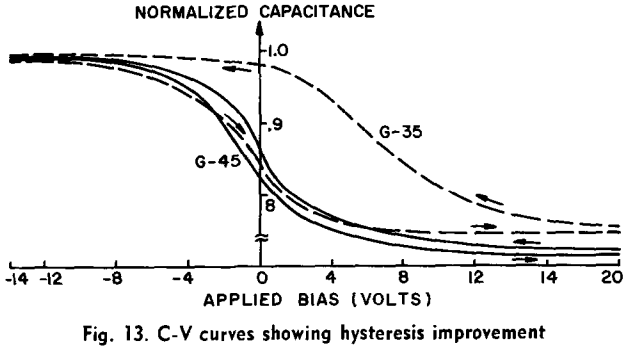

Fig. 13. C-V curves showing hysteresis improvement

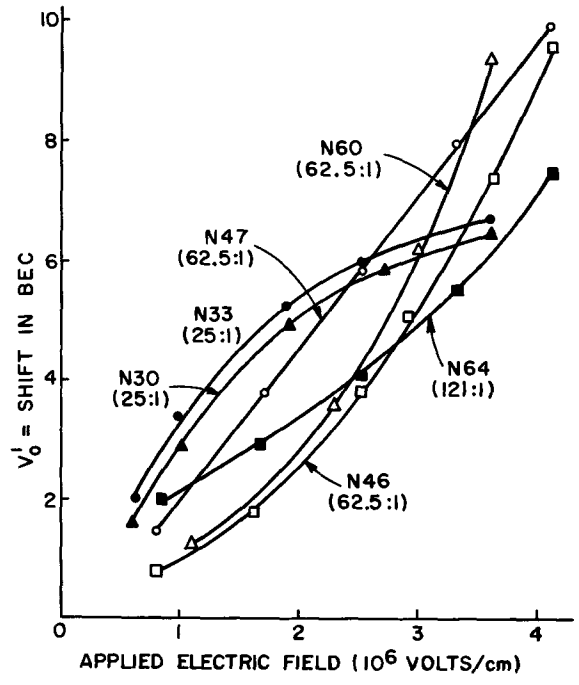

Fig. 14. Curve shift for n-type samples with positive applied voltage.

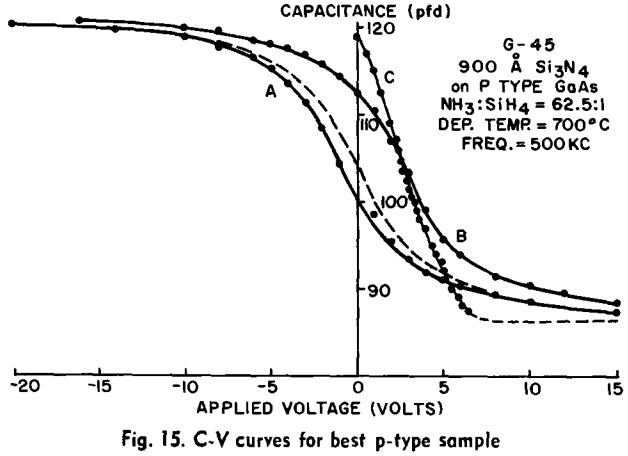

Fig. 15. C-V curves for best p-type sample

This is due to the fact that the traps were first filled before taking Curve *B*. Since the traps empty very slowly until negative voltages are reached, this curve gives the minimum effect of hysteresis as far as determining surface state density. The fact that the curve is shifted to the right of the equilibrium Curve *A* does not affect surface state density measurements. Such a shift is analogous to that produced by a non-zero ϕ_{MS} (metal-semiconductor work function difference) and has no effect on determination of surface state density.

Curve *C* in Fig. 15 is the calculated theoretical C-V curve (45) for values of surface potential, ψ_S, ranging from 0 to +1.1V. This corresponds to the Fermi level going from 0.1V above the valence band ($\psi_S = 0$) to 0.2V below the conduction band ($\psi_S = 1.1$). The surface state density was calculated from Curves *B* and *C* and is shown in Fig. 16. N_{SS} is the effective density of surface states per square centimeter per unit voltage. N_{SS} is in the 10^{12}-10^{13} range—being highest for low values of ψ_S. Values of ψ_S between 0 and 0.1V correspond to negative values of the applied voltage. The emptying of traps in this region could account for the large increase in N_{SS}. The lowest value of N_{SS} is 1 x 10^{12} for ψ_S of 0.4-0.5V.

Summary

The predominant characteristic of the Si_3N_4-GaAs interface is the presence of hysteresis due to the filling and emptying of traps in the Si_3N_4 near the interface. The spatial distribution of these traps from the interface is strongly dependent on the $NH_3:SiH_4$ ratio. The amount of this hysteresis was minimized to less than 2V for fields below 1.7 x 10^6 V/cm for the best p-type sample. Best results were obtained at a deposition temperature of 700°C and a $NH_3:SiH_4$ ratio of 62.5:1.

The relaxation (emptying) of filled traps with no applied bias is extremely slow and logarithmic in time. Recovery times as long as 20,000 years are indicated. The refilling of traps to equilibrium after removal of a negative bias is exponential in time with time constants of a few minutes in the dark. Surface states at the interface appear to be negative when below the Fermi level and account for the opposite polarity of flat band voltage for n- and p-samples.

A method was found for obtaining repeatable C-V measurements. This involved the establishing of a zero bias equilibrium condition—ZBEC. This condition could be achieved in a few minutes by relaxation after the application of a negative bias.

Surface state density for the best p-sample was in the 10^{12}-10^{13} range. Repeatability on p-type samples was good—apparently being primarily determined by repeatability of the processing. Repeatability for n-type samples was relatively poor for reasons not yet determined.

Some further reduction in the amount of hysteresis is needed before stable gates can be fabricated from GaAs-Si_3N_4 FET's.

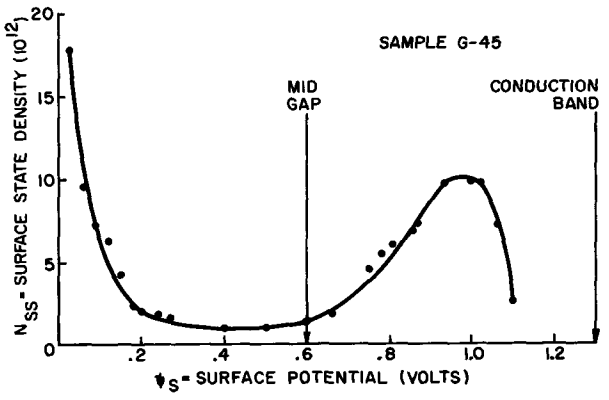

Fig. 16. Surface state density for best p-sample

Manuscript submitted Feb. 4, 1970; revised manuscript received *ca.* June 22, 1970.

Any discussion of this paper will appear in a Discussion Section to be published in the June 1971 JOURNAL.

REFERENCES

1. H. T. Minden, *Solid State Technol.*, 25 (April 1969).
2. A. S. Grove, "Physics and Technology of Semiconductor Devices," pp. 323-326, John Wiley & Sons, Inc. (1967).
3. V. Y. Doo, *Electron Devices*, **ED-13**, 561 (1966).
4. V. Y. Doo, D. R. Nichols, and G. A. Silvey, "Vapor Detection of Silicon Nitride," Paper presented at Electrochem. Soc. Meeting, Buffalo, N. Y., Oct. 10-14, 1965.
5. J. V. Dalton, "Sodium Drift and Diffusion in Silicon Nitride Films," Paper presented at Electrochem. Soc. Meeting, Cleveland, Ohio, May 1-6, 1966.
6. W. van Gelder and V. E. Hauser, *This Journal*, **114**, 869 (1967).
7. T. L. Chu, C. H. Lee, and G. A. Gruber, *ibid.*, **114**, 717 (1967).
8. V. Y. Doo, D. R. Nichols, and G. A. Silvey, *ibid.*, **113**, 1279 (1966).
9. K. E. Bean, P. S. Gleim, and R. L. Yeakly, *ibid.*, **114**, 733 (1967).
10. D. M. Brown, W. E. Engeler, M. Garfinkel, and F. K. Heumann, *ibid.*, **114**, 730 (1967).
11. Sugano *et al.*, *Japan. J. Appl. Physics*, **7**, 122 (1968).
12. S. M. Sze, *J. Appl. Phys.*, **38**, 2951 (1967).
13. S. Yoshioka and S. Takayanagi, *This Journal*, **114**, 962 (1967).

14. T. L. Chu, J. R. Szedon, and C. H. Lee, *This Journal*, **115**, 318 (1968).
15. M. J. Grieco, Paper 148 presented at Electrochem. Soc. Meeting, Philadelphia, Oct. 9-14, 1966.
16. H. Sterling and R. Swann, *Solid State Electron.*, **8**, 653 (1967).
17. S. M. Hu, *This Journal*, **113**, 693 (1966).
18. T. L. Chu, J. Szedon, and C. H. Lee, *Solid State Electron.*, **10**, 897 (1969).
19. N. C. Tombs *et al.*, *Proc. IEEE*, **54**, 87 (1966).
20. S. M. Hu and L. V. Gregor, *This Journal*, **114**, 826 (1967).
21. R. S. Levitt and W. K. Zucker, *ibid.*, **114**, 1192 (1967).
22. E. J. Kendall, *Brit. J. Appl. Phys., Ser. 2*, **1**, 1409 (1950).
23. V. Y. Doo, D. R. Kerr, and D. R. Nichols, *This Journal*, **115**, 61 (1968).
24. F. K. Heumann, D. Brown, and E. Mets, *ibid.*, **115**, 99 (1968).
25. N. C. Tombs and F. A. Sewell, *ibid.*, **115**, 101 (1968).
26. A. N. Saxena and O. N. Tkal, *ibid.*, **115**, 227 (1968).
27. J. R. Yeargan and H. L. Taylor, *ibid.*, **115**, 273 (1968).
28. P. F. Schmidt and D. R. Wonsidler, *ibid.*, **114**, 603 (1967).
29. R. C. G. Swann, R. R. Mehta, and T. P. Cauge, *ibid.*, **114**, 713 (1967).
30. B. E. Deal and P. J. Fleming, *ibid.*, **115**, 300 (1968).
31. D. M. Brown *et al.*, *ibid.*, **115**, 311 (1968).
32. M. J. Griers, F. L. Worthing, and B. Schwartz, *ibid.*, **115**, 525 (1968).
33. M. V. Coleman and D. J. Thomas, *Phys. Stat. Solidi*, **25**, 241 (1968).
34. E. J. M. Kendall, *Can. J. Phys.*, **46**, 2509 (1968).
35. D. J. D. Thomas, *Phys. Stat. Solidi*, **20**, 131 (1967).
36. A. S. Grove, B. E. Deal, E. H. Snow, and C. T. Sah, *Solid State Electron.*, **8**, 145 (1965).
37. K. H. Zaininger and G. Warfield, *IEEE Trans. Electron Devices*, **ED-12**, 179 (1965).
38. E. S. Schlegel, *ibid.*, **ED-14**, 728 (1967).
39. E. S. Schlegel, *ibid.*, **ED-15**, 951 (1968).
40. J. Drowart and P. Goldfinger, *J. Chem. Phys.*, **55**, 721 (1958).
41. M. V. Sullivan and G. A. Kolb, *This Journal*, **110**, 585 (1963).
42. K. H. Zaininger and G. Warfield, *IEEE Trans. Electron Devices*, **ED-12**, 179 (1965).
43. F. P. Heiman and G. Warfield, *ibid.*, **ED-12**, 167 (1965).
44. E. C. Ross and J. T. Wallmark, *RCA Rev.*, **30**, 366 (1969).
45. K. H. Zaininger, "Surface-State Density from High Frequency Capacitance Measurements," *RCA Product Engr.*, pp. 50-52 (1968).

The Orientation Dependence of Epitaxial $InAs_xP_{(1-x)}$ on GaAs

H. A. Allen*

Texas Instruments Incorporated, Dallas, Texas 75222

ABSTRACT

The orientation dependence of the deposition of $InAs_xP_{1-x}$ epitaxial layers on GaAs using an AsH_3, PH_3, indium, and HCl vapor-deposition system was studied. The total flow rate and the ratio of Group III to total Group V components were held constant while deposits were made simultaneously on (100), (110), (111)A, and (111)B substrates. Similar deposits were made under the same conditions on spherical, single-crystal GaAs substrates. Growth on these spheres exhibited facets that correspond to slow growth and high-perfection orientations. The sphere surface morphologies were similar to the planar substrates over much of the composition range.

Many of the properties of the $InAs_xP_{(1-x)}$ alloy system have been known for some time. It has only been more recently that this material has been grown epitaxially by chemical-vapor deposition on InAs (1), GaAs, and GaP (2) substrates. The perfection of hetero-epitaxial layers is, generally, strongly dependent on the substrate orientation and in binary alloy systems, the preferred orientation can also be a function of alloy composition. In order to determine which is the preferred growth orientation for a given alloy, a systematic investigation under controlled growth conditions is necessary. The goal of this investigation is to define the preferred growth planes of the $InAs_xP_{(1-x)}$ alloy system on GaAs as a function of alloy composition.

Materials Preparation

An open-tube deposition system constructed of fused quartz was used in these studies (2) (Fig. 1). Purified hydrogen and high-purity AsH_3 and PH_3 each in hydrogen gas are mixed in a mixing chamber prior to introduction to the reactor. Anhydrous HCl gas (purchased from the Matheson Company) which has also been mixed with purified hydrogen, is passed through the heated indium reservoir and transports the volatile InCl to the deposition zone (1, 2). In these experiments 4% AsH_3 and 4% PH_3 each in hydrogen obtained from the Matheson Company, were sources. Elemental indium was six-nines pure and was purchased from Cominco American Incorporated. The composition of the deposited alloys was controlled by the relative flow rates of the AsH_3 and PH_3 gases and was reproducible to a standard deviation of 1% in alloy composition. The flow rates could be varied continuously from 0 to about 250 cc/min for AsH_3 and

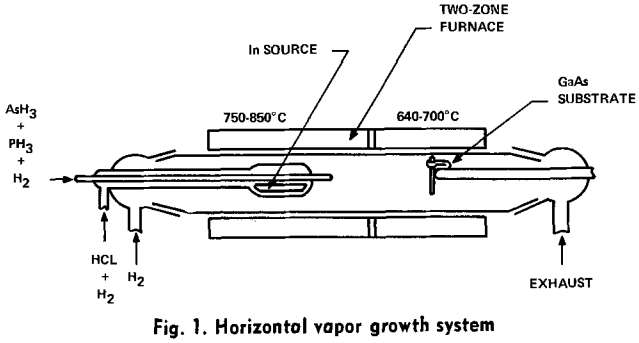

Fig. 1. Horizontal vapor growth system

* Electrochemical Society Active Member.
Key words: III-V semiconductor alloys, infrared materials, chemical vapor deposition.

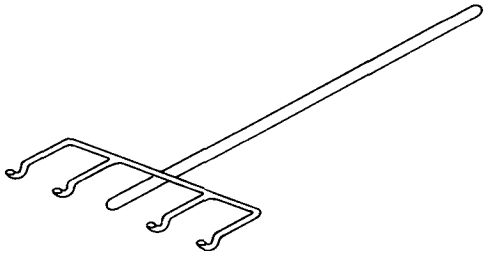

Fig. 2. Four-slice seed holder

PH_3 in hydrogen. The total flow rate was held constant at 300 cc/min. The Group III to Group V ratio was held constant at 5:4 with an anhydrous HCl flow of 14 cc/min and a total Group V flow of 11.3 cc/min.[1] The flow rates of AsH_3 and PH_3 relative to the alloy composition were determined in earlier studies (1, 2).

A two-zone resistance furnace provided temperature control of the indium reservoir and the GaAs substrates. The indium zone was controlled at 800°C and the substrate temperature was controlled at a temperature between 640° and 700°C; the seed temperature was increased from 640°C for InP to 700°C for InAs (2). The temperature gradient in the system was gradual within the indium reservoir and the seed being separated by 3-4 in. In most runs the seed or seeds were held normal to the direction of gaseous flow by quartz pins through a hole in the slice (Fig. 2). All temperatures were maintained at ± 2°C throughout a given run.

The GaAs substrates used in this investigation were from Czochralski-grown crystals that had been sawed in the (100), (110), (111)A, and (111)B planes and polished to about 20 mils in thickness. These substrates were sawed to within ± 0.5° of the given direction as evidenced by x-ray diffractometer readings of the slices. The substrates were chemically polished with 8:1:1(H_2SO_4:H_2O_2:H_2O) immediately prior to use. The GaAs spheres were mechanically ground from cubes which had been sawed from Czochralski-grown crystals. The spheres were between 0.063 and 0.125 cm in diameter. Immediately prior to use, the spheres were polished with the nonpreferential 40HCL:$4H_2O_2$:$1H_2O$ etch (3). The deposition times were 20 min for all substrates and 2-3 hr for the sphere deposits. Layer thicknesses varied between 8 and 20 μm and were determined by cleave or angle lap-and-stain techniques (2).

Large Area Deposits

The regular substrate deposits are referred to as large area as compared to the hypothetical point locations of each orientation on a sphere.

The (100), (110), (111)A, and (111)B substrates were suspended normal to the gas flow in the same run by use of a four-hooked fused silica seed holder (Fig. 2). Thus, in each run a nearly constant set of growth conditions was maintained. Very shiny deposits with smooth substrate-epitaxy interface could be grown reproducibly on the (111)A substrates from compositions consisting of pure InP up to about 80% InAs. The alloy deposits above 80% were generally polycrystalline in nature with the frequency of the poly layers increasing with the InAs concentration in alloy. Figure 3 is photomicrographs of representative (111)A deposits.

The (111)B deposits were erratic throughout the composition range and were generally polycrystalline in nature. The (110) deposits were similar in trend to the (111)A, but the frequency of poly layers was much higher above 75% and below 25% InAs. The deposits on (100) substrates, below 75% InAs, were practically all poly. The highest perfection InAs layers

[1] Assuming a 1:1 ratio of indium transported to HCl introduced.

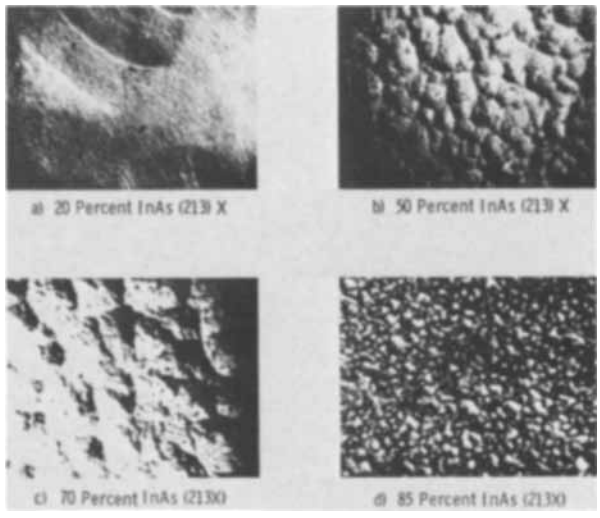

Fig. 3. Undoped $(InAs)_x$ $(InP)_{1-x}$ (III)A surfaces

were grown on this orientation. Representative photomicrographs of the (111)B, (110), and (100) surfaces are shown respectively in Fig. 4-6.

The compositions of the above samples were obtained by electron microprobe analysis and checked by x-ray diffraction techniques (4). The crystallinity was determined by x-ray diffraction and Laue backreflection techniques (5). Single crystals had well-defined Laue patterns as well as diffractometer peaks sharp enough to enable composition analysis to ± 2%. Table I gives the results of these measurements.

Sphere Deposits

Deposition on a sphere, ideally, makes it possible to have all orientations present at the same time. The

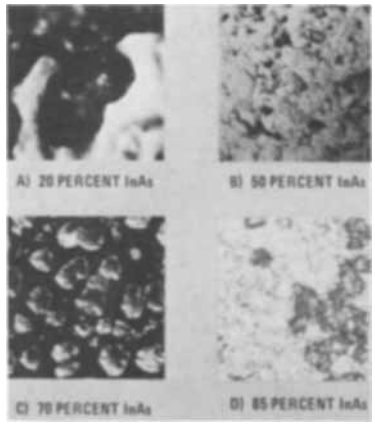

Fig. 4. $(InAs)_x$ $(InP)_{1-x}$ (III)B surfaces. 213×

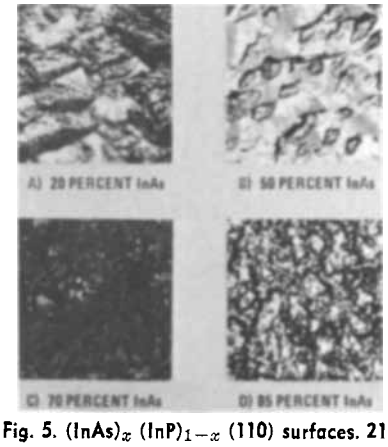

Fig. 5. $(InAs)_x$ $(InP)_{1-x}$ (110) surfaces. 213×

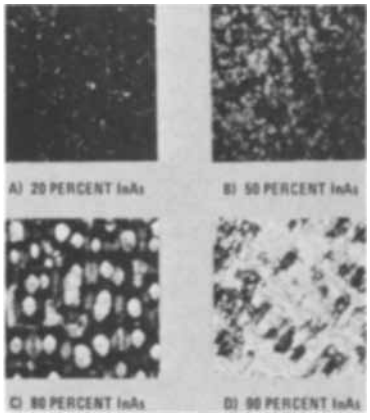

Fig. 6. $(InAs)_x$ $(InP)_{1-x}$ (100) surfaces. 213×

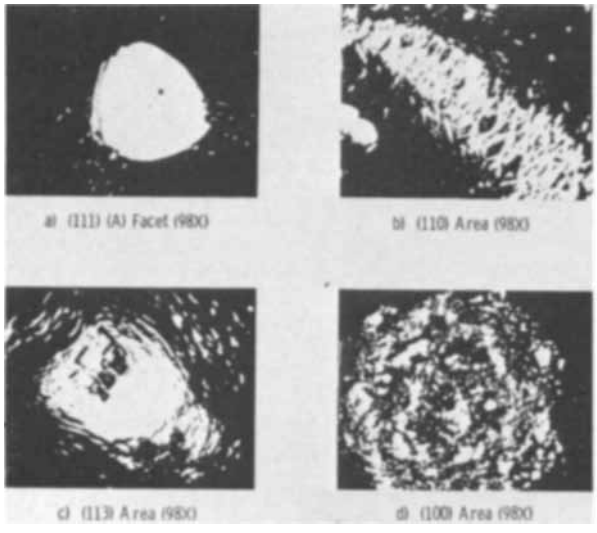

Fig. 7. InP sphere facets

faster growing planes will "grow out" leaving only the slower growing orientations as facets. In general, these facets represent optimum growth directions for high-perfection crystal growth. This proved to be the case with the epitaxial growth of InP on a GaAs sphere. The only true facet was a (111)A, with the (110) and (113) directions exhibiting shiny, shingled flats. The (100) and (111)B area could be located and were dull in appearance. The (111)A facet was distinguished by its surface similarity with control slices included in the run. Figure 7 is the facets observed on the InP deposited sphere.

Table I. Mole per cent InAs

Orientation	Run numbers								
	18	19	12	21	23	24	25	26	27
(111)A	0	17	25	50	77	80	79	89	93
(110)	0	17	24	52	66	83	82	87	95
(111)B	0	18	24	49	78	85	79	85	
(100)	0	22	30	55	80	87	85	84	94

Note: — denotes single crystallinity.

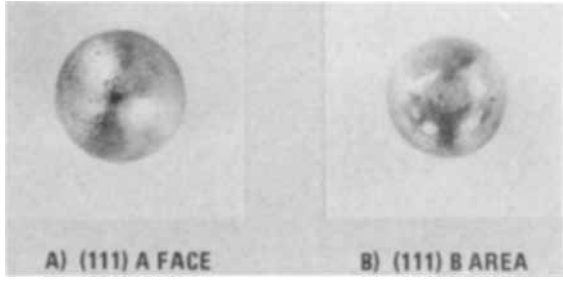

Fig. 8. $(InAs)_{0.50}$ $(InP)_{0.50}$ on GaAs sphere

Unfortunately, the InP deposited GaAs sphere was the only one which lent itself to such a straightforward explanation. Five more spheres were deposited with various compositions of the alloy between an InAs composition of 20 and 90 m/o (mole per cent). In all cases the only discernible facet was a (111)A with the (111)B direction identifiable by a triangular banded area 180° from each (111)A facet as shown in the (111)A and (111)B polar photographs in Fig. 8. No other identifiable facets were seen on these spheres.

Discussion

The composite of the large area and sphere deposits indicate that the (111)A direction of GaAs is the best plane for high-perfection epitaxial $InAs_xP_{(1-x)}$ alloy layers in the 0-80% InAs range. There is a pronounced orientation shift in large-area 85-100% InAs alloys to the (100) as the preferred growth. The above results were observed as the general rule through many depositions; it was occasionally possible to grow a high-perfection layer on an orientation which had previously given all poly deposits. Though no extensive experiments were conducted, the general trends stated in the test were seen on selected deposits with temperature conditions varied widely (± 75°C), on the seed and feed and with change in the Group III to Group V ratio between 0.5 and 3.0.

The fact that there were no identifiable facets on the alloy sphere deposits other than (111)A and in particular no (100) facets for alloy layers of greater than 85% InAs, is not well understood. It should be stressed that although one expects agreement, large-area and sphere deposits are very different. As was mentioned earlier, with a sphere each orientation is only a point on the sphere's surface and therefore, only slow-growing orientations tend to increase this point to a real geometrical area as growth occurs. Thus, it is possible that a preferred growth direction could be fast growing and not produce a facet on a sphere. Obviously, this would not be a problem with large-area deposit.

Manuscript submitted April 1, 1970; revised manuscript received *ca.* June 22, 1970.

Any discussion of this paper will be published in a Discussion Section to be published in the June 1971 JOURNAL.

REFERENCES

1. J. J. Tietjen, H. P. Maruska, and R. B. Clough, *This Journal*, **116**, 492 (1969).
2. H. A. Allen and E. W. Mehal, *This Journal*, **117**, 1081 (1970).
3. D. W. Shaw, *Proc. 1968 Sym. on GaAs* (London Inst. of Phys. and Phys. Soc.), Paper 8.
4. J. K. Howard and R. P. Dobrott, *This Journal*, **113**, 567 (1966).
5. H. F. Buckley, "Crystal Growth," John Wiley & Sons, Inc., New York (1951).

Phase Diagram of the CdTe-CdSe Pseudobinary System

Alan J. Strauss* and Jacques Steininger

Lincoln Laboratory, Massachusetts Institute of Technology, Lexington, Massachusetts 02173

ABSTRACT

The liquidus and solidus curves of the CdTe-CdSe pseudobinary system have been determined by thermal analysis of cooling and heating curves, respectively, for homogenized liquid and solid alloy samples. The phase diagram has a eutectic point at 1091° ± 1°C near 20 m/o (mole per cent) CdSe. Above the eutectic composition both liquidus and solidus temperatures increase monotonically and sublinearly with increasing CdSe content. In this region the experimental values of the liquidus-solidus gap do not exceed 11 m/o and are in excellent agreement with the ideal thermodynamic liquidus-solidus relationship. The phase diagram below the solidus has been investigated by x-ray diffraction measurements on alloy powders annealed between 770° and 1050°C and quenched. It consists of two broad single-phase regions, one of alloys with the zinc blende structure of CdTe and the other of alloys with the wurtzite structure of CdSe, separated by a two-phase region only about 3 m/o wide, whose boundaries shift toward increasing CdSe content with decreasing temperature. For compositions between 30 and 45 m/o CdSe, either structure could be obtained at room temperature, depending on annealing temperature and rate of cooling. In addition, a polytype of unknown structure, which appears to be a metastable intermediate in the wurtzite-to-zinc blende transformation, was observed in two melt-grown furnace-cooled ingots containing 45-50 m/o CdSe.

The II-VI compounds CdTe and CdSe have the cubic zinc blende and hexagonal wurtzite structures, respectively, when prepared by solidification of stoichiometric melts or nonstoichiometric Cd-Te or Cd-Se solutions. [Other methods of preparation can be used to obtain CdTe with wurtzite structure (1) or CdSe with zinc blende structure (2).] The phase diagram of the CdTe-CdSe system has not been determined previously but x-ray diffraction studies (3, 4) on a limited number of samples prepared by solidifying stoichiometric melts indicate that pseudobinary solid solutions are formed over the entire composition range. According to these studies, undoped alloys containing less than about 40 m/o CdSe have the zinc blende structure, those containing at least 70 m/o CdSe have the wurtzite structure, and those with intermediate compositions may have either structure.

In this investigation, the liquidus and solidus curves in the CdTe-CdSe pseudobinary system have been determined by thermal analysis measurements on homogenized liquid and solid alloy samples. The cubic-hexagonal transition in the solid phase has been studied by x-ray diffraction analysis of annealed and quenched alloy powders. The x-ray data show that the cubic and hexagonal phase fields are separated by a two-phase region about 3 m/o wide, whose boundaries shift toward increasing CdSe content with decreasing temperature. Therefore, within a certain composition range, alloys can be obtained with either cubic or hexagonal structure, as reported earlier (3, 4), depending on the annealing temperature and rate of cooling. In addition to these two phases, a previously unreported polytype of unknown structure can also be formed as shown by x-ray diffraction data for two melt-grown, furnace-cooled ingots containing 45-50 m/o CdSe.

Experimental Procedure

Alloys for thermal analysis and x-ray diffraction studies were prepared from CdTe and CdSe. The CdTe was synthesized by fusion of the elements (nominal purity 99.9999%) in forepump-evacuated and sealed fused silica ampoules coated with pyrolytic graphite. To prepare CdSe, the elements (same nominal purity) were combined in an open-tube fused silica reactor (5) heated to 1050°-1100°C under helium gas at 1 atm. The composition of the CdSe was then adjusted by sublimation in a dynamic vacuum in order to remove the excess of unreacted elements and reduce the vapor pressure during subsequent high temperature annealing.

To prepare each alloy for x-ray analysis, a 10g mixture of the two powdered compounds was sealed in a fused silica ampoule containing helium gas (pressure of about 400 Torr at room temperature), annealed at 950°C for 21 days or longer, and quenched by dropping the ampoule into water. Annealing was continued until x-ray diffraction measurements gave no evidence of inhomogeneity, and the measured lattice parameters were consistent with the nominal compositions.

Samples for thermal analysis were either alloy powders annealed in the manner described or unannealed mixtures of CdTe and CdSe powders. A sample weighing about 10g was sealed in an evacuated fused silica ampoule and placed in a DTA apparatus described previously (6), together with a similar ampoule containing about 8g of silicon used as a reference. The sample and reference temperatures were measured with Pt-Pt, 13% Rh thermocouples inserted into reentrant wells in the ampoules. Calibration with a gold sample (melting point 1063.0°C) gave melting and freezing arrests of 1063.0°C ± 0.1°C and showed that no correction of the sample temperature readings was necessary. Solidus temperatures were obtained from thermal arrests observed either during initial heating of the annealed powder samples or during heating of both types of samples after they had been melted, frozen, and then homogenized by annealing in the DTA apparatus for 16 hr at about 20°C below the solidus temperature. The two types of experiments gave solidus temperatures which agreed to within a fraction of a degree. The liquidus temperatures were obtained from the thermal arrests observed when the samples were cooled after homogenization in the DTA apparatus for 16 hr at about 50°C above the liquidus temperature. Liquidus temperatures reproducible to ±1°C were obtained from repeated runs on the same sample. Rates of 1°-2°C/min were used for both heating and cooling. Supercooling was observed during most of the cooling runs but was limited to only a few degrees (Table I). When supercooling occurred, the liquidus arrest temperature was taken to be the

* Electrochemical Society Active Member.

Key words: phase diagram, cadmium telluride, cadmium selenide, alloys, polytypes, crystal growth.

Table I. Thermal analysis data

Composition CdTe	Composition CdSe	Cooling curves Super-cooling, °C	Cooling curves Liquidus arrest, °C	Cooling curves Reproducibility, °C	Heating curves Solidus arrest	Heating curves Reproducibility
1.000	0	0	1091.8	±0.2	1091.8	±0.2
0.900	0.100	0	1092.9	±0.1	1089.6	±0.1
0.800	0.200	3.3	1092.3	±0.4	1091.3	—
0.700	0.300	5.0	1100.0	0	1097.0	—
0.675	0.325	7.0	1101.0	±0.3	1098.5	0
0.650	0.350	2.0	1108.3	±0.4	—	—
0.625	0.375	6.6	1106.8	±0.2	1099.8	±0.2
0.600	0.400	0.9	1107.2	±0.2	1101.5	—
0.550	0.450	3.7	1118.4	±1.0	—	—
0.500	0.500	0.1	1125.8	±0.2	1110.5	—
0.450	0.550	0.3	1136.7	±1.0	—	—
0.400	0.600	4.0	1147.3	±1.0	1125.0	—
0.300	0.700	0.2	1169.5	±1.0	1143.5	—
0.200	0.800	2.3	1196.0	±0.5	—	—
0.100	0.900	0.3	1222.0	±0.5	1200.5	—
0	1.00	0	1252.3	±0.2	1252.3	—

maximum in the recalescence curve. Otherwise, both liquidus and solidus arrest temperatures were obtained from the intersection of the practically straight lines below and above the break in the sample temperature curve. Because of the large thermal effects in this system, differential temperature recording was used only as a confirmation of the arrests observed on the sample temperature curve. The over-all accuracy is estimated to vary from within ± 1°C near the terminal compounds to within a few degrees in the middle of the composition range.

To investigate the cubic-hexagonal transition below the solidus, pairs of homogenized alloy powders with the same composition, in the range 30-50 m/o CdSe, were preannealed so that one was initially cubic and the other initially hexagonal. Portions of the samples weighing 1-2g were then sealed in separate fused silica ampoules containing helium gas, annealed at temperatures between 770° and 1050°C, quenched by dropping the ampoules into water, and ground to minus 325 mesh. The phases present were determined from x-ray diffractometer patterns obtained with Cu Kα radiation. Annealing was repeated if necessary until both samples were either single-phase cubic, single-phase hexagonal, or two-phase. The total annealing times ranged from 16 hr at 1050°C to 30 days at 800°C. A sample was taken to be single-phase cubic if the noncoincident (111) hexagonal line in the vicinity of $2\theta = 23°$ was not detected, and single-phase hexagonal if the noncoincident (400) cubic line in the vicinity of $2\theta = 58°$ was not detected. [Use of these criteria gives a considerably lower detection limit for the hexagonal phase than for the cubic phase, since the (111) hexagonal line is 5-10 times more intense than the (400) cubic line.]

X-ray diffraction patterns were also obtained with a Debye-Scherrer camera for all the alloys following initial homogenization and for a number of samples after subsequent annealing. These patterns were used to calculate the cubic or hexagonal lattice parameters to an accuracy of ±0.001Å by a least-squares extrapolation method (7).

In addition to the alloys prepared by annealing mixtures of powdered CdTe and CdSe, a number of polycrystalline alloy ingots each weighing 150g were obtained by the Bridgman method of crystal growth. Stoichiometric melts containing up to 60 m/o CdSe, which were prepared from the elements in evacuated and sealed fused silica ampoules coated with pyrolytic graphite, were frozen directionally by lowering the ampoules at the rate of about 1 mm/hr out of a vertical resistance-heated furnace. One ingot, containing 35 m/o CdSe, was quenched by pulling the ampoule out of the furnace with part of the material still molten. The others were allowed to cool in the furnace after the power had been turned off. Portions of the ingots were analyzed with an electron microprobe (8) to determine their alloy composition, and a number of these and other portions were ground for x-ray diffraction analysis with the diffractometer and/or Debye-Scherrer camera.

Results

The phase diagram determined for the CdTe-CdSe system is shown in Fig. 1. The compositions plotted are the nominal compositions calculated from the weights of CdTe and CdSe used to prepare the alloys. The thermal analysis data are listed in Table I, which gives the liquidus and solidus arrest temperatures, the amount of supercooling observed during the liquidus determinations, and the reproducibility when repeated runs were made. Melting and freezing arrests of 1091.8° ± 0.2°C were obtained for CdTe, in good agreement with the literature values of 1090° ± 2°C [Ref. (9)], 1092° ± 3°C [Ref. (10)], and 1091° ± 2°C [Ref. (11)]. The liquidus and solidus temperatures for 10 and 20 m/o CdSe do not differ significantly from each other or from the melting point of CdTe and suggest the presence of a eutectic point at 1091° ± 1°C and near 20 m/o CdSe. (The separation between liquidus and solidus curves in this region is not shown in Fig. 1 because of the small scale of the diagram.) Above 20 m/o CdSe, both liquidus and solidus temperatures increase monotonically and sublinearly with increasing CdSe content. The liquidus-solidus gap in this region remains rather narrow, never exceeding 11 m/o. Melting and freezing arrests of 1252.5° ± 0.5°C were obtained for CdSe, in fair to good agreement with previously reported values of 1239° ± 3°C [Ref. (12)], 1250° ± 2°C [Ref. (11)], 1258° ± 3°C [Ref. (13)], 1259° ± 4°C [Ref. (14)], and 1264° ± 10°C [Ref. (15)].

The results of the x-ray diffractometer measurements on annealed and quenched powders are represented by circles in Fig. 1—closed circles for single-phase cubic samples, open circles for single-phase hexagonal samples, and half-closed circles for two-phase samples. (There was no evidence for ordering of the Te and Se atoms in either the cubic or hexagonal structure.) Over the limited composition range where the relationship between structure and temperature has been studied in detail, the cubic and hexagonal phase fields are separated by a two-phase region only about 3 m/o wide. The boundaries of this region are well represented by parallel straight lines, along which the temperature decreases with increasing CdSe content. According to these lines, the two-phase field extends from 26 to 29 m/o CdSe at 1000°C and from 46.5 to 49.5 m/o CdSe at 800°C. The composition range investigated was not extended to lower CdSe content because of the difficulty anticipated in retaining the hexagonal phase by quenching as the hexagonal-cubic transformation temperature increased. The range was not ex-

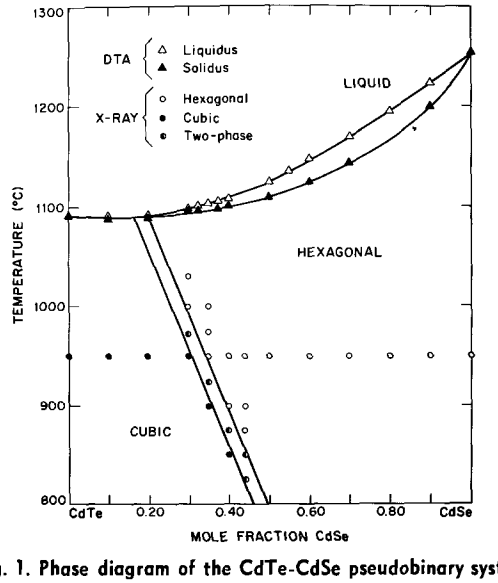

Fig. 1. Phase diagram of the CdTe-CdSe pseudobinary system

tended to higher CdSe content because the time required to attain equilibrium in the solid phase became inconveniently long as the transformation temperature decreased. (Some two-phase samples may have been incorrectly identified as single-phase because the quantity of the minor phase was too small to be detected by the x-ray diffraction method used. Errors of this kind would tend to make the width of the two-phase region shown in Fig. 1 somewhat less than the actual width.)

As shown in Fig. 1, when extrapolated linearly the lower and upper boundaries of the two-phase field intersect the solidus curve at 17 and 20 m/o CdSe, respectively, consistent with a eutectic point near 20 m/o CdSe. Linear extrapolation to lower temperatures gives an hexagonal-cubic transformation temperature around 250°C for pure CdSe, although such an extended extrapolation is obviously of limited significance. Partial transformation from cubic to hexagonal CdSe after annealing for 10 hr at 130°C has been reported (2).

The cubic (a_0) and hexagonal (a_0, c_0) lattice parameters measured for annealed single-phase alloy powders are listed in Table II, together with the values calculated from them for the unit cell volume (V) and for the c/a ratio of the hexagonal alloys. (Where duplicate results are given for the same composition, they were obtained for independent samples, not for aliquots of the same sample.) The c/a ratios range from 1.631 to 1.638, compared with the theoretical value of 1.633 for the wurtzite structure. For CdTe, the measured a_0 is 6.481Å, compared with literature values of 6.480-6.483Å [Ref. (3, 16-18)]. [The value of 6.423Å given by Litwin (4) is obviously incorrect.] For CdSe, a_0 = 4.301Å and c_0 = 7.016Å, compared with literature values of a_0 from 4.297 to 4.309Å, and values of c_0 from 7.007 to 7.034Å [Ref. (3, 4, 14, 19)]. Most of the lattice parameters reported previously (3, 4) for the alloys with cubic structure agree fairly well with the present ones, but there is greater disagreement among the parameters for the hexagonal alloys.

The values of a_0 for cubic samples, a_0 and c_0 for hexagonal samples, and V for all samples are plotted against nominal alloy composition (expressed in mole fraction CdSe, x) in Fig. 2, 3, and 4, respectively. The three lattice parameters vary linearly with composition, according to the following expressions which correspond to the straight lines in Fig. 2 and 3: a_0 (cubic) (Å) = 6.481-0.411x; a_0 (hexagonal) (Å) = 4.580-0.279x; c_0 (Å) = 7.502-0.486x. Except at the extremes of the composition range, the values of V fall slightly below the straight line joining the unit cell volumes of CdTe and CdSe. For the region ($0.3 \leq x \leq 0.45$) in which both cubic and hexagonal samples have been obtained, the values of V are generally somewhat lower for cubic samples than for hexagonal.

For the $CdTe_{1-x}Se_x$ ingots which were prepared by directional freezing of stoichiometric melts, the results of electron microprobe analysis of small sections close to the tip are qualitatively consistent with the liquidus-solidus relationships shown in Fig. 1. If solidification of an alloy occurs under equilibrium conditions, the first-to-freeze composition is the solidus composition corresponding to the liquidus composition given by the nominal ingot composition. For $CdTe_{1-x}Se_x$ ingots with nominal x up to 0.3, within the error of the microprobe (estimated to be ±3%) the measured compositions are the same as the nominal ingot compositions, presumably because the gap between liquidus and solidus compositions is quite small in this region. For 3 ingots with nominal x = 0.4, 0.4, and 0.5, the measured compositions were x = 0.41, 0.45, and 0.55, respectively, compared with the solidus compositions of x = 0.50, 0.50, and 0.61 given by the phase diagram. The measured compositions are all less than the corresponding

Table II. Lattice parameters of $CdTe_{1-x}Se_x$ alloys

x	Cubic a_0(Å)	Cubic V(Å³)	Hexagonal a_0(Å)	Hexagonal c_0(Å)	Hexagonal c_0/a_0	Hexagonal V(Å³)
0	6.481	68.06				
0.1	6.444	66.90				
0.2	6.398	65.47				
0.25	6.381	64.95				
0.3	6.359	64.28	4.489	7.355	1.638	64.18
0.35	6.336	63.59	4.484	7.333	1.635	63.84
0.4	6.316	62.99	4.465	7.310	1.637	63.10
			4.466	7.308	1.636	63.12
0.44	6.295	62.36	4.456	7.293	1.637	62.70
0.5			4.442	7.257	1.634	62.00
			4.441	7.262	1.635	62.02
0.6			4.414	7.206	1.633	60.79
0.7			4.380	7.169	1.637	59.55
			4.383	7.163	1.634	59.59
0.8			4.355	7.114	1.634	58.42
			4.354	7.125	1.636	58.49
0.9			4.328	7.070	1.634	57.34
1.0			4.301	7.016	1.631	56.20

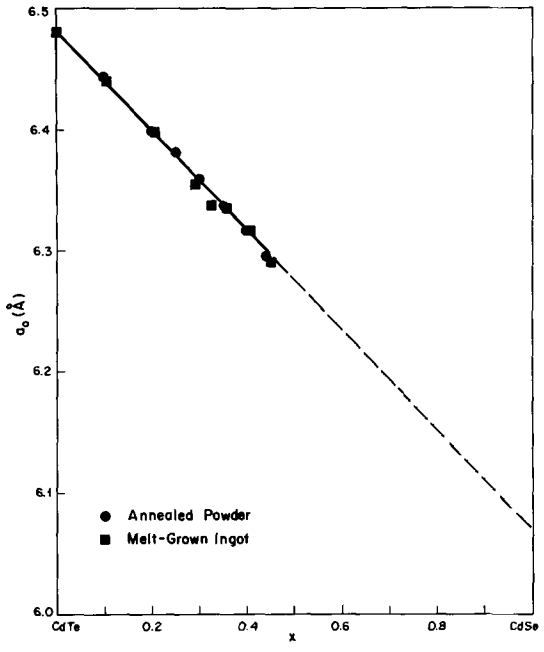

Fig. 2. Lattice parameter a_0 as a function of mole fraction CdSe in $CdTe_{1-x}Se_x$ alloys with cubic structure.

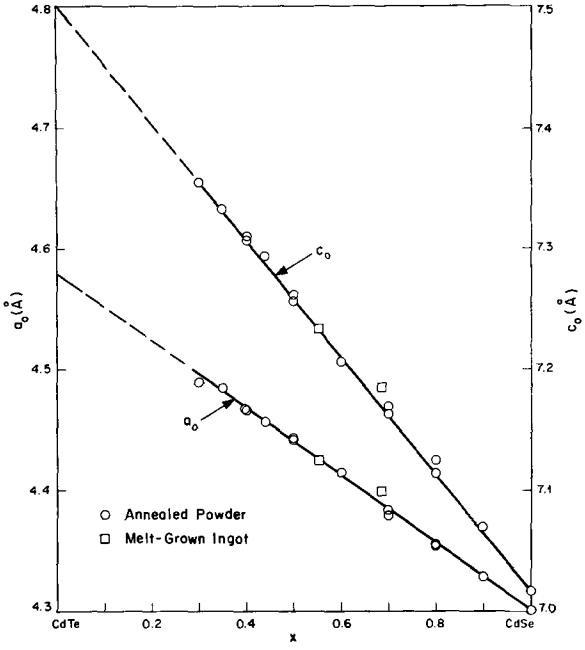

Fig. 3. Lattice parameters a_0 and c_0 as a function of mole fraction CdSe in $CdTe_{1-x}Se_x$ alloys with hexagonal structure. The ordinate scale for a_0 is at the left side of the figure and the scale for c_0 is at the right side.

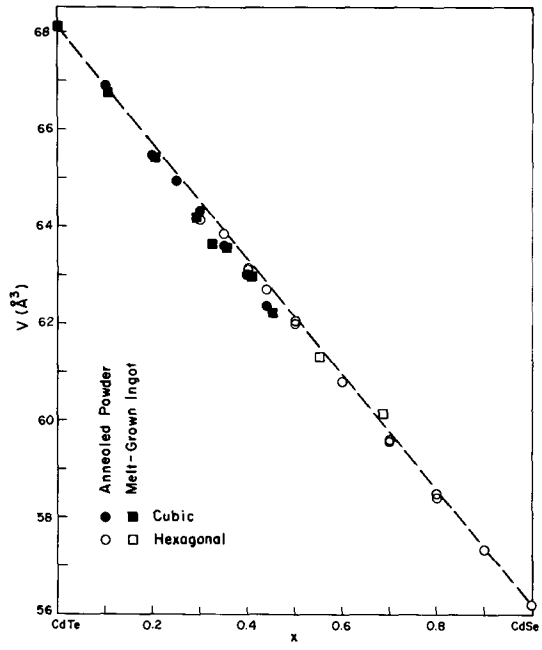

Fig. 4. Unit cell volume (V) as a function of mole fraction CdSe in $CdTe_{1-x}Se_x$ alloys.

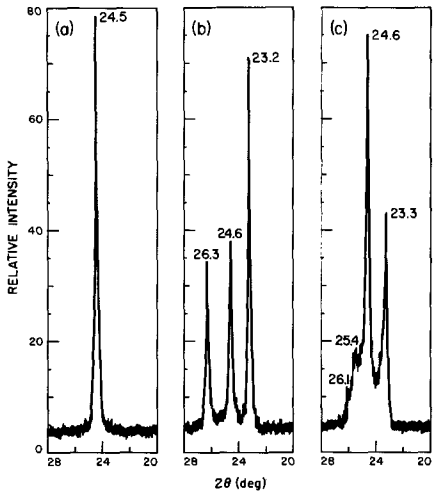

Fig. 5. X-ray diffraction patterns over the angle range $20° \leq 2\theta \leq 28°$ for $CdTe_{1-x}Se_x$ alloys with $x \sim 0.5$: *(a)* cubic, *(b)* hexagonal, *(c)* polytype.

solidus compositions; these discrepancies are in the direction expected if the rate of solidification was too high for equilibrium to be established between the liquid and solid or if the samples analyzed were too far removed from the first-to-freeze region.

Although the x-ray diffractometer measurements made on the alloy ingots were not extensive, the data are sufficient to show that the phases present depend on ingot composition, the location of the sample in the ingot, and the method of cooling. Thus all samples from ingots with $x \leq 0.2$ are cubic, and all those from an ingot with $x = 0.6$ are hexagonal. (The compositions quoted in this discussion are nominal, and the ingots were furnace cooled unless otherwise specified.) The first-to-freeze portions of ingots with $x = 0.3$, 0.4, and 0.45 are either entirely cubic or contain a small amount of the hexagonal phase in addition to the cubic. A sample frozen later in one of the ingots with $x = 0.4$ contains a larger proportion of the hexagonal phase but is still primarily cubic. In contrast, samples from an ingot with x of only 0.35, which had been air quenched by removing the growth ampoule from the hot furnace, are entirely hexagonal.

For two ingots with $x = 0.45$ and 0.5, the first-to-freeze portions are single-phase cubic and hexagonal, respectively. However, a number of other samples from these ingots give diffractometer patterns which cannot be attributed to these two phases. Part of one such pattern is shown in Fig. 5, together with the same angle range ($20° \leq 2\theta \leq 28°$) from patterns for single-phase cubic and hexagonal samples of about the same composition. The unusual features of the new patterns are: (*a*) the appearance of new although poorly defined lines at 25.4° and 42.9°; (b) an increase in the relative intensity of the line at 24.6°, which cannot be attributed to the cubic phase because the characteristic cubic line at 58.8° is either weak or absent; and (*c*) a marked decrease in the relative intensities of the lines at 26.3°, 44.4°, and 76.5° which appear in the wurtzite pattern. We attribute these features to the presence of a polytype, like those observed for ZnS and SiC, whose structure is intermediate between the zinc blende structure (with entirely cubic close packing) and the wurtzite structure (with entirely hexagonal close packing). In the ingot with $x = 0.5$, the region containing the polytype is in the interior, completely surrounded by a thin outer shell of the wurtzite phase. The two regions are easily distinguished by visual observation of a lapped cross section.

In addition to the diffractometer patterns for ingot samples, Debye-Scherrer patterns were also obtained for a number of such samples which were powdered after they had been analyzed with the electron microprobe. The lattice parameters and unit cell volumes measured for single-phase cubic and hexagonal samples, which are plotted in Fig. 2-4 as a function of the measured composition, are the same within experimental error (including the error of the microprobe analysis) as those for annealed alloy powders.

Discussion

The qualitative features of the CdTe-CdSe phase diagram (Fig. 1) reflect the fact that the crystal structures of CdTe and CdSe are different but very closely related. Because of their difference in structure, the compounds cannot form a complete series of solid solutions along the solidus curve. Therefore the CdTe-CdSe diagram has the eutectic form, rather than the simple lens form of the II-VI pseudobinary CdTe-ZnTe [Ref. (6)] and HgTe-HgSe [Ref. (20)] diagrams. In each of the latter systems, involving two binary compounds with zinc blende structure which exhibit complete mutual solid solubility, both liquidus and solidus temperatures increase monotonically and sublinearly with increasing ZnTe or HgSe content across the entire diagram. Thus the liquidus and solidus curves in these systems resemble those for the hexagonal branch of the CdTe-CdSe diagram (*i.e.*, the region between about 20 m/o CdSe, the eutectic composition, and pure CdSe). Over this entire region $CdTe_{1-x}Se_x$, alloys with wurtzite structure are stable along the solidus curve, according to a linear extrapolation of the hexagonal phase boundary from lower temperatures.

Liquidus-solidus relationship.—For a binary alloy system of completely miscible components A and B, by expressing the equality of the partial free energies of mixing in the liquid and solid phases, it has been shown (21) that the liquidus and solidus compositions in equilibrium at temperature T are related by

$$RT\left(\ln\frac{X_A^s}{X_B^s}-\ln\frac{X_A^l}{X_B^l}\right)=\Delta H_A\left(1-\frac{T}{T_A}\right)-\Delta H_B\left(1-\frac{T}{T_B}\right)-D \quad [1]$$

with

$$D=\frac{\partial\Delta G_{e,m}^s}{\partial X_A^s}-\frac{\partial\Delta G_{e,m}^l}{\partial X_A^l}$$

where X_i^l and X_i^s are the mole fractions of component i in the liquid and solid phases, respectively, T_i and ΔH_i are the temperature and enthalpy of fusion of the pure component, and $\Delta G_{e,m}^s$ and $\Delta G_{e,m}^l$ are the excess molar free energies of mixing in the respective phases. Equation [1] is a general thermodynamic expression which is applicable to any system. If both liquid and solid solutions are ideal, the excess free energies of mixing are zero and $D = 0$. The ideal form of Eq. [1] with $D = 0$ has also been found to fit the experimental data for a large number of binary and pseudobinary alloy systems (metallic, semiconducting, and ionic) in which the liquidus and solidus temperatures vary monotonically with composition (21). Although in general the liquid and solid phases in these systems are not ideal solutions, the ideal liquidus-solidus expression is applicable because the deviations from ideality in the two phases are comparable, and therefore, the difference between the partial excess free energies of mixing is small enough to be neglected. (An excellent fit to Eq. [1] with $D = 0$ is obtained for the CdTe-ZnTe system but not for the HgTe-HgSe system. We believe that the deviations between experiment and calculation in the latter case are probably due to errors in the experimental determination of the solidus curve.)

The ideal form of Eq. [1] can be used to calculate one of the boundaries of the two-phase field when the other boundary and the enthalpies of fusion of the pure components are known. In the present study this expression has been used to calculate the solidus curve for the CdTe-CdSe system from the experimental liquidus data and the enthalpies of fusion of CdTe and CdSe determined by Kulwicki (11) (12.0 and 10.5 kcal/mole, respectively). As shown in Fig. 6, the calculated curve is in excellent agreement with the experimental solidus data for the hexagonal branch of the diagram. (The root mean square of the difference between calculated and experimental temperatures for 8 data points is 2.4°C.) The agreement indicates that over this composition range the deviations from ideality are comparable for the liquid and solid phases, as in systems where the liquidus and solidus temperatures vary monotonically over the whole range of composition. The agreement between calculation and experiment for the hexagonal branch also implies that the zinc blende and metastable wurtzite structures of CdTe do not differ greatly in free energy, since the temperature and enthalpy of fusion used in the calculations were measured for CdTe with zinc blende structure.

It should be noted that calculation of the solidus curve from our initially limited liquidus data facilitated the selection of temperatures close to the solidus for annealing the frozen alloy samples. Because homogenization was accelerated by the increased rates of diffusion, the heating curves for such samples annealed for only 16 hr at these high temperatures gave thermal arrests almost as sharp as those obtained with powder samples annealed at 950°C for 3 weeks or more.

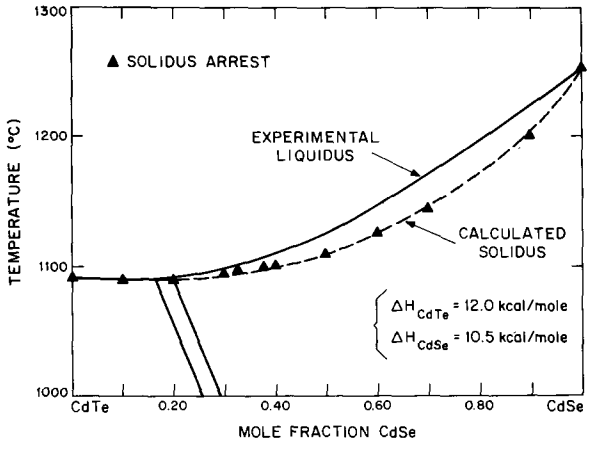

Fig. 6. Comparison of calculated solidus curve with experimental solidus data for CdTe-CdSe system.

Sub-solidus phases.—The zinc blende and wurtzite structures have the same primary coordination, with each cation surrounded by four nearest-neighbor anions in tetrahedral configuration, and *vice versa*. This close structural relationship, together with the chemical similarity between Te and Se, explains the broad range of mutual solid solubility exhibited by CdTe and CdSe. Within the temperature region where the boundaries of the cubic and hexagonal phases have been determined, the miscibility gap at a fixed temperature is only about 3 m/o, and its position shifts sufficiently with temperature to permit formation of solid solutions over the whole range of compositions.

According to the phase diagram of Fig. 1, for any composition up to 17 m/o CdSe the zinc blende structure is stable at all temperatures below the solidus curve. For any other composition, this structure is stable only up to a transition temperature which decreases quite rapidly with increasing CdSe content. Above this temperature there is an interval of about 15°C in which no solid solution of this composition is stable, and at still higher temperatures the wurtzite structure is stable. The same sequence of low-temperature zinc blende, intermediate two-phase, and high-temperature wurtzite regions has recently been observed by Shalimova *et al.* (19) for fixed compositions near 40 m/o CdSe in the pseudobinary system formed by CdSe and ZnSe, which like CdTe has the zinc blende structure. According to their results for annealing temperatures between 800° and 1200°C, the phase diagram below the solidus in this system is similar to that of the CdTe-CdSe system, since it too consists of cubic and hexagonal phase fields separated by a narrow two-phase region whose boundaries shift toward increasing CdSe content with decreasing temperature.

For ZnS, the prototype compound for both structures, the zinc blende structure is the low-temperature form and the wurtzite structure the high-temperature form, just as in the two alloy systems. The fact that in all three cases there is a temperature at which the two phases have the same free energy is another result of their close structural relationship. In each case, at constant composition the free energy of the zinc blende phase increases more rapidly with increasing temperature than that of the wurtzite phase. [For the alloys, the temperature of equal free energy lies in the region where neither structure is stable with respect to the formation of a mixture of two phases with different compositions. Shalimova *et al.* (19) claim that the zinc blende and wurtzite structures are both stable for any composition and temperature within the two-phase region of the CdSe-ZnSe system. This is thermodynamically impossible.]

Although the zinc blende and wurtzite structures have the same primary coordination, transformations from one to the other require the breaking of nearest-neighbor bonds (22). Such reconstructive transformations involve an appreciable activation energy, and their rates therefore depend approximately exponentially on temperature. It is this strong temperature dependence which makes it possible to establish equilibrium phase relations for elevated temperatures by means of phase determinations at room temperature on samples which have been annealed and quenched. The use of this method requires the transformation rates to be high enough at the annealing temperature for equilibrium to be achieved in a convenient time and low enough at any phase boundary for the high-temperature phase to be retained by quenching. In our investigation of the CdTe-CdSe system, these conditions were apparently satisfied for small powder samples with compositions between 30 and 44 m/o CdSe, corresponding to transition temperatures between about 950° and 800°C at the upper boundary of the cubic phase field. Within this range single-phase sam-

ples of a given composition were prepared with both wurtzite and zinc blende structures by annealing above or below the transition temperature, respectively. No attempt was made to prepare hexagonal samples containing less than 30 m/o CdSe, because of the difficulty anticipated in cooling rapidly enough to prevent conversion to the cubic phase at temperatures of 1000°C and above. Cubic samples containing more than 44 m/o CdSe were not prepared because it would have taken too long to transform them from the hexagonal phase at temperatures below 800°C.

In the two earlier investigations (3, 4) of the structure of CdTe-CdSe alloys, the samples studied were prepared by solidification from the melt. Those containing up to 30 m/o CdSe were entirely cubic. Stuckes and Farrell (3) found that samples containing 40 and 50 m/o CdSe were cubic with only a trace of the hexagonal phase, and Litwin (4) observed both phases for compositions of 36, 50, and 60 m/o CdSe. Only samples containing at least 70 m/o CdSe were entirely hexagonal. According to the phase diagram of Fig. 1, however, alloys containing more than about 20 m/o CdSe crystallize from the melt in the hexagonal structure. Therefore the presence of the cubic phase in samples containing 30-60 m/o CdSe must have resulted from the partial or complete transformation of the hexagonal phase during cooling, after the temperature had fallen below the hexagonal-to-cubic transition temperature. The cubic phase was not formed for compositions exceeding 60 m/o CdSe because of the decrease in the transition temperature with increasing CdSe content and the decrease in transformation rate with decreasing temperature. In this range, the cubic phase becomes stable at such low temperatures (less than about 700°C) that the transformation rate was never high enough for appreciable transformation to occur at the cooling rates used. Since cooling rates were not discussed in either paper, it can be assumed that they were neither extremely fast nor extremely slow, and that times of the order of hours were probably required to cool to room temperature. This indicates that the rates of the hexagonal-to-cubic transformation were much faster for solid samples than for the powdered samples annealed in our investigation at fixed temperatures, which required many days for complete transformation to the cubic phase even at 800°C.

Increased transformation rates in solid samples were also observed for ingots prepared in our investigation by directional solidification of stoichiometric melts. The hexagonal phase was retained without transformation in a 35 m/o CdSe ingot which was air quenched to room temperature from above the transition temperature, while transformation occurred in furnace-cooled ingots containing up to 45 m/o CdSe. In one such furnace-cooled ingot containing 30 m/o CdSe, cubic single-crystal regions up to about 1 cm on a side were identified by sandblasting, which reveals the grain boundaries in these alloys. Thus under suitable experimental conditions the transformation to the cubic phase can occur without introducing polycrystallinity. This is another consequence of the close relationship between the zinc blende and wurtzite structures.

This relationship is also reflected by the rather close agreement in unit cell volume measured at room temperature (Fig. 4) between alloys with the zinc blende and wurtzite structures. The volume difference for a given composition does not exceed 0.6% in the range ($0.3 \leq x \leq 0.45$) where both structures have been obtained. However, the significance of the comparison is limited because the wurtzite structure is metastable at room temperature in the overlapping range and also for compositions considerably richer in CdSe—quite possibly for CdSe itself. A valid comparison would require x-ray diffraction measurements at temperatures high enough for each structure to be stable over a wide composition range. Such high-temperature measurements would also be necessary to satisfactorily test the conformity of the CdTe-CdSe alloys to Vegard's law. According to the room temperature volume data, the alloys with zinc blende structure deviate by as much as 0.8% from the straight line shown in Fig. 4, while the wurtzite alloys generally exhibit smaller deviations.

As a final result of the zinc blende-wurtzite relationship, we note the formation of a polytype in two furnace-cooled ingots with nominal compositions of 45 and 50 m/o CdSe. A large number of polytypes with structures intermediate between zinc blende and wurtzite are known for ZnS and SiC, but to our knowledge none has been reported for a ternary alloy. No attempt has been made to identify the polytype by single-crystal x-ray diffraction analysis, but calculations of the powder diffraction patterns for the 4H, 6H, 8H, 12H, and 15R polytypes of $CdTe_{0.5}Se_{0.5}$ indicate that it is probably not one of these.

Apparently the polytype was formed as an intermediate stage in the hexagonal-to-cubic transformation because the rate of cooling was too slow to permit retention of the hexagonal phase but too fast to permit complete transformation to the cubic phase. (The first-to-freeze tip of the ingot containing 45 m/o CdSe was cubic, apparently because it reached the transition temperature and transformed before the furnace was shut off. In the ingot containing 50 m/o CdSe, a thin outer shell remained hexagonal because it cooled rapidly enough to prevent transformation, but the center was converted to the polytype because it cooled more slowly.) Our experiments do not give any evidence that the polytype is a thermodynamically stable phase rather than a metastable intermediate, since it was not observed in any of the powdered samples which were quenched after annealing. Polytype formation as an intermediate step in the cubic-to-hexagonal transformation of thin films of ZnS has recently been reported (23).

Acknowledgments

This work was sponsored by the Department of the Air Force.

The authors wish to acknowledge the assistance of R. E. England and Mrs. M. C. Plonko in the phase diagram determination, R. L. MacLean in crystal growth, Mary C. Finn in electron microprobe analysis, and E. L. Mastromattei and Mrs. M. J. Button in the x-ray measurements. They are also indebted to J. M. Longo and R. F. Brebrick for discussions of the crystallographic and thermodynamic properties of the alloys.

Manuscript submitted March 31, 1970; revised manuscript received *ca.* July 8, 1970.

Any discussion of this paper will appear in a Discussion Section to be published in the June 1971 JOURNAL.

REFERENCES

1. M. Weinstein, G. A. Wolff, and B. N. Das, *Appl. Phys. Letters*, **6**, 73 (1965).
2. A. S. Pashinkin and R. A. Sapozhnikov, *Soviet Phys.—Cryst.*, **7**, 501 (1962).
3. A. D. Stuckes and G. Farrell, *J. Phys. Chem. Solids*, **25**, 477 (1964).
4. J. Litwin, *Phys. Stat. Sol.*, **5**, 551 (1964).
5. T. B. Reed and W. J. LaFleur, Solid State Research Report, Lincoln Lab., M.I.T. (1968:1), p. 19.
6. J. Steininger, A. J. Strauss, and R. F. Brebrick, *This Journal*, **117**, 1305 (1970).
7. J. B. Nelson and D. P. Riley, *Proc. Phys. Soc.*, **57**, 160 (1945).
8. M. C. Finn, *Anal. Chem.*, **42**, 1084 (1970).
9. D. de Nobel, *Philips Res. Rept.*, **14**, 361 (1959).
10. M. R. Lorenz, *J. Phys. Chem. Solids*, **23**, 939 (1962).
11. B. M. Kulwicki, Ph.D. Dissertation, Univ. of Michigan (1963).
12. A. Reisman, M. Berkenblit, and M. Witzen, *J. Phys. Chem.*, **66**, 2210 (1962).
13. D. R. Mason and D. F. O'Kane, *Proc. Intern. Conf. Semicond. Phys., Prague, 1960*, p. 1026 (1961).

14. W. R. Cook, *J. Am. Ceram. Soc.*, **51**, 518 (1968).
15. L. A. Sysoev, E. K. Raiskin, and V. R. Gur'ev, *Inorg. Mater.*, **3**, 341 (1967).
16. P. W. Davis and T. S. Shilliday, *Phys. Rev.*, **118**, 1020 (1960).
17. J. C. Woolley and B. Ray, *J. Phys. Chem. Solids*, **13**, 151 (1960).
18. G. A. Slack and S. Galginaitis, *Phys. Rev.*, **133**, A253 (1964).
19. K. V. Shalimova, A. F. Botnev, V. A. Dmitriyev, M. Z. Kognovitskaya, and V. V. Starostin, *Sov. Phys. Cryst.*, **14**, 531 (1970).
20. T. C. Harman "Physics and Chemistry of II-VI Compounds," M. Aven and J. S. Prener, Editors, p. 786, John Wiley & Sons, Inc., New York (1967).
21. J. Steininger, *J. Appl. Phys.*, **41**, 2713 (1970).
22. A. R. Verma and P. Krishna, "Polymorphism and Polytypism in Crystals," p. 50, John Wiley & Sons, Inc., New York (1966).
23. K. N. Rai, O. N. Srivastava, and P. Krishna, *Bull. Am. Phys. Soc.*, **14**, 1187 (1969).

Phase Equilibria Relations in the Ternary System BaO-SrO-Nb_2O_5

J. R. Carruthers and M. Grasso

Bell Telephone Laboratories, Incorporated, Murray Hill, New Jersey 07974

ABSTRACT

Phase equilibria in the binary system SrO-Nb_2O_5 and the Nb_2O_5-rich region of the ternary system BaO-SrO-Nb_2O_5 were investigated by DTA, x-ray diffraction, strip heater, and Curie temperature measurement techniques. The ternary-phase fields of three tetragonal-tungsten-bronze type structures have been located. Only one of these structures is a ternary compound; it is located along the $SrNb_2O_6$-$BaNb_2O_6$ binary join, extending from 20 to 80 m/o $BaNb_2O_6$, and melts congruently near 50% $BaNb_2O_6$. The ternary solubility extends from about 4% excess (Ba + Sr) to about 1% excess Nb_2O_5. This phase possesses observable orthorhombic distortion in the $BaNb_2O_6$-rich region of the solid solution. The implications of the phase diagram for the crystal growth of these compounds are briefly discussed.

The existence of a ferroelectric compound $Ba_xSr_{(1-x)}Nb_2O_6$ (BSN) was independently reported in 1960 by Francombe (1) and Ismailzade (2). The structure was found to be closely related to the tetragonal tungsten bronze structure. The existence regions were found to be $0.30 \leq x \leq 0.80$ by Francombe and $0.35 \leq x \leq 0.75$ by Ismailzade. No indication of the extent of solid solution in the ternary region was given. Both workers reported that the tetragonal structure was distorted to orthorhombic over a part of the range; however, Francombe found the orthorhombic structure for $x < 0.45$, while Ismailzade found the values $x > 0.40$ corresponded to this structure. Both workers also reported that the Curie temperatures varied from 50°C at the high $SrNb_2O_6$ end of the solution to 200°-300°C at the high $BaNb_2O_6$ end. Ismailzade reported that the paraelectric phase was tetragonal over the entire solid solution range.

The first large BSN single crystals were grown in this system by Ballman and Brown (3) over a range of melt compositions $0.25 \leq x \leq 0.75$. Chemical analysis indicated that the solid compositions were quite similar to those of the melt. Also the Curie temperature was found to vary in a similar manner to that found for the ceramic specimens. These crystals have been used by Jamieson, Abrahams, and Bernstein (4) for structure determination as well as Glass (5, 6) for investigations of the electrical properties with special reference to the pyroelectric detection of infrared radiation. These crystals have also been shown to have interesting electro-optic properties (7).

The crystal structure was determined by Jamieson *et al.* (4) for the composition $x = 0.27$ (grown from a melt with $x = 0.25$). In agreement with Ismailzade, the structure was found to be tetragonal tungsten bronze and to belong to the space group P4bm. This structure consists of a framework of NbO_6 octahedra sharing corners so that there are three different types of interstitial sites, two of which may be occupied by Ba or Sr ions. There are five formula units per unit cell so that the five Ba/Sr ions can be distributed on six possible interstitial sites (two A1 sites with distorted tetragonal symmetry and four A2 sites with distorted trigonal symmetry). In addition, it was found, for $x = 0.27$, that only Sr ions were found in the two A1 sites with an occupancy factor of 82.2% and Sr and Ba ions in the four A2 sites with occupancy factors 50.3 and 34.4%, respectively. As Glass (6) points out, if the A1 site continues to be occupied only by Sr ions as the Sr/Ba ratio changes, then the entropy of distribution of the ions becomes a minimum when $x = 0.67$. At this composition, only Sr ions occupy the A1 sites and Ba ions occupy the A2 sites (for the same occupancy factors).

The electrical properties of BSN were investigated by Glass (6) over the solid-solution range and from 10°-500°K. His dielectric constant and electrical conductivity measurements showed a behavior at the Curie temperature which correlated with the degree of randomness in the Ba/Sr distribution. Glass also measured the field and frequency dependence of the dielectric properties and the specific heat and pyroelectric coefficients of BSN.

There have been no phase equilibria studies of the ternary BaO-SrO-Nb_2O_5 system or of the SrO-Nb_2O_5 system. The BaO-Nb_2O_5 system was reported by Roth and Waring (8). The ternary oxide system SrO-NbO_2-Nb_2O_5 has been reported by Ridgley and Ward (9). These studies showed that the compounds $SrNb_2O_6$ (SN) and $BaNb_2O_6$ (BN) existed and possessed a complex and an orthorhombic crystal structure, respectively. In addition, the compounds $3BaO.5Nb_2O_5$ (B_3N_5) and $BaO.3Nb_2O_5$ (BN_3) were observed with distorted tungsten-bronze-type structures. The structures of both SN and BN have been

Key words: phase equilibria, barium strontium niobate, nonlinear optical materials.

observed to be quite sensitive to the valence state of the Nb. Partial reduction of the Nb causes SN to become cubic perovskite with characteristics of the tungsten bronzes (8) while in the case of BN, less direct evidence suggests that a hexagonal phase is stabilized which is apparently an intermediary structure between orthorhombic BN and the tungsten-bronze type structures.

The present investigation was undertaken to complete the ternary BaO-SrO-Nb_2O_5 phase diagram around the tungsten-bronze structures in this system. We wished to establish the crystal-growth equilibria and existence regions for these compounds.

Experimental Procedure

Specimen preparation.—Specimens were prepared from dried $Ba(NO_3)_2$ and $Sr(NO_3)_2$ (Fisher reagent grade) and Nb_2O_5 (CIBA optical grade). Specimens were multiply ground, pelletized, and sintered in air at temperatures 50°C below solidus temperatures. The ternary region along the binary join SN-BN possessed some strange reactivity problems to be discussed later which required the use of a strip heater to obtain completely reacted samples.

Measurements.—DTA measurements were made on a DuPont 1600 Thermoanalyzer. X-ray diffraction measurements were performed on a Nonius-Guinier focusing camera using monochromatic $CuK\alpha$ radiation. Curie temperature (T_c) measurements were made on small ceramic pellets (~ 2 mm on a side) using a General Radio 1673A capacitance bridge at 1 kHz with platinum electrodes. Firm electrode pressure was essential for these measurements. Silver paste electrodes, although used on most specimen surfaces, were found not to be necessary. The Curie temperature was reported as the position of the capacitance maximum, although Glass (6) has shown that this does not exactly coincide with the actual Curie temperature. Nevertheless we are only interested in relative changes in the position of the peak with composition.

Experimental Results

SrO-Nb_2O_5 *system.*—The DTA and x-ray results are shown in Fig. 1. In addition to SN, three new compounds were observed, S_5N_2, S_2N, and S_2N_5. The *d*-spacings for the compounds SrO, S_5N_2, S_2N, and SN are shown in Table I. SrO has a simple cubic structure while S_5N_2 has a hexagonal structure which resembles its counterpart B_5N_2 in the BaO-Nb_2O_5 system (8). The structures of S_2N and SN are seen to be complex and will not be considered further. The structure of S_2N_5 is of the tungsten-bronze type and is identical to that of BN_3. This compound will be discussed later in more detail.

Table I. *d*-Spacings of compounds in the SrO-Nb_2O_5 system

SrO		$(SrO)_5(Nb_2O_5)_2$		$(SrO)_2(Nb_2O_5)$		$SrNb_2O_6$	
d(Å)	*I*	*d*(Å)	*I*	*d*(Å)	*I*	*d*(Å)	*I*
4.80	1	3.00	10	18	<1	5.50	<1
4.15	1	2.83	10	5.3	<1	5.02	3
2.92	10	2.05	8	4.4	<1	4.50	1
2.06	5	1.77	3	3.92	1	4.20	1
1.66	5	1.655	5	3.89	1	3.95	4
1.455	3	1.625	4	3.53	2	3.88	4
1.310	2	1.495	3	3.35	3	3.45	3
		1.405	3	3.22	3	3.40	<1
		1.320	3	3.05	10	3.15	4
		1.275	3	2.94	5	3.05	10
				2.88	3	3.00	2
				2.85	5	2.91	2
				2.77	7	2.84	2
				2.16	3	2.80	5
				2.12	1	2.78	2
				2.06	3	2.75	1
				1.97	5	2.59	1
				1.94	2	2.46	1
				1.82	1	2.38	1
				1.805	<1	2.37	1
				1.730	1	2.33	1
				1.735	1	2.24	3
				1.710	1	2.22	3
				1.690	1	2.13	1
				1.670	1	2.08	3
				1.620	4	2.04	1
				1.615	4		

Liquidus temperatures in excess of 1500°C in Fig. 1 were determined by means of an optical pyrometer using SN as a calibration and an iridium strip as the heating source. This method minimized SrO volatilization for these compositions and also insured completion of the reaction. Sintering temperatures of 1400° were insufficient to achieve solid-state reaction over this composition range (0-30% Nb_2O_5).

$SrNb_2O_6$-$BaNb_2O_6$ *pseudobinary system.*—The DTA and x-ray results for the SN-BN binary join are shown in Fig. 2. The structure of $(BSN)_I$ is of the tetragonal tungsten bronze type and will be discussed later. At room temperature, compositions greater than $x = 0.55$ (where x = mole fraction $BaNb_2O_6$) showed orthorhombic splittings in agreement with the work of Ismailzade (2).

It is of some interest here to mention the reactivity problem encountered in this system. Attempts to

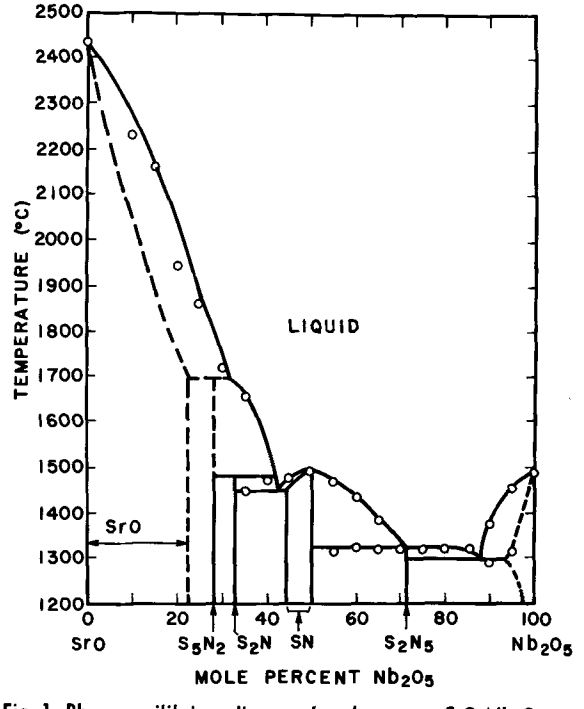

Fig. 1. Phase equilibrium diagram for the system SrO-Nb_2O_5

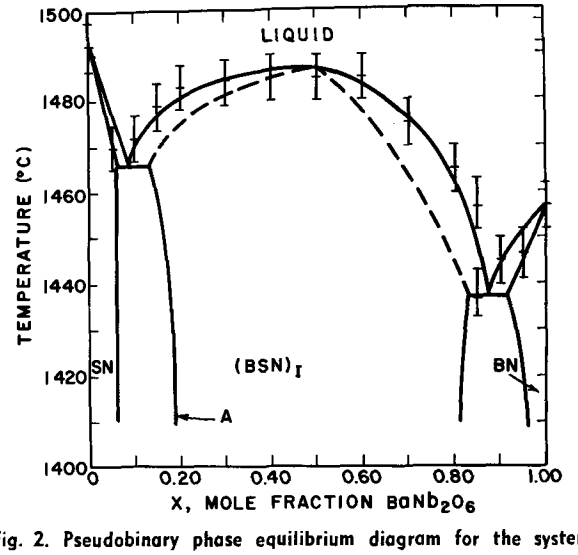

Fig. 2. Pseudobinary phase equilibrium diagram for the system $SrNb_2O_6$-$BaNb_2O_6$.

produce a single-phase BSN by sintering at 1000°C failed completely, even with ten regrindings and using a reducing ambient of 15% H_2-85% N_2 for 6 hr. As the sintering temperature was progressively raised by 100°C increments to 1400°C, the single-phase field opened up starting with the BN-rich end. The solvus line, A, in Fig. 2 moved to the left and was located at 35% BN after sintering at 1400°C. The final location of solvus line A at 20% BN was determined by melting these specimens on a platinum strip heater, slowly freezing under a microscope, and looking for second-phase SN lines with the Nonius-Guinier camera.

The liquidus shown in Fig. 2 is flat within experimental error over the composition range 20-60% BN. The location of the liquidus maximum and associated congruently melting composition was determined with the aid of T_c measurements described later. The solidus lines (shown as dashed lines) were located approximately using the composition shifts reported by Ballman and Brown (3) as guidelines and also the end-points of the eutectic arrest lines (which are observable by DTA).

BaO-SrO-Nb_2O_5 *ternary system.*—The compositions investigated in the ternary oxide region are shown in Table II together with the x-ray and DTA results. The room temperature existence regions are reproduced in Fig. 3 where the compounds $(BSN)_I$, $(BSN)_{II}$, $(BSN)_{III}$, and $(BSN)_{IV}$ have been identified. Data points have been omitted for clarity. These compounds all have tetragonal-tungsten-bronze type structures and the *d*-spacings are given in Table III. Compound I and its orthorhombic modification, II, is the compound shown in the binary join (Fig. 2) and was the subject of the introduction of this paper. Compound III corresponds to the ternary solid solution of B_3N_5, while compound IV corresponds to the ternary solid-solution range of the isomorphous S_2N_5-BN_3 series. Both III and IV show othorhombic splittings as can be seen in Table III.

The high-temperature phase equilibria for these ternary compounds may be seen from the isopleth taken at 25% BaO shown in Fig. 4. The DTA data points are shown as well as the solid-solution extent of the three bronze structures in this particular section. The solidus curves for $(BSN)_I$ are seen to be quite steep, especially in comparison to their behavior in the binary join of Fig. 2. This indicates that growth from melts with compositions off the binary SN-BN join will readily give rise to the usual types of compositional variations in the grown crystals. Compounds $(BSN)_{III}$ and $(BSN)_{IV}$ both melt peritectically in agreement with the behavior observed by Roth Waring (8) in the end members, B_3N_5 and BN_3, respectively.

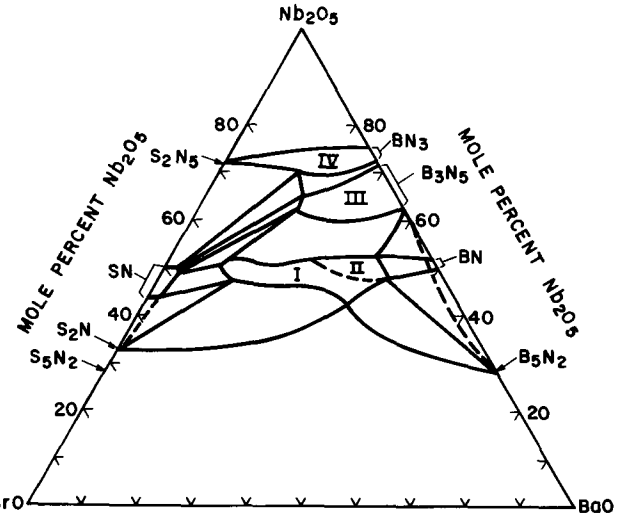

Fig. 3. Ternary phase relationships in the room-temperature isotherm of the system BaO-SrO-Nb_2O_5. Phases I, II, III, IV have tetragonal-tungsten-bronze type structures and the *d*-spacings shown in Table III.

Table II. Experimental data for compositions in the ternary system BaO-SrO-Nb_2O_5

Sample designation	Composition BaO	SrO	Nb_2O_5	Phases present	Temperature arrests, °C
BSN 160	0.05	0.20	0.75	$(BSN)_{IV}$ + Nb_2O_5	1323
163	0.10	0.15	0.75	$(BSN)_{IV}$ + Nb_2O_5	1323
167	0.15	0.10	0.75	$(BSN)_{IV}$ + Nb_2O_5	1316
153	0.20	0.05	0.75	$(BSN)_{IV}$	1323
150	0.25	—	0.75	$(BSN)_{IV}$	1323
149	0.25	0.025	0.725	$(BSN)_{IV}$	1308, 1312
159	0.05	0.25	0.70	$(BSN)_{IV}$ + SN	1320
162	0.10	0.20	0.70	$(BSN)_{IV}$ + SN	1316
166	0.15	0.15	0.70	$(BSN)_{IV}$ + SN	1312
152	0.20	0.10	0.70	$(BSN)_{IV}$	1312
148	0.25	0.05	0.70	$(BSN)_{III}$ + $(BSN)_{IV}$	1312
147	0.25	0.075	0.675	$(BSN)_{III}$	1312
158	0.05	0.30	0.65	SN + $(BSN)_{IV}$	1320
161	0.10	0.25	0.65	SN + $(BSN)_{IV}$	1323
165	0.15	0.20	0.65	SN + $(BSN)_{III}$ + $(BSN)_{IV}$	(1312), 1319
151	0.20	0.15	0.65	$(BSN)_{III}$	1312, 1335
146	0.25	0.10	0.65	$(BSN)_{III}$	1312, 1330
154	0.30	0.05	0.65	$(BSN)_{III}$	1305
145	0.25	0.125	0.625	$(BSN)_{II}$ + $(BSN)_{III}$	1292, 1312, 1384
157	0.05	0.35	0.60	SN + $(BSN)_{IV}$	1312, 1402
100A	0.10	0.30	0.60	SN + $(BSN)_{III}$ + $(BSN)_{IV}$	1312, 1395
164	0.15	0.25	0.60	SN + $(BSN)_{III}$ + $(BSN)_{I}$	1312, 1392
101	0.20	0.20	0.60	$(BSN)_{I}$ + $(BSN)_{III}$	1312, 1411
144	0.25	0.15	0.60	$(BSN)_{III}$	1315, 1411
102	0.30	0.10	0.60	$(BSN)_{III}$	1307, 1391
136	0.175	0.25	0.575	$(BSN)_{I}$ + $(BSN)_{III}$	1312, 1442
137	0.20	0.225	0.575	$(BSN)_{I}$ + $(BSN)_{III}$	1312, 1448
138	0.25	0.175	0.575	$(BSN)_{II}$ + $(BSN)_{III}$	1312, 1430
139	0.30	0.125	0.575	$(BSN)_{II}$ + $(BSN)_{III}$	1298, 1425
140	0.325	0.10	0.575	$(BSN)_{II}$ + $(BSN)_{III}$	1303, 1427
141	0.35	0.075	0.575	$(BSN)_{II}$ + $(BSN)_{III}$	1296, 1407
156	0.05	0.40	0.55	SN + $(BSN)_{III}$ + $(BSN)_{IV}$	1312, 1442
111	0.10	0.35	0.55	SN + $(BSN)_{I}$ + $(BSN)_{III}$	1308, 1439
132	0.15	0.30	0.55	$(BSN)_{I}$ + $(BSN)_{III}$	1321, 1456
133	0.20	0.25	0.55	$(BSN)_{I}$ + $(BSN)_{III}$	1312, 1456
134	0.25	0.20	0.55	$(BSN)_{II}$ + $(BSN)_{III}$	1312, 1456
135	0.30	0.15	0.55	$(BSN)_{II}$ + $(BSN)_{III}$	1312, 1456
103	0.35	0.10	0.55	$(BSN)_{II}$ + $(BSN)_{III}$	1294, 1447
142	0.375	0.075	0.55	$(BSN)_{II}$ + $(BSN)_{III}$	(1303), 1429
125	0.10	0.38	0.52	$(BSN)_{I}$	1460
126	0.15	0.33	0.52	$(BSN)_{I}$ + $(BSN)_{III}$	1300, 1463
127	0.20	0.28	0.52	$(BSN)_{I}$ + $(BSN)_{III}$	1312, 1481
128	0.25	0.23	0.52	$(BSN)_{I}$ + $(BSN)_{III}$	(1384), 1474
129	0.30	0.18	0.52	$(BSN)_{II}$	(1429), 1470
130	0.35	0.13	0.52	$(BSN)_{II}$	(1429), 1465
131	0.38	0.10	0.52	$(BSN)_{II}$	1472
143	0.40	0.08	0.52	$(BSN)_{II}$ + BN	1447
112	0.10	0.42	0.48	SN + $(BSN)_{I}$	1447, 1456
113	0.15	0.37	0.48	$(BSN)_{I}$	1420, 1468
114	0.20	0.32	0.48	$(BSN)_{I}$	1438, 1472
115	0.25	0.27	0.48	$(BSN)_{I}$	1429, 1465
116	0.30	0.22	0.48	$(BSN)_{I}$	1471
117	0.35	0.17	0.48	$(BSN)_{II}$	1420, 1465
118	0.40	0.12	0.48	$(BSN)_{II}$	1456
110	0.10	0.45	0.45	SN + S_2N + $(BSN)_{I}$	1461
119	0.15	0.40	0.45	SN + $(BSN)_{I}$	1442
120	0.20	0.35	0.45	SN + $(BSN)_{I}$	1438
121	0.25	0.30	0.45	SN + $(BSN)_{I}$	1429
122	0.30	0.25	0.45	SN + $(BSN)_{I}$	1420, 1452
123	0.35	0.20	0.45	SN + $(BSN)_{I}$	1414, 1456
124	0.40	0.15	0.45	BN + $(BSN)_{I}$	1361, 1434
104	0.45	0.10	0.45	BN + $(BSN)_{I}$	1335, 1384, 1429
109	0.10	0.50	0.40	$(BSN)_{I}$ + S_2N	1344, 1466
108	0.20	0.40	0.40	$(BSN)_{I}$ + S_2N	1420, 1510
155	0.25	0.35	0.40	$(BSN)_{I}$ + S_2N	1420, 1470
107	0.30	0.30	0.40	$(BSN)_{I}$ + S_2N	1413, 1420, 1438
106	0.40	0.20	0.40	$(BSN)_{I}$ + B_5N_2	1384, 1411
105	0.50	0.10	0.40	$(BSN)_{I}$ + B_5N_2	1384, 1406

Curie temperature measurements.—The results of the capacitance measurements are shown in Fig. 5 where (a) shows the behavior across the pseudo-binary join (48 and 50% Nb_2O_5, isopleths) and (b) shows the behavior along the 25% BaO isopleth. Also shown in Fig. 5(a) are the Curie temperatures for

Table III. X-ray diffraction data for ternary BSN tungsten-bronze type structures

(BSN)I [BSN-40] d(Å)	I	(BSN)II [BSN-80] d(Å)	I	(BSN)III [BSN-146] d(Å)	I	(BSN)IV [BSN-149] d(Å)	I
				8.80	2	8.80	2
				6.30	2	6.25	2
		5.60	2				
				4.40	1	4.40	1
		3.99	4	3.99	8	3.97	8
3.95	7	3.95	4	3.93	6	3.92	6
				3.87	1		
				3.79	1		
						3.70	2
						3.65	2
				3.62	2		
				3.53	2		
3.45	7	3.47	7	3.45	7	3.43	7
3.31	1	3.35	4	3.33	4	3.33	4
3.20	9	3.25	10	3.22	8	3.21	8
3.10	1	3.11	1	3.10	1	3.15	1
				3.08	1	3.10	1
3.00	9	3.02	10	3.00	10	3.00	10
		2.95	6	2.94	6	2.93	6
2.92	7	2.94	3	2.93	3	2.92	6
				2.91	2		
				2.90	1		
				2.85	1	2.85	1
						2.84	1
		2.80	8	2.78	8	2.78	8
2.78	10	2.79	5	2.77	5	2.77	5
						2.70	1
						2.67	1
2.59	4	2.60	4	2.62	2	2.60	4
				2.60	4		
				2.51	1		
2.43	2	2.45	2	2.44	2	2.43	3
				2.40	1		
				2.30	1	2.30	1
2.30	1	2.31	1	2.27	1	2.26	1
				2.25	1		
2.12	2	2.13	3	2.13	3	2.13	3
				2.12	3		
				2.06	1	2.06	1
1.955	5	1.982	6	1.98	6	1.975	6
		1.960	3	1.95	3	1.955	3
1.860	1	1.870	1	1.89	1		
1.840	3	1.850	3	1.842	3	1.840	3
				1.840	3		
1.820	3	1.835	3	1.822	2		
1.745	5	1.758	5	1.750	6	1.750	7
1.730	4	1.740	4	1.730	3	1.735	3
1.695	2	1.715	2	1.710	2	1.710	2
						1.700	1
1.662	2	1.675	2	1.670	2	1.670	3
1.635	4	1.655	4	1.645	5	1.645	5
				1.635	2	1.635	2
		1.610	3	1.601	3	1.601	1
1.597	5	1.600	5	1.599	5	1.599	3

Note: d-spacings of tetragonal bronzes in barium strontium niobate (orthorhombic splittings denoted by braces).

crystals grown from the melt compositions (shown on the abscissa) as reported by Glass (6). Ceramic specimen results are given in terms of solid composition.

The results of Fig. 5(a) will be discussed first. The relationship between the Curie temperature of crystals and ceramics has been used in the binary lithium niobate (10) and lithium tantalate (11) systems to locate the congruently melting composition and establish liquidus-solidus tie lines. It is not strictly possible to use this procedure in ternary systems because the ternary tie lines move on three dimensional surfaces. Nevertheless the technique can be useful in pseudobinary regions such as the SN-BN join. A comparison of the slopes of the solidus curves of Fig. 2 and 4 suggests that melt compositions on the binary join freeze along the binary join. In fact the low values of T_c measured in the 48.0% Nb_2O_5 isopleth support this conclusion. These two observations do not agree with the composition shifts reported by Ballman and Brown (3) on the basis of chemical analysis. The error in the ceramic T_c measurements is quite large in the region 20-50% BN because of the very broad dielectric peaks in this region. This agrees with the results of Glass (6) on crystals in this composition range. We estimate the uncertainty in T_c as ± 8°C at 50% BN. Thus the location of the congruently melting composition is 54 ± 4% BN in the 50% Nb_2O_5 isopleth.

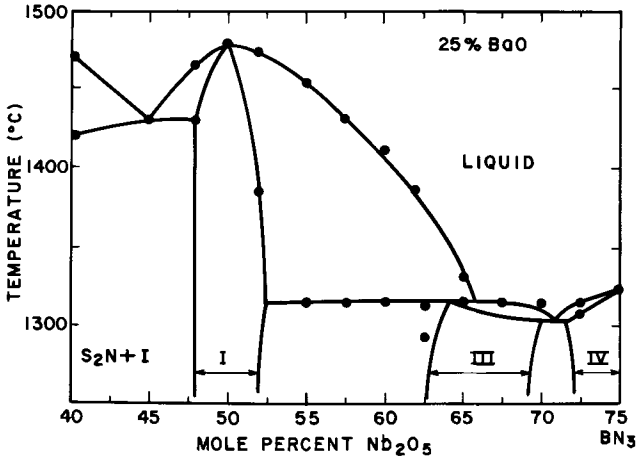

Fig. 4. High-temperature portion of 25% BaO isopleth shown as a function of Nb_2O_5 concentration.

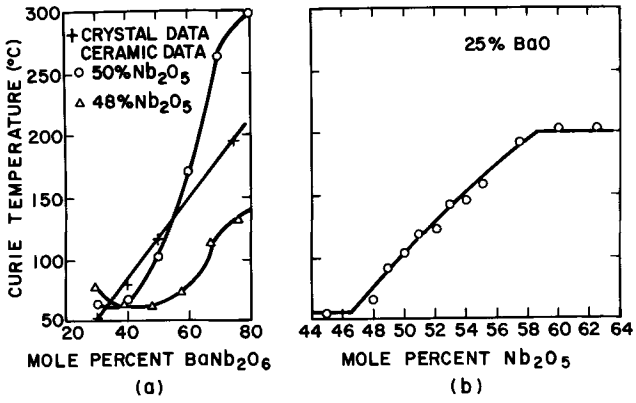

Fig. 5. Curie temperatures as a function of composition (a) along the binary join $SrNb_2O_6$-$BaNb_2O_6$ and (b) along the 25% BaO isopleth (ceramic specimens).

The variation of T_c with Nb_2O_5 concentration is shown for ceramic specimens in Fig. 5(b) along the 25% BaO isopleth. The composition range, 46-52% Nb_2O_5, represents the solid-solution range of $(BSN)_I$ traversed by this isopleth at room temperature. The composition range 52-60% Nb_2O_5 represents the two-phase region $(BSN)_I + (BSN)_{III}$, and the change in T_c corresponds to the change in composition of $(BSN)_I$ along this direction in the two-phase region. An internal check on the consistency of this data is provided by noting that the composition corresponding to the constant value of T_c = 200°C from Fig. 5(b) on the binary section [Fig. 5(a)] is 63% BN. If this point is joined by a straight line to pure Nb_2O_5 on Fig. 3, the line can be seen to pass through the coordinates (60% Nb_2O_5, 25% BaO) at the solid-solution boundary of $(BSN)_{III}$ as would be expected.

The dielectric properties of $(BSN)_{III}$ and $(BSN)_{IV}$ were not studied because the phase diagram indicates that these compounds melt incongruently and cannot be easily prepared as large single crystals. We did observe a capacitance peak at 287°C for specimen No. 150 (compound BN_3). However we observed no capacitance peak for $(BSN)_{III}$ specimens up to 400°C.

Some mention should be made of the early Curie temperature work of Francombe (1) where regions of constant T_c were observed in ceramic specimens across the binary join [phase $(BSN)_I$ and $(BSN)_{II}$]. Our observations in Fig. 5(a) show that T_c varies smoothly. However, very small variations in the (BaO + SrO)/Nb_2O_5 ratio cause large shifts in T_c, and it may be conceivable that Francombe's specimens possessed a variable ratio due to insufficient reaction and consequently scatter in the transition temperature. It is also possible that the disorder of Ba/Sr ions on the A1 and A2 sites may influence T_c in a fashion

similar to that reported by Burns and O'Kane (12) for barium sodium niobate. We observed no shift by fast air cooling from 1000°C. Since our specimens were all furnace cooled to 1000°C, it remained possible that the degree of cation ordering could be influenced by the cooling rate through the range 1300°-1000°C. Although Francombe did not report his preparation technique in detail, it is probable that his specimens were removed from the furnace at 1300°C and air cooled to room temperature in view of the short (1 hr) sintering times used. A check on several of our $(BSN)_I$ specimens with x near 0.5 showed that air cooling from the furnace at 1200°C did in fact decrease T_c by 20°-40°C. We were thus satisfied that the T_c measurements shown in Fig. 5 were made on specimens properly equilibrated with respect to both temperature and composition.

The crystal growth of ferroelectric compounds of controlled or uniform composition and properties requires a knowledge of the high-temperature phase equilibria for the particular system. Recent investigations have been undertaken for lithium niobate (13-15), barium sodium niobate (16-18), strontium potassium niobate (19), and potassium lithium niobate (20). These are all systems which exhibit a wide solid-solution range and a congruently melting composition which is substantially different from the "stoichiometric" composition. In practical crystal growth, we wish to operate as closely to a congruently melting composition as possible in order to avoid the problems associated with the redistribution of an excess component at the growing interface. However the desired properties, such as phase matching temperatures above room temperature, may be obtainable only at noncongruently melting compositions. Consequently, a system such as barium sodium niobate, where the congruently melting composition has desirable properties, is of more practical interest. In the present system, we can therefore eliminate compounds $(BSN)_{III}$ and $(BSN)_{IV}$ as being potential crystal growth candidates, since neither melts congruently at any point in the ternary solid-solution range. However the compound BSN [representing $(BSN)_I$ and $(BSN)_{II}$], which has been grown as large single crystals by Ballman and Brown (3), can be seen from Fig. 2 to melt congruently near 50% BN. Furthermore, the liquidus and solidus curves are very close together for this compound across the pseudobinary SN-BN section. This behavior is reminiscent of the SN-rich region of strontium potassium niobate (19) and the BN-rich region of barium sodium niobate (17, 18). Thus it is possible to prepare large crystals of reasonable optical perfection at compositions other than the congruent composition in this compound. This fact allowed Glass (5, 6) to use crystal compositions in the SN-rich region where there are large pyroelectric effects.

Summary

This investigation of the phase equilibria in the BaO-SrO-Nb_2O_5 system shows the existence of three tetragonal-tungsten-bronze type structures as well as the ternary phase fields. Only one of these structures is a ternary compound; it has the formula $Ba_xSr_{(1-x)}Nb_2O_6$ and has been estimated to melt congruently near $BaO:SrO:Nb_2O_5 = 0.27:0.23:0.50$. This phase possesses a large existence region along the binary $SrNb_2O_6$-$BaNb_2O_6$ join and some adjacent ternary solubility. This structure possesses observable orthorhombic distortion in the $BaNb_2O_6$-rich region.

Acknowledgments

We wish to thank A. A. Ballman and A. M. Glass for many discussions and for providing us with single crystals. We also thank R. A. Laudise for discussions and suggestions.

Manuscript submitted April 22, 1970; revised manuscript received *ca.* June 22, 1970. This was Recent News Paper 352 presented at the Los Angeles Meeting of the Society, May 10-15, 1970.

Any discussion of this paper will appear in a Discussion Section to be published in the June 1971 JOURNAL.

REFERENCES

1. M. H. Francombe, *Acta Cryst.*, **13**, 131 (1960).
2. I. G. Ismailzade, *Kristallografiya*, **5**, 268 (1960).
3. A. A. Ballman and H. Brown, *J. Cryst. Growth*, **1**, 311 (1966).
4. P. B. Jamieson, S. C. Abrahams, and J. L. Bernstein, *J. Chem. Phys.*, **48**, 5048 (1968).
5. A. M. Glass, *Appl. Phys. Letters*, **13**, 147 (1968).
6. A. M. Glass, *J. Appl. Phys.*, **40**, 4699 (1969).
7. P. V. Lenzo, E. G. Spencer, and A. A. Ballman, *Appl. Phys. Letters*, **11**, 23 (1967).
8. R. S. Roth and J. L. Waring, *J. Res. NBS*, **65A**, 337 (1961).
9. D. Ridgley and R. Ward, *J. Am. Chem. Soc.*, **77**, 6132 (1955).
10. J. R. Carruthers, G. E. Peterson, P. M. Bridenbaugh, and M. Grasso, To be submitted to *J. Appl. Phys.*
11. R. L. Barns and J. R. Carruthers, Submitted to *J. Appl. Cryst.*
12. G. Burns and D. F. O'Kane, *Phys. Letters*, **28a**, 776 (1969).
13. P. Lerner, C. Legras, and J. P. Dumas, *J. Cryst. Growth*, **3, 4**, 231 (1968).
14. G. E. Peterson and J. R. Carruthers, *J. Solid State Chem.*, **1**, 98 (1969).
15. J. R. Carruthers, G. E. Peterson, M. Grasso, and P. M. Bridenbaugh, Submitted to *J. Appl. Phys.*
16. B. A. Scott, E. A. Giess, and D. F. O'Kane, *Mat. Res. Bull.*, **4**, 107 (1969).
17. J. R. Carruthers and M. Grasso, *ibid.*, **4**, 413 (1969).
18. E. A. Giess, B. A. Scott, B. L. Olson, G. Burns, and D. F. O'Kane, *J. Am. Ceram. Soc.*, **53**, 14 (1970).
19. B. A. Scott, E. A. Giess, D. F. O'Kane, and G. Burns, *ibid.*, **53**, 106 (1970).
20. B. A. Scott, E. A. Giess, B. L. Olson, G. Burns, A. W. Smith, and D. F. O'Kane, *Mat. Res. Bull.*, **5**, 47 (1970).

Thermodynamics of the Iron-Nickel-Oxygen System at 1000°C

A. D. Dalvi** and W. W. Smeltzer*

Department of Metallurgy and Materials Science, McMaster University, Hamilton, Ontario, Canada

ABSTRACT

The isothermal section of the Fe-Ni-O system at 1000°C has been defined by determining the compositions and structures of the equilibrated solid phases. Wustite can coexist with Fe-Ni alloys containing up to 79.6 a/o (atomic per cent) Ni. The three-phase field wustite-spinel-alloy consists of wustite containing 0.51 a/o Ni, spinel containing 0.6 a/o Ni, and an alloy containing 79.6 a/o Ni. The three-phase field, spinel-nickel oxide-alloy, consists of nickel ferrite, nickel oxide containing 6.5 a/o Fe, and an alloy containing 99.5 a/o Ni. Tie lines in the spinel-alloy field were investigated in detail. Wustite-nickel oxide solid solutions exhibited nonideal behavior.

The properties of the Fe-Ni-O system at high temperatures where the iron-nickel alloys occur in the form of austenitic solid solution have not been intensively investigated. Brabers and Birchenall (1) determined the equilibrium compositions of wustite, spinel oxide, and alloys containing up to 60 w/o (weight per cent) Ni at 1050°C. The latest available results obtained for temperatures in the range 700°-1100°C are those reported by Viktorovich and Lisovskii (2) and Viktorovich *et al.* (3) for compositions within the wustite-alloy phase field including the limiting compositions of wustite and alloy coexisting with spinel. Values for the dissociation pressures of wustite containing nickel in solid solution have been reported for the temperature of 1000°C by Oriani (4) and Roeder and Smeltzer (5). Accordingly, the purpose of this work has been to obtain more complete knowledge of this ternary system at 1000°C by investigating the nickel-rich region of the phase diagram.

Experimental

Specimens were prepared by two methods. Mixtures of powders containing iron and nickel (99.99 w/o pure) in given proportions and one or more of the C.P. reagent grade oxides (99.6 w/o pure)—nickel oxide, hematite. and nickel ferrite—were compressed into tablets, 12.5 mm diameter and 2 mm thick, at a pressure of 6.5 tons/cm^2 by means of a hydraulic press. In the second method, alloy plates, 2 x 1 x 0.05 cm of various compositions ranging from 40 to 95% Ni were oxidized to desirable degrees in oxygen at 1000°C. The tablets and oxidized alloy specimens were sealed in quartz tubes containing argon [99.99 v/o (volume per cent) pure]. All encapsulated specimens were equilibrated at 1000° ± 2.5°C and then cooled to room temperature within 5 min by means of an air quench. Tablets were equilibrated for 30 days, while the oxidized alloy plates were equilibrated for periods up to 75 days. The phases in the quenched specimens were identified by x-ray techniques using a diffractometer equipped with a copper tube and nickel filter.

Specimens were mounted in epoxy cold setting resin, polished on silicon carbide papers 200 through 600 grit with kerosene as lubricant, then polished on a wax lap impregnated with 30μ alumina. This procedure resulted in best retention of oxide grains and in obtaining a flat surface. The final polishing was done on 6 and 1μ diamond wheels with napless cloths and kerosene as lubricant. It was necessary to etch the specimens for identification of phases by optical microscopy. A 5% concentrated hydrochloric acid solution in ethyl alcohol was used to preferentially etch wustite in structures containing wustite, spinel, and alloy. A 50% concentrated hydrochloric acid solution in water, which preferentially etched spinel, was used as etchant for structures containing nickel ferrite, nickel oxide, and alloy.

Chemical analyses were carried out by means of a CAMECA electron-probe microanalyzer operating at 15 kev with an x-ray beam take-off angle of 18°. This instrument was calibrated according to the method described by Friskney and Haworth (6, 7). Essentially the method consisted of successively applying atomic number (8), absorption (9, 10), and fluorescence (11, 12) corrections to an assumed set of compositions for a solid phase and calculating the intensity ratio for each metal to that for the pure metal. This procedure yielded iron and nickel calibration curves for each solid. In all cases, the fluorescence correction was significant. The atomic number correction was significant only for the oxides due to the presence of oxygen. Standards used to check the calibration curves for the alloys were alloys of several known compositions. The calibration procedure for the wustite phase could be verified only for pure wustite. For spinel oxide, the calibration procedure was verified for magnetite and nickel ferrite. The homogeneity of each phase in a specimen was determined by subjecting different areas to point counts. In addition, x-ray and electron back-scatter pictures were used for phase identification and to determine qualitatively the metal compositions in the coexisting phases.

Results

The photomicrographs in Fig. 1 and 2 illustrate typical oxide-alloy structures of equilibrated specimens. The structures obtained from both compacts and oxidized alloy plates exhibited an essential feature in that the different phases, which were bonded to one another, were sufficiently large for accurate analyses by the electron microprobe. At the acceleration voltage of 15 kev used for these analyses, the diameter of the x-ray production zone was only about 2μ and hence the minimum size of the particle for accurate analysis was about 5μ. The minimum size of particles analyzed in this investigation was 15μ. Identification of the phases present in a specimen by x-ray diffraction and microscopic observation showed complete agreement.

Information given by the electron probe micrographs was very useful. For example, the micrographs shown in Fig. 3 were obtained from a specimen consisting of spinel containing 1.4 w/o Ni and 71 w/o iron, and an alloy containing 84 w/o Ni. In the electron back-scatter image, the alloy was black and the spinel completely white. Also, the x-ray intensities clearly defined the amounts of iron and nickel in the different phases.

The compositions for the coexisting oxide and alloy phases are recorded in Table I. The mass concentra-

** Electrochemical Society Student Associate Member.
* Electrochemical Society Active Member.
Key words: thermodynamics, Fe-Ni-O system, Gibbs-Duhem relations, phase composition of wustite, nickel, ferrite, spinel, nickel oxide, iron-nickel alloys.

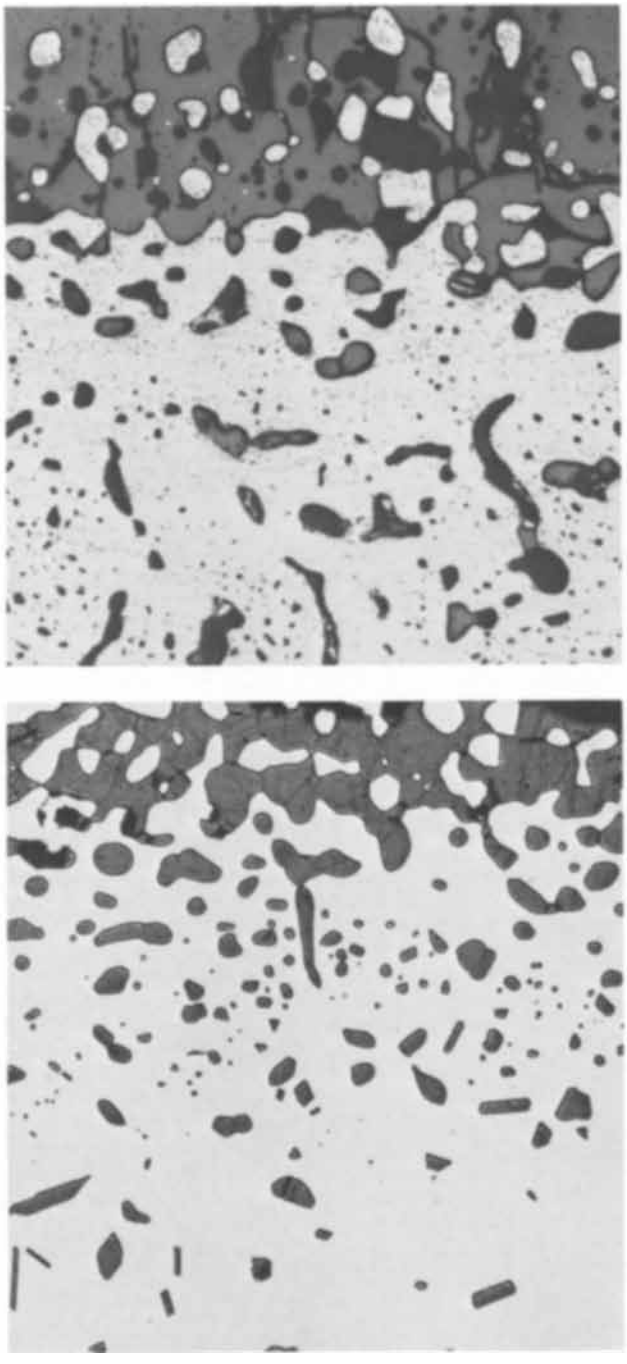

Fig. 1. Equilibrium two-phase fields wustite-alloy and the spinel-alloy. In both micrographs, the dark phases are the oxide phases and the bright phase is the alloy phase: (a) upper micrograph—wustite + alloy etched in 5% HCl in ethyl alcohol, 250X; (b) lower micrograph—spinel + alloy etched in 50% HCl in water, 320X.

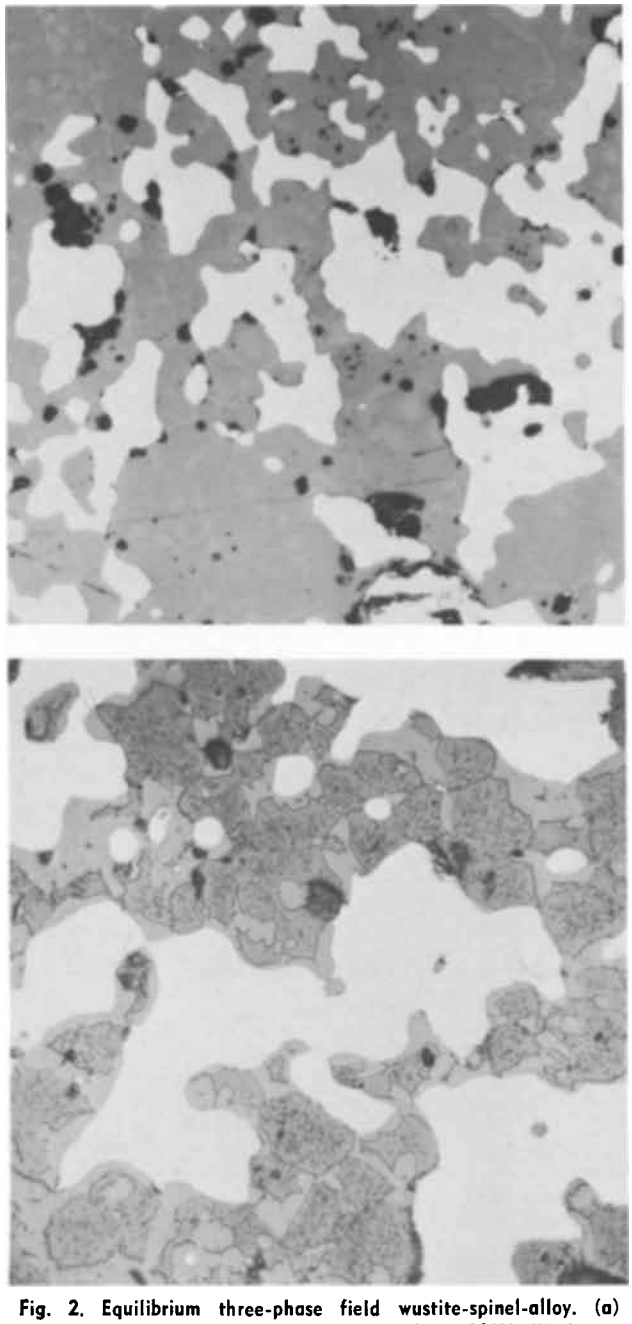

Fig. 2. Equilibrium three-phase field wustite-spinel-alloy. (a) Upper micrograph—microstructure before etching, 200X. (b) Lower micrograph—specimen surface after etching in 5% HCl in ethyl alcohol, 400X; bright phase—alloy, dark matrix phase—wustite, gray precipitates—spinel.

tions obtained experimentally were converted to atomic concentrations which are also given in Table I. Wustite coexisted with alloys containing up to 79.6 a/o Ni, the maximum nickel solubility in wustite being 0.51 a/o. It was found that spinel coexisted with alloys containing from 79.6 to 99.5 a/o Ni. The spinel in equilibrium with wustite and alloy contained 0.6 a/o Ni, while the compositions of the spinel in equilibrium with nickel oxide and alloy corresponded to stoichiometric nickel ferrite. The maximum iron solubility in nickel oxide was 6.5 a/o.

Discussion

The isothermal section of the phase diagram at 1000°C constructed from the compositional determinations is illustrated in Fig. 4. The oxygen solubilities in the alloys have been magnified for clarity and are in fact negligibly small and unknown. The diagram is symmetric about the spinel-alloy field which is bounded by three-phase fields containing wustite-spinel-alloy and nickel oxide-spinel-alloy. These fields are bounded in turn by two-phase fields containing wustite and alloy on the iron-rich side and nickel oxide and alloy on the nickel-rich side of the diagram. Wustite, which exhibits only a small nickel solubility, is stable over a wide range of alloy composition; on the other hand, nickel oxide exhibits a relatively large iron solubility but its stability is confined to a very narrow range of alloy composition. The tie lines in the wustite-alloy and spinel-alloy fields are not proportionately spaced. They fan out from oxide in the iron-rich region and from the alloy in the nickel-rich region of the diagram.

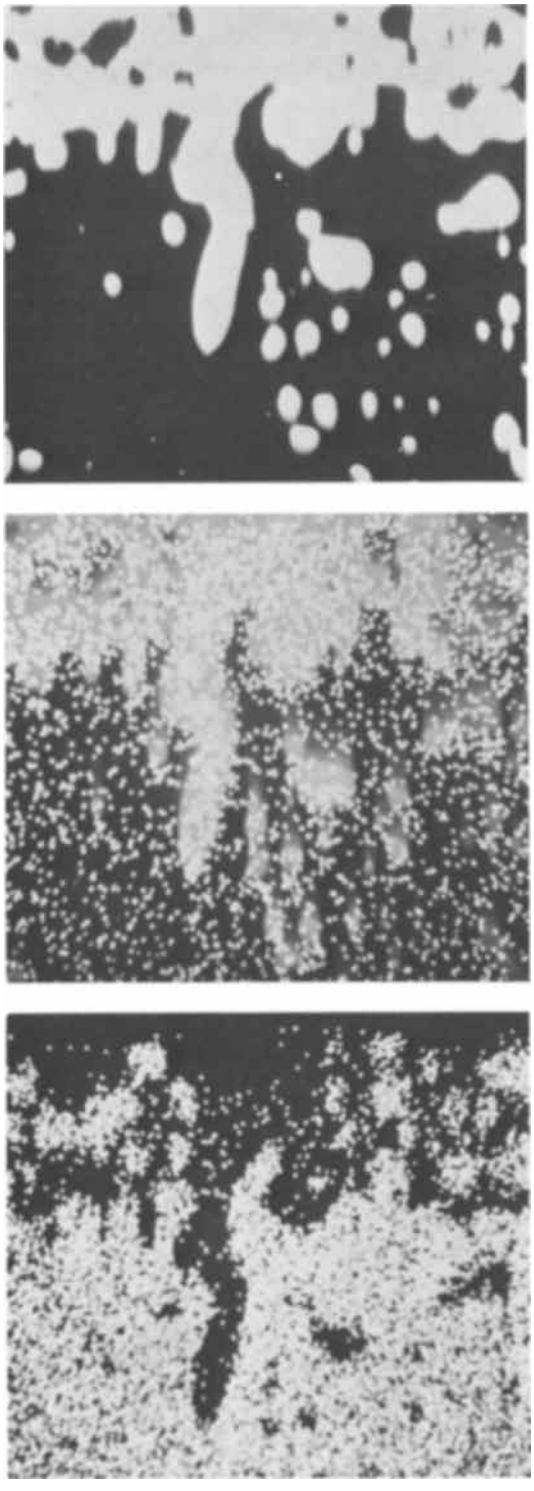

Fig. 3. Electron probe images of sample in the two-phase field spinel + alloy, 1000X. (a) Upper micrograph—electron backscatter image. The spinel phase appears as bright and the alloy phase appears as dark. (b) Middle micrograph—Fe-K_α x-ray image showing distribution of iron in the two phases. (c) Lower micrograph—Ni-K_α x-ray image showing nickel distribution.

A terminal nickel solubility of 0.51 a/o in wustite agrees with a reported value (2) and it lies between two determinations where the nickel contents were reported virtually absent (1) and 1.3 a/o (5). The iron concentration as well as the total metal concentration in wustite decreased with increasing nickel content of the alloy. At the terminal composition, the total amount of metal was 46.7 a/o. Since this value is equal to the iron concentration in wustite upon its equilibration with magnetite, it would appear that there is an isomorphous substitution of nickel for iron in the wustite lattice. The nickel composition of 0.6 a/o for spinel S_1, shows wide divergence from an earlier determination of 5 a/o (1). Magnetite exhibits an inverse spinel structure with ferrous ions occupying octahedral sites and ferric ions occupying both octahedral and tetrahedral sites between oxygen ions (13). Apparently, nickel replaces iron in the divalent sites in the spinel up to the terminal composition corresponding to nickel ferrite (14, 15).

The values reported for the dissociation pressures and nickel contents of wustite are sufficient for thermodynamic evaluation of the solution behavior of nickel in wustite. Values reported for the dissociation pressures of wustite containing nickel in solid solution are compared to that for pure wustite in Fig. 5. The Gibbs-Duhem relationship may be applied to the alloy and oxide phases because these pressures determine oxygen activities

$$N_O{}^A \, d\ln a_O{}^A + N_{Ni}{}^A \, d\ln a_{Ni}{}^A + N_{Fe}{}^A \, d\ln a_{Fe}{}^A = 0 \quad [1]$$

$$N_O{}^W \, d\ln a_O{}^W + N_{Ni}{}^W \, d\ln a_{Ni}{}^W + N_{Fe}{}^W \, d\ln a_{Fe}{}^W = 0 \quad [2]$$

where N is a mole fraction and a is an activity in the alloy (A) and wustite (W) phases. At equilibrium, Eq. [1] and [2] yield the variation of oxygen activity with respect to nickel activity, for

$$\frac{d\ln a_O}{d\ln a_{Ni}} = -\frac{N_{Ni}{}^A - N_{Ni}{}^W N_{Fe}{}^A/N_{Fe}{}^W}{N_O{}^A - N_O{}^W N_{Fe}{}^A/N_{Fe}{}^W} \quad [3]$$

Since the oxygen solubility in the metal is extremely small, 0.0003-0.015 w/o (16, 17), we may neglect the term $N_O{}^A$ in integrating Eq. [3]. Therefore

$$\ln P_{O_2}/P^o{}_{O_2} = 2\int_0^{N_{Ni}{}^A} \left\{ \frac{N_{Ni}{}^A - N_{Ni}{}^W N_{Fe}{}^A/N_{Fe}{}^W}{N_O{}^W N_{Fe}{}^A/N_{Fe}{}^W} \right\} d\ln (\gamma_{Ni}{}^A N_{Ni}{}^A) \quad [4]$$

where $P^o{}_{O_2}$ is the dissociation pressure of pure wustite. This equation was integrated numerically by means of a computer since values are available for the mole fractions of iron, nickel, and oxygen in wustite as well as the activity coefficients of nickel in the alloy (2, 4, 18, 19).

Equation [3] may be simply integrated to the following expression if it is additionally assumed that the small concentration of nickel in wustite approximates to zero and that the mole fractions of iron and oxygen are equal as for stoichiometric wustite

$$\log P_{O_2}/P^o{}_{O_2} = 2 \log (1/1 - N_{Ni}{}^A) \quad [5]$$

This expression is also obtained by comparing the dissociation pressures of pure wustite with that of wustite equilibrated with the alloy

$$FeO^W \leftrightarrows Fe^A + \tfrac{1}{2} O_2 \quad [6]$$

under the approximations of unit activity for wustite and ideal solution behavior of iron in the alloy.

Comparison of the values for the dissociation pressures calculated by means of Eq. [4] and [5] to those determined experimentally are shown in Fig. 5. Although there are large uncertainties in the evaluations of the alloy compositions in the case where dissociation pressures were determined for wustite-alloy compacts (5), both equations serve as a first approximation to the experimental results. The better fit, however, is obtained by Eq. [4] where account has been given to the degree of nickel solubility in wustite and to the activity coefficients for the alloy components. Equation [4] gives the invariant oxygen partial pressures in the wustite-spinel-alloy phase field as 3.26×10^{-14} atm, a value considerably larger than the dissociation pressure of pure wustite, $P^o{}_{O_2} = 1.32 \times 10^{-15}$ atm. Since

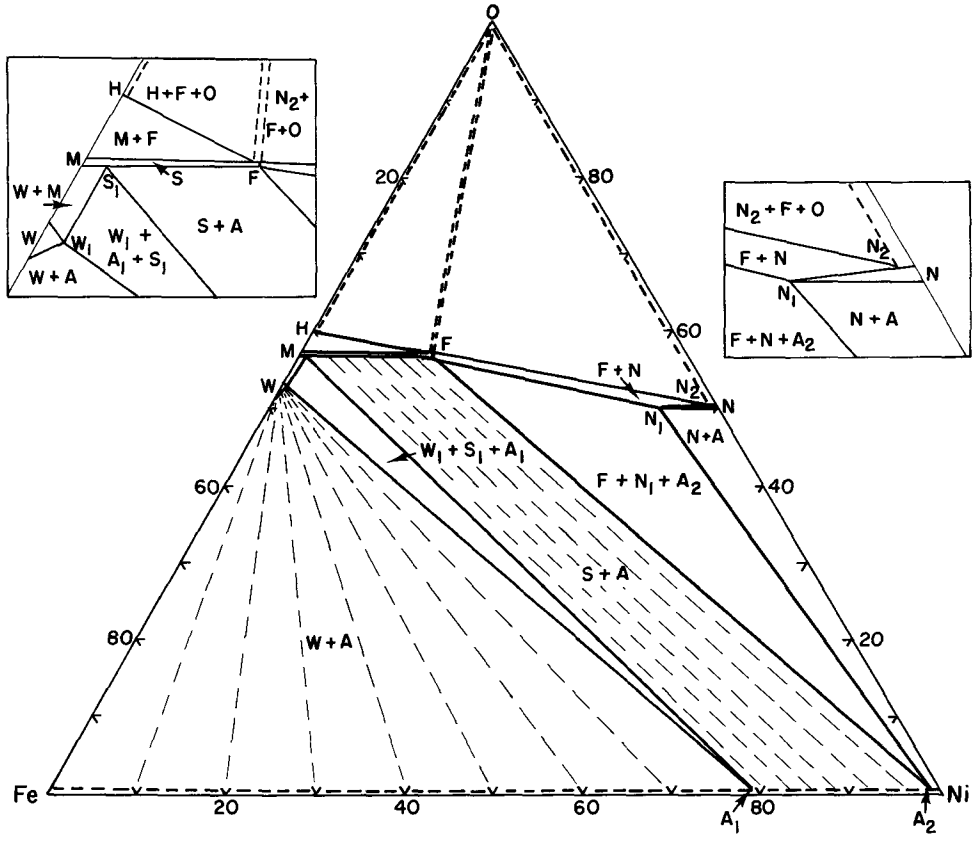

Fig. 4. Iron-nickel-oxygen phase diagram at 1000°C (a/o). W_1—$Ni_{0.01}Fe_{0.87}O$ (wustite); S_1-$Ni_{0.04}Fe_{2.96}O_4$ (spinel). A_1—79.6 a/o Ni, 20.4 a/o Fe (alloy). F—$NiFe_2O_4$ (ferrite); N_1-$Fe_{0.13}$-$Ni_{0.87}O$ (nickel oxide). A_2—99.5 a/o Ni, 0.5 a/o Fe (alloy). N_2—$Fe_xNi_{1-x}O$ where $x \simeq 0.0005$ (nickel oxide). Phase notations: W—*wustite*, $Ni_xFe_{1-(x+y)}O$; M—magnetite, Fe_3O_4. H—*hematite*, Fe_2O_3; N—*nickel oxide*, $Fe_xNi_{1-x}O$. The dashed line across the bottom of the diagram represents oxygen solubilites in the alloy magnified for clarity. Dashed lines in the vicinity of the oxygen corner represent undetermined boundaries of phase fields involving oxygen. The insets on either side represent corresponding phase regions on an expanded scale.

the dissociation pressure of wustite containing the maximum nickel content is less than that for wustite-magnetite equilibrium, 1.62 x 10^{-13} atm, it can be inferred, as was found, that the limiting nickel content of wustite, 0.51 a/o, should be less than the corresponding value for spinel, 0.60 a/o.

A useful approximation to the wustite solid solution may be made by assuming that nickel dissolves in wustite as nickel oxide. The following displacement reaction may then be considered

$$Fe^A + NiO^W \rightleftarrows Ni^A + FeO^W \qquad [7]$$

where

$$K = \frac{a_{Ni}^{(A)} \cdot a_{FeO}^{(W)}}{a_{Fe}^{(A)} \cdot a_{NiO}^{(W)}} = \frac{(\gamma_{Ni} \cdot N_{Ni})_A \cdot (\gamma_{FeO} \cdot N_{FeO})_W}{(\gamma_{Fe} \cdot N_{Fe})_A \cdot (\gamma_{NiO} \cdot N_{NiO})_W} \qquad [8]$$

The value of K is determined to be 186 at 1000°C from electromotive force measurements of Kiukkola and Wagner (20). Since the values of the activity coefficients for the alloy components are known, the nickel oxide content of wustite was calculated for the case of oxide ideal solid solution behavior as a function of nickel content of the alloy phase. This relationship and the experimental relationship are shown in Fig. 6. The curve through the experimental points was determined by a least-squares analysis using a computer. Division of the corresponding values obtained by these two relationships yields the activity coefficient ratio, $\gamma_{NiO}/\gamma_{FeO}$, as a function of equilibrium alloy composition. The curve representing this activity coefficient ratio is also shown in Fig. 6. It can be seen that the ratio of the activity coefficient remains constant at 3.72 for the alloy composition range of 0-40 a/o Ni and then decreases to a value of 2.33 at the limiting alloy compositon for stability of wustite. Consequently, nickel oxide solubility in wustite displays a Henry law be-

Table I. Electron microprobe analysis of coexisting alloy and oxide phases at 1000°C

Sample No.	Composition of alloy						Oxide phase identification	Composition of oxide phases					
	w/o Ni	U†	w/o Fe	U†	a/o Ni	a/o Fe		w/o Ni	U†	w/o Fe	U†	a/o Ni	a/o Fe
1	60.0	0.5	40.0	0.4	48.8	41.2	W	0.13	0.05	76.0	0.4	0.1	47.7
2	62.9	0.5	37.1	0.4	61.8	38.2	W	0.13	0.05	75.9	0.4	0.1	47.6
3*	81.0	0.5	19.6	0.4	79.7	20.3	W	0.84	0.05	75.4	0.4	0.50	53.3
							S	0.91	0.05	71.5	0.4	0.51	42.2
4*	80.5	0.5	20.1	0.4	79.1	20.9	W	0.85	0.05	75.4	0.4	0.51	53.3
							S	1.08	0.05	71.4	0.4	0.51	42.1
5*	81.1	0.5	19.3	0.4	80.0	20.0	W	0.85	0.05	75.4	0.4	0.51	53.3
							S	1.10	0.05	71.4	0.4	0.62	42.1
6	84.0	0.5	16.0	0.4	83.3	16.7	S	1.4	0.1	71.0	0.4	0.79	42.1
7	86.3	0.5	14.0	0.4	85.3	14.6	S	1.7	0.1	70.5	0.4	0.96	41.7
8	88.0	0.5	12.1	0.4	87.4	12.6	S	2.3	0.2	70.1	0.4	1.29	41.4
9	88.5	0.5	12.2	0.4	87.6	12.4	S	2.7	0.2	69.8	0.4	1.51	41.2
10	93.8	0.6	6.0	0.4	93.6	6.4	S	5.9	0.3	66.5	0.4	3.32	39.3
11	96.0	0.6	4.5	0.4	95.4	4.8	S	9.0	0.3	63.5	0.4	5.07	37.6
12	97.5	0.6	3.7	0.3	96.2	3.8	S	11.7	0.3	60.8	0.4	6.60	36.1
13	98.7	0.6	1.5	0.2	98.4	1.6	S	16.8	0.5	55.6	0.4	9.53	33.1
14	98.9	0.6	1.2	0.2	98.8	1.2	S	20.0	0.5	52.4	0.4	11.37	31.3
15**	99.5	+0.3 −0.7	0.5	0.1	99.5	0.5	S	25.0	0.5	47.4	0.5	14.26	28.4
							N	68.7	0.5	9.8	0.3	43.5	6.5

* Three-phase field wustite-spinel-alloy.
** Three-phase field *nickel ferrite-nickel oxide-alloy*.
† U corresponds to the uncertainty in the experimental determinations. Phase symbols correspond to: W—wustite; S—spinel; N—nickel oxide.

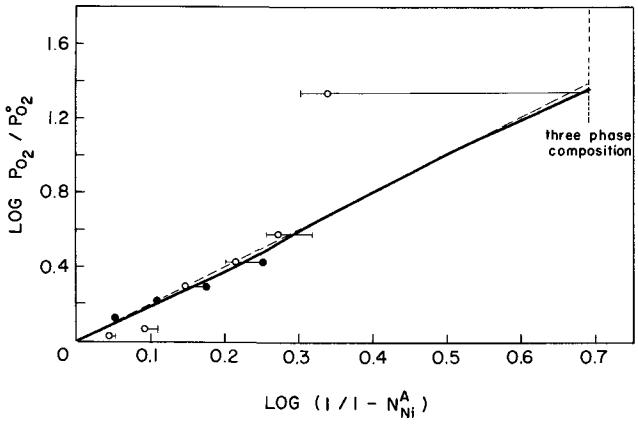

Fig. 5. Equilibrium oxygen partial pressure in the two-phase field wustite-alloy as a function of alloy composition. The solid and dashed curves were calculated according to Eq. [4] and [5], respectively. The data were obtained from Ref. (4) (●) and Ref. (5) (○).

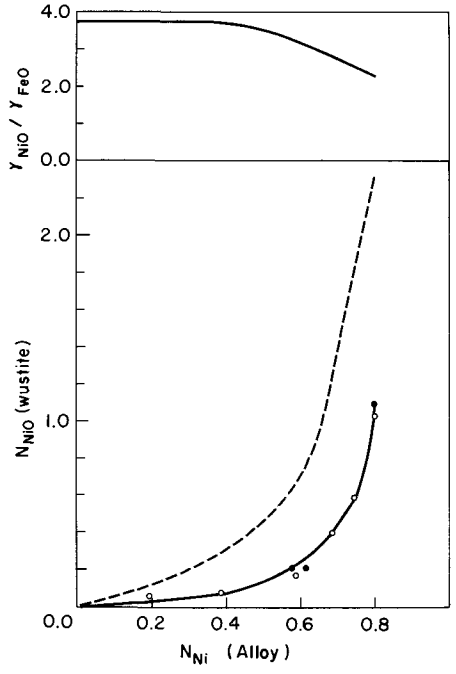

Fig. 6. Solubility of nickel oxide in wustite as a function of equilibrium alloy composition. The dashed curve was obtained with the assumption of ideality for the wustite-nickel oxide system. The data for the experimental curve were obtained from this investigation (●), and from Ref. (2) (○). The activity coefficient ratio $\gamma_{NiO}/\gamma_{FeO}$ for the wustite phase as a function of equilibrium alloy composition was obtained from the above two curves on dividing calculated values obtained on the assumption of ideality by the corresponding experimental values, Eq. [8].

havior only to a mole fraction of 0.008. A similar calculation using Eq. [8] yields $\gamma_{FeO}/\gamma_{NiO} = 4.88$ at the limiting tie line of the nickel oxide-alloy region where the alloy composition is 99.5 a/o Ni, the activity coefficients of nickel and iron in the alloy are 1.0 and 0.78, respectively, and the mole fraction of wustite in nickel oxide is 0.13. Consequently, wustite-nickel oxide solid solutions exhibit positive deviation from ideal behavior at oxygen partial pressures for equilibration with Fe-Ni alloys.

The iron contents of the nickel oxide, N_2, and the alloy, A_2, occurring in the spinel-nickel oxide-oxygen and in the spinel-nickel oxide-alloy regions, respectively, may be evaluated from appropriate standard free energies of formation. The following reactions may be considered

$$NiFe_2O_4 = Ni + 2Fe + 2\,O_2 \quad [9]$$

$$FeO = Fe + \tfrac{1}{2}\,O_2 \quad [10]$$

$$NiO = Ni + \tfrac{1}{2}\,O_2 \quad [11]$$

Since the standard free energies for these reactions at 1000°C are 152, 43, and 30 kcal, respectively (21, 22), we obtain for the equilibrium constants in terms of standard oxygen activities for the pure metals and oxides

$$K_9 = (a_O^{\circ})_9^4 = a_{Ni}\,a_{Fe}\,a_O^4 = 7.65 \times 10^{-27} \quad [12]$$

$$K_{10} = (a_O^{\circ})_{10} = a_{Fe}\,a_O/a_{FeO} = 4.14 \times 10^{-8} \quad [13]$$

$$K_{11} = (a_O^{\circ})_{11} = a_{Ni}\,a_O/a_{NiO} = 7.06 \times 10^{-6} \quad [14]$$

In the three-phase region spinel-oxygen-nickel oxide, $a_O \simeq 1$ and $a_{NiO} \simeq 1$. Therefore, $a_{FeO} \cong 10^{-3}$. Accordingly, the iron content in nickel oxide, N_2, corresponds to approximately 0.05 a/o. In the three-phase region spinel-nickel oxide-alloy, $N_{NiO} \simeq 0.9$ and $a_{Ni} \simeq 1$. Therefore, $a_{FeO} = 0.38$ and $a_O = 6.35 \times 10^{-6}$. Accordingly, the mole fraction of iron in the alloy, A_2, $N_{Fe} = a_{Fe}/\gamma_{Fe} = 0.0047/0.78 \simeq 0.006$. That is, the nickel-iron alloy existing in equilibrium with spinel and nickel oxide contains approximately 0.6 a/o iron. This calculated value is to be compared to the experimentally determined value of 0.5 a/o.

Conclusions

The phase boundaries of the two-phase fields wustite-alloy, spinel-alloy, and nickel oxide-alloy, and the three-phase fields wustite-spinel-alloy and spinel-nickel oxide-alloy were determined at 1000°C. Chemical analyses indicated that nickel solubility in wustite was governed by isomorphic replacement of iron by nickel. It was inferred that, in the spinel phase extending from magnetite to stoichiometric nickel-ferrite, ferrous ions in the octahedral interstitial sites were replaced by divalent nickel ions. The spinel phase in equilibrium with alloys extends from $Ni_{0.04}Fe_{2.96}O_4$ to $NiFe_2O_4$. The wustite-spinel-alloy field consists of wustite containing 0.51 a/o Ni, spinel containing 0.60 a/o Ni, and an Fe-Ni alloy containing 79.6 a/o Ni. The spinel-nickel oxide-alloy field consists of nickel ferrite, nickel oxide containing 6.5 a/o Fe, and an alloy containing 0.5 a/o Fe. The iron content of nickel oxide in equilibrium with spinel and oxygen was calculated to be approximately 0.05 a/o. By means of the Gibbs-Duhem relationship, the dissociation pressures of wustite were related to the compositions of the alloy. Solution of nickel oxide in wustite was shown to exhibit positive deviations from ideal solid solution behavior.

Acknowledgments

This work was carried out by A. D. Dalvi in partial fulfillment of the requirements for award of the Ph.D. degree at McMaster University. He wishes to acknowledge the award of an International Nickel Company of Canada Fellowship for graduate research. The authors are indebted to Professor Carl Wagner for discussion relating to this problem. This research was carried out under auspices of the Defence Research Board and the National Research Council of Canada.

Manuscript submitted Dec. 12, 1969; revised manuscript received June 26, 1970. This was Paper 206 presented at the Detroit Meeting of the Society, Oct. 5-9, 1969.

Any discussion of this paper will appear in a Discussion Section to be published in the June 1971 JOURNAL.

REFERENCES

1. M. J. Brabers and C. E. Birchenall, *Corrosion*, **14**, 179 (1958).
2. G. S. Viktorovich and D. I. Lisovskii, *Tsvetnye Metally. (Eng. Transl.)*, **7** (11), 49 (1966).
3. G. S. Viktorovich, V. A. Gutin, and D. I. Lisovskii, *ibid.*, **7** (12), 54 (1966).

4. R. A. Oriani, *Acta Met.*, **1**, 448 (1953).
5. G. A. Roeder and W. W. Smeltzer, *This Journal*, **111**, 1074 (1964).
6. C. A. Friskney and C. W. Haworth, *Brit. J. Appl. Phys. Ser. 2*, **1**, 873 (1968).
7. C. A. Friskney and C. W. Haworth, *J. Sci. Instr., Ser. 2*, **1**, 753 (1968).
8. P. Duncumb and S. J. B. Reed, Nat. Bur. Std. (U.S.) Spec. pub. No. 298 (1968).
9. J. Philibert, X-Ray Optics and X-Ray Microanalysis, Proc. Third Int. Symp., Stanford (1962).
10. P. Duncumb and P. K. Shields, "The Electron Microprobe," p. 284, T. D. McKinley, K. F. J. Heinrich, and D. B. Wittry, Editors, John Wiley (1966).
11. R. Castaing, Thesis, University of Paris (1951).
12. M. Green and V. E. Cosslett, *Proc. Phys. Soc. (London)*, **78**, 1206 (1961).
13. K. Hauffe, "Oxidation of Metals," p. 23, Plenum Press (1965).
14. S. I. Youssef, M. G. Natera, R. J. Begum, B. J. Srinivasan, N. S. Murthy, *J. Phys. Chem. Solids*, **30**, 1948 (1969).
15. A. E. Paladino, Jr., *J. Am. Ceram. Soc.*, **42**, 168 (1959).
16. M. Hansen, "Constitution of Binary Alloys," p. 1024, Mc-Graw Hill (1958).
17. J. Swisher and E. T. Turkdogan, *Trans. Met. Soc. AIME*, **239**, 626 (1967).
18. R. Hultgren, R. L. Orr, P. D. Anderson, and K. K. Kelley, "Selected Values of Thermodynamic Properties of Metals and Alloys," John Wiley (1963).
19. O. Kubaschewki and O. Von Goldbeck, *Trans. Faraday Soc.*, **45**, 959 (1949).
20. K. Kiukkola and C. Wagner, *This Journal*, **104**, 379 (1957).
21. G. G. Charette and S. J. Flengas, *ibid.*, **115**, 796 (1968).
22. J. D. Tretjakow and H. Schmalzried, *Berichte der Bunsengesellschaft*, **69**, 396 (1965).

Technical Notes

Surface Polarity and Etching of Beta-Silicon Carbide

Robert W. Bartlett* and Malcom Barlow

Stanford Research Institute, Menlo Park, California 94025

Beta-silicon carbide has the zinc blende structure and solution-grown crystals are in the form of octahedral platelets (1). Although the silicon and carbon layers alternate in the stacking sequence, the interatomic spacing in the octahedral direction, [111], is not uniform. The terminating plane for the (111) surface is ideally composed of silicon atoms, while the terminating plane for the $(\bar{1}\bar{1}\bar{1})$ surface is composed of carbon atoms.

If use is made of the anomalous phase shift, differences in x-ray diffraction intensity are detectable and the two opposite sides of noncentrosymmetric crystals can be identified (2). This method has been used by Warekois and co-workers (3, 4) to identify faces of several III-V and II-VI compounds, and Brack (5) has used it to determine polarity in α-silicon carbide.

Polarity Determination

X-ray diffraction intensities from octahedral platelets of β-silicon carbide were measured on a Norelco diffractometer, using filtered CuK_α radiation. The standard sample holder was replaced by a single-crystal goniometer to facilitate orientation and mounting of the crystals, and the x-ray beam was collimated to about 1 mm diameter. Intensities of the scattered beams were determined by a Geiger counter with chart recorder, each reflection being scanned slowly through the Bragg angle. Filters limited the intensities to the linear counting rate region of the counter.

The diffracted intensities are proportional to $|\mathbf{F}(hkl)|^2$. The theoretical ratios of $|\mathbf{F}(hkl)|^2/|\mathbf{F}(\bar{h}\bar{k}\bar{l})|^2$, calculated from the anomalous dispersion correction, are

$$\frac{|\mathbf{F}(111)|^2}{|\mathbf{F}(\bar{1}\bar{1}\bar{1})|^2} = 0.94, \quad \frac{|\mathbf{F}(222)|^2}{|\mathbf{F}(\bar{2}\bar{2}\bar{2})|^2} = 1.00, \quad \frac{|\mathbf{F}(333)|^2}{|\mathbf{F}(\bar{3}\bar{3}\bar{3})|^2} = 1.06$$

Three crystals were examined repeatedly, and the experimental ratios of intensities for the $(111)/(\bar{1}\bar{1}\bar{1})$ reflections were always smaller than 1, while the experimental ratios of intensities for the $(333)/(\bar{3}\bar{3}\bar{3})$ reflections were always larger than 1.

Etching

Etching studies were made on β-silicon carbide platelets grown from solution and on vapor-deposited β-silicon carbide grown epitaxially on platelets (6). Two etchants were used: (*a*) a gas mixture containing 6% chlorine and 26% oxygen in argon at 850° to 900°C and (*b*) a fused salt mixture of 75% NaOH and 25% Na_2O_2 at 700°C. The polarity of the crystals was determined from the ratio of x-ray diffraction intensities. Although the rate of attack was different, the same surface characteristics were observed with both etchants. Etch pits developed on the (111) face but did not develop on the $(\bar{1}\bar{1}\bar{1})$ face. Except for the etch pits, the (111) face remains smooth. These results correspond with the etching of α-silicon carbide in similar etchants (7, 8) where etch pits are observed to form on the smooth face, which was identified by Brack (5) as the (0001) face terminating in silicon atoms, although pits do not usually form on the rough $(000\bar{1})$ face. Similar results have been observed for other zinc blende and wurtzite structures among III-V and II-VI compounds (3, 4).

The depth of etch pits is much less than the thickness of silicon carbide uniformly removed during etching. Uniform etch rates for the chlorine-oxygen gas etchant were obtained by measuring step heights between etched regions and the regions protected by a thermally grown oxide film. On solution-grown crystals the etch rate at 900°C was 0.3 to 0.5 μM/min. Although the etch-pitting characteristics of β-silicon carbide grown epitaxially by vapor deposition were essentially the same as those of the solution-grown platelets, there were marked differences in the uniform etching rates under identical etching conditions. The chlorine-oxygen gas-etching rate of undoped epitaxially grown

* Electrochemical Society Active Member.

Key words: silicon carbide, etching, surfaces, noncentrosymmetric crystals, semiconductors.

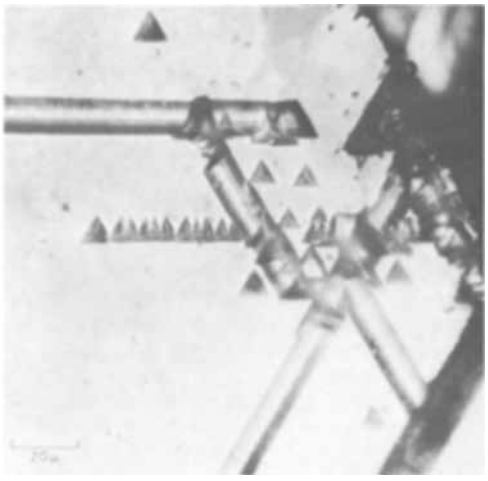

Fig. 1. Solution-grown β-SiC (111) surface etched in $NaOH-Na_2O_2$.

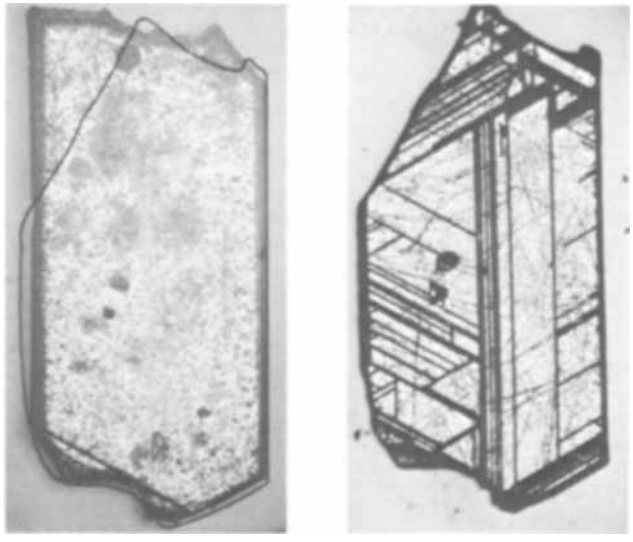

Fig. 2. Etch pit rows extending from the substrate through the epitaxial layer: (left) Etched boron-doped epitaxial layer; (right) after removal of epitaxial layer and re-etching.

crystals was less than 0.02 μM/min at 900°C. The mechanism leading to this difference in rates is not known but may be related to differences in the concentrations of specific impurities present in amounts below the detection limits of neutron activation analysis or emission spectrography.

The etch pits on solution-grown platelets have a marked tendency to cluster in rows as shown in Fig. 1. The pits are frequently sufficiently large and closely spaced to form a groove often running the entire length of the crystal. The axis of these etch pit rows is always a <110> direction. X-ray topographic studies (9) show that the etch pits correspond to surface-terminating partical dislocations with a <112> Burgers' vector that are associated with closely spaced parallel {111} stacking faults.

These dislocations continue in the vapor-deposited silicon carbide grown epitaxially on solution-grown substrates. Etch pits on the surface of the epitaxially grown layer are observed in exactly the same locations as the underlying substrate. This indicates that the stacking faults are also extending from the substrate through the epitaxy layer. This effect is demonstrated by the two micrographs of the same crystal shown in Fig. 2. Correspondence between the etch pit patterns in these micrographs is readily apparent. Both surfaces shown were given identical $NaOH-Na_2O_2$ etching treatments. The lefthand micrograph was taken after lapping off the epitaxial layer with 1μ diamond paste and re-etching the surface. Note that a small section of the crystal was broken during lapping. The epitaxial layer was more resistant to the $NaOH-Na_2O_2$ etchant than was the substrate, which is consistent with the results observed with the chlorine-oxygen gas etchant.

Etch pits that were not extensions from the substrate were also observed on (111) surfaces of epitaxially grown β-silicon carbide. These pits occur in short <110> oriented rows often grouped to form one or more sides of an equilateral triangle, as shown in Fig. 3. These rows are usually no longer than 25μ. The chlorine-oxygen gas etching also causes a few large craters to form in the (111) epitaxial surface, also shown in Fig. 3. Although these craters are oriented in conformance with the octahedral morphology of the smaller etch pits, they are not observed on similarly etched solution-grown substrates. On the $(\bar{1}\bar{1}\bar{1})$ face of epitaxially grown β-silicon carbide the chlorine-oxygen gas etch rounds off twinning hillocks that were formed during vapor deposition. The nodules that result are faintly visible on the back face of the transparent crystal shown in Fig. 3.

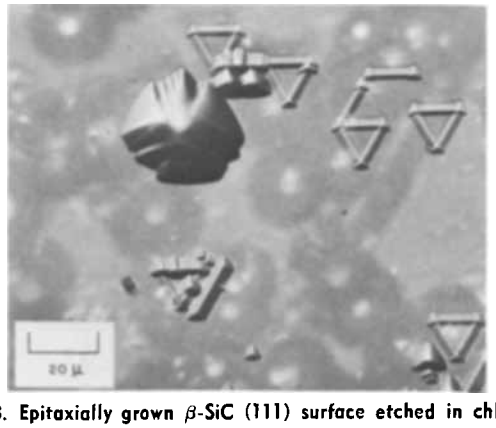

Fig. 3. Epitaxially grown β-SiC (111) surface etched in chlorine-oxygen gas mixture.

Acknowledgments

The authors wish to express their appreciation to Charlotte Meredith and David Dionne for experimental assistance. This work was sponsored by the Air Force Cambridge Research Laboratories, Office of Aeronautical Research, under Contract F19628-67-C0243.

Manuscript submitted Oct. 3, 1969; revised manuscript received *ca.* July 10, 1970.

Any discussion of this paper will appear in a Discussion Section to be published in the June 1971 JOURNAL.

REFERENCES

1. W. E. Nelson, F. A. Halden, and A. Rosengreen, *J. Appl. Phys.*, **37**, 333 (1966).
2. R. W. James, "Optical Principles of the Diffraction of X-Rays," Chap. IV., G. Bell & Sons Ltd., London (1958).
3. E. P. Warekois and P. H. Metzger, *J. Appl. Phys.*, **30**, 960 (1959).
4. E. P. Warekois, M. C. Levine, A. N. Mariano, and H. C. Gatos, *J. Appl. Phys.*, **33**, 690 (1962).
5. K. Brack, *J. Appl. Phys.*, **36**, 3560 (1965).
6. R. W. Bartlett and R. A. Mueller, *Mater. Res. Bull.*, **4**, S-341 (1969).
7. V. J. Jennings, *ibid.*, **4**, S-199 (1969).
8. V. J. Jennings, A. Sommer, and H. C. Chang, *This Journal*, **113**, 728 (1966).
9. R. W. Bartlett and G. W. Martin, *J. Appl. Phys.*, **39**, 2324 (1968).

Sputtering of Bismuth-Titanium Two-Phase Cathodes

R. T. Shoemaker, C. E. Anderson,*[1] and G. L. Liedl

Purdue University, Lafayette, Indiana 47907

In recent years there has been an increased interest in the development of sputtered films for electronic applications. A wide variety of elements has been investigated in the past with particular emphasis on single element films. Recently more emphasis has been placed on multiple component films produced by a number of methods such as sputtering from multiple component cathodes, reactive sputtering, or some post reaction process.

Winters, Raimondi, and Horne (1) have recently proposed a model for thin film composition by considering only the mechanisms affecting the composition at the substrate. An influence on the flux of atoms leaving the cathode has been illustrated by Anderson (2).

It is also of importance to determine the influence of the cathode morphology on the thin film structure and properties. This study is concerned with the influence of the cathode morphology on the stoichiometry of the resulting thin film. The bismuth-titanium system was selected for this study because of the large difference in the self-sputtering rates of bismuth and titanium (3).

Theory

To relate the composition of the film to the cathode, it is assumed that the number of each type of atom reaching the substrate is a function of the number of atoms of that type leaving the cathode and the probability that these atoms will reach and adhere to the substrate. Therefore, the composition of the film produced on the substrate is given by

$$y_i = N_i P_i \alpha_i / \Sigma_j N_j P_j \alpha_j \qquad [1]$$

where N_i is the number of atoms of element i leaving the cathode per unit area per second, P_i is the probability that atom i will reach the substrate, and α_i is the sticking coefficient.

The number of atoms of element i leaving the cathode is a function of the cathode morphology, the areal coverage of each phase, the composition of each phase, and the sputtering rate of each phase. For a two-element two-phase cathode where the two phases are pure elements, the number of type i atoms leaving the cathode is

$$N_i = x_i f_i \qquad [2]$$

where x_i is the atom fraction of element i in cathode and f_i is the function relating areal coverage to atom fraction and sputtering rate to sputtering parameters.

If we assume a probability function which describes the probability of each species reaching the substrate as

$$P_i = \exp\left[-d(K_{1i}X_i - K_{2i})\right] \qquad [3]$$

where d is the interelectrode separation, X_i is the atomic fraction, and the constants K_{1i} and K_{2i} are dependent on the cathode morphology and atomic collisions.

Therefore, the form of Eq. [1] for the atom fraction composition of the thin film produced from a two-element two-phase cathode is

$$y_1 = \frac{\alpha_1 x_1 f_1 \exp\left[-d(k_{11}x_1 + k_{22})\right]}{\alpha_1 x_1 f_1 \exp\left[-d(k_{11}x_1 + k_{21})\right] + \alpha_2 x_2 f_2 \exp\left[-d(k_{22}x_2 + k_{22})\right]} \qquad [4]$$

which can be rewritten, by assuming that $\alpha_2 f_2/\alpha_1 f_1$ is equal to one, as

$$y_1 = \left[1 + \frac{1 - x_1}{x_1} \exp\left(Ax_1 + B\right)\right]^{-1} \qquad [5]$$

The relationship of the coefficients A and B to the various parameters is dependent on several unknown factors, such as the cathode morphology, sticking coefficients, relative densities of sputtered molecules in the glow discharge, and the energy of the sputtered particles. A detailed model to describe the probability function is currently in progress.

Experimental Procedure

The cathodes were prepared by sintering 100 mesh powders of 99.9 w/o bismuth and titanium powders. Eleven disk-shaped cathodes 2½ in. in diameter and ½ in. thick were prepared with compositions varying from pure titanium to pure bismuth at 10 w/o intervals. The powders were mixed by tumbling and compressed to a pressure of 8000 psi. The green cathodes were placed in capsules which were evacuated to 2 x 10^{-5} Torr and were sintered at temperatures ranging from 250° to 1000°C depending on composition.

The sputtering was carried out in a conventional 4-in., oil-pumped, liquid nitrogen baffled vacuum system. Initially, the system was evacuated to 5 x 10^{-6} Torr. The 99.9% argon sputtering gas was then introduced through a calibrated leak valve at a constant flow rate of about 100 cc/min and the total pressure was set at 20μ by throttling the diffusion pump. The sputtering power source was a 5 kV-d-c source, and sputtering voltages varied from 2.0 kV to 4.5 kV. The sintered cathodes were presputtered for 30 min. The substrates used in this study were soft glass microscope slides.

The segregation of the elements in the thin film were analyzed with an ARL-AMX electron probe microanalyzer, and the composition of the film was determined from the ratio of the bismuth to titanium characteristic x-ray intensities calibrated for films less than bulk thickness (4). Some of the films were stripped from the substrate and examined in transmission with the electron microscope for morphology and structure characterization. The thickness of each film was measured with a multiple beam interferometer.

Results

The sintered cathodes yielded consistent results for longer sputtering times and after presputtering. However, the sintering of the cathodes did result in some problems. It was not possible to get high density sintering because of the wide discrepancies in melting point of the two elements.

Figures 1 through 3 show the relation between the composition of the cathode and the resulting thin film for 2, 3, and 4 kV sputtering potential. These results agree favorably with the predicted form as shown by the fit of Eq. 5 in Fig. 1 through 3. An attempt to fit the data to the model of Winters, Raimondi, and Horne (1) was unsuccessful. The parameters A and B obtained by fitting Eq. [5] to the experimental data are given in Table I. It should be noted that the low bismuth and low titanium composition determinations are inherently the most inaccurate values, and therefore, the intermediate compositions were weighted

* Electrochemical Society Active Member.
[1] Present address: Radiation, Inc., Melbourne, Florida.
Key words: selected sputtering, sintered cathodes.

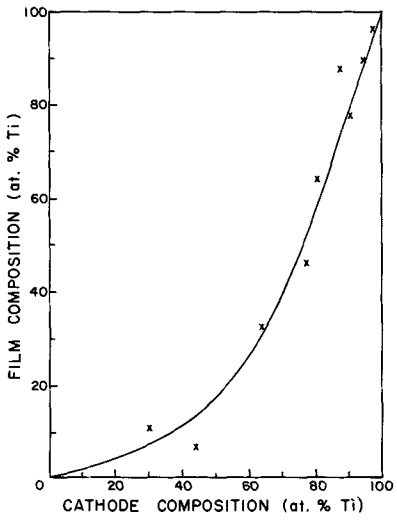

Fig. 1. Experimental and theoretical variation of titanium concentration for films sputtered at 2 kV and 20μ argon pressure from sintered bismuth-titanium cathodes.

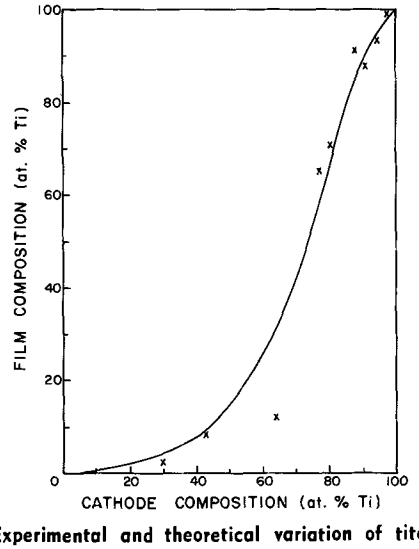

Fig. 2. Experimental and theoretical variation of titanium concentration for films sputtered at 3 kV and 20μ argon pressure from sintered bismuth-titanium cathodes.

more than the low compositions in fitting the equation. Since the probability function is empirical, no particular significance could be applied to the values found for the parameters. However, two factors are apparent. Since bismuth has a higher sputtering efficiency than titanium, bismuth composition in the film should be higher than in the cathode, especially for high bismuth cathodes. This effect contradicts the observed

Table I. Fitted parameters for equation relating titanium composition of sintered cathodes to sputtered film composition

kV	A	B
2	−1.74	2.16
3	−3.94	3.54
4	−7.42	5.24

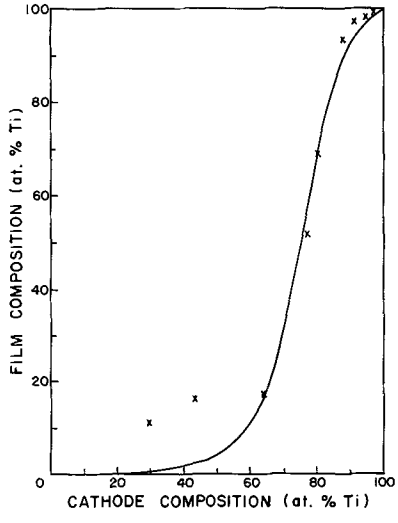

Fig. 3. Experimental and theoretical variation of titanium concentration for films sputtered at 4 kV and 20μ argon pressure from sintered bismuth-titanium cathodes.

excess titanium in the film for the high titanium cathodes. The observed S-shaped curves, especially for the higher sputtering voltages, could be the result of either a significant variation in the sticking coefficient with composition or, more likely, a net change in the flux leaving the cathode due to shape changes of the phases in the cathode.

The analysis of the electron diffraction patterns showed that the film sputtered from the 30.2 a/o titanium cathode contained at least two phases: a solid solution of titanium in bismuth and an unknown phase or phases. The films sputtered from the 87.8 a/o titanium cathode contained a solid solution of titanium in bismuth and $BiTi_2$, while a very thin film sputtered from the same cathode at the same pressure and voltage contained a solid solution of bismuth in titanium and $BiTi_2$. This result indicates a possible change in the sputtering rates of the two elements during the earlier stages of growth. A third film sputtered from the 96.8 a/o titanium cathode contained a solid solution of bismuth in titanium.

The results of this study verify a selective sputtering in two-phase cathodes and indicate either a composition dependence on the sticking coefficients or a morphology effect in the cathode.

Acknowledgment

The authors wish to thank the Advanced Research Projects Agency, Contract SD-102, for its support of this research.

Manuscript submitted Dec. 15, 1969; revised manuscript received *ca.* July 8, 1970.

Any discussion of this paper will appear in a Discussion Section to be published in the June 1971 JOURNAL.

REFERENCES

1. H. R. Winters, D. L. Raimondi, and D. E. Horne, *J. Appl. Phys.*, **40**, 2996 (1969).
2. G. S. Anderson, *ibid.*, **40**, 2884 (1969).
3. M. Kaminsky, "Atomic and Ionic Impact Phenomena on Metal Surfaces," p. 156, Academic Press, Inc., New York (1965).
4. W. E. Sweeney, R. E. Seebold, and L. S. Birks, *J. Appl. Phys.*, **31**, 1061 (1960).

Dielectric Properties of Surface Oxides on Aluminum

S. H. A. Begemann[1] and A. W. Smith

Boeing Scientific Research Laboratories, Box 3981, Seattle, Washington 98124

The impedance of barrier layer oxides on aluminum have frequently been characterized by an equivalent circuit of series-parallel resistor-capacitor combinations or by relaxation processes with a wide spread of relaxation times (1). Work on porous oxides have often used simplified models of the oxide itself while complicating the equivalent circuit with the introduction of pore resistance (2). The present work is an attempt to study the relaxation processes themselves. To make measurements as a function of temperature, a capacitor is formed by evaporating aluminum on top of the surface oxide. Measurements of capacitance and dissipation between 10 Hz and 200 kHz will be reported on both barrier layer and porous oxides between 100° and 500°K.

Experimental

A sample holder was built to allow evaporation of aluminum onto the surface of the oxide and to make measurements of the dielectric properties. This is shown in Fig. 1. The copper sample holder can be cooled with liquid nitrogen and heated electrically. Contact to the outer electrode was made by affixing a wire with a dot of colloidal silver paint at the edge of the area on which aluminum was evaporated. An NRC, Model 3114 vacuum coater was used for the evaporation and as a sample chamber. A General Radio, Type 716-C capacitance bridge was used in combination with a null detector system consisting of a Hewlett-Packard wave analyzer, Model 302A, a low noise preamplifier and filter. This allowed signal amplitudes of 20 mV to be used. The experiment has been discussed in detail elsewhere (3).

Results

Barrier layer oxides.—Aluminum specimens of 99.99% purity, were degreased and etched with 1*N* NaOH for 5 min and rinsed with distilled water. The anodizing was carried out in a 3% by weight ammonium tartrate solution adjusted to *p*H 7. An aluminum cathode was used. The voltage was raised in 10 V steps, and the current allowed to decay to a nearly constant value after each step.

The inverse capacitance/anodizing voltage ratio is close to that obtained by McMullen and Pryor for the same anodizing conditions but measured in the electrolyte solution (4). The frequency dependence of the dissipation for samples formed at several voltages, measured in ambient atmosphere, is shown in Fig. 2. The dissipation factor of these barrier layer oxides is only slightly dependent on atmospheric humidity. The dissipation decreases by at most 20% on application of vacuum and heating to 200°C. The values of the dissipation factor and its decrease with film thickness are similar to that reported by VanGeel and Scholte (5).

Figure 3 shows the temperature dependence of the dissipation factor for a 100V film measured at 1 kHz. Peaks with background subtracted out are shown at 142° and 245°K. At 50 kHz these peaks occurred at 230° and 287°K.

Porous oxides.—The formation of porous oxide layers was carried out on a commercial alloy, 2024-T3. After degreasing and alkaline cleaning, they were etched in a sulfuric acid, sodium dichromate solution. The anodizing was carried out at 36°C, the voltage reaching 40V in 10 min and held there for 30 min. The anodizing solution was a 3% by weight solution of chromic acid.

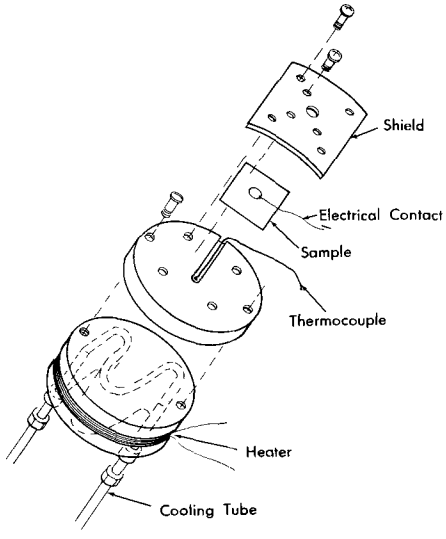

Fig. 1. Schematic drawing of sample holder

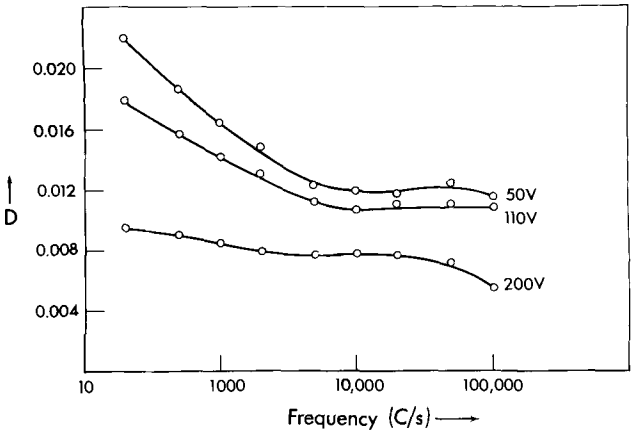

Fig. 2. Dissipation *vs.* frequency for barrier layer films with different anodizing voltages.

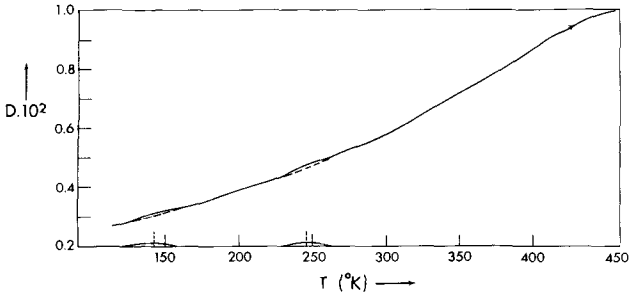

Fig. 3. Temperature *vs.* dissipation for a barrier layer film, anodized in a 3% ammonium tartrate solution at 100V. Measured at 1 kHz in vacuum.

Measurements made with a sodium sulfate solution counterelectrode gave results, agreeing with Dekker and Urguhart (6), that the solution penetrates the porous layer, and the measured capacity depends only on the underlying barrier layer. Results using the evaporated aluminum electrode depend on the porous layer as well, and show the sensitivity to humidity

[1]Present address: Laboratorium voor Technische Natuurkunde, Universiteitscomplex Paddepoel, Groningen, The Netherlands.

Key words: dielectric properties, aluminum oxide, anodic layer, dissipation, hydration.

noted by Jason and Wood (2). This was attributed by them to adsorption of water and consequential conduction down the walls of the pores.

To study the properties of the oxide layer without pore wall conduction, measurements must be made in high vacuum. Figure 4 shows typical results for the variation of dissipation with temperature below room temperature. Similar results to those of the barrier layer oxide were obtained. In one case, peaks occurred at 140° and 214°K for measurements at 1 kHz and at 235° and 270°K for measurements at 50 kHz. As shown in Fig. 4, partial sealing of the oxide with hot water increased the background dissipation with only little increase in the dissipation peaks. Although these dissipation peaks, as well as those for the barrier layer oxides, are small, they occur consistently and the temperature shift with frequency is appropriate for processes with activation energies between 0.1 and 0.5 eV.

Peaks of a much greater magnitude were observed above room temperature with the porous oxide. Figure 5 shows the dissipation factor *vs.* temperature for several frequencies. Two peaks occur, but only one varies in position on the temperature scale with frequency. The higher temperature peak remains at about 405°K.

There is a considerable irreversible decrease in the dissipation due to the first heating cycle. The curves show no hysteresis on further heating, however. It was difficult to remove the background from the lower temperature peak to determine an activation energy, due to overlap with the second peak. The assumption was made (to be discussed later) that the second peak was a decrease in dissipation at 405°K, on a background which increased with temperature. Figure 6 is an example of this background removal.

Figure 7 is an Arrhenius plot of the log frequency *vs.* reciprocal temperature of this dissipation peak. An activation energy of 0.76 eV was obtained.

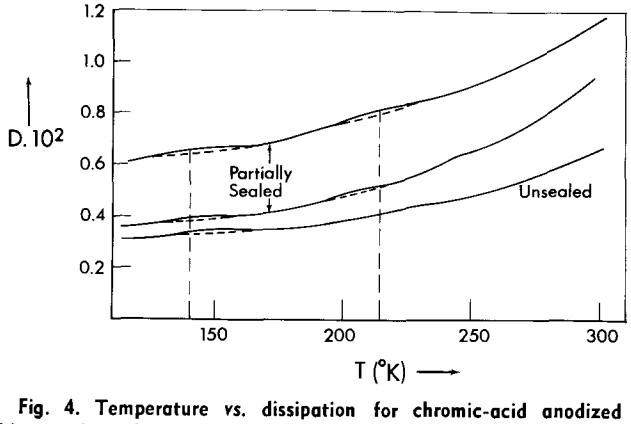

Fig. 4. Temperature *vs.* dissipation for chromic-acid anodized films with different sealing treatments. Measured at 1 kHz in vacuum.

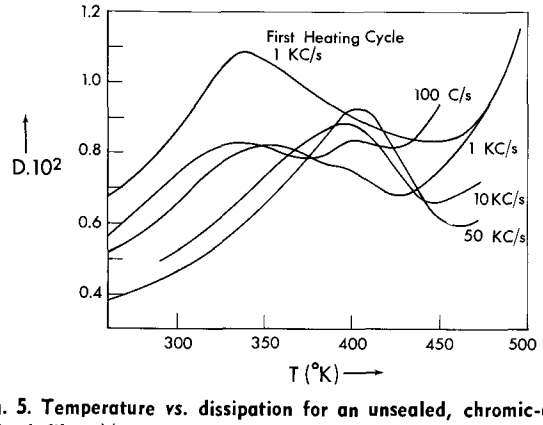

Fig. 5. Temperature *vs.* dissipation for an unsealed, chromic-acid anodized film. Measured in vacuum at different frequencies (500 Hz omitted for clarity purposes).

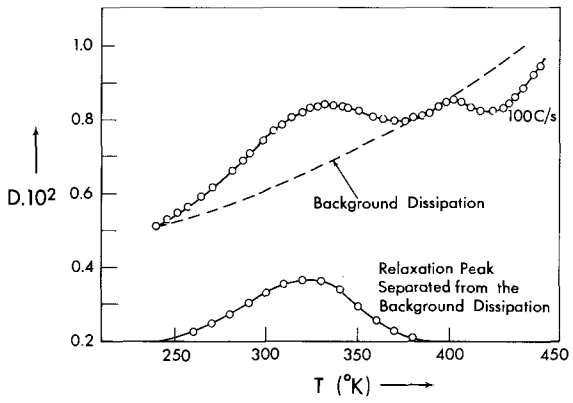

Fig. 6. Temperature *vs.* dissipation for an unsealed, chromic-acid anodized film. Measured in vacuum after the first heating cycle.

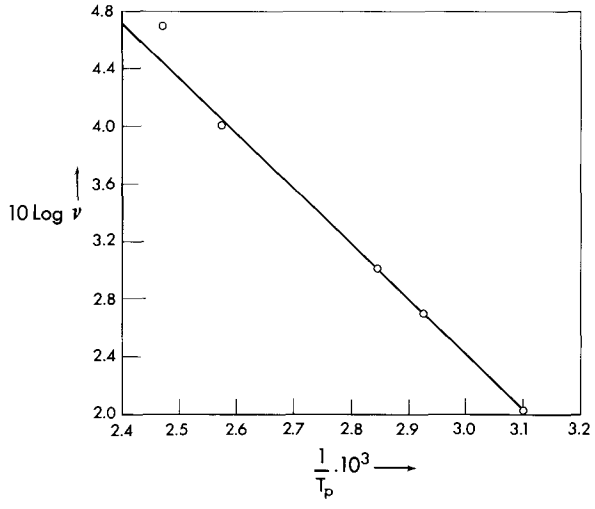

Fig. 7. Log ν *vs.* $1/T_p \cdot 0.10^3$ plot for anodized and partially "sealed" films. T_p = peak temperature.

Discussion

McMullen and Pryor measured the dielectric loss for a barrier layer film at low temperatures (4). Their data also show a peak at about 230°K which they do not discuss. These peaks may be the same as those found here. In addition, they find a large peak just below room temperature in ambient atmosphere which disappears under vacuum. No such peak was found in the present work. However, their apparatus has a thick porous anodic film in parallel with the barrier layer film as an insulator. At high humidities the pore walls would conduct well, and the impedance of this film may become low enough to affect their measurements.

The physical identity of the two species causing the two low temperature peaks is not apparent from the data since they are not very sensitive to humidity or heat treatment. If they are hydroxide groups, then they are stable above the 550°K outgassing used here. Boehmite is stable above this temperature (7).

The 0.76 eV dissipation peak at high temperatures for the porous oxides seems to correspond to the peak for Boehmite for which Mata-Arjona and Fripiat found an activation energy of 0.68 eV (7). Porous oxides do contain some moisture (8). The 0.76 eV relaxation peak is therefore assigned to hydroxide ions as was proposed for Boehmite (7).

It is suggested that the dissipation peak at 405°K is in fact a decrease in dissipation on a rising background curve. This can be due to an order-disorder transition (9). Such an effect was sought by Wickershen and Korpi for Boehmite in dielectric constant measurements (10). Apparently this effect shows up here in the more sensitive dissipation measurements and not in the measurements of dielectric constant.

Manuscript submitted April 16, 1970; revised manuscript received *ca.* July 31, 1970.

Any discussion of this paper will appear in a Discussion Section to be published in the June 1971 JOURNAL.

REFERENCES

1. L. Young, "Anodic Oxide Films," Academic Press, New York (1961).
2. A. C. Jason and J. L. Wood, *Proc. Phys. Soc.*, **B.68**, 1105 (1955).
3. S. H. A. Begemann and A. W. Smith, Boeing Scientific Research Lab. Document D1-82-0824, Feb. 1969, AD 685577.
4. J. J. McMullen and M. J. Pryor, "1st International Congress on Metallic Corrosion," p. 52, Butterworths, London (1962).
5. W. Ch. VanGeel and J. W. A. Scholte, *Philips Res. Repts.*, **6**, 54 (1951).
6. A. J. Dekker and H. M. A. Urguhart, *Can. J. Res.*, **28B**, 541 (1950).
7. A. Mata-Arjona and J. J. Fripiat, *Trans. Faraday Soc.*, **63**, 2936 (1967).
8. H. W. Phillips, "Institute of Metals Monograph and Report," Vol. 13, p. 237 (1953).
9. Frohlich, "Theory of Dielectrics," 2nd Ed., Clarendon Press, Oxford, (1958).
10. K. A. Wickersheim and G. K. Korpi, *J. Chem. Phys.*, **42**, 579 (1965).

JOURNAL OF THE ELECTROCHEMICAL SOCIETY

ELECTROCHEMICAL TECHNOLOGY

NOVEMBER 1970

Diffusional Processes in Solid Electrolyte Fuel Cell Electrodes

R. L. Zahradnik

Department of Chemical Engineering, Carnegie-Mellon University, Pittsburgh, Pennsylvania 15213

ABSTRACT

A mechanism is proposed to account for the polarization voltage loss encountered in the electrochemical oxidation of CO at porous, high-temperature, solid-electrolyte fuel cell anodes. The mechanism involves the transport of gaseous CO and oxygen ions to reaction sites, followed by slow electrochemical reaction. The mechanism results in an involved polarization expression, which under certain conditions simplifies to the familiar Tafel form.

High-temperature fuel cells employing either calcia or yttria stabilized zirconia electrolyte have received considerable attention as potential power generators using gaseous fuels derived from coal (1, 2). At the 1000°C operating temperature of solid electrolyte fuel cells, such coal-derived gases as well as prospective fuels such as reformed hydrocarbons will contain large amounts of CO. Oxidation of CO at metallic and mixed oxide fuel cell anodes, however, is accompanied by large polarization losses (3). The presence of hydrogen reduces this loss somewhat, but it is not clear that either the high current densities which are expected from such cells or the complete combustion of CO to CO_2 can be achieved without incurring severe voltage losses. For this reason, it is important to understand in a fundamental way the irreversibilities which occur at solid-electrolyte fuel cell anodes. The purpose of this paper is to propose a possible scheme by which this polarization occurs and to derive the equations which quantitatively relate polarization voltage loss to electrode current density.

Many such analyses for liquid electrolyte fuel cell electrodes have appeared in the literature, and a complete review of the work in this area is not presented here. The pioneering work of Will should be mentioned, however, since it was the first to treat partially immersed electrodes and proposed a method for treating the electrolyte meniscus which considerably clarified the polarization phenomena (4). Will's work has been reviewed and generalized by Lightfoot, who included effects of convection as well as concentration polarization in his analysis (5).

Not all liquid electrolyte fuel cell electrodes follow the thin-meniscus model, however, and analyses of flooded porous fuel cell electrodes have been made, *e.g.* Brown and Rockett (6).

With a liquid electrolyte, it is possible for the gaseous species participating in the electrode reaction to reach the electrode reaction site either through a meniscus film or bulk electrolyte phase, and the reported polarization studies analyze the various ways this transport can occur. In the case of a solid electrolyte, however, such transport is impossible and alternate mechanisms must be responsible for electrode polarization. One possibility is for the reactants (CO and oxygen ions) to counterdiffuse to a mutually acceptable location somewhere on the electrode, and there react. In an earlier paper, Zahradnik analyzed this situation for a one-dimensional electrode (7). In this paper, the analysis is extended to cover two-dimensional effects. In order to simplify the analysis, the concept of a single, rectangular pore is introduced.

Key words: fuel cell, porous electrode, polarization (and/or) overvoltage, diffusion, limiting current, Damkohler number.

A Single Rectangular Pore

Noble metals, nonnoble metals, conducting oxides, and mixtures of oxides and metals have been used at one time or other as high-temperature fuel cell anodes (3). The physical structure of all these materials has been porous, and hence it is reasonable to idealize the structure as a single pore, normal to the electrolyte surface—Fig. 1. In order to simplify the ensuing mathematics and notation, the pore is considered to be rectangular and of infinite extent in the direction normal to the paper. The distance coordinate y is introduced, directed normal to the electrolyte, with origin at the electrode-electrolyte interface and value $y = b$ at the bulk gas phase boundary. The distance coordinate x is introduced, directed parallel to the electrolyte. Its origin is at the centerline of the electrode and it has the value $x = a$ at the pore wall.

The electrode is taken to operate isothermally, and the electrochemical reaction between CO and oxygen

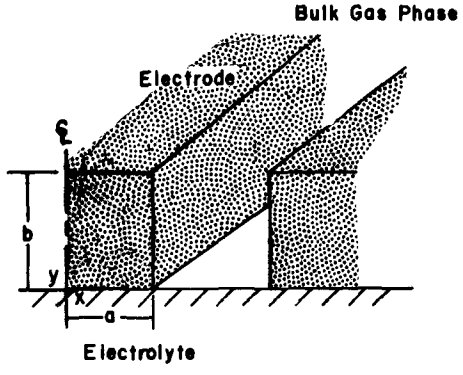

Fig. 1. Idealized pore structure

ions is assumed to occur at the walls of the pore

$$CO + O^{=} \rightarrow CO_2 + 2e^{-} \qquad [1]$$

The rate at which this reaction proceeds per unit of pore wall area, in units of current, is symbolized by $i(y)$.

A number of kinetic expressions have been proposed for $i(y)$ but no generally accepted kinetic description is available (8, 9). At the conditions under which high-temperature solid electrolyte fuel cell anodes operate, however, it seems likely that the following, often proposed, equation is applicable (10)

$$i(y) = 2\mathbf{F}k\, e^{-\left(\frac{\Delta F^{\neq} + \alpha 2\mathbf{F}V}{RT}\right)} [CO]\,[O^{=}] \qquad [2]$$

where k = Constant, including units of rate
$\Delta F^{\neq}$ = Standard state free energy of activation
R = Gas law constant
T = Temperature
α = Fraction of generated voltage which contributes to increasing free energy of activation

Equation [2] represents only the forward rate of reaction [1]. Under most conditions of high-temperature fuel cell operation, the forward rate alone is satisfactory, although provision to include a term for the reverse reaction could be made should electrode operation be near the equilibrium condition of reaction [1].

It is assumed that the oxygen ions diffuse from the electrode-electrolyte interface under the influence only of a concentration gradient. That is, the electrode is assumed to be equipotential, so that no voltage gradient is present as an additional driving force. Under these assumptions, the oxygen ion flow is described by the following steady-state conduction equation

$$\frac{\partial^2[O^{=}]}{\partial x^2} + \frac{\partial^2[O^{=}]}{\partial y^2} = 0 \qquad [3]$$

The nature of the oxygen ion flow need not be completely specified at this time. That is, the diffusion is assumed to be bulk diffusion, such as lattice, grain boundary, or short-circuit diffusion, but no further specification is made. In any case, Eq. [3] would have a similar form (11, 12). Also, the diffusivity of oxygen ions has been assumed to be the same in both the x- and y-direction.

The boundary conditions which apply to Eq. [3] are: at

$$x = 0, \quad \frac{\partial[O^{=}]}{\partial x} = 0 \qquad 0 < y < b \qquad [4]$$

$$y = b, \quad \frac{\partial[O^{=}]}{\partial y} = 0 \qquad 0 < x < a \qquad [5]$$

$$y = 0, \quad [O^{=}] = [O^{=}]_e \qquad 0 < x < a \qquad [6]$$

$$x = a, \quad -D_O = \frac{\partial[O^{=}]}{\partial x} = K[CO]_b\,[O^{=}] \qquad 0 < y < b \qquad [7]$$

where K = A convenient kinetic parameter, representing the terms premultiplying the concentrations on the right-hand side of Eq. [2]
$D_{O^{=}}$ = Diffusivity of $O^{=}$

Equation [4] states that there is no flux across the electrode centerline; Eq. [5] similarly denies oxygen ions admission into the bulk gas phase. At the electrode-electrolyte interface, the oxygen ions have a constant concentration, $[O^{=}]_e$—Eq. [6]. Equation [7] equates the diffusive flux of oxygen ions to the flux due to chemical reaction. In this equation, the concentration of CO is taken to be equal to $[CO]_b$, the bulk gas phase composition. This assumption is reasonable in the light of the high value of diffusivity CO has at cell operating temperatures. However, if so desired, provision could be made to account for small changes in CO concentration due to changes in current level—in the manner used by Zahradnik in his one-dimensional analysis (7). This is not done here, however, since its effect is small.

Solution to Electrode Equations

The solution to the system of Eq. [2]-[7] can be expressed in terms of a Fourier series; the result is from Carslaw and Jaeger (13) (p. 168, Eq. [17])

$$[O^{=}] = 2K\,[O^{=}]_e\,[CO]_b \sum_{n=1}^{\infty} \frac{\cos \alpha_n x \cosh \alpha_n (b - y)}{[(\alpha_n^2 + D_m^2)\, a + D_m] \cos \alpha_n a \cosh \alpha_n b} \qquad [8]$$

where α_n represents the solution to the following

$$\alpha_n a \tan \alpha_n a = D_m = \frac{K\,[CO]_b\,[O^{=}]_e}{\frac{D_{O^{=}}\,[O^{=}]_e}{a}} \qquad [9]$$

The right-hand side of Eq. [9] is the ratio of the maximum reaction rate to a characteristic diffusion rate of $O^{=}$. Such a ratio represents an electrode Damkohler number, and is symbolized as D_m.

The total pore current per unit of length normal to the xy-plane, I, is obtained by integrating the oxygen ion flux at $x = a$ over the entire height of pore wall

$$I = \int_0^b -D_{O^{=}} \frac{\partial\,[O^{=}]}{\partial x}\bigg|_{x=a} dy$$

$$I = \int_0^b D_{O^{=}}\, 2K\,[O^{=}]_e\,[CO]_b \sum_{n=1}^{\infty} \frac{\tan \alpha_n a \cosh \alpha_n (b - y)}{[(\alpha_n^2 + D_m^2)\, a + D_m] \cosh \alpha_n b}\, \alpha_n\, dy$$

This expression can be written as the ratio of I to $I_D = D_{O^{=}}\,[O^{=}]_e/a$, a characteristic oxygen ion flux

$$\frac{I}{I_D} = 2\, D_m^2 \left(\frac{a}{b}\right) \sum_{n=1}^{\infty} \frac{\tanh \alpha_n b}{\alpha_n a\,[\alpha_n^2 a^2 + D_m^2 + D_m]} \qquad [10]$$

Since it is the current-polarization relationship which is of most interest from a fuel-cell point of view, Eq. [10] can be modified slightly to indicate how these two quantities are related.

Current-Polarization Relationship

K is given explicitly by the following

$$K = 2\,\mathbf{F}k\, e^{-\frac{\Delta F^{\neq}}{RT}}\, e^{-\frac{2\alpha \mathbf{F}V}{RT}}$$

At this point it is convenient to utilize the fact that, on an IR free basis, electrode voltage, V, is given by the following thermodynamic relationship

$$V = E_t - \eta = -\frac{\Delta F^{\circ}}{2\mathbf{F}} - \frac{RT}{2\mathbf{F}} \ln \left\{ \frac{[CO_2]_b}{[CO]_b} [O^{=}]_e \right\} - \eta$$

where
η = Electrode polarization
ΔF° = Standard free energy change of reaction [1]

Hence, it is possible to relate D_m to polarization η

$$D_m = D_m^{0}\, e^{\frac{2\alpha \mathbf{F}\eta}{RT}}$$

where D_m^{0} denotes the value of D_m at zero polarization.

Figure 2 is a plot of $\ln (I/I_O)$ *vs.* $\ln D_m = \ln D_m^{0} + 2\alpha\mathbf{F}\eta/RT$, for various aspect ratios.

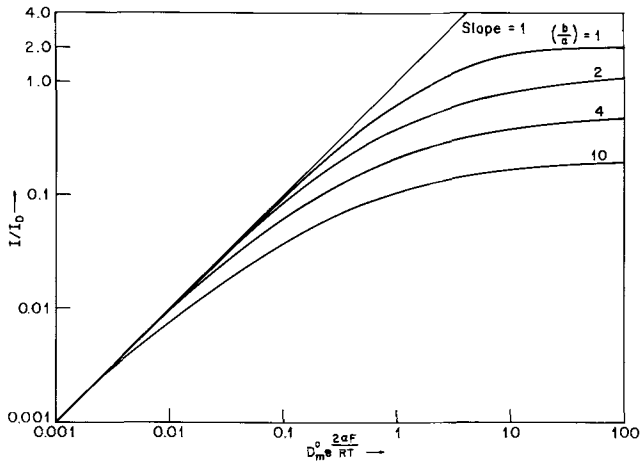

Fig. 2. Current-polarization relationship

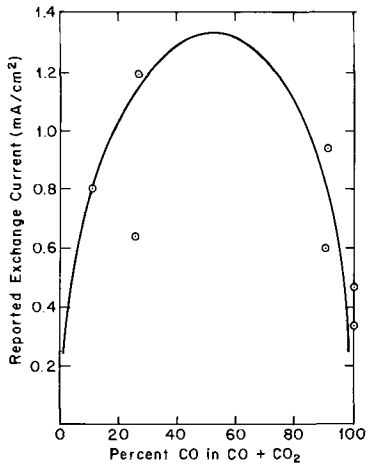

Fig. 3. Reported values of exchange current as function of per cent CO for sintered platinum electrodes (1). Curve is predicted by Eq. [12].

Notice that for small values of current these two expressions are equal, suggesting that

$$\ln I/I_D = \ln D_m{}^0 + \frac{2\alpha \mathbf{F}\eta}{RT} \text{ (small } I\text{)}$$

If $D_m{}^0\ I_D$ is denoted as an exchange current, I_0, this equation reduces to the familiar Tafel form

$$\eta = \frac{RT}{2\alpha \mathbf{F}} \ln I/I_0 \qquad [11]$$

Archer, Elikan, and Zahradnik have obtained polarization data for zirconia-based fuel cells equipped with sintered platinum anodes operating on CO-CO_2 mixtures (3). They report a successful fit of their data using Eq. [11]. Although a consistent value of $\alpha = \frac{1}{2}$ was obtained over a range of compositions, the authors were unable to draw any firm conclusions about trends of the exchange current with composition. However, a simple dependency of (I_0) on bulk gas phase composition may be obtained

$$(I_0) \propto [CO]_b{}^{1-\alpha}\,[CO_2]_b{}^{\alpha}$$

Consider

$$[CO_2]_b = (1 - y_{CO})\ C_b$$

and

$$[CO]_b = (y_{CO})\ C_b$$

where C_b = Bulk gas phase concentration
y_{CO} = Mole fraction CO in bulk gas phase

Then if the value of α is taken to be $\frac{1}{2}$, for a constant C_b, the proportionality between (I_0) and y_{CO} is given by the following

$$\boxed{(I_0) \propto [y_{CO}(1 - y_{CO})]^{1/2}} \qquad [12]$$

The data reported by Archer, Elikan, and Zahradnik are plotted in Fig. 3 *vs.* bulk gas phase percentage of CO in the CO + CO_2 mixture. The relationship suggested by Eq. [12] is also plotted in Fig. 3, with the proportionality constant adjusted to give a best fit to the data. The agreement is quite reasonable, considering the variety of conditions under which the data were obtained. Unfortunately, no data were reported in the 50% CO range.

As I increases, the current-polarization curve starts to deviate from the linear relationship. No other region is encountered where an equation of the Tafel form is a good approximation. This conclusion is different from the one based on a one-dimensional counter diffusion (7), where a second region was observed in which an equation of the Tafel form served as a good approximation to the exact equation.

In order to demonstrate that the current-polarization curve predicted by Eq. [10] does provide a good fit for

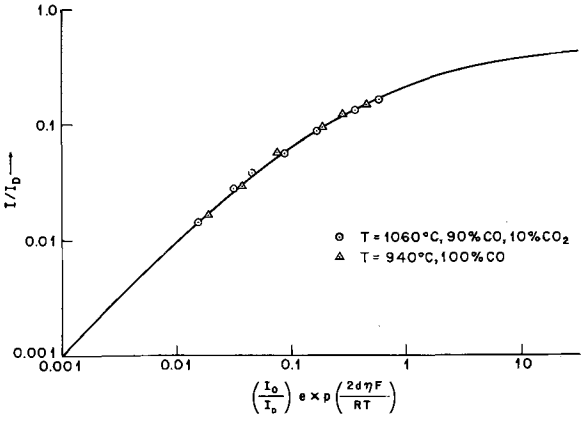

Fig. 4. Experimental data for sintered platinum electrodes (1). Curve is predicted from Eq. [10] with $(b/a) = 4$.

experimental data, some of the results reported by Archer, Elikan, and Zahradnik (3) are plotted in Fig. 4 in the format prescribed by Eq. [10]. The data were obtained at two temperatures, 940° and 1060°C, with a fuel of 100% CO and 90% CO plus 10% CO_2, respectively.

The curve derived from Eq. [10] which is used to correlate these data is for an aspect ratio $(b/a) = 4$. This ratio is felt to be reasonable for the sintered platinum electrodes used in the experiments. The sintering process causes the platinum to coalesce into individual particles whose mean diameter is about one third times the electrode thickness. If the pores are viewed as passages through a matrix of connected particles, then an aspect ratio of four to six would be expected.

The data reported in Fig. 4 were obtained with a test cell whose electrode area was 27.6 cm^2. From Fig. 3, it is noted that exchange current densities of about 0.3 and 0.6 mA/cm^2 can be expected for the 100% CO and the 90% CO fuels, respectively. This would correspond to I_0 values of 8 and 16 mA, respectively, and these were the values used to plot the data. The value of α was taken to be $\frac{1}{2}$.

For the 940°C, 100% CO data, the correlation was obtained with an I_D value of 1500 mA. The 1060°C, 90% CO data was correlated with an I_D value of 1700 mA. It can be seen that only the low current points are in the region of the Tafel kinetics.

The limiting current, I_L, can be obtained from Eq. [10] by letting D_m become large. The result may be expressed as

$$I_L = \left(\frac{D_{O^=}[O^=]_e}{b}\right) \lim_{D_m \to \infty} 2D_m \sum_{n=1}^{\infty} \frac{\tanh\left[(b/a)\,\alpha_n a\right]}{\alpha_n a[\alpha_n^2 a^2 + D_m^2 + D_m]}$$

The first bracketed term shows the limiting current to be inversely proportional to electrode thickness as expected. The exact constant of proportionality depends on the electrode aspect ratio (b/a) as seen from the second term. For (b/a) values larger than 2, this last term is relatively insensitive to (b/a) however.

The data shown in Fig. 4 correspond to limiting currents of 900 mA at 940°C and 1000 mA at 1060°C. While these values are quite low on a current density basis, it should be pointed out that the test cell did employ a thick electrode and that other cells have been operated with much thinner electrodes and consequently much higher limiting currents.

Discussion

The analysis presented here allows a number of interesting conclusions to be drawn about solid electrolyte fuel cell anodes. At low current levels, polarization is controlled by slow chemical reaction, and familiar Tafel behavior is observed. As current increases, the slope of the ln I *vs.* η curve decreases continuously, and no other characteristic region is noted until the limiting current is reached.

Since the object of a properly designed electrode is to support large current densities while sustaining only small polarization losses, it is clear that such an electrode should have large $D_m{}^0$. This requirement means that the kinetics of the electrochemical reaction [1] should be fast. The data reported for platinum electrodes indicate that such is not the case for platinum. However, other materials are suitable as anodes, and one criterion in their selection should be the rate at which reaction [1] proceeds on their surface.

If an anode material of sufficient catalytic level, either natural or induced by special treatment, can be found, the fuel cell behavior would be characterized by large $D_m{}^0$ values. It is interesting to observe what happens to the current distribution in such cases. The net current at any electrode position, $I(y)$, may be obtained directly by differentiating the expression for $[O^=]$, and is given by the following equation

$$\frac{I(y)}{I} = 1 - \sum_{n=1}^{\infty} \frac{\sinh \alpha_n b\,(1-y)}{\alpha_n a[\alpha_n^2 a^2 + D_m^2 + D_m]} \qquad [13]$$

For small values of D_m, this equation is nearly linear (Fig. 5). However, as D_m increases, the relationship is no longer linear, but distinctly curved, as shown in Fig. 5. At high values of D_m, the current is generated largely near the electrode-electrolyte interface and the distribution is distinctly nonuniform. Similar distributions are found along the meniscus of a liquid electrolyte fuel cell electrode (8). However, in the case of solid electrolyte fuel cell anodes, the high current densities that are developed in the vicinity of the electrode-electrolyte interface will produce large heat effects, due to resistance heating in the electrode, which may in turn lead to rupture of the electrode-electrolyte contact. A careful analysis will have to be made of the local heat effects produced in electrodes capable of supporting high current densities.

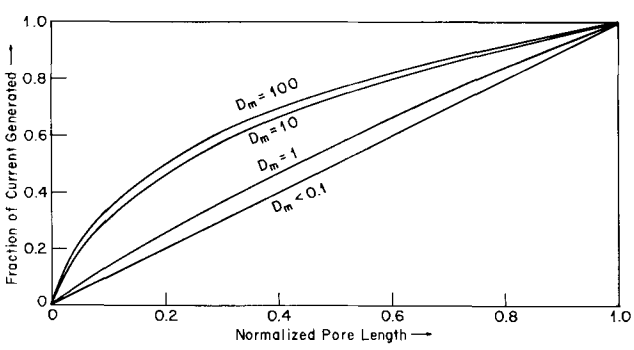

Fig. 5. Current distribution as function of electrode Damkohler number for aspect ratio = 1.

Manuscript submitted Dec. 5, 1969; revised manuscript received July 1, 1970.

Any discussion of this paper will appear in a Discussion Section to be published in the June 1971 JOURNAL.

REFERENCES

1. D. H. Archer, E. F. Sverdrup, and R. L. Zahradnik, *Chem. Eng. Progr.*, **60**, 64 (1964).
2. R. L. Zahradnik, L. Elikan, and D. H. Archer, pp. 343-355 in "Fuel Cell Systems," Am. Chem. Soc. (1965).
3. D. H. Archer, L. Elikan, and R. L. Zahradnik, pp. 51-75 in "Hydrocarbon Fuel Cell Technology," Academic Press, Inc., New York (1965).
4. F. G. Will, *This Journal*, **110**, 152 (1963).
5. E. N. Lightfoot, *ibid.*, **113**, 614 (1966).
6. Ralph Brown and J. A. Rockett, *ibid.*, **113**, 865 (1966).
7. R. L. Zahradnik, "Mechanism of CO Polarization at High-Temperature Solid Electrolyte Fuel Cell Anodes," Troisiemes Journees Internationales D'Etude Des Piles a Combustible, Bruxelles, Presses Academiques Europeennes, pp. 125-130, 1969.
8. D. N. Bennion and C. W. Tobias, *This Journal*, **113**, 593 (1966).
9. E. A. Grens, R. M. Turner, and Theodore Katan, *Advanced Energy Conversion*, **4**, 109 (1964).
10. L. G. Austin, *Proc. IEEE*, **51**, 820 (1963).
11. Karl Hauffe, "Oxidation of Metals," Plenum Press, New York (1965).
12. Per Kofstad, "High-Temperature Oxidation of Metals," John Wiley & Sons, Inc., New York (1966).
13. H. S. Carslaw and J. C. Jaeger, "Conduction of Heat in Solids," Oxford University Press (1959).

NOMENCLATURE

English

a	Electrode distance
b	Electrode thickness
C_b	Bulk gas phase molar concentration (g/cm³)
$D_{O^=}$	Diffusivity of $O^=$ (cm²/sec)
E_t	Thermodynamic voltage for reaction [1]
$\Delta F^{\neq}$	Activation energy for absolute rate expression for reaction [1] (kcal/g mole)
ΔF°	Standard free energy of reaction [1] (kcal/g mole)
$\mathbf{F}$	Faraday Number (coulomb/g mole equivalent)
$i(x)$	Local rate of reaction [1] (A/cm²)
I	Operating electrode current
$I(x)$	Local electrode current
I_D	Characteristic electrode current (A)
(I_0)	Exchange current
I_L	Limiting current (A)
k	Kinetic parameter with units of rate
K	Convenient kinetic parameter
R	Gas law constant (kcal/g mole °K)
T	Electrode temperature (°K)
V	Electrode potential (V)
x	Distance coordinate parallel to electrolyte
y	Distance coordinate normal to electrolyte
y_{CO}	Bulk gas phase CO mole fraction

Greek

α	Parameter indicating portion of anode voltage which increases activation energy of intermediate complex for reaction [1]
α_n	Solution to Eq. [9]
η	Polarization voltage loss (V)

Subscripts

e	Electrode-electrolyte interface
b	Bulk gas phase-electrolyte interface

The Corrosion of Titanium Carbide

R. D. Cowling and H. E. Hintermann*

Laboratoire Suisse de Recherches Horlogères, Neuchâtel, Switzerland

ABSTRACT

In 2*N* H_2SO_4, the anodic dissolution of titanium carbide begins at about 0.8V (SHE). Trivalent titanium ions could not be detected in the nitrogen-saturated solution, although this does not rule out the possibility that Ti(III) is formed in the dissolution reaction. However, at 0.8V oxidation to Ti(IV) would readily occur. The results of potentiostatic and galvanostatic experiments indicate that the subsequent passivation of the electrode, which occurs between 1.2 and 1.7V when it is polarized potentiostatically, is due to Ti(IV) oxide. At potentials above 1.7V, oxidation to Ti(VI) occurs. During the initial dissolution of the carbide, both CO and CO_2 were detected.

Although titanium carbide is an important refractory material, characterized by its extreme hardness and its relative inertness, very little attention has been given to its chemical properties. The stability of the Group IV, V, and VI transition metal carbides toward acid and alkali solutions has been examined (1), but, while a patent exists (2) for an anode incorporating titanium carbide, there appear to have been no studies on the anodic behavior of this material. It was felt that one point of interest in such a study would be to determine the nature of products arising from the bonded carbon. Thus Ervin *et al.* (3), in describing the use of titanium carbide anodes for the extraction of titanium metal in molten salt electrolysis, state that the carbide behaves during electrolysis as though it were a metal with high carbon content. From this, one might expect dissolution of titanium, leaving free carbon. On the other hand, various attempts have been made to describe the bonding in carbides (4-6), and it is more reasonable to suppose that the carbon gives rise to at least one gaseous corrosion product.

It was the aim of the present study to investigate the behavior of titanium carbide anode in sulfuric acid solution, to identify the dissolution products, and to define the limit beyond which this material cannot be regarded as inert.

Experimental

Titanium carbide was deposited onto steel disks (C, 1.4%; Cr, 1.3%) by chemical vapor deposition from a mixture of hydrogen, methane, and titanium tetrachloride vapor at high temperature (7).

The nature of the deposit was confirmed by x-ray diffraction studies. Unfortunately this method cannot be used to determine the stoichiometry of the carbide, due to the high degree of scatter in the measured lattice parameter. Chemical analyses have been performed on representative samples of carbide, in order to obtain the stoichiometry. The analysis of metallic impurities was performed by spectrographic and atomic absorption methods. Determination of oxygen and nitrogen was carried out by vacuum extraction and chemical methods, respectively, and of total carbon by oxidation to CO_2 which was subsequently determined by coulometric titration. Free carbon was determined by dissolving the sample in HF and HNO_3, filtering the free carbon on asbestos and burning it to CO_2 in a tube furnace.

Compositions vary between nearly stoichiometric ($TiC_{0.98}$) and about $TiC_{0.9}$. The variation must be due to experimental factors which may be controllable (temperature, gas composition, *etc.*) or not (aging of the apparatus). A systematic study of this problem has not yet been undertaken. Analysis of the impurities showed about 4% each of iron and chromium, which arise either by diffusion from the substrate or by high-temperature attack on the reactor walls by the gas stream. The level of these impurities is not high enough to affect the general characteristics of the corrosion behavior of the carbide, but uncertainties in the stoichiometry and purity made a detailed kinetic study impossible.

Anodes.—Deposits of titanium carbide 10-15 μm thick were obtained on disks of 2 mm thickness. The carbide on one surface was planed away, and the steel then dissolved in warm hydrochloric acid, leaving flakes of titanium carbide.

Cell and instrumentation.—Experiments were performed in a simple cell at room temperature, using Reagent Grade acid solutions. A large cylindrical platinum counterelectrode was used. The basic instrument for both potentiostatic and galvanostatic experiments was a Tacussel[1] type PRT 2000 potentiostat. For potential scans this was coupled to a drive unit, type Servovit 2, and current-potential curves were obtained directly on a Sefram[2] XY recorder.

Results

Potentiostatic measurements.—Figure 1 shows a typical polarization curve for TiC in 2*N* H_2SO_4, obtained at a potential scan rate of 10 mV/min. At about 2V,[3] rapid dissolution of the electrode occurs. The passivation of TiC at about 1V is a process which, at a low rate of scanning, undergoes reactivation when the potential is made progressively less positive. At a higher rate of scan, little reactivation occurs. This is shown in Fig. 2. The *p*H-dependence of the potential of the peak maximum was found to be -0.045 ± 0.005 mV/*p*H unit, the potential becoming more positive as the *pH* decreases. Although plots of log *i* *vs.* *E* during the initial stages of dissolution showed a well-defined Tafel relationship, the slopes were not sufficiently constant to enable reliable kinetic data to be extracted.

Galvanostatic measurements.—When a titanium carbide electrode was charged at constant current in the range 2×10^{-3} to 1×10^{-2} A cm^{-2} in 0.1*N* H_2SO_4, two plateaus in the potential-time curve were found. These occurred at about the same potentials as those at which the two active regions were found during potentiostatic polarization. A typical *E/t* curve is shown in Fig. 3. The process giving rise to the first plateau was assumed to have finished after a time, τ, which was arbitrarily marked by the intersection of two straight lines, extrapolated from the region of rising potential and from the second plateau, in the

* Electrochemical Society Active Member.

Key words: anodic, dissolution, polarization.

[1] Tacussel, 2, rue Carry, Lyon 3, France; Ryaby Associates, 38 Wall St., Passaic, N.J. 07055.

[2] Sefram, 74, rue de la Fédération, Paris XV, France.

[3] All potentials reported in this paper are referred to the standard hydrogen electrode.

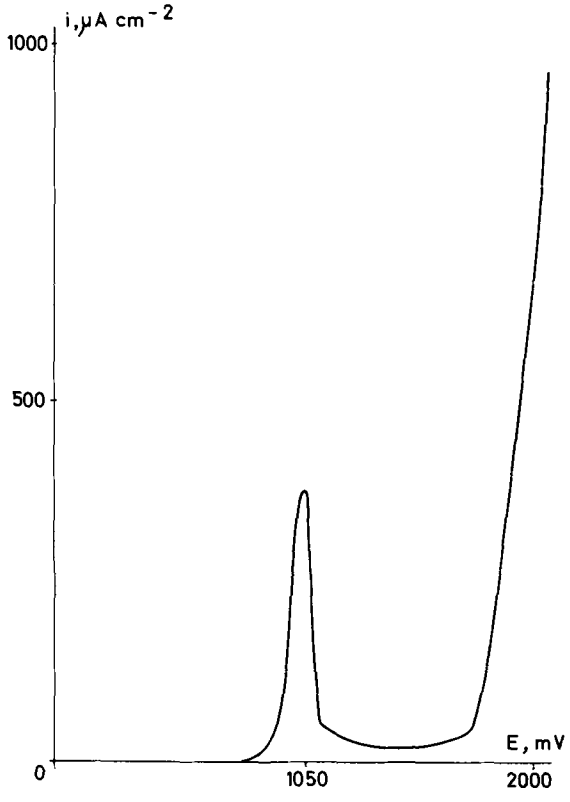

Fig. 1. Polarization of TiC in 2N H_2SO_4, 10 mV min^{-1}

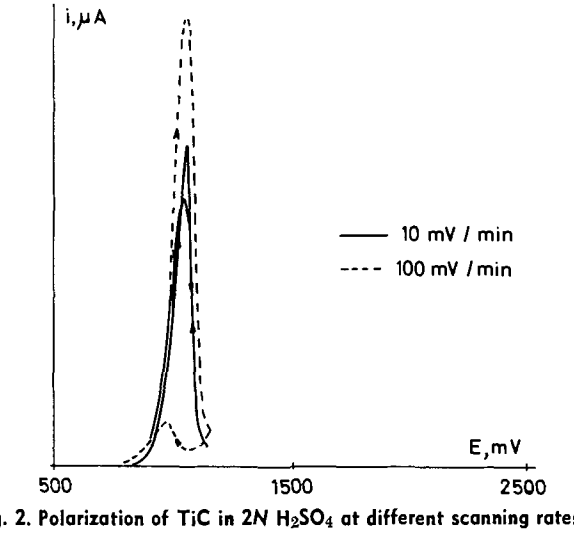

Fig. 2. Polarization of TiC in 2N H_2SO_4 at different scanning rates

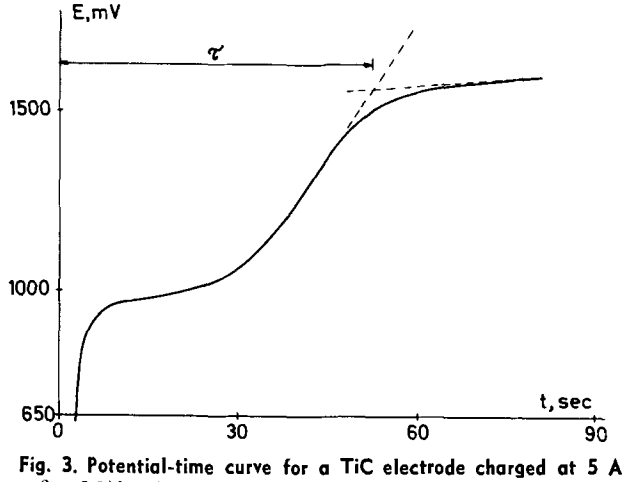

Fig. 3. Potential-time curve for a TiC electrode charged at 5 A cm^{-2} in 0.1N H_2SO_4.

Table I. Transition times for galvanostatic charging of TiC in 0.1N H_2SO_4

$i \times 10^3$, A cm^{-2}	10	9	8	7	6	5	4	3
τ_1 sec	18	23	26	32	41	53	70	107
τ_2	18	23	27	33	42	53	68	104
τ_3	19	23	27	33	42	53	68	104
$i\tau^{1/2}$	43	44	41	40	39	36	33	35

manner indicated in Fig. 3. At each current, three charging curves were obtained, each one after prior polarization to the point of hydrogen evolution, and the mean value of τ recorded. At any one current, the reproducibility in the values of τ was generally excellent. Typical results are shown in Table I.

Identification of the dissolution products.—From the titanium.—Several attempts were made to detect the presence of Ti(III) in the solution during the anodic dissolution of titanium carbide. In a standard solution of Ti(IV) in 2N H_2SO_4, containing 5 ppm of Ti and saturated with nitrogen, a platinum wire electrode was polarized cathodically to the point of vigorous hydrogen evolution. After about 5 min, the electrode was charged with a constant anodic current of 3 μA. The *E/t* curve showed a plateau at 0.47V due to the oxidation of Ti(III) to Ti(IV). A titanium carbide electrode was then charged at 500 μA in 2N H_2SO_4 saturated with nitrogen. After a sufficient time had elapsed to put a detectable amount of titanium into solution, a platinum wire electrode in the solution was charged anodically at 3 μA, and the *E/t* curve recorded. No plateau corresponding to the oxidation of Ti(III) could be found. Thus, while this test was not intended to give a quantitative microanalysis of Ti(III), it indicated at least that the concentration of this ion did not build up during the dissolution to a level which was comparable to the concentration of titanium in the solution, and that therefore this titanium is almost certainly in its tetravalent oxidation state.

A similar attempt to detect the presence of Ti(III) as a result of the dissolution of TiC was made by potentiometric titration with a Ce(IV) solution. This also gave a negative result.

From the bonded carbon.—A titanium carbide electrode was charged galvanostatically at 100 μA for 6 days, in 5 ml of 2N H_2SO_4 contained in a tube sealed with a silicon rubber bung. A platinum wire was used as the cathode. The cell voltage was recorded continuously, and was always less than 1.3V. At the end of the charging period, samples of the gas above the solution were taken by direct injection of a 1 ml syringe. This gas was analyzed with a permanent-gas chromatograph,[4] using a silica gel, and a molecular sieve, column. The presence of both CO_2 and CO was confirmed.

Repeat experiments were performed on single crystals of titanium carbide, and in every case both gases were detected.

Discussion

The equilibrium potential-pH diagram for the system titanium-H_2O shows (8) that the most stable species at pH = 0 and at potentials in the region of 1V is the tetravalent ion TiO^{2+}. In fact, at this pH the domain of stability of this ion extends from about zero to about 1.8V. As all attempts to detect the presence of Ti^{3+} during the anodization of titanium carbide failed, it is reasonable to suppose that the initial dissolution produces TiO^{2+}. The actual mechanism cannot be elucidated at this stage, although further work is in progress with pure single crystals of the carbide.

It is quite possible that the dissolution actually produces Ti^{3+}, but that this species is subsequently oxidized to TiO^{2+} at the surface of the corroding

[4] H. Feichtinger, Schaffhausen, Switzerland.

electrode. From Pourbaix (8), the equilibrium potential for the redox couple Ti^{3+}/TiO^{2+} at $pH = 0$ and at $TiO^{2+}/Ti^{3+} = 6$ is about 0.46V. Since the potential of the titanium carbide is above 0.8V during its dissolution, it is clear that any Ti^{3+} formed would be quickly oxidized to TiO^{2+}. Thus, while the present work cannot distinguish whether titanium carbide is oxidized directly to Ti(IV) or whether this occurs through the intermediate formation of Ti(III), the net result is clearly an oxidation to the tetravalent state. Further experiments are planned to examine this question more fully, with the aid in particular of a rotating ring-disk electrode, and it is hoped to report these results in a further communication. It is therefore proposed here that the passivation observed between about 1.2 and 1.7V is due to a tetravalent oxide (or hydrated oxide) of titanium. The peak at about 1V in Fig. 1 can thus be attributed to the sequence

$$TiC(s) \rightarrow TiO^{2+}(aq) \rightarrow TiO_2 \cdot H_2O(s)$$

Figure 4 shows that the formation of the oxide is kinetically possible at potentials above 0.91V. At this point, the i/t curve at constant potential first shows a gradual decay, due to the depletion of active surface by the formation of solid oxide.

During the second active region, one would then expect the oxidation to produce Ti(VI) ions. The potential at which this region begins is in fact in good agreement with that indicated by Pourbaix for the process $TiO_2 \cdot H_2O \rightarrow TiO_2^{2+}$. Direct experimental evidence is given by the fact that, during the dissolution of titanium carbide at about 2V, the solution gradually becomes yellow. It shows exactly the same absorption maximum (410 nm) as the yellow solution formed by the reaction of titanium(IV) ions with hydrogen peroxide, which is due to the ion TiO_2^{2+}.

Figure 2 confirms that this oxide is relatively soluble. Reactivation on the reverse scan occurs only at slow sweep speeds; at higher scan rates, dissolution of the oxide film is not sufficiently fast to allow reactivation. It would appear, then, that passivation is not due to anhydrous TiO_2 (rutile), which has a very low solubility, but rather to the hydrated oxide TiO_2 H_2O.

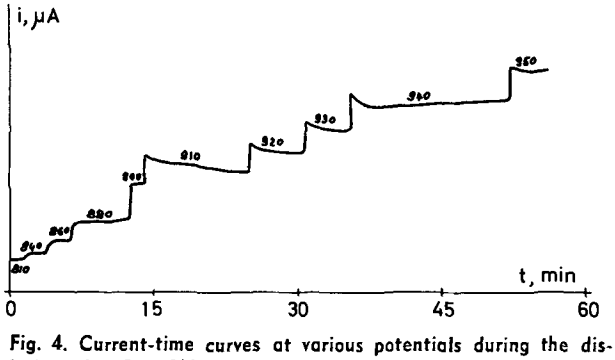

Fig. 4. Current-time curves at various potentials during the dissolution of TiC in 2N H_2SO_4; numbers refer to potential in millivolts.

The gaseous corrosion products being CO_2 and CO, the initial dissolution may proceed according to the reactions

$$TiC + 3\,H_2O = TiO^{2+} + CO_2 + 6\,H^+ + 8e^-$$

and

$$TiC + 2\,H_2O = TiO^{2+} + CO + 4\,H^+ + 6e^-$$

for which dE/dpH is -0.044 and -0.039V, respectively. This corresponds with the observed pH-dependence of -0.045 ± 0.005V.

The potentiostatic experiments therefore indicate that the initial corrosion of TiC produces TiO^{2+}, and that at a certain potential (0.910V in 2N H_2SO_4) the formation of solid oxide ($TiO_2 \cdot H_2O$) begins. At about 1.05V, the rate of formation of oxide exceeds the rate of its dissolution, and the electrode becomes passivated. At about 1.75V, oxidation to TiO_2^{2+} occurs, and severe corrosion of the TiC follows.

This picture is confirmed by the galvanostatic experiments. The charging curve shown in Fig. 3 contains only two plateaus, of which the potential of the first clearly corresponds to the dissolution of TiC as TiO^{2+}. In general during such galvanostatic charging, where the initial corrosion product is freely soluble, the current density, i, and the time, τ, required for passivation to occur are related by: $i\tau^{1/2}$ = constant. In the present case, although the transition times were very long and were rather arbitrarily determined, this relationship held reasonably well above about 6×10^{-3} A cm^{-2} (see Table I).

The second plateau in Fig. 3 occurs at a potential which corresponds closely to that found potentiostatically for the oxidation to Ti(VI). The absence of an intermediate plateau is further evidence that the net reaction during the first active region is an oxidation to the tetravalent state of titanium.

Manuscript submitted April 13, 1970; revised manuscript received July 15, 1970.

Any discussion of this paper will appear in a Discussion Section to be published in the June 1971 JOURNAL.

REFERENCES

1. V. P. Kopyleva, *Zh. Prikl. Khim.*, **34**, 1936 (1961).
2. A. M. Suggs, U.S. Pat. 2,636,856 (Cl. 204-290), April 28, 1953.
3. G. Ervin, H. F. G. Ueltz, and M. E. Washburn, *This Journal*, **106**, 144 (1959).
4. S. P. Denker, *J. Phys. Chem. Solids*, **25**, 1397 (1964).
5. S. P. Denker, "Bonding Stability and Formation of Cubic Refractory Monocarbides, Mononitrides and Monoxides," Report No. CU-3553-5, U.S. Atomic Energy Contract No. AT(30-1)-3553.
6. E. Dempsey, *Phil. Mag.*, **8**, 285 (1963).
7. H. E. Hintermann and H. Gass, *Schweiz. Archiv. Angew. Wiss. Tech.*, **33**, 3 (1967).
8. M. Pourbaix, "Atlas d'Equilibres Electrochimiques à 25°C," Gauthier-Villars, Paris (1963).

A Comparison of Various 24K Gold Electrodeposits

S. E. Craig, Jr.,* R. E. Harr,* J. Henry,[1] and P. Turner[2]

Chemical Engineering, School of Engineering, College of Engineering Sciences, Arizona State University, Tempe, Arizona 85281

ABSTRACT

Thick electrodeposits of 24K gold were prepared from 14 types of plating solutions in both new and replenished-used conditions. The deposits were examined by x-ray, scanning electron microscope, gravimetric, and electrical techniques. It was found that the purity, microstructure, and apparent density were functions of the plating solution type and age. The crystal lattice constants were found to be independent of both type and age.

Deposit Preparation

Fourteen types of plating solutions were selected as representative of modern commercial plating practice. They contained 8-15 g/liter gold and were operated at 3 mA/cm^2. The bath components are given in Table I. The used baths were taken from various production lines. They had all been "turned over" at least 10 times. The amount of use and degree of contamination could not be precisely determined for these baths. However, a partial determination is given in Table III. Before using the old baths, they were filtered, analyzed, and regenerated by adjusting the pH, density, and gold concentration to the nominal values.

Plating was accomplished in a vigorously agitated 4 liter, constant-temperature tank. The anodes were platinum-plated titanium and had approximately 5 times the area of the cathodes. During plating, small quantities of gold were periodically added to the bath to insure that the gold concentration never fell below 90% of its nominal value. The cathodes were copper plates 2.5 x 5 cm. One side of each cathode was mirror smooth while the other side had a fine mat finish. Four cathodes were used for each bath and the gold was deposited on both sides of each cathode. Immediately after deposition, the samples were cut and the copper etched away with nitric acid. The samples were ultrasonically washed in water, trichloroethylene, and methanol, dried, and stored for later examination.

* Electrochemical Society Active Member.
[1] Present address: U.S. Army, Ft. Bliss, Texas.
[2] Present address, Texas Instruments, Inc., Dallas, Texas.
Key words: gold, electrodeposits, purity, crystal structure, resistivity, density.

The deposits were very thick (127 μm) so that effects from the bath could be separated from effects of the copper substrate.

The properties investigated were appearance, density, purity, crystal structure, and preferred orientation. In all cases, the samples from the smooth side of the copper cathodes had the same characteristics as those from the mat side of the copper.

Visual Appearance

The visual appearances of the solution side of the deposits are tabulated in Table I. Except for deposits from baths 1, 13, and 14, the surfaces were fairly similar in appearance. They differed only in relative brightness, smoothness, and fineness of the mat. Bath 13 produced unique, smooth, uniformly brown, dull surfaces. Bath 14 produced bright, shiny, perfectly smooth surfaces. The sparkly, bright appearance of the new hot cyanide deposit is due to its large, individual grains, while the dull, orange or brown color seen in deposits 8u, 11u, and 13 is caused by many small, individual grains. Deposits from used baths tended to be duller and smoother than deposits from new baths. The addition of brighteners and hardeners caused the baths to produce a finer mat surface.

The sides of the deposit adjacent to the copper cathodes were visual replicas of the copper surface even when viewed at 30,000X.

Density

The density of each sample was determined from its weight in air and in diiodomethane. The results, corrected for buoyancy of air and further corrected

Table I. Gold-plating deposits investigated

Bath* No.		Ref.	pH	Density ° Baumé	Visual appearance	Density g/cm^3
1n	Hot cyanide, phosphate, carbonate	(1)	12	15-30	Sparkly bright, very coarse mat.	19.22
1u					Very coarse mat.	19.13
2n	Citrate, phosphate in equal amounts	(2)	5.7-6.0	15-25	Bright, coarse mat.	19.26
2u					Dull, smooth.	19.25
3n	Same as 2 plus 25 g/liter polyamino acid com-		5.7-6.0	15-25	Bright, fine mat.	19.27
3u	plex				Dull, fine mat.	19.27
4n	Same as 2 plus 10 g/liter metallic brightener		5.5-6.0	15-25	Fine mat.	19.26
4u					Fine mat.	19.26
5n	Same as 4 plus 20 g/liter potassium chromium		5.5-6.0	15-25	Dull, fine mat.	19.25
5u	sulfate hardener				Dull, smooth.	19.26
6n	Same as 5 plus 25 g/liter boric acid inhibitor		5.5-6.0	15-25	Very fine mat.	19.25
7n	Citrate plus 6 g/liter hydrazine sulfate redox	(3)	4.2-4.5	14-16	Fine mat.	19.26
7u	agent				Fine mat.	19.25
8n	Phosphate plus 6 g/liter hydrazine sulfate	(4)	5.5-6	14-16	Fine mat.	19.27
8u					Dull, fine mat, orangeish stains.	19.26
9n	Ammonium citrate plus 20 g/liter potassium	(5)	4.5	12	Very fine mat.	19.25
9u	chromium sulfate hardener				Dull, very fine mat.	19.27
10u	Borocitrate plus tetraethylene pentamine		5.0-6.0	20-25	Dull mat.	19.26
11u	Phosphate		6	17-18	Dull mat, orangeish stains.	19.27
12u	Phosphate		9-10	23	Dull, very fine mat.	19.27
13n	Gold sulfite with excess sulfate and sulfite	(6)	9-10	10-12	Very dull, smooth, brownish.	19.23
13u					Dull, smooth, orangeish.	19.25
14n	Same as 13 plus 15 ppm arsenic		9-10	10-12	Bright, shiny, very smooth.	19.13
14u					Bright, shiny, smooth.	19.24

* "n" and "u" signify new and used baths respectively.
Source of gold is $KAu(Cn)_2$ for all baths, except 13 and 14. All unspecified cations are potassium. The conducting salts had concentrations of approximately 100 g/liter as required to provide the lower Baumé for new baths and the higher for used baths.

to 25°C, are shown in column 7 of Table I. Most of these densities are within 0.2% of the density of pure gold. The exceptions are deposits from baths 1, 13, and 14. The low density of deposits from bath 1 is a result of the large pores within the deposits. The lower density of the deposits from bath 13 are caused by the 5 ppm sulfur contained in this deposit and by the microscopic voids barely visible in the photomicrographs. The arsenic in bath 14 further reduces the deposit density.

Electrical Resistivity—Procedure

Strips approximately 1 mm wide and 25 mm long were cut from the deposits and tested for electrical resistivity using a standard four-contact technique. The measurements were made at room temperature, 298°K, and liquid nitrogen temperature, 77°K. The main uncertainty in any individual resistivity measurement resulted from geometric uncertainties. However, when the resistivity at room temperature is divided by the resistivity of the same sample measured at liquid nitrogen temperature, all geometric factors cancel and a ratio. R_{298}/R_{77}, is obtained which is a function of the material only. This ratio does not include the effects of voids, pores, or electrically inactive inclusions. It does include the effect of chemical purity and, to a lesser extent, grain size.

This ratio serves as a sensitive indicator of relative chemical purity. However, it yields no information as to the concentration or types of impurities present.

White and Wood (7) report R_{298}/R_{77} equals 5.0 for 99.999% pure, vacuum-annealed gold. The highest value obtained in this work was 4.91. The difference probably represents a normal amount of dissolved gases, since most of these deposits are 99.999+% pure on a metallic basis.

Deposits from new baths without special additives (baths 1, 2, 7, 8) typically had a resistivity ratio of about 4.9, while used baths without special additives yield deposits with R_{298}/R_{77} in the range of 4.6-4.8. This reduction in purity is typical of the contamination obtained in normal industrial usage.

The high value of R_{298}/R_{77} for the deposits from bath 4 indicates an extremely low amount of codeposition of the brightener.

The addition of hardeners reduced R_{298}/R_{77} into the 4.6 range. However, as the baths were used and the special agents were depleted, the value of R_{298}/R_{77} for deposits from these baths approached the value from used baths without special additives.

Deposits from bath 13 had a lower value of R_{298}/R_{77} than expected. When these deposits were annealed to 400°C for 8 hr, the value of R_{298}/R_{77} increased to about 4.4 which still indicates a fairly high level of impurities. The exceptionally low resistivity level for deposits from bath 14 is a direct result of the 15 ppm arsenic included in the deposit.

The high value of the resistance ratio for deposits from used baths 3 and 10 indicates a very high purity of deposit. This purity can be traced to the low level of contamination of these baths and to the effectiveness of the chelating agent in preventing the deposition of contaminants.

Crystalline Structure

The crystalline structure of the deposits was examined by x-ray diffraction techniques, by Berg-Barret X-Ray Topology (8) and by Scanning Electron Microscopy (SEM). Prior to SEM examination, the sample cross sections were etched in a solution of 2.5% $(NH_4)_2S_2O_8$ and 2.5% KCN for 5-30 min at 25°C to bring out the crystal structure. Typical SEM photomicrographs are shown in Fig. 1 through 8.

Generally, the surface microstructure can be divided into four categories. The first is that produced by the alkaline cyanide baths (Fig. 1). These surfaces are composed of uniform, very large (60-120 μm) grains separated by open grain boundaries which penetrate deeply into the deposit. The second category includes most of the solutions. For this category, nonuniform grains of 5-50 μm are connected by distinct, tight-grain boundaries. Deposits from baths 4, 5, and 6, which contain a codepositing metallic brightener, show more small (1-5 μm) grains. In these first two categories, deposit surfaces made from new baths tended to contain many smooth planes, sharp angles, and straight lines identifiable with the underlying crystal structure (Fig. 2 and 4). Deposits made from used baths exhibited a less-organized structure made up of rounded surfaces and curved lines and often contained randomly distributed small (<1 μm) pits (Fig. 3 and 5). A notable exception to this is the deposit from bath 3 and to a lesser extent the deposit from bath 10, where the chelating agents have caused deposits from used baths to have the surface characteristics of new baths.

The third category of surface microstructure is exhibited by the pure sulfite bath, bath 13, Fig. 7. The grains are small and fairly uniform in size 0.2-5 μm). The grain boundaries are distinct and do not appear to

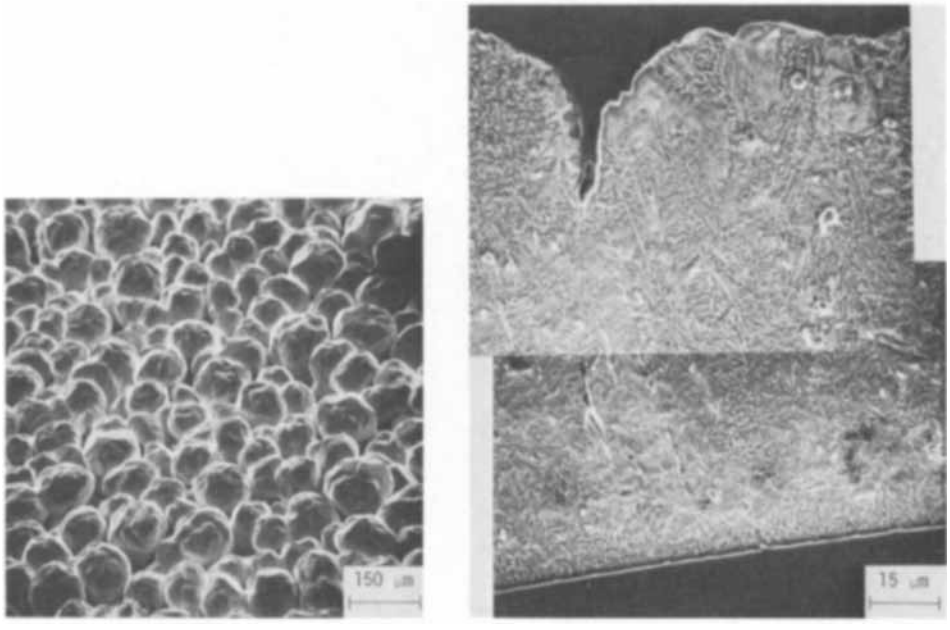

Fig. 1. SEM photomicrographs of deposit 1n from a hot cyanide solution.

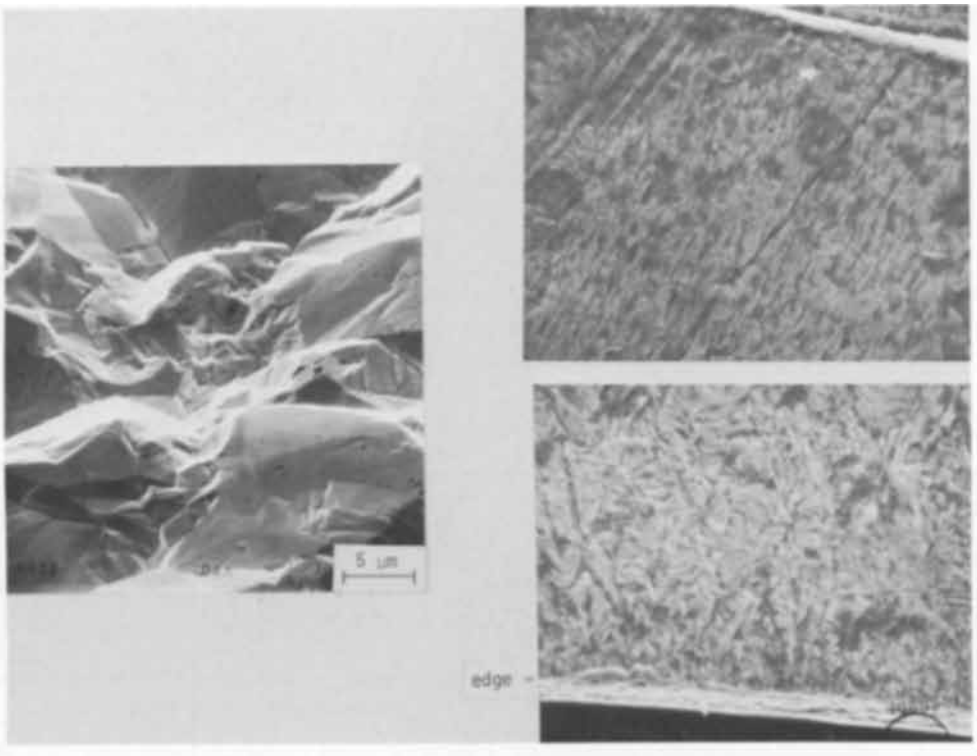

Fig. 2. SEM photomicrographs of deposit 2n. The center 2/3 of the cross section is removed. The lower picture is the copper edge of the deposit, while the upper picture is the solution edge. Surfaces and sections of deposits 3u, 7n, 10u, and, to a lesser extent, 8n, were similar.

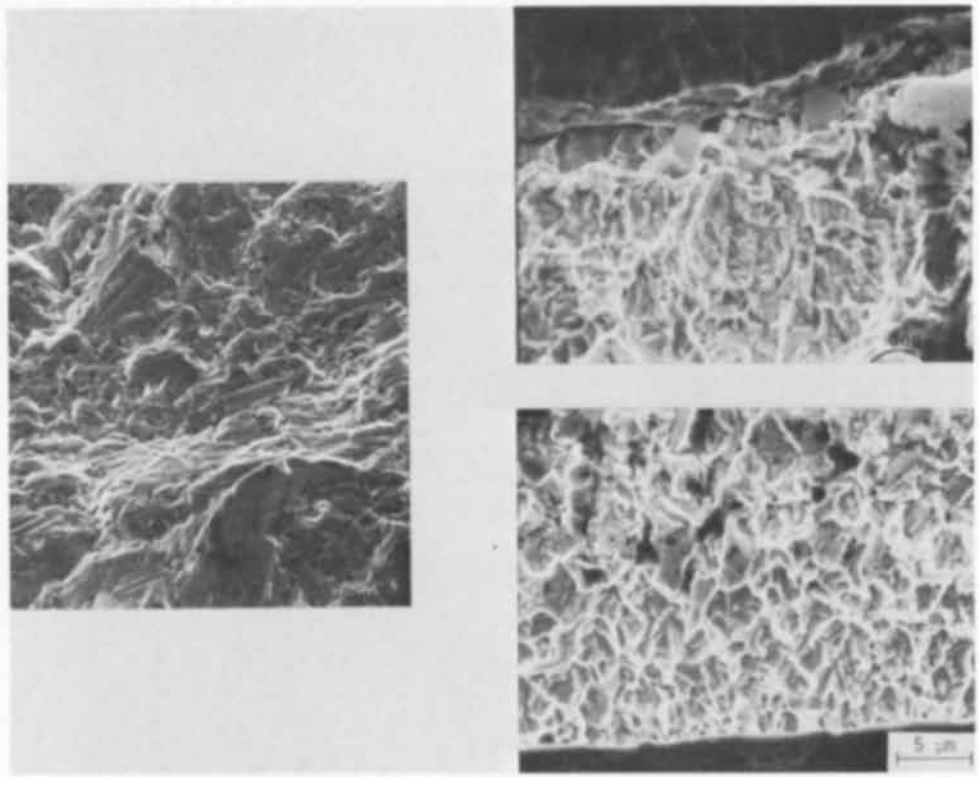

Fig. 3. SEM photomicrographs of deposit 2u.

be tightly closed. The fourth category is exhibited by bath 14. Surfaces from this bath were completely featureless even when viewed at 30,000X.

The SEM photomicrographs of cross sections may also be divided into four categories. The first is the coarse grain structure with deeply penetrating pores found in the hot cyanide bath deposits, Fig. 1. The second category includes the majority of the deposits and shows grains less than 0.5 μm in diameter on the substrate side of the deposit and crystallites 5-30 μm in diameter on the solution side of the deposits. Many of these crystallites can be followed for 20-60 μm through the deposit. Those deposits containing hardeners and brighteners, baths 4, 5, 6, and 9, fall at the lower end of the crystallite size ranges. Deposits from used baths tend to fall in the center of the range, while deposits from new baths which do not contain metallic impurities and from used baths containing chelating agents have crystallites in the upper end of the size range. The two anomalous structures in this group are from new solution 3 which appeared almost amorphous and from new solution 9 which exhibited a distinct columnar structure (Fig. 6).

The third category consists of deposits from the non-cyanide solution, bath 13, which had extremely small grains throughout the deposit (Fig. 7).

The last category is from the non-cyanide solution containing arsenic, bath 14. Cross sections of these

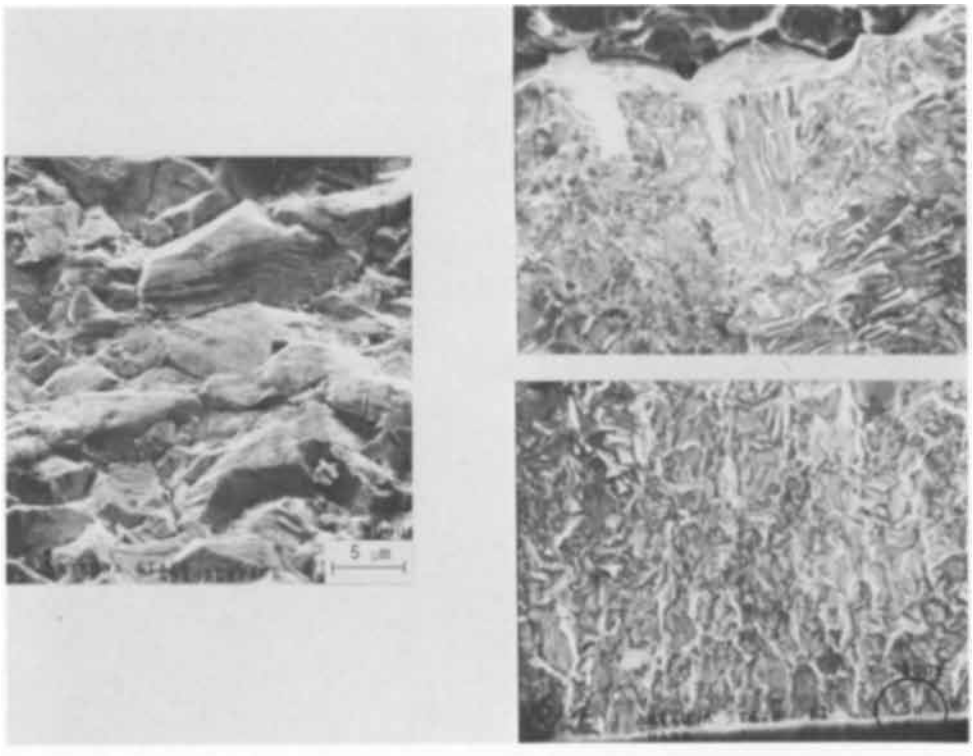

Fig. 4. SEM photomicrographs of deposit 4n. Deposits from 5n and 6n were fairly similar.

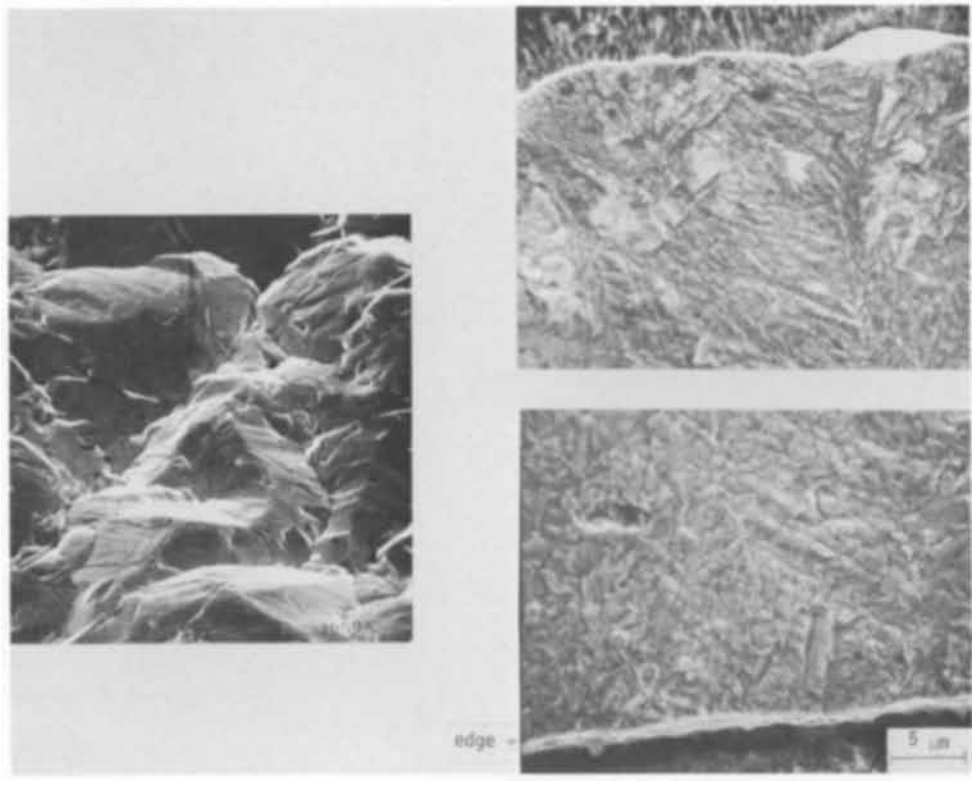

Fig. 5. SEM photomicrographs of deposit 4u.

deposits are amorphous in appearance (Fig. 8). The deposit from the new bath also shows a layered structure similar to those often found for alloy deposits (8). The deposit from a used bath shows only a random porosity.

The crystal lattice parameters were determined by x-ray back reflection. Within the limits of the equipment used, the lattice parameters were those for pure gold. Thus the density variations shown in Table I are caused by impurities, pores, inclusions, *etc.*, but not by lattice expansion.

X-ray line broadening was used to determine the average crystal size (9). This technique is precise for crystallite sizes under 0.1 μm, but for larger values the accuracy degenerates quickly and only a lower limit can be placed on the size. The results of the line-broadening measurements are shown in columns 3 and 4 of Table II.

Berg-Barrett X-Ray Topology (10) was used to determine the maximum crystallite size. With the film used, crystals larger than 3 μm were resolved. The results are shown in parentheses in columns 3 and 4 of Table II. Where values are not reported, no individual crystals could be resolved by this technique.

The first crystals to nucleate from new baths not containing metallic impurities (baths 1, 2, 3) grew to average sizes greater than 0.1 μm. However, the first crystals to grow from all other baths were much

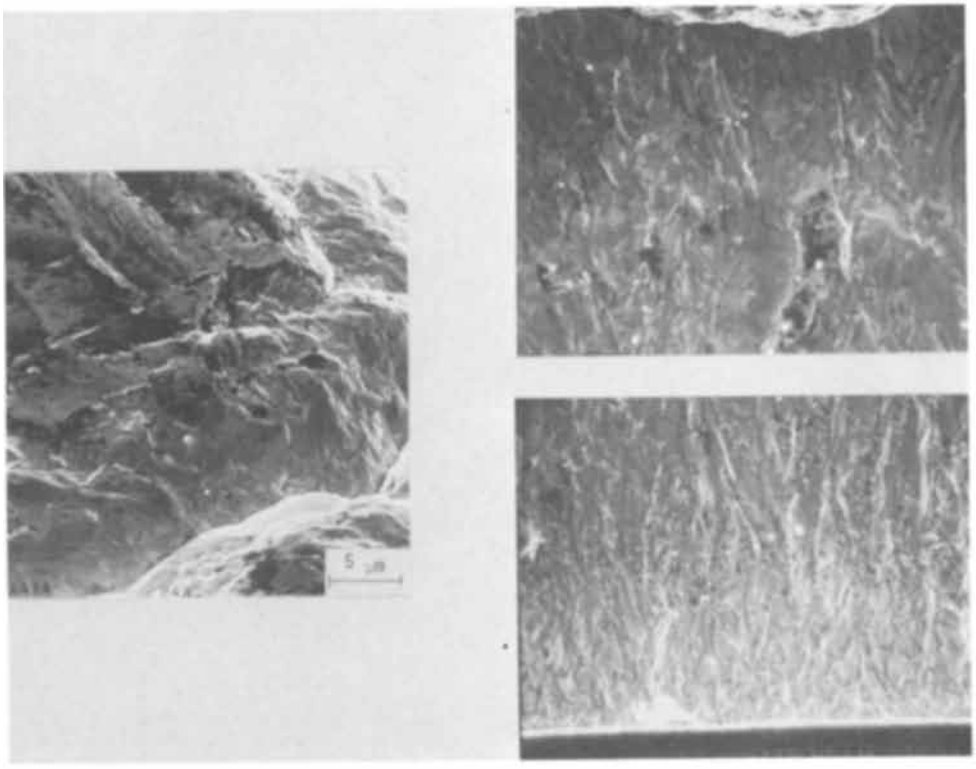

Fig. 6. SEM photomicrographs of deposit 9n.

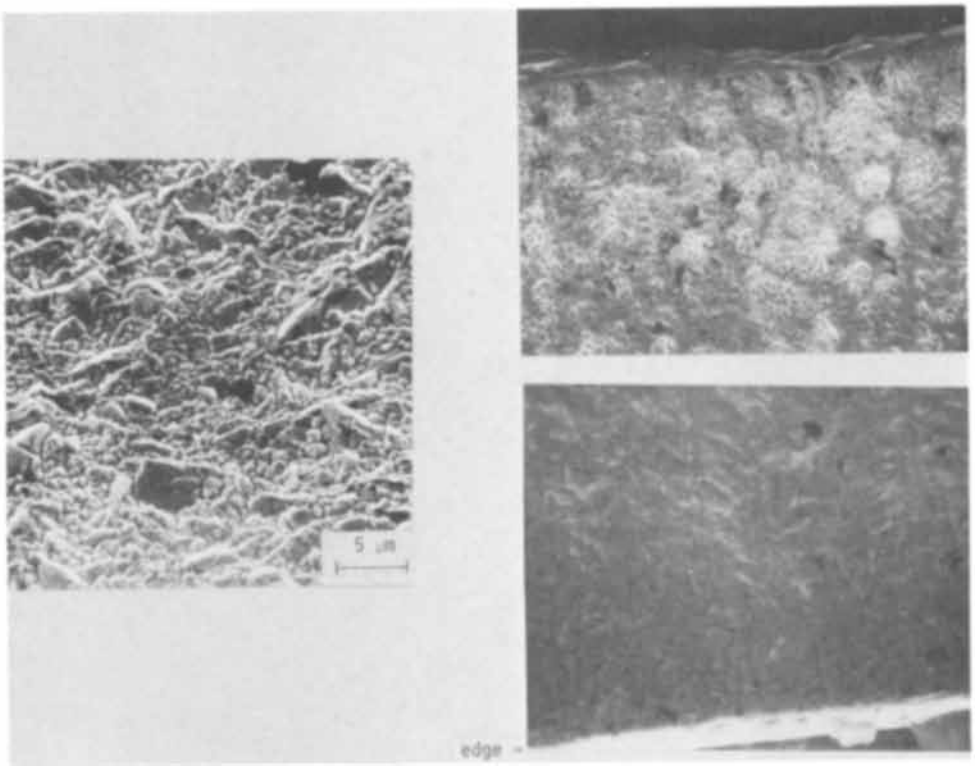

Fig. 7. SEM photomicrographs of deposit 13n. Deposit 13u was similar, but finer grained.

smaller in size (about 0.03 μm). These other baths, with the exception of 7 and 8, all contained metallic impurities either because of normal contamination from use or because of addition of hardeners and brighteners. It appeared that these codepositing metallic impurities facilitated nucleation on the copper substrate so that the average crystal size was smaller. Hydrazine sulfate (baths 7 and 8) performed the same function although the mechanism by which this occurred was not clear.

The average crystallite size on the solution side of the deposit was a good indication of the ability of hardeners and brighteners to control average crystal size. New baths 4, 5, 6, and 9, with these additives, show average solution side crystal sizes of about 0.06 μm, while new baths without these addition agents produce crystals in excess of 0.1 μm. As the baths were used and replenished, the effectiveness of the brighteners and hardeners in controlling crystal size was diminished. This was probably caused by a failure to replenish the baths with these additives at the same rate they were consumed. At the same time, all baths picked up impurities during use. These impurities, unless counteracted with chelating agents as in baths 3 and 10, tended to decrease the grain size. The net result was that baths with and without the

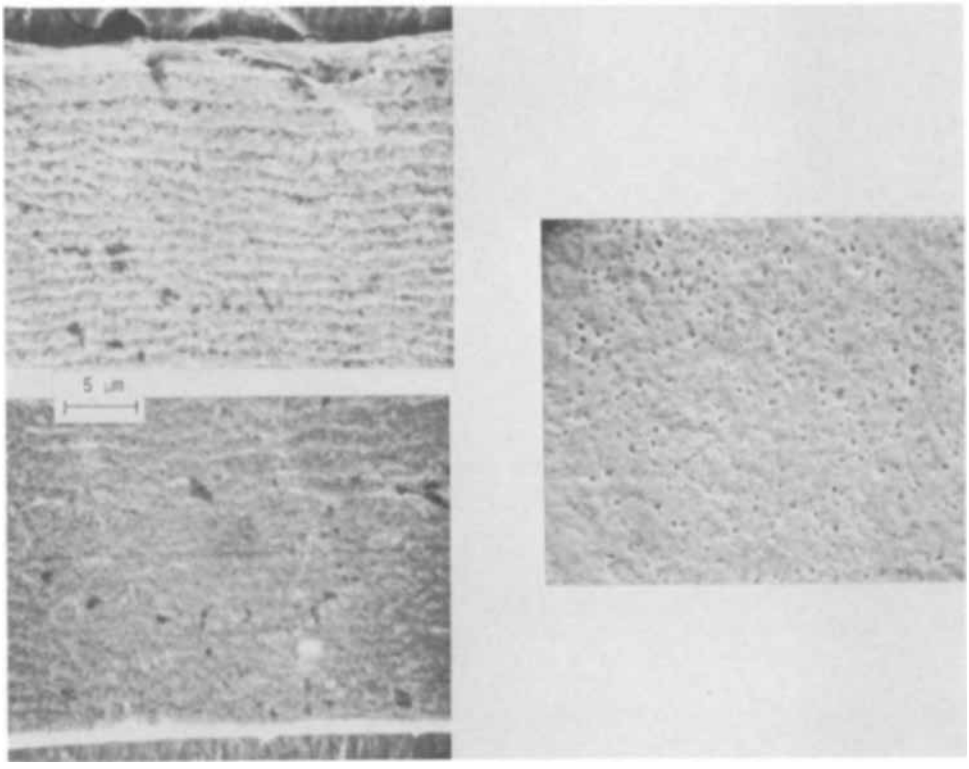

Fig. 8. SEM photomicrographs of sections of deposits 14n and 17u. Surfaces were featureless.

special additives took on the same character as they became contaminated with use.

Except for baths 1 and 14, the maximum crystallite size obtained by the deposits differed only slightly from bath to bath. Bath 14 was the only bath to produce resolvable crystals on the copper side of the deposit. The used bath 14 produced many extremely large single crystals on the solution side of the deposit. These crystals exhibited internal structure, possible parallel slip planes, and long range order between crystals. Since these crystals were not resolved in SEM photomicrographs of either the section or the surface, we conclude that these crystals are extremely thin and oriented parallel to the surface. Crystal platelets of this type are believed to be major contributors to the smooth, shiny surfaces of these deposits.

Table II. Deposit characteristics

Bath No.	R_{298}/R_{77}	Crystallite size μm Copper side	Crystallite size μm Solution side	Preferred orientation* Copper side	Preferred orientation* Solution side
1n	4.82	>0.1	>0.1 (20)	(111)	r, −(111)
1u	4.77	0.05	>0.1 (20)	(311), r	r, −(111)
2n	4.91	>0.1	>0.1 (12)	(111)	(311), (511)
2u	4.70	0.03	0.05 (7)	(311)	(311), (511), −(111)
3n	4.79	>0.1	0.06 (6)	(111)	(311), (422)
3u	4.92	0.03	>0.1 (7)	(111), (311)	(311), (511)
4n	4.70	0.06	0.08 (9)	(220), (311)	(220), (311)
4u	4.86	0.04	>0.1 (7)	(311), r	(311), (511)
5n	4.62	0.03	0.06 (8)	r	r
5u	4.69	0.03	>0.1 (10)	(220), (311)	(220) (311)
6n	4.72	0.03	0.06 (9)	(111)	(311)
7n	4.91	0.03	>0.1 (10)	(111), (311)	(311)
7u	4.60	0.03	0.08 (15)	(311), r	r
8n	4.87	0.03	>0.1 (15)	(311)	(220), (311)
8u	4.83	0.04	0.07 (9)	(311)	(311), (511)
9n	4.36	0.03	0.05 (11)	(111)	(111)
9u	4.65	0.03	0.05 (11)	(111)	(311)
10u	4.88	0.03	>0.1 (10)	(111)	(311), (511)
11u	4.91	0.04	>0.1 (10)	(311)	(200) (311), (511)
12u	4.82	0.06	0.06 (10)	(111)	(311)
13n	4.12	0.03	0.06 (6)	(220)	(220)
13u	4.14	0.05	>0.1 (8)	(111), r	r
14n	2.67	0.05 (8)	0.05 (3)	(200)	(200), (220)
14u	3.73	0.06 (10)	>0.1 (50)	(220)	(200)

* "r" signifies a nearly random orientation. Underlined orientations are strongly preferred orientation. Doubly underlined orientations are very strongly preferred. Orientations preceded by a minus sign are significantly diminished.

X-ray diffraction was used to determine the preferred orientation of the deposits. For each side of each deposit, the x-ray intensities of the the first 10 diffraction peaks were measured. These peaks represent crystal orientation from (111) to (511). Intensities for redundant peaks such as (200) and (400) were combined. The intensities were then normalized and compared with NBS data for random deposits (11) and with a pure gold powder sample. The results are shown in columns 5 and 6 of Table II. A major feature of some diffraction patterns was the suppression of a particular peak intensity. This is shown in Table II by a minus sign in front of the associated orientation.

With the exception of the non-cyanide baths and acid phosphate baths, new baths without hardeners or brighteners tended to nucleate and grow (111) initially. As growth of these deposits continued, the (111) orientation was suppressed and higher order orientations, particularly the (311), became dominant. This is in keeping with the general concept that close-packed orientations are natural for heterogeneous nucleation but form the slowest growing crystal faces.

The addition of hardeners, brighteners, or normal operational contaminants usually suppressed the initial (111) nucleation so that both sides of the deposit tended to have a (311) preferred orientation or to be more nearly random. However, two baths, 6 and 9, which contained hardeners, produced deposits with strongly preferred initial (111) orientation. In addition to hardeners and brighteners, bath 6 contained boric acid as a copper conditioner. New bath 9, which contained the hardener and ammonium ion, produced a strong (111) preferred orientation throughout the deposit. The chelating agents in baths 3 and 10 were effective in controlling contaminations so that deposits from these used baths had orientations typical of deposits from new baths. The acid

Table III. Metallic constituents in used baths

Bath No.	1u	2u	3u	4u	7u	9u	10u	14u
Gold	7.45	6.24	4.61	6.34	8.06	7.20	6.44	10.14
Silver						0.025		
Nickel	0.21	0.11	<0.01	0.019	0.017	0.01	0.052	<0.01
Copper	0.44	0.01	0.056	0.02	0.015	<0.01	N.D.	0.10
Cobalt	N.D.	0.07	N.D.	N.D.	0.07	N.D.	N.D.	N.D.
Iron	0.19	0.27	<0.01	0.044	0.026	0.08	0.054	N.D.
Lead	0.014	0.01	0.18	<0.01	<0.01	<0.01	N.D.	0.011
Zinc	N.D.	N.D.	0.50	N.D.	<0.01	0.02	N.D.	N.D.
Chromium						0.14		
Arsenic								0.40

Values are in grams per liter for baths taken from production lines.

phosphate baths (8 and 11) were unique in showing a strong tendency to (311) nucleation and growth.

The observations on preferred orientation do not correlate with the observations of crystal size, surface appearance, or grain structure, except in the case of new bath 9. The columnar structure that runs through this deposit is a direct result of the strong (111) preferred orientation for both nucleation and growth.

Conclusions

With the exceptions of the large grain porous structure of deposits from the hot cyanide bath, the very fine grain, brown deposit from bath 13, and the bright shiny deposits from bath 14, the deposits investigated were fairly similar. Special hardeners and brighteners added to new baths decreased the grain size and affected the orientation of the crystals and the surface appearance. However, as the baths were used and regenerated, the differences in deposits tended to diminish. Chelating agents were found to be effective in controlling impurity deposition from used baths.

Manuscript submitted Nov. 5, 1969; revised manuscript received July 6, 1970. This was Paper 151 presented at the Detroit Meeting of the Society, Oct. 5-9, 1969.

Any discussion of this paper will appear in a Discussion Section to be published in the June 1971 JOURNAL.

REFERENCES

1. "Metal Finishing Guidebook Directory," p. 279, Metals and Plastics Publications, Inc., Westwood, N. J. (1968).
2. B. Ostrow and F. Nobel, French Pat. 1,479,984 (1966).
3. R. Duva and D. G. Foulke, U.S. Reissue, 25,883 (1965).
4. D. G. Foulke, U.S. Pat. 3,156,634 (1964).
5. K. Schumpelt, U.S. Pat. 3,367,853 (1968).
6. P. T. Smith, U.S. Pat. 3.057,789 (1962).
7. G. K. White and S. B. Woods, *Phil. Trans. Roy. Soc. (London)*, **A251**, No. 995, 273 (1959).
8. R. Duva and D. G. Foulke, *Plating*, **55**, 10, 1056 (1968).
9. H. P. Klug and L. E. Alexander, "X-Ray Diffraction Procedures," John Wiley & Sons, Inc., New York (1954).
10. C. S. Barrett, *Trans AIME*, **161**, 15 (1945).
11. H. E. Swanson and E. Tatge, *Nat. Bur. Std. (U.S.) Circ. 539*, I, 33 (1953).

Electrophoretic Deposition of Luminescent Materials

P. F. Grosso, R. E. Rutherford, Jr., and D. E. Sargent

Applied Physics Department, CBS Laboratories, Stamford, Connecticut 06905

ABSTRACT

Electrophoretic deposition of luminescent materials such as $2CaO \cdot MgO \cdot 2SiO:Ce:Li$ has been accomplished by the adsorption of inorganic cations of Mg^{++}, Ca^{++}, Ba^{++}, Sr^{++}, Al^{+++}, Na^{+}, K^{+}, Li^{+} or NH_4^{+}, from nitrates, chlorides, and bromides, in polar liquids such as isopropyl alcohol with a critical concentration of about 1% H_2O. An explanation of the adsorption charging and the pertinent factors which effect cataphoretic deposition for a calcium magnesium silicate-magnesium nitrate system is presented. Acetone has been found to have a beneficial depolarizing effect, while magnesium salts produce a cementing action on the deposited phosphor layer.

The electrophoretic deposition of powdered phosphors to form fluorescent screens offers several advantages over the usual gravitational sedimentation-cementation processes: (*a*) Curved or irregularly-shaped objects can be coated uniformly; deposition can even be accomplished in an upward direction to prevent the settling out of large phosphor aggregates onto the screen. (*b*) Very fine particle-size screens can be deposited quickly from suspensions that flocculate or settle very slowly (due to the similar charge on each particle); in fact, in electrophoresis, the fine particles move and are deposited more rapidly than larger particles. (*c*) Definite control can be exercised over the amount and character of the final particle cementing agent; desirable cementing agents may be generated simultaneously with particle deposition by combining electrolytic with electrophoretic effects. (*d*) Very smooth screens of uniform and controlled thickness and density can be prepared.

Key words: electrophoresis, deposition, luminescent materials, phosphors, cathode-ray screens.

In these laboratories in the past, phosphor suspensions for electrophoretic deposition have been prepared by stone-milling phosphor powders in polar organic liquids such as alcohols, acetone, *etc.*, for substantial periods of time. Milling does indeed yield "charged" suspensions, but usually also damages the phosphor (light output and efficiency are lower than the original powder). The mechanism of this damage is not completely understood, but appears to result from severe

physical shear, production of many particles below optimum size for efficient fluorescence, thermal damage caused by high local impact temperatures, surface chemistry such as oxidation-reduction reactions, loss or absorption of various substances (*e.g.* analysis shows that phosphors milled with flint stones have absorbed aluminum), *etc.*

During the present study, methods have been sought for "charging" phosphor suspensions without the attendant damage of stone milling. Most attention has been focused on the addition of soluble electrolytes to suspensions of various phosphors in essentially nonaqueous media, but auxiliary means such as stirring, classification by settling (elutriation), and ultrasonic dispersion have also been employed.

In the experimental work described, calcium magnesium silicate (2CaO·MgO·2SiO:Ce:Li) was used.

Experimental Procedure

In order to compare the efficacy of various added electrolytes and various nonaqueous liquid suspending media for promoting the cataphoretic deposition of various phosphors the following test procedure was employed.

The electrophoretic deposition cell consisted of an unstirred vessel of 300 ml capacity, which was provided with a stainless steel frame which supported a 1 in. diameter test blank in a vertical position. The test blanks were either conductive glass or stainless steel. These blanks, one of which was used as the cathode in each experiment, were cleaned ultrasonically with acetone and were weighed before each deposition experiment. Facing the blank cathode and separated from it by a distance of ⅝-¾ in. was a row of three ¼ in. carbon rods held in a vertical position. These rods were the anode in each experiment. Any inert material, such as platinum, can be used as an anode. A variable d-c power supply capable of providing potentials up to 500V and currents up to 250 mA was used to promote electrophoretic deposition.

In typical operation, 250 mg of the phosphor powder under test was added to 250 cc of the fluid suspending media in which the electrolyte under test had previously been dissolved. The phosphor was allowed to equilibrate with the liquid medium by stirring for 5 min, and the resulting suspension was then poured into the test cell. Sufficient potential was immediately applied to yield a current of 10 mA and the deposition was allowed to proceed at 25°C without stirring. The test cathode blank was then withdrawn, dried, and weighed. The appearance of the deposited phosphor layer was examined and noted.

Pertinent Factors

Cataphoretic deposition is a complex phenomenon in which several variables play significant roles. First, the liquid suspending medium must be carefully chosen. It must be a suitable solvent for the added electrolytes under test, but must not yield solutions having high conductivities. It is desirable to maintain a high potential difference between the anode and the cathode, but high current flow with resultant resistance heating is not desirable. Deposition of the suspended powder rather than electrolysis of the liquid medium is desired. In addition, the liquid medium should have a low viscosity so that the charged particle can migrate at the maximum rate under the applied field. For practical reasons, it should be inexpensive, water miscible, and low in toxicity.

Previous work in these laboratories (1-3) and elsewhere (4) has shown that polar liquids such as the water soluble lower molecular weight alcohols and ketones provide good media for electrophoretic deposition. In the present study, isopropyl alcohol and acetone have been used almost exclusively, either separately or mixed together and usually with some water added. Water can be used to advantage in electrophoretic systems, but is very important to carefully control the amount added. This may be illustrated by

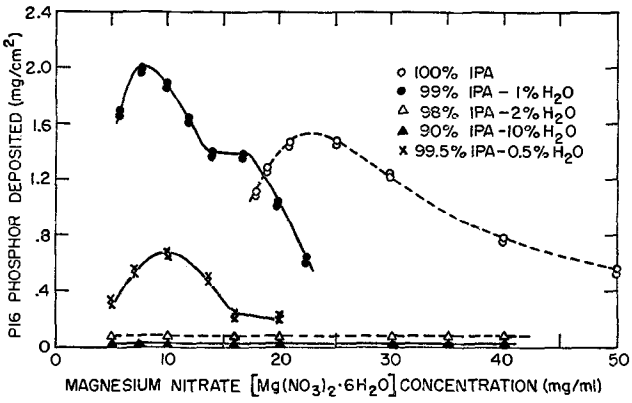

Fig. 1. Effect of magnesium nitrate and water concentrations on amount of phosphor deposited. Deposition conditions: carbon anode-stainless steel cathode; electrode spacing 5/8 in.; current 10 mA, voltage 25-100V; time 5 min; P16 phosphor concentration in suspension 1 mg/ml.

examination of 2CaO·MgO·2SiO:Ce:Li (P16 phosphor) deposition curves shown in Fig. 1. In the experiments represented by the curves, increasing amounts of magnesium nitrate $Mg(NO_3)_2 \cdot 6H_2O$ was added to either 100% isopropyl alcohol, 99.5% isopropyl alcohol +0.5% water, 99% isopropyl alcohol +1% water, 98% isopropyl alcohol +2% water, or 90% isopropyl alcohol +10% water. It will be noted that the highest mass deposition efficiency of phosphor (greater weight deposited during the standard 5 min time interval) occurred when about 8 mg of the magnesium nitrate was added to the 1% water system (250 mg phosphor in 250 cc 99% isopropyl alcohol +1% water). Addition of more or less magnesium nitrate gave less deposition of phosphor. In the experiments in which water was not added, the maximum deposition occurred with approximately 22.5 mg of the nitrate. Addition of more or less than 1% water also gave less deposition of phosphor than 1% water. Use of 98% isopropyl alcohol +2% water, 90% isopropyl alcohol +10% water gave very poor results at all levels of added magnesium nitrate. The higher water concentrations increased the conductivity to allow electrolysis to predominate over electrophoretic deposition. Lower water concentration did not allow satisfactory ionization to take place. It is then evident that the amount of water present, as well as the amount of electrolyte added, is critical.

In the 1% water system, addition of the optimum amount of magnesium nitrate (8 mg) apparently gives good "charging" of the calcium magnesium silicate (P16) phosphor since the weight of deposited phosphor is high. Simultaneously, the conductivity of the system appears to increase, for without the phosphor present 20 mg of magnesium nitrate would be required to give the same conductivity. In order to explain this phenomenon, it may be suggested that the phosphor, known to have excess calcium oxide on its surface, may undergo the following type of absorption-desorption reaction:

$$2(\text{P16}) - \text{SiO} \cdot \text{CaO} - \text{OH} + 2\text{Mg}^{++} + 2\text{NO}_3^- \rightarrow \left((\text{P16}) - \text{SiO} - \text{Mg}^{+} \right)_2 + 2\text{Ca}^{++} + 2\text{OH}^- + 2\text{NO}_3^- \quad [1]$$

The phosphor thus becomes "charged" and the ionic concentration (conductivity) of the suspending medium is simultaneously increased. When less than the optimum magnesium nitrate concentration is added, maximum charging is not attained, and the weight of phosphor deposition is decreased. If greater than the optimum magnesium nitrate concentration is used, the amount of phosphor deposited also decreases because either (*a*) the increase in conductivity causes electrolysis instead of electrophoretic deposition or

(b) the increasing electrolyte concentration may actually diminish the positive charge on the phosphor particles through the increased absorption of negative ions (5). This same type of maximum is noted in the anhydrous system but at higher electrolyte concentrations.

It was also found that acetone is an effective cathode depolarizer, *e.g.*, that when present, it largely prevents the appearance of gaseous hydrogen, presumably by acting as an acceptor of any electrolytic hydrogen generated.

$$2H^+ + CH_3COCH_3 + 2e \rightarrow CH_3CHOHCH_3 \quad [2]$$

Acetone Isopropyl alcohol

When no hydrogen is evolved, very smooth, compact phosphor screens may be deposited. Experiments were conducted to determine the optimum combination of acetone, water, and alcohol.

Excellent results were obtained with 25% isopropyl alcohol +74% acetone +1% water (by volume) as the suspending fluid and electrolyte solvent. Below 70% acetone concentration yielded coarse phosphor screens due to gas evolution during deposition. Above 80% acetone yielded thin, nonuniform phosphor screens of low adherence.

Choice of Added Electrolyte

A large number of inorganic compounds were found to be capable of "charging" calcium magnesium silicate positively so that deposition at the cathode could be achieved. The suitability of these various additives was determined by dissolving 1 mg/ml of the inorganic compound to be investigated to either 99% isopropyl alcohol +1% water or to 74% acetone +25% isopropyl alcohol +1% water (by volume), and then suspending 1 mg/ml of the phosphor in the above fluid and determining whether favorable rates of deposition and good quality screens were obtained. With promising candidate additive compounds, the concentration was varied until the maximum deposition rate and screen quality was established.

Since cataphoresis rather than electroplating was desired, principal attention was given to inorganic compounds having anions which cannot be reduced in aqueous media. Thus soluble salts of magnesium, calcium, barium, strontium, aluminum, sodium, potassium, lithium, and ammonium were evaluated. Divalent magnesium, calcium, and strontium all gave positive results. It is interesting to note that all of these cations form rather insoluble silicates and it is not surprising that they are well absorbed on and "charge" calcium magnesium silicate (probably due to reaction with exposed SiOH or SiO groups). Because of its relatively high ionic charge, low mass, low toxicity, and low solubility in combination with a variety of anions, magnesium was chosen as the preferred cation, with aluminum as a close second choice.

Insofar as the preferred anion is concerned, nitrate and chloride (and to a lesser extent, bromide) appeared to be preferable to several other anions evaluated. While the nitrates and chlorides of magnesium, aluminum, and lithium gave good deposition, the sulfates of these and other metals gave uniformly poor results. It is possible that the sulfate ion was too well removed from solution by the phosphor. When fluoride, phosphate, formate, acetate, citrate, hydroxide, etc., were introduced in the form of acids and bases, the results were also not satisfactory.

P16 phosphor ($2CaO \cdot MgO \cdot 2SiO:Ce:Li$) appears to have a "basic" surface (shown by pH of moist powder against pH paper), probably due to the presence of MgO and/or CaO or the corresponding hydroxides. It may also be "charged" by the addition of hydrochloric acid (presumably by conversion of the oxides and/or hydroxides to magnesium and calcium ions to form the oppositely charged counter layer). The addition of hydrofluoric, phosphoric, sulfuric, formic, acetic, and citric acids do not give favorable "charging." The failure of hydrofluoric, phosphoric, and sulfuric acids may be explained on the basis that the anions of these acids form insoluble calcium salts (the surface is coated with an insoluble compound rather than converted to an ionized double layer), but the failure of formic, acetic and citric acids is more difficult to explain. Perhaps these acids too well "sequester" calcium and magnesium, *i.e.*, actually remove them from the surface of the phosphor, making it impossible for a double layer to form.

The behavior of nitric acid is anomalous. It should yield calcium and magnesium nitrates by reaction with the surface of the phosphor, and these nitrates are known to give favorable depositions. But when nitric acid was added to a system containing isopropyl alcohol, no deposition resulted. Perhaps it is too rapidly consumed in oxidizing the easily oxidized alcohol.

Heavier, more easily reduced cations do not give satisfactory results in general. Thus, the nitrates of lead, iron (ferric), zinc, copper, the chlorides of nickel, cobalt, manganese, palladium, and chromium sulfate either gave no deposit, very discolored deposits (probably containing the respective metals or lower valence compounds), or poorly adhering deposits. This is to be expected in view of the ease of reduction of these metallic ions at a cathode.

Added Advantage of Magnesium and Related Metallic Salts

When magnesium salts are electrolyzed, hydrogen rather than magnesium is liberated at the cathode. In the system we have been investigating, the hydrogen is apparently taken up by acetone (see above). Regardless of the fate of the hydrogen, there is an increase in hydroxyl ion concentration (or pH) in the vicinity of the cathode. This results in the formation (and deposition) of an interesting and adherent form of magnesium hydroxide which can apparently act as a cementing agent for the simultaneously cataphoretically deposited phosphor. The cathode reactions involved may be represented as follows

$$(2CaO \cdot MgO \cdot 2SiO)Mg^{++} + 2HOH + CH_3COCH_3 + 2e \rightarrow (2CaO \cdot MgO \cdot 2SiO) - Mg(OH)_2\downarrow + CH_3CHOHCH_3 \quad [3]$$

That an adherent magnesium hydroxide film is formed under the conditions employed is also indicated by the following: The addition of phenolphthalein to the system with the omission of phosphor gives a very adherent, bright red film on the cathode when current is passed. This is probably a combined film of magnesium hydroxide and the magnesium salt of the phthalein (colored, basic form). Other dyestuff compounds have also been bonded to the cathode by this process, but extensive discussion of these is beyond the scope of this paper.

Conclusions

An electrophoretic deposition process for the formation of luminescent phosphor screens has been developed which does not employ the use of stone milling to disperse and charge phosphor particles. The charging of calcium magnesium silicate phosphor particles is achieved by the adsorption of nonreducible inorganic cations of Mg^{++}, Ca^{++}, Ba^{++}, Sn^{++}, Al^{+++}, Na^+, K^+, Li^+, and NH_4^+ on the phosphor surface. The adsorbed cations cause the phosphor particles to migrate in a suitable suspending media under the influence of an electric field to the electrode of opposite charge. Salts of these cations produce a cementing action between the deposited phosphor layer and the substrate to be coated.

The resulting phosphor coating is tenacious to the substrate, uniform, dense, fine grained, and does not exhibit a decrease in luminous efficiency.

Water concentration is extremely critical with magnesium nitrate as the charging cation. Above and below 1% H_2O decreased the phosphor deposition efficiency.

Acetone has been found to be an effective depolarizing agent, thereby preventing gaseous evolution during the deposition.

Manuscript submitted December 10, 1969; revised manuscript received *ca.* July 22, 1970.

Any discussion of this paper will appear in a Discussion Section to be published in the June 1971 JOURNAL.

REFERENCES

1. P. Grosso, CBS Lab., "Development of Phosphor Screens for High Resolution Display Devices," Technical Documentary Report No. AL-TDR-64-94, Contract No. AF 33(657)-10632, Project 4156, Air Force Avionics Lab., Wright-Patterson AFB, Ohio, May 1964.
2. P. Grosso and R. Rutherford, Jr., CBS Lab., "Cataphoretic Screen Studies," Final Report, Contract No. DA44009 ENG 5196, Project 8F23-02-1-03, USAERDL, Fort Belvoir, Va., May 1963.
3. R. Rutherford, Jr., and K. Speigel, CBS Labs., "Research and Investigation on Phosphor Screens for High Resolution Display Devices," Technical Documentary Report No. ASD-TDR-62-1097, Contract No. AF33(616)8509, Wright-Patterson AFB, Ohio, Nov. 1962.
4. N. F. Cerulli, "Methods of Electrophoretic Deposition of Luminescent Materials and the Product Resulting Therefrom," U.S. Pat. 2,851,408, Sept. 9, 1958.
5. S. Glasstone, "Textbook of Physical Chemistry," p. 1225, D. Van Nostrand Co. (1946).

Technical Notes

Synergistic Effects of Anions in the Corrosion of Aluminum Alloys

A. M. McKissick, Jr., A. A. Adams, and R. T. Foley*

Department of Chemistry, The American University, Washington, D. C. 20016

Aluminum and aluminum alloys are susceptible to pitting and general corrosion in chloride solutions and the fact that nitrate ion can inhibit this corrosion has been reported by several investigators. Callendar (1) measured the corrosion of Al and three Al-Cu alloys in tap water to which were added various concentrations of $NaNO_3$, NaCl, and $K_2Cr_2O_7$. He reported that a critical amount of $NaNO_3$, 0.008% for his tap water, was required to achieve passivation of the Al-Cu alloy and he directly related the rate of reduction of nitrate to the concentration required to achieve passivation. Blanchard and Goucher (2) in their studies of aluminum corrosion in microbial culture media containing a number of salts, including $CaCl_2$ and $FeCl_3$, observed that a 12 mM (millimolar) concentration of KNO_3 protected aluminum alloys 2024 and 7075. At a Cl^-/NO_3^- ratio of 20 there was a slight stimulation of corrosion (about 20% increase). Kassyura and Zaretskii (3) recently reported on the anodic behavior of A-99 aluminum in 1*N* and 3*N* solutions of $NaNO_3$ with various chloride additions. They noted that in a specific concentration range for NaCl the region of the passive state decreased with increased chloride ion concentration. Böhni and Uhlig (4) noted that $NaNO_3$ additions to NaCl solutions moved the pitting potential of 99.99% Al in the noble direction and the relationship between chloride activity and inhibiting nitrate activity followed the equation

$$\log (Cl^-) = 0.65 \log (NO_3^-) - 0.78$$

From the review of the literature it may be concluded that nitrate is an inhibitor for aluminum corrosion in chloride solutions, and that the Cl^-/NO_3^- ratio is important. In connection with an investigation of the chemistry of stress-corrosion cracking of high-strength aluminum alloys we have examined the effect of a number of anions on aluminum and aluminum alloys. Certain effects that have been observed are felt to be sufficiently unusual to warrant a preliminary report. We note, particularly, certain synergistic effects that could not be predicted from a knowledge of the behavior of individual ions.

Experimental

The work reported here consists of immersion tests with three aluminum alloys. Alloy 1199-H14 was supplied by the Reynolds Metals Company and alloys 2024-T3 and 7075-T6 by the Kaiser Aluminum Company. Samples 38 x 26 x 0.81 mm were cleaned in the conventional manner. The strip was immersed in NaOH solution (5 g/100 ml) at 75°-80°C for 1 min, rinsed thoroughly, dipped in NHO_3 (1:3) for 1 min at room temperature, and thoroughly rinsed in distilled water and acetone. Samples were immersed in triplicate in solutions of various salt concentrations for periods of 14 days at 22° ± 1°C. Following exposures, the corrosion product was removed with a stripping solution of 20g of chromic acid and 32.25 ml of 85% phosphoric acid/liter. The weight loss reported was the difference in weight of the sample before the test and that after the stripping. The latter was corrected with the weight loss of an uncorroded metal specimen in the stripping solution.

Results and Discussion

The weight losses for the three aluminum alloys in 0.01*N* NaCl solutions are given in Table I. The corrosion observed with unalloyed aluminum is of the pitting type, whereas that of the alloys progresses rapidly after the first day to a general attack over the entire surface. Also noted here is the inhibiting effect of $NaNO_3$ in concentrations of 0.05*N* and higher in solutions of 0.01*N* NaCl, *i.e.*, a NO_3^-/Cl^- ratio of 5. These two effects, corrosion in chloride solution and inhibi-

* Electrochemical Society Active Member.

Key words: inhibition, chloride, nitrate, aluminum alloy 7075, aluminum alloy 2024.

Table I. Weight changes of aluminum alloys after 2 week immersion in salt solutions

Alloy	Electrolyte	Weight loss (mg/cm²) (±σ)*
1199	0.01*N* NaCl	0.02 ± 0.007
2024	0.01*N* NaCl	1.17 ± 0.21
7075	0.01*N* NaCl	1.44 ± 0.04
7075	0.01*N* NaCl/0.05*N* $NaNO_3$	0.01 ± 0.01
2024	0.01*N* NaCl/0.10*N* $NaNO_3$	0.14 ± 0.02
7075	0.01*N* LiCl	0.17 ± 0.003
7075	0.01*N* KCl	0.54 ± 0.01

* These are average values. A minimum of three replicates were run but most of these represent averages of about 12 samples run by two different investigators.

Table II. Weight changes of aluminum alloys after 2 week immersion in salt solutions of various nitrate chloride ratios

Alloy	Electrolyte	Weight loss (mg/cm²) (±σ)
2024	0.01*N* NaCl/0.01*N* $NaNO_3$	6.80 ± 0.8
7075	0.01*N* NaCl/0.01*N* $NaNO_3$	10.1 ± 0.75
7075	0.01*N* NaCl/0.005*N* $NaNO_3$	8.8 ± 0.48
7075	0.01*N* KCl/0.01*N* KNO_3	0.31 ± 0.03
7075	0.01*N* LiCl/0.01*N* $LiNO_3$	0.08 ± 0.001
1199	0.01*N* NaCl/0.009*N* $NaNO_3$	0.07 ± 0.03
1199	0.01*N* NaCl/0.003*N* $NaNO_3$	0.07 ± 0.03

tion at some critical NO_3^-/Cl^- ratio have been reported previously, at least qualitatively.

Table II lists typical results wherein the NO_3^-/Cl^- ratio is reduced to one and below. Corrosion is increased by an order of magnitude in the sodium salt solutions. The effect is graphically represented in Fig. 1. The maximum effect is exhibited at a NO_3^-/Cl^- ratio of about 0.7. Tables I and II also indicate that the corrosion rate is not independent of the cation, which is contrary to previously reported observations. The corrosion rate for the 7075 alloy varies, as follows

$$NaCl > KCl > LiCl$$

$$8.5 > 3.2 > 1.0$$

for corrosion under the stated conditions. Also, there is no synergistic effect with potassium or lithium salt solutions.

There is an alloy effect observed here and in other measurements as well. Thus in chloride solution the rates are in the following order

$$7075 > 2024 > 1199$$

$$72 > 59 > 1$$

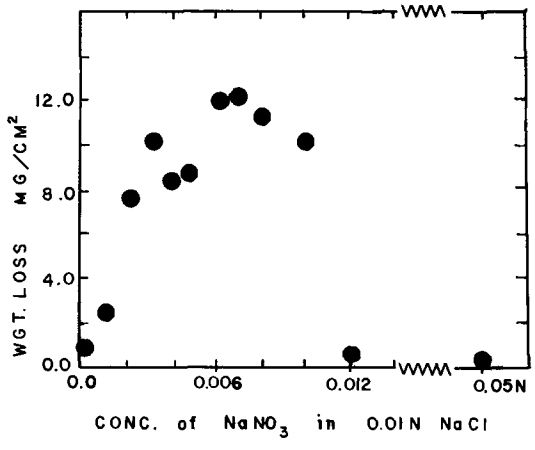

Fig. 1. Effect of $NaNO_3$ additions to 0.01*N* NaCl solutions on the corrosion of aluminum alloy 7075.

The synergistic effect was noted with both alloy types 7075 and 2024 but not with 1199. The physical appearance of the samples corroded in the nitrate-chloride solutions is different from those corroded in chloride solution, being characterized by large blisters suggesting considerable gas evolution during corrosion. After about 1 day's exposure the sample turns black, suggestive of a dealuminification type of attack. Continual exposure over a period of weeks produces a voluminous corrosion product often in the form of streamers (probably hydrated aluminum oxide). Metallographic cross section reveals considerable roughening of the sample.

At this point we are not able to offer a good explanation for these observations. The simple descriptions based on oxide films or competitive adsorption do not appear adequate. We have considered the physical properties of the salts. For example, the activity coefficients at 0.01M are given (5) as

NaCl	0.904
KCl	0.901
LiCl	0.89

These values are not significantly different. The radii of the ions (6) are in the following order

Li^+	0.60
Na^+	0.95
K^+	1.33

This rules out any effect dependent on a trend in size, but not an optimum size for some adsorption process.

The accelerating effect may be related to the reduction of nitrate to nitrite. Nitrite ion is not an inhibitor for aluminum but actually accelerates corrosion. Under conditions comparable to those given in Table II alloy type 7075 exhibits a weight loss in a 0.01*N* NaCl + 0.01*N* $NaNO_2$ of 13.3 mg/cm². This explanation, however, would not account for the cation effect.

We are looking for an explanation of these effects along two lines: The first, potentiostatic experiments to establish the effect of anion ratio on pitting inception time when the alloy is held in the passive range; the second, x-ray and metallographic studies of structural changes in the corrosion product.

Generally, it must be concluded that if these observations are borne out by future experiments we must revise our concept of "anion" effects and include cation effects as well.

Acknowledgment

The authors are pleased to acknowledge the support of the Advanced Research Projects Agency of the Department of Defense, ARPA Order No. 878, under Contract No. N 00014-68-A-0245.

Manuscript submitted May 29, 1970; revised manuscript received *ca.* July 21, 1970.

Any discussion of this paper will appear in a Discussion Section to be published in the June 1971 JOURNAL.

REFERENCES

1. L. H. Callendar, *Engineering*, **120**, 340 (1925).
2. G. C. Blanchard and C. R. Goucher, *Electrochem. Technol.*, **5**, 79 (1967).
3. V. P. Kassyura and E. M. Zaretskii, *Zaschita Metallov.*, **4**, 376 (1968).
4. H. Böhni and H. H. Uhlig, *This Journal*, **116**, 906 (1969).
5. W. M. Latimer, "Oxidation Potentials," p. 355, Prentice-Hall, Inc., Englewood Cliffs, N. J. (1952).
6. L. Pauling, "The Nature of the Chemical Bond," p. 346, Cornell University Press, Ithaca, N. Y. (1940).

Composite Film Metallizing for Ceramics[1]

E. L. Hollar, F. N. Rebarchik, and D. M. Mattox

Sandia Laboratories, Albuquerque, New Mexico 87115

There are two primary approaches to forming a solderable/brazable surface on oxide ceramics: (*a*) react an oxygen active metal on the surface at high temperatures (active-metal metallizing) (1), or (*b*) fuse a glass-metal composite to the ceramic surface (dispersion metallizing) (2).

In the active-metal metallizing technique, the oxygen active metal reacts with the oxide surface at high temperatures to form an interfacial complex oxide system which may act as the intermediate bonding agent, as has been suggested for the glass-on-metal system (3-5). Not all of the active metal is allowed to react with the oxide, thus a brazable metal surface remains. In the dispersion-metallizing technique, the glass phase reacts with the ceramic and, by the selection of the correct coefficients of expansion, provides good bonding to the ceramic. The metal phase which is dispersed in the glass then provides the brazable surface. Both of these techniques require high temperatures to allow chemical reaction and diffusion to take place between the metallizing layer and the ceramic surface. These techniques also allow irregular penetration of the metallizing into the ceramic, particularly in the polycrystalline ceramics having a high glass content in the grain boundaries.

In some cases, design restrictions make these metallizing techniques impractical. Some of these cases are: (*a*) ceramics which cannot withstand high temperatures without decomposition or distortion, (*b*) thin ceramics where the interfacial region must be kept very thin and carefully controlled, (c) ceramic applications where the irregular penetration of the conventional metallizing imposes problems with dielectric breakdown, and (*d*) metallizing techniques which are incompatible with other processing.

The usual method of obtaining an adherent coating in these cases is to sputter, or vacuum evaporate, an oxygen active material on the surface and promote substrate-coating reaction by limited heating (6, 7). Without extensive heating the transitional interface region which is formed is limited in extent and the stress distribution across the interface, which is necessary to obtain a good bond (8), is not developed.

We propose that a transitional interface region, conducive to good bonding, may be formed by deposition of an oxygen-active metal in a controlled gaseous environment. In this technique, the deposition of the active metal is begun in a partial pressure of oxygen to allow partial oxidation of the deposited material and thus form a transition oxide and suboxide interfacial region. By decreasing the partial pressure of oxygen during the deposition, the composition of the interfacial region may be "graded" from the substrate material through a metal oxide-metal composite region to the pure metal. It has previously been noted that better adhesion can be obtained with oxygen active materials on glass when there is a poor vacuum (9, 10). Since the oxygen-active metals are often difficult to braze, a more brazable surface may be formed by the co-deposition of some easily brazed material during the active metal deposition and then grading to the pure brazable metal by gradually decreasing the deposition rate of the active metal.

This investigation was primarily concerned with metallizing fused silica for a high-temperature brazing operation. Fused silica develops large internal strains when other chemical species are diffused into the surface or when recrystallization (devitrification) occurs at high temperature. These strains can crack the fused silica. Therefore, metallizing must be done at moderate temperature with controlled chemical reaction between the metallizing and the fused silica. In addition, the low thermal expansion coefficient of fused silica compared to most glasses and metals causes high stress to be developed in the interfacial region on cooling from high temperatures when conventional metallizing is used. This problem can be averted by using a thin metallizing layer and/or a ductile metal coating.

The choice of materials is dictated by the processing involved. The oxygen-active metal should be insoluble in the braze alloy so that it will not be "scavenged" from the ceramic surface during the brazing operation. In addition, it should not exhibit grain growth at the brazing temperature. The brazable metal should be relatively insoluble in the active metal to prevent excessive diffusion and should not alloy rapidly with the braze material at the brazing temperature.

To prevent scavenging, a refractory material was used in contact with the silica. Of the four refractory metals (niobium, tantalum, tungsten, and molybdenum) investigated, niobium seemed to be the most stable under brazing conditions, and the system niobium-silver with a copper-silver eutectic braze was used. The niobium and silver were deposited in a hot cathode triode sputtering system shown in Fig. 1. The relative sputtering rates were controlled by varying the bias on the sputtering cathodes. The oxygen content in the discharge was controlled using commercial argon-oxygen mixtures and pure argon with valving and a variable leak as shown. The oxygen content in the system was monitored using a differentially pumped mass spectrometer. Recorders were used to monitor the cathode current during deposition.

The sequence of steps in a typical metallizing operation was as follows. The fused quartz substrate was thoroughly cleaned by scrubbing with Alconox until water would wet the entire surface. After multiple rinses in distilled water, the fused silica was etched for 1 min in a 5 v/o (volume per cent) hydrofluoric acid solution and rinsed again. The final precleaning step was air firing at 800°C for 15 min. The cleaned substrate was then placed in the sputtering chamber and the chamber evacuated to 1×10^{-5} Torr. The system was then backfilled with an Ar/5% O_2 mixture to a pressure of approximately 8×10^{-3} Torr while the chamber was continuously pumped. A hot

[1] This work is supported by the U. S. Atomic Energy Commission.
Key words: ceramic metallizing, composite films, thin film metallizing, sputter deposition.

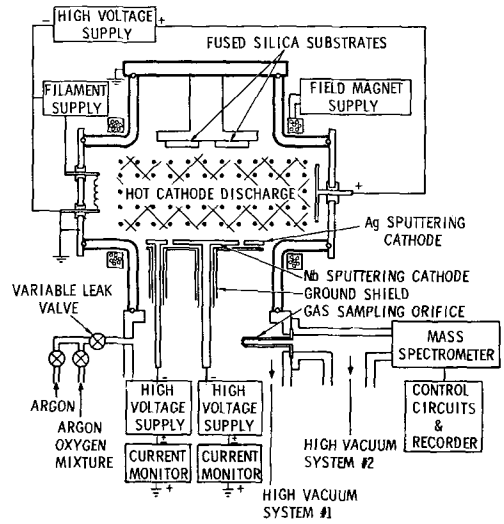

Fig. 1. Hot cathode-dual cathode sputtering apparatus showing disk niobium cathode and concentric ring-shaped silver cathode.

cathode discharge was established, and the substrate was glow-discharge cleaned (11) in the discharge plasma. The sputtering of the niobium was begun by applying a negative 2 kV bias to the niobium sputtering cathode. After a predetermined time necessary to give about 500Å of oxide, the gas flow was switched to pure argon. As the oxygen in the system was pumped out, the film became more metallic and the deposition was continued until about 1500Å of niobium were deposited. At this point, the negative bias on the silver sputtering cathode was gradually increased to codeposit silver with the niobium. The bias on the niobium cathode was then gradually decreased until pure silver was being deposited. The silver deposition was continued until a total thickness of about 10,000Å

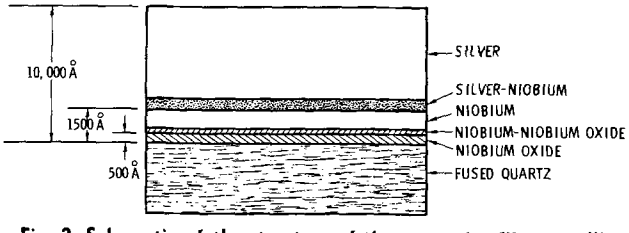

Fig. 2. Schematic of the structure of the composite film metallizing showing composition of regions which are graded into each other.

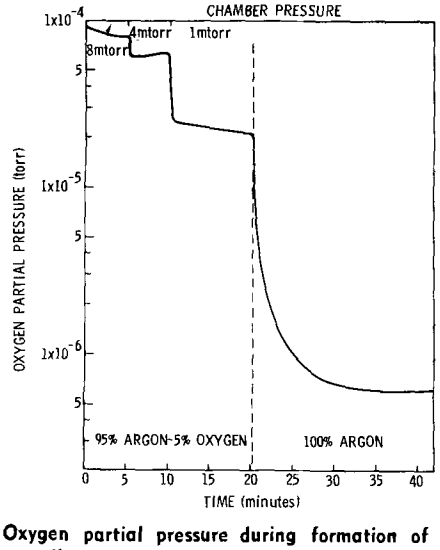

Fig. 3. Oxygen partial pressure during formation of the composite film metallizing.

Table I

Operation	Gas composition and pressure	Sputtering bias	Time (min)
1. Sputter niobium	Ar/5% O_2 @ 8 mTorr	−2 kV	5
2. Sputter niobium	Ar/5% O_2 @ 4 mTorr	−2 kV	5
3. Sputter niobium	Ar/5% O_2 @ 1 mTorr	−2 kV	10
4. Sputter niobium	Pure Ar @ 1 mTorr	−2 kV	30
5. Sputter niobium		−1.5 kV (niobium)	
&	Pure Ar @ 1 mTorr		5
Sputter silver		−0.5 kV (silver)	
6. Sputter niobium		−1.0 kV (niobium)	
&	Pure Ar @ 1 mTorr		10
Sputter silver		−1.0 kV (silver)	
7. Sputter niobium		−0.5 kV (niobium)	
&	Pure Ar @ 1 mTorr		5
Sputter silver		−1.5 kV (silver)	
8. Sputter silver	Pure Ar @ 1 mTorr	−2 kV	90

had been deposited. Figure 2 shows the resulting composition of the composite metallized surface.

The times necessary to deposit the various thicknesses of niobium and silver with a given gas composition, discharge conditions, cathode current density, and cathode bias were determined by stopping the deposition at various stages and measuring the film thicknesses with a Talysurf. Table I summarizes the sequence of steps and the times involved. Care was taken to insure that silver from the previous run was cleaned from the niobium cathode. If this is not done, silver will be deposited on the silica surface and a poor bond will be obtained.

Figure 3 shows the oxygen content of the discharge in a typical metallizing operation. Chemical and ion pumping of oxygen by the discharge substantially reduced the oxygen content of the discharge gas in the initial phase of the process. In order to have excess oxygen available during the initial niobium deposition, high gas pressure was required. The gas pressure was then reduced as the discharge electrodes were saturated and as the discharge chemical pumping decreased.

The fused silica surfaces thus metallized were then brazed with a copper-silver eutectic braze. After being subjected to the brazing operation the seals thus formed were vacuum tight, and when tested to failure the joint fractured in the fused silica.

Where a low temperature–high strengh bond was desired, the aluminum-silver composite system was used. This system provided surfaces which may be soft soldered and is useful for electroding ferroelectric materials and in joining materials having large differences in coefficient of expansion such as alumina and brass.

Manuscript submitted Mar. 31, 1970; revised manuscript received June 29, 1970.

Any discussion of this paper will appear in a Discussion Section to be published in the June 1971 JOURNAL.

REFERENCES

1. W. H. Kohl, "Handbook of Materials and Techniques for Vacuum Devices," p. 451, Reinhold Publishing Corp., New York (1967).
2. R. N. Fulrath and E. L. Hollar, *Am. Ceram. Soc. Bull.*, **47**, 493 (1968).
3. M. P. Boron and J. A. Pask, *J. Am. Ceram. Soc.*, **49**, 1 (1966).
4. R. M. Pillar, T. G. Carruthers, and J. Nutting, *J. Mater. Sci.*, **2**, 28 (1967).
5. T. E. Hutchinson and K. H. Olsen, *J. Appl. Phys.*, **38**, 4933 (1967).
6. J. L. Vossen, *Electrochem. Technol.*, **3**, 56 (1965).
7. J. M. Seeman, *Trans. Vacuum Met. Conf. 1965*, p. 269, L. M. Bianchi, American Vacuum Soc., Boston, Mass. (1966).
8. D. M. Mattox, "Interface Formation and the Adhesion of Deposited Thin Films," Sandia Corp. Report, SC-R-65-852 (1965).
9. P. Benjamin and C. Weaver, *Proc. Roy. Soc. (London)*, **A252**, 177 (1960).
10. P. Benjamin and C. Weaver, *ibid.*, **A261**, 516 (1961).
11. L. Holland, "The Properties of Glass Surfaces," p. 290, John Wiley & Sons, New York (1964).

JOURNAL OF THE ELECTROCHEMICAL SOCIETY

ELECTROCHEMICAL SCIENCE

DECEMBER 1970

Crystallogenic Modification in the Formation Process at the Lead Electrode by the Addition of a Lignin Derivative

J. R. Pierson and P. Gurlusky

Globe-Union, Inc., Milwaukee, Wisconsin 53201

A. C. Simon*

U. S. Naval Research Laboratory, Washington, D. C. 20390

and S. M. Caulder*

International Lead-Zinc Research Organization Research Associate at the U. S. Naval Research Laboratory, Washington, D. C. 20390

ABSTRACT

Microscopic investigation of the effect of lignin and $BaSO_4$ on the negative lead electrode showed that lignin was able to modify the lead crystal structure produced during the forming operation, in addition to its effect on the structure of the $PbSO_4$ crystals formed on discharge. The effect of the lignin was to reduce the size and complexity of the dendritic lead crystals in the formed plate. The presence of $BaSO_4$ had no appreciable effect on the microstructure of the formed plate.

At low temperatures and at high discharge rates, the capacity of lead-acid batteries of the pasted plate type is usually controlled by the negative lead electrode. This limiting action is the result of increased polarization at the negative electrode which seriously limits reaction. Of the factors responsible for this polarization, the resistive component is the most serious in its effect. That is to say that low temperature increases the viscosity of the electrolyte, decreases diffusion, lowers conductivity, and otherwise increases the resistance to current flow and reaction at both electrodes. The process at the negative, in addition, produces highly resistive and passivating films of lead sulfate on the reacting lead electrode. Although lead sulfate is also produced on the lead dioxide electrode, the passivating effect in this case is less severe so that the reaction at this electrode can be faster than at the lead electrode.

It has been found that certain substances, called expanders, can decrease the polarization and passivation at the negative electrode. Lamp black, barium sulfate, and certain lignin derivatives have been found to change but not entirely eliminate the limiting character of the negative electrode.

Of these additives, barium sulfate and lampblack have been used almost as long a time as have pasted electrodes and there is now no means of determining if their first use was the result of fortuity or deliberate planning. Lignin, however, was deliberately used to restore desirable properties attributed to products leached from wood separators, as this need became evident when the industry converted from wood to synthetic separators.

The effect of $BaSO_4$ and lignin derivatives on low-temperature, high-rate discharge capacity has been reported by Willihnganz (1), Ritchie (2), Zachlin (3), Popova and Kabanov (4), Kasporov, Yampol'skaya, and Kabanov (5), Barnes (6), Yampol'skaya, Ershova, Astakhov, and Kabanov (7), and Simon (8). The effect of organic materials on the discharge characteristics of the lead electrode has also been the source of many patents claiming specific improvement by certain materials.

While there is disagreement as to the exact mechanism, it is generally agreed that $BaSO_4$ and an organic expander material are most effective when used together. Even here the objection has been made that the effectiveness of the $BaSO_4$ may depend on unidentified organic impurities. The maximum effectiveness of the organic expanders has been reported to occur after a number of charge-discharge cycles, while the effectiveness of the $BaSO_4$ is immediately available (3). Since the size of the $PbSO_4$ crystals has been demonstrated to depend on the size of the $BaSO_4$ crystals added to the original mix, it is generally agreed that the $BaSO_4$ crystals must remain undissolved in the plate to act as nuclei when lead sulfate is being formed. This is thought to prevent or hinder the formation of $PbSO_4$ films on the lead crystals and thus to reduce passivation. As to the function of the organic material, there is less general agreement but such a material seems to require electrolytic oxidation or reduction for maximum effectiveness and it probably then adsorbs on the growing faces

* Electrochemical Society Active Member.

Key words: expander, microstructure, lead-acid, battery, negative plate.

of the $PbSO_4$ crystals, enabling a more porous layer to be formed. There seems to be quite general agreement that a definite small amount of organic material produces expander action and that an excess can be very harmful to the functioning of the electrode. This would appear to indicate a definite adsorption of a monomolecular layer of some portion of the lignin on all or at least the reactive part of the available surface. This adsorbed layer could then produce modification in the crystallization occurring at certain crystal faces.

The foregoing work has emphasized the effect of expanders on the $PbSO_4$ crystals formed on discharge of the lead electrode and has said nothing about any effect on the structure of the lead crystals grown during the charge process. Barnes (6), however, had suggested, without experimental verification, that expanders might also modify the lead crystals formed during charge, leading to an increased surface area. It is, of course, well known that various organic additives have a modifying effect on the growth of specific crystals and this has also been demonstrated for certain metal crystals formed by reduction from solution. There was therefore good reason to expect the same modification in the case of lead crystals.

An investigation was initiated, using microscopic study and other available means, to determine the nature of the modification produced in the lead sulfate crystallization films through the use of lignin derivatives or barium sulfate. Examination of the negative electrodes which were to be used in this investigation, following their electrolytic reduction to lead from the oxide paste, revealed that the microstructure of the lead crystals was different in the plates with, and in those without, lignin. $BaSO_4$ on the other hand, had no appreciable effect on the electrolytic formation of the negative plate.

Preparation of the Electrodes

The positive PbO_2 electrodes used in these experiments were obtained from Globe-Union factory production and they were of a proprietary formulation. The negative lead electrodes, on the other hand, were of an experimental formulation and the necessary mixing and pasting of these electrodes were done at the Globe-Union Laboratory.

The negative paste was prepared from Eagle-Picher 34U Oxide. Various amounts of $BaSO_4$ and lignin were added to separate portions of this dry oxide, as shown in Table I. These dry mixtures were then mechanically blended for 1 hr to insure thorough mixing. After blending, the portions were individually placed in a mixer and dry mixed for 2 min. Following this, 111 ml of water, at approximately 23°C, were added to 3 lb portions of the oxide during 1 min of mixing, after which the paste was mixed for 4 min more. The required amount of acid, 138 ml (1.325 sp gr., 23°C) was then added over a 5 min period. The paste was then mixed for 15 min more. In the case of paste without lignin, it was necessary to increase the water addition to 121 instead of 111 ml.

Numbered and weighed grids from factory production were then hand pasted to contain approximately the same final weight of paste. After pasting, these plates were cured for a minimum of 72 hr. After curing, the plates were joined together into groups of 4 positives or 5 negatives by burned-on connector straps. The cell groups so produced were then formed electrolytically in 1.050 sp gr acid at 6.6 A/cell, for a period of 20 hr. After formation, the cells were disassembled and the positive and negative groups separated.

Table I. Negative paste mixes used in this investigation (relative amounts of lignin and $BaSO_4$ used in mix)

% $BaSO_4$	% Lignin		
0	0	0.5	1.0
0.5	0	0.5	1.0
1.0	0	0.5	1.0

Both the negative and positive groups were then washed in a stream of water for 3-4 hr. Without further preparation, the positive plates were then dried at 65°C in an oven.

The negative plates, to avoid oxidation, were placed in a drying oven at room temperature which was then purged with nitrogen by three times drawing a vacuum and then releasing it by the introduction of nitrogen. After the third purge, the nitrogen was kept continuously flowing while the temperature was raised to 82°C and maintained for 5 hr. The plates were then cooled to 50°C while still in the nitrogen environment.

After further cooling, the positive and negative groups were then cut apart and the individual plates were analyzed by x-ray diffraction, differential thermal analysis, thermogravimetric analysis, and microscopy. Only the microscopic examination proved of much value in the examination of the formed negative electrode, which consisted almost entirely of lead. Therefore, the present paper deals only with the microscopy of the formed lead electrode.

General and Microscopic Observations of the Formed Lead Electrode

Effectiveness of the lignin in prevention of cracking.—From the preliminary examination of the formed lead electrodes, it was evident that extensive cracking of the active material had occurred only in those electrodes that contained no lignin. Those to which lignin had been added had either no cracks or cracks so small and limited in extent as to make difficult their detection without optical magnification. It was also noted that the electrodes containing no lignin cracked to the same extent whether or not $BaSO_4$ was present.

Apparent variation of electrode surface texture with the amount of lignin present.—Examination of the formed lead electrode by low magnification stereomicroscopy, before the plastic impregnation, indicated that the surface structure varied from electrode to electrode quite noticeably. It seemed that the greatest porosity and the coarsest surface structure was found in plates with 1.0% lignin, while plates containing no lignin appeared to be less porous and to have a finer structure. The presence or absence of $BaSO_4$ seemed to make no difference.

The significance of the above observations was greatly reduced, however, when cross sections of the electrodes were examined at high magnification. To obtain these cross sections, portions of the electrode were impregnated with a polyester, which, after hardening, permitted the sample to be sectioned and polished. Examination at higher magnification of this cross section revealed that the electrodes made from each of the mixes had a structure at the surface and for a few mils below the surface that was quite unlike that which existed in the interior of the electrodes (Fig. 1 and 2). This same difference was found at both plate surfaces. In general, the lead crystals at or near the surface were larger and much further apart than those which were present in the interior.

In addition, there were often large voids just below the surface (Fig. 2). These voids were always a small distance beneath the surface and they were covered over with a layer of surface crystals, so that it is unlikely that these voids could have been seen during the surface examination that took place before the electrodes were impregnated with plastic. Moreover, the electrodes containing 1.0% lignin showed no such voids as appeared in Fig. 2. However, in the actual surface of the 1.0% lignin electrodes the particles

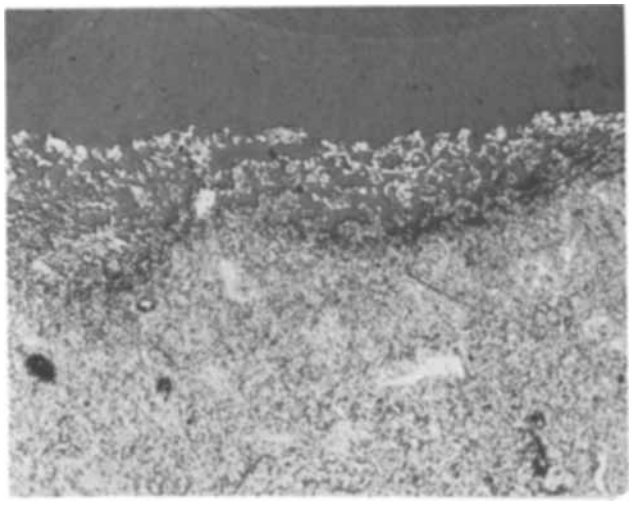

Fig. 1. Cross-sectional view of negative plate, including surface layer. Plate made from paste mix with 1.0% lignin and no $BaSO_4$. Bright particles are lead dendritic crystals. Center of plate is below the lower edge of photograph, while surface of the plate is above the center of the photograph. Dark area at top of photograph is the plastic embedding material. Note different structure at, and just below, surface. Magnification 120X.

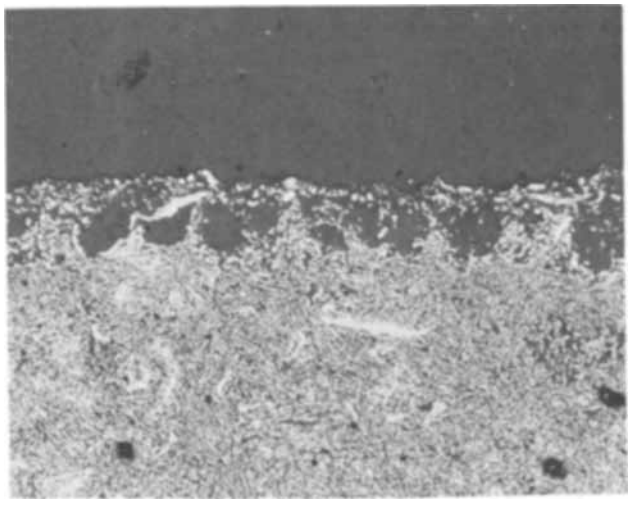

Fig. 2. Cross-sectional view of negative plate, including surface layer. Plate was made from paste mix with no lignin but 0.5% $BaSO_4$. Same relative position as Fig. 1. Note large voids below plate surface. Magnification 120X.

seemed to be larger, or else had formed conglomerates, thus suggesting larger particles, than those that were seen in the other electrodes. Therefore, it seemed likely that in the earlier examination the spaces between these large surface particles had been mistaken for voids when comparison was made with electrodes containing much finer particles. In any case, the differences in size of particles in the surfaces of the different electrodes, as viewed in cross section, were not as obvious as had seemed the case when viewed from above the surface with a stereomicroscope.

It may have been significant that the plates representing mixes with 1.0% lignin had no subsurface voids. It should be noted, however, that there was considerable variation in the appearance of the surface layer, even in the same electrode. It was also true that the amount of material involved in this phenomenon was small as compared with the total area of the cross section. There is also considerable evidence at hand to suggest that the difference at the surface may be, at least partially, the result of the slight sulfation that occurs when the plates stand for a time in the forming electrolyte before the actual electrolysis begins. In this case the phenomenon would probably be independent of the type or amount of expanders being used. Similar differences between the surface and interior of the plate have been noticed in commercial plates of many different manufacturers and have been seen in both positive and negative plates.

Modification of the crystalline lead structure by the presence of lignin.—The most noticeable change in crystalline structure in the presence of lignin was in the central portion of the plate. The thin surface layer of different structure remained unchanged in the presence or absence of $BaSO_4$ and lignin, although this surface layer contained less large holes in the presence of lignin, as previously mentioned.

The interior structure of plates with lignin consisted of smaller and less complex dendritic crystals than that in lignin-free plates. No significant changes of structure could be attributed to the presence of the various amounts of $BaSO_4$ in any of the electrodes. The relative amount of lignin added may have been significant but the effect of changing the amount was small as compared with its complete absence. Therefore, the following description of structure modification by lignin is confined to a comparison of electrodes in which lignin was present and in which lignin was absent, without considering the smaller changes produced by varying the quantity of lignin. It should also be mentioned that the interior microstructure for any given electrode was not entirely uniform and occasional areas were observed in both the electrodes with and without lignin that did not fit the following description. However, the following description represents the structure found in most areas.

In the electrodes containing no lignin (Fig. 3), the individual lead filaments were very long, sometimes with a dozen or more practically parallel filaments extending as a group in straight lines for distances in the range of 200-375μ. This parallel filament structure seemed to be most extensive in the area of the grid bars and to sweep outward from their vicinity. Usually, however, no direct contact with the grid was found. The crystals were randomly oriented except in the vicinity of the grid. They did not seem to grow into the surface layer, so that a distinct boundary could be marked between the surface and the interior. In contrast to the very long, slender lead filaments of the interior, the surface particles were coarse, nondescript, and seldom parallel.

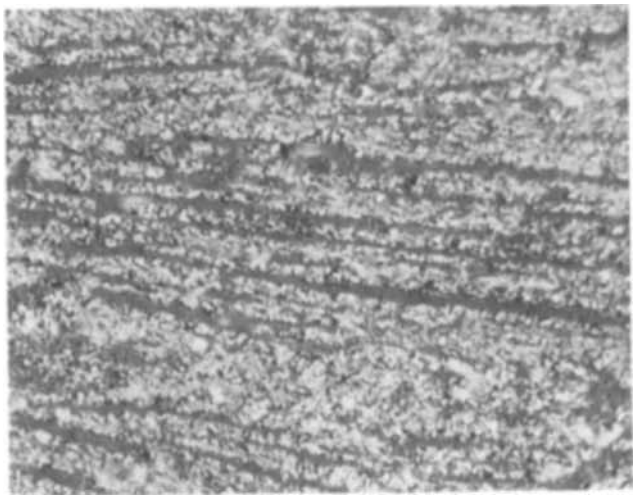

Fig. 3. Formed negative plate cross section, showing the many parallel rows of what appear to be needlelike lead filaments. Paste mix used in the preparation of this plate contained neither lignin nor $BaSO_4$. Magnification 800X.

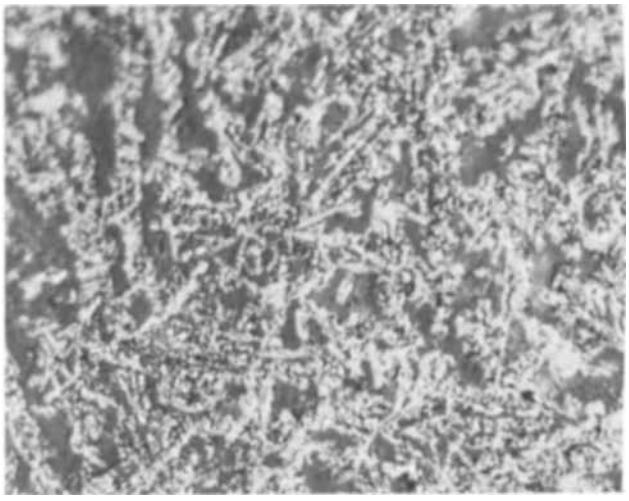

Fig. 4. Cross section of formed negative plate containing 0.5% lignin but no $BaSO_4$. Magnification 800X.

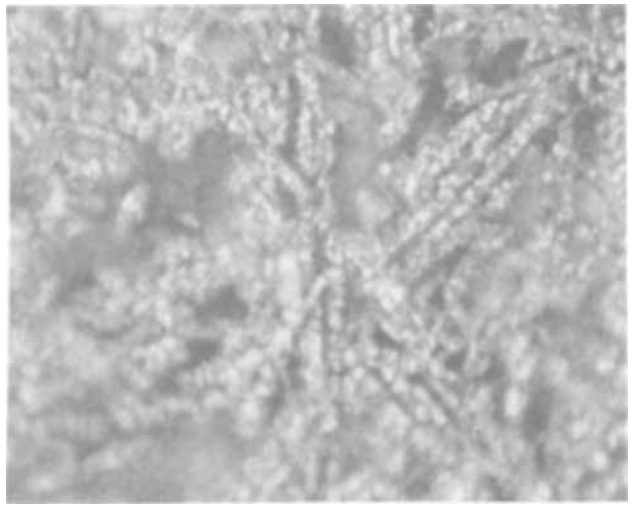

Fig. 6. Same view as Fig. 4, but at the higher magnification of 1600X. Note relatively simple needles as compared with Fig. 5.

In most areas of the plates containing lignin (Fig. 4), on the other hand, parallel filaments of lead were rarely found to exceed 30μ in length and there were rarely more than three or four parallel filaments in a group. Growth direction was also completely random.

Figures 3 and 4 represent a magnification of 800X, about the lowest that could be used to encompass a sufficient area to give an idea of the general structure and yet furnish sufficient detail to enable one to see the individual particles. Figures 5 and 6, taken at 1600X magnification, give a clearer view of the essential differences of the electrodes with and without lignin.

At the magnification of Fig. 4, there seems to be an almost complete lack of parallel filaments, but if one looks closely at Fig. 6, at the higher magnification of 1600X, it is possible to detect very closely spaced parallel filaments. The corresponding photographs of the type of structure found in lignin-free plates (Fig. 3 and 5) very clearly show the many practically parallel filaments of lead that are present in lignin-free electrodes.

Figures 5 and 6 were obtained with an oil immersion objective which not only changes the contrast and general appearance of the lead filaments but also lowers the reflectivity of the polished sample section to some extent. This permits portions of the sample which are beneath the sectioning level to be examined but has the disadvantage that crystal identification by means of differing surface reflectivity is made correspondingly more difficult.

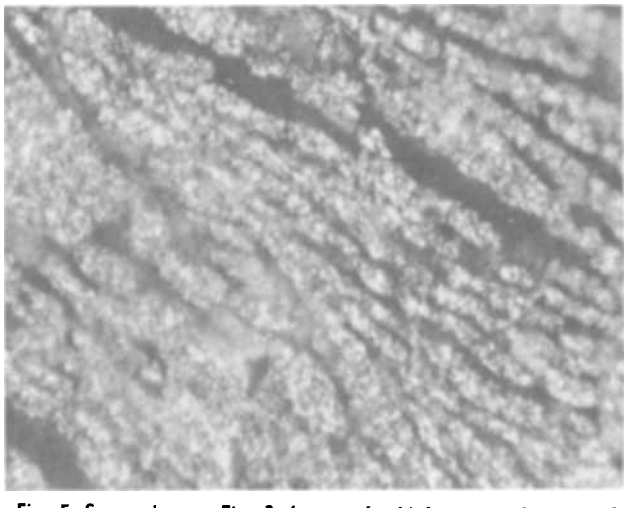

Fig. 5. Same view as Fig. 3, but at the higher magnification of 1600X.

Examination of plates at lower magnifications, such as those of Fig. 3 and 4, seemed to show a number of very small crystals of reflectivity different from that of the lead. This is most evident in Fig. 4. Their general appearance suggested that they were lead sulfate crystals. These crystals seemed to be more numerous in the plates that contained lignin. If true, this might indicate a clue for the reason for the structural differences shown by electrodes containing lignin. Unfortunately, when using oil immersion objectives, for the reasons given above, these crystals could not be clearly differentiated from the lead so that no definite conclusions as to the relative amounts present in lignin-free and lignin-containing plates could be drawn.

It was concluded from the microscopic examination that the complexity of dendritic growth of the lead crystals, and total crystal size, had been reduced by the presence of lignin.

Possibility of lignin migration during forming.—It is the usual practice to add the lignin and $BaSO_4$ to the original paste mix. This mix is then pasted into the grids used for the negative electrodes and is subsequently dried. The negative electrode is then immersed in an acid electrolyte and electrolytically formed to sponge lead. It is not definitely known what happens to the lignin during this process. The $BaSO_4$, on the other hand, because of its lack of solubility, is believed to remain in the negative plate. During the electrolytic forming, the original paste of the negative electrode, consisting of basic lead sulfates, PbO, lignin, and $BaSO_4$, is converted almost entirely to dendritic lead crystals. This conversion presumably liberates the lignin which may either diffuse into the surrounding electrolyte and even to the positive electrode, or immediately deposit on the surfaces of the growing lead crystals as they form.

In the original experimental arrangement, each of the cells contained a positive electrode consisting of four commercial plates and a negative electrode consisting of five plates. The three inside negative plates were laboratory mixes which contained various amounts of $BaSO_4$ and lignin as shown in Table I. In every case, however, the two outside plates were production negatives containing both lignin and $BaSO_4$. After the forming, these two outer plates were discarded and were not given any examination. In the subsequent examination of the experimental plates, the presence of $BaSO_4$ and lignin in the two

outer commercial plates did not seem to have any effect on the structure of the inner experimental plates of the same electrode.

To test the correctness of this observation, however, five additional cells were prepared and electrolytically formed in the same manner as the earlier cells. These additional cells contained the following experimental arrangements in the negative electrode:

(*a*) All five plates were laboratory preparations containing 0.5% $BaSO_4$ but no lignin.

(*b*) Two laboratory prepared plates containing 0.5% $BaSO_4$ but no lignin were sandwiched between three production negatives containing lignin and $BaSO_4$

(*c*) All five plates were production negatives containing $BaSO_4$ and lignin.

(*d*) An electrode was assembled from five laboratory prepared plates containing 0.5% $BaSO_4$ but no lignin. Just prior to formation lignin was added to the electrolyte.

(*e*) An electrode was assembled from five laboratory prepared plates containing 0.5% lignin and 0.5% $BaSO_4$.

The individual plates from each of these electrodes were examined after the formation and their structure was found to confirm the previous conclusions. The structure of the lignin-free plates was the same as that of the two plates containing no lignin which had been sandwiched between production negatives.

The plates which contained no lignin, formed in the electrolyte to which lignin had been added, may have undergone a very slight modification of structure. For the most part the structure found in this electrode was quite similar to that in the electrodes in which all plates were lignin free, except that there seemed to have been a slight reduction in crystal size near the surface of the plate. However, the somewhat different structure usually found at the surface of the plate, as previously noted, made it difficult to be sure. It can only be said that, if lignin added to the electrolyte had any effect on the structure developed during electrolytic forming, such an effect was slight. It was concluded that lignin must remain in the plate and that it is not released into the electrolyte during the formation process.

Discussion and Conclusions

Lignin definitely reduced the complexity of the structure in lead crystals during the original electrolytic formation that produced the so-called "sponge lead" electrode. Therefore, it is important to consider just what is the lead crystal structure. Polished cross sections of electrodes that contained no lignin showed groups of parallel lead filaments extending for considerable distances until their path was interrupted by similar groups of parallel filaments extending in other directions.

What was seen cannot be filaments, however. The possibility would be extremely remote that such small-diameter filaments would extend for any distance parallel to a randomly selected plane section, and for this to occur with the observed frequency would be incredible. Despite their appearance, therefore, the apparent filaments or needlelike lead structures must have represented some other configuration.

The idea of parallel tabular crystals or laminar-like growths suggests itself immediately but was rejected in favor of an ordered dendritic growth for the following reasons:

(*a*) Cross sectioning at any angle through a laminar structure would always produce apparently continuous filaments in the surface of the section. This is not the actual case, however. Sections contained areas both of the needlelike, parallel, pseudo-filaments and areas where small irregular particles appeared, usually roughly circular or ovoid, separated by considerable and usually uniform distances. These particles did not show visible connection with one another. That these irregular particles were dendritic extensions of a larger growth could be easily demonstrated by repeated grinding and re-examination of the same area whereby it was found that particles remained in approximately the same position although the depth of material removed by grinding greatly exceeded their apparent diameters. That they were interconnected at certain levels was also established in this manner.

(*b*) Focusing down through the clear plastic made possible examination of some subsurface areas. It was noted in some cases that pointed projections could be seen below the surface. These appeared to be the ends of dendritic type branched structure, and they were most numerous in areas where the ovoid or circular particles were found. When such areas were ground down, cross sections of these particles were identical with those seen elsewhere and since laminar structure was never noted in this manner it was assumed that the pointed extensions and the sectioned irregular particles were cross sections through a dendritic crystal near a growth boundary. It was indicated that the pointed projections seen beneath the surface were the same as those that had been sectioned, except that growth had stopped short of the plane of section.

(*c*) Disintegration of the plate either by mechanical crushing and grinding, ultrasonic vibration, or the vigorous shaking of suspensions did not reveal any platelets or foil-like structures in the residue. Since lead is malleable, some evidence of such structure should have survived the plate disintegration, if it indeed existed. On the other hand, short lead needles of irregular circumference were abundant in the residue.

(*d*) It has been our experience that sectioning of material containing platelets or tabular crystals gives some evidence of their presence in the polished microsection. The appearance of irregular thin platelets, formed by the sectioning of tabular crystals at angles very close to paralleling their surfaces, is one such indication. Although it is granted that the psuedo-lead filaments seen in the sections of negative plates would indicate very thin laminae, if laminae were indeed present, it would seem that there should be at least an occasional occurrence of such sectioning parallel or nearly parallel to their surfaces. This is especially true since the psuedo-lead filaments occurred in such abundance. Actually no such indications were found, indicating that laminar or tabular forms are not present.

(*e*) The smallness of the psuedo-lead filaments, the closeness of their spacing, and the limited depth to which high magnification objectives are able to be focused below the surface of the section make it impossible to follow inclined surfaces to a sufficient depth below the surface of cutting to obtain much information, but it was noted that such inclined surfaces as could be inspected appeared to have very irregular appearance and that they contained many knoblike protrusions and otherwise more nearly resembled dendritic structure than laminar.

(*f*) Finally, attempts to study the growth of lead crystals by electrochemical reduction from other solutions and from assorted jells has always resulted in a dendritic type of growth rather than a foil-like or laminar one, except where a foil-like structure may eventually develop from a dendritic origin, as is to be discussed.

Much has been learned of lead crystal structure from a study of lead crystals grown by electrolysis from a lead-rich solution, when such crystals were

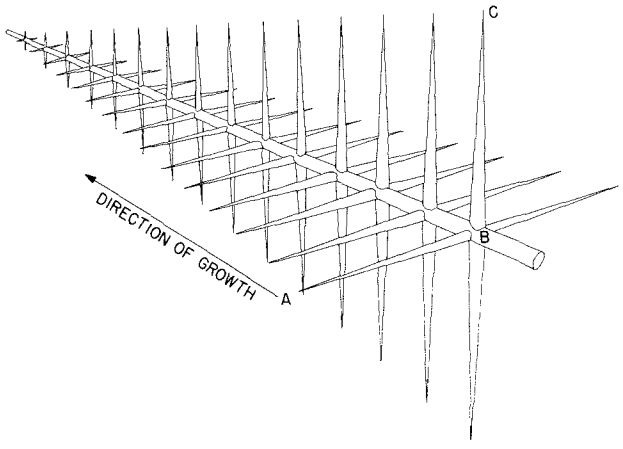

Fig. 7. Simplified drawing of branched structure produced during growth of lead crystals by electrochemical reduction from solution.

grown so that other crystals did not interfere. Figure 7 gives a greatly simplified sketch of such a crystal. The reader is undoubtedly familiar with such skeletal crystals, commonly referred to as dendritic crystals. The observed growth of dendritic lead crystals, however, showed them to be unbelievably complex and far from the simple form shown in Fig. 7. The primary stem, while continuing to grow in a straight line, produced numerous secondary branches growing at right angles to the original growth direction, as in Fig. 7. The process did not stop there, however, because the secondary branches also continued to grow and to produce tertiary branches, at right angles to the growth direction of the secondaries. The process even continued beyond this point to produce branches of an even higher order of branching.

Each branch of such a dendritic crystal grew first into a long, slender needle, much longer in proportion to breadth than shown in Fig. 7. At a later stage numerous platelets or crystallites formed along the length of the needle. These platelets obscured the simple needlelike shape first formed and, when cut, formed very unsymmetrical cross sections. This is illustrated in Fig. 8, which shows an actual photograph of a very small portion of a crystal electrolytically grown from solution. The portion shown does not represent the original primary stem but it was in an area where tertiary branches grew from a secondary. It will be noted that tertiary branches occurred at right angles to one another and at closely spaced intervals along the secondary. Had the process not been stopped at this point, some of the small platelets growing from the tertiary branches may eventually have formed additional branches of higher order. It can be seen that the combination of closely spaced tertiary branches and the growth of the small platelets into the spaces between them produced an almost continuous surface, or foil. In such a structure there are preferred growth directions so that, in essence, parallel laminae result, although with a dendritic origin and without smooth and uninterrupted surfaces. Such a form of growth produces a three-dimensional grid and when cross sectioned at any angle there will be produced in the sectioned surface cross sections of dendritic branches which will be arranged in parallel rows.

This is shown by Fig. 7. If only the quadrant represented by ABC is considered, this can be drawn in slightly greater detail, with some secondary and tertiary branching included, as in Fig. 9. Then imagine that the plane ABCD represents the plane of the electrode cross section. It can be seen how the highly symmetrical branches of the crystal, when intersected in this way, can produce parallel rows of branch cross sections on the surface of the microscopic specimen. Remember also that in the actual crystals the branches are very closely spaced and have overgrowths that not only help to produce cross sections of irregular shape but also help to close up any space left between members of the row. This helps to give the illusion that one is viewing a continuous filament rather than a row of cross sections. In real crystals the dendritic branches were less uniform in diameter, sometimes bent because of their weight, and perhaps with less uniform spacing of branches. Nevertheless, the structure in cross sections would be produced in the same manner as described. (Fig. 10).

This somewhat lengthy description of dendritic growth is not intended to imply that such dendritic growth is unique to lead but only to illustrate how the psuedo-lead filaments are produced that appear in the microscopic cross sections and also how these psuedo lead filaments may indicate the presence of a considerably more complex structure. Whether or not this explanation is correct has no bearing on the reality of the considerably less complex microstructure found in the electrodes containing lignin. Whatever the explanation of the observed microstructures,

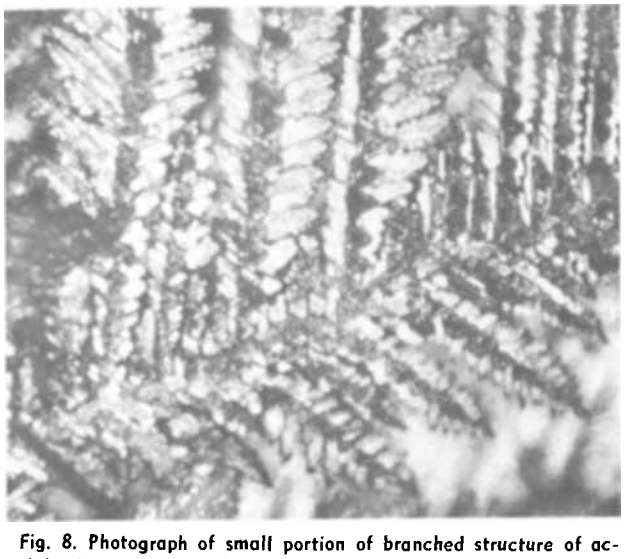

Fig. 8. Photograph of small portion of branched structure of actual lead crystal grown by electrochemical reduction from solution. Magnification 640X.

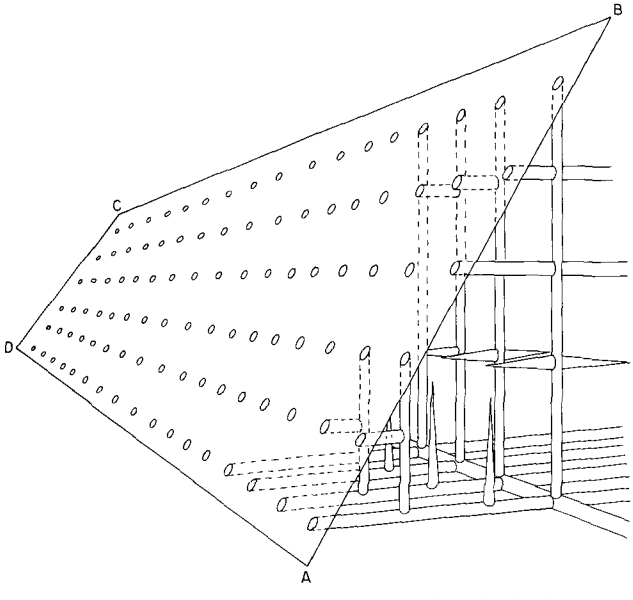

Fig. 9. Drawing made to indicate method by which illusion of parallel lead filaments is created in surface of sections cut through dendritic branched crystals.

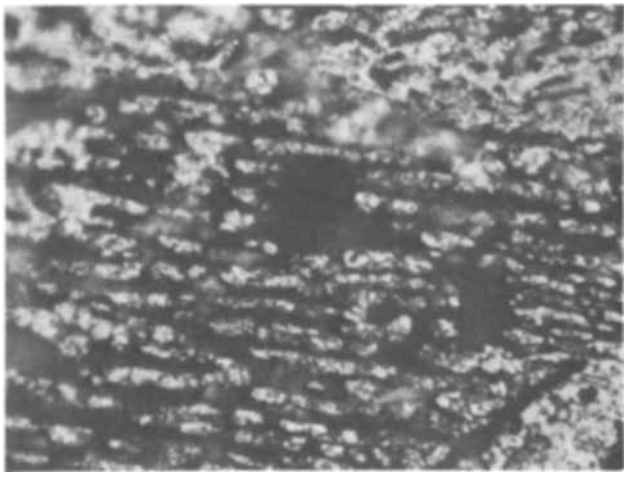

Fig. 10. Photograph of a portion of the psuedo-filaments of lead, indicating the pronounced tendency to be discontinuous even though the individual particles maintain pronounced alignment. Magnification 1600X.

that in the electrodes containing lignin was definitely less complex than that in lignin-free plates.

If this explanation of the observed microstructure is correct, however, the parallel filaments as seen in a lignin-free electrode are evidence of a much more extensive and complex structure either above or below the plane of the cross section made for examination. It should be evident that random sectioning would rarely show the full length of the underlying crystal, so that it would be expected that many of the crystals were actually larger and more complex than the part seen in the section would indicate.

In watching the dendritic growth of lead crystals from solution, it was determined that the diameter was roughly uniform along the entire length of a dendritic branch except at the growing tip where it narrowed to a sharp point. Branch diameter, branch spacing, and total crystal complexity varied with the concentration, current density, temperature, and other factors. Considerable variation in these factors is also noted in different areas of the same formed electrode.

Artistic license is taken in Fig. 7 and 9 which show the branches tapering along their entire length, a completely false impression. Since the branches are all so uniform in diameter, it would appear that added growth to the diameter of the crystal, during the initial rapid stage of growth, is prevented by a sudden depletion of lead ion in the dendritic branch's vicinity as a steep concentration gradient develops.

After the sudden growth of a dendritic branch through a given area, an equilibrium condition is gradually restored and secondary branching occurs. Microscopic examination of dendritic crystals grown in solution showed that the original growth of a branch through the area produced a needlelike cylindrical structure with practically smooth sides. After a time very small crystallites began to form on the original dendritic branches and these continued to increase in size (Fig. 8). At more or less regular intervals along the length of the dendritic branch, some of these crystallites were able to outgrow the others and initiated another sequence of dendritic branching. This in turn set up new concentration gradients that suppressed the growth of the crystallites that remained between those able to outstrip the others.

Very small differences were found in the diameter of dendritic branches of lignin-free and lignin-containing electrodes. This would indicate that lignin exerts little influence in the initial stages of growth during which primary stems are forming. It is apparently the secondary or higher branching that the lignin suppresses. More likely, it is the formation of the small platelets that is suppressed, so that higher order branching is not possible. It is assumed, therefore, that lignin must deposit at once on the newly formed primary stems and further lead growth can occur only by nucleation of new crystals. Presumably, the primary dendritic stem could be as long in a lignin-containing plate as in a lignin-free plate, but no extensive branching would occur. Without a symmetrical and extensive secondary branching, such a long primary stem would probably never be detected, as there would be infinitesimal chance of sectioning so as to reveal the entire length, or even any great portion, of such a long primary stem.

The sections of lignin-containing plates show only short psuedo-filaments and very little paralleling, so that it can be deduced that the underlying crystals are quite simple, close packed, and very numerous.

It is doubtful that the modification in crystal structure brought about by the lignin offers any real advantage at the beginning, although this cannot be definitely ascertained until all phases of this investigation are completed. BET measurement of the surface of the lignin-free and lignin-containing electrodes showed nearly the same surface area to be present in the two cases.

It was noted that lignin seemed to reduce the cracking that occurred during the drying of the formed negative electrodes. This is puzzling since it would seem that the complex lead structure found in the lignin-free plates would form more interlocking and a more coherent plate than would the less intricate crystals of the lignin-containing electrode.

However, perhaps the less complex structure in the lignin-containing plate resulted in more efficient packing so that such a plate was more resistant to the surface tension produced by the evaporation of the electrolyte. Or perhaps the simpler structure of the crystals in the lignin-containing plates is more resistive to compressive forces than are the long, complex, many-branched crystals of the lignin-free plates.

In conclusion, mention should be made of the work of Hauel (9), who studied the change in permeability of the negative electrode during formation and concluded that $BaSO_4$ was beneficial to the process. This conclusion was based on the observed decrease in permeability at the end of formation in plates containing $BaSO_4$ but no organic material, and on the assumption that decreased permeability was the result of the formation of smaller crystals and consequently smaller pores. As mentioned previously, no evidence was found in the present investigation that $BaSO_4$ changed the lead crystal structure in any manner, nor could evidence be found to otherwise explain the decreased permeability in the presence of $BaSO_4$ that was observed by Hauel.

Acknowledgments

The authors wish to thank both the U.S. Naval Research Laboratory and Globe-Union, Inc., for permission to publish this paper, and for their part in the joint effort that has made possible the extensive investigation of lead electrode behavior of which this paper is only a preliminary report. Appreciation is also expressed to the International Lead-Zinc Research Organization, Inc., which has contributed to this and other investigations of electrochemical power sources by maintaining at the Naval Research Laboratory the position of Postdoctoral Research Associate for one of the authors.

Grateful acknowledgment is also made to Dr. Victor R. Deitz of the U.S. Naval Research Laboratory who made the BET surface area determinations.

Manuscript submitted May 7, 1970; revised manuscript received *ca.* Aug. 12, 1970.

Any discussion of this paper will appear in a Discussion Section to be published in the June 1971 JOURNAL.

REFERENCES

1. E. Willihnganz, *Trans. Electrochem. Soc.*, **92**, 281 (1947).
2. E. J. Ritchie, *ibid.*, **92**, 229 (1947); *ibid.*, **100**, 53 (1953).
3. A. C. Zachlin, *This Journal*, **98**, 325 (1951).
4. T. I. Popova and B. N. Kabanov, *Zh. Prikl. Khim.*, **32**, 326 (1959), English transl. p. 339.
5. Ya. B. Kasporov, E. G. Yampol'skaya, and B. N. Kabanov, *ibid.*, **37**, 1936 (1964), English transl. p. 1922.
6. S. C. Barnes, *Proc. Intern. Conf. Lead, 2nd, Arnhem*, Oct. 4-7, 1965.
7. E. G. Yampol'skaya, M. I. Ershova, I. I. Astakhov and B. N. Kabanov, *Elektrokhimiya*, **2**, 1327 (1966), English transl. p. 1211.
8. W. Simon, *Bosch. Techn. Berichte*, **1**, 234 (1966).
9. A. P. Hauel, *Trans. Electrochem. Soc.*, **78**, 231 (1940).

Oxygen and Hydrogen Peroxide Reduction at a Ferric Phthalocyanine-Catalyzed Graphite Electrode

A. Kozawa,* V. E. Zilionis,* and R. J. Brodd*

Union Carbide Corporation, Consumer Products Division, Research Laboratory, Cleveland, Ohio 44101

ABSTRACT

When deposited on graphite, ferric phthalocyanine has been found to be a good catalyst for electrochemical oxygen reduction in near neutral isotonic saline electrolytes (*p*H 7.22). In this study, the electrochemical reduction of oxygen and hydrogen peroxide at the ferric phthalocyanine-graphite electrode was investigated over a wide range of *p*H-values by linear sweep voltammetry in order to characterize the catalyst system. The results are compared with those at platinized platinum and graphite electrodes. The activity of the ferric phthalocyanine-graphite electrode is approximately equal to that of the platinized platinum electrode in 1M KOH. In acid solution, the ferric phthalocyanine-graphite electrode has a fair activity but becomes inactive once a fairly negative potential is imposed.

In the search for a specific catalyst for the oxygen cathode of an implantable fuel cell that could power an artificial heart device, ferric phthalocyanine-catalyzed graphite was found to be an excellent electrode for oxygen reduction in saline solution (1, 2). Metal phthalocyanines such as cobalt phthalocyanine (3, 4) and ferric phthalocyanine (5) have been reported to be good catalysts for the oxygen cathode of a fuel cell. Although the performance of fuel cells or half cells having such catalysts on or in the porous cathode have been reported, basic electrochemical studies of such a catalyst under relatively simple conditions have not been reported. In previous studies, 35% KOH or 4.5*N* H_2SO_4 solutions were used as electrolytes (3, 5). The *pH* range in the present investigation is limited to that between 1M KOH and 0.5M H_2SO_4.

In this study, in order to establish the electrochemical characteristics and capabilities of the ferric phthalocyanine-graphite electrode, the electrochemical reductions of oxygen and hydrogen peroxide were investigated at ferric phthalocyanine-graphite, platinized platinum, and graphite electrodes over a wide *p*H range (*p*H 0.3-13.5). Investigations of the ferric phthalocyanine-graphite electrode in widely varying media should be helpful in defining important characteristics of electrocatalysts, since many catalysts for oxygen cathodes generally do not work equally well in both alkaline and acid solutions.

Experimental Procedure

A platinum or pyrolytic graphite rotating disk electrode described previously was used (1). The areas of the disk electrodes were 0.196 and 0.268 cm^2 for platinum and graphite electrodes, respectively. The cell was a glass vessel having a water jacket to control the temperature. Both the counterelectrode and the reference electrode were saturated calomel electrodes (SCE). All potentials were measured and reported *vs.* SCE. All the current-potential (*i-E*) curves were taken starting at the open-circuit potential and sweeping toward more negative potentials at a rate of 0.1 V/min at 23° ± 1°C. The *i-E* curves were recorded with an X-Y recorder.

Platinum black electrodes were prepared by electrodepositing platinum black on the surface of a polished platinum disk from a chloroplatinic acid solution containing lead acetate. The surface was completely covered with a black deposit. The pyrolytic graphite surface was polished in the usual metallographic manner using a 0.3μ alumina suspended in water, with water on microcloth for the final polish. Ferric phthalocyanine catalyst was deposited on the polished graphite surface from a concentrated sulfuric acid solution by diluting the solution with water. By this method, approximately 1 $\mu g/cm^2$ of ferric phthalocyanine was deposited on the graphite surface. Ferric phthalocyanine was determined spectrophotometrically from the absorbance of pyridine solutions at 655 mμ. The platinized platinum electrode was kept in distilled water and used repeatedly. However, a fresh ferric phthalocyanine-graphite electrode was prepared for each experiment.

The following six electrolytes were prepared from analytical grade reagents:

1. 0.5M H_2SO_4
2. 0.05M H_2SO_4 + 0.15M NaCl (*p*H 1.55)
3. 0.15M NaCl + 0.05M sodium-potassium phosphate buffer (*p*H 7.22)
4. 0.15M NaCl + 0.05M sodium acetate (*p*H 7.7)
5. 0.1M KOH + 0.15M NaCl (*p*H 11.58)
6. 1M KOH.

The *i-E* curves were taken in nitrogen-saturated solution, oxygen-saturated (1 atm) solutions, and in nitrogen-saturated solutions containing hydrogen peroxide. The hydrogen peroxide solution was prepared from 90% hydrogen peroxide (which was a stabilizer-free product supplied by FMC Corporation). The ap-

* Electrochemical Society Active Member.

Key words: oxygen reduction, H_2O_2 reduction, ferric phthalocyanine graphite.

proximate hydrogen peroxide concentration in the nitrogen-saturated solution was 0.001M.

In order to compare the capability of the ferric phthalocyanine-graphite electrode with that of a platinized platinum electrode, the i-E curves for both electrodes were taken in the same solution. Equivalent measurements at an uncatalyzed graphite electrode gave the basic activity of the substrate material since the ferric phthalocyanine catalyst may not completely cover the surface of the graphite electrode.

Results

Figures 1-6 show the i-E curves taken at platinized platinum, ferric phthalocyanine-graphite, and graphite electrodes in various oxygen-saturated, acid, neutral, and alkaline solutions. Regardless of the pH value of the solution used in this work, the current due to oxygen reduction at a graphite electrode is practically zero up to about −0.3V *vs.* SCE. In neutral and alkaline electrolytes, the current at the platinized platinum or ferric phthalocyanine-catalyzed graphite electrodes becomes diffusion limited before that potential.

In acid solutions (Fig. 1 and 2), the loss in activity of the ferric phthalocyanine-graphite electrodes for oxygen reduction is noted once the electrode is swept beyond −0.3V *vs.* SCE. The current is much lower for the second i-E curve than for the initial sweep. In fact, the activity of the catalyzed electrode is reduced to that of a plain (uncatalyzed) graphite electrode after an extended voltage excursion to potentials more negative than −0.8V as noted in curves 2 and 3 of Fig. 2.

It should be kept in mind when examining the i-E curves that essentially all the oxygen reaching the platinized platinum electrode surface by diffusion is reduced to water ($O_2 + 4H^+ + 4e^- \rightarrow 2H_2O$) by a four-electron transfer reaction in the potential range more negative than +0.4V in 0.5M H_2SO_4.

Assuming the plateau current at the platinized platinum disk electrode is the diffusion-limiting current for the oxygen reduction reaction ($O_2 + 4H^+ + 4e^- = 2H_2O$), the maximum current for the ferric phthalocyanine-graphite electrode can be calculated from the ratio of their surface areas. A current value of 300 μA was observed for platinized platinum electrodes. The limiting current value for the ferric phthalocyanine-graphite electrode is calculated to be 400 μA; that is, 0.268 cm^2/0.196 cm^2 x 300 μA = 400 μA.

In neutral and alkaline electrolytes (Fig. 3-6), the ferric phthalocyanine-graphite electrode gives a plateau current value that is close to the diffusion-limiting current as previously calculated over a wide potential range. Also, the electrode maintains its activity upon repeated sweeps, even when it has been swept to very negative potentials.

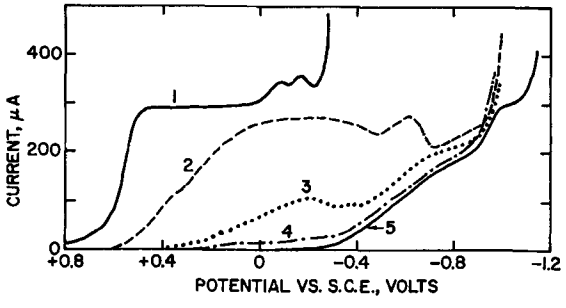

Fig. 1. Current-potential curves in 0.5M H_2SO_4 (oxygen-saturated). Curve 1, platinized platinum electrode (apparent surface area: 0.196 cm^2); curve 2, ferric phthalocyanine-graphite electrode (apparent surface area: 0.268 cm^2), (1st sweep); curve 3, ferric phthalocyanine-graphite electrode (2nd sweep, immediately after curve 2); curve 4, ferric phthalocyanine-graphite electrode (previously swept once in N_2-saturated H_2SO_4 from +0.4 to −1.0V); curve 5, graphite electrode (apparent surface area: 0.268 cm^2).

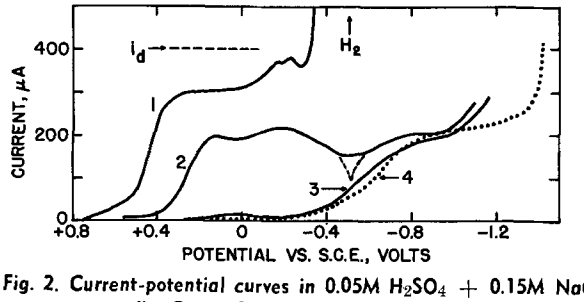

Fig. 2. Current-potential curves in 0.05M H_2SO_4 + 0.15M NaCl (oxygen-saturated). Curve 1, platinized platinum electrode (apparent surface area: 0.196 cm^2); curve 2, ferric phthalocyanine-graphite electrode (apparent surface area: 0.268 cm^2), (1st sweep); curve 3, ferric phthalocyanine-graphite electrode (2nd sweep, immediately after curve 2); curve 4, graphite electrode (apparent surface area: 0.268 cm^2).

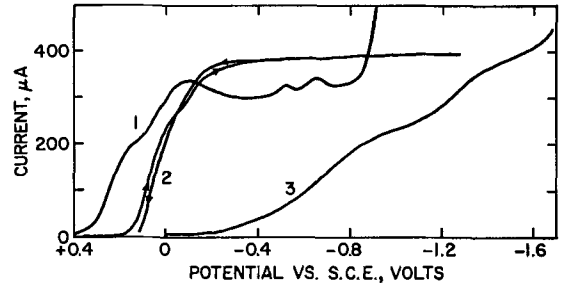

Fig. 3. Current-potential curves in 0.15M NaCl +0.05M phosphate buffer (pH 7.22), (oxygen-saturated). Curve 1, platinized platinum electrode (apparent surface area: 0.196 cm^2); curve 2, ferric phthalocyanine-graphite electrode (apparent surface area: 0.268 cm^2), (arrows show direction of the voltage sweep); curve 3, graphite electrode (apparent surface area: 0.268 cm^2).

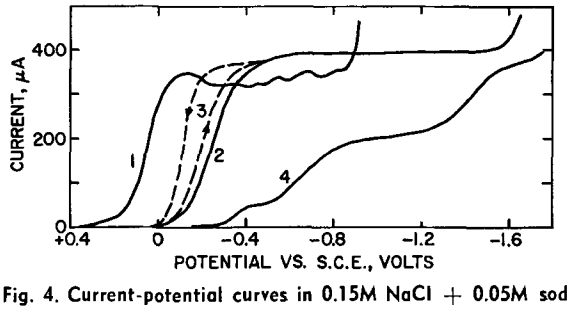

Fig. 4. Current-potential curves in 0.15M NaCl + 0.05M sodium acetate (pH 7.7), (oxygen-saturated). Curve 1, platinized platinum electrode (apparent surface area; 0.196 cm^2); curve 2, ferric phthalocyanine-graphite electrode (apparent surface area: 0.268 cm^2), (1st sweep); curve 3, ferric phthalocyanine-graphite electrode (2nd sweep, immediately after curve 2); curve 4, graphite electrode (apparent surface area: 0.268 cm^2).

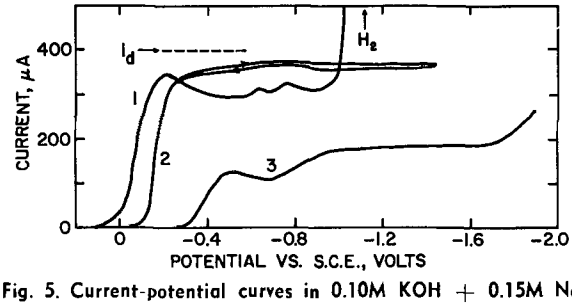

Fig. 5. Current-potential curves in 0.10M KOH + 0.15M NaCl (oxygen-saturated). Curve 1, platinized platinum electrode (apparent surface area: 0.196 cm^2); curve 2, ferric phthalocyanine-graphite electrode (apparent surface area 0.268 cm^2), (arrows show direction of the sweep); curve 3, graphite electrode (apparent surface area: 0.268 cm^2).

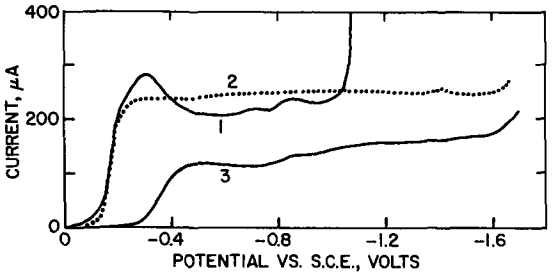

Fig. 6. Current-potential curves in 1M KOH (oxygen-saturated). Curve 1, platinized platinum electrode (apparent surface area: 0.196 cm^2); curve 2, ferric phthalocyanine-graphite electrode (apparent surface area: 0.268 cm^2); curve 3, graphite electrode (apparent surface area: 0.268 cm^2).

An anion effect was noted in the two neutral solutions. It is seen that the i-E curve at the ferric phthalocyanine-graphite electrode is almost reversible in the phosphate-containing solution (curve 2, Fig. 3); that is, the direction of the sweep does not influence the shape of the curve. In the acetate-containing solution, however, the i-E curve is less reversible and the electrode becomes activated (*i.e.*, the i-E curve is shifted toward a more positive potential) when repeated cyclic sweeps are made (curves 2 and 3, Fig. 4).

A well-platinized platinum electrode is considered to be one of the most active electrodes for cathodic oxygen reduction. In neutral and 0.1M KOH + 0.15M NaCl solutions (Fig. 3-5), the half-wave potentials of the i-E curves at the ferric phthalocyanine-graphite electrode are fairly close (100-200 mV) to the value at the platinized platinum electrode. In 1M KOH solution, the half-wave potentials of the i-E curves (Fig. 6) for the ferric phthalocyanine-graphite electrode and the platinized platinum electrode are essentially identical, and there is little difference between the two electrodes in the oxygen reduction capability.

Discussion

Deactivation of the ferric phthalocyanine-graphite electrode in acid.—Deactivation of the ferric phthalocyanine-graphite electrode is seen clearly in acid solution (curve 2, Fig. 2). Around −0.3V the current begins to decrease and passes through a minimum. This may be associated with the oxygen reduction current at a plain graphite electrode which increases around that potential, although the catalyst (ferric phthalocyanine) loses its activity. In order to correlate this behavior with the redox nature of the ferric phthalocyanine-graphite electrode itself, i-E curves were taken in nitrogen-saturated solution (Fig. 7) where the only reactions occurring should be associated with redox reactions of the catalyst. The current values are very low, but four peaks can be seen between −0.3 and −0.8V. Since there are no peaks in the i-E curve (curve 3) taken at a graphite electrode, these four peaks may be attributed to the ferric phthalocyanine catalyst. Although these four peaks are always observed on freshly catalyzed electrodes, they are not exactly reproducible in shape and relative height from one electrode to another. The reduction processes that are responsible for these reduction currents are not known. It is interesting to note that the potential (about −0.3V) at which the first peak begins to appear (see Fig. 7) corresponds to the point where the current decreases in curve 2 of Fig. 2. There may be a correlation between the reduction of the catalyst and the loss of the oxygen reduction activity. This loss of activity in the acid solution was not necessarily permanent. A ferric phthalocyanine-graphite electrode, which was deactivated in acid by sweeping to −0.8V, showed almost full activity when operated in oxygen-saturated 0.1M KOH solution. Therefore, the loss in activity is not associated with loss of the catalyst from the electrode.

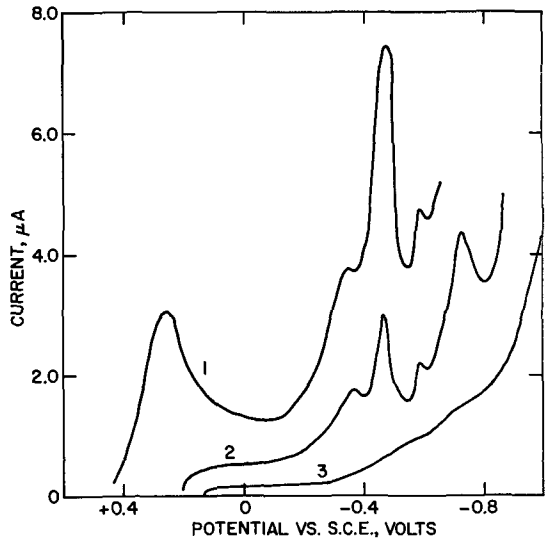

Fig. 7. Current-potential curves in 0.05M H_2SO_4 + 0.15M NaCl (nitrogen-saturated). Curve 1, ferric phthalocyanine-graphite electrode (apparent surface area: 0.268 cm^2); curve 2, ferric phthalocyanine-graphite electrode (2nd sweep); curve 3, graphite electrode (apparent surface area: 0.268 cm^2).

It is possible that the change in activity of ferric phthalocyanine catalyst may be associated with a change in the anion associated with the test. The catalyst is deposited in a thin layer, and an ion exchange which was dependent on the solution composition could occur. It is not clear exactly how the anion would influence the catalytic activity.

Hydrogen peroxide reduction.—Hydrogen peroxide is known to be an intermediate in the cathodic reduction of oxygen at various electrodes (6-8) including graphite and platinum in acid, neutral, and alkaline solutions. A proposed scheme of oxygen reduction is given below.

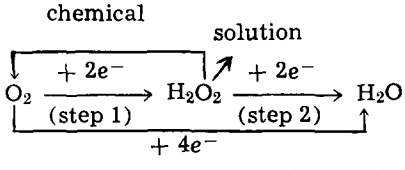

[1]

A study of hydrogen peroxide reduction in nitrogen-saturated solution should yield some useful information on the kinetics of the electrochemical oxygen reduction. Suppose an electrode does not reduce hydrogen peroxide electrochemically, although oxygen is reduced to water at the electrode. In such a case, oxygen must be reduced either by a direct four-electron step or through a step involving chemical decomposition of hydrogen peroxide.

Figures 8-11 show the results of hydrogen peroxide reduction in nitrogen-saturated acid, neutral, and alkaline solutions. The graphite electrode has little or no ability to reduce hydrogen peroxide electrochemically over most of the potential range studied. The current plateau at the platinized platinum electrode is an experimental measure of the total hydrogen peroxide reduction current. The i-E curves (Fig. 9-11) at the ferric phthalocyanine-graphite electrode in neutral and alkaline hydrogen peroxide solutions contain two steps and differ considerably from the i-E curves taken in the oxygen-saturated solutions. In alkaline and neutral solutions, the ferric phthalocyanine-graphite electrode can reduce hydrogen peroxide, but in acid solution (Fig. 8) the electrode has no activity for hydrogen peroxide reduction. This behavior suggests that step 2 in Eq. [1] does not proceed at reasonable rates at the ferric phthalocyanine-graphite electrode in acid solution. Catalytic decomposition of hydrogen peroxide on ferric phthalocyanine in the absence of

applied potentials has been studied by Cook and George since its structure is similar to hemin and catalase (9, 10). According to Cook's study, ferric phthalocyanine was an outstanding catalyst for decomposing hydrogen peroxide. He attributed the activity to its central iron ion. As yet, the electrochemical oxygen reduction mechanism at the ferric phthalocyanine-graphite electrode is not known. However, a speculative explanation of the two reduction steps could be given here. The hydrogen peroxide decomposition rate should be potential dependent. At low potentials where the rate is small, the spontaneous decomposition of peroxide could produce enough dissolved oxygen to give a significant current. Thus the first step could be attributed to reduction of oxygen produced by the spontaneous catalytic decomposition of peroxide by the catalyst. The second step could be attributed to direct reduction of the hydrogen peroxide molecule to water on the electrode.

In 1M KOH, the current capability of the ferric phthalocyanine-graphite electrode remained fairly close to that of the platinized platinum electrode, as shown in Fig. 12. However, an indication of a kinetic limitation for the ferric phthalocyanine-graphite electrode is noted at the higher rotational speeds. It

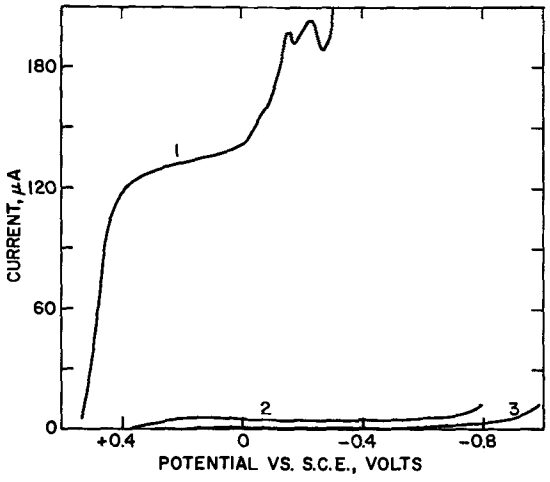

Fig. 8. Current-potential curves in 0.05M H_2SO_4 + 0.15M NaCl (pH 1.55), (nitrogen-saturated) containing about 0.001M H_2O_2. Curve 1, platinized platinum electrode (apparent surface area: 0.196 cm^2); curve 2, ferric phthalocyanine-graphite electrode (apparent surface area: 0.268 cm^2); curve 3, graphite electrode (apparent surface area: 0.268 cm^2).

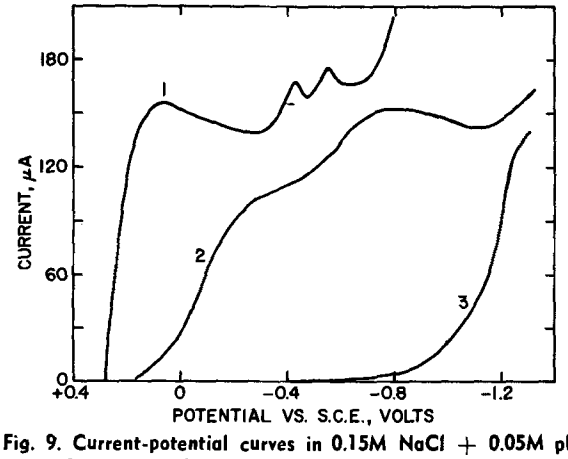

Fig. 9. Current-potential curves in 0.15M NaCl + 0.05M phosphate buffer (pH 7.22) containing about 0.001M H_2O_2. Curve 1, platinized platinum electrode (apparent surface area: 0.196 cm^2); curve 2, ferric phthalocyanine-graphite electrode (apparent surface area: 0.268 cm^2); curve 3, graphite electrode (apparent surface area: 0.268 cm^2).

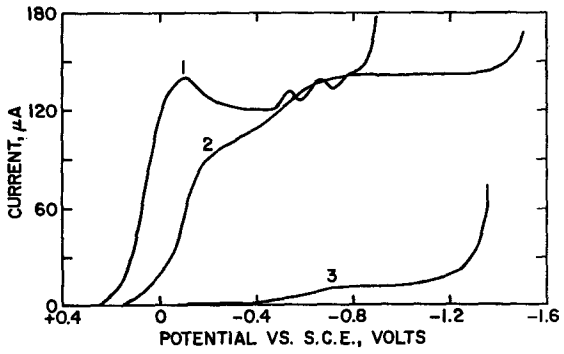

Fig. 10. Current-potential curves in 0.15M NaCl + 0.05M sodium acetate (pH 7.7), (nitrogen-saturated) containing about 0.001M H_2O_2. Curve 1, platinized platinum electrode (apparent surface area: 0.196 cm^2); curve 2, ferric phthalocyanine-graphite electrode (apparent surface area: 0.268 cm^2); curve 3, graphite electrode (apparent surface area: 0.268 cm^2).

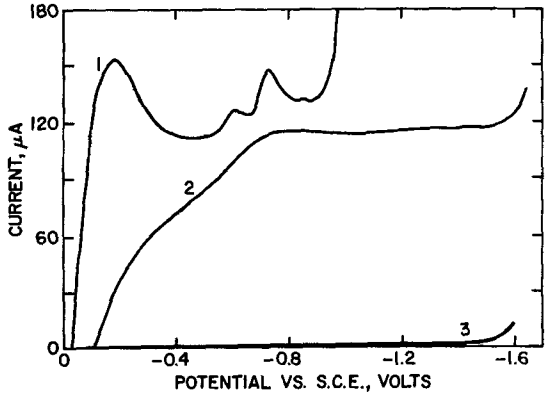

Fig. 11. Current-potential curves in 0.1M KOH + 0.15M NaCl solution (nitrogen-saturated) containing about 0.001M H_2O_2. Curve 1, platinized platinum electrode (apparent surface area: 0.196 cm^2); curve 2, ferric phthalocyanine-graphite electrode (apparent surface area: 0.268 cm^2); curve 3, graphite electrode (apparent surface area: 0.268 cm^2).

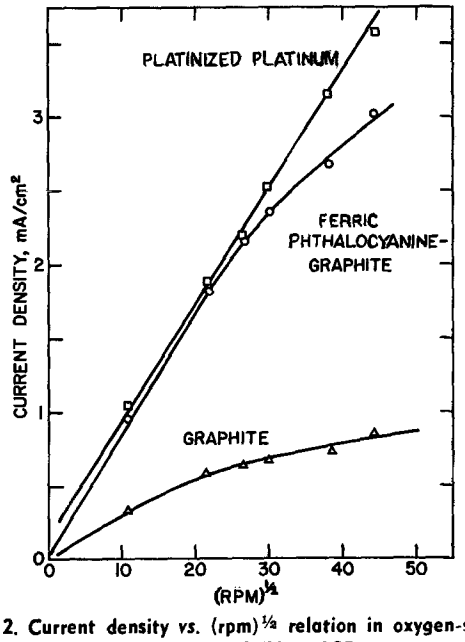

Fig. 12. Current density *vs.* $(rpm)^{1/2}$ relation in oxygen-saturated 1M KOH for three electrodes at —0.4V *vs.* SCE.

should be noted in Fig. 13 that the graphite electrode itself has practically no activity for oxygen reduction up to —0.3V *vs.* SCE in the saline solution. Therefore the function of ferric phthalocyanine cata-

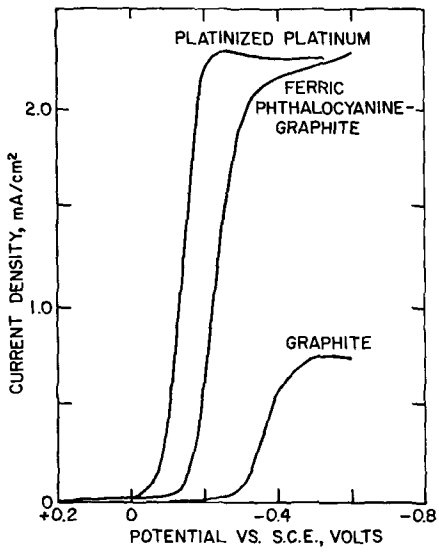

Fig. 13. Current-potential curves at rotating platinized platinum, ferric phthalocyanine-graphite, and graphite disk electrodes in oxygen-saturated 1M KOH solution at 23°C and at 720 rpm.

lyst applied on the surface is solely responsible for the oxygen reduction current at the ferric phthalocyanine-graphite electrode.

Acknowledgment

The research on which this report is based was performed pursuant to Contract No. PH-43-68-1391 with the Artificial Heart Program, National Heart and Lung Institute, Department of Health, Education, and Welfare.

Manuscript submitted April 22, 1970; revised manuscript received July 20, 1970. This was Paper 35 presented at the Detroit Meeting of the Society, Oct. 5-9, 1969.

Any discussion of this paper will appear in a Discussion Section to be published in the June 1971 JOURNAL.

REFERENCES

1. A. Kozawa, V. E. Zilionis, R. J. Brodd, and R. A. Powers, Artificial Heart Program Conference Proceedings, National Heart Institute, June 9-13, 1969, Washington, D. C., Chap. 71, p. 849.
2. A. Kozawa, V. E. Zilionis, and R. J. Brodd, *This Journal*, **117**, 1474 (1970).
3. R. Jasinski, *ibid.*, **112**, 526 (1965).
4. J. A. S. Bett, W. M. Vogel, K. Ronsis, and S. B. Anderson, Am. Chem. Soc., Div. of Fuel Chem., Preprints of Papers Presented at New York Meeting, Sept. 7-12, 1969, Vol. 13, No. 3, pp. 44-49.
5. H. Jahnke and M. Schönborn, "Electrocatalysis on Organic Semiconductors," Paper presented at the 19th CITCE Meeting, Detroit (September 26, 1968).
6. W. G. Berl, *Trans. Electrochem. Soc.*, **83**, 253 (1943).
7. A. Kozawa, *J. Electroanal. Chem.*, **8**, 20 (1964).
8. P. Delahay, *This Journal*, **97**, 198, 205 (1950).
9. A. H. Cook, *J. Chem. Soc.*, **1938**, 1761, 1768, 1774, 1845.
10. P. George, *J. Biochem.*, **43**, 287 (1948).

Electrode Materials and Catalysts for Oxygen Reduction in Isotonic Saline Solution

A. Kozawa,* V. E. Zilionis,* and R. J. Brodd*

Union Carbide Corporation, Consumer Products Division, Research Laboratory, Cleveland, Ohio 44101

ABSTRACT

The cathode for an implantable fuel cell that could power an artificial heart requires both a specific catalyst and an appropriate electrode material for oxygen reduction. In search of such an electrode structure, various graphites, carbides, metals, and catalytic agents were evaluated using linear sweep voltammetry for oxygen reduction activity in neutral saline solutions. The effect of blood additions on electrode performance was also investigated. An electrode of pyrolytic graphite catalyzed with ferric phthalocyanine was found to be a good specific electrode structure. Characteristics of this electrode in near neutral saline (0.15M NaCl + phosphate buffer, pH 7.22) solution were studied using the rotating disk electrode technique. A kinetic limitation on the limiting diffusion current for oxygen reduction was noted at higher rotational speeds.

An implantable fuel cell that could power an artificial heart requires a specific catalyst for oxygen reduction at the cathode. This means that the catalyst applied on the cathode when used in a blood stream should be selective for electrochemical oxygen reduction and should not promote a direct chemical reaction between molecular oxygen and glucose or other organic substances coexisting in the blood.

In order to fabricate such a cathode to be used in blood, a good oxygen catalyst as well as an appropriate substrate or electrode material having good electrical conductivity is necessary. For this purpose, various possible electrode materials such as graphites, carbides, borides, and a large number of metals, including zirconium and titanium which are known to be corrosion resistant in salt solutions (1), have been evaluated for oxygen reduction in an isotonic saline solution. Also, various organic compounds were tested as possible catalysts. It was noted in the early stage of this work that blood itself contains a substance that promotes oxygen reduction on a graphite electrode. Therefore, our attention focused on iron-containing porphyrin-type compounds such as catalase, hemin, hemoglobin, and metal phthalocyanines. The results of the effect of catalase and hemin on the reduction of oxygen have been reported elsewhere (2) and are not included in this paper.

* Electrochemical Society Active Member.

Key words: oxygen reduction, isotonic saline, ferric phthalocyanine, rotating disk electrode.

Although many papers have been published concerning the electrochemical reduction of oxygen in general (3), these studies were made mostly in concentrated KOH (pH ≅ 16) or H_2SO_4 (pH ≅ 0) electrolytes. Studies of oxygen reduction in neutral salt solutions are very limited [Delahay (4), Kozawa (5), and Laitinen and Kolthoff (6)]. The effect of blood additions on oxygen electrode performance has not been previously reported.

Cobalt phthalocyanines have been reported to be good catalysts for an oxygen cathode in alkaline solution (35% KOH, pH ≅ 16) by Jasinski (7), and iron phthalocyanine in acid solution (4.5*N* H_2SO_4, pH ≅ 0) by Jahnke and Schönborn (8). Neither the activity nor the substrate effect on activity of these compounds for oxygen reduction in neutral salt solution has been reported. In this study, the significance of the substrate effect, particularly the uniqueness of graphite and carbon as substrates for the phthalocyanine compound, are demonstrated.

Experimental Procedure

Electrode materials, chemicals, and blood.—Most of the metals were in the form of wire or a strip and were relatively pure (at least 99.9%). Most of the graphites, carbides, and borides are commercially available items. General information on pyrolytic graphite was published previously (9), and ZTA and other graphites are described in a bulletin (10). Ferric phthalocyanine was obtained from Distillation Products Industries (Division of Eastman Kodak Company) and used as received without purification. The pyridine, used as a solvent for the phthalocyanines, was Fisher Infrared Spectroanalyzed grade. Fresh human blood was obtained from Parma Community General Hospital and stored in a refrigerator at 4°C. The blood contained ethylenediaminetetraacetic acid as an anticoagulant.

Solution.—An isotonic saline solution (0.15M NaCl + 0.05M phosphate buffer, pH 7.22) was prepared from reagent grade chemicals. It was used without further purification. Phosphate buffer was used because it is one of the major pH buffer systems in the blood (11).

Linear sweep voltammetry.—Current-potential (*i-E*) curves were taken in quiescent nitrogen- or oxygen-saturated solution with a Controlled Potential and Derivative Voltammeter (Model ORNL-1988A) (12). The test electrode was placed in one arm of a polarographic H-cell filled with isotonic saline solution. The electrode surface exposed to the solution was about 0.25 cm^2. Paraffin was used to mask off the unused portion of the surface. The potential sweep rate was 0.25 V/min. Usually the *i-E* curve was first taken in a nitrogen-saturated solution, then twice consecutively in an oxygen-saturated solution, and finally in the solution to which blood (10% by volume) was added. All potential measurements were made with respect to a saturated calomel reference electrode (SCE).

Rotating disk electrode.—The rotating disk apparatus used was described in a previous paper (2). The area of the pyrolytic graphite rotating disk electrode was 0.268 cm^2 and that of the platinum electrode was 0.196 cm^2. The electrode was press fitted in a Teflon holder concentric to the rotating shaft. Electrical connection was established by a spring-loaded silver graphite contact in the shaft. Epoxy resin was used to seal the imperfections between the Teflon and the electrode to prevent oxygen from diffusing into the test cell from the back side of the electrode. This also prevented solution from creeping up into the joint.

The rotational speed was varied between 120 and 1980 rpm. The speed was monitored continuously by an electronic counter using a photocell. The voltage scanning rate was 0.1 V/min.

Before deposition of the catalyst, the pyrolytic graphite rotating disk electrode was polished using standard metallurgical techniques. An alumina (0.3μ) suspension in water was used, always ending with a wet polish on the plain microcloth. After deposition of the catalyst, the electrode was washed with distilled water and mounted on the rotating disk apparatus.

Results and Discussion

Oxygen reduction on graphites, carbides, and others.—As noted in Fig. 1 and 2, the shape and the current level of the *i-E* curve are largely dependent on the electrode material. Some of the electrode materials (for example, pyrolytic graphite) gave a two-step *i-E* curve similar to the polarogram of dissolved oxygen at a dropping mercury electrode. Among the electrode materials of this group (Table I), the material which displayed the highest oxygen reduction current at the most anodic potential was ZTA graphite (high density graphite). When blood (10% by volume) was added to the isotonic saline solution, the oxygen reduction current generally increased as shown in Fig. 3 for the case of the ZTA graphite electrode. Table I summarizes the results for all the electrode materials tested of this group. This in-

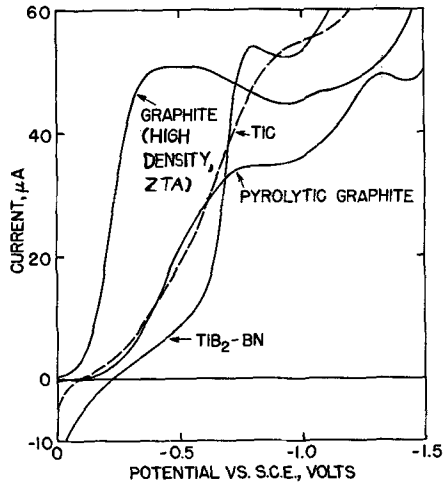

Fig. 1. Current-potential curves taken with various electrodes by linear sweep voltammetry in 0.15M NaCl (+ phosphate buffer, pH 7.22) at 24°C. The solution was saturated with oxygen (1 atm) and the curves were taken in quiescent solution.

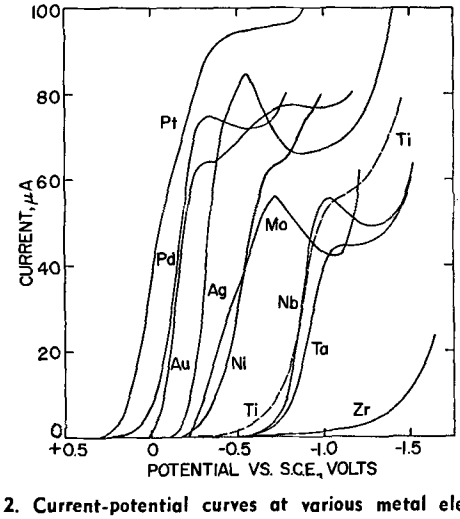

Fig. 2. Current-potential curves at various metal electrodes in 0.15M NaCl solution (phosphate buffer, pH 7.22) saturated with oxygen gas (1 atm) at 23° ± 1°C. The curves were taken in quiescent solution. The electrode surface exposed to the solution was approximately 0.25 cm^2 (not more than 10% deviation).

Table I. Comparison of various electrode materials for oxygen reduction activity

Electrode material*	Solution** condition	Current density at −0.25V (μA/cm²)	Current density at −0.5V (μA/cm²)	Current density at plateau (μA/cm²)
1. Graphite (ZTA)	O_2-saturated	124.0	186.6	
	Plus blood	123.3	232.9	
2. Graphite (ATJS)	O_2-saturated	75.7	176.2	172.4
	Plus blood	71.4	228.5	212.8
3. Graphite (exper. high density)	O_2-saturated	94.3	203.3	201.6
	Plus blood	33.3	229.7	219.1
4. Graphite (ATJ)	O_2-saturated	43.8	164.4	164.8
	Plus blood	15.4	181.1	196.5
5. Graphite (AUC)	O_2-saturated	24.3	167.0	148.1
	Plus blood	5.8	207.0	194.6
6. Graphite (pyrolytic)	O_2-saturated	11.7	88.7	145.2
	Plus blood	6.1	110.4	228.3
7. TiB_2-BN	O_2-saturated	17.5	20.8	
	Plus blood	16.1	12.7	
8. Ti carbide	O_2-saturated	16.4	69.3	
	Plus blood	16.6	76.3	
9. TiB_2	O_2-saturated	17.3	40.3	
	Plus blood	16.1	44.4	
10. TiB_2 (95%)-TiN (5%)	O_2-saturated	—	60.4	
	Plus blood	—	64.0	
11. Boron carbide	O_2-saturated	3.4	17.6	
	Plus blood	2.1	12.1	

* Materials manufactured by Union Carbide Corp., Carbon Products Div.
** In 0.15M NaCl (+ phosphate buffer, pH 7.22) saturated with oxygen (1 atm), and in the NaCl solution to which 10% (by volume) of human blood was added.

creased activity with blood additions suggests that some material present in the blood either acts as a catalyst for the electrochemical oxygen reduction or is itself reduced in the isotonic saline solution. The background current for nitrogen-saturated blood (10% by volume) solutions was negligible, that is, essentially the same as that shown for nitrogen-saturated saline solutions. Therefore, materials present in the blood act as catalysts and are not reduced under the conditions of the experiments.

Oxygen reduction on various metals.—The current level and the potential where the oxygen reduction starts on metal electrodes are widely distributed over the potential range as shown in Fig. 2. The ability to reduce oxygen in neutral saline solution appears to be highly dependent on the nature of the metal. Of the metals evaluated, the best electrode was platinum, as expected. The poorest one was zirconium, on which practically no oxygen reduction took place over a wide potential range. Although all these electrodes were polished with silica powder and water before the experiments, some of the metals, such as zirconium, probably form a surface oxide film under the test conditions which could account for their poor activity.

The effects of blood additions are shown in Fig. 3, 4, and 5 for platinum, graphite, silver, and niobium. In the case of silver (Fig. 4), the oxygen reduction was hindered slightly at the beginning portion of the i-E curve and the plateau current was increased somewhat. The behavior of silver with blood additions was typical of most of the electrode materials studied. The niobium electrode (Fig. 5) is an example of a metal which exhibited a large shift in the i-E curve when blood was added. In the case of the platinum electrode (Fig. 3), not only was the oxygen reduction hindered at the beginning of the i-E curve, but also the plateau current was considerably decreased. This

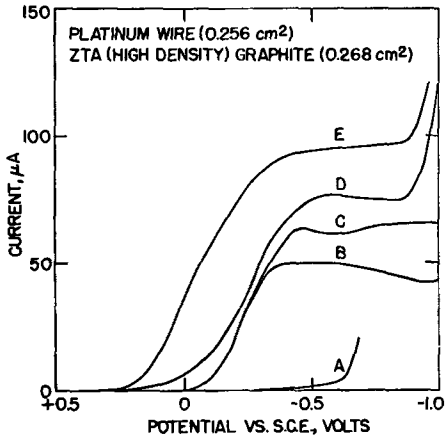

Fig. 3. Current-potential curves taken at platinum and ZTA graphite electrodes by linear sweep voltammetry in 0.15M NaCl (+ phosphate buffer, pH 7.22) at 24°C. The curves were taken in quiescent solution. Curve A, in nitrogen-saturated solution (platinum electrode); curve B, in oxygen-saturated (1 atm) solution (ZTA graphite electrode); curve C, in oxygen-saturated solution + 10% blood (by volume), (ZTA graphite electrode); curve D, in oxygen-saturated solution + 10% blood (by volume), (platinum electrode); curve E, in oxygen-saturated (1 atm) solution (platinum electrode).

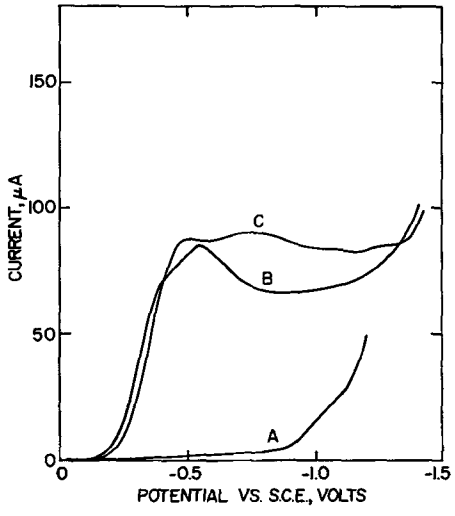

Fig. 4. Current-potential curves taken at a silver electrode (exposed area: 0.258 cm²) by linear sweep voltammetry in 0.15M NaCl (+ phosphate buffer, pH 7.22) at 24°C. The curves were taken in a quiescent solution. Curve A, in nitrogen-saturated solution; curve B, in oxygen-saturated (1 atm) solution; curve C, oxygen-saturated solution + 10% blood (by volume).

effect may be caused by a direct chemical reaction between the dissolved molecular oxygen and an organic substance (for example, glucose) present in the blood at the platinum surface and/or due to strong adsorption of blood component(s) on the electrode surface which would hinder the electrochemical oxygen reduction process. In Fig. 3, the results of the ZTA graphite electrode are also shown for comparison with the platinum electrode performance. The oxygen reduction activity for the ZTA graphite and platinum electrodes is almost the same in the solution containing blood.

Search for catalysts.—As noted, some blood components act as a catalyst for oxygen reduction in saline solution. Since it is generally accepted that hydrogen peroxide is an intermediate in the cathodic oxygen reduction process, a catalyst which decomposes hydrogen peroxide rapidly should be a good

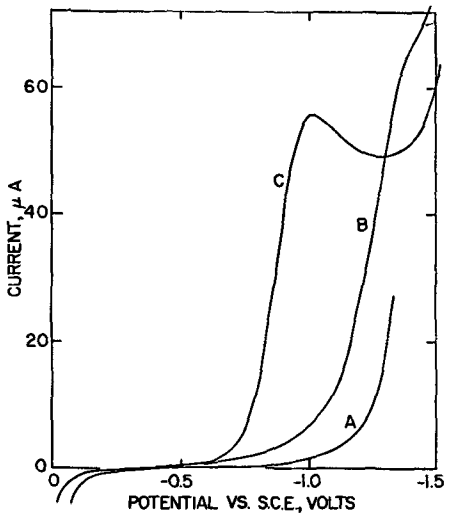

Fig. 5. Current-potential curves taken at a niobium electrode (exposed area: 0.275 cm^2) by linear sweep voltammetry in 0.15M NaCl (+ phosphate buffer, pH 7.22) at 24°C. The curves were taken in a quiescent solution. Curve A, in nitrogen-saturated solution; curve B, in oxygen-saturated solution + 10% blood (by volume); curve C, in oxygen-saturated (1 atm) solution.

catalyst for the oxygen cathode reaction. Therefore, catalase, hemin, hemoglobin, various metal phthalocyanines, and metal porphyrazines were tested by dissolving them in the saline solution or by depositing them on a pyrolytic graphite substrate. Ferric phthalocyanine was the best catalyst of the materials tested. The effectiveness of ferric phthalocyanine as a catalyst appears to be dependent on the nature of the substrate material. The results for catalase, hemin, and various metal phthalocyanines have been presented previously (2).

Substrate effect on the activity of ferric phthalocyanine catalyst.—In these experiments, a small amount of a solution of ferric phthalocyanine in pyridine (50 mg of ferric phthalocyanine in 200 ml of pyridine) was applied to a cleaned nickel or pyrolytic graphite surface. The solvent was evaporated by blowing hot air (70°-80°C) across the electrode surface. The total amount of ferric phthalocyanine on the electrode surface was approximately 45 $\mu g/cm^2$. Figure 6 shows the difference in the activity of the ferric phthalocyanine when deposited on a nickel substrate and on a pyrolytic graphite substrate. In the case of the pyrolytic graphic electrode, the oxygen reduction activity was enhanced considerably when the ferric phthalocyanine was applied; whereas, in the case of nickel, the oxygen reduction activity was decreased

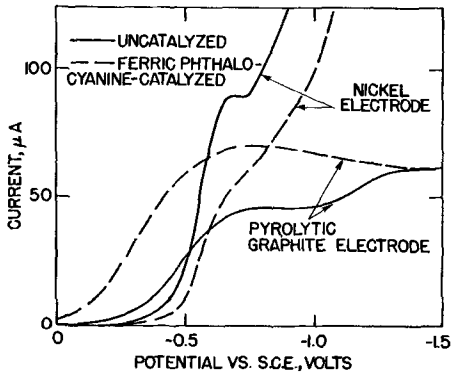

Fig. 6. Current-potential curves at uncatalyzed and ferric phthalocyanine-catalyzed nickel and pyrolytic graphite electrodes in 0.15M NaCl solution (0.05M phosphate buffer added, pH 7.22) at 23°C. Electrode area: 0.27 ± 0.01 cm^2.

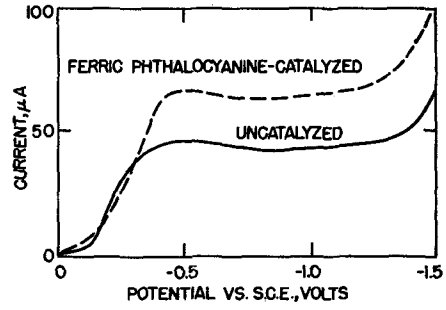

Fig. 7. Current-potential curves at ferric phthalocyanine-catalyzed and uncatalyzed ZTA graphite electrodes in 0.15M NaCl (+ phosphate buffer, pH 7.22) at 23°C. Electrode area: 0.27 ± 0.01 cm^2.

somewhat when the ferric phthalocyanine was applied. If a sintered porous nickel plaque, such as is commonly used in fuel cells and nickel-cadmium batteries, was used as a substrate, slightly better activity was observed with the ferric phthalocyanine present than was observed with the nickel plaque substrate alone. The special structure of the carbonyl nickel particles or a nickel oxide film on the surface may be responsible for this effect. In any event, the current increase obtained when ferric phthalocyanine was applied to a nickel plaque was far less than that observed with the graphite substrate. The ZTA graphite electrode itself had a good activity for oxygen reduction as previously mentioned. When ferric phthalocyanine was applied to a ZTA graphite substrate, the oxygen reduction activity was further enhanced as shown in Fig. 7. This behavior is very similar to that noted for pyrolytic graphite.

Various materials (metals, carbides, borides, *etc.*) were tested as substrates for the ferric phthalocyanine catalyst in the same manner as previously described. The results are summarized in Table II. Of these materials, the only substrate that exhibited a substantial current increase in the *i-E* curve was graphite. This suggests that the graphite substrate does not function merely as an electronic conductor for the electrode, but is indispensable in developing the remarkable activity of the ferric phthalocyanine catalyst for electrochemical oxygen reduction. It is well known in the field of catalysis that the supporting substance greatly influences the activity of the catalyst or sometimes determines the specific activity. The graphite and carbon substrates in this case seem to be specific supports and can be considered part of the catalyst system, since neither ferric phthalocyanine nor graphite (or carbon) alone are catalytically active.

Current capability of the ferric phthalocyanine-graphite electrode.—A comparison of the current capabilities of ferric phthlocyanine-catalyzed graphite electrodes and platinum electrodes is found in Fig. 8 and 9.

In the neutral NaCl solution (Fig. 8), the initial oxygen reduction activity at the ferric phthalocyanine-graphite electrode was very good and was close to that of the platinized platinum electrode. It is

Table II. Effect of ferric phthalocyanine on the *i-E* curve compared with that for the uncatalyzed electrode

Increases current significantly (Group A)	Essentially no effect (Group C)	Slight decrease in current (Group D)	Considerable decrease in current (Group E)
Pyrolytic graphite	Gold	Platinum	Tantalum
ZTA graphite	Molybdenum	Nickel	TiB_2-BN
	Zirconium	Niobium	
	TiB_2-TiN	Titanium	
	TiC	Silver	
	TiB_2	Boron carbide	

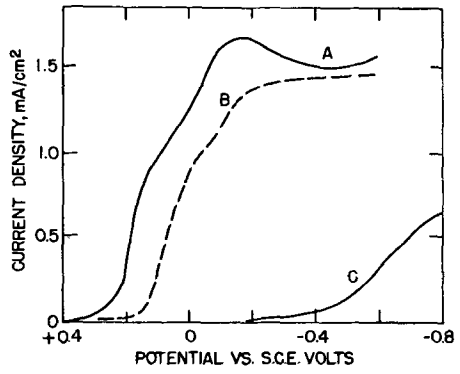

Fig. 8. Current-potential curves at rotating platinized platinum, ferric phthalocyanine-graphite, and graphite disk electrodes in oxygen-saturated 0.15M NaCl (+ phosphate buffer, pH 7.22) at 23°C and at 720 rpm. Curve A, platinized platinum; curve B, ferric phthalocyanine-graphite; curve C, graphite.

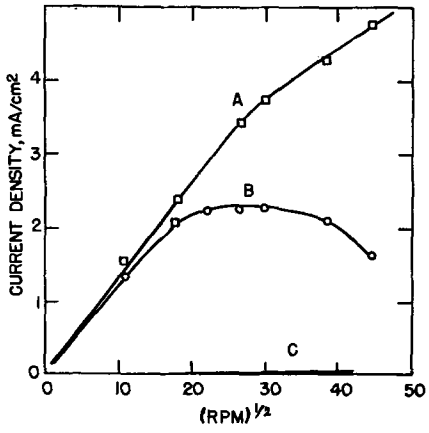

Fig. 9. Current density vs. $(rpm)^{1/2}$ curves in 0.15M NaCl (+ 0.05 phosphate buffer, pH 7.22) for three electrodes at —0.2V vs. SCE. Curve A, platinized platinum; curve B, ferric phthalocyanine-graphite; curve C, graphite.

also noted in Fig. 9 that the current density *vs.* $(rpm)^{1/2}$ relation between 120 and 1980 rpm was not linear at this electrode. This behavior is indicative of a kinetic limitation for the ferric phthalocyanine-catalyzed graphite electrode at —0.2V.

Acknowledgment

The authors gratefully acknowledge the assistance of W. L. Adams in carrying out part of the experimental portion of this study.

The research on which this report is based was performed pursuant to Contract No. PH-43-68-1391 with the Artificial Heart Program, National Heart and Lung Institute, Department of Health, Education, and Welfare.

Manuscript submitted April 22, 1970; revised manuscript received July 20, 1970. This was Paper 34 presented at the Detroit Meeting of the Society, Oct. 5-9, 1969.

Any discussion of this paper will appear in a Discussion Section to be published in the June 1971 JOURNAL.

REFERENCES

1. "Rate Metals Handbook," C. A. Hample, Editor, Reinhold Publishing Corp., New York (1961).
2. A. Kozawa, V. E. Zilionis, R. J. Brodd, and R. A. Powers, Artificial Heart Program Conference Proceedings, National Heart Institute, June 9-13, 1969, Washington, D. C., Chap. 71, p. 849.
3. J. P. Hoare, "The Electrochemistry of the Oxygen Electrode," Reinhold Publishing Corp., New York (1968).
4. P. Delahay, *This Journal*, **97**, 198, 205 (1950).
5. A. Kozawa, *J. Electroanal. Chem.*, **8**, 20 (1964).
6. H. A. Laitinen and I. M. Kolthoff, *J. Phys. Chem.*, **45**, 1061 (1941).
7. R. Jasinski, *This Journal*, **112**, 526 (1965).
8. H. Jahnke and M. Schönborn, "Electrocatalysis on Organic Semiconductors," Paper presented at the 19th CITCE Meeting, Detroit (Sept. 26, 1968).
9. A. W. Moore, *Ned. Tijdschr. Natuurk*, **32**, 221 (1966). Also A. R. G. Brown, A. R. Hall, and W. Watt, *Nature*, **172**, 1145 (1953).
10. Advanced Material Information Bulletin No. 3 (Union Carbide Corp., Carbon Products Div., May 1962). Also The Industrial Graphite Engineering Handbook (Union Carbide Corp., Carbon Products Div.).
11. H. A. Harper, "Review of Physiological Chemistry," p. 167, Lange Medical Publications, Los Altos, Calif. (1965).
12. M. T. Kelly, H. C. Jones, and D. T. Fischer, *Anal. Chem.*, **31**, 1475 (1959).

The Anodic Polarization Behavior of Copper

H. P. Leckie

Inland Steel Research Laboratories, Inland Steel Company, East Chicago, Indiana 46312

ABSTRACT

The anodic polarization characteristics of copper have been studied under a variety of environmental conditions. In dilute acid solutions at room temperature, copper may dissolve at rates limited by a diffusion-controlled current; increasing the acid concentration results in an increased tendency for passivation. Lowering the temperature promotes the establishment of passivity. A passivation reaction was observed in all the alkaline solutions studied. Galvanostatic charging and decay curves show the existence of several potential plateaus which have been correlated with probable potential-dependent surface reactions.

The present study was undertaken in an attempt to clarify the anodic polarization characteristics of copper, over which controversy has existed for some time. A variety of experimental techniques has been employed in order to gain some insight into the factors affecting the active/passive transition in copper under various environmental conditions.

Key words: oxides, potential current, thermodynamics, kinetics, dissolution.

Anodic polarization of copper may result in either general dissolution or film formation, depending primarily on the pH of the electrolyte. Thus Hickling and

Taylor (1) showed that copper passivated in an alkaline solution forming oxides of Cu_2O and CuO, while in acid solution, copper dissolves to give soluble salts and does not develop a passive protective film. Stolica and Uhlig (2) and Osterwald and Uhlig (3) have studied the effect of alloying elements (nickel and nickel plus zinc) on the anodic behavior of copper in sulfuric acid. These authors showed that the addition of critical amounts of alloying elements to copper would induce passivity in acid solutions. Hedges, (4) however, showed that unalloyed copper could be passivated in acid solutions by lowering the temperature. At −11°C copper became passive in concentrated nitric acid due to the formation of a dark gray film of cupric oxide. In a study of anodic transients for the system copper/hydrochloric acid, Cooper (5) showed the formation of, first solid cuprous chloride followed by cuprous oxide. Copper single crystals immersed in water containing oxygen have been shown by Kruger (6) to oxidize first to cuprous and then cupric oxide. Further studies on the electrochemical dissolution of copper single crystals have been conducted by Jenkins (7). An excellent four-part paper covering the thermodynamic, kinetic, and electrochemical aspects of the corrosion of copper has been written by Ives and Rawson (8).

In the present study, the anodic polarization behavior of copper has been related to *pH*, temperature, galvanostatic current density, and potentiodynamic polarization rate.

Experimental

Copper electrodes (total surface area 10 cm^2) were cut from sheet and prepared by abrasion on 3/0 emery paper followed by a 2-min immersion in 20% nitric acid at 25°C. Each specimen had a tag to which electrical connection could be made.

The all-glass cell used for polarization studies incorporated the following features: (*i*) provision for the centrally located copper anode between and equidistant from two platinum cathodes of the same dimensions, (*ii*) an inlet and outlet for nitrogen agitation, and (*iii*) a further inlet to permit a Luggin capillary from a saturated calomel reference electrode to reach near the anode surface.

Before polarizing, a period of about 15 min was allowed for the specimen to reach a steady open-circuit potential. In the present studies, the electrolyte was exposed to oxygen in the atmosphere and it was noted that the copper electrodes formed a thin surface film during the short time required to reach the open-circuit potential. All potentials quoted are with respect to the saturated calomel reference electrode (SCE). Charging curves were also conducted by first controlling the potential at 1.0V active to SCE and subsequently switching to a preset anodic current density. This procedure eliminated the formation of the oxide film which spontaneously formed under open-circuit immersion conditions.

Solutions were prepared from distilled water made acid or alkaline using sulfuric acid or sodium hydroxide. Low-temperature passivation studies were conducted having the cell enclosed in a freezing mixture of an aqueous calcium chloride solution. This, in turn, was immersed in a bath of acetone to which solid carbon dioxide was added from time to time. By this method, the temperature at −10°C could be maintained within ±0.2°C. In these low-temperature experiments, the calomel electrode was connected to the cell through a bridge. The relatively small potential deviations due to thermal gradients were neglected.

Results

Figure 1 shows the anodic polarization curves for copper in 1M H_2SO_4 at 0° and 25°C. At 25°C only a maximum diffusion-controlled current was observed at noble potentials with no decrease in current density usually associated with passivity. At 0°C, however, there is some evidence of partial passivation as shown

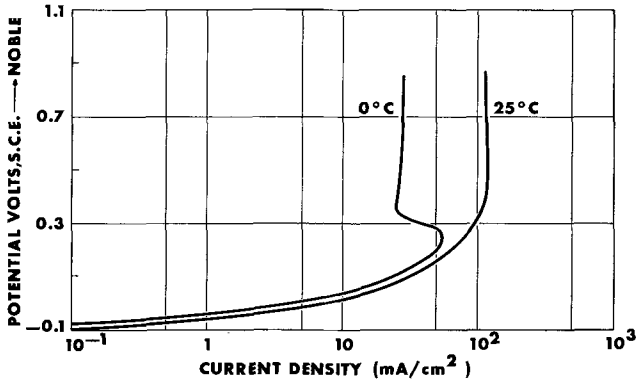

Fig. 1. Potentiodynamic anodic polarization of copper in 1M H_2SO_4 at 0° and 25°C.

by a reduction in the maximum current density as the potential shifts in the noble direction. As the sulfuric acid concentration is increased to 10M, a pronounced passivation reaction is observed even at 25°C (Fig. 2). Lowering the temperature to −11°C further increases the tendency for passivation. Figure 2 also shows that a reduction in temperature from 25° to −11°C lowers the current density for copper in 10M H_2SO_4 at noble potentials by a factor of 4. Anodic polarization curves for copper in a series of sulfuric acid solutions at 25°C ranging from five to ten molar are shown in Fig. 3. It can be seen that the higher the acid concentration, for a given temperature, the more pronounced is the passivation tendency for copper. Between 5 and 6M H_2SO_4, the anodic polarization curves show that copper undergoes a transition from general active dissolution with diffusion-controlled current densities to behavior indicative of film formation. In acid solutions there was no visible film formation at the open-circuit potential.

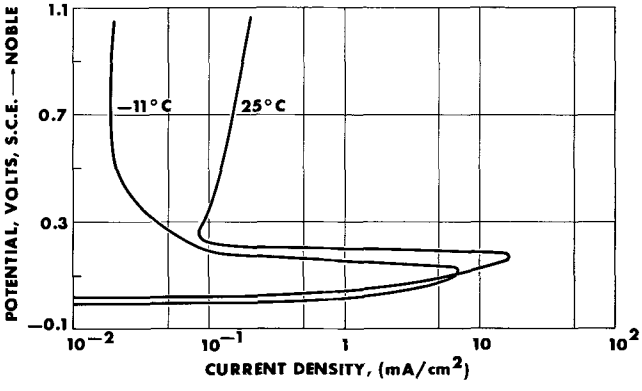

Fig. 2. Potentiodynamic anodic polarization of copper in 10M H_2SO_4 at −11° and 25°C.

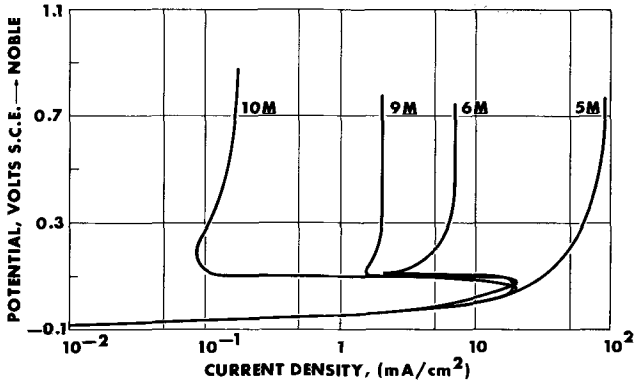

Fig. 3. Potentiodynamic anodic polarization of copper in 5, 6, 9, and 10M H_2SO_4 at 25°C.

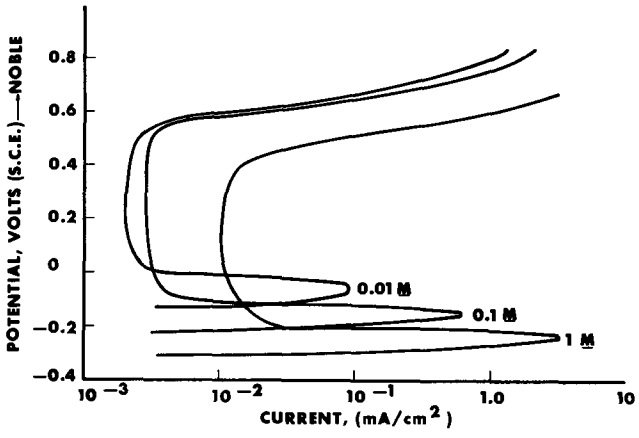

Fig. 4. Potentiodynamic anodic polarization of copper in 0.01, 0.1, and 1.0M NaOH at 25°C.

Figure 4 shows the potentiodynamic polarization curves for copper in 1.0, 0.1, and 0.01M sodium hydroxide solution at 25°C, obtained at a polarization rate of 400 mV/hr. Passivation was observed at all concentrations. The critical current density for passivity in sodium hydroxide solution increases with increase in pH. The passivation potential shifts in the noble direction with decreasing pH according to the relationship $E_{pp} = E^{o}_{pp} - 0.086\ pH$ (Fig. 5).

The anodic polarization curves for copper in the same sodium hydroxide solutions, obtained under galvanostatic conditions, are shown in Fig. 6. A linear relationship was found between pH and the logarithm of the critical current density for passivity

$$\log i_{crit} = KpH + K' \qquad [1]$$

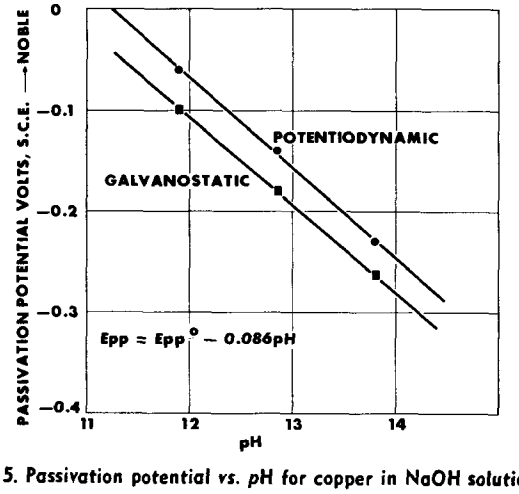

Fig. 5. Passivation potential vs. pH for copper in NaOH solution

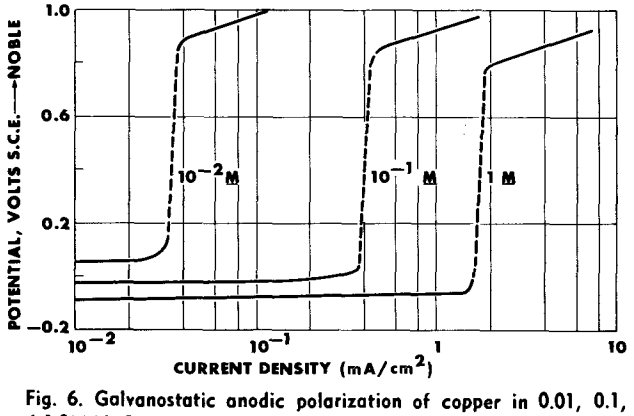

Fig. 6. Galvanostatic anodic polarization of copper in 0.01, 0.1, and 1.0M NaOH solution.

A similar relationship was found for data obtained both from potentiodynamic and galvanostatic techniques. The value of the intercept changes due to differences in the polarization rate. Thus, under galvanostatic conditions, the equation relating critical current density and pH is of the form

$$\log i_{crit} = KpH + K'' \qquad [2]$$

The relationships between pH and critical current density for passivity for copper, obtained from both galvanostatic and potentiodynamic polarization methods are shown in Fig. 7.

Constant current charging curves for copper in 1M NaOH are shown for various current densities in Fig. 8. Three distinct plateaus were observed at −0.57, −0.32, and +0.7V. The exact potential of the plateaus was dependent on applied current density. Potential values quoted here are the most active observed, chosen to minimize overvoltage effects associated with higher applied current densities. Prior to the application of anodic charging currents, specimens were controlled at a potential of −1.0V for a period of 5 min to insure complete removal of all surface films.

With more extended studies of the potential/time behavior of copper in 1M NaOH solution, it was possible to distinguish a further transient plateau in the region of 0 to +0.15V as shown in Fig. 9. In these experiments, polarization was started after the specimen had been allowed to stand at open circuit for some time.

Potential decay curves from the oxygen evolution region, either under open-circuit or forced current decay conditions, show the existence of a plateau at +0.52V. This effect was not observed during anodic charging, probably being obscured by the potential plateau for oxygen evolution. Figure 10 shows the potential decay curves for various current densities from the oxygen evolution potential region to −1.0V. The significance of the various plateaus, each denoting

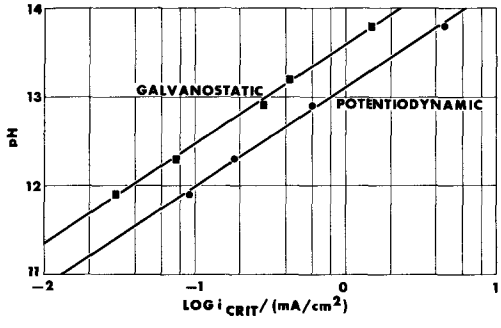

Fig. 7. Critical current density for passivity vs. pH for copper in NaOH solution.

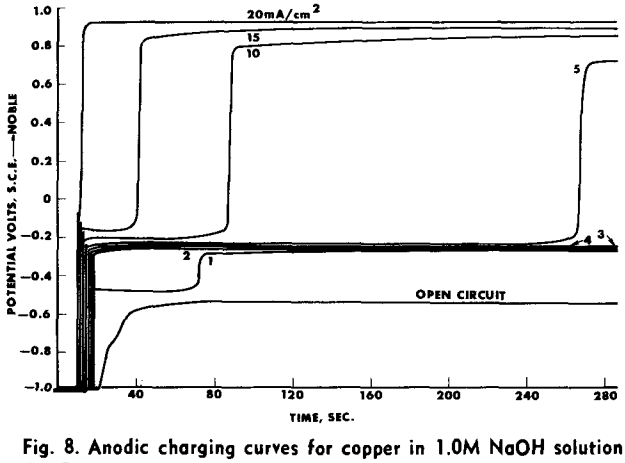

Fig. 8. Anodic charging curves for copper in 1.0M NaOH solution at 25°C.

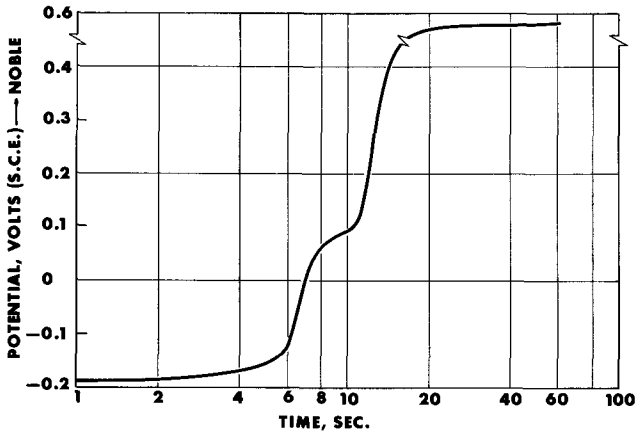

Fig. 9. Anodic charging curve for copper in 1.0M NaOH solution at 25°C (10 mA/cm^2) after prolonged exposure at the open-circuit potential.

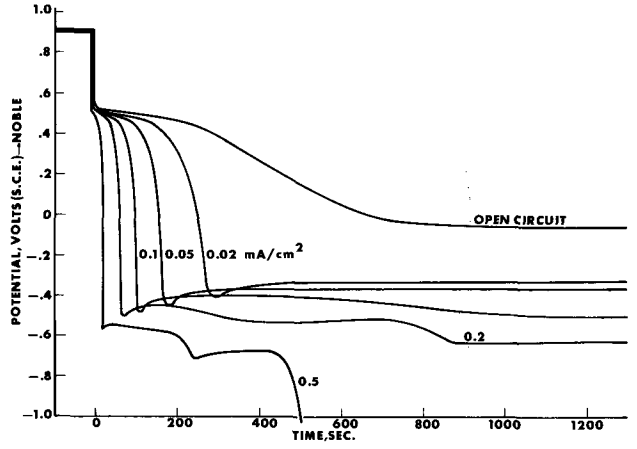

Fig. 10. Potential decay curves on cathodic charging for copper in 1.0M NaOH solution at 25°C.

a distinct potential-dependent surface reaction, is discussed in the following section.

Decay curves from the oxygen evolution region after prepolarizing to various potentials are shown in Fig. 11. Prepolarizing to potentials more noble than −0.3V (for a period of 15 min) resulted in a very pronounced plateau at +0.52V, whereas, prepolarizing to more active potentials than −0.3V resulted in a rapid decay to the $Cu_2O/Cu(OH)_2$ potential between −0.3 and −0.35V.

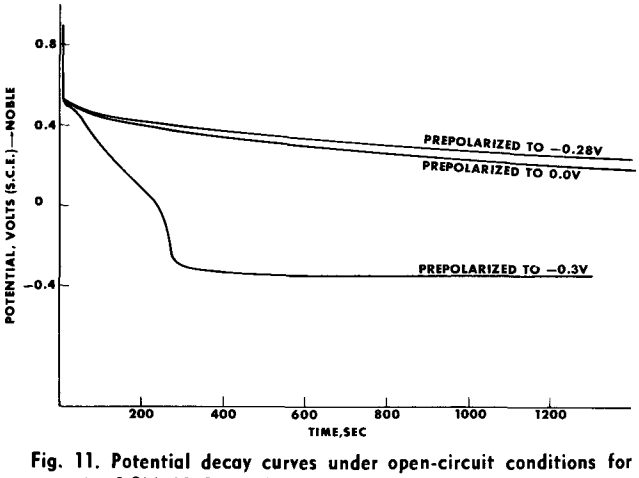

Fig. 11. Potential decay curves under open-circuit conditions for copper in 1.0M NaOH solution at 25°C after prepolarizing to various potentials.

Discussion

The anodic polarization behavior of copper in highly concentrated (10M) solutions of sulfuric acid at room temperature and below shows an active/passive transition characterized by a critical current density and a passivation potential. Lowering the temperature shifts the passivation potential in the active direction and reduces the critical current density. Both of these factors are more conducive to the establishment of passivity.

According to Latimer (9), the free energy of formation of Cu_2O is −34.98 kcal. From thermodynamics the free energy for the following reaction

$$2Cu + H_2O \rightarrow Cu_2O + 2H^+ + 2e \qquad [3]$$

may be calculated to be −21.71 kcal. The equilibrium potential for the formation of Cu_2O according to the above reaction is then 0.23V (SCE).

The passivation potential for copper in 10M H_2SO_4 at 25°C (Fig. 2) occurring at 0.21V, corresponds very closely with the above calculated formation potential of Cu_2O, indicating that the passivation reaction may well be associated with the formation of Cu_2O. The absence of passivity in more dilute acid solutions (1M H_2SO_4) may be attributed to the increased solubility of the corrosion products. In the strongly ionized, more dilute acid solutions, the copper reacts to form $CuSO_4$.

Similarly, the passivation tendency of copper in 1M H_2SO_4 at 0°C may be attributed to the reduced solubility of the corrosion product film at the lower temperature. The fact that such films were readily visible even at very low temperatures, however, indicates that they were porous and offered little protection against further dissolution of the base metal during their initial stages of formation. The increased stability of passivity found in 1M H_2SO_4 at low temperatures is in agreement with the observations made by Hedges (4) on iron, nickel, cobalt, copper, zinc, and magnesium.

In all the alkaline solutions investigated, an active/passive transition was observed. Allmand (10) measured the equilibrium potentials of copper and copper oxide in sodium hydroxide solution and reported the following values (recalculated with respect to SCE): $Cu\text{-}Cu_2O$ = −0.588V, $Cu_2O\text{-}CuO$ = −0.396V, and $Cu_2O\text{-}Cu(OH)_2$ = −0.318V.

It is apparent from Fig. 4 that the potentiodynamic polarization curves do not show the existence of several oxides on the metal surface as only one active/passive transition was observed. Under galvanostatic polarization conditions again only one critical potential was observed where the potential shifted suddenly in the noble direction to the oxygen evolution region. It was therefore not possible to follow the polarization behavior through the various oxidation states of copper by observing the potential/current density relationship utilizing either potentiodynamic or galvanostatic polarization techniques.

The critical current density for passivity *vs.* *p*H dependence in alkaline solutions showed a logarithmic relationship of the form of Eq. [1].

With increasing *p*H, higher critical current densities were required to induce passivity. It is of interest to note that in acid to neutral solutions, King and Uhlig (11) and Leckie (12) have shown, for Fe-25% Cr and various stainless steels, respectively, that the critical current density for passivity decreases with increase in *p*H, but again following a logarithmic dependence.

An increase in the passivation index, $it^{1/2}$ (i = current, t = time taken at all potential steps during polarization), for copper with increase in *p*H has been reported by Shams El Din and Abd El Wahab (13), again showing increased difficulty associated with the passivation of copper at high *p*H values. The difficulty in passivation is probably associated with the dissolution of copper hydroxide in strongly alkaline solutions to form CuO_2^{--}.

The potential/time curves during galvanostatic anodic charging of copper, starting at a potential of −1.0V (to insure a film-free surface) showed three plateaus at potentials corresponding to −0.57, −0.32, and 0.00V. Finally, in all cases, the potentials rose rapidly to some value more noble than 0.7V at which oxygen evolution was observed. The potential plateau close to 0.00V (Fig. 8) was observed only under carefully controlled conditions. With increased current densities, the plateaus corresponding to the various compound formation potentials were shifted in the noble direction, in accordance with the increased overvoltage associated with higher current densities.

The two most active potential plateaus occurring at −0.57 and −0.32V were pronounced and correspond very closely to the thermodynamically calculated formation potentials of Cu_2O and $Cu(OH)_2$ according to the following reactions (calculated for *p*H 14)

$$2Cu + 2\,OH^- \rightarrow Cu_2O + H_2O + 2e \; E_{SCE} = -0.57V \quad [4]$$

and

$$Cu_2O + 2\,OH^- + H_2O \rightarrow 2Cu(OH)_2 + 2e \; E_{SCE} = -0.32V \quad [5]$$

The work of other authors (13) has fairly well established these two reactions as those taking place at the two most active plateaus and the present data is in good agreement with their findings. The existence and nature of the third plateau at approximately 0.00V, however, is the subject of some controversy. Shams El Din and Abd El Wahab (13) found this plateau only after repeated cycling from anodic to cathodic potentials and attribute it to the formation of cuprate ion according to one of the following reactions

$$Cu + 3\,OH^- \rightarrow H\,CuO_2^- + H_2O + 2e \quad [6]$$

or

$$Cu_2O + 4\,OH^- \rightarrow 2H\,CuO_2^- + H_2O + 2e \quad [7]$$

Marcovic and Atlic (14) also attribute this plateau to the formation of cuprate ion according to one of the following equations

$$Cu + 2H_2O \rightarrow H\,CuO_2^- + 3H^+ + 2e \; E^\circ_{SCE} = 1.02V \quad [8]$$

or

$$Cu_2O + 3H_2O \rightarrow 2H\,CuO_2^- + 4H^+ + 2e \; E^\circ_{SCE} = 1.54V \quad [9]$$

where the equilibrium potential of these reactions is both a function of *p*H and $H\,CuO_2^-$ activity. Ohse (15), on the other hand, attributed the potential of −0.01V to the formation of Cu_2O_3. Shams El Din and Abd El Wahab contend that the formation of cuprate ion at approximately −0.01V is a prerequisite to the formation of Cu_2O_3 at the more noble potential of +0.52V according to the reactions

$$2H\,CuO_2^- \rightarrow Cu_2O_3 + H_2O + 2e \quad [10]$$

$$2CuO_2^{--} \rightarrow Cu_2O_3 + \tfrac{1}{2}\,O_2 + 4e \quad [11]$$

The potential plateau found by these authors could be determined only by potential decay curves from the oxygen evolution region and, according to their observations occurred only after sufficient cuprate had formed in the solution by repeated anodic and cathodic polarization cycles.

The potential decay curves shown in Fig. 10 show a distinct plateau commencing at 0.52V. Various experiments were conducted to determine the effect of the presence of cuprate ion on the stability of this plateau. Possible reactions for the oxidation of copper and copper compounds to Cu_2O_3 are according to Eq. [10], [11], [12], and [13].

$$2Cu(OH)_2 + 2\,OH^- \rightarrow Cu_2O_3 + 3H_2O + 2e \quad [12]$$

$$2Cu + 3H_2O \rightarrow Cu_2O_3 + 6H^+ + 6e \quad [13]$$

It is most unlikely, however, that reaction [12] would take place in one step. The formation of Cu_2O_3 probably occurs through the oxidation of either cuprate ion or copper hydroxide. Results from tests where copper was held at various potentials from 0 to −0.3V for various times, instantly polarized to +0.9V and the potential allowed to decay (Fig. 11) show that even at prepolarizing potentials of −0.28V, the potential plateau at +0.52V remained quite pronounced on subsequent decay from the oxygen evolution region. A potential of −0.28V would not appear to be sufficiently noble to sustain the reaction

$$Cu + 2H_2O \rightarrow H\,CuO_2^- + 3H^+ + 2e \quad [8]$$

even at *p*H 14, yet Cu_2O_3 is apparently formed (as shown by the decay curves) without the prior formation of cuprate ion. The prepolarizing potential of −0.28V is sufficiently noble to sustain the formation of $Cu(OH)_2$ from the reaction

$$Cu_2O + 2OH^- + H_2O \rightarrow 2Cu(OH)_2 + 2e \; E_{SCE} = -0.32V \quad [5]$$

Even though cuprate ion will not form directly from copper at such an active potential (−0.28V), it may be possible to form this compound from a direct chemical reaction between $Cu(OH)_2$ and hydroxyl ion at high *p*H values according to the equations

$$Cu(OH)_2 + OH^- \rightarrow H\,CuO_2^- + H_2O \quad [14]$$

$$H\,CuO_2^- + OH^- \rightarrow CuO_2^{--} + H_2O \quad [15]$$

Using neo-cuproine as a complex former, it was possible to detect the presence of soluble copper in the region of the $Cu_2O/Cu(OH)_2$ plateau. This would indicate the presence of cuprate ion (CuO_2^{--}) in this potential range, possibly formed according to reactions [14] and [15]. Table I shows the soluble copper analysis figures for 50 ml aliquots of solution taken at various times during the polarization cycles. Immediately after shifting to the oxygen evolution region, the solution showed a sudden increase in soluble copper. This effect may be accounted for by the copper being polarized through the potential region (plateau at ~0.00V) where $H\,CuO_2^-$ is considered to form directly from copper according to Eq. [5].

Table I. Amount of soluble copper found at various potentials after times shown

Potential, mV	Time, min	Soluble copper, mg/50 ml aliquot
−280	0.25	2.0
−280	8.0	2.5
−280	20.0	10.0
+600	24.0	17.0
+620	35.0	17.0

Cuprate ion may thus be formed during anodic polarization of copper in two ways: first, by the reaction of $Cu(OH)_2$ with hydroxyl ions (Eq. [14] and [15]) and second, at more noble potentials by direct formation from copper.

The present study therefore gives rise to the belief that the primary reactions accompanying the anodic polarization of copper in alkaline solutions may be summarized as follows

$$2Cu + 2\,OH^- \rightarrow Cu_2O + H_2O + 2e$$

$$Cu_2O + 2\,OH^- + H_2O \rightarrow 2Cu(OH)_2 + 2e$$

$$Cu(OH)_2 + OH^- \rightarrow H\,CuO_2^- + H_2O$$

$$H\,CuO_2^- + OH^- \rightarrow Cu_2O^{--} + H_2O$$

$$Cu + 3\,OH^- \rightarrow H\,CuO_2^- + H_2O + 2e$$

$$H\,CuO_2^- + OH^- \rightarrow Cu_2O^{--} + H_2O$$

$$2CuO_2^{--} \rightarrow Cu_2O_3 + \tfrac{1}{2}\,O_2 + 4e$$

Manuscript submitted April 24, 1970; revised manuscript received July 24, 1970.

Any discussion of this paper will appear in a Discussion Section to be published in the June 1971 JOURNAL.

REFERENCES

1. A. Hickling and D. Taylor, *Trans. Faraday Soc.*, **44**, 262 (1948).
2. N. Stolica and H. H. Uhlig, *This Journal*, **110**, 215 (1963).
3. J. Osterwald and H. H. Uhlig, *ibid.*, **108**, 515 (1961).
4. E. S. Hedges, *J. Chem. Soc.*, 969 (1928); 561 (1930).
5. R. Cooper, *This Journal*, **103**, 307 (1956).
6. J. Kruger, *ibid.*, **106**, 847 (1959).
7. L. Jenkins and J. Steigler, *ibid.*, **109**, 467 (1962).
8. D. Ives and A. Rawson, *ibid.*, **109**, 447 (1962).
9. W. Latimer, "Oxidation Potentials," Prentice Hall Inc. (1952).
10. A. Allmand, *J. Chem. Soc.*, 2151 (1914).
11. H. H. Uhlig, *This Journal*, **108**, 327 (1961).
12. H. P. Leckie, *Corrosion*, **24**, 70 (1968).
13. A. Shams El Din and F. Abd El Wahab, *Electrochim. Acta*, **9**, 113 (1964).
14. Van T. Marcovic and E. Atlic, *Werkstoffe und Korrosion*, 958 (1965).
15. R. W. Ohse, *Phys. Chem. (NF)*, **21**, 406 (1959).

Electron Injection into Anodic Tantalum Oxide Assisted by Ionic Interface Polarization

Gerhart P. Klein* and Nils I. Jaeger*

P. R. Mallory & Co. Inc., Laboratory for Physical Science, Burlington, Massachusetts 01803

ABSTRACT

The investigation of electronic conduction processes in anodic tantalum oxide films with electrolytic and solid contacts is generally hampered by parallel ionic conductivity at high fields and the uncertain contributions of flaws, even in the case of high-purity materials. We found that electronic conductivity could be induced reproducibly and with homogeneous current densities in the presence of thin layers of semiconducting oxides, such as Fe_2O_3 and MnO_2 which were deposited by reactive sputtering. Experiments were carried out with electrolyte contact. The electronic current was found to follow log i prop. $V^{1/2}$ in a wide range of current densities. A Poole-Frenkel mechanism is proposed in which the current is controlled by thermionic emission at the Ta_2O_5/MeO-interface. Electronic conductivity increases as a time dependent activation process lowers the emission barrier through ionic interface polarization. The contribution of flaws to the electronic conductivity was investigated by means of the anodic printing technique. The electronic current resulting from the activation process was found to be of uniform density and unrelated to any physical flaws in the anodic tantalum oxide.

Oxide films generated electrochemically by anodic oxidation on valve metals (1), among them tantalum oxide as the relatively best defined, are characterized by high insulation resistance. Their resistivity is dependent on the substrate metal and its degree of chemical purity. The resistivity of anodic Ta_2O_5 on high-purity Ta has been estimated to exceed 10^{15} ohm cm (2). Any lower resistivities found experimentally must be caused by chemical impurities or flaws.

The intrinsic conductivity of anodic Ta_2O_5 is too low to measure, which means that the current-voltage characteristics of Ta/Ta_2O_5-electrodes are usually those of impure Ta_2O_5, after corrections have been made for ionic current contributions. The distribution of electronic conductivity (e.c.) due to impurities is mostly nonhomogeneous (3).

The study of conduction mechanisms in flaws is of some practical, but little theoretical interest, since it is hardly possible to create well-defined experimental conditions. One may ask, however, whether leakage conduction can be understood in terms of explanations such as have been advanced in the literature assuming the existence of fissures (4), and flaws (5), or whether a more fundamental conduction mechanism is at work. Some indication of this was given in an earlier paper (3) which attempted to establish some typical conduction patterns for commonly encountered impurities and physical flaws in Ta_2O_5. Aside from the tentative conclusion that impurities had to be present in all cases where e.c. was observed, we found a behavior of the e.c. which indicated that certain modifications of the Ta_2O_5/electrolyte-interface were responsible for the observed e.c.

The anodization of Ta which had been alloyed with Fe or Ni, among others, resulted in the formation of oxides of the impurities on top of Ta_2O_5. This process was accompanied by sharply increasing e.c. By dissolving the impurity oxide the cause of e.c. was eliminated until, on further anodization, it would gradually return.

In the present investigation we have further explored the conditions under which anodic Ta_2O_5 exhibits e.c. of sufficient magnitude to be measured by electrochemical techniques. Instead of Ta substrates alloyed with metallic impurities we used anodic oxide films on high-purity substrates and deposited thin films of transition metal oxides, *e.g.*, Fe_2O_3 and MnO_2 by means of thermal decomposition of the respective nitrates, or by reactive sputtering. We found on return of the specimens to the electrochemical cell that reproducible, uniformly distributed e.c. could be developed by applying voltage close to the original formation voltage of the anodic Ta_2O_5.

The detailed investigation of this effect revealed an electronic conduction mechanism that is controlled by the properties of the contact between the two oxides. The properties of the contact are modified under the influence of an applied field that leads to ionic migration.

The experimental system, a Ta/Ta_2O_5/MeO-electrode with aqueous electrolyte contact, is shown schematically in Fig. 1. It is in many ways similar to metal/insulator/metal systems which have been studied extensively (6, 7) and for which models have been developed to account for electronic conduction processes. In our system, one of the metal electrodes was replaced by an electronically conducting metal oxide combined with a redox electrolyte that supplies electronic charge to the oxide. Experimentally, metal/in-

* Electrochemical Society Active Member.

Key words: electron injection, anodic tantalum oxide, ionic interface polarization, thin film conduction.

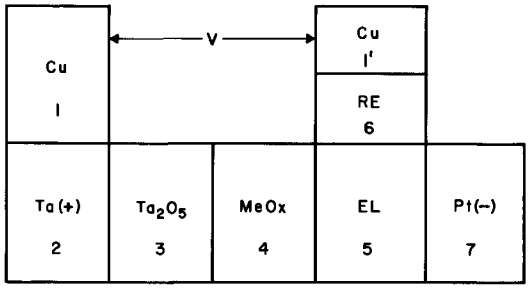

Fig. 1. Schematic of experimental system: V applied voltage, El electrolyte, RE reference electrode, Pt counterelectrode.

sulator/metal systems are hard to work with due to the difficulties of preparing well-defined thin layers of insulators and providing them with electrodes. Nonhomogeneous current distribution, lack of quantitative reproducibility, and current instabilities are common problems which make for a scarcity of unambiguous experimental results.

The advantage of electrolytic contact to insulators, such as insulating anodic oxides, is due to the control of the field distribution in the system by ionic processes. Additional film growth tends to equalize the field in the insulator. Even though this provides an electrically stable condition, the contact properties can be influenced only in a very limited way, *e.g.*, through the redox potential of the electrolyte.

By combining a semiconducting oxide and a redox electrolyte, the advantages of the electrolyte contact are maintained while, at the same time, a means of influencing the contact properties is introduced. The contact remains uniform and the effects of air gaps, dust, etc., are eliminated. At the same time, the oxide limits the ionic processes without entirely blocking them, as would be the case with metal contact, and thus provides some stabilizing effect. In cases where the electronic conductivity of the system is controlled by the contact, this allows one to study the conduction mechanism at fields which in case of metal contact might lead to early breakdown.

The availability of an electrochemical method for the determination of the electronic current distribution (8, 9) on a micro scale is an additional advantage over metal electrodes. A quantitative study of conduction processes in thin films is impossible without detailed information about the density and distribution of the electronic current.

Experimental

Capacitor grade tantalum foil was cleaned in the usual way. Chemical polishing (10) in a mixture of 5 pt H_2SO_4, 2 pt HNO_3, and 1.5 pt HF (all reagent grade, concentrated) was followed by dipping in HF, rinsing in distilled water, and vacuum annealing at 2100°C for 3 hr at 10^{-5}-10^{-6} mm Hg. Anodic oxide films were formed at room temperature in dilute H_2SO_4. Formation current density was 1 mA/cm^2 followed by stabilization at final voltage for 30 min. Film thickness was calculated on the basis of a thickness equivalent of 16.4 Å/V for formation at 1 mA/cm^2 to voltage. The thickness of stabilized films was determined by reforming at this current density and extrapolating the voltage time curve to zero time.

Reactive sputtering of Fe_2O_3 and MnO_2 was carried out in a CVC Bendix D.C. triode sputtering system. The sputtering conditions were, typically: 1000V, 60 mA, 5% oxygen in argon, 12μ pressure, and a target to substrate distance of 8 cm. The deposition rate was approximately 12 Å/min. The target consisted of 9 x 9 cm metal disks without cooling. Iron oxide was sputtered from a high-purity (99.99%) iron target, while manganese targets were prepared by vapor deposition of manganese on a tantalum substrate. The substrate holder was water cooled, and specimens were held in intimate contact with the substrate support by means of a spring loaded mask. Sputter deposition of the metal oxide on the substrate was preceded by sputter cleaning of the target with pure argon. No special treatment was given to the Ta/Ta_2O_5 electrode prior to sputtering. After admission of the sputtering gas mixture, sputtering continued onto a shutter until a stationary sputtering condition had been established. After cleaning the sputtering rate was high, and oxides of low oxidation state were formed. With increasing oxidation of the target the sputtering rate dropped and became constant. The oxides sputtered under this condition were close to Fe_2O_3 and MnO_2 in composition. Electron diffraction experiments showed the films to be polycrystalline. Electron micrographs indicated that the films were continuous. Best results were obtained with oxide films of the order of some hundred angstroms, typically 200Å.

Reactive sputtering of oxides can take place by a number of mechanisms (11). The low sputtering rates prevailing after a stationary condition had been established suggest that the surface of the target was oxidized and that the oxide itself was being sputtered. High energy sputtering may lead to the injection of ions into the anodic oxide. However, in our case the energies of the sputtered ions were relatively low and, in addition, sputtering was done at pressures of 1-10μ and target to substrate distances of 5-8 cm, much greater than the mean free path of any sputtered ions. This made it likely that deposition of MeO took place in the form of neutral molecules by diffusion.

MnO_2 was also deposited by pyrolytic conversion of manganese nitrate. The specimen was coated with a dilute solution of $Mn(NO_3)_2$ in water to which a surface active agent had been added to insure complete wetting of a larger foil area. After thermal conversion to MnO_2 at about 200°C, the foil was carefully rubbed with a cotton swab and water to remove any of the voluminous MnO_2. Only a thin, firmly adherent film was left after this treatment.

After sputtering or pyrolytic deposition the specimen was returned to the electrolyte cell shown in Fig. 2a. It consisted of a glass container with mantle for thermostating, a magnetic stirrer, a platinum counterelectrode, and a saturated calomel reference electrode (SCR). All potentials were referred to the hydrogen electrode in the electrolyte used. The electrolyte was 0.5m standard acetate buffer solution (25°C) in which the sputtered oxides were insoluble.

The electronic circuit (Fig. 2b) consisted of a Kepco Model ABC 200 power supply, a Keithley Model 610C electrometer and a Hewlett-Packard Model 3430A digital voltmeter to measure potential, and a Mosley Model 7100B strip chart recorder to measure current.

Anodic printing, a technique used to make the distribution of the electronic conductivity visible, was described previously (8). For high resolution printing the experiments were performed under the microscope.

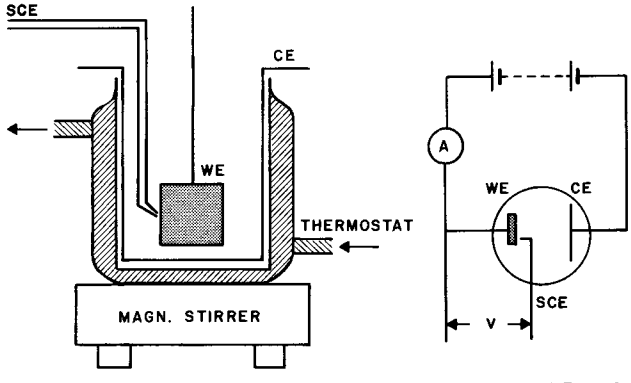

Fig. 2. Electrochemical cell and electrical schematic: WE working electrode, CE counterelectrode, SCE standard calomel electrode. Fig. 2a left, Fig. 2b right.

The experimental details have been described elsewhere (9).

Results

Anodic activation.—A typical experiment to demonstrate the effect of anodic electronic activation (referred to as activation) was performed as follows: A 200Å film of Fe_2O_3 or MnO_2 was sputtered reactively onto a tantalum substrate which previously had been anodized at 120V for 30 min. The specimen was then returned to the cell shown in Fig. 2 and constant voltage applied. Near the original formation voltage the current increased sharply with time (Fig. 3a-c). For comparison the reformation behavior of a similar Ta/Ta_2O_5 electrode without sputtered oxide on its surface is also shown (Fig. 3d). In the latter case the observed current is largely ionic and decays with time after an initial overshoot. In the former case the current is largely electronic and continually increases with time. Figure 3 gives three examples of "activation curves" (log i_{el} *vs.* time). One for Fe_2O_3 deposited by sputtering, (a) and two for MnO_2 deposited by sputtering (b) and thermal conversion (c) of $Mn(NO_3)_2$. The rate of electronic current increase with time ("rate of activation") is considerably lower for MnO_2. This is attributed to its higher ionic conductivity as compared to Fe_2O_3. This tends to lead to some additional growth of Ta_2O_5 (21) during activation. The activation curves show an initial overshoot which is similar to the overshoot observed with Ta/Ta_2O_5 electrodes. The current goes through a minimum followed by an exponential increase of the electronic current with time to current densities of 10^{-2} A/cm^2 and higher.

In some instances, activation curves with one or several plateaus were observed. This behavior appeared to be related to the composition of the sputtered oxide. The present study is concerned only with the exponential section of the activation curve which is regularly observed with oxides of high oxidation state.

With continuing activation at constant voltage the rate of increase of the electronic current diminished.

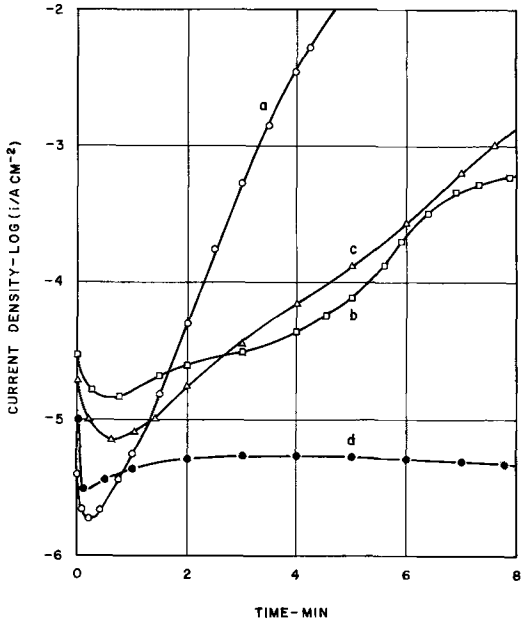

Fig. 3. Current-time characteristic of the activation process for three Ta/(2310Å) Ta_2O_5/MeO electrodes. Anodization of Ta/Ta_2O_5 at 120V, 25°C, 30 min; activation voltage V_A. (a) MeO = sputtered (200Å) Fe_2O_3 film, V_A = 118V, (c) MeO = MnO_2 by thermal conversion of $Mn(NO_3)_2$, V_A = 118V, 75°C; (b) MeO = sputtered (200Å) MnO_x film, V_A = 122V; (d) reanodization curve of Ta/Ta_2O_5 electrode at 118V after activation of the Ta/Ta_2O_5/Fe_2O_3 electrode and subsequent dissolution of the Fe_2O_3 film. This curve is identical to the reanodization trace of the Ta/Ta_2O_5 electrode before deposition of MeO and activation.

This was most pronounced with thin Ta_2O_5 films and was thought to be due to changes in the potential distribution as activation progresses.

The activation process does not destroy the anodic Ta_2O_5 film. In particular, no catastrophic breakdown or scintillations were observed during activation. The current increased steadily with time without giving any indication of noise due to carrier multiplication. After activation and subsequent dissolution of the sputtered oxide film the Ta/Ta_2O_5 electrode could be reformed to voltages in excess of the original formation voltage. Microscopic inspection did not reveal any breakdown or scintillation patterns.

The current-time curve of reformation at constant voltage after dissolution of the Fe_2O_3 film following activation to 10^{-2} A/cm^{-2} was identical to the reformation curve obtained with the original Ta/Ta_2O_5 electrode prior to any deposition of Fe_2O_3 (Fig. 3d). This indicated that the effect of Fe_2O_3 was temporary and that no modification of the bulk of Ta_2O_5 had taken place during activation.

A direct experimental distinction between ionic and electronic current can be made by means of the printing technique. These and all subsequent prints were obtained while increasing the applied voltage at a constant rate. A typical series of prints is shown in Fig. 4 for a Ta/Ta_2O_5/Fe_2O_3 electrode. The example chosen shows both uniform activation near the anodization voltage and nonuniform e.c. at lower voltage. The onset of activation led to the uniform development of opacity due to the formation of the starch-iodine complex. At higher current density levels gassing of the electrode due to oxygen evolution was observed.

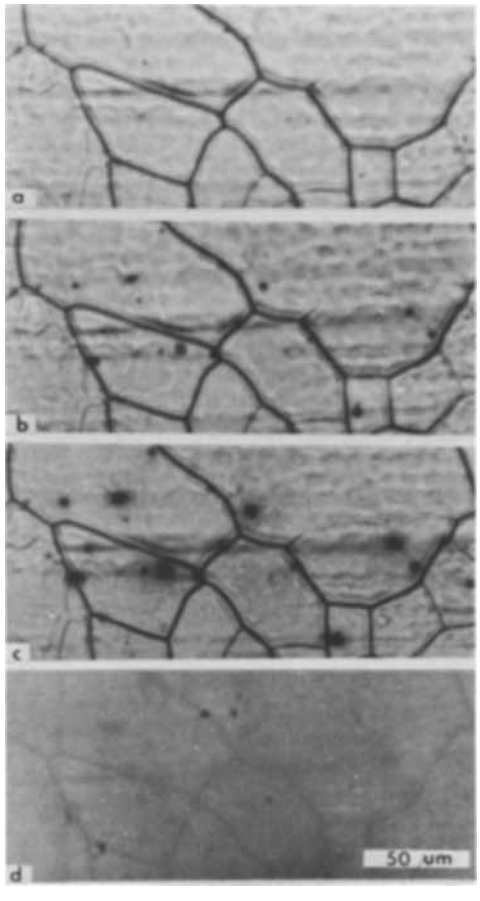

Fig. 4. Series of four anodic prints obtained from a Ta/(2000Å) Ta_2O_5/(200Å) Fe_2O_3 electrode anodized at 100V, 25°C for 1 hr; voltage scan rate 20 V/min; a, at 0V; b, at 80V; c, at 90V; and d, after 30 sec at 95V. Note: Grain boundaries appear dark because they are out of focus.

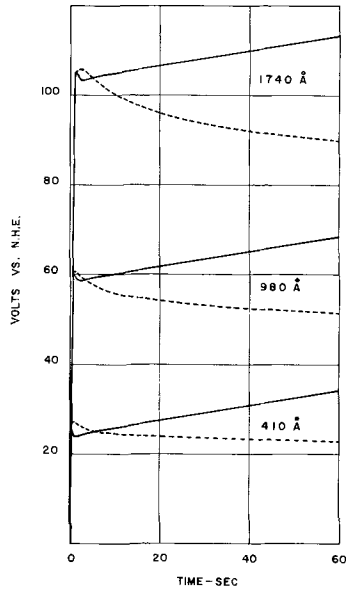

Fig. 5. Activation of three Ta/Ta_2O_5/(200Å) Fe_2O_3 electrodes (- - - -) at constant current (0.5 mA/cm^2). For comparison, the voltage-time curves of anodization for the same Ta/Ta_2O_5 electrodes (————) are also given.

Activation under galvanostatic conditions is shown in Fig. 5 for three Ta/Ta_2O_5/Fe_2O_3 electrodes with different Ta_2O_5 thicknesses. At constant current the voltage increases linearly with time for Ta/Ta_2O_5 electrodes, while it drops steadily toward a constant value when activation takes place in the presence of Fe_2O_3. An initial overshoot is observed in both cases.

Activation as a function of field.—The process responsible for electronic activation depends on the applied field. Figure 6 shows the increase of the electronic current with time for Ta/(1360Å)Ta_2O_5/(200Å)Fe_2O_3 electrodes as a function of the applied voltage (field). The rate of log i increase with time (rate of activation) rises sharply with increasing field strength. The ionic current at these fields is determined by $i_{ion} = A \exp BF$ (1) (F field across Ta_2O_5, A, B, empirical constants). With typical values for A and B given in the literature (2) the ionic current at the highest fields used is estimated to $i_{ion} < 10^{-6}$ A/cm^2. The ionic current is small but finite, and it appears that the activation process shows some correlation with ionic charge displacement.

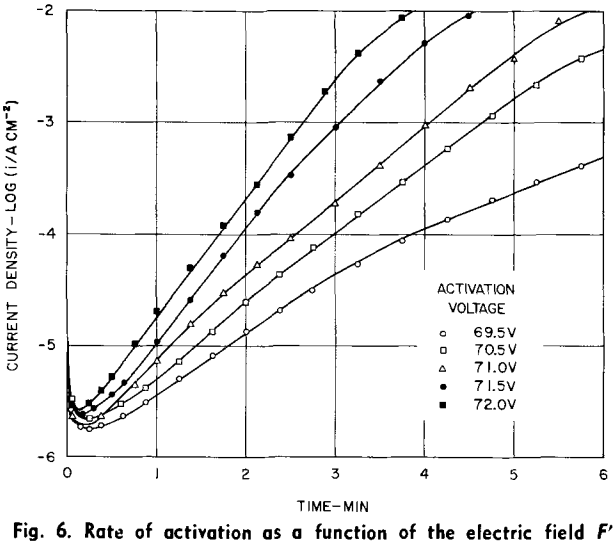

Fig. 6. Rate of activation as a function of the electric field $F' = V/d$ for Ta/(1360Å)Ta_2O_5/(200Å) Fe_2O_3 electrodes. The Ta/Ta_2O_5 electrode was anodized at 70V, 25°C, for 30 min. ○, 5.11 MV/cm; □, 5.18 MV/cm; △, 5.22 MV/cm; ●, 5.26 MV/cm; ■, 5.30 MV/cm.

The activation behavior as a function of Ta_2O_5 thickness is shown in Fig. 7. The Fe_2O_3 thickness was 200Å in all cases. As in Fig. 6, all activation curves were measured at fields that were determined from the actual voltage V as measured against the reference electrode and the thickness d of the particular Ta_2O_5 film. The activation curves of Fig. 7 start out at about the same current level if measured at the same field V/d, but the slopes of the curves increase from the thinnest to the thickest film. The slopes of the activation curves of the thicker films approach a constant value. For the 2310Å film the activation curve is essentially linear over two decades of current. The activation curves of the thin films, *e.g.*, the 410Å film, start out with the lowest slopes, and the slopes decrease further with time of activation.

These differences in the rates of activation may be related to the nonidentity of the applied voltage and the actual potential drop across the Ta_2O_5 film. It was necessary to examine the distribution of the applied voltage over the experimental system shown in Fig. 1 in order to determine whether the activation process was in fact dependent on the field in Ta_2O_5. The constant voltage V does not drop fully across Ta_2O_5 but includes voltage drops across interfaces and the bulk of the MeO film. Also, the potential distribution in the electrostatic condition without ionic or electronic current flow will be different from the distribution during activation. During this transition, the potential drop across Ta_2O_5 may change with a corresponding effect on the rate of activation. For example, the rate of activation would be expected to decline as the field across Ta_2O_5 decreased which, at constant applied voltage, could be caused by increasing interface polarizations, increasing voltage drop across MeO, or by additional growth of Ta_2O_5. Conversely, an increase in the rate of activation could be expected to take place if an electrostatic potential drop across MeO or other parts of the system was shifted to Ta_2O_5.

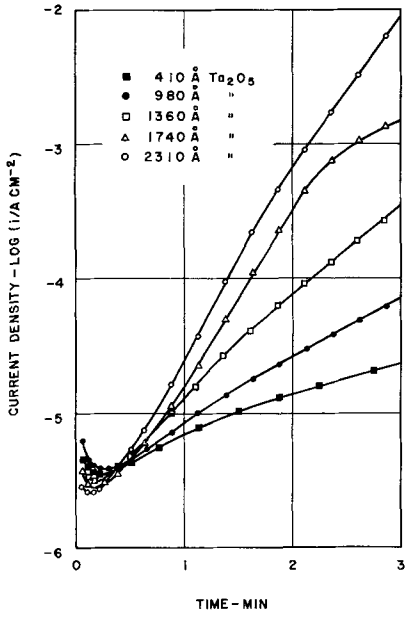

Fig. 7. Rate of activation as a function of Ta_2O_5 thickness at the same field $F' = V/d = 5.2$ MV/cm.

Ta_2O_5, Å	Anodization V min	Applied voltage, V
○ 2310	120, 30	120
△ 1740	90, 30	91
□ 1360	70, 30	71
● 980	50, 30	51
■ 410	20, 30	21.3

Potential distribution in the experimental system.— The voltage V measured against a reference electrode is made up of the following contributions: $V = \Delta V + V_4 + \Sigma\psi_{ij} + \Sigma\eta_{ij}$ with ΔV voltage drop across Ta_2O_5, V_4 voltage drop across MeO, $\Sigma\psi_{ij}$ sum of Galvani potential differences, $\Sigma\eta_{ij}$ sum of overvoltages. Any ohmic potential drop (η_Ω) across MeO is also included in this sum. Under electrostatic conditions ($i_{ion} = 0$, $i_{el} = 0$) $\Sigma\eta_{ij} = 0$.

The sum of Galvani potentials is made up of the respective interface Galvani potential differences as indicated in Fig. 1: $\Sigma\psi_{ij} = \psi_{12} + \psi_{23} + \psi_{34} + \psi_{45} + \psi_{56} + \psi_{61}$; with $\psi_{12} = \psi_1 - \psi_2$, $\psi_{23} = \psi_2 - \psi_3$ etc. The sum of overvoltages is similarly composed of the respective contributions from the various interfaces affected by ionic and electronic current passage: $\Sigma\eta_{ij} = \eta_{23} + \eta_{34} + \eta_{45}$.

In a series of experiments at constant field in Ta_2O_5 where only the thickness of the Ta_2O_5 film is being varied a correction of the applied voltage is required which takes into account the potential distribution across the system. This correction which affects the field in Ta_2O_5 becomes the more significant the thinner the Ta_2O_5 film. In the initial phases of the activation process the overvoltage contribution is negligible and the correction is constant. This appears to be the range in which the rate of activation (log scale) is constant. As overvoltages develop in various parts of the system, the rate of activation decreases, and this decrease is again the more pronounced the thinner the Ta_2O_5. Also, additional Ta_2O_5 growth may occur and thus lower the field under constant voltage conditions. Only two factors will be examined more closely in the context of this paper: first, the importance of a redistribution of potential between Ta_2O_5 and Fe_2O_3; and second, an attempt to determine the constant contribution to the applied voltage arising from Galvani potential differences. The contribution from overvoltages other than ohmic potential drop in Fe_2O_3 will not be considered, and the discussion of the activation process will be restricted to the range in which a linear activation characteristic is observed.

Potential redistribution between Ta_2O_5 *and* Fe_2O_3.— The experimental evidence presented so far suggests that the activation process is tied to the migration of ions in Ta_2O_5. This is more clearly demonstrated by Fig. 8 which shows a comparison of the initial parts of an activation curve (e) for a $Ta/Ta_2O_5/Fe_2O_3$ electrode with reanodization curves (a-d) of Ta/Ta_2O_5 electrodes at four constant voltage levels. By varying the reanodization voltage one can find a reanodization curve (c) which closely matches the initial part of the activation curve (e). The two curves match during the initial overshoot and begin to separate only after the current minimum has been reached. The initial overshoot is caused by ionic polarization processes (1, 6) with oxide formation taking place during the overshoot. The identity of the two curves is assumed to signify identical ionic processes in the Ta_2O_5 layer of both specimens. This congruence is regarded as a reference condition for which the field is assumed to be equal in the Ta_2O_5 layer of each electrode. The presence of Fe_2O_3 in one of the electrodes requires a somewhat higher applied voltage to match the reformation curve of the Ta/Ta_2O_5 electrode. From Fig. 8, the difference in the applied voltage was determined to $\Delta V_{Fe_2O_3} = (0.5 \pm 0.5)V$. This represents the initial voltage drop across Fe_2O_3 before electronic conduction sets in. The maximum voltage that could be transferred from across Fe_2O_3 to across Ta_2O_5 would, therefore, be the order of 1V. This will have to be compared to the maximum ohmic drop across Fe_2O_3 as a consequence of the electronic current in order to determine the significance of potential redistribution in the activation process.

The resistivity of Fe_2O_3 as deposited by reactive sputtering is not known, but it can be estimated if it is assumed that the decrease in the rate of activation

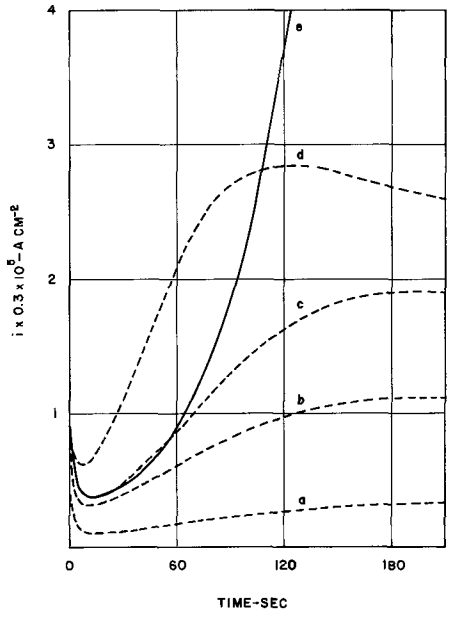

Fig. 8. Comparison of the initial part of the activation curve for a Ta/(1360Å)Ta_2O_5/(200Å)Fe_2O_3 electrode (e) with reanodization curves for Ta/(1360Å)Ta_2O_5 electrodes at different voltages V (a-d). - - -, Ta/Ta_2O_5 (a) 68V; (b) 70V; (c) 70.5V; (d) 72V. ——, $Ta/Ta_2O_5/Fe_2O_3$ (e) 70V.

at high electronic current densities is caused by the ohmic potential drop. It was found that $\sigma_{Fe_2O_3} < 9 \times 10^7$ ohm cm, which leads to a potential drop $\eta_\Omega < 0.9V$ at 5 mA/cm² for a 200Å Fe_2O_3 film. η_Ω becomes significant at current densities of the order of mA/cm² for thin Ta_2O_5 films.

Contribution from Galvani potential differences.—If the rate of activation (log scale) was in fact a function of the ionic processes in Ta_2O_5, as suggested by the experiments presented so far, one would then expect the slopes of the activation curves to be identical for all Ta_2O_5 thicknesses at the same field in Ta_2O_5. Figure 9 shows activation curves with the same slope for the $Ta/Ta_2O_5/Fe_2O_3$ electrodes of Fig. 7. The voltages $V = \Delta V + \Sigma\psi_{ij}$ that had to be used experimentally to obtain equal slopes are given in Table I. The resulting fields $F' = V/d$ are different for all Ta_2O_5 thicknesses. This is attributed to the error made by not taking into account the constant additive voltage arising from $\Sigma\psi_{ij}$. The later is found by computing that value of $\Sigma\psi_{ij}$ that minimizes the difference between the fields. The resulting field $F = (5.06 \pm 0.4)$ MV/cm is then the true field in Ta_2O_5 for all thicknesses. The contribution to the applied voltage from Galvani potentials was found to be $\Sigma\psi_{ij} = (2.35 \pm 0.30)V$.

It was concluded from these estimates that the corrections arising from potential redistributions between Fe_2O_3 and Ta_2O_5 can become significant for thin Ta_2O_5 films. The electrostatic shift appeared to be small in our experiments, but the effect of the ohmic drop was clearly noticeable at the higher electronic current densities. Also, by making allowances for the constant contribution from interface potential drops to the voltage V it was found that the rate of activation (log scale) at constant field in Ta_2O_5 was in fact independent of the thickness of the tantalum oxide.

Table I. Voltages used experimentally to obtain equal slopes

$d_{Ta_2O_5}$, Å	Voltage V, V	Field F', MV/cm	$\Sigma\psi_{ij}$, V	Field F, MV/cm
410	23.0	5.61		
980	52.5	5.36		
1360	71.5	5.26	2.35	5.06
1740	90.0	5.17	±0.30	±0.04
2310	118	5.12		

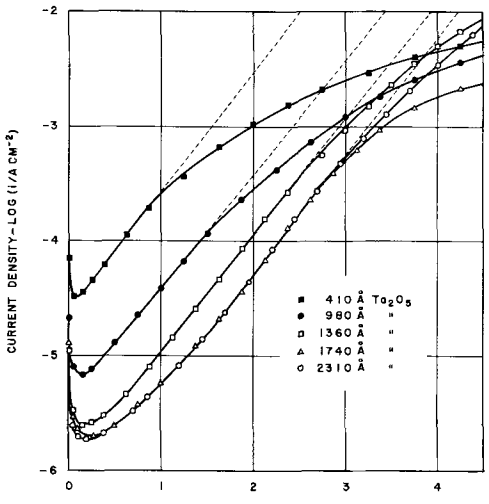

Fig. 9. Activation curves for five Ta/Ta_2O_5/(200Å) Fe_2O_3 electrodes with different Ta_2O_5 thicknesses. Activation voltages were selected to yield equal rates of activation.

Ta_2O_5, Å	Anodization, V min	Voltage, V
○ 2310	120, 30	118
△ 1740	90, 30	90
□ 1360	70, 30	71.5
● 980	50, 30	52.5
■ 410	20, 30	23

The continuing decrease in the rate of activation observed in Fig. 7 and 9 which was most pronounced in the curves for the thinnest Ta_2O_5 films is attributed to the effects of overvoltages developing at the various interfaces of the Ta/Ta_2O_5/Fe_2O_3 electrode due to the electronic current and to some additional growth of Ta_2O_5.

Current-field characteristic of the electronic conduction process resulting from activation.—The current-field characteristic of Ta/Ta_2O_5/Fe_2O_3 electrodes was measured after activation to different electronic current levels. The measurements were made at decreasing field. The results for a 1740Å Ta_2O_5 film are shown in Fig. 10 which gives the activation curve and the current-voltage curves related to the activation levels as indicated by horizontal lines. The current-field (voltage) characteristics are linear over several decades of electronic current if log i is plotted *vs.* $F^{1/2}$.

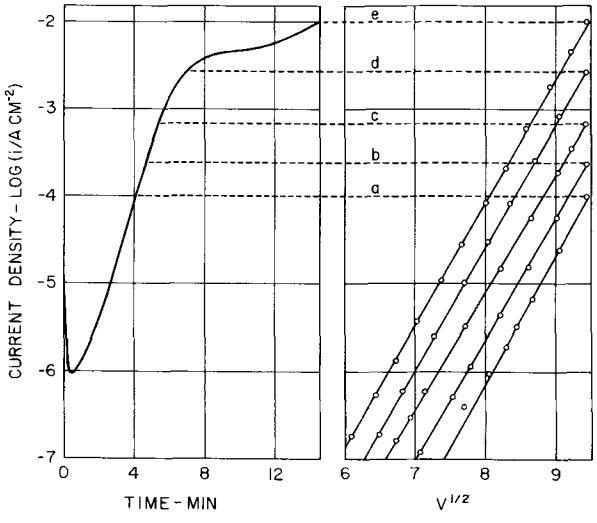

Fig. 10. Activation curve (left) and current-field characteristics (right) for a Ta/(1740Å) Ta_2O_5/(200Å) Fe_2O_3 electrode. Current-field characteristics were measured after activation to the current levels as indicated. Ta_2O_5 was anodized at 90V, 25°C, for 30 min; activation at 89V.

The activation curve shown in Fig. 10 is characterized by a section in which log i *vs.* time is linear, followed by a plateau, and further increase with time. The particular shape of the activation curve is believed to be due to the composition of the sputtered Fe_2O_3 layer. It has no significant effect on the i-F characteristic of the electronic current.

Bulk vs. interface control.—For the interpretation of the activation process and the current-field characteristic of the electronic current to be meaningful it was important to determine the location of the rate-limiting step in the transfer of electrons from the electrolyte to the tantalum substrate. The dependence of electronic current on field would seem to support bulk control. However, there is convincing experimental evidence that it is the injection of electrons into Ta_2O_5 which is rate limiting. In the case of electrolyte contact to Ta_2O_5 the injection rate of carriers is extremely small. In the presence of MeO an electronically conductive state can be created, which must be directly related to a modification of the Ta_2O_5/MeO interface since chemical dissolution of MeO after the active condition had been established removed the cause of electronic conductivity. No indication of any modification of the bulk of Ta_2O_5 as a consequence of the activation process was found.

This behavior of specimens with deposited MeO films is paralleled by the behavior of tantalum that had been alloyed with iron (3). The observations were then interpreted in terms of a competitive migration of tantalum and impurity ions under the effect of the field whereby the impurity ions were faster than tantalum ions. The impurity ion-rich surface layer was thought to be responsible for the observed e.c. Ta_2O_5 layers immediately adjacent to the oxide/electrolyte interface must also have been highly contaminated, but could not be reached by the hydrochloric acid. It is significant that little e.c. was found in an extended interval of continued formation after dissolution of the surface oxide, since it showed that doping of the Ta_2O_5 did not seem to lead to e.c. unless surface oxides were present.

Current distribution.—The question of current distribution is of equal importance for the interpretation of the activation effect since it is well known that high flaw densities can be present in anodic Ta_2O_5 (12). What appeared as uniform e.c. macroscopically could, therefore, be due to large numbers of minute structural flaws. Naturally, assigning the cause for e.c. to flaws would only shift the problem to flaws without solving it. In order to establish the distribution of e.c. one must be able to resolve the current distribution on a microscale. Techniques such as area variation can detect only rather coarse heterogeneity and cannot resolve conduction due to microscopically small flaws of high density. Scanning a surface with various kinds of probes suffers from similar problems. By contrast, anodic printing in its modified form allowed direct observation of the surface of the specimen and, at the same time, its e.c. distribution as revealed by the coloration of the printing electrolyte. It permitted a direct correlation between microscopically visible flaws and their contribution to the electronic conductivity with a resolution of up to 10^8 point flaws/cm^2.

The purpose of the following experiments was to establish the distribution of electronic conduction under the conditions of activation. Macroscopically, the distribution was found to be homogeneous; however, it could not be decided whether this homogeneity was in fact the result of microscopic heterogeneity due to flaws in the anodic oxide.

The following tabulation lists common types of "heterogeneities."

I. Structural	(a) thermal crystalline oxides, nitrides
	(b) "field" crystals
	(c) carbides
	(d) inclusions of foreign phases
	(e) cracks, pores, pinholes, etc.
II. Chemical	(a) metallic impurities in solid solution
	(b) inclusions from electrolyte
	(c) surface impurities

High flaw densities are usually due to structural flaws and those listed under I, a-c are the most common ones. Methods of generating such flaws have been described previously (12-14). In the following high resolution anodic prints obtained with specimens containing various densities of such structural flaws are shown.

Thermal oxide flaws.—Thermal crystalline oxide forms on Ta foil when heated in air at temperatures of 300°-700°C. Different amounts of thermal oxide were generated by heating Ta foil at 500°C in air for 2, 5, 10, and 30 min. Preparation for the printing experiment included anodizing at 80V and sputtering of a 200Å Fe_2O_3 film. Prints for the 5-min sample are shown in Fig. 11. The first of the micrographs shows the Ta foil before anodization with a typical pattern of Ta_2O_5 crystallites. The two anodic prints at 85 and 90V show increasing uniform activation which is most clearly seen at the grain boundaries. These show up quite strongly in the first prints because they are out of focus but disappear gradually as the opacity of the printing electrolyte increases due to the formation of the starch-iodine complex. The prints show homogeneous and uniform opacity and none of the typical distributions of crystallites which vary in density from grain to grain. Uniform opacity was observed even in cases where the anodic Ta_2O_5 contained patches of different color due to high thermal oxide concentration.

"Field"-crystallite flaws.—"Field" crystals in anodic Ta_2O_5 were generated by anodizing Ta foil in 2% nitric acid at 80V, 90°C, for 4 hr. The prints of Fig. 12 were obtained with a sputtered 200Å Fe_2O_3 film. Figure 12a shows the specimen before application of voltage, b at 112V, and c at 117V. Uniform opacity is observed at the highest voltage indicating that the activation proceeded uniformly over the whole surface. At the lower voltage the crystallites led to electronic leakage which could be distinguished clearly from the uniform activation current that occurred at the higher voltage level.

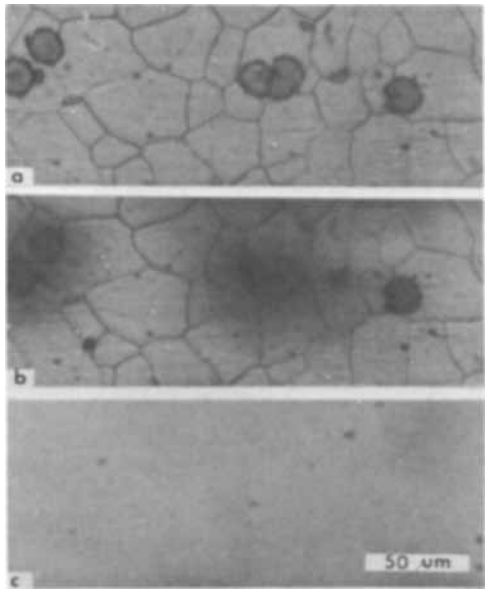

Fig. 12. Anodic microprints of a Ta/(2280Å)Ta_2O_5/(200Å)Fe_2O_3 electrode. "Field" crystals were generated by anodizing in 2% HNO_3 at 80V, 90°C, for 4 hr; voltage scan rate 20 V/min. a, Specimen with "field" crystals, no voltage applied; b, anodic print at 112V; c, anodic print at 117V.

Tantalum carbide flaws.—Carbide flaws were generated in anodic Ta_2O_5 by evaporation of carbon on Ta foil followed by annealing in vacuum at 1800°C for 30 min. Anodization was carried out at 120V, 25°C, for 30 min. The prints of Fig. 13 were obtained after sputtering a 200Å Fe_2O_3 film on Ta_2O_5. The center grain in the specimen shown in Fig. 13 contained the highest car-

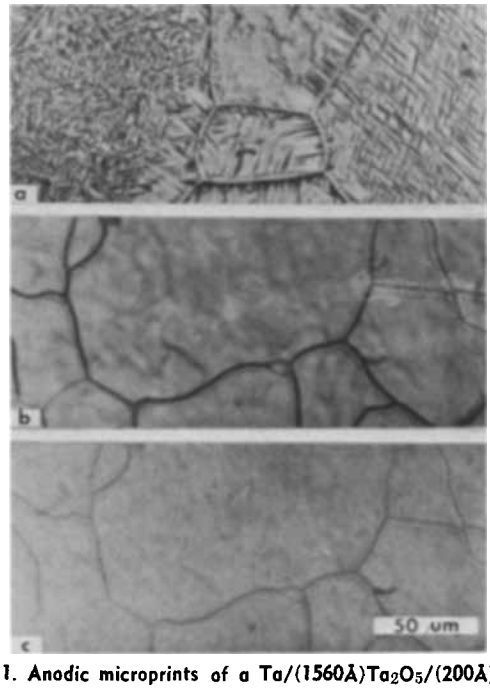

Fig. 11. Anodic microprints of a Ta/(1560Å)Ta_2O_5/(200Å)Fe_2O_3 electrode. Ta foil with thermal oxide by heating in air at 500°C for 5 min. Ta_2O_5 anodized at 80V, 25°C, for 30 min; voltage scan rate 20 V/min. a, Ta foil with Ta_2O_5 crystallites before anodization; b, anodic print at 85V; c, anodic print at 90V.

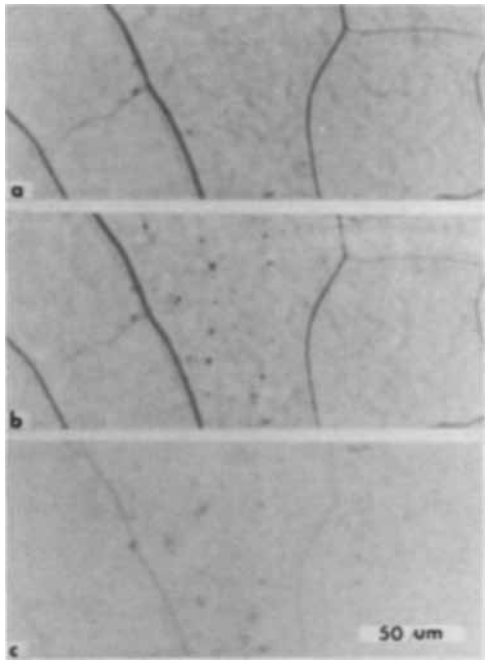

Fig. 13. Anodic microprints of a Ta/(2310Å)Ta_2O_5/(200Å)Fe_2O_3 electrode. Ta foil carburized before anodization at 120V, 25°C, for 30 min; voltage scan rate 20V/min. a, Anodic print at 80V; b, anodic print at 100V; b, anodic print at 115V.

bide concentration which was estimated to be of the order of 10^8 carbide flaws per cm^2. The color of the anodic oxide on this grain was substantially different from that of the surrounding grains. The print at 100V shows discrete electronic leakage sites with a density of about 5 x $10^4/cm^2$. The number of active sites remains constant until uniform activation occurs at 115V. Activation at this voltage was uniform and did not show any variation from grain to grain even though the carbide concentration varied greatly.

Other types of flaws.—Impurities, if present in sufficient quantity, will precipitate under favorable conditions. Tantalum used in these investigations was of high purity and elemental impurities were present in parts per million quantities only after chemical polishing and vacuum annealing. With rapid cooling after annealing conditions were unfavorable for the formation of any precipitates. Such material is characterized by flaw densities of less than $10^4/cm^2$. Anodic prints of less pure $Ta/Ta_2O_5/Fe_2O_3$ electrodes showed the effects of impurity islands with random distribution and shape. In Fig. 5 electronically active flaws are present in a density of 10^4-$10^5/cm^2$. In highly impure material the density of discrete active flaws may increase further. However, high impurity content usually leads to distributed e.c.

Pores, cracks, and pinholes have also been cited as possible contributors to e.c. A sensitive method to detect any of these types of flaws was the deposition of MnO_2 by means of pyrolytic conversion of $Mn(NO_3)_2$ followed by printing. The liquid penetrated pores and cracks and anodic prints revealed any such flaws at low voltage. Since this behavior was rarely, if ever, observed with flat high-purity specimens we could exclude such flaws from further consideration.

Conclusions from printing experiments.—Electronic conduction in flaws could be distinguished clearly from uniform e.c. by means of the high resolution printing technique. Uniform e.c. was observed at the same field strength for all specimens whether they were of highest purity with low flaw density, or whether they were prepared with the highest flaw densities. This was shown most strikingly in samples where different grains of widely varying flaw density exhibited identical activation behavior. Carbide containing samples were of particular interest because nonuniform e.c. was observed within those grains with the highest flaw densities. However, this localized type of e.c. was observed at significantly lower fields and was clearly distinguishable from the uniform e.c. at the activation field strength.

Electronically active sites were usually found to be present in much smaller densities than visible flaws and often appeared in patterns that reflected random contamination rather than distinctive distributions along grain boundaries or definite crystal orientations.

The density of active sites in some grains with high carbide flaw density was higher than in others with lower flaw density. But similar grains in other areas had no active sites at all. Therefore, no direct correlation existed between carbide flaws and e.c.

Thermal oxidation led to vastly greater e.c. occasionally, even though the specimen was thought to be one of high purity. Anodic printing revealed that thermal crystalline oxide was not the source of e.c., but that it originated in typical impurity patterns. This was attributed to the accumulation of impurities at the surface during thermal oxidation. This means that no direct correlation existed between thermal oxide or carbide flaws and e.c. under the conditions of anodic activation. This conclusion should be qualified to the effect that the properties of flaws may depend on the formation voltage. For the purpose of resolving the distribution of the activation current this is of no relevance since activation is observed at all Ta_2O_5 thicknesses.

Typically, electronically active flaws appeared in anodic prints at voltages far enough below the level of uniform activation to be clearly distinguishable. Even though a distribution in size and intensity was usually found to exist it is significant to note that flaws appeared first at rather distinct voltage levels. Their number was, by and large, determined at this level, and no significant increase in number was observed as the voltage increased further. The absence of a voltage dependent distribution of electronically active flaws in these cases allowed one to exclude the possibility that uniform activation was the result of many small flaws of the same kind as the larger ones that had appeared at the lower voltage levels.

Some kinds of flaws can become sources of e.c. in contact with sputtered or pyrolytically deposited MeO. "Field" crystals were one example, cracks, pores and breakdown sites, another. Their density was usually found to be several orders of magnitude smaller than that of oxide or carbide flaws. Again, they were found to conduct at voltage levels below those of uniform conduction and could, therefore, be excluded from consideration in the activation effect.

Summary of experimental results.—The e.c. of Ta/Ta_2O_5 electrodes in aqueous electrolytes was found to be extremely low in the absence of impurities. No obvious correlation between physical flaws as observed microscopically and e.c. was observed. The distribution of e.c. depended on the distribution of impurities present and had to be established experimentally.

With $Ta/Ta_2O_5/MeO$ electrodes (MeO = Fe_2O_3, MnO_2) e.c. was established in a time-dependent activation process on polarization in contact with electrolyte to potentials at which ionic migration set in.

Activation was observed at all Ta_2O_5 thicknesses and was characterized by an exponential increase of the electronic current with time at constant field in Ta_2O_5. In some cases deviations from this behavior were found and attributed to the properties of MeO.

The distribution of e.c. due to activation was found to be uniform and homogeneous. Electronically active flaw sites were found to be active at fields below those required for uniform activation. Therefore, the e.c. observed in the presence of MeO could not be attributed to flaws.

The electronically active condition persisted after activation had taken place and current field characteristics could be measured at fields below those used for activation. The active state slowly reverted to a less active state. The rate was dependent on the nature of MeO.

The dissolution of MeO removed the cause of e.c. The rate-limiting step for electron transport after activation was found to be localized in the Ta_2O_5/MeO interface.

The current-field characteristic of the e.c. was found to be that of thermionic emission, *i.e.*, log i_{el} proportional $F^{1/2}$, over several decades of current.

Discussion

Mechanism of activation.—Any physical model of the experimental system must be able to explain the dependence of the electronic conduction phenomena on the ionic processes preceding them. Experimentally, it was found that the electronic conductivity of the $Ta/Ta_2O_5/MeO$ electrode was as low as that of the Ta/Ta_2O_5 electrode until some ionic conduction had taken place. It is necessary, therefore, to first discuss the ionic processes which take place in Ta_2O_5 with electrolyte and MeO/electrolyte contacts. The two systems are shown in schematic form in the following figures.

The behavior of the Ta/Ta_2O_5 electrode (Fig. 14) is characterized by ionic migration as fields of the order of 10^6-10^7 V/cm are applied (Eq. [1]). Close to 80% of the ionic current is carried by anions (II), the rest by cations (I) (15). Reaction (II) leads to additional oxide growth at the Ta/Ta_2O_5 interface while reaction

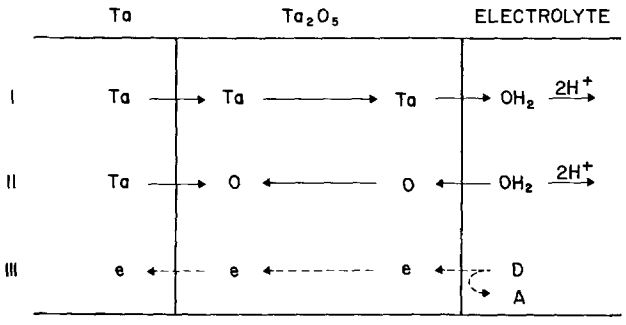

Fig. 14. Schematic of Ta/Ta_2O_5 electrode with electrolyte contact under anodic polarization. D = A + e redox system with D electron donor, A acceptor. Arrows indicate migration currents under a gradient of the electrochemical potential. Charge signs on ions have been omitted.

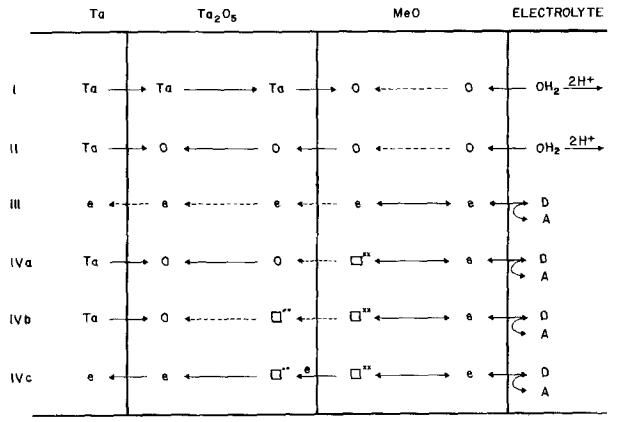

Fig. 15. Schematic of $Ta/Ta_2O_5/MeO$ electrode with electrolyte contact under anodic polarization. MeO = Fe_2O_3, MnO_2. D = A + e, redox system with D electron donor, A acceptor. $\square^{xx}$ oxygen vacancy with positive charge compensated by electrons, $\square^{\circ\circ}$ oxygen vacancy, positively charged. Full line arrows indicate migration currents under a gradient of the electrochemical potential; broken arrows indicate that the reaction is strongly hindered; double arrows indicate equilibrium. Charge signs on ions have been omitted.

(I) leads to growth at the Ta_2O_5 electrolyte interface. (The arrows indicate gradients of the electrochemical potential due to the applied field. Double arrows indicate equilibrium, broken lines indicate that the reaction is strongly hindered.) Oxide growth proceeds with nearly theoretical current efficiency, unless impurities are present in Ta_2O_5. This means in fact that the Ta/Ta_2O_5 electrode is an insulator electrode, since the electronic current even at the highest fields experimentally accessible is small compared to the ionic current.

The properties of metal-insulator electrodes have recently been reviewed (16). They are characterized by the lack of intrinsic electronic charge carriers in the insulator. A steady space charge limited electronic current is observed only if charge carriers can be injected at the insulator-electrolyte interface. An injecting or "ohmic" contact (17) is formed if the electrochemical potential of electrons in the electrolyte (Fermi energy) is sufficiently close to the energy of one of the band edges of the insulator, and if "band bending" allows electron exchange between energy levels in the electrolyte and the surface of the insulator. This condition is not satisfied for the Ta/Ta_2O_5 electrode in aqueous electrolytes as can be concluded from the absence of measurable space charge limited current flow. Also, the absence of measurable electronic current at high fields is evidence of negligible field induced charge injection or carrier generation in the bulk of the oxide. In Fig. 14 the electronic reaction (III) is characterized by the redox system D = A + e in the electrolyte (D donor, A acceptor species), blocked electron injection and a steep gradient of the electrochemical potential in the Ta_2O_5 which sweeps all mobile as well as most of the trapped electrons into the metal substrate. The potential distribution is characterized by a large drop across Ta_2O_5 and polarization at both of its interfaces. The ionic reactions I and II determine the magnitude of these overvoltages. In electrochemical terms the Ta_2O_5/electrolyte-contact is a blocking one for electrons because the overvoltage, as determined by the ion transfer reaction, is insufficient to establish the interface potential difference required for electron injection. Only by increasing the overvoltage of the ionic reaction can this condition for electron injection be met.

In the $Ta/Ta_2O_5/MeO$ electrode (Fig. 15) a second oxide film has been inserted between the insulating Ta_2O_5 and the electrolyte. The consequences regarding the ionic and electronic reactions will now be discussed. MeO (= Fe_2O_3 or MnO_2) is a transition metal oxide which exhibits electronic conductivity according to its nonstoichiometry and impurity content. Two assumptions are made regarding its e.c.

1. Electron equilibrium is established across the MeO/electrolyte interface and throughout MeO.

2. The electronic conductivity of MeO is much larger than its ionic conductivity. This means that the electrolyte contact to MeO is "ohmic" and that a Me/MeO-electrode would correctly measure the redox potential of the electrolyte (18). Electrons will be in equilibrium across MeO as long as its electronic charge carrier concentration is reasonably high and the current drawn remains low.

The effect on the migration of ions of a field applied across Ta_2O_5 will be the same as in the previous case but in contrast to electrolyte contact to Ta_2O_5, oxygen ions will not be readily available at the Ta_2O_5/MeO interface and a metal excess will result at this interface. We assume, for the purpose of this discussion, that the metal excess results from oxygen deficiency. This assumption would seem to be a reasonable one in view of the experimental evidence of amphoteric or n-type behavior of the oxides involved (19, 20). The reactions that lead to a depletion of oxygen ions on either side of the Ta_2O_5/MeO interface are illustrated in Fig. 15, IV a-c. At first, oxygen vacancies are being created on the MeO side as a result of the migration of oxygen ions away from the interface under the influence of the potential gradient across Ta_2O_5 and their limited availability from the electrolyte due to dominant electronic conductivity in MeO. The doubly positive charge of oxygen vacancies is compensated by electrons which are freely available from the redox reaction. This process creates additional electronic energy levels at the MeO side of the MeO/Ta_2O_5 interface.

As the depletion of oxygen ions spreads to the Ta_2O_5 side of the interface, positively charged oxygen vacancies (IV b) are formed inside Ta_2O_5. Their positive charge will remain largely uncompensated as any electrons crossing the barrier will be swept across Ta_2O_5 under the influence of the high applied field. As the oxygen depletion increases on both sides, a double layer charge builds up which is equivalent to saying that the overvoltage at the Ta_2O_5/MeO interface increases. The insertion of the MeO layer between Ta_2O_5 and the electrolyte thus leads to a limitation of the oxygen ion supply required for further Ta_2O_5 growth. The consequence of this limitation is increased interface polarization. This in turn leads to a reduction of the energy barrier for electron injection into Ta_2O_5 and allows larger electronic currents to pass from the electrolyte to the substrate metal. This is the condition that is indicated by reaction (IVc): The electrons are in equilibrium across the electrolyte/MeO interface and MeO and follow the electrochemical potential gradient across the MeO/Ta_2O_5 interface and Ta_2O_5.

Interaction of ionic and electronic processes at the Ta_2O_5/MeO *interface.*—No direct experimental evidence for the modification of the Ta_2O_5/MeO interface due to ion depletion can be given at this time. However, strong support for the contention that ionic migration contributes to the establishment of electronic conductivity comes from the following considerations. First, the activation process takes place at fields where ionic current (1) is known to flow according to

$$i = A \exp BF \quad [1]$$

where A, B = empirical constants and F = electric field. The activation process is time dependent, and the rate of increase of the electronic conductivity is a function of the applied field. Second, in cases where MeO shows some small degree of ionic conductivity, as for example in the case of MnO_2, one can detect some additional growth of Ta_2O_5 underneath MeO (21). Third, after activation has proceeded to a certain conductivity level one finds this condition to persist in the absence of the field for extended periods of time, but with a general tendency to decline over longer periods of time. The reversion to the inactive condition is considerably faster in the case of MnO_2 which shows somewhat higher ionic conductivity than Fe_2O_3. This points to the participation of ionic migration also in the reversion process which proceeds, it is believed, under the driving force of a gradient of the electrochemical potential of the depleted ions.

A quantitative correlation between the ionic current and the activation process as characterized by the increase in electronic conductivity will now be given. The electronic current (i_{el}) follows the current-field characteristic of thermionic emission (7)

$$i_{el} = i_{o,el} \exp (e\beta F^{1/2} - \phi_o)/kT \quad [2]$$

where

ϕ_o = energy barrier at zero field
e = electronic charge
k = Boltzmann constant
T = absolute temperature
β = field lowering coefficient

At constant field

$$\log_{10} i_{el} = D - 0.43\, \phi_o/kT \quad [3]$$

with

$$D = 0.43\, (\log_{10} i_{o,el} + e\beta F^{1/2}/kT)$$

The assumption is made that the ionic polarization at the Ta_2O_5/MeO interface leads to a reduction of the zero field energy barrier ϕ_o, and it is further assumed that the reduction is proportional to the ionic charge that has been displaced. The polarization process can be regarded as the charging of the double layer capacitance in the interface between Ta_2O_5 and MeO by the ionic current as given by Eq. [1]

$$d\eta = i_{ion}\, dt/C \quad [4]$$

$$= A\, (\exp BF)\, dt/C \quad [5]$$

where C = capacitance of polarization double layer formed in Ta_2O_5/MeO interface, η = interface overvoltage. This leads to an expression for the energy barrier as a function of time (t)

$$\phi = \phi_o - et\, d\eta/dt \quad [6]$$

$$= \phi_o - (eAt/C) \exp BF \quad [7]$$

From [7] and [3]

$$\log_{10} i_{el} = D - 0.43\, \phi_o/kT - (0.43\, eAt/CkT) \exp BF \quad [8]$$

From this equation the electronic activation current follows log i_{el} prop exp BF, with B the field constant of the ionic current. B was determined by plotting the slope s of the activation curves ($\log_{10} i_{el}$ *vs.* t, Fig. 6) *vs.* the applied field. From [8]

$$s = (0.43\, eA/CkT) \exp BF$$

$$\log_{10} s = \text{const.} + 0.43\, BF$$

The slope of $\log_{10} s$ *vs.* F yields the field constant of the ionic current. The result that was obtained for three Ta_2O_5 film thicknesses is shown in Fig. 16. The slope of the least-mean-square line gives a value of $B = (4.95 \pm 0.2) \times 10^{-6}$ cm V^{-1}. The close correspondence of this value with $B = 5.2 \times 10^{-6}$, the value given in the literature (1) as determined from studies of the ionic current-field relationship, provides conclusive evidence for the interaction of ionic and electronic processes in the activation effect.

Electronic leakage current due to impurities in Ta/Ta_2O_5 *electrodes.*—The role of impurities in causing electronic leakage in Ta/Ta_2O_5 electrodes may be understood similarly in terms of the activation model. The anodization of contaminated Ta may result in an accumulation of impurity oxide at the Ta_2O_5 electrolyte interface if competitive migration favors this and if the resulting impurity oxide is not dissolved by the electrolyte. This has been found to be the case with Ta contaminated with Fe, for example (3). The surface layer of impurity oxide will now restrict the supply of oxygen ions and thus lead to a degree of interface polarization. This in turn will permit the injection of electrons into Ta_2O_5. As long as the impurity oxide is sufficiently thin and of low electronic conductivity continuing anodization under the impurity oxide will be observed. This mechanism would explain why electronically active sites persist over wide voltage intervals of anodization without significant changes in their relative intensity. In cases where increasingly thicker impurity oxide films are formed the formation of additional anodic Ta_2O_5 will cease and all current will eventually become electronic. Subsequently, excessive current densities may destroy the underlying Ta_2O_5 film.

Impurities may also act as dopants for Ta_2O_5 and thus lead to discrete or quasi-continuous electron conduction levels in the forbidden gap. This would mean that the barrier for electron injection into Ta_2O_5 was reduced under anodization conditions and that conduction took place in impurity levels. A combination of both leakage conduction mechanisms appears possible. However, in the case of Ta contaminated with Fe the experimental observations strongly suggested that doping was not a contributing factor.

The current-field characteristic of impurity conduction will depend on the properties of the impurity oxide, such as its electronic conductivity, thickness, and solubility in the electrolyte, among others. In addition, the energy level distribution in all phases, *i.e.*, Ta_2O_5, the impurity oxide, and the redox electrolyte will also have a major influence.

Mechanism of charge transfer from the electrolyte to Ta *substrate.*—A more detailed discussion of the energy levels of electrons in the Ta/Ta_2O_5/MeO electrode in an aqueous redox electrolyte will now be

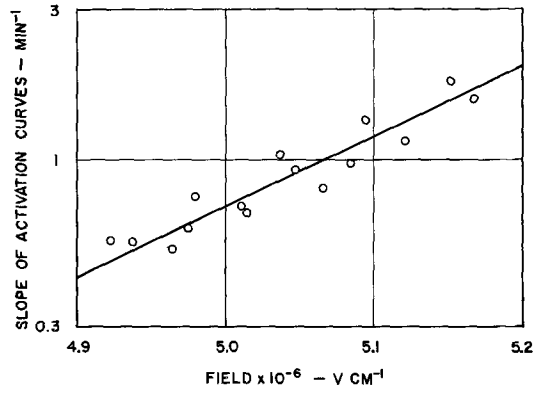

Fig. 16. Slope of activation curves (from Fig. 6) *vs.* the true field $F = \Delta V/d$ in Ta_2O_5.

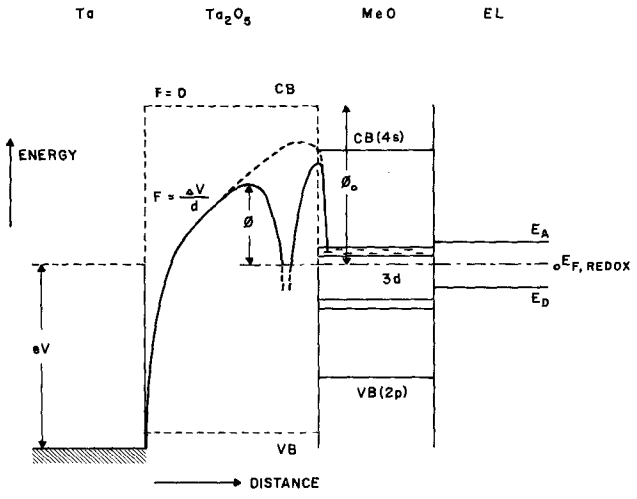

Fig. 17. Electronic energy diagram for $Ta/Ta_2O_5/MeO$ electrode with redox electrolyte contact. For details see text. CB conduction band; VB valence band; redox electrolyte: E_A acceptor level, E_D donor level, $_oE_{F,redox}$ Fermi level; V applied voltage; ΔV potential drop across Ta_2O_5.

given. Figure 17 shows, in schematic form, the electronic energy distribution for the system. The Ta electrode is characterized by its Fermi level E_F (Ta), the anodic Ta_2O_5 by the forbidden energy gap [of the order of 4.5 eV (1)]. The contact is nonblocking with Ta positive. The amorphous nature of anodic Ta_2O_5 may lead to a distribution of quasi-localized energy levels in the forbidden gap (7).

The electronic energy level diagrams of transition metal oxides such as Fe_2O_3 or MnO_2 are not known in any great detail (22-24). For the purpose of this discussion we assume the two transition metal oxides to be characterized by two narrow bands which result from crystal field splitting of the degenerate 3d levels of the transition metal cations under the influence of the strong electric field set up by the oxygen ions. Two wide bands resulting from oxygen 2p and cation 4s electrons are assumed to be too far from 3d levels to affect their occupancy. The location of the 3d energy bands of MeO with respect to the Ta_2O_5 band gap is not known. It is assumed that the 3d band energy levels are far removed in energy from the conduction levels of Ta_2O_5. The Ta_2O_5/MeO electrolyte contact is nonohmic before activation.

The redox system is characterized (25) by its Fermi level, $E_{F,redox}$ which is equivalent to the chemical potential of the electrons in the electrolyte. Donor (E_D) (occupied, reduced) and acceptor (E_A) (unoccupied, oxidized) energy levels show a distribution in energy due to thermal fluctuations of the hydration shell of each ion. The position of the electrolyte Fermi level depends on the redox potential and varies, therefore, with the kind and concentration of the redox system in contact with the $Ta/Ta_2O_5/MeO$ electrode.

In Fig. 17 the effect of an electric field across Ta_2O_5 has been illustrated. With zero field the barrier is rectangular with height ϕ_o. Under a low field the barrier for electrons is of such magnitude and shape that electron transfer is negligibly small. As the field increases the bands in Ta_2O_5 slope sharply downward resulting in a triangular barrier of reduced height. The maximum band bending is obtained when ionic migration sets in. At this point the barrier is still such as to prevent electrons from being injected into Ta_2O_5. As described previously, ionic migration then leads to polarization of the Ta_2O_5/MeO interface and the generation of positively charged centers in Ta_2O_5 close to this interface. The effect of positive ionic charges on the shape of interface barriers has been discussed by Schmidlin (26) and Korzo *et al.* (27). Tunnelling through and/or thermionic emission over a barrier ϕ of reduced height as shown in Fig. 17 must be considered as possible charge transfer mechanisms. The experimental results presented in this study strongly suggest that thermionic emission is the dominant mechanism.

Thermionic current-field characteristic of the electronic activation current.—The experimental results in conjunction with the model of the activation process provide the basis for the interpretation of the current field (voltage) characteristic of the electronic conduction process. The current-field characteristic of the electronic current measured after activation to a certain current level (Fig. 10) showed log i to be proportional to $F^{1/2}$. This characteristic is commonly associated with thermionic emission (Eq. [2]) which may follow one of two mechanisms, which have been reviewed extensively (6, 7, 28).

1. The Schottky effect (S) describes thermionic emission over a field-lowered barrier. The field lowering coefficient β_S is given by

$$\beta_S = (e/4\pi\epsilon_o\epsilon)^{1/2} \quad [9]$$

where ϵ_o = permittivity of vacuum and
ϵ = relative dielectric constant.

2. The Poole-Frenkel effect (PF) is the field assisted thermally activated release of electrons from traps or, more generally, coulombic potential wells. The current-field characteristic of the Poole-Frenkel effect also follows Eq. [2] with a field lowering coefficient which is twice that of the Schottky effect

$$\beta_{PF} = 2\beta_S = (e/\pi\epsilon_o\epsilon)^{1/2} \quad [10]$$

The Schottky effect is normally considered to be an interface effect, while the Poole-Frenkel effect applies to the bulk. The only criterion for an experimental differentiation between the two is the field lowering coefficient which gives the slope of the log i *vs.* $F^{1/2}$ curve. β contains only fundamental constants, with the dielectric constant the only one somewhat uncertain. The slope of the experimental log i *vs.* $F^{1/2}$ curve was used to calculate the dielectric constant. Our measurements for the $Ta/Ta_2O_5/Fe_2O_3$ electrode gave the following results:

ϵ_S	ϵ_{PF}	$\epsilon^{\infty}_{Ta_2O_5}$ (1)	$\epsilon^{\infty}_{Fe_2O_3}$ (29)
1.18	4.7	5.1	~9

There is general agreement in the literature (6, 7) that the high-frequency dielectric constant should apply to both mechanisms. The above comparison of dielectric constants clearly favors the Poole-Frenkel mechanism since there is close agreement between the high-frequency dielectric constant of Ta_2O_5 and the dielectric constant calculated from the Poole-Frenkel field lowering coefficient and the experimentally determined slope of the current-voltage curve.

At first sight it might be surprising that electron emission from an interface should follow the Poole-Frenkel mechanism. In the schematic electronic energy diagram (Fig. 17) it has been assumed that traps are generated inside Ta_2O_5 and that electrons may tunnel freely from the MeO electron levels through the narrow energy barrier at the interface to the traps. The energy barrier of thermionic emission according to Poole-Frenkel would therefore be the barrier seen by electrons trapped in a coulombic potential well as required by the theory. The field in Ta_2O_5 will assist the release of these electrons, and it is believed that it is this step in the electronic conduction process which is rate limiting.

Manuscript received May 22, 1970.

Any discussion of this paper will appear in a Discussion Section to be published in the June 1971 JOURNAL.

REFERENCES

1. L. Young, "Anodic Oxide Films," Academic Press Inc., New York (1961).

2. D. A. Vermilyea, "Advances in Electrochemistry," Vol. 3, p. 211ff, P. Delahay, Editor, Interscience Publishers, Inc., New York (1963).
3. G. P. Klein, *This Journal*, **113**, 348 (1966).
4. L. Young, *Trans. Faraday Soc.*, **55**, 842 (1958).
5. D. A. Vermilyea, *J. Appl. Phys.*, **36**, 3663 (1965).
6. W. S. Goruk, L. Young, and F. G. R. Zobel, "Modern Aspects of Electrochemistry," Vol. 4, p. 176ff, J. O'M Bockris, Editor, Plenum Press, New York (1966).
7. A. K. Jonscher, *Thin Solid Films*, **1**, 213 (1967).
8. G. P. Klein, *This Journal*, **113**, 345 (1966).
9. G. P. Klein, *ibid.*, **117**, 1581 (1970).
10. W. J. McG. Tegart, "The Electrolytic and Chemical Polishing of Metals," Pergamon Press Ltd., London (1956).
11. R. S. Clark, *Trans. Met. Soc. AIME*, **233**, 592 (1965).
12. D. A. Vermilyea, *This Journal*, **110**, 250 (1963).
13. D. A. Vermilyea, *Acta Met.*, **6**, 166 (1958).
14. D. A. Vermilyea, *This Journal*, **102**, 207 (1955).
15. J. S. P. Pringle, Paper 11 presented at the New York Meeting of the Society, May 4-9, 1969.
16. W. Mehl and J. M. Hale, "Advances in Electrochemistry," Vol. 6, p. 399ff, P. Delahay, Editor, Interscience Publishers Inc., New York (1967).
17. W. Mehl, J. M. Hale, and F. Lohmann, *This Journal*, **113**, 1166 (1966).
18. K. J. Vetter, "Elektrochemische Kinetik," p. 607, Springer Verlag Berlin, Heidelberg, New York (1961).
19. P. Kofstad, *This Journal*, **109**, 776 (1962).
20. K. Hauffe, "Reaktionen in und an festen Stoffen," p. 177ff, Springer Verlag Berlin, Heidelberg, New York (1966).
21. D. M. Smyth, *This Journal*, **113**, 19 (1966).
22. F. J. Morin, "Semiconductors," N. B. Hannay, Editor, p. 600ff, Reinhold Publishing Corp., New York (1959).
23. G. H. Jonker and S. van Houten, "Halbleiterprobleme," Vol. 6, p. 118ff, Friedrich Vieweg und Sohn, Braunschweig (1961).
24. D. Adler, "Solid State Physics," Vol. 21, 1 ff, Academic Press, New York, London (1968).
25. H. Gerischer, "Advances in Electrochemistry," Vol. 1, p. 139ff, P. Delahay, Editor, Interscience Publishers Inc., New York (1961).
26. F. W. Schmidlin, *J. Appl. Phys.*, **37**, 2823 (1966).
27. V. F. Korzo and G. A. Lyashenko, *Sov. Phys. Solid State*, **10**, 2665 (1969).
28. J. G. Simmons, *Phys. Rev.*, **166**, 166 (1968).
29. Handbook of Chemistry and Physics, 42nd ed., The Chemical Rubber Publishing Co. (1961).

Mechanism of the Electrochemical Reduction of Enolized 1,3-Diketones

Raymond C. Buchta[1] and Dennis H. Evans

Department of Chemistry, University of Wisconsin, Madison, Wisconsin 53706

ABSTRACT

A mechanism for the electrochemical reduction of 1,3-diphenyl-1,3-propanedione (**1**) and other enolized 1,3-diketones in aprotic solvents has been developed on the basis of cyclic voltammetric studies. The over-all reaction is a 0.5-electron process producing the enolate anion of the 1,3-diketone and the dimeric pinacol. The central feature of the mechanism is a one-electron reversible reduction to the radical anion of the 1,3-diketone followed by a fast, reversible proton transfer from unreacted diketone to the radical anion forming enolate and a neutral radical. The neutral radicals then undergo rapid coupling reactions. The electrochemical behavior of 1,3-diketones existing in the diketo form is contrasted with the above scheme.

Previous investigations have characterized the over-all electrode reactions involved in the electrochemical reduction of representative enolized 1,3-diketones in ethanol-water (1) and dimethylsulfoxide (2). In the present communication the results of detailed studies of the mechanism of the reduction of 1,3-diphenyl-1,3-propanedione **1** (or dibenzoylmethane, DBMH) and other enolized 1,3-diketones in dimethylsulfoxide (DMSO) will be presented.

The reduction of DBMH in DMSO proceeds by an over-all 0.5-electron process (2) with the stoichiometry given in Reaction [1]

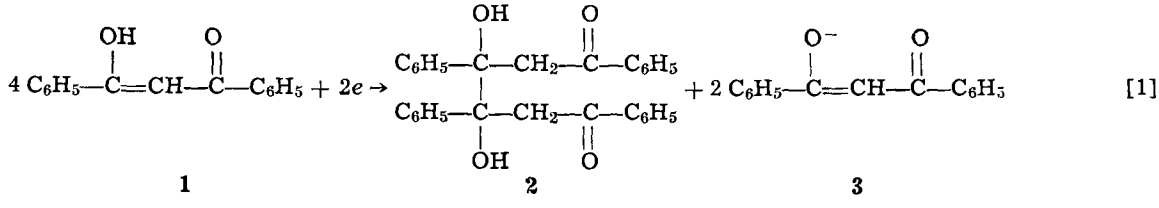

[1]

1 **2** **3**

Several chemical properties of 1,3-diketones have proven to be extremely important determining factors in the electrochemical reduction of these compounds. The first and most obvious is the keto-enol tautomerism. Those compounds which exist in the diketo form possess a much different pattern of reactivity (3) than the enolized compounds. The most important difference is the fact that the enol proton in compounds like **1** is sufficiently acidic that the 1,3-diketone acts as a proton donor during its reduction in aprotic solvents leading to the stoichiometry of Reaction [1] in which the conjugate base (enolate ion **3**) of the starting material is one of the products.

Another important property is the tendency for 1,3-diketones to undergo cleavage reactions in basic solution. This is particularly important during the reduction of diketo tautomers in aprotic solvents (3). Metal ions form a variety of complexes with 1,3-diketones

[1] Present address: Jackson Laboratory, E. I. du Pont de Nemours and Company, Wilmington, Delaware 19898.

Key words: cyclic voltammetry, tautomerism, dimethylsulfoxide, dimerization, coulometry.

and the electrochemical behavior of some of these has been reported (4,5). An effect of lithium ions on the electrochemical reduction of DBMH was observed in the present investigation, but the general area of the effect of metal ions on 1,3-diketone electrochemistry remains largely unexplored.

Cyclopropanediols are possible two-electron reduction products of 1,3-diketones. Recently, such products have been isolated after chemical reduction of several cyclic 1,3-diketones (6). Cyclopropanediol derivatives are produced in certain electrochemical reductions (7). However, this particular reaction path appears to be unimportant for the acyclic compounds discussed in this paper.

Experimental

Reagents.—Dimethylsulfoxide (J. T. Baker Reagent, 0.05% or 30 m*M* water) was stirred over calcium hydride for at least 12 hr and distilled under reduced pressure just before use. Tetra-*n*-butylammonium perchlorate (Matheson) was used as received for polarography and controlled potential coulometry. For cyclic voltammetric studies it was recrystallized from ethyl acetate and vacuum dried. Lithium perchlorate (G. F. Smith) was vacuum dried before use. Prepurified nitrogen (Airco) was used for solution deaeration.

Various 1,3-diketones and other materials (Eastman) were used as received: 1,3-diphenyl-1,3-propanedione, 1,3-bis(*p*-fluorophenyl)-1,3-propanedione, 1,3-bis(*p*-methoxyphenyl)-1,3-propanedione, 1-phenyl-1,3-butanedione, isobutyrophenone, acetophenone. Preparations of tetra-*n*-butylammonium dibenzoylmethide (2), 2,2-dimethyl-1,3-diphenyl-1,3-propanedione (8), 2-*t*-butyl-1,3-diphenyl-1,3-propanedione (3), and 1,4-dibenzoyl-2,3-diphenyl-2,3-butanediol (1) have been described.

The nmr spectra of DBMH, 1,3-bis(*p*-fluorophenyl)-1,3-propanedione, 1,3-bis(*p*-methoxyphenyl)-1,3-propanedione, and 1-phenyl-1,3-butanedione were obtained in d_6-DMSO and *d*-chloroform. In consonance with earlier studies (9) these substances were found to exist almost entirely in the enol form. These conclusions were based on the fact that the proper ratios between the integrals of the olefinic proton resonance and the other resonances were found. In addition, no resonance attributable to the methylene protons of the keto form was detected. A broad enol resonance was found for each compound in the 15-17 ppm range. The nmr spectra of 2-*t*-butyl-1,3-diphenyl-1,3-propanedione indicated that it was almost completely in the diketo form. Substitution in the 2-position causes a marked preference for the diketo tautomer as, for example, with 2-methyl-1,3-diphenyl-1,3-propanedione (9c).

Apparatus and procedure.—Instrumentation, cells, electrodes, and procedures for polarography and controlled potential coulometry have been described (2).

Cyclic voltammetric experiments were carried out using an instrument based on conventional circuits (10) and utilizing solid-state operational amplifiers. Philbrick SP65A amplifiers were used for the current follower, voltage sweep, and controller amplifiers. The voltage follower was a Philbrick P25AH. Up to and including a voltage scan rate of 0.3 V/sec, the direction of the scan was changed manually. For voltage scan rates greater then 0.3 V/sec, the triangular waveform of a signal generator (Wavetek Model 112) was employed in conjunction with the above instrument. An X-Y recorder (Hewlett Packard-Moseley Division, Model 2D-2A) was used to record voltammograms up to 0.3 V/sec and for faster scan rates an oscilloscope (Tektronix Type 564 with two Type 2A63 plug-ins) was employed. Oscilloscope traces were photographed (C-12 camera) using Polaroid Type 107 film. Voltage scan rates were measured using the calibrated time axis of the recorder or oscilloscope (Type 2B67 plug-in).

The working electrode was a microburette-type hanging mercury drop electrode (Brinkmann Instruments, Inc.). Necessary precautions in the use of such electrodes have been described (11). The size of the mercury drop was determined from the mass of a known number of drops.

The cell for cyclic voltammetry was the same as that described for polarography (2). The temperature of the test solution was maintained at 25.0° ± 0.1°C using the cell water jacket in conjunction with a pump and controlled temperature bath. The microburette electrode occupied the central inlet of the cell and the other inlets were used for nitrogen deaeration, counter and reference electrodes. The reference electrode was either an aqueous saturated calomel electrode in a cracked glass probe (2) or a platinum quasi-reference electrode (12) sealed in a Luggin capillary. The tip of the capillary could be positioned within one drop diameter of the working electrode. The electrolyte concentration was increased to 0.2*M* to minimize resistance effects. The base line for the measurement of the anodic peak current was obtained by stopping the scan at a convenient potential past the cathodic peak and recording the resulting current-time curve (13). Residual currents were obtained using solutions containing only electrolyte and solvent.

In the cyclic voltammetric studies of the reduction of DBMH it was necessary to use relatively large concentrations (0.5-2.0 m*M*) in order to obtain a significant amount of following chemical reaction at practical scan rates. Consequently, the peak currents were rather large and the cyclic voltammograms were slightly distorted by uncompensated resistance effects. For example, with 2.00 m*M* **1** the cathodic peak current was 56 μA at a scan rate of 5.00 V/sec. The separation of peak potentials was 96 mV compared with 57 mV predicted for a reversible, one-electron process with no distortion due to uncompensated resistance. The effect also manifests itself in a diminished cathodic peak current. Corrections have been discussed by Delahay (14) and Nicholson (15). The approximate correction due to Delahay (14) was applied to all results. The largest correction of the cathodic peak current function was 8%. All corrections were less than 2% for scan rates less than 1.0 V/sec. The efficacy of the correction procedure was demonstrated in a study of the reduction of 2.05 m*M* acetophenone with scan rates varying from 0.050 to 5.00 V/sec and attendant peak potential separations of 70-123 mV. The corrections varied from 3 to 14% and the resulting current functions were constant with an average deviation of 1.0%. The use of this correction procedure assumes that the standard rate constant of the heterogeneous electron transfer reaction is large enough to prevent deviation of the waves from their reversible shape at the highest scan rates employed.

Results and Discussion

Representative cyclic voltammograms of 2.00 m*M* DBMH in dimethylsulfoxide (DMSO) containing 0.2 *M* tetra-*n*-butylammonium perchlorate are shown in Fig. 1. On the cathodic portion of the voltage scan, waves are found having peak potentials of −1.42, −1.72, and −2.28V *vs.* SCE. The first is the main reduction wave for DBMH. The latter two correspond to those observed for the pinacol **2** (−1.73V) and the enolate **3** (−2.27V). On the anodic portion of the voltage scan an oxidation wave occurs at −1.36V. This is due to the oxidation of the primary product formed at the first cathodic wave. If the anodic scan is extended to potentials more positive than those in Fig. 1, a reversible couple at −0.05V is detected. This process is also found with solutions of the enolate **3**. It is probably caused by anodic reactions yielding 1,3-diketone complexes of mercury. It is absent when a platinum working electrode is used.

The cyclic voltammograms in Fig. 1 were recorded at two different scan rates, 0.1(A) and 1.0(B) V/sec. The waves for the pinacol and the enolate show the expected dependence on scan rate, *i.e.*, they are smaller relative to the main wave at faster scan rates. This, of

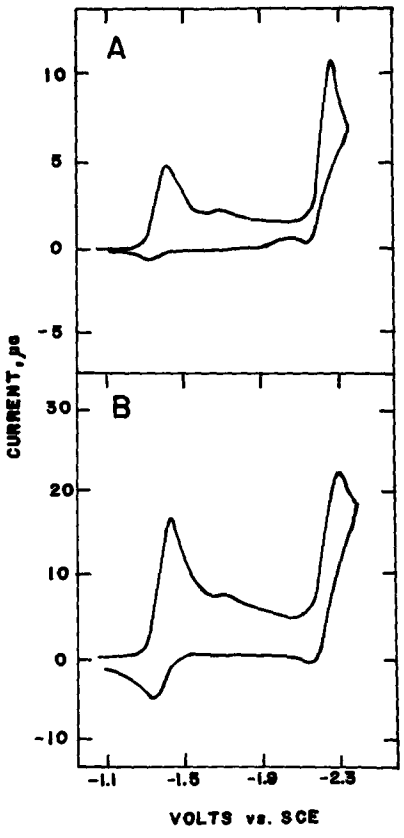

Fig. 1. Cyclic voltammograms of 2.00 mM dibenzoylmethane in 0.2M tetra-n-butylammonium perchlorate in DMSO. A. 0.100 V/sec. B. 1.00 V/sec.

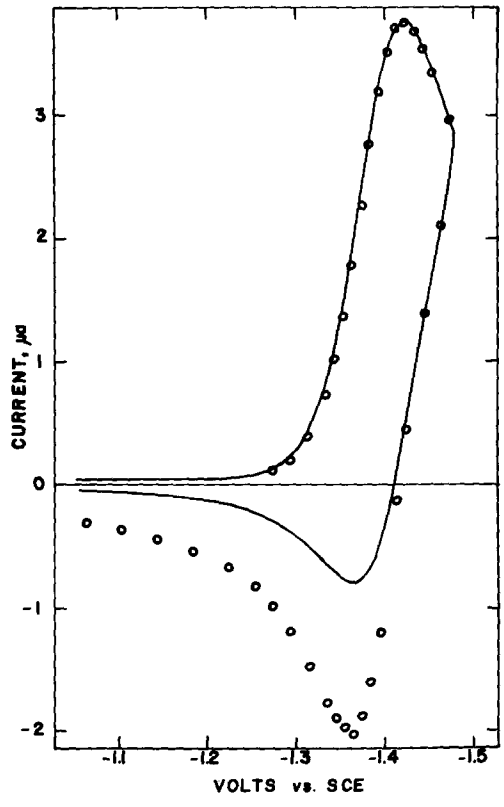

Fig. 2. Cyclic voltammogram of 1.01 mM dibenzoylmethane in 0.2M tetra-n-butylammonium perchlorate in DMSO, 0.100 V/sec. Circles are theoretical points for a reversible one-electron reduction with no following reaction.

course, indicates that given less time for the following chemical reactions to occur, less pinacol and enolate will be formed. It was also found that the pinacol and enolate waves were smaller relative to the main wave at lower DBMH concentrations. This dependence of the rate of the following reactions on concentration indicates that the reactions are of an order higher than first.

The most fundamental process characterizing this system is associated with the main wave at −1.42V. The other waves that have been observed result from products of this reaction. Therefore, experimental efforts were concentrated on the characterization of this process.

Before performing detailed studies of this reaction, it was necessary to establish that Reaction [1] is an adequate stoichiometric description of the process. From earlier studies (2) it was known that controlled potential coulometry of DBMH at −1.50V yielded an average n-value of 0.55. The two products (pinacol 2 and enolate 3) could be detected in the final electrolysis solution by polarography. The yellow color of 3 was completely discharged by the addition of dilute perchloric acid which converted it to DBMH which could then be detected by polarography. The pinacol 2 has been isolated after large scale electrolysis of DBMH in acetonitrile (16), a solvent in which the electrochemical behavior is very similar to that in DMSO.

Finally, the per cent yield of pinacol 2 was determined after controlled potential electrolysis of 49.9 mg of DBMH. A polarographic standard addition method employing the first polarographic wave of the pinacol was developed. Addition of known amounts of pure pinacol resulted in an increase in diffusion current with no change in the wave shape. The yield of pinacol was 107% based on the stoichiometry of Reaction [1]. Thus it is concluded that this reaction is an adequate description of the over-all process occurring at the first wave. Reactions other than [1] can consume no more than about 10% of the DBMH.

The first fact which may be obtained from the cyclic voltammogram of the first wave is the number of electrons in the primary electrode reaction. In Fig. 2 an experimental cyclic voltammogram of the first wave is presented together with the theoretical (13) curve for a reversible one-electron reaction with no following reaction. Excellent agreement is found between experiment and theory except, of course, the anodic peak current is diminished because of the following chemical reactions. Thus the primary product of the electrode reaction is probably the radical anion of DBMH.

There are three major properties of cyclic voltammetry which may be used to characterize a chemical reaction following the electrode reaction. These are the cathodic peak current function, the cathodic peak potential, and the ratio of anodic peak current to cathodic peak current, i_a/i_c (13). For the reaction rates found in this system, the last is the most sensitive and informative measure of the effect of the following reaction.

Representative data for three concentrations of DBMH and scan rates from 0.050 to 5.00 V/sec are summarized in Table I. The values of i_a/i_c increase with increasing scan rate and approach the limiting value of 1.00 at scan rates rapid enough to prevent appreciable following reaction. At a given scan rate the values of i_a/i_c are relatively higher at lower concentrations of DBMH.

To gain some qualitative information about the nature of the reaction, the i_a/i_c values were compared with the predictions for a similar but considerably simpler reaction scheme, *viz.*, a reversible electrode reaction followed by irreversible dimerization of the product (17). The values of k included in Table I are apparent rate constants for dimerization calculated from the i_a/i_c data. The values of k are reasonably independent of scan rate and concentration, although the

Table I. Cyclic voltammetric data for reduction of dibenzoylmethane[a]

Scan rate, V/sec	0.510 mM			1.01 mM			2.00 mM		
	$i_c/v^{1/2}C^*_O$[b]	i_a/i_c	k[c]	$i_c/v^{1/2}C^*_O$[b]	i_a/i_c	k[c]	$i_c/v^{1/2}C^*_O$[b]	i_a/i_c	k[c]
0.050	1.17	0.602	2.9	1.07	0.570	1.8	1.06	0.478	2.1
0.075	1.14	0.642	3.0	1.08	0.620	1.8	1.07	0.523	2.1
0.100	1.21	0.684	3.2	1.13	0.636	2.1	1.10	0.542	2.1
0.200	1.20	0.756	4.2	1.13	0.706	2.2	1.13	0.620	2.1
0.500	1.24	0.887	3.0	1.27	0.857	2.1	1.25	0.757	2.3
1.00	1.25	0.922	4.0	1.26	0.920	2.0	1.28	0.832	2.5
1.50	1.26	0.948	—	1.25	0.933	—	1.30	0.857	—
2.00	—	—	—	1.27	0.948	—	1.29	0.894	—
5.00	1.26	0.981	—	1.28	0.980	—	1.35	0.927	—

[a] 0.2M tetra-n-butylammonium perchlorate in DMSO. Temperature 25.0° ± 0.1°C. Current functions and peak current ratios are averages (typically 2-3 determinations). Radius of hanging mercury drop electrode: r_o = 0.0485 cm.
[b] Cathodic peak current function × 10^2, A-sec$^{1/2}$ $v^{-1/2}$ M^{-1}. Peak current has been corrected for sphericity effects and small distortions caused by uncompensated resistance. Separation of peak potentials range from 57 mV at low concentrations and slow scan rates to about 100 mV at high concentrations and rapid scan rates. v: scan rate (V/sec).
[c] Apparent second order dimerization rate constant × 10^{-3}, M^{-1} sec^{-1}. Switching time parameter, $a\tau$ (17), was calculated from each voltammogram. Typical values of $a\tau$ were 3.0-4.0.

average apparent rate constant for 0.510 mM DBMH is significantly larger than those obtained with the higher concentrations of DBMH. Thus in terms of i_a/i_c values, the process under study bears resemblance to a simple dimerization reaction. This resemblance is illustrated further in Fig. 3 where additional i_a/i_c data are plotted *vs.* the logarithm of the scan rate. Theoretical curves for an apparent dimerization rate constant of 2200 M^{-1} sec^{-1} are shown and a typical (k = 4 sec^{-1}) theoretical curve for a first-order following reaction (13) is presented for comparison.

The values of the cathodic peak current function are also included in Table I. For the dimerization mechanism, the peak current function will be almost independent of scan rate (17), exhibiting a slight increase at slow scan rates. The experimental values show a significant decrease at slow scan rates. This reflects the fact that the following chemical reactions consume additional starting material (DBMH) leaving less available for the electrode reaction. This effect is largest, of course, at slow scan rates where the extent of the following reaction is largest. The high scan rate limit is about 0.013 A sec$^{1/2}$ V$^{-1/2}$ M^{-1}. This corresponds to a diffusion coefficient of 2.7 x 10^{-6} cm^2/sec for DBMH.

A proposed reaction sequence consistent with the results just discussed is presented in Chart I. The central elements of this scheme are the reversible one-electron reduction of DBMH to its radical anion DBMH$^{\cdot-}$ and the subsequent rapid equilibrium reaction in which unreacted DBMH transfers a proton to DBMH$^{\cdot-}$ producing a neutral radical (DBMH$_2^{\cdot}$) and the enolate 3 (DBM$^-$). Three types of dimerization reaction are included: (*i*) dimerization of neutral radicals characterized by rate constant k_1; (*ii*) coupling of a neutral radical and an anion radical giving an anion of the pinacol. This reaction is characterized by rate constant k_2. It must be followed by protonation of the pinacol anion by DBMH; and (*iii*) coupling of two radical anions characterized by rate constant k_3. Charge interaction considerations suggest that k_3 is smaller than either k_1 or k_2.

Chart I

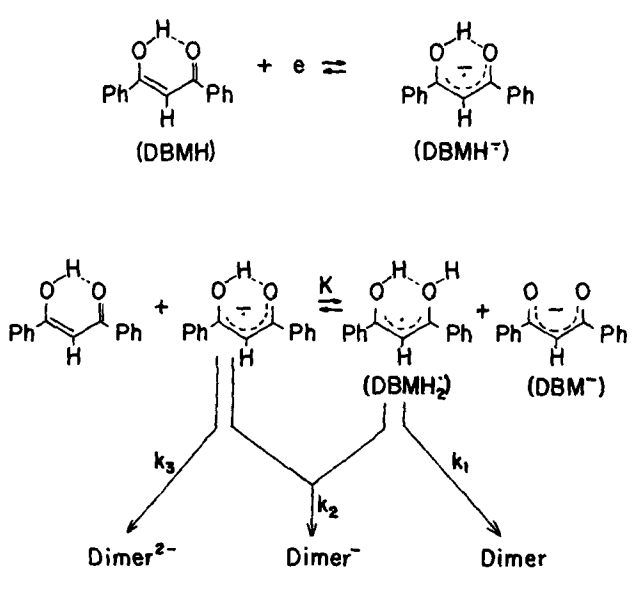

In this scheme the oxygen atom has been chosen as the site of protonation of the radical anion. Thus the pinacol 2 would be produced in the enol form requiring subsequent tautomerization. Protonation of the radical anion at the central carbon atom cannot be ruled out at this point.

So far no evidence has been found suggesting that reactions of radical species with DBMH to give dimeric radicals (18) are important in this system and such reactions have been omitted from the scheme in Chart I.

This reaction sequence is considerably more complex than the simple dimerization mechanism which was used in the analysis of the i_a/i_c data. It differs in two major ways: (*i*) the species which are dimerizing exist in an equilibrium mixture of two forms, protonated and unprotonated; and (*ii*) the following chemical reactions consume starting material. The latter point is consistent with the observed scan rate dependence of the cathodic peak current function discussed above.

The agreement of the observed i_a/i_c data with the predictions of the simple dimerization model may signify that the theoretical i_a/i_c values corresponding to

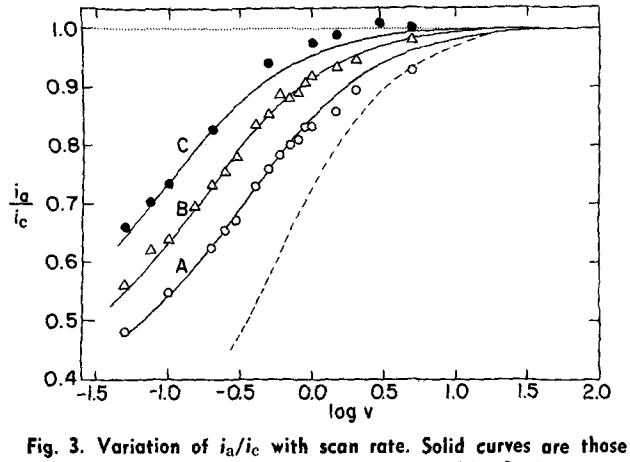

Fig. 3. Variation of i_a/i_c with scan rate. Solid curves are those predicted for a simple dimerization reaction (17). Dashed curve is a typical (k = 4 sec^{-1}) predicted curve for a first-order following reaction (13). The value of the parameter $a\tau$ is 3.4 for all theoretical curves and experimental data. Dibenzoylmethane concentrations: Curve A and ○: 2.00 mM; k = 2200 M^{-1} sec^{-1}. Curve B and △: 1.01 mM; k = 2200 M^{-1} sec^{-1}. Curve C and ●: 2.00 mM + 7.96 mM enolate 3, k = 550 M^{-1} sec^{-1}. Scan rate in V/sec.

the more complex scheme in Chart I would differ only slightly from those for simple dimerization (17). The larger values of apparent rate constant found at the lowest concentration of DBMH studied may signal the breakdown in the similarity of the two schemes. A few double potential step experiments were carried out with 2.00 m*M* DBMH and the disparity between experimental results and theory for a simple dimerization (19) was more readily detected. The calculated values of apparent rate constant showed little dependence on switching time just as they were almost independent of scan rate in the cyclic voltammetric experiments. However, the shape of the anodic portion of the current-time curve was incorrect, causing larger values of the apparent rate constant to be obtained from data points considerably past the switching point. Thus the actual mechanism differs from a simple following dimerization. The apparent rate constants computed from the cyclic voltammetric data should be regarded only as indications of the relative rate of the following reactions.

The succeeding chemical equilibrium plays a central role in the mechanism given in Chart I. The rapid coupling reactions are thought to involve the protonated neutral radical, $DBMH_2^{\cdot}$. Any alteration in experimental conditions which would cause less $DBMH_2^{\cdot}$ to be formed, should cause a concomitant decrease in the rate of the following reactions. One way of effecting such a decrease would be to increase the concentration of the enolate **3** (DBM^-). This should cause the equilibrium to be shifted to the left resulting in less $DBMH_2^{\cdot}$ being formed and a smaller over-all rate of the coupling reactions.

Data for the reduction of 2.00 m*M* DBMH in the presence of various amounts of the tetra-*n*-butylammonium enolate salt of DBMH are summarized in Table II. It is clear that the addition of enolate **3** has a pronounced effect on the rate of the following reactions. Substantial increases in the values of i_a/i_c were observed with an enolate concentration of 1.99 m*M* and again when the concentration was increased to 7.96 m*M*. The effect appears to be leveling off, however, as evidenced by the relatively modest increases in i_a/i_c found when the enolate concentration was increased to 15.0 m*M*. Apparent dimerization rate constants calculated from the data of Table II are roughly 1000 M^{-1} sec^{-1} at 1.99 m*M* enolate and 500 M^{-1} sec^{-1} at 7.96 and 15.0 m*M* enolate. Additional data for 7.96 m*M* enolate are plotted in Fig. 3 along with a theoretical curve for $k = 550$ M^{-1} sec^{-1}. Enolate ion causes a substantial decrease in the rate of the following reactions in consonance with the scheme in Chart I.

The addition of large amounts of enolate has at least one additional effect. The cathodic peak current functions are larger than the *ca.* 1.3 x 10^{-2} A $sec^{1/2}$ $V^{-1/2}$ M^{-1} value (*cf.* Table I) characteristic of DBMH reduction with negligible following reactions. For example, at 0.100 V/sec with 2.00 m*M* DBMH plus 15.0 m*M* enolate the cathodic peak current function was 1.68 x 10^{-2}. This does not signify a change in the over-all reaction scheme because the coulometric *n*-value for electrolysis of 2.0 m*M* DBMH in 15 m*M* enolate was still 0.55. The cause of the increased current functions in the presence of enolate remains to be discovered.

Table II. Effect of enolate on the cyclic voltammetry of dibenzoylmethane[a]

Scan rate, V/sec	i_a/i_c 2.00 m*M* DBMH	2.00 m*M* DBMH + 1.99 m*M* DBM⁻	2.00 m*M* DBMH + 7.96 m*M* DBM⁻	2.00 m*M* DBMH + 15.0 m*M* DBM⁻
0.050	0.478	0.562	0.661	0.695
0.100	0.542	0.632	0.731	0.755
0.200	0.620	0.722	0.826	0.854
0.500	0.757	0.842	0.942	0.954
1.00	0.832	0.904	0.974	0.995
5.00	0.927	0.954	1.00	1.00

[a] Experimental conditions are the same as those given in Table I.

Further evidence that the DBMH radicals are more stable when enolate is present may be found in the fact that an electron spin resonance spectrum may be obtained during electrolysis of DBMH in 0.1*M* tetra-*n*-butylammonium enolate as supporting electrolyte. Unequivocal identification of this radical as the radical anion of DBMH has not been accomplished. A similar spectrum was obtained by reduction of DBMH in tetrahydrofuran at −60°C.

The addition of water has little effect on the cyclic voltammetry of DBMH. When a 2.00 m*M* DBMH solution in DMSO was made 300 m*M* in water, the i_a/i_c ratio decreased only 2% and the cathodic peak current decreased 3% (scan rate: 0.1 V/sec). The acidity of DBMH is about the same as that of phenol (20). DBMH is apparently much more effective than water in donating a proton to $DBMH^{\cdot-}$ in the scheme in Chart I causing water to be relatively ineffective in increasing the rates of the following reactions.

The electrochemical behavior of DBMH is quite similar when 0.1*M* lithium perchlorate is used as supporting electrolyte in place of tetra-*n*-butylammonium perchlorate. The over-all process is still given by Reaction [1]. The pinacol **2** and the enolate **3** were detected in an electrolysis solution. The average *n*-value from controlled potential coulometry was 0.51. Just as was observed in the absence of lithium ion, the pinacol **2** decomposed by an electrolytic autocatalytic process (2) giving benzil[2] and acetophenone. The latter was determined in the electrolysis mixture by a polarographic standard addition technique and was found to be produced in 95% over-all yield from DBMH. The benzil was detected as its radical anion by esr spectroscopy. The somewhat distorted, broad-lined spectrum which was obtained was identical to that obtained during electrolysis of authentic benzil in 0.1*M* lithium perchlorate in DMSO. An exact assignment of splitting constants was not possible. Nevertheless, it was clear that some interaction between the benzil radical anion and a lithium ion (^7Li; $I = 3/2$) was occurring.

Thus the over-all reaction of DBMH reduction in lithium perchlorate is the same as it is in tetra-*n*-butylammonium perchlorate (2). The major difference is that the rates of the following reactions are much greater in the presence of lithium ion. Qualitative evidence for this may be found in the observation that the solution remains colorless during the reduction of DBMH in 0.1*M* lithium perchlorate in DMSO. When the tetraalkylammonium salt is used (2), the solution develops a light green color during the electrolysis presumably because of a higher steady-state concentration of the DBMH radicals.

Even very small amounts of lithium perchlorate have a profound effect on the cyclic voltammetry of DBMH. For example, the addition of 2.0 m*M* lithium perchlorate to 2.00 m*M* DBMH in 0.2*M* tetra-*n*-butylammonium perchlorate completely obliterated the anodic wave for the radical anion at sweep rates less than 0.5 V/sec. The value of i_a/i_c was only 0.534 at 1.00 V/sec and 0.815 at 5.00 V/sec (*cf.* Table I). These i_a/i_c values signify an approximately ten-fold increase in the apparent dimerization rate constant. The increased rates of the following reactions also affect the cathodic peak current function. At slow scan rates the current function is about 0.8 x 10^{-2} A $sec^{1/2}$ $V^{-1/2}$ M^{-1}. These low values (*cf.* Table I) are caused by the fact that the reactions following charge transfer consume DBMH. As the scan rate is increased and the i_a/i_c values approach 1.00, the current function increases toward the limiting value of 1.3 x 10^{-2} characteristic (*cf.* Table I) of insignificant following reactions.

[2] It has been reported that benzil exhibits only a single, two-electron wave in 0.1*M* lithium perchlorate in DMF, whereas there are two separate one-electron waves when tetra-*n*-butylammonium iodide or tetraethylammonium perchlorate is used as supporting electrolyte (21). By contrast, we find two closely spaced one-electron waves for benzil in 0.1*M* lithium perchlorate in DMSO. The half-wave potentials are −1.03 and −1.13V *vs.* SCE.

The effect of lithium ion may be explained in two ways. First the lithium ions may interact with the enolate **3** forming a stable 1:1 complex. The equilibrium in Chart I would be shifted to the right causing relatively more neutral radicals ($DBMH_2^{\cdot}$) to be formed and bringing a commensurate increase in the over-all dimerization rate. This explanation is reasonable in view of the relatively stable lithium-acetylacetonate complex formed in acetonitrile (4).

Second, lithium ions may interact with DBMH radical anions forming ion pairs which may exhibit an enhanced rate of dimerization since electrostatic repulsion has been reduced. The relative importance of these two effects cannot be determined from the present data and available theory.

Other symmetrical, enolized 1,3-diketones behave in a manner similar to DBMH. Cyclic voltammograms of 2.00 m*M* 1,3-bis(p-methoxyphenyl)-1,3-propanedione showed i_a/i_c values of 0.592 and 0.676 at 0.100 and 0.200 V/sec, respectively. These correspond to an apparent dimerization rate constant about 60% of that observed for DBMH. On the other hand, 2.00 m*M* 1,3-bis(p-fluorophenyl)-1,3-propanedione gave i_a/i_c values of 0.478 and 0.534 at 0.100 and 0.200 V/sec, respectively. These indicate an apparent rate constant about twice that observed for DBMH.

These relatively small substituent effects do not appear to be related to the ability of electron-withdrawing substituents to lower the unpaired spin density at the coupling site and consequently decrease the rate constant. The effect is actually the opposite. Electron-withdrawing substituents cause increased apparent rate constants.

The effect may be interpreted in terms of a substituent effect on the equilibrium constant of the equilibrium step in Chart I. This equilibrium constant is equal to the ratio K'/K'' where K' is the acidic dissociation constant for DBMH ($DBMH \rightleftarrows DBM^- + H^+$), and K'' is the acidic dissociation constant for $DBMH_2^{\cdot}$ ($DBMH_2^{\cdot} \rightleftarrows DBMH^{\cdot} + H^+$). The electronic properties of the substituents suggest that K' and K'' should be greatest for the difluoro DBMH, less for DBMH, and least for the dimethoxy DBMH. If K' is more susceptible to substituent effects than K'', the equilibrium constants for the difluoro and dimethoxy compounds would be largest and smallest, respectively, in agreement with the observations. Very little is known about substituent effects on radical anion basicity so the above argument can be offered only as a suggestion.

Role of Keto-enol Tautomerism

We may now compare the electrochemical behavior of symmetrical, enolized 1,3-diketones as discussed above with the behavior of symmetrical 1,3-diketones which exist in the diketo form (3). Any of these compounds may exist as the diketo tautomer, **4**, the enol tautomer, **5**, or a mixture of the two.

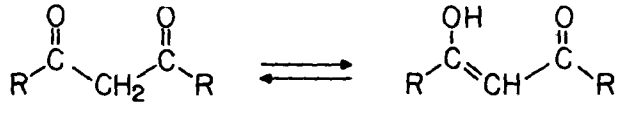

4 **5**

All of the compounds discussed in the first section are almost completely enolized. By substitution of alkyl groups at the 2-position, compounds may be prepared which cannot exist in the enol form. An example is 2,2-dimethyl-1,3-diphenyl-1,3-propanedione, **6**. Other compounds which conceivably could enolize, show a distinct preference for the diketo form. An example of this class is 2-*t*-butyl-1,3-diphenyl-1,3-propanedione, **7**, which exists almost completely in the diketo form. We have not yet found a compound whose diketo and enol tautomers can be isolated and studied separately.

The diketo compounds differ from the enolized compounds with respect to at least three properties: coulometric n-values, stability of the radical anions, and nature of the reactions of the radical anions.

The n-values obtained by controlled potential coulometry differ markedly for the two kinds of compounds. As was discussed earlier (2) the n-values for reduction of the enolized compounds are all about 0.5 and the over-all reaction is given by [1]. The diketo compounds do not possess the relatively acidic enol proton and the rapid protonation by starting material which is a part of Reaction [1] is no longer possible. Consequently the n-values for the diketo compounds are about one, or specifically, $n = 0.99$ for **6** and $n = 1.1$ for **7**.

The relative stability of the primary product of the electrode reaction, the radical anion, also depends on tautomerism. The radical anions of all the enolized compounds undergo the protonation-dimerization reactions discussed earlier and thus their life-times are relatively short. The radical anions of the diketo compounds have longer lives. For example, the electron spin resonance spectrum of the radical anion of **6** is readily obtained by electrolysis in a cell in the microwave cavity of the spectrometer (3). Under similar conditions the enolized compounds do not give spectra of the primary radical anion, but rather spectra of species formed by subsequent chemical and electrochemical reactions (2). Cyclic voltammetric studies of **6** also indicate an enhanced life-time of the radical anion. The cathodic peak current function was 0.013 $A \cdot sec^{1/2} \cdot V^{-1/2} \cdot M^{-1}$, the same as that obtained for DBMH at fast scan rates (Table I).

The radical anions of diketo compounds are subject to decomposition but the nature of the reactions differs from those of the radical anions of the enolized compounds. The most important reactions are cleavage reactions (3). For example, after the electrolysis of **6** ($n = 0.99$), no polarographic waves for the radical anion can be detected. Instead a wave for a cleavage product, isobutyrophenone, is present and its diffusion current indicates that it has been produced in 80-90% yield. Further evidence of the formation of isobutyrophenone is found in the acquisition of the electron spin resonance spectrum of isobutyrophenone radical anion on further electrolysis of the solution. A cleavage product, 3,3-dimethyl-1-phenyl-1-butanone, is also found after the electrolysis of **7**. No evidence has been found indicating cleavage reactions during the electrolysis of enolized 1,3-diketones. Such reactions may become important under conditions in which the second-order dimerization reactions are slow, *viz.*, low concentrations (*cf.* Table I) and in the presence of added enolate **3** (*cf.* Table II). Another possible reaction of the radical anions of enolized 1,3-diketones is a decomposition to hydrogen gas and enolate ion.[3] Under the conditions utilized in this study, however, Reaction [1] is the major over-all reaction for symmetrical, enolized 1,3-diketones.

One unsymmetrical, enolized compound, 1-phenyl-1,3-butanedione, was studied. Its behavior is more complex. The coulometric n-value for electrolysis on its first wave is 0.75. Some formation of a pinacol is indicated by the characteristic current-time maximum obtained during electrolytic autocatalytic decomposition of pinacols and by the acquisition of an electron spin resonance spectrum for the radical anion of 1-phenyl-1,2-propanedione (2). Yet the high n-value and the formation of acetophenone (2) may indicate that cleavage reactions are also occurring. Further study of unsymmetrical, enolized 1,3-diketones is in progress.

Acknowledgment

This research was supported by National Science Foundation grant number GP-8350, the National Science Foundation Chemistry Research Instruments Program and the Wisconsin Alumni Research Foundation.

[3] Such a pathway for the radical anion of **1** was suggested by Bauld and Brown (22). It is also the major reaction observed for the electrochemical reduction of acetylacetone in acetonitrile (23).

Manuscript submitted April 6, 1970; revised manuscript received ca. July 24, 1970. This was Paper 311 presented at the Los Angeles Meeting of the Society, May 10-15, 1970.

Any discussion of this paper will appear in a Discussion Section to be published in the June 1971 JOURNAL.

REFERENCES

1. D. H. Evans and E. C. Woodbury, *J. Org. Chem.*, **32**, 2158 (1967).
2. R. C. Buchta and D. H. Evans, *Anal. Chem.*, **40**, 2181 (1968).
3. R. C. Buchta and D. H. Evans, *J. Org. Chem.*, **35**, 2844 (1970).
4. R. W. Murray and L. K. Hiller, Jr., *Anal. Chem.*, **39**, 1221 (1967).
5. W. R. Heineman, J. N. Burnett, and R. W. Murray, *ibid.*, **40**, 1970 (1968).
6. W. Reusch and D. B. Priddy, *J. Am. Chem. Soc.*, **91**, 3677 (1969).
7. T. J. Curphey, C. W. Amelotti, T. P. Layloff, R. L. McCartney, and J. H. Williams, *ibid.*, **91**, 2817 (1969).
8. I. Smedley, *J. Chem. Soc.*, **97**, 1484 (1910).
9. (a) K. H. Meyer, *Chem. Ber.*, **47**, 826 (1914); (b) J. L. Burdett and M. T. Rogers, *J. Am. Chem. Soc.*, **86**, 2105 (1964); (c) G. Allen and R. A. Dwek, *J. Chem. Soc.*, (*B*), 161 (1966).
10. W. L. Underkofler and I. Shain, *Anal. Chem.*, **35**, 1778 (1963).
11. R. H. Wopschall and I. Shain, *ibid.*, **39**, 1527 (1967).
12. D. J. Fisher, W. L. Belew, and M. T. Kelley in "Polarography 1964," Vol. 2, p. 1043, G. J. Hills, Editor, Macmillan, London (1966).
13. R. S. Nicholson and I. Shain, *Anal. Chem.*, **36**, 706 (1964).
14. P. Delahay, "New Instrumental Methods in Electrochemistry," pp. 132-135, Interscience Publishers, Inc., New York (1954).
15. R. S. Nicholson, *Anal. Chem.*, **37**, 667 (1965).
16. V. Y. Liu, Unpublished experiments, University of Wisconsin, 1967.
17. M. L. Olmstead, R. G. Hamilton, and R. S. Nicholson, *Anal. Chem.*, **41**, 260 (1969).
18. J. P. Petrovich, M. M. Baizer, and M. R. Ort, *This Journal*, **116**, 743 (1969).
19. M. L. Olmstead and R. S. Nicholson, *Anal. Chem.*, **41**, 851 (1969).
20. L. G. VanUitert, C. G. Haas, W. C. Fernelius, and B. E. Douglas, *J. Am. Chem. Soc.*, **75**, 455 (1953).
21. R. H. Philp, Jr., R. L. Flurry, and R. A. Day, Jr., *This Journal*, **111**, 328 (1964); R. H. Philp, Jr., T. Layloff, and R. N. Adams, *ibid.*, **111**, 1189 (1964).
22. N. L. Bauld and M. S. Brown, *J. Am. Chem. Soc.*, **89**, 5413 (1967).
23. R. W. Murray, Professor, University of North Carolina, Private communication.

Use of the Potential-Step Method to Measure Surface Oxides

D. E. Icenhower,* H. B. Urbach,* and J. H. Harrison

Naval Ship Research and Development Laboratory, Annapolis, Maryland 21402

ABSTRACT

A new potential-step method was used to determine oxygen coverage on platinum, gold, and rhodium. The procedure was based, in part, on the use of an electronic coulometer. Experimental evaluation of the coverage and its theoretical interpretation was obtained by the use of the potential-step method in conjunction with the potential-sweep method. The advantage of the step method over the potential-sweep method for evaluating the degree of coverage is that the step method gives invariant results regardless of whether the technique is anodic or cathodic. The pH was found to have profound effects on the oxygen coverage. In general, changing the pH alters the degree of coverage by oxygen-containing species probably including carbon dioxide. Changes produced by pH alteration in the potential-sweep patterns of noble metals may be ascribed in part to the adsorption of carbonaceous impurities and to the pH-activated amphoteric character of the surface oxides. The oxygen coverage on platinum, a linear function of potential above 0.8V, may be explained in terms of platinum oxide dipoles.

The literature indicates general disagreement with regard to experimental techniques and results obtained by anodic and cathodic methods (1-4). To resolve questions relative to the merits of these techniques it was decided to measure the oxide coverage by the potential-sweep method and the potential-step method (5-9). The potential-step method employed in this study utilized electronic integration of the current in a way which permitted precision measurements of the oxide coverage and which exhibited no hysteresis in the results regardless of the direction of the potential sweep.

Experimental

Electrochemical cell.—A cell consisting of three compartments separated by sintered glass disks was used for all experiments. Prepurified nitrogen was bubbled through the main compartment and the counterelectrode compartment in order to flush out dissolved oxygen and hydrogen. Giner's (9) dynamic hydrogen reference electrode was used to measure the potential of the working electrode relative to the reversible hydrogen electrode (RHE) in the same solution, and platinum wire was used as the counterelectrode. The individual working electrodes were 5 cm long, 10-mil wires of platinum and gold. They were sealed in soft glass tubing and had small glass balls on the ends to eliminate edge effects.

All solutions were prepared from reagent-grade chemicals and triple-distilled water. Acid and caustic solutions were prepared from sulfuric acid and potassium hydroxide, respectively. Potassium sulfate was added to solutions with pH values of 2.4 and 12.7 to establish approximately constant ionic strength for all electrolytes, which were pre-electrolyzed overnight in a separate vessel prior to use. The pH was

* Electrochemical Society Active Member.

Key words: potential step coulometry, oxide coverage, electronic current integration, platinum oxides, gold oxides.

measured after pre-electrolysis. Measurements were carried out at an average of 27°C.

Electronic equipment.—In the sweep method of studying oxygen adsorption, a Hewlett-Packard Model 3300A, low-frequency function generator produced the triangular potential-time sequences. The function generator programmed a Wenking 61TR potentiostat, which controlled the potential of the working electrode with respect to the reference electrode. The apparatus is shown in block form in Fig. 1. The d-c potential level, the potential span, and rate of change of potential were adjusted easily. The instantaneous potential produced by the passage of the cell current through the calibrated 1000-ohm resistor, was recorded directly on the X-Y recorder as current-potential plots. By insertion of the integrator as shown by the dashed lines, charge-potential rather than current-potential plots were obtained. The integrator consisted of a Philbrick P2 (high common-mode rejection ratio) differential operational amplifier with a 10K input resistor and a 5 mfd output capacitor, which was short-circuited, when desired, by a switch to reset the integrator to zero charge.

Procedure.—Initially the potential was fixed at 1.8V so that oxygen was liberated on the electrode to burn off oxidizable impurities (11). Then the electrode was maintained below the visible oxygen-evolution potential at 1.4V to permit molecular oxygen to diffuse away from the surface. In the third step, the potential was lowered to some empirical value at which the metal oxide was reduced to provide a clean, metal surface. Next, the potential of interest was established. The potential in the last step was the same as that of the third step. The value of the potential employed in the third step was determined from a study of the sweep data on the given electrode at each pH in order to insure that the surface of the metal was indeed free of oxides. The electrode potential in the third step was 0.45V on platinum and 0.5V on gold.

The experimental evaluation of the oxide coverage was performed as follows. Current-time curves associated with the fast potential step similar to that in Fig. 2 were observed by means of an oscilloscope. When the potential was stepped, the current first rose rapidly to some relatively high value and then fell asymptotically to some nonvanishing residual value. This residual current is largely unrelated to the formation of a new state of charge of the surface occasioned by the step in potential, but it arises from the diffusion of oxidizable and reducible impurities to the interface. In order to integrate these current-time plots manually, and thus obtain the total quantity of electricity associated with the desired reaction, some approximation must be made to account for the presence of the diffusion current. Typical plots of the integrated current are shown in Fig. 3. The abrupt rise and fall of the coverage in millicoulombs at 2.5 and 22 sec is due to potential steps. The tangent to the linear sections of the rising curves (between 2.5 and 22 sec) was extrapolated to zero time. This extrapolation to the time of the step (2.5 sec) yielded the coverage in millicoulombs.

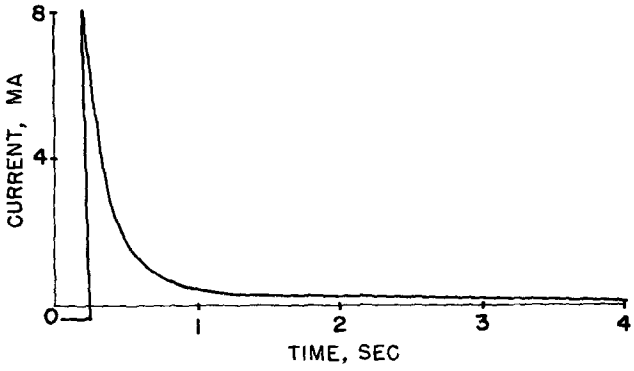

Fig. 2. Typical current-time plot obtained in the potential-step method.

Results

Platinum.—Potential-sweep measurements were employed to eliminate uncertainties with regard to the critical potential region where the oxide layer is reduced without simultaneous formation of a hydrogen layer. Therefore sweep data were obtained to facilitate each study involving the potential steps. Sweep data were obtained for the metals at 0.01 and 0.1 Hz at sweep speeds corresponding to 320 and 32 mV/sec. Some results for these sweep studies at pH values of 0.3, 2.4, 12.7, and 14 are illustrated in Fig. 4.

The sweep curves shown in Fig. 4 represent results previously detailed by Breiter and others (1, 2, 12, 13). The referenced papers furnish adequate discussion. However it is useful to recall that the oxide reduction peak b is flattened in alkaline solutions. It is clear from the above sweep data that a successful potential-step method will require that the cathodic end of the step terminate in the neighborhood of 0.45V at least in acid solution. However in alkaline solution the fusion of the oxide reduction wave with the hydrogen-atom-formation wave would suggest that some error might result due to incomplete reduction. However, use of the 0.45V value in alkaline solution yielded reproducible data independent of step direction indicating

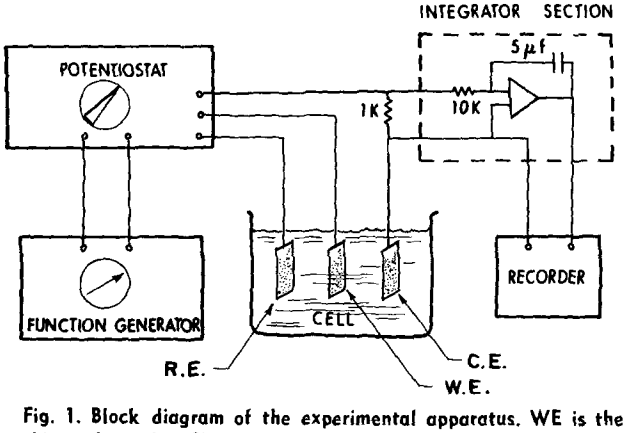

Fig. 1. Block diagram of the experimental apparatus. WE is the working electrode, CE the counterelectrode, RE is the hydrogen reference anode of a dynamic cell. F represents fritted glass walls and B bubble offs.

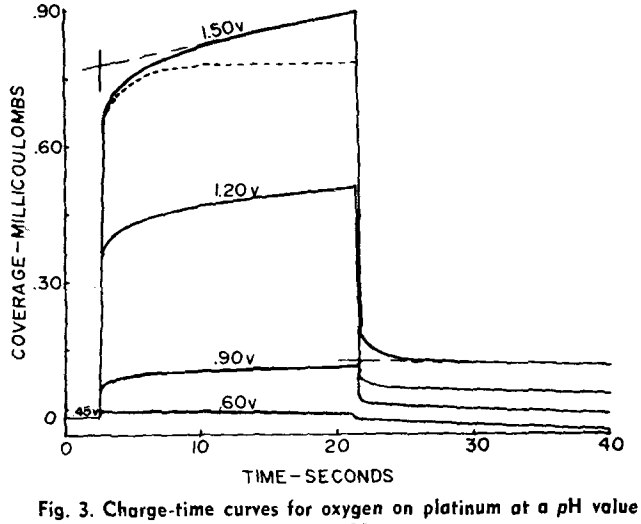

Fig. 3. Charge-time curves for oxygen on platinum at a pH value of 2.4. Extrapolations are to 2.5 and 22 sec.

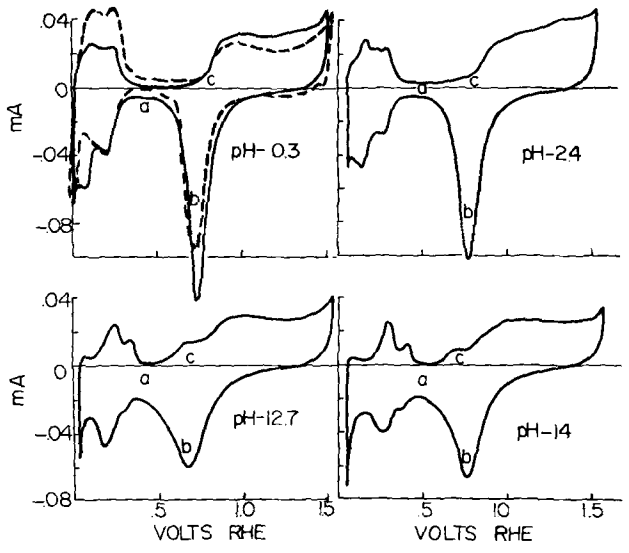

Fig. 4. Effect of pH on the triangular potential sweeps on platinum. Solids lines represent 0.01 Hz. Dashed lines represent 0.1 Hz (multiply current scale by 10).

that oxide reduction is complete at 0.45V provided sufficient time is allowed.

The triangular potential-sweep traces were integrated by the electronic procedure described above. Figure 5 represents the integral form of the sweep curves for two speeds. The dashed curve represents data for 0.01 Hz and the solid curve is for 0.1 Hz. The thickness of the double-layer region is greater in the slow sweep because the integral of the constant diffusion current over a longer period of time results in a larger number of coulombs. The charge representative of oxygen adsorption is apparently independent of the sweep time according to the figure, *i.e.*, $Q(0.1) = Q(0.01)$. However, it must be noted that the comparisons are made over different potential limits. The relatively straight line in the oxygen zone (a) represents the oxygen coverage obtained by the potential-step method (to be discussed). The form of these curves is similar to results obtained by Will and Knorr (2) using manual integration of the sweep curves. However, the negative character of the charge in the hydrogen region is explicitly indicated by the present technique. The electronic integration used here measures the double-layer charge (zone b) in addition to charge associated with oxygen coverage. The degree of reversibility in the hydrogen region of the curves is indicated by the fact that the quantities of electricity obtained during the anodic and cathodic sweep (Q_a and Q_c, respectively) differ only by the charge due to diffusion current at the end of the sweep. Careful manipulation of the potential limits is necessary to obtain isocoulombic (closed) curves which in essence bring about the balance of charge due to positive and negative diffusion currents. If the potential span is too far to the right, then $Q_a > Q_c$ due to oxygen evolution and/or oxidation currents of diffusing impurities and the curves shift continuously upward. Similarly, if the potential span lies in the regions too far to the left of the double layer, there is a shift downward due to reduction currents such as those arising from hydrogen evolution. Figure 6 illustrates the latter case for gold electrodes.

The results of the potential-step method on platinum are shown in Fig. 7. A comparison of the results with the sweep method of Will and Knorr has been indicated in Fig. 5. The step data are in better agreement with the anodic rather than the cathodic sweep data. The charge-potential curve representing oxygen coverage is rather linear at all pH values. Effects of pH are noticeable at potentials in the "double-layer" region below 0.8V, where the bend of the charge-potential curve is indicative of substantially more coverage in alkaline solutions than in acid solutions, as was observed in the sweep data.

Gold.—The results on gold (Fig. 8) show several differences from results in platinum. Hydrogen does not electrosorb on gold in the regions of interest in this study (13, 14). Oxygen does not adsorb on the electrode surface below a potential of approximately 1.35V in the acid solution (13, 14).

The reduction of the gold oxide in acid solution is associated with the appearance of a narrow peak near 1.15-1.20V, but in alkaline solution two shallow peaks are observed. The flattened peak at 1.10-1.15V in alkaline solution may correspond with the narrow peak (1.15-1.20V) in acid solution. Anomalous peaks

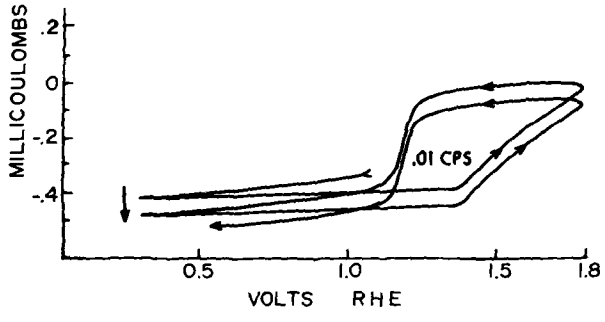

Fig. 6. Nonisocoulombic charge-time curves for gold at a pH of 2.4.

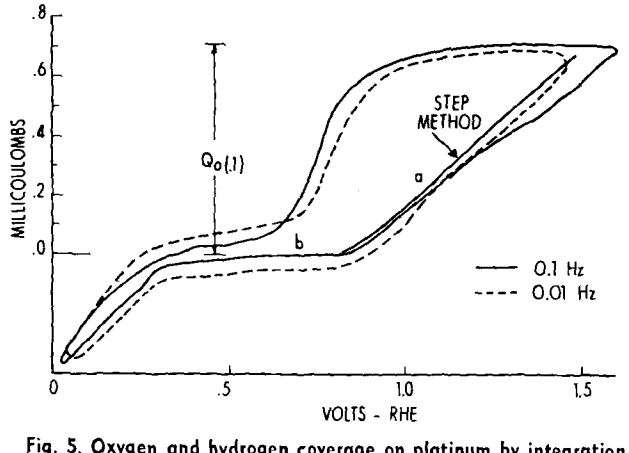

Fig. 5. Oxygen and hydrogen coverage on platinum by integration of sweep and step curves.

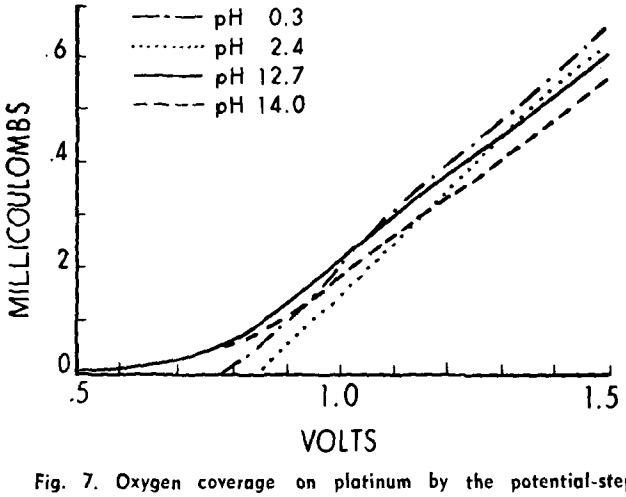

Fig. 7. Oxygen coverage on platinum by the potential-step method.

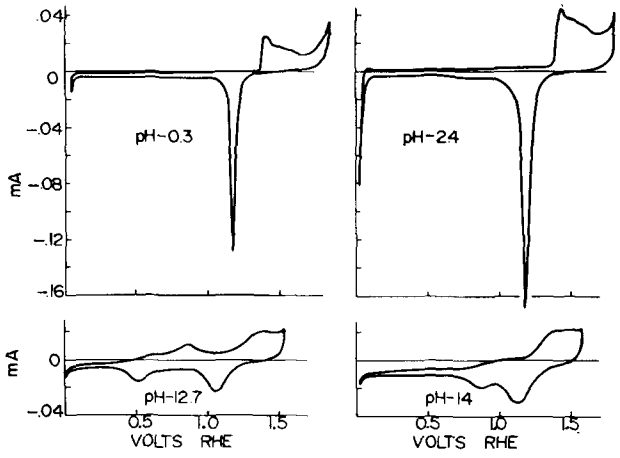

Fig. 8. Potential sweeps on gold

at other values probably represent the oxidation and reduction of organic adsorbates (see Discussion).

The results of the electronic integration of the triangular-potential sweep curves at 0.01 Hz are illustrated in Fig. 6 for gold at a *p*H of 2.4. Gold forms an oxide layer on its surface above the extended double-layer region at about 1.4V. There is a definite fall-off in the rate of oxygen adsorption at about 1.55V corresponding to the fall-off from the first peak in the current-potential plot of Fig. 8 (acid *p*H values). A similar fall-off in the rate of oxygen adsorption has been observed by Brummer and Makrides (14) at 1.45V using a galvanostatic stripping technique. The step method (acid *p*H) indicates a change of slope (Fig. 9) at about 1.55V. The region representative of the reduction and oxidation of hydrogen on platinum is absent in the case of gold (13, 14).

Sweep data on gold (Fig. 8) indicate that at a *p*H of 12.7 there is a broad plateau in the current *vs.* potential curve which may be associated with the adsorption of organic species on the surface of the gold, similar to that of platinum (see Fig. 7). In addition, at alkaline *p*H values the quantity of charge associated with the formation of organic sorbates on the gold appears to be greater at low potentials.

Rhodium.—The potential-sweep data for rhodium (Fig. 10) show a reduction peak at 1.3V in alkaline media. The charge which corresponds to this reduction peak is approximately the same as that for the oxidation peak (see curve for *p*H of 14). The relative magnitude of the oxygen and hydrogen waves in alkaline solution far exceeds the 2 to 1 ratio expected for monolayer coverage in alkaline solution. The

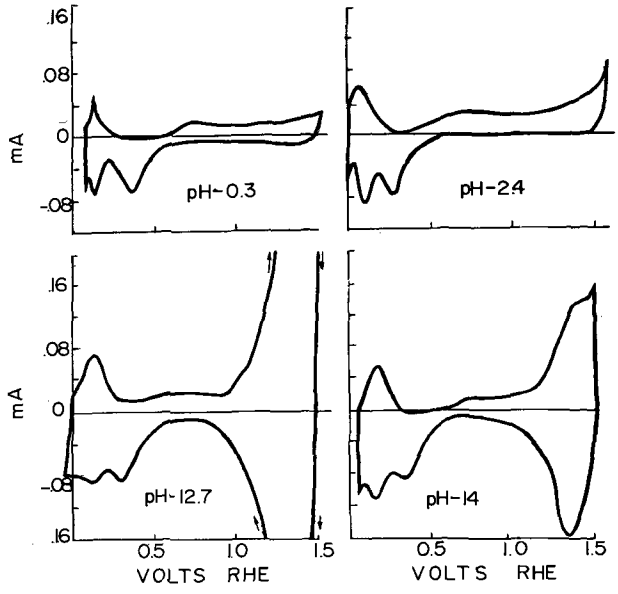

Fig. 10. Potential sweeps on rhodium

normal metal reduction waves between 0.25 and 0.35V appear unchanged in character at all *p*H values.

The hydrogen formation peaks in some cases nearly fuse with the oxide-reduction wave at 0.3V as noted by Bold and Breiter (1). In the *p*H systems corresponding to 2.4 and 12.7 the double-layer region loses the well-defined character shown in the *p*H system at 0.3. Curves obtained at high *p*H for fast sweeps (not illustrated) show less oxidation current relative to hydrogen than do the curves for the slow sweep.

The results of the potential-step experiments on rhodium are illustrated in Fig. 11. The presence of the large, new reduction waves in alkaline media noted in the potential-sweep experiments is confirmed by the very large wave that appears at approximately 1.2V.

Discussion

The experimental results reported here suggest a need for further clarification. An analysis of some areas is presented here, including the theory of the potential-step technique, the nature of the *p*H effects, and the linearity of the charge-potential curves on platinum.

Theory of the potential-step method.—Previous researchers who measured the area under the current-time curves such as that in Fig. 2 have simply terminated the zone of integration arbitrarily in the region where the curve appeared to be leveling. In addition, manual extrapolation to zero time was not

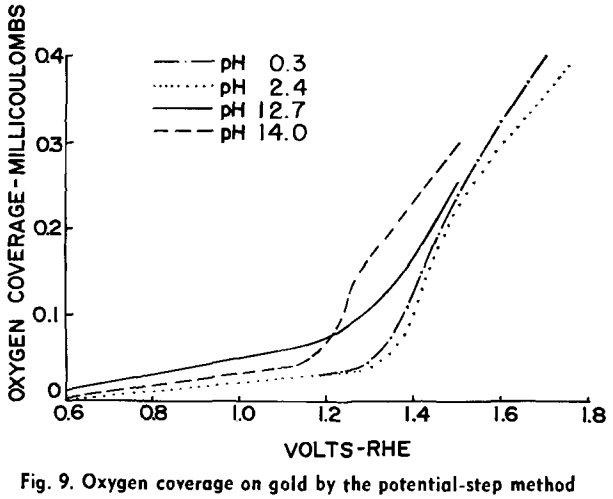

Fig. 9. Oxygen coverage on gold by the potential-step method

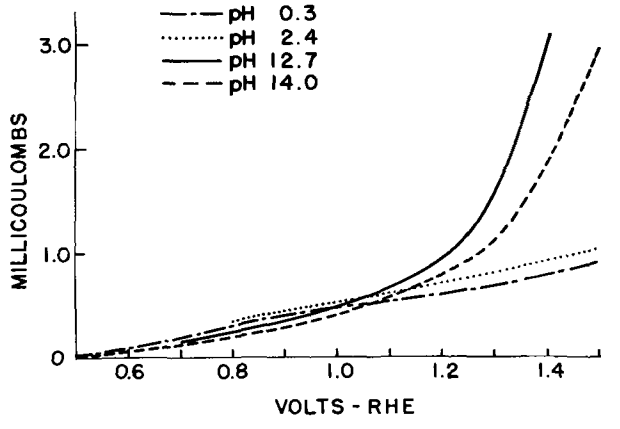

Fig. 11. Oxygen coverage on rhodium by the potential-step method.

performed. This procedure is neither rigorous nor satisfactory. In the typical integrated current-time curves in Fig. 3, the degree of linearity of the plots increases with the length of time from the potential step. Therefore the precision of the extrapolation from the "linear" section increased with time. (In this discussion it is assumed that diffusion currents remain uniform.) If the extrapolation process is repeated for sections of the coulomb-time curve which are doubled in length ad infinitum, the deviations between successive extrapolated values appears to decrease geometrically rather than arithmetically so that the coulomb value converges on some meaningful limit. Therefore this limit is a function of surface area and independent of time in contrast with methods where integration involves measurement of area with arbitrary limits. The quantity of charge, Q, obtained by extrapolating the straight-line portion of the curve back to zero time was found to be independent of the direction of the step. This fact supports the above conclusion that the charge, Q, is also independent of time. At low levels of charging, the scatter between values of Q for the forward and reverse step was as much as 10%. For large levels of charging (large potential steps) values of Q were within 2%.

It is clear from these results that hysteresis between surface charge measurements for anodic and cathodic methods observed elsewhere (3) are not supported here.

The fact that a numerical value close to unity independent of potential and pH is indeed attained must be attributed to the unique ability of the potential-step method to remove from the data extraneous contributions of charge due to residual diffusion currents. If the contributions of the residual currents shown by the dashed extrapolated line in Fig. 3 are subtracted from the experimentally observed charge-time curves, one obtains the corrected curve (short dashes), which rapidly approaches a horizontal asymptote. It is possible to obtain the general behavior of this corrected charge-time curve from the following form of the charge-transfer limited, current-potential relation for the case when the transfer coefficient[15] is 0.5. That is

$$i = 2i_o \sinh\left(\frac{n\mathbf{F}}{2RT}\eta\right) \qquad [1]$$

where i is current density, i_o is exchange current density, n is the number of electrons for the rate-controlling reaction, $\mathbf{F}$ is Faraday's constant, R is the gas constant, T is the absolute temperature, and η is the polarizing potential. The polarization, η, is assumed to be $E_f - E(Q)$, where E_f is the final potential at the end of the potential step and $E(Q)$ is the potential corresponding to the charge, Q, on the surface. Now $E(Q)$ is given by $E_o + Q/C$ where E_o is the starting potential, and where C is the slope of the experimental charge-potential plot of the electrode which is assumed to be constant because of the linearity of the charge-potential curves above 0.8V in Fig. 7. Replacing η by its definition, we obtain

$$\frac{dQ}{dt} = 2i_o \sinh\left(\frac{n\mathbf{F}}{2RT}\right)\left(E_f - E_o - \frac{Q}{C}\right) \qquad [2]$$

An expression involving the quantity of charge on the surface in the argument of an exponential function was derived by Feldberg, Enke, and Bricker (3) in a similar manner. However, they ignored the back reaction which is contained in the hyperbolic sine function. Equation [2] was written only for a step over a linear charge-potential region which in this case requires that E_o be approximately 0.8V. Thus, the equation is applicable only to the anodic sweep on platinum. Integration of Eq. [2] yields

$$-\log\frac{\tanh\frac{n\mathbf{F}}{4RT}\left(E_f - E_o - \frac{Q}{C}\right)}{\tanh\frac{n\mathbf{F}}{4RT}(E_f - E_o)} = \frac{n\mathbf{F}i_o t}{CRT} \qquad [3]$$

Equation [3] behaves like the dashed curve of Fig. 3 which was obtained by subtracting the area due to the diffusion current (the triangle formed by the extrapolation of the coulomb-time curve to zero). Equation [3] has the desirable property that at infinite time the charge, Q, is finite, whereas the mathematical results of previous workers (3) predict an infinite charge. Their charge-time curves showed a logarithmic dependence on the time. A tendency to approach infinite charge has in fact been experimentally observed by Laitinen and Enke (16) at 1.35V and above.

However at 1.25V and below, their results indicate that the charge remains fixed after a finite period (60 sec) of time. Their data and the results reported herein suggest that the coverage (charge divided by true area) is a function of potential rather than time below 1.25V. Two factors associated with the logarithmic increase of charge with time are probably the increase of surface roughness with time and formation of multilayers. Above 1.35V, the charge and coverage increase with time and the coverage approaches infinity, *i.e.*, the pure metal is consumed.

One other aspect of the charge-time curves of Fig. 3 is worthy of attention. The rounding of the curves after the initial jump is indicative of a slow reaction probably associated with the final crystallization steps in oxide formation which is discussed in more detail below. It is clear from the rapid rise of the curves that the majority of the charge transfer takes place within a fraction of a second.

Effects of pH.—Bold and Breiter (1, 12) observed a shift of the triangular potential sweep curves of −0.059 V/pH unit in acid regimes. In addition they noted changes in the structure of the sweep curves when the pH was altered from acid to alkaline character which are similar to those recorded at c in Fig. 4. Gilman (4) and others have suggested that the appearance of such changes in structure arise from the adsorption of carbon dioxide which is generally present in alkaline hydroxides. Radiometric data obtained in this laboratory (17) show that concentrations of less than 10^{-4} molar carbonate yield coverages of the order of 0.05 which can easily account for observed currents. The adsorption of carbon dioxide tends to suppress the magnitude of the current peaks arising from hydrogen adsorption and oxidation (see region a of Fig. 4) below 0.4V.

In the formation of adsorbed metal oxide, hydroxide surface species represent intermediate forms between states representative of water adsorption and those representative of oxygen adsorption.

The formation of oxides on the surface may be analogous to the formation of the bulk oxides of amphoteric metals. In the bulk systems elevation of the pH normally brings about precipitation of the hydroxide. As the pH continues to increase, the metal hydroxides may lose the elements of water. Also, additional hydroxide may be adsorbed with dissolution of hydroxide precipitates. Both insoluble and soluble species may continue to lose elements of water forming oxides (amphoteric acids).

In some cases, the hydroxide is so unstable that on precipitation, it immediately decomposes to the oxide. For each metal the hydroxide will exhibit a pH of maximum stability which for many transition metals will be quite acid. These hydroxides will maintain gelatinous structures or solid structures containing large quantities of water of hydration. These relatively soft structures form quite stable or inert

"hard oxides" through loss of water which may occur not only by dessication but by change of pH. These hard oxides (*e.g.*, silica, alumina, taconite) display a relatively low chemical reactivity compared with the soft oxides since their structures permit considerable resonance stabilization.

Advanced inorganic texts such as Cotton and Wilkinson (18) do not mention the existence of a divalent platinum of the form Pt(II)O. They point out that the divalent hydrous oxide $Pt(II)(OH)_2$ exists, but it is unstable with respect to Pt and PtO_2. It cannot be expected that the divalent surface oxides exhibit different behavior. In the formation of species such as PtO_2 considerable geometric inversion of oxide sites should be anticipated. These inverted species should therefore be part of the basic structure of the hard oxide. These species should account for the great hysteresis between the oxidation and reduction waves of platinum oxide shown in Fig. 4 and 5.

Bold and Breiter have noticed a flattening of the oxide-reduction peak occurring at about 0.8V (see peaks at b in Fig. 4) in experimental triangular sweep curves at high pH values. In fact, they noticed this change at a pH value even as low as 3. A plausible explanation for this behavior may be found in the fact that the cathodic formation of platinum hydroxide is acid catalyzed (see similar discussion under gold below). The thermodynamics of the reduction do not appear to have changed, since the relative position of the peaks shifts 0.059 mV per unit pH. Only the kinetics are affected.

Linearity of the charge-potential curves on platinum.—A significant feature of the charge-potential curves on platinum (Fig. 7) is their linearity above 0.8V. It is possible to explain this linearity by assuming that multilayer formation of the oxide occurs only after a complete monolayer is formed. It is convenient to discuss the charged oxide surface in terms of dipoles (19). The charging process is visualized to begin with a platinum surface on which is adsorbed a layer of water in roughly equal amounts of the "up" and "down" configuration. This surface state is assumed to have little or no charge due to cancellation of dipole fields. Finally the platinum surface is covered by a monatomic layer of platinum hydroxide and oxide. The positive image of the negative oxide species in the platinum represents the positive end of dipoles making up the double layer. We note that the surface potential (20) is given by the expression

$$\chi = 4\pi n\mu/\epsilon \qquad [7]$$

where n is the number of dipoles (represented by the oxide atom and its positive image) per square centimeter, μ is the effective dipole moment of the individual dipoles, and ϵ is the dielectric constant. Now μ is $2rq$ where q is the charge transfer between the metal and the oxide and r is the radius of the oxide species. Substituting μ into Eq. [7] there is obtained

$$\chi = 8\pi rnq/\epsilon = 8\pi rQ/e \qquad [8]$$

where Q is the charge per square centimeter. But this expression represents precisely a linear behavior between charge and potential which was observed. Differentiation of the potential with respect to Q yields a capacitance per square centimeter which represents the process of placing a monolayer of oxide dipoles with moment, μ, on the surface

$$C = \frac{\epsilon}{8\pi r} \qquad [9]$$

(In cgs units this expression represents the capacity per unit area of the oxide region in cm^{-1}.) Using 1.4Å for the radius (21) based on a doubly charged oxide species, we obtained a calculated value of 134 for ϵ which may be compared to the value *ca.* 80 for water. The result suggests a more highly polarized layer in the oxide due to closer stacking of the atoms.

Effects of pH on gold.—Gold also exhibits profound pH effects. As in the case of platinum, the pH effects may be ascribed to various forms of oxide-containing species, *i.e.*, hydrous and hard oxide forms. The step-potential data (Fig. 9) are most easily explained in terms of the mechanisms described above for platinum. However, the sweep data (Fig. 8) are much more complicated. In acid solution one would expect that the abundance of hydrogen ions might lead to rapid formation of hydroxide species in the reduction wave characterized by the peak occurring at 1.20-1.25V. In alkaline solution the formation of this reduction peak is delayed by a lack of hydrogen ions or by reaction of hydroxide ions with the relatively acidic hydroxide species formed by the gold. In other words, the reduction is acid catalyzed. The oxidation is base catalyzed. These effects are illustrated by the following equations

$$e^- + AuO + H_2O \rightleftarrows AuOH + OH^- \qquad [13]$$

$$Au + OH^- \rightleftarrows AuOH + e^- \qquad [14]$$

Thus the cathodic formation of gold hydroxide is hindered by high pH, whereas the anodic formation on gold hydroxide is aided by high pH in agreement with the results.

Areas of uncertainty associated with errant peaks below 0.9V may arise from the presence of organic adsorbates. These adsorbates may be similar to the reduced carbon dioxide species observed on platinum.

Effects of pH on rhodium.—The most unusual feature of the rhodium data is that enormous quantities of charge appear in the anodic sweep at high pH values. There is some evidence of multiple-layer formation, even at a pH of 2.4. At pH values of 12.7 and 14, a new reduction wave characterized by symmetry with the anodic oxidation wave appears. The reduction peak for oxidized rhodium at *ca.* 0.3V is found at all pH's. The magnitude of the oxidation and reduction peaks at high pH's may be explained by assuming multilayer formation (and some dissolution) because the value of 2 characteristic of the monolayer oxide-hydride charge ratio is far exceeded. The different behavior of rhodium at high pH may be attributed to the amphoteric behavior of the rhodium oxides in the manner described above.

Summary

A potential-step method which makes use of an electronic coulometer has been described. The method indicates the extent of oxide coverage on noble metal surfaces without evidence of hysteresis between the data regardless of whether anodic or cathodic steps are employed. The method eliminates arbitrary procedures previously employed in the evaluation of the total surface charge.

The pH profoundly influences the degree of oxide coverage on several metals. Coverage arising from the adsorption of reduced carbon dioxide increases in the double-layer region with increasing pH at least on platinum. The broadening of the oxide reduction wave of platinum with pH is related to the acid catalyzed reduction of the amphoteric oxide.

The hysteresis observed between anodic and cathodic charge obtained by potential sweep methods on platinum may be due to the formation of inert "hard" oxides.

The linear relationship between potential and charge may arise from uniform oxide build-up on platinum. The dielectric constant of the oxide was calculated on this basis.

Acknowledgment

The authors are pleased to acknowledge the helpful discussions of the techniques and theory of the paper

with Dr. E. Gileadi and Dr. J. O'M. Bockris. In addition they give their thanks to R. J. Bowen for his assistance in times of crisis.

(The opinions or assertions expressed herein are those of the authors and are not to be construed as official or reflecting the views of the Department of the Navy or the naval service at large.)

Manuscript submitted Aug. 15, 1966; revised manuscript received July 27, 1970.

Any discussion of this paper will appear in a Discussion Section to be published in the June 1971 JOURNAL.

REFERENCES

1. W. Bold and M. Breiter, *Electrochim. Acta*, **5**, 145 (1961).
2. F. G. Will and C. A. Knorr, *Z. Elektrochem.*, **64**, 258, 270 (1960).
3. S. W. Feldberg, C. G. Enke, and C. E. Bricker, *This Journal*, **110**, 828 (1963).
4. S. Gilman, "Electroanalytical Chemistry," Vol. 2, pp. 132-189, A. J. Bard, Editor, Marcel Dekker, Inc., New York (1967).
5. F. C. Anson, *Anal. Chem.*, **38**, 54 (1966); **36**, 932 (1964).
6. J. Christie, G. Lauer, and R. A. Osteryoung, *J. Electroanal. Chem.*, **7**, 60 (1964).
7. J. Christie, G. Lauer, R. A. Osteryoung, and F. C. Anson, *Anal. Chem.*, **35**, 1979 (1963).
8. E. Gileadi and B. E. Conway, "Modern Aspects of Electrochemistry," Vol. III, J. O'M. Bockris and B. E. Conway, Editors, Butterworths, London (1964).
9. D. E. Icenhower, H. B. Urbach, and J. H. Harrison, Abstract No. 21 of the Extended Abstracts of Papers of the Battery Division presented at the Buffalo Meeting of the Society, Oct. 1965, Vol. 10, p. 61.
10. J. Giner, *This Journal*, **111**, 376 (1964).
11. S. Gilman, *J. Phys. Chem.*, **67**, 78 (1963).
12. M. W. Breiter, *Ann. New York Acad. Sci.*, **101**, 709 (1963).
13. M. W. Breiter, *Electrochem. Acta*, **8**, 973 (1963).
14. S. B. Brummer and A. C. Makrides, *This Journal*, **111**, 1122 (1964).
15. K. J. Vetter, "Electrochemical Kinetics," p. 118, Academic Press, New York (1967).
16. H. A. Laitinen and C. G. Enke, *This Journal*, **107**, 773 (1960).
17. H. B. Urbach, L. G. Adams, and R. E. Smith, Submitted for publication.
18. F. A. Cotton and G. Wilkinson, "Advanced Inorganic Chemistry," p. 847, Interscience Publishers, New York (1962).
19. H. B. Urbach, *Electrochim. Acta*, **11**, 1651 (1966). See also H. B. Urbach and J. H. Harrison, Abstract No. 22 of the Extended Abstracts of Papers of the Battery Division presented at the Philadelphia Meeting of the Society, Oct. 1966.
20. R. Parsons, "Modern Aspects of Electrochemistry," Vol. I, p. 106, J. O'M. Bockris and B. E. Conway, Editors, Academic Press, Inc., New York (1954).
21. L. Pauling, "Nature of the Chemical Bond," p. 346, Cornell University Press, Ithaca, New York (1948).

Galvanostatic Overpotential Transients and Electrocrystallization Processes on Copper Single Crystals in Solutions of Cupric Sulfate[1]

L. H. Jenkins* and R. B. Durham[2]

Solid State Division, Oak Ridge National Laboratory, Oak Ridge, Tennessee 37830

ABSTRACT

Overpotential transients have been measured on copper single-crystal surfaces oriented (100), (110), (111), or (321) which were undergoing galvanostatic dissolution or deposition in acidic solutions of $CuSO_4$. In the current density range below 800 μA cm^{-2}, it is shown that observed overpotential maxima contained both electrocrystallization and charge-transfer components. Deposited material up to the equivalent of $\approx$50 atom layers affected subsequent anodic overpotential-time relationships in a manner related quantitatively to the extent of the deposit. Overvoltage-current relationships are shown to be insensitive to the densities of steps distributed more or less evenly over the various surfaces, but sensitive to orientation and to arrangements and distributions of steps.

Mattsson and Bockris (1) used galvanostatic measurements to demonstrate that, at geometric current densities $>$ 10 mA cm^{-2}, the Cu^{2+}/Cu^{+} redox reaction was rate determining for a system of polycrystalline copper electrodes in acidic copper sulfate solutions. It was suggested that at lower current densities adion diffusion over the electrode surface became kinetically critical. Bockris and Enyo (2) confirmed these observations and assumed further that the factor defining the limits of surface diffusion control was the number of dislocations intersecting electrode surfaces. Studies of the effects of electrode preparative methods on parameters sensitive to the structure of electrode surfaces in the $Cu/CuSO_4$ system were extended by Bockris and Kita (3). Confirmation that at higher current densities in this system the redox reaction indeed was the slowest process was obtained by Brown and Thirsk (4) using another experimental technique.

All these reports cited concerned systems of polycrystalline copper in acidic copper sulfate solutions and the vast majority of the data and observations reported were obtained under experimental conditions such that surface processes were not rate controlling. Damjanovic, Setty, and Bockris (5) examined growth

* Electrochemical Society Active Member.

[1] Research sponsored by the U.S. Atomic Energy Commission under contract with Union Carbide Corporation.

[2] Cooperative student from the University of Tennessee.

Key words: electrocrystallization, electrodeposition, copper crystals, facets, electrode kinetics.

forms of copper deposited from such solutions on various copper single-crystal surfaces of specific orientation and measured current-potential relationships for the growing surfaces as a function of time. At deposition times corresponding, on the average, to $\sim 10^2$ and 10^5 atom layers of copper over the initial substrate, the overpotentials measured on the surfaces existing at these moments at various geometric current densities indicated the same relationships for electrode kinetics previously reported (1-4). However, small differences due to orientations and/or growth forms were observed and, again, most of the data reported were obtained under conditions such that surface processes could not be considered rate determining. Similar results were obtained by Hayashi *et al.* (6) who also observed effects which were attributed to the "free acid" content in both cupric perchlorate and cupric sulfate solutions. Recently data have been reported for single crystalline copper electrodes in acid cupric perchlorate systems under experimental conditions such that surface processes were rate determining and initial surfaces were not altered appreciably before data pertinent to establishing electrode kinetics were obtained (7). Also, it was shown that relatively thin electrodeposits did not behave exactly as the substrates supporting them. These latter data and their interpretations are in sufficient disagreement with the previously suggested models of surface processes on copper electrodes (2, 3, 5) to make desirable a similar study in copper sulfate solutions at reaction rates lower than were previously examined in detail.

Materials and Experimental Methods

The growth, manipulation, surface preparation, and final electropolishing and washing of the copper crystals used in this work were as previously reported (7-9). Solutions 0.20M in $CuSO_4$, pH adjusted to ≈ 1 by addition of H_2SO_4, were used in all these studies and their preparation, storage, transfer to reaction cells, etc., were also in the manner previously described (7, 10). The two types of reaction cells used, one for obtaining galvanostatic current-potential data and the other permitting microscopic observation and photography of reacting surfaces, were the same as those used in the $Cu/Cu(ClO_4)_2$ systems (7).

Experimental Results

Changes in surface structure.—Observations of changes in surface structures resulting from both dissolution and deposition processes on surfaces oriented (100), (110), (111), and (321) were made and photographed. While data were taken in duplicate for both anodic and cathodic processes on all orientations at 4, 40, and 400 $\mu A\ cm^{-2}$ original surface area, the structural changes observed did not differ enough from those reported for perchlorate systems to warrant extended comment. However, the following comparisons of observations between the two systems are of interest:

(a) Structures developed on the (100) in the sulfate system seemed of about equal size after passage of equivalent charge at the two higher current densities for both deposition and dissolution. This was not observed in perchlorate solutions in which relatively smaller structures with more sharply defined singularities developed on the (100) at progressively higher current densities.

(b) The detailed structure and orientations developed on (110), (111), and (321) were similar in every case in either perchlorate or sulfate systems: Reaction on the (111) occurred by the bunching of steps to form ledges, the (110) developed sharply defined typical ridge-valley arrangements, etc. However, it was noted in sulfate solutions that the relative sizes of structures developed on all orientations other than (100) decreased with increasing current density as compared with those grown under comparable circumstances in perchlorate.

Figure 1 illustrates the structures obtained on the (100) at current densities of 4 $\mu A\ cm^{-2}$. At such low reaction rates, occasional pits or pyramids would develop faster than the rest of the surface. However, as could best be determined, initial deposition or dissolution and early growth stages occurred uniformly over the surface. Note that pit edges, preferred growth direction, etc., are not nearly so well defined in the anodic as in the cathodic case. As stated earlier, structural development of characteristic features at higher current densities occurred completely uniformly over the surface. The figure also illustrates the ledges formed by step aggregation due to deposition at 400 $\mu A\ cm^{-2}$ on the (111). Large, flat areas can be seen clearly separated by relatively low ledges.

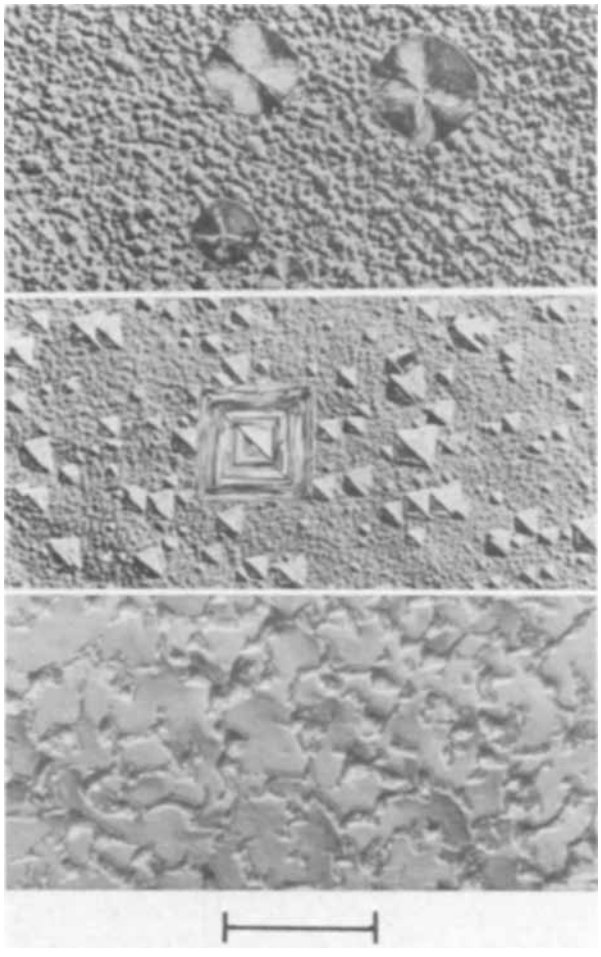

Fig. 1. Upper and middle photomicrographs illustrate structures developed on the (100) due to dissolution and deposition, respectively, at 4 $\mu A\ cm^{-2}$ to the extent of 1.7 coulombs cm^{-2}. The lower illustration is of a (111) after deposition at 400 $\mu A\ cm^{-2}$ to a total of 1.4 coulombs cm^{-2}. The reference mark is equivalent to 4μ in the upper two photographs and to 20μ in the lower.

Current-potential data.—Under galvanostatic conditions, overpotential *vs.* time curves exhibited maxima of the type reported for perchlorate solutions. Also, as in those solutions, a "deposition anomaly" was observed in that times to formation and absolute values of overpotential maxima were changed if the immediately preceding process on the electrode had been deposition. These phenomena are discussed later, but it must be understood that all overpotential relationships discussed as a function of current density are, first of all, values of the observed maxima. Secondly, following every cathodic process on surfaces on which current *vs.* potential data were being determined, an anodic pulse of equal intensity and duration was applied. This latter pulse was disregarded and equilibrium established in the system before the next electrode process of interest was initiated and data recorded.

Figure 2 illustrates the current *vs.* potential relationships obtained for surfaces of the indicated orientations. The treatment given the copper crystals before mounting in the cells was exactly that of those in the previously reported perchlorate systems. The crystals were never annealed after growth and the final pre-experimental treatment consisted of the normal electropolish in an acid copper phosphate bath, followed by standard washing procedures. For purposes of later discussion, these will be termed "standard" surfaces. Obviously it was impossible to focus on these flat, specular surfaces with the microscope in order to obtain meaningful photomicrographs.

Since one of the authors had previously argued that overvoltage *vs.* time and/or current values were changed drastically by the arrangement and distribution of steps over crystal surfaces (7), current *vs.* potential measurements were also obtained on other than standard surfaces. Figure 3 shows such data for surfaces produced by annealing standard surfaces under an H_2 atmosphere at 400°C for 4 hr. Following annealing, all surfaces appeared unchanged to the eye and, while with the optical microscope examinations of these "standard annealed" surfaces showed no observable changes on (100) and (110) orientations, small facets were detected on the (111) and (321). Facet development on the (111) is illustrated in the phase-contrast photomicrograph shown in Fig. 4. The low facet density can be seen and interference fringe shift measurements indicated the average facet to be $\approx 0.1\mu$ high.

Mechanical polishing always leaves fine scratches in the surfaces of soft metals such as copper and these scratches afford sites for possible facet development. Therefore, mechanically polished surfaces, although bright and mirrorlike to the eye, were given a standard electropolish and wash treatment in order to remove $\approx 10\mu$ from the surface in case any impurities were introduced by the mechanical polish. The crystals then were annealed in an H_2 atmosphere at 950°C

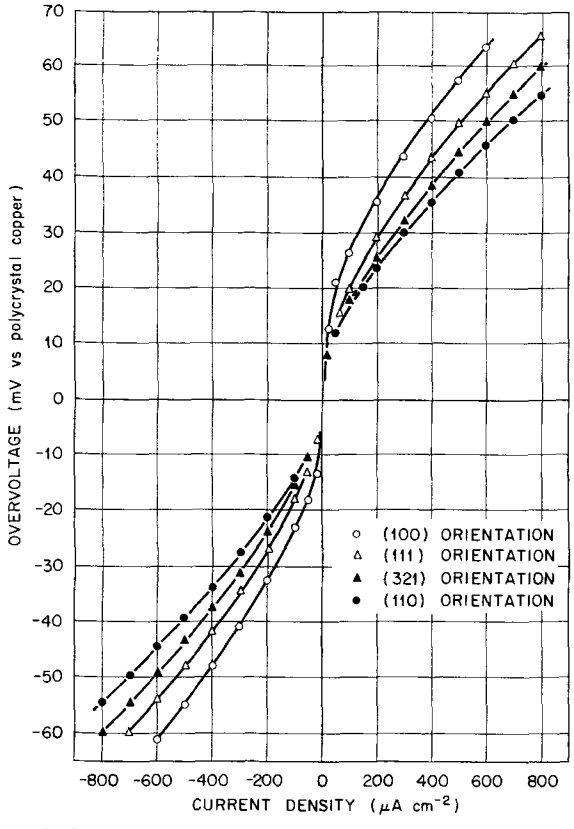

Fig. 2. Overvoltage *vs.* current relationships for "standard" copper single-crystal surfaces in 0.2M $CuSO_4$ + H_2SO_4 (pH $\approx$ 1) at 23°C.

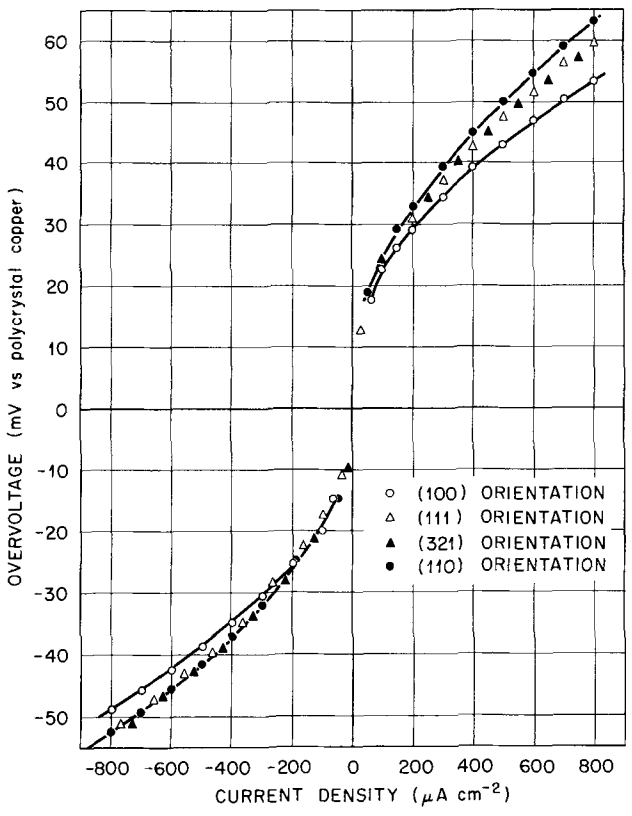

Fig. 3. Overvoltage *vs.* current relationships for "standard annealed" copper single-crystal surfaces in 0.2M $CuSO_4$ + H_2SO_4 (pH $\approx$ 1) at 23°C.

for 16 hr. Following annealing, the samples again appeared bright and flat to the eye, but microscopic examination revealed that all surfaces contained facets whose development was related to, among other things, the mechanical polish. For purposes of comparison, the (111) surface treated in this manner is also shown in Fig. 4. The effects of the mechanical polish are evident in the long, ridged facets. Average structures on all orientations were $\approx 1\mu$ high, although differing markedly, of course, in detail from the (111) illustrated. The current-potential relationships obtained on these "mechanically treated" surfaces are illustrated in Fig. 5.

Finally, in order to develop a high degree of faceting on all surfaces, standard surfaces were vacuum annealed at 950°C for 24 hr so that thermal facets could develop. Following this treatment, all surfaces appeared changed to the eye since facets had grown to such an extent. The (321) and (110) had a milky-pink appearance due to an extremely high density of very small facets estimated to extend less than 0.1μ in any direction and with no preferred orientations developed. Both the (111) and (100) were completely covered by pits which on the (111) were semihexagonally shaped. Pits on the (100) are illustrated in Fig. 4. Pits on the (111) were not quite as well formed as those on the (100) and the former also had a relatively smaller density of the larger pits observed on the latter. The largest pits observed on either surface were less than 2μ deep. The detail in all the illustrations is due to the characteristics of interference-contrast photomicrography, and the sides of the deepest pits on the (100) illustrated in Fig. 4, for example, were only 2° at most from horizontal to the original surface. Current *vs.* potential relationships obtained for these samples are indicated in Fig. 6.

Potential vs. time data.—In general, the potential-time relationships observed for standard crystal surfaces in the sulfate solutions reported here were the same as those previously observed in perchlorate solutions (7) where the same type of surface was used

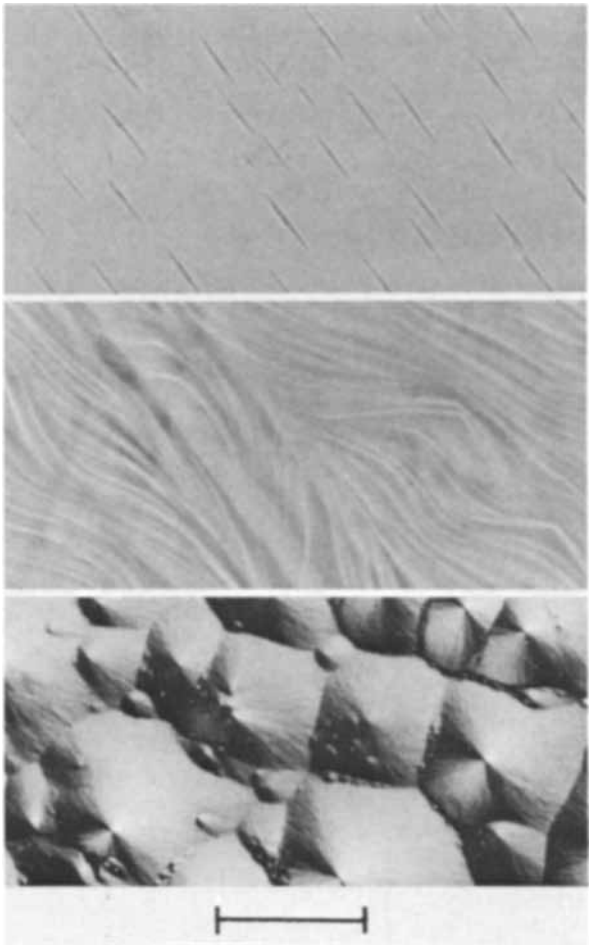

Fig. 4. Upper and middle photomicrographs are of (111) surfaces which were "standard annealed" and "mechanically treated," respectively. The lower illustrates pits on a "vacuum-annealed" (100). The reference mark is equivalent to 25, 50, and 100μ, top to bottom.

exclusively and where it was shown that maxima were established long after the time required to charge the double layer. Also, similar to the latter systems, it was observed that deposition on a standard surface produced anomalous effects on following anodic voltage-time relationships which could persist for periods up to hours unless all the deposited material was removed by an anodic pulse. Not only were times to establishment of succeeding anodic maxima delayed until the time at which the previous deposit had been removed, but also the absolute values of overvoltage maxima were decreased. Since no significant differences were noted in sulfate systems from the well-documented evidence previously reported, oscilloscope traces of voltage-time transients illustrating the phenomena are not shown. However, the effect was observed not only on all standard surfaces, but also on standard annealed and mechanically treated surfaces at current densities of 50, 150, and 450 μA cm^{-2} for deposits equivalent to an average of 50 atom layers. The largest current density or thickest deposit at which the effect could be obtained on these surfaces was not established. However, although the phenomena were observed on all vacuum-annealed surfaces at 50 and 150 μA cm^{-2}, and for all but the (321) at 300 μA cm^{-2}, the effect on all such surfaces ceased to be quantitative at about 150 μA cm^{-2}. Thus it seems established that, also in sulfate solutions, material initially deposited did not diffuse rapidly over the surface to kink-step sites and become indistinguishable from the substrate material.

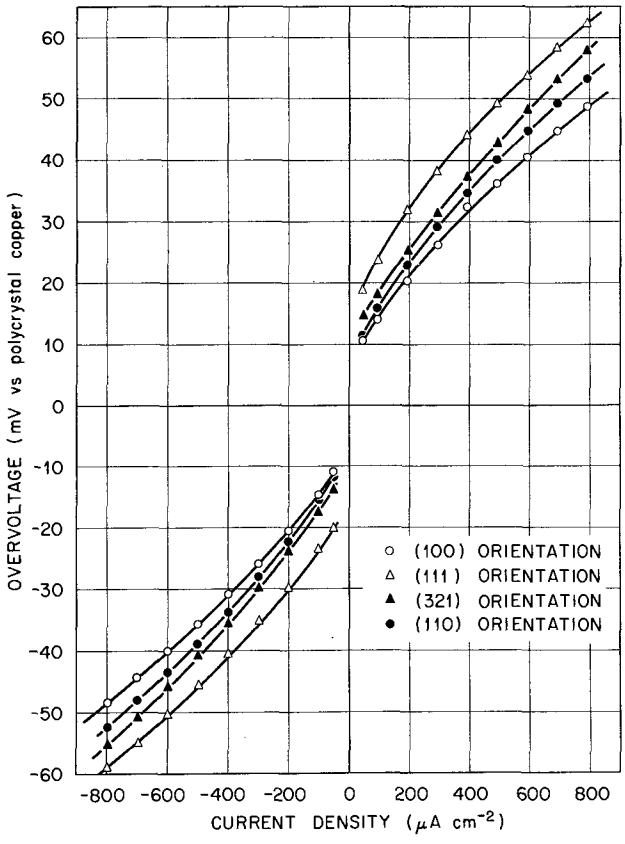

Fig. 5. Overvoltage vs. current relationships for "mechanically treated" copper single-crystal surfaces in 0.2M $CuSO_4$ + H_2SO_4 (pH $\approx$ 1) at 23°C.

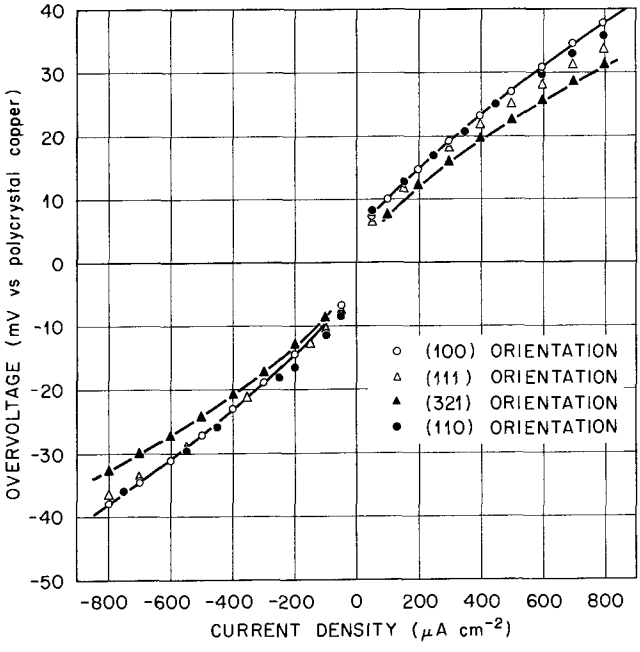

Fig. 6. Overvoltage vs. current relationships for "vacuum-annealed" copper single-crystal surfaces in 0.2M $CuSO_4$ + H_2SO_4 (pH $\approx$ 1) at 23°C.

Discussion

Overpotential maxima and current density relationships.—Three reactions must be examined in the systems reported here: a redox reaction

$$Cu^+ \leftrightarrows Cu^{2+} + e \qquad [i]$$

the reaction between adatoms and cuprous ions

$$A \leftrightarrows Cu^+ + e \qquad [ii]$$

and the exchange of adatoms with the metal lattice

$$M \leftrightarrows A \qquad [iii]$$

Previously (7) it was shown that, although transient processes, maxima treated in the manner of steady-state phenomena would yield the relationship

$$2\eta = \frac{RT}{\mathbf{F}} \ln \frac{(\hat{a}_{Cu2+})}{(\hat{a}_{Cu2+})_{eq}} + \eta_i + \eta_{ii} + \eta_{iii} \qquad [1]$$

where η values are either the total overvoltage measured, or that associated with the reaction appropriate to the subscript notation, and other symbols represent their usual quantities. Also, it should be noted that Vetter's (11) definition of crystallization overvoltage, η_c, is such that

$$\eta_c \equiv \frac{RT}{\mathbf{F}} \ln \frac{(\hat{a}_A)_{eq}}{(\hat{a}_A)} = \eta_{iii} \qquad [2]$$

Others (1-6) have shown that, at higher current densities than those reported here, reaction [i] was the rate-controlling process and, further, that $2\eta = \eta_i$, which as Bertocci (12) pointed out required that $(\hat{a}_{Cu2+})$ not depart from the equilibrium value and that reaction [ii] occur completely reversibly ($\eta_{ii} = 0$). But, obviously, it is also required that $\eta_{iii} = 0$, if the explanation of the data at higher current densities is valid.

On the basis of the deposition anomaly observed in perchlorate systems, which was interpreted to mean that deposited atoms did not occupy half crystal positions and further possessed adatom-like character, and also because of the measured relatively high overvoltages, it was assumed that maxima were established before reaction [iii] had occurred to a significant extent and that $\eta_i \to 0$. The model seemed justified (7) since the data could be treated by the expression

$$i = K\left\{\exp\left[\frac{\alpha z \mathbf{F}\eta_*}{RT}\right] - \exp\left[\frac{-(1-\alpha)z\mathbf{F}\eta_*}{RT}\right]\right\} \qquad [3]$$

where i = current density
K = an orientation-sensitive factor with the dimensions of current density
α = a transfer coefficient which can be orientation sensitive
z = a factor relating the observed overvoltage maxima to the electrocrystallization overvoltage
η_* = value of overpotential maxima

and the remaining terms have their usual significance. In the perchlorate systems $\alpha = 0.50$ for orientation with symmetrical anodic and cathodic current-potential relationships and, of course, z had a value of 2 since the assumptions that $\eta_i \to 0$, $(\hat{a}_{Cu2+}) = (\hat{a}_{Cu2+})_{eq}$, and η_{ii} established that $2\eta = \eta_{iii}$.

Under the experimental conditions reported here, it is only reasonable to assume that certainly the cupric ion activity did not depart from the equilibrium value and that the value of η_{ii} remains zero. Therefore, the expression to be considered is

$$2\eta = \eta_i + \eta_{iii} \qquad [4]$$

and the response of the data to treatment by Eq. [3] will determine whether $\eta_i \to 0$.

Standard surfaces.—However, since the overvoltages measured on standard orientations in sulfate solutions are much lower than those for corresponding conditions in perchlorate solutions, it would seem unlikely that in the range of current densities studied here the situation should be realized in which $\eta_i \to 0$. That this assumption is valid is illustrated by treating the overpotential maxima data from standard surfaces in the manner shown in Fig. 7. (Note that a value of 0.5 is assumed for α since the data illustrated in Fig. 2

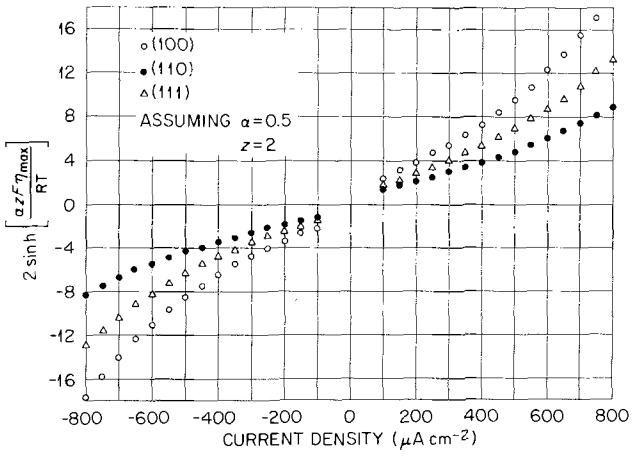

Fig. 7. Relationships between functions of overpotential maxima and current densities for "standard surface" data shown in Fig. 2. All symbols have their usual significance except for z which is a factor relating the crystallization overvoltage to the measured value.

have symmetric anodic and cathodic branches and, therefore, in sulfate systems α is not orientation dependent.) As opposed to the perchlorate case, both anodic and cathodic data from a given orientation do not fall on a straight line passing through the origin. It seems clear that, in sulfate systems, low current density overpotential maxima contain components of both η_i and η_{iii} and that $2\eta \neq \eta_{iii}$. The maxima themselves of course reflect the departures from equilibrium activities of cuprous ions at the interface and adatoms on the metal surface, again as in the perchlorate systems, and the subsequent changes in activities of these two species in an effort to establish the desired steady-state conditions. Other qualitative differences noted between standard data in the two solutions is that, while in both cases higher maxima were established on the (100) than on any other surface, in sulfates the (110) is displaced lower than in perchlorate with respect to the (111) and (321). Also, the asymmetry of (111) and (321) cathodic branches seen in perchlorate systems is not found in the sulfate where all standard orientations had symmetric anodic and cathodic branches. This suggests it would be easier to grow more perfect crystals over these two substrates in sulfate solutions, if the explanation advanced for the cause of asymmetry in perchlorates is correct (7).

Overpotential maxima and surface types.—Although comparison between current-potential curves of a single orientation from different types of surfaces in sulfate systems is difficult due to the manner in which the data are shown, by consideration of Fig. 2, 3, 5, and 6 the following relationships can be verified:

(*a*) Vacuum-annealed surfaces of all orientations yield data considerably different from those obtained on surfaces prepared in other ways.

(*b*) Only standard annealed surfaces produced results which showed a significant asymmetry between anodic and cathodic branches of any one orientation, and all orientations so treated yielded cathodic data which were slightly lower than their anodic counterparts.

(*c*) Both anodic and cathodic branches of (321) data were little affected by any method of surface preparation other than vacuum annealing.

(*d*) Anodic data from standard, standard annealed, and mechanically treated (111) surfaces differ only slightly from each other. However, the cathodic branches of these three surfaces differ significantly, particularly so in the differences of the latter two types from the first.

(*e*) Standard and mechanically treated (110) surfaces yield almost identical data. While cathodic data

from the standard annealed surface do differ from the two former, the anodic portion of the curve shows the highest values observed for any orientation treated in this manner. Indeed, this (110) is the only example observed in which any other than standard treatment created a significant increase in overpotentials over the entire current density range.

(*f*) All other (100) surfaces produced results markedly different from those obtained on the standard (100).

Initially it might be thought that the great differences in current-potential characteristics measured on vacuum-annealed surfaces could be due to changes in surface area. However, consider the extreme case; the dimensions of the pits on the (100) illustrated in Fig. 4, the most heavily faceted surface of all tested, can be shown from simple geometric considerations to increase the surface area from that of the original (considered to lie in the plane of the page) only by $\approx 0.1\%$!

As previously pointed out (7), standard surfaces could not be prepared absolutely flat, but contained gentle long-range undulations such that over the surface the orientation deviated $\approx \pm 0.1°$ from that desired. For purposes of estimation of average monatomic step densities resulting from such slight misorientations, the low index orientations of copper which all contain in excess of 10^{15} atoms cm^{-2} can be considered from the standpoint of fcc hard ball models. Again simple geometric relationships can be used to demonstrate that deviations of 0.1° from a low index plane result in an average monatomic step density of $\sim 10^5$ cm^{-1} due solely to this slight misorientation. Similar relationships show that the average step density arising from misorientation in the pits illustrated in Fig. 4 was $\sim 10^6$ cm^{-1}. However, the hard sphere model reveals that the standard (321) step density approaches 10^7 cm^{-1}; moreover, the steps are continuously kinked such that no atom on a step occupies a half lattice position. Further, neither removal nor addition of material at steps can alter this situation if the orientation is maintained. Thus it seems an unavoidable conclusion that the magnitudes of overpotential maxima were not directly related to average step densities of the various orientations or to the meager changes in surface areas produced by facet formation, and that a barrier exists to reaction at steps. However, large differences related solely to orientation could be observed.

The small differences in anodic data on the (111) surfaces prepared by other than vacuum annealing also suggest maxima were established before significant reaction at steps had occurred. However, the cathodic behavior of other than standard surfaces indicates that deposition occurred over the facets as well as on the (111). The rather extreme sensitivity of both anodic and cathodic processes on the (100) and (110) orientations to method of surface preparation could indicate that facets formed on these orientations serve as preferred sites for supporting the electrode processes. These observations agree with the conclusions reached for perchlorate systems that surface processes such as diffusion and/or step motion seem to be much more difficult over the (100) and (110) than on the (111) and (321).

The observance of the deposition anomaly on the standard (321), as well as on the highly faceted, vacuum-annealed (100), surely must indicate that initial deposition at these low current densities did not occur by the diffusion of adatoms to steps where they were incorporated into the lattice, even on a surface with near maximum step density. Some barrier to diffusion and/or incorporation must be overcome before this can occur. It would appear then that attempts to grow more perfect crystals over like substrates should be made at higher current densities than those reported here, since direct reaction at steps (ledges) under the former conditions is a well-documented phenomenon (13).

It should be said that the term "standard" surface was selected solely because this method of electrode preparation is so universally used. There is no intent to imply that only such surfaces yield data useful in the study of electrocrystallization kinetics. However, it does seem significant that only surfaces prepared in this manner permitted duplication of data from one experimental cell to another. Still, it is quite possible that the practical lower limit of $\sim 10^5$ steps cm^{-1} arising from unavoidable, very slight misorientations from close-packed orientations on any surface prepared in this manner already is too great to afford a true indication of the effects of a few steps spaced more or less uniformly over the surfaces. However, a lack of correlation between average step densities and the magnitude of overvoltage maxima does seem well established. Conversely, it is equally clear that maxima are extremely sensitive to the manner in which steps are arrayed over surfaces, for, although the standard (321) had a higher step density than any other-than-standard surface, all the latter, with but two minor exceptions, exhibited lower overvoltages at comparable current densities. These relationships must have resulted solely from the arrangements of steps over the surface since surface areas remained essentially unchanged in all systems. It is only reasonable to conclude that, given a certain number of steps on a surface, observed overvoltages decrease as step interactions increase to form ledges and/or facets. Since the relative sizes of maxima decrease with decreasing overvoltage such that they also form and decay quite slowly at overvoltages $\simeq$ 10 mV, it is not surprising that they are either unobserved or identified as "pseudo steady state" on surfaces highly faceted as a result of extensive measurements at high reaction rates.

The ranges of higher current densities and overpotentials reported here correspond to the lowest ranges measured by Bockris and Enyo (2) and Bockris and Kita (3), where charge-transfer was not the rate-determining process. Their preparative treatments and the extent of processes necessarily sustained by their electrodes in order to supply the data suggest the research was conducted on surfaces resembling more the vacuum-annealed structures than any others in this present study. Comparison of data in Fig. 6 with those illustrated in Fig. 2, 3, and 5 indicates then that the conclusions of Bockris *et al.* regarding surface processes such as adion diffusion rates, charge-transfer rates on various types of surfaces, relative adion concentrations, predominance of (100) orientations, *etc.*, all must be regarded, at best, as highly speculative because of the uncertainties of the structures of the electrodes yielding the data.

Manuscript submitted July 1, 1970; revised manuscript received *ca.* Aug. 17, 1970.

Any discussion of this paper will appear in a Discussion Section to be published in the June 1971 JOURNAL.

REFERENCES

1. E. Mattsson and J. O'M. Bockris, *Trans. Faraday Soc.*, **55**, 1586 (1959).
2. J. O'M. Bockris and M. Enyo, *ibid.*, **58**, 1187 (1962).
3. J. O'M. Bockris and H. Kita, *This Journal*, **109**, 928 (1962).
4. O. R. Brown and H. R. Thirsk, *Electrochim. Acta*, **10**, 383 (1965).
5. A. Damjanovic, T. H. V. Setty, and J. O'M. Bockris, *This Journal*, **113**, 429 (1966).
6. T. Hayashi *et al.*, *J. Electrochem. Soc. Japan*, **37**, 64 (1969).
7. L. H. Jenkins, *This Journal*, **117**, 630 (1970).
8. F. W. Young, Jr., and T. Wilson, *Rev. Sci. Instr.*, **32**, 559 (1961).
9. L. H. Jenkins and U. Bertocci, *This Journal*, **112**, 517 (1965).

10. L. H. Jenkins and J. Stiegler, *ibid.*, **109**, 467 (1962).
11. K. J. Vetter, "Electrochemical Kinetics," Academic Press, New York (1967).
12. U. Bertocci, *Electrochim. Acta*, **11**, 1261 (1966).
13. F. W. Young, Jr., and L. D. Hulett, Jr., "Metal Surfaces," W. D. Robertson and N. A. Gjostein, Editors, Am. Soc. Metals, Metals Park, Ohio (1963).

Reduction of Oxygen on Teflon-Bonded Platinum Electrodes

W. M. Vogel* and J. T. Lundquist

Advanced Materials Research and Development Laboratory, Pratt & Whitney Aircraft, Middletown, Connecticut 06458

ABSTRACT

By using specially prepared Teflon-bonded electrodes, it was possible to eliminate the internal *IR* drop across the porous electrode and the concentration overvoltage associated with diffusion of oxygen in the gas filled pores of the electrode structure. After this elimination, the apparent exchange current and kinetic parameters for the reduction of oxygen on Pt-black in KOH, H_2SO_4, and H_3PO_4 electrolytes can be determined by using Tafel plots. The data indicate that although the rate of the transfer reaction is the same in the two acids, H_3PO_4 is the poorer electrolyte for an acid fuel cell because of the much slower transport of oxygen. The kinetic data differ only moderately from those reported for smooth Pt surfaces.

A problem common to the development of fuel cell electrodes and to the evaluation of electrocatalysts has always been the difficulty of separating the effects of the electrode structure from the intrinsic activity of the catalyst. In the past this problem has been attacked theoretically by assuming a model.

Generally, the theoretical approach is in effect a method of curve fitting, employing a large number of adjustable parameters. The rather ambiguous results obtained exclusively in this way are, not surprisingly, usually of little value. To reduce the number of these parameters we can use kinetic data obtained on smooth surfaces of the catalyst. Even if such a surface can be prepared, we cannot assume that the catalytic properties, referred to unit true area, are the same for platinum black as for smooth Pt. In addition, of course, it is extremely difficult to eliminate impurities from the electrolyte to such an extent that they no longer influence the O_2 reduction reaction on smooth surfaces. As a result of these difficulties, in many instances neither the intrinsic activity of the electrocatalyst nor the structural details of a given electrode could be determined. There is, therefore, a critical need for additional tools with which to study catalyst blacks and porous electrode structures. This paper describes a new approach to this problem.

The aim was to determine, for a given platinum black, the kinetic parameters of the oxygen reduction free of ohmic and transport limitations. We used Teflon bonded electrodes (1) for this purpose. For very thin electrodes of this type the internal *IR* drop across the electrode and the concentration changes in the gas phase should both be negligible. The electrode thickness should be proportionate to the catalyst loading, *L*, if the Teflon content is constant and if the structure does not change. Under these conditions plots of current density *vs. L* should have linear portions at low loadings. Tafel plots of the initial slopes of these curves (dimension current/unit weight) are the *IR*-free polarization curves, reflecting transfer polarization and concentration overvoltage associated with diffusion of oxygen in the liquid filled pores of the electrode structure. By superimposing the Tafel plots of electrodes of different catalyst content, it is possible to cover a very wide range of current densities. The apparent exchange current and kinetic parameters of the oxygen reduction can be determined from these composite plots.

Experimental

It is essential when employing the procedure just outlined that electrodes be made in such a way that a change in the loading does not produce a qualitatively different structure. Ideally only the electrode thickness should vary. The experimental results indicate clearly whether one is successful in this undertaking. However, we know of no method which will predictably produce the desired results.

It was found that a number of different methods produce satisfactory electrodes. The kind described below were found to be the easiest to make and the most reliable.

A layer of Teflon of approximately 1 mg/cm^2 was sprayed on aluminum foil. The spray mixture was prepared from Teflon 30 (E. I. du Pont de Nemours), containing 60 w/o (weight per cent) solid and 6 w/o Triton X-100, by diluting approximately 1:1 with distilled water. This layer was air dried, vacuum dried, and subsequently sintered to produce a thin porous sheet of TFE. Upon this layer was sprayed catalyst containing Pt-black (Engelhard Industries) and 30 w/o TFE. The catalyst spray mixture was made by first barely wetting the dry Pt-black with water, adding the required amount of Teflon 30 and further adding water to produce a relatively thick soupy consistency of the mix. At 30 w/o TFE content the maximum performance at high currents was obtained, falling off at higher and lower values. The catalyst layer was air dried at 60°C and then lightly compacted with a roller pressed down by hand. Subsequently the electrode was vacuum dried at 150°C for 30 min and finally sintered in air at 250° to 310°C for 5 min. A current collector screen was pressed lightly into the catalyst layer. The screen material was pure nickel (for experiments in KOH) or gold plated tantalum (for acids). Finally the aluminum foil was dissolved by treatment with the respective electrolyte to be used. The electrode was washed with distilled water and dried at 120°C.

The test electrodes were mounted in a screw cap holder, and current pick up was made via a platinum ring in contact with the current collector screen of the electrode. The electrode holder was made of Plexiglas (Rohm and Haas) for use in KOH or of Lexan (General Electric Company) for use in the acids.

The reference was a hydrogen electrode in the same medium used in conjunction with a Luggin capillary.

* Electrochemical Society Active Member.

Key words: cathodes—fuel cell, fuel cell cathodes, porous electrodes, oxygen reduction, platinum black.

The cell was a 500 ml jacketed glass reaction kettle. The temperature was controlled by means of an external circulating constant temperature bath. Reagent grade chemicals were used without further purification and solutions were prepared using singly distilled water. The instrumentation consisted of standard commercially available equipment.

Electrode potentials, E^*, were measured at constant current against a hydrogen electrode in the same medium. The applied current was established in less than 3 μsec and was constant within 1%. The external IR drop between electrode surface and Luggin capillary was determined by the interruptor method.

The electrodes were prepolarized for a few seconds at a potential of approximately 500 mV to remove the initial oxygen coverage from the platinum surface. The potentials were measured after about 1 min and were stable for at least 10 to 15 min.

The specific surface area of the Pt-black is being determined routinely by another laboratory at Pratt & Whitney Aircraft using the hydrogen stripping and the BET methods. Both methods give the same results. The particular black used by us had a surface of (24 $\pm$ 2) m^2/g. This value was rechecked on finished electrodes and found to be the same as for the original Pt-black.

Results

Typical experimental results are presented in Fig. 1-4 for 85% H_3PO_4 at 120°C for oxygen (1 atm) and for air (1 atm) respectively. Similar data were measured in 30% KOH, 20% H_2SO_4 and in 50% H_3PO_4, all at 70°C and with oxygen and air. The data follow the same general pattern as those in Fig. 1-4.

Within the initial approximately linear portion of these curves the internal IR loss is very small, certainly smaller than the reproducibility of the results. This means that the potential does not change across the thickness of the electrode, and it is physically meaningful to normalize the data by dividing the observed currents by the catalyst loading. The resulting specific current, i_m (per mg of catalyst), is proportional to the true current density at the Pt-electrolyte interphase if the concentration overvoltage is negligible, *i.e.* at low currents and especially on pure oxygen.

Semilogarithmic plots of specific current *vs.* potential, obtained from data for several electrodes of differ-

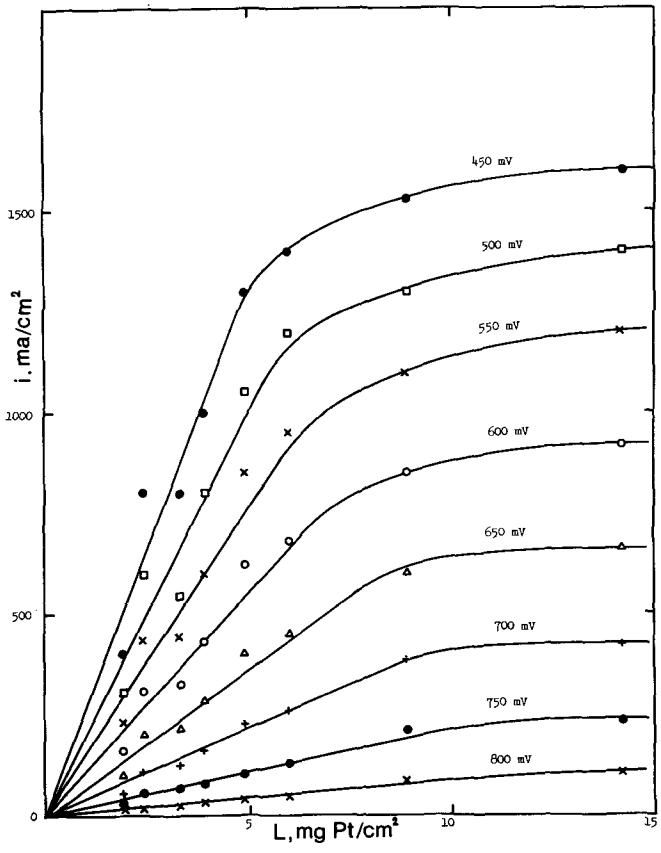

Fig. 2. Performance curves on air; 85% H_3PO_4, 120°C

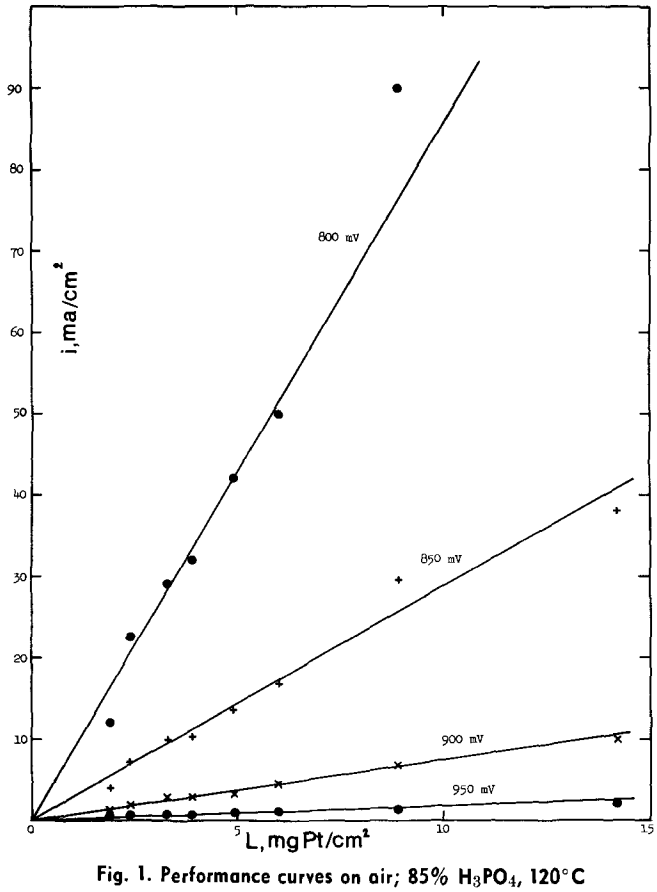

Fig. 1. Performance curves on air; 85% H_3PO_4, 120°C

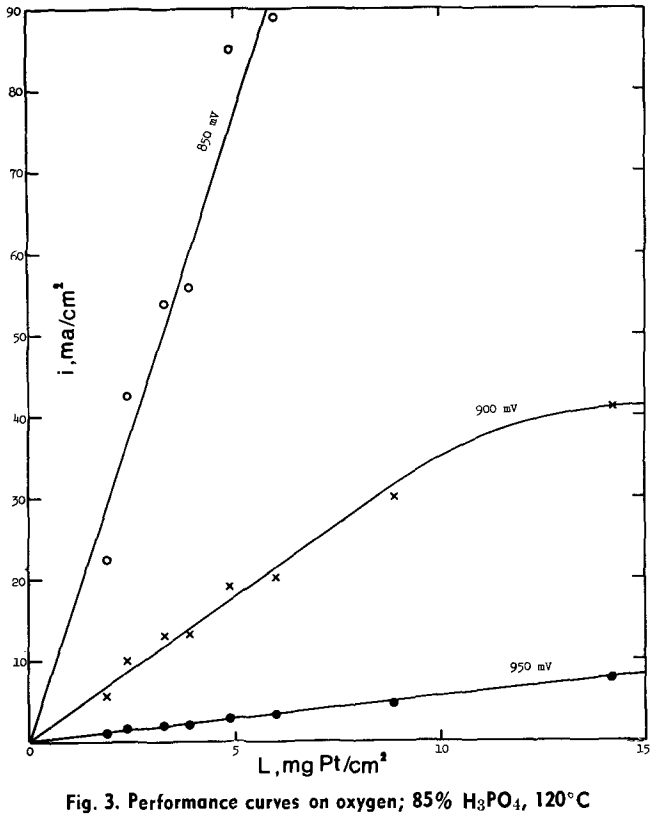

Fig. 3. Performance curves on oxygen; 85% H_3PO_4, 120°C

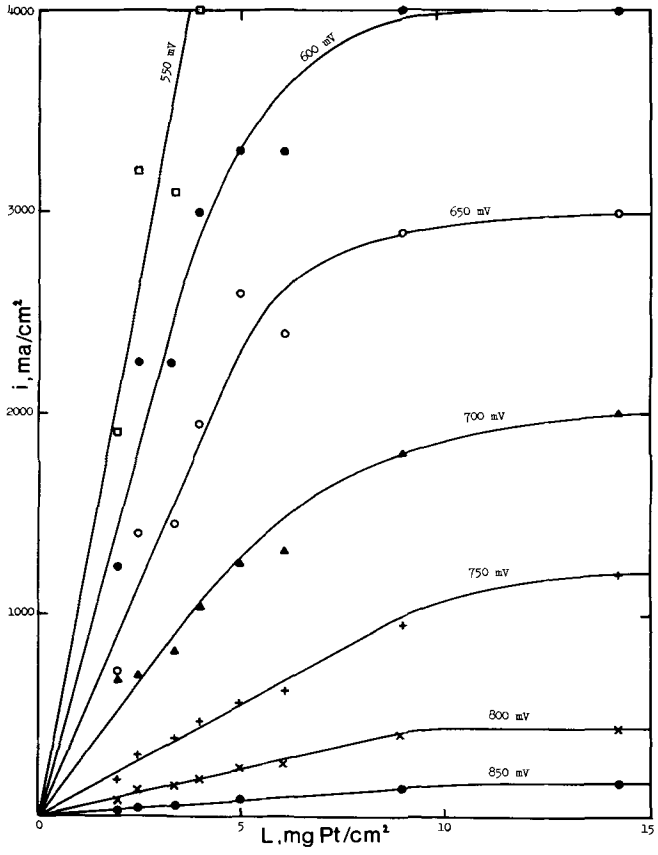

Fig. 4. Performance curves on oxygen; 85% H_3PO_4, 120°C

ent loadings are presented in Fig. 5 and 6. The curves on oxygen (Fig. 5) show linear portions of two (H_3PO_4) to four orders of magnitude, allowing us to calculate apparent exchange currents referred to unit

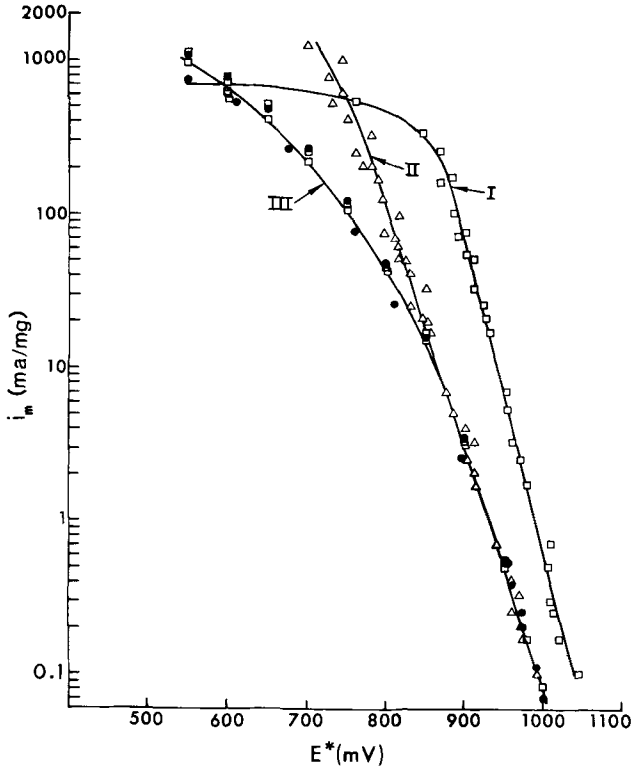

Fig. 5. Polarization curves for oxygen; curve I: 30% KOH, 70°C, curve II: 20% H_2SO_4, 70°C, curve III: 50% H_3PO_4, 70°C (●) and 85% H_3PO_4, 120° C (■).

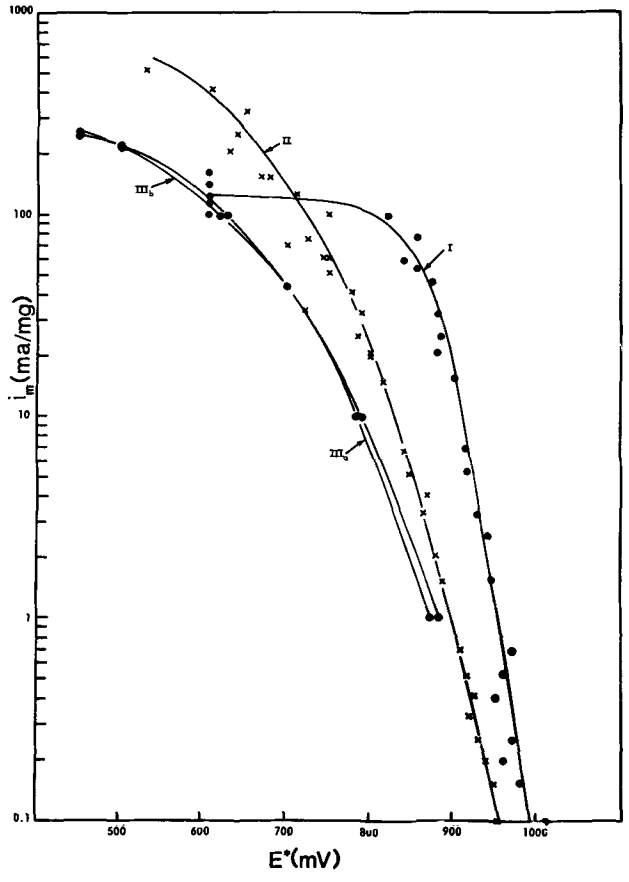

Fig. 6. Polarization curves for air; curve I: 30% KOH, 70°C, curve II: 20% H_2SO_4, 70°C, curve IIIa: 85% H_3PO_4, 120°C, curve IIIb: 50% H_3PO_4, 70°C.

weight of catalyst $(i_o)_m$ and Tafel slopes, b.

The results are summarized in Table I. Values for $(i_o)_m$ and b were also obtained by analyzing the oscillographic traces after current interruption. For this purpose we assumed that the only process taking place after interruption is the charging of the double layer, assuming constant double layer capacity C^*. We further assumed that the concentration overvoltage remains constant. These two assumptions restrict the analysis to potentials below approximately 800-850 mV and to relatively short times. Under these conditions, the method is that developed by Frumkin (3). This method involves plotting potential E^* *vs.* log $(K_2 + t)$ according to

$$E^* = K_1 + b \log (K_2 + t)$$

$$K_1 \equiv b \log (2.3\ kc/b\ C^*)$$

$$K_2 \equiv (b\ C^*/2.3\ kc) \exp [2.3\ E^*\ (t = 0)/b] \quad [1]$$

where k is a constant and c is the concentration of oxygen at the metal-liquid interface. In Fig. 7 plots of

Table I. Values for the apparent exchange currents and Tafel slopes at $P_{O2} + P_{H2O} = 1$ atm obtained from steady state data

Electrolyte	Temperature	b (mV)	$(i_o)_m$ (mA)/mg	i_o' amp[a]/cm²	$E^*_{eq.}$ (mV)[b]
30% KOH	70°C	50 ± 5	7 × 10^{-5}	3 × 10^{-10}	1195
20% H_2SO_4	70°C	64 ± 5	9 × 10^{-5}	4 × 10^{-10}	1186
50% H_3PO_4	70°C	60 ± 5	8 × 10^{-5}	3 × 10^{-10}	1191
85% H_3PO_4	120°C	60 ± 5	11 × 10^{-5}	5 × 10^{-10}	1175

[a] Apparent exchange C.D. referred to unit true Pt surface area; calculated with 24 m²/g for specific surface area of the Pt black.
[b] Equilibrium potential measured against the hydrogen electrode (p = 1 atm) in the same medium. Standard potentials from ref. (2).

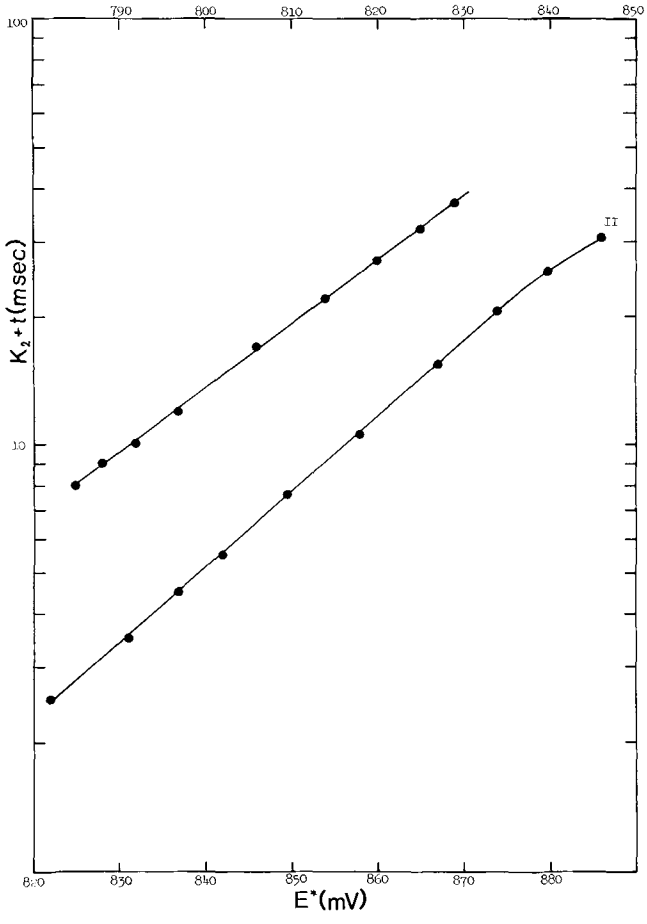

Fig. 7. Determination of kinetic parameters (i_o and b) from oscillographic E^*-t traces after current interruption; curve I (lower E^* scale): 20% H_2SO_4 (70°C), curve II (upper E^* scale): 85% H_3PO_4 (120°C).

log $(K_2 + t)$ *vs.* E^* are given for the following two cases:

(I) 20% H_2SO_4	(II) 85% H_3PO_4
$P_{O_2} + P_{H_2O} = 1$ atm	$P_{O_2} + P_{H_2O} = 1$ atm
70°C	120°C
$L = 4.9$ mg Pt/cm²	$L = 4.9$ mg Pt/cm²
$i = 300$ mA/cm²	$i = 300$ mA/cm²

The parameters of these curves (Fig. 7) are presented in Table II.

The value for the exchange current in H_2SO_4 is for saturation concentration at $P_{H_2O} + P_{O_2} = 1$ atm since the concentration overvoltage in this case was negligible (see Fig. 5). The value for $(i_o)_m$ in Table II for H_3PO_4 refers to an unknown value for the oxygen concentration which, however, was less than the solubility at $P_{H_2O} + P_{O_2} = 1$ atm. This is shown in Fig. 5 where, at the employed current density (61 mA/mg), a deviation from the Tafel line already exists which indicates non-negligible concentration overvoltage. Because of the inherent limitations of the transient method the data for $(i_o)_m$ in Table II are considered less reliable than those in Table I.

Table II. Determination of Tafel parameters from oscilloscopic E^*-t traces after current interruption for Experiments I and II above

	K_1 (mV)	K_2 (msec)	b (mV)	$\left(\frac{dE^*}{dt}\right)_{t=0}$ $\left(\frac{\text{Volt}}{\text{sec}}\right)$	C^* (μf/mg)	kc (mA/mg)	$(i_o)_m$ (mA/mg)
I (H_2SO_4)	766	...	66	3.56	17.2	2.0×10^{13}	2.2×10^{-5}
II (H_3PO_4)	760	2.5	57	9.90	6.2	3.3×10^{15}	8.8×10^{-6}

Table III. Exchange currents and Tafel slopes for oxygen reduction on Pt black at $P_{O_2} + P_{H_2O} = 1$ atm

Electrolyte	Temperature	i_o' (A/cm²)	b
30% KOH	70°C	4×10^{-10}	(50 ± 5) mV Steady state
30% KOH	70°C	—	50 mV Transient
20% H_2SO_4	70°C	4×10^{-10}	(64 ± 5) mV Steady state
20% H_2SO_4	70°C	0.9×10^{-10}	66 mV Transient
50% H_3PO_4	70°C	4×10^{-10}	(60 ± 5) mV Steady state
85% H_3PO_4	120°C	4×10^{-10}	(60 ± 5) mV Steady state
85% H_3PO_4	120°C	4×10^{-10}	(60 ± 5) mV Steady state
85% H_3PO_4	120°C	—	57 mV Transient

Similar analyses were performed for all electrolytes. The results are compiled in Table III. Values obtained from steady state data (Fig. 5) are included for comparison.

Discussion

The values for i_o' and b for H_3PO_4 are the same at 70°C and 120°C (Table I). This has probably little theoretical significance because of the different electrolyte concentrations which were used at the two temperatures. For fuel cell applications, however, the independence of temperature is of real significance since different concentrations have to be used to keep vapor pressure and cell resistance small. Thus the activation polarization cannot practically be lowered by raising the temperature.

Somewhat surprisingly, in the region of activation control, phosphoric and sulfuric acid act very similarly as supporting electrolytes. If, as is indicated by the large difference in the values for C* (Table II), the double layer is different in the two acids, it has apparently little or no effect on the rate of O_2 reduction.

All data in Fig. 5 and 6 are practically free of all ohmic polarizations and concentration polarization caused by oxygen depletion in the gas phase. The difference between the extrapolated Tafel lines and the actual polarization curves is therefore caused by the diminishing utilization of catalyst due to oxygen starvation at the interior, flooded portions of the catalyst agglomerates. The current derived from these interior, flooded portions approaches zero for high polarizations. It is in this potential region where the two acids differ. The combination of higher concentration overvoltage and lower Pt utilization makes H_3PO_4 a much poorer electrolyte for fuel cell cathodes, not a higher activation polarization.

The only data for smooth Pt surfaces which are directly comparable with the present data are those of ref. (4). Thus at 116°C and for 85% H_3PO_4 these authors report $i_o' = 5 \times 10^{-9}$ A/cm² and $b = 80$ mV for what they consider oxide-free Pt. Their "active" Pt yielded $i_o' = 1.1 \times 10^{-7}$ A/cm² and $b = 125$ mV. Because of similar prepolarization our data should correspond to their oxide free surface.[1] The remaining difference may reflect a genuine difference between a black and a smooth surface or it may be due to incomplete removal of impurities in the experiments with smooth surfaces. We have no reason to prefer one possibility to the other. Even if the difference reflects entirely the different catalytic activity it is surprisingly small for what are supposedly vastly different surfaces.

At very low potentials the linear range of curves like those in Fig. 1-4 is restricted to very thin electrodes. Such electrodes are difficult to make with the described method of spraying the catalyst on the supporting Teflon film. As a result the present data are insufficient to extend the curves for acids in Fig. 5 and 6. Relatively thin electrodes, although not assuredly free of internal IR drops at the highest currents, nevertheless show defined limiting currents as can be seen in Fig. 8.

[1] Note: At high potentials ($\epsilon^* \gtrsim 950$ mV) an increase in the polarization begins to become noticeable after 10 to 20 min. This change may be due to poisoning by impurities diffusing into the porous electrode from the bulk electrolyte or it may be due to poisoning by the increasing oxygen coverage. At present we cannot distinguish between these two possibilities.

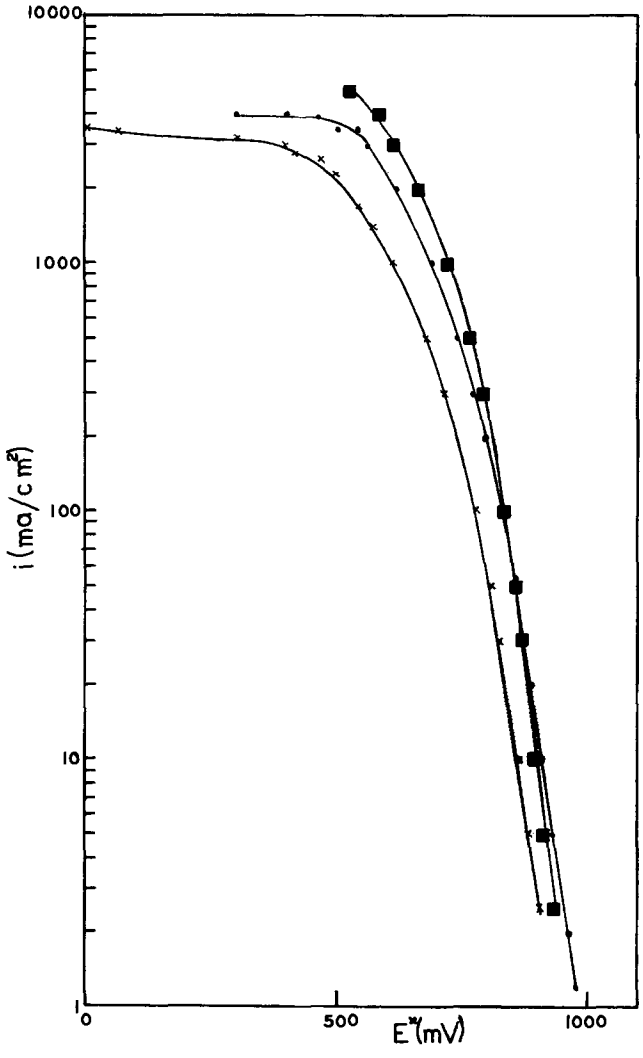

Fig. 8. Polarization curves for single electrodes. ● oxygen, 120°C, 85 w/o H_3PO_4, L = 4.2 mg Pt/cm²; X air, 70°C, 20 w/o H_2SO_4, L = 2.3 mg Pt/cm²; ■ oxygen, 70°C, 20 w/o H_2SO_4, L = 2.3 mg Pt/cm².

Limiting currents on oxygen in H_2SO_4 were not obtained because of the very high current density. If the catalyst loading becomes too high, the current increases slowly without showing a defined limiting current before H_2 evolution begins at the front of the electrode.

An interesting feature of the polarization curves in Fig. 5, 6, and 8 is the shape for KOH. The potential region where the polarization changes from pure activation control with perfect utilization of the catalyst to a limiting current which is obviously controlled by a liquid film is much narrower for KOH than it is for the acids. Although the limiting currents in the acids are at least as high as those in KOH, the starvation of O_2 begins, in the acids, at much lower currents relative to these limiting values. As a matter of fact, the curves for KOH can be described formally by the following equation:

$$\eta - \eta_a = K \log [1 - (i/i_{lim})] \quad [2]$$

where η is the total polarization, η_a is the activation polarization (obtained by extrapolating the linear portions) and i_{lim} is the observed limiting current. Equation [2], of course, describes the behavior of a smooth electrode.

No explanation can be given for this very different behavior of the electrode in acid and in base. The theoretical models proposed for the operation of gas diffusion electrodes usually do not take account of several processes which become important at high current densities. Thus the electrolyte concentration in the catalyst pores changes with the applied current density (5). This change is in opposite directions in acid and in base and depends on the thickness of the electrode. As a result, not only the vapor pressure of the electrolyte changes, but the oxygen solubility and diffusivity become current dependent. In addition, Teflon bonded cathodes in KOH tend to exude electrolyte at their gas-side: The degree of this pumping action increases reversibly with the applied current and the gas-side of the electrode becomes, except in severe cases, immediately dry again at open circuit. This behavior indicates that the catholyte within the catalyst pores is under an overpressure which depends on the current and is sufficiently large to overcome the capillary forces of the catalyst structure. Such an overpressure would tend to increase the thickness of the liquid film on the porous catalyst agglomerates which also would depend on the applied current density.

Manuscript submitted November 17, 1969; revised manuscript received *ca.* May 18, 1970.

Any discussion of this paper will appear in a Discussion Section to be published in the June 1971 JOURNAL.

LIST OF SYMBOLS

- b, Tafel slope, mV
- c, Concentration of oxygen, moles/liter
- C^*, Double layer capacity referred to unit weight of catalyst, μf/mg
- E^*, Potential measured against a hydrogen electrode (P_{total} − 1 atm) in the same medium, mV
- $E^*_{eq.}$, Equilibrium potential, mV
- I, Current, mA
- i, Current density referred to external surface area of the electrode, mA/cm²
- i_m, Current referred to unit weight of Pt-black, mA/mg
- $(i_o)_m$, Exchange current referred to unit weight of Pt-black, mA/mg
- i_o', Exchange current density referred to unit true surface area of Pt-black, A/cm²
- L, Catalyst content, mg Pt/cm²
- p, Pressure, atm
- t, Time, sec
- η Polarization, mV

REFERENCES

1. L. W. Niedrach and H. R. Alford, *This Journal*, **112**, 117 (1965).
2. J. Llopis and J. Giner, *Quimica*, L. (B) 921 (1954).
3. A. Frumkin, *Acta Physico Khim., USSR*, **18**, 23 (1943); see also K. J. Vetter, "Elektrochemische Kinetik," p. 434, Berlin (1961).
4. A. J. Appleby and A. Borucka, Paper 257 presented at Electrochem. Soc. Meeting, New York, May 4-9, 1969.
5. J. T. Lundquist and W. M. Vogel, *This Journal*, **116**, 1066 (1969).

Rotating Ring-Disk Electrodes

III. Catalytic and ECE Reactions

Keith B. Prater[1] and Allen J. Bard*

Department of Chemistry, The University of Texas at Austin, Austin, Texas 78712

ABSTRACT

Digital simulation techniques were employed to calculate the ring and disk currents at the rotating ring-disk electrode (RRDE) for the cases where the intermediate generated at the disk electrodes undergoes first- or second-order processes producing electroactive species: either the original starting material (a catalytic reaction) or a new species (an ECE reaction). Working curves which allow the detection of these mechanisms and the determination of rate constants of the homogeneous reactions from current-rotation rate data are provided. The determination of the rate constant of the iron(II)-hydrogen peroxide reaction by examination of the reduction of iron(III) in a hydrochloric acid medium at a carbon paste RRDE is described.

A digital simulation treatment of the rotating ring-disk electrode (RRDE) in the absence of following chemical reactions has been presented previously (1). The results of this treatment were in excellent agreement with the work of Albery and Bruckenstein (2). This digital simulation technique has also been applied to those cases in which a following first- or second-order chemical reaction results in a nonelectroactive product (an EC mechanism) (3). These results were in good agreement with the approximate treatments of Albery and Bruckenstein (4-7) within the range of their approximations. In this paper, results of the digital simulation of two mechanisms in which the products of the following chemical reaction are electroactive at the potential of the disk electrode are presented.

In the first mechanism, the ECE (electrochemical-chemical-electrochemical) mechanism, species B, which is generated at the disk electrode by

$$A \pm n_1 e \rightarrow B \qquad [1]$$

undergoes a homogeneous reaction to yield species D which immediately undergoes a further electrochemical reaction at the disk electrode. The homogeneous reaction may be either first- or second-order. In the first-order case

$$B \xrightarrow{k_1} D \qquad [2]$$

while in the second-order case

$$B + C \xrightarrow{k_2} D + Y \qquad [3]$$

In either case, species D is immediately oxidized or reduced at the disk by

$$D \pm n_2 e \rightarrow Z \qquad [4]$$

and species C, Y, and Z are considered to be nonelectroactive at the potentials of the ring and disk electrodes. At the ring electrode, A is regenerated from B by the reaction

$$B \pm ne \rightarrow A \qquad [5]$$

The second mechanism is the so-called catalytic mechanism in which one of the products of the homogeneous reaction is the initial species, A. In the common second-order catalytic mechanism, the intermediate, B, reacts with species C, to yield A and Y, where C and Y are nonelectroactive. That is

$$B + C \xrightarrow{k_2} A + Y \qquad [6]$$

In the limit of large concentrations of species C, the second-order catalytic case simplifies to the first-order case given by

$$B \xrightarrow{k_1} A \qquad [7]$$

In each case, the chemical reaction is instantaneously followed by the re-oxidation or re-reduction of A to B as shown in Eq. [1]. As before, the reaction at the ring electrode is given by Eq. [5].

Digital Simulation

The ECE mechanism.—The general approach to the simulations and the notation to be used has been described in previous communications (1, 3). In the ECE mechanism, the ring current-dependent parameter, *ZR*, calculated for a given value of the rate parameter *XKT* for a first-order reaction or *XKTC* for a second-order reaction, is identical with that calculated for the analogous EC case (3). The difference in the collection efficiency curves for the EC and ECE mechanisms is a result of the effect of the ECE reaction on the disk current parameter, *ZD*. Although the EC reaction does not change the disk current from that observed in the absence of a following reaction, the ECE reaction gives rise to increased disk current. Thus the collection efficiency working curves for the first- and second-order ECE mechanisms can be generated by calculating the ECE disk current for a specified value of the rate parameter and dividing the analogous EC ring current by that disk current.

The simulation of the first- and second-order ECE disk currents is quite similar to the previous RRDE simulation (1, 3) except that only the $K = 1$ boxes need to be considered and thus radial convection can be ignored. The dimensionless rate parameters, *XKT* and *XKTC*, are identical to those for the EC cases. The only major differences between the EC and ECE calculations are that in the ECE case, the boundary conditions at the disk electrode and the current parameter, *ZD*, must take into account the fact that both species A and species D are being consumed at the disk and that both are contributing to the total disk current. Thus in this case the parameter, *ZD*, will be the sum of the currents due to (*i*) diffusion of A into the disk box ($J = 1$, $K = 1$), (*ii*) diffusion of D into the disk box, and (*iii*) electrolysis of any D generated in the disk box. Since the fractional concentrations of A and D in the disk box are zero, the

* Electrochemical Society Active Member.
[1] Present address: University of Texas at El Paso, El Paso, Texas 79999.
Key words: digital simulation, electrode reactions, rotating disk electrode.

contribution to the current due to diffusion of A and D into the disk box will be

$$IA = DM_AF_A(2,1)\,(L/DM_A)^{1/2} \quad [8]$$

$$ID_{dif} = DM_DF_D(2,1)\,(L/DM_A)^{1/2} \quad [9]$$

The contribution to ZD due to electrolysis of D produced in the disk box will be

$$ID_{elec} = F_D(1,1)\,(L/DM_A)^{1/2}/2 \quad [10]$$

The factor of 1/2 occurs because the disk box is only $x/2$ wide. Thus in this case

$$ZD = IA + ID_{dif} + ID_{elec} \quad [11]$$

The simulated limiting disk currents as functions of the appropriate dimensionless rate parameters for the first- and second-order ECE mechanisms are shown in Fig. 1. The first-order curve agrees with that simulated by Feldberg *et al.* (8). The disk currents have been normalized by the disk current one would observe in the absence of any following reactions. These disk currents were calculated assuming the stoichiometry given in Eq. [3] and assuming that the number of electrons transferred per molecule is the same for the A to B reaction and the D to Z reaction. In those cases where $n_1 \neq n_2$ or where the stoichiometry is not 1 to 1, the disk current curves can easily be generated by multiplying the amount by which the disk current is enhanced by the appropriate factor. Also shown in Fig. 1 are the associated ring currents from the EC calculations for an electrode with $IR1 = 83$, $IR2 = 94$, and $IR3 = 159$. These, too, have been normalized by the ring current in the absence of any following reaction. The collection efficiency working curves for the first- and second-order ECE mechanisms are shown in Fig. 2. As must be the case, the collection efficiency is lower for an ECE curve than for the analogous EC curve.

The catalytic mechanism.—In the case of the catalytic mechanism, the ring current parameters, ZR, are not the same as the corresponding parameters in the EC mechanism, because the homogeneous reaction regenerating A at the disk is followed by reduction of A to B, so that a greater flux of B to the ring electrode is observed. The simulation, however, is entirely analogous to the simulation of the EC and ECE cases except for the appropriate changes in the boundary conditions and current parameters.

The simulated limiting disk currents for the catalytic mechanism as compared with those in the absence of a following reaction are shown in Fig. 3 as functions of XKT and $XKTC$. The limiting disk currents for this

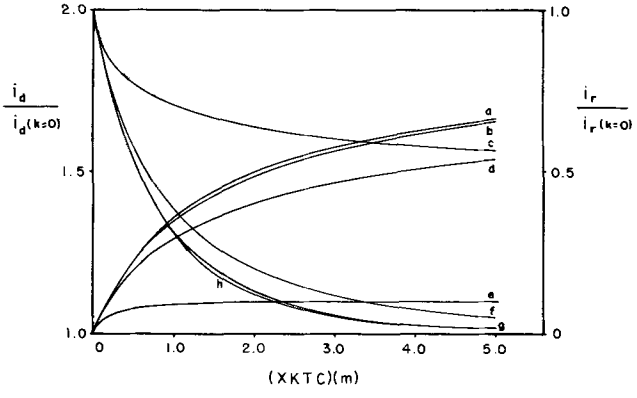

Fig. 1. Simulated limiting ring and disk currents for the ECE mechanism for various values of $m = C°_C/C°_A$. a. Disk current: first-order; b. disk current: $m = 10.0$; c. ring current: $m = 0.1$; d. disk current: $m = 1.0$; e. disk current: $m = 0.1$; f. ring current: $m = 1.0$; g. ring current: $m = 10.0$; h. ring current: first-order. $IR1 = 83$, $IR2 = 94$, $IR3 = 159$. $XKTC = k_2C°_A\omega^{-1}\nu^{1/3}D^{-1/3}(0.51)^{-2/3}$.

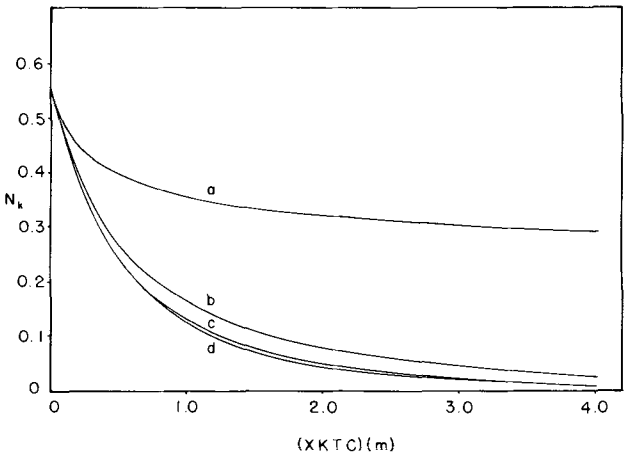

Fig. 2. Simulated collection efficiency vs. $(XKTC)\,(m)$ for the ECE mechanism for various values of m. a. 0.1; b, 1.0; c. 10.0; d. first-order. $IR1 = 83$, $IR2 = 94$, $IR3 = 159$. $XKTC = k_2C°_A\omega^{-1}\nu^{1/3}D^{-1/3}(0.51)^{-2/3}$. $m = C°_C/C°_A$.

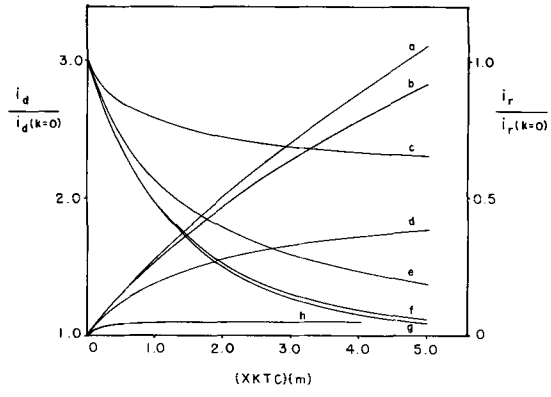

Fig. 3. Simulated limiting ring and disk currents for the catalytic mechanism for various values of m. a. Disk current: first-order; b. disk current: $m = 10.0$; c. ring current: $m = 0.1$; d. disk current: $m = 1.0$; e. ring current: $m = 1.0$; f. ring current: $m = 10.0$; g. ring current: first order; h. disk current: $m = 0.1$. $IR1 = 83$, $IR2 = 94$, $IR3 = 159$. $XKTC = k_2C°_A\omega^{-1}\nu^{1/3}D^{-1/3}(0.51)^{-2/3}$. $m = C°_C/C°_A$.

case have been treated by Koutecky and Levich (9), by Haberland and Landsberg (10), and by Beran and Bruckenstein (11). The treatment by Koutecky and Levich assumed that the reaction layer thickness was very small compared with the diffusion layer thickness, that is, it assumed that k/ω was large. Beran and Bruckenstein treated a rather complex system under pseudo-first order conditions. The simulation results agree very well with the more general treatment of Haberland and Landsberg. This is shown in Fig. 4 in which some of their data for the Fe^{+3}/H_2O_2 system are compared with points calculated from their data in the absence of the following reaction, the rate constant which they calculated, and the simulation results.

While the simulated disk currents are valid for any geometry, the limiting ring currents which are also shown in Fig. 3 were calculated for an electrode with $IR1 = 83$, $IR2 = 94$, and $IR3 = 159$. From the ring and disk currents, one can obtain the collection efficiency working curves shown in Fig. 5.

At this point it is appropriate to compare the simulated collection efficiency working curves for the EC, ECE, and catalytic mechanisms. In all useful ranges of the rate parameters, the ECE curves differ significantly from the analogous EC and catalytic curves. The collection efficiency found for the ECE mechanism for a given value of $XKTC$ and m, where $m = C°_C/C°_A$, is always smaller than that found for the

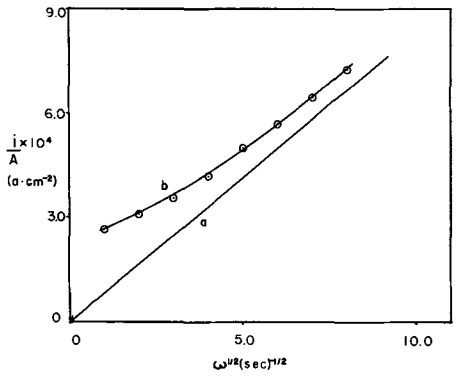

Fig. 4. Comparison of simulated disk current for the catalytic mechanism with results of Haberland and Landsberg (10) for the Fe^{+3}/H_2O_2 system. a. Limiting disk current in the absence of H_2O_2; b. simulated limiting disk current based on curve a, the homogeneous rate constant (k_2 = 145 liters/mole sec) calculated by Haberland and Landsberg and for $C_{H_2O_2} = 10\ C_{Fe^{+3}}$. ⊙ Experimental limiting currents found by Haberland and Landsberg for $C_{H_2O_2} = 1.6 \times 10^{-2}M$, and $C_{Fe^{+3}} = 1 \times 10^{-3}M$ in 1M KCl.

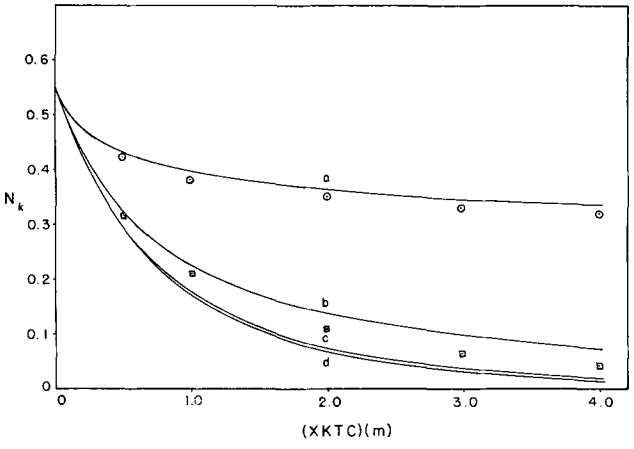

Fig. 5. Simulated collection efficiency *vs.* *XKTC(m)* for the catalytic mechanism for various values of m. a. 0.1; b. 1.0; c. 10.0; d. first-order. *IR1* = 83, *IR2* = 94, *IR3* = 159. $XKTC = k_2 C^\circ_A \omega^{-1} \nu^{1/3} D^{-1/3} (0.51)^{-2/3}$. $m = C^\circ_C / C^\circ_A$. ⊙ Simulated collection efficiency for the EC mechanism, m = 0.1. ⊡ Simulated collection efficiency for the EC mechanism, m = 1.0.

EC or catalytic mechanisms with the same values of $XKTC$ and m. On the other hand, the EC and catalytic curves are, for most values of the rate parameters, quite similar. In fact, the first-order curves for the two mechanisms are indistinguishable as are the analogous curves for m — 10.0. The m = 1.0 and m = 0.1 curves for the two mechanisms are experimentally indistinguishable for values of $(XKTC \cdot m) < 0.5$. Thus, it is not surprising that Albery *et al.* (6) obtained reasonable results when they treated a pseudo-first order catalytic system with a theory developed for the EC mechanism. Although the collection efficiency data are insufficient for differentiating between the EC and catalytic mechanism, examination of the limiting ring and disk currents allows the two mechanisms to be easily distinguished. The limiting disk current for the EC mechanism is identical to that found in the absence of any following reaction, while the limiting disk current, i_{lim}, for the catalytic mechanism is significantly larger and $i_{lim}/\omega^{1/2}$ varies with ω. Thus, it seems advisable to carry out the RRDE experiment in a manner which yields both collection efficiency and limiting ring and disk current data.

Transient behavior.—The simulated ring current transients for the ECE mechanism are identical to those for the EC mechanism. For the first- and second-order catalytic reactions, the value of $\omega t (D/\nu)^{1/3} (0.51)^{2/3}$ at which the ring current is one-half of the steady-state value is observed to be a function of XKT or $XKTC$ as in the EC case. Unlike the EC transients, however, the catalytic transients do not exhibit maxima.

Results and Discussion

To test the simulation results for a second-order catalytic reaction, the reduction of iron(III) in the presence of hydrogen peroxide was investigated. This reaction, previously investigated at a RDE by Haberland and Landsberg (10), was studied by reduction of ferric ion at the disk and analysis for the ferrous ion at the ring, that is

$$Fe^{+3} + e \rightarrow Fe^{+2} \qquad \text{disk electrode}$$

$$Fe^{+2} + 1/2H_2O_2 \xrightarrow{k_2} Fe^{+3} + OH^-$$

$$Fe^{+2} - e \rightarrow Fe^{+3} \qquad \text{ring electrode}$$

The electrode was a carbon paste RRDE with dimensions r_1 = 0.237 cm, r_2 = 0.268 cm, and r_3 = 0.455 cm. It was calibrated by determining the limiting disk and ring currents in a solution containing 6.4 x $10^{-3}M$ iron(III) and 2M HCl. Typical results are shown in Fig. 6, curves b and c. The experimental collection efficiency, 0.545 ± 0.003, compares quite well to that for the simulation in the absence of perturbing reactions, 0.551. A second determination of the collection efficiency, involving oxidation of 5.7 x $10^{-4}M$ o-dianisidine in 1M H_2SO_4 at the disk electrode yielded a collection efficiency of 0.548 ± 0.003.

The limiting disk currents and corresponding limiting ring currents for the solution which was 6.4 x $10^{-3}M$ in ferric ion and 0.64 x $10^{-3}N$ in hydrogen peroxide were found to be identical to those obtained in a solution which contained 6.4 x $10^{-3}M$ ferric ion and no hydrogen peroxide. This indicated that at this ratio of the concentration of ferric ion to hydrogen peroxide, the rate of the ferrous-hydrogen peroxide reaction was so slow that its effect on the ring and disk currents could not be detected.

When limiting ring and disk currents were obtained for the solution which was 6.4 x $10^{-3}N$ in both ferric ion and hydrogen peroxide, it was obvious that the reaction was significantly affecting the ring and disk currents. These currents along with the collection efficiencies at various rotation rates are shown in Table I. Also shown in Table I are the values of $XKTC$ corresponding to the observed collection efficiencies as obtained from the m = 1.0 working curve in Fig. 5. The

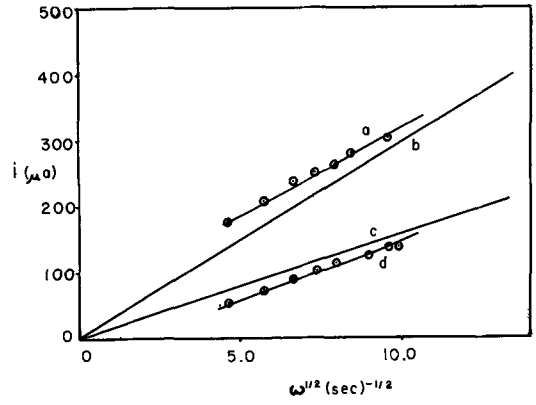

Fig. 6. Experimental limiting ring and disk currents for the ferrous-hydrogen peroxide reaction as compared with simulated values. a. Simulated limiting disk current in the presence of a catalytic following reaction. b. Limiting disk current in the absence of a following reaction. c. Limiting ring current in the absence of a following reaction. d. Simulated limiting ring current in the presence of a catalytic following reaction. ⊙ Experimental results.

Table I. RRDE data for the iron(III)-hydrogen peroxide system[a]

ω (sec^{-1})	Disk current i_d (μA)	Ring current i_r (μA)	N_k[b]	$XKTC$[c]	$(XKTC) \times (\omega)$	k_2 (liter/mole sec)
21.4	177	53	0.300	0.59	12.6	100
32.6	208	73	0.351	0.40	13.1	104
43.9	238	91	0.383	0.305	13.4	105
53.6	250	104	0.416	0.23	12.3	98
62.8	264	114	0.432	0.20	12.6	100
91.4	302	136	0.450	0.16	14.6	116
97.8	297	136	0.458	0.14	13.7	109
					Avg. $k_2 = \overline{105} \pm 5$	

[a] The solution was 6.4 x $10^{-3}N$ in both Fe(III) and H_2O_2 and $2M$ in HCl. The carbon paste RRDE had the dimensions $r_1 = 0.237$ cm, $r_2 = 0.268$ cm, $r_3 = 0.455$ cm. The temperature was 23°C.
[b] $N_K = -i_r/i_d$.
[c] Calculated using simulated curves in Fig. 5.

product of the rotation rate and the value of $XKTC$

$$(\omega)(XKTC) = k_2 C^o_A (\nu/D_A)^{1/3} (0.51)^{-2/3}$$

should also be a constant. The values of this product and also the value of k_2 calculated for each rotation rate using a value of the diffusion coefficient, D_A, of 5 x 10^{-6} cm^2/sec and a value of the kinematic viscosity, ν, of 1 x 10^{-2} cm^2/sec, are also given in Table I.

The average value of k_2, 105 liters/mole-sec, compares favorably with reported values which range from $k_2 = 96$ liters/mole-sec in a solution containing $2M$ chloride ion and 4 x $10^{-3}M$ hydrogen ion at 35°C (12), to $k_2 = 145$ obtained in a $1M$ potassium chloride solution (10). This average value of k_2, calculated using the collection efficiencies, can also be employed to compare the predicted values of disk and ring current to the experimental ones. Curves a and d in Fig. 6 are the results of simulations of i_d and i_r at different values of ω employing a k_2 of 105 liters/mole-sec and parameters from the experimental ring and disk currents in the absence of hydrogen peroxide. Also shown in Fig. 6 are the experimental values of i_d and i_r from Table I, which are in satisfactory agreement with the simulated values.

Experimental

The carbon paste RRDE was fabricated from a cylinder of Quickmount (E. H. Sargent Company, Chicago, Illinois) molded onto a precision steel shaft (13). A Motormatic E-550 motor and controller (Electrocraft Corporation, Hopkins, Minnesota) was used as a rotator. A 1/4-in. chuck was mounted directly onto the motor shaft and held the RRDE. A dual-potentiostat similar to that described by Napp, Johnson, and Bruckenstein (14) was used to control the potentials of the disk and ring electrodes independently.

The standard iron(III) solution was prepared by dissolving ferric chloride in $2M$ HCl. This solution, standardized by reducing an aliquot with hydroquinone and determining the ferrous ion spectrophotometrically as the ferrous 1,10-phenanthroline complex, was found to contain $0.064M$ ferric ion.

A stock solution of hydrogen peroxide was prepared by diluting an approximately 30% hydrogen peroxide solution with water to produce about a 5 x $10^{-3}M$ solution. The hydrogen peroxide concentration of this solution was determined shortly before the experiment by reacting an aliquot of this solution with an aliquot of a standard solution of ferrous ammonium sulfate and determining the amount of ferrous ion remaining in solution spectrophotometrically. The hydrogen peroxide solution was found to be 5.9 x $10^{-3}M$ in hydrogen peroxide, or 1.18 x $10^{-2}N$ as an oxidant in the ferrous-hydrogen peroxide reaction. Test solutions were prepared from these stock solutions.

Solutions more concentrated than 6.4 x $10^{-3}N$ in hydrogen peroxide were found to be unstable with respect to decomposition into oxygen and water. Even in a solution which was 6.4 x $10^{-3}N$ in hydrogen peroxide, bubbles were observed at the electrode surfaces. This required wiping the electrode before each measurement and making the measurement as rapidly as possible. All measurements were carried out at 23° ± 0.5°C.

Acknowledgment

The support of the Mobil Oil Corporation and the Eastman Kodak Company for fellowships to one of us (K.B.P.) the Robert A. Welch Foundation, and the National Science Foundation are gratefully acknowledged.

Manuscript submitted April 7, 1970; revised manuscript received July 22, 1970.

Any discussion of this paper will appear in a Discussion Section to be published in the June 1971 JOURNAL.

REFERENCES

1. K. B. Prater and A. J. Bard, *This Journal*, **117**, 207 (1970).
2. W. J. Albery and S. Bruckenstein, *Trans. Faraday Soc.*, **62**, 1920 (1966).
3. K. B. Prater and A. J. Bard, *This Journal*, **117**, 335 (1970).
4. W. J. Albery and S. Bruckenstein, *Trans. Faraday Soc.*, **62**, 1946 (1966).
5. W. J. Albery and S. Bruckenstein, *ibid.*, p. 2584.
6. W. J. Albery, M. L. Hitchman, and J. Ulstrup, *ibid.*, **64**, 2831 (1968).
7. W. J. Albery, M. L. Hitchman, and J. Ulstrup, *ibid.*, **65**, 1101 (1969).
8. L. S. Marcoux, R. N. Adams, and S. Feldberg, *J. Phys. Chem.*, **73**, 2611 (1969).
9. J. Koutecky and V. G. Levich, *Zhur. Fiz. Khim.*, **32**, 1565 (1958).
10. D. Haberland and R. Landsberg, *Z. Elektrochem.*, **70**, 724 (1966).
11. P. Beran and S. Bruckenstein, *J. Phys. Chem.*, **72**, 3630 (1968).
12. C. F. Wells and M. A. Salam, *Trans. Faraday Soc.*, **63**, 620 (1967).
13. P. A. Malachesky, K. B. Prater, G. Petrie, and R. N. Adams, *J. Electroanal. Chem.*, **16**, 41 (1968).
14. D. T. Napp, D. C. Johnson, and S. Bruckenstein, *Anal. Chem.*, **39**, 481 (1967).

Technical Notes

The Effect of Potential and Time on Deposition Characteristics of Zinc on a Zinc Single Crystal in KOH

F. Mansfeld*[1] and S. Gilman*

NASA/Electronics Research Center, Cambridge, Massachusetts 02139

Employing *in situ* microscopy, Powers (1) demonstrated that the morphology of the zinc electrodeposit in alkaline solutions obtained on the basal plane of a zinc single crystal is markedly different at polarizations in the ranges of −100 mV and −200 mV *vs.* zinc. Details of early growth of the zinc electrodeposit are accessible through the use of the scanning electron microscope (SEM). Although SEM studies have been made of zinc electrodeposits (2, 3), these were not made under conditions of potentiostatic control and are, therefore, not exactly comparable to the results of Powers (1) or to the results obtained by the present authors (4, 5) in their studies of the effect of additives on the morphology of the electrodeposit.

The present studies were performed in a cell similar to that of Powers (1) in a solution of 6*N* KOH containing 20 g/liter of ZnO. Test samples were obtained by cleavage of single crystal rods in a dry box under argon [for details of the experimental procedure, see ref. (4)]. The growth process at a constant potential was followed for a prescribed period of time, employing *in situ* light microscopy. The sample was then removed and examined with the SEM.

Observations of the zinc electrodeposit at −100 mV polarization with the *in situ* light microscope revealed epitaxial growth in the form of hexagonal pyramids. Such pyramids grew in size and decreased in number as already observed by Powers (1). After approximately 15 min, a new growth feature appeared (Fig. 1) at the base of the growth pyramids. These new protrusions appear as black dots and have been called sponge or moss by various authors. They have been observed in the present experiment to be particularly numerous along cracks in the crystal introduced by cleavage. When viewed with the SEM (Fig. 2), it is apparent that these protrusions start to grow directly on the surface of the crystal; still visible are

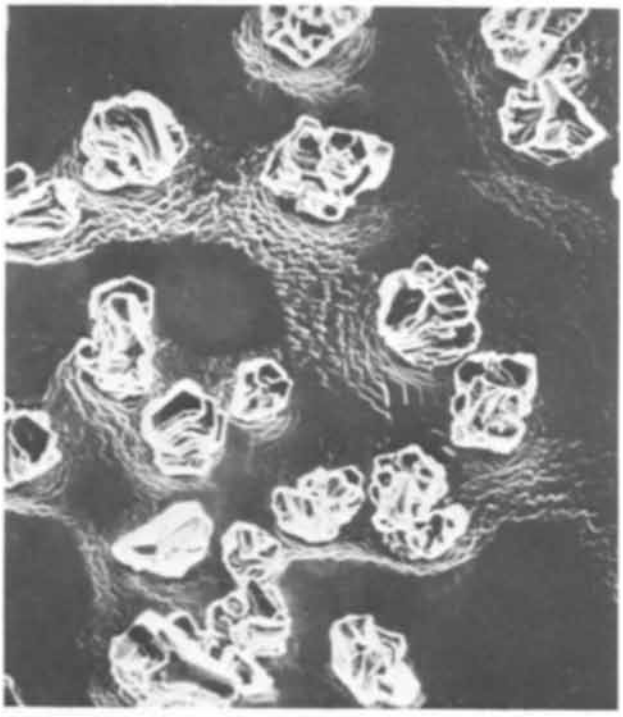

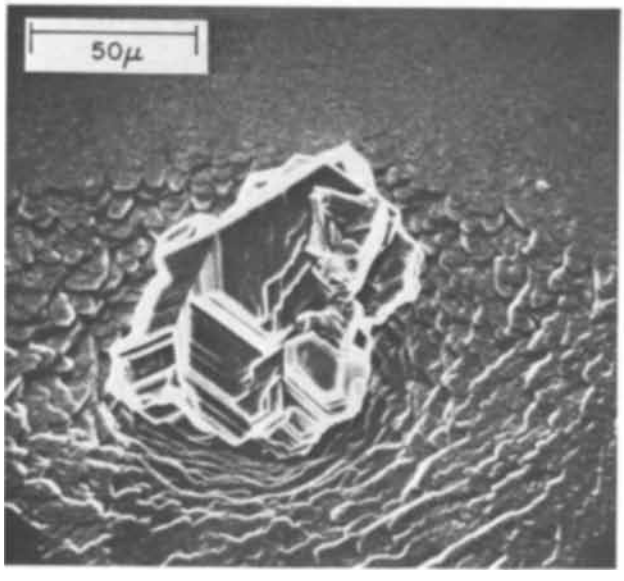

Fig. 2. Deposit at −100 mV from 6*N* KOH + 20 g/liter ZnO after 20 min. SEM, 34°. (a) (top) 280X; (b) (bottom) 140X.

* Electrochemical Society Active Member.

[1] Present address: Science Center, North American Rockwell Corporation, Thousand Oaks, Calif. 91360.

Key words: epitaxial growth, dendritic growth, nucleation, *in situ* microscopy.

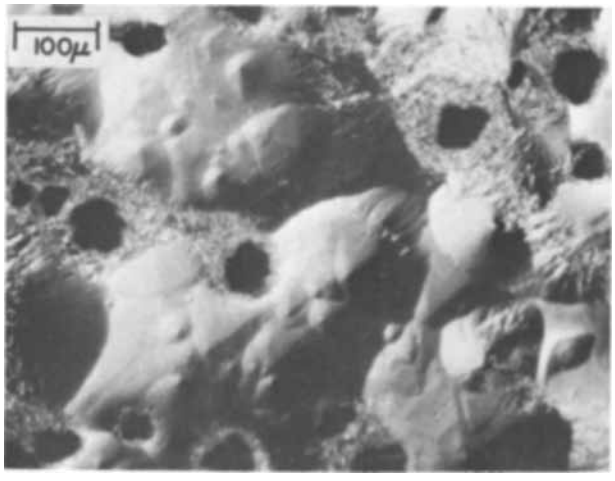

Fig. 1. Deposit at −100mV from 6*N* KOH + 20 g/liter ZnO after 20 min. Nomarski Interference Contrast, 110X.

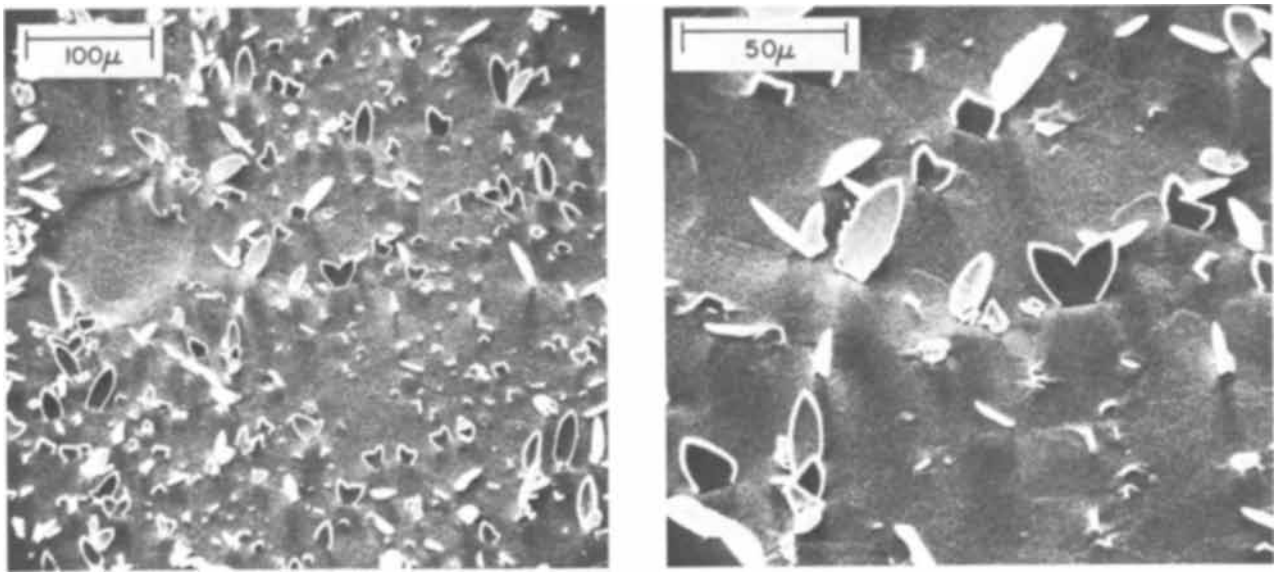

Fig. 3. Deposit at —200 mV from 6N KOH + 20 g/liter ZnO after 5 min. SEM, 34°. (a) (left) 170X; (b) (right) 440X

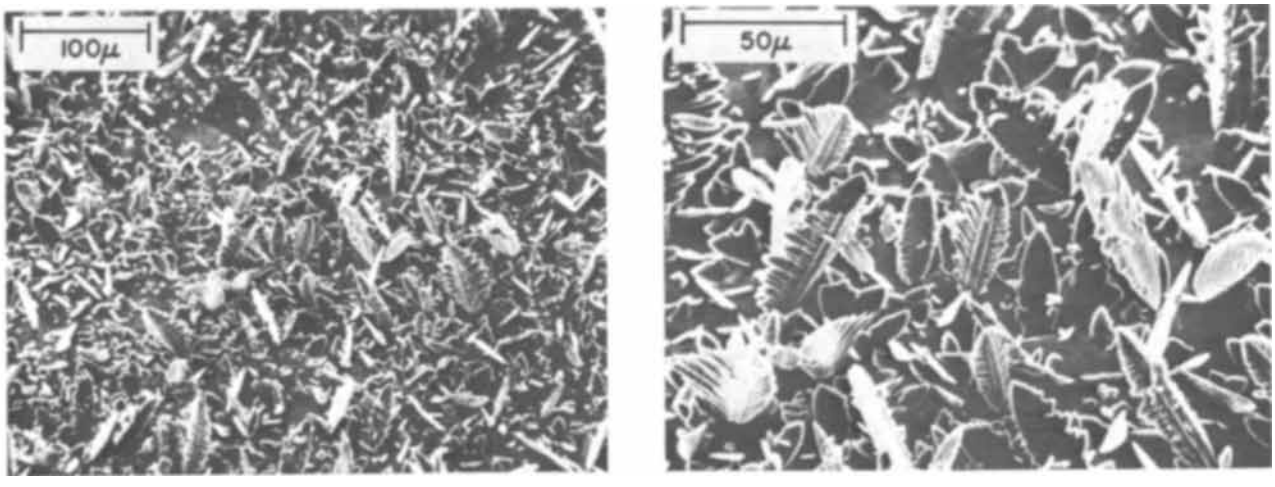

Fig. 4. Deposit at —200 mV from 6N KOH + 20 g/liter ZnO after 10 min. SEM, 34°. (a) (left) 170X; (b) (right) 440X

the layers that formed the growth-pyramids. Fig. 2b shows in more detail the structure of one of the protrusions which were already observed in an earlier study of the authors (Fig. 8 of ref. 4). They consist of many layers with certain crystallographic orientations. It seems reasonable to conclude that both types of growth occur on different sites, which might be screw dislocations in the case of pyramids, while the protrusions seem to nucleate at macroscopic defects or impurity centers (including such regions of macroscopic crystalline disorder as cracks). Comparison of Fig. 2 of this communication with Fig. 6 of ref. 4 reveals the dramatic effect produced by the addition of lead ions to the solution. The epitaxial growth and discrete crystalline protrusions observed here are replaced by microcrystalline hillocks with a pipelike structure in the valleys.

At —200 mV polarization, observation of the zinc electrodeposit with the *in situ* light microscope again reveals initial pyramidal epitaxial growth, the number of pyramids being higher than at —100 mV as observed in ref. 4. As at —100 mV, protrusions appear in the valleys between the growth pyramids, but the protrusions at the more cathodic potential occur early (within minutes) and develop into classical flat dendrites. Features of the dendritic growth are evident in the SEM photographs of Fig. 3 and Fig. 4. Such dendritic growth is suppressed in the presence of additions of lead (4) or tin (5) ions.

The effect of time on morphology of zinc deposits at —200 mV was studied at 5, 10, and 15 min. As can be seen better resolved with the light microscope (Fig. 5) (which in turn does not allow good resolution of the structure of the dendrites), dendrites are initi-

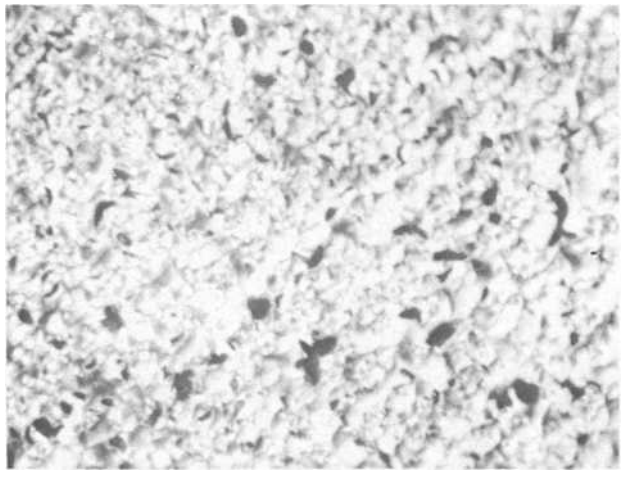

Fig. 5. Deposit at —200 mV from 6N KOH + 20 g/liter ZnO after 5 min. Nomarski Interference Contrast, 110X.

ated at the feet of the growth pyramids, probably at the same sites as the protrusions observed at −100 mV. Figure 3 shows growth after 5 min, and Fig. 4, growth after 10 min. It is obvious that the dendrites not only grow in size but also in number. Often two dendrites start at the same site, producing a heartlike structure. Figure 3b shows details of the observed growth including dendrites at the very early stages of growth. After 10 min of deposition the dendrites already have all features of classical dendrites observed after long plating times—a stem consisting of many plates and sidebranches as can be seen from Fig. 4b at a higher magnification. Examples for deposits after 15 min are shown in Fig. 2 of ref. 5.

In summary our results show that the deposition time and potential play an important role in morphology of zinc deposits on the basal plane of zinc in alkaline solutions. At −100 mV polarization, only epitaxial growth is observed for times below approximately 15 min. For longer times a second structure appears which grows probably from macroscopic defects. At −200 mV dendrites can be observed at times shorter than 5 min, possibly nucleated at the same sites as the protrusions formed at −100 mV. The dendrites grow in size and number with time. A comparison with results in the presence of lead ions (4) and tin or tetraethylammonium ion (5) shows that these additives suppress dendrite growth, although to different extents.

It will be noted that our results do not support a theory concerning the mechanism of dendritic electrocrystallization of zinc proposed by Diggle, Despic, and Bockris (6). In this model the initiation of a dendrite is treated in terms of growing pyramids on the substrate surface. It is assumed that "the rotation of the spiral, within the linear diffusion boundary surrounding the sphere, gives rise to a decrease of the effective radius of curvature of the dendrite tip" until a critical radius is obtained, which is the condition for dendrite initiation (6). In the present work, it has never been found that a dendrite initiated at the top of a pyramid; on the contrary the protrusions at −100 mV always start to grow at the foot of pyramids after these have stopped to grow further (Fig. 2b). At −200 mV, where classical dendrites are observed, these start to grow almost instantaneously between pyramids. It is hard to understand how the heartlike structure as shown in Fig. 3b should grow from the tip of a pyramid after this had reached the critical—very small—radius. It seems more likely that pyramids and protrusions or dendrites grow independently and from different sites.

Acknowledgment

One of the authors (F. M.) wishes to acknowledge support under a National Academy of Sciences Research Associateship. Scanning electron micrographs were taken with the help of Mr. J. Herman of Prof. Ogilvie's laboratory, Massachusetts Institute of Technology.

Manuscript submitted June 1, 1970; revised manuscript received *ca.* Aug. 18, 1970.

Any discussion of this paper will appear in a Discussion Section to be published in the June 1971 JOURNAL.

REFERENCES

1. R. W. Powers, *Electrochem. Technol.*, **5**, 429 (1967).
2. R. D. Naybour, *Electrochim. Acta*, **13**, 763 (1968).
3. R. D. Naybour, *This Journal*, **116**, 520 (1969).
4. R. Mansfeld and S. Gilman, *ibid.*, **117**, 588 (1970).
5. F. Mansfeld and S. Gilman, *ibid.*, **117**, 1154 (1970).
6. J. W Diggle, A. R. Despic, and J. O'M. Bockris, *ibid.*, **116**, 1503 (1969).

The Preparation of $FeSn_2$ Coatings by Electrodeposition

Henry Leidheiser, Jr.* and Jyotin Sachdev

Center for Surface and Coatings Research, Lehigh University, Bethlehem, Pennsylvania 18015

$FeSn_2$ is a very corrosion-resistant material (1) and plays a major role at the iron-tin interface in controlling the corrosion behavior of commercial electrolytic tinplate used in container applications. Previous work has shown that small amounts of $FeSn_2$ are formed during the electrodeposition of tin from the alkaline bath on steel substrates (2) and Barry and Phillips (3) have shown that $FeSn_2$ is also formed at the interface during electrodeposition from the acid bath. A method is described herein for the formation of $FeSn_2$ coatings on steel and copper substrates utilizing electrodeposition of an iron-tin alloy followed by heat treatment.

Izmailov and Kudryavtseva (4) have developed an electroplating bath for depositing iron-tin alloys over a wide composition range and have studied the effect of bath composition, pH, and current density on the composition of the alloy. Experiments were carried out which confirmed the essential correctness of their observations. Electron microprobe analysis indicated that the iron and tin were homogeneously distributed throughout the deposit.

Iron-tin alloys of the approximate composition 33 a/o Fe-67 a/o Sn were deposited at 55 ± 5% current efficiency under the following conditions modified from those used by Izmailov and Kudryavtseva: bath composition—$FeCl_3 \cdot 6H_2O$ 27 g/liter, $SnCl_2 \cdot 2H_2O$ 4.0 g/liter, $Na_4P_2O_7 \cdot 10\ H_2O$ 150 g/liter; pH 8.4; temperature, 80°C; current density, 0.5 A/dm^2; graphite anodes. Deposits were typically 0.0002-0.0005 cm in thickness as determined by time of deposition. They were matte, smooth, and dull gray in color. X-ray diffraction analysis indicated the presence of elemental iron, elemental tin, and a small amount of $FeSn_2$. These results are in accord with the phase diagram which indicates that the stable phases at low temperature are iron containing a small amount of dissolved tin, FeSn, $FeSn_2$, and tin (5).

Deposits were heated for 24 hr at 150°-200°C, and the resulting alloy was studied by x-ray diffraction. A small amount of residual tin was present on samples heated at 150°C (residual iron could not be determined because of interference from the steel substrate); complete conversion to $FeSn_2$ occurred at 175°; and small amounts of FeSn were detected on samples heated at 200°C. Presumably above 175°C interaction between the substrate and the deposit becomes significant. Diffraction analysis of deposits formed on copper substrates confirmed that the iron was converted to $FeSn_2$ during heating at 175°C. The use of a copper substrate complicated the analysis since Cu_3Sn was also formed and appreciable amounts of FeSn were observed.

Two forms of $FeSn_2$ are claimed to exist, a tetragonal form and a pseudohexagonal form. Gabe (6) summarizes the diffraction data reported by a number of investigators. Although there are only minor differences between the diffraction patterns of these

* Electrochemical Society Active Member.
Key words: coating, $FeSn_2$, iron-tin, electrodeposition.

two crystalline forms of $FeSn_2$, our data are in better accord with the pattern for the pseudohexagonal form.

The data of Frankenthal and Loginow (7) indicate that one can expect 0.15 mg/cm^2 of $FeSn_2$ to be formed in 24 hr at 175° when tin electrodeposits on steel substrates are heated. In the case of our deposits of thickness equivalent to 3-6 mg/cm^2 there was complete conversion to $FeSn_2$ at 175°C. The higher amount of conversion to the alloy is to be expected in our experiments because of the intimate mixture of iron and tin crystallites in the electrodeposit before heating.

The presence of detectable amounts of FeSn in samples heated at 200°C is interesting because FeSn is not generally observed after commercial tinplate is heated during manufacture.

Acknowledgment

Support of this research by the Materials Research Council of Lehigh University is gratefully acknowledged.

Manuscript submitted June 19, 1970; revised manuscript received Aug. 20, 1970.

Any discussion of this paper will appear in a Discussion Section to be published in the June 1971 JOURNAL.

REFERENCES

1. W. E. Hoare, *J. Iron Steel Inst. (London)*, **129**, 253 (1934); R. A. Covert and H. H. Uhlig, *This Journal*, **104**, 537 (1957).
2. W. R. Buck, III, and H. Leidheiser, Jr., *This Journal*, **112**, 243 (1965).
3. B. T. K. Barry and D. L. Phillips, *Electrochem. Technol.*, **6**, 394 (1968).
4. A. V. Izmailov and V. A. Kudryavtseva, *Izv. Vysshykh Uchebn. Zavedenii, Khim. i Khim. Tekhnol.*, **10**, 1031 (1967); U.S.S.R. Pat. 187, 476, Oct. 11, 1966.
5. M. Hansen, "Constitution of Binary Alloys," pp. 718-720, McGraw-Hill Book Co., New York, (1958).
6. D. R. Gabe, *Iron Steel (London)*, **40**, 118 (1967).
7. R. P. Frankenthal and A. W. Loginow, *This Journal*, **107**, 920 (1960).

On the Conductivity of Electrolytes Simulating Those Found in AgCl-Mg, Fresh Water-Activated Batteries

Duane W. Faletti

Applied Physics Laboratory, University of Washington, Seattle, Washington 98105

Experimental determinations were made of the electrolytic conductivity of simulated electrolytes (aqueous $MgCl_2$ solutions) of AgCl-Mg batteries operated in fresh water.

Studies of high-drain, water-activated AgCl-Mg alloy batteries have been conducted. The conductivities of the effluents from such batteries operated in the open sea over the range of concentration (4.5 to 19 °/$_{oo}$ chlorinity) of interest to the battery designer have been presented (1). The development of voltage control systems that maintain a desired battery voltage by recycling a portion of the effluent and adjusting the intake of new electrolytes permits operation of these batteries in both fresh and brackish water. Since fresh water can be thought of as sea water with a chlorinity of zero, the data presented here are not only applicable to the operation of batteries in fresh water, but, by suitable interpolations in chlorinity with the results of Ref. (1), are applicable to operation in brackish water. The rationale for the use of aqueous $MgCl_2$ solutions as simulated effluents of AgCl-Mg alloy batteries when operated in fresh water is given in the following section.

Electrolyte Composition

In addition to the electrochemical reaction

$$2AgCl + Mg \rightarrow MgCl_2 + 2Ag \qquad [1]$$

which has the effect of adding magnesium chloride to the electrolyte, secondary reactions between the anode and water occur:

$$Mg + 2H_2O \rightarrow Mg(OH)_2 + H_2 \qquad [2a]$$

$$Al + 3H_2O \rightarrow Al(OH)_3 + 3/2H_2 \qquad [2b]$$

$$Zn + 2H_2O \rightarrow Zn(OH)_2 + H_2 \qquad [2c]$$

$$Mn + 2H_2O \rightarrow Mn(OH)_2 + H_2 \qquad [2d]$$

$$Pb + 2H_2O \rightarrow Pb(OH)_2 + H_2 \qquad [2e]$$

With pure Mg only reaction [2a] occurs. With AZ61, the most common anode material, reactions [2a] through [2d] occur. With AP65, a recently developed anode, all five of the reactions occur.

Since the hydroxides are insoluble, one would expect them to be quantitatively precipitated, leaving only the $MgCl_2$ from reaction [1] in solution. Analyses of the effluents from batteries that use either AZ61 or AP65 showed that this is the case (2).

The above should be true for any battery using Mg alloy anodes with constituents that form insoluble hydroxides. Therefore, an aqueous $MgCl_2$ solution closely simulates the effluent from a fresh water-activated AgCl-Mg alloy battery.

Experimental Studies

The methods we used to determine the electrolytic conductivities have been reported (2). The electrolytes were prepared from a stock solution made from analytical grade $MgCl_2 \cdot 6H_2O$. Values of the $MgCl_2$ concentration of the stock solution were calculated from chloride and magnesium determinations. The two methods gave results which agreed to within 0.57% of each other. The composition given by the intrinsically more precise chloride determination was used in formulating the electrolytes utilized in this study.

Taking into account uncertainties in cell constant, resistance, temperature, $MgCl_2$ concentration, and the effects of evaporation, maximum uncertainties in electrolytic conductivity ranged from ±1.5% at room temperature or below up to +2.2 to −1.5% at 75°C, where evaporation errors were significant. These uncertainties are based on an error analysis presented in Ref. (1) with a 0.5% maximum uncertainty in the value of $MgCl_2$ concentration in the stock solution.

Key words: electric conductors, electrolytes, aqueous electrolytes, aqueous $MgCl_2$ solutions, conductivity of electrolytes, AgCl-Mg batteries, AgCl, Mg, battery electrolytes.

Table I. Conductivity of aqueous $MgCl_2$ solutions, $(ohm\text{-}cm)^{-1}$

Temperature, °C	$MgCl_2$ concentration, g/liter							
	2.5	5.0	10.0	15.0	20.0	40.0	55.0	70.0
5.0	0.00335	0.00626	0.0118	0 0169	0.0216	0.0388	0.0493	0.0594
10.0	0.00383	0.00719	0.0134	0.0192	0.0247	0.0441	0.0565	0.0676
15.0	0.00435	0.00816	0.0152	0.0217	0.0280	0.0498	0.0639	0.0760
20.0	0.00486	0.00913	0.0170	0.0243	0.0312	0.0557	0.0714	0.0849
25.0	0.00541	0.01014	0.0189	0.0270	0.0346	0.0617	0.0791	0.0942
45.0	0.00776	0.01449	0.0270	0.0383	0.0491	0.0875	0.1118	0.1330
75.0	—	—	0.0399	0.0572	0.0732	0.1290	0.1633	0.1935

Results

The electrolytic conductivities obtained from this study are presented in Table I. They agree to within 0.5% or better with the results of Shedlovsky and Brown (3), which should be more precise than those of this study since they used a more accurate method of formulating $MgCl_2$ solutions and since they also used more accurate techniques for determining conductivity.

Kondrat'ev and Nikich (4) determined the electrolytic conductivity of $MgCl_2$ solutions over a temperature range of 25°-300°C (requiring autoclave-type equipment). Their results differed from the results of this study by ±2% at 25°C and ±4% at 35°C. At both temperatures the disagreement decreased from positive values at 5.0 weight per cent (w/o) to negative values at 2.0 w/o, indicating that a systematic error in composition may have existed in their solutions. No systematic error in the concentration was likely in our study as a single stock solution was used to formulate all the electrolytes.

Kondrat'ev and Gorbachev (5) described the cell used by Kondrat'ev and Nikich but did not mention the use of platinized platinum. They simply stated that the electrodes were composed of platinum wire. Thus, the possibility exists that a lack of platinized platinum might also account for the observed discrepancies.

Comparisons were made with the data of Urazov and Tavkesheva (6), who used stock solutions whose concentration was based on the assumption of saturation (great care was taken by them to assure saturation). Good agreement (−1.04%) was observed at 6 w/o $MgCl_2$, but very poor agreement (+6.35% and +8.14%) was obtained at 2.0 and 4.0 w/o, respectively. Since the technique used by Urazov and Tavkesheva to determine the electrolytic conductivity appeared to be reliable, the lack of agreement is more likely due to errors in concentration. As stated previously, Urazov and Tavkesheva diluted their saturated solutions to obtain solutions of the desired concentration. Although they checked the concentrations of their saturated solutions by density determinations, these checks could allow significant errors in concentration, for example, 6% at 4 w/o.

Although the above hypotheses on possible errors in the work of Kondrat'ev *et al.* and Urazov *et al.* cannot be substantiated because the information given in the literature is inadequate, the results presented in Table I are believed to be accurate to within the maximum uncertainties given for this study because (*a*) a proven technique was used, the electrolytic conductivities obtained for sea water using the same method and equipment agreed to within 0.7% with those of Thomas *et al.* (7), and (*b*) the agreement with Shedlovsky and Brown's (3) results was excellent.

Acknowledgments

Dr. William R. Davis, assistant director of the Applied Physics Laboratory, and staff, Mr. William Felton and Mr. Rodney Lipp, contributed to the success of this effort. Their contributions are gratefully acknowledged.

This work was supported by the Naval Ordnance Systems Command, U. S. Navy Department.

Manuscript submitted Dec. 15, 1969; revised manuscript received Aug. 14, 1970.

Any discussion of this paper will appear in a Discussion Section to be published in the June 1971 JOURNAL.

REFERENCES

1. D. W. Faletti and M. A. Gackstetter, *This Journal*, **114**, 299 (1967).
2. D. W. Faletti, M. A. Gackstetter, and J. A. Arne, *ibid.*, **116**, 552 (1969).
3. T. Shedlovsky and A. Brown, *J. Am. Chem. Soc.*, **56**, 1066 (1934).
4. V. P. Kondrat'ev and V. I. Nikich, *Russ. J. Phys. Chem., (English Transl.)*, **37**, 47 (1963).
5. V. P. Kondrat'ev and S. V. Gorbachev, *ibid.*, **35**, 326 (1961).
6. G. G. Urazov and S. M. Tavkesheva, *Izv. Sektora Fiz. Khim. Analiza, Inst. Obshch. Neorgan. Khim., Akad. Nauk SSSR (Proc. Sect. Physical-Chem. Anal., Acad. Sci. USSR)*, **26**, 275 (1955).
7. B. D. Thomas, T. G. Thompson, and C. L. Utterback, *J. Conseil, Conseil Perm. Intern. Exploration Mer*, **9**, 28 (1934).

On the Relation between Standard Potentials and Activity of Interstitial Silver Ions in AgCl and AgBr

Arnold Hoffman

Research Laboratories of Polaroid Corporation, Cambridge, Massachusetts 02139

There have been several reports (1, 2) indicating that interstitial silver ions, Ag^+_i, are involved in the reduction of a silver halide. Awad (3) recently pointed out that it is likely that the potential of a silver electrode varies with the activity of Ag^+_i in an adhering silver bromide crystal in an analogous manner to the activity of silver ions, Ag^+, in solution.

It is the purpose of this note to show that the difference in the standard potentials between a Ag/AgCl electrode and a Ag/AgBr electrode, $\Delta E°$, can be ascribed to the difference in activity of Ag^+_i in the respective silver halide crystals.

The thermodynamic relations of lattices can be found in textbooks of solid-state physics or chemistry.

Key words: silver chloride, silver bromide, interstitial silver ions, Frenkel defects.

For the sake of clarity these relations will be stated for the special case of silver halides, *e.g.*, AgCl, AgBr, where the defects are mainly of the cationic Frenkel type.

Using the notation of Kröger (4) and Honig *et. al.* (5, 6), a vacant site is denoted by V^{z}_{J-D}, an interstitial ion by J^{z}_{i-D}, and an ion on a normal lattice site by K_{J-D}, where J and K denote chemical species (J and K may be the same chemical species), D the specific silver halide lattice, V vacancy, i interstitial and z formal charge. The number of vacancy and interstitial ions are related by electroneutrality and chemical equilibrium; *e.g.*, for a pure silver halide, the total number of negative defects is equal to the total number of positive defects, *i.e.*

$$[V^{-}_{Ag-D}] + [X^{-}_{i-D}] = [V^{+}_{X-D}] + [Ag^{+}_{i-D}] \quad [1]$$

where

V^{-}_{Ag-D} = silver ion vacancy

X^{-}_{i-D} = interstitial halide ion

V^{+}_{X-D} = halide ion vacancy

Ag^{+}_{i-D} = interstitial silver ion

and

$$V^{-}_{Ag-D} + Ag^{+}_{i-D} \rightleftarrows Ag_{Ag-D} \quad [2]$$

where

Ag_{Ag-D} = silver ion in lattice position (An occupied lattice site is considered to have zero formal charge.)

For a pure silver halide

$$[V^{+}_{X-D}] = [X^{-}_{i-D}] \approx 0 \quad [3]$$

and Eq. [1] becomes

$$[V^{-}_{Ag-D}] = [Ag^{+}_{i-D}] \quad [4]$$

i.e., the number of interstitial silver ions is equal to the number of silver ion vacancies.

The thermodynamics of defects in solids can be treated in a manner analogous to the thermodynamics of solutes in solution. The vacancies and interstitial ions are to be compared to anions and cations, respectively. The silver halide lattice is to be compared to the solvent. On the assumption of ideal behavior, chemical potentials μ_{J-D}, can be expressed as functions of standard chemical potentials μ°_{J-D}, concentration of lattice sites N_{L-D}, of interstitial silver ions N_{i-D}, and of vacant silver sites N_{V-D} (N_i, $N_V \ll N_L$, N can be expressed in mole/cm^3).

The silver ion in a normal lattice position is chosen as the reference point for the thermodynamic scale (5, 6). On the assumption of ideal behavior, a silver ion in a AgCl lattice position is at the same thermodynamic point as a silver ion in a AgBr lattice position. Since this has been chosen as the reference point for the thermodynamic scale, the difference in the chemical potential of silver ions between AgCl and AgBr can be expressed in terms of the respective population of defects, *i.e.*, interstitials and vacancies.

Hence, for a silver halide crystal, with mole fractions $X_{J-D} = N_{J-D}/N_{L-D}$ introduced, we may write

$$\mu_{i-D} = \mu^{\circ}_{i-D} + RT \ln [X_{i-D}/\beta] \quad [5]$$

where β denotes the number of available interstitial sites per silver ion. (For AgBr and AgCl $\beta = 2$.)

$$\mu_{V-D} = \mu^{\circ}_{V-D} + RT \ln X_{V-D} \quad [6]$$

$$\mu_{AgAg-D} = \mu^{\circ}_{AgAg-D} + RT \ln X_{AgAg-D} \quad [7]$$

but,

$$X_{AgAg-D} \approx 1$$

and

$$\mu^{\circ}_{AgAg-D} \equiv 0 \qquad \text{(reference state)}$$

therefore

$$\mu_{AgAg-D} = 0 \quad [8]$$

If equilibrium has been attained for reaction [2], then the difference in the chemical potential of silver ions in the product and reactant states, $\Delta\mu_D$, equals zero, *i.e.*

$$\Delta\mu_D = \mu_{AgAg-D} - (\mu_{i-D} + \mu_{V-D}) = 0 \quad [9]$$

Substituting [8] into [9]

$$\Delta\mu_D = -(\mu_{i-D} + \mu_{V-D}) = 0 \text{ (at equilibrium)} \quad [10]$$

Substituting [5] and [6] into [10]

$$\mu^{\circ}_{i-D} + RT \ln[X_{i-D}/\beta] + \mu^{\circ}_{V-D} + RT \ln X_{V-D} = 0 \quad [11]$$

but from Eq. [4]

$$X_{i-D} = X_{V-D} \quad [12]$$

Substituting [12] into [11]

$$(\mu^{\circ}_{i-D} + \mu^{\circ}_{V-D}) = -RT \ln [(X_{i-D})^2/\beta] = (\mu^{\circ}_{I} + \mu^{\circ}_{V})_D \quad [13]$$

If D represents AgBr, then

$$\tfrac{1}{2}(\mu^{\circ}_{i} + \mu^{\circ}_{V})_{AgBr} = RT \ln (1/X_{i-AgBr}) + \tfrac{1}{2}RT \ln \beta \quad [14]$$

For AgCl (assuming $\mu^{\circ}_{AgAg-AgCl} = \mu^{\circ}_{AgAg-AgBr} = 0$, Eq. [8] is applicable).

$$\tfrac{1}{2}(\mu^{\circ}_{i} + \mu^{\circ}_{V})_{AgCl} = RT \ln (1/X_{i-AgCl}) + \tfrac{1}{2}RT \ln \beta \quad [15]$$

The difference in standard chemical potential of silver ions between AgCl and AgBr is given by

$$\tfrac{1}{2}(\mu^{\circ}_{i} + \mu^{\circ}_{V})_{AgCl} - \tfrac{1}{2}(\mu^{\circ}_{i} + \mu^{\circ}_{V})_{AgBr} = RT \ln [X_{i-AgBr}/X_{i-AgCl}] \quad [16]$$

The electrical work done on a charge, q, when its potential is changed ΔV, is $q\Delta V$. In transferring positive charge (interstitial silver ions) from the negative (AgBr) electrode to the positive (AgCl) electrode, electrical work is done on the cell. The work is equal to $+ nF\Delta E^{\circ}_s$, where nF is the number of charges per mole ($n = 1$), and ΔE°_s is the potential difference between AgCl and AgBr. Therefore, in the cell

$$(-)\ Ag/AgBr/Br^{-}//Cl^{-}/AgCl/Ag(+)$$

Eq. [16] becomes

$$\Delta E^{\circ}_s = [\tfrac{1}{2}(\mu^{\circ}_{i} + \mu^{\circ}_{V})_{AgCl} - \tfrac{1}{2}(\mu^{\circ}_{i} + \mu^{\circ}_{V})_{AgBr}]/F = RT/F \ln [X_{i-AgBr}/X_{i-AgCl}] \quad [17]$$

The values of $(\mu^{\circ}_{i} + \mu^{\circ}_{V})_{AgCl}$ and of $(\mu^{\circ}_{i} + \mu^{\circ}_{V})_{AgBr}$ [as obtained from application of the Boltzmann distribution law to data of ionic conductivity *vs.* temperature (7)] are 1.4 and 1.1 eV, respectively, or 1.4 and 1.1 volt-faradays per mol (1 $V\mathbf{F}$ = 96487 joules = 23061 calories). Substituting these values into Eq. [17] gives

$$\Delta E^{\circ}_s = RT/n\mathbf{F} \ln[X_{i-AgBr}/X_{i-AgCl}] = +150 \text{ mV} \quad [18]$$

This value is in excellent agreement with the difference in the standard Gibbs-Stockholm potentials between Ag/AgCl and Ag/AgBr electrodes: + 0.2222V and + 0.0713V, (*vs.* standard hydrogen electrode), respectively (8). Thus, the difference in standard potentials reflects the differences in equilibrium population of interstitials. It would seem, therefore, that the suggestion above, that the potential of a silver electrode varies with the activity of Ag^{+}_{i} in an adhering silver halide crystal in an analogous manner to the activity of silver ions, Ag^{+}, in solution, is correct.

Manuscript submitted May 12, 1970; revised manuscript received Aug. 7, 1970.

Any discussion of this paper will appear in a Discussion Section to be published in the June 1971 JOURNAL.

REFERENCES

1. W. R. Ruby and C. G. Tremmel, *J. Electroanal. Chem. Interfacial Electrochem.*, **18**, 231 (1968).
2. L. E. Brady and J. F. Hamilton, *J. Appl. Phys.*, **35**, 1565 (1964).
3. S. A. Awad, *J. Electroanal. Chem. Interfacial Electrochem.*, **21**, 483 (1969).
4. F. A. Kröger, *J. Phys. Chem. Solids*, **26**, 901 (1965).
5. E. P. Honig, *Trans. Faraday Soc.*, **64**, 2248 (1969).
6. E. P. Honig and J. H. Th. Hengst, *J. Colloid Interface Sci.*, **31**, 545 (1969).
7. C. Kittel, "Introduction to Solid State Physics," 3rd ed., p. 564, J. Wiley & Sons, Inc., New York (1967).
8. A. J. de Bethune, "Table of Standard Aqueous Electrode Potentials and Temperature Coefficients at 25°C," in "The Encyclopedia of Electrochemistry," C. A. Hampel, Editor, Reinhold Publishing Co., New York (1964).

Rapid Mass Transport to Electrodes in Foamed Electrolyte

Leonard Nanis* and Frank McLarnon[1]

School of Chemical Engineering, University of Pennsylvania, Philadelphia, Pennsylvania 19104

Foamed electrolyte, prepared by adding commercially available foaming agents to KOH and H_2SO_4 solutions has certain potentially attractive features. Gas saturation should proceed rapidly by diffusion into the foam bubble walls. The open foam structure should also permit ready removal of reaction products. By comparison, the porous electrodes used in conventional fuel cells must permit the transport and reaction of fuel gases as well as waste products removal within the complex pathways of the pore structure. Foam may be readily produced by the dispersion of fuel gas in concentrated electrolytes containing nonelectrochemically active foaming agents. Overpotential-current density studies have been made with smooth platinum electrodes immersed completely in the liquid electrolyte which is stirred by the entry of fuel gas to provide a comparison for similar measurements with electrodes totally in foam.

Experimental

The apparatus consisted of two standard Pyrex reaction kettles (500 cc) joined by a simple inverted U-tube electrolyte bridge. The kettle tops were fitted with rubber stoppers through which passed the bridge, reference and working electrodes, and a gas inlet (hydrogen, oxygen, helium) connected to a standard dispersion tube (15-20μ pore size). The anode compartment is shown in Fig. 1. The working platinum electrodes were spot-welded to a Pt wire sealed into a glass tube which was vertically movable to permit electrode positioning. A platinized-platinum electrode in contact with hydrogen saturated anolyte (either liquid or foam) provided a hydrogen reference electrode (shown schematically as the probe in Fig. 1) for the anode studies. A silver electrode was used for convenience in the cathode compartment and was frequently checked for stability against the hydrogen reference. For background studies with helium gas, a hydrogen reference electrode was separated from the anolyte by a fritted glass barrier, obtained conveniently by the use of a gas dispersion tube. The cell was operated in a driven mode in a simple constant current circuit obtained with a d-c power supply with current regulated with a decade resistance box. Electrode overpotentials were measured with a Hewlett-Packard 3430A digital voltmeter (10^7 ohm input impedance).

Electrolytes were prepared with once-distilled water and technical grade reagents without further purification. The pretreatment sequence consisted of purging each cell for about 1 hr with helium gas at about 15 cc/min through each of the 500 cc compartments. Midway through this purging, the platinum electrodes were activated with a current of about 20 mA/cm^2 reversed once a second for about twenty seconds as recommended by Petrii and Shchigorev (2). The same pretreatment sequence was used for H_2 and O_2 bubbled through the anode and cathode compartments, and for background current determinations in the presence of helium stirring. Gas purities were: H_2, 99.8%; O_2, 99.5%; He, 99.995. All gases were used without further purification.

In 4*N* H_2SO_4, the current reversal treatment gave an open circuit cell potential of 1.0V within a few minutes

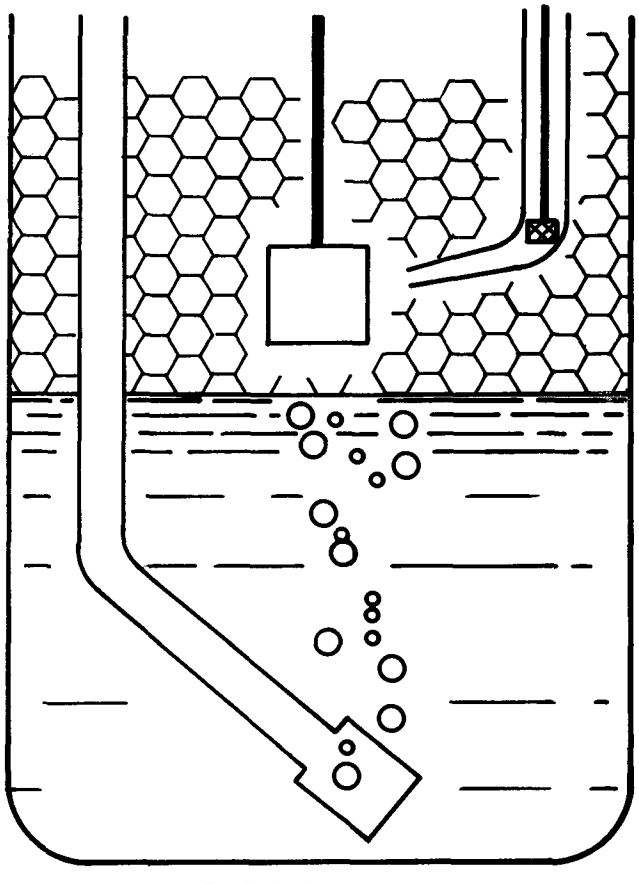

Fig. 1. Anode compartment

* Electrochemical Society Active Member.

Key words: fuel cell, foam, mass transport, hydrogen, bubbles.

[1] Present address: Department of Chemical Engineering, University of California, Berkeley, California 94720.

after treatment, declining gradually to about 0.85V after 5-10 min. In KOH (2-6*N*), the potential reached about 1.0-1.1V within 1-5 min after activation, changing very little thereafter.

Following helium pretreatment, a blank test with helium stirring was conducted. Anode and cathode overpotentials were recorded for current density steps of 10 μA/cm^2 up to 100 μA/cm^2 both in the electrolyte well-stirred by helium bubbles and in the foam above the electrolyte. After H_2 and O_2 pretreatment, anode and cathode overpotentials were recorded for 0.1 mA/cm^2 steps to 1.0 mA/cm^2 for the electrolyte immersed completely in the well-stirred liquid electrolyte, and at 0.5 mA/cm^2 intervals up to 12 mA/cm^2 for the electrode withdrawn completely into the foam. At each current, steady potentials were recorded with the time for attainment of steady overpotentials usually less than 30 sec except near the limiting current density where times on the order of one minute were needed. For studies of the anode (square electrode, Fig. 1) immersed in liquid, stirring was provided by positioning the electrode directly in the ascending stream of hydrogen bubbles.

For a typical run (using 0.2 weight per cent [w/o] Carboxane TW-100, Textilana Corp., Hawthorne, Calif.) in 4*N* H_2SO_4 electrolyte at 22°C, the foam height measured from the liquid-foam interface increased from 3 cm to 10 cm as the gas flow rate was increased from 0.5 cc/min to 20 cc/min. As the temperature was increased from 7° to 65°C, the foam level (for a flow rate of 4 cc/min) decreased from 5 cm to 1 cm. However, the anodic limiting current density remained at 9 ± 0.5 mA/cm^2 over the temperature range. For foam height under 2 cm, the upper section of the 2 x 1.4 cm smooth platinum electrode was uncovered by foam.

For studies with 0.2 w/o Actrasol PSR foamant (A. C. Trask Co., Chicago, Illinois), the foam level at constant gas flow rate decreased from 5 cm to essentially no foam (even at gas flow rates greater than 100 cc/min) as the KOH electrolyte concentration was increased from 2 to 6*N*.

Results and Discussion

Various foaming agents were initially tested in both 4*N* H_2SO_4 and 2*N* KOH. Oxidizable or reducible agents, as determined by current passage in the blank helium test, were rejected. Foaming agents chosen for study generally produced an order of magnitude improvement in current when the electrodes were withdrawn from the liquid electrolyte into the foam.

In 4*N* H_2SO_4, best results were obtained with Carboxane TW-100, an alcohol ethoxylate, which gave a nearly constant foam level and essentially invariant overpotential-current density response at foamant concentrations ranging from 0.02 to 1.0 w/o. In KOH, the agent giving the greatest current increase was Actrasol PSR, potassium sulfo-ricinoleate, used at 0.2 w/o in 2-6*N* KOH. Comparison of various foamants is shown in Table I.

The current density-overpotential behavior for H_2 oxidation in liquid and in foam for Carboxane TW-100 in 4*N* H_2SO_4 is shown in Fig. 2. The lowest curve, designated "in foam" (triangle points), was obtained for foam produced by helium bubbling. A nearly similar curve (not shown) was obtained for the helium-stirred liquid background anode determination. Clearly defined anode limiting current densities (*cf.* Fig. 2) were obtained for hydrogen oxidation in all solutions tested and were used to compute an equivalent mass transfer boundary layer thickness, assuming uniform current density distribution. Hydrogen diffusion and solubility data (uncorrected from 30°C) of Ruetschi (1) were used in the expression

$$J_{lim} = \frac{nF\mathcal{D}C_b}{\delta} \qquad [1]$$

Results are shown in Table I. Clear resolution of cathodic limiting current densities was not generally obtained, so that δ values were not calculated. However, cathodic currents were always greater in foam than in bubble-stirred electrolyte. An index of the foam effect is the ratio of cathodic oxygen reduction current in foam to current in stirred liquid at a potential of 0.4V with respect to the hydrogen reference electrode of the anode compartment. The foam-liquid current ratio ranged from 26 for Actrasol PSR in 4*N* KOH to low values of 3.7 for Aromox T/12 in 2*N* KOH and 1.6 for BRIJ 30 in 4*N* H_2SO_4. At a potential of 0.1V, the foam-liquid current ratio for BRIJ 30 in 4*N* H_2SO_4 increased to 3.4, while the ratio for Aromox T/12 in 2*N*

Table I. Anode mass transport

Additive (0.2 w/o)	Electrolyte	H_2 flow rate (cc/min)	Boundary layer thickness δ (μ) In liquid electrolyte	In foam
Carboxane TW-100[1]	2*N* KOH	15.0	—	9.6
Carboxane TW-100[1]	4*N* H_2SO_4	4.0	74	2.8
Actrasol PSR[2]	2*N* KOH	15.0	48	5.7
Actrasol PSR[2]	3*N* KOH	15.0	29	2.9
Actrasol PSR[2]	4*N* KOH	4.0	46	3.3
Actrasol PSR[2]	5*N* KOH	100	16	3.1
Aromox C/12[3]	4*N* H_2SO_4	4.0	61	3.5
Aromox C/12[3]	2*N* KOH	4.0	61	10.8
Aromox T/12[4]	4*N* H_2SO_4	9.0	74	3.9
Aromox T/12[4]	2*N* KOH	4.0	86	14.3
FC—95[5]	4*N* H_2SO_4	4.0	74	3.7
FC—408[6]	4*N* H_2SO_4	4.0	83	12.1
BRIJ—30[7]	4*N* H_2SO_4	4.0	51	4.1

[1] Alcohol ethoxylate, Textilana Corp., Hawthorne, California.
[2] Potassium sulfo-ricinoleate, A. C. Trask Co., Chicago, Illinois.
[3] bis (2-hydroxyethyl) cocoamine oxide, Armour, Chicago, Illinois.
[4] bis (2-hydroxyethyl) tallowamine oxide, Armour, Chicago, Illinois.
[5] Anionic fluorocarbon, 3M Co., St. Paul, Minnesota.
[6] Amphoteric fluorocarbon, 3M Co., St. Paul, Minnesota.
[7] Polyoxyethylene (4) lauryl ether, Atlas Chemical Industries, Wilmington, Delaware.

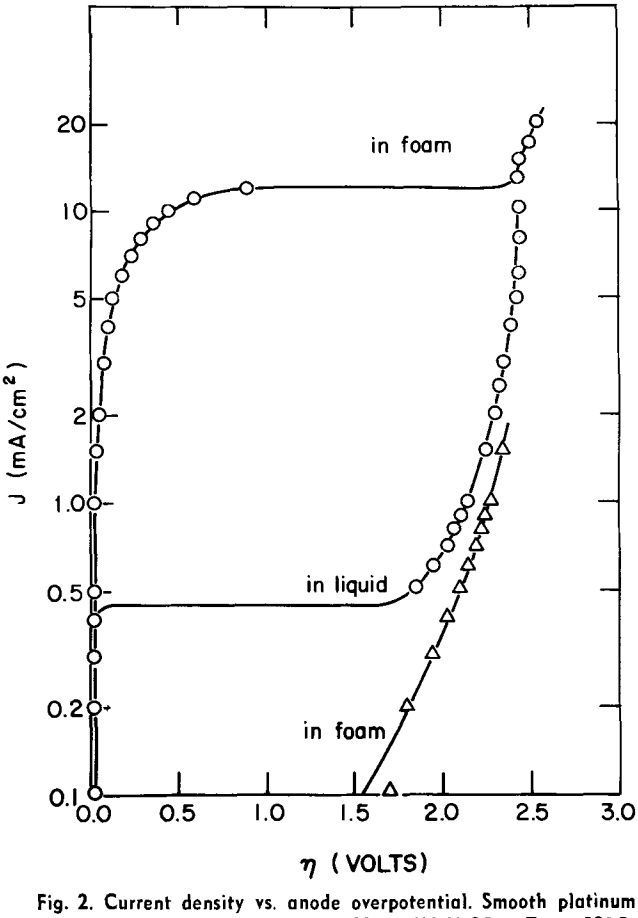

Fig. 2. Current density vs. anode overpotential. Smooth platinum electrode; 0.1 w/o Carboxane TW-100 in 4*N* H_2SO_4; T = 23°C; P = 1 atm; gas flow at 4 cc/min; △, helium; ○, hydrogen.

KOH was 5.8. It should be noted that the foam-liquid current ratio for Actrasol PSR in 4*N* KOH was essentially constant over a wide potential range (32 at 0.65V, 30 at 0.1V). Cathode current density in foam ranged from 3 mA/cm^2 at 0.65V to 9 mA/cm^2 at 0.1V. Table I shows that boundary layer thickness for the anode immersed in electrolyte stirred by hydrogen varies between 46 and 83μ as the flow rate varies from 9 to 4 cc/min in 500 cc of liquid, *i.e.*, as expected, smaller δ was associated with high flow rates. In the foam, the equivalent boundary layer thicknesses are very much less than for the well-stirred electrolyte, with the calculated values grouped chiefly around 3-4μ with an apparent second range of 10-14μ.

The 3-4μ values (Table I) may be explained in terms of a thin film of electrolyte covering the electrode when it is in the foam. Many researchers (3-8) have noted a similar increase in current when electrodes were partially withdrawn from liquid electrolyte into a gas atmosphere. For instance, Will (5) has determined that for a partially withdrawn platinum electrode, the rate-controlling step for hydrogen oxidation is the diffusion of the gas through a thin electrolyte film completely covering the electrode. Also, Burshtein (4) and Müller (9) have optically determined the establishment of an electrolyte film thickness on the order of several microns covering an electrode partially withdrawn from solution. Since present electrochemical determination indicates a mass transfer layer of a few microns in thickness in the foam region, it may be considered that the foam acts to stabilize an electrolyte film on the electrode. Insufficient data are presently available for speculation about the interaction of foamants in electrolytes which produce the 10-14μ range of computed layers.

Will (5), Bennion and Tobias (7), and Burshtein *et al.* (4) have determined that most of the current on a partially immersed electrode is passed in a critical reaction zone, on and near the meniscus. In the foam, since the electrode is completely withdrawn from the solution, there can be no conventional meniscus, and the more uniform film permits more useful electrode surface to be available for reaction.

Further studies of foam conductivity, current distribution and applications of the foam method to electrode reactions will be reported shortly.

Acknowledgments

Financial support of NASA (NSG-316), the NSF Undergraduate Research Program and Matthey-Bishop is gratefully acknowledged as well as the generous loan of platinum electrodes from Matthey-Bishop Inc., Malvern, Pennsylvania, and of foaming agents from the various companies cited in Table I in the text.

Manuscript submitted April 6, 1970; revised manuscript received *ca.* July 30, 1970.

Any discussion of this paper will appear in a Discussion Section to be published in the June 1971 JOURNAL.

REFERENCES

1. P. Ruetschi, *This Journal*, **114**, 301 (1967).
2. O. Petrii, and I. Shchigorev, *Soviet Electrochem.*, **4**, 332 (1968).
3. V. Shepelin, T. Zalkind, and V. Veselovskii, *ibid.*, **2**, 946 (1966).
4. R. Burshtein, M. Tarasevich, S. Chernyshov, and Y. Chirkov, *ibid.*, **4**, 1154 (1968).
5. F. Will, *This Journal*, **110**, 145 (1963).
6. F. Will, *ibid.*, **114**, 138 (1967).
7. D. Bennion and C. Tobias, *ibid.*, **113**, 589 (1966).
8. V. Belokopytov and N. Aladzhalova, *Soviet Electrochem.*, **2**, 1149 (1966).
9. R. Müller, *This Journal*, **113**, 943 (1966).

DISCUSSION SECTION

This Discussion Section includes discussion of papers appearing in the *Journal of The Electrochemical Society*, Vol. 116, No. 7 and 11, July and November, 1969, and Vol. 117, No. 1 and 5, January and May, 1970.

Study of the Lithium Oxide-Nickel Oxide System. I. Thermodynamics of Dilute Solid Solutions

S. Pizzini, R. Morlotti, and V. Wagner
(pp. 915-920, Vol. 116, No. 7)

J. Deren and **G. Róg**[1]: By measurements of emf of appropriate solid galvanic cells Pizzini *et al.* determine in their work the thermodynamic properties of solid solutions of Li_2O in NiO. There are some remarks which we would like to make in connection with this problem.

1. In their work Pizzini *et al.* assume the possibility of only one mechanism of incorporation of lithium in an oxidizing atmosphere

$$0.5\,Li_2O + 0.25\,O_2 \rightleftharpoons Li^{\cdot}_{Ni} + O_o + h \qquad [1]$$

As we showed in 1964[2] the mechanism of lithium incorporation is more complicated. In the region of low concentrations of lithium, up to about 0.1 a/o, a number of phenomena have been observed which can be explained only by accepting another mechanism of lithium incorporation in this concentration region. The possible ways of formation of low-concentration solutions of Li_2O in NiO have been suggested also.[2,3] Recent studies on the emf of the appropriate solid cells confirmed the different behavior of the low- and high-concentration solutions.[4,5]

2. In our laboratory we carried out the methodological investigations of measurement of solid galvanic cells given by the scheme

$$Pt|Ni, NiO_{pure}||\text{solid electrolyte}||NiO_{doped}, Ni|Pt \qquad [2]$$

with the use of the lime-zirconia electrolye/0.85 ZrO_2 + 0.15 CaO.[6] In contrast to Pizzini we did not observe the drop of the voltage with time to values close to zero. As may be seen from the data listed in our Table I, a very good constancy of the emf value is observed during the measurement carried out for 10 hr at 900°C.

3. The suggestion of the authors ascribing the observed drop of the voltage (see above) to irreversible migration of lithium from the left-hand compartment to the right-hand one, when $x_2 > x_1$, is not clear to us. As is known, the zirconia-lime electrolyte is defective practically solely in the anion sublattice. It is possible that incorrect sintering of the electrolyte caused the possibility of lithium migration along the grain boundaries. The reproducibility of our results amounted to 0.02 mV.[4,7]

4. Application by the authors of α-Li_2SO_4 as the solid electrolyte raises the question whether, during heating of the samples in the course of measurements conducted at temperatures 570°-850°C, the diffusion of

[1] Institute of Solid State Chemistry, School of Mining and Metallurgy, Kraków, Poland.
[2] A. Bielanski, K. Dyrek, Z. Kluz, J. Sloczynski, and T. Tobiasz, *Bull. Acad. Polon. Sci., Ser. sci. chim.*, 12, 657 (1964).
[3] J. Deren, J. Nowotny, and J. Ziólkowski, *Bull. Acad. Polon. Sci., Ser. sci. chim.*, 16, 657 (1968).
[4] J. Deren and G. Róg, *Bull. Acad. Polon. Sci., Ser. sci. chim.*, 16, 491 (1968).
[5] J. Deren and G. Róg, *Bull. Acad. Polon. Sci., Ser. sci. chim.*, 17, 327 (1969).
[6] K. Kiukkola and C. Wagner, *This Journal*, 104, 308 (1957).
[7] G. Róg, Thesis, Kraków, 1970.

Table I. Dependence of emf of solid galvanic cells given by scheme 2 on the time of measurement. Lithium concentration $c_{Li} = 2.50$ a/o

t, min	EMF, mV
15	31,124
30	31,123
45	31,135
60	31,120
90	31,112
120	31,126
150	31,123
180	31,130
210	31,141
240	31,130
270	31,128
300	31,116
330	31,119
360	31,125
390	31,121
420	31,113
450	31,126
480	31,124
510	31,116
540	31,131
570	31,122
600	31,121

Table II. Activity coefficients of Li_2O (f_{Li_2O}) in solid solution Li_2O in NiO

c_{Li}, a/o	f_{Li_2O} 700°	750°	800°	850°	900°
1	2	3	4	5	6
0.20	0.016	0.020	0.024	0.028	0.033
0.24	0.016	0.020	0.024	0.028	0.033
0.30	0.016	0.020	0.024	0.028	0.033
0.38	0.016	0.020	0.024	0.028	0.033
0.50	0.016	0.020	0.024	0.028	0.033
0.60	0.017	0.020	0.024	0.029	0.033
0.80	0.017	0.020	0.024	0.029	0.034
0.85	0.017	0.020	0.024	0.029	0.034
1.28	0.017	0.021	0.025	0.029	0.034
1.40	0.017	0.021	0.025	0.029	0.034
2.00	0.018	0.021	0.026	0.030	0.035
2.50	0.018	0.022	0.026	0.031	0.036
3.40	0.019	0.023	0.027	0.032	0.037

lithium from the electrolyte to solid solutions of lithium in nickel oxide did not take place. If such diffusion were possible, the cell would then become irreversible. Relatively poor reproducibility of the emf measurements, 5-10 mV, observed in experiments in which this value was low, up to 80 mV, may imply the occurrence of such processes. The studies carried out by us[5,7] on the solid cell given by the scheme

$$Pt|Ni, NiO||0.85ZrO_2 + 0.15CaO||NiO, Li_2O, Ni|Pt \quad [3]$$

indicate that for these temperatures incorporation of Li into the parent lattice of NiO occurs relatively fast, resulting in the formation of the appropriate electromotive force.

5. It appears from the paper that the authors regard solid solutions of lithium oxide in nickel oxide containing below 1.5 a/o Li as ideal solutions. Our studies show that even in this concentration range the solutions cannot be classified as ideal. However, they behave as the regular solutions. In the region of concentration under discussion the activity coefficients depend only slightly on the concentration of Li incorporated, $f_1 \approx f_2$.[7] This is illustrated by the data of our Table II. In our opinion it is due to this fact that the Nernst equation

$$E = \frac{RT}{F} \ln \frac{a_1}{a_2} = \frac{RT}{F} \ln \frac{f_1 x_1}{f_2 x_2} \approx \frac{RT}{F} \ln \frac{x_1}{x_2} \quad [4]$$

is obeyed.

S. Pizzini[7a] and **R. Morlotti:** The work of both Professor Deren and ourselves on the lithium oxide-nickel oxide system was concluded in the same month and independently so we learned only later, unfortunately of the alternative approach used by the authors in footnote 4.

[7a] Now at the Institute of Electrochemistry, University of Milano, Italy.

Table I. Effect of lithium diffusion

	Li ppm in the electrode	Li ppm in the electrolyte	Li ppm in the electrode
Before the experiment	91	—	1860
After the experiment	243	320	1430

With regard to the first point of Professor Deren's remarks, about the possibility that other defect mechanisms, different from the purely substitutional one, which is described by our Eq. [1]

$$0.5\ Li_2O + 0.25\ O_2 \rightarrow Li_{Ni} + O_O + h^{\cdot} \quad [1]$$

could be operative in the range of dilute solutions, we stress the point that we carried out our measurements in a concentration range of dissolved lithium ($x_{Li} > 0.1$ a/o) where also according to footnotes 9 and 10 only the mechanism described by Eq. [1] is active. The omission of comments about other mechanism, however, could have raised some misunderstandings about the role of other defects, such as nickel vacancies in the range of the very dilute solutions. As to the second point, we would like to mention that the cell used by Deren and Rog[8,11,12] is different from that used preliminarily by us, since we fitted lime zirconia (in oxidizing atmosphere) with two electrodes which did not contain any metallic nickel. Table I, published here, which was omitted in our paper, shows the effect of lithium diffusion in the electrolyte, after having operated the cell for some days at 1000°C. Lower temperature (900°C) and excess nickel in the reducing atmosphere might well be responsible for the reduced reactivity of the system, so that we do not see any contradiction between our results and those of Deren and Rog.

We do not exclude the possibility that lithium migration could have taken place along grain boundaries, but this, in our opinion, has nothing to do with the incorrect sintering of the electrolyte. In all polycrystalline materials, and when the temperature is lower or of the order of magnitude of the Tamann temperature, one could never exclude contributions from surface or grain boundary migration. Moreover, it has been demonstrated recently that protons[13] could diffuse with the interstitial mechanism in stabilized zirconia, the order of magnitude of the diffusion coefficient being 10^{-6} cm^2 sec^{-1} at 900°C.

It seems therefore not entirely surprising that a small size ion such as lithium ion is, could diffuse in stabilized zirconia.

As to the other points, it is our opinion that it is rather difficult to compare directly our results with those of footnotes 8, 11, 12. Our results, in fact, refer to samples with known lithium content and known Ni^{3+} content (for details see footnotes 14 and 15 as well as the paper now in discussion) which have been never equilibrated with metallic nickel. Analysis of lithium and Ni^{3+} content before and after each measurement permits the care of the negligible influence of the Li_2SO_4 decomposition in oxygen atmosphere on the lithium content in the electrodes and of the negligible deviations from the 1:1 ratio between the lithium added and entirely dissolved and Ni^{3+} found.

Professor Deren's results, on the contrary, all refer to samples of known lithium content (but possibly not entirely dissolved) and of unknown Ni^{3+} content,

[8] J. Deren and G. Róg, *Bull. Acad. Polon. Sci.* (*Engl.*) **16**, 9, 491 (1968).
[9] J. Deren and J. Ziólkowski, *Bull. Acad. Polon. Sci.* (*Engl.*) **14**, 7, 443, (1966).
[10] A. Bielanski and J. Deren, from "Symposium on electric phenomena in chemisorption and cathalisis on semiconductors," K. Hauffe and Th. Wolkenstein, Editors, W. de Gruyters, Berlin (1969).
[11] J. Deren and G. Róg, *Bull. Acad. Polon. Sci.* (*Engl.*) **17**, 6, 327 (1969).
[12] J. Deren and G. Róg, *Zesz. Nauk. Akad. Gorn. Hutn.*, **207**, 125 (1969).
[13] C. Wagner, *Ber. Bunsengesell*, **72**, 7, 778 (1968).
[14] C. J. Toussaint and C. Vos, *J. Appl. Cryst.*, **I**, 187 (1968).
[15] C. Geel, R. Morlotti and S. Pizzini, Euratom Rep. 4390 (1970).

which is presumably inadequate over the 1:1 ratio, due to the presence of metallic nickel.

In our opinion, so far there is no experimental evidence that excess nickel does not influence the 1:1 ratio within the dissolved lithium and localized electron holes (or Ni^{3+}); one has to treat the solutions with and without nickel excess as different solutions. We also raise some doubts on the reliability of the regular solution approach used by Professor Deren and colleagues, just on the basis of the experimental temperature coefficients of concentration cells, calculated with the classical Hildebrand approach from the results reported in footnote 12, which largely differ from the theoretical purely configurational values.

On the Breakdown of Passivity on Stainless Steels in Halide Media

B. E. Wilde and E. Williams, (pp. 1539-1540, Vol. 116, No. 7)

N. D. Greene[16] and **W. D. France, Jr.**[17]: The authors explanation that slight changes in critical pitting potentials are "related to the presence of nonionic, nonelectroactive constituents in the corrodent" prompts this discussion. In our recent study[18] of the critical breakdown potential, E_c, we noted that oxygen produces effects different from other oxidizers because its reduction yields hydroxide. Oxygen reduction can occur during anodic polarization in aerated solutions because of the noble redox potential of the O_2/OH^- couple. As a result, the pH increases at the metal-electrolyte interface which shifts the breakdown potential in the noble direction.[19] Thus, our theoretical model predicts that E_c should become more noble as the O_2 content increases.

Our concept is qualitatively confirmed by the results of Mueller and Greener.[20] The experiments of Wilde and Williams also can be viewed as supporting this mechanism, that is, E_c is more noble in oxygenated solutions than in deaerated media. However, the Wilde-Williams data do not exhibit a direct correlation between E_c and oxygen levels at low concentrations where it appears that the reported oxygen contents are beyond both the accuracy and repeatability of the Beckman Model 778 Process Oxygen Analyzer[21] employed. The accuracy of this instrument is limited by its polarographic sensing probe to $\pm 1\%$. At the lowest range, 2.5 ppm, this introduces an error of ± 0.025 ppm. Consequently, we would be interested in learning more about the author's measurements of oxygen in solution, especially any refinements that were used to obtain the degree of accuracy reported.

B. E. Wilde and **E. Williams:** We would like to thank Drs. Greene and France for their interest in our paper and their comments. In reply, we shall clarify the issues raised in two parts: 1, details regarding the analysis of dissolved oxygen, and 2, the effect of oxygen on the critical pitting potential.

1. Since we made no statements regarding the accuracy of our measurements in our communication, we can only assume that Drs. Greene and France are referring in their discussion to the sensitivity[22] of the oxygen probe measurements. In this regard in connection with other work, one of us (BEW) has determined the limits of sensitivity of an identical polarographic probe to oxygen in pressurized water using an independent method of analysis[23] modified to operate in the range of 0.01-0.1 ppm O_2. Briefly, we exposed a Beckman probe to recirculating pure water at 1200 psig, the oxygen content of which was controlled in the range 0.01-0.1 ppm O_2 by conventional gas sparging techniques.[24] It was found, by using a recorder connected to the Beckman amplifier output, that changes in oxygen concentration in the range 0.025 to 0.05 ppm and up, could be detected, although the absolute accuracy was no better than $\pm 25\%$. However, in no case was a reading observed where the probe output was not qualitatively related to the oxygen content of the water. That is, readings always reflected incremental increases and decreases of oxygen in a qualitative manner. As a matter of interest, the above correlation was not confined to one probe, but was observed on a number of probes used throughout the investigation.

In view of this, we feel that the reported oxygen contents in our paper are qualitatively correct, *e.g.*, more dissolved oxygen resulted after purging with hydrogen than that resulting from argon, etc. We have to concede that the absolute magnitudes of the oxygen concentrations may be somewhat different than the reported values at the lowest levels, but we feel that this point is of minor significance in view of the over-all objectives of our communication.

2. The purpose of our communication was to draw attention to the fact that experimental values of the critical pitting potential could vary (in the case of Type 430 stainless steel in 1*N* NaCl at 25°C) from -0.185 to -0.035 V_{SCE}, depending on whether hydrogen or oxygen, respectively, were employed to purge the corrodent. It was also noted that apparently such nonionic and nonelectroactive substances as argon and nitrogen could also affect E_c by a significant amount rather than a "slight change" as described by Greene and France.

In an attempt to explain this behavior, we suggested that (*a*) hydrogen could be oxidized to H^+ on the anode surface, and (*b*) oxygen could be reduced; these reactions may account for the variation in E_c. More recent studies[25] have shown that the effect of oxygen is due to local pH changes at the metal/electrolyte interface following cathodic reduction of oxygen, a fact which apparently Greene and France surmized in a footnote in their recent paper,[26] yet overlooked in their conclusions regarding the correlation between electrochemical and chemical pitting tests. We could not and still cannot explain the effect of argon and nitrogen.

While there may be some uncertainty about the absolute magnitude of dissolved oxygen resulting from purging with argon and hydrogen as discussed earlier, we feel that two significant facts emerge from the data: (*a*) the variations in E_c observed in argon and nitrogen purged solutions cannot be explained on the oxygen content of the solution alone and (*b*) more importantly we have shown[27] that the pronounced effect of oxygenation on E_c is the cause of the reported lack of correlation between electrochemical and chemical accelerated pitting tests on stainless steels.

Oxidation of C-25 w/o Cr at High Temperatures

P. K. Kofstad and A. Z. Hed (pp. 1542-1550, Vol. 116, No. 11)

S. Mrowec and **T. Werber**[28]: In their interesting papers concerning kinetics and mechanism of oxidation of Co-Cr alloys, Kofstad and Hed[29-31] consider some gen-

[16] Institute of Materials Science, The University of Connecticut, Storrs, Connecticut 06268.
[17] Research Laboratories, General Motors Technical Center, Warren, Michigan 48090.
[18] W. D. France, Jr. and N. D. Greene, Paper 128 presented at the NACE Annual Conference, Houston, Texas, March 1969; *Corrosion*, 26, 1 (1970).
[19] H. P. Leckie and H. H. Uhlig, *This Journal*, 113, 1262 (1966).
[20] H. J. Mueller and E. H. Greener, *J. Biomed. Mat. Res.*, 4, 29 (1970).
[21] Beckman Model 778 Process Oxygen Analyzer, Bulletin 0-4041, Beckman Instruments, Inc. Process Instruments Division, Fullerton, California 92634.
[22] A. J. Duncan, "Quality Control and Industrial Statistics," p. 649, Richard D. Irwin Inc. (1955).
[23] B. E. Wilde and F. G. Hodge, *Ind. Eng. Chem., Product R&D*, 8, 408 (1969).
[24] W. L. Pearl, M. D. Fitzsimmons, and M. Siegler, G.E.A.P. Report No. 3748, June 6, 1961.
[25] B. E. Wilde, E. Williams, and C. D. Kim, To be published.
[26] W. D. France, Jr. and N. D. Greene, *Corrosion*, 26, 1 (1970).
[27] B. E. Wilde and E. Williams, *This Journal*, 117, 775 (1970).
[28] Institut of Solid State Chemistry, School of Mining and Metallurgy, Cracow, Poland.
[29] P. K. Kofstad and A. Z. Hed, *This Journal*, 116, 224 (1969).
[30] P. K. Kofstad and A. Z. Hed, *This Journal*, 116, 229 (1969).
[31] P. K. Kofstad and A. Z. Hed, *This Journal*, 116, 1542 (1969).

which is presumably inadequate over the 1:1 ratio, due to the presence of metallic nickel.

In our opinion, so far there is no experimental evidence that excess nickel does not influence the 1:1 ratio within the dissolved lithium and localized electron holes (or Ni^{3+}); one has to treat the solutions with and without nickel excess as different solutions. We also raise some doubts on the reliability of the regular solution approach used by Professor Deren and colleagues, just on the basis of the experimental temperature coefficients of concentration cells, calculated with the classical Hildebrand approach from the results reported in footnote 12, which largely differ from the theoretical purely configurational values.

On the Breakdown of Passivity on Stainless Steels in Halide Media

B. E. Wilde and E. Williams, (pp. 1539-1540, Vol. 116, No. 7)

N. D. Greene[16] and **W. D. France, Jr.**[17]: The authors explanation that slight changes in critical pitting potentials are "related to the presence of nonionic, nonelectroactive constituents in the corrodent" prompts this discussion. In our recent study[18] of the critical breakdown potential, E_c, we noted that oxygen produces effects different from other oxidizers because its reduction yields hydroxide. Oxygen reduction can occur during anodic polarization in aerated solutions because of the noble redox potential of the O_2/OH^- couple. As a result, the pH increases at the metal-electrolyte interface which shifts the breakdown potential in the noble direction.[19] Thus, our theoretical model predicts that E_c should become more noble as the O_2 content increases.

Our concept is qualitatively confirmed by the results of Mueller and Greener.[20] The experiments of Wilde and Williams also can be viewed as supporting this mechanism, that is, E_c is more noble in oxygenated solutions than in deaerated media. However, the Wilde-Williams data do not exhibit a direct correlation between E_c and oxygen levels at low concentrations where it appears that the reported oxygen contents are beyond both the accuracy and repeatability of the Beckman Model 778 Process Oxygen Analyzer[21] employed. The accuracy of this instrument is limited by its polarographic sensing probe to $\pm 1\%$. At the lowest range, 2.5 ppm, this introduces an error of ± 0.025 ppm. Consequently, we would be interested in learning more about the author's measurements of oxygen in solution, especially any refinements that were used to obtain the degree of accuracy reported.

B. E. Wilde and **E. Williams:** We would like to thank Drs. Greene and France for their interest in our paper and their comments. In reply, we shall clarify the issues raised in two parts: 1, details regarding the analysis of dissolved oxygen, and 2, the effect of oxygen on the critical pitting potential.

1. Since we made no statements regarding the accuracy of our measurements in our communication, we can only assume that Drs. Greene and France are referring in their discussion to the sensitivity[22] of the oxygen probe measurements. In this regard in connection with other work, one of us (BEW) has determined the limits of sensitivity of an identical polarographic probe to oxygen in pressurized water using an independent method of analysis[23] modified to operate in the range of 0.01-0.1 ppm O_2. Briefly, we exposed a Beckman probe to recirculating pure water at 1200 psig, the oxygen content of which was controlled in the range 0.01-0.1 ppm O_2 by conventional gas sparging techniques.[24] It was found, by using a recorder connected to the Beckman amplifier output, that changes in oxygen concentration in the range 0.025 to 0.05 ppm and up, could be detected, although the absolute accuracy was no better than $\pm 25\%$. However, in no case was a reading observed where the probe output was not qualitatively related to the oxygen content of the water. That is, readings always reflected incremental increases and decreases of oxygen in a qualitative manner. As a matter of interest, the above correlation was not confined to one probe, but was observed on a number of probes used throughout the investigation.

In view of this, we feel that the reported oxygen contents in our paper are qualitatively correct, *e.g.*, more dissolved oxygen resulted after purging with hydrogen than that resulting from argon, etc. We have to concede that the absolute magnitudes of the oxygen concentrations may be somewhat different than the reported values at the lowest levels, but we feel that this point is of minor significance in view of the over-all objectives of our communication.

2. The purpose of our communication was to draw attention to the fact that experimental values of the critical pitting potential could vary (in the case of Type 430 stainless steel in 1*N* NaCl at 25°C) from -0.185 to -0.035 V_{SCE}, depending on whether hydrogen or oxygen, respectively, were employed to purge the corrodent. It was also noted that apparently such nonionic and nonelectroactive substances as argon and nitrogen could also affect E_c by a significant amount rather than a "slight change" as described by Greene and France.

In an attempt to explain this behavior, we suggested that (*a*) hydrogen could be oxidized to H^+ on the anode surface, and (*b*) oxygen could be reduced; these reactions may account for the variation in E_c. More recent studies[25] have shown that the effect of oxygen is due to local pH changes at the metal/electrolyte interface following cathodic reduction of oxygen, a fact which apparently Greene and France surmized in a footnote in their recent paper,[26] yet overlooked in their conclusions regarding the correlation between electrochemical and chemical pitting tests. We could not and still cannot explain the effect of argon and nitrogen.

While there may be some uncertainty about the absolute magnitude of dissolved oxygen resulting from purging with argon and hydrogen as discussed earlier, we feel that two significant facts emerge from the data: (*a*) the variations in E_c observed in argon and nitrogen purged solutions cannot be explained on the oxygen content of the solution alone and (*b*) more importantly we have shown[27] that the pronounced effect of oxygenation on E_c is the cause of the reported lack of correlation between electrochemical and chemical accelerated pitting tests on stainless steels.

Oxidation of C-25 w/o Cr at High Temperatures

P. K. Kofstad and A. Z. Hed (pp. 1542-1550, Vol. 116, No. 11)

S. Mrowec and **T. Werber**[28]: In their interesting papers concerning kinetics and mechanism of oxidation of Co-Cr alloys, Kofstad and Hed[29-31] consider some gen-

[16] Institute of Materials Science, The University of Connecticut, Storrs, Connecticut 06268.
[17] Research Laboratories, General Motors Technical Center, Warren, Michigan 48090.
[18] W. D. France, Jr. and N. D. Greene, Paper 128 presented at the NACE Annual Conference, Houston, Texas, March 1969; *Corrosion*, 26, 1 (1970).
[19] H. P. Leckie and H. H. Uhlig, *This Journal*, 113, 1262 (1966).
[20] H. J. Mueller and E. H. Greener, *J. Biomed. Mat. Res.*, 4, 29 (1970).
[21] Beckman Model 778 Process Oxygen Analyzer, Bulletin 0-4041, Beckman Instruments, Inc. Process Instruments Division, Fullerton, California 92634.
[22] A. J. Duncan, "Quality Control and Industrial Statistics," p. 649, Richard D. Irwin Inc. (1955).
[23] B. E. Wilde and F. G. Hodge, *Ind. Eng. Chem., Product R&D*, 8, 408 (1969).
[24] W. L. Pearl, M. D. Fitzsimmons, and M. Siegler, G.E.A.P. Report No. 3748, June 6, 1961.
[25] B. E. Wilde, E. Williams, and C. D. Kim, To be published.
[26] W. D. France, Jr. and N. D. Greene, *Corrosion*, 26, 1 (1970).
[27] B. E. Wilde and E. Williams, *This Journal*, 117, 775 (1970).
[28] Institut of Solid State Chemistry, School of Mining and Metallurgy, Cracow, Poland.
[29] P. K. Kofstad and A. Z. Hed, *This Journal*, 116, 224 (1969).
[30] P. K. Kofstad and A. Z. Hed, *This Journal*, 116, 229 (1969).
[31] P. K. Kofstad and A. Z. Hed, *This Journal*, 116, 1542 (1969).

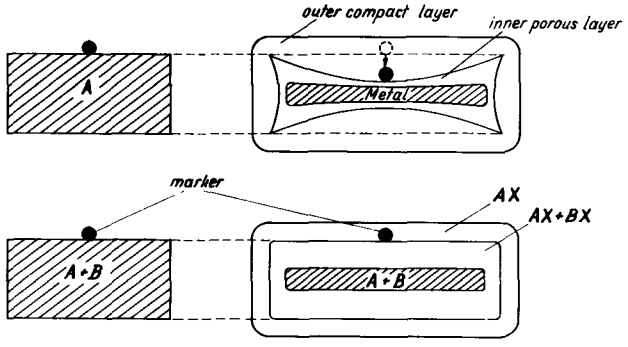

A — more noble base metal (Cu, Ni, Fe, Co)
B — alloying addition (Zn, Cr, Si, Al)
X — oxidizer

Fig. 1. Schematic representation of limiting cases

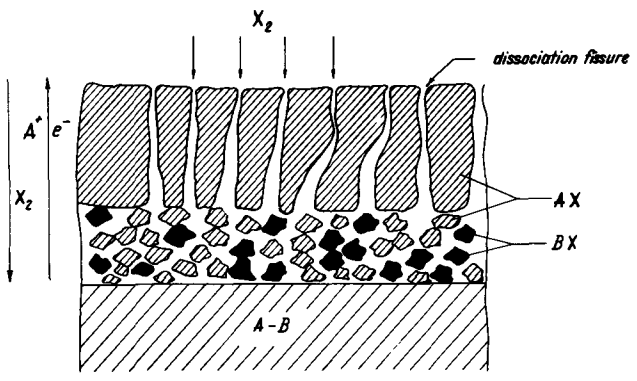

Fig. 2. Schematic representation of outward lattice diffusion of the basis metal and of inward diffusion of the oxidant.

eral problems involved in the theory of oxidation of metals and alloys. In particular these authors pay much attention to the mechanism of transport of matter through the scale in the course of oxidation of Co-Cr alloys. This problem has been extensively studied also in our laboratories.[32-41] On the basis of model studies carried out on the Ag-Zn-S, Cu-Zn-S, Ni-Cr-S, and Fe-Cr-S systems we proposed a new model for the mechanism of formation of double layer, heterophase scales on binary alloys. The model pertains to the systems in which the oxidation products of the alloy components do not form solid solutions, and the defect structure of which is confined solely to the cation sublattice. It was shown that the heterophase scale grown on the alloys of this type (Cu-Zn, Fe-Cr, Ni-Cr, Co-Cr, etc.) is composed as a rule of two layers: the outer monophase layer and the inner heterophase layer. The outer layer is built of the compound of the base metal with an oxidant, the base metal being in the alloys of this type the nobler one. The inner layer on the other hand is built of the heterophase mixture of compounds of both alloy components with an oxidant, and in the case when these compounds form the spinel phases, the inner scale layer may by triple or even multiphase. The scales of this type show as a characteristic feature a complete or practically complete lack of the plastic flow of the reaction products, which is reflected in the characteristic morphologic cross section of the scale. The boundary between the two scale layer corresponds, irrespective of the reaction time and the shape and size of the element under oxidation, to the initial surface of the alloy specimen. Another proof of the lack of the plastic flow of the scale is provided by the location of a marker, which, irrespectively of the reaction time, *i.e.*, of the scale thickness, is found at the boundary between the two scale layers. On the other hand in the case of monophase scales on pure metals, or on alloys, the scale in the region of flat surfaces undergoes considerable plastic deformation, resulting in the shift of the marker together with the scale toward the metallic core. The two limiting cases mentioned above are illustrated schematically in Fig. 1.

Lack of plastic flow in the case of the heterophase scale on alloys constitutes the main reason for the different mechanism of the scale formation in this case as compared with the mechanism of formation of the monophase scales. The islets of phase BX formed on the core surface made impossible, practically from the first moments of the reaction, preservation of the full contact between outer AX layer and the metallic core. This leads to dissociative decomposition of the outer layer, which occurs mainly along the perpendicular to the core grain boundaries of the scale crystals. Since dissociation commences in the case under discussion practically instantaneously after formation of the primary outer layer, the anisotropic decomposition results in the instantaneous destruction of the layer compactness in its entire cross section. Further growth of the scale proceeds then due to the outward lattice diffusion of the basis metal A and the inward diffusion of the oxidant as shown schematically in Fig. 2. As mentioned above the dissociative model of the mechanism governing formation of the double-layer heterophase scales on alloys, is based on the results of model experiments carried out with the use of radioactive isotope of sulfur ^{35}S.[32-41] Veracity of this model with respect to oxide scales was confirmed in experiments with the use of the stable isotope of oxygen ^{18}O.[42]

Extensive studies by Hed and Kofstad concerning morphologic structure of heterophase scales on Co-Cr alloys allow one to suppose that the mechanism of formation of these scales is in accordance with the dissociative model proposed by Brückman, Mrowec, and Werber, Fig. 2. Such a conclusion is supported particularly by the fact that the boundary between the two scale layers corresponds to the initial surface of the alloy. In contradiction to Hed and Kofstad's suggestions we believe that this fact implies the absence of the plastic flow of the scale. Further proof for the dissociative mechanism of formation of the scales under consideration is provided by the porosity of both scale layers observed by Hed and Kofstad. They indeed ascribe the porosity of the outer layer to the existence of the dissociative mechanism; however, they do not draw consistent conclusions from this fact. The works of Hed and Kofstad contain a number of experimental proofs confirming the dissociative mechanism proposed by us. Some of their facts cannot even be explained satisfactorily in terms of the other theories. In particular these authors have shown the presence in the outer scale layer of micropores situated perpendicular to the core, grouped mainly along grain boundaries (Fig. 14[29] and Fig. 13a[31]). A further experimental fact which has not been explained satisfactorily consists of the formation at the corners of the alloy sample Co-25% Cr, oxidated at low pressures of oxygen, of the heterophase scale, whereas at the same time in the region of flat surfaces the monophase scale composed of chromic oxide was observed. Such a structure of the scale results evidently from the dissociative mechanism. At the sample corners namely, plastic

[32] S. Mrowec and T. Werber, *Corrosion Sci.*, 5, 717 (1965).
[33] S. Mrowec, T. Werber, and M. Zastawnik, *Bull. Acad. Polon. Sci., Ser. Sci. Chim.*, 13, 27, 545, 551 (1965).
[34] A. Brückman, S. Mrowec, and T. Werber, *Z. physik Chem.*, 231, 375 (1966).
[35] S. Mrowec, T. Werber, and M. Zastawnik, *Corrosion Sci.*, 6, 47 (1966).
[36] A. Brückman, *Corrosion Sci.*, 7, 51 (1967).
[37] S. Mrowec, *Corrosion Sci.*, 7, 563 (1967).
[38] S. Mrowec and T. Werber, *Werkstoff und Korrosion*, 18, 116 (1967).
[39] A. Brückman, J. Gilewicz-Wolter, and S. Mrowec, *Bull. Acad. Polon. Sci., Ser. Sci. Chim.*, 15, 11 (1967).
[40] A. Brückman, S. Mrowec, and J. Wolter, *Oxidation of Metals*, 1 (1969).
[41] A. Brückman and J. Romanski, *Corrosion Sci.*, 5, 185 (1965).
[42] A. Brückman, S. Mrowec, and P. Emerich, *Oxidation of Metals*, To be published.

deformations of the monophase scale are considerably hindered owing to geometrical rigidity of the system.[34-39] Therefore in this region anisotropic dissociation leads practically instantaneously to the destruction of the compactness of the primary Cr_2O_3-layer and consequently to the formation of the heterophase scale. In the region of the flat surface on the other hand, the monophase scale is subjected to plastic deformations, which ensures its considerably longer contact with the metallic core, and thus good compactness of the scale during the longer reaction time.

We would like to conclude that the results of the studies by Kofstad and Hed may be readily interpreted in terms of the dissociative model of the mechanism governing formation of heterophase scales on binary alloys.

Solid Ionics—Solid Electrolyte Cells

T. Takahashi and O. Yamamoto (pp. 1-5, Vol. 117, No. 1)

G. Pistoia and **B. Scrosati**[43]: The authors report that the x-ray diffraction pattern of $RbAg_4I_5$, prepared according to the method described by Owens and Argue,[44] showed lattice parameter identical with that reported in literature. Nevertheless the authors found a $RbAg_4I_5$ specific conductivity of 0.170 ohm^{-1} cm^{-1}, a value which is 0.090 ohm^{-1} cm^{-1} less than that found by Oxley and Humphrey.[45] Since this difference in conductivity values cannot certainly be included in the experimental errors, do the authors have some explanation for their low conductivity data? In this respect it may be useful to report an observation made in our laboratory when measuring the specific conductivity of $RbAg_4I_5$ pellets in function of the compression pressure. We found that the conductivity depends to a certain extent on the compression pressure of the electrolyte pellets.[46] Since Takahashi and Yamamoto report that the electrolyte pellets utilized in their solid state cells were compressed at 5 tons/cm^2, it seems reasonable to believe that also the pellets for the conductivity measurements were compressed at the same pressure. If this assumption is valid, the relatively low conductivity value found by the authors may find its explanation since we have found that at 5 tons/cm^2 the $RbAg_4I_5$ conductivity is of the order of 0.178 ohm^{-1} cm^{-1}.

For a cell using a mixture of $Te,RbAg_4I_5,Ag_2Te$ and graphite as cathode, the authors claim an internal resistance of 1 ohm at room temperature. From the cell discharge curves, reported in Fig. 8 of the paper, however, the internal resistance results in average to be of the order of 15 ohms, a value which seems to be more realistic.

Furthermore, from the polarization curve at 25°C of Fig. 3 it results that at 10 mA/cm^2 the anodic polarization becomes severe. Nevertheless flat discharge curves at 10 mA/cm^2 are reported in Fig. 9. It seems very difficult to give an explanation of this point unless considering that the charging process has some depolarizing effect on the anode.

In conclusion our opinion is that the work of Professors Takahashi and Yamamoto is interesting because it shows the feasibility of selenium and tellurium as cathode materials in $RbAg_4I_5$ solid electrolyte cells, and therefore we would appreciate some comments on the relatively low value of the conductivity of the electrolyte, on the discrepancy between the reported internal resistance value and the one derived from the discharge curves, and finally, on the discharge curves at 10 mA/cm^2.

T. Takahashi: The difference between the conductivity values of $RbAg_4I_5$ measured by us and by Oxley and Humphrey seems to be due to the difference of the state of the electrode used. We used a silver plate as the electrode while Oxley used a mixture of silver powder and $RbAg_4I_5$. This sort of discrepancy in conductivity value has been pointed out by Owens and Argue[47] comparing their value with that obtained by Bradley and Greene.[48] We have obtained a conductivity value of 0.24 ohm-cm^{-1} at 25°C using the mixture of silver powder ond $RbAg_4I_5$ as electrode. This value is somewhat smaller than that obtained by Oxley, and this is considered to be due to the difference of the contact resistance between the electrode and the electrolyte and the difference of the moulding pressure of the specimen as pointed out by Professor Scrosati.

The internal resistance 1 ohm of the cell Ag/$RbAg_4I_5$/Te, $RbAg_4I_5$, graphite was the value measured by 1,000 Hz a-c bridge, and the internal resistance obtainable by Fig. 8 should be higher than 1 ohm owing to the polarization resistance at anode and cathode being added. The value of the resistance measured by the interrupter method was 1 ohm.

In the anode polarization measurement shown in Fig. 3, the silver plate electrode was used, while in the cell shown in Fig. 9, a mixture of silver powder and $RbAg_4I_5$ was used as the electrode. This is the reason why the appreciable polarization was not found in the case of Fig. 9 at the apparent current density of 10 mA/cm^2.

Galvanostatic Overpotential Transients and Electrocrystallization Processes on Copper Single Crystals in Solutions of Cupric Perchlorate

L. H. Jenkins (pp. 630-640, Vol. 117, No. 5)

R. Piontelli, B. Rivolta,[49] **G. Poli,**[50] and **G. Serravalle**[51]: The systematic work on the single crystal electrodes carried out by Dr. Jenkins, with the aim of throwing some light on the dark mystery of the kinetics and morphology of the electrocrystallization and electrodemolition processes of metals, is fully acknowledged. No doubt, the use of single crystal electrodes is an indispensable step in view of any true progress along this route.

The very extensive research work carried out here in this field[52] has clearly shown, however, the difficulties encountered in controlling: (*a*) the nature and density of the defects interesting the electrode surface, and (*b*) the surface states.

As a matter of fact, the most carefully prepared surfaces appear to be especially sensitive to the various contamination sources, arising not only from the preparation and handling of the electrodes, but from traces of organic matter on the walls of the measurement cells or present in the solution.

The influence of the ensuing contamination may concern both morphology and kinetic laws (especially in the low current density range). It is a predominant source of the appearance of transient overvoltage maxima in galvanostatic conditions with single crystal electrodes and especially with perchlorate baths.

Overvoltage maxima have been observed by us too at the start of our work: (*a*) in the deposition on foreign cathodes,[53] and (*b*) in anodic and cathodic exchange processes of the ions of the electrode metal.

A test of credibility for the meaning of these phenomena appeared to us to be the quite regular obedience to the (generalized) Tafel-law.

We noticed moreover a conspicuous influence of the anion, a point deserving successive comments.

[43] Istituto Chimico, Università di Roma, Rome, Italy.
[44] B. B. Owens and G. R. Argue, *Science*, 157, 308 (1967).
[45] J. E. Oxley and J. R. Humphrey, Atomics Int. Final Report, July 22-Oct. 22, 1968.
[46] Submitted for publication to *This Journal*.
[47] B. B. Owens and G. R. Argue, *Science*, 157, 308 (1967).
[48] J. N. Bradley and P. D. Greene, *Trans. Faraday Soc.*, 63, 424 (1967).
[49] Laboratory of Physical Chemistry, Milan Polytechnic, Milan, Italy.
[50] University of Pisa, Pisa, Italy.
[51] University of Palermo, Palermo, Italy.
[52] For an extensive literature until 1965 see R. Piontelli, *Electrochim. Metallorum*, 1, 5 (1966).
[53] See in particular R. Piontelli and M. Guerci, CITCE: C.R. 2me Réunion (Milan 1950); Milan 1961, p. 149.

For (b), however, the decisive progress in experimental techniques, successively attained here[54] have led to the systematic disappearance of the maxima from our oscillographic recordings, together with a strong reduction of the quasi-steady overvoltages.

Among the necessary cares, we recall: (i) the use of only glass-metal cells, whose form and interior wall-surface must allow a very radical cleaning before use, and (ii) the prolonged galvanic prepurification of the solution[55] in a separate compartment of the cell, from which the solution may be successively introduced (by inert gas pressure) in the measurement compartment, where the electrode has been previously placed, in accurately controlled surface conditions.

For the $Cu/Cu(ClO_4)_2$ electrodes, the Jenkins result may be compared with those obtained here, with the techniques above, by G. Poli and B. Rivolta.[56]

The bath utilized by Poli and Rivolta was $Cu(ClO_4)_2$ 0.5M + $HClO_4$ 1M [for Jenkins: $Cu(ClO_4)_2$ 0.2M; pH 1] and the explored c.d. range 2-100 A/m^2 (instead of 0.01-4 A/m^2 for Jenkins.

Our experiments[57] indicate:

1. dissymmetry between anodic and cathodic overvoltages (higher for the last) on all of the studied orientations: (111), (110), (100) (in the Jenkins experiments only for (111));
2. the anodic quasi-steady cathodic overvoltages decrease in the order: (100) > (111) > (110) according to both Jenkins and our experiments;
3. on the cathodic side, at c.d. lower than about 40 A/m^2, the overvoltages (in absolute value) decrease in the order (100) > (111) > (110), while, in the c.d. range over 40 A/m^2, the order is (111) > (100) > (110); while Jenkins finds (100) > (110) > (111);
4. for (100), at 2 A/m^2, the quasi-steady anodic overvoltage lies in the range of 3 mV, while the oscillographic records of Jenkins at 1.5 A/m^2, indicate overvoltages in the order of 35 mV.

Again for (111), at 2 A/m^2, the anodic and cathodic quasi-steady overvoltages lie in the range of 1.2 and 1.4 mV, respectively, as compared with values in the order of 25 mV at 1.5 A/m^2 for Jenkins.

Jenkins finds moreover at this c.d. transient maxima: for (100) in the order of 50 mV, and for (111) 38 mV on the anodic side and −33 mV on the cathodic one.

In our experiments, the above mentioned cares lead to a total disappearance of the transient maxima, previously found by us also.[58]

Of course we do not exclude the occurrence of transient overvoltage maxima (sometimes strong) in cases in which nucleation may assume a kinetically very decisive role, for instance on foreign cathodes in the absence of alloy formation, or on nearly ideal surfaces. Quite modest maxima may be foreseen in various conditions. One may thus consider the hypothesis the surfaces investigated by Jenkins to be ideally flat.

On the basis of our results, concerning not only Cu but also Ag, Pb, Cd and other single crystal electrodes, however, we are forced to consider the intervention of contamination sources in a part at least of these results.

A special comment appears to deserve the influence exerted, in this field, too, like every one of the electrochemistry of metals[59] by anions.[60]

In the usual inorganic-anion series, the perchlorate baths utilized by Jenkins and by Poli and Rivolta, among the various investigated, are quite peculiar. In these baths the highest quasi-permanent galvanostatic overvoltages and transient maxima are encountered as a rule; moreover, the baths themselves are especially sensitive to the prepurification policy.

The last in this case leads to the strongest (absolute and relative) reduction of these effects.

One could attempt, of course, simply correlating the high quasi-steady overvoltages with the high transients by admitting a direct inhibitive influence of the perchlorate ions themselves.

This does not explain the influence of the purification policy. On the contrary, the general phenomenological results and the comparison with the other anions (among which chlorides are, in general, at the opposite extreme, as well known in corrosion), appear to suggest a more convincing explanation.

Due to their want of selective adsorption on the electrode surface, perchlorate anions are also the less able to exert a "competitive adsorption,"[61] by which the anions may displace from the electrode surfaces the contamination sources or other adsorbed species.[62]

In our opinion, the differences in the sensitivity of the different baths in respect to the purification policy is the most convincing evidence of the importance the competitive adsorption may assume in deciding the influence of anions in the kinetics of electrode processes (either anodic or cathodic).

L. H. Jenkins: It was an awareness of the pioneering work of Professors Piontelli, Poli, Rivolta, and Serravalle which aided in the decision of the Surface Studies Group at Oak Ridge National Laboratory to investigate electrocrystallization phenomena as a means of understanding the effects of structure on the reactivity of metal surfaces. Since much of the group effort has been concerned with other than electrochemical phenomena, it might be useful to call attention to some of this work. Members of the group were the first to grow metallic crystals (copper) with a dislocation density conclusively proven to be as low as $\simeq 50$ cm^{-2}. From crystals of such high perfection it was possible to obtain Borrmann x-ray transmission stereotopographs and to demonstrate a correspondence between dislocation images in the topographs and etch pits at sites where dislocations intersected specimen surfaces.[63] The use of electron microscopy of surface replicas[64,65] and interference and phase-contrast optical microscopy,[66,67] as well as neutron irradiation hardening as an aid in handling and manipulating samples,[68] are some of the many techniques routinely used by the group. The group's ability to prepare specifically oriented surfaces and to characterize them in terms of their structure is well documented.[66,67,69,70] Therefore,

[54] R. Piontelli, G. Serravalle, and G. Poli, *Rend. Accad. Lincei*, 25, 431 (1958); R. Piontelli and G. Poli, *Rend. Ist. Lomb.*, 92(A), 601 (1958).

[55] Following our purification policy, the prolonged electrolysis is carried out at low current-density with cathodes, or both electrodes, of the same metal to be utilized in the measurement. The especially good results thus obtained may be credited to the progressive elimination (by adsorption and occlusion) at least of those contamination sources, and also of oxygen, in respect of which the measurement electrode may result specifically sensitive.

[56] *Rend. Ist. Lomb.*, 93, 262 (1959).

[57] In all of these experiments the electrode surfaces examined by electron diffraction gave very neat Kikuchi lines while the details of the diffractograms confirm the surfaces are usually exempt from any distortion or covering films and are smooth.

[58] The influence of the prepurification is different for the different orientations, being definitely greater for (100), that is, the orientation corresponding to the highest overvoltages, a result which appears to be in line with our general views on the kinetics of the electrode processes.

[59] R. Piontelli, CITCE: C.R. 2^{me} R. (Milan 1950) Milan 1951, p. 185; *Z. Elektrochem.*, 55, 128 (1951); *Corrosion*, 9, 115 (1953).

[60] For Cu, however, on the cathodic side, the overvoltages are a little greater in sulfate bath than in perchlorate, a result that may indicate an inhibitive influence of the sulfate ion. This last hypothesis finds support in the systematic study carried out here on the influence of addition of neutral salts including potassium sulfate. Also the influence of the "free" acid in sulfate baths could thus find a partial explanation.

[61] R. Piontelli and G. Serravalle, *Z. Elektrochem.*, 62, 759 (1958); R. Piontelli, *Electrochim. Metallorum*, 1, 5 (1966).

[62] We consider this one of the main reasons why chlorides may be thus effective in preventing and destroying passivation and passivity.

[63] F. W. Young, Jr., "Crystal Growth," H. Steffen Peiser, Editor, pp. 789-800, Pergamon Press, New York (1967).

[64] L. H. Jenkins, *This Journal*, 107, 371 (1960).

[65] L. D. Hulett, Jr. and F. W. Young, Jr., *This Journal*, 113, 410 (1966).

[66] L. D. Hulett, Jr. and F. W. Young, Jr., *J. Phys. Chem. Solids*, 26, 1287 (1965).

[67] U. Bertocci, L. D. Hulett, Jr., and L. H. Jenkins, *This Journal*, 110, 1190 (1963).

[68] F. W. Young, Jr. and J. R. Savage, *J. Appl. Phys.*, 35, 1917 (1964).

[69] U. Bertocci and T. S. Noggle, *Rev. Sci. Inst.*, 37, 1750 (1966).

[70] U. Bertocci, C. Bertocci, and F. W. Young, Jr., *J. Appl. Phys.*, 40, 1674 (1969).

it does not appear unjustified to conclude that the surfaces discussed here were exceptionally well characterized in terms of the density and nature of the defects intersecting the electrode surface. No comment can be made regarding control of "surface states" since the meaning of the term used by Piontelli *et al.* is not clear in this context.

As for the experimental systems, we also have noted a pronounced "anion effect." If nothing else, the observations demonstrate quite conclusively that the usual model of adatoms diffusing over a bare surface to monatomic steps is inappropriately simplistic. All surface processes must be affected by the water, anions, adatoms, etc., on the electrode surface. However, it is difficult to say more than that it is possible impurities adsorbed in sufficient quantity at significant sites should contribute to the effect. Moreover, the concept of selective or competitive adsorption in solutions assumed to contain minute quantities of unidentified impurities is such a general argument that it is of limited usefulness. From completely reasonable assumptions of values for adsorption coefficients, number of sites, impurity levels in solution, etc., it can be used to demonstrate that (*a*) no system can be properly purified, or (*b*) any system is sufficiently pure unless containing a measurable quantity of specific inhibitors, or (c) any stage between these two extremes is a proper description. This concept applied to data obtained in "clean" systems at different laboratories does have the virtue of supplying a vague, nonspecific means for rationalization of conflicting results.

In the work under discussion here very careful precautions were taken to ensure the cleanliness of all components of the system.[71] Certain aspects of the experimental results such as the quantitative relationships between the extent of deposition and time-to-formation of maxima, long-lived aspects of this deposition anomaly, asymmetry of cathodic and anodic branches of the (321) and (111) current *vs.* potential relationships, as well as the near coincidence of their cathodic values, symmetry of the two processes on the (100) and (110), and other data and arguments presented in the paper led to the conclusion that in this case maxima could not result from impurities adsorbed on the crystal surfaces. As a matter of fact, much of the earlier stages of investigation not reported in the paper were spent establishing the fact that use of all the cleaning techniques of Piontelli *et al.*, did not eliminate maxima from these systems. In attempting to understand this discrepancy the following observations were made:

1. Maxima were extremely sensitive to the presence of dissolved oxygen and were altered when absolutely all oxygen was removed. This phenomenon could be understood on the basis that, by oxidizing the cuprous ions to cupric, equilibrium was destroyed in a system in which the observed overvoltage was extremely sensitive to the cuprous ion concentration (*see* Eq. [8] in original text). Moreover, it was demonstrated[72] that while singular orientations of copper crystals reacted completely uniformly over the surface when the sole driving force for the reaction was an applied external emf, the same systems undergoing corrosion at reaction rates even an order of magnitude greater due to the reactions

$$\frac{1}{2}O_2 + H_2O + 2Cu^+ \rightleftarrows 2Cu^{++} + 2OH^- \quad [1]$$

$$Cu^{++} + Cu^\circ \rightleftarrows 2Cu^+ \quad [2]$$

were not uniformly attacked over the surface. Therefore, it was concluded that nonuniform attack due to corrosion and the concomitant effects on interfacial cuprous ion activities, at the very least, affected the formation of maxima in oxygen-containing systems. However, it was soon established that the complete removal of dissolved oxygen changed the absolute values of observed maxima, but did not cause them to disappear.

2. Nevertheless, after many measurements at current densities in excess of ~ 1 mA/cm^{-2} had been made on any one surface it was observed that overvoltage values decreased markedly. Initially this was assumed to be due to an attendant increase in surface area. However, examination of such surfaces by optical and surface replication electron microscopy revealed that no change in surface area had occurred, but rather that the steps initially evenly distributed over electropolished surfaces due to even slight ($\sim$0.1°) misorientations from low-index planes had interacted and bunched into ledges and facets. This suggested that in systems initially at equilibrium overvoltages were extremely sensitive to the arrangement and distribution of steps over a surface. Extensive investigations of various step distributions on different orientations of copper crystals in solutions of copper sulfate unequivocally confirmed this to be the case.[73]

It is well known and easily demonstrated that on an electropolished copper surface in either perchlorate or sulfate solutions a current of 10 mA/cm^{-2} flowing for as little as 5 sec will produce a change in surface structure sufficient to be easily observable with an optical microscope. Therefore, when extensive data are obtained in such systems at current densities $\gtrsim$1 mA/cm^{-2} they are from surfaces whose structures are changing constantly during the course of observations. Because of the deposition anomaly demonstrated in the paper under discussion, this is particularly true of surfaces on which measurements have resulted in a net deposition, an observation confirmed by the results of Bockris and Enyo.[74] Moreover, as facet and ledge formation increase, the overvoltage decreases markedly even though the faceting is to a degree much too small to alter the surface area.[73] Also, it is well known that maxima decrease with the overvoltage such that at $\lesssim 10$ mV they are quite small and slow both to form and decay. This last fact seems to be acknowledged by Piontelli *et al.* who refer to their observed overvoltages as "quasi-steady."

For all these reasons it seems completely justifiable to conclude that the experimental data of all the many researchers discussed here were obtained from "clean" systems. As concluded in the paper under discussion and confirmed by work currently in press,[73] it seems to the author that experimental evidence supports the opinion that many of the differing results obtained in various laboratories reflect differences in surface structures yielding the data rather than indeterminate differences in ill-defined trace impurity levels.

[71] L. H. Jenkins and J. O. Stiegler, *This Journal*, 109, 467 (1962).
[72] L. H. Jenkins, *This Journal*, 113, 75 (1966).
[73] L. H. Jenkins and R. B. Durham, *This Journal*, 117, 1506 (1970).
[74] J. O'M. Bockris and M. Enyo, *Trans. Faraday Soc.*, 58, 1187 (1962).

JOURNAL OF THE ELECTROCHEMICAL SOCIETY

SOLID STATE SCIENCE

DECEMBER 1970

A New Class of High-Conductivity Solid Electrolytes: Tetraalkylammonium Iodide-Silver Iodide Double Salts

Boone B. Owens*

Gould Ionics Incorporated, Canoga Park, California 91304

ABSTRACT

Double salts, formed by the combination of silver iodide with tetraalkylammonium iodide salts, have been found to exhibit very high ionic mobilities in the solid state over the temperature range from 100° down to −50°C. In the system AgI-diethyldimethylammonium iodide, the composition dependence of the ionic conductivity at 22°C passes through a maximum value of 0.06 $(\text{ohm-cm})^{-1}$ at a composition of 87 m/o (mole per cent) AgI. Results are presented for a number of related salts in the silver tetraalkylammonium iodide class.

Takahashi and Yamamoto (1-6) have extensively investigated the electrolyte Ag_3SI and the solid electrolyte cell $Ag/Ag_3SI/I_2$. This system has been of especial interest because the electrolyte has a specific electrical conductivity of 0.01 $(\text{ohm-cm})^{-1}$ at 20°C, orders of magnitude more conductive than most other solid electrolytes at ambient temperatures. However, this electrolyte has the disadvantage of a low decomposition emf (7). Another solid-state battery was reported by Gutmann, Hermann, and Rembaum (8); however, no completely dry, high-conductivity solid electrolyte was reported, and the cell discharge reaction has recently been re-evaluated (9).

The highly conducting group of salts KAg_4I_5, $RbAg_4I_5$, and $NH_4Ag_4I_5$ was more recently reported to have ionic conductivities of 0.2 $(\text{ohm-cm})^{-1}$ at 20°C (10, 11). This group of electrolytes suffers from a thermodynamic instability at 20°C, with respect to the reaction

$$2MAg_4I_5 \rightarrow M_2AgI_3 + 7AgI \qquad [1]$$

where $M = K$, Rb, or NH_4 (10, 12). The MAg_4I_5 electrolytes can be quenched in at very low temperatures; however, at temperatures near to or below ambient they may decompose, according to Eq. [1], in the presence of H_2O vapor or upon being ground.

Because of the number of silver halide or silver halide containing salts that exist in structures that permit high Ag^+ ion mobility, it appeared that new high-conductivity solid electrolytes would be complex salts of the type $MX \cdot nAgI$ where MX represents an unspecified salt and n is the mole ratio of AgI to MX in the conducting compound. In considering other iodide salts that might form high-conductivity products with AgI, substituted ammonium iodide compounds were investigated (13). The initial successful experiments on this group were carried out prior to Bradley and Greene's conflicting report that Me_4NI did not combine with AgI to form a conductive product (10). The present paper reports the properties of high-conductivity solid electrolytes formed by the combination of silver iodide with the tetraalkylammonium iodides.

The new set of solid electrolytes has ionic conductivities of 0.01-0.06 $(\text{ohm-cm})^{-1}$ at 20°C. Furthermore, these materials appear to be thermodynamically stable at subambient temperatures, and as such they represent the most conductive stable solid electrolytes known at temperatures below 25°C.

Experimental

Materials.—The quaternary tetraalkylammonium iodide salts (QI) were obtained from Eastman Kodak or prepared from the tertiary amines and the alkyl iodide; the silver iodide was supplied by Mallinckrodt Chemical. The double salts were prepared by the combination reaction

$$QI + n\ AgI \rightarrow QAg_nI_{n+1} \qquad [2]$$

where n is the mole ratio of AgI to QI.

The reactants were intimately mixed, compacted, and then annealed in closed Pyrex vessels under an inert Ar atmosphere at elevated temperatures ranging from 125° to 165°C. Multiple compactions and anneals were carried out to permit the system to come to equilibrium.

Alternately the products were prepared by adding a small amount of H_2O to the reactants to form a paste. This material was vacuum dried at 80°C, ground, pelletized, and then annealed at 120°C for 8-16 hr in a sealed tube under an Ar atmosphere. The compaction and annealing were repeated once.

Compositions were prepared with n values varying from 0 to about 20. The conductivities of these compositions were determined and from the variation in conductivity with composition the approximate stoichiometry of the conducting phase was determined.

Resistance measurements.—The method for measuring the pellet resistance of ½ in. diameter cells Ag, $RbAg_4I_5$/Sample/Ag, $RbAg_4I_5$ has been described elsewhere (11, 14). The temperature dependence of the resistance was also determined, following essentially

* Electrochemical Society Active Member.

Key words: conductivity, quaternary ammonium iodide, silver iodide, solid electrolyte, solid-state electrochemistry, substituted ammonium iodide, tetraalkylammonium iodide.

the same procedure as previously reported (11, 14). The low-temperature environment was maintained by placing the conductivity cells in a Missimer environmental chamber that had been adapted to have a flowing Ar atmosphere and external electrical contacts for reading the resistance of samples within the atmosphere. The temperature range was from −80° to 200°C.

Density.—Densities were determined by pressing the products into ½ in. diameter pellets at pressures of 45,000 psi. The pellet dimensions were determined with a micrometer and the weight was determined with an analytical balance.

Results and Discussion

Me_4NI-AgI *system.*—The composition of the tetramethylammonium iodide-silver iodide samples varied from 0 to 97.5 m/o AgI. Generally, the products would contain two phases; a single phase product would be formed only at compositions corresponding to compounds stable at the synthesis temperature. The one intermediate compound reported to form in this system is $(Me_4N)Ag_2I_3$ at 66 2/3 m/o AgI (15). The density results are reported in Table I, with those for the Me_2Et_2NI and Et_4NI systems.

The specific conductivities for samples of composition ranging from 0 to 100 m/o AgI are reported in Table II, column 2. In the composition range from $(Me_4N)I$ to $(Me_4N)Ag_2I_3$ there is no evidence of a high-conductivity electrolyte having been formed. However, between the compounds $(Me_4N)Ag_2I_3$ and AgI, the conductivity passes through a maximum at 87 m/o as shown by the plot in Fig. 1 of specific conductivity *vs.* mole per cent AgI. Smyth, Tompkins, and Ross (16) recently reported that silver iodide, comelted with Me_4NI, at a mole ratio of 6 to 1 forms a solid product with conductivity of 0.04 $(ohm\text{-}cm)^{-1}$, in good agreement with the results shown in Fig. 1. The position of the maximum indicates that the formula of the conducting compound is close to $(Me_4N)Ag_{6.7}I_{7.7}$. However, this method of measurement is not precise enough to determine the exact formula. An x-ray structure determination has been carried out by Geller and Lind who found the compound stoichiometry to be $(Me_4N)Ag_{6.5}I_{7.5}$ (17).

Table I. Density of pelletized polycrystalline salts QAg_nI_{n+1} at 22°C[a]

m/o AgI	Density in g/cc, where QI is		
	Me_4NI[b]	Me_2Et_2NI	Et_4NI
0	1.84 (1.83)	1.54	(1.56)
66.6	3.37	3.07	2.83
80	4.10	3.89	3.56
88	4.67	4.47[c]	4.27[c]
100	5.76	5.76	5.76

[a] Chemical handbook values in parentheses.
[b] The x-ray density of $(Me_4N)_2Ag_{13}I_{15}$ is 4.59 g/cc (17), compared to a value of 4.55 g/cc for the 86.5 m/o AgI composition, obtained in the present investigation.
[c] Interpolated value.

Table II. Specific conductivity of pelletized polycrystalline salts QAg_nI_{n+1} at 22°C

m/o AgI	Conductivity in $(ohm\text{-}cm)^{-1}$, where QI is		
	Me_4NI	*Me_2Et_2NI*	*Et_4NI*
0	$\sim 10^{-8}$		
33.3	$\sim 10^{-8}$		$\sim 10^{-8}$
50	$\sim 10^{-8}$		
66.7	$\sim 10^{-8}$	$\sim 10^{-8}$	$\sim 10^{-8}$
75	6.3×10^{-4}	8.0×10^{-5}	6.4×10^{-4}
80	1.1×10^{-3}	6.2×10^{-3}	3.2×10^{-3}
85	3.4×10^{-2}	4.0×10^{-2}	1.1×10^{-2}
86	4.0×10^{-2}	5.2×10^{-2}	1.5×10^{-2}
87	4.1×10^{-2}	6.4×10^{-2}	2.0×10^{-2}
88	4.0×10^{-2}	6.3×10^{-2}	2.2×10^{-2}
89	3.4×10^{-2}	5.2×10^{-2}	2.1×10^{-2}
90	2.9×10^{-2}	4.6×10^{-2}	1.7×10^{-2}
97	1.7×10^{-3}		2.4×10^{-3}
100	2.8×10^{-4}	2.8×10^{-4}	2.8×10^{-4}

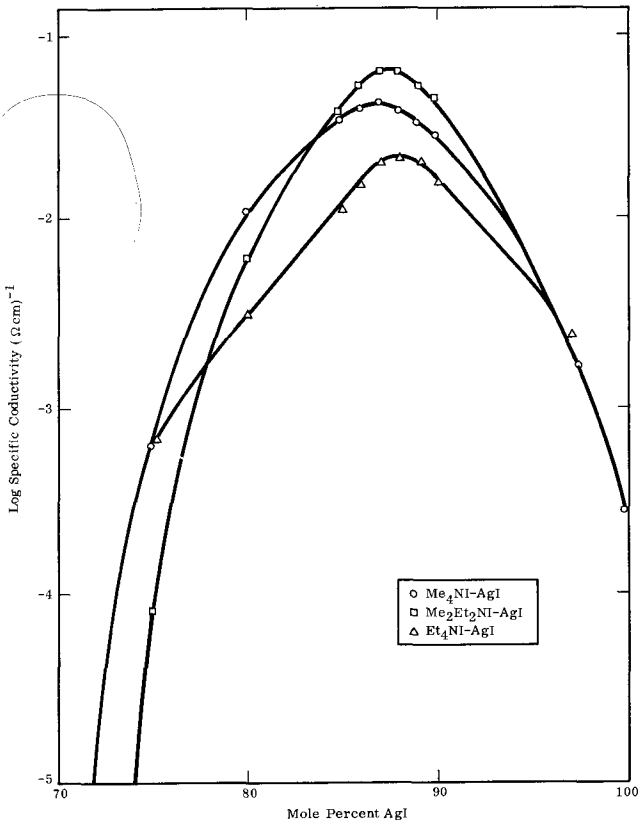

Fig. 1. Composition dependence of the specific conductivity of the binary solid electrolyte systems Me_4NI-AgI, Me_2Et_2NI-AgI, and Et_4NI-AgI, at 22°C.

In the present investigation some of the initial syntheses were carried out at 160°C. From both conductivity measurements and powder pattern analysis of the products evidence was obtained for another high-conductivity compound forming at a composition near 80 m/o AgI. When syntheses were carried out at 120°C this compound was not formed; it therefore appears to be a high-temperature compound, unstable at temperatures below 120°C. The conductivity at 22°C of quenched samples of this high-temperature phase was about 0.01 $(ohm\text{-}cm)^{-1}$.

The conductivity curves of Fig. 1 were not corrected for contact resistance. These corrections were obtained for the 87 m/o AgI composition following the procedure previously described (14). The specific conductivity of the 87 m/o AgI-Me_4NI composition at 22°C is $4.2 \pm 0.7 \times 10^{-2}$ $(ohm\text{-}cm)^{-1}$.

Other high-conductivity electrolytes have been found to be thermodynamically unstable at and below ambient temperatures (10-12). No thermodynamic data for the $(Me_4N)_2Ag_{13}I_{14}$ compound have been reported, and therefore its stability with respect to decomposition reactions such as

$$(Me_4N)_2Ag_{13}I_5 \rightarrow 2\ (Me_4N)Ag_2I_3 + 9\ AgI \qquad [3]$$

is unknown. However, the conducting compound has not exhibited any tendency to decompose during storage under ambient conditions, in contrast to the behavior of the MAg_4I_5 group of high-conductivity electrolytes (10, 11). In addition, a sample of the $(Me_4N)_2Ag_{13}I_{15}$ compound was prepared out of water by refluxing a slurry of AgI in a solution of Me_4NI and then cooling the reaction vessel to 0°C. The solid phase that was then isolated was predominately $(Me_4N)_2Ag_{13}I_{15}$ as evidenced by x-ray powder analysis, indicating that this compound is stable at least over the temperature range from 0° to 120°C.

Me_2Et_2NI-AgI *system.*—The investigation of the diethyldimethylammonium iodide-silver iodide system

was carried out, following the same procedures as just described for the tetramethylammonium iodide-silver iodide system. The results are shown in Tables I and II and Fig. 1. This system is analogous to the preceding one in that there appears to be a nonconducting compound QAg_2I_3, and a conductive compound at a composition near 87½ m/o AgI. The maximum conductivity observed was 6.4 x 10^{-2} $(ohm\text{-}cm)^{-1}$. The precise formula of the conducting compound is unknown. The conductivity results suggest $(Me_2Et_2N)Ag_7I_8$ (87½ m/o AgI); however, the formula may be the same as that of the preceding system, $(Me_2Et_2N)_2Ag_{13}I_{15}$ (17). No structural results have been reported for the high conducting compound.

Et_4NI-AgI *system.*—The tetraethyl ammonium iodide-silver iodide system was similarly investigated, and a maximum in the conductivity curve was found at 88 m/o AgI. Results are also shown in Tables I and II and Fig. 1. The maximum value of 2.2 x 10^{-2} $(ohm\text{-}cm)^{-1}$ was observed at 88 m/o AgI.

Conductivity of QAg_6I_7 *as function of* Q.—The results thus far reported have shown that high-conductivity electrolytes are formed between AgI and the tetraalkylammonium iodide salts Me_4NI, Me_2Et_2NI, and Et_4NI. In order to investigate the extent to which other tetraalkylammonium iodide salts will combine with AgI to form conductive products a series of different QI salts were combined with AgI in the mole ratio of 1 to 6. The conductivity of these products (which would generally be expected to contain two phases) was then determined, and these results are given in Table III. The conductivity of the pure AgI determined by the present procedure was 3 x 10^{-4} $(ohm\text{-}cm)^{-1}$. Conductive products were formed by all the salts from tetramethylammonium iodide through butyldiethylmethylammonium iodide. The most conductive compound was formed with the diethyldimethylammonium iodide. As the tetraalkyl group changed from butyldiethylmethyl to butyltriethyl a sharp decrease by a factor of 10^4 was observed in the conductivity. This result suggests that these larger quaternary ammonium ions are forming new nonconductive compounds with AgI. If no compound formation were occurring, then the dilution effect of a second phase on the conductivity of AgI should result in a specific conductivity of about 10^{-4} $(ohm\text{-}cm)^{-1}$, as was observed for the very large asymmetric hexadecyltrimethyl ammonium ion.

Temperature dependence of conductivity.—The temperature dependence of the resistance was determined for samples of Me_4NI, Me_2Et_2NI, and Et_4NI combined with AgI in the mole ratio of 1/7. The results of several temperature cycles are shown in Fig. 2, where the conductivity curves are compared to those of AgI, Ag_3SI, and $RbAg_4I_5$. The Me_4NI and Me_2Et_2NI compounds remained conductive down to −50°C, with Arrhenius activation energies of 4.0 and 3.6 kcal/mole, respectively. The Et_4NI compound has an activation energy of 5.7 kcal/mole at 20°C. It gave some indication of transforming into a nonconductive phase, as the conductivity dropped to less than 10^{-4} at −50°C, as shown in Fig. 2. Contact resistance contributes to the total resistance measured on these cells; the contribution was determined for samples at 22°C but not at other temperatures. This effect could modify the slopes of the curves in Fig. 2. The log conductivity-reciprocal temperature plots for these three compounds are compared to those of other high-conductivity electrolytes in Fig. 2. Below 27°C this new group of electrolytes contains the most conductive, thermodynamically stable solid electrolyte known (12).

Table III. Electrical conductivity of tetraalkylammonium iodide-silver iodide compositions of empirical formula QAg_6I_7 at 22°C

Tetraalkylammonium ion	σ $(ohm\text{-}cm)^{-1}$
Tetramethyl	4 × 10^{-2}
Ethyltrimethyl	4 × 10^{-2}
Diethyldimethyl	6 × 10^{-2}
Trimethylisopropyl	4 × 10^{-2}
Trimethylpropyl	3 × 10^{-2}
Triethylmethyl	3 × 10^{-2}
Tetraethyl	1 × 10^{-2}
Diethylmethylisopropyl	2 × 10^{-3}
Triethylpropyl	2 × 10^{-3}
Butyldiethylmethyl	8 × 10^{-4}
Butyltriethyl	6 × 10^{-8}
Methyltripropyl	3 × 10^{-8}
Tetrapropyl	3 × 10^{-8}
Tributylmethyl	3 × 10^{-7}
Butyltripropyl	2 × 10^{-7}
Tributylethyl	3 × 10^{-7}
Tetrabutyl	1 × 10^{-7}
Hexadecyltrimethyl	1 × 10^{-4}

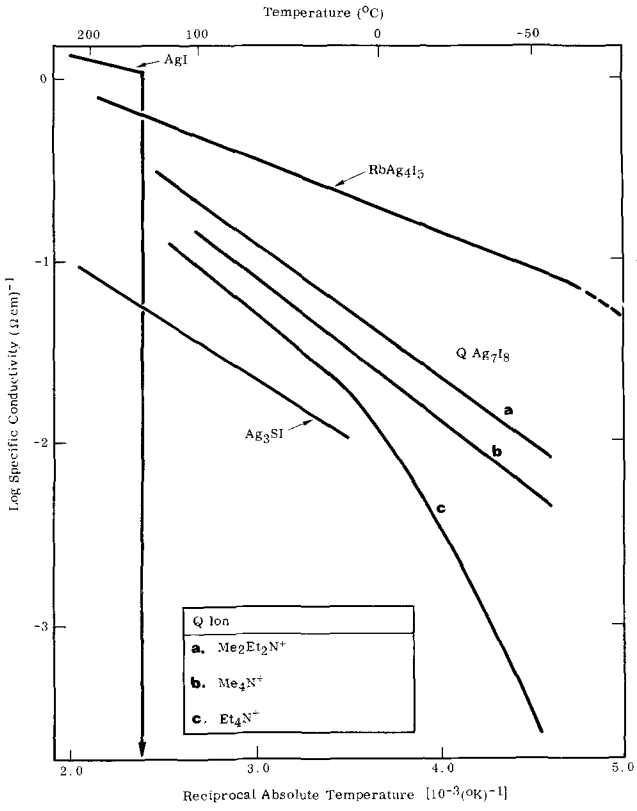

Fig. 2. The temperature dependence of the specific conductivity of $(Me_4N)Ag_7I_8$, $(Me_2Et_2)NAg_7I_8$, and $(Et_4N)Ag_7I_8$ from −50° to 100°C.

Electronic conductivity.—Measurements of the electronic conductivity in some of these compounds have been carried out by Oxley and Humphrey (18). Polarization cells Ag/electrolyte/Pt were analyzed by their current-voltage relationships. Results indicate the electronic conductivities are less than 1 x 10^{-10} $(ohm\text{-}cm)^{-1}$ in these materials.

Transport number measurements.—The ionic transport numbers in the electrolyte compositions Me_4N-Ag_7I_8 and $Et_4NAg_7I_8$ were determined by Topol (19). The Hittorf method of correlating weight changes in the electrodes of cells of the type

$$Ag/QAg_7I_8/C$$

with the transport of current was used, as previously described (12). The result for both materials was that Ag^+ ion carried all of the current. Thus, it is probable that in this entire class of electrolytes Ag^+ ion carries all of the current as it does in the previously reported high-conductivity electrolyte class MAg_4I_5 (10, 12).

Conclusions

The results indicate that the formation of conductive quaternary ammonium iodide-silver iodide compounds is a fairly general phenomenon, including all ions from $C_4H_{12}N^+$ to $C_9H_{22}N^+$. It is probable that under non-

ambient conditions of pressure and temperature there will be not only transformations from conductive to resistive phases (as observed for $Et_4N\,Ag_7I_8$ at low temperatures), but also some transformations from resistive to conductive phases by the compositions containing the larger tetraalkylammonium ions. Structural studies have shown that in the $RbAg_4I_5$ crystal lattice the Ag^+ ions (16 per unit cell) are distributed over a large number of sites (20, 21). Geller reported there are 56 iodide tetrahedra per unit cell, which share faces to permit rapid Ag^+ ion diffusion within the immobile lattice of iodide anions (20).

Geller and Lind (17) have recently reported the crystal structure of $(Me_4N)_2Ag_{13}I_{15}$. The hexagonal unit cell contains 39 Ag^+ ions distributed over 123 tetrahedral sites. These sites are formed by iodide tetrahedra that again share faces in a manner to permit Ag^+ ion diffusion throughout the anion lattice.

In the solid electrolyte group KAg_4I_5, $RbAg_4I_5$, and $NH_4Ag_4I_5$ the compounds are isomorphous and form complete solid solutions (11). A comparison of powder photographs of the present series of tetraalkylammonium silver iodide electrolytes gives no evidence for isomorphous structures. However, the similarity of ionic transport suggests there should be similar diffusion paths in these crystals. Structural studies of this series should prove to be very enlightening as to the detailed processes involved in the Ag^+ ion transport.

Acknowledgment

The author wishes to thank Mr. Louis D. Hermo who carried out much of the experimental phase of this investigation. The work was performed under the North American Rockwell Corporation Independent Research and Development Program.

Manuscript received May 25, 1970. This was Paper 331 presented at the Los Angeles Meeting of the Society, May 11-15, 1970.

Any discussion of this paper will appear in a Discussion Section to be published in the June 1971 JOURNAL.

REFERENCES

1. T. Takahashi and O. Yamamoto, *Denki Kagaku*, **32**, 610 (1964).
3. T. Takahashi and O. Yamamoto, *ibid.*, **32**, 664 (1964).
3. T. Takahashi and O. Yamamoto, *ibid.*, **33**, 364 (1965).
4. T. Takahashi and O. Yamamoto, *ibid.*, **33**, 518 (1965).
5. T. Takahashi and O. Yamamoto, *Electro. Chim. Acta*, **11**, 779 (1966).
6. T. Takahashi and O. Yamamoto, *ibid.*, **11**, 911 (1966).
7. B. B. Owens, G. R. Argue, I. J. Groce, and L. D. Hermo, *This Journal*, **116**, 312 (1969).
8. F. Gutmann, A. M. Hermann, and A. Rembaum, *ibid.*, **114**, 323 (1967).
9. R. A. Friedel, *ibid.*, **115**, 614 (1968).
10. J. N. Bradley and P. D. Greene, *Trans. Faraday Soc.*, **63**, 424 (1967).
11. B. B. Owens and G. R. Argue, *Science*, **157**, 308 (1967).
12. L. Topol and B. B. Owens, *J. Phys. Chem.*, **72**, 2106 (1968).
13. B. B. Owens, U.S. Pat. 3,476,606, Solid State Electrochemical Device (1969).
14. B. B. Owens and G. R. Argue, *This Journal*, **117**, 898 (1970).
15. R. Kuhn and H. Schretzmann, *Angew. Chem.*, **67**, 785 (1955).
16. D. M. Smyth, C. H. Tompkins, Jr., and S. D. Ross, "Solid Electrolyte Batteries with Modified AgI Electrolytes," Paper presented at the 24th Annual Power Sources Symposium, May 19-21, 1970, Atlantic City, N. J.
17. S. Geller and M. D. Lind, *J. Chem. Phys.*, In press (1970).
18. J. E. Oxley and J. R. Humphrey, Private communication (1968).
19. L. Topol, Private communication (1967); AI-68-TDR-11.
20. S. Geller, *Science*, **157**, 312 (1967).
21. J. N. Bradley and P. D. Greene, *Trans. Faraday Soc.*, **63**, 2516 (1967).

Oxidation of an Fe-30% Ni Alloy in Oxygen at 700°-1000°C

I. A. Menzies and J. Lubkiewicz[1]

Corrosion Laboratories, Department of Chemical Engineering, The University of Manchester Institute of Science and Technology, Manchester 1, England

ABSTRACT

The oxidation of an Fe-30% Ni alloy has been studied at 700°-1000°C using thermogravimetric, metallographic, and electron probe microanalysis techniques. At all temperatures, parabolic kinetics was observed and the activation energy for the process was 37.8 ± 5 kcal $mole^{-1}$. At all temperatures, $Ni_xFe_{3-x}O_4$ and Fe_2O_3 were present in the external scale and oxidation was accompanied by a progressive Ni enrichment of the underlying alloy. In this alloy, the Ni enrichment reached values of ~60% even after short periods of oxidation at 700°C and Ni concentrations of 75-85% were recorded after longer times and at higher temperatures. The Ni concentration in the $Ni_xFe_{3-x}O_4$ scale layer rapidly attained concentrations corresponding to $x > 0.5$. There was no internal oxidation at 700°C although some was observed at 800°-900°C. Considerable internal oxidation was observed at 1000°C. In this alloy, there was relatively uniform precipitation of internal oxide particles with no evidence of intergranular oxidation. The mechanism of oxidation of the alloy is discussed in the light of present knowledge concerning the Fe-Ni-O system.

It was clear from a detailed review of the literature (1, 2) that there was considerable disagreement concerning the growth morphology and composition of oxide scales formed on Fe-Ni alloys containing ≤ 30 w/o (weight per cent) Ni in air and in oxygen. Furthermore, there was little information concerning the kinetics and scaling of Fe-Ni alloys in CO_2 or CO_2/CO mixtures. Since that time, considerable information dealing with the behavior of alloys containing ≤ 50 w/o Ni in CO_2 and CO_2/CO mixtures has been given (3-6). The present study is a continuation of more

[1] Present address: Instytut Mechaniki Precyzyjnej, Warsaw, Poland.

Key words: oxidation, iron-nickel alloys, kinetics, oxide morphology, electron probe microanalysis.

recent investigations of the behavior of an Fe-12% Ni alloy in oxygen at atmospheric pressure at 700°-1000°C (7) and deals with scale development and internal oxidation as a function of time and temperature. Since completion of the present investigation, additional information concerning the behavior of Fe-Ni alloys at 0.2 atm and 200 Torr oxygen pressure at 977°-1000°C has become available (8) and these recent observations are discussed with the present results.

Experimental

The alloy used was of high purity and was supplied by the British Iron and Steel Research Association in the form of cold-rolled strips. The composition of the alloy was as follows: Ni, 30.2%; C, 0.006%; S, < 0.03%; Sb, < 0.005%; Bi, < 0.005%; Pb, < 0.005%; P, 0.001%; Si, 0.004%; CW, < 0.05%; Nb, < 0.05%; Sn, < 0.01%; Cr, 0.008%; Co, 0.014%; Mo, < 0.01%. Specimens 0.5-0.8 cm x 1.0 cm x 1.6 cm were cut from the sheet and a small suspension hole drilled in each specimen for a fine Pt suspension wire.

All specimens were abraded on 600 SiC paper and chemically cleaned in an acid mixture as previously described (3-5). After water washing, the specimens were dipped in a mixture of 2 parts of H_2SO_4 and 1 part HNO_3 and again rinsed thoroughly. The specimens were then allowed to stand in a solution containing 50 g/liter KCN for 1 hr. They were then washed in water, rinsed in acetone, and allowed to stand in this solvent until required.

Weight gain determinations were made continuously using a quartz spring thermobalance as previously described (9). Oxygen containing $\not>$10 ppm hydrocarbons, $\not>$50 ppm Ar, $\not>$0.15 g/m^3 H_2O, 5 ppm CO_2 was further purified before use to remove CO_2 and to reduce the moisture level to <10 ppm. In all runs, the chemically etched specimen was suspended in the cool part of the balance while the chamber was evacuated and flushed with purified oxygen for 15-30 min. The specimen was then lowered into the hot zone of the furnace by means of a winching device, and cathetometer readings were commenced as soon as possible. All experiments were carried out in an atmosphere of oxygen at atmospheric pressure. At the end of each run, the specimen was winched out of the furnace over a period of 2-3 min and cooled in oxygen in the top section of the balance.

All specimens for metallographic examination and electron probe microanalysis were vacuum impregnations mounted in an Araldite resin with powdered calcite as a hardener (10). Specimens for electron probe microanalysis were then given a thin (100-500Å) coating of carbon to render them electrically conducting. Iron and nickel profiles were measured using a Cambridge Mk II Misroscan at several scanning speeds in the range 4-40 μm/min and the peak values of Ni enrichment were checked by direct measurement of Bragg angles at these points. An accelerating voltage of 25 kV was used throughout and the results were corrected for background radiation, paralysis time, absorption, and fluorescence. The quantitative traces for Fe and Ni shown in the various figures have been fully corrected at the points indicated and the complete curves adjusted accordingly. In all cases, several traces were obtained at various scanning speeds to insure appropriate sensitivity of measurement and allow elimination of statistical errors. All values of interfacial contents of oxides and metal with respect to Ni are accurate to within ±2% of the measured value and were obtained from the corrected line scans.

Results

Kinetics of oxidation.—The specimen weight gains are given in Fig. 1 as a function of time. The results shown are the average of at least five experimental runs at each temperature. The parabolic law was obeyed throughout the entire exposure period and no rate transitions were apparent. The parabolic rate constants are given in Table I. An Arrhenius function was plotted using the method of least mean squares and the value obtained for the activation energy was 37.8 ± 5 kcal mole^{-1}. The value of the rate constant at 900°C was lower than expected from the over-all pattern of results at other temperatures.

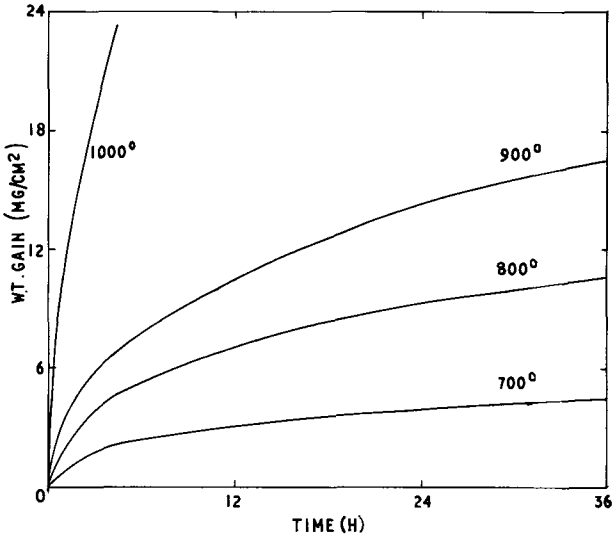

Fig. 1. Weight gain as a function of time for the oxidation of an Fe-30% Ni alloy in oxygen at atmospheric pressure at 700°-1000°C.

Oxide morphology and composition, and Ni *redistribution in the alloy.*—To facilitate comparison with other studies (7), the main investigations were carried out at 700° and 900°C. In addition, specimens oxidized for 46 hr at 800°C and 3 and 7 hr at 1000°C were also examined.

Examination of specimens oxidized at 700°C.—Specimens oxidized for 0.25, 3.5, 9.0, and 40 hr were examined. Similar morphological features were found throughout the entire exposure period and details of all major features are presented collectively in Table II. The outer scale consisted of a two-layer oxide, the layers being of almost the same thickness (Fig. 2). Beneath the external scale in each specimen was a Ni-rich rim which increased in thickness with time of exposure, being ~2 μm thick after 0.25 hr oxidation and ~10 μm thick after 40 hr. No internal oxidation was detected within this rim. Linear scans for Fe and Ni along lines normal to the metal-oxide interface in Fig. 2 yielded the profiles shown in Fig. 3. The spinel compositions at the inner interface in contact

Table I. Parabolic rate constants for the oxidation of an iron-30% nickel alloy in O_2 at 700°-1000°C

Temp, °C	Oxidation rate, g^2/cm^4/sec
1000	1.99 ± 0.3 × 10^{-8}
900	2.7 ± 0.4 × 10^{-9}
800	1.36 ± 0.3 × 10^{-9}
700	1.85 ± 0.2 × 10^{-10}

Table II. Major features of specimens of an Fe-30% Ni alloy oxidized at 700°C

Duration of oxidation (hr)	Wt gain (mg/cm^2)	scale thickness (μm)	Ni content of $Ni_xFe_{3-x}O_4$ at interfaces: Scale/subscale (%)	Spinel/hematite %	Ni concentration in enriched alloy (%)
0.25	0.39	6	7	<0.5	59
3.5	1.97	13	11	<0.5	68
9.0	2.78	17	8	<0.5	69
40.0	5.1	30	16	<0.5	75

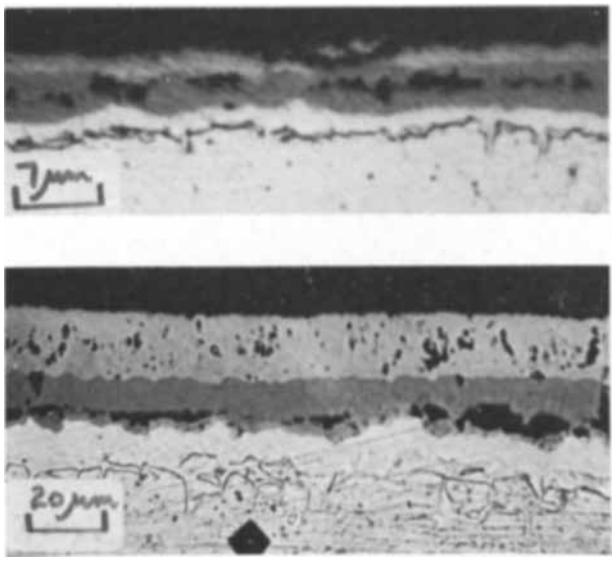

Fig. 2. Cross sections of an Fe-30% Ni alloy oxidized at 700°C (2% nital etch): *(a) top*—0.25 hr, *(b) bottom*—40 hr.

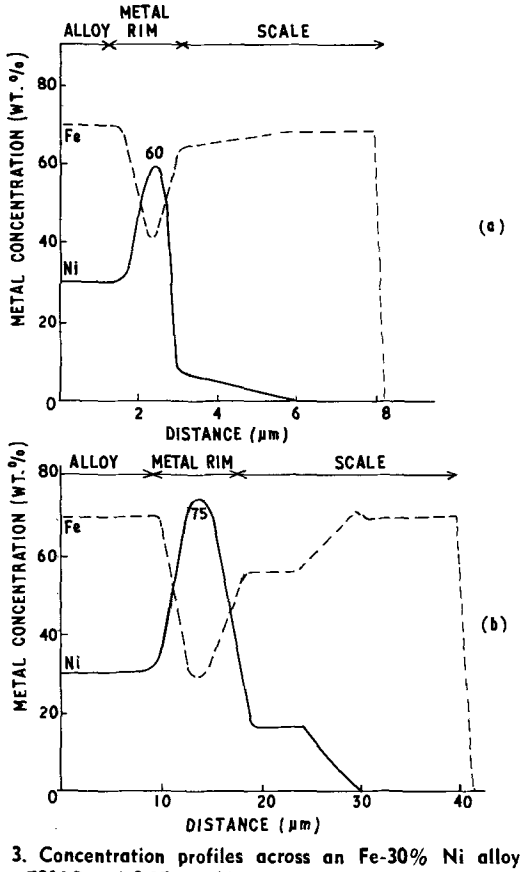

Fig. 3. Concentration profiles across an Fe-30% Ni alloy oxidized at 700°C: *(a)* 0.25 hr, *(b)* 40 hr.

with the metal were as follows: 0.25 hr—$Ni_{0.29}Fe_{2.71}O_4$; 9 hr—$Ni_{0.33}Fe_{2.67}O_4$; and 40 hr—$Ni_{0.66}Fe_{2.34}O_4$. In specimens oxidized up to 9 hr there was a Ni concentration gradient across the spinel phase (*cf.* Fig. 3a), whereas after 40 hr (Fig. 3b) the spinel phase in contact with the metal showed little change in Ni concentration over a thickness of ~7 μm. Thereafter there was a concentration gradient to the hematite interface.

The metal rim always contained ≥60% Ni but the apparent rise in Ni concentration with increasing amounts of oxidation may be due to an increase in the accuracy of the analyses with increasing thickness of the enriched zone.

Table III. Major features of specimens of an Fe-30% Ni alloy oxidized at 900°C

Duration of oxidation (hr)	Wt gain (mg/cm²)	Scale thickness (μm)	Ni content of $Ni_xFe_{3-x}O_4$ Inner interface %	Inner interface x	Outer interface %	Outer interface x	Ni concentration in enriched alloy (%)	Composition of internal oxide Fe, %	Ni, %
1	3.9	30	14	0.57	<1	<0.04	76	—	—
4	5.8	40	13	0.53	<1	<0.04	88	—	—
9	8.8	50	14	0.57	<1	<0.04	80	69	4
21.5	12.4	80	18	0.74	18	0.74	85	71	1
46	18.4	90	19	0.78	19	0.78	85	69	3

Examination of specimens oxidized at 900°C.—Overall, the results at 900°C were similar to those at 700°C except that some internal oxidation occurred. The major features are summarized in Table III. After all exposures, the external scale consisted of two oxides of approximately the same thickness.

After 0.25 hr oxidation (0.9 mg/cm²), a few isolated oxide particles were apparent within the metal rim beneath the external scale (Fig. 4). The Ni enrichment behind the external scale was 65% even at this stage (Fig. 5). The Ni concentration in the spinel layer decreased from ~20% at the scale/alloy interface to <1% at the spinel hematite interface and thus the inner region of the external scale corresponded to oxide compositions in the range $Ni_{0.82}Fe_{2.18}O_4$ to $Ni_{0.04}Fe_{2.96}O_4$. The internal oxide particles were too small to allow accurate analysis. After 1 and 4 hr, similar features were observed (Table III) and the internal oxide particles were 1-2 μm diameter still too small for accurate analysis.

After 9 hr oxidation, the general features of the specimen were similar but, contrary to previous speci-

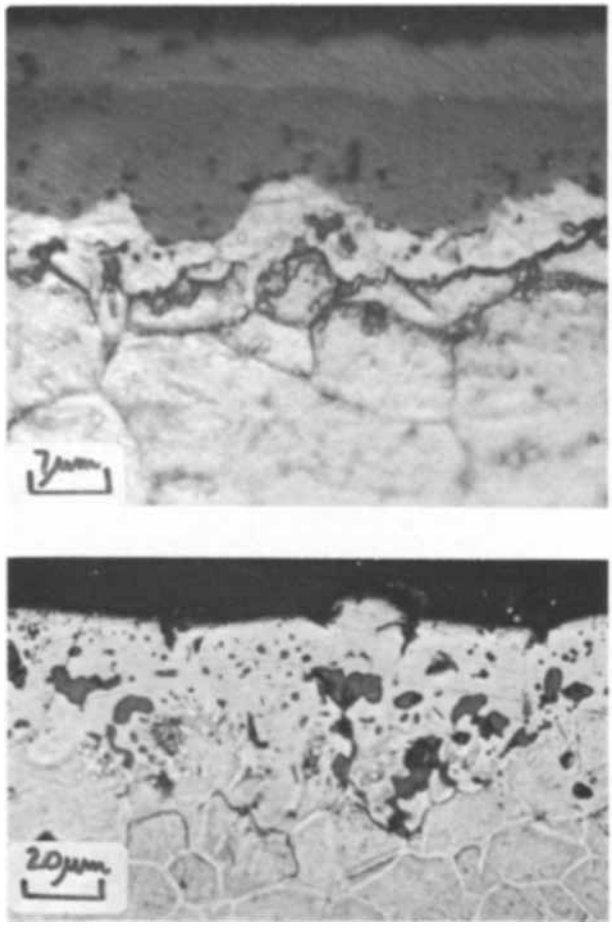

Fig. 4. Cross sections of an Fe-30% Ni alloy oxidized at 900°C (2% nital etch): *(a) top*—0.25 hr, *(b) bottom*—46 hr. (Internal oxide particles.)

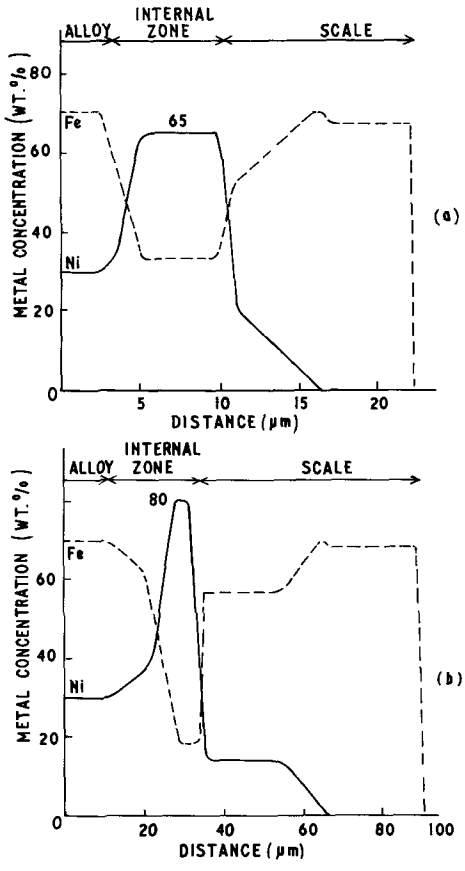

Fig. 5. Concentration profiles across an Fe-30% Ni alloy oxidized at 900°C: *(a)* 0.25 hr, *(b)* 9 hr.

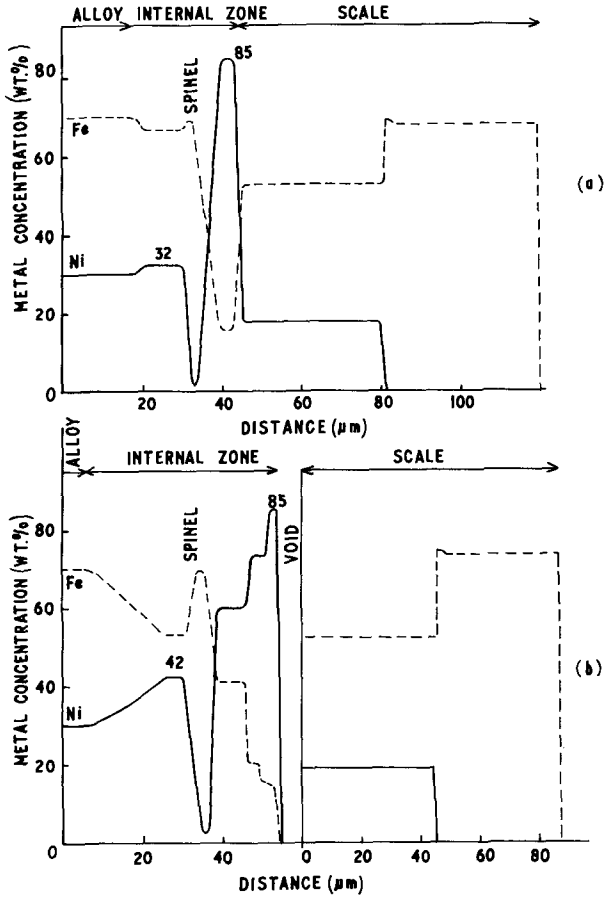

Fig. 6. Concentration profiles across an Fe-30% Ni alloy oxidized at 900°C: *(a)* 21.5 hr, *(b)* 46 hr.

mens at this temperature, the Ni concentration profile in the spinel region of the external scale showed little change in Ni concentration in the innermost 15 μm of this layer (Fig. 5b), although there was a gradient in the outermost regions of the layer. In specimens oxidized for longer periods (21.5 and 46 hr), there was little evidence of concentration gradients anywhere across the spinel layer (Fig. 6). Metallographic examination of cross sections of specimens exposed for 9-46 hr indicated that the size of the internal oxide particles increased with increasing exposure time. The particles were of irregular shape, discontinuous, and randomly distributed (*cf.* Fig. 4b). These internal oxide particles contained surprisingly little Ni having compositions corresponding to: 9 hr—$Ni_{0.12}Fe_{2.88}O_4$; 21 hr—$Ni_{0.04}Fe_{2.96}O_4$; 46 hr—$Ni_{0.1}Fe_{2.9}O_4$. After 9 hr exposure, the Ni enrichment in the alloy was recorded as a single peak (Fig. 5b), whereas after long exposures (Fig. 6) the Ni build-up was in the form of steps ~5 μm long indicating some stratification of the Ni enrichment of the alloy.

Clearly Ni concentration gradients were observed in the spinel in the outer scale. When the Ni build-up had attained ~80% in the internal zone of the alloy, uniform Ni profiles were recorded in the spinel region of the external scale.

Examination of specimens oxidized at 800° and 1000°C.—The early stages of oxidation were not investigated at either temperature. The major results are summarized in Table IV. Again, features similar to those observed at 700° and 900°C were evident at 800°. The external scale and degree of internal oxidation were similar to those observed in specimens oxidized for 9-21.5 hr at 900°C (*cf.* Fig. 7). The internal zone contained a number of small (1-2 μm diam) particles and the concentration profiles obtained were similar to those in Fig. 6a. Thus, results from the terminal specimen at 800°C were consistent with those obtained at 700° and 900°.

In general, the scale morphology at 1000°C was similar to that at 700°-900°C (Table IV), the major difference being the pattern of internal oxidation at 1000°C (*cf.* Fig. 7b,c). Here the proportion of oxide (~50%) in the internal zone was considerably greater in specimens exposed at 1000°C than in specimens of corresponding weight gain at 900°C (*cf.* 3 hr at 1000°C and 46 hr at 900°C). The internal zones of the specimens oxidized for 3-7 hr at 1000°C were analyzed along lines normal to the metal/oxide interface. In the 3 hr specimen (Fig. 8), three different spinel areas were analyzed and found to have the following compositions: (*A*) $Ni_{0.78}Fe_{2.22}O_4$; (*B*) $Ni_{0.24}Fe_{2.76}O_4$; (*C*) $Ni_{0.29}Fe_{2.71}O_4$. In the 7 hr specimen, the internal oxide particles had the composition $Ni_{0.12}Fe_{2.88}O_4$. The Ni enrichment in the alloy within the internal zone was recorded in both specimens as 70-80%. These

Table IV. Major features of specimens of an Fe-30% Ni alloy oxidized at 800° and 1000°C

Temp, °C	Duration of oxidation (hr)	Wt gain	scale thickness	Ni content of $Ni_xFe_{3-x}O_4$ Inner interface		Outer interface		Ni concentration in enriched alloy (%)	Composition of internal oxide		Proportion of internal oxide in the zone (%)
		(mg/cm²)	(μm)	%	x	%	x		Fe, %	Ni, %	
800	46	10.3	56	12	0.49	<1	0.04	85	—	—	<5
									65	7	
1000	3	16.6	70	11	0.45	<1	0.04	80	53	18	~50
1000	7	23.6	140	13	0.53	<1	0.04	79	69	3	~50

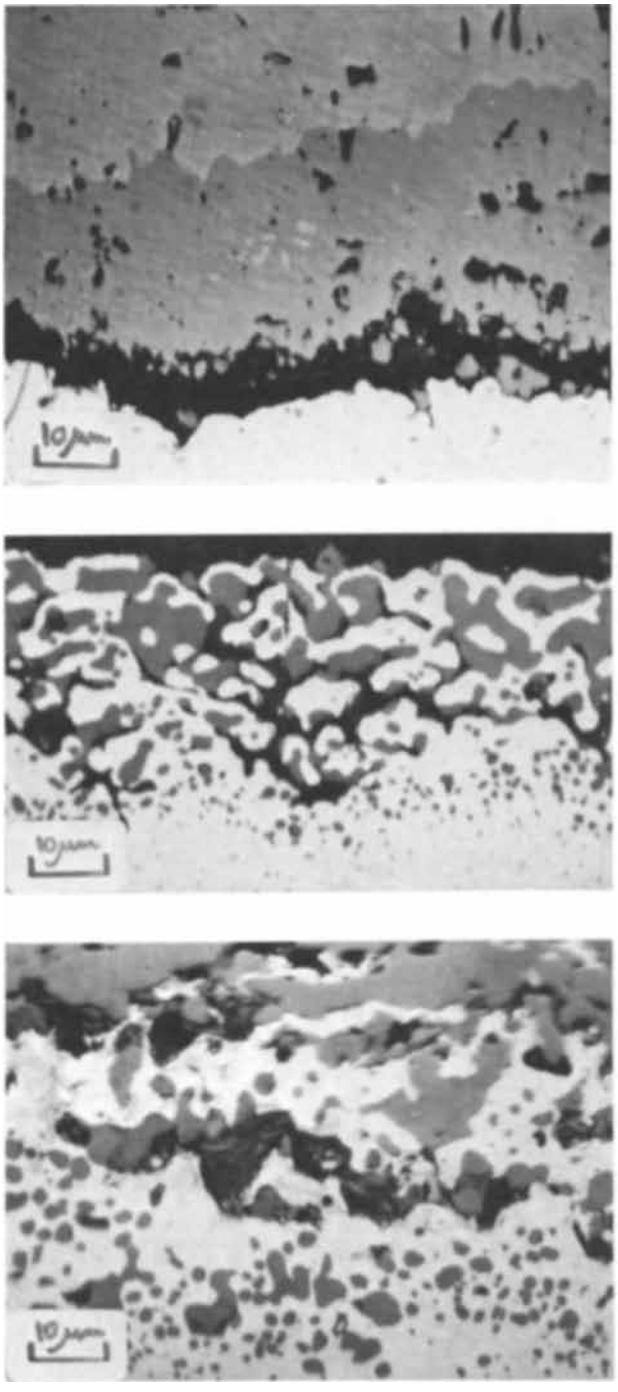

Fig. 7. Cross sections of an Fe-30% Ni alloy oxidized at 800° and 1000°C (2% nital etch): *(a) top*—46 hr at 800°C, *(b) center*—3 hr at 1000°C, *(c) bottom*—7 hr at 1000°C.

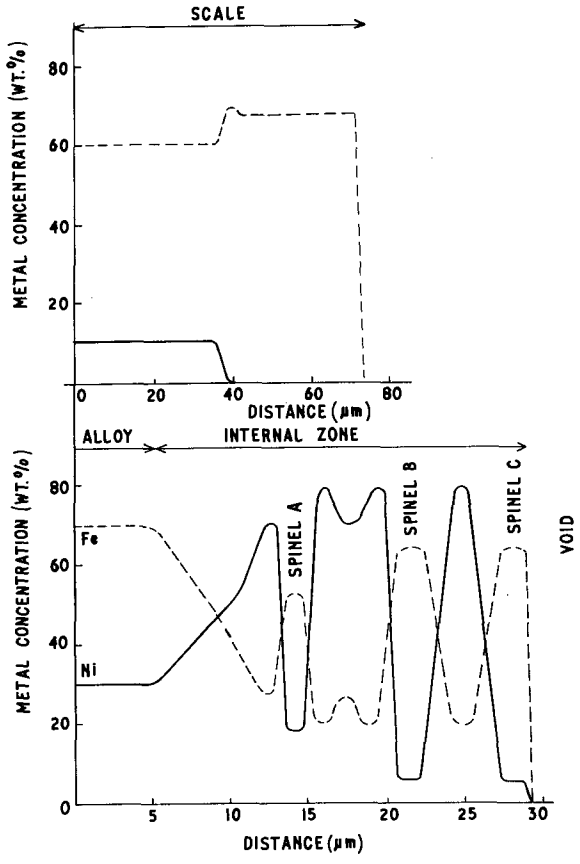

Fig. 8. Concentration profiles across an Fe-30% Ni alloy oxidized at 1000°C for 3 hr.

concentrations may in some instances have been low due to excitation of iron from immediately adjoining areas of spinel oxide. The nickel concentration profiles in the outer spinel phase in both specimens oxidized at 1000°C were uniform.

Discussion and Interpretation

Satisfactory reproducibility in the kinetic studies was achieved by careful attention to surface preparation of the specimens prior to exposure, in agreement with previous work (1-5, 7). The observed oxidation rates at 900° and 1000°C were close to those reported by Foley and Guare (11), whereas those at lower temperatures were somewhat higher than those reported previously (11). The activation energy of 37.8 ± 5 kcal mole^{-1} is in agreement with the values of 41.8 kcal mole^{-1} obtained for an Fe-30% Ni alloy in air (11). Thus, although the establishment of the morphological pattern of oxidation is more important than the oxidation kinetics, the kinetic data and their reproducibility and agreement with other work in the literature give confidence that the observed morphological features are typical of the system.

One of the main features of the oxide scales was the absence of FeO in agreement with recent work (7, 8) but contrary to results reported earlier by Bénard and Moreau (12, 13). Under all conditions of exposure, the scale consisted of an inner layer of nickel ferrite spinel ($Ni_xFe_{3-x}O_4$) and an outer layer of hematite (Fe_2O_3). It should be made clear that the structures of the oxides of composition $Ni_xFe_{3-x}O_4$ have not been examined in detail. It seems most likely from the evidence available in the literature, however, that this is a reasonable assumption (14, 15). Lattice parameter measurements in oxides across gradients of the type shown in Fig. 3, 5, 6, and 8 would be difficult to interpret because of the variations in Fe:O ratio in magnetite and in the Fe:Ni ratio in nickel ferrite. In the case of the Fe-30% Ni alloy, nickel entered the spinel layer from the commencement of oxidation and rapidly increased in concentration to values of x in $Ni_xFe_{3-x}O_4$ close to or greater than 0.5. Indeed, at temperatures >700°C, values of x significantly less than 0.5 were not observed even after relatively short periods of exposure. This is in agreement with the rapid rise in Ni concentration in the underlying alloy to >60% at lower temperatures and >80% at higher temperatures. Thus, from known equilibria in the Fe-Ni-O system (14-17), FeO would not be expected to be present, in agreement with the experimental observations. Oxide growth was regular and the additional oxide phase, NiO containing 10-20% Fe, reported (8) for the oxidation of an Fe-35% Ni alloy at 1000°C did not appear which suggests that 30% Ni is probably closer to the true composition limit for

Type 2 alloys of the Wulf, Carter, Wallwork classification.

Internal oxidation was of quite a different pattern from that observed for an Fe-12% Ni alloy (7) where grain boundary precipitation predominated. In the Fe-30% Ni alloy there appeared to be no preferential sites for internal oxidation (Fig. 7) at 1000°C and at all temperatures <1000°C the amount of internal oxidation in the 30% Ni alloy was very much less than that observed after similar exposures of an Fe-12% Ni alloy (7). Indeed, with the Fe-30% Ni alloy there was no internal oxidation at 700°C, whereas internal oxidation of the Fe-12% Ni was considerable. Thus the decrease in the amount of internal oxidation with increasing Ni content of the alloy corresponds with greater Ni enrichment in the alloy behind the oxide scale and a rapid enrichment of the spinel scale layer in Ni to compositions of $Ni_xFe_{3-x}O_4$ where $x \geq 0.5$. This is of particular interest since it has been reported (18) that solid solutions of $NiFe_2O_4$ in Fe_3O_4 are ideal solutions up to Ni concentrations corresponding to $Ni_{0.5}Fe_{2.5}O_4$, whereas at higher Ni concentrations (*i.e.*, $x > 0.5$) nonideal behavior occurs. Thus there may be some changes in diffusion or transport processes which take place when Ni concentrations exceed the limits of ideality and this may be of particular significance in relation to the reduction in internal oxidation as compared with the Fe-12% Ni alloy (7), particularly at lower temperatures (700°-900°C). Initially, preferential oxidation of iron occurs and in the case of the Fe-30% Ni alloy there is a rapid uniform build-up of Ni in the underlying alloy. There was no evidence of grain boundary enrichment in nickel although the general increase in nickel concentration would be expected to lead to an increase in the solubility of oxygen in the underlying Ni-enriched zone and possibly to the presence of oxygen gradients, assuming that oxygen becomes available. It seems clear that in the case of the Fe-30% Ni alloy sytem at 700°-900°C there is much less oxygen mobility than in the Fe-12% Ni alloy (7). This may be due to changes in interfacial equilibria between Ni-enriched metal and Ni-rich Ni ferrite as compared with the situations in the Fe-12% Ni alloy (7) where the spinel phase contains much less Ni. It has previously been suggested (7) that some anion diffusion may occur in $Ni_xFe_{3-x}O_4$ where $x < 0.4$ and that this may contribute toward providing a supply mechanism for oxygen which then goes into solution in the alloy and gives internal oxidation. In the present work, the observations for the Fe-30% Ni alloy suggest that at 700°-900°C when $x > 0.5$ such anion diffusion processes no longer contribute to internal oxidation which consequently decreases. The position is less clear at 1000°C where internal oxidation takes place to a considerable extent in alloys containing 12-30% Ni although there is some evidence of a change in the form of the internal oxide. Clearly, further data are required to substantiate these views which must be regarded as tentative.

Over-all, however, despite those possibilities of changes in anion diffusion in the spinel phase and their possible significance in relation to internal oxidation, such processes are of limited significance in relation to the over-all rate-controlling process. This is clearly the rate of cation diffusion in the nickel ferrite spinel phase. This work also indicates that for alloys containing ~30% Ni the problem of internal oxidation at lower temperatures (~700°C) is much less severe than that encountered in lower alloys (~12% Ni) under similar conditions where the total amounts of oxidation involved are similar. This is of considerable practical significance since the presence of internal oxide may be extremely damaging under service conditions.

Acknowledgments

We wish to thank Professor T. K. Ross for the provision of laboratory facilities and one of us (J.L.) wishes to acknowledge the receipt of Departmental Research Bursary. We also wish to thank Mr. B. Lambert for his valuable assistance and advice concerning the electron probe microanalyses.

Manuscript submitted May 7, 1970; revised manuscript received ca. July 27, 1970.

Any discussion of this paper will appear in a Discussion Section to be published in the June 1971 JOURNAL.

REFERENCES

1. R. J. Foley, *This Journal*, **109**, 1202 (1962).
2. W. J. Tomlinson, Ph.D. Thesis, Univ. of Manchester, Manchester, England (1965).
3. I. A. Menzies and W. J. Tomlinson, *J. Iron and Steel Inst., (London)*, **204**, 1239 (1966).
4. I. A. Menzies and W. J. Tomlinson, *J. Mater. Sci.*, **2**, 529 (1967).
5. I. A. Menzies and W. J. Tomlinson, *Brit. Corrosion J.*, **2**, 235 (1967).
6. L. A. Morris and W. W. Smeltzer, *Acta Met.*, **15**, 1591 (1967).
7. I. A. Menzies and J. Lubkiewicz, "Oxidation of Metals" (1971), In press.
8. G. L. Wulf, T. J. Carter, and G. R. Wallwork, *Corrosion Sci.*, **9**, 689 (1969).
9. I. A. Menzies and K. N. Strafford, *ibid.*, **3**, 193 (1965).
10. I. A. Menzies and D. Mortimer, *ibid.*, **6**, 517 (1966).
11. R. T. Foley and C. J. Guare, *This Journal*, **106**, 936 (1959).
12. J. Bénard and J. Moreau, *Rev. Met.*, **47**, 317 (1950).
13. J. Bénard and J. Moreau, *Compte Rend. (Paris)*, **232**, 1842 (1951).
14. M. J. Brabers and C. E. Birchenall, *Corrosion*, **14**, 179t (1958).
15. M. J. Brabers, W. J. Heideger, and C. E. Birchenall, *J. Chem. Phys.*, **53**, 810 (1956).
16. D. I. Lisovskii *et al.*, *Tsvetnye Metally*, **5**, 50 (1962).
17. G. S. Viktorovich, V. A. Gutkin, and D. I. Lisovskii, *ibid.*, **39**, 47 (1966).
18. T. Gordeev and M. Tretyakov, *Vestn. Mosk. Univ., Ser. II, Khim*, **18**, No. 2, 32 (1963).

Ellipsometric Studies of Anodic Oxide Films Formed on Tantalum in Dilute Phosphoric Acid

C. J. Dell'Oca** and L. Young*

Department of Electrical Engineering, University of British Columbia, Vancouver 8, British Columbia

ABSTRACT

Further ellipsometric data which confirm the two-layer nature of the anodic oxide films grown on tantalum in dilute phosphoric acid are reported. The two layers are believed to arise, respectively, from growth at the oxide/solution interface due to metal ion transport and from growth at the metal/oxide interface due to oxygen ion transport. The outer layer has a lower refractive index and dielectric constant due to phosphate incorporation. The effects have been observed in dilute phosphoric acid but not in the previous work in dilute sulfuric acid and citric acid of comparable concentration since phosphate is incorporated relatively strongly during the growth process. A model with a linear gradient of index is shown not to give an adequate representation of the optical results.

One of the most unexpected experimental findings in the study of the growth of anodic oxide films on tantalum is that both metal and oxygen ions are mobile to comparable extents. The situation as shown by the most recent tracer studies of Pringle (1) is especially puzzling in that the results are, as he pointed out, quite inconsistent with conventional models of ionic transport. Thus it was found that layers of rare gas marker atoms embedded in thin oxide films were spread out during subsequent growth of the films. The amount of spreading was greater the lower the mass of the rare gas atoms. However, the position of center of the distribution with respect to the metal surface was independent of the mass of the atoms. The amounts of new oxide produced on either side of the marker layer were determined by Pringle and used to calculate the metal ion transport number for anodization in 0.2*N* sulfuric acid at various current densities. It appears that the film grows simultaneously at the metal/oxide and oxide/solution interfaces: thus, tracer studies by Randall, Bernard, and Wilkinson (2) showed that the outer part of the film contains a uniform and in some cases a quite large amount of species from the electrolyte. The effect was particularly marked with phosphoric acid, and it was shown that the incorporated phosphate decreased the permittivity and ionic conductivity of the oxide compared to films made in dilute sulfuric acid. The oxide produced at the metal/oxide interface was found to be free from incorporated electrolyte species, as would be expected if the incorporated species are not mobile within the film. Ellipsometric measurements already reported (3) and further extended below give a clear confirmation of this picture of two homogeneous layers for films made in dilute phosphoric acid. In 0.2*N* sulfuric acid the effect of incorporated sulfate is less and optical methods (4-7) have either indicated a homogeneous film or have detected a deviation from a uniform oxide only in the form of an apparent very thin outer absorbing layer for films made in dilute sulfuric acid (5) although marked optical inhomogeneity through the thickness of the film was found for films made in more concentrated acid. Recent ellipsometric measurements by Muth (8) on films made in citric acid and dilute sulfuric acid have also indicated an optically uniform film and have given a permittivity close to that found for films made in 0.2*N* sulfuric acid (4) as compared to the lower value found by Klerer (9) using "Talysurf" measurements for the thickness.

* Electrochemical Society Active Member.
** Electrochemical Society Student Member. Present address: Fairchild Research & Development Laboratories, Palo Alto, California.
Key words: ellipsometry, anodic oxide films, tantalum.

Experimental Procedures

The polycrystalline Fansteel capacitor grade tantalum specimens were prepared by abrasion with metallurgical papers followed by either (*a*) mechanical polishing with alumina on a polishing wheel followed by a 5-sec dip in 48% HF, (*b*) electropolishing (5), or (*c*) mechanical polishing followed by electropolishing. It is believed that large-scale deviations from flatness should introduce only an averaging error due to the range of angles of reflected light accepted by the ellipsometer. Small-scale deviations would make the metal behave as though it were "tapered" in density but should disappear due to the smoothing inherent in anodizing. In practice electropolishing gave 1 or 2% higher current efficiencies for oxide production but a more wavy surface than did mechanical polishing. More careful empirical optimization of procedures is needed to obtain a good electropolished surface with polycrystalline than with single crystal metal.

Formation procedures and ellipsometry measurements were essentially as described in previous papers (3, 7). A detailed analysis of ellipsometric errors was made (thesis by Dell'Oca).

Results and Discussion

Two layer nature of the films.—The evidence from the tracer work is that the transport number is independent of total thickness at constant current density. To the extent that one may assume as a first approximation that the thickness of oxide formed per coulomb is the same for the two parts of the film, then the ratio of increments in the thickness of the outer layer to increments in total thickness is equal to the metal ion transport number. The ellipsometric results were fitted on the basis of the ratio of the thickness of the two parts being constant at constant current density. The parameters were initially chosen by comparison of experimental ellipsometric curves with computer curves. Later a program was used which adjusted the parameters in turn to minimize the mean square deviation of the experimental points from the computed curve with the Ψ values weighted by a factor of 4.[1]

The characteristic feature of the two layer model is that, with two layers which are nearly equal in index and thickness, when the thickness of the film has been increased so that the phase change of light traversing the whole film in-and-out has increased by 2π, the exponential terms in the ellipsometry equation which involve the phase changes in the individual parts of the film have changed corresponding to an approximate π change of phase, *i.e.*, have changed sign. After a fur-

[1] Ellipsometry gives the ratio of the complex reflectivities in p and s light: $R_p/R_s \equiv \tan\psi \exp i\Delta$.

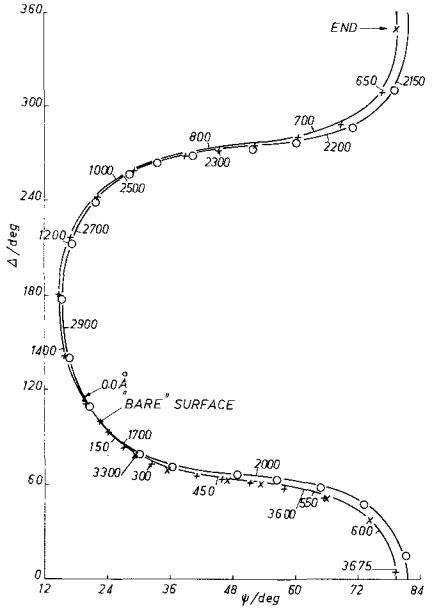

Fig. 1. Experimental results and calculated curve for *in situ* ellipsometric measurements on tantalum specimen anodized in dilute H_3PO_4 (Table I, line 7). Successive cycles denoted + O X. Wavelength 5461Å, angle of incidence 67.5° (also applies to Fig. 2, 4).

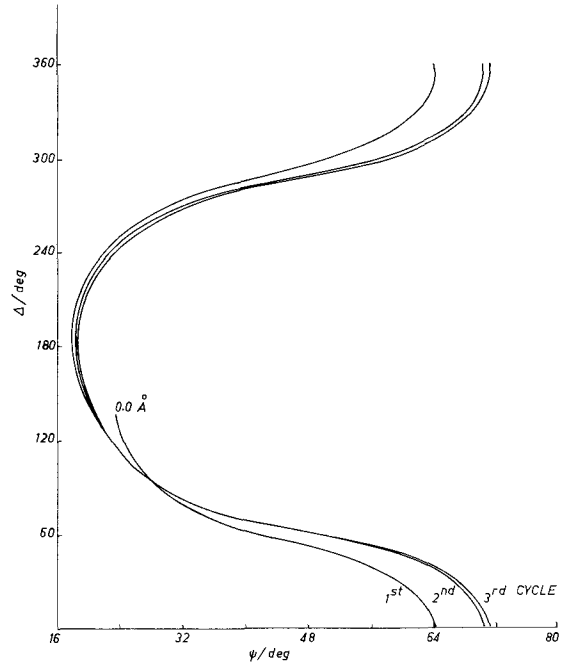

Fig. 2. Computed ellipsometric curve for a linear gradient of index modelled by 56 homogeneous layers. Indices at inner and outer surface fixed at 2.22 and 1.70, respectively. Metal index 3.3 − 2.3*j*.

ther 2π total phase change these terms have nearly returned to their original values. Hence the plot of Ψ *vs.* Δ tends to return close to its original track on what would be the third cycle for a uniform film. This is illustrated by calculated and experimental data in Fig. 1.

Some numerical results are given in Table I which contains the values of the parameters which gave the best fit to each of a set of specimens for both two layer and single layer films. The root mean square deviation in Δ and Ψ is also given and clearly confirms a better fit with the two layer model. The qualitative aspect of "recycling" on the third cycle (3) is, however, perhaps the most conclusive feature.

With electropolished surfaces a value of 3.3-2.3*j* for the refractive index of the metal (5-7) gave the best fit, but with mechanically polished metal a lower value of absorption index 2.25 was preferred. However, the optical properties of the oxide seemed unaffected by method used in surface preparation of the metal. The index of the inner oxide was found to be 2.22, *i.e.*, close to the value at this wavelength found in previous work (7) for films made in 0.2*N* H_2SO_4. The index of the outer layer depended on both the concentration and nature of the electrolyte, since these things affect the nature and amount of incorporated electrolyte species. As in previous work, no evidence for two layers was found in 0.2*N* H_2SO_4.

What might seem an obvious alternative model is that involving a continuous monotonic gradient of index through the film rather than two individually homogeneous layers. Physically this might correspond to the incorporated species continuously moving inward as the film grew, and in this case fixed values of index at the interfaces might be expected. The case of a linear gradient with fixed end values was computed using a stepwise approximation with 56 steps, *i.e.*, 56 thin homogeneous layers. This model fairly unequivocally does not fit the data since on the third cycle there is no tendency to return to the curve traced out on the first cycle (Fig. 2.).

Experimentally, there is clearly no reason why the measurement errors should produce the recycling effect.

Table I. Parameters giving best fit to ellipsometry data for oxides grown in various ways using a one or two layer optical model for the oxide. For oxides grown in H_3PO_4 both the double and single layer fit is given. (Single layer is distinguished by absence of values for n_2 and G where G = thickness of outer part divided by total thickness.) The value $n_m = 3.3$ is assumed

Growth conditions*	No. of ellipsometry cycles-points	Optical parameters				RMS deviations		Final thickness, Å
		n_1	n_2	$N_m = n_m - jk_m$	G	Δ	Ψ	
1 aDSA	1-13	2.210		3.3-2.25*j*		0.270	0.140	1410
1 bDSA	<2-29	2.215		3.3-2.29*j*		0.488	0.155	2143
1 aDSW	>1-19	2.20		3.3-2.23*j*		1.790	0.170	1889
1 aDPA	>3-69	2.145	2.22	3.3-2.25*j*	0.510	0.295	0.089	4468
		2.150		-2.18*j*		1.08	0.386	4569
1 bDPA	>2-41	2.145	2.215	-2.29*j*	0.525	0.494	0.138	3278
		2.155		-2.23*j*		0.834	0.342	3316
1 cDPA	>2-18	2.145	2.225	-2.30*j*	0.520	0.319	0.122	3259
		2.155		-2.22*j*		1.630	0.147	3306
1 aDPW	>2-52	2.14	2.20	-2.24*j*	0.50	1.600	0.288	3683
		2.165		-2.24*j*		1.980	0.374	3689
10 cDPA	>2-33	2.140	2.225	-2.30*j*	0.565	0.537	0.155	3124
		2.155		-2.23*j*		0.950	0.367	3166
10 cDPW	>2-29	2.145	2.20	-2.31*j*	0.56	2.500	0.330	2930
		2.155		-2.25*j*		3.360	0.408	2949
1 aCPA	<1-21	1.980	2.22	-2.24*j*	0.65	0.390	0.105	1246
		2.000-0.028*j*		-2.18*j*		0.990	0.250	1305

* Code indicates: current density (1 or 10 mA/cm²); specimen preparation (a, b, or c); growth in 0.2*N* H_2SO_4 (DS), 0.23*N* H_3PO_4 (DP), or 85% H_3PO_4 (CP); measured in air (A) or *in situ* (W).

Table II. Comparison of goodness of fit by a single layer and by a two layer model of measurements at three angles of incidence on a single film. The index of the metal was taken as $3.3 - 2.3j$ and the other parameters were varied to obtain the best fit. The best values were: single layer; $n = 2.17$; two layers $n_1 = 2.15$, $n_2 = 2.22$, $G = 0.52$ (= outer film thickness/total film thickness). ϕ = angle of incidence, T = thickness

	Experimental		Single layer fit			Two layer fit		
ϕ	ψ	Δ	ψ	Δ	T (A)	ψ	Δ	T (A)
75°	50.04	10.6	49.956	10.287	1924.71	49.986	10.435	1894.25
67.5°	54.71	4.64	54.718	4.575	1924.70	54.786	4.683	1895.3
60°	60.03	339.98	60.094	339.916	1923.81	60.143	339.876	1895.67

Measurements were also made on each of three films at three angles of incidence to test the two layer model. As might be expected the data for each film can *a priori* be fitted equally well by a single layer model, as illustrated for one film in Table II.

The relative permittivity of the outer layer of films formed in 0.23*N* phosphoric acid was determined by assuming that the inner layer has the same permittivity as the effective value 27.6 found for films formed in 0.2*N* sulfuric acid under specified conditions (4). This is justified by the model in which the oxide formed at the metal/oxide interface is not affected by the nature of the electrolyte, and provided that the effect of the incorporated sulfate in films made in dilute sulfuric acid may be neglected, as is confirmed by the interpretation of the ellipsometer data in which the refractive index of the inner layer of films made in phosphoric acid was equal to the effective value for films made in dilute sulfuric acid. The value obtained was 25 for formation at 1 mA/m^{-2} and 25°C, measured at the same temperature.

Metal ion transport member.—Ellipsometry provides a nondestructive method of estimating transport number. The values obtained for 0.23*N* phosphoric acid at 25°C were 0.51 to 0.52 at 1 mA/cm^{-2} and 0.56 at 10 mA/cm^{-2}. These, as shown in Fig. 3 are in excellent agreement with the tracer data of Randall *et al.* (2), as might be expected since both methods use the incorporated electrolyte species as markers. It is perhaps worth noting that the only case for which both the method using inert gas and that using the electrolyte species as markers have been applied is formation at 1 mA/cm^{-2} at 25°C in 0.2*N* sulfuric acid and that the results were in disagreement [0.256 (1) as compared to 0.48 (2)].

Sequential Formation in Different Electrolytes

If a film is formed first in concentrated and then in dilute acid it is expected that the oxide produced consists of three layers. An inner layer which represents the inner undoped portion of the oxide formed in each anodization. A middle layer containing a uniform high concentration of phosphate typical of formation in concentrated H_3PO_4 and an outer layer typical of the outer layer formed in the dilute acid; this is provided

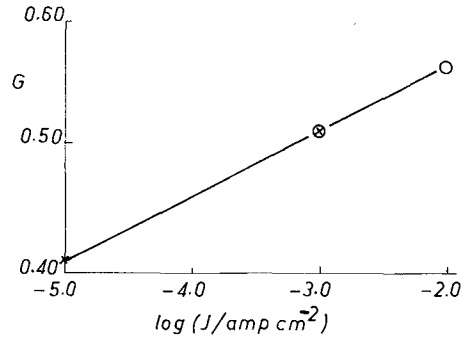

Fig. 3. Ratio of thickness of outer layer to total thickness vs. current density for film grown in dilute H_3PO_4 at 25°C. X Randall *et al* (2); O present work.

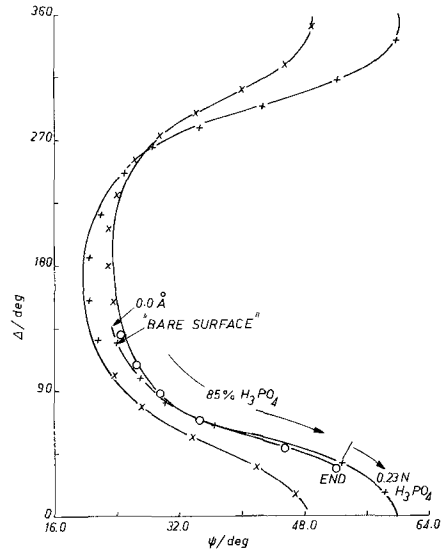

Fig. 4. Experimental points and computed curve for anodization in concentrated followed by dilute phosphoric acid. The computer curve is based on the model that the already existing oxide is unchanged by further anodization, the oxide produced is determined by the electrolyte in use. Cycles denoted + X O.

that the incorporated species are immobile. Knowing the thickness of each layer of the oxide produced in the concentrated acid anodization and assuming that the refractive index of each portion of the oxide for the two anodizations would be the same as for formation entirely in each electrolyte, then the ellipsometry results of the second anodization could only be fitted if the separate layers occur in the sequence outlined above. Figure 4 shows fitted and observed data for the case where 0.23*N* H_3PO_4 was the second electrolyte. In curve fitting, values from Table I of $n_1 = 2.14$, $n_2 = 1.98$, and $n_3 = 2.22$ for the index of refraction of outer, middle, and inner layers were used, and the best fit to the data was found by varying G, the ratio of the outer layer to total new oxide produced in the second electrolyte, where the initial oxide now acts as a marker layer. A G of one half was found which agrees well with formation entirely in dilute H_3PO_4 as in Table I. Similar results were obtained from fitting the previously reported data (3) where the second electrolyte was 0.2*N* H_2SO_4 (except $n_1 = 2.22$ was used). All formations were at 1 mA/cm^2 at 25°C.

It might be pointed out that oxide formation in concentrated phosphoric acid is supported to about 95V at 1 mA/cm^2. The range of oxide thickness obtained is not sufficient to produce a complete ellipsometry cycle (3); however, a model of two nonabsorbing layers fits these results better than a single absorbing layer (1 aCPA Table I) and much better than a single nonabsorbing layer (not shown). Furthermore, the fit to the results from sequential formation in different electrolytes was obtained only if the initial oxide formed in concentrated acid consisted of two nonabsorbing layers.

Acknowledgment

The authors wish to thank the Sprague Electric Company for a grant which supported this work and J. P. S. Pringle for communication of his recent results before their publication.

Manuscript submitted Feb. 12, 1970; revised manuscript received *ca.* July 10, 1970. This was paper 14 presented at the New York Meeting of the Society, May 4-9, 1969. This paper was based on the Ph.D. thesis of one of the authors (C. J. D.'O.).

Any discussion of this paper will appear in a Discussion Section to be published in the June 1971 JOURNAL.

REFERENCES
1. J. P. S. Pringle, Extended Abstract 11, Electrochemical Society Meeting, New York 1969; personal communication. For earlier work see: J. A. Davies, B. Domeij, J. P. S. Pringle, and F. Brown, *This Journal*, **112**, 675 (1965).
2. J. J. Randall, W. J. Bernard, and R. R. Wilkinson, *Electrochim. Acta*, **10**, 183 (1965).
3. C. J. Dell'Oca and L. Young, *Surface Sci.*, **16**, 331 (1969).
4. L. Young, *Proc. Roy. Soc.*, **A244**, 41 (1958).
5. L. Masing, J. E. Orme, and L. Young, *This Journal*, **108**, 428 (1961).
6. S. Kumagai and L. Young, *ibid.*, **111**, 1411 (1964).
7. L. Young and F. G. R. Zobel, *ibid.*, **113**, 277 (1966).
8. D. G. Muth, *Vac. Sci. and Tech.*, **6**, 749 (1969).
9. J. Klerer, *This Journal*, **112**, 896 (1965).

High Field Ionic Conduction in Tantalum Anodic Oxide Films with Incorporated Phosphate

C. J. Dell'Oca and L. Young***

Department of Electrical Engineering, University of British Columbia, Vancouver 8, British Columbia

ABSTRACT

The dependence of the ionic current density J on the mean field $\overline{E}$ in oxides grown on tantalum in H_3PO_4 electrolyte was studied using ellipsometry to estimate the thickness. The field in the outer layer which is believed to grow due to metal ion motion is higher because of phosphate incorporation. The field in this layer was estimated by assuming that the field in the inner undoped layer was the same as the mean field at the same current density and temperature in films made in dilute sulfuric acid, which are less affected by electrolyte incorporation. The results indicate that the effect of phosphate on the ionic conductivity may be due to its reducing the permittivity and hence the effective field. It is pointed out that electrolyte incorporation gives two effects which contribute to the nonlinearity of log J *vs.* $\overline{E}$ plots. Thus, since the metal ion transport number increases with J so does the proportion of the film which contains phosphate and requires a higher field. Also the concentration of phosphate increases with J. The incorporation leads to history effects which are not removed by subsequent formation, since the profile of phosphate records the sequence of current densities used. The time dependence of the field on changing the electrolyte is consistent with the field locally determined by the local film material.

An investigation is reported on the effects of incorporated phosphate (1) on the ionic conduction process using the ellipsometer techniques described in the preceding paper.

In the earlier work on ionic conduction in anodic oxide films the current density J was expected to depend on the field E according to $J = J_0 \exp(-(W - \alpha E)/kT)$. Experimental results were at one time thought to show an anomaly of the type that $\partial \log J/\partial E$ was independent of the temperature (2). Later (3) it was claimed that the steady state J could be described by $J = J_0 \exp(-(W - \alpha E + \beta E^2)/kT)$ *i.e.*, the slope of log J *vs.* E plots varied as expected with temperature at constant E but was not independent of E. The earlier anomaly arose because experimentally a mean slope over a fixed range of J was calculated. The rationale of this form of expression was that the activation energy for sufficiently large fields should be detectably nonlinear in the field. Several mechanisms have since been proposed by various authors which must lead to this type of effect with homogeneous oxide, whether or not they are experimentally significant. The theory of ionic conduction is based on the idea that the potential energy of the moving ion can be written as a periodic function of its own position coordinates only, plus a ramp due to the applied field. This model gives nonlinearity as a second order effect as was noted in the above paper (2) where it was supposed to be small. (It depends on the shape of the potential energy function.) Random variations in activation energy from site to site such as are expected in an amorphous oxide were shown to be capable of giving this effect but not the analogous one in the transient case where the sudden changes in J due to sudden changes in E are observed (4).

Later it was suggested that electrostriction might be responsible (5), but Dignam (6) and later Dignam and Gibbs (7) showed that, if so, the electrostriction must be much greater than in halide crystals. It is certainly likely to be greater, and electrostriction has been claimed and disputed to dominate the electro-optic effect shown by these films (8, 9). Dignam, Goad, and Sole (10) have found a similar experimental behavior with aluminum. Dignam (6) and Dignam and Gibbs (7) have considered in some detail the question of the effects of the shape of the periodic potential energy function and conclude that the curvature may be accounted for by this. Young and Zobel (12), who extended the experimental result to niobium, suggested that an expected model for these oxides would be ions moving fairly freely down channels with occasional coulombic traps. This model corresponds to $J = J_0 \exp(-(W - \gamma E^{1/2})/kT)$ which represents the data quite well with one less parameter. It is a mistake to suppose (7) that this model is incorrect because the quadratic expression gives a better fit. One cannot expect an accurate fit for an approximate treatment of a simplified model; the point is whether the fit is accurate enough to suggest that the model contains the essential features of the real system. Further theoretical treatments have been based on the shape of the potential energy-distance relation and on dielectric effects treated by transition state theory (13, 14). Dreiner and Tripp (15)

* Electrochemical Society Active Member.
** Electrochemical Society Student Member. Present address: Fairchild Research & Development Laboratories, Palo Alto, California.
Key words: tantalum, anodic oxide films, ellipsometry, ionic conduction at high fields, dielectric films.

[*cf.* Dreiner (16)] have recently confirmed experimentally the quadratic form for tantalum over an extended temperature range using a pressure vessel.

Most of the work has been done on films made in dilute solutions of electrolyte which are not strongly taken up by the oxide. It will be shown in the present paper that two effects, due to the incorporation of electrolyte, lead to curvature of log J *vs.* $\bar{E}$ plots where $\bar{E}$ is the average field in the oxide. This has not been noted before although in the first report of the effect (3) it was shown that the curvature is larger for films made in more concentrated sulfuric acid solutions which were known to be inhomogeneously taken up.

The experimental procedures were as described in the accompanying paper which also deals with the ellipsometric techniques used.

Results and Discussion

The constant field required for a constant ionic current up to quite large thicknesses suggests that the bulk of the oxide is electrically neutral at fields which give ionic conduction. The field required for a given current must then, according to conventional models, be determined by the concentration of the mobile species in the electrically neutral oxide. However, this concentration could be controlled by the nature of the bulk oxide or by interface effects, *e.g.*, if space charge compensation occurred due to double injection of positive and negative ions. A partial test is provided by formation successively in two electrolyte solutions. In the case of bulk control, if the existing oxide is not modified by the change of electrolyte, then the mean field is a function of the thicknesses and characteristic fields of the various layers. Thus for formation in 14.7M phosphoric acid followed by formation in 0.23*N* phosphoric acid, an inner layer which is essentially pure oxide, a second layer containing a high concentration of phosphate and a third, outer layer containing a lower concentration of phosphate are produced. Ellipsometric data were fitted well by this model as shown in the previous paper. Figure 1 shows that the computed and observed fields are consistent with the idea that the field in each individual layer is characteristic of that layer and independent of whatever other layers were present. In the computation 8.15 x 10^6 V/cm and 6.46 x 10^6 V/cm, respectively, represent the fields typical of formation in the first and second electrolyte and the oxide produced in the first electrolyte was 552Å.

In previous work with 0.2*N* sulfuric acid (3), experiments were made in which films were grown either completely at a given current density to a given final voltage, or partly at a higher current density and then finally at the same lower current density to the same final voltage. The optical thickness was found to be indistinguishable provided a quite small minimum charge was passed at the final current

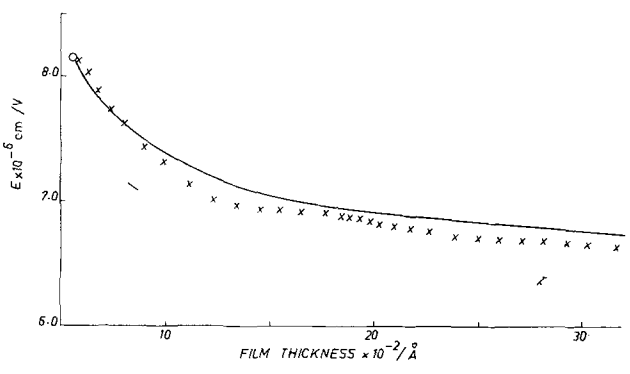

Fig. 1. Average field as function of thickness after changing electrolyte. The line is calculated on the basis that the field in each part of the film is characteristic of the material in that region.

Table I. Comparison of films made in 0.23*N* H_3PO_4 at 25°C

1. at 10 mA/cm^{-2} to 136V followed by 9.5 μA/cm^{-2} to 115.8V
2. at 9.5 μA/cm^{-2} to same final voltage.

	ψ	Δ
1.	41.60	300.16
2.	32.75	280.28

Assumed refractive indices				Apparent total thickness, Å	
Outer film	Inner film	Metal	G	Formation 1	Formation 2
2.22	2.22	3.3-2.30*j*	(single film)[a]	1989	2077
2.14	2.21	3.3-2.26*j*	0.56[b]	2040	2135
2.14	2.21	3.3-2.26*j*	0.51[c]	2038	2133

[a] As in the case of oxide grown in dilute H_2SO_4.
[b] and [c] As in the case of growth at 10 and 1 mA/cm^2, respectively, in H_3PO_4.

density. Also the relation between J and $\bar{E}$ was indistinguishable within 1% of field values for formation at constant voltage and constant field, respectively (12). On the present model one should expect the distribution of incorporated electrolyte to be a function of the formation procedures, and, since the incorporated phosphate is thought to be immobile, no amount of formation at a final current density should bring the film into the same state as complete formation at this current density. If this is indeed the case, the effect went undetected in dilute sulfuric acid only because it was too small. In 0.23*N* phosphoric acid the effect was detected as shown in Table I.

Dependence of ionic current density on field.— Figure 2 shows the mean field in the oxide *vs.* the ionic current density for growth of films in 0.23*N* phosphoric acid. The data were obtained by first growing to 99V at 10 mA/cm^{-2} giving about 1400Å of oxide. A constant 100V was then applied. The thickness was estimated using ellipsometric measurements made during successive interruptions of film growth. A two layer model with the metal ion transport number taken as 0.56 was employed as an approximation,

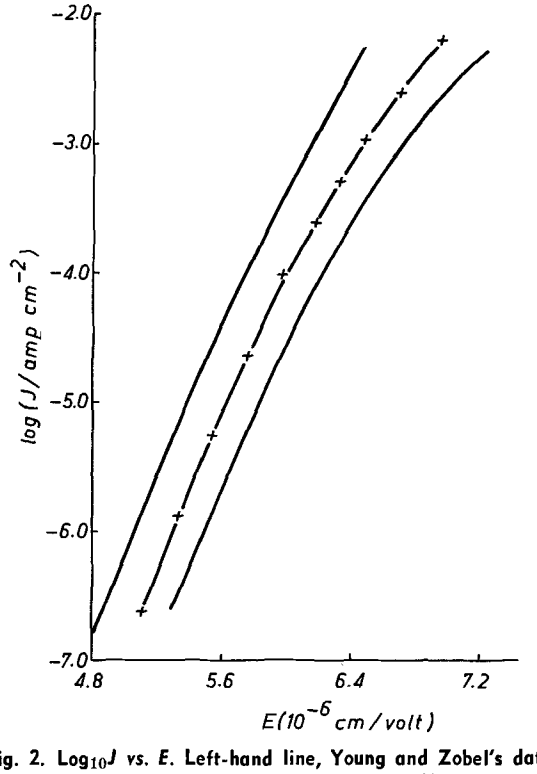

Fig. 2. $\text{Log}_{10}J$ *vs.* E. Left-hand line, Young and Zobel's data for 0.2*N* H_2SO_4; middle line, present data for 0.23*N* H_3PO_4; right-hand line, field in outer part of film obtained from middle line by assuming that the field in the inner part is the same as the mean field for formation in 0.2*N* H_2SO_4.

since most of the film was grown at the high current densities for which this transport number was found. The total ionic current density was found by differentiating the thickness-time data. Also shown in Fig. 2 is a curve which represents the data of Young and Zobel (12) for formation in 0.2N H_2SO_4 with the same procedure except that a uniform film was assumed.

In agreement with Randall *et al.* (1) the mean field is higher with the phosphoric acid due to the greater effects of phosphate compared to sulfate.

The results at 25°C are described by

$$J = J_1 \exp (q(\alpha E - \beta E^2)/kT)$$

where $q = 5e$ and

$J_1 = 10^{-38.42}$ A/cm^{-2}, $\alpha = 10.69$Å, $\beta = 6.51$ Å/10^{7}vcm^{-1}

as compared to

$10^{-28.71}$A/cm^{-2}, 6.995Å, 3.34 Å/10^{7}vcm^{-1}

for 0.2N H_2SO_4. To obtain the field in the outer layer, the field in the layer near the metal was approximated by the mean field for formation in 0.2N sulfuric acid, analogous to what was done in the accompanying paper to estimate the permittivity. The result is shown in Fig. 2. Changes during the constant voltage formation in the ratio G of the thickness of the outer film to the total thickness were estimated by assuming that the instantaneous transport number at a given J was the same as the steady-state value at this J (see preceding paper).

Curvature of log J vs. $\bar{E}$ plot.—Two effects associated with electrolyte incorporation cause curvature. First, the metal ion transport number has been found experimentally to increase with J. Thus the higher J the larger the fraction of the film that requires a higher field because of phosphate incorporation. Second, concentration of incorporated electrolyte is found to increase with J. The precise curvature produced depends on the conditions, *i.e.*, constant voltage or constant current formation. If the assumptions made in dissecting the film to evaluate the field in the outer layer were correct, then any curvature in the plot in Fig. 2 would be due to this second effect plus any curvature shown by homogeneous oxide.[1]

It is interesting to note that the fields in the two layers are roughly inversely proportional to their permittivities. This is shown in Fig. 3 when log J is plotted against $\epsilon_r E = D/\epsilon_0$ (D = electric displacement). This continuity of D across the interface between the two layers is not the result of an electrostatic boundary condition between dielectrics as assumed by Dignam (17) and by the reviewers: the layers act as conductors not dielectrics and the boundary condition is continuity of current density. There is no reason why charges should not accumulate at the interface to give any required change in D.

[1] It is perhaps useful to give some trivial equations showing that (for constant J formation) curvature is implied by the empirical facts of dependence of transport number, and concentration of incorporated phosphate on J, and of the constancy of D. Thus, experimentally (1) at constant temperature $G = A + B \ln(J/C)$ where A, B, C and further similar quantities below are temperature dependent parameters. Clearly, this relation can be valid only over a limited range of J. The mean field is $\bar{E} = E_i(1 - G) + E_0 G$ where E_i and E_0 are the fields in the inner and outer layers. We assume that the permittivity may also be taken as linearly dependent on $\ln(J/C)$ and that the effect of phosphate is solely on the effective field, *i.e.*, $J = C \exp HE_i = C \exp KE_0$, where $K = (1 - L \ln(J/C))M$. Hence, $\bar{E} = \left(\frac{1-A}{H} + \frac{A}{M}\right)\ln\left(\frac{J}{C}\right) + \left(\frac{B}{M} - \frac{B}{H} + \frac{AL}{M}\right)\left(\ln\left(\frac{J}{C}\right)\right)^2 + \left(\frac{BL}{M}\right)\left[\ln\left(\frac{J}{C}\right)\right]^3$ provided $1/(1 - L \ln(J/C)) \simeq 1 + L \ln(J/C)$. In Fig. 3 the difference in curvature between the plots for the inner and outer layers, on the assumptions made, is due to no allowance having been made for L. Also, in this experiment the concentration of phosphate in the outer layer will not have been constant, since the current density and mean field were decreasing throughout as the thickness increased at constant voltage.

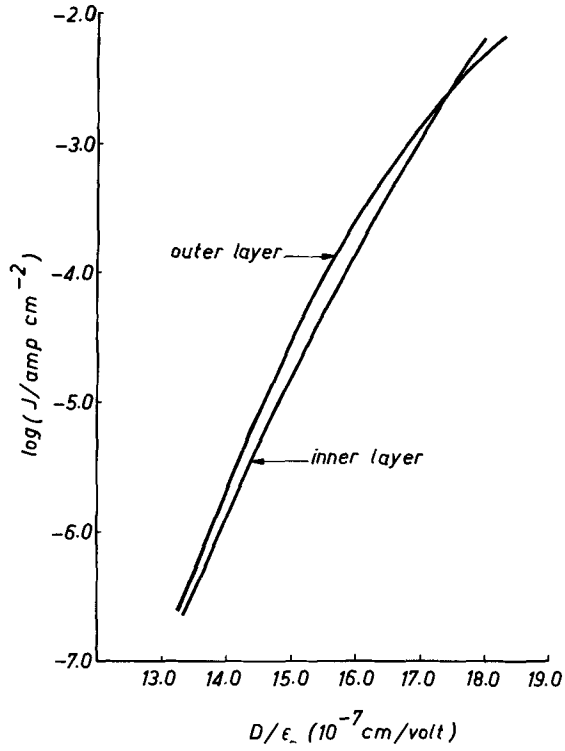

Fig. 3. $\text{Log}_{10} J$ vs. $\epsilon_r E = D/\epsilon_0$ for inner and outer parts of films made in 0.2N H_3PO_4.

Charges are supposed to exist close to the metal/oxide and oxide/solution interfaces to adjust the fields at these interfaces with respect to those in the interior of the film.

The near-equality of D seems to mean that an effective field should be taken as driving the ions in the ordinary model. For high ϵ_r the effective field will be essentially proportional to ϵ_r. The long-noted parallelism (1, 18) between ϵ_r and ionic conductivity cannot be ascribed to both being due to lattice point defects since little change occurs with phosphate doping in the audio frequency dielectric dispersion. The difference in permittivity is partly due to ultraviolet frequency effects (as shown by the change in refractive index) and most of the rest must be due to infrared polarization processes.

Both sources of curvature are indicated by the tracer results (1) to be present in films made in 0.2N H_2SO_4. The question is, therefore, whether any detectable curvature would be present in truly homogeneous oxide. To resolve this question, experiments are needed on films made in very dilute solutions of electrolytes which have minimum tendency to be incorporated. However, some clues are possibly as follows. First the idea of nonlinear activation energy removes the temperature anomaly in $\partial \log J/\partial E$ for both steady-state (3) and transient experiments (4). Second, the history of current densities was found experimentally to have little effect with 0.2N H_2SO_4 on the $\bar{E}$ for a given J provided a quite small charge was passed at the final J. Finally, it is surprising that the curvature effects should be shown by tantalum, aluminum, and niobium. In all these considerations a basic difficulty is that, in our opinion, no theory, which would be at all convincing in the absence of the experimental data, explains the comparable order of mobility of metal and oxygen ions. Possibly some momentum transfer process, such as is required (4) to explain the time development of J at constant E with films previously made at low J, will eventually explain this, but such a process is not taken account of in the ordinary theories of steady-state ionic con-

duction. We refer to Pringle's (19) and Dignam's approaches to this problem (20).

Thermal recrystallization.—Another process which involves atomic movement is the thermal recrystallization of the films (21-24). In this case local electric fields and concentration gradients near the crystalline nuclei drive the transport process. It might be expected that electrolyte incorporation effects might be seen also in this process although the facts that the inner layer is thought to be free of electrolyte, and that ion movement occurs more freely in this layer, might equally be expected to cancel out the effect. Brandon *et al.* in the discussion of their paper (24) have in fact reported observing electrolyte effects on thermal recrystallization.

Films of about 500Å were made on tantalum which had been chemically polished. The films were detached by the cathodic technique (2), mounted on platinum grids, and annealed at temperatures in the range of 650°-750°C in groups on a silica support in a silica-tube furnace in an atmosphere of oxygen. They were then examined in a Hitachi 11AB electron microscope at 100 kV. The reproducibility as regards the absolute amount of recrystallization was poor. However, the percentage of recrystallization was consistently greater for films made in dilute sulfuric acid than for films made in dilute phosphoric acid. The general appearance of the recrystallized films was also different.

Acknowledgment

The authors thank the Sprague Electric Company for a grant which supported this work.

Manuscript submitted Feb. 12, 1970; revised manuscript received *ca.* July 10, 1970. This was Paper 14 presented at the New York Meeting of the Society, May 4-9, 1969. This paper was based on the Ph.D. thesis of one of the authors (C. J. D.'O.).

Any discussion of this paper will appear in a Discussion Section to be published in the June 1971 JOURNAL.

REFERENCES

1. J. J. Randall, W. J. Bernard, and R. R. Wilkinson, *Electrochim. Acta*, **10**, 183 (1965).
2. For references see: L. Young, "Anodic Oxide Films," Academic Press, London & New York (1961).
3. L. Young, *Proc. Roy. Soc.*, **A258**, 496 (1960).
4. L. Young, *ibid.*, **A263**, 395 (1961).
5. L. Young, *This Journal*, **110**, 589 (1963).
6. M. J. Dignam, *Can. J. Chem.*, **42**, 1155 (1964).
7. M. J. Dignam and D. B. Gibbs, *J. Phys. Chem. Solids*, **30**, 375 (1969).
8. B. J. Holden and F. G. Ullman, *This Journal*, **116**, 280 (1969).
9. A. Frova and P. Migliorato, *Appl. Phys. Letters*, **13**, 328 (1968).
10. M. J. Dignam, D. Goad, and M. Sole, *Can. J. Chem.*, **43**, 800 (1965).
11. M. J. Dignam and D. Goad, *This Journal*, **113**, 382 (1966).
12. L. Young and F. G. R. Zobel ,*ibid.*, **113**, 277 (1966).
13. N. Ibl, *Electrochim. Acta*, **12**, 1043 (1967).
14. S. G. Christov and S. Ikonopisov, *This Journal*, **116**, 56 (1969).
15. R. Dreiner and T. B. Tripp, Abstract 21 in Extended Abstracts, Electrochemical Society Spring Meeting, New York (1969).
16. R. Dreiner, *This Journal*, **111**, 1350 (1964).
17. M. J. Dignam, Abstract 10 in Extended Abstracts, Electrochemical Society Spring Meeting, New York (1969).
18. L. Young, *Can. J. Chem.*, **38**, 1141 (1960).
19. J. P. S. Pringle, Abstract 11 in Extended Abstracts, Electrochemical Society Spring Meeting, New York (1969); and personal communication.
20. M. J. Dignam, *This Journal*, **112**, 722 (1965).
21. J. Harvey and H. Willman, *Acta Cryst.*, **14**, 278 (1967).
22. J. Spyridelis, P. Delavignette, and S. Amelinckx., *Phys. Stat. Sol.*, **19**, 683 (1967).
23. R. E. Pawel and J. J. Campbell, *This Journal*, **111**, 1230 (1964).
24. D. G. Brandon, J. Zahari, A. Aladjem, and J. Yaholom, *J. Vac. Sci. Techol.*, **6**, 783 (1969).

A Doped Oxide Deposition System for Antimony Diffusion

F. L. Gittler* and R. A. Porter

Bell Telephone Laboratories, Inc., Allentown, Pennsylvania 18103

ABSTRACT

A doped oxide diffusion system for antimony diffusion is described. The system has been shown to be feasible for base diffusion in PNP transistors. It appears to be superior to presently used systems for buried layers in integrated circuit slices.

The apparatus consists of a hot plate which heats a turntable on which slices to be deposited are placed. The associated gas train is automatic and can be programmed to deliver $(CH_3)_3Sb$ (the antimony source), SiH_4 and oxygen, to make the oxide, and nitrogen. The gas reaches the slice through an inverted fritted funnel. The deposition occurs at the desirably low temperature of 315°C and typically takes less than 5 min. The layer before the drive-in diffusion consists of an Sb_2O_5 or mixed SiO_2-Sb_2O_5 layer. This is then capped with an SiO_2 layer to prevent Sb evaporation from the surface. The drive-in is accomplished at normal diffusion temperatures.

The diffusion coefficient at 1200°C of 8.3×10^{-13} cm^2 sec^{-1} was calculated using an erfc distribution. A surface concentration of 5×10^{19} cm^{-3} was determined from published curves (13). The diffusion coefficient is somewhat higher than published values, which may be due to the availability of excess Sb_2O_5 at all times during the diffusion run.

The system is recommended for silicon device processing and has recently been shown to be useful for germanium diffusion.

Antimony diffusions have customarily been accomplished by use of solid Sb_2O_3 in a two-zone furnace (1). Some of the surface problems generated by use of the solid source were described by LaRocque *et al.* (2). The surface eroded during diffusion due to high concentration Sb areas. Runyan has used $SbCl_5$ as a diffusion source with some success (1). A liquid source has also been reported (3) which performs well.

The dopant used in this investigation is $(CH_3)_3Sb$, trimethylstibine. It was diluted in nitrogen and pur-

* Electrochemical Society Active Member.

Key words: diffusion in silicon, antimony diffusion coefficient, silane oxide diffusion.

chased from Air Products and Chemicals Company, Allentown, Pennsylvania. Methods of preparation are cited in Morgan (4). $(CH_3)_3Sb$ is a colorless liquid, boiling point—80.6°C, melting point—87.6°C.

In the work described here, the source is admitted in the vapor state mixed with nitrogen. The apparatus used is an improved modification, described below, of the version used by Conser *et al.* (5).

The major advantages of this diffusion system are the preservation of surface perfection, inexpensive deposition apparatus, and a furnace system in which gas flow patterns are inconsequential, because only the drive-in is accomplished in the high temperature furnace. Flow patterns in the deposition apparatus may be important, when mixed Sb_2O_5-SiO_2 is deposited. However, this deposition is a low temperature, 300°, procedure. $(CH_3)_3Sb$ was chosen for this application, because the hydride H_3Sb, is unstable and $(CH_3)_3Sb$ was the volatile compound with the highest antimony content available (6). The most important use of the method described here is for "buried layer" applications for integrated circuit designs and for base layers in PNP transistors. The method works equally well for germanium.

Experimental Procedure

In Fig. 1 is a schematic representation of the experimental apparatus. The gas flow is controlled automatically by timers. Entering at the top of the reaction chamber are the reactants SiH_4 and $(CH_3)_3Sb$. The cylinders containing the gases are shown on the left. The silane used was a 3% mixture in nitrogen and the trimethylstibine was a 1% mixture in nitrogen. These concentrations were not checked.[1] The only other reactant required, oxygen, entered on the left and right of the reaction chamber. The temperature of the hot plate was 360° ± 0.5°C stabilized by the controller. The slice temperature, determined by means of a color changing indicator was 315°C. It can easily be seen that all or any combination of the 3 reactants can be admitted to the reaction chamber.

The object of this procedure was to deposit the dopant onto the slices located on the turntable. Subsequent treatment in a furnace at temperatures in excess of 1200°C resulted in a diffused silicon layer in a slice. When only $(CH_3)_3Sb$ or SiH_4 was admitted, no deposition occurred. In order to make a run, the hot plate turntable was lowered from the reaction chamber. Slices were placed on the turntable as shown, the turntable raised to meet the reaction chamber, timers set for desired time, and the start button pushed. After completion of the prescribed automatic cycle, the slices were removed by lowering the turntable. Between runs, N_2 was usually allowed to flush to keep the system dry.

The reactions presumed to occur are

$$SiH_4 + 2\,O_2 = SiO_2 + 2\,H_2O$$
$$2\,(CH_3)_3\,Sb + 13\,O_2 = Sb_2O_5 + 6\,CO_2 + 9\,H_2O$$
$$SiH_4 + 2(CH_3)_3Sb + 15\,O_2 = SiO_2 + Sb_2O_5 + 6\,CO_2 + 11\,H_2O \quad [1]$$

[1] The concentration of SiH_4 was obtained by mixing the pure gases. The $(CH_3)_3Sb$ was weighed in an ampoule, which was then broken in the nitrogen contained in the cylinder. All runs were made by use of a single cylinder of each of the gas mixtures.

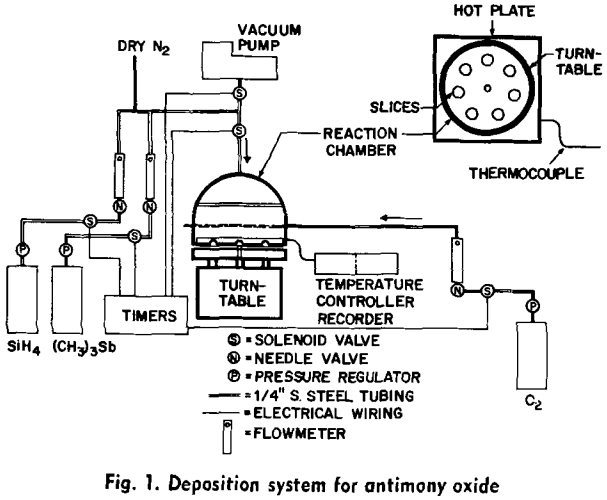

Fig. 1. Deposition system for antimony oxide

Experimental Results

Deposition experiments.—The purpose of this series of experiments was to find the rate of deposition of SiO_2 and Sb_2O_5 on silicon substrates. Six runs were made with flow conditions given in Table I. Shown in Fig. 2 is a plot of weight gain *vs.* time of deposition for pure or mixed oxides on silicon substrates at 317°C. The volume ratios shown are flow rates of $(CH_3)_3Sb$-N_2 and SiH_4-N_2 mixtures. Note that to obtain the volume ratios 0.3, 0.5, and 1, the flow rate of SiH_4-N_2 was maintained constant and the flow rate of $(CH_3)_3Sb$-N_2 varied. The run at volume-ratio-of-2 was made at one-half the SiH_4 flow.

One would expect that weight gains of runs 2, 3, and 4 with additional $(CH_3)_3Sb$ would be larger than for pure SiH_4. This is not the case as shown by the results in Fig. 2. The maximum weight gain per minute if complete reaction occurred and all products deposited on one slice only, is given in Table II. Of course, not all reaction products deposit on one slice, but the relative amounts should be in proportion with Table II.

A plot normalized at volume ratio of 0.3 is shown in Fig. 3. It is not clear how the added $(CH_3)_3Sb$ could cause such a decrease in deposition rate. The layer deposited with equal volumes of SiH_4 and $(CH_3)_3Sb$ was analyzed and found to be 95% Sb_2O_5 and 5% SiO_2. Several explanations are plausible. The addition of $(CH_3)_3Sb$ may act as a chain breaker in the oxidation of SiH_4 believed by some to be a chain reaction. Or the surface, which is required for deposi-

Table I. Experimental flow conditions

Run number	1 Ratio $\frac{(CH_3)_3Sb}{SiH_4}$	2 Flow of SiH_4-N_2 3% nominal $cm^3\ min^{-1}$	3 Flow of $(CH_3)_3Sb$-N_2 1% nominal $cm^3\ min^{-1}$	4 Flow of O_2 $cm^3\ min^{-1}$
1	Pure SiH_4	250	—	100
2	0.3	250	83	100
3	0.5	250	125	100
4	1	250	250	100
5	2	125	250	100
6	Pure $(CH_3)_3(Sb)$	—	250	100

Table II. Theoretical weight gain

Run number	Calculated weight gain due to SiH_4* mg min^{-1}	Calculated total weight gain due to $(CH_3)_3Sb$ + SiH_4 mg min^{-1}
1	20.85	20.85
2	20.85	31.82
3	20.85	37.38
4	20.85	53.91
5	10.33	43.39
6	0	33.06

* For conditions see Table I.

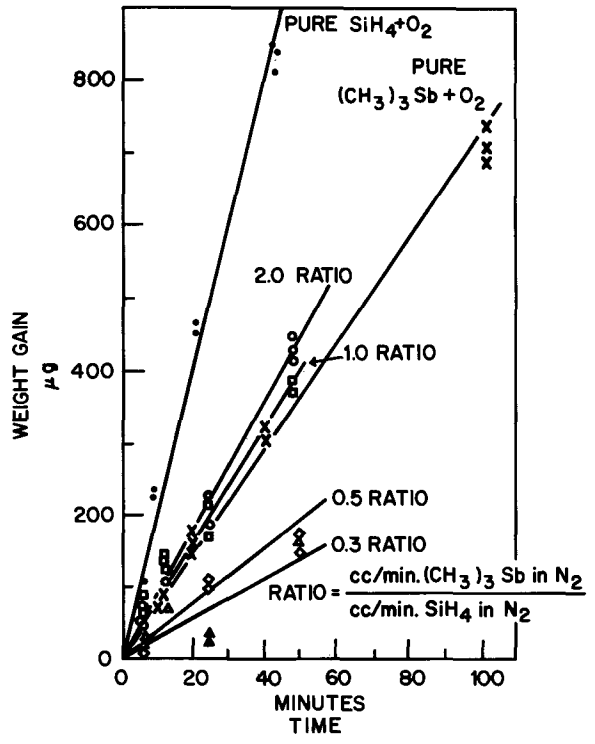

Fig. 2. Weight gain of silicon slices as a function of gas composition and time of deposition.

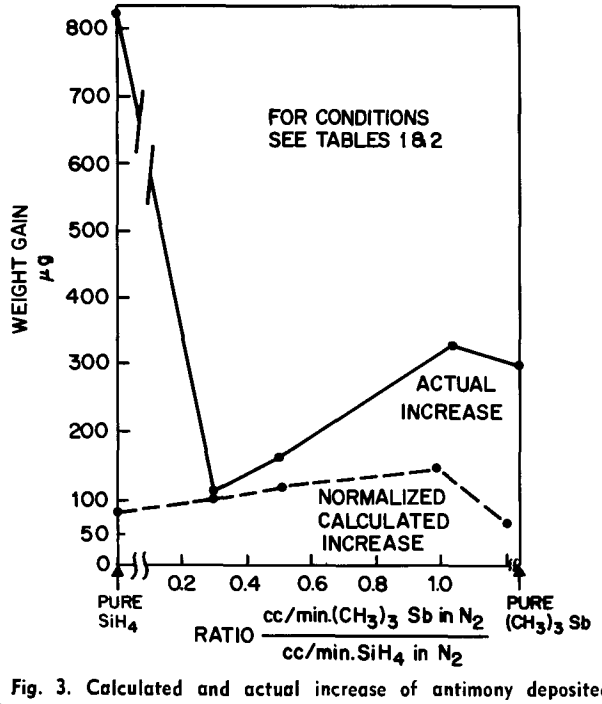

Fig. 3. Calculated and actual increase of antimony deposited slices.

tion of SiO_2 and Sb_2O_5, catalyzes the Sb_2O_5 formation but not the SiO_2 formation. Or, even though oxygen was in excess, SiO_2 molecules did not deposit with the same efficiency as Sb_2O_5 and, therefore, unreacted SiH_4 and nondeposited SiO_2 left the reaction chamber.

The molecular species deposited in the silicon slice was determined by microprobe analysis (7). As noted above, Sb_2O_5 and SiO_2 were found, hence Eq. [1] is consistent with the analysis.

Diffusion experiments.—One of the problems with Sb_2O_5 is its volatility since Sb_2O_5 evaporates during the diffusion necessary to redistribute the Sb from

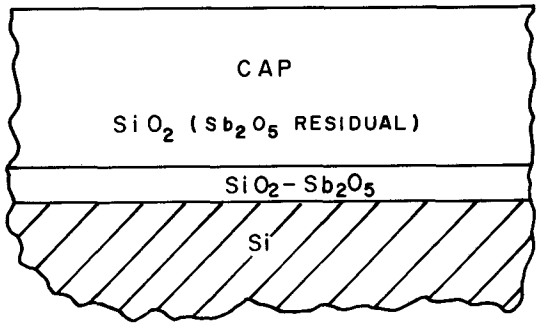

Fig. 4. Structure after deposition

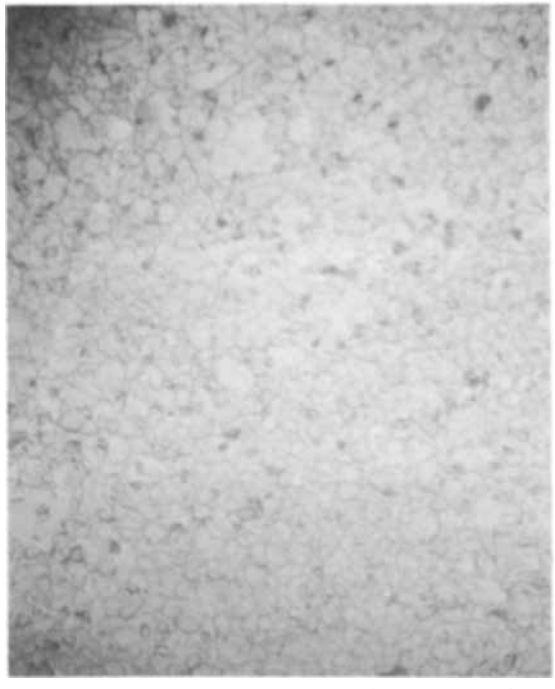

Fig. 5. Surface of slice after diffusion, when excessive deposition times are used.

the surface into the silicon to avoid the escape of Sb_2O_5 during drive-in-diffusion, an "oxide-cap" is grown as shown in Fig. 4. Such a structure is produced by first admitting a mixture of $(CH_3)_3Sb$, SiH_4 and oxygen and then only SiH_4 and oxygen. If very low sheet resistances were desired, pure $(CH_3)_3Sb$ and O_2 were admitted. The SiO_2 cap is directly responsible for the success of this method; however, in addition to the cap, it was necessary to restrict deposition times to less than 3 min or poor surfaces resulted. An example is shown in Fig. 5. Thin deposition layers resulted in no visible surface deterioration during diffusion.

A wide range of sheet resistivities can be obtained by varying the trimethylstibine to silane ratio. Sheet resistivities from 15 to 290 ohm-square^{-1} were obtained by changing the flow ratios from 0.03 to 1.0 and drive-in temperatures from 1200° to 1284°C as shown in Fig. 6. An example of a typical run is given in Table III.

The deposition time of 4 min is favorable for mass processing. Since only a flat temperature-profile-furnace is required for drive-in diffusion, a number of hot plates can be used to deposit the slices and several hundred slices can then be driven-in at the same time. Junction depths can easily be predicted as shown in Fig. 7. The junction depth is a function of $\sqrt{t}$.

Reproducibility of the runs is shown in Table IV. Each run consisted of 4 slices deposited with pure

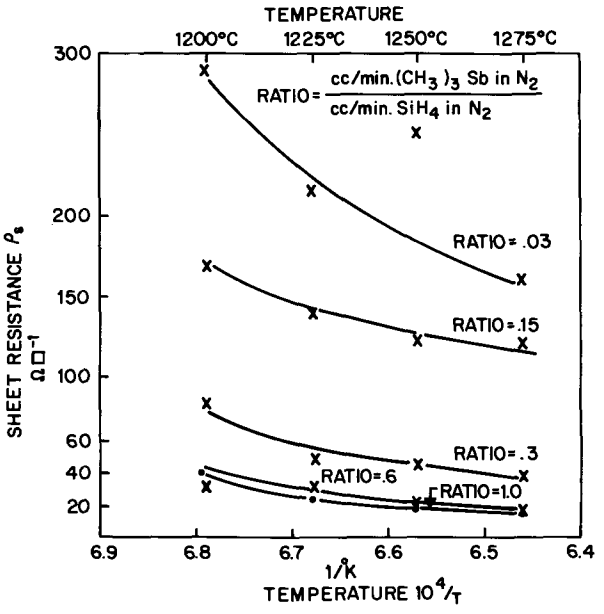

Fig. 6. Resistivity as a function of stibine ratio and diffusion temperature.

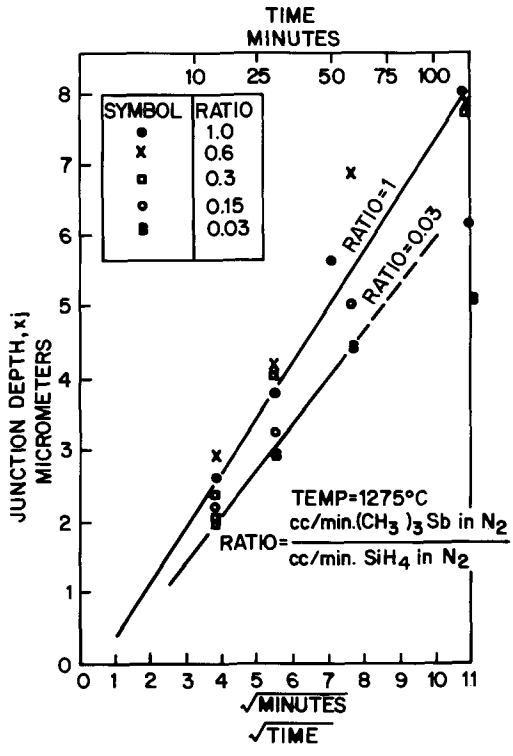

Fig. 7. Junction depth as a function of diffusion time

$(CH_3)_3Sb+O_2$, capped with SiO_2, and diffused for 2 hr at the temperatures indicated. One slice was angle lapped in each run and surface concentrations were computed using the complementary error function profile. The resistivities measured on each of the 4 slices in each run were 2% of the average resistivity for that run.

The error function distribution was assumed in the solution of the diffusion equation, though an infinite source may not actually have been available. Rather a rate-limiting step may have to be assumed, because the antimony in the silicon diffuses faster than in the oxide. Smits and Miller derived a solution for a rate-limiting transfer step which they solved for the gaseous case (8). In the situation at hand, diffusion occurs both into the oxide cap and the silicon. For simplicity and since no diffusion constants in the oxide were known, a complementary error function in the silicon was assumed. This is a good assumption, since diffusion occurred from pure Sb_2O_5.

Since diffusion times are known, it is possible to calculate effective diffusion coefficients, which are shown in Table V. The higher diffusion coefficient found in this work may be due to the more concentrated source used.

Many device slices have been diffused using the doped oxide deposition system and both good surfaces and good device yields have been produced.

Table III. Example of procedure for Sb diffusion of silicon slice with $(CH_3)_3Sb$

Minutes	Operation	N_2 cc/min	$(CH_3)_3Sb$ cc/min	SiH_4 cc/min	O_2 cc/min	Temperature
10	Flush	7500	None	None	None	362
1	Codeposit	7500	250	250	100	360
3	Cap	7500	None	250	100	360
5	Flush	500	None	None	None	360
120	Drive-in	2000	None	None	40	1284

Table IV. Concentration and sheet resistance

Run No.	Temp, °C	ρs Ω□-1	Junction depth micrometer	$C_s \times 10^{-19}$ (13) cm^{-3}
59	1275	17.4	4.86	4.8
57	1277	15.2	5.60	4.8
58	1278	14.0	6.18	4.8
56	1284	12.7	5.89	5.2

Table V. Diffusion coefficients for Sb diffusion at 1200°C

Investigator	Reference	D × 10^{13} at 1200°C
Fuller and Ditzenberger	9	2.5 cm^2 sec^{-1}
Thurston and Tsai	10	1.5
Rohan *et al.*	11	3.8
Petrov	12	1.7*
Gittler	3	2.4
This investigation		8.3

* Calculated from their data.

Acknowledgments

The authors thank Mr. R. E. Caffrey for his support during this work and J. W. Colby for the microprobe analysis.

Manuscript submitted March 11, 1970; revised manuscript received July 14, 1970.

Any discussion of this paper will appear in a Discussion Section to be published in the June 1971 JOURNAL.

REFERENCES

1. W. R. Runyan, "Silicon Semiconductor Technology," p. 146, McGraw-Hill, New York (1965).
2. A. LaRocque, R. Yatsko, and A. Quade, Semiconductor Electronics **2**, 317, (1959) and *This Journal*, **105**, 254C (1958).
3. F. L. Gittler, Paper 94 presented at the Dallas Meeting of the Society May 7-12, 1967.
4. G. T. Morgan, "Organic Compounds of Arsenic and Antimony," p. 53, Lomans Green and Co., London (1918).
5. Development of Integrated Circuits Utilizing Complementary Transistor. Radio Corp. of America, Interim Development. Report: Number 1; Contract Number: NOBSR-93365; Project Serial No.: SR008-0303; Task Number: 9631.
6. M. Dub, Editor, "Organometallic Compounds," 2nd ed., Vol. III, p. 654, Springer Verlag-New York (1968).
7. J. W. Colby and R. A. Porter, Private communication.
8. F. M. Smits and R. C. Miller, *Phys. Rev.*, **104**, 1242-1245 (1956).
9. C. S. Fuller and J. A. Ditzenberger, *J. Appl. Phys.*, **27**, 549 (1956).

10. M. C. Thurston and J. Tsai, Report 1233-40 AD274, 969 February, 1962.
11. J. J. Rohan, N. E. Pickenig, and J. Kennedy, *This Journal*, **106**, 705-709 (1959).
12. D. A. Petrov, I. M. Shashkov, and I. P. Akimchenko, "Questions of the Metallurgy and Physics of Semiconductors" (Transactions of the Second Conference on Semiconductors Materials, January, 1956), Akademiia Nauk Press, Moscow (1957), Translated by Morris D. Friedman, Inc., Needham Heights 94, Mass.
13. J. C. Irvin, *Bell System Tech. J.*, **41**, 387 (1962).

Exposure of Photoresists

II. Electron and Light Exposure of a Positive Photoresist

Barret Broyde

Engineering Research Center, Western Electric Company, Inc., Princeton, New Jersey 08540

ABSTRACT

Less energy is required to solubilize AZ-1350 when the exposure is accomplished with kilovolt electrons than when light is used to expose the photoresist. In contrast to overexposure with light, overexposure by electrons causes an insoluble cross-linked product to form. The solubilization reaction is enhanced by the addition of small amounts of benzotriazole, indazoles, and imidazoles, while the cross-linking reaction is inhibited by these additives.

Photosensitive materials called photoresists are used during the manufacture of semiconductor devices to protect selected areas of semiconductors and other surfaces against chemical attack. Conventionally, the desired pattern in the photoresist is obtained by exposing the photoresist-coated surface to light through a mask. However, electron beam pattern generators, in which a controlled electron beam writes on the photoresist, offer the advantage of exposing narrow sharp lines. After exposure with either electrons or light, the pattern is developed by rinsing the photoresist with a solvent. Negative resists are those that are insolubilized on exposure while positive resists are solubilized.

The light and electron flux necessary to expose resists has been reported by several workers (1-3). It appears that positive resists are less sensitive to both light and electrons than are negative resists. In conventional positive photoresist processing this lower sensitivity sometimes requires that exposure times be longer than desirable. But, more important, the low sensitivity usually leads to very long exposure times when either projection photolithography or writing electron beams are used to pattern the resist.

This work reports that members of the benzotriazole, imidazole, and indazole families decrease the flux and hence energy required for the light and electron exposure of a high resolution positive photoresist, AZ-1350.[1] The energy required can be determined from the flux if the fraction absorbed is known. Previous work at Western Electric has shown how this can be calculated for electron exposure (4) while absorptivity data are reported here for the experiments involving light exposure.

Experimental

Layers of AZ-1350, 6000Å thick, were prepared by spinning techniques. The resist was then baked at 60°C for 10 min, allowed to cool, exposed and then dip-developed for 4 min in the Shipley AZ-Developer (full strength). The thickness of the resist before and after development was measured by profilometer techniques described previously (4). Electron exposure was carried out at 2×10^{-5} Torr with an electron beam focused to give a 2.5 cm^2 spot. The current was measured with a Faraday cup before and after exposure. Light exposures were carried out with a 150W xenon lamp held 1m from the resist. Glass filters allowed only wavelengths longer than 3100Å to irradiate the resist. Chromium-coated glass plates were used as the substrates for the electron exposure experiments, while quartz plates were used to study the light exposure.

When the effects of additives were examined, the additive was dissolved in the photoresist solution at least 16 hr before use. Occasionally, it was found that films of the resist with additive required shorter development times.

Key words: photoresists, electron beams, light exposure.

[1] A proprietary product of the Shipley Company, Newton, Massachusetts.

Results and Discussion

Electron exposure of AZ-1350.—Typical behavior of 6000Å thick layers of AZ-1350 after exposure to 15 keV electrons and development is given in Fig. 1, curves A and B. The electron flux required to expose unsensitized AZ-1350 depends on the energy of the exposing electrons as well as the time that the resist has been stored. Typically, 6 $\mu coul/cm^2$ of 15 keV electrons are required to expose newly purchased solutions while the same resist 4 months later requires about 40 $\mu coul/cm^2$ for exposure. The loss of sensitivity of the resist on storage may arise from the same cause as the loss in sensitivity of the resist when it is heated (5). When AZ-1350 is overexposed to the extent that it has absorbed about 20×10^{21} eV/cm^3, it cannot be removed by AZ-Developer. This overexposed spot is also insoluble in acetone and benzene.

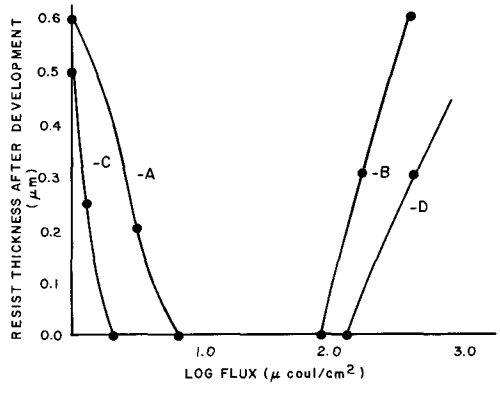

Fig. 1. Exposure of AZ-1350 by 15 keV electrons. Curves A and B, newly purchased resist; curves C and D, newly purchased AZ-1350 containing 2% benzotriazole. The initial thickness of resist was 0.6 μm.

Varying the electron accelerating potential between 5 and 20 kV changes the flux required to expose newly purchased AZ-1350 from 3 to 9 μcoul/cm^2. Using the model previously described (4) to calculate the amount of energy transferred from the beam to thin layers, the amount of absorbed energy required to solubilize fully newly purchased resist is 1.5 $\pm$ 0.05 x 10^{21} eV/cm^3. The range of 5 keV electrons in AZ-1350 has been measured here as 6500 $\pm$ 200Å, and this value was used for this calculation.

Harwood and Hunter have identified the reactive moiety in AZ-1350 as 3,4-dihydroxybenzophenone-4-[naphthoquinone-(1,2) diazide (2)] sulfonate and have found that it constitutes 23% of the weight of the solids in the photoresist (6). Since the density of dried AZ-1350 films is 0.9, there are 1.6 x 10^{16} sensitizer molecules in a square centimeter of film 6000Å thick. If all the sensitizer molecules have reacted when the film is fully solubilized, then the G value (number of molecules that react per 100 eV absorbed) for solubilization is about 18. This rather high value implies that energy transfer from the electron beam to a reactive site in AZ-1350 is much more efficient than in negative resists.

The mechanisms of the reactions involved in the response of AZ-1350 to electron radiation have not been determined yet, but it is likely that a cross-linking reaction of its phenol-formaldehyde polymer (6) leads to the insoluble product (*see* below). It is also likely that the solubilization reaction is the same one that occurs with light; quinone diazide groups are converted to carboxylic acids (7). Solubilization arising from a scission reaction of the phenol-formaldehyde polymer in which indiscriminate bond breakage occurs and soluble low molecular-weight compounds result cannot be fully excluded, but it is not probable because scission would have to predominate at low exposures and cross-linking at high exposures.

Exposure of AZ-1350 by light.—Htoo has shown that an exposure of 3.6 x 10^{18} eV/cm^2 is needed for a 6000Å-thick film of the resist with 3654Å radiation (1). Since K. H. Cho of this laboratory has shown the absorptivity of these films to be 0.32 at this wavelength, this exposure corresponds to an absorbed energy of 1.7 x 10^{18} eV/cm^2 and a quantum yield of 0.032 for the solubilization process. Absorbed light energy therefore is only 5% as efficient in causing solubilization as is electron energy. The higher efficiency of solubilization during electron exposure is unexpected, since the primary process of electron energy absorption leads to a large variety of excited bonds and molecules, while during light absorption only the quinone diazide groups are excited.[2] Overexposure by wavelengths greater than 3100Å does not lead to an insoluble product, but when the resist is exposed to 2537Å radiation it forms an undevelopable spot. Since the phenol-formaldehyde polymer absorbs radiation at this wavelength but not at the longer wavelengths, it is probably undergoing a cross-linking reaction.

Sensitization of AZ-1350.—When dilute solutions of benzotriazole in AZ-1350 are prepared and spun to films, it is found that a lower flux of both electrons and light is required to solubilize the resist. Typical results for electron exposure are shown by curve C of Fig. 1 and, for light exposure, by Fig. 2. Benzotriazole also inhibits the cross-linking that occurs with high electron fluxes (curve D, Fig. 1). The edges of exposed and developed lines in the photoresist both with and without sensitizer were examined under an optical microscope. The resolution of the microscope is about 0.33 μm which is insufficient to distinguish any difference in edge gradients.

[2] Htoo has shown that less than 8.1 x 10^{15} eV/cm^2 of light are needed for the exposure of 6000Å KTFR films, while 4.6 x 10^{16} eV/cm^2 of electron energy are needed, so that light exposure of KTFR is more efficient than electron exposure. In ref. (4), Htoo's work is incorrectly quoted.

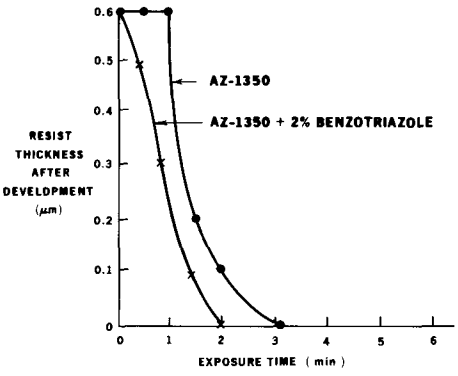

Fig. 2. Effect of benzotriazole on the exposure of AZ-1350 by light. The initial thickness of resist was 0.6 μm. A 150W xenon lamp 100 cm from the sample was used.

Benzotriazole is not the only efficacious additive. All members of the benzotriazole, imidazole, and indazole families that are soluble and that have a hydrogen atom bonded to a nitrogen atom also decrease the flux needed to expose AZ-1350. These additives also sensitize the response of other quinone diazide resists *e.g.*, AZ-1350-H (a Shipley product) and KAR-3 which is manufactured by Eastman Kodak.

The mechanisms in sensitizing the solubilization reaction and in inhibiting the cross-linking reaction are still being investigated. Since neither the absorption spectrum nor the penetration range of electrons of the resist change significantly when low levels of benzotriazole additives are added to the resist, sensitization of the solubilization probably involves better energy transfer from the site of absorption to the reaction site. Benzotriazole-type additives also cause energy to be transferred away from cross-linking sites, since 2% solutions in KTFR cause an increase in the electron energy needed to reach the gel point from 2.5 x 10^{20} eV/cm^3 to 11 x 10^{20} eV/cm^3. Benzophenone and hexaphenyldilead, which reduce the electron flux needed to reach the gel point of KTFR, also cause a reduction in the flux that cause overexposure in AZ-1350.

Conclusions

1. Electron exposure is more efficient in solubilizing AZ-1350 than is light exposure.
2. Overexposure by electrons causes a cross-linking reaction which renders AZ-1350 undevelopable.
3. Benzotriazole-type additives increase the efficiency of the solubilization reaction caused by both electron and light absorption while retarding the cross-linking reaction caused by electrons.

Acknowledgments

The author is indebted to Dr. H. H. Loar, M. W. Sagal, and W. R. Samaroo of the Western Electric Company, Inc., for many stimulating discussions and to Mr. C. A. Adams for his invaluable technical assistance.

Manuscript submitted May 5, 1970; revised manuscript received *ca.* July 20, 1970. This was Paper 250 presented at the Los Angeles Meeting of the Society, May 10-15, 1970.

Any discussion of this paper will appear in a Discussion Section to be published in the June 1971 JOURNAL.

REFERENCES

1. M. S. Htoo, *Photo Sci. Eng.*, **12**, 169 (1968).
2. R. K. Matta, *Electrochem. Technol.*, **5**, 382 (1967).
3. M. Hatzakis, *This Journal*, **116**, 1033 (1969).
4. B. Broyde, *ibid.*, **116**, 1241 (1969).
5. H. A. Levine in "Polymer Preprints," Am. Chem. Soc., **10**, 337 (1967).
6. M. G. Harwood and D. N. Hunter, DDC, AD846184.
7. A. Mustafa in "Advances in Photochemistry," Vol. II, p. 113 ff, W. A. Noyes, Jr., G. S. Hammond, and J. N. Pitts, Jr., Editors, J. Wiley & Sons Inc., New York (1964).

Properties of Cathodochromic Sodalite

William Phillips

RCA Laboratories, Princeton, New Jersey 08540

ABSTRACT

Cathodochromic behavior of iron-doped sodalites containing Br, I, or mixtures of halogens has been investigated in addition to that of chloride sodalite. Ultraviolet excitation of these materials produces an optically bleachable absorption band whose peak moves from 5250 to 6025Å as the halogen composition is changed from Cl to I. Electron beam excitation produces nearly identical absorption, but exposures above a certain threshold produce, in addition to optically bleachable absorption, residual absorption that is insensitive to light. Residual absorption is at a minimum in iodide sodalite.

Cathode-ray tubes utilizing a cathodochromic screen material instead of a phosphor have a number of valuable attributes in display-storage applications. The behavior of tubes of this type made with sodalite as the screen material has been described earlier (1). In this publication we describe in some detail the properties of iron-doped sodalite materials that have been synthesized for cathodochromic applications.

Sodalite is an aluminosilicate compound having the ideal formula $Na_8Al_6Si_6O_{24}Cl_2$. The basic structural unit consists of a cage formed of AlO_4 and SiO_4 tetrahedra linked together by their oxygen atoms. In the center of this cage is a Cl^- surrounded by four Na^+ ions. The sodalite cage can, and often does, accommodate a number of anions other than Cl^-. Br^-, I^-, OH^-, and SO_4^{2-} are frequently occurring substitutions. Sodalite usually occurs in nature as a blue-colored mineral. A photochromic variety of sodalite also occurs and is known as hackmanite.

The synthesis of sodalite for photochromic studies was reported by Medved in 1953 (2) and 1954 (3). He used a powder sintering technique and found that his sodalite had to be reduced, preferably in a hydrogen atmosphere, before photochromic properties appeared. Medved suggested a model for the switching of sodalite in which electrons were transferred from U-centers to F-centers under the influence of uv excitation. Also in 1954 a paper by Kirk (4) appeared emphasizing the role of sulfur as an activator in sodalite. Further work on sodalite was reported by Radler and others in 1962 through 1964 (5). Radler reported that the color of the switched sodalite could be altered by substituting other halogens for the chlorine.

The ESR spectrum of the photochromic color center of sodalite was reported in 1967 by Hodgson, Brinen, and Williams (6) and found to be consistent with the F-center model. The photochromic properties of this material were described in a subsequent paper by the same authors (7). They found, in agreement with Kirk, that photochromic behavior appeared only when sulfur was present in their materials. Cathodochromic properties of sulfur-doped sodalite have been reported recently by Forrester *et al.* (8).

In this paper we describe the photochromic and cathodochromic behavior of sodalites containing Cl, Br, I, and mixtures of these halides. These materials differ from those reported in ref. (6) through (8) in that they are activated by the presence of iron. Sulfur does not appear to play a significant role in their switching behavior.

Synthesis and Optical Properties

Most of the material used in the present research was prepared by a hydrothermal synthesis method at the Airtron Division of Litton Industries. The pressures utilized were considerably higher than those reported in ref. (7) (25,000 psi instead of 4000 psi), and a temperature gradient was applied to the apparatus to encourage transport and crystallization of the sodalite at the top of the vessel. The resultant material has the form of a coarse crystalline gravel, containing well-formed dodecahedra with faces occasionally as large as 5 mm across. In order to induce photochromic properties the material is crushed, if necessary, to smaller than 12 mesh, then annealed in a reducing atmosphere, usually hydrogen, for several hours at 850°-950°C.

Reduced sodalite prepared as described above is colorless, but develops a magenta coloration when exposed to uv or to electron beam excitation. The coloration is nearly identical for the two types of excitation, but we find that little or no coloration can be induced or bleached by optical excitation unless the material contains appreciable amounts of iron (see section on the Influence of Dopants).

The optically induced and electron beam induced absorption spectra measured by transmission through an iron-doped chloride sodalite single crystal are shown in Fig. 1. The optical samples used to obtain this and the following figure were cut from the largest available hydrothermal crystals. To obtain the cathodochromic spectrum the reduced samples were aluminized and then colored (on both sides) in a demountable electron beam apparatus at approximately 30 kV. The aluminum was removed and the crystals measured within about 10 min of coloration.

When bromine is substituted for the chlorine in sodalite the resultant photochromic material develops a purple color rather than magenta, because the position of the induced absorption band is moved to a longer wavelength (5550Å instead of 5250Å). The shape and intensity of the induced absorption band are similar to those of chloride sodalite (*see* Fig. 2). In sodalite synthesized with iodine as the halogen, the absorption peak occurs at even longer wavelengths (6025Å) as shown in Fig. 3. Intermediate positions for the peak of the induced absorption band are produced in sodalites containing mixtures of halogens.

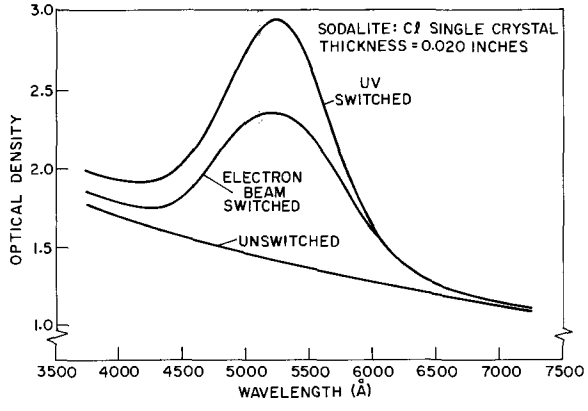

Fig. 1. Unswitched, uv switched, and electron beam switched absorption spectra of a sodalite:Cl single crystal.

Key words: photochromic, dark trace, display, storage.

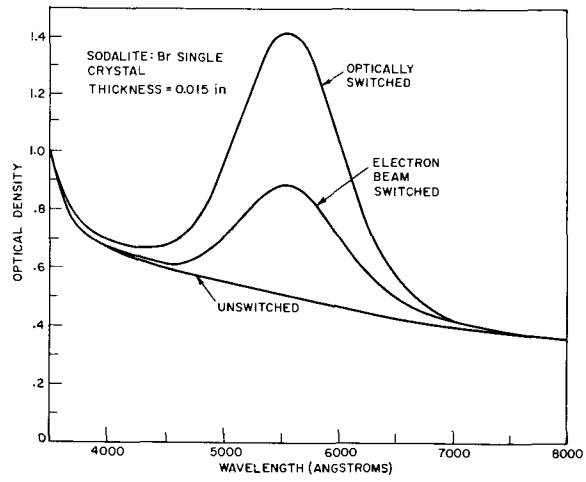

Fig. 2. Unswitched, uv switched, and electron beam switched absorption spectra of a sodalite:Br single crystal.

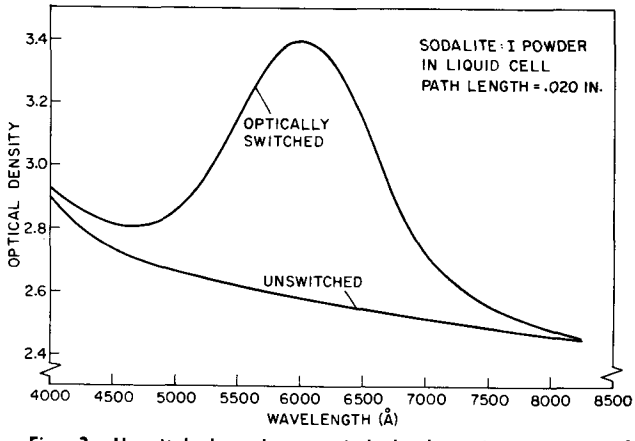

Fig. 3. Unswitched and uv switched absorption spectra of sodalite:I powder dispersed in an index-matched liquid.

The position of the photochromic absorption band in sodalite in fact appears to be determined by the lattice constant of the material as is the case for the F-band in alkali halides (9). Figure 4 shows the position of the peak of the induced absorption band as a function of lattice constant for the materials mentioned above, and also for sodalites having the compositions $Na_8Al_6Si_6O_{24}ClBr$ and $Na_8Al_6Si_6O_{24}BrI$. The linewidths for the latter materials are about the same as for pure chloride and bromide, *i.e.*, 1000-1100Å. The dependence of wavelength on lattice constant found in Fig. 4 is much steeper than that found for alkali halides. The results in Fig. 4 are in general agreement

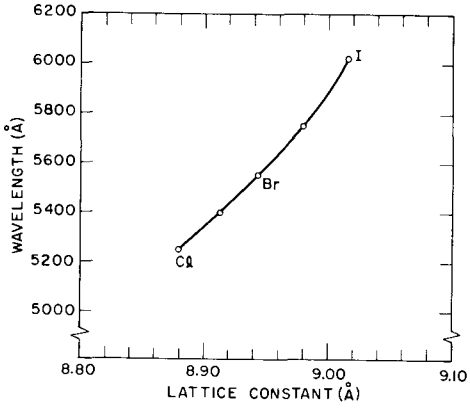

Fig. 4. Position of the peak of the photochromic absorption band of sodalite vs. the lattice constant of the material.

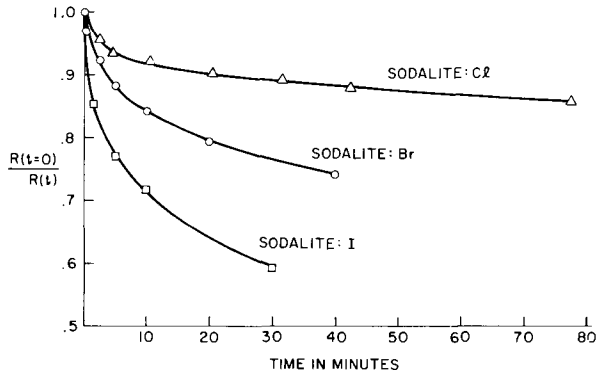

Fig. 5. Thermal decay of the induced change in reflectance of chloride, bromide, and iodide sodalite powdered samples measured at room temperature. $R(t=0)/R(t)$ is the reflectance immediately after coloring the sample divided by the reflectance at time t.

with those reported in ref. (8), except that the positions of the absorption peaks in the present work consistently occur at 80-160Å shorter wavelengths. This may result from the absence of sulfur from the present materials.

The thermal decay rate of the materials also changes with composition. The decay of the optically induced reflectance change of powdered chloride, bromide, and iodide sodalites was measured, at the peak of the induced absorption band, on a spectrophotometer equipped with integrating spheres. The results are reproduced in Fig. 5 (10).

The induced absorption coefficient inferred from Fig. 1 for sodalite:Cl is $\alpha = 68$ cm^{-1}. This value is typical of chloride and bromide sodalite crystals and powdered specimens excited to saturation with 3650Å radiation. Iodide sodalite crystals and powders are usually found to be less strongly absorbing when optically excited, for reasons that are not clearly understood (*see* Table I). Using the Smakula equation and assuming that the oscillator strength of the photochromic transition if $f = 0.5$ (about the same as for the F center in alkali halides), one can estimate the density of color centers in the materials. These estimates are shown in Table I.

Bleaching of the optically induced coloration in sodalite is accomplished by irradiation with light within the induced absorption band. This is also the case for the electron beam induced coloration provided that the degree of coloration is held below a particular level. If this level is exceeded in many sodalite specimens, a portion of the induced coloration is found to linger after optical bleaching is attempted. The residual coloration of chloride and bromide sodalites cannot be removed by optical irradiation nor does it show any significant thermal decay at room temperature. It can, however, be removed by heating the crystal to 200°-250°C. The extent to which residual coloration occurs varies with the material composition. It will be discussed in greater detail in the following section.

Electron Beam Coloration of Sodalite Powders

The major portion of the study of the cathodochromic behavior of sodalite has been performed using powdered material. The procedure has been to prepare 2 in. square glass slides by settling the powder from aqueous suspension in much the same manner as phos-

Table I. Typical optical properties of sodalites

Sodalite type	Absorption peak, Å	Absorption coefficient at peak, cm^{-1}	Density of color centers, cm^{-3}
Cl	5250	70	5×10^{17}
Br	5550	70	5×10^{17}
I	6025	40	3×10^{17}

phor CRT screens are formed. Early experimentation established approximate optimum powder parameters for these slides. The values used for sodalite usually fall in the range 10-37μ for the particle size and 3-7 mg/cm^2 for the screen weight. The slides are aluminized to increase their whiteness and to render them completely opaque.

Test slides are evaluated by mounting them in a demountable electron beam apparatus and exciting them over a known area with a measured electron beam current. The accelerating voltage is held at 28 $\pm$ 1 kV, and the exposures are typically made at current densities ranging from 0.05 to 5 μA/cm^2 for 1, 2, or 5 sec. The slides are illuminated with a regulated tungsten light source at an angle of 45°. The source intensity is adjusted until the diffuse reflected screen luminance, as measured by a spot brightness meter normal to the slide, reaches a convenient value, usually 1 or 10 ft-L. At these illuminations the contrast ratio is essentially independent of light level, and the decay rate of the coloration is long compared with the exposure time. After electron beam exposure the luminance is again determined and the contrast ratio calculated from the relation

$$C.R. = \frac{\text{reflectivity unswitched}}{\text{reflectivity switched}} = \frac{\text{luminance unswitched}}{\text{luminance switched}}$$

Successively larger exposures are made, and the slides are erased after each exposure. In this way a curve of contrast *vs.* electron beam exposure is obtained. As the exposure is increased one usually reaches a point where residual coloration begins to appear. The contrast ratio measured on a slide after the optically erasable portion of the coloration is removed is referred to as the residual contrast. A typical electron-beam exposure curve, showing the onset of residual coloration, is shown in Fig. 6. (The accumulated residual coloration in Fig. 6 and 7 is shown as a function of the sum of those exposures which exceed the residual coloration threshold.)

The coloration behavior illustrated in Fig. 6 is characteristic of chloride and of bromide sodalites as well. The behavior of iodide sodalite differs in several important respects. As shown in Fig. 7, the residual coloration in iodide sodalite is much smaller than in chloride and bromide sodalites at any given exposure level. Under continuous excitation at current densities typical of many CRT applications (3 μA/cm^2), the residual contrast ratio of some iodide samples saturates between 1.1 and 1.2. The residual coloration built up under these circumstances can be removed by exposure to a high intensity visible light source (7500 ft-c) for a period of about 1 hr. An iodide sodalite CRT of this nature has been in operation for many months. Although it needs occasionally to be flooded with light from a slide projector to remove residual images, there has been no permanent degradation of its contrast capabilities or background screen color.

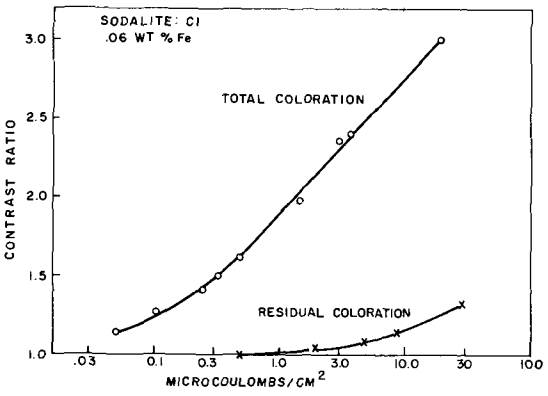

Fig. 6. Electron beam exposure curve for a chloride sodalite test slide.

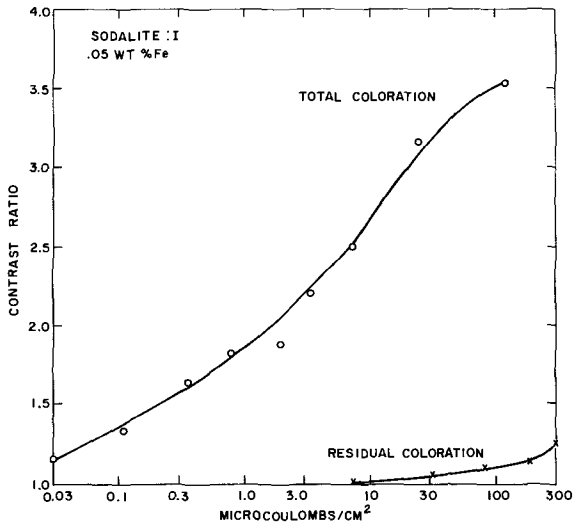

Fig. 7. Electron beam exposure curve for an iodide sodalite test slide.

Influence of Dopants

The role of iron.—Iron-free sodalite colors in a manner comparable to iron-doped sodalite under electron beam excitation. However, residual coloration begins to appear at very low exposure levels in the iron-free material. The results of electron-beam measurements on a number of sodalite samples, having a variety of iron concentrations, are summarized in Fig. 8. Except for the points marked with an S (*see* Role of Sulfur below), the materials have sulfur concentrations less than or about equal to 0.012 w/o.

The data points represent the contrast ratio at which residual coloration first appears during exposure curve measurements, as a function of the measured or estimated iron concentration in the sample. The filled-in points represent materials for which iron concentrations were determined by atomic absorption spectroscopy. The open points represent estimated iron concentrations based on the nominal doping and checked by emission spectrographic analysis. The estimated concentrations are usually found to agree with the measured concentrations to within 20%. Exceptions occur in the low concentration range, where residual iron levels (typically 0.001-0.005 w/o) become comparable to or exceed the intentional doping.

The data of Fig. 8 indicate a rapid rise of the residual coloration threshold with increasing iron concentration to about 0.03 w/o, followed by a slower rise at higher concentrations. At low concentrations the optically induced contrast capabilities of the materials

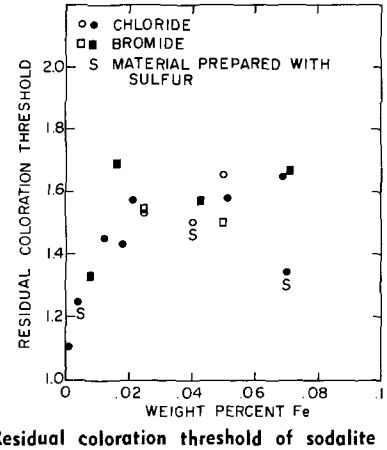

Fig. 8. Residual coloration threshold of sodalite test slides *vs.* amount of iron in the sodalite. Closed points; iron concentration determined by atomic absorption spectroscopy; open points, estimated iron concentration.

are quite similar to the results shown in Fig. 8. The sodalites prepared for this study containing 0.001 w/o or less iron show little or no photochromism. At iron concentrations greater than 0.03 w/o, however, the optical switching tends to fall off somewhat (10, 11), whereas no fall-off is discernible in Fig. 8. The reasons for this discrepancy are not clear.

It has not been possible to extend this investigation to iron concentrations higher than about 0.07 w/o because the solubility of iron, at least under the synthesis conditions used until now, appears to saturate in this region. It is expected, however, that in future work this solubility limit can be raised by charge-compensation techniques.

The Role of Sulfur.—The data of Williams *et al.* (7) show a strong correlation between the amount of photochromic coloration of chloride sodalite and the amount of sulfur present in the material. These authors find that the optimum concentration of sulfur lies between 0.3 and 0.6 w/o, and the lowest concentrations for a measurable effect are "less than .014 percent."

Most of the iron-doped sodalite samples studied in the present work have residual sulfur concentrations of about 0.012 w/o as determined by mass spectroscopy. In spite of this low concentration, it was necessary to rule out the possibility that some or all of the reversible switching properties of these materials derive from the presence of sulfur. To determine if the residual sulfur concentration does indeed contribute to the switching we evaluated sodalite prepared with highly purified starting materials and doped with iron in the normal way. In these samples the sulfur concentration was measured to be about 0.0015 w/o, yet they colored and bleached at least as well as the nonpurified sodalite, both under optical and electron-beam excitation.

To extend the tests in the direction of high sulfur concentrations, a few samples were prepared containing approximately the optimum sulfur concentration, 0.5 w/o as reported in ref. (7). The performance of these samples under electron beam excitation is indicated in Fig. 8 by the points marked with an S. They tend to have residual coloration thresholds lower than or about equal to the materials containing an equal amount of iron but no added sulfur.

From the available data it appears that sulfur does not contribute to the cathodochromic switching performance of the iron-doped sodalite synthesized in the present study and that its presence may in fact be detrimental in materials with high iron concentrations.

On the other hand Forrester *et al.* (8) have synthesized sodalites activated by sulfur and containing very little iron, with properties closely resembling the present iron-doped materials in many respects. It is probable that both iron and sulfur can play the role of activators in sodalite and that the synthesis conditions used in the present study tend to be favorable for the formation of iron-activated sodalite and rather unfavorable for sulfur-activated sodalite.

Density Changes and Fused Salt Anneals

During the reduction of sodalite in hydrogen (the step that induces cathodochromic behavior) a considerable amount of HCl and NaCl is evolved, leading to a large change in the density of the material. These changes were measured by floating batches (typically 4-8g) of the material in question on mixtures of S-tetrabromoethane and methanol (densities 2.96 and 0.73). As additional methanol is titrated into the mixture and stirred, some of the floating material goes into suspension and finally sinks. Histograms such as those shown in Fig. 9 and 10 were plotted from visual estimates of the amount of material remaining afloat after discrete amounts of methanol are added.

Some density loss occurs for all types of sodalite, but the amount that occurs varies from one batch to the next. It is found that for given hydrogen reduction

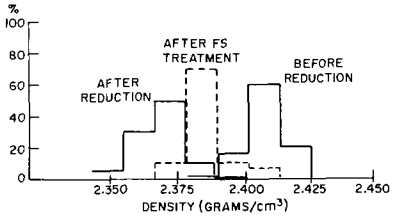

Fig. 9. Density history of a typical sodalite:Br sample

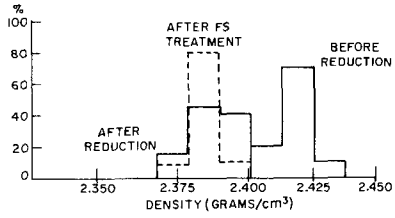

Fig. 10. Density history of a sodalite:Br sample that underwent a relatively small density decrease during reduction.

conditions, the density loss is at a minimum for sodalite batches containing particularly clear and well-formed crystalline material. This type of material is characterized by occurring at the high end of the density spectrum of the unreduced sodalite (*see* Fig. 9 and 10). It is also found that this type of material yields cathodochromic screens with the highest residual coloration thresholds. The mean densities before reduction and the minimum density losses observed for chloride, bromide, and iodide sodalites are shown in Table II.

The density data may be used to estimate the number of halogen vacancies generated in the reduction process. This has been done for two limiting cases, one in which it is assumed that all the loss is due to halogen evolution and another in which it is assumed that all the loss is due to sodium halide evolution. The results are summarized in the last two columns of Table II. In some cases lattice expansion is responsible for a significant portion of the density deficit, but this does not alter the fact that at least two orders of magnitude more halogen vacancies are created than actually participate in the switching process. An iron-doping level of 0.05 w/o corresponds to a density of 1.25×10^{19} iron atoms/cm^3 in chloride sodalite. Thus, considerably more iron is present in these materials than is required to account for the number of reversible color centers.

A series of experiments was performed in which sodalite samples were annealed in fused NaCl or NaCl-NaBr baths. The anneals were generally carried out at a temperature of 850°-950°C for 4 hr in a hydrogen atmosphere. It was found that this treatment could restore a portion of the density loss. This is illustrated in Fig. 9 for a rather typical sodalite:Br sample. About half of the lost density of the reduced material has been replaced in the fused salt anneal. A different situation is illustrated in Fig. 10. This material underwent a relatively small density decrease during reduction, and the fused-salt treatment does not produce any significant change in its density.

Regardless of whether or not the reduced material undergoes an increase in density during the fused-salt

Table II. Halogen vacancy density in reduced sodalites

Sodalite type	Density before reduction, g/cm^3	Minimum density change, %	Lattice volume expansion, %	Vacancy density, cm^{-3}	
				Halogen lost	Sodium halide lost
Cl	2.27	0.73	~0	2.9×10^{20}	1.7×10^{20}
Br	2.41	1.0	0.41	1.1×10^{20}	8.5×10^{19}
I	2.55	0.55	0.25	3.7×10^{19}	3.2×10^{19}

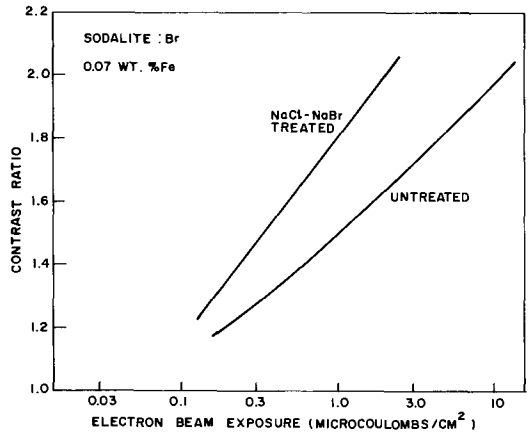

Fig. 11. Electron beam exposure curves for the material of Fig. 10 before and after fused-salt treatment.

anneal, there is usually a large increase in the electron-beam sensitivity of the material. Figure 11 shows a sensitivity curve for a sample of the material of Fig. 10 untreated, compared to material that was treated. Approximately six times more electron beam exposure is required to color the untreated material to a given contrast than is needed to color the treated material. Similar results are obtained for most other samples, with the exception of those which already have high sensitivities (*i.e.* 1.5 microcoulomb/cm² or less required to achieve a 2 to 1 contrast ratio). The sensitivity increase is accompanied by an increase in the residual coloration threshold as shown in Fig. 12. The data points in Fig. 12 that are linked by lines represent the residual coloration thresholds for the same material untreated and fused-salt treated (marked FS). In most cases there is an increase in the threshold for the treated material. These effects appear to be most profound for materials with high iron concentrations.

Conclusions

Sodalites synthesized with Cl, Br, I or mixtures of these halides form a family of photochromic and cathodochromic materials whose properties can be varied continuously as a function of composition and doping. These materials are of particular interest because they can be used to fabricate display-storage devices having uniquely simple configurations. Therefore, it is of importance to try to further improve their contrast capabilities and other pertinent properties.

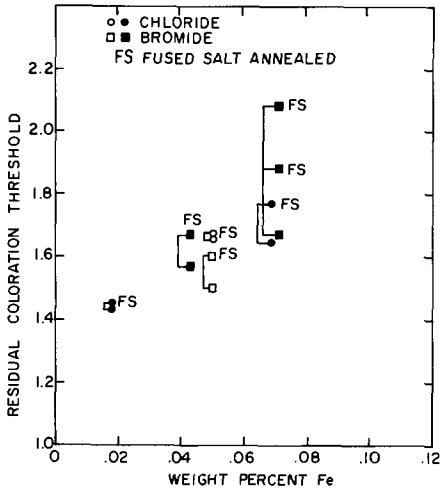

Fig. 12. Residual coloration thresholds of samples of sodalite materials before and after fused-salt treatment.

The photochromic switching of the sodalites involves the reversible transfer of an electron from a thermally stable level which may be provided by iron or sulfur, to a halogen vacancy in which it is thermally unstable. Optically reversible cathodochromism appears to involve the same centers, and the cathodochromic electron transfer process is thought to be closely related to the photochromic process (11, 12). From the data on the relative densities of halogen vacancies and reversible color centers it appears that the number of thermally stable centers limits the degree of reversible switching that occurs. A more serious practical limitation of sodalite, however, is the occurrence of residual coloration. A detailed understanding of this phenomenon would be most helpful to increase the usefulness of the sodalites in cathodochromic display applications.

Acknowledgment

The author is indebted to R. C. Puttback of the Airtron Division of Litton Industries for his continued cooperation during the project, to R. L. Quinn for his assistance with the materials preparation and measurements, to P. E. Norris for his helpful collaboration during a portion of the project and to B. W. Faughnan for many helpful discussions. Thanks are due H. H. Whitaker, R. J. Paff, and W. L. Harrington for, respectively, emission spectrographic and atomic absorption, x-ray, and mass spectrographic analyses of sodalite samples. The research reported herein was jointly sponsored by the Naval Ship Systems Command, Washington, D. C. under Contract No. N00024-68-C-1173 and RCA Laboratories, Princeton, New Jersey.

Manuscript submitted May 21, 1970; revised manuscript received July 30, 1970.

Any discussion of this paper will appear in a Discussion Section to be published in the June 1971 JOURNAL.

REFERENCES

1. W. Phillips and Z. J. Kiss, *Proc. IEEE*, **56**, 2072 (1968).
2. D. B. Medved, *J. Chem. Phys.*, **21**, 1309 (1953).
3. D. B. Medved, *Am. Mineralogist*, **39**, 615 (1954).
4. R. D. Kirk, *This Journal*, **101**, 461 (1954); *see* also R. D. Kirk, *Am. Mineralogist*, **40**, 22 (1955).
5. Technical Documentary Report No. ASD-TDR-62-305, April 1962; R. Radler, ASD-TDR-63-172, March 1963; R. Radler and D. Chenot, Al-TDR-64-170, Oct. 1964.
6. W. G. Hodgson, J. S. Brinen, and E. F. Williams, *J. Chem. Phys.*, **47**, 3719 (1967).
7. E. F. Williams, W. G. Hodgson, and J. S. Brinen, *J. Am. Ceramic Soc.*, **52**, 139 (1969).
8. P. A. Forrester, D. J. Marshall, S. D. McLaughlan, and M. J. Taylor, in Conference Proceedings No. 50, *Opto-Electronics Signal Processing Techniques*, NATO Advisory Group for Aerospace Research and Development (Technical Editing and Reproduction Ltd., London, England, 1970).
9. J. H. Schulman and W. D. Compton, "Color Centers in Solids," p. 52ff, Pergamon Press, New York (1963).
10. P. E. Norris, Unpublished work.
11. R. C. Duncan, B. W. Faughnan, and W. Phillips, *Appl. Optics*, **9**, 2236 (1970).
12. Z. J. Kiss and W. Phillips, *Phys. Rev.*, **180**, 924 (1969).

Reflection X-Ray Topography of GaAs and GaP Cleavage Faces

G. A. Rozgonyi and S. E. Haszko

Bell Telephone Laboratories, Incorporated, Murray Hill, New Jersey 07974

ABSTRACT

X-ray topography has been applied to cleaved cross sections of GaAs and GaP wafers. Experimental procedures for cleavage face x-ray topography are described in this paper, and the wide range of use for this method is shown. Using this technique a measure of the depth of damage introduced into the material during cutting and polishing, as well as during device fabrication, *e.g.*, the application of ohmic contacts, is obtained. The relative defect density in GaP substrates and epitaxial layers can be determined from the topographs. Damage introduced at the substrate-epitaxial layer interface can also be readily identified.

The relation between crystal imperfections and the performance of semiconductor devices has been well established during the last decade (1). Although most of this work has been on silicon, there is plenty of evidence that defects play an equally important role in compound semiconductors as well (2). One of the more powerful techniques for the analysis of defects in semiconductors has been x-ray topography (XRT) (3). Recently several workers have applied XRT techniques to the study of imperfections in GaAs substrates as well as in GaAs and $GaAs_xP_{1-x}$ epitaxial layers (4-6). Both the reflection (Berg-Barrett) and transmission (Lang) geometries have been employed to study surface and bulk defects of wafers during processing and after epitaxial thin film growth. Attempts have been made (6) to analyze selectively the defects as a function of depth by adjusting the diffraction conditions such that only the top 5-20μ of the sample are active in the diffraction process. There are several factors limiting the usefulness of this approach. For example, in samples with deep surface damage, the diffraction contrast is overpowered by enhanced diffraction from the deformed surface regions. In this case the depth of damage can only be determined after the damaged layer is removed. Also, for studies of film-substrate interfaces, the region of most interest, the interface itself, is not explicitly delineated and may actually be deeper than the penetration depth of the x-rays, which is generally 6-12μ for Cu $K_{\alpha 1}$ depending on the angle of incidence of the x-rays with the surface (6).

An alternate approach to the problem of obtaining a profile or "in-depth" analysis is to cleave the wafer. Since (100)- and (111)-oriented samples are used for practically all devices, it is easy to obtain cleavage faces which expose a cross section normal to the large area growth surface of the wafer. A reflection x-ray topograph of the cleavage face will, therefore, yield the following information:

(*i*) a profile of the strain field at the free surface,
(*ii*) the distribution and density of defects in the bulk and in the layer, and
(*iii*) the imperfection density at the film-substrate interface.

Considering the amount of information obtained with a single topograph it is surprising how little cleavage face topography has been used. Aside from a recent report by Schiller (7) and a single XRT in a paper by Howard and Dobrott (6) the technique has been neglected. In the present report we wish to show that once the sample alignment procedures are optimized there are many phenomena associated with thin film-substrate processing steps that can be readily observed and studied with cleavage face XRT. This information can then be used in conjunction with the electrical or optical evaluation of the material to relate the effectiveness of a particular processing step, or type of defect, with the final performance of specific devices.

Key words: defects, III-V compounds, semiconductor processing.

Equipment and Sample Alignment Procedures

A Jarrell-Ash microfocus x-ray unit with a line focus and Cu $K_{\alpha 1}$ characteristic radiation has been used. A standard Jarrell-Ash Lang camera was adapted for use in the reflection mode to obtain Berg-Barrett topographs of $(\bar{1}10)$ and $(1\bar{1}0)$ cleavage faces of GaAs and GaP wafers. Figure 1 shows schematically the relation between x-ray source, cleavage face, and photographic plate. The x-ray beam is ~3 cm high and 1 mm in cross section when it reaches the sample. Since the sample is at a small angle to the incident radiation it is quite easy to image reasonably large cleavage faces. In fact, using this geometry for normal

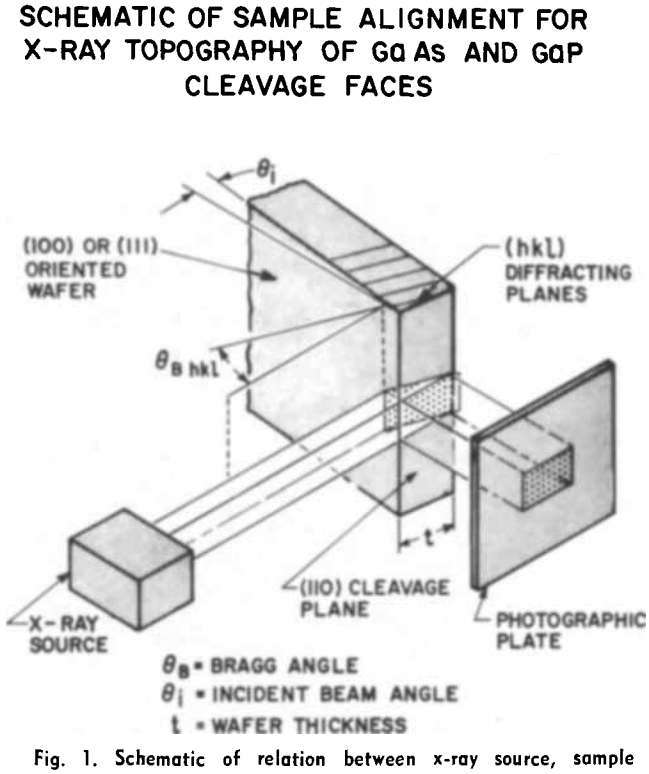

Fig. 1. Schematic of relation between x-ray source, sample cleavage face, and photographic plate.

Table I. Crystallographic data for alignment of GaAs and GaP cleavage faces using Cu $K\alpha_1$ radiation

Material	Orientation of wafer surface	hkl Diffracting planes	$\theta_{110/hkl}$	$\theta_{B_{hkl}}$	θ_i	$2\theta_{B_{hkl}}$	θ_{roll}
GaAs	111	531	44.18	53.71	9.53	107.42	11.0
		422	30.0	41.87	11.87	83.74	19.47
	100	333	35.26	45.07	9.81	90.14	Zero
GaP	111	531	44.18	56.74	12.56	113.48	11.0
		422	30.0	43.82	13.82	87.64	19.47
	100	333	35.26	47.26	12.00	94.52	Zero

Berg-Barrett XRT of plane wafer surfaces, it is possible to image 5 x 30 mm samples without scanning.

In order to obtain topographs of maximum resolution with minimum distortion it is necessary to place the photographic plate close to the sample and also have it intercept the diffracted beam at 90°. Therefore, the (hkl) diffracting planes are chosen such that the angle of incidence, θ_i, is small, *i.e.*, less than ~20°, and the diffracted beam is as close to the normal to the cleavage face as possible, *i.e.*, $2\theta_B - \theta_i \approx 90°$. θ_i is easily calculated as the difference between θ_{Bhkl} and the angle between the $(1\bar{1}0)$ cleavage face and the (hkl) planes. Table I lists the data necessary to select a suitable diffraction plane for (100) and (111) oriented wafers of GaAs and (111) wafers of GaP. It should be mentioned that it is sometimes necessary to tilt or "roll" the sample about the $[1\bar{1}0]$ axis in order to obtain a zero-layer reflection. That is, for minimum distortion of the XRT image, it is necessary to keep the incident and diffracted beams and the cleavage face normal in the same plane. For example, from Table I it is seen that for a (111) oriented wafer of GaP the $(4\bar{2}2)$ reflection gives $2\theta_B = 87.64°$ and $\theta_i = 13.82°$. However, referring to the $(\bar{1}10)$ stereographic projection of Fig. 2 it is found that the $(4\bar{2}2)$, or equivalently the $(2\bar{1}1)$, does not lie along the line from $(1\bar{1}0)$ to (111). Since the GaP was oriented (111), the sample must be rolled 19.47° toward the (001) until it coincides with the (112) zone. The sample is now properly aligned for a zero-layer $(4\bar{2}2)$ topograph.

The diffracted beam is initially recorded on dental x-ray film with a 3-5 min exposure to check the sample alignment. With thin wafers this is quite important because the samples bend and overlapping

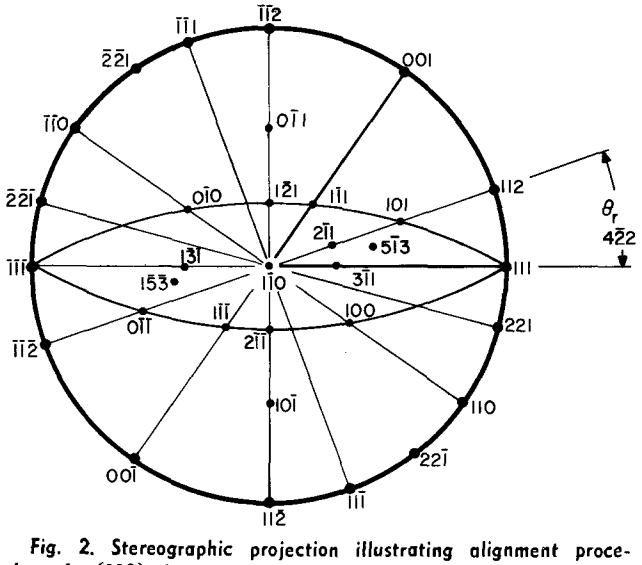

Fig. 2. Stereographic projection illustrating alignment procedures for {110} cleavage faces.

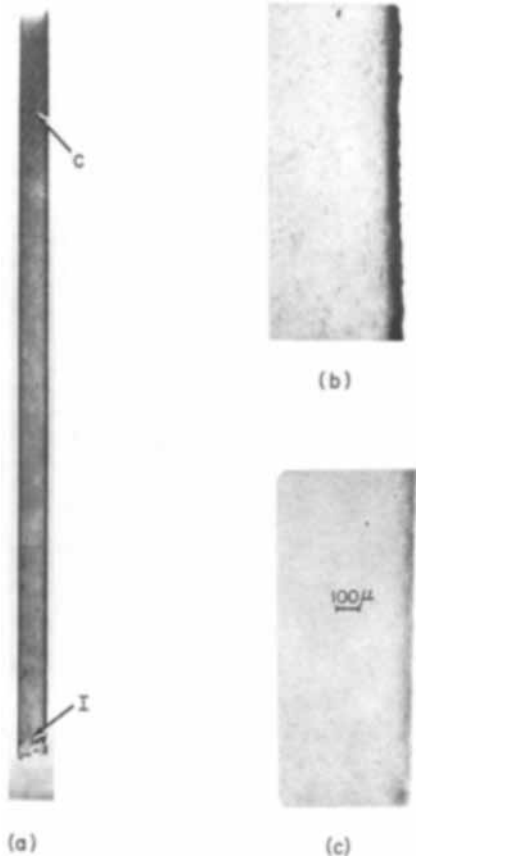

Fig. 3. CF-XRT of saw-cut GaAs wafers: (a) Czochralski crystal (~6X); (b) Czochralski crystal (~35X); (c) boat-grown crystal (~35X).

spurious images may occur. Ilford nuclear plates, either type G-5, exposure times ½-1 hr, or type L-4, exposure times of 2-4 hr, are then used depending on the resolution required for the sample. The distance between x-ray source and exit slit is ~42 cm, while a power level of 200W was used.

As examples of cleavage face x-ray topography (CF-XRT), several topographs from Czochralski and boat-grown GaAs substrate wafers are shown in Fig. 3. The wafers have been cut to ~0.030 in. on an ID saw and then cleaved with a razor blade. Aside from localized damage at the impact point of the razor blade, marked I in Fig. 3(a), and the cleavage steps in the upper portion of the sample, marked C in Fig. 3(a), the cleaving operation does not seriously affect the major portion of the wafer. The dark region on the right-hand side[1] of the higher magnification CF-XRT's in Fig. 3(b) and 3(c) represents the surface damage and associated strain field introduced by the sawing operation. The photographs have the same contrast as the original plate; therefore, defects show up as dark areas. The intense dark areas arise because the angular range of Bragg reflection by a perfect crystal is small compared to the divergence of the incident beam. Therefore, a distorted, damaged, or dislocated region reflects a larger fraction of the incident flux in the diffracted beam direction than does the more perfect surrounding material.

An estimate of the dislocation density can be obtained by counting the strain fields in the center of the crystal, *i.e.*, the number of dark lines per unit area. A value of 10^3-10^4/cm^2 has been seen in most of the GaAs Czochralski crystals, *see* Fig. 3(b), while boat-grown material is much lower and approaches zero for some

[1] The surface of interest is always presented as the right-hand edge of our CF-XRT's since the left-hand or "leading edge" side is often over-exposed due to x-rays which enter the front face of the wafer and exit from the cleavage face, see Fig. 1. Therefore, we generally trim the left-hand side of our pictures, where practical.

ingots, *see* Fig. 3(c). It should be noted that the saw damage and associated strain field in the low dislocation, boat-grown material is substantially less than that in the Czochralski crystals, and that both bulk imperfections and surface damage can be examined in the single CF-XRT.

Applications of Cleavage Face XRT

Polishing damage in GaP substrates.—Figure 4 is a composite of 3 CF-XRT of GaP wafers cut from a Czochralski crystal grown by the liquid encapsulation method. The right-hand edge of Fig. 4(a) shows the surface of a wafer cut with an ID saw which shows greatly enhanced diffraction to a depth of ~1 mil. There is also a gray area extending ~2 mils deeper, which is most likely the extent of the elastic strain field due to the gross surface damage. In Fig. 4(b) the sample has been mechanically polished on both sides to a mirror finish, initially with American Optical Type 305 abrasive, followed by 3.0μ and then 0.1μ diamond paste to remove a total of 3 mils. There is a corresponding reduction in the depth of heavy damage at the surface, but the crystal is still obviously highly strained. In order to remove the surface damage and associated strain field and still maintain a flat, highly polished surface we had the wafers chemically polished. A total of ~1.2 mils was removed from the "B" or phosphorous-face. The uniform contrast of the topograph in Fig. 4(c) shows that the chemical treatment does in fact remove the saw damage and leave the surface strain free. These observations can be related to the electroluminescent properties of liquid phase epitaxial layers subsequently grown on chemically and mechanically polished substrates (8).

LPE layer—substrate profiles.—Two examples of film-substrate combinations which are well suited to examination by CF-XRT are shown in Fig. 5 and 6. The films are GaP and have been deposited by liquid phase epitaxy (LPE) onto Czochralski GaP substrates. A thin dark line can be seen at the film-substrate interface in Fig. 5, while a region of gross deformation exists at the outer surface of the LPE layer. The strain field due to interfacial defects is readily detected and, for this film, it is on the order of 5-10μ in width. Note that the film-substrate interface does not act as a barrier to line defects which readily cross over from substrate to film. We would, therefore, expect the LPE film defect concentration to be comparable to that in the substrate. The origin of the large surface damage or "skin effect" is not understood at present. However, we note that the surface damage is now comparable to that in the raw cut wafer shown in Fig. 4(a). We might expect that an ohmic contact or the growth of another LPE layer would be severely influenced by this type of surface. Application of chemical polishing

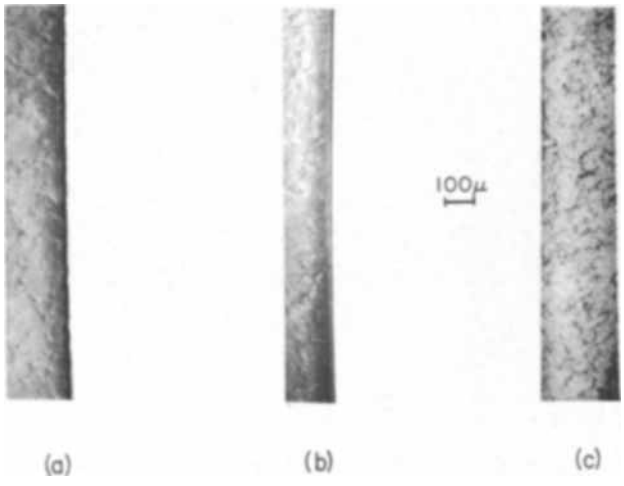

Fig. 4. CF-XRT of GaP wafers (~45X): (a) saw-cut; (b) mechanically polished; (c) chemically polished.

Fig. 5. CF-XRT of GaP substrate — single LPE film profile (~90X).

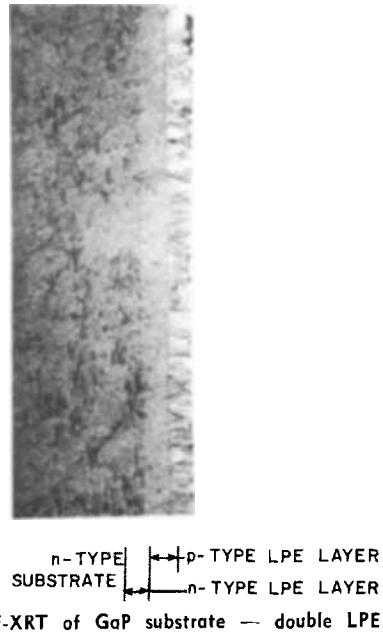

Fig. 6. CF-XRT of GaP substrate — double LPE film profile (~75X).

to remove 20μ of surface removed the damage and a CF-XRT revealed uniform contrast across the LPE layer.

A "double tipped" layer, *i.e.*, a p-type LPE layer on a previously grown n-type LPE layer, is shown in Fig. 6. In this example we note a large difference in the defect concentration in the first layer when compared to the substrate. Also, the film substrate interface is not a distinct line as in Fig. 5 but shows up as a barrier for the defects in the substrate. Unfortunately, the p-n interface is not nearly as good, and a continuous line of defects appears. In addition, a series of large strain fields are observed traversing the width of the p-type layer. A subsequent powder x-ray diffraction analysis of the outer layer revealed the presence of polycrystalline Ga_2O_3 which is not detected in samples free of this particular contrast feature. We have, therefore, attributed these defects to the strain field around precipitated inclusions of Ga_2O_3 (9).

Ohmic contacts to GaAs thin films.—A recurring problem with the device fabrication of Gunn and LSA oscillators is the quality of ohmic contacts. A popular contacting procedure is the evaporation of Ag and/or

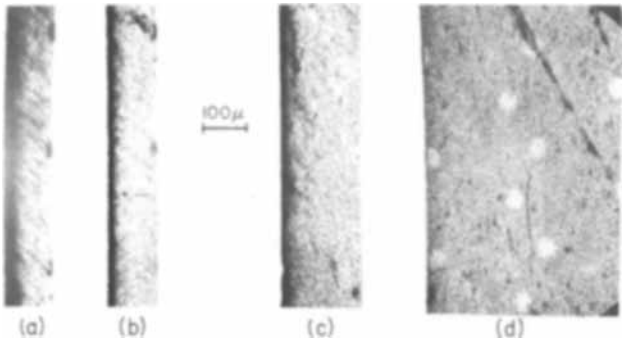

Fig. 7. CF-XRT of ohmic contacts to GaAs thin films (~60X). (a) Sn-Ag; (b) Ag; (c) Au-Ge; (d) (100) wafer surface.

alloys of Ag with Sn, In, and Ge followed by heating to 600°C in forming gas at a pressure of 5×10^{-3} Torr. Because of the rather high temperature involved and the variety of Ag compounds under consideration it was decided to supplement the normal electrical measurements with CF-XRT. Typical results illustrating good and bad alloy contacts and also a new lower temperature vacuum evaporated Au-Ge contact are shown in Fig. 7. The contacts are initially evaporated on the GaAs through a mask with a staggered array of 0.002 in. diameter holes. A CF-XRT of a poor contact is expected to show excessive damage whenever the cleavage face intercepts a contacted region of the wafer. A Sn-Ag contact on a 6μ thick epitaxial GaAs layer vapor deposited on a substrate now thinned to 0.004 in. is shown in Fig. 7(a). It is readily seen that the processing damage and associated strain field extends up to 20μ below the surface. This is considerably deeper than the 6μ thick epitaxial film. A defective, high resistance device resulted from this procedure. A CF-XRT from an Ag contact, also heated to 600°C, is shown in Fig. 7(b). Once again the location of the damaged regions near a contact is quite evident. However, in this case the extent of damage is substantially reduced, and an ohmic contact was obtained. Finally, an Au-Ge alloy evaporated in vacuum at 250°C onto an outgassed GaAs film-substrate combination was examined. The result is a topograph with no evidence of a strain gradient due to the contact, see Fig. 7(c). A normal Berg-Barrett XRT of the array of 0.002 in. dots is shown in Fig. 7(d) alongside the CF-XRT in order to pinpoint the location of the contacts. As expected the electrical properties of the evaporated Au-Ge contact have proven to be consistently better than the Ag alloys (10).

Discussion and Conclusions

The examples presented above have been chosen to illustrate the range of applicability of cleavage face x-ray topography to everyday problems in semiconductor device processing. Obviously many other examples could have been presented, but these cover the range from cutting a substrate wafer to the contacting of a layered device. It has been our experience that many attempts at device fabrication involving a series of materials preparation and device processing steps have been unsuccessful because the quality of the initial material or the effectiveness of a processing step is judged primarily by the operation of the device itself. We believe that CF-XRT when used in conjunction with other metallurgical, electrical, optical, etc., tests offers a means of establishing optimum semiconductor shaping processes and a meaningful in-process quality control.

It should be pointed out that by concentrating on a profile of a cross section we have sacrificed one of the usual advantages of XRT, *i.e.*, the ability to obtain information over the entire surface or bulk of the sample. Therefore, a CF-XRT should be coupled with a Lang or Berg-Barrett XRT if any doubt exists as to the general applicability of the results. This dual-XRT approach was taken in the present paper, see Fig. 7(c) and 7(d), in locating the GaAs contacts. Figure 7(d) also shows that the cleavage operation does not affect the surface of the sample. In terms of sample preparation, cleaving is the only step required.

The results presented above were obtained from cleavage faces normal to the large area surface of the wafer. In the future we plan to cleave along the (101) plane, which leaves an angle of 35° and 45° with the (111) and (100) surfaces, respectively, *see* Fig. 2. In this way interfacial defects, such as misfit dislocations, which would appear as a dot or a line in a normal cleavage, would be exposed as a cross grid network.

Another possible area of improvement is in reducing exposure times by diffracting off more intensely reflecting planes. The use of Cr radiation in place of Cu and an analysis similar to that in Table I would reveal the (311) plane as the most favorable diffracting plane for (111) oriented wafers. This should reduce the exposure times for L-4 plates to less than an hour. A (311) reflection would also reduce θ_{roll} to zero.

In conclusion, it has been shown that CF-XRT is a powerful technique for examining defects in GaAs and GaP substrates and epitaxial layers as a function of thickness. As a consequence of this initial study several results have already been obtained which have aided in the improvement of GaAs and GaP device fabrication. Specifically, ohmic contacts to GaAs thin films are now made by vacuum evaporation of Ge-Au in place of the high-temperature Ag and Ag(In, Sn, Ge) procedures previously used. Also, by using a chemical polishing procedure it has been possible to improve the electroluminescent properties of LPE GaP diodes over that obtained from mechanically polished substrates. In addition, a qualitative means of estimating the depth of damage due to saw cutting and evaluating the most effective polishing technique for its removal has been described. Similarly, residual surface damage in GaP LPE layers has been observed and subsequently removed by chemical polishing. Other applications to problems related to defects introduced by ion implantation and thermal diffusion are obvious and will be pursued in the future.

Acknowledgments

The authors would like to thank A. A. Bergh for initially suggesting they examine cleavage faces and for his comments on this work. The GaP Czochralski crystals were supplied by H. W. Verleur and chemically polished by A. J. Sayko. The contacts to GaAs films were provided by T. Riley and B. Pruniaux. Comments on the initial manuscript by B. Schwartz, R. H. Saul, and T. Iizuka are appreciated. The authors would also like to acknowledge numerous discussions with F. B. Koch on x-ray phenomena.

Manuscript submitted March 16, 1970; revised manuscript received *ca.* July 16, 1970. This was Paper 146 presented at the Los Angeles Meeting of the Society, May 10-15, 1970.

Any discussion of this paper will appear in a Discussion Section to be published in the June 1971 JOURNAL.

REFERENCES

1. "Semiconductor Silicon," R. R. Haberecht and E. L. Kern, Editors, pp. 585-653 and references therein. The Electrochemical Society, New York, (1969).
2. K. H. Zschauer, *Solid State Commun.*, **7**, 335 (1969).
3. E. S. Meieran, *Siemans Rev.*, 4th Special Issue **37**, 1 (1970).
4. E. S. Meieran, *Trans. Met. Soc. AIME*, **242**, 413 (1968).
5. J. K. Howard and R. H. Cox, *Advan. X-Ray Anal.*, **9**, 35 (1966).
6. J. K. Howard and R. D. Dobrott, *This Journal*, **113**, 567 (1966).
7. C. Schiller, *J. Appl. Cryst.*, **2**, 223 (1969).
8. G. A. Rozgonyi and R. H. Saul, Paper 163 presented at the Atlantic City Meeting of the Society, Oct. 4-8, 1970.
9. The presence of Ga_2O_3 in p-type LPE layers was initially observed by M. Kowalchik using optical microscopy. See M. Kowalchik, A. S. Jordan, and M. H. Read, RNP 250, presented at the Atlantic City Meeting of the Society, October 4-8, 1970.
10. B. R. Pruniaux, Private communication.

Concentration and Behavior of Carbon in Semiconductor Silicon

Tadashi Nozaki

Institute of Physical and Chemical Research, Yamatomachi, Saitama, Japan

and Yoshifumi Yatsurugi and Nobuyuki Akiyama

Komatsu Electronic Metals Company, Hiratsuka, Japan

ABSTRACT

The concentration of carbon in semiconductor silicon and the behavior of carbon in the fusion and crystallization of silicon have been studied by the use of charged particle activation analysis. The solubility of carbon in solid silicon has been found to be 3.5 x 10^{17} at./cm^3 or slightly less at the melting point, and the equilibrium distribution coefficient of carbon between solid and liquid silicon has been determined to be 0.07 ± 0.01. Carbon content over the above solubility value has seldom been observed in silicon single crystals produced by modern industrial techniques. The content appears to depend more on the growth conditions of the single crystal than on the chemical purification method. The phase diagram of the C-Si system in the extremely low carbon concentration range is given, together with a discussion of the kinematics of the carbon behavior in zone melting. Also, a new technique for studying the evaporation of carbon from the silicon melt is shown.

Although reliable information about the concentration and behavior of carbon in semiconductor silicon has been required, analytical results reported for carbon vary anomalously according to the analytical method used (1). We have proved that charged particle activation analysis by the $^{12}C(^3He, \alpha)^{11}C$ reaction is the most sensitive and most reliable for this analysis (2). Using this method, we have analyzed semiconductor silicon of various origins and specifications, and determined the following two constants: (*i*) the solubility of carbon in solid silicon at the melting point, and (*ii*) the equilibrium distribution coefficient of carbon between solid and liquid silicon.

Experimental

Analytical method.—Details concerning the charged particle activation analysis for carbon, nitrogen, and oxygen in semiconductor silicon are described in a separate paper (2). This technique has a lower limit of sensitivity for carbon down to 1 x 10^{15} at./cm^3. For carbon concentrations between 4 x 10^{16} and 3.5 x 10^{17} at./cm^3, this method has given results which agree fairly well with those of the infrared absorptiometry (3), as will be shown in a separate paper. (The former method gave results smaller by a factor of 0.7 than the latter.) About 160 samples including device-grade silicon and carbon-doped silicon have been analyzed. Uncertainty in the results of the activation analysis is estimated to be about 10 and 30% for carbon concentrations of 2 x 10^{17} and 5 x 10^{15} at./cm^3, respectively. The lowest result obtained for the apparent carbon content has been 2.0 x 10^{15} at./cm^3, indicating that the various possible interferences in this analysis are not serious for carbon concentrations over 5 x 10^{15} at./cm^3 (2).

When the carbon is precipitated as silicon carbide, the activation analysis involving the chemical separation usually gives lower results because the precipitate is not readily decomposed by the chemical treatment. This was found by measuring the ^{11}C activity formed in some carbon-doped samples before and after the chemical separation. For carbon concentrations up to about 3.5 x 10^{17} at./cm^3, results of the nondestructive measurement have always agreed with those of the separation and measurement, but for higher concentrations, the latter has given distinctly lower results than the former. However, as will be made clear later, carbon concentrations under about 3.5 x 10^{17} at./cm^3 is usually not precipitated.

Key words: concentration of C in semiconductor Si, solubility of C in solid Si at its mp, equilibrium distribution coefficient of C between solid and liquid Si, phase diagram of C-Si system.

Preparation of carbon-doped silicon.—Commercial semiconductor silicon usually does not contain enough carbon for the reliable measurement of its solubility in solid silicon and its equilibrium distribution coefficient. Various quantities of carbon (10, 30, and 100 ppm) in aqueous suspension (Aquadag) were painted uniformly on silicon rods (2.5 cm diameter, 30 cm length), and molten zones were passed through them (about 7 mm width, 3.5 mm/min traveling velocity). Then, in several parts of one of the resultant rods, molten zones (7 mm width) were passed with various traveling velocities to give a sample from which distribution coefficient measurements were made. All the zone meltings were carried out in a vacuum, and the above sample was not exposed to air in the intervals between the zone meltings. Also, Czochralski crystals were pulled from pyrolytic graphite crucibles.

Results

Solubility of carbon in solid silicon at the melting point.—When passing molten zones through the carbon-covered silicon rods, silicon carbide powder appeared on the surfaces of the melts; the larger the quantity of carbon, the sooner the appearance of the particles. The resultant carbon distribution in one of the samples is shown in Fig. 1. Carbon concentration just prior to the appearance of silicon carbide was always found to be 3.5 ± 0.4 x 10^{17} at./cm^3 regardless of the quantity of carbon painted on the rod. This is explained clearly by the phase rule. When three condensed phases, *e.g.*, solid silicon, liquid silicon, and silicon carbide, coexist in equilibrium in a two-component system, *e.g.*, silicon and carbon, the composition of each phase should be uniquely determined. Therefore, 3.5 ± 0.4 x 10^{17} at./cm^3 is an observed value for the solubility of carbon in solid silicon at its melting point. Also, this value is consistent with the following experimental results: (*i*) Czochralski crystals from graphite crucibles exhibit approximately the same carbon content; and (*ii*) as described in the preceding section, when carbon exceeded this concentration, different behavior was observed in the chemical treat-

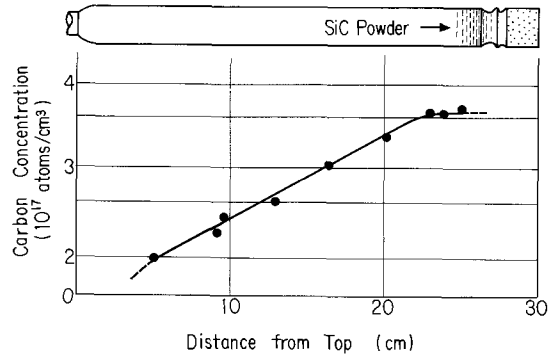

Fig. 1. Carbon distribution after a single zone pass through a carbon-painted silicon rod.

ment. This value, however, may be slightly overestimated, as the solid-liquid boundary could be dendritic and thus the growing solid phase would capture a small fraction of the liquid phase.

Equilibrium distribution coefficient of carbon between solid and liquid silicon (K_{eq}).—The solubility of carbon in liquid silicon has been reported by several authors (4-6). This value can be regarded as about 35 x 10^{17} at./cm³, or slightly higher, at the melting point of silicon. Thus, K_{eq}, which is the ratio of the solubility in the solid to that in the liquid, is calculated to be about 0.1, or slightly less.

By another method, K_{eq} was obtained with more certainty. Carbon distributions in the sample described above are shown in Fig. 2. From these distributions, the effective distribution coefficients, K_{eff}, are obtained in relation to the zone velocities, as shown in Fig. 3. By extrapolating the curve in Fig. 3 to zero velocity, K_{eq} is obtained as 0.06 or 0.07. This value may be slightly underestimated, due to the evaporation of part of the carbon from the molten silicon in the course of the zone pass. This evaporation, however, can be regarded as insignificant because no notable amount of oxygen was available to form carbon monoxide (see below). Therefore, K_{eq} has been determined to be 0.07 ± 0.01.

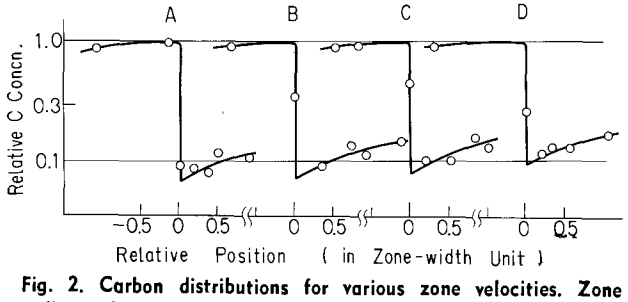

Fig. 2. Carbon distributions for various zone velocities. Zone traveling velocity: A, 0.4 mm/min; B, 0.8 mm/min; C, 1.2 mm/min; D, 1.6 mm/min.

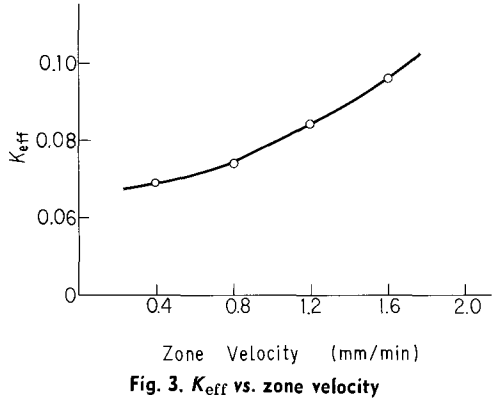

Fig. 3. K_{eff} vs. zone velocity

Carbon content of commercial semiconductor silicon.—The carbon content of various kinds of commercial semiconductor silicon produced by modern industrial techniques is shown in Table I, together with their oxygen content as measured by the charged particle activation analysis (2). All values are below the solubility in solid silicon at the melting point. In general, the carbon content of single-crystal silicon appears to depend more significantly on the conditions in the single-crystal formation than on the chemical purification method. The carbon content of dislocation-free samples shows no obvious difference from ordinary float-zone silicon. The high carbon and oxygen contents of the Czochralski crystals can be explained as contaminations from the graphite heating device and silica crucible used in the process.

Change of the carbon content in an industrial process.—Table II shows the change of the carbon and oxygen content in the course of the production of single-crystal silicon. The polycrystalline silicon used as the raw material for all the single crystals, was produced by the monosilane process in Komatsu Electronic Metals Company, Japan, and carbon content was very uniform and constant.

Single crystals with the lowest carbon and oxygen content were obtained by float-zone melting in a vacuum. After multiple zone passes, the concentrations have been found to be reduced, but reach a value which seems to be determined by several conditions in the process. For example, in order to reduce the carbon content below about 5 x 10^{15} at./cm³, special care should be taken to prevent the back diffusion of vacuum pump oil. Silicon crystals after float-zone melting in argon have been found to contain varying quantities of carbon, although the concentrations are always lower than the polycrystal content. Probably, the purity of the argon is a critical factor in determining the carbon content.

Discussion

Phase diagram of C-Si *system.*—From the information described above, the phase diagram of the C-Si system in the extremely low carbon concentration range can be drawn (*see* Fig. 4). The lowering of the melting point was calculated by the formula: $\Delta T = RT^2_m x/\Delta H$, which is an integrated form of the Clausius-Clapeyron equation using Raoult's law, and allowing for a dilute solution $\ln(1-x) \approx -x$ where x is the mole fraction of the solute. R is the gas constant, T_m is the melting point, x is the mole fraction of solute, and ΔH is the molar heat of fusion.

Table I. Carbon and oxygen content of commercial semiconductor silicon

	Carbon content, 10^{17} at./cm³	Oxygen content, 10^{17} at./cm³
Polycrystal	0.20 ~ 0.50 [0.82]*	0.80 ~ 3.0 [0.04]*
Single crystal		
FZ in argon	0.080 ~ 0.35	0.05 ~ 0.20
FZ in vacuum	0.030 ~ 0.40	0.010 ~ 0.030
CZ in argon	0.30 ~ 3.0	2.0 ~ 10
Dislocation-free FZ	0.40, 0.13, 0.016, 0.30	0.013, 0.019, 0.026, 0.10

* Figures in the brackets are exceptional values.

Table II. Change of carbon content in an industrial process

	Carbon content, 10^{17} at./cm³	Oxygen content, 10^{17} at./cm³
Crude	>40	10
Polycrystal	0.20 ~ 0.25	0.80 ~ 0.85
FZ in argon*		
(Single pass)	0.15	0.06
FZ in vacuum*		
Single pass	0.03	0.03
Three passes	0.02	0.015
CZ in argon*	1.0	4

* Middle portion of the rod.

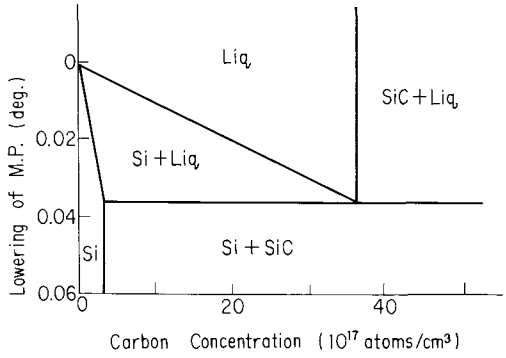

Fig. 4. Phase diagram of C-Si system in extremely low carbon concentrations.

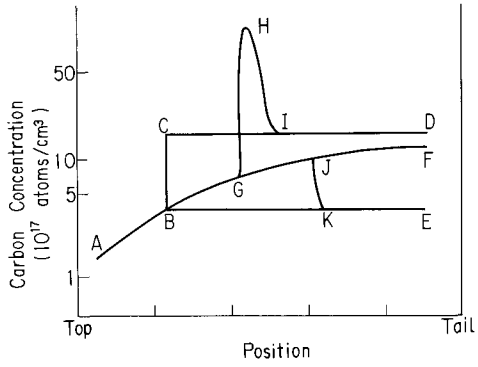

Fig. 5. Various possible carbon distributions after a single zone pass. ABCID, no supersaturation of the liquid phase and no removal of the silicon carbide; ABKE, no supersaturation but complete removal; ABGJF, supersaturation throughout; ABGHID, supersaturation up to G and then no removal; ABGJKE, supersaturation up to J and then complete removal.

The technique described above, *i.e.*, combination of charged particle activation analysis with zone melting, will provide useful information concerning the phase diagrams of carbon, nitrogen, and oxygen in ultrapure substances. More detailed thermodynamic discussions concerning these impurity elements in semiconductor silicon will be forthcoming in a separate paper.

Kinematical considerations of the carbon behavior.—In the solidification of the liquid eutectic C-Si mixture, it is quite natural for carbon to behave differently from the one component of an ordinary binary alloy due to the phenomena: (*i*) usually silicon carbide will not precipitate immediately when the liquid phase has become supersaturated; and (*ii*) silicon carbide appearing on the solid-liquid boundary can be removed to the liquid-gas surface, leaving only the solid silicon rather than the solid eutectic mixture.

In order for the carbon to precipitate, many carbon atoms must condense. The probability of their encounter, however, should be quite small because of their low concentration. This is especially true in the float-zone melting process where none of the nucleation centers, such as foreign substances, imperfections in the solid phase, and special spots on container walls, are readily available. Therefore, the liquid, and also the solid phases are likely to become supersaturated.

We have actually observed phenomenon (*ii*). In general, the van der Waals' attraction between the surface of a solid phase and the surrounding liquid phase is much smaller when the solid is only slightly soluble in the liquid as compared to the highly soluble conditions. The silicon carbide powder, therefore, can be positioned on the liquid-gas surface with more stability in free energy than on the solid-liquid boundary. Turbulence in the molten zone caused by the radio-frequency heating carries the silicon carbide powder to the more stable position.

According to whether the removal of the silicon carbide and the supersaturation of the liquid phase take place or not, varying types of the resultant carbon distribution are possible after a single zone pass of a silicon rod with a relatively high original carbon content. This is shown in Fig. 5. The original carbon content is about 15 x 10^{17} at./cm^3, and the liquid phase has become saturated at Location B. The carbon level at C, I, and D should be equal to the original carbon content. Practically, distributions corresponding to the partial removal of the silicon carbide probably occur more frequently than those in Fig. 5.

From these kinematic considerations, carbon contents of silicon single crystals exceeding the solubility in the solid at the melting point can be explained. Such high carbon concentrations were sometimes found in old silicon crystals, but rarely in modern products. This is probably due mainly to the difference in the carbon content of the raw polycrystals. It is natural that silicon carbide precipitates when silicon containing over 3.5 x 10^{17} at./cm^3 of carbon is kept at 1100°C (7).

Evaporation of carbon.—A parallel can be found between the carbon and oxygen concentrations in Table I and Table II. This suggests the evaporation of carbon as carbon oxide from the molten silicon. In order to obtain proof of this evaporation, the following new radiochemical technique has been devised: (*i*) bombard semiconductor silicon of known carbon and oxygen content with ^{3}He particles accelerated over 40 MeV energy to produce ^{11}C in the silicon by the reaction of the matrix itself (2); (*ii*) fuse the bombarded silicon by radio-frequency heating, and analyze the evolved gas for the ^{11}C by radio gas chromatography; and (*iii*) measure the ^{11}C remaining in the silicon. The evaporation of the carbon has thus been proved, although data are still being acquired in this study.

Future problem.—Effects of the carbon on the semiconductor properties still remain obscure, although a correlation between the lattice parameter and the carbon concentration has been reported (8). At the present, any remarkable effect on the electronic properties has not been documented. In more elaborate and elegant uses of the semiconductor, however, it is possible for the carbon to play some role. This will be the topic of future study.

Acknowledgment

The authors would like to express their thanks to the Cyclotron Group of the Institute of Physical and Chemical Research for their bombardment services, and to Mr. Yoshiyuki Endo, of the Komatsu Electronic Metals Company, for his aid in the analytical practice.

Manuscript submitted March 31, 1970; revised manuscript received *ca.* July 21, 1970.

Any discussion of this paper will appear in a Discussion Section to be published in the June 1971 JOURNAL.

REFERENCES

1. E. Spenke, "Semiconductor Silicon," R. R. Haberecht and E. L. Kern, Editors, p. 1, Electrochemical Society, New York (1969).
2. T. Nozaki, Y. Yatsurugi, and N. Akiyama, *J. Radioanal. Chem.*, **4**, 87 (1970).
3. R. C. Newman and J. B. Willis, *J. Phys. Chem. Solid*, **26**, 373 (1964).
4. R. N. Hall, *J. Appl. Phys.*, **29**, 914 (1958).
5. R. I. Scace and G. A. Slack, *J. Chem. Phys.*, **30**, 1551 (1959).
6. F. A. Halden, "Silicon Carbide," J. R. O'Connor and J. Smiltens, Editors, p. 115, Pergamon, Oxford (1960).
7. R. C. Newman, *Proc. Phys. Soc. London*, **76**, 993 (1960).
8. J. A. Baker, T. N. Tucker, N. E. Moyer, and R. C. Buschert, *J. Appl. Phys.*, **39**, 4365 (1968).

Structure of Silicon Films Deposited on Oxidized Silicon Wafers

A. L. Fripp and R. L. Stermer
NASA Langley Research Center, Hampton, Virginia 23365

and A. Catlin
Materials Science Department, University of Virginia, Charlottesville, Virginia 22904

ABSTRACT

The effect of substrate temperature on the preferred orientation of polycrystalline silicon films deposited on thermally grown silicon dioxide has been investigated. The films were deposited by the pyrolytic decomposition of silane and were examined by x-ray diffraction and scanning electron microscopy. For films grown to a thickness of 16μ, the preferred orientation first increased in the <110> direction as deposition temperature was increased to 1000°C; as deposition temperature was increased above 1000°C the preferred {110} orientation decreased. The measurement of preferred orientation as a function of film thickness indicated that the strong {110} preferred orientation at 1000°C was due to accelerated {110} growth and not preferred {110} nucleation orientation.

The deposition of silicon on oxidized silicon wafers is of interest in microelectronic applications of dielectric isolation and selected area epitaxy. Silicon may be deposited on these surfaces by physical or chemical methods. Chemical deposition of silicon from the halide onto the oxidized surface has been reported as often needing a nucleating agent, such as a sodium salt, to produce a uniform coating of polycrystalline silicon (1). Silane has been used to deposit polycrystalline silicon on silicon dioxide covered silicon wafers, but no information was given on the structure of the films (2).

Silicon wafers used in microelectronic applications are polished single crystals and are usually sliced parallel to a low index crystallographic plane, but silicon oxide grown on the single crystal surface is amorphous with a short range crystobalite structure (3, 4). Hence, deposition on oxidized single crystal silicon is deposition on an amorphous substrate. Previous papers, where silicon was vacuum evaporated onto heated fused quartz substrates, report that the deposited film habit has a strong temperature dependence. Random polycrystalline silicon films were reported at substrate temperatures above 550°C, and evidence of (111) preferred orientation above 1000°C was shown (5, 6). Mountvalla (7) reports random films in the range between 700° and 765°C with a preferred {110} orientation between 765° and 900°C. At 1000°C Mountvalla (7) reports a mixed {110} and {111} orientation.

The purpose of this paper is to report the use of silane for silicon deposition on oxidized silicon wafers and to report the effect of substrate temperature on the preferred orientation of the deposits.

Experimental

The wafers were polished 0.005 ohm-cm boron doped single crystal silicon orientated within 2° of the {111} face. They were then oxidized in a quartz tube furnace at 1100°C by bubbling nitrogen through a heated water bath. The final oxide was approximately 1μ thick.

The deposition apparatus was an induction heated silicon horizontal tube epitaxial reactor (Fig. 1). Pure (50 ohm-cm) silane was fed through a flowmeter and mixed with sufficient hydrogen to produce a silane atmosphere of 0.37% by volume in the 7-cm-diameter by 75-cm-long quartz glass reaction chamber. The oxidized substrates were placed on either a silicon carbide coated graphite susceptor or a quartz envelope containing a graphite susceptor. The susceptor was placed in the quartz reactor tube at a point midway in the induction coil and at a small angle with respect to the horizontal.

The primary control variable for these experiments was substrate temperature which was varied from 840° to 1265°C (corrected from optical pyrometer readings). Silane flow rate was a constant 50 cc/min which produced a deposition rate of 0.8 μ/min. In a standard run the substrate was rapidly brought to temperature and then held at temperature for 7 min before introducing the silane gas for a 20-min run. A hydrogen atmosphere was used during both preheat and cooling periods. The preheat conditions and deposition time were varied for some runs, as will be described in the section "Results."

The preferred orientation was examined using an x-ray diffractometer. The {111} oriented silicon wafers did not produce a diffraction pattern since they were slightly misoriented. To give accurate comparison of preferred orientations of the different samples, all x-ray scans were run at identical settings, except for the counts-per-second scale.

Results

A total of 18 samples were prepared under various processing conditions. Table I shows sample identification numbers, process conditions, and relative x-ray intensities.

Macroscopically flat layers of polycrystalline silicon were deposited on the oxidized silicon substrates for all test temperatures except 1265°C. At a substrate temperature of 1265°C, the reduction and erosion of the silicon dioxide was too rapid to hold the deposited silicon. Examination of the wafer after the run showed that all oxide had been removed, and random crystallites had nucleated and grown on the single crystal surface (Fig. 2). The remainder of this paper will be a discussion of test results for substrate temperatures of 840°-1170°C only.

The texture of the 16μ-thick deposits was strongly temperature dependent. The absolute x-ray intensity

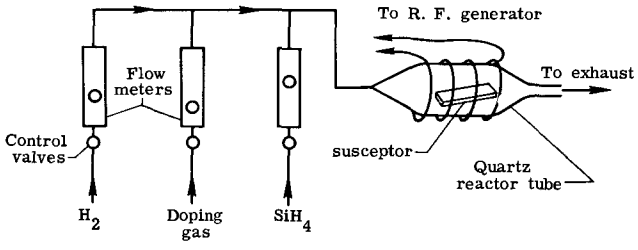

Fig. 1. Simplified block diagram of reactor system

Key words: microelectronics, dielectric insulation, preferred orientation, silane.

Table I. X-ray data

Sample	Deposition time	I(220), counts per sec	Temp, °C	{111}/{220} %	{311}/{220} %	{400}/{220} %	{331}/{220} %
ASTM				167	58	13.5	22
2-1	20 min	195	840	11	3	—	7.5
2-8	20 min	690	840	1	—	—	1
2-2	20 min	1360	860	—	—	—	2
2-3	20 min	2600	980	—	—	3	2
2-18	20 min	1950	980	2	—	—	1
2-9	20 min	1740	990	—	—	1	1
2-10	20 min	1900	995	—	—	3	—
2-4	20 min	620	1095	26	—	12	10
2-5	20 min	300	1160	55	7	7	13
2-11	20 min	250	1168	60	3	4	9
2-6	20 min	160	1170	105	10	12	16
2-19	1 min	0	975	—	—	—	—
2-20	5 min	150	975	47	—	23	8
2-21	5 min	145	980	45	—	20	11
2-17	8.5 min	370	985	17	—	19	7.5
2-14	20 min	4000	1125 preheat 970 run	—	—	—	—
2-15	20 min	110	985, 5 min 1165, 15 min	80	12	110	65
2-13	20 min	425	1150, 5 min 985, 15 min	19	2	3.5	10

of the {110} crystal planes showed an increase with increasing temperature until 1000°C, and then the {110} intensity decreased with further increases in temperature (Fig. 3). The relative intensities of the other low index crystallographic planes increased as the absolute {110} intensity decreased (Table I). That is, the films have an increasing preferred {110} orientation for deposition temperatures up to 1000°C; and even though the {110} orientation predominates, it reduces in strength at higher temperature to approach the surface coverage of {100} orientated crystallites. Even in the high-temperature deposits the relative intensities of the {111}, {311}, and {331} orientations are depressed from the standard ASTM (8) values. It should be noted that in an x-ray diffraction pattern, a {400} peak which is 13.5% of the {220} peak implies that there are as many {100} oriented crystallites on the wafers as there are crystallites oriented in the {110} direction.

An example of the x-ray diffractometer data is shown in Fig. 4 where the diffraction peaks from sample 2-3 are compared to the peaks in sample 2-4 (see Table I). Both patterns were taken with identical machine settings. The upper curve shows a very strong {220} peak, and the lower curve shows a weaker {220} peak, but the relative (and in this case, the absolute) intensities of the {111}, {400}, and {331} peaks have increased. The surfaces on samples 2-3 and 2-4 were examined by scanning electron microscopy. The surface of sample 2-4, which has the more random distribution of the crystallites, is shown in Fig. 5. Sample 2-3, which has a strong {110} preferred orientation, is similar to Fig. 5 except that the surface appears more uniform.

To test for possible causes of preferred orientation, the standard deposition run, as described above, was perturbed. The methods of perturbation and the results are described below:

1. Sample 2-9 which was deposited initially at 990°C was heat-treated in hydrogen at 1165°C for 30 min. The purpose of this test was to see if a high-temperature treatment would produce an orientation similar to a high-temperature deposition. The x-ray diffraction pattern was not changed by this treatment.

2. The oxide coated substrate was preheated at 1125°C for approximately 8 min before deposition; the

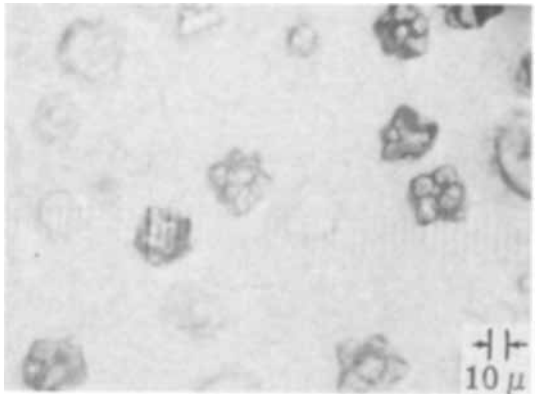

Fig. 2. Silicon crystallites on eroded substrate

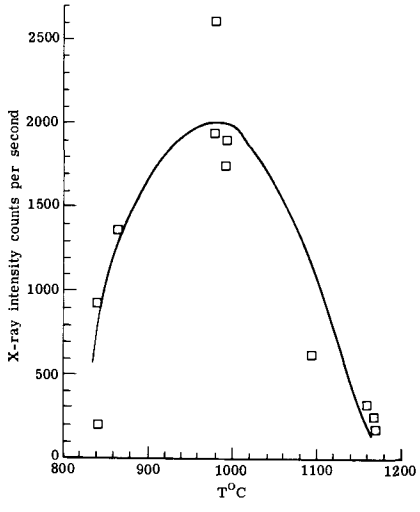

Fig. 3. Intensity of {220} diffraction peak as a function of substrate temperature.

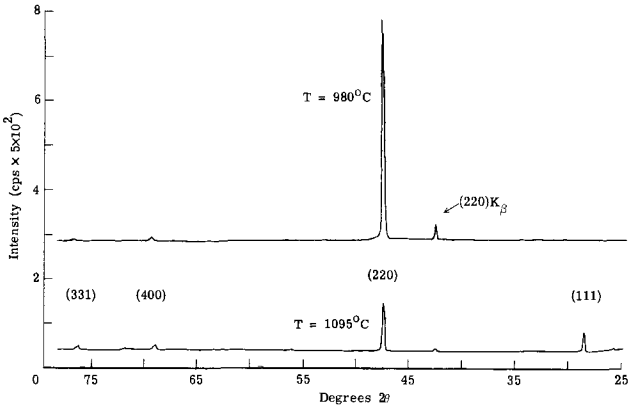

Fig. 4. X-ray diffraction intensity of low index planes for deposits made at 980° and 1095°C.

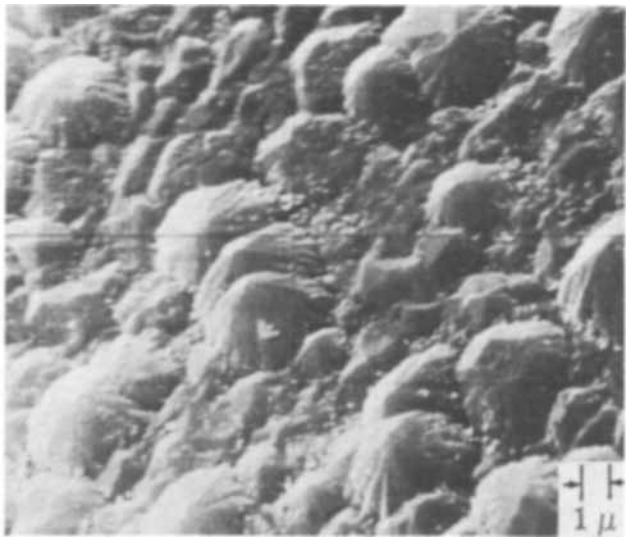

Fig. 5. SEM photomicrograph of film deposited at 980°C

temperature was then lowered to 970°C for normal deposition. This test was made to see if the preferred orientation was due to the oxide heat-treatment or to the actual deposition temperature. This test resulted in a stronger {110} preferred orientation than would normally be obtained at a deposition temperature of 970°C (see data on sample 2-14 in Table I).

3. Two sets of samples were made by depositing each at two different temperatures. That is, on one set of samples deposition was started at 985°C and continued for 5 min, then deposition was stopped and the temperature was raised to 1165°C, in the hydrogen atmosphere, and deposition proceeded for the remaining 15 min of the 20-min run. In another run the above temperatures were reversed, except that the high temperature was 1150°C. These tests were conducted to see if the temperature of the initial deposition would be controlling for future changes in temperature. The data, obtained from the high-temperature start, fell on the curve of {220} peak *vs.* substrate temperature as though the entire run was made at 1150°C; however, the run started at 970°C, had a low intensity {220} similar to a run made at 1165°C and a relatively strong {400} peak indicating a {100} preferred orientation (see data on samples 2-15 and 2-13 in Table I).

4. Data were taken in which deposition time was the independent variable, and temperature was held constant at approximately 980°C. Deposition times of 1, 5, and 8.5 min were used. These data were taken to see if the preferred orientation was due to nucleation orientation or growth orientation. The x-ray data for the 1-min run gave no distinguishable diffraction pattern. The 5-min run had a combination {110} and {100} preferred orientation with the {100} being the stronger of the two. Finally, in the 8.5-min run the {110} peak was clearly showing its strong preferred orientation (see data on samples 2-19, 2-21, and 2-17 in Table I).

Discussion

The preferred orientation of thin silicon films deposited on thermally grown silicon dioxide by the pyrolytic decomposition of silane is both temperature and thickness dependent. Substrate temperatures of approximately 1000°C produced a very strong {110} preferred orientation when the films were grown to a thickness of approximately 16μ, but thinner films ($t \simeq 4\mu$) tend to have a near random orientation with the {100} crystallographic plane predominating. This thickness dependence of preferred orientation indicates that the films have a preferred {100} nucleation orientation, but the {110} orientated crystallites have more favorable growth conditions in the intermediate temperature (970°-1000°C) range. The strongest {100} preferred orientation for all samples was produced by starting deposition at 985°C and then going to 1165°C for the majority of the run (see data for sample 2-15). These data not only indicate that the lower temperature produces a greater nucleation {100} orientation than a higher temperature, but that the growth {100} orientation is greater at the higher temperature.

However, in a deposit started at a high temperature ($T \approx 1150$°C), and continued at an intermediate temperature ($T \approx 980$°C), the preferred {110} orientation was weak as compared to deposits made entirely at 980°C. This implies that the nucleation orientation may be random at high temperatures. The preferred {110} orientation that does exist in this sample is due to growth orientation at the reduced temperature, but there were less {110} oriented nuclei to start with due to initial growth at the higher temperature.

A high-temperature (1125°C) predeposition treatment of the substrate tends to enhance the nucleation orientation of {110} crystal planes since sample 2-14 has the strongest {110} orientation of all runs. A post deposition heat-treatment ($T \approx 1165$°C, initial run at $T \approx 990$°C) had no measurable effect on the crystallography of the deposits.

In summary, both nucleation and growth contributions to preferred crystallographic orientation of silicon deposits on silicon dioxide appear to be temperature dependent. Temperatures in the neighborhood of 1000°C produce a preferred {100} nucleation orientation but strongly favor the {110} orientation in growth kinetics. Substrate temperatures in the range of 1150°C appear to favor a more random distribution of oriented nuclei and favor a {100} growth orientation.

Manuscript received April 27, 1970.

Any discussion of this paper will appear in a Discussion Section to be published in the June 1971 JOURNAL.

REFERENCES

1. E. G. Alexander and W. R. Runyan, *Trans. Met. Soc. AIME*, **236** 284 (1966).
2. K. E. Bean, H. P. Hentzschel, and D. Colman, "Semiconductor Silicon," p. 747, R. R. Haberecht and E. L. Kern, Editors, The Electrochemical Society, Inc., New York (1969).
3. P. V. Pavlov and E. V. Shitova, *Soviet Phy. Crystallography*, **12**, 95 (1967).
4. A. N. Knopp and R. Stickler, *Electrochem. Technol.*, **5**, 37 (1967).
5. F. M. Collins, *Trans. Eighth National Vacuum Symposium*, Vol. 2, p. 899, The Macmillan Co., New York (1961).
6. Y. Katooka, *J. Phys. Soc. Japan*, **17**, 967 (1962).
7. A. J. Mountvalla and G. Abowitz, *Vacuum*, **15**, 359 (1965).
8. ASTM Card No. 5-065, American Society for Testing Materials, Philadelphia, Pa.

Reaction Equilibria in the Growth of GaAs and GaP by the Chloride Transport Process

D. J. Kirwan[1]

Monsanto Company, St. Louis, Missouri 63166

ABSTRACT

The equipment and procedures used for the measurement of high temperature heterogeneous reaction equilibria are described. The results of these measurements for four reactions of primary importance to the epitaxial growth of GaAs and GaP by the chloride transport process are reported and compared with literature values.

The epitaxial growth of III-V compounds is based upon the departure from equilibrium of reactions of the type

$$3GaCl(g) + 1/2As_4(g) = 2GaAs(s) + GaCl_3(g)$$

with a similar reaction applying for GaP. Also, in the presence of hydrogen the reaction

$$GaCl_3(g) + H_2(g) = GaCl(g) + 2HCl(g)$$

is important. The crystal growth rate will be dependent upon the departure of the above reactions from equilibrium, and the equilibrium constants are temperature dependent. The purpose of this work was the experimental determination of the equilibrium constants for the above reactions and others pertinent to the manufacture of GaAs and GaP.

The results of a literature survey of available reaction equilibria data for reactions involved in the growth of GaAs and GaP from the vapor by the chloride transport process are presented in Table I. In all cases the standard state is taken as the pure material at one atmosphere pressure. In the last column the references for the data are given as well as whether the equilibrium constant was obtained by direct experimental observation or calculated from thermochemical data. Redundant reactions are included for the convenience of the user.

[1] Present address: Department of Chemical Engineering, University of Virginia, Charlottesville, Virginia 22901.

Key words: gallium arsenide, gallium phosphide, vapor transport, epitaxial growth, reaction equilibrium.

The thermochemical data tabulated by Fergusson and Gabor (1) are used in Table I when available. There is a significant discrepancy between their value of the standard heat of formation of GaCl and that reported in (2) (−16.2 kcal/mole *vs.* −19.0 kcal/mole). The equilibrium constants for reactions 17-21 involving GaP were obtained by computing the chemical potential of GaP from the vapor pressure measurements of Johnston (3).

Direct experimental observations are available for only three of the reactions listed in Table I and in one case (reaction 4) the value is not in agreement with that calculated from thermochemical data. Also, the extreme sensitivity of the value of the equilibrium constant to the accuracy of the standard enthalpy and entropy of reaction (at 1000°K an uncertainty of 5 kcal in the enthalpy of reaction changes the equilibrium constant by more than an order of magnitude) makes direct measurement of equilibrium constants of interest advisable. In this work the equilibrium constants for reactions 4, 6, 12, and 20 in Table I are measured as a function of temperature.

Experimental

Since the reactions of interest have a net change in the total number of moles of gaseous species, the equilibrium constants can be obtained from closed tube pressure-temperature measurements similar to those of Silvestri and Lyons (4) and Zeugel (5). In this method the total pressure in the reactor is measured as the reactor is heated to various temperature levels.

Table I. Gallium arsenide, gallium phosphide reaction equilibria

Reaction No.	Reaction	$Log_{10}K$ atm. units	Temp range, °K	Ref.
1	$Ga(l) + 1/2Cl_2(g) = GaCl(g)$	$6.46 + 3.69 \times 10^3/T - 0.47 \ln T$	300-2000	Calculated from data in (1, 10, 11, 6)
2	$Ga(l) + 3/2Cl_2(g) = GaCl_3(g)$	$-1.96 + 2.25 \times 10^4/T - 0.17 \ln T$	300-2000	Calculated from data in (1, 10, 11, 6)
3	$GaCl(g) + Cl_2(g) = GaCl_3(g)$	$-8.37 + 1.87 \times 10^4/T + 0.30 \ln T$	300-2000	Calculated from data in (1, 10, 11, 6)
4	$GaCl_3(g) + 2Ga(l) = 3GaCl(g)$	$21.1 - 1.13 \times 10^4/T - 1.23 \ln T$	300-2000	Calculated from data in (1, 10, 11, 6)
		$14.42 - 1.19 \times 10^4T$	693-903	Exp. Value (5)
		$4.87 - 4.66 \times 10^3T$	800-1200	Exp.Value (10)
5	$1/2H_2(g) + 1/2Cl_2(g) = HCl(g)$	$2.79 + 4.56 \times 10^3/T - 0.31 \ln T$	400-2000	Calculated from data in (1)
6	$GaCl_3(g) + H_2(g) = GaCl(g) + 2HCl(g)$	$13.95 - 9.58 \times 10^3T - 0.92 \ln T$	400-3000	Calculated from Rx. (3) and (5)
7	$As_4(g) = 2As_2(g)$	$11.6 - 1.36 \times 10^4T - 0.43 \ln T$	400-3000	Calculated from data in (10, 6)
8	$1/4As_4(g) + 3/2H_2(g) = AsH_3(g)$	$3.65 - 7.52 \times 10^3/T - 1.0 \ln T + 0.6 \times 10^{-3}T$	298-2000	Calculated from data in (1, 10, 6)
9	$1/4As_4(g) + 3/2Cl_2(g) = AsCl_3(g)$	$-6.18 + 1.76 \times 10^4/T + 0.37 \ln T$		Calculated from data in (1, 10, 6)
10	$Ga(l) + 1/4As_4(g) = GaAs(s)$	$-4.62 + 6.15 \times 10^3T + 0.35 \times 10^{-3}T$	300-2000	Calculated from data in (1, 10, 13)
11	$2GaCl + 1/2As_4(g) = 2GaAs(s) + Cl_2(g)$	$-21.6 + 4.86 \times 10^3/T + 1.1 \ln T$	300-2000	Calculated from data in (1)
12	$3GaCl(g) + 1/2As_4(g) = 2GaAs(s) + GaCl_3(g)$	$-30.1 + 2.36 \times 10^4T + 1.4 \ln T + 0.7 \cdot 10^{-3}T$	300-2000	Calculated from Rx.
13	$GaCl(g) + 1/4As_4(g) + 1/2H_2 = GaAs(s) + HCl(g)$	$-18.79 + 2.28 \times 10^4/T$	913-1253	Exp. Value (5)
		$-8.04 + 6.99 \times 10^3/T + 0.22 nT + 0.35 \cdot 10^{-3}T$	300-2000	Calculated from Reactions (12) and (6)
14	$P_4(g) = 2P_2(g)$	$11.5 - 1.21 \times 10^4/T - 0.5 nT$	298-1500	Calculated from data in (10 and (12)
15	$1/4P_4(g) + 3/2H_2(g) = PH_3(g)$	$4.88 + 1.47 \times 10^3/T - 1.2 nT$	298-1500	Calculated from data in (10 and (12)
16	$1/4P_4(g) + 3/2Cl_2(g) = PCl_3(g)$	$-6.21 + 1.79 \times 10^4/T + 0.25 nT$	298-1500	Calculated from data in (10, 12, 13)
17	$Ga(l) + 1/2P_2(g) = GaP(s)$	$-5.36 + 9.41 \times 10^3/T$	1054-1278	Exp. Value (3)
18	$Ga(l) + 1/4P_4(g) = GaP(s)$	$-2.46 + 6.385 \times 10^3/T - 0.13 nT$	1054-1278	Calculated from Rx. (14) and (17)
19	$2GaCl(g) + 1/2P_4(g) = 2GaP(s) + Cl_2(g)$	$-18.00 + 5.39 \times 10^3/T + 0.68 nT$	1054-1278	Calculated from Rx. (18) and (1)
20	$3GaCl(g) + 1/2P_4(g) = 2GaP(s) + GaCl_3(g)$	$-26.46 + 2.41 \times 10^4/T + 0.98 nT$	1054-1278	Calculated from Rx. (19) and (3)
21	$GaCl(g) + 1/4P_4(g) + 1/2H_2(g) = GaP(s) + HCl(g)$	$-6.08 + 7.255 \times 10^3/T + 0.03 nT$	1054-1278	Calculated from Rx. (18), (6) and (4)

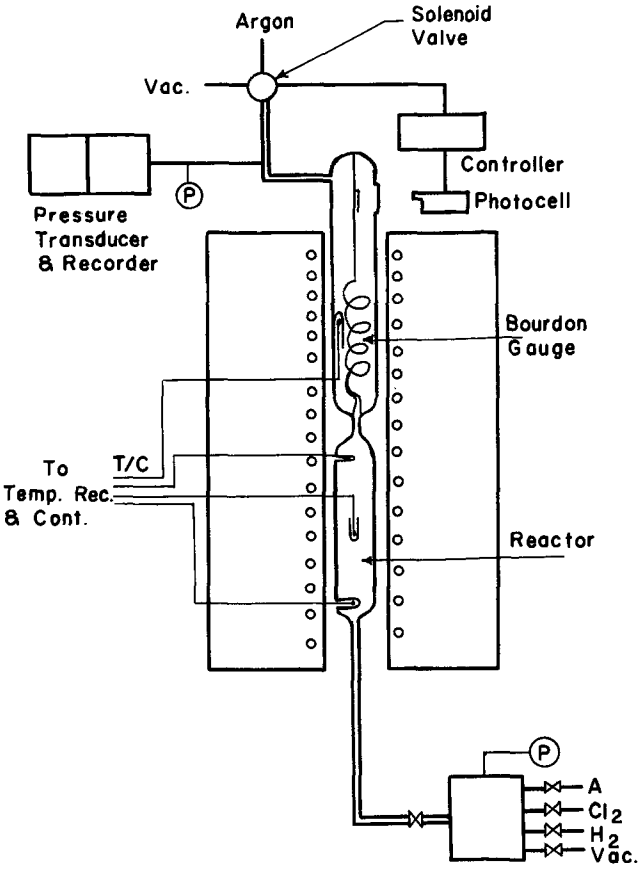

Fig. 1. Closed reactor system

From atom balances, a knowledge of the initial charge of reactants, and the temperature and pressure measurements, the partial pressure of each species may be calculated; hence, the equilibrium constant can be obtained at each temperature.

Equipment.—The experimental system selected was a batch reactor consisting of a quartz tube placed within a furnace capable of reaching approximately 1200°C. The principal items of equipment shown schematically in Fig. 1 included:

1. A reactor pressure sensing system consisting of a quartz helix bourdon tube attached to the reactor through a capillary tube, a photocell and a controller. The quartz bourdon gauges are manufactured by Worden Quartz Products, Inc., Houston, Texas. A mirror attached to the end of the helix rotated when the pressure within the tube changed causing a deflection of a light beam coming from the photocell. The reflected light beam was received by a photocell assembly coupled to a controller which operated a solenoid valve which restored the mirror to the null position by adjusting the argon gas pressure in the enclosure about the helix. The pressure in the enclosure was then read from a Wallace and Tiernan absolute pressure gauge and continuously recorded using a potentiometric type pressure transducer.

Some further comment on the quartz bourdon gauges is perhaps in order. Since condensed phases (GaAs, GaP, Ga) were present during these reactions even at the highest temperatures, it is necessary that the pressure measuring system be capable of being heated above the temperature in the reactor to prevent deposition. These all quartz gauges can be heated to above 1100°C in a corrosive atmosphere. They do have some drawbacks. The quartz helix is very fragile and quite easily broken from mechanical shock. Quartz is subject to weakening and eventual breakdown due to devitrification at high temperatures. This process is hastened by water vapor and basic oxides. Hence it is necessary that the quartz be kept clean and not handled with the hands or fingers before placing in the furnace. To obtain reproducible readings it is necessary to anneal the gauges prior to use. For the gauges used in this work approximately 30 hr at 1070°C were required.

2. As shown in Fig. 1, a muffle furnace having three separately controlled windings was used to maintain a uniform temperature along the reactor with the bourdon tube about 20°C higher than the reactor.

3. A gas handling system was used for evacuating the reactor and charging the gaseous reactants. Two Wallace and Tiernan absolute pressure gauges (0-1800 and 0-800 Torr) were used for pressure measurements.

4. Temperatures were measured and controlled by Type K, Iconel sheathed, thermocouples placed in wells at three locations along the length of the reactor and in a well in the bourdon gauge.

5. The reactor, a 24 mm ID quartz tube approximately 7 in. long, was designed to insure separation of gaseous and liquid or solid reactants until the reactor had been sealed and the initial charge of gas determined. This was accomplished by sealing the solid or liquid within a quartz ampoule with a breakaway tip. The ampoule was placed at the bottom of a vertical tube within the reactor. An iron rod, encased in quartz, was placed on top of the ampoule. At the start of the run, this rod was raised by an external magnet and then allowed to drop breaking the tip and allowing reaction to begin.

Procedure.—The determination of an equilibrium constant consisted of the following steps:

1. An ampoule containing the appropriate solid or liquid reagent was placed in the reactor with the bourdon assembly attached.

2. The reactor was evacuated and heated with a torch to remove any adsorbed species. After a number of alternate fillings and evacuations with argon and then with the gaseous reactants, the reactor was filled to the desired pressure and sealed with a torch.

3. The exact gaseous charge was determined by observing the pressure in the reactor as a function of temperature with the ampoule unbroken. At these low pressures (50-200 Torr) all the gases of interest behave ideally. This determination was carried out in a constant temperature air bath operating between room temperature and approximately 250°C. When the material in the ampoule was nonvolatile, *e.g.* GaAs, the muffle furnace was used, permitting higher temperatures to be obtained and a more accurate calculation of the molar density of gas charged.

4. With the reactor in the furnace, the pressure sensing system was nulled at the true pressure in the reactor as determined in step 3. The ampoule was broken and the total pressure observed at a series of temperatures. The pressure transducer used with a recorder was useful for determining when the total pressure had become constant and the reading could be taken. Data were taken during both heating and cooling to insure that equilibrium had been attained in the reactor.

Further details of the procedure will be given when the individual reactions are discussed.

Results and Discussion

Reaction A: $3GaCl(g) + \frac{1}{2}As_4(g) = 2GaAs(s) + GaCl_3(g)$.—The measurement of the equilibrium constant of this reaction follows the method of Zeugel (5). It consisted of charging a known amount of chlorine gas (>99.5%) and a sealed ampoule containing an excess of GaAs (Monsanto, melt grown) to the reactor. At low temperatures the chlorine completely reacts with GaAs forming chlorides of gallium and arsenic (possibly free arsenic also). Above approximately 600°C these reactions are complete and the only species present are $GaCl_3$, GaCl, As_4 (small amounts of As_2)

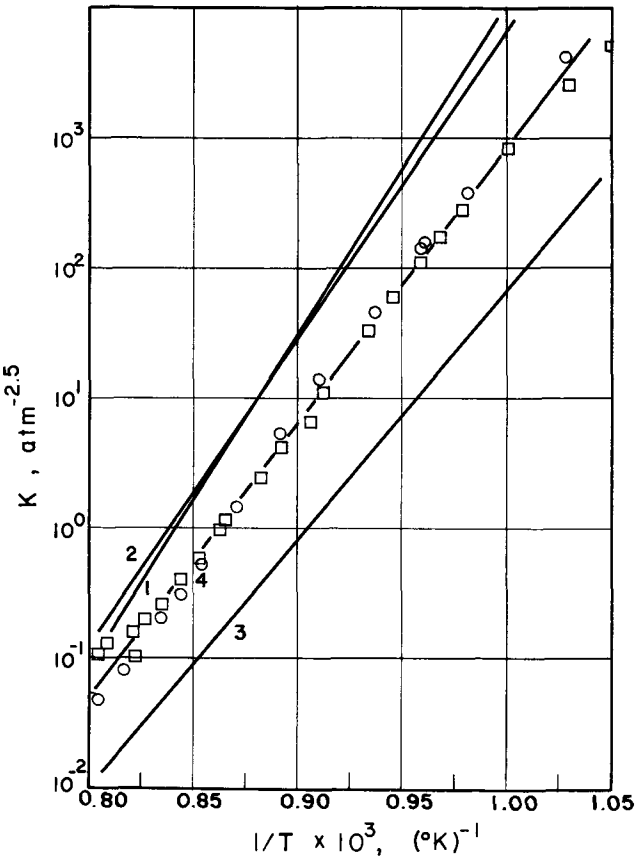

Fig. 2. Equilibrium constant: $3GaCl + \frac{1}{2}As_4 = 2\ GaAs + GaCl_3$. Curve 1, (5); curve 2, (1); curve 3, (2); curve 4, this work (two runs).

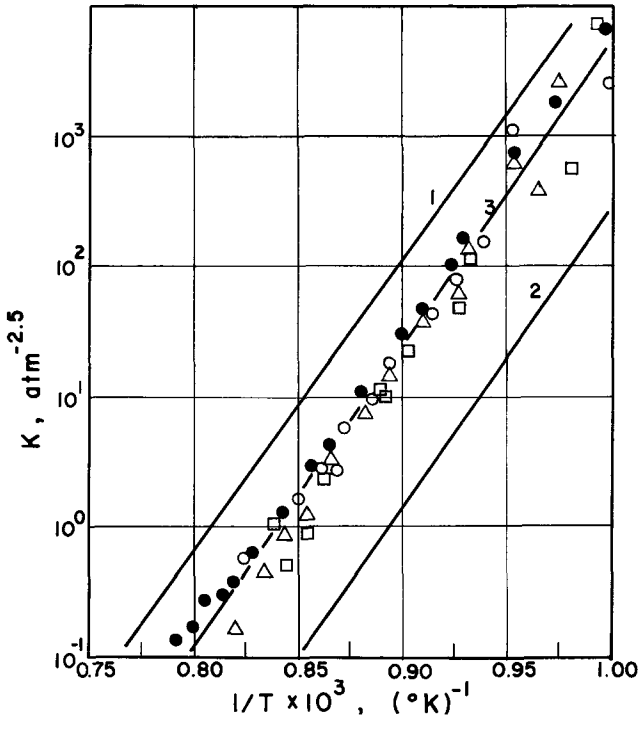

Fig. 3. Equilibrium constant: $3GaCl + \frac{1}{2}P_4 = 2GaP + GaCl_3$. Curve 1, (1, 3, 6); curve 2, (2); curve 3, this work (four runs).

and GaAs. A correction for the amount of arsenic present as As_2 in equilibrium with As_4 was made using the data of Stull and Sinke (6) as correlated by Zeugel (5). The equilibrium constant for the reaction was then calculated from total pressure measurements as the temperature was raised in steps from 600°C to about 1000°C and then lowered. The calculations were performed on a CDC 6400 computer.

The values of the equilibrium constant obtained in this work are presented in Fig. 2. Also shown are a correlation of the experimental results of Zeugel (5) and two sets of values calculated from thermochemical data. As mentioned earlier, the only difference between the literature curves is due to the use of different values for the standard heat of formation of GaCl(g). The least squares correlation of the equilibrium constants measured in this work is given in Table II along with information on the uncertainty of the correlating equation and the temperature range over which it applies.

Zeugel's experimental values are in good agreement with values calculated from Fergusson and Gabor's (2) thermochemical data while the results of this work lie between the two literature curves. Some recent results obtained in this laboratory on the growth and etching rates of GaAs support the equilibrium constant reported here (7). Finally, as has been previously noted, the value of the equilibrium constant calculated from thermochemical data is very sensitive to small changes in the heats and entropies of reaction. For example, if Thurmond's (8) value for the heat of formation of GaAs, which is only 700 cal less than that of Fergusson and Gabor, were used, the literature curve would be much closer to the experimental values obtained here.

Reaction B: $3GaCl(g) + \frac{1}{2}P_4(g) = 2GaP(s) + GaCl_3(g)$.—The procedure for measuring equilibrium constants for this reaction is analogous to that for reaction *A* except, of course, excess GaP (Monsanto, melt grown) was placed in the quartz ampoule. A correction for the presence of $P_2(g)$ was made using the equilibrium data of Stull and Sinke (6) for the dissociation of $P_4(g)$ to the dimer. It was noted that chlorine did not react very rapidly with GaP at room temperature. To increase the reaction rate the temperature was raised to about 1000°C and data taken during cooling first and then taken during heating. This also had the effect of removing material from the ampoule and distributing it throughout the reactor which reduced mass transfer resistance in the reactor and thereby shortened the time required to come to equilibrium at a given temperature.

The results of four runs on this system are presented in Fig. 3. Similar to those of GaAs, the equilibrium constant data lie between the two literature curves which again differ only in the value used for $\Delta Hf°_{298}$ of GaCl(g). The equilibrium constants measured in this work were correlated and the resulting equation is given in Table II.

Reaction C: $GaCl_3(g) + H_2(g) = GaCl(g) + 2HCl(g)$.—The equilibrium of this reaction is of importance because epitaxial deposition of GaAs, GaP or $GaAs_xP_{1-x}$ occurs in the presence of a high partial pressure of hydrogen. Under such conditions the partial

Table II. Experimental equilibrium constant data

Reaction	$Log_{10}K_p$ (atm units)	Var. of slope	Std. error of estimate	Temperature range (°K)
$3GaCl(g) + 1/2As_4(g) = 2GaAs(s) + GaCl_3(g)$	$2.10 \times 10^4/T - 18.0$	4.5×10^4	0.11	900-1300
$3GaCl(g) + 1/2P_4(g) = 2GaP(s) + GaCl_3(g)$	$2.20 \times 10^4/T - 18.6$	1.8×10^5	0.21	1000-1250
$GaCl_3(g) + H_2(g) = GaCl\ (g) + 2HCl(g)$	$-1.00 \times 10^4/T + 8.5$	3.6×10^4	0.14	900-1330
$GaCl_3(g) + 2Ga(l) = GaCl_3(g)$	$-1.16 \times 10^4/T + 14.0$	6.2×10^4	0.11	720-920

pressure of $GaCl_3$ is so reduced by reaction C that the deposition reaction is often written as

$$2GaCl(g) + \tfrac{1}{2}As_4(g) + H_2(g) = 2GaAs(g) + 2HCl(g)$$

The equilibrium constant for this reaction is simply the product of the equilibrium constants of reactions *A* and *C*. It is not possible to determine the equilibrium constant of the above reaction directly using a closed reactor system; hence the equilibrium constant for reaction *C* was measured and combined with that of reaction *A* to obtain the desired result.

The reactor was charged with hydrogen gas (>99.9%) and $GaCl_3$ (Monsanto produced, purity ~98%) crystals in a quartz ampoule. The amount of $GaCl_3$ charged was determined by an analysis of the reactor pressure between 550°K and 750°K where the reaction with hydrogen has not yet begun, but all of the $GaCl_3$ is in the vapor phase. The analysis is complicated by the presence of $GaCl_3$ in both monomer and dimer forms in the vapor. The equilibrium constant for the dissociation of the dimer as measured by Laubengayer and Schirmer (9) was used in the calculation of the amount of $GaCl_3$ present.

The total pressure measurements were complicated by high temperature diffusion of hydrogen through the thin-walled quartz helix of the bourdon gauge and the reactor walls themselves. Since in this system no condensed phases exist above about 250°C (a temperature where the diffusion rate is negligible), the bourdon tube was maintained at this temperature throughout a run. Diffusion through the reactor walls was slower but significant at the higher temperatures when the hydrogen partial pressure is high. To minimize this effect a large $GaCl_3/H_2$ ratio was used so that at the higher temperatures most of the hydrogen has reacted. This, of course, makes the calculation of the hydrogen partial pressure and, therefore, the equilibrium constant more uncertain in the high temperature region.

In a number of runs the data were not reproducible and log *K* *vs.* 1/T plots did not give straight lines. These problems were attributed to contamination of the $GaCl_3$. Gallium trichloride is strongly hygroscopic and easily contaminated if contacted with air. Data from such runs were, of course, disregarded.

In Fig. 4 are presented data from two runs in which the $GaCl_3/H_2$ ratio was large, the data reproducible during heating and cooling and no evidence of contamination was observed. Also shown are the literature values calculated from the data of Fergusson and Gabor (1) and that using the NBS value for $\Delta Hf°_{298}$ of GaCl(g). The data indicate a heat of reaction 15 to 25 per cent higher than the literature values and do not agree with either literature curve. The observed equilibrium constants were correlated and the resulting equation is given in Table II.

The growth rate studies, mentioned previously (7) as supporting the equilibrium constant values for reaction *A*, actually gave values of the equilibrium constant for the reaction,

$$2GaCl(g) + \tfrac{1}{2}As_4(g) + H_2(g) = 2GaAs(s) + 2HCl(g)$$

The values obtained were in agreement with the combined values of the measured equilibrium constants for reactions *A* and *C*. Consequently, those studies give support to the results obtained here for both reactions *A* and *C*.

Reaction D: $GaCl_3(g) + 2Ga(l) = 3GaCl(g)$.—As well as providing further thermodynamic information on the chlorides of gallium, the equilibrium of this reaction is important to the epitaxial growth of GaAs in two ways. First, gallium is commonly supplied to an epitaxial reactor by bubbling HCl through a gallium contactor held at high temperature. The reaction of interest is

$$2HCl(g) + 2Ga(l) = 2GaCl(g) + H_2(g)$$

whose equilibrium constant is simply the equilibrium constant of reaction *D* divided by that of reaction *C*.

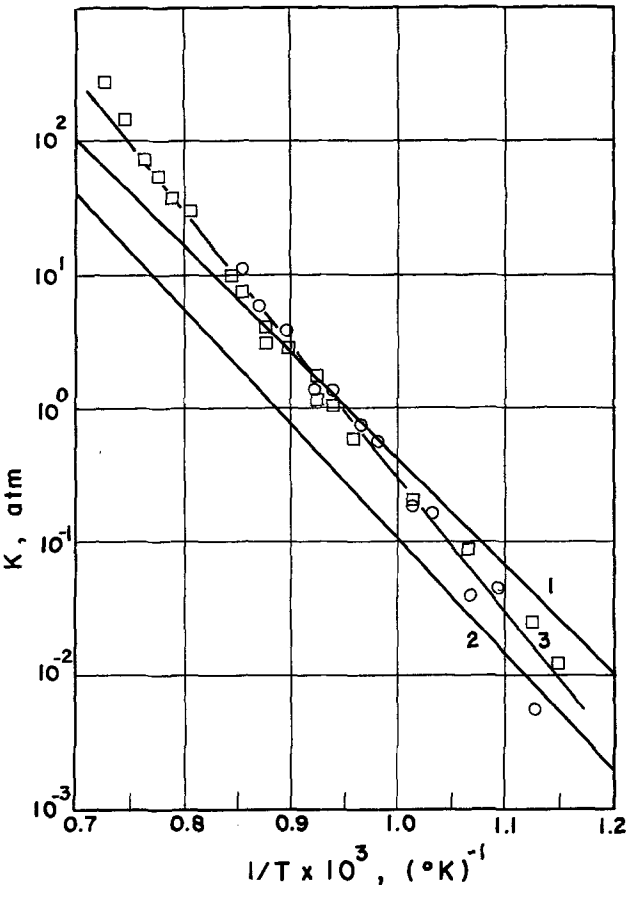

Fig. 4. Equilibrium constant: $GaCl_3 + H_2 = GaCl + 2HCl$. Curve 1, (2); curve 2, (1); curve 3, this work (two runs).

A knowledge of this equilibrium constant provides the value of the maximum conversion to GaCl to be expected in the contactor. Second, the disproportionation of GaCl(g) to free gallium and GaCl(g) has been suggested as a step in the mechanism of the growth of GaAs by the chloride transport process.

The procedure for carrying out the measurement of this equilibria consists of charging chlorine gas and an ampoule containing excess liquid gallium (99.99%) to the reactor. At lower temperatures the chlorine completely reacts forming a mixture of $GaCl_3$ and $GaCl_2$. The $GaCl_2$ decomposes above 300°C to Ga(l) and $GaCl_3$(g). Above approximately 400°C the reaction of interest then occurs.

The results of the two runs made are compared with the literature data in Fig. 5. The data are in excellent agreement with the experimental measurements of Zeugel (5) and lie between the literature curves using different values for $\Delta Hf°_{298}$ of GaCl. The values obtained in our work were correlated with the equation listed in Table II.

Thermochemical data.—We had hoped that the equilibrium constants of these four reactions would permit the calculation of new values of the more uncertain thermochemical data, particularly that of GaCl. Inspection of Fig. 2-5 suggests that, since the measured values lie between the two literature curves corresponding to different values of $\Delta Hf°_{298}$ of GaCl, the thermochemical data of GaCl may be in error. The only other species common to all four reactions is $GaCl_3$; however, since it is stable at room temperature, it would be expected that its thermochemical properties would be more easily measured and therefore more reliable.

The chemical potential of GaCl as a function of temperature was calculated from each of the measured equilibrium constants assuming that the literature values of the entropies and enthalpies of all other

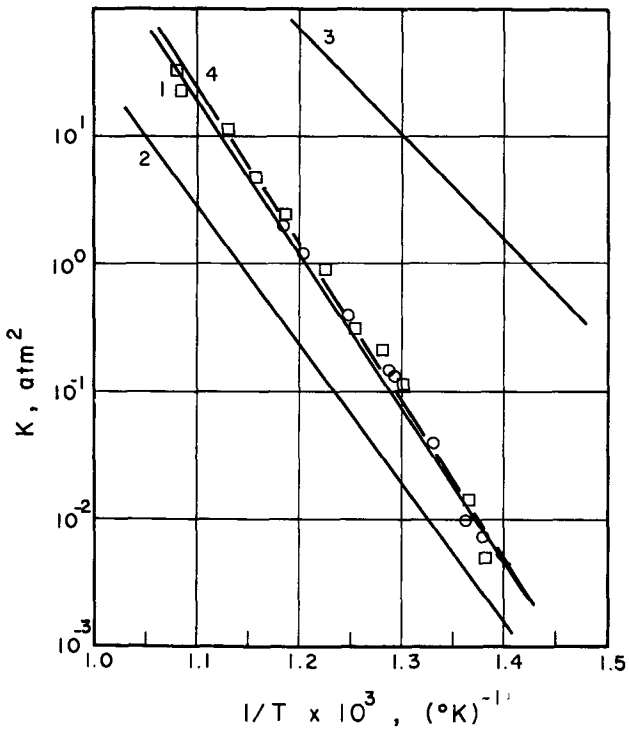

Fig. 5. Equilibrium constant: 2Ga + $GaCl_3$ = 3GaCl. Curve 1, (5); curve 2, (1); curve 3, (2); curve 4, this work (two runs).

species were correct. The results, which generally lay between the two literature values, varied, at most, by 4 kcal/mole (out of approximately 80 kcal/mole) depending upon which reaction was used. $\Delta Hf°_{298}$ for GaCl calculated from these data also varied as much as 4 kcal/mole with an average value of 17.5 kcal/mole. The discrepancy in $\Delta Hf°_{298}$ and hence in the chemical potential of GaCl between the two literature values [Ref. (1) and (2)] is 2.8 kcal/mole. Although the measured equilibrium data are reasonably self-consistent, they are not accurate enough to settle the discrepancy in the literature values. The true value of $\Delta Hf°_{298}$ of GaCl probably does lie between the literature values.

Equilibrium alloy composition.—The equilibrium constants for the reactions depositing pure GaAs and GaP may be used to predict the composition of a mixed crystal, $GaAs_{1-x}P_x$, in equilibrium with a vapor of given composition.

Consider the formation of a solid solution of GaP and GaAs. The condition of thermodynamic equilibrium of the deposition reactions yields the equations

$$\frac{P_{GaCl_3}(\gamma_A X_A)^2}{P^3_{GaCl}\, P^{1/2}_{As4}} = K_A \qquad [1]$$

$$\frac{P_{GaCl_3}(\gamma_P X_P)^2}{P^3_{GaCl}\, P^{1/2}_{P4}} = K_B \qquad [2]$$

where γ_A and γ_P are the activity coefficients of GaAs and GaP in a solid solution of mole fraction, $X_A = 1 - X_P$, of GaAs and of mole fraction, X_P, of GaP. K_A and K_B are the equilibrium constants of reactions A and B discussed previously. Equation [2] divided by [1] yields a relation between the phosphorous composition in the solid and that in the vapor.

$$\frac{\gamma_P X_P}{\gamma_A(1 - X_P)} = \left(\frac{K_B}{K_A}\right)^{1/2} \left(\frac{p_{P4}}{p_{As4}}\right)^{1/4} \qquad [3]$$

In the absence of better information it is reasonable to assume that the solid solution is approximately ideal ($\gamma = 1$). Equation [3] can be solved for the mole fraction of GaP in the solid.

$$X_P = \frac{(K_B/K_A)^{1/2}\,(P_{P4}/P_{As4})^{1/4}}{1 + (K_B/K_A)^{1/2}\,(P_{P4}/P_{As4})^{1/4}} \qquad [4]$$

The partial pressure ratio, p_{P4}/p_{As4}, is not simply the ratio of phosphorus to arsenic in the feed because these species partially dissociate into the dimer forms at the temperatures of interest. The true ratio of tetramers, accounting for the dissociation, is given by the equation

$$\frac{P_{P4}}{P_{As}} = \frac{y_P P_V + K_P/8 - (K^2_P/64 + y_P P_V K_P/4)^{1/2}}{(1 - y_P)P_V + K_{As}/8 - (K^2_{As}/64 + (1 - y_P)P_V K_{As}/4)^{1/2}} \qquad [5]$$

where y_P is the fraction of group V element that is phosphorus, P_V is the total pressure of group V elements computed as if all were in the tetramer form, and K_{As} and K_P are the equilibrium constants for the dissociation reactions: $As_4 = 2As_2$, $P_4 = 2P_2$. Equations [4] and [5] may then be used to calculate the equilibrium alloy composition for a given temperature, group V partial pressure and fraction of group V elements that is phosphorus, provided the temperature dependencies of the equilibrium constants are known. In Fig. 6 are presented some calculated values of the equilibrium alloy composition for typical conditions of epitaxial growth of $GaAs_xP_{1-x}$ (T = 800°, 850°C, 1 atm pressure and 0.375 mole per cent group V elements).

Summary and Conclusions

The equilibrium constants measured in this work are listed below.

1. $3GaCl(g) + \frac{1}{2}As_4(g) = 2GaAs(s) + GaCl_3(g)$

$$\log_{10} K\ (atm^{-2.5}) = 2.10 \times 10^4/T - 18.0$$

2. $3GaCl(g) + \frac{1}{2}P_4(g) = 2GaP(s) + GaCl_3(g)$

$$\log_{10} K\ (atm^{-2.5}) = 2.20 \times 10^4/T - 18.6$$

3. $GaCl_3(g) + H_2(g) = 2HCl(g) + GaCl(g)$

$$\log_{10} K\ (atm) = -1.00 \times 10^4/T + 8.5$$

4. $2Ga(l) + GaCl_3(g) = 3GaCl(g)$

$$\log_{10} K\ (atm^2) = -1.16 \times 10^4/T + 14.0$$

Acknowledgments

This work was partially supported by the Electronics Branch, Manufacturing Technology Division, Air Force

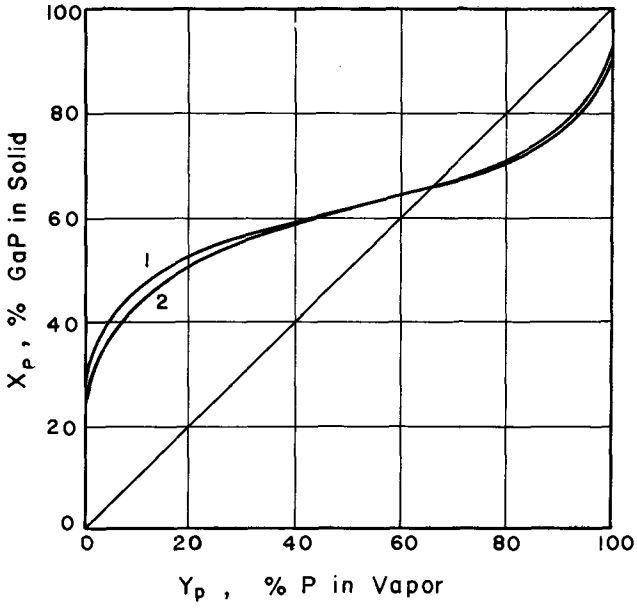

Fig. 6. Equilibrium alloy composition. P_V = 0.00375 atm. Curve 1, T = 800°C; curve 2, T = 850°C.

Materials Laboratory, Wright-Patterson Air Force Base under Contract No. AF 33(615)-3618, Project No. 9-531.

The author acknowledges the helpful advice of Drs. B. M. Kocatas and L. A. Goettler and appreciates the assistance of D. G. Schneider in the construction and operation of the equipment.

The permission of the Monsanto Company to publish this work is appreciated.

LIST OF SYMBOLS

$\Delta Hf°_{298}$	Standard enthalpy of formation at 298°K, kcal/mole
K_A	Equilibrium constant for reaction A, atm units
P	Partial pressure, atm
P_V	Total pressure of group V elements, atm
X_P	Mole fraction of GaP in the solid
y_P	Mole fraction of group V element in vapor that is phosphorus

GREEK SYMBOLS

γ	Activity coefficient in solid.

Manuscript submitted September 11, 1969; revised manuscript received *ca.* July 17, 1970.

Any discussion of this paper will appear in a Discussion Section to be published in the June 1971 JOURNAL.

REFERENCES

1. R. Fergusson and T. Gabor, *This Journal*, **111**, 585 (1964).
2. D. Wagman, *et al.*, "Selected Values of Chemical Thermodynamic Properties," National Bureau of Standards Technical Note 270-3, 219 (1965).
3. W. Johnston, *This Journal*, **110**, 117 (1963).
4. V. J. Silvestri and V. Lyons, *ibid.* **109**, 963 (1962).
5. M. Zeugel, *ibid.*, **112**, 1153 (1965).
6. D. R. Stull and G. C. Sinke, *Advan. Chem. Ser.*, **18**, (1956).
7. L. A. Goettler, "Diffusion and Surface Kinetics in the Epitaxial Vapor Deposition of Gallium Arsenide," Presented at Atlanta AIChE meeting, Feb. 1970.
8. C. Thurmond, *J. Phys. Chem. Solids*, **26**, No. 5, 785 (1965)
9. A. Laubengayer and F. Schirmer, *J. Am. Chem. Soc.*, **67**, 1578 (1940).
10. "Contribution to the Data on Theoretical Metallurgy," U.S. Dept. of Commerce, Bureau of Mines, Bulletin 584 (1960).
11. L. Quill, "Chemistry and Metallurgy of Miscellaneous Materials," McGraw-Hill Book Co., Inc., New York (1950).
12. F. Rossini, "Selected Values of Thermodynamic Properties," National Bureau of Standards, Circ. 500 (1952).
13. "Chemical Engineer's Handbook," R. Perry, Editor, 3rd Ed., McGraw-Hill Book Co., Inc., New York (1950).
14. "Manufacturing Methods for Epitaxially Growing Gallium Arsenide-Gallium Phosphide Single Crystal Alloys," Final Report, Contract No. AF 33(615)-3618.

On the Redistribution of Boron in the Diffused Layer during Thermal Oxidation

J. S. T. Huang and L. C. Welliver

Solid State Electronics Center, Honeywell, Inc., Plymouth, Minnesota 55427

ABSTRACT

This work is concerned with the investigation of the impurity redistribution process in a two step p-type diffusion. A simple theoretical model is formulated from which a closed form expression for the impurity profile is obtained. The experimental results verify the theoretical prediction of the profile. From these results, the segregation coefficient of boron at the oxide-silicon interface is determined, and the total number of impurity atoms that have escaped into the oxide can also be estimated.

In integrated circuit technology, two step boron diffusion involving a deposition step followed by a drive-in step is commonly encountered. The drive-in process is usually performed in oxidizing atmosphere, resulting in redistribution of boron within the semiconductor. This redistribution process during thermal oxidation was studied by Grove *et al.* (1) using uniformly doped substrates of semi-infinite extent. Their model is therefore not applicable to the case where diffused layers are used. For instance, their conclusion that the concentration at the interface is independent of the oxidation time certainly will not hold true for the diffused layer. Kato and Nishi (2) studied the redistribution of the boron diffused layer over a limited temperature range, but their analysis was so complicated that a computer was needed to obtain numerical results. In this paper, a simple theoretical model is first developed. A closed-form solution is then obtained for the impurity profile. The only unknown is the segregation coefficient at the interface which is determined by fitting the experimental result to the theoretical plots for various values of the segregation coefficient.

With the mathematical form of the impurity distribution available, many semiconductor properties such as the Hall coefficient and piezoresistive coefficient of a diffused layer can be characterized by effective values averaged over the impurity distribution in the layer.

Key words: semiconductor, diffusion, oxidation.

Theoretical Model

The boron deposition process gives rise to a complementary error function distribution of impurities. The total impurity atoms per unit area is given by

$$Q = 2C_s\sqrt{\frac{D_1 t_1}{\pi}} \qquad [1]$$

where C_s is the surface concentration usually limited by the solid solubility of the diffusant; D_1 and t_1 are the diffusion constant during the deposition and the time of deposition, respectively. The subsequent oxidation and drive-in will result in a total oxide thickness of x_o. The corresponding thickness of silicon oxidized is mx_o, where m is experimentally determined to be 0.38 (3). Figure 1 shows the diffusion model. At $t = 0$, the original Si surface is at $y = 0$ and the oxide-silicon interface as a function of time is indicated by $y_o(t)$.

The problem can be divided into two parts. First, consider that there is no flow of impurity atoms into

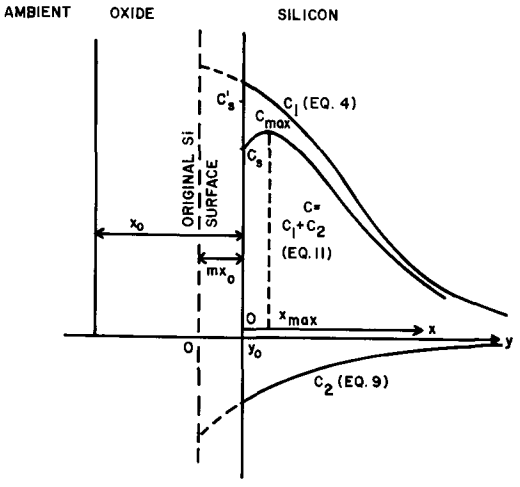

Fig. 1. Diffusion model

the oxide from the silicon, and the original Si surface is impermeable. The oxidation will cause an amount of impurity contained within mx_o to be absorbed by the oxide. The impurity distribution is then given by the solution of the diffusion equation

$$\frac{\partial C_1}{\partial t} = D\frac{\partial^2 C_1}{\partial y^2} \qquad \text{for } y > y_o \qquad [2]$$

where D is the boron diffusion constant in silicon during the drive-in. Since the extent of junction penetration of the deposited profile is small compared to that of the final profile after the drive-in, the total impurity distribution may be approximated by a delta function. The solution is then

$$C_1(y,t) = \frac{Q}{\sqrt{\pi Dt}}\exp(-y^2/4Dt) \qquad \text{for } y > y_o \quad [3]$$

Let x be the distance measured from the oxide-silicon interface as shown in Fig. 1, then $y = x + mx_o$. The oxide growth is assumed to be parabolic, *i.e.*, $x_o = \sqrt{Bt}$ where B is the growth rate constant. By the coordinate transformation $y = x + m\sqrt{Bt}$, [3] can be written as

$$C_1(x,t) = \frac{Q}{\sqrt{\pi Dt}}\exp\left[-\left(\frac{x}{2\sqrt{Dt}} + \frac{m}{2}\sqrt{\frac{B}{D}}\right)^2\right] \quad [4]$$

There is a net flow of impurities across the silicon-oxide interface because of the segregation coefficient at two solid interfaces, the finite diffusion probability of the dopant in the oxide, and the mass transfer at the oxide-ambient interface. For simplicity, assume that the diffusion constant of boron in oxide is negligible compared to that in silicon. Consider a small time interval dt during which a layer of silicon $m dx_o$ is converted into oxide of thickness dx_o. The amount of impurity in the original silicon was $C_s(y_o,t)\,m dx_o$ and the amount in the oxide is

$$C'_s(y_o,t)\,dx_o = kC_s(y_o,t)\,dx_o \qquad [5]$$

where k is the segregation coefficient. The difference, $(k-m)C_s(y_o,t)\,dx_o$, must outdiffuse from the semiconductor. Hence, the rate of flow is

$$D\frac{\partial C_2}{\partial y}\Big]_{y=y_o} = (k-m)\,C_s(y_o,t)\frac{dx_o}{dt} = \frac{(k-m)\,C_s(y_o,t)}{2}\sqrt{\frac{B}{t}} \quad [6]$$

The conditions for the second part of the solution are $C_2(y,0) = 0$ and $C_2(\infty,t) = 0$. Initially, assume zero impurity concentration in the silicon. The subsequent outdiffusion of the boron into the oxide will result in a mathematically negative concentration at the oxide-silicon interface. The solution of the diffusion equation is

$$C_2(y,t) = A\,\text{erfc}\left(\frac{y}{2\sqrt{Dt}}\right) \qquad [7]$$

where A is a constant to be determined. From [6] and [7], and $y_o = m\sqrt{Bt}$, the constant A can be expressed as

$$A = -\frac{k-m}{2}\sqrt{\frac{\pi B}{D}}\,C_s(y_o,t)\exp\left(\frac{m}{2}\sqrt{\frac{B}{D}}\right)^2 \qquad [8]$$

With reference to the x-coordinate, [7] and [8] can be combined to give

$$C_2(x,t) = -\frac{k-m}{2}\sqrt{\frac{\pi B}{D}}\exp\left(\frac{m}{2}\sqrt{\frac{B}{D}}\right)^2 \times C_s\,\text{erfc}\left(\frac{x}{2\sqrt{Dt}} + \frac{m}{2}\sqrt{\frac{B}{D}}\right) \quad [9]$$

The solutions $C_1(x,t)$ and $C_2(x,t)$ are sketched in Fig. 1. Since the diffusion equation and its associated boundary conditions are linear, the resulting impurity distribution is obtained by adding [4] and [9] to give

$$C(x,t) = \frac{Q}{\sqrt{\pi Dt}}\exp\left[-\left(\frac{x}{2\sqrt{Dt}} + \frac{m}{2}\sqrt{\frac{B}{D}}\right)^2\right] - \frac{k-m}{2}\sqrt{\frac{\pi B}{D}}\exp\left(\frac{m}{2}\sqrt{\frac{B}{D}}\right)^2 \times C_s\,\text{erfc}\left(\frac{x}{2\sqrt{Dt}} + \frac{m}{2}\sqrt{\frac{B}{D}}\right) \quad [10]$$

By setting $x = 0$ in Eq. [10], the surface concentration $C_s(0,t)$ is determined from [10]. Finally, the expression for the concentration profile is given by

$$C(x,t) = \frac{Q}{\sqrt{\pi Dt}}\exp\left[-\left(\frac{x}{2\sqrt{Dt}} + \frac{m}{2}\sqrt{\frac{B}{D}}\right)^2\right] - \frac{k-m}{2D}\sqrt{\frac{B}{t}} \times \frac{Q}{1 + \frac{k-m}{2}\sqrt{\frac{\pi B}{D}}\exp\left(\frac{m}{2}\sqrt{\frac{B}{D}}\right)^2\text{erfc}\left(\frac{m}{2}\sqrt{\frac{B}{D}}\right)} \times \text{erfc}\left(\frac{x}{2\sqrt{Dt}} + \frac{m}{2}\sqrt{\frac{B}{D}}\right) \quad [11]$$

Equation [11] is not as complex as it appears because the coefficient of the second term is independent of x. The distance at which the maximum concentration occurs is found by differentiating [11] to give

$$x_{\text{max. conc.}} = \sqrt{\frac{B}{D}}\sqrt{Dt} \times \left\{\frac{k-m}{1 + \frac{k-m}{2}\sqrt{\frac{\pi B}{D}}\exp\left(\frac{m}{2}\sqrt{\frac{m}{D}}\right)^2\text{erfc}\left(\frac{m}{2}\sqrt{\frac{B}{D}}\right)} - m\right\} \quad [12]$$

By setting $x = 0$ in [11] and also substituting [12] into [11], the ratio of maximum concentration C_{max} to surface concentration C_s is found to be independent

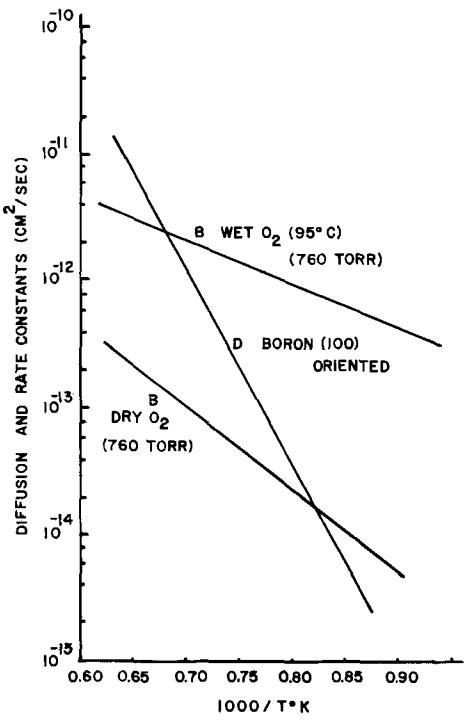

Fig. 2. Temperature dependences of oxide growth rate and diffusion constant of boron.

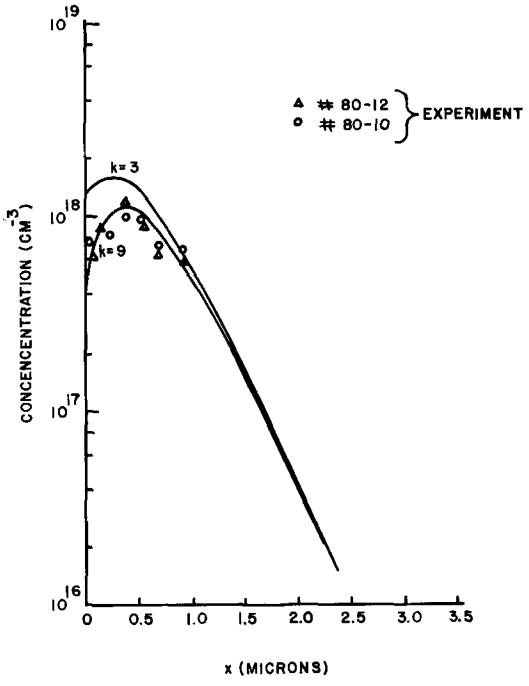

Fig. 3. Impurity profiles after oxidation in wet O_2 at 1100°C for 2 hr.

of the diffusion time and the total impurity Q prior to oxidation. However, the values of C_{max} and C_s depend critically on the diffusion temperature and the oxidation condition (wet or dry). Figure 2 shows the oxidation rate constants in dry and wet oxygen together with the diffusion constant of boron in (100) orientation. The diffusion constant of boron is taken from the measurements of Kurtz and Yee (4) corrected for (100) orientation based on the experimental results of Wills (5).[1] For cases in which both wet and dry cycles are involved, the effective rate constant is given by

$$B = \frac{B_w t_w + B_d t_d}{t_w + t_d} \qquad [13]$$

where the subscripts w and d indicate wet and dry oxidations, respectively.

The total impurity left in the silicon after oxidation can be found by integrating [11] from $x = 0$ to $x = x_j$ where x_j is the junction depth. Thus

$$Q' = Q\left\{\operatorname{erfc}\left(\frac{m}{2}\sqrt{\frac{B}{D}}\right) - \frac{\frac{k-m}{\sqrt{\pi}}\sqrt{\frac{B}{D}}\exp\left[-\left(\frac{m}{2}\sqrt{\frac{B}{D}}\right)^2\right] - \frac{m(k-m)}{2}\frac{B}{D}\operatorname{erfc}\left(\frac{m}{2}\sqrt{\frac{B}{D}}\right)}{1 + \frac{k-m}{2}\sqrt{\frac{\pi B}{D}}\exp\left(\frac{m}{2}\sqrt{\frac{B}{D}}\right)^2\operatorname{erfc}\left(\frac{m}{2}\sqrt{\frac{B}{D}}\right)}\right\} \qquad [14]$$

For a typical oxidation process, the impurity lost to the oxide, *i.e.*, $(Q - Q')/Q$, is generally greater than 60%.

Experimental Results

The materials used in this work were all 2-5 ohm-cm (100) n-type silicon wafers polished on both sides. The deposition was accomplished by heating boron nitride disks and the silicon wafers together at 925°C. The sheet resistivity, as measured by a four-point probe, was 80 ohm/□. The total impurity concentration was determined to be 6.3 x 10^{14} at./cm^2. The wafers were then divided into three groups subject to wet oxidation (oxygen bubbled through 95°C water) at 1100°, 1200°, and 1250°C for 2, 1, and ½ hr, respectively.

To obtain the experimental profile the oxide was stripped off each wafer and the wafer was then subjected to successive etching in KOH at 60°C. After each etch, the weight loss of the slice was found to determine the depth of the etch, and the sheet resistivities were measured using a four-point probe.

The surface concentrations of the diffused layer were obtained independently from the capacitance-voltage characteristics of MOS structures (6). By comparing the surface concentration obtained this way with the change of resistivities after the first etching step, the effective mobility value for the diffused layer was obtained from which the impurity concentration was determined for the subsequent etches. The mobility values used in the calculation are listed in Table I together with other results discussed later.

The theoretical profile is given by [11] for which appropriate values of the diffusion and oxidation rate constants corresponding to the oxidation temperature are to be found in Fig. 2. The theoretical profiles for different oxidation temperatures are plotted in Fig. 3 through 5 for two values of the segregation coefficient:

Table I. Comparison of results

Oxidation temperature	1100°C	1200°C	1250°C
Oxidation time	2 hr	1 hr	½ hr
Oxidation conditions	wet O_2	wet O_2	wet O_2
Diffusivity, cm²/sec	3.5×10^{-13}	1.9×10^{-12}	4.2×10^{-12}
Growth constant, cm²/sec	1.55×10^{-12}	2.3×10^{-12}	2.8×10^{-12}
Mobility, cm²/V-sec	145	135	130
Resistivities, ohm/□ (calculated)	410	250	210
Resistivities, ohm/□ (measured)	440	280	200
Initial boron cnc Q cm⁻²	0.63×10^{15}	0.63×10^{15}	0.63×10^{15}
Remaining boron, cm⁻²	0.11×10^{15}	0.19×10^{15}	0.22×10^{15}
% Boron lost	83%	70%	65%
Segregation coefficient	9	9	9

[1] The boron diffusion constants plotted in Fig. 2 are in good agreement with the experimental result recently reported in a paper by Chan and Mai, *Proc. IEEE*, pp. 588-589, April, 1970.

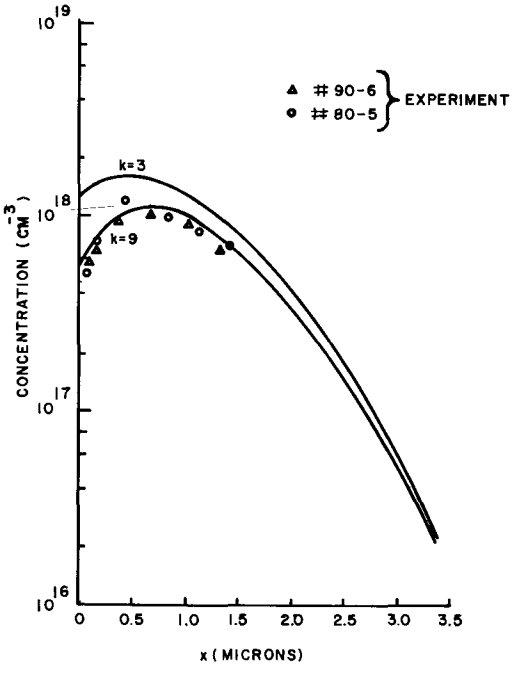

Fig. 4. Impurity profiles after oxidation in wet O_2 at 1200°C for 1 hr.

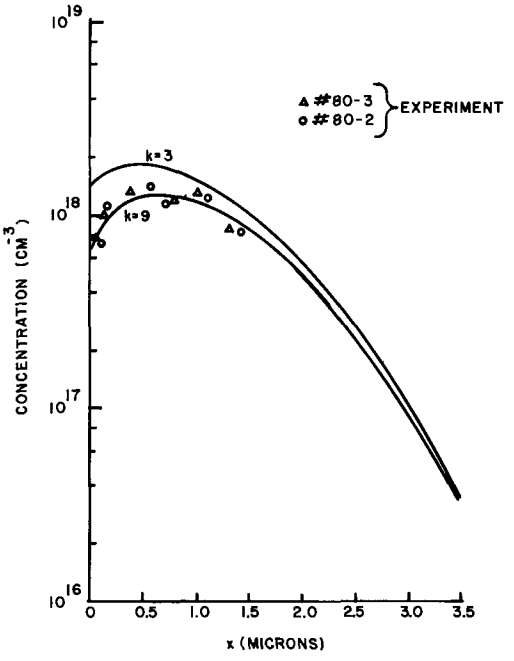

Fig. 5. Impurity profiles after oxidation in wet O_2 at 1250°C for ½ hr.

$k = 3$ and $k = 9$. The experimental results are also shown as points is these figures. It is seen that the experimental points fit quite well to the curves with $k = 9$. Thus it may be concluded that, for boron, the segregation coefficient is approximately 9 and is independent of oxidation temperatures and conditions. This value is in general agreement with the value of 10 found by Kato and Nishi (2) for dry oxidation conditions with diffused layers. It should be noted that had redistribution of boron in the oxide been ignored, the surface concentration as calculated from [3] would be about an order of magnitude higher than the actual surface concentration.

The total impurity atoms that remained in the silicon are calculated from [14]. The results are shown in Table I indicating that the amount of boron lost during oxidation is so large that it more than compensates for the increase of mobilities.

Discussion of Results

The scattering of experimental points is to be expected because errors arising from measurements of this type are unavoidable. Some deviations of the experimental result from the theoretical prediction can also be explained by uncertainties in diffusion and rate constants used in our calculations. It should be pointed out that there exist discrepancies in mobility values reported in the literature. However, in our work, uncertainties in mobility values are mitigated because they are measured by the MOS capacitance technique. Inspection of the results shown in Fig. 3 through 5 indicates generally good agreement between theory and experiment thus validating the diffusion model we proposed.

This model, together with Fig. 2, furthers the understanding and control of the redistribution process in p-type diffused layers. For example, at low temperatures the oxidation rate is higher than the diffusion rate resulting in large depletion of boron at the interface. Silicon surfaces with low boron concentrations are prone to inversion. For oxidation at 1250°C, faster diffusion and slower oxidation rates have brought about a decreased depletion of boron and less loss of total boron atoms even though the junction is deeper.

Acknowledgment

The authors wish to thank K. Gilliksen for her contribution to the experimental portion of this work.

Manuscript submitted May 6, 1970; revised manuscript received July 27, 1970.

Any discussion of this paper will appear in a Discussion Section to be published in the June 1971 JOURNAL.

REFERENCES

1. A. Grove, O. Leistiko, Jr., and C. T. Sah, *J. Appl. Phys.*, **35**, 2695 (1964).
2. T. Kato and Y. Nishi, *J. Appl. Phys., Japan*, **3**, 377 (1964).
3. L. C. Perham, Private communication.
4. A. D. Kurtz and R. Yee, *J. Appl. Phys.*, **31**, 303 (1960).
5. G. N. Wills, *Solid State Electronics*, **12**, 133 (1969).
6. B. Deal, A. Grove, E. Snow, and C. T. Sah, *This Journal*, **112**, 308 (1965).

Technical Notes

High Resolution Print-Out of the Electronic Conductivity Distribution of Anodic Tantalum Oxide

Gerhart P. Klein*

P. R. Mallory & Co. Inc., Laboratory for Physical Science, Burlington, Massachusetts 01803

The distribution of the electronic conductivity (e.c.) of valve metal oxides and other thin film dielectrics is frequently nonuniform on a microscale. This may be due to impurities or flaws arising from many causes. Experimental results, *e.g.*, current-voltage characteristics, cannot be interpreted meaningfully unless the current distribution is known. In many instances it is desirable to identify the sources of e.c., especially when arising from heterogeneities on a microscale, such as grain boundaries, inclusions, *etc.*

This communication reports on some recent improvements in the resolution of the redox print-out technique which has been described elsewhere (1). Originally, the potassium iodide/starch printing gel was spread on the specimen while hot and filter paper was used as a backing material. The paper with a thin film of gel which contained the image of the e.c. distribution was lifted off the specimen after current had been passed through the oxide film. The coloration on the print provided a direct replica of the electronic charge that had been passed through the specimen. In this form, the print-out technique is particularly well suited for replicating relatively large areas.

In the study of oxide films, one is frequently interested in determining whether or not there is a direct correlation of the e.c. with microscopically visible surface features. In this case, the microdistribution of the e.c. might provide clues as to its source. In other cases, the interpretation of the electronic current-voltage characteristic of oxide electrodes may depend on whether the current is truly homogeneous on a microscale or whether it is in fact heterogeneous but only appears uniform due to high flaw density.

Experimental

To obtain high resolution, the printing experiments were performed under the microscope. This allowed one to observe, at the same time, the surface of the specimen and the passage of electronic charge as reflected in the coloration of the starch/potassium iodide gel electrolyte. The distribution of the e.c. could be followed as a function of time and voltage without the need to reapply the electrolyte as was required in the older technique if interval prints were desired.

In the micro redox print-out technique, the specimen was masked with tape and provided with a counter-electrode, as shown in Fig. 1. For masking, pressure-sensitive polyester tape with silicone adhesive was used. Pressure-sensitive aluminum tape served as the counterelectrode. Holes punched through both tapes exposed circular areas of the specimen. A drop of liquid printing gel was applied to the test area and a cover glass was pressed on the masking tape. A thin layer of printing gel was thus formed in the test area. The edge of the aluminum tape acted as the counter-electrode (negative). The specimen itself was connected to the positive terminal of a suitable power source.

The experiments were carried out by applying linearly increasing voltage to the specimen. In some cases, it was desirable to follow the change in e.c. with time at constant applied voltage.

A LEITZ Ortholux microscope was used with automatic Orthomat camera and an achromatic objective 32X/0.60 with a free working distance of 5.7 mm. A magnification of 100X on 35 mm film was obtained, before additional photographic magnification. Photographic reproduction of the prints in black and white posed serious problems since the substrate, when anodized, provided a colored background which reduced the contrast between it and the coloration of the printing gel in areas of current flow. Color prints or slides would be more satisfactory in this regard than black and white prints.

Results and Discussion

The following examples of microprints were obtained with tantalum foil. They have been selected to illustrate the capability of the micro print-out technique to resolve the electronic conductivity distribution on a micro scale, to correlate its distribution with structural features of the substrate, and to identify sources of leakage current after introducing defined heterogeneities in the anodic oxide film or subjecting the specimen to characteristic pretreatments.

Detection of impurities in substrate.—Tantalum foil in the "as-rolled" condition did not show grains either before or after chemical polishing. In the course of heating in vacuum (*e.g.*, 1 hr at 2100°C and 10^{-5} mm Hg), a grain structure was developed with the grain boundaries clearly delineated. Surface impurities were plentiful in the "as-rolled" condition; however, after the vacuum-annealing treatment, very few electronically active flaws remained.

The e.c. of flaws is often low which makes detection by the print-out technique difficult. Recently (2), it was shown that uniformly distributed e.c. could be developed in high-purity Ta_2O_5 after depositing thin layers of certain metal oxides, Fe_2O_3 and MnO_2

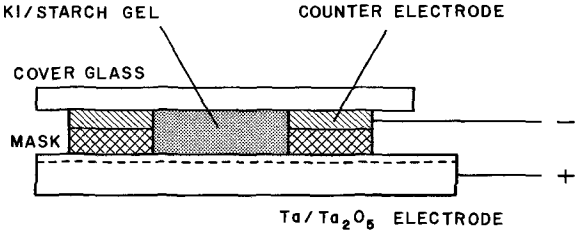

Fig. 1. Specimen as prepared for micro print-out experiment

* Electrochemical Society Active Member.

Key words: anodic oxide films, tantalum oxide, electronic leakage current, current distribution, print-out technique, starch-iodide electrolyte, flaw conduction.

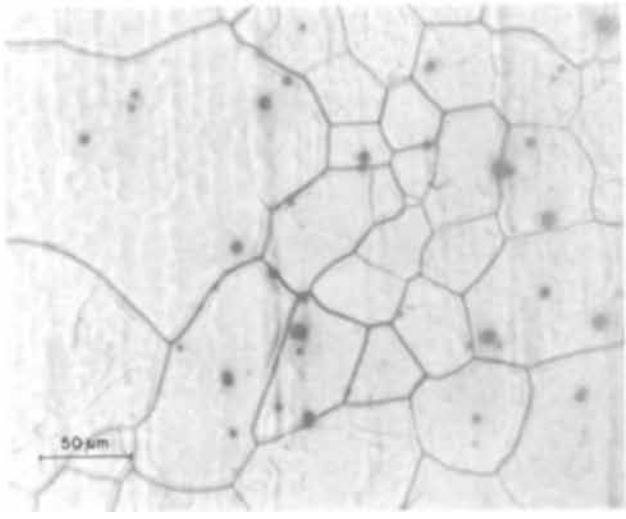

Fig. 2. Print-out of Ta/Ta_2O_5 specimen pretreated as described in text.

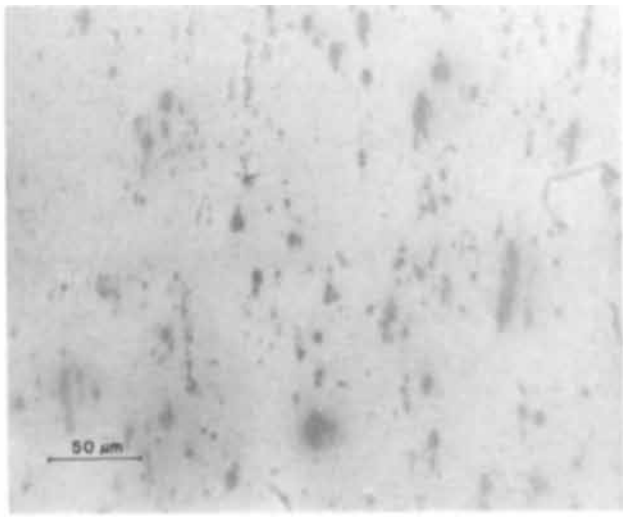

Fig. 3. Print-out of Ta/Ta_2O_5 specimen without special pretreatment.

among others, on the anodized substrate and reanodizing at a voltage close to the original anodization voltage of the oxide film. In addition, certain kinds of flaws in the oxide showed leakage at voltage levels below those at which uniform e.c. was found when such additional impurity oxide films were present. This method was employed in some of the examples shown here to enhance the e.c. of any flawed areas and thus increase the sensitivity and contrast of the micro print-out technique.

Figure 2 shows the print-out of Ta foil that was prepared as follows: Metallurgical grade Ta foil after chemical polishing and annealing in vacuum at 2100°C for 1 hr was oxidized for 5 min at 500°C in air, anodized at 100V for 1 hr, and sputtered with a 200A film of Fe_2O_3 (2). The print obtained at 90V shows randomly distributed leakage sites. The grain boundaries stand out because they are out of focus. At the grain boundaries, no electronic current was observed in any of the specimens studied. The density of electronically active sites in the specimen of Fig. 2 was of the order of $6 \times 10^4/cm^2$.

Chemical polishing and vacuum heating had removed many of the impurities of the rolled stock leaving a reasonably clean surface which did not show a sufficient density of leakage sites when evaluated by means of the print-out technique.

Thermal oxidation of tantalum in air was found to bring out sources of e.c. buried below the cleaner surface which were not in evidence after heating in vacuum. This is attributed to the preferential oxidation and diffusion of impurities to the surface. Thermal oxidation caused leakage sites to appear in a pattern typical for random contamination. The additional deposition of Fe_2O_3 served to amplify the intensity of the electronic current at such impurity sites.

The print-out shown in Fig. 3 was obtained with tantalum foil as used above, however without chemical polishing or vacuum heating. The surface was sufficiently contaminated to yield a high density of electronically active sites. In this case, additional thermal oxidation and Fe_2O_3 deposition would have increased their density beyond the limits of resolution and was thus omitted. The density of leakage sites was of the order of $5 \times 10^5/cm^2$ after anodization to 40V. Most conducting sites are unrelated to any surface features visible before or after anodization.

Anodic crystals.—In the print-out shown in Fig. 4, physical heterogeneities were generated deliberately in the anodic oxide by anodically crystallizing the

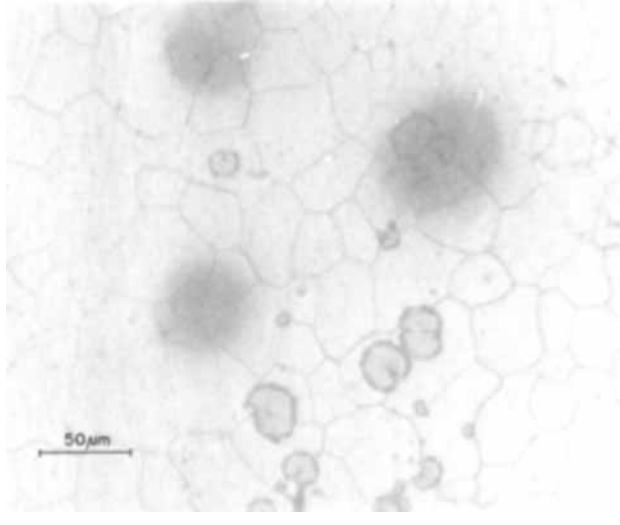

Fig. 4. Print-out of Ta/Ta_2O_5 specimen with "field" crystals

specimen (3) (no chemical polishing or vacuum heating) at 100V, 90°C, for 2 hr in 2% nitric acid solution. A print-out of the sample after crystallization revealed few sites with electronic conductivity within the sensitivity of the technique. After deposition of a 200A Fe_2O_3 film, the print shown in Fig. 4 was obtained at 90V. The striking feature of this print is that there seems to be some correlation between anodic crystals and electronic conductivity. Three dominant conducting sites happen to be on crystal sites; however, many more crystals show no e.c. at all at this voltage. In addition, the e.c. in the areas around the crystals is distributed over an area much larger than the crystals themselves. Observation of the growth of the spots revealed that they did not spread out from the crystals but intensified uniformly over the whole area. This, together with an observation of the over-all leakage pattern led to the conclusion that the three crystals located within the electronically conducting areas had to be associated with impurities in the substrate, while crystals by themselves did not exhibit any noticeable e.c. at the voltage applied in this print.

Tantalum carbide.—In the following example, chemically polished and vacuum-treated Ta foil was carburized by vapor deposition of a 1000A carbon film and subsequent heat treatment in vacuum at 1800°C for 30 min. After anodization at 80V, the interference

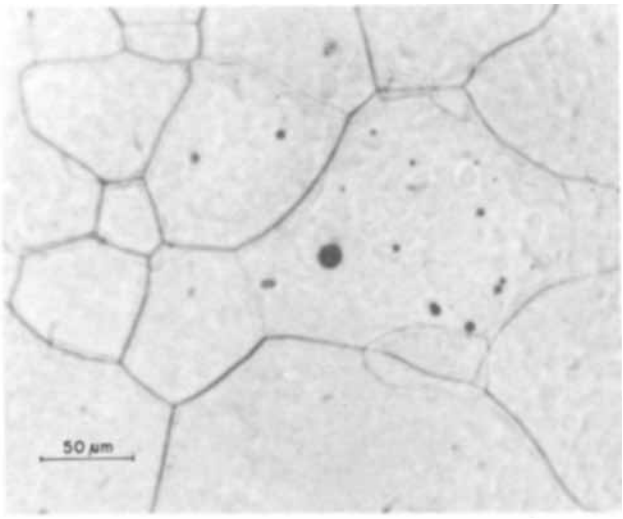

Fig. 5. Print-out of Ta/Ta_2O_5 specimen containing tantalum carbide.

color of the oxide film varied from grain to grain depending on the concentration of tantalum carbide crystals intersecting the surface of the grains. The large grain in the center of Fig. 5 showed the highest concentration of carbide. Under high magnification (1000X), individual flaws (4) could be identified by their color. Their density was estimated to exceed $10^8/cm^2$. The grains surrounding the one with the highest flaw concentration still contained fairly high concentrations of carbide flaws but the effect on the color of the anodic oxide was less visible.

The print-out after anodization to 80V (not shown) revealed only weak e.c. in isolated spots. After the deposition of a 200A film of sputtered Fe_2O_3, the print-out shown in Fig. 5 was obtained. A limited number of electronically active sites were found, being most numerous within the grain with the highest flaw density. However, their density was of the order of 10^4-$10^5/cm^2$ as compared to 10^8 for tantalum carbide flaws.

The examples given in Fig. 4 and 5 should caution one when trying to infer the cause of e.c. from the kind of pretreatment given to the specimen. Figure 4 shows that the e.c. is not associated with field crystallization even though the print shows leakage at some of the crystals. In the case of Fig. 5, the presence of tantalum carbide in high concentration did not lead to quasi homogeneous electronic leakage as one might expect considering the high concentration of carbide flaws present. Although e.c. was observed, its distribution did not correspond to the distribution and density of carbide flaws which was about four orders of magnitude higher than the density of leakage sites. Still the number of leakage sites tended to be highest in grains with the highest carbide concentration, but not consistently so. No attempt is made to resolve this apparent contradiction. It illustrates convincingly the need for high power resolution of the distribution of e.c. in all studies of the effects of impurities and flaws on the e.c. of anodic oxide films.

Sensitivity.—The maximum resolution of anodic micro prints was estimated to be of the order of 10^7-10^8 electronically conducting sites per square centimeter. This estimate is based on the analysis of prints such as the one shown in Fig. 3. Obviously, the resolution depends on the nature of the sources of e.c., their size, and distinctness. Additional processing of the photographic image using microdensitometric techniques could increase the resolution further.

The sensitivity of the print-out technique depends on the size and the intensity of the electronically active sites that can be detected at the limit of resolution. It was found that a charge density of 10 mcoulombs/cm^2 let to a pronounced coloration of the printing gel. Using this charge density, the electronic current was estimated for the spots in Fig. 2. With a printing time of 60 sec and an average spot diameter of 7 μm, the apparent geometric current density was 3.5×10^{-6} A/cm^2, and the current per electronically active site was of the order of 10^{-10} to 10^{-11}A. This should not be considered an absolute limit since smaller spots can still be resolved under favorable conditions.

Manuscript submitted June 3, 1970; revised manuscript received *ca.* Aug. 13, 1970.

Any discussion of this paper will appear in a Discussion Section to be published in the June 1971 JOURNAL.

REFERENCES

1. G. P. Klein, *This Journal*, **113**, 345 (1966).
2. G. P. Klein and N. I. Jaeger, *This Journal*, **117**, 1483 (1970).
3. D. A. Vermilyea, *This Journal*, **102**, 207 (1955).
4. D. A. Vermilyea, *ibid.*, **110**, 250 (1963).

Measurement of P-Etch Rates for Boron-Doped Glass Films

Ahmed H. El-Hoshy

General Electric Research and Development Center, Schenectady, New York 12301

Pliskin (1) has pointed out that glasses that are rich in either lead or boron have faster P-etch[1] rates than glasses with no lead or boron oxide in them. Earlier, he used the selective etching property of the P-etch to establish that oxygen is the diffusing species when silicon dioxide is grown thermally (2). Recently use has been made of pyrolytically deposited boron-doped glasses as a diffusion source in semiconductor processing (3). For a specific diffusion time and temperature, both the surface concentration and junction depth are determined by the glass composition. The boron-doped glasses are particularly useful in MOS processing where their properties match those of the thermally grown silicon dioxide, while providing additional insulation for subsequent metallization steps.

In the course of using boron-doped glass, two aspects requiring elucidation were found: (a) the need to monitor glass composition and (b) the necessity of providing a fast etch. Both spectrophotometry (4) and infrared absorption (5) have been used successfully to determine glass composition. The following experiment demonstrates that etch rate measurement can serve the same purpose. During the experiment P-etch rates were found to be much faster than those of buffered HF, thereby providing a basis for mixing fast etches for boron-doped glasses.

[1] 15 parts HF (49%), 10 parts HNO_3 (70%), and 300 parts H_2O.

Key words: P-etch rates, boron-doped glass films.

Experiment

One ohm-cm, P-type (100) silicon wafers are coated with boron-doped glass of variable composition at 300°C. The ratio of boron oxide to silicon dioxide is controlled by the ratio of diborane to silane in the main gas stream. The deposited glass thickness is a few thousand angstroms. Subsequent to glass deposition the wafers are fired in argon at ~1050°C for several minutes. Half the wafer is then masked by dipping it into molten glycol-phthalate. The glass is dissolved from the unmasked half. After removal of the glycol-phthalate, the sample is ready for etch rate measurement.

The height of the deposited glass is measured using a Sloan Dektak instrument. A series of immersions in P-etch, each followed by a measurement of the step height, is made for each sample. Figure 1 shows a set of such measurements. The accuracy of height measurement is better than 25Å.

Results and Discussions

Figure 2 shows the etch rate in Å per minute as a function of the molar fraction of diborane to diborane and silane in the reaction chamber. Spectrophotometric measurements indicate an increase of the molar fraction of B_2O_3 in the deposited glass from 14 to 34% with the increase in molar fraction of $B_2H_6/B_2H_6 + SiH_4$ from 15 to 42% (6). The etch rate is observed to increase markedly with diborane concentration; in particular, it seems to have an exponential dependence on the diborane molar concentration.

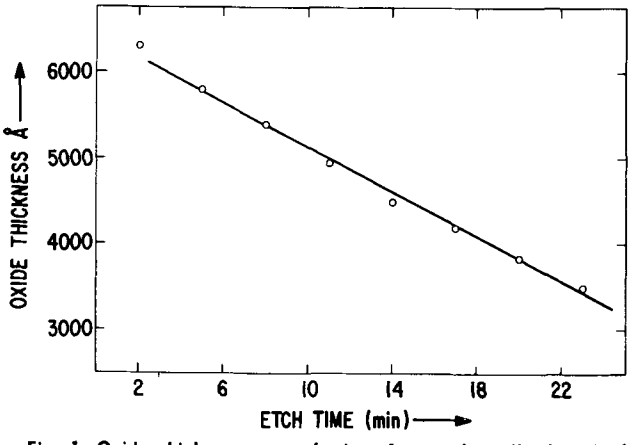

Fig. 1. Oxide thickness vs. etch time for pyrolytically deposited undoped glass.

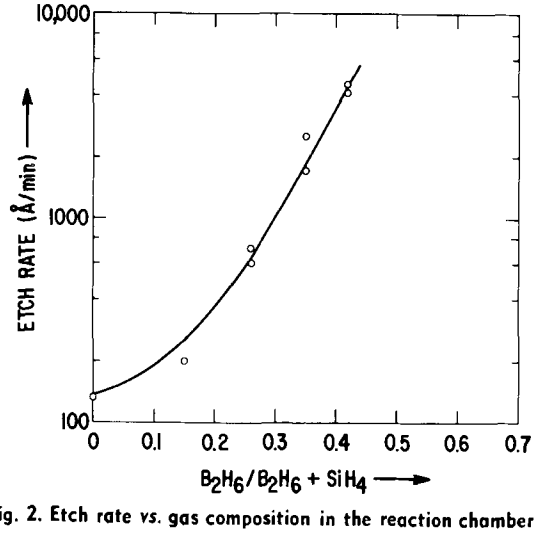

Fig. 2. Etch rate vs. gas composition in the reaction chamber

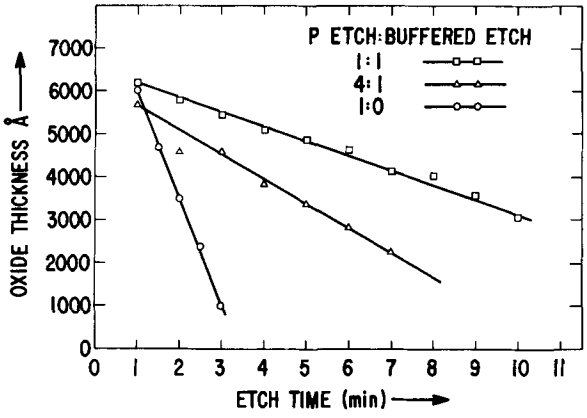

Fig. 3. Oxide thickness vs. etch time for three different etches $\left(\frac{B_2H_6}{B_2H_6 + SiH_4} = 0.35 \text{ for the glass}\right)$.

The increase in P-etch rate with boron content seems to indicate that the dissolution rate is limited by the amount of silicon dioxide present in the glass. This conclusion is further supported by measured dissolution rates of B_2O_3 in dilute HNO_3 solutions of about 10^4 Å/sec at room temperature (7). The reported decrease in buffered HF etch rates with boron content strongly suggests that the etch rate in this case is limited by the dissolution of B_2O_3 present in the glass. It is, therefore, possible to control the etch rate of boron-doped glasses by using an etch that varies in composition from 100% P-etch to 100% buffered HF. Figure 3 shows the effect of etch composition on etch rate.

Summary

P-etch rates can be used as a sensitive measure of boron concentration in pyrolytically deposited boron glasses. By mixing P-etch with buffered HF, fast etches are obtainable for boron glasses.

Manuscript submitted June 12, 1970; revised manuscript received *ca.* Aug. 20, 1970.

Any discussion of this paper will appear in a Discussion Section to be published in the June 1971 JOURNAL.

REFERENCES

1. W. A. Pliskin, in "Measurement Techniques for Thin Films," B. Schwartz and N. Schwartz, Editors, p. 168, The Electrochemical Society, New York (1967).
2. W. A. Pliskin and R. P. Gnall, *This Journal*, **111**, 872 (1964).
3. A. W. Fisher, J. A. Amick, H. Hyman, and J. H. Scott, Jr., *R C A Rev.*, **29**, 533 (1968).
4. M. L. Barry and P. Olofsen, *This Journal*, **116**, 854 (1969).
5. R. M. Valletta, W. A. Pliskin, D. W. Boss, and V. Y. Doo, Paper 43 presented at the New York Meeting of the Electrochem. Soc., May 4-9, 1969.
6. D. M. Brown and P. R. Kennicott, To be published.
7. V. M. Imamutdinova and A. Kh. Bikchurova, *J. Appl. Chem. USSR English Transl.*, **40**, 1552 (1967).

Brief Communication

Chemical Transport Epitaxy of Silicon by Organic Compounds

Y. Avigal and M. Schieber

Department of Physics, Hebrew University, Jerusalem, Israel

Epitaxial growth of silicon by chemical transport is performed mainly by the reaction: $SiCl_4 + 2H_2 = Si + 4HCl$ (1-3) which takes place at about 1200°C. Besides the high temperature (4) the process has the disadvantage of handling corrosive products.

More recent investigations use the pyrolytic decomposition of silane to deposit silicon: $SiH_4 = Si + 2H_2$. This reaction takes place at somewhat lower temperatures of about 1100°C but is considered to be hazardous due to the presence of H_2. It should be mentioned that both the hydrogenation of $SiCl_4$ and the decomposition of SiH_4 take place at relatively low temperatures of about 600°C while the epitaxial reaction occurs above 1100°C. Recent work has proved both theoretically (5) and experimentally (6) that absorption of hydrogen is responsible for the high temperature used for the epitaxial crystallization of silicon. So, for instance, in order to remove mechanically the adsorbed hydrogen, it was possible to obtain epitaxial (6) growth of silicon at temperatures below 1000°C. The present work describes an intrinsic way to avoid the presence of H_2 during the epitaxy of silicon. The following chemical reaction is used:

$$Si(CH_3)_4 = Si + \text{byproducts}$$

The first experiments were performed at relatively high temperatures of 1100°C because we used H_2 to clean the substrates. It is anticipated that etching with HCl (7) should lower the crystallization temperature below 1000°C because it would avoid the use of hydrogen in any stage of the epitaxial process.

Experimental Method

The apparatus used to prepare epitaxial films by the pyrolysis of the organic compound of silicon (shown in Fig. 1) consists of a source of pure hydrogen and a source of pure helium, a saturator, reaction chamber, and a radio frequency generator for external heating.

Key words: epitaxy, thin films of silicon, chemical transport deposition, MOS technology.

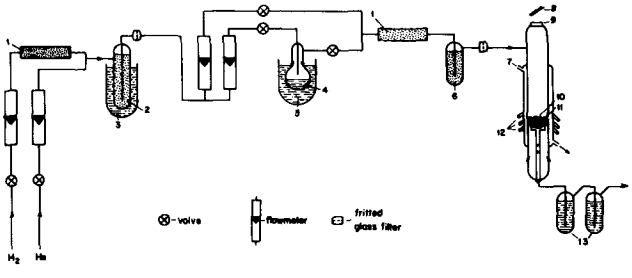

Fig. 1. Apparatus for the preparation of thin films of silicon by the pyrolysis of $Si(CH_3)_4$: 1—Palladium deoxo; 2—Linde molecular sieves; 3—liquid air trap; 4—$Si(CH_3)_4$; 5—cooling solution; 6—phosphor pentaoxide; 7—water sleeves; 8—mirror; 9—optical flat window for inspection; 10—substrate; 11—pedestal; 12—R.F. coil; 13—silicon oil traps.

The hydrogen and helium gases are purified by passing through a trap of "palladium deoxo" to remove oxygen. A trap of molecular sieves type-5A refrigerated with liquid air to remove water and another "palladium deoxo" purifier and a trap containing phosphorpentaoxide in order to remove any traces of water.

A mixture of hydrogen diluted with helium passes directly to the reaction chamber to etch the substrate. After etching, one part of the helium used as a gas carrier of the $Si(CH_3)_4$ is mixed with free flowing helium and introduced in the reaction chamber for epitaxy. The temperature of the saturator and the ratio between the two parts of the helium gives the desired mole fraction of $Si(CH_3)_4$ in the gas mixture. The pyrolytic reaction takes place in a water-cooled quartz tube. The substrate is supported in a graphite pedestal acting as a susceptor. The (111) mirror polished silicon substrate wafers are etched by 40% HF solution and then washed with deionized water and dried under an inert gas. Prior to film deposition the silicon wafer is etched in dry hydrogen at about 1300°C for half an hour after which the temperature is lowered to about 1100°C, and a mixture composed of $Si(CH_3)_4$ and He is introduced in the reactor. The parameters which control the deposition rate are temperature, $Si(CH_3)_4$/He molar ratio, flow rate, and time of reaction. A typical example for an epitaxial growth is: 1150°C, molar ratio, $Si(CH_3)_4/He = 0.05$ and 17 min during which a thickness of 7μ is obtained.

The film thickness was measured by polishing a 5° bevel on the coated surface of the wafer, stained with a mixture of $HF\text{-}HNO_3$ 100:1 which delineated the film region at the top of the bevel. The thickness is then determined by measuring the width of the film region under microscope and calculating the film thickness accordingly.

Monocrystalline films were grown in the temperature range of: 1100°-1300°C. At the upper part of this range of temperatures the film surfaces were of mirror perfection. Experiments using HCl etching to replace H_2 and heteroepitaxial growth on spinel and sapphire substrates and doping experiments with phosphine and borane in both homo- and heteroepitaxy are progressing and will be reported separately. The carbon contamination of thin films produced by this method is published elsewhere (8).

Acknowledgments

The authors wish to thank the Robert Szold Foundation for Applied Research for the financial support which has covered part of the expenses of this project.

Manuscript received March 5, 1970.

Any discussion of this paper will appear in a Discussion Section to be published in the June 1971 JOURNAL.

REFERENCES

1. H. C. Theuerer, *This Journal*, **108**, 649 (1961).
2. A. Mark, *ibid.*, **108**, 880 (1961).

3. D. M. Jackson, *Trans. Met. Soc. AIME*, **273**, 23 (1965).
4. S. Nakanuma, *IEEE Trans. Electron Devices*, **13**, 578 (1966).
5. B. A. Joyce and R. R. Bradley, *This Journal*, **110**, 1235 (1963).
6. D. Richman and R. A. Arlett, *ibid.*, **116**, 872 (1969).
7. W. Bond and E. Smits, *Bell System Tech. J.*, **35**, 1209 (1956).
8. Y. Avigal and M. Schieber, *J. Cryst. Growth*, **9** (1971).

DISCUSSION SECTION

This Discussion Section includes discussion of papers appearing in the *Journal of The Electrochemical Society*, Vol. 116, No. 7, July 1969, and Vol. 117, No. 4, 5, and 7, April, May, and July 1970.

Infrared Reflection Studies of the Oxidation of Copper and Iron

G. W. Poling (pp. 958-963, Vol. 116, No. 7)

Robert R. Rahn[1]: I have studied the oxidation of copper with a technique similar to that used by Poling, the main difference being the angles of incidence. Poling used 73° and I used near grazing incidence, 85°-90°. Poling's statement that "Infrared oxide band intensities were found to be directly proportional to film thickness over the range of about 0-5000Å" is not supported by his data for an oxide thickness greater than 1000Å. My data,[2] on Cu films oxidized at 145°C and an oxygen pressure of 175 Torr, show that the band intensity at 655 cm^{-1} (close to Poling's maximum at 640 cm^{-1}) is linear to about 1000Å, is maximum at about 2000Å, and then decreases. For incidence angles of 85° and 89°, calculations by Schwartz[3] indicate that there is an optimum oxide thickness for which this band intensity is a maximum. The apparent disagreement between Poling's statement and my observations may very well be due to the complicated and critical dependence of band intensity on the angles of incidence.

Poling does not mention the copper oxide, $CuO_{0.67}$, which is a defect structure of Cu_2O. At a temperature of 150°C and an oxygen pressure of 100 Torr, the defect oxide should be formed on the copper surface rather than Cu_2O.[4-6] Since some of Poling's samples were oxidized at 140°C in air, $CuO_{0.67}$ must have been present in those oxide films. I mention this defect oxide because many people are not aware of its existence. This does not change Poling's conclusions, because the defect structure and Cu_2O both have the same strong absorption band.

I would like to acknowledge the contribution to this work by Professor Robert Greenler. The work was supported by a research grant from the National Science Foundation.

G. W. Poling: R. Rahn's data on *IR* band intensity *vs.* copper oxide film thickness for incidence angles of 85°-90° cannot be compared directly with our data obtained using 73° incidence. It is to be expected that the range of "approximate" linearity between band intensity and film thickness will decrease as the incidence angle increases. We have many data indicating that at 73° incidence good linearity is observed up to film thicknesses of approximately 2500Å. Results of one experiment indicated that reasonable linearity extended up to about 5000Å film thickness. This latter result should certainly be checked.

[1] Physics Department and Laboratory for Surface Studies, University of Wisconsin—Milwaukee, Milwaukee, Wis. 53201; present address: Department of Metallurgy and Mining Engineering, University of Illinois, Urbana, Ill. 61801.
[2] R. R. Rahn, Master's Thesis, University of Wisconsin, Milwaukee (1969).
[3] J. P. Schwartz, Master's Thesis, University of Wisconsin, Milwaukee (1968).
[4] H. Wieder and A. W. Czanderna, *J. Appl. Phys.*, 37, 184 (1966).
[5] H. Wieder and A. W. Czanderna, *J. Phys. Chem.*, 66, 816 (1962).
[6] M. G. Hapase, *Surface Sci.*, 9, 87 (1968).

There seems little doubt that, as Mr. Rahn pointed out, several of the oxide films that we studied would better have been described as $CuO_{0.67}$ and not Cu_2O. Although we referenced the paper of Wieder and Czanderna [Ref. (24) in subject paper] which initially reported the occurrence of $CuO_{0.67}$, we did not distinguish between Cu_2O and $CuO_{0.67}$ in our paper. Neither the infrared spectra, x-ray diffraction patterns, nor electron diffraction patterns that we observed could distinguish Cu_2O from $CuO_{0.67}$ since the latter is a defect structure of Cu_2O. Although our paper did not contribute data on film stoichiometry, we should nevertheless have mentioned this aspect and thank Mr. Rahn for his reminder.

Structure and Electrical Properties of $FeO-P_2O_5$ Glasses

D. L. Kinser (pp. 546-548, Vol. 117, No. 4)

Mary Splann Mizzoni[7]: In his study of an iron-phosphate glass system, Dr. Kinser has attributed the dielectric dispersions that he observed to a Maxwell-Wagner-Sillars heterogeneous loss mechanism. He was able to do this because he observed no dispersion in two specimens—one with no observable crystallites and one with large crystals. He presents his data as evidence that the dispersions cannot be attributed to an electron-hoping mechanism which Dr. K. W. Hansen and I had previously proposed in our paper[8] on the same glass system.

Dr. Kinser could not have come to his conclusions had he found dispersion peaks in his noncrystalline specimen and in his large-crystal specimen (Fig. 2 and 5 of his paper). Most likely, he would have found these peaks if he had subtracted the d-c conductivity from the total a-c conductivity. He claims that this is not necessary. However, an approximation of the total a-c conductivities of these two specimens indicates that the d-c conductivities are an appreciable part of these totals. Approximations were made, as Kinser reported no capacitance or dielectric constant data.

[7] Research and Development Laboratory, Corning Glass Works, Corning, N. Y. 14830.
[8] K. W. Hansen and M. T. Splann, *This Journal*, 113, 895 (1966).

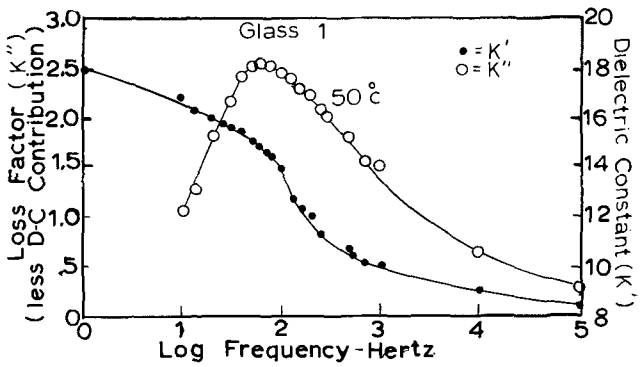

Fig. 1. Dielectric constant and loss factor (minus the d-c contributions) *vs.* the logarithm of frequency for Glass 1 at 50°C.

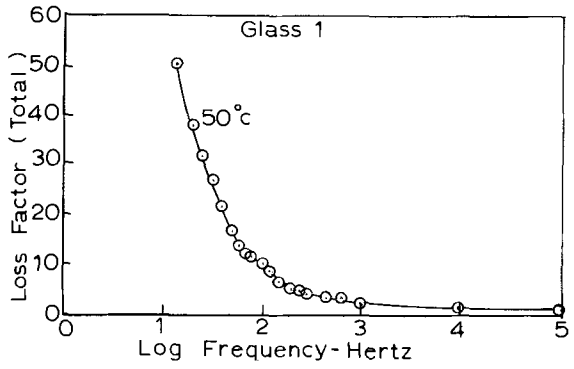

Fig. 2. Loss factor (total) vs. the logarithm of frequency for Glass 1 at 50°C.

To illustrate more exactly the effect of the d-c conductivity on the total a-c conductivity, I have plotted data presented in our paper and that same data *without* the d-c contributions removed, as shown in Fig. 1 and 2, respectively. It is readily seen that the d-c conductivity masks the dispersions in our data. There were no observable crystals in our glasses.

Kinser reports that the oxidation of the glassy matrix was altered by the formation of crystals, thereby changing the electrical properties. Without forming crystals, we obtained this change in oxidation of the glassy matrix, accompanied by changing electrical properties. It appears that *this* is the difference in our work, rather than an explanation for the conduction mechanism.

D. L. Kinser: The comments of Mrs. Mizzoni with reference to my possible conclusion as to Maxwell-Wagner-Sillars loss behavior in these glasses are quite true and they are appreciated. As a result of discussions with her, I have subtracted the d-c contributions from all the data reported. These calculations have not revealed any dielectric dispersions in any samples where none were observed in the $\tan\delta_{Total}$ observations.

Several of these calculations were made prior to publication, and these were taken to be representative of all these glasses because of the relatively small d-c conductivity changes upon thermal treatment. My original assertion that this calculation is unnecessary thus stands unmodified. No dielectric dispersion was observed in either $\tan\delta_{Total}$ or $\tan\delta_{a.c.}$ in the as cast or 1 hr at 600°C samples. From this I concluded that the mechanism of the loss is M-W-S in origin and not a result of electron hopping. To further substantiate this conclusion, I might add that an electron resonance—even of a partially bound electron—seems unlikely in the audio-frequency range.

Examination of Mrs. Mizzoni's uncorrected loss factor data (Fig. 2, Discussion Mizzoni) reveals a clear indication of the dispersion at about 100 Hz. This dispersion is clearer and obviously easier to handle after the calculation, but nonetheless it is evident without corrections. Most of my reported results are at higher temperatures and are considerably clearer without correction.

Analogous behavior with thermal treatment was observed by the author (Ref. (3), abstract only) in a Na_2O-V_2O_5-P_2O_5 glass, and this result is also cited as an independent argument that the loss is M-W-S in origin rather than electron resonance.

Recent continuation of this work by A. Dozier and myself to other $Fe^{3+}/Fe^{3+} + Fe^{2+}$ glasses has revealed analogous behavior in all compositions examined. This work is being prepared for publication at this time.

With reference to Mrs. Mizzoni's final comment regarding an explanation for the conduction mechanism, I had no intention of disputing the electron-hopping model for conduction in these systems. I did assert and now reaffirm that the dielectric dispersion which she observed can be attributed to a heterogenous loss mechanism rather than an electron resonance.

The Theory of Anomalous Diffusion in Solids Near Diffusant Saturation Concentrations: Example—Phosphorus in Silicon

P. E. Bakeman, Jr. and J. M. Borrego

(pp. 688-690, Vol. 117, No. 5)

D. Shaw[9]: Bakeman and Borrego have proposed a model, referred to here as the BB model, to explain the concentration dependence of the chemical diffusion coefficient of P in Si. The authors supported the validity of their model by fitting it to the radiotracer data of Tannenbaum.[10] There are however further consequences of the BB model which appear to make it untenable:

1. According to the BB model, D (in the notation of the model) is independent of P concentration, yet two values of D ($4{\cdot}8 \times 10^{-13}$ and $7{\cdot}4 \times 10^{-13}$ cm^2/sec) were required in order to fit Tannenbaum's results on two samples diffused under identical conditions. It is implicit in the BB model that at one temperature there should only be one value of D.

2. Tannenbaum's[10] radiotracer data are rather unsatisfactory because (*a*) It is not clear whether radiotracer concentrations were measured right up to the surface or whether a considerable extrapolation was involved (*e.g.* Fig. 7 of Tannenbaum's study);[10] (*b*) It is not known to what extent the neutron activation affected the P distribution; there is evidence that neutron irradiation can cause an enhanced penetration of an impurity;[11] (*c*) It is not known what effect the anneal (3 min at 1050°C) following the neutron activation had on the P distribution.

Maekawa's[12] experiments avoided these three difficulties and application of the Matano method of analysis[13] to the data in his Fig. 3 gives the variation of the chemical diffusion coefficient of P in Si with P concentration shown in Fig. 1. It is manifest that this variation cannot be explained by the BB model, which predicts a monotonic dependence of diffusion coefficient on concentration.

[9] Physics Department, The University of Hull, Hull, England.
[10] E. Tannenbaum, *Solid-State Electron.*, 2, 123 (1961).
[11] A. I. Koifman and O. R. Niyazova, *Soviet Phys. Semicond.*, 3, 1173 (1970).
[12] S. Maekawa, *Japan. J. Phys.*, 17, 1592 (1962).
[13] P. G. Shewmon, "Diffusion in Solids," p. 29, McGraw-Hill Book Co., New York (1963).

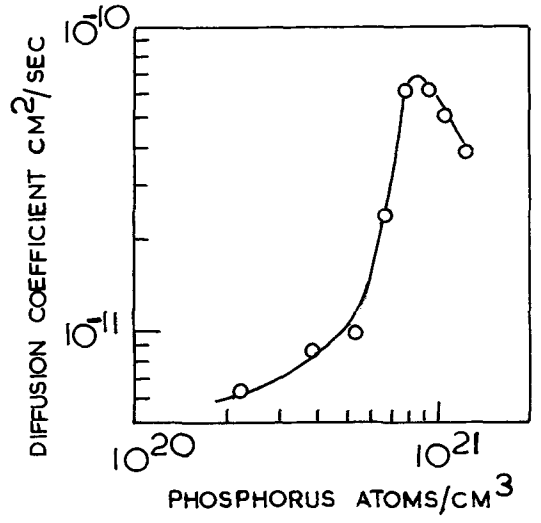

Fig. 1. The variation of the chemical diffusion coefficient of P in Si with P concentration at 1200°C from the data of Maekawa.[12]

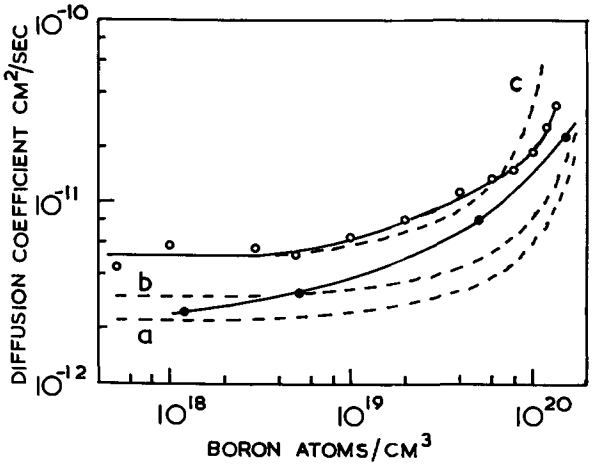

Fig. 2. The variation of the chemical diffusion coefficient of B in Si with B concentration. The solid lines represent the data of Vick and Whittle[14] (●) and Okamura[15] (○). The dashed curves show the variations according to the BB model with (a) $D = 2{\cdot}2 \times 10^{-12}$ cm²/sec, surface concentration $= 2{\cdot}2 \times 10^{20}$ cm^{-3}; (b) $D = 3 \times 10^{-12}$ cm²/sec, surface concentration $= 2{\cdot}2 \times 10^{20}$ cm^{-3}; (c) $D = 5 \times 10^{-12}$ cm²/sec, surface concentration $= 1{\cdot}35 \times 10^{20}$ cm^{-3}.

3. It is stated in the paper discussed that the results of Vick and Whittle[14] for B chemical diffusion in Si are also in accord with the BB model. In Fig. 2 an attempt has been made to fit the BB model to the data of Vick and Whittle[14] at 1150°C (their Fig. 4). In this case the surface concentration is well defined ($=2{\cdot}2 \times 10^{20}$ cm^{-3}). Okamura[15] has also studied B diffusion in Si and shows that the chemical diffusion coefficient of B varies as the square root of B concentration (his Fig. 8). Objection however can be made to his method of evaluating the concentration dependence of the diffusion coefficient which basically assumes that the diffusion coefficient is independent of concentration! Application of the Matano analysis[13] to the B distribution given by Okamura[15] in his Fig. 7 gives the dependence shown in Fig. 2. The surface concentration is again well defined at $1{\cdot}35 \times 10^{20}$ cm^{-3}, and an attempt to fit the BB model is shown. The best that can be said about the BB model and the chemical diffusion of B in Si is that it shows the same trend as the experimental data.

4. As propounded it would seem that the BB model should apply equally well to the radiotracer distribution in isoconcentration diffusion experiments whereas it is well known that in such experiments the radiotracer distribution is given by a complementary error function, *i.e.*, a constant diffusion coefficient.[16]

Although there is general agreement in the literature that in the chemical diffusion of P and B in Si the diffusion coefficient is concentration dependent, there seems to be a lack of agreement on the form of this dependence which obviously must be established before a proper theory can be advanced.

P. E. Bakeman, Jr. and **J. M. Borrego:** We thank Professor Shaw for his comments and will answer them in the same order as they are presented. It should be noted that the BB model is an attempt to incorporate impurity atom interaction into diffusion theory in a physical way. Other effects which undoubtedly also occur have been neglected, but we feel that the theory properly accounts for many of the anomalous high-concentration diffusion results presented in the literature.

1. In short high-concentration diffusions such as the phosphorus diffusions performed by Tannenbaum, the rate of impurity dissolution is extremely high. It is probable, therefore, that the density of vacancies in the host material is less than the equilibrium density characteristic of the host material at the diffusion temperature. This vacancy deficiency is expected to vary from run to run causing differing reductions in low-level diffusion constants throughout the crystal.

2. (*a*) Concentration *vs.* depth data is required to obtain the results presented in Tannenbaum's Fig. 9. As the samples were anodically sectioned in approximately 400Å layers, it is probable that the appropriate data were used.

(*b*) Koifman and Niyazova consider the case of exposing a silicon wafer coated with metallic gold to a neutron flux. The conclusion generated from their work cannot be generalized to cover the case in hand.

(*c*) Further, Tannenbaum indicates that the sheet resistivity of the samples was identical before irradiation and after annealing. Any change in the phosphorus profile would have lowered the sheet resistivity of the samples.

Maekawa's experiments do not show that Tannenbaum's results were incorrect. In fact, there is acceptable agreement between Maekawa's results as presented by Shaw, in his Fig. 1, and the BB theory for concentration of less than 8×10^{20} phosphorus atoms/cm³. It is quite possible that a second phase formed at concentrations higher than this.

3. As there are no radioactive isotopes of boron, impurity profiles of sufficient accuracy to determine concentration-dependent diffusion coefficients are not available.

4. The BB model does apply to the radiotracer distribution in isoconcentration diffusion experiments. The diffusion coefficient is concentration-dependent and given by

$$D' = D\frac{C_{max} + C(x)}{C_{max} - C(x)}$$

where $C(x)$ is the sum of radioactive and nonradioactive diffusant concentrations. As $C(x)$ is not a function of x, a complementary error function diffusion profile is expected.

[13] G. L. Vick and K. M. Whittle, *This Journal*, 116, 1142 (1969).
[15] M. Okamura, *J. Appl. Phys. Japan*, 8, 1440 (1969).
[16] B. J. Masters and J. M. Fairfield, *J. Appl. Phys.*, 40, 2390 (1969).

Growth and Characterization of Lead Telluride Epitaxial Layers

John W. Wagner and Alan G. Thompson

(pp. 936-940, Vol. 117, No. 7)

A. J. Crocker and **D. C. L. Wiffen**[17]: Wagner and Thompson state that the solubility of Te in molten Pb

[17] Zenith Radio Research Corporation (U.K.) Ltd., Stanmore, Middlesex, England.

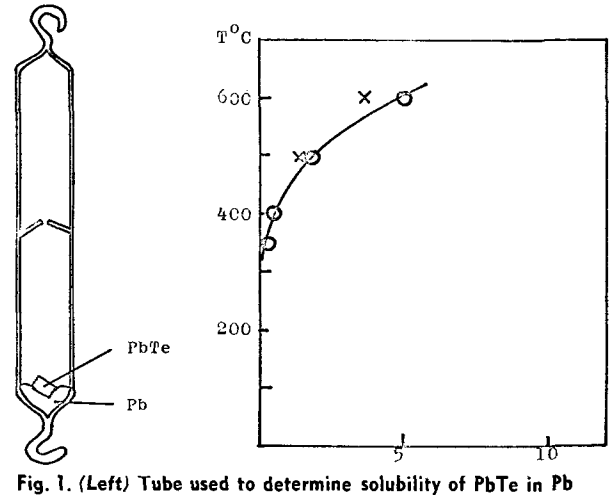

Fig. 1. *(Left)* Tube used to determine solubility of PbTe in Pb
Fig. 2. *(Right)* Liquidus curve of the Pb-Te system for low concentrations of Te. ○ = Crocker and Wiffen. X = Wagner and Thompson.

has not been reported in the more recent literature. We have investigated methods of fabricating diodes similar to those of Wagner and Thompson and thought it would be of interest to describe our method of determining this solubility.

A weighed cube of PbTe (6 mm edge, p-type $\sim 10^{18}$ cm^{-3}) was sealed in an evacuated tube (Fig. 1) together with a known weight ($\sim$10g) of Pb (99.99% pure). The Pb and PbTe were heated at various temperatures for 24 hr with occasional shaking. The tube was then inverted and shaken and kept inverted at the temperature in question for 30 min. The assembly was then cooled at $\sim$40°C/hr.

The contents of the tube were etched in a solution of H_2O_2/acetic acid. This solution rapidly dissolves Pb but has little or no effect on PbTe. The original PbTe source was reweighed after etching. From the change in weight of the lead telluride source and the original weight of Pb, the solubility of PbTe (*i.e.* Te) in Pb could be determined and is shown in Fig. 2. Good agreement with the data of Wagner and Thompson is found. Since a closed tube was used, there is no loss of Te such as that reported by Wagner and Thompson.

The solution grown crystals, grown from the highest temperature were cage and solid cubes together with some dendrites. As the starting temperature decreased the size of the crystals decreased and there was an increased tendency to form dendrites.

JOURNAL OF THE ELECTROCHEMICAL SOCIETY

ELECTROCHEMICAL TECHNOLOGY

DECEMBER 1970

Catholyte Studies in Copper Oxide-Magnesium Thermal Cells

Lawrence H. Thaller*

Lewis Research Center, National Aeronautics and Space Administration, Cleveland, Ohio 44135

ABSTRACT

The present investigation concludes the study of the performance of copper oxide-magnesium thermal cells operating at 450°C. The objective of this present study was to investigate the cause of the 0.25V step drop in open-circuit voltage that occurred during the latter stages of discharge of these cells.

The investigation consisted of two parts:

(*A*) Cells were equipped with a reference electrode between the anode and cathode and discharged. These tests showed that the step drop in the open-circuit voltage was due to a sudden drop in the activity of the cuprous ion in the vicinity of the cathode. This two-order-of-magnitude drop in the cuprous ion activity was attributed to the formation of a complex. Other cells were discharged which had additions of either magnesium chloride or lithium oxide in the electrolyte. Additions of lithium oxide brought about the formation of this complex, and additions of magnesium chloride retarded the formation of this complex at the expense of a much higher rate of self-discharge. (*B*) Potentiometric titrations were performed to more fully investigate the stoichiometry of the complex. These titrations were performed in solutions of the lithium chloride-potassium chloride eutectic. When 1.5 moles of lithium oxide were added per mole of cuprous oxide, an end point in the titration occurred. The difference in electromotive force (emf) of a copper electrode placed in a saturated solution of cuprous oxide and one placed in a saturated solution of the cuprous complex was the same as the emf difference that occurred at the voltage step during discharge of complete cells. Additions of magnesium chloride to this solid complex returned the cuprous ion to solution by precipitating the oxide ion (as MgO) associated with the complex.

Based on these and our previous findings, a model is presented that explains essentially all the significant features of cell behavior during discharge. This model suggests that, during the initial stages of discharge, magnesium ions move to the catholyte, where they are precipitated as magnesium oxide. During the latter stages of discharge, lithium ion predominates in the charge neutralization process and creates conditions favorable for the formation of the cuprous complex. This lowers the open-circuit and operating voltages of these thermal cells.

A continuing program (1-4) at Lewis has been directed toward the investigation of a high-temperature primary cell having an operating time of several days at a temperature of 450°C. The anodes used are magnesium; the cathodes, mixed copper oxides; and the electrolyte, the eutectic mixture of lithium chloride and potassium chloride. One of the objectives of this program was to understand the over-all electrochemical and chemical reactions that take place during the discharge of these cells and how they are influenced by mass-transport processes.

In the first phase of these studies (1), the open-circuit voltage during the early stages of discharge of complete cells was shown to be the result of the following half-cell reactions:

$$Mg \rightarrow Mg^{+2} + 2e^- \qquad \text{at anode}$$

$$Cu^{+1} + e^- \rightarrow Cu \qquad \text{at cathode}$$

The cupric ion is chemically reduced to the cuprous state by reaction with copper according to the reaction

$$Cu^{+2} + Cu \rightarrow 2Cu^{+1}$$

In the second phase (2), methods of reducing the self-discharge rates of these cells were investigated. It was determined that the rate of transport of copper ions from the cathode to the anode controlled the over-all rate of self-discharge. In the third phase (3), the performance of two different cell designs was investigated as a function of the amount of electrolyte, discharge rate, and electrode geometry. One of the important findings of this study was that cell failure under the test conditions was probably due to freezing of the electrolyte. This must have been caused by a change in electrolyte composition during the course of the discharge; specifically, an increase in magnesium ion content.

This situation was investigated more completely in anode half-cell studies (4) employing electrolyte compositions which simulated different stages of discharge in actual cells. It was shown that under certain conditions of temperature, composition, and current density, the electrolyte adjacent to the anode (anolyte) partially froze next to the anode and thus caused extreme concentration and *IR* polarization.

One of the remaining unanswered questions in the study of this thermal cell was the origin of the 0.25V

* Electrochemical Society Active Member.

Key words: thermal cell, battery, molten salts.

drop in the open-circuit voltage that was observed at greater than about 45% depth of discharge of complete cells (1-3). It had already been shown (2) that, in the latter stages of discharge, lithium oxide was one of the products of reaction in the vicinity of the cathode. Also, a compound of unknown composition (compound X) was located in the region of the discharged cathode (catholyte) in cases which showed the 0.25V drop in open-circuit voltage. It was suggested that this unknown compound may be a complex species of lithium oxide and cuprous ion or cuprous oxide, which could explain the abrupt drop in the open-circuit voltage.

This present study was undertaken in order to explore this point in more detail. It consisted of two sets of experiments:

(*A*) A study of the anode and cathode polarization during the discharge of complete cells by means of a reference electrode.

(*B*) Potentiometric titrations to explore the complex ion chemistry of the electrolyte in the catholytes.

Materials

The electrolyte used was the eutectic mixture of lithium chloride and potassium chloride. This material, purified according to the modified Laitinen process (5), was ground to a suitable particle size (<3 mm). A nitrogen-filled (from liquid boiloff) drybox was used to store the materials and to carry out all the experimental procedures (weighing, mixing, heating, *etc.*). The cathode material was the wire form of cupric oxide (a mixture of cuprous and cupric oxide), and the anodes were primary magnesium. The chemical compositions of the materials used, determined by analytical techniques already described (1), are listed in Table I. In some of the experiments, reagent-grade, anhydrous powders of cuprous oxide, lithium oxide, and magnesium chloride were used. It was assumed that water in the cuprous oxide and magnesium chloride accounted for the discrepancy from 100.0%.

The reference electrodes (6) were of the disposable type. Silver wire (99.99% Ag) was immersed in a 0.13*M* (molal) silver chloride solution of the lithium chloride-potassium chloride eutectic. This mixture was contained in a glass melting point tube which acted as a membrane between the reference electrolyte and the cell electrolyte.

Procedure

Cell discharge studies.—Open-top vertical cells, shown in Fig. 1, were discharged in a small, electrically heated, temperature-controlled furnace located inside the drybox. The cells, with reference electrodes placed between the anode and cathode, were discharged for 2 hr in a regime programmed as follows:

(*a*) Fixed external resistance equal to R_1, 100 min
(*b*) Fixed external resistance equal to $R_1 + R_2$, 10 min
(*c*) No load, 10 min

Table I. Composition of materials[a]

Material	Content, w/o	Material	Content, w/o
Cuprous oxide:		Cupric oxide (wire form):	
Cu_2O	96.60	CuO	72.6
CuO	2.07	Cu_2O	27.4
H_2O (by difference)	1.33		
Magnesium chloride:		Magnesium:	
$MgCl_2$	97.4	Mg	99.8
Mg	1.4	Mn	0.15
H_2O (by difference)	1.2	Cu	~0.02
		Lithium oxide:	
		Li_2O	99.9
		CaO	0.1

[a] LiCl-KCl used as received from manufacturer. Silver wire had a silver content of 99.99%, as analyzed by manufacturer.

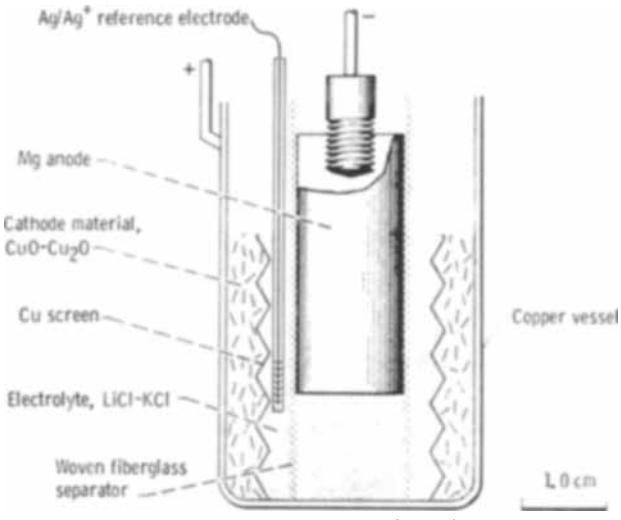

Fig. 1. Cell with reference electrode

This program was repeated as necessary until the cell voltage dropped to the arbitrary cutoff voltage of 0.5V. The voltage of the cell, as well as the current flowing through the discharge circuit, was recorded continuously. The details of the discharge circuit are described in Ref. (2). For the sake of this discussion, the term open-circuit voltage is defined as the cell voltage at the end of each 10-min no load period.

The cells were assembled for discharge with weighed amounts of anode and cathode material. The anode was covered with two layers of tightly woven glass fabric to reduce the possibility of internal short circuits. The cell, minus electrolyte and reference electrode, was placed in the furnace and allowed to preheat to 450°C. The desired amount of powdered electrolyte was added to the cell and melted. At this point, electrolyte additives (lithium oxide or magnesium chloride) were mixed with the molten electrolyte. After insertion of a reference electrode, the discharge was begun and was continued until the cell voltage dropped below the 0.5V cutoff point.

Potentiometric titration studies.—Figure 2 shows the details of the cell used for the potentiometric titrations. The copper vessel (identical to those used for the discharge studies) served as the indicator electrode (Cu/Cu^{+1}) and contained the mixture to be titrated. About 30g of the lithium chloride-potassium chloride eutectic was the solvent. After a weighed amount of the cuprous salt had been added to the solvent, the cell was placed inside the furnace (the same as used for the discharge studies) and allowed to equilibrate for ½ hr after melting. Either the saturated solutions of cuprous oxide with excess solid on the bottom of

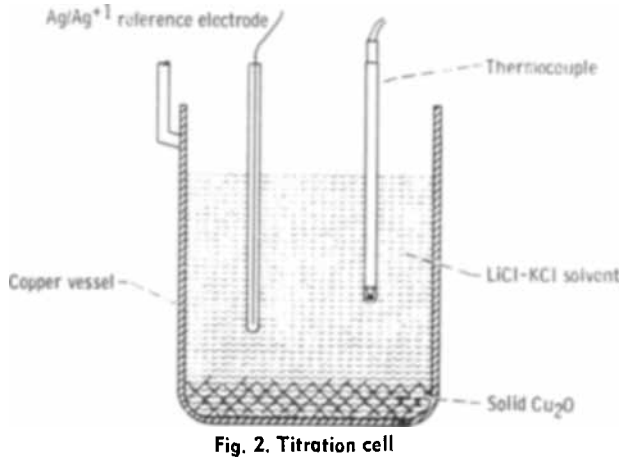

Fig. 2. Titration cell

the vessel or the unsaturated solutions of cuprous chloride were used as starting mixtures for the titrations.

After a silver/silver ion reference electrode was placed in the cell and the emf between the reference electrode and the coper electrode became constant within 2 mV, the titration was begun. Weighed additions of lithium oxide or magnesium chloride were made to the electrolyte, and the emf of the Cu/Cu^{+1} electrode was followed relative to the Ag/Ag^{+1} reference electrode. Between additions, ample time was allowed for the re-establishment of equilibrium conditions. Electromotive force was recorded continuously on a strip-chart recorder fed from a high-impedance ($>10^{14}$ ohms), battery-operated electrometer.

Results and Discussion

Cell discharge studies.—As pointed out in the introduction, previous studies indicated that the origin of the 0.25V drop in open-circuit voltage was the formation of a cuprous ion complex which would reduce the cuprous ion activity in the vicinity of the cathode. Further, it was indicated that lithium oxide was implicated in some way with the complex formation. For these reasons, cells were discharged that had a reference electrode placed between the anode and cathode so that individual electrode potentials could be obtained.

Figure 3 shows the open circuit voltages between the anode and the reference electrode and between the cathode and the reference electrode recorded during the discharge of a cell. Clearly evident is the 0.3V change in the emf of the cathode at about 70% depth of discharge. This change in the cathode potential, together with the gradual decline of 0.05V in the anode emf, leads to a net decrease in cell potential of about 0.25V at the step. Based on this information this potential drop is associated with decreased cuprous ion activity at the cathode.

The chemical analytical work described previously (2) had revealed that lithium oxide, as well as compound X, was present in large amounts in the catholyte during the latter stages of discharge. Based on these facts it was speculated that the lithium oxide was in some way responsible for the change in the cathode half-cell potential. To verify this hypothesis, another cell was discharged that had 1g of lithium oxide dissolved in the 20g of electrolyte prior to discharge. Figure 4 compares this discharge to the previous one in which no lithium oxide was added. Only the open-circuit anode-to-cathode voltages are plotted as a function of depth of discharge. The drop in open-circuit voltage of the cell with the added oxide occurred at a much smaller depth of discharge. These two cells differed only in electrolyte composition. They contained about the same amounts of active materials, were discharged through the same fixed external resistance, and delivered essentially the same number of ampere-hours of electricity. This amounted to about 95% of their theoretical capacity (based on the cathode) (see Table II). So, although the activity of the cuprous ion was reduced about two orders of magnitude, as evidenced by the change in open-circuit voltage, there was no decrease in the electrochemical accessibility of this complex form of the cuprous ion.

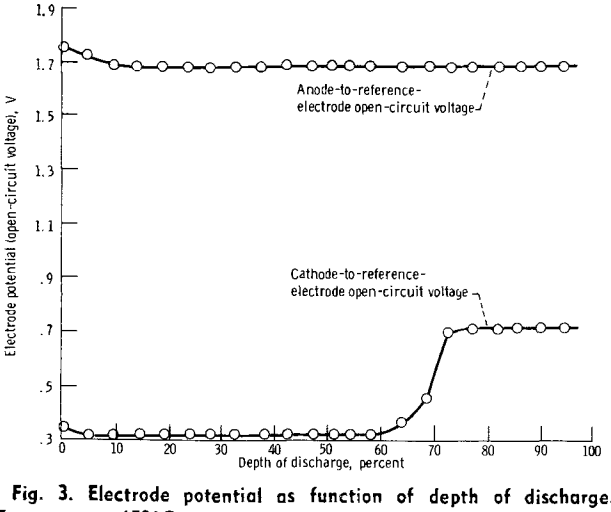

Fig. 3. Electrode potential as function of depth of discharge. Temperature, 450°C.

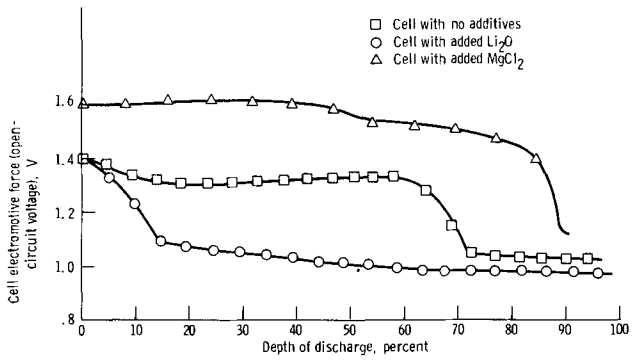

Fig. 4. Cell voltages (open-circuit voltage) as function of depth of discharge.

If the addition of lithium oxide accelerates the appearance of the step in the open-circuit voltage, the addition of magnesium chloride should have the opposite effect. This can occur because soluble magnesium ion should precipitate more of the oxide ion freed by the discharge of the copper oxides than the amount of magnesium ion diffusing over from the discharging anode. Also shown in Fig. 4 are the open-circuit voltages of a cell discharged with 3.7g of magnesium chloride dissolved in the electrolyte prior to discharge. It should be noted that the predicted behavior is observed; namely, that the step in the open-circuit voltage is delayed to the end of the discharge.

In connection with these results, it is important to compare several other aspects. In Table II, all the pertinent parameters are listed for the three cells. The two most important parameters to compare are (*a*) the step placement factor, χ, defined previously (3), which is the depth of discharge at which the voltage step occurs; and (*b*) the average rate of self-discharge. As the amount of soluble oxide in the cell is reduced, χ increases. However, the addition of the magnesium chloride leads to a 34-fold increase in the rate of self-discharge when compared with the cell that had no additives. This is caused by a shift in the copper oxide solubility equilibrium to favor dissolution as the soluble oxide ions are removed by precipitation. The resulting increase in concentration of copper ions leads to an increase in the rate of self-discharge.

Titration studies.—Although the cell discharge studies were fully adequate to detect the presence of the cuprous complex and identify lithium oxide as one of the constituents, there was no way of ascertaining the stoichiometry of the complex species. Potentiometric titration studies were undertaken to investigate this matter.

Table II. Cell operating parameters

Parameter	Cell 1	Cell 2	Cell 3
Weight, g:			
Mg anode (initial)	5.87	6.13	6.10
CuO-Cu_2O cathode (initial)	10.0	10.0	10.0
LiCl-KCl	19.0	19.0	19.0
Li_2O	0	1.0	0
$MgCl_2$	0	0	3.7
Cell life (to 0.5V), hr	42	42	22
Cell output (to 0.5V) A-hr	6.07	5.97	3.25
Average cell current, mA	145	142	148
Average self-discharge current, mA	3.1	15	102
Step placement factor, χ	0.68	0.10	0.87

In the titrations described in this section, the emf (relative to the Ag/Ag^{+1} reference) of the copper indicator electrode is plotted against what is referred to as the oxide ratio. The oxide ratio is defined as the moles of oxide that are either in solution or can be forced into solution (by shifts of equilibrium) for every 2 moles of cuprous ion. When the data are plotted in this manner, inflection points in the emf at certain oxide ratios will denote the composition at which a large change in cuprous ion activity has occurred. It is presumed that this corresponds to complex formation. It must be re-emphasized here that only the cuprous ion can be in equilibrium with metallic copper. Copper in any higher oxidation state is reduced by the metal to form cuprous ion (Cu^{+1}). Hence, only cuprous compounds were investigated.

Figure 5 shows a typical titration curve. The starting mixture was a saturated solution of cuprous oxide with excess solid on the bottom of the container. Slightly soluble cuprous oxide has an oxide ratio of 1.0 (1 mole $O^{=}$/2 moles Cu^{+1}) and this is the starting point of the titration curve at about 0.32V relative to the 0.13*M* silver-silver ion reference electrode. The circular data points represent the successive additions of lithium oxide. A very strong complex is formed at an oxide ratio of about 2.5; that is, 1.5 moles of lithium oxide and 1 mole of cuprous oxide are required for its formation. The extent of the emf shift from the solution saturated with cuprous oxide to that saturated with respect to the complex is about 0.3V, which is identical to the magnitude of the cathode potential shift in the cell discharge studies. This complex was a light-green solid material that was partially soluble in the melt. The squares in the figure represent back-titration data points using magnesium chloride, which is very soluble. It appears that the very low solubility of magnesium oxide shifts the complex formation equilibrium so that the complex is quantitatively dissociated. During the course of this back titration, one insoluble material (MgO) is being formed at the expense of another insoluble material (stoichiometric $Cu_2O \cdot 1.5\ Li_2O$). The exact composition of the cuprous complex has not been determined, but the preceding representation is convenient for the purposes of discussion. These reactions are summarized as follows: Complex formation:

$$Cu_2O_{(S)} + 1.5\,Li_2O \rightarrow Cu_2O \cdot 1.5\,Li_2O_{(S)}$$

Complex dissociation:

$$Cu_2O \cdot 1.5\,Li_2O_{(S)} + 1.5\,Mg^{+2} \rightarrow Cu_2O_{(S)} + 1.5\,MgO_{(S)} + 3\,Li^{+}$$

This evidence for complex formation was by no means unexpected considering the changes that took place in the cathode potentials during cell discharge, which have already been discussed. However, further studies of this cuprous complex did lead to some unexplainable results. Figure 6 shows another titration that started with excess cuprous oxide as before. Magnesium chloride was added first to force the cuprous ions into solution as magnesium oxide was precipitated; that is

$$Cu_2O_{(S)} + Mg^{+2} \rightarrow MgO_{(S)} + 2Cu^{+1}$$

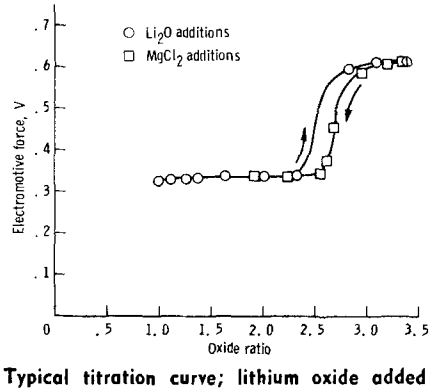

Fig. 5. Typical titration curve; lithium oxide added first, then magnesium chloride. Temperature, 450°C.

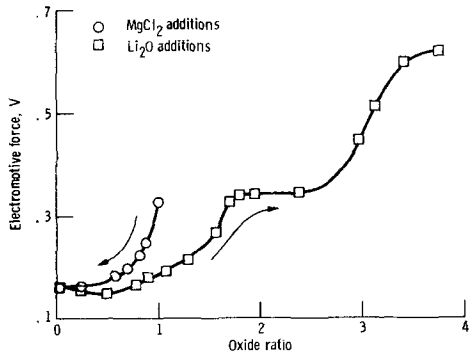

Fig. 6. Further titration study; magnesium chloride added first, then lithium oxide. Temperature, 450°C.

Note here that oxide in the form of magnesium oxide does not contribute to the oxide ratio since it is too insoluble. Enough magnesium chloride was added to reduce the oxide ratio from 1.0 to almost zero (0.012). Starting from this point, lithium oxide was added. The emf from an oxide ratio of about zero to 1.0 was not retraced, but two inflection points were obtained: one at an oxide ratio of about 1.5 and the other at about 3.0. A simple precipitation of cuprous ion $2Cu^{+1} + O^{=} \rightarrow Cu_2O_{(S)}$ would have resulted in an inflection point at an oxide ratio of 1.0. Clearly, cuprous ion does not precipitate as the oxide in a simple manner, but forms at least two different species as lithium oxide is added to the solution.

From the values of emf at an oxide ratio of 1.0 in the two titration curves, namely 0.18V (Fig. 6) and 0.32V (Fig. 5), it can be noted that the activity of cuprous ion is greater when lithium oxide is added to cuprous ion alone than when cuprous oxide itself is placed in the melt. This indicates that the solution process of cuprous ion is itself coupled with complex formation involving lithium ions from the melt.

In contrast to the differences noted at oxide ratio of 1.0, at ratios of 2.0 both titration curves show a rather constant emf of about 0.34V. Also, both titrations show the final formation of a complex that has an emf of about 0.62V.

This information on the complex forms of the cuprous ions may now be added to the information obtained from the discharge of complete cells to form a more accurate concept of the over-all chemical and electrochemical reactions that take place inside an operating thermal cell. Figure 7 depicts the over-all reactions as they are now understood. There are essentially two limiting cases, depending on whether the magnesium ion or the lithium ion carries the current (*i.e.*, has a transport number of 1.0). In actual cell operation, there will, of course, be a combination of these two processes, depending on such factors as the current drain and the depth of discharge. It is assumed here that the transport numbers of the chloride ion and oxide ion are zero. This is justified since no magnesium oxide was ever found in the anolytes of discharged cells (2). Although it is not proven that the transport number of the chloride ion is zero at all times, the point is irrelevant to the following argument.

First, the case where the transport number of the magnesium ion is 1 is discussed. For lack of evidence to the contrary, it is assumed that cupric oxide dissolves in a simple manner at the cathode. The cupric ion then oxidizes metallic copper to form cuprous ions which are electrochemically reduced. Meanwhile, in the anode compartment, a magnesium ion is generated and migrates to the catholyte where it precipitates the oxide ion liberated when the cupric oxide dissolved.

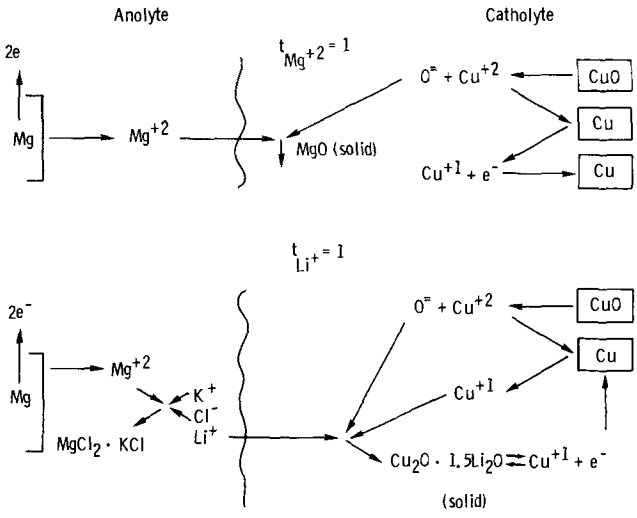

Fig. 7. Over-all reactions involved during cell discharge

This over-all situation would be characterized by a cell open-circuit voltage of 1.5-1.3V. The distribution of reaction products and cell emf agrees with that observed during the early stages of cell discharge (2). Since the data agree with the proposed model, the assumption that chloride ion plays little or no part in the charge neutralization process appears to be valid.

Later in the discharge, as it becomes more difficult for the magnesium ions to move through the layer of discharge products, the smaller lithium ion predominates in the charge neutralization process. As a consequence, a solid cuprous complex is formed in the catholyte. This results in a cell emf of 1.1-0.9V. It also results in a magnesium ion enrichment of the anolyte causing an increase in the melting point (4), which leads eventually to partial freezing of the electrolyte next to the discharging anode. Once again, the model is consistent with experimental facts and provides an explanation for the 0.25V drop in the open-circuit voltage of cells in the later stages of discharge and the sharp cutoff at the end of their service lives which occurs before all the active materials have been consumed.

Summary of Results

This is the conclusion of a program to evaluate the performance of copper oxide-magnesium thermal cells at 450°C. The present study was conducted to verify the presence of solid cuprous complexes in the vicinity of the cathode during the latter stages of discharge of complete cells and, further, to study these complexes using potentiometric titrations. The significant findings are as follows:

1. Cells that were discharged with a reference electrode placed between the anode and cathode revealed that the step drop in the open-circuit voltage during the latter stages of discharge was due to a change in the half-cell reaction at the cathode.
2. This change in half-cell reaction could be brought about earlier in the discharge by the addition of lithium oxide to the cell electrolyte.
3. This change in half-cell reaction could be made to occur later in the discharge by the addition of magnesium chloride to the cell electrolyte. This addition caused a very large increase in the rate of self-discharge of otherwise identical cells.
4. In the titration studies, the addition of 1.5 moles of lithium oxide per mole of cuprous oxide in a lithium chloride-potassium chloride solvent brought about the formation of an insoluble cuprous complex compound. The difference in electromotive force (emf) of a copper electrode placed in a saturated solution of cuprous oxide and one placed in a saturated solution of the cuprous complex was the same as the emf difference that occurred at the voltage step during the discharge of complete cells.
5. Cuprous ions that were precipitated by lithium oxide in the lithium chloride-potassium chloride solvent formed two different complexes, indicating that cuprous oxide does not dissolve in a simple manner.
6. Finally, based on this and our previous studies, a model is presented that explains essentially all the significant features of cell behavior during discharge.

Manuscript received April 24, 1970.

Any discussion of this paper will appear in a Discussion Section to be published in the June 1971 JOURNAL.

REFERENCES

1. L. H. Thaller, *This Journal*, **113**, 309 (1966).
2. L. H. Thaller, *ibid.*, **115**, 116 (1968).
3. L. H. Thaller, NASA TN D-4790 (1968).
4. L. H. Thaller, NASA TN D-5657 (1969).
5. H. A. Laitinen, W. S. Ferguson, and R. A. Osteryoung, *This Journal*, **104**, 516 (1957).
6. J. O'M Bockris, G. J. Hill, D. Inman, and L. Young, *J. Sci. Instr.*, **33**, 438 (1956).

Efficiency of Hydrazine-Peroxide Fuel Cells[1]

H. B. Urbach* and R. J. Bowen*

Naval Ship Research and Development Laboratory, Annapolis, Maryland 21402

ABSTRACT

Studies of the efficiency of single hydrazine-hydrogen-peroxide fuel cells were undertaken as part of a continuing program on electrode materials providing input data for hydrazine-peroxide-fuel-cell power. Experimental results for single fuel cells constructed of pressed platinum-Teflon electrodes indicate that oxygen-purge rates equivalent to 1-2 A/ft^2 are adequate. Most significant is the fact that coulombic efficiencies of both fuel and oxidant exhibit a broad maximum exceeding 88% between 60 and 100 A/ft^2. Thus, a minimum reactant weight-energy ratio appears to lie between these current density limits.

Hydrazine fuel cells may be a contender in some future applications of fuel-cell power. However, the precise evaluation of the hydrazine fuel cell relative to other cells requires a knowledge of their realizable experimental coulombic efficiencies which are hitherto unreported. Losses in efficiency result largely from the self-decomposition of the hydrazine, from cross diffusion of hydrazine and oxygen through the porous structure of the cell, and by purge of oxygen from the cell. A general procedure necessary for the determina-

[1] The opinions or assertions made in this paper are those of the authors and are not to be construed as official or reflecting the views of the Department of the Navy or the naval service at large.

* Electrochemical Society Active Member.

Key words: fuel-cell efficiency, fuel-cell purge requirements, hydrazine anode, oxygen cathode, efficiency, coulombic.

tion of such inefficiencies is presented here based on laboratory studies employing a single 6- by 6-in. cell. Coulombic and power efficiencies as a function of purge rate, hydrazine concentration, oxygen pressure, load, total pressure, and temperature are reported in detail. The results will be useful in the engineering evaluation of hydrazine fuel-cell plants and systems. However, the specific assignment of numerical values of efficiency to other systems should be employed only with the knowledge that considerable variation exists not only between different systems but within individual systems.

Experimental Equipment and Procedure

Most of the studies of experimental efficiencies were performed at atmospheric pressure. Cells 6- by 6-in. square (232 cm^2) were employed in all studies. The anodes were commercially (American Cyanamid, Type AB-6) supplied electrodes prepared from pressed Teflon-platinum powders on gold-plated nickel screens with platinum loadings of 9 mg/cm^2. The cathodes were the same except that the platinum loadings were 40 mg/cm^2. The electrodes were separated by an electrolyte-saturated, 0.030 in. thick asbestos matrix. Expanded metal nickel screen was used as manifolding behind both electrodes. The anolyte consisting of 5M KOH and hydrazine was circulated behind the anode by a magnetically coupled polypropylene centrifugal pump. High-purity (Matheson "gold label" grade) oxygen was maintained at a 3 psi differential pressure relative to the electrolyte by a diaphragm regulator. The study is based on the anticipated decomposition of hydrogen peroxide into oxygen before feed to the cathode. Oxygen use was measured by a calibrated float-type flowmeter. Oxygen purge and anolyte gas-evolution rates were measured by wet test gas meters at room temperature and atmospheric pressure. Analyses of the gases were obtained by means of a Beckman oxygen analyzer and a Fisher-Hamilton gas partitioner.

To analyze losses resulting from pressurized operation, studies were performed using similar cells exposed to typical oxygen pressures and hydrazine concentrations. High ambient pressures were developed in a system described previously (1) employing high-pressure argon and oxygen compressed above cylinder pressure by diaphragm compressors. The cross-diffusion of oxygen and hydrazine through the 0.030 in. electrolyte matrix was measured as a function of oxygen pressure and hydrazine concentration by potentiostatic procedures referenced previously (1).

Polarization data were obtained by programming the current sweep of a 30 ampere Kordesch-Marko-type current interrupter and gate, and recording sequentially by means of a stepping switch the cell potential and cell potential corrected for ohmic losses. The hydrazine coulombic efficiencies calculated from gas-evolution data were verified by comparing the number of coulombs measured on a current integrator with the change in hydrazine concentration after a period of cell operation.

Experimental Results

The inefficiencies in the hydrazine-oxygen fuel cell are derived from self-decomposition of the fuel, from cross diffusion of the oxidant and fuel, and from purge of the oxidant. The experimental data on self-decomposition are illustrated in Fig. 1. The arrows associated with the experimental points indicate the rate of gas evolution during increasing or decreasing load (current density). Gas-evolution rates include both hydrogen and nitrogen evolution normalized to 1.0 ft^2 of electrode area. The dashed line showing increasing gas evolution with load represents the theoretical nitrogen evolution discussed below. The ascending solid line was constructed parallel to the theoretical line of nitrogen evolution in the manner which best approximates the experimental points. The descending solid

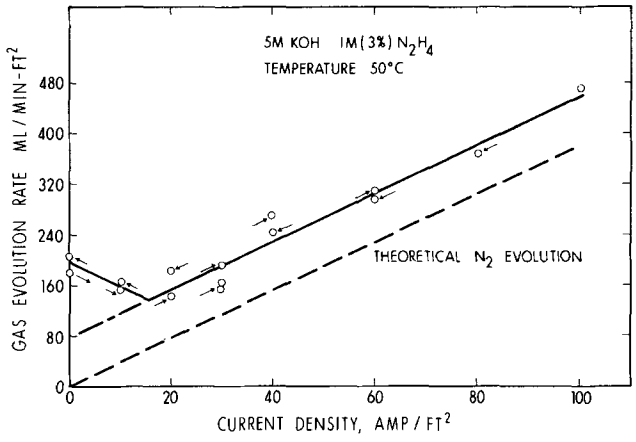

Fig. 1. Gas evolution at platinum-Teflon anodes exposed to hydrazine solution.

line, by construction a straight line which best fitted the points, approaches, at its junction with the ascending branch, a minimum at approximately 128 ml/min-ft^2, almost 67% of the open-circuit value of 200 ml/min-ft^2.

Figure 2 is a graph of experimental data for the cross diffusion of hydrazine from the anolyte through the anode and cell matrix to the cathode compartment where the hydrazine reacts with oxygen to form water and nitrogen. The cross diffusion is measured by analysis of the evolved gases rather than by electrochemical analyses (1). The diffusion is dependent on the applied load as well as the hydrazine concentration. The hydrazine loss is given in ml N_2/min-ft^2 and in the equivalent current density. Gas volumes are reported in the water-saturated condition at 25°C in all graphs and tables.

The most significant fact relative to efficiency is that the cross-diffusion losses of hydrazine decrease rapidly with increasing load. At low concentrations of hydrazine the ratio of cross-diffusion losses at open circuit and at load is much higher than the ratio at high concentrations of hydrazine. For example, at 1% hydrazine

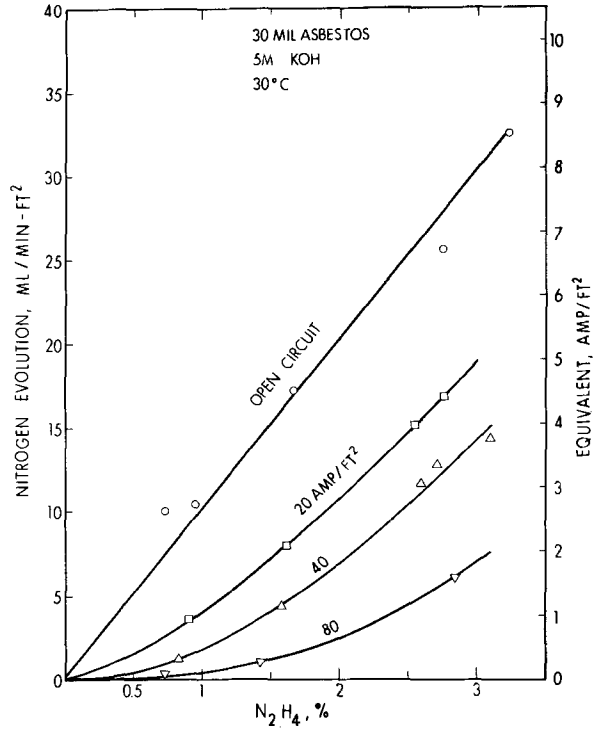

Fig. 2. Effect of hydrazine concentration on the nitrogen evolution rate (resulting from hydrazine diffusion) at the cathode.

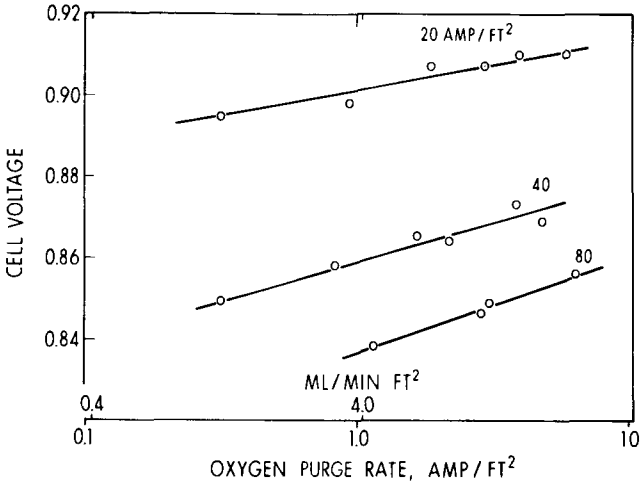

Fig. 3. Effect of load and oxygen purge rate on the output potential of a hydrazine-oxygen cell.

the ratio is approximately 20, whereas at 3% the ratio is approximately 4.5.

Figure 3 illustrates the effect of steady oxygen-purge rates on the cell potential at various loads. The cell potential is logarithmically dependent on the purge rate within the experimental limits of study. However, the logarithmic dependence is not uniform with current density, exhibiting increasing slope with the load. Thus, purge rates increase cell output most strongly at high loads.

Discussion

Self-decomposition losses.—Experimental gas-evolution data for hydrazine decomposition have been reported previously (2). It is possible to rationalize such experimental data if it is assumed that the mechanism of self-decomposition of hydrazine proceeds according to the following half-cell and over-all reactions:

$$N_2H_4 + 4\,OH^- \rightarrow N_2 + 4H_2O + 4e^- \quad [1]$$

$$4H_2O + 4e^- \rightarrow 2H_2 + 4\,OH^- \quad [2]$$

$$N_2H_4 \rightarrow 2H_2 + N_2 \quad [3]$$

Others have proposed electrochemical mechanisms (3-12).

Equation [1] for the anodic reaction is not reversible. Although reaction [2] is reversible, there is no hydrogen except that arising from the decomposition of hydrazine to produce the reverse of Eq. [2]. Polarization curves for the reactions of Eq. [1] and [2] may be approximated by dashed curves shown in Fig. 4. The open-circuit potential is of course a mixed potential, E_m, which occurs when the anodic and cathodic currents are equal in accordance with Eq. [4]. The superscripts (see glossary for meaning of symbols)

$$I_a^\circ = I_c^\circ \quad [4]$$

of Eq. [4] indicate the values of the anodic and cathodic current at the mixed potential. To assist in the analysis it is assumed that the polarization curves are linear and parallel.

The linear cathodic hydrogen line is drawn through the reversible hydrogen potential, 0.0V at vanishing current. The anodic line is constructed parallel to the cathodic hydrogen curve. These assumptions are quite crude as Fig. 4 shows, but the procedure is easily generalized to take into account the precise functional relationship between the half-cell currents and potential. The assumptions are justified if they facilitate analysis utilizing unsimplified experimental data.

The observed external current, I, is given by Eq. [5]

$$I = I_a - I_c \quad [5]$$

The relationship between the number of moles of nitrogen, hydrogen, and current is given by Faraday's

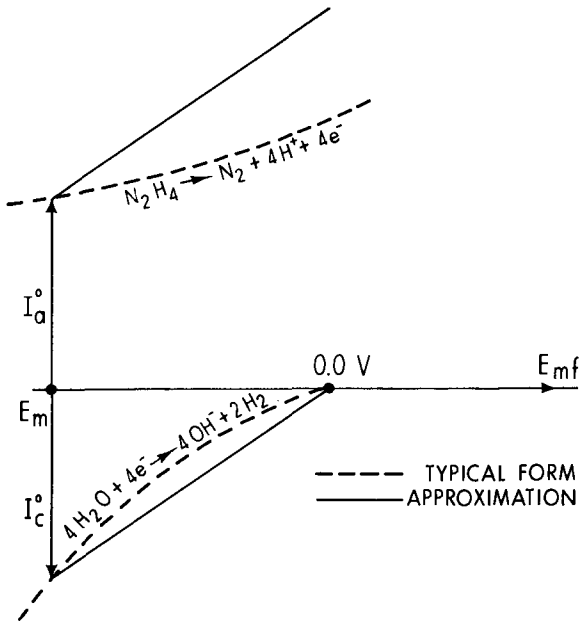

Fig. 4. Form of polarization curves for the half-cell reactions of Eq. [1] and [2].

law as written in Eq. [6] and [7], where K is (298/273) (22.4 x 60)/96.5

$$V_n = \frac{KI_a}{4} \quad [6]$$

$$V_h = \frac{KI_c}{2} \quad [7]$$

As the potential becomes anodic, the anodic and cathodic currents may be expressed in terms of the current at the mixed potential. By construction from Fig. 4

$$I_a \doteq I_a^\circ + \frac{I}{2} \quad [8]$$

$$I_c \doteq I_a^\circ - \frac{I}{2} \quad [9]$$

where the coefficient ½ arises from the assumption of parallel polarization curves. (Employing the actual unsimplified polarization curves, the coefficients of I in Eq. [8] and [9] would be r and $-(1-r)$ where $0 \leq r \leq 1$ and r is a function of I. Equations [8] and [9] would then be precise.) Employing either approximate or precise coefficients of I, Eq. [8] and [9] are consistent with Eq. [5].

Inserting Eq. [8] and [9] in Eq. [6] and [7] yields

$$V_n = V_n^\circ + \frac{KI}{8}; \quad I \leq \frac{8V_n^\circ}{K} \quad [10]$$

$$V_h = 2V_n^\circ - \frac{KI}{4}; \quad I \leq \frac{4V_h^\circ}{K} \quad [11]$$

When $I > 8V_n^\circ/K$, I_c vanishes. The total gas evolution is given by the sum of Eq. [10] and [11].

$$V_t = 3V_n^\circ - \frac{KI}{8}; \quad I < \frac{8V_n^\circ}{K} \quad [12]$$

$$V_t = \frac{KI}{4}; \quad I > \frac{8V_n^\circ}{K} \quad [13]$$

Equations [12] and [13] yield the theoretical gas evolution. They predict a minimum gas evolution obtained by equating [12] and [13] whence

$$2V_n^\circ = \frac{KI}{4} \quad [14]$$

which states that the minimum gas evolution is 2/3 its value at open circuit.

Thus, Eq. [12], [13], and [14] predict a gas-evolution-current curve with a descending branch, an ascending branch which has the theoretical faradaic slope, and a minimum which is 67% of the open-circuit gas evolution. These predictions are in agreement with the data of Daniel'-Bek and Vivitskaya (2). Likewise, they are in agreement with the data of this study (Fig. 1). The slope of the ascending branch is in agreement with the theoretical value of $KI/4$ in conformity with Faraday's law.

An area of divergence between theory and experimental result exists in the fact that the extrapolated ascending branch of the curve does not pass through the origin. This result suggests that some self-decomposition takes place on metallic or catalytic surfaces which cannot accommodate electrochemical discharge of the evolved hydrogen. This self-decomposition is independent of the current passed through the external circuit. The amount of the self-decomposition can be calculated from the deviation of the actual experimental curve from the theoretical curve in Eq. [13].

The approximate procedure described here suggests that precise measurement of gas evolution from hydrazine cells may be used to define the true anodic hydrazine polarization curves.

Cross-diffusion losses.—The results of Fig. 2 obtained by analysis of purged gases may be compared with previous studies of cross diffusion (1) obtained by a potentiostatic analysis of hydrazine under open-circuit conditions. The potentiostatic data, interpolated to 30°C, yield an equivalent cross-diffusion loss of approximately 9.5 A/ft² in good agreement with the value of 8 A/ft² obtained from Fig. 2 (at 3% hydrazine) considering the differences in the experimental conditions.

The significant features of the data in Fig. 2 (namely, that losses arising from cross diffusion decrease with load) arise from the fact that under load part of the available hydrazine is anodically consumed. Most interesting is the fact that the cross-diffusion loss at lower concentrations of hydrazine is significantly less than half the loss at higher concentrations. In particular, for example, at 80A loads, the loss at 2% hydrazine is only 35% of the loss at 3%.

The possibility that cross diffusion of oxygen decreases with load is suggested by these results.

Purge losses.—The data of Fig. 3 represent not only purge losses but cross diffusion of hydrazine. The nitrogen which is observed in the purged oxygen was originally part of the hydrazine which was transported by diffusion from the anolyte flowing past the back side of the anode through the asbestos separator. Convection plays a negative role in the transport of this hydrazine because the pressure gradient in the cell is normally against the direction of hydrazine flow.

The logarithmic dependence of the cell potential on oxygen-purge rate suggests that the cathode potential is exhibiting a Nernst-like response to the oxygen concentration which therefore should be linearly related to the purge rate. While logarithmic proportionality may exist, the slopes of the curves do not correspond to expected values for typical Nernst behavior. In addition, the slopes change with current density, indicating more complex relationships.

Hydrazine fuel requirements.—A formulation of fuel and oxidant requirements is simply stated if it is assumed that there are only four significant elements of fuel-cell inefficiency: the diffusion of hydrazine to the cathode, D_h; the diffusion of oxygen to the anode, D_o; the purge of oxygen from the cathode space, P; and the decomposition of hydrazine, S. The weight per kilowatt-hour of hydrazine, W_h, in terms of the weight per kiloampere-hr, M_h (0.663 lb/kA-hr for pure hydrazine), is

$$W_h = \frac{M_h}{E}\left(\frac{I + D_h + D_o + S}{I}\right) \qquad [15]$$

Table I. Fuel requirements

I, A/ft²	D_h, A/ft²	$D_o + S$, A/ft²	$\frac{I+D_h+D_o+S}{I}$	E, volt	(100%) Hydrazine, lb/kW-hr	(90%) Hydrazine, lb/kW-hr	Oxygen purge, A/ft²	Coulombic efficiency, %
20	5.7	6.5	1.61	0.895	1.19	1.33	0.3	62.1
20	5.8	6.5	1.62	0.899	1.19	1.32	0.9	61.9
20	5.8	6.5	1.62	0.907	1.18	1.31	1.8	61.9
20	5.7	6.5	1.61	0.907	1.18	1.31	2.8	62.1
20	5.7	6.5	1.61	0.910	1.17	1.30	5.5	62.1
40	3.5	6.5	1.25	0.849	0.976	1.08	0.3	80.0
40	3.5	6.5	1.25	0.858	0.966	1.07	0.8	80.0
40	3.7	6.5	1.26	0.865	0.962	1.07	1.6	79.7
40	3.5	6.5	1.25	0.864	0.959	1.07	2.1	80.0
40	3.5	6.5	1.25	0.869	0.954	1.06	4.5	80.0
80	3.8	6.5	1.13	0.838	0.893	0.992	1.1	88.6
80	3.4	6.5	1.12	0.846	0.881	0.979	2.7	89.0
80	4.2	6.5	1.13	0.849	0.886	0.984	2.9	88.2

where E is the cell potential. The oxygen-purge term does not enter into the expression for fuel requirements.

Table I is a compilation of raw laboratory and derived data used in subsequent calculations and figures. Losses have been expressed in amperes per square foot for consistency. The loss due to diffusion of oxygen, D_o (see column 3 which contains the sum of D_o and S), is obtained from Fig. 5 which is reproduced from Ref. (1). The value of D_o is negligible at atmospheric pressure. The value of the self-decomposition term, S, is 6.5 A/ft² and is derived from Fig. 1 in accordance with the discussion above. The average values for the cross diffusion of hydrazine, D_h (namely, 5.7, 3.7, and 3.8 A/ft² corresponding to the 20, 40, and 80 ASF level), were obtained experimentally and deviate from the values 7.8, 5.5, and 2.6 obtained from Fig. 2 and corrected for temperature. The results of Fig. 2 represent a separate independent study at 30°C. The disparities result from aging processes and from difficulties associated with maintaining constant oxygen-purge, hydrazine diffusion rates, and differential pressures in a dynamic system. The results of Fig. 2 exhibit a larger fall-off in the cross-diffusion rate as load increases than is apparent from column 2 of Table I. In fact, according to Table I, the average cross diffusion, D_h is slightly higher at 80 than at 40 A/ft². Figure 2 indicates that such behavior is anomalous. The data of Table I represent measurements over a period of several hours in contrast with the data of Fig. 2. Thus,

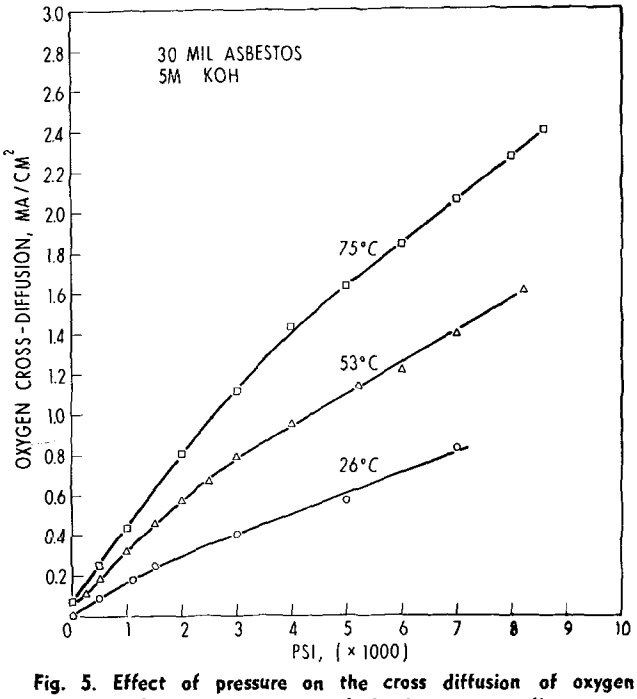

Fig. 5. Effect of pressure on the cross diffusion of oxygen through an asbestos separator in a hydrazine-oxygen cell.

they may represent changes in the nitrogen bubble content of the asbestos matrix and changes in the differential pressure between anode and cathode spaces which modify the diffusion processes by superposition of convective flow patterns.

In the following analysis, the values of hydrazine diffusion, D_h, employed in subsequent calculations are those listed in Table I. The inconsistency described in the previous paragraph colors the results of the following analyses to the extent of +4% to +2% in the most discrepant cases. The discrepancy is on the conservative side in the most likely operating ranges.

Columns 6 and 7, the hydrazine fuel requirement calculated by use of Eq. [15], are plotted as a function of the purge rates (column 8) in Fig. 6. The immediate conclusion to be drawn is that the oxygen-purge rate within the range of 1-5 A/ft² does not change the fuel requirement by more than 1.5% and is therefore not the most significant factor in hydrazine fuel requirements.

Peroxide requirements.—A formulation of peroxide requirements is given in Eq. [16] based on an anticipated 100% conversion of peroxide to oxygen. The weight per kilowatt-hour of peroxide, W_o, in terms of the weight of peroxide required per kiloampere-hour, M_o (1.398 lb/kA-hr for 100% peroxide), is

$$W_o = \frac{M_o}{E}\left(\frac{I + D_o + D_h + P}{I}\right) \qquad [16]$$

The self-decomposition term, S, in Eq. [15] is replaced by the oxygen-purge rate, P, in Eq. [16]. The value of D_o is again negligible at atmospheric pressure. The values of D_h and P are taken directly from the measured raw data of Fig. 3. See Table II for a compilation of the input raw data and calculated values of weights per kilowatt-hour. The required weights are plotted against purge rate in Fig. 7. The significant fact again is that, at current densities where operation is likely because of high efficiency, purge rates between 1 and 4 A/ft² have negligible effect.

Fuel-oxidant requirements.—Figure 8 indicates that fuel-oxidant requirements per kilowatt-hour (derived from Fig. 6 and 7 and listed in Table III) exhibit broad minima with respect to oxygen-purge rate. The significant conclusion, as before, is that the oxygen-purge rate is not a significant factor at operating current densities such as 40 A/ft² or greater which would be desirable for reasonable coulombic efficiency.

Figure 9 represents the specific fuel-oxidant requirements per kilowatt-hour under varying load as determined by Fig. 8. The effect of purge rate is again seen to be small compared to the effect of load. In contrast with behavior observed in hydrogen-oxygen fuel cells, the fuel-oxidant weight-energy ratio decreases with load to approximately 80 A/ft². The specific fuel-oxidant requirements probably increase above 80 A/ft² where life characteristics of hydrazine fuel cells represent an uncertain area. Assuming acceptable life characteristics, a minimum reactant weight-to-energy ratio appears to occur between 60 and 100 A/ft².

Table II. Peroxide requirements

I, A/ft²	$D_h + P$, A/ft²	$\frac{I + D_o + D_h + P}{I}$	E, volt	100% H_2O, lb/kW-hr	90% H_2O_2, lb/kW-hr	Purge, A/ft²	Coulombic efficiency, %
20	6.0	1.30	0.895	2.03	2.26	0.3	76.9
20	6.7	1.33	0.899	2.07	2.31	0.9	74.9
20	7.6	1.38	0.907	2.13	2.36	1.8	72.5
20	8.5	1.42	0.907	2.20	2.44	2.8	70.2
20	11.2	1.56	0.910	2.40	2.66	5.5	64.1
40	3.8	1.09	0.849	1.80	2.00	0.3	91.3
40	4.3	1.10	0.858	1.80	2.00	0.8	90.3
40	5.3	1.13	0.865	1.83	2.03	1.6	88.3
40	5.6	1.14	0.864	1.84	2.05	2.1	87.7
40	8.0	1.20	0.869	1.93	2.14	4.5	83.3
80	4.9	1.06	0.838	1.77	1.97	1.1	94.3
80	6.1	1.07	0.846	1.78	1.98	2.7	92.9
80	7.1	1.08	0.849	1.79	1.99	2.9	91.8

Table III. Fuel-oxidant requirements

I, A/ft²	Fuel, lb/kW-hr	Oxidant, lb/kW-hr	Total lb/kW-hr (100%)	Total lb/kW-hr (90%)	Purge, A/ft²
20	1.19	2.03	3.22	3.58	0.3
20	1.19	2.07	3.26	3.63	0.9
20	1.18	2.13	3.31	3.68	1.8
20	1.17	2.20	3.37	3.75	2.8
20	1.17	2.40	3.57	3.97	5.5
40	0.97	1.80	2.77	3.09	0.3
40	0.96	1.80	2.77	3.08	0.8
40	0.96	1.83	2.79	3.10	1.6
40	0.95	1.84	2.80	3.12	2.1
40	0.95	1.93	2.88	3.21	4.5
80	0.89	1.77	2.66	2.96	1.1
80	0.88	1.78	2.66	2.95	2.7
80	0.88	1.79	2.67	2.97	2.9

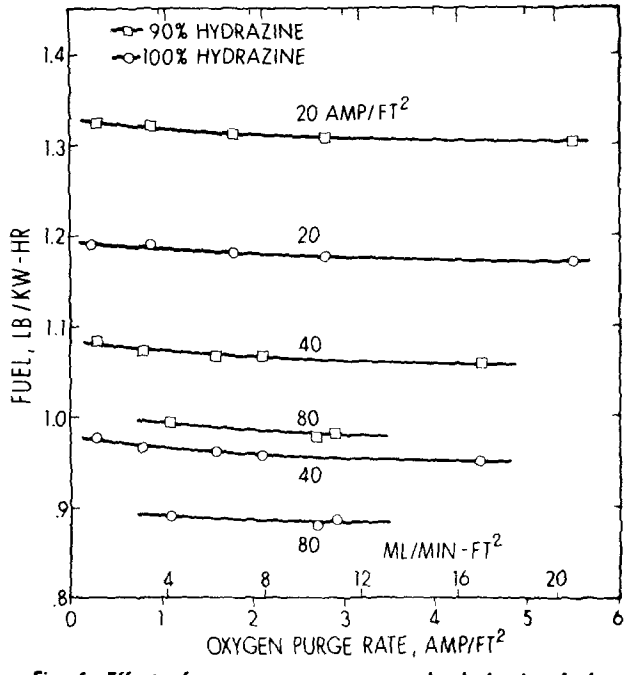

Fig. 6. Effect of oxygen purge rate on the hydrazine fuel requirements per kilowatt-hour.

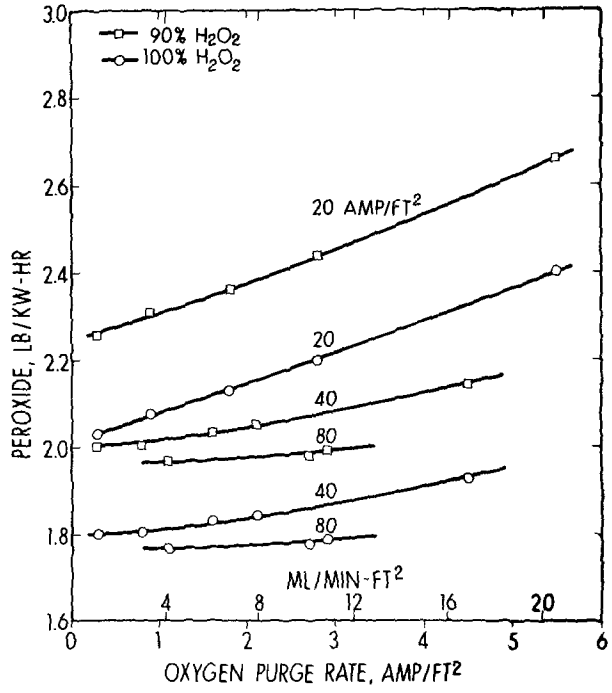

Fig. 7. Effect of oxygen purge rate on peroxide requirements per kilowatt-hour.

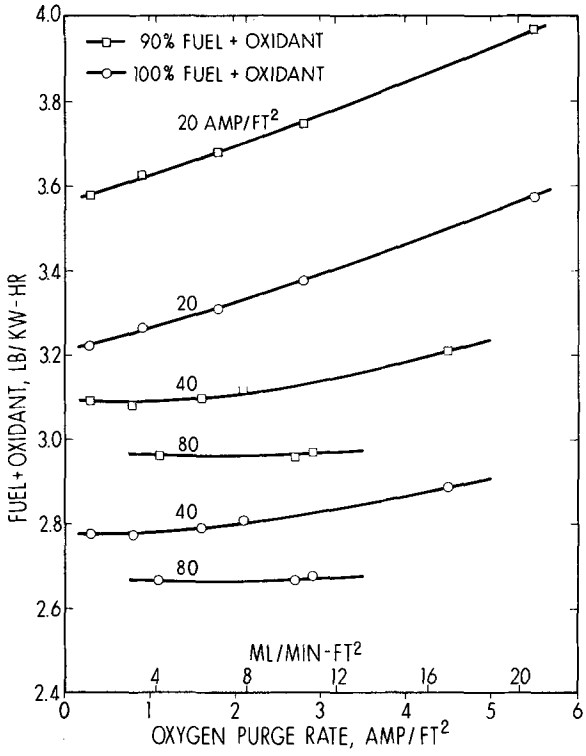

Fig. 8. Effect of oxygen purge rate on hydrazine-peroxide requirements per kilowatt-hour.

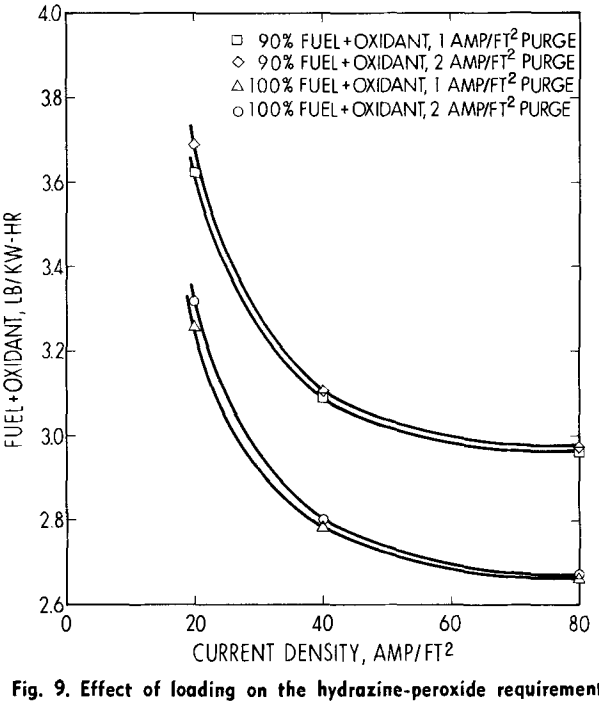

Fig. 9. Effect of loading on the hydrazine-peroxide requirements per kilowatt-hour.

Coulombic efficiencies.—Figure 10 shows that the coulombic efficiency of the peroxide (oxygen) cathode is a function of purge rate. On the other hand, Fig. 11 shows that the coulombic efficiency of the hydrazine anode is independent of oxygen-purge rate over the range studied. Figures 12 and 13 show again that load rather than purge is the significant over-all factor in coulombic efficiency as in the weight-energy ratio.

Summary

The coulombic efficiency and material requirements per energy unit of a hydrazine-peroxide single cell

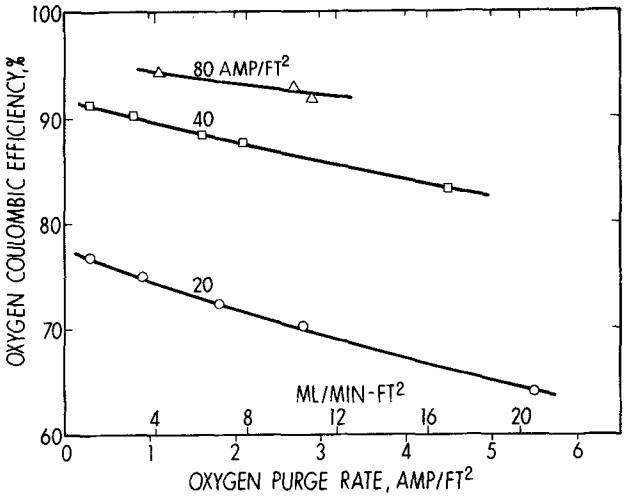

Fig. 10. Effect of oxygen purge rate on the coulombic peroxide (oxygen) efficiency.

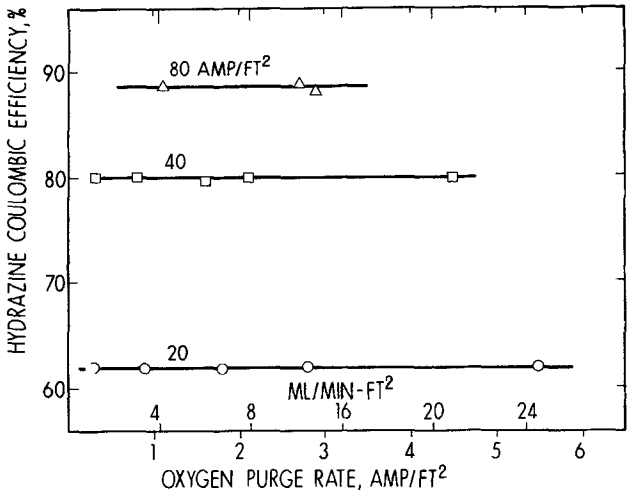

Fig. 11. Effect of oxygen purge rate on the coulombic hydrazine efficiency.

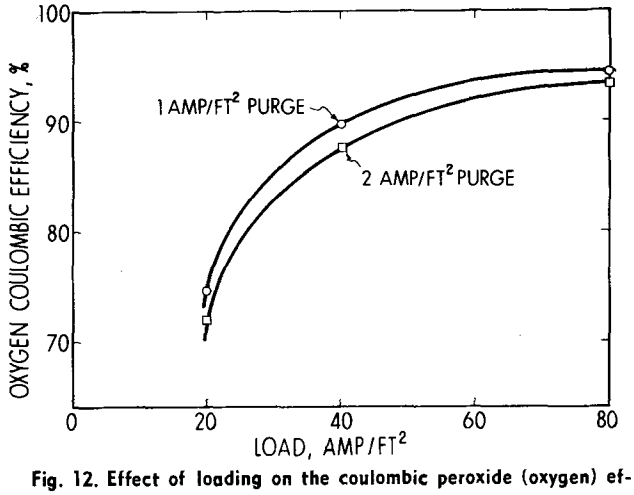

Fig. 12. Effect of loading on the coulombic peroxide (oxygen) efficiency.

were studied. Electrodes were a commercially supplied variety prepared from pressed platinum and Teflon powders in 6- by 6-in. squares. Analysis of the gas evolution at hydrazine anodes indicates that at high load the self-decomposition losses of hydrazine may be negligible. Cross diffusion of hydrazine (and possibly oxygen) decreases rapidly with load. Increased oxy-

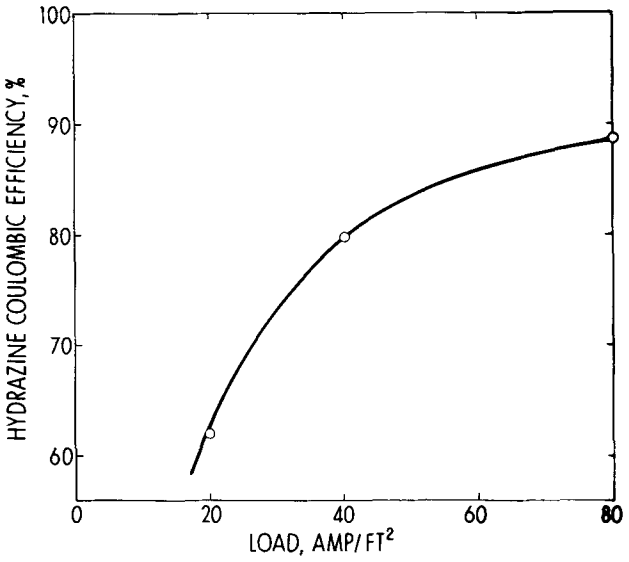

Fig. 13. Effect of loading on the coulombic hydrazine efficiency

gen-purge rates increase the cell potential most strongly at high load.

Hydrazine requirements decrease only slightly with oxygen-purge rate. On the other hand, peroxide requirements increase with purge rate although at high loads the increase is small. Combined fuel-oxidant requirements per energy unit show broad minima with respect to oxygen-purge rate. Moreover, at high current densities where operation is most efficient, the fuel-oxidant requirements are essentially independent of purge rate. However, they are strongly dependent on load. Minimum reactant weight-energy ratios and maximum coulombic efficiency may occur between 60 and 100 A/ft^2.

The results are peculiar to the particular system studied. In any systems analysis, numerical assignment of efficiencies should be based on experimental evaluation of the fuel-cell modules actually contemplated for application.

The results suggest that hydrazine-peroxide fuel cells of the type studied should be operated at current densities of the order of 60 and 100 A/ft^2 to achieve minimum reactant weight-energy ratios.

Acknowledgments

This work is part of a program of exploratory development sponsored by the Naval Ship Systems Command under the management of Bernard B. Rosenbaum and the technical cognizance of Ronald R. Nilson of the Naval Ship Engineering Center. The authors are pleased to acknowledge the support and encouragement of their supervisor, John H. Harrison.

GLOSSARY OF SYMBOLS

D_h	Diffusion loss of hydrazine in amperes per square foot
D_o	Diffusion loss of oxygen in amperes per square foot
E	Cell potential in volts
I	Current density in amperes per square foot
I_a	Current density for the anodic reaction
I_c	Current density for the cathodic reaction
I^o	Current density at the mixed potential
K	A constant
M	Mass requirements per kiloampere-hour
M_h	Weight of pure hydrazine per kiloampere-hour
M_o	Weight of pure peroxide per kilowatt-hour
P	Purge loss of oxygen in amperes per square foot
S	Self-decomposition loss of hydrazine
r	The fraction of the external current which produces a change in the anodic current
V_h	Volume of hydrogen in milliliters produced per minute per square foot
V_n	Volume of nitrogen in milliliters produced per minute per square foot
V_t	Volume of all gases in milliliters produced per minute per square foot
V^o	Volume of gas produced at the mixed potential at open circuit
W_h	Weight of hydrazine per kilowatt-hour
W_o	Weight of peroxide per kilowatt-hour

Manuscript submitted April 27, 1970; revised manuscript received Aug. 19, 1970.

Any discussion of this paper will appear in a Discussion Section to be published in the June 1971 JOURNAL.

REFERENCES

1. R. J. Bowen *et al.*, "The Hydrazine-Oxygen Fuel Cell at Ambient Deep Sea Pressures," NAVSHIPRANDLAB Annapolis R&D Rept. 2671, Feb. 1969 [published for the Intersociety Energy Conversion Engineering Conference in "IECEC '68 Record" by the Institute of Electrical and Electronics Engineers, Inc., New York (1968)].
2. V. S. Daniel'-Bek and G. V. Vivitskaya, *Elektrokhimiya*, **3**, 973 (1967).
3. R. Jasinski, *Electrochem. Technol.*, **3**, 129 (1965).
4. G. E. Evans and K. V. Kordesch, *Science*, **158**, 1148 (1967).
5. W. Vielstich, *Z. Instrumentenk.*, **71**, 29 (1963).
6. S. Karp and L. Meites, *J. Am. Chem. Soc.*, **84**, 906 (1962).
7. S. Susbielles and O. Bloch, *Compt. Rend.*, **255**, 685 (1962).
8. A. J. Bard, *Anal. Chem.*, **35**, 1602 (1963).
9. S. P. Szpak, P. Stonehart, and T. Katan, *Electrochim. Acta.*, **10**, 563 (1965).
10. B. P. Nesterov and N. V. Korovin, *Elektrokhimiya*, **2**, 1296 (1966).
11. B. E. Conway, M. Marinic, D. Gilroy, and E. Rudd, *This Journal*, **113**, 1144 (1966).
12. T. N. Glasatova and V. S. Daniel'-Bek, *Elektokhimiya*, **3**, 396 (1967).

Electrochemical Characteristics of Armco Iron in Acidic Solutions Containing Benzoic Acid—Effect of pH and Chloride Ions

D. L. Piron* and Ken Nobe**

School of Engineering and Applied Science, University of California, Los Angeles, California 90024

ABSTRACT

The effect of chloride ions and solution pH on the electrochemical behavior of Armco iron in sulfuric acid in the absence and presence of benzoic acid has been investigated. The corrosion rate of inhibited and uninhibited iron decreased with increase in solution pH. The capacitance increased linearly with immersion time although the corrosion rate remained essentially constant. The slope of the capacitance-immersion time curve was less for inhibited than for uninhibited iron and decreased with increase in solution pH. A minimum in the corrosion rate was observed for inhibited and uninhibited iron in pH 0.3 solutions containing 0.01M NaCl. This minimum was not observed for solutions of pH 1.0 and 1.7.

This paper reports on the effects of benzoic acid and chloride ions on the electrochemical behavior of Armco iron in acidic sulfate solutions at various pH values. Workers in this laboratory have previously investigated the electrochemical behavior of Armco iron in 1*N* H_2SO_4 containing ring-substituted anilines (1) and benzoic acids (2).

Experimental

The electrodes of Armco iron were cut from a ½ in. diameter rod and a thin layer of the cylindrical surface was milled off on a lathe to remove the scale. Electrodes were degreased with benzene in a soxlet extraction apparatus for 3 hr and finally vacuum annealed at 900°C for 1 hr and cooled slowly to room temperature in about 7 hr while still under vacuum.

The electrochemical cells and the electrode assembly have been described previously (3). All solutions were prepared from 1*N* H_2SO_4 and the pH was adjusted by addition of a concentrated NaOH solution. For solutions containing the inhibitor, benzoic acid, the concentration of the organic compound was maintained at 0.02M. The specific concentrations of chloride ions were obtained by addition of sodium chloride in the desired amounts to the solution. Sodium chloride concentrations of 0.01, 0.02, 0.1, and 0.2M were used in this study. All solutions were deaerated with the prepurified nitrogen for at least 3 hr before insertion of the electrodes. The electrodes were activated in 5*N* H_2SO_4 for 10 min immediately before immersion in the electrolyte. All experiments were performed at room temperature.

Five second current pulses, which were sufficient to reach steady state, were utilized for cathodic polarization. The corrosion current was determined by extrapolation of the cathodic Tafel line to the corrosion potential. The differential capacitance was determined by the d-c pulse method.

Results

The corrosion potential of inhibited iron in the absence of chloride ions shifted to slightly more noble potential indicating a greater effect of the benzoic acid on the anodic dissolution reaction than on the cathodic process, the hydrogen evolution reaction [see Ref. (4)]. With the exception of pH 1.7 solutions, the corrosion potential of iron was not appreciably affected by chloride ions. In pH 1.7 solutions, there was a small but consistent shift in the corrosion potential in the noble direction with increase in concentration of chloride ions.

The cathodic polarization of inhibited and uninhibited iron in sulfuric acid at pH 0.3, 1.0, and 1.7 in the absence of chloride ions is shown in Fig. 1. For solutions of pH 0.3 and 1.0, the rate of the hydrogen evolution reaction (h.e.r.) on iron was less in the presence of benzoic acid. However, no effect of the inhibitor on the rate of the h.e.r. was observed for iron in pH 1.7 solutions.

Tafel lines were obtained for both inhibited and uninhibited iron with cathodic Tafel slope of 80 mV as shown in Fig. 1. The electrochemical reaction orders of the h.e.r. with respect to the hydrogen ions were determined by plots of log i_c *vs.* pH. For both inhibited and uninhibited iron

$$\left(\frac{\partial \log i_c}{\partial \text{pH}}\right)_{\psi} \approx -1$$

The effect of chloride ions on the rate of the h.e.r. on both inhibited and uninhibited iron in pH 0.3 solutions is shown in Fig. 2. It is seen that the h.e.r. rate on iron in 0.01M NaCl was less than in 0.02M benzoic acid compound. Comparison of the decrease in the rate of the h.e.r. on iron in solutions containing 0.01M NaCl and 0.02M benzoic acid separately and together suggest that at these concentrations the inhibition of the h.e.r. is the result of adsorption of both chloride ions and benzoic acid. Iron in pH 0.3 solutions containing chloride ions of 0.02, 0.1, and 0.2M NaCl behaved similarly; *i.e.*, chloride ions decreased the rate of the h.e.r. on both inhibited and uninhibited iron. The same effect of chloride ions was observed for iron in pH 1.0 solutions. However, for pH 1.7 solutions the

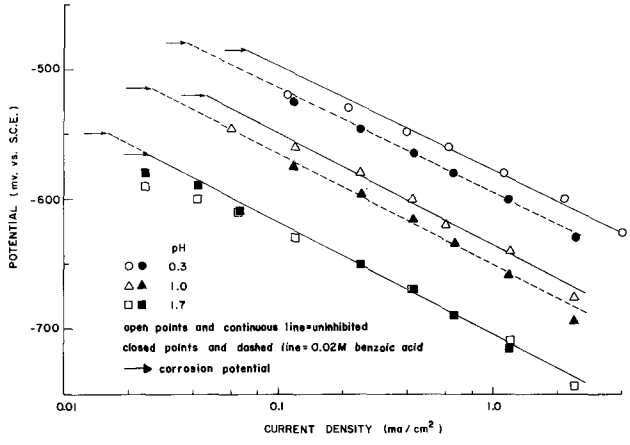

Fig. 1. Cathodic polarization of iron in H_2SO_4

* Electrochemical Society Student Associate Member.
** Electrochemical Society Active Member.
Key words: corrosion inhibition, hydrogen evolution.

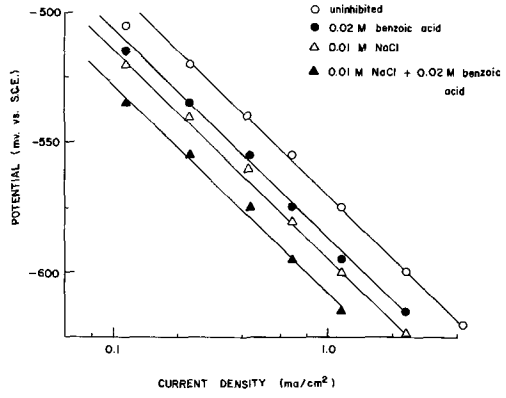

Fig. 2. Effect of low concentrations of chloride ions on the cathodic polarization of iron.

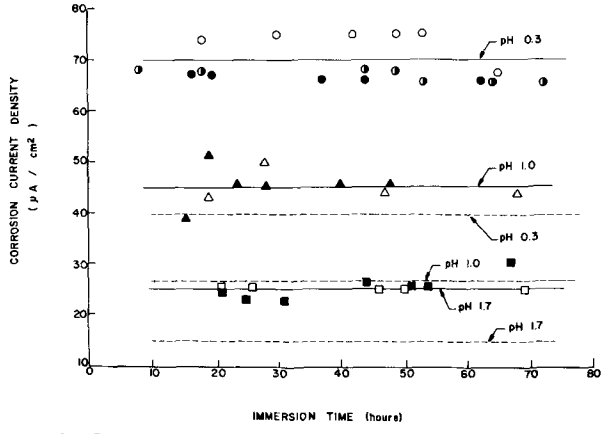

Fig. 3. Corrosion rate of iron in H_2SO_4 vs. immersion time. Points and continuous line represent uninhibited iron. Dashed line represents inhibited iron (0.02M benzoic acid).

rate of the h.e.r. on inhibited and uninhibited iron was stimulated by the presence of chloride ions.

The corrosion rates of uninhibited iron in sulfuric acid solutions of *p*H 0.3, 1.0, and 1.7 as a function of immersion time are given in Fig. 3. The corrosion rates were essentially constant with immersion time, and the averaged rates were 70, 44, and 25 μA/cm^2, respectively.

The corrosion rates of iron in sulfuric acid solutions of *p*H 0.3, 1.0, and 1.7 containing 0.02M benzoic acid were also constant with immersion time. The averaged corrosion rates were 40, 27, and 15 μA/cm^2, respectively, and are shown in Fig. 3. For both inhibited and uninhibited iron, the corrosion rate decreased with increase in the solution *p*H.

Table I shows the effect of chloride ions on the corrosion rate of inhibited and uninhibited iron. It is seen that a minimum in the corrosion rate was observed for both inhibited and uninhibited iron in 1*N* H_2SO_4 + 0.01M NaCl. Corrosion inhibition of iron by benzoic acid was maintained for all concentrations of chloride ions studied in this work ($\leq$0.2M NaCl). A minimum in the corrosion rate was also observed by Mazza and Greene (5) who investigated the corrosion of 304 stainless steel in 1*N* H_2SO_4 containing sodium chloride of various concentrations. The sharp minimum and subsequent increase in corrosion rate observed for iron in *p*H 0.3 solutions was not observed for iron in *p*H 1.0 and 1.7 solutions. For *p*H 1.0 solutions, the corrosion rate decreased with introduction of chloride ions but leveled off to a reasonably constant value with increase in chloride ions. For *p*H 1.7 solutions, the corrosion rate increased slightly with introduction of chloride ions and leveled off to an approximately constant value with increase in concentration of sodium chloride. Table I shows that the effect of chloride ions on the corrosion rate of inhibited and uninhibited iron in sulfuric acid solutions is influenced by the solution *p*H.

Table I. Averaged steady-state corrosion rate (μA/cm^2)

NaCl conc (M)	Uninhibited pH			Inhibited pH		
	0.3	1.0	1.7	0.3	1.0	1.7
0.00	70 ± 6	44 ± 1	25 ± 1	40 ± 7	27 ± 6	15 ± 2
0.01	40 ± 8	30 ± 7	28 ± 2	20 ± 4	22 ± 4	20 ± 1
0.02	48 ± 15	19 ± 4	31 ± 1	30 ± 5	23 ± 7	20 ± 1
0.10	66 ± 4	21 ± 4	33 ± 3	37 ± 3	20 ± 4	20 ± 1
0.20	70 ± 2	25 ± 5	35 ± 1	47 ± 6	22 ± 3	20 ± 2

The initial capacitance of inhibited and uninhibited Armco iron in sulfuric acid in the presence and absence of chloride ions ranged from 30 to 35 μf/cm^2. Thus, there was no significant effect of benzoic acid and chloride ions on the initial capacitance of iron.

For *p*H 0.3 and 1.0 solutions, the capacitance of inhibited and uninhibited iron in H_2SO_4 increased linearly with immersion time as shown in Fig. 4 and 5, respectively. The slope of the capacitance *vs.* immersion time curve decreased with increase in *p*H and with addition of benzoic acid. For *p*H 1.7 solutions, the capacitance remained constant with immersion time and was not affected by the presence of benzoic acid. The capacitance increase with immersion time of Armco iron in 1*N* H_2SO_4 in the absence and presence of benzoic acid has been reported previously (2, 6).

Figures 4 and 5 also show a typical effect of chloride ions on the capacitance of inhibited and uninhibited Armco iron in *p*H 0.3 solutions. For uninhibited and inhibited iron in *p*H 0.3 solutions, the rate of increase of capacitance with immersion time decreased with addition of chloride ions. However, the rate of increase in capacitance of inhibited and uninhibited iron

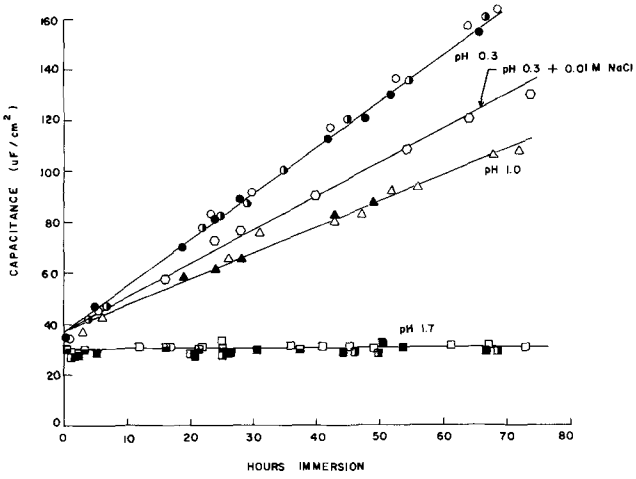

Fig. 4. Open-circuit capacitance of iron in H_2SO_4 vs. immersion time.

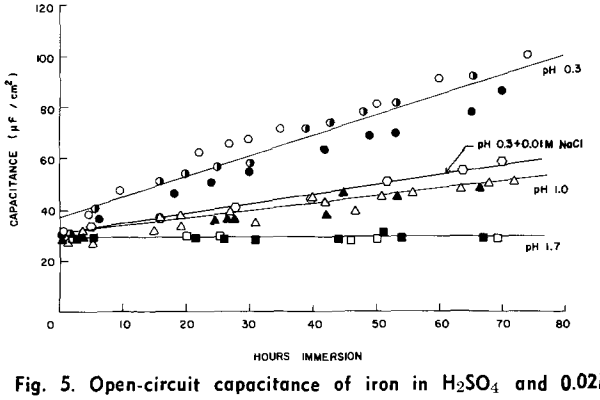

Fig. 5. Open-circuit capacitance of iron in H_2SO_4 and 0.02M benzoic acid vs. immersion.

in pH 1.0 and 1.7 solutions was not appreciably affected by chloride ions.

Discussion

The open-circuit capacitance of iron in 1*N* $HClO_4$ and HCl solutions did not increase appreciably with immersion time in contrast to the capacitance increase observed for iron in sulfuric acid solutions of less than pH 1.7. The results of the open-circuit capacitance experiments indicate that the anion, HSO_4^-, plays a significant role in the capacitance-immersion time behavior of Armco iron in H_2SO_4 of pH 0.3 and 1.0. Since the corrosion rate of both inhibited and uninhibited Armco iron remained constant with immersion time as shown in Fig. 3, it is apparent that the increase in capacitance with immersion time was not due to an increase in surface roughness.

In a separate series of experiments, it has been observed that the large capacitance (pseudocapacitance) obtained after long immersion times can be substantially reduced by prolonged cathodic polarization. Furthermore, it has been observed previously that, after removal of the electrode from the solution for a prolonged period of time and then reimmersion in electrolyte, the Armco iron resumed the capacitance increase with immersion time (7). Sayano (8) observed that the large open-circuit capacitance after a long immersion time could be reduced to the original value by anodic passivation of iron at +600 mV *vs.* SCE and subsequent self-activation to the corrosion potential. After activation the initial capacitance value was attained again and, subsequently, the capacitance increased linearly with immersion time as observed previously. These results provide further evidence that the capacitance increase was not due to an increase in surface area, but rather to the formation of a surface species which involves the anion, HSO_4^-.

In view of the above experimental observations, a possible mechanism to account for the anodic dissolution and open-circuit capacitance behavior of iron in H_2SO_4 is as follows:

$$Fe + H_2O \underset{k_{-1}}{\overset{k_1}{\rightleftharpoons}} [FeOH]_{ads} + H^+ + e \qquad [1]$$

$$[FeOH]_{ads} \xrightarrow[k_2]{\text{RDS}} FeOH^+ + e \qquad [2]$$

$$[FeOH]_{ads} + HSO_4^- \underset{k_{-2a}}{\overset{k_{2a}}{\rightleftharpoons}} [FeOH_2SO_4]_{ads} + e \qquad [2a]$$

$$FeOH^+ + H^+ \xrightarrow[\text{fast}]{k_3} Fe^{++} + H_2O \qquad [3]$$

$$[FeOH_2SO_4]_{ads} \xrightarrow{k_{3a}} Fe^{++} + HSO_4^- + H_2O \qquad [3a]$$

where k_1, k_{-1}, and $k_3 >> k_2 >> k_{2a}$

Bockris *et al.* (9) proposed reaction steps [1], [2], and [3], with step [2] the rate-determining step, as the mechanism for the anodic dissolution of iron. Step [2a] is similar to one of the reaction steps in the mechanism proposed by Florianovich *et al.* (10). The slow but steady increase in the open-circuit capacitance with immersion time is surmised to be an adsorption pseudocapacitance due to formation of an electroactive surface complex intermediate, $FeOH_2SO_4$, as in step [2a], which is a parallel reaction to the rate-determining step [2]. Pseudocapacitance due to adsorbed hydrogen atoms has been precluded in light of Devanathan and Stachurski's results (11). A plausible alternative mechanism would include a slow reaction step, a reaction between Fe and the bisulfate ion to form an electroactive surface intermediate, parallel to step [1]. The depletion of the surface complex during passivation of iron at +600 mV and the subsequent reattainment of the initial capacitance, as observed by Sayano (8), may be ascribed to a reaction as step [4]

$$[FeOH_2SO_4]_{ads} \xrightarrow{k_4} Fe^{+++} + SO_4^= + H_2O + e \qquad [4]$$

Acknowledgment

This work was supported by a grant from the Office of Saline Water, U. S. Department of the Interior.

Manuscript submitted Jan. 30, 1970; revised manuscript received June 22, 1970.

Any discussion of this paper will appear in a Discussion Section to be published in the June 1971 JOURNAL.

REFERENCES

1. F. M. Donahue, A. Akiyama, and Ken Nobe, *This Journal*, **114**, 1006 (1967).
2. A. Akiyama and Ken Nobe, *This Journal*, **117**, 999 (1970).
3. R. R. Sayano and Ken Nobe, *Corrosion*, **22**, 81 (1966).
4. H. Kaesche and N. Hackerman, *This Journal*, **105**, 191 (1958).
5. F. Mazza and N. D. Greene, *2nd Symp. Europ. sur Les Inhibiteurs de corr.*, 401, Ferrara, Italy (1965).
6. A. Akiyama, R. E. Patterson, and Ken Nobe, *Corrosion*, 26, 51 (1970).
7. Francis M. Donahue, Ph.D Dissertation, Univ. of California, Los Angeles, Sept. 1965.
8. R. R. Sayano, Ph.D. Dissertation, Univ. of California, Los Angeles, March 1967.
9. J. O'M. Bockris, D. Drazic, and A. R. Despic, *Electrochim. Acta*, **4**, 325 (1961).
10. G. M. Florianovich, L. A. Sokolova, and Y. M. Kolotyrkin, *Electrochim. Acta*, **12**, 879 (1967).
11. M. A. V. Devanathan and Z. Stachurski, *This Journal*, **111**, 619 (1964).

The Preparation of Dithionites by the Electrolytic Reduction of Sulfur Dioxide in Water

Colin Oloman

B.C. Research, Vancouver 167, Canada

ABSTRACT

This paper reports the results of experimental studies on the cathodic reduction of sulfur dioxide in water solution. The system is discussed in terms of the chemical and electrochemical reactions which accompany the flow of current. Experimental results demonstrate the effect of principal process variables on current efficiency and chemical yield. The work described is directed toward the development of an electrolytic process for the production of dithionite solution for industrial use.

Background

The dithionites are strong reducing agents which are commercially valuable as bleaching chemicals. Consequently, the preparation of these salts has received considerable attention.

The common method of making dithionites is through the direct reduction of a solution of sulfur dioxide or sodium bisulfite in water with metallic zinc (1, 2). The reduction can be carried out successfully using sodium amalgam (3) and metallic iron has been considered for the same purpose (4). Dithionites can also be made by the reaction of such reducing agents as sodium borohydride with sulfur dioxide.

Apart from chemical reduction, the electroreduction of sulfurous solutions has long been recognized as a source of dithionites.

In 1857 Schonbein (5) observed the reddish brown color formed by the electrolysis of sulfur dioxide solutions and noted that the resulting liquid is a strong reducing agent. In 1877 Gerout (6) reported the electrolysis of sulfurous acid to obtain a yellow solution of "hydrosulfurous" acid and the electrolysis of sulfur dioxide in water was adopted by Worsley (7) in 1924 as a method of producing "hydrosulfurous" acid for bleaching purposes. However, dithionous acid is very unstable and, since this early work, the electroreduction of simple solutions of sulfur dioxide in water has received little attention.

The decomposition of dithionite in an electrochemical cell can be partly avoided by using as the catholyte nearly neutral solutions of sulfites and bisulfites. This technique has been the subject of investigations since about 1900 (8-12) and is the basis of several patented processes for the electrochemical manufacture of dithionites (13, 14).

Despite considerable work on the subject, the electroreduction process has not been made to compete commercially with the conventional zinc reduction process for dithionite manufacture. In an evaluation written in 1924 (15), McKee and Woldman explain how limitations on chemical yield and current efficiency impair the value of the electrochemical process. Their concise summary of the situation is probably still pertinent today.

Nevertheless, the potential cost reduction through the direct use of electric power in the preparation of dithionite makes a successful application of the electrochemical method an attractive goal. The work described in this paper has been directed toward the development of a useful process for producing dithionite solutions by the electroreduction of sulfur dioxide in water.

Cathode reactions.—The standard electrode potentials for the reduction of sulfurous solutions to dithionite under acidic and basic conditions are given by Latimer (16) as

$$2H_2SO_3 + H^+ + 2e^- \rightarrow HS_2O_4^- + 2H_2O \qquad -- E_o = -0.08V$$

$$2SO_3^= + 2H_2O + 2e^- \rightarrow S_2O_4^= + 4\,OH^- \qquad ---- E_o = -1.12V$$

The corresponding hydrogen discharge potentials are 0.0 and −0.83V, respectively. However, the existence of a hydrogen overvoltage of a few tenths of a volt on most metal cathodes will allow the preferential formation of dithionite in acid solution. With rising *p*H, dithionite formation should be possible only with high overvoltage cathodes at relatively low current densities.

Apart from the discharge of the hydrogen ion, further secondary reactions at the cathode can involve the reduction of dithionite itself to thiosulfate

$$S_2O_4^= + 2H^+ + 2e^- \rightarrow S_2O_3^= + H_2O \text{ ---- } E_o \approx +0.88V$$

and possibly the reduction of thiosulfate to free sulfur. The existence of these alternative electrode reactions explains, in part, the difficulty of obtaining useful concentrations of dithionite in the electroreduction process.

The stoichiometry of dithionite formation in the electrolytic process is commonly given as

$$2HSO_3^- + 2H^+ + 2e^- \rightarrow S_2O_4^= + 2H_2O$$

This equation implies that the bisulfite ion is the reactive species in the primary cathode reaction. However, from their study of the reduction of sulfurous solutions at a dropping mercury electrode, Kolthoff and Miller (17) conclude that sulfur dioxide or sulfurous acid is the depolarizer in the primary cathode reaction.

It follows that dithionite is formed most easily through the electroreduction of a solution of low *p*H containing a high concentration of sulfur dioxide.

Chemical decomposition of dithionite.—The principal barrier to the efficient electrolytic preparation of dithionites lies in the chemical instability of dithionous acid. Practical current densities can be attained only in acid conditions which promote decomposition of the product dithionite and consequently limit the process yield.

The mechanism of the decomposition of dithionite is complex. McKee and Woldman (18) summarize the work of early investigators of this subject and present data which show the decomposition of dithionite in neutral and acid sulfite solutions to be a simple reaction, second order with respect to dithionite concentration. This reaction is presented as

$$H_2O + 2S_2O_4^= \rightarrow S_2O_3^= + 2HSO_3^-$$

More rigorous examinations of the decomposition kinetics (19, 20) have showed that in the *p*H range

Key words: *primary*—dithionites; *co-term*—electrolytic, preparation, reduction, sulfur dioxide. *Primary*—sulfur dioxide; co-*term*—dithionites, electrolytic, reduction.

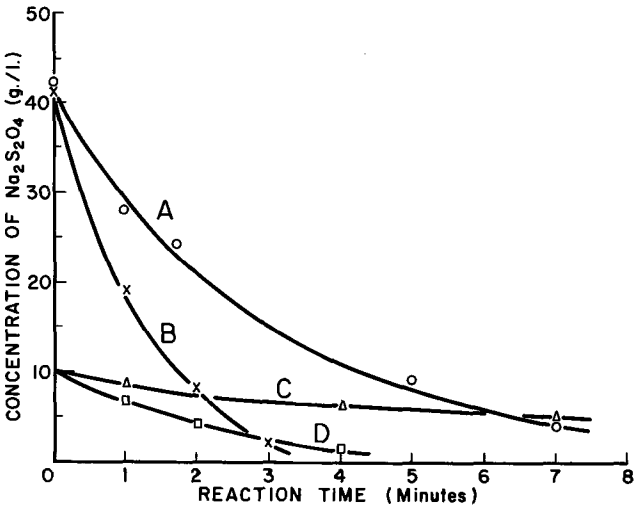

Fig. 1. Decomposition of dithionite in solution with sulfur dioxide and thiosulfate. Temperature 18°C; SO_2 concentration, 8 weight per cent (w/o); pH, 0.8; nitrogen purge; initial $[S_2O_3^=]$, A, 0.008M; B, 0.04M; C, 0.002M; D, 0.04M.

4.5-7 the rate is raised by increases in the concentration of dithionite, bisulfite, thiosulfate, and hydrogen ions. Under some circumstances, the decomposition of dithionite is autocatalytic.

Both zinc (21) and cadmium (22) have been observed to stabilize dithionite, while transition metal ions are generally believed to increase the rate of decomposition.

It is certain that the rate of decomposition of dithionite increases with decreasing pH. However, published studies give no quantitative account of the decomposition of dithionite in solutions with a pH below 4. Specific data on the decomposition of dithionite in a strong solution of sulfur dioxide is given here in Fig. 1. The 8% sulfur dioxide solution has a pH of about 0.8 and under this condition the dithionite disappears very rapidly. Thiosulfate appears to be an autocatalytic agent and the decomposition rate is largely determined by an interaction between the effects of dithionite and thiosulfate concentration. The form of this dependence is not known.

Similar studies have shown that the rate of decomposition of dithionite in an 8% sulfur dioxide solution is increased about fivefold by raising the reaction temperature from 10° to 28°C.

The Electrodeposition of Sulfur Dioxide in Water

Process.—The production of dithionites by the cathodic reduction of sulfurous solutions always involves a competition between the rate of formation of dithionite at the cathode and the rate of decomposition of dithionite in the bulk of the catholyte.

In such a process, the dithionite yield and the current efficiency for production of dithionite depend on the interaction of several factors. Most important of these are:

(*a*) The concentration of depolarizer in the catholyte, the condition of turbulence at the cathode surface, and the cathode material, which together determine the current density that can be usefully applied to the cathode.

(*b*) The ratio of cathode area to cathode chamber volume, which together with the current density gives the current concentration and hence the rate of dithionite formation within the catholyte.

(*c*) The concentration of dithionite and thiosulfate, the pH, and the temperature of the catholyte, which determine the rate of dithionite decomposition.

When a simple solution of sulfur dioxide is used as the catholyte in this process, the rate of dithionite decomposition is very high but the presence of free sulfur dioxide allows the application of a correspondingly high current density. Under these conditions, dithionite can be obtained in reasonable yields from a reactor with a high ratio of cathode surface area to cathode chamber volume which operates at a low temperature and employs a low catholyte residence time.

The method adopted for the preparation of sodium dithionite by the electroreduction of sulfur dioxide in water is represented in Fig. 2. In this process, sulfur dioxide in water is converted to dithionite in a single pass across an active cathode plate. A cation specific membrane separates the anode and cathode chambers of the cell and sodium ions are supplied to the catholyte from a recycling anolyte solution of a convenient sodium salt. The primary electrode reactions occurring in the cell are:

at the anode

$$4NaOH \rightarrow 4Na^+ + O_2 + 2H_2O + 4e^-$$

at the cathode

$$4SO_2 + 4e^- \rightarrow 2S_2O_4^=$$

net reaction

$$4NaOH + 4SO_2 \rightarrow 2Na_2S_2O_4 + O_2 + 2H_2O$$

The balance between the rate of formation and decomposition of the dithionite makes it impractical to carry the sulfur dioxide conversion to 100%. Thus the catholyte solution leaving the reactor contains sodium dithionite, sodium bisulfite, and sodium thiosulfate, together with unconverted sulfur dioxide which must be neutralized to preserve the dithionite.

Apparatus and procedure.—The conditions required for the preparation of sodium dithionite by electroreduction of sulfur dioxide in water are fulfilled by the

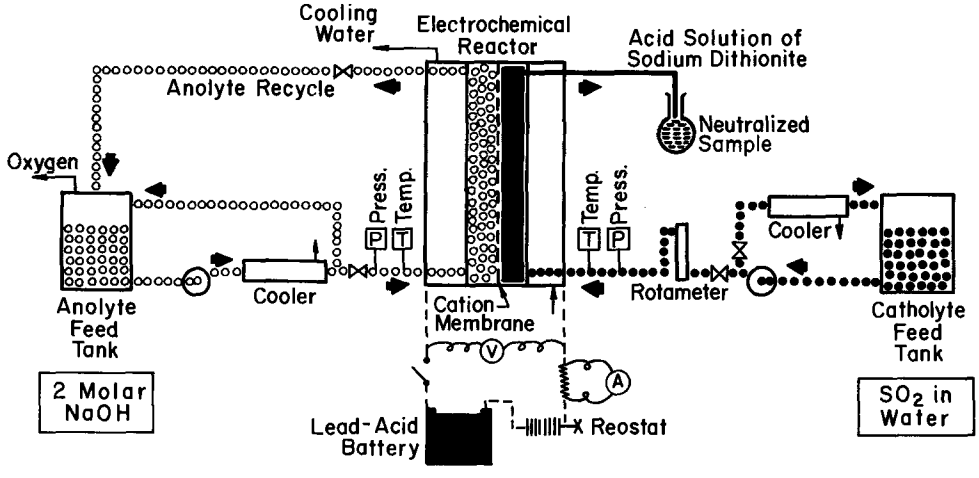

Fig. 2. Apparatus used in experimental production of sodium dithionite.

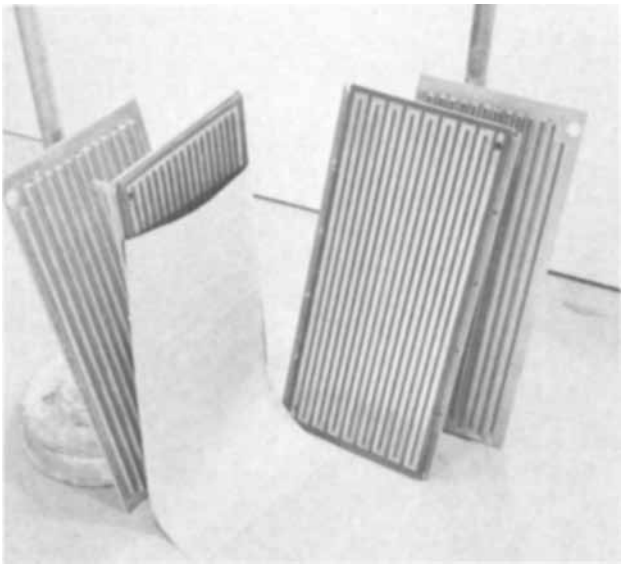

Fig. 3. Single cell used in electroreduction of sulfur dioxide in water.

electrochemical cell shown open in Fig. 3. This cell consists of a cathode and anode plate, both of 316 stainless steel, separated by a cation membrane. The membrane is supported by a nylon mesh not shown in the photograph. Cathode and anode chambers are formed on the electrodes by fingered neoprene gaskets which direct the solutions across the electrodes so that the catholyte flows through the cathode channels in series while the anolyte moves through the anode channels in parallel. The channels are all 1 cm wide and about 0.15 cm deep and the total active cathode area is 1000 cm^2 for a single cell or 800 cm^2 for each cell used in series. Electrode plates are 1/32 in. thick and are backed by 1/16 in. aluminum current distribution plates which in turn are cooled by water flowing through external chambers. Several of these cells may be put together in series to increase the cathode area of the reactor.

In operation of the reactor, a catholyte solution of 2-12% sulfur dioxide in water was precooled to 10°C and pumped through the cathode chamber. The anolyte consisted of a 2M (molar) solution of sodium hydroxide which was kept at a temperature between 10° and 15°C while recycling around the anode circuit at a rate of about 1 liter/min/cell. With a flow of 100 ml/min of a catholyte solution containing 95 g/liter of sulfur dioxide, the decomposition potential of each cell was 1.2V and the electrical resistance some 24 ohm · cm^2.

Both the anolyte and catholyte were made up with water from the city mains containing about 0.5 ppm of both iron and copper. However, in the experiments the anode was dissolved slowly at the higher current densities and this was responsible for the presence of transition metal ions in the catholyte product up to concentrations of about 10 ppm.

Direct current was supplied to the reactor from a set of lead-acid batteries and controlled to individual cells through separate carbon block rheostats.

In each of a series of experimental runs, the reactor produced a continuous flow of a reddish-brown solution of sodium dithionite with unconverted sulfur dioxide. This product stream was sampled directly into an excess of sodium hydroxide solution and analyzed within 30 min. Routine analysis for dithionite alone was done by titration into an acid indigo carmine solution under a nitrogen purge (23), while the complete analysis for dithionite, thiosulfate, and sulfite was carried out by a detailed iodometric method (24). No systematic account was made of the sulfide content of the product solutions but occasional checks showed sulfide to be present in relatively small amounts.

The dithionite yield from sulfur dioxide and the current efficiency for the process were calculated as:

$$\text{Dithionite yield} = \frac{2[S_2O_4^{=}] \text{ in product}}{[SO_2] \text{ in feed}}$$

$$\text{Current efficiency} = \frac{\text{Mole/min of } S_2O_4^{=} \text{ in product}}{\text{Applied current}} \times \frac{193{,}000}{60}$$

Results and discussion.—(a) Effects of catholyte flow rate, sulfur dioxide concentration, and cathode current density.—The effects of flow rate, sulfur dioxide concentration, and current density on the current efficiency and chemical yield for dithionite are illustrated by the factorial results of Tables I and II. The corresponding equations are the results of a stepwise multiple linear regression analysis of the data and contain the factors which were shown to be significant up to the 10% level.

From the statistical analysis, most of the variation in current efficiency and yield could be attributed to the effects of the primary variables and their linear interactions. Residual errors are probably due to experimental error to the uncontrollable variation of the process temperature between 10° and 15°C.

In Table I it is apparent that the current efficiency is increased with sulfur dioxide concentration and flow rate. This is a consequence of the independent effects that these variables have on the concentration of reactive species at the cathode surface. Increasing current density always lowers the current efficiency as the cathode becomes polarized with respect to sulfur dioxide and the cathode potential favors the occurrence of secondary reactions. This effect is diminished with increasing sulfur dioxide concentration.

Other interactions are indicated in Table I but their analysis is confused by chemical decomposition effects due to the varying composition of the catholyte.

Table I. Current efficiency for dithionite in electroreduction of sulfur dioxide in water

Catholyte flow rate (cc/min)	SO_2 concentration—w/o: 3.5, Current density, A/cm^2			7.2, Current density, A/cm^2			11.5, Current density, A/cm^2		
	0.025	0.05	0.1	0.025	0.05	0.10	0.025	0.05	0.10
	Current efficiency—per cent								
60	42	6	1	62	41	14	69	61	34
100	58	9	4.5	69	53	30	67	68	54
200	70	32	12	78	58	33	74	71	64

Catholyte temperature = in 15°C; out 10°C.
Cathode area = 1000 cm^2.
Cathode chamber volume = approx 150 cm^3.
Current efficiency = 45 + 1.97 (SO_2 conc) + 0.12 (flow) − 806 (current density) + 43 (SO_2 conc) (current density).
Correlation coefficient = 0.93.

Table II. Chemical yield for dithionite in electroreduction of sulfur dioxide in water

Catholyte flow rate (cc/min)	SO_2 concentration—w/o: 3.5, Current density, A/cm^2			7.2, Current density, A/cm^2			11.5, Current density, A/cm^2		
	0.025	0.05	0.1	0.025	0.05	0.10	0.025	0.05	0.10
	Dithionite yield—per cent								
60	19	5.5*	2*	14	19*	11*	10	18	19*
100	16	5.5*	5*	9	14	15*	6	12	18
200	10	10	6.7*	5	8	9	3.5	6	11

* Indicates appearance of H_2 gas and free sulfur.
Catholyte temperature = in 15°C; out 10°C.
Cathode area = 1000 cm^2.
Cathode chamber volume = approx 150 cm^3.
Dithionite yield = 15 + 0.35 (flow) − 193 (current density) − 0.98 (SO_2 conc) (flow) + 27 (SO_2 conc) (current density).
Correlation coefficient = 0.82.

The results for chemical yield (Table II) are also complicated by several interactions. The observed effects and the natural result of a process in which the dithionite yield is determined by a competition between formation and decomposition reactions in the catholyte.

An increase in current density should generally improve the dithionite yield as it raises the rate of dithionite formation at the cathode. However, this effect is limited by the polarization of the cathode, which promotes alternative and/or destructive cathode reactions. Consequently, the positive effect of current density is only seen at a high sulfur dioxide concentration. Similarly, the negative effects of flow rate and sulfur dioxide concentration are reversed at a high current density because increases in flow or concentration restore the balance of cathode reactions to favor dithionite accumulation.

The curves of Fig. 4 and 5 described the action of the cell in more detail. Figure 4 shows how an increasing current density on the cathode causes the current efficiency to fall due to the effects of secondary electrode reactions and chemical decomposition. Corresponding results for dithionite yield from sulfur dioxide show that with increasing current density the dithionite yield rises until it reaches a maximum at a critical current density. Higher current densities lead to a loss of yield through secondary electrode reactions. Experimentally, the critical current density is that at which hydrogen bubbles appear in the product catholyte, higher current densities give free sulfur and cause the disappearance of the typical orange color in the product dithionite solution.

The effect of sulfur dioxide feed concentration and catholyte flow rate on the critical current density is reflected in Fig. 6 and 7. These results are indicative of the importance of mass transfer to the kinetics of dithionite accumulation in the catholyte during the electroreduction of sulfur dioxide in water.

The utilization of electric current in the various cell reactions is shown in Fig. 8. At low current densities dithionite is the principal product of the cathode reaction, with small amounts of thiosulfate and hydrogen. As the current density increases thiosulfate formation becomes more important, until hydrogen and dithionite degeneration products are the only results of current applied in excess of the critical current density.

Figure 8 also shows the value of lead as a cathode material. Lead has a higher hydrogen overvoltage than stainless steel, but it appears that the lower hydrogen loss is compensated by increased thiosulfate formation. The maximum dithionite yield is not increased by using a lead cathode, although the critical current density is somewhat higher than that obtained with a stainless steel cathode.

(b) Effect of ratio of cathode surface to cathode chamber volume.—Figure 9 demonstrates that increasing the ratio of cathode surface area to cathode cham-

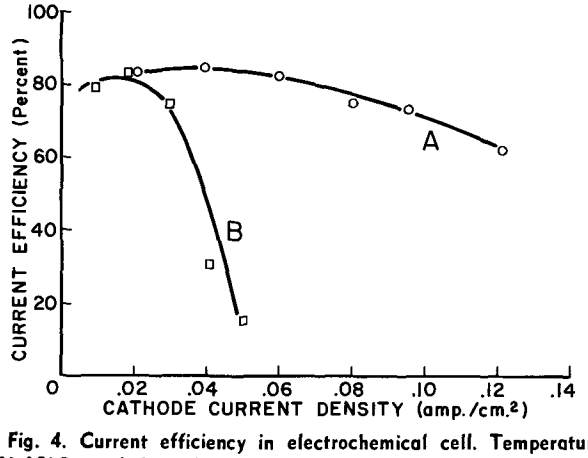

Fig. 4. Current efficiency in electrochemical cell. Temperature, 10°-15°C; catholyte flow, 100 ml/min; cathode area, 1000 cm^2; cathode area/chamber volume, 15 cm^2/cm^3; SO_2 feed concentration: A, 95 g/liter; B, 26 g/liter.

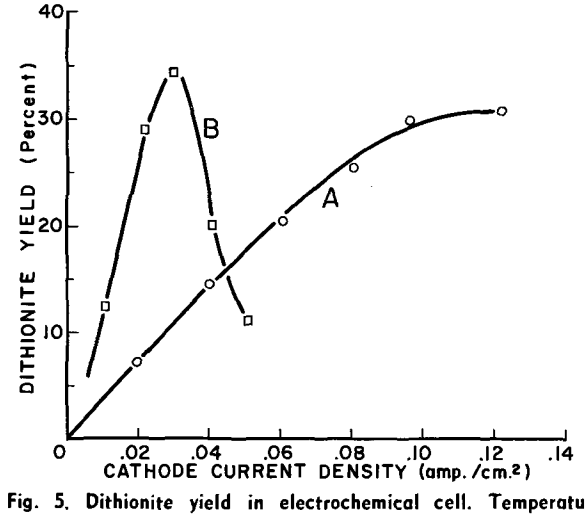

Fig. 5. Dithionite yield in electrochemical cell. Temperature, 10°-15°C; catholyte flow, 100 ml/min; cathode area, 1000 cm^2; cathode area/chamber volume, 15 cm^2/cm^3; SO_2 feed concentration: A, 95 g/liter; B, 26 g/liter.

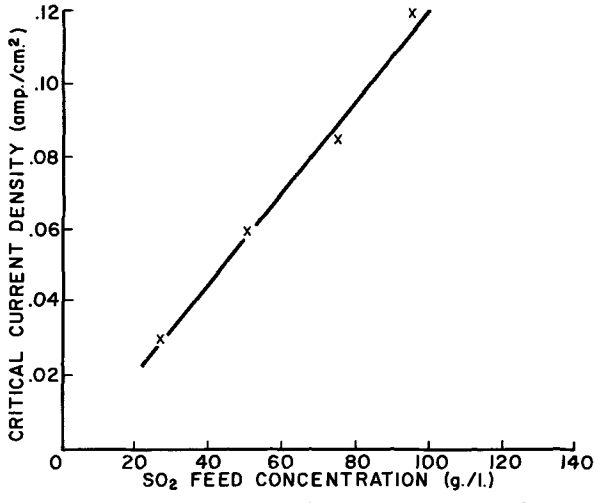

Fig. 6. Effect of sulfur dioxide feed concentration on the critical current density. Temperature, 15°C; catholyte flow, 100 ml/min; cathode area, 800 cm^2; cathode area/chamber volume, 15 cm^2/cm^3.

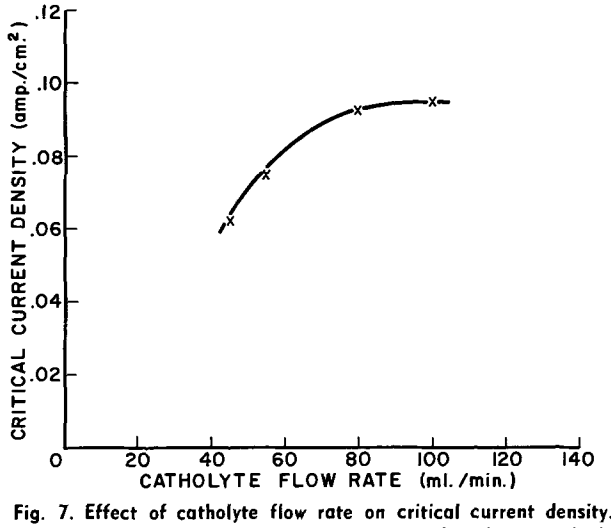

Fig. 7. Effect of catholyte flow rate on critical current density. Temperature, 15°C; SO_2 feed concentration, 80 g/liter; cathode area, 800 cm^2; cathode area/chamber volume, 15 cm^2/cm^3.

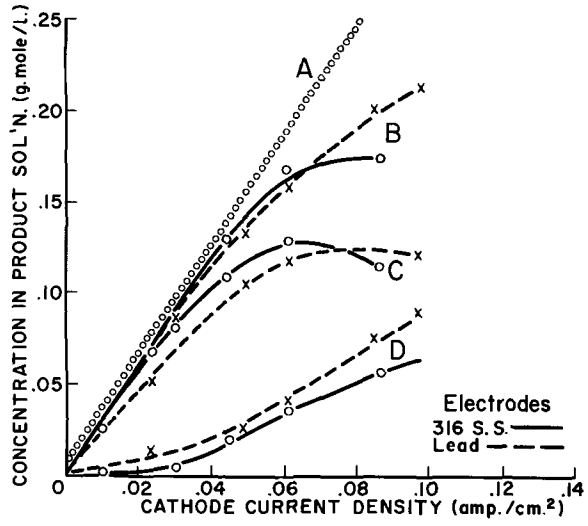

Fig. 8. Current utilization in electrochemical cell. Temperature, 10°-15°C; catholyte flow, 100 ml/min; SO_2 feed concentration, 50 g/liter; cathode area 1000 cm^2; cathode area/chamber volume, 15 cm^2/cm^3: A, applied current; B, thiosulfate + dithionite; C, dithionite; D, thiosulfate.

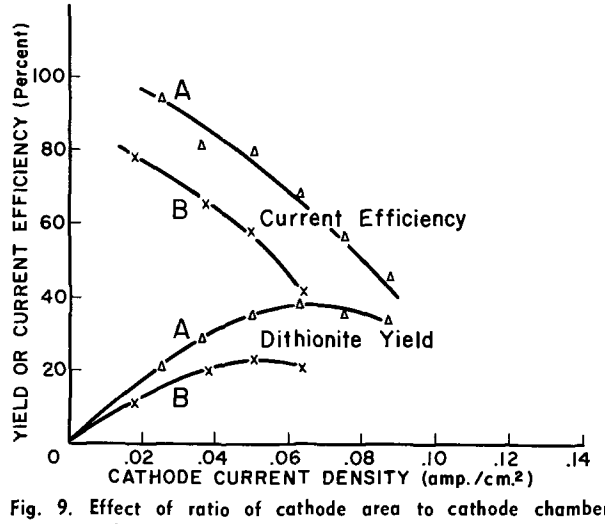

Fig. 9. Effect of ratio of cathode area to cathode chamber volume on yield and current efficiency for dithionite. Temperature, 15°C; catholyte flow, 50 ml/min; SO_2 feed concentration, 80 g/liter; cathode area, 800 cm^2. Ratio of cathode area to chamber volume: A, 15 cm^2/cm^3; B, 8 cm^2/cm^3.

ber volume increases the maximum dithionite yield from a single cell. This ratio is raised from 8 to 15 cm^2/cm^3 by packing the cathode chamber with inert beads and is responsible for increasing the maximum dithionite yield from 28 to 38%. The effect here is that of increasing the rate of dithionite formation relative to its rate of decomposition and possibly of helping sulfur dioxide transfer through increasing the turbulence in the catholyte.

(c) Effect of total cathode area.—The conversion of sulfur dioxide can be increased, while still employing subcritical current densities, through using more than one cell in series. The result of using two cells in series, thus increasing the total cathode area from 800 to 1600 cm^2, is shown in Fig. 10. In the experiments represented by Fig. 10, the current was supplied to the two cells in parallel with the same potential drop across each cell and the current density averaged over the total electrode area.

The effect of doubling the cathode area was to increase the maximum yield of dithionite from 38 to 48%, while the corresponding total applied current was raised from 50 to 70 A.

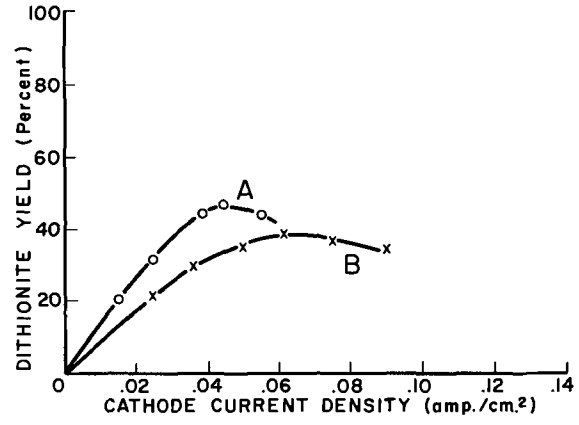

Fig. 10. Effect of cathode area on dithionite yield. Temperature, 15°C; catholyte flow, 50 ml/min; SO_2 feed concentration, 80 g/liter; cathode area/chamber volume, 15 cm^2/cm^3. Cathode area: A, 1600 cm^2; B, 800 cm^2.

It is apparent from these results that, as the sulfur dioxide conversion rises, the current density which can be usefully applied to the catholyte must fall. This decreasing current density means a decreasing rate of dithionite formation but coincides with an increasing rate of dithionite decomposition. The difficulty is compounded by the high order kinetics of dithionite decomposition but is balanced by the rising catholyte *p*H shown in Fig. 11. The consequence of these interactions is an area of diminishing returns where the use of greater cathode areas eventually leads to a loss of dithionite yield.

Within the limitations of the experimental apparatus, the dithionite yield obtained with four cells in series was no greater than that obtained from two cells, and sometimes less. The highest dithionite yield measured was 48% and corresponded to a current efficiency of 72% with a product concentration of 52 g/liter of sodium dithionite.

(d) Effect of catholyte pH.—The consequence of increasing the catholyte feed *p*H with a constant total sulfurous sulfur content is illustrated in Fig. 12. For a given current density, the current efficiency on a stainless steel cathode falls with increasing catholyte *p*H. These curves are some evidence that the formation of dithionite is favored by the presence of free sulfur dioxide and that the bisulfite ion, which in Fig. 12 has its highest concentration at a *p*H of 2.1, is not relevant to the primary cathode reaction.

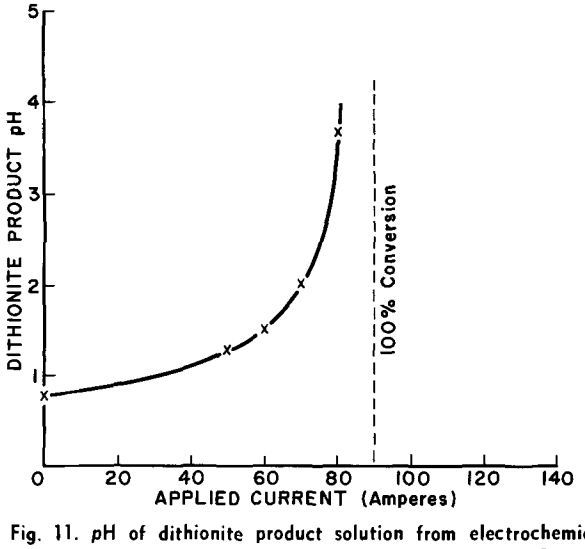

Fig. 11. *p*H of dithionite product solution from electrochemical reactor. Temperature, 15°C; catholyte flow, 50 ml/min; SO_2 feed concentration, 80 g/liter; cathode area, 800 cm^2.

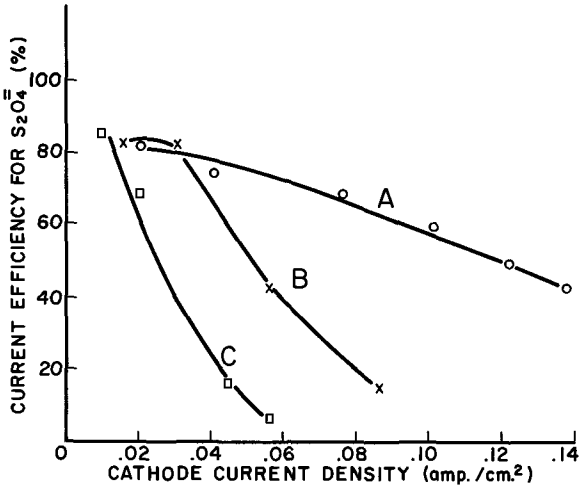

Fig. 12. Effect of catholyte *p*H on current efficiency in electrochemical cell. Temperature, 10°-15°C; catholyte flow, 100 ml/min; cathode area, 1000 cm^2; cathode area/chamber volume, 8 cm^2/cm^3. Catholyte composition: A, 95 g/liter SO_2; *p*H = 0.75; B, 95 g/liter SO_2 + 60 g/liter NaOH, *p*H = 2.1; C, 95 g/liter SO_2 + 90 g/liter NaOH, *p*H = 6.0.

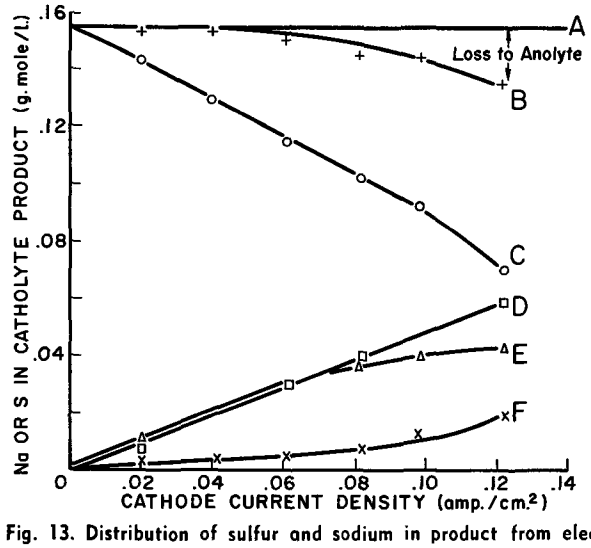

Fig. 13. Distribution of sulfur and sodium in product from electrochemical cell. Temperature, 10°-15°C; catholyte flow, 100 ml/min; SO_2 feed concentration, 95 g/liter; cathode area, 1000 cm^2, cathode area/chamber volume, 15 cm^2/cm^3. A, total S in feed; B, total S in product; C, S in sulfite; D, Na^+ in product; E, S in dithionite; F, S in thiosulfate.

(e) Sodium and sulfur balance.—The movement of sulfur and sodium across the membrane is an important aspect of the operation of the electrolytic cell. Figure 13 shows the effect of current density on the quantities of sulfur and sodium appearing in the catholyte product. That the membrane is selective for cations is evident in the relation between total sulfur in the catholyte feed and that in the catholyte product. These lines are identical for low current densities, but at high current densities they show a gap, corresponding to a loss of negative sulfur radicals into the anolyte. Sodium ions appear to be the principal current carrier across the membrane.

Conclusion

Sodium dithionite can be made by the electroreduction of a simple solution of sulfur dioxide in water in a divided cell.

In this process, the formation of dithionite is favored by the presence of free sulfur dioxide in the catholyte. However, the low *p*H of the catholyte promotes the decomposition of dithionite, which effect is compounded by the catalytic influence of thiosulfate in the product solutions.

The natural difficulties in producing dithionite through the electroreduction of sulfur dioxide in water can be partly overcome in the design of the reactor used for this purpose. A continuous bench-scale reactor, operating at 10°C on a catholyte feed of 8% sulfur dioxide in water, has been made to give a solution containing 52 g/liter of sodium dithionite with a corresponding current efficiency for dithionite of 72%, and a dithionite yield of 48%.

The process is one of diminishing returns in which the yield is limited by the increasingly unfavorable balance between dithionite formation and decomposition with rising sulfur dioxide conversion.

Manuscript submitted Dec. 1, 1969; revised manuscript received *ca.* Aug. 3, 1970. This was Paper 207 presented at the New York Meeting of the Society, May 4-9, 1969.

Any discussion of this paper will appear in a Discussion Section to be published in the June 1971 JOURNAL.

REFERENCES

1. L. A. Pratt, *Ind. Eng. Chem.*, **16**, 676 (1924).
2. B.I.O.S. Final Report No. 1373 (1948).
3. J. A. A. Ketelaar, *Chem. Ing. Tech.*, **35**, 372 (1963).
4. F. E. Murray *et al.*, *Pulp Paper Mag. Can.*, **68**, T-28 (1967).
5. J. W. Mellor, "A Comprehensive Treatise on Inorganic and Theoretical Chemistry," Vol. 10, p. 166, Longman, Green and Co. Ltd., London (1930).
6. A. Gerout, *Compt. Rend. T.*, **LXXXV**, No. 4, 225 (1877).
7. A. Worsley, Brit. Pat. 218,347, "Improvements in and Relating to the Production of Hyposulfurous Acid and the Use thereof," July 3, 1924.
8. E. H. Ekker, "Sur la formation de l'hydrosulfite de sodium par le courant électrique," *Rec. Trav. Chim.*, p. 57 (1895).
9. A. R. Frank, *Z. Elektrochem.*, No. 28, p. 450 (1904).
10. K. Elbs and K. Becker, *ibid.*, No. 21, p. 361 (May 1904).
11. K. Jellinek, *ibid.*, No. 7, p. 245 (April 1911).
12. A. McGlynn and O. W. Brown, *J. Phys. Chem.*, **33**, 1665 (1929).
13. O. Nitzschke, *et al.*, U.S. Pat. 2,193,323, "Manufacture of Hyposulfites," March 12, 1940. Also, Brit. Pat. 475,000.
14. M. S. Spencer, Brit. Pat. 1,045,675, "Process for the Electrolytic Production of Dithionites," Oct. 12, 1965.
15. R. McKee and N. Woldman, *Color Trade J. and Textile Chemist*, **15**, 98 (1924).
16. W. M. Latimer, "Oxidation Potentials," Prentice Hall Co., New York (1952).
17. I. Kolthoff and C. Miller, *J. Am. Chem. Soc.*, **63**, 2818 (1941).
18. R. McKee and N. Woldman, *Color Trade J. and Textile Chemist*, **15**, 1 (1924).
19. R. Rinker, *et al.*, *Ind. Eng. Chem. Fundamentals*, **4**, 282 (1965).
20. M. S. Spencer, *Trans. Faraday Soc.*, **64**, 2510 (1967).
21. O. Ingruber and J. Kopandis, *Pulp Paper Mag. Can.*, **68**, T-258 (1967).
22. Wayman, *et al. TAPPI*, **51**, 89 (1969).
23. R. McKee and N. Woldman, *Color Trade J. and Textile Chemist*, **15**, 180 (1924).
24. I. Kolthoff *et al.*, "Volumetric Analysis," Vol. 3, p. 297, Interscience Publishers Inc., New York (1957).

Technical Notes

Electroplating of Osmium

A. J. Appleby*

Institute of Gas Technology, Chicago, Illinois 60616

Although electroplating of the remaining platinum-group metals has been widely studied, there are no references in the literature to bright osmium plating. When the subject was last reviewed (1), a number of methods were available for bright ruthenium plating, including aqueous (for instance, nitrosochloride) baths, and a high-temperature process originally described for noble metal stripping by Atkinson (2) and for iridium electrodeposition by Withers and Ritt (3), and extended to platinum and ruthenium coatings by Rhoda (4). A fused alkali cyanide bath is used in the latter method, with dissolving noble metal anodes. Electrodeposited coatings were described (4) as being of much better quality than those available from aqueous ruthenium or platinum baths, and could be produced in flaw-free layers up to several mils in thickness. Owing to the instability of the cyanide complexes of palladium and apparently also of rhodium, no satisfactory results were obtained with these metals. No attempts were made to plate osmium by a similar method.

Khomchenko and co-workers examined aqueous osmates or perosmates (5), together with hexachlorosmates (6) for preparing electrodeposited osmium black catalyst electrodes. Although previous studies by the same workers (7) showed that bright ruthenium deposits could be prepared under certain conditions from analogous ruthenium baths (ruthenates), they report no work on obtaining bright osmium deposits. Black deposits were also obtained by Llopis and Vasquez using a similar method (8).

In the present work, an osmium electrode for oxygen electrode and redox studies was required. A bright deposit with the lowest possible roughness factor was most desirable, as this is easier to interpret kinetically. Gold foils of 1 cm^2 area were used as the substrate.

Some initial experiments were carried out in 2% aqueous hexachlorosmate solutions using a gold cathode and carbon anode at current densities varying from 1 to 20 mA/cm^2. At low current densities (lower than about 4 mA/cm^2, no osmium was deposited. At higher current densities, black nonadherent deposits resulted. At low current densities, it appears that Os^{2+} is formed.

Accordingly, an attempt was made to obtain a bright electrodeposit on gold using a modification of the molten salt method (2-4). A mixture of 8% osmium trichloride in equal parts of KCN-NaCN was heated to 600°C under nitrogen in an alumina crucible.[1]

Not all the osmium salt appeared to be soluble; some decomposition occurred. Using a gold cathode and a graphite anode, current densities in the range 1-50 mA/cm^2 were explored. Below about 5 mA/cm^2 no deposit appeared, but at about 10-20 mA/cm^2 a bright and adherent, though granular, deposit (*i.e.*, showing many-faceted crystals) was obtained. At higher current densities, black deposits again resulted.

In the present work, no attempts were made to make deposits thicker than 2-5μ, as this was sufficient for the purpose of making an electrode. Initial current efficiency was on the order of 20-40%, based on Os^{3+}. Attempts to obtain thicker coatings in the apparatus used were not successful, owing to deterioration of the bath. It would appear that more careful control of the atmosphere over the melt than was possible with nitrogen flow over an open crucible is necessary to prevent loss of osmium as OsO_4. It was observed that electrodeposited osmium films dissolved in the bath when small anodic currents (~1 mA) were applied.

Roughness factors of the electrodeposited coatings were measured by the electrolytic hydrogen-charging method, using constant current chronocoulometry in nitrogen-saturated dilute sulfuric acid. This method has been shown to give results that are consistent with BET measurements (5), and it is not affected by the presence of gold, which does not adsorb hydrogen in this potential range (9). Typical roughness factors for the granular bright deposits were 6-7.

It thus appears that bright osmium electrocoatings, using dissolving osmium anodes in molten cyanides, are a practical proposition.

Acknowledgments

The author wishes to thank the sponsors of the TARGET fuel cell program and Pratt & Whitney Aircraft Division of United Aircraft Corporation, for permission to publish this work.

Manuscript submitted Feb. 5, 1970; revised manuscript received *ca.* Aug. 14, 1970.

Any discussion of this paper will appear in a Discussion Section to be published in the June 1971 JOURNAL.

REFERENCES

1. F. H. Reid, *Met. Rev.*, **8**, 167 (1963).
2. R. H. Atkinson, U.S. Pat. 2,093,406 (Sept. 1937).
3. J. C. Withers and P. E. Ritt, *Tech. Proc. Am. Electroplaters' Soc.*, **44**, 124 (1957).
4. R. N. Rhoda, *Plating*, **49**, 69 (1962).
5. G. P. Khomchenko, N. G. Ul'ko, and G. D. Vovchenko, *Electrokhimiya*, **1**, 659 (1965).
6. T. M. Grishina, G. P. Khomchenko, and G. D. Vovchenko, *Vestn. Mosk. Univ., Ser. II, Khim.*, **17**, No. 2, 53 (1962).
7. T. N. Stoyanovskaya, G. P. Khomchenko, and G. D. Vovchenko, *ibid.*, **17**, No. 5, 30 (1962); **18**, No. 2, 20 (1963).
8. J. Llopis and M. Vazquez, *Anales Real Soc. Espan. Fis. Quim. (Madrid)*, **B63**, 273 (1967).
9. F. G. Will and C. A. Knorr, *Z. Elektrochem.*, **64**, 270 (1960).

* Electrochemical Society Active Member.

Key words: osmium, electrodeposition of osmium, fused-salt osmium baths.

[1] The osmium electrodeposits obtained during the course of this work were only for the purpose of making test electrodes for experimental redox and oxygen electrode studies. For these experiments a thin coating of osmium was satisfactory. No facilities were available to extend the study to examination of the conditions for obtaining thicker coatings. The control of atmosphere above the melt was not particularly satisfactory, and this probably accounts for the instability of the bath. However, we were able to show that bright osmium flash coatings can be produced by this method and, with more careful control of atmosphere and using dissolving osmium anodes to insure a constant concentration of Os ions in the melt, it seems probable that more satisfactory coatings of considerable thickness can be obtained.

Observations on Imperfections in Silicon Material Using the Spreading Resistance Probe

D. C. Gupta,* J. Y. Chan, and P. Wang*,[1]

The Bayside Research Center of General Telephone & Electronics Laboratories Incorporated, Bayside, New York 11360

The spreading resistance probe is a versatile technique for measuring resistivity, resistivity profiles, resistivity variations, mobility, and the hardness of silicon (1-7). In this paper, the applications of this probe to study resistivity striations and lateral variations in resistivity are described. Further, it is shown that the probe can also be used to locate strain regions and various imperfections in bulk and epitaxial silicon which affect the electrical properties of the material.

The spreading resistance probe technique, as discussed elsewhere (1, 2), is based on the measurement of the total contact resistance or conductance of a metal-to-semiconductor point contact. The radius of contact is influenced by mechanical vibration, the pressure on the probe, the specimen surface preparation, and the damage of the region under the contact due to Joule heating during measurement. It is, therefore, necessary to control all these parameters to make the measurements reproducible. The measurements reported in this paper were made by using a semiautomatic spreading resistance probe in a constant output voltage mode and with a constant impact of the probe to the specimen as described by Gupta and Chan (1). With this probe, the reproducibility of the resistivity measurements on (111)-oriented n-type bulk silicon was found to be $\pm$ 0.39% (3σ) over a wide range. Similar reproducibility was also obtained on p-type silicon material.

Application of the Technique to Study Imperfections

The technique is applicable for locating regions of resistivity striations and impurity segregation in highly doped bulk silicon. It has also been shown to be useful in identifying deformed regions and strain areas. Figure 1 shows striations in a low-resistivity phosphorus-doped silicon slice cut in (111)-plane as depicted on an x-ray topograph; the numbers represent resistivity values obtained by spreading resistance probe and normalized such that the value at the center of the slice was one. As the spiral grew out from the center, higher resistivity values were obtained.

Figure 2 shows the x-ray topograph of a slice cut in (110)-plane from a low-resistivity phosphorus-doped silicon grown in a <111> direction. The striations were in the form of closely spaced lines because of the angle in which the crystal was cut. Resistivity measurements were made with the spreading resistance probe and values represented a variation of up to 14%.

Figure 3 is a photograph of strain field on the back side of a n/n^+ silicon epitaxial wafer as seen through the scanned Infrared Laser Microscope (8). The substrate of the wafer was Sb doped to approximately 0.008 ohm-cm or 7×10^{18} atoms/cm^3, the solubility limit. Darker areas in the photograph represented high absorption areas where free carrier concentrations were higher. These dark regions did not result from strains in the silicon due to lattice mismatch because regions with greater strain should be more transparent to infrared radiation. High concentration areas were also verified by the spreading resistance probe measurement data taken on the back side surface. These areas on the slice could actually be located by carefully mapping the resistivity values as shown in normalized form on this micrograph; low values were obtained in the darker areas and high values in the light-shaded areas.

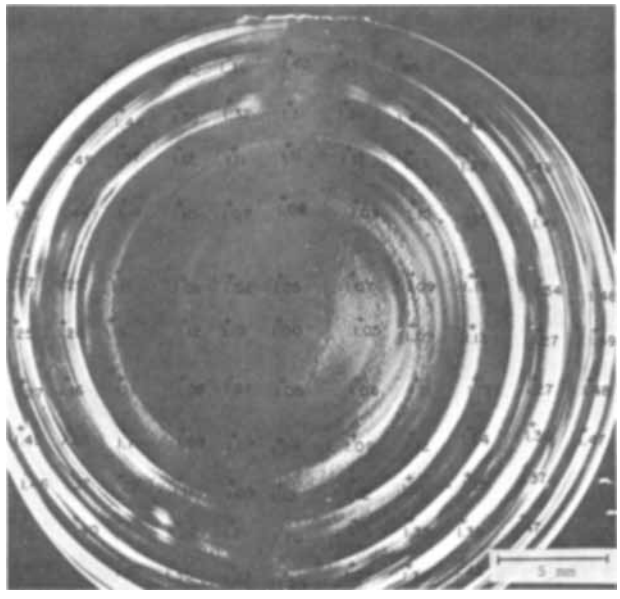

Fig. 1. Numbers showing resistivity values in normalized units as measured with the spreading resistance probe (1.0 represents 0.004 ohm-cm) superimposed on an x-ray topograph of the striations in a low-resistivity phosphorus-doped silicon slice cut in (111)-plane.

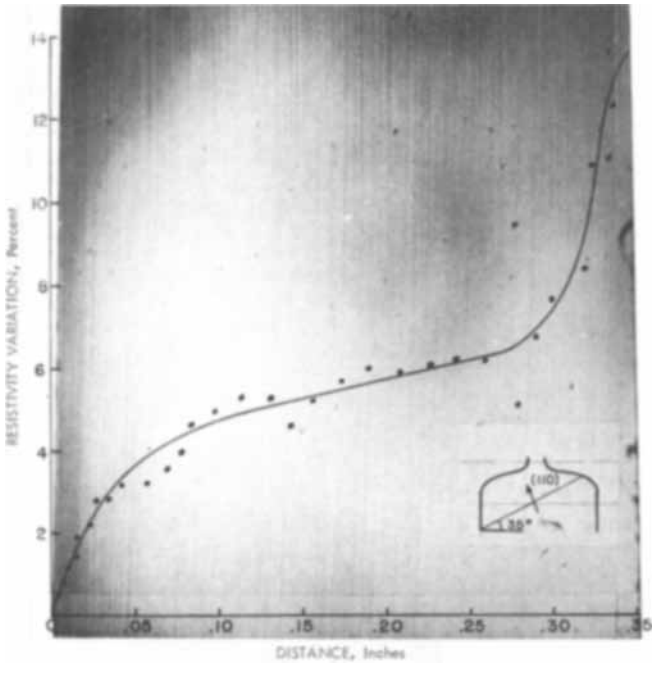

Fig. 2. Measured resistivity variations are superimposed on an x-ray topograph of a low-resistivity phosphorus-doped silicon slice cut in (110)-plane from a crystal (diam 1 in.) grown in <111> direction.

* Electrochemical Society Active Member.
[1] Present address: Texas Instruments, Inc., Dallas, Texas 75222.

Key words: silicon, spreading resistance probe, resistivity inhomogeneities, growth imperfections, micro-defects in bulk and epitaxial silicon.

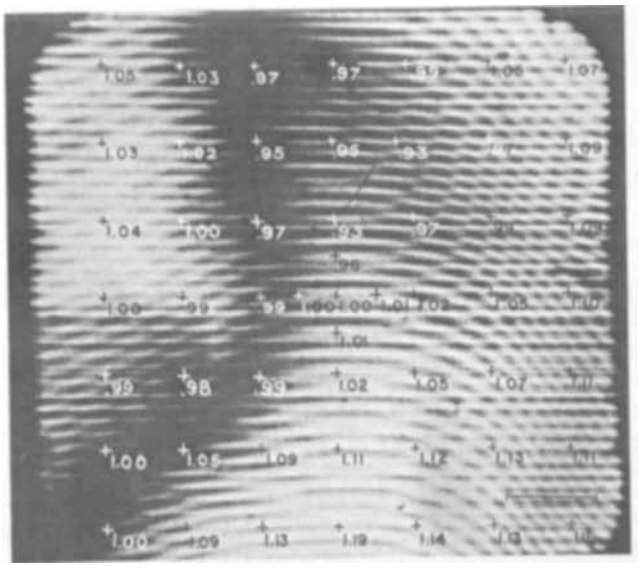

Fig. 3. Photograph of strain field on the backside of n/n$^+$ silicon epitaxial wafer with Sb-doped substrate as seen through the Scanned Laser Infrared Microscope (8). Numbers show resistivity values in normalized units, 1.0 represents 0.0089 ohm-cm, $\Delta\rho/\rho \simeq$ 26%.

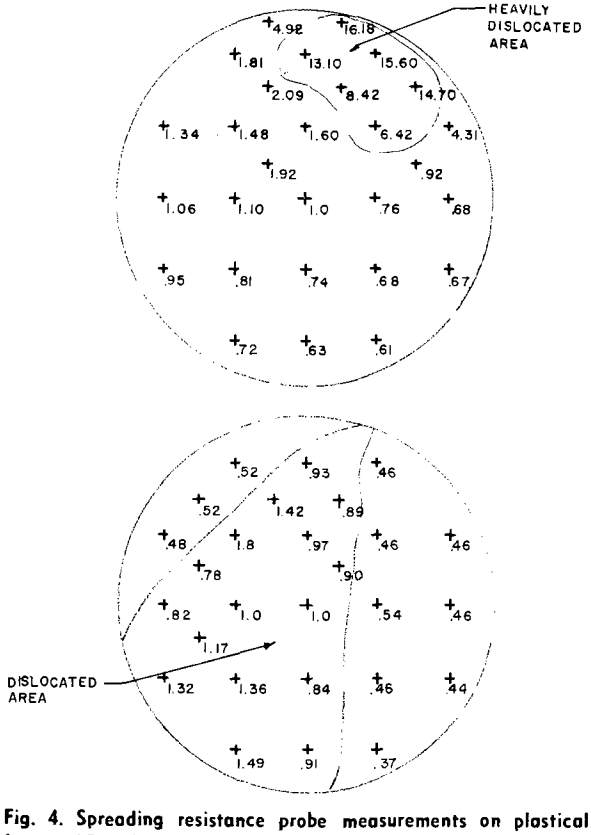

Fig. 4. Spreading resistance probe measurements on plastically deformed IC-wafers after isolation diffusion: (a) severely deformed specimen, (b) not-so-severely deformed. Numbers show resistivity values in normalized units.

Spreading resistance probe measurements made on an epitaxial wafer that contained a large number of stacking faults did not reveal any significant variations in resistivity. Either these stacking faults were not electrically active or this spreading resistance probe was incapable of locating the microvariations due to stair-rod dislocations (9).

Normalized spreading resistance measurements data on two partially plastically deformed silicon slices are shown in Fig. 4. The wafer shown in Fig. 4(a) was more severely deformed than that shown in Fig. 4(b). In the more severely deformed wafer, high-resistivity values were found to correspond to regions with high dislocation density observed by x-ray transmission topography. In the less severely deformed specimen, the regions with high dislocation densities still yielded higher resistivities, but the change in the resistivity values in deformed and not-deformed areas was relatively minor. These results may be explained partly in terms of Read's theory modified to include the scattering of carriers. The scattering results in a reduction of mobility as shown experimentally by Glaenzer and Jordan (10). Their results, however, are not directly applicable here because the dislocations in the silicon samples used in their work were intentionally aligned in one direction, whereas the dislocations in the silicon wafers used in the present work were not oriented in any particular direction.

Figure 5 is an x-ray transmission topograph of an integrated circuit wafer taken after isolation diffusion. This wafer was severely deformed by the high temperature and high surface concentration boron diffusion step for formation of the isolation junctions. The extent of plastic deformation in five different regions is shown in the enlarged micrographs strategically placed on the over-all view. The spreading resistance probe measurements taken on the back side surface were normalized and are plotted on this micrograph. Several features are prominent in this figure:

(a) Higher resistivities corresponded to higher dislocation density.
(b) The deformation was due to localized stress caused thermally or mechanically rather than to the high boron surface concentration used in the diffusion.
(c) The bright spot, a strain region probably due to probe damage, had no effect on resistivity, supporting our previous observation.

Conclusions

The spreading resistance probe is shown to be useful in detecting inhomogeneities and strain areas in bulk and epitaxial silicon without the use of sophisticated photographic techniques. To detect these, however, the probe needs to be a precise instrument capable of high spatial resolution. Such a probe can be designed with the careful consideration of all the parameters that affect spreading resistance measurements (1, 3). The quality of the surface of the specimens is required to be the same as that of the bulk calibration standards. Wherever possible, vapor-etched or chemically mechanically polished, mirrorlike surfaces should be used. These surfaces yield reproducible results (11). The technique is simple, speedy, and nondestructive. As with all electrical measurements, the technique has the drawback of being nonspecific as to the characteristics of the defects.

Acknowledgments

The authors acknowledge the assistance of the late John Sciola for the x-ray topography work and E. D. Jungbluth for the investigations on the Scanned Laser Infrared Microscope.

Manuscript submitted March 30, 1970; revised manuscript received Aug. 10, 1970. This was Paper 101 presented at the New York Meeting of the Society, May 4-9, 1969.

Any discussion of this paper will appear in a Discussion Section to be published in the June 1971 JOURNAL.

REFERENCES

1. D. C. Gupta and J. Y. Chan, *Rev. Sci. Instr.*, **41**, 176 (1970).
2. R. G. Mazur and D. H. Dickey, *This Journal*, **113**, 255 (1966).
3. J. M. Adley, M. R. Poponiak, C. P. Schneider, P. A. Schumann, Jr., and A. H. Tong, "Semiconductor Silicon," R. R. Haberecht and E. L. Kern, Editors, p. 721, ECS Softbound Symposium Series (1969).
4. D. C. Gupta, *This Journal*, **116**, 670 (1969).
5. A. H. Tong and M. R. Poponiak, *ibid.*, **114**, 275C (1967).

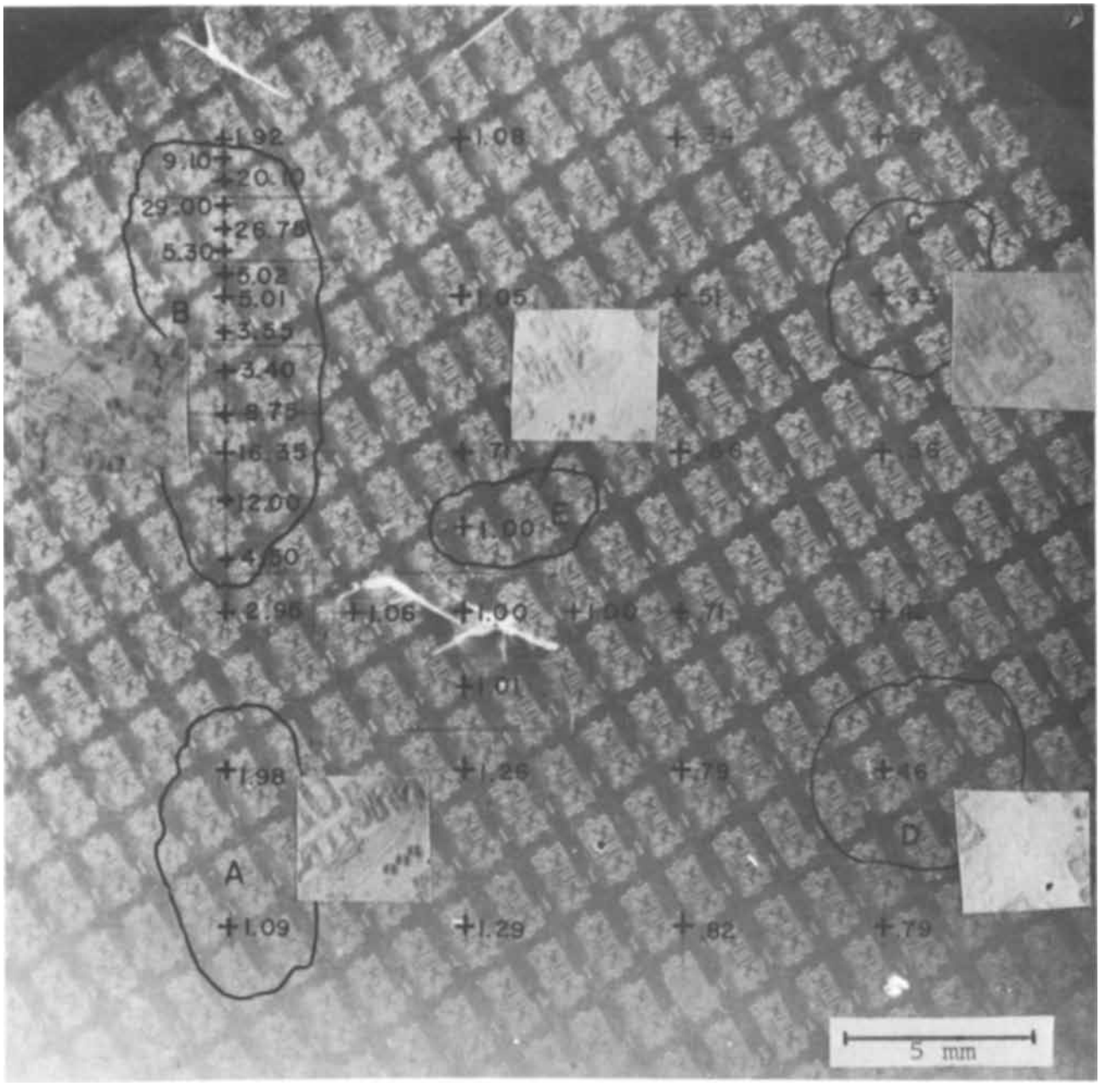

Fig. 5. X-ray transmission topograph of a plastically deformed IC-wafer after isolation diffusion. Numbers represent resistivity values in normalized units as measured with the spreading resistance probe.

6. H. F. John, J. W. Faust, Jr., and R. Stickler, *IEEE Trans. PMP*, **2**, 51 (1966).
7. R. G. Mazur, *This Journal*, **114**, 255 (1967).
8. B. Sherman and J. F. Black, *Appl. Opt.*, **9**, 802 (1970).
9. H. J. Queisser and A. Goetzberger, *Phil. Mag.*, **8**, 1063 (1963).
10. R. H. Glaenzer and A. G. Jordan, *Solid-State Electron.*, **12**, 259 (1969).
11. D. C. Gupta, J. Y. Chan, and P. Wang, *Rev. Sci. Instr.*, To be published.

DISCUSSION SECTION

This Discussion Section includes discussion of papers appearing in the *Journal of The Electrochemical Society*, Vol. 116, No. 3 (March 1969), and Vol. 117, No. 3, March 1970.

Plating Stresses from Electroless Nickel Deposition on Beryllium

R. M. Shemenski, J. G. Beach, and R. E. Maringer
(pp. 402-409, Vol. 116, No. 3)

E. Meisler and **D. Banerjee**[1]: Messrs. Shemenski, Beach, and Maringer have applied the theory of bimetallic beams in order to determine the stress resulting from electroless nickel plating on beryllium. For the problem considered by the authors, the failure to satisfy continuity and equilibrium conditions simultaneously leads to an unduly high value for both the resulting loads and stresses. The results of this investigation indicate that in this case the authors' use of the theory is inapplicable. Before this theory can be successfully applied, one must investigate its applicability and limitations.

The theory presented by Timoshenko[2] as applied by the authors is valid if the following conditions are met:

(*a*) The resulting deflections are small with respect to the thickness of the beam
(*b*) The elastic moduli and the thicknesses of the respective metals must obey the relationship that

$$E_1 t_1^2 = E_2 t_2^2$$

The impact of these conditions can be shown as follows. The free body diagram of the plating and the basis material is shown in Fig. 2 published here. In order that there be no separation at the interface, the relationship between the radii of curvature of the plating and the substrate must be

$$\rho_2 = \rho_1 + \frac{t_1 + t_2}{2} \qquad [i]$$

If the deflections are small, the resulting radii of curvature are very large with respect to the term

$$\frac{t_1 + t_2}{2}$$

Hence, the following approximation can be made

$$\rho_2 \approx \rho_1 = \rho \qquad [ii]$$

Using the beam equation for beam 1 and 2, results in the following relationships

$$\frac{P_1 t_1}{2} = \frac{E_1 I_1}{\rho_1} \qquad [iii]$$

$$\frac{P_2 t_2}{2} = \frac{E_2 I_2}{\rho_2} \qquad [iv]$$

Substituting [ii] in [iii] and [iv] and solving for P results in

$$P_1 = \frac{E_1 b t_1^2}{6\rho_1} \qquad [v]$$

$$P_2 = \frac{E_2 b t_2^2}{6\rho_2} \qquad [vi]$$

Equilibrium considerations demand that P_1 be equal to P_2. No separation at interface demands $\rho_1 = \rho_2$. Hence, in order to satisfy both the condition of continuity, *i.e.*, no separation at the interface and the condition of equilibrium, the following must be satisfied

$$E_2 t_2^2 = E_1 t_1^2 \qquad [vii]$$

One way of satisfying Eq. [vii] is to have $E_1 = E_2$ and $t_1 = t_2$.

The values presented by the authors show that the substrate is approximately twice as thick as the plating and that the elastic modulus of the substrate is 1.5 times the elastic modulus of the plating which results in the following

$$E_2 t_2^2 = 6.0 E_1 t_1^2$$

The immediate inference from this result is that conditions of equilibrium and nonseparation at interface are not satisfied simultaneously. This means that, if one assumes a common radius of curvature for beams 1 and 2, one cannot have a common P for both of them and *vice versa*. The authors, however, ignore this inherent contradiction in the theory and proceed to calculate a common P for beams 1 and 2 while assuming a common radius of curvature (Eq. [A-15]). The effect of this erroneous assumption is illustrated by the values of P in the authors' Table II. It shows values of P as high as 44 lb. A simple experiment performed during the course of this investigation demonstrated that a mere 350g axial load caused buckling and a permanent bow-out of 0.39 in. on a 0.010 in. thick, 0.5 in. wide, and 4 in. long beryllium strip. A simple computation of Euler buckling loads for the type of strip considered by the authors shows the first critical buckling load to be about ½ lb, second critical buckling load to be about 2 lb, and so on. All these clearly show that Eq. [A-15] used by the authors for computing P

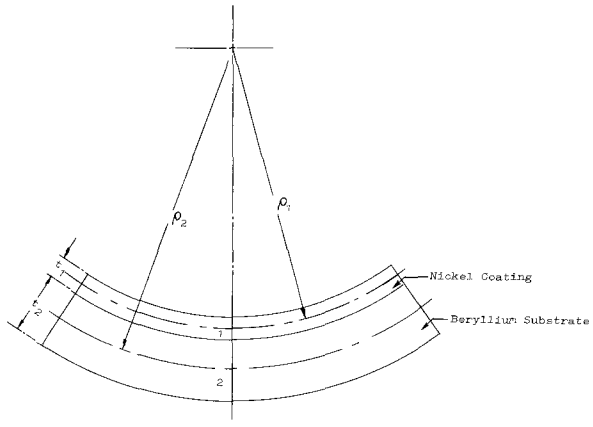

Figure 1

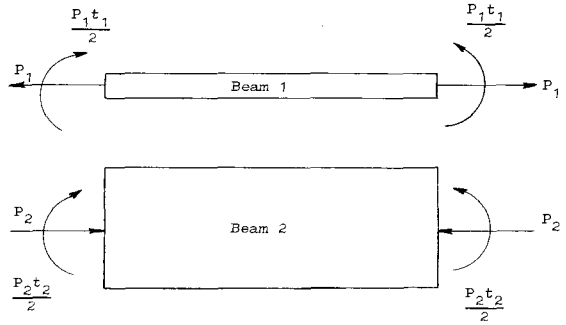

Figure 2

[1] Advanced Development Group, Speedring Systems, 7111 East Eleven Mile Rd., Warren, Mich. 48090.
[2] S. Timoshenko, *J. Opt. Soc. Am.*, **11**, 233 (1925).

for the present problem is not valid and gives unrealistically high values. Consequently, the stress equations, [A-16], [A-17], [A-18], and [A-19], will give erroneous stress values.

The discrepancy is further corroborated if one computes the bow-out based on the authors' Eq. [1] and [2] by using the values of $\Delta\alpha$ from Fig. 4 and compares it with measured values of bow-out presented in Table II. The computed values differ by as much as 100% from the measured values and are on the lower side.

Ignoring the basic assumptions leads the authors to compute stress and load values which are very high and totally unrealistic.

A Simple Procedure for Mounting Sodium-Tungsten Bronze Electrodes

R. S. Alwitt and A. K. Vijh (pp. 413-414, Vol. 117, No. 3)

A. Belanger, G. Belanger, and A. K. Vijh[3]: We have recently applied the suggested procedure of electrode mounting to graphite rod electrodes (National "Spectroscopic Electrodes" obtained from the Carbon Products Division of Union Carbide of U.S.A.; diameter of the electrodes 1/16 in.) and found that some modifications are needed. The graphite rod electrodes were initially prepared as described in the above publication (with contact to a copper wire through a mercury drop) and were tried as anodes for the electrolysis of aqueous sodium chloride solutions. It was observed that the chlorine evolved migrates through the graphite rod and attacks severely the mercury contact and the copper wire forming chemical compounds which are presumably insulating, thus giving rise to terribly bad contact, in addition to creating unwanted, solid-state electrochemical couples. The ease with which chlorine migrates through this graphite electrode suggests presence of some porosity in the graphite. The porosity, however, is definitely not high enough to allow diffusion of the electrolyte solution through the graphite. In any case, if a corrosive gas diffuses through the bulk of an electrode material (with or without porosity) the procedure of Alwitt and Vijh has to be somewhat modified. For graphite rod electrodes, we have changed this procedure slightly in the following way: A platinum wire was first flame-sealed into the Pyrex "trubore" tubing; the outer end of this platinum wire was heated into a small bead and was mechanically fitted into a matching tiny vertical hole drilled into the graphite rod. The bead is unnecessary if a thicker platinum wire which fits tightly into the drilled hole is available. The glass-(platinum)-graphite boundary was masked by the Flotite Teflon tubing (as in the paper under discussion). The mechanical seal between graphite and platinum, though far from being a perfect electrical connection, yields a contact which is satisfactory for most of the laboratory experiments since the ohmic resistance is less than *ca.* 0.2 ohms. A graphite electrode thus mounted is shown schematically in Fig. 1 published here. This electrode assembly has been found to be quite satisfactory for prolonged anodic evolution of chlorine.

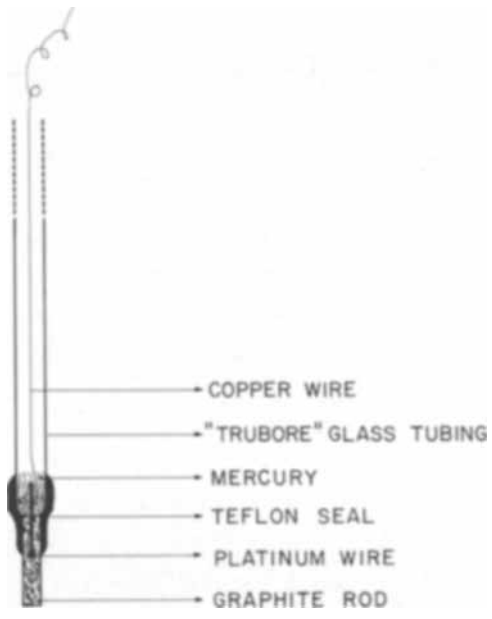

Figure 1

[3] Hydro-Quebec Institute of Research, Varennes, Que., Canada.

JOURNAL OF THE ELECTROCHEMICAL SOCIETY

REVIEWS AND NEWS — SEPTEMBER 1970

Physical and Mechanical Properties of Electrodeposited Copper

III. Deposits from Sulfate, Fluoborate, Pyrophosphate, Cyanide, and Amine Baths[1,2]

Vernon A. Lamb,[3] Christian E. Johnson,[4] and Donald R. Valentine[5]

National Bureau of Standards, Washington, D. C. 20234

ABSTRACT

This paper is the third published report on the results of a broad program on properties of electrodeposited copper, sponsored jointly by the American Electroplaters' Society, The International Copper Research Association, Inc., The Copper Development Association, and the National Bureau of Standards. The first paper is a comprehensive review of the literature to 1965. The second paper is an interim report on experimental results. The present and final paper, which incorporates the data in the second, includes data from the baths designated in the title, for deposits prepared under a wide range of operating conditions and with use of a variety of addition agents. Properties measured include tensile strength, yield strength, elongation, modulus of elasticity, fatigue strength, hardness, internal stress, density, electrical resistivity, and thermal expansivity. Properties were measured for as-plated deposits, deposits after annealing at several temperatures, after cold-working, and at low and high ambient temperatures. Structure of deposits was examined by optical, electron micrograph, and x-ray methods. Content of impurities in deposits was determined. Correlations are developed among properties, structure, impurity content, type of bath, and operating conditions.

I. Introduction

The properties of wrought metals can be varied over wide ranges by alloying, by various heat treatments, or by mechanical working. By these procedures, properties are tailored to fit various applications. Electrodeposited metals are often and increasingly used for electroforming and other engineering applications for which specific properties are required or would be advantageous. As with wrought metals, properties of a particular electrodeposited metal can also be varied over wide ranges. This may be done by varying the type and composition of the plating bath, by use of addition agents or alloying constituents in the bath, or by varying the operating conditions, *e.g.* current density, bath temperature, agitation, or use of modulated current. Properties of electrodeposited metals may also be modified subsequent to formation by heat treatment or mechanical working. Although interest in properties of electrodeposited metals is not new, early applications of plating were such that the need for data on properties was limited, and therefore no comprehensive data had been reported. Special military applications during World War II stimulated work in this area and led to an extensive study of the properties of electrodeposited chromium (1). From 1948 to 1952, a comprehensive project on determination of the properties of electrodeposited nickel was carried out under joint sponsorship of the American Electroplaters' Society and the National Bureau of Standards (2).

Except for nickel, more copper is electrodeposited for technical and engineering applications than any other metal. A considerable amount of data on properties of electrodeposited copper was available prior to the present program. However, there were many gaps and inconsistencies. A broad program to determine physical and mechanical properties of electrodeposited copper was therefore initiated at the National Bureau of Standards, sponsored jointly by the American Electroplaters' Society, the International Copper Research Association, the Copper Development Association, and the National Bureau of Standards.

Key words: electrodeposited copper, copper electrodeposits, copper-electrolytic sulfate, copper-electrolytic fluoborate, copper-electrolytic pyrophosphate, copper-electrolytic cyanide, copper-electrolytic amine, physical properties-electrolytic copper, mechanical properties-electrolytic copper, tensile strength-electrolytic copper, yield strength-electrolytic copper, ductility-electrolytic copper, modulus-electrolytic copper, fatigue strength-electrolytic copper, hardness-electrolytic copper, internal stress-electrolytic copper, density-electrolytic copper, electrical resistivity-electrolytic copper, thermal expansivity-electrolytic copper, annealing-electrolytic copper, cold working-electrolytic copper, hot properties-electrolytic copper, low temperature properties-electrolytic copper, structure-electrolytic copper, impurity content-electrolytic copper.

[1] AES Project 21 Report No. III. Sections I-III published here are the first of three installments of this paper: part 2 (Sections IV-VII) will appear in the October issue and part 3 (Sections VIII-XI) in the November issue.

[2] Sponsors and Committee Members of AES Project 21:

Sponsors

The Research Committee of the American Electroplaters' Society, Inc.
The National Bureau of Standards of the Department of Commerce
The International Copper Research Association, Inc.
The Copper Development Association, Inc.

Committee Members

Dr. M. M. Beckwith, R. O. Hull & Company, Inc.
Dr. William Blum, Consultant
Dr. Abner Brenner, National Bureau of Standards
Stuart Lyman, Copper Development Association, Inc.
Dr. Owen B. Mathre, E. I. du Pont de Nemours & Co., Inc.
Robert E. Ehrhardt, Bell Telephone Laboratories, Inc.
Dr. Abraham Max, Purdue University
Charles W. Ostrander, Allied Research Products, Inc.
Dr. Harold J. Read, Pennsylvania State University
W. H. Safranek, Battelle Memorial Institute
Clarence H. Sample, International Nickel Company, Inc.
E. J. Smith, National Steel Corporation
Dr. D. A. Swalheim, E. I. du Pont de Nemours & Co, Inc
Dr. Dennis Turner, Bell Telephone Laboratories, Inc.
G. C. Van Tilburg, American Metal Climax, Inc.
M. L. Whitehurst, Radio Corporation of America
Dr. Charles I. Whitman, International Copper Research Association, Inc.

[3] Project Director, AES Project 21, at the NBS.

[4] Research Associate from the AES at the NBS 1965-1968.

[5] Research Associate from the AES at the NBS 1963-1965.

Table I. Summary of mechanical and physical properties of as-deposited copper [a,b]

Part A. Deposits from the sulfate bath

Line No.	Panel No.	Bath[c] symbol	Addition agent[d] Name	Addition agent[d] Conc. g/l or other variable	Bath temp, °C	Current density, A/dm²	Tensile[e] strength, ×10³ = psi	Yield[e,f] strength, ×10³ = psi	Elongation in 2 in. (5 cm), %	Young's[e] modulus of elasticity, ×10⁶ = psi	Fatigue[e] strength No. of cycles 10⁶ ×10³ = psi	Fatigue[e] strength No. of cycles 10⁷ ×10³ = psi	Hardness[g] KHN 200g load, kg/mm²	Internal[e,h] stress, psi	Density 25°C, g/cm³	Elec. resistivity 25°C, ×10⁻⁶ = ohm-cm
1	48	Cu1-H1	None		20	0.5	27	8	18				56	−70	8.922	
2	47				30	2	30	8	37				49	400	8.920	1.72
3	52				40	0.5	30	10	24				57	80	8.922	
4	53				40	4	29	8	32				46	530	8.921	
5	55	Cu1-H2	None		20	2	31	9	28	16			59	3,300	8.921	
6	56				30	2	25	7	15				58	570	8.921	
7	58				40	2	24	8	13				47	370		
8	60	Cu1-H3	None		30	0.5	20	8	8				56	−110	8.919	1.72
9	59				30	2	28	8	16				58	1,800	8.919	1.72
10	61				30	4	31	11	16				77	3,800	8.925	
11	62, 63				30	4	36	15	14				80			
12	54	Cu2-H1	None		30	2	30	8	32				48	560	8.922	1.72
13	274		None		40	8	32	10	36				61	1,400	8.925	1.75
14	64		Gelatin	0.003	30	2	40	19	26	17			91		8.914	
15	65		Gelatin	0.003	30	2	41	22	23				88	750	8.915	
16	68		PSA	1.0	30	2	36	15	31				97	−370	8.924	
17	110	Cu2-H2	None		20	0.5	26	7	25	14			105	−510	8.928	1.78
18	94				20	2	32	11	33				61	1,500	8.925	1.73
19	106				20	2	32	10	34							1.74
20	23			5 mils	20	2				16						
21	104			2.5 mils	20	2	45		10	16						1.80
22	22				20	4	33	12	29				67	4,300	8.920	
23	15				32	0.5	23	7	11	13[i]			87	−700	8.924	1.71
24	13				30	2	25	8	14		13	11	88	550	8.921	1.73
25	25				30	2	26	7	19							1.71
26	322, 323				30	2	32	11	39	14	14	12	55		8.925	1.73
27	44				30	4	30	9	24				53	2,200	8.922	1.72
28	51				40	2	22	7	10				85			
29	16, 18				45	2	21	8	10	12[i]			49	−320	8.923	1.73
30	27				45	4	24	7	14				57	190	8.924	
31	66		Gelatin	0.003	30	2	45	28	8	15[i]			82	1,000	8.914	1.76
32	69		PSA	0.7	30	2	33	11	35				73		8.922	
33	70		PSA	1.0	30	2	36	15	34				99	250	8.923	
34	277	Cu2-H3	None		20	2	37	15	41	16[j]			78	2,000	8.926	
35	332				30	0.5	33	10	41				62	−90	8.926	1.71
36	276				30	2	28	9	17	14			54	180	8.924	1.73
37	307				30	2	29		21							
38	308				30	4	34	11	46				66	1,500	8.925	1.73
39	278				30	8	32	14	24				75	4,300	8.926	1.74
40	285				40	8	37	15	44				80	2,600	8.926	1.75
41	286				60	8	27	10	18				58	380	8.925	1.76
42	297				60	20	20	7	5				58	1,400	8.86	1.90
43	5-4		Dextrin	0.02	30	2	22		5[k]				60			
44	5-6		Dextrose	0.05	30	2			Zero							
45	219		EA + M	0.3, 2.0	30	2	27	13	9				61	1,500	8.922	1.73
46	81		Gelatin	0.01	30	2	53	31	10	17[j]			131	860		1.77
47	83		Gelatin	0.1	30	2	40	34	0.4	15[i]			148	−4,200	8.86	2.10
48	5-5		Glycerol	1.0	30	2	33		11[k]				62			
49	5-2		Glycine	0.1	30	2	31		4[k]				79			
50	214		LA	0.05	30	2	25	8	10				78	800	8.929	1.72
51	215		LA, thickness, 2 mils	0.05	30	2	29		3							
52	160		β-NQ	0.1	30	2	36	14	8				119	5,300	8.923	1.78
53	162		β-NQ, thickness, 2 mils	0.1	30	2	46		9							
54	91		NDS	1.8	30	2	31	9	29				67	300	8.923	1.71
55	114		NDS	1.8	30	2	29	6	29				98		8.923	1.73
56	114F		NDS, thickness 6 mils	1.8	30	2	35	15	39							

Table I. (contd.)

Line No.	Panel No.	Bath[c] symbol	Addition agent[d] Name	Addition agent[d] Conc, g/l or other variable	Bath temp, °C	Current density, A/dm²	Tensile[e] strength, ×10³ = psi	Yield[e,f] strength, ×10³ = psi	Elongation in 2 in. (5 cm), %	Young's[e] modulus of elasticity, ×10⁶ = psi	Fatigue[e] strength No. of cycles 10⁶ ×10³ = psi	Fatigue[e] strength No. of cycles 10⁷ ×10³ = psi	Hardness[e] KHN 200g load, kg/mm²	Internal[e,h] stress, psi	Density 25°C, g/cm³	Elec. resistivity 25°C, ×10⁻⁶ = ohm-cm
57	114A	CU2-H3	NDS, thickness 1.3 mils	1.8	30	2	36		10							1.74
58	73		PSA	1.0	20	2	40	18	28				93	1,600	8.923	
59	71		PSA	1.0	30	2	34	13	32				84	100	8.923	1.72
60	71B		PSA	1.0	30	2	36	14	34				90			
61	—		PSA	1.0	30	8								5,000		
62	72		PSA	1.0	40	2	30	9	23				88	380	8.923	1.71
63	76		PSA	1.0	40	4	33	12	31				87	−260	8.922	
64	166		SeO_2	10^{-4} Se	30	2	47	17	21				123	2,300	8.929	1.76
65	168		SeO_2, thickness, 2 mils	10^{-4} Se	30	2	54		11							
66	172		SeO_2	10^{-3} Se	30	2	44	16	24	16	19	14	108	2,800	8.928	1.75
67	173		SeO_2, thickness, 2 mils	10^{-3} Se	30	2	50	28	20							
68	5-1		Sorbitol	0.1	30	2	30		4[k]				51			
69	86		TU	0.005	30	2	20	6	10				70	−120	8.922	1.76
70	88		TU	0.015	30	2	28	12	9				76	−40	8.918	1.77
71	216		TU + NDS	0.015, 0.5	30	2	39	13	20				99	900	8.923	1.76
72	93		TIPA	3.5	30	2	41	19	26	15[i]			109	2,100	8.923	1.73
73	108, 109		TIPA	3.5	30	2	39	19	7	16			129	2,100	8.923	1.76
74	109F		TIPA, thickness, 6 mils	3.5	30	2	53		13	16						
75	109A		TIPA, thickness, 1.4 mils	3.5	30	2	57		9							1.78
76	337-341		TIPA	3.5	30	5	71	43	7	15	25	18	144	7,100	8.913	1.89
77	226		Prop. A[m]		22	4	51	40	14				137		8.917	1.82
78	230		Prop. A[m]		28	4	52	40	19				128	2,900	8.918	
79	306		None	PR cycle, 5-2 sec	30	4	43	20	26				106	4,100	8.925	1.76
80	321	Cu3-H3	None		20	4	32	12	42				64	3,100	8.925	1.73
81	29				30	0.5	27	8	16				57	−90	8.920	1.71
82	310				30	2	30	9	29				55	620	8.924	1.72
83	31				45	0.5	32	10	34				57		8.919	
84	28				45	4	26	8	15				51	1,400	8.921	1.70
85	30				60	4	30	8	41				53		8.925	1.72
86	32				60	4	31	8	43				57			
87	309				60	8	31	10	33				59	620	8.925	1.75
88	77		PSA	1.0	30	2	34	13	32		19		82	−420	8.921	
89	78C	Cu2-H2	None	Spangled deposit	20	2	15	6	8				85		8.923	2.08
					Part B. Deposits from the fluoborate bath											
90	342	F-1	None		30	2	20	9	7				53	Zero	8.925	1.73
91	343-345				30	8	37	16	31	12	16	13	81	700	8.926	1.73
92	346				60	8	32	11	16				56	−200	8.925	1.73
93	347	F-2	None		30	8	36	15	31				71	800	8.926	1.74
94	348				50	20	33	12	29		16		60	1,600	8.925	1.75
					Part C. Deposits from the pyrophosphate bath											
95	317-320	Pyrophos-phate	None	Air agitation	50	2	38	20	39	17	22	17	83	−1,600	8.926	1.75
96	312			Mech. agitation Thickness, 8 mils	50	4	42	23	23							1.73
97	313			Mech. agitation Thickness, 16 mils	50	4	40	22	31				90			1.74
98	314			Air agitation	50	4	40	22	33		22			1,700		1.74
99	315			Violent air + mech agitation	50	4	41	23	35				92		8.926	1.74
100	316			Air agitation	60	4	39	20	39				80	−1,900	8.926	1.74

Table I. (contd.)

Line No.	Panel No.	Bath[c] symbol	Addition agent[d] Name	Addition agent[d] Conc, g/l or other variable	Bath temp, °C	Current density, A/dm²	Tensile[e,n] strength, ×10³ = psi	Yield[e,f] strength, ×10³ = psi	Significant strain	Young's[e] modulus of elasticity, ×10⁶ = psi	Fatigue[e] strength No. of cycles 10⁶ ×10⁶ = psi	Fatigue[e] strength No. of cycles 10⁷ ×10⁶ = psi	Hardness[g] KHN 100g load, kg/mm²	Internal[e,h] stress, psi	Density 25°C, g/cm³	Elec. resistivity 25°C, ×10⁻⁶ = ohm-cm
							Part D. Deposits from the cyanide bath									
101	128	CN-1	None		40	1	66		6 × 10⁻²	17			162	14,000	8.898	1.79
102	125			Thickness, 0.35 mil			47		1.1							1.81
103	130			Thickness, 0.30 mil												1.87
104	125A			Thickness, 0.25 mil			33		0.4							
105	136	CN-2	None		40	1	57		10	17			119	8,600	8.913	1.74
106	138					2	53		14				147	6,900	8.909	1.78
107	133			Thickness, 0.20 mil												1.87
108	143				60	1	66		18	16			135	7,400	8.908	1.76
109	140			Thickness, 0.40 mil												1.80
110	145-147					2	81		4				159	7,800	8.913	1.75
111	142			Thickness, 0.40 mil			46		1.2							1.80
112	142A			Thickness, 0.30 mil			28		0.4							
113	153	CN-3	None		60	2	56		16	17			133	9,500	8.907	1.80
114	150			Thickness, 0.40 mil												1.81
115	197	CN-4	None		40	2	52		10				150	9,200	8.916	1.81
116	201, 202					4	44		7				144	7,500	8.900	1.80
117	158				60	2	53		24	16			129	9,200	8.904	1.78
118	154			Thickness, 0.7 mil			61		1							1.78
119	205					4	50		12	16			132	9,500	8.908	1.84
120	208, 209				80	2	51		25				139	6,100	8.917	1.77
121	210, 212					4	51		22				131	6,400	8.908	1.79
122	178, 180	CN-5	None		40	2	49		13				143	9,300	8.915	1.83
123	182					4	48		14				136	7,600	8.918	1.83
124	184, 186				60	2	54		12	15			123	9,700	8.907	1.78
125	187, 188					4	63		5	16			152	9,500	8.900	1.81
126	191				80	2	53		14				139	6,200	8.917	1.75
127	194, 195					4	78		6				131	6,700	8.912	1.79
128	234-236	CN-6	None		40	2	44		19				116	5,200	8.913	1.76
129	242-244				60	1	43		57				141	3,500	8.918	1.88
130	239, 240					2	64		40				143	5,500	8.919	1.88
131	245, 247					4	58		9				135	4,400	8.919	1.86
132	249				80	2	57		22				158	5,800	8.920	1.87
133	252, 253	CN-7	None		60	2	38		34				92	8,100	8.920	1.74
134	256, 258				80	4	45		25				113	9,100	8.919	1.77
135	260-263	CN-8	None		80	4	37		22				114	4,500	8.919	1.80
136	264, 265			Air agitation			35		41				96			1.77
137	266, 267			N_2 agitation			35		33				96			1.76
138	268-270					6	40		49				98	4,500	8.925	1.76
139	271-273					8	39		50				129	3,900		1.76
140	280			PR, cycle 15-5 sec	80	6	61		31					4,600		1.78
141	281			PR, cycle 15-5 sec Thickness, 18 mils		6	64[o]	38[o]	12[o]		25		147			1.82
142	279			PR, cycle 15-5 sec		8	60		23				151			1.76
143	293, 294, 296			KCNS 2 g/l PR, cycle 15-5 sec Thickness, 18 mils	80	6	86[o]	57[o]	10[o]	17	28	20	144	5,100	8.917	2.02
144	295			Ditto line 143, except PR cycle 30-10 sec			79[o]	46[o]	10[o]		25		193			1.98
145	300	CN-9	Prop. B		80	4	26		9					11,000		1.82
146	305			Thickness, 9 mils			28[o]	12[o]	22[o]				74		8.923	1.80
147	303					6	24		10				76			1.81
148	304			PR, cycle 15-5 sec			66		45				224			1.96

Table I. (contd.)

Line No.	Panel No.	Bath[c] symbol	Addition agent[d] Name	Conc. g/l or other variable	Bath temp., °C	Current density, A/dm²	Tensile[e,n] strength, × 10³ = psi	Yield[e,f] strength, × 10³ = psi	Significant strain	Elongation % in 2 in.	Young's[e] modulus of elasticity, × 10⁶ = psi	Fatigue[e] strength No. of cycles 10⁷ × 10³ = psi	Hardness[g] KHN 200g load 100g load, kg/mm²	Internal[e,h] stress, psi	Density 25°C, g/cm²	Elec. resistivity 25°C, × 10⁻⁶ = ohm-cm
Part E. Deposits from the amine bath							Pull values						200g load			
149	328	Amine	None	Thickness, 5 mils	55	2	69	41		4			202	−5,700	8.891	2.08
150	329			Thickness, 10 mils			50	43		1			169	−6,000	8.906	2.10
151	326-330			Thickness, 5 mils		4	60	44		4						2.10

FOOTNOTES TO TABLE I

[a] Agitation. Air agitation was used for all baths except cyanide baths, except as noted in the "other variable" column in the table. Agitation of cyanide baths CN-1 through CN-4 was effected by pumping the solution upward past the specimen panel. Baths CN-5 through CN-9 were agitated by a combination of pumped solution and propeller stirring, except as noted in lines 136 and 137.
[b] Deposit thickness. Deposits from sulfate, fluoborate, and pyrophosphate baths are 15-20 mils (375-500 μm) thick, except as noted.
[c] Bath symbols are defined in Tables II, III, and IV.
[d] Abbreviations: EA + M, ethyl alcohol plus molasses; LA, lactic acid; β-NQ, β-naphthoquinoline; NDS, 1, 5-naphthalenedisulfonic acid; PSA, phenolsulfonic acid; TU, thiourea; TIPA, triisopropanolamine; Prop. A, proprietary brightener for sulfate bath, containing a sulfonate and an azo dye; Prop. B, proprietary brightener of the selenium type for cyanide bath; PR, periodically reversed current.
[e] One pound per square inch (psi) = 0.000704 kilogram per square millimeter (kg/mm²).
[f] 0.05% offset.
[g] KHN = Knoop hardness number.
[h] Negative values represent compressive stresses.
[i] Determined from beam deflection measurements.
[j] Determined from stress-strain curve. Values not designated [i] or [j] determined by measuring strain with resistance strain gauges.
[k] Per cent elongation in 1 in.
[m] Copper sulfate concentrations in the proprietary baths were in the range specified by the vendor, 225 and 200 g/l, respectively, of $CuSO_4 \cdot 5H_2O$.
[n] Values for tensile strength for thin deposits from the cyanide bath, measured by the bulge method, are based on the initial thickness of the deposits. They are, thus, approximately comparable with values measured by tensile pull.
[o] Tensile and yield strengths and elongation for these thick deposits were measured by tensile pull. Strains are elongation, % in 2 in.

The objectives of the project were as follows: to obtain data on the more important mechanical and physical properties of electrodeposited copper, prepared from all of the commonly used types of plating baths under a range of operating conditions; to correlate the properties with these conditions and with the structure and chemical composition of the deposits; and to examine correlations among the various properties.

Availability of systematic data of this character will make it possible for designers and producers of items incorporating engineering-type copper deposits to select and control optimum types of baths and operating conditions, and should stimulate uses of copper deposits for this kind of application. In addition, extensive data of this sort are likely to reveal relationships and disclose questions that will stimulate basic or theoretical researches in the field.

The following properties have been measured in the present study; tensile strength, yield strength, elongation, Young's modulus of elasticity, fatigue strength, internal stress, hardness, density, electrical resistivity, thermal expansivity, tensile strength and ductility at low (−78°C) and elevated (150° and 325°C) temperatures, and effects of annealing and cold-working on several of the preceding properties. In addition, concentrations of impurities and structures have been determined for a representative sampling of deposits.

The values of most of these properties for as-plated deposits are summarized in Table I. Data showing effects of temperature, annealing, and cold-working are summarized in Table XXVII (to be published in November).

This is the third and final paper based on the work done under this project. The first paper was a comprehensive survey of the literature through 1965 on properties of copper electrodeposits (3). The second was a preliminary report on properties of deposits from the sulfate bath (4). In the present paper, in order to make a complete and consistent presentation, we have included the data previously published in Ref. (4). In addition, the present paper includes data from fluoborate, pyrophosphate, cyanide, and amine types of baths.

II. Preparation of Plating Solutions and Deposits

A. Solutions

Composition and operating conditions for all of the baths used are given in Tables II, III, and IV. The black areas in Table II represent conditions under which deposits from sulfate baths were made. They were chosen so as to give several 2-4 point compari-

Table II. Composition of baths and operating conditions under which deposits were prepared from the sulfate bath without addition agents

(shaded areas represent conditions that were used)

Temp., °C		20			30				40				60		
		Current Density, A/dm²													
Bath Symbol		0.5	2	4	0.5	2	4	8	0.5	2	4	8	4	8	20
Cu-1	H1	■				■					■				
	H2		■		■		■			■					
	H3														
Cu-2	H1					■						■			
	H2	■	■	■			■			■	■				
	H3				■			■					■	■	■
Cu-3	H1														
	H2										■				
	H3			■	■	■			■				■	■	

Definition of Bath Symbols

$CuSO_4 \cdot 5H_2O$				H_2SO_4			
Symbol	Moles/l	g/l	oz/gal	Symbol	Moles/l	g/l	oz/gal
Cu-1	0.35	87	12	H1	0.25	25	3.3
Cu-2	0.75	187	25	H2	0.40	39	5.2
Cu-3	1.1	275	36	H3	0.75	74	9.8

Table III. Composition of plating baths

Constituents and conditions	Fluoborate bath, Bath symbol F-1*, moles/l	F-1*, Conc g/l	F-1*, Conc oz/gal	F-2, moles/l	F-2, Conc g/l	F-2, Conc oz/gal	Pyrophosphate bath, Constituents and conditions	moles Cu^{++} per liter	g/l	oz/gal	Amine bath, Constituents and conditions	moles/l	g/l	oz/gal
$Cu(BF_4)_2$	0.75	177	24	1.55	366	45	$Cu_2P_2O_7 \cdot 3H_2O$	0.5	90	12	$CuSO_4 \cdot 5H_2O$	0.4	100	13
HBF_4		12	1.6		22	3	$K_4P_2O_7$		350	47	$(NH_4)_2SO_4$		20	2.7
H_3BO_3		12	1.6		22	3	K_3PO_4		80	11				
											Ethylenediamine		80 ml/l	10 fl oz/gal
							KNO_3		15	2				
pH		0.8-1.0			0.4-0.6		NH_3, conc aq		2 ml/l	0.25 fl oz/gal	NH_3, conc aq		4 ml/l	0.5 fl oz/gal
Temp, °C		30, 60			30, 50									
C.D. A/dm^2		2, 8			8, 20		NH_3 replenishment		1 ml/l/day		NH_3 replenishment		3-5 ml/l/day	
C.D. A/ft^2		18.6, 75			75, 185									
							P_2O_7/Cu, wt ratio		7.2					
											Temp, °C		55	
							pH		8.5					
							Temp, °C		50, 60				2, 4	
							C.D. A/dm^2		2, 4		C.D. A/dm^2		18.6, 37	
							C.D. A/ft^2		18.6, 37		pH		9.3-9.7	

* The copper metal concentration in F-1 is the same as in the Cu-2 sulfate baths.

sons for a given variable with all other variables constant. Variables not included in Table II, such as addition agents, periodic current reversal, *etc.*, are covered in other tables that are discussed in subsequent sections.

The range of conditions investigated with the fluoborate, pyrophosphate, and amine baths (Table III) is much smaller than with the sulfate bath, but sufficient sets were used to show the effects of the major variables. Cyanide baths, Table IV, were extensively studied. Basis for choice of levels of variables and other details regarding these baths are discussed in the sections containing the results for the respective baths.

Sulfate baths were prepared either from analytical reagent or National Formulary grades of chemicals. The copper fluoborate concentrate, the copper pyrophosphate, and the copper cyanide were plating-grade salts from reliable suppliers. Analytical grade chemicals were used to provide the minor constituents in these baths. Distilled water was used in all cases for both original make-up and maintenance of bath level.

Data in the literature indicate that chloride as an impurity in sulfate baths may have marked effects on deposit properties (3). These baths were therefore checked after purification and periodically during use for chloride content. In new purified baths, chloride was not detected (<1 ppm).[6] In used baths, 2-3 ppm were occasionally found. At this level, chloride has no measureable effect (5).

All baths were purified before use by treatment with 10 g/l of activated carbon, followed by filtration through filter paper. Some of the sulfate baths were also treated with hydrogen peroxide, 1 ml/l, followed by heating to 60°C prior to filtering. Deposits from baths purified by either procedure had the same tensile strength. Following the above treatments, all baths were pre-electrolyzed with a corrugated copper cathode for approximately 10 A-hr/l, at a current density of 0.5 A/dm^2.

As a check on adequacy of purification, spectrographic analyses of several typical deposits were made[7] (Table V). It is seen that only a few metallic impurities were detected, and that these were present at concentrations of only a few parts per million. In a bath that has been operated for some time, equilibrium with the anodes is approached, and bath and deposit purity may depend more on the purity of the anodes than on that of the original bath. Therefore, samples of two of the types of anodes that we used were also analyzed (Table V). No impurities were found at levels that would be expected to cause significant contamination of deposits.

B. Control of Operating Variables

1. Bath concentrations.—Concentrations of the major constituents of each bath were determined by standard analytical procedures (6, 7). The aim was to control the concentration of constituents in operating baths to ±2%. For the most part, this was achieved. In a few cases, slightly larger deviations occurred but were insufficient to produce significant effects on deposits.

2. Temperature and current density.—Temperature was controlled to ±1°C with automatic equipment. Consistent use of vigorous agitation insured uniformity within this range throughout the bath. Current density was controlled to ±5%. Current for most overnight runs was monitored with a recorder.

C. Equipment

1. Tanks.—Plating baths were contained in glass battery jars. Two shapes were used, 8 x 13 in. and 12 x 12 in. in horizontal section. Filled to a depth of 14 in., they contained 27 and 30 liters of solution, respectively. A few panels (serial No. 68-77, addition agent phenolsulfonic acid) were plated in a polypropylene tank.

[6] ppm signifies parts per million by weight.
[7] Determinations were made by Virginia C. Stewart, Analytical Chemistry Division, NBS.

Table IV. Composition and operating conditions of cyanide baths

Constituents and conditions	Bath symbol	CN-1	CN-2	CN-3	CN-4	CN-5	CN-6	CN-7	CN-8	CN-9
		Concentrations								
CuCN	moles/liter	0.17	0.28	0.45	0.45	0.45	0.45	0.45	0.84	0.84
	g/liter	15	25	40	40	40	40	40	75	75
	oz/gal	2	3.4	5.4	5.4	5.4	5.4	5.4	10	10
Free NaCN	g/liter	6	6	6	6	10	6			
	oz/gal	0.8	0.8	0.8	0.8	1.3	0.8			
Free KCN	g/liter							8	10	22.5
	oz/gal							1.1	1.3	3
Na_2CO_3	g/liter	15	15	15	30	30	30			
	oz/gal	2	2	2	4	4	4			
K_2CO_3	g/liter							40		
	oz/gal							5.4		
Rochelle salt	g/liter						45	45		
	oz/gal						6	6		
KOH	g/liter								40	22.5
	oz/gal								5.4	3
Addition agent	g/liter								KCNS,[b] 2	Prop. B[c]
	oz/gal								0.27	
pH Initial		11.4		11.7	11.7	11.8	11.6	11.8	13.6	
pH Worked[a]		12.8		12.7	12.8	12.8	12.8	12.6	13.6	
Temp, °C		40	40, 60	60	40, 60, 80	40, 60, 80	40, 60, 80	60, 80	80	80
C.D. A/dm²		1	1, 2	2	2, 4	2, 4	1, 2, 4	2, 4	4, 6, 8	4, 6
C.D. A/ft²		9.3	9.3, 18.6	18.6	18.6, 37	18.6, 37	9.3, 18.6, 37	18.6, 37	37, 55, 75	37, 55

[a] Stable pH after working bath 5 to 10 A-hr/liter.
[b] KCNS used only for deposits listed in lines 143 and 144, Table I.
[c] Proprietary brightener of the selenium type.

Table V. Impurities in copper electrodeposits and anodes[a]

Line No., Table I	Panel No.	Bath symbol	Bath temp, °C	Current density, A/dm²	Content of impurity, % by weight							
					Silver	Calcium	Iron	Magnesium	Manganese	Nickel	Lead	Silicon
26	324	Cu2-H2	30	2	<0.001		0.000X	<0.001			0.000X	<0.001
91	345	F-1	30	8	<0.001		<0.001	<0.001	<0.001		<0.001	<0.001
95	317	Pyrophosphate	50	2	0.000X	0.000X	0.000X	<0.001	<0.001		<0.001	<0.001
141	281	CN-8[b]	80	6	<0.001	0.000X	0.000X	<0.001	<0.001	<0.001	0.000X	<0.001
Electrolytic sheet anode					0.001-0.01	<0.001	<0.001	<0.001	<0.001	<0.001	0.000X	<0.001
Oxygen-free anode					0.001-0.01	<0.001	<0.001	<0.001	<0.001	0.000X	<0.001	<0.001

[a] Values were determined by semiquantitative spectrographic analysis. Where no value is shown, the content was less than 0.0001%. The designation 0.000X indicates a probable trace in the range 0.0001-0.001%. Other elements checked for but not detected in the deposits, *i.e.* if present their levels were less than 0.0001%, include Al, As, Au, B, Ba, Be, Bi, Cd, Ce, Co, Cr, Ga, Ge, Hf, Hg, In, Ir, La, Na, Nb, Os, Pd, Pt, Rh, Ru, Sb, Sc, Sn, Sr, Ta, Te, Th, Ti, Tl, U, V, W, Y, Zn, Zr.
[b] Deposited with periodically reversed current, 15-5 sec cycle.

2. Cathode boxes.—Uniform current distribution and deposit thickness were obtained on specimen panels by boxing them closely with a nonconducting shield. In the jar with 8 x 13 in. horizontal section, boxing was supplied by the bottom and sides of the jar itself, with the 8 x 14 in. panel set against one short side of the jar. In the jar with 12 x 12 in. horizontal section, the panel was enclosed in a cathode box, open at the top and toward the anodes. The width of the sides was 6 in. An air distribution channel was built into the lower front edge of these boxes. It contained six evenly spaced outlet holes, 1/16 in. in diameter. The line of holes was parallel to the panel and spaced 4 in. from it. Discharge of air or liquid through these holes provided agitation that was uniform along the width of the specimen panel.

Early preliminary experiments with the sulfate bath yielded panels that varied in hardness from top to bottom if the air was discharged close to the panel (*e.g.*, 1 in.) or if the rate of air flow was appreciably less than that given in the next paragraph. Various box materials were used, namely, methyl methacrylate polymer, polypropylene, and Teflon. The methylmethacrylate was used only in the sulfate baths. Experiments described in Section III showed that contact of the baths with these resins did not affect properties of deposits.

3. Heating, cooling, pumps, filters, and agitation.—Heaters were quartz electric units.

A 1 hp commercial chilling unit was used for maintaining the bath temperature during high current density operation and for operation at 20°C. The chiller maintained a low temperature in a water ballast tank. Ballast tank water was circulated with a thermostatically controlled pump through a water jacket surrounding the plating tank when cooling was required.

Pumps for circulating the plating solution, and filter bodies, were made of either polyvinylchloride or polypropylene. In the early work with sulfate baths (panel serial No. 1-67), solution was pumped continuously into a large glass funnel containing a paper filter. For subsequent deposits from sulfate baths, a commercial filter-pump unit was used with a cotton filter cartridge. The reason for the choice of the cotton is discussed later. A cotton filter was also used for the fluoborate baths, but for all other baths cartridge filter units of polypropylene were used.

For the early sulfate deposits, air for agitation from the building supply line was filtered through a 4 ft long column of cotton. Air for all subsequent deposits was obtained from an oil-less blower, with the output filtered through a mixture of cotton and granular carbon, packed in a 20 liter bottle. The rate of flow of the air was approximately 10 l/min. This provided vigorous agitation, judged to be comparable to what would normally be used in a commercial installation. In general, air was used for agitating all baths except the cyanide types, though it was also used for the latter for a few deposits from the high-efficiency bath (CN-8). Some exceptions are noted in Table I.

For cyanide baths CN-1 through CN-4, agitation was provided by pumping plating solution through the same cathode-box distribution holes that were otherwise used for air distribution. Flow rate was approximately 4 l/min. This agitation was supplemented by the natural flow induced by evolution of hydrogen at the panel surface. For deposits from cyanide baths CN-5 through CN-9, additional agitation was found to be necessary to prevent excessive top-to-bottom variation of deposit thickness. It was provided by a non-

conducting propeller blade, 3 in. diameter, located about 1 in. below the center of the panel, rotated at about 400 rpm.

4. *Anodes and anode bags.*—Three types of anodes were used: electrolytic sheet, oxygen-free, and phosphorized. There were no significant impurities in the first two types (Table V). Phosphorized anodes were not analyzed because they were used only in the proprietary bright sulfate bath, in accordance with the vendor's recommendation. The electrolytic sheet anodes were used in all sulfate baths. Before use, they were heated to 600°C for 1 hr to carbonize any organic inclusions that might be present, such as glue. The oxygen-free anodes were used in all cyanide baths.

Anode bags made of polyvinylchloride fabric were used for the early sulfate deposits and bags made of napped polypropylene for all later baths. Before use, bag materials were thoroughly freed of weaving lubricants by a combination of solvent cleaning and leaching with portions of plating bath which were discarded. (Filter units were treated similarly.)

D. Deposits

The standard thickness of specimen deposits was 18-20 mils (500 μm). A few thinner deposits were made for determining the effects of thickness on properties. Deposits were formed on Type 304 stainless steel starting sheets, 8 x 14 x 0.03 in. The sheets were polished as required to remove surface imperfections, buffed with a fine emery compound, degreased, scrubbed with fine pumice, and dipped for 1 min in 1:1 nitric acid to passivate the surface. A flash plate of nickel about 0.1 mil thick was applied from a Watts bath and the panel transferred after rinsing with distilled water to the copper plating bath.

The nickel starting plate was used because it covered the stainless steel more uniformly and quickly than did copper, and separated easily, whereas copper plated directly on the stainless steel, at least from the acid baths, occasionally exhibited sufficient local adhesion to make separation difficult. On completion of plating, the copper deposit was freed from the starting sheet by trimming the edges. It separated easily. The nickel flash, which adhered to the starting face of the copper, was removed by stripping it anodically in a solution containing, in parts by volume, 50 of conc H_2SO_4, 50 of 85% H_3PO_4, and 5 of water. The stripping operation removed about 0.01 mil of copper. This did not affect the measured values of tensile strength and elongation. A band 1 in. wide all around the panel was trimmed and discarded. The remaining portion, with dimensions of 6 x 12 in., was uniform in thickness within ±5% for most deposits. It was more difficult to obtain uniform top-to-bottom thickness of deposits from cyanide baths. In general, these varied in thickness about ±10%.

The various specimens required for measurements of properties were cut from these panels.

III. Deposits from Sulfate Baths

A. Mechanical Properties

1. *Methods of measurement: tensile and yield strengths, elongation, Young's modulus of elasticity, and hardness.*—Tensile specimens were made by milling a stacked bundle of specimen stock that had been sheared to ¾ x 6 in. Dimensions of finished specimens conformed to ASTM specifications except for a shorter grip length (8). The width of the reduced section of a standard specimen was 0.5 in. and gauge length 2 in. The specification also describes a subsize specimen with a reduced section ¼ in. wide and 1 in. gauge length. A few subsize specimens were used, identified in Table I by listings of elongation as per cent in 1 in. Ultimate tensile strengths were determined by testing specimens in a standard tensile machine, which plotted load and elongation. Yield strengths were determined from these curves. The linear speed of loading for the tensile test was 0.030 in./min. Cross-sectional area of a specimen was determined from its width, measured by micrometer caliper, and its thickness calculated from its weight and area. Three specimens were usually made from each panel, from top, center, and bottom zones.

For triplicate specimens from the same panel, the deviation of tensile strength from the mean for about 80% of the panels was within ±5%. For the remaining 20% of the panels, deviations ranged from ±6 to ±15%.

Elongation measurements were more variable. Again, for triplicate specimens from the same panel, the deviation from the mean for about 80% of the panels was within ±5%. For the remainder, the deviation ranged up to ±33%. The high deviations were mainly for specimens having a low elongation, so that a relatively small absolute deviation corresponded to a large relative deviation. It is therefore more meaningful in the case of elongation to express deviation in absolute rather than relative terms. A deviation of ±5 absolute percentage points encompassed all but two of the panels.

Three procedures were used for obtaining modulus of elasticity, namely, measurement of the slope of the initial part of the stress-strain curve plotted by the tensile machine, measurement of beam deflection, and measurement of strain for small loads with resistance strain gauges. For the beam deflection procedure, a strip of specimen stock 1 x 15 cm was mounted as a cantilever and its vertical deflection with dead-weight loads measured with a microscope. In the strain-gauge method, gauges were cemented to both sides of a standard tensile specimen, using the manufacturer's recommended adhesives and procedures. The specimens were stressed in a sensitive, small-capacity pulling unit and strain measured in terms of change of resistance with a Mueller Bridge having a sensitivity of 0.0001 ohm. Elongation sensitivity was about 1 μin. In calculating the modulus, allowance was made for the contribution of the gauge and cement to the strength of the assembly. The strain-gauge method was the most accurate and reliable of the three and was used for obtaining most of the values given in Table I and the various subtables. Data that were obtained by the other methods are noted in the tables.

The values reported for modulus of elasticity are judged to be accurate to ±1 x 10^6 psi.

Hardnesses of deposits were measured on metallographically mounted and polished cross sections. A Tukon microhardness tester was used, with a Knoop indentor. For the thicker deposits, a 200g load was used. For most of the thin deposits from the cyanide baths a 100g load was used, but for a few of the thinnest deposits a 50g load was used. Where intercomparisons between hardnesses determined with different loads are made in some of the subsequent tables and figures, corrections have been made to place all values on a 200g load-basis, by substracting 11 hardness units from values determined with a 50g load, and 6 hardness units from values determined with a 100g load. These difference factors for load effect were determined from comparative measurements on our specimens.

Hardnesses were usually run in duplicate, with specimens from top and bottom zones of a panel. Most of the individual values were within ±5 KHN[8] units of the tabulated average values.

2. *Reproducibility of properties.*—It is important that a deposit obtained from a particular type of bath under particular operating conditions be representative of those conditions and that observed properties can be reproduced under like conditions at any time. The purification and control procedures described above were thought to be adequate to achieve reproducibility, but evidence was required. Among properties that we considered for monitoring the reproducibility of deposits were tensile strength, hardness, electrical resistivity, and polarization. Hardness, which served this

[8] Knoop hardness number, kg/mm².

purpose for nickel (2), was found to be unsuitable for deposits from the sulfate bath because of low correlation with other properties. Our preliminary measurements showed this, as did the results of our literature survey (3) and the work of Read (9). Electrical resistivity was found to vary too little with change of independent variables to provide a good criterion of reproducibility. Polarization measurements should, in principle, serve the purpose, but we found them impractical because of the time and effort required to check their reliability and reproducibility. Tensile strength appeared to be the property best suited as a monitor of reliability and reproducibility of baths and deposits.

Results of some checks on reproducibility of properties are shown in Table VI, in which comparable members of pairs are juxtaposed. In the cases of lines 18-19 (line numbers refer to serial positions in Table I), 24-25, and 54-55, the compared specimens were made at different times with different bath preparations. Panels represented in lines 14-15 and 85-86 were made from the same baths and at close time positions. Tensile strengths and elongations are seen to agree closely for members of pairs. The exception of elongation on line 26 is discussed below.

Reproducibility of hardness was good for pairs on lines 14-15 and 85-86, but poor on lines 24-26 and 54-55. The variation for lines 24-26 is related to that for elongation and is also discussed below. The poor agreement on lines 54-55 may be an addition agent effect. Baths containing naphthalenedisulfonic acid (NDS) require prolonged pre-electrolysis, which causes a change in composition of the addition agent, associated with a change of color, and may be also related to deposit hardness even though tensile strength and elongation were not affected.

We concluded from such comparisons that reasonable reproducibility was achieved with the purification and control procedures that had been adopted. However, at a point about one year along in the project, difficulties were encountered. Baths that had given deposits with properties as in lines 18-19 began to yield deposits with properties like those in line 89 (last line in Table VI), characterized by very low strength and ductility. In appearance these deposits had a coarsely faceted, spangly surface, whereas the deposits that had been obtained previously had a relatively fine-grained, smooth surface. The degree to which this effect occurred varied. The deposit of line 89 was intermediate. Some deposits were more coarsely faceted than this and so weak that they bent under their own weight. On bending such a deposit to a short radius, cleavage occurred between facets. Others, only slightly faceted, showed perhaps half the reduction of strength seen for panel No. 78C (line 89). To identify these deposits, we refer to them in succeeding discussion as "spangled." A few deposits of this type had been obtained early in the program. At that time we ascribed the cause to accidental impurities, because a repurified bath generally yielded the fine-grained deposits that we considered to be normal. Spangled deposits became a persistent problem when we put into operation a new plating installation that we thought would improve the maintenance and control of baths and operating conditions and permit faster production of specimen stock. The plating had previously been done in the 8 x 13 in. glass jar units with continuous filtration of the plating solution through a paper filter in a large funnel, as described above (Par. II-C-3).

The new installation employed a 12 x 24 x 18 in. deep polypropylene tank, equipped with a high-speed polypropylene filter-pump unit containing a polypropylene filter cartridge, a methacrylate resin cathode box, polyvinylchloride piping, and an anode diaphragm of polyvinylchloride fabric. A new air supply from an oil-less compresser was also used. All of the polymeric materials were reputed to introduce no contamination into plating baths. However, the obvious hypothesis, which we assumed initially, was that one or more of these polymers, large areas of which contacted the bath, was introducing a harmful impurity that caused spangling.

Many experiments were performed to locate the source of the supposed contamination. Without describing all of the details, it may be said that the general procedure and results were as follows. Starting with a bath that was yielding the smooth strong type of deposit, it was subjected in turn to contact with all of the suspect materials; alternatively, a bath producing spangled deposits was repeatedly purified after each of the suspect materials was removed from contact with the bath, one by one. The conclusion reached from these experiments was that none of these materials caused the trouble. In the course of the experiments, it was observed on several occasions that a bath freshly repurified with activated carbon and batch-filtered through filter paper yielded a few normal deposits and then reverted to spangling. After the batch filtration, subsequent filtration was done through a polypropylene cartridge. A related observation made about the same time was that, when the filter paper previously used in the funnel for continuous filtration of a bath in our smaller original unit was replaced with a napped polypropylene cloth filter, spangling soon developed.

The conclusion, or hypothesis, that we have reached as a result of these experiments is as follows. The natural form of a deposit from a highly purified copper sulfate bath approaches a mixture of separate crystals, such as is characteristic of deposits of silver or lead from nitrate baths or cadmium from a sulfate bath. Traces of impurities in the plating solution, which act as grain-refining addition agents, are necessary to prevent coarse, faceted deposits. In our case, the impurity was a cellulosic derivative of the filter paper, perhaps a sulfonate. In commercial baths, muslin or wool fabrics (6) have commonly been used as filter media. Hydrolysis of wool would introduce small concentrations of glue-type compounds. Furthermore,

Table VI. Reproducibility of measurements of properties

Line No., Table I	Panel No.	Bath symbol	Addition agent		Bath temp, °C	Current density, A/dm²	Tensile[c] strength, psi	Elongation in 2 in. (5 cm), %	Hardness KHN 200g load, kg/mm²
			Name	Conc, g/liter					
14	64	Cu2-H1	Gelatin	0.003	30	2	40 × 10³	19	91
15	65						41	22	88
18	94	Cu2-H2	None		20	2	32	33	61
19	106						32	34	
24	13	Cu2-H2	None		30	2	25	14	88
25	25						26	19	
26	322, 323						32	39	55
54	91	Cu2-H3	NDS[a]	1.8	30	2	31	29	67
55	114						29	29	98
85	30	Cu3-H3	None		60	4	30	41	53
86	32						31	43	57
89	78C[b]	Cu2-H2	None		20	2	15	8	85

[a] 1,5-Naphthalenedisulfonic acid.
[b] Spangled deposit.
[c] One pound per square inch (psi) = 0.000704 kilogram per square millimeter (kg/mm²).

addition agents have been almost universally intentionally added to commercial baths. Thus, the conditions that we encountered that caused spangling would be rarely observed.

Similar coarsely faceted deposits were obtained by Shreir (10). He reported a correlation with cathode polarization, with low polarization for faceted, and high for smooth, deposits. A higher polarization is the expected effect of an addition agent. However, Shreir's interpretation was different. He believed that the smooth deposits were "normal," and that the coarse deposits, which he obtained after working of a bath, were the result of the presence in the bath of cathodic reduction products of the sulfate ion that caused a lowering of cathode polarization. However, his data were not all consistent with this interpretation. Barnartt (11) has reported copper deposits from a sulfate bath for which he claims a purity of 99.999% which were smooth and fine grained at a thickness of 7 mils. However, it is conceivable that an unsuspected grain-refining impurity may have been present.

Our experiences described above led us to the conclusion that we could not complete the work with the sulfate bath without using a grain-refining addition agent. One alternative would be to continue the slight contamination with cellulose extract to control spangling. The cellulose has a mild effect, producing deposits with nearly the same strength as annealed wrought copper.

A second alternative was to search for an addition agent in the form of a definite compound that would have a mild effect similar to that of the cellulose, but preferable because of its definite characterization. For this purpose we tried dextrin, dextrose, glycerol, glycine, and sorbitol. The results are shown in Table I, lines 43, 44, 48, 49, and 68, respectively. Tensile strengths for the last three were in the correct range and none of them produced appreciable grain refinement. However, they all caused significant embrittlement. We, therefore, returned to the use of a cellulosic filter. However, at this point we were well along with production of deposits from other types of baths, had abandoned the funnel-type filter, and were using solely the equipment consisting of the 12 x 12 in. glass jar with a high-speed filter pump unit. We, therefore, completed the preparation of deposits from sulfate baths in this unit, using a cotton-wound filter cartridge. All deposits from sulfate baths with panel serial numbers of 274 or higher were made in this manner. In Table VI we show a comparison of physical properties as affected by this change in conditions. The deposits averaged in line 26 are duplicates of lines 24-25, except for the more drastic exposure to cellulose of the bath from which the deposits of line 26 were made. It is seen that the later deposits (higher cellulose) are about 20% stronger, are much more ductile, and somewhat softer.

The effect on structure of the difference in the degree of exposure to cellulose is shown in Fig. 1-1 and 1-2. The structures of both deposits are of similar columnar type, but the grain size in panel No. 322 (line 26), which had the more drastic exposure to cellulose, is appreciably smaller than that in panel No. 25.

The structure in Fig. 1-3 (Table VI, line No. 18) is the typical columnar type, whereas the spangled deposit in Fig. 1-4 (Table VI, line No. 89) contains smaller equiaxed grains, reminiscent of an annealed structure. Although the structure of the spangled deposit is distinctly different from that of the other deposits in Fig. 1, it is not obvious from its structure that it should be so much weaker.

The starting surface of the deposits in Fig. 1, and in all succeeding photomicrographs, is at the bottom of the photomicrograph.

3. Effect of thickness on properties of deposits.—The initial layers of an electrodeposit tend to continue the structure of the basis metal for a short distance. If this structure is fine, a transition zone occurs where the deposit grains grow with thickness from the initial fine structure to a coarser structure characteristic of the deposit (12). Properties therefore tend to change with thickness. Examination of the structures of deposits from sulfate baths in Fig. 1 and in later structure figures shows this fine initial grain and the transition zone extending for 3-5 mils. Beyond this zone, the structure changes little with increase in thickness.

A few experiments were conducted to determine the effect of thickness (Table VII, Fig. 2 and 3). Thin deposits, 1-6 mils, are significantly stronger but less ductile than deposits 18 mils thick (Fig. 2). Because of lack of data for intermediate thicknesses or for thicknesses greater than 18-20 mils, the curves in Fig. 2 are drawn as straight lines. Actual curves are probably similar in form to the dotted curves at the top and bottom of Fig. 2. This postulate is reinforced by the form of the resistivity curve in Fig. 3 (curve No. 4) for which a value at an intermediate thickness was

Table VII. Effect of thickness on properties of deposits from sulfate baths

Line No., Table I	Panel No.	Bath symbol	Addition[a] agent Name	Conc, g/l	Bath temp, °C	Current density, A/dm²	Thickness,[c] mils	Tensile[c] strength, psi	Elongation in 2 in. (5 cm), %	Young's[c] modulus of elasticity, psi	Hardness KHN 200g load, kg/mm²	Elec. resistivity 25°C, ohm-cm
21	104	Cu2-H2	None		20	2	3	45 × 10³	10	16 × 10⁶		1.80 × 10⁻⁶
20	23						5			16		
18	94						18	32	33			1.73
34	277	Cu2-H3	None		20	2	18			16[b]		
23	15	Cu2-H2	None		32	0.5	1				77	
							10				87	
							20				93	
24A	10				30	2		28	5		93	1.79
24	13						10				89	
							20	26	19		82	1.73
53	162	Cu2-H3	β-NQ	0.1	30	2	2	46	9			
52	160		β-NQ	0.1			18	36	8			
51	215		LA	0.05			2	29	3			
50	214		LA	0.05			18	25	10			
57	114A		NDS	1.8			1.3	36	10			1.74
56	114F		NDS	1.8			6	35	39			1.72
54, 55	91, 114		NDS	1.8			18	30	29			1.72
65	168		SeO_2	10^{-4} Se			2	54	11			
64	166		SeO_2	10^{-4} Se			18	47	21			
67	173		SeO_2	10^{-3} Se			2	50	20			
66	172		SeO_2	10^{-3} Se			18	44	24			
75	109-A		TIPA	3.5			1.4	57	9			1.78
74	109-F		TIPA	3.5			6	53	13	16		
72, 73	93, 108, 109		TIPA	3.5			18	40	17	16		1.75

[a] β-NQ, β-naphthoquinoline; LA, lactic acid; NDS, 1,5-naphthalenedisulfonic acid; TIPA, triisopropanolamine.
[b] Determined from stress-strain curve.
[c] Metric conversions; one mil (0.001 in.) = 25 μm; one pound per square inch (psi) = 0.000704 kilogram per square millimeter (kg/mm²).

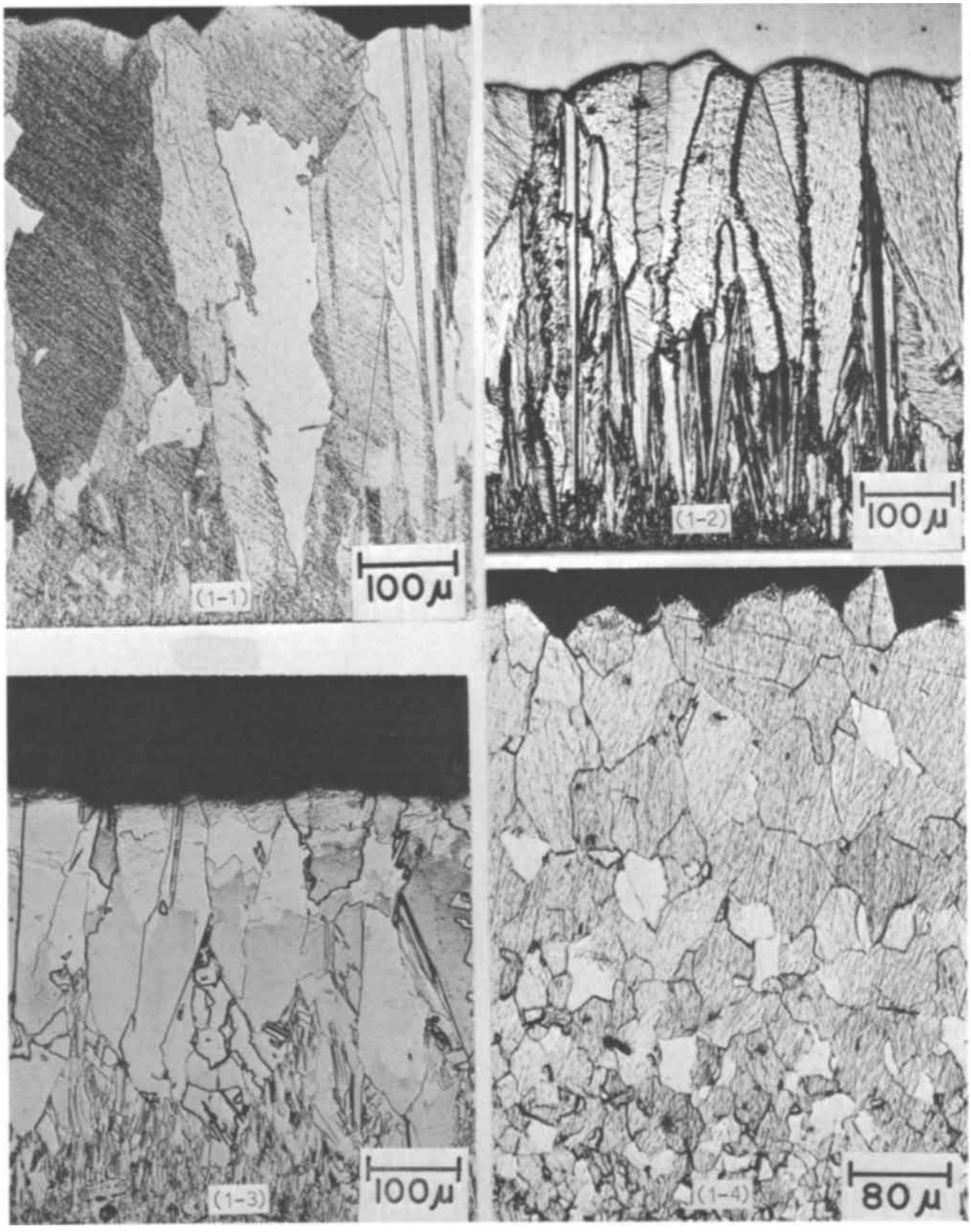

Fig. 1. Effect of contact of sulfate plating baths with cellulose on the structure of copper deposits: Cu2-H2, 30°C, 2 A/dm²—(1-1) Mild exposure to cellulosic filter; (1-2) severe exposure to cellulosic filter. Cu2-H2, 20°C, 2 A/dm²—(1-3) Mild exposure to cellulosic filter; (1-4) Spangled deposit from highly purified bath, no known exposure to any grain-refining agent.

determined. The effect of thickness on tensile strength, elongation, and resistivity is consistent with the transition from the fine-grain structure of the deposit at the starting surface to large grains at a thickness of about 5 mils (Fig. 1).

From Table VII it is seen that the modulus of elasticity is independent of thickness. Data presented later show that there is some variation of modulus with strength, but variations in strength in the present data are too small to reveal an effect on modulus.

Variation of hardness with thickness is indeterminate from our data. If thickness has an effect on hardness, it is minor.

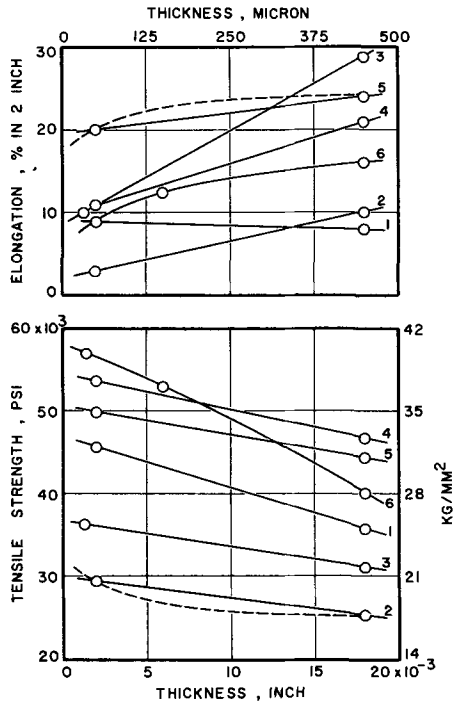

Fig. 2. Relationships between thickness, tensile strength, and elongation of copper deposits from the Cu2-H3 bath at 30°C, 2 A/dm², and containing addition agents as follows: 1—0.1 g/l β-naphthoquinoline; 2—0.05 g/l lactic acid; 3—1.8 g/l 1,5-naphthalenedisulfonic acid; 4—10^{-4} g/l Se; 5—10^{-3} g/l Se; 6—3.5 g/l triisopropanolamine.

Changes of properties with thickness also occur in deposits from standard cyanide baths, but probably for a different reason, to be discussed later. Because of their uniform grain size, one would not expect thickness to affect the properties of deposits from pyrophosphate, amine, or high efficiency type cyanide baths to the same extent as it does those of deposits from sulfate baths (see Fig. 34 and 59).

If an addition agent had sufficient effect to completely suppress a columnar structure (see Fig. 20-9, 20-10), one would not expect properties to vary with thickness. However, none of the addition agents shown in Table VII completely suppressed the columnar

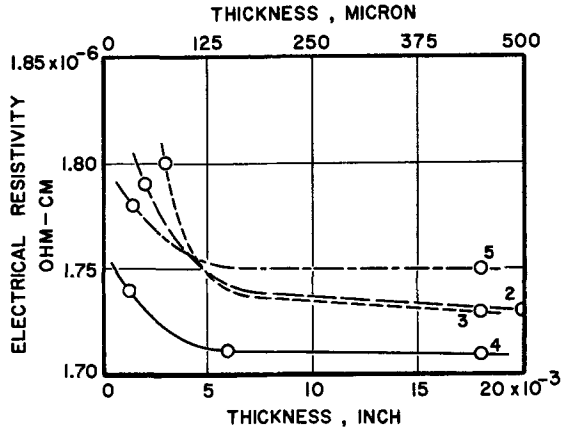

Fig. 3. Relationship between thickness and electrical resistivity of copper deposits from the sulfate bath: 2—Cu2-H2, 30°C, 2 A/dm²; 3—Cu2-H2, 20°C, 2 A/dm²; 4—Cu2-H3 plus naphthalenedisulfonic acid, 1.8 g/l, 30°C, 2 A/dm²; 5—Cu2-H3 plus triisopropanolamine, 3.5 g/l, 30°C, 2 A/dm².

structure of sulfate bath deposits (Fig. 20-2 to 20-8), with the result that the properties of these deposits, as well as those from nonaddition agent baths, vary with thickness.

4. Effect of operating conditions and bath composition.—a. Bath temperature.—Data on the effect of bath temperature on mechanical properties of deposits from sulfate baths are collected in Table VIII. Variation of tensile strength and elongation with temperature is plotted in Fig. 4. Both of these properties decrease with increase in bath temperature in most cases. The reverse effect for tensile strength, seen in two curves in Fig. 4 and in lines 39-41 and 80-86 of Table VIII, has a maximum magnitude of ±9.5%; thus, its significance is doubtful (Section III-A-1). A similar analysis applies to the data for elongation. We conclude that increase of temperature generally causes a decrease of tensile strength and elongation. Since the magnitudes of the effects are small, they may be obscured by minor variations in other conditions or by inherent errors of measurement.

Values of yield strengths as a function of temperature are given in Table VIII. In general, yield strength parallels tensile strength, and is similarly related to bath temperature.

Table VIII. Effect of bath temperature on properties of deposits from the sulfate bath

Line No., Table I	Panel No.	Bath symbol	Current density A/dm²	Bath temp, °C	Tensile[a] strength, psi	Yield[a,b] strength, psi	Elongation in 2 in. (5 cm), %	Young's[a] modulus of elasticity, psi	Hardness KHN 200g load, kg/mm²	Internal[a,c] stress, psi	Density 25°C, g/cm³	Elec. resistivity 25°C, ohm-cm
1	48	Cu1-H1	0.5	20	27 × 10³	8 × 10³	18		56	−70	8.922	
3	52			40	30	10	24		57	80	8.922	
5	55	Cu1-H2	2	20	31	9	28	16 × 10⁶	59	3300	8.921	
6	56			30	25	7	15		58	570	8.921	
7	58			40	24	8	13		47	370		
17	110	Cu2-H2	0.5	20	26	7	25	14	105	−510	8.928	
23	15			32	23	7	11	13[d]	87	−700	8.924	1.71 × 10⁻⁶
18	94		2	20	32	11	33	16	61	1500	8.925	1.73
24, 25	13, 25			30	26	8	17	14	88	550	8.921	1.72
28, 29	51, 16, 18			40, 45	22	8	10	12[d]	67	−320	8.923	1.73
22	22		4	20	33	12	29		67	4300	8.920	
27	44			30	30	9	24		53	2200	8.922	1.72
30	27			45	24	7	14		57	190	8.924	
34	277	Cu2-H3	2	20	37	15	41	16[e]	78	2000	8.926	
36, 37	276, 307			30	29	9	19	14	54	180	8.924	1.73
39	278		8	30	32	14	24		75	4300	8.926	1.74
40	285			40	37	15	44		80	2600	8.926	1.75
41	286			60	27	10	18		58	380	8.925	1.76
81	29	Cu3-H3	0.5	30	27	8	16		57	−90	8.920	1.71
83	31			45	32	10	34		57		8.919	
80	321		4	20	32	12	42		64	3100	8.925	1.73
84	28			45	26	8	15		51	1400	8.921	1.70
85, 86	30, 32			60	31	8	42		55		8.925	1.72

[a] One pound per square inch (psi) = 0.000704 kilogram per square millimeter (kg/mm²).
[b] 0.05% offset.
[c] Negative values represent compressive stresses.
[d] Measured by beam deflection method.
[e] Determined from stress-strain curve.

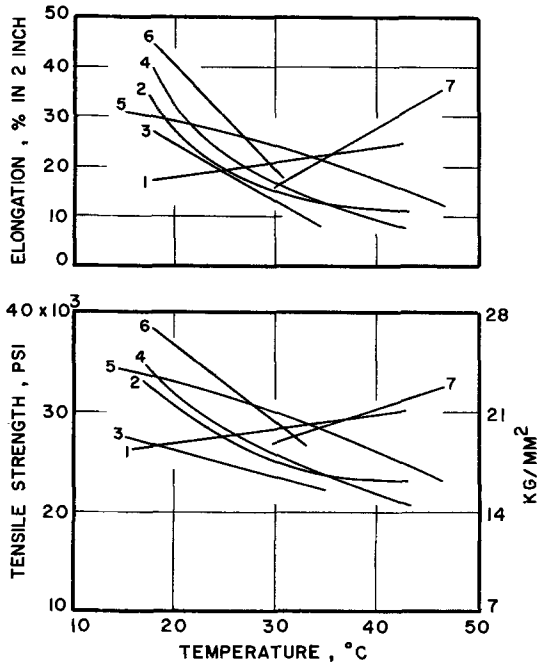

Fig. 4. Relationships between bath temperature, tensile strength, and elongation for deposits from sulfate baths: 1—Cu1-H1, 0.5 A/dm²; 2—Cu1-H2, 2 A/dm²; 3—Cu2-H2, 0.5 A/dm²; 4—Cu2-H2, 2 A/dm²; 5—Cu2-H2, 4 A/dm²; 6—Cu2-H3, 2 A/dm²; 7—Cu3-H3, 0.5 A/dm².

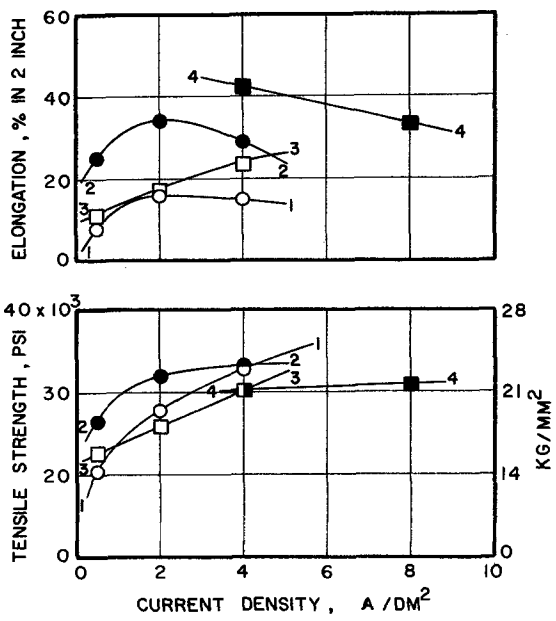

Fig. 5. Relationships between current density, tensile strength, and elongation of copper deposits from sulfate baths: 1—Cu1-H3, 30°C; 2—Cu2-H2, 20°C; 3—Cu2-H2, 30°C; 4—Cu3-H3, 60°C.

The data for hardness in Table VIII are analyzed as follows. Out of nine sets of data, hardness decreases with increase in temperature in six of the sets and is unaffected in two. In three of the 3-member sets, minor reversals of effect occur, smaller than the ±5 KHN units shown in Section III-A to be the variability range of duplicates. These reversals are therefore not significant. In only one set (lines 18-29) do the data deviate significantly from the general trend. Thus, the statement made above regarding tensile strength and ductility also applies to hardness; namely, the predominant trend is a decrease of hardness with increase in bath temperature. However, the effect is generally small and it may be obscured in specific cases by the effect of other variables or by inherent errors of measurement.

b. Current density.—Data on the effect of current density on properties are assembled in Table IX. Variations of elongation and tensile strength with current density are shown in Fig. 5. The dominant trend is increase of both elongation and tensile strength with increase of current density, but the effects are not large. A few deviations from the dominant trend occurred.

The reversed relationship noted in comparing the data on lines 41 and 42 requires explanation. It was evident from the appearance of panel No. 297 (line 42) that the deposit approached a "burnt" condition. The current density of 20 A/dm² at 60°C was obviously too high to yield a sound deposit. The decrease of tensile strength and ductility with current density is therefore real and significant in this case. The abnormality of this deposit (panel No. 297) may be seen

Table IX. Effect of current density on properties of deposits from sulfate baths

Line No., Table I	Panel No.	Bath symbol	Bath temp, °C	Current density, A/dm²	Tensile[a] strength, psi	Yield[a,b] strength, psi	Elongation in 2 in. (5 cm), %	Young's[a] modulus of elasticity, psi	Hardness KHN 200g load, kg/mm²	Internal[a,c] stress, psi	Density 25°C, g/cm³	Elec. resistivity 25°C, ohm-cm
3	52	Cu1-H1	40	0.5	30 × 10³	10 × 10³	24		57	80	8.922	
4	53			4	29	8	32		46	530	8.921	
8	60	Cu1-H3	30	0.5	20	8	8		56	−110	8.919	1.72 × 10⁻⁶
9	59			2	28	8	16		58	1800	8.919	1.72
10, 11	61-63			4	34	13	15		79	3800	8.925	
17	110	Cu2-H2	20	0.5	26	7	25	14 × 10⁶	105	−510	8.928	1.78
18, 19	94, 106			2	32	11	34	16	61	1500	8.925	1.74
22	22			4	33	12	29		67	4300	8.920	
23	15		32	0.5	23	7	11	13[d]	87	−700	8.924	1.71
24, 25	13, 25		30	2	26	8	17	14	88	550	8.921	1.72
27	44		30	4	30	9	24		53	2200	8.922	1.72
28	51		40	2	22	7	10		85			
29	16, 18		45	2	21	8	10	12[d]	49	−320	8.923	1.73
30	27		45	4	24	7	14		57	190	8.924	
35	332	Cu2-H3	30	0.5	33	10	41		62	−90	8.926	1.71
36, 37	276, 307			2	28	9	19	14	54	180	8.924	1.73
38	308			4	34	11	46		66	1500	8.925	1.73
39	278			8	32	14	24		75	4300	8.926	1.74
41	286		60	8	27	10	18		58	380	8.925	1.76
42	297			20	20	7	5		58	1400	8.86	1.90
81	29	Cu3-H3	30	0.5	27	8	16		57	−90	8.920	1.71
82	310			2	30	9	29		55	620	8.924	1.72
83	31		45	0.5	32	10	34		57		8.919	
84	28			4	26	8	15		51	1400	8.921	1.70
85, 86	30, 32		60	4	31	8	42		55		8.925	1.72
87	309			8	31	10	33		59	620	8.925	1.75

[a] One pound per square inch (psi) = 0.000704 kilogram per square millimeter (kg/mm²).
[b] 0.05% offset.
[c] Negative values represent compressive stress.
[d] Measured by beam deflection method.

in its structure (Fig. 17-C-4) and in its high content of impurities (Table XXXII), in comparison with the normal deposit (panel No. 323).

Data on the effect of current density on hardness given in Table IX indicate no definite relationship between current density and hardness. However, it is shown later that, if *all* nonaddition agent deposits from the sulfate bath are considered, there is a loose correlation between tensile strength and hardness (Fig. 15). Since tensile strength was shown above to have a small positive correlation with current density, it follows that there must be on the average a small increase of hardness with increase of current density. However, the effect is too small to be evident from examination of individual cases.

c. Concentration of copper sulfate.—It is seen from Table X that copper sulfate concentration does not have a significant effect on tensile strength or hardness. There is a sufficient predominance of cases where elongation increased with increase of concentration of copper sulfate to indicate a real effect.

In Table X some properties of commercial wrought copper have been included for comparison with those of electrodeposits from the sulfate bath. It is seen that the tensile strengths of the electrodeposits are nearly the same as that of annealed tough-pitch copper. The latter has a tensile strength of 31,000 psi, whereas the average for all nonaddition agent deposits is 29,000 psi. On the other hand, the average elongation of the electrodeposits, 24%, is considerably less than the 45% of the annealed tough-pitch copper, and the average hardness of the electrodeposits, 60 KHN, is significantly higher than the value of 45 KHN for the annealed tough-pitch copper.

d. Concentration of sulfuric acid.—The effect of the concentration of sulfuric acid on properties of deposits is shown in Table XI. Several sets of data relating tensile strength and elongation to concentration of sulfuric acid are plotted in Fig. 6. There is a consistent trend to increase in strength and elongation for an increase from the intermediate to the high concentration of acid. In the two cases where data were obtained relating the low to intermediate acid concentration, the reverse effect occurs. Thus, the curves in Fig. 6 pass through a minimum. We hesitate to conclude that this is a true relationship without additional evidence. The generally observed parallelism between tensile strength and ductility that occurs with nonaddition agent deposits from the sulfate bath is well illustrated in Fig. 6.

One sees on examining the results for hardness in Table XI that, again, the correlation with the composition variable is equivocal. However, the preponderant

Table X. Effect of concentration of copper sulfate on properties of deposits from the sulfate bath

Line No., Table I	Panel No.	Bath temp, °C	Current density, A/dm²	Bath symbol[a] H_2SO_4	Bath symbol[a] $CuSO_4$	Tensile[g] strength, psi	Yield[b,g] strength, psi	Elongation in 2 in. (5 cm), %	Young's[g] modulus of elasticity, psi	Hardness KHN 200g load, kg/mm²	Internal[c,g] stress, psi	Density 25°C, g/cm³	Elec. resistivity 25°C, ohm-cm
5	55	20	2	H2	Cu1	31 × 10³	9 × 10³	28	16 × 10⁶	59	3300	8.921	
18, 20	23, 94				Cu2	32	11	33	16	61	1500	8.925	1.73 × 10⁻⁶
8	60	30	0.5	H3	Cu1	20	8	8		56	−110	8.919	1.72
35	332				Cu2	33	10	41		62	−90	8.926	1.71
81	29				Cu3	27	8	16		57	−90	8.920	1.71
2	47	30	2	H1	Cu1	30	8	37		49	400	8.920	1.72
12	54				Cu2	30	8	32		48	560	8.922	1.72
6	56, 57	30	2	H2	Cu1	25	7	15		58	570	8.921	
24, 25	13, 25				Cu2	26	8	17		88	550	8.921	1.72
26	322, 323				Cu2	32	11	39	14	55		8.925	1.73
9	59	30	2	H3	Cu1	28	8	16		58	1800	8.919	1.72
36, 37	276, 307				Cu2	29	9	19	14	54	180	8.924	1.73
82	310				Cu3	30	9	29		55	620	8.924	1.72
10, 11	61-63	30	4	H3	Cu1	34	13	15		79	3800	8.925	
38	308				Cu2	34	11	46		66	1500	8.925	1.73
7	58	40	2	H2	Cu1	24	8	13		47	370		
28, 29	51, 18				Cu2	22	7	10	12[d,e]	85, 49[e]	−320[e]	8.923[e]	1.73[e]
41	286	60	8	H3	Cu2	27	10	18		58	380	8.925	1.76
87	309				Cu3	31	10	33		59	620	8.925	1.75
	Commercial electrolytic tough-pitch copper			Annealed		31	10	45	13-16	45		8.92-8.93	1.74
				Half-hard		45	38	14	16[f]	80		8.907[f]	1.76
				Hard		54	48	6	15-18	100		8.89	1.77

[a] See Table II.
[b] 0.05% offset.
[c] Negative values represent compressive stress.
[d] Measured by beam deflection. Values for which no method is indicated were determined by the resistance strain gauge method.
[e] Bath temperature 45°C.
[f] Values measured by authors. Other data for commercial copper are from published sources. Literature Ref. No. (20), (35).
[g] One pound per square inch (psi) = 0.000704 kilogram per square millimeter (kg/mm²).

Table XI. Effect of concentration of sulfuric acid on properties of deposits from the sulfate bath

Line No., Table I	Panel No.	Bath temp, °C	Current density, A/dm²	Bath symbol $CuSO_4$	Bath symbol H_2SO_4	Tensile[a] strength, psi	Yield[a,b] strength, psi	Elongation in 2 in. (5 cm), %	Young's[a] modulus of elasticity, psi	Hardness KHN 200g load, kg/mm²	Internal[a,c] stress, psi	Density 25°C, g/cm³	Elec. resistivity 25°C ohm-cm
18	94	20	2	Cu2	H2	32 × 10³	11 × 10³	33	16 × 10⁶	61	1500	8.925	1.73 × 10⁻⁶
34	277				H3	37	15	41	16[d]	78	2000	8.926	
23	15	32	0.5	Cu2	H2	23	7	11	13[e]	87	−700	8.924	1.71
35	332	30			H3	33	10	41		62	−90	8.926	1.71
2	47	30	2	Cu1	H1	30	8	37		49	400	8.920	1.72
6	56				H2	25	7	15		58	570	8.921	
9	59				H3	28	8	16		58	1800	8.919	1.72
12	54	30	2	Cu2	H1	30	8	32		48	560	8.922	1.72
24, 25	13, 25				H2	26	8	17	14	88	550	8.921	1.72
36, 37	276, 307				H3	29	9	19	14	54	180	8.924	1.73
27	44	30	4	Cu2	H2	30	9	24		53	2200	8.922	1.72
38	308				H3	34	11	46		66	1500	8.925	1.73
13	274	40	8	Cu2	H1	32	10	36		61	1400	8.925	1.75
40	285				H3	37	15	44		80	2600	8.926	1.75

[a] One pound per square inch (psi) = 0.000704 kilogram per square millimeter (kg/mm²).
[b] 0.05% offset.
[c] Negative values represent compressive stresses.
[d] Determined from stress-strain curve.
[e] Measured by beam deflection method.

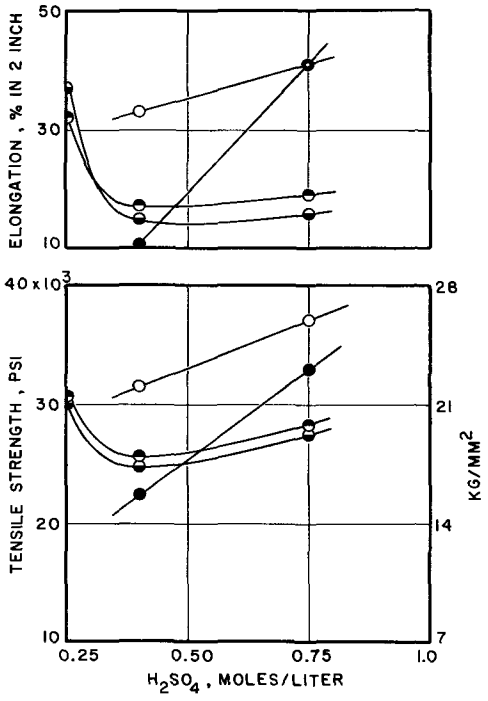

Fig. 6. Relationships between sulfuric acid concentration, tensile strength, and elongation of copper deposits from sulfate baths: ○—Cu-2, 20°C, 2 A/dm²; ●—Cu-2, 30°, 0.5 A/dm²; ◒—Cu-1, 30°, 2 A/dm²; ◓—Cu-2, 30°, 2 A/dm².

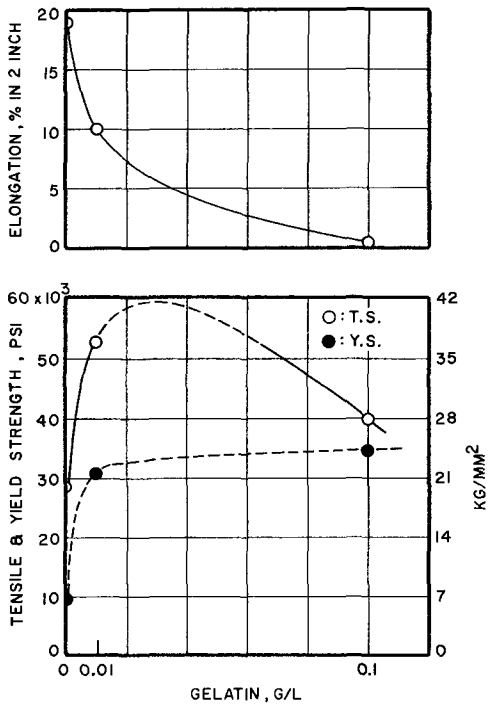

Fig. 7. Relationships between gelatin concentration and tensile strength, yield strength, and elongation of copper deposits from the sulfate bath (Cu2-H3, 30°C, 2 A/dm²).

effect is an increase in hardness with increase in acidity.

e. Addition agents.—Data relating addition agents to properties are summarized in Tables XII and XIII and Fig. 7. In both tables, data for the corresponding non-addition agent deposits are shown so that a direct evaluation of the effects of the addition agents can be made. We refer to these as "control deposits." As little as 3 mg/l of gelatin are seen to produce a significant effect on strength, more so than any of the operating or composition variables discussed in the preceding sections. This concentration of gelatin also produces a moderate decrease in ductility and increase in hardness. The effects of concentration of gelatin are shown graphically in Fig. 7. Concentrations of gelatin between 0.003 and 0.1 g/l cause a regular change of ductility and yield strength, with the effect leveling off at about 0.1 g/l. However, tensile strength passes through a maximum, probably at a concentration of gelatin somewhat higher than 0.01 g/l. The high ratio of yield strength to tensile strength at 0.1 g/l is abnormal and probably indicates that the true tensile strength was higher than that observed, and that premature failure occurred due to brittleness (the elongation was nearly zero).

The higher concentrations of gelatin produced a marked increase in hardness (148 KHN at 0.1 g/l).

Phenolsulfonic acid (Table XII, PSA) was used at a concentration of 1.0 g/l and deposits were made over a range of operating conditions. The average tensile strength for all of these deposits was 33,000 psi *vs.* 28,000 psi for the control deposits. The increase is small, but is probably real because it is consistent. PSA has a comparable small but consistent effect in raising ductility and a more definite effect on hardness, with an increase from an average hardness of 57 KHN for the control deposits to 88 KHN for the PSA deposits.

Table XII. Effect of addition agents on properties of deposits from sulfate baths

Line No., Table I	Panel No.	Addition[a] agent: Name	Conc, g/l	Bath symbol	Bath temp, °C	Current density, A/dm²	Tensile[b] strength, psi	Yield[b,c] strength, psi	Elongation in 2 in. (5 cm), %	Young's[b] modulus of elasticity, psi	Hardness KHN 200g load, kg/mm²	Internal[b,d] stress, psi	Density 25°C, g/cm³	Elec. resistivity 25°C, ohm-cm
12	54	None		Cu2-H1	30	2	30 × 10³	8 × 10³	32		48	560	8.922	1.72 × 10⁻⁶
14, 15	64, 65	Gelatin	0.003		30	2	41	21	25	17 × 10⁶	90	750	8.915	
24-26	13, 25 322	None		Cu2-H2	30	2	28	9	24	14	72	550	8.923	1.72
31	66	Gelatin	0.003		30	2	45	28	8	15[e]	82	1000	8.914	1.76
36, 37	276, 307	None		Cu2-H3	30	2	29	9	19	14	54	180	8.924	1.73
46	81	Gelatin	0.01		30	2	53	31	10	17[f]	131	860		1.77
47	83		0.1		30	2	40	34	0.4	15[e]	148	−4200	8.86	2.10
16	68	PSA	1.0	Cu2-H1	30	2	36	15	31		97	−370	8.923	
32	69	PSA	0.7	Cu2-H2	30	2	33	11	35		73		8.922	
33	70	PSA	1.0		30	2	36	15	34		99	250	8.923	
58	73	PSA	1.0	Cu2-H3	20	2	40	18	28		93	1600	8.923	
59, 60	71, 71B	PSA	1.0		30	2	35	14	33		87	100	8.923	1.72
62	72	PSA	1.0		40	2	30	9	23		88	380	8.923	1.71
63	76	PSA	1.0		40	4	33	12	31		87	−260	8.922	
82	310	None		Cu3-H3	30	2	30	9	29		55	620	8.924	1.72
88	77	PSA	1.0		30	2	34	13	32		82	−420	8.921	

[a] PSA = phenolsulfonic acid.
[b] One pound per square inch (psi) = 0.000704 kilogram per square millimeter (kg/mm²).
[c] 0.05% offset.
[d] Negative values represent compressive stresses.
[e] Measured by beam deflection method.
[f] From stress-strain curve.

Table XIII. Effect of addition agents on properties of deposits from sulfate baths[a]

Line No., Table I	Panel No.	Addition[b] agent: Name	Addition[b] agent: Conc, g/l	Bath temp, °C	Current density, A/dm²	Tensile[c] strength, psi	Yield[c,d] strength, psi	Elongation in 2 in. (5 cm), %	Young's[c] modulus of elasticity, psi	Hardness KHN 200g load, kg/mm²	Internal[c,e] stress, psi	Density 25°C, g/cm³	Elec. resistivity 25°C, ohm-cm
36, 37	276, 307	None	—	30	2	29×10^3	9×10^3	19	14×10^6	54	180	8.924	1.73×10^{-6}
43	5-4	Dextrin	0.02	30	2	22		5[f]		60			
44	5-6	Dextrose	0.05	30	2			Zero					
45	219	EA + M	0.3, 2.0	30	2	27	13	9		61	1500	8.922	1.73
48	5-5	Glycerol	1.0	30	2	33		11[f]		62			
49	5-2	Glycine	0.1	30	2	31		4[f]		79			
50	214	LA	0.05	30	2	25	8	10		78	800	8.929	1.72
52	160	β-NQ	0.1	30	2	36	14	8		119	5300	8.923	1.78
54, 55	91, 114	NDS	1.8	30	2	30	8	29		83	300	8.923	1.72
64	166	SeO_2	10^{-4} Se	30	2	47	17	21		123	2300	8.929	1.76
66	172	SeO_2	10^{-3} Se	30	2	44	16	24	16	108	2800	8.928	1.75
68	5-1	Sorbitol	0.1	30	2	30		4[f]		55			
69	86	Thiourea	0.005	30	2	20	6	10		70	−120	8.922	1.76
70	88	Thiourea	0.015	30	2	28	12	9		76	−40	8.918	1.77
71	216	Thiourea + NDS	0.015 0.5	30	2	39	13	20		99	900	8.923	1.76
72, 73	93, 108 109	TIPA	3.5	30	2	40	19	17	16	119	2100	8.923	1.75
76	337-341	TIPA	3.5	30	5	71	43	7	15	144	7100	8.913	1.89
77	226	Prop. A		22	4	51	40	14		137		8.917	1.82
78	230	Prop. A		28	4	52	40	19		128	2900	8.918	

[a] All deposits were made from the Cu2-H3 bath.
[b] Addition agent symbols are defined as follows: EA + M, ethyl alcohol + molasses; β-NQ, β-naphthoquinoline; LA, lactic acid; NDS, 1,5-naphthalenedisulfonic acid; TIPA, triisopropanolamine; Prop. A, proprietary bright acid copper bath containing a sulfonate and an azo dye.
[c] One pound per square inch (psi) = 0.000704 kilogram per square millimeter (kg/mm²).
[d] 0.05% offset.
[e] Negative values represent compressive stress.
[f] Per cent elongation in 1 in. (2.5 cm).

Lines 58-62 in Table XII show the effect of bath temperature on tensile strength and ductility of deposits from baths containing PSA. The decrease in tensile strength is more pronounced than for corresponding nonaddition agent deposits, with the effect of the PSA largely lost at 40°C. Bath temperature has a smaller effect on ductility.

The effects of a variety of other addition agents are shown in Table XIII. Most of these addition agents have only small effects on tensile strength. Dextrin, lactic acid, and thiourea cause small decreases, especially thiourea. Ethyl alcohol plus molasses is neutral in its effect. The addition agents that were most effective in increasing strength were selenium dioxide, triisopropanolamine (13) (TIPA), and the proprietary brightener designated as "A."[9] TIPA was most effective at a relatively high current density. It is possible that the effects of some of the other addition agents might be larger at higher current densities. All of these addition agents resulted in smoother deposits with a visual appearance of grain refinement, but none except Proprietary A yielded bright deposits. TIPA tended to yield deposits peppered with small nodules on a fine-grained background. Efforts to eliminate this defect were not entirely successful. The tendency to cause nodules appears to be an inherent characteristic of this addition agent. Its concentration was also difficult to control due to rapid depletion. Control of selenium dioxide was also difficult. This is natural because of its very low concentration in the bath.

Selenium dioxide and 1,5-napthalenedisulfonic acid (NDS) caused increases in ductility. The effects on ductility of thiourea plus NDS and of Proprietary A were not significant. The other addition agents resulted in significant decreases in ductility, but in no case to the extent of extreme brittleness.

All the addition agents caused significant increases in hardness. β-Naphthoquinoline, selenium dioxide, TIPA, and Proprietary A were most effective, yielding hardnesses in the range of 120-140 KHN.

f. Periodic current reversal (PR).—Plating with periodically reversed current, as developed by Jernstedt (14) and applied to high efficiency copper cyanide baths, results in marked improvements in physical properties, smoothness, and ability to form thick deposits. Periodic current reversal (PR) has less pronounced, but significant, effects on deposits from acidic baths. Applications of PR have been reviewed in previous publications (3, 15).

A clock-type timer system and a large-capacity relay unit were used to control the periodically reversed current. Cycle periods were adjusted to ±5%. A thorough investigation of the effect of PR would require variation of the PR cycle and other operating conditions. We intended only a limited study, to show whether PR significantly affects properties. The cycle used was based on information in the review references cited above.

Our data on the effect of PR on properties of copper deposits are given in Table XIV for deposits from both sulfate and cyanide baths. At this point we consider only the former. Comparing the data in line 79 with that in the next two lines, it is seen that tensile and yield strengths and hardness are increased significantly by use of PR. Comparisons are made with direct current deposits formed at both 2 and 4 A/dm² because, while the instantaneous plating rate with PR is 4 A/dm², the net plating rate is only $4(5 - 2/5 + 2) = 1.7$ A/dm².

The elongation of the PR deposit is between those of the two direct current deposits. The data in Table XIV by themselves are not sufficient to permit a definite conclusion regarding effect of PR on elongation. However, in conjunction with other elongation data shown in Fig. 14, discussed in Section III-E, we conclude that tensile strength and elongation vary inversely for PR deposits.

B. Internal Stress in Deposits from Sulfate Baths

1. Method of measurement and reproducibility.—Data on internal stress are of interest from the theoretical standpoint and are of practical concern in engineering applications, where excessive stress may cause warping and cracking of an electrodeposit. Stress was measured with the Brenner-Senderoff spiral contractometer, using the precautions described by these authors (16). The estimated accuracy of individual determinations of stress is ±300 psi (0.21 kg/mm²).

2. Effect of Thickness of Deposit.—Partly for convenience and partly because internal stress in sulfate deposits, with which we worked first, did not usually increase significantly with increase in thickness beyond 1 mil, this was chosen as the thickness on which to base our measurements. Variation of stress with thickness for several representative types of deposit is shown in Fig. 8 and 9. The curve in Fig. 8 for a deposit from a sulfate bath containing naphthalenedisulfonic

[9] This proprietary addition agent is reported to contain a cationic azo dye and an organic sulfonic acid.

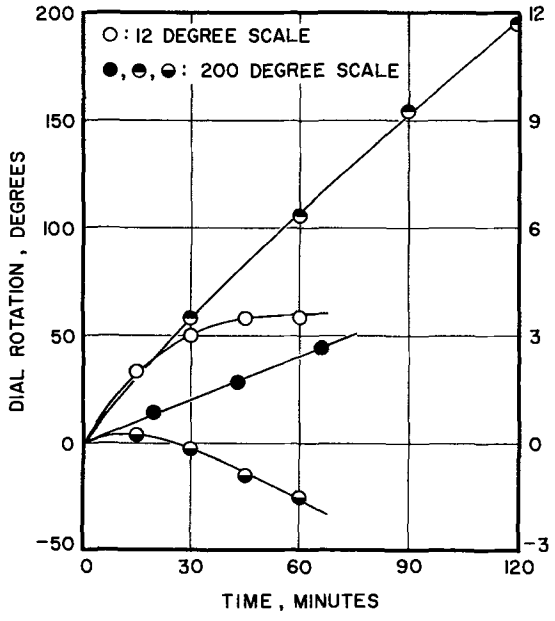

Fig. 8. Increase of internal stress with thickness (plating time) for various types of copper deposits. Dial rotation of 1° equals 70±20 psi, depending on thickness. Negative rotation designates compressive stress. The terminal point of each curve corresponds to a deposit thickness of approximately 1 mil (25 μm). ○—Cu2-H3 containing 1.8 g/l 1,5-naphthalenedisulfonic acid, 30°C, 2 A/dm²; ●—Cu2-H3, 30°, 4 A/dm², PR cycle 5-2 sec; ◓—CN-2, 40°, 1 A/dm²; ◒—pyrophosphate, 50°, 2 A/dm².

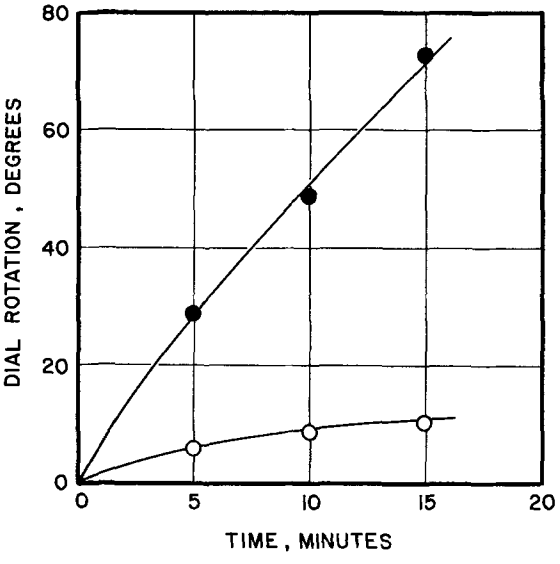

Fig. 9. Increase of internal stress with thickness (plating time) for copper deposits from a sulfate and a fluoborate bath. Dial rotation of 1° equals approximately 65 psi. The terminal point of each curve corresponds to a deposit thickness of approximately 1 mil (25 μm). ○—F-1, 30°C, 8 A/dm²; ●—Cu2-H3, 30°, 8 A/dm².

acid is fairly typical of low-strength deposits from sulfate baths. It is seen that the rate of increase of stress has become nearly zero at a thickness of about 1 mil. This was also the behavior of the deposit from a fluoborate bath (Fig. 9). Stress was still changing at a significant rate at this thickness in deposits of the other types illustrated in Fig. 8 and 9. In these latter deposits, the stress ultimately developed is higher than the value we have reported. However, we conclude on qualitative grounds that the increase in stress, with one exception, soon ceases to increase with thickness, because deposits, after separating from the starting sheet, did not warp and curl. This indicates that either the stress-free later "layers" of the deposit were more predominant in thickness or that stresses were relieved by room-temperature annealing.

The one exception was the deposit made from a sulfate bath with periodic current reversal (Fig. 8 and Table I, line 79). Residual stress was evident in this deposit, causing warping of the 18 mils thick panel. Apparently, reversal of current causes each new layer, cycle after cycle, to deposit with stress comparable to that in the initial layer of a continuous deposit. In general, the deposits that show continued increases in stress at a thickness of 1 mil and which have the higher reported levels of stress have small-grain structures (Fig. 20, 21, 34, 59).

The pyrophosphate deposit (Fig. 8), in which stress is compressive, first went through a brief period in which the stress was tensile. This may be caused by an abnormal initial structure induced by the substrate, with conversion to a structure typical of the conditions as thickness increases.

3. Effect of operating conditions and bath composition.—a. Bath temperature.—Increase of bath temperature causes the internal stress of deposits from sulfate baths to decrease. This is true in an algebraic sense; *i.e.*, if the stress is compressive, increase of temperature makes it more compressive. This is illustrated in Table VIII and Fig. 10 and 11.

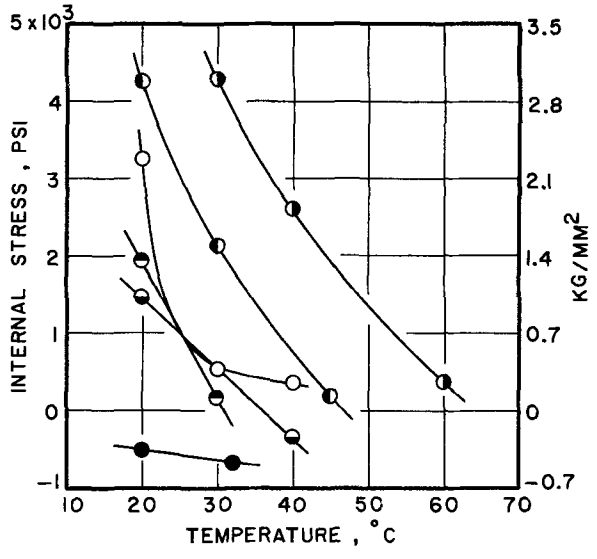

Fig. 10. Relationship between bath temperature and internal stress in copper deposits from sulfate baths. Negative stress is compressive. ○—Cu1-H2, 2 A/dm²; ●—Cu2-H2, 0.5 A/dm²; ◒—Cu2-H2, 2 A/dm²; ◐—Cu2-H2, 4 A/dm²; ◓—Cu2-H3, 2 A/dm²; ◑—Cu2-H3, 8 A/dm².

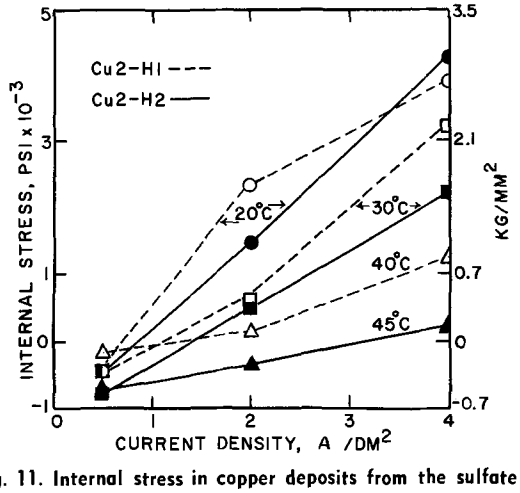

Fig. 11. Internal stress in copper deposits from the sulfate bath: effect of bath temperature, current density, and concentration of sulfuric acid. Negative stress is compressive.

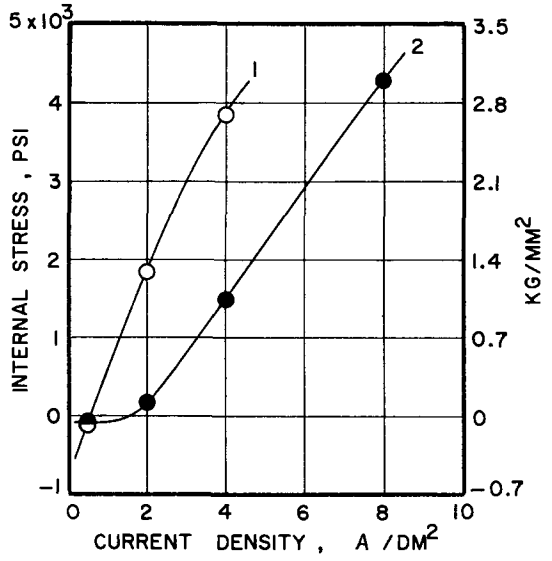

Fig. 12. Relationship between current density and internal stress in copper deposits from sulfate baths. Negative stress is compressive. 1—Cu1-H3, 30°C; 2—Cu2-H3, 30°.

b. Current density.—The effect of current density on internal stress is shown in Table IX and in Fig. 11 and 12. The effect is unequivocal, with significant and consistent increase in stress with increase in current density in each instance.

c. Concentration of copper sulfate.—If the concentration of copper ions in the cathode film is relatively low, this might be expected to cause small grain size and high stress. However, the effect might be small in magnitude unless limiting current conditions were approached. On these hypotheses, one might expect minor effect from change of concentration of copper sulfate in a high concentration range, but that, in passing from an intermediate to a low concentration, increase in stress would be larger. On the other hand, this conclusion is modified by consideration of current density and temperature. If current density is sufficiently low or bath temperature sufficiently high, the tendency for stress to increase with decrease in concentration of copper ion might be nullified. These hypotheses fit the data tabulated in Table X rather closely. Thus, in the first set of data (lines 5, 18, 20), where bath temperature is low, stress increases significantly with decrease of copper sulfate from the intermediate (Cu-2) to the low concentration (Cu-1). In the second set (lines 8, 35, 81), stress does not change significantly with change of copper sulfate concentration and this insensitivity is associated with a very low current density. In the third, fourth, and seventh sets (lines 2-12; 6-24, 25; and 7-28, 29), differences in stress are not significant and this is associated with high bath temperatures (relative to the first set). In the fifth set (lines 9-82), the difference due to the change from Cu-2 to Cu-3 is not significant (less than ±300 psi), in agreement with the hypothesis. There is a significant increase in stress with decrease of copper from Cu-2 to Cu-1. In this case, the concentration of sulfuric acid is high, and this would tend to depress the copper ion concentration by means of the common-ion effect, thus causing an increase in stress. In the sixth set (lines 10-38) the situation is similar to that for the first pair of the fifth set, except that one would expect the effect to be larger because the current density is higher in the sixth set, and a larger effect did occur. Finally, in the eighth set (lines 41-87), due to the high bath temperature and high range of copper concentration, we might anticipate that stress would be little affected by the change of copper concentration, and this is what is observed.

The data in Table X have been discussed in this detail to emphasize that, in all of the interrelationships we have attempted to simplify, many variables interact with complex effects. This may result in apparent discord which might disappear if the effects of all variables could be simultaneously analyzed.

d. Concentration of sulfuric acid.—Data showing the effect of concentration of sulfuric acid on stress are summarized in Table XI and Fig. 11. Counting sets of three as two pairs, there are 17 pairs of data for deposits made with different acid concentrations in Table XI and Fig. 11, jointly. In 13 of these pairs, differences in stress are within or nearly within our estimate of reproducibility of ±300 psi. Two pairs show a small but significant increase of stress with increase of acidity, and two a decrease. We can only conclude that, within the range of concentrations of sulfuric acid that we used, the effect of change of concentration of sulfuric acid is small and its direction undetermined.

One might predict a dual effect: *e.g.*, if conditions are borderline with respect to maintenance of an ample concentration of copper ions in the cathode film, due to a low concentration of copper in the bath, high current density, or low temperature, increase of acidity might, due to the common ion effect referred to in Section III-B-3-c, cause sufficient further reduction of concentration of copper ion in the cathode layer to result in significant grain refinement and increase of stress. Another situation would be that in which the concentration of acid was sufficiently low that basic material codeposited, causing high stress. Increase in acidity might then cause *decrease* of stress. Additional experiments would be required to evaluate this speculation.

e. Addition agents. Effects of addition agents on stress are shown in Tables XII and XIII and Fig. 13.

A concentration of gelatin in the plating bath of 0.003 or 0.01 g/liter results in an increase in stress, whereas with 0.1 g/liter the stress has a large compressive value (Table XII, Fig. 13). Thiourea and Rochelle salt have been reported to have a similar effect (17, 18). The concentration of thiourea that we used (Table XIII) was not large enough to produce stress reversal.

The effect of phenolsulfonic acid is shown in Table XII. Comparing the values of stress in pairs, lines 12 *vs.* 16, 24-26 *vs.* 33, 36-37 *vs.* 59-60, and 82 *vs.* 88, we see that phenolsulfonic acid consistently causes a reduction of stress. This is analogous to the effect of organic sulfonates in nickel baths. On the other hand, 1,5-naphthalenedisulfonic acid (line 54-55, Table XIII) causes a small but not significant increase in stress. The stress value in line 58, Table XII, shows that

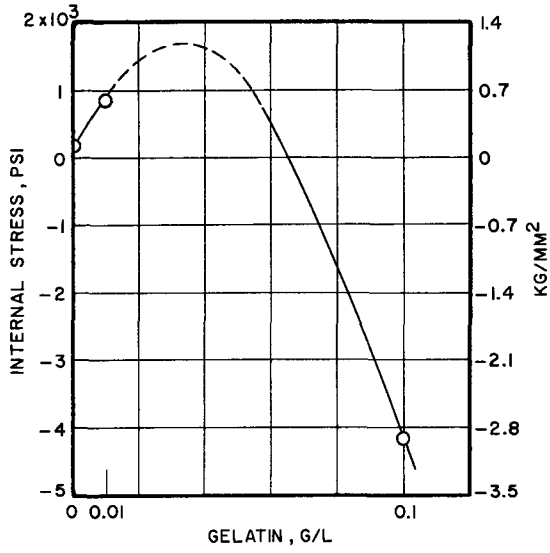

Fig. 13. Relationship between gelatin concentration in the bath and internal stress in copper deposits from sulfate baths (Cu2-H3, 30°C, 2 A/dm²).

decrease of temperature from 30° to 20°C causes a significant increase in stress of a deposit from a bath containing phenolsulfonic acid ($\Delta psi = +1500$). Thus, the effect of temperature is the same as in a non-addition agent bath.

The addition agents listed in Table XIII that are not referred to in the preceding paragraph all caused significant increases in stress. The largest effects were produced by β-naphthoquinoline, selenium dioxide, triisopropanolamine (TIPA), and the proprietary addition agent. However, none of the stresses seen in Table XIII is high enough to cause trouble in most applications of electrodeposits.

f. Periodic current reversal.—Effect of periodic current reversal on stress is shown in the first three lines of Table XIV. It is seen that PR causes a marked increase of internal stress. This has already been discussed in Section III-B-2 in its relation to deposit thickness. It is hypothesized that the high stress may be the result of forming deposit, layer after layer because of the cycling, that has the high stress characteristic of the fine-grained zone next to the substrate in d-c deposits.

C. Density of Deposits from Sulfate Baths

1. Method of measurement and reproducibility.—Knowledge of density is of interest primarily because it depends on purity and structure of deposits. Density was measured by obtaining the mass of a specimen by weighing in air and the volume of the specimen by measuring the buoyant force on it when immersed in a liquid. Precautions required for precision density measurements have been described (19) and were followed with some abridgments. For deposits through panel serial No. 96, the immersion liquid used was water containing a wetting agent. The immersion liquid for subsequent panels was tetrabromoethane. Specimens were made from broken segments of tensile specimens or from rectangular strips ¾ x 5 in. A comparison of the density of a pulled and unpulled specimen showed that the cold-working of a tensile specimen did not affect its density measurably. Triplicate specimens were usually used, each taken from a different position on the panel; from some panels only duplicates were used. No significant effect of position on the panel was found.

Weighings were made to 0.05 mg. Balance case temperature was constant to ±1°C. Temperature of the submersion liquid was measured to 0.1°C. All data were corrected to 25°C. The average variation among duplicate or triplicate sets was ±0.001 and the maximum ±0.004 g/cm³. The accuracy of the reported values is judged to be ±0.005 g/cm³.

2. Results.—Examination of the data in Tables VIII to XI shows maximum variations within given sets of pairs or triplets of ±0.002, ±0.004, ±0.004, and ±0.002 g/cm³ due to the largest applied variations of bath temperature, current density, concentration of copper sulfate, and concentration of sulfuric acid, respectively. Corresponding average densities, respectively, are 8.924, 8.924, 8.923, and 8.923 g/cm³. These data illustrate the remarkably small change of density with change of bath composition or operating conditions.

One exception to this constancy appears in Table IX, line 42, panel 297. This is the high current density deposit referred to in Section III-A-4-b. Its low density of 8.86 correlates with its other abnormal properties.

Some addition agents cause marked lowering of density, while others have little, if any, effect. As little as 3 mg/liter of gelatin cause a significant lowering, while 0.1 g/liter results in the very low value of 8.86 g/cm³ (Table XII). Among the other addition agents used (Tables XII and XIII), only triisopropanolamine at 5 A/dm² caused significant reduction of density.

Periodically reversed current has no measurable effect on density of deposits from the sulfate baths (see Table XIV, first three lines).

Densities of deposits from sulfate baths are summarized in Table XV, in which comparative values for other preparations of copper are also assembled.

D. Electrical Resistivity of Deposits from Sulfate Baths

1. Method of measurement and reproducibility.—Specimens used for measuring electrical resistivity were strips 0.5 x 15 cm. They were clamped in a jig with current contacts at the ends and intermediate voltage contacts 10 cm apart. Two methods were used for the electrical measurements. In the first method, conventional equipment was used for measuring voltage between the two contacts while a measured current was passed. This method was used for specimens from all panels through No. 96. Measurements on specimens from panels made subsequent to No. 96 were made with a commercial milliohmmeter, which operated on the same principle as above, and which had an accuracy of ±1% in the range of resistance within which measurements were made. In both procedures, the equipment was calibrated and measurements of experimental specimens were directly intercompared with a 1 mohm standard resistor. The resistance of experimental specimens was of this order. Two, or usually three, specimens were taken from each panel, from top, middle, and bottom positions. Position did not affect resistivity. Cross-sectional area of specimens was obtained from length and mass. Small corrections were made for surface roughness, as described previously (4). The average deviation from the mean within sets of duplicates or triplicates was ±0.8%, considering all thick deposits (84 sets; thin deposits from cyanide baths excluded). Among these 84 sets, variation exceeded ±1% for only eight sets. Calculated values of resistivity reported in Table I and in the various subtables have been corrected to 25°C by assuming that the temperature coefficient of resistivity of the deposits is the same as that for pure copper (0.0068×10^{-6} ohm-cm/°C) (20).

2. Results.—Variation of electrical resistivity with thickness of deposits from sulfate baths has already been discussed (Section III-A-3, Table VII).

Analysis of resistivity data in Tables VIII to XI shows the following:

	Electrical resistivity, μohm-cm	
	Maximum variation within sets	Average, all sets
Table VIII, effect of bath temperature	±0.035	1.73
Table IX, effect of current density	±0.02	1.73
Table X, effect of concentration of copper sulfate	±0.005	1.73
Table XI, effect of concentration of sulfuric acid	±0.005	1.73

The variations are too small to permit definite conclusions as to the effects of the various parameters. It is seen in these tables that the few cases of maximum resistivity (1.75-1.78 μohm-cm) correspond to either a low temperature (20°C) or a high current density (8 A/dm²) and this is probably significant.

Not included in the above analysis is the deposit made at 60°C and 20 A/dm² (line 42, Table IX) which has been referred to in previous sections as abnormal. It also has an abnormally high resistivity, 1.90 μohm-cm.

Periodic reversal of current caused a small increase in resistivity of a deposit from a sulfate bath (Table XIV, line 79). This is consistent with the fine-grain structure of the deposit and with the higher resistivity of thin deposits (Section III-A-3, Table VII).

Relationships between the resistivity of deposits and addition agents in sulfate baths are shown in Tables XII and XIII. It is seen that gelatin, 0.1 g/l, triisopropanolamine, and the proprietary addition agent produce significant increases in resistivity. Gelatin, 0.003 or 0.01 g/l β-naphthoquinoline, SeO_2, sorbitol, and thiourea cause an increase of about 0.04 μohm-cm, only slightly larger than possible measurement variability, but probably real. Effects of phenolsulfonic acid, ethyl alcohol plus molasses, lactic acid, and naptha-

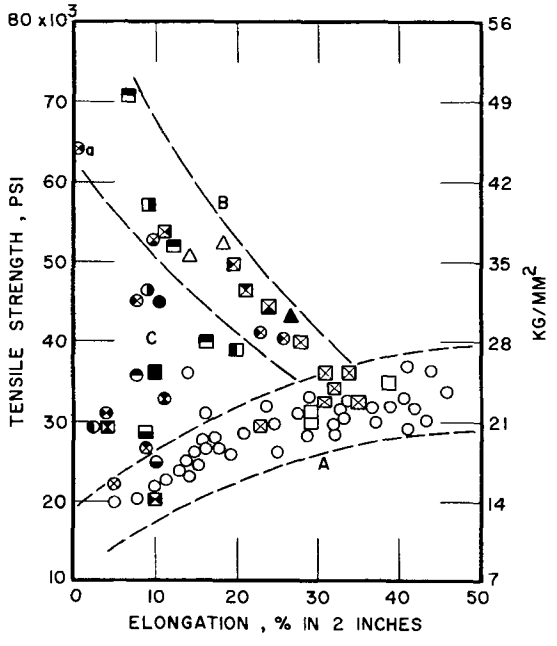

Fig. 14. General relationship between elongation and tensile strength for all copper deposits from sulfate baths. A—*Direct relationship between elongation and tensile strength:* ○—all nonaddition agent sulfate baths; ⊗—Cu2-H3 containing 0.02 g/l dextrin, 30°C, 2 A/dm²; ◒ Cu2-H3 containing 0.05 g/l lactic acid, 30°, 2 A/dm²; □—Cu2-H3 containing 1.8 g/l naphthalenedisulfonic acid, 30°, 2 A/dm²; □—all baths containing 1.0 g/l phenolsulfonic acid; ⊠ Cu2-H3 containing 0.005 g/l thiourea, 30°, 2 A/dm². B—*Inverse relationship between elongation and tensile strength:* ⊗—Cu2-H3 containing 0.1 g/l gelatin, 30°C, 2 A/dm²; ⊗—Cu2-H3 containing 0.01 g/l gelatin, 30°, 2 A/dm²; ⊗—Cu2-H1 containing 0.003 g/l gelatin, 30°, 2 A/dm²; ⊠—Cu2-H3 containing 10^{-4} g/l selenium, 30°, 2 A/dm²; ⊠—Cu2-H3 containing 10^{-4} g/l selenium, 30°, 2 A/dm², thin deposit (2 mils); ⊠—Cu2-H3 containing 10^{-3} g/l selenium, 30°, 2 A/dm²; ⊠—Cu2-H3 containing 10^{-3} g/l selenium, 30°, 2 A/dm², thin deposit (2 mils); ▭—Cu2-H3 containing 3.5 g/l triisopropanolamine, 30°, 5 A/dm²; ▯—Cu2-H3 containing 3.5 g/l triisopropanolamine, 30°, 2 A/dm², thin deposit (2 mils); △—proprietary bright acid copper, 22° and 28°, 4 A/dm²; ▲—Cu2-H3, 30°, 4 A/dm², PR cycle 5-2 sec. C—*Transitional relationship between elongation and tensile strength:* ●—thin nonaddition agent sulfate deposit (2 mils) ⊗—Cu2-H3 containing 0.3 g/l and 2.0 g/l ethyl alcohol and molasses, respectively, 30°C, 2 A/dm²; ⊗—Cu2-H3 containing 1.0 g/l glycerol, 30°, 2 A/dm²; ⊗ Cu2-H3 containing 0.1 g/l glycine, 30°, 2 A/dm²; ◓—Cu2-H3 containing 0.1 g/l β-naphthoquinoline, 30°, 2 A/dm²; ◑—Cu2-H3 containing 0.1 g/l β-naphthoquinoline, 30°, 2 A/dm², thin deposit (2 mils); ◐—Cu2-H3 containing 0.05 g/l lactic acid, 30°, 2 A/dm², thin deposit (2 mils); ▬—Cu2-H3 containing 0.015 g/l thiourea, 30°, 2 A/dm²; ◧—Cu2-H3 containing 0.015 g/l and 0.5 g/l thiourea and naphthalenedisulfonic acid, respectively, 30°, 2 A/dm²; ■—Cu2-H3 containing 1.8 g/l 1,5-naphthalenedisulfonic acid, 30°, 2 A/dm², thin deposit (2 mils); ⊠—Cu2-H3 containing 0.1 g/l sorbitol, 30°, 2 A/dm². a—Calculated value, see section III-A-4-e.

lenedisulfonic acid on resistivity are smaller than the sensitivity of our measurements.

Some comparative values of resistivity for wrought copper are shown in Table X. The average resistivity of the deposits from nonaddition agent sulfate baths is about the same as that of annealed electrolytic tough-pitch copper (1.73 and 1.74 μohm-cm, respectively). Resistivity values of many individual deposits in Tables VIII to XI are in the range of 1.70-1.72 μohm-cm, which compares with 1.71 reported for high-purity copper (3). Resistivity data therefore indicate a high degree of purity for most of the deposits from nonaddition agent sulfate baths.

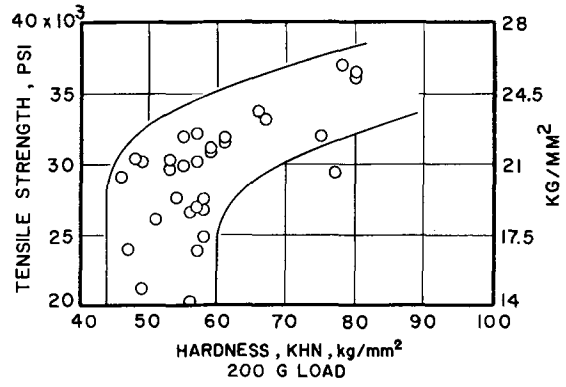

Fig. 15. General relationship between hardness and tensile strength of copper deposits from all nonaddition agent sulfate baths at various operating conditions.

E. Relationships between Properties of Deposits from Sulfate Baths

1. Tensile strength and elongation.—The usual relationship between tensile strength and elongation for wrought metals is inverse; *i.e.*, a high tensile strength is associated with a low ductility and *vice versa*. In Fig. 14 we have plotted values of tensile strength and elongation for all as-plated deposits from sulfate baths, including those containing addition agents. The points fall into three main groups: those enclosed by envelopes A and B, and the group in the intermediate area designated as C.

With a few minor exceptions, the "A" envelope includes all deposits from nonaddition agent baths (except for thin deposits) and deposits from baths containing addition agents that have little effect on tensile strength. These addition agents are dextrin, lactic acid, the two sulfonic acids, and thiourea, 0.005 g/l.

Contrary to the usual relationship, the ductility of these deposits increases with increase in tensile strength. This anomalous relationship has been previously noted by Safranek (21), Read (9), and the present authors (4). The points enclosed in envelope "B" show the expected inverse relationship between tensile strength and elongation. It is seen that this group includes deposits from baths that contain effective addition agents, such as triisopropanolamine and Proprietary A. The deposit made with periodic current reversal is also in this group.

Area C may be referred to as a transition zone. In this zone are found points representing deposits from baths containing addition agents of intermediate effectiveness and points for thin deposits.

Examination of the photomicrographs in Fig. 16-21 reveals that size and type of grain is correlated with these differences in relationships between tensile strength and ductility. The deposits represented in envelope A are composed predominantly of relatively large columnar grains. Those represented by points in envelope B have a fine grain structure and in area C an intermediate grain size. It is assumed that the thin deposits, represented in both envelope B and area C, have a relatively fine structure similar to that of the initially formed portion of the structures seen in Fig. 16-21.

The direct relationship between tensile strength and ductility exemplified by envelope A in Fig. 14 is also seen in Fig. 4, 5, and 6 for nonaddition agent deposits. The inverse relationship corresponding to envelope B in Fig. 14 is further illustrated in Fig. 2. Again, the influence of the finer grain of thin deposits is noted.

It is clear from Fig. 14 and the above discussion that a consequence of the dual relationship between tensile strength and elongation is that low ductility may be associated with either high tensile strength and fine grain structure, or with low tensile strength and coarse grain structure. On the other hand, high ductility is associated with a narrow range of tensile strength. The association of low ductility with either very fine

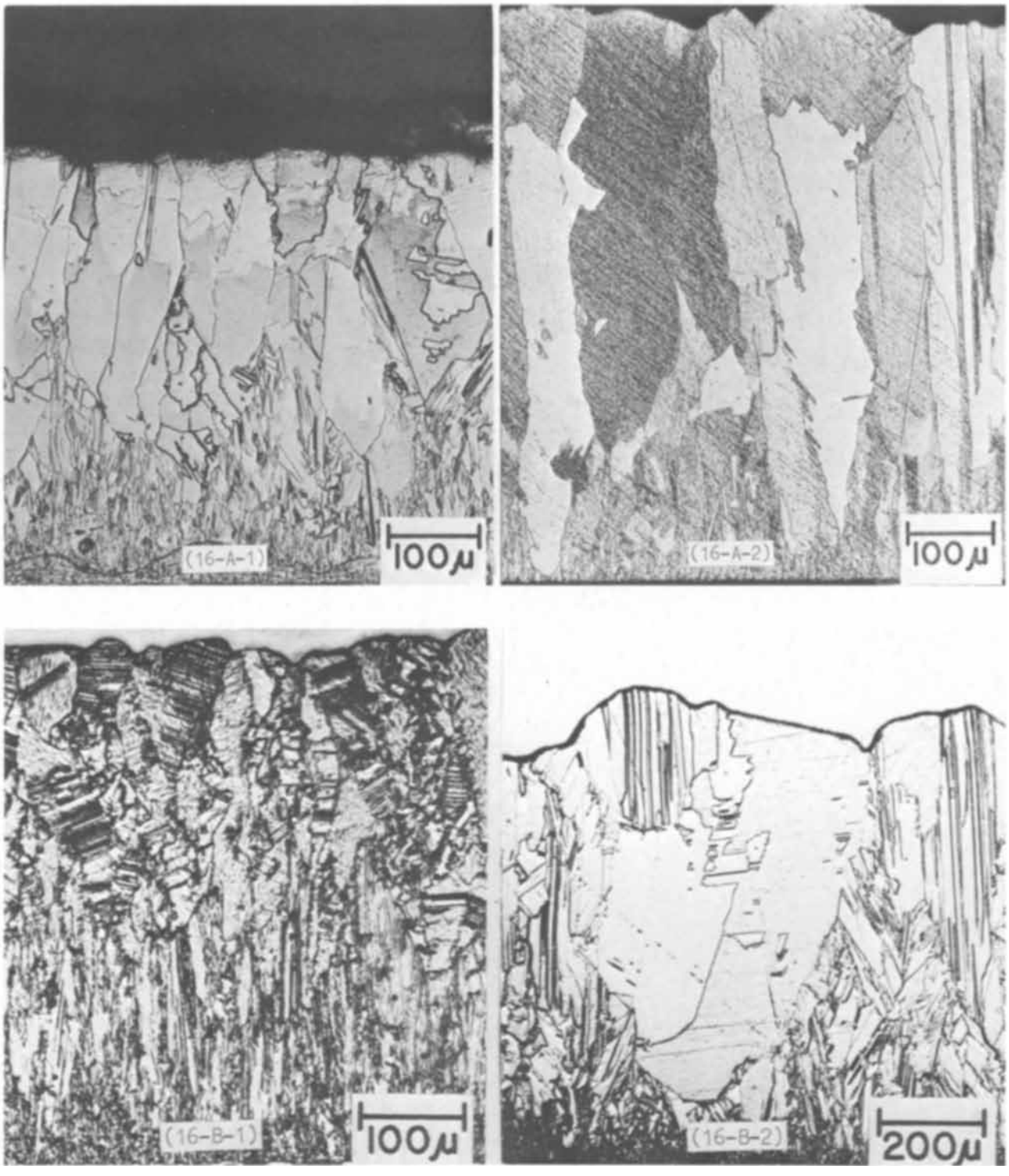

Fig. 16. Effect of bath temperature on the structure of copper from sulfate baths. Part A: Cu2-H2, 2 A/dm^2—(16-A-1) 20°C; (16-A-2) 30°C. Part B: Cu3-H3, 4 A/dm^2—(16-B-1) 20°C; (16-B-2) 60°C.

or very coarse grain structure has been noted by others.[10]

2. Tensile strength and hardness.—Hardness usually increases linearly with the tensile strength of wrought metals. The same relationship has been observed for electrodeposited nickel (2). In Fig. 15 tensile strength is plotted as function of hardness for all deposits from nonaddition agent sulfate baths. It is seen that in the range of tensile strength of 20,000-30,000 psi and hardness from 46 to 60 KHN, distribution of points is quite random, with no apparent correlation. At higher strengths and hardnesses, there is an approximate direct correlation. Data for three deposits that are abnormally hard in combination with low strength, due to a small degree of spangling, were omitted from Fig. 15. In Table XIII, it is seen that deposits made with some addition agents, such as lactic acid (line 50) and thiourea (line 69) have relatively high hardness but abnormally low strength. On the other hand, the addition agents that have been described in preceding sections as "active" or "effective," such as triisopropanolamine and proprietary A, cause increase of both hardness and strength. Thus, addition agents affect hardness and tensile strength independently, so that no general correlations are seen.

[10] A. M. Max, Engineering Department, Purdue University, Indianapolis, Indiana, Private communication.

F. Structure of Deposits from Sulfate Baths

1. General.—Structure of copper electrodeposits has been more extensively studied than any other property. However, in much of this work there has been no effort to correlate structure with mechanical and physical properties of deposits. The literature on this subject was reviewed in the first paper of this series (3). An extensive study of structure was not a part of this research, although photomicrographs of a sufficient sampling of deposits were prepared to show broad interrelationships.

Standard metallographic procedures were used for preparing specimens. To avoid changes of structure caused by annealing during mounting, the specimens were mounted in a room-temperature curing thermosetting casting resin. Most specimens were given a thick back-up plate of electrodeposited nickel prior to mounting, to protect edges during polishing. Approved polishing procedures were used (20, 22). The final polishing of most of the specimens was mechanical, but several were electropolished also and the structures obtained by the two methods compared to make sure that structure alterations due to surface working were not occurring. Good agreement of structure was obtained. Some of the specimens were etched with an ammonia-peroxide etch (NH_4OH, conc, 5; H_2O_2, 3% grade, 5; water, 5 parts by volume) and some with a dichromate etch (K_2CrO_7, 5g; H_2SO_4, conc, 3 ml; water, 100 ml).

2. Effect of operating variables and bath composition.—*a. Bath temperature.*—Structures for two pairs of deposits with temperature the only variable are shown in Fig. 16. Increase in grain size and decrease in the thickness of the fine-grained basal layer with increase of temperature are seen in both pairs.

b. Current density.—Microstructures for three sets of deposits with current density the only variable within each set are shown in Fig. 17. The series in part A shows a decrease of grain size with increase in current density. Between 0.5 and 2 A/dm² (17-A-1 and 17-A-2), the difference is most marked in the basal zone of Fig. 17-A-2. A significant change of structure to a randomly oriented fine grain is seen on going to 4 A/dm² (17-A-3). This is the only deposit of this character among those we examined from nonaddition agent baths. A minimum concentration of copper, a maximum acid concentration, and a moderately high cur-

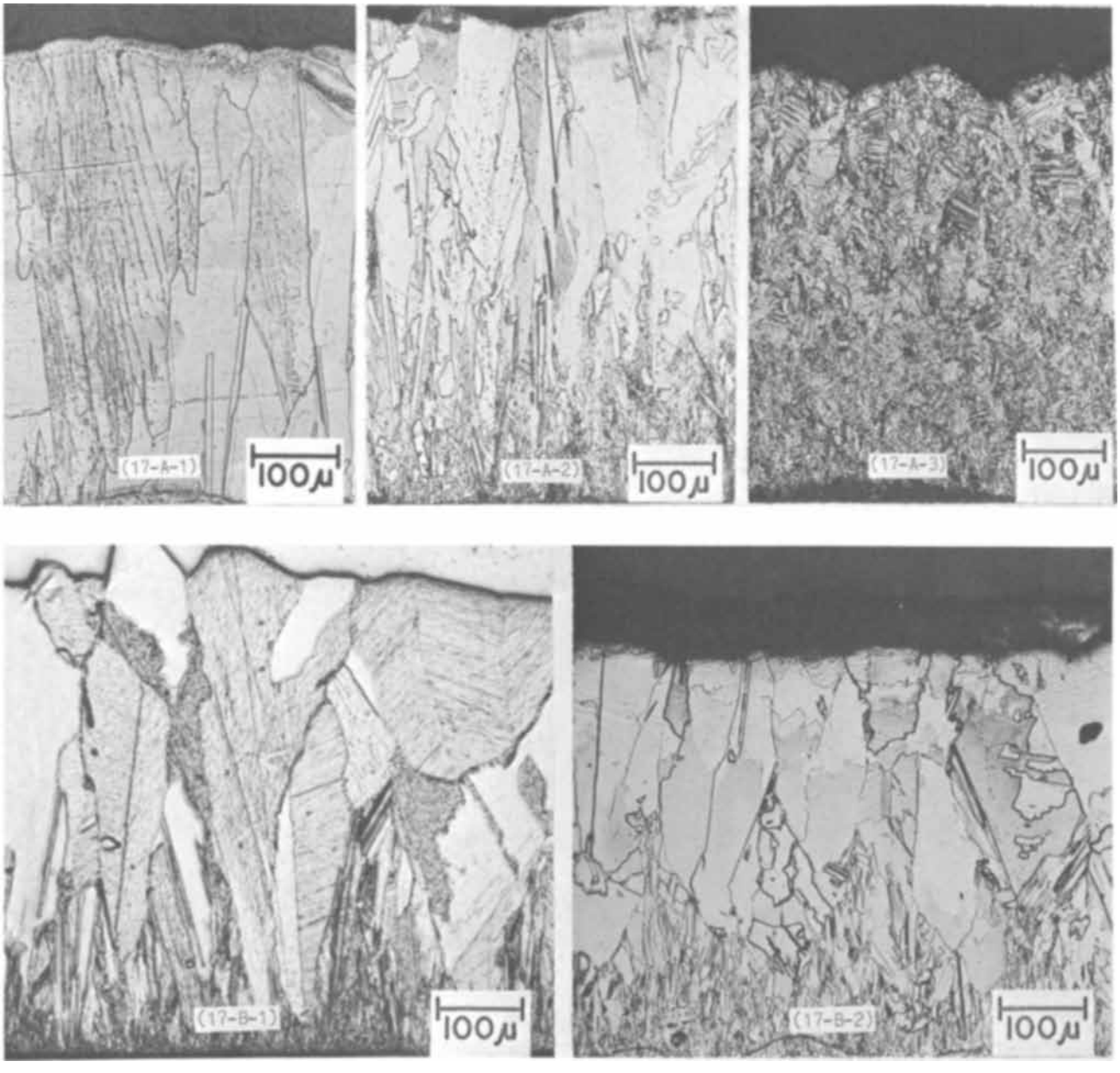

Fig. 17. Effect of current density on the structure of copper from sulfate baths. Part A: Cu1-H3, 30°C—(17-A-1) 0.5 A/dm²; (17-A-2) 2 A/dm²; (17-A-3) 4 A/dm². Part B: Cu2-H2, 20°C—(17-B-1) 0.5 A/dm²; (17-B-2) 2 A/dm².

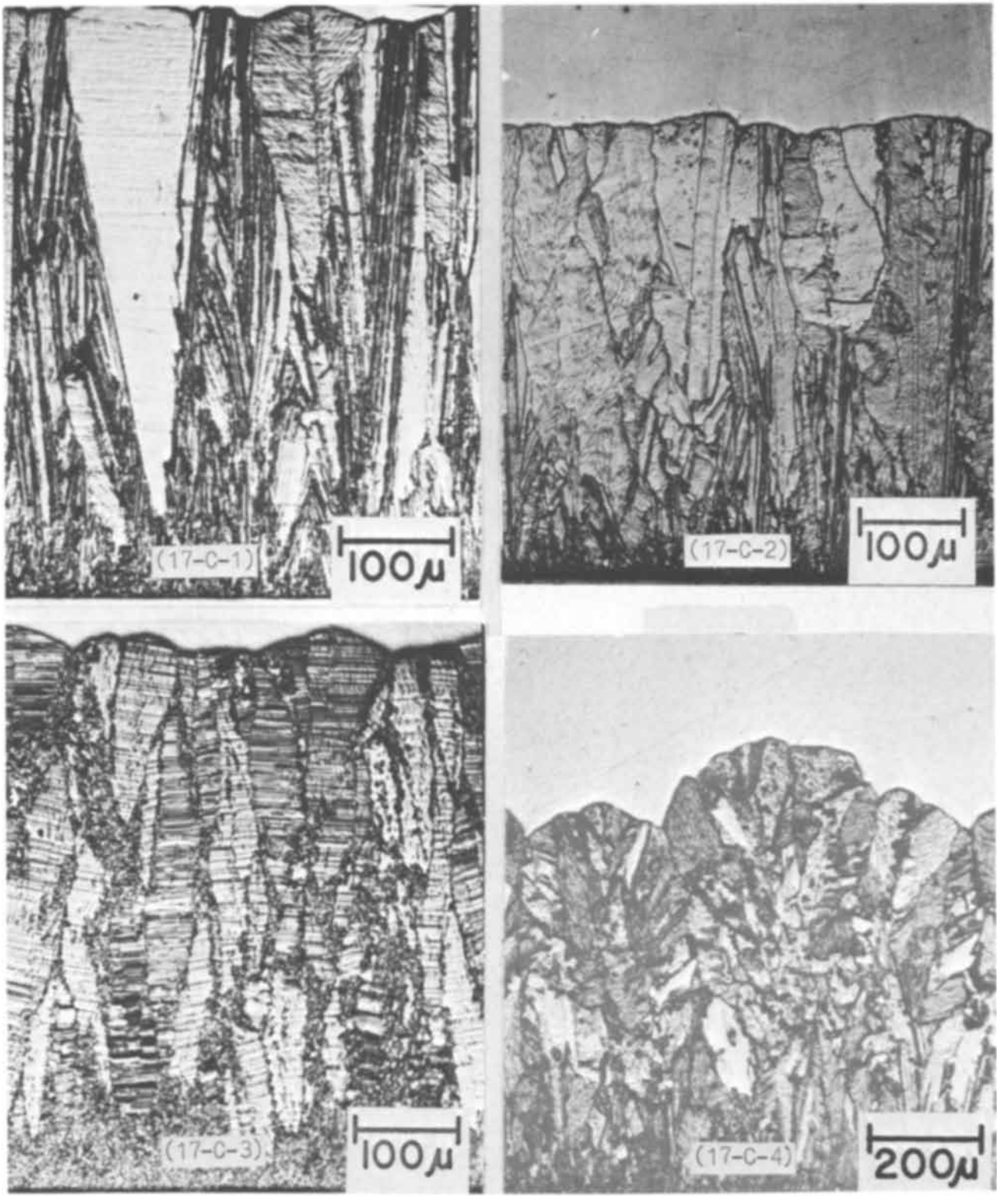

Fig. 17 (contd.). Effect of current density on the structure of copper from sulfate baths. Part C: Cu2-H3, 30°C—(17-C-1) 0.5 A/dm^2; (17-C-2) 2 A/dm^2; (17-C-3) 8 A/dm^2. Part C: Cu2-H3, 60°C—(17-C-4) 20 A/dm^2.

rent density probably combine to produce this effect. Decrease of crystal size with increase of current density is confirmed in Fig. 17-B and 17-C-1 to 3. Figure 17-C-4 is not strictly part of this series but is included here to show the contrast due to a very high current density (20 A/dm^2). This deposit, though not fine grained, is seen to be very nodular. To the naked eye it had a "burnt" appearance and was very weak, as discussed previously in Section III-A-4-b.

c. Concentration of copper sulfate.—The effect of the concentration of copper sulfate on structure is shown in Fig. 18. Even though the structures of the various deposits in this figure are not identical, they are similar to the extent that all of them contain large columnar grains, with no characteristic shift of structure with increase of concentration of copper ion. We conclude that, within the range studied, copper concentration has little effect on structure.

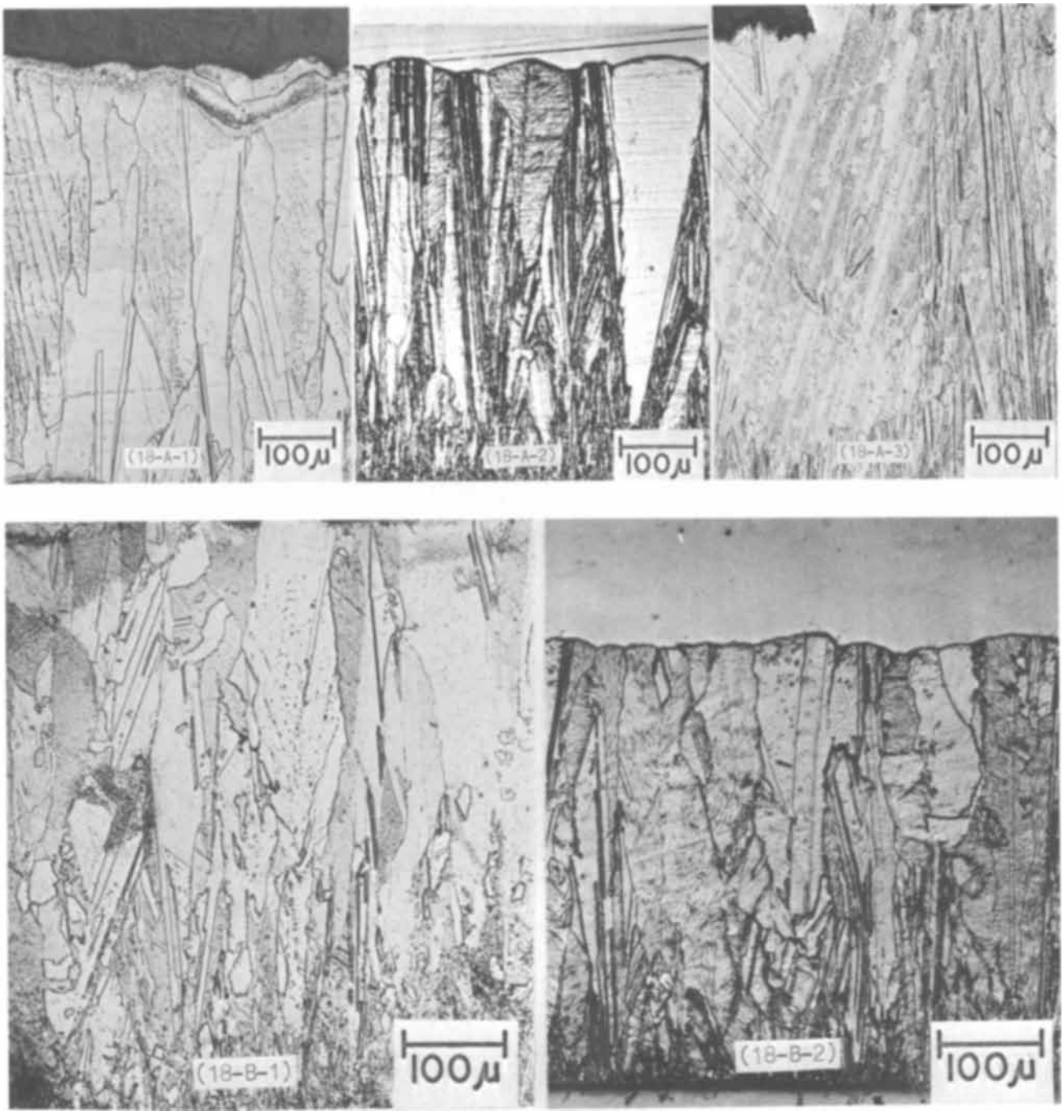

Fig. 18. Effect of concentration of copper in the bath on structure of deposits from sulfate baths. Part A: H-3, 30°C, 0.5 A/dm^2—(18-A-1) Cu-1; (18-A-2) Cu-2; (18-A-3) Cu-3. Part B: H-3, 30°C, 2 A/dm^2—(18-B-1) Cu-1; (18-B-2) Cu-2.

d. Concentration of sulfuric acid.—Figure 19 shows the effect of concentration of sulfuric acid on structure. In both Part A (sulfuric acid, 0.25 and 0.75 molar, respectively) and Part B (sulfuric acid, 0.4 and 0.75 molar, respectively) there is a shift from long columns to somewhat broken columns, but no marked change in grain size.

e. Addition agents.—Effects of addition agents are shown in Fig. 20. Figure 20-1 shows the structure of a nonaddition agent deposit from the Cu2-H3 bath, temperature 30°C, current density 2 A/dm^2. It is included for comparison since all of the other deposits were made under the same conditions except for the presence in the bath of the addition agent (Fig. 20-10, a deposit made from a bath containing the proprietary addition agent, is an exception with respect to both composition and operating conditions. (See line 77, Table I).

Two addition agents that had minor effects on properties are lactic acid and naphthalenedisulfonic acid (NDS) (Fig. 20-2 and 20-3, respectively). Lactic acid causes the structure to be somewhat acicular, but the grain size is nevertheless rather large. NDS causes a change in crystal form but does not appear to reduce the grain size. The small effects of these addition agents on structure are thus correlated with their small effects on properties. All of the other addition agents result in marked grain refinement, especially triisopropanolamine and proprietary A (Fig. 20-9 and 20-10, respectively). Figure 20-7 shows an unusual structure; it is a deposit from a bath containing a mixture of thiourea and NDS. It shows cyclic lamina-

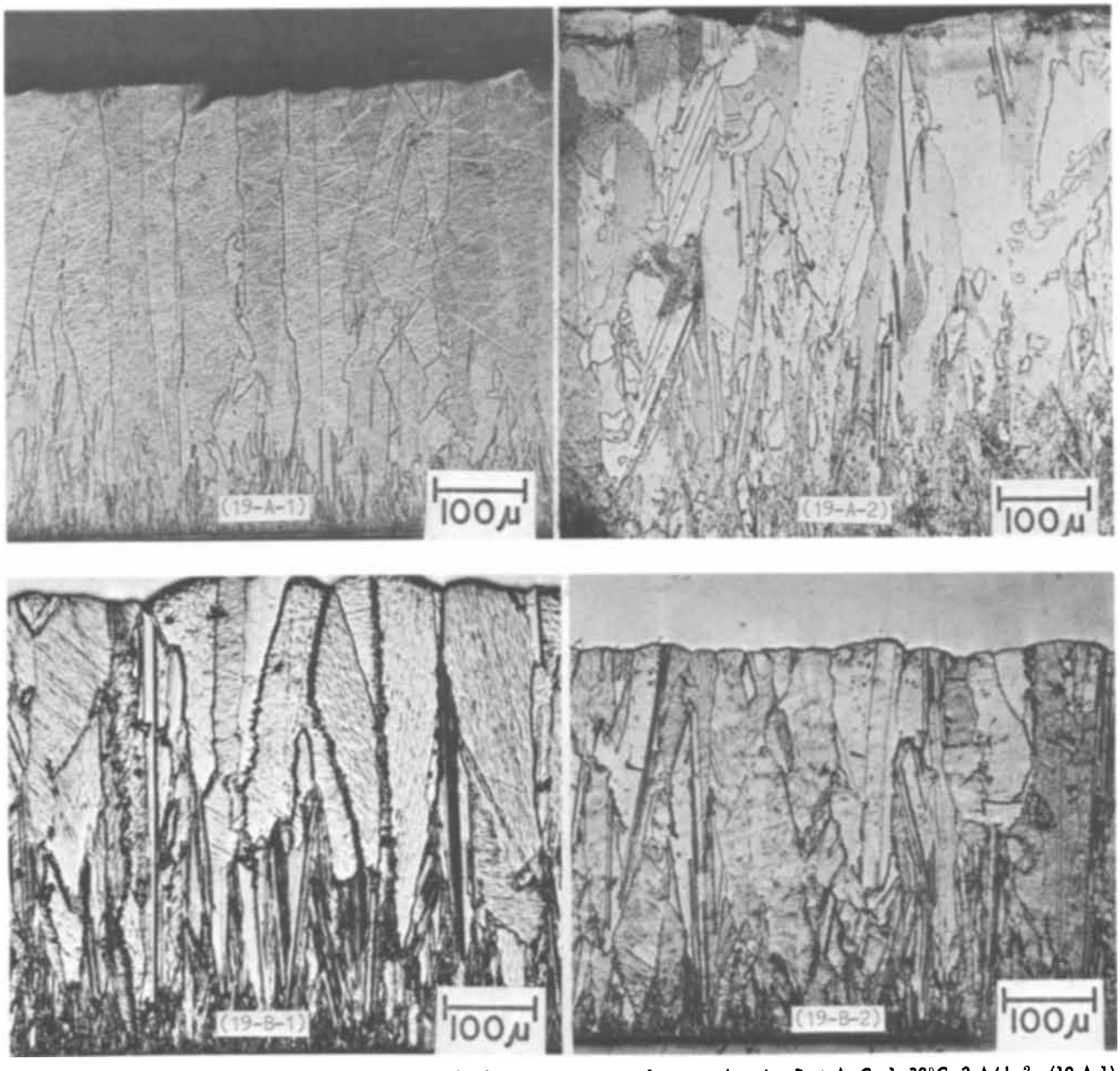

Fig. 19. Effect of concentration of sulfuric acid in the bath on structure of copper deposits. Part A: Cu-1, 30°C, 2 A/dm^2—(19-A-1) H-1; (19-A-2) H-3. Part B: Cu-2, 30°C, 2 A/dm^2—(19-B-1) H-2; (19-B-2) H-3.

tions parallel to the base and simultaneously a fine columnar structure that persists through the laminations. A structure of this type has been reported previously in a cobalt-tungsten alloy deposit (23). The deposit was examined by electron probe measurements to see whether a cyclic concentration of carbon or sulfur could be detected corresponding to the visible laminar structure.[11] The average lamination width is about 3 mils and the probe resolution was less than 1 mil. The probe was therefore adequate with respect to resolution. Neither carbon nor sulfur was detected. This result was not unexpected, because the probe sensitivity was only of the order of 1-2% for carbon and 0.1% for sulfur. It is probable that cyclic concentrations of these impurities would be less than these sensitivity limits.

The structures of several other deposits from addition agent baths were examined visually and are briefly described as follows:

[11] Electron probe measurements were made by D. L. Vieth, Analytical Chemistry Division, NBS.

Line No. Table I	Addition agent	Character of deposit: Crystal form	Character of deposit: Average grain diameter (mil)
43	Dextrin	Broken columnar	~3
48	Glycerol	Regular columnar	~4
49	Glycine	Regular columnar	~4
68	Sorbitol	Broken columnar	~4

f. Periodic current reversal.—The structure of the sulfate deposit made with periodic current reversal (Table XIV, line 79) is shown in Fig. 21-3, together with direct current deposits for comparison. The deposit in Fig. 21-1 was made at the same temperature and current density and approximately the same plating rate as the net rate for the PR deposit. The deposit in Fig. 21-2 was made at the same instantaneous rate as the PR deposit. Other conditions do not quite match, but the effect of the differences on the structure of Fig. 21-2 should be small. It is seen that PR causes a marked reduction in grain size to yield a fine fibrous structure (Fig. 21-3). The nodule seen in this view is characteristic. In appearance, these deposits were semi-bright but marred by a fairly high density of small

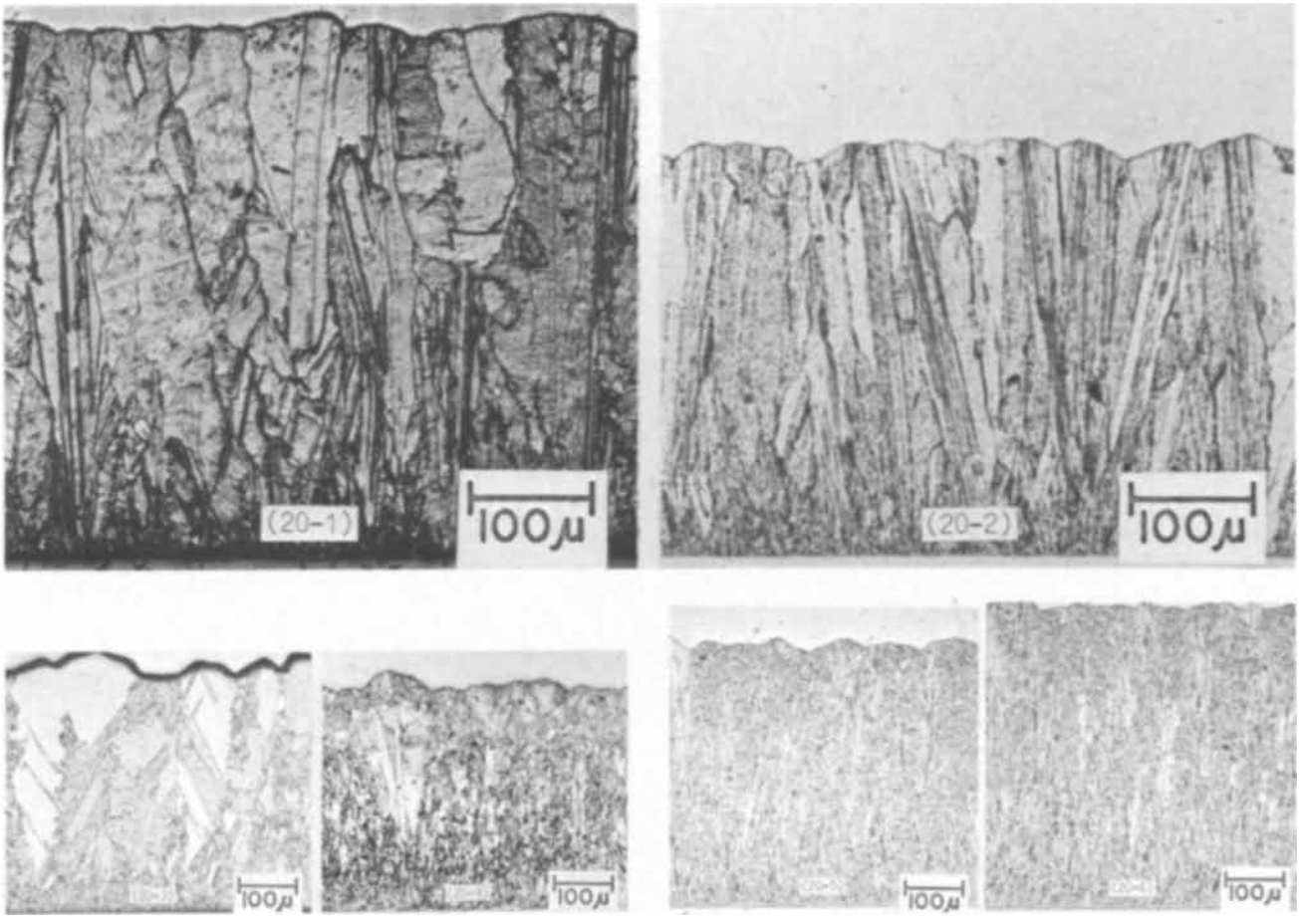

Fig. 20. Effect of addition agents on structure of copper deposits from sulfate baths. All deposits are from bath Cu2-H3 operated at 30°C and 2 A/dm^2, except as noted under 20-9 and 20-10: (20-1) No addition agent; (20-2) 0.05 g/l lactic acid; (20-3) 1.8 g/l naphthalenedisulfonic acid; (20-4) 0.1 g/l β-naphthoquinoline; (20-5) 10^{-4} g/l selenium; (20-6) 10^{-3} g/l selenium.

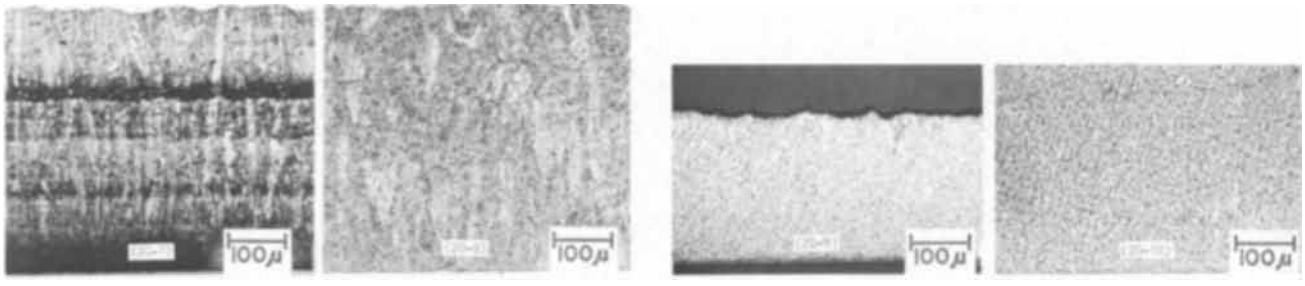

Fig. 20 (contd.). (20-7) 0.015 g/l thiourea plus 0.5 g/ naphthalendisulfonic acid; (20-8) 3.5 g/l triisopropanolamine; (20-9) 2 g/l triisopropanolamine, 5 A/dm^2; (20-10) proprietary brightener (Prop. A), 22°C, 4 A/dm^2.

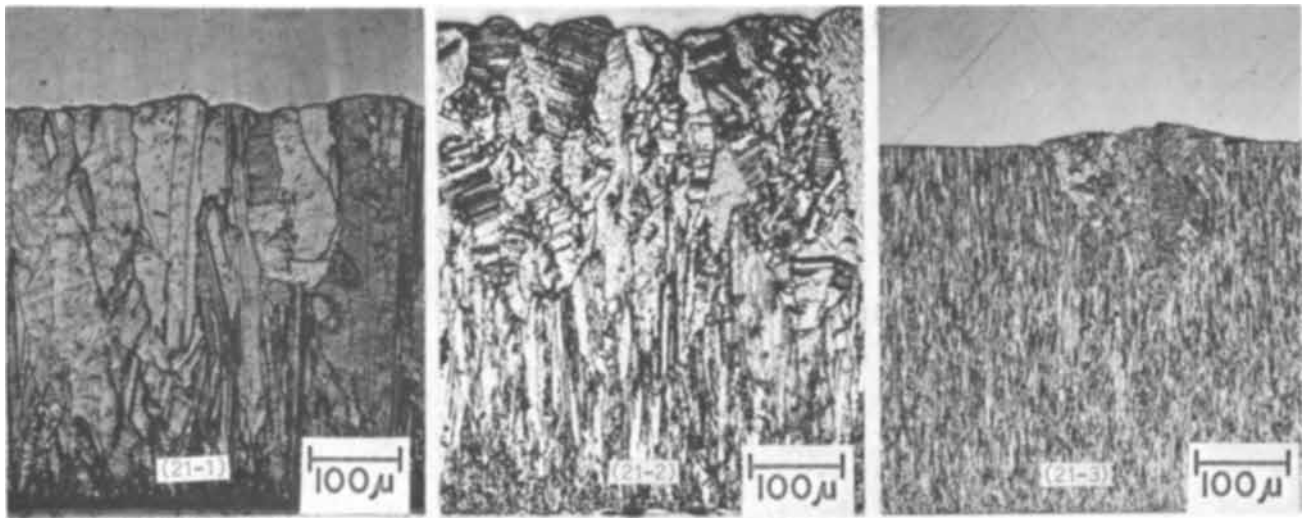

Fig. 21. Effect of periodic current reversal (PR) on the structure of copper deposits from a sulfate bath (Cu2-H3): (21-1) 30°C, 2 A/dm^2, continuous current; (21-2) 20°C, 4 A/dm^2, continuous current; (21-3) 30°C, 4 A/dm^2, PR, 5 sec cathodic, 2 sec anodic.

Table XIV. Effect of periodic reversal of current on properties of copper deposits

Line No., Table I	Panel No.	Bath symbol	Addition agent Name	Addition agent Conc, g/l	Bath temp, °C	Current density, A/dm²	PR cycle Cathodic sec	PR cycle Anodic sec	Tensile[a] strength, psi	Yield[a,b] strength, psi	Elongation in 2 in. (5 cm), %	Hardness KHN 200g load, kg/mm²	Internal[a] stress, psi	Density 25°C, g/cm³	Elec. resistivity 25°C, ohm-cm
79	306, 325	Cu2-H3	None		30	4	5	2	43 × 10³	20 × 10³	26	106	4100	8.925	1.76 × 10⁻⁶
36, 37	276, 307					2	Direct current		29	9	19	54	180	8.924	1.73
38	308					4	Direct current		34	11	46	66	1500	8.925	1.73
140, 141	280, 281	CN-8	None		80	6	15	5	61[c]	38	31[d]	147	4600		1.80
142	279					8	15	5	60[c]		23[d]	151			1.76
143	293, 294,		KCNS	2	80	6	15	5	86	57	10	144	5100	8.917	2.02
	296						30	10	79	46	10	193			1.98
144	295														
135	260, 263		None		80	4	Direct current		37		22	114	4500	8.919	1.80
138	268, 270					6	Direct current		40		49	98	4500	8.925	1.76
148	304	CN-9	Prop. B			6	15	5	66[c]		45[d]	224			1.96
145, 146	300, 305					4	Direct current		26[c]		9[d]	74			1.80
147	303					6	Direct current		24[c]		10[d]	76			1.81

[a] One pound per square inch (psi) = 0.000704 kilogram per square millimeter (kg/mm²).
[b] 0.05% offset.
[c] Nominal tensile strength from bulge measurements.
[d] 100 × significant strain from bulge measurements. Values not designated [c] or [d] are from tensile pull measurements.

Table XV. Density of copper from sulfate baths with comparative values

	Density at 25°C, g/cm³
Deposits from non-addition agent baths	8.919-8.928
Deposits from addition agent baths	8.86-8.929
Wrought sheet, half hard	
Our value	8.907
Literature values (20)	8.90-8.92
Single crystal,* our value	8.931
Spectrographically pure copper (20)	8.96
Calculated from lattice constant	8.94

* Supplied by courtesy of Mr. Theodore Orem, Metallurgy Division, National Bureau of Standards.

nodules that we were unable to eliminate and that seemed to be characteristic. No laminations corresponding to PR cycles can be seen at the magnification of 200X, which is to be expected, since with an over-all cycle period of 7 sec, the thickness per cycle is less than 2 μin.

3. Correlation of structure with properties.—It has already been shown (Section III-E-1) that there is a correlation between structure and tensile strength and elongation. Correlation between structure and hardness is inconsistent. Among the nonaddition agent deposits, there is no consistent correlation. Among the fine-grained addition agent deposits, higher hardness is associated with a fine-grain structure.

In Section III-B-2 it was shown that there is a correlation between internal stress and structure, with a higher stress associated with the finer structure in the basal zone of a deposit. In Sections III-F-2-a and b, a decrease in grain size with decrease of temperature or with increase of current density was demonstrated, and in Sections III-B-3-a and b the latter two variables were seen to cause an increase of stress. One would therefore deduce that decrease of grain size is associated with increase of internal stress. When one considers addition agents, the same relationship exists in some cases, *e.g.* for deposits from baths that contain β-naphthoquinoline or selenium dioxide (Table XIII). On the other hand, gelatin in higher concentrations causes deposits to have a very fine grain structure (24), yet they are compressively stressed. Other instances of anomalous structure-stress relationships have been reported (3).

The significant lowering of density and increase of resistivity noted in Sections III-C and D, caused by the addition agents that produce significant grain refinement, indicates that there is a correlation between these properties and grain size.

Manuscript received April 8, 1970.

Any discussion of this paper will appear in a Discussion Section to be published in the June 1971 JOURNAL.

REFERENCES

1. A. Brenner, P. Burkhead, and C. Jennings, *J. Res. Nat. Bur. Stds.*, **40**, 31 (1948).
2. V. Zentner, A. Brenner, and C. W. Jennings, *Plating*, **39**, 865 (1952).
3. V. A. Lamb and D. R. Valentine, *ibid.*, **52**, 1289 (1965).
4. V. A. Lamb and D. R. Valentine, *ibid.*, **53**, 86 (1966).
5. W. H. Gauvin and C. A. Winkler, *This Journal*, **99**, 71 (1952).
6. W. Blum and G. B. Hogaboom, "Principles of Electroplating and Electroforming," 3rd Ed., McGraw-Hill Book Co., Inc., New York (1949).
7. K. E. Langford, "Analysis of Electroplating and Related Solutions," 3rd Ed., Robert Draper, Ltd., Teddington, Middlesex, England (1962).
8. Specification No. E8-66, Tension Testing of Materials, 1967 Book of ASTM Standards, Part 31, p. 204, American Society for Testing and Materials, Philadelphia, Pa. 19103.

9. H. J. Read, *Plating*, **49**, 602 (1962).
10. L. L. Shreir, *This Journal*, **98**, 193 (1951).
11. S. Barnartt, *ibid.*, **107**, 1004 (1960).
12. See reference No. (3), p. 1306.
13. A. M. Max, U.S. Pat. 2,475,974 (1949); A. M. Max and C. M. Vance, U.S. Pat. 2,482,354 (1949).
14. G. W. Jernstedt, *Proc. Am. Electroplaters' Soc.*, **37**, 151 (1950).
15. J. W. Dini, *Metal Finishing*, **61**, No. 7, 52 (1963).
16. A. Brenner and S. Senderoff, *J. Res. Nat. Bur. Stds.*, **42**, 89 (1949).
17. N. P. Fedot'ev and Yu. M. Pozin, *J. Appl. Chem. (USSR)*, **31**, 406 (1958). (English translation Consultants Bureau, Inc., N.Y.)
18. Yu. V. Lyzlov and A. G. Samartsev, *Zh. Fiz. Khim*, **33**, 1345 (1959); *Plating*, **46**, 266 (1959).
19. C. T. Collett, *J. Res. Nat. Bur. Stds.*, **52**, 201 (1954); H. A. Bowman, R. M. Schoonover, and M. W. Jones, *ibid.*, **71C**, 179 (1967).
20. American Society for Metals, "Metals Handbook," 7th Ed., Cleveland, Ohio (1948).
21. American Society for Testing and Materials, Philadelphia, Pa. Symposium on Electroforming—Applications, Uses, and Properties of Electroformed Metals. ASTM Special Technical Publication No. 318 (1962).
22. Specification No. E3-62, Standard Methods of Preparation of Metallographic Specimens, 1968 Book of ASTM Standards, Part 31, American Society for Testing and Materials, Philadelphia, Pa. 19103.
23. A. Brenner, P. Burkhead, and E. Seegmiller, *J. Res. Nat. Bur. Stds.*, **39**, 351 (1947).
24. H. Fischer, P. Huhse, and F. Pawlek, *Z. Metallk.*, **47**, 43 (1956).

JOURNAL OF THE ELECTROCHEMICAL SOCIETY

REVIEWS AND NEWS

OCTOBER 1970

Physical and Mechanical Properties of Electrodeposited Copper

III. Deposits from Sulfate, Fluoborate, Pyrophosphate, Cyanide, and Amine Baths[12]

Vernon A. Lamb, Christian E. Johnson, and Donald R. Valentine

National Bureau of Standards, Washington, D. C. 20234

IV. Deposits from Fluoborate Baths

A. General

The compositions of the fluoborate baths are shown in Table III. The concentration of copper metal (molarity) in the low-concentration bath (F-1) was the same as in the Cu-2 sulfate baths. The high-concentration bath (F-2) was similar to a bath described by Diggin (21) and by the commercial suppliers of fluoborate concentrates. Control of the concentration of copper fluoborate was based on chemical analysis. Fluoboric acid control was based on measurement of *p*H with sensitive *p*H paper. Equipment used was the same as for sulfate baths with one exception. To avoid attack of the glass tank by fluoborate, a lining of polyethylene sheet was used. A cotton filter, the same as used in the later sulfate baths, was used for the fluoborate baths. Air agitation was used.

B. Effect of Operating Conditions and Bath Composition on Properties of Deposits

1. Bath temperature.—Data on the effect of bath temperature on tensile strength, elongation, hardness, and internal stress, tabulated in Table XVI, are plotted in Fig. 22. Each of these properties decreases with increase of temperature. Attention is directed to the fact that, as with non-addition agent sulfate baths, ductility decreases with decrease of tensile strength.

Neither density nor electrical resistivity undergoes significant change with change of bath temperature (Table XVI).

2. Current density.—Effect of current density is also shown in Fig. 22. Increase in current density causes tensile strength, elongation, hardness, and internal stress to increase. Again, elongation parallels tensile strength.

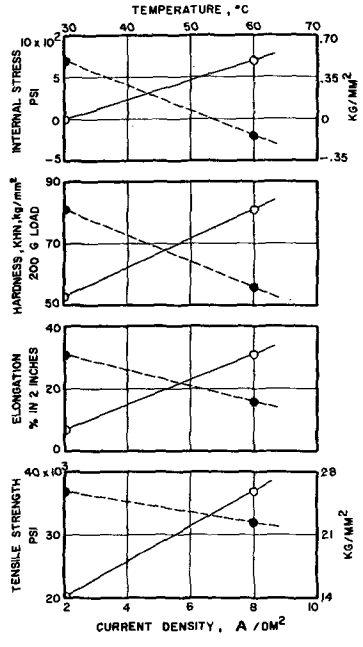

Fig. 22. Relationships of current density and bath temperature to tensile strength, elongation, hardness, and internal stress of copper deposits from a fluoborate bath (F-1). ○—current density, ●—bath temperature.

As with temperature, current density has no significant effect on either density or electrical resistivity.

3. Concentration of copper fluoborate.—The effect of concentration of copper fluoborate on properties may be seen by comparing lines 91 and 93 in Table XVI. The differences due to concentration are insignificant for all of the properties shown except hardness. The small

[12] AES Project 21 Report, part 2. Sections IV-VII published here are the second of three installments of this paper. Part 1 (Sections I-III) appears on pages 291C-318C of the September issue, and part 3 (Sections VIII-X) will appear in the November issue.

Table XVI. Effects of temperature, current density, and concentration of copper fluoborate on properties of deposits from the fluoborate bath

Line No., Table I	Panel No.	Bath symbol	Conc of $Cu(BF_4)_2$, g/l	Bath temp, °C	Current density, A/dm²	Tensile[a] strength, psi	Yield[a,b] strength, psi	Elongation in 2 in. (5 cm), %	Hardness KHN 200g load, kg/mm²	Internal[a,c] stress, psi	Density 25°C, g/cm³	Elec. resistivity 25°C, ohm-cm
90	342	F-1	177	30	2	20 × 10³	9 × 10³	7	53	Zero	8.925	1.73 × 10⁻⁶
91	343-345				8	37	16	31	81	700	8.926	1.73
92	346			60	8	32	11	16	56	−200	8.925	1.73
93	347	F-2	336	30	8	36	15	31	71	800	8.926	1.74

[a] One pound per square inch (psi) = 0.000704 kilogram per square millimeter (kg/mm²).
[b] 0.05% offset.
[c] Negative values represent compressive stresses.

Table XVII. Comparison of properties of deposits made at high current density from sulfate and fluoborate baths

Line No., Table I	Panel No.	Bath[a] symbol	Conc Cu^{++}, g/l	Bath temp, °C	Current density, A/dm^2	Tensile[c] strength, psi	Yield[b,c] strength, psi	Elongation in 2 in. (5 cm), %	Hardness KHN 200g load, kg/mm^2	Internal[c] stress, psi	Density 25°C, g/cm^3	Elec. resistivity 25°C, ohm-cm
42	297	Cu2-H3	47	60	20	20×10^3	7×10^3	5	58	1400	8.86	1.90×10^{-6}
94	348	F-2	90	50	20	33	12	29	60	1600	8.925	1.75

[a] No addition agent in either bath; identical air agitation.
[b] 0.05% offset.
[c] One pound per square inch (psi) = 0.000704 kilogram per square millimeter (kg/mm^2).

decrease from 81 to 71 KHN with increase of concentration is in the expected direction. It is possible that larger effects exist at lower bath temperatures or at higher current densities.

C. Comparison of Deposits Made with High Current Densities from Fluoborate and Sulfate Baths

A comparison between properties of deposits from fluoborate and sulfate baths, both made at a high current density, 20 A/dm^2, is shown in Table XVII. The general character and properties of the deposit from the fluoborate bath are nearly the same as those of the deposits shown in Table XVI that were made at lower current densities. On the other hand, the deposit from the sulfate bath was weak, brittle, had a very low density and high resistivity, and a high impurity content (see Section VIII-G), properties indicating that the limiting current density was exceeded. These results confirm the reputed high current density capability of the fluoborate bath in comparison with the sulfate bath. The comparison is in one sense unfair, since the concentration of copper ion in the fluoborate bath is nearly twice that in the sulfate bath. However, the solubility of $CuSO_4$ makes it impractical to operate the sulfate bath with a significantly higher concentration than we used, whereas operation of the fluoborate bath with a concentration of copper ion equal to that shown in Table XVII or higher is practicable.

D. Structure

The structure of the deposit represented on line 91, Table XVI, is shown in Fig. 59-2. It has a more fibrous character than the deposit from the corresponding non-addition agent sulfate bath (Fig. 59-1). It is possible, however, that under other conditions fluoborate baths may yield large-grained deposits. Thus, if grain size correlates with strength, one might expect the very weak deposit on line 90, Table XVI, made at a low current density, to have a coarse structure.

V. Deposits from the Pyrophosphate Bath

A. General

Only one bath composition was used for making deposits from the pyrophosphate bath (Table III). The selection of the concentrations of the various constituents was based on recommendations made by several authors (25-27). No addition agents were used. Deposits were bright as plated.

B. Effect of Operating Conditions on Properties of the Deposits

1. Bath temperature.—Comparing lines 98 and 100 in Table XVIII, it is seen that the only property that is affected significantly by a change of temperature of 10°C is internal stress. The change from 1700 psi tensile to 1900 psi compressive with increase of temperature is in the same direction as has been observed for the sulfate and fluoborate baths but is larger.

2. Current density.—The data on lines 95 and 98 of Table XVIII show that increase of internal stress is the only significant change of property due to increase of current density from 2 to 4 A/dm^2.

3. Agitation.—Propeller agitation was tried initially in the pyrophosphate bath. Since the deposits were not uniformly bright over the entire area and tended to be nodular, other means of agitation were tried, as described in Table I, lines 95-100. Air agitation gave the best results, and was used for the deposits for which data are given in Table XVIII. However, several properties of the deposits prepared with other modes of agitation were measured. The results appear in Table I. It is seen that these properties were not affected appreciably by the variations in agitation.

C. Structure

Photomicrographs of the deposit on line 95, Table XVIII, are shown in Fig. 59-3 and 59-4. The structure differs markedly from that of deposits from sulfate or fluoborate baths. There is indication of large columnar crystals with a very fine substructure. Tensile strength and other properties of these deposits vary from those of large-grained sulfate deposits in the direction that one would expect if the grain size were smaller, but the effect is not as large as it is with the finer-grained deposits from addition agent sulfate baths.

Additional data on the structure of these deposits are discussed in Section VIII-F.

VI. Deposits from the Amine Bath

A. General

Several researches have been reported on attempts to develop commercially useful baths based on copper-

Table XVIII. Effects of temperature and current density on properties of deposits from the pyrophosphate and amine baths

Line No., Table I	Panel No.	Bath temp, °C	Current density, A/dm^2	Tensile[a] strength, psi	Yield[a,b] strength, psi	Elongation in 2 in. (5 cm), %	Hardness KHN 200g load, kg/mm^2	Internal[a,c] stress, psi	Density 25°C g/cm^3	Elec. resistivity 25°C, ohm-cm
				A. Pyrophosphate bath						
95	317-320	50	2	38×10^3	20×10^3	39	83	−1600	8.926	1.75×10^{-6}
98	314		4	40	22	33	90	1700	8.926	1.74
100	316	60	4	39	20	39	80	−1900	8.926	1.74
				B. Amine bath						
149	328	55	2	69	41	4	202	−5700	8.891	2.08
151	326-330		4	60	44	4	169	−6000	8.906	2.10

[a] One pound per square inch (psi) = 0.000704 kilogram per square millimeter (kg/mm^2).
[b] 0.05% offset.
[c] Negative values represent compressive stresses.

amine complexes (27-29). Although the baths that have been described have not achieved significant use, it was thought that since the amine bath is a rather different type than the others used in this project it deserved a limited investigation to see whether the deposits had any unusual properties. Several of the baths described in the literature were tried. Most of them did not yield sound thick deposits. Sound deposits were obtained from the bath shown in Table III, which is similar to one described by Greenspan (29). Deposits were fairly smooth at a thickness of 10 mils, but became excessively rough, with a tendency for filamentary growths to start at larger thickness.

B. Effect of Current Density on Properties of Deposits

Because current density is a relatively uncontrollable variable when irregularly shaped objects are plated, it seemed most important in a limited study to include current density as a variable. This was the only variable studied. The results shown in Table XVIII indicate that a change of current density from 2 to 4 A/dm^2 does not significantly change the properties of the deposits.

It is seen that the deposits are fairly strong and very hard. However, their low ductility is adverse. Their high compressive internal stress is noteworthy. Their low density and high electrical resistivity indicate a probable high content of impurity, but this was not investigated.

C. Structure

A photomicrograph of the deposit on line 151, Table XVIII, is shown in Fig. 59-6. The structure is seen to be very fine, with unresolved grains at a magnification of 500X.

VII. Deposits from Cyanide Baths

A. General

Concentrations of the various constituents of the cyanide baths and levels of operating variables were chosen on the basis of a review of the recommendations made in various publications (6, 26, 27). The brightener system identified in Table IV as "Proprietary B" is reported by the vendor to be a selenium type (26).

B. Mechanical Properties

1. The bulge method for measuring tensile strength and ductility.—a. Apparatus.—It is difficult to prepare, handle, and test deposits in the thickness range of 0.001-0.002 in. by the standard tensile pull method. To avoid these difficulties, Read and co-workers have adapted the hydraulic bulge test to the measurement of tensile strength and ductility of thin electroformed deposits (30, 31). Since most of our deposits from cyanide baths were 0.001-0.002 in. thick, the bulge test was the preferred test method. Besides avoiding the technical difficulties referred to above, the method has the advantage that specimens can be made very easily and at low cost by simply cutting out a disk of the material with scissors.

The basic principle of the bulge tester is illustrated in Fig. 23, Part I. The test specimen, in the form of a disk cut from a specimen panel, is clamped between the thick steel base plate and the clamp ring. Oil is pumped through the opening under the copper disk, causing it to expand into the opening in the clamp ring. In our apparatus, the diameter of the disk is 2⅜ in., and of the hole in the clamp ring, 1.5 in. Tensile strength can be calculated from the fluid pressure and bulge height, and degree of elongation or ductility can be determined from the linear stretch of a unit length at the top of the bulge at rupture. We constructed the apparatus that we used. It is the same in principle as the apparatus described by Read and co-workers but differs in details of design. A photograph is shown in Fig. 23, Part II, in which the major components are identified. The gear pump, with a capacity of 1000 psi, was powered by a 1/6 hp integrally coupled motor. Oil was drawn from the reservoir through the filter and pumped through the throttle valve into a parallel

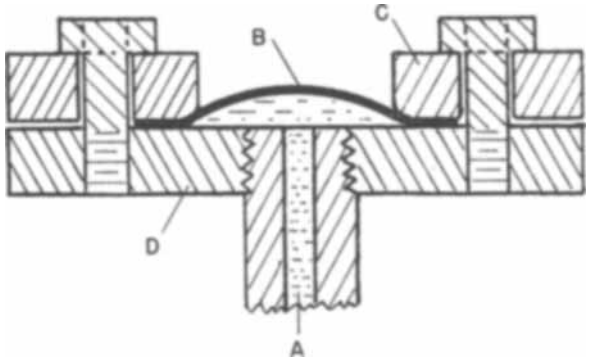

Fig. 23-I. Cross section of head of bulge tester: A—oil inlet, B—bulged disk, C—clamping ring, D—base plate.

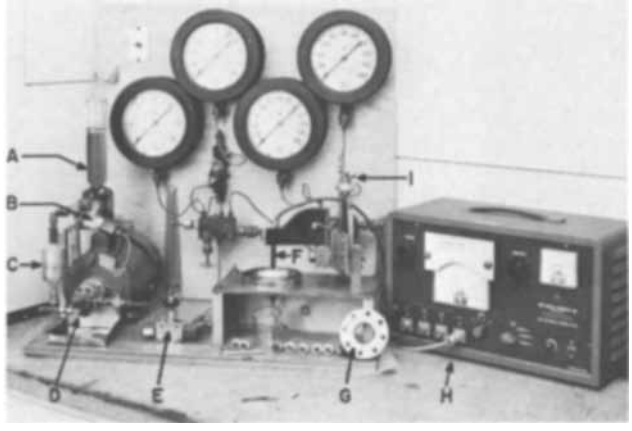

Fig. 23-II. Photograph of complete bulge tester: A—oil reservoir, B—bypass valve, C—oil filter, D—pump, E—throttle valve, F—Dermitron probe, G—clamping ring, H—Dermitron unit, I—vertical micrometer.

array of tubing, one to the bulge and one to each of the four gauges. The line to each gauge was equipped with a cut-off valve. If the pressure limit for the first gauge (30 psi) was exceeded, its valve was closed and pressure read on the second gauge (100 psi), *etc.*, through the third (300 psi) and fourth (1000 psi). Good sensitivity of pressure measurement was thus obtained for any magnitude of pressure encountered. Flow rate and bulge growth were controlled by combined settings of the bypass valve and throttle valve.

An expanded disk is shown in place on the base plate. Oil released on rupture of the disk is caught in the shallow tray surrounding the base plate and flows into the small beaker. The height of the bulge is measured with the Dermitron[13] unit (32) in the following manner. A dummy specimen is laid on the base plate and the probe is lowered with the probe-height control screw until it just touches the specimen, then raised about 0.005 in. The Dermitron controls are then adjusted so that, at this arbitrary distance between the probe face and the specimen, the Dermitron thickness meter reads at the midpoint of the scale and the sensitivity is about 0.001 in. for full-scale needle deflection. Without changing the Dermitron adjustments, the probe is raised sufficiently by the screw to permit placement and clamping of the test specimen. The probe is then returned to its former position, minor readjustments in Dermitron control settings are made if necessary, and the starting height of the probe is read on the micrometer screw. The bulge is then slowly expanded. As it grows, the probe is raised simultaneously with the screw so that the original clearance between the probe face and the specimen is maintained, as indicated by a constant reading at the center point of the Dermitron meter. When the specimen ruptures, growth stops, and, simultaneously, advance of the

[13] An eddy current type of thickness gauge.

screw is stopped. The difference between the reading of the probe-height micrometer screw at this point and at the beginning gives the height of the bulge. The advantages of this height-measuring procedure are (*a*) that the bulge is not mechanically contacted by the measuring device and, hence, not mechanically damaged and (*b*) the procedure is sufficiently simple that one operator can control bulge growth and height measurement simultaneously. We estimate that the measured values of bulge height are accurate to about ±0.001 in. and those of pressure to about ±5% of the observed value. A minimum of six replicate disks from each panel was tested. Variations in pressure among the six were often as much as ±25%. The large variation is judged to result from premature failure of some of the specimens because of the presence of flaws. However, within a given set of specimens, bulge height and pressure were usually closely correlated. The formulas in the next section show that tensile strength is approximately proportional to the ratio of pressure to bulge height and, therefore, even though variations of pressure and height among replicates were rather large, calculated values of tensile strength seldom varied more than ±5%.

b. Bulge test relationships.—(i) Basic relationships.— The following relationships for obtaining tensile strength and ductility values from bulge measurements are stated without development. For more detail the reader is referred to Read and co-workers (30, 31):

$$\text{Nominal tensile strength} = \frac{PR}{2t} \qquad [1]$$

where P is pressure at fracture, R is the radius of curvature of the bulge at fracture, and t is the initial thickness of the specimen, which was determined from area and mass.

$$\text{True stress} = \sigma = \bar{\sigma} = \frac{PR}{2t_i} \qquad [2]$$

in which true stress, σ, is equal to the load divided by the simultaneously measured cross-sectional area. Use in Eq. [2] of t_i, the simultaneously measured thickness, yields true stress. "Significant stress," $\bar{\sigma}$, is a generalized function which is a measure of the stress under any type of loading. The equality shown in Eq. [2] applies to isotropic material tested either in simple tension or in balanced biaxial tension; the latter is the situation in the bulge test (30).

To obtain values for t_i for substitution in Eq. [2], a grid was printed on the flat specimen before bulging. From the elongation of the grid after bulging, t_i can be calculated on the assumption that the volume of metal underlying an initial grid square remains constant. The radius of curvature, R, is obtained from

$$R = \frac{r^2 + h^2}{2h} \qquad [3]$$

where r is the radius of the hole in the clamp ring and h is the height of the bulge.

Nominal tensile strength (Eq. [1]) is calculated and tabulated in all of the succeeding tables of data obtained by bulge testing. The values are thus approximately comparable to those already discussed which have been determined by tensile pull, which are calculated on the basis of the initial cross section of the test specimen. In one exception, Fig. 25, discussed later in this section, significant stress is used.

Ductility was determined from bulge measurements by measuring the amount of stretch at fracture of a grid printed on the specimens. The grid pattern was transferred with printer's ink from an intaglio engraving in a steel block. Line spacing was 0.05 in. The lengths of four or five grid squares near the peak of the bulge were measured, after bulging, with a microscope. Both axes of grids were measured. The average length of the bulged grid, calculated from these measurements, is designated as L. The initial grid length is designated L_o. "True strain," δ, is defined by the relation

$$\delta = \int_{L_o}^{L} \frac{dL}{L} = \ln \frac{L}{L_o} \qquad [4]$$

The following remarks are intended to show in a brief manner the significance of δ. Consider a uniaxial tensile test, *i.e.* a test of a standard pull specimen. For small values of elongation, *e.g.* up to 10%, $\Delta L/L_o$ is nearly equal to $\ln L/L_o$, where ΔL is the difference between initial and final length of a grid unit. Therefore, for a brittle material that elongates uniformly and does not undergo necking, true strain from Eq. [4], multiplied by 100, is approximately equal to elongation expressed as per cent of a given gauge length such as 2 in. However, for a ductile material with a nominal elongation larger than about 10%, the arithmetic and logarithmic ratios deviate significantly. Also, necking may occur, resulting in a much larger true elongation at the point of rupture than the average over the gauge length. Therefore, while true strain and per cent elongation are both measures of ductility, they are, in general, not numerically comparable.

In tensile pull, strain occurs in only one direction. In bulge testing, strain occurs in all directions radially from the center of the disk. The ability of the metal to elongate in a given radial direction is reduced by its simultaneous elongation in other radial directions. Thus, δ for a bulge specimen will be less than the strain obtained with the same stress applied to a tensile pull specimen. Read shows that a quantity designated as $\bar{\delta}$, significant strain, is identical to true strain in the case of a specimen pulled in simple tension, but that in the case of the biaxial loading of a bulge specimen

$$\bar{\delta} = 2\,\delta \qquad [5]$$

Significant strain from bulge measurements is comparable to true strain from tensile pull, but is not comparable to nominal elongation for the reasons given in the preceding paragraph.

As already indicated above, bulge height and, hence, $\bar{\delta}$ for individual specimens within sets of six sometimes varied as much as ±25%, especially for the relatively brittle deposits. This is comparable to the situation in tensile pull, where, *e.g.*, the difference between 5 and 10% elongation in our measurements (a relative variation of ±50%) is scarcely significant. It is, therefore, not feasible for us to assign a definite evaluation of accuracy to our data on significant strain. However, small differences, *e.g.* ±10%, cannot be considered to be significant.

(ii) Data relating significant stress and significant strain for several types of baths.—It was not practicable to print grids and measure elongation directly for every specimen. Therefore, grids were printed on a substantial sampling of disks from deposits of a given type of bath. Values of $\bar{\delta}$ calculated from the grid data were then plotted as a function of bulge height. The same curves were then used to obtain $\bar{\delta}$ from bulge height for unprinted specimens.

A plot of $\bar{\delta}$ *vs.* bulge height is shown in Fig. 24. The curves for most of the deposits are closely clustered, showing that there is not much difference in what may be termed, by analogy with tensile pull, as their necking characteristics. Curves for two types of deposits do not fit the main pattern. The deposits from a sulfate bath containing 1,5-naphthalenedisulfonic acid addition agent (curve 2, panel No. 114A-E) had significantly higher $\bar{\delta}$ for a given bulge height than the other deposits; *i.e.*, for a given height of bulge, the degree of stretch at the peak of the bulge was abnormally high and, hence, thickness at the peak of the bulge abnormally low. In other words, this deposit showed a pronounced "necking" tendency. Deposit No. 303 (curve

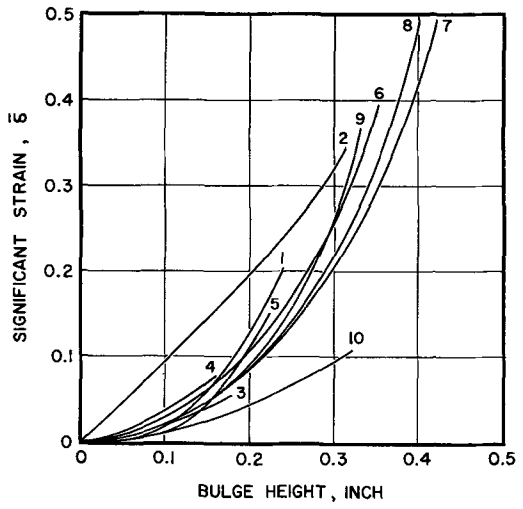

Fig. 24. Relationship between bulge height and significant strain for thin copper deposits from various baths: (1)—Cu2-H3 containing 3.5 g/l triisopropanolamine, 30°C, 2 A/dm^2; (2)—Cu2-H3 containing 1.8 g/l 1,5-naphthalenedisulfonic acid, 30°C, 2 A/dm^2; (3)—CN-2, 60°C, 2 A/dm^2; (4)—CN-5, 80°C, 4 A/dm^2; (5)—CN-4, 80°C, 2 A/dm^2; (6)—CN-6, 60°C, 2 A/dm^2; (7)—CN-7, 60°C, 2 A/dm^2; (8)—CN-8, 80°C, 6 A/dm^2; (9)—CN-8, 80°C, 6 A/dm^2, PR, cycle 15-5 sec; (10)—CN-9, 80°C, 6 A/dm^2.

10), a deposit from the high efficiency cyanide bath containing the proprietary selenium-type addition agent, showed the opposite effect, indicating relatively uniform stretch over most of its area, or lack of necking. One might expect this property to be associated with brittleness, yet specimens from panel No. 303, while of low ductility, were not as brittle as specimens from panels 146 or 195 (Table XXII), which fall in the central group in Fig. 24.

Relationship between significant stress and significant strain for a variety of deposit types is shown in Fig. 25. Most of them show a nearly linear stress-strain relationship up to a fairly definite yield point. Two of them, specimens represented by curves 3 and 4, show brittle failure. A very wide range of ultimate strength is seen, from a low of 28,000 psi for the proprietary high efficiency deposit (curve 10, panel No. 303) to 85,000 psi for a deposit from a standard cyanide bath (curve

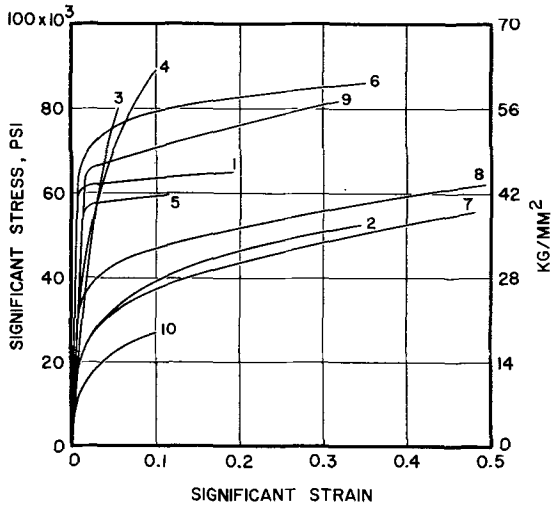

Fig. 25. Relationship between significant strain and significant stress for thin copper deposits from various baths: (1)—Cu2-H3 containing 3.5 g/l triisopropanolamine, 30°C, 2 A/dm^2; (2)—Cu2-H3 containing 1.8 g/l 1,5-naphthalenedisulfonic acid, 30°C, 2 A/dm^2; (3)—CN-2, 60°C, 2 A/dm^2; (4)—CN-5, 80°C, 4 A/dm^2; (5)—CN-4, 80°C, 2 A/dm^2; (6)—CN-6, 60°C, 2 A/dm^2; (7)—CN-7, 60°C, 2 A/dm^2; (8)—CN-8, 80°C, 6 A/dm^2; (9)—CN-8, 80°C, 6 A/dm^2, PR, cycle 15-5 sec; (10)—CN-9, 80°C, 6 A/dm^2.

4, panel No. 195). Only one cyanide-type deposit with a higher strength was encountered in this research (not included in Fig. 25), namely, a deposit made with periodic current reversal from a bath containing thiocyanate (line 143, Table XIV).

c. Comparison of tensile properties obtained by pull and bulge methods.—Table XIX contains comparative values of tensile strength and elongation from pull and bulge measurements. Except for the deposits from cyanide baths on lines 141 and 146, all deposits from both sulfate and cyanide baths were in the range of thickness from 1 to 3 mils.

The first group of data, lines 53-75, is for deposits from sulfate baths. It is seen that, for each deposit, both pull and bulge methods yield the same value for tensile strength, within the normal range of variability of the measurements. On lines 57 and 75 are shown comparisons between our results and those obtained by Read[14] from measurements on specimens from duplicate panels that we supplied to him. Close agreement is seen.

The strength values measured by tensile pull for the deposits from cyanide baths on lines 101 through 125 are seen, with one exception, to be consistently lower than the bulge values. This is probably because premature rupture occurs during tensile pull. As discussed above, tensile pull specimens, when thin and brittle, are more subject to damage in preparation and handling than are bulge disks, and premature failure may be expected. Good agreement is seen in lines 140-146 between tensile pull values of strength for thick cyanide deposits and bulge values for corresponding thin deposits. Good agreement is seen in lines 119 and 121 between our values and those determined by Read.

Turning to comparisons of ductility determined by the two methods (Table XIX), agreement cannot be expected in light of the preceding discussion in Section VII-B-1-b. In both the sulfate and cyanide groups, per cent elongation from tensile pull is significantly less than 100 x $\bar{\delta}$, with one exception in each group. The tensile pull specimens in the sulfate group underwent varying degrees of necking, which would cause differences between the two methods in the direction that is seen. In the cyanide group the differences are probably due mainly to premature rupture of the tensile pull specimens, since the latter were relatively brittle and did not undergo noticeable necking. Good agreement is seen between our values of significant strain and those determined by Read.

2. Effect of thickness on properties of deposits from cyanide baths.—Effects of deposit thickness for several deposits from cyanide baths are shown in Table XX and Fig. 26. Tensile strength and significant strain increase with increase of thickness, while electrical resistivity decreases. The directions of the effects for tensile strength and significant strain are opposite to those for sulfate deposits (Section III-A-3, Table VII, Fig. 2, 3). However, the comparisons are made in a somewhat different range of thickness. The thinnest sulfate deposit was 0.5 mil and most of the thin deposits were 1.0-2.0 mils, whereas the thicknesses of several of the thinnest cyanide deposits are 0.2-0.3 mil. Our explanation of the effects in the case of the cyanide deposits is that these very thin deposits contain pores and defects which cause them to have abnormally low strength and ductility and high resistivity. At a thickness of about 2 mils these effects were diminishing.

3. Effects of operating conditions and bath composition on mechanical properties of deposits from cyanide baths.—a. Bath temperature.—The effect of bath temperature on tensile strength is shown in Table XXI and Fig. 27. Counting sets of three in Table XXI as two pairs, there are 12 pairs. The data for all of these are plotted in Fig. 27. It is seen that for four pairs the effect is minor and for one pair tensile strength decreases with increase of temperature. For the other seven

[14] H. J. Read, Pennsylvania State University, University Park, Pa., Private communication.

Table XIX. Comparisons of tensile strengths and elongations measured by pull and bulge methods

Line No., Table I	Panel No.	Bath symbol	Addition agent		Tensile strength[b,c]		Ductility	
			Name[a]	Conc g/l	Pull	Bulge	Elongation in 2 in. (5 cm) %	By bulge method Significant strain
					psi			
53	162	Cu2-H3	β-NQ	0.1	46	47	9	25
57	114A, C		NDS	1.8	36	35	10	32
	114D[e]		NDS	1.8		33		
65	168		SeO_2	10^{-4} Se	54	62	11	21
67	173		SeO_2	10^{-3} Se	50	56	20	22
75	109A, D		TIPA	3.5	57	57	9	18
	109C[e]		TIPA	3.5		55		19
101	128	CN-1	None		57	66	2	6
105	136	CN-2			43	57	1	10
108	143	CN-2			51	66	2	18
119	205	CN-4			41	50	2	12
	203[e]	CN-4				54		9
121	210, 212	CN-4			58	51	2	22
	210[e]	CN-4				50		16
124	184, 186	CN-5			44	54	7	12
125	187, 188	CN-5			39	63	8	5
140	280	CN-8				61		31
141	281[d]				64		12	
145	300	CN-9	Prop. B			26		9
146	305[d]				28		22	

[a] β-NQ: β-naphthoquinoline; NDS: 1,5-naphthalenedisulfonic acid; TIPA: triisopropanolamine; Prop. B: proprietary brightener for high efficiency cyanide bath, selenium type.
[b] Both pull and bulge values, for comparability, are based on initial thickness of specimens.
[c] Values determined by Dr. H. J. Read, Pennsylvania State University, University Park, Pa.
[d] Specimens 281 and 305 are 18 and 9 mils (450 and 225 μm) thick, respectively. All others are 1-3 mils (25-75 μm) thick.
[e] One pound per square inch (psi) = 0.000704 kilogram per square millimeter (kg/mm^2).

Table XX. Effect of thickness on properties of deposits from cyanide baths

Line No., Table I	Panel No.	Bath No.	Bath temp, °C	Current density, A/dm^2	Thickness,[a] mil	Tensile[a] strength, psi	Significant strain	Elec. resistivity 25°C, ohm-cm
104	125A	CN-1	40	1	0.25	33×10^3	0.4×10^{-2}	
103	130				0.30			1.87×10^{-6}
102	125				0.35	47	1.1	1.81
101	128				1.4	66	6	1.79
107	133	CN-2	40	2	0.2			1.87
106	138				1.4			1.78
109	140		60	1	0.4			1.80
108	143				1.4			1.76
112	142A			2	0.3	28	0.4	
111	142				0.4	46	1.2	1.80
110	145				2.0	81	2	1.75
114	150	CN-3	60	2	0.4			1.81
113	153				2.0			1.80
140	280	CN-8, PR[b]	80	6	3.0	61	31	1.78
141	281				18	64[c]	12[c]	1.82

[a] Metric conversions: one mil (0.001 in.) = 25 μm; one pound per square inch (psi) = 0.000704 kilogram per square millimeter (kg/mm^2).
[b] PR cycle 15 sec cathodic, 5 sec anodic.
[c] Determined by tensile pull. Elongation for specimen No. 281 is per cent in 2 in. All other values in this table were determined by bulge measurements.

Table XXI. Effect of bath temperature on properties of deposits from cyanide baths

Line No., Table I	Panel No.	Bath symbol	Addition agent or other variable	Current density, A/dm^2	Bath temp, °C	Tensile[a] strength, psi	Significant strain	Young's[a] modulus of elasticity, psi	Hardness KHN 100g load, kg/mm^2	Internal[a] stress, psi	Density 25°C, g/cm^3	Elec. resistivity 25°C, ohm-cm
105	136	CN-2	None	1	40	57×10^3	10×10^{-2}	17×10^6	119	8600	8.913	1.74×10^{-6}
108	143				60	66	18	16	135	7400	8.908	1.76
106	138			2	40	53	14		147	6900	8.909	1.78
110	145, 146				60	81	2		159	7800	8.913	1.75
115	197	CN-4	None	2	40	52	10		150	9200	8.916	1.81
117	158				60	53	24	16	129	9200	8.904	1.78
120	208, 209				80	51	25		139	6100	8.917	1.77
116	201, 202			4	40	44	7		144	7500	8.900	1.80
119	205				60	50	12		132	9500	8.908	1.84
121	210, 212				80	51	22		131	6400	8.908	1.79
122	178, 180	CN-5	None	2	40	49	13		143	9300	8.915	1.83
124	184, 186				60	54	12	15	123	9700	8.907	1.78
126	191				80	53	14		139	6200	8.917	1.75
123	182			4	40	48	14		136	7600	8.918	1.83
125	187, 188				60	63	5	16	152	9500	8.900	1.81
127	194, 195				80	78	3		131	6700	8.912	1.79
128	234-236	CN-6	None	2	40	44	19		116	5200	8.913	1.76
130	239, 240				60	64	29		143	5500	8.919	1.88
132	249				80	57	22		158	5800	8.920	1.87

[a] One pound per square inch (psi) = 0.000704 kilogram per square millimeter (kg/mm^2).

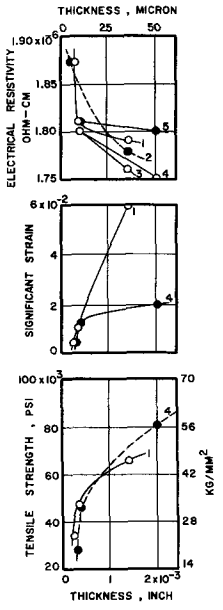

Fig. 26. Relationships between thickness, tensile strength, significant strain, and electrical resistivity of copper deposits from cyanide baths: (1)—CN-1, 40°C, 1 A/dm²; (2)—CN-2, 40°C, 2 A/dm²; (3)—CN-2, 60°C, 1 A/dm²; (4)—CN-2, 60°C, 2 A/dm²; (5)—CN-3, 60°C, 2 A/dm².

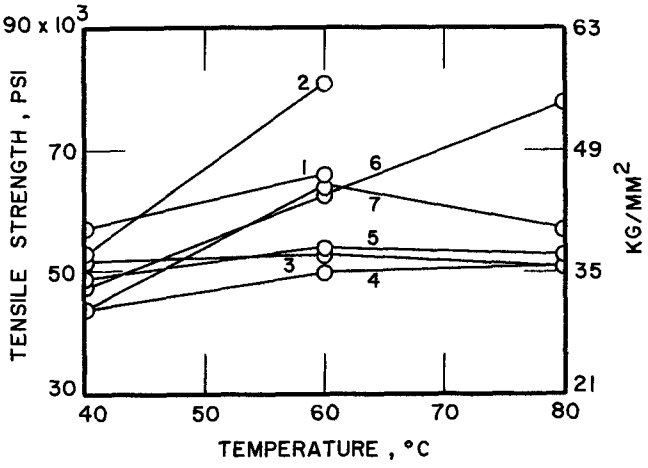

Fig. 27. Relationship between bath temperature and tensile strength of copper deposits from cyanide baths: (1)—CN-2, 1 A/dm²; (2)—CN-2, 2 A/dm²; (3)—CN-4, 2 A/dm²; (4)—CN-4, 4 A/dm²; (5)—CN-5, 2 A/dm²; (6)—CN-5, 4 A/dm²; (7)—CN-6, 2 A/dm².

pairs tensile strength increases with increase of temperature. With one exception, the effect is smaller between 60° and 80°C than between 40° and 60°C. We judge that the predominant effect, increase of deposit strength with increase of bath temperature, which is unexpected, is real. The following hypothesis may explain the effect: In cyanide-type baths current efficiency, and, hence, plating rate, increases markedly with increase in bath temperature. Thus, with other conditions constant, increase in temperature may lead to depletion of copper ions in the cathode film, with consequent decrease of grain size and increase of strength. This effect would be countered by increase in rate of diffusion of complex cyanide ions into the cathode film with increase of temperature, but the latter might be the minor effect because of the large size of the complex ions.

The effect of bath temperature on significant strain is indefinite, as seen in Table XXI. Most of the values vary randomly in the range of 0.1-0.25. The only clues to a relationship are seen in the second and sixth sets of data (lines 106-110 and 123-127, respectively) which show an appreciable decrease of significant strain with increase in temperature.

Variation of modulus with temperature is in the range $(16 \pm 1) \times 10^6$ psi, not a significant variation.

Hardness is not markedly affected by bath temperature. However, there is a small but predominant trend toward increase of hardness with increase of bath temperature. The relationship is, thus, parallel to that between tensile strength and bath temperature, and our explanation is the same.

b. Current density.—Complete data on the effects of current density on mechanical properties are shown in Table XXII. Figure 28, which contains data for those cases where the effects were significant, shows that the predominant tendency is for tensile strength and hardness to increase with increase in current density, and for significant strain to decrease. Several cases

Table XXII. Effect of current density on properties of deposits from cyanide baths

Line No. Table I	Panel No.	Bath symbol	Addition agent or other variable	Bath temp, °C	Current density, A/dm²	Tensile[a] strength, psi	Significant strain	Young's[a] modulus of elasticity, psi	Hardness KHN 100g load, kg/mm²	Internal[a] stress psi	Density 25°C, g/cm³	Elec. resistivity 25°C, ohm-cm
105	136	CN-2	None	40	1	57 × 10³	10 × 10⁻²	17 × 10⁶	119	8,600	8.913	1.74 × 10⁻⁶
106	138				2	53	14		147	6,900	8.909	1.78
108	143			60	1	66	18	16	135	7,400	8.909	1.76
110	145, 146				2	81	4		159	7,800	8.913	1.75
115	197	CN-4	None	40	2	52	10		150	9,200	8.916	1.81
116	201, 202				4	44	7		144	7,500	8.900	1.80
117	158			60	2	53	24	16	129	9,200	8.904	1.78
119	205				4	50	12	16	132	9,500	8.908	1.84
120	208, 209			80	2	51	25		139	6,100	8.917	1.77
121	210, 212				4	51	22		131	6,400	8.908	1.79
122	178, 180	CN-5	None	40	2	49	13		143	9,300	8.915	1.83
123	182				4	48	14		136	7,600	8.918	1.83
124	184, 186			60	2	54	12	15	123	9,700	8.907	1.78
125	187, 188				4	63	5	16	152	9,500	8.900	1.81
126	191			80	2	53	14		139	6,200	8.917	1.75
127	194, 195				4	78	6		131	6,700	8.912	1.79
129	242-244	CN-6	None	60	1	43	57		141	3,500	8.918	1.88
130	239, 240				2	64	40		143	5,500	8.919	1.88
131	245, 247				4	58	9		135	4,400	8.919	1.86
135	260-263	CN-8	None	80	4	37	22		114	4,500	8.919	1.80
138	268-270				6	40	49		98	4,500	8.925	1.76
139	271-273				8	39	50		129	3,900		1.76
141	281		PR, 15-5 sec cycle, 18 mils	80	6	64[c]	12[c]		147			1.76
142	279		Ditto PR, 3 mils		8	60	23		151			1.76
145-146	300, 305	CN-9	Prop. B[b]	80	4	26	9		74	11,000	8.923	1.80
147	303				6	24	10		76			1.81

[a] One pound per square inch (psi) = 0.000704 kilogram per square millimeter (kg/mm²).
[b] Proprietary brightener, selenium type.
[c] Values measured by tensile pull. Elongation unit is per cent in 2 in. (5 cm).

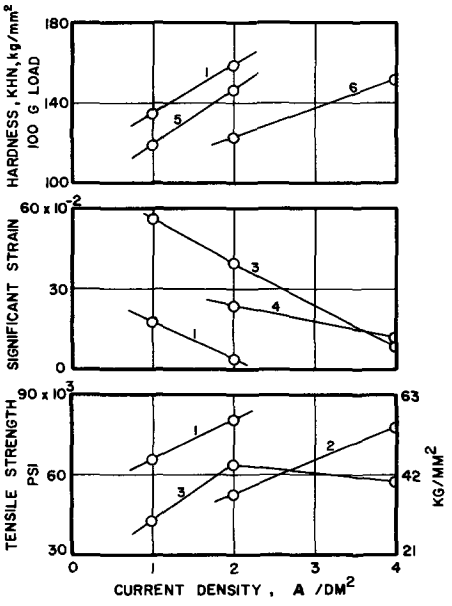

Fig. 28. Relationships between current density, tensile strength, significant strain, and hardness of copper deposits from cyanide baths: (1)—CN-2, 60°C; (2)—CN-5, 80°C; (3)—CN-6, 60°C; (4)—CN-4, 60°C; (5)—CN-2, 40°C; (6)—CN-5, 60°C.

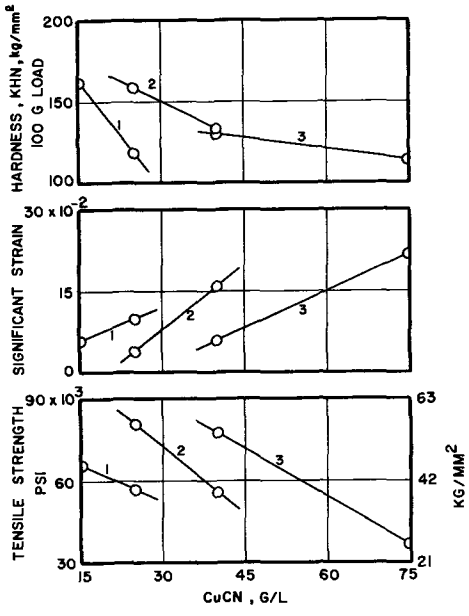

Fig. 29. Relationships between copper cyanide concentration, tensile strength, significant strain, and hardness of deposits from cyanide baths: (1)—CN-1 and CN-2, 40°C, 1 A/dm²; (2)—CN-2 and CN-3, 60°C, 2 A/dm²; (3)—CN-5 and CN-8, 80°C, 4 A/dm².

where there was no appreciable effect are seen in Table XXII.

The range of variation of the modulus is (16 ± 1) x 10^6 psi; *i.e.*, change of current density does not affect the modulus significantly.

c. Concentration of copper cyanide.—The effects of concentration of copper cyanide on mechanical properties are shown in Table XXIII and Fig. 29. There is a consistent decrease of tensile strength and hardness and a trend toward increase of ductility with increase

Table XXIII. Effect of concentration of copper cyanide on properties of deposits from cyanide baths

Line No., Table I	Panel No.	Bath symbol	Bath temp, °C	Current density, A/dm²	Conc CuCN, g/l	Tensile[a] strength, psi	Significant strain	Young's[a] modulus of elasticity, psi	Hardness KHN 100g load, kg/mm²	Internal[a] stress, psi	Density 25°C, g/cm³	Elec. resistivity 25°C, ohm-cm
101	128	CN-1	40	1	15	66 × 10^3	6 × 10^{-2}	17 × 10^6	162	14,000	8.898	1.79 × 10^{-6}
105	136	CN-2			25	57	10	17	119	8,600	8.913	1.74
110	145, 146	CN-2	60	2	25	81	4		159	7,800	8.913	1.75
113	153	CN-3			40	56	16	17	133	9,500	8.907	1.80
127	194, 195	CN-5	80	4	40	78	6		131	6,700	8.912	1.79
135	260-263	CN-8			75	37	22		114	4,500	8.919	1.80
145	300	CN-9			75	26	9		74	11,000	8.923	1.80

[a] One pound per square inch (psi) = 0.000704 kilogram per square millimeter (kg/mm²).

Table XXIV. Effects of concentrations of free sodium cyanide and sodium carbonate on properties of deposits from cyanide baths

A. Effect of free cyanide

Line No., Table I	Panel No.	Bath symbol	Bath temp, °C	Current density, A/dm²	Conc free NaCN, g/l	Tensile[a] strength, psi	Significant strain	Young's[a] modulus of elasticity, psi	Hardness KHN 100g load, kg/mm²	Internal[a] stress, psi	Density 25°C, g/cm³	Elec. resistivity 25°C, ohm-cm
115	197	CN-4	40	2	6	52 × 10^3	10 × 10^{-2}		150	9200	8.916	1.81 × 10^{-6}
122	178, 180	CN-5			10	49	13		143	9300	8.915	1.83
116	201, 202	CN-4		4	6	44	7		144	7500	8.900	1.80
123	182	CN-5			10	48	14		136	7600	8.918	1.83
117	158	CN-4	60	2	6	53	24	16 × 10^6	129	9200	8.904	1.78
124	184, 186	CN-5			10	54	12	15	123	9700	8.907	1.78
119	205	CN-4		4	6	50	12	16	132	9500	8.908	1.84
125	187, 188	CN-5			10	63	5	16	152	9500	8.900	1.81
120	208, 209	CN-4	80	2	6	51	25		139	6100	8.917	1.77
126	191	CN-5			10	53	14		139	6200	8.917	1.75
121	210, 212	CN-4		4	6	51	22		131	6400	8.908	1.79
127	194, 195	CN-5			10	78	6		131	6700	8.912	1.79

B. Effect of sodium carbonate

					Conc Na_2CO_3, g/l							
113	153	CN-3	60	2	15	56 × 10^3	16 × 10^{-2}	17 × 10^6	133	9500	8.907	1.80 × 10^{-6}
117	158	CN-4			30	53	24	16	129	9200	8.904	1.78

[a] One pound per square inch (psi) = 0.000704 kilogram per square millimeter (kg/mm²).

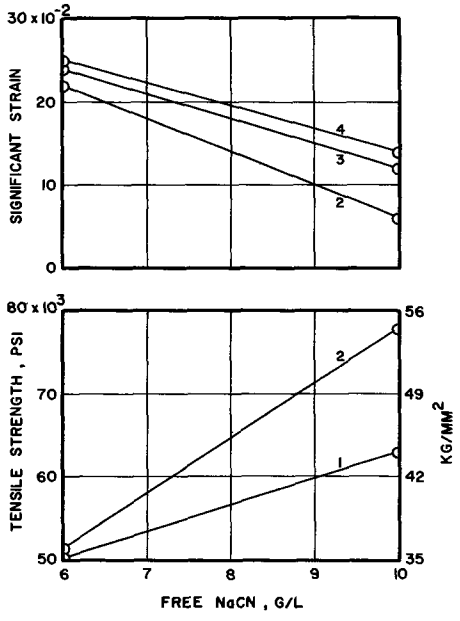

Fig. 30. Relationships between free cyanide concentration, tensile strength, and significant strain of copper deposits from cyanide baths: (1)—CN-4 and CN-5, 60°C, 4 A/dm²; (2)—CN-4 and CN-5, 80°C, 4 A/dm²; (3)—CN-4 and CN-5, 60°C, 2 A/dm²; (4)—CN-4 and CN-5, 80°C, 2 A/dm².

of concentration of copper cyanide. The modulus of elasticity is unaffected.

d. Concentration of free cyanide and sodium carbonate.—Increase in concentration of free cyanide results in increase in tensile strength and decrease in significant strain in most instances. The cases in which a significant effect occurs are shown in Fig. 30. However, examination of Table XXIV shows several cases in which the effect was negligible. Neither modulus of elasticity nor hardness were affected significantly (Table XXIV).

The data in Table XXIV also show that a twofold increase of concentration of sodium carbonate did not produce an appreciable effect on any of the properties except significant strain, which was increased.

e. Concentration of Rochelle salt and effect of potassium ion.—Examination of the data summarized in Table XXV does not give a clear conclusion regarding the effect of Rochelle salt on mechanical properties. Differences are small and tend in both directions. We can only conclude that the effects are minor.

Effect of an all-potassium bath may be seen by comparing lines 130 and 133 in this table. Potassium ion, as compared with sodium, causes significant decreases of strength, ductility, and hardness.

f. pH.—Table IV shows the variation of pH with duration of electrolysis of cyanide baths. Variation of pH is not normally controlled in these baths, which operate at a "natural" pH. It is seen that the initial pH for all except bath No. CN-8 is in the range 11.4-11.8 and increases after working to a stable value in the range 12.6-12.8. This is the direction of shift to be expected due to the low cathode efficiency. Bath No. CN-8 is initially higher in pH due to its high content of KOH, and does not change with working, due to its high cathode efficiency. Under the above circumstances, effect of pH on properties of deposits is of only academic interest. However, a few measurements were made to compare the tensile strength and ductility of panels made at the lower limit of the pH ranges shown in Table IV with those of panels made at the upper limit of the range. No measurable effect was observed.

g. Proprietary brightener.—Baths No. CN-8 and CN-9 are fairly similar in composition, as may be seen in Table IV, except for the presence in CN-9 of the proprietary addition agent of the selenium type. Both are based on potassium salts and have the same copper content. CN-9 is higher in free cyanide and lower in KOH but it is probable that effects of these differences on properties of deposits are less than that of the addition agent.

Comparing lines 135 and 138 with lines 145 and 147 of Table XXII, we see that tensile strength, ductility, and hardness are all significantly smaller for the deposits from the bath containing the selenium-type addition agent. The value of the addition agent lies in its effect on smoothness and brightness rather than in its effect on properties.

h. Periodic current reversal (PR).—The effects of periodic current reversal on properties of deposits from baths CN-8 and CN-9 are summarized in Table XIV. Comparing line 140 with 135-138 we see that PR produces a marked increase in tensile strength. Addition of KCNS (line 143) produces a further significant increase. Deposits from bath No. CN-9 made with PR (line 148) are more than twice as strong as non-PR deposits (lines 145-147). Neither change of current density nor change of PR cycle had significant effects on strength (lines 140 *vs.* 142 and 143 *vs.* 144, respectively). Under none of these conditions used by us was the tensile strength as high as has been claimed by some authors (3).

Effects of PR on ductility are less consistent, but the conclusion in summary is that, for deposits from bath CN-8, the stronger PR deposits are less ductile than the weaker non-PR deposits (*cf.* line 138 with 140-141 and line 135 with 143-144). The strongest deposits (lines 143, 144) have the lowest ductility. On the other hand, the moderately strong PR deposit from bath CN-9 (line 148) has the very high elongation of 45%, which is evidently due to a specific effect of the addition agent.

Hardness is much increased by PR for deposits from baths CN-8 and CN-9 (Table XIV). Whereas variation of the PR cycle had no effect on strength and ductility, the deposit made with the 30-10 sec cycle is significantly harder than that made with the 15-5 sec cycle. The PR deposit from bath CN-9 (line 148) is the hardest encountered in this research, namely, 224 KHN.

Table XXV. Effect of Rochelle salt on properties of deposits from cyanide baths

Line No., Table I	Panel No.	Bath symbol	Bath temp, °C	Current density, A/dm²	Conc Rochelle salt, g/l	Tensile[b] strength, psi	Significant strain	Hardness KHN 100g load, kg/mm²	Internal[b] stress, psi	Density 25°C, g/cm³	Elec. resistivity 25°C, ohm-cm
115	197	CN-4	40	2	0.0	52 × 10³	10 × 10⁻²	150	9200	8.916	1.81 × 10⁻⁶
128	234-236	CN-6			45	44	19	116	5200	8.913	1.76
117	158	CN-4	60	2	0.0	53	24	129	9200	8.904	1.78
130	239, 240	CN-6			45	64	40	143	5500	8.919	1.88
133	252, 253	CN-7[a]			45	38	34	92	8100	8.920	1.74
119	205	CN-4		4	0.0	50	12	132	9500	8.908	1.84
131	245, 247	CN-6			45	58	9	135	4400	8.919	1.86
120	208, 209	CN-4	80	2	0.0	51	25	139	6100	8.917	1.77
132	249	CN-6			45	57	22	158	5800	8.920	1.87

[a] "All-potassium" bath.
[b] One pound per square inch (psi) = 0.000704 kilogram per square millimeter (kg/mm²).

C. Internal Stress in Deposits from Cyanide Baths

1. Effect of thickness.—The uppermost curve in Fig. 8 shows that the cumulative internal stress of a deposit from bath CN-2 (line 105, panel 136, Tables XXI-XXIII) increases nearly linearly with time (*i.e.*, with thickness) to the limit of thickness over which stress was measured (approximately 1.5 mil). With respect to internal stress, this deposit is fairly typical of deposits from cyanide baths. This relationship between stress and thickness is in marked contrast to that for deposits from sulfate baths, such as the deposit from a bath containing naphthalenedisulfonic acid. Internal stress in the latter deposit levels off, with no further increase after reaching a thickness of about ¾ mil (Fig. 8). These contrasting effects correlate with the increase in grain size with increase of thickness for the sulfate deposits (Fig. 20-3), and with the constancy of grain size of the cyanide deposits (Fig. 34).

2. Effect of operating conditions and bath composition on internal stress of deposits from cyanide baths.—*a. Bath temperature.*—Effect of bath temperature on internal stress is shown in Fig. 31 and Table XXI. At first sight the results, shown fully in Fig. 31, appear to form no consistent pattern. However, some relationships may be deduced as follows. Consider first the deposits from baths CN-2, CN-4, and CN-5. The general pattern is that, for these deposits, stress tends to go through a maximum with increase of bath temperature. Of 10 pairs of data involved, only one (curve No. 1) has a contrary trend. Deposits from bath CN-6 (Rochelle type, curve No. 7) have significantly lower stress than the deposits from the other baths and their stress is nearly unaffected by bath temperature.

b. Current density.—There is no consistent relationship between internal stress and current density and in no case is the effect very large (Table XXII). There is indication that the effect of current density on stress tends to be lost at the higher operating temperatures.

c. Concentration of copper cyanide.—The preponderant effect indicated by the data summarized in Table XXIII is decrease of internal stress with increase of concentration of copper cyanide. The effect is definite for lines 101 *vs.* 105 and 127 *vs.* 135. However, there is a borderline reverse effect in lines 110 *vs.* 113.

The high value of stress seen in line 145 is an addition agent effect, discussed in paragraph *f* below.

d. Concentration of free cyanide and sodium carbonate.—There is consistently no significant effect on internal stress due to changes of concentration of either free cyanide or sodium carbonate (Table XXIV).

e. Concentration of Rochelle salt and effect of potassium ion.—The data in Table XXV show that addition of Rochelle salt to a cyanide bath consistently causes a decrease of internal stress.

Comparison of lines 130 and 133 shows that converting a sodium to a potassium Rochelle bath results in a significant increase in internal stress of the deposits. The same change caused decreases of tensile strength, ductility, and hardness, illustrating the lack of correlation of these properties with stress.

f. Proprietary brightener.—Comparison of the values for internal stress on lines 135 and 145 of Table XXII shows that addition of the proprietary selenium-type brightener to a high efficiency bath causes a marked increase in internal stress.

g. Periodic current reversal (PR).—Data relating the effect of PR to internal stress of deposits from cyanide baths are available only for bath No. CN-8 (Table XIV). Comparing lines 140 and 143 with lines 135 and 138, it is seen that stress is only slightly higher in the PR deposits. The large effect observed with sulfate deposits does not occur with cyanide deposits because, as seen in Section VII-C-1 above, stress does not decrease with increase of thickness of the latter.

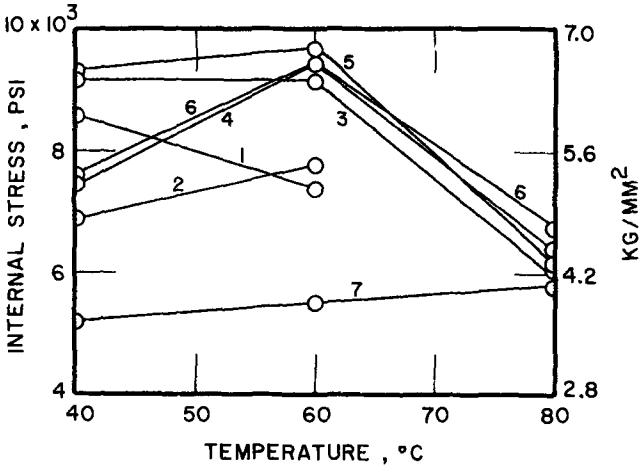

Fig. 31. Relationship between bath temperature and internal stress in copper deposits from cyanide baths: (1)—CN-2, 1 A/dm²; (2)—CN-2, 2 A/dm²; (3)—CN-4, 2 A/dm²; (4)—CN-4, 4 A/dm²; (5)—CN-5, 2 A/dm²; (6)—CN-5, 4 A/dm²; (7)—CN-6, 2 A/dm².

D. Density of Deposits from Cyanide Baths

Excluding the deposits from baths CN-8 and CN-9, which will be referred to subsequently, the average density of all deposits listed in Tables XXI through XXV is 8.911, with extremes of 8.898 and 8.920 g/cm³. For these thin deposits, the accuracy of our measurements (±0.01 g/cm³) was not sufficient to enable us to detect any effect of temperature, current density, and bath composition on density.

It is noted in Table XXII that the densities of the deposits from the high efficiency baths (lines 135, 138, and 146) range from 8.919 to 8.925 g/cm³, significantly higher than the average 8.911 of the low-copper cyanide baths. We believe that these higher values of high-efficiency deposits, in the same range as the densities of deposits from sulfate baths, are real, particularly since some of these high values were obtained from measurements on thick deposits for which accuracy of measurements is judged to be ±0.005 g/cm³ (*e.g.*, line 146, Table I).

E. Electrical Resistivity of Deposits from Cyanide Baths

An analysis similar to that given above for density leads to the following conclusions regarding the effects of various variables on electrical resistivity:

Table No.	Variable	Effect on resistivity
XIV	PR	None
XIV	Added KCNS + PR	Significant increase
XIV	Added proprietary addition agent + PR	Significant increase
XXI	Temperature increase	Variable, minor
XXII	Current density increase	Very small increase
XXII	*Added proprietary addition agent (without PR)*	*None*
XXIII	CuCN increase	None
XXIV	Free CN increase	None
XXIV	Na_2CO_3 increase	None
XXV	Rochelle salt addition	Small increase
XXV	Potassium ion (*vs.* sodium)	Significant decrease

F. Relationships between Properties of Deposits from Cyanide Baths

1. Tensile strength and ductility.—Tensile strength as a function of significant strain is plotted in Fig. 32, which contains points representing all deposits from cyanide baths. In general, significant strain decreases with increase in strength. This is the relationship that usually occurs for wrought metals, and was observed for certain addition agent sulfate deposits. It is the opposite of the relation between strength and ductility for nonaddition agent deposits from sulfate and fluoborate baths (Fig. 14 and Fig. 22, respectively). The two deposits that most conspicuously fail to conform to the general pattern are (*a*) the deposit from the proprietary high-efficiency bath made with direct current, which has low ductility for its strength, in comparison with the main pattern; and (*b*) the corresponding PR deposit, which has abnormally high ductility.

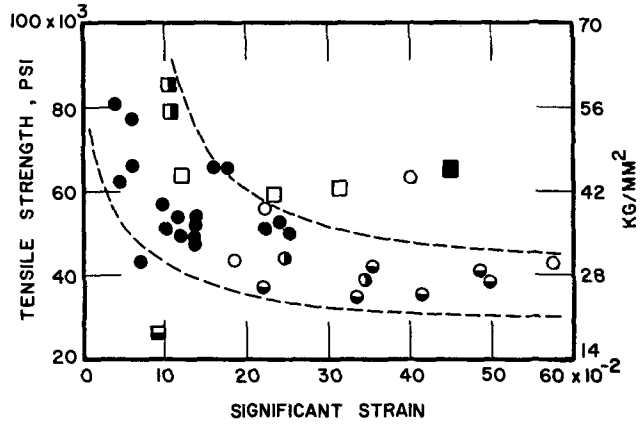

Fig. 32. General relationship between significant strain and tensile strength of copper deposits from various cyanide baths. ●—CN-1 through CN-5, all operating conditions; ○—CN-6, sodium Rochelle salt bath, all operating conditions; ◑—CN-7, potassium Rochelle salt bath, all operating conditions; ◒—CN-8, all operating conditions; □—CN-8 with periodic current reversal (PR), no addition agent; ◧—CN-8 plus 2 g/l KCNS, with PR; ▣—CN-9, proprietary bright bath; ■—CN-9 with PR.

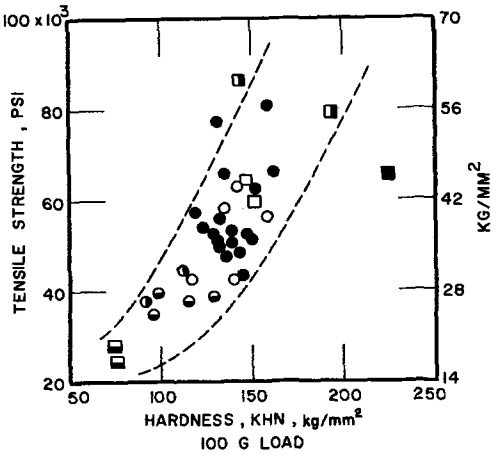

Fig. 33. General relationship between hardness and tensile strength of copper deposits from various cyanide baths. The code defining deposits is the same as for Fig. 32.

2. Tensile strength and hardness.—The general relationship between tensile strength and hardness for all deposits from cyanide baths is shown in Fig. 33, in which there is seen to be a positive correlation between hardness and tensile strength. The relationship is more definite than that for sulfate deposits (Fig. 15).

G. Structure of Deposits from Cyanide Baths

1. Effect of type of bath on structure.—Optical micrographs of several typical deposits from cyanide baths are shown in Fig. 34. Included for comparison are a strike bath deposit, a deposit from a typical low-concentration bath, deposits from both sodium and potassium Rochelle-type baths, a deposit from a standard high-efficiency bath, and a deposit from a high-efficiency bath containing a selenium-type proprietary brightener. The deposits from the low-concentration baths (Fig. 34-1 and 34-2) show a fine columnar structure, which is surprising, because literature references commonly refer to deposits from these baths as being extremely fine grained (33). On the other hand, a cyanide deposit with a structure similar to that of Fig. 34-1 has been reported by R. R. Bair and A. K. Graham [Ref. (26), p. 167]. To verify the structure seen in Fig. 34-1 and to check the possibility that it might be an erroneous work-induced structure, an entirely new section was prepared and examined by both optical and electron micrography. The electron micrographs, shown in Fig. 36, were made from a specimen prepared by a deep electropolish. The same results were obtained, indicating that the observed structure is a true representation of the deposit. The significant features noted in the electron micrographs are:

a. Small micro-twin and columnar grains extending the thickness of the deposit.

b. Surface rippling in the areas below nodules on the upper surface (Fig. 36-2). The electron micrographs were made for us by D. B. Ballard of the NBS Metallurgy Division. Details are given in section X, Appendix.

The addition of Rochelle salt (Fig. 34-3) is seen to cause grain refinement. The deposit from the potassium Rochelle bath (Fig. 34-4) does not contain the nodular structures of the deposit from the sodium salt bath and shows some indication of the presence of fairly large equi-axed grains. The deposit from the high-efficiency bath (Fig. 34-5) is fine grained, whereas that from the proprietary bright bath (Fig. 34-6) shows large columnar grains extending the thickness of the deposit. This structure correlates with its low strength and ductility (Table XXII).

2. Effect of periodic current reversal on structure.—Effect of periodic current reversal on structure is

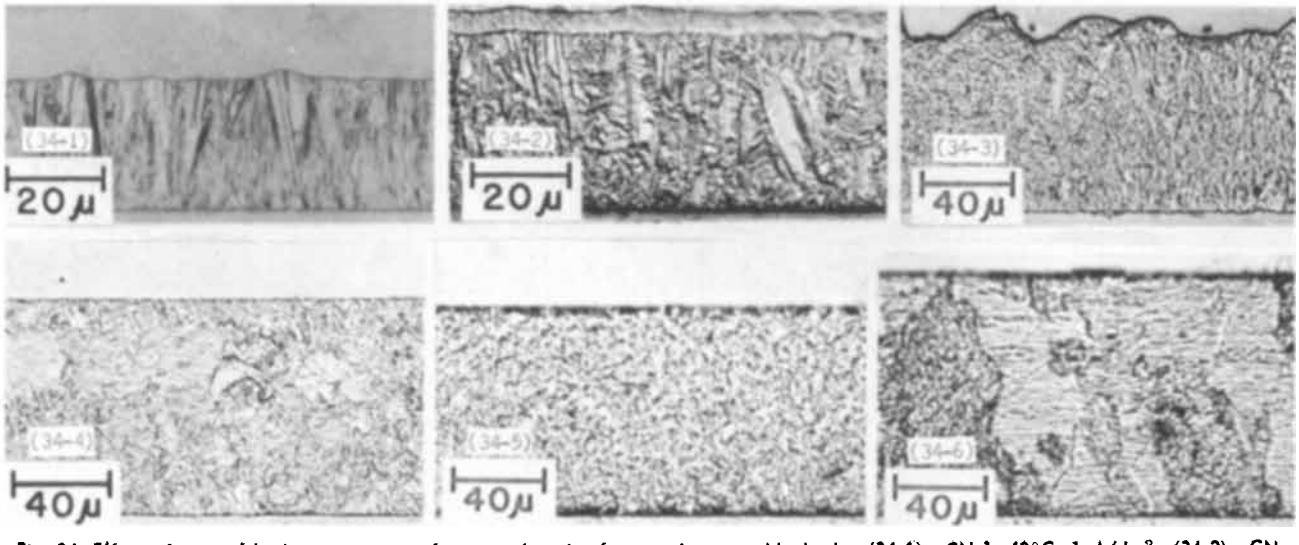

Fig. 34. Effect of type of bath on structure of copper deposits from various cyanide baths: (34-1)—CN-1, 40°C, 1 A/dm²; (34-2)—CN-5, 60°C, 2 A/dm²; (34-3)—CN-6, 60°C, 2 A/dm²; (34-4)—CN-7, 60°C, 2 A/dm²; (34-5)—CN-8, 80°C 6 A/dm²; (34-6)—CN-9, 80°C, 6 A/dm².

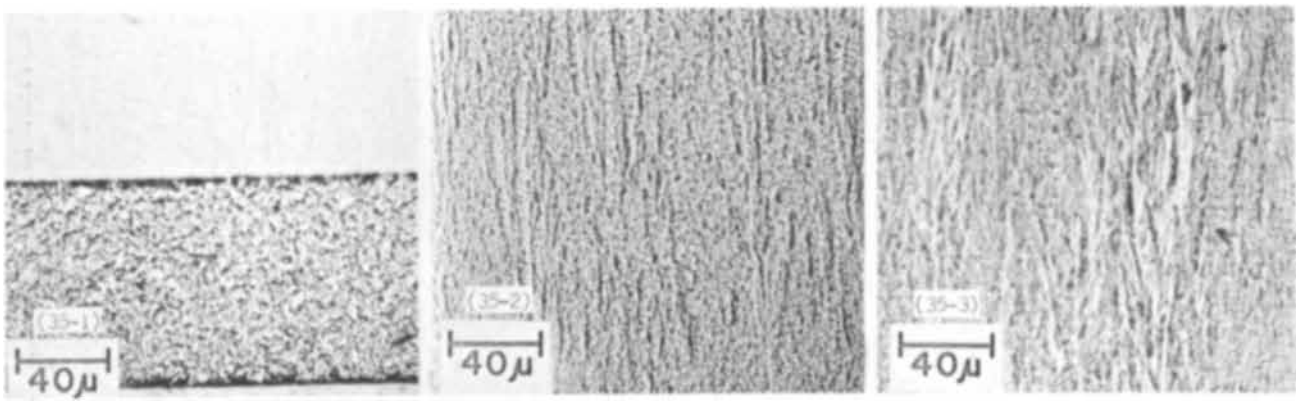

Fig. 35. Effect of periodic current reversal (PR) on structure of copper deposits from a high-efficiency cyanide bath: (35-1)—CN-8, 80°C, 6 A/dm^2, continuous current; (35-2)—CN-8, 80°C, 6 A/dm^2, no addition agent, PR, 15 sec cathodic, 5 sec anodic; (35-3)—CN-8 plus 2 g/l KCNS, 80°C, 6 A/dm^2, PR, 15 sec cathodic, 5 sec anodic.

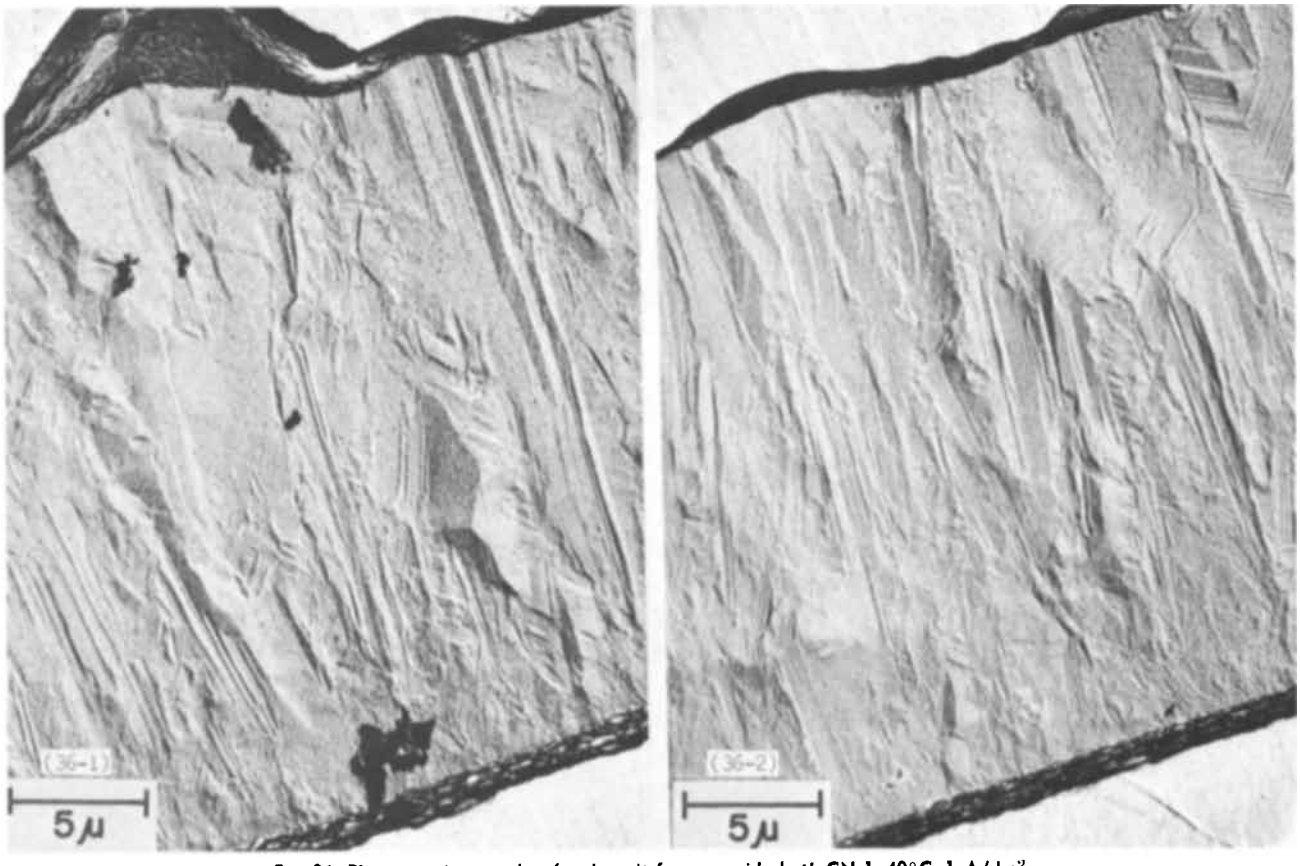

Fig. 36. Electron micrographs of a deposit from cyanide bath CN-1, 40°C, 1 A/dm^2

shown in Fig. 35. Figure 35-1 is a deposit from bath CN-8 made without PR, 35-2 the same with PR, and 35-3 the same as 35-2 except for addition of potassium thiocyanate to the bath. The latter two deposits were both built to a thickness of 18 mils. The addition of the thiocyanate resulted in a brighter final surface and less tendency for nodules to form. Both of the PR structures appear to be finer than the non-PR but with a distinct fibrous character. This shift of structure is consistent with the higher strength and hardness of these deposits (Table XIV). The laminations in Fig. 35-2 and 35-3 due to current interruption are not as distinct as have been shown in other published PR structures (14, 26). This is because the short cycle time that we used (15 sec cathodic, 5 sec anodic) resulted in a thickness per layer of only about 0.04 mil, which is resolvable and faintly visible in the original photographs at 500X but may not show in published prints.

REFERENCES

25. J. W. Dini, H. R. Johnson, and J. R. Helms, *Plating*, **54**, 1337 (1967).
26. F. A. Lowenheim, Editor, "Modern Electroplating," 2nd Ed., John Wiley & Sons, Inc., New York (1963).
27. R. Pinner, "Copper and Copper Alloy Plating," 2nd Ed., Copper Development Association, London, W.I. (1964).
28. A. V. Ryabchenkov, A. A. Gerasimenko, and E. S. Naydena, *Zashchita Metallov.*, **2**, No. 2, 232 (1966).
29. L. Greenspan, *Trans. Electrochem. Soc.*, **78**, 303 (1940).
30. T. A. Prater and H. J. Read, *Plating*, **36**, 1221 (1949); **37**, 830 (1950).
31. H. J. Read and T. J. Whalen, *Proc. Am. Electroplaters' Soc.*, **46**, 318 (1959).
32. F. P. Brodell and A. Brenner, *Plating*, **44**, 591 (1957).
33. H. Fischer, "Elektrolytische Abscheidung und Elektrokristallisation von Metallen," p. 486, Springer-Verlag, Berlin (1954).

Report of the Electrolytic Industries for the Year 1969[1]

Robert G. Milner*

Union Carbide Corporation, Carbon Products Division, Cleveland, Ohio 44101

Thomas C. Jeffery*

PPG Industries, Industrial Chemical Division, Lake Charles, Louisiana 70601

Chlorine-Caustic Soda

I. Production.—The production of chlorine increased in 1969 to a new record of 9,427,000 tons in the United States, according to The Chlorine Institute, Inc. (1). This tonnage represents a gain of approximately 11.2% over the 1968 production of chlorine gas. The 1969 production of chlorine in Canada also reached a new high, 887,000 tons, which is up 14.4% over 1968 figures. During the period 1959-1969, the average annual growth rate has been 8.0% in the U.S. and 11.5% in Canada.

From December 1968 to December 1969, daily capacity increased 12.2% to 28,276 tons in the U.S. and increased 6.4% to 2636 tons in Canada.

Manufacturing in the U.S. operated at 95.6% of capacity, while Canadian producers operated at 93.3% in 1969.

During 1969, the unusual situation of a snug caustic soda market was the rule rather than the exception. Although generally caustic has experienced a slower growth trend than chlorine, lower prices have brought other markets into range (2). Caustic has already taken over most of the alumina processing market, and is making inroads into pulp and paper production at the expense of soda ash. There is some hope that the trend will extend to the glass industry, but most feel business in this area will come slowly.

A 7.5%/yr growth prediction for caustic soda and an 8.0%/yr growth for chlorine would indicate that supplies of caustic will continue to exceed market growth. In addition, theoretical yield of caustic is about 1.1 tons per ton of chlorine. Production figures, however, do not indicate that this yield is achieved in practice.

Some chlorine, approximately 4%, is a by-product of making metallic sodium from salt, with no coproduction of caustic. Production of lithium chloride, soda ash, potassium hydroxide, and in-plant use of caustic account for most of the rest of the discrepancy between the theoretical and the actual output ratio for chlorine and caustic.

Dow Chemical leads U.S. producers of caustic with 30% of the total capacity, followed by PPG with about 9%, Allied and Diamond Shamrock with about 8% each, Olin Mathieson and Hooker with about 6%, Wyandotte 5%, and with FMC, Stauffer, Pennwalt, B. F. Goodrich, Alcoa, and Kaiser rounding out the list of major companies in the industry.

In marked contrast to chlorine, exports of caustic grew at 12%/yr during the period 1960-1967. Most of this production was tied to bauxite processing.

No attempt is made to pinpoint caustic prices due to the many grades, type, and volume of shipments, *etc.*, but it does appear that discounting has been eliminated to a great extent. Most major producers announced \$3-\$4/ton increases, to the \$66/ton range, effective the third quarter of 1969 (3).

II. Expansions.—The best estimates of The Chlorine Institute, Inc., indicate that by the end of 1970 projects now under way will increase combined U.S. and Canadian daily capacity by about 6.5% or to approximately 12 million tons (4, 5).

Company & location	Type of cell	Capacity (tons/day)	Completion date
(A) Shutdown			
Arkla Chemical Corp., Pine Bluff, Ark.	Hooker S-1 Diaphragm	75	Oct. 1969
Stauffer Chemical Co., Huntsville, Ala.	Hooker S-1 Diaphragm	100	Aug. 1969
Stauffer Chemical Co., Dominguez, Calif.	BASF Mercury	150	
(B) Production started			
General Aniline and Film Corp., Linden, N. J.	BASF-Krebs Mercury	250	Nov. 1969
Interprovincial Cooperative Ltd., Saskatoon, Saskatchewan	Kureha HD-4 Mercury	70 Exp.	Jan. 1969
Kaiser Aluminum & Chemical Corp., Gramercy, La.	Hooker S-3B Diaphragm	300 Exp.	May 1969
PPG Industries, Lake Charles, La.	DeNora Mercury	600	Feb. 1969
Reactive Metals, Inc., Ashtabula, Ohio	Downs	50% Exp. metallic sodium-chlorine	Dec. 1969 1st stage
Velsicol Chemical Co., Memphis, Tenn.	Hooker S-4 Diaphragm	Hooker S-1 removed	June 1969
Wyandotte Chemicals Corp., Geismar, La.	Hooker S-4B Diaphragm	350	April 1969
C. Building or planned			
American Magnesium, Snyder, Texas	Magnesium cells	30,000 tons/yr	Bal. 1970
Conso Chemicals Ltd., Abercrombie Point, Nova Scotia	ICI Mercury	\$8 million	Early 1970
Dow Chemical Co.,	Dow	24,000 tons/yr	Late 1971
Dallesport, Wash.	Dow	24,000 tons/yr Magnesium (100,000 tons/yr Cl_2)	Late 1973
Dow Chemical Co., Freeport, Texas	Dow Diaphragm	Expansion planned	
Dow Chemical Co., Midland, Mich.	Dow Diaphragm	Modernization planned	1971-1972
Dow Chemical Co., Pittsburg, Calif.	Dow Diaphragm	450	Mid-1970
Dow Chemical Co., Plaquemine, La.	Dow Diaphragm	\$2.2 million	2nd Quarter 1970
National Lead Co., Grantsville, Utah	BASF	45,000 tons/yr Magnesium	Late 1971
Oregon Metallurgical Co., Albany, Ore.	Alcan	10,000 tons/yr Magnesium	1st Quarter 1970
PPG Industries Inc., Guayanilla, Puerto Rico	DeNora Mercury	500	Late 1970
Standard Chemical Ltd., Beauharnois, Quebec	Uhde Mercury	220	1970
Stauffer Chemical Co., St. Gabriel, La.	Uhde 30 m^2 Mercury	500	1st Quarter 1970

III. New developments.—A. Pricing.—In the last quarter of 1969, the price of chlorine was raised \$2/ton to the \$75/ton range, in single unit tankcars, F.O.B. plants, freight equalized. Higher manufacturing and distributing costs were given as the reason for the increase. For that small percentage of total production sold in ton containers, the price was also increased \$2 to \$97/ton (6, 7).

B. Mercury.—Mercury consumption increased 5% during 1969 with the larger users being the manufacturers of chlorine and caustic soda, catalysts, pulp and paper, and pharmaceutical products.

Mine production was estimated at 29,000 76-lb flasks; secondary production was 50% less than 1968, mainly as a result of a drop in government sales. California and Nevada supplied 63% and 28%, respectively, of the mercury produced in the U.S., with the balance from Alaska, Arizona, Idaho, Oregon, and Texas. The value of primary production was placed at \$14,600,000 (8).

Imports of mercury increased approximately 20%. Spain is the largest producer with British Columbia,

[1] This report is sponsored by the Industrial Electrolytic Division of The Electrochemical Society. While it is primarily a summary of production and developments in the chlor-alkali industry, reports of other electrolytic industries are included.

The material presented herein has been gathered from many sources, noted in the References, and does not necessarily represent the opinions of the authors.

* Electrochemical Society Active Member.

Algeria, Turkey, and Yugoslavia also contributing to the world production.

The price of mercury has been as low as $182/flask in August 1963, and as high as $700/flask in June 1965. Lately it has fallen from about $585 to less than $500/flask (9).

Government officials recently said they would like to sell about 73,700 flasks from surplus stockpiles eventually; however, opposition is expected from the domestic industry and through diplomatic channels. The government has been offering stockpiled mercury this year at the rate of 1500 flasks a month.

C. BASF-Wyandotte.—Badische Anilin and Soda-Fabrik AG of Ludwigshafen, West Germany, announced that it is acquiring 98.5% of the outstanding stock of Wyandotte Chemicals Corporation, Wyandotte, Michigan. This represents an investment of about $95 million. In the next three or four years, BASF expects to spend around $105 million on plant expansions and modernization.

In 1968 BASF had sales of $1.4 billion, while Wyandotte's sales were $147 million (10).

Other Alkalies and Electrolytic Processes

Sodium Chlorate.—Production of sodium chlorate in the U.S. was approximately 183,000 tons in 1969, with a projected demand of 244,000 tons by 1973. Of this, 72% goes to the pulp and paper industry, 14% is used in the manufacture of chlorates and perchlorates, and 9% is used for herbicides. The pulp and paper industry employs chlorates for the generation of chlorine dioxide to bleach paper. Cotton defoliation and clearing railroad rights-of-way account for most of the herbicide use.

The domestic producers of sodium chlorate are listed (11):

Producer	Capacity (short tons/yr)
American Potash and Chemical Corp., Hamilton, Miss.	23,500
American Potash and Chemical Corp., Henderson, Nev.	30,000
Brunswick Pulp and Paper Co., Brunswick, Ga.	7,000
Georgia-Pacific Corp., Bellingham, Wash.	5,000
Hooker Chemical Corp., Columbus, Miss.	55,000
Hooker Chemical Corp., Niagara Falls, N. Y.	15,500
Reigel Paper Corp., Butler, Ala.	4,000
Reigel Paper Corp., Reigelwood, N. C.	7,000
Pacific Engineering and Production Co., Henderson, Nev.	6,000
Penn-Olin Chemical Co., Calvert City, Ky.	31,000
Pennwalt Corp., Portland, Ore.	15,000
PPG Industries Inc., Lake Charles, La.	15,000
	214,000 Total

Caustic potash.—Caustic potash facilities currently operable in the U.S. are shown below (12):

Producer	Capacity (short tons/yr)
Allied Chemical Co., Syracuse, N. Y.	30,000*
Diamond Shamrock Corp., Delaware City, Del.	16,000
Diamond Shamrock Corp., Muscle Shoals, Ala.	40,000
Dow Chemical Co., Pittsburg, Calif.	10,000
Hooker Chemical Corp., Niagara Falls, N. Y.	36,000*
International Minerals and Chemical Corp., Niagara Falls, N. Y.	23,000*
Monsanto Co., Sauget, Ill.	45,000
Pennwalt Corp., Calvert City, Ky.	25,000
PPG Industries, Inc., Corpus Christi, Texas	7,000*
PPG Industries, Inc., New Martinsville, W. Va.	8,000
	240,000 Total*

* Includes solid or flake production.

Published price for liquid, in carload or truckload quantities, was $3.80/cwt., F.O.B. producing plant. Flake prices increased during the year from $11.10/cwt. to $11.60/cwt.

Soda ash.—Natural soda ash production reached a total of 2,500,000 tons in 1969; this quantity was valued at $47,800,000 (13). The production rate noted reflects continued price degradation, as the quantity increased 23%, but the value dropped 14% compared to last year. While some production came from the dry lake beds in California, the bulk of U.S. needs was supplied by Green River, Wyoming, as in previous years. Food Machinery Corporation's three shafts in Green River are operating at near capacity of 1,250,000 tons/yr; a fourth shaft is planned, commencing a $5,000,000 expansion program (14). In addition, nearly 2,000,000 tons of sodium carbonate were produced synthetically (15).

Year-end price for both dense and light 58% soda ash climbed 5% from 1968, listing: bagged, $2.20/cwt. and bulk, $1.65/cwt. (16).

Aluminum.—Primary aluminum production in the U.S. increased to 3,800,000 tons in 1969, up from 3,250,000 tons in 1968. Canadian production of aluminum was reported to total approximately 1,063,000 tons in 1969.

Apparent use of aluminum in the U.S., based on shipments of primary metal, net imports, and recovery from scrap, increased to approximately 4,800,000 tons. This year of relatively steady production served to reduce imports of aluminum metal to a level less than 1968, when strikes at plants of two major domestic producers forced consumers to rely on foreign supply (17).

Aluminum ingot capacity under construction or planned for 1969 was as follows (18):

Producer	Capacity (short tons/yr)
Aluminum Co. of America, Rockdale, Texas	50,000
Aluminum Co. of America, Evansville, Ind.	50,000
Gulf Coast Aluminum Corp., Lake Charles, La.	35,000
Kaiser Aluminum & Chemical Corp., Tacoma, Wash.	20,000
Reynolds Metals Co., Longview, Wash.	40,000
National-Southwire Aluminum Co., Hawesville, Ky.	180,000

The price of unalloyed primary aluminum ingot, which had been raised to 27¢/lb early in January 1969, was raised again to 28¢/lb in mid-October.

Domestic production of bauxite rose to 1,800,000 long tons, while imports were 12,000,000 long tons. Approximately 60% of the bauxite imports in 1969 came from Jamaica, 20% from Surinam, and the majority of the balance from the Dominican Republic, Haiti, and Guyana. It is estimated that 67% of the alumina imports were from Australia and about 25% from Surinam (19). Generally speaking, 4 tons of bauxite are required to produce 2 tons of alumina which will yield 1 ton of primary aluminum.

Beryllium.—This year marks the fifth straight year that the use of beryl (a beryllium-aluminum-silicate) has increased, and the U.S. consumption for 1969 exceeded 6000 tons (20). Nearly half of the beryllium metal consumed is used in high-speed aircraft, and the remainder employed in missile components, the nuclear industry, and copper and nickel alloys (to impart fatigue resistance) (21, 22).

Domestic sources for beryllium production are the states of South Dakota, Maine, and Colorado, in that order, for hand-sorted beryl; and Utah for mined bertrandite (another beryllium-aluminum-silicate). General imports of beryl for 1969 should exceed 6400 tons, valued at $2,600,000; interestingly, while the tonnage is nearly a 40% increase over 1968, the foreign value of this material dropped 15%.

The industrial activity evident in 1969 is probably in response to the steadily growing beryllium market. Kawecki Berylco Industries, Inc., and Brush Beryllium Company processed hand-sorted beryl into beryllium metal and alloys; and some concentrates have been shipped from the new (September) Brush Beryllium's Spor Mountain processing plant near Delta, Utah. General Astrometals Corporation has leased the electrofining facilities of Beryllium Metals and Chemicals Corporation. Topaz Beryllium Company (subsidiary of The Anaconda Company) has acquired land in Juab County, Utah, for a proposed beryllium ore concentration plant.

Government inventories at mid-year listed 7387 tons of beryllium-copper master alloy and 229 tons of beryllium metal (exactly the amounts reported for

mid-year 1968); the 11% BeO-bearing beryl figure was 26,559 tons, which is slightly down from a year ago. The General Services Administration sales of beryl in 1969 (including a December 1968 sale) totaled 3475 tons; the price varied from $50.52 to $52.67/short ton unit.

Chromium.—The three leading consumers of chromite increased their usage during the year, as inventories dropped. The metallurgical industry used 739,000 tons in 10 months, an 8.5% increase over 1968, reflecting the high level of stainless steel production. The chemical and refractory industries consumed 175,000 and 253,000 tons, respectively. This was a 5% increase in chromite use by the chemical industry, while the 8% decrease in use for the refractory group continued last year's trend (23).

The metallurgical industry had to turn to surplus chromite from government stockpiles to supplement supply, with the continued economic sanction against Southern Rhodesia imposed in early 1967. The General Services Administration has sold 789,000 tons since January 1967 with 206,000 tons delivered in the first 10 months of 1969.

Negotiations for a plant to produce ferroalloy in Puerto Rico were announced by Air Reduction Company. The plant is to have two furnaces with a combined rating of 40,000 kW; full production is estimated for late 1971 or early 1972. A chromium chemical plant to be built in Wilmington, North Carolina, was announced by Diamond Shamrock Corporation.

Metallurgical-grade chromite prices moved upward for the third successive year. Quoted prices per long ton at Atlantic ports were as follows: Russian, 48% Cr_2O_3, 4-1 ratio $49-$52; Russian 54-56% Cr_2O_3, 4-1 ratio, $55.10-$59.60; and Turkish 48% Cr_2O_3, 3-1 ratio, $47.50-$48.50.

Copper.—In its first full year of operation since 1966, the U.S. Copper Industry posted significantly optimistic gains in 1969.

A record 9% jump in mine production of recoverable copper was recorded, up to 1,560,000 tons over the 1,429,000-ton 1966 previous high (24). Of this amount, more than half (51%) came from Arizona with the states of Utah, New Mexico, Montana, and Nevada contributing another 40% which accounts for the bulk of U.S. production. The U.S. share of free world mine output is now up to about 30% (25).

Based on tonnages of domestic primary material only, smelter production was up almost 32% over 1968, to a projected total for 1969 of 1,520,000 tons. Refinery output of domestic material jumped 35% over last year, and is expected to post 1,450,000 tons for 1969.

Reversing a two-year trend, consumption of refined copper increased (over 2,000,000 tons used in 1969), but fell short of the 2,400,000-ton record year of 1966. Wire and cable alone accounted for 1,300,000 tons (up 9% over 1968); defense programs, primarily for ammunition, took 225,000 tons of copper.

In conjunction with increased U.S. mine production, imports of blister and refined copper dropped this year and are estimated below 1968 receipts by 8% and a plummeting 69%, respectively.

Primary world copper prices have risen 200% in the past ten years, using the London Metal Exchange as a measure; domestic wholesale price indexes show a 60% rise. For the year 1969, the LME average price per pound for copper went from 56¢ to 72¢; U.S. prices mirrored this increase, going from 42¢ to 52¢ in three steps. However, a balance in the copper market is anticipated with the expected elimination of World-U.S. price differentials.

In the recovery field, Powdered Metals Corporation of Phoenix, Arizona, has announced construction plans for the first plant which will employ the new Harlan (George E. Harlan) Process to obtain copper powder from oxide ores (26). The ore is leached with a demineralized water-sulfuric acid solution and the leach liquor is then filtered and electrolyzed. The process is said to reduce the cost of present smelting and electrowinning techniques by 40%. Most of the reduction results from utilization of inexpensive equipment and avoiding costly milling, flotation, and furnacing units. In addition, the components are so simple and light that a portable plant can be trucked to operate on-site at ore deposits once considered too small or remote. Ore-to-powder requires only 4 hr compared to several days using conventional means.

Lithium.—The following companies are involved in processing lithium raw material to lithium primary products: Foote Mineral Company at Sunbright, Virginia, and Silver Peak, Nevada; American Potash and Chemical Corporation, Trona, California; and Lithium Corporation of America, Bessemer City, North Carolina (27). Production data are not available.

Use of lithium in 1969 was at an all-time high. Products employing lithium in their manufacture include: ceramics and glass, greases, welding and brazing fluxes, air conditioning equipment, rubber, and pharmaceuticals. Some newer uses include aluminum reduction cells, and bleaches and sanitizers.

Lithium metal was priced at $7.75/lb in 1000-lb lots; lithium carbonate at $0.46/lb in carload lots; and lithium chloride at $0.85/lb.

The reports on cesium and rubidium, normally included in this section, are omitted this year since the Mineral Industry Survey fails to make any mention of these metals.

Magnesium.—For the year 1969, production of primary magnesium is projected at 89,500 tons, up 2% over 1968; and shipments at 107,000 tons, up 16%. Secondary magnesium recovery is expected to be 15,000 tons. While there was only a minimal rise in exports (4500 tons), imports increased 43% netting about 24,000 tons. The U.S. accounts for over 60% of the world 162,000-ton annual production figure.

The consumption of primary magnesium in 1969 was 100,000 tons, which represents a 3% drop from the 103,000 tons in 1968, as reported by the U.S. Bureau of Mines (28). In contrast, *Business Week* reports 1969 as the sixth consecutive year that magnesium demand has risen, and the third year in a row that demand has exceeded capacity (29). However, all sources agree that magnesium is on the verge of a Cinderella boom; expansions of present capacity are predicted to double by 1971 and reach 300,000 tons/yr in 1972 (30).

The ultimate target of the expanding magnesium industry is an anticipated 400,000-ton potential automotive market within 10-15 years. In the near term, the largest single market for magnesium is in the aluminum-magnesium alloys used in commercial aircraft; machinery is next, and the chemical industry third. The lightweight metal is making a strong bid to replace aluminum; while it still costs more than aluminum, the price differential may shrink with the activity the magnesium producers are exhibiting. New products include rapid transit systems, motors, cameras, power tools for home use, photoengraving, corrosion-resistant paint, and battery casings.

One big name in the industry dropped out in the third quarter of 1969: Alamet Division of Calumet and Hecla Corporation shut down its dolomite (highest grade magnesium, but most expensive process) plant at Selma, Alabama. The major producers now in the field are: Dow Chemical Company, with a 48,000-ton/yr plant to go on stream the last half of 1971 and reach design capacity in 1976 at Dallesport, Washington (31, 32); National Lead Company with a 45,000-ton plant under construction at Salt Lake, due for completion in 1971 (33, 34); American Magnesium Company began operation of its scheduled 30,000-ton plant at Snyder, Texas; and Oregon Metallurgical Corporation at Albany, Oregon, plans to complete its 10,000-ton plant in early 1975 (35). In addition, two large aluminum producers, Alcoa and Kaiser, own property in the magnesium-rich Salt Lake area (36); and two steelmakers, USS and National are taking a close look at producing magnesium themselves (37).

Magnesium compound production increased over 1968 by 14% in volume and 16% in value. Imports of refractory magnesium declined about 20% for the year.

Manganese.—In 1969, approximately 1,800,000 tons of manganese ore containing 35% or more manganese were imported from Brazil, Gabon, Australia, and the Congo. Ferromanganese imports increased to 300,000 tons for the year, primarily from the Republic of South Africa, France, India, and West Germany. Manganese metal imports were down to 1428 tons for the first three quarters, with the majority from the Republic of South Africa.

Domestically, approximately 2,300,000 tons of ore were produced. Montana and New Mexico continued to mine ore containing 35% manganese, but at lower levels than in 1968. International Minerals and Chemical Corporation shut down their blast furnace in Sheridan, Pennsylvania, and stopped producing ferromanganese. High imports and large inventories were given as reasons for this change (38).

December quotations for ore with a content of 46-48% manganese were 49-53¢/long ton. Foote Mineral announced price increases effective January 1, 1970 on all grades of electrolytic manganese, with a typical increase being No. 1 chip to 31.25¢ from 30.25¢/lb (39).

Deepsea Ventures Inc., a subsidiary of Tenneco Inc., was active in carrying on the deep-sea mineral investigations formerly pursued by Newport News Shipbuilding and Dry Dock Company. This work, off the Georgia and Florida coasts, has yielded over 40 tons of manganese nodules that are to be treated in process pilot plants.

Nickel.—International Nickel Company of Canada, Ltd. (Inco) operations in Ontario were closed by a strike of the United Steelworkers of America from July 10 until November 17, 1969. While Inco's Manitoba facilities continued to produce nickel, these account for only 30% of the company's total capacity. In addition, Falconbridge Nickel Mines, Ltd., was out of operation from August 21 until November 22, 1969, because of a strike by the Mine, Mill, and Smelter Workers Union (40). These two stoppages reduced the free world's production of nickel approximately 50%. Upon resumption of work, the increased wage and fringe benefits (worth $1.35/hr) increased Inco's employment costs by approximately 35% (41).

A total of 29 million pounds of nickel has been released from Government stockpiles thus far, compared to the 150 million pounds International Nickel claims to have lost during the four month strike. The stocks must be replaced with the government by July 1972, so it seems certain the shortage will continue (42).

World production of nickel was estimated at 530,000 tons. Imports into the U.S. from all sources were expected to be 125,000 tons with exports at 30,000 tons.

The producer price for cathodes started the year at $1.03/lb F.O.B. shipping point. Following settlement of the 128-day strike, Inco raised the price to $1.28 which was followed by other major producers. Quotations for dealer cathodes according to *Metals Week* were $1.65-$1.75/lb early in the year, but reached $6.65-$7.15 in October. Prices in the $8-$10/lb range were said to have been obtained for small quantities of special forms.

A hydrometallurgical nickel refining process, developed by Sherritt Gordon Mines, Ltd. (Toronto, Canada), has come to the attention of others due to the nickel shortage. Sherritt Gordon has been using this process since 1954 and recently licensed the process to Western Mining Corporation of Australia. A 50-million lb/yr refinery was announced for completion in 1971 or 1972 by The Philippine's Marinduque Mining and Industrial Corporation, using a modified version of the process (43).

International Nickel announced construction of an $80-million refinery marking the first commercial use of the Inco Pressure Carbonyl (IPC) process. This highly automated plant at Copper Cliff, Ontario, is scheduled for completion in 1971. Capacity is stated to be 100 million lb/yr of pellets and 25 million lb/yr of powder (44).

Sodium.—The use of sodium metal was up slightly over 3% in 1969 compared to last year; the 3% figure confirms the growth estimated in this industry for the next 3 years (45). While the sodium business recovered from the 1967-1968 drop, projected quantities based on 8-month figures show the 1969 total at 162,000 tons, which is still under the 1966 165,000-ton high. Of the sodium metal produced, 83% was used to manufacture tetramethyl and tetraethyl lead, 6% was used as a reducing agent in the production of titanium sponge, and the remaining 11% found miscellaneous uses (peroxide production, sodium hydride descaling of metals, chemical and drug intermediaries, and coolant in nuclear power stations) (46).

All major producers increased metallic sodium prices effective on spot in mid-November and on January 1, 1970 for contract business. Brick price (drummed, in 18,000-lb lots) rose 2¢/lb to 24½¢; reactor grades increased to 29¢; and carload lots increased to 18¾¢/lb.

Titanium.—Titanium sponge metal (refined ore) production rose 12% in 1969; sponge consumption leaped 35% over 1968, to about 19,500 tons (47). Foreign sponge imports for the first 9 months indicated a total receipt of 6230 tons. At year's-end, domestic sponge of 99.3% purity held at $1.32/lb, while import (from Japan and the United Kingdom, principally) dropped 0.05 to $1.20/lb (48). Only a small amount of titanium sponge was sold by the General Services Administration in 1969.

Through October, titanium metal (unwrought, waste, and scrap) was imported for consumption in an amount projected to equal 6500 short tons at a value expected to exceed $10,500,000. The bulk of the imports came from Japan (70%), with Russia (15%) and the United Kingdom (10%) making up most of the remainder. Exports, mostly scrap, were up 20%, totaling 3400 tons for 1969.

The price reduction reported last year (49) seems to have produced the desired result as the burgeoning consumption in 1969 indicated. Gains in chemical and construction uses are difficult to measure accurately, but aerospace and the aircraft industry are still prime markets.

No rutile was produced domestically in 1969, and imports increased 15%. To expand domestic rutile production, in June of 1967 the Office of Emergency Preparedness (OEP) reduced the war stockpile of rutile from 200,000 to 100,000 short dry tons. In 1969, import price for 96% TiO_2 rose to a high of $160 per short ton over last year's close at $125.

Ilmenite imports of the mineral concentrate rose 50% over 1968 in the face of a 3% drop in domestic production. Ilmenite is used mostly in making titanium oxide pigment. Quoted prices for 1969 held firm at $30-$35 per short ton for domestic 60% TiO_2-content stocks; and at $20-$21 per long ton for imported 54% TiO_2 material.

Zinc.—Reversing a three-year trend, U.S. mine production of zinc for 1969 rose 4%, to 546,000 tons (50). In conjunction with the expanding lead industry, 33,000 tons of zinc supplied from new mines alone placed Missouri as one of the country's leading zinc producers. While the historically higher zinc producing states increased their output, zinc production in others dropped, which offset the potential gain.

Smelter production of slab zinc zoomed the first half of 1969, but fell off the last half; still, projected output was up from the previous record year of 1966 by 5% and exceeded 1968 by 8%, totaling 1,160,000 tons. To add to this bright picture, shipments led production by a net 9000 tons for the year, considering customer's stores accumulation. Zinc imports of ore and metal approximated those of 1968. The principal suppliers were Canada, Mexico, Australia, and Peru.

Total consumption of zinc for 1969 was 1,800,000 tons with slab accounting for 1,400,000 and the other 400,-

000 tons made up of direct ore use (135,000) and scrap (265,000). In line with the increases noted in production, consumption also equalled the record year 1966. The largest advances in the industry were posted by zinc-base alloys (585,000 tons), zinc oxide (44,000), and in copper-base alloys as a result of full-year operation of brass mills (184,000 tons).

The General Services Administration sales amounted to 25,440 tons from the existing zinc disposal authorization; 22,610 tons remain in inventory.

Prime Western Grade zinc price rose 2¢ during the year, in three steps, to finish 15½¢/lb. The London Metal Exchange price, after fluctuating throughout the year, ended at 14¢/lb.

Electrical Energy

U.S. Generation.—The utility companies and industrial plants in the U.S. combined to produce 1.43 trillion kilowatt hours (kWhr) of electricity this year (51). Reflecting ever-increasing power consumption, this represents an 8.8% gain over 1968, substantially greater than the 5.2% growth in 1968, and the 7.4% average for the 5-year period ending 1967.

Utility production (representing 93% of the nation's total electrical energy capacity) held at the same 9.3% increase over the previous year, to a new record total of 1.33 trillion kWhr. The breakdown by production means shows: 16.7% hydroelectric, 82.7% by steam electric plants, and the balance (0.6%) by internal combustion engines and gas turbines. Each category reached a new high, exceeding 1968 levels by 0.3, 11.2, and 16.9%, respectively.

Steam electric generation using nuclear fuel showed a gain compared to 1968, of from 7.7 to a total of 12.3 billion kWhr; this increase (60%) is still only 0.86% of the country's total energy need. However, it is predicted that, by the year 2000, 50% of the nation's electrical energy requirements will be met by nuclear facilities (52). In 1969, consumption of coal reached 297 million tons, gas nearly 3.15 trillion cubic feet, and oil 188 million barrels. In keeping with the production increases, use of each fuel also rose. Hydroelectric generation also set a record high of 52.8 million kW, topping 1968 by 3.3%. It is estimated that, of the country's total hydroelectric potential (178.5 million kW), only 48.8 million kW, or 27%, has been developed.

There has been some concern regarding the rate at which present resources are being dissipated. Coal, gas, and oil have been carefully studied, and it is estimated that existing supplies will suffice for from 200 to 1000 years (53).

Utility generating capacity posted a record 8.1% increase this year, adding 21,806,000 kW, to a new high of installed capacity totaling 291,058,000 kW. This total capability is ample to supply current U.S. needs. Looking to the future, however, demand for electricity in the U.S. is expected to match the growth rate of the past three decades, which means doubling the generating capacity each ten years (54).

Coupled with the capacity and consumption increases seen in 1968, the industry also experienced delays. Some generating plants and transmission lines were not put into service on schedule, primarily as a result of shortages of skilled labor.

Nuclear Power.—In the U.S. Generation section of this report, it was reported that the total percentage of electrical energy derived from nuclear sources was very small (less than 1%). The past year still succeeded in chalking up a 60% production increase over 1968, even though it was a declining year for orders in the nuclear business. Furthermore, though recent rising construction costs (now about $1.45/kW for conventional *vs.* $2.00/kW for nuclear) have made utility companies hesitate to go the nuclear route, 1972 is predicted as the turning point for the swing to nuclear power (55, 56).

Historically, fossil-fueled steam generating plants have been the major source of electrical energy (57). In 1957, a government-sponsored program to develop and demonstrate the feasibility of nuclear reactors for civilian application was introduced to the electric utility industry. By 1964, $3 billion in study had indicated the cost advantage of a nuclear installation as typically slightly over 5 mills/kWhr, compared to 5-6 mills/kWhr for a fossil-fired plant. In addition, nuclear plants will require considerably less expense for pollution control. Following these findings, a rash of orders were placed for nuclear plants in 1966 and 1967. The explanation for the difference between the fast start and the current restrained status of the nuclear power industry is simply growing pains.

The power plant supply industry was pushed beyond its capacity, as neither facilities nor trained workmen were available to begin; construction costs and inflation have been steadily rising; and delays were experienced in educating a public concerned with thermal and radiation effects. On-stream service has been postponed as much as two years, and the original five years have been stretched to the present 6½-7 years for expansion planning.

The U.S. is well established as the world leader in enriched-uranium light water type nuclear power reactors, but the present generation of nuclear reactors employ less than 2% of uranium's potential energy. For this reason, the government and private industry are actively investigating fast (breeder) reactors for electrical power generation. Breeder reactors will utilize 50% of the latent energy in uranium and will, in fact, produce or "breed" more fissionable material than they consume. The major effect of the fast reactors will be to stabilize the supply and price of uranium; however, commercial exploitation of fast reactors is not expected to begin before the 1980's. Accordingly, power rates will probably fluctuate little in the next ten years, and only begin to drop as a result of breeders in the succeeding ten years.

D-C power.—In evaluating the power transmission figures of the last few years, the recent use of extra-high-voltage (EHV) lines must be taken into account. Power transfer capability increases as the square of the voltage, so comparing only miles of transmission line installed is not comprehensive. The decrease in actual miles from 18,452 in 1968 to 14,555 in 1969 illustrates the point well; in terms of voltage-miles, power transmission installation increased 32% in 1969 (58).

Currently, utility transmission installations are limited to 500-kilovolt (kV) lines, but this year saw the first 765-kV line become operable. Tests are in progress to utilize 1100- and even 1500-kV lines. Also, additional exploration is under way to examine the benefits directly related to direct current EHV transmission systems working in conjunction with alternating current systems.

There was a delay in completing the 853-mile, 750-kV[2] d-c transmission line between the Dalles Substation (on the Columbia River in Oregon) of the Bonneville Power Administration and the Slymar Substation of the Los Angeles Department of Water and Power. Start-up service was rescheduled for Spring of 1970.

Developments of Interest

Petrochemicals by electrolysis.—Electrolysis in organic syntheses has been studied for many years; however, very few processes have reached a commercialized scale. Electrolytic routes to organics may be applicable where product selectivity may be superior to known chemical methods (59).

A good example is the Monsanto process for electrohydrodimerization of acrylonitrile producing adiponitrile in a single, high-selectivity step; it is recognized that existing thermal and catalytic dimerization methods give inferior yields and/or lower conversions. Asahi Chemical of Japan is reported to be planning a 20-million-lb/yr adiponitrile facility. BASF is also said to be working on a similar process.

[2] Erroneously reported as an 825-mile, 800-kV line in the Report for 1968.

When objectional co-products may be avoided, the electrolysis method may have merit. An example would be the electrolytic chlorohydrin process for propylene oxide, eliminating the unwanted production of calcium chloride.

Conversion by chemical means may require reaction conditions so severe in terms of pressure, temperature, residence time, catalyst life, or corrosivity that the cost of the electrolysis system is justified. Direct handling of troublesome reagents may be eliminated, as in 3M's electrolytic fluorination process, and the bromination process developed by Sohio. The use of lower cost raw materials and useful products from both anode and cathode reactions may provide economic advantages.

Continued research in this area is indicated and, when any of the above advantages or a combination of them offset the high power and cell cost, an attractive process will result.

The Kel-Chlor process.—At the April 1969 American Chemical Society meeting in Minneapolis, Dr. Alex G. Oblad, Vice-President of Research and Development for the M. W. Kellogg Company (New York), presented the chemistry involved and the potential market impact of a breakthrough nonelectrolytic process for the manufacture of chlorine (60-62). Essentially, the Kellogg development provides a successful way to oxidize hydrogen chloride to chlorine.

The basic idea is not new. In the same manner, chlorine was first produced in the laboratory by the Swedish chemist Karl Wilhelm Scheele (63), and the concept was refined to commercial use about a century ago by Deacon and Hurter. They employed solid copper chloride as a catalyst; but, by using air as the oxidizing medium, the resultant chlorine was highly diluted with nitrogen, though acceptable for those times. More recent attempts to upgrade the process include increased catalytic activity, which has not proved attractive, or introduction of an organic molecule to react with chlorine and thus drive the reaction equilibrium toward more complete oxidation. The latter are generally termed oxychlorinations, and are useful but limited in application.

With the present-day availability of cheap oxygen, the Kellogg process employs two novel keys to push its descendant of the Deacon reaction to completion: nitrogen oxides as homogeneous (gas phase) catalysts, and sulfuric acid to absorb oxides and steam (64). Briefly, gaseous hydrogen chloride is reacted with hot recycled nitrosyl sulfuric acid to form nitrosyl chloride; in the first oxidation chamber, nitrosyl chloride with oxygen breaks down to chlorine and nitric oxide; conversion is completed in a second oxidizing step, where sulfuric acid absorbs water (steam) and reacts with the nitrogen oxides to yield nitrosyl sulfuric acid, which is recycled. The product chlorine is quite pure and relatively dry and meets the specifications of some applications as is; for more stringent uses, it can be easily upgraded.

In the past, attempts to commercialize hydrogen chloride oxidation processes have stumbled on economically insurmountable corrosion problems. Kellogg reports, however, that in its new process corrosion is not a difficulty and that "available" materials are utilized. Continuous operation of a one-ton/day unit is said to have proven the Kel-Chlor process, and Kellogg is prepared to offer it for license. Operating costs will vary, depending on plant size, from $17 to $10/ton of chlorine produced.

Dr. Oblad points out that, for the first time, the production of chlorine is exceeding that of caustic, dumping more caustic in an already saturated market. In addition, by-product hydrogen chloride from organic chlorinations is also creating an increasing disposal problem. Its developer offers the Kel-Chlor process as the solution to this situation. Neither the electrolysis of aqueous hydrogen chloride nor the electrolysis of magnesium chloride is geared to American market requirements, according to Dr. Oblad.

Two major areas are suitable targets: the production of elemental chlorine itself, and the use of chlorine in chlorination reactions (the largest of which is manufacture of vinyl chloride). As to the hydrogen chloride charge, four processes are listed as adequate sources: 1—steam hydrolyzed magnesium chloride, 2—the by-product from Solvay Process ammonium chloride, 3—the reaction of sulfuric acid with sodium chloride, and 4—the fertilizer industry's conversion of potassium chloride to the more potent potassium phosphate or nitrate.

Manuscript received June 11, 1970. This report was presented at the Industrial Electrolytic Division Luncheon at the Los Angeles Meeting of the Society, May 10-15, 1970.

Any discussion of this report will appear in a Discussion Section to be published in the June 1971 JOURNAL.

REFERENCES

1. Robert F. Schultz, President, Chlorine Institute (Feb. 4, 1970).
2. *Chemical Week*, p. 55, April 19, 1969.
3. *Wall Street Journal*, June 12, 1969.
4. The Chlorine Institute, Inc.
5. *Chem. Eng.*, p. 120, Oct. 20, 1969.
6. *Oil, Paint & Drug Reporter*, Sept. 15, 1969.
7. *Chemical Week*, p. 53, Sept. 13, 1969.
8. Mineral Industry Surveys, U.S. Dept. of the Interior, Annual Preliminary, "Mercury in 1969."
9. *Business Week*, p. 32, Feb. 14, 1970.
10. *Oil, Paint & Drug Reporter*, Nov. 10, 1969.
11. *Ibid.*, Oct. 13, 1969.
12. PPG Industries, Verbal communication.
13. Mineral Industry Surveys, U.S. Dept. of the Interior, Annual Preliminary, "Sodium Compounds in 1969."
14. *Chemical Week*, p. 25, Dec. 24, 1969.
15. Current Industrial Reports, Inorganic Chemicals, U.S. Dept. of Commerce, Oct. 1969.
16. *Oil, Paint & Drug Reporter*, Dec. 29, 1969.
17. Mineral Industry Surveys, U.S. Dept. of the Interior, Annual Preliminary, "Aluminum in 1969."
18. Yearbook of the American Bureau of Metal Statistics, 48th Annual Issue, June 1969.
19. U.S. Industrial Outlook 1970, U.S. Dept. of Commerce (BDSA).
20. Henry C. Meeves, U.S. Dept. of the Interior, Verbal communication.
21. Mineral Industry Surveys, U.S. Dept. of the Interior, Annual Preliminary, "Beryllium in 1969."
22. "Chemical Engineer's Handbook," 2nd Ed., John H. Perry.
23. Mineral Industry Surveys, U.S. Dept. of the Interior, Annual Preliminary, "Chromium in 1969."
24. Mineral Industry Surveys, U.S. Dept. of the Interior, Annual Preliminary, "Copper in 1969."
25. U. S. Industrial Outlook 1970, U.S. Dept. of Commerce (BDSA).
26. *Chem. Eng.*, p. 96, Sept. 8, 1969.
27. Mineral Industry Surveys, U.S. Dept. of the Interior, Annual Preliminary, "Lithium in 1969."
28. Mineral Industry Surveys, U.S. Dept. of the Interior, Annual Preliminary, "Magnesium and Magnesium Compounds for 1969."
29. *Business Week*, p. 52, May 31, 1969.
30. *Chem. Eng.*, p. 60, Aug. 25, 1969.
31. *Oil Paint & Drug Reporter*, June 16, 1969.
32. *Chem. Eng. News*, p. 15, June 9, 1969.
33. *Ibid.*, p. 21, April 21, 1969.
34. *Chem. Eng.*, p. 43, May 5, 1969.
35. *Ibid.*, p. 123, Oct. 20, 1969.
36. *Chemical Week*, p 15, Sept 6, 1969.
37. *Ibid.*, p. 36, May 17, 1969.
38. Mineral Industry Surveys, U.S. Dept. of the Interior, Annual Preliminary, "Manganese in 1969."
39. *Chemical Week*, p. 56, Dec. 17, 1969.
40. Mineral Industry Surveys, U.S. Dept. of the Interior, Annual Preliminary, "Nickel in 1969."
41. *Chem. Eng. News*, p. 16, Nov. 24, 1969.
42. *Ibid.*, p. 15, Dec. 22, 1969.
43. *Chem. Eng.*, p. 108, April 7, 1969.
44. *Ibid.*, p. 106, May 19, 1969.
45. *Oil, Paint & Drug Reporter*, May 19, 1969.
46. *Ibid.*, Nov. 17, 1969.
47. Mineral Industry Surveys, U.S. Dept. of the Interior, Annual Preliminary, "Titanium in 1969."
48. *American Metal Market*. p. 24, Dec. 26, 1969.

49. "Report of the Electrolytic Industries for the Year 1968," *This Journal*, **117**, 9C (1970).
50. Mineral Industry Surveys, U.S. Dept. of the Interior, Annual Preliminary, "Zinc in 1969."
51. Federal Power Commission, Annual Report, 1969.
52. *Chem. Eng. News*, p. 34, Oct. 27, 1969.
53. J. E. Curry, "The Effect of Energy Sources on Electrochemistry," Paper given at Niagara Section Meeting of Electrochem. Soc. Nov. 17, 1969.
54. U.S. Industrial Outlook 1970, U.S. Dept. of Commerce (BDSA).
55. *Chem. Eng. News*, p. 36, Oct. 27, 1969.
56. Federal Power Commission, Annual Report, 1969.
57. U.S. Industrial Outlook 1970, U.S. Dept. of Commerce (BDSA).
58. Federal Power Commission, Annual Report, 1969.
59. *Hydrocarbon Processing*, p. 159, June 1969.
60. *Chem. Eng. News*, p. 14, April 21, 1969.
61. *Chemical Week*, p. 83, April 26, 1969.
62. *Chem. Eng.*, p. 39, May 5, 1969.
63. *Ind. Eng. Chem.*, p. 23, July 1969.
64. *Chem. Eng. News*, p. 14, May 5, 1969.

F. M. Becket Memorial Award

The Electrochemical Society will offer the F. M. Becket Memorial Award to a qualified graduate student for the summer of 1971. This Award commemorates F. M. Becket, a man of great research and administrative ability and a former President of the Society, whose accomplishments in science and industry were outstanding. The stipend valued at $1500 provides a grant-in-aid toward a summer's (at least two months) research and study overseas in the laboratory of a recognized research institute or institution of higher learning, selected from the approved list maintained by the F. M. Becket Memorial Award Committee.

The objectives of this Award are to stimulate and encourage education and participation in the fields of electrochemical science and industry concerned with specialty materials and processes as follows:

a) **Materials** such as refractory metals and compounds, intermetallics, graphite, fused salts, and rare earth metals;

b) **Equipment** for the utilization of electrical energy in materials synthesis;

c) **Processes** using arcs, vacua, plasmas, and electron and ion beams; and

d) **High temperature kinetics and thermodynamics phenomena** such as melting, vaporization, reactions, sintering, diffusion or oxidation occurring at high temperatures, high pressures, or vacua involving high temperature materials.

To be eligible for the Award, the entrant must qualify in one of the two following categories. He must be either (1) a graduating senior of demonstrated ability, regularly enrolled in any recognized college, university, or institute of technology in continental United States or Canada, who intends to seek an advanced degree, or (2) a graduate student, similarly enrolled, who is seeking an advanced degree. No limitations of sex, race, nationality, or religion are to be imposed by the Award Committee in determining the recipient of the Award.

The Award shall be presented on the basis of the following material:

1. A complete transcript of the student's academic record.

2. Two copies of a letter, over the signature of the head of the College or Department in which the student is enrolled, describing briefly his academic work, his campus activities, and presenting an estimate of his abilities.

3. Two copies of a letter, over the student's signature, containing a brief biographical sketch, a detailed description of the nature and extent of his academic work, particularly as it may relate to the field of the Award, and an outline of his plans for the future. The student shall indicate, from the list provided by the Award Committee, his choice of a place of residence under the Award.

Application forms are available from the Executive Secretary, Mr. Ernest G. Enck, The Electrochemical Society, Inc., 30 East 42nd Street, New York, N. Y. 10017. Deadline for receipt of completed applications will be February 1, 1971; and the Award winner will be announced on April 1, 1971.

JOURNAL OF THE ELECTROCHEMICAL SOCIETY

REVIEWS AND NEWS — NOVEMBER 1970

Physical and Mechanical Properties of Electrodeposited Copper

III. Deposits from Sulfate, Fluoborate, Pyrophosphate, Cyanide, and Amine Baths*

Vernon A. Lamb, Christian E. Johnson, and Donald R. Valentine

National Bureau of Standards, Washington, D. C. 20234

VIII. Comparisons of Deposits from All Types of Baths: Fatigue Strength, Thermal Properties, Cold Working, Structure, Composition, and General Correlations

A. Fatigue Strength

1. Introduction, method, and apparatus.—Fatigue strength is of interest primarily in applications in which vibration or other cyclic stressing of plated or electroformed parts may cause fracture. Several studies of the effect of plating on the fatigue strength of a basis metal have been reported, but very little information on fatigue properties of separated deposits has come to our attention [Ref. (2) for nickel, Ref. (21), p. 55, for copper].

The method that we used for measuring fatigue strength was designed by J. A. Bennett of the NBS Metallurgy Division. It is an adaptation of the Amsler "Vibrophore" test method[15] to thin sheet stock (34). Specimens were milled from panel stock to the form shown in Fig. 37. They were then bent into a "U" as shown at "1" in Fig. 38. The bending procedure was as follows. A ¼ in. diameter rod was placed transversely across the center of the flat specimen, which was supported on a deep (2-3 in.) sponge-rubber pile which acted as a female mandrel. With a small press, the rod and sheet were forced into the sponge-rubber pile. The action of the test machine is illustrated in Fig. 38. The formed specimen was attached to blocks 2 and 3 with screws through clamping plates (not shown). Block 2 was rigidly attached to the frame of the machine. Block 3 oscillated vertically, driven by the force, *P*. This produced lateral oscillation of the top of the specimen, as indicated by the arrows above "1." Thus, each of the four faces of the specimen was alternately stressed in tension and compression, with maximum stress at the position of minimum width. The mean load was zero; *i.e.*, the maximum deflections of the specimen to either side of the zero-load position were equal. Oscillation rate was 1800 cycles/min. The maximum load, *P*, was determined from machine adjustments; lateral displacement of the top of the specimen, illuminated with a stroboscope, was measured with a micrometer microscope. The relationships by means of which stress and strain in the specimen are determined from *P* and the lateral displacement of the specimen are developed in the Appendix, paragraphs X-B-1 and X-B-2.

2. Results.—The fatigue characteristics of several typical kinds of copper deposits are shown in Fig. 39, in which stress amplitude is plotted as a function of the number of cycles required to produce failure by cracking. The character of the curves is typical, similar to those obtained for wrought metals. The pertinent data from these curves are summarized in Table XXVI. Stress-strain parameters for three types of copper representing high and low extremes and a mid-value of

* AES Project 21 Report. Sections VIII-X published here are the third and last installment of this paper. Part 1 (Sections I-III) appears on pages 291C-318C of the September issue, and part 2 (Sections IV-VII) on pages 341C-352C of the October issue.

[15] Alfred J. Amsler & Co., Schaffhouse, Switzerland; Hirschmann Corporation, Roslyn Heights, New York.

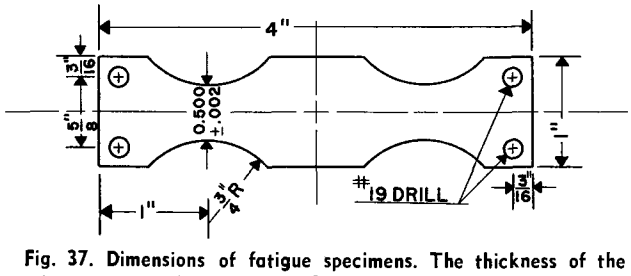

Fig. 37. Dimensions of fatigue specimens. The thickness of the specimens ranged from 0.015 to 0.02 in. (375-500 μm).

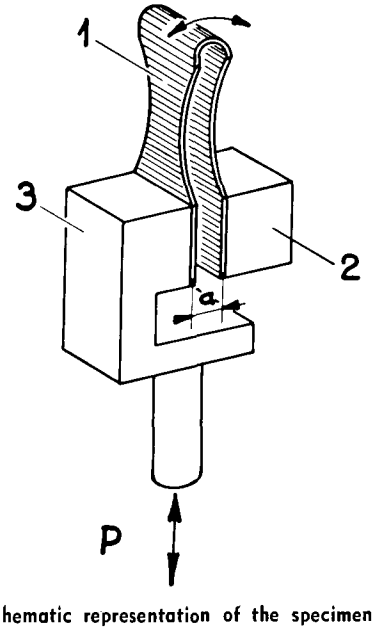

Fig. 38. Schematic representation of the specimen mounting for fatigue testing of electroformed copper. The specimen, 1, is attached to holders, 2 and 3, with screws and clamping plates (not shown). Holder, 2, is rigidly attached to the frame of the machine. Application of the pulsating force, *P*, causes holder, 3, to oscillate vertically, resulting in lateral oscillation of the specimen as indicated by the curved arrows. The distance "*a*" is 0.300 in. (7.5 mm).

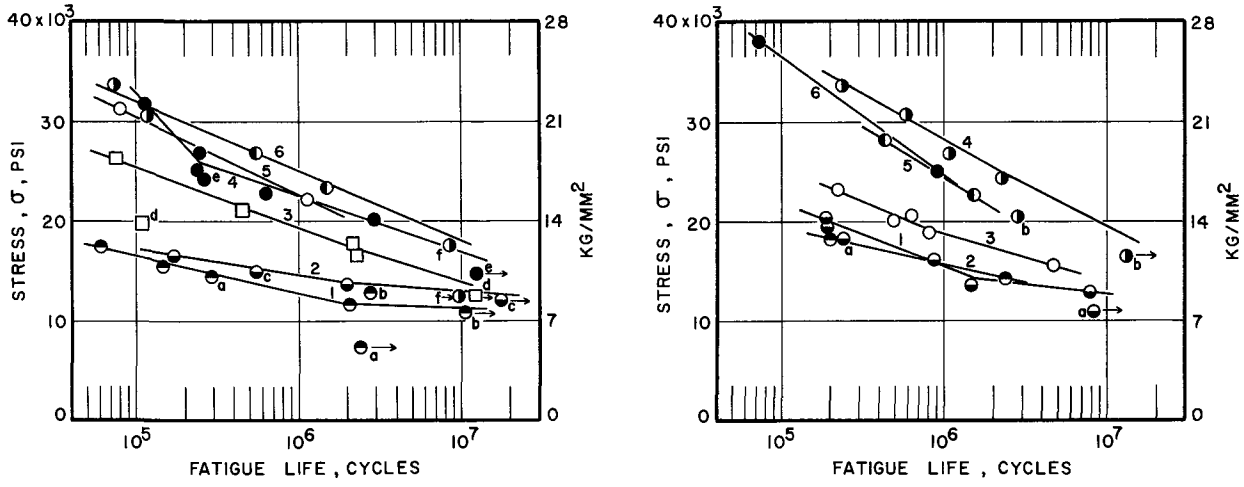

Fig. 39. Relationship between fatigue life (cycles) and stress for electroformed copper. *Part A (left):* (1) Cu2-H2, mild cellulosic exposure, 30°C, 2 A/dm^2; (2) Cu2-H2, severe cellulosic exposure, 30°C, 2 A/dm^2; (3) Cu2-H3 containing 1 mg/liter selenium, 30°C, 2 A/dm^2; (4) pyrophosphate, 50°C, 2 A/dm^2; (5) pyrophosphate, 50°C, 4 A/dm^2; (6) Cu2-H3 containing 3.5 g/l triisopropanolamine, 50°C, 5 A/dm^2. *Part B (right):* (1) F-1, 30°C, 8 A/dm^2; (2) F-2, 50°C, 20 A/dm^2; (3) Cu3-H3 containing 1 g/l phenolsulfonic acid, 30°C, 2 A/dm^2; (4) CN-8 containing 2 g/l KCNS, 80°C, 6 A/dm^2, PR, cycle 15 sec cathodic, 5 sec anodic; (5) CN-8 containing 2 g/l KCNS, 80°C, 6 A/dm^2, PR, cycle 30 sec cathodic, 10 sec anodic; (6) CN-8, 80°C, 6 A/dm^2, no addition agent, PR, cycle 15 sec cathodic, 5 sec anodic. Specimens that did not fail are indicated by a letter and an arrow. These specimens were tested further with larger loads. The point representing the retest conditions is designated by the corresponding letter.

fatigue strength are plotted in Fig. 40.[16] The curves for the non-addition agent sulfate deposits and for the pyrophosphate deposits are linear, indicating that in testing these deposits the elastic limit was not exceeded. The small deviation from linearity at the top of the stress range for the deposit from a sulfate bath containing triisopropanolamine has questionable significance.

In Table XXVI, the stress level at failure is shown for two life periods, 10^6 and 10^7 cycles. For 10^6 cycles, two values of stress are shown for lines 76 and 147, designated as σ_c and σ_m. σ_c represents a "calculated" value, obtained from the basic mechanical relationships developed in Appendix B-1. σ_m represents a "measured" value, determined from direct microscope measurements of strain on statically displaced specimens. The procedure is described in Appendix B-2. The magnitudes of the fatigue strength obtained by the two methods are in reasonable agreement.

The value of σ_c will first be considered in relation to the yield strength (Table XXVI). Fatigue failure would be expected to occur rapidly if the yield strength were exceeded. It is seen that several of the deposits were stressed beyond our values for yield strength, but nevertheless had fatigue lives of 10^6 or 10^7 cycles. This indicates that the tabulated values of yield strength, which are based on the arbitrarily selected offset of 0.05%, may be too low, or that dynamic yield strengths are higher than static yield strengths. Whatever the explanation, the results show that at the stress levels applied for lives of 10^6 to 10^7 cycles, plastic deformation must not have occurred.

It is of interest to intercompare the endurance ratio, *i.e.*, the ratio of the fatigue strength to the tensile strength, for the various plated coppers and for wrought copper. The ratio varies from a low of 0.32 for a PR deposit from bath CN-8 to a high of 0.61 for a deposit from the pyrophosphate bath. Ratios for deposits from the sulfate and fluoborate baths are close

[16] Explanation of stress-strain parameters in Fig. 40: From Eq. [12] of Appendix B-1, it is seen that stress is proportional to P/t^2 since a and b are constants. From Fig. 72 it can be readily shown that $\delta = t/2R$, where δ is the strain in the surface fibers of the specimen. Since R is approximately inversely proportional to the horizontal deflection of the top of the specimen, we have $R = K/D$, where K is the proportionality constant and D the deflection. Substituting this value of R in the preceding equation gives $\delta = tD/2K$. Thus, surface strain is approximately proportional to tD. See Appendix B-1 for definitions of symbols.

Table XXVI. Fatigue characteristics of electrodeposited copper

Line No., Table I	Panel No.	Bath symbol	Addition agent	Bath temp, °C	Current density, A/dm^2	Fatigue strength[a] σ_c 10^6	σ_m No. of cycles 10^6 psi	σ_c 10^7	Yield[a,b] strength, psi	Tensile[a] strength, psi	Endurance ratio σ_c, 10^6 / T.S.	Internal[a,c] stress, psi
24	13	Cu2-H2	None	30	2	13 × 10³		11 × 10³	8 × 10³	25 × 10³	0.54	550
26	323	Cu2-H2	None	30	2	14		12	11	32	0.47	
88	77	Cu3-H3	PSA[d]	30	2	19			13	34	0.58	−420
66	172	Cu2-H3	SeO_2	30	2	19		14	16	44	0.44	2800
76	337, 341	Cu2-H3	TIPA[d]	30	5	25	31 × 10³	18	43	71	0.36	7100
91	345	F-1	None	30	8	16		13	16	37	0.44	700
94	348	F-2	None	50	20	16			12	33	0.49	1600
139	281	CN-8	None, PR[e]	80	6	25			38	64	0.39	
147	294	CN-8	KCNS, PR[e]	80	6	28	33	20	57	86	0.34	5100
148	295	CN-8	KCNS, PR[f]	80	6	25			46	79	0.32	
95	318	Pyrophos-	None	50	2	22		17	20	38	0.61	−1600
98	314	phate	None	50	4	22			22	40	0.59	1700
	Commercial copper[g]		Annealed			15		12	10	31	0.48	
			Half hard			23		18	38	45	0.51	
			Hard			24		18	48	54	0.44	

[a] One pound per square inch (psi) = 0.000704 kilogram per square millimeter (kg/mm^2).
[b] 0.05% offset.
[c] Negative values represent compressive stress.
[d] PSA = phenolsulfonic acid; TIPA = triisopropanolamine.
[e] PR cycle 15 sec cathodic, 5 sec anodic.
[f] PR cycle 30 sec cathodic, 10 sec anodic.
[g] Data from Ref. (35).

to 0.5, about the same as the ratios for wrought copper.

With respect to quality of deposits as measured by fatigue strength, deposits from non-addition agent sulfate and fluoborate baths are about the equal of annealed wrought copper, but poorer than cold-worked wrought copper. On the other hand, deposits from the sulfate baths containing addition agents and from the cyanide and pyrophosphate baths are equal or superior in fatigue strength to cold-worked wrought copper.

For a given type of bath, variation of operating conditions did not affect the fatigue strength significantly (Table XXVI). For example, changes in the following variables produced either no change or negligible change: degree of exposure of the sulfate bath to cellulose (lines 24, 26); bath temperature and current density (fluoborate bath, lines 91, 94 and pyrophosphate bath, lines 95, 98); and PR cycle (lines 147, 148).

Residual tensile stress adds to deformation stress to produce a higher total stress, which may be expected to hasten fatigue failure. One might, therefore, expect a relationship between fatigue strength and internal stress (Table XXVI). There are some positive correlations. For example, compare lines 26 and 88. The tensile strength is nearly the same, but the fatigue strength of the latter, with a compressive stress, is significantly higher. On the other hand, two of the highest values of fatigue strength appear in lines 76 and 147, both associated with high internal stress. At first sight this appears to be a reversal of the expected effect. However, we note that these high stress values corrrelate with the lowest endurance ratios. It is thus probable that, if these deposits were to retain their high strength and also had a low internal stress, the endurance ratio would be in the "normal" range of 0.5 and the fatigue strength would then be about 40,000 instead of 25,000-28,000 psi. The difference is a measure of the reduction due to the high internal stress. The correlation with internal stress fails in the case of the pyrophosphate deposits, where an apparently significant variation in internal stress does not affect the fatigue strength.

Several failed specimens were examined by J. A. Bennett to determine the character of the failure cracks, with the following results:

Panel No.	Structure type	Character of cracks
13	Large columnar, fairly fine starting grain	Cracks started on final (coarse) surface, propagated between dendrites
295	Fine uniform grain	Cracks started on both sides. Grain too fine to evaluate position of cracks with respect to grains at magnification used.
345	Like No. 13, U-bend with final surface outside	Like No. 13, cracks started on outside surface.
345	Same as above, but U-bend with final surface inside	Like No. 13, but cracks started on inside surface, in this case also the coarse surface.

The above results are what one would expect. The comparison between the two specimens from Panel No. 345 shows that the characteristics of the machine and the test procedure were such that inside and outside surfaces of the "U" were equally stressed.

B. Properties of Annealed Deposits

1. *Annealing procedures.*—Specimens were made from panel stock before annealing, *i.e.*, operations such as machining and stripping of nickel were carried out on the as-plated stock. Annealing[17] was done either in vacuum or in an argon atmosphere. Specimens were held at temperature for the times indicated in Table XXVII. They were put into and removed from a cold furnace, so the actual total annealing period was longer than the nominal period. The heat-up and cool-down periods ranged from about 15 min for 150°C to 45 min for 500°C.

Since it was not feasible to procure the extended data shown in Table XXVII for a large number of copper deposits, a representative sampling was chosen, including typical soft deposits from sulfate and fluoborate baths, deposits of a hard strong type from a sulfate bath containing an addition agent, typical pyrophosphate deposits, and PR deposits from bath CN-8 containing KCNS as an addition agent. The latter was chosen because it has good properties as plated and can be produced as thick electroforms. Limited measurements were also made with thin deposits from other cyanide baths, namely CN-2, a typical low-concentration bath, CN-8 without an addition agent or PR, and CN-9, the proprietary high-efficiency bright-plating bath.

[17] Annealing was done in part by G. E. Hicho of the Metallurgy Division, NBS, and in part by the authors.

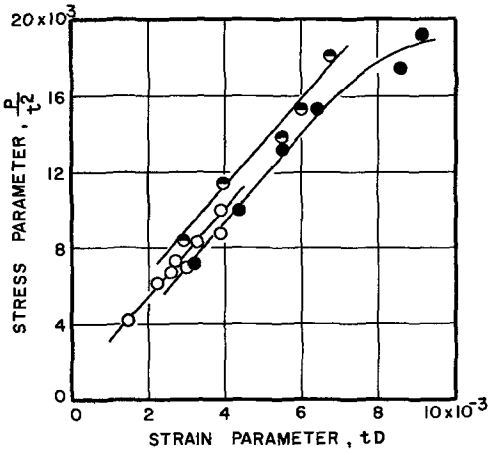

Fig. 40. Relationship between stress and strain at the surface of copper fatigue specimens from three types of baths at the point of minimum width: ○—Cu2-H2, 30°C, 2 A/dm²; ●—Cu2-H3 containing 3.5 g/l triisopropanolamine, 30°, 5 A/dm²; ◓—pyrophosphate, 50°, 2 A/dm². The specimen thickness is represented by "*t*", the magnitude of the horizontal deflection of the top of the specimen by "*D*," and the applied load by "*P*."

2. *Effects of annealing on mechanical properties.*—Data are summarized in Table XXVII and in Fig. 41, 42, and 43. In Fig. 41, it is seen that in general annealing caused decrease of tensile strength and increase of ductility. However, the changes are small for deposits that are initially soft and ductile, namely those from the non-addition agent sulfate bath, the fluoborate bath, and the pyrophosphate bath. The deposit from the sulfate bath containing triisopropanolamine resists change to a fairly high annealing temperature (325°-400°C), then abruptly loses strength and gains ductility. The PR cyanide deposit, on the other hand, undergoes significant changes in the same directions at the lowest annealing temperature of 150°C. The tensile strength and elongation of all of the deposits tend to the same values after annealing at 500°-550°C.

Effects of both annealing and cold rolling on modulus and hardness are illustrated in Fig. 42 and 43. In general, cold rolling has less effect on modulus than does annealing. The magnitude of the shifts due to cold rolling is within our estimated accuracy of $\pm 1 \times 10^6$ psi and the direction is random. On the other hand, annealing at 500°C causes a significant decrease of modulus in all but one case (PR deposit from bath CN-8).

The effect of annealing on hardness (Fig. 43) is similar to its effect on tensile strength. The deposits that are initially soft or fairly soft (non-addition agent sulfate, fluoborate, and pyrophosphate) undergo minor additional softening. The deposits from the triisopropanolamine sulfate bath (TIPA) and the PR CN-8 bath undergo marked reduction of hardness. The abnormally low hardness, 32 KHN, of the TIPA deposit is an "apparent" value due to an "exploded structure" of the deposit resulting from heating to 500°C. This has other related effects that are referred to subsequently.

Cold rolling in all cases causes a significant increase of hardness.

Table XXVII. Effects of annealing[p] and cold working on properties of electrodeposited copper, and properties at low and high temperatures

Line No., Table I	Panel No.	Bath symbol	Addition agent	Bath temp, °C	Current density, A/dm²	Tensile strength[a]								Yield strength[b,e]					Elongation							
						As deposited	Annealed, °C 150, 2 hr	Annealed, °C 325, 15 min	Annealed, °C 500, 15 min	Pulled at temp, °C −78	Pulled at temp, °C 150	Pulled at temp, °C 325	Cold rolled 50% reduction	As deposited	Annealed, °C 150, 2 hr	Annealed, °C 325, 15 min	Annealed, °C 500, 15 min	Cold rolled 50% reduction	As deposited	Annealed, °C 150, 2 hr	Annealed, °C 325, 15 min	Annealed, °C 500, 15 min	Pulled at temp, °C −78	Pulled at temp, °C 150	Pulled at temp, °C 325	Cold rolled 50% reduction
						× 1000 = psi								× 1000 = psi					% in 2 in. (5 cm)							
26	322-324	Cu2-H2	None	30	2	32	31	31	30	38	20	11	51	11	9	10	5	46	39	41	40	44	41	13	7	2
76	337-341	Cu2-H3	TIPA,[f] 3.5 g/l	30	5	71	62	62[g]	32[h]	78	39	12	72	43	34	34	11[h]	45	7	8	11	32[h]	14	3	4	7
																15[g]					46[g]					
91	343-345	F-1	None	30	8	37	35	33	28	44	28	14	54	16	14	13	3	47	31	33	29	41	33	22	8	2
95	317-320	Pyrophosphate	None	50	2	38	38	36	31	49	29	16	61	20	18	15	8	50	39	42	46	56	39	47	25	4
143	293, 294, 296	CN-8	KCNS, 2 g/l PR cycle 15-5 sec	80	6	86	39	38	35	80	42	20	82	57	21	20	16	50	10	23	33	39	11	16	7	5
110	147	CN-2	None	60	2	81[m]		33[m]	33[m]										4[i]		12[i]	12[i]				
138	269	CN-8	None	80	6																					
147	303	CN-9	Prop. B[k]	80	6																					
	Commercial sheet or rod								31[d]	40-75[d]		17[c] 20[d]	54[d] 45[d] (half hard)				10[c]	48[d] 38[d] (half hard)				45[d]	35-60[d]	18[c] 15-40[d]	6[d] 14[d] (half hard)

Line No., Table I	Panel No.	Bath symbol	Addition agent	Bath temp, °C	Current density, A/dm²	Elastic modulus[o]			Hardness, KHN 200g load					Density at 25°C			Electrical resistivity at 25°C						Linear[f] thermal expansion	
						As deposited	Annealed 500°C 15 min	Cold rolled 50% reduction	As deposited	Annealed, °C 150, 2 hr	Annealed, °C 325, 15 min	Annealed, °C 500, 15 min	Cold rolled 50% reduction	As deposited	Annealed 500°C 15 min	Cold rolled 50% reduction	As deposited	Annealed, °C 150, 2 hr	Annealed, °C 325, 15 min	Annealed, °C 500, 15 min	Cold-rolled reduction 50%	Cold-rolled reduction 90%	× 10⁻⁶ = parts per unit length per °C Temp range, °C 20-200	20-400
						× 10⁶ = psi			kg/mm²					g/cm³			microhm-cm							
26	322-324	Cu2-H2	None	30	2	14	12[a]	15[a]	55		62	54	122	8.925	8.925	8.924	1.73	1.73	1.72	1.70	1.76	1.78	17.1	17.8
76	337-341	Cu2-H3	TIPA,[f] 3.5 g/l	30	5	15	10[g] 10[h]	14[a]	144		115	32[c,h] 61[a]	158	8.913	7.35[h]		1.89		1.82	1.94	1.87		18.9	25.8
91	343-345	F-1	None	30	8	13	6[a]	16	81		62	61	129	8.926			1.73	1.74	1.73	1.70	1.77		16.7	17.6
95	317-320	Pyrophosphate	None	50	2	17	14[a]	17[a]	83	84	75	60	159	8.926	8.926		1.75	1.74	1.74	1.70	1.84		16.7	17.5
143	293, 294, 296	CN-8	KCNS, 2 g/l PR cycle 15-5 sec	80	6	16	15[a]	14	138		81	61	153	8.917	8.917		2.02	1.95	1.83	1.79	1.99		16.7	16.9
110	147	CN-2	None	60	2												1.75	1.76	1.71	1.70				
138	269	CN-8	None	80	6				98		77						1.76	1.74	1.74					
147	303	CN-9	Prop. B[k]	80	6												1.81	1.81	1.80					
	Commercial sheet or rod						13-15[d]	16[c] 15-18[d]				45[d]	100[d] 80[d] (half hard)		8.92-8.93[d]	8.89[d] 8.907[c] (half hard)				1.71[d]	1.77[d]	17.3[c]	18.1[c]

[a] These values are from stress-strain curves. Values not so marked are from resistance strain-gauge measurements.
[b] Yield strength corresponds to 0.05% offset.
[c] Values for commercial wrought material measured by authors.
[d] Values for commercial wrought material from literature [Ref. (20, 35)].
[e] Apparent value, excessively low due to porosity.
[f] Values are for the first heating of as-deposited specimens.
[g] 400°C.
[h] 550°C.
[i] ÷ 100 = significant strain.
[j] Triisopropanolamine.
[k] Proprietary brightener.
[m] Bulge values, based on initial thickness of specimens.
[n] Value for panel No. 225, TIPA, 2 g/l.
[o] One pound per square inch (psi) = 0.000704 kilogram per square millimeter (kg/mm²).
[p] All mechanical properties of annealed deposits were measured at room temperature.

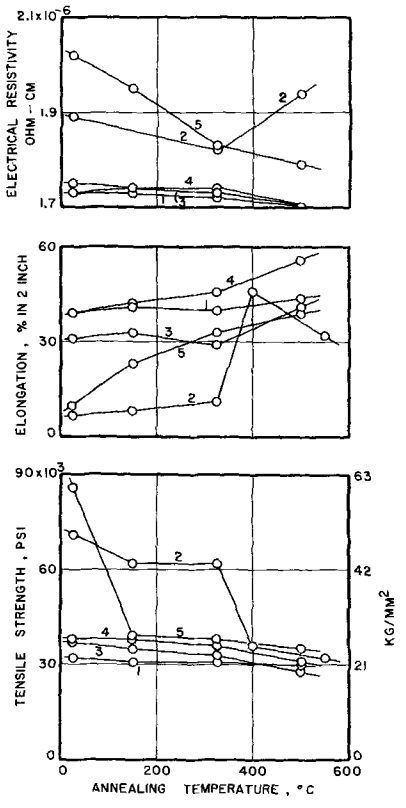

Fig. 41. Relationships between annealing temperature and tensile strength, elongation, and electrical resistivity of copper deposits from various baths: (1) Cu2-H2, 30°C, 2 A/dm²; (2) Cu2-H3 containing 3.5 g/l triisopropanolamine, 30°C, 5 A/dm²; (3) F-1, 30°C, 8 A/dm²; (4) pyrophosphate, 50°C, 2 A/dm²; (5) CN-8 containing 2 g/l KCNS, 80°C, 6 A/dm², PR, cycle 15 sec cathodic, 5 sec anodic.

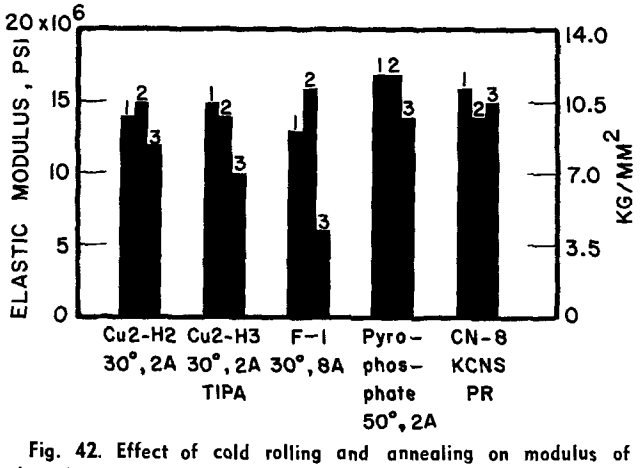

Fig. 42. Effect of cold rolling and annealing on modulus of elasticity of copper deposits from various types of baths: 1—deposits as plated; 2—deposits cold rolled, 50% reduction; 3—deposits annealed at 500°C for 15 min.

Yield strength decreases with annealing for all of the deposits, reaching the extremely low value of 3000 psi for the fluoborate deposit annealed at 500°C (Table XXVII).

3. Effect of annealing on density.—Since the effects of annealing on density were in general small, data were obtained only for deposits annealed at 500°C. The results are compared with as-deposited values in Table XXVII. No measurable effect was found except for the TIPA deposit. It underwent a very large decrease of density, 18%, due to "explosion" and formation of interior voids. (The effect of the same

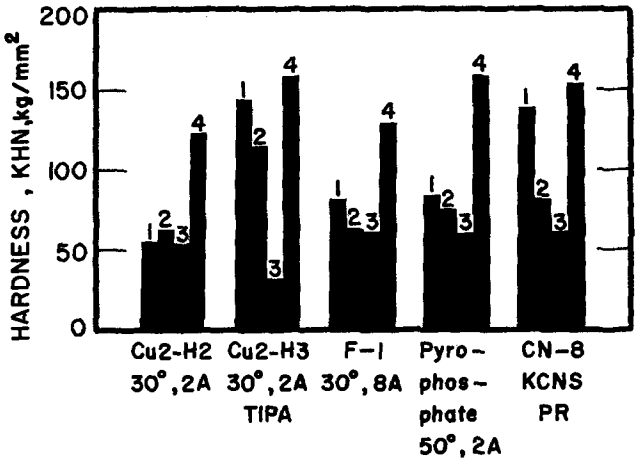

Fig. 43. Effect of annealing and cold rolling on hardness of copper deposits from various types of bath: 1—deposits as plated; 2—deposits annealed at 325°C for 15 min; 3—deposits annealed at 500°C for 15 min; 4—deposits cold rolled, 50% reduction.

phenomenon on hardness was described above in Section VIII-B-2.) The voids are shown in Fig. 45-3.

4. Effect of annealing on electrical resistivity.—Effect of annealing on electrical resistivity is shown in Fig. 41. As in the cases of the other properties already discussed, the deposits that are soft and have low resistivity as plated undergo little change, although their resistivity does decrease slightly. The anomalous behavior of the TIPA deposit is seen again. Its resistivity is high as plated and undergoes significant decrease after annealing at 325°C. However, after annealing at 500°C, its resistivity *increases*. Our interpretation is that, after heating at 325°C, the deposit still has a normal structure, with grain growth that correlates with the lower resistivity. After heating at 500°C, void formation has occurred which causes the true cross section of the deposit to be less than the nominal cross section, hence, the resistivity increases. The PR deposit from the CN-8 bath undergoes a marked regular decrease of resistivity as the annealing temperature is increased, but even after heating at 500°C its resistivity is higher than that of high-purity copper.

5. Effect of annealing on the structure of various deposits.—*a. A deposit from a non-addition agent sulfate bath.*—In Fig. 44 are shown the structures of specimens from panel No. 322-323 (Table XXVII, line 26), as plated, annealed at 325°C, and annealed at 500°C. At 325°C recrystallization and grain growth have involved mainly the originally fine-grained basal portion of the deposit. After annealing at 500°C, complete recrystallization has occurred, with large grains extending through the entire thickness of the deposit. The columnar character of the structure is retained.

It was seen in the preceding Sections VIII-B-2, 3, and 4, that properties of this type of deposit varied but little as a result of annealing. The change of structure is sufficient that a somewhat larger effect on properties might have been predicted.

b. A deposit from a sulfate bath containing an addition agent.—In Fig. 45 are shown the structures of an as-plated deposit from a sulfate bath containing 2 g/l of triisopropanolamine, the same deposit after annealing at 500°C, and a deposit from a bath containing 3.5 g/l of the addition agent after annealing at 500°C. The deposit from the bath containing the low concentration of addition agent has equiaxed grains of medium size after annealing, whereas the deposit from the bath containing the high concentration of addition agent contains many voids (black areas). This condition is discussed in detail in subsequent Section VIII-E-2. It causes the abnormally low hardness and density already described.

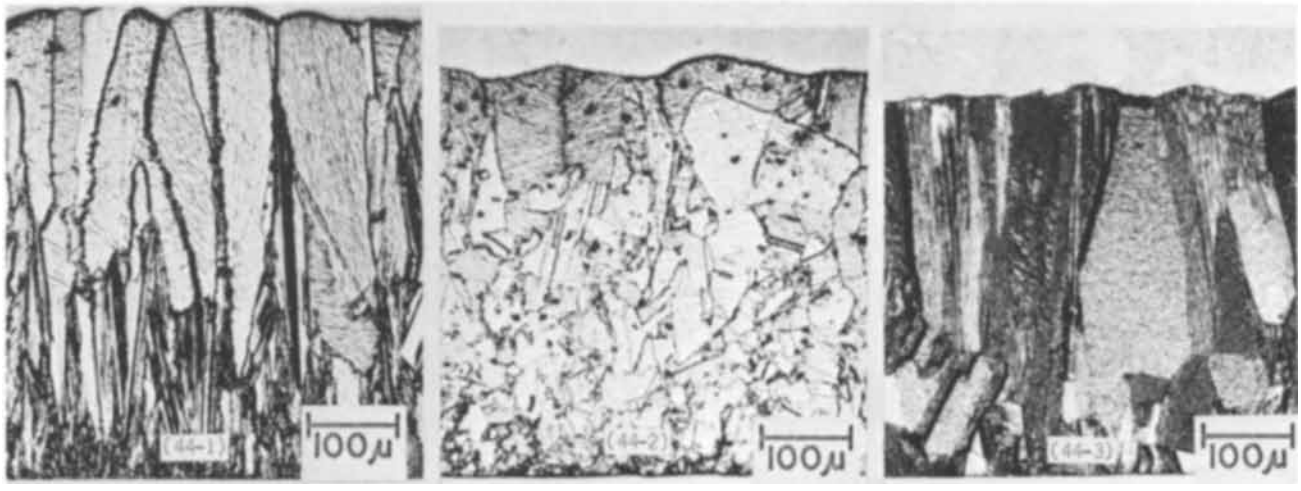

Fig. 44. Effect of annealing on structure of a copper deposit that is coarse grained as plated; from sulfate bath Cu2-H2, 30°C, 2 A/dm^2: (44-1) as plated; (44-2) annealed 15 min at 325°C; (44-3) annealed 15 min at 500°C.

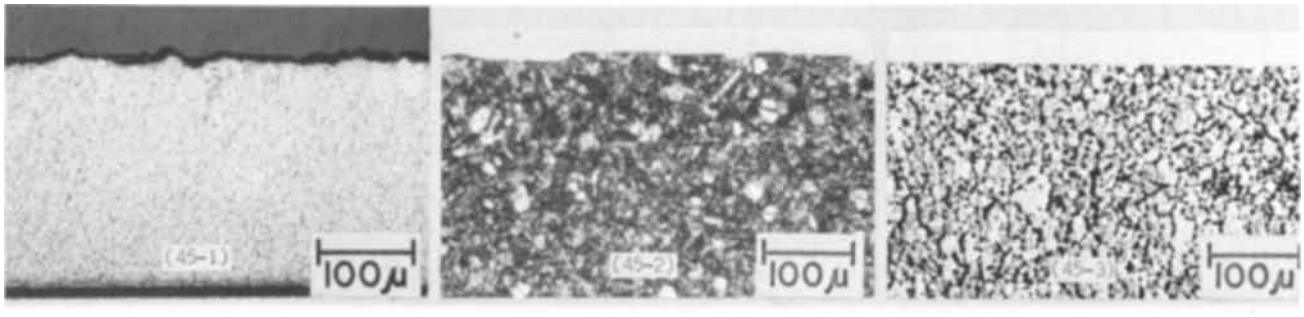

Fig. 45. Effect of annealing on structure of copper deposits that are fine grained as plated. Deposits made in a Cu2-H3 bath containing triisopropanolamine (TIPA), 30°C, 5 A/dm^2. Note voids caused by gas-forming impurities entrapped in the deposit from the high-TIPA bath. (45-1) 2 g/l TIPA, as-plated deposit; (45-2) 2 g/l TIPA, deposit annealed 15 min at 500°C; (45-3) 3.5 g/l TIPA, deposit annealed 15 min at 500°C.

Fig. 46. Effect of annealing on structure of a copper deposit from fluoborate bath F-1, 30°C, 8 A/dm^2: (46-1) as plated; (46-2) annealed 15 min at 325°C; (46-3) annealed 15 min at 500°C.

In Table XXVII we see that the hardness of the deposit shown in Fig. 45-2 is normal (footnote[n]), which correlates with the absence of voids.

c. *A deposit from the fluoborate bath.*—The effect of annealing on the structure of a deposit from a fluoborate bath is shown in Fig. 46. The character of the changes is so similar to those for the non-addition agent sulfate deposit discussed above in paragraph "*a*" that the same remarks apply. However, there is a larger difference in grain size before and after annealing at 500°C, which correlates with a somewhat larger effect on properties than occurred in the case of the sulfate deposit.

d. A deposit from the pyrophosphate bath.—The effect of annealing of a deposit from a pyrophosphate bath is shown in Fig. 47. There is scarcely any effect at 150°C (47-2) and only a small effect at 325°C (47-3). However, the specimen annealed at 500°C shows marked grain growth. The same specimen at a higher magnification (500X) is shown in Fig. 47-5. Large columnar grains with a fine substructure are seen. The magnitude of the properties and the relatively small

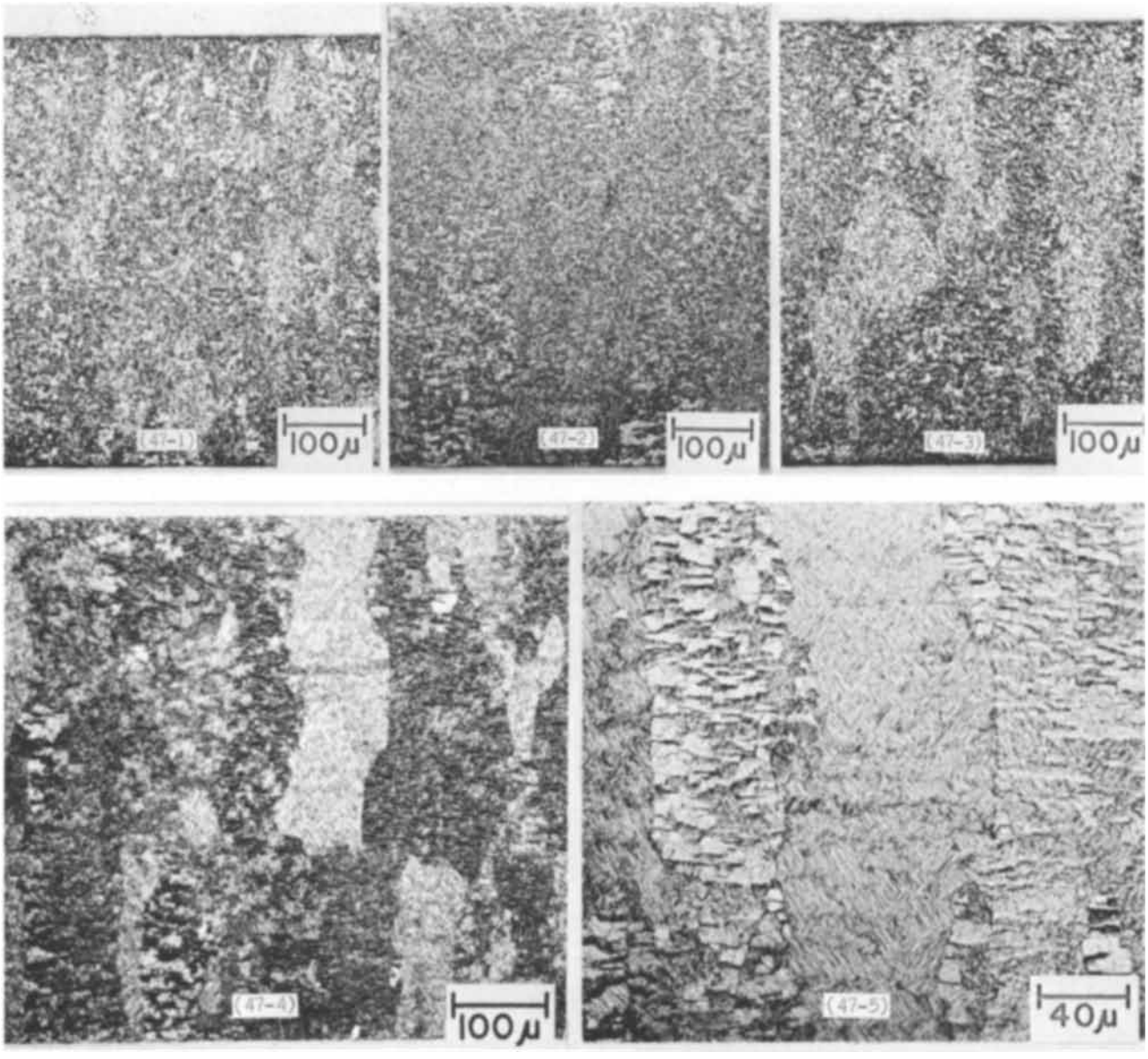

Fig. 47. Effect of annealing on structure of a copper deposit from the pyrophosphate bath, 50°C, 2 A/dm^2: (47-1) as plated; (47-2) annealed 2 hr at 150°C; (47-3) annealed 15 min at 325°C; (47-4) and (47-5) annealed 15 min at 500°C.

degree of change on annealing, in comparison with the TIPA and the CN-8 deposits (Section VIII-B-2, 3, 4; Table XXVII), indicate that possibly fairly large grains as seen in Fig. 47-5 are present in the unannealed deposit and that annealing delineates the boundaries.

e. A deposit from cyanide bath CN-8, made with periodically reversed current.—The effect of annealing on the structure of a deposit made with PR in bath CN-8 is shown in Fig. 48. Annealing at 325°C (48-2) has resulted in the loss of the fibrous character of the as-plated deposit, but no distinct grains can be seen. After annealing at 500°C, fairly large equiaxed grains appear. The black spots are apparently an etch effect and do not represent voids, since the density did not change with annealing (Table XXVII, line 143). The marked changes of properties of this deposit due to annealing, seen in Table XXVII and discussed in Sections VIII-B-2, 3, and 4, correlate with the large increase of grain size.

C. Properties of Cold-Rolled Deposits

1. Cold-rolling procedures.—Cold rolling was done with a small hand mill. Strips of panel stock 1 in. wide, with the nickel flash removed, were rolled to 50% and 10% of their original thickness. Rolling to 10% (90% reduction) was done primarily to determine whether the deposits were sufficiently malleable to permit such drastic reduction. All of the deposits in Table XXVII did submit to this treatment, without annealing and with no edge-cracking apparent to the naked eye. However, reductions were not carried out in one pass. About three passes were used for 50% reduction, with additional fine-adjustment passes to obtain the exact thickness desired and to straighten the strips. Specimens for measurements of properties were cut from the reduced strips.

2. Effects of cold rolling on several properties and on structure.—a. Mechanical properties.—Results are shown in Table XXVII and Fig. 49. Division of deposits into the same type-groups that occurred with annealed deposits is noted for cold working. Thus, the soft as-plated sulfate, fluoborate, and pyrophosphate deposits undergo significant strengthening and embrittlement due to cold reduction (Fig. 49). The initially strong deposits from the sulfate TIPA bath and the CN-8 bath with PR are only slightly affected.

The effects of cold reduction on yield strength are closely parallel to the effects on tensile strength. All deposits acquire a yield strength in the range of 45,000-50,000 psi after 50% reduction, essentially the

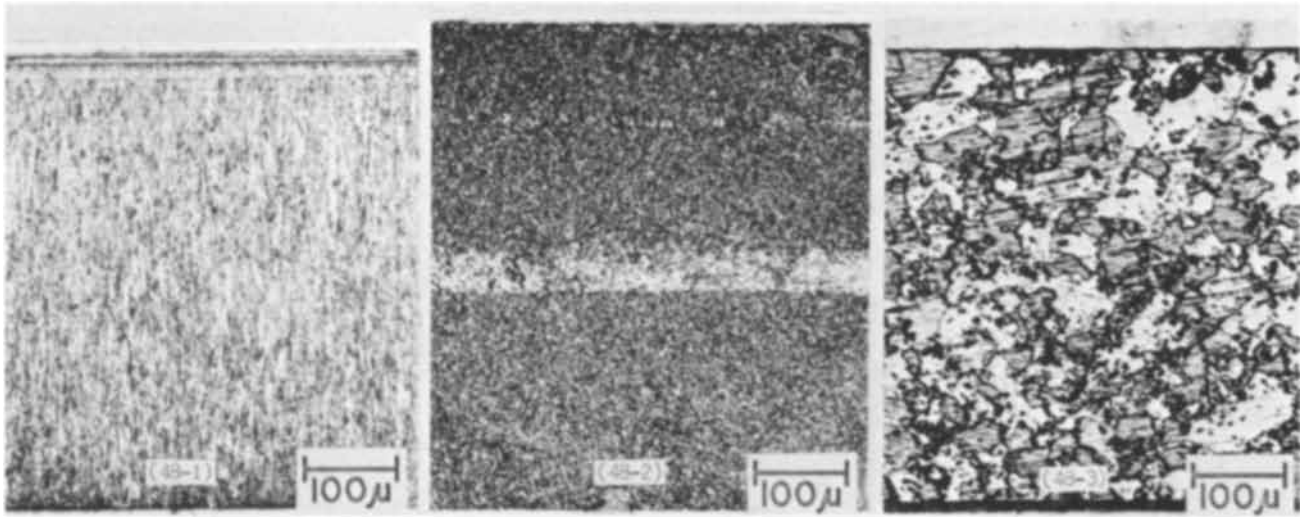

Fig. 48. Effect of annealing on structure of a copper deposit from cyanide bath CN-8 containing 2 g/l KCNS, 80°C, 6 A/dm², PR, 15 sec cathodic, 5 sec anodic: (48-1) as plated; (48-2) annealed 15 min at 325°C; (48-3) annealed 15 min at 500°C.

same as that of similar wrought copper (48,000 psi).[18]

The effects of cold rolling on modulus and hardness were already discussed above (Section VIII-B-2, Fig. 42 and 43).

b. Density.—Only one determination of the effect of cold rolling on density was made (Table XXVII, line 26). The decrease of 0.001 g/cm³ for a soft sulfate deposit is not a significant change. Data from the literature for wrought copper (Table XXVII, last line) indicate that cold working causes a small decrease of density.

[18] The values in Table XXVII from the literature for cold reduced wrought copper that have no temper designation are for material that has been cold reduced 50%. Temper designation for this degree of reduction is *extra hard*. The values included for half-hard materials (21% cold reduction) are for comparative purposes. For example, the material cold reduced 50% is appreciably stronger than that reduced 21%, or half hard, namely, 54,000 and 45,000 psi, respectively. Magnitudes of effects on yield strength, elongation, and hardness also depend on degree of cold reduction.

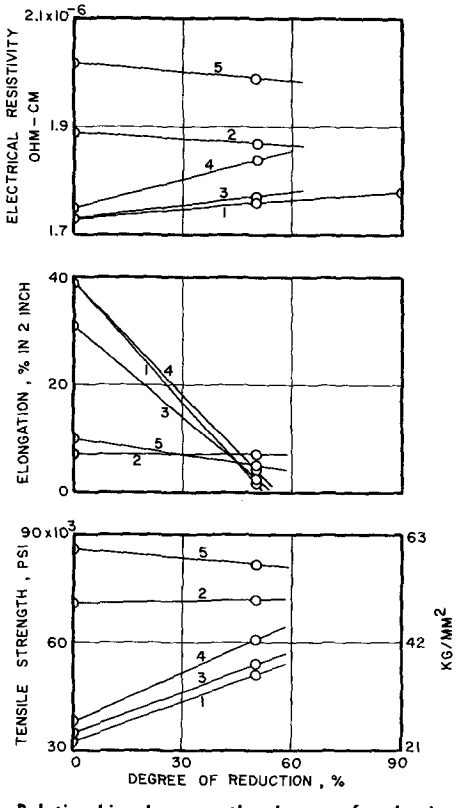

Fig. 49. Relationships between the degree of reduction by cold rolling and tensile strength, elongation, and electrical resistivity of copper deposits from various types of baths: (1) Cu2-H2, 30°C, 2 A/dm²; (2) Cu2-H3 containing 3.5 g/l triisopropanolamine, 30°C, 5 A/dm²; (3) F-1, 30°C, 8 A/dm²; (4) pyrophosphate, 50°C, 2 A/dm²; (5) CN-8 containing 2 g/l KCNS, 80°C, 6 A/dm², PR, cycle 15 sec cathodic, 5 sec anodic.

c. *Electrical resistivity.*—Resistivity is increased by cold rolling of the three soft-type deposits (Fig. 49). The resistivity of the soft sulfate deposit (Table XXVII, line 26) is slightly higher after 90% reduction than after 50% reduction. The hard deposits (TIPA and CN-8, PR) undergo a small decrease of resistivity with cold rolling. However, the change is of borderline significance. The small effect is what might be expected of deposits that have very fine grain and high resistivity as plated.

d. Structure.—The effects of cold rolling on structure are shown in Fig. 50-54, inclusive, for the five types of deposits appearing in Table XXVII. The soft sulfate and fluoborate deposits (Fig. 50 and 52, respectively) show elongation of grains in the direction of rolling, and irregular crumpling of columnar grains, but little reduction of grain size.

In general appearance, the effects of cold rolling on the deposit from sulfate TIPA bath, the pyrophosphate bath, and the CN-8 bath with PR are similar (Fig. 51, 53, and 54, respectively). The cold-rolled specimens in Fig. 51 and 53 show a hint of conversion from a perpendicular to a longitudinal fiber, and Fig. 54 shows a conversion from a perpendicular fiber to an equiaxed, slightly finer structure. It will be noted that the reduced specimens are not exactly half the thickness of the as-plated specimens. This is because the two were made from different but duplicate panels which were not identical in thickness.

D. Tensile Strength and Elongation of Deposits at Low and High Ambient Temperatures

1. Methods of measurement. Tensile strength and elongation were measured by the tensile pull method. Specimens were pulled with the same test machine that was used for measurements of modulus (Section III-A-1). Three temperatures were used, −78°, 150°, and 325°C. The specimens pulled at 150°C were preannealed at 150°C for 1 hr to avoid the necessity of holding them for this period at 150°C in the test machine before pulling. The specimens pulled at 325°C were held at this temperature in the test machine for 15 min before pulling. Specimens pulled at −78°C were pulled immediately with no hold at temperature. To provide the various ambient temperatures, a lightweight aluminum can was attached to the lower specimen grip and extended upward to sufficient height to enclose the specimen and the upper grip. The inside

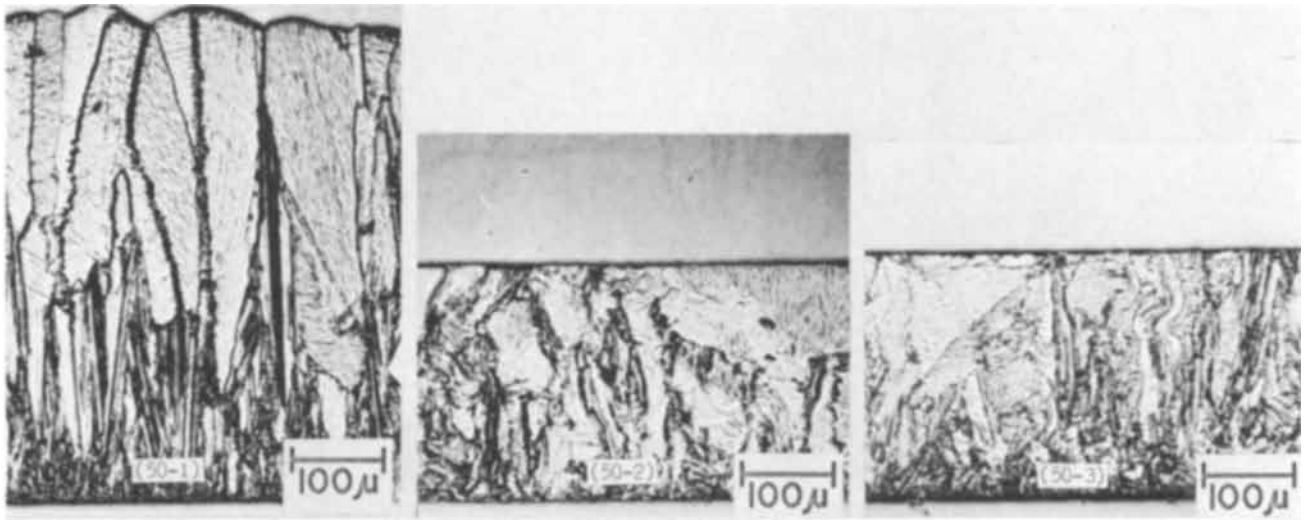

Fig. 50. Effect of cold rolling on structure of a large-grained type of deposit from copper sulfate bath Cu2-H2, 30°C, 2 A/dm^2: (50-1) as plated; (50-2) 50% reduction, cross section parallel to direction of rolling; (50-3) 50% reduction, cross section normal to direction of rolling.

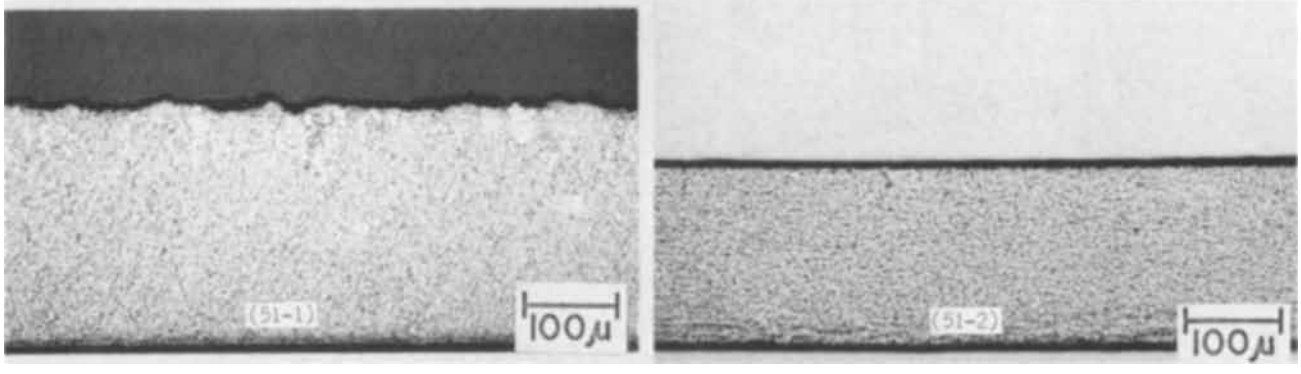

Fig. 51. Effect of cold rolling on structure of a fine-grained copper deposit from sulfate bath Cu2-H3 containing 2 g/l triisopropanolamine, 30°C, 5 A/dm^2: (51-1) as plated; (51-2) 50% reduction, cross section parallel to direction of rolling.

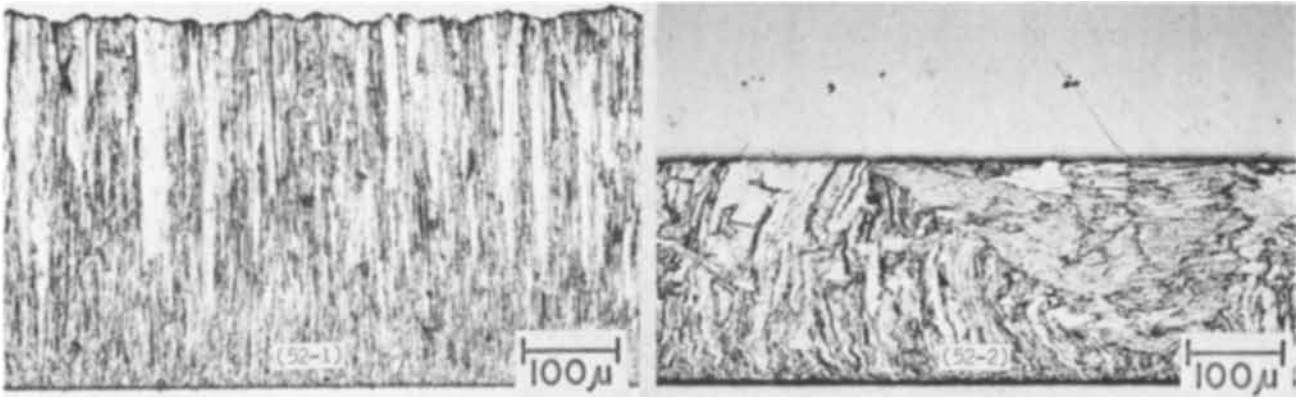

Fig. 52. Effect of cold rolling on structure of a deposit from fluoborate bath F-1, 30°C, 8 A/dm^2: (52-1) as plated; (52-2) 50% reduction, cross section parallel to direction of rolling.

diameter of the can was 2 in. A Nichrome winding and thermal insulation surrounded the can. Controlled current through the winding provided the elevated temperatures. Tubes with an outside diameter of ¼ in. were welded to the lower and upper ends of the can to provide inlet and exit, respectively, for argon, to provide a nonoxidizing atmosphere. A thermocouple close to the center of the tensile specimen was used to measure its temperature, which was maintained constant to ±1°C. Prior determination of vertical temperature gradient within the can showed that vertical variation over the active length of the deposit was not more than 2°C. For pulling at −78°C, the can was filled with a cryogenic mixture of solid carbon dioxide and absolute alcohol.

2. Effects of low and high ambient temperatures on tensile strength and elongation.—The data on tensile strength and elongation at the ambient temperatures listed in Table XXVII are plotted in full in Fig. 55. Several relationships of interest may be seen. Tensile strength of all deposits increases as ambient temperature decreases from 325° to −78°C. The one exception in the case of the deposit from the CN-8 bath, between 25° and −78°C, is probably not significant, because the difference between 80,000 and 86,000 psi is within our normal accuracy range of ±5%. The same type-grouping of deposits occurs as was seen above in Sections VIII-B and C. The soft sulfate, fluoborate, and pyrophosphate deposits remain close together in strength with parallel decreases with increase in tem-

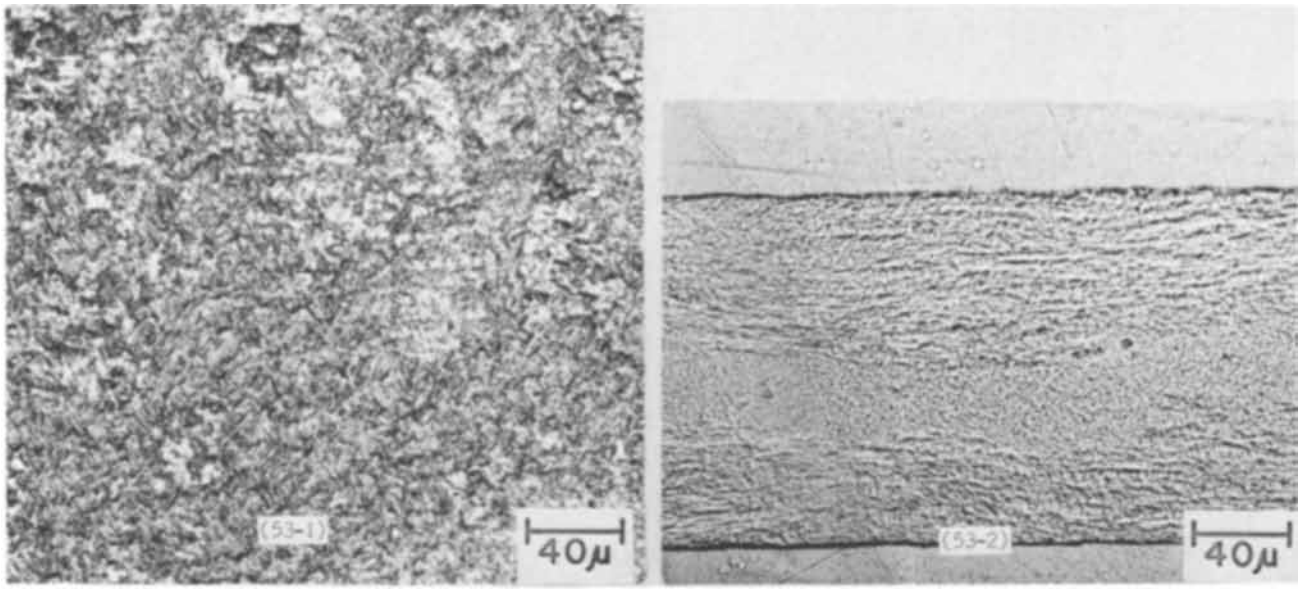

Fig. 53. Effect of cold rolling on structure of a copper deposit from a pyrophosphate bath, 50°C, 2 A/dm^2: (53-1) as plated; (53-2) 50% reduction, cross section parallel to direction of rolling.

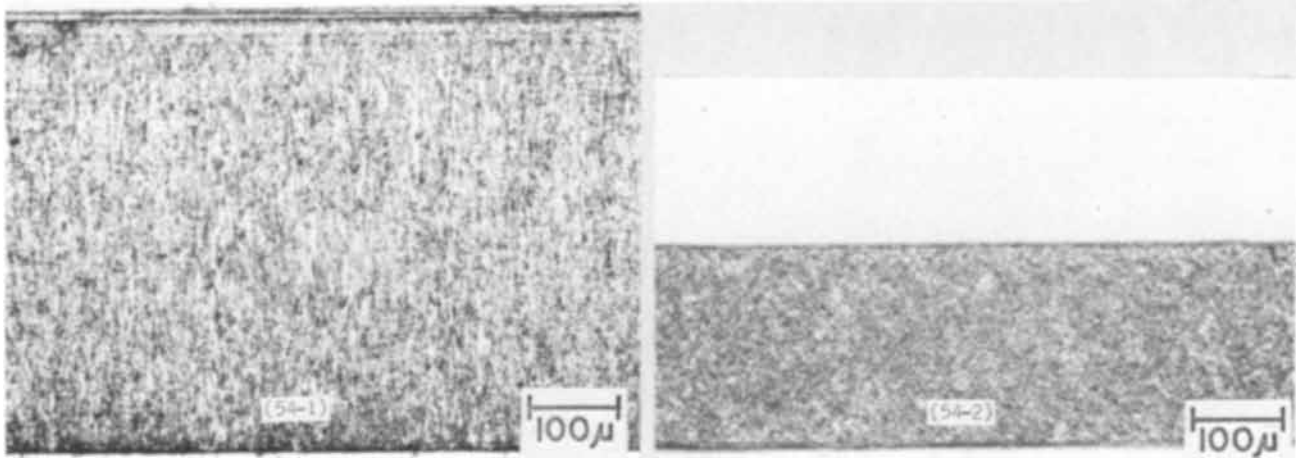

Fig. 54. Effect of cold rolling on structure of a copper deposit from cyanide bath CN-8 containing 2 g/l KCNS, 80°C, 6 A/dm^2, PR, 15 sec cathodic, 5 sec anodic: (54-1) as plated; (54-2) 50% reduction, cross section parallel to direction of rolling.

perature. The deposits of the other group (TIPA; CN-8, PR) have higher strengths at room temperature, but lose strength more rapidly with increase of temperature; thus, deposits of both groups approach the same strength at 325°C. The CN-8 deposit, with a strength of 20,000 psi at 325°C, remains slightly stronger than the other deposits at this temperature.

The relationship between tensile strength and elongation of deposits tested at ambient elevated temperatures is opposite to that for deposits that are annealed and then tested at room temperature. In the first case, *both* tensile strength and elongation decrease with increase of ambient temperature. In the second case, annealing causes tensile strength to decrease, but elongation to increase, with increase of annealing temperature. The same relationships have been reported for wrought copper (35).

The type-grouping referred to above is seen again with respect to elongation. Except for two partial aberrations, ductility for both groups decreases with increase of ambient temperature. However, the soft-type deposits, which at low temperature have markedly higher ductility, decrease in ductility more rapidly with increase of temperature so that, at 325°C, all but the pyrophosphate deposit have very low and nearly equal elongation (Fig. 55).

The deviation of the elongation of the pyrophosphate deposit from the main pattern is large enough that it is probably real and indicates that a difference in structure or a difference in rate of annealing exists that accounts for its significantly higher ductility at 325°C.

E. Thermal Expansivity

1. Introduction and method of measurement.— Knowledge of thermal expansivity may be needed in cases where distortion might occur due to differential expansion of coating and basis metal or of electroformed assemblies made of more than one kind of metal. Cracking due to differential thermal forces, which may occur with chromium or brittle nickel deposits, is not likely in the case of copper deposits. We know of no published data on thermal expansivity of as-plated copper (3).

Specimens were made from sheet panel stock cut into pieces ¾ in. x 6 in. These were made into 6 in.-long tubes, ¼ in. diameter, by forming over a mandrel. Several small holes were drilled adjacent to each long edge of the sheet before forming. A lacing of fine copper wire through these holes, inserted after forming, bound the edges together and prevented deformation of the tube during heating.

To measure thermal expansivity, we used an apparatus of fused quartz described by Hidnert and Souder (36). Length changes were measured with a dial gauge accurate to 0.1 mil. It was calibrated against a standard gauge block. An inert atmosphere was

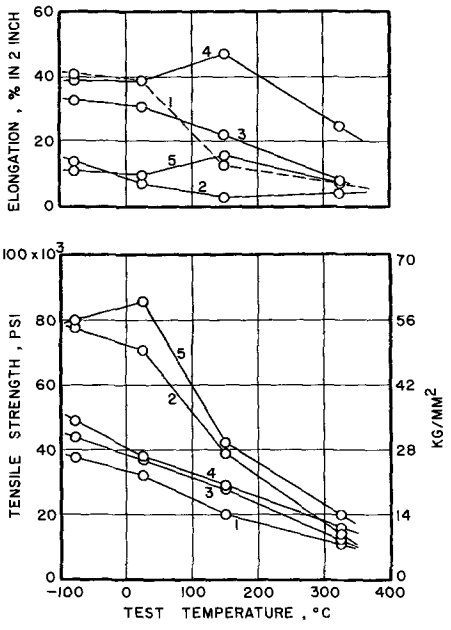

Fig. 55. Relationships between actual test temperature at which properties were measured and tensile strength and elongation of copper deposits from various types of baths: (1) Cu2-H2, 30°C, 2 A/dm²; (2) Cu2-H3 containing 3.5 g/l triisopropanolamine, 30°C, 5 A/dm²; (3) F-1, 30°C, 8 A/dm²; (4) pyrophosphate, 50°C, 2 A/dm²; (5) CN-8 containing 2 g/l KCNS, 80°C, 6 A/dm², PR, cycle 15 sec cathodic, 5 sec anodic.

maintained in the specimen container while it was heated. Calibrated thermocouples were located near each end and at the center of the specimen. End-to-end temperature variation was not more than 2°C and average temperature of a specimen over its length was known to within less than 1°C. Measurements were made at two temperatures, 200° and 400°C. Measurements were made during both heating and cooling portions of the cycle, and several of the specimens were measured through more than one cycle.

We estimate the accuracy of our measured expansivities to be ±1%, equivalent conservatively to an uncertainty in the coefficient of expansion of ±0.2 x 10^{-6} parts per unit length per °C.

As described below, the deposit from the sulfate TIPA bath underwent a large permanent expansion as a result of heating. We, therefore, decided that a limited study of the expansivity characteristics of other deposits from addition agent baths, the amine bath, *etc.*, should be made, to determine whether permanent changes in length occur due to heating. For these limited measurements, specimens were flat strips, ¼ in. x 6 in. Their as-plated lengths were measured accurately, after which they were heated at 500°C for 15 min. After cooling to room temperature, their lengths were again measured.

2. Measured values of thermal expansivity.—The types of deposits selected for expansivity measurements are the same as were used for annealing, cold rolling, *etc.* Complete expansivity data for these deposits are given in Table XXVIII. Hysteresis curves are shown in Fig. 56, 57, and 58.

The expansivity of the soft deposit from the sulfate bath (Table XXVIII, line 26) is seen to be nearly identical with the values obtained by us for cold-rolled commercial sheet and with the values reported in the literature for high-purity electrolytic copper, melted, cast, and cold drawn (37). There is indication that the expansivity of this deposit is slightly higher on first heating after annealing at 500°C, but it reverts to the "normal" value on second heating.

The expansivities of the fluoborate, pyrophosphate, and CN-8 deposits are about 2% less than that of the sulfate deposit.

Table XXVIII. Coefficients of linear thermal expansion of electrodeposited copper

Line No., Table I	Panel No.	Bath symbol	Addition agent or other variable: Name	Conc, g/l	Bath temp, °C	Current density, A/dm²	Condition of specimen	Test cycle	Average coefficient ×10⁻⁶ = parts per unit length per °C: 20°-200°C	20°-400°C	Permanent change in specimen length after heating, in. in 6 in.
26	324	Cu2-H2	None		30	2	As plated	1st heating	17.1	17.8	
								1st cooling	16.7		−0.0001
								2nd heating	17.1	18.0	
								2nd cooling	17.0		0.0000
							Annealed at 500°C 1 hr	After 500° anneal			0.001
								1st heating	17.4	18.3	
								1st cooling	17.6		0.0000
								2nd heating	17.1	18.0	
								2nd cooling	17.0		0.0000
—	224	Cu2-H3	TIPA[a]	2[b]	30	5	Preheated to 470°C	1st heating	17.0	18.0	
								1st cooling	17.0		0.003
76	339	Cu2-H3	TIPA	3.5	30	5	As plated	1st heating	18.9	25.8[c]	
								1st cooling	34.9		0.02
								2nd heating	18.1	27.3[c]	
							Annealed at 550°C 1 hr	After 550° anneal			0.14
								1st heating	18.7	19.0	
								1st cooling	17.6		0.0000
91	343	F-1	None		30	8	As plated	1st heating	16.7	17.6	
								1st cooling	16.2		0.0000
95	320	Pyrophosphate			50	2	As plated	1st heating	16.7	17.5	
								1st cooling	15.9		−0.001
								2nd heating	16.9	17.1	
								2nd cooling	16.8		−0.0003
143	293	CN-8	KCNS PR cycle, 15-5 seconds	2	80	6	As plated	1st heating	16.6	17.1	
								1st cooling	15.0		−0.002
143	296	CN-8	KCNS PR cycle, 15-5 seconds	2	80	6	As plated	1st heating	16.7	16.7	
								1st cooling	14.1		−0.003
		Cold-rolled sheet—half hard From P. Hidnert and H. S. Krider, *J. Res. NBS*, 39, 419 (1947).						1st heating	17.3[d]	18.1[d]	
								1st cooling	17.0[d]		−0.0001
									17.3	20°-300°C 17.7	

[a] TIPA = triisopropanolamine.
[b] Estimated concentration.
[c] Due to the large absolute expansion it was necessary to limit the temperature in these two cases to about 325°C to avoid exceeding the limit of our gauge. This effect and the large permanent elongation is caused by formation of voids. See Fig. 45-3 and corresponding value for density, Table XXVII.
[d] Values measured by authors of present research.

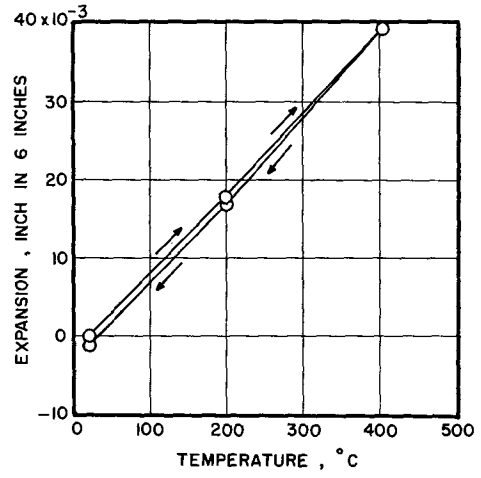

Fig. 56. Thermal expansion of a copper deposit from a pyrophosphate bath, 50°C, 2 A/dm². Curve shows first heating and cooling cycle. Hysteresis effect was much smaller on second cycle (not plotted). Specimen length, 6 in.

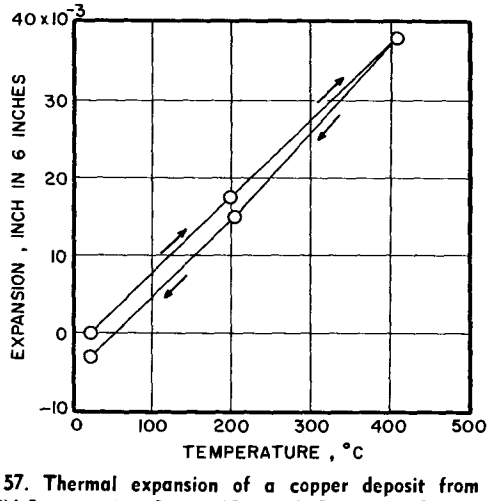

Fig. 57. Thermal expansion of a copper deposit from cyanide bath CN-8 containing 2 g/l KCNS, 80°C, 6 A/dm², PR, cycle 15 sec cathodic, 5 sec anodic. Curve shows first heating and cooling cycle. Specimen length, 6 in.

The expansivities of the deposits from the sulfate TIPA bath were quite irregular. The irregular behavior of these deposits was first noted when a large permanent expansion of a specimen from panel No. 224 caused loss of data because the range of our micrometer dial gauge was exceeded. The bath from which this deposit was made contained approximately 2 g/l TIPA, whereas the bath from which panel No. 339 was made contained 3.5 g/l. It is seen that the specimen from panel No. 224 had normal expansivity after heating to 470°C, but still underwent an additional small permanent expansion. A specimen from panel No. 339 yielded very high expansivities and underwent large permanent expansion. Annealing at 550°C stabilized the specimen so that no further permanent expansion occurred, but the expansivity is about 5% higher than for the other deposits. Figure 58 shows expansion curves for two cycles for the deposit from the sulfate TIPA bath. The first cycle shows the large permanent expansion. This behavior is undoubtedly due to incorporation of addition agent or other gas-generating impurities into the deposit during plating. Gas generation on heating expands the deposit (Fig. 45-3) and causes decrease of density, hardness, and strength as noted in previous sections. The expansivity specimen from panel No. 339, after final heating, was distorted, brittle, and friable.

The pyrophosphate and cyanide deposits, which had low expansivities, underwent small permanent con-

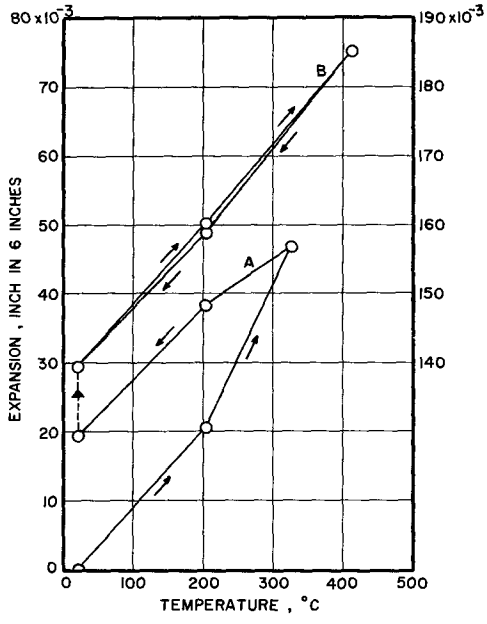

Fig. 58. Thermal expansion of a copper deposit from sulfate bath Cu2-H3 containing 3.5 g/l triisopropanolamine, 30°C, 5 A/dm². Curve A shows first heating and cooling cycle—use scale on left. Curve B shows third cycle after specimen was annealed at 550°C for 1 hr—use scale on right. Permanent expansion of 0.12 in. occurred between heatings represented by curves A and B. Specimen length, 6 in.

tractions. The contraction and the low expansivity are undoubtedly related. The pyrophosphate deposit on second heating had nearly normal expansivity. Expansion curves for these deposits are shown in Fig. 56 and 57. They show the small hysteresis effect associated with the slightly smaller expansivity always noted on the cooling cycle. The effect is larger for the CN-8 deposit (Fig. 57) than for the pyrophosphate deposit (Fig. 56).

3. Qualitative tests of thermal expansion.—The results of the qualitative tests described above in Section VIII-E-1 are tabulated in Table XXIX. The amine deposit undergoes significant permanent expansion, but only about 1/15 that of the TIPA deposit (Table XXVIII). The proprietary bright sulfate deposit undergoes about 50% more permanent elongation than the TIPA deposit and is quite brittle after heating. The deposit from the sulfate bath containing 0.1 g/l gelatin is the only other deposit that underwent marked permanent expansion. It was very brittle, but this was also its condition before heating. None of the deposits in Table XXIX showed distortion of shape except the amine deposit, which was severely blistered.

It is probable that the deposits in Table XXIX that undergo only a small permanent expansion have thermal expansivities very close to the value for the deposit in Table XXVIII, line 26.

F. Structure of Deposits

1. Optical micrographs.—Structure in relation to various parameters has already been illustrated with many optical micrographs in preceding figures. In this section we restrict the consideration of optically determined structure to comparisons between typical deposits from various types of baths (Fig. 59).

In Fig. 59-1 and 59-2, deposits from non-addition agent sulfate and fluoborate baths are compared. The concentration of copper was the same in each bath, and operating conditions (bath temperature, current density, and cellulose filter) were the same for each deposit. The finer, more fibrous structure of the deposit from the fluoborate bath must, therefore, be ascribed to some unique effect of the fluoborate anion. The finer

Table XXIX. Effect of heating on dimensions and ductility of a variety of copper deposits
Deposits held 15 min at 500°C

Line No., Table I	Panel No.	Bath symbol	Operating conditions: Bath temp, °C	Operating conditions: C.D., A/dm²	Addition agent: Name	Addition agent: Conc, g/l	Increase in length[a] % = $\frac{(l_{500,25} - l_{25})\ 100}{l_{25}}$	Ductility[d] After heating: No. of bends
150	329	Amine	55	2	None		0.16[b]	<1
79	306	Cu2-H3	30	4	None	PR, 5-2 sec	0.00	3
77	226	—	22	4	Prop. A[c]	—	3.6	<1
43	5-4	Cu2-H3	30	2	Dextrin	0.02	0.06	3
44	5-6	Cu2-H3	30	2	Dextrose	0.05	0.04	2
45	219	Cu2-H3	30	2	EA + M[c]	0.3, 2.0	0.01	2
15	65	Cu2-H1	30	2	Gelatin	0.003	0.05	2
46	81	Cu2-H3	30	2	Gelatin	0.01	0.02	3
47	83	Cu2-H3	30	2	Gelatin	0.1	1.2	0
48	5-5	Cu2-H3	30	2	Glycerol	1.0	0.03	4
49	5-2	Cu2-H3	30	2	Glycine	0.1	0.00	4
50	214	Cu2-H3	30	2	LA[c]	0.05	0.00	4
54	91	Cu2-H3	30	2	NDS[c]	1.8	0.04	3
52	160	Cu2-H3	30	2	β-NQ[c]	0.1	0.14	2
59	71	Cu2-H3	30	2	PSA[c]	1.0	0.03	3-4
64	166	Cu2-H3	30	2	SeO_2	10^{-4} Se	0.06	3
68	5-1	Cu2-H3	30	2	Sorbitol	0.1	0.00	3
70	88	Cu2-H3	30	2	TU[c]	0.015	0.4	<1

[a] Nominal length of specimens: 6 in. $l_{500,25}$ is length at 25°C, after cooling from 500°C. l_{25} is initial length at 25°C.
[b] Blisters formed during heating of the deposit from the amine bath.
[c] Prop. A = proprietary addition agent containing a sulfonate and an azo dye; EA + M = ethyl alcohol plus molasses; LA = lactic acid; NDS = 1,5-naphthalenedisulfonic acid; β-NQ = β-naphthoquinoline; PSA = phenolsulfonic acid; TU = thiourea.
[d] A qualitative check of physical damage caused by heating. Specimens were bent onto themselves and creased with pliers, opened, and repeated.

structure is associated with slightly better mechanical properties than those of the sulfate deposit.

The pyrophosphate deposit, Fig. 59-3 and 59-4, appears to have a fine random structure. However, this conclusion is in conflict with the magnitudes of the properties of this deposit, with its behavior on annealing (already discussed in Section VIII-B-5-d), and with the results of x-ray diffraction examination presented in the next section.

The deposit from the high-efficiency cyanide bath, the structure of which is shown in Fig. 59-5, is similar to that from the pyrophosphate bath and involves similar contradictions. It appears to have a fine random grain, in conflict with its properties and with the x-ray data. An explanation for these anomalies is suggested in the next section following the presentation of the x-ray data. Similar contradictory data on grain size, as determined optically and by x-ray, have been noted by Read.[19]

The deposit from the amine bath, shown in Fig. 59-6, appears to have a very fine, random structure with no resolved crystals. The properties of this deposit, such as fairly high strength, low ductility, and high hardness, summarized in Section VIII-H, confirm the reality of its fine structure.

2. X-ray diffraction.—a. Back-reflection patterns.— Back-reflection patterns were obtained from both the final and starting faces of the six deposits listed in Table XXX to obtain information on grain size. Ilford CX film was used to enhance resolution. Specimens were used as plated; *i.e.*, the faces were not polished. Specimens were positioned normal to the beam, with 6 cm between specimen and film. Filtered radiation from an iron target was used, collimated to a beam diameter of 1 mm.

Grain size is estimated from the degree of resolution of spots in the back-reflection patterns (Fig. 60). However, accurate values of grain size cannot be determined by this method unless the following conditions are met: (*a*) specimens must be free of internal stress; (*b*) grain orientation should be random; (*c*) grain size should be uniform. While some as-plated electrodeposits approach these criteria, most fail in one or more of them. Furthermore, grain size estimated by the x-ray method and by optical methods under ASTM standards is not comparable because a twin is not regarded as a new grain in optical determinations, but does give rise to a new x-ray spot. Because of these factors, the grain sizes given in Table XXX can be regarded only as qualitative and as showing relative fineness of grain for the various deposits.

In Fig. 60, the diffraction index of the outer ring is 311 (Kα), middle ring 222 (Kα), and inner ring 400 (Kβ). The absence of the resolution of the Kα doublets may be due to internal stress or to very small grain size.

Following are interpretations of the patterns shown in Fig. 60:

1—Panel No. 323 (line 26), a soft-type deposit from a sulfate bath. Figure 60-1-F shows the pattern for side F, the final plated surface. It shows blurring to very large spots, indicating a wide range of grain size. Figure 60-1-B shows the pattern for side B, next to the basis metal. It contains continuous rings with doublets resolved, indicating very small grain size and low stress.

2—Panel No. 337 (line 76), a hard, strong deposit from a sulfate bath containing triisopropanolamine. Figures 60-2-F and 60-2-B show the patterns for sides F and B, respectively. The rings are continuous, with doublets unresolved, indicating a uniform fine grain throughout the deposit.

3—Panel No. 343 (line 91), a soft-type deposit from a fluoborate bath. Figure 60-3-F shows the pattern for side F. The 222 and 400 lines are absent, indicating texture. The 311 line contains 2 large spots and a very faint continuous line, indicating a mixture of fine and large grains. The rings for Fig. 60-3-B, with no resolution of spots and poor resolution of doublets, indicate a very fine structure of the fluoborate deposit in the basal zone. These x-ray results for panels No. 323, 337, and 345 confirm the grain sizes seen in the optical micrographs, Fig. 59-7, 59-8, and 59-2, respectively.

4—Panel No. 320 (line 95), a deposit from a pyrophosphate bath. Figures 60-4-F and 4-B show the patterns for the final and starting surfaces of the deposit, respectively. Both show large isolated spots with some faint blurring, indicating large grains intermixed with some fine grains. The indicated grain size in the basal zone is not quite as large as in the final plated zone. The absence of the 222 reflection indicates that the deposit is textured.

The x-ray evidence in the preceding paragraph, physical property data, and behavior on annealing (Section VIII-B) indicate that the pyrophosphate deposit has a large grain size. However, contradictory evidence was found by optical examination (Fig. 59-3 and 59-4). Since evidence for a relatively large grain

[19] H. J. Read, Pennsylvania State University, University Park, Pennsylvania, Private communication.

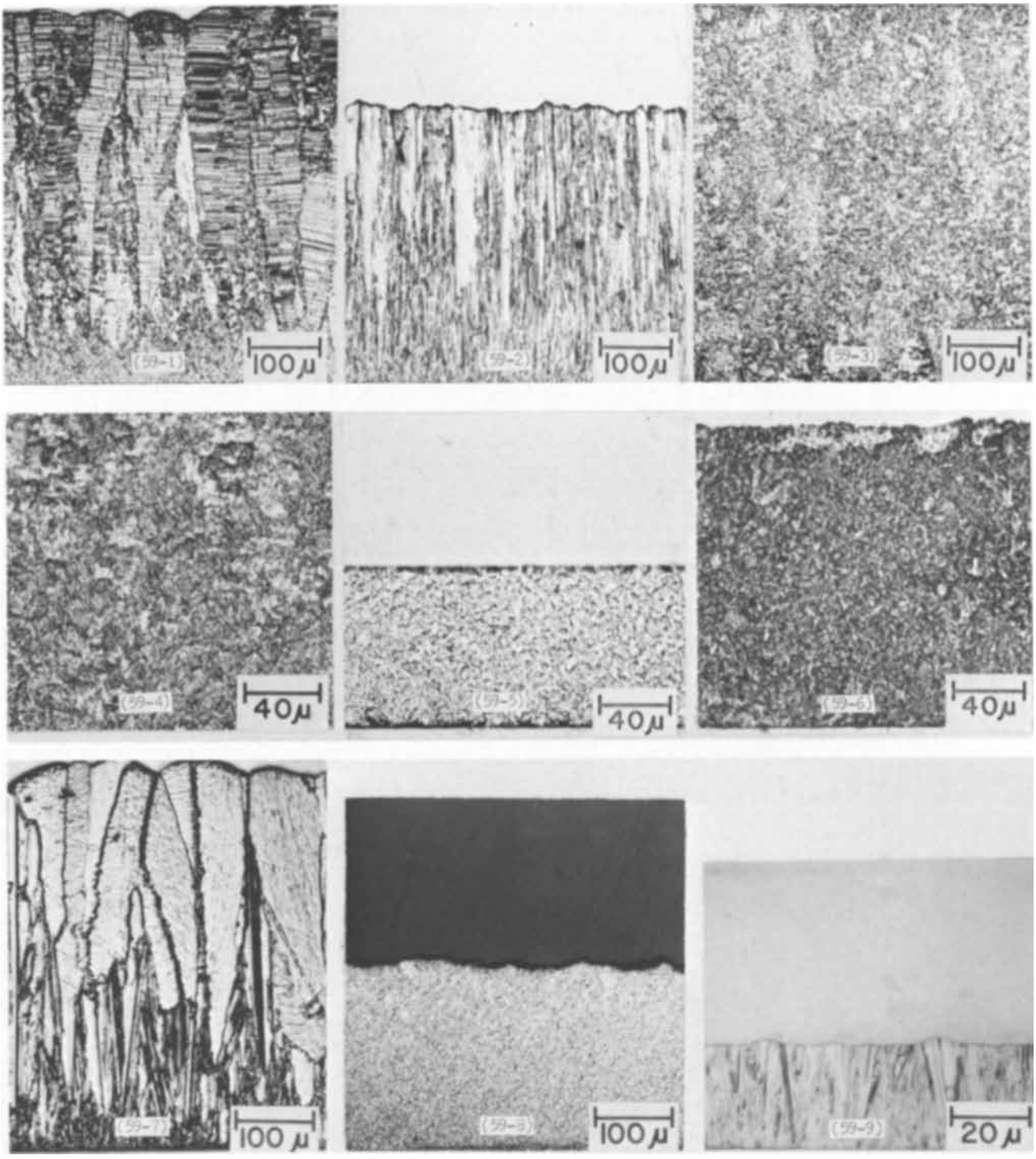

Fig. 59. Comparison of structure of deposits of copper from all types of baths: (59-1) Cu2-H3, 30°C, 8 A/dm^2; (59-2) F-1, 30°C, 8 A/dm^2; (59-3) and (59-4) pyrophosphate, 50°C, 2 A/dm^2; (59-5) CN-8, 80°C, 6 A/dm^2; (59-6) amine bath, 55°C, 4 A/dm^2; (59-7) Cu2-H2, 30°C, 2 A/dm^2; (59-8) Cu2-H3 containing 2 g/l triisopropanolamine, 30°C, 5 A/dm^2; (59-9) CN-1, 40°C, 1 A/dm^2.

size is preponderant, we conclude that the optical structure is misleading. We suggest the following two theories to account for the apparent discrepancy: (*a*) A columnar structure such as seen in Fig. 47-4 and 47-5 after annealing may be present in the as-plated deposit, but the etching technique used for preparing the photomicrograph specimen was inadequate to reveal it. (b) The fine structure seen in Fig. 59-3 and 59-4 represents an end-view of crystals whose main axes lie in the plane of the deposit. The pyrophosphate photomicrographs would thus be analogous to a view normal to the surface of, *e.g.*, the fluoborate deposit, Fig. 59-2. This theory would require that the grains in the pyrophosphate deposit grow in a directional parallel to, or nearly parallel to, the plane of the deposit. This could occur by a mechanism in which shallow crystal steps are located with their faces nearly normal to the plane of the deposit, with growth occurring by build-up on these faces (38). We favor this theory, as it is also in accord with the semibrightness of the pyrophosphate deposits.

5—Panel No. 128 (line 101), a deposit from a strike-type cyanide bath, CN-1. The diffraction lines, Fig. 60-5-F and 5-B, which are continuous, indicate fine grain size on both the final plated side and in the basal zone of the deposit. The photomicrograph (Fig. 59-9) and the electron micrographs (Fig. 36) show columnar grains, of the order of 1 μm in diameter, in agreement with what the x-ray sees in a view normal to the plane of the deposit.

Table XXX. Structural features of copper deposits determined from x-ray diffraction and optical micrographs and their relationships to properties and impurities

Line No., Table I	Panel No.	Bath symbol	Addition agent	Bath temp, °C	Current density, A/dm²	Panel[a] surface	Type of surface	Crystal[b] size (estimated) μm	Preferential orientation[c] of diffraction plane parallel to surface (111)	(200)	(220)	(311)	Photomicrograph structure	Tensile[d] strength, psi	Hardness KHN, kg/mm²	Elec. resistivity 25°C, ohm-cm	Total impurities, w/o
26	323	Cu2-H2	None	30	2	F	Matte	1 to 60	0.06	0.06	10.9	0.2	Large-grained columnar. Fine in basal zone.	32 × 10³	55	1.73 × 10⁻⁶	0.0035
						B		1	1.0	0.6	2.0	1.1					
76	337	Cu2-H3	TIPA 3.5 g/l	30	5	F	Matte	<1	0.5	0.5	1.8	0.9	Fine. No visible texture or grain resolution.	71	144	1.89	0.022
						B		<1	1.3	0.4	1.3	0.9					
91	343, 345	F-1	None	30	8	F	Matte	1 to 50	0.08	1.2	32.7	0.2	Fibrous columnar. Finer than line 26. Fine in basal zone.	37	81	1.73	0.0041
						B		<1	0.5	0.4	3.8	0.6					
95	320	Pyrophosphate	None	50	2	F	Semibright	1 to 100	13.8	0.06	0.04	0.1	Very fine lamellae, visible at 500X (Fig. 59-4).	38	83	1.75	0.003-4
						B		1 to 40	0.5	0.4	0.3	1.0					
101	128	CN-1	None	40	1	F	Matte	1	0.5	0.6	2.0	0.7	Very fine columnar grains.	66	162	1.79	0.01
						B		1	1.3	1.2	0.8	1.0					
138	268	CN-8	None	80	6	F	Semibright	1 to 25	0.9	1.3	0.4	0.5	Similar to line 95.	40	98	1.76	0.0053
						B		1 to 25	0.6	12.4	0.1	0.3					

[a] F, x-ray beam directed at final plated surface; B, beam directed at starting surface, *i.e.*, the surface that was adjacent to the basis metal.
[b] Estimated values of crystal size are qualitative.
[c] The magnitude of the number for a given plane indicates the ratio of the intensity of diffraction by that plane to the intensity that would occur if orientation were random. If the orientation were random, the number would be unity for all planes.
[d] One pound per square inch (psi) = 0.000704 kilogram per square millimeter (kg/mm²).
[e] Values from Table XXXI. For panel 337, sulfur was taken as the same as that for panel 323. For panel 320, phosphorus was estimated by analogy with 323. For panel 128, impurity content is assumed to be similar to that of panel 145 (line 110 in Table XXXI), which was made under similar conditions.

6—Panel No. 268 (line 138), a deposit from a high-efficiency cyanide bath, CN-8, containing no addition agent, made without periodic current reversal. Individual spots in the back-reflection patterns are resolved, although smaller than those in the patterns of the large-grained deposits. There is no significant difference between the final plated side and the basal side (Fig. 60-6-F and 6-B). An intermediate grain size is indicated, as shown in Table XXX.

The optical micrograph for this deposit, Fig. 59-5, shows a very fine grain. Thus, for this deposit we have the same contradictions as for the pyrophosphate deposit, and the discussion above in paragraph 4 applies.

b. *Texture analysis.*—A preferred orientation, or fiber texture, of crystals in electrodeposits has been noted and studied by many authors. The results of these studies of copper deposits were reviewed briefly in the first paper of this series (3). Most deposits from sulfate baths have been reported to contain a predominance of crystals oriented with the (110) plane in the plane of the deposit. Quantitative measurement of the angular distribution of the degree of preferred orientation of the (110) plane about the normal to the surface of a copper deposit was made by Ogburn and Newton (39). Under certain conditions, (100) and (111) textures occur in deposits from sulfate baths (40-42). According to the results of a recent publication (43), a shift of orientation from (110) to (113) to (210) planes parallel to the plane of the deposit occurs with increase in current density. The (113) and (210) orientations were obtained at current densities in the range of 60-200 A/dm² with violent agitation. In the upper part of the range the deposits were arboreal and very weak. Most nickel deposits have a (100) texture (2).

The present measurements were made with a diffractometer, using a cobalt target. The radiation was monochromated with the (111) plane of a lithium fluoride crystal at the receiving detector. The front and back surface of each specimen was step-scanned over the diffraction peaks indicated, at 0.05 deg 2θ steps, with a counting period at each step of 100 sec. Background was substracted and area integrated by the Simpson 1/3 rule. A number representing the relative intensity of the diffraction peak from the planes listed in Table XXX to its expected intensity was then calculated. This number, given in Table XXX, is the ratio of the intensity of diffraction by a given plane to the intensity that would occur if orientation were random. If orientation were random, the number would be unity for all planes.

Since the 220 diffraction peak is the second order of the (110) plane, the results in Table XXX show a fairly strong preferred orientation of the (110) plane in the plane of the deposit for panel No. 323, the non-addition agent sulfate deposit, and still stronger identical orientation in the fluoborate deposit. The basal zone of both of these deposits shows a small preferred orientation of the same plane. The strike-type deposit from the cyanide bath, which shows a columnar grain orientation, shows a small degree of preferred orientation, also of the (110) plane.

Orientation in the deposit from the sulfate bath containing triisopropanolamine is nearly random, with just a hint of preferred (110) orientation.

The deposits from the pyrophosphate and high-efficiency cyanide baths depart from the above pattern in that the former shows a high degree of preferred orientation with the (111) plane in the plane of the deposit, and the latter the (200) plane, equivalent to the (100) plane, in the plane of the deposit. The latter is unusual in that the orientation is strong in the basal zone but has become random at the final surface.

It was noted that the intensity of diffraction from the oriented plane in the final plated surface of specimens No. 323, 320, and especially 345, approached that from a single crystal. It should be noted that the method used did not give a complete survey of all

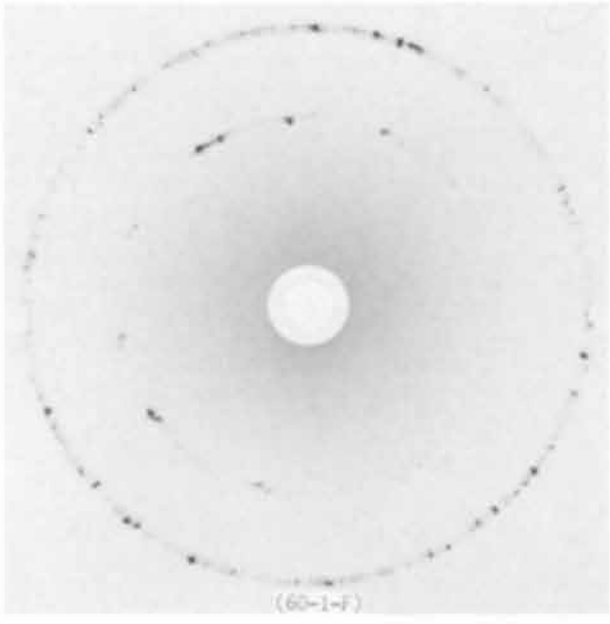
(60-1-F)

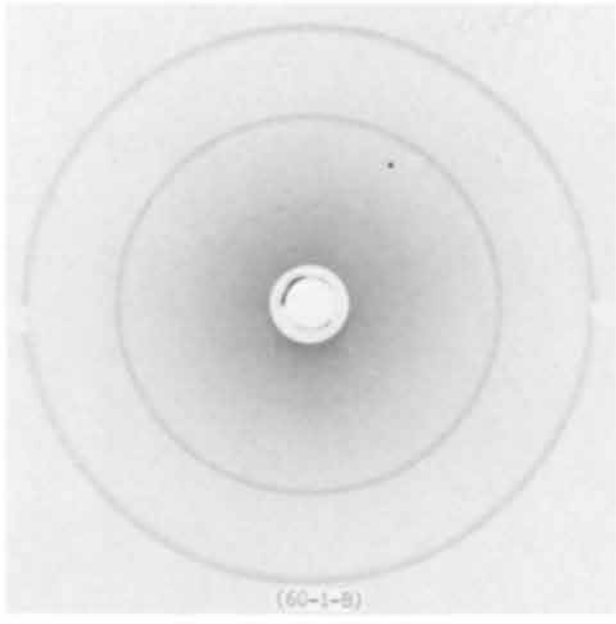
(60-1-B)

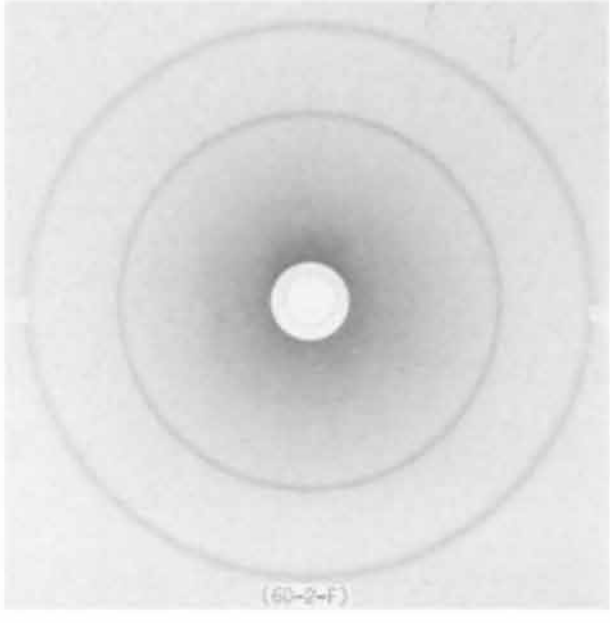
(60-2-F)

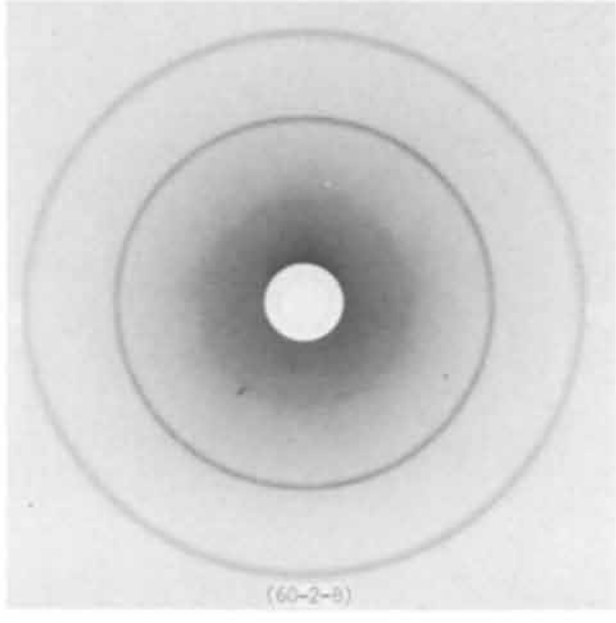
(60-2-B)

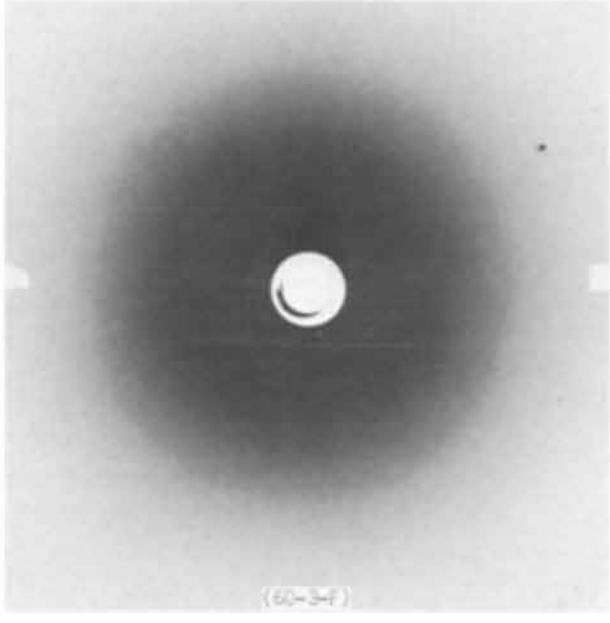
(60-3-F)

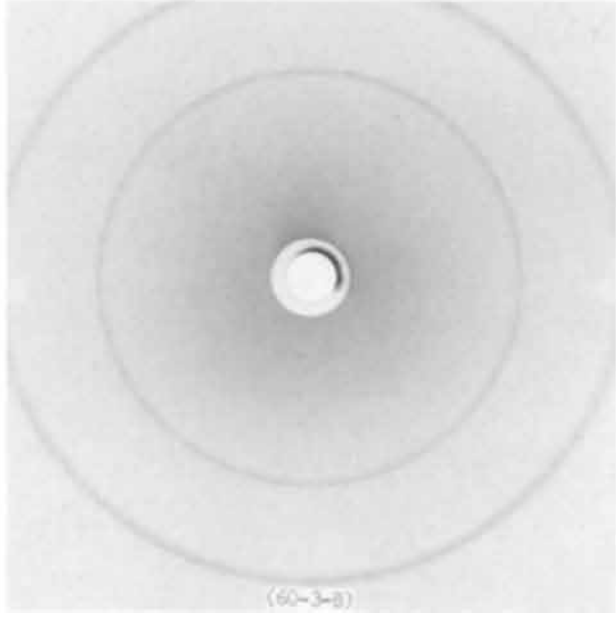
(60-3-B)

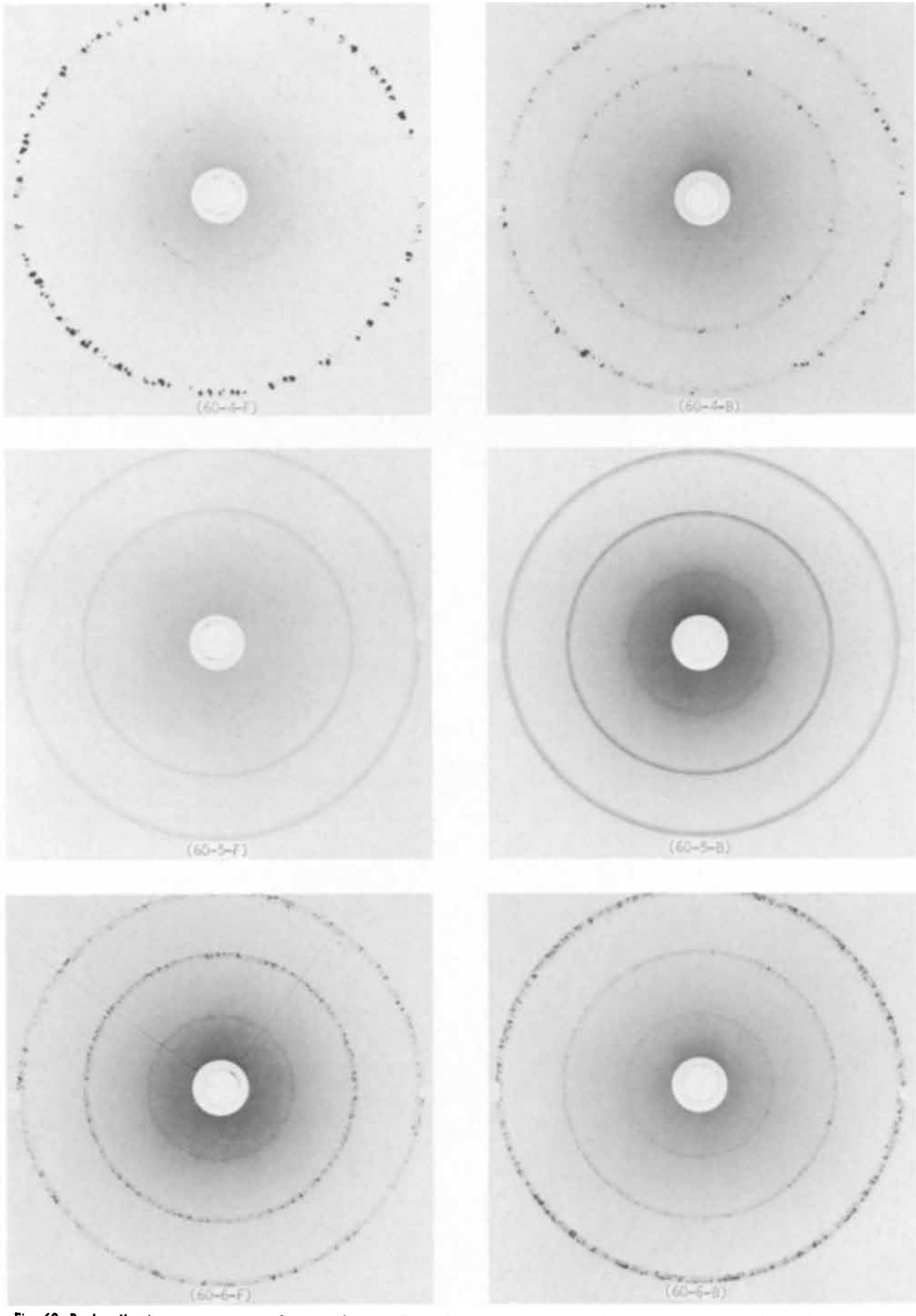

Fig. 60. Back-reflection x-ray patterns of copper deposits. F and B represent patterns with the beam directed at the final plated surface and the starting surface, respectively. (60-1-F and B) Cu2-H2, 30°C, 2 A/dm^2; (60-2-F and B) Cu2-H3 plus 3.5 g/l triisopropanolamine, 30°C, 5 A/dm^2; (60-3-F and B) fluoborate F-1, 30°C, 8 A/dm^2; (60-4-F and B) pyrophosphate, 50°C, 2 A/dm^2; (60-5-F and B) cyanide CN-1, 40°C, 1 A/dm^2; (60-6-F and B) cyanide CN-8, 80°C, 6 A/dm^2.

Table XXXI. Nonmetallic impurities in copper electrodeposits

Line No., Table I	Panel No.	Bath symbol	Addition agent		Other variable	Bath temp, °C	C.D., A/dm²	Content of impurity, % by weight							
			Name	Conc, g/l				Oxygen	Hydrogen	Ratio, O/H	Nitrogen	Carbon	Boron	Fluorine	Selenium	Sulfur
26	323	Cu2-H2				30	2	0.00038	<0.0001	>4	0.0010	0.0005				0.0011
								0.00054[a]				0.0015[b]				
42	297					60	20	0.0094	0.0003	40						0.0039
								0.0136[a]								
46	81	Cu2-H3	Gelatin	0.01		30	2	0.0021[a]	0.00015	14	0.0021					
47	83			0.1		30	2	0.0350	0.0040	8.8	0.0530	0.0530[b]				
66	172		SeO_2	0.001 Se		30	2									
76	337		TIPA[c]	3.5		30	5	0.0050	0.0006	8.3	0.0094	0.0062			0.00006	
91	345	F-1				30	8	0.0008	<0.0001	>8	0.0017		<0.0001	0.0017		
								0.00053[a]								
95	320	Pyrophos-phate				50	2	0.00058	<0.0001	>7	0.0015					
								0.00078[a]								
110	145	CN-2				60	2	0.0033	<0.0001	>33	0.0055					
127	193	CN-5				80	4	0.0013[a]	<0.0001	>13	0.0036	0.0005				
138	269	CN-8				80	6	0.0010	<0.0001	>10	0.0021					
141	281	CN-8			PR, 15-5 sec	80	6	0.00051[a]				0.0022[b]				
147	303	CN-9	Prop. B[c]			80	6								0.0011	

[a] and [b] Values designated [a] and [b] were determined at the laboratories of American Metal Climax, Inc., and E. I. du Pont de Nemours & Co., Inc., respectively. All other determinations were made at NBS.
[c] TIPA: triisopropanolamine; Prop. B: proprietary brightener, selenium type.

possible preferentially oriented planes. For example, the (211) plane was not examined.

We are indebted to C. J. Bechtoldt of the NBS Metallurgy Division, Lattice Defects and Microstructure Section, for the x-ray measurements and for interpretation of the results.

3. Correlations among structure, properties, and impurities.—The deposits in Table XXX fall into two distinct groups, those with medium to large grain size (non-addition agent sulfate, fluoborate, pyrophosphate, and high-efficiency cyanide), and those with fine grain (sulfate-TIPA, and cyanide, CN-1). The deposits in the coarse-grained group have low to medium tensile strength, hardness, and resistivity, and a small content of impurities. The deposits in the fine-grained group have high tensile strength, hardness, resistivity, and impurity content.

As discussed by Brenner (2) and others, the primary factor that determines properties of electrodeposits is impurity content. A high content of impurities interferes with crystal growth, causing fine grain and associated high values of properties. Impurity content in turn is determined primarily by type of bath and by the kind and concentration of addition agent used. Variations in operating conditions of baths, in the normal range, have minor effects in comparison with type of bath and addition agent. This theory is confirmed for copper by the results summarized in Table XXX. Thus, the total impurity content of the four large-grained deposits is in the range of 0.003-0.005%, whereas that of the fine-grained deposits (lines 76 and 101) is much larger, namely, 0.022 and 0.01%, respectively.

G. Composition and Impurity Content of Deposits

1. Introduction.—It is generally recognized that impurities in deposits may significantly affect their structure and properties. About 20 papers dealing with this aspect of electrodeposited copper were reviewed in the first paper of this series (3). In the present work we have determined metallic and nonmetallic impurities in several representative types of deposits.

Determinations of metallic impurities in both anodes and deposits were made, mainly to monitor the effectiveness of our purification procedures. The results of these determinations, already presented in Table V, were discussed in Section II-A.

In this section we consider nonmetallic impurities in several typical kinds of deposits.

2. Results of determinations of nonmetallic impurities in copper deposits.—a. Hydrogen and oxygen.—Content of hydrogen and oxygen in various deposits is shown in Table XXXI. Values of oxygen designated "*a*" in Table XXXI were determined in the laboratories of American Metal Climax, Inc.[20] The other values of both oxygen and hydrogen were determined at NBS.[20] Reasonable agreement is seen between values determined at the two laboratories.

The ratio of O/H in nickel and chromium deposits has been found to be close to 8 on the average, indicating that they enter these metals in the form of adsorbed water or hydrated salts (1, 2). Ratios of O/H for copper deposits calculated from our data range from 4 to 40, with 5 out of the 10 values equal or close to 8 (Table XXXI). One might conclude that in a significant proportion of deposits the hydrate theory is indicated, but that in several kinds of deposits other factors must be acting. For example, the high value of 40 for the sample from panel No. 297 (line 42) is shown below to be probably caused by the inclusion of sulfate ion in the deposit.

With one exception, only 1/10 to 1/2 as much oxygen is present in the three soft-type deposits (non-addition agent sulfate, fluoborate, and pyrophosphate) as in the addition agent and cyanide deposits.

[20] Determinations at American Metal Climax, Inc., were made by courtesy of G. C. Van Tilburg. Oxygen, hydrogen, and nitrogen were determined by J. T. Sterling of the Analytical Chemistry Division, NBS, by a vacuum fusion method.

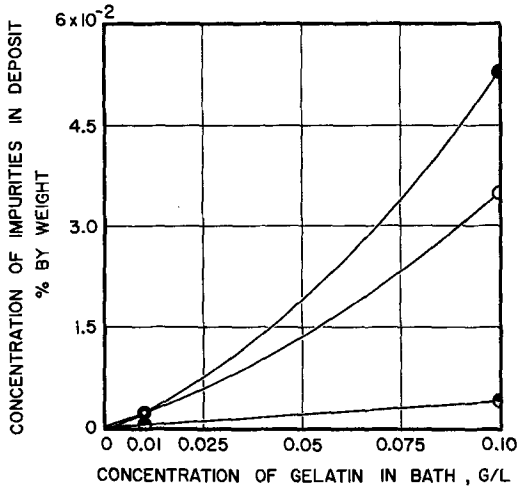

Fig. 61. Relationship between concentration of gelatin in a sulfate bath and concentration of impurities in deposits from the baths. Bath: Cu2-H3, 30°C, 2 A/dm². ○—oxygen; ●—nitrogen or carbon; ◓—hydrogen.

One would expect the concentrations of oxygen and hydrogen in deposits from acid-type copper baths to be lower than in deposits from nearly neutral nickel baths. This is the relationship that occurs. On the average, we found the content of oxygen and hydrogen in copper deposits to be less than 1/10 of that reported in nickel deposits (2).

The effect of concentration of an addition agent in the bath on concentration of impurities in the deposit is seen in Fig. 61. The concentration in the deposit increases more rapidly than that in the bath. This relationship implies that part of the impurities in the deposit may be entrapped by a mechanism other than adsorption, because, as is well known, the amount of a material adsorbed on a surface increases less rapidly than its concentration in the contacting fluid.

b. Nitrogen.—The possibility exists that nitrogen will enter deposits from sulfate baths that contain a nitrogen compound as an addition agent (gelatin, TIPA) and from pyrophosphate and cyanide baths, both of which contain nitrogen compounds. Nitrogen was found in these deposits in reasonable relative concentrations (Table XXXI). It is surprising that nitrogen was found in the deposits from the non-addition agent sulfate bath or from the fluoride bath. The source of the small amounts in the latter deposits could be accidental, e.g., contamination of the surface of the samples that were analyzed, although precautions were taken to minimize surface contamination.

c. Carbon.—The relatively high content of carbon[21] in the gelatin and TIPA deposits is to be expected, due to adsorption of these carbon-containing addition agents (Table XXXI).

The amount of carbon in the cyanide deposits is small, indicating that the amount of cyanide ion adsorbed by the deposit is small. If the carbon in the cyanide deposits does enter *via* adsorption of CN ion, the ratio C/N might be expected to be close to 12/14 = 0.86. Since the deposits in lines 138 and 141 are similar, it is valid to use the concentration of carbon in one and nitrogen in the other to obtain C/N, which is seen to equal 1.05. This is close enough to 0.86 to indicate that carbon and nitrogen do enter the deposit as CN ion. On the other hand, the ratio for the deposit from bath CN-5 (line 127) is about 7, a large deviation. Not much weight can be given to this speculation, based on only two determinations.

d. Boron and fluorine in deposits from the fluoborate bath.—The very low concentrations of boron[22] and fluorine[22] in the deposits from the fluoborate bath indicate that there is very little inclusion of fluoborate ion in the deposits (Table XXXI).

[21] Determinations of carbon were made in the laboratories of E. I. du Pont de Nemours and Company, Inc., by courtesy of O. B. Mathre. Carbon was also determined, by combustion, by J. R. Baldwin of the Analytical Chemistry Division, NBS.

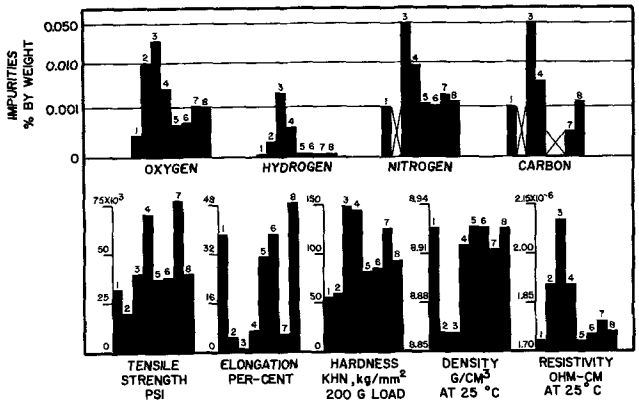

Fig. 62. Correlations between impurities in deposits and properties of deposits for various types of baths: 1—sulfate bath Cu2-H2, 30°C, 2 A/dm²; 2—sulfate bath Cu2-H3, 60°C, 20 A/dm²; 3—sulfate bath Cu2-H3 containing 0.1 g/l gelatin, 30°C, 2 A/dm²; 4—sulfate bath Cu2-H3 containing 3.5 g/l triisopropanolamine, 30°C, 5 A/dm²; 5—fluoborate bath F-1, 30°C, 8 A/dm²; 6—pyrophosphate bath, 50°C, 2 A/dm²; 7—cyanide bath CN-5, 80°C, 4 A/dm²; 8—cyanide bath CN-8, 80°C, 6 A/dm². Note pseudo-logarithmic impurity scale. Metric conversion: one pound per square inch (psi) = 0.000704 kilogram per square millimeter (kg/mm²).

e. Selenium in deposits from baths containing selenium compounds as addition agents.—Selenium[23] is present in the deposits from the sulfate bath containing SeO_2 and in the deposit from the high-efficiency cyanide bath containing the proprietary selenium-type brightener (Table XXXI). Evidently very small concentrations of selenium in copper deposits produce marked effects on structure and properties. (Sections III-A-4-e, III-B-3-e, III-F-2-e, VII-B-3-g, VII-C-2-f, VII-G-1, and Fig. 20 and 34).

f. Sulfur in deposits from sulfate baths.—The low concentration of sulfur[24] in the deposit from the non-addition agent sulfate bath (Table XXXI, line 26) indicates very little inclusion of sulfate ion in normal deposits. The high current density deposit (line 42) contains more than three times as much, which correlates with the high value of the ratio, O/H, for this deposit.

3. Correlations between concentrations of impurities and properties of deposits.—Correlations between impurity content and properties for eight representative types of deposit are shown in the bar graphs in Fig. 62, from which one can visualize the interrelationships. While some variations from regular correlations will be noted, there are, in general, fairly close correlations between, on the one hand, concentrations of the various impurities, and, on the other hand, between these impurities and the various properties. It should be noted that the correlations with impurities are inverse in the case of elongation and density. Close study of this figure will reveal many details regarding correlations that we leave to the reader to ferret out. Relationships between total impurity content, structure, and properties were discussed above (Table XXX, section VIII-F-3).

H. Summary of Properties and General Correlations

In this section we present a general analysis and correlation of all properties for all as-plated deposits.

[22] Boron was determined by quantitative spectrography by Virginia C. Stewart and fluorine by a wet method by J. R. Baldwin, both of the staff of the Analytical Chemistry Division, NBS.

[23] Selenium was determined by neutron activation analysis by D. A. Becker of the Analytical Chemistry Division, NBS.

[24] Sulfur was determined by combustion by J. R. Baldwin of the Analytical Chemistry Division, NBS.

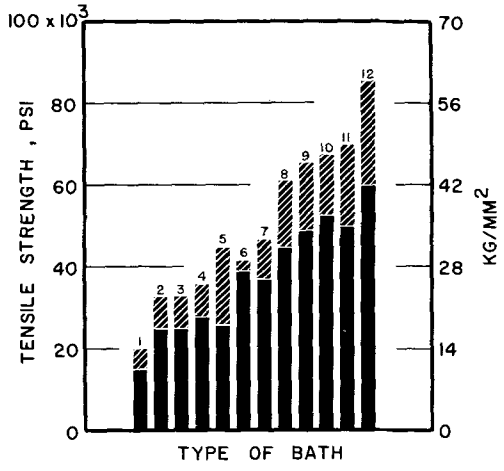

Fig. 63. Ranges and comparative magnitudes of tensile strength of copper deposits from various types of baths: 1—Sulfate baths: plus thiourea (0.005 g/l) and spangled deposits. 2—Sulfate baths, no addition agent, all conditions. 3—Sulfate bath plus addition agents with small effect on strength: dextrin, ethyl alcohol and molasses, glycerol, glycine, lactic acid, 1,5-naphthalenedisulfonic acid, sorbitol, thiourea (0.015 g/l). 4—Fluoborate baths, all conditions. 5—Cyanide baths that yield deposits with lower strengths than those from low-concentration baths: CN-7, CN-8, CN-9. 6—Pyrophosphate bath, all conditions. 7—Sulfate baths plus addition agents or other conditions that cause a moderate increase in strength: gelatin, β-naphthoquinoline, phenolsulfonic acid, selenium dioxide, thiourea plus 1,5-naphthalenedisulfonic acid, thin deposits (2 mils), periodic current reversal (PR). 8—Cyanide bath, sodium ion Rochelle salt type, CN-6. 9—Cyanide baths, all low-concentration types, CN-1 through CN-5, all conditions. 10—Amine bath. 11—Sulfate baths plus addition agents or other conditions that cause a large increase in strength: proprietary A, selenium dioxide (thin deposits, 2 mils), triisopropanolamine. 12—Cyanide baths plus addition agents or other conditions that cause a large increase in strength: CN-8 plus PR, CN-8 containing KCNS plus PR, CN-9 plus PR.

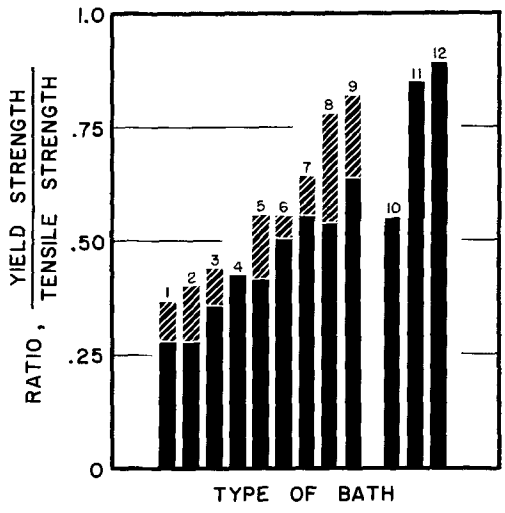

Fig. 64. Ranges and comparative magnitudes of the yield ratio of copper deposits from various types of baths: 1—Sulfate baths, non-addition agent, all conditions. 2—Sulfate baths plus addition agents that cause minor change in yield ratio: lactic acid, β-naphthoquinoline, 1,5-naphthalenedisulfonic acid, phenolsulfonic acid, selenium dioxide, thiourea (0.005 g/l), thiourea plus 1,5-naphthalenedisulfonic acid. 3—Fluoborate baths, all conditions. 4—Cyanide bath, CN-9. 5—Sulfate baths plus addition agents or other conditions that cause a moderate increase in yield ratio: ethyl alcohol plus molasses, thiourea (0.015 g/l), triisopropanolamine, periodic current reversal (PR), thin deposits (2 mils) from bath containing 1,5-naphthalenedisulfonic acid. 6—Pyrophosphate bath, all conditions. 7—Cyanide bath, CN-8 plus PR. 8—Sulfate baths plus addition agents or other conditions that cause a large increase in yield ratio: gelatin, proprietary A, thin deposits (2 mils) from a bath containing selenium dioxide. 9—Amine bath. 10—Commercial wrought copper, annealed. 11—Commercial wrought copper, half hard (21% reduction). 12—Commercial wrought copper, extra hard (50% reduction).

1. Correlations between tensile strength and types of deposits.—In Fig. 63, values of tensile strength are plotted for all deposits that we studied. The data are shown for groups of deposits, classified in part on the basis of bath and in part on magnitude of tensile strength, arranged with increasing strength from left to right on the graph. The limits of the shaded zones at the tops of the bars represent minimum and maximum values of tensile strength for the group. The limits plotted for each group are based mainly on the average deviation from the mean within the group. However, if several deposits within the group had values appreciably lower or higher than the limits defined by the average deviation, the range plotted was enlarged to take account of these deviant deposits. The plotted values are thus somewhat subjective, but in our judgment best represent the group. This procedure was followed for determining the plotted values of upper and lower limits for Fig. 63-65 and 67-70, inclusive.

Figures 63 to 70 were prepared primarily to serve as a convenient visual reference summary, and are therefore discussed only briefly. For example, it is seen in Fig. 63 that the over-all range of strength varies by a factor of four, with spangled sulfate deposits the weakest and PR cyanide deposits the strongest. Changes of tensile strength due to large-effect variables, such as type of bath or addition agents, are readily seen. However, changes in strength due to small-effect variables, such as current density, are not revealed. For the latter type of information, the reader must refer to the appropriate preceding section.

2. Correlations between the yield strength-tensile strength ratio and types of deposits.—The ratio, yield strength/tensile strength, is very low (about 25%) for soft-type deposits, considerably lower than that of annealed wrought copper (55%). The ratio increases progressively with strength, approaching that of cold-worked wrought copper for the strongest electrodeposits.

3. Correlations between elongation and types of deposits.—Figure 65 discloses a general inverse relationship between elongation and type of bath, as compared with Fig. 63 for tensile strength. Thus, the deposits from the amine bath, among the highest in tensile strength, are the most brittle, and the soft-type sulfate deposits, next to weakest, are third from most ductile. The deposits from the pyrophosphate and high-efficiency cyanide baths, with the highest ductilities, are somewhat more ductile than would be predicted from their position in Fig. 63. This could be the result of the crystal orientation hypothesized in Section VIII-F-2-a.

4. Correlations between modulus of elasticity, tensile strength, and types of deposits.—A general correlation between tensile strength and modulus is seen in Fig. 66. However, the higher range of modulus, 16 and 17 x 10^6 psi, embraces a rather large range of tensile strength (40,000-86,000 psi). Modulus values for wrought copper are seen to be located in the mid-range of the correlation band. Correlations between modulus and type of deposit are similar to those between tensile strength and type of deposit, although the fluoborate and sulfate-TIPA deposits deviate conspicuously from the predominant pattern, having abnormally low moduli.

5. Correlations between hardness and types of deposits.—The type-grouping for hardness, Fig. 67, is closely parallel to that for tensile strength, Fig. 63.

6. Correlations between internal stress and types of deposits.—Examination of the groupings in Fig. 68 shows many deviations from the group order that

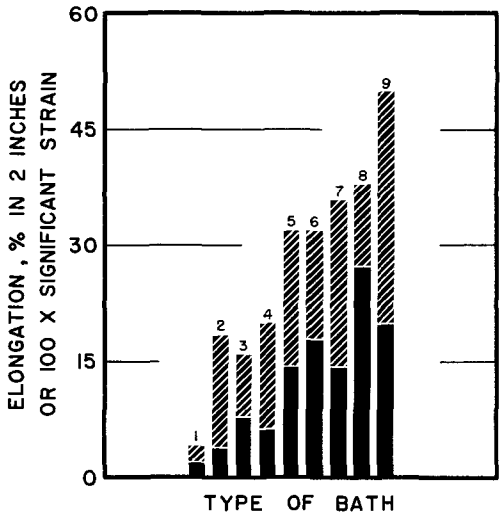

Fig. 65. Ranges and comparative magnitudes of elongation of copper deposits from various types of baths: 1—Amine bath. 2—Sulfate baths plus addition agents or other conditions that cause significant lowering of ductility: dextrin, ethyl alcohol plus molasses, glycerol, glycine, lactic acid, β-naphthoquinoline, sorbitol, thiourea (0.005 and 0.015 g/l), triisopropanolamine, proprietary A, non-addition agent thin deposits (2 mils), thin deposits (2 mils) from baths containing 1,5-naphthalenedisulfonic acid or selenium dioxide, spangled deposits. 3—Cyanide baths, all low-concentration types, CN-1 through CN-5, all conditions. 4—Cyanide baths, high concentration types that yield deposits with ductility nearly the same as those from low concentration baths: CN-8 containing KCNS plus periodic current reversal (PR), CN-9. 5—Fluoborate baths, all conditions. 6—Sulfate baths plus addition agents or other conditions that cause minor effect on ductility: gelatin (0.003 g/l), 1,5-naphthalenedisulfonic acid, phenolsulfonic acid, selenium dioxide, thiourea plus naphthalene disulfonic acid, PR. 7—Sulfate baths, no addition agent, all conditions. 8—Pyrophosphate bath, all conditions. 9—Cyanide baths that yield deposits that are significantly more ductile than those from low-concentration baths: CN-6, CN-7, CN-8, CN-8 plus PR, CN-9 plus PR.

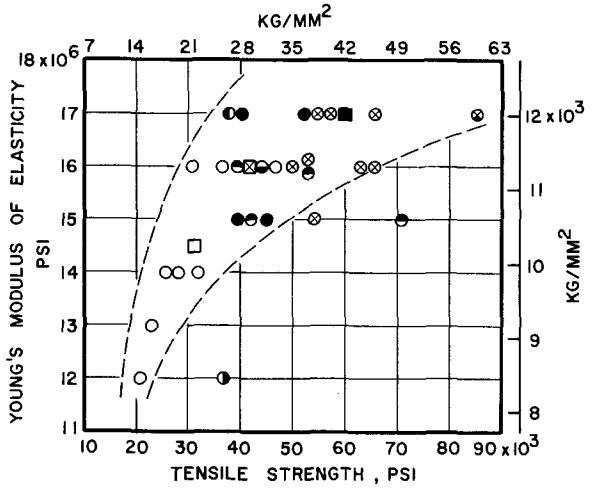

Fig. 66. Relationship between tensile strength and modulus of elasticity of copper deposits from various types of baths: ○—non-addition agent sulfate baths; ●—sulfate baths containing gelatin; ◒—sulfate bath containing selenium dioxide; ◓—sulfate bath containing triisopropanolamine; ◑—fluoborate bath; ◐—pyrophosphate bath; ⊗—cyanide baths, CN-1 through CN-5; ⊗—CN-8 containing KCNS plus periodic current reversal (PR); □—commercial wrought copper, annealed; ⊠—commercial wrought copper, half hard (21% reduction); ■—commercial wrought copper, extra hard (50% reduction).

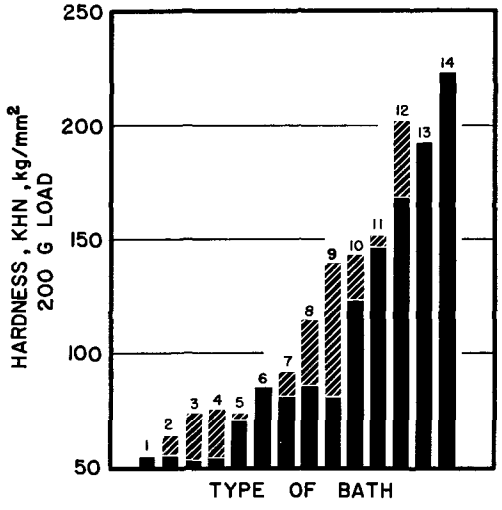

Fig. 67. Ranges and comparative magnitudes of hardness of copper deposits from various types of baths: 1—Sulfate bath, Cu2-H3, 30°C, 2 A/dm^2, severe exposure to cellulose. 2—Sulfate baths plus addition agents that have minor effect on hardness: dextrin, ethyl alcohol plus molasses, glycerol, sorbitol. 3—Sulfate baths, no addition agent, all conditions. 4—Fluoborate baths, all conditions. 5—Cyanide bath, CN-9. 6—Sulfate bath, spangled deposit. 7—Pyrophosphate bath, all conditions. 8—Cyanide baths, CN-7 and CN-8, all conditions. 9—Sulfate baths plus addition agents: includes all addition agents in Table XIII except those in "2" above. 10—Cyanide baths, CN-1 through CN-6, all conditions. 11—Cyanide baths: CN-8 plus periodic current reversal (PR); CN-8 plus KCNS plus PR, cycle 15 sec cathodic, 5 sec anodic. 12—Amine bath. 13—Cyanide bath, CN-8 plus KCNS plus PR, cycle 30 sec cathodic, 10 sec anodic. 14—Cyanide bath, CN-9 plus PR.

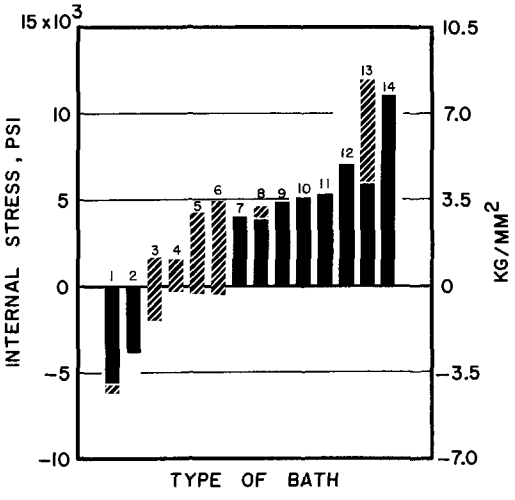

Fig. 68. Ranges and comparative magnitudes of internal stress in copper deposits from various types of baths. Negative stress is compressive. 1—Amine bath. 2—Sulfate bath containing 0.1 g/l gelatin. 3—Pyrophosphate bath, all conditions. 4—Fluoborate baths, all conditions. 5—Sulfate baths, no addition agent, all conditions. 6—Sulfate baths plus all addition agents in Table XIII except gelatin (0.1 g/l), β-naphthoquinoline, triisopropanolamine (30°, 5 A/dm^2). 7—Sulfate bath plus periodic current reversal (PR). 8—Cyanide baths: CN-8, CN-8 plus PR. 9—Cyanide bath, CN-6. 10—Cyanide bath, CN-8 plus 2 g/l KCNS plus PR. 11—Sulfate bath plus β-naphthoquinoline. 12—Sulfate bath plus triisopropanolamine (30°, 5 A/dm^2). 13—Cyanide baths: CN-1 through CN-5, CN-7, all conditions. 14—Cyanide bath, CN-9.

exists in the other graphs in this set (Fig. 63-70). This individuality of internal stress, or lack of consistent relationships with other properties, has been previously noted.

7. Correlations between density and types of deposits.—Except for the low values of density seen in

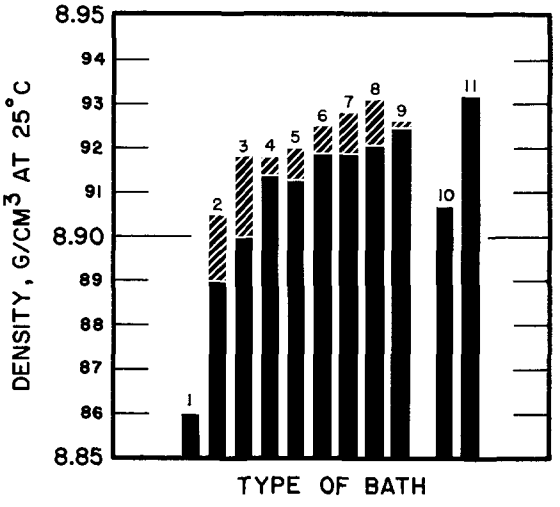

Fig. 69. Ranges and comparative magnitudes of density of copper deposits from various types of baths: 1—Sulfate baths plus addition agents or other conditions that cause a large decrease of density: gelatin, 0.1 g/l; Cu2-H3, 60°C, 20 A/dm^2 (high current density). 2—Amine bath. 3—Cyanide baths: CN-1 through CN-5, all conditions. 4—Sulfate baths plus addition agents that have slight lowering effect on density: gelatin, 0.003 g/l; triisopropanolamine, 30°, 5 A/dm^2; proprietary brightener A. 5—Cyanide baths: CN-6 and CN-7, all conditions; CN-8 plus KCNS plus periodic current reversal (PR). 6—Cyanide baths: CN-8, CN-9. 7—Sulfate baths, no addition agent, all conditions. 8—Sulfate baths plus addition agents or other conditions that have no significant effect on density: ethyl alcohol plus molasses, lactic acid, 1,5-naphthalenedisulfonic acid, β-naphthoquinoline, phenolsulfonic acid, selenium dioxide, thiourea, thiourea plus naphthalenedisulfonic acid, triisopropanolamine, 30°, 2 A/dm^2; periodic current reversal; spangling. 9—Fluoborate and pyrophosphate baths, all conditions. 10—Commercial sheet, half hard (21% reduction). 11—Single crystal.

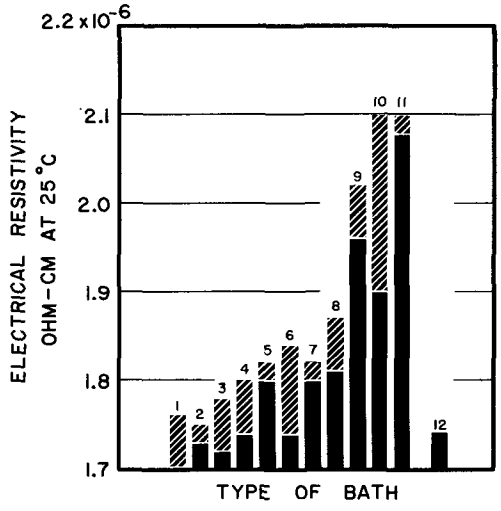

Fig. 70. Ranges and comparative magnitudes of electrical resistivity of copper deposits from various types of baths: 1—Sulfate baths, no addition agent, all conditions. 2—Fluoborate and pyrophosphate baths, all conditions. 3—Sulfate baths containing addition agents that have minor effect on resistivity: ethyl alcohol plus molasses, β-naphthoquinoline, gelatin (0.003 and 0.01 g/l), lactic acid, naphthalenedisulfonic acid, phenolsulfonic acid, selenium dioxide, thiourea, thiourea plus naphthalene disulfonic acid, triisopropanolamine (30°C, 2 A/dm^2), periodic current reversal (PR). 4—Cyanide baths: CN-7 and CN-8, all conditions; CN-8 plus PR. 5—Sulfate baths plus factors that have medium effect on resistivity: thin deposits (2 mils); proprietary brightener A. 6—Cyanide baths: CN-1 through CN-5, all conditions. 7—Cyanide bath: CN-9 (proprietary B). 8—Cyanide baths: thin deposits (0.25 mil) from CN-1 through CN-3; CN-6, all conditions. 9—Cyanide baths: CN-8 plus KCNS plus PR; CN-9 (proprietary B) plus PR. 10—Sulfate baths plus addition agents or other factors that have large effect on resistivity: Cu2-H3, 60°, 20 A/dm^2 (high current density); gelatin (0.1 g/l); triisopropanolamine plus high current density (5 A/dm^2); spangling. 11—Amine bath. 12—Commercial wrought copper: annealed electrolytic tough pitch.

the first two groups of Fig. 69, all deposits have rather high density, with only small differences between groups. Nevertheless, the lower density of cyanide deposits and the reduction of the density of sulfate deposits due to "active" addition agents is apparent.

8. Correlations between electrical resistivity and types of deposits.—Type groupings for electrical resistivity, Fig. 70, are quite parallel to those for tensile strength and hardness (Fig. 63 and 67, respectively).

9. General correlations among properties and types of deposits.—Some of the properties of the main types of deposits are represented in Fig. 71. In the first group, the seven types of deposits are arranged in increasing order of tensile strength. The same order, type 1 to 7 serially, is maintained in the representations of the other properties, so that deviations from regular correlations will be apparent. There is general parallelism between tensile strength, hardness, and resistivity, and to some extent internal stress, and inverse correlation of these properties with elongation and density.

The higher than "normal" elongation of the deposits from the high-efficiency cyanide bath and pyrophosphate bath is apparent, as is the inverse relationship between ductility and tensile strength of the deposits from the amine bath and from sulfate baths containing high-effect addition agents. The average hardness of the latter group of deposits is lower than normal. This is the only significant deviation from a regular hardness pattern.

We have remarked several times that internal stress is the most unique property in that it is least correlated with other properties. While this is true, Fig. 71 does show several regular correlations. Abnormally low stress of the pyrophosphate and amine baths is the main deviation from normal correlation.

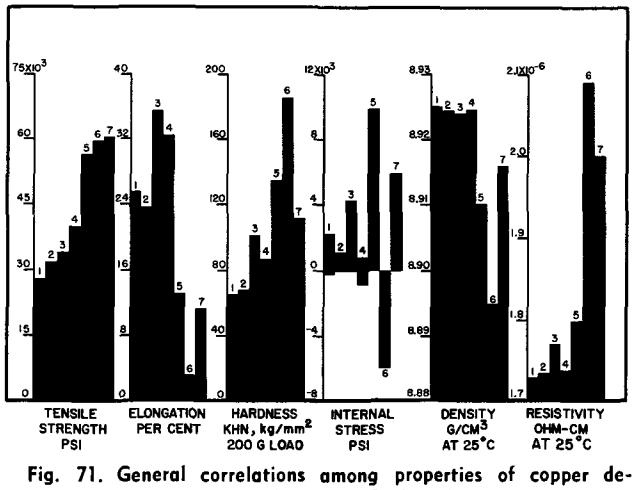

Fig. 71. General correlations among properties of copper deposits from various types of baths: 1—Sulfate baths, all non-addition agent deposits. 2—Fluoborate baths, all conditions. 3—Cyanide bath, CN-8, all conditions except no addition agent nor periodic current reversal (PR). 4—Pyrophosphate bath, all conditions. 5—Cyanide baths, CN-1 through CN-5, all conditions. 6—Amine bath. 7—Sulfate baths plus large effect addition agents. Notes: Elongation is in per cent in 2 in. except for column "5" which is 100X significant strain. Negative values of internal stress represent compressive stress. Metric conversion: one pound per square inch (psi) = 0.000704 kilogram per square millimeter (kg/mm^2).

Considering density, correlation is regular except for the same reversed positions between the deposits from the amine bath and the sulfate bath containing high-effect addition agents, also noted for elongation

and hardness, and repeated again for electrical resistivity. The low value of resistivity of the pyrophosphate deposit is also apparent. The consistent deviation of the properties of the pyrophosphate deposits from the normal, in general in favorable directions, is the most apparent phenomenon shown in these comparisons. It is quite likely that it is associated with a unique structure, as hypothesized in Section VIII-F-2-a.

IX. Acknowledgments

The authors acknowledge the assistance of the following for help with experimental work: J. F. Berkeley and G. I. Reid of the Electrolysis and Metal Deposition Section, NBS, for preparation of metallographic specimens, measurements of expansivity, and preparation of photomicrographs, and T. R. Shives of the Metallurgy Division, NBS, for measurements of hardness. The assistance of many other members of the staff of NBS has been acknowledged at appropriate points in the text.

We also acknowledge the valuable help and advice given by the following: C. H. Sample, District Supervisor, Project 21; R. A. Ehrhardt and A. M. Max, previous and present chairman of the Project 21 committee; and members W. Blum, A. Brenner, S. Lyman, O. B. Mathre, C. W. Ostrander, H. J. Read, D. A. Swalheim, G. C. Van Tilburg, M. L. Whitehurst, and C. I. Whitman.

We gratefully acknowledge the donation of anodes by American Metal Climax, Inc.

Financial support for the project was supplied jointly by the American Electroplaters' Society, Inc., through the Research Board, and by the International Copper Research Association, Inc., the Copper Development Association, and the National Bureau of Standards.

X. Appendix

A. Procedures Used for Preparation of Electron Micrographs (Fig. 36)[25]

Mechanically polished cross sections were electropolished in a commercial electropolishing unit with a proprietary polishing solution containing H_3PO_4, 250 ml; distilled water, 500 ml; ethanol, 250 ml; propanol, 50 ml; urea, 5g; proprietary constituent, 2 ml. Conditions were: time, 5 sec; temperature, 25°C; current, 0.6A. Contact to one specimen was made with a solder spot at the base of the mount and to another with silver paint. No significant difference in structure was seen due to the brief heating during soldering. After electropolishing, chemical etching was done in the etch mixture: NH_4OH, 30 ml; H_2O_2-3%, 30 ml; H_2O, 30 ml; 5 sec, 25°C.

Replicas were made with cellulose acetate tape. The negative replicas were rotary shadowed at an angle of 25° with palladium and backed with carbon at an angle of 90°.

B. Development of Fatigue Relationships

1. Calculation of σ_c in Table XXVI.—The fatigue specimen is represented in Fig. 72 with exaggerated thickness and curvature and with the U-bend at the top replaced with an equivalent rigid bar so that the rotational moments may be visualized. The lower end of the right-hand strip is rigidly fixed. The vertical force, P, causes bending as shown. We consider the bending of only one arm, recognizing that the same forces are present in both. Thus, the force, P, may be thought of as divided in two equal parts, $P/2$, each part causing the bending of one arm. Therefore, the moment causing rotation about O and corresponding bending about O' is

$$\frac{P}{2} \cdot a = M \qquad [1]$$

M, the moment about O', is also equal to the integral

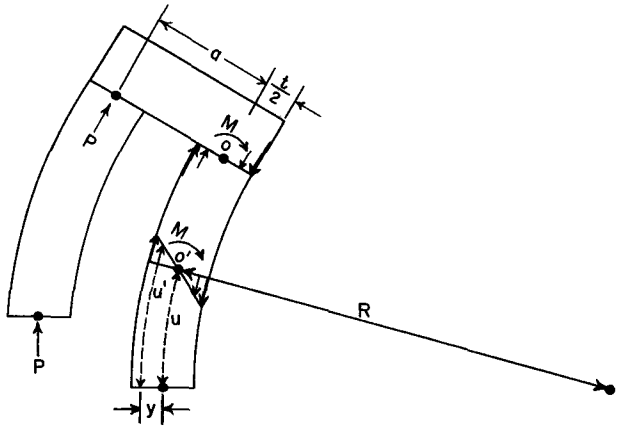

Fig. 72. Stresses and moments in a flexed fatigue specimen

over the cross section of the specimen of the product of the fiber stresses (represented by the small arrows) and their respective moment arms. It is thus expressed as

$$M = \int \sigma y \, dA \qquad [2]$$

where σ is the fiber stress at distance y from the neutral plane of the strip and dA is an element of area in a normal plane. By definition

$$\sigma = E\delta \qquad [3]$$

where E is Young's modulus of elasticity and δ is strain. From Fig. 72, $\delta = (u' - u)/u$. Substituting in [3]

$$\sigma = E\left[\frac{u' - u}{u}\right] \qquad [4]$$

Again from Fig. 72

$$\frac{R}{R + y} = \frac{u}{u'} \qquad [5]$$

from which

$$u' = u + \frac{yu}{R} \qquad [6]$$

Substituting u' from [6] in [4]

$$\sigma = \frac{Ey}{R} \qquad [7]$$

Substituting for σ from [7] in [2]

$$M = \frac{E}{R}\int y^2 dA = \frac{EI}{R} \qquad [8]$$

where $I = \int y^2 dA$, the geometrical moment of inertia around O'.

For a rectangular beam of width b and thickness t, $dA = b\,dy$; hence

$$I = b\int y^2 dy = 2b\left|\frac{y^3}{3}\right|_0^{t/2} = \frac{bt^3}{12} \qquad [9]$$

Equation [7] gives the actual stress in any given plane at distance y from the neutral plane. The distance y to the outer plane is $t/2$. Therefore the surface stress is given by

$$\sigma = \frac{E}{R} \cdot \frac{t}{2} \qquad [10]$$

From Eq. [8], $E/R = M/I$. Substituting this in [10]

$$\sigma = \frac{M}{I} \cdot \frac{t}{2} \qquad [11]$$

Substituting the value of M from [1] and the value of I from [9] in Eq. [11] gives

$$\sigma = \frac{Pa}{2} \cdot \frac{12}{bt^3} \cdot \frac{t}{2} = \frac{3Pa}{bt^2} \qquad [12]$$

Equation [12] gives surface stress, and is the relation

[25] Electron micrographs were made by D. B. Ballard, NBS Metallurgy Division, Lattice Defects and Microstructure Section, who also supplied the data on procedures used.

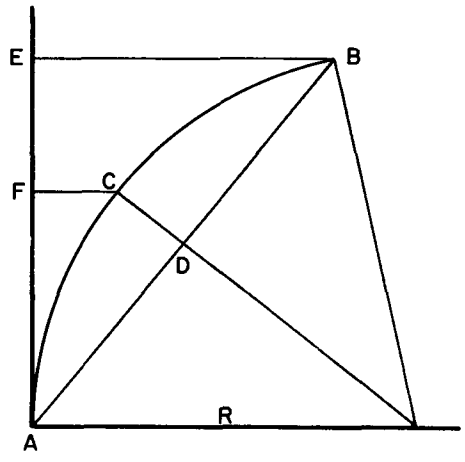

Fig. 73. Relationship between radius of curvature and deflection of an arc.

used for calculating σ_c in Table XXVI. P is obtained from the machine calibration, a is 0.30 in. for our specimens, b is 0.50 in., and t is the measured thickness of the specimen.

2. Calculations of σ_m in Table XXVI.—The arc ACB in Fig. 73 represents an edge view of a short segment of one arm of a flexed fatigue specimen. C is the longitudinal center, *i.e.*, the point of minimum width. Index marks were placed on the edge of the specimen at C and at points A and B, with $\overline{AC}$ and $\overline{CB}$ each equal to 1/8 in. The variation in width of the specimen over the span $\overline{AB}$ is small, so that the curvature is nearly uniform. The specimen was statically flexed and clamped in the flexed position in a jig. The distances $\overline{EB}$, $\overline{FC}$, $\overline{AE}$, and $\overline{AF}$ were then measured with a micrometer microscope to an accuracy of 0.1 mil. Their values were then plotted on large paper on a magnified scale of 100X. From the plot, $\overline{CD}$ and $\overline{AD}$ were measured. The following right triangle relationship is apparent from Fig. 73

$$(R - \overline{CD})^2 + \overline{AD}^2 = R^2 \qquad [13]$$

Expanding [13] and solving for R gives

$$R = \frac{\overline{CD}^2 + \overline{AD}^2}{2\overline{CD}} \qquad [14]$$

From Eq. [10] in the preceding Section X-B-1

$$\sigma = \frac{E}{R} \cdot \frac{t}{2} \qquad [10]$$

Substituting in [10] the value of R from [14]

$$\sigma = \frac{Et}{2}\left[\frac{2\overline{CD}}{\overline{CD}^2 + \overline{AD}^2}\right] \qquad [15]$$

This is the value of σ designated as σ_m in Table XXVI. The values of E (modulus) used in [15] were determined by us or estimated from values for similar deposits. $\overline{CD}$ and $\overline{AD}$ were determined from the direct measurements and graphical evaluation just described.

REFERENCES

34. G. Földes, *Sheet Metal Ind.*, **34**, 749 (1957).
35. R. P. Reed and R. P. Mikesell, "Low Temperature Mechanical Properties of Copper and Selected Copper Alloys," *Nat. Bur. Std. (U.S.) Monograph*, **101**, (1967), Supt. of Documents, U.S. Govt. Printing Office, Washington, D.C. 20402.
36. P. Hidnert and W. Souder, *Nat. Bur. Std. (U.S.) Circ.*, No. 486 (1950).
37. P. Hidnert and H. S. Krider, *J. Res. Nat. Bur. Std.*, **39**, 419 (1947).
38. J. O'M. Bockris and B. E. Conway, "Modern Aspects of Electrochemistry—No. 3," p. 293, Butterworths, Washington, D. C. (1964).
39. F. Ogburn and C. Newton, *This Journal*, **110**, 1148 (1963).
40. H. Leidheiser and A. T. Gwathmey, *Trans. Electrochem. Soc.*, **91**, 95 (1947).
41. S. Okada and S. Magari, *This Journal*, **102**, 580 (1955).
42. S. C. Barnes, *ibid.*, **111**, 296 (1964).
43. L. Krushev, V. Pangarova, and N. Pangarov, *Plating*, **55**, 841 (1968).